



**CHL
LIBRARY**

VOLUME 1

Edited by Billy L. Edge

Coastal Engineering 1996

Proceedings of the
twenty-fifth international conference

ASCE

Volume 1

Coastal Engineering 1996

Proceedings of the
twenty-fifth international conference

September 2-6, 1996
The Peabody Hotel
Orlando, Florida

Held under the auspices of the
Coastal Engineering Research Council of the
American Society of Civil Engineers

Edited by Billy L. Edge

Published by the

ASCE *American Society
of Civil Engineers*

345 East 47th Street
New York, New York 10017-2398

Abstract:

This proceedings contains over 370 papers presented at the 25th International Conference on Coastal Engineering which was held in Orlando, Florida, 2-6 September, 1996. The book is divided into six parts: 1) Characteristics of coastal waves and currents; 2) long waves and storm surges; 3) coastal structures; 4) coastal processes and sediment transport; 5) coastal, estuarine and environmental problems; and 6) case studies. The individual papers include such topics as the effects of wind, waves, storms and currents as well as the study of sedimentation, erosion and beach nourishment. Special emphasis is given to case studies of completed engineering projects. With the inclusion of both theoretical and practical information, these papers provide the civil engineer and professionals in related fields with a broad range of information on coastal engineering.

Library of Congress Cataloging-in-Publication Data

Coastal engineering 1996 : proceedings of the twenty-fifth international conference, September 2-6, 1996, The Peabody Hotel, Orlando, Florida / edited by Billy L. Edge.

p. cm.

"Held under the auspices of the Coastal Engineering Research Council of the American Society of Civil Engineers."

ISBN 0-7844-0242-6

1. Coastal engineering--Congresses. 2. Ocean waves--Congresses. 1. Edge, Billy L. II. Coastal Engineering Research Council (U.S.) III. International Conference on Coastal Engineering (25th : 1996 : Orlando, Fla.)

TC203.5.C6184 1997

97-10664

627'.58--dc21

CIP

The Society is not responsible for any statements made or opinions expressed in its publications.

Photocopies. Authorization to photocopy material for internal or personal use under circumstances not falling within the fair use provisions of the Copyright Act is granted by ASCE to libraries and other users registered with the Copyright Clearance Center (CCC) Transactional Reporting Service, provided that the base fee of \$4.00 per article plus \$.25 per page is paid directly to CCC, 222 Rosewood, Drive, Danvers, MA 01923. The identification for ASCE Books is 0-7844-0242-6/97/\$4.00 + \$.25 per copy. Requests for special permission or bulk copying should be addressed to Permissions & Copyright Dept., ASCE.

Copyright © 1997 by the American Society of Civil Engineers,
All Rights Reserved.

Library of Congress Catalog Card No: 97-10664

ISBN 0-7844-0242-6

Manufactured in the United States of America.

Cover: One year after nourishment at Palm Beach, Florida. Photo courtesy of Applied Technology & Management, Inc. and Aerial Photography, Inc.

FOREWORD

The *Silver Conference* represents the 25th International Conference on Coastal Engineering. The first conference was held in Long Beach, California, in 1950, approximately a half a century ago. This conference series has maintained and still represents the major forum for presentation and discussion of the ongoing research in the field of coastal engineering, applications to design projects and case histories of completed projects. Moreover, the conference is not limited to just coastal engineers but it is open to other related disciplines including geologists, meteorologists, oceanographers and construction for example. Traditionally, each conference was hosted by a different country to allow the problems and solutions of that country to be shared with others attending from around the world. This also provided a unique opportunity for the young engineers to benefit by having a coastal engineering conference hosted in their country which they could more easily attend. As the conference series evolved, many formats have been introduced to help promote the discussion and learning opportunities, but the conference series has remained dedicated to the highest standard of presentation and dissemination of information that can aid the practitioners as well as the researchers. The competition to present work at the conference has continued to increase as the research has increased and the works become ever larger and more exciting.

In recognition of the *Silver Conference* (also know as ICCE96) and celebration of our "Coastal Engineering History and Heritage," the organizers of the conference commissioned a coastal engineer in each of the countries which had hosted a conference in the series to prepare a history of coastal engineering in that country. Papers were prepared by authors representing 15 countries, presented at the conference and published in a separate volume¹ edited by the Conference co-chair Dr. Nicholas C. Kraus. The volume is available from the American Society of Civil Engineers.

The *Silver Conference* was the largest in the long series with largest number of papers being submitted for consideration. The 850 papers were each reviewed by four members of the technical review panel. Unfortunately, only 435 papers could be accepted for presentation during the week long conference. This necessitated changing the normal 30 minute presentations to 20 minute presentations in order to accommodate the large number of presentations --nearly 100 more papers than previous conferences have accommodated. The technical aspects of ICCE96 were very successful and to support the discussions, informative field trips to the East and West shorelines of Florida were arranged and well attended. This allowed participants to view the coastal engineering solutions to problems in inlet management, beach fill technology, shoreline and environmental protection and restoration and coastal water quality.

Lastly, the 25th International Conference on Coastal Engineering was a family oriented meeting with special emphasis on an "American Experience." Being located in Orlando, Florida, near such facilities as Disneyworld, Epcot Center, MGM Studios and Sea World, provided many opportunities for family and social interaction.

¹ Kraus, Nicholas C. 1996. *History and Heritage of Coastal Engineering*. American Society of Civil Engineers. New York, NY.

The first 25 conferences have been held at venues noted in the table below; the table also includes the upcoming ICCE conferences which have been selected.

Conference	Year	Venue
1	1950	Long Beach, California
2	1951	Houston, Texas
3	1952	Cambridge, Massachusetts
4	1953	Chicago, Illinois
5	1954	Grenoble, France
6	1957	Gainesville, Florida
7	1960	The Hague, The Netherlands
8	1962	Mexico City, Mexico
9	1964	Lisbon, Portugal
10	1966	Tokyo, Japan
11	1968	London, United Kingdom
12	1970	Washington, D.C.
13	1972	Vancouver, Canada
14	1974	Copenhagen, Denmark
15	1976	Honolulu, Hawaii
16	1978	Hamburg, Germany
17	1980	Sydney, Australia
18	1982	Cape Town, South Africa
19	1984	Houston, Texas
20	1986	Taipei, Taiwan
21	1988	Torremolinos, Spain
22	1990	Delft, The Netherlands
23	1992	Venice, Italy
24	1994	Kobe, Japan
25	1996	Orlando, Florida
26	1998	Copenhagen, Denmark
27	2000	Sydney, Australia

The Editor would like to acknowledge the work of the Local Organizing Committee in developing a very successful conference. Being a member of the LOC brings into sharp focus the amount of work required to develop and conduct a successful conference. The members of the LOC worked tirelessly to ensure the success of the ICCE96. In addition to the Local Organizing

Committee, the work of the eight members of the technical review panel were critical to selecting the highest quality papers to be presented. Each reviewer was responsible for a critical review of 425 abstracts in a very brief period of time. One special person deserving of recognition who continues to support the conference and the preparation of the *Proceedings* and communicates with authors of papers is Becky Edge. She has unselfishly given her time and energy to producing the databases from which the conference and *Proceedings* are maintained and over the years has developed a network among those who contribute papers to the Conference. To the above and to the many others who have helped to produce these *Proceedings*, I say "Thanks."

Billy L. Edge
b-edge@tamu.edu
Ocean Engineering Program
Department of Civil Engineering
Texas A&M University

ACKNOWLEDGMENTS

LOCAL ORGANIZING COMMITTEE

Co-Chairmen:

Robert G. Dean, University of Florida
Nicholas C. Kraus, Texas A&M University Corpus Christi
and Coastal and Hydraulics Laboratory, Corps of Engineers

Organizing Committee:

Robert A. Dalrymple, University of Delaware
Richard A. Davis, Jr., University of South Florida
Billy L. Edge, Texas A&M University
Karyn M. Erickson, Applied Technology & Management, Inc.
James R. Houston, Coastal Engineering Research Center, Corps of Engineers
David L. Kriebel, U. S. Naval Academy
William G. McDougal, Oregon State University

ICCE '96 Secretariat:

East Meets West Productions, Inc.
710 Buffalo Street, Suite 810
Corpus Christi, Texas 78401
USA

COASTAL ENGINEERING RESEARCH COUNCIL (ASCE)

Chairman:

Robert G. Dean

Vice-Chairman

Orville T. Magoon

Secretary:

Billy L. Edge

Members:

Kees d'Angremond
Robert A. Dalrymple
Kyoshi Horikawa
J. William Kamphuis
Nobuhisa Kobayashi
Ronald M. Noble
Thorndike Saville, Jr.

FINANCIAL SUPPORT

The Conference Organizing Committee expresses sincere gratitude to the exhibitors for their financial support of the conference.

SUPPORTING ORGANIZATIONS

American Geophysical Union
Canadian Society for Civil Engineering
Florida Shore and Beach Preservation Association
Institution of Civil Engineers, United Kingdom
international Association for Hydraulic Research, Maritime Hydraulics Section
Japan Society of Civil Engineers, Committee on Coastal Engineering
Permanent International Association of Navigation Congresses (PIANC)
Royal Institution of Engineers in The Netherlands
Society of Danish Engineers
U. S. Geological Survey
U. S. Army Corps of Engineers, Waterways Experiment Station

CONTENTS

Part I Characteristics of Coastal Waves and Currents

CHAPTER 1	
Experimental Study of Breaking Waves over a Shoal	2
<i>Arun Chawla, H. Tuba Ozkan-Haller, James T. Kirby</i>	
CHAPTER 2	
A Method for Estimating Standardized Bimodal Directional Spectra	16
<i>Ryuichi Fujiwara, Masahiko Isobe</i>	
CHAPTER 3	
The Effects of Currents on Estimations of Directional Wave Spectra	30
<i>Yasuyuki Nakagawa, Hiroichi Tsuruya, Noriaki Hashimoto</i>	
CHAPTER 4	
A Method for Estimating Directional Spectra in a Field of Incident and Reflected Waves	43
<i>Hiromune Yokoki, Masahiko Isobe</i>	
CHAPTER 5	
Active Absorption of Multidirectional Waves	55
<i>Hemming A. Schaffer, Jesper Skourup</i>	
CHAPTER 6	
Time-Averaged Wave Field Evolution in Coastal Zone	67
<i>Jianlu Xu, Rodney J. Sobey</i>	
CHAPTER 7	
Quality Control of GEOSAT Wave Data for Engineering Applications	81
<i>M. Siddabathula, Vijay G. Panchang</i>	
CHAPTER 8	
Boussinesq Type Equations with High Accuracy in Dispersion and Nonlinearity	95
<i>P.A. Madsen, B. Banijamali, H.A. Schaffer, O.R. Sorensen</i>	
CHAPTER 9	
Wave Kinematics Computations Using Boussinesq Models	109
<i>J. Bosboom, G. Klopman, J.A. Roelvink, J.A. Battjes</i>	
CHAPTER 10	
Effects of Mode Truncation and Dissipation on Predictions of Higher Order Statistics ...	123
<i>James M. Kaihatu, James T. Kirby</i>	
CHAPTER 11	
Field Observation of Movement of Sand Body Due to Waves and Verification of Its Mechanism by Numerical Model	137
<i>Takaaki Uda, Yoshimichi Yamamoto, Naoki Itabashi, Kosuke Yamaji</i>	

CHAPTER 12	
Wave Groups in the Surf-Zone: Model & Experiments	151
<i>J. Veeramony, I. A. Svendsen</i>	
CHAPTER 13	
Simulation of Propagating Nonlinear Wave Groups	165
<i>Paul de Haas, Maarten Dingemans, Gert Klopman</i>	
CHAPTER 14	
Cross-Shore Momentum Flux Due to Shear Instabilities	175
<i>Ad Reniers, Jurjen A. Battjes</i>	
CHAPTER 15	
Modelling Post-Wave Breaking Turbulence and Vorticity	186
<i>T.C.D. Barnes, M. Brocchini, D.H. Peregrine, P.K. Stansby</i>	
CHAPTER 16	
A Turbulent Flow Model for Breaking Waves	200
<i>Nguyen The Duy, Tomoya Shibayama, Akio Okayasu</i>	
CHAPTER 17	
Turbulence Structures in the Surf Zone	214
<i>T.R. Haydon, D.B. Hann, P. Davies, C.A. Greated, T.C.D. Barnes</i>	
CHAPTER 18	
Experiments on Design Wave Height in Shallow Water	221
<i>J. William Kamphuis</i>	
CHAPTER 19	
Time-Dependent Quasi-3D Modeling of Breaking Waves on Beaches	233
<i>Entin A. Karjadi, Nobuhisa Kobayashi</i>	
CHAPTER 20	
Models of Wave Height and Fraction of Breaking Waves on a Barred Beach	247
<i>Yoshiaki Kuriyama</i>	
CHAPTER 21	
A Parametric Model for Random Wave Deformation by Breaking on Arbitrary Beach Profiles	261
<i>Hyuck-Min Kweon, Yoshimi Goda</i>	
CHAPTER 22	
Generation Characteristics of Wave Sounds as a Factor of Beach Amenity	275
<i>Hitoshi Murakami, Sadahiko Itoh, Yoshihiko Hosoi, Hideo Araki and Tsuyoshi Koyabu</i>	
CHAPTER 23	
Measurements of Wave Breaking in the UK Coastal Research Facility	286
<i>Howard N. Southgate, Stuart Stripling</i>	
CHAPTER 24	
A New Type Breaker Forming a Giant Jet and Its Decaying Properties	300

CHAPTER 25	
Wave Climate Cycles and Coastal Engineering Practice	314
<i>Douglas L. Inman, Scott A. Jenkins, M. Hany S. Elwany</i>	
CHAPTER 26	
Stability of Design Wave Estimates	328
<i>Jan Rossouw, Josep R. Medina</i>	
CHAPTER 27	
An Evaluation of Two Wave Forecast Models for the South African Region	340
<i>M. Rossouw, D. Phelp</i>	
CHAPTER 28	
A Comprehensive Wind, Wave, and Current Measurement Program in the South China Sea	354
<i>Jagat N. Sharma, S. Tryggestad, J. Bian</i>	
CHAPTER 29	
Wave Height and Period Distributions from Long-Term Wave Measurement	368
<i>Chung-Chu Teng, Ian M. Palao</i>	
CHAPTER 30	
Interference of Small Structures in the Vicinity of Large Structures	380
<i>Subrata K. Chakrabarti, Sumita Chakrabarti</i>	
CHAPTER 31	
Wave Dynamics at Coastal Structures: Development of a Numerical Model for Free Surface Flow	389
<i>Zoheir A. Sabeur, N. William H. Allsop, Robert G. Beale, John M. Dennis</i>	
CHAPTER 32	
Scale Effects in Oxygenation in the Breaker Zone of Coastal Structures	403
<i>V.K. Tsoukala, C.I. Mouzouris</i>	
CHAPTER 33	
Wave Actions on a Vertical Cylinder in Multi-Directional Random Waves	415
<i>Yu-xiu Yu, Ning-chuan Zhang, Qun Zhao</i>	
CHAPTER 34	
Wind/Wave Relation and the Pressure Gradient Effect	429
<i>Spiros M. Gouloumis</i>	
CHAPTER 35	
Non-Reflected Multi Directional Wave Maker Theory and Experiments of Verification ..	443
<i>Kazunori Ito, Hidehiro Katsui, Masashi Mochizuki, Masahiko Isobe</i>	
CHAPTER 36	
Fifty Years of Wave Growth Curves	457
<i>Paul C. Liu</i>	

CHAPTER 37	
Development of a Third Generation Shallow-Water Wave Model with Unstructured Spatial Meshing	465
<i>Michel Benoit, Frederic Marcos, Francoise Becq</i>	
CHAPTER 38	
New Optimization Method for Paddle Motion of Multi-Directional Wavemaker	479
<i>Akira Matsumoto, Minoru Hanzawa</i>	
CHAPTER 39	
Generation of Second-Order Long Waves by a Wave Group in a Laboratory Flume and Its Control	493
<i>M. Mizuguchi, H. Toita</i>	
CHAPTER 40	
Kinematic Predictions in Large Shallow Water Waves	502
<i>Susan Smith, Christopher Swan</i>	
CHAPTER 41	
Fetch Limited Spectral Evolution in Finite Depth Water	516
<i>I.R. Young, L.A. Verhagen</i>	
CHAPTER 42	
Measurement of Breaking Waves Using Particle Image Velocimetry	527
<i>Kuang-An Chang, Philip L.-F. Liu</i>	
CHAPTER 43	
Computation of the Near-Bottom Kinematics of Shoaling Waves	537
<i>Luc Hamm</i>	
CHAPTER 44	
Formulation and Validation of Vertically 2-D Shallow-Water Wave Model	551
<i>Bradley D. Johnson, Nobuhisa Kobayashi, Daniel T. Cox</i>	
CHAPTER 45	
Particle Velocity Distribution in Surface Waves	565
<i>Geir Moe, Oivind A. Arntsen</i>	
CHAPTER 46	
A Comparison of Analysis Methods for Wave Pressure Data	575
<i>Murray Townsend, John D. Fenton</i>	
CHAPTER 47	
A Nonlinear Model for Wave Propagation	589
<i>Ting-Kuei Tsay, Philip L.-F. Liu, Nan-Jing Wu</i>	
CHAPTER 48	
Application of a Digital Particle Image Velocimetry (DPIV) System to Breaking Waves in the Surf Zone	602
<i>Kenneth R. Craig, Robert J. Thieke</i>	

CHAPTER 49	
Wave Gauging Networks Worldwide - An Overview616
<i>J. Michael Hemsley</i>	
CHAPTER 50	
Improvement of Submerged Doppler-Type Directional Wave Meter and its Application to Field Observations629
<i>Noriaki Hashimoto, Masao Mitsui, Yoshimi Goda, Toshihiko Nagai, Tomoharu Takahashi</i>	
CHAPTER 51	
Comparison of Directional Wave Data Quality from Two Different Monitoring Systems .	.643
<i>Lihwa Lin, Sidney Schofield, Hsiang Wang</i>	
CHAPTER 52	
The Digital Simulation of Non-Linear Random Waves657
<i>Kyungmo Ahn</i>	
CHAPTER 53	
The “SWAN” Wave Model for Shallow Water668
<i>N. Booij, L.H. Holthuijsen, R.C. Ris</i>	
CHAPTER 54	
Generation Depths from Water Wave Data677
<i>J. Ernest Breeding, Jr.</i>	
CHAPTER 55	
Wave Climate Assessment in the South Aegean Shelf689
<i>Spiros Christopoulos, Christos Solomonidis</i>	
CHAPTER 56	
Sea State Parameterisation Using Empirical Orthogonal Functions703
<i>Witold Cieslikiewicz, Jerzy Graff</i>	
CHAPTER 57	
Fully Nonlinear Properties of Periodic Waves Shoaling over Slopes717
<i>Stephan T. Grilli, Juan Horrillo</i>	
CHAPTER 58	
Water Wave Fluctuations Induced by Irregular Bathymetry731
<i>Lulin Guo, Robert A. Dalrymple</i>	
CHAPTER 59	
Integral Control Data Assimilation in Wave Predictions743
<i>L.H. Holthuijsen, N. Booij, M. van Endt, S. Caires, C. Guedes Soares</i>	
CHAPTER 60	
Two-Dimensional Analysis of Wave Transformation by Rational-Approximation-Based, Time-Dependent Mild-Slope Equation for Random Waves754
<i>Toshimasa Ishii, Masahiko Isobe, Akira Watanabe</i>	

CHAPTER 61	
Nonlinear Wave Transformation Due to a Submerged Breakwater	767
<i>Masahiko Isobe, Akira Watanabe, Shogo Yamamoto</i>	
CHAPTER 62	
Observed and Modeled Wave Results from Near-Stationary Hurricanes	781
<i>Charles L. Vincent, Robert E. Jensen</i>	
CHAPTER 63	
Estimation of Persistence Statistics of the Waves Observed on Japanese Coast in the Light of Recent Studies	794
<i>Hajime Kato, Hisamichi Nobuoka</i>	
CHAPTER 64	
Probabilistic Modeling of Long-Term Wave Climate	808
<i>V.M. Leyden, W.R. Dally</i>	
CHAPTER 65	
Monte Carlo Simulation for Nearshore Wave Statistics in Southern California	822
<i>Chia-Chi Lu, R. Rea Strange III</i>	
CHAPTER 66	
Bottom Friction Dissipation in the Belgian Coastal Regions	836
<i>Weimin Luo, Jaak Monbaliu, Jean Berlamont</i>	
CHAPTER 67	
Weakly non-Gaussian Model of Wave Height Distribution for Nonlinear Random Waves .	.850
<i>Nobuhito Mori, Takashi Yasuda</i>	
CHAPTER 68	
An Attempt at Applying the Chaos Theory to Wave Forecasting	864
<i>Takao Ohta, Akira Kimura</i>	
CHAPTER 69	
Transition of Stochastic Characteristics of Waves in the Nearshore Zone	878
<i>David J. Robillard, Michel K. Ochi</i>	
CHAPTER 70	
Monitoring and Modelling on Shallow Water Wave Propagations in “El Saler” Beach ..	.889
<i>Jose C. Santos, Jose M. de la Pena, Jose Lozano</i>	
CHAPTER 71	
Intercomparison of Parameter Estimation Methods in Extremal Wave Analysis	900
<i>Masataka Yamaguchi</i>	
CHAPTER 72	
Influences of Spectral Shapes on the Statistical Properties of Simulated Random Waves .	914
<i>John Z. Yim, M.-Y. Lai</i>	
CHAPTER 73	
Second-Order Interaction between Random Wave and Submerged Obstacle	927

CHAPTER 74	
A Uniform Mild-Slope Model for Waves over Varying Bottom	941
<i>Libang Zhang, Billy L. Edge</i>	
CHAPTER 75	
Bragg Reflection of Shallow-Water Waves on a Sloping Beach	955
<i>Yong-Sik Cho, Jong-In Lee, Jong-Kyu Lee</i>	
CHAPTER 76	
Reflection Analysis with Separation of Cross Modes	968
<i>John Gronbech, Thomas Jensen, Henning Andersen</i>	
CHAPTER 77	
Wave Runup on Beaches	981
<i>John P. Ahrens, William N. Seelig</i>	
CHAPTER 78	
Field Study on Wave Run-Up on Seadykes	994
<i>Joachim Grune</i>	
CHAPTER 79	
Wave Run-Up on Revetments with Composite Slopes	1008
<i>Zeya Wang, Joachim Grune</i>	
CHAPTER 80	
Landward Transport of Spray Generated from a Wave Absorbing Sea Wall	1022
<i>Misao Hashida, Nobuhiro Matsunaga, Isao Irie</i>	
CHAPTER 81	
Irregular Wave Kinematics from a Pressure Record	1034
<i>Christopher H. Barker, Rodney J. Sobey</i>	
CHAPTER 82	
Nonlinear Refraction-Diffraction of Surface Waves over Arbitrary Depths	1048
<i>Serdar Beji, Kazuo Nadaoka</i>	
CHAPTER 83	
Boussinesq Equations with Improved Doppler Shift and Dispersion for Wave/Current Interaction	1060
<i>Qin Chen, Per A. Madsen, Ole R. Sorensen, David R. Basco</i>	
CHAPTER 84	
The Propagation of Water Waves in Prismatic Channels	1074
<i>Li Li, Robert A. Dalrymple, Jeffrey M. Mlynarski</i>	
CHAPTER 85	
A Statistical Approach for Modeling Triad Interactions in Dispersive Waves	1088
<i>Y. Eldeberky, V. Polnikov, J. A. Battjes</i>	

CHAPTER 86	
A Fully Nonlinear 3D Method for the Computation of Wave Propagation	1102
<i>Andrew B. Kennedy, John D. Fenton</i>	
CHAPTER 87	
A Fourth Order Boussinesq-Type Wave Model	1116
<i>Mauricio F. Gobbi, James T. Kirby</i>	
CHAPTER 88	
Fast Methods for Computing the Shoaling of Nonlinear Waves	1130
<i>J.D. Fenton, A.B. Kennedy</i>	
CHAPTER 89	
Structure of Frequency Domain Models for Random Wave Breaking	1144
<i>James T. Kirby, James M. Kaihatu</i>	
CHAPTER 90	
A Hamiltonian Model for Nonlinear Water Waves and Its Applications	1156
<i>A.K. Otta, M.W. Dingemans, A.C. Radder</i>	
CHAPTER 91	
The Role of Wave-Induced Shear Stresses in the Momentum Balance Equations	1168
<i>Francisco J. Rivero, Agustin S.-Arcilla</i>	
CHAPTER 92	
Nonlinear Wave Dynamics in the Surf Zone	1178
<i>O.R. Sorensen, P.A. Madsen, H.A. Schaffer</i>	
CHAPTER 93	
A Boussinesq Breaking Wave Model with Vorticity	1192
<i>I.A. Svendsen, Ke Yu, J. Veeramony</i>	
CHAPTER 94	
Roller Contributions as Inferred from Inverse Modelling Techniques	1205
<i>D.J.R. Walstra, G.P. Mocke, F. Smit</i>	
CHAPTER 95	
Wave-Current Interaction in Inlets	1219
<i>Michael J. Briggs, Zeki Demirbilek, Debra R. Green</i>	
CHAPTER 96	
Wave Climate of Large Reservoirs and a Revised Wave Hindcast Formula	1233
<i>Pierre Dupuis, Jean-Pierre Tournier, Octave Caron</i>	
CHAPTER 97	
Spectral Modelling of Current Induced Wave-Blocking	1247
<i>R.C. Ris, L.H. Holthuijsen</i>	

Part II Long Period Waves, Storm Surges and Wave Groups

CHAPTER 98	
Uncertainties in the Validation of Harbor Wave Models	1256
<i>Zeki Demirbilek, Bingyi Xu, Vijay Panchang</i>	
CHAPTER 99	
Field Measurements and Numerical Modeling of Harbor Oscillations During Storm Waves	1268
<i>W.M. Jeong, J.W. Chae, W.S. Park, K.T. Jung</i>	
CHAPTER 100	
Performance of a Resonator Designed by the Wave Filter Theory - Applicability to a Harbor	1280
<i>Takayuki Nakamura, Hitoshi Mochizuki, Satoshi Morita</i>	
CHAPTER 101	
The Generation of Waves by a Landslide: Skagway, Alaska - A Case Study	1293
<i>Fredric Raichlen, Jiin Jen Lee, Catherine Petroff, Philip Watts</i>	
CHAPTER 102	
Laboratory Experiment on Long Wave Generation by Time-Varying Breakpoint	1307
<i>Satoru Nagase, Masaru Mizuguchi</i>	
CHAPTER 103	
Laboratory Experiments on Generation of Long Waves in the Surf Zone	1321
<i>Akio Okayasu, Teruki Matsumoto, Yasuyuki Suzuki</i>	
CHAPTER 104	
Generation of Infragravity Waves	1335
<i>A. R. van Dongeren, I.A. Svendsen, F.E. Sancho</i>	
CHAPTER 105	
Responses of Coastal Topography to Sea-Level Rise	1349
<i>Nobuo Mimura, Eiichi Kawaguchi</i>	
CHAPTER 106	
Numerical Study of Low Frequency Surf Zone Motions	1361
<i>H. Tuba Ozkan-Haller, James T. Kirby</i>	
CHAPTER 107	
Neptune - An Integrated Approach to Determining NW European Coastal Extremes ...	1375
<i>Jerzy Graff, Witold Cieslikiewicz</i>	
CHAPTER 108	
A Stochastic Typhoon Model and Its Application to the Estimation of Extremes of Storm Surge and Wave Height	1389
<i>Yoshio Hatada, Masataka Yamaguchi</i>	

CHAPTER 109	
Design of Vertical Walls Against Storm Surge	1403
<i>A. Kortenhaus, C. Miller, H. Oumeraci</i>	
CHAPTER 110	
Nearshore, Wave and Topographic Effects in Storm Surges	1417
<i>Gary Watson, Takao Yamashita</i>	
CHAPTER 111	
The Swash Zone: A Focus on Low Frequency Motion	1431
<i>Adam M. Shah, J. William Kamphuis</i>	
CHAPTER 112	
The Development of an On-Line, Interactive, Tsunami-Information Resource	1443
<i>Benjamin Cook, Catherine Petroff</i>	
CHAPTER 113	
Long Wave Runup on Coastal Structures	1452
<i>Utku Kanoglu, Costas Emmanuel Synolakis</i>	
CHAPTER 114	
Offshore Tsunami Profiles Observed at the Coastal Wave Stations	1465
<i>Toshihiko Nagai, Noriaki Hashimoto, Kazuyoshi Shimizu, Fujio Kitamura</i>	
CHAPTER 115	
A Realistic Model for the 1992-96 Tidal Waves	1478
<i>Srinivas Tadepalli, Costas Emmanuel Synolakis</i>	
CHAPTER 116	
Long-Period Oscillations in a Harbour Caused by Typhoon	1491
<i>Wataru Kioka</i>	
CHAPTER 117	
Estimation of Wave Groups Parameter from Wave Climate Statistics	1503
<i>Satoshi Nakamura</i>	

Part III Coastal Structures

CHAPTER 118	
Reflection Coefficients of the Step-Shaped Slit Caisson on the Rubble Mound	1516
<i>Sung Mo Ahn, Ryuichi Fujiwara, Hiroshi Matsunaga, Katsuhiko Kurata, Shohachi Kakuno</i>	
CHAPTER 119	
Berm Breakwater Trunk Exposed to Oblique Waves	1528
<i>A. Alikhani, G.R. Tomasicchio, J. Juhl</i>	
CHAPTER 120	
Interaction Between Main Armour and Toe Berm Damage	1542
<i>P. Aminti, A. Lamberti</i>	

CHAPTER 121	
Stability of Artificial Roughness Elements and Run-Up Reduction	1556
<i>M. Klein Breteler, K.W. Pilarczyk</i>	
CHAPTER 122	
Wave Induced Velocities at a Rubble Mound Breakwater	1569
<i>Bruno Brunone, Giuseppe R. Tomasicchio</i>	
CHAPTER 123	
Natural Periods of Armor Stones	1583
<i>Fred E. Camfield</i>	
CHAPTER 124	
Reliability Based Optimal Design of Vertical Breakwaters Modelled as a Series System of Failure	1589
<i>E. Christiani, H.F. Burcharth, J. Dalsgaard Sorensen</i>	
CHAPTER 125	
Overall Slope Stability Analysis of Rubble Mound Breakwaters	1603
<i>Julien De Rouck, Luc Van Damme</i>	
CHAPTER 126	
Interactions in the Stability of Toe-Berm and Main-Armour for Rubble-Mound Breakwaters: An Experimental Study	1617
<i>Philippe Donnars, Michel Benoit</i>	
CHAPTER 127	
Potential Uses for the Rapidly Installed Breakwater System	1631
<i>Jimmy Fowler, Donald Resio, Michael Briggs, Cheryl Pollock</i>	
CHAPTER 128	
Stability of Reshaping Breakwaters with Special Reference to Stone Durability	1640
<i>P. Frigaard, T. Hald, H.F. Burcharth, Sigurdur Sigurdarson</i>	
CHAPTER 129	
Field Investigations on Wave-Dissipating Concrete Blocks Covering Vertical Wall Breakwater	1652
<i>Michio Gomyoh, Kazuhiko Sakai, Tomotuka Takayama, Kojiro Suzuki, Shigeo Takahashi</i>	
CHAPTER 130	
New Stability Formula for Wave-Dissipating Concrete Blocks Covering Horizontally Composite Breakwaters	1665
<i>Minoru Hanzawa, Hirokazu Sato, Shigeo Takahashi, Kenichiro Shimosako, Tomotsuka Takayama, Katsutoshi Tanimoto</i>	
CHAPTER 131	
Breakwater Stability under Regular and Irregular Wave Attack	1679
<i>Thomas Jensen, Henning Andersen, John Gronbech, Etienne P.D. Mansard, Michael H. Davies</i>	
CHAPTER 132	
Roundhead Stability of Berm Breakwaters	1693

CHAPTER 133	
Improvement of Composite Breakwater on Solid Bottom Against Severe Tsunamis	1707
<i>Yoshiaki Kimura, Hideo Kondo, Shinji Kuwabara, Akira Kawamori</i>	
CHAPTER 134	
Hydraulic Stability Analysis of Leese Slopes of Overtopped Breakwaters	1721
<i>M.D. Kudale, N. Kobayashi</i>	
CHAPTER 135	
Influence of the Core Configuration on the Stability of Berm Breakwaters	1735
<i>Nikolay Lissev, Alf Torum</i>	
CHAPTER 136	
Model Study of Reservoir Riprap Stability	1748
<i>Etienne P. D. Mansard, Michael H. Davies, Octave Caron</i>	
CHAPTER 137	
Prototype Measurements of Wave Pressures on a Wave Screen: Comparison to Physical and Analytical Models	1762
<i>F.L. Martin, M. A. Losada, C. Vidal, J.L. Diaz Rato</i>	
CHAPTER 138	
Velocity Field Measurements over Breakwater Heads under 3D Waves	1776
<i>Yoshiharu Matsumi, Akira Kimura, Kenichi Ohno</i>	
CHAPTER 139	
Wave Climate Simulation and Breakwater Stability	1789
<i>Josep R. Medina</i>	
CHAPTER 140	
Incipient Motion of Breakwater Armor Units	1803
<i>J. A. Melby, N. Kobayashi</i>	
CHAPTER 141	
Overtopping Reduction in Crownwall Design	1816
<i>Jose Luis Monso, Alfonso Vidoar, Cristina Cadevall, Cristina Garcia</i>	
CHAPTER 142	
Stable Profiles of Reshaping Breakwaters with a Berm Below the Water Level	1826
<i>C.I. Moutzouris</i>	
CHAPTER 143	
Experiments on a Non-Wave Overtopping Type Seawall	1840
<i>Keisuke Murakami, I. Irie, Y. Kamikubo</i>	
CHAPTER 144	
A Condition and Performance Rating System for Breakwaters and Jetties	1852
<i>John Oliver, Don Plotkin, John Lesnik, Douglas Pirie</i>	

CHAPTER 145	
Wave Overtopping and Stability of Armor Units under Multidirectional Waves	1862
<i>T. Sakakiyama, R. Kajima</i>	
CHAPTER 146	
Numerical Modeling of Breach Growth in a Sanddike	1876
<i>Guus S. Stelling, Willem T. Bakker, Christine van Kuik, Christel Somers</i>	
CHAPTER 147	
Aging and Stability of Placed Block Revetments	1888
<i>Theo Stoutjesdijk, Hans Johanson, Mark Klein Breteler</i>	
CHAPTER 148	
Experimental Analysis of the Settlement Failure Mechanism Shown by Caisson-Type Seawalls	1902
<i>Shigeo Takahashi, Kojiro Suzuki, Katsumasa Tokubuchi, Ken-ichiro Shimosako</i>	
CHAPTER 149	
Full Scale Measurements of Wave Attenuation Inside a Rubble Mound Breakwater . . .	1916
<i>Peter Troch, Marc De Somer, Julien De Rouck, Luc van Damme, Dierik Vermeir, Jean-Pierre Martens, Conan van Hove</i>	
CHAPTER 150	
Numerical Modelling of Wave Interaction with Dynamically Stable Structures	1930
<i>Marcel R.A. van Gent</i>	
CHAPTER 151	
Monitoring of Zeebrugge Breakwaters	1944
<i>Luc van Damme, Julien de Rouck</i>	
CHAPTER 152	
Influence of Rock Shape and Grading on Stability of Low-Crested Structures	1957
<i>Jentsje W. van der Meer, W.H. Tutuarima, G. Burger</i>	
CHAPTER 153	
Toe Stability of Rubble Mound Breakwaters	1971
<i>Ton van der Meulen, Gerrit J. Schiereck, Kees d'Angremond</i>	
CHAPTER 154	
Seawall Effects on Historically Receding Shorelines	1985
<i>Bryan N. Jones, David R. Basco</i>	
CHAPTER 155	
Control of Wave Propagation Angle by Tapered-Submerged Breakwater	1998
<i>Satoshi Takewaka, Isao Irie</i>	
CHAPTER 156	
Multidirectional Wave Loads on Vertical Breakwaters	2008
<i>Claudio Franco, Jentsje W. Van der Meer, Leopoldo Franco</i>	

CHAPTER 157	
Modelling the Impact of Detached Breakwaters on the Coast	2022
<i>K.J. Bos, J.A. Roelvink, M.W. Dingemans</i>	
CHAPTER 158	
Evaluation of Beach Modelling Techniques Behind Detached Breakwaters	2036
<i>Philip Axe, Suzana Ilic, Andrew Chadwick</i>	
CHAPTER 159	
Numerical Modelling of Bed Evolution Behind a Detached Breakwater	2050
<i>Philippe Pechon, Charles Teisson</i>	
CHAPTER 160	
Combined Diffraction and Transmission of Water Waves around a Porous Breakwater	
Gap	2063
<i>Xiping Yu, Hiroyoshi Togashi</i>	
CHAPTER 161	
Prediction of Wave Reflection from Rock Structures: An Integration of	
Field & Laboratory Data	2077
<i>Mark A. Davidson, Paul A.D. Bird, David A. Huntley, Geoff N. Bullock</i>	
CHAPTER 162	
Performance Evaluation of Buoy-Membrane Wave Barriers	2087
<i>M.H. Kim, B. L. Edge, S.T. Kee, L. Zhang</i>	
CHAPTER 163	
An Improved Design Method for the Riprap of Earthfill Dams of Large Reservoirs ...	2101
<i>Jean-Pierre Tournier, Pierre Dupuis, Raymond Ares</i>	
CHAPTER 164	
Geotextile Systems in Coastal Engineering - An Overview -	2114
<i>Krystian W. Pilarczyk</i>	
CHAPTER 165	
Groynes on the East Frisian Islands: History and Experiences	2128
<i>Hans Kunz</i>	
CHAPTER 166	
Permeable Pile Groins	2142
<i>Thomas Trampenau, Frank Goricke, Arved J. Raudkivi</i>	
CHAPTER 167	
The Effect of Groundwater on Scour Near Structures	2152
<i>John H. Loveless, Geoffrey T. Grant, Robert I. Karlsson</i>	
CHAPTER 168	
Abrasion of Steel Pipe Piles by Sediment Motion in Coastal Zones	2166
<i>Gaku Matsuoka, Shinichi Ito, Toshihiko Yamashita, Hiroshi Saeki, Yoshihisa Kariyazono, Koichi Sato</i>	

CHAPTER 169	
A Viscous Rotational Model for Wave Overtopping over Marine Structure	2178
<i>Fei Zhuang, Jiin-Jen Lee</i>	
CHAPTER 170	
Overtopping of Waves at a Wall: A Theoretical Approach	2192
<i>M. Jervis, D.H. Peregrine</i>	
CHAPTER 171	
Wind Effects on Runup and Overtopping of Coastal Structures	2206
<i>Donald L. Ward, Jun Zhang, Christopher G. Wibner, Charles M. Cinotto</i>	
CHAPTER 172	
Wave Overtopping of Vertical Structures Including Wind Effect	2216
<i>Johannes P. de Waal, Patrick Tonjes, Jentsje W. van der Meer</i>	
CHAPTER 173	
Bridge Pier Scour Assessment for the Northumberland Strait Crossing	2230
<i>C.D. Anglin, R.B. Nairn, A.M. Cornett, L. Dunaszegi, J. Turnham, G.W. Annandale</i>	
CHAPTER 174	
Wave Setup at River Entrances	2244
<i>David J. Hanslow, Peter Nielsen, Kevin Hibbert</i>	
CHAPTER 175	
Scour at Coastal Inlet Structures	2258
<i>Steven A. Hughes, J. William Kamphuis</i>	
CHAPTER 176	
Probability Distribution of the Maximum Wave Height along a Sea Wall with Finite Width	2272
<i>Akira Kimura, Takao Ohta</i>	
CHAPTER 177	
Beach Response in Front of Wave-Reflecting Structures	2284
<i>Roy C. Seaman, Tom O'Donoghue</i>	
CHAPTER 178	
Fundamental Characteristics of Wave Transformation around Artificial Reefs	2298
<i>Toshio Aono, Eric C. Cruz</i>	
CHAPTER 179	
Performance of a Submerged Breakwater for Shore Protection	2312
<i>Albert E. Browder, Robert G. Dean, Renjie Chen</i>	
CHAPTER 180	
Nonlinear Wave Transformation over a Submerged Triangular Breakwater	2324
<i>Lifen Dong, Akira Watanabe, Masahiko Isobe</i>	
CHAPTER 181	
Breaking Limit, Breaking and Post-Breaking Wave Deformation Due to Submerged	

Structures2338
<i>Koichiro Iwata, Koji Kawasaki, Do-Sam Kim</i>	
CHAPTER 182	
Italian Experience on Submerged Barriers as Beach Defence Structures2352
<i>Alberto Lamberti, Alessandro Mancinelli</i>	
CHAPTER 183	
Resonant Reflection and Refraction-Diffraction of Surface Waves Due to Porous Submerged Breakwaters2366
<i>Hajime Mase, Akira Kimura, Hiroshi Sakakibara</i>	
CHAPTER 184	
BEM-FEM Combined Analysis of Nonlinear Interaction between Wave and Submerged Breakwater2377
<i>N. Mizutani, W.G. McDougal, A.M. Mostafa</i>	
CHAPTER 185	
Regulation of Nearshore Circulation by Submerged Breakwater for Shore Protection .	.2391
<i>Hisamichi Nobuoka, Isao Irie, Hajime Kato, Nobuo Mimura</i>	
CHAPTER 186	
Submerged Breakwaters for the Defence of the Shoreline at Ostia - Field Experiences, Comparison2404
<i>Ugo Tomasicchio</i>	
CHAPTER 187	
Wave Transmission of Low-Crested Structures2418
<i>Kees d'Angremond, Jentsje W. van der Meer, Rutger J. De Jong</i>	
CHAPTER 188	
Effect of Submerged Breakwater on Profile Development2428
<i>Martin D. Groenewoud, Jan van de Graaff, Edward W.M. Claessen, Stephan C. van der Biezen</i>	
CHAPTER 189	
Cause and Characteristics of Impact Pressure Exerted by Spilling and Plunging Breakers on a Vertical Wall2442
<i>Seyed Ali Azarmsa, Takashi Yasuda, Hidemi Mutsuda</i>	
CHAPTER 190	
Dynamic Response of Vertical Elastic Walls to Breaking Wave Impact2456
<i>Masatato Hattori, Nobuaki Tsujioka</i>	
CHAPTER 191	
Wave Transmission Past Vertical Wave Barriers2470
<i>David L. Kriebel, Chad A. Bollmann</i>	
CHAPTER 192	
Physical Study of the Nature of High Peak Wave Pressures2484
<i>Jordan Marinski</i>	

CHAPTER 193	
A Design Short-Crested Wave Force Model for Vertical Deep-Water Breakwaters2494
	<i>S.-Y. Tzang, S.-R. Liaw</i>
CHAPTER 194	
New Design Methods for Wave Impact Loadings on Vertical Breakwaters and Seawalls . .	.2508
	<i>N.W.H. Allsop, J.E. McKenna, D. Vicinanza, T.T.J. Whittaker</i>
CHAPTER 195	
Scale Effects of Wave Impact Pressures on Cob Armour Units2522
	<i>M.W. Howarth, N.W.H. Allsop, A.M. Vann, R.J. Jones, J.P. Davis</i>
CHAPTER 196	
Wave Impact Loading of Vertical Face Structures for Dynamic Stability	
Analysis - Prediction Formulae -2534
	<i>P. Klammer, A. Kortenhaus, H. Oumeraci</i>
CHAPTER 197	
Analysis on the Interaction of Waves with Flexible Floating Structure	
by BE-FE Combined Method2548
	<i>Xiaodong Liu, Shigeki Sakai</i>
CHAPTER 198	
Design Wave Height Related to Structure Lifetime2560
	<i>Zhou Liu, Hans F. Burcharth</i>
CHAPTER 199	
Wave Impact Beneath a Horizontal Surface2573
	<i>D.J. Wood, D.H. Peregrine</i>
CHAPTER 200	
Wave Impulse Prediction for Caisson Design2584
	<i>Michael J.A. Walkden, Peter J. Hewson, Geoffrey N. Bullock</i>
CHAPTER 201	
Wave Overtopping Rate and Reflection Coefficient for Obliquely Incident Waves2598
	<i>Yoichi Moriya, Masaru Mizuguchi</i>
CHAPTER 202	
Sediment Transport and Wave Reflection near a Seawall2612
	<i>Jonathon R. Miles, Paul E. Russell, David A. Huntley</i>

Part IV Coastal Processes and Sediment Transport

CHAPTER 203	
Wave Energy Dissipation in Kelp Vegetation2626
	<i>Alfonse Dubi, Alf Torum</i>
CHAPTER 204	
Experimental Study on the Effect of Gravity Drainage System on Beach Stabilization . .	.2640
	<i>Hiroshi Kanazawa, Fumihiko Matsukawa, Kazumasa Katoh, Iwao Hasegawa</i>

CHAPTER 205	
Field Experiment on the Effect of Gravity Drainage System on Beach Stabilization . . .	2654
<i>Kazumasa Katoh, Shin-ichi Yanagishima</i>	
CHAPTER 206	
On the Change of Velocity Field in Nearshore Zone Due to Coastal Drain and the Consequent Beach Transformation	2666
<i>Michio Sato, Tadaihiro Fukushima, Ryuichiro Nishi, Masahiko Fukunaga</i>	
CHAPTER 207	
Evaluation of a Beach Dewatering System: Nantucket, USA	2677
<i>William R. Curtis, Jack E. Davis, Ian L. Turner</i>	
CHAPTER 208	
Sediment Transport Processes at Ocean Beach, San Francisco, California	2691
<i>Robert T. Battalio, Dilip Trivedi</i>	
CHAPTER 209	
Two Treatments of Shore Erosion in Extreme Floods on U.S. Great Lakes	2705
<i>Robert J. Hallermeier</i>	
CHAPTER 210	
Long-Term Beach Response to Shore Stabilization Structures on the Oregon Coast . . .	2718
<i>G.E. Hearon, W.G. McDougal, P.D. Komar</i>	
CHAPTER 211	
Profile Volumes as a Measure of Erosion Vulnerability	2732
<i>Timothy W. Kana, Ram Krishna Mohan</i>	
CHAPTER 212	
Breach Growth: Experiments and Modelling	2746
<i>Harry de Looff, Henk J. Steetzel, Arie W. Kraak</i>	
CHAPTER 213	
The Impact of an Extreme Event on the Sediment Budget: Hurricane Andrew in the Louisiana Barrier Islands	2756
<i>Jeffrey H. List, Mark E. Hansen, Asbury H. Sallenger, Jr., Bruce E. Jaffe</i>	
CHAPTER 214	
Beach Maintenance Strategies, a Comparison for a Recreational Beach	2770
<i>M. Pluijm, G. Kant, R. Nolten, A.P. de Looff</i>	
CHAPTER 215	
Littoral Impact of Ocean City Inlet, Maryland, USA	2779
<i>Julie Dean Rosati, Bruce A. Ebersole</i>	
CHAPTER 216	
Extreme Water Levels, Wave Runup and Coastal Erosion	2793
<i>P. Ruggiero, P.D. Komar, W.G. McDougal, R.A. Beach</i>	

CHAPTER 217	
A Morphological “Mixed-Type” Model for the Ebro Delta Coast	2806
<i>Agustin Sanchez-Arcilla, Jose A. Jimenez</i>	
CHAPTER 218	
Sea Dike Erosion and Coastal Retreat at Nam Ha Province, Vietnam	2820
<i>Ton That Vinh, G. Kant, Nguyen Ngoc Huan, Z. Pruszk</i>	
CHAPTER 219	
Beach Profile Analysis around Indian River Inlet, Delaware, U.S.A	2829
<i>Kirk F. Bosma, Robert A. Dalrymple</i>	
CHAPTER 220	
Improved 3-D Beach Evolution Model Coupled with the Shoreline Model (3D-SHORE)	2843
<i>Takuzo Shimizu, Takahiro Kumagai, Akira Watanabe</i>	
CHAPTER 221	
Evaluation of Shoreface Nourishments by Line Modelling	2857
<i>Martin D. Groenewoud, Willem T. Bakker, Jan van de Graaff, Ruud Spanhoff, Christian Laustrup</i>	
CHAPTER 222	
Beach Monitoring Program of Valencia (Spain)	2871
<i>Jose Serra, Josep R. Medina</i>	
CHAPTER 223	
Bar Migration and Duneface Oscillation on Decadal Scales	2884
<i>Marcel J.F. Stive, Jorge Guillen, Michele Capobianco</i>	
CHAPTER 224	
Morphological Development of the Terschelling Shoreface Nourishment in Response to Hydrodynamic and Sediment Transport Processes	2897
<i>P. Hoekstra, K.T. Houwman, A. Kroon, B.G. Ruessink, J.A. Roelvink, R. Spanhoff</i>	
CHAPTER 225	
Justification for Beach Nourishment	2911
<i>John G. Housley</i>	
CHAPTER 226	
Beach Nourishment Versus Shore Protection Structures	2918
<i>Alexander Khabidov, Yuri Bazhenov, Marina Glodenis, Nadya Ivanova, Liya Kaskevitch, Oleg Rybak, Valery Savkin, Anatoly Trizno, Grigory Zelensky, Veniamin Yedapin</i>	
CHAPTER 227	
Comparison of Beach and Shoreface Nourishment Torsminde Tange, Denmark	2927
<i>Christian Laustrup, Holger Toxvig Madsen, Per Sorensen, Ida Broker</i>	
CHAPTER 228	
Mathematical and Physical Modeling of Beach Nourishment Projects	2941
<i>W. Eric Rogers, Paul A. Work</i>	

CHAPTER 229	
Coastal Zone Dynamics during Artificial Nourishment	2955
<i>Elzbieta Zawadzka</i>	
CHAPTER 230	
Dune Damage Curves and Their Use to Estimate Dune Maintenance Costs	2969
<i>David R. Basco, Cheol S. Shin</i>	
CHAPTER 231	
Hurricane Opal Induced Changes on Natural and Nourished Beaches, West-Central Florida	2982
<i>Richard A. Davis, Jr., Ping Wang</i>	
CHAPTER 232	
Modelling Sand Transport and Profile Evolution on Macrotidal Beaches	2994
<i>Paul R. Fisher, Tim J. O'Hare</i>	
CHAPTER 233	
Beach Evolution Under Random Waves	3006
<i>Patrick Holmes, Thomas E. Baldock, Ray T.C. Chan, M. Ahmad L. Neshaei</i>	
CHAPTER 234	
Beach Profile Surveys Along the U.S. Pacific Coast 1945-1947	3020
<i>Nicholas C. Kraus, Robert L. Wiegel, Willard N. Bascom</i>	
CHAPTER 235	
Mechanism and Calculation of Sand Dune Erosion by Storms	3034
<i>Ryuichiro Nishi, Nicholas C. Kraus</i>	
CHAPTER 236	
Simulation of Coastal Profile Development Using a Boussinesq Wave Model	3048
<i>K.A. Rakha, R. Deigaard, P.A. Madsen, I. Broker, J.K. Ronberg</i>	
CHAPTER 237	
Cross-shore Sediment Transport and Beach Deformation Model	3062
<i>RattanapitikonWinyu , Tomoya Shibayama</i>	
CHAPTER 238	
Experimental Study on Sediment Transport in Surf and Swash Zones Using Large Wave Flume	3076
<i>Takao Shimizu, Masaaki Ikeno</i>	
CHAPTER 239	
The Influence of Long Waves on Macrotidal Beach Morphology	3090
<i>David J. Simmonds, Tim J. O'Hare, David A. Huntley</i>	
CHAPTER 240	
Mathematical Models for Waves and Beach Profiles in Surf and Swash Zones	3104
<i>Akira Watanabe, Mohammad Dibajnia</i>	

CHAPTER 241
Comparisons of Erosion Models for Storms at Ocean City, Maryland3115
Jie Zheng, Robert G. Dean

CHAPTER 242
Measurements of Wave Generated Bedforms3129
Christopher D. Jette, Daniel M. Hanes

CHAPTER 243
Field Measurement of Bed Roughness for Waves on an Offshore Reef3143
Raymond C. Nelson

CHAPTER 244
Effect of Wave-Induced-Pressure on Seabed Configuration3155
Tetsuo Sakai, Hitoshi Gotoh

CHAPTER 245
The Measurement of Bed Form Shapes in Hydraulic Models3169
Ian E. Shepherd

CHAPTER 246
Asymmetric Boundary Layer Flow above Sand Ripples under Progressive Waves3183
Takao Toue, Kazuo Nadaoka, Hidehiro Katsui

CHAPTER 247
Undertow Profiles in the Bottom Boundary Layer under Breaking Waves3194
Daniel T. Cox, Nobuhisa Kobayashi

CHAPTER 248
**A Comparison of Field Observations and Quasi-Steady Linear Shear Instabilities
of the Wave Bottom Boundary Layer**3207
D.L. Foster, A.J. Bowen, R.A. Beach, R.A. Holman

CHAPTER 249
Wave Boundary Layer Flows and Pore Pressures in Permeable Beds3219
H.H. Hwung, K.S. Hwang, B.H. Lee

CHAPTER 250
Backfilling of Trenches Exposed to Waves3231
Jacob Hjelmager Jensen, Jorgen Fredsoe

CHAPTER 251
A Closed-Form Solution for Turbulent Wave Boundary Layers3244
Magnus Larson

CHAPTER 252
Observed Suspended Sediments in Storm Conditions3257
*J.J. Williams, C.P. Rose, P.D. Thorne, L.E. Coates, J.R. West, P.J. Harcastle, J.D. Humphery,
S.P. Moores, D.J. Wilson*

CHAPTER 253	
Ebb Tidal Delta Evolution of Coastal Inlets	3270
<i>Michael R. Dombrowski, Ashish J. Mehta</i>	
CHAPTER 254	
Adjustments toward Equilibrium of a Large Flood -Tidal Delta after a Major Dredging Program, Tauranga Harbour, New Zealand	3284
<i>Terry Healy, Joseph Mathew, Willem de Lange, Kerry Black</i>	
CHAPTER 255	
Laboratory Mobile Bed Model Studies on Ebb Tidal Shoal Evolution	3295
<i>Xu Wang, Lihwa Lin, Hsiang Wang</i>	
CHAPTER 256	
Interaction of the Colorado River Project, Texas, with Longshore Sediment Transport ..	3309
<i>Daniel J. Heilman, Billy L. Edge</i>	
CHAPTER 257	
A Comprehensive Field Study of Tidal Inlet Processes at Ponce de Leon Inlet, Florida ..	3323
<i>Gary L. Howell</i>	
CHAPTER 258	
Transport of Fluid Mud Generated by Waves on Inclined Beds	3337
<i>Thijs van Kessel, C. Kranenburg, J.A. Battjes</i>	
CHAPTER 259	
Wave on Pebble Beach and Deformation of Pebble Beach	3349
<i>Ichiro Deguchi, Masanobu Ono, Toru Sawaragi</i>	
CHAPTER 260	
Wind-Induced Waves and Currents in a Nearshore Zone	3363
<i>Nobuhiro Matsunaga, Misao Hashida, Hiroshi Kawakami</i>	
CHAPTER 261	
Predicting Large-Scale, Cross-Shore Sediment Movement from Orbital Speeds	3378
<i>Edward B. Hands, John P. Ahrens, Donald T. Resio</i>	
CHAPTER 262	
Small-scale Morphology Related to Wave and Current Parameters Over a Barred Beach	3391
<i>A.F. Garcez Faria, E.B. Thornton, T.P. Stanton</i>	
CHAPTER 263	
Prediction of Shoreline Change Considering Cross-Shore Sediment Transport	3405
<i>Yoshimichi Yamamoto, Kiyoshi Horikawa, Katsutoshi Tanimoto</i>	
CHAPTER 264	
The Influence of Rollers on Longshore Currents	3419
<i>Daniel A. Osiecki, William R. Dally</i>	

CHAPTER 265	
Velocity Field Measurements in a “Coastal Buffer Zone”	3431
<i>Hiroshi Yagi, Hirofumi Hinata, Kazuo Nadaoka</i>	
CHAPTER 266	
Development of Underwater Beach Profile by Monochromatic and Random Waves ...	3442
<i>Karsten Peters, Jurgen Newe, Hans-H. Dette</i>	
CHAPTER 267	
Turbulent Stresses in the Surf-Zone: Which Way Is Up?	3453
<i>John W. Haines, Guy Gelfenbaum</i>	
CHAPTER 268	
Asymmetric and Irregular Wave Effects on Bedload: Theory Versus Laboratory and Field Experiments	3467
<i>Leszek M. Kaczmarek, Rafal Ostrowski</i>	
CHAPTER 269	
Kinematics and Shear Stresses from Combined Waves and Longshore Currents in the UK Coastal Research Facility	3481
<i>Richard R. Simons, Ruairi D. MacIver, Wameidh M. Saleh</i>	
CHAPTER 270	
Movable Bed Roughness in the Flow of Irregular Waves and Currents Over Movable Beds	3495
<i>Zai-Jin You, Peter Nielsen</i>	
CHAPTER 271	
Seabed and Foundation Response to Wave Loading	3507
<i>Michael H. Davies</i>	
CHAPTER 272	
Interannual Shoreline Variations at Duck, NC, USA	3521
<i>Nathaniel Plant, Rob Holman</i>	
CHAPTER 273	
Long Term Behaviour of the Sediment Volume inside a Tidal Basin after Poldering ...	3534
<i>Ernst Schroeder, Roland Goldenbogen, Hans Kunz</i>	
CHAPTER 274	
Wave Groups in a Barred Nearshore	3546
<i>B. Boczar-Karakiewicz, W. Romanczyk, J.L. Bona, B. Greenwood</i>	
CHAPTER 275	
Coastal Morphodynamic Instabilities	3560
<i>Albert Falques, Amadeu Montoto, Vicente Irazo</i>	
CHAPTER 276	
On Validation of a Sand Waves and Sand Banks Model	3574
<i>Suzanne J.M.H. Hulscher</i>	

CHAPTER 277	
Transverse Bars in Duck, North Carolina	3588
<i>Kathryn M. Konicki, Rob A. Holman</i>	
CHAPTER 278	
On the Systematic Offshore Decay of Breaker Bars	3600
<i>Kathelijne M. Wijnberg</i>	
CHAPTER 279	
Longshore Bed-Load Transport	3614
<i>Jesper S. Damgaard, Richard L. Soulsby</i>	
CHAPTER 280	
Design Capacity of a Longshore Current Recirculation System for a Longshore Sediment Transport Laboratory Facility	3628
<i>David G. Hamilton, Julie D. Rosati, Jimmy E. Fowler, Jane M. Smith</i>	
CHAPTER 281	
Influence of Nearshore Hardbottom on Regional Sediment Transport	3642
<i>Paul C.-P. Lin, R. Harvey Sasso</i>	
CHAPTER 282	
Improvement of the Most Accurate Longshore Transport Formula	3652
<i>J.S. Schoonees, A.K. Theron</i>	
CHAPTER 283	
Cross-shore Structure of Longshore Currents during Duck94	3666
<i>Falk Feddersen, R.T. Guza, Steve Elgar, T.H.C. Herbers</i>	
CHAPTER 284	
Three-Dimensional Hydrodynamics on a Barred Beach	3680
<i>Tae-Myoung Oh, Robert G. Dean</i>	
CHAPTER 285	
Rip Current Generation on a Plane Beach	3694
<i>D.A. Suriamihardja, Yoshito Tsuchiya</i>	
CHAPTER 286	
Nearshore Placement of Sand	3708
<i>Scott L. Douglass</i>	
CHAPTER 287	
Influence of Nearshore Berm on Beach Nourishment	3722
<i>Paul A. Work, Emre N. Otay</i>	
CHAPTER 288	
Accuracy of Sand Volumes as a Function of Survey Density	3736
<i>Jennifer L. Irish, W. Jeff Lillycrop, Larry E. Parson</i>	
CHAPTER 289	
Shoreline Analysis Using Digital Photogrammetry	3750

CHAPTER 290	
Application of Satellite Images to the Detection of Coastal Topography	3762
<i>Ji Wu, Jea Tzyy Juang</i>	
CHAPTER 291	
Sediment Transport in Swash Zone under Obliquely Incident Waves	3770
<i>Toshiyuki Asano</i>	
CHAPTER 292	
Sheet Flow Modelled As Pure Convection	3784
<i>Stephen Clark, Peter Nielsen</i>	
CHAPTER 293	
A Transport Rate Formula for Mixed-Size Sands	3791
<i>Mohammad Dibajnia, Akira Watanabe</i>	
CHAPTER 294	
Modelling of 3D Sediment Transport in the Surf Zone	3805
<i>Berry Elfrink, Ida Broker, Rolf Deigaard, Erik Asp Hansen, Peter Justesen</i>	
CHAPTER 295	
A Numerical Model of Sheet Flow Sediment Transport	3818
<i>Sadakazu Katori, Masaru Mizuguchi, Akira Watanabe</i>	
CHAPTER 296	
Numerical Modeling of Nearshore Morphological Changes under a Current-Wave Field	3830
<i>Taerim Kim, Hsiang Wang</i>	
CHAPTER 297	
An Analysis of Particle Saltation Dynamics	3846
<i>Michael R. Krecic, Daniel M. Hanes</i>	
CHAPTER 298	
Sediment Movement and Stress Condition in Sea Bed	3860
<i>Yoshihiko Maeno, Motoyasu Ishikawa, Kozo Bando, Yoshinobu Akiyama, Kouichi Yabe</i>	
CHAPTER 299	
Application of the Depth of Closure Concept	3874
<i>Robert J. Nicholls, William A. Birkemeier, Robert J. Hallermeier</i>	
CHAPTER 300	
Numerical Modeling of Sediment Transport for Various Mode	3888
<i>Masanobu Ono, Ichiro Deguchi, Toru Sawaragi</i>	
CHAPTER 301	
Nearbed Sediment Concentration from Tracer Studies	3901
<i>Zbigniew Pruszk, Ryszard Wierzchnicki, Andrzej Owczarczyk, Ryszard B. Zeidler</i>	

CHAPTER 302	
A Sloping Duct for the Study of Sediment Transport	3913
<i>Jesper S. Damgaard, Richard J.S. Whitehouse, Richard L. Soulsby</i>	
CHAPTER 303	
Sediment Dynamics and Profile Interactions: DUCK94	3921
<i>Donald K. Stauble, Mary A. Cialone</i>	
CHAPTER 304	
A Study on Flow Structure and Suspended Sediment Concentration over Seaweed Bed ..	3935
<i>Gozo Tsujimoto</i>	
CHAPTER 305	
An Energetics Approach for Suspended Sand Transport on Macrotidal Ridge and Runnel Beaches	3948
<i>George Voulgaris, Travis Mason, Michael B. Collins</i>	
CHAPTER 306	
Field Tests of Suspended-Load Transport Theories Used in Numerical Models	3962
<i>Thomas E. White</i>	
CHAPTER 307	
Shore Protection Studies for Ras-Elbar Area, Egypt	3976
<i>John B. Herbich, Abd-Elfattah Elfiky, Abd-Elmohsen Elmongy; Ali Elbahrawy, Gamal Elsaed</i>	
CHAPTER 308	
Stabilizing Beaches Downcoast of Harbor Extensions	3986
<i>John R.C. Hsu, Richard Silvester</i>	
CHAPTER 309	
Observation of Nearshore Currents and Beach Changes around Headlands Built on the Kashimanada Coast, Japan	4000
<i>K. Saito, T. Uda, K. Yokota, S. Ohara, Y. Kawanakajima, K. Uchida</i>	
CHAPTER 310	
Nourished Beach Control Between Balis and Arenys Harbours (Spain)	4014
<i>F. Javier Escartin, Alfonso Vidoar, A.M. Castaneda, Nuria Lupon</i>	
CHAPTER 311	
Numerical Simulation of Shoreline Change with Longshore Sand Waves at Groins . . .	4024
<i>Hans Hanson, Michelle M. Thevenot, Nicholas C. Kraus</i>	
CHAPTER 312	
Erosive Waves in Shoreline Change Due to the Reduction of a River Delta	4038
<i>Yoshito Tsuchiya</i>	
CHAPTER 313	
DELILAH, DUCK94 & SandyDuck: Three Nearshore Field Experiments	4052
<i>William A. Birkemeier, Charles E. Long, Kent K. Hathaway</i>	

CHAPTER 314	
Eulerian Mean Velocities under Non-Breaking Waves on Horizontal Bottoms	4066
<i>Peter Nielsen, Zai-Jin You</i>	
CHAPTER 315	
Reynolds Stress and Small-Scale Morphology Measurements during DUCK94	4079
<i>Timothy P. Stanton, Edward B. Thornton</i>	
CHAPTER 316	
Studies on the Suspended Concentration in the Surf Zone	4088
<i>Ching-Her Hwang, Li-Hung Tsai, Po-Ching Lin, Chin-Chi Tsai</i>	
CHAPTER 317	
Suspended Sediment Mixing in the Surf Zone	4098
<i>Jose A. Jimenez, Francisco J. Rivero, Agustin Sanchez-Arcilla, Vicente Gracia, Andres Rodriguez</i>	
CHAPTER 318	
Sand Suspension Events and Intermittence of Turbulence in the Surf Zone	4111
<i>R.D. Kos'yan, H. Kunz, S.Yu. Kuznetsov, N.V. Pykhov, M.V. Krylenko</i>	
CHAPTER 319	
Mechanisms of Beach Ground Water and Swash Interaction	4120
<i>Andrew J. Baird, Travis E. Mason, Diane P. Horn</i>	
CHAPTER 320	
The Equations for Integral and Mean Flow Properties in the Swash Zone	4134
<i>M. Brocchini, D.H. Peregrine</i>	
CHAPTER 321	
Wave Overwash of Subaerial Dunes	4148
<i>Yukiko Tega, Nobuhisa Kobayashi</i>	
CHAPTER 322	
Pressure Gradients Within Sediment Beds	4161
<i>Thomas E. Baldock, Patrick Holmes</i>	
CHAPTER 323	
Analysis of Mud Mass Transport under Waves Using an Empirical Rheological Model ..	4174
<i>Qin Jiang, Akira Watanabe</i>	
CHAPTER 324	
Countermeasures Against Wind-Blown Sand on Beaches	4188
<i>Shintaro Hotta, Kiyoshi Horikawa</i>	
CHAPTER 325	
Sea Breeze Effects on Nearshore Coastal Processes	4200
<i>Charitha Pattiaratchi, Gerhard Masselink</i>	
CHAPTER 326	
Wind Blown Sand at Castroville, California	4214
<i>Douglas J. Sherman, Bernard O. Bauer, Paul A. Gares, Derek W.T. Jackson</i>	

Part V Coastal, Estuarine and Environmental Problems

CHAPTER 327	
Pipeline Protection in the Surf Zone	4228
<i>Gerrit J. Schiereck, Henri L. Fontijn</i>	
CHAPTER 328	
Modeling Tidal Circulation in Florida Bay	4242
<i>Y. Peter Sheng, Justin Davis</i>	
CHAPTER 329	
Recent Developments in Coastal Defence Policy and Guidance in England	4253
<i>Reg Purnell</i>	
CHAPTER 330	
Structural Restoration of Coral Reefs Damaged by Vessel Groundings	4261
<i>Kevin R. Bodge</i>	
CHAPTER 331	
Dredging and Disposal within the Limits of a National Park	4274
<i>H. A. Manzenrieder, J.M. de Vries</i>	
CHAPTER 332	
Storm-Derived Bar/Sill Dynamics in a Dredged Channel	4289
<i>Sean O'Neil, Keith W. Bedford, David P. Podber</i>	
CHAPTER 333	
Bivalve Habitat Based on Sediment-Transport Mechanics	4300
<i>Hitoshi Gotoh, Tetsuo Sakai</i>	
CHAPTER 334	
Hydraulic Controls on Tidal Wetlands	4314
<i>R. Eric Katmarian, Philip A. McKee, Timothy W. Kana</i>	
CHAPTER 335	
Enhanced Mixing Through Perforated Discs on Round Buoyant Jet	4325
<i>Lilun Wu, Jiin-Jen Lee</i>	
CHAPTER 336	
Assessing Coastal Flood Risks	4339
<i>Roger Maddrell, Chris Fleming, Chris Mounsey</i>	
CHAPTER 337	
Experimental Study on the Behavior of Bivalves by Oscillatory Flow	4353
<i>Toshihiko Yamashita, Akira Wada, Gaku Matsuoka, Kenji Yano, Sadamitsu Akeda</i>	
CHAPTER 338	
Wind- and Sea Level-Induced Shore Evolution in Poland	4364
<i>Ryszard B. Zeidler, Marek Skaja, Grzegorz Rozynski, Jarka Kaczmarek</i>	

CHAPTER 339	
Ashdod Port's Effect on the Shoreline, Seabed and Sediment	4376
<i>Abraham Golik, Dov S. Rosen, Arik Golan, Maxim Shoshany Dan DiCastro, Pinkhas Harari</i>	
CHAPTER 340	
Tweed River Sand Bypass: Concepts and Progress	4390
<i>Russell J. Murray, R.P. (Jock) Brodie, Mark Porter, David A. Robinson</i>	
CHAPTER 341	
Design Considerations for Coastal Projects in Cold Regions	4397
<i>Craig B. Leidersdorf, Peter E. Gadd, Kennon D. Vaudrey</i>	
CHAPTER 342	
Experimental Study on Deformation and Fracture of Ice Sheet by Propagating Water Wave	4411
<i>Shigeki Sakai, Xiaodong Liu, Makoto Sasamoto, Shigeo Kanada and Koh Izumiyama</i>	
CHAPTER 343	
An Attempt to Determine the Spanish Public Domain Border	4418
<i>R. Medina, I.J. Losada, F. Mendez, A.J. Fernandez</i>	
CHAPTER 344	
Education of Coastal Engineers for the 50th ICCE	4431
<i>Henk Jan Verhagen</i>	
CHAPTER 345	
Risk-Based Analysis of Coastal Projects	4440
<i>Edward F. Thompson, Michael Wutkowski, Norman W. Scheffner</i>	
CHAPTER 346	
Designing for Propeller Action in Harbours	4451
<i>G.A. Hamill, J.A. McGarvey</i>	
CHAPTER 347	
Modeling Inlet Sand Bypassing	4464
<i>Christopher G. Creed</i>	
CHAPTER 348	
An Approach to Modeling Inlet and Beach Evolution	4477
<i>Mark B. Gravens</i>	
CHAPTER 349	
Hydrodynamics of a Bar in a Flood Channel - the Westerschelde Estuary	4491
<i>Claire Jeuken</i>	
CHAPTER 350	
Interactions between a Sand Barrier and Flood Terrace at the Abukuma River Mouth ..	4505
<i>Akira Mano, Masaki Sawamoto</i>	
CHAPTER 351	
A Unique Look at Oregon Inlet, NC USA	4517

CHAPTER 352	
Impacts of Inlet Structures on Channel Location	4531
<i>William C. Seabergh, Mary A. Cialone, Donald K. Stauble</i>	
CHAPTER 353	
Complete Closure of the Nanakita River Mouth in 1994	4545
<i>Hitoshi Tanaka, Fumihiko Takahashi, Atsushi Takahashi</i>	
CHAPTER 354	
The Erosion of a Salt Wedge Trapped Behind a Barrage Across An Estuary	4557
<i>S.A. Walker, G.A. Hamill, H.T. Johnston</i>	
CHAPTER 355	
Near-Field Measurements of a Buoyant Jet in Waves and Currents	4569
<i>K.H. Kwan, C. Swan</i>	
CHAPTER 356	
Cost Effectiveness of Wave Power Extraction at Erosive Coasts	4583
<i>Hideo Kondo</i>	
CHAPTER 357	
Feasibility Tests of New Pendular-Type Wave Energy Conversion Apparatus	4591
<i>Senji Osanai, Hideo Kondo, Yuzo Mizuno and Tomiji Watabe</i>	
CHAPTER 358	
Watertable Dynamics in Coastal Areas	4601
<i>Hong-Yoon Kang, Peter Nielsen</i>	
CHAPTER 359	
Long Range Positive Effects of the Delray Beach Nourishment Program	4613
<i>Kim E. Beachler, Douglas W. Mann</i>	
CHAPTER 360	
Effectiveness of a Combined Beach and Shoreface Nourishment on the Island of Norderney/East Frisia, Germany	4621
<i>Hanz D. Niemeyer, Ralf Kaiser, Heiko Knaack</i>	

Part VI Case Studies

CHAPTER 361	
Nearshore Berm Performance at Newport Beach, California, USA	4636
<i>Chuck Mesa</i>	
CHAPTER 362	
San Gabriel River to Newport Bay Erosion Control Project, Orange County, California—30 Years of Periodic Beach Replenishment	4650
<i>Arthur T. Shak, Joseph A. Ryan</i>	

CHAPTER 363	
A Ten-Year History of Dolos Monitoring at Crescent City	4664
<i>William S. Appleton, Thomas Kendall, Jeffrey A. Melby</i>	
CHAPTER 364	
Breakwater Damage in Okushiri Port Due to the Hokkaido Nansei-oki Earthquake Tsunami	4676
<i>Katsutoshi Kimura, Yuzo Mizuno, Hiroichi Tsuruya, Yasuyuki Nakagawa</i>	
CHAPTER 365	
Richards Bay North Breakwater - Repair of a Roundhead: Monitoring, Model Testing, Design and Construction	4689
<i>D. Phelp, A. McClarty, A. Bartels</i>	
CHAPTER 366	
Thyboron Coastal Investigations 1995: New Lessons from an Old Coastal Problem ...	4703
<i>I. Broker, J.A. Zyserman, Per Roed Jakobsen</i>	
CHAPTER 367	
Probabilistic Risk Assessment of Beach Erosion at Pevensey Bay in England	4717
<i>Ping Dong, Keith J. Riddell</i>	
CHAPTER 368	
Beach Nourishment in Altafulla, Spain: Verification of Theoretical Models	4730
<i>J. Galofre, F.J. Montoya, R. Medina</i>	
CHAPTER 369	
Alternatives to Beach Stabilization: Cambrils Coast Case Study (Spain)	4744
<i>Nuria Lupon, Alfonso Vidaor, Jordi Galofre, F. Javier Escartin</i>	
CHAPTER 370	
The Effect of Grain Sorting on Profile Stability of Nourished Beaches	4756
<i>Ram K. Mohan, Timothy W. Kana</i>	
CHAPTER 371	
The Use of Data Assimilation to Improve Wave Hindcast Results	4770
<i>Jon M. Hubertz</i>	
CHAPTER 372	
Grain-Size Influence on Sand Transport in Oscillatory Sheet Flow	4779
<i>C. Marjolein Janssen and Jan S. Ribberink</i>	
CHAPTER 373	
Cross-Shore Sediment Transport Mechanisms in the Surfzone on a Timescale of Month to Years	4793
<i>Klaas T. Houwman and Gerben Ruessink</i>	
CHAPTER 374	
Numerical Prediction of Breaking Waves and Currents with a Boussinesq Model	4807
<i>Okey George Nwogu</i>	

CHAPTER 375

The Effect of the CL-Vortex Force in 3D Wave-Current Interaction4821
M. W. Dingemans, J. A. Th. M. van Kester, A. C. Radder and R. E. Uittenbogaard

Subject Index4833

Author Index4847



Measurement of waves and sediment at Field Research Facility, Duck, North Carolina. Photo courtesy of Billy L. Edge.

PART I

Characteristics of Coastal Waves and Currents



Lark and the CRAB at Field Research Facility, Duck, North Carolina. Photo courtesy of Billy L. Edge.

CHAPTER 1

EXPERIMENTAL STUDY OF BREAKING WAVES OVER A SHOAL

Arun Chawla, H. Tuba Özkan-Haller and James T. Kirby¹

ABSTRACT: The aim of this paper is to study the transformation of irregular directional waves over a circular shoal. An experimental study has been carried out. The resulting data has been used to test the accuracy of an existing refraction-diffraction model. Model to data comparisons have been carried out for the entire basin region including about 3 shoal diameters downwave of the shoal, with satisfactory results. Several physical processes have been identified which lead to possible disparities in the comparisons.

INTRODUCTION

Wave modeling of random waves over a varying bathymetry is a subject of considerable importance to coastal engineers. The development of the classical mild slope equation by Berkhoff (1972) allowed coastal engineers to study the combined effects of refraction and diffraction. A wide family of equations have been derived from the mild slope equation to increase the accuracy and the speed of the models. One such set of equations are the parabolic equations, first derived for ocean waves by Radder (1979), which have gained popularity because of their speed of computation, even though they have a fixed direction of propagation and a limited range of angles from the assumed propagation direction over which they are valid. Nonlinear formulations of parabolic equations (Kirby and Dalrymple 1983) have been found to give more accurate results than the linear mild slope equation (Kirby and Dalrymple 1984). The limitation in the range of angles has been relaxed using Padé approximants (Booij, 1981).

Although relatively accurate parabolic models have been developed to study the evolution of waves over an irregular bottom, all these models have been derived for monochromatic waves only. Coastal engineers have traditionally approximated the offshore irregular sea states by representative monochromatic waves in order to use these models to make predictions. However, investigators such as Goda (1985) (using an analytical approach), Vincent and Briggs (1989) (by conducting an experimental study) and Panchang *et al.* (1990) (using a numerical approach) have shown that such an approximation may result in large errors due to vast dissimilarities in the refraction-diffraction patterns of the two

¹Center for Applied Coastal Research, Department of Civil and Environmental Engineering, University of Delaware, Newark, DE 19716, USA. Correspondence e-mail: cwla@coastal.udel.edu

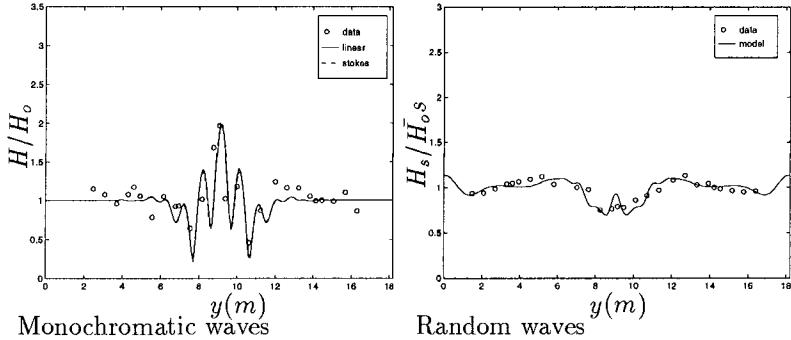


Figure 1: Wave height distribution behind a shoal for a monochromatic wave and a directional sea state

wave fields. Our own experiments confirm this and Figure 1 shows the vast differences in the wave height distribution along a transect (transect D-D in Figure 2) behind a submerged shoal.

Recently, methods for computing the evolution characteristics of a directional spectral sea state using parabolic models for monochromatic waves have been developed. Panchang *et al.* (1990), Grassa (1990) and Izumiya and Horikawa (1987) have developed models using a spectral calculation method which consists of discretizing the offshore spectrum into individual monochromatic directional components, determining the wave transformations of each component with the help of monochromatic wave models, and then assembling the wave components by linear superposition at the respective grid points in the domain to obtain the statistical characteristics of the spectrum at those points.

In this paper a numerical model which has been developed using the parabolic formulation of Kirby (1986a), is tested against data for a range of breaking wave conditions. Experimental study of random directional waves breaking over a submerged circular shoal has been carried out for two different directional spreadings and energy variances to study their effects on wave height distribution. Extensive surface elevation measurements have been made on top of and around the shoal, and some aspects of the frequency spectra have been looked into.

NUMERICAL MODEL

The parabolic model for spectral wave conditions used here simulates the evolution of directional random waves in the nearshore zone. The model predicts the effects of refraction, diffraction, shoaling and breaking. Therefore, the model is particularly applicable to regions where an incoming random sea propagates over complicated bathymetry towards shore. The bathymetry may include a shoal formation at the mouth of an inlet or estuary, where refraction, diffraction, shoaling and depth-limited breaking will be simultaneously important.

The model requires the specification of the incoming directional random sea at the offshore boundary. The random sea is represented by a two-dimensional spectrum which is discretized into wave components, resulting in wave components of amplitude A with associated frequency f and angle of incidence θ to

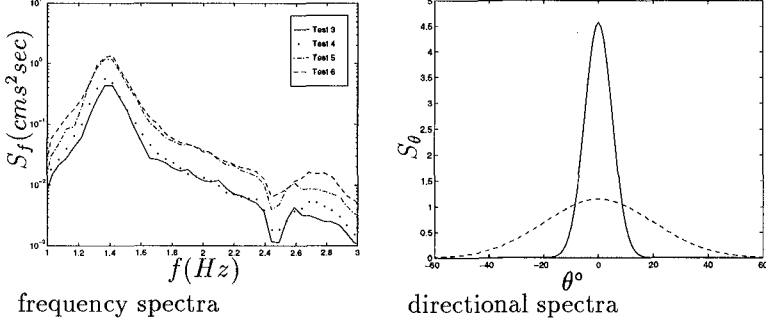


Figure 3: Design frequency and directional spectra for the 4 directional sea states

Table 1: Test particulars for the random wave experiments

Test no.	$H_{0s}(m)$	$T_p(sec)$	θ_m	Range
3	0.0139	0.73	0	$\pm 15^\circ$
4	0.0156	0.73	0	$\pm 45^\circ$
5	0.0233	0.73	0	$\pm 15^\circ$
6	0.0249	0.71	0	$\pm 45^\circ$

$$\begin{aligned}
 & (C_{gn} + U)(A_n)_x - 2\Delta_1 V(A_n)_y + i(\bar{k}_n - a_0 k_n)(C_{gn} + U)A_n \\
 & + \left\{ \frac{\sigma_n}{2} \left(\frac{C_{gn} + U}{\sigma_n} \right)_x - \Delta_1 \sigma_n \left(\frac{V}{\sigma_n} \right)_y \right\} A_n + i\Delta'_n \left[\left((CC_g)_n - V^2 \right) \left(\frac{A_n}{\sigma_n} \right)_y \right]_y \\
 & - i\Delta_1 \left\{ \left[UV \left(\frac{A_n}{\sigma_n} \right)_y \right]_x + \left[UV \left(\frac{A_n}{\sigma_n} \right)_x \right]_y \right\} + \alpha A_n \\
 & + \frac{-b_1}{k_n} \left\{ \left[\left((CC_g)_n - V^2 \right) \left(\frac{A_n}{\sigma_n} \right)_y \right]_{yx} + 2i \left(\sigma_n V \left(\frac{A_n}{\sigma_n} \right)_y \right)_x \right\} \\
 & + b_1 \beta_n \left\{ 2i\omega_n U \left(\frac{A_n}{\sigma_n} \right)_x + 2i\sigma_n V \left(\frac{A_n}{\sigma_n} \right)_y - 2UV \left(\frac{A_n}{\sigma_n} \right)_{xy} \right. \\
 & + \left. \left[\left((CC_g)_n - V^2 \right) \left(\frac{A_n}{\sigma_n} \right)_y \right]_y \right\} - \frac{i}{k_n} b_1 \{ (\omega_n V)_y + 3(\omega_n U)_x \} \left(\frac{A_n}{\sigma_n} \right)_x \\
 & - \Delta_2 \left\{ \omega_n U \left(\frac{A_n}{\sigma_n} \right)_x + \frac{1}{2} \omega_n U_x \left(\frac{A_n}{\sigma_n} \right) \right\} + ik_n \omega_n U (a_0 - 1) \left(\frac{A_n}{\sigma_n} \right) = 0 \quad (3)
 \end{aligned}$$

where U and V are the currents in the x and y directions, α is a dissipation coefficient for wave breaking, \bar{k}_n is a representative wave number corresponding

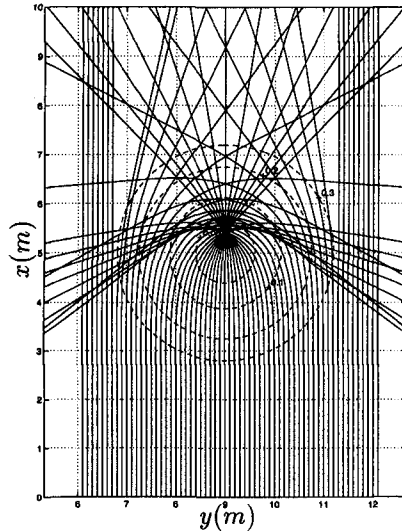


Figure 4: Refraction diagram at peak frequency, $f_p = 1.37 \text{ Hz}$ for the given bathymetry.

to the peak frequency, and

$$\begin{aligned}
 \sigma_n &= \omega_n - k_n U, \\
 \beta_n &= \frac{(k_n)_x}{k_n^2} + \frac{(k_n ((CC_g)_n - U^2))_x}{2k_n^2 ((CC_g)_n - U^2)}, \\
 \Delta_1 &= a_1 - b_1, \\
 \Delta_2 &= 1 + 2a_1 - 2b_1, \\
 \Delta'_n &= a_1 - b_1 \frac{\bar{k}_n}{k_n}.
 \end{aligned} \tag{4}$$

The model coefficients

$$a_0 = 1; \quad a_1 = -0.75; \quad b_1 = -0.25 \tag{5}$$

recover the Padé approximant of Booij(1981).

The statistical information obtained after each step in the parabolic scheme is used to construct a model for the dissipation of energy due to breaking. To determine the energy dissipation, a simple model by Thornton and Guza (1983) is used. The energy dissipation model is built into the model equation using an additional breaking term αA_n in (3), so that it is unnecessary to have any criterion for turning breaking on or off. The coefficient α is given by

$$\alpha = \frac{3\sqrt{\pi} \bar{f} B^3}{4 \gamma^4 h^5} H_{rms}^5. \tag{6}$$

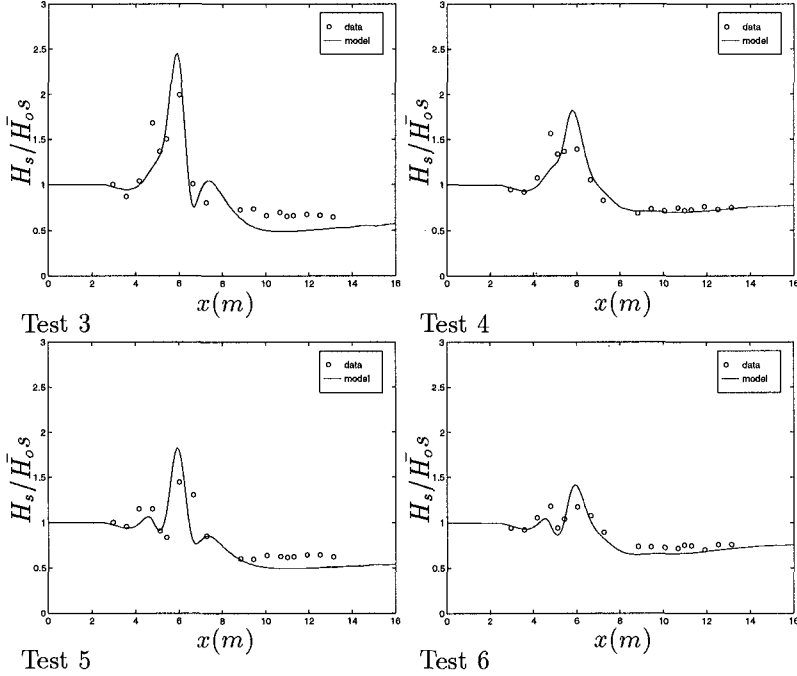


Figure 5: Significant wave height distribution along transect A-A

where h is the local water depth and \bar{f} is a representative frequency for the frequency spectrum and is chosen to be the peak frequency. B and γ are constants and are chosen to be equal to 1 and 0.6, respectively (Mase and Kirby, 1992). H_{rms} is the root-mean-square wave height, and is obtained as a statistical quantity from the wave model,

$$H_{rms}(x, y) = 2 \sqrt{\sum_{n=1}^N |A(x, y)_n|^2} \quad (7)$$

The dissipation model of Thornton and Guza (1983) was originally derived assuming that the waves continue breaking once they have started, and has been validated for waves breaking on a monotonic beach. Though we can see from (6) that the dissipation term α is artificially reduced with increase in local water depth h we are not certain if this correctly simulates the reforming of waves with increased water depth. Also, no modifications have been made in the dissipation model to account for directional effects. Only change in energy flux in the x direction is considered, and energy flux in the y direction does not take part in the dissipation model.

EXPERIMENTAL SETUP

The experiments were conducted at the Center for Applied Coastal Research, University of Delaware. The wave basin is approximately 18.2m long and 18.2m

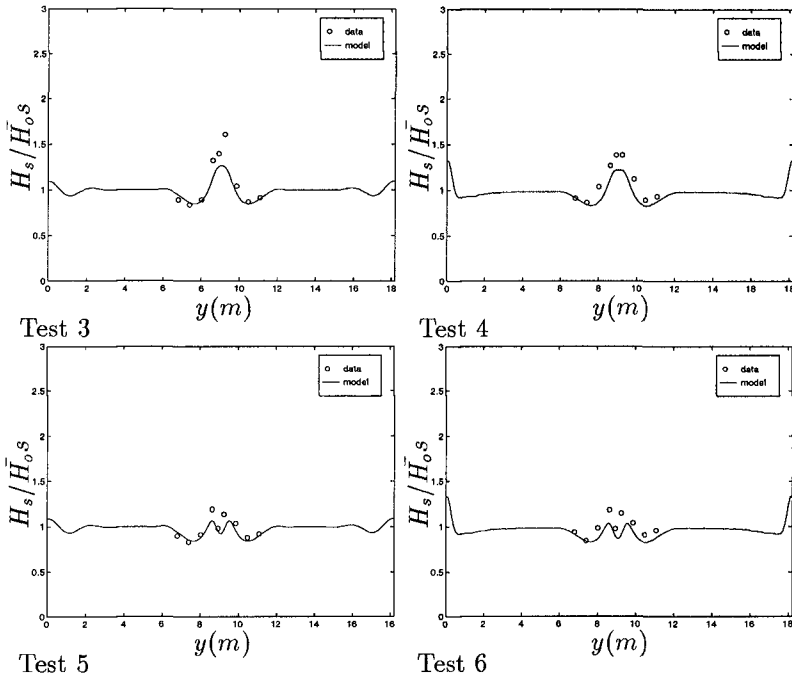


Figure 6: Significant wave height distribution along transect F-F

wide. It has a three-dimensional wavemaker at one end, consisting of 34 flap type paddles which creates the desired wave field. The bottom is flat except for a circular shoal in the center, and a stone beach at the far end minimizes the reflections. A schematic view of the experimental layout, together with the gage locations is given in Figure 2.

A total of ten capacitance wave gages were used in the experiment, of which nine were placed on an array. This array was then placed at fourteen different positions (denoted by thick lines in Figure 2) to obtain a total of 126 measuring points around the shoal. Depending upon their orientation, one or more array positions form a transect along which comparisons are made with the numerical model. There is one longitudinal transect (A-A) going over the top of the shoal and six transverse transects (B-B, C-C, D-D, E-E, F-F and G-G) behind and on top of the shoal (see Figure 2).

The circular shoal has a diameter of $5.2m$ and a maximum height of $37cm$. Geometrically it is the top portion of a circular sphere of radius $9.1m$. The center of the shoal is placed at $x = 5m$ and $y = 8.98m$. The equation for the perimeter of the shoal is given by

$$(x - 5)^2 + (y - 8.98)^2 = (2.57)^2 \quad (8)$$

and for the bathymetry is given by

$$z = -h + \sqrt{82.81 - (x - 5)^2 - (y - 8.98)^2} - 8.73 \quad (9)$$

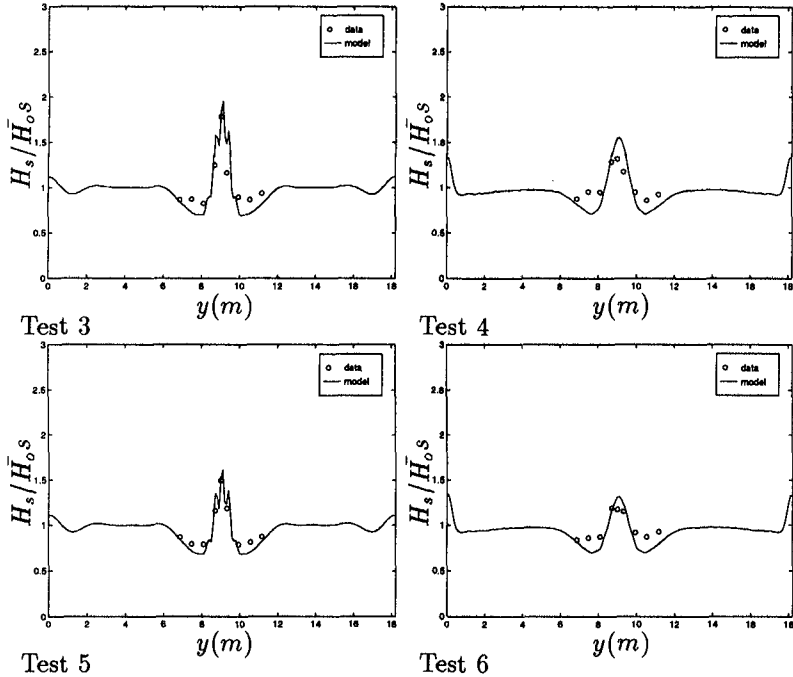


Figure 7: Significant wave height distribution along transect E-E

where h is the water depth away from the shoal.

Four different directional sea test conditions (Test 3, Test 4, Test 5 and Test 6) were run with a TMA spreading function (Bouws *et al.*, 1985) in frequency, and a wrapped normal directional spreading function (Borgman, 1984) in direction. The water depth away from the shoal (h in (9)) was 40cm, and the water depth on top of the shoal was 3cm. All four tests had similar frequency spreadings except that the energy variance in Tests 3 and 4 were lower, and the frequency spectra for the four test cases is given in Figure 3. In all the four cases the waves were breaking on top of the shoal, with more waves breaking for Tests 5 and 6. Two different directional spreadings were used (Figure 3), with the mean angle normal to the wavemaker ($\theta_m = 0^\circ$). Tests 3 and 5 have a narrow directional spread ($\pm 11^\circ$), while Tests 4 and 6 have a broad directional spread ($\pm 45^\circ$).

The initial significant wave height (H_{0s}), peak period (T_p), mean angle (θ_m) and the range of directional spreading for the four different test cases are given in Table 1. Data was collected at a sampling rate of 50Hz for 655 seconds (32768 sample points) at all the gages.

DATA TO MODEL COMPARISONS

Significant wave height information was obtained from the data using a zero-upcrossing method, while from the model it was obtained from the statistics assuming a Rayleigh wave height distribution. Reflections from the beach at the

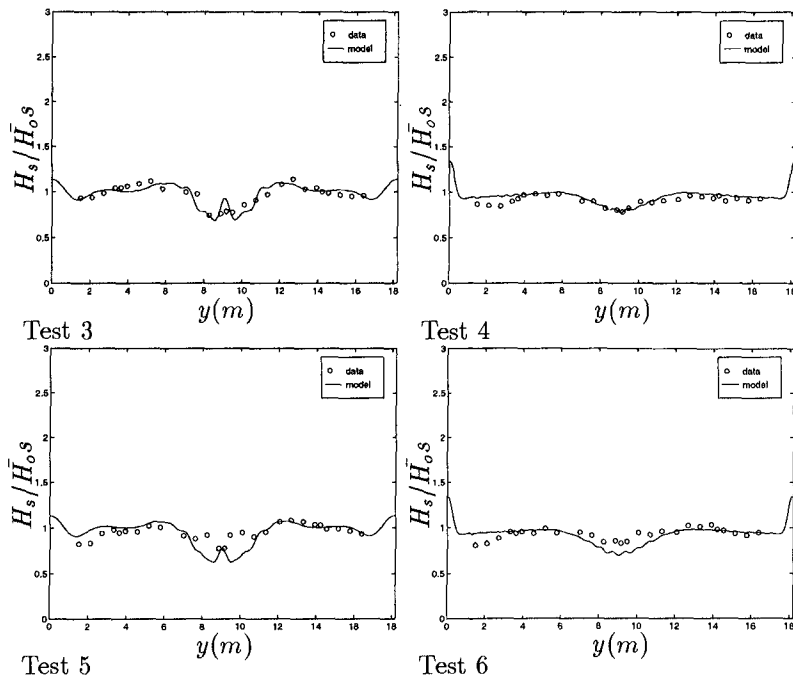


Figure 8: Significant wave height distribution along transect D-D

far end of the basin (see Figure 2) are a matter of concern but have been ignored here since the reflected wave field could not be separated from the incident wave field. In each case the input frequency spectrum to the model was directly measured from the wave data. The input directional spectrum was taken to be the same directional spreading function used to generate incident waves for the respective test cases (Figure 3).

A wave refraction pattern for the peak frequency (Figure 4) shows that the focusing is quite severe on top of the shoal, and that some of the wave rays are moving at angles greater than 90° . Since the model can predict wave conditions accurately only within a range of wave angles of $\pm 45^\circ$, some discrepancies between model and data results are expected in this region.

For each test case, all significant wave height comparisons have been normalized by the respective initial significant wave height (H_{0s}) given in Table 1. Figure 5 gives the wave height comparisons along transect A-A. The model tends to overpredict the wave height distribution near the region of focus. This is probably due to the severe focusing in this region (Figure 4), which the model cannot properly simulate. Since the focusing is taking place inside the surf zone, another probable cause for the discrepancy could be the limitations of the breaking model, and a different breaking model might give more accurate results.

Comparisons along the six transverse transects are shown in Figures 6 – 10. In all the cases the model predicts large wave heights at the side walls. This is because the no flux boundary condition at the side wall causes the waves to

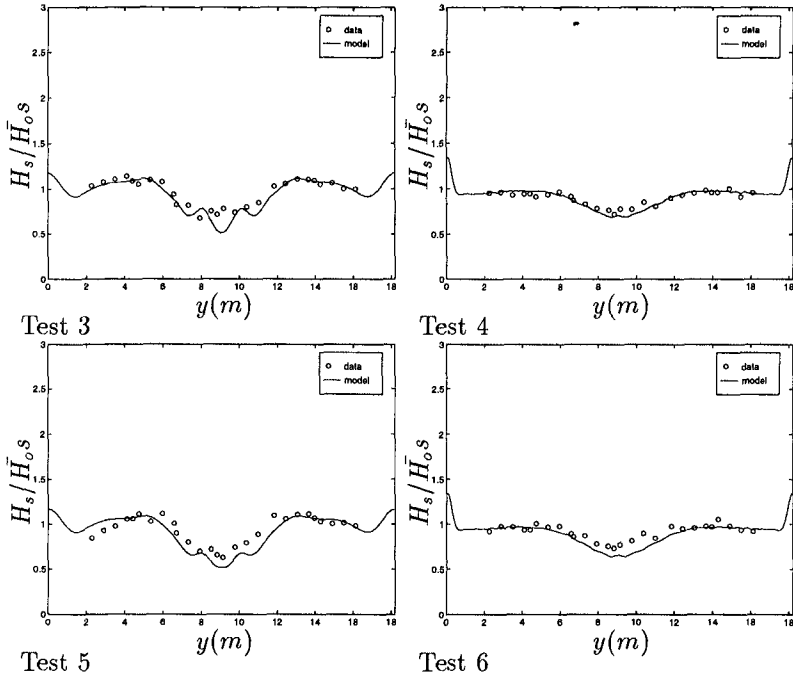


Figure 9: Significant wave height distribution along transect C-C

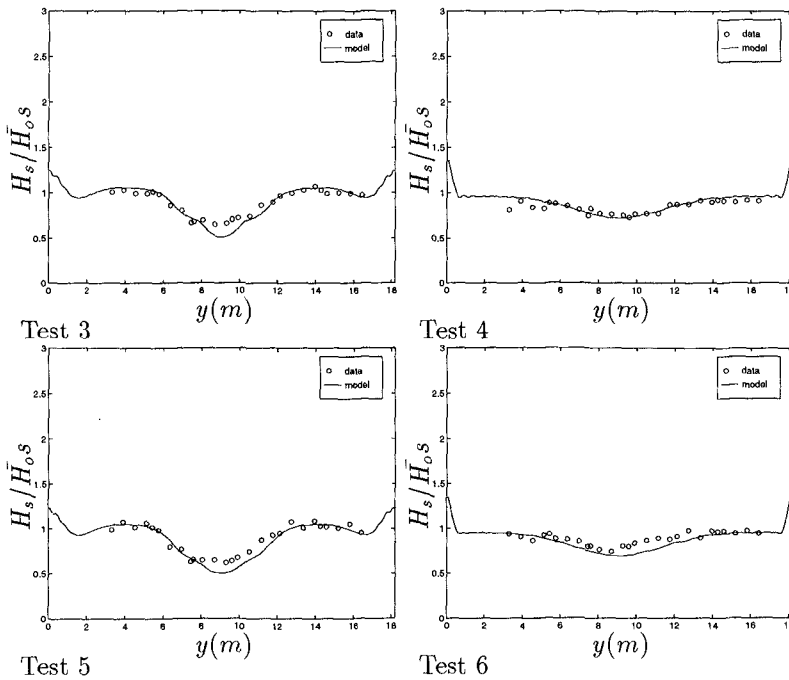


Figure 10: Significant wave height distribution along transect B-B

form an antinode there for each wave component, which when superimposed lead to large significant wave heights. On top of the shoal (Figure 6) and along transect E-E (Figure 7) where the waves are breaking and focusing, the same energy discrepancy that was seen in Figure 5 is observed, but the spread of the wave heights is simulated reasonably well by the model. The comparisons further behind the shoal (Figures 8 – 10) on the other hand are extremely good. In general we see that the wave height distribution behind the shoal is more smoothed out for the broad directional test cases (Tests 4 and 6) as compared to the narrow directional test cases (Tests 3 and 5). An interesting observation is that behind the shoal the wave height distributions are more a function of the type of directional distribution of the input spectrum, instead of being a function of the energy content of the spectrum. Before the focusing takes place (Figure 6), the wave height distributions for Tests 3 and 4, and Tests 5 and 6 are quite similar, while after focusing (Figures 6 – 10) Tests 3 and 5, and Tests 4 and 6 have similar wave height spreadings. This effect can also be seen clearly in Figure 5, where the wave height distribution till $x = 5m$ is a function of the energy content of the spectrum, and beyond that depends on the directional spreading of the spectrum.

Though the model gives reasonable significant wave height comparisons, it is unable to predict wave-wave interactions since it is based on a linear superposition of monochromatic wave components. These interactions lead to the formation of higher harmonics in nature, and become more pronounced with increased nonlinearity. A comparison of model spectra to data spectra on top of

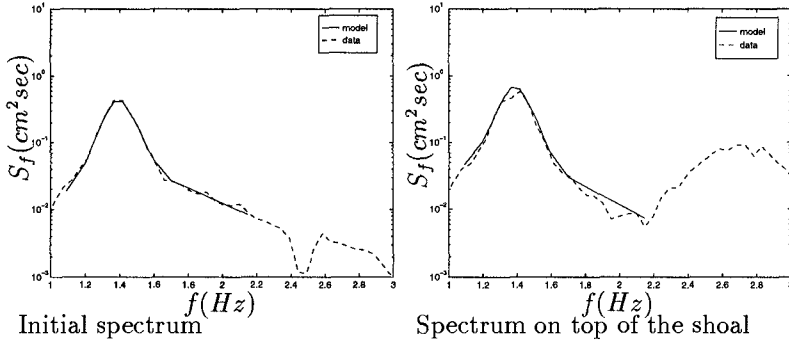


Figure 11: Frequency spectra comparisons (Test 3) showing nonlinear wave-wave interactions on top of the shoal

the shoal (Figure 11) shows this disparity quite clearly. The higher harmonics (second peak) in the data have considerable amount of energy compared to the primary wave field (first peak), all of which are not predicted by the model. These higher harmonics are seen in the data on top of the shoal and in the region of focus where the wave field is highly nonlinear.

CONCLUSIONS

A parabolic model for simulating the evolution of wave spectra over a gently sloping bottom has been tested with experimental data. Wave height comparisons have shown that the model works reasonably well in simulating wave height distributions for breaking random waves. Some discrepancies exist in the region of focus which could be due to the parabolic limitations of the model. Discrepancies could also be due to limitations of the breaking model, and in predicting non-linear effects. To get a better idea as to whether the discrepancy between the data and the model on top of the shoal is due to the limitations of the numerical model, or errors in the experimental data, comparisons need to be made to a model which will be able to simulate waves with no limitations on the range of angles and also predict the generation of higher harmonics on top of the shoal.

Nonetheless, we find that the spectral model works well in simulating transformations of a random wave field over an irregular bathymetry, even for broad directional spectra. Although certain aspects of the frequency spectrum cannot be obtained accurately from the model, it can be used to obtain useful estimates of significant wave heights.

ACKNOWLEDGMENTS

This research has been sponsored by the U.S. Army Corps of Engineers, Coastal Engineering Research Center (Contract No. DACW 39-90-D-0006-D002) and by NOAA Office of Sea Grant, Department of Commerce, under Grant No. NA/6RG0162-01 (Project No. R/OE-9). The U.S. Government is authorized to produce and distribute reprints for governmental purposes, not withstanding any copyright notation that may appear hereon.

REFERENCES

- Berkhoff, J. C. W. (1972) "Computation of combined refraction diffraction", *Proc. 13th Intl. Conf. Coastal Engrng.*, ASCE, Vancouver.
- Booij, N. (1981) "Gravity waves on water with non-uniform depth and current", Reprt No. 81-1, *Communication on Hydraulics*, Department of Civil Engineering, Delft University of Technology.
- Borgman, L. E. (1984) "Directional spectrum estimation for the S_{xy} gages", *Technical Report*, Coastal Engrg. Res. Center, Vicksburg, 1-104.
- Goda, Y. (1985) *Random Seas and Design of Maritime Structures*, Univ. of Tokyo Press, Japan.
- Grassa, J. M. (1990) "Directional random waves propagation on beaches", *Proc. 22nd Intl. Conf. Coastal Engrng.*, Delft, 798-811.
- Isobe, M. (1987) "A parabolic model for transformation of irregular waves due to refraction, diffraction and breaking", *Coastal Engineering in Japan*, 30, 33-47.
- Izumiya, T. and Horikawa, K. (1987) "On the transformation of directional waves under combined refraction and diffraction", *Coastal Engineering in Japan*, 30, 49-65.
- Kirby, J. T. (1986a) "Higher-order approximations in the parabolic equation for water waves", *J. Geophys. Res.*, 91, 933-952.
- Kirby, J. T. (1986b) "Rational approximations in the parabolic equation method for water waves", *Coastal Engineering*, 10, 355-378.
- Kirby, J. T. and Dalrymple, R. A. (1983) "A parabolic equation for combined refraction diffraction of Stokes waves by mildly varying topography", *J. Fluid Mech (1983)*, 136, 453-466.
- Kirby, J. T. and Dalrymple, R. A. (1984) "A verification of a parabolic equation for propagation of weakly nonlinear waves", *Coastal Engineering*, 8, 219-221.
- Mase, H. and Kirby J. T. (1992) "Modified frequency-domain KdV equation for random wave shoaling", *Proc. Intl. Conf. Coast. Engrng.*, Venice.
- Mei, C. C. (1992) *The Applied Dynamics of Ocean Surface Waves*, World Scientific, New Jersey
- O'Reilly, W. C. and Guza, R. T. (1991), "Comparison of spectral refraction and refraction-diffraction wave models", *J. Waterway, Port, Coastal and Ocean Engrng.*, 117, 199-215.
- Özkan, H. T. and Kirby, J. T. (1993) "Evolution of breaking directional spectral waves in the nearshore zone", *Proceedings of the Second International Symposium*, New Orleans, 849-863.

- Panchang, V. G., Wei, G., Pearce, B. R. and Briggs, M. J. (1990) "Numerical simulation of irregular wave propagation over shoal", *J. Waterways, Port, Coastal and Ocean Engrg.*, 116, 324-340.
- Radder, A. C. (1979) "On the parabolic equation method for water wave propagation", *J. Fluid Mech (1979)*, 95, 159-176.
- Thornton, E. B. and Guza, R. T. (1983) "Transformations of wave height distribution", *J. Geophys. Res.*, 88, 5925-5938.
- Vincent, C. L. and Briggs, M. J. (1989) "Refraction-diffraction of irregular waves over a mound", *J. Waterways, Port, Coastal and Ocean Engrg.*, 115, 269-284.

CHAPTER 2

A Method for Estimating Standardized Bimodal Directional Spectra

Ryuichi Fujiwara¹ and Masahiko Isobe²

Abstract

Random sea waves are described by directional spectra which sometimes have bimodal distributions. Frequency spectra are often expressed in standardized forms which contain several parameters. This makes it easy to accumulate and analyze a large number of data obtained in various fields and to specify incident wave conditions in designing practice. In the present study, a method is proposed for estimating directional spectra in the form of a standardized bimodal distribution. The validity of the method is verified by numerical simulation for a three-component array (water surface elevation and horizontal two components of the water particle velocity). Furthermore, several applications to field data are shown.

Introduction

Many of methods have been proposed for estimating directional spectra : e.g. DFTM (Barber, 1963), parametric method (Longuet-Higgins *et al.*, 1963, Panicker and Borgman, 1974; Mitsuyasu *et al.*, 1975), MLM (Capon, 1969), EMLM (Isobe *et al.*, 1984), MEP (Kobune and Hashimoto, 1986) and BDM (Hashimoto and Kobune, 1988). In the last few years, it has become possible to estimate directional spectra accurately and stably. Degrees of freedom of estimated directional spectra, however, are too large to derive a standard form except for parametric method.

In recent years field observations have been carried out in deep area for

¹ Senior Research Engineer, Hydraulic Engineering Laboratory, Technical Research Institute, Toyo Construction Co. Ltd., 3-17-6 Naruohama, Nishinomiya, Hyogo 663, Japan

² Dr. Eng., Professor, Department of Civil Engineering, University of Tokyo, 7-3-1 Hongo, Bunkyo-ku, Tokyo 113, Japan

investigating directional spectra property. To utilize the data in designing practice, it is important to express directional spectra in a standardized form which has a limited number of parameters. This makes it easy to accumulate and analyze a large number of data, and then to specify incident wave conditions in designing coastal and ocean structures as is done for frequency spectra.

In the present study, a method for estimating directional spectra with a standardized bimodal distribution is proposed by taking into consideration, the statistical variability of the Fourier coefficients which have Gaussian distributions.

Theory

(1) Bimodal directional spectrum

A bimodal directional spectrum is expressed in a standard form which is a superposition of two unimodal distribution functions. The unimodal distribution function employed is proposed by Mitsuyasu *et al.* (1975). Then the directional spectrum, $S(f, \theta)$, is expressed by Eq.(1) :

$$S(f, \theta) = \sum_{i=1}^2 P_i(f) \frac{2^{2S_i(f)-1} \Gamma^2 \{S_i(f) + 1\}}{\pi \Gamma \{2S_i(f) + 1\}} \cos^{2S_i(f)} \left\{ \frac{\theta - \theta_i(f)}{2} \right\} \quad (1)$$

where, $P_i(f)$, $\theta_i(f)$ and $S_i(f)$ are, respectively, the power spectrum, the peak wave direction and the directional concentration parameter of each unimodal directional spectrum, Γ the gamma function, f the frequency, and θ the wave direction. To estimate the directional spectrum for a certain frequency f , the unknown parameters are $P_1(f)$, $P_2(f)$, $\theta_1(f)$, $\theta_2(f)$, $S_1(f)$ and $S_2(f)$. For simplicity, we omit “(f)” hereinafter. Next, by the following relationship, we transform the spectrum parameters to P , α , θ_1 , θ_2 , S_1 and S_2 which are denoted by λ_1 , λ_2 , λ_3 , λ_4 , λ_5 and λ_6 , respectively:

$$P = \alpha P + (1 - \alpha) P = P_1 + P_2 \quad (2)$$

A component directional distribution function should have the following two properties: first, it has only one peak and varies smoothly; second, it can express both narrow and broad banded distributions.

(2) Definition of cross-power spectrum

The general relationship between the cross-power spectrum, ϕ_{mn} , of m -th and n -th quantities in the irregular wave field, and the directional spectrum, $S(f, \theta)$, is derived by Isobe *et al* (1984) as:

$$\phi_{mn} = \int_0^{2\pi} H_m(f, \theta) \overline{H_n(f, \theta)} \exp\{-ik(\mathbf{x}_n - \mathbf{x}_m)\} S(f, \theta) d\theta \quad (3)$$

where \mathbf{k} is the wave number vector, \mathbf{x}_m and \mathbf{x}_n the measuring locations, H_m the transfer function from the water surface elevation to the m -th quantity and $\overline{\quad}$ denotes the complex conjugate.

(3) Definition of likelihood

When the directional spectrum, $S(f, \theta)$, are expressed in a standard form, the expected cross-power spectrum, ϕ_{mn} , becomes a function of prescribed parameters, $\lambda_i (i=1, 6)$. The maximum likelihood method is employed to determine the most probable values of these parameters. The likelihood, L , is defined by Isobe(1990) as:

$$L(A^{[j]}; \phi) = \left\{ p(A^{[1]}) \times p(A^{[2]}) \times \cdots \times p(A^{[j]}) \times \cdots \times p(A^{[J]}) \right\}^{1/J} \quad (4)$$

$$= \frac{1}{(2\pi\Delta f)^M |\phi|} \exp\left(-\sum_{m=1}^M \sum_{n=1}^M \phi_{mn}^{-1} \hat{\phi}_{nm}\right)$$

$$\hat{\phi}_{nm} = \frac{1}{2J\Delta f} \sum_{j=1}^J \overline{A_n^{[j]}} A_m^{[j]} \quad (5)$$

where $p(A^{[j]})$ is a joint probability density function of the Fourier coefficients, $A^{[j]}$ the Fourier coefficients of the time series, Δf the frequency interval, and $|\phi|$ the determinant of the matrix, ϕ_{mn} and $\hat{\quad}$ denotes the quantity obtained from measured data.

The likelihood takes the maximum value, L_{\max} when the expected cross-power spectrum corresponding to the assumed directional cross-power spectra agrees with the measured one:

$$L_{\max} = \frac{e^M}{(2\pi\Delta f)^M |\phi|} \quad (6)$$

Therefore, we can define a degree of fitting by computing the ratio, L/L_{\max} .

(4) Most probable values of parameters

The most probable values of the parameters λ_i in Eq.(4) are obtained by maximizing the likelihood, L , through the relationship between ϕ_{mn} and λ_i . The most probable values of the parameters are determined so that all the partial derivatives of L with respect to directional spectrum parameters vanish:

$$\frac{\partial L}{\partial \lambda_i} = \sum_{k=1}^M \sum_{l=1}^M \frac{\partial L}{\partial \phi_{kl}} \frac{\partial \phi_{kl}}{\partial \lambda_i} = 0 \quad (7)$$

Substitution of Eq.(4) with Eq.(7) yields

$$\sum_{k=1}^M \sum_{l=1}^M \left\{ -\phi_{lk}^{-1} + \sum_{m=1}^M \sum_{n=1}^M \phi_{ln}^{-1} \hat{\phi}_{mn} \phi_{mk}^{-1} \right\} \frac{\partial \phi_{kl}}{\partial \lambda_i} = 0 \quad (8)$$

The solution of Eq.(8) are obtained numerically by using the Newton-Raphson method. First, the left-hand side is defined as a function of the parameters λ_i :

$$f_i(\lambda_i) = \sum_{k=1}^M \sum_{l=1}^M \left\{ -\phi_{lk}^{-1} + \sum_{m=1}^M \sum_{n=1}^M \phi_{ln}^{-1} \hat{\phi}_{nm} \phi_{mk}^{-1} \right\} \frac{\partial \phi_{kl}}{\partial \lambda_i} \quad (9)$$

The values of $\lambda_i^{(j+1)}$ at the $(j+1)$ -th iteration of the calculation is expressed in terms of the previous values, λ_i^j , as follows:

$$\lambda_i^{(j+1)} = \lambda_i^{(j)} - \left[\sum_{i'=1}^M \left[\frac{\partial f_i}{\partial \lambda_{i'}} \right]^{-1} f_{i'} \right]_{\lambda_i = \lambda_i^{(j)}} \quad (10)$$

where $\partial f_i / \partial \lambda_{i'}$ is expressed by Eq.(11) :

$$\begin{aligned}
\frac{\partial f_i}{\partial \lambda_{i'}} &= \sum_{k=1}^M \sum_{l=1}^M \left\{ -\phi_{lk}^{-1} + \sum_{n=1}^M \sum_{m=1}^M \phi_{ln}^{-1} \hat{\phi}_{nm} \phi_{mk}^{-1} \right\} \frac{\partial^2 \phi_{kl}}{\partial \lambda_{i'} \partial \lambda_i} \\
&\quad - \sum_{k'=1}^M \sum_{l'=1}^M \sum_{k=1}^M \sum_{l=1}^M \frac{\partial \phi_{k'l'}}{\partial \lambda_{i'}} \frac{\partial \phi_{kl}}{\partial \lambda_i} \\
&\quad \times \left[-\phi_{l'k}^{-1} \phi_{lk'}^{-1} + \left\{ \begin{aligned} &\phi_{lk'}^{-1} \sum_{m=1}^M \sum_{n=1}^M \phi_{ln}^{-1} \hat{\phi}_{nm} \phi_{mk}^{-1} \\ &+ \phi_{l'k}^{-1} \sum_{m=1}^M \sum_{n=1}^M \phi_{ln}^{-1} \hat{\phi}_{nm} \phi_{mk'}^{-1} \end{aligned} \right\} \right]
\end{aligned} \tag{11}$$

Application to three-component array

A three-component array is composed of the water surface elevation and horizontal two components of the water particle velocity. The main reason for choosing this array is that it is able to detect bimodal directional spectra (Isobe, 1990). Other reasons are: since it is a point sensor, it is easy to implement in the field; and since cross-power spectra of this array are represented theoretically as real values, the theoretical development becomes simple.

By applying Eq.(3) to a three-component array, the cross-power spectra, ϕ_{mn} , have real values as:

$$\phi_{\eta\eta} = P \tag{12}$$

$$\phi_{\eta u} = PH_u \{ \alpha m_{11} \cos \theta_1 + (1 - \alpha) m_{12} \cos \theta_2 \} \tag{13}$$

$$\phi_{\eta v} = PH_u \{ \alpha m_{11} \sin \theta_1 + (1 - \alpha) m_{12} \sin \theta_2 \} \tag{14}$$

$$\phi_{uu} = PH_u^2 \{ \alpha (\frac{1}{2} + m_{21} \cos 2\theta_1) + (1 - \alpha) (\frac{1}{2} + m_{21} \cos 2\theta_1) \} \tag{15}$$

$$\phi_{vv} = PH_u^2 \{ \alpha (\frac{1}{2} - m_{21} \cos 2\theta_1) + (1 - \alpha) (\frac{1}{2} - m_{22} \cos 2\theta_2) \} \tag{16}$$

$$\phi_{uv} = PH_u^2 \{ \alpha m_{21} \sin 2\theta_1 + (1 - \alpha) m_{22} \sin 2\theta_2 \} \tag{17}$$

where

$$m_{11} = S_1 / (S_1 + 1) \tag{18}$$

$$m_{12} = S_2 / (S_2 + 1) \tag{19}$$

$$m_{21} = S_1(S_1 - 1) / \{2(S_1 + 1)(S_1 + 2)\} \quad (20)$$

$$m_{22} = S_2(S_2 - 1) / \{2(S_2 + 1)(S_2 + 2)\} \quad (21)$$

and H_u is the transfer function from a water surface elevation to horizontal component of a water particle velocity. Subscripts, η , u and v represent the water surface elevation and horizontal two components of the water particle velocity, respectively.

Numerical calculation

(1) Procedure

Numerical simulation is performed to verify the validity of the present method. The method to estimate the directional spectrum is independent of the wave frequency, the simulation is performed under a fixed frequency. The procedure is summarized as follows:

- ① Define a true directional spectrum, $S(f, \theta)$ as Eq.(1).
- ② For a given data set, compute the cross-power spectra, ϕ_{mn} , using Eq.(12) to Eq.(17)
- ③ Calculate the estimated directional spectrum parameters using Eq.(10).
- ④ The estimated directional spectrum is compared with the true one.

(2) Simulated cross-power spectrum

The simulated cross-power spectra for the three-component array are given by in Eq.(12) to Eq.(17). In the present study, we created sets of cross-power spectra by using the Mitsuyasu-type directional distribution function with the directional spectrum parameters given in **Table 1**.

(3) Initial values for numerical calculation

For the three-component array, estimated directional spectrum by EMLM (Extended Maximum Likelihood Method) is able to represent the bimodal distribution (Horikawa ed.,1985). The following three parameters are available to estimate in the iteration procedure.

First, directional splitting parameter, γ'/γ , are defined as follows:

Table 1: Values of the directional spectrum parameters

P ($m^2 \cdot s$)	S_1	S_2	θ_1 (deg.)	θ_2 (deg.)	$P_2/P_1 =$ ($1 - \alpha$)/ α
1.0	100	100	0	10	1.0
		50			
		10			
	50	100			20
		50			30
		10			60
		10			90
	10	100			120
		10			150
		5			160
		1			170
		1			180
	5	50			0.5
		10			
		1			
1	10	0.2			
	10				
1	10	0.1			
	10				

$$\left(\frac{\gamma'}{\gamma}\right)^2 = \frac{4}{\gamma^2} \left[m_{00}(m_{20}m_{02} - m_{11}^2) + 2m_{10}m_{01}m_{11} - (m_{10}^2m_{02} + m_{01}^2m_{20}) \right] / \left[3m_{00}(m_{20} + m_{02})^2 - 4(m_{10}^2 + m_{01}^2)(m_{20} + m_{02}) + m_{00} \left\{ (m_{20} - m_{02})^2 + 4m_{11}^2 \right\} \right] \quad (22)$$

where γ is the long crestedness parameter, and m_{pq} are the normalized cross power spectra defined as follows:

$$m_{00} = \phi_{\eta\eta} \quad (23)$$

$$m_{20} = \phi_{uu} / H_u^2 \quad (24)$$

$$m_{02} = \phi_{vv} / H_u^2 \quad (25)$$

$$m_{10} = \phi_{\eta u} / H_u = \phi_{u\eta} / H_u \quad (26)$$

$$m_{01} = \phi_{\eta v} / H_u = \phi_{v\eta} / H_u \quad (27)$$

$$m_{11} = \phi_{uv} / H_u^2 = \phi_{vu} / H_u^2 \quad (28)$$

if small amplitude wave theory is used to evaluate H_u , errors due to nonlinear

effect or inaccurate will be included. Therefore, the following definition of the transfer function is used:

$$H_u = \sqrt{(\phi_{uu} + \phi_{vv})/\phi_{\eta\eta}} \quad (29)$$

Secondly, intersecting angle, Δ , of the two peak directions is defined as follows:

$$\Delta = 2 \cos^{-1} \frac{\sqrt{(m_{01}m_{11} - m_{10}m_{02})^2 + (m_{10}m_{11} - m_{01}m_{20})^2}}{\sqrt{\left\{ (m_{10}^2 - m_{01}^2) - m_{00}(m_{20} - m_{02}) \right\}^2 + 4(m_{10}m_{01} - m_{00}m_{11})^2}} \quad (30)$$

Thirdly, the bias of wave energies in the two directions is defined as follows:

$$r_p = \frac{\tan(\theta_m - \theta'_c)}{\tan(\Delta/2)} \quad (31)$$

where θ_m is the mean wave direction, θ'_c , the median wave direction defined as follows:

$$\theta'_c = \tan^{-1} \left\{ \frac{2(m_{10}m_{01} - m_{00}m_{11})}{(m_{10}^2 - m_{01}^2) - (m_{00}m_{20} - m_{00}m_{02})} \right\} \quad (32)$$

Now, the initial values of θ_1 , θ_2 and α are given as follows:

$$(\theta_1)_0 = (\theta'_c \pm \delta_1) - (\Delta + \delta_2)/2 \quad (33)$$

$$(\theta_2)_0 = (\theta'_c \pm \delta_1) - (\Delta + \delta_2)/2 \quad (34)$$

$$(\alpha)_0 = (1 - r_p)/2 \quad (35)$$

where $\delta_1 = 10^\circ$, 20° and 30° and $\delta_2 = 0^\circ$, 10° , 20° and 30° are tried to obtain

the largest value of L . For S_1 and S_2 , initial values are derived under the assumption that degrees of directional concentration are the same. First, S is derived by Eq.(37) from γ_1 which is calculated by Eq.(22) and Eq.(36), and $(S_1)_0$ and $(S_2)_0$ are given as $0.5S$. Also, $(P)_0$ is given as $\phi_{\eta\eta}$.

$$(\gamma'/\gamma)^2 = (1/\gamma)^2 \gamma_1^2 \quad (36)$$

$$\gamma_1 = (2S + 1) / (S^2 + S + 1) \quad (37)$$

(4) Directional spectra

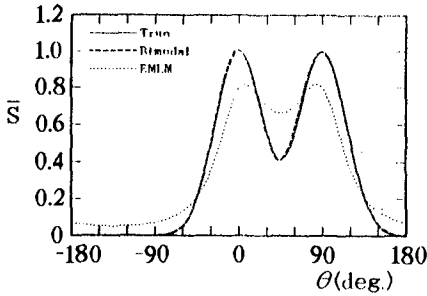
Before examining the present method, a few remarks should be made concerning the solution by the three-component array. The directional spectrum parameters cannot be determined uniquely by the three-component array, since the number of independent cross-power spectrum is less than that of directional spectrum parameters. Thus, even when the likelihood is equal to L_{\max} , the estimated values of the directional spectrum parameters are not always equal to the true values. The directional spectrum for these parameters, however, agrees well with the true directional spectra. Moreover, it is observed that, when both S_1 and S_2 are greater than 5, and α is between 0.3 and 0.7, the estimated values of the directional spectrum parameters almost agree with the true values.

The following figures show the result of closer examination of the present method. **Figure 1** shows examples of estimated directional spectrum parameters : $\theta_1 = 0^\circ$, $\theta_2 = 90^\circ$, and $(1 - \alpha) / \alpha (=P_2/P_1) = 1.0, 0.1$. The abscissa represents the wave direction, and the ordinate represents the normalized directional spectrum. Also, the results of EMLM are included in the figure for comparison. The results of estimation agree well with the true directional functions.

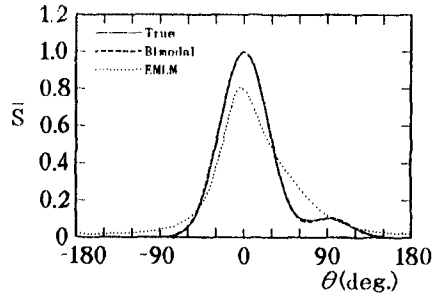
The accuracy of the method, however, becomes poor as the difference between S_1 and S_2 becomes large. Nevertheless, the accuracy of this method is higher than that of EMLM. **Figure 2** shows examples in which $S_1/S_2 = 0.1, 10$ and $\theta_1 = 0^\circ$ and $\theta_2 = 90^\circ$.

Figure 3 shows examples for small intersection angles or small $(1 - \alpha) / \alpha$. The results estimated as unimodal directional spectra are also included in the figure for comparison. These estimated distribution agree well with true values. In these cases, assumption of bimodal spectrum is almost the

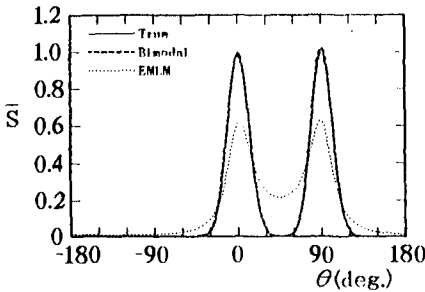
same as that of unimodal spectrum.



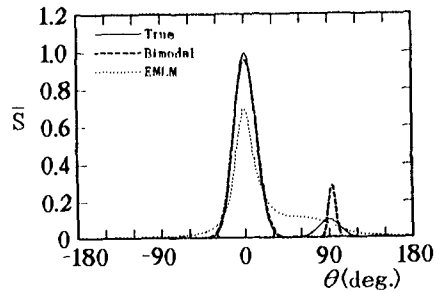
(a) $S_1=10, S_2=10, P_2/P_1=1.0$



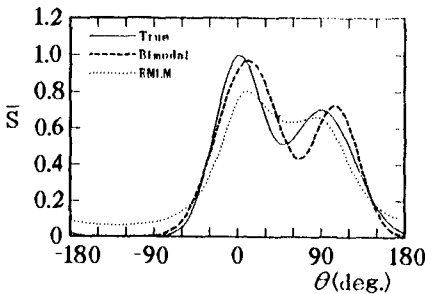
(b) $S_1=10, S_2=10, P_2/P_1=0.1$



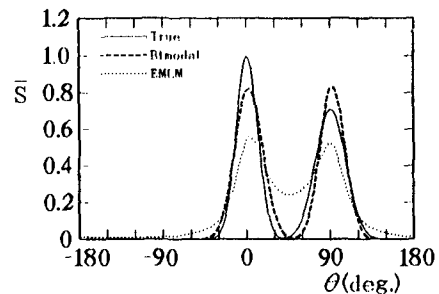
(c) $S_1=50, S_2=50, P_2/P_1=1.0$



(d) $S_1=50, S_2=50, P_2/P_1=0.1$



(e) $S_1=10, S_2=5, P_2/P_1=1.0$



(f) $S_1=50, S_2=25, P_2/P_1=1.0$

Figure 1 Directional spectra computed by the estimated directional spectrum parameters(1) : $\theta_1 = 0^\circ$ and $\theta_2 = 90^\circ$

(5) Directional spectrum parameters

Figure 4 shows the accuracy of the estimated directional spectrum parameters. The estimated values of P , α , θ_1 and θ_2 agree well with true values. The accuracy of estimated S_1 and S_2 , however, becomes poor in comparison with the other parameters.

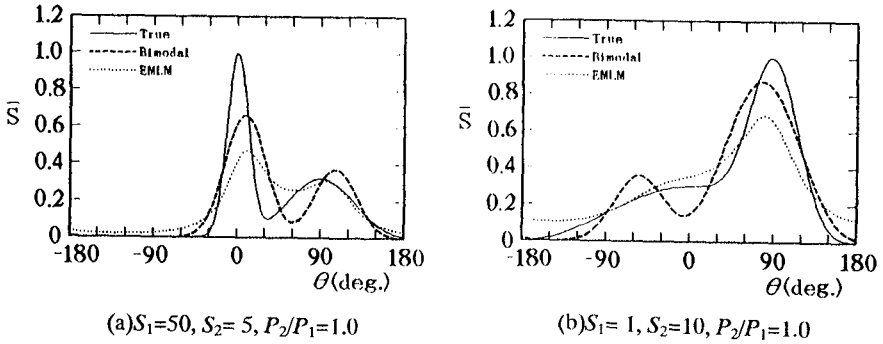


Figure 2 Directional spectra computed by the estimated directional spectrum parameters(2) : $\theta_1 = 0^\circ$ and $\theta_2 = 90^\circ$

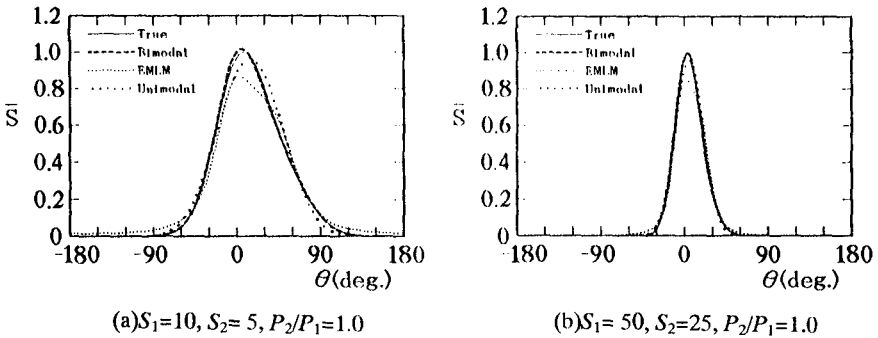


Figure 3 Directional spectra computed by the estimated directional spectrum parameters(3) : $(1 - \alpha) / \alpha = 1.0$

Application to field data

Figure 5 shows the arrangement of three-component arrays in the observation field in east coast of Japan facing to the Pacific Ocean. The water depth at the measurement points are about 20m. A three-component array consists of an ultrasonic wave gage and a two-component electromagnetic current meter, and all the devices are packed together in one container. A pressure-type wave gage is also packed in the same container to increase the reliability of measurement.

Point A is affected by reflected waves from upright caissons; however, phase lags are considered to be random between incident waves and reflected waves because of a fairly large distance from the caisson. Point B, on the other hand, is not affected by reflected waves. **Figure 6** shows examples of the estimated directional spectra at Points A and B. It is clear that the directional

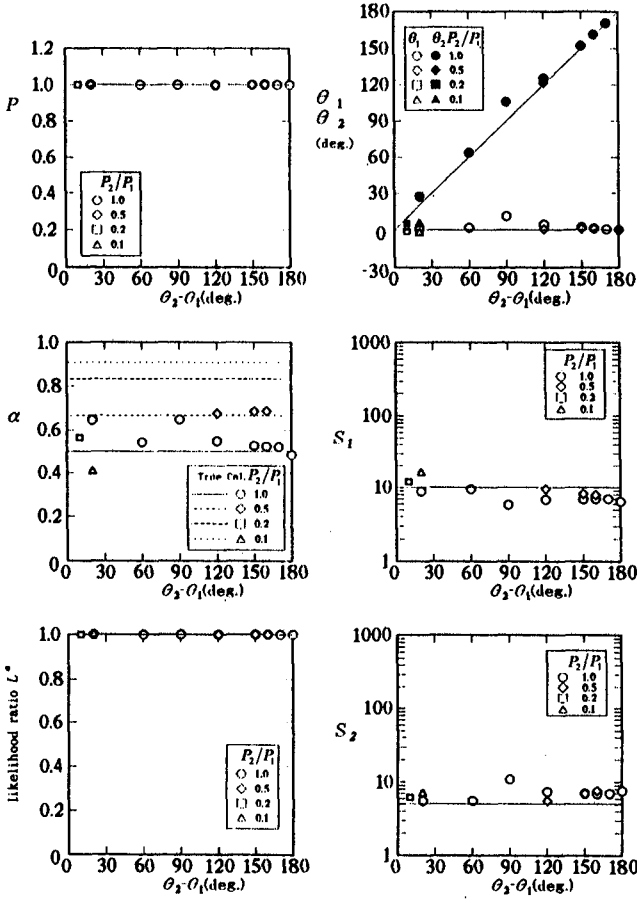


Figure 4 Estimated directional spectrum parameters

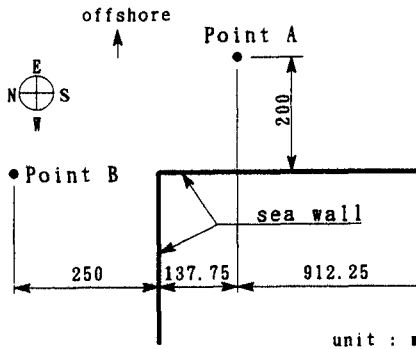


Figure 5 The arrangement of the three-component array in the observation field

spectrum have a bimodal distribution at Point A because of the reflected waves. Therefore, significant wave height, $H'_{1/3}$, of the incident waves was estimated from the wave energy contained in the range of incident wave direction:

$$H'_{1/3} = H_{1/3} / \sqrt{1 + K_R^2}, \quad K_R = \sqrt{E_R / E_I}$$

($H_{1/3}$: total significant wave height, E_I and E_R : incident and reflected wave energy).

The range of the incident wave direction is defined as **Figure 6**. **Figure 7** shows the relationship between $H'_{1/3}$ at Point A and $H_{1/3}$ at Point B. Good agreement suggests that the directional spectra are reasonably estimated.

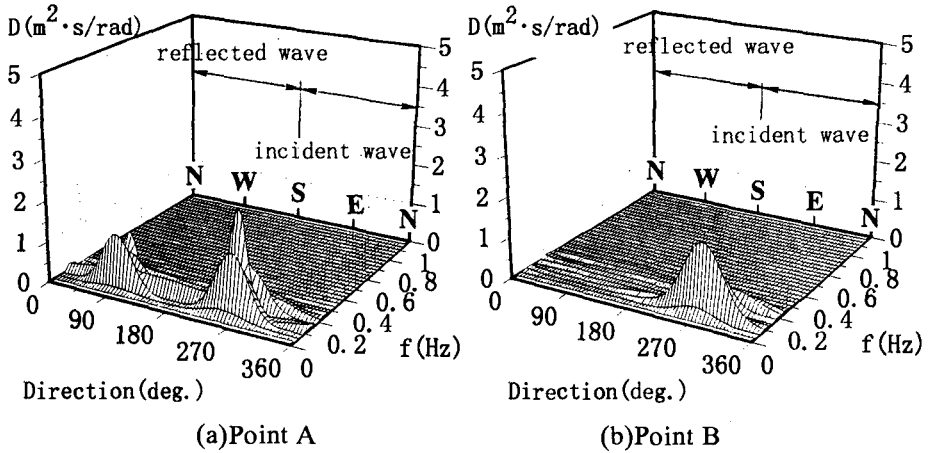


Figure 6 Estimated directional spectra

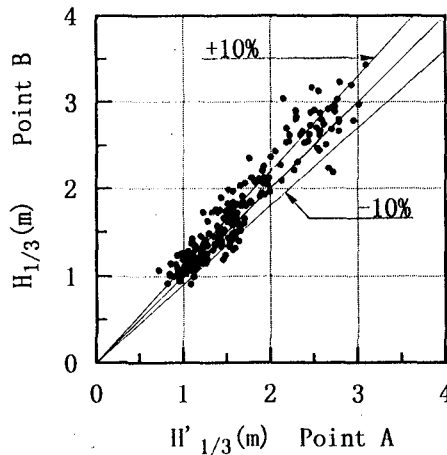


Figure 7 The relationship between the estimated significant wave height at Point A and the significant wave height at Point B

Conclusion

The following conclusions are obtained in this study.

- A method is proposed to estimate a bimodal directional spectrum expressed in a standard form.
- The validity of the method is verified by numerical simulation for a three-component array which is easy to be implemented in the field.
- Application to field data yields reasonable results.

Reference

- Barber, N. F. (1963): The directional resolving power of an array of wave detectors, *Ocean Wave Spectra*, Prentice-Hall, Eaglewood Cliffs, New Jersey, pp.137-150.
- Capon, J. (1969): High-resolution frequency-wave number spectrum analysis, *Proc. Inst. Electr. Electron. Eng.*, Vol.57, pp. 1408-1418.
- Hashimoto, N. and K. Kobune (1988): Directional spectrum estimation from a Bayesian approach, *Proc. 21st ICCE*, pp. 62-76.
- Horikawa, K. ed (1985): *Near shore Dynamics and Coastal Process*, University of Tokyo Press, pp. 506-524, in Japanese.
- Isobe, M., K. Kondo and K. Horikawa (1984): Extension of MLM for estimating directional wave spectrum, *Proc. Symp. on Description and Modelling of Directional Seas*, pp.A-6-1 - A-6-5.
- Isobe, M (1990): Estimation of directional spectrum expressed in standard form, *Proc. 22nd ICCE*, pp. 647-660.
- Kobune, K. and N. Hashimoto (1986): Estimation of directional spectra from the Maximum Entropy Principle, *Proc. 5th Int. Offshore Mech. and Arctic Eng. Symp.*, pp. 80-85.
- Longuet-Higgins, M. S., D. E. Cartwright and N. D. Smith (1963): Observations of the directional spectrum of sea waves using the motions of a floating buoy, *Ocean Wave Spectra*, Prentic-Hall, Inc., New Jersey, pp. 111-136.
- Mitsuyasu, H., F. Tasai, T. Suhara, S. Mizuno, M. Ohkusu, T. Honda and K. Rikiishi (1975): Observations of directional spectrum of ocean wave using a cloverleaf buoy, *Jour. of Physical Oceanography*, Vol. 5, pp. 750-760.
- Panicker, N. M. and L. E. Borgmann (1974): Enhancement of directional wave spectrum estimate, *Proc. 14th ICCE*, pp. 258-279.

CHAPTER 3

THE EFFECTS OF CURRENTS ON ESTIMATIONS OF DIRECTIONAL WAVE SPECTRA

Yasuyuki Nakagawa¹, Hiroichi Tsuruya¹, Noriaki Hashimoto¹

Abstract

To investigate the effects of currents on estimations of directional wave spectra, the problems with the existing methods for obtaining directional wave spectra are discussed when they are applied to wave fields in the existence of currents. The characteristics of distortion of the estimated spectra by current effects are examined through numerical simulations and analyses of experimental data. Both the numerical and experimental tests with wave gages, show that the directional spread of estimated spectra becomes narrower than that of the actual wave field and the value of the spectral peak is overestimated for the case of adverse currents. The extent of these distortions depends on the relative speed and direction of the current and waves. The relation of the error and these factors is summarized in the present study.

Introduction

Several methods have been developed for estimating directional wave spectra. These techniques, however, are generally restricted for the analysis of directional random sea waves in the absence of currents. When conventional methods are applied to wave fields with currents, misinterpretations of the actual phenomena may result. Methods are, therefore, needed to evaluate how currents will modify conventional directional spectral analyses so that corrective measures can be taken. This paper discusses the limitations associated with the existing methods for computing directional spectra of waves on currents. The effects of uniform currents on spectra are then estimated using numerical simulation techniques and these results are compared with the estimated directional spectra of wind waves propagating on uniform currents in an experimental channel.

¹ Port and Harbour Research Institute, 3-1-1 Nagase, Yokosuka 239, JAPAN.

Estimation of Directional Wave Spectra on Currents

(1) Existing methods

The basic equation for estimating directional wave spectra is described as the simultaneous integral equation,

$$\Phi_{mn}(f) = \int_0^{2\pi} H_m(f, \theta) \cdot H_n^*(f, \theta) \times \left[\cos\{k(x_{mn} \cos\theta + y_{mn} \sin\theta)\} - i \sin\{k(x_{mn} \cos\theta + y_{mn} \sin\theta)\} \right] \times S(f, \theta) d\theta, \quad (1)$$

where $\Phi_{mn}(f)$ is the cross power spectrum between the m -th and n -th wave motion parameters, $H(f, \theta)$ is the transfer function from surface elevation to other wave motion parameters and * denotes their complex conjugates. $S(f, \theta)$ is the directional spectrum, $x_{mn} = x_m - x_n$, and $y_{mn} = y_m - y_n$.

Based on some assumptions and approximations to directional distribution functions in Equation (1), the existing methods try to determine the unique solution of a directional spectrum with a limited number of wave motion parameters (See e.g. Hashimoto *et al.* 1994). In the process of getting a solution with these methods, the wave numbers and the transfer functions of wave components with arbitrary wave frequency are evaluated by using linear wave theory, and do not consider the presence of currents. Therefore, simply applying the existing methods to the analysis of the combined wave-current field may not produce accurate results. The following points have to be noted when analyzing such cases.

(2) Dispersion Relation in Currents

When the analysis is carried out with wave records measured at separate locations, e.g. a measurement with an array of wave gages, the wave number has to be put into Equation (1) corresponding to arbitrary frequency. In order to do this, the existing methods use the following equation as a dispersion relation,

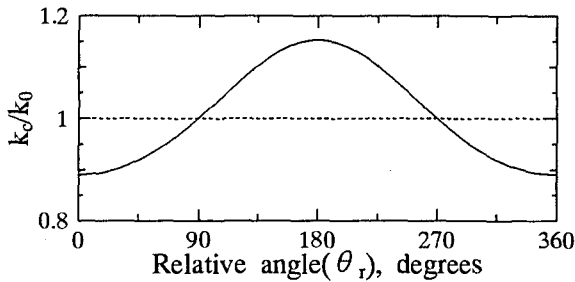
$$\omega^2 = (2\pi f)^2 = gk_0 \tanh k_0 h, \quad (2)$$

where k_0 is the wave number, and h is the water depth. The subscript 0 denotes in the absence of currents. This relation is, however, not appropriate in the wave field on currents. For the simple case, assuming the propagation of waves in a uniform current in space and time, the relation becomes,

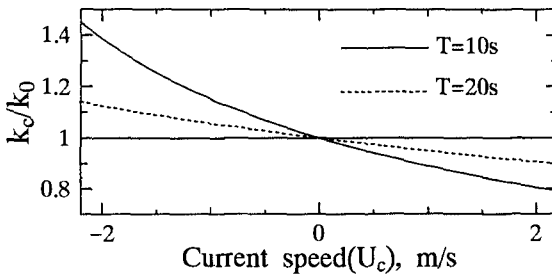
$$(\omega - U_c k_c \cos\theta_r)^2 = (2\pi f - U_c k_c \cos\theta_r)^2 = gk_c \tanh k_c h, \quad (3)$$

where U_c is the speed of the uniform current, and θ_r is the relative angle between the directions of current and wave propagation. The subscript c denotes in the presence of currents. This equation shows that, the wave number for a wave of given frequency

depends on the direction and the speed of the current. **Figure 1(a)** shows this dependence of the change in wave number with the relative direction of the current. Here the wave period is assumed to be 10 s, the water depth 100 m and the speed of the current 1.0 m/s. In the region where adverse currents are dominant, around $\theta_r = 180^\circ$, the wave numbers become larger than that of the wave of the same period and depth condition in the absence of a current. The computation of wave numbers with Equation (2), therefore, can not describe the distribution of the wave number correctly in the current field. This is one source of inaccuracies in present methods. These deviations of wave numbers are also governed by the speed of currents in relation to the wave celerity as shown in **Figure 1(b)**. In the figure, where a negative current speed means adverse current, the deviation of the wave number increases with the magnitude of the current speed. The effect of the currents is significant for waves of higher frequency.



(a) Variation of wave numbers in relation to the relative angle



(b) Variation of wave numbers in relation to current speed

Figure 1. Deviations of wave numbers by the effect of currents

(3) The Transfer Functions

As a set of data for the analysis, several wave motion parameters measured at the same location are also used for the computation of directional wave spectra. In this case, the appropriate transfer functions from free surface elevation to other wave properties must be evaluated for the estimation procedure with the existing methods. For example, the transfer function to the horizontal particle velocities induced by the

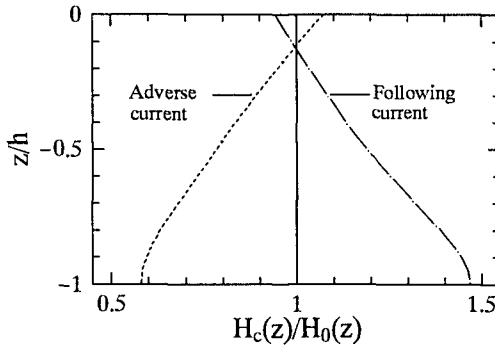
wave motion is expressed as,

$$H_0(f, \theta) = \frac{gk_0}{\omega} \frac{\cosh k_0(h+z)}{\cosh k_0h}, \quad (4)$$

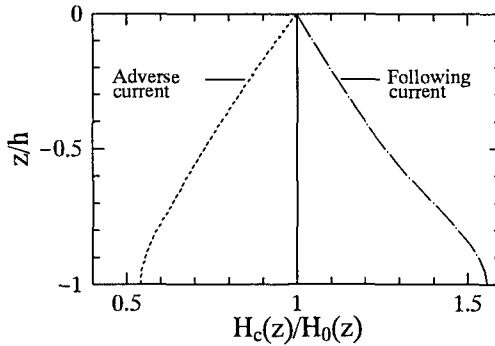
where z is the vertical coordinate with positive value taken upwards from the mean water level and k_0 is determined by the relation of Equation(2). Assuming again that the current is uniform, the expression becomes,

$$H_c(f, \theta) = \frac{gk_c}{(\omega - U_c k_c \cos \theta_r)} \frac{\cosh k_c(h+z)}{\cosh k_c h}, \quad (5)$$

where the relation between frequencies and wave numbers, k_c , is based on Equation (3). Since the wave numbers are modified by the currents, as mentioned in the previous



(a) Horizontal water particle velocities



(b) Hydrodynamic pressure

Figure 2. Deviations of transfer functions by the effect of currents

section, the transfer function also changes depending on the relative speed and direction of the current to the direction of wave propagation. The deviation of the transfer function of horizontal water particle velocities with frequency in the adverse and following current cases are shown in **Figure 2(a)** as a ratio of the function in currents, $H_c(z)$, to that in no current, $H_0(z)$. In the figure, it is seen that the deviation of the functions are maximum at the bottom, and the trend decreases towards the surface, and reverses just below the free surface. This means that estimations based on data of horizontal water particle velocities may be different depending on the depth of the measuring instruments such as a current meter.

In the case of the transfer function of the hydrodynamic pressure it is expressed, in the absence of currents, as,

$$H_0(f, \theta) = \rho g \frac{\cosh k_0(h+z)}{\cosh k_0 h} \quad (6)$$

It can be shown that the hydrodynamic pressure transfer function in a uniform current is identical to Equation (6), with wave number and frequency governed by Equation (3). Their ratio is compared in **Figure 2(b)** for the same condition as **Figure 2(a)**. The maximum deviations by currents are at the bottom in the same manner as the horizontal water particle velocities. The transfer function ratio in a following current is greater than one and less than one in an adverse current, at all depths. Therefore the estimation, by existing methods which do not consider these differences, may also lead to inaccurate results of the directional wave spectrum.

Numerical Simulations

(1) Procedure of Simulation

To investigate the effects of currents on the directional spectrum estimation, a series of numerical simulations was performed by using an existing estimation method, known as Extended Maximum Entropy Principle method, EMEP by Hashimoto *et al.* (1994). The numerical tests were conducted in the same manner as the examination of another estimation method, Extended Maximum Likelihood Method, EMLM by Isobe *et al.* (1984). Prior to the estimation of the directional spectrum in the simulation, the cross power spectra of wave motions with target frequency are computed by numerical integration of the basic equations expressed by Equation (1). The directional spreading function is given arbitrarily as a model function. In the present study, since the objective wave field is supposed to be in uniform currents, the dispersion relation expressed by Equation (2) is used to obtain the cross power spectra. Based on the computed cross power spectra for the assumed wave field with currents, the analyses with the existing method are used to estimate directional spectra. Since the presence of currents is ignored at this stage of the estimating procedure, the estimation results may be distorted from the model function due to the incompatibilities of the existing methods, as mentioned in the previous section. In the following sections, some estimation results and their comparisons with the model function are demonstrated.

(2) Results of Simulation

A 10 s wave propagating in a uniform current of 1.0 m/s, in a water depth of 100 m was used as the target wave field for the simulation. The model function is expressed here as a conventional cosine-powered function,

$$G(\theta) = \cos^{2S} \left(\frac{\theta - \theta_w}{2} \right), \tag{7}$$

where S is the spreading parameter and θ_w the principal wave direction. The estimated directional spreading functions by the EMEP for the above condition are shown in **Figure 3**. A star array consisting of four wave gages is assumed as the simulated observation condition. In the case of adverse currents to the principal wave propagation, the estimated directional spectrum shows a narrower distribution and

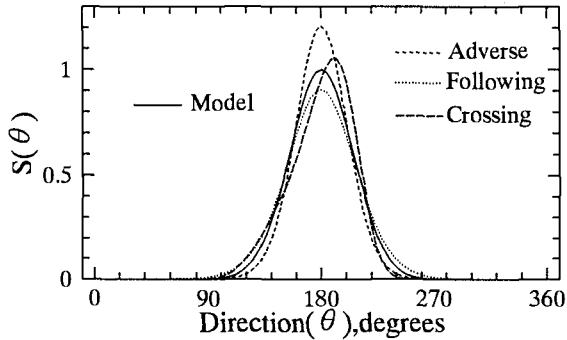


Figure 3. Estimated directional wave spectra by EMEP for various current directions using star array

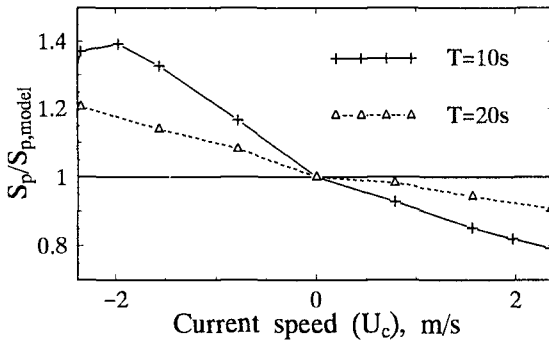


Figure 4. Relative errors of estimated peak value in relation to current speed

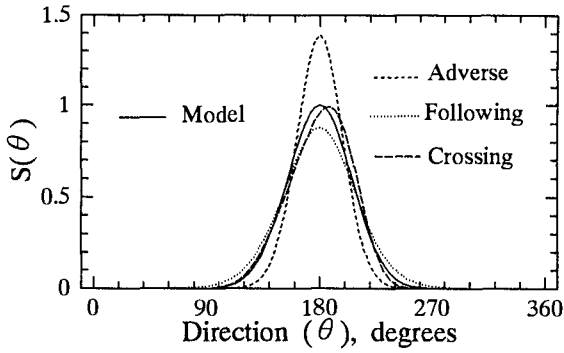
higher peak value than the model function which is represented by the solid line. The opposite trend appears in the following current case. When the direction of wave propagation and the current direction are at right angles, the peak of the estimated function is shifted downstream of the current but the effect of this current is considerably less than the adverse and following current cases. The over- and under-estimation of the peak of the directional distribution in the adverse and following current cases, respectively, are shown in **Figure 4**. In relation to the change in the wave numbers by the effect of currents shown in **Figure 1(b)**, the error in estimation results increases with the speed of currents and is greater for higher frequency waves.

Similar results have been obtained for the case of the three measured quantities; sea surface elevation and two components of horizontal water particle velocity at the same location. These results are shown in **Figure 5(a)**, with the water particle velocities assumed to be measured at the free surface. **Figure 5(b)** shows the estimated result for the same condition as in **Figure 5(a)** except now the depth at which the particle velocities were measured is 20 m. It should be noted that the trend of the error in the estimated results (**Figure 5(b)**) are opposite to the results obtained in **Figure 5(a)**. For example when the spectrum is estimated for the following current case using water particle velocities measured at the surface, the estimated peak is lower and the shape is wider than the model. For the same current scenario using water particle velocities measured 20 m below the surface, the estimated directional spectrum has a higher peak and is narrower than the model. This is ascribed to the deviation of the transfer functions and their vertical distribution in the presence of currents as shown in **Figure 2(a)**. The ratios of the transfer functions for adverse and following currents cross unity at a depth beneath the surface. This introduces a distortion of the estimated directional wave spectra depending on the depth at which the wave motion parameters were measured.

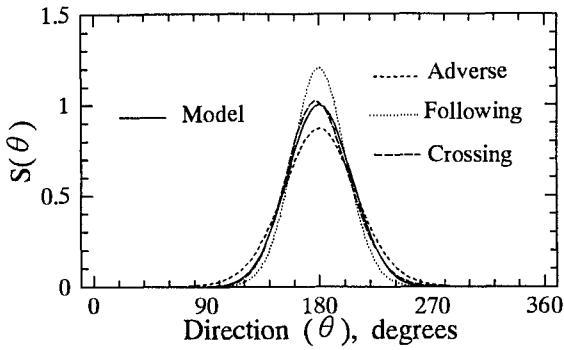
In shallow water regions near coasts, it is possible to use a measurement system at the sea bottom with sensors that measure hydrodynamic pressure and horizontal water particle velocities for directional spectra analysis. Assuming such observation conditions, directional wave spectra were estimated in cases for a wave period of 10 s, water depth 30 m and a current speed of 1.0 m/s. The results are shown in **Figure 6**. For reference, another estimated result is shown in **Figure 7** where the free surface elevation and horizontal water particle velocities at the surface were used as a measurement system for the same conditions as for the previous case in **Figure 6**. By the comparison of these figures, it is clear that the errors in **Figure 6** are extremely large. The reason of the large errors is that the deviation of the transfer functions for the wave properties are maximum at the bottom as explained in the previous section.

(3) Simulations with Consideration of Currents

As shown in the previous section, when the existing methods are applied to the wave field with currents, the estimated directional spectra are distorted by the effects of the current. Under the assumption of a uniform current, if the current speed is known, the wave numbers and the transfer functions can be modified appropriately by using Equations (3) and (5). The results of simulations using these modifications for the same following current conditions as **Figure 3** are shown in **Figure 8** by the dots.



(a) Using horizontal water particle velocities at $z = 0$ m



(b) Using horizontal water particle velocities at $z = -20$ m

Figure 5. Estimated directional wave spectra by EMEP for various current directions

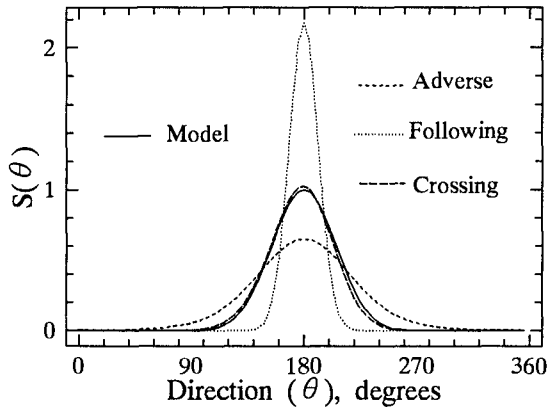


Figure 6. Estimated directional wave spectra by EMEP for various current directions using u , v , and p at the bottom

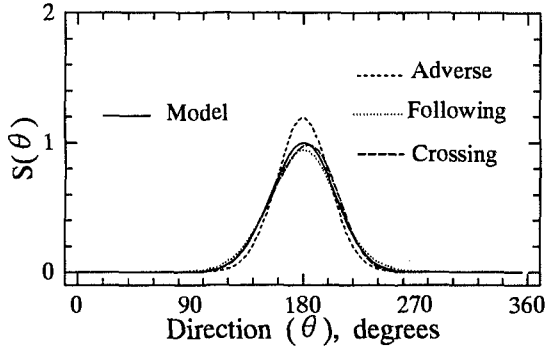


Figure 7. Estimated directional wave spectra by EMEP for various current directions using u , v , at the mean water level and η

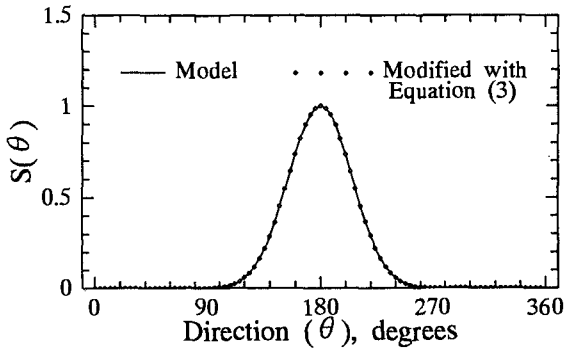


Figure 8. Estimated directional wave spectrum by EMEP with the modification of wave numbers by Equation (3)

It can be seen that the simulated results show almost complete agreement with the model. Simulations for adverse and crossing current scenarios were also conducted using Equation (3) with equally good agreements to the model.

In order to reduce the calibration error of field data measured at the same location, it was proposed by Isobe *et al.* (1984) to use the ratio between the power spectra of different wave properties instead of using theoretical expressions like Equation (7). The following expression was used for wave data to include surface elevation and the two components of horizontal water particle velocities,

$$H(\omega) = \sqrt{\frac{S_{uu}(\omega) + S_{vv}(\omega)}{S_{\eta\eta}(\omega)}} \quad (8)$$

Here $S_{uu}(\omega)$, $S_{vv}(\omega)$ and $S_{\eta\eta}(\omega)$ represent the power spectra of horizontal water particle velocities, u and v and the surface elevation, η , respectively. The estimation result of the directional spectra for the same conditions as in **Figure 3** are shown in **Figure 9**, where Equation (8) is used for the determination of the transfer function. In each case, the degree of distortion is substantially diminished. The reason for this good agreement with the model function may be explained with **Figure 10**. In this figure, the transfer functions approximated with Equation (8) in the following and adverse current cases are indicated by the horizontal lines. Although they may not approximate the model transfer function in all directions, they come very close to the true transfer functions for the direction where the wave energy is highly concentrated. That is, for the estimation of directional spectra, the complete agreement with the theoretical function is not required for the directions where the wave energy does not exist. Equation (8) makes it possible to get reasonable transfer functions near the peak of the directional wave spectrum. Therefore, the analysis with Equation (8) is very effective in estimating directional spectra for wave fields with currents when the wave directionality is narrow.

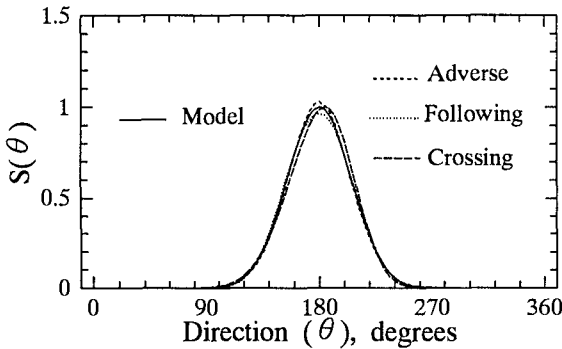


Figure 9. Estimated directional wave spectra by EMEP for various current directions with the transfer function approximated by Equation (8)

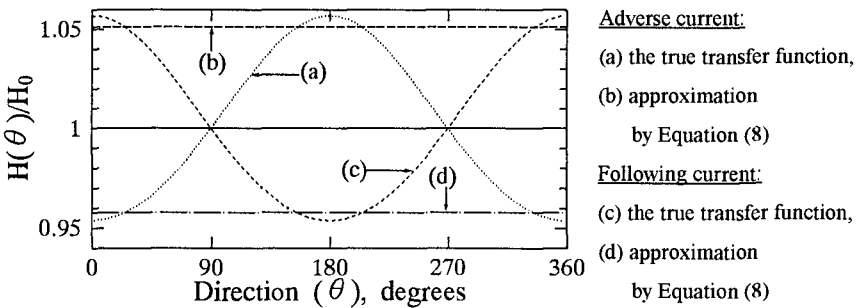


Figure 10. Approximation of transfer functions by Equation (8) for various currents

Analysis of Experimental Data

Estimations of directional spectra have also been carried out using the experimental data of directional waves in a wind-wave channel at the Port and Harbour Research Institute (PHRI). The channel is 30 m in length, 1.5 m in width, and has a water depth of 0.5 m as shown in **Figure 11**. The waves were generated by wind blowing into the channel at a speed of 10.4 m/s at 40 cm above the still water level. Uniform currents were superimposed on the waves in following and adverse directions to the waves. For this analysis, surface elevations were measured with four wave gages installed at the location as shown in **Figure 11**. The sampling frequency was 50 Hz and the sampling duration was 2.5 minutes. The frequency power spectra of the wind waves on the currents are shown in **Figure 12**. The difference in peak frequencies of the spectra are

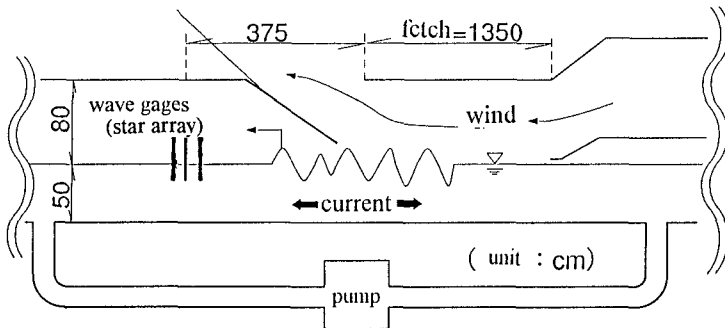


Figure 11. Sketch of wind-wave and current channel

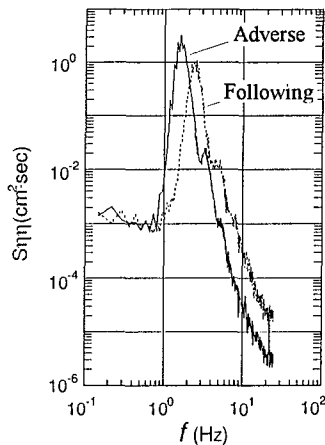


Figure 12. Power spectra of wind waves for various current directions

caused by the change in the effective fetch length (Kato and Tsuruya, 1978). By using these data, the analysis of directional spectra was estimated by EMEP. **Figures 13** and **14** show the results of estimated directional spectra near the peak frequency, for following and adverse currents, respectively. The dashed lines represent the estimated spreading function and the solid lines represent the results with the modification of wave numbers per Equation (3). In the following current case, **Figure 13**, the function estimated by EMEP predicts a wider distribution than the modified estimation. Under adverse current conditions, **Figure 14**, the estimated distribution has a narrower shape and a higher peak than the modified case. The trend of the results are the same as those obtained by the numerical simulations.

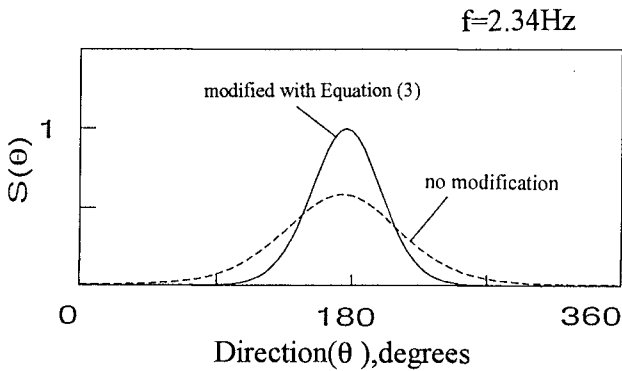


Figure 13. Estimated directional wave spectrum (following current)

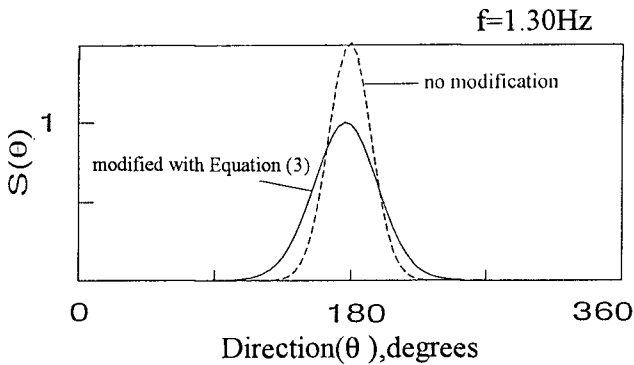


Figure 14. Estimated directional wave spectrum (adverse current)

Conclusion

Numerical simulations of directional wave spectra estimations for wave fields with currents have shown that the degree and trend of the distortion of wave spectra by the currents depends not only on the relative speed and direction of the waves and current but also on the measuring system of the wave properties. To reduce the errors of these estimation results, modifications of wave numbers and transfer functions by the theoretical relations for currents have been confirmed to be effective in uniform current cases. The transfer function defined as the ratio of each power spectra is particularly useful in reducing the error of estimated directional spectra in the presence of currents when the directionality of the waves is narrow. From analyses of experimental data with a wind wave channel, similar distortion trends to those estimated by the numerical simulations have been observed.

Acknowledgment

We wish to express our sincere gratitude to Mr. Sidney W. Thurston III, National Sea Grant Fellow of NOAA, who kindly gave us many valuable comments and advice on the present study.

REFERENCES

- Hashimoto, N., T. Nagai and T. Asai (1994). Extension of the Maximum Entropy Principle Method for Directional Wave Spectrum Estimation, Coastal Engineering, ASCE, pp.232-246.
- Isobe, M., K. Kondo and K. Horikawa (1984). Extension of MLM for estimating directional wave spectrum, Proc. Symp. on Description and Modeling of Directional Seas, Paper No. A-6, 15p.
- Kato, H. and H. Tsuruya (1978). Experimental Study of Wind Waves Generated on Currents, Coastal Engineering, ASCE, pp.742-755.

CHAPTER 4

A METHOD FOR ESTIMATING DIRECTIONAL SPECTRA IN A FIELD OF INCIDENT AND REFLECTED WAVES

Hiromune Yokoki¹ and Masahiko Isobe²

Abstract

A method for estimating the directional spectrum as well as the reflection coefficient in a incident and reflected random wave field is developed for practical use. In the method, the directional spectrum is assumed to be expressed by a circular normal distribution which includes three parameters. Then the parameters are estimated by the maximum likelihood method. The present method is applied to laboratory data, and the parameters are estimated for two kinds of wave gauge arrays. A measure of accuracy of the estimated parameters is also proposed.

Introduction

Recently it has become usual in the design of coastal, harbor and ocean structures to take into account the randomness of sea waves with respect to wave direction as well as to wave frequency. Directional wave spectra can describe the randomness of sea waves as the distribution of wave energy among the wave frequency and direction. However, there are a lot to be studied in the estimation of directional spectra, especially in a field composed of incident and reflected waves. No existing method can estimate the reflection coefficient accurately enough for practical use.

In this paper, we propose a method for estimating the directional spectrum in a short-crested random wave field by introducing a standard directional function which is expressed by the circular normal distribution function (Yokoki *et al.*,

¹Assistant Professor, Department of Urban & Civil Engineering, Ibaraki University, 4-12-1, Nakanarusawa, Hitachi, Ibaraki, 316, JAPAN. E-mail: yokoki@hit.ipc.ibaraki.ac.jp

²Professor, Department of Civil Engineering, University of Tokyo, 7-3-1, Hongo, Bunkyo, Tokyo, 113, JAPAN. E-mail: isobe@kowan.t.u-tokyo.ac.jp

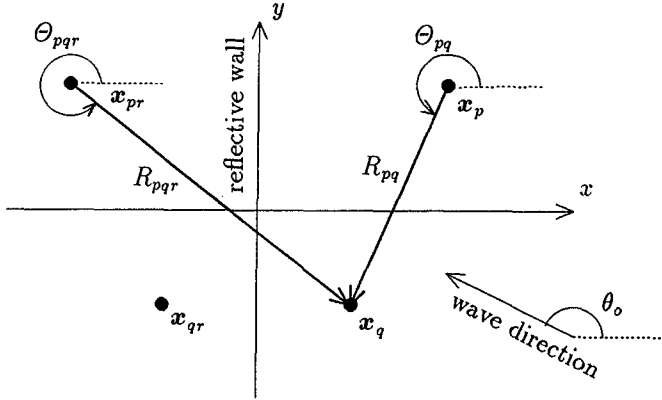


Figure 1: Definitions of variables

1992, 1994). The parameters in the function are determined by the Maximum Likelihood Method (Isobe, 1990).

Then we apply the method to laboratory data. The estimated results confirm its applicability to the existing data.

A method is also proposed for measuring the accuracy of the estimated parameters by means of the root-mean-square values of the errors. We propose the appropriate configurations of wave gauge arrays for estimating the directional spectrum parameters accurately.

Theory

Cross-power spectrum

In a wave field which consists of incident and reflected waves, the cross-power spectrum, $\Phi_{pq}(\sigma)$, between the water surface fluctuations at points p and q is represented as Eq. (1) (e.g., Horikawa, 1988; Isobe and Kondo, 1984):

$$\Phi_{pq}(\sigma) = \int_{\mathbf{k}} S(\mathbf{k}, \sigma) \{ \exp(i\mathbf{k}\mathbf{x}_p) + r \exp(i\mathbf{k}\mathbf{x}_{pr}) \} \times \{ \exp(-i\mathbf{k}\mathbf{x}_q) + r \exp(-i\mathbf{k}\mathbf{x}_{qr}) \} d\mathbf{k} \quad (1)$$

where $S(\mathbf{k}, \sigma)$ is the directional spectrum, \mathbf{k} the wave number vector, \mathbf{x}_p the measuring position vector, \mathbf{x}_{pr} the point symmetrical to \mathbf{x}_p with respect to the reflective wall (y -axis), and r the reflection coefficient (Fig. 1).

We rewrite Eq. (1) by using the transformation of variables as follows.

$$\left. \begin{aligned} \mathbf{k} &= (k \cos \theta, & k \sin \theta &) \\ \mathbf{x}_p - \mathbf{x}_q &= (R_{pq} \cos \Theta_{pq}, & R_{pq} \sin \Theta_{pq} &) \\ \mathbf{x}_{pr} - \mathbf{x}_{qr} &= (R_{pq} \cos(\pi - \Theta_{pq}), & R_{pq} \sin(\pi - \Theta_{pq}) &) \\ \mathbf{x}_{pr} - \mathbf{x}_q &= (R_{pqr} \cos \Theta_{pqr}, & R_{pqr} \sin \Theta_{pqr} &) \\ \mathbf{x}_p - \mathbf{x}_{qr} &= (R_{pqr} \cos(\pi - \Theta_{pqr}), & R_{pqr} \sin(\pi - \Theta_{pqr}) &) \end{aligned} \right\} \quad (2)$$

The definitions of variables are also indicated in Fig. 1. Substituting Eq. (2) into Eq. (1), we obtain the expression of the cross power spectrum, $\Phi_{pq}(f)$:

$$\begin{aligned} \Phi_{pq}(f) &= \int_0^{2\pi} S(f, \theta) \\ &\times [\exp\{ikR_{pq} \cos(\theta - \Theta_{pq})\} + r^2 \exp\{ikR_{pq} \cos(\theta - \pi + \Theta_{pq})\}] \\ &+ r \exp\{ikR_{pqr} \cos(\theta - \Theta_{pqr})\} + r \exp\{ikR_{pqr} \cos(\theta - \pi + \Theta_{pqr})\}] d\theta \end{aligned} \quad (3)$$

where f represents the frequency connected with the wave number, $|\mathbf{k}|$, by the dispersion relation, and r the reflection coefficient of the reflective wall.

In the present study, we assume the directional spectrum, $S(f, \theta)$, is expressed by using the circular normal distribution function, so that we can obtain the cross power spectrum analytically and the numerical calculation becomes faster. Thus, the directional spectrum, $S(f, \theta)$, is expressed by Eq. (4):

$$S(f, \theta) = P(f) \frac{1}{2\pi I_0(a)} \exp\{a \cos(\theta - \theta_0)\} \quad (4)$$

where I_0 is the modified Bessel function of zero order.

Then the relationship between the cross-power spectrum and the parameters is written as follows:

$$\Phi_{pq}(f) = \left\{ \begin{array}{l} \varphi(a, \theta_0, R_{pq}, \Theta_{pq} | f) \\ + r^2 \varphi(a, \theta_0, R_{pq}, \pi - \Theta_{pq} | f) \\ + r \varphi(a, \theta_0, R_{pqr}, \Theta_{pqr} | f) \\ + r \varphi(a, \theta_0, R_{pqr}, \pi - \Theta_{pqr} | f) \end{array} \right\} \times (1 + \delta_{pq} \varepsilon_p) P(f) \quad (5)$$

$$\begin{aligned} \varphi(a, \theta_0, R, \Theta | f) &= \frac{1}{2\pi I_0(a)} \int_0^{2\pi} \exp\{-ikR \cos(\theta - \Theta)\} \exp\{a \cos(\theta - \theta_0)\} d\theta \end{aligned} \quad (6)$$

where R and Θ , respectively, indicate the length and the angle of the vector $\mathbf{x}_p - \mathbf{x}_q$, and R_r and Θ_r those of the vector $\mathbf{x}_{pr} - \mathbf{x}_q$.

Finally, the cross-power spectrum, $\Phi_{pq}(f)$, becomes a function of five parameters: the degree of directional concentration, a ; the peak wave direction, θ_0 ; the reflection coefficient, r ; the frequency spectrum, $P(f)$, of the incident wave; and the ratio, ε_p , of the noise component to the power at the point p .

Most probable values of parameters

The five directional spectrum parameters including the reflection coefficient should be determined so that the cross-power spectrum, $\Phi_{pq}(f)$, in Eq. (5) would approximate the observed cross-power spectrum, $\hat{\Phi}_{pq}(f)$. In the present study, the parameters are determined by the Maximum Likelihood Method (MLM). The likelihood L is defined by Isobe (1990):

$$L = \frac{1}{(2\pi\Delta f)^M |\Phi|} \exp \left(- \sum_{p=1}^M \sum_{q=1}^M \Phi_{pq}^{-1} \hat{\Phi}_{qp} \right) \quad (7)$$

where Δf is the interval of the frequency, M the number of measuring points, and $|\Phi|$ the determinant of the cross-power spectrum matrix, Φ_{pq} .

The maximum likelihood method implies that the most probable values of the parameters, λ_i , are the solutions of the equation:

$$\frac{\partial L}{\partial \lambda_i} = \sum_{j=1}^M \sum_{l=1}^M \frac{\partial L}{\partial \Phi_{jl}} \frac{\partial \Phi_{jl}}{\partial \lambda_i} = 0 \quad (8)$$

Equation (8) is expressed as a nonlinear simultaneous equation through some algebraic calculation (Yokoki *et al.*, 1994) as follows:

$$\sum_{j=1}^M \sum_{l=1}^M \left\{ -\Phi_{lj}^{-1} + \sum_{p=1}^M \sum_{q=1}^M \Phi_{lp}^{-1} \hat{\Phi}_{qp} \Phi_{pj}^{-1} \right\} \frac{\partial \Phi_{jl}}{\partial \lambda_i} = 0 \quad (9)$$

The directional spectrum parameters, λ_i , which satisfy Eq. (9) for all i ($i = 1 \sim 7$) are the most probable values.

The modified Marquardt method (*ex.* Fletcher, 1971) is adopted instead of the Newton-Raphson method to solve Eq. (9) iteratively, and thus the solutions are obtained more robustly and quickly.

In the modified Marquardt method, the values of $\lambda_i^{(k+1)}$ at the $(k+1)$ -th iteration is expressed in terms of the previous values, $\lambda_i^{(k)}$, as follows:

$$\boldsymbol{\lambda}^{(k+1)} = \boldsymbol{\lambda}^{(k)} - \left[\mathbf{A} + \mu^{(k)} \{ \mathbf{E} + \text{diag}(\mathbf{A}) \} \right]^{-1} \mathbf{f}^{(k)} \quad (10)$$

where $\boldsymbol{\lambda}$ is the vector expression of λ_i , $\mathbf{A} = [A_{ij}] = [\partial f_i / \partial \lambda_j]$, $\mathbf{f} = [f_i]$, f_i is the left hand side of Eq. (9), $\text{diag}(\mathbf{A})$ the diagonal matrix of \mathbf{A} , and \mathbf{E} the unit matrix.

If Eq. (9) is strongly nonlinear, the parameter μ increases during in the iterations, and finally Eq. (10) reduces as follows:

$$\lambda_i^{(k+1)} \approx \lambda_i^{(k)} - \left(1 + \frac{\partial f_i}{\partial \lambda_i} \right)^{-1} f_i^{(k)} \quad (11)$$

If μ is small, Eq. (9) reduces to the same form as the Newton-Raphson method.

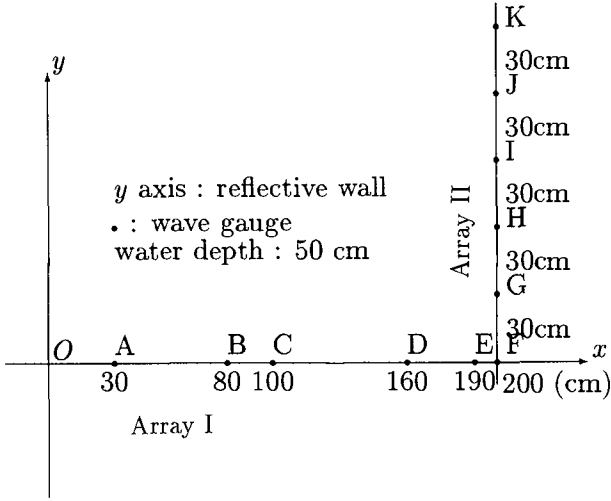


Figure 2: Layout of positions of wave gauges

Table 1: Incident wave conditions

Case No.	$H_{1/3}$ (m)	$T_{1/3}$ (s)	θ_0 ($^\circ$)	s_{max}	Array of wave gauges
4151	0.04	1.25	180	75	I
4191	0.05	1.00	180	10	I
4152	0.04	1.25	180	75	II
4192	0.05	1.00	180	10	II

Application to Laboratory Data

Laboratory data

To verify the validity of the present method, we applied it to experimental data. Figure 2 shows the layout of wave gauges in the multi-directional wave basin, where the water depth is uniformly 50cm, the reflective wall (y -axis) is vertical and no wave absorber is installed. The water surface elevations were measured by two kinds of wave gauge arrays: The array I is linear and normal to the reflective wall, and the array II parallel to the reflective wall.

Multi-directional incident waves were generated by using the Bretschneider-Mitsuyasu spectrum proposed by Mitsuyasu *et al.* (1975). The incident wave conditions and the corresponding wave gauge arrays are listed in Table 1.

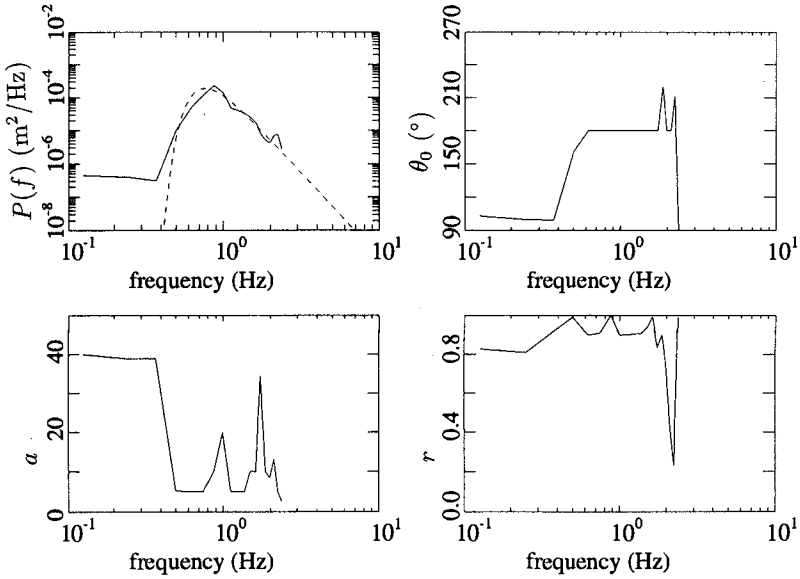


Figure 3: Estimated values of parameters (No. 4151)

Estimated parameters

Figure 3 shows the estimated values of the parameters by the array I composed of the wave gauges A, B and C, for which the incident wave condition is No. 4151 in Table 1. Figure 4 shows the estimated values for the incident wave condition No. 4191. The dashed lines in the graphs for the power, $P(f)$, indicate the frequency spectrum of the incident waves. From these figures, we can see that the array I estimates the reflection coefficient and the peak wave direction accurately around the peak wave frequency, but not the directional concentration.

Figures 5 and 6 show the estimated values of the parameters by the array II composed of the wave gauges F, G and I, for which the incident wave conditions are No. 4152 and 4192 respectively. These figures show that the peak wave direction and the directional concentration are accurately estimated by the array II, though the reflection coefficient cannot be estimated accurately.

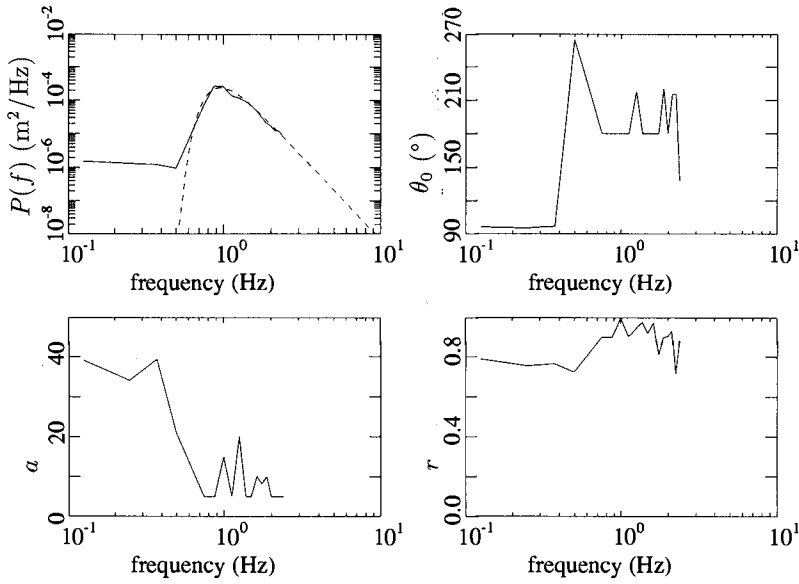


Figure 4: Estimated values of parameters (No. 4191)

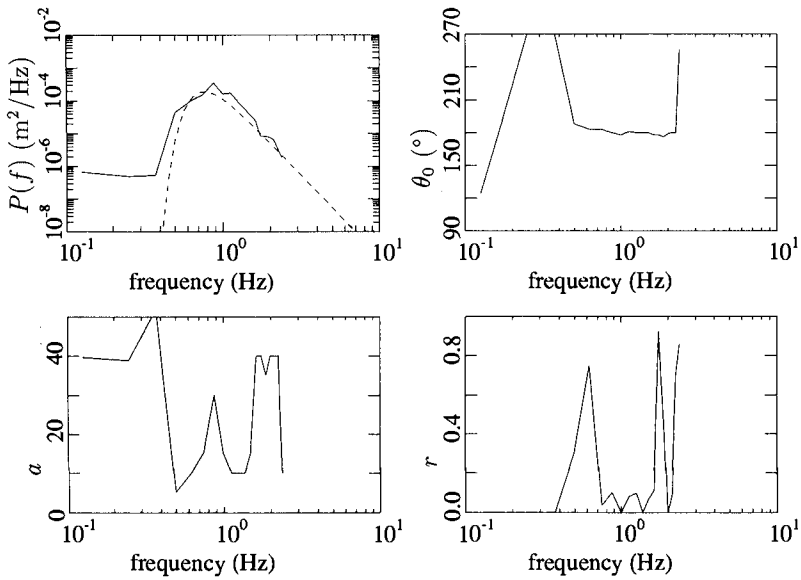


Figure 5: Estimated values of parameters (No. 4152)

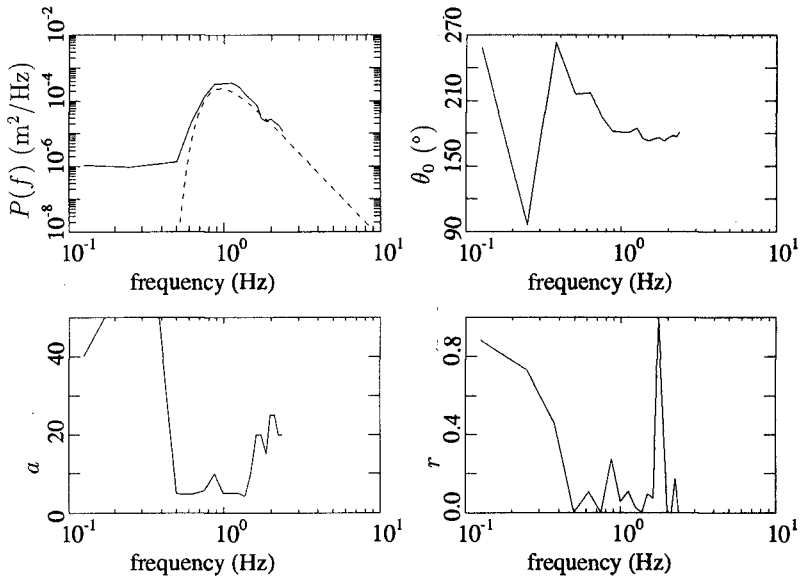


Figure 6: Estimated values of paramters (No. 4192)

Table 2: Incident wave conditions and reflection coefficient

θ_0 ($^\circ$)	s_{\max}	r
$\left\{ \begin{array}{c} 180 \\ 135 \\ 95 \end{array} \right\}$	$\left\{ \begin{array}{c} 10 \\ 25 \\ 75 \end{array} \right\}$	$\left\{ \begin{array}{c} 0.1 \\ 0.5 \\ 0.9 \end{array} \right\}$

Accuracy of Estimated Parameters

Definition of accuracy of parameters

In this section, we show how to evaluate the performance of wave gauge arrays for estimating the directional spectrum parameters. We proposed Eq. (12) as a measure of the accuracy of the estimated parameters:

$$\text{Err}(\lambda_i) = \frac{1}{\bar{\lambda}_i} \sqrt{\frac{1}{N_{\text{total}}} \sum_{j=1}^{N_{\text{total}}} (\lambda_{i,j} - \bar{\lambda}_i)^2} \quad (12)$$

where $\lambda_{i,j}$ is the estimated values of the parameter, λ_i in the j -th sample, $\bar{\lambda}_i$ is the (given) true value, N_{total} is the total number of samples, and $\bar{\lambda}_i$ is the value by which the error is normalized.

Equation (12) is regarded as the normalized root-mean-square value of the error. We used Eq. (12) to evaluate the performance of the array for the twenty-seven incident wave conditions shown in Table 2. In all cases, the incident directional wave spectra are calculated by using the Bretschneider-Mitsuyasu frequency spectrum, and the directional function proposed by Mitsuyasu *et al.* (1975). The significant wave height, $H_{1/3}$, is 0.1m and the significant wave period, $T_{1/3}$, is 1.0s.

Errors were calculated for the parameters estimated by the various arrays shown in Fig. 7: two kinds of linear arrays, and the three kinds of triangular arrays. The errors are calculated for each array by changing the distance, D_p , from the reflective wall and the interval, D , of the wave gauges.

Calculated accuracy

Figure 8 shows calculated errors in the peak wave direction, θ_0 , the directional concentration, a , and the reflection coefficient, r .

We can see from Fig. 8 that the linear array (1) and the triangular array (3) cannot estimate the peak wave direction accurately, and the linear array (2) cannot estimate the reflection coefficient accurately, either. In other words, the linear array parallel to the reflective wall and the triangular array can estimate

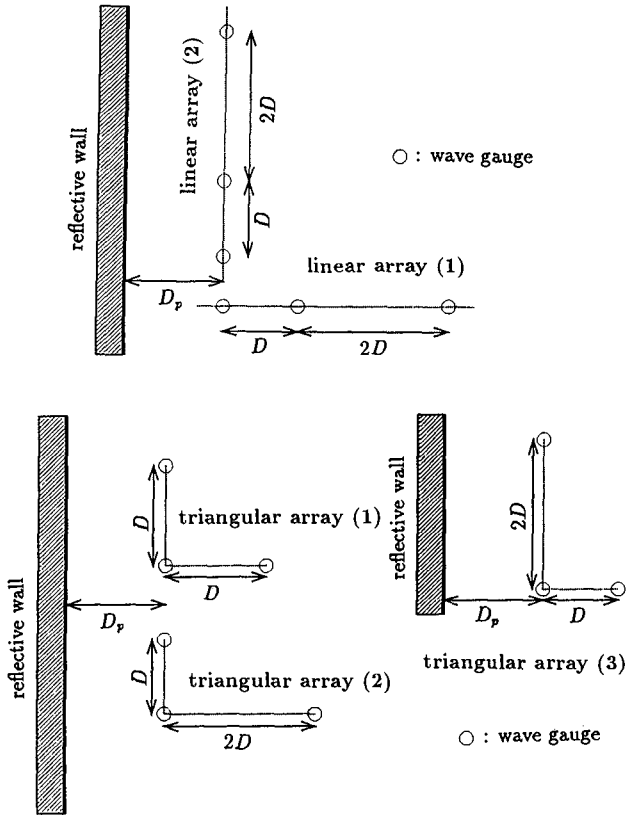


Figure 7: Arrays of wave gauges

the peak wave direction accurately, and the linear array normal to the reflective wall and the triangular array can estimate the reflection coefficient accurately. No particular trends relationship was found for the the directinal concentration.

Concluding Remarks

Major concluding remarks of the present study are as follows:

1. A method is derived for estimating the directional spectrum in a field of incident and reflected waves using the cicular normal distribution function.
2. The method is proved to be valid for data in laboratory experiments.
3. The performance of wave gauge arrays is estimated through the root-mean-square error of the estimated paramters.

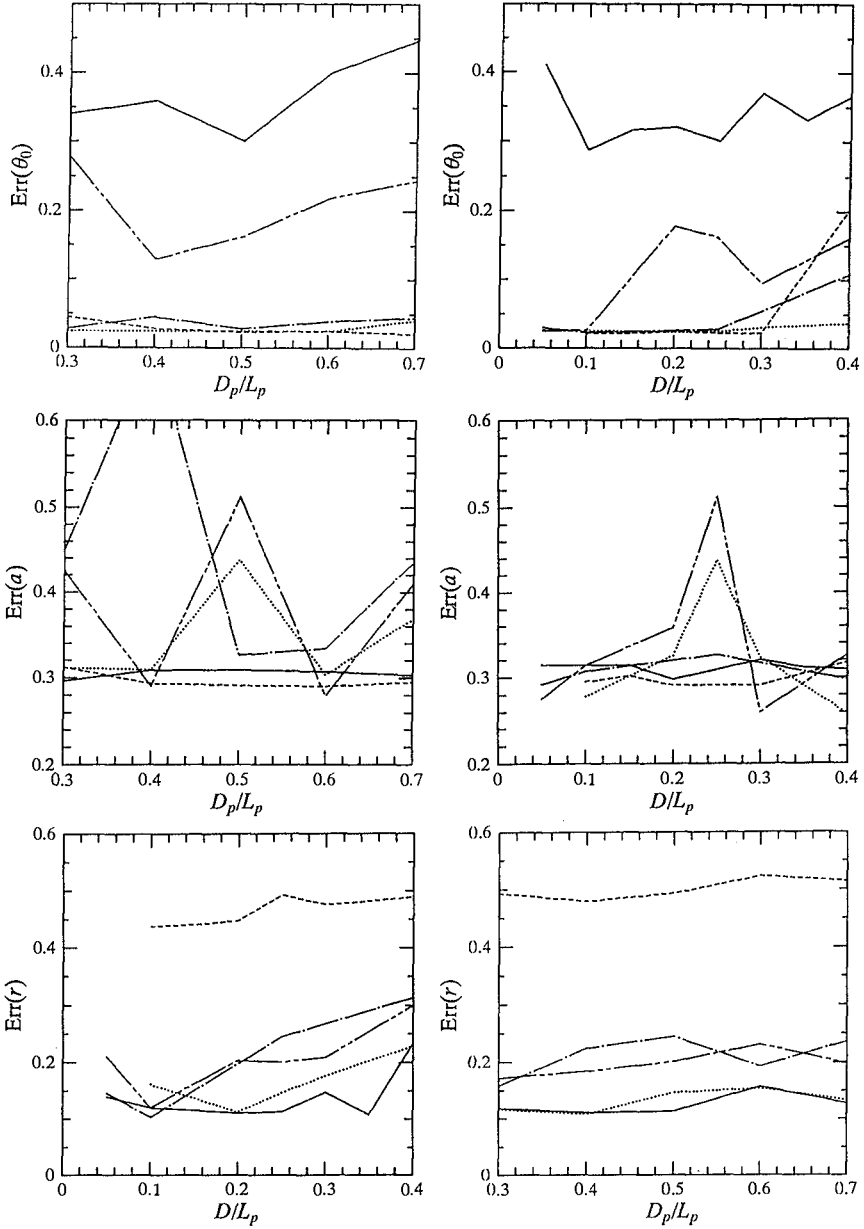


Figure 8: Evaluated errors

- : linear array (1); - - -: linear array (2);
-: triangular array (1); - · - ·: triangular array (2);
- - - -: triangular array (3)

Acknowledgment

The authors thank Prof. Akira Watanabe, University of Tokyo, Japan, for his valuable advice to this study, and also thank Dr. Masaaki Ikeno, Central Research Institute of Electric Power Industry, Japan, for providing experimental data.

References

- [1] Fletcher, R. (1971): A modified Marquardt subroutine for nonlinear least squares, Harwell Report, AERE-R, 6799.
- [2] Horikawa, K. (ed.) (1988): Nearshore Dynamics and Coastal Processes, Univ. Tokyo Press, Part. V, pp. 407-411.
- [3] Isobe, M. and K. Kondo (1984): Method for estimating directional wave spectrum in incident and reflected wave field, Proc. 19th Int. Conf. on Coastal Eng., pp. 467-483.
- [4] Isobe, M. (1990): Estimation of directional spectrum expressed in standard form, Proc. 22nd Int. Conf. on Coastal Eng., pp. 647-660.
- [5] Mitsuyasu, H., F. Tasai, T. Suhara, S. Mizuno, M. Ohkusu, T. Honda and K. Rikiishi (1975): Observations of directional spectrum of ocean waves using a cloverleaf buoy, Jour. of Physical Oceanography, Vol. 5, pp. 750-760.
- [6] Yokoki, H., M. Isobe and A. Watanabe (1992): A method for estimating reflection coefficient in short-crested random seas, Proc. 23rd Int. Conf. on Coastal Eng., pp. 765-776.
- [7] Yokoki, H., M. Isobe and A. Watanabe (1994): On a method for estimating reflection coefficient in short-crested random seas, Proc. 23rd Int. Conf. on Coastal Eng., pp. 719-730.

CHAPTER 5

ACTIVE ABSORPTION OF MULTIDIRECTIONAL WAVES

Hemming A. Schäffer¹⁾ and Jesper Skourup²⁾

Abstract

The development of a control system for active absorption of multidirectional waves is described. The present work is an extension of a two-dimensional flume system to include the wave propagation direction. The hydrodynamic feedback necessary for the active absorption is taken to be the surface elevation measured at each segment of the multidirectional wavemaker. A frequency-direction domain transfer function relating the paddle position to the measured and desired elevations is derived. For practical applications a two-dimensional digital filter is used for a time-space realization of the generation/absorption procedure. Experimental verification is made in a numerical wave tank using a Boundary Element Model. The numerical setup includes a moving boundary representing a segmented wavemaker. This ensures a realistic reproduction of evanescent wave modes, which can be important for the system performance. The numerical tests show that a quasi three-dimensional system consisting of an array of absorbing wavemakers developed for wave flumes is far better than having no active absorption. The present fully three-dimensional absorption system is shown to further reduce spurious reflections to around one third in the examples treated. Although the system is capable of simultaneous wave generation and active absorption, only the absorption ability was used in these preliminary tests.

1. Introduction

Spurious wave reflection remains an important problem in physical as well as numerical model testing of coastal and offshore structures. Open boundaries are often modelled by passive absorbers using e.g. physical perforated plates and numerical sponge layers. In numerical models the absorption performance is often poor for very oblique waves and unwanted diffraction into the sponge layer is a problem for waves travelling along such boundaries. In physical models spurious re-reflection from the wavemaker can lead to considerable distortion of the incident wave field or even to spurious resonance in the model.

²⁾ International Research Centre for Computational Hydrodynamics (ICCH)
at ¹⁾ Danish Hydraulic Institute, Agern Allé 5, DK-2970 Hørsholm, Denmark

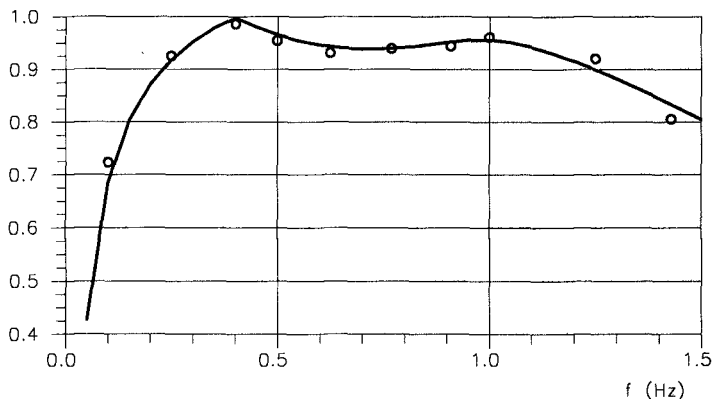


Figure 1 Absorption coefficients for active absorption tests in a numerical wave flume using 2D-AWACS. The full curve gives the theoretical performance. Water depth 1m.

This work primarily regards the problem of active absorption from a physical model point of view, but the system developed is also relevant for numerical modelling. The performance of the system is actually analysed using a numerical wave tank.

Recently, the original electric system used for active absorption in flumes at the Danish Hydraulic Institute was revised, leading to a digital Active Wave Absorption Control System called AWACS. The theoretical background and preliminary performance results are given in Schäffer et al. (1994). Since then, enhancements of the recursive filters involved have further improved the results. Applying the technique used in the AWACS, Skourup and Schäffer (1995) demonstrated that the absorption performance could be investigated using a numerical wave flume based on a Boundary Element Model (BEM). Figure 1 compares numerically determined absorption coefficients (found by analysing surface elevation time series from the numerical simulation) with theoretical values (given by the theory behind the active wave absorption system). Similar results were obtained from physical model tests and it appears that the BEM is well suited for a numerical test of an active absorption system for multidirectional waves, as pursued in this work.

The most simple way of introducing active absorption for a segmented multidirectional wavemaker is to apply a system developed for a wave flume to the control of each segment. This was done by e.g. Hirakuchi et al. (1992) using the flume system of Hirakuchi et al. (1990). However, this method only works well for weakly oblique waves. The trouble is that the system overreacts for oblique waves resulting in spurious wave generation.

When generating waves by the snake principle it is well known that for a fixed wave height, oblique waves require a smaller stroke than normally emitted waves. Specifically, the transfer function relating the wavemaker paddle stroke to the amplitude of the progressive wave is proportional to $\cos \theta$ where θ is the angle of emission (zero for normally emitted waves). Since active absorption is the reverse process of wave generation (i.e. reversing time), this $\cos \theta$ should also

be accounted for in the absorption of oblique waves. When the hydrodynamic feedback to the control system is taken as the elevation measured on the paddle front the presence of evanescent modes can be important. In this case the simple $\cos \theta$ -variation of the involved transfer function is changed to a more complicated one which not only includes a θ -dependent amplitude but also a θ -dependent phase shift.

The flume AWACS has two inputs and one output. At each time step the inputs are the elevation of the desired incident waves and the elevation measured at the paddle of the wavemaker. The output is the position of the wavemaker paddle. The two inputs are combined in a simple manner reducing the system to a single-input-single-output system. For the multidirectional wave case a general multiple-input-multiple-output system is in principle required. The input represents desired incident waves and the hydrodynamic feedback, e.g. surface elevation measured on each paddle, and the output is the position of each paddle. Using a number of flume systems in parallel (which is the equivalent of making the approximation $\cos \theta = 1$) the multiple-input-multiple-output system is simplified to a number of parallel single-input-single-output systems. However, if $\theta \neq 0$ is to be accounted for, each paddle should at least be influenced by the hydrodynamic feedback at neighbouring flaps. Such a system is developed allowing for any number of directions to be represented at each frequency. Analysis of the system performance is made using the BEM to simulate the physical wave tank including the moving boundary representing the segmented wavemaker.

Since the 2D-AWACS is the basis for the present 3D system the next chapter gives a short review. In Chapter 3 the theory for multidirectional active wave absorption is derived and Chapter 4 gives some basic ideas for the practical inclusion of directional information. The general approach taken for the 3D-AWACS is shown in Chapter 5 and verification by experiments in a numerical wave tank is given in Chapter 6. Finally, summary and conclusions are presented in Chapter 7.

2. Review of the 2D-AWACS

The active wave absorption control system for wave flumes (2D-AWACS) presented by Schäffer et al. (1994) is based on a frequency domain expression for the wavemaker paddle position which may be formulated as

$$X_a = (2A_I - A_0) F_0; \quad F_0 \equiv \frac{1}{\sum_{j=0}^{\infty} c_j^*} \quad (1)$$

in which “*” denotes complex conjugation and i is the imaginary unit. Here A_I and A_0 are the complex amplitudes of the desired incident wave elevation and the elevation measured on the wave board. F_0 is a complex transfer function based on a real transfer function c_0 and some imaginary transfer functions c_j . Here c_0 , which is sometimes called the Biésel transfer function, relates the amplitude of the generated wave to the amplitude of the paddle motion in the case of pure wave generation. The rest of the series in (1) is imaginary, and it relates the amplitude of the evanescent modes at the wave board to the amplitude of the paddle motion. For a piston type wavemaker we have

$$c_j = \frac{4 \sinh^2 k_j h}{2k_j h + \sinh 2k_j h} \quad (2)$$

see e.g. Schäffer (1996) for results for different types of wave paddles. Here k_j is the j 'th solution to

$$\omega^2 = gk_j \tanh k_j h \quad (3)$$

which is the linear dispersion relation generalized to complex wave numbers. It has one real solution, say k_0 , and an infinity of purely imaginary solutions k_j , $j \geq 1$, where $ik_j > 0$.

Practical application in the time domain is made by use of the recursive digital filter

$$v_n = \sum_{k=0}^M a_k u_{n-k} + \sum_{k=1}^N b_k v_{n-k} \quad (4)$$

where the input u_n is $2\eta_I - \eta_0$ evaluated at time $t = n\Delta t$ and the output v_n is the wavemaker position, $X(n\Delta t)$. The transfer function of this recursive filter was fitted to match the transfer function F_0 over a wide frequency range by optimization of the filter coefficients (a_k, b_k) under stability constraints (see e.g. Antoniou, 1979). With these coefficients (4) provides the instantaneous paddle position for irregular as well as regular waves. The system only needs the instantaneous elevations of the desired incident-wave elevation, η_I and the elevation measured at the wave board, η_0 . No a priori knowledge on the waves to be generated or absorbed is required.

3. Absorption theory – frequency-direction representation

Let $\eta_I(x, y, t)$ denote the elevation of the desired incident wave (i.e. the wave emitted from the wavemaker), let $\eta_0(y, t)$ be the elevation measured on the paddles of the wavemaker and let the position of these paddles be $X(y, t)$. Here (x, y) is a Cartesian coordinate system with $x = 0$ on the wavemaker.

In a linear representation the wave field to be absorbed or generated can be described as a superposition of a number of unidirectional monochromatic wave components. Thus, in this section active absorption is examined in the frequency domain concentrating on just one frequency and one wave propagation direction. Let A_I, A_0 , and X_a be complex amplitudes and let c.c. denote the complex conjugate of the preceding term, then we have

$$X = \frac{1}{2} \{ X_a e^{i(\omega t - k_y y)} + \text{c.c.} \} \quad (5)$$

$$\eta_I = \frac{1}{2} \{ A_I e^{i(\omega t - k_x x - k_y y)} + \text{c.c.} \} \quad (6)$$

$$\eta_0 = \frac{1}{2} \{ A_0 e^{i(\omega t - k_y y)} + \text{c.c.} \} \quad (7)$$

where (k_x, k_y) are the components of the wave number vector. Since waves impinging on the wavemaker will typically be reflections from some beach or structure their complex amplitude will be denoted A_R and their re-reflections from the wavemaker are termed A_{RR} . Thus, the waves emitted from the wavemaker are due to both the paddle motion and re-reflections:

$$A_I = iX_a e_0 + A_{RR} \quad (8)$$

Here e_0 is a frequency and direction dependent transfer function defined below and i is the imaginary unit representing a 90° phase shift. When no reflections

are present there will be no re-reflections and (8) reduces to an expression for pure wave generation. On the other hand, when pure active absorption is wanted then $A_I \equiv 0$ and thus the paddle generates progressive waves cancelling the re-reflections. The elevation measured on the paddle front includes both reflections and re-reflections as well as the waves generated by the movement of the paddle including the evanescent modes due to the mismatch between the shape of the paddle and the vertical structure of a progressive wave:

$$A_0 = iX_a \sum_{j=0}^{\infty} e_j + A_R + A_{RR} \quad (9)$$

Assuming full reflection at the wave paddle, we further have

$$A_R = A_{RR} \quad (10)$$

Eliminating (A_R, A_{RR}) from (8)–(10) and solving for X_a yields

$$X_a = (2A_I - A_0) F; \quad F \equiv \frac{1}{i \sum_{j=0}^{\infty} e_j^*} \quad (11)$$

in which “*” denotes complex conjugation. This simple relation is the frequency-direction basis for the control of simultaneous generation and active absorption. For practical application this needs to be transformed to a time-space domain representation as shown in Chapter 5. The transfer functions constituting F are

$$e_j = \begin{cases} \frac{1}{\sqrt{1 - k_y^2/k^2}} c_0 = \frac{1}{\cos \theta} c_0 & \text{for } j = 0 \\ \frac{1}{\sqrt{1 + k_y^2/|k_j^2|}} c_j & \text{for } j = 1, 2, \dots \end{cases} \quad (12)$$

where (k_j, c_j, e_j) are real for $j = 0$ and imaginary for $j = 1, 2, \dots$. This is for the normal case, where $(k_y < k)$, so that e_0 corresponds to progressive waves. If $(k_y > k)$, then e_j is imaginary even for $j = 0$ and all modes are evanescent. For the two-dimensional case (11) reduces to (1). The transfer functions given by (12) do not account for spurious wave generation due to finite segment width of the directional wavemaker.

In addition to the frequency variation (11) also depends on the wave direction. Thus, the task is now to formulate this in the time domain somehow including the directional information. Our first ideas on how this could be done are still useful for illustrating the more general approach finally adopted. These ideas are given in the next chapter.

4. Basic ideas for inclusion of directional information

In this chapter the discussion is simplified by disregarding evanescent wave modes and considering monochromatic, unidirectional, oblique waves. Under these assumptions (11) reduces to

$$X_a = (2A_I - A_0) \frac{\cos \theta}{i c_0} \quad (13)$$

where the factor $\cos \theta$ makes the only difference from the flume case. Thus, for a known wave direction the correct time domain response can be obtained by replacing $2\eta_I - \eta_0$ by $(2\eta_I - \eta_0) \cos \theta$ in the instantaneous evaluation of the position of each paddle. Skourup (1996) used a numerical wave tank to show examples where this worked very well. However, generally θ is not known and an online determination of $\cos \theta$ is needed. Including the variation along the wavemaker in the amplitudes, (13) becomes

$$\hat{X}_a = \left(2\hat{A}_I - \hat{A}_0\right) \frac{\cos \theta}{ic_0} \quad (14)$$

where

$$\left(\hat{X}_a(y), \hat{A}_0(y), \hat{A}_I(y)\right) \equiv (X_a, A_0, A_I)e^{-ik_y y}; \quad k_y = k \sin \theta \quad (15)$$

The idea is now to differentiate this expression in order to obtain some kind of directional variation. The n 'th derivative

$$\frac{\partial^n}{\partial y^n} \left(2\hat{A}_I - \hat{A}_0\right) = (ik \sin \theta)^n \left(2\hat{A}_I - \hat{A}_0\right) \quad (16)$$

provides a directional variation in terms of $\sin^n \theta$, but since a cosine was the goal, we use the expansion

$$\cos \theta = \sum_{n=0}^N a_{2n} \sin^{2n} \theta \quad (17)$$

where a_{2n} are expansion coefficients and N is the order of the expansion. Using (16) and (17), we get

$$\left(2\hat{A}_I - \hat{A}_0\right) \cos \theta = \sum_{n=0}^N \frac{b_{2n}}{k^{2n}} \frac{\partial^{2n}}{\partial y^{2n}} \left(2\hat{A}_I - \hat{A}_0\right) \quad (18)$$

where

$$b_{2n} = (-1)^n a_{2n} \quad (19)$$

In principle (18) provides the input for the absorption system. In a time domain representation instantaneous elevations would replace the amplitudes. These elevations would then be given by their discrete values in time and in space along the wavemaker, typically with a spacing equal to the segment width of the wavemaker. A second derivative would then e.g. be evaluated by a central difference including three points: the elevation at the actual segment and at the two neighbouring segments. Generally, the evaluation of the $2n$ 'th derivative would involve (at least) $2n + 1$ points i.e. n neighbouring points to each side.

Since we have avoided nonlinear relations (e.g. for expressing the cosine in terms of sines) the formulation is not restricted to one direction at one particular frequency. Application to irregular waves requires that the frequency dependent factors $1/k^{2n}$ are replaced by time domain recursive digital filters, approximating $1/k^{2n}$ for their frequency domain transfer function. Since $k \sim \omega$ in shallow water (and even $\sim \omega^2$ in deep water) $1/k^{2n}$ represents a low pass filter

of increasing order for increasing n . This filter just balances the amplification at high frequency caused by the differentiations in (18). For the general case of irregular waves the procedure outlined above involves a separate fitting of the coefficients b_{2n} and coefficients for the recursive filters representing $1/k^{2n}$. Furthermore, it relies on the neglect of evanescent modes and altogether it is more suited for explaining the principles than for practical application.

In conclusion to this chapter, differentiations of the elevations along the wavemaker are in principle able to provide the directional information required for active absorption of oblique waves. Since differentiation is equivalent to convolution with a set of filter weights it appears natural to formalize this in terms of a digital filter in space regarding the segmentation of the wavemaker as the spatial discretization. Since, for irregular waves, recursive filtering was already used with respect to the time variable, the general approach calls for a two-dimensional digital filter in time and space.

5. General approach to the time-space realization

We now return to the general case including the evanescent modes i.e. without a restriction to rather shallow water. Equation (11) in Chapter 3 gives a frequency-direction recipe for simultaneous generation and active absorption. Inspired by the above ideas we now take a general two-dimensional filter approach to the practical time-space realization of this recipe. The input to the system is a combination of desired and measured elevations and the output is the paddle position. Both input and output are regarded as functions of the coordinate along the wavemaker, y , and of time, t , sampled at $(n\Delta t, m\Delta y)$. The two-dimensional Fourier transform relates (t, y) -space to (ω, k_y) -space. Thus, we need to regard the target transfer function F from (11) as a function of (ω, k_y) instead of (ω, θ) . From this point of view we can use a two-dimensional digital filter for practical time-space application:

$$v_{n,m} = \sum_{l=-M_2}^{M_2} \sum_{k=0}^{M_1} a_{kl} u_{n-k, m-l} + \sum_{l=-N_2}^{N_2} \sum_{k=1}^{N_1} b_{kl} v_{n-k, m-l} \quad (20)$$

Here the input $u_{n,m}$ is $2\eta_I - \eta_0$ evaluated at $(t, y) = (n\Delta t, m\Delta y)$ and the output $v_{n,m}$ is $X(n\Delta t, m\Delta y)$. Like the filter given in (4) for the flume case, this filter must be causal in time as the future is unknown. Thus, the counter k only takes non-negative values. However, this restriction does not apply in space, and thus the counter l runs through negative as well as positive values. The transfer function of this recursive filter was fitted to match the transfer function $F(\omega, k_y)$ over a wide range of frequencies and directions by optimization of the filter coefficients (a_{kl}, b_{kl}) . Generally, the stability constraints for two-dimensional recursive filters are very complicated. At present, we omit the recursive element with respect to the spatial part of the filter, i.e. restricting ourselves to $N_2 = 0$ in (20). Furthermore, $M_2 = 1$ is used which means that at each time step the evaluation of the paddle position is only influenced by the signals at neighbouring segments. With our choice of $(\Delta t, \Delta y) = (0.025s, 0.5m)$ this allows information to travel with a speed of $\Delta y/\Delta t = 20m/s$ along the wavemaker. Since F is an even function of k_y , we get $a_{k,l} = a_{k,-l}$. It can be shown that by these restrictions the formulation basically contains the spatial

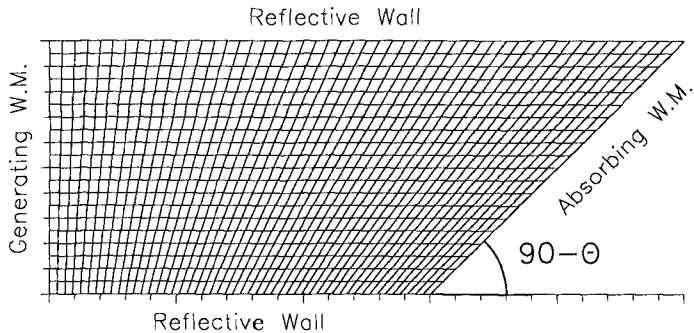


Figure 2 Top view of the numerical wave tank with a distorted rectangular grid. Wave generation at the west boundary, fully reflecting walls on the two sides and an absorbing segmented wavemaker on the oblique boundary.

derivatives from the preliminary analysis leading to (18). Only now the coefficients are found directly by fitting to the general transfer function F from (11) including evanescent-mode effects.

6. Experimental verification in a numerical wave tank

Skourup et al. (1992) developed a three-dimensional Boundary Element Model solving an integral equation for the potential flow problem in combination with an explicit time stepping procedure for updating the boundaries of the computational domain, including the free surface. Applications to a numerical wave tank equipped with a moving boundary to simulate a segmented wavemaker was described by Skourup (1996), who considered active absorption of oblique waves where the propagation direction was known a priori. In the present work this facility is used for a performance test of the 3D-AWACS as if it was a physical wave tank. However, the flexibility available in a numerical wave tank is used in the experimental setup as shown in Fig. 2. Longcrested regular waves are generated at the west boundary and propagate unaffected by the perpendicular side walls until they reach the oblique eastern boundary simulating the absorbing segmented wavemaker. The computations were made on a distorted rectangular grid fitting the boundaries. Different orientations of the oblique boundary was used to obtain a variety of different angles of wave attack relative to the absorbing wavemaker. Regular waves at two different frequencies and at angles of attack ranging from zero to 60 degrees were investigated. We first look at a frequency $f = 0.4Hz$ at which the 2D-AWACS has an almost ideal performance, cf. Fig. 1. For a wave attack of 45 degrees Fig 3 shows the instantaneous picture of the free surface after 12 periods of simulation time. Three different conditions were used on the oblique boundary to show the difference between having no absorption at all (Fig. 3a), using independent 2D-AWACS's for each

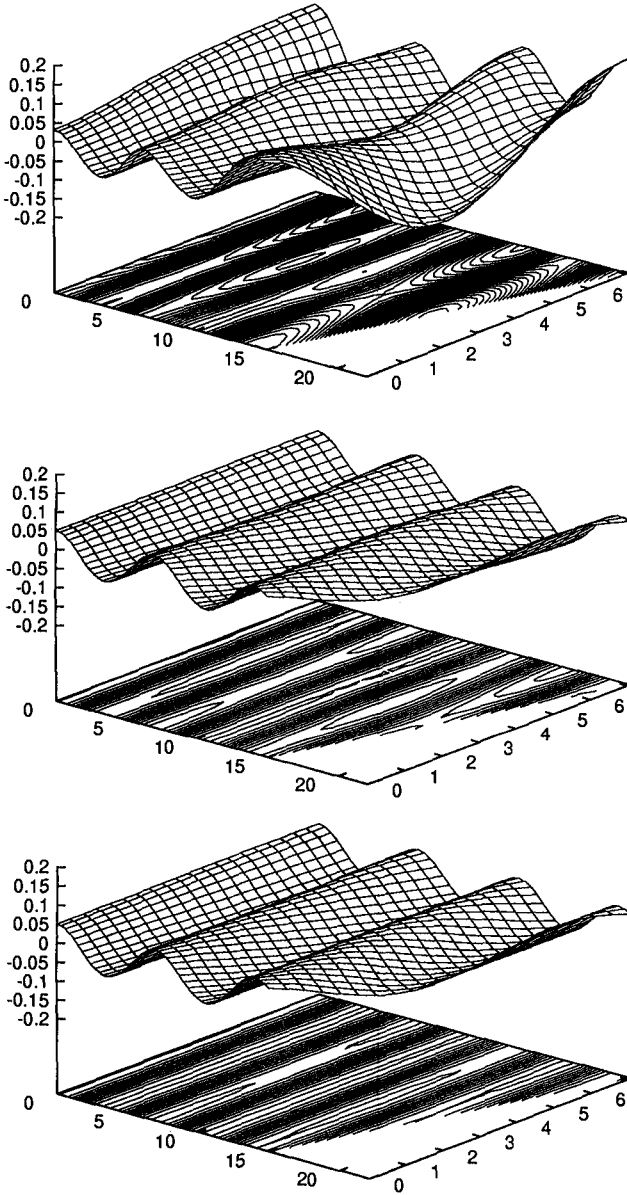


Figure 3 Waves of frequency $0.4Hz$ generated at the west boundary reflected or absorbed at the oblique boundary using a) no boundary movement b) partial absorption using 2D-AWACS c) better absorption using 3D-AWACS. Water depth 1m.

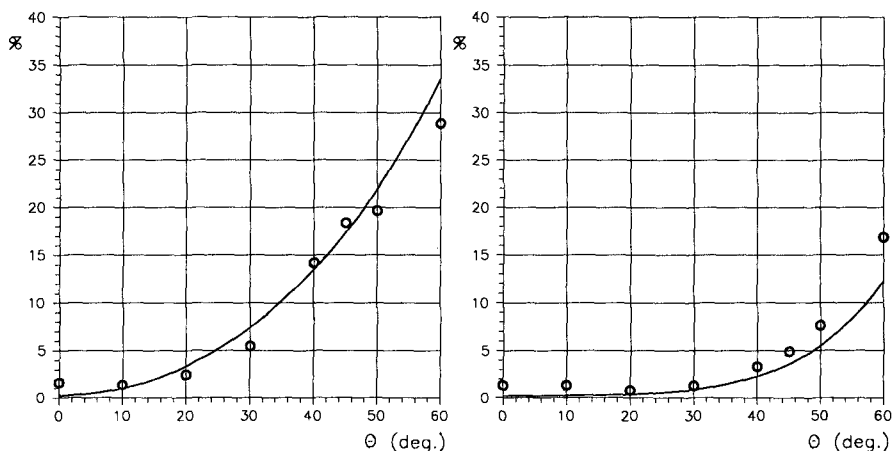


Figure 4 Reflection coefficients (%) for regular waves of frequency $0.4Hz$ versus angle of attack for a) 2D-AWACS and b) 3D-AWACS. The full curves give the theoretical performance. Water depth 1m.

segment (Fig. 3b), and using the 3D-AWACS (Fig. 3c). The pronounced cross-wave pattern for the fully reflective case (Fig. 3a) is significantly improved by use of the 2D-AWACS (Fig. 3b). Further improvement is obtained by using the 3D-AWACS.

In order to quantify the performance, time series of surface elevation and components of vertical velocity at a point in the vicinity of the absorbing wavemaker were analysed assuming the presence of three wave components: 1) One of direction θ impinging on the absorbing wavemaker 2) its (small) reflection and 3) its re-reflection from the side wall. In the postprocessing of the numerical data the angles of these three components were known and their amplitudes were calculated and used for estimation of the (small) reflection coefficients from the absorbing wavemaker. The markers on Fig. 4 show this reflection coefficient for angles θ ranging from vanishing obliqueness, $\theta = 0$ to $\theta = 60$ degrees. The performance of the 2D-AWACS is shown in Fig. 4a, while Fig. 4b gives the results for 3D-AWACS. The full curve gives the theoretical variation of the coefficient. For both systems this can be determined from the theory behind the 3D-AWACS. Again it appears that the 2D-AWACS is far better than having no absorption at all, i.e. the coefficients are small compared to 100%. The use of the 3D-AWACS further reduces the reflection to approximately one third.

The second frequency to be studied is $f = 0.7Hz$ at which the absorption coefficient of the 2D-AWACS has a local minimum, i.e. the poorest performance within a wide frequency range. Figure 5 shows the resulting reflection from the absorbing wavemaker. For the 2D-AWACS (Fig. 5a) the trend is the same as for $f = 0.4Hz$ that increasing obliqueness gives increasing reflection. However, for the 3D-AWACS, the performance is actually best around $\theta = 30$ degrees.

For these preliminary tests the aspect ratio of the boundary elements was rather high near the absorbing wavemaker in case of large θ . This gave unreliable results at $f = 0.7Hz$ and $\theta > 40$ degrees, explaining why these data do not appear in Fig. 5.

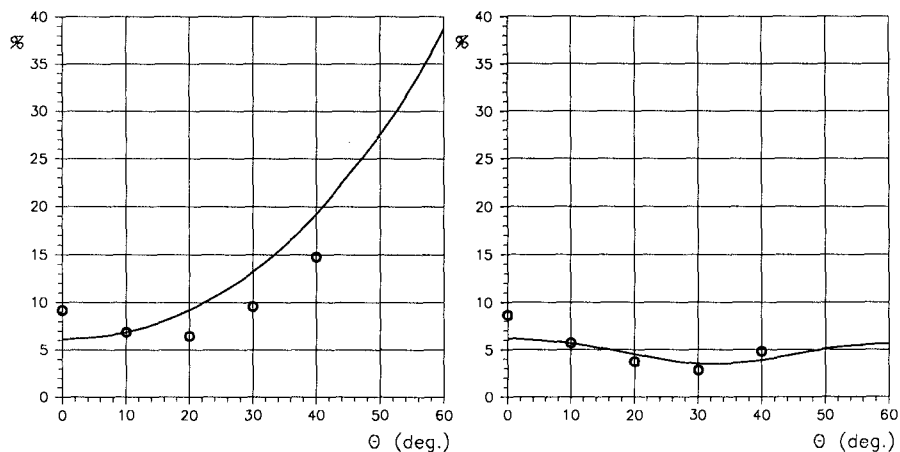


Figure 5 As Fig. 4, but for a frequency of $0.7Hz$.

7. Summary and conclusions

The development of an Active Absorption Control System for multidirectional waves called 3D-AWACS has been outlined. The theoretical basis has been derived in the frequency-direction domain and practical realization has been shown to be possible by use of a two-dimensional digital filter operating in the time-space domain, where the spatial coordinate runs along the absorbing wavemaker.

The preliminary performance of the system has been tested in a numerical wave tank including a moving boundary to simulate the segmented absorbing wavemaker. Comparative tests with a quasi three-dimensional system consisting of an array of two-dimensional absorption systems (2D-AWACS) in parallel shows that the 2D system is very much better than no active absorption and that the 3D-AWACS can further reduce spurious reflection significantly. Although the system is capable of simultaneous wave generation and active absorption, only the absorption ability was shown in these preliminary tests.

Acknowledgement. The numerical work was funded by the the Danish National Research Foundation. Their support is greatly appreciated.

Antoniou, A. (1979). *Digital Filters: Analysis and Design*. McGraw-Hill, New York, New York, USA.

Hirakuchi, H., R. Kajima, and T. Kawaguchi, 1990. Application of a piston-type absorbing wavemaker to irregular wave experiments. *Coastal Eng. in Japan JSCE* **33**(1), 11-24.

Hirakuchi, H., R. Kajima, T. Shimizu and M. Ikeno, 1992. Characteristics of absorbing directional wavemaker. Proc. 23rd Int. Conf. Coastal Eng., Venice Italy, 1992, ASCE, New York, 1993, 281-294.

Schäffer, H.A., 1996. Second order wavemaker theory for irregular waves. *Ocean Engng.* **23**(1), 47-88.

- Schäffer, H.A., T. Stolborg and P. Hyllested, 1994. Simultaneous generation and active absorption of waves in flumes. Proc. *Waves - Physical and numerical modelling*, Vancouver, B.C., Canada, 90-99.
- Skourup, J., M.J. Sterndorff and E.A. Hansen, 1992. Numerical modelling of wave-structure interaction by a three-dimensional nonlinear boundary element method: A step towards the numerical wave tank. *Ocean Engng.* **19**(5), 437-460.
- Skourup, J. and H.A. Schäffer, 1995. Active absorption in boundary element modelling of nonlinear water waves. Proc. 3rd Int. Congr. on Indust. and Appl. Maths. (ICIAM), Hamburg, Germany.
- Skourup, J., 1996. Active absorption in a numerical wave tank. Proc. 6th Int. Offshore and Polar Engrg. Conf. (ISOPE), Los Angeles, USA, May, 31-38.

CHAPTER 6

TIME-AVERAGED WAVE FIELD EVOLUTION IN COASTAL ZONE

Jianlu Xu¹ and Rodney J. Sobey²

1. Introduction

Flow circulation and the field variation of wave height and setup are important data in coastal engineering practice. This paper presents a wave-averaged model for simulating wave transformation and associated mean flow circulation in coastal regions. It is intended for applications where interest centers on the evolution of wave-averaged parameters such as wave height, setup and wave-induced current, and where the resolution of wave phase is unnecessary.

2. Governing Equations

An analysis technique used in turbulent shear flow is adapted to develop the governing equations for wave height, wave setup and mean flow. Variables are decomposed into a slowly varying mean flow and a fluctuating residual which includes both wave and turbulent components. For example, a general velocity vector is decomposed into a wave-averaged velocity vector ($\bar{u}, \bar{v}, \bar{w}$) and a fluctuating velocity vector ($\tilde{u}, \tilde{v}, \tilde{w}$).

Subsequently the conservation equations of mass, momentum and energy are averaged over a wave period and integrated over water depth. The time-averaging introduces apparent stress- or Reynolds stress-style terms corresponding to the time scale of the wave period. The wave-averaged and depth-integrated continuity equation reads (Sobey & Thieke 1988).

$$\frac{\partial \bar{\eta}}{\partial t} + \frac{\partial}{\partial x} \int_{-h}^{\eta_c} \bar{u} dz + \frac{\partial}{\partial y} \int_{-h}^{\eta_c} \bar{v} dz = 0 \quad (1)$$

where x, y and z denote the Cartesian coordinates with z directed upward, t denotes the time, $\bar{\eta}$ is the local wave setup, η_c is the local wave crest elevation, and h is the local water depth from a datum plane in the global SWL. Equation (1) is identical to the long wave continuity equation.

The depth-integrated and wave-averaged x - and y -momentum equations are

-
1. Hydraulic Engineer, Bechtel Environmental Inc. San Francisco, CA 94119, USA
 2. Professor, Department of Civil and Environmental Engineering, University of California at Berkeley, CA 94720, USA.

$$\begin{aligned} \frac{\partial}{\partial t} \int_{-h}^{\eta_c} \bar{u} dz + \frac{\partial}{\partial x} \int_{-h}^{\eta_c} \bar{u}^2 dz + \frac{\partial}{\partial y} \int_{-h}^{\eta_c} \bar{u} v dz = \\ -g(h + \bar{\eta}) \frac{\partial \bar{\eta}}{\partial x} + \frac{1}{\rho} \left[\frac{\partial}{\partial x} \int_{-h}^{\eta_c} s_{xx} dz + \frac{\partial}{\partial y} \int_{-h}^{\eta_c} s_{xy} dz - \tau_{bx} \right] \end{aligned} \quad (2)$$

$$\begin{aligned} \frac{\partial}{\partial t} \int_{-h}^{\eta_c} \bar{v} dz + \frac{\partial}{\partial x} \int_{-h}^{\eta_c} \bar{u} v dz + \frac{\partial}{\partial y} \int_{-h}^{\eta_c} \bar{v}^2 dz = \\ -g(h + \bar{\eta}) \frac{\partial \bar{\eta}}{\partial y} + \frac{1}{\rho} \left[\frac{\partial}{\partial x} \int_{-h}^{\eta_c} s_{xy} dz + \frac{\partial}{\partial y} \int_{-h}^{\eta_c} s_{yy} dz - \tau_{by} \right] \end{aligned} \quad (3)$$

where s_{xx} , s_{xy} , s_{yy} are wave apparent stresses, and τ_{bx} and τ_{by} are the bottom shear stress components in the x and y direction, respectively. The wave energy equation is written as

$$\begin{aligned} \frac{1}{2} \frac{\partial}{\partial t} \int_{-h}^{\eta_c} (\bar{u}^2 + \bar{v}^2 + \bar{w}^2) dz + g \bar{\eta}^2 + \frac{\partial}{\partial x} \int_{-h}^{\eta_c} \left[\frac{\bar{p}_d \bar{u}}{\rho} + \frac{1}{2} (\bar{u}^3 + \bar{u} \bar{v}^2 + \bar{u} \bar{w}^2) \right] dz \\ - \frac{\partial}{\partial y} \int_{-h}^{\eta_c} \left[\frac{\bar{p}_d \bar{v}}{\rho} + \frac{(\bar{v} \bar{u}^2 + \bar{v}^3 + \bar{v} \bar{w}^2)}{2} \right] dz = - \frac{\partial}{\partial x} \int_{-h}^{\eta_c} \bar{u} (\bar{u}^2 + \bar{v}^2 + \bar{w}^2) dz - \frac{\partial \bar{u}}{\partial x} \int_{-h}^{\eta_c} \bar{u}^2 dz \\ - \left(\frac{\partial \bar{v}}{\partial x} + \frac{\partial \bar{u}}{\partial y} \right) \int_{-h}^{\eta_c} \bar{u} \bar{v} dz - \frac{\partial}{\partial y} \int_{-h}^{\eta_c} \bar{v} (\bar{u}^2 + \bar{v}^2 + \bar{w}^2) dz - \frac{\partial \bar{v}}{\partial y} \int_{-h}^{\eta_c} \bar{v}^2 dz - D_{bf} - D_{wb} \end{aligned} \quad (4)$$

where D_{bf} and D_{wb} are energy dissipation due to bottom friction and wave breaking, respectively.

3. Closure Solution Surfaces

Equations (1)-(4) contain wave setup, mean flow velocity and wave apparent stresses, among other unknowns. The number of the unknowns far exceeds the number of governing equations. This is the apparent stress closure problem familiar in turbulence. As our closure hypothesis, the Reynolds stress-style terms are established as a function of wave height, wave period and water depth from Fourier approximation wave theory. For simplicity, the closure variables are defined in the propagation direction of plane waves. In addition, a two-layer flow structure is assumed with the kinematics above wave trough (surface layer) being dominated by wave motion and the mean flow current being confined below the wave trough (bottom layer). The closure parameters for the local layer-averaged wave apparent stresses are, e.g., defined as

$$S_s = \frac{1}{H} \int_{\eta_{tr}}^{\eta_c} [-\Delta p + \rho(\bar{w}^2 - \bar{u}^2)] dz \quad \text{for the surface layer} \quad (5)$$

$$S_b = \frac{1}{h - \eta_{tr}} \int_{-h}^{\eta_{tr}} \rho(\bar{w}^2 - \bar{u}^2) dz \quad \text{for the bottom layer} \quad (6)$$

where η_{tr} is the local wave trough elevation, and Δp is the local pressure residual due to the partial submergence of a point above the wave trough during a wave period. Sixteen closure variables (η_{tr} , \hat{U}_s , U_{rms} , \hat{U}_b^2 , \bar{U}_b^2 , S_s , S_b , N_s , N_b , W_s , W_b , $\bar{\eta}^2$, F_s , F_b , K_s and E_p) are similarly established and these closure variables are normalized by angular

wave frequency ω and the acceleration due to gravity, g . For example, S_s and S_b are normalized by $\rho\omega^2/g^2$. Following the above procedure, closure solution surfaces are established with water depth ranging from deep to shallow and wave height upto the breaking limit.

Upon substituting the closure parameters into Equations (1) to (4), a closed system for the wave height, H , wave setup, $\bar{\eta}$, and mean flow velocity, U_b and V_b , is developed. The integral, dimensionless continuity equation reads

$$\frac{\partial \bar{\eta}}{\partial t} + \frac{\partial}{\partial x} [(H U_s \cos \phi) + (h + \bar{\eta} + \eta_{tr}) U_b] + \frac{\partial}{\partial y} [(H U_s \sin \phi) + (h + \bar{\eta} + \eta_{tr}) V_b] = 0 \quad (7)$$

The integral x- and y-momentum equations are

$$\begin{aligned} \frac{\partial}{\partial t} [H U_s \cos \phi + (h + \bar{\eta} + \eta_{tr}) U_b] + \frac{\partial}{\partial x} [H U_s^2 \cos^2 \phi + (h + \bar{\eta} + \eta_{tr}) U_b^2 + (h + \frac{\bar{\eta}}{2}) \bar{\eta}] \\ + \frac{\partial}{\partial y} [H U_s^2 \frac{\sin 2\phi}{2} + (h + \bar{\eta} + \eta_{tr}) U_b V_b] = -\bar{\eta} \frac{\partial h}{\partial x} - \frac{\partial}{\partial x} [H(S_s + \sin^2 \phi N_s) \\ + (h + \bar{\eta} + \eta_{tr})(S_b + \sin^2 \phi N_b)] - \frac{\partial}{\partial y} [\frac{\sin 2\phi}{2} (H N_s + (h + \bar{\eta} + \eta_{tr}) N_b)] - \frac{\tau_{bx}}{\rho} \end{aligned} \quad (8)$$

$$\begin{aligned} \frac{\partial}{\partial t} [H U_s \sin \phi + (h + \bar{\eta} + \eta_{tr}) V_b] + \frac{\partial}{\partial x} [H U_s^2 \cos^2 \phi + (h + \bar{\eta} + \eta_{tr}) U_b V_b] \\ + \frac{\partial}{\partial y} [H U_s^2 \sin^2 \phi + (h + \bar{\eta} + \eta_{tr}) V_b^2 + (h + \frac{\bar{\eta}}{2}) \bar{\eta}] = -\bar{\eta} \frac{\partial h}{\partial y} - \frac{\partial}{\partial x} \{ [\frac{\sin 2\phi}{2} (H N_s \\ + (h + \bar{\eta} + \eta_{tr}) N_b)] \} + \frac{\partial}{\partial y} [H(S_s + \cos^2 \phi N_s) + (h + \bar{\eta} + \eta_{tr})(S_b + \cos^2 \phi N_b)] - \frac{\tau_{by}}{\rho} \end{aligned} \quad (9)$$

And the integral wave energy equation is

$$\begin{aligned} \frac{1}{2} \frac{\partial}{\partial t} [\bar{\eta}^2 + H W_s + (h + \bar{\eta} + \eta_{tr}) W_b] + \frac{\partial}{\partial x} \{ \cos \phi [H(F_s + K_s) + F_b (h + \bar{\eta} + \eta_{tr})] \} + \\ \cos^2 \phi H N_s \frac{\partial U_s}{\partial x} + (N_b \cos^2 \phi + \frac{W_b}{2}) (h + \bar{\eta} + \eta_{tr}) \frac{\partial U_b}{\partial x} + \frac{U_b}{2} \frac{\partial}{\partial x} [W_b (h + \bar{\eta} + \eta_{tr})] + \\ H N_s \frac{\sin 2\phi}{2} (\frac{\partial U_s}{\partial y} + \frac{\partial V_s}{\partial x}) + (h + \bar{\eta} + \eta_{tr}) N_b \frac{\sin 2\phi}{2} (\frac{\partial V_b}{\partial x} + \frac{\partial U_b}{\partial y}) + \\ \frac{\partial}{\partial y} \{ \sin \phi [H(F_s + K_s) + (h + \bar{\eta} + \eta_{tr}) F_b] \} + (h + \bar{\eta} + \eta_{tr}) (N_b \frac{\sin 2\phi}{2} + \frac{W_b}{2}) \frac{\partial V_b}{\partial y} + \\ \frac{V_b}{2} \frac{\partial}{\partial y} [(h + \bar{\eta} + \eta_{tr}) W_b] + H N_s \sin^2 \phi \frac{\partial U_s}{\partial y} = -\frac{2}{3\pi} f_w \bar{U}_b^3 - f_{wb} \omega H^2 \end{aligned} \quad (10)$$

where H is the wave height, ϕ is the direction of wave propagation from the x-axis, f_w is the bottom friction factor and f_{wb} is a dimensionless factor for predicting energy dissipation rate due to wave breaking.

4. Simulation of Mean Wave Parameters in One Spatial Dimension

In a one-dimensional space with x denoting the direction of wave propagation, the integral continuity equation reads

$$\frac{\partial \bar{\eta}}{\partial t} + \frac{\partial}{\partial x} [H U_s + (h + \bar{\eta} + \eta_{tr}) U_b] = 0 \quad (11)$$

The dimensionless integral momentum equation becomes

$$\begin{aligned} \frac{\partial}{\partial t} [H U_s + (h + \bar{\eta} + \eta_{tr}) U_b] + \frac{\partial}{\partial x} [H U_s^2 + (h + \bar{\eta} + \eta_{tr}) U_b^2] = \\ -(h + \bar{\eta}) \frac{\partial \bar{\eta}}{\partial x} + \frac{\partial}{\partial x} [H S_s + (h + \bar{\eta} + \eta_{tr}) S_b] - \frac{\tau_{bx}}{\rho} \end{aligned} \quad (12)$$

and the dimensionless integral wave energy equation becomes

$$\begin{aligned} \frac{1}{2} \frac{\partial}{\partial t} [E_p + H W_s + (h + \bar{\eta} + \eta_{tr}) W_b] + \frac{\partial}{\partial x} [H F_s + (h + \bar{\eta} + \eta_{tr}) F_b] \\ = -\frac{\partial}{\partial x} (K_s H) - H N_s \frac{\partial U_s}{\partial x} - [(N_b + \frac{W_b}{2})(h + \bar{\eta} + \eta_{tr})] \frac{\partial U_b}{\partial x} \\ - \frac{U_b}{2} \frac{\partial}{\partial x} [W_b (h + \bar{\eta} + \eta_{tr})] - \frac{2}{3\pi} f_w \bar{U}_b^3 - f_{wb} \omega H^2 \end{aligned} \quad (13)$$

4.1 Characteristic Equations and Numerical Solution

The integral equations (11)-(13) can be written into a quasilinear system

$$\frac{\partial \bar{q}}{\partial t} + A \cdot \frac{\partial \bar{q}}{\partial x} = S(x, t, \bar{q}) \quad (14)$$

where \bar{q} is a dependent variable vector,

$$\bar{q} = [H, \bar{\eta}, U_b]^T \quad (15)$$

S is a source or sink vector, and A is a 3×3 Jacobian coefficient matrix. The propagation of the information described by Equation (14) can be characterized using the eigenvalues of the coefficient matrix, A . The eigenvalue of a matrix is defined as

$$\det[\lambda I - A] = 0 \quad (16)$$

where \det denotes the determinant, λ is the eigenvalue, and I is a 3×3 unit matrix. Equation (16) is generally a third order polynomial in λ . If all three roots of the polynomial, λ_1 , λ_2 and λ_3 , are real and distinct, the system is hyperbolic. For a hyperbolic system, each eigenvalue denotes the propagation speed of some particular information. It is advantageous to obtain the numerical solutions of Equation (14) by the method of characteristics since the corresponding characteristic equations are ordinary differential equations.

The characteristic equations are established by combining the original system equations with an eigenvector of the coefficient matrix as follows

$$\bar{l}_i \cdot \left[\frac{\partial}{\partial t} + A \frac{\partial}{\partial x} \right] \bar{q} = \bar{l}_i \cdot S \quad i = 1, 2, 3 \quad (17)$$

where \bar{l}_i is the left eigenvector such that

$$\bar{l}_i \cdot [\lambda I - A] = 0 \quad (18)$$

Equation (17) can be written as ordinary differential equations

$$\bar{l}_i \cdot \frac{d\bar{q}}{dt} = \sum \bar{l}_i \cdot S \quad i = 1, 2, 3 \quad (19)$$

along the characteristic curve

$$\frac{d}{dt} = \frac{\partial}{\partial t} + \lambda_i \cdot \frac{\partial}{\partial x} \quad (20)$$

The numerical solutions, say at a point "o" and at time level n , can be obtained by

solving three characteristic equations integrated over the characteristic curves

$$\bar{\ell}_i \cdot (\bar{q}_o^n - \bar{q}_{x_j}^{n-1}) = \Delta t \cdot \sum \bar{\ell}_i \cdot S \quad i, j=1,2,3 \quad (21)$$

where Δt is the time step, x_1, x_2 and x_3 denote three points traced back from the point “o” through three characteristic curves over one time step. Numerical stability requires that the Courant condition is satisfied

$$\frac{\Delta t \cdot |\lambda|_{\max}}{\Delta x} \leq 1 \quad (22)$$

where Δx is the spacing step and $|\lambda|_{\max}$ is the maximum eigenvalue throughout the entire simulation period and over the entire computational domain.

To provide some insight into the characteristics of this system, eigenvalues and the corresponding eigenvectors are computed for three typical coastal conditions as shown in Table 1. T is the wave period, and L is the local wave length.

Table 1 Characteristics for Three Typical Coastal Conditions

Case	H (m)	T (sec)	h (m)	h/L	C _L (m/s)	C _g (m/s)	Eigenvalue (m/s)	Eigenvector		
								ℓ ₁	ℓ ₂	ℓ ₃
A	1.0	10	100	0.64	31.32	7.80	31.32	0.01	0.50	1.00
							8.32	1.00	-0.01	-0.01
							-31.32	0.01	-0.50	1.00
B	1.0	10	10	0.11	9.90	8.02	10.00	0.28	1.00	0.61
							7.85	1.00	-0.19	-0.10
							-9.90	0.01	1.00	-0.61
C	1.0	10	2	0.04	4.43	4.45	5.24	0.63	1.00	0.23
							3.84	-0.61	1.00	0.29
							-4.48	0.01	1.00	-0.26

Cases A, B and C represent deep, intermediate and shallow water condition, respectively. The linear long wave speed $C_L=(gh)^{1/2}$ and wave group speed C_g estimated from Fourier approximation wave theory are included Table 1 for comparison with the eigenvalues. Based on the above investigation, the following observations are appropriate:

- In each of the three cases, the three eigenvalues are real and distinct. Thus the system is generally hyperbolic.
- In both Case A and Case B, the first and third eigenvalues are almost equal to the linear long-wave speed in magnitude. This is expected since the mean flow part of the system is similar to the shallow water wave equations, as stated in Section 2. The characteristics corresponding to these eigenvalues are termed wave characteristics(Katopodes and Strelkoff 1979).
- The second eigenvalue in each case is almost equal to the wave group speed. Thus the characteristics corresponding to this eigenvalue describes wave energy transfer, and they are accordingly termed energy characteristics(Xu 1996).
- As implied in Equation (17), the eigenvector measures the interaction among the characteristic equations. In Case A, the first component of the eigenvectors for the wave characteristics is always much smaller than the second and third components, while the first component of the eigenvector for the energy

characteristics is much greater than the other two components. This suggests that the wave energy transfer in deep waters is little affected by the mean flow circulation, and vice versa. From Case A to Case C, the first component ℓ_1 of the first eigenvector increases, suggesting that interaction between the mean flow and the wave energy transfer becomes stronger as the water shallows.

- In all three cases, the first component of the eigenvector of the third eigenvalue (negative) is always much smaller than other two components. This indicates that the backward propagation of the information described by the wave characteristics is little affected by the forward wave energy transfer.

4.2 Open Boundary Conditions

Numerical simulation in coastal engineering normally focuses on only a small portion of a larger system. Open boundaries are present at the locations of truncation from the larger system. In the numerical model, open boundary conditions must be specified to allow information to cross the open boundaries unhampered, as would be in the real situation.

For this case, three constraints are necessary and sufficient at the boundary. To permit interior information to propagate out of the domain, the characteristic equations corresponding to the eigenvalue denoting outgoing propagation should be used as part of the boundary conditions. In general, additional constraints would be required to supplement the characteristic equations for outgoing information. Ideally field data should meet such a need, but field data is only rarely available. Instead, additional (and artificial) conditions are generally called for. These extra boundary conditions coupled with the characteristic equations for outgoing information should be non-reflective or at most weakly reflective.

In this study, the Hedstrom(1979) approximate open boundary conditions are used whenever necessary. Hedstrom's approximate boundary conditions for a three-equation hyperbolic system are briefly described here. Suppose that of the three eigenvalues, $m(<3)$ eigenvalues denote outgoing characteristics. The boundary conditions

$$\bar{\ell}_i \bullet \frac{\partial \bar{q}}{\partial t} = 0 \quad (m < i \leq 3) \quad (23)$$

prevents back reflection of waves into the solution domain from the boundary if there are only simple waves going out. In a linear case, the eigenvalues and eigenvectors are constant. The condition described by Equations (23) is equivalent to

$$\bar{\ell}_i \bullet \bar{q} = \text{constant} \quad (m < i \leq 3) \quad (24)$$

This is the Riemann invariant along the incoming characteristics, i.e., the projection of the dependent variable vector on the incoming characteristic curve is constant.

Wave height is normally given at the offshore boundary as external forcing. Then only one of the Equation (23) conditions is needed, because the given wave height and the characteristic equation corresponding to outgoing waves would provide two boundary conditions. The extra condition corresponding to the wave characteristics should be used because the specification of wave height makes the condition corresponding to the energy characteristic redundant.

4.3 Application to Wave Propagation at Egmond Beach

The cross shore bottom profile at Egmond beach (Derks and Stive 1984) is shown in Figure 1. The incident wave period and height are 8.7 seconds and 2.46m, respectively. The wave forcing is suddenly imposed at the offshore boundary and persists throughout the simulation. The system is assumed to be initially quiescent, with wave height, wave setup and current all zero at the beginning of the simulation.

The computational domain is about 3000 m long, with a water depth at the offshore boundary of about 16 m. A uniform space step of 10 m is used with a corresponding time step of 0.7 second.

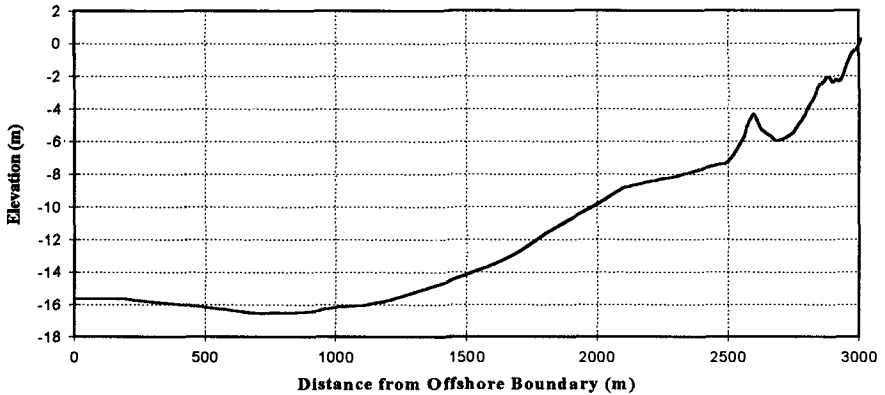


Figure 1 Bathymetric Profile At Egmond Beach

The wave height, wave setup and undertow velocity at eight time levels are shown in Figures 2 through 4. After seven minutes, a steady state wave height profile is established. It takes about fourteen minutes for the wave setup and undertow current to reach an equilibrium state. As waves approach to the shoreline, the mass transport is predominantly shoreward, causing a significant water surface pulse (Figure 3) and shoreward mass transport. After waves reach the shoreline, seaward undertow current develops (Figure 4). The transient wave setup and undertow current are much greater than steady state wave setup and undertow current, suggesting that the transient dynamics in coastal process could be very important. The observed (Derks and Stive 1984) wave height and setup are also plotted in Figures 2 and 3 as the small circles. Good agreement is found for both wave height and wave setup.

The above case study leads to the following conclusions: (1) the numerical scheme is appropriate for simulating the evolution of mean wave parameters in one spatial dimension; (2) the open boundary conditions work satisfactorily.

5. Simulation of Mean Wave Parameters in Two Spatial Dimensions

The integral governing equations in two spatial dimensions, Equations (7) through (10), can be written in the quasilinear form

$$\frac{\partial \bar{q}}{\partial t} + A_x \frac{\partial \bar{q}}{\partial x} + A_y \frac{\partial \bar{q}}{\partial y} = S \quad (25)$$

where \bar{q} is the dependent variable vector, $\bar{q} = [H, \bar{\eta}, U_b, V_b]$, A_x and A_y are the

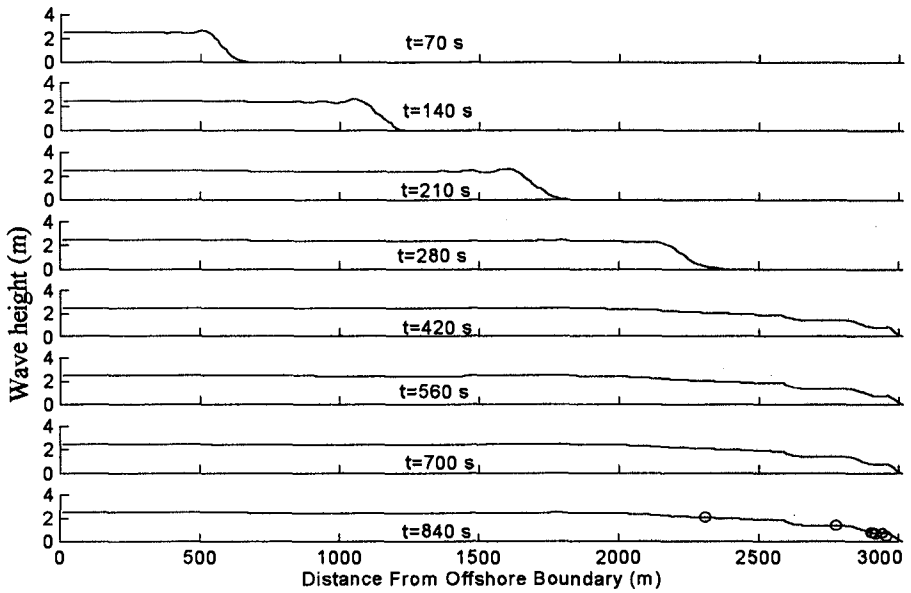


Figure 2 Evolution of Wave Height Profile

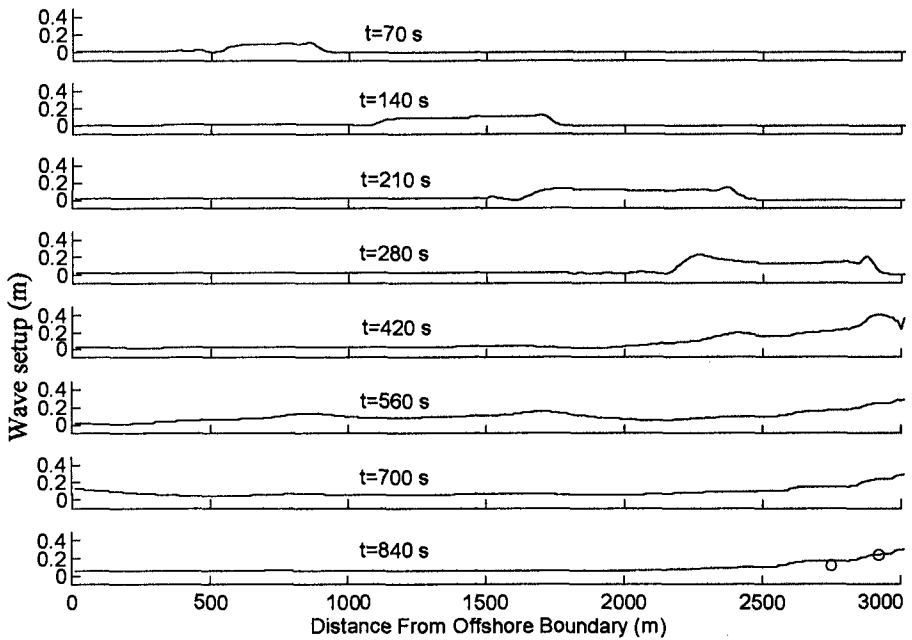


Figure 3 Evolution of Mean Water Surfaces

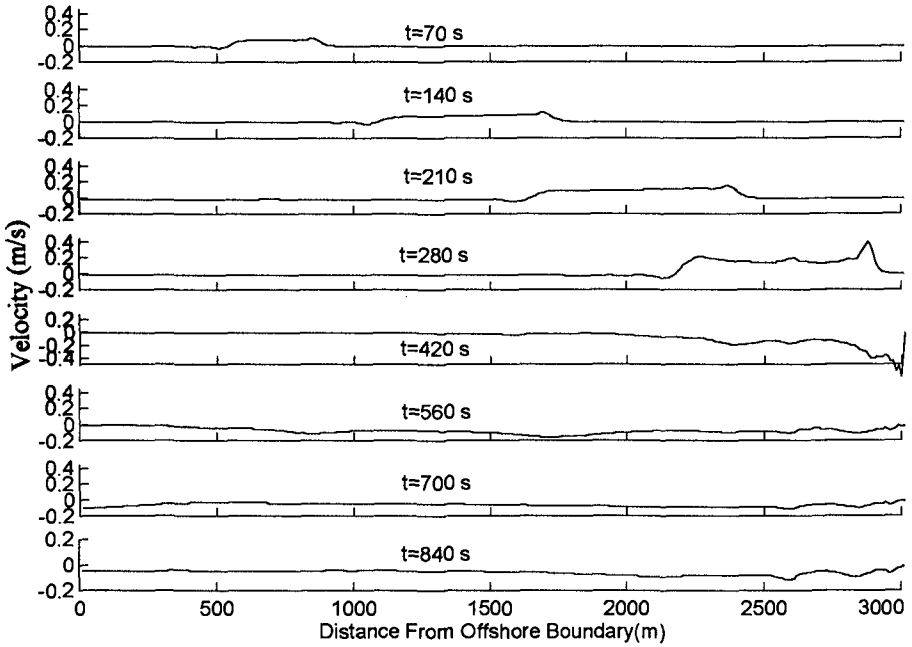


Figure 4 Evolution of Undertow Velocity

coefficient matrices, and S denotes the sink or source vector. Due to the limit of space for this paper, the complexity of the integral equations and, the introduction of closure variables, the exact expressions for the coefficient matrices and the sink terms are not presented here; see Xu (1996) for details.

5.1 Characteristic Equations and System Properties

Again the information propagation described by equation (25) can be characterized using the eigenvalues of the coefficient matrices, A_x and A_y . In two spatial dimensions, however, the eigenvalues are azimuth-dependent. If the azimuth on the x - y plane is denoted by a normal vector $\vec{n} [\cos(\theta), \sin(\theta)]$, then the eigenvalues for Equation (25) are defined as

$$\det[\lambda \cdot I - A_x \cos(\theta) - A_y \sin(\theta)] = 0 \quad (26)$$

which in general is a fourth order polynomial in λ . If the four roots of λ are all real and distinct, the system is hyperbolic. The eigenvalues for the entire range of the azimuth form a family of characteristic surfaces with its normal vector defined as $[-\lambda, \cos(\theta), \sin(\theta)]$. These characteristic surfaces are generally inscribed by a cone. The generation lines of the cone are termed bi-characteristics. The characteristic equations can be derived by linearly combining the system equations through the eigenvector of the coefficient matrices

$$\bar{\ell}_j \left(\frac{\partial \bar{q}}{\partial t} + A_x \frac{\partial \bar{q}}{\partial x} + A_y \frac{\partial \bar{q}}{\partial y} \right) = \bar{\ell}_j S \quad j = 1, 4 \quad (27)$$

where $\bar{\ell}_j$ is the left eigenvector

$$\bar{\ell}_i \left[\lambda \cdot I - A_x \cos(\theta) - A_y \sin(\theta) \right] = 0 \quad (28)$$

On the characteristic surfaces, the characteristic equations can be written with differentiations in two directions only, conventionally along the bi-characteristics and a cross-direction which is almost perpendicular to the bi-characteristics. Such characteristic equations are still partial differential equations. There are infinite sets of eigenvalues and characteristic equations at a point since they are azimuth-dependent.

To appreciate the characteristics of this system, the eigenvalues are computed numerically for the following condition: wave direction $\phi = \pi/2$, wave height = 1.0 m, water depth $h = 10$ m, mean water elevation $\bar{\eta} = 0$, and mean flow velocities under wave trough $U_b = 0.5$ m/s and $V_b = 0.5$ m/s. The eigenvalues as a function of the azimuth in the range from 0 to 2π are shown in Figure 5. Also shown in the figure are the three eigenvalues of the shallow water wave equations under the same condition along with their analytical expressions. Of the four eigenvalues at each azimuth, two are identified by λ_w , denoting wave characteristics, one labeled by λ_e , referring to the energy characteristic, and the fourth by λ_f denoting the flow characteristic (Katopodes 1979). The flow characteristics is an extra characteristic family in the two spatial dimensions. The magnitude of the eigenvalue of the flow characteristics is the same order of the magnitude as the flow velocity. The following observations are appropriate:

- This system is generally hyperbolic because the four eigenvalues at any azimuth under the given condition are real and distinct.
- Under the assumed condition, the eigenvalues of wave and flow characteristics are almost identical to those for the shallow water wave equations. The eigenvalue of the energy characteristics may be approximated by $C_g \cos(\phi - \theta)$, in which C_g is the plane wave group speed.

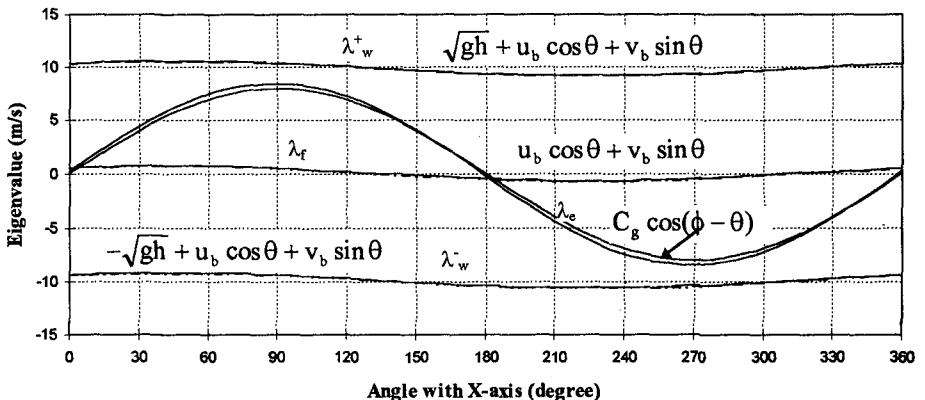


Figure 5 Variation Of Eigenvalue λ With Azimuth θ

- The eigenvalues λ_w^+ and λ_w^- of the wave characteristics are identical when considering the entire range of azimuth (0, 2π) since $\lambda_w^+(\theta) = -\lambda_w^-(\theta + \pi)$. Only one of them, conventionally λ_w^+ , is used in describing wave characteristics. The eigenvalues of the wave characteristics vary slightly with azimuth. Information spreads out at an almost uniform speed.
- The maximum eigenvalue is of particular importance to numerical simulation because it defines the domain of influence or dependence. The direction corresponding to the maximum eigenvalue is termed a principal direction (Xu 1996). In the principal direction, the eigenvalues and characteristic equations of the shallow water wave equations in two spatial dimensions are the same as those in one spatial dimension

5.2 Numerical Scheme

The method of characteristics is used to obtain numerical solutions. The major issues in numerically simulating the evolution of mean wave parameters in two spatial dimensions are (1) evaluation of wave propagation direction, which is used in the closure of wave apparent stresses, (2) development of a numerical scheme recognizing that there are infinite characteristic equations, (3) open boundary conditions, and (4) evaluation of derivatives in the cross direction (cross-derivatives). Due to the limit of space here, the evaluation of wave direction is not discussed.

The bi-characteristic method proposed by Bulter (1962) is adapted to develop a numerical scheme for the present system. This method is based on the combination of the characteristic equations along several bi-characteristics to minimize the coefficients of the cross derivatives. A total of six directions are involved in this case.

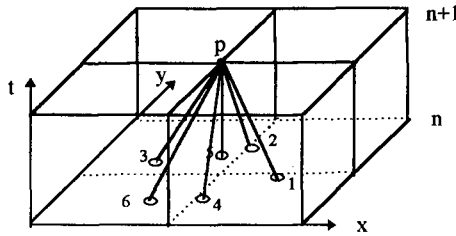


Figure 6 Illustration of Bi-characteristics Scheme

The six points traced back from point “p” by the respective characteristic velocity are labeled as 1 to 6 at time level n. Of the six points, 1,2,3 and 4 are on the wave bi-characteristics corresponding to azimuth $\theta=0, \pi/2, \pi$ and $3\pi/2$, respectively. Point 5 is on the flow path, and point 6 is along the wave propagation direction. The coordinates of the points 1 through 6 can be estimated by using the following expressions with sufficient accuracy (Xu 1996)

$$\begin{aligned}
 x_{2,4,5} &= x_p - U_b \Delta t; & x_{1,3} &= x_p - (U_b \mp C) \Delta t; & x_6 &= x_p - \lambda_e \Delta t \cos \phi \\
 y_{2,4,5} &= y_p - V_b \Delta t; & y_{1,3} &= y_p - (V_b \mp C) \Delta t; & y_6 &= y_p - \lambda_e \Delta t \sin \phi
 \end{aligned}
 \tag{29}$$

where C is the long wave speed and ϕ is the wave propagation direction. The values at these points are interpolated from the values at surrounding grid points.

The integration of the energy characteristic equation along 6-p gives

$$\begin{aligned} \ell_1^6 H_p + \ell_2^6 \bar{\eta}_p + \ell_3^6 U_{b,p} + \ell_4^6 V_{b,p} = & \ell_1^6 H_6 + \ell_2^6 \bar{\eta}_6 + \ell_3^6 U_{b,6} + \ell_4^6 V_{b,6} + [a_6 \frac{\partial H}{\partial x} \\ & + b_6 \frac{\partial H}{\partial y} + c_6 \frac{\partial \bar{\eta}}{\partial x} + d_6 \frac{\partial \bar{\eta}}{\partial y} + e_6 \frac{\partial U_b}{\partial x} + f_6 \frac{\partial U_b}{\partial y} + g_6 \frac{\partial V_b}{\partial x} + h_6 \frac{\partial V_b}{\partial y} + S_6] \cdot \Delta t \end{aligned} \quad (30)$$

Summing up the four wave characteristic equations along 1-p, 2-p, 3-p and 4-p and subtracting twice the continuity equation along 5-p gives

$$\begin{aligned} (\sum_{i=1,4} \ell_1^i) H_p + (\sum_{i=1,4} \ell_2^i - 2) \bar{\eta}_p + (\sum_{i=1,4} \ell_3^i) U_{b,p} + (\sum_{i=1,4} \ell_4^i) V_{b,p} = \\ [\sum_{i=1,4} \ell_1^i H_i + (\sum_{i=1,4} \ell_2^i \bar{\eta}_i - 2\bar{\eta}_5) + \sum_{i=1,4} \ell_3^i U_{b,i} + \sum_{i=1,4} \ell_4^i V_{b,i} + \\ (\sum_{i=1,4} a_i) \frac{\partial H}{\partial x} + (\sum_{i=1,4} b_i) \frac{\partial H}{\partial y} + (\sum_{i=1,4} c_i) \frac{\partial \bar{\eta}}{\partial x} + (\sum_{i=1,4} d_i) \frac{\partial \bar{\eta}}{\partial y} + \\ (\sum_{i=1,4} e_i) \frac{\partial U_b}{\partial x} + (\sum_{i=1,4} f_i) \frac{\partial U_b}{\partial y} + (\sum_{i=1,4} g_i) \frac{\partial V_b}{\partial x} + (\sum_{i=1,4} h_i) \frac{\partial V_b}{\partial y} + (\sum_{i=1,4} S_i)] \cdot \Delta t \end{aligned} \quad (31)$$

Subtracting the wave characteristic equation along 1-p from that along 3-p gives

$$\begin{aligned} (\ell_1^1 - \ell_1^3) H_p + (\ell_2^1 - \ell_2^3) \bar{\eta}_p + (\ell_3^1 - \ell_3^3) U_{b,p} + (\ell_4^1 - \ell_4^3) V_{b,p} = \\ \ell_1^1 H_1 - \ell_1^3 H_3 + \ell_2^1 \bar{\eta}_1 - \ell_2^3 \bar{\eta}_3 + \ell_3^1 U_{b,1} - \ell_3^3 U_{b,3} + \ell_4^1 V_{b,1} - \ell_4^3 V_{b,3} + \\ [(a_1 - a_3) \frac{\partial H}{\partial x} + (b_1 - b_3) \frac{\partial H}{\partial y} + (c_1 - c_3) \frac{\partial \bar{\eta}}{\partial x} + (d_1 - d_3) \frac{\partial \bar{\eta}}{\partial y} + (e_1 - e_3) \frac{\partial U_b}{\partial x} \\ + (f_1 - f_3) \frac{\partial U_b}{\partial y} + (g_1 - g_3) \frac{\partial V_b}{\partial x} + (h_1 - h_3) \frac{\partial V_b}{\partial y} + S_1 - S_3] \cdot \Delta t \end{aligned} \quad (32)$$

Similarly, subtracting the characteristic equation along 2-p from that along 4-p gives

$$\begin{aligned} (\ell_1^2 - \ell_1^4) H_p + (\ell_2^2 - \ell_2^4) \bar{\eta}_p + (\ell_3^2 - \ell_3^4) U_{b,p} + (\ell_4^2 - \ell_4^4) V_{b,p} = \\ \ell_1^2 H_2 - \ell_1^4 H_4 + \ell_2^2 \bar{\eta}_2 - \ell_2^4 \bar{\eta}_4 + \ell_3^2 U_{b,2} - \ell_3^4 U_{b,4} + \ell_4^2 V_{b,2} - \ell_4^4 V_{b,4} + \\ [(a_2 - a_4) \frac{\partial H}{\partial x} + (b_2 - b_4) \frac{\partial H}{\partial y} + (c_2 - c_4) \frac{\partial \bar{\eta}}{\partial x} + (d_2 - d_4) \frac{\partial \bar{\eta}}{\partial y} + (e_2 - e_4) \frac{\partial U_b}{\partial x} \\ + (f_2 - f_4) \frac{\partial U_b}{\partial y} + (g_2 - g_4) \frac{\partial V_b}{\partial x} + (h_2 - h_4) \frac{\partial V_b}{\partial y} + S_2 - S_4] \Delta t \end{aligned} \quad (33)$$

It can be verified that the coefficients of the cross derivatives through these combinations are much smaller than those without using such combinations. Equations (30) through (33) are used to obtain the solutions for H , $\bar{\eta}$, U_b and V_b .

5.3 Open Boundary Conditions

At an open boundary, some bi-characteristics lie outside the computational domain. So only some of Equations (30) through (33) can be derived. As a result, extra boundary conditions need to be specified.

In the study of the characteristics of the shallow water wave equations, it is found that the characteristics along a flow path in a two dimensional space behave exactly the same as in a one-dimensional space (Xu 1996). Heuristically, the Hedstrom open boundary conditions introduced in Section 4.2 may be extended approximately to two spatial dimensional problems as long as the open boundary conditions are applied in the flow direction.

If there are m outgoing characteristics, then the 4- m Hedstrom approximate

boundary conditions in the flow direction are formed as

$$\vec{\lambda}_j \cdot \frac{\partial \vec{q}}{\partial t} = 0 \quad j = m. 4 \tag{34}$$

5.4 Simulation of Oblique Wave Propagation

To test the performance of the numerical scheme and open boundary conditions, the numerical model is applied to simulate oblique wave propagation. Waves are assumed to propagate into an initially quiescent square domain from the left lower corner at an angle of 45° with the x-axis. The water depth of the domain is 10 m, and the incident wave height is 0.5 m with a wave period of 10 seconds. A uniform grid with Δx=Δy=10m is used, coupled with a time step of 0.5 second. Wave height is gradually imposed at the inflow boundaries over three time steps.

The computed wave height surfaces at six time levels are shown in Figure (7). At time 50 seconds, waves pass through the computational domain, and a steady state wave field is established. The solutions at the inflow and outflow boundaries are smooth at all six time levels, demonstrating that the imposed boundary conditions do not cause any appreciable numerical reflection at the boundaries.

The propagation speed is estimated by dividing the distance by the time interval. The estimated speed of energy transfer is 8.25 m/s, which is close to the wave group speed estimated from Fourier approximation wave theory of 8.34 m/s.

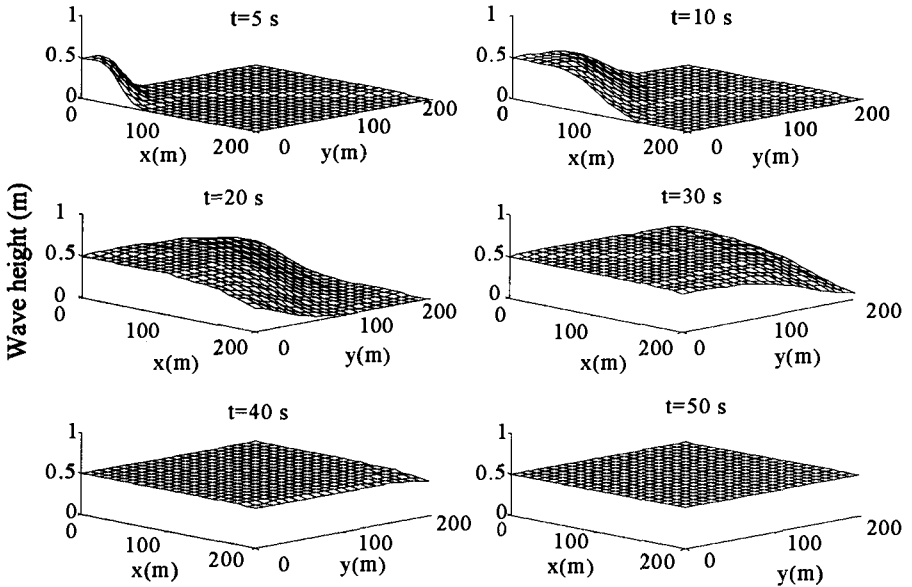


Figure 7 Evolution of Wave Height Envelops

6. Summary

In this study, a wave-averaged depth-integrated model for the evolution of mean wave parameters was developed. This model is valid for both shoaling waves and surf zones provided that periodic motion is dominant over turbulence. The physical processes that this model can simulate include wave shoaling, refraction, diffraction, wave-current interaction and mean flow circulation, etc. The proposed numerical scheme can be used to obtain the numerical solutions effectively and with negligible reflection at open boundaries. The transient behavior in the evolution of mean wave field can be adequately modeled.

It was clearly shown in this study that transient dynamics may be important for coastal evolution. The wave-driven current and mean water surface variation are significantly greater than the respective steady state values. Since the wave conditions in deep water are rarely invariant, the simulation of transient behavior is a significant feature of this model.

References

- Bulter, D.S., 1960. *The Numerical Solution of Hyperbolic Systems of Partial Differential Equations in Three Independent Variables*. Proc. Royal Soc.(London), 255A, pp.232-252
- Derks, H. and Stive, M.J.F., 1984. *Field Investigation in the TOW Study Programme for Coastal Sediment Transport in the Netherlands*: . Proc. 19th Conf. Coastal Eng., Houston, Volume II, Chapter 123, pp. 1830-1845.
- Hedstrom, G.W., 1979. *Non-reflecting Boundary Conditions for Nonlinear Hyperbolic Systems*. Computational Physics, Vol.30, pp.222-237.
- Katopodes, N. and Strelkoff, T., 1979. *Two Dimensional Shallow Water-Wave Models*. Journal of Engineering Mechanics, Vol.105, No. EM2. pp. 317-334.
- Sobey, R.J. and Thieke, R.J., 1989. *Mean Flow Circulation Equations For Shoaling And Breaking Waves*. Journal of Engineering Mechanics. 115: 285-303.
- Xu, Jianlu. 1996. *A Time-Averaged Approach to Wave Evolution from Deep Water to Shallow Water*. Ph.D. Thesis, University of California at Berkeley [Available from University Microfilms].

CHAPTER 7

Quality Control of GEOSAT Wave Data for Engineering Applications

M. Siddabathula¹ and Vijay G. Panchang²

Introduction

Engineers are often confronted by a paucity of useful wave data needed for a variety of applications. Available information is presently derived from three sources: wave buoy measurements, wave model calculations, and ship observations. Of these, buoy measurements constitute the only reliable data source. However, they provide exceedingly sparse spatial resolution. (For instance, there are only about 45 wave buoys in operation in US waters (Franklin 1992)). Wave modeling (with models such as WAM and the Army Corps' Wave Information Studies) provide a data base of uniform spatial and temporal resolution, but despite many advances, wave modeling must still be considered an evolving field and model results are not fully reliable. Visual ship observations have been used to construct global wave climatologies (e.g. the US Navy Marine Climatic Atlas of the world). However, ship-reported wave observations are irregular and usually regarded as highly imprecise.

This difficulty with traditional data sets may be overcome to some extent by using the large amounts of data collected in recent years by satellites (GEOS-3, SEASAT, Geosat etc.). The US Navy satellite GEOSAT has recorded ocean wave data for almost 5 years. Circling the globe about 15 times a day, GEOSAT gave the densest coverage compared with all existing data. After the initial 18 months of its mission (31 March 1985 to 30 September 1986), it was maneuvered into an exact repeat mission (ERM; November 1986 to January 1990), when the satellite executed 17-day repeat cycles. Global oceanographic information for some 30 oceanographic parameters were recorded every second. These data have been processed by the National Ocean Service (Cheney et al. 1991a, b) and are disseminated to the user community on CD-ROM's. The data are in the form of "Geophysical Data Records" (or GDR's) for the ERM period and "Crossover Difference Records" (or XDR's) for the initial 18 month period. Significant wave heights (SWH) measured by an on-board altimeter were calculated as an average of 10 values recorded every second. About 50,000 measurements, made every 6.4 km along track, were reported daily.

The quality of GEOSAT SWH measurements has been examined by Dobson et al. (1987) and others by comparing them with buoy data. The agreement has been found to be generally good. Of course satellite measurements do not always coincide

¹Programming Analyst, Valanki Information Systems, Somerset, NJ 07783.

²Associate Professor, Civil Engg Dept., University of Maine, Orono, ME 04469.

with buoy measurements in space and time, and allowing various windows of separation, they report the following differences (not "errors" but differences):

Max Separation	Average Separation	Separation		Difference in SWH	
Distance	Time	Separation	Time	rms	mean
50 km	30 min.	35 km	15 min.	0.49 m	0.36 m
50 km	15 min.	35 km	8 min.	0.1 m	
20 km.	30 min.	14 km	15 min.	0.2 m	

Table 1: Comparison of satellite and buoy wave heights (after Dobson et al. 1987)

It is clear that when the two measurements coincide in space and time, the difference between satellite and buoy measurements of significant wave heights are insignificant, at least for most practical uses. Dobson and Porter (1989) and Young (1994) have used these data for their global climatological studies.

In spite of the above observations, there remains some uncertainty regarding the accuracy of GEOSAT SWH data as disseminated to the user community on the CD-ROM's, especially in regions close to land. No comparison has been made with wave data close to land. A closer inspection of the GEOSAT SWH dataset performed here indicates that it contains several erroneous values. Some of the reported measurements are extremely large and have the potential to adversely influence wave statistics calculated on the basis of this dataset (Panchang et al. 1997). In addition, the unintentional use of faulty data on the CD-ROM's is likely to hinder other applications of these data e.g. wave model/data comparisons.

A rigorous assessment of the quality of the GEOSAT SWH data was therefore performed. As noted by Young (1994), quality control of satellite data is difficult; this work involved manual inspection of the satellite and buoy data on a track-by-track basis. This is necessary to eliminate erroneous records from the dataset and to prevent inclusion of similar erroneous records from future satellite missions. A computer program was developed in this study to (a) conveniently extract SWH data in any desired region from the CD-ROM's (since they use a format which is somewhat cumbersome for routine use), and (b) apply rigorous quality control criteria to the SWH data.

Existing Quality Control Criteria

Several quality control criteria were used during the processing of the satellite altimeter data prior to installation on the CD-ROM's (Cheney et al. 1991a, b). Laxon & Rapley (1987), Brooks & Lockwood (1990) and Hayne & Hancock (1990) also describe techniques to flag data of poor quality as measured by SEASAT & GEOSAT satellites. However, these techniques apply to the sensory data records, i.e. the raw satellite data which are not generally available; even if they were, it would be extremely tedious for the user to reprocess the raw data. This study deals only with the data as presented to the end-user on the CD-ROM's. For assessing the quality of these SWH's, the parameters given in Table 2 (out of the 34 oceanographic parameters presented in the GDR's) are of relevance to this study.

During previous studies that have utilized Geosat wave data, some effort had been devoted towards quality control. For instance, Dobson and Porter (1989) discarded those GDR's which had the following criteria: (1) $\sigma_h > 10$ cm; (2) the height bias and satellite attitude were out of range, as determined from bit 2 in the

"Flags" parameter; (3) no value of attitude was available on the GDR (attitude = 0); (4) any one of the 10 per second heights was flagged as bad (as determined by bit 3 in the "Flags" parameter). See Table 2 for a definition of the symbols.

Similarly, in a comparison of wave model and satellite data, Romeiser (1993) used the following criteria to discard measurements: (1) attitude is outside the interval between 0.25° and 1.2°; (2) AGC < 18 dB; (3) $\sigma_0 < 6$ dB; (4) $\sigma_{swh} > 12$ cm. In the remainder of this paper, the above criteria will be referred to as the D&P criteria and the R criteria, respectively. Young (1994) also has used certain quality control criteria in his global climatological studies using the ERM data. His criteria, however, are based on the examination of 50 consecutive records, which tend to eliminate large quantities of coastal wave data.

Date, Time	Provided in the Universal Time Constant format.
Latitude	Latitude in degrees (positive for north, negative for south).
Longitude	Longitude in degrees (positive for east, negative for west).
H	1-second average sea surface height derived from 10 per second heights recorded.
σ_h	Standard deviation from a linear fit to the 10 per second sea surface height values used in computing H.
SWH	Significant wave height as an average of 10 values recorded in one second.
σ_{swh}	Standard deviation of the 10 per second wave height values used in computing SWH.
AGC	Automatic gain control determined onboard the spacecraft at a rate of 10 per second. Indicates signal strength at the altimeter receiver.
σ_{agc}	Standard deviation of the 10 per second values used to compute AGC
σ_0	Backscatter coefficient computed from AGC. Also referred to as normalized radar cross section
Flags	A 16 bit integer, where each bit conveys information about the GDR; of these the following are relevant here: bit 0 = 1 if over water (based on a 1/12 degree mask) or 0 if over land; bit1 = 1 if over water depth over 1000 m . bit2 = 1 if there is height bias reported bit3 = 1 if any of 10 per second values of surface height are bad, (marked 32767)
Attitude	Spacecraft off-nadir orientation angle estimated by ground processing of the return waveform trailing edge.

Table 2: Partial list of GDR parameters (after Cheney et al. 1991b)

In a study of the GEOSAT wave data in the Gulf of Maine, it was found that the above criteria were inadequate. A rigorous examination was therefore performed of the satellite measurements in this region in conjunction with data from several buoys. The Gulf of Maine is particularly well-suited to this study because of the availability of 5 buoys which were operational during the satellite mission and their relative proximity to the satellite tracks (Fig. 1). The adequacy of the D&P and the R quality control criteria was examined and new criteria were developed as necessary. A computer program was then developed to automatically eliminate questionable data. The new criteria and the program were then tested against satellite data in the Gulf of Mexico (Fig. 2).

Wave Data in the Gulf of Maine

There are 14 tracks pertaining to the ERM period of the Geosat mission in the Gulf of Maine. Ascending tracks are denoted here by 0a, 1a, 2a, ... 7a and descending tracks are denoted by 0d, 1d, 2d, ... 5d (Fig. 1). However, the GDR's associated with tracks 0a, 7a, and 0d were found to contain negligible quantities of data in the Gulf of Maine and were hence not used for assessing the quality of the SWH's. It must be noted that even during the ERM phase, the tracks were not exactly self-repeating. As determined from the GDR's, successive passes have a small lateral displacement. Therefore, the lines denoting the tracks in Fig. 1 actually represent a group of closely-clustered tracks. For assessing the quality of the satellite wave measurements, data for the following wave buoys were obtained from NDBC on CD-ROMs (Franklin, 1992): Buoy 44005 (42.7° lat, 68.3° long), buoy 44007 (43.5° lat, 70.1° long), buoy 44008 (40.5° lat, 69.5° long), buoy 44011 (41.1° lat, 66.6° long), and buoy 44013 (42.4° lat, 70.8° long).

As seen in Fig. 1, the satellite tracks never coincide with the exact location of the buoys. Moreover, buoys provide SWH's every hour, while the satellite provides them every second. Therefore, there is never an exact overlap of the measurements for comparison. Automatic comparison of the measurements is thus not sufficient for quality control of the satellite data; differences in the measurements may be entirely attributable to the space/time offset. It was therefore necessary to perform a manual comparison, using as much data as possible as well as a significant level of individual judgment for accepting or discarding satellite data. A complete listing of the satellite data on a track-by-track basis along with the buoy data at the nearest half-hour in the vicinity of the satellite tracks is given in Siddabathula and Panchang (1996).

Quality Control of Satellite Data in the Gulf of Maine

We first performed a detailed examination of the data from the track 2d. The 33 ERM tracks belonging to this class emanate from the west of the Bay of Fundy and proceed southwest past the Cape Cod (Fig. 1). A typical satellite pass in Gulf of Maine region reported 40 to 80 measurements. This variation was due to the fact that sometimes the satellite started tracking several seconds after emerging over water relative to the rest of the tracks in this class. Immediately after emerging over water from west of the Bay of Fundy, the satellite flew over a group of islands; similarly, proximity to land was also encountered near the Cape Cod area. Data from these tracks were examined in detail in conjunction with data from buoys 44005, 44007, 440013 and 44008. Buoy 44011 was considered to be too remote for validation of the data from track 2d.

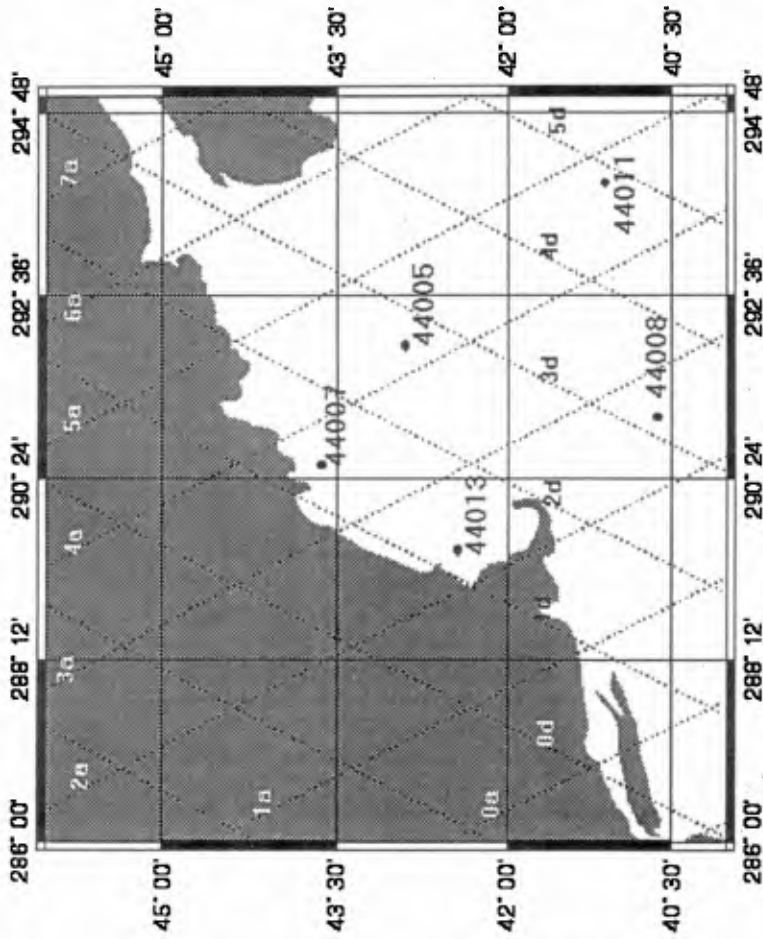


Fig. 1 Geosat Satellite ground tracks and buoys in the Gulf of Maine

The D&P criteria would have detected a total of 99 erroneous measurements; this amounts to 5% of the GDR's (See summary Table 12). Detailed visual examination of these data revealed, however, a number of additional erroneous data records. The R criteria, on the other hand, eliminated almost 50% of the GDR's in this class of tracks (Table 12). There were instances (e.g. the track on 2 March 1987, Siddabathula and Panchang, 1996) where a complete track was flagged as erroneous by the R criteria while visual examination showed that the altimeter data did agree very well with buoy measurements (Siddabathula, 1996). It can therefore be inferred that the R criteria are too stringent for the 2d tracks. The D&P criteria (all but the third) were therefore used as a baseline. Errors which escape detection by the D&P criteria appear to fall in 3 categories for the 2d tracks. These are denoted as E1, E3 and E4. These errors and ways to detect them are described below.

Error type 1 (E1): Consider the following record pertaining to the 2d track (a complete listing can be found in Siddabathula and Panchang, 1996):

Date	Time	Latit.	Longit.	σ_h	SWH	σ_{swh}	bit0	bit1	bit2	bit3
				(cm)	(m)	(cm)				
870109	222251	41.677	290.117	365	0.29	27	1	0	0	0
870109	222253	41.570	290.045	8	10.17	73	1	0	0	0

Table 3: Subset of 2d track data for 9 Jan 1987

At the closest half-hour, the buoys measurements were about 1.5 m (Table 4):

Buoy	Closest Distance from track (km)	SWH(m)
44005	58	1.5
44007	99	0.3
44008	97	1.5
44011	248	2.5
44013	94	0.2

Table 4: Buoy-SWH data for 9 Jan 1987 in the Gulf of Maine.

Clearly the satellite measurement of 10.17 m appears to be in error. This error would not have been detected by the D&P criteria. (Although detected by the R-criteria since $\sigma_{swh} \geq 12$ cm, this criterion, on its own eliminates too many acceptable GDR's, as seen in Table 7). This error appears to stem from a jump in the recording sequence, i.e. no measurement is reported for some time (1 sec in this case, more in some other cases). This may be due to the altimeter shutting off for an interval of time or due to criteria that prevented any faulty data during this time from being installed on the CD-ROM's in the first place. Such errors were found more than 10 (tracks) times out of 33 inspected. Wave heights seemed erroneous each time such a gap in sequence is detected. To automatically detect such faulty data, we have routinely eliminated the first reported record after a gap in the time sequence.

Error type 2 (E2): To be disregarded (Siddabathula, 1996).

Error type 3 (E3): Consider the subset of 2d track data for 16 July 1987 shown in Table 5 (reproduced from Siddabathula and Panchang, 1996). The SWH measurements reported by nearby buoys are shown in Table 6:

Date	Time	Latit.	Longit.	σ_h	SWH	σ_{swh}	bit0	bit1	bit2	bit3
870716	114257	41.176	289.769	23	12.51	51	1	0	0	0
870716	114258	41.122	289.733	141	2.53	25	1	0	0	0
870716	114259	41.069	289.697	324	19.92	0	1	0	0	0
870716	114300	41.016	289.661	39	17.80	79	1	0	0	0
870716	114301	40.962	289.626	13	13.56	51	1	0	0	0
870716	114302	40.909	289.590	10	12.33	42	1	0	0	0
870716	114303	40.855	289.554	5	11.63	39	1	0	0	0
870716	114304	40.802	289.519	6	7.55	22	1	0	0	0
870716	114305	40.748	289.483	5	5.47	13	1	0	0	0
870716	114306	40.695	289.448	4	3.33	7	1	0	0	0

Table 5: Subset of 2d track data for 16 July 1987.

Buoy	Closest Dist. from track (km)	SWH(m)
44005	59	0.8
44007	99	0.2
44008	85	0.8
44011	248	-
44013	94	0.4

Table 6: Buoy-SWH data for 16 July 1987 in the Gulf of Maine.

After careful inspection, it appears that SWH data in all GDR's except the last one are suspect. The first five SWH measurements in Table 5 are discarded by D&P criterion #1. It was also noted that the average SWH is about 1.5m - 2m in the remainder of the track (Siddabathula, 1996). With buoy data showing waves smaller than 1 m, it appears that the last 5 records in Table 5, with SWH of the order of 5.4 m to 12.33 m, are probably erroneous. Also, these records have an $\sigma_{swh} > 12\text{cm}$. The SWH measurement returns to normal once the σ_{swh} value falls below 12cm, which in this example, occurs for the last record. This phenomenon of consecutive erroneous SWH measurements occurred especially in descending tracks. It mostly occurred at the beginning of the 2d tracks and in the proximity of Cape Cod area.

This example is indicative of a typical descending satellite track near coastal regions. This error has occurred about 24 times (72%) out of total 33 tracks. The threshold value of 12cm for σ_{swh} was chosen on the basis of visual inspection. For quality control, all GDRs with $\sigma_{swh} \geq 12\text{cm}$ occurring immediately after a series (one or more) of GDRs with a land flag or a GDR with $\sigma_h > 10\text{cm}$ were regarded as faulty.

Error type 4 (E4): It was found that a GDR has an erroneous SWH measurement if σ_h is equal 10 cm. Consider the following subset of GDR's (Table 7):

Date	Time	Latit.	Longit.	σ_h	swh	σ_{swh}	bit0	bit1	bit2	bit3
881226	011611	42.737	290.844	4	2.35	0	1	0	0	0
881226	011612	42.684	290.807	3	2.25	13	1	0	0	0
-	-	-	-	-	-	-	-	-	-	-
-	-	-	-	-	-	-	-	-	-	-
881226	011618	42.365	290.583	2	2.29	0	1	0	0	0
881226	011619	42.312	290.546	2	2.52	15	1	0	0	0
881226	011620	42.259	290.509	7	2.17	12	1	0	0	0
-	-	-	-	-	-	-	-	-	-	-
-	-	-	-	-	-	-	-	-	-	-
881226	011634	41.513	289.997	13	5.87	21	1	0	0	0
881226	011635	41.460	289.961	10	4.09	0	1	0	0	0
881226	011636	41.406	289.925	2	2.12	13	1	0	0	0

Table 7: Subset of 2d track data for 26 Dec 1988.

The nearest buoy 44005, about 58 km from the satellite track, has reported an SWH = 2.6 m (not shown). It appears that while the last record in Table 7 represents a viable SWH value, the one above it (4.09 m) may be considered suspect. A closer visual inspection of complete listing of the data for this track indicate waves of about 2m and the fact that $\sigma_{swh} = 0$ further justifies its elimination. This criterion can be considered as a refinement of the D&P criterion #1. It appears that in coastal regions, this threshold value for σ_h is necessary to eliminate errors which would escape all the above criteria as well as D&P criteria. This kind of error was observed 5-6 times in 2d tracks.

In order to fine-tune the editing criteria, a detailed examination of data pertaining to 3d and 1d tracks (Fig. 1) was performed. This led to 2 new criteria. Tracks belonging to the 3d class encounter close proximity (the shortest distance being 15 km) with buoy 44005 in the middle and buoy 44008 at the outskirts of the Gulf of Maine. Similar proximity to buoy 44007 (near Portland) and buoy 44013 (near Boston) occurs for track 1d. Therefore data from these tracks were examined in detail in conjunction with data from buoys 44005, 44007, 44013 and 44008. There are 34 tracks in the 3d class and 17 in 1d class. The reason for the small number of 1d tracks is perhaps its proximity to the coastline and the inherent lateral displacement among passes (as noted earlier), resulting in some passes falling largely on land.

Error type 5 (E5): Consider the partial listing of 3d track data for 21 October 1988 in the Gulf of Maine shown in Table 8. Some GDR's in Table 8 depict SWH's as small as 2 cm. These values do not appear to be consistent with the somewhat rougher sea state in the Gulf of Maine region as deduced from the wave buoy measurements in given in Table 9. These small wave heights are probably erroneous and escape detection by all the earlier criteria. This kind of error is found often, about 10 times out of 34 tracks in the 3d tracks and 7 times out of 17 tracks in the 1d class. Detailed examination revealed that satellite SWH's below 0.2 m are almost always suspect, when compared with the buoy measurements near the track and also with successive measurements in the rest of the track. A GDR is thus marked for elimination if the $SWH \leq 0.2$ m.

Date	Time	Latit.	Longit.	σh	swh	σswh	bit0	bit1	bit2	bit3
881021	203208	42.990	292.5	3	32767	32767	1	0	0	0
881021	203209	42.937	292.462	1	0.06	5	1	0	0	0
881021	203210	42.884	292.424	2	0.02	0	1	0	0	0
881021	203211	42.831	292.387	2	0.02	0	1	0	0	0
881021	203212	42.778	292.349	2	0.08	8	1	0	0	0
881021	203213	42.724	292.312	2	0.13	8	1	0	0	0
881021	203214	42.671	292.274	3	0.15	7	1	0	0	0
881021	203215	42.618	292.237	2	0.02	0	1	0	0	0
881021	203216	42.565	292.2	1	32767	32767	1	0	0	0
881021	203217	42.512	292.162	1	0.1	8	1	0	0	0
881021	203218	42.459	292.125	2	0.15	8	1	0	0	0
881021	203219	42.406	292.088	2	32767	32767	1	0	0	0

Table 8: Subset of 3d track data for 21 Oct 1988

Buoy #	Closest Dist. from track (Km)	SWH(m)
44005	39	0.6
44007	198	0.5
44008	15	1.3
44011	149	1.2
44013	194	0.9

Table 9: Buoy-SWH data for 21 Oct 1988 in the Gulf of Maine.

Error type 6 (E6): Consider the following partial listing of 3d track data for reported on 4 July 4 1989 in the Gulf of Maine (Table 10).

Date	Time	Latit.	Longit.	σh	swh	σswh	bit0	bit1	bit2	bit3
890704	144332	40.617	290.873	2	32767	32767	1	0	0	0
890704	144333	40.564	290.837	2	32767	32767	1	0	0	0
890704	144334	40.510	290.802	0	32767	32767	1	0	0	0
890704	144335	40.457	290.767	3	32767	32767	1	0	0	0
890704	144336	40.403	290.732	3	0.22	0	1	0	0	0
890704	144337	40.350	290.697	2	32767	32767	1	0	0	0
890704	144338	40.296	290.661	2	32767	32767	1	0	0	0

Table 10: Subset of 3d track data for 4 July 1989.

In all likelihood, the 5th record in the above table is erroneous, even though the flags field and rest of the parameters (associated with the D&P criteria) do not indicate so. Although reasonable close to buoy measurements (Table 11), this altimeter record may be suspect because the GDR is sandwiched between the other faulty GDRs (having, for example, on board instrumentation error denoted by 32767). Also, the parameter $\sigma_{swh} = 0$ for this GDR, which is doubtful. Such values are therefore considered erroneous and a criterion (E6) is used to flag them. Automatic detection of such errors is done by checking whether there are one or more "32767" type GDR's or other faulty GDR's preceding and following (thus sandwiching) the GDR in question.

Buoy #	Closest Dist. from track (Km)	SWH(m)
44005	39	0.7
44007	198	0.5
44008	15	0.7
44011	149	1.1
44013	194	0.3

Table 11: Buoy-SWH data for 4 July 1989 in the Gulf of Maine.

In tracks belonging to other classes in the Gulf of Maine, the behavior of erroneous SWH measurements is similar to that of those associated with 2d, 3d and 1d classes of tracks. A detailed analysis of data belonging to the other classes is therefore not presented. It can also be inferred that the cases discussed so far are representative of the editing criteria needed for data pertaining to satellite wave data covering any region in general. Table 12 gives a summary of the relative performance of each of the editing criteria applied to all the tracks in Gulf of Maine region. It is interesting to note that for tracks 1d & 2a, the new criteria actually eliminate more GDR's than the R criteria which are generally too stringent.

Data Extraction and Quality Control Program

The Gulf of Maine study described above led to the following criteria which were found to successfully and optimally eliminate GDR's (as presented on the CD-ROM's) with erroneous SWH measurements:

1. $\sigma_h \geq 10$ cm. [D&P, R and E4]
2. The height bias and satellite attitude were out of range determined from Flags field bit 2. [D&P]
3. Any one of the 10 per second heights was flagged as bad (Flags field bit 3). [D&P]
4. First record reported after a gap in the time sequence. [E1]
5. All GDRs with σ_{swh} greater than or equal to 12cm until σ_{swh} falls below 12cm, occurring immediately after a series (one or more) of GDRs with a land flag or a GDR with σ_h greater 10cm. [E3, R]
6. $SWH \leq 0.2$ m. [E5]
7. Record sandwiched between one or more GDRs above and below with instrumentation errors (32767 in SWH or σ_{swh} field) or other faulty GDRs.[E6]

GEOSAT data (during the ERM phase) presented to users on CD-ROM's (Cheney et al. 1991b) are sequential in time. Data for some of 34 oceanographic parameters are presented at intervals of 1 second during the satellite's spirograph-like track. This format is cumbersome if only SWH data for a particular area are needed. (The complexity is greater for the XDR's). To facilitate efficient usage, a computer program was developed to read the satellite data from the CD-ROMs, to filter the data according to the above criteria, and to output a filtered dataset for any rectangular region specified by 4 latitude/longitude coordinates.

track_0d	Total	%	track_1d	Total	%
Records	69		Records	417	
Landpoints(L)	69	100	Landpoints(L)	129	30.94
D&P	0	0	D&P	29	6.95
R	0	0	R	63	15.11
Q.C.Program (E)	0	0	Q.C.Program (E)	73	17.51

track_2d	Total	%	track_3d	Total	%
Records	1982		Records	2694	
Landpoints(L)	62	3.13	Landpoints(L)	0	0
D&P	99	4.99	D&P	69	2.56
R	917	46.27	R	942	34.97
Q.C.Program (E)	265	13.37	Q.C.Program (E)	191	7.09

track_4d	Total	%	track_5d	Total	%
Records	1293		Records	1265	
Landpoints(L)	14	1.08	Landpoints(L)	0	0
D&P	19	1.47	D&P	6	0.49
R	271	20.96	R	428	35.05
Q.C.Program (E)	73	7.81	Q.C.Program (E)	46	3.77

track_1a	Total	%	track_2a	Total	%
Records	1163		Records	738	
Landpoints(L)	72	6.19	Landpoints(L)	205	27.78
D&P	54	4.64	D&P	25	3.39
R	230	19.78	R	60	8.13
Q.C.Program (E)	120	10.32	Q.C.Program (E)	78	10.57

track_3a	Total	%	track_4a	Total	%
Records	3513		Records	3815	
Landpoints(L)	281	8	Landpoints(L)	120	3.15
D&P	25	0.71	D&P	36	0.94
R	465	13.24	R	519	13.60
Q.C.Program (E)	136	3.87	Q.C.Program (E)	105	2.75

track_5a	Total	%	track_6a	Total	%
Records	3964		Records	1528	
Landpoints(L)	97	2.45	Landpoints(L)	0	0
D&P	38	0.96	D&P	222	14.53
R	457	11.3	R	368	24.08
Q.C.Program (E)	131	3.3	Q.C.Program (E)	364	23.82

Table 12: Relative performance of editing criteria applied to data in the Gulf of Maine.

Validation of Data Extraction & Quality Control Program

The quality control program described above was based on data in the Gulf of Maine region (Fig. 2). In order to test the reliability and usefulness of the new criteria and the program, the program was applied to satellite wave data in the Gulf of Mexico region, bounded by coordinates [24° N, 268.5° E], [31° N, 268.5° E], [31° N, 274.25° E], [24.2° N, 274.25° E]. There are a total of 24 ERM tracks in the Gulf of Mexico region. Fig. 2 also shows the location of several buoys in this region. This

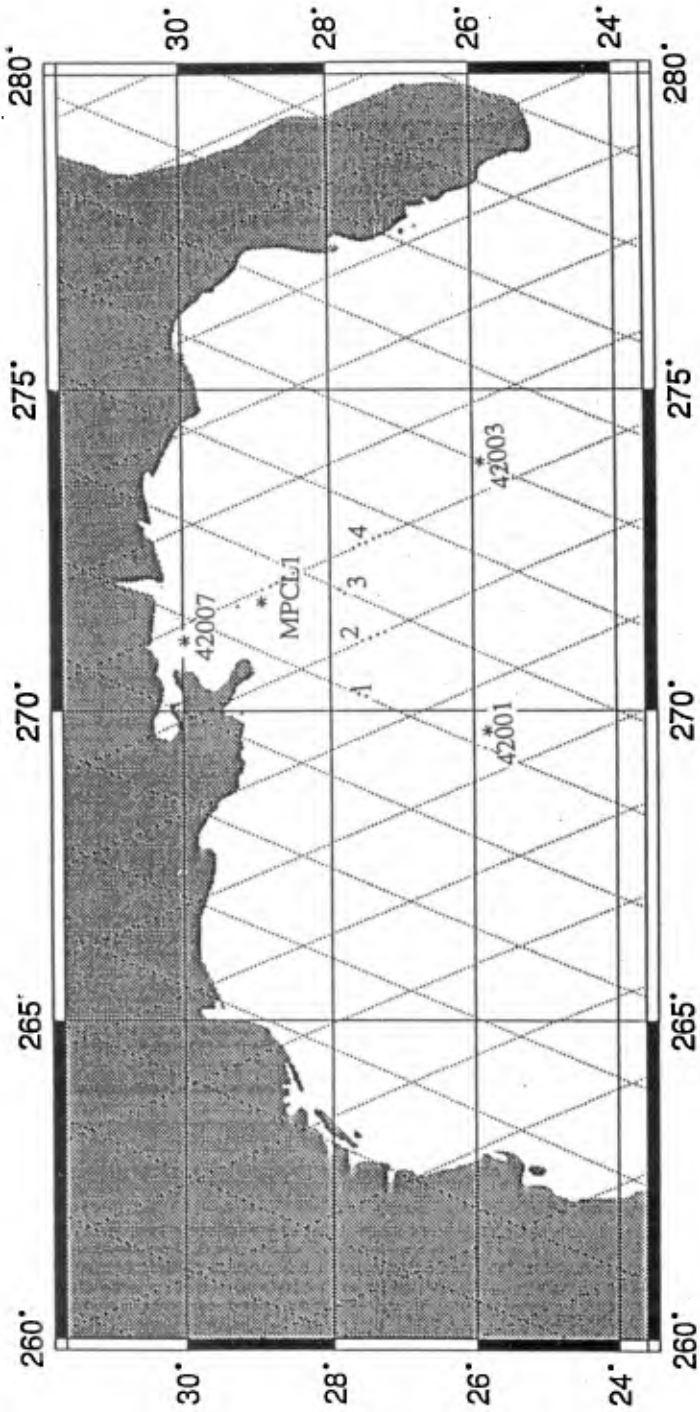


Fig. 2 Geosat satellite ground track and buoys in Gulf of Mexico

region is larger than the primary test site (i.e. Gulf of Maine). For the purpose of validation, data pertaining to 4 ERM tracks (each of which is a cluster of self-repeating tracks in the ERM phase of the satellite mission) falling in the study area were examined in detail. The satellite wave data are compared with measurements from the following 4 wave buoys in this region: 42001, 42003, MPCL1 and 42007. There are a total of 171 tracks, which fall into 4 track classes: 1, 2, 3, and 4 as shown in Fig. 2.

It was found that the program was extremely effective in automatic elimination of questionable data. The D&P criteria would have eliminated only 270 erroneous measurements, allowing several errors to escape detection. The R criteria, on the other hand, would eliminate 2067 records, many of which contain acceptable wave measurements. (In some instances data for the entire pass was discarded by the R criteria, even though most measurements agreed very well with buoy measurements). Application of the program developed here eliminates 1422 data records. The relative performance is given in Table 13. (For additional details, see Siddabathula, 1996).

Statistics for	Gulf Of	Mexico	Statistics for	Gulf of	Maine data
		data			
Records	17414		Records	22441	
Landpoints(L)	322	1.85	Landpoints (L)	1049	4.67
D&P	270	1.55	D&P	622	2.77
R	2067	11.87	R	4720	21.03
Q. C. Progr. (E)	1422	8.17	Q. C. Progr.(E)	1582	7.049

Table 13: Relative performance of editing criteria

Concluding Remarks

The Geosat wave data provide the most exhaustive ocean wave data ever obtained and the potential for using them for a variety of engineering applications (e.g. Panchang et al. 1997) is great. However the dataset available to the user community contain several erroneous wave measurements. Previous efforts at quality control have been largely driven by the synoptic use of these data and have led to criteria that either eliminate large quantities of acceptable data or allow erroneous data to escape detection. Unintentional use of these data can have an adverse influence on various applications. For example, Table 3 shows an SWH measurement of 10.17 m, which, as shown, is probably incorrect and can adversely influence wave statistics calculated with these data (e.g. Young, 1994; Panchang et al. 1997) or data assimilation for wave modeling (e.g. Lionello et al. 1992).

A visual examination of all of the ERM SWH data in the Gulf of Maine on a track-by-track basis in conjunction with wave buoy data led to a set of new criteria which eliminated nearly all the erroneous measurements with minimal loss of acceptable data. A computer program was developed to facilitate SWH data extraction from the CD-ROM's and to perform automatic quality control for any region bounded by 4 latitude/ longitude coordinates. This program may be obtained from the authors.

The criteria and the program were validated by application to satellite wave data in the Gulf of Mexico region. The overall results in Table 13 indicate that the

criteria were effective for quality control in the GDR's in both study areas. Application of the program developed here can prevent cumbersome visual inspection of SWH data by users (as done by Young, 1994; Romeiser, 1993). It may be also used for the Geosat Follow-On mission for post-processing the results of existing data-processing algorithms prior to installation on CD-ROMs for the users.

Acknowledgments: This work was supported in part by NASA and NOAA (Gulf of Maine-RMR Program).

References

- Brooks R. L., D. W. Lockwood and D. W. Hancock III (1990): Effects of Islands in the Geosat Footprint. *Jnl. Geophys. Res.*, v95, c3, 2849-2855.
- Cheney R. E. et al. (1991a): Geosat Altimeter Crossover Difference Handbook. NOAA Manual NOS NGS 6.
- Cheney, R.E., N.S. Doyle, B.C. Douglas, R.W. Agreen, L. Miller, E.L. Timmerman, and D.C. McAdoo (1991b). The complete Geosat altimeter GDR handbook, NOAA Manual NOS NGS 7, National Ocean Service, Rockville, MD.
- Dobson E. and Porter D. (1989). World statistics of wind speed and significant wave height from the Geosat altimeter. JHU/APL S1R89U-007.
- Dobson E., F. Monaldo, J. Goldhirsh & J. Wilkerson (1987). Validation of Geosat Altimeter-Derived Wind Speeds and Significant Wave Heights Using Buoy Data. *Jnl. Geophys. Res.*, v92, c10, 10719-10731.
- Franklin B. H. (1992). NDBC Data Availability Summary. Stennis Space Center., US Dept. of Commerce, National Oceanic and Atmospheric Administration.
- Hayne G. S. and D. W. Hancock III (1990): Corrections for the Effects of Significant Wave Height and Attitude on Geosat Radar Altimeter Measurements. *Jnl. Geophys. Res.*, v95, c3, 2837-2842.
- Lionello P., H. Gunther, and P. A. E. M. Janssen (1992). Assimilation of Altimeter Data in a Global Third-Generation Wave Model. *Jnl. Geophys. Res.* 97, c9, 14,453-14,474.
- Laxon S.W. and C. G. Rapley (1987). Radar altimeter data quality flagging. *Adv. Space Res.*, v7, No.11, 11315-11318.
- Romeiser R. (1993). Global Validation of the Wave Model WAM Over a One-Year Period Using Geosat Wave Height Data. *Jnl. Geophys. Res.*, v98. c3, 4713-4726.
- Panchang, V. G., L. Zhao, & M. Siddabathula (1997). Estimation of Extreme Wave Heights using GEOSAT Data. Submitted, Jnl Waterways, Port, Coastal & Ocean Engg.
- Siddabathula M. (1996). Quality Control of Geosat satellite and buoy measurements in Gulf of Maine. M.S. thesis, Dept. of Civil & Environmental Eng. Univ. of Maine, Orono, ME 04469.
- Siddabathula M. and Panchang V. G. (1996). Wave data from Geosat satellite and buoy measurements in Gulf of Maine. Tech Report, Dept. of Civil & Environmental Engg. Univ. of Maine, Orono.
- Young I. R. (1994). Global ocean wave statistics obtained from satellite observations. *Applied Ocean Research*, v16, No.4, 235-248.

CHAPTER 8

BOUSSINESQ TYPE EQUATIONS WITH HIGH ACCURACY IN DISPERSION AND NONLINEARITY

P.A. Madsen*, B. Banijamali*, H.A. Schäffer* and O.R. Sørensen*

Abstract

Two sets of Boussinesq type equations with high accuracy in dispersion as well as in nonlinearity are presented. The first set, which is expressed in terms of the depth-averaged velocity, includes up to fifth-derivative terms in the momentum equation, while the second set, which is expressed in terms of the velocity at an arbitrary z-level, includes up to third-derivative terms in the continuity equation as well as in the momentum equation. Both sets of equations provide linear dispersion characteristics, which are accurate for wave numbers (kh) up to 6, and nonlinear characteristics which are superior to previous Boussinesq formulations. The high quality of dispersion is also achieved for the Doppler shift in connection with wave-current interaction. A numerical model based on the new equations in two horizontal dimensions is presented and verified with respect to nonlinear transformation of waves in shallow water and refraction-diffraction in deep and shallow water.

1. Introduction

The classical Boussinesq equations as formulated by e.g. Peregrine (1967) are known to incorporate only weak dispersion and weak nonlinearity. For many applications the weak dispersion is the most critical limitation and it has achieved considerable attention in the last 5 years, where a number of alternative lower order Boussinesq type equations have been presented with the purpose of improving the linear dispersion characteristics (see e.g. Madsen et al., 1991; Nwogu, 1993; Schäffer and Madsen, 1995). It has been demonstrated that the accuracy of the dispersion for larger wave numbers is sensitive to the choice of velocity equa-

* International Research Centre for Computational Hydrodynamics (ICCH). Located at the Danish Hydraulic Institute, Ager Alle 5, DK-2970 Hørsholm, Denmark

tions, and with minor modifications the lower order Boussinesq type equations can incorporate significantly improved dispersion characteristics. A similar improvement of the nonlinear properties is more difficult to obtain and will be addressed in this work.

This paper presents two sets of Boussinesq type equations with high accuracy in dispersion (μ) as well as in nonlinearity (ϵ). The first set, which is expressed in terms of the depth-averaged velocity, includes dispersive terms of order μ^4 and nonlinear terms up to order $\epsilon^5\mu^4$ (Chapter 3). The second set, which is expressed in terms of the velocity at an arbitrary z -level, includes dispersive terms of order μ^2 and nonlinear terms up to order $\epsilon^3\mu^2$ (Chapter 4). Using the technique suggested by Madsen et al. (1991) and Schäffer and Madsen (1995) we enhance the new equations and obtain excellent linear dispersion characteristics corresponding to a Pade [4,4] expansion of linear Stokes theory. A Fourier analysis also demonstrates that the accuracy of the nonlinear energy transfer is improved considerably compared to previous Boussinesq formulations. This allows for a much more accurate description of wave-wave interactions in irregular wave trains. Finally, it turns out that the high quality of dispersion is also achieved for the Doppler shift in connection with wave-current interaction and it allows for a study of wave-blocking due to opposing currents. These aspects will be studied in a companion paper at this conference by Chen et al. (1996).

A numerical model based on the new equations from Chapter 4 is presented in Chapter 5 and it is verified with respect to nonlinear transformation of waves in shallow water and refraction-diffraction in deep and shallow water.

2. Derivation of Boussinesq type equations

In the following presentation the adopted coordinate system is Cartesian with the x' -axis and y' -axis located at the still water level (SWL) and with the z' -axis pointing vertically upwards. The fluid domain is bounded by the sea bed at $z' = -h'(x', y')$ and the free surface at $z' = \eta'(x', y', t')$. Non-dimensional variables (denoted without primes) are introduced in the conventional way (see e.g. Nwogu, 1993) by the use of a characteristic water depth (h_0), wave length (l_0) and wave amplitude (a_0) and we introduce the classical measures of nonlinearity and frequency dispersion by $\epsilon = a_0/h_0$ and $\mu = h_0/l_0$.

With the usual assumptions of irrotational flow in an incompressible fluid, the nondimensional form of the governing equations and boundary conditions read:

$$\Phi_{zz} + \mu^2 \nabla^2 \Phi = 0, \quad -h < z < \epsilon \eta \quad (1a)$$

$$\Phi_z + \mu^2 \nabla h \cdot \nabla \Phi = 0, \quad z = -h \quad (1b)$$

$$\Phi_t + \eta + \frac{\epsilon}{2} \left((\nabla\Phi)^2 + \frac{1}{\mu^2} (\Phi_z)^2 \right) = 0, \quad z = \epsilon\eta \quad (1c)$$

$$\Phi_z - \mu^2(\eta_t + \epsilon\nabla\eta \cdot \nabla\Phi) = 0, \quad z = \epsilon\eta \quad (1d)$$

where Φ is the velocity potential and ∇ the horizontal gradient operator.

The basic idea in Boussinesq-type derivations is to reduce the three dimensional description to a two-dimensional one and this is achieved by expanding the velocity potential as a power series in the vertical coordinate:

$$\Phi(x, y, z, t) = \sum_{n=0}^{\infty} z^n \Phi^{(n)}(x, y, t) \quad (2)$$

by which $\Phi^{(0)}(x, y, t) = \Phi(x, y, 0, t)$. While traditional Boussinesq theory assumes $\mu < 1$ and $\epsilon = O(\mu^2)$, the present expansion allows for arbitrary ϵ .

The individual steps in the derivation of Boussinesq-type equations are as follows: Firstly, the velocity potential is determined in terms of spatial derivatives of $\Phi^{(0)}$ by combining (2) with (1a) and (1b). By the use of the gradient operator this also defines the horizontal velocity vector in terms of the velocity, \hat{u} at the still water level. Secondly, the velocity potential is inserted in the dynamic free surface condition (1c), and by using the horizontal gradient operator a momentum equation is derived in terms of \hat{u} . Thirdly, the horizontal velocity vector expressed in terms of \hat{u} is substituted into the depth-integrated continuity equation. The resulting equations in terms of \hat{u} can be found in Madsen & Schäffer (1996) and will not be given here.

3. Equations in terms of the Depth-Averaged Velocity

Traditionally, Boussinesq models are not based on equations formulated in terms of the velocity at the still water level. This is partly because of the rather complicated form of the continuity equation expressed in this variable and partly because of the relatively poor dispersion characteristics of these equations. A more common choice is the depth-averaged velocity U which is defined by

$$U \equiv \frac{1}{h + \epsilon\eta} \int_{-h}^{\epsilon\eta} u dz \quad (3)$$

One of the obvious advantages of using this variable is that the continuity equation becomes exact and relatively simple,

$$\eta_t + \nabla \cdot (\bar{h} + \epsilon \eta) \mathbf{U} = 0 \quad (4)$$

3.1. Formulation of momentum equations

In order to formulate the momentum equation in terms of \mathbf{U} we use the procedure as follows: Firstly, a relation in which \mathbf{U} is expressed in terms of \hat{u} is established by the use of (2) and (3). Secondly, this relation is inverted into a relation in which \hat{u} is expressed in terms of \mathbf{U} , by the use of successive substitutions starting at lowest order in μ^2 . Now \hat{u} can be eliminated from the momentum equation and replaced by functions of \mathbf{U} . The resulting higher order momentum equations truncated at the order μ^6 take the form of

$$\mathbf{U}_t + \nabla \eta + \frac{\epsilon}{2} \nabla (U^2) + \mu^2 \mathbf{\Gamma}_2^I + \mu^4 \mathbf{\Gamma}_4^I = 0 (\mu^6) \quad (5)$$

where

$$\mathbf{\Gamma}_2^I \equiv [\mathbf{\Lambda}_{20}^I + \epsilon \mathbf{\Lambda}_{21}^I + \epsilon^2 \mathbf{\Lambda}_{22}^I + \epsilon^3 \mathbf{\Lambda}_{23}^I] \quad (6a)$$

$$\mathbf{\Gamma}_4^I \equiv [\mathbf{\Lambda}_{40}^I + \epsilon \mathbf{\Lambda}_{41}^I + \epsilon^2 \mathbf{\Lambda}_{42}^I + \epsilon^3 \mathbf{\Lambda}_{43}^I + \epsilon^4 \mathbf{\Lambda}_{44}^I + \epsilon^5 \mathbf{\Lambda}_{45}^I] \quad (6b)$$

Notice that $\mathbf{\Lambda}_{mn}^I$ is used to express the Boussinesq terms, where subscript m accounts for the power of μ (dispersion) and subscript n for the power of ϵ (non-linearity). The equations include full nonlinearity up to the truncated order of dispersion, i.e. retaining $\epsilon^3 \mu^2$ and $\epsilon^5 \mu^4$ -terms, and involve higher order spatial derivatives incl. third and fifth-derivative terms. The actual expressions for the $\mathbf{\Lambda}_{mn}^I$ -terms can be found in Madsen & Schäffer (1996) and will not be given here. We note that if only terms up to the order $O(\epsilon, \mu^2)$ are retained we obtain the classical Boussinesq equations by Peregrine (1967) and if terms of order $O(\epsilon \mu^2, \mu^4)$ are retained as well we obtain the higher order Boussinesq equations by Dingemans (1973).

The final step in the derivation procedure is to apply the technique introduced by Madsen et al. (1991) and Schäffer & Madsen (1995) for improving the dispersion characteristics of (4) and (5). This procedure is illustrated on a horizontal bottom in the following: Firstly, (5) is truncated omitting $O(\mu^4)$, the gradient operator is applied twice and the result is multiplied by $\alpha \mu^2 h^2$, where α is a free parameter of the order $O(1)$:

$$\alpha \mu^2 h^2 \nabla^2 \left(\mathbf{U}_t + \nabla \eta + \frac{\epsilon}{2} \nabla (U^2) + \mu^2 \mathbf{\Gamma}_2^I \right) = 0 (\mu^6) \quad (7a)$$

Secondly, (5) is truncated omitting $O(\mu^2)$, the gradient operator is applied four times and the result is multiplied by $\beta\mu^4h^4$, where β is a free parameter of the order $O(1)$:

$$\beta\mu^4h^4\nabla^4\left(\mathbf{U}_t + \nabla\eta + \frac{\epsilon}{2}\nabla(U^2)\right) = O(\mu^6) \quad (7b)$$

We can now consistently modify (5) by subtracting (7a) and adding (7b), which yields an enhanced set of higher order Boussinesq equations truncated at $O(\mu^6)$. The coefficients α and β are yet to be determined.

3.2. Fourier Analysis for weakly nonlinear waves

Although the equations have been derived under the assumption of $\mu \ll 1$ and $\epsilon = O(1)$, we shall analyse the imbedded linear and nonlinear characteristics by assuming that $\epsilon < 1$ while μ is arbitrary. We look for analytical solutions of the form

$$\eta = a_1\cos(\omega t - kx) + \epsilon a_2\cos(2\omega t - 2kx) \quad (8a)$$

$$U = U_1\cos(\omega t - kx) + \epsilon U_2\cos(2\omega t - 2kx) \quad (8b)$$

At first order (ϵ^0) non-trivial solutions require the dispersion relation

$$\frac{\omega^2}{k^2h} = \frac{1 + \alpha k^2h^2 + \beta k^4h^4}{1 + \left(\alpha + \frac{1}{3}\right)k^2h^2 + \left(\beta + \frac{\alpha}{3} - \frac{1}{45}\right)k^4h^4} \quad (9)$$

which should be compared with Stokes relation for linear waves on arbitrary depth, i.e. $\tanh(kh)/kh$. The ratio between the two expressions is shown as a function of kh in Fig 1. If we omit the enhancement of the higher order equations using $(\alpha, \beta) = (0, 0)$ the resulting dispersion relation (9) corresponds to a Padé [0,4] expansion in kh of the Stokes relation. For these equations the deviation is significant and in fact a singularity occurs for $kh = 4.2$. This singularity shows up in numerical calculations as an instability even in the case of initially calm water, and actually makes (5) quite useless without the enhancement. On the other hand, by using the enhanced equations incl. (7a-b) with $\alpha = 1/9$ and $\beta = 1/945$ the resulting dispersion relation (9) corresponds to a Padé [4,4] expansion. This is an extremely good approximation to the exact linear relation even for kh as large as 6. The dispersion relation of lower order Boussinesq equations is obtained by ignoring the k^4h^4 terms in (9). With $\alpha = 0$ (Padé [0,2]) this corresponds to the classical equations of Peregrine (1967) and with $\alpha = 1/15$ it corresponds to the Padé

[2,2] formulation introduced by Madsen et al. (1991). Both cases are shown as a reference in Fig 1.

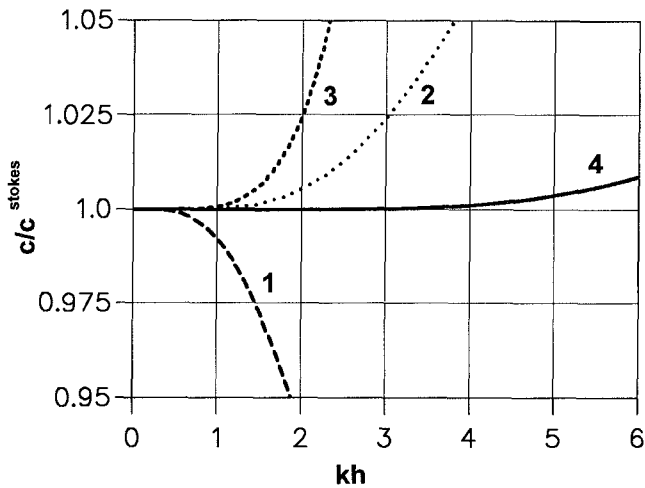


Fig 1 Relative phase celerity, c/c^{Stokes} , for various forms of the Boussinesq equations. 1: Padé [0,2]; 2: Padé [2,2]; 3: Padé [0,4]; 4: Padé [4,4].

Extending the Fourier analysis to second order we determine a_2 in terms of a_1^2/h times a transfer function. In this respect the target solution is

$$a_2^{\text{Stokes}} = \frac{1}{4} \frac{a_1^2}{h} kh \coth(kh) (3 \coth^2(kh) - 1) \quad (10)$$

according to Stokes second order theory. Fig 2 shows the variation of a_2/a_2^{Stokes} as a function of kh . The curve corresponding to the new higher order equations is seen to be superior to the results obtained from the equations of Dingemans (1973) and Peregrine (1967).

It is straight-forward to extend the Fourier analysis to second order sub-harmonics and super-harmonics and the results can be found in Madsen and Schäffer (1996).

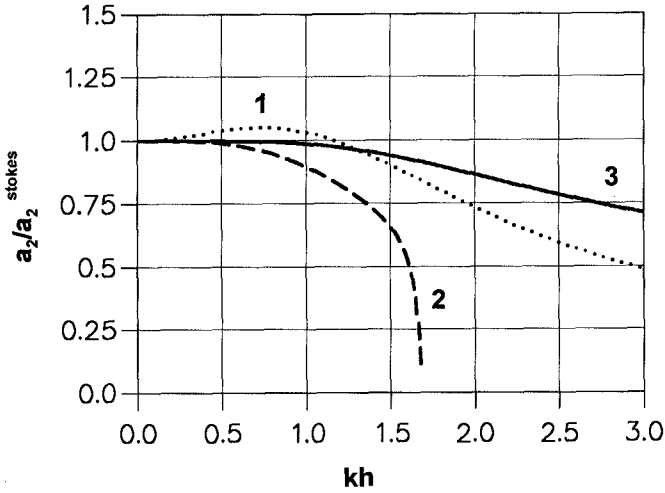


Fig 2 Ratio of second harmonic, a_2/a_2^{Stokes} . 1: Peregrine (1967); 2: Dingemans (1973) 3: Present e.g. eqs. (4) & (5) with (7a-b), $\alpha=1/9$, $\beta=1/945$.

3.3 Ambient currents and Doppler shift

Yoon and Liu (1989) introduced separate scaling of waves and currents and showed that additional terms were to be added to the classical formulation of Peregrine (1967) if a correct Doppler shift was to be obtained in connection with ambient currents. In the present work we analyse the new equations for the case of a strong but constant ambient current U_c and obtain the following dispersion relation,

$$\frac{(\omega - kU_c)^2}{k^2h} = \frac{1 + \alpha k^2h^2 + \beta k^4h^4}{1 + \left(\alpha + \frac{1}{3}\right)k^2h^2 + \left(\beta + \frac{\alpha}{3} - \frac{1}{45}\right)k^4h^4} \quad (11)$$

This provides a correct Doppler shift including Padé [4,4] dispersion characteristics. Fig. 3 shows lines of 2 per cent wave number errors as a function of $(F, h/L_0)$, F being the Froude number (U_c/\sqrt{gh}) of the current and L_0 being the deep water wave length for the case of no currents. The application range of the Padé [4,4] curve is seen to be superior to the Padé [0,2] corresponding to Yoon & Liu's formulation as shown for comparison.

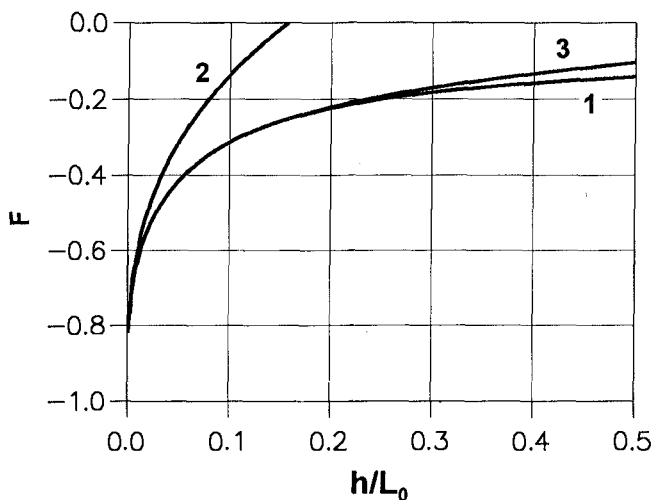


Fig 3 Waves on ambient currents. 1: Blocking curve according to Stokes theory. Tracks of 2 per cent wave number errors, $(k-k^{\text{Stokes}})/k^{\text{Stokes}}$:
 2: Yoon & Liu (1989), Padé [0,2]; 3: New equations (11), Padé [4,4]

4. Equations in terms of the velocity at an arbitrary z-location

In the previous section we have demonstrated that highly accurate linear dispersion and nonlinear characteristics can be obtained by formulating higher order equations including up to fifth-derivative terms in the momentum equation. In this section we shall, however, show that almost the same accuracy can be obtained with only third-derivative terms, if the lower order equations are formulated in terms of the velocity vector at an arbitrary z-location i.e.

$$\tilde{\mathbf{u}} \equiv \mathbf{u}(x, y, \tilde{z}, t) \quad (12)$$

This variable was introduced by Nwogu (1993).

From the expression derived for the velocity potential we can establish an expression for $\tilde{\mathbf{u}}$ in terms of $\hat{\mathbf{u}}$. This relation is then inverted into a relation in which $\hat{\mathbf{u}}$ is expressed in terms of $\tilde{\mathbf{u}}$, by the use of successive substitutions starting at lowest order in μ^2 . Now $\hat{\mathbf{u}}$ can be eliminated from the original mass and momentum equations and replaced by functions of $\tilde{\mathbf{u}}$ and the resulting equations truncated at the order μ^4 take the form of

$$\eta_t + \nabla \cdot (\tilde{\mathbf{u}}(h + \epsilon \eta) + \mu^2 \Gamma_2'') = 0(\mu^4) \quad (13a)$$

$$\tilde{u}_t + \nabla\eta + \frac{\epsilon}{2}\nabla(\tilde{u}^2) + \mu^2\Gamma_2^{III} = O(\mu^4) \quad (13b)$$

where

$$\Gamma_2^{II} \equiv \left[\Lambda_{20}^{II} + \epsilon\Lambda_{21}^{II} + \epsilon^2\Lambda_{22}^{II} + \epsilon^3\Lambda_{23}^{II} \right] \quad (14a)$$

$$\Gamma_2^{III} \equiv \left[\Lambda_{20}^{III} + \epsilon\Lambda_{21}^{III} + \epsilon^2\Lambda_{22}^{III} + \epsilon^3\Lambda_{23}^{III} \right] \quad (14b)$$

These equations, which were first derived by Wei et al. (1995), include full nonlinearity up to the truncated order of dispersion i.e. retaining $\epsilon^3\mu^2$. If only terms up to the order $O(\epsilon, \mu^2)$ are retained we obtain the equations of Nwogu (1993). With a specific choice of the z-location defining the velocity variable, Nwogu and Wei et al. achieved Padé [2,2] dispersion characteristics.

Here we shall further enhance the equations (13a-b) to improve dispersion as well as nonlinearity. Again we apply the technique as described in section 3 and illustrate the procedure on a horizontal bottom: Firstly, (13a & b) are truncated omitting $O(\mu^2)$, the gradient operator is applied twice and the results are multiplied by μ^2h^2 and two free parameters (α, β) which are of the order $O(1)$:

$$\alpha\mu^2h^2\nabla^2\left(\tilde{u}_t + \nabla\eta + \frac{\epsilon}{2}\nabla(\tilde{u}^2)\right) = O(\mu^4) \quad (15a)$$

$$\beta\mu^2h^2\nabla^2(\eta_t + \nabla\cdot(\tilde{u}(h+\epsilon\eta))) = O(\mu^4) \quad (15b)$$

We can now consistently modify (13a-b) by subtracting (15a-b), which yields an enhanced set of lower order Boussinesq equations. The detailed formulation is given in Madsen & Schäffer (1996).

The linear dispersion relation of the enhanced equations reads

$$\frac{\omega^2}{k^2h} = \frac{1 + \left(\alpha + \beta - \gamma - \frac{1}{3}\right)k^2h^2 + \alpha\left(\beta - \gamma - \frac{1}{3}\right)k^4h^4}{1 + (\alpha + \beta - \gamma)k^2h^2 + \beta(\alpha - \gamma)k^4h^4} \quad (16)$$

where

$$\gamma \equiv \frac{\tilde{z}}{h} + \frac{1}{2}\left(\frac{\tilde{z}}{h}\right)^2 \quad (17)$$

As shown by Schäffer & Madsen (1995) Padé [4,4] characteristics can be obtained by choosing one of four different sets of parameters. It turns out that one of these

sets is superior with respect to nonlinear properties, hence we recommend the parameter set

$$(\gamma, \beta, \alpha) = \left(\frac{-3 - \sqrt{23/35} - 2\sqrt{19/7}}{18}, \frac{28 - 2\sqrt{133}}{126}, \frac{105 - 3\sqrt{805}}{1890} \right) \quad (18)$$

Extending the Fourier analysis to second order we determine a_2 in terms of a_1^2/h times a transfer function. Fig 4 shows the variation of a_2/a_2^{Stokes} as a function of kh . We notice that the curve corresponding to the new enhanced equations is superior to the results obtained from Nwogu's and Wei et al's equations as shown for comparison. A full analysis of second order sub-harmonics and super-harmonics can be found in Madsen and Schäffer (1996).

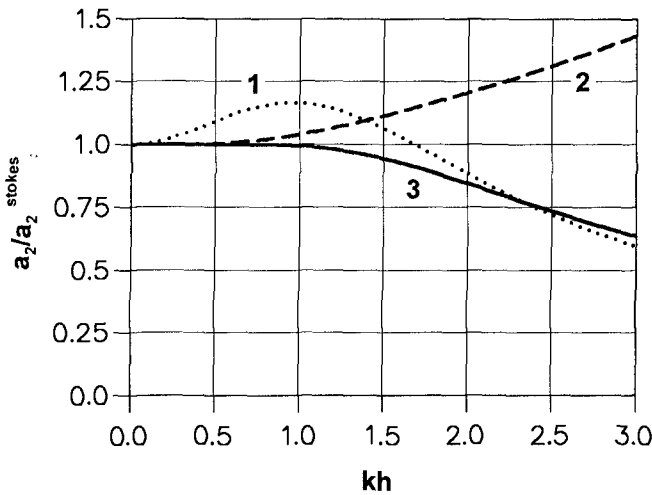


Fig 4 Ratio of second harmonic, a_2/a_2^{Stokes} . 1: Nwogu (1993); 2: Wei et al. (1995); 3: Present e.g. eqs. (13a-b) with (15a-b) & (18).

5. Numerical model and its verification

A numerical model has been developed to solve the two-dimensional equations formulated in Chapter 4. The equations are discretized in space by applying higher order central-differencing with the variables defined on a space-staggered rectangular grid while the temporal integration is performed by using a fourth order Adams-Bashforth-Moulton predictor-corrector method. More details about the numerical method can be found in Banijamali et al. (1997).

5.1 Wave transformation over a submerged bar

One of the most demanding tests for Boussinesq-type models is the study of wave transformation over a submerged bar. In this case nonlinearity increases considerably during the propagation at the upward slope and results in energy transfer to the higher harmonics. As long as the depth is decreasing the higher harmonics will be bound or phase-locked to the primary wave train, but on the downward slope the harmonics will be released and propagate as free waves. This introduces the peculiarity that a linear regular shallow water wave will be converted into a linear irregular deep water wave after the passage over the bar. This situation calls for highly accurate dispersion characteristics and for this reason most Boussinesq models fail to predict the process.

Beji and Battjes (1993) and Luth et al. (1994) presented a series of accurate measurements of wave transformation over a trapezoidal bar with an upward slope of $1/20$, a downward slope of $1/10$, a depth of 40 cm on both sides of the bar and 10 cm on top of the bar (Fig 6a). The data have previously been used in an inter-comparison study in MAST-G8M, see Dingemans (1994). As one example from this test series we have selected the case of a wave period of 2.02s and a wave height of 2.0 cm.

Fig 5 shows the measured time series of surface elevations at three locations: We notice the transformation from a sinusoidal, linear-wave profile at $x=5.2\text{m}$, to a profile of a strongly nonlinear wave at $x=13.5\text{m}$ and back to a profile of a fairly linear wave at $x=19.0\text{m}$, where the significant frequency obviously has been doubled.

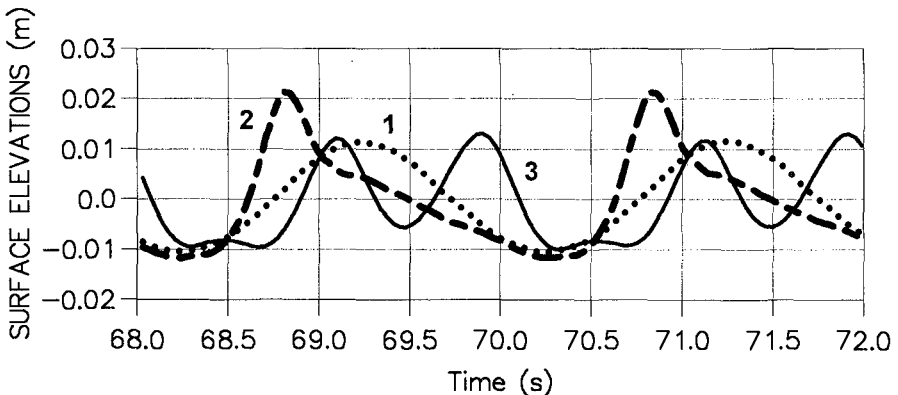


Fig 5 Harmonic generation over a submerged bar.
Measured timeseries of surface elevations at three locations
Input: wave period=2.02s, wave height=0.02m, 1: $x=5.2\text{m}$;
2: $x=13.5\text{m}$ and 3: $x=19.0\text{m}$.

The energy transformation to higher harmonics is in fact seen more clearly in Fig 6b-c, which is based on FFT analysis of time series from a numerical solution of the Boussinesq equations. Here we clearly notice the rapid growth of the second

(and third) harmonics at the upward slope and the release of these harmonics after the bar.

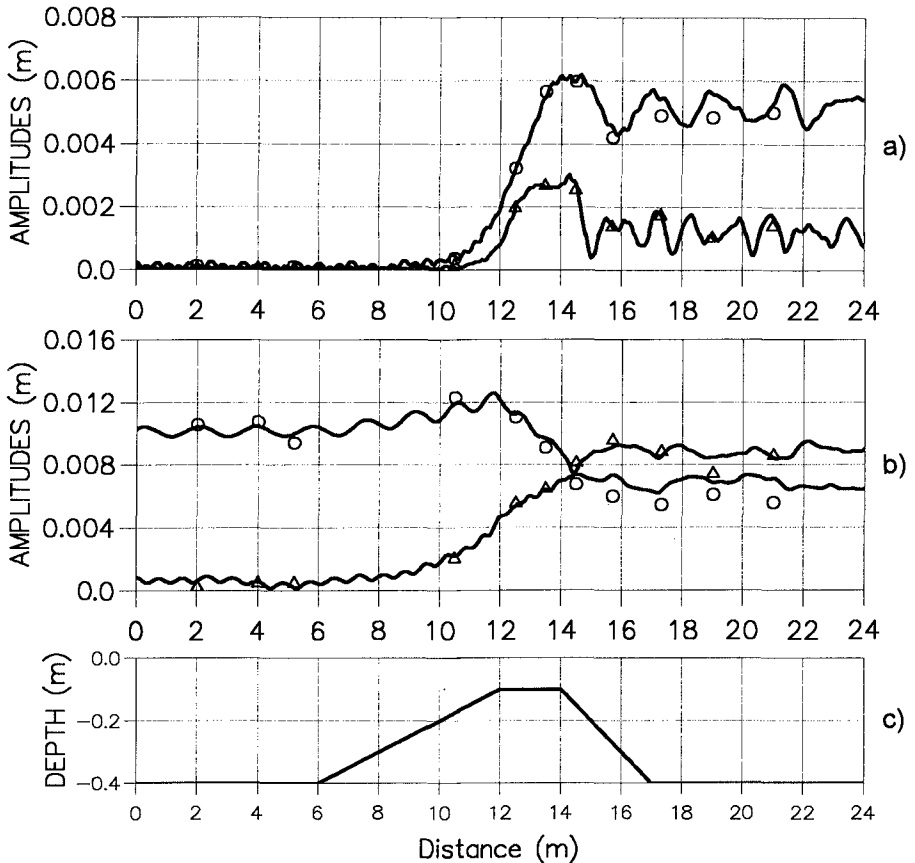


Fig 6 Harmonic generation over a submerged bar
 a) Spatial evolution of harmonics (third & fourth); b) Spatial evolution of harmonics (first & second); c) Bathymetry
 Markers are measurements.

In Fig 7 we compare the measured time series at $x=21.0$ m with the numerical results corresponding to two different versions of the Boussinesq model: One using $(\gamma, \alpha, \beta) = (-2/5, 0, 0)$ leading to Padé [2,2] dispersion characteristics (corresponding to the model of Wei et al., 1995) and one using the parameter set of (18) leading to Padé [4,4] characteristics.

The latter is seen to be superior and it provides a highly accurate result.

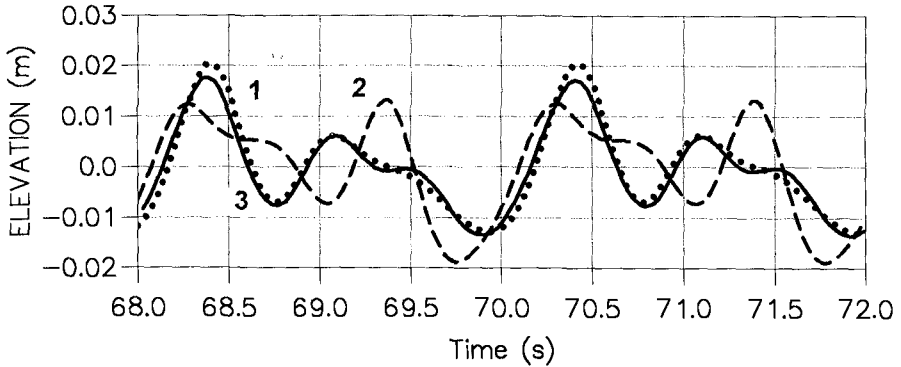


Fig 7 Computed and measured surface elevations at $x=21\text{m}$
 1: Eqs. (13a-b) with (15a-b) & (18), Padé [4,4] 2: Wei et al. (1995), Padé [2,2] 3: Measurements

5.2 Nonlinear refraction-diffraction

As a second demanding test for the Boussinesq model we study nonlinear refraction-diffraction over a semicircular shoal with depth contours varying between 0.4572m and 0.1524m as investigated experimentally by Whalin (1971).

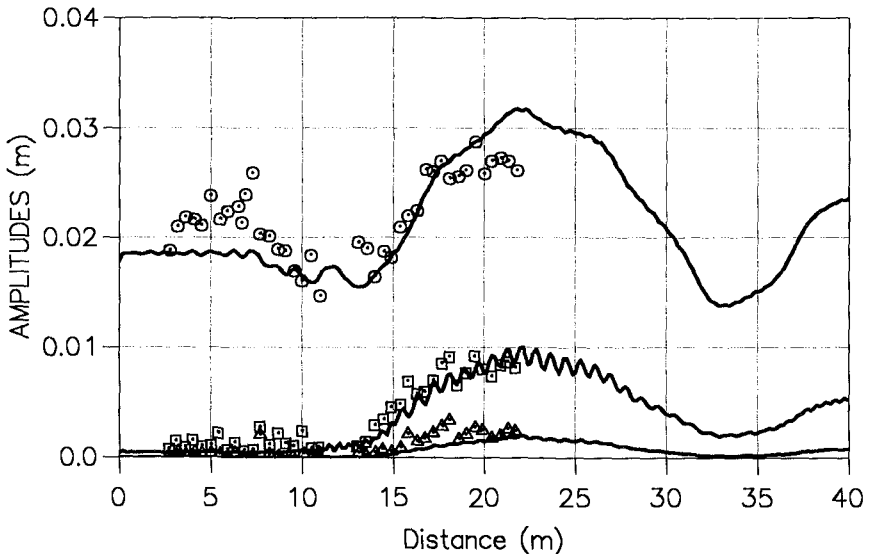


Fig 8 Whalin's nonlinear refraction-diffraction. Spatial evolution of first and second harmonics along the centreline. Input: wave period = 1.0s, wave height = 0.039m. Markers are measurements.

In the present work we focus on the case of incoming regular waves with period 1.0s and wave height 0.039m. At the boundary the waves are linear but after the focusing on the shoal higher harmonics become significant due to nonlinear effects. An FFT analysis of time series in each grid point along the centreline has been computed and the resulting spatial evolution of first and second harmonics is compared with Whalin's experimental data in Fig 8. The agreement is found to be most acceptable.

Acknowledgement

This work has been financed by the Danish National Research Foundation. Their support is greatly appreciated.

References

- Beji, S. and J.A. Battjes (1993), "Experimental investigation of wave propagation over a bar", *Coastal Engineering*, Vol. 19, pp 151-162.
- Banijamali, B., O.R. Sørensen, and P.A. Madsen (1997), "A numerical model for enhanced Boussinesq type equations", In preparation.
- Chen, Q., P.A. Madsen, O.R. Sørensen, and D. Basco (1996), "Boussinesq type equations with improved Doppler shift for wave/current interaction", ICCE, Orlando 1996.
- Dingemans, M. (1973), "Water waves over an uneven bottom; a discussion of long-wave equations". Delft Hydraulics Report R729 part 2, 88p.
- Dingemans, M. (1994), "Comparison of computations with Boussinesq-like models and laboratory measurements", MAST-G8M note, H1684, Delft Hydraulics, 32pp.
- Luth, H.R., G. Klopman, and N. Kitou (1994), "Project 13G: Kinematics of waves breaking partially on an offshore bar; LDV measurements for waves with and without a net onshore current". Delft Hydraulics Report H1573, March 1994, 40pp.
- Madsen, P.A., R. Murray and O.R. Sørensen (1991), "A new form of the Boussinesq equations with improved linear dispersion characteristics. Part 1", *Coastal Engineering*, Vol 15, pp 371-388.
- Madsen, P.A. and H.A. Schäffer (1996), "Higher order Boussinesq-type equations - Derivation and Analysis". Submitted for publication, 80 pp.
- Nwogu, O. (1993), "Alternative form of Boussinesq equations for nearshore wave propagation", *J. WatWays, Port, Coastal Ocean Engrg.*, ASCE, 119(6), pp 618-638.
- Peregrine, D.H. (1967), "Long waves on a beach", *Journal of Fluid Mechanics*, Vol 27, pp 815-827.
- Schäffer, H.A. and P.A. Madsen (1995), "Further enhancements of Boussinesq-type equations". *Coastal Engineering*, Vol 26, pp 1-14.
- Yoon, S.B. and P.L.-F. Liu (1989), "Interactions of currents and weakly nonlinear water waves in shallow water", *Journal of Fluid Mechanics*, Vol 205, pp 397-419.
- Wei, G., J.T. Kirby, S.T. Grilli, and R. Subramanya (1995), "A fully nonlinear Boussinesq model for surface waves", *Journal of Fluid Mechanics*, Vol 294, pp 71-92.
- Whalin, R.W. (1971), "The limit of applicability of linear wave refraction theory in a convergence zone", Res. Rep. H-71-3, U.S. Army Corps of Engineers, Waterways Expt. Station, Vicksburg, MS.

CHAPTER 9

WAVE KINEMATICS COMPUTATIONS USING BOUSSINESQ MODELS

J. Bosboom^{1,2}, G. Klopman^{1,2}, J.A. Roelvink^{1,2}, J.A. Battjes¹

ABSTRACT

Existing Boussinesq models are extended to include the computation of the vertical structure of the horizontal velocity. A time-domain model is tested against laboratory measurements of the vertical profile of the horizontal velocity in regular waves; good results are obtained, especially in the near-bed zone. A spectral model, which includes a dissipation formulation to account for wave breaking, is tested against laboratory measurements of bottom velocities in (partially) breaking irregular waves. For moderately long waves, the comparison on velocity variance and skewness, which are relevant to sediment transport, yields good results.

1. INTRODUCTION

The development of numerical models capable of reproducing the hydrodynamics field in the shoaling region and the surf zone is of particular interest to coastal morphological problems. From an evaluation of sediment transport formulations (Bailard, 1981; Roelvink and Stive, 1989), it appears that the third and fourth order oscillatory velocity moments ($\langle u^3 \rangle$ and $\langle |u|^3 u \rangle$ respectively), are the most important parameters in determining the magnitude of the wave-induced sediment transport. These moments are non-zero only for asymmetric (non-linear) motions such as occur in shallow water. Boussinesq equations, describing (weakly) non-linear, relatively long waves propagating in water of varying depth, are suitable for the description of these asymmetries.

Many different forms of Boussinesq equations exist, which differ in frequency-dispersion and shoaling characteristics. Efforts have recently been spent on

-
- 1) Netherlands Centre for Coastal Research (NCK), Department of Civil Engineering, Delft University of Technology, PO Box 5048, 2600 GA Delft, The Netherlands
 - 2) DELFT HYDRAULICS, PO Box 177, 2600 MH Delft, The Netherlands

improving the linear frequency dispersion with respect to the conventional Boussinesq equations. Reference is made to Witting (1984), Madsen et al. (1991), Madsen and Sørensen (1992), Nwogu (1993), Dingemans (1994b) and Schröter (1995).

On the basis of these time-domain formulations, frequency-domain formulations have been developed leading to coupled evolution equations for slowly-varying complex Fourier amplitudes. Applications and verifications of spectral evolution equations valid for a mildly sloping bottom and non-breaking waves (Freilich and Guza, 1984) were reported in numerous papers (Elgar and Guza, 1985, 1986; Elgar et al., 1990; Freilich et al., 1990). Spectral evolution equations with improved frequency dispersion were presented by Madsen and Sørensen (1993). They concluded that the agreement between the evolution equations and the time-domain counterpart is most satisfactory, except for the peak values of the highest waves which are underestimated by the spectral evolution equations.

Attempts have also been made to include a formulation for wave breaking in Boussinesq equations to extend their applicability to the surf zone. The concept of surface rollers (Deigaard, 1989) was incorporated in conventional time-domain Boussinesq equations by Schäffer et al. (1993). Eldeberky and Battjes (1996) supplemented the spectral evolution equations of Madsen and Sørensen (1993) with a spectral breaking term which accounts for the energy dissipation due to wave breaking (see, also, Battjes et al., 1993).

Only few efforts have been spent on testing Boussinesq models against velocity data. Verification of conventional Boussinesq models (Brocchini et al., 1992 and Quinn et al., 1994) with a description of the breaking process according to Schäffer et al. (1993) against velocity data for waves breaking partially on a gently sloping beach showed fairly good agreement with measured vertical profiles, especially in the near-bed zone. Elgar et al. (1990) obtained accurate estimates of the velocity variance and skewness in the shoaling region using the model of Freilich and Guza (1984).

The purpose of this paper is to verify the Boussinesq modelling of horizontal velocities under (breaking) waves, especially in the near-bed zone. We use a time-domain model (Dingemans, 1994a) for non-breaking waves and a spectral Boussinesq model (Elderberky and Battjes, 1996) assuming a parabolic expression for the calculation of the vertical structure of the horizontal particle velocities, as is consistent with the Boussinesq approximation.

2. TIME-DOMAIN MODEL

The time-domain equations with improved frequency-dispersion and good shoaling behaviour (Dingemans, 1994a) read in one horizontal dimension:

$$\frac{\partial \zeta}{\partial t} + \frac{\partial}{\partial x} [(h + \zeta)\bar{u}] = 0 \quad (1a)$$

$$\frac{\partial \bar{u}}{\partial t} + \bar{u} \frac{\partial \bar{u}}{\partial x} + g \frac{\partial \zeta}{\partial x} = h \frac{\partial}{\partial t} \left[\left(\frac{1}{2} + b \right) \frac{\partial^2 (h\bar{u})}{\partial x^2} - \frac{1}{6} h \frac{\partial^2 \bar{u}}{\partial x^2} \right] + b g h \frac{\partial^2}{\partial x^2} \left[h \frac{\partial \zeta}{\partial x} \right] \quad (1b)$$

where b is a fitting parameter for obtaining the best agreement with the frequency dispersion according to Stokes' first order theory. For $b = 1/15$ the phase celerity errors are minimized over the whole range of kh (see Madsen and Sørensen, 1992 and Dingemans, 1994b).

Solution of Eqs. (1) yields values for the surface elevation and the computational (depth-averaged) horizontal velocity. The vertical structure of the horizontal velocity is related to the computational velocity through a parabolic expression depending on the vertical coordinate (Dingemans, 1994b):

$$u(x, z, t) = \bar{u} - \left[\frac{1}{2} h + z \right] (h\bar{u})_{xx} + \left[\frac{1}{6} h^2 - \frac{1}{2} z^2 \right] \bar{u}_{xx} \quad (2)$$

where $z = 0$ corresponds to the undisturbed position of the free surface.

The numerical integration is based on the scheme as applied by Beji and Battjes (1994), which is essentially based on the formulation by Peregrine (1967). The finite difference equations, in which central difference formulations are used both for time and space derivatives, are solved by using a predictor-corrector method.

The extension to reconstruct the horizontal velocity profile is implemented by discretizing the second-order derivatives in the parabolic expression (2) using central differences in space. A low-pass filter is applied to the values of \bar{u} to obtain stable estimates of the second-order derivative \bar{u}_{xx} and $(h\bar{u})_{xx}$.

3. VERIFICATION OF THE TIME-DOMAIN MODEL

Experimental data

The model described above was verified against laboratory measurements of non-breaking monochromatic waves performed by Luth et al. (1994) in a wave flume with a submerged trapezoidal bar (see Fig. 1) as part of the EU-sponsored Large Installations Plan. The flume was 45 m long, 1 m wide and had a still water depth of 80 cm on each side of the bar. The incident wave conditions are $T =$

1.50 s and $H = 0.06$ m. Velocity measurements were carried out at different points in the vertical at 15.50 m and 21.72 m from the wave maker using two 3-beam, 2-component Laser Doppler Velocimeters.

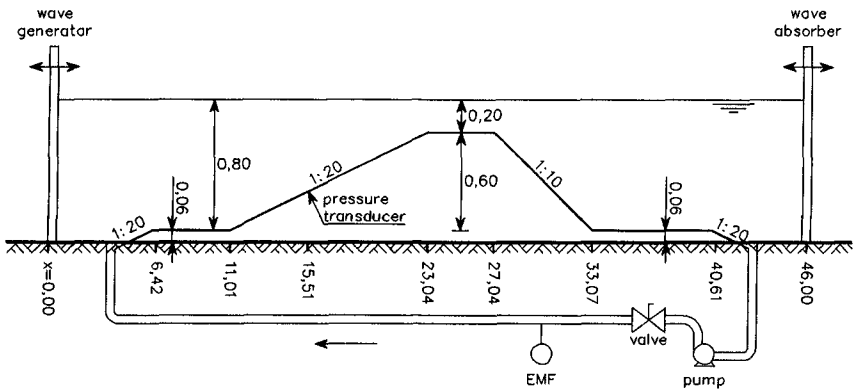


Fig 1 Experimental set-up, all dimensions in m, from Luth et al (1994)

Computational parameters

The time and spatial steps used in the computation were approximately equal to 1/150 of the incident wave period and wave length, respectively. At the seaward boundary, the Courant number $c(\Delta t/\Delta x)$ was approximately one.

Discussion of results

Fig. 2 shows for both stations time-domain comparisons of the measured and computed bottom velocity as well as the velocity evaluated at a level close to where the depth-averaged velocity may be found ($z \approx -0.4 h$). For the measured bottom velocity in Fig. 2, the value at approximately 2 cm from the bed, just outside the boundary layer, was taken. The time-window in Fig. 2 was chosen in such a way that permanent wave profiles are obtained in the computations. Fig. 3 gives the vertical profiles of the horizontal velocity profile for two different wave phases, corresponding to a crest and a trough in the computations.

Fig. 2 shows that the asymmetry about the horizontal axis occurring on the seaward slope is well represented. The depth-averaged velocity at the crest is slightly overestimated by the Boussinesq model, while the agreement is very good for the trough values. It was found that the surface elevation exhibits a similar overestimation of the crest values. The bottom velocities are predicted quite well, with a small overestimation of the trough values by the model.

Fig. 3 shows a fair agreement between the measured and computed velocity profiles, especially for the lower half of the profile. A small but systematic overestimation of the velocity is found, which is particularly evident for the crest values near the surface.

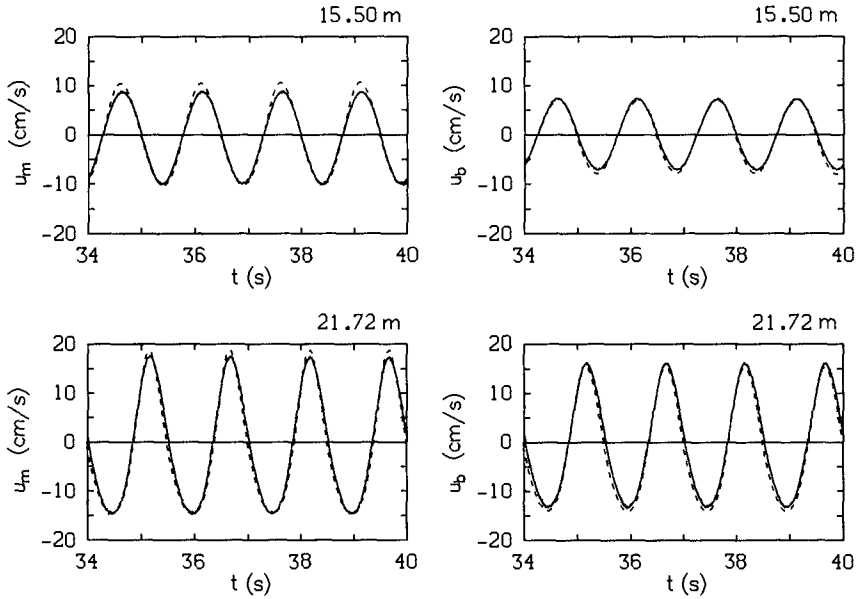


Fig. 2 Measured (solid line) and computed (dotted line) horizontal velocity u_m , evaluated at a level close to where the depth-averaged velocity may be found (top), and near-bed velocity u_b , evaluated at approximately 2 cm from the bed (bottom), for $x = 15.50$ and 21.72 m respectively.

4. FREQUENCY DOMAIN MODEL

Assuming slowly-varying complex Fourier amplitudes and uni-directional wave propagation, evolution equations for the complex amplitudes were derived by Madsen and Sørensen (1993) and extended by Eldeberky and Battjes (1996) with a formulation for dissipation of energy due to breaking which reduces the spectral amplitudes in the same proportion without affecting the spectral shape. Starting point of the derivation of the spectral evolution equations were time-domain Boussinesq equations (Madsen and Sørensen, 1992) valid for a slowly-varying bottom ($|dh/dx| \ll kh$).

Madsen and Sørensen (1993) formulated solutions for the free-surface elevation in terms of Fourier series with spatially varying coefficients:

$$\zeta(x,t) = \sum_{p=-\infty}^{\infty} A_p(x) \exp[i(\omega_p t - \psi_p(x))] , \quad (3)$$

where p indicates the rank of the harmonic, A_p is the complex Fourier amplitude, ω_p is the angular frequency and $d\psi_p/dx = k_p(x)$ is the wave number in the linear

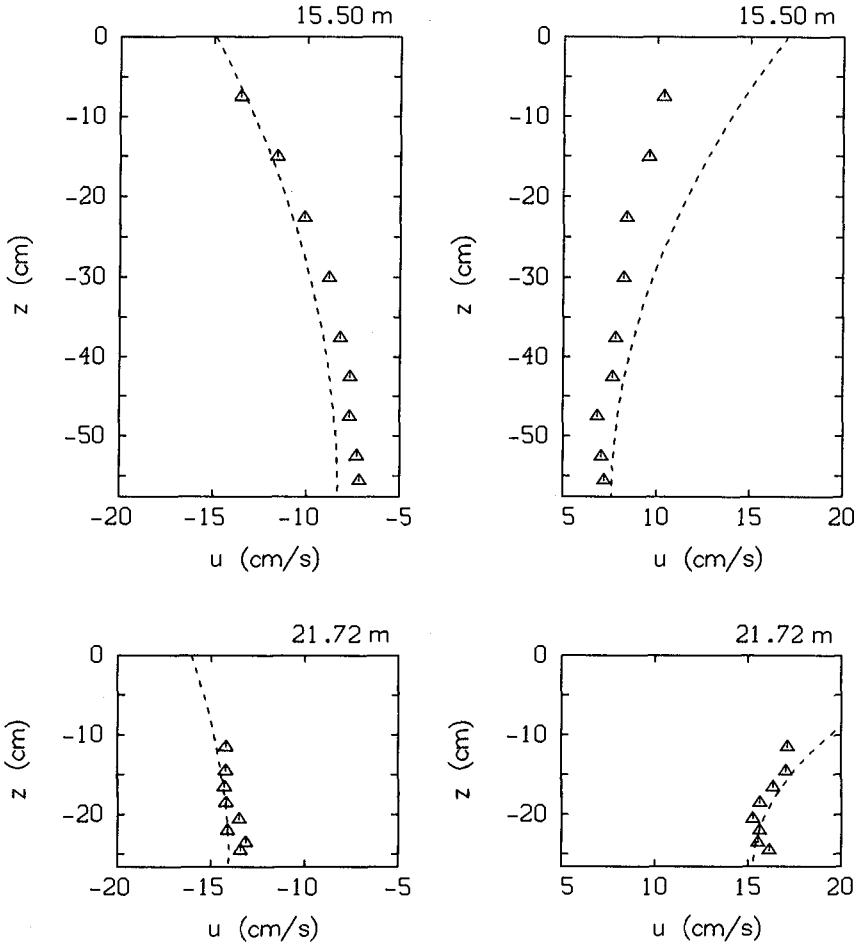


Fig. 3 Comparison of measured (triangles) and computed (dotted line) horizontal velocity vertical profile at $x = 15.50$ m and 21.72 m respectively, for two different wave phases corresponding to a trough (left) and a crest (right)

approximation. Note that $\omega_p = -\omega_p$, $\psi_p = -\psi_p$, $A_p = A_p^*$ with "*" denoting the complex conjugate. The frequencies are determined by $\omega_p = p\Delta\omega$ where $\Delta\omega$ is the lowest frequency of interest. The wave number k_p can be determined from the linear dispersion relation of the equations.

The evolution equations read, with p covering the interval from $p = 1$ to ∞ ,

$$\frac{dA_p}{dx} = -\beta_5 \frac{h_x}{h} A_p - i2g (F_p^+ + F_p^-) - \frac{1}{2} \frac{D}{F} A_p, \quad (4)$$

where the first term in the right-hand side of Eqs. (4) represents linear shoaling, the second and the third term represent the triad sum and difference interactions respectively and the last term is the dissipation term representing the contribution due to wave breaking. Here F is the total local rate of energy flux per unit width and D is the total local rate of random-wave energy dissipation per unit area due to breaking. Expressions for the terms F_p^+ and F_p^- and the shoaling coefficient β_5 can be found in Madsen and Sørensen (1993). The energy dissipation rate D can be computed using the energy dissipation model of Battjes and Janssen (1978) or comparable methods (e.g. Thornton and Guza, 1983); here we use the model of Battjes and Janssen (1978).

In the linear approximation, the depth-averaged velocity is expressed in terms of surface elevation using the lowest-order approximation for the volume flux q in a progressive wave:

$$\bar{u}(x,t) \approx \frac{q}{h} \approx \sum_{p=-\infty}^{\infty} \frac{\omega_p}{k_p h} A_p(x) \exp[i(\omega_p t - \psi_p(x))] . \quad (5)$$

Note that in this way only the purely oscillating part of the horizontal velocity is predicted by the model; the time-averaged component of the velocity is eliminated upon linearization.

In order to compute the horizontal velocity profile as a function of the depth, we use the parabolic profile for the constant depth situation (Eq. 2 with h -derivatives omitted). Substituting Eq. (5) while neglecting all x -derivatives of A_p , k_p and h , yields the following expression for the horizontal velocity profile in terms of Fourier series:

$$u(x,z,t) = \sum_{p=-\infty}^{\infty} \frac{\omega_p}{k_p h} A_p(x,z) \left[1 + k_p^2 \left[\frac{1}{3} h^2 + zh + \frac{1}{2} z^2 \right] \right] \exp[i(\omega_p t - \psi_p(x))] . \quad (6)$$

The evolution equations which are first-order ordinary differential equations are numerically integrated using a fourth-order Runge-Kutta method. The upwave boundary condition for the integration is a set of complex amplitudes A_p ($p = 1, 2, 3 \dots P$).

5. VERIFICATION OF THE FREQUENCY DOMAIN MODEL

Experimental data

The prediction of horizontal velocities and velocity moments was verified against wave channel measurements of irregular (partially) breaking waves propagating over a concave sandy beach. The experiments were carried out within the framework of the EU-sponsored Large Installations plan (Arcilla et al., 1993; Roelvink and Reniers, 1995). Two different experimental data sets (i.e. test 1a and 1c) were used. The incident peak period T_p and significant wave height H_{m0} are $T_p = 4.9$ s and $H_{m0} = 0.9$ m and $T_p = 8.0$ s and $H_{m0} = 0.6$ m for tests 1a and 1c respectively. In the experiments the low frequency energy is kept at a reasonable level by an active wave absorption system at the wave-maker. Surface elevations and velocities were measured at several locations along the wave channel. The velocity measurements were carried out at several distances from the bed. Since the spectral model only predicts the purely oscillating part of the velocity the time-averaged velocity component was filtered from the measured signals.

In experiment 1a the wave breaking is strong. The monotonic sandy beach profile (Fig. 4) allows for wave breaking to take place over a large distance; the experiments showed a gradual decrease of the significant wave height at distances from 100 m up to about 140 m from the wave board, beyond which the wave breaking gets strong. In experiment 1c on the contrary, a barred beach profile is present (Fig. 5). The wave breaking is mild and is concentrated behind the bar, the crest of which is located around 138 m.

The upwave boundary conditions used in the numerical computations are obtained from the measured surface elevations at 20 m by the use of a standard FFT algorithm.

Computational parameters

Besides the bottom geometry and the upwave boundary, the model input comprises the breaking coefficient $\gamma = H_m/h$ in which H_m is the maximum wave height, the bandwidth Δf , the number of frequency components P and the spatial step Δx . The spatial step was chosen $\Delta x = 0.5$ m and the breaking coefficient $\gamma = 0.85$ in accordance with the γ -value used by Eldeberky and Battjes (1996). A cut-off frequency of 1 Hz was used in the simulations. The length of the simulated time record was $T = 2048$ s for both experiments, resulting in a number of frequency components $P = 2048$ and a bandwidth $\Delta f = 4.883 \cdot 10^{-4}$ Hz.

Analysis of time-series

The comparison between measurements and computations was carried out on amongst others velocity variance and third order velocity moments, the latter being the most important variable in determining the magnitude of the net bed-load transport rate. In computing the variance and third order moment of the

bottom velocity it was assumed that the total oscillatory velocity signal u consists of a short wave averaged low-frequency component u_{lo} and a short wave component u_{hi} . The lowest short wave frequency was set to half the peak frequency.

Assuming u_{lo} and u_{hi} to be uncorrelated, the velocity variance is given by:

$$\langle u^2 \rangle = \langle u_{hi}^2 \rangle + \langle u_{lo}^2 \rangle , \quad (7a)$$

where the $\langle \rangle$ indicate time-averaging over the short wave and wave group scale.

Assuming in addition that $u_{lo} \ll u_{hi}$, Roelvink and Stive (1989) demonstrated that the most important contributions of the oscillatory part of the velocity to the third order velocity moment are given by:

$$\langle u^3 \rangle = \langle u_{hi}^2 u_{hi} \rangle + 3 \langle u_{hi}^2 u_{lo} \rangle + \dots . \quad (7b)$$

The first term in the right-hand side of Eq. (7b) is related to the short wave asymmetry, whereas the second term is associated with the interaction between the long wave velocity and the slowly-varying short wave velocity variance.

For both the measured and the computed bottom velocity time series, the three terms in Eqs. (7a-b) were separately calculated and plotted.

Discussion of results

Fig. 4 shows that, except for the last station behind the bar, the short wave velocity variance is very well predicted, indicating that the spectral energy density for the higher frequencies is well reproduced by the model. The model slightly underestimates the total velocity variance for the stations closest to the bar. This can be seen to originate from the inaccurate reproduction of the long wave velocity variance for these stations. This may be the result of a standing low-frequency wave pattern present in the channel with a node in the low-frequency surface elevation and hence large velocity amplitudes around station 5, which are not reproduced by the model because of the assumption of uni-directional wave propagation. Another possible cause could be a too strong reduction of the low frequency energy by the wave breaking formulation.

The third order velocity moment, which can be seen to be dominated by the short wave asymmetry, is largely underestimated by the model. This appeared to be a result of an underestimation of the peak values of the highest waves, which was already reported by Madsen and Sørensen (1993). The agreement is reasonable for the last two stations where strong wave breaking occurs. The long wave contribution is predicted rather well. Increasing the maximum frequency and the frequency resolution did not improve the numerical results.

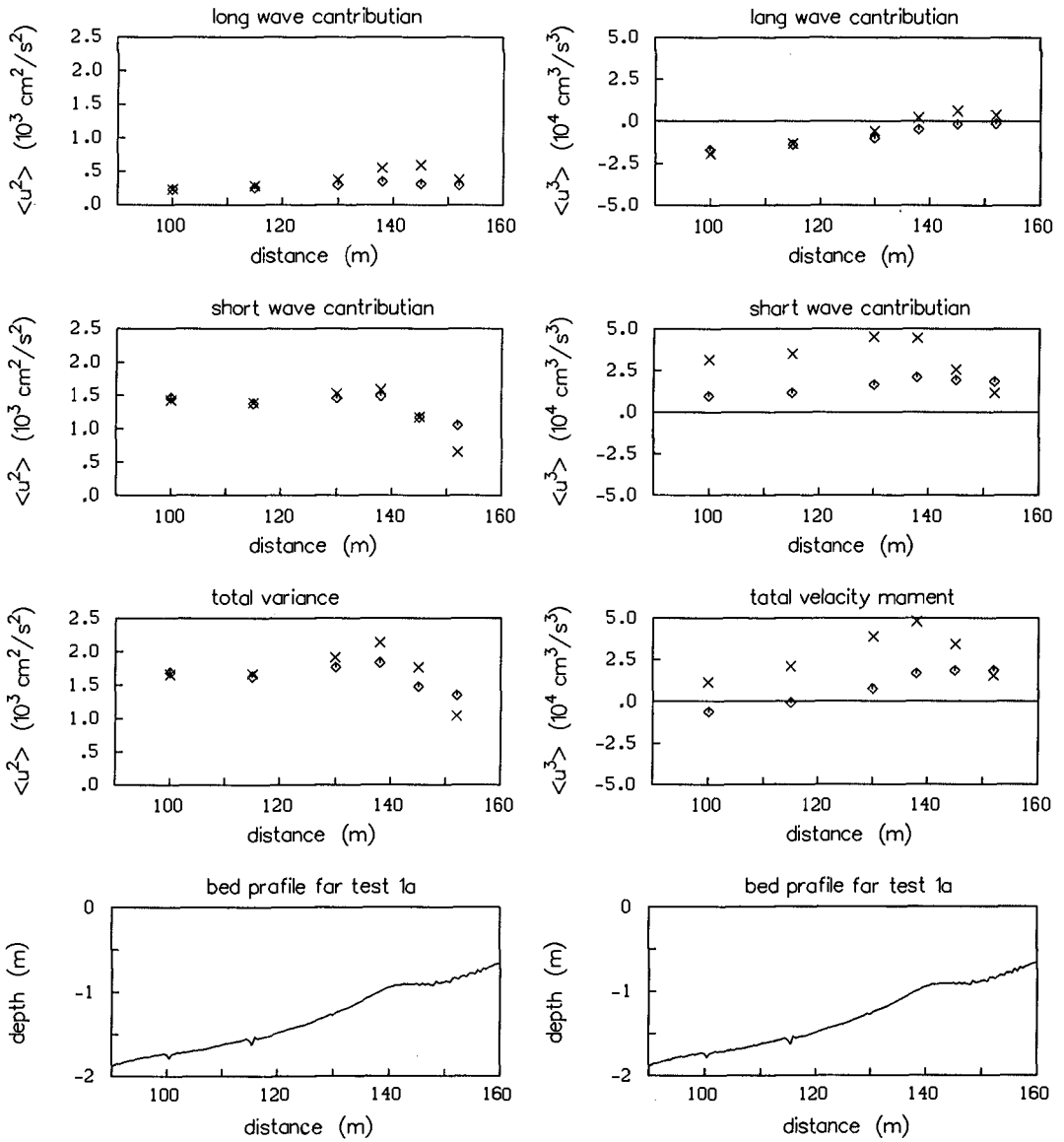


Fig. 4

Comparison of measured (crosses) and computed (diamonds) bottom velocity variance (left) and third order moments (right): long wave contribution, short wave contribution and total moment respectively; experiment 1a. Reprinted from J. Coastal Eng., Bosboom et al., 1996, with kind permission from Elsevier Science-NL, Amsterdam, The Netherlands.

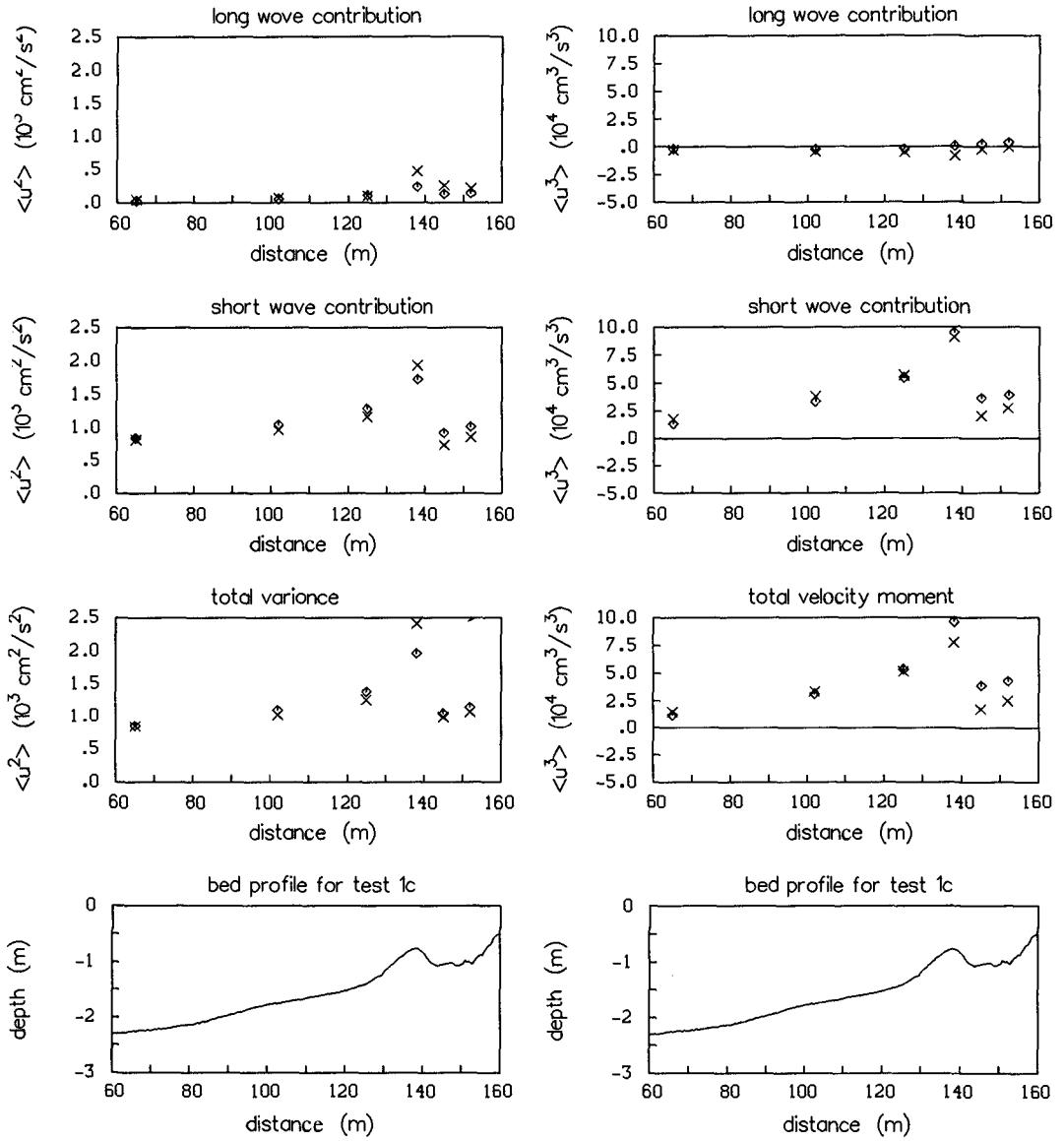


Fig. 5 Comparison of measured (crosses) and computed (diamonds) bottom velocity variance (left) and third order moments (right): long wave contribution, short wave contribution and total moment respectively; experiment 1c. Reprinted from J. Coastal Eng., Bosboom et al., 1996, with kind permission from Elsevier Science-NL, Amsterdam, The Netherlands.

Test 1c shows an encouraging agreement between measured and predicted variance and third order moments (Fig. 5), especially up to the bar crest. The underestimation of the peak values was found to be less significant than for test 1a. The less good agreement beyond the bar crest, also found by Eldeberky and Battjes (1996) for surface elevation spectra, can possibly be ascribed to the relatively steep bottom beyond the bar crest ($|h_x|/kh = 0.52$ for the primary wave) which is in contrast with the assumption of slowly-varying bottom ($|h_x|/kh \ll 1$).

The velocity variance in test 1c (Fig. 5) is predicted well. The difference between the total velocity variance determined from the computed and measured time series at the bar crest is for the larger part the result of the incorrect representation of the long wave energy. As for test 1a, this is can possibly be ascribed to a standing wave pattern in the wave channel or to a too strong reduction of low-frequency energy by the breaking formulation.

It can be concluded that for test 1c the third order velocity moments compare very well with the measurements. For test 1a as well as 1c, the short wave energy is predicted well by the model. The underprediction of the short wave asymmetry by the model in test 1a is therefore the result of an incorrect representation of the phases of the harmonic components. This might be partly due to the larger degree of non-linearity as compared to test 1c, such that the wave breaking already occurs at 100 m from the wave board and continues for a large propagation distance. Besides, the peak period is smaller in test 1a which decreases the accuracy of the frequency dispersion as well as the validity of the assumption of slowly-varying complex amplitudes underlying the evolution equations.

6. CONCLUSIONS

The modelling of horizontal velocities in non-breaking and breaking waves on a beach using Boussinesq-type models has been studied. Time-domain simulations of regular waves indicate that the use of a parabolic vertical distribution of the horizontal particle velocity yields realistic predictions, especially in the near-bed zone.

Horizontal velocities in the near-bed zone in (partially) breaking random waves have been simulated using a frequency-domain Boussinesq model. A fair prediction of the velocity variance was found. For the test with the longer wave period, the third order velocity moments are predicted well by the model. The shorter wave test however, shows an underestimation of the velocity moments due to an underestimation of the crest values of the highest waves. This was seen to be the result of an inaccurate representation of the phases of the higher harmonics.

Further research is necessary to determine whether the discrepancies result from the water-depth restrictions of the Boussinesq equations or from additional assumptions made in the derivation of the evolution equations. Further, attention

should be paid to the inclusion of higher-order derivatives in the spectral evolution equations and the mean velocity in the velocity computation.

ACKNOWLEDGEMENTS

This work was undertaken as part of the MAST-2 G8 Coastal Morphodynamics Research Programme. It was funded jointly by Delft Hydraulics, Delft University of Technology and the Commission of the European Communities, Directorate General for Science, Research and Development under contract no. MAS2-CT92-0027. The laboratory data used were obtained during experiments in the framework of the "Access to Large-scale Facilities and Installations Programme" (LIP), which were funded by the Commission of the European Communities, Directorate General for Science, Research and Development under contract no. GE1*-CT91-0032 (HSMU).

REFERENCES

- Arcilla, A.S., J.A. Roelvink, B.A. O'Connor, A. Reniers and J.A. Jimenez, 1994. The Delta Flume '93 Experiment. *Proc. Coastal Dynamics Conf.*, UPC, Barcelona, Feb. 1994: 488-502.
- Bailard, J.A., 1981. An energetics total load sediment transport model for a plane sloping beach. *J. Geophys. Res.*, 86(C11): 10938-10954.
- Battjes, J.A. and J.P.F.M. Janssen, 1978. Energy loss and set-up due to breaking of random waves. *Proc. 16th Int. Conf. Coastal Eng.*: 569-587. ASCE, New York.
- Battjes, J.A., Y. Eldeberky and Y.S. Won, 1993. Spectral Boussinesq modelling of breaking waves. In *Ocean Wave Measurement and Analysis*, edited by O.T. Magoon and J.M. Hemsley. ASCE, New York, pp. 813-820.
- Beji, S. and J.A. Battjes, 1994. Numerical simulation of nonlinear wave propagation over a bar. *Coastal Eng.*, 23: 1-16.
- Bosboom, J., G. Klopman, J.A. Roelvink and J.A. Battjes, 1996. Boussinesq modelling of wave-induced horizontal particle velocities. *Coastal Eng.*, submitted for publication.
- Brocchini, M., M. Drago and L. Iovenitti, 1992. The modelling of short waves in shallow waters. Comparison of numerical methods based on Boussinesq and Serre equations. *Proc. 23rd Int. Conf. Coastal Eng.*, ASCE, New York, 4: 76-88.
- Deigaard, R., 1989. Mathematical modelling of Waves in the Surf Zone. Prog. Report 69, ISVA, *Technical University of Denmark*, Lyngby, pp. 47-59.
- Dingemans, M.W., 1994a. Comparison of computations with Boussinesq-like models and laboratory measurements. *Mast-G8M Note*, Project 1, 30 pp.
- Dingemans, M.W., 1994b. Water Wave Propagation Over Uneven Bottoms. *Ph.D. Thesis, Delft University of Technology*, November 1994, 780 pp. Extended version to be published by World Scientific, Singapore, 1996.
- Eldeberky, Y. and J.A. Battjes, 1996. Spectral modelling of wave breaking:

- Application to Boussinesq equations. *J. Geophys. Res.*, 101(C1): 1253-1264.
- Elgar, S. and R.T. Guza, 1985. Shoaling gravity waves: comparisons between field observations, linear theory, and a non-linear model. *J. Fluid Mech.*, 158: 47-70.
- Elgar, S. and R.T. Guza, 1986. Non-linear model predictions of bispectra of shoaling surface gravity waves. *J. Fluid Mech.*, 167: 1-18.
- Elgar, S., M.H. Freilich and R.T. Guza, 1990. Model-data comparisons of moments of non-breaking shoaling surface gravity waves. *J. Geophys. Res.*, 95: 16,055-16,065.
- Freilich, M.H. and R.T. Guza, 1984. Nonlinear effects on shoaling surface gravity waves. *Phil. Trans. R. Soc. Lond.*, A311: 1-41.
- Freilich, M.H., R.T. Guza and S. Elgar, 1990. Observations of nonlinear effects in directional spectra of shoaling gravity waves. *J. Geophys. Res.*, 95: 9645-9656.
- Luth, H.R., G. Klopman and N. Kitou, 1994. Project 13G: Kinematics of waves breaking partially on an offshore bar; LDV measurements for waves with and without a net offshore current. *Delft Hydraulics*, Report H1573, 40 pp.
- Madsen, P.A., R. Murray, and O.R. Sørensen, 1991. A new form of the Boussinesq equations with improved linear dispersion characteristics. *Coastal Eng.*, 15: 371-388.
- Madsen, P.A. and O.R. Sørensen, 1992. A new form of the Boussinesq equations with improved linear dispersion characteristics. Part 2: A slowly-varying bathymetry. *Coastal Eng.*, 18: 183-204.
- Madsen, P.A. and O.R. Sørensen, 1993. Bound waves and triad interactions in shallow water. *Ocean Eng.*, 20(4): 359-388.
- Nwogu, O., 1993. An alternative form of the Boussinesq equations for modelling the propagation of waves from deep to shallow water. *J. of Waterway, Port, Coastal and Ocean Eng.*, 119(6): 618-638.
- Peregrine, D.H., 1967. Long waves on a beach. *J. Fluid Mech.*, 27(4): 815-827.
- Quinn, P.A., M. Petti, M. Drago and C.A. Greated, 1994. Velocity field measurements and theoretical comparisons for non-linear waves on mild slopes. *Mast-G8M Workshop*, Sept. 1994.
- Roelvink, J.A. and A.J.H.M. Reniers, 1995. LIP 11D Delta Flume experiments. *Delft Hydraulics*, Report H2130.
- Roelvink, J.A. and M.J.F. Stive, 1989. Bar-generating cross-shore flow mechanisms on a beach. *J. Geophys. Res.*, 94(C4): 4785-4800.
- Schäffer, H.A., P.A. Madsen and R. Deigaard, 1993. A Boussinesq model for waves breaking in shallow water. *Coastal Eng.*, 20: 185-202.
- Schröter, A., 1995. Nichtlineare zeitdiskrete Seegangssimulation im flachen und tieferen Wasser. *Institut für Strömungsmechanik und Elektron. Rechnen im Bauwesen, Universität Hannover*, Bericht Nr. 42/1995.
- Thornton, E.B. and R.T. Guza, 1983. Transformation of wave height distribution. *J. Geophys. Res.*, 88(C10): 5925-5938.
- Witting, J.M., 1984. A unified model for the evolution of nonlinear water waves. *J. Comp. Phys.*, 56: 203-236.

CHAPTER 10

EFFECTS OF MODE TRUNCATION AND DISSIPATION ON PREDICTIONS OF HIGHER ORDER STATISTICS

James M. Kaihatu¹ and James T. Kirby, Member, ASCE²

Abstract

We investigate the effects mode truncation and dissipation characteristics have on predictions of wave shape statistics such as skewness and asymmetry. We demonstrate the effect of mode truncation by calculating wave shape statistics for data from a laboratory experiment using an increasing number of frequency components each calculation. We find that the values of skewness and asymmetry converge to a maximum as more components are retained, with the maximum values attained when components out to the Nyquist frequency are kept. We run a lowest order Boussinesq shoaling model and a nonlinear dispersive shoaling model with the data, retaining more components with each simulation. Both models show the same convergence characteristics as the data as the number of retained frequency components increases. The lowest order Boussinesq model, despite its shallow water formalism, yields skewness and asymmetry values closer to those of the data than those of the dispersive model. This is likely due to the phase mismatches in the dispersive model, which become large in deep water and thus violate the slowly-varying amplitude assumption. We also investigate the effect of spectral dissipation on these predictions. We run the lowest order Boussinesq shoaling model with different proportions of frequency-dependent dissipation and calculate wave shape statistics. We find that the distribution must take into account some aspect of $(f)^2$ variation in the dissipation for reliable wave shape statistics.

Introduction

The Boussinesq equations (Peregrine 1967) are robust predictors of weakly nonlinear wave propagation in shallow water. The “consistent” frequency domain Boussinesq model of Freilich and Guza (1984) has been used in a number of studies (e.g., Elgar and Guza 1985; Elgar et al. 1990) concerning nearshore wave propagation; they have shown that this model does predict shallow water wave spectra reliably provided that $kh \ll O(1)$, where k is the wave number and h the water depth.

¹ Oceanographer, Oceanography Division (Code 7322), Naval Research Laboratory, Stennis Space Center, MS 39529-5004

² Professor, Center for Applied Coastal Research, University of Delaware, Newark, DE 19716

In recent years, however, frequency domain models with fewer restrictions on the value of kh have been developed (e.g., Madsen and Sorensen 1993; Agnon et al. 1993; Kaihatu and Kirby 1995). These models, because of their dispersive nature, can be applied in greater water depths (and take into account a greater frequency range) than the lower-order Boussinesq-type models. Application of these models to laboratory data have shown their utility.

A different test of these frequency domain models would be to evaluate their ability to replicate surface shape characteristics. This involves evaluating quantities such as skewness and asymmetry. These higher order statistical quantities track the free surface characteristics of waves, and thus lend insight into the effect nonlinear energy exchange has on the evolution of the wave shape.

Elgar et al. (1990) have investigated skewness and asymmetry predictions from the consistent model of Freilich and Guza (1984) and compared these quantities to field data taken at both Torrey Pines, CA and Santa Barbara, CA in 1980. Because of the lowest order dispersion characteristics of the model, the simulations required an upper frequency cutoff that was based on the relative magnitude of the dispersion parameter kh . This upper frequency was established prior to simulation and analysis so that no nonlinear interaction with frequencies beyond the cutoff could occur. They found good data-model agreement for relatively narrow banded spectra, but somewhat poorer agreement for broad banded spectra. This is primarily due to the spectral energy content beyond the cutoff frequency for the broad spectra data.

No corresponding studies have been undertaken for the more dispersive frequency domain models, particularly as applied to field measurements. The ability of these models to simulate processes at frequencies beyond the small kh limit is particularly germane to this problem. Bowen (1994) showed that the calculation of skewness and asymmetry varied significantly with the number of harmonics of the spectral peak retained. He used his laboratory data of shoaling irregular waves on a slope to calculate these quantities with varying numbers of harmonics of the spectral peak, and found that the values of skewness and asymmetry converged to a maximum as the number of components retained increased. The maximum values of skewness and asymmetry were reached when the upper limit cutoff frequency reached the Nyquist limit. Bowen (1994) also noted that the differences between the values of skewness and asymmetry as the number of components increased were most marked in the breaking zone. This would likely be due to the increased nonlinear shifting of energy to the higher frequency components. The dependence of skewness and asymmetry on the number of retained components was not evident in the work of Elgar et al. (1990) due to the dispersion-based upper frequency cutoff for both model and data. This upper frequency cutoff is not a function of kh in the more dispersive frequency domain models, so a different criteria needs to be applied to determine this cutoff. Kaihatu and Kirby (1995), for example, use percentage of total variance. Other concerns, such as upper frequency limitations on pressure to surface conversions

(required when deducing free surface fluctuations from pressure records), can also affect the choice of cutoff frequency.

In this study we wish to investigate the effect the upper frequency cutoff has on simulating these higher order statistics. We will first investigate skewness and asymmetry values gleaned from experimental data. This will also lend insight into the sensitivity of these statistics to cutoff frequency. We will then run two shoaling models and determine the effect that retaining various numbers of components has on the reliability of predictions of skewness and asymmetry. We will find that the nature of the model has a strong effect on the predictions.

Skewness and Asymmetry in the Wavefield

As waves in the nearshore shoal, nonlinear effects become more important. The wave crests become sharper and the crests flatter. This is represented as an increase in skewness (asymmetry about a horizontal plane). As the waves begin to approach breaking, the front face of the wave becomes steeper. This is quantified as an increase in negative asymmetry (in this context, referring to asymmetry about a vertical plane).

Skewness is defined as:

$$skewness = \frac{\langle \eta^3 \rangle}{\langle \eta^2 \rangle^{\frac{3}{2}}} \quad (1)$$

and asymmetry as:

$$asymmetry = \frac{\langle H(\eta^3) \rangle}{\langle \eta^2 \rangle^{\frac{3}{2}}} \quad (2)$$

where the brackets denote a time average, η is the free surface elevation and H is the Hilbert transform.

We will be working with the Case 2 data of Mase and Kirby (1992); full details of the experimental setup can be found therein. The tank consisted of a constant depth section ($h=47cm$) of $10m$ length, and a 1:20 slope. A Pierson-Moskowitz spectrum was input at the wave paddle. For Case 2, the value of kh at the spectral peak in the deep portion of the tank was 1.9, a severe test of the dispersive wave models. In this experiment, the sampling rate $\Delta t = 0.05s$ with the data divided into seven realizations at 2048 points each. The Nyquist frequency was $10Hz$. The evolution characteristics of this data are shown in Figure 1. This figure shows the spectra at several gages taken out to the Nyquist frequency. It is apparent that the high frequency tail increases in energy, particularly in shallow water.

We use (1) and (2) to calculate the higher order statistics from the data. For each calculation we retain in turn 300, 500, 700, 900, and 1024 frequency

components (1024 components takes the calculation to the Nyquist limit). Plots of H_{rms} (root-mean-square wave height), skewness and asymmetry appear in Figure 2. There is not much difference between the measured H_{rms} values for different numbers of retained components; this implies that $N=300$ retains a significant percentage of the energy content in the spectrum. However, the skewness and asymmetry values clearly indicate that the number of retained frequency components has a profound effect on the calculation of high order statistics, with an increase in the number of components evidencing a convergence to a maximum value. The differences are most apparent in the nearshore, as nonlinearity becomes more prevalent in the wavefield. Additionally, the skewness measure for the $N=300$ case is clearly less than those for more retained components even in the offshore area, an indication that this number of components is insufficient to describe the evolution of the shape of the wavefield. This is in spite of the fact that $N=300$ retains sufficient energy for H_{rms} quantification.

Shoaling Models

Now that we have demonstrated the effect the number of retained components has on the evaluation of skewness and asymmetry, we now wish to determine how this affects our ability to accurately model these effects. This is more germane for the dispersive models, since the linear characteristics of the higher frequencies could be more accurately modeled

The consistent model of Freilich and Guza (1984) is:

$$A_{nx} + \frac{h_x}{4h} A_n - \frac{in^3 k^3 h^2}{6} A_n + \frac{3ink}{8h} \left(\sum_{l=1}^{n-1} A_l A_{n-l} + 2 \sum_{l=1}^{N-n} A_l^* A_{n+l} \right) = -\alpha_n A_n \quad (3)$$

where A is the complex amplitude, and N is the index of the highest frequency component considered. The right hand side is a dissipation term that removes energy from the spectrum in accordance with the probabilistic dissipation expression of Thornton and Guza (1983). The distribution of that dissipation over the frequency range is discussed in a later section. The second term in (3) is the Green's Law shoaling term.

The nonlinear finite-depth shoaling model of Kaihatu and Kirby is:

$$A_{nx} + \frac{C_{gnx}}{2C_g} A_n + \frac{i}{8\omega_n C_{gn}} \left(\sum_{l=1}^{n-1} R A_l A_{n-l} e^{i\Theta} + 2 \sum_{l=1}^{N-n} S A_l^* A_{n+l} e^{i\Psi} \right) = -\alpha_n A_n \quad (4)$$

where R and S are interaction coefficients, and:

$$\Theta = \int k_l + k_{n-l} - k_n dx \quad (5)$$

$$\Psi = \int k_{n+l} - k_l - k_n dx \quad (6)$$

are referred to as “phase mismatches” since they determine the relative amount of detuning away from resonance in x . They have the capacity to become quite large in deep water, thus causing the nonlinear term to oscillate. The expansion technique used to derive (4) assumes that the amplitudes are slowly varying in space, an assumption which may be violated in deep water.

We use the shoaling models to determine the effect of the cutoff frequency on the simulation of these higher order statistics. Both models utilized error-checked variable stepsize ODE integration schemes; the consistent model used the Bulirsch-Stoer method with Richardson extrapolation, while the dispersive model used a fourth order Runge-Kutta scheme. We note that the consistent model of Freilich and Guza (1984) is formally invalid in this water depth. The lack of phase mismatch in the model is due to the nondispersive nature of the

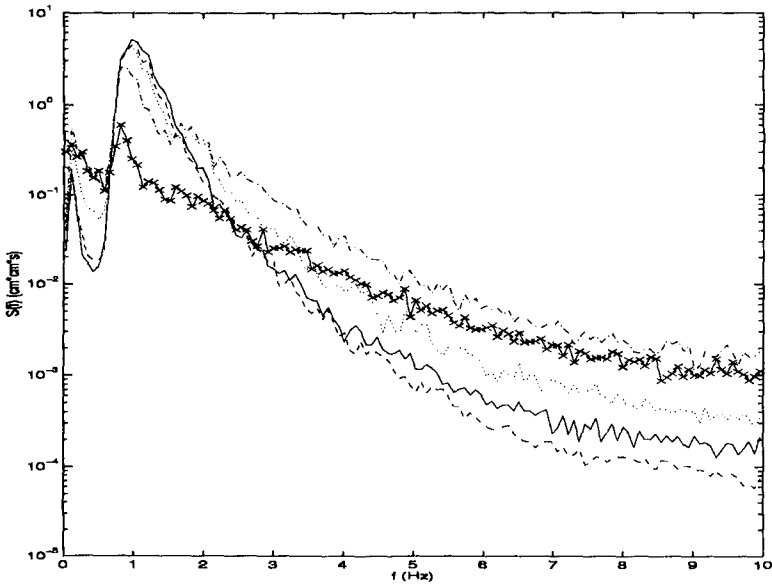


Figure 1. Evolution of spectra in experiment of Mase and Kirby (1992). Top figure: $h=47\text{cm}$ (solid), $h=25\text{cm}$ (dashed), $h=15\text{cm}$ (dotted), $h=7.5\text{cm}$ (dash-dot), $h=2.5\text{cm}$ (dash-x)

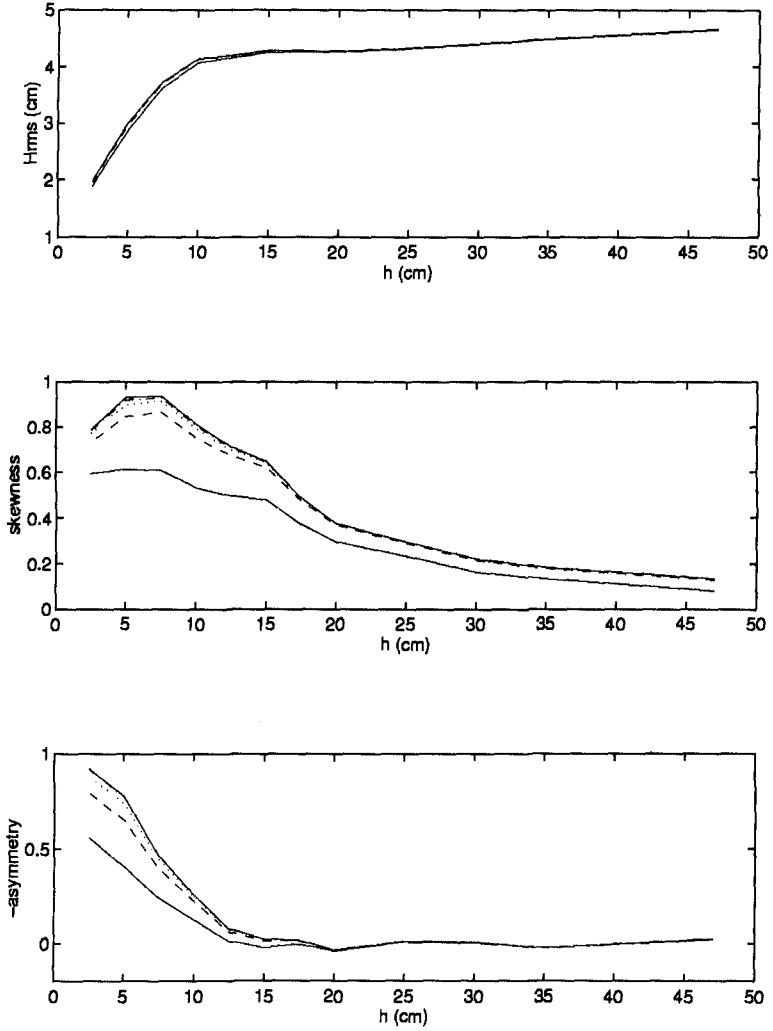


Figure 2. Statistics calculated from Case 2 data of Mase and Kirby (1992). In each figure: $N=300$ (bottom solid), $N=500$ (dashed), $N=700$ (dotted), $N=900$ (dash-dot), $N=1024$ (top solid). Top figure: H_{rms} . Middle figure: skewness. Bottom figure: - asymmetry.

nonlinear terms; in shallow water $k_n = nk_l$, where k_l is the wavenumber associated with the lowest frequency ω_l in the spectrum. This causes the phase mismatches to become zero. The dispersive models, with the finite phase mismatches, have linear characteristics that work well in deep water, but have nonlinear terms that may oscillate fast enough in deep water to cause difficulty in replicating the wave shape. The phase mismatches are a consequence of the somewhat misordered derivation of the dispersive models.

We ran the two models with increasing numbers of components ($N=300, 500, 700, 900$ and 1024) to simulate the experiment of Mase and Kirby (1992). Then we filter the data similarly, and calculate H_{rms} and third moments. The comparisons between the consistent model and the data are shown in Figure 3. We were able to simulate the spectrum out to the Nyquist frequency with this model; it is relatively expedient compared to the more computationally intensive dispersive model (4). Even so, the consistent model with $N=900$ and $N=1024$ requires substantial computational resources. Most runs were performed on the US Army Waterways Experiment Station Cray YM-P. The $N=900$ and $N=1024$ runs, however, required a Cray batch queue with a very low assigned priority; thus these were done, one realization at a time, on a Silicon Graphics Indy.

Figure 3 shows that the consistent model greatly overpredicts the H_{rms} values of the data. This is not surprising, since the model is clearly outside its area of validity; Green's Law, the linear shoaling mechanism in the consistent model, overpredicts the shallow water spectral amplitudes when initialized in deep water. In addition, the model results for all simulations agree, which indicates that $N=300$ is sufficient for describing the energy level in the spectrum. The skewness and asymmetry values, on the other hand, agree reasonably well with the data. This seems inconsistent with the fact that the consistent model is far outside its range of validity. Additionally, the model results show the same tendency to converge to a maximum value as N increases as shown by the data.

The dispersive model (4) required significantly more computational resources than the consistent model. This is primarily due to the phase mismatches of the dispersive model; their size in deep water causes difficulty in solving the sets of equations. Available computational resources only allowed the $N=300$ and $N=500$ cases to be run with this model.

Figure 4 shows the comparisons between the statistics from the experiment of Mase and Kirby (1992) and the dispersive model (4). The H_{rms} comparison is not unexpected, since the dispersive model does have the ability to reliably model spectral shoaling from deep to shallow water. The third moment comparisons, however, look worse than those of the consistent model. This is somewhat surprising, since the dispersive model has linear characteristics that can be applied to deeper water. However, the likely cause of these deleterious comparisons are the phase mismatches. We define a normalized phase mismatch:

$$M = \frac{|k_1 - k_{N-1} - k_N|}{k_N} \quad (7)$$

The magnitude of M when $N=1024$ is 25 in the deep portion of the tank. This magnitude of mismatch can induce oscillations which have deleterious effects on the replication of the free surface. Thus, these phase mismatches serve to keep the wave from attaining a realistic form. This is not evident in spectra comparisons shown in studies of dispersive frequency domain models (e.g., Agnon et al. 1993; Kaihatu and Kirby 1995) since these effects are averaged.

One feature that is apparent with both the consistent and dispersive model simulations is that the model results underpredict the skewness and asymmetry values seen in the data for each particular cutoff frequency; this is true even at the Nyquist frequency. One reason for this underprediction for $N < 1024$ is that all frequencies of the data have undergone nonlinear energy exchange with all others, while the model simulations are limited to those below the cutoff.

Effect of Dissipation Mechanism on Statistics

Both models have a dissipation mechanism that removes energy in the spectrum based on a probabilistic decay function developed by Thornton and Guza (1983). This dissipation mechanism is:

$$\alpha_n = \alpha_{n0} + \left(\frac{f_n}{f_{peak}} \right)^2 \alpha_{n1} \quad (8)$$

where:

$$\alpha_{n0} = F\beta(x) \quad (9)$$

$$\alpha_{n1} = \left(\beta(x) - \alpha_{n0} \right) \left(\frac{f_{peak}^2 \sum_{n=1}^N |A_n|^2}{\sum_{n=1}^N f_n^2 |A_n|^2} \right) \quad (10)$$

where f_{peak} is the peak frequency of the spectrum, f_n is the n^{th} frequency, F is a weighting factor, and $\beta(x)$ is the simple dissipation model of Thornton and Guza:

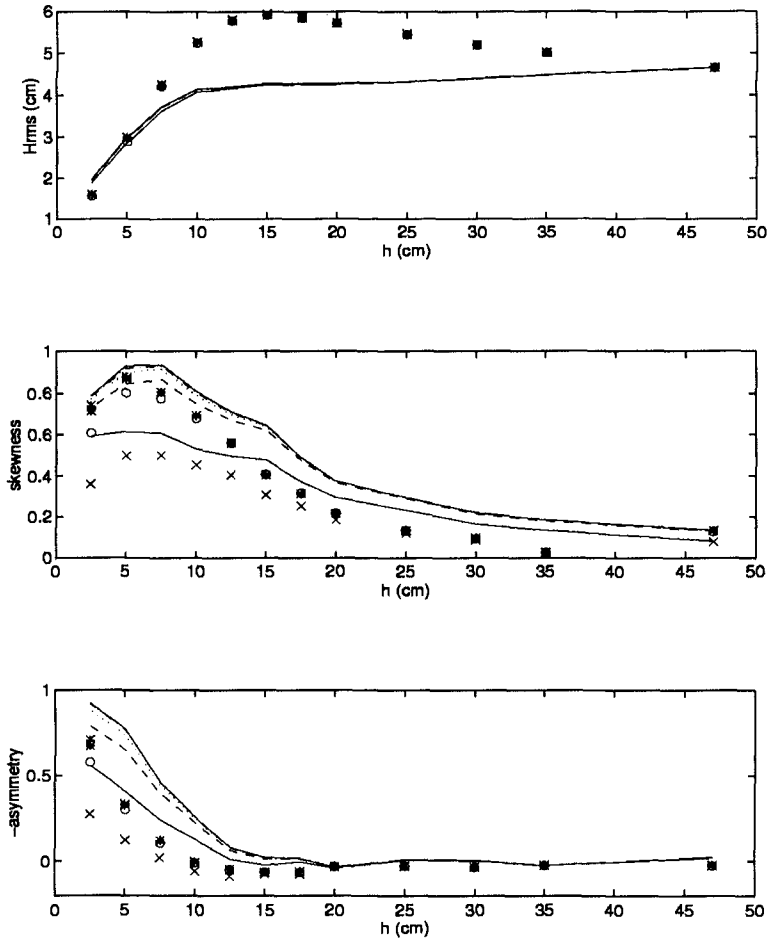


Figure 3. Comparison of modeled statistics to data of Mase and Kirby (1992) using the consistent model of Freilich and Guza (1984). In each figure: $N=300$ (bottom solid line is data, bottom “x” is model), $N=500$ (dashed line is data, “o” is model), $N=700$ (dotted line is data, “*” is model), $N=900$ (dash-dot line is data, “+” is model), $N=1024$ (top solid line is data, top “x” is model). Top figure: H_{rms} . Middle figure: skewness. Bottom figure: -asymmetry.

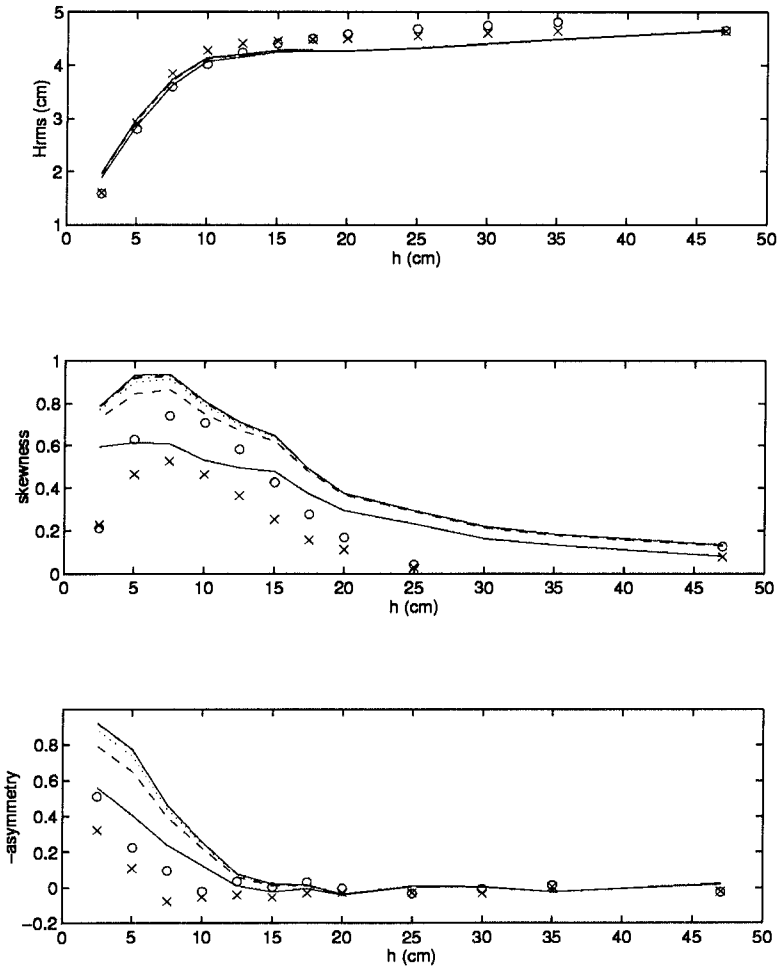


Figure 4. Comparison of modeled statistics to data of Mase and Kirby (1992) using the dispersive model of Kaihatu and Kirby (1995). In each figure: $N=300$ (bottom solid line is data, bottom "x" is model), $N=500$ (dashed line is data, "o" is model), $N=700$ (dotted line is data), $N=900$ (dash-dot line is data), $N=1024$ (top solid line is data). Top figure: H_{rms} . Middle figure: skewness. Bottom figure: -asymmetry.

$$\beta(x) = \frac{3\sqrt{\pi}B^3\bar{f}H_{rms}^5}{4\sqrt{gh}\gamma^4h^5} \quad (11)$$

where B and γ are free parameters set to 1.0 and 0.6, respectively. The mean frequency \bar{f} is taken to be the peak frequency. These values are close to those found by Thornton and Guza (1983). The proper value of F is a matter of some discussion; this weighing factor determines the dependence of the dissipation on frequency. Setting $F=1.0$ causes the dissipation to be equal across all frequencies, while setting $F=0$ weights the dissipation proportionally to $(f)^2$. Physical arguments for the proper value of F are presented elsewhere (Eldeberky and Battjes 1996; Kirby and Kaihatu 1996) and thus will not be presented here. The primary intent in this section is to discern the effect the particular value of F has on higher order statistics.

Realizing that we will not obtain accurate predictions of these quantities (for the reasons described earlier), we instead look for the effect various values of F have on the *trends* of the skewness and asymmetry values as waves propagate into shallow water. We ran both the consistent model of Freilich and Guza (1984) for various values of F , using $N=300$. Figure 5 shows skewness and asymmetry results for the consistent model with $F=0., 0.25, 0.5, 0.75,$ and 1.0 . The skewness results indicate that $F=0.75$ follows the trend of the data best, while the asymmetry results show that $F=0.5$ is most representative. However, what is more instructive are the comparisons between the simulations. The skewness values for $F=0, F=0.25$ and $F=0.5$ show a decrease at the last three gages. These values of F weight the dissipation higher towards higher frequencies, thus suppressing the nonlinear energy transfer to higher frequencies. The converse trend is evident in the asymmetry predictions. The $F=0$ has the most negative asymmetry for water depths up to $7.5cm$, at which point the negative asymmetry unexpectedly decreases in the inner surfzone. The fact that the $F=0$ curve exhibits the most negative asymmetry until its sudden downturn is indicative of the sawtooth shape of the breaking waves, which are in line with an $(f)^2$ distribution of dissipation. Kirby and Kaihatu (1996) discuss the physical basis behind this supposition. As mentioned before, the $F=0.5$ best matches the trend of the data for the entire range of water depths. The fact that the $F=1.0$ curves are not the best representations of the skewness and asymmetry trends indicates that some weighting of the dissipation toward higher frequencies is required to simulate this reliably, contrary to Eldeberky and Battjes (1996), who indicate that no such weighting need take place. In fact, it may be that if all components of the spectrum out to the Nyquist frequency were retained we can rely solely on the $(f)^2$ representation of the dissipation distribution, and that retention of α_{n_0} in (8) is an artifact of the truncation of the spectrum below the Nyquist frequency. Additionally, the sudden downturn of both skewness and asymmetry from the model results in the inner surf zone may also be an artifact of the mode truncation; Kirby and Kaihatu

(1996) show a comparison of third moments between the Case 2 data of Mase and Kirby (1992) and the time-domain extended Boussinesq code of Wei et al. (1995). This comparison, which utilized the entire unfiltered data set in the model simulation, showed that the time-domain model can reliably replicate third moment statistics.

Conclusions

We used the data of Mase and Kirby (1992) and two nonlinear shoaling models to investigate the effect mode truncation and dissipation mechanisms have on the prediction of third order statistics. We found that the number of components used in the calculation has a strong effect on the skewness and asymmetry values; this was true for both the data and the model simulations. The consistent model of Freilich and Guza (1984), though formally invalid for the peak kh values of the experiment, actually modeled the third order moments better than the dispersive model of Kaihatu and Kirby (1995). This is due to the phase mismatches in the dispersive model; their size in deep water causes the nonlinear term to oscillate considerably, keeping the wave from attaining a realistic form. We also looked at the effect different weightings of frequency dependent dissipation mechanisms have on the predictions of these statistics, and found that these mechanisms must contain some frequency dependence to model skewness and asymmetry realistically. This is contrary to Eldeberky and Battjes (1996), who maintained that a constant distribution of dissipation over frequency is optimum. Further work in this area will focus on continued development of the dissipation models.

Acknowledgments

The first author was supported by the Office of Naval Research through the Naval Research Laboratory and a JOI/Core Post-Doctoral Fellowship. Computer time on the CEWES Cray YM-P was provided by the DoD High Performance Computing Center. The second author was supported by the Army Research Office, Grant DAAL 03-92-G-0116. This paper, NRL contribution PP/7322--96-0035, is approved for public release; distribution unlimited.

References

- Agnon, Y., Sheremet, A., Gonsalves, J., and Stiassnie, M., "Nonlinear evolution of a unidirectional shoaling wave field," *Coastal Engineering*, 20, pp 29-58, 1993.
- Bowen, G., "Shoaling and breaking random waves on a 1:35 laboratory beach," M.S. Thesis, Civil Engineering Dept., University of Delaware, Newark, DE, 94p., 1994.

- Eldeberky, Y., and Battjes, J., "Spectral modelling of wave breaking: application to Boussinesq equations," *Journal of Geophysical Research*, vol. 101, no. C1, pp. 1253-1264, 1996.
- Elgar, S., and Guza, R., "Shoaling gravity waves: comparisons between field observations, linear theory, and a nonlinear model," *Journal of Fluid Mechanics*, vol. 158, pp. 47-70, 1985.
- Elgar, S., Freilich, M., and Guza, R., "Model-data comparisons of moments of nonbreaking shoaling surface gravity waves," *Journal of Geophysical Research*, vol. 95, no. C9, pp. 16055-16063, 1990.
- Freilich, M., and Guza, R., "Nonlinear effects on shoaling surface gravity waves," *Proceedings of the Royal Society of London*, A311, pp. 1-41, 1984.
- Kaihatu, J., and Kirby, J., "Nonlinear transformation of waves in finite water depth," *Physics of Fluids*, vol. 7, no. 8, pp. 1903-1914, 1995.
- Kirby, J., and Kaihatu, J., "Structure of frequency domain models for random wave breaking," *Proceedings of the 25th International Conference on Coastal Engineering*, Orlando, FL, to appear, 1996.
- Madsen, P., and Sorensen, O., "Bound waves and triad interactions in shallow water," *Ocean Engineering*, vol. 18, pp. 183-204, 1993.
- Mase, H., and Kirby, J., "Hybrid frequency-domain KdV equation for random wave transformation," *Proceedings of the 23rd International Conference on Coastal Engineering*, Venice, Italy, pp. 474-487, 1992.
- Thornton, E., and Guza, R., "Transformation of wave height distribution," *Journal of Geophysical Research*, vol. 88, no. C10, pp. 5925-5938, 1983.
- Wei, G., Kirby, J.T., Grilli, S.T., and Subramanya, R., "A fully nonlinear Boussinesq model for surface waves. Part 1. Highly nonlinear steady waves," *Journal of Fluid Mechanics*, vol. 294, pp. 71-92, 1995.

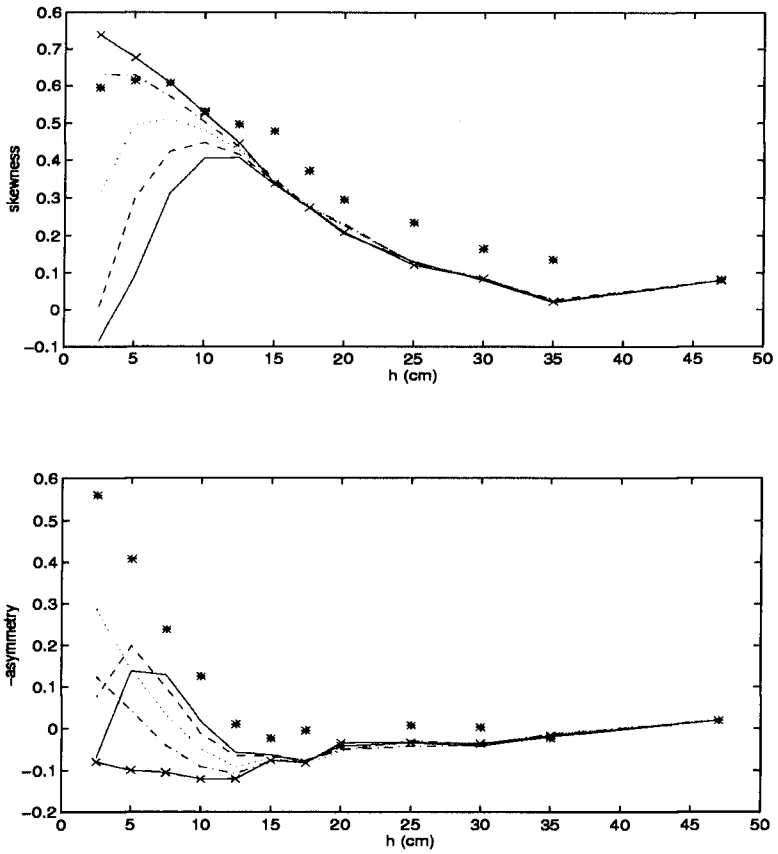


Figure 5. Skewness and asymmetry comparisons between the consistent model of Freilich and Guza (1984) and Case 2 data of Mase and Kirby (1992) for different values of F . In each figure: data (*); $F=0$ (solid); $F=0.25$ (dashed); $F=0.5$ (dotted); $F=0.75$ (dash-dot), $F=1.0$ (dash-x). Top figure: skewness. Bottom figure: - asymmetry.

CHAPTER 11

FIELD OBSERVATION OF MOVEMENT OF SAND BODY DUE TO WAVES AND VERIFICATION OF ITS MECHANISM BY NUMERICAL MODEL

Uda, Takaaki ¹, Yoshimichi Yamamoto ², Naoki Itabashi ² and Kosuke Yamaji ²

ABSTRACT

Bottom sounding data collected from 1983 to 1993 on the Shizuoka coast were analyzed. The results reveal the existence of a sand body moving downcoast at a velocity of about 233m/yr. It is the first time that this kind of phenomenon was observed in the quantitative sense including the spatial and temporal changes in longitudinal profile of the beaches, and this propagation mode is a very interesting phenomenon. In this study, sand movement shoreward and offshoreward of the detached breakwaters is modeled, and a model to predict successive contour line changes is developed, taking into account of time lag caused by the obstruction effect of longshore sand transport due to the detached breakwater. The new phenomenon observed on the Shizuoka coast is well explained by the present model. The propagation velocity of the sand body reproduced by this model is 230m/yr and it is well in agreement with the field observation value.

I . INTRODUCTION

Recently, beach erosion has proceeded at many coasts in Japan. According to the analysis of beach erosion, many of the beach deformations are caused by the imbalance of the longshore sand transport by the obstruction of continuous longshore sand transport due to breakwater, etc., decrease in sediment supply from rivers/sea cliffs, or change in wave field due to the construction of a large-scale harbor breakwater. In all these cases, the basic principle itself of beach deformation is already known, but there still remain many unknown points regarding the quantitative evaluation of the longshore sand transport and an external force of the topographic change, especially the research is insufficient on the change in mechanism of the longshore sand transport associated with the installation of shore protection facilities against erosion such as detached breakwater and headland. This leads to the decreased accuracy in predicting the beach deformation when countermeasures against erosion are taken, and in order to enhance the accuracy of the prediction, this kind of problem must be clarified.

Of the beach deformations due to the above three factors, this study

-
- 1) Dr. Eng., Research Coordinator for Hydraulic Structures, Public Works Research Inst., Ministry of Const., Asahi 1, Tsukuba, Ibaraki Pref. 305, Japan. (FAX. +81- 298-64-1168).
 - 2) Coastal Engineering Department, INA Corporation, Sekiguchi 1-44-10, Bunkyo-ku, Tokyo 112, Japan. (FAX. +81-3-3268-8256).

focuses on the beach deformation due to a sharp decrease in sediment discharge from a river and the Shizuoka coast facing Suruga Bay is selected as the case study area. Through the analysis recent recovery process of the sandy beach due to the increase of the sediment discharge is discussed. As for beach deformation of the Shizuoka coast, Uda et al.(1994) found out that the sediment supplied from the Abe River was moved downdriftward by the longshore sand transport while forming a large mass of sediment (hereinafter called sand body) along the coastline. Tsuchiya(1995) also discussed erosional waves on the Shizuoka coast on the basis of the field data of Toyoshima et al.(1981). As for the shoreline change, this phenomenon is classified into the longshore sand waves recently discussed by Thevenot-Kraus(1995) or can be classified as a type of phenomenon in which the wave-like shoreline propagates alongshore while keeping its form. In addition, there are various names for the longshore sand waves. Sonu(1968) calls them cusp-type sand waves, Bruun(1954) and Grove et al.(1987) migrating sand humps, Inman(1987) accretion and erosion waves, and Verhagen(1989) simply sand waves. Of these studies, especially the accretion and erosion waves by Inman(1987) are produced when a coastal structure such as a groin is installed or the sediment supply from a river or the source of littoral drift, is sharply increased due to flood, and they propagate along the coastline while being accompanied by weak diffusion.

On the Shizuoka coast, the erosion waves were produced from the beginning of the 1970s to around 1983 before the movement of the sand body, and propagated alongshore, and this is completely the same phenomenon as the erosion waves mentioned by Inman(1987). On the Shizuoka coast, seawalls, many wave dissipating armour units and detached breakwaters were installed on the eroded beach after the erosion waves were gone, and the foreshore was almost completely lost. Subsequently, the movement of the sand body started. Such a characteristic change has shown that the sediment was accumulated only when the leading portion of the sand body arrived. In all the past studies, the sand waves propagated alongshore on the coast with a continuous sandy beach. And in this respect, the longshore sand waves subject to this study are remarkably different from others. In this study, a soliton, instead of many waves, propagated alongshore while being accompanied by weak diffusion, and so this may be called by the movement of a sand body different from other types and its occurrence mechanism will be discussed.

As to the theoretical study on the longshore sand waves, Thevenot-Kraus(1995) numerically solved a diffusion equation including the advection term on the shoreline change, and they well explain the propagation of the longshore sand waves on Southampton Beach, New York, U.S.A. But their study is on the predictive model of shoreline change and has not reached the level of predicting the three-dimensional beach deformation. On the Shizuoka coast a number of detached breakwaters have been installed, and they are considered to be closely related to the movement of the sand body, which suggests the necessity of modeling of the obstruction effect of littoral transport by the detached breakwaters. For this reason, in this study, contour line change model which can predict three-dimensional topographic changes by assuming the depth distribution of the longshore sand transport rate, is applied to the Shizuoka coast to clarify the movement of the sand body.

II. OBSERVATION OF MOVEMENT OF SAND BODY ON SHIZUOKA COAST

(1) General

The Shizuoka coast is located on the west shore of Suruga Bay and is a sandy beach extending 7.8km northeastward from the Abe river mouth, as shown in Fig.1, Fig.2 shows the sea bottom contours off the Shizuoka and Shimizu coasts. On the Shizuoka coast as well as the Shimizu coast, it is very steep as 1/10 near the shoreline. In the offshore zone ranging from 10m to 30m depth, a continental shelf of mild slope of 1/150 spreads, but the bottom slope at the tip of the Mihono-matsubara sand spit is steep at about 1/5.

During the Jomon Transgression of the sea level, it is considered that hill side of Mt. Kuno was eroded to supply sediment toward the Mihono-matsubara sand spit, but at the present sea level, the only supply source of sediment to the sand spit is the Abe River. In the Abe River, the river bed excavation was carried out extensively before 1967, causing sharp decrease of the sediment discharge of this river and then serious beach erosion was triggered from near the river mouth and spread out northeastward. Presently, the most severely eroded portion of the beach is approaching the tip of the Mihono-matsubara sand spit. Much sediment supplied from the Shimizu coast is transported from the northeast end of the Mihono-matsubara sand spit into submarine canyons.

The study area ranges from No. 0, 7.8km away northeastward from the Abe River mouth, to No. 78 of the Abe river mouth, as shown in Fig. 2. The interval of the measuring line is 100m. On the Shizuoka coast, bottom soundings have been done along these measuring lines once a year. According to the sampling test of bottom materials conducted at 9 points in 1km intervals alongshore from the Abe River mouth on February 20, 1989, the median diameter of the beach materials near the shoreline of the Shizuoka coast is around 7.5mm

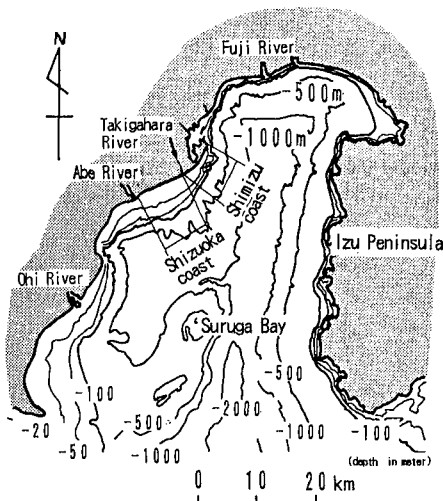


Fig.1 Location of Shizuoka coast in Suruga Bay.

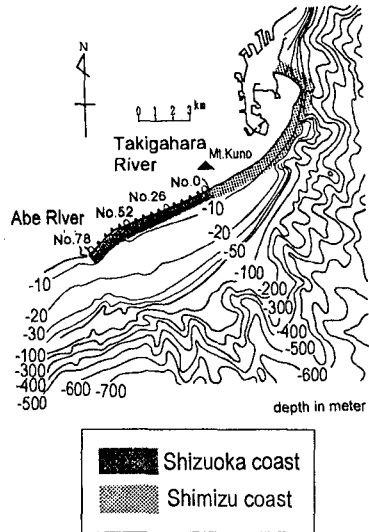


Fig.2 Sea bottom contours of Shizuoka and Shimizu coasts and alignment of measuring lines.

(2) Change in Shoreline Position and Longitudinal Profile on Shizuoka coast

On the basis of the bottom sounding data, the change in shoreline position by selecting 1989 as the reference year, is shown in Fig. 3. In the figure, No. 78 is located next to the left bank of the Abe River mouth, and the origin of the longshore distance is set at 7.8km east-northeast from the river mouth. On the top of the figure, approximate locations of various shore protection facilities (detached breakwater, seawall, groin, wave dissipating armour units and jetty) are shown.

The main change in shoreline position started near the Abe River mouth, the source of the littoral drift on the Shizuoka coast. In the beginning, the erosion concentrated on the south side of the jetty of the Hama River as the boundary, but after 1990, the erosion spread fast northward of the jetty of the Hama River. Simultaneously with the northward spread of the accretion area, the shoreline retreated fast in the areas (e.g. section between No. 66 and No. 70 in 1987) where the shoreline had been remarkably advancing in the beginning, and as a whole, the aggregate of sediment (sand body) moved northward with mild deformation. In 1993, north of No. 38 where the leading edge of the sand body seems to have arrived, the shoreline hardly moved in comparison with the southern side, indicating that the beach was completely eroded and there is no sediment to move because the area is totally covered with seawalls and wave-dissipating armour units and no foreshore exists. From Fig. 3, the propagation velocity of the leading edge of the sand body between 1984 and 1993 is calculated to be 233m/yr.

The profile change of the beach associated with this sand body movement is investigated in two sections : No. 67 between breakwaters in the area where the shoreline greatly advanced until 1988 but retreated subsequently, No. 62 without breakwaters.

Fig. 4 shows the profile change of No. 67. Until 1988, the accretion took place in the area shallower than -4m, but subsequently the accretion occurred in a wide area shallower than 7m depth. Taking into account of the fact that the breakwaters were installed at a depth of 3m in this area, it is found that the accretion occurred shoreward of the breakwaters until 1988, but after that the area was filled with sand, littoral drift started to pass through the offshore side of the breakwaters, causing the accretion in that area. In the period between 1983 and 1993, remarkable profile changes were seen mostly in the area shallower than -7m.

As to the profile change of No. 62 shown in Fig. 5, much sediment

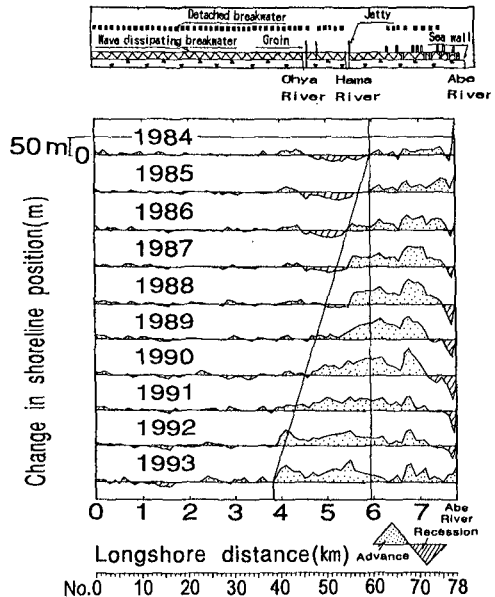


Fig.3 Change in shoreline position on Shizuoka coast (reference year:1983)

accumulated in the area shallower than -4m until 1989, but subsequently an erosion occurred. In this profile, too, the topographic changes were seen mostly in the area shallower than -7m, but the bottom fluctuation between -5m and -7m was small in contrast to the remarkable bottom changes between -5m and -7m at No. 67 located between breakwaters.

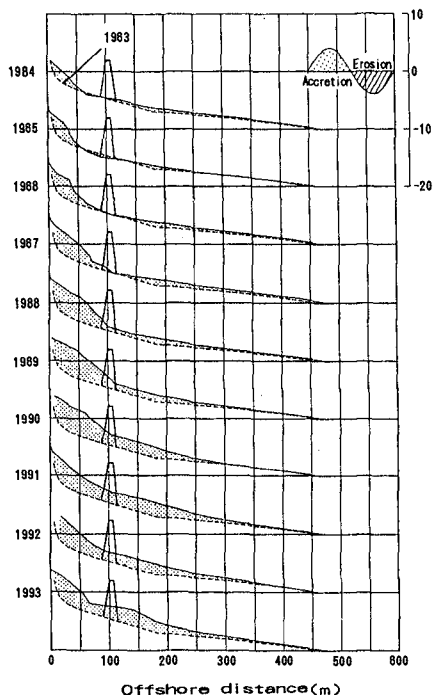


Fig.4 Change in longitudinal profile along measuring line No. 67 on Shizuoka coast.

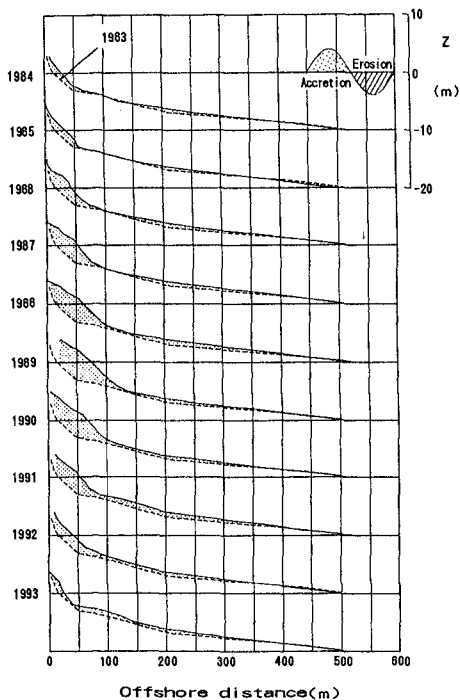


Fig.5 Change in longitudinal profile along measuring line No. 62 on Shizuoka coast.

(3) Littoral Drift and Propagation Velocity of Center of Gravity of Sand Body

As to beach deformation of the Shizuoka coast, it was found that the sea bottom slope greatly changed with the accretion of sediment. As an index of the change in cross-sectional area, the change in cross-sectional area of the beach between +5m and -3m equivalent to the water depth at the shore end of the detached breakwaters, and between +5m and -7m equivalent to the critical depth for sand movement were determined and their spatial and temporal changes were investigated.

The sand volume shallower than -7m was increasing with the elapse of years, but the longshore stretch where the remarkable volume change was observed was limited in each year. Therefore, the region shown in Table 1 was selected in each year, and the volume change was calculated and the time change in sand volume together with the change in the foreshore area is shown in Fig. 6. From this, it is realized that on the average from 1983 to 1993, the total sand volume increased at the rate of $10 \times 10^4 \text{ m}^3/\text{yr}$, though some fluctuation existed. In this area, as a whole,

northeastward littoral drift is dominant, and the only sediment supply source is the Abe River. On the northeast side of the tip of the sand body, seawalls and wave-dissipating armour units

Table 1 Integration region of sand volume and location of center of gravity of sand body.

Measured year	Integretion region	Longshore distance of accretion zone(m)	Longshore distance(m) of center of gravity from No.78
1984	No. 60~No. 78	1,800	471
1985	No. 60~No. 78	1,800	508
1986	No. 55~No. 76	2,100	997
1987	No. 55~No. 76	2,100	1,247
1988	No. 55~No. 75	2,000	1,376
1989	No. 46~No. 72	2,600	1,586
1990	No. 46~No. 72	2,600	1,773
1991	No. 38~No. 72	3,400	2,078
1992	No. 39~No. 72	3,300	2,263
1993	No. 38~No. 78	4,000	2,373

have been installed, and no beach deformation has been observed, and in fact, the littoral drift rate is considered as 0. Therefore, the increase rate of the total sand volume shown in Fig. 6 should be equal to the littoral transport rate supplied to this area from the Abe River mouth. Uda·Yamamoto(1994) estimated, on the basis of the time change in beach topography, that the littoral transport rate on the Shimizu coast was about $13 \times 10^4 \text{ m}^3/\text{yr}$. Before the Shizuoka and Shimizu coasts were eroded, almost the same littoral transport rate was considered to exist over the entire area, and therefore the littoral transport rate in this area is also assumed to be about $13 \times 10^4 \text{ m}^3/\text{yr}$. The littoral transport rate after 1983 is about 77% in comparison with this.

The foreshore area and total sand volume in the zone higher than 0m and shallower than -3m shown in Fig. 6 increased until 1989, but thereafter they remained almost at certain values, implying that although the accretion seems to have stopped in view of the change in sand volume shoreward of the detached breakwaters, actually the accretion continues in the offshore zone.

Fig. 7 shows the time change of the longshore distance from No.78 of the center of gravity of the accretion area. In all cases except the period of 1983-1984, the center of gravity of the sand body moved monotonously northward and the average propagation velocity of the center of gravity is 235m/yr. The fact that the propagation velocity of the center of gravity is identical in all three types of integration regions means that almost the

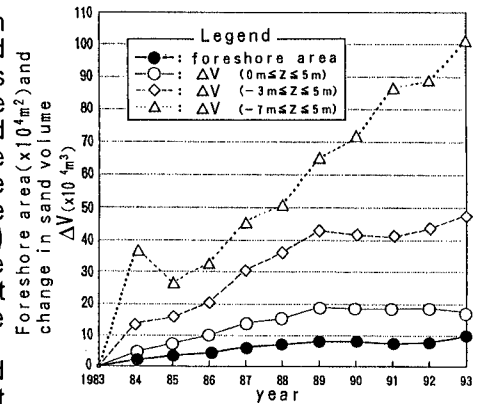


Fig.6 Time change in sand volume and foreshore area of the beach (reference year:1983)

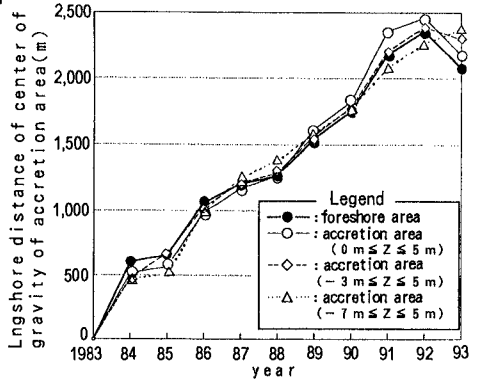


Fig.7 Movement of center of gravity of sand body.

same propagation velocity of the center of gravity existed at any place. While the sand volume of the beach shoreward of the detached breakwaters saturated in 1989, the center of gravity moved with keeping almost the same velocity. This means that although the sand volume shoreward of the detached breakwaters does not change, it, as a whole, is also moving at the same velocity. Uda·Yamamoto(1994) estimated from the shoreline changes that the phase velocity of the erosion wave before the construction of the detached breakwaters was 0.5 to 0.8km/yr. In comparison with this value, it is realized that the propagation velocity was reduced to 0.47-0.29 times due to the installation of the detached breakwaters.

III. REPRODUCTION OF PROPAGATION PHENOMENON OF SAND BODY BY CONTOUR LINE CHANGE MODEL

(1) Contour Line Change(CLC) Model

Uda-Kawano(1996) developed a model which can predict the spatial and temporal changes of the contour line by assuming depth change in littoral transport rate. This model is designed for a coast with a steep slope near the shoreline and without the existence of bar/trough topography and it can model the effects of coastal structures such as groin, seawall and breakwaters. But in the former study it was difficult to model the permeable detached breakwaters installed in the breaker zone. For this reason, here modeling of the permeable breakwaters is carried out.

The Shizuoka coast has a steep slope near the shoreline and has no bar/trough, suggesting that the beach deformation is caused only by the action of the littoral transport even around the breakwaters. From this, the CLC model to predict the topographic changes due to the littoral transport may be applicable for reproducing the propagation phenomenon of the sand body. With the CLC model, it is possible to predict the three-dimensional topographic changes including the profile changes of the beach by assuming the depth change in littoral transport rate.

The fundamental equations of the model is shown below. If the breaker angle of waves is assumed to be sufficiently small using the Savage formula, Eq.(1) stands.

$$Q = F_0 \left(\tan \alpha_0 - \frac{\partial y_s}{\partial x} \right) \quad (1)$$

Where Q : littoral transport rate, F_0 : a coefficient of littoral transport rate dependent on wave energy flux, α_0 : breaker angle, x : longshore distance, and y_s : shoreline position measured normal to x axis. Eq.(1) is established under the assumption that the beach profile makes parallel movement in time and space.

Now a region is divided by n contour lines, and the littoral transport rate at each water depth corresponding to $k=1 \dots n$ is set to be q_k and if a similar relationship is assumed to be satisfied between the contour line position y_k and q_k in analogy with Eq. (1), the following equation is obtained.

$$q_k = F_{0k} \left(\tan \alpha_0 - \frac{\partial y_k}{\partial x} \right) \quad (2)$$

Where $F_{0k} = F_0 \cdot \mu_k$, $\sum \mu_k = 1$. Eq. (2) assumes that the littoral transport

rate in each layer is governed by the relationship between each contour line and incident wave direction at breaking point. In the CLC model, therefore, the contour lines do not need to make parallel movement like the shoreline change model, and this makes it possible for the littoral transport to pass the offshore zone of the detached breakwaters. This is because even if the shoreline is perpendicular to the direction of the breaking waves, they are obliquely incident to the offshore contour lines, which makes it possible for the littoral transport to move. From the above, the littoral transport rate in the shoreline change model and the littoral transport obtained by integrating littoral transport rate in each layer in the CLC model are not equal except in the case of parallel contour lines.

μ_k is a coefficient to give the littoral transport rate for each water depth and is calculated using Eq. (3) by giving the depth change of the littoral transport rate.

$$\mu_k = \int_{z_k}^{z_k+1} \xi(z) dz / \int_{-h_c}^{h_r} \xi(z) dz \quad (3)$$

where z is the vertical distance with reference to the still water level as the reference, h_r wave run-up height and h_c critical depth for sand movement. The continuity equation of the littoral transport is given as follows :

$$\frac{\partial q_k}{\partial x} + h_k \frac{\partial y_k}{\partial t} = 0 \quad ; \quad k = 1 \dots n \quad (4)$$

where h_k ($k = 1 \dots n$) is the characteristic height of beach changes as given by Eq.(5)

$$h_k = Z_k - Z_{k-1} \quad (5)$$

If the functional form of $\xi(z)$ is given, μ_k is calculated by Eq. (3), and so the contour line change for each depth is calculated by simultaneously solving Eqs.(2) and (4). The depth change in littoral transport rate may be assumed to have such a distribution that it varies between the wave run-up height(h_r) and critical depth for sand movement(h_c), so as to satisfy empirically the field and experimental data.

$$Z^* = Z / H_b \quad , \quad h_c^* = h_c / H_b \quad (6)$$

When $-h_c \leq z \leq h_r$,

$$\xi(Z^*) = 2 / h_c^{*3} (h_c^* / 2 - Z^*) (Z^* + h_c^*)^2 \quad (7)$$

When $z < -h_c$ and $z > h_r$,

$$\xi(Z^*) = 0 \quad (8)$$

In this model stabilization mechanism of beach profile is taken into account as described in detail in Uda-Kawano(1996). If the bottom slope between contours exceeds a critical slope on the foreshore the sea bottom, the local slope is reset by the critical slope and the position of the contour lines is adjusted so as to satisfy the eroded and accreted areas in the profile are equivalent.

In the calculation it is necessary to determine the wave height and breaker angle. There are various methods for predicting wave field. Here the numerical calculation method of the energy balance equation by Karlsson(1969) is used, including the refraction, shoaling and diffraction effects for irregular waves. Wave dissipation effect is calculated using the method of Takayama et al.(1991) and wave breaking was evaluated by Goda's breaker index. Since this study deals with the permeable detached breakwater, wave energy transport is set to be proportional to the square of the wave transmission coefficient of the detached breakwater.

(2) Modeling of Detached Breakwater

Without detached breakwaters, the depth change in littoral transport rate is given by Eqs.(7) and (8). Even when there are detached breakwaters, these equations are applicable if the breaking point is located shoreward of the detached breakwaters, but the dominant sand movement zone is narrowed because the breaker height is decreased. If, on the other hand, the breaking point is off the detached breakwaters, further modeling is required. This is because under such a condition that the breaking point moves off the detached breakwaters, and the cusped spit has been already developed behind the detached breakwaters. Since the detached breakwaters are permeable, the cusped spit does not become the tombolo to completely reach the detached breakwaters, leaving seawater surface between the cusped spit and the detached breakwaters. In this case, the cusped spit, like the groin, obstructs the longshore sand movement, but sand can still pass in the gap between the cusped spit and detached breakwaters.

Now, the depth change in littoral transport off the detached breakwaters is calculated by Eqs.(7) and (8) using the breaker height in the offshore zone, and the distribution of littoral transport rate shoreward of the detached breakwaters is calculated by multiplying the littoral transport rate given by these equations by the obstruction rate (ϵ) of the littoral transport. Since it may be considered that the obstruction rate of the littoral transport is proportional to the cross-sectional shape of the cusped spit, the following expression is assumed.

$$\epsilon = 1.0 - \left(\frac{y_1}{y_{d0}} \right)^n \quad (9)$$

Where the offshore distance from the seawall to the detached breakwaters is y_{d0} and the distance from the seawall to each contour line (including the contour lines of the land portion) is y_1 (see Fig. 8).

If the obstruction rate (ϵ) of the littoral transport is equal to 1.0, the littoral transport rate passing behind the detached breakwaters is 0, equivalent to that of the impermeable groin. At $\epsilon = 0.0$, the littoral transport rate passing behind the detached breakwaters is completely the same as that of the natural sandy beach.

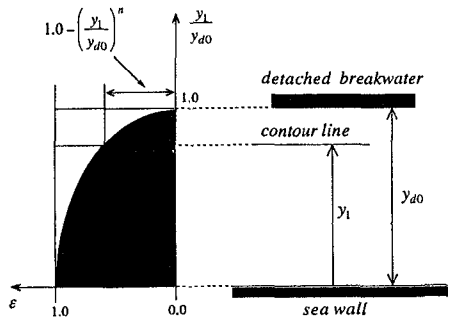


Fig.8 Definition of obstruction rate of littoral transport due to detached breakwater.

(3) Application of Model

In Fig. 3, the extension of the area where the remarkable movement of the sand body was observed is about 4km from the Abe River mouth. As shown in Fig. 2, the Abe River mouth forms a river-mouth delta with a considerably protruded shoreline, and in this area the movement of

the sand body is not clear, whereas in the area with almost parallel contour lines on the northeast side of the mouth, remarkable movement is observed. From this reason, the parallel contour lines are simply assumed in this study. But the existence of the detached breakwaters is important for investigating the movement of the sand body, and so due attention must be paid to the modeling of the detached breakwaters. Fig. 9 shows the contour of initial topography. The slope near the shoreline is steep and the offshore is a flat bottom. Along this coastline, seawall and wave-dissipating armour units have been installed and the contour line cannot retreat from the initial position, and therefore the contour line shape given by the initial topography is regarded as the retreat limit. The validity of this assumption will be realized from the fact that in the profile change along the measuring line No. 62 as shown in Fig. 5, the shoreline advanced, but was again eroded and returned to the original concave profile vertically upward. In Fig. 9, 28 detached breakwaters of 80m long are installed at intervals of 40m. Actually the detached breakwaters on the Shizuoka coast have been installed over years, but here the detached breakwaters are installed at the same time to simplify the calculation.

For the numerical calculation, the finite difference method is used, and the area shown in Fig. 9 is meshed at intervals of 10m. The wave transmission coefficient of the detached breakwaters is set at 0.4.

As to the wave conditions, from the observation results of 1976 to 1991 at the Irozaki Observatory of the Meteorological Agency, 3.0m significant wave with the occurrence rate of 2% is selected as the high wave to give a dominant effect on the topographic change, and the period is set at 9s from the correlation of the wave height/period based on the same observation results. In the calculation, the continuous period of the above mentioned high wave is set at 27 days per year so that the incident energy of the waves per year is approximately equal to the measured value. As to the wave direction, SSE is set based on the predominant wave direction observed at the Mochimune Fishery Harbor located 2.5km southwest of the Abe River mouth. The time step for the topographic change calculation is 10min. As the topography changes, the wave field also changes. The repetitive time interval must be set in consideration of the situation of the topographic change. Here the calculation aims at the prediction of the long-term and relatively mild topographic changes, and so the repetitive time was set at 3 days, sufficiently shorter than the annual order (27 days).

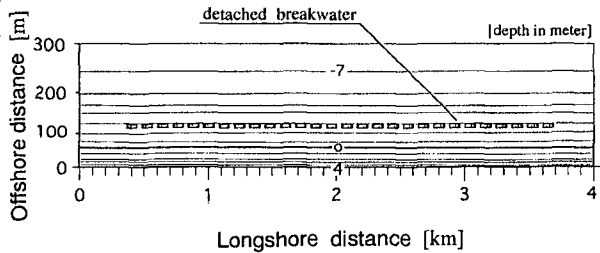


Fig.9 Model beach for movement of sand body.

In the calculation, h_c and h_r were set to be 4.0m and 7.0m, and the contour line deformation is predicted at intervals of 1m.

The boundary condition of sediment supply greatly depends on the flood. Due to the flood records since 1980 at a location 4.7km upstream from the river mouth, floods of $1000\text{m}^3/\text{s}$ or larger in daily average of flood discharge occurred seven times between 1980 and 1993 as shown in Table 2, and especially

Table 2 Flood discharge of Abe River.

DATE	Daily average of flood discharge [m^3/s]	Maximum flood discharge [m^3/s]
Aug. 2, 1982	1,129	} 3,857
Aug. 3, 1982	1,466	
Sep. 12, 1982	1,723	
Aug. 2, 1983	1,731	2,981
July. 2, 1985	1,523	————
Aug. 10, 1990	1,005	————
Sep. 2, 1991	1,396	2,511

on September 12, 1982, the flood of the largest discharge $3857\text{m}^3/\text{s}$ occurred, but thereafter large-scale floods hardly occurred. From this, as a boundary condition, the constant sand supply of $10 \times 10^4\text{m}^3/\text{yr}$ was given as the total littoral transport from $x=4.0\text{km}$ and distributed to the littoral transport rate for each contour line by Eq.(7). On the other hand, the $x=0.0\text{km}$ was set as the passing boundary.

In Case 1, the power n ($n=1.0$) of Eq.(9) is assumed as the obstruction rate of the littoral transport behind the detached breakwaters. In this case, the propagation velocity of the sand body becomes excessive in comparison with the measured value, and in Case 2, the power $n=1.6$ was used.

In the calculation of the topographic changes around the detached breakwaters using the present model under the above mentioned conditions, the contour lines around the detached breakwaters tend to locally protrude with the elapse of time, and there are some cases in which the condition that the breaker angle of waves is sufficiently small is not satisfied even after the wave refraction. In such a case, in order to enhance the stability of the calculation, even if the reproduction of the local shape of the leading edge of the sand body is somewhat sacrificed, the upper limit is set to be 30° for the angle (θ) between the contour line and the wave crest line at the breaking point.

(4) Results of the Calculation

First the topographic change in Case 1 is shown in Fig. 10. Sand is supplied from $x=4.0\text{km}$ and from there sand passes through a group of the detached breakwaters located on the downcoast. Sand clearly moves as the sand body downdriftward, and sand supplied from the river mouth does not show rapid diffusion pattern. Although the mechanism of the sand transport is due to the littoral transport associated with wave breaking, the diffusion of sand is suppressed because of the existence of the detached breakwaters and instead of this, the sand body movement is observed. In this case, the propagation velocity of the leading edge of the sand body is $360\text{m}/\text{yr}$, 56% higher than observed $233\text{m}/\text{yr}$.

It is considered as the cause that the obstruction rate of the littoral transport behind the detached breakwaters is too small(that is, the passing rate of littoral transport is excessive), and in Case 2, therefore, the obstruction rate of the littoral transport behind the detached breakwaters was increased by setting the power n in Eq.(9) as $n = 1.6$. The results are shown in Fig. 11. The beach changes are similar to those of

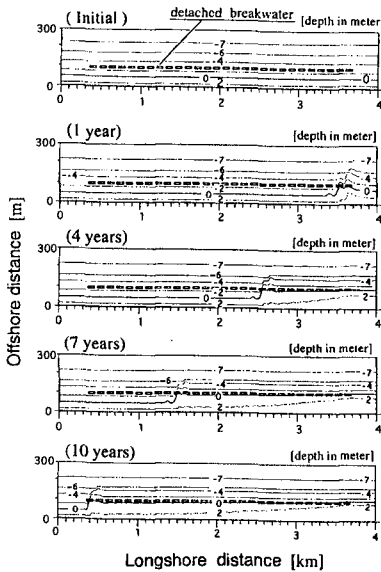


Fig.10 Predicted beach changes (case ①).

Case 1, but the propagation velocity of the leading edge of the sand body is 230m/yr, in agreement with the 233m/yr of the observed result. Since the obstruction rate of the littoral transport shoreward of the detached breakwaters increased, +2m contour line further advanced.

In the topographic changes shown in Figs. 10 and 11, the profile changes on the updrift side of the littoral transport monotonously with time, and therefore it is sufficient to show the profile change at one section. Fig. 12 shows the profile changes of the section passing at the center of the detached breakwaters shown by A-A' in Fig. 11.

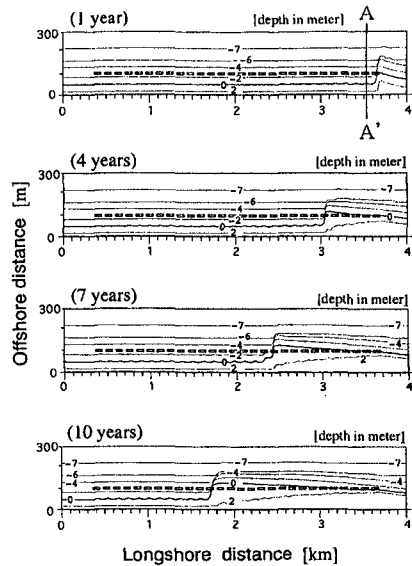


Fig.11 Predicted beach changes (case ②)

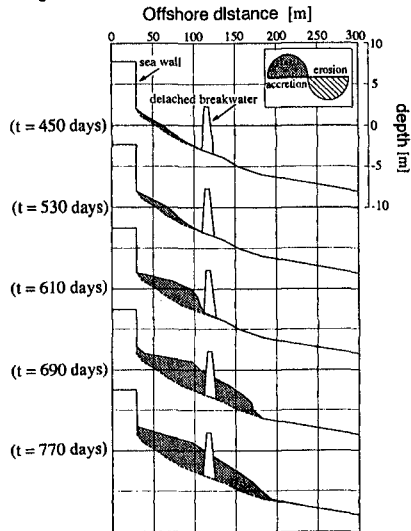


Fig.12 Predicted beach profile changes

It is clearly understood that in the beginning accretion concentrated shoreward of the detached breakwaters, and when the accretion in the zone between the detached breakwater and the seawall becomes full, the accretion advances off the detached breakwaters. As shown in the beach profile after 770 days, the cusped spit is sufficiently developed, but even in this stage, the littoral drift pass over the foreshore behind the detached breakwaters. The accretion off the detached breakwaters well corresponds to the observed results on the Shizuoka coast shown in Figs. 4 and 5.

IV. DISCUSSION

In this study, the propagation phenomenon of the sand body was discovered through the analysis of the field data of the Shizuoka coast and investigated its occurrence mechanism by means of the CLC model. Occurrence of the sand body can be summarized as follows. First, the littoral transport sand is supplied from the updrift side of the coast provided with detached breakwaters, and when it passes through a group of the detached breakwaters, sand accumulates behind each detached breakwater. When the sand volume accumulated behind the detached breakwater becomes sufficiently large, the sand passes off the detached breakwaters and moves downdriftward, and in the meantime, time lag occurs. As a result, when many detached breakwaters are installed, the propagation phenomenon such as the sand body occurs and looks as if the solitary wave propagates. In comparison with the already clarified propagation velocity of the erosion wave in the eroded area on the Shizuoka coast, the propagation velocity of the sand body is smaller (0.47 to 0.29 times), and this means that the detached breakwaters obstruct it. Presently, the Shimizu coast located northeast of the Shizuoka coast is exposed to severe erosion, but since the velocity of the movement of the sand supplied from the Abe River mouth to the Shimizu coast is greatly reduced, it will take about 30 years for the sand body to move 8.2km from the leading edge of the sand body of the Shizuoka coast to the remarkably eroded point of Shimizu coast (where detached breakwaters are installed as in the case of the Shizuoka coast). This indicates that the countermeasures against erosion on the Shimizu coast must be considered without expecting the sand supply from the upcoast over about 30 years in the future. During this period the sand supply it is required will be minimal, and so to carry out beach nourishment until the sediment reaches the Shimizu coast in order to maintain the sandy beach.

IV. CONCLUSIONS

The main conclusions of this study is summarized as follows.

(1) Observing the beach deformation in the period of 1983 to 1993 on the Shizuoka coast, it was found that the sediment aggregate (sand body) moved downdriftward while deforming. The propagation velocity of the center of gravity of the sand body was 235m/yr, 0.47 to 0.29 times the phase velocity of the erosion wave before the detached breakwaters were installed in the same area.

(2) In this sand body area, the sediment of $10 \times 10^4 \text{ m}^3/\text{yr}$ was accumulated from 1983 to 1993. The sediment supply source of the Shizuoka coast is the Abe River only, and since it is considered that the outflow of sediment beyond the leading edge of the sand body is very small, this accumulated volume is equal to the sand volume supplied from the Abe River into this area. This drift sand volume is about 77% of the estimated sand volume of $13 \times 10^4 \text{ m}^3/\text{yr}$ before the remarkable erosion occurred.

(3) The contour line change model so far limited to the utilization for predicting the topographic changes at the natural sandy beach and around the groin, seawall, and breakwater was extended so that it can be also utilized for predicting the topographic changes around the permeable detached breakwaters installed within the breaker zone. This makes it possible for the contour line change model, so far limited to the application to steep-sloped coasts, to be utilized for predicting

topographic changes around all the structures normally installed on coasts.

(4) By applying this model for reproducing the propagation phenomenon of the sand body observed at the Shizuoka coast, it is found to be attributable to the existence of the detached breakwaters installed along the coastline and the occurrence of floods of the Abe River, the sediment supply source to this coast. That is, when the drift sand flows from the upstream side, accretion develops first shoreward of the detached breakwaters, and when the shore-side area becomes full, accretion develops off detached breakwaters, making it difficult for the drift sand to pass through around the detached breakwaters, and this is the main factor for the propagation phenomenon of the sand body.

References

- Bruun, P. (1954): Migrating sand waves or sand humps, with special reference to investigations carried out on the Danish north coast sea, *Proc. 5th Coastal Eng. Conf.*, ASCE, New York, pp.269-295.
- Goda, Y. (1970): On the breaker indices, *Proc. of JSCE*, Vol. 180, pp.39-49. (in Japanese)
- Grove, R.S., Sonu, C.J. and Dykstra, D.H. (1987): Fate of massive sediment injection on a smooth shoreline at San Onofre, California, *Proc. Coastal Sediments '87*, ASCE, New York, pp.531-538.
- Inman, D.L. (1987): Accretion and erosion waves on Beaches, *Shore & Beach*, Vol.55, No. 3 and 4, pp.61-64.
- Karlsson, T. (1969): Refraction of continuous ocean wave spectra, *Proc. of ASCE*, Vol.95, No. WW4, pp.437-448.
- Sonu, C.J. (1968): Collective movement of sediment in littoral environment, *Proc. 11th Coastal Eng. Conf.*, ASCE, New York, pp.378-398.
- Takayama, T., N.Ikeda and T.Hiraishi (1991): Wave deformation calculation in consideration of wave breaking and reflection, *Rep. of P.H.R.I., Ministry of Transport*, Vol.30, No. 1, pp.21-67. (in Japanese)
- Thevenot, M.M. and N.C.Kraus (1995): Longshore sand waves at Southampton Beach, New York: observation and numerical simulation of their movement, *Mar.Geol.*, 126, pp.249-269.
- Toyoshima, O., S.Takahashi and I.Suzuki (1981): Erosion characteristics of Shizuoka coast, *Proc. of Japan Coastal Eng.*, Vol.28, pp.360-364. (in Japanese)
- Tsuchiya, Y. (1995): Wave characteristics of beach erosion (1) -an example of Shizuoka coast, *Proc. of Japan Coastal Eng.*, Vol. 42, pp.551-555. (in Japanese)
- Uda, T. and K.Yamamoto (1994): Beach erosion around a sand spit -an example of Mihono-matubara Sand Spit, *Proc. 24th Coastal Eng. Conf.*, ASCE, pp.2726-2740.
- Uda, T., T.Suzuki, M.Ohishi, Y.Yamamoto and N.Itabashi (1994): Longshore sand transport rate on Shizuoka coast and evaluation of its distribution, *Proc. of Japan Coastal Eng.*, Vol.41, pp.536-540. (in Japanese)
- Uda, T. and S.Kawano (1996): Development of contour line change model for predicting beach changes, *Proc. of JSCE*, No.539/II -35, pp.121-139. (in Japanese)
- Verhagen, H.J. (1989): Sand waves along the Dutch coast, *Coastal Eng.*, 13, pp.129-147.

CHAPTER 12

Wave Groups in the Surf-Zone: Model & Experiments

J. Veeramony and I. A. Svendsen¹

Abstract: Experiments were conducted with regular wave groups incident on a plane beach to analyze the behaviour of the groups in the breaking region and in the surf-zone. The groups were composed of individual cnoidal waves. Emphasis was laid on obtaining measurements in the breaking region and in the surf-zone. It was found that the location of the start of breaking of the individual waves was affected by the groupiness of the waves. The structure of the groups were also seen to be different inside the surf-zone, which changes the forcing for the long wave. The long wave motion is forced at the group frequency and can be resolved into two components, an incident forced wave, which varies along the tank and a free standing wave. The standing wave is generated because the free outgoing long wave is reflected at the wavemaker, where there was no absorption of waves. A conservation model was developed using the kinematic conservation equation and the energy conservation equation. The dispersion relation was used to close the system of equations. Cnoidal theory was used in the shoaling region and bore theory was used in the surf-zone. It was found that the model accurately predicts the group structure and the individual wave location in the shoaling region, but does not do well in the surf-zone.

1. Introduction.

Wave groups have been long recognized as one of the primary driving mechanisms for long wave generation (Kostense, 1984; Watson et al. 1994; Longuet-Higgins & Stewart, 1962; Symonds et al, 1982; Schäffer & Svendsen, 1988; Schäffer, 1993; List 1991). However, the lack of comprehensive data in the breaking region and in the surf-zone has precluded the understanding of how the groups develop in that region.

The first part of this study reports experimental results for the development of wave groups in the shoaling region and in the inner surf-zone. The experiments also provide information about the variation of the break point of the individual

¹Center for Applied Coastal Research, Ocean Engineering Lab, University of Delaware, Newark, DE 19716, USA. Correspondence e-mail: jay@coastal.udel.edu

waves in the group. The long wave motion will also be analyzed from the measurements (for further details on the experimental results, see also Svendsen and Veeramony, 1995).

In the second part, we will focus on efforts to model the development of the wave groups on the basis of two conservation equations, namely kinematic conservation and energy conservation. The results of the model will be compared to the measurements described in the experimental part of the study.

2. Experimental set-up.

The experiments were conducted in a wave flume (figure 1) which is 30 m long, 0.75 m wide and 1.0 m deep. The water depth for the experiments was maintained at 0.4 m. The wave flume has a 1:35 beach, the toe of which starts at 11.85 m from the mean position of the piston type wavemaker.

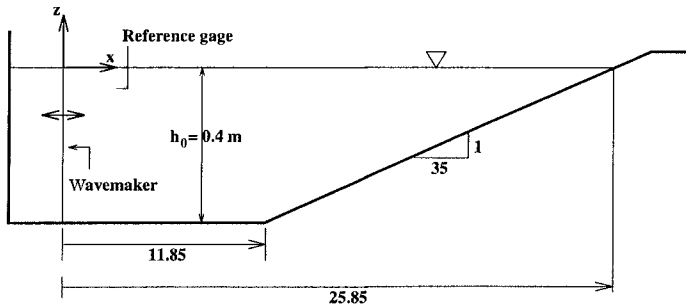


Figure 1: Definition sketch of the experimental setup.

The wave groups were composed of a series of five cnoidal waves, each of which was generated according to the method given by Goring (1978). The individual cnoidal waves were joined at the mean water line to form a group (figure 2). The height of the waves in the group was specified as

$$H_i = H_m \left(1 + \frac{G}{2} \sin \frac{2\pi i}{n} \right); \quad i = 1, \dots, 5 \quad (1)$$

where H_i represents the height of the i^{th} wave in the group, H_m the mean wave height, and $G = \Delta H / H_m$ is the variation of the wave height in the group.

In all, seven experiments were conducted. In this paper, discussion will be limited to three of those experiments, the parameters of which are shown in table 1.

Each experiment was repeated many times with different positions of the wave gages. It is therefore important to verify the repeatability of the experiments.

Figure 3 shows the measured wave groups at three different locations for experiment W06. At the reference gage [Figure 3(a)], the variation from wave group to group is seen to be negligible. Inside the breaking region [Figure 3(b)] and inside the surf-zone [Figure 3(c)], there is seen to be some variability which is expected. To an extent, this is caused by the variations in the horizontal position of the waves in the group.

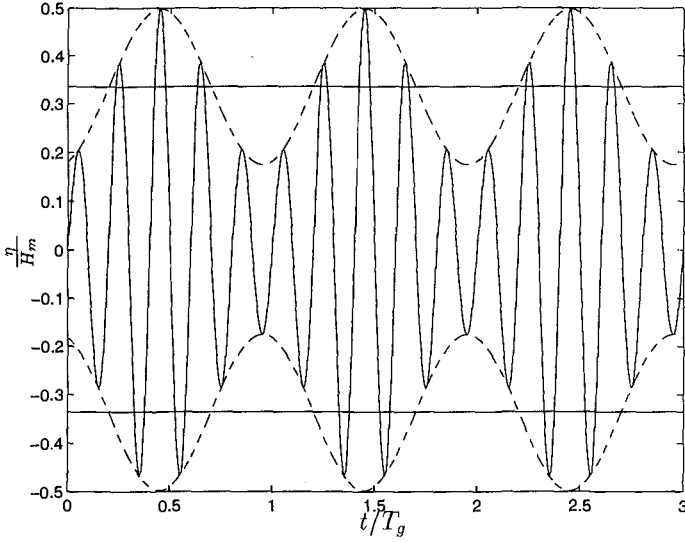


Figure 2: Schematic of the wave group generated at the wavemaker.

Experiment number	H_m/h_0	$T_m\sqrt{g/h_0}$	Groupiness factor G
W01	0.167	7.43	$\pm 10\%$
W03	0.237	12.38	$\pm 20\%$
W06	0.25	7.92	$\pm 50\%$

Table 1: Wave parameters at the wavemaker. H_m is the mean height of the short waves, T_m is the period of the short waves and h_0 is the water depth at the wavemaker.

To eliminate the effect of initial disturbances and surges in the tank, the data collection for each run was not started until 30 minutes after the start of wave generation.

3. Wave breaking.

One of the important questions is how the wave groupiness affects the individual wave breaking. There is no one method for the prediction of wave height or water depth at breaking, even for monochromatic waves. All current methods for predicting wave breaking are based on empirical formulations extracted from existing data. However, it is known that both the wave height and the wave height to water depth ratio have a maximum at or near the breaking point. In this analysis, we use the maximum of the wave height to water depth ratio as the definition of the break point, which can be expressed mathematically as

$$\left(\frac{H}{h}\right)_b \equiv \left(\frac{H}{h}\right)_{max}. \quad (2)$$

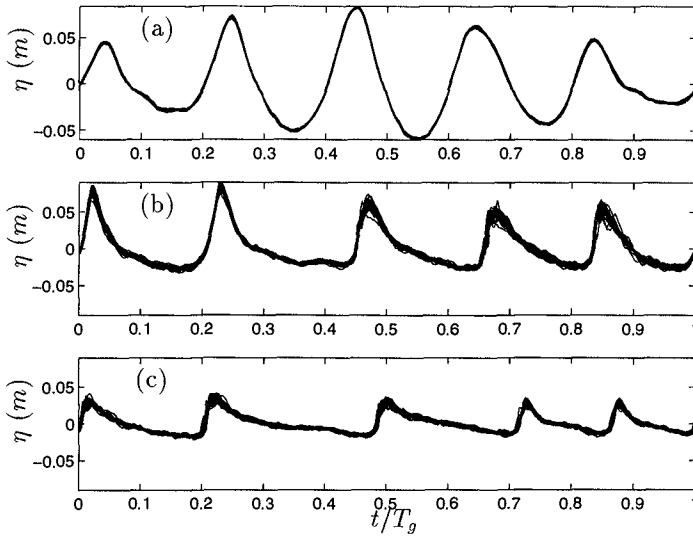


Figure 3: The variability of the wave profiles at three different positions in the tank: (a), at the reference gage, $x = 4.0$ m; (b), inside breaking region, $x = 20.9$ m; and (c), inside surf-zone, at $x = 23.1$ m, for experiment W06. Breaking occurs between $x = 19.2$ m and $x = 21.4$ m.

The wave heights, wave periods and phase speed obtained from the data, using the zero-upcrossing analysis was used to find other parameters such as the wave length and the slope parameter $S \equiv h_x L/h$, defined as the change in water depth over one wavelength L and h_x is the bottom slope.

The experimental data is compared with similar results obtained for regular waves by Svendsen & Hansen (1976). They found that the H/h ratio at breaking was very well predicted by the local value of S . Svendsen (1987) suggested the following empirical formula as a fit to the experimental data:

$$\left(\frac{H}{h}\right)_b = 1.9 \left(\frac{S_b}{1 - 2S_b}\right)^{\frac{1}{2}} \quad (3)$$

where the subscript b denotes the value at breaking. Hansen (1990) gives a simpler approximation to the data for the range $0.25 < S < 1$ as

$$\left(\frac{H}{h}\right)_b = 1.05 S^{0.20} \quad (4)$$

Figure 4(a) shows the result for W01, which has a groupiness of $\pm 10\%$. It is seen that, for this case, the two empirical formulae predict the wave breaking height very accurately. Note that wave 3, which is the highest wave at the wavemaker, has the lowest ratio of $(H/h)_b$, and wave 1, the smallest wave at the wavemaker has the highest ratio of $(H/h)_b$.

Figure 4(b) shows the results for W03 (groupiness of $\pm 20\%$) and figure 4(c) shows the results for W06 (groupiness of $\pm 50\%$). The empirical formulae again

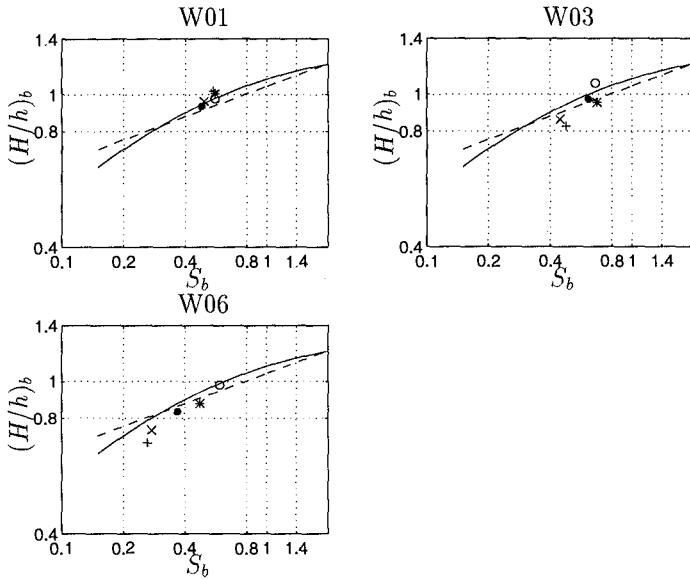


Figure 4: Variation of break point for W01, W03 and W06. The curves shown are from Svendsen, 1987 (—) and Hansen, 1990 (---). The points shown are for the individual waves in the group, wave 1 (*), wave 2 (o), wave 3 (●), wave 4 (x) and wave 5 (+).

predict the breaking height accurately although the spread in the breaking region is larger. The two smaller waves at the wavemaker have the largest $(H/h)_b$ ratio.

The variation in breaker height combined with variations in the position of the breaking determines the height of each individual wave in the surf-zone. The resulting surf-zone wave motion generally shows a shift in groupiness as demonstrated below.

4. Structure of the wave groups.

This variation in the start of breaking implies that the structure of the groups change as the waves propagate shoreward. To illustrate this, we look at the phase averaged wave groups at different locations in the tank, from the shoaling region through to the inner surf-zone.

First, we look at the shoaling region (figure 5). The vertical axis shows the x -location and the horizontal axis shows the time. The solid line is the phase-averaged η , the filled circles are the zero-upcrossing locations of the individual waves and the broken line show the location of the waves if they were traveling at speed \sqrt{gh} .

Wave 3 is the highest wave at the toe of the beach and the form of the group is essentially unchanged in the shoaling region. The individual waves are seen to travel slightly slower than the shallow water wave speed (\sqrt{gh}).

Figure 6 shows the groups around the breaking region. Up until breaking, wave 3 is the highest wave in the group. As the individual waves start to break, they lose energy and the wave height decreases rapidly. The highest wave, which

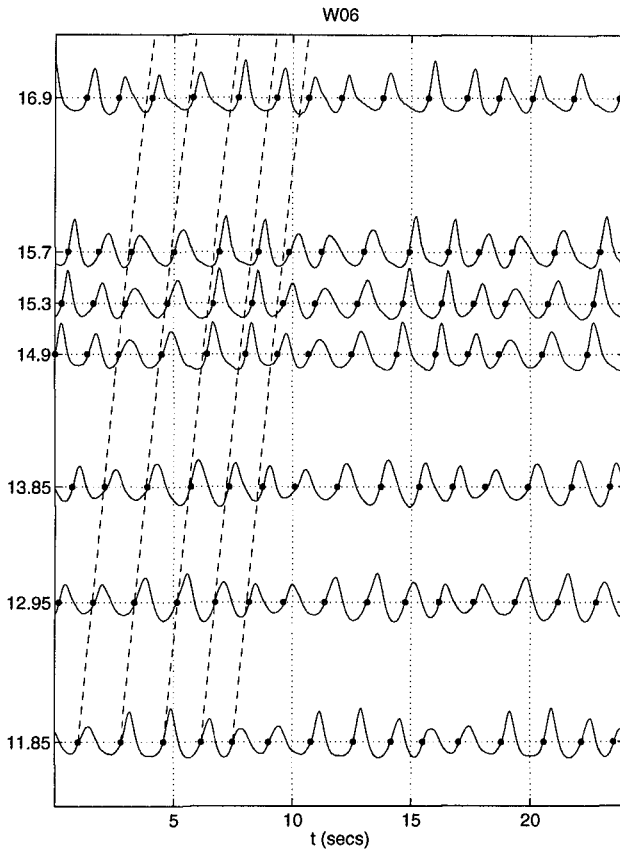


Figure 5: Development of the form of the wave groups for W06 in the shoaling region. $x = 11.85 \text{ m}$ is at the toe of the beach.

breaks at the largest depth (although, as seen before, the ratio H/h is not the largest), loses energy rapidly enough that, at the end of the breaking region, it is no longer the largest wave in the group. Wave 2 is seen to be the largest wave in the group at that location. Also, the wave speed after breaking is seen to be larger than \sqrt{gh} , which is expected.

Figure 7 shows the development of the structure in the inner surf-zone. The waves groups have evolved such that the smallest wave at the wavemaker is the largest wave here and the wave height is the smallest for wave 4. Note also that as the waves approach the shoreline, wave 4 is captured by wave 5 around $x = 25 \text{ m}$. For further details, see Svendsen & Veeramony (1995).

5. Analysis of the long wave motion.

The wavemaker only generates the amplitude modulated short waves. Therefore, the set-down wave associated with the wave groups is generated as the groups propagate shoreward, taking energy out of the short wave motion. No

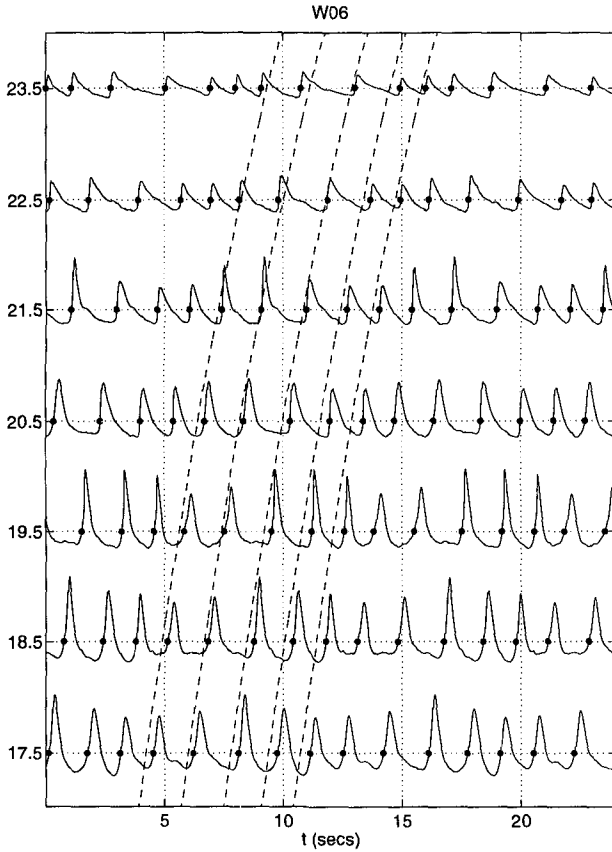


Figure 6: Development of the form of the wave groups for W06 in the breaking region. Breaking starts between $x = 19.20$ m and $x = 21.60$ m.

attempt was made to verify whether the set-down wave has reached an equilibrium value before the group reaches the toe of the beach. On the slope, the transformation of the groups represents a change in the forcing, which implies that the long wave motion changes continuously towards the shoreline.

It was clear, from watching the long period motion of the shoreline, that, apart from viscous effects, the long wave motion was fully reflected from the shore and essentially, sent back out as a free wave. This wave is re-reflected from the wavemaker, and over time, this process creates a standing long wave component. Hence, the total long wave motion in the tank can be analyzed as a forced wave propagating shoreward and a standing free long wave, both at the group frequency. At each gage, therefore, the long wave motion can be represented by an expression of two such components

$$\eta_l(x_j, t) = a(x_j)e^{i(kx_j - \omega t)} + bJ_0\left(\frac{2\omega}{\sqrt{gh}}(l - x_j)\right)e^{-i\omega t} \quad (5)$$

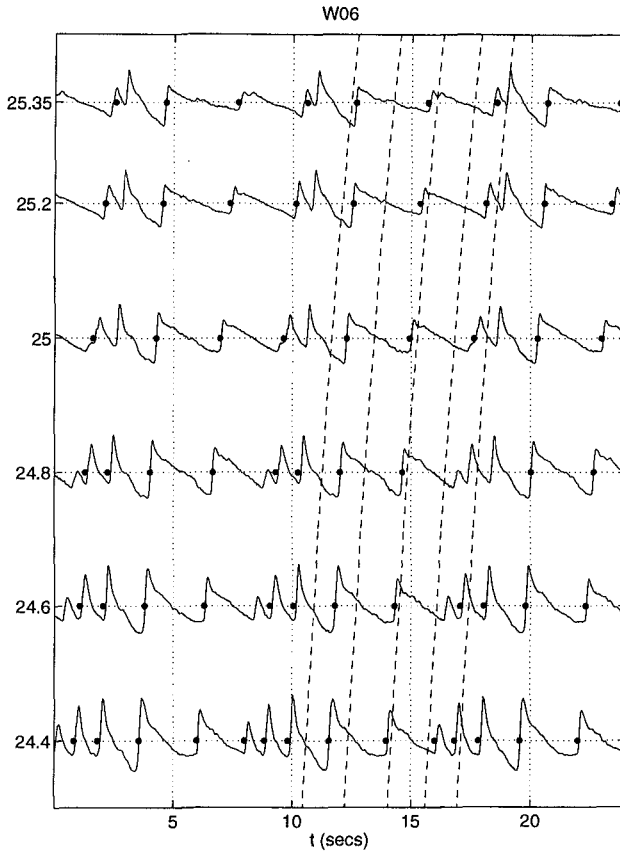


Figure 7: Wave profile development for experiment W06 in the region near the shore-line where wave 4 in the group ceases to exist. (Vertical scale changed from Fig. 5 & Fig. 6).

where $a(x)$ is the amplitude of the forced wave which includes both the shoaling and the variation caused by the short wave forcing and b is the amplitude of the standing wave component.

The coefficients a and b are determined from the data. The results of this analysis is shown in figure 8. Figure 8(a) shows the total long wave water surface elevation (\bullet), η , at a time when η due to the standing wave is zero (which is essentially the forced wave motion) and also the total long wave water surface elevation when η due to the standing wave is maximum (\circ). Figure 8(b) shows the amplitude variation of the forced wave, obtained from the data shown in (a). It is seen that, after an initial increase, the energy in the forced wave decreases steadily up to the breaking region ($x = 19.2 \text{ m}$ to $x = 21.6 \text{ m}$). After breaking, energy is fed back into the forced wave which reaches a constant value inside the surf-zone. Figure 8(c) shows the standing wave water surface elevation, calculated from the data (\bullet) and from the linear representation given in equation (5) (—). It can be seen that the standing wave is quite well represented by the zeroth-order

bessel function.

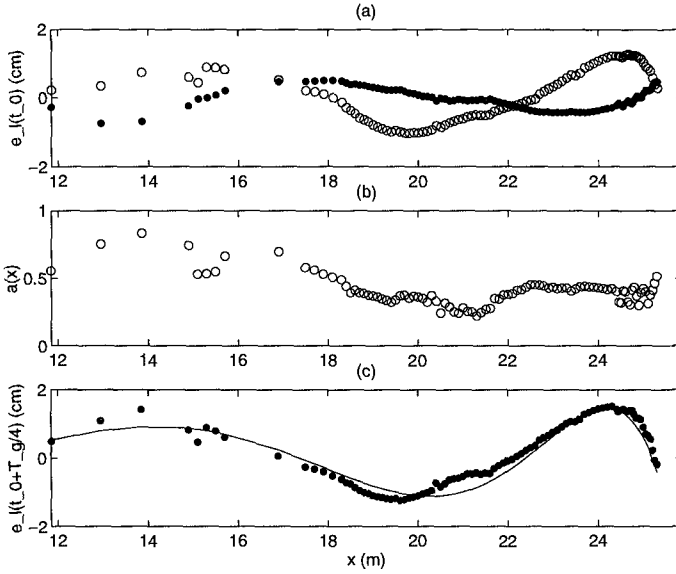


Figure 8: Long wave motion in the tank for W06: (a) water surface elevation of the propagating long wave at time $t = t_0$, (b) amplitude of the propagating long wave as a function of the distance from the wave maker, (c) the standing long wave in the tank at $t = t_0 + T_g/4$ ('•' is data and 'o' is the least-squares fit).

6. Modelling of short wave properties.

In this section, the short wave motion, described in the previous section, is modelled using the kinematic conservation equation and the energy conservation equation. The dispersion relation is used to close the system. Since cnoidal waves are generated by the wavemaker, the same theory is used in the modelling to evaluate the necessary coefficients.

We limit our consideration to a 1-D wave motion and the basic assumption made about the waves is that they are slowly varying in space and time. The effect of the horizontal particle velocity, u_l , of the long wave is assumed equivalent to that of a time varying current.

For such a case, the kinematic conservation equation for the short wave motion can be expressed as

$$\frac{\partial k_s}{\partial t} + \frac{\partial (c_s + u_l) k_s}{\partial x} = 0 \tag{6}$$

where k_s is the wavenumber of the short waves, c_s , the short wave celerity and u_l is the orbital velocity under the long wave. The equation for the evolution of the wave averaged short wave energy density is given by (see Phillips, 1980)

$$\frac{\partial \mathcal{E}}{\partial t} + \frac{\partial [\mathcal{E} (u_l + c_g)]}{\partial x} + S_{xx} \frac{\partial u_l}{\partial x} = D \tag{7}$$

where c_g is the group velocity for the short wave motion, S_{xx} is the radiation stress and \mathcal{D} is the energy dissipation.

The dispersion relation is given by cnoidal theory in the shoaling region and bore theory in the surf-zone as

$$\frac{c_s^2}{gh} = \begin{cases} 1 + \frac{H}{mh} \left(2 - m - 3 \frac{E(m)}{K(m)} \right) & \text{for } h > h_b \\ 1 + \left(-\frac{3}{2} + 3\delta \right) \frac{H}{h} + \left(\frac{1}{2} - 3\delta + 3\delta^2 \right) \left(\frac{H}{h} \right)^2 \\ + \left(\frac{1}{2}\delta - \frac{3}{2}\delta^2 + \delta^3 \right) \left(\frac{H}{h} \right)^3 & \text{for } h \leq h_b \end{cases} \quad (8)$$

where m is the elliptic parameter, $K(m)$ is the elliptic integral of the first kind, $E(m)$ is the elliptic integral of the second kind, h_b is the depth at breaking and $\delta \equiv \eta_c/H$ with η_c in the surf-zone given by (Hansen, 1990)

$$\delta = 0.5 + [\delta_b - 0.5] \left(\frac{h}{h_b} \right)^2 \quad (9)$$

The short wave averaged energy can be written as

$$\mathcal{E}(x, t) = \rho g H^2 B \quad (10)$$

where B is the shape parameter, which can be expressed outside the surf-zone using cnoidal theory. Inside the surf-zone, the empirical formula suggested by (Svendsen, 1984) is used

$$B = \begin{cases} \frac{1}{m^2} \left[\frac{1}{3} \left(3m^2 - 5m + 2 + (4m - 2) \frac{E}{K} \right) - \left(1 - m - \frac{E}{K} \right)^2 \right] & \text{for } h > h_b \\ B_0(B_{0b}, h_x, \frac{H_0}{L_0}) + \frac{1}{2} \frac{A}{H^2} \frac{c_s}{gT} & \text{for } h \leq h_b \end{cases} \quad (11)$$

where A is the area of the roller, T is the wave period and Hansen's (1990) expression is used for B_0 .

For simplicity, linear theory is used for S_{xx} . The energy dissipation is assumed to be negligible outside the surf-zone and inside the surf-zone can be calculated, using bore theory, as (Svendsen, 1984)

$$\mathcal{D} = -\frac{\rho g H^3}{4hT} \frac{1}{\left(1 + \delta \frac{H}{h} \right) \left(1 + \frac{H}{h} (\delta - 1) \right)} \quad (12)$$

The equations are solved in conservation form using the MacCormack predictor-corrector scheme. The criteria for breaking used in the model is the one given by equation (3). At breaking, a matching condition is required for each of the governing equations. Continuity in frequency and energy flux are used as matching conditions at the break point.

Thus, we are also assuming that the transition from a regular wave to a bore takes place over an infinitesimally small region. Since the break point varies in

time, the matching conditions have to be evaluated at each time step. The model domain extends from the toe of the beach to the location where $\min(h + a_l) = 0$, where a_l is the amplitude of the long wave. The wave envelope, which is the input to the model, is obtained at the toe of the beach using the Hilbert Transform (Melville, 1983). The zero-upcrossing points at the toe of the beach are also input to the model.

7. Comparison between model and data.

Figures 9-11 show the results of the comparison between the model results and the experimental data from W06. In each of these figures, the abscissa shows the time and the ordinate shows the location of the measurement, — — is the measured η , ——— is the predicted envelope of $H(x, t)$, - - - - is the predicted speed of the individual waves and \bullet is the upcrossing point of the individual waves.

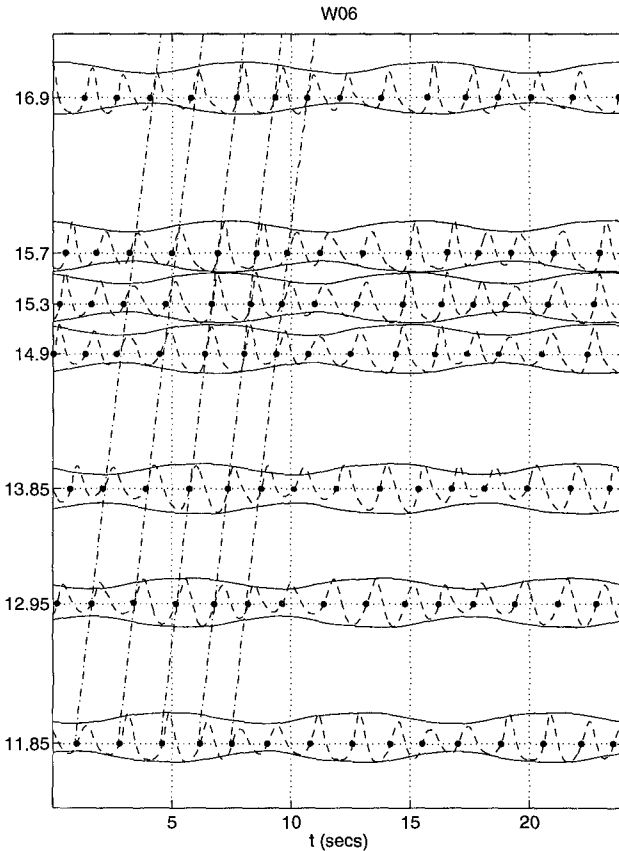


Figure 9: Comparison between model and W06 in the shoaling region showing η (— —), zero upcrossing point (\bullet), wave location from model (- - - -) and the envelope from model (———).

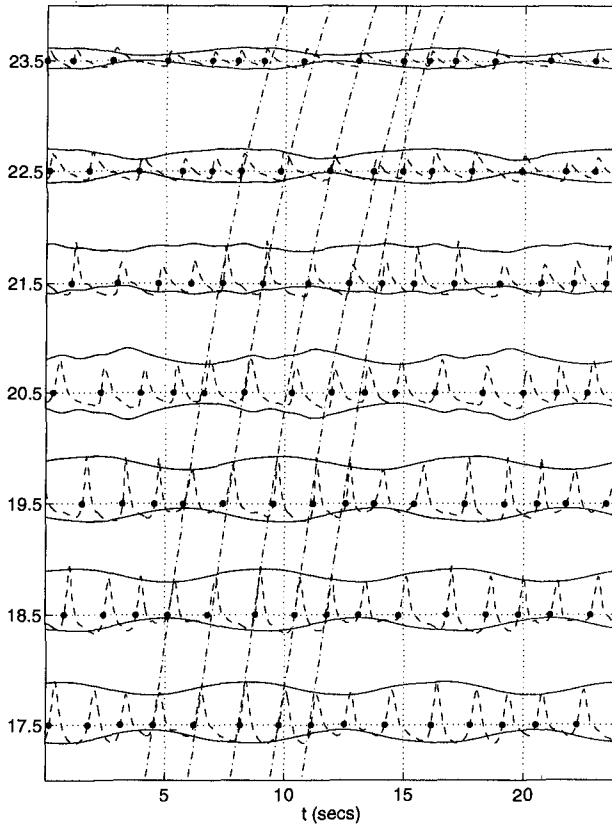


Figure 10: Comparison between model and W06 shoreward from breaking, showing η (---), zero upcrossing point (\bullet), wave location from model (-·-·-) and the envelope from model (—). Breaking region from data is between $x = 19.10\text{ m}$ and $x = 21.40\text{ m}$ and in model is between $x = 19.48\text{ m}$ and $x = 22.30\text{ m}$.

In this experiment, the groupiness factor at the wavemaker was $\pm 50\%$, the short wave period was 1.6 s and the mean wave height at the wavemaker was 0.1 m . In the shoaling region (figure 9), the wave envelope and the wave speed are predicted extremely accurately by the model.

The results for the breaking region are shown in figure 10. The prediction of the wave envelope is poor in the breaking region, although the prediction seems to improve as the shoreline is approached. It is seen from figure 10 and 11 that in spite of the fact that the wave speed in the model is represented by the bore velocity, the highly nonlinear kinematics, in particular in the inner parts of the surf-zone, is poorly predicted. This may in part be due to errors in predicting the precise breaking region (model predicts breaking between $x = 19.48\text{ m}$ and $x = 22.3\text{ m}$ whereas the analysis of the data gives the breaking region to be between $x = 19.2\text{ m}$ and $x = 21.4\text{ m}$), in part due to the fact that the surf-zone is very wide and the waves near the shoreline are small.

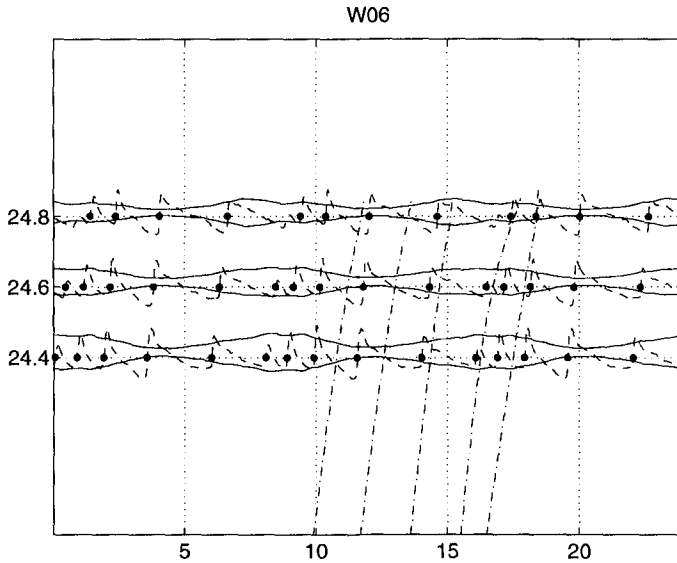


Figure 11: Comparison between model and W06 in the inner surf-zone, showing η (— — —), zero upcrossing point (\bullet), wave location from model (---) and the envelope from model (——).

8. Conclusions.

Experiments were conducted to analyze the behaviour of wave groups in the breaking region and in the surf-zone.

It was found that the location of the individual wave break point is affected by the groupiness of the waves. The altered structure of breaking causes the group structure to be completely different inside the surf-zone. The long wave motion is mainly forced at the group frequency. These long waves can be resolved into a forced wave travelling shoreward and a free standing long wave. The amplitude of the incident forced wave varies along the tank, whereas the standing wave is shown largely to agree with a linear representation of a free standing wave system.

The model is seen to predict the behaviour of the group very well until the breaking region. Inside the surf-zone, the breaking waves interact strongly with each other and with the long wave motion, which the model predicts poorly.

Acknowledgements

This work was sponsored by the US Army Research Office, University Research Initiative under contract No. DAAL 03-92-G-0016. The United States government is authorized to produce and distribute reprints for government purposes notwithstanding any copyright notation that may appear herein.

- Abdelrahman, S.M. and Thornton, E.B., 1988. Changes in the short wave amplitude and wave number due to the presence of infragravity waves. *Proceedings of the ASCE Special Conference on Coastal Hydrodynamics*, pp. 458-478.
- Goring, D.G., 1978. Tsunamis-The propagation of long waves onto a shelf. *Rep. No. KH-R-38, W.M.Keck Lab. of Hydraulics and Water Res., CalTech, Pasadena, California.*
- Hansen, J.B., 1990. Periodic waves in the surf zone : Analysis of experimental data. *Coastal Engineering, Vol 14*, pp. 19-41.
- Kostense, J.K., 1984. Measurements of surf beat and set-down beneath wave groups. *Proceedings of the 19th International Conference on Coastal Engineering*, pp. 724-740.
- Longuet-Higgins, M.S. and Stewart, R.W., 1962. Radiation stress and mass transport in gravity waves, with application to surf beats. *Journal of Fluid Mechanics, Vol. 13*, pp. 481-504.
- List, J.H., 1991. Wave groupiness variations in the nearshore. *Coastal Engineering, Vol. 15*, pp. 475-496.
- Phillips, O.M., 1980. The dynamics of the upper ocean. *Cambridge University Press, Cambridge.*
- Schäffer, H.A., 1990. Infragravity water waves induced by short-wave groups. *Series paper # 50, Institute of Hydrodynamics and Hydraulic Engineering, Technical University of Denmark.*
- Schäffer, H.A. and Svendsen, I.A., 1988. Surf beat generation on a mild slope beach. *Proceedings of the 21st International Conference on Coastal Engineering*, pp. 1058-1072.
- Svendsen, I.A., 1987. Analysis of surf zone turbulence. *Journal of Geophysical research, Vol. 92.*, pp. 5115-5124.
- Svendsen, I.A. and Hansen, J.B. 1976. Deformation up to breaking of periodic waves on a beach. *Proceedings of the 15th International Conference on Coastal Engineering*, pp. 477-496.
- Symonds, G. Huntley, D.A. and Bowen, A.J., 1982. Two-dimensional surf beat: long wave generation by time varying break point. *Journal of Geophysical Research, Vol. 87*, pp. 492-498.
- Svendsen, I. A. and Veeramony, J., 1995. Groups of breaking waves: Experiments. *Submitted to the ASCE Journal of Waterways, Port, Coastal and Ocean Engineering.*
- Watson, G., Barnes, T.C.D. and Peregrine, D.H., 1994. The generation of low-frequency waves by a single wave group incident on a beach. *Proceedings of the 24th International Conference on Coastal Engineering*, pp. 776-790.

CHAPTER 13

SIMULATION OF PROPAGATING NONLINEAR WAVE GROUPS

Paul de Haas^{1, 2}, Maarten Dingemans¹ and Gert Klopman¹

Abstract

Propagating nonlinear waves can be computed with a time-domain numerical method based on a boundary element method. For the simulation of propagating wave groups a domain decomposition method is used to increase the efficiency of the model and to enable simulation over many wave periods. In the computations described in this paper several nonlinear formulations for an initial wave group signal are used to investigate their ability to describe a wave group of fixed form. A difficulty consists of the imposition of the boundary conditions at the unknown free-surface elevation. The nonlinear contributions to the first-order signal are related to the generation of free waves as computed by the model.

1 Introduction

Long-wave motion is usually split up between a bound part which is due to nonlinear difference interactions between short sea and swell waves and a free part which are waves that move with their own celerity according to an appropriate dispersion relation. It is known that when waves travel over an uneven bottom, energy in the bound component of the long waves is transformed to the free components.

In this paper we present a two-dimensional (2DV) time-domain numerical method, based on a boundary element method, which computes the propagation of waves with the exact nonlinear boundary conditions over an arbitrary bottom geometry. It is therefore able to simulate the generation of free long waves due to an uneven bottom. A model problem used by Dingemans et al. [3], is used as reference for the computations presented here. Different formulations of the nonlinear wavegroup signal are tested for their suitability to describe a wave group of fixed form over a horizontal bottom. Such a signal can then be used

¹Delft Hydraulics, P.O. Box 177, 2600 MH Delft, The Netherlands

²University of Twente, Faculty of Applied Mathematics, P.O. Box 217, 7500 AE Enschede, The Netherlands

as an initial signal for problems with a bottom topography in order to study the generation of free long-wave components.

Because the study of such problems requires large computational effort, the use of efficient numerical techniques is imperative. Here we will present a domain decomposition method which reduces the computational costs of the boundary element method considerably.

This paper is organized as follows. First the numerical method is described in Section 2. In Section 3 the domain decomposition method is described and its efficiency is discussed. In Section 4 some nonlinear formulations of a wave group signal are discussed and used as initial signal for the computations. Finally some conclusions will be stated in Section 5.

2 Numerical method

In the mathematical model for nonlinear water waves considered here, the motion of the water is described by the usual potential-flow equations for inviscid irrotational fluid motion with a free surface on water of varying depth. It is described by the field equation for the velocity potential ϕ (Laplace's equation)

$$\Delta\phi = 0, \quad (1)$$

and the boundary conditions on the free surface $\partial\Omega_{FS}$

$$\left. \begin{aligned} \frac{D\phi}{Dt} &= \frac{1}{2}(\nabla\phi)^2 - gz - \frac{p}{\rho} \\ \frac{D\mathbf{x}}{Dt} \cdot \mathbf{n} &= \frac{\partial\phi}{\partial n} \end{aligned} \right\} \mathbf{x} \in \partial\Omega_{FS} \quad (2)$$

and on the bottom $\partial\Omega_B$

$$\frac{\partial\phi}{\partial n} = 0, \quad \mathbf{x} \in \partial\Omega_B. \quad (3)$$

Appropriate in- and outflow boundary conditions are formulated on the lateral boundaries.

The numerical method consists of a time marching scheme for the evolution of the free surface and its boundary conditions. At every time-step, Laplace's equation for the velocity potential has to be solved. This is done with a boundary element method (BEM). In the BEM, Laplace's equation is solved by writing it as a set of integral equations over the boundary (one equation for every node). These integral equations are first discretized. Then, by using the boundary conditions a system of linear equations is built and subsequently solved. Insertion into equations (2) of the solution obtained in this way, provides the time derivatives which are needed for the time marching scheme.

Boundary element methods are very suitable for solving Laplace's equation on such domains because they only require a discretization of the boundary of the domain. Compared with field discretization methods, the advantages of a BEM are a much smaller amount of grid points and a natural description of the evolution of the free surface. See [1] for a description of a three-dimensional

method. The computations described here were performed with a code developed for two-dimensional simulations based on the work of these authors.

For the computation of large-scale wave problems the solution algorithm for Laplace's equation is the bottleneck. It involves both the discretization of the boundary integral equations and the solution of the resulting system of linear equations. The time marching scheme requires a minor part of the total CPU-time. Furthermore, memory requirements for solving Laplace's equation depend quadratically on the number of grid points. These problems can be reduced considerably by the use of a domain decomposition method.

3 Domain decomposition

3.1 Description

The domain decomposition method described here consists of a division of the computational domain into subdomains (see Figure 1) and an iterative procedure which generates a sequence of solutions on the subdomains that converges towards the solution on the original domain.

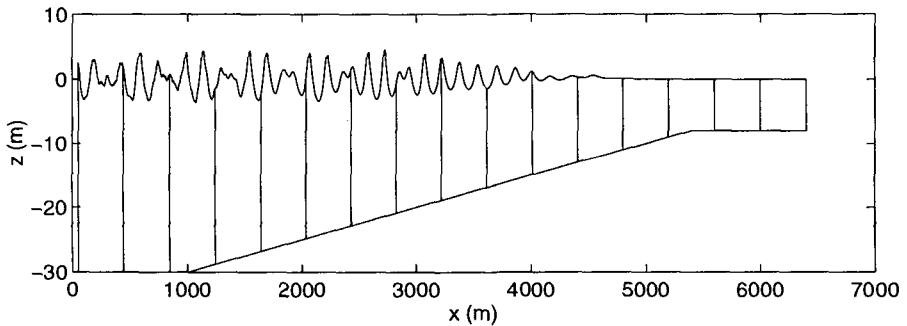


Figure 1: Decomposed domain

Every step of the iterative procedure consists of first solving Laplace's equation for the potential ϕ on the separate subdomains simultaneously and secondly formulating new boundary conditions on the subdomain interfaces. In the latter part the subdomain problems are coupled.

There are many possibilities in the way information can be exchanged between the subdomains. We have chosen here to use the so-called DD/NN-scheme. Every odd step of the iterative procedure Dirichlet conditions are imposed on all interfaces. Neumann conditions are imposed at all even steps. These steps are illustrated in Figure 2 for the first two steps of a two-subdomain problem.

This scheme is also known as a Neumann-Neumann preconditioner in the context of domain decomposition methods for field discretization techniques. See e.g. [4]. In the field of time-domain BEM's a similar technique was used by Wang

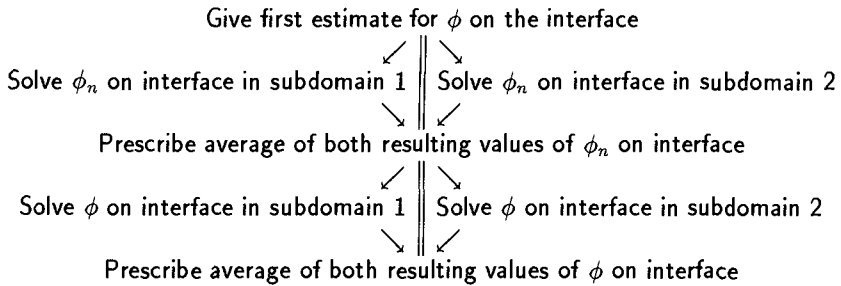


Figure 2: Schematic representation of the DD/NN-scheme

et al. [8]. In their work interfaces are used to formulate a block-structured matrix which is then solved iteratively. For a general impression of work being done in the field of domain decomposition the reader can consult [7].

3.2 Convergence characteristics

The performance of the domain decomposition method is determined here by the convergence of the iterative process. The convergence of the process can be judged by considering the jump across the interface between the solutions on both sides of each interface. The convergence on different interfaces depends on the geometrical form of the subdomains. This aspect has been subject of previous investigations [2] and the main conclusions given there are:

- The convergence of the iterative procedure deteriorates as the length-to-height ratio of the subdomains decreases and if there is more asymmetry near the interfaces due to a disturbed free surface or an uneven bottom.
- Therefore, given a fixed length of the computational domain, the convergence of the iterative procedure deteriorates as the number of subdomains N increases.
- Given a fixed length-to-height ratio of the subdomains, the convergence rate does not change as the number of subdomains increases, in the case of rectangular subdomains of equal size. In applications with a disturbed free surface we have seen that convergence is determined by the interface with the worst convergence. The number of iterations has an upper bound which is independent of N .

3.3 Efficiency

The efficiency of the domain decomposition technique is of course related to the convergence of the iterative method. It can be considered for the two cases mentioned above.

- If for a computational domain with a fixed length the number of subdomains is increased, on the one hand the number of required iterations will increase. On the other hand, the CPU-time to solve Laplace's equation per subdomain decreases, since the subdomains becomes smaller. It appears that there is a certain optimal number of subdomains (with respect to CPU-time) to solve a given water-wave problem. See [2].
- If subdomains are used with a fixed length-to-height ratio, the number of iterations and therefore the computational costs per subdomain, have an upper bound independent of the number of subdomains. This implies that the computational cost per time step depend at most linearly on the size of the computational domain.

In the application of the domain decomposition technique to the time-domain numerical method described here, it is possible to subdivide the domain differently every time step, adjusted to the presence of a wave signal. We have chosen to use a fixed initial subdivision of the computational domain with subdomains of equal size so that no reorganization of data over the subdomains is necessary and the number of grid points in all subdomains is the same.

4 Simulation of some nonlinear wave group signals

4.1 Introduction

In Liu and Dingemans [5] and Dingemans et al. [3] a mathematical model is described for the wave envelope A of a carrier wave signal. In this model third-order equations are derived with a multiple-scales technique for a first-order carrier wave signal given in complex notation by

$$\eta_1(x, t) = \frac{1}{2}(Ae^{i\chi_0} + *) \quad (4)$$

and

$$\phi_1(x, z, t) = \frac{1}{2} \left(-\frac{g \cosh(k_0(z+h))}{\omega \cosh(k_0 h)} i A e^{i\chi_0} + * \right) \quad (5)$$

with $\chi_0 = k_0 x - \omega_0 t$, being the phase function of the carrier wave. The $*$ -symbol denotes the complex conjugate of the preceding term.

From solvability conditions of the third order equations, evolution equations are derived for the envelope A . For a horizontal bottom these equations simplify to a nonlinear Schrödinger (NLS) equation. See also Mei [6]. This equation admits several steady solutions for A which can be used to create an initial signal for a simulation.

In our computations we have chosen a soliton-solution described by the envelope function A as:

$$A(x, t) = a \operatorname{sech} \left(\sqrt{\frac{-\nu_1}{\partial C_g / \partial k_0}} a \cdot (x - C_g t) \right) \exp \left\{ -i \frac{\nu_1 a^2}{2} t \right\} \quad (6)$$

in which a and C_g are the amplitude and the group velocity of the carrier wave. ν_1 is a long expression in terms of characteristic quantities of the carrier wave and is given in Dingemans et al. [3], p. 364. The parameters have been evaluated for $a = 1$ m, $\omega_0 = 2\pi/6$ rad/s and $h = 12$ m. The corresponding wave length L_0 and group velocity C_g according to linear theory are equal to 50.73 m and 5.52 m/s respectively. Based on an elevation $1 \cdot 10^{-3}$ times the maximum elevation, the wave group has a length of approximately 1850 m.

In the computations a known elevation $\eta(x, t)$ is required as the initial disturbance of the free surface. The panel method furthermore requires an initial value of the potential ϕ on the free surface which imposes the initial velocity field on the free surface. In the third-order model it is, just as η , given in terms of the third-order perturbation serie. Because of the large and complex expressions associated with the series, we have tried a number of alternatives and have studied the degree in which they describe a signal that propagates undisturbed over a horizontal bottom. These alternatives will be described next.

4.2 Formulations for free-surface elevation and potential

A difficulty of simulating nonlinear wave signals consists of the imposition of the boundary conditions at the unknown free-surface elevation. In perturbations techniques, one usually expands free-surface elevation and potential around the still-water level $z = 0$ and the potential is evaluated at the still-water level. In the numerical approach, the grid points are located at $z = \eta$ so that evaluations there deviate from those of the perturbation approach. A Taylor expansion for ϕ can be used to account for the location of the free surface at $z = \eta$:

$$\phi(x, z, t)|_{z=\eta} = \phi(x, 0, t) + \eta(x, t) \frac{\partial \phi}{\partial z}(x, 0, t) + O(\eta^2). \quad (7)$$

Besides the first order expressions given in equations (4) and (5) we have used a Stokes' second-order contribution given by

$$\eta_2(x, t) = \frac{1}{2} \left(\frac{1}{4} \frac{k_0 \cosh(k_0 h)}{\sinh^3(k_0 h)} [2 + \cosh(2k_0 h)] A^2 e^{2ix_0} + * \right) \quad (8)$$

and

$$\phi_2(x, z, t) = \frac{1}{2} \left(\frac{3 \omega \cosh(2k_0(z + h))}{8 \sinh^4(k_0 h)} i A^2 e^{2ix_0} + * \right). \quad (9)$$

and a bound long-wave contribution based on the linearized depth-integrated mean-flow equations. See [3]. The free-surface elevation ζ and potential ϕ_{bl} of this wave are given by

$$\zeta(x, t) = \frac{2c_g/c - \frac{1}{2}}{2(c_g^2 - gh)} g \left(|A(-c_g t)|^2 - \langle |A|^2 \rangle \right) \quad (10)$$

and

$$\phi_{bl}(x, t) = \int_{-\infty}^x \frac{\partial \phi}{\partial x'} dx' = \int_{-\infty}^x u dx' = \int_{-\infty}^x \frac{c_g}{h} \zeta dx' \quad (11)$$

$$= \frac{2c_g/c - \frac{1}{2} c_g g}{2(c_g^2 - gh)} \frac{c_g g}{h} \int_{-\infty}^x (|A|^2 - \langle |A|^2 \rangle) dx'. \quad (12)$$

$\langle |A|^2 \rangle$ denotes the mean value of $|A|^2$ over a time interval much longer than the wave group period. For the soliton solution (6), $\langle |A|^2 \rangle = 0$.

4.3 Results

For our computations we have selected a number of formulations which are tabulated in Table 1. These initial signals were used in simulations over 60 wave

Table 1: Initial signal for the various computations

	η	ϕ	using formula (7)
run 1	η_1	ϕ_1	no, ϕ evaluated at $z = \eta$
run 2	η_1	ϕ_1	no, ϕ evaluated at $z = 0$
run 3	η_1	ϕ_1	yes
run 4	$\eta_1 + \eta_2$	$\phi_1 + \phi_2$	no, ϕ evaluated at $z = 0$
run 5	$\eta_1 + \zeta$	$\phi_1 + \phi_{bl}$	no, ϕ evaluated at $z = 0$
run 6	$\eta_1 + \eta_2 + \zeta$	$\phi_1 + \phi_2 + \phi_{bl}$	no, ϕ evaluated at $z = 0$

periods in a computational domain with length 5000 m. Free-surface collocation points were distributed over $z = \eta(x)$ with equal horizontal distances. The resolution of the computational configuration was taken the same for all simulations and is given by $\Delta x = 2.5 \text{ m} \approx L_0/20 \text{ m}$ on the free surface and $\Delta t = T_0/20 \text{ s}$.

The results are illustrated best by showing the free-surface elevation at $t = 45T$ for the different computations. Run 1 has been shown separately in a larger plot in order to show the details better. The result of run 3 is similar to that of run 1, because the vertical profile of ϕ_1 is almost linear in the range $-\eta \leq z \leq \eta$ and differences between the evaluation of ϕ_1 at $z = \eta$ (run 1) and the use of equation (7) (run 3) are hardly discernible. Therefore results of run 3 are not shown here.

A typical feature common to all computations is the generation of small left-going signals. In Figure 3 wave groups with carrier waves with a wave period of approximately 6.0 s (around $x = 200 \text{ m}$) and 3.8 s (around $x = 700 \text{ m}$) can be seen. Their group velocities are equal to 4.4 and 3.1 m/s respectively. Not visible in Figures 3 and 4 is a small left-going *long* wave ($c = 11.1 \text{ m/s}$) which at this point of the computation has already left the computational domain. The left-going signal is the smallest in runs 2 and 5.

There is also a right-going free-long wave (around $x = 4400 \text{ m}$) in all computations. The computed phase velocity of this wave equals 11.1 m/s where as \sqrt{gh}

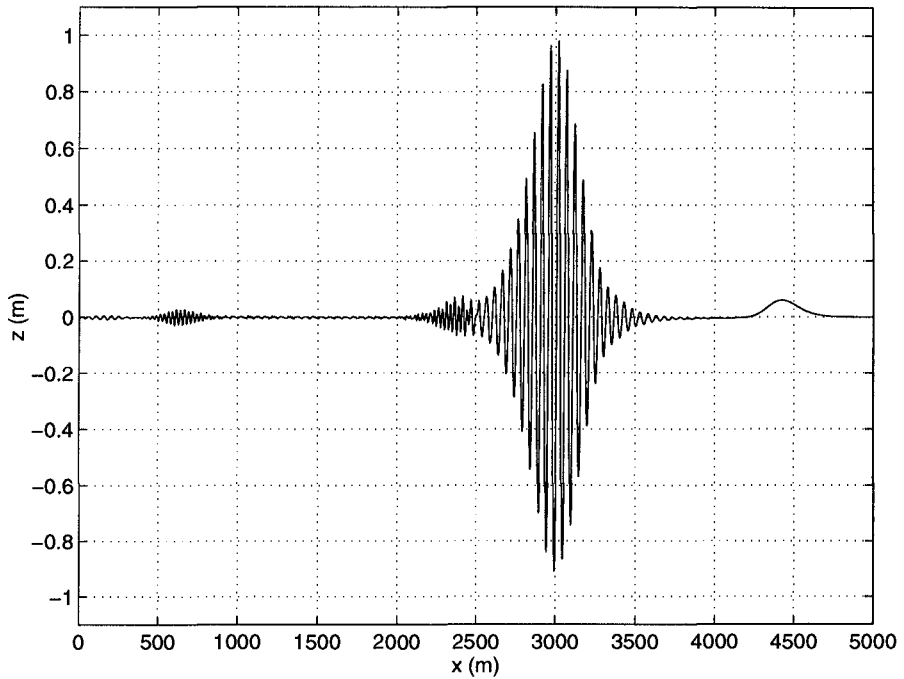


Figure 3: Surface elevation at $t = 45T$ for run 1

equals 10.85 m/s here. The computations with a contribution of ζ and ϕ_{bl} show a reduction of the amplitude of this wave from 6.0 to 2.5 cm.

At the back of the wave group a smaller wave group evolves consisting of carrier waves with wave period approximately 4.2 s. Its amplitude is smallest in run 4 and 6 which contain the second-order contribution η_2 and ϕ_2 .

In summary it can be said that the differences between the computations presented here can be explained satisfactory by relating them to the contributions to the initial wave signal. However, the second-order contributions in runs 4, 5 and 6 do not prevent the generation of free waves nor do they prevent the generation of a left-going wave signal. At this point it is not clear whether this is due to the imposition of the boundary condition at the actual free surface or to the restriction to only second-order contributions. The use of formula (7) on the second-order part of the wave signal and the use of more higher-order contributions may improve the stationary character of the signal. Nevertheless it is possible to investigate the influence of bottom topography on the generation of free-long waves, but one has to take into account the generation of the spurious waves shown in these computations.

A closer study should also include the effect of the dispersive and dissipative

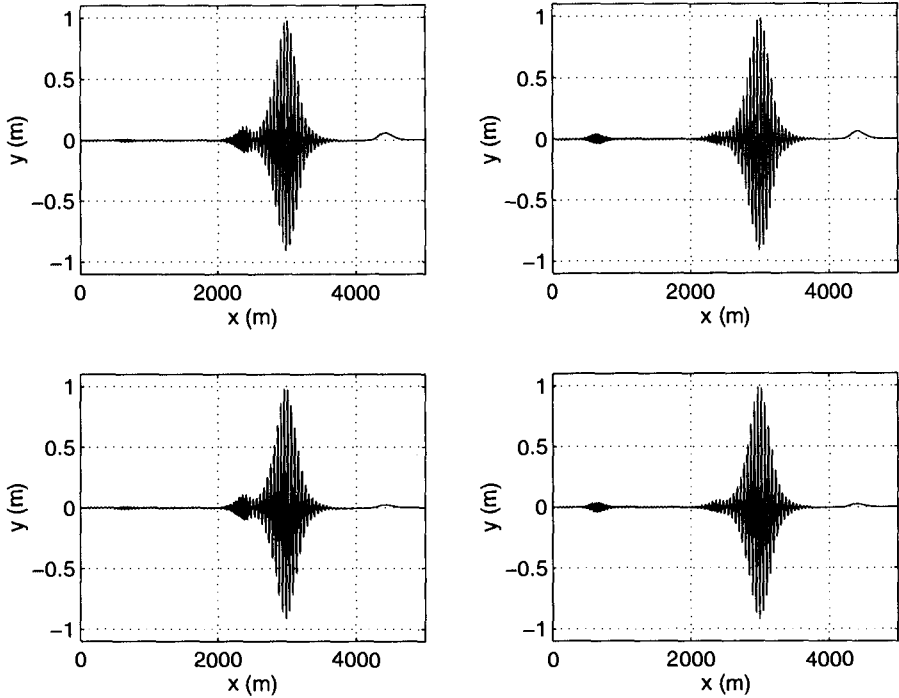


Figure 4: Surface elevation at $t = 45T$ for: run 2 (upper left), run 4 (upper right), run 5 (down left) and run 6 (down right)

character of the numerical scheme. Although very small for the resolution used, they may become relatively important when smaller contributions to the wave signal are considered.

The simulations over 60 wave periods took about 1.5 hours on a Cray C98 computer at a computational speed of about 125 Mflop/s. The required memory was approximately 56 MByte. The use of a single domain for this simulation would have exceeded the capacity of the Cray computer. Moreover it is questionable whether the system of linear equations in this case is numerically solvable within the required accuracy.

With an eye to larger problems involving a bottom topography it is remarked again that the computational costs per time step depend at most linearly with the size of the computational domain. For comparison with the results of Dingemans et al. [3] on a domain with a length of 15 km, this implies three times as much computational costs per time step. However, a longer simulation time is required for this domain. The computational costs per simulation will then be an additional factor larger than those presented in this paper. Studies including bottom topography will be continued in due time.

5 Conclusions

By using a domain decomposition method in a numerical method for nonlinear waves, it is possible to simulate the propagation of wave groups over large simulation times. For the formulation of a stationary propagating wave group it is important to include higher-order contributions. The release of free waves from the wave group can be explained from second-order contributions to the first-order signal. The question remains however, how to impose an initial signal to obtain a propagating wave group of fixed form over a horizontal bottom.

Acknowledgements

These investigations were supported by the Dutch Technology Foundation (STW). The use of supercomputer facilities was provided by NCF.

References

- [1] Broeze, J., E.F.G. van Daalen and P.J. Zandbergen, (1993), *Comp. Mech.*, **13**, pp. 12-28.
- [2] De Haas, P.C.A. and P.J. Zandbergen, (to appear), The application of domain decomposition to time-domain computations of nonlinear water waves with a panel method, *J. Comp. Phys.*
- [3] Dingemans, M.W., H.A.H. Petit, Th.J.G.P. Meijer and J.K. Kostense, (1991), Numerical evaluation of the third-order evolution equations for weakly nonlinear water waves propagating over uneven bottoms. In: *Computer Modelling in Ocean Engineering 91*, Barcelona, pp. 361-370.
- [4] Le Tallec, P., (1994), Domain decomposition methods in computational mechanics, *Comp. Mech. Adv.*, **1**, pp. 121-220.
- [5] Liu, P.L-F. and M.W. Dingemans, (1989), Derivation of the third-order evolution equations for weakly nonlinear water waves propagating over uneven bottoms. *Wave Motion*, **11** pp. 41-64.
- [6] Mei, C.C., (1983), The applied dynamics of ocean surface waves, Advanced Series on Ocean Engineering (Vol. 1), World Scientific, Singapore.
- [7] Quarteroni, A., Ed., (1994), *Proc. Sixth Int. Symp. on Domain Decomposition Methods for Partial Differential Equations*, Como, June 1992 (AMS, Providence).
- [8] Wang, P., Y. Yao and M.P. Tulin, (1994), *Int. Journ. of Offshore and Polar Eng.*, **4**, pp. 200-205.

CHAPTER 14

CROSS-SHORE MOMENTUM FLUX DUE TO SHEAR INSTABILITIES

Ad Reniers¹ and Jurjen A. Battjes

Abstract

Results obtained from a laboratory experiment on shear instabilities in wave-driven longshore currents were used to analyse the cross-shore structure of the shear instability induced momentum flux. As the shear instabilities grew in the downstream direction, a significant cross-shore momentum flux occurred. However, the expected changes in the mean longshore current velocity profile were not observed.

Introduction

In spring 1994 an experiment on the generation of shear instabilities in wave-driven longshore currents was performed in a large wave basin. Shear instabilities were found to occur when using obliquely incident waves to create an alongshore uniform current over a barred beach (Reniers et al., 1994).

Shear instabilities are assumed to cause a cross-shore redistribution of mass and momentum in the surfzone. The redistribution depends on the cross-shore structure of the shear instabilities and the phase coupling between the horizontal velocity components. Numerical studies (Dodd and Thornton, 1990, 1993, Putrevu and Svendsen, 1992) indicate an inflection point in the redistribution of momentum, resulting in a smoothing of the initial longshore current velocity profile. These predictions can now be checked quantitatively.

First a brief layout of the experimental set-up is given. For a more detailed description reference is made to Reniers et al. (1996). Next proof is given of the existence of shear instabilities using a spectral analysis method (MEM) to obtain the frequency wave-number spectrum based on the fact that the shear instability signature is outside the gravity-wave range. This enables us

¹Faculty of Civil Engineering, Delft University of Technology, P.O. Box 5048, Delft, The Netherlands, ad.reniers@wldelft.nl

to establish which energy corresponds to shear instabilities only. Phase coupling between the u and v velocity components results in cross-shore flux of momentum. This is examined in detail using cross-shore spectral analysis to compute the frequency distribution of the momentum flux induced by shear instabilities. The total transfer is obtained by integration over the frequency domain. The results are compared to the other terms in the longshore momentum equation used to compute the longshore current velocity.

Experimental set-up

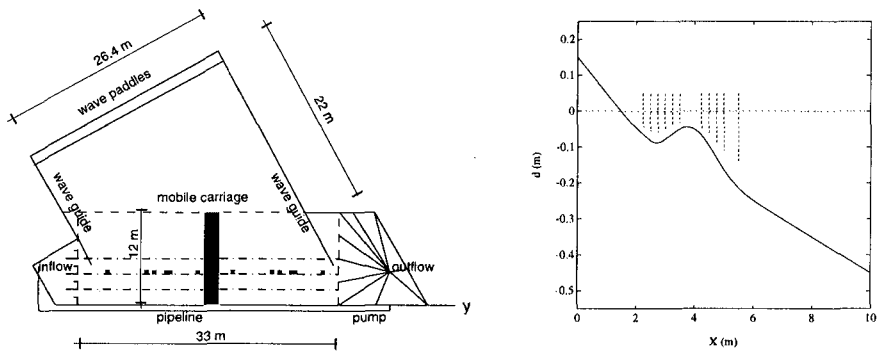


Figure 1: Left panel: plan view experimental set-up. Instrument positions of alongshore arrays indicated by the '*' signs. Right panel, bottom profile and deployment positions alongshore array indicated by the dashed lines.

The experimental set-up is shown in Figure 1. The left panel shows the plan view of the experimental layout. Incident waves are generated by a multi-paddle wave maker. Given the oblique alignment of the beach with respect to the wave maker the paddles could be operated in phase, generating longcrested waves. The longshore current generated by the waves breaking over the barred profile (right panel Figure 1) was recirculated using a pump system to prevent spurious recirculations in the basin (Visser, 1984, Reniers and Battjes, 1996). To further increase the alongshore uniformity the pumped discharge was redistributed at the inflow opening. The cross-shore distribution of the longshore current velocity profile was measured with instruments attached to the mobile carriage. Two alongshore arrays of six spatially lagged current velocity meters (see left panel Figure 1) were used to measure the velocities up-and downstream respectively and thus the alongshore development of the shear instabilities. Detailed measurements of the cross-shore structure for a particular wave condition, monochromatic waves with a wave height of 8 cm and a 1 s period, were obtained by reposition-

ing the alongshore arrays perpendicular to the beach (see right panel Figure 1). During the repositioning the input wave and flow conditions were maintained. Measurements would restart after the disturbances induced by the repositioning of the instruments had disappeared (estimated duration less than half an hour). Note that instruments could not be positioned at the bar crest given the strong wave breaking induced turbulence.

Shear instabilities

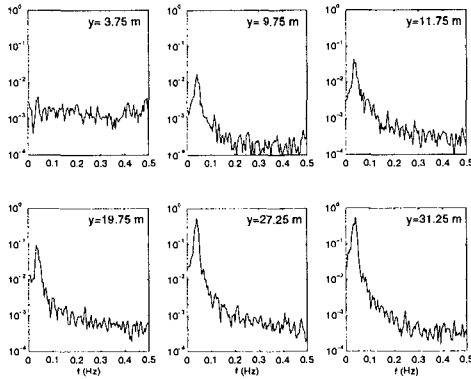


Figure 2: Alongshore development of low-frequency spectral density of alongshore velocity $(\text{m/s})^2/\text{Hz}$ obtained from measurements at $x = 4.5 \text{ m}$, from the inflow opening (upper left panel) to the outflow opening (lower right panel). Distance to the inflow opening given by y .

An example of the downstream development of the low-frequency spectrum of the alongshore velocity, measured with the two alongshore arrays positioned offshore of the bar ($x = 4.5 \text{ m}$), is shown in Figure 2. It clearly shows the strong growth of the energy density in the 0 to .1 Hz frequency band. At this point it is not known whether energy in this frequency band corresponds to shear instabilities.

A spectral analysis technique based on maximum entropy was used to estimate the spectral distribution of energy density with alongshore wave number (k_y) of selected frequencies so as to determine which part of the energy density belonged to the shear instabilities (Reniers et al., 1996). Two results obtained at the downstream end of the basin, offshore of the bar and in the trough respectively, are shown in Figure 3. The zero-mode edge-wave dispersion curve (for a plane beach) is also shown as a reference. It is obvious that all energy density is outside the gravity wave range indicated by the area below the edge wave dispersion line, i.e. belonging to shear instabilities only.

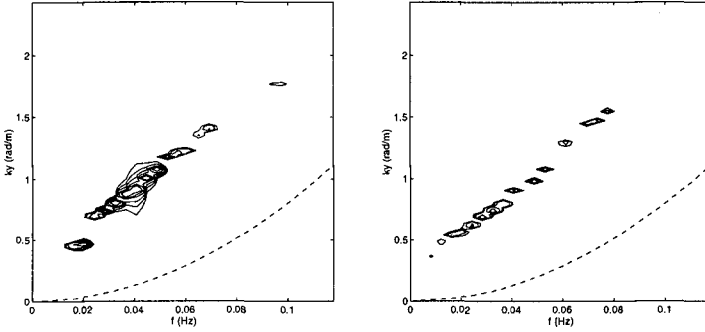


Figure 3: Left panel, $f - k_y$ -spectrum at $x = 4.5m$. Right panel, $f - k_y$ -spectrum at $x = 2.75m$. Zero-mode edge wave dispersion curve denoted by the dashed line.

From the almost linear dispersion lines of the shear instabilities it can be seen that the energy density propagates with approximately the same speed, $c = O(0.35)$ m/s, at both locations.

Cross-shore momentum flux

The momentum flux at the cross-shore measurement locations, denoted by the subscript i , in a single transect may be obtained from:

$$R(x_i) = \rho d(x_i) \langle u(x_i, t)v(x_i, t) \rangle \quad (1)$$

with u and v being the cross-shore and alongshore velocities associated with the shear instabilities, $\langle \rangle$ denotes time averaging, d the local water depth and ρ the water density. The resulting flux depends on the spatial structure, mentioned in the previous paragraph, and the phase coupling between the velocity components. First we have a closer look at the frequency distribution of the momentum flux associated with the shear instabilities using cross-spectral analysis. To that end the velocity time series are written in Fourier series:

$$u(x_i, t) = \sum_n A_n e^{i\omega_n t} + * \quad (2)$$

$$v(x_i, t) = \sum_n B_n e^{i\omega_n t} + * \quad (3)$$

The momentum flux as function of frequency can be obtained from the co-spectral values:

$$R'(x_i, \omega_n) = d(x_i)(A_n B_n^* + A_n^* B_n) \delta \omega \quad (4)$$

The results of the frequency dependent momentum flux at 27,25 m from the inflow opening is shown in Figure 4. The intermediate values have been obtained from linear interpolation in frequency and space. The flux is spa-

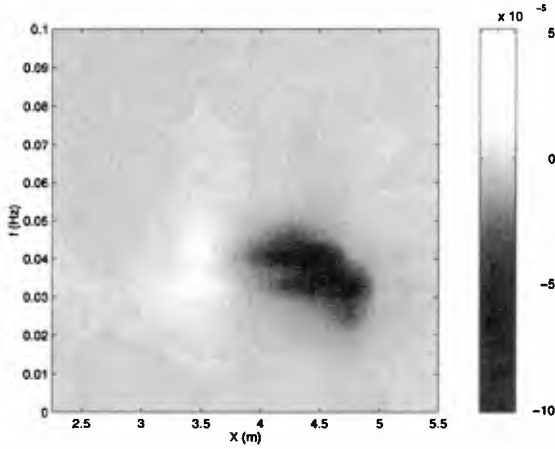


Figure 4: Frequency distribution of shear instability momentum flux, R' , at 27.25 m from the inflow opening expressed in $\frac{m^3}{s^2}$ rad/s

tially concentrated at both sides of the bar crest ($x \simeq 3.75$ m), with maximum contributions around the peak shear instability frequency. At the shoreward side of the bar crest ($x < 3.75$ m) the momentum flux seems to be bimodal in frequency space. The frequency where the maximum flux is located decreases with increasing x -values, i.e. going further offshore, indicating that the higher frequencies, having smaller spatial scales, contribute less. The same can be seen going toward the shoreline, though to a lesser extent.

Importance in longshore current modelling

For alongshore uniform steady state conditions the wave averaged longshore momentum equation is given by:

$$\frac{\partial S_{xy}}{\partial x} = \bar{\tau}_{y,b} \quad (5)$$

with the following contributions to the term on the left-hand side due to

waves:

$$\frac{\partial}{\partial x} \rho \int_d \tilde{u} \tilde{v} dz \quad (6)$$

turbulence:

$$\frac{\partial}{\partial x} \rho \int_d u'v' dz = \rho \frac{\partial}{\partial x} \left(d\nu_t \frac{dV}{dx} \right) \quad (7)$$

and shear instabilities:

$$\frac{\partial}{\partial x} \rho \int_d uv dz \quad (8)$$

which are balanced by the alongshore directed wave-averaged bottom shear stress given by the term on the right hand side. In the following the shear instability contribution is compared to the other components in the longshore momentum equation.

The total momentum flux due to the shear instabilities, R , is obtained by integrating R' over all frequencies (see Figure 5). It shows the measured

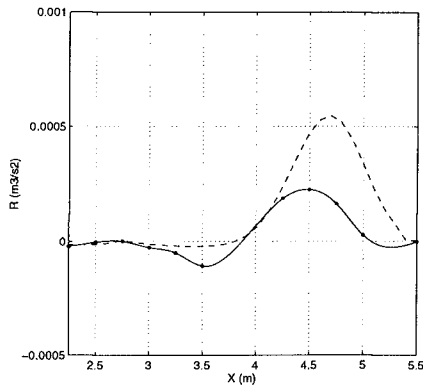


Figure 5: Total momentum transfer at $y = 27.25$ m from the inflow opening

flux, indicated by the dots, through which a spline has been fitted, in comparison to the horizontal mixing induced by wave breaking turbulence which is estimated from the measurements:

$$R_{\nu_t}(x) = d(x)\nu_t(x) \frac{dV}{dx} \quad (9)$$

using the measured longshore current velocity, V and the measured wave height, H , as input. The turbulent eddy viscosity, ν_t , is obtained from (Batjes, 1975):

$$\nu_t = H(x) \left(\frac{D(x)}{\rho} \right)^{\frac{1}{3}} \quad (10)$$

where the estimated wave dissipation is obtained from the measured wave transformation. It shows a significant contribution of the shear instabilities to the momentum flux at 27.25 m from the inflow opening, though almost everywhere smaller than the estimated horizontal mixing. The cross-shore profile of the momentum flux is not unlike results obtained from linear stability results (Church et al., 1992), though in this case the contribution in the trough seems to be considerably less. Given the fact that the shear instability intensity increases in the downstream direction the corresponding flux also evolves in this direction, which is apparent from the sequence of panels shown in Figure 6.

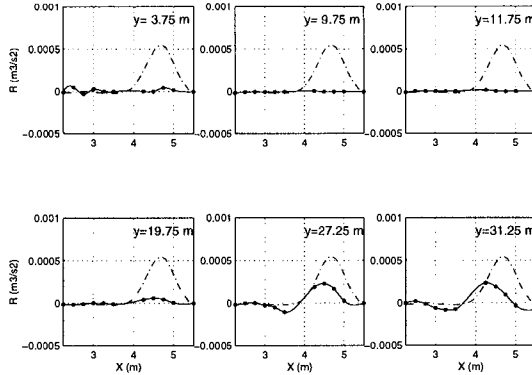


Figure 6: Alongshore development of total momentum transfer from the inflow opening (upper left panel) to the outflow opening (lower right panel). Distance to the inflow opening given by y .

At the upstream end of the basin little evidence of additional mixing is available, except in the very first panel in the upper left corner, which can be associated with the redistribution of the pumped discharge at the inflow opening. It takes until EMF07, located 19.75 m from the inflow opening, for the cross-shore momentum flux by shear instabilities to become evident.

After that a strong build-up is apparent, though never reaching values as indicated by the wave-breaking induced horizontal mixing. Note that the contribution in the trough stays small all along the beach.

Next we have a look at the cross-shore gradient of the mixing, using the spline, which contributes to the longshore momentum equation in computing the longshore current velocity profile:

$$F = \frac{\partial R}{\partial x} \quad (11)$$

The alongshore directed wave forcing, estimated from the measurements, is included as a reference:

$$F_w = \frac{\partial E_w \sin(\theta) \cos(\theta)}{\partial x} \quad (12)$$

where E_w represents the wave energy (obtained from the measured wave transformation) and θ the angle of incidence (using Snell's law).

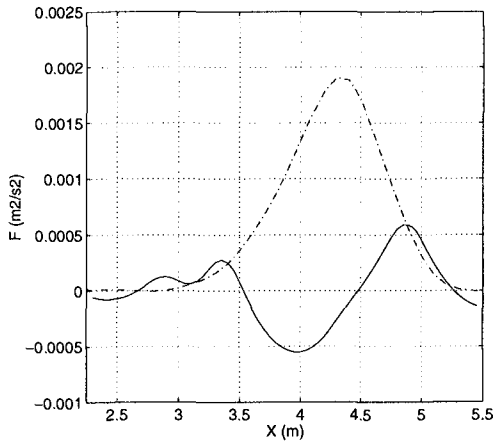


Figure 7: Contribution of shear instabilities to the longshore momentum balance at $y = 27.25$ m from the inflow opening (solid line). The alongshore-directed wave forcing is shown as a reference (dashed line)

The results at 27.25 m from the inflow opening, Figure 7, indicate a significant contribution to the longshore momentum balance. Based on this, it is expected that the maximum current velocity will decrease, given the

opposite signs of the contribution by the shear instabilities and wave forcing at the bar crest. Furthermore, the shear instability contribution at the seaward side of the bar indicates a broadening of the longshore current velocity. Only minor differences in the current velocity over the trough are expected to occur.

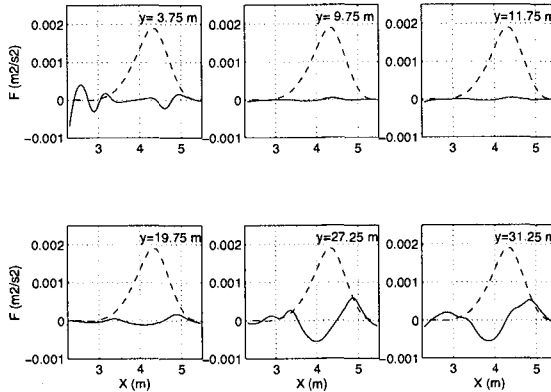


Figure 8: Alongshore development of shear instability contribution to longshore momentum balance (solid lines) from the inflow opening (upper left panel) to the outflow opening (lower right panel). The alongshore-directed wave forcing is shown as a reference (dashed lines)

The alongshore development of the shear instability contribution to the longshore momentum (see Figure 8) is in line with the results previously shown for the momentum flux. In all cases the contribution is considerably smaller than the alongshore directed wave forcing. It is worth to note that the development of the shear instability contribution to the longshore momentum balance stays small in the trough.

Finally we have a look at the measured development of the longshore current velocity (see Figure 9). There is no clear evidence of the effects of the shear instability induced cross-shore mixing on the alongshore development of the mean longshore current velocity profile.

Conclusions

A detailed analysis of the cross-shore momentum flux due to the presence of finite amplitude shear instabilities in a wave-driven longshore current was made based on the measurements obtained during a laboratory experiment.

It showed an alongshore increasing cross-shore flux, becoming of compa-

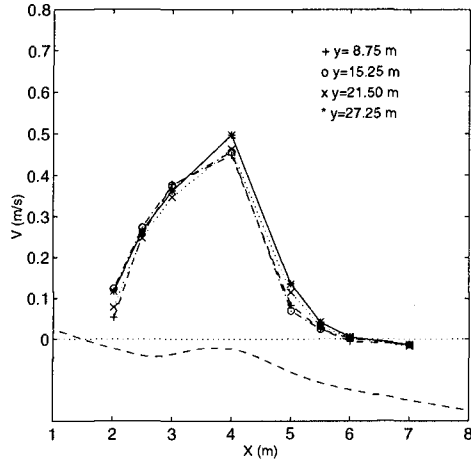


Figure 9: Longshore current velocity at four different transsects

rable order as the mixing associated with breaking wave induced turbulence at the downstream end of the basin.

However, no significant downstream changes in the mean longshore current velocity profile were detected. This can be explained by the fact that the shear instabilities take only effect near the outflow opening, whereas the wave forcing is present all along the beach.

Acknowledgements. The experiments, performed in the large multidirectional wave-basin at Delft Hydraulics, were funded by the European Community in the framework of the European Large Installations Plan (LIP), project 19 M. Ad Reniers was funded by the J.M. Burgers Centre for Fluid Mechanics in Delft.

References

- Battjes, J.A., 1975: Modelling of turbulence in the surfzone. Proc. Symp. Model. Techniques, San Francisco, pp. 1050-1061.
- Church C.C., E.B. Thornton and J. Oltman-Shay, 1992: Mixing by shear instabilities of the longshore current. Proc. 23rd Int. Conf. Coastal Eng., Venice, pp. 2,999:3,011.
- Dodd, N. and E.B. Thornton, 1990: Growth and energetics of shear waves in the nearshore. J.Geophys.Res., 95, C9, pp. 16,075:16,083.
- Dodd, N. and E.B. Thornton, 1993: Longshore current instabilities: growth to finite amplitude. Proc. 23rd Int. Conf. Coastal Eng., Venice, pp. 2655-2668.
- Putrevu, U and I.A. Svendsen, 1992: Shear instability of longshore currents: A numerical study, J.Geophys. Res., 97, C5, pp. 7283-7303.
- Reniers, A.J.H.M., J.A. Battjes, A. Falques and D.A. Huntley, 1994: Shear wave laboratory experiment. Proceedings IAHR waves conference, Vancouver, Canada, pp. 356-365.
- Reniers, A.J.H.M., and J.A. Battjes, 1996: A laboratory study of longshore currents over barred and non-barred beaches. To appear in Journal of Coastal Eng.
- Reniers, A.J.H.M., J.A. Battjes, A. Falques and D.A. Huntley, 1996: A laboratory study on the shear instability of longshore currents. To appear in JGR.
- Visser, P.J., 1984: Uniform longshore current measurements and calculations. Proc. 19th Int. Conf. Coastal Eng., Houston, pp. 2192-2207.

CHAPTER 15

Modelling Post-Wave Breaking Turbulence and Vorticity.

T.C.D.Barnes, M.Brocchini,[†] D.H.Peregrine[‡] and P.K.Stansby[§]

1. Abstract

A brief review is given of the initial development of two approaches to the modelling of the flow that occurs after a water wave breaks. The first approach aims to model the turbulence generated by a spilling breaker riding on an unsteady wave. The turbulent volume of water in a spiller is modelled as a thin layer.

The second approach is applied to model the region of strong vorticity generated by a plunging breaker. The vorticity is modelled using two-dimensional discrete vortices. The behaviour of both a single vortex and a ‘cloud’ of vortices near a free surface is described.

2. Introduction

Water wave breakers, whether in deep or shallow water are mainly categorized as spilling or plunging breakers with no clear distinction between them. In particular intermediate types certainly exist, where there is a small initial plunging event which initiates tumbling white water as in a spiller. The strongly vortical and turbulent flow which results from all types of breaker is the interest of our studies. We distinguish between the turbulence and the vorticity of the mean flow. For example, a plunging breaker frequently creates a strong vortical flow about a horizontal axis. First steps in using discrete vortices in a two-dimensional model with a fully nonlinear free surface are described in the second part of this paper. The first section describes the modelling of a thin layer of turbulence in a spilling breaker.

[†]Research assistants, School of Mathematics, University of Bristol, University Walk, Bristol, BS8 1TW, UK, (*Tim.Barnes@bristol.ac.uk*, *M.Brocchini@bristol.ac.uk*)

[‡]Professor of Applied Mathematics, School of Mathematics, University of Bristol, (*D.H.Peregrine@bristol.ac.uk*)

[§]Professor of Civil Engineering, Department of Engineering, University of Manchester. (*pkstansby@fs1.eng.man.ac.uk*)

3. Turbulence and vorticity in a spilling breaking wave

In their analysis of spilling breakers, bores and hydraulic jumps Peregrine & Svendsen (1978) suggested that the volume of turbulent flow in a spilling breaker resembles a turbulent mixing layer. The roller model in which the turbulent region is modeled as a separate flow region passively riding the wave crest is seen to be only a partial solution as it is evident that the fluid content of the roller itself is continually mixing with the rest of the turbulent fluid in the wave.

Peregrine (1992) also suggests that a spilling breaker may be considered as a quasi-steady system in a frame of reference moving with the wave where deformations of the spiller shape occur at longer time scales than those typical of the motion of water through the turbulent region. The structure of such a quasi-steady breaker is thus an initial mixing layer region, followed by a region beneath the crest of the wave where gravity influences and restrains the turbulent motions near the surface.

This view leads to consideration of a turbulent layer where turbulence is generated at the leading edge (toe of the wave) by shear stresses due to the relative motion between the turbulent wave surface and the water in which the wave propagates. Turbulence, generated near the free surface, propagates within the body of the wave and the turbulent layer evolves from a mixing layer type flow near the leading edge towards a wake type flow where most of the turbulent kinetic energy is dissipated.

This scenario is now documented for a small, quasi-steady spilling breaker, a recent experimental analysis of which is given by Lin & Rockwell (1995). It is found that the breaker originates from a region where the free surface abruptly changes slope (toe of the wave). The magnitude of the velocity is virtually unaltered until the abrupt onset of curvature of the free surface is encountered. At this location, there is a drastic nearly discontinuous reduction in magnitude of the velocity. The change in the velocity field is accompanied by a sudden increase in elevation of the free surface and represents an abrupt transformation from an undisturbed, essentially uniform velocity field to a very low velocity separated region existing beneath the free surface. The essentially discontinuous slope of the surface, in the presence of flow separation beneath it, serves as a source of vorticity giving rise to vorticity concentrations in a separated mixing layer, or shear layer.

We report on modelling of an unsteady thin turbulent layer (to be used in the modelling of a spilling breaking wave). One of the main assumptions is that the vertical extent of turbulent flow is much smaller than its streamwise extent. The motion of the wave is to be modelled by any suitable model for irrotational flows (e.g. boundary integral method) while the turbulent region of the breaker is modelled by a simplified $k - \epsilon$ model for a thin layer of fluid similar to that of Madsen & Svendsen (1983). The main new features of the present model are concerned with the correct representation of stretching, curvature, acceleration and local rotation that the layer of turbulent flow undergoes. Particular care has been put in analyzing the effects of curvature on the turbulent flow in the thin layer.

In figure 1 the global geometry of the present model for a spilling breaking wave is shown. Two regions of turbulent flow are identified. The 'surface layer'

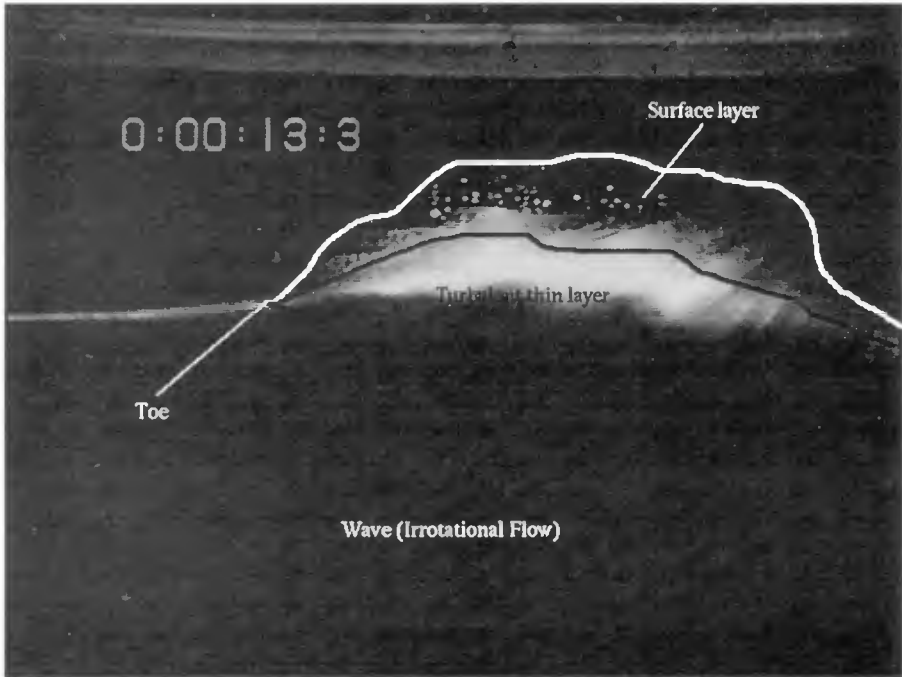


Figure 1: Global geometry adopted in the model for the system wave - turbulent thin layer - surface layer. Frame of video taken at the Fluid Dynamics unit of the University of Edinburgh.

region represents that portion of the turbulent thin layer where the instantaneous free surface fluctuates around the mean free surface. When turbulent eddies cause the interface to splash into the air phase a situation occurs in which space is occupied by two substances which have different properties (e.g. air and water) and can be distinguished from each other (Brocchini & Peregrine, 1997a). Thus, the flow is essentially a two-phase flow. Beneath the 'surface layer' a second layer is found where the flow is still turbulent but single-phase (water). A summary on the modelling of the single-phase turbulent thin layer follows.

Brocchini & Peregrine (1997a) analyses in detail the boundary conditions for a turbulent air-water mixture ('surface layer') occurring at a splashing free surface. In order to obtain conditioned equations for each phase (i.e. air and water) a phase function or intermittency function is introduced such that

$$I(\mathbf{x}, t) = \begin{cases} 1 & \text{probe at } \mathbf{x} \text{ is in the water at time } t \\ 0 & \text{probe at } \mathbf{x} \text{ is in the air at time } t. \end{cases} \quad (1)$$

An integral method has been used to assess the flow equation for the water phase. Exact boundary conditions have been obtained by integrating in the crossflow direction the equations for the water flow. These boundary conditions are com-

plicated and cannot be directly used in simple turbulence models (e.g. $k - \varepsilon$) because they are written in terms of the flow properties in the water phase rather than in terms of the ordinary mean flow variables. Approximations and closure assumptions are made to obtain simpler approximate boundary conditions for use in the modelling of the spilling breaker. The intermittency factor

$$\langle I(\mathbf{x}, t) \rangle = \gamma(\mathbf{x}, t) \quad (2)$$

is the ensemble average of $I(\mathbf{x}, t)$ and is the most important statistical parameter to characterize a specific surface layer. Thus, closure is based on a suitable definition for γ for each flow regime (see figure 2).

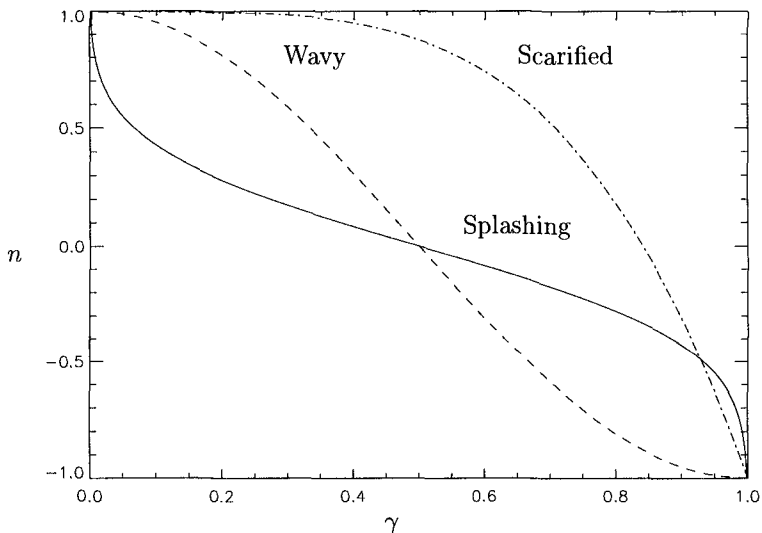


Figure 2: The intermittency factor (or residence time) γ for: (a) wavy air-water interface (dashed line), (b) periodically scarified interface (dot-dashed line) and (c) turbulent splashing interface (solid line).

Since the main aim of the modelling is to correctly represent the stretching, curvature, acceleration and local rotation that the layer of turbulent flow undergoes we use the tools of curvilinear tensor analysis to derive the flow equations and derive a more general version of Svendsen & Madsen, (1984) thin, hydrostatic layer for a shallow water flow. Here the underlying irrotational wave motion is supposed to be modelled by an accurate flow solver, such as that of Dold & Peregrine (1986), modified to use the following thin layer equations as a boundary condition.

We start from Euler's equation for a Newtonian, incompressible, perfect fluid

of constant density ρ :

$$\rho \frac{Du_i}{Dt} = \rho F_i - p_{,j}. \quad (3)$$

where the comma refers to partial covariant differentiation. The left hand side of this equation contains the total derivative of the flow velocity. The two contributions on the right hand side are due to the external forces (here only gravity) and to the pressure p . A set of two-dimensional orthogonal coordinates (ξ_1, ξ_2) is defined as follows (Moore, 1978).

Consider a smooth time-dependent two-dimensional curve $\Upsilon(t)$ (see Figure 3) given parametrically by the equation

$$\mathbf{r} = \mathbf{R}(\alpha, t) \quad (4)$$

where t is time and α is an arbitrary parameter. The curve $\Upsilon(t)$ represents either the wave free surface when no breaking occurs or an interface between the irrotational flow region (below) and the region containing turbulent flow (above). Due to the typical entrainment of irrotational flow into the region of turbulence the curve $\Upsilon(t)$ is not a material surface when turbulence is present, i.e. water particles which at time $t = t_0$ are on the surface $\Upsilon(t)$ at a later time $t = t_1$ will not be on the surface any more.

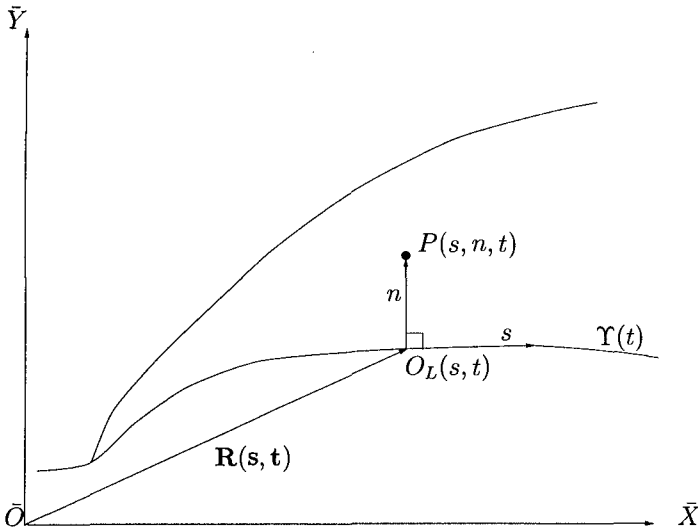


Figure 3: Definitions for geometry and coordinates used for the thin turbulent layer.

With each "convected point" $O_L(\alpha(s), t)$ of the curve we associate a unit tangent vector $\hat{\mathbf{s}}(\alpha(s), t)$ to the curve defined by

$$\hat{\mathbf{s}} = \frac{\partial \mathbf{R}}{\partial s} \quad \text{so} \quad \frac{\partial \mathbf{R}}{\partial \alpha} = \frac{\partial s}{\partial \alpha} \frac{\partial \mathbf{R}}{\partial s} = \frac{\partial s}{\partial \alpha} \hat{\mathbf{s}}; \quad (5)$$

and also a unit normal vector $\hat{\mathbf{n}}(\alpha(s), t)$. For the sake of simplicity much of the following analysis is carried out by referring differential quantities to the arc length s rather than to the convected coordinate α , hence the position of each convected point $O_L(s, t)$ in the fixed frame of reference $\bar{O}\bar{X}\bar{Y}$ is:

$$\mathbf{r} = \mathbf{R}(s, t). \quad (6)$$

For any general point P , which is in the turbulent layer (i.e. above Υ) we assume that it is close enough to Υ that there is only one normal to the curve passing through O_L towards P and the distance $O_L P = n$ is also defined. This is positive if P is on the left hand side of Υ when this is described in the s -increasing direction (i.e. above Υ). Moreover the position of the point P within the thin layer is determined by two coordinates $\xi^1 = s$, $\xi^2 = n$ which form a mobile curvilinear coordinate system.

With this convention the position of P in $\bar{O}\bar{X}\bar{Y}$ is :

$$\mathbf{r}_P(s, n, t) = \mathbf{R}(s, t) + \hat{\mathbf{n}}(s, t)n. \quad (7)$$

The metric tensor g_{ij}^M can be identified more clearly by analysing the infinitesimal distance between two points P and Q and is:

$$ds^2 = d\mathbf{r} \cdot d\mathbf{r} = (1 - \kappa n)^2 ds^2 + dn^2 = g_{ij}^M d\xi_i d\xi_j. \quad (8)$$

where κ is the local curvature.

The model comprises four equations for the mean flow. Mean flow variables are in capital letters (e.g. U, V, P) while turbulent fluctuations are in lower case (e.g. u, v). A first equation states the conservation of mass:

$$\frac{\partial U}{\partial s} + \frac{\partial}{\partial n} [(1 - \kappa n)V] = n \frac{\partial \Omega}{\partial s}. \quad (9)$$

Here two extra terms due to the angular velocity Ω and to the curvature κ influence the mean motion.

The two equations for the conservation of momentum in the streamwise and crossflow direction are respectively:

$$(1 - \kappa n) \frac{\partial U}{\partial t} + (1 - \kappa n) \left[\left(V + \hat{\mathbf{n}} \cdot \frac{\partial \mathbf{R}}{\partial t} \right) \frac{\partial U}{\partial n} + \frac{\partial \langle uv \rangle}{\partial n} \right] + \frac{\partial \langle u^2 \rangle}{\partial s} - 2\kappa \langle uv \rangle \quad (10)$$

$$+ \left(U + \hat{\mathbf{s}} \cdot \frac{\partial \mathbf{R}}{\partial t} - n\Omega \right) \left(\frac{\partial U}{\partial s} - n \frac{\partial \Omega}{\partial s} - \kappa V \right) = (1 - \kappa n) \left(V\Omega + \frac{\partial(n\Omega)}{\partial t} + \hat{\mathbf{s}} \cdot \mathbf{g}' \right) - \frac{1}{\rho} \frac{\partial P}{\partial s},$$

and

$$\frac{\partial V}{\partial t} + \hat{\mathbf{n}} \cdot \frac{\partial \mathbf{R}}{\partial t} \frac{\partial V}{\partial n} + \frac{1}{2} \frac{\partial V^2}{\partial n} + \frac{\partial \langle v^2 \rangle}{\partial n} + \frac{1}{(1 - \kappa n)} \hat{\mathbf{s}} \cdot \frac{\partial \mathbf{R}}{\partial t} \left(\frac{\partial V}{\partial s} + \kappa U \right) + \frac{(U - n\Omega)}{(1 - \kappa n)} \left(\frac{\partial V}{\partial s} + \kappa U \right)$$

$$+ \frac{1}{(1 - \kappa n)} \frac{\partial \langle uv \rangle}{\partial s} + \frac{\kappa \langle u^2 \rangle - \langle v^2 \rangle}{(1 - \kappa n)} = n\Omega^2 - U\Omega + \hat{\mathbf{n}} \cdot \mathbf{g}' - \frac{1}{\rho} \frac{\partial P}{\partial n}. \quad (11)$$

where $\langle \cdot \rangle$ is the average operator and \mathbf{g}' is the 'reduced' gravity factor

$$\mathbf{g}' = \mathbf{g} - \frac{\partial^2 \mathbf{R}}{\partial t^2}. \quad (12)$$

The above are the Reynolds' equations for our two-dimensional mean flow. As usual Reynolds' decomposition of non-linear convective terms introduces Reynolds' stress terms $\langle u_i u_j \rangle$ and isolates the effects of fluctuations on the mean flow.

These equations resemble the equations used in the modelling of a curved thin layer of turbulence (e.g. Gibson & Rodi, 1981). One of the main differences is that in the present case there is interactive coupling (through $\partial \mathbf{R} / \partial t$ and \mathbf{g}') between the motion of the thin layer of turbulence and that of the irrotational wave below.

Finally, modelling of the turbulence may be achieved by means of a simplified $k - \varepsilon$ model in which a first order closure is adopted such that we only solve a transport equations for the turbulent kinetic energy k :

$$\begin{aligned} \frac{\partial k}{\partial t} + \frac{1}{(1 - \kappa n)} \left(U + \hat{\mathbf{s}} \cdot \frac{\partial \mathbf{R}}{\partial t} - n\Omega \right) \frac{\partial k}{\partial s} + \left(V + \hat{\mathbf{n}} \cdot \frac{\partial \mathbf{R}}{\partial t} \right) \frac{\partial k}{\partial n} = \frac{1}{(1 - \kappa n)^2} \frac{\partial}{\partial s} \left(\nu_t \frac{\partial k}{\partial s} \right) \\ + \frac{\partial}{\partial n} \left(\nu_t \frac{\partial k}{\partial n} \right) + (\langle u^2 \rangle - \langle v^2 \rangle) \frac{\partial V}{\partial n} - \frac{\langle uv \rangle}{(1 - \kappa n)} \left[(1 - \kappa n) \frac{\partial U}{\partial n} + \frac{\partial V}{\partial s} + \kappa U \right] - \varepsilon. \end{aligned} \quad (13)$$

Here ε and ν_t are respectively the energy dissipation and the eddy viscosity such that:

$$\varepsilon \approx \frac{k^{3/2}}{\delta}, \quad \text{and} \quad \nu_t \approx \frac{k^2}{\varepsilon} \quad (14)$$

where δ is the thickness of the turbulent layer.

Modelling the dynamics of the thin layer of turbulence provides suitable boundary conditions for the irrotational flow of the wave. The turbulence/wave interaction occurring at lower boundary ($n = 0$) of the turbulent layer is represented by mass entrainment across the boundary and by extra pressure at the boundary. These extra terms are to be incorporated respectively in the kinematic and in the dynamic boundary condition for the irrotational wave along $\Upsilon(t)$. For example the kinematic boundary condition for the irrotational wave is:

$$\hat{\mathbf{s}} \cdot \frac{\partial \mathbf{R}}{\partial t} + \frac{\partial s}{\partial t} = \frac{1}{(1 - \kappa n)} \frac{\partial \phi}{\partial s}, \quad (15)$$

$$\hat{\mathbf{n}} \cdot \frac{\partial \mathbf{R}}{\partial t} = \frac{\partial \phi}{\partial n} + \mathcal{V} \quad (16)$$

where ϕ is the velocity potential for the irrotational flow and \mathcal{V} is the 'entrainment velocity' i.e. the velocity at which the turbulent layer entrains irrotational flow across the boundary $n = 0$. Increasing entrainment is such that the interface $\Upsilon(t)$ is lowered. The velocity \mathcal{V} is parameterized in terms of the local amount of turbulence in the thin layer.

We refer to Brocchini (1996) and Brocchini & Peregrine (1997b) for a detailed description of the derivation of the model equations.

4. Modelling of Waves and Concentrated Vorticity

For large organised vortical motions that are generated by plunging breakers, we add point vortices to the two-dimensional fully nonlinear free surface boundary integral solver for irrotational flow described by Cooker *et al* (1990). The numerical model solves the following equations, the usual equations for inviscid, incompressible and irrotational potential flow with the full nonlinear boundary conditions:

$$\begin{aligned}
 \nabla^2\Phi &= 0 && \text{in fluid} - \{\mathbf{x}_i^v\} \\
 \frac{D\mathbf{x}}{Dt} &= \nabla\Phi && \text{on free surface} \\
 \frac{D\Phi}{Dt} &= \frac{1}{2}|\nabla\Phi|^2 - gy && \text{on free surface} \\
 \frac{\partial\Phi}{\partial n} &= 0 && \text{on solid boundaries}
 \end{aligned} \tag{17}$$

where $\mathbf{x} = (x, y)$, $\Phi(\mathbf{x}, t)$ is the velocity potential and g is the acceleration due to gravity. The velocity potential, Φ is composed of a regular part ϕ_r and a singular part ϕ_s . The singular part is due to a system of point vortices, centres $\{\mathbf{x}_i^v\}$ while the regular part is due to the free surface. The potential due to a single point vortex is augmented by its images in both the bed ($y = -h$) and the line $y = h$ above the free surface, which gives the following expression

$$\begin{aligned}
 \phi_s &= \kappa(\tan^{-1}[\coth[s(x - x^v(t))]\tan[s(y - y^v(t))]] \\
 &\quad - \tan^{-1}[\coth[s(x - x^v(t))]\tan[s(y + y^v(t) + 2h)]])
 \end{aligned} \tag{18}$$

where $s = \pi/4h$, $(x^v(t), y^v(t))$ is the position of the point vortex and κ its strength. The extra images are helpful in giving a singular solution which decays rapidly in space. The circulation around the point vortex is then $\Gamma = 2\pi\kappa$, $\Gamma > 0$ denotes circulation in the counter-clockwise direction. We define a Froude number $Fr = \kappa/\sqrt{(gL^3)}$ where L is some characteristic length scale, usually the distance of a vortex from the free surface. The system is non-dimensionalised with g and L , all results presented are dimensionless.

Tong (1991) computed the evolution of a single point vortex as it interacted with a free surface. He used the two dimensional fully nonlinear free surface potential flow numerical solver which solves the equations shown to model the free surface deformation (Cooke *et al* 1990). A single point vortex modelling the effect of vorticity, moving under the effect of its images and the free surface. We have extended the method to include a system of point vortices in order to model the effect of larger regions of vorticity.

In the extended model each point vortex moves under the influence of the free surface, the other vortices and its images. The free surface moves under the

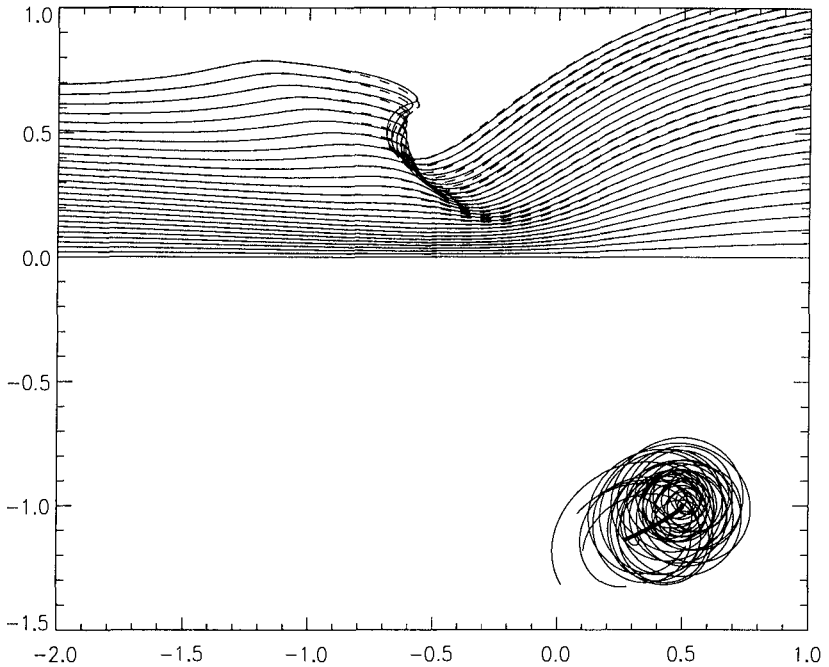


Figure 4: Stacked free surface deformation due to a single (solid) and 10 (dashed) vortices.

influence of the vortices and gravity. The numerical method which we use time-steps the free surface using a Taylor series expansion truncated at the sixth power of the time-step. The inclusion of the point vortices necessitates the computation of every partial derivative of the vortex potential in every combination of x , y and t up to the third derivative in order to maintain the accuracy of the scheme. The time step criterion must also be modified to include the vortices, as velocities are very high close to the singular core of a point vortex.

We present some preliminary results here: figure 4 shows the free surface deformation and vortex movement due to a single impulsively started vortex (dotted) with strength $\kappa = 0.5$ initial position $(0.5, -1)$, and due to a system of 10 vortices whose strengths are all constant, positive and sum to 0.5, initially grouped around $(0.5, -1)$.

We can see that the two cases are remarkably similar, and give us some hope that the point approximation can model patches of vorticity well. Clearly a very diffuse patch of vorticity will not be well modelled by a point vortex. Our model will allow us to define the limits within which a single point vortex is sufficient

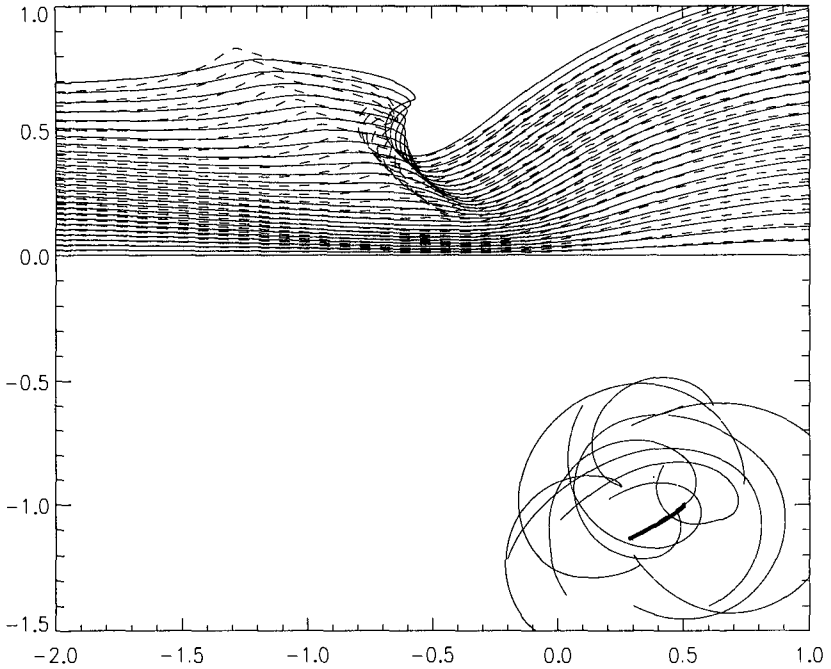


Figure 5: Stacked free surface deformation due to a single (solid) and 10 (dashed) vortices.

to model the free surface deformation due to a patch of vorticity.

We define the centre of the patch of vorticity to be the centroid of vorticity, the point defined by $\mathbf{X}_c^v = \frac{\sum_i \kappa_i \mathbf{x}_i^v}{\sum_i \kappa_i}$. Then the radius of the patch of vorticity is

defined as $R^v = \sqrt{\frac{\sum_i \kappa_i (\mathbf{x}_i^v - \mathbf{X}_c^v)^2}{\sum_i \kappa_i}}$. These definitions are also useful when defining centres and radii of patches of vorticity in experiments.

Figure 4 also shows the individual vortex paths. The thin lines are the paths of the system of 10 vortices, we can see that they co-rotate under their mutual influence, and drift under the influence of the free-surface. The thick line is the path of the single vortex and the centroid of the 10 vortices, which are virtually indistinguishable.

If the patch of vortices are sufficiently diffuse then there are variations from the behaviour in the single vortex case. Figure 5 shows such a case, where the free surface deformation is clearly different in the two cases. However similarities still exist, just outside the limits of the plot the free surface deformation is very

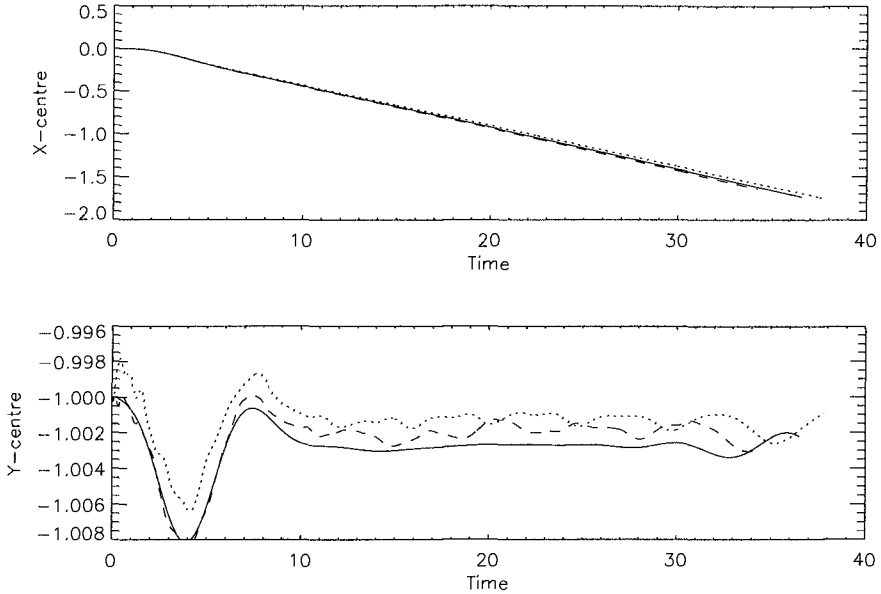


Figure 6: Path of single (solid), five (dashed) and ten (dotted) vortices sum strength 0.1

similar. Also the centre of the system of vortices and the single vortex still move along almost the same path, the thick line.

In certain cases the free surface deformation due to a patch of vorticity and a point vortex appear to be fairly similar. In such cases another interesting feature to study is the longer time evolution of a patch of vorticity which does not induce surface breaking. If the patch is modelled with a single point vortex then, for sufficiently weak vortices, the vortex moves as it would under a rigid wall. The image required to satisfy the rigid wall boundary condition predicts a vortex core velocity of $(-\kappa/2L, 0)$ for a point vortex located at $(x, -L)$. Individual point vortices in a patch of vorticity moving under the influence of the free surface alone will move with different velocities resulting in a diffusion of vorticity. So their interaction with each other and the free surface will determine the evolution of the patch of vorticity.

The solid line graphs in figure 6 show the paths of a single point vortex, strength $\kappa = 0.1$, initial position $(0, -1)$. After an initial transient period the vortex settles down to a constant x -velocity -0.049 with a small varying y -velocity, the rigid wall theory predicts a velocity of $(-0.05, 0)$. Note that the vortex takes some time to reach a steady state, initially sitting almost still. This is in qualitative agreement with the behaviour of vortices which we see in our

experiments (Quinn *et al* 1995 and Haydon *et al* 1996), which appear to take some time to start moving after being left by a plunging breaker.

The dotted and dashed path superimposed on figure 6 show the paths of the centres of systems of five and ten point vortices whose strengths sum to 0.1. We note that even the very small y -variations are fairly similar for all three cases. The radius of the patches is plotted in figure 7.

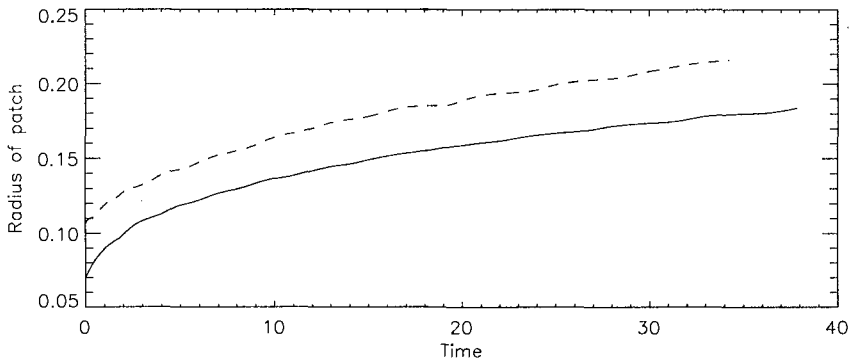


Figure 7: Radius of the patches in figure 6, five vortices (solid), ten vortices (dashed).

More importantly the free-surface generated in these three cases is also very similar, and rather complicated. It is also worth noting that the computations all fail at similar times due to a lack of points caused by a stretching of part of the free surface. This can be overcome by invoking a regridding procedure, we halt the computation at this point as it seems unlikely to yield any more interesting results.

Finally, we include the variation in the radius of the vortex cloud. Figure 7 shows the variation in the radius of the vortex clouds for the present example. We see that the cloud becomes steadily more diffuse, behaviour which is replicated in all cases which we have tried.

5. Conclusions

The work described in this paper continues. The thin layer model of a spilling breaker is being developed to add to boundary integral methods. The detailed analysis of the toe of the spiller is still in progress.

The discrete vortex system under a free surface is demonstrated to be practicable and may be of value for problems other than plunging breakers. For example the flows over many structures result in vortex shedding, which could be well described using the present methods.

6. Acknowledgments

Support from Engineering and Physical Sciences Research Council GR/J/43899 and GR/H/96836, European Union, Directorate General XII, contracts ERBCH-BICT930678 and MAS2-CT92-0047 is gratefully acknowledged.

7. References

- Brocchini, M. (1996). *Flows with freely moving boundaries: the swash zone and turbulence at a free surface*. Ph.D Dissertation. University of Bristol, Bristol.
- Brocchini, M. & Peregrine, D.H. (1997a). *The dynamics of a turbulent free surface. Part 2. The boundary conditions*. (in preparation).
- Brocchini, M. & Peregrine, D.H. (1997b) *The dynamics of a turbulent free surface. Part 3. A model for a spilling breaking wave*. (in preparation).
- Cooker, M.J., Peregrine, D.H., Vidal, C. and Dold, J.W. (1990) *The interaction between a solitary wave and a submerged semicircular cylinder*, J. Fluid Mech. **215**, 1-22.
- Dold, J.W. & Peregrine, D.H. (1984). *Steep unsteady waves: an efficient computational scheme*. Proc. 19th Int. Conf. Coastal Eng. **1**, 955-967.
- Gibson, M.M. & Rodi, W. (1981) *A Reynolds-stress closure model of turbulence applied to the calculation of a highly curved mixing layer*. J. Fluid Mech. **103**, 161-182.
- Haydon, T.A., Hann, D.B., Davies, P. and Greated, C.A. (1995) *Turbulence Structures in the Surf Zone*. Submitted to ICCE '96.
- Lin, J.C. & Rockwell, D. (1995). *Evolution of a quasi-steady breaking wave*. J.Fluid Mech., **302**, 29-44.
- Lugt, H.J. & Ohring, S. (1992) *The oblique ascent of a viscous vortex pair toward a free surface*. J.Fluid Mech. **236**, 461-476.
- Madsen, P.A. & Svendsen, I.A. (1983) *Turbulent bores and hydraulic jumps*. J. Fluid Mech. **129**, 1-25.
- Moore, D.W. (1978). *The equation of motion of a vortex layer of small thickness*. Stud. Appl. Maths., **58**, 119-140.
- Peregrine, D.H. (1992) *Mechanisms of water-wave breaking*. In Breaking waves. IUTAM Symposium, Sydney. (ed. M.L.Banner & R.H.J. Grimshaw), 39-53.
- Peregrine, D.H. & Svendsen, I.A. (1978) *Spilling breakers, bores and hydraulic jumps*. Proc. 16th Int. Conf. Coastal Eng., 540-550.

Quinn, P.A., Barnes, T., Lloyd, S.T., Greated, C.A. and Peregrine, D.H., (1995), *Velocity Measurements of Post-Breaking Turbulence Generated by Breaking Waves*. Proceedings of Coastal Dynamics '95 Conference, 293-304.

Stansby, P.K. & Slaouti, A. (1984) *On nonlinear wave interaction with cylindrical bodies: a vortex sheet approach*. Appl. Ocean Res., **6**, 108-115.

Svendsen, I.A. & Madsen, P.A. (1984). *A turbulent bore on a beach*. J. Fluid Mech. **148**, 73-96.

Tong, R.P., (1991) *Unsteady Flow with a Free Surface: A Study of Numerical Approximations in the Boundary Integral Method*. Ph.D. Thesis, University of Bristol.

CHAPTER 16

A Turbulent Flow Model For Breaking Waves

Nguyen The Duy¹, Tomoya Shibayama² and Akio Okayasu²

Abstract

This paper presents the formulation and solution of a numerical model for breaking waves on uniform sloping bottoms. The model is based on the two-dimensional vertical (2DV) Reynolds-averaged Navier-Stokes equations. The effect of breaker-generated turbulence is modeled by the Reynolds stress terms in the momentum equations, together with an eddy viscosity model. A transformation technique is utilized to solve numerically the governing equations in a variable grid system. At each time level of computation, it is possible to determine directly the following wave quantities for the surf zone: water surface elevation, pressure field and velocity field. The numerical results are verified with various cases of laboratory data.

1. Introduction

The breaking of waves results in the transformation of irrotational wave motion into turbulent rotational motion, which is characterized by vortex motion of various scales; and due to this turbulent motion, the wave energy transported from the offshore is dissipated throughout the surf zone. It has been known that turbulence generated by breaking waves has important effects on most processes within the surf zone such as wave transformation, diffusion of materials, etc. Therefore, in order to obtain a realistic and reasonable simulation of surf zone processes, it is necessary to include the effect of turbulence in the formulation of the wave equations. In addition, information on the vertical structure of wave variables such as wave pressure and water particle velocities is necessary to solve important problems of the nearshore area. For instance, the vertical profile of wave pressure can be applied to determine acting force used in the design of coastal structures, or the near-bottom velocity can be used as a boundary condition to determine the bed shear stress and to solve the flow inside the bottom boundary layer which, in turn, play an important role in the prediction of beach profile

¹Dr. Eng., Dept. of Civil Eng., Ho Chi Minh City Univ. of Technology, 268 Ly Thuong Kiet, Q. 10, Ho Chi Minh City, Vietnam.

²Dr. Eng., Assoc. Prof., Dept. of Civil Eng., Yokohama National Univ., Hodogaya-ku, Yokohama 240, Japan.

change due to sediment transport. An useful and effective wave model, therefore, must be capable of computing directly the vertical distribution of wave variables.

Recently, rapid development in the memory capacity and computational speed of personal computers makes it possible to solve the full 2DV Navier-Stokes equations for water waves. The solution of 2DV wave models may be one among preliminary steps to achieve a complete picture of the modeling of coastal hydrodynamics in a near future, when water waves can be simulated by solving the full three-dimensional Navier-Stokes equations.

Petit et al. (1994) computed breaking waves on a submerged bar by applying the Volume of Fluid method to solve the 2DV Navier-Stokes equations. Shibayama and Duy (1994) presented a 2DV model for waves propagating on sloping bottoms and verified it with laboratory data of non-breaking and breaking waves, however, they could not attain reasonable numerical results for the velocity field in the surf zone.

This paper presents a hydrodynamic model for breaking waves on uniform sloping bottoms, in which the effect of breaker-generated turbulence and the depth variation of the wave variables are included in the model.

2. Governing Equations

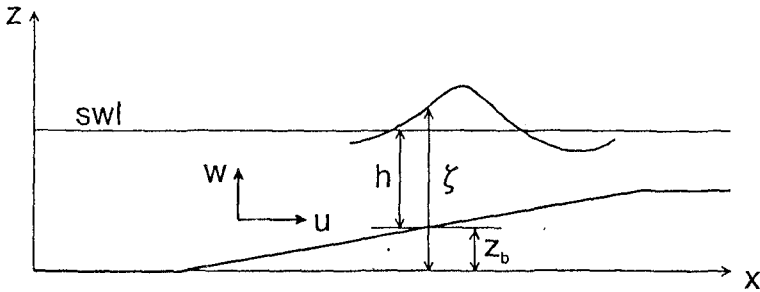


Figure 1: Definition sketch of coordinates system

For a free surface domain, the 2DV Reynolds-averaged Navier-Stokes equations are written as

$$\frac{\partial u}{\partial x} + \frac{\partial w}{\partial z} = 0 \quad (1)$$

$$\frac{\partial u}{\partial t} + \frac{\partial(u^2)}{\partial x} + \frac{\partial(uw)}{\partial z} = -\frac{1}{\rho} \frac{\partial P}{\partial x} + M_x \quad (2)$$

$$\frac{\partial w}{\partial t} + \frac{\partial(uw)}{\partial x} + \frac{\partial(w^2)}{\partial z} = -g - \frac{1}{\rho} \frac{\partial P}{\partial z} + M_z \quad (3)$$

$$\frac{\partial \zeta}{\partial t} + \frac{\partial}{\partial x} \int_{z_b}^{\zeta} u dz = 0 \quad (4)$$

where (u, w) : Reynolds-averaged velocity vector; P : Reynolds-averaged pressure; ζ : water surface elevation; z_b : sea bottom elevation; g : gravity acceleration. The

momentum transports due to fluctuating velocity components of turbulent motion (Reynolds stress terms), M_x and M_z , can be expressed as follows, by using eddy viscosity model

$$M_x = 2 \frac{\partial}{\partial x} \left(\nu_T \frac{\partial u}{\partial x} \right) + \frac{\partial}{\partial z} \left[\nu_T \left(\frac{\partial u}{\partial z} + \frac{\partial w}{\partial x} \right) \right] \quad (5)$$

$$M_z = \frac{\partial}{\partial x} \left[\nu_T \left(\frac{\partial u}{\partial z} + \frac{\partial w}{\partial x} \right) \right] + 2 \frac{\partial}{\partial z} \left(\nu_T \frac{\partial w}{\partial z} \right) \quad (6)$$

where ν_T is the eddy viscosity. In the above equations, since $\nu \ll \nu_T$, the diffusive terms due to molecular viscosity ν are neglected.

In the surf zone, the mean value (time-averaged over one wave period) of ν_T , $\bar{\nu}_T$, has been previously determined by fitting computed currents velocities to measured data. For instance, Longuet-Higgins (1970) simulated longshore currents by using

$$\bar{\nu}_T \approx 0.01h\sqrt{gh} / s \quad (7)$$

where h is the mean water depth and s the beach slope.

On the other hand, in the modeling of cross-shore currents, Okayasu et al. (1988) applied a mean eddy viscosity in the form

$$\bar{\nu}_T = 0.3\sqrt{g(d_t + H)} s z' \quad (8)$$

in which d_t is the depth to wave trough, H the wave height and z' the vertical distance from the bottom, while Svendsen and Hansen (1988) suggested that

$$\bar{\nu}_T = (0.007 - 0.03)h\sqrt{gh} \quad (9)$$

Based on Eq. (9) and the Prandtl-Kolmogorov assumption, Shibayama and Duy (1994) derived approximately a time-varying eddy viscosity for the area outside the bottom boundary layer of the surf zone as follows

$$\nu_T = f_v \sqrt{gh} (\zeta - z_b) \quad (10)$$

In Eq. (10), f_v is a constant and was found to have an average value of 0.125 from the computations of breaking waves. Shibayama and Duy (1994) showed that the use of a fixed value of f_v for all computational cases can produce good agreements between computed and measured wave heights in the surf zone, however, simulated wave profiles and velocity field generally exhibit certain discrepancies compared to measured data, in particular for the near-breaking area. These discrepancies may be caused by the fact that the eddy viscosity commonly increases within certain distance from the breaking point, as shown by laboratory measurements of Okayasu et al. (1988). In order to take into account this effect in the simulation, the constant f_v is slightly modified to become

$$f_v = \begin{cases} 0.03 e^{h_b/h} & \text{if } h_b / h < 1.5 \\ 0.03 e^{1.5} & \text{if } h_b / h \geq 1.5 \end{cases} \quad (11)$$

where h is the still water depth, and h_b the breaking water depth. Eq. (11) expresses a variation range of f_v from a minimum value of 0.082 at the breaking point ($h_b / h = 1$) to a maximum value of 0.134.

Boundary Conditions:

- *Water surface boundary* ($z = \zeta$):

The water surface is a moving boundary in the model. The position of this boundary must be determined at each time level with its own boundary conditions as follows.

For u , a zero shear stress condition is assumed at the water surface

$$\frac{\partial u}{\partial z} = 0 \tag{12}$$

For w , the kinematic boundary condition at a free surface is applied:

$$w = \frac{\partial \zeta}{\partial t} + u \frac{\partial \zeta}{\partial x} \tag{13}$$

and the boundary condition for P is

$$P = 0 \tag{14}$$

- *Bottom Boundary* ($z = z_b$):

A non-slip condition is applied for w :

$$w = 0 \tag{15}$$

In the numerical mesh, the first grid point of u is not located at the bottom (Fig. 2) and therefore, a direct use of the non-slip condition is not necessary. Instead, the boundary condition of u is given implicitly in the form

$$u_{i+0.5,1} + u_{i+0.5,2} = 0 \tag{16}$$

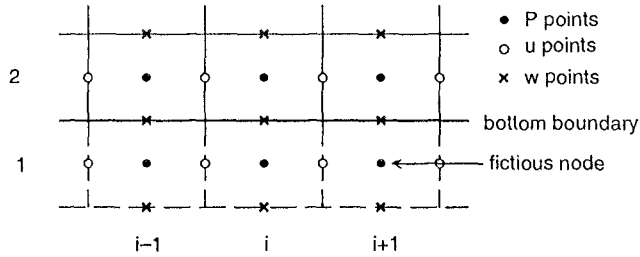


Figure 2: Bottom boundary

Using the continuity equation, Eq. (1), and the non-slip condition, a Neumann boundary condition for pressure is obtained from the z -momentum equation, Eq. (3):

$$\frac{\partial P}{\partial z} = \rho \left[-g + 2\nu_T \frac{\partial^2 w}{\partial z^2} \right] \tag{17}$$

- *Seaward Boundary* ($x = 0$)

The boundary conditions for ζ , u , w and P of incident wave are obtained by applying cnoidal wave theory or Stokes wave theory, depending on the calculated Ursell parameter, Ur , at the seaward boundary (Nishimura et al., 1977):

$$U_r = \frac{HL^2}{h^3} \begin{cases} \geq 25 & : \text{cnoidal waves} \\ < 25 & : \text{Stokes waves} \end{cases} \quad (18)$$

The reflected wave from the domain inside, if existing, will be treated to pass freely and undisturbed through the open seaward boundary. In the model, the actual water surface at each time level t is computed as the sum of the incident and reflected waves.

After determining the water surface elevation $\zeta(t)$, the other variables at the seaward boundary (u, w, P) can be determined approximately by using cnoidal or Stokes wave theory depending on the value of Ursell parameter.

- *Shoreline Boundary* ($x = x_{\max}$)

For u , an absorbing boundary condition is applied at the shoreline boundary (Zienkiewicz and Taylor, 1991):

$$\frac{\partial u}{\partial t} + c \frac{\partial u}{\partial x} = 0 \quad (19)$$

where c is the wave celerity at the shoreline boundary. For outflow at the shoreline boundary, typical boundary condition for w is (Fletcher, 1991)

$$\frac{\partial w}{\partial x} = 0 \quad (20)$$

Assuming that the effect of viscosity in the region adjacent to the shoreline is negligible, a Neumann boundary condition for pressure P can be derived by using the x-momentum equation, Eq. (2), and the absorbing condition, Eq. (19). The resultant equation is

$$\frac{\partial P}{\partial x} = -\rho \left[(2u - c) \frac{\partial u}{\partial x} + \frac{\partial(uw)}{\partial z} \right] \quad (21)$$

- *Breaking Location* ($x = x_b$)

The breaking point is determined by Goda's breaking indices (1975):

$$\frac{H_b}{L_0} = A \left\{ 1 - \exp \left[-1.5 \frac{\pi h_b}{L_0} (1 + 15s^{4/3}) \right] \right\} \quad (22)$$

where H_b : breaking wave height; L_0 : deep water wave length; s : beach slope; and A is an empirical constant taken to be 0.17.

3. Numerical Formulation

In the physical domain, the upper surface is a moving boundary due to wave motion, and the sea bottom also changes in space,

$$\zeta = \zeta(x, t) \quad (23)$$

$$z_b = z_b(x) \quad (24)$$

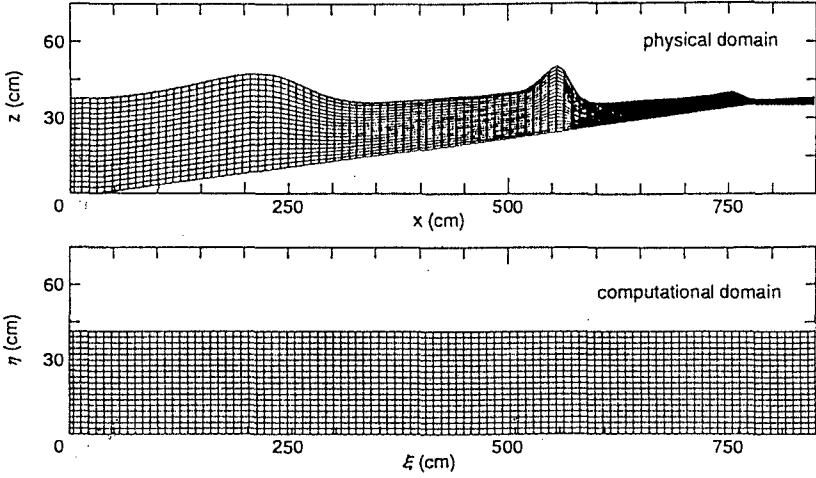


Figure 3: Physical and computational domain

The generated grid for numerical computation is thus also a moving system in space and time (Fig. 3). It is difficult to solve the governing equations numerically in this moving and curvilinear grid. Therefore, a coordinate transformation is carried out to map the moving grid to a fixed and linear one, in which the boundaries are parallel to the coordinate-axes (Fig. 3). The relationships between the physical domain (x, z, t) and the computational domain (ξ, η, τ) are expressed as follows

$$x = \xi \quad (25)$$

$$z = z_b + f(\eta^*) (\zeta - z_b) \quad (26)$$

$$t = \tau \quad (27)$$

where $\eta^* = \eta / \eta_m$ and η_m is the maximum value of η .

Depending on the form of the function $f(\eta^*)$, different types of numerical mesh can be generated for the physical domain (Fletcher, 1991). To obtain constant vertical mesh intervals in the physical domain, we choose

$$f(\eta^*) = \eta^* \quad (28)$$

The first derivatives of the velocity components, u and w , with respect to x , z , and t are expressed in terms of the new variables ξ , η , τ as follows:

$$\begin{bmatrix} \frac{\partial u}{\partial x} & \frac{\partial u}{\partial z} & \frac{\partial u}{\partial t} \\ \frac{\partial w}{\partial x} & \frac{\partial w}{\partial z} & \frac{\partial w}{\partial t} \end{bmatrix} = \begin{bmatrix} \frac{\partial u}{\partial \xi} & \frac{\partial u}{\partial \eta} & \frac{\partial u}{\partial \tau} \\ \frac{\partial w}{\partial \xi} & \frac{\partial w}{\partial \eta} & \frac{\partial w}{\partial \tau} \end{bmatrix} \begin{bmatrix} \frac{\partial \xi}{\partial x} & \frac{\partial \xi}{\partial z} & \frac{\partial \xi}{\partial t} \\ \frac{\partial \eta}{\partial x} & \frac{\partial \eta}{\partial z} & \frac{\partial \eta}{\partial t} \\ \frac{\partial \tau}{\partial x} & \frac{\partial \tau}{\partial z} & \frac{\partial \tau}{\partial t} \end{bmatrix} \quad (29)$$

where the Jacobian matrix J of the transformation is determined by using Eqs. (25) through (27)

$$J = \begin{bmatrix} \frac{\partial \xi}{\partial x} & \frac{\partial \xi}{\partial z} & \frac{\partial \xi}{\partial t} \\ \frac{\partial \eta}{\partial x} & \frac{\partial \eta}{\partial z} & \frac{\partial \eta}{\partial t} \\ \frac{\partial \tau}{\partial x} & \frac{\partial \tau}{\partial z} & \frac{\partial \tau}{\partial t} \end{bmatrix} = \begin{bmatrix} 1 & 0 & 0 \\ -\frac{[\eta_m z_{bx} + \eta(\zeta_x - z_{bx})]}{\zeta - z_b} & \frac{\eta_m}{\zeta - z_b} & -\eta \frac{\zeta_t}{\zeta - z_b} \\ 0 & 0 & 1 \end{bmatrix} \quad (30)$$

where ζ_x and z_{bx} denote the derivatives of ζ and z_b with respect to x , respectively.

With the obtained Jacobian matrix J , at each time level the variable physical domain (x, z, t) can be transformed to the fixed computational domain (ξ, η, τ) . The governing equations, Eqs. (1) through (4), in the computational domain are then given as:

$$\frac{\partial u}{\partial \xi} + \eta_x \frac{\partial u}{\partial \eta} + \eta_z \frac{\partial w}{\partial \eta} = 0 \quad (31)$$

$$\frac{\partial u}{\partial \tau} + \eta_t \frac{\partial u}{\partial \eta} + \frac{\partial(u^2)}{\partial \xi} + \eta_x \frac{\partial(u^2)}{\partial \eta} + \eta_z \frac{\partial(uw)}{\partial \eta} = -\frac{1}{\rho} \left(\frac{\partial P}{\partial \xi} + \eta_x \frac{\partial P}{\partial \eta} \right) + M_\xi \quad (32)$$

$$\frac{\partial w}{\partial \tau} + \eta_t \frac{\partial w}{\partial \eta} + \frac{\partial(uw)}{\partial \xi} + \eta_x \frac{\partial(uw)}{\partial \eta} + \eta_z \frac{\partial(w^2)}{\partial \eta} = -g - \frac{\eta_z}{\rho} \frac{\partial P}{\partial \eta} + M_\eta \quad (33)$$

$$\frac{\partial \zeta}{\partial t} + \frac{\partial}{\partial x} \int_{z_b}^{\zeta} u dz = 0 \quad (34)$$

where

$$M_\xi = 2 \left(\frac{\partial v_T}{\partial \xi} + \eta_x \frac{\partial v_T}{\partial \eta} \right) \left(\frac{\partial u}{\partial \xi} + \eta_x \frac{\partial u}{\partial \eta} \right) + \eta_z^2 \left(\frac{\partial v_T}{\partial \eta} \frac{\partial u}{\partial \eta} + v_T \frac{\partial^2 u}{\partial \eta^2} \right) + 2v_T \left[\frac{\partial^2 u}{\partial \xi^2} + \eta_x^2 \frac{\partial^2 u}{\partial \eta^2} + 2\eta_x \frac{\partial^2 u}{\partial \xi \partial \eta} + \frac{\partial u}{\partial \eta} \left(\frac{\partial \eta_x}{\partial \xi} + \eta_x \frac{\partial \eta_x}{\partial \eta} \right) \right] \quad (35)$$

$$M_\eta = \left(\frac{\partial v_T}{\partial \xi} + \eta_x \frac{\partial v_T}{\partial \eta} \right) \left(\frac{\partial w}{\partial \xi} + \eta_x \frac{\partial w}{\partial \eta} \right) + 2\eta_z^2 \left(\frac{\partial v_T}{\partial \eta} \frac{\partial w}{\partial \eta} + v_T \frac{\partial^2 w}{\partial \eta^2} \right) + v_T \left[\frac{\partial^2 w}{\partial \xi^2} + \eta_x^2 \frac{\partial^2 w}{\partial \eta^2} + 2\eta_x \frac{\partial^2 w}{\partial \xi \partial \eta} + \frac{\partial w}{\partial \eta} \left(\frac{\partial \eta_x}{\partial \xi} + \eta_x \frac{\partial \eta_x}{\partial \eta} \right) \right] \quad (36)$$

The boundary conditions are also transformed to the computational domain in the similar way. The transformed equations and corresponding boundary conditions can be solved numerically by the finite difference method. The numerical computation is carried out on a staggered grid. In this staggered grid, P is defined at the centre of each cell and u, w are defined at the cell faces. In discretizing Eqs. (31), (32), (33), (34), finite difference expressions centered at grid point (i, j) , $(i+0.5, j)$, $(i, j+0.5)$, and (i, j) are used, respectively. These allow all derivatives can be discretised in second-order accuracy with smallest number of involved grid points. The use of the staggered grid also permits coupling of the u, w and P solutions at adjacent grid points. This in turn prevents the appearance of oscillatory

solutions, particularly for P , that can occur if centred differences are used to discretise all derivatives on a non-staggered grid.

A semi-implicit scheme is utilized to solve numerically the discretized forms of Eqs. (31) through (34). At each time step, a main set of linear equations for pressure is solved for the total number of grid points and subordinate sets of linear equations for velocities are solved along the boundaries. The result of pressure distribution is then used to compute the velocity field. For the water surface, two computational steps are necessary to determine this moving boundary at each time step as follows.

(i) At the beginning of a time step $n+1$, an approximate solution for the water surface is obtained by applying an explicit finite difference scheme for Eq. (31), using velocity profiles at the previous time step n . The water surface obtained is then used to evaluate the elements of the Jacobian matrix, and therefore the transformed equations (31) through (34) can be solved in the computational domain.

(ii) At the end of the time step $n+1$, after finishing the velocity computation, an improvement on the water surface computation is achieved by applying the Crank-Nicolson scheme for Eq. (31), using velocity profiles at both time steps n and $n+1$.

4. Numerical results

The total computational time required for the model to get the final results depends mainly on the number of grid points used in the mesh. Using a HP9000/720, it takes approximately 1 hour to complete one simulation for a mesh of 2000 grid points.

A typical illustration of the convergence and stability characteristic of the present model is presented in Fig. 4, which are the computed wave profiles at different sections in the surf zone. With the still water level (horizontal line) is set as the initial condition of the computation, it can be seen that after only about two waves coming from the offshore boundary, the computed wave profile at each section already converts to its final solution. This behavior indicates a rapid convergence characteristic of the model. After the convergence point, the stability of the solution can also be seen through the periodical results of the computed wave profiles.

A typical example of the numerical results of the hydrodynamic model are shown in Figs. 5 and 6. The model results are verified with the laboratory data obtained by Okayasu et al. (1988). In the figures, the variable X denotes horizontal distance from the shoreline of the still water, subscript " b " denotes the breaking point, and z' is the vertical elevation from the bottom.

Fig. 5 shows that the time history of water surface elevation follows an asymmetric pattern: the rise of water surface occurs much faster than the fall one. In general, the model is capable of simulating the highly nonlinear and asymmetric characteristics of wave profiles in the surf zone, as shown through the comparisons with measured data. However, as a common result, large discrepancies between

the computed and measured wave profiles are observed at sections close to the shoreline. These discrepancies may have been caused by the effect of the shoreline boundary. The verifications also show that the present model is capable of

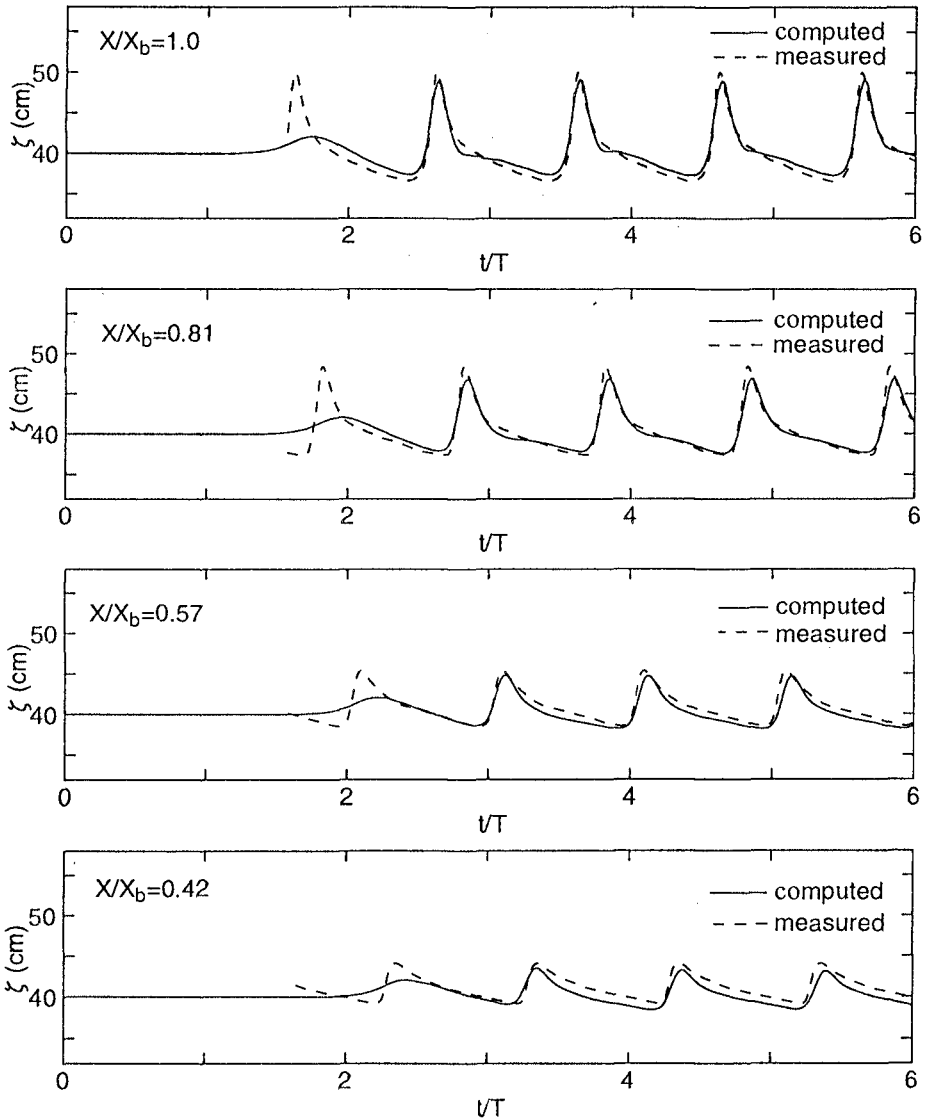
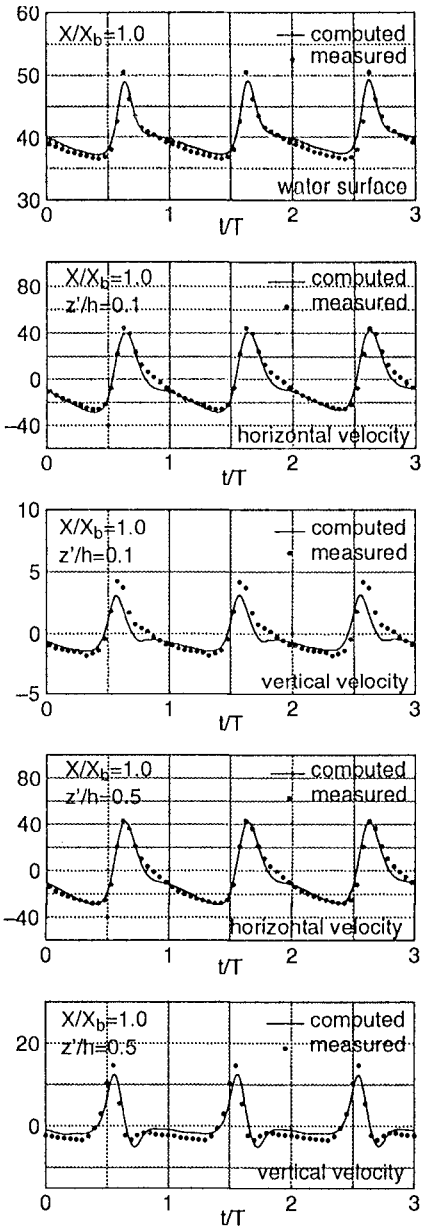
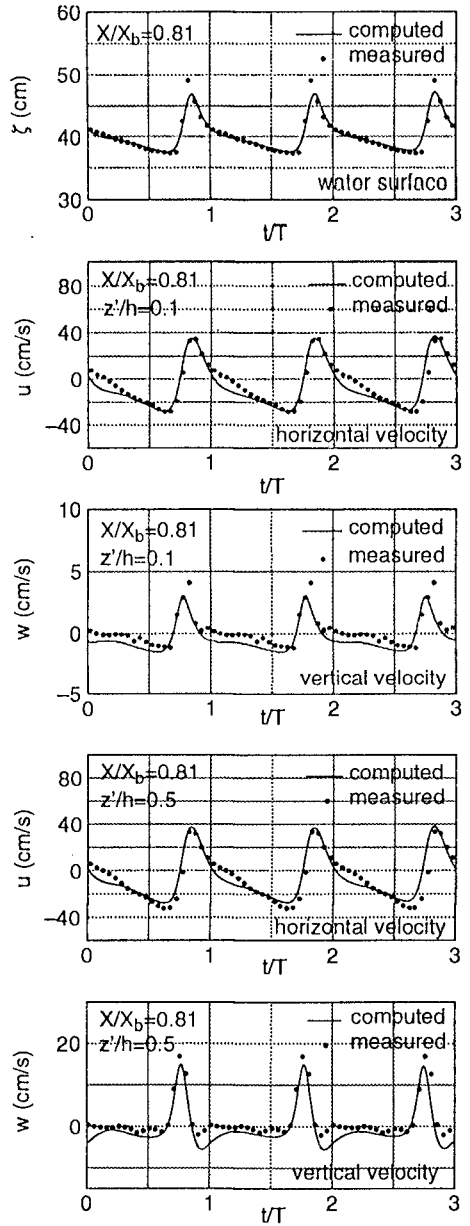


Figure 4: Convergence and stability characteristics of the present model, illustrated through the time series of equi-phase mean water surface elevation ($H_0 = 8.5\text{cm}$, $T = 2\text{s}$, $h_0 = 40\text{cm}$, $s = 1/20$).



(a)



(b)

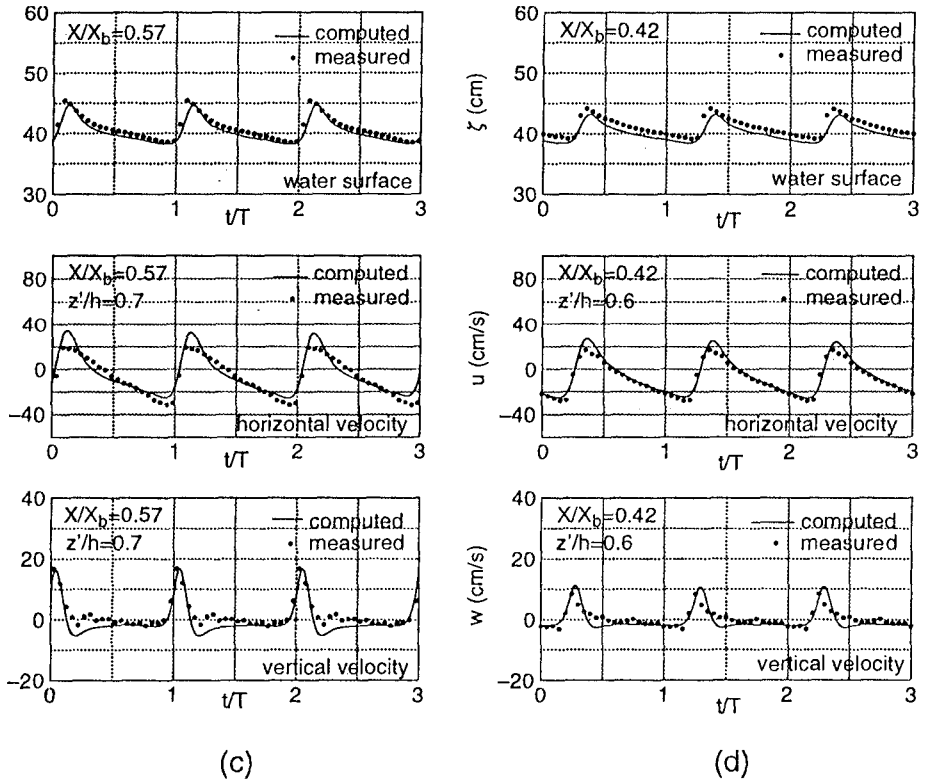


Figure 5: Time histories of water surface elevation ζ , horizontal velocity u and vertical velocity w at different sections and elevations in the surf zone ($H_0 = 8.5\text{cm}$, $T=2s$, $h_0 = 40\text{cm}$, $s=1/20$).

simulating the deformation of the velocity profiles as the wave propagates shoreward and of producing the high nonlinearity and asymmetry of the velocity profiles in shallow water area (Fig. 5). Generally, reasonable agreements, both in magnitude and phase, are obtained between the computed velocities and the laboratory data. In the vicinity of the breaking point, however, the vertical velocity is somewhat underestimated by the model. And at sections close to the shoreline, the model overestimates the peak value of the horizontal velocity. The simulation results also show that, in the surf zone, the vertical velocity magnitude at most elevations is considerable compared to the horizontal velocity magnitude and therefore cannot be neglected in the computation as is done in most existing wave models.

The equi-phase mean velocity vectors in the measured area of the surf zone are plotted in Fig. 6, for different phases in one wave period. A fairly good agreement in the direction and the magnitude between the computed and measured velocity vectors can be observed, but there exist small discrepancies in the near-bottom area. In bottom area, the simulated velocity vectors exhibit smaller values than the measured ones. Small discrepancies between the computed and measured velocity vectors can also be seen in the vicinity of the shoreline. This may be due to the fact that the real shoreline boundary has not yet been simulated perfectly in the model and may cause certain effects on the computed velocity field.

5. Conclusions

- In the present model, the hydrodynamics of breaking waves in the surf zone was investigated based on the governing equations of turbulent flow: the Reynolds-averaged Navier-Stokes equations. The effect of breaker-generated turbulence was included in the model and the vertical distribution of wave variables (P , u , w) can be computed directly by the model. The numerical results agree reasonably well with laboratory data of 2DV velocity field and water surface elevation in the surf zone.
- A time-dependent eddy viscosity was introduced in the present study to solve the 2DV Reynolds-averaged Navier-Stokes equations. The derived eddy viscosity has been verified to be applicable in the modeling of breaking waves. However, this is only one of the possible alternatives in determining the eddy viscosity. The present model may be tested with other solutions of the eddy viscosity in order to seek for possible improvements of the simulation results.
- In the model, it is possible to determine only the vertical distribution of horizontal velocity from the water surface to the first grid point above the bottom. The horizontal velocity profile below this grid point, which is affected by the bottom boundary layer (BBL), has not yet been computed by the model. The inclusion of the effect of the BBL requires a very fine mesh interval, whose order is about $0.1mm$, in order to model the large velocity gradient in the near-bottom area. However, at present, a 2DV hydrodynamic simulation of the entire surf zone, in which the BBL is included, is still not economical in sense of the CPU time required.
- Disagreements between the numerical results and the laboratory data commonly occur in the area close to the shoreline. As already mentioned, these poor agreements may have been caused by the effect of the shoreline boundary. Due to certain technical problems encountered in the formulation of a 2DV model, some assumptions have been made to simplify the implementation of the shoreline boundary conditions such as the absorbing condition for u , the uniform condition for w . These assumptions may not reflect properly the realistic phenomena at the shoreline boundary. Therefore, a more reasonable implementation of the shoreline boundary conditions is necessary to obtain better simulation results in the area close to the shoreline.

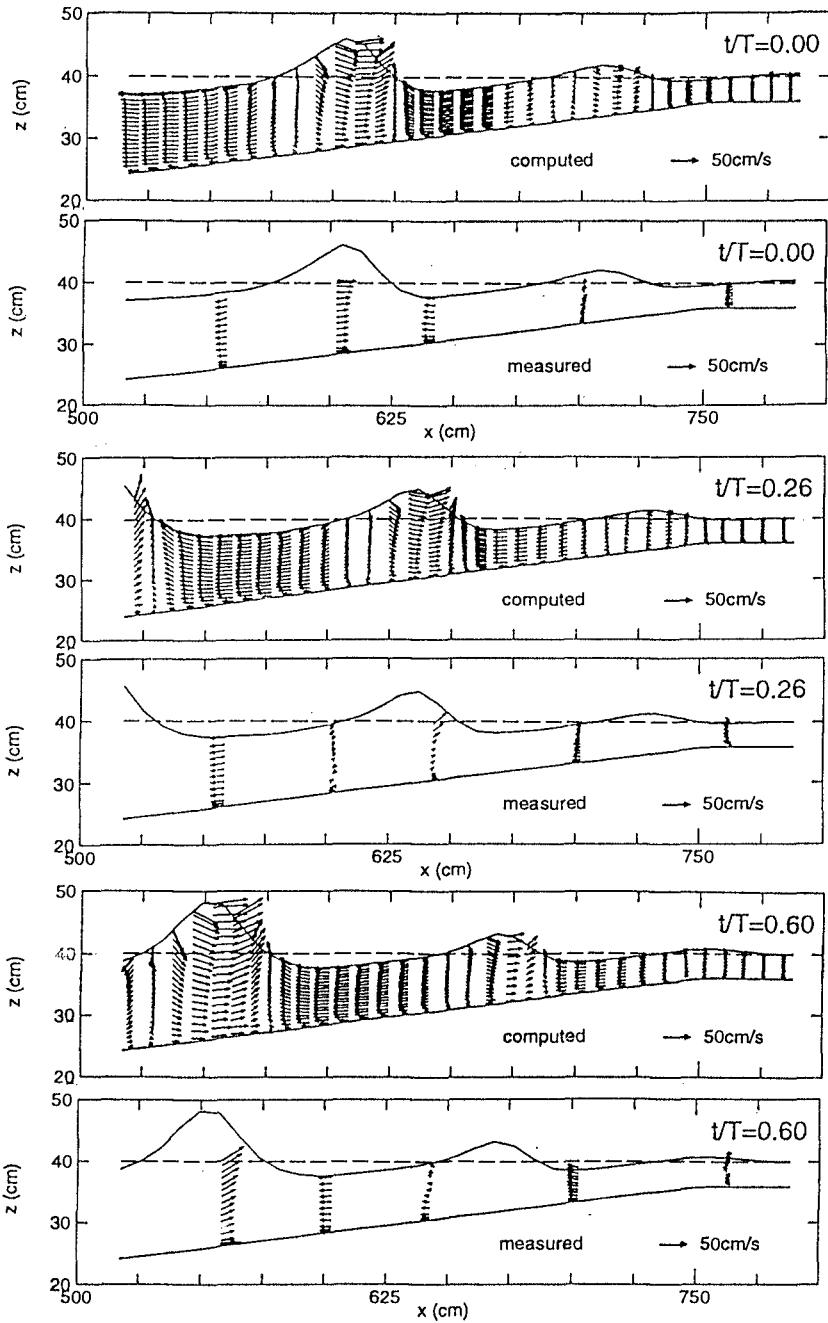


Figure 6: Comparison of equi-phase mean velocity vectors in the surf zone ($H_0 = 9.87\text{cm}$, $T = 1.17\text{s}$, $h_0 = 40\text{cm}$, $s = 1/20$).

References

- Fletcher, C.A.J. (1991). *Computational Techniques for Fluid Dynamics*. Vol. 1,2, 2nd edition, Springer-Verlag, Berlin Heidelberg, 299-328.
- Goda, Y. (1975). Deformation of irregular waves due to depth-controlled wave breaking. *Report of the Port and Harbour Tech. Res. Inst.*, 14-(3).
- Longuet-Higgins, M.S. (1970). Longshore currents generated by obliquely incident sea waves. *J. of Geophys. Res.*, 75, 6790-6801.
- Nishimura, H., M. Isobe, and K. Horikawa (1977). Higher order solutions of the Stokes and the cnoidal waves. *J. Fac. Eng., Univ. of Tokyo, B-34, No. 2*, 267-293.
- Okayasu, A., T. Shibayama, and K. Horikawa (1988). Vertical variation of undertow in the surf zone. *Proc. 21st ICCE, ASCE*, 478-491.
- Petit, H.A.H., P. Tonjes, M.R.A. van Gent, and P. van den Bosch (1994). Numerical simulation and validation of plunging breakers using a 2D Navier-Stokes model. *Proc. 23rd ICCE, ASCE*, 511-524.
- Shibayama, T. and N.T. Duy (1994). A 2D vertical model for wave and current in the surf zone based on the turbulent flow equations. *Coastal Eng. in Japan, JSCE*, 37-(1), 41-65.
- Svendsen, I.A., and J.B. Hansen (1988). Cross-shore currents in surf zone modeling. *Coastal Eng., Elsevier*, 12, 23-42.
- Zienkiewicz, O.C. and R.L. Taylor (1991). *The Finite Element Method*. Vol. II, McGraw-Hill, 4th edition, 807 pages.

CHAPTER 17

Turbulence Structures in the Surf Zone.

T.R.Haydon D.B.Hann *, P.Davies † C. A.Greated‡ and T.C.D.Barnes§

Abstract

Turbulence due to breaking waves is an important factor in the ocean as it has a direct effect on coastal erosion, sediment transport and marine life. The laboratory study of this phenomenon is important to produce controlled simulations of processes that occur at sea, and has mainly consisted of temporal point measurements. In this paper the results obtained from using PIV to study the turbulence in the laboratory are presented. PIV is a spatial technique and yields unique information on the turbulence structure in such a flow. Of particular interest in this paper are the evolution of the wavenumber spectra and the form of the turbulent energy decay with time and space. This is used to characterise the decay of turbulence from 2-d to 3-d. Separation of the turbulence from the mean motion is important and the method used here is justified. The main results and conclusions are compared with other research, with similarities and differences emphasised and discussed.

1. Introduction

Little is known about the nature of the turbulence produced by a breaking wave event. It is a very difficult flow to model numerically and equally hard to measure experimentally. The traditional approach to experimental investigation has been to use point measuring techniques such as Laser Doppler Anemometry (LDA) [5, 4]. This does not enable the spatial structures of the flow and the way in which the associated vorticity and energy is dissipated, to be measured. Particle Image Velocimetry (PIV) is a well documented velocity measuring technique, yielding full field instantaneous flow information [12]. The implementation of a high resolution digital camera and an image shifting device allows the problem of measuring multi-directional velocities to be solved, imparting a constant velocity throughout the flow that can be subtracted after analysis.

Previous research on laboratory generated single breaking waves is fairly scarce, however a comprehensive study using LDA was done by Rapp and Melville [5] along with other interesting work from Battjes and Sakai [2]. The results obtained by these researchers will be referenced and comparisons made, with results obtained here. There are two main objectives to be addressed in this paper, firstly the validation of PIV as a technique for studying this type of complex flows, and secondly the exploitation of the advantages inherent in using PIV, to characterise the turbulent flow spatially and temporally.

2. Experimental facility

The experiments described in this paper were carried out in the Edinburgh University wave flume. The flume is 9m long 0.4m wide and 1m deep, with the water depth being 0.75m. The wavemaker is a hinged paddle that has a force feedback mechanism, designed to limit reflections. Breaking waves are formed by the superposition of differing frequencies formed by the paddle which are focussed to create a breaking event. The walls of the flume are glass to allow easy optical access. At the far end of the flume there is an absorbing wedge of foam which disperses the remaining wave energy and limits reflections.

Wavegauges can be used to measure the surface elevations during experimentation and in these experiments four were used, two positioned before breaking and two after. These yield important information on the spectral contents of the wave used in the investigation and also the enable the repeatability of the wavemaker to be verified.

*Research Student, Physics Dept, University of Edinburgh, Edinburgh, UK

†Professor, University of Dundee

‡Professor, University of Edinburgh

§Research Student University of Bristol.

3. PIV

An in depth explanation of PIV is not going to be undertaken in this paper as it has been covered many times before [3]. However there are recent improvements made to the technique that have increased its versatility, which will be outlined here.

Image shifting overcomes the problems that PIV has with measuring multi-directional flows or flows that have a large dynamic range of velocities (for a detailed description see Morrison[6]). The PIV image is obtained through the reflection in a rotating mirror which imparts a constant shift to all the velocities in the flow. It has the effect (when optimised) to shift all the velocities into the range measurable with PIV. The velocity imparted can be removed after the analysis stage, leaving the original flow velocities. There is an added complication, due to the fact that there are differing optical path lengths to the various parts of the mirror, (and hence to the flow region) meaning that the shift velocity is not exactly uniform over the whole flow. However averaging many velocity maps recorded in still water gives the full-field shifting velocity map, which can be subtracted from all measurements.

The use of a high resolution CCD camera for image acquisition has many advantages over the previously used photographic film method. Obviously the primary advantage is the saving in time on the analysis which is done digitally on a PC. Using very large CCD array sizes, however, does create very large image files which fill memory up very quickly. The memory on the frame grabber used in this research was extended to 32mb so that a maximum of seven sequential pictures could be taken, limited only by the frame rate of the camera.

Image analysis is done digitally using an auto-correlation routine which yields the magnitude and direction of the velocity within small areas of the image.

4. Experiments

Both deep water and beach waves were investigated. Four different types of deep water breaker were used, ranging from severe plunging to gently spilling. For the beach experiments a 1:20 beach was built into the flume. Due to the nature of the wavemaker paddle a solitary wave breaking on the beach due to shoaling was not feasible. Therefore the beach waves used broke due to a combination of focusing and shoaling. This was not a huge problem, because the main objective was to see how the shallow water affected the turbulence structures present.

Images of the flow were captured beginning from approximately 3 seconds after the initial breaking event. This was the earliest that the flow could realistically be studied, due to the large amount of aeration that is caused by the breaking. The triggering of the camera was controlled by an external pulse from the wavemaking software which triggered the image-shifter, which in turn triggered the camera at the precise moment the mirror has rotated to an angle of 45° to the line of the flume. The choice of shift velocity was dictated by a number criteria. Firstly the limitation that the same shift had to be used for all images acquired in one sequence, meant that it had to be of a sufficient velocity to shift the earliest flow field into the analysable range of velocities. It is however generally advantageous to use as small a shift as possible, so the loss of resolution is kept to a minimum.

For each different wave used in this experiment a number of different positions of the camera were used in order to cover the full extent of the turbulence and vorticity produced by breaking, which was generally spread over quite a large area. This tends to be split into distinct separate patches of turbulence, which become more merged together as the wave goes from plunging to spilling.

5. Results

Figures 1-6 show vorticity information, on the same scale, derived from a sequence of PIV velocity fields obtained after breaking. These show the evolution of a dominant vortex patch which appears to consist of two counter rotating vortices. The vorticity is shown to be concentrated and fairly focussed soon after breaking. The patch becomes visibly weaker, deepens slightly and occupies a slightly larger area. A notable feature

is that the structures do not seem to translate significantly across the flow. The area shown in these plots are about 60cm wide and 50cm deep.

The vorticity maps give a visual representation of the post-breaking flow, showing a number of significant features. However, in order to make comparisons with the results of other experimenters it was necessary to compute more detailed properties of the turbulence.

The wavenumber spectra for the turbulent velocities obtained at two different times 4s and 17s after breaking are shown in figure 7. The information is shown on a log/log plot with a k^{-3} and a $k^{-5/3}$ line shown for comparison. This can be related to theories on 2-d and 3-d turbulence originally conjectured by Kraichnen [8] and further reviewed by Kraichnen and Montgomery [7] and Lesieur [10]. The proposed slope of the wavenumber spectrum for two-dimensional turbulence is k^{-3} . This seems to suggest that after breaking the flow is dominated by two-dimensional turbulence which decays to three-dimensional turbulence as the structures become smaller and less coherent. This supports the work of Lemmin and George *et al* [9, 11], who also note this spectral change.

The flow measured using PIV cannot be said to be a solely turbulent flow, as it contains a mixture of mean and turbulent components. A simple method of local averaging was used in order to separate out these two components. Each velocity point was averaged using the nearby velocities, with this average then subtracted from the central velocity value. All turbulent information was obtained using this method.

Figure 8 shows the decay of turbulent energy with time for a deep water post breaking field averaged over four repeats. This is shown for two separate positions after breaking, position 2 being closer to the breaking point. The reciprocal of the mean square turbulence level at position 2 appears to decay approximately in proportion to time. This is analogous to the way in which grid generated turbulence decays with the distance behind the grid. Position 1 does not show such a decay relationship, probably because it is close to breaking where the structures are moving forward more than at subsequent positions, hence leading to a significant flow of turbulent energy out of the region.

Figures 9 and 10 show some examples of turbulent energy depth profiles, averaged across each line of velocities at each depth for a deep water breaker and a beach wave. The essential features of the two cases are that in deep water there is a strong decay of the turbulence level with depth, whereas the turbulence in the beach case is spread out more evenly, with only a slight decay with depth. The two instances in figure 9 correspond to the vorticity plots shown in figures 1 and 2. The spike in turbulence between 20 and 30cm depth clearly falls from the first instant to the second.

6. Conclusions

PIV has been effectively applied to the complex turbulent flow generated by breaking waves, producing a visual representation of the structures and the way in which they decay and dissipate. The characterisation of the turbulence in order to make direct comparisons with the work of others has been attempted and early results suggest a good agreement. Further analysis to examine the mixing process in more depth is planned for both the deep and beach waves.

7. Acknowledgements

The authors wish to acknowledge the financial support from the Natural Environment Research Council and the Engineering and Physical Sciences Research Council, in the UK, for this research.

References

- [1] Agrawal, Y. C., Terray, E. A., Donelan, M. A., Hwang, P. A., Williams III, A. J., Drennan, W. M., Kahma, K. K. and Kitaigorodskii, S. A. (1992) *Enhanced dissipation of kinetic energy beneath surface waves* Nature 359:219-20

- [2] Battjes, J. A. and Sakai, Y (1981) *Velocity field in a steady breaker* Journal of Fluid Mechanics 111:421-437
- [3] Greated, C. A., Skyner, D. J. and Bruce, T. (1992) *Particle Image Velocimetry in the coastal engineering laboratory*. Proc. 23rd Int. Conf. on Coastal Engineering, Venice 1992.
- [4] Nadaoka, K., Hino, M., Koyano, Y. (1989) *Structure of the turbulent flow field under breaking waves in the surf zone* J. Fluid Mech 204:359-387
- [5] Rapp, R.J., Mellville, W.K. (1990) *Laboratory Measurements of Deep Water Breaking Waves*. Phil. Trans. R. Soc. Lond. A 331:735-800.
- [6] Morrison, I.G. (1995) *The hydrodynamic performance of an oscillating water column wave energy converter*. PhD Thesis, The University of Edinburgh.
- [7] Kraichnen, R.H., Montgomery, D. (1980) *Two-dimensional turbulence* Reports Progr. Phys 43:547-619
- [8] Kraichnen, R.H. (1967) *Inertial ranges in two-dimensional turbulence* Phys. Fluids 10:1417-1423
- [9] Lemmin, U. Scott, J.T. and Czapski, U.H. (1974) *The development from two-dimensional to three-dimensional turbulence generated by breaking waves* J. Geophys Res 79:3442-3448
- [10] Lesieur, M. (1990) *Turbulence in Fluids* 2nd edition. Kluwer, Dordrecht.
- [11] George, R., Flick, R.E., Guza, R.T. (1994) *Observations of turbulence in the surf zone* J. Geophys Res 99:801-809
- [12] Skyner, D.J. *The Mechanics of Extreme Water Waves*. PhD Thesis, The University of Edinburgh.



Figure 1: Vorticity at $T=3.125s$.



Figure 2: Vorticity at $T=3.875s$.



Figure 3: Vorticity at $T=4.625s$.



Figure 4: Vorticity at $T=5.375s$.



Figure 5: Vorticity at $T=6.125s$.



Figure 6: Vorticity at $T=7.625s$.

Evolution of wavenumber spectra with time

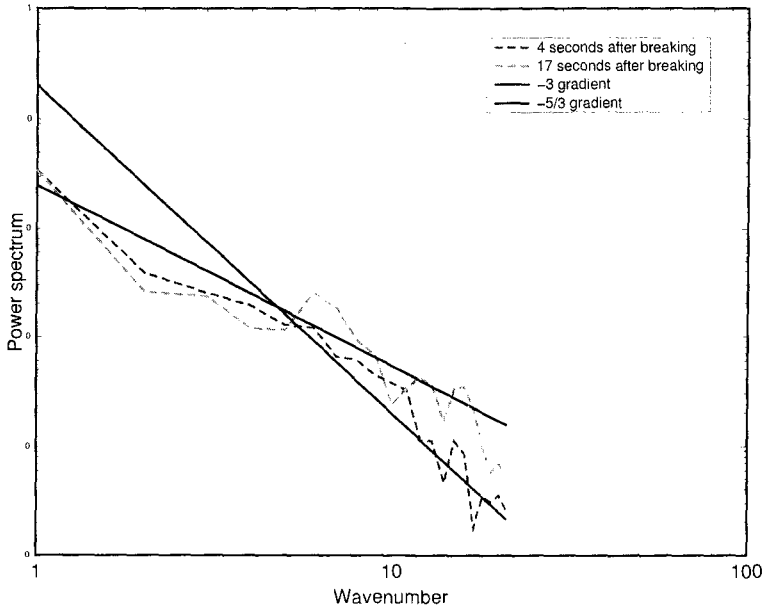


Figure 7

Graph showing the decay of turbulence with time

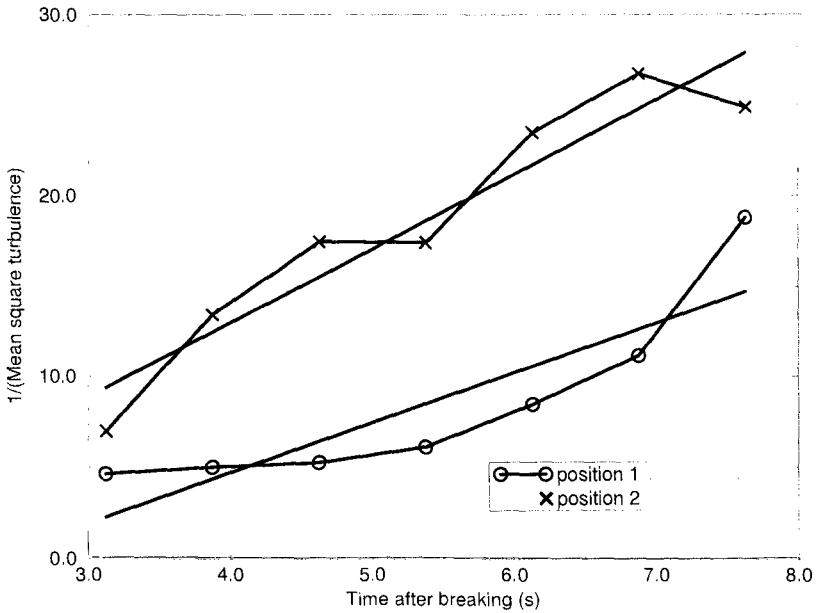


Figure 8

Energy depth profiles—deep water

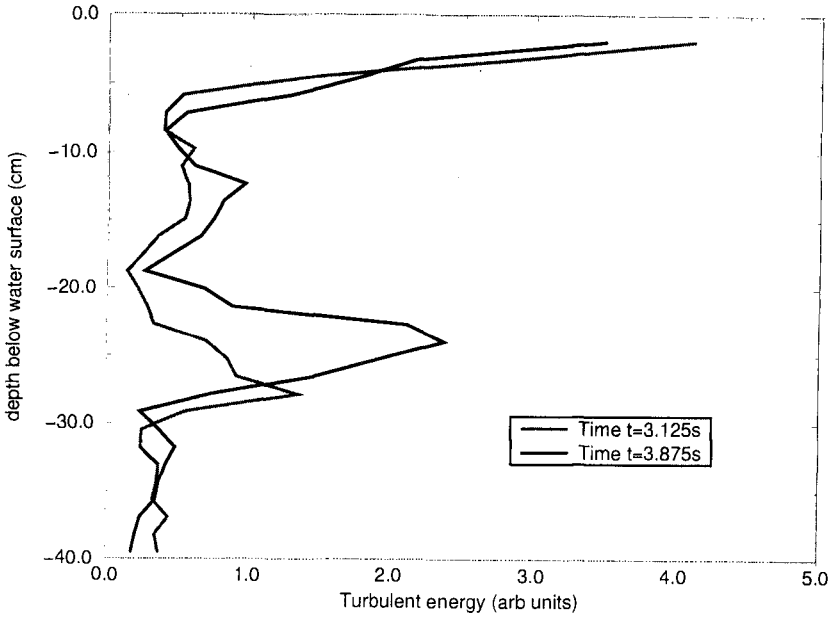


Figure 9

Energy depth profile—beach wave

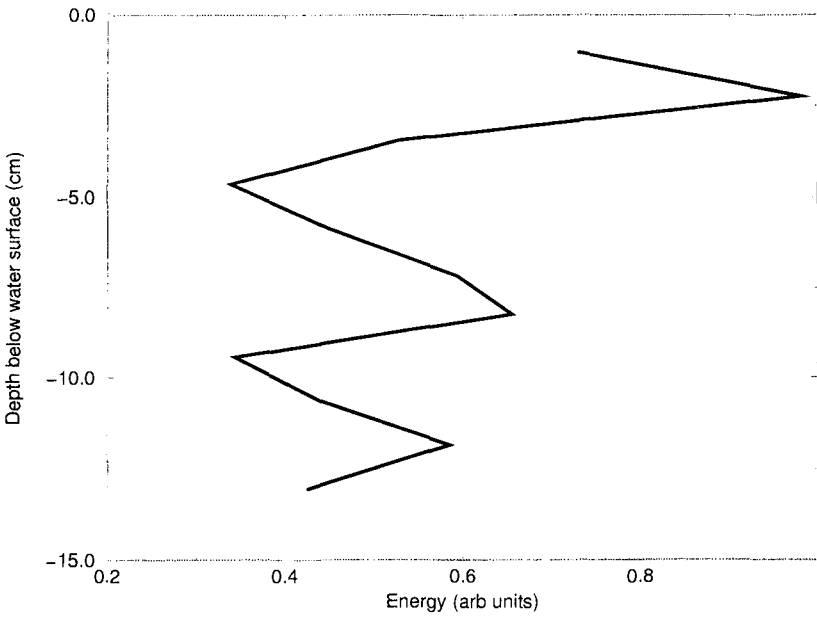


Figure 10

CHAPTER 18

Experiments on Design Wave Height in Shallow Water

J. William Kamphuis, M. ASCE.¹

Abstract

Traditional depth-limited criteria for design of structures in shallow water were found not to be valid in hydraulic model tests with irregular waves. An extensive series of experiments showed that in addition to the height of the short period waves and the depth at the structure, the design wave height is a function of long wave action and wave setup at the structure. The additional effects are related to incident wave height and they result in an increase in depth at the structure. Thus, a simple design expression was developed by introducing a depth modification into a standard depth-limited design equation.

1. Depth-Limited Design

For many years, the design wave for structures in shallow water has been considered to be depth limited, meaning that the design conditions are controlled by the water depth at the structure. The maximum breaking wave reaching the structure is considered to be the design wave height. It is approximated by the wave that breaks exactly on the structure. Any wave breaking further offshore is expected to have lost enough energy that it results in a smaller breaking wave at the structure. Any wave that has not broken by the time it arrives at the structure is by definition smaller than the breaking wave and will result in smaller “non-breaking” wave forces. The design wave (H_{des}) may thus be approximated by the maximum breaking wave height at the toe of the structure, $(H_b)_{max,T}$, which is a function of the water depth at the toe (d_T).

$$H_{des} = (H_b)_{max,T} = \gamma d_T \quad (1)$$

¹ Prof. of Civil Eng., Queen’s Univ., Kingston, Ontario, Canada, K7L 3N6; Kamphuis@civil.queensu.ca.

Equation 1 was developed for regular waves. With irregular waves, a wave height distribution (normally assumed to be Rayleigh) needs to be introduced. The entire Rayleigh distribution is commonly represented by the Significant Wave Height (H_s) as determined by time domain (Zero Crossing) analysis or the Zero Moment Wave Height (H_{m0}) as determined from frequency domain (Wave Spectrum) analysis. Introducing these into Eq 1 yields:

$$H_{des} = (H_{s,b})_{max,T} = (H_{m0,b})_{max,T} = \gamma d_T \quad (2)$$

where γ is normally defined as a constant, which may vary from 0.78 down to values as low as 0.4, depending on the wave height definitions used.

This type of depth-limited calculation has been used in practice for many years and the adequacy of Eq 1 was repeatedly demonstrated to the undergraduate students at Queen's University through a final year project that ended with the design and hydraulic model testing of a rubblemound breakwater section. However, when this exercise was "updated" using irregular waves, Eq 2 was found not to be valid. The following difficulties were identified:

- a. H_{des} was not only a function of water depth at the structure, but increased with incident wave height. Damage to the structure increased with wave height, even when the incident wave broke a long distance offshore.
- b. The use of H_s or H_{m0} is not correct for design when structure damage is cumulative.

The inadequacy of Eq 2 was first investigated with several short experiments, but every one of these indicated that the problem was not simple and that the solution required more thorough investigation. Thus, a comprehensive set of tests was finally embarked upon to try to solve what everyone thought had been solved long ago. This paper provides a summary of these tests, examples from the initial analysis of the results and a simple design expression.

2. Experiments

Experiments were carried out in the 2 m wide irregular wave flume at the Queen's University Coastal Engineering Research Laboratory (Fig 1). The model was 0.6 m wide; the remaining width of the flume was reserved to minimize reflection of long wave action in the flume. The model consisted of a 1:50 plywood slope with a rubble mound breakwater at the end. Water level fluctuations were measured at 64 locations on the ramp for each incident wave height. Each test consisted of 6 to 11 different incident JONSWAP spectra with offshore wave heights (H_{m0}) varying from 0.04 to 0.18 m. Sixteen tests were performed (Table 1), resulting in some 7000 records of water level fluctuation. The results for Test 7 will be used to provide a consistent example in Figs 3 to 6. All other results were very similar to Test 7.

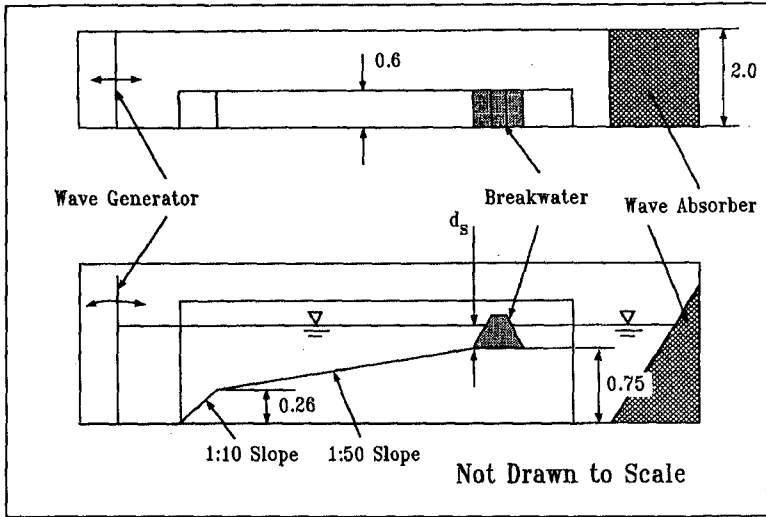


Figure 1 Experimental Setup

TABLE 1
Test Numbers for the Various Combinations of Water Depth and Wave Period

Wave Period (sec)	Depth of Water at Toe (m)			
	0.04	0.05	0.064	0.08
0.8	6	2	9	10
1.0	4	3	1	11
1.2	5	7	8	12
1.5	13	14	15	16

3. Initial Analysis

Each record was analyzed in frequency domain (Wave Spectrum Analysis) and some records were analyzed in the time domain (Zero-Crossing Analysis). Significant wave height (H_s) was virtually identical to H_{m0} everywhere but very close to the toe of the structure, where H_s is smaller than H_{m0} , as shown in Fig 2. The difference was a function of d_T . All wave heights quoted in this paper are zero moment wave heights (H_{m0}), derived from the frequency analysis. An example of wave heights calculated from the records is given in Fig 3. If the concept of depth-limited design as expressed in Eq 2 were valid, then H_{m0} at the structure should decrease (or at least remain the same) as the offshore wave height increases and the breaker moves

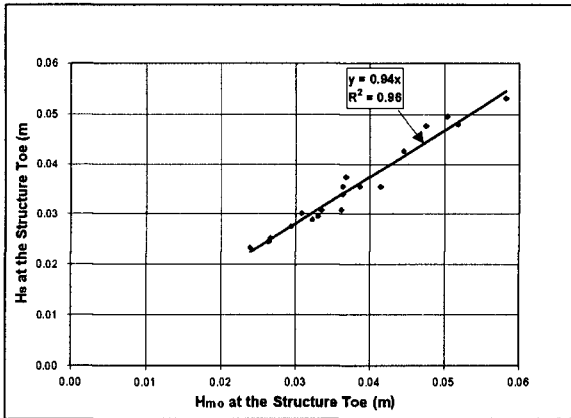


Figure 2 H_s as a Function of H_{m0} at the Structure Toe for Test 7

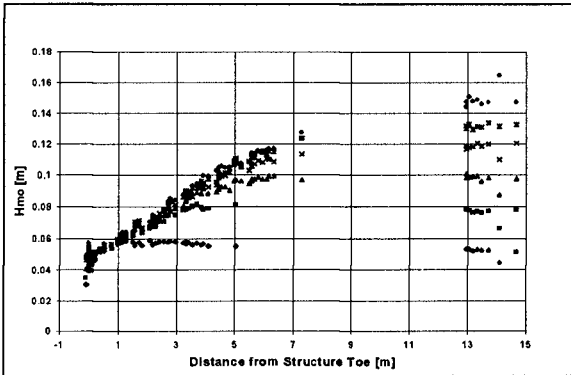


Figure 3 Profile of H_{m0} with Distance for Test 7

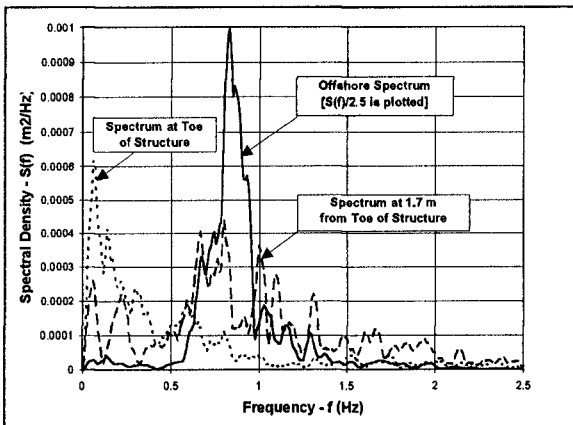


Figure 4 Growth of Long Wave Components for Test 7

further offshore. Figure 3 shows that H_{m0} at the toe of the structure is almost depth limited, but there is clearly a small increase with the incident offshore wave height as mentioned in Point a) of Section 1. Figure 3 also shows an unexpected sudden increase in H_{m0} near the structure toe.

During the tests, visual observations indicated that, in addition to the incident short wave action, which decayed as it travelled from the breaking point to the structure, substantial long wave activity and wave setup existed, which increased from the breaking point to the structure. Both the short wave and long wave action could be clearly identified both by time domain and frequency domain analysis. Zero-Crossing Analysis of both long wave and short wave components indicated that both were essentially Rayleigh distributed, even at the toe of the structure. Wave Spectra at three locations for a medium height wave of Test 7 are shown in Fig 4. The long wave component clearly grows as the wave approaches the structure, while the energy of the short wave component decreases. The complicated wave spectrum at 1.72 m indicates, however, that this transformation is not simple and involves major re-organization of wave energy. Figure 4 also shows a minimum spectral density near $f=f_p/2$, where f_p is the peak frequency of the offshore spectrum. This minimum occurred in all the tests and was used to separate long wave and short wave energy for all results, providing H_{m0} values for the long wave component ($f < f_p/2$) and the short wave component ($f > f_p/2$). In addition to the long waves and short waves, there is substantial wave setup at the structure.

Figure 5 shows some profiles of the short wave component of Test 7. The sudden increase in H_{m0} near the structure, shown in Fig 3 has now disappeared, indicating it to be the effect of the long wave component, which is largest near the structure. A credible explanation for the wave height profile with distance of the short wave component is also shown in Fig 5. The simulation proposed by Kamphuis (1994) was used. Rakha and Kamphuis (1995) also show this method to be valid. The wave was shoaled up to the breaking point, using linear shoaling and friction. The breaking point was defined using either the depth-related breaker criterion:

$$\frac{H_{s,b}}{d_b} = \gamma_{s,b} = 0.56 e^{3.5m} \quad (3)$$

or the wave steepness-related breaker criterion:

$$\frac{H_{s,b}}{L_{p,b}} = 0.095 e^{4.0m} \tanh\left(\frac{2\pi d_b}{L_{p,b}}\right) \quad (4)$$

developed by Kamphuis (1991). Here $H_{s,b}$ is the significant height of the breaking waves, $L_{p,b}$ is the wave length of the breaking waves, calculated using the peak frequency and m is the beach slope offshore of the breaking zone. The test results

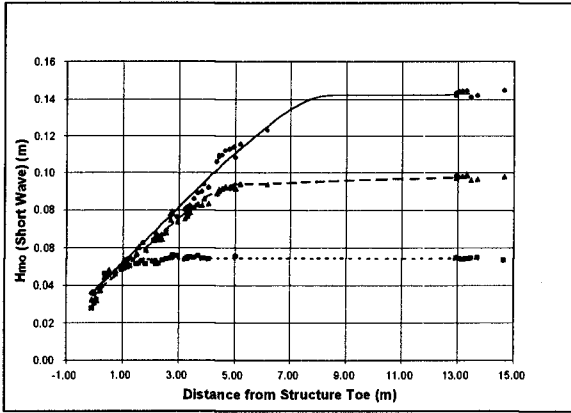


Figure 5 Calculated and Measured Short Wave Profiles for Test 7

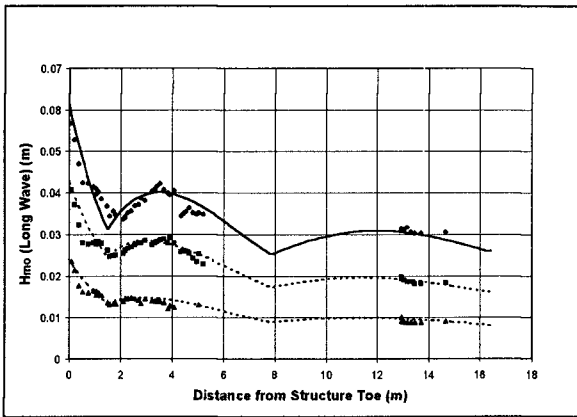


Figure 6 Calculated and Measured Long Wave Profiles for Test 7

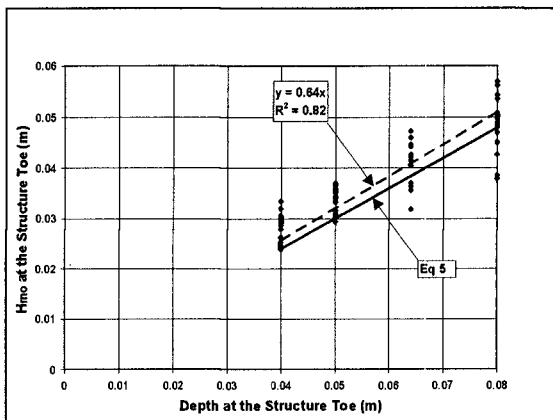


Figure 7 Depth-Limited Design Using Equation 5

showed that H_s and H_{m0} at breaking were virtually identical. Wave decay after breaking was related to excess wave energy, a concept originally developed by Dally, Dean and Dalrymple (1986) for regular waves and adapted by Kamphuis (1994) for irregular waves. Similar wave height profiles were also obtained using the method of Battjes and Janssen (1978).

Figure 6 shows an initial explanation of the complicated long wave profile. Similar to Shah and Kamphuis (1996), the long wave profile was assumed to consist of a shoaling, incident bound long wave, that becomes a shoaling, free long wave upon breaking. This wave is partially absorbed and partially reflected, with an antinode at the structure. It is important to note that seiche at the natural frequency of the wave flume was not (and did not need to be) included in this computation. The transition from the bound long wave to the free long wave is gradual through the breaking zone and involves a 180° phase shift of the long wave energy, relative to the wave groups. Offshore, the highest short waves in the wave group accompany the trough of the bound long wave, but at the structure the highest short waves travel on the crest of the free long wave.

4. Waves at the Toe of the Structure

Analysis of the complete data set to determine of the transformation of H_{m0} approaching a structure is underway. The purpose of the present paper is to provide a design expression for structures in shallow water and including the complete wave transformation would be too cumbersome. Therefore the remainder of this paper will concentrate on the waves at the toe of the structure. Two wave gauges were located at the toe for each test. The long waves calculated from both records were virtually identical. The short wave heights showed small differences, that were not systematic. The wave heights quoted at the structure toe are therefore the averaged values of the two measurements.

The long wave influences certain design aspects directly, such as, crest elevation and wave overtopping, which involve water levels. For design parameters involving velocities and accelerations, such as stability of rubble mound armour or of a vertical breakwater, however, it may be assumed that the long wave does not generate large enough fluid velocities and accelerations to influence stability. Although the long wave may influence the actual short wave heights slightly, this paper concentrates on the all-important short wave design component.

Figure 3 indicated that the depth-limited design concept does not quite apply, but it is clear that the effect of increasing offshore wave heights is only of second order. Therefore we propose to work with the depth-limited design equation (Eq 2) and modify it.

Applying strict depth-limited design for the moment and ignoring Point b) from Section 1, Eqs 2 and 3 can be combined to estimate the design wave height as:

$$H_{des} = (H_{mo,b})_{max,T} = 0.56 d_T e^{3.5m} \quad (5)$$

Fig 7 plots all the measured values of H_{mo} for the short waves at the structure toe, against depth at the structure toe. It shows that Eq 5 describes the trend correctly but underpredicts the maximum values. Figure 8 indicates that both the underprediction and some of the scatter may be approached through a relatively simple, linear relationship with wave height. To provide the most accurate representation of the changing incident wave height, the breaking wave height as calculated by Eqs 2 to 4 was chosen here, in lieu of the offshore wave height. The bias and part of the scatter in H_{mo} at the toe of the structure are, in fact, the result of:

- wave setup
- the incoming bound and free long waves
- the antinode of the reflected long wave.

All three of these influences in this complicated, interactive system add to the depth of water at the structure and all are more or less proportional to incoming wave height. Since the influence of the above causes is relatively small, it is possible to use Eq 5 with a modified depth:

$$d_T' = d_T + \alpha H_{s,b} = d_T + \alpha H_{mo,b} \quad (6)$$

The experiments showed the best-fit value of α to be 0.1 and hence the revised design expression is:

$$H_{des} = (H_{mo,b})_{max,T} = 0.56 d_T' e^{3.5m} = 0.56 (d_T + 0.1 H_{mo,b}) e^{3.5m} \quad (7)$$

Figure 9 shows that the best-fit coefficient is 0.52, but that Eq 7 is a better design expression since it represents the maximum values of H_{mo} . Another design formula, based on Eq 4, is shown in Fig 10. It is:

$$H_{des} = (H_{mo,b})_{max,T} = 0.095 L_{p,b} e^{4.0m} \tanh\left(\frac{2\pi (d_T + 0.1 H_{mo,b})}{L_{p,b}}\right) \quad (8)$$

5. Design Wave

Equations 7 and 8 give H_{des} , corresponding to H_{mo} , at the toe of a breakwater, but this does not take into account Point b) of Section 1, which addresses cumulative damage. Because the waves impacting a structure in shallow water are basically

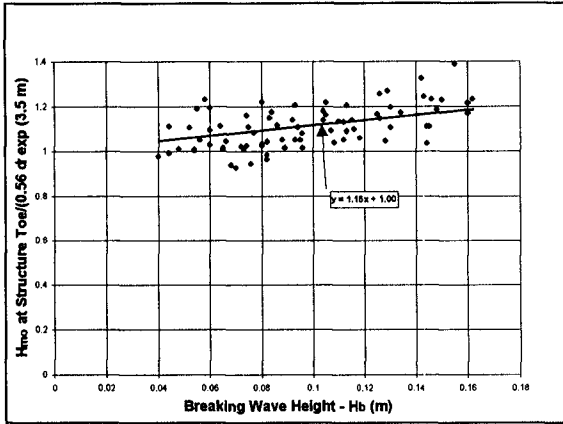


Figure 8 Effect of Wave Height

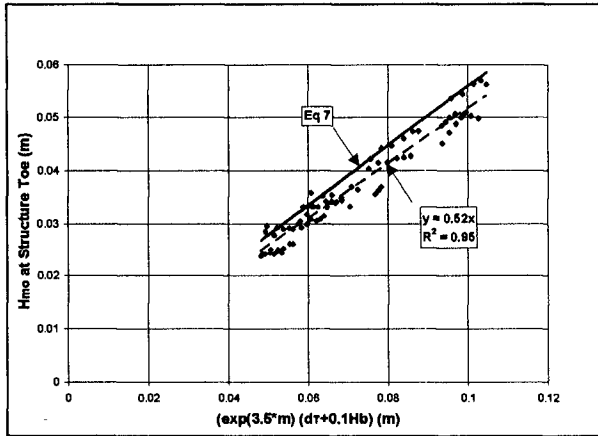


Figure 9 Modified Depth-Limited Design Using Equation 7

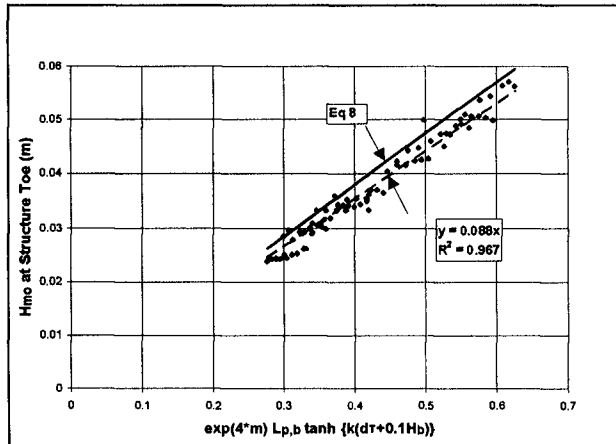


Figure 10 Modified Depth-Limited Design Using Equation 8

depth limited, design return period exerts only a minor influence on H_{des} . Table 2 presents an example for $m=0.02$ and a design return period of 50 yrs. It is seen that Eq 7 increases H_{des} by 10 % (forces increase by 33%) over Eq 5. Table 2 also shows that H_{des} varies only slightly with return period. This means that wave heights very close to the 50 year return period wave height will occur often during the structure lifetime.

Table 2
Wave Height as a Function of Return Period

Return Period (yrs)	Breaking Wave Height (m)	Depth at Structure (m)	Modified Depth (m)	H_{des} Eq (7) (m)	H_{des} Eq (5) (m)
50	4.0	4.0	4.40	2.64	2.40
1	3.5	4.0	4.35	2.61	
0.1	3.0	4.0	4.30	2.58	

Thus it becomes necessary to distinguish between design parameters that, when exceeded, do not result in cumulative damage (such as wave overtopping, breakwater crest height, etc.) and design parameters that, when exceeded, result in damage that is added to any earlier damage (such as damage to rubble mound armour layers and sliding of a vertical structure). Non-cumulative damage may be related to H_{mo} or H_s , which represents a rather high wave and which comes directly from the available long term data. Equations 7 and 8 may be used directly.

For cumulative damage, however, it is absolutely necessary to design for zero damage, each time the design wave occurs (or almost occurs). Therefore design must be for the highest possible waves, which may be defined by:

$$(H_{max}) = K_H (H_{mo}) \quad (9)$$

If the wave height distribution is Rayleigh, K_H is a function of storm duration and may be approximated by values in excess of 2. Goda (1985) uses 1.8. Rakha (1995) found $K_H=1.5$ for stable, irregular breaking waves on a horizontal slope and $K_H=1.7$, when the stable waves are reflected. For waves breaking a substantial distance offshore and travelling over a slowly sloping bottom toward a rubble mound structure, $K_H=1.5$ is probably realistic; For vertical breakwaters, $K_H=1.7$ is probably better. Thus the design wave may finally be defined as:

$$H_{des} = 0.56 K_H e^{3.5m} (d_T + 0.1H_{mo,b}) \quad (10)$$

or

$$H_{des} = 0.095 K_H L_{p,b} e^{4.0m} \tanh \left(\frac{2\pi (d_T + 0.1 H_{m0,b})}{L_{p,b}} \right) \quad (11)$$

where

$$(K_H)_{\text{damage not cumulative}} = 1.0 \quad \text{and} \quad (K_H)_{\text{damage cumulative}} = 1.5 \text{ to } 1.7 \quad (12)$$

6. Discussion

Equations 10 to 12 are based on recordings taken in a wave flume at the toe of a rubble structure. Do they apply to other structures such as vertical breakwaters or sloping seawalls? Wave setup at the toe of a structure is a function of the breaking wave height and the bottom slope. Thus the shape of the structure has only a small influence on wave setup. Only the reflected portion of the long wave is affected by the reflectivity of the structure. Since the rubble mound reflected much of the long wave energy, the shape of the structure is again not expected to exert a major influence on the results. Incident wave angle must of course be taken into account in the usual manner. The perpendicular angle of wave approach in a wave flume obviously results in the maximum effect and a mitigating term related to the cosine of the incident wave angle needs to be introduced. Thus, Eqs 10 to 12 are expected to be robust and applicable to a variety of design conditions and structures.

Equations 10 to 12 also provide a physical basis for determining the design parameters. This is much to be preferred over other, rather subjective adjustments found in the literature, such as an arbitrary increase from H_s to a higher wave height definition for different structures, providing different "damage coefficients" for breaking and non-breaking waves, or basing the design on the estimated number of waves that impact the structure during its lifetime.

Figures 3 and 6 show that analysis of the wave record without due regard for long and short wave components will lead to incorrect results, particularly near the structure. Figure 6 also demonstrates that the common laboratory practice of measuring the waves in a model without the structure in place, misses any influence from reflected long wave action entirely.

7. Summary

- The simple concept of depth-limited design was originally developed for regular waves.
- It was shown not to be correct for irregular waves.
- The design wave increases as incident offshore wave height increases (Fig 3).

- The complete system involves wave setup and the transformation of both long waves and short waves (Figs 5 and 6).
- The analysis of the short wave and long wave profiles, as the waves approach a structure is underway.
- It was possible to develop a relatively simple modification of the depth-limited design equations to incorporate the influence of wave setup and long waves.
- The wave setup and the incident and reflected long waves that accompany a train of irregular waves increase as they approach the structure. They effectively increase the depth at the structure.
- The depth increase may be related to incident wave height, using a modified depth (Eq 6).
- The design wave height can be rather simply related to the modified depth of water at the toe of the structure, which is introduced into existing breaking criteria and depth-limited design expressions (Eqs 7 and 8).
- The design wave height is also a function of whether or not exceedence of the design criterion causes cumulative damage (Eqs 10 and 11).

8. Acknowledgments

The study was funded by the Natural Sciences and Engineering Research Council of Canada through its operating grants program. The experimental work by Steffen Christensen and the contributions by Adam Shah are gratefully acknowledged.

7. References

- Battjes, J.A. and J.P.F.M. Janssen (1978), "Energy loss and set-up due to breaking of random waves", *Proc. 16th Int Conf. on Coastal Eng., ASCE*, Hamburg, pp 569-589.
- Dally, W.R., R.G. Dean and R.A. Dalrymple (1986), "Transformation of random breaking waves on Beaches", *Proc. 20th Int. Conf. on Coastal Eng., ASCE*, Taiwan, pp 82-89.
- Goda, Y (1985), "*Random seas and design of maritime structures*", Univ. of Tokyo Press, 323 pp.
- Kamphuis, J.W. (1991), "Incipient wave breaking", *Coastal Eng.* Vol 15, pp 185-203.
- Kamphuis, J.W. (1994), "Wave height from deep water through the breaking zone", *J. Waterway, Port, Coastal and Ocean Eng., ASCE*, Vol 120, pp 347-367.
- Rakha, K.A. (1995), "A numerical and physical study of beach evolution near a seawall", *Ph.D. Thesis, Queen's University*, 488 pp.
- Rakha, K.A. and J.W. Kamphuis (1995), "Numerical and hydraulic model study of wave decay on a shelf beach", *Coastal Eng.* Vol 121, pp 275-296.
- Shah, A. M. and J.W. Kamphuis (1996), "The swash zone: a focus on low frequency motion", *Proc. 25th Int. Conf. on Coastal Eng., ASCE*, Orlando.

CHAPTER 19

TIME-DEPENDENT QUASI-3D MODELING OF BREAKING WAVES ON BEACHES

Entin A. Karjadi¹ and Nobuhisa Kobayashi²

ABSTRACT: A time-dependent quasi-3D numerical model is developed to predict the temporal and cross-shore variations of the free surface elevation and fluid velocities in the surf and swash zones under obliquely incident waves. This model, which includes the dispersion due to the vertical variations of the instantaneous horizontal velocities, is an extension of the two-dimensional model of Kobayashi and Karjadi (1994, 1996). The developed model is compared with available laboratory and field data for planar beaches as well as field data for a barred beach. For planar beaches, the dispersion effects on the longshore current are significant for regular waves but secondary for irregular waves. For a barred beach, the model under the assumption of alongshore uniformity cannot predict the broad peak in the longshore current profile. The small alongshore variation of wave setup induced by a small alongshore variation of obliquely incident irregular waves is shown to significantly modify the driving force and longshore current profile in the bar trough region. On the other hand, for planar beaches, the alongshore current profile is shown to be insensitive to the small alongshore variation of obliquely incident waves. This may explain why existing longshore current models based on the assumption of alongshore uniformity were regarded to be adequate before their comparisons with the barred beach data.

INTRODUCTION

The time-averaged quasi-3D nearshore currents below the wave trough level have been modeled by various researchers (*e.g.*, DeVriend and Stive 1987; Svendsen and Lorenz 1989). These time-averaged models assume that the oscillatory wave motion is known, although no realistic model is available to predict the velocity field of breaking waves on beaches. Alternatively, a time-dependent quasi-3D numerical model, which runs on a workstation, is developed herein to predict the oscillatory and mean components of the 3D velocity field of obliquely incident breaking waves on beaches. This model is an extension of the time-dependent two-dimensional model of Kobayashi and Karjadi (1994, 1996) which is simply referred to as KK hereafter.

¹Department of Civil Engineering, Bandung Institute of Technology, Jalan Ganesha 10, Bandung 40132, Indonesia. E-mail: entin@coastal.udel.edu

²Professor and Associate Director, Center for Applied Coastal Research, University of Delaware, Newark, DE 19716, USA. E-mail: nk@coastal.udel.edu

KK neglects the dispersion due to the vertical variations of the horizontal velocities although wave breaking produces vertical variations in the horizontal velocity and resulting energy dissipation. As a result, KK cannot reproduce the longshore current profile induced by regular waves breaking on planar beaches because it does not model the transition zone and lateral mixing. In this paper, KK is expanded to include the dispersion due to vertical variations of the horizontal velocities. Very little is known of the dispersion effects on surf zone hydrodynamics apart from the analysis of Svendsen and Putrevu (1994) that showed the importance of the dispersion effect due to the nonlinear interaction of cross-shore and longshore currents in explaining the measured cross-shore variations of long-shore currents induced by regular breaking waves. They used linear wave theory with depth-limited breaker height to describe the wave motion. The present analysis deals with the vertical variations of instantaneous horizontal velocities.

The dispersion terms due to the vertical variations of the horizontal velocities express additional cross-shore and alongshore momentum fluxes in the depth-integrated momentum equations. To predict these unknown momentum flux corrections, two new equations are derived from the corresponding three-dimensional shallow-water momentum equations using a method of moments. The quasi-3D model is compared with the same regular and irregular wave data for planar beaches as KK and with the field data of Smith *et al.* (1993) for a barred beach. The measurements of longshore currents on the barred beach during the DELILAH experiment generally indicated a broad peak in the bar trough region. Under the assumption of alongshore uniformity, the 3D model cannot explain this data. Low-frequency components and alongshore variations of incident irregular waves are examined to explain the broad peak of the longshore current. The longshore current profile on the barred beach is then shown to be sensitive to the alongshore variability unlike the longshore current profile on the planar beaches.

NUMERICAL MODEL

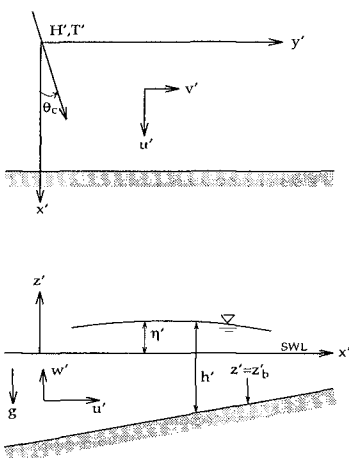


Figure 1: Definition sketch.

The approximate continuity and momentum equations used in this paper is derived from the three-dimensional continuity and Reynolds equations (Karjadi 1996) in a manner similar to the derivation for the two-dimensional case presented by Kobayashi and Wurjanto (1992). The symbol used in the derivation are depicted in Figure 1 where the prime indicates the physical variables that will be normalized later; x' =horizontal coordinate normal to the shoreline and positive landward; y' = horizontal coordinate parallel to the shoreline and positive in the downwave direction; z' = vertical coordinate and positive upward with $z' = 0$ at the still water level (SWL); z'_b =elevation of the seabed which is assumed to be impermeable and fixed; η' = free surface elevation

above SWL; h' =total water depth given by $h' = (\eta' - z'_b)$; u' =cross-shore velocity; v' =alongshore velocity; w' = vertical velocity; and g =gravitational acceleration. Limiting to waves in shallow water, the coordinates x' , y' , and z' are normalized by $\sigma H'$, $\sigma H'/\theta_c$ and H' , respectively, where $\sigma = T' \sqrt{g/H'}$, whereas T' , H' , and θ_c are the characteristic wave period, height and incident angle in radian used for the normalization. The corresponding fluid velocity components u' , v' , and w' in the x' , y' , and z' directions are normalized by $\sqrt{gH'}$, $\theta_c \sqrt{gH'}$ and H'/T' , respectively. The normalized continuity and momentum equations are then simplified under the assumptions of $\sigma^2 \gg 1$ and $\theta_c^2 \ll 1$ for shallow water waves with small angles of incidence. The simplified equations are integrated from $z = z_b$ to $z = \eta$ using the kinematic boundary conditions at $z = z_b$ and η and the boundary conditions of zero tangential stresses at $z = \eta$. The derived continuity and horizontal momentum equations for $\sigma^2 \gg 1$ and $\theta_c^2 \ll 1$ are expressed in the following normalized forms (Kobayashi *et al.* 1997, Karjadi 1996)

$$\frac{\partial h}{\partial t} + \frac{\partial}{\partial x}(hU) = 0 \tag{1}$$

$$\frac{\partial}{\partial t}(hU) + \frac{\partial}{\partial x}(hU^2 + m) = -h \frac{\partial \eta}{\partial x} - \tau_{bx} \tag{2}$$

$$\frac{\partial}{\partial t}(hV) + \frac{\partial}{\partial x}(hUV + n) = -h \frac{\partial \eta}{\partial y} - \tau_{by} \tag{3}$$

with

$$m = \int_{z_b}^{\eta} (u - U)^2 dz \quad ; \quad n = \int_{z_b}^{\eta} (u - U)(v - V) dz \tag{4}$$

in which t = time, U = depth-averaged cross-shore velocity; V = depth-averaged alongshore velocity; τ_{bx} = cross-shore bottom shear stress; τ_{by} = alongshore bottom shear stress. The dispersion terms m and n defined in (4) express the cross-shore and alongshore momentum fluxes due to the vertical variations of u and v , respectively. The dispersion terms result from the vertical integration of the horizontal momentum equations.

The normalized variables without the primes in these equations are defined as

$$t = \frac{t'}{T'} \quad ; \quad x = \frac{x'}{\sigma H'} \quad ; \quad y = \frac{y'}{\sigma H'/\theta_c} \quad ; \quad z = \frac{z'}{H'} \quad ; \quad z_b = \frac{z'_b}{H'} \quad ; \quad \eta = \frac{\eta'}{H'} \tag{5}$$

$$h = \frac{h'}{H'} \quad ; \quad u = \frac{u'}{\sqrt{gH'}} \quad ; \quad v = \frac{v'}{\theta_c \sqrt{gH'}} \quad ; \quad U = \frac{U'}{\sqrt{gH'}} \quad ; \quad V = \frac{V'}{\theta_c \sqrt{gH'}} \tag{6}$$

$$\nu_t = \frac{\nu'_t}{H'^2/T'} \quad ; \quad \tau_{bx} = \frac{\tau'_{bx}}{\rho \sqrt{gH'} H'/T'} \quad ; \quad \tau_{by} = \frac{\tau'_{by}}{\rho \theta_c \sqrt{gH'} H'/T'} \quad ; \quad \sigma = \frac{T' \sqrt{gH'}}{H'} \tag{7}$$

in which ρ = fluid density; ν_t = normalized eddy viscosity used to express the turbulent stresses $\tau_x = \nu_t \partial u / \partial z$ and $\tau_y = \nu_t \partial v / \partial z$; and the parameter σ defined in (7) is the ratio of the cross-shore and vertical length scales. It is noted that the pressure is assumed to be approximately hydrostatic and the lateral turbulent stresses can be shown to be negligible for shallow-water breaking waves (Karjadi 1996).

For obliquely incident waves with $\theta_c^2 \ll 1$, the cross-shore fluid motion governed by (1) and (2) with $m = 0$ is the same as that for normally incident waves

obtained by Kobayashi and Wurjanto (1992). Furthermore, the variations in the y -direction appear only in the term $\partial\eta/\partial y$ in (3) and along the seaward boundary of the computation domain.

In this model, the bottom boundary layer is not analyzed explicitly and the bottom stresses for $\theta_c^2 \ll 1$ are expressed as

$$\tau_{bx} = f_b |u_b| u_b \quad ; \quad \tau_{by} = f_b |u_b| v_b \quad ; \quad f_b = \frac{1}{2} \sigma f'_b \quad (8)$$

in which u_b and v_b are the cross-shore and alongshore velocities immediately outside the bottom boundary layer, respectively, and f'_b = bottom friction factor which is assumed constant. KK assumes that $m = 0$, $n = 0$, $u_b = U$ and $v_b = V$.

In this quasi-3D model, the equations for m and n are derived from the three-dimensional momentum equations using the algebraic procedure which may be called a method of moments. The resulting equations for m and n can be shown to be expressed as (Kobayashi *et al.* 1997, Karjadi 1996)

$$\frac{\partial m}{\partial t} + \frac{\partial}{\partial x} (3mU + m_3) = 2 \left(U \frac{\partial m}{\partial x} - \tilde{u}_b \tau_{bx} - D_B \right) \quad (9)$$

$$\frac{\partial n}{\partial t} + \frac{\partial}{\partial x} (nU + mV + n_3) = V \frac{\partial m}{\partial x} - n \frac{\partial U}{\partial x} - \tilde{v}_b \tau_{bx} - \tilde{u}_b \tau_{by} - 2D_n \quad (10)$$

with

$$\tilde{u}_b = u_b - U \quad ; \quad \tilde{v}_b = v_b - V \quad (11)$$

$$m_3 = \int_{z_b}^{\eta} (u - U)^3 dz \quad ; \quad n_3 = \int_{z_b}^{\eta} (u - U)^2 (v - V) dz \quad (12)$$

$$D_B = \int_{z_b}^{\eta} \nu_t \left(\frac{\partial u}{\partial z} \right)^2 dz \quad ; \quad D_n = \int_{z_b}^{\eta} \nu_t \frac{\partial u}{\partial z} \frac{\partial v}{\partial z} dz \quad (13)$$

The thickness of the bottom boundary layer is assumed to be much smaller than the water depth $h = (\eta - z_b)$, and the lower limit z_b of the integrations in (12) and (13) should be interpreted at the elevation immediately outside the bottom boundary layer. The contributions of the boundary layer flow, which needs to satisfy $u = 0$ at the bed, to the second moments m and n in (4) and the third moments m_3 and n_3 are assumed to be negligible. The normalized energy dissipation rate D_B due to the vertical variations of τ_x and u outside the boundary layer is the same as the dissipation rate due to breaking of normally incident waves used by Svendsen and Madsen (1984). The energy dissipation rate inside the bottom boundary layer corresponding to D_B is estimated as $u_b \tau_{bx}$ (Kobayashi and Wurjanto 1992) and is taken into account in (9). The boundary layer contribution corresponding to D_n is assumed to be given by $v_b \tau_{bx}$ and accounted for in (10) where $u_b \tau_{by} = v_b \tau_{bx}$ by use of (8).

To obtain h , U , V , m and n using (1)–(3), (9) and (10), u_b , v_b , m_3 , n_3 , D_B and D_n need to be expressed in terms of the five unknown variables. As a first attempt to deal with this closure problem, the horizontal velocities u and v outside the bottom boundary layer are assumed to be expressed as

$$u = U + \tilde{u}_b F(\zeta) \quad ; \quad v = V + \tilde{v}_b F(\zeta) \quad ; \quad \zeta = (z - z_b)/h \quad (14)$$

in which F is assumed to be a function of ζ only with $\zeta = 0$ at the bottom and $\zeta = 1$ at the free surface. The definitions of \tilde{u}_b and \tilde{v}_b in (11) require $F = 1$ at $\zeta = 0$. Furthermore, the turbulent eddy viscosity ν'_t is assumed to be given by $\nu'_t = (C_\ell h')^2 |\partial u' / \partial z'|$ outside the bottom boundary layer where the turbulence measurements by Cox *et al.* (1994) indicate that the mixing length parameter C_ℓ is on the order of 0.1. Accordingly, the normalized eddy viscosity ν_t is expressed as

$$\nu_t = \sigma C_\ell^2 h^2 \left| \frac{\partial u}{\partial z} \right| \tag{15}$$

Substitution of (14) and (15) into (4), (12) and (13) yields

$$m = C_2 h \tilde{u}_b^2 \quad ; \quad n = C_2 h \tilde{u}_b \tilde{v}_b \quad ; \quad C_2 = \int_0^1 F^2 d\zeta \tag{16}$$

$$m_3 = C_3 h \tilde{u}_b^3 \quad ; \quad n_3 = C_3 h \tilde{u}_b^2 \tilde{v}_b \quad ; \quad C_3 = \int_0^1 F^3 d\zeta \tag{17}$$

$$D_B = C_B \sigma C_\ell^2 |\tilde{u}_b|^3 \quad ; \quad D_n = C_B \sigma C_\ell^2 |\tilde{u}_b| \tilde{u}_b \tilde{v}_b \quad ; \quad C_B = \int_0^1 \left| \frac{dF}{d\zeta} \right|^3 d\zeta \tag{18}$$

in which the constants C_2 , C_3 and C_B can be found for the specified functional form of F . To find \tilde{u}_b using $m = C_2 h \tilde{u}_b^2$ for given $h \geq 0$ and $m \geq 0$, it is assumed that $\tilde{u}_b \leq 0$ for $U \geq 0$ and $\tilde{u}_b > 0$ for $U < 0$ to ensure $|u_b| \leq |U|$ where $u_b = (U + \tilde{u}_b)$ is the near-bottom cross-shore velocity used in (8). After \tilde{u}_b is obtained, $\tilde{v}_b = n / (C_2 h \tilde{u}_b)$, $v_b = (V + \tilde{v}_b)$, and (17) and (18) yield m_3 , n_3 , D_B and D_n .

Finally, the function F needs to be specified. Svendsen and Madsen (1984) assumed a cubic profile for their analysis of a single turbulent bore on a beach. For regular and irregular breaking waves on beaches, the following cubic profile is tentatively assumed:

$$F = 1 - (3 + 0.75a)\zeta^2 + a\zeta^3 \quad \text{for } 0 \leq \zeta \leq 1 \tag{19}$$

in which a = cubic velocity profile parameter. Comparison of (19) and the cubic profile assumed by Svendsen and Madsen (1984) suggests that a is about 3. The shear stresses at the surface are zero only if $a = 4$. For the range $a = 3-4$, F is not very sensitive to a , $C_2 = 0.49-0.55$, $C_3 = -0.07-0.00$, and $C_B = 12.3-15.2$ (Johnson *et al.* 1996). The computed results using $C_\ell = 0.1-0.2$ in (15) and $a = 3-4$ in (19) are found to be very similar. The typical values of $C_\ell = 0.1$ and $a = 3$ are hence employed for the computed results presented in this paper.

The numerical method used in the quasi-3D model is an extension of the numerical method devised in KK to solve (1)-(3) with $m = 0$ and $n = 0$. The computer program developed for the quasi-3D model solves (1)-(3), (9) and (10) along with (8), (11) and (16)-(18) using the MacCormack method (MacCormack 1969). The procedure is described in detail in Karjadi (1996).

COMPARISON WITH AVAILABLE DATA

1 Comparison with Laboratory and Field Data for Planar Beaches

The comparisons of the 2D model of KK and the quasi-3D model with the laboratory experiments 2-5 of Visser (1991) and the field data of Thornton and Guza (1986) on February 5 and 6, 1980 are presented in Kobayashi *et al.*

(1997). The 3D computations are made in the same way as the corresponding 2D computations presented in KK. For regular waves, the dispersion term n in the alongshore momentum equation (3) definitely improves the prediction of the cross-shore variation of longshore current. The bottom friction factor f'_b in (8) is adjusted somewhat for experiments 4 and 5 to obtain better agreement. The alongshore bottom shear stress τ_{by} in (3) is important in determining the magnitude of \bar{V} but modifies its profile little as expected from the previous work (*e.g.*, Longuet-Higgins 1970).

For irregular waves, the dispersion term n improves the agreement somewhat if the bottom friction factor f'_b is reduced to $f'_b = 0.01$ from $f'_b = 0.015$ used for the 2D model. Moreover, the dispersion effects on the longshore currents induced by breaking irregular waves are secondary in comparison to breaking regular waves. To confirm this conclusion, the time-averaged alongshore momentum equation corresponding to (3) is expressed as

$$\frac{\partial}{\partial x} S_{xy} + \frac{\partial \bar{\eta}}{\partial x} + \bar{h} \frac{\partial \bar{\eta}}{\partial y} + \frac{1}{2} \frac{\partial}{\partial y} \overline{(\eta - \bar{\eta})^2} = \bar{\tau}_{by} \quad (20)$$

in which $S_{xy} = \overline{hUV}$ is the alongshore radiation stress based on U and V . The third and fourth terms in (20) are zero for the case of alongshore uniformity. The computed cross-shore variations of dS_{xy}/dx and $d\bar{\eta}/dx$ for regular and irregular waves are presented in Kobayashi *et al.* (1997). For regular waves, the term $d\bar{\eta}/dx$ included in the 3D model decreases the force driving the longshore current near the breaker point but increases this force near the shoreline. On the other hand, for irregular waves the term $d\bar{\eta}/dx$ is secondary in the alongshore momentum equation (20).

2 Comparison with Field Data for A Barred Beach

On a barred beach, conceptually, waves will break on the bar, reform and break again on the beach face producing two peaks in the longshore current distribution. Contrary to this concept, the measurements of longshore currents on a barred beach obtained during the DELILAH experiment (Smith *et al.* 1993) generally indicated a broad peak in the bar trough region. Existing time-averaged models for longshore currents, which couple four governing equations for the wave height, wave angle, mean water surface elevation, and longshore current, have not been able to predict these broad peak longshore current data (Smith *et al.* 1993).

Smith *et al.* (1993) developed a one-dimensional time-averaged numerical model for longshore current that included the effect of turbulence due to wave breaking through a general transport equation for the mean turbulent kinetic energy. Their model produced an unrealistic high peak on the beach face. Church and Thornton (1993) developed a model using a spatially varying bottom friction coefficient based on a one-dimensional turbulent kinetic energy equation associated with the breaking-wave induced turbulence. However, this model was unable to satisfactorily predict the broad peak of the longshore current distribution observed in the DELILAH experiment. Momentum fluxes associated with mass transport above the trough level of broken waves, which were ignored in the other models, were included in the model developed by Kuriyama (1994). His model with additional empirical coefficients was compared with field data

in Japan. At present, there is no model available to predict the broad peak of the longshore current on a barred beach in a physically satisfactory manner.

To assess whether the developed model including the dispersion effects is capable of predicting the longshore current on a barred beach, the 3D model is compared with the DELILAH field data of Smith *et al.* (1993) on October 14, 1990 at 1900 EST which included the cross-shore variations of the measured root-mean-square wave height and longshore current. The frequency spectrum measured at the 8 m water depth was narrow banded in frequency with symmetric directional distributions about a mean oblique wave direction. The wave conditions at the 8 m depth were: the root-mean-square wave height $H'_{\text{rms}} = 0.83$ m; the spectral peak period $T'_p = 12.0$ sec; and the dominant incident wave direction $\theta_i = 18^\circ$. The bathymetry was nearly uniform in the alongshore direction.

The seaward boundary of the numerical model based on the assumption of shallow water waves is taken at the water depth $d' = 3.64$ m below the still water level where the measured root-mean-square wave height H'_{rms} was 1.02 m. The measured frequency spectrum at $d' = 8$ m is used to estimate the assumed unidirectional frequency spectrum and the predominant incident wave direction at $d' = 3.64$ m using the computer program RESHOAL developed by Poff and Kobayashi (1993) as explained briefly in the following.

RESHOAL assumes a straight shoreline with parallel bottom contours. For a given incident directional random wave spectrum at a deeper water depth, RESHOAL computes the directional random wave spectrum at a specified shallow water depth using linear finite-depth wave theory for directional random wave shoaling and refraction (LeMéhauté and Waug 1982). The incident directional random wave spectrum at the deeper water depth $d' = 8$ m is assumed to be given by the product of the TMA frequency spectrum and the Mitsuyasu-type directional spreading function. The input parameters for RESHOAL at the deeper water depth $d' = 8$ m are: H'_{mo} = spectral estimate of significant wave height; T'_p = spectral peak period ($T'_p = 12$ s for this data); γ = spectral peak enhancement factor; θ_i = dominant incident wave direction ($\theta_i = 18^\circ$); s_{max} = maximum value of the spreading parameter. RESHOAL computes the directional spectrum, frequency spectrum and directional spreading function at the shallower water depth $d' = 3.64$ m. The parameters H'_{mo} , γ , and s_{max} need to be calibrated such that the root-mean-square of wave height at the 3.64 m depth is equal to the measured value of $H'_{\text{rms}} = 1.02$ m and the assumed incident directional wave spectrum at the 8 m water depth is similar to the measured spectrum. The calibrated values are $H'_{\text{mo}} = 1.35$ m; $\gamma = 5$; and $s_{\text{max}} = 120$ at the 8 m water as shown in Figure 2. It is noted that the assumption of $H'_{\text{rms}} = H'_{\text{mo}}/\sqrt{2}$ yields $H'_{\text{rms}} = 0.95$ m for $H'_{\text{mo}} = 1.35$ m, which is slightly larger than the measured value $H'_{\text{rms}} = 0.83$ m. This might indicate wind effects on wind waves between the 8 m and 3.64 m water depths.

Figure 2 shows the measured and fitted frequency and directional spectra at the 8 m water depth and the computed frequency and directional spectra at the seaward boundary $d' = 3.64$ m. The fitted directional spectrum at the 8 m depth is the TMA frequency spectrum with $\gamma = 5$ and $H'_{\text{mo}} = 1.35$ m with the Mitsuyasu-type directional spreading function with $s_{\text{max}} = 120$. The computed frequency spectrum with $T'_p = 11.9$ s at $d' = 3.64$ m is used to compute the incident wave trains at the seaward boundary required as the input to the 3D

model. This incident frequency wave spectrum does not include low-frequency wave components as shown in Figure 2. The computed dominant incident wave direction is $\theta_i = 12^\circ$ at $d' = 3.64$ m as may be seen from the computed directional spectrum at $d' = 3.64$ m in Figure 2 which suggests that the assumption of unidirectional random waves may be reasonable.

Similar to the computations made in KK, the normalized computation duration is taken as $t_{\max} = 500$ corresponding to $t'_{\max} \simeq 99$ min. The sampling rate $\Delta t'_s$ is taken to be the same as the sampling rate of the field data, $\Delta t'_s = 0.125$ s. The bottom friction factor is assumed to be $f'_b = 0.015$. The computed results presented in the following are based on the normalization using the wave conditions at the seaward boundary of $d' = 3.64$ m, *i.e.*, the measured root-mean-square wave height $H' = H'_{\text{rms}} = 1.02$ m; the computed spectral peak period $T' = T'_p = 11.9$ sec; and the computed dominant wave direction $\theta_i = 12^\circ$. Correspondingly, $\sigma = T'(g/H')^{1/2} = 37$ and $\theta_c = \theta_i = 0.21$ in radians. The assumptions of $\sigma^2 \gg 1$ and $\theta_c^2 \ll 1$ are satisfied for this data. The normalized grid spacings are taken as $\Delta x \simeq \Delta y = 0.0106$ corresponding to the dimensional cross-shore and alongshore grid spacings of $\Delta x' = 0.40$ m and $\Delta y' = 1.91$ m, respectively.

Figure 3, with the parameter $\delta_\eta = 0$ for the case of uniform incident wave conditions in the alongshore direction, shows the comparisons between the measured and computed cross-shore variations of the local root-mean-square wave height H_{rms} and the longshore current \bar{V} together with the measured bottom profile. The computed temporal variation of η for $200 \leq t \leq 500$ is used to obtain H_{rms} based on the zero-up crossing method whereas the computed longshore current \bar{V} is obtained by averaging the temporal variation of the depth-averaged alongshore velocity V for the duration $200 \leq t \leq 500$. Figure 3 with $\delta_\eta = 0$ shows that the 3D model without the incident low-frequency wave components underpredicts the root-mean-square wave height in the bar trough region. Moreover, the model predicts a peak in the longshore current at the seaward edge of the bar crest in contrast to a broad peak in the bar trough region.

As a first attempt to explain the broad peak in the longshore current distribution, the effects of incident low-frequency waves on the cross-shore distribution of longshore current are examined because incident low-frequency waves might modify the wave breaking on the bar crest and resulting longshore current profile. The incident wave spectrum at the seaward boundary shown in Figure 2 does not include low-frequency components. As a first approximation, uniform low-frequency components are added to the incident wave spectrum to examine the effects of these low-frequency components to the longshore current profile. The additional low-frequency components are found to modify the longshore current profile little (Karjadi 1996). Consequently, the broad peak of the longshore current in the bar trough cannot be explained by incident low-frequency waves.

The effect of alongshore non-uniformity on the longshore current profile is examined in the following. Longshore currents have been primarily modeled assuming alongshore uniformity, although it has been known that alongshore non-uniformities affect longshore currents (*e.g.*, Putrevu *et al.* 1995). To study the effect of the alongshore variation of incident wave conditions within the limitation of the 3D model based on three cross-shore lines as discussed in KK,

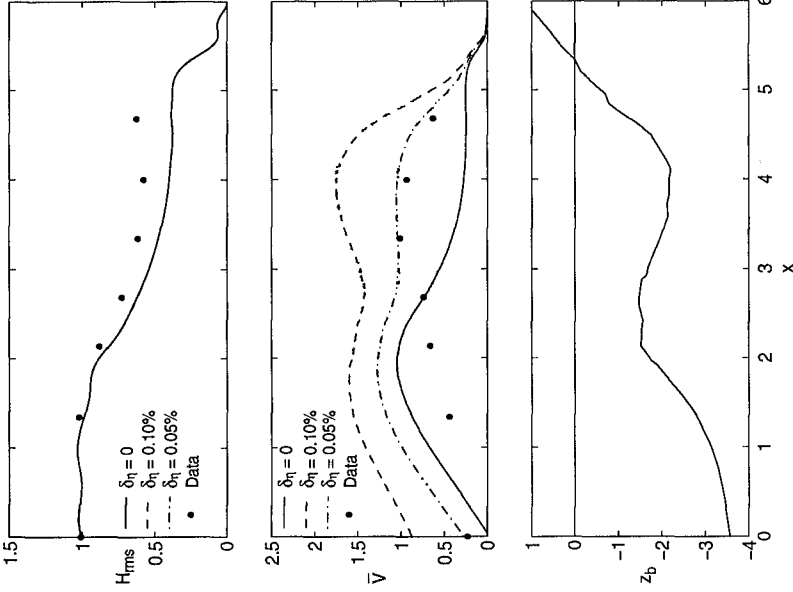


Figure 3: Measured and computed cross-shore variations of H_{rms} and longshore current \bar{V} together with normalized bottom profile for DELLAH experiment with $\delta_\eta \geq 0$.

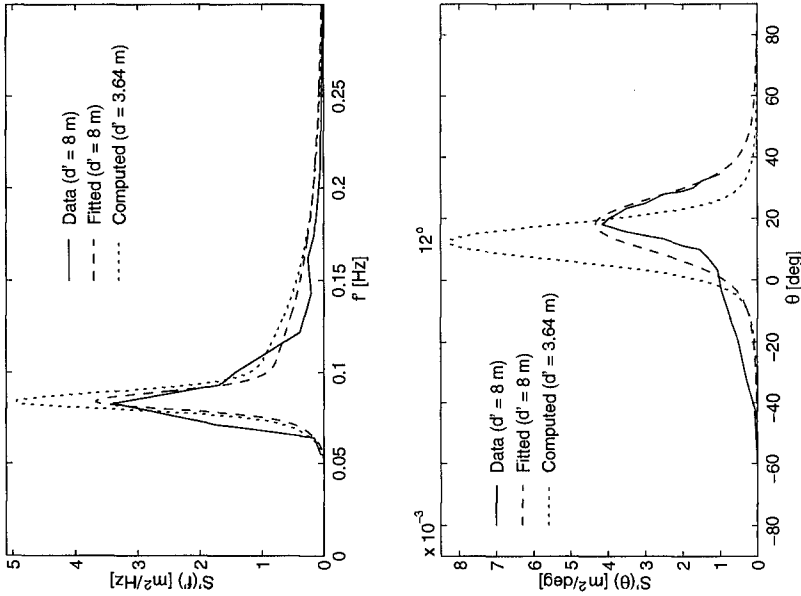


Figure 2: Measured and fitted frequency and directional spectra at depth $d' = 8$ m and the shoaled and refracted frequency and directional spectra at $d' = 3.64$ m.

the incident wave trains η_i specified as new input to the model are modified as follows:

$$\begin{aligned} \text{Line 1: } & \text{new } (\eta_i)_1 = \text{old } (\eta_i)_1 \\ \text{Line 2: } & \text{new } (\eta_i)_2 = \text{old } (\eta_i)_2 \times (1 - \delta_\eta) \\ \text{Line 3: } & \text{new } (\eta_i)_3 = \text{old } (\eta_i)_3 \times (1 - 2\delta_\eta) \end{aligned}$$

where the old time series $(\eta_i)_1$, $(\eta_i)_2$ and $(\eta_i)_3$ have been computed for incident unidirectional random waves of alongshore uniformity. The distance between two adjacent lines is $\Delta y' = 1.91$ m. The dimensionless parameter δ_η is taken to be much less than unity to satisfy the assumption of gradual alongshore variation. The incident wave intensity decreases or increases in the down-wave direction depending on $\delta_\eta > 0$ or $\delta_\eta < 0$, respectively.

The computed results using these new incident wave trains are shown in Figures 3 and 4 for the cases of $\delta_\eta = 0, 0.0005$ and 0.001 and for the cases of $\delta_\eta = 0$ and -0.001 , respectively. The root-mean-square wave height changes very little since the specified change in the incident wave train is very small. For the wave intensity decreasing in the down-wave direction, the longshore current profile increases almost uniformly across the shoaling region and over the bar crest. The increase in the longshore current is larger in the bar trough region, whereas the increase is smaller in the swash zone. The broad peak in the bar trough region in Figure 3 is similar to the broad peak observed in the field. For the wave intensity increasing in the down-wave direction as shown in Figure 4 the longshore current in the bar trough region is decreased significantly and becomes negative.

To explain the computed results shown in Figures 3 and 4, Figure 5 shows the cross-shore variations of the driving forces on the left hand side of (20) for the cases of $\delta_\eta = 0.001$ and -0.001 . The terms of $\partial\bar{\eta}/\partial x$ and $\frac{1}{2}\partial(\overline{\eta - \bar{\eta}})^2/\partial y$ are on the order of 0.005 or less in the bar trough region and secondary in comparison to the other two terms plotted in these figures. For both cases, the cross-shore gradient of the alongshore radiation stress, $\partial S_{xy}/\partial x$, driving the longshore current is very small in the bar trough region. The additional term $\bar{h}\partial\bar{\eta}/\partial y$ associated with the alongshore wave setup gradient modifies the driving force significantly in the bar trough region where the incident wave intensity and resulting wave setup decrease or increase in the down-wave direction depending on $\delta_\eta > 0$ or $\delta_\eta < 0$, respectively.

To examine the effects of the alongshore non-uniformity on planar beaches, the modified incident wave trains for the cases of $\delta_\eta = 0.0005$ and 0.001 are also specified for the computations for the regular wave experiment 2 of Visser (1991) and the irregular wave data of Thornton and Guza (1986) on February 5. For the planar beaches as shown in Figure 6, the longshore current increases almost uniformly in the shoaling and surf zones except in the swash zone. Contrary to the computed results for the barred beach shown in Figure 3, the longshore current profile shape on the planar beaches is not sensitive to the alongshore non-uniformity. To explain this difference, Figure 7 shows the cross-shore variations of the driving forces in the time-averaged momentum equation (20) for the regular and irregular waves on the planar beaches. The additional driving force terms $\bar{h}\partial\bar{\eta}/\partial y$ and $\frac{1}{2}\partial(\overline{\eta - \bar{\eta}})^2/\partial y$ due to the alongshore variations are small

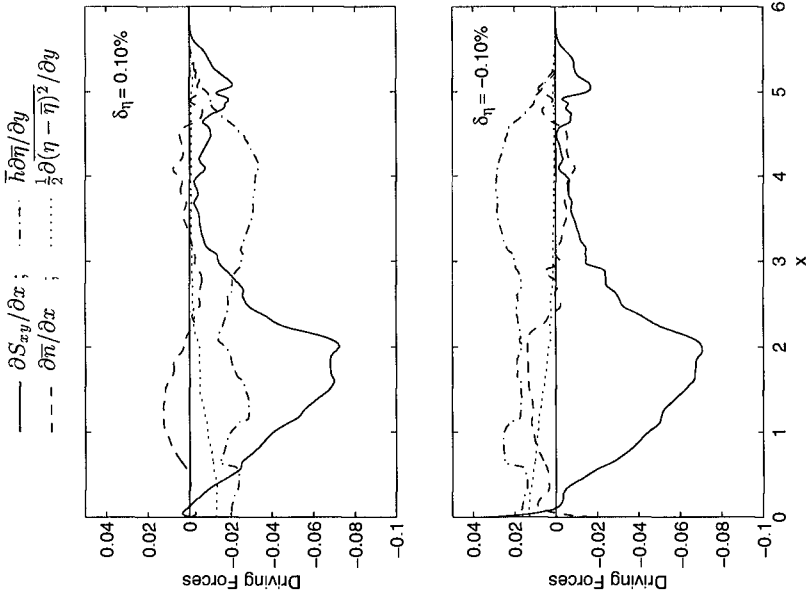


Figure 5: Computed cross-shore variations of driving forces in time-averaged alongshore momentum equation (20) for a barred beach.

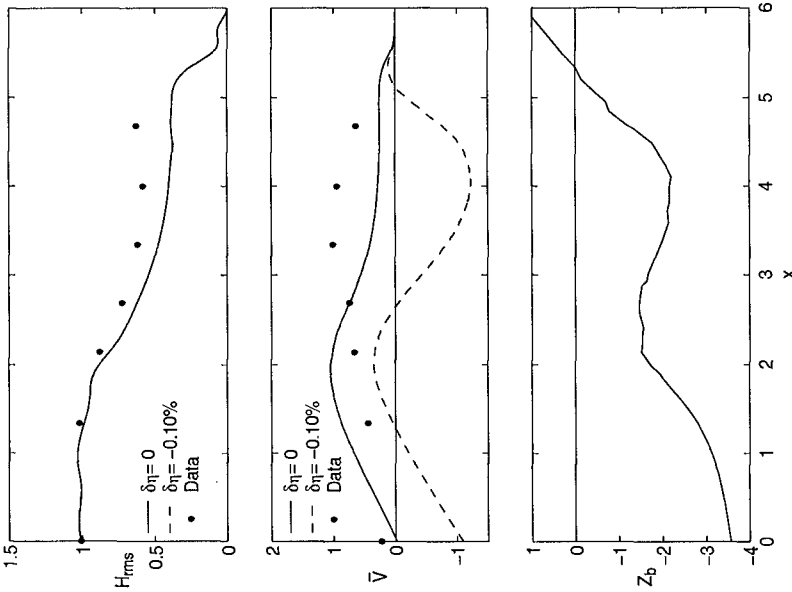


Figure 4: Measured and computed cross-shore variations of H_{rms} and longshore current \bar{V} together with normalized bottom profile for DELILAH experiment with $\delta_\eta \leq 0$.

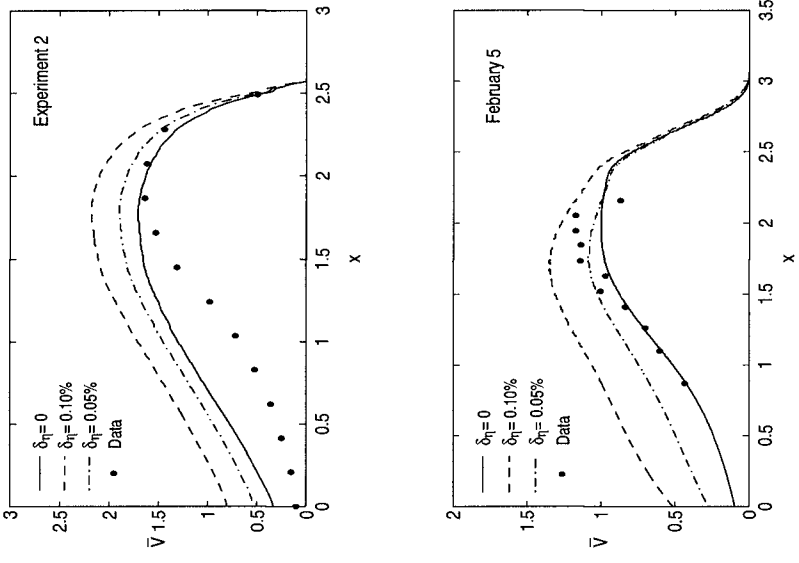


Figure 6: Effects of alongshore decrease of incident wave intensity on the longshore current profile for planar beaches.

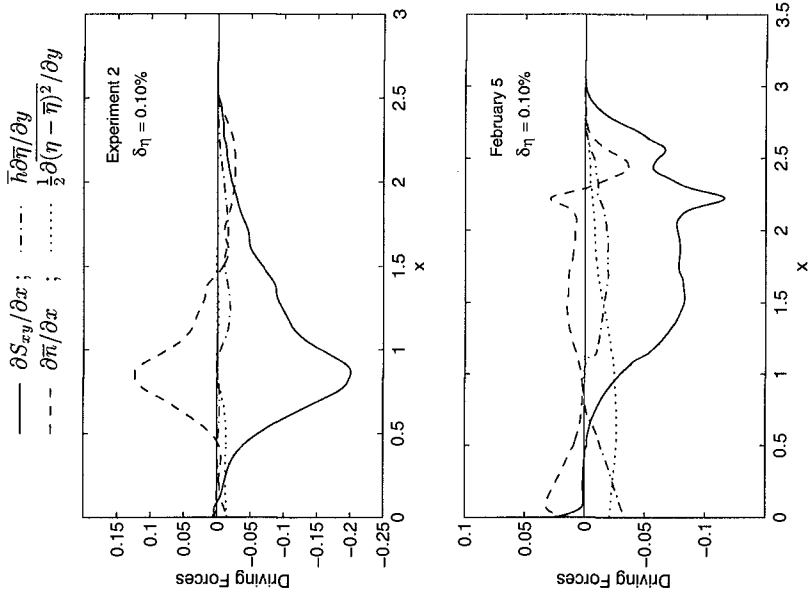


Figure 7: Computed cross-shore variations of driving forces in time-averaged alongshore momentum equation (20) for planar beaches.

in comparison to the main driving force, $\partial S_{xy}/\partial x$, causing the almost uniform increase in the longshore current without changing its shape as shown in Figure 6. It is noted that the term $\partial \bar{\eta}/\partial x$ in (20) is important for regular waves as discussed in relation to (20).

The computed results discussed above imply that the broad peak of the longshore current on a barred beach can be caused by the very small alongshore variation of wave height and setup. This may explain why existing longshore current models based on the assumption of alongshore uniformity were regarded to be adequate before their comparisons with the barred beach data. For planar beaches, the effect of alongshore non-uniformity, even if it exists, can be accounted for by adjusting the constant bottom friction factor which changes the longshore current profile shape little. On the other hand, for barred beaches, the very small alongshore variation of wave height and setup modifies the longshore current profile shape which cannot be changed much by adjusting the constant bottom friction factor.

CONCLUSIONS

A time-dependent quasi three-dimensional numerical model is developed to predict the temporal and cross-shore variations of the free surface elevation and fluid velocities in the surf and swash zones under obliquely incident waves. This model is used to clarify the dispersion effects due to the vertical variation of the horizontal velocities in the surf zone. For planar beaches, the dispersion effects on the cross-shore variations of the wave height and setup are shown to be minor, indicating that the cross-shore dispersion term m may be neglected in the depth-integrated cross-shore momentum equation (2) as anticipated by Kobayashi and Wurjanto (1992). On the other hand, the dispersion effects on the longshore current profile are significant for regular waves but secondary for irregular waves, especially in view of the uncertainties associated with the bottom friction factor.

The 3D model is also compared with the DELILAH field data for a barred beach (Smith *et al.* 1993). Under the assumption of alongshore uniformity, the model cannot explain the observed broad peak in the longshore current in the bar trough region. Small alongshore variations of the incident wave intensity and resulting wave setup are shown to modify the longshore current profile in the bar trough region significantly. The cross-shore gradient of the alongshore radiation stress driving the longshore current is very small in this bar trough region. The alongshore gradient of wave setup is shown to alter the force driving the longshore current significantly in this region and produces a broad peak in the longshore current. Contrary to the computed results for the barred beach, the longshore current profile on planar beaches is found to be insensitive to the alongshore variations of the incident wave intensity and resulting wave setup. As a result, the prediction of the longshore current profiles on barred beaches will require the knowledge of small alongshore variability that is very difficult to measure accurately.

ACKNOWLEDGMENT

This work was supported by the U.S. Army Research Office, University Re-

search Initiative under Contract No. DAAL03-92-G-0116, by the NOAA Office of Sea Grant, Department of Commerce, under Grant No. NA85AA-D-SG033 (Project SG95 R/OE-18), and by the National Science Foundation under Grant No. CTS-9407827.

REFERENCES

- Church, J.C. and Thornton, E.B., 1993. "Effects of breaking wave induced turbulence within a longshore current model." *Coast. Engrg.*, **20**, 1–28.
- Cox, D.T., Kobayashi, N. and Okayasu, A. (1994). "Vertical variations of fluid velocities and shear stress in surf zones." *Proc. 24th Coast. Engrg. Conf.*, ASCE, **1**, 98–112.
- DeVriend, H.J. and Stive, M.J.F. (1987). "Quasi-3D modelling of nearshore currents." *Coast. Engrg.*, **11**, 565–601.
- Johnson, B.D., Kobayashi, N. and Cox, D.T. (1996). "Formulation and validation of vertically two-dimensional shallow-water wave model." *Proc. 25th Coast. Engrg. Conf.*, ASCE (in press).
- Karjadi, E.A. (1996). "Numerical models for obliquely incident waves in surf and swash zones." Ph.D. dissertation, Univ. of Delaware, Newark, Del.
- Kobayashi, N. and Karjadi, E.A. (1994). "Swash dynamics under obliquely incident waves." *Proc. 24th Coast. Engrg. Conf.*, ASCE, **2**, 2155–2169.
- Kobayashi, N. and Karjadi, E.A. (1996). "Obliquely incident irregular waves in surf and swash zones." *J. Geophys. Res.*, **101**(C3), 6527–6542.
- Kobayashi, N. and Karjadi, E.A., and Johnson, B.D. (1997). "Dispersion effects on longshore currents in surf zones." *J. Wtrwy, Port, Coast. and Oc. Engrg.*, ASCE (in press).
- Kobayashi, N. and Wurjanto, A., 1992. "Irregular wave setup and run-up on beaches." *J. Wtrwy, Port, Coast. and Oc. Engrg.*, ASCE, **118**(4), 368–386.
- Kuriyama, Y., 1994. "Numerical model for longshore current distribution on a bar-trough beach." *Proc. 24th Coast. Engrg. Conf.*, ASCE, **2**, 2237–2251.
- LeMéhauté, B. and Wang, J.D., 1982. "Wave spectrum changes on a sloped beach." *J. Wtrwy, Port, Coast. and Oc. Engrg.*, ASCE, **108**(1), 33–47.
- Longuet-Higgins, M.S., 1970. "Longshore currents generated by obliquely incident sea waves, 1 and 2." *J. Geophys. Res.*, **75**(C3), 6778–6801.
- MacCormack, R.W., 1969. "The effects of viscosity in hypervelocity impact cratering." *Paper 69-354*, American Institute of Aeronautics and Astronautics, New York.
- Poff, M.T. and Kobayashi, N., 1993. "Computer program for refraction of directional random waves." *Res. Rept. No. CACR-93-04*, Ctr. for Applied Coast. Res., Univ. of Delaware, Newark, DE.
- Putrevu, U., Oltman-Shay, J. and Svendsen, I.A., 1995. "Effect of alongshore nonuniformities on longshore current predictions." *J. Geophys. Res.*, **100**(C8), 16119–16130.
- Smith, J.M., Larson, M. and Kraus, N.C. (1993). "Longshore current on a barred beach: field measurements and calculation." *J. Geophys. Res.*, **98**(C12), 22727–22731.
- Svendsen, I.A. and Lorenz, R.S. (1989). "Velocities in combined undertow and longshore currents." *Coast. Engrg.*, **13**, 55–79.
- Svendsen, I.A. and Madsen, P.A., 1984. "A turbulent bore on a beach." *J. Fluid Mech.*, **148**, 73–96.
- Svendsen, I.A. and Putrevu, U., 1994. "Nearshore mixing and dispersion" *Proc. Roy. Soc. London*, A(445), 561–576.
- Thornton, E.B. and Guza, R.T. (1986). "Surf zone longshore currents and random waves: Field data and models." *J. Phys. Oceanogr.*, **16**, 1165–1178.
- Visser, P.J. (1991). "Laboratory measurements of uniform longshore currents." *Coast. Engrg.*, **15**, 563–593.

CHAPTER 20

Models of Wave Height and Fraction of Breaking Waves on a Barred Beach

Yoshiaki Kuriyama¹

Abstract

Models for wave height and the fraction of breaking waves were developed; the models employ a wave-by-wave approach, in which the shoaling, breaking and reforming of individual waves are calculated. The performance of the models calibrated with experimental data was not satisfied; the fractions of breaking waves estimated by the models were smaller than the values measured over troughs in the field. The models therefore were calibrated and verified with the field data. Furthermore, the validity of the models calibrated with the field data was confirmed by comparison with large-scale experiment data.

Introduction

The fraction of breaking waves, defined as the ratio of the number of breaking/broken waves to the total number of waves, strongly affects various phenomena in the surf zone, such as nearshore currents, sediment suspension, and morphology changes. This is because various surf zone phenomena are mainly caused by turbulence, mass flux and momentum flux induced by breaking/broken waves, which are much greater than those induced by non-breaking waves. For example, Kuriyama (1994) carried out numerical simulations to show that the longshore current distribution over a longshore bar and trough is dependent on the cross-shore distribution of the fraction of breaking waves. Hence, to predict longshore current velocities as well as undertow velocities, suspended sediment concentrations and topography changes, it is essential to estimate accurately the fraction of breaking waves Q_b .

Several models have been proposed to estimate Q_b and wave height H . Battjes and Janssen (1978) simulated variations in H within the surf zone, assuming a modified Rayleigh distribution truncated at the breaking wave height H_b , where breaking and broken waves have the same value of H_b . According to the assumption, the value of Q_b is estimated with the root-mean-square wave height H_{rms} and H_b . Battjes and Stive (1985), Roelvink (1993) and Southgate and Nairn (1993) compared Q_b estimated by Battjes and Janssen's model with results of field and laboratory measurements on

1) Senior Research Engineer, Marine Environment Division, Port and Harbour Research Institute, Ministry of Transport, Nagase 3-1-1, Yokosuka, Kanagawa 239, JAPAN

planar beaches. Although the estimated values of Q_b were smaller than those measured, the estimated cross-shore distributions of Q_b qualitatively agreed with the measurements.

Thornton and Guza (1983) improved Battjes and Janssen's model; an unmodified Rayleigh distribution, not truncated at the breaking wave height, was assumed at every location inside and outside the surf zone and wave breaking was allowed to occur at any wave height. The value of Q_b was taken to be a function of H , H_{rms} and water depth h . They measured Q_b on a planar beach in the field, and found that Q_b calculated by their model agreed well with the measured values.

Recently, Dally (1992) simulated variations in wave height by applying another algorithm, a wave-by-wave approach, in which the shoaling, breaking and reforming of individual waves are calculated. Because the mode of wave breaking of an individual wave (breaking, broken, or non-breaking) is clarified at any point through the calculation for the individual wave, Q_b can be directly estimated as the ratio of the number of breaking/broken waves to the total number of waves. By comparing calculated results with those measured over a longshore bar in the field by Ebersole (1987), Dally showed that Q_b calculated at the seaward slope of the bar correlated well with measured values, though the calculated values were smaller than the measured values.

The models reviewed above accurately predicted the cross-shore distributions of Q_b quantitatively or at least qualitatively on planar beaches and on the seaward slopes of longshore bars. Over troughs, however, the models could not predict the distributions of Q_b even qualitatively. Rivero et al. (1994) as well as Southgate and Nairn (1993) compared Q_b estimated by Battjes and Janssen's model with the values measured in experiments, and showed that Battjes and Janssen's model considerably underestimated Q_b over troughs. Dally's model also significantly underestimated Q_b over a trough (Dally, 1992; Nishi, 1994). Although Thornton and Guza's model has not been compared with measurements over troughs, their model is expected to have the same problem because it considers only wave breaking and not wave reforming.

To overcome the weakness of these models, Southgate and Wallace (1994) introduced the "persistence length" into Battjes and Janssen's model; beyond the persistence length, a broken wave reforms regardless of the wave condition. This length was assumed to be proportional to H_b , where the coefficient of the proportionality was determined by fitting the model results to Q_b measured in large-scale experiments. The use of the "persistence length" improved the accuracy of determining Q_b over troughs (Southgate and Wallace, 1994). The values of Q_b over troughs, however, were still underestimated. To predict the fraction of breaking waves more precisely, a more reliable criterion for wave reforming is required.

In this study, I hence develop two models for predicting H and Q_b that include a criterion for wave reforming proposed on the basis of field data. The models are calibrated and verified with both field and large-scale experiment data.

Formulation of models

The two models developed here employ a wave-by-wave approach in the manner of Dally (1992); the shoaling, breaking and reforming of individual waves are calculated. The values of significant wave height $H_{1/3}$ and Q_b are estimated using the simulation results of individual waves. The only difference between the two models is in the estimation of wave energy dissipation due to wave breaking. One, called Model 1, contains a periodic bore dissipation sub-model used by Thornton and Guza (1983), while the other, called Model 2, uses a dissipation sub-model developed by

Dally et al. (1985), in which stable wave height is included.

(1) Model 1

The shoaling of a wave is calculated with a shoaling coefficient proposed by Shuto (1974); the coefficient has been derived under the consideration of wave nonlinearity.

As a criterion for wave breaking, Model 1 adopts a formula proposed by Seyama and Kimura (1988), who experimentally measured wave height deformation of individual, irregular waves in the surf zone, and investigated the wave height-water depth ratio at wave breaking H_b/h_b . The formula is expressed in terms of beach slope $\tan \beta$ and the ratio of breaking water depth to the offshore wavelength h_b/L_0 as

$$\frac{H_b}{h_b} = 0.16 \frac{L_0}{h_b} [1 - \exp(-0.8\pi \frac{h_b}{L_0} (1 + 15 \tan^4 \beta))] - 0.96 \tan \beta + 0.2. \quad (1)$$

Because the experiment data of Seyama and Kimura (1988) are scattered around the values predicted by Eq.(1) with a standard deviation of $0.08H_b/h_b$, the values of H_b/h_b in Model 1 are assumed to distribute around those predicted by Eq.(1) with a normal distribution having a standard deviation of $0.08H_b/h_b$.

After wave breaking, the energy dissipation of a wave of frequency f , energy E and group velocity C_g is evaluated using

$$\frac{\partial(EC_g)}{\partial x} = \frac{1}{4} \rho g f \frac{(BH)^3}{h}, \quad (2)$$

where x is the cross-shore coordinate directed positive offshore, ρ is the density of sea water, g is the acceleration of gravity, and B is a dimensionless coefficient.

Thornton and Guza (1983) used Eq.(2) to calculate the total wave energy dissipation applying the same value of B to all waves irrespective of wave heights. By comparing H_{rms} measured in the field with the values estimated by Eq.(2), they determined that $B=1.5$. Model 1, however, predicts variations in H of individual waves, for which $B=1.5$ has not been proved to be optimum. The optimum B for individual waves has therefore been investigated with Seyama and Kimura's experimental results on wave deformation in the surf zone (1988), and has been found to be

$$B = 1.6 - 0.12 \ln(H_0/L_0) + 0.28 \ln(\tan \beta). \quad (3)$$

Wave reforming is judged by a formula proposed by Kuriyama and Ozaki (1996) on the basis of field data. They measured water surface elevations and the modes of wave breaking (non-breaking, breaking, or broken) of individual waves over longshore bars and troughs at the Hazaki Oceanographical Research Station (HORS), which is a 427 m long field observation pier on the Kashima-nada coast of Japan facing the Pacific Ocean, and investigated the wave height-water depth ratio at wave reforming H_r/h_r . The formula proposed is expressed as

$$H_r/h_r = -0.0624 \ln(h_r/L_0) + 0.142. \quad (4)$$

Because the field data are scattered around the values predicted by Eq.(4) (Kuriyama and Ozaki, 1996), H_r/h_r in Model 1 are assumed to distribute randomly in the region between Eq.(4)-0.2 and Eq.(4)+0.2.

While wave reforming is determined on the basis of Eq.(4), a transition zone where a broken wave does not reform even though the wave height-water depth ratio is less than that estimated by Eq.(4) is introduced in the model for the following reason. After wave breaking, a bore gradually develops on the front of a broken wave. Bore development appears to be strongly influenced by the wave condition at the wave breaking point, whereas it appears to be only slightly influenced by the wave condition shoreward of the wave breaking point. Consequently, even though $H < H_r$, the bore under development is supposed to advance toward the shore without vanishing.

The length of the transition zone l is determined based on experimental data of Seyama and Kimura (1988); they reported that the variation in H within the surf zone consists of three phases: an increase in H immediately after wave breaking, a sharp decrease in H after reaching the maximum wave height and a moderate decrease in H from the middle of the surf zone to the shoreline. The length l is assumed to be equal to the distance between the point of the maximum wave height and the point where a change occurs in the rate of decrease of H/H_b versus h/h_b , because bore development is supposed to end at the latter point; Seyama and Kimura (1988) reported the appearance of stable bores at the latter point. The length of l is expressed accordingly as

$$l = \frac{h_b}{\tan\beta} \left[1 - 0.93 \exp(-9.21 \tan\beta) - \frac{0.02}{0.72 \exp(6.11 \tan\beta)} \right]. \quad (5)$$

The transition zone introduced in Model 1 seems to be equivalent to the persistence length proposed by Southgate and Wallace (1994). However, these are slightly different; Model 1 assumes that a broken wave cannot reform if $H > H_r$, regardless of wave position, whereas Southgate and Wallace's model assumes that a broken wave must reform beyond the persistence length, regardless of wave condition.

Naturally, wave shoaling is calculated again after wave reforming.

(2) Model 2

Because Model 2 uses the same methods as Model 1 to calculate shoaling, wave breaking and wave reforming of an individual wave, only the method for estimating the wave energy dissipation due to wave breaking is described here.

Wave energy dissipation is estimated by the following equation, proposed by Dally et al. (1985),

$$\frac{\partial(EC_g)}{\partial x} = (EC_g - E_s C_g) \frac{K}{h}, \tag{6}$$

$$E_s = \rho g H_s^2 / 8, \quad H_s = \Gamma h,$$

where K and Γ are dimensionless coefficients, and H_s represents the stable wave height, defined as the value of H at which wave breaking ends on a shelf beach composed of an upward sloping bottom and a flat bottom. Dally et al. (1985) showed that by setting $K=0.15$ and $\Gamma=0.4$, H could be estimated in good agreement with the experimental data by Horikawa and Kuo (1966).

Since H_s represents the height of a stable wave, which is non-breaking after reforming, Γ can be considered as the wave height-water depth ratio at wave reforming. In this model, hence, Γ is replaced by a value estimated by Eq.(4), while $K=0.15$ is maintained as a constant.

Calibration

The values of $H_{1/3}$ and Q_b estimated by Models 1 and 2 were compared with 11 sets of field data obtained at HORS (Kuriyama and Ozaki, 1996). The offshore boundaries in the calculations were set at the most seaward measurement points where few waves were broken. Figure 1 shows four examples of the comparisons of $H_{1/3}$ and Q_b measured in the field with values estimated with Model 1 and Model 2. Table 1 lists the wave conditions for the measurements shown in Figure 1.

Table 1 Wave and wind conditions during the measurements: significant wave heights in deep water ($H_{1/3}0$), significant wave periods in deep water ($T_{1/3}0$), and the wave directions visually observed at the bar crests θ_b , which are defined relative to the shoreward direction and are positive counterclockwise.

Case	Time	$(H_{1/3})_0$ (m)	$(T_{1/3})_0$ (s)	θ_b (deg.)
1	Mar. 3, 1994, 13:20-14:50	1.28	11.2	10
2	Mar. 10, 1994, 13:10-14:40	2.27	9.5	5
3	June 14, 1994, 13:20-14:40	1.50	9.2	-5
4	Nov. 22, 1994, 10:10-11:40	1.68	7.0	0

Good agreements exist between the results of Model 1 and Model 2 for Q_b and $H_{1/3}$. The values of Q_b estimated by the models are, however, smaller than the measured values over the troughs, and even over the seaward slopes of the longshore bars. Furthermore, $H_{1/3}$ estimated by the models are smaller than the measured values over the troughs. These results show that waves simulated in the models tend to break less and decay more than actual waves in the field. I attribute this tendency of the waves in the models to a scale effect; all coefficients in the models, except those of the wave reforming criterion, were determined on the basis of experimental data.

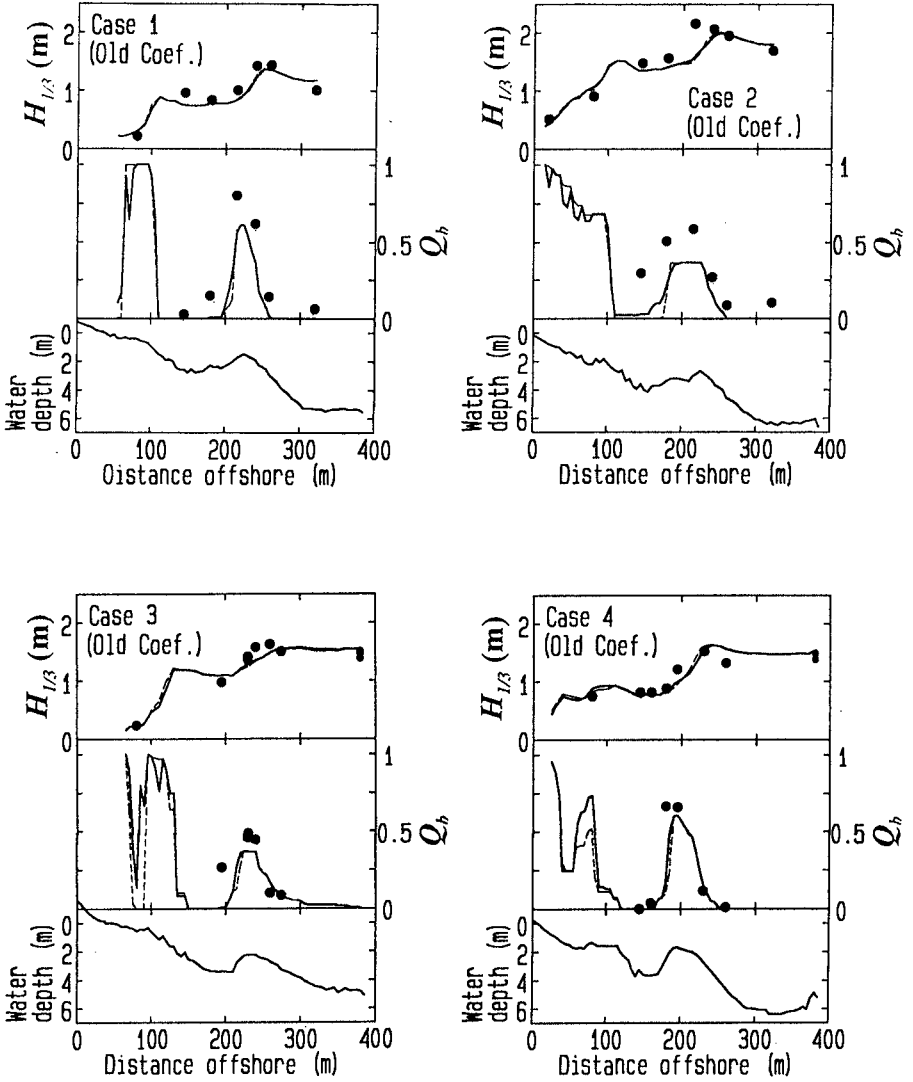


Figure 1 Comparison of $H_{1/3}$ and Q_b measured in the field (solid circles) with those estimated by Model 1 (thick solid lines) and Model 2 (thin dashed lines).

Hence, new coefficients were introduced and the models were calibrated with the field data.

Instead of Eq.(1), which is the criterion for wave breaking in the models, the following equation with a dimensionless coefficient C_{br} was introduced.

$$\frac{H_b}{h_b} = C_{br} (0.16 \frac{L_0}{h_b} [1 - \exp(-0.8\pi \frac{h_b}{L_0} (1 + 15 \tan^4 \beta))] - 0.96 \tan \beta + 0.2). \quad (7)$$

Equation (3), used for the calculation of wave energy dissipation in the Model 1, was replaced by

$$B = C_B (1.6 - 0.12 \ln(H_0/L_0) + 0.28 \ln(\tan \beta)), \quad (8)$$

where C_B is a new dimensionless coefficient.

A calibration for Model 1 was conducted by varying the values of C_{br} and C_B , and by determining the optimum values that minimize errors between predicted and measured values of $H_{1/3}$ and Q_b ; the value of C_{br} was varied from 0.8 to 1.1 at intervals of 0.05, and C_B was varied from 0.5 to 1.2 at intervals of 0.1. An error index $\epsilon(C_{br}, C_B)$ was defined to determine the optimum coefficients. This error index was calculated according to the following procedure.

1) The error in $H_{1/3}$ for all data sets, denoted as $\epsilon_H(C_{br}, C_B)$, and that in Q_b , denoted as $\epsilon_Q(C_{br}, C_B)$, are given by

$$\begin{aligned} \epsilon_H(C_{br}, C_B) &= \sum_{i=1}^{N_s} \sqrt{\sum_{n=1}^{N_{H,i}} ((H_{1/3,p})_n - (H_{1/3,m})_n)^2 / N_{H,i} / N_s}, \\ \epsilon_Q(C_{br}, C_B) &= \sum_{i=1}^{N_s} \sqrt{\sum_{n=1}^{N_{Q,i}} ((Q_{b,p})_n - (Q_{b,m})_n)^2 / N_{Q,i} / N_s}, \end{aligned} \quad (9)$$

where $N_{H,i}$ and $N_{Q,i}$ are the numbers of values of $H_{1/3}$ and Q_b in the i -th data set, and N_s is the number of the data sets. The subscripts p and m denote the values predicted and measured, respectively.

2) If ϵ_H and S_H are the mean and the standard deviation of $\epsilon_H(C_{br}, C_B)$ at $0.8 \leq C_{br} \leq 1.1$ and $0.5 \leq C_B \leq 1.2$, and ϵ_Q and S_Q are those of $\epsilon_Q(C_{br}, C_B)$, then the error index $\epsilon(C_{br}, C_B)$ is defined as

$$\epsilon(C_{br}, C_B) = \frac{(\epsilon_H(C_{br}, C_B) - \bar{\epsilon}_H)}{S_H} + \frac{(\epsilon_Q(C_{br}, C_B) - \bar{\epsilon}_Q)}{S_Q}, \quad (10)$$

In a calibration for Model 2, an error index $\epsilon(C_{br}, K)$ was similarly defined; C_{br} was varied from 0.8 to 1.1 at intervals of 0.05, and K was varied from 0.025 to 1.5 at intervals of 0.025.

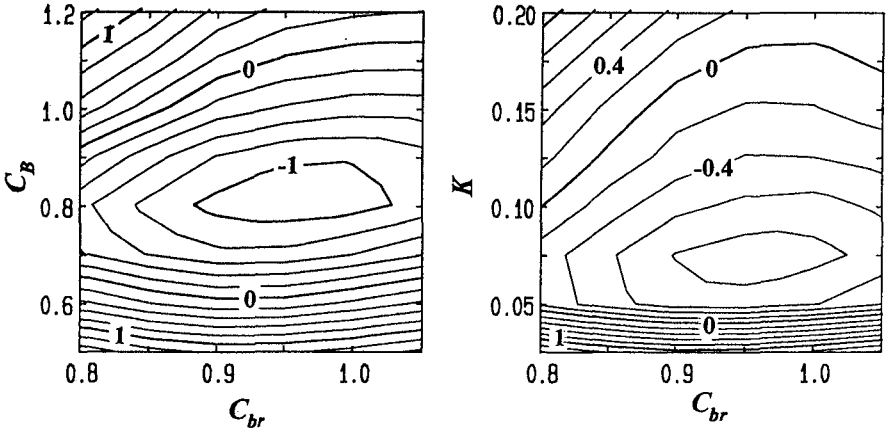


Figure 2 Contour plots of $\epsilon(C_{br}, C_B)$ and $\epsilon(C_{br}, K)$.

Figure 2 shows contour plots of $\epsilon(C_{br}, C_B)$ and $\epsilon(C_{br}, K)$. The optimum values of the coefficients were found to be $C_{br}=0.95$ and $C_B=0.8$ for Model 1, and $C_{br}=0.95$ and $K=0.075$ for Model 2.

I compared $H_{1/3}$ and Q_b measured in the field with those calculated with Models 1 and 2 containing the new coefficients, and show the results in Figure 3. The shortcomings of the models containing the old coefficients were lessened; the accuracy of Q_b estimated with the new coefficients increased. The values of Q_b estimated by the models containing the new coefficients agree with the field data over the longshore bars as well as over the troughs.

The differences between Q_b as estimated by the two models are small, but Q_b estimated by Model 2 decrease more over the troughs toward the shore and are more sensitive to the change in water depth near the shorelines than those estimated by Model 1.

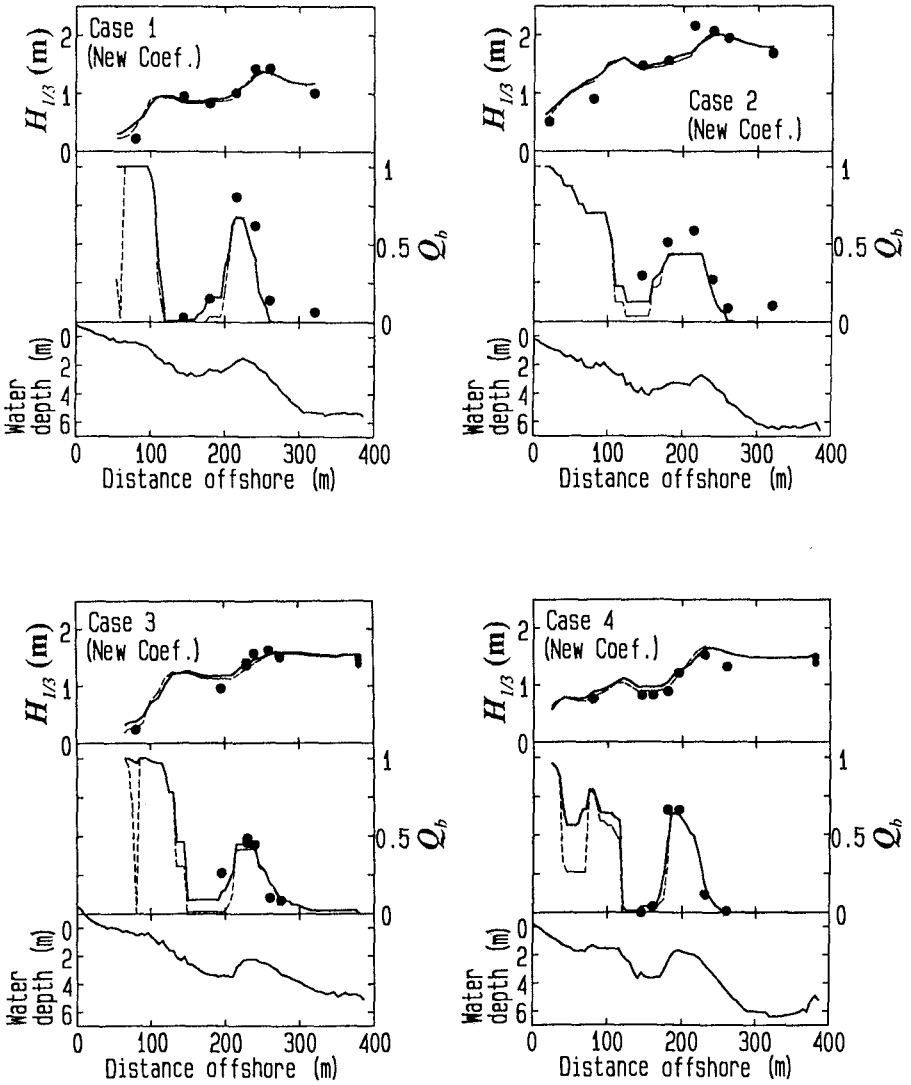


Figure 3 Comparison of $H_{1/3}$ and Q_b measured in the field (solid circles) and those estimated by the newly calibrated Model 1 (thick solid lines) and Model 2 (thin dashed lines).

Verification

The models were then compared with large-scale experiment data of the Delta Flume '93 Experiments (Rivero et al., 1994). The data shown by Rivero et al. (1994) are Q_b and H_{m0} , defined as

$$H_{m0} = 4.004 \eta_{rms}. \quad (11)$$

The present models cannot predict H_{m0} because that variable is estimated from a series of water surface elevation, which the present models cannot predict. Thus, a relationship between η_{rms} and $H_{1/3}$ is required to compare the results of the present models with those of the large-scale experiments.

Outside the surf zone, using field data, Goda (1983) has investigated the relationship between $H_{1/3}/\eta_{rms}$ and a wave nonlinearity parameter $\pi_{1/3}$, defined as

$$\pi_{1/3} = \frac{H_{1/3}}{L} \left(\tanh \frac{2\pi h}{L} \right)^{-3}, \quad (12)$$

where L is the wavelength at the water depth of h . He reported that $H_{1/3}/\eta_{rms}$ increases with increasing $\pi_{1/3}$ when $\pi_{1/3} \geq 0.1$, while $H_{1/3}/\eta_{rms}$ is constant and about 3.8 when $\pi_{1/3} < 0.1$.

Although the relationship between $H_{1/3}/\eta_{rms}$ and $\pi_{1/3}$ for waves out of the surf zone was investigated, no relationship between them for waves in the surf zone has been reported. Hence, I investigated this relationship with the field data for the 11 cases mentioned above, and show the results in Figure 4.

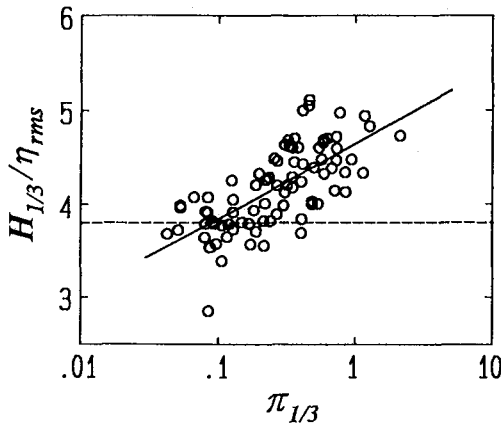


Figure 4 Relationship between $H_{1/3}/\eta_{rms}$ and $\pi_{1/3}$. The solid line shows the relationship obtained with the method of least squares, and the dashed line shows $H_{1/3}/\eta_{rms} = 3.8$.

The value of $H_{1/3}/\eta_{rms}$ in the surf zone increases with increasing $\pi_{1/3}$ when $\pi_{1/3} \geq 0.1$, while $H_{1/3}/\eta_{rms}$ is remaining constant at about 3.8 when $\pi_{1/3} < 0.1$. Thus I assumed that

$$\begin{aligned} H_{1/3}/\eta_{rms} &= 0.349 \ln \pi_{1/3} + 4.648, & \pi_{1/3} \geq 0.1, \\ H_{1/3}/\eta_{rms} &= 3.8, & \pi_{1/3} < 0.1. \end{aligned} \tag{13}$$

The upper equation of Eq.(13) for $\pi_{1/3} \geq 0.1$ was obtained by the method of least squares.

With the relationship expressed as Eq.(13), $H_{1/3}$ predicted by Model 1 and 2 were translated to H_{m0} , and the translated H_{m0} and the predicted Q_b were compared with the values measured in cases 1A, 1B, and 1C of the Delta Flume '93 Experiment (Rivero et al., 1994). The comparisons are shown in Figure 5. In all cases, the values of H_{m0} predicted by Model 1 are almost equal to those predicted by Model 2, and both agree with the measured values quite well. Hence, the discussion is focused on the fraction of breaking waves. On the planar beach of case 1A, the predicted Q_b agree with the measured values although the predicted values are somewhat smaller. On a barred beach of case 1B, Q_b predicted over the trough do not decrease toward the shore, and agree with the measured values, while the present models overestimated Q_b out of the trough. On another barred beach, case 1C, although the predicted values of Q_b decrease slightly toward the shore over the trough, the predicted Q_b agree with the measured values. Out of the trough, the present models also overestimated Q_b . Compared with Q_b predicted by Southgate and Wallace (1994) for cases 1A, 1B and 1C, Q_b predicted by the present models are insensitive to the change in water depth over the troughs, and Q_b variations predicted by the present models are smooth.

Discussion

The models developed in this study incorporate the wave reforming criterion proposed on the basis of field data and the coefficients calibrated with the field data. Through the calibrations of the models, scale effects were recognized in H_b/h_b and in the rate of wave energy dissipation due to wave breaking. In the field, values of H_b/h_b and the energy dissipation seem to be smaller than those in small-scale experiments.

While the cause of the scale effects on H_b/h_b is unknown, the scale effects on wave energy dissipation are considered to be due to the size of the vortex and turbulence generated by wave breaking. Differences in the size of the vortex and turbulence probably results in difference in the energy dissipation process.

Although scale effects on wave energy dissipation due to wave breaking, which strongly influence wave height variation in the surf zone, were recognized in this study, a comparison of wave height variations at different scales on planar beaches (Stive, 1985) revealed that scale effects on wave height variations in the surf zone were negligible. On a planar beach, waves continuously break and few waves reform. On the other hand, at a trough on a barred beach, few waves newly break and some waves reform. The difference in wave conditions seems to result in the difference in the appearance of scale effects.

Although the present models predict well $H_{1/3}$ and Q_b in the surf zone, models employing the wave-by-wave approach, like the present models, have a serious limitation; changes in wave period due to wave decomposition cannot be predicted

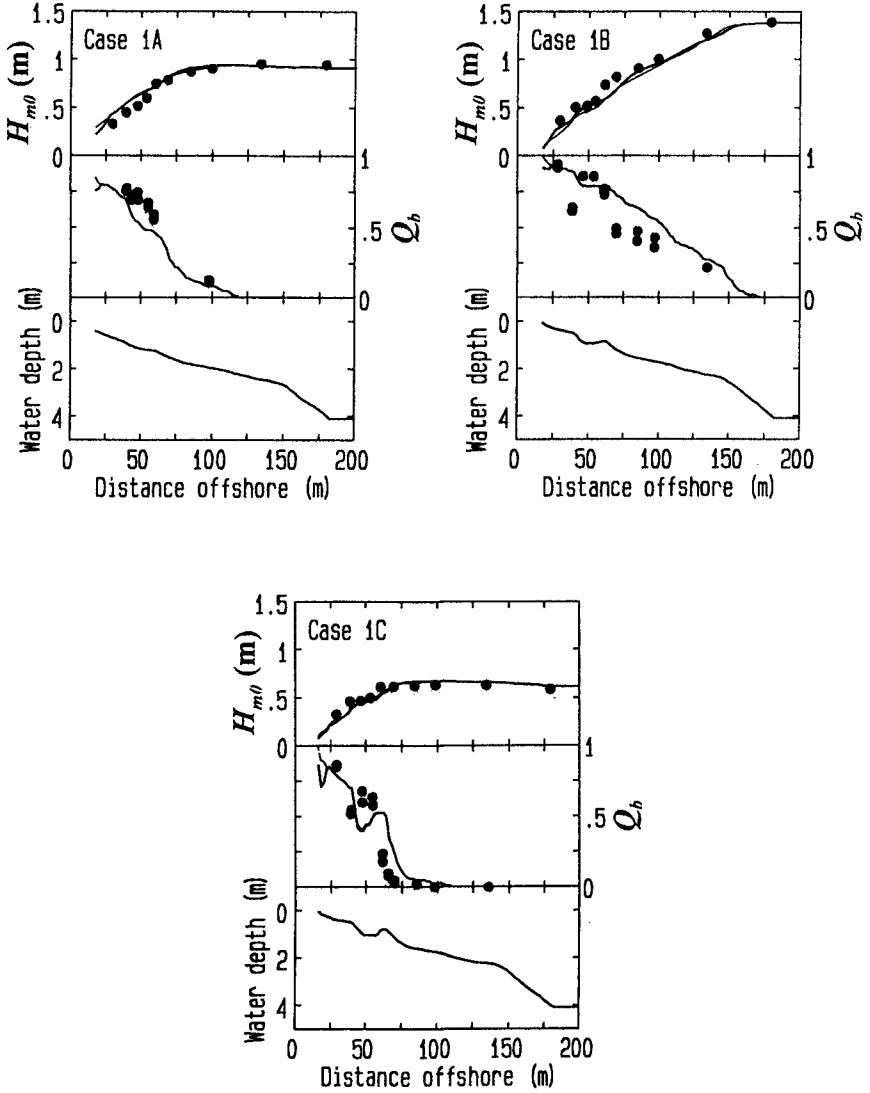


Figure 5 Comparison of H_{m0} and Q_b measured in large-scale experiments (solid circles) and those estimated by Model 1 (thick solid lines) and Model 2 (thin dashed lines).

because the models assume the number of waves to be constant. Wave decomposition frequently occurs over longshore bars, and results in a decrease in wave period. Future improvement of the models will be required to overcome this limitation.

Summary and Conclusions

Models for calculating $H_{1/3}$ and Q_b employing a wave-by-wave approach were developed. The performance of the models containing sub-models for wave breaking and energy dissipation calibrated with experimental data was not satisfactory; Q_b values estimated by these models were smaller than those measured over troughs. New coefficients were therefore introduced, and the models were calibrated with the field data. The models calibrated with the field data predict $H_{1/3}$ and Q_b well over the longshore bars as well as over the troughs. The validity of the models was also verified by comparison with large-scale experiment data.

Acknowledgements

The author would like to thank Mr. Yasushi Ozaki for conducting the field experiments at HORS.

References

- Battjes J.A. and J.P.F.M. Janssen (1978) : Energy loss and set-up due to breaking of random waves, Proc. 16th Coastal Eng. Conf., ASCE, pp.569-587.
- Battjes J.A. and M.J.F. Stive (1985) : Calibration and verification of a dissipation model for random breaking waves, J. Geophys. Res., Vol.90, No.C5, pp.9159-9167.
- Dally W.R., R.G. Dean and R.A. Dalrymple (1985) : Wave height variation across beaches of arbitrary profile, J. Geophys. Res., Vol.90, No.C6, pp.11,917-11,927.
- Dally W.R. (1992) : Random breaking waves: field verification of a wave-by-wave algorithm for engineering application, Coastal Eng., 16, pp.369-397.
- Ebersole B.A. (1987) : Measurement and prediction of wave height decay in the surf zone. Coastal Hydrodynamics, ASCE, pp.1-16.
- Goda Y. (1983) : A unified nonlinearity parameter of water waves, Rep. Port and Harbour Res. Inst., Vol.22, No.3, pp.3-30.
- Horikawa K. and C.T. Kuo (1966) : A study on wave transformation inside surf zone, Proc. 10th Coastal Eng. Conf., ASCE, pp.217-233.
- Kuriyama Y. (1994) : Numerical model for longshore current distribution on a bar-trough beach, Proc. 24th Coastal Eng. Conf., ASCE, pp.2237-2251.
- Kuriyama Y. and Y. Ozaki (1996) : Wave height and fraction of breaking waves in a bar-trough beach -Field measurements at HORS and modeling-, Rep. Port and Harbour Res. Inst., Vol.35, No.1, pp.1-38.
- Nishi R. (1994) : Probability of wave breaking on a plane beach, Proc. of International Symposium: Waves- Physical and Numerical Modelling, pp.773-782.
- Rivero F.J., A.S.- Arcilla and D. Beyer (1994) : Comparison of a wave transformation model with LIP-11D data, Coastal Dynamics '94, ASCE, pp.518-532.
- Roelvink J.A. (1993) : Dissipation in random wave groups incident on a beach, Coastal Eng., 19, pp.127-150.
- Seyama A. and A. Kimura (1988) : The measured properties of irregular wave breaking and wave height change after breaking on the slope, Proc. 21st Coastal Eng. Conf., pp.419-432.
- Shuto N. (1974) : Nonlinear long waves in a channel of variable section, Coastal Eng. Japan, Vol.17, pp.1-12.
- Southgate H.N. and R.B. Nairn (1993) : Deterministic profile modelling of nearshore processes. Part1. waves and currents, Coastal Eng., 19, pp.27-56.

- Southgate H.N. and H.M. Wallace (1994) : Breaking wave persistence in parametric surf zone models, Coastal Dynamics '94, ASCE, pp.543-555.
- Stive M.J.F. (1985) : A scale comparison of waves breaking on a beach, Coastal Eng., 9, pp.151-158.
- Thornton E.B. and R.T. Guza (1983) : Transformation of wave height distribution, J. Geophys. Res., Vol.88, No.C10, pp.5925-5938.

CHAPTER 21

A Parametric Model for Random Wave Deformation by Breaking on Arbitrary Beach Profiles

Hyuck–Min Kweon¹ and Yoshimi Goda²

Abstract

The process of wave energy dissipation after breaking has been investigated with a number of random wave tests. To obtain the data for wave breaking and its deformation, experiments have been conducted by utilizing a horizontal step adjoining to a combined slope of 1/20 and 1/10.

After breaking, the wave height decreases by dissipation but attains a certain value at some distance from the breaking point. Experimental results show that the stable wave height is not constant but affected considerably by the wave period. The study has yielded a general formulation of stable wave height due to the random wave breaking.

A new one-dimensional random wave deformation model is proposed, being coupled with nonlinear shoaling coefficient formula before wave breaking and the new energy dissipation term after breaking. The model is compared with the experimental data, large wave tank data, and field data. It predicts well the wave height deformation and the change of mean water level before and after wave breaking on arbitrary bottom profiles.

1 Introduction

Random wave breaking is one of the most important phenomena in coastal engineering. Since around 1970, various models have been proposed to predict wave height variations in the surf zone. Many models assume planar beach profiles. However, in the natural sea there are step type beach profiles, and longshore bars appear in the breaking zone. Thus, a workable model applicable to arbitrary beach profiles is needed.

The difference among existing models lies on how to express the dissipation

1) Researcher, TETRA Co., Ltd., 2-7 Higashi Nakanuki, Tsuchiura, Ibaraki, 300, Japan

2) Professor, Department of Civil Engineering, Yokohama National University, 79-5 Tokiwadai, Hodogaya-ku, Yokohama, 240 Japan

term. Takayama et al. (1991) proposed a model that calculates the dissipation term with a modified Rayleigh distribution. Battjes and Janssen (1978) represented it with a bore model. The concept of stable wave height after wave breaking was introduced by Dally et al. (1985). That is, after breaking, the wave height decreases by dissipation but attains a stable value at some distance from the breaking point. However, existing models have certain problems. Some models are applicable to plane beaches only, some requires clumsy computation for a joint probability density of wave heights and periods, and some others need calibration with individual wave data in the field.

The present study gives a formulation of the stable wave height due to the random wave breaking and aims at presenting a model simple enough but reasonably accurate.

2 Experiments

2-1 Experimental conditions

Tests were conducted in a glass walled tank of 17 m long, 0.5 m wide, and 0.55 m as shown in Fig. 1. A horizontal step of 6 m long was set, adjoining to the combined slopes of 1/10 with the length 2.0 m and 1/20 with the length 1.0 m. The motion of the wave generator was controlled to absorb waves reflected from slopes. The crushed stone slope of 13/100 was built at the end of horizontal step. Buoyant artificial material was also used as a dissipater together with the crushed stone. The height of horizontal step was 25 cm.

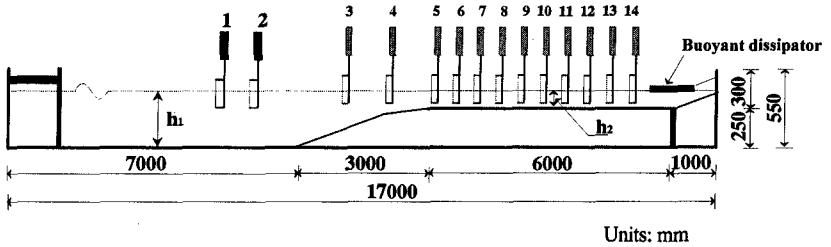


Fig. 1 Experimental section and measuring points for obtaining stable wave height

The wave profiles were recorded at 14 points. Measurements were made at 8 points simultaneously. Gauge #1 was fixed at the distance 3 m from the wave paddle and gauge #2 changed its location depending on the wave period for separation of incident and reflected waves utilizing the Goda and Suzuki (1976) method. Gauge #5 was set at the tip of horizontal step. On the horizontal step, 9 wave gauges from gauge #6 to #14 were set with the interval of 60 cm each.

Experiments are divided into two groups. One is for estimation of the bottom friction effect. The other is for obtaining fundamental data of wave height decay.

Firstly, nonbreaking waves were utilized for the estimation of wave attenuation due to bottom friction on a horizontal step. In total, 18 cases were tested with the water depth on the step of 9 cm and 11 cm, 3 types of spectrum, and 3 combinations of wave periods and heights.

Secondly, wave profiles were measured for obtaining the data of wave height decay by breaking and stable wave height. With 3 different shapes of spectrum, 2 water depths, 3 periods, and 3 wave heights, a total of 54 cases was tested. Wave heights were measured at 14 points as shown in Fig. 1. The sampling interval was 0.05 sec and 8192 data were collected at one run. Wave heights were determined from the surface elevation records using the zero down-crossing method.

2-2 Analysis of wave data

Investigation of wave spectra at gauges #1 or #2 indicated a presence of appreciable low frequency energy. However, there was a noticeable drop of spectral density between the main wave component and the low frequency components. The frequency of spectral density drop was indentified for each case, and the wave components lower than that frequency was filtered out. The filtered wave profiles were produced by the inverse FFT technique.

The frequency range for separating incident and reflected waves was from 0.6 to 3 times the peak frequency. The magnitude of wave attenuation in wave height due to friction was estimated with the data of nonbreaking waves. The wave profiles obtained from gauges #5 to #14 on the horizontal step were analyzed by the FFT method for the Fourier coefficients.

Iwagaki et al. (1965) derived the solution of wave attenuation by bottom friction based on the laminar flow theory. The solution was used to yield the following formula for wave amplitude correction.

$$a_{cor} = a_{mes} \exp(-C_{amp} \epsilon_{b+w} x/L) \quad (1)$$

where

$$\epsilon_{b+w} = (4\pi^2/\beta L)(1 + 1/\psi_0)(\sinh 2kd_0 + 2kd_0) \quad (2)$$

$$\beta = (\pi/\nu T)^{1/2} \quad (3)$$

$$\psi_0 = k B/\sinh 2kd_0 \quad (4)$$

in which a_{cor} is the amplitude of corrected Fourier coefficient, a_{mes} the amplitude of measuring data, C_{amp} (≥ 1.0) an amplifier coefficient, x the distance from the initiation of horizontal step, L the wave length at a local point, T the wave period, k the wave number, d_0 the still water depth, ν the kinematic viscosity of water, and B the width of a water tank. The value of C_{amp} was estimated with nonbreaking waves corresponding to different shapes of spectrum. The results were 1.48 for the JONSWAP-type spectrum with $\gamma=1.0$, 1.74 for the spectrum with $\gamma=3.3$, and 2.19 for an extremely high concentrated spectrum with $\gamma=10.0$, respectively.

The decomposed Fourier amplitudes were corrected for the bottom friction

effect with eq. (1). Then, all the corrected amplitudes were utilized in the inverse FFT method to reproduce wave profiles. Wave heights were determined from the reproduced profiles.

3 Estimation of Stable Wave Heights after Random Wave Breaking

The stable height at some distance from the breaking point is proportional to the local water depth. In the experiments of Horikawa and Kuo (1966) the test bottom profile consisted of a steep slope section of 1 to 5 followed by a less steep slope (up to 1 to 20) or a horizontal section. The incident waves were forced to break at the end of the steep slope section and the wave height decay after breaking was monitored. It was fitted by exponential functions toward a stable wave height that is equal to about 0.4 times of the local water depth (d_0) for all conditions. The results of Horikawa and Kuo were interpreted by Dally et al. (1985) in terms of a wave height stabilizing at a constant value (cessation of breaking) lower than that related to the initiation of breaking.

The present study re-analyzed the Horikawa and Kuo (1966) data, by fitting the following exponential function:

$$H = H_0 \exp(-\varepsilon_{b+w}x/d_0) + H_S \tag{5}$$

where H_0 is the wave height at the initiation of the horizontal step. The stable wave height H_S was estimated with a bisection method.

All the stable wave heights were classified by water depth and wave period of 20 groups. Dally et al (1985) assumed that the stable height is proportional of water depth only. However, the height-to-depth ratio is not constant but affected considerably by the wave period as shown in Fig. 2 for the cases of regular waves. As shown in Fig. 2, the longer the wave period is, the higher the stable wave height is.

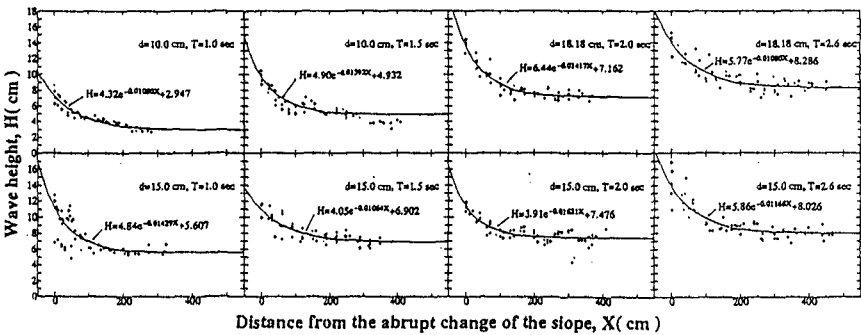


Fig. 2 The effect of wave period to a stable wave height

With the same procedure, the stable wave heights after random wave breaking

were estimated. In the random wave system, however, the stable wave heights have different levels corresponding to the definition of representative wave heights such $H_{1/3}$ and H_{rms} . The experimental results are plotted in Fig. 3.

Figure 3 indicates that the stable wave height is a function of the relative water depth d_0/L_0 . For the experimental data, the following formulation has been applied in an analogy to Goda's breaker index:

$$H_s = \Gamma d \quad (6)$$

where

$$\Gamma = A(d_0/L_0)^{-1} [1 - \exp(-1.5\pi d_0/L_0)] \quad (7)$$

$$d = d_0 + \bar{\eta} + \bar{\xi} \quad (8)$$

in which A is the coefficient for stable wave height. The symbol d_0 refers to the still water depth, L_0 the deep water wave length corresponding to the significant wave period, $\bar{\eta}$ the wave set-up, and $\bar{\xi}$ the representative amplitude of surf beat.

The curves in Fig. 3 represents the computation with eqs. (6) to (8).

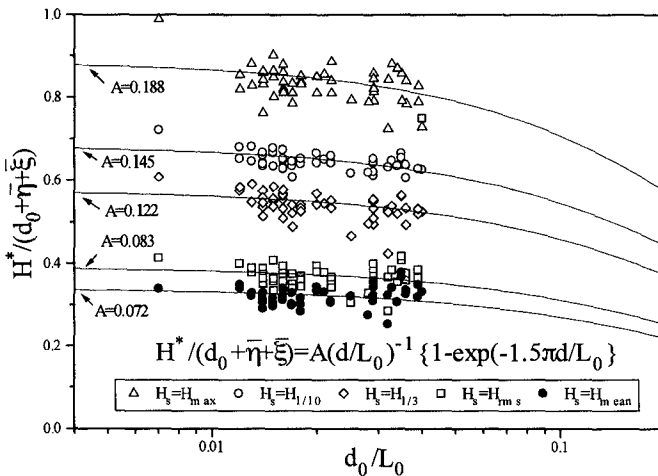


Fig. 3 The general form of stable wave heights due to breaking of random wave

The total water depth including the representative surf beat amplitude was assumed as below.

$$d_0 + \bar{\eta} + \bar{\xi} = d_0 + \chi \bar{\eta} \quad (9)$$

By assuming the value of χ at 1, 2, and 3, the least square method was applied for the relationship between the ratio of the significant wave height to the total depth and the relative water depth. It was found the linear fitting has the least value when χ is equal to 2. That means, it is best to set the representative surf beat amplitude $\bar{\xi}$ equal to the

wave set-up $\bar{\eta}$.

Table 1 lists the best fitted values of stable wave height coefficient A in eq. (7), for various representative wave heights.

Table 1 The stable wave height coefficients of A for various representative waves.

H	mean	rms	1/3	1/10	max
A	0.072	0.083	0.122	0.145	0.188

4 Modeling of Random Wave Deformation

4-1 Governing equation

Dally et al (1985) proposed a model to describe wave decay in the surf zone assuming that the energy dissipation per unit surface area due to breaking is proportional to the excess energy flux relative to a stable energy flux, which is depth dependent.

$$\frac{\partial EC_g}{\partial x} = -\frac{K_d}{d_0} \left[EC_g - (EC_g)_s \right] \quad (10)$$

where E is the energy density, C_g the group velocity, x the onshore coordinate, K_d the wave decay coefficient, and d_0 the still water depth. The energy density and group velocity are given by the linear theory relationships.

Rewriting eq. (10) in terms of wave height, it becomes as below:

$$\frac{\partial [H^2 C_g]}{\partial x} = -\frac{K_d}{d} C_g [H^2 - H_s^2] \quad (11)$$

where $H_s = \Gamma d$.

The present model adopts eq. (11) as the basis of computation and employs the stable wave height expressed by eq. (7). The wave decay coefficient K_d is specified with a gradually varying value, the treatment of which is discussed in detail in the next section.

The wave-induced set-up and set-down are determined from the time-averaged momentum balance equation neglecting inertial effects and bed-shear stress, as follows :

$$\frac{d\bar{\eta}}{dx} = -\frac{1}{\rho g(d + \bar{\eta})} \frac{dS_{xx}}{dx} \quad (12)$$

in which S_{xx} is the onshore radiation stress. The radiation stress component S_{xx} for the organized wave motion is calculated by the linear theory as

$$S_{xx} = \frac{1}{16} \rho g H_{rms}^2 \left[1 + \frac{4kd}{\sinh 2kd} \right] \tag{13}$$

where ρ is the density of water, g the acceleration due to gravity, k the wave number, and d the total water depth ($d = d_0 + \bar{\eta} + \bar{\xi}$).

4-2 Treatment of wave decay coefficient

The dissipation term with the wave decay coefficient K was originally proposed by Dally and Dean (1985) who gave a constant value. For the analysis of random wave deformation, however, a modification is made on the decay coefficient in such a way that its value gradually increases over some distance.

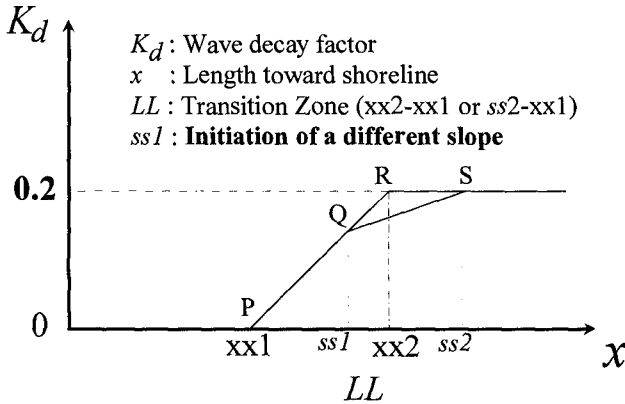


Fig. 4 Treatment of wave decay coefficient, K_d

The modification reflects the fact that waves have the different locations of initiation of breaking in a random wave system. Figure 4 shows the treatment of wave decay coefficient. For a single slope, K_d rises along the line PR over the locations between $xx1$ and $xx2$ and then takes a constant value of 0.2. The distance between $xx1$ and $xx2$ is calculated as the horizontal length corresponding to the change in water depth equivalent to the vertical distance of H_0' . If the slope becomes milder at the location $ss1$, then K_d follows the line QS. By introducing such a gradually varying wave decay coefficient, it becomes possible to calculate the wave decay successfully with the representative waves of a random wave system. It is also possible to analyze the wave deformation across beaches of arbitrary shapes.

The model has been calibrated with the Goda model (1975) for random wave breaking on a plane beach. The maximum value for the wave decay coefficient K_d and the transition length LL are calibrated to yield the best agreement between the present and Goda models. The comparison of the present and Goda model is shown in Fig. 5.

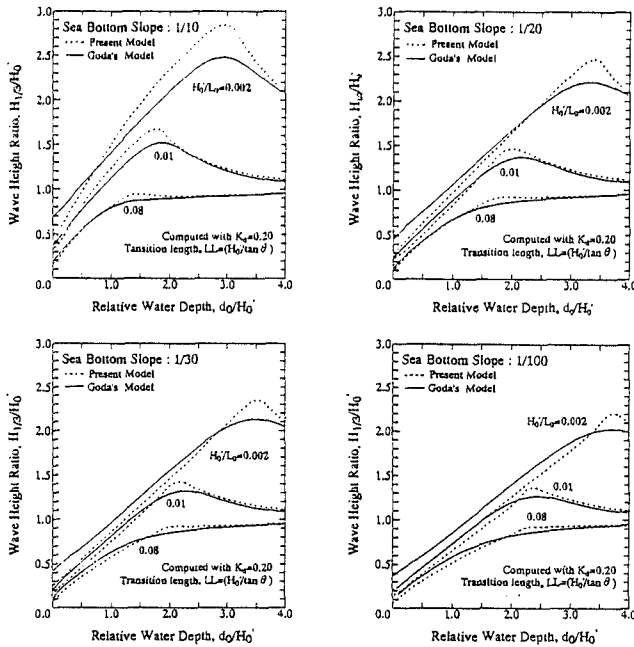


Fig. 5 Comparison of the present model with $K_d=0.2$ and the Goda model on plane beach

4-3 Procedure of calculation

Calculation is proceeded by a forward-difference numerical solution scheme from the offshore end of the numerical grid. The incident wave conditions of the model are the representative wave heights and the significant wave period. The non-linear wave shoaling is considered in the model.

Because eq. (11) produces a linear wave shoaling before wave breaking, the resultant wave height is amplified by the factor β of the following

$$\beta = K_s / K_{s0} \tag{14}$$

where

$$K_s = K_{s0} + 0.0015(d_0 / L_0)^{-2.87} \left(H_0' / L_0 \right)^{1.27} \tag{15}$$

in which K_s is a nonlinear shoaling coefficient, K_{s0} the linear shoaling coefficient, and H_0' the equivalent deep water significant wave height. The nonlinear shoaling coefficient of eq. (14) is obtained by the trial and error method as an approximation to Shuto's (1974) shoaling coefficient for non-breaking nonlinear wave based on cnoidal wave theory.

For initiation of wave breaking, Goda's breaking index of the following is adopted:

$$H_b = \Gamma_b d \quad (16)$$

where

$$\Gamma_b = A(d_0/L_0)^{-1} \left\{ 1 - \exp \left[-1.5 \frac{\pi d_0}{L_0} \left(1 + 15 \tan^{4/3} \theta \right) \right] \right\} \quad (17)$$

in which H_b refers to the respective breaker heights of representative waves such as $H_{1/3}$ and A is the coefficient listed in Table. 1.

After wave breaking is initiated, the wave decay coefficient K_d in eq. (11) is assigned the value which rises up following the path PR or PQS and the energy dissipation is evaluated. For the calculation of nonlinear wave decay height, the stable wave height is modified as

$$(H_s)_A = \frac{1}{1 + \beta_b} (H_s)_F \quad (18)$$

where $(H_s)_A$ is the linear stable wave height, $(H_s)_F$ the non-linear stable wave height which was attained by experiments as in eq. (6), and β_b is the amplification factor of shoaling coefficient ratio at the initiation point of breaking.

After wave breaking has occurred, a check is always made for the possibility of wave reformation. That is, if the calculated wave height falls below the stable wave height even though the K_d does not attain the maximum value of 0.2, K_d is reset as zero at that point. Then calculation starts again in the process of shoaling change.

Calculation of radiation stress by eq. (13) is needed before that of wave set-up by eq. (12). The root-mean-square wave height is calculated from $H_{1/3}$ with the assumption of Rayleigh distribution.

$$H_{rms} = H_{1/3}/1.416 \quad (19)$$

The computation of wave height and set-up is carried out twice. In the first run, the wave set-up at the shoreline where the still water depth is zero is linearly extrapolated from the adjacent two grid points. In the second run, the wave set-up and representative surf beat amplitude are added to the still water depth to yield the total depth. The present model finishes the calculation for all points at the second run because the difference of wave set-up between the 2nd and 3rd runs becomes below 2%.

5 Verification of the Model

5-1 Laboratory tests on a horizontal step adjoining to slope

Figure 6 shows the comparison of the model calculation and experimental data obtained from the present study. The increment of x in the calculation is 5 cm. The data with the JONSWAP-type spectrum ($\gamma=3.3$) are selected for comparison. Three

sets of data in which the wave steepness is almost the same but the water depth is different are shown here. As seen in Fig. 6, even when the water depth is extremely shallow, the model predicts the wave decay height quite well.

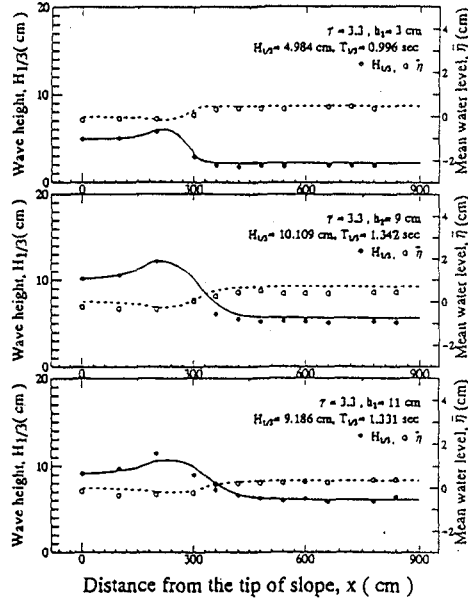


Fig. 6 Comparison of the model and experimental data on a horizontal step adjoining to slopes

5-2 Laboratory tests on a bar type beach profile

For obtaining data in a bar type beach profile, experiments were conducted with the section shown in Fig. 7. The wave profiles were measured at 14 points. Waves were expected to break between gauges #3 to #5 and to attain stable wave height between gauges #9 to #11. After waves become stable, waves start a shoaling change and re-break around gauges #12 to #13. Gauges #4 to #13 were set with the interval of 50 cm. The distance between gauges #13 and #14 was changed depending on wave period from 50 cm to less than 50 cm. The wave conditions included 3 diffe-

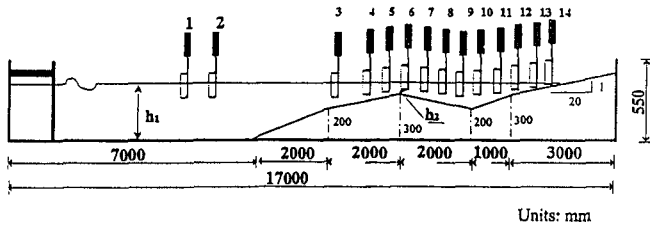


Fig. 7 Experimental setup for bar type beach profile

rent shapes of spectrum, 2 water depths, 3 wave periods, and 3 wave heights, and 54 cases were tested totally. The water depth in front of the wave paddle was $h_1=39$ cm and the depth on top bar was $h_2=9$ cm.

A selected set of experimental data with the JONSWAP-type spectrum ($\gamma=1.0$) is compared with the model calculation in Fig. 8. As shown in Fig. 8, the significant wave height (closed circles) shows good agreement except for the case with the largest wave steepness (top figure). However, the root-mean-square wave height (closed triangle) is predicted well by the model. During the wave decay height, it arrives a stable wave and increase with shoaling change. And it breaks again and decays toward the shoreline

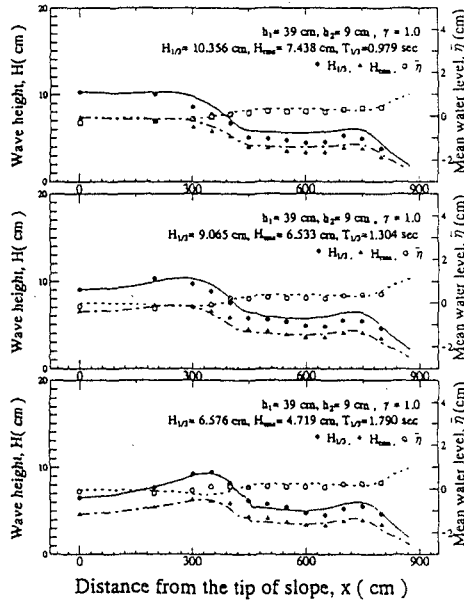


Fig. 8 Comparison of the model and data on a bar type profile

Moreover, variation of wave set-up (open boxes) is predicted quite well by the present model. Though not presented in this paper, experimental data with other spectral shapes have also shown good agreement with the calculation by the present model. Thus, the model is applicable broadly to different shapes of spectrum.

5-3 SUPERTANK data

Four cases from the SUPERTANK Data Collection Project (Kraus et al. 1992) were selected to validate the random wave deformation model for normally incident waves under controlled conditions. SUPERTANK was conducted to investigate cross-shore hydrodynamic and sediment transport process using the large wave tank at Oregon State University, Corvallis, Oregon. In this study, the statistical data are utilized and no spectral information is used.

In the case A0517A, a pronounced bar was present with the crest located at a water depth of about 0.6 m. Case A0914A belongs to the same run as the previous case, but the bar was located further offshore. In the case S0913A a narrow-crested mound was constructed. A broad-crested mound was built in the offshore in the case S1208B.

Table 2 Wave conditions for compared SUPERTANK data

Run Number	Case number	Incident wave height		Wave period (sec)
		<i>rms</i> (m)	$H_{1/3}$ (m)	
ST10	A0517A	0.56	0.79	2.9
ST10	A0914A	0.51	0.71	3.8
STJ0	S0913A	0.45	0.63	2.8
STK0	S1208B	0.45	0.64	2.7

The data of $H_{1/3}$, H_{rms} and $\bar{\eta}$ are plotted in Fig. 9 with the symbols of closed boxes, closed circles, and open circles, respectively. The computed results are shown by the dash-dot lines, continuous lines, and dashed lines, respectively.

In the case A0517A, the wave breaking by computing starts prior to the data. The significant wave height is predicted well by the model. Case A0914A belongs to the same run as previous case but has longer wave period. The decay in H_{rms} and $H_{1/3}$ through the surf zone are well produced. However, it seems that the wave height nearest to the bar is affected by concentrating of wave breaking. The starting of set-up is affected by the initiation of breaking points.

In the case S0913A, the decays in H_{rms} and $H_{1/3}$ are faithfully produced by the model. However, the wave set-up is lower than the computation. In the case S1208B which has the broader bar, the model overestimates the wave heights around crest of the bar. It seems that on the crest the waves are not strongly affected by the wave nonlinearity.

5-4 Field data

Hotta and Mizuguchi (1980) carried out field measurements in 1978 at Ajigaura beach facing the Pacific Ocean located at the southern end of Tokai coast about 200 km from Tokyo. A breaker bar was present in the surf zone as shown in Fig. 10. In the nearshore zone, about sixty poles were placed on the sea bed at intervals of about 2 m normal to the shore over a total distance of 120 m. The significant wave at the latter pole was about 0.8 m in height and 9.4 sec in period.

Figure 10 shows the measured and computed wave heights. The computed wave heights before breaking are greater than the measured ones. The measured wave heights do not increase much in the zone between 120 to 100 m. The reason is not quite clear. It may be related to the bathymetry of the field. Dally and Dean(1986) also made comparison of their model and the data. Their prediction shows underestimation of the data because they used the linear shoaling.

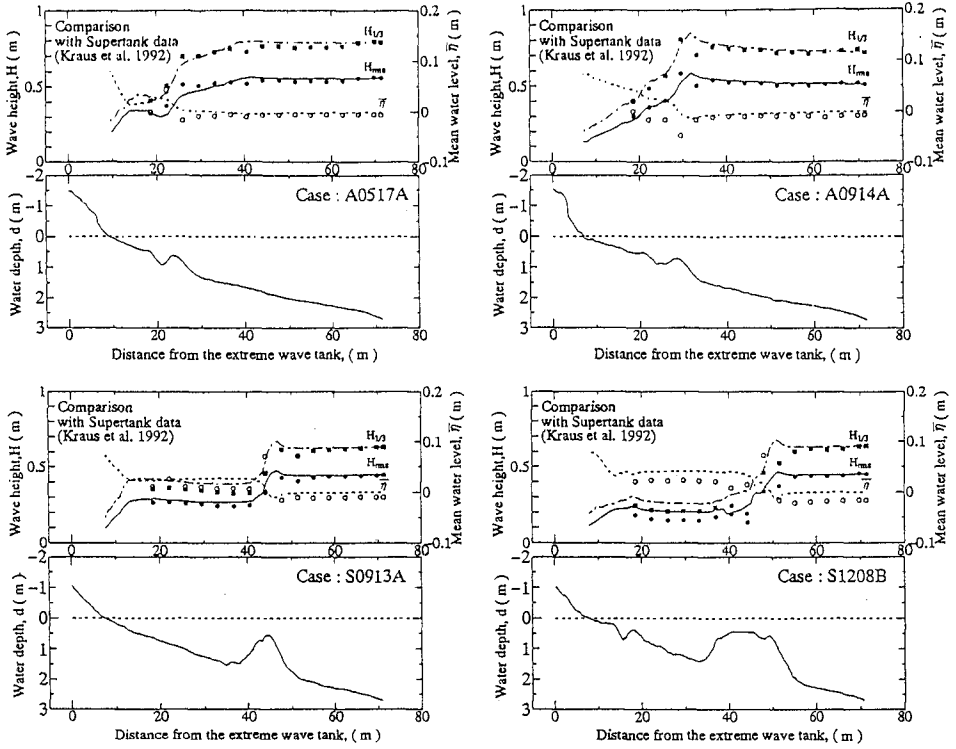


Fig. 9 Comparison of the model and SUPERTANK data

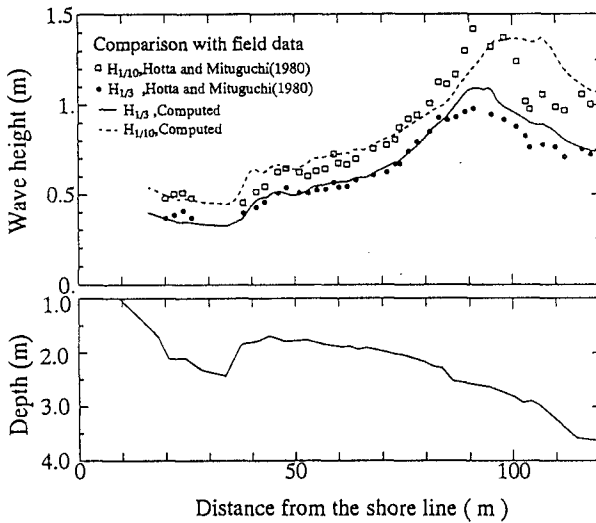


Fig. 10 Comparison of the model and field data

6 Conclusion

The merits of the present model are summarized as follows:

- 1) The model is applicable to any shapes of bottom profiles.
- 2) It requires the input data of incident wave heights and periods only without necessity of coefficient calibration with field data.
- 3) Its computation time is minimal because it deals with representative waves directly.

In addition, the model can easily be programmed as a subroutine for a large scheme to drive numerical models of nearshore circulation and sediment transport problems.

Acknowledgment

The authors would like to thank Dr. Kraus, Dr. Smith and all the members who participated the SUPERTANK project. They offered valuable data for verification of the present model.

References

- Battjes, J. A. and J.P.F.M. Janssen, 1978. Energy loss and setup due to breaking of random waves. Proc. 16th Coast. Eng. Conf., pp.567-587.
- Dally, W.R., 1992. Random breaking waves : field verification of a wave-by-wave algorithm for engineering application, Coastal Eng., Vol. 16, pp. 369-397.
- Dally, W.R. and R.G Dean, 1986. Transformation of random breaking waves on surf beat. Proc. 20th Coast. Eng. Conf., Vol. 1, pp. 109-123.
- Dally, W.R., R.G. Dean, and R.A. Dalrymple, 1985. Wave height variation across beaches of arbitrary profiles, J. Geophys. Res., 90(C6), pp. 11917-11927.
- Goda, Y., 1975. Irregular wave deformation in the surf zone. Coast. Eng. Jpn, Vol. 18, pp. 12-26.
- Mase, H. and Y. Iwagaki, 1982. Wave height distribution and wave grouping in surf zone. Proc. 18th Coast. Eng. Conf., pp. 58-76.
- Horikawa, K and C.T. Kuo, 1966. A study on wave transformation inside surf zone. Proc. 16th Coast. Eng. Conf., Vol. 1, pp. 217-233.
- Hotta, S. and M. Mizuguchi, 1980. A field study of waves in the surf zone. Coastal Eng. Jpn., Vol. 23, pp. 59-81.
- Iwagaki, Y. and Y. Tsuchiya, 1966. Laminar damping of oscillatory waves due to bottom friction. Proc. 10th Coast. Eng. Conf., pp. 149-174.
- Kraus, N. C., J. M. Smith, and C. K. Sollitt, 1992. SUPERTANK laboratory data collection project. Proc., 23th Coast. Eng. Conf., pp. 2191-2204.
- Larson, M., 1995. Model for decay of random waves in surf zone. J. Wtrwy., Port, Coast., Oc., Engrg., ASCE, pp. 1-12.
- Shuto, N., 1974. Non-linear long waves in a channel of variable section. Coastal Eng. Jpn., Vol. 17, pp. 1-12.

CHAPTER 22

Generation Characteristics of Wave Sounds as a Factor of Beach Amenity

Hitoshi Murakami¹, Sadahiko Itoh², Yoshihiko Hosoi³,
Hideo Araki⁴ and Tsuyoshi Koyabu⁵

Abstract

This study deals with the comfortableness of wave sounds from physiological and psychological aspects. Firstly, the difference of wave sound generation mechanism between plunging and spilling breakers is discussed on basis of the variation characteristics of sound pressure level and the volume of air bubbles in water. Secondly, the comfortableness of wave sounds is investigated based on the generation characteristics of the brain wave and the result of questionnaire surveys of auditory test.

Introduction

Many artificially nourished beaches have been created as part of the improvement works related to coastal environment. The visual, auditory and olfactory factors are considered important factors of beach amenities.

Recently, much importance has been attached to the roles of desirable sounds in environment. The term "Sound Scape" named by R.M.Schafer(1977) has been used in much the same way as the term "Land Scape". More attention must be paid to the sound environment of the coastal zone.

As a matter of fact, the sensory tests on psychological responses to wave sound

-
- 1.Fac.of Eng.,The Univ.of Tokushima, Minami-josanjima,Tokushima 770,Japan.
 - 2.Fac.of Eng.,Kyoto Univ.,kyoto 606-01,Japan.
 - 3.Fac.of Eng.,Tottori Univ., Koyamacho-minami,Tottori 680,Japan.
 - 4.Fac. of Integrated Arts and Sciences., The Univ. of Tokushima, Minami-josanjima, Tokushima 770,Japan.
 - 5.Nikken Consultants Inc., Higashi-gotanda,Shinagawa-ku,Tokyo 141,Japan

have shown that the auditory factor such as breaking wave sounds is one of the most important factors affecting the amenities of the beach environment just as much as visual and olfactory factors(Nadaoka et al,1991a,b. Murakami et al, 1991). Authors have also investigated the characteristics of breaking wave sounds in laboratory tests and field observations(Murakami et al,1993). However, the exact physical mechanism of sound generation due to wave breaking remains under debate.

The purpose of this study is to investigate fundamental characteristics of the wave sound generation and to examine the difference of the sound generation mechanism in two types of wave breaking, the plunging and spilling breakers. Furthermore, the relationship between wave sound and its comfortableness is discussed from physiological and psychological aspects.

Characteristics of Wave Sound Generation of Air Bubbles in Wave Breaking

1) Experimental Methods

A wave tank with a pendulum-type wave generator at one end, which was 30m long, 1m wide and 0.9m deep, was used as shown in Fig.1. The bottom slopes θ were 1/10 and 1/15, and 45 kinds of waves which had different surf similarity parameters ξ_0 were induced.

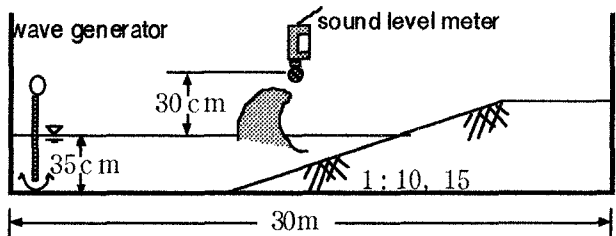


Fig.1 Experimental Apparatus

Table 1 Experimental Conditions

beach slope $\tan\theta$	wave period T (sec)	equivalent deepwater waveheight H_0' (cm)	surf similarity parameter ξ_0
1/10	0.8~2.0	1.8~13.4	0.397~2.045
1/15	0.8~2.0	2.9~13.3	0.214~0.894

Wave sounds were recorded by a sound level meter at the upper point 30cm from still water surface. The video pictures of breaking waves were taken simultaneously at the distance of 1.5m from the side wall of wave tank to observe air bubbles in water induced by wave breaking. The water depth h was kept at a constant of 35 cm. The wave period T was changed from 0.8 to 2.0 sec.

Experimental conditions of wave breaking were shown in Table 1.

The surf similarity parameter ξ_0 as a breaker type index is defined as follows(Battjes,1974):

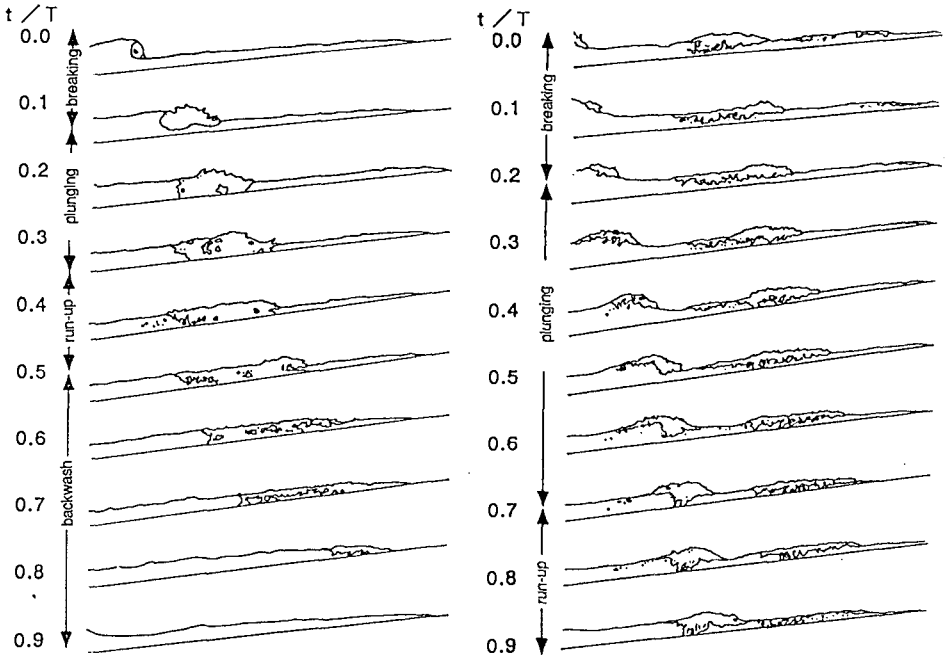
$$\xi_0 = \tan \theta / \sqrt{H_0'/L_0}$$

Spilling breaker, if $\xi_0 < 0.5$. Plunging breaker, if $0.5 < \xi_0 < 3.3$. Surging breaker, if $\xi_0 > 3.3$. In which, H_0' ; equivalent deepwater wave height, L_0 ; deepwater wave length. ξ_0 in this study are in the range of 0.2-2.0 . This means the experiments include both spilling and plunging breakers.

2) Characteristics of Generation of Air Bubbles and Wave Sounds

Fig.2 shows an example of the wave breaking process and air bubble generation during a wave period for the plunging and spilling breaker, respectively. Nondimensional phase $t/T=0$ means the onset of wave breaking. Generally, the behavior of wave breaking is divided into the following four phases; breaking , plunging, run-up and backwash.

For the plunging breaker, the wave begins to break and folds over air at the breaking phase. At the plunging phase, a large quantity of air bubbles are generated.



(1) plunging breaker

($H_0'/L_0=0.01, \tan \theta =1/15$)

(2) spilling breaker

($H_0'/L_0=0.12, \tan \theta =1/15$)

Fig.2 Breaking Process and Air Bubble Generation

Subsequently air entrainment occurs and the air bubble cloud reaches the sea bottom. After that , the air bubble cloud spreads out gradually to create the patch of foam at the run-up and backwash phases.

On the other hand, for the spilling breaker , the air bubble cloud induced by the former wave breaking remains without appearance over a wide area, even when a new wave begins to break at the wave crest in the breaking phase. The air bubble cloud near the wave crest spreads radially in every direction at the breaking and plunging phases. Finally, it combines with the former air bubble cloud .

From this experiment, the difference of generation and disappearance mechanism of air bubbles for the two types of wave breaking was revealed to

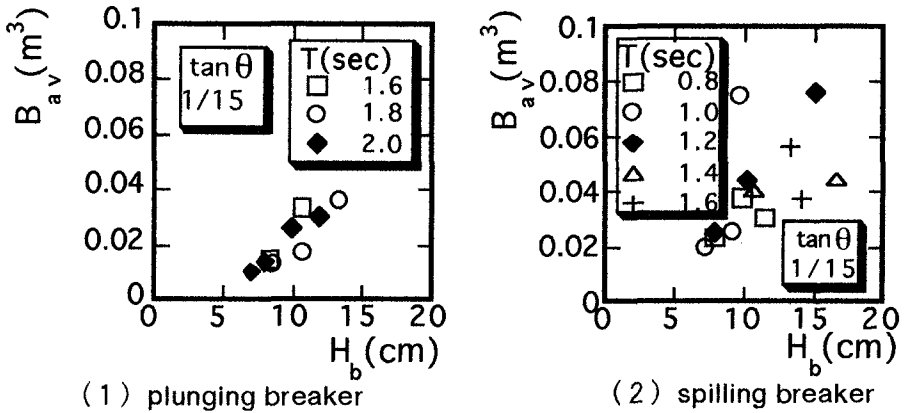


Fig.3 Relationship between B_{av} and H_b

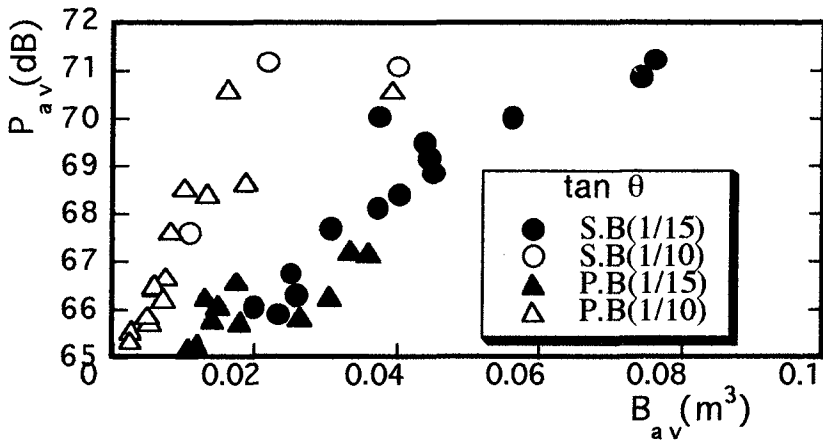


Fig.4 Relationship between P_{av} and B_{av}

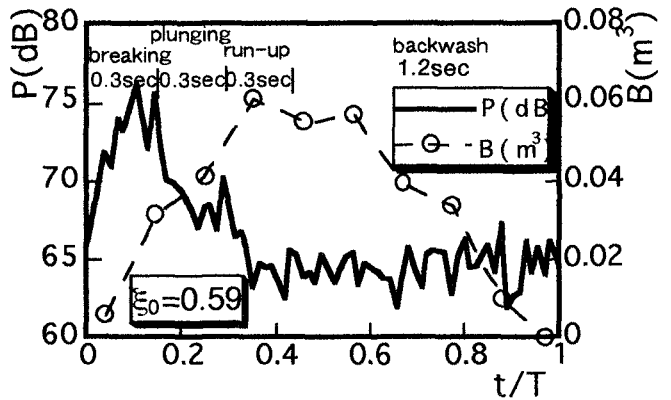
some degree. The volume of air bubbles, however, depends on the breaking wave height. In addition, the wave sound must be related to the volume of air bubbles.

Fig.3 shows the relationship between the average volume of air bubbles per one wave B_{av} and a breaking wave height H_b in the case of the bottom slope 1/15. It is difficult to measure directly a volume of air bubbles. The volume of air bubbles B at an arbitrary phase of wave is conveniently defined so that B can be obtained by multiplying a bubble cloud cross section area projected on the glass wall of wave tank with a wave tank width. An average volume of air bubbles B_{av} was obtained from the average value at the 5 different wave phases in a one wave period.

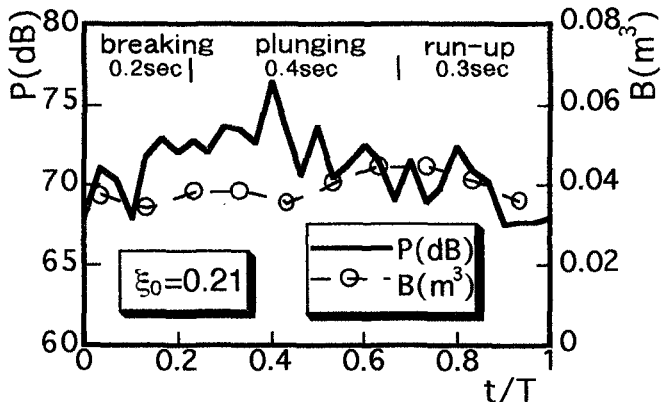
It can be seen that B_{av} increases with an increase of H_b . However, it shows a partially opposite tendency in the spilling breaker's long period wave. The relationship between an average sound pressure level P_{av} and B_{av} is shown in Fig.4. P_{av} increases with an increase of B_{av} regardless of the breaking type. The rate of increase of P_{av} , however, is more distinct with a steeper bottom slope.

The sound pressure level is also closely related to the volume of air bubbles.

Furthermore, let us consider the correlation between



(1) plunging breaker ($H'_0/L_0 = 0.01, \tan\theta = 1/15$)



(2) spilling breaker ($H'_0/L_0 = 0.12, \tan\theta = 1/15$)

Fig.5 Temporal fluctuation of P and B

the variation of sound pressure level P and the volume of air bubbles B in time in order to clarify the sound generation mechanism .

Fig.5 shows the temporal fluctuations of P and B for two types of wave breakers. Let us first consider the variation characteristics of P for the plunging breaker. P takes the maximum value in the middle of breaking and plunging phases. P decreases rapidly at the run-up and backwash phases. On the other hand, B takes the maximum value in the middle of run-up and backwash phases. It is significant that the maximum sound is not generated when the volume of air bubbles is at a maximum . It means a dominant sound is generated only in the short time when a water wave plunges on to the water surface, however, air bubbles are only slightly generated. Subsequently, even if the volume of air bubbles increases gradually after breaking, these bubbles are not an important factor in the generation of dominant sounds.

Secondly, let us consider the characteristics of the spilling breaker. P does not fluctuate so noticeably, though it increases slightly at the breaking phase in comparison with other phases. The fluctuation of B is smaller than that of P . It can be recognized that the mechanism of wave sound generation for the spilling breaker is attributed to the strong turbulence and bursting of air bubbles in the vicinity of the water surface.

Comfortableness of Wave Sounds due to Auditory Tests

1) Experimental Methods

In order to investigate the comfortableness of wave sounds, the brain wave test and questionnaire surveys were carried out simultaneously with 8 students of the University of Tokushima being the subjects.

Fig.6 shows an outline of brain wave measurement . First of all, a subject listened to various kinds of recording tapes of wave sounds on the headphones. The brain waves at the central zone Cz and occipital one Oz were measured and recorded in the FM data recorder whilst the subject's eyes were open for 3-6 min. The brain

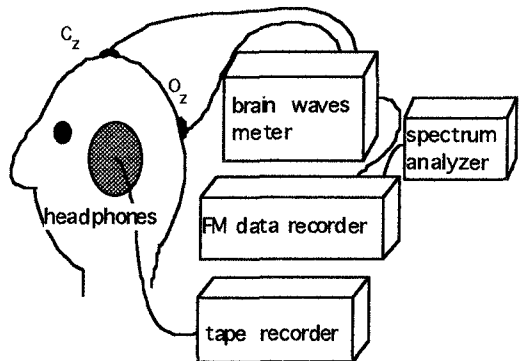


Fig.6 Outline of Brain Wave Measurement

Table 2 Experimental Conditions of Auditory Tests

sound factor	wave sound		subject
	kind	condition	
strength	field observation sounds	$P_{av}(dB)$ 54,62,74	students male4,female1
wave period	artificial sound	$T(sec)$ 4,6,8,10,12	male7
sound tone	field observation sounds	$f^{-1/2}, f^{-1}$	male8

wave spectrum was obtained by a spectrum analyzer. In addition, the questionnaire surveys were conducted to find the most desirable sound by the same subjects.

The experimental conditions used in the brain wave tests and questionnaire surveys are shown in Table 2. Field observation wave sounds and artificial sounds made from white noise by FM radio were used as wave sounds in the tests. The effects of sound strength, sound wave period and sound tone as physical sound factors on the comfortableness of wave sounds were examined. The sound tone spectra at the backwash phase used here is shown in Fig.7. One is having minus 1/2 power of frequency f at the higher frequency region. The other is having minus 1st power of frequency f .

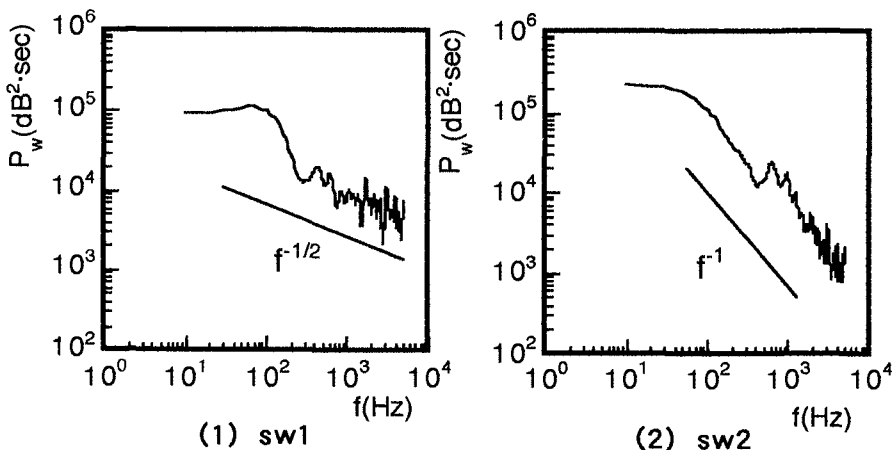


Fig.7 Sound Tone Spectra at Backwash Phase

2) Effects of Wave Sound Strength on Comfortableness

Fig.8 shows the relationship between the average power of α -wave(8-13Hz) P_w and an average sound pressure level SP_{av} over 6 min. Sign N in the transverse axis means non-sound. P_w decreases slightly with an increase of SP_{av} at the central zone Cz. On the other hand, P_w at the occipital zone Oz has the maximum value for the 62 dB sound. Especially, it should be noted that the power of α -wave for the 74 dB sound is smaller than that for the two others.

Fig.9 shows the result of a questionnaire survey on the relationship between the

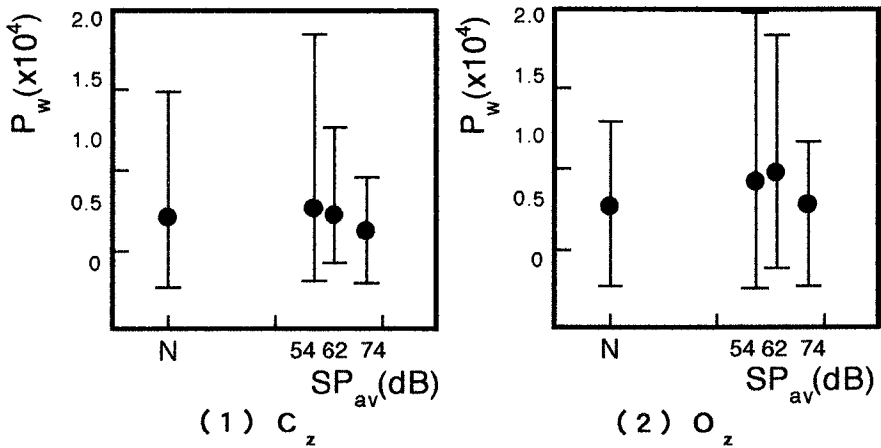


Fig.8 Relationship between P_w and SP_{av}

comfortableness and the average sound pressure level P_{av} . The vertical axis indicates the number of persons, who gave the most suggestive response from the three sounds. From this test, the 62dB sound is the most comfortable of the three which corresponds to as the tendency of the brain wave tests at Oz. No one felt any comfortableness from on the 74dB sound to the subjects. The 74dB sound seemed to be felt as if it were stormy sea.

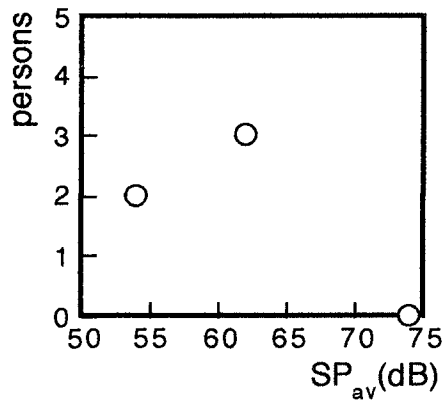


Fig.9 Effect of SP_{av} on Comfortableness

3) Effects of Sound Wave Period on Comfortableness

The authors have already pointed out from the questionnaire survey of the 67 students that the subjects feel the comfortableness for 6-8 sec of the sound wave period, but do not feel the comfortableness under 6 sec of the wave period. It has been pointed out this desirable value is nearly equivalent to the period of our breathing(Murakami et al,1992).

Fig.10 shows the effect of the sound wave period on the brain wave. The power of α -wave P_w has the muxmum value in 8 -10 sec of wave period in both figures. In the case of the wave period being under 6 sec, P_w has less than the power at non-sound.

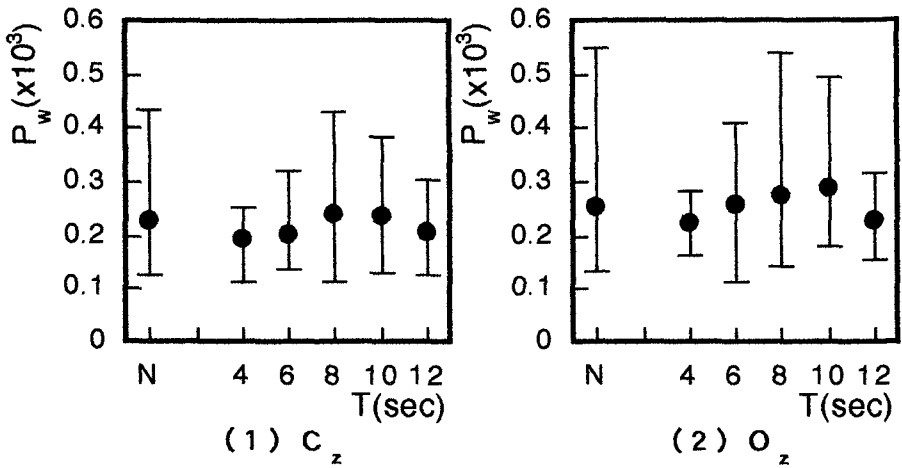


Fig.10 Relationship between P_w and T

Fig.11 shows the results of the points obtained from the questionnaire survey of the five grade estimations with a score of 5 to 1 points for each wave period. The tendency in this figure is similar to the result of brain wave tests, though the tendency of the two in 12 sec of the wave period is different.

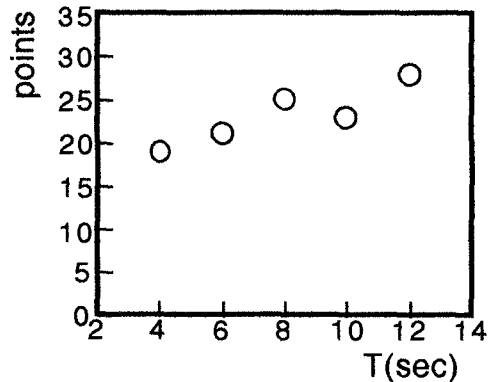


Fig.11 Effect of T on Comfortableness

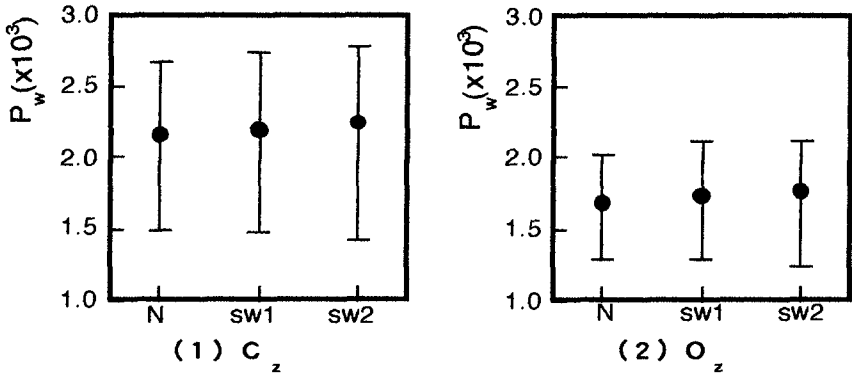


Fig.12 Effect of Power Spectrum Shape on Comfortableness

4) Effects of Sound Tone on Comfortableness

The subjects listened to wave sounds which had two kinds of sound tone spectra as shown in Fig.7.

Fig.12 shows the effects of wave sound tone on the α -wave power. As a result, it can be seen that the power on sw2 is only slightly bigger than that on sw1. It is widely noted the α -wave power increases in the case of sound tone with the minus 1st power of frequency at a higher frequency region.

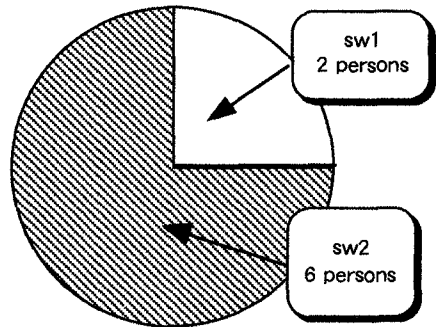


Fig.13 Comfortableness of Sound Tone

Fig.13 shows the comparison of the comfortableness of two kinds of sound tone on the basis of the questionnaire survey. The sound tones with sw2 and sw1 are in the ratio 6:2. This is the same tendency as the result of the brain wave test.

Conclusion

The generation mechanism of wave sound for two types of wave breakers was discussed on the basis of measurement of sound pressure level and volume of air bubbles. The effects of sound factors on comfortableness were examined from the physiological and psychological aspects. As a result, the wave sounds should be emphasised as being one of the most important factors of beach amenities. The

results are summarized as follows.

1) The difference of the sound generation mechanism between the plunging and spilling breakers was clarified. It was confirmed the behavior of air bubbles generated by wave breaking was closely connected with the characteristics of wave sounds.

2) It was proved that the comfortableness of wave sounds was affected by the factors of sound pressure level, sound wave period and sound tone and so on through the power of α -wave in the brain wave test and questionnaire surveys.

Acknowledgement

The authors would like to acknowledge the assistance of Mr Kazuto Iida and Mitsuhiro Sato who contributed their efforts for the accomplishment of many of the experiments.

Reference

- 1) Battjes, J.A.: Surf Similarity, Proc. 14th Conf. on Coastal Eng., ASCE, pp.466-480, 1974.
- 2) Murakami, H. Hosoi, Y. and Y. Kozuki: Wave Sounds as a Factor of Coastal Environment and Their Generation Characteristics, Environmental Sanitary Engineering Research, Vol.6, No.3, pp.148-153, 1992 (in Japanese).
- 3) Murakami, H. Itoh, S. Hosoi, Y. Ogawa, Y. and T. Koyabu, Consideration on Generation Characteristics of Breaking Wave Sounds, Proc. of Coastal Engineering, Vol.40, pp.1116-1120, 1993 (in Japanese).
- 4) Nadaoka, K. and T. Tokumi: Sounds of Breaking Waves as a Factor Constituting Amenity in Beach Space, Coastal Engineering in Japan, Vol. 34, No.1, pp.105-116, 1991.
- 5) Nadaoka, K. and K. Tamashima: Auditory Characteristics of Wave Sounds on Beaches, Coastal Engineering in Japan, Vol.34, No.1, pp.117-126, 1991.
- 6) Schafer, R.M.: The Tuning of the World, Arcana Editions, Ontario, 1977.

CHAPTER 23

Measurements of Wave Breaking in the UK Coastal Research Facility

Howard N Southgate¹ and Stuart Stripling¹

Abstract

Many experiments have been carried out on wave breaking in the past, but these have mainly been for regular, normally-incident waves. This paper describes experiments in the UK Coastal Research Facility in which over a hundred separate tests were carried out, covering regular, random, normally-incident, angled and multidirectional waves. Measurements were made of wave parameters as the waves underwent breaking in shallow water on a 1:20 slope. Analysis of the data to determine the wave breaking criterion, γ , for three random wave categories is presented.

Introduction

The criteria for values of wave height and water depth at which waves start to break in shallow water are an essential part of most computational models of nearshore wave propagation, and hence of many types of coastal engineering projects. A recent review (Southgate, 1995) has collated a large number of theoretical studies, laboratory experiments and field data sets which provide information for determining these criteria. Despite the large amount of work carried out, there remain important gaps in our understanding of the factors that influence breaker height criteria, with consequent uncertainties in the expressions used in wave prediction models. In particular, more information is required on breaker height criteria for random, angled and multidirectional waves.

This paper describes experiments carried out in the UK Coastal Research Facility (hereafter referred to as the CRF) to provide data for this purpose and for other aspects of wave propagation in shallow water regions where waves are breaking. About 100 tests were done in total, and five categories of wave were

¹HR Wallingford Ltd., Wallingford, Oxon, OX10 8BA, U.K..

investigated. These were:

- 1) Regular waves, normal incidence
- 2) Regular waves, 25 degrees to the normal
- 3) Random long-crested waves, normal incidence
- 4) Random long-crested waves, 25 degrees to the normal
- 5) Multi-directional waves, mean direction at normal incidence

These tests were designed so that, as far as possible, equivalent average input wave heights and periods were tested in each category. This has enabled a direct comparison of trends in wave behaviour across the different categories to be made.

In addition, this paper presents an initial evaluation of breaker height criteria for three categories of random waves (random at normal incidence, random at 25° incidence, and multidirectional waves).

Experimental Arrangement

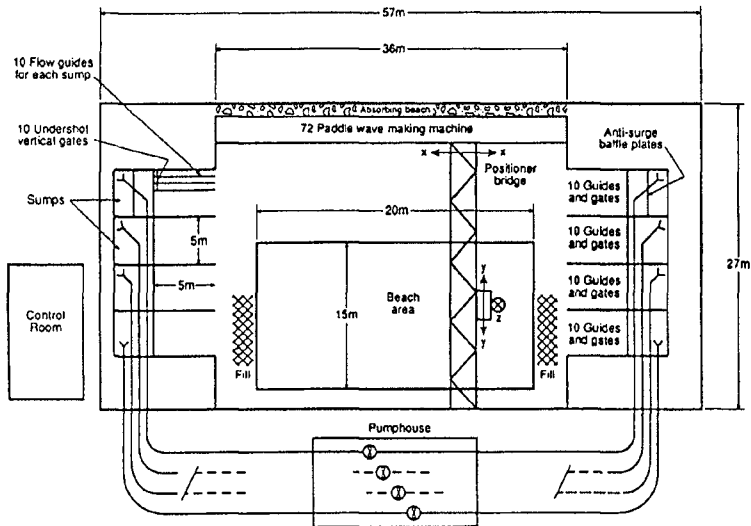


Figure 1. Layout of the CRF

The CRF is a state-of-the-art shallow-water wave basin constructed at HR Wallingford. The basin measures 36m by 27m and has a working area of about 20m by 15m. The wave-maker is 36m long and consists of 72 independent paddles capable of generating regular, random or multidirectional waves at normal or

oblique incidence. In front of the wave-maker is a flat area followed by a 1:20 smooth concrete slope parallel to the wave-maker. The depth of water in the flat area is 0.5m. The overall layout is shown in Figure 1, and the main features of the CRF are described in more detail in Simons et al (1995).

For each test, wave conditions were measured at 14 locations along a line perpendicular to the coastline roughly midway between the two side boundaries of the basin. Measurements were made with twin-wire resistance probes. Most of the probes were clustered within and just offshore from the breaking region, giving a high spatial resolution in this region. Three probes were also positioned a short distance in front of the wave-maker in order to make measurements of the input wave conditions. These probes were positioned on a line parallel to the wave-maker, with the central probe on the same cross-shore line as the inshore cluster of probes.

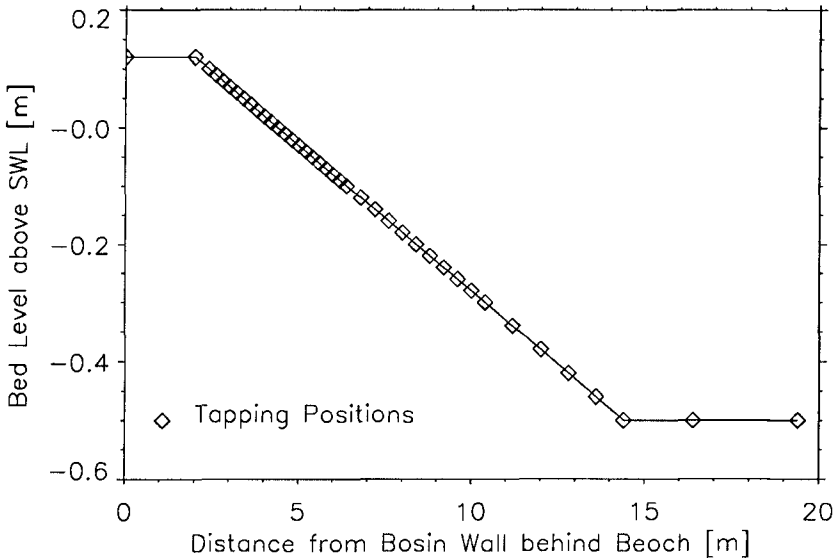


Figure 2. Cross-Shore Locations of Pressure Tappings

In addition to measurements of wave conditions, data was obtained on set-up of the water level caused by the breaking of waves. To measure the set-up, holes (known as pressure tappings) were drilled at spatial intervals into the basin floor along the cross-shore line (see Figure 2). These holes were connected via smooth nylon hydraulic tubes to individual stilling pots. Measurements of the water levels in each pot were made using the same type of twin-wire probes as for the wave measurements. This system of pressure tappings and stilling pots was installed specifically for this study and is now a permanent feature of the CRF. In all, 38 pressure tappings and stilling wells were installed, but only a subset of these were

used in each test. For identification, each pressure tapping is given a number, with 1 closest inshore and 38 furthest offshore. Wave probe positions were selected to be coincident with a pressure tapping location so that corresponding values of wave parameters and water level set-up could be obtained.

A range of input wave heights from 0.03m to 0.1m was tested. Obviously, the higher waves broke further offshore and had a wider surf zone than the smaller waves. Therefore, in order to get the best spatial coverage and resolution, the locations of the probes needed to be changed according to the input wave height (the probes would need to be more spaced out for the higher waves). However, too much moving around of the probes would use up valuable experimental time, so a compromise was adopted in which there were two arrangements of probes. The first arrangement had the probes closely bunched near the waterline, and was used for low wave conditions (input wave height between 0.03m and 0.08m). The second arrangement had the probes more widely spaced, and was used for high wave conditions (input wave height of 0.09m and 0.1m). In each case every probe was located over a pressure tapping point. Figure 3 shows the relative locations of the probe positions for 'low' and 'high' wave conditions (the West Wall is the basin wall behind the beach, and the bed elevation is relative to the flat area in front of the wavemaker). Further details on the experimental arrangements can be found in CRF test report (Beresford and Channell, 1995)

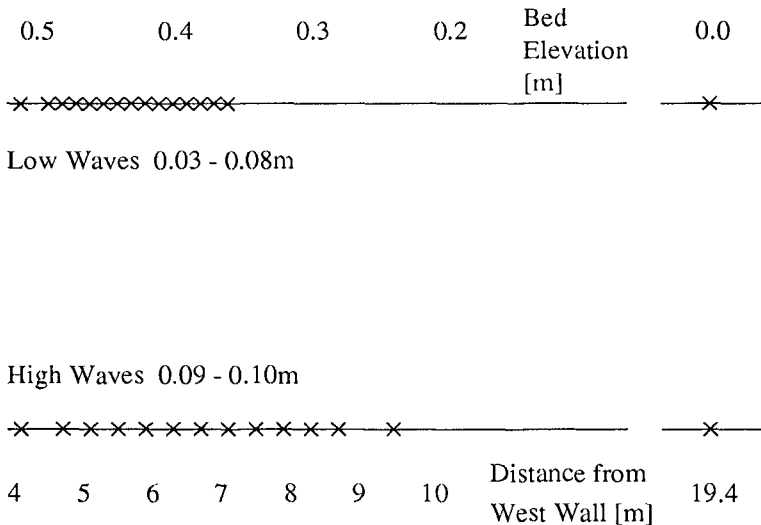


Figure 3. Locations of wave probes

Test Programme

A total of 125 tests was planned. Due to time constraints, only 108 tests were actually carried out. Of these, data from seven tests were found to be corrupted as a result of a hardware problem in the logging computer. Therefore, a total of 101 tests produced data successfully for subsequent analysis.

The following procedure was adopted in carrying out the test programme. Firstly, the water was allowed to settle to a quiescent state and then 'zero levels' (ie the digital readings corresponding to the still water level) for each probe were logged. The waves were started and run until transient effects had died away. This was checked by monitoring up to four of the probes online. After this, data collection for the first test started, and tests continued in sequence for about two hours. The wave-maker was then switched off, and the water allowed to settle. New zero readings were taken and testing was restarted.

The regular wave tests were performed first. The duration of these tests was the equivalent of 100 wave periods or 180 seconds, whichever was the longer. The two wave directions tested were at 0 degrees and 25 degrees to the normal to the shoreline. At the end of each test, the data quality was assessed. The data from the three offshore probes was analysed (by a wave counting method) and the average wave height over the three probes was calculated. The test was accepted if this wave height was within 10% of the target wave height. If not, the test was discarded and then repeated.

The random and multidirectional wave tests were then performed. For all the tests, the frequency spectrum was based on the JONSWAP formulation (Hasselmann et al., 1976), with a peak enhancement factor equal to 3.3. As with the regular wave tests, the directions tested were 0 degrees and 25 degrees. For the multidirectional wave tests, the directional spectrum used a standard Cos-squared spreading function centred on 0 degrees. The length of each random wave test needed to be considerably longer than the regular wave tests to ensure that there were a sufficient number of the longest period waves in the spectrum for reliable statistical analyses to be carried out. Accordingly the length of each random wave test was set at 1200 seconds. The procedure for carrying out the random wave tests was the same as the regular wave tests, but a more stringent data quality criterion was applied. One of the main purposes of the experiment was to compare results of different wave categories for equivalent wave input (ie waves with the same average wave height and period). A random test was repeated if its input root-mean-square wave height differed by more than 5% from the input wave height in the equivalent regular wave test.

For all the tests, signals from all the 30 probes were sampled at a rate of 30 Hz. This is sufficient to determine maximum wave heights by wave counting analysis to an accuracy of better than 0.5% (Tayfun, 1993). This rate is more than

is necessary for spectral analysis, but does not adversely affect the analysis.

Table 1 below summarises the numbers of tests carried out for each wave category.

Wave Run Category	Wave Height Range (cm)	Steepness Range	Wave Period Range (sec)	Number of Performed Runs	Number of Successful Runs
Regular Waves. Normal Incidence	3 - 10	0.005 - 0.055	1 - 3	25	23
Regular Waves. 25 Degrees Incidence	3 - 10	0.005 - 0.055	1 - 3	25	25
Random Waves. Normal Incidence	6 - 10	0.015 - 0.055	1 - 3	20	20
Random Waves. 25 Degrees Incidence	6 - 10	0.015 - 0.055	1 - 3	18	15
Multi-Dir Waves. Normal Incidence	6 - 10	0.015 - 0.055	1 - 3	20	18
Totals	-	-	-	108	101

Table 1. Summary of Tests Performed for each Wave Category

Within each category, input wave height and steepness values were chosen systematically within the ranges 0.03m to 0.1m for wave height, and 0.005 to 0.055 for wave steepness. Pairs of values were chosen to give wave periods between 1s and 3s. These ranges of wave height and period represented the allowed operating ranges of the wave-maker. The random wave parameters that are designed to be matched to the equivalent regular waves are the *root-mean-square* wave height, and the *peak* period.

A feature of the wave-maker software for random and multidirectional waves normal to the shoreline is set-down compensation. Set-down is a natural feature in random (but not regular) seas that refers to the raising of the water level under groups of lower waves and lowering of the water level under groups of higher waves. The software allows the movement of the paddles to be modified to ensure that the set-down propagates correctly without unwanted second-order wave effects. For the normal-incidence random and the multidirectional wave tests, the set-down compensation was switched on. However, for both wave categories an extra test was done with the set-down compensation switched off, in order to assess the differences in the final results. In both cases the differences turned out to be very minor, and substantially less than differences between equivalent runs for different wave categories. The random wave tests at 25 degree incidence were done

without set-down compensation (the software at the time was only applicable to normally incident waves). Further details of the design input conditions for each test are given in Southgate et al (1996).

Spectral Analysis of Data

The CRF data has been analysed spectrally, and all the results in this paper are based on this analysis. The software uses a fast Fourier transform (FFT) algorithm, which requires the data to consist of exactly 2^n values, where n is a positive integer. Accordingly the data series for each probe in each run were truncated to 2^{12} (=4096) for the regular wave tests, and 2^{15} (=32768) for the random and multidirectional wave tests. One potential problem was the presence of a number of spikes in the time series data of water surface elevations. However, the spikes were narrow (usually consisting of only one data point) and few in number. Tests showed that they had a negligible effect on the statistical quantities of the whole time series, and therefore no action was taken to remove them.

The results of the spectral analysis are in two forms: a) frequency spectra (in 32 bands each of width 0.434Hz) for each of the wave probes, and b) statistical data derived from the frequency spectrum for each wave probe and corresponding stilling well probe. These latter data are:

- 1) The root-mean square wave height (H_{rms}), defined as $2\sqrt{2.m_0^{1/2}}$, where m_0 is the zero spectral moment.
- 2) The spectral period (T_m), defined as $(m_0/m_2)^{1/2}$, where m_2 is the second spectral moment.
- 3) The mean water level, derived from the stilling well probe data (the still water level is 0.5m).

Tabulated examples are shown in Southgate et al (1996). In deriving the data for b), the spectrum was truncated at high frequencies and only the first 16 frequency bands were considered (covering wave frequencies between 0Hz and about 7Hz). Wave energy at higher frequencies appeared to be 'noise' and represented only a small contribution to the total. Low-frequency wave energy is included in the analysis. A separate investigation of the low-frequency part of the spectrum would require a reanalysis with smaller band widths.

The spectral analysis has provided results in the form of wave frequency spectra, rms wave heights, spectral wave periods and wave setup at each probe location for each run. An example of the wave height results has been plotted in Figure 4 (diamonds) along with a computational model prediction with a best-fit breaker criterion, γ_{min} (full line). A full set of results for wave height decay and wave setup is shown in Southgate et al (1996).

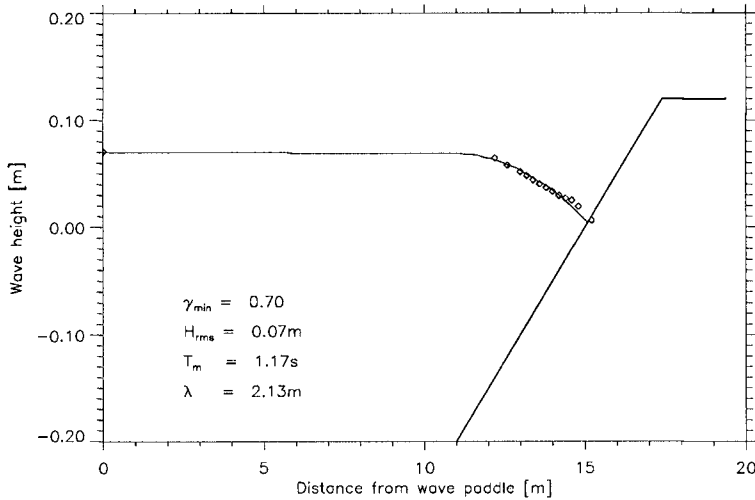


Figure 4. Random waves, Normal Incidence

From the full set of results some initial observations can be made:

- a) Angled waves are generally slightly lower than normally incident waves. This can be explained by the angled waves undergoing refraction.
- b) Regular waves are generally higher than random waves immediately before breaking and decay to lower values immediately after breaking. This is explained by regular waves breaking over a much narrower zone than random waves. Also the increase in wave height due to non-linear effects immediately before breaking is noticeable.
- c) Multidirectional waves and random normally incident waves show very similar heights and patterns of decay
- d) There is substantial spreading of wave energy to both lower and higher frequencies, and a reduction in the spectral period values as one travels inshore. The effect is particularly strong for regular waves.
- e) Setup caused by regular normal waves starts further landward and reaches higher values than that caused by random normal waves or multidirectional waves.
- f) Setup caused by random normal waves tends to be higher than that caused by random oblique waves or multidirectional waves.

Other plots of this data are possible, for example spectral period vs cross-shore distance, or spectral density vs wave frequency (at each location). Other modes of analysis are also possible, for example wave counting analysis, or spectral analysis using different frequency bands.

Determination of Breaker Height Criterion for Random Wave Categories

This data set has been used to illustrate how to derive an expression for the breaker height criterion, γ , for three categories of random wave (normal incidence, 25 degrees incidence, and multidirectional waves). γ is defined as the ratio of wave height to water depth when waves initially break in shallow water, and is a key input parameter in most computational models of shallow water wave processes. Many experiments have been carried out in the past to derive values of γ , but these have mainly been flume experiments, most commonly with regular waves. The present experiments provide the opportunity to derive expressions for γ for the three types of random wave categories with equivalent input wave conditions. For random waves the wave height in the definition of γ is the rms value.

For random waves, γ has a different interpretation than for regular waves. In the case of regular waves, γ refers to the wave height to depth ratio at initial breaking for *individual waves*. For random waves, γ is a single value representing an average value of wave height to depth ratio at initial breaking for a range of waves of different heights and wavelengths. In parametric surf zone wave models, it needs to be regarded as a parameter in the representation of the average rate of wave decay through the surf zone.

The most extensive previous study of breaker height criteria for random waves was done by Battjes and Stive (1985) who analysed twenty results from three separate laboratory exercises and two field exercises. Their analysis showed no systematic dependence of γ on bed slope, but a dependence on deep-water wave steepness. They used a hyperbolic tangent function to give a best fit to the data:

$$\gamma = 0.5 + 0.4 \tanh(33H_0/L_0)$$

The method of determining γ from the present experiments follows that used by Battjes and Stive. The idea is to use a parametric model of wave decay through the surf zone and repeat the runs for many different trial values of γ . For each run, the rms error of predicted wave height vs measured wave height at all points across the profile for which there are measurements is calculated. The value of γ which gives the minimum error is selected. The model used for this purpose was the wave part of the morphodynamic profile model, COSMOS-2D (Southgate and Nairn, 1993).

Model runs were performed for each experiment in each of the three random wave categories, stepping through a range of values of γ from 0.4 to 1.0 with

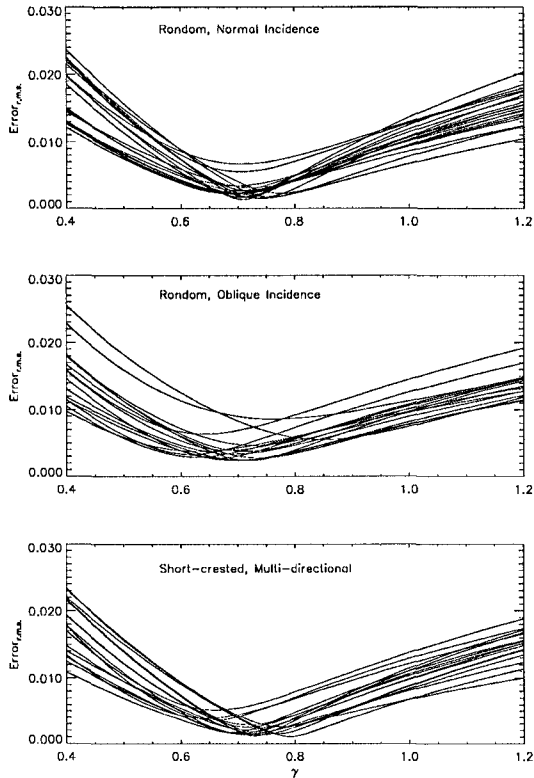


Figure 5. rms Error in Wave Height vs γ

increments of 0.01. At each value of γ , the root-mean-square (rms) error between the wave height measurements and the wave height profile predicted by the model at each measurement point was calculated. Figure 5 shows the range of γ values plotted against the rms error between the measured and the predicted wave height profiles. It can be seen that each wave has an optimum value of γ which provides a minimum rms error. This was taken to be the wave breaking coefficient for that wave.

Results

Figure 6 shows a plot of the deep water wave steepness against the optimum γ value, γ_{\min} . To calculate the deep water wave steepness, the average rms wave height and wavelength (calculated by the linear dispersion relation from the peak period) at the three probes in front of the wavemaker were refracted out to deep water using Snell's law. In this plot, r is the correlation coefficient and sd is the standard deviation of the data from the linear regression line obtained using the method of least squares. It can be seen that the normally incident random waves

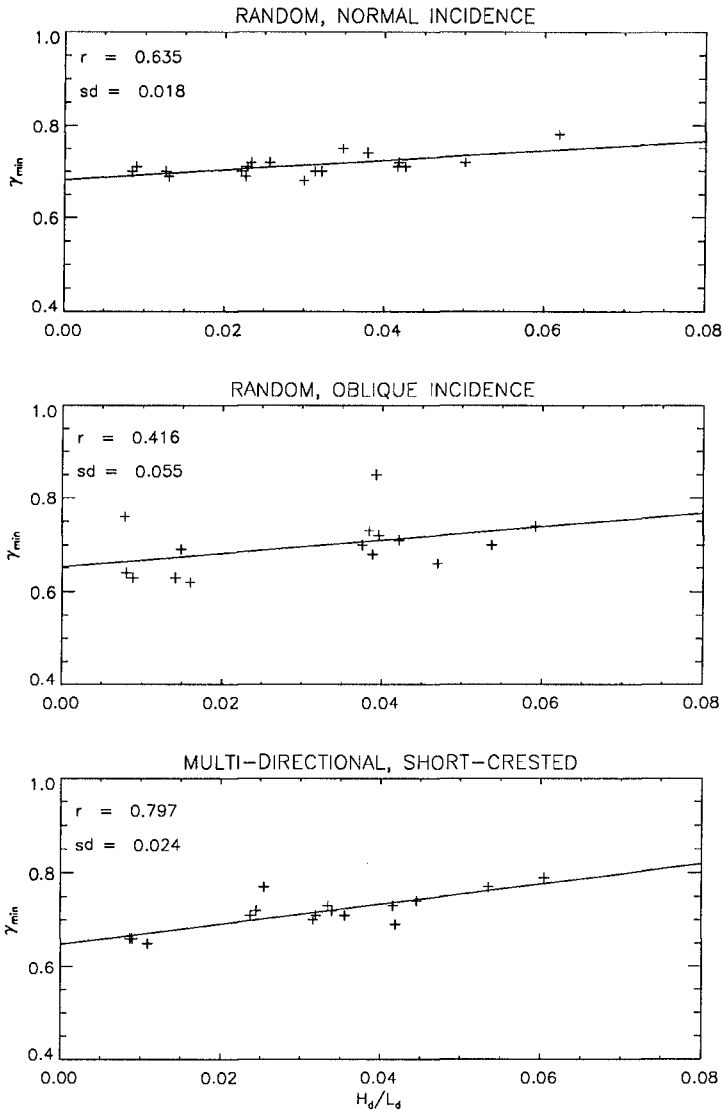


Figure 6. γ_{min} vs Deep Water Wave Steepness

and the multidirectional waves have quite high values of the correlation coefficient, but that random oblique incident waves have a lower value.

Figure 7 shows a plot of the deep water Iribarren number, I_d , where I_d is the beach slope divided by the square root of the deep water wave steepness. It can be seen here that the correlation coefficients are lower for the random normal and oblique incident waves than for the deep water steepness plotted in Figure 6. The

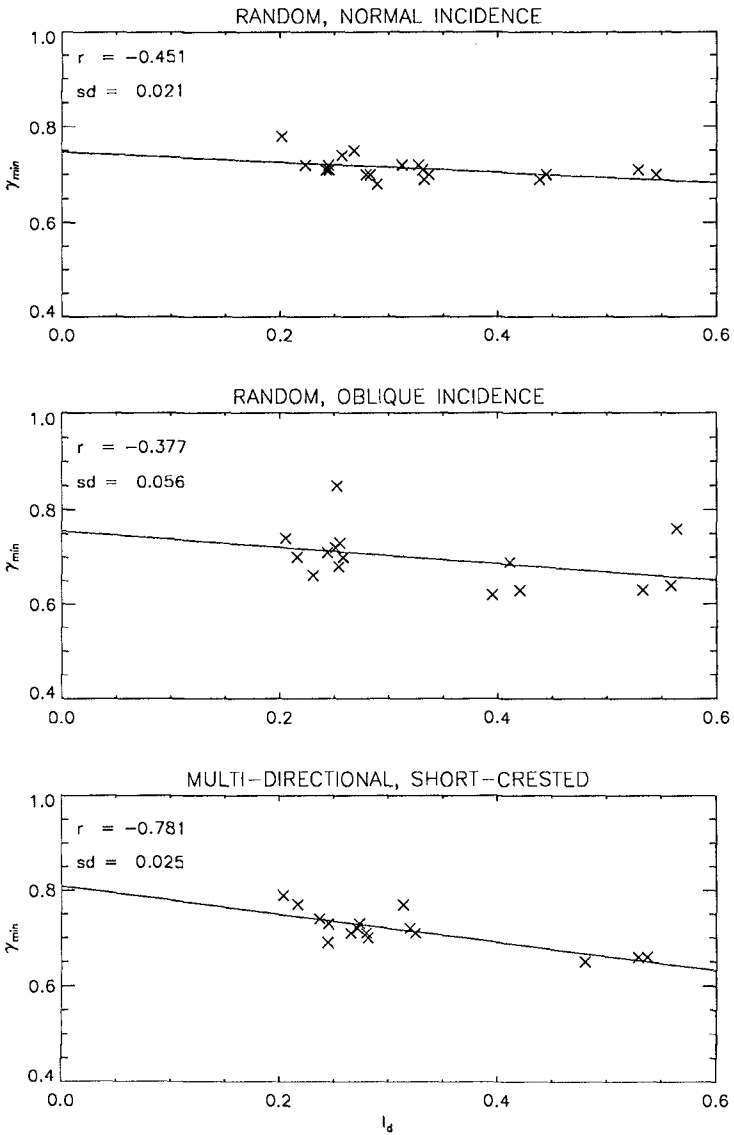


Figure 7. γ_{min} vs Deep Water Irribarren Number

multidirectional waves, however, still have a high correlation coefficient. This suggests that the deep water wave steepness is a more appropriate parameter than deep water Irribarren number to predict γ .

Figure 8 shows the deep water wave steepness regression lines and the trend line of Battjes and Stive (1985). The differences with Battjes and Stive appear

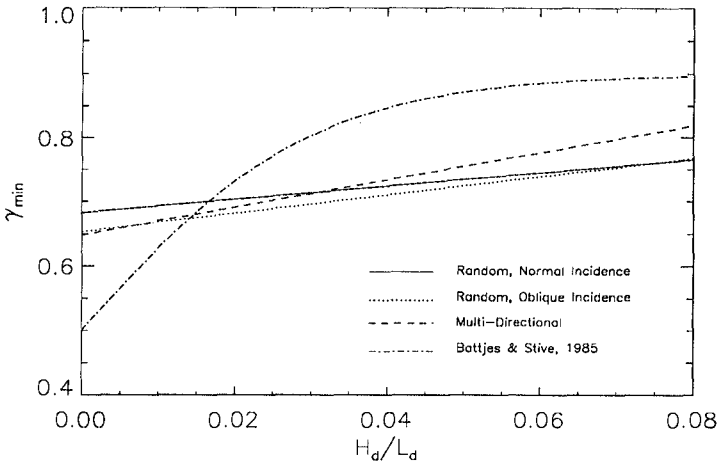


Figure 8. γ_{\min} vs Deep Water Wave Steepness (trend lines)

quite large, but almost all the wave steepness values in Battjes and Stive's data lay between 0.01 and 0.03.

Conclusions

A series of experiments in the UK Coastal Research Facility have been performed to provide data on wave transformation and decay in the nearshore breaking region in a systematic manner using five different categories of input waves. This data has been processed by spectral analysis to provide information suitable for investigating nearshore wave processes and evaluating wave models. An initial, visual comparison of the results across the different wave categories is summarised in the section on spectral analysis. If necessary the data could also be reanalysed using alternative methods. Typical examples of applications of this data set would be:

- a) Criteria for initial breaking of waves
- b) Wave height transformation and decay
- c) Wave setup and the 'transition zone' length (the distance between where waves start to break and where radiation-stress-driven phenomena start to appear, as revealed by wave setup)
- d) Wave energy transfer between frequency spectral components
- e) The fraction of waves breaking at any location (for random and multidirectional runs) determined from analysis of video records.

An analysis of the data for three categories of random wave (normal incidence, oblique incidence and multidirectional) has been carried out to determine breaker height criteria and their functional dependence on deep water wave steepness. However, to establish the most reliable expressions for breaker height criteria, it is recommended that this data set is combined with others, such as those used in Battjes and Stive (1985), so that the overall data set is as large as possible and covers as wide a range as possible of laboratory and field conditions.

Acknowledgements

This work was funded by the UK Ministry of Agriculture, Fisheries and Food (Flood and Coastal Defence Division) as part of the CAMELOT Commission (FD1001).

References

1. Battjes J A and Stive M J F (1985). "Calibration and verification of a dissipation model for random breaking waves", Proc. 19th ICCE, ASCE, Vol. 1, pp649-660.
2. Beresford P J and Channell A R (1995). "Breaking waves. Physical model tests in the CRF". Report IT 426, HR Wallingford.
3. Hasselman K et al (1976). "Parametric Wave Prediction Model", Journal of Physical Oceanography, Vol. 6, No. 2.
4. Simons R, Whitehouse R J S, MacIver R D, Pearson J, Sayers P, Zhao Y and Channell A R (1995). "Evaluation of the UK Coastal Research Facility". Proc. Coastal Dynamics '95, Gdansk, Poland.
5. Southgate H N (1995). "Prediction of wave breaking processes at the coastline". Article in "Advances in Fluid Mechanics". Ed. M Rahman, Pub. Computational Mechanics Publications.
6. Southgate H N and Nairn R B (1993). "Deterministic profile modelling of nearshore processes. Part 1. Waves and currents", Coastal Engineering, Vol.19, pp27-56.
7. Southgate H N, Beresford P J, Channell A R and Adams R (1996). "Wave breaking experiments in the UK Coastal Research Facility. Data report", Report TR2, HR Wallingford.
8. Tayfun M A (1993). "Sampling rate errors in statistics of wave heights and periods". J. Waterway, Port, Coastal and Ocean Eng., ASCE, 119(2), pp172-192.

CHAPTER 24

A New Type Breaker Forming a Giant Jet and its Decaying Properties

Takashi Yasuda¹, M.ASCE Hidemi Mutsuda², Atsushi Oya³,
Akihide Tada⁴ and Tadashi Fukumoto⁴

Abstract

Experiments in a wave flume(1m × 2m × 65m) with 16 wave gages and numerical simulations using a fully nonlinear BIM(Boundary Integral Method) in a super-computer(VP2600) are conducted to make clear the characteristics and occurrence condition of a new type breaker. Further, its deformation and wave height decay after breaking are investigated. It is shown that the new type breaker forms a giant jet with the size exceeding three times of the maximum jet size of usual type breakers and therefore is very efficient to wave control because of strong turbulence excited by plunging of the giant jet and the resultant remarkable absorption.

1. Introduction

Wave control and shore protection works utilizing artificial reef and submerged breakwater have many advantages over usual coastal structures such as offshore breakwater. However, since most breaking waves caused by the submerged coastal structures are spilling or plunger and they cannot excite sufficiently strong turbulence responsible to the required wave absorption, the problem that the efficiency of wave absorption is insufficient arises from those submerged structures. For that reason, in order to increase the efficiency and develop the artificial reef work to a desirable wave control and shore protection work, it is required to generate a breaker exciting much stronger turbulence and strengthen the absorption due to wave breaking.

However, a good understanding and information of the mechanism for breaker types that are essentially important for the energy absorption are still very limited. Nevertheless, most breaking waves have been supposed to be classified into four breaker types, spilling, plunging, collapsing and surging, based on

¹Prof., Dept. of Civil Eng., Gifu Univ., Yanagido 1-1 Gifu 501-11, Japan

²Res. Assoc., ditto

³Graduate student, Graduate school of Gifu Univ., ditto

⁴Res. Eng., Tech. Res. Inst., Nishimatsu Construction Co. Ltd., Yamato 242, Japan

the visual observations of periodic waves regarding uniformly sloping bottoms, and accordingly little attention has been given to the possibility of new breaker types.

Cooker et al.(1990) studied the interaction between a solitary wave and a submerged semicircular cylinder, and found that the breaker forms are governed by the extent of the crest exchanges between the incident crest and the 2nd crest excited on the downward side of the cylinder. The results show that the breaker suffering the crest exchange is clearly different from the breaking of nonlinear long waves, in which the higher parts of an incident wave travel faster due to shallow water steepening and finally overturns to eject a jet, and reveals various behaviors and forms dependent on the interaction between the incident crest and the 2nd one.

In order to find out a new type breaker forming a giant jet and being efficient to wave absorption, we have been investigating basically the mechanism and characteristics of the breakers caused by submerged obstacles. As a result, such a breaker forming a giant jet was found to occur when a solitary wave strikes a reef having two steps, referred here to as a double reef. This breaker could be expected applicable to efficient wave control because it excites strong turbulence by plunging of the giant jet. Further, the new type breaker could be generated independently of these kinds of waves and bottom topography, only if the given conditions can be satisfied.

In this study, a solitary wave is made as an incident wave and is allowed to strike reefs having single and two steps with various heights, in order to reduce the number of parameters related to wave breaking as few as possible. Numerical simulations of the overturning of solitary waves on reefs are carried out until the jets ejected from their crests begin to fall, in order to investigate the characteristics of breaking wave profile and jet size and make clear the occurrence condition of the aforementioned new type breaker forming a giant jet. Further, experiments are conducted to verify the generation of the new type breaker in real fluid. At the same time, the accuracy of the simulated results is examined and the properties of wave deformation and wave height decay after breaking is made clear.

2. Method and Condition

2.1 Computations

Numerical computations using a fully-nonlinear BIM irrotational-flow model (Yasuda et al., 1990) are carried out of the overturning of solitary waves on reefs having single and two steps (Fig .1) until the jet-fall initiation, defined as when the overhanging face beneath the jet becomes just horizontal and the maximum

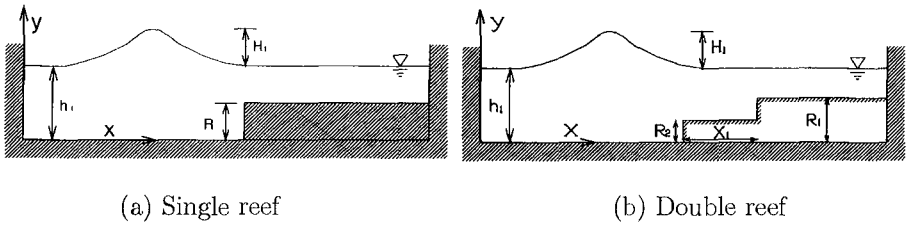


Figure 1: Coordinates and symbols for computations

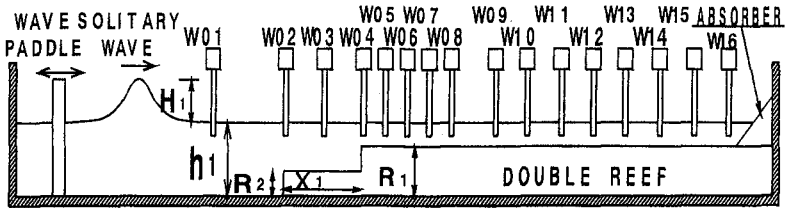


Figure 2: Wave flume and locations of wave gages

gradient angle θ of the front face at each time step reaches 180° . Here, while a reef shown in Fig.1(a) is referred to as a single reef, a reef having two steps is referred to as a double reef.

The accuracy of the computations was previously examined by comparing a computed solitary wave with its exact solution and further verifying the validity of the computed surface profiles and water particle velocities at the breaking against carefully controlled experiments (Yasuda et al., 1992, 1993).

As an initial condition, a solitary wave represented by the exact solution (Tanaka, 1986) of a fully-nonlinear irrotational flow theory is given over the flat bed of the left-hand side of each reef as illustrated in Fig.1, and is assumed to propagate toward the reef. The numerical computations were undertaken under the condition that the error for energy conservation law is always less than 1%.

2.2 Experiments

Experiments were conducted in a 65m long, 1m wide and 2m high wave flume with a side window. Solitary waves with incident wave heights of 9.15cm \sim 16.90cm were generated using a computer-controlled piston wave maker. The still water depth h_1 was fixed to 31.0cm. Reef models made of steel plate were built on the plane bottom, 30.0m distant from the wave paddle. The height R of a single reef is 26.3cm, and the lower crown height R_2 and the upper one R_1 of a double reef are 13.1cm and 26.3cm respectively. A relative distance X_1 between

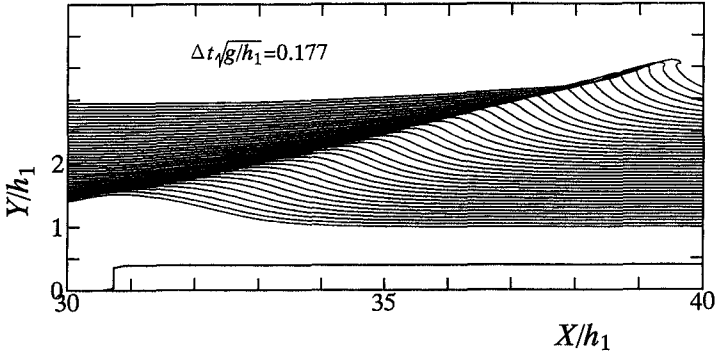
the 1st step and 2nd one of a double reef was changed from 0.0cm to 250.0cm. The case of $X_1 = 0.0\text{cm}$ corresponds to the single reef ($R_2 = 0.0\text{cm}$).

16 capacitance wave gages were installed to measure the temporal water surface elevation at each location shown in Fig.2. The gage W01 was placed in front of the reef to measure the incident wave profile and height. A high-speed video camera(unic, HSV-400) with a speed of 200 frames per second was used simultaneously to record the profile and size of the overturning jet.

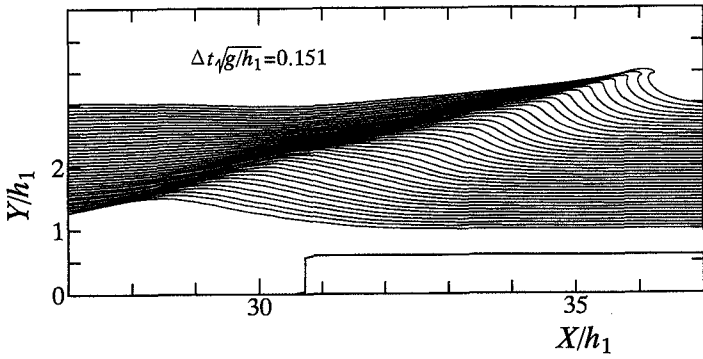
3. Wave Breaking on a Single Reef

Time evolutions of spatial surface profiles of a solitary wave incident to single reefs with $R/h_1 = 0.4, 0.6$ and 0.9 are introduced here. The evolutions up to jet-fall initiation are illustrated in Fig.3, in which $\Delta t \sqrt{g/h_1}$ indicates the non-dimensionalized time increment of each evolution. The incident wave shown in Fig.3(a) does not accompany the 2nd crest and steepens to eject a small jet from the crest point at the location of $X/h_1 \approx 8$. This breaker therefore could be regarded as a spiller type. In the case of a single reef with a relative crown height of $R/h_1 = 0.6$, the breaker could be regarded as a plunger type because it had a larger jet than that of a spiller type. Further, the 2nd crest is generated from the front face and grows to eject a jet from the crest at the position of $X/h_1 \approx 4$ through the crest exchange with the incident crest, while the incident crest vanishes after having finished the crest exchange. Although this crest exchange is apparently similar with the soliton-soliton overtaking interaction as pointed out by Cooker et al.(1990), more information about it needs to be known. Furthermore, in the case of a single reef with $R/h_1 = 0.9$, the 2nd crest is generated far before the incident crest approaches the step, and then promptly ejects the jet at the position of $X/h_1 \approx 2$ during the crest exchange, while the incident crest keeps a height exceeding the 2nd crest. As a result, the jet seems to be ejected from lower part of the front face of the incident wave and therefore is regarded as a collapsing breaker.

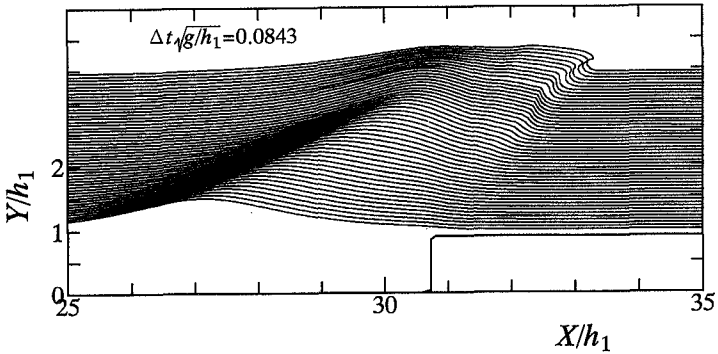
In order to examine the relation of the profile and size of the jet to the relative crown height R/h_1 , comparisons of surface profiles around the jet are made for the solitary waves incident to single reefs with $R/h_1 = 0.25 \sim 0.90$, and their profiles at the breaking limit, defined as an instant that the forward face first becomes vertical and the maximum gradient angle θ just reaches 90° , and the jet-fall initiation are shown in Fig.4. It is found from the surface profiles at $\theta = 90^\circ$ that their horizontal asymmetries correspond well to the crown heights of reefs. It is also noticed that the vertical location of the jet tip at $\theta = 180^\circ$ becomes lower with the increasing of the reef height. However, the size of the jet seems to grow with the increase of the reef height while the profile of the jet keeps similarity.



(a) $R/h_1 = 0.4$

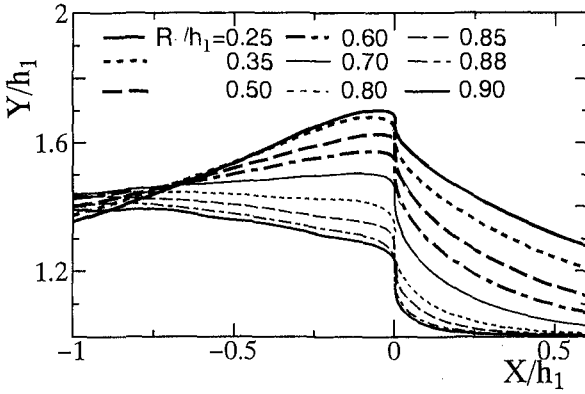


(b) $R/h_1 = 0.6$

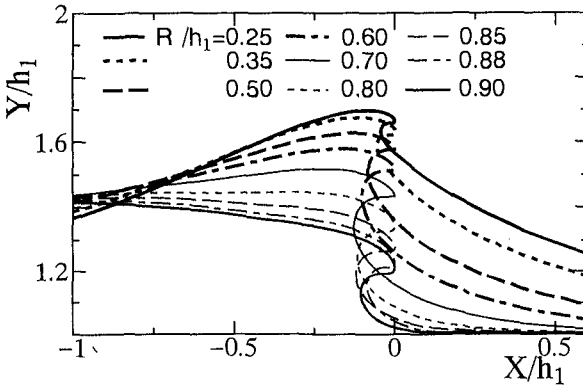


(c) $R/h_1 = 0.9$

Figure 3: Propagation process up to overturning of a solitary wave with $H_1/h_1 = 0.5$ on single reefs with $R/h_1 = 0.4, 0.6$ and 0.9



(a) Breaking limit($\theta = 90^\circ$)



(b) Jet-fall initiation($\theta = 180^\circ$)

Figure 4: Comparisons of wave profiles at the breaking limit($\theta = 90^\circ$) and jet-fall initiation($\theta = 180^\circ$)

Further, in order to examine a quantitative relationship between the jet size and the reef height, we first define the horizontal jet length γ and the jet height η_J at the jet-fall initiation ($\theta = 180^\circ$), as illustrated in Fig.5, and further show the correlation under the incident wave heights of $H_1/h_1 = 0.4, 0.5$ and 0.6 between the relative jet size $S = \gamma\eta_J/H_1^2$ and the relative reef height R/h_1 in Fig.6. The relative jet size S is found not to grow monotonically with the increase of the reef height but to have the maximum value dependent on the value of H_1/h_1 . This shows that the breaking waves accompanying the jet of which size exceeds 0.06 under the incident wave heights of $H_1/h_1 = 0.4, 0.5$ and 0.6 never occur on single reefs even if the reef height R increases up to the water depth h_1 .

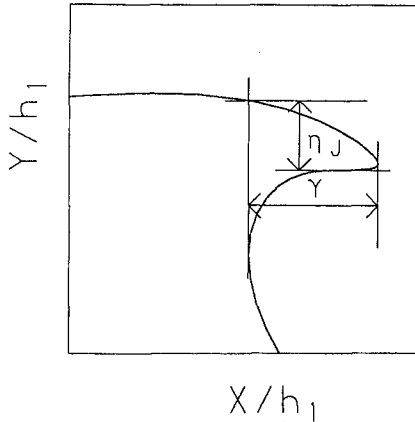


Figure 5: Definition diagram of the horizontal jet length γ and the jet height η_J at the jet-fall initiation

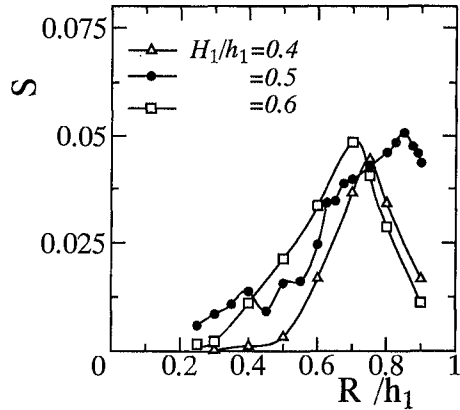


Figure 6: Relations of the jet size parameter S to the ratio of incident wave height to water depth H_1/h_1 and the relative crown height of the single reef R/h_1

4. New Type Breaker on a Double Reef

The surface profiles of a new type breaker on a double reef are shown in Photo 1. It is clearly found from the profiles that the new type breaker is characterized by the height of the location ejecting a jet, which is not the crest point and lower-half part of the wave, but is the upper part of the front face, and by the overturning jet form having a triangular crown. Such a breaker can never be categorized by the usual four types defined by Galvin(1968), and therefore, should be recognized as a new type breaker out of doubt. The snapshots further demonstrate the generation of the 2nd crest from the forward face and the formation of a giant jet excited by the coupling of the near-breaking incident crest and the 2nd one. Thus, the new type breaker is characterized by the formation of the giant jet having a triangular crown through the composition of both the crests and therefore is referred to as a composite breaker.

Figure 7 shows time evolutions of the numerically computed spatial surface profile of a solitary wave with $H_1/h_1 = 0.5$ incident to a double reef with $R_1/h_1 = 0.8$, $R_2/h_1 = 0.4$ and $X_1/h_1 = 6.5$, in which the 2nd step is located near the point of breaking of the incident wave caused by the 1st step. The features of the composite breaker demonstrated by the snapshots are clearly found in the computed results. The 2nd crest generated from the forward face grows fast to eject the jet through the crest exchange with the near-breaking incident crest, as found from the distance between the 2nd step and the position of the ejection

of the jet.

The incident crest suffers the decaying effect due to the crest exchange with 2nd crest and the shoaling effect due to the 2nd step, and consequently, its steep profile is strongly held under the nonlinear interaction. This strongly held triangular crest joins up with the 2nd crest to form a giant jet. Thus, the composite breaker is supposed to be generated by the composition of the triangular incident crest strongly held by the reciprocal effects of decaying and shoaling and the overturning 2nd crest.

Figure 8 indicates comparisons of the breaking wave profiles shown in Photo 1 between the results processing from the images captured with the high-speed video camera and the computed ones shown in Fig.7. The computed profiles agree very well with the experimental ones, although the numerical computation was performed under the assumption of irrotational flow in an incompressible and inviscid fluid. The results obtained assure again that the present BIM is applicable for investigating the breaking wave problem without performing any experimental work, and further, verify that a new type breaker forming a giant jet, that is, a composite breaker can be generated on a double reef.



Photo 1 : Snapshots of the composite breaker from the generation of the 2nd crest to the jet-fall initiation

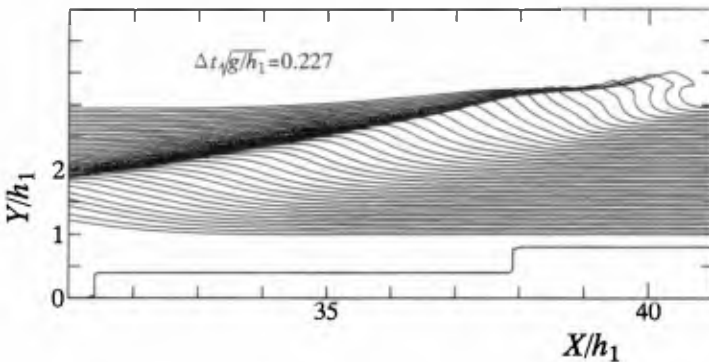


Figure 7: Propagation process of a solitary wave leading to composite breaker on a double reef with $R_1/h_1 = 0.8$, $R_2/h_1 = 0.4$ and $X_1/h_1 = 6.5$.

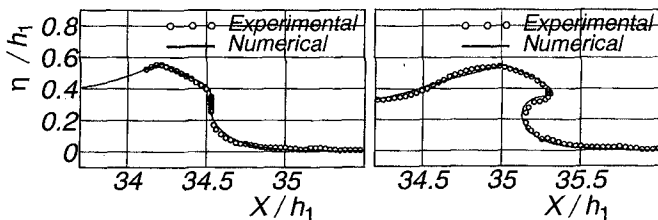
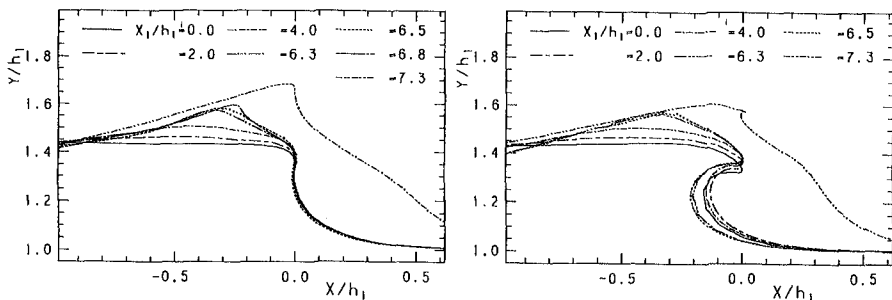


Figure 8: Comparisons of spatial surface profiles at breaking and jet-fall initiations between the results processed from images captured with a high-speed video camera and the numerically computed ones



(a) Breaking limit($\theta = 90^\circ$) (b) Jet-fall initiation($\theta = 180^\circ$)

Figure 9: Relations of wave profiles at the breaking and jet-fall initiations to the relative step distance X_1/h_1 of the double reef

In order to examine the relation of the profile and size of the jet to the relative step distance X_1/h_1 , comparisons of surface profiles around the jet at the breaking and jet-fall initiations are made for a solitary wave with $H_1/h_1 = 0.5$ incident to the double reefs with $R_1/h_1 = 0.8$, $R_2/h_1 = 0.4$ and $X_1/h_1 = 0.0 \sim 7.3$ and their results are shown in Fig.9. The incident crest turns to reveal triangular form and its height exceeds that of the breaker on a single reef($X_1/h_1 = 0.0$), as the relative step distance X_1/h_1 increases. However, when the value of X_1/h_1 exceeds about 7.0, a small jet is ejected from the incident crest before the incident crest gets to be combined with the 2nd one and then a giant jet is formed. For that reason, the jet size remarkably decreases in $X_1/h_1 = 7.3$ as shown in Fig.9(b).

Further, in order to make clear quantitatively the relation of the jet size S of breakers on double reefs to the relative 1st step height R_2/h_1 and step distance X_1/h_1 , we show the relations under the conditions of $H_1/h_1 = 0.5$, $R_1/h_1 = 0.8$, $R_2/h_1 = 0.3 \sim 0.6$ and $X_1/h_1 = 0.0 \sim 10.0$ in Fig.10. While the jet sizes of usual

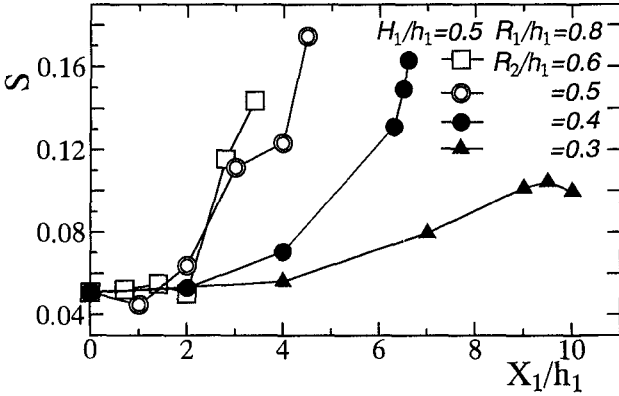


Figure 10: Relations of the jet size parameter S of the breaking wave with an incident wave height $H_1/h_1 = 0.5$ caused by double reefs with $R_1/h_1 = 0.8$, $R_2/h_1 = 0.3 \sim 0.6$ and $X_1/h_1 = 0.0 \sim 10.0$.

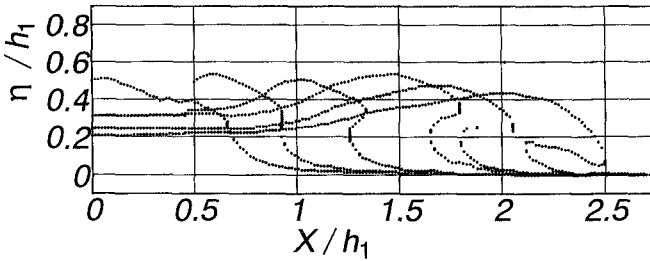


Figure 11: Overturning process of a composite breaker obtained by image processing

type breakers generated on a single reef can never exceed the maximum value as previously shown in Fig.6, the jet size of the composite breaker generated on a double reef grows with an increase in X_1/h_1 and at last exceeds 0.16, that is, three times of the maximum jet size $S \doteq 0.05$ of usual type breakers introduced in Fig.6 when the location of the 2nd step is close to the breaking point of the incident wave.

5. Deformation and Decay After Breaking

Deformation of wave profile and decay of wave height after breaking are investigated and then their characteristics for composite breaker are made clear, by analyzing the data of water surface elevations at 16 measuring points.

Figure 11 shows the time evolution up to the touch down of the water surface

profiles of a composite breaker captured with the high speed video camera. The surface profile demonstrates that a remarkably large jet is formed by the composite breaker and is ejected from the 2nd crest developed by the coupling with the incident crest.

Figure 12 shows spatial changes of water surface elevations at measuring points from W01 to W16 of composite breakers with $H_1/h_1 = 0.30, 0.42$ and 0.55 on a double reef with $R_1/h_1 = 0.85, R_2/h_1 = 0.43$ and $X_1/h_1 = 8.06$. Each incident wave begins to break near the measuring point of W07. After that, the overturning jet from the 2nd crest touches down on the front face as shown in Fig.11, and further a bore front accompanying strong energy dissipation is formed.

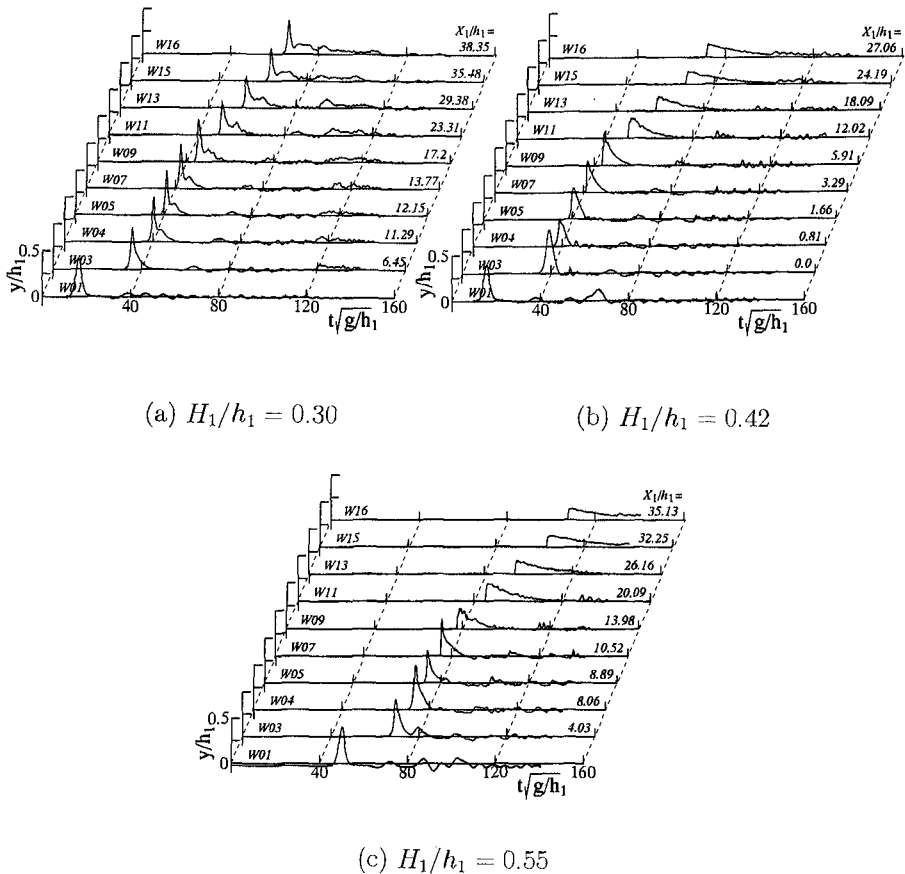


Figure 12: Temporal water surface elevations at representative measuring points of the composite breaker

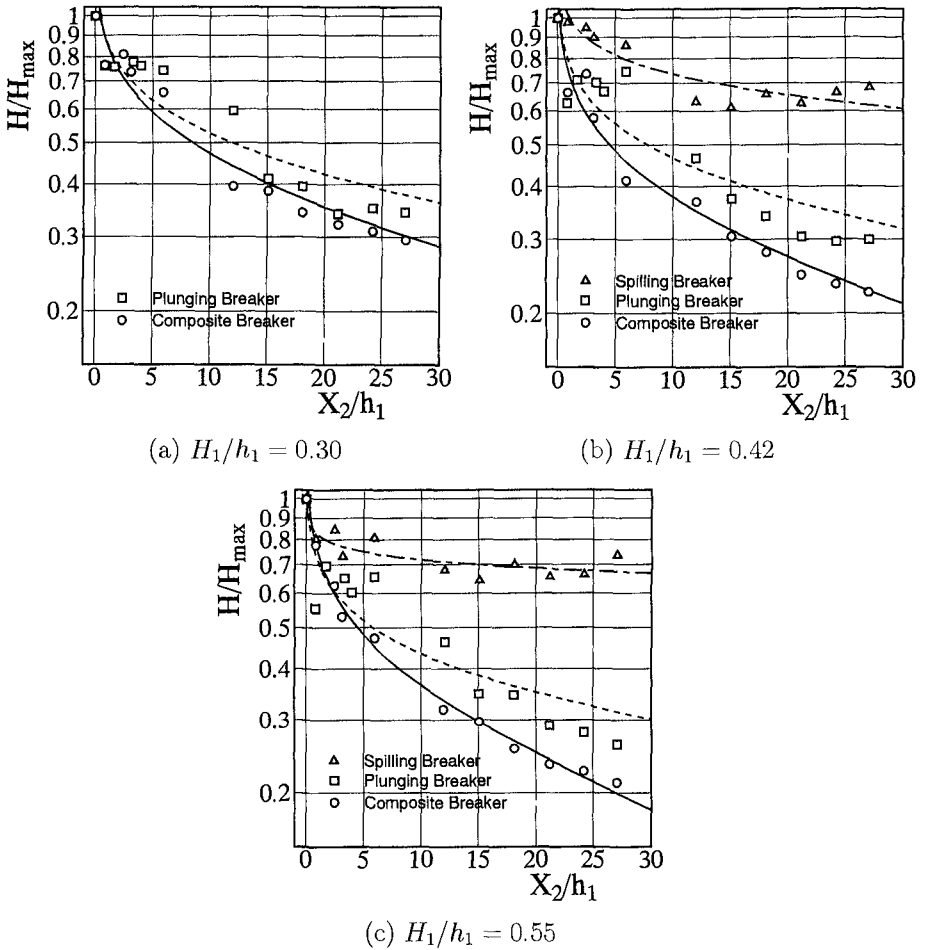


Figure 13: Wave height decay after breaking of the composite breaker

As a result, wave absorption is pronounced and the breaking wave propagates as bore-like wave while keeping a similar profile.

Figure 13 shows spatial variations of the wave height ratio H/H_{max} of the composite breakers on a double reef shown in Fig.12, together with those of a spilling breaker on a single reef of $R/h_1 = 0.43$ and a plunging breaker on a single reef of $R/h_1 = 0.85$. The value of H/H_{max} strongly depends on breaker type ; the wave height of the composite breaker remarkably decays with the propagation distance after breaking, while those of the spilling breaker and the plunging one reach nearly stable state at $X_2/h_1 \approx 10$ and 20 respectively.

Figure 14 shows the relations of the transmission coefficient K_T and reflec-

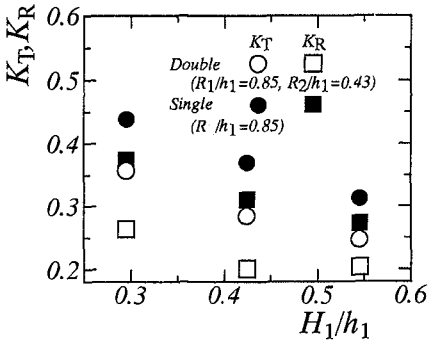


Figure 14: Comparisons of the transmission coefficient K_T and reflection one K_R between the composite breaker and plunging one under the same incident wave height H_1/h_1

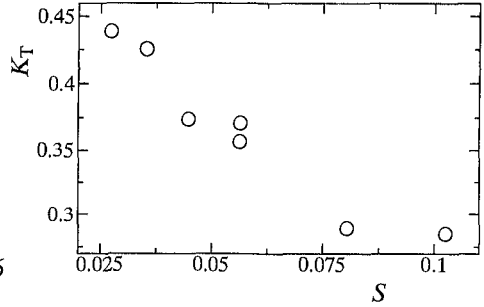


Figure 15: Relationships between the transmission coefficient K_T and the relative jet size S

tion coefficient K_R to the incident wave height ratio H_1/h_1 . The incident waves break on a double reef as a composite breaker, while they break on a single reef as a plunging breaker. Even if the incident wave is identical and further the crown height R_1 of the double reef is the same with the crown height R_1 of the single reef, both the coefficients K_R and K_T for waves incident to a double reef largely decrease in comparison with those for waves incident to a single reef, respectively by the depth change due to two steps and the generation of the composite breaker on the reef. Thus, by remodelling a single reef with $R_1/h_1 = 0.85$ to a double reef with $R_1/h_1 = 0.85$, $R_2/h_1 = 0.43$ and $X_1/h_1 = 8.06$, it becomes possible to reduce both the values of K_T and K_R by more than 23% against the incident waves with $H_1/h_1 = 0.30 \sim 0.55$.

Figure 15 shows the relationships of the transmission coefficient K_T to the jet size S of various type breakers on single and double reefs. It is clearly found that the value of K_T decreases proportionally to the increase of the jet size and wave height decay after breaking is governed by the jet size itself. This result shows that the generation of the breaker forming a jet with larger size, that is, the generation of the composite breaker is efficient to the improvement of wave absorption.

6. Conclusions

A new type breaker forming a giant jet, referred here to as a composite breaker, is generated by the composition of fast growing 2nd crest and near-breaking incident crest suffering the reciprocal effect; the decaying effect due to the crest exchange with the 2nd crest generated by the 2nd step of a double reef and the shoaling effect due to the 2nd step. The reciprocal effect forms the strongly held triangular crown and produces a giant jet by incorporating the triangular crown into the 2nd crest. Such a breaker has not ever been known and are supposed to excite strong turbulence by its diving and cause the resultant remarkable dissipation. Therefore, development of a new wave control system utilizing a composite breaker could be expected.

References

- Cooker, M.J., D.H.Peregrine, C.Vidal and J.W.Dold(1990) : The interaction between a solitary wave and a submerged semicircular cylinder, *J.Fluid Mech.*, 125, 51-55.
- Galvin, C.L.(1968) : Breaker type classification on these laboratory beaches, *J. Geophys. Res.*, 73/12, 3651-3659.
- Tanaka, M.(1986) : The stability of solitary waves, *Physics of Fluids*, 29, 650-655.
- Yasuda, T., H.Hara and M.Tanaka(1990) : A computational model of the deformation including overturning of a solitary wave over a submerged obstacle, *Proc. 3rd Int. Sympo. Fluid Dynamics, Nagoya, Japan*, 919-924.
- Yasuda, T., Y.Sakakibara and M.Hara(1992) : BIM simulation on deformation up to breaking of solitary waves over uneven bottoms, *Proc. HY-DROSOFT92, Valencia, Spain*, 523-535.

CHAPTER 25

WAVE CLIMATE CYCLES AND COASTAL ENGINEERING PRACTICE

Douglas L. Inman,¹ Scott A. Jenkins,¹ M. Hany S. Elwany¹

Abstract

El Niño-Southern Oscillation (ENSO) events are major factors in changing wave climate at coastal sites. These events are triggered by extreme anomalies in the global seasonal climate; and in recent years they have become quasi-predictable from certain antecedent conditions. Judicious application of the global concepts leading to (ENSO) events will improve our understanding and prediction of wave climate.

Introduction

Design of coastal structures and planning for beach remedial systems depend upon statistics determined from the study and measurement of past events and upon models using those statistics as primary inputs. The value of the statistic is usually assumed to depend solely upon the accuracy and duration of the observational series. This leads to common statistics such as a "design wave" height based on a recurrence history that defines the storm of the decade and century, and to shoreline changes based upon simple statistics such as the mean and standard deviation of beach width.

The limitation of our statistic is usually not the quality or resolution of the observations it is based upon, but rather that the statistics do not take into consideration the episodic nature of larger,

¹ Center for Coastal Studies, Scripps Institution of Oceanography, La Jolla, California 92093-0209

controlling systems that govern the intermediate to long-term wave climate and sediment budget. For example, wave climate is an end product of meteorological climate and subject to the cyclicities and uncertainties associated with that subject. Beach width is an end effect of the position within a littoral cell and is subject to all of the factors that influence the littoral sediment budget, including source, transport paths and sinks of sediment, as well as the variability in wave climate. Also, in the case of beaches, there is an element of inertia that causes beach erosion to be influenced more by the successive occurrence of clusters of average storms rather than by the isolated occurrence of a single extreme storm.

Climatic events such as El Niño-Southern Oscillation (ENSO) effect wave climate on a world-wide basis by altering the global atmospheric circulation paths, introducing periods of abrupt chaotic or episodic change. El Niños are harbingers of more intense wave climate along the temperate west coast of the Americas, but result in milder wave climates for the temperate east coasts of the Americas (Inman and Masters, 1994; Neelin et al 1994). El Niños also modify rainfall, causing droughts in some areas and flooding and maximum sediment yield in others. Along the southern California coast decades of relatively stable, mild wave climate are interrupted by El Niño events characterized by groups or clusters of intense storms and heavy rainfall. The El Niño of 1982/83 and its associated cluster storms completely denuded beaches that had been stable for the preceding 30 years. Thus, it is apparent that the usual statistical techniques based upon limited record lengths for predicting beach width and littoral drift rates and directions would lead to conclusions that are invalid for episodic periods of significant wave climate change.

Seasonal Climate: An Introduction to ENSO Events

The seasonal variations in the exposure of the hemispheres to the sun produce interannual changes in the duration of daylight and the angle of the sun's irradiance. These effects modulate solar heating, resulting in the interannual variation of the earth's atmospheric pressure field which in turn introduces seasonal climatic effects. Interannual variations are enhanced by the higher

convective effects of land and the greater concentration of land mass relative to water in the temperate latitudes of the northern hemisphere. In January, a large intense area of high pressure forms over the Asian continent (Figure 1a). This occurs because the convective slopes of Asia are inclined away from the sun with short periods of daylight that shutdown upslope convection, resulting in subsidence of air mass and an increase in pressure at ground level. In July, the convective slopes are inclined towards the sun with longer periods of daylight that increase solar irradiance and fuel upslope convection and lower surface pressure. Note that, in contrast to a rigid-lid system, the free motion of air in the convective atmosphere results in an inverse relation between temperature and pressure.

The northeast monsoons of southern Asia maximize in January, mainly in response to downslope anticyclonic flowing air caused by subsidence under the large area of Asian high pressure (Figure 1a). The cold descending air converges with tropical air to form a wet monsoon. The northeast monsoon in the Indian Ocean is less intense because of lower pressure gradients and the blocking effect of the Asian and African continental mountains. During July, the combination of upslope flow towards the low pressure area over the Himalaya mountains and the cyclonic geostrophic flow generates a strong southwest monsoon over the Indian Ocean (Figure 1b). This brings heavy rainfall over India and the high Ethiopian plateau (Quinn, 1992). The latter causes the Nile River floods that maximize during July. In contrast to the Indian Ocean, the southwestern monsoon is weak and relatively dry over southeast Asia because of lower pressure gradients and blocking by high inland topography.

The ENSO System

Upon occasion the typical seasonal weather cycles discussed above are abruptly and severely modified on a global scale. These intense global modifications are signalled by anomalies in the pressure fields between the tropical eastern Pacific and Malaysia known as the *El Niño/Southern Oscillation* (ENSO) (e.g., Diaz and Markgraf, eds., (1992). The intensity of the oscillation is often

measured in terms of the *Southern Oscillation Index* (SOI), defined as the monthly mean sea level pressure anomaly in mb normalized by the standard deviation of the monthly means for the period 1951-1980 at Tahiti, minus that at Darwin, Australia (Figure 2). A

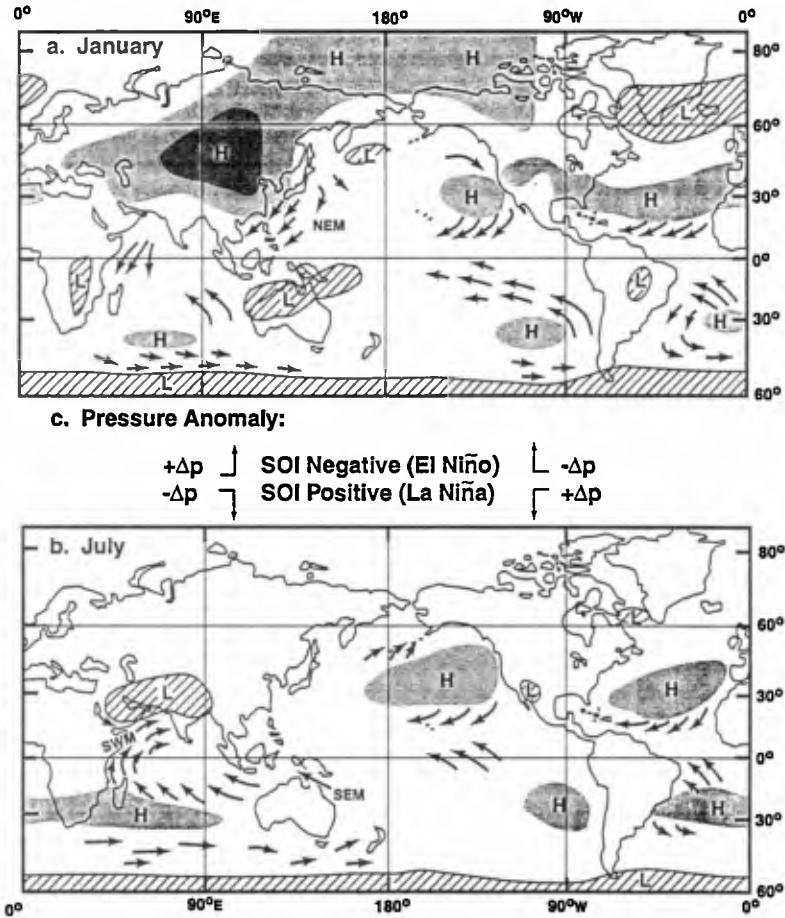


Figure 1. Seasonal pressure and winds for (a) January and (b) July. Contours of 1020 mb and 1000 mb are shown around areas of high (H) and low (L) pressure respectively. Prevailing winds are indicated by arrows: NEM, SEM, SWM designate northeast, southeast and southwest monsoons. (c) The pressure anomaly, Δp centered around longitudes 105° E and 105° W for negative and positive Southern Oscillation Indices (SOI).

Asian low pressure area will be intensified, spinning up a strong southwestern monsoon in the Indian Ocean, causing increased rain in India and over the Ethiopian plateau. In July, the air flow over the northern Indian Ocean is dominated by the large Asian low pressure system centered over Afghanistan. This intensifies the southwesterlies and draws the *intertropical convergence zone* (ITCZ) north over the Ethiopian plateau. The ITCZ is the zone of collision between the converging tradewinds of the northern and southern hemispheres. Its primary features are surface doldrums and vertical convection with considerable cumulus development, rain and thunder storms. For intense La Niñas, the resulting convergence of air masses in the ITCZ brings heavy rainfall that causes floods on the Nile River (Quinn, 1992). Application of $-\Delta p$ anomaly to the southern hemisphere tropics in the vicinity of 105° E lowers the pressure over northern Australia and New Guinea. This modifies the pattern of the southeast monsoon and brings heavy monsoonal rainfall to Australia (e.g., Nicholls, 1992).

Of course, the above suggestions based on an intensified seasonal pattern are vastly oversimplified and tell us nothing about why or when ENSO events occur or how long they will last. However, climatic events characterized by intense El Niños and La Niñas affect wave climates on a world-wide basis in the sense that atmospheric circulation paths are altered globally (Neelin, et. al., 1994; Philander, 1989). Spectral analysis of coral growth rates shows that over the past century El Niño events have occurred with recurrence periods centered approximately on 3 and 7 years with more intense events occurring every decade or so (Cole et al, 1992; 1993). Although the events are not clearly understood, there is evidence that ocean-atmosphere interactions act as an oscillator which drives large-scale ocean waves known as equatorial Kelvin waves. However, this oscillator interacts with Earth's annual cycles, producing nonlinear resonances (Jin et al, 1994; Tziperman et al, 1994). The ENSO cycles jump irregularly among these nonlinear resonances, exhibiting chaotic behavior. Thus, there may be relatively long periods of uniform annual climate response, interrupted by periods of abrupt change.

El Niños are harbingers of more intense wave climates along the temperate west coast of the Americas, but may result in milder

measured in terms of the *Southern Oscillation Index* (SOI), defined as the monthly mean sea level pressure anomaly in mb normalized by the standard deviation of the monthly means for the period 1951-1980 at Tahiti, minus that at Darwin, Australia (Figure 2). A

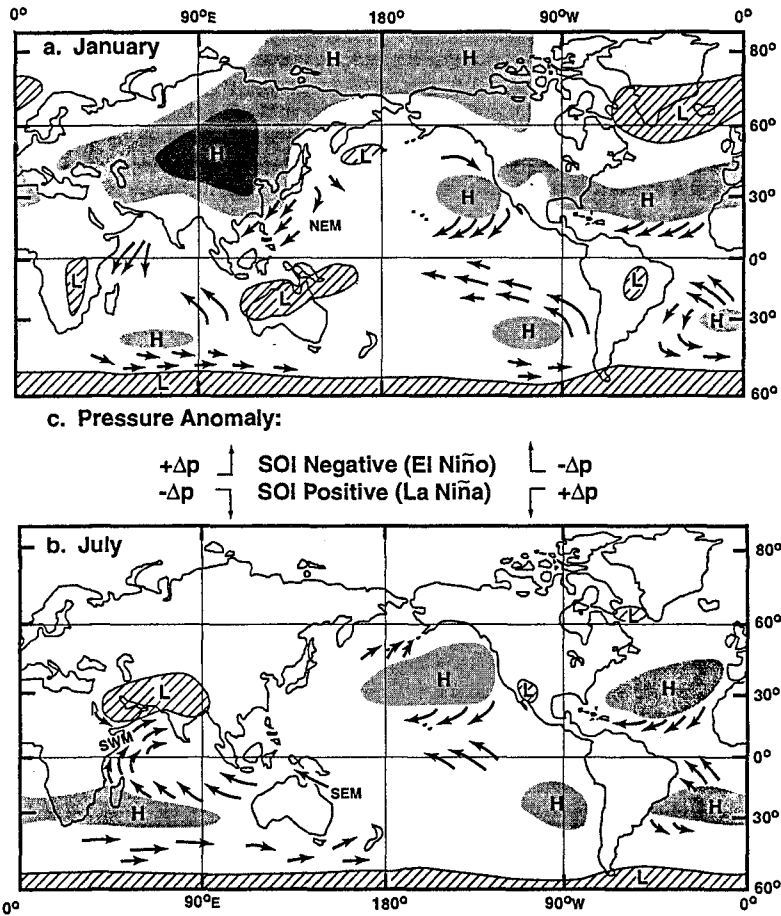


Figure 1. Seasonal pressure and winds for (a) January and (b) July. Contours of 1020 mb and 1000 mb are shown around areas of high (H) and low (L) pressure respectively. Prevailing winds are indicated by arrows: NEM, SEM, SWM designate northeast, southeast and southwest monsoons. (c) The pressure anomaly, Δp centered around longitudes 105° E and 105° W for negative and positive Southern Oscillation Indices (SOI).

negative SOI (lower pressure at Tahiti, higher pressure at Darwin) is known as an El Niño or warm ENSO event, because of the arrival

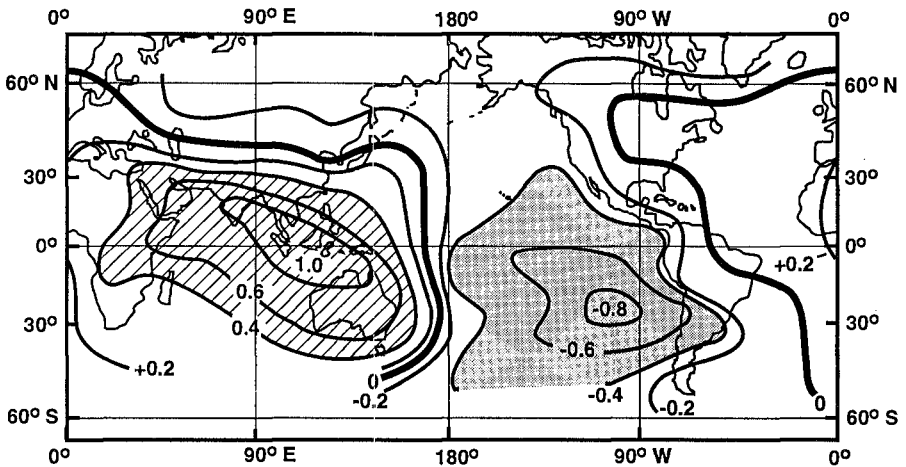


Figure 2. Global distribution of the correlation coefficient of annual pressure anomalies with simultaneous pressure anomalies at Jakarta (107° E longitude). Redrawn from Berlage (1957) and centered on 180° to show the southern oscillation.

of unusually warm surface water off the coast of Peru at the time of Christmas; hence, the term El Niño. Warm water also occurs along the coast of California and both regions experience unusually heavy rainfall. A positive SOI is known as La Niña and it signals the occurrence of colder than normal surface water in the eastern Pacific, but stronger southwest monsoons in the Indian Ocean with heavy rainfall in India and in the Ethiopian plateau. The latter causes flooding of the Nile River. Thus, the terms warm and wet vs cold and dry ENSO events that accompany El Niños and La Niñas respectively apply to the waters and coastal areas of the tropical-subtropical eastern Pacific Ocean and not necessarily to other parts of the globe.

It has been shown that the pressure changes associated with ENSO events are global in extent, and follow a pattern of alternate positive and negative correlation coefficients centered around

wave climates for the temperate east coasts of the Americas (Dolan et al, 1990 and Seymour, 1996). As El Niño events and groups of intense storms (referred to as "cluster storms") alter the wave climate, models of the nearshore must be adjusted to these changes in order to account for the abrupt and often long-lived coastal changes induced by these events.

The El Niño system

El Niño systems involve a complex set of interactions between the atmospheric and ocean circulation at tropical to middle latitude. The large-scale wind patterns and the companion mid-latitude high pressure systems described previously have a complementary feature in the ocean circulation referred to as "gyres". The gyres are the dynamic equivalent of the mid-latitude highs in the atmosphere, and are the result of an elevated sea level in the center of the ocean basin caused by a convergence of the Ekman drift from the trades and the mid-latitude westerlies. A large pool of warm water is established in the western Pacific which is ultimately regulated by the strength of the tradewind-driven component of gyre circulation.

This warm pool extends from the Philippine Islands south to the mid-Australian coast (Figure 3). Associated with these prevailing conditions is a stationary area of low atmospheric pressure, centered on Darwin, Australia, as compared with the relatively higher sea level pressure in the eastern Pacific from Tahiti to the coast of the Americas. El Niño events are associated with the release to the east of the warm water pool and a reversal of the relative pressure fields at Darwin as compared with Tahiti and the coast of the Americas (Figure 1a,c). These changes in the pressure fields in the lower layers of the atmosphere redirect the upper level jet streams that steer the tracks of traveling storms and markedly alter the wave climate of the world's coastline. The sequences within an El Niño event are illustrated in Figure 3 by numbers (1) through (5). The trade winds setup and confine a pool of warm surface water on the western side of the equatorial Pacific Ocean (1). Fluctuations in the prevailing trade wind intensity may release a series of eastward-flowing pulses of warm water. The warm El

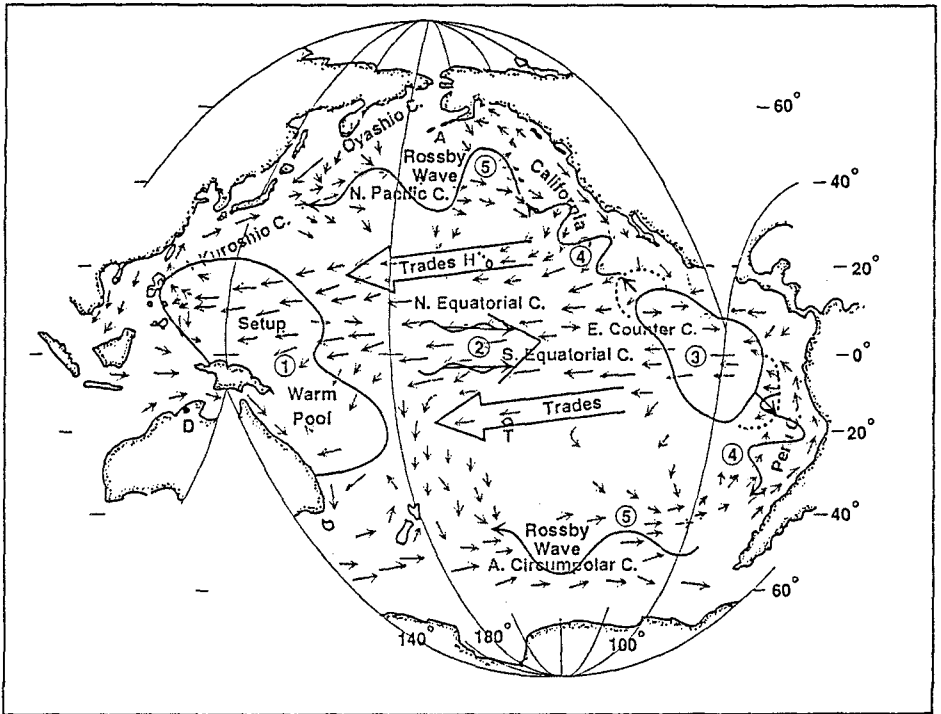


Figure 3. Schematic illustration of the five sequences leading to a fully developed El Niño event. See text for description.

Niño event begins when the trade winds relax and release a large "slosh" from this warm water pool which travels to the east along the equator (2). These sloshes travel as soliton-like internal features that are low-mode, baroclinic Kelvin waves channeled in the equatorial wave guide by the north-south gradients in planetary vorticity. Planetary vorticity is the spin imparted to a fluid particle by the local surface-normal vector component of the earth's angular velocity. These Kelvin waves have a phase speed determined by the density difference, $\Delta\rho$, at the thermocline, such that their phase speed is order:

$$C = [(\Delta\rho/\rho_2)gh_1]^{1/2} = 150 \text{ cm/sec,}$$

where h_1 is the depth of the thermocline. The equatorial Kelvin waves pump warm water into the eastern equatorial Pacific (3),

where it is spread poleward by barotropic Kelvin waves with topographically trapped modes propagating along the continental margins (4). These waves oppose the flow of the California and Peru currents. In turn, the shelf-trapped Kelvin waves appear to excite Rossby planetary waves that propagate slowly to the west against the flows of the North Pacific Current and the Antarctic Circumpolar Current (5). In addition to slowing the ocean current system, the Rossby waves induce sea surface temperature anomalies which modify surface pressures in the lower atmosphere that ultimately decrease the intensity of the westerlies, further slowing the overall circulation of water in the large Pacific gyres.

Sequences (1) through (5) in the El Niño event are all interactive among themselves and with the atmospheric circulation in very complex ways that are poorly understood. The conditions triggering the beginning of an El Niño event or those leading to its demise are not yet known. However, it is clear that, once started, the Kelvin-Kelvin-Rossby sequences all provide positive feedback that enhance each other and work toward a spin-down in the intensity of the prevailing anticyclonic oceanic gyres.

Changing Wave Climate

ENSO events leading to significant changes in seasonal trends of wave climate are usually associated with SOI values greater than about ∓ 0.5 . Figure 4 shows hemispheric contour plots of the pressure height anomalies (meters) for SOI positive (La Niña) and SOI negative (El Niño). Pressure gradients cause winds, and height anomalies show where persistent pressure gradients occur. The strongest pressure gradients occur along the boundaries of the height anomalies. The height anomalies in the figure show the mean location and intensities of the pressure changes during the ENSO events, and their boundaries indicate the likely location of storm paths. Figure 4a (La Niña) shows large areas of high pressure over the North Pacific and eastern North Atlantic. These high pressure areas would enhance storm tracks as shown by the two arrows for waves approaching North America and Europe. The El Niño condition is characterized in Figure 4b by a large area of negative height anomaly over the North Pacific ocean and a

relaxation in intensity but an increase in area of the positive height anomaly in the eastern North Atlantic. Thus, the La Niña/El Niño pattern over the North Pacific is bipolar and would be expected to give distinct changes in the storm track locations for the two conditions. In contrast either extreme would tend to enhance storm tracks approaching the coasts of Europe and the southeastern Mediterranean coast.

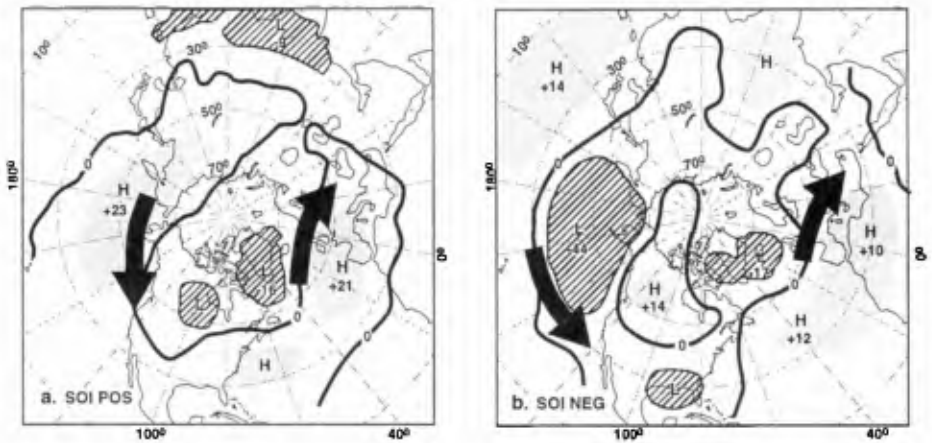


Figure 4. Height anomalies of the 700 mb atmospheric pressure surface derived from averaging winters (October-March) between 1947 and 1992 with preceding June-November for 11 SOI of +0.5 or greater (a) and for 12 SOI of -0.5 or less (b) (data from Redmond and Cayan, 1994). Shading and hatching indicate areas of negative (L) and positive (H) anomalies with maximum departure in meters. Arrows show position of storm-track enhancement associated with the anomalies.

Along many coasts, there are decades of relatively stable weather interrupted by shorter periods characterized by more variable weather, often accompanied by severe storms. The most recent period of mild-stable weather along the southern California

coast occurred during the 30 years between the mid-1940's and mid-1970's when mild La Niña type weather prevailed. Winters were moderate with low rainfall (Figure 5), and winds were predominantly from the west-northwest. The principal wave energy was from Aleutian lows having storm tracks which usually did not reach southern California (Figure 4a). Summers were mild and dry with principal wave energy coming from the southern hemisphere.

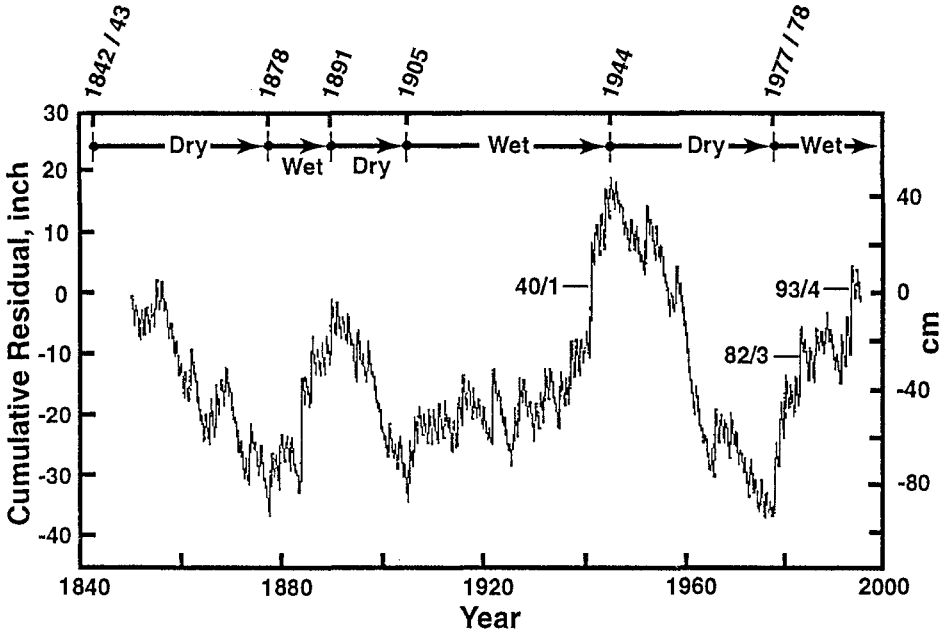


Figure 5. Cumulative residual rainfall in San Diego illustrating wet and dry periods that correlate with El Niño trends.

The wave climate in Southern California changed, beginning with the El Niño years of 1979/80 and 1982/83. The prevailing northwesterly winter waves have been replaced by waves approaching from the west (Figure 4b), and the previous southern hemisphere swell waves of summer have been replaced by tropical storm waves from the waters off Central America. The net result appears to be a decrease in the southerly component of the longshore transport of sand that prevailed during the preceding thirty years (Inman and Masters, 1994). Previous southward drift

rates of 200,000 m³/yr. have decreased to 50,000 m³/yr. and have reversed direction for protracted periods of time.

Conclusions

The clue to successful application of time series to engineering practice lies in long record lengths, and in the identification of supposedly anomalous trends. These anomalous trends can be identified by observables that either have intrinsically long record length or correlate with certain cause and effect mechanisms. For example, rainfall records, tree rings, railroad surveys and old newspaper articles can be used to correlate beach width and wave erosion with past El Niño's. Fluctuations in rainfall and wave intensity both follow the ENSO cycle which links them. For the modern records, a number of techniques are available to help elucidate this problem of cause and effect, including spectral and cross-spectral approaches and numerical progressions such as those resulting in cumulative residuals (Figure 5).

Acknowledgments

This research was funded by the Office of Naval Research, Ocean Modeling and Prediction program, under grant N00014-95-1-0005 with the University of California, San Diego.

References

- Berlage, H. P., 1957, "Fluctuations of the general atmospheric circulation of more than one year, their nature and prognostic value," *Koninklijk Nederlands Meteorologisch Instituut, Mededelingen en Verhandelingen*, 69, 152 p.
- Cole, J. E., G. T. Shen, K. G. Fairbanks and M. Moore, 1992, "Coral monitors of El Niño/Southern oscillation dynamics across the equatorial Pacific," pp. 349-375 in H. F. Diaz and V. Markgraf, eds., *El Niño, Historical and Paleoclimatic Aspects of the Southern Oscillation*, Cambridge Univ. Press, Cambridge, U. K., 476 p.

- Cole, J. E., R. G. Fairbanks and G. T. Shen, 1993, "Recent variability in Southern oscillation: isotopic results from a Tarawa Atoll coral," *Science*, v. 260, p. 1790-93.
- Diaz, H. F. and V. Markgraf, eds., 1992, "El Niño, historical and Paleoclimatic aspects of the Southern oscillation," *Cambridge Univ. Press, Cambridge, U. K.*, 476 pp.
- Dolan, R., D. L. Inman and B. Hayden, 1990, "The Atlantic coast storm of March 1989," *Jour. Coast. Res.*, v. 6, n. 3, p. 721-25.
- Inman, D. L. and P. M. Masters, 1994, "Status of research on the nearshore," *Shore and Beach*, v. 72, n. 3, p. 11-20.
- Jin, F-F, J. D. Neelin, and M. Ghil, 1994, "El Niño on the Devil's staircase: annual subharmonic steps to chaos," *Science*, v. 264, p. 70-72.
- Neelin, J. D., M. Latif and F-F Jin, 1994, "Dynamics of coupled ocean-atmosphere models: the tropical problem," *Annual Rev. Fluid Mech.*, v. 26, p. 617-659.
- Nicholls, N., 1992, "Historical El Niño/Southern oscillation variability in the Australasian region," pp. 151-173 in H. F. Diaz and V. Markgraf, eds., *El Nino, Historical and Paleoclimatic Aspects of the Southern Oscillation*, Cambridge Univ. Press, Cambridge, U.S., 476 pp.
- Philander, S. G., 1989, "El Niño, La Niña, and the southern Oscillation," *Int. Geophy. Ser.*, v. 46, Acad. Press, S.D., 293 pp.
- Quinn, W. H., 1992, A study of Southern Oscillation-related climatic activity for A. D. 622-1900 incorporating Nile River flood data," p. 119-194 in H. F. Diaz and V. Markgraf, eds., *El Nino, Historical and Paleoclimatic Aspects of the Southern Oscillation*, Cambridge Univ. Press, Cambridge, UK, 476 pp.
- Redmond, K. T. and D. R. Cayan, 1994, "El Niño/Southern oscillation and western climate variability," *6th AMS Conf. on Climate Variations*, Nashville, Tenn.
- Seymour, R., 1996, "Wave climate variability in southern California," *Jour. Waterway, Port, Coastal, and Ocean Engineering*, v. 122, n. 4.
- Tziperman, E., L. Stone, M. A. Crane, and H. Jarosh, 1994, "El Niño chaos: overlapping of resonances between the seasonal cycle and the Pacific Ocean-atmosphere oscillator," *Science*, v. 264, p. 72-74.

CHAPTER 26

STABILITY OF DESIGN WAVE ESTIMATES

Jan Rossouw¹, Josep R Medina²

ABSTRACT

Design wave heights are estimated for the Atlantic coasts of Southern Africa and the Iberian peninsula using the best available recorded data sets from the more exposed sites along these coasts. By spatial integration of the available data for a region and relaxing conditions with respect to independent sampling, stable estimates of design wave heights are obtained. Clear patterns are found in which the predicted design wave heights are strongly correlated with latitude. The recommendations of the IAHR committee on methods for design wave estimation are discussed and reservations are expressed about their recommendation to use only one method for design wave estimation.

INTRODUCTION

The estimation of design wave heights from recorded data is a subject that has received attention from many designers, engineers, statisticians and scientists in the past. Standard procedures for these estimates have however not been established and a variety of methods are presently being used. An international committee appointed by the IAHR, published a recommended procedure for design wave estimation in 1994 (Mathiesen et al, 1994). The committee recommended that only one method should be used. This method fits a three parameter Weibull distribution to data selected by means of a peaks over threshold (POT) sampling method.

This paper describes an alternative approach to design wave estimation favoured by the authors for areas such as the Atlantic ocean off South Africa and the Iberian peninsula. These areas are free of cyclones and similar storm events occur with great regularity during the winter months. Clear patterns in parameters such as the mean and standard deviation of the recorded wave heights exist in these areas. By using the method of moments to fit an Extreme 1 distribution to a total sample from the winter months, stable design wave estimates are obtained. Using this method, a very

¹ Senior Lecturer, Department of Civil Engineering, University of Stellenbosch, Stellenbosch 7600 South Africa

² Professor, Universidad Politecnica de Valencia, 46022 Valencia, Spain

interesting pattern in design wave heights emerges which is compatible with the known weather patterns in the area. Design waves estimated by this method are often much higher than with the method recommended by the IAHR committee.

In this paper an overview of the weather systems responsible for generating large waves in the Atlantic is given. Patterns in recorded wave heights are described and the knowledge of the weather and wave patterns are used to estimate design waves. The results obtained are discussed and compared with the results from studies by the IAHR committee

WAVE CLIMATE OF THE STUDY AREAS

The Atlantic coastlines off South Africa and the Iberian peninsula are free of cyclones as illustrated in Figure 1

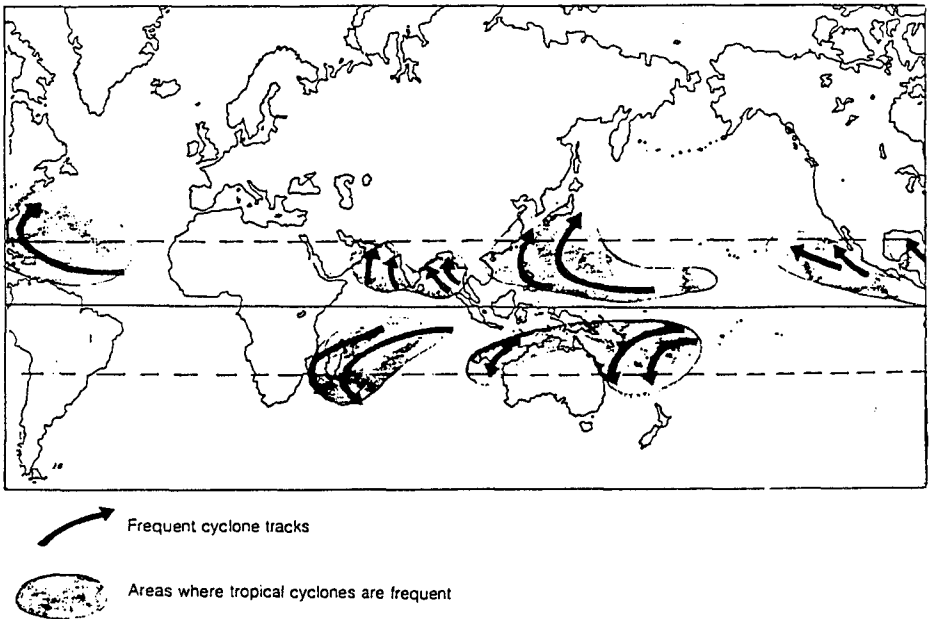


Figure 1: Frequent cyclone tracks of the world

(Hurry and van Heerden, 1982)

All major wave events in these areas are caused by large frontal systems which occur with great regularity during the winter months. Because of the size of the frontal systems and the speed at which they move on their path from west to east towards and past the coastline, similar wave heights are recorded over large coastal areas during major wave events. This is illustrated in Figure 2 for the South African coast for a few events during August 1980.

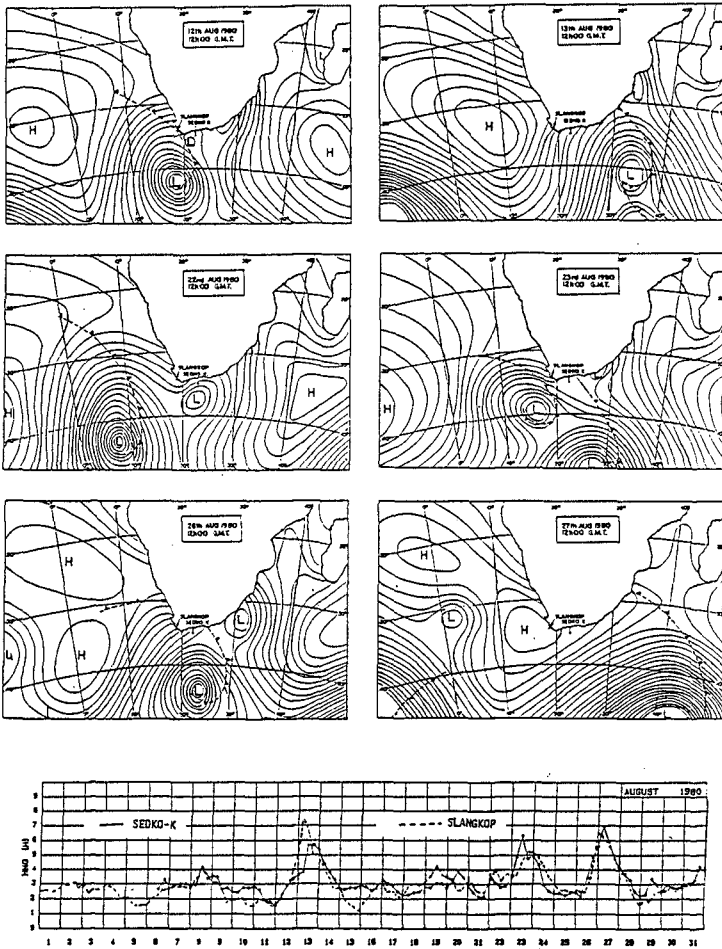


Figure 2: Waves recorded during August 1980

The similarity in wave heights recorded at two stations 300 km apart is apparent from this figure. Not only are the wave heights during major wave events similar over large areas, but the mean and standard deviation of the recorded wave heights over longer periods also show a remarkable similarity. In Figure 3 this similarity for 3 stations off the Iberian peninsula is illustrated.

The seasonal variation in wave height is also apparent from Figure 3. Extreme events can therefore be expected to occur in the winter months. In Figure 4 a comparison is made of the mean and standard deviation of the wave heights recorded in winter at a number of stations in the north Atlantic.

A clear pattern of increasing wave height with latitude is evident as can be expected due to the increasing intensity of the frontal systems at higher latitudes. A similar pattern is evident along the South African Atlantic coast.

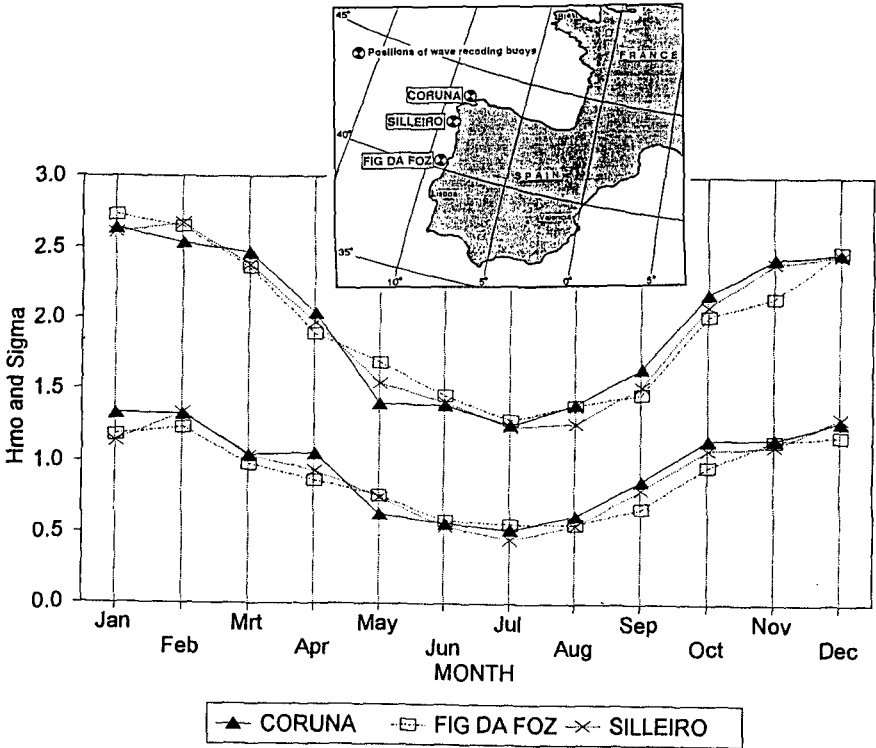


Figure 3: Mean and standard deviation of Hmo - Iberian Peninsula

The similarity in extreme and average wave conditions recorded along these coasts, together with the knowledge of the weather systems, lead to the following conclusions related to design wave estimation:

- Extreme waves are invariably caused by similar frontal systems and the extreme wave heights at exposed coastal stations must belong to the same extreme distribution.

- Due to the absence of cyclones and the seasonal variation in wave heights, identical data would be ensured if only data from the stormy winter months are selected
- The paths of the frontal systems are such that their intensity increase towards the higher latitudes. An increase in design wave heights should therefore occur with increasing latitude. Recording stations at similar latitudes should have similar design wave heights.

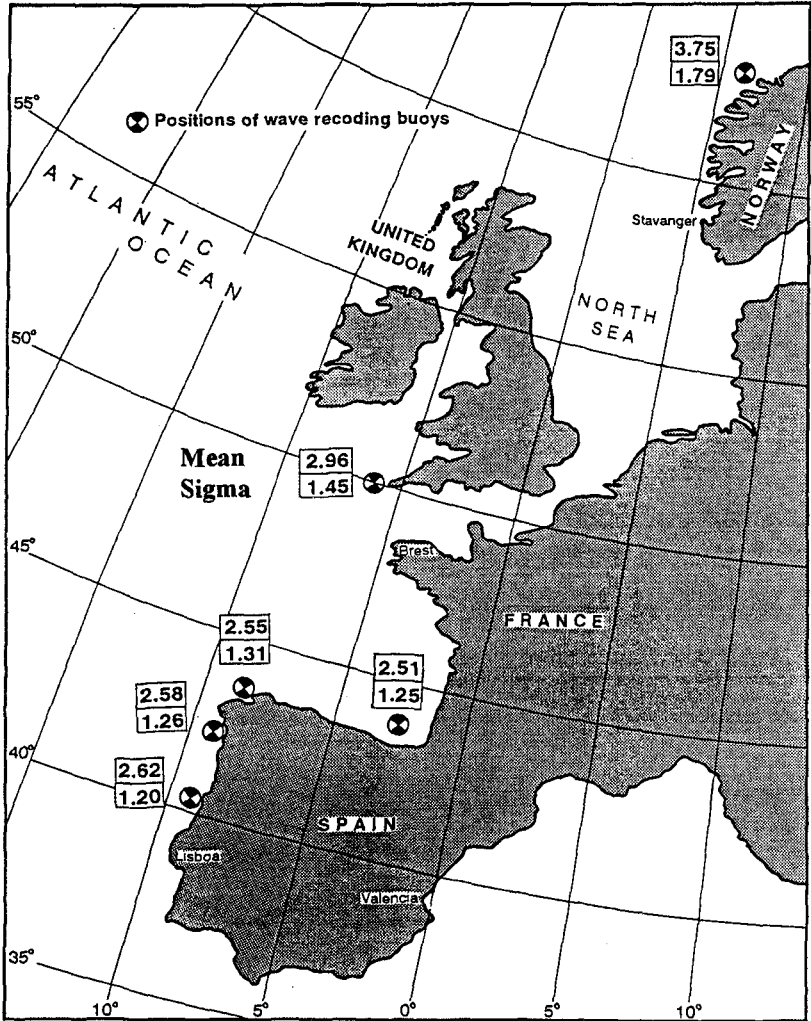


Figure 4: Mean and standard deviation of H_{mo} - European Atlantic

ESTIMATES BASED ON EXTREME 1 DISTRIBUTION AND TOTAL SAMPLE

The method preferred by the authors for estimating design wave heights, uses the method of moments to fit an Extreme 1 distribution to a total sample from the winter months. In this method the parameters of the distribution are based only on the mean (\bar{H}_{mo}) and standard deviation (σ) of the recorded wave heights in winter. The distribution is given by

$$(\bar{H}_{mo}) = A - B \cdot \ln(-\ln p) \quad \text{with}$$

$$B = 0.78 \cdot \sigma \quad \text{and}$$

$$A = (\bar{H}_{mo}) - 0.5772 \cdot B$$

$$p = \text{probability of non-exceedance of } H_{mo}.$$

A graph of H_{mo} versus $\ln(-\ln p)$ gives a straight line with slope B and a abscissa A as shown in Figure 5.

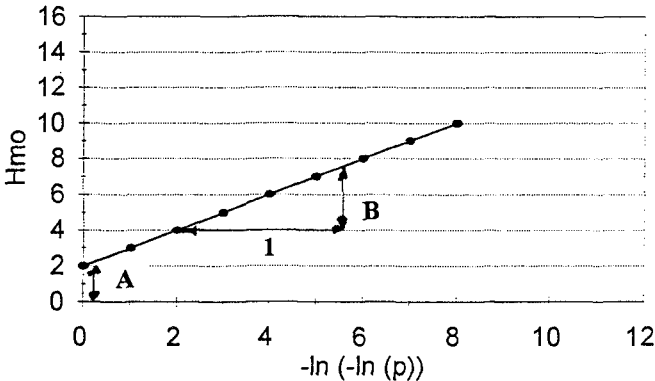


Figure 5: Extreme 1 distribution

This method makes maximum use of the available data as well as of the clear pattern that exists in the mean and standard deviations of the recorded wave heights

The fit of the data to the Extreme 1 distribution for all the stations along the South African west coast is shown in Figure 6.

The distribution generally fits the data well although deviations occur near the upper tail of the data. The deviations of the data at the upper tail are both above and below the fitted distribution. Although it will be possible to obtain a better fit at individual stations by employing a three parameter distribution, the overall fit is acceptable if the same distribution is used at all the stations along the coast. Inspection of the data shows that the stations where the data at the upper tail exceeds the fitted curves, included the more severe storms recorded on the coast. A downward deviation occur where these storms are not included in the data set. These deviations are considered

to be due to variations in the wave climate and deficiencies in the data rather than variation in the underlying distributions. Too much emphasis on this upper tail will lead to unstable design wave estimates that vary haphazardly from station to station.

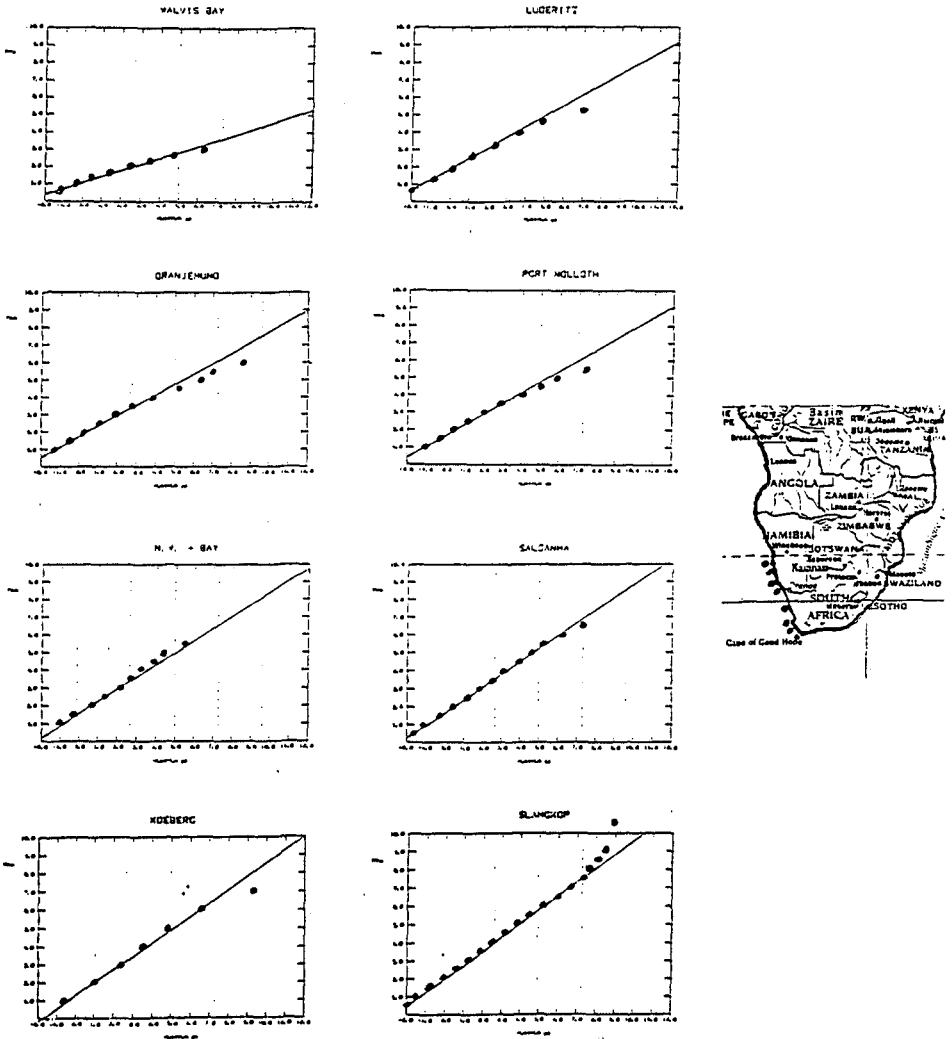


Figure 6: Extreme 1 fit to RSA data

The 100 year return period waves (H_{m0}) with a duration of 3 hours are shown in Figure 7 for the south and north Atlantic. Added to the data off the South African and Iberian Atlantic is data off the British isles and Norway.

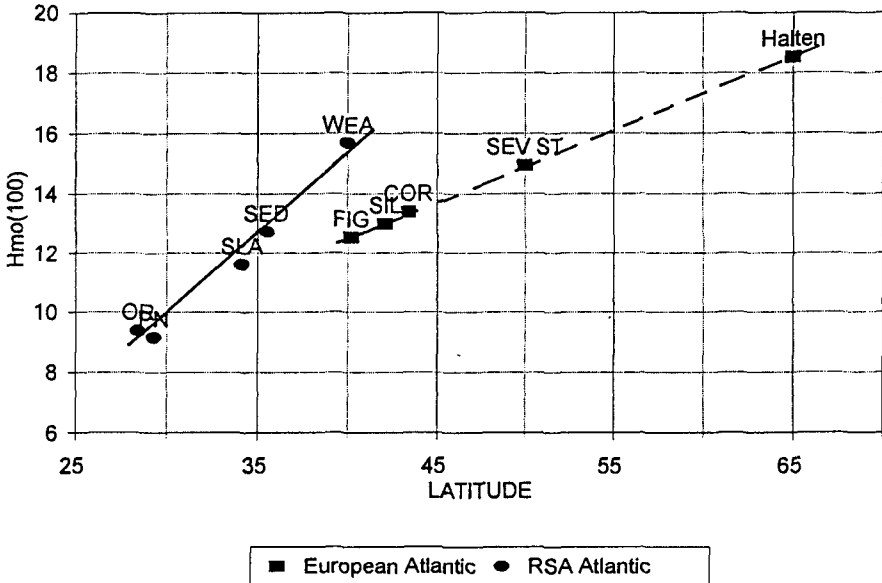


Figure 7: Design $H_{m0}(100)$ - 3 hour duration

A strong correlation between the design waves and the latitude is evident from this figure.

The 100 year wave as estimated here is compared to the largest waves recorded at various sites in the north Atlantic in Figure 8. The 100 year wave predicted at all the stations exceed the maximum recorded wave height by between 30 and 50 per cent. The maximum difference occur at Haltenbanken where the 100 year wave of 18.5 m exceeds the maximum recorded wave by 6m or nearly 50 per cent. This design wave seems extraordinarily high and is much higher than the 15.0 m predicted by the members of the IAHR committee using the same data (van Vledder, 1993). The question obviously arises whether there should be a physical limit to the height a wave can reach. A wave height (H_s) of 17.4 m was recorded at the Weather Station India in the North Atlantic (Draper, 1986), at a latitude lower than the Haltenbanken site, giving some credibility to this high design height. The probable reason for the large difference between the two methods of design wave estimation in the case of Haltenbanken lies in the difference in emphasis placed on the upper tail of the data by the two methods. This will be further discussed in the next section.

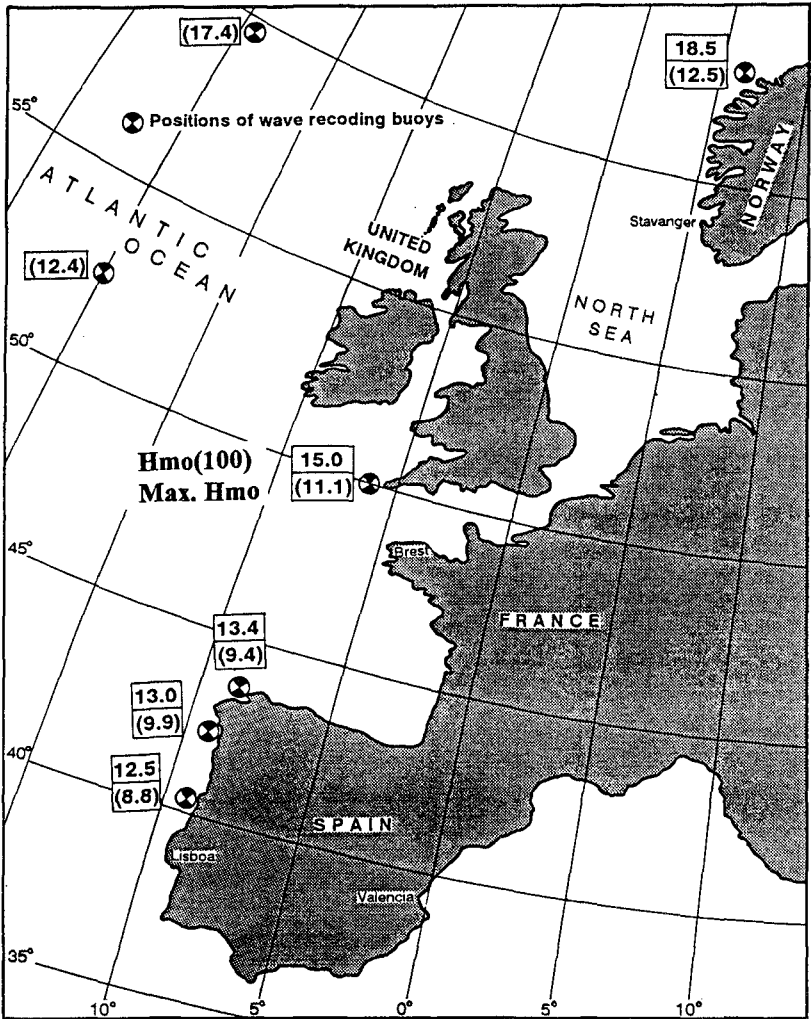


Figure 8: $H_{mo}(100)$ and maximum H_{mo} recorded

ESTIMATES BASED ON 3 PARAMETER WEIBULL DISTRIBUTION AND POT SAMPLING

The method for design wave estimation recommended by the IAHR group, differ from the method described above. To ensure independent and identical data, a peaks over threshold sampling technique is used. The highest wave recorded between the up and down crossing of a chosen threshold (POT) is used as data. A three parameter Weibull distribution is fitted to the selected data. This method inherently places the emphasis on the upper tail of the data in that only the largest storms are included in

the data and that the use of three parameters allows the fit to follow the data deviations at the upper tail.

With the South African data it was found that the two methods described above lead to similar design values in cases where a long data record is available and where the upper tail of the data follows the Extreme 1 distribution. With shorter data sets or in cases where a deviation from Extreme 1 distribution occur at the upper tail of the distribution, large differences occur between the two methods. Because of the emphasis on the upper tail by the IAHR method, much lower design wave heights are predicted when the data deviates downward at the upper tail. This is thought to be the reason for the large differences at Haltenbanken discussed in the previous section. Similarly the IAHR method will predict higher waves where the deviation is upward. The emphasis on the upper tail destroys the clear pattern in design waves illustrated in Figure 6. Copeiro (1978) already warned against placing too much emphasis on the upper tail of the distribution.

APPROPRIATE METHOD

Two methods have been presented which essentially differs in the procedure for data selection and in the choice of extreme value distributions. The question arises as to which procedure is most appropriate.

The advantages of using a total sample from the winter months and a simple two parameter Extreme 1 distribution in areas such as the open coasts of the South African and European Atlantic are:

- Maximum use is made of the available data.
- Design wave estimates are not sensitive to the upper tail of the data. The loss of data during storms and outliers in the data do not influence the estimates unduly.
- Estimates of design waves stabilise after a few years of data. This method is therefore ideal where short data records must be used.
- The Extreme 1 distribution fits the data well if all the data of an area is considered rather than data at individual recording stations
- Maximum use is made of clear spatial patterns that exist in the mean and standard deviation of the recorded wave heights

Criticisms against the method are:

- The data used are not independent. For areas such as the South African and Iberian Atlantic, where storms occur with great regularity, the use of correlated data do not seem to bias the estimates (Rossouw,1988). This method however will only work in areas where one can expect a strong correlation between mean and extreme conditions. It will not work in areas prone to cyclones, semi-protected areas where refraction, diffraction and other shallow water effects will influence the data or in areas where mixed distributions are present.

- The selection of the probability associated with a given return period requires a decision with respect to the duration of the storm peak. This in the opinion of the authors is an advantage since the significant wave height of one hour duration during the peak of the storm can be expected to be higher than the height for three hour duration. This is also the reason why an increase in the peak H_{m0} value can be expected if the recording interval is decreased. Rossouw and Medina (1995) show that the selection of the duration of storm peaks varying from 1 to 6 hours, although affecting the value of the design H_{m0} , does not influence the design H_{max} values.

Advantages of the method recommended by the IAHR committee are as follows:

- The POT method of sampling should ensure independent and identical data.
- The use of a three parameter Weibull distribution allows a good fit to most data sets

Problems with this method are however:

- The POT method of sampling is sensitive to the level of the threshold that is chosen. This was illustrated by the IAHR committee in van Vledder et al (1993).
- There is an emphasis on the upper tail of the distribution. This emphasis increases with increasing threshold values
- The use of a 3 parameter distribution increases the emphasis on the upper tail of the distribution.
- The use of only one data point in each storm makes the method very sensitive to outliers in the data, loss of records near the peak of the storm, the recording interval, etc. Long data records are also required before stable design wave estimates are obtained.

It is concluded that both these methods have their merits. The method recommended by the IAHR committee is expected to be superior in cases where there is a danger of using non identical data. Such areas would be cyclone prone areas, semi protected areas such as inside bays where directionality plays a major role and where mixed systems are present.

The simple method favoured by the authors seem to be applicable to areas where storms of identical origin occur with great regularity. In such areas a correlation between the mean and extreme conditions should exist and the estimate of design waves based on mean wave heights seems reasonable.

For either method the integration of the data over space should help to add stability to the estimates. Knowledge of the generating systems should be incorporated in the integration process.

CONCLUSIONS

The recommendation of the IAHR committee to use only one method for design wave estimation seems unrealistic. Their recommended method will work well in areas where different systems are responsible for wave generation for example in areas where cyclones occur regularly. In areas such as the Iberian and South African Atlantic, the methods used by the authors are preferred, especially at stations with short recording histories. In areas such as the South African east coast where cyclones occur very irregularly, i.e only once every few years, neither these methods are applicable.

Clear patterns exist in the recorded wave data. This is to be expected taking into account the present knowledge of the weather systems over the oceans. Design wave estimates, especially over large bodies of open water, can be improved by the spatial integration of the available data. Efforts to do this in the South African and Iberian Atlantic produces promising results. A global approach and co-operation between the countries involved in wave recording, will enhance our knowledge of extreme wave events and will lead to better estimates of design wave conditions.

REFERENCES

- Copeiro, E. (1978): Extremal prediction of significant wave height, Proc. 16th Int. Conf Coastal Eng., Hamburg.
- Draper L. (1986): Wave measurements at north Atlantic weather stations India and Juliett in the nineteen seventies. IOS Report No. 222. 1986.
- Hurry L. and van Heerden J. (1982): South African weather patterns, Via Africa Ltd, Cape Town, 1982.
- Mathiesen, M. et al (1994): Recommended practice for extreme wave analysis, Journal of Hydraulic Research, Vol. 32, No. 6, 1994.
- Rossouw, J. (1988): Design waves and their probability density functions. Proc. 21st Int. Conf. Coastal Eng., Malaga, Spain.
- Rossouw J. and Medina J.R. (1995): Design wave estimation - a robust approach: Proc. 4th Int. Conf. on Coastal and Port engineering in developing countries, Rio de Janeiro, Brazil. September 1995.
- Van Vledder et al (1993): Case studies of extreme wave analysis: a comparative analysis, Proc. WAVE93 Conf. New Orleans, USA.

CHAPTER 27

AN EVALUATION OF TWO WAVE FORECAST MODELS FOR THE SOUTH AFRICAN REGION

by
M. Rossouw¹, D. Phelp¹

ABSTRACT

The forecasting of wave conditions in the oceans off Southern Africa is important for both offshore and coastal marine operations in the area. The accuracy of wave forecasts for the area from models operated in Europe has, however, not been high. One of the main reasons is that the local measurement of waves has not been taken into account. Since the necessary infrastructure for operational wave forecasting is locally available in South Africa, a decision has been taken to establish a local facility whereby a numerical wave forecast model will be implemented. This paper focuses on the comparison of two operational wave forecast models in order to assist in the selection of an appropriate model for the South African region.

1. INTRODUCTION

The South African ocean route is one of the major shipping routes in the world (approximately 120 million tonnes of oil were transported around the tip of Africa in 1991). In addition, the offshore activities such as oil exploration, diamond mining and also coastal construction operations are increasing.

The Southern African waters are renowned for their treacherous sea, especially during winter. The already established weather forecast service provided by the South African Weather Bureau (SAWB) has up till now depended largely on information obtained from the global forecast model data, especially for wave forecasts. However, the wave conditions are represented relatively poorly as the input data sources are sparse in the Southern Atlantic Ocean where most of the wave energy is generated which reaches the South African coast. Only a few weather data sources are available (a couple of islands and a number of weather buoys).

¹Research Engineers, CSIR, P O Box 320, Stellenbosch, 7599, South Africa

The maritime activities need a reliable and accurate maritime weather forecast service which includes the prediction of the wave conditions. Local input data sources should be incorporated, including the local wave conditions. This information should result in a reduction in the risk of shipping accidents and could improve the planning for offshore exploration and operational activities.

Therefore, an appropriate wave forecast model should be implemented and operated in conjunction with the already established weather forecast service. This paper focuses on the comparison of two operational wave forecast models in order to assist in selecting an appropriate model for the South African region (CSIR, 1995).

2. DATA SOURCES

The data sources used for this exercise included the wave forecast data from the UKMO and WAM numerical wave models, wave data collected by wave recording buoys and also remotely sensed wave height data recorded by the ERS-1 satellite. In a number of cases the synoptic weather charts were also consulted for the identification of weather systems. These data sources are discussed briefly in the following sections.

2.1 Forecast Wave Data

UKMO model

The data of the UKMO model from the British Meteorological Office in Bracknell (UKMO) were received via the South African Weather Bureau (SAWB). Two forecasts per day were received, for 00:00 and 12:00 hours.

The forecasts covered an area delineated by latitudes 20° to 65° S and longitudes 0° to 40° E at a 2,5° grid spacing. The data included the significant wave height (H_{mo}), the significant wave height and wave direction for the swell, and the swell and sea wave period. Each forecast covers 120 hours (five days) at the following intervals:

$$T+0, 12, 24, 36, 48, 72, 96 \text{ and } 120 \text{ hours } (T = 00:00 \text{ and } 12:00)$$

WAM model

The WAM model data were received directly from the Royal Dutch Meteorological Institute (KNMI) in the Netherlands via e-mail. One forecast per day was received, for 12:00 hours.

The forecasts covered an area delineated by latitudes 21° to 60° S and longitudes 9° to 39° E at a 3,0° grid spacing. The data included the significant wave height (H_{mo}) and wave direction, the significant wave height and wave direction for the swell, and the significant wave height and wave direction for the sea component. The forecast covered a period 72 hours (three days) at six hourly intervals.

2.2 Recorded Wave Data

Wave recording buoys

The wave data used in this study were collected by wave recording buoys at locations offshore of Mōwe Bay, Port Nolloth, Slangkop and Durban in water depths of 100m, 100m, 76m and 50m, respectively (Figure 1).

Wave records of approximately 17,5 minute duration were routinely recorded at three-hourly intervals at all these stations. These records were subsequently spectrally analysed and interpreted in terms of the significant wave height and period. However, these records do not contain the wave direction and are therefore omnidirectional.

Remotely sensed data

The only remotely sensed data used in this study were obtained from the ERS-1 satellite. These data, consisting of significant wave height, were used to investigate specific forecasts during the period of interest. It was possible to compare observed and predicted wave heights over a large area.

3. COMPARISON METHODOLOGY

The study used a number of methods to compare the predicted data with that observed. It should, however, be noted that only the significant wave height could be analysed as it was the only parameter common to all three data sets. Although the wave direction parameter is included in the forecasts, it is not part of the suite of wave parameters obtained from the recorded data, as non-directional wave recording buoys were used. The methods of comparison are discussed below.

3.1 Data Processing

Both the UKMO and WAM data were received in a grid format. For comparison with measured data at specific locations, the most appropriate grid points had to be identified in the UKMO and WAM data sets. Therefore, the closest grid points to the wave recording buoy locations were selected as shown in Figure 1. Although two UKMO forecasts per day were available, only the 12:00 hour forecasts were used to compare with the 12:00 WAM forecast and the measured data.

For comparison with the offshore wave data from both models, the measured data had to be adjusted for the shallow water effects. Shoaling was therefore taken into account by applying linear shoaling as described in the Shore Protection Manual (CERC, 1984). However, as no wave directions were available, the refraction-effect could not be considered. The bathymetry in the vicinity of all four locations is fairly uniform and the water depth relatively large, thus wave energy-loss due to refraction will not be significant.

3.2 Time-series Comparisons

In order to establish the effectiveness of a wave forecast over a certain period, one can compare the entire forecast with the observed (measured) wave conditions. If the forecast predicted the actual conditions well enough one would have confidence in that forecast. It should, however, be remembered that there can be some variation in the predictions as these are based on meteorological information that is not always 100 per cent correct. One must, therefore, include an estimation of uncertainties for short-term sea state parameters in the wave forecast.

For the purposes of this study a factor " σ " (normalised standard deviation) was applied to both UKMO and WAM data sets. This factor was taken as $\sigma=0,2$ in accordance with standards for wave predictions (PIANC, 1992). Thus, the following formula was implemented:

$$H_{\min} = H - (H * \sigma) \quad \text{and} \quad H_{\max} = H + (H * \sigma)$$

where H = significant wave height (H_{m0})

These two parameters, H_{\min} and H_{\max} , thus provide a range in which the observed wave height could occur for a satisfactory prediction.

3.3 Specific Timeslots

Another way of comparing the wave forecasts with measured data is to consider specific forecast timeslots. Both the model data sets have predictions for 12, 24, 48 and 72 hours ahead. It was therefore possible to compare the predicted and measured data at the specific timeslots, graphically and statistically.

Scatter plots of the predicted and measured total wave height were prepared at all four locations for the above mentioned timeslots. Statistical parameters such as the correlation coefficient and the root mean square error (RMSe) were also determined for these comparison sets (Khandekar, 1989). The RMSe is given by the following expression:

$$RMSe = \sqrt{\frac{1}{N} \sum (Model - Observed)^2}$$

where:

Model = predicted value; Observed = observed value; N = number of values

3.4 Wave Contours

As mentioned previously both the UKMO and WAM data come in a grid format. It is thus possible to present these data sets in a contour plot. Predicted wave conditions for a large section of the Southern Atlantic Ocean can therefore be presented. These were plotted with the ERS-1 satellite tracks. The predicted wave heights along the satellite tracks could then be compared to wave heights recorded

by the ERS-1 satellite.

Due to the vast number of individual predictions (every timeslot), it is not practical to prepare a contour plot for each of them. Therefore, only a selected number were chosen which could be examined.

4. RESULTS

4.1 Time-series Comparisons

Using the procedure described in Section 3.2, both UKMO and WAM forecasts were plotted with the observed data recorded off Möwe Bay, Port Nolloth, Slangkop and Durban for the period 14 November to 31 December 1994. Examples of the comparisons are presented in Figure 2 for Möwe Bay, Port Nolloth, Slangkop and for Durban.

For the purposes of this study the assumption was made that up to a two-day-ahead (48 hours) and three-day-ahead (72 hours) wave forecasts are practical. The observed values had to fall within approximately 80 per cent of the predicted ranges in each wave forecast in order for the forecast to be deemed satisfactory. This meant that only one prediction value of the UKMO forecasts for both the 48 and 72 hours could be out of range. As the WAM data produced more values, two predictions in 48 hours and three predictions in 72 hours could be out of range and the forecast would still be acceptable. However, if the erroneous prediction values were consecutively out of range, the forecast was rejected.

Based on these criteria, the percentage of satisfactory wave forecasts are presented in Table 1. For each location and for the two models these percentages are given for the 48 hour and 72 hour forecast period. It is evident that the WAM model produced more satisfactory forecasts than the UKMO model for the Möwe Bay, Port Nolloth and Slangkop area. For example, at Möwe Bay 92 per cent of the WAM wave forecasts were satisfactory while 67 per cent of the UKMO forecasts were satisfactory. Both models produced better results over the 48 hour forecast period than over the 72 hour period. The low percentage of acceptable forecasts for the Slangkop location is again addressed in Section 4.2.

TABLE 1: Percentage satisfactory wave forecasts

Location	UKMO model (%)		WAM model (%)	
	48 hour	72 hour	48 hour	72 hour
Möwe Bay	67	64	92	89
Port Nolloth	60	44	81	73
Slangkop	39	11	56	44
Durban	64	51	45	33

4.2 Specific Timeslots

Using the procedure described in Section 3.3, scatter plots were done for both the UKMO and WAM forecasts with the observed data recorded off Möwe Bay, Port Nolloth, Slangkop and Durban for the period 14 November to 31 December 1994.

UKMO data

Two examples of the scatter plots are presented in Figure 3, showing the 24 and 48 hour timeslot results for Slangkop. The solid line also shown in the figures represents the 1-to-1 (1:1) ratio of the predicted versus the observed wave heights. The correlation coefficient and RMSe values for the 24 hour timeslot are given in Table 2.

TABLE 2: UKMO statistics: 24 hour timeslot

Location	Average wave height (m)		Correlation coefficient	RMSe (m)
	Measured	Predicted		
Möwe Bay	1,86	1,84	0,644	0,34
Port Nolloth	2,01	1,82	0,652	0,53
Slangkop	2,22	1,86	0,631	0,69
Durban	1,81	2,00	0,503	0,53

From the results it appears that the values for Möwe Bay, Port Nolloth and Durban locations are distributed fairly symmetrically around the 1:1 line. However, at the Slangkop location there is a definite bias towards under-prediction. This was evident in the scatter plots of all four timeslots. In order to eliminate this bias, linear regression was performed on the 12-hour data set. The regression line should coincide with the 1:1 line if perfect agreement between observed and predicted data exists. In order to eliminate the under estimation of the predicted results, data points were adjusted proportionately to get better correlation between observed and predicted values. The data sets of the other three timeslots (24, 48 and 72 hours) were also adjusted in a similar manner using the 12 hour regression function. These re-analysed results are presented in Table 3. Using this regression function it was possible to improve the comparison of the predicted with the observed wave heights for all four timeslots at Slangkop.

In general the correlation between the observed and predicted values was found to be low. As can be expected, the correlations decreased over time with the 12 hour timeslot having the highest correlations. The average correlation coefficients for the 12, 24, 48 and 72 hour timeslot (for all four locations combined) were found to be approximately 0,6, 0,6, 0,5 and 0,4 respectively. In general, the predictions, therefore, do not compare all that well with the observed conditions. However, by applying the regression function to the Slangkop data, an average coefficient of about

0,8 was found. As was expected, the correlation for 72 hour forecasts was the lowest on average.

TABLE 3: UKMO: Re-calculated Slangkop statistics

Timeslot (hours)	Average wave height (m)		Correlation coefficient	RMSe (m)
	Measured	Predicted		
12	2,35	2,35	0,88	0,45
24	2,22	2,11	0,86	0,40
48	2,20	2,20	0,80	0,45
72	2,21	2,24	0,62	0,65

The RMSeS on the other hand, range from approximately 0,3 m to 0,85 m; the lowest RMSe values being in the 12 hour timeslot. It is also noteworthy that Möwe Bay has the lowest values for all timeslots, on average 0,36 m. This implies the predictions for Möwe Bay were the most accurate of the locations considered. By applying σ (0,2) to the average predicted wave height (Tables 2 and 3), an uncertainty value of 0,38 is determined. Therefore, because this value compares well with the RMSe, one can conclude that the prediction for Möwe Bay should be satisfactory and typically within ± 20 per cent of the actual wave height.

The average RMSe for the Slangkop location was found to be 0,71 m while an average uncertainty value of 0,39 m was calculated. This difference of 0,32 m and the low correlation indicates that the predictions for this location are unsatisfactory. However, following the re-analysis the high correlation coefficient of 0,8 and the average RMSe of 0,49 m suggest reasonable predictions. Based on the average predicted wave height an uncertainty value of 0,45 m was determined. This value therefore compares well with the average RMSe. Thus, the predictions close to the Slangkop location appear to have been reasonable. Satisfactory forecasts can therefore be obtained with some level of calibration.

Durban has the highest RMSe value, 0,84 m (72 hour) with an average value of approximately 0,65 m. Application of σ to the average predicted wave height yields an uncertainty value of 0,41 m which is about 0,2 m less than the average RMSe. Apart from inadequate input data for the wave forecast model, these discrepancies could also be attributed to the effect of the Agulhas Current on wave conditions along the south and south-east coast of South Africa.

The average RMSe at the Port Nolloth location was found to be 0,61 m while the average uncertainty value of 0,4 m was calculated. Therefore, these forecasts for this location could not be rated as satisfactory as a correlation coefficient of 0,6 was obtained.

WAM data

Figure 3 also presents two examples of the scatter plots showing the 24 and 48 hour timeslots for Slangkop. The solid line also shown in the figures represents the 1-to-1 (1:1) ratio of the prediction versus the observed wave heights. The correlation coefficient and RMSe values for the 24 hour timeslot are given in Table 4.

TABLE 4: WAM statistics: 24 hour timeslot

Location	Average wave height (m)		Correlation coefficient	RMSe (m)
	Measured	Predicted		
Möwe Bay	1,84	1,89	0,86	0,23
Port Nolloth	2,00	2,05	0,87	0,33
Slangkop	2,19	2,41	0,77	0,53
Durban	1,77	2,18	0,45	0,76

From the figures it appears that the values for Möwe Bay and Port Nolloth locations are distributed fairly symmetrically around the 1:1 line. However, at the Slangkop location there was also a slight bias towards over-predicting wave heights below 2,5 m and under-predicting wave heights above 2,5 m. In order to eliminate this bias, linear regression was performed on the 12-hour data set, as in the case of the UKMO data (Section 4.2). The data sets of the other three timeslots were also adjusted in a similar manner using the 12 hour regression function. These re-analysed results are presented in Table 5.

TABLE 5: WAM: Re-calculated Slangkop statistics

Timeslot (hours)	Average wave height (m)		Correlation coefficient	RMSe (m)
	Measured	Predicted		
12	2,32	2,32	0,90	0,41
24	2,19	2,18	0,90	0,33
48	2,17	2,17	0,89	0,34
72	2,18	2,15	0,82	0,42

The correlation between the observed and predicted values was found to be quite satisfactory, except for the Durban location. As expected, the correlations decreased over time with the 12 hour timeslot having the highest correlations.

The average correlation coefficients for the 12, 24, 48 and 72 hour timeslots were found to be approximately 0,7, 0,7, 0,7 and 0,6 respectively. The average

correlation coefficients for the Möwe Bay, Port Nolloth, Slangkop and Durban location were found to be about 0,8, 0,8, 0,7 and 0,4 respectively. In general, the predictions, therefore, compare well with the observed conditions except at the Durban location. However, by applying the "regression" function to the Slangkop data, an average coefficient of almost 0,9 was found at this location. As was expected, the correlation of 72 hour forecast was, on average the lowest on average.

The RMSe's on the other hand range from approximately 0,2 m to 0,8 m. The lowest RMSe values being in the 12 hour timeslot. It is also noteworthy that Möwe Bay has the lowest values for all timeslots, on average 0,26 m. By applying σ (0,2) to the average predicted wave height, an average uncertainty value of 0,39 m is determined. Therefore, because this value compares well with the RMSe, and the correlation is good for Möwe Bay, one can conclude that the forecasts are satisfactory.

The average RMSe for the Slangkop location was found to be 0,56 m while an average uncertainty value of 0,47 m was calculated (Section 3.2). Although the difference is quite small and the correlation fair, the re-analysis resulted in a high correlation coefficient of 0,9 and an average RMSe of 0,38 m suggesting satisfactory predictions. Based on the average predicted wave height an average uncertainty of 0,44 was determined. This value therefore compares well with the average RMSe. Thus, reliable wave forecasts close to the Slangkop location can be obtained with some level of calibration.

As in the case of the UKMO forecasts, the Durban location has the highest RMSe value, 0,76 m (for the 24 hour timeslot) with an average value of approximately 0,69 m. Application of σ to the average predicted wave height yields an average uncertainty value of 0,42 m which is about 0,3 m less than the average RMSe. This implies a greater than 20 per cent uncertainty in the predicted wave height. Apart from inadequate input data for the wave forecast model, these discrepancies could also be attributed to the effect of the Agulhas Current on wave conditions along the south and south-east coast of South Africa.

The average RMSe at the Port Nolloth location was found to be 0,36 m while the average uncertainty value of 0,42 m was calculated. Thus, the forecasts for this location also appear to be reasonable as a correlation coefficient of 0,8 was obtained.

4.3 Wave Contours

Five case studies were selected to present specific predictions spatially together with the ERS-1 data. All the forecasts used were produced at 12:00 (T = 12:00).

An example of the predicted wave height contours of the UKMO and WAM forecasts as well as the ERS-1 tracks are presented in Figure 4. The wave height versus latitude plots are also given in these figures. The ERS-1 tracks were selected so that they would correspond with the time of the predicted wave heights.

It would be difficult to determine which model produced the best wave forecasts as only five cases were examined. However, these results give an indication of how well specific predictions compared spatially using the ERS-1 data.

5. DISCUSSION

The time-series comparisons determined for the UKMO and WAM wave forecasts, revealed that the WAM model produced a larger percentage of satisfactory forecasts than the UKMO model. However, the UKMO forecasts appear to have been more successful at the Durban location. As expected all cases the forecasts for the 48 hour forecast period were more reliable than for the 72 hour period.

It appears that during calm and also gradually varying conditions both models predict wave heights quite well. Wave height conditions that increased over a period of a day or more were predicted satisfactorily on a number of occasions. However, when the wave height increases rapidly (less than a day), the predictions tended to be poor. Under these storm conditions, WAM forecasts compared better with the observed wave heights than the UKMO forecasts. The UKMO forecasts also frequently under-predicted the wave heights during these events.

By examining the results of the timeslot-comparison, it was found that the RMSe's of the WAM forecasts are, on average, more than 20 per cent lower than the RMSe's of the UKMO forecasts. The correlation coefficients, on the other hand, are 33 per cent higher at the Möwe Bay and Port Nolloth locations and, 12 per cent higher at Slangkop. At the Durban location these coefficients were found to be approximately the same.

The five cases selected for plotting the wave height contours are not enough to unequivocally determine which model produced the best results. In order to determine this, more specific predictions (i.e., 24, 36, 48, 72 hours) of every forecast would have to be used.

Although it has been established that the forecasts of the WAM model compare most favourably with the observed data, the wave forecasts can still be improved. It should also be recognised that this study was performed in the summer season when mild to moderate wave conditions prevail for most of the time. During the winter season (June to August) extreme wave conditions prevail more frequently and are also more variable. These large fluctuations in wave height are coupled to the passage of intense low pressure systems which are more frequent during the winter months.

For both forecast values, the mathematical formulation used to determine the generation and propagation of wave conditions are state-of-the-art and are continuously being improved. However, the input data (the atmospheric forces) used to drive these models determines the reliability of a wave forecast to a large extent. In the southern hemisphere the input data are unfortunately sparse which results in

poor spatial data representation. Currently the input data consist mainly of data from coastal weather stations and some remotely sensed data sources. To improve the wave forecasts in the Southern Atlantic Ocean, it would be essential to improve the number and quality of input data sources. This could be done through the deployment of more offshore weather buoys. In addition the use of wave recording buoys off the coast of South Africa for verification purposes, would contribute to greater reliability of wave forecasts.

6. CONCLUSIONS

Considering the three comparative methods that were used to compare the UKMO and WAM forecasts with the observed data, obtained from wave recording buoys offshore of Möwe Bay, Port Nolloth, Slangkop and Durban as well as wave height data remotely sensed by the ERS-1 satellite, the following conclusions can be drawn:

The time-series comparison results showed that the WAM model produced a larger percentage of satisfactory wave forecasts than the UKMO model at the locations of Möwe Bay, Port Nolloth and Slangkop. On average, the WAM model produced over 35 per cent more satisfactory forecasts than the UKMO model.

By analysing the wave forecasts in terms of correlations coefficients and Root Mean Square errors (RMSes) it was found that the forecasts produced by the WAM model provided the best results.

The RMSes of the WAM forecasts are, on average, more than 20 per cent lower than the RMSes of the UKMO forecasts. The correlation coefficients are 33 per cent higher at the Möwe Bay and Port Nolloth locations and 12 per cent higher at Slangkop. At the Durban location these coefficients were found to be approximately the same.

Although it was not possible to determine which model produced the best results by comparing the predicted wave heights with remotely sensed wave heights along satellite tracks, it was found that this method may be useful in establishing the spatial reliability of the forecasts in terms of specific predictions (timeslots).

This comparative study was done during the months of November and December with mild to moderate wave conditions prevailing for most of the time. These results should therefore be considered to be more relevant for the summer season than for the winter season.

The differences between the results of the two models could amongst other things be attributed to the following factors:

- The UKMO is a second generation model whereby the non-linear transfer of wave energy is parameterised. The WAM model, which is a third generation model, solves the non-linear wave energy transfer function.

- In addition, different atmospheric input data sets are used to drive the two models, which would influence the output of these models.

It is concluded that the WAM model produces the most favourable results. However, these forecasts can still be improved by increasing the number of the input data sources (offshore weather stations) and also by evaluating the numerical modelling procedures of the wave forecast model.

7. RECOMMENDATIONS

Based on the conclusions the following recommendations can be made:

The WAM model should be implemented locally for providing the necessary wave forecasts for the South African region. (Note: the model has been installed at the head office of the SAWB; the model is presently running on a trial basis).

In order to establish the effectiveness of the WAM and UKMO forecasts during storm conditions, a similar comparison study should be conducted for the autumn and winter seasons (March to August).

The Agulhas Current is also a prominent feature along the south and south-east coast and influences the wave conditions in this region. This current-wave interaction should therefore also be investigated for incorporation in the wave forecast models in order to have reliable forecasts along both the south and south-east coast.

An essential component of the numerical modelling of the atmospheric forces and wave conditions are the data sources. As these are sparse in the southern hemisphere, especially in the Southern Atlantic Ocean, data coverage should be increased by, for example, the deployment of offshore weather buoys. The present network of wave recording buoys along the coast of South Africa (called WAVENET) and maintained by the CSIR, could be used for verification purposes in the wave forecasting procedures. These strategies should improve the reliability of the wave forecasts and also the general weather forecasts.

REFERENCES AND BIBLIOGRAPHY

- CERC (1984). *Shore Protection Manual*. Coastal Engineering Research Centre. Washington D.C. 1984.
- CSIR (1995). Evaluation of Two Wave Forecast Models for the South African Region. CSIR Report EMAS-C 95003.
- PIANC (1992). Analysis of Rubble Mound Breakwaters. Report of Working Group no. 12 of the Permanent Technical Committee II. Permanent International Association of Navigational Congresses. *Supplement to Bulletin N° 78/79*, 1992: 15 - 17.
- Khandekar, M.L. (1989). *Operational Analysis and Prediction of Ocean Wind Waves*. Coastal and Estuarine Studies. Springer-Verlag, New York.
- Benjamin, J.R. and Cornell, C.A. (1970). *Probability, Statistics, and Decision for Civil Engineers*. McGraw-Hill, New York, N.Y.

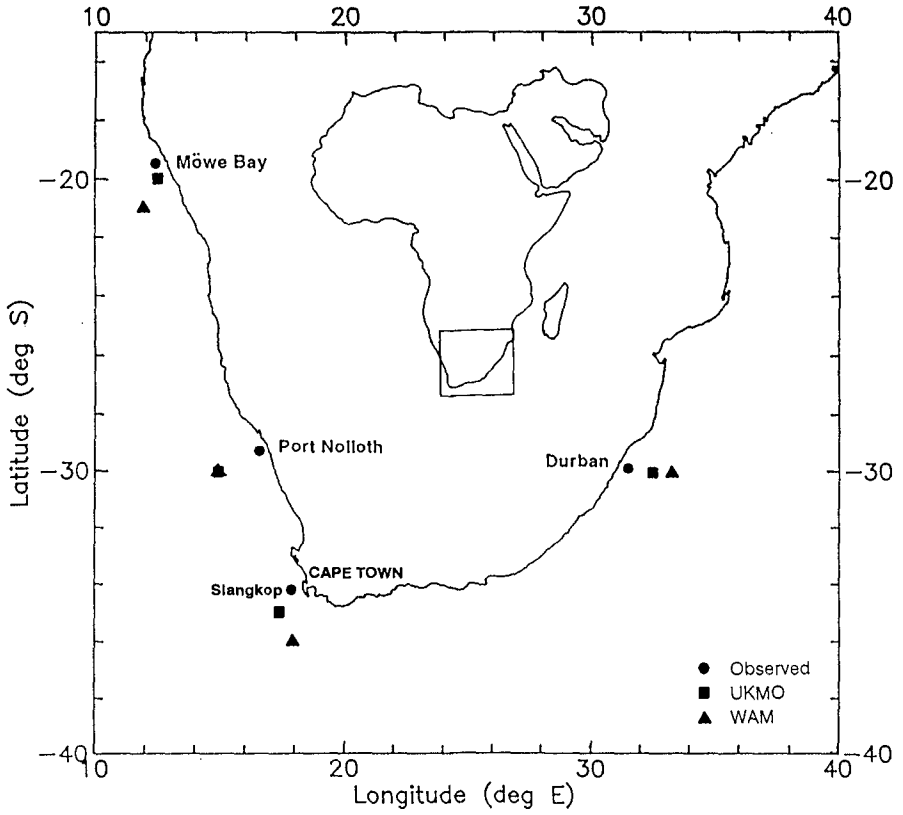


Figure 1: Location map

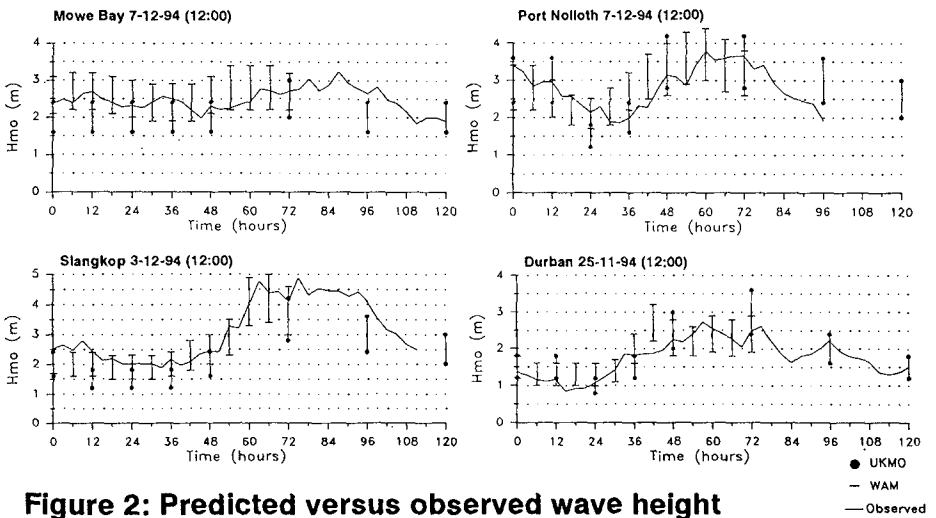


Figure 2: Predicted versus observed wave height

LOCATION: SLANGKOP

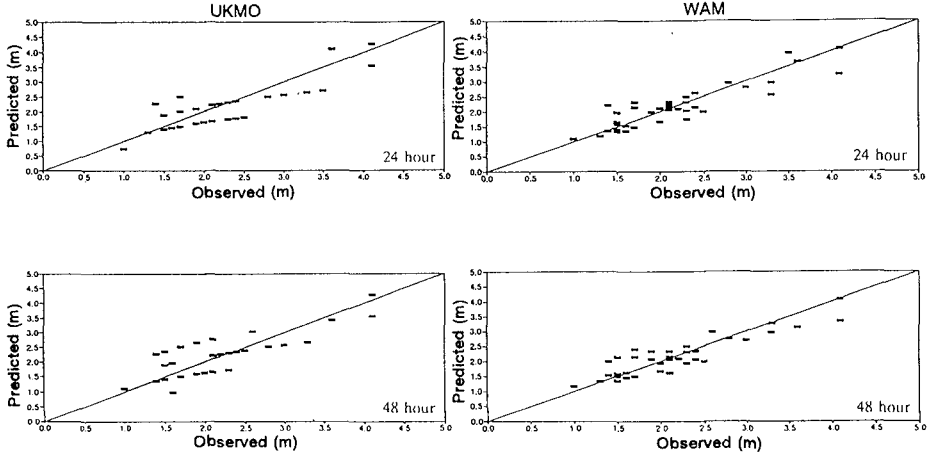


Figure 3: Scatter plots for Slangkop location

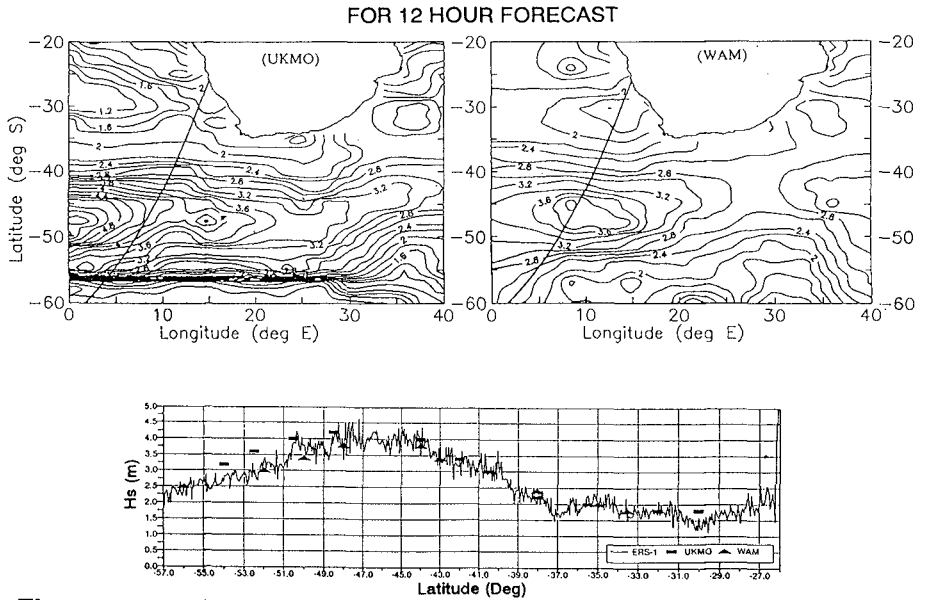


Figure 4 Predicted and recorded wave heights along ERS-1 track

CHAPTER 28

A Comprehensive Wind, Wave and Current Measurement Program in the South China Sea

by Jagat N. Sharma,¹ S. Tryggestad,² and J. Bian³

Abstract

The South China Sea has been a prolific fishing ground and a busy shipping lane, and has recently become an important source of offshore oil and a center of rapidly growing economic activities. However, little systematic scientific study of the area has been carried out (Anonymous 1985 and Wyrski 1961). Recently, several Metocean (meteorological and oceanographic) studies were performed to support the offshore petroleum production in the area. This paper summarizes these and other studies, and then, describes a comprehensive Metocean measurement program (Sharma et. el. 1991). Many distinctive and unique features of the measurement program are presented and discussed. Published samples of wind, waves, and current data are used to illustrate the complexity of oceanographic conditions in the area. Economic benefits of the measurement program are estimated approximately and found to be many times the cost of the program. While many important design decisions can be made with the 18 months of data, many other decisions need to be made conservatively in the absence of a multi-year Metocean dataset. A comparison with the condition in the Gulf of Mexico reveals many similarities and some differences. Future data needs and their possible benefits are also discussed briefly.

Introduction

The South China Sea (Figure 1) is a semi-enclosed sea very similar to the Gulf of Mexico. It has been a prolific fishing ground and a busy shipping lane, and now, some of the fastest growing nations of the Asia-Pacific region surround it. As economic activity grows in the

¹ President, COMET: Coastal, Ocean, Marine, Environmental Technology, Inc., 7714 S. 75th E. Ave., Tulsa, OK 74133-3511, USA.

² Manager, OCEANOR: Oceanographic Company of Norway A/S, Pir-Senteret, P.O. Box 2514 Fjordgata, N-7002 Trondheim, NORWAY.

³ President & General Manager, COTC: Shenzhen China Ocean Technology Company Ltd, Huaqiang N. Rd. Shangbu Industrial Zone, Room 411B East 4/Floor, 204# Building, Shenzhen, CHINA.

area, the need for more and better meteorological and oceanographic will grow in this area. First, we briefly review various studies conducted in this area to support economic activities. Then, we summarize a comprehensive Metocean measurement program with which we were closely involved. Benefits of past studies are conservatively estimated and it is found that a similar future measurement program could be very cost effective. Future data

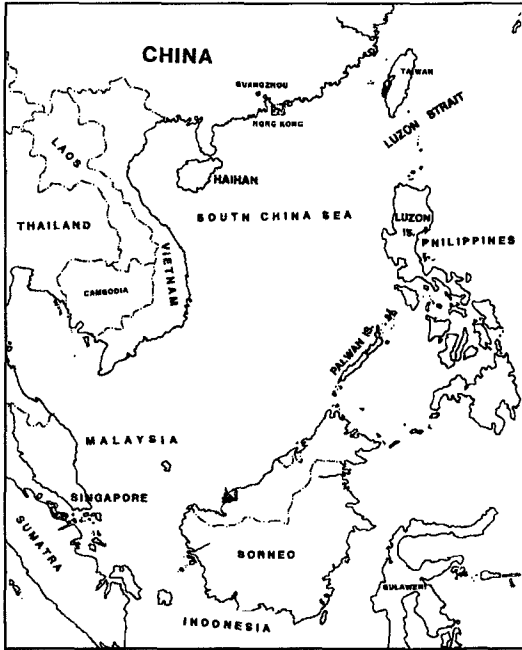


Figure 1. Location Map

needs are briefly discussed.

Finally, we present our conclusions and recommendations.

When China granted offshore leases to western companies in 1979, the only available Metocean information consisted of Wyrski 19961 and SSMO (Synoptic Ship Meteorological Observation) data which consists of visual observations from ships in the area. For few preliminary planning purposes, these data are adequate, but are inadequate for final design criteria preparation. Inadequacy of general understanding of the South China Sea Oceanography became very apparent when Glomar Java Sea sank near Hainan Island in a minimal typhoon.

Prior Measurements & Analysis in the South China Sea

In 1959-61, a hydrographic survey of the area was conducted and the results were published as a report by Wyrski (Wyrski 19961). In 1979-1982, Academia Sinica conducted several oceanographic surveys in the area. Western visiting scientists went on many of these cruises. A summary of the collected data has been published as a report in Chinese (Anonymous 1985). Several other oceanographic studies have modeled transport in and out of South China Seas. Results of these studies are useful in understanding the oceanography of the area. However, these studies did not include collection of wind, wave, and current data for model verification and calculation of operational and extreme design criteria.

Recently to meet some offshore industry needs, Oceanweather Inc. performed a proprietary hindcast study covering the entire basin using a third generation wave model. Wind, wave and depth averaged currents were hindcast in two hundred severest tropical storms during past 50 years. The same parameters were also hindcast for a continuous 10-year

period. Using the hindcast results, extreme and normal operating criteria can be prepared. For more details, please refer to Cardone (Cardone 1994). This study's strong points include basin-wide coverage, excellent use of historical meteorological data such as surface weather maps and tropical cyclone summary data. However, to verify the model results the study could use only limited wave measurements in shallow water in the southern part of the basin.

There is no high-quality measured wave data available in the public domain. Several high-quality long term data sets have been acquired recently in the northern part of the South China Sea. Unfortunately, these data are proprietary and unavailable except for limited data which appear in published papers (Yuan 1988, Sharma 1991). Some of the published results will be presented here to illustrate the complexities of South China Sea Oceanography.

Many other proprietary studies have been performed to support specific project needs. Several design criteria studies were performed by China Ocean Technology Company, Oceanweather Inc., and possibly others. To support the needs of specific projects, many operators measured specific features affecting their operations. Some of those data are of oceanographic interest but unavailable for research.

To support the construction and maintenance of their gas pipeline from Hainan Island to Hong Kong, Arco measured currents along their pipeline route. Currents in several typhoons were measured. During their drilling programs, Oxy and Amoco Orient vessels experienced very strong soliton currents. The measurement yielded some of the strongest soliton currents ever, and these measurements were subsequently useful in developing environmental design criteria.

To support their many offshore operations, Arco developed and implemented a typhoon emergency response plan. Corona et. al. (Corona 1996) presented the results of their implementation at the 1996 Offshore Technology Conference in Houston. In one year evaluation period, the study prevented 1,200 round trip helicopter flights (2,400 flight hours) transporting equivalent of 24,000 personnel. Besides saving the cost of flight time and vessel downtime, the emergency response plan greatly reduced the inherent transportation risks associated with flights in inclement weather. From the information provided in the paper, it is conservatively estimated that the total savings could easily exceed several tens of million dollars. A similar proprietary study was performed for the Lihua project. The results of the study are unavailable to public. An informal evaluation of the method indicated that savings in evacuation cost and downtime were several million dollars.

A better and simpler typhoon evacuation method has been developed recently (Sharma 1996). In this method, it is recognized that the long lead time needed for shutting down offshore operations presents special problems because the historical forecast errors for such long lead time are very high. Meteorological forecasts are used as received along with a few simple and easy measurements at site. Many oceanographic and meteorological features which consistently affect typhoon parameters are used in such a way that safety is not compromised. Using this method the essential operations could be continued by delaying total evacuation without risking even a single life. The method is implemented in a simple calculation method using PC applications such as

Excel, Lotus or Project. The calculation method is activated when a typhoon is about 800 miles away from the operating area. At this time, the safety engineer enters the number of helicopters available, their passenger capacities, round trip time and total number of personnel on the rig in order of their evacuation priority. From this information, time needed for various levels of evacuation including total evacuation is calculated. Meteorological forecasts without any modification are used in this method. From the forecast parameters, the arrival time of the edge of severe wind conditions unsuitable for helicopter operations is calculated. At all forecast time steps, the total evacuation time is maintained smaller than the quickest possible arrival time of the adverse edge of the typhoon. This could be achieved either by partial evacuation or by chartering more and/or bigger helicopters. Full evacuations are avoided most of the time because only a small fraction of all typhoons occurring within say 400 nautical miles of a site come close enough to affect operations. Using this method, operation managers could delay, or possibly avoid complete shut down without risking any life.

Many proprietary Metocean studies were performed to evaluate the possible exploitation of a difficult prospect named Lihua in 1000 feet water depth located at 150 miles Southeast of Hong Kong in the South China Sea. Very little results of these proprietary studies are available in journal papers or conference proceedings. The following description of a comprehensive meteorological and oceanographic measurement program are based on scant published results.

Lihua Measurement Program

In 1987-88, a consortium of Chinese Scientific Agencies and Oceanor of Norway deployed the following measuring instruments:

- two acoustic Doppler current profilers,
- four Aandera current meters,
- an ultrasonic current meter (UCM-30),
- Marex buoy for waves and wind,
- directional Wavec buoy,
- anemometers at four different elevations on a drilling rig,
- water temperature, oxygen content, and salinity,
- air pressure, tidal elevation.

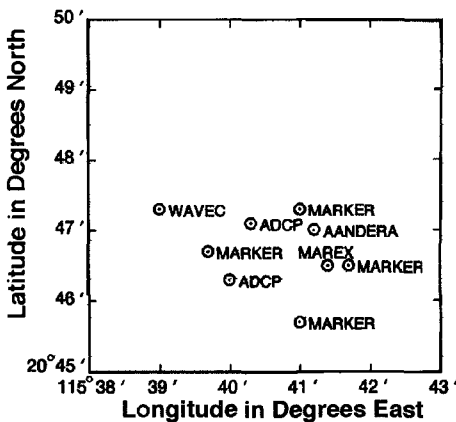


Figure 2. Instrument Location

The instruments were spread out in a well thought out pattern to allow future 3-dimensional current studies (Figure 2). As presented on the figure 2, four different current meters are located at the corners of a trapezoid with each side equal to about one nautical mile. So, the upstream and downstream current meters registered a soliton pulse current about 15 to 20 minutes apart. Also, eddy currents can be clearly resolved with a suitable computer program.

Recognizing that the measurement program was in a frontier area, many unique and special steps were taken to insure success. Some of the **unique** and **distinctive** features of the measurement program were:

- global cooperative project organization,
- careful planning to overcome extremely unfavorable logistics,
- satellite search and rescue methods,
- redundant instruments for reliability,
- patrolling of instrument area to prevent theft, and
- quality control at every step.

As a result, the actual data recovery was substantially higher (about 95%) than the initial overall goal of 80%. Eighteen months of nearly continuous wind, wave, current, water temperature data were recorded. The measured data contains many features of special scientific and design interest. The following are some of the most important features:

- complex storm current profiles,
- interaction of typhoon and cyclonic eddy,
- interaction of typhoon and monsoon,
- waves higher than forecast from wind,
- intense current of a short duration (possible internal soliton signature), and
- relation between current and sea temperature.

To illustrate the above oceanographic features, sample data are presented and discussed.

Meteorological & Oceanographic Features

Wind, wave current and other meteorological parameters were continuously measured from August 1987 to February 1989. The instruments in the operating area were affected by 11 typhoons and 12 winter monsoon storms. The following paragraphs briefly describe some of the most important meteorological and oceanographic features:

Typhoons

Four typhoons registered significant wave heights over 7 meters (23 feet) and one over 9 meters (30 feet). Seven other distant passages of typhoons were recorded. Significant wave heights much greater than those predicted by a parametric model were measured in typhoons embedded in monsoon winds. Typhoon Nina passed over the instrument area while it was in its tropical storm stage. A maximum wind of 22 meters per second was measured by the two wind instruments mounted on the Marex buoy at a 6 meter elevation, but the measured waves were much higher than expected for a 22 meters per second typhoon.

Wind, waves and currents measured in Typhoons Betty and Cary are presented here (Figure 3) to demonstrate the quality and quantity of the collected data. Typhoon Cary followed Typhoon Betty within 6 days. Typhoon Betty entered the South China Sea in the evening of the same day the instruments were deployed. Even though the measuring instruments experienced only the outer periphery of the typhoon, the forceful presence of a dangerous typhoon is visible in the recorded data. Typhoon winds were from the east superimposed on southwest monsoon wind.

A diurnal cycle in the measured wind speeds can be seen on the plot. This cycle corresponds to a land breeze sea breeze effect at the site. This effect so far from land was unexpected.

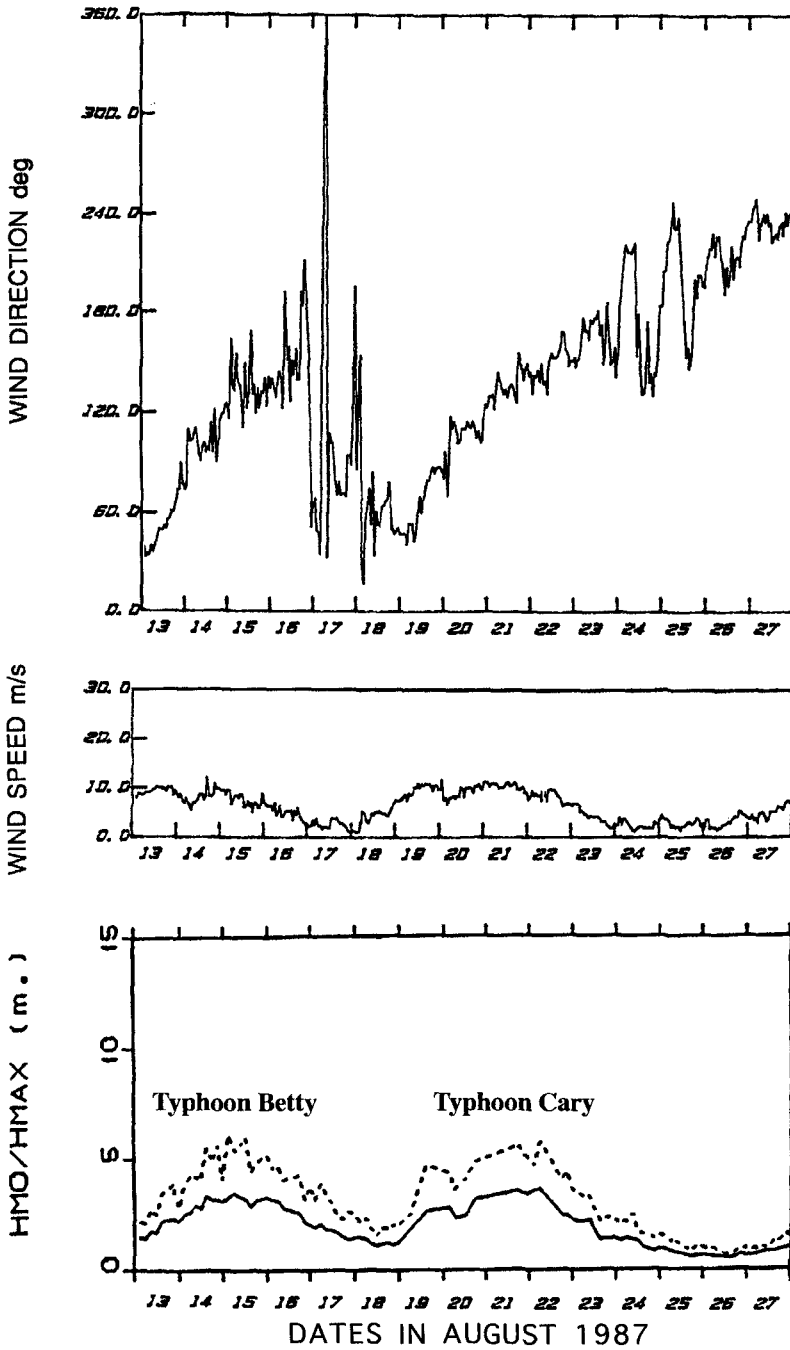


Figure 3. Wind direction, wind speed and wave in Typhoons Betty and Cary.

The waves reflect the distant passage of Typhoons Betty and Cary. A maximum significant wave height of 3.5 meters was recorded in both typhoons.

While the wind and wave responses were similar in the two typhoons, the current responses were entirely different (Figure 4). The mean current during Typhoon Betty increased without any significant change in the diurnal current amplitude. In contrast, the mean current during Typhoon Cary increased only slightly, but the diurnal current amplitude increased significantly. The combined maximum current measured during the two typhoons are nearly equal.

If the sharp spike in the beginning of data had been measured by only one current meter, it could have been rejected as a spurious noise. In this case, the same spike was measured by all three current meters, and the spike could not be rejected. Similar spikes are seen

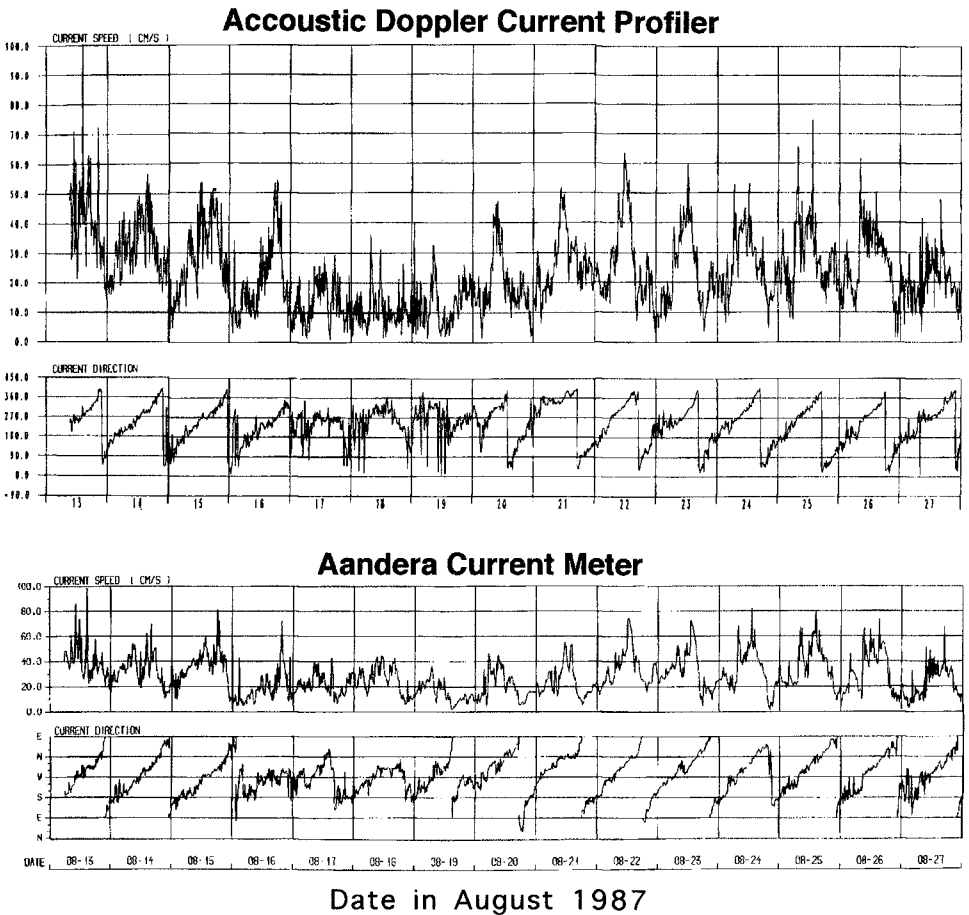


Figure 4. Currents measured by an ADCP and an Aandera current meter in Typhoons Betty and Cary.

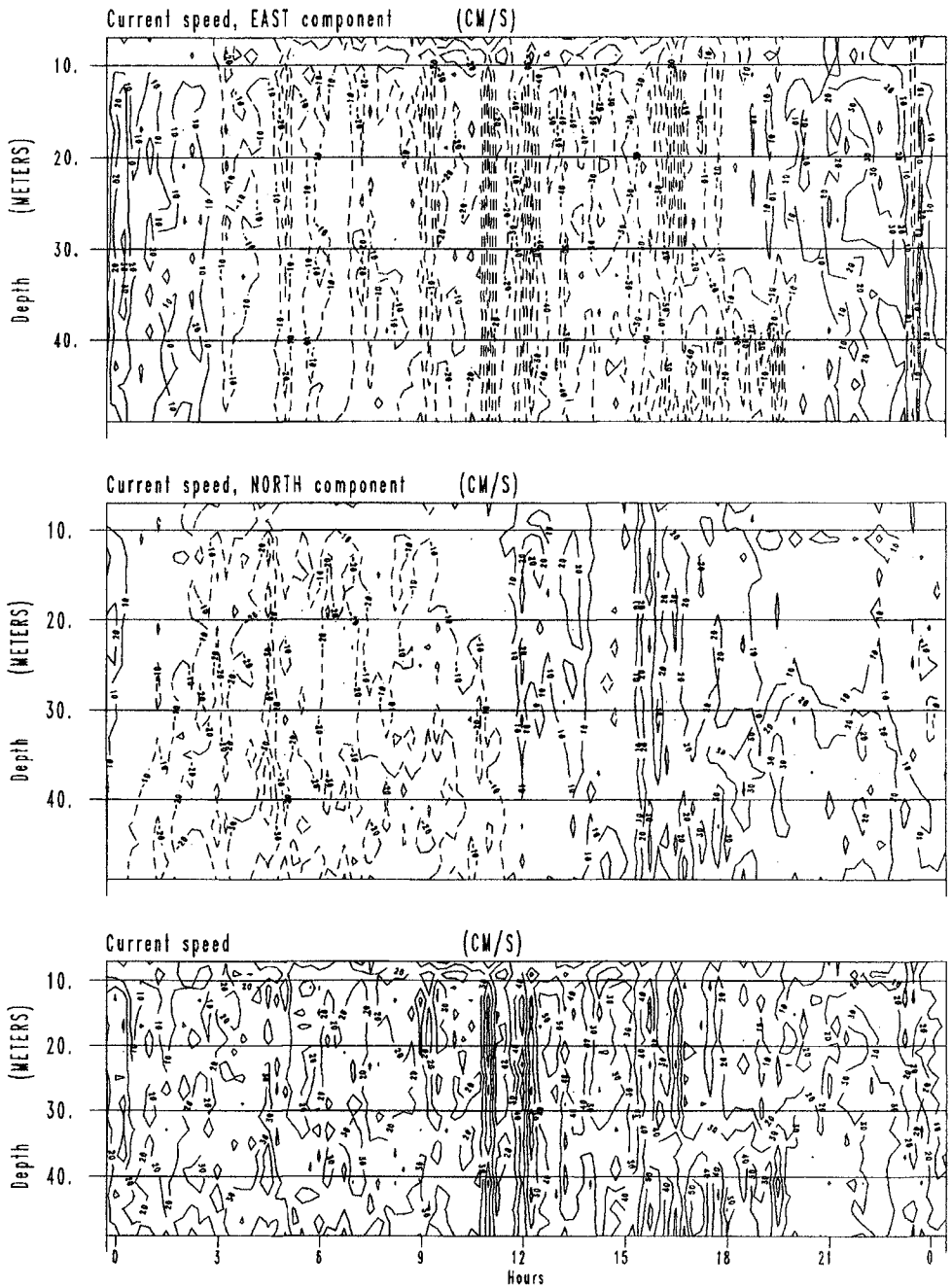


Figure 5. Contour plot of currents at all depth bins and time steps measured by an ADCP at -65 meter on August 14, 1987

when 1 to 2-minute average soliton data are converted to the same averaging period as used in this measurement program.

Acoustic Doppler Current Profiler Data

The data collected by the acoustic Doppler current profiler at -65 meter at two meter depth bins and all hours of August 14 are presented in Figure 5 as a contour plot. On this plot we see a strong current at about 1300 hours UTC. The currents are the combined effect of wind, tide and oceanic currents.

Figure 6 shows hourly current data recorded at every two-meter-depth with the acoustic Doppler current profiler at -65 meters on August 22, 1987 at 11 hours 43 minutes and 43 seconds UTC. Currents are nearly equal throughout the mixed layer depth. The current directions are also nearly constant from the sea surface to -55 meters. Currents are nearly constant between -20 and -55 meters depths. There is a sharp decrease in current at -15 meter, then a still sharper increase at -10 meters. The depth resolution in this case is 2 meters and the standard error in velocity measurement is 4 cm per sec. Data from three bins near the surface and close to the acoustic Doppler current profiler are suspect and excluded from our presentation.

The slab like measured currents are of special scientific and design interest. The design

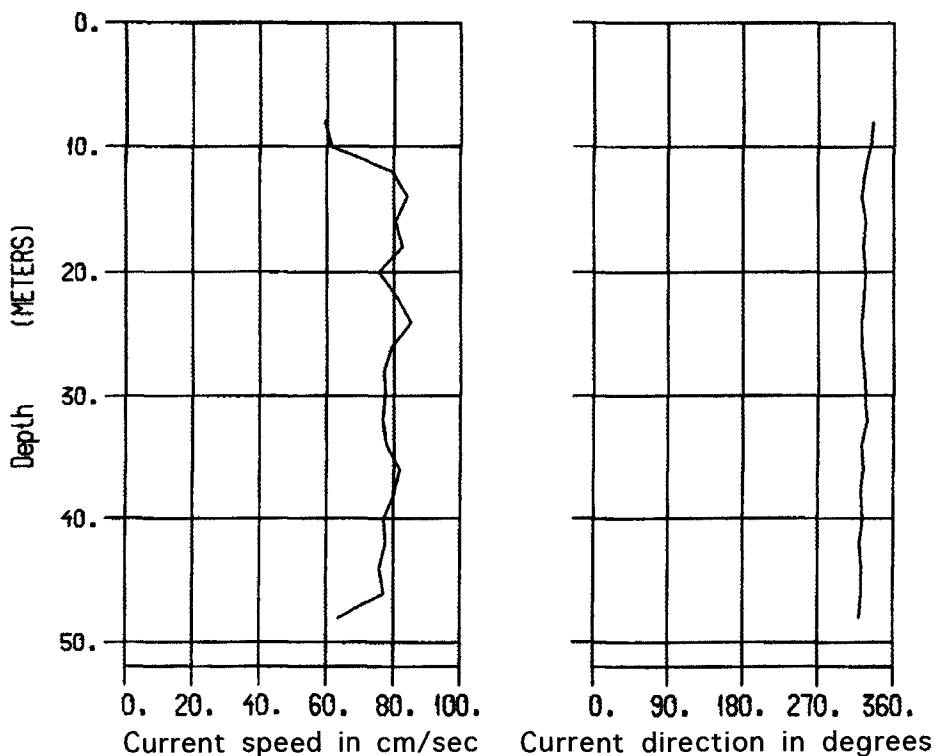


Figure 6. A sample current profile in the upper mixed layer.

current near sea surface which should be associated with the design wind and wave could be very different depending on whether a shear or a slab current profile (Figure 7) is

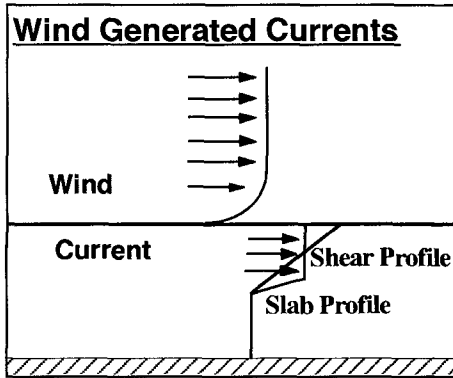


Figure 7. Wind generated current profiles for design use.

acceptable. The cost of building offshore structures with large projected area near surface (such as a tension leg platform or a floating unit) could be up to 20% lower if a slab current profile is acceptable.

Tidal and Oceanic Current

Figure 8 presents an example of relation between sea water temperature and tidal and oceanic currents measured by the Aandera current meter at -50 meters from October 16 to October 20, 1987. The tidal currents are predominantly diurnal. Current speed and temperature appear to be correlated.

change in temperature from 24.C to 28.C over several tidal cycles suggests the ingress and egress of the Dongsha cold eddy over the instrument area (Figure 9). These and

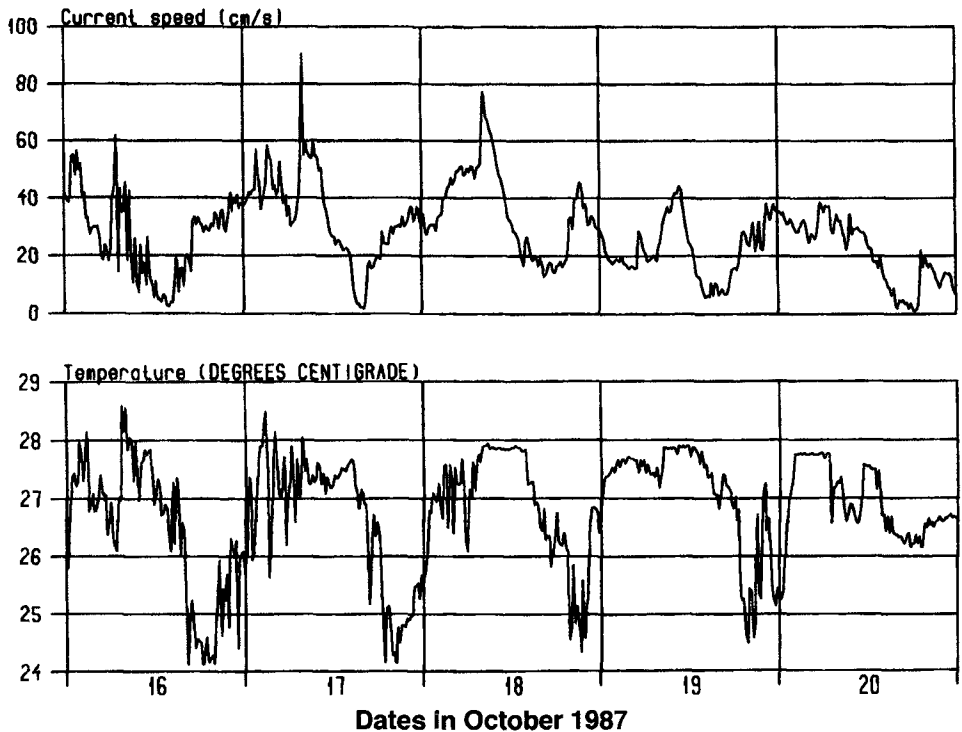


Figure 8. Current and temperature measured by Aandera current meter at -50 meter.

other aspects of eddy and oceanic current effects need to be pursued by acquiring sea surface temperature images for the periods in question.

It should be noted that the current directions make a complete loop in each tidal cycle. In such currents, a floating tanker will weathervane one full circle during each tidal cycle.

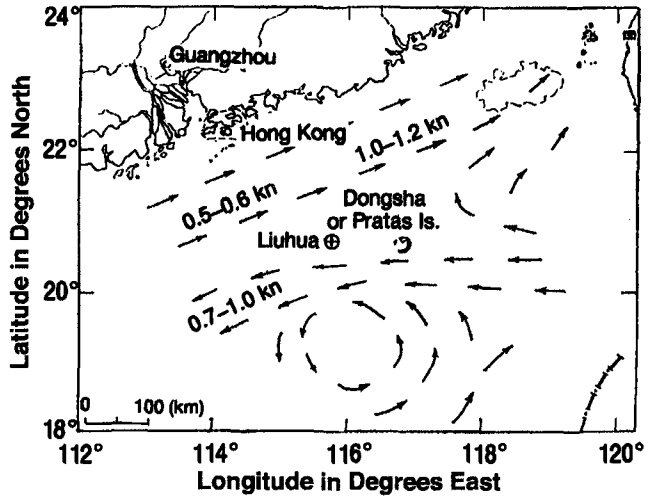


Figure 9. Dongsha Eddy Current in Summer

Strong Cold Front Passage

Wind, wave and current during the passage of a strong cold front are interesting because wind speed and direction change rapidly. With the passage of a strong cold front on the evening of September 25 immediately following our deployment, the wind velocity jumped from less than 2 meters per second to 12 meters per second within three hours. Also, the wind direction changed from north to south and then north again. During the passage of this cold front through Hong Kong, wind gusts up to 60 kilometer per hour were recorded by land based anemometers.

While the sudden jump in wind is very clearly seen in the wind record, the wave record shows a smaller jump from calm seas to about 3 meters significant. Interestingly enough, the effect on current is entirely unnoticeable. This is to be expected because during a sudden passage of a cold front, wind speeds and directions change so fast that the sea does not have enough time to respond.

Marine Fouling

Although marine fouling caused malfunctioning of the Aandera current meter at -50 m, photographs of marine growth constitute an important data base for marine fouling, which is an important parameter in design and operations. All other current meters and buoys functioned properly despite marine growth.

Every type of surface within about 100 meters of the sea surface were fouled mainly by two barnacles species (*pollicipes polymerus* and *lepas anatifera*). Near the surface, the fouling clusters were large and populated by bigger specimens (up to 2 inch). Both the cluster size and their density decreased with increasing depth. Macroscopic fouling was not observed below -100 meters. However, we cannot rule out long-term fouling of the structural elements below 100 meters, because the surfaces were not examined for short-term microscopic fouling.

Comparison with the Gulf of Mexico

A comparison of the meteorological and oceanographic conditions in the South China Sea and the Gulf of Mexico is instructive and has many practical uses. While tidal currents are very small in both the Gulf of Mexico and the South China Sea, severe tropical storms affect both basins. Maximum intensities of tropical storms in both operating areas are comparable, but the frequency of occurrence in the South China Sea is about 3 times that in the Gulf of Mexico.

The deep water Gulf of Mexico operations are occasionally shut down by strong oceanic currents caused by the Loop Current and its anti-cyclonic eddies. In the South China Sea, the background oceanic current is weak but appears to intensify under the influence of a typhoon during the Northeast Monsoon. Cyclonic wind field in a hurricane or typhoon has been known to interact with weak cyclonic eddies in both basins. The effect of this interaction on design and operation is poorly understood because no simultaneous measurement of good quality is available.

Before a hurricane approaches an operating area in the Gulf of Mexico, sky is usually clear with no wind, wave or current (in the absence of the Loop Current or its eddies). In the South China Sea, similar conditions exist before a typhoon approaches during the Southwest Monsoon (April-August). However during the Northeast Monsoon (September-March), strong wind, wave and current may be present even before a typhoon approaches. As a result, even a low intensity storm could produce very high waves with rapidly changing intensity and directions of wind, wave and current. Such events were recorded during the measurement program. Extreme design conditions could be governed by such conditions, and operating conditions could be more dangerous than the intensity of a typhoon may suggest.

Both basins have only few straits connecting them with open ocean. Even though most oceanic conditions, such as stratification, etc. are similar in the two basins, soliton induced strong currents have been noted only in the South China Sea.

While many comprehensive Metocean studies have been performed for the Gulf of Mexico, but very few similar studies have been performed for the South China Sea.

Applications & Benefits

The collected data has been applied to meet a variety of industry needs. Some of the most notable applications include:

- Wind and wave measurements were used in real time for operational planning and weather forecasting.
- Collected data were used extensively in developing both extreme and operational design criteria.
- Typhoon wave and current hindcast models were evaluated using the measured data. Monsoon effects on typhoon waves and currents are especially significant.

Possible future applications of data include:

- Complex measured currents could be studied to improve extreme and operational design criteria particularly using joint probability methods.

- Wave and current models could be evaluated using all data.
- Duration analysis of benign and inclement weather could be performed for operational planning.
- Real time wind, wave and current measurement integrated with a forecasting model could improve accuracy of forecasting in both NE Monsoon and typhoon resulting in lower cost of day-to-day operations, and enhanced safety of personnel & production platforms.
- Collected data could be used in future to develop better design criteria.

Only a very crude estimate of the benefits of the measurement program is possible. Even a rough conservative estimate shows that the value of benefits is many times the 2.2 million dollars spent on the measurement program.

First, drilling and testing operations during the measurement program benefited from the improved accuracy of forecasts, and many days of operating costs were saved at daily rates of up to \$500,000. Eighteen months of good quality data enabled safety evaluation of many unconventional but cheaper alternative production systems. Even assuming only 2% savings in the total cost of the final production system, the savings would be about 15.2 million dollars. Similar dollar amount savings are possible in the cost of a Tension Leg Platform if measured average slab current profiles are used in design.

Conclusions

Comprehensive Metocean data has been collected in a difficult area to support economic development. In comparison with other areas of similar interest, quantity of Metocean information available for the South China Sea is very small.

Some of the most important conclusions are presented below:

- A difficult measurement program in a remote area has been completed successfully to provide a valuable service to the industry.
- Extremely valuable deep water current data has been collected for operational planning purposes, especially for remotely controlled underwater operations.
- Pure tidal current ellipses will cause floating tankers to weather vane full circle in each tidal cycle in the absence of wind driven currents.
- Dongsha cold eddy appears to move in and out of the operating area during a tidal cycle. Wind velocity and direction also influence the location of the cold cyclonic eddy.
- Measured currents are much more complex than expected.
- The operational wind and wave climate is most severe during the winter monsoon.
- Typhoons imbedded in winter monsoons could be the worst weather conditions.
- A cost-effective measurement program is possible in a remote area.
- Site-specific data can improve the accuracy of monsoon and typhoon forecasts.
- Estimated benefits of a metocean measurement program are many times the cost of the measurement.

Recommendations

Countries surrounding the South China Sea have some of the fastest economic growth rates within the Asia-Pacific region. Here, coastal and marine economic activities are growing exponentially. However, very little comprehensive meteorological and oceanographic data are available to support these economic activities. The finished measurement program and

studies provide acceptable data for preliminary design criteria purposes, but, are insufficient to resolve many important design criteria issues, such as (i) joint occurrence probability of the northeast monsoon and a typhoon, (ii) joint probability of wind, wave, and current in a storm, and (iii) the role of complex currents in design criteria. Safe but economic design criteria are needed to design infrastructures for offshore oil production, a coastal plant or a harbor. Day-to-day operations could be interrupted by severe weather or typhoon. With good knowledge, one could plan operations to minimize downtime without compromising safety. Therefore, it is recommended that

- More environmental data should be collected preferably through a joint industry project.
- Ongoing site-specific Metocean measurement should be made part of economic activities in an offshore area.
- Measured data should be integrated with day-to-day weather forecasting and severe storm warning services.
- Collected data should be archived and made readily available for research and design criteria development.
- Extended current analysis of collected data could improve our understanding of the complex currents in the area resulting in safer and more cost-effective design and operating criteria.

Acknowledgments

We gratefully appreciate the financial and logistics support of Amoco Orient Petroleum Company and China National Offshore Nanhai East Oil Company during the measurement program.

References

- Anon, "Report of the Multidisciplinary Investigation of Northeast Waters of the South China Sea, (II)," Science Press, 1985.
- Cardone, V. J., and Grant, C. K., "South East Asia Meteorological and Oceanographic Hindcast Study (SEAMOS)," 10th Offshore South East Asia Conference, 1994.
- Corona, E. N., Lynch, R. D., Riffe, D., Cardone, V. J., Cox, A. and Chen, H., "Typhoon Emergency Response Planning for the South China Sea," Proceeding of the Offshore Technology Conference, 1996.
- Sharma, J. N., Tryggstad, S., and Bian, J., "Eighteen Months of Metocean Measurement Program in the South China Sea," Proceeding of the Offshore Technology Conference, 1991.
- Sharma, J. N., "A New Typhoon Evacuation Method to Minimize Downtime Without Compromising Safety," COMET Proposal, January 1997.
- Wyrski, K., "Physical Oceanography of the Southeast Asian Waters, Scientific Results of Marine Investigation of the South China Sea and Gulf of Thailand 1959-61," Naga Report No. 2, 1961.
- Yuan, Y., P. Zengdi and Z. Jiansheng, "LGFD Numerical Forecast Method of Sea Waves, Part 1 Numerical Forecast Model," Journal of Oceanology of Huanghai & Bohai Seas, 1988, 6, pp 1-5.

CHAPTER 29

WAVE HEIGHT AND PERIOD DISTRIBUTIONS FROM LONG-TERM WAVE MEASUREMENT

Chung-Chu Teng¹ and Ian M. Palao²

Abstract

Both the univariate and joint distributions of the significant wave height (H_s) and the zero-crossing wave period (T_z) are studied using 16 years of hourly wave data measured from five National Data Buoy Center (NDBC) buoy stations. For the univariate distribution, the log-normal distribution fits both the H_s and the T_z well. The modified log-normal distribution proposed by Fang and Hogben (1982) does improve the fit at the high H_s end and at the peak for some stations. For H_s , the Weibull distribution, with parameters computed from the maximum likelihood (ML) method, fits the upper tail of the cumulative distribution; however, it underpredicts both the probability peak and the probability density at the high end. For the joint distribution, the marginal Weibull/conditional log-normal distribution best describes the measured data of the steeper sea states and has the best overall fit.

Introduction

The theoretical distribution and characteristics of individual wave heights and periods have been extensively studied and verified using measured data (see Tucker 1991). Unlike individual waves, distributions of H_s and T_z , which are important for ocean and coastal engineering, need to be determined empirically from real measurements. Thus, both the univariate and joint distributions of the two wave parameters have not been extensively studied in the past due to a lack of reliable, long-term wave measurements. However, the early studies conducted by Ochi (1978) and Fang and Hogben (1982) provide a very useful basis for studying distributions of H_s and T_z . Some recent studies (e.g., Ochi (1992); Mathisen and Bitner-Gregersen (1990); and Athanassoulis, et al. (1994)) present many ideas and useful results on this topic.

In this study, 16 years of hourly wave data measured at five NDBC buoy stations are used to study both the univariate and the joint distributions of H_s and T_z .

¹ Principal Engineer/Project Manager, National Data Buoy Center, Stennis Space Center, MS 39529-6000, U.S.A.

² Senior Scientist, Computer Sciences Corporation, Stennis Space Center, MS 39529-6000, U.S.A.

Measured Wave Data

Data used in the present study were obtained from five NDBC buoy stations, designated as stations 46001, 46002, 46003, 46005, and 46006. All five buoy stations, as shown in Figure 1, are located in the northeastern Pacific Ocean. Water depths (in meters) at these buoy stations are listed in parentheses below the station numbers in the figure. These buoy stations were chosen for this study mainly because they are located in very deep water, so that wave height and period are not affected by shallow water effects, and they have longer periods of available wave data. These buoy stations measure both meteorological and wave data and report hourly data in nearly real time through the Geostationary Operational Environmental Satellite (GOES).

Wave data are processed onboard the buoys by transforming the time-series data into wave frequency spectra. The processed wave data, together with meteorological data, are transmitted to shore via GOES. Then, the wave information received are further processed and analyzed (e.g., conducting transform function, noise correction, and data quality control). H_s and T_z are derived from the wave spectrum: $H_s = 4(m_0)^{1/2}$ and $T_z = 2\pi(m_0/m_2)^{1/2}$, where m_0 and m_2 are the zero-th and the second spectral moments, respectively.

Sixteen years (from 1980 through 1995) of hourly wave data measured at these buoy stations are used in this study. During these 16 years, periods of missing data were present in the wave records for all of the stations. These data gaps were caused by a number of different factors: sensor failure, payload failure, periodic loss of data during transmission, or the buoy not being on station due to refurbishment or mooring failure. Table 1 shows the monthly distribution of the available data points during the 16 years for all five stations. Data for these five stations cover 76% (46006) to 90% (46001) of the all possible hourly data. From the distribution, it is clear that the data gaps or missing data did not concentrate on any

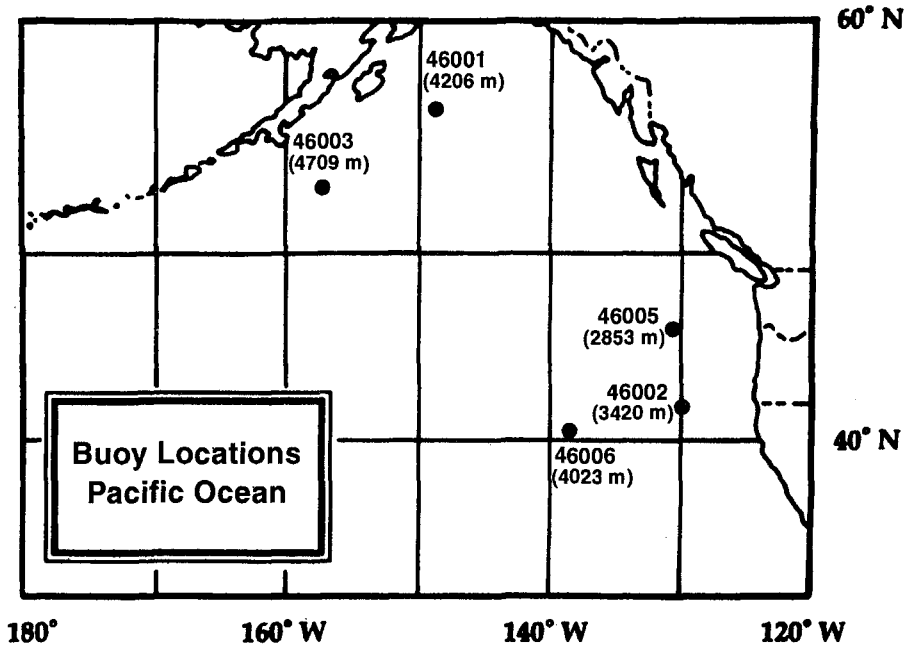


Figure 1. Locations of the five NDBC buoy stations used in this study

Table 1. Monthly distributions and total numbers of available data

	46001	46002	46003	46005	46006
January	10,917	9,368	9,322	10,141	9,023
February	9,483	8,703	7,053	9,343	7,931
March	9,886	9,448	8,348	10,179	8,271
April	8,897	8,602	8,765	9,546	7,526
May	10,351	8,104	8,134	9,347	7,880
June	10,567	9,459	8,616	9,031	7,975
July	10,836	9,878	9,289	10,145	8,752
August	11,326	9,975	9,029	10,915	9,649
September	11,069	9,930	10,447	9,133	9,838
October	10,994	10,473	9,570	9,347	10,242
November	10,610	9,583	9,016	8,471	9,792
December	10,876	9,433	10,242	9,216	9,650
Total	125,692	112,956	107,831	114,814	106,529

particular month or season. In addition, the whole data set was carefully examined, and no data gap that could significantly affect long-term wave statistics was found. Thus, it can be assumed that the missing data or data gaps in this data set will not affect the long-term distributions of H_s and T_z .

Data Analysis

Univariate Distributions

For univariate (or marginal) distributions of H_s and T_z , two commonly used probability distribution functions are studied: the log-normal and the three-parameter Weibull distributions. Parameters in these two distributions are computed by three different methods: the least square (LS) method, the ML method, and the method of moments. More details of these methods are presented in Teng, et al. (1994) and Palao, et al. (1994).

(1) *Log-Normal Distribution*

$$p(x) = \frac{1}{\sqrt{2\pi\sigma x}} e^{-\frac{1}{2}\left(\frac{\ln(x)-\mu}{\sigma}\right)^2}$$

where μ and σ are parameters of the distribution.

The modified log-normal distribution, which includes a skew factor to make a better fit at high values (Fang and Hogben, 1982), is also examined in this study.

(2) *Three-Parameter Weibull Distribution*

$$p(x) = \frac{\beta(x-\gamma)^{\beta-1}}{\alpha^\beta} e^{-\left(\frac{x-\gamma}{\alpha}\right)^\beta}$$

where α , β , and γ are the shape, scale, and location parameters, respectively.

Joint Distributions

For joint distributions of H_s and T_z three frequently used distribution functions are examined: bivariate log-normal distribution, bivariate two-parameter Weibull distribution, and marginal three-parameter Weibull/conditional log-normal distribution. More details of these distributions can be found in Mathisen and Bitner-Gregersen (1990). In the following equations, x represents T_z and y represents H_s .

(1) *Bivariate Log-Normal Distribution*

$$p(x,y) = \frac{0.5}{\sqrt{1-\alpha_{xy}^2} \pi \sigma_x \sigma_y xy} e^{-\frac{0.5}{1-\alpha_{xy}^2} \left[\frac{(\ln(x)-\mu_x)^2}{\sigma_x^2} - \frac{2\alpha_{xy}(\ln(x)-\mu_x)(\ln(y)-\mu_y)}{\alpha_x \sigma_y} + \frac{(\ln(y)-\mu_y)^2}{\sigma_y^2} \right]}$$

where μ_x , μ_y , σ_x , σ_y , and α_{xy} are parameters of the distribution.

Computationally, μ_x and μ_y are the expected values of $\ln(x)$ and $\ln(y)$; σ_x and σ_y are the standard deviations of $\ln(x)$ and $\ln(y)$; and α_{xy} is the correlation coefficient between $\ln(x)$ and $\ln(y)$. The modified bivariate log-normal distribution, proposed by Fang and Hogben (1982), is also examined in this study for reference purposes. The modified distribution is identical to the bivariate log-normal distribution except for the addition of a multiplicative term describing the skewness of $\ln(y)$.

(2) *Bivariate Weibull Distribution*

$$p(x,y) = \left[\frac{\zeta y^{\zeta-1}}{\eta^\zeta} e^{-\left(\frac{y}{\eta}\right)^\zeta} \right] \left[\frac{\beta x^{\beta-1}}{\alpha^\beta} e^{-\left(\frac{x}{\alpha}\right)^\beta} \right]$$

where α , β , η , and ζ are parameters of the distribution.

This distribution uses two two-parameter Weibull distributions (i.e., one for H_s and one for T_z) as a joint model. The parameters are calculated using the LS method. The marginal distribution is used for T_z while the estimation of the distribution of H_s is conditional on T_z through the use of the η parameter.

(3) *Marginal Weibull/Conditional Log-Normal Distribution*

$$p(x,y) = \left[\frac{1}{\sqrt{2\pi}\sigma} e^{-\frac{1}{2}\left(\frac{\ln(x)-\mu}{\sigma}\right)^2} \right] \left[\frac{\beta(y-\gamma)^{\beta-1}}{\pi\alpha^\beta} e^{-\left(\frac{y-\gamma}{\alpha}\right)^\beta} \right]$$

where α , β , γ , σ , and μ are parameters.

This distribution is calculated by using a three-parameter Weibull for H_s along with a log-normal for T_z . The parameters of this distribution are identical to the corresponding univariate distributions. The LS method is used to calculate the three Weibull parameters and the two log-normal parameters. Note the log-normal parameters are calculated for every 0.5-m wave height interval.

Results and Discussion

Figure 2 shows the comparisons between histograms of the measured H_s , and the univariate distributions for the five buoy stations. From visual judgment, the log-normal distribution, in general, fits the data better than the Weibull distribution. For the log-normal distribution, results obtained from the three different methods of parameter estimation are almost identical. The log-normal distribution slightly overpredicts the peak for the two northern stations (46001 and 46003) and slightly misses the peak location for two of the three southern stations (46005 and 46006). For the Weibull distribution, different parameter estimate methods produce different parameters and have different effects on the distribution shapes. The LS method always underpredicts the high wave range and overpredicts the location of the peak. The ML method provides much better prediction of the peak location and at high H_s , but significantly underpredicts the height of the peak and overpredicts at the lower range. The Weibull fits, based on the method of moments, are much poorer than the other two methods and are not presented in the figures.

Two goodness-of-fit statistics, the Kolmogorov-Smirnov statistic (K-S) and Chi-square statistic (χ^2), are used to evaluate the degree of fit between the data and the fitted distributions. Table 2 summarizes the values of these two statistics for the two distributions for each of the five buoy stations. Note the values of χ^2 are computed based on a wave height interval of 0.1 m. For the Weibull distribution, the goodness-of-fit values for the ML method, which are listed in the table, are always smaller (i.e., the fits are better) than those from the other two methods. Based on the two goodness-of-fit statistics, the log-normal distribution fits the data better than the Weibull distribution, regardless of the parameter estimate method used.

To further examine the fit of the univariate distributions of H_s , comparisons between the empirical cumulative distribution from the measured data and the theoretical cumulative distributions are made. Figure 3(a) shows an example of this comparison for station 46001. The log-normal distribution fits the data well, except for the upper tail (i.e., cumulative probability greater than 0.9) where it slightly underpredicts the empirical cumulative distribution. This trend was also reported by many previous studies (e.g., Ochi (1978); Fang and Hogben (1982)). However, among the five stations, stations 46001 and 46003 clearly show

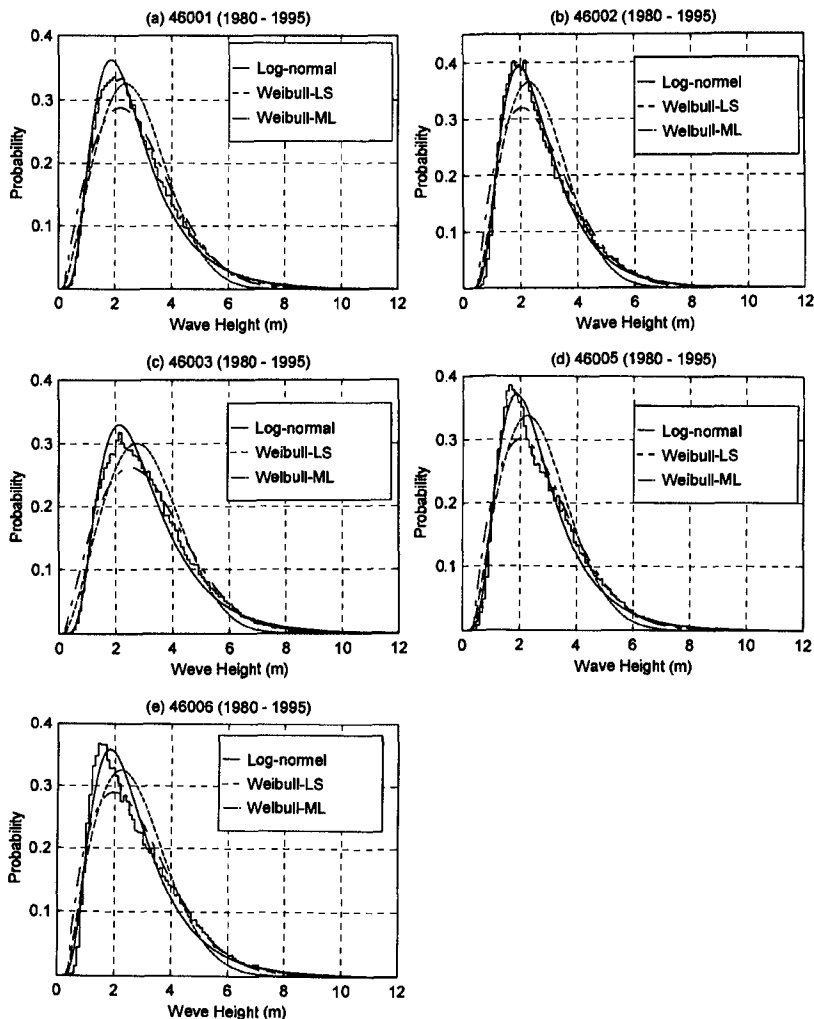


Figure 2. Comparisons of H_s between histograms and the univariate distributions for all five buoy stations

Table 2. Values of χ^2 and K-S for distributions of the zero-crossing wave period

	Log-Normal		Weibull	
	K-S	$\chi^2 (\times 10^{-6})$	K-S	$\chi^2 (\times 10^{-6})$
46001	0.01560	1.01749	0.03438	1.01889
46002	0.03862	0.91254	0.03086	0.91537
46003	0.01440	0.87029	0.03172	0.87135
46005	0.03021	0.92694	0.03337	0.92846
46006	0.02717	0.86185	0.02981	0.86325

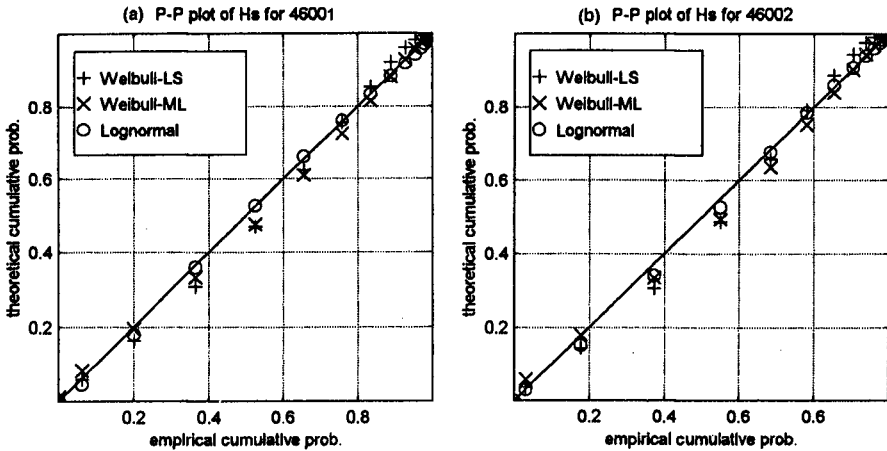


Figure 3. Comparisons of cumulative distribution for H_s between measured data and univariate distributions for (a) station 46001 and (b) station 46002

the underprediction. For other stations, there is very little or no underprediction from the log-normal distribution at the upper tail, as shown in Figure 3(b) for station 46002. For the Weibull distribution, the LS method overpredicts both the upper and lower tails for all five stations, while the ML method predicts well at the upper tail but underpredicts at the lower tail.

Figure 4 shows, for H_s at 46001, the histograms and univariate distributions including the Weibull, the log-normal, and the modified log-normal (Fang and Hogben (1982)) distributions. It is clear that the modified log-normal distribution significantly improves the fitting at high values and at the peak. The improvement is significant for stations 46001 and 46003. For other stations, there is very little or no improvement. Note the Weibull distribution, with parameters computed from the ML method, underpredicts the distribution at high values despite the better fit of the cumulative distribution at the high end. This trend is valid for all five stations.

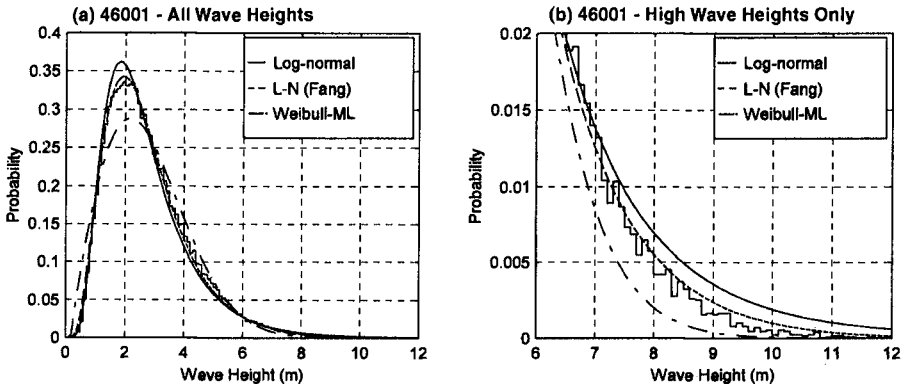


Figure 4. Comparisons of H_s between histograms and the univariate distributions for station 46001

For T_z , comparisons between the histograms and the univariate distributions are presented in Figure 5. Similar to H_s , the parameters of the log-normal distribution for T_z computed from the three methods of parameter estimation are almost identical. In addition, variations of these parameters from station to station are very small. The parameter μ varies from 1.88 to 1.96, and the parameter σ varies from 0.187 to 0.202. The log-normal distribution fits very well for the two northern stations (i.e., 46001 and 46003). For the three southern stations (i.e., 46002, 46005, and 46006), the histograms show broader peaks, and neither of the two distributions predicts the peak very well. Similar to their effects on H_s , the Weibull distribution based on the ML method predicts the upper range best and underpredicts the peak, while the LS method underpredicts the high range and does not predict the peak well. Again, the method of moments is much worse than the other two methods, and its results are not presented.

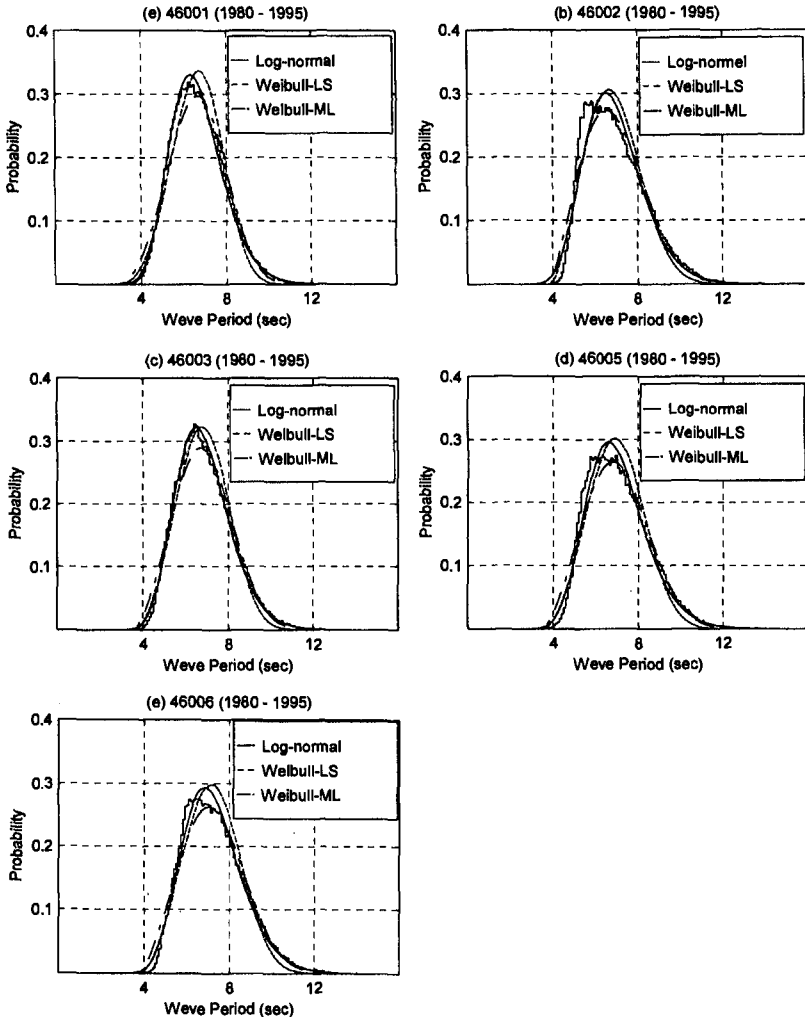


Figure 5. Comparisons of T_z between histograms and the univariate distributions for all five buoy stations

Table 3 presents values of K-S and χ^2 for T_z . Based on the two statistics, the log-normal distribution fits better than the Weibull distribution (using the ML method). Figure 6 presents comparisons between the empirical and fitted cumulative distributions of T_z for stations 46001 and 46002. For the log-normal distribution, unlike that for H_s , there is no underprediction at the upper tail of the cumulative distribution of T_z for all five stations. Performances of the Weibull distribution in modeling T_z using the LS and ML methods are similar to those for H_s .

The contour plots of the joint probability between H_s and T_z for station 46001 are presented in Figure 7. It is clear that both the bivariate log-normal and the bivariate Weibull distributions overpredict the joint probability for the steeper sea states, as indicated by the straight line. The marginal Weibull/conditional log-normal distribution fits this steeper sea range well. This trend was also shown by Mathisen and Bitner-Gregersen (1990) using wave data collected from the Norwegian Sea. The bivariate Weibull distribution also performs poorly at high wave periods. Except for steep seas, the bivariate log-normal distribution generally fits the data well. The modified bivariate log-normal distribution, proposed by Fang and Hogben (1982), was also studied. Its results are very similar to those from the original distribution and, thus, are not presented in this paper. Although the marginal Weibull/conditional log-normal distribution generally fits the data, it seems that it does not predict the very high probability location very well. The trends observed for station 46001 are also applicable to all other stations, but these results are not shown in this paper due to space limitations.

Table 3. Values of χ^2 and K-S for distributions of the significant wave height

	Log-Normal		Weibull	
	K-S	χ^2 ($\times 10^{-6}$)	K-S	χ^2 ($\times 10^{-6}$)
46001	0.02270	1.01465	0.04155	1.01859
46002	0.02113	0.91402	0.04693	0.91566
46003	0.02720	0.86907	0.03510	0.88058
46005	0.02652	0.92650	0.04303	0.92890
46006	0.03183	0.86031	0.04202	0.86336

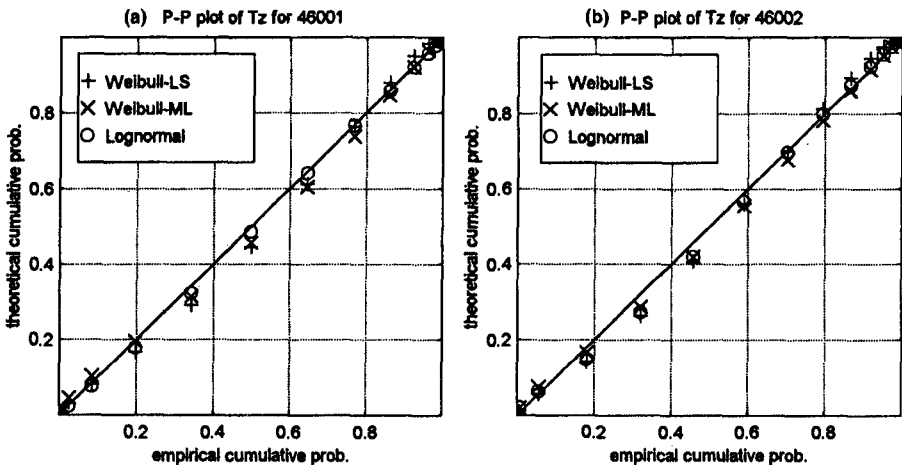


Figure 6. Comparisons of cumulative distribution for T_z between measured data and univariate distributions for (a) station 46001 and (b) station 46002

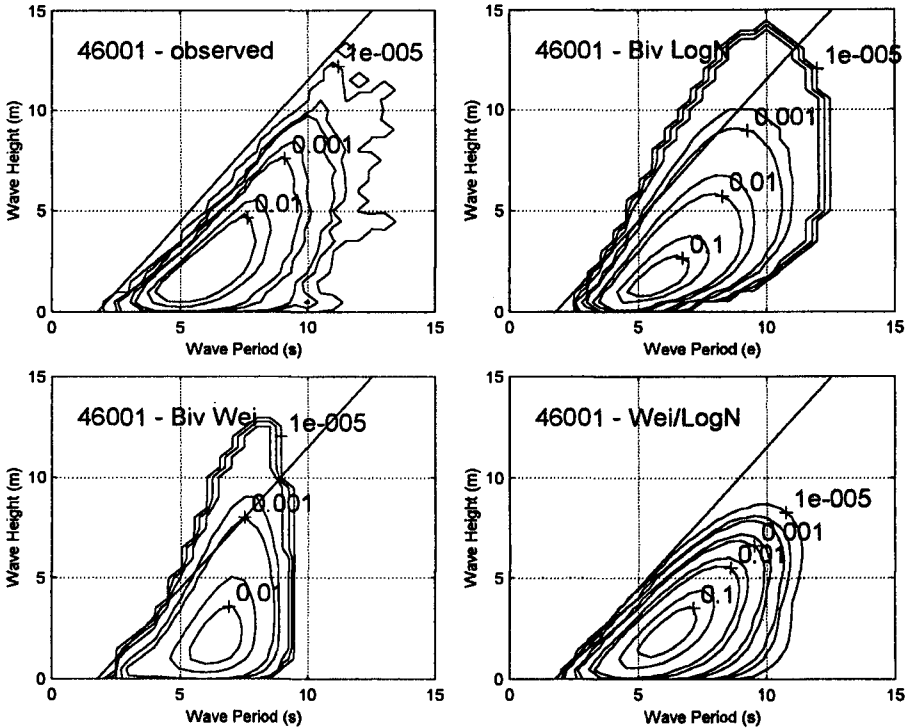


Figure 7. Contour plots of joint probability between H_s and T_z for (a) measured data, (b) bivariate log-normal distribution, (c) bivariate Weibull distribution, and (d) marginal Weibull and conditional log-normal distribution

The theoretical joint probability distributions are compared to the distribution of the observed data based on the correlation coefficients. For H_s , a correlation coefficient is computed for each 0.5-m wave height bin. For each wave height bin, the corresponding values of observed frequencies and frequencies calculated from the joint distributions across the 0.5-s T_z bins form a paired data set. A correlation analysis is then performed on the two paired data (i.e., observed frequencies versus calculated frequencies). The correlation coefficients for every 0.5-s T_z bin are computed similarly. Note the correlation coefficient at both the upper and lower ends may not be reliable due to limited data observations. Negative coefficient values show a polarity between the deviations of observed frequencies and the deviations of calculated frequencies. This shows a very poor fit between the measured data and the joint distribution. Figure 8 shows the correlation coefficients for all the H_s and T_z bins for all five stations. For H_s , it is clear that the marginal Weibull/conditional log-normal distribution fits better than other distributions. The bivariate Weibull distribution's performance is very poor and, therefore, unacceptable. All joint distributions have high correlation coefficients for the T_z fit. Note the bivariate Weibull distribution does not have correlation values for periods higher than 10 seconds because there are no calculated frequencies from which to compute the coefficients.

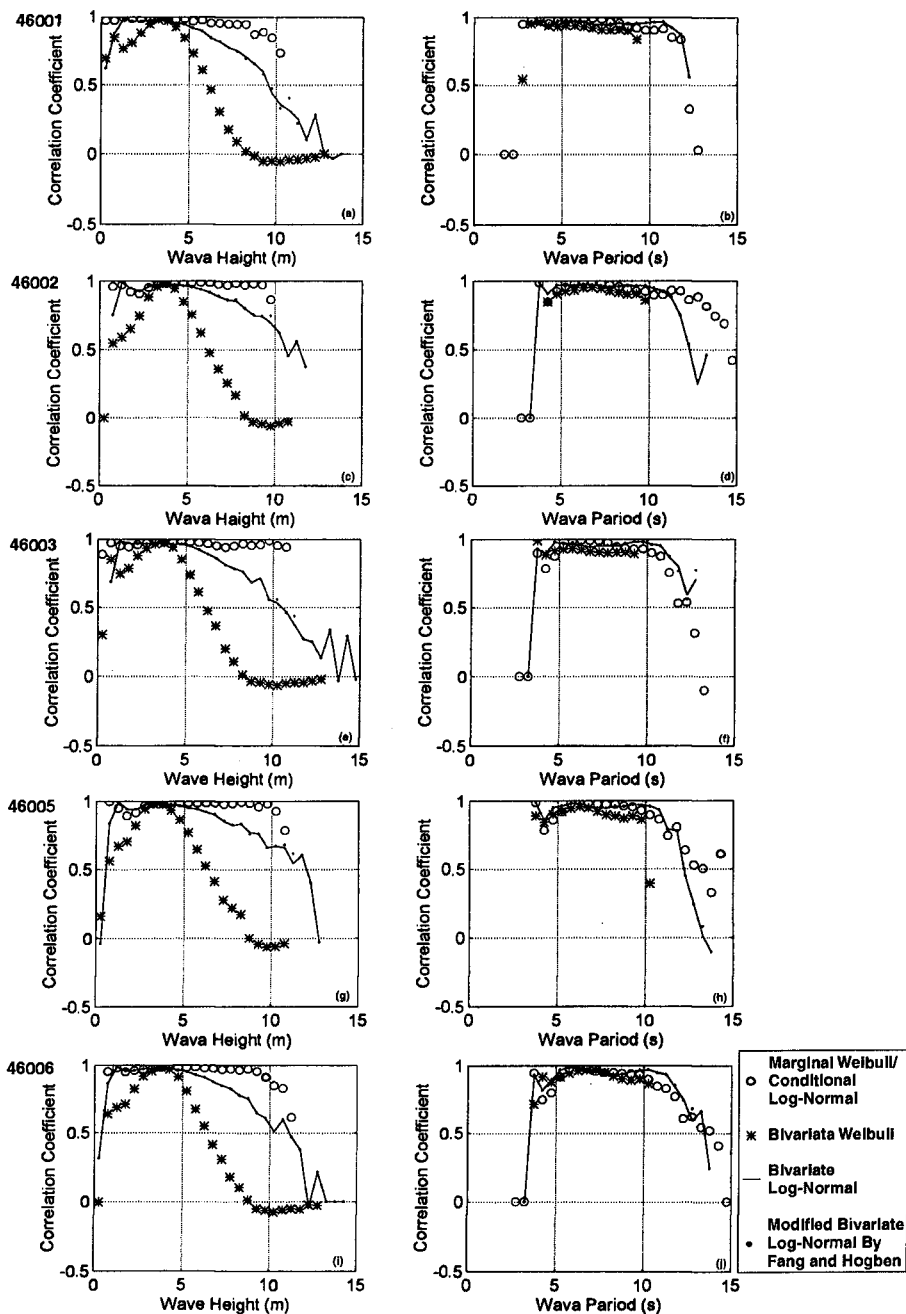


Figure 8. Coefficients of correlation between measured data and joint distributions for various H_s and T_z values for all five buoy stations

Conclusions

The results show that the log-normal distribution best fits both H_s and T_z for the five buoy stations. The modified log-normal distribution, proposed by Fang and Hogben (1982), significantly improves the fitting at the high H_s end and at the peak for some stations. For the three-parameter Weibull distribution, different methods of parameter estimation produce different parameters and distribution shapes. In general, the ML method is better than both the LS method and the method of moments. Although the Weibull distribution with parameters computed from the ML method fits the upper tail of the cumulative distribution for the H_s , it underpredicts both the probability peak and the probability density values at the high values.

Although the fit between various joint distributions and the measured data depends on the wave height and period range, the marginal Weibull/conditional log-normal distribution has the best overall fit based on the visual inspection and the correlation coefficients. Also, this joint distribution better estimates the data of the steeper sea states. Both the bivariate log-normal and the bivariate Weibull distributions overpredict the steeper sea states. The bivariate Weibull distribution also poorly fits the high wave period data.

References

- ATHANASSOULIS, G.A., SKARSOULIS, E.K., and BELIBASSAKIS, K.A., "Bivariate Distributions With Given Marginals With an Application to Wave Climate Description," *Applied Ocean Research*, Vol. 16, pp. 1-17, 1994.
- FANG, Z.S., and HOGBEN, N., "Analysis and Prediction of Long-Term Probability Distributions of Wave Heights and Periods," Technical Report, National Maritime Institute, London, 1982.
- MATHISEN, J., and BITNER-GREGERSEN, E., "Joint Distributions for Significant Wave Height and Wave Zero-Up-Crossing Period," *Applied Ocean Research*, Vol. 12, No. 2, pp. 93-103, 1990.
- OCHI, M.K., "Wave Statistics for the Design of Ships and Ocean Structures," *Transactions, Society of Naval Architects and Marine Engineers*, Vol. 86, pp. 47-76, 1978.
- OCHI, M.K., "New Approach for Estimating the Severest Sea State From Statistical Data," *Proceedings of International Conference on Coastal Engineering*, pp. 512-525, 1992.
- PALAO, I.M., TENG, C.C., TIMPE, G.L., and BROWN, D.A., "An Extremal Analysis of Significant Wave Height Measured From NDBC Data Buoys," Technical Report 1804-07.01, National Data Buoy Center, May 1994.
- TENG, C.C., TIMPE, G., and PALAO, I., "The Development of Design Waves and Wave Spectra for Use in Ocean Structure Design," *Transactions, Society of Naval Architects and Marine Engineers*, Volume 102, pp. 475-499, 1994.
- TUCKER, M.J., *Waves in Ocean Engineering*, Ellis Horwood, 431 pp., 1991.

CHAPTER 30

INTERFERENCE OF SMALL STRUCTURES IN THE VICINITY OF LARGE STRUCTURES

Subrata K. Chakrabarti, F. ASCE and Sumita Chakrabarti

Abstract



The purpose of this paper is to investigate the effect of large structures in the vicinity of small structures in the determination of wave forces on the small structures. The structures considered in this study are circular cylinders and analytical expressions are derived. It is shown that if the small cylinders are placed in close proximity of large cylinders (center distance/ caisson radius < 2.0), the wave forces on the small cylinder are largely influenced by the large cylinder.

INTRODUCTION

When large structures placed underwater encounter incoming waves, the waves alter in form in the vicinity of the structure. The problem is generally solved as a boundary value problem based on a linear velocity potential due to the incident wave. The diffraction effect of large coastal or offshore structures in waves is well-known. For an arbitrary shape of the structure the wave diffraction effect is solved numerically. For a fixed large caisson, this problem was solved by MacCamy and Fuchs (1955) in a closed form for Airy waves. This solution has been extended to the second-order wave theory [e.g., Molin (1979)]. For large cylinders in the vicinity of one another, the problem of multiple cylinder interaction is well-known [Chakrabarti(1978)]. In this case multiple diffraction from the neighboring cylinders is taken into account.

For structures which are placed near each other and are allowed to move independently, the problem of multiple radiation is taken into account in addition to multiple diffraction. Several research works addressed this problem in the diffraction regime, e.g., Ohkusu (1976).

The present study addresses the situation in which only one part of the structure is large enough to encounter diffraction effect. The other structure dimension is such that its effect on the waves is local and its presence has little influence on the large structure. Examples of such applications are composite structures, e.g., the Maurcen gravity platform in the North Sea and piles in the neighborhood of large caisson as shown in Fig. 1.

In this case, the small structure, such as, the pile, will experience a wave that is a combination of the incident wave and the scattered wave from the neighboring large structure. The size of the small structure is such that it falls in the Morison force regime in that both the inertia and drag effects are important.

¹Offshore Structure Analysis, Inc. 191 E. Weller Dr. North, Plainfield, IL 60544

²Biomedical Engineering Dept., Northwestern University, Evanston, IL 60201

Two different cases are considered in this study. In the first case, a pile is placed near a large caisson. Expressions of the forces on the pile are derived in the presence of the caisson based on the MacCamy-Fuchs theory. In the second case, the presence of large multiple cylinders on a small diameter member is investigated. Here, multiple scattering effect of waves on the small member is considered. An example of this situation may be found in the presence of multi-legged gravity offshore structure on risers.

Analytical solutions are derived for the total velocity potential at a point in the wave field which includes the wave scattering effect. The wave kinematics are derived based on this velocity potential. The forces on the small member are then expressed in terms of the wave kinematics. Numerical results are presented in all cases. Comparisons are made for the forces on the small structure with and without the presence of the large structure. In particular, the effect of spacing between the large and small structures is shown. The region where the influence of the large structure is significant in the design of the small structure is discussed.

LARGE VERTICAL CYLINDER

For a large vertical cylinder an analytical solution for the linear diffraction problem has been derived by McCamy and Fuchs (1954). In this case the expression for the incident wave is written in a convenient cylindrical polar coordinate (Fig. 1). The expression for the total potential at a point (r, θ) in the fluid field is obtained as

$$\Phi = \frac{H\omega}{2k} \frac{\cosh ks}{\sinh kd} \sum_{m=0}^{\infty} \delta_m i^{m+1} \left[J_m(kr) - \frac{J'(ka)}{H_m^{(1)'}(ka)} H_m^{(1)}(kr) \right] \cos m\theta \exp(-i\omega t) \quad (1)$$

in which H = wave height, ω = wave frequency, k = wave number, s = vertical distance from the ocean floor, d = water depth, a = caisson radius, and t = time. The quantities J_m and $H_m^{(1)}$ are the Bessel and Hankel functions of the first kind of order m respectively and prime denotes derivatives with respect to their arguments. Note that $H_m^{(1)} = J_m + iY_m$ where Y_m is the Bessel function of the second kind of order m . The value of δ_m is 1 for $m=0$ and 2 for $m>0$. The first term inside the bracket corresponds to the incident waves while the contribution of the scattered wave from the cylinder surface to the potential function is given by the second term within the bracket involving the Hankel function.

Note that while the above equation is written in complex form for mathematical convenience, only the real part of the expression matters. The horizontal water particle velocities are given in terms of Φ by

$$u_r = \frac{\partial \Phi}{\partial r} \quad (2)$$

and

$$u_\theta = \frac{1}{r} \frac{\partial \Phi}{\partial \theta} \quad (3)$$

Using the expression for Φ in Eqs. 2 and 3, we have

$$\bar{u}_r = \frac{\cosh ks}{\sinh kd} \sum_{m=0}^{\infty} \delta_m i^{m+1} \left[J_m'(kr) - \frac{J_m'(ka)}{H_m^{(1)}(ka)} H_m^{(1)'}(kr) \right] \cos m\theta \exp(-i\omega t) \quad (4)$$

and

$$\bar{u}_\theta = -\frac{1}{kr} \frac{\cosh ks}{\sinh kd} \sum_{m=0}^{\infty} m \delta_m i^{m+1} \left[J_m(kr) - \frac{J'(ka)}{H_m^{(1)'}(ka)} H_m^{(1)}(kr) \right] \sin m\theta \exp(-i\omega t) \quad (5)$$

where bar denotes nondimensional quantities and the velocities are normalized by dividing by the quantity $(H\omega/2)$. In Cartesian coordinate system the horizontal particle velocity and acceleration components at the pile center are

$$\begin{aligned} \bar{u}_x &= \bar{u}_r \cos\theta - \bar{u}_\theta \sin\theta \\ \bar{u}_z &= \bar{u}_r \sin\theta + \bar{u}_\theta \cos\theta \\ \bar{\dot{u}}_x &= -i\omega \bar{u}_x \\ \bar{\dot{u}}_z &= -i\omega \bar{u}_z \end{aligned} \quad (6)$$

where the coordinate x is the direction of waves and z normal to this direction. The derivation thus far has been carried out in the complex field. However, in order to apply the expressions for the kinematics in the Morison force, it is necessary to use the real parts of these quantities. The forces on a unit section of the pile in the neighborhood of the single cylinder are computed based on these kinematics using the Morison equation. The forces along and transverse to the wave direction respectively are

$$\bar{f}_x(\omega t) = -\pi C_M \frac{D}{H} \operatorname{Re}\{\bar{i}\bar{u}_x \exp(-i\omega t)\} + C_D \left| \operatorname{Re}\{\bar{u}_x \exp(-i\omega t)\} \right| \operatorname{Re}\{\bar{u}_x \exp(-i\omega t)\} \quad (7)$$

and

$$\bar{f}_z(\omega t) = -\pi C_M \frac{D}{H} \operatorname{Re}\{\bar{i}\bar{u}_z \exp(-i\omega t)\} + C_D \left| \operatorname{Re}\{\bar{u}_z \exp(-i\omega t)\} \right| \operatorname{Re}\{\bar{u}_z \exp(-i\omega t)\} \quad (8)$$

in which D = pile diameter, C_M = inertia coefficient and C_D = drag coefficient. The forces in the above expressions are nondimensionalized by the quantity $1/2 \rho D (H\omega/2)^2$.

While the Morison equation in general will not produce a transverse horizontal force on a pile, the diffraction effect of the wave from the caisson is expected to introduce a transverse force.

Note that these expressions do not state anything about the vortex induced lift force as the Morison equation fails to describe this phenomenon. The description of the transverse force in this case is complicated by the fact that the scattered wave introduces a flow field which has a direction different from that of the incident wave and depends on the location of the fluid field.

It is considered interesting to compare these forces with the forces on the same pile in the absence of the large caisson. The force on the pile in the x-direction (Morison force is absent in the z-direction) written in the same nondimensional form is expressed as

$$\bar{f}_{xa} = -\pi C_M \frac{D}{H} \bar{u} \sin \omega t + C_D \bar{u}^2 |\cos \omega t| \cos \omega t \quad (9)$$

where the nondimensional force has the same form as in Eq. 7 and

$$\bar{u} = \frac{gk}{\omega^2} \quad (10)$$

This last quantity approaches a value of one in deep water.

LARGE MULTIPLE CYLINDERS

Assume that the pile resides in the neighborhood of a multi-legged vertical structure whose legs represent large vertical cylinders. The pile experiences multiple diffraction from these cylinders. The effect of the waves on the pile, as before, is considered small in developing the theory. Considering the interaction of the waves with all large cylinders in the flow field, the total potential is described with reference to the coordinate system described at the center of the δ th cylinder as

$$\Phi^\delta = \frac{iH\omega}{2k} \frac{\cosh ks}{\sinh kd} \left\{ \begin{array}{l} \sum_{n=-\infty}^{\infty} -J_n(kr_\delta) \exp(in(\theta_\delta - \theta_\omega + \pi/2)) \\ + A_n^\delta H_n(kr_\delta) \exp(in\theta_\delta) \\ + (\sum_{\mu=1}^{\delta-1} + \sum_{\mu=\delta+1}^{\Delta}) \sum_{m=-\infty}^{\infty} A_n^\mu H_{n+m}(kr_{\delta\mu}) J_m(kr_\delta) \\ \exp(im(\theta_{\delta\mu} - \theta_\delta)) \exp(in\theta_{\mu\delta}) \end{array} \right\} \exp(-i\omega t) \quad (11)$$

in which Δ = total number of large cylinders, θ_ω = angle of incident wave with respect to the positive x-axis, r_δ , θ_δ = location of field point with respect to the center of δ th cylinder (see Fig. 2). For convenience, the center of the coordinate system is located at the center of the caisson δ . To numerically compute the potential function, the infinite sums in the above equation are

replaced by a finite sum from -N to N where N is the number of symmetric images provided of the caisson in question. The first term within the bracket is due to the incident wave, the second term arises from the scattering from the reference δ th cylinder and is similar to the MacCamy-Fuchs expression. The third series term is due to scattering from the balance of the cylinders in the neighborhood where the Bessel's addition theorem has been used to transfer the coordinate system to the reference cylinder.

The expression for Φ^δ satisfies Laplace's equation and all boundary conditions except the cylinder surface condition. As for the single cylinder, when this condition is applied, a matrix equation in the unknown coefficients A_n^δ is derived.

$$\left\{ \begin{aligned} & \sum_{\mu=1}^{\delta-1} \sum_{m=-N}^N A_m^\mu H_{n+m}(kr_{\delta\mu}) \exp(im\theta_{\mu\delta}) J'_n(ka_\delta) \exp(in\theta_{\delta\mu}) + A_{-n}^\delta H'_{-n}(ka_\delta) \\ & + \sum_{\mu=\delta+1}^{\Delta} \sum_{m=-N}^N A_m^\mu H_{n+m}(kr_{\delta\mu}) \exp(im\theta_{\mu\delta}) J'_n(ka_\delta) \exp(in\theta_{\delta\mu}) \\ & = J'_{-n}(ka_\delta) \exp(ikr_{0\delta} \cos(\theta_{0\delta} - \theta_\omega)) \exp(-in(-\theta_\omega + \pi/2)) \end{aligned} \right\}, n = -N, \dots, N \quad (12)$$

In the above, the higher the value of N, the better is the accuracy in Φ^δ . The order of the matrix is given by $(2N+1)\Delta$. The coefficients A_n^δ are computed by the matrix inversion.

Once the velocity potential at a field point, r_δ, θ_δ is known, the particle kinematics are computed as before from Eqs. 2 and 3 so that the forces on the pile may be obtained from the Morison equation. The spatial part of the radial and tangential velocities at the center of the pile (r_δ, θ_δ) is obtained from

$$\bar{u}_r^\delta = i \frac{\cosh ks}{\sinh kd} \left\{ \begin{aligned} & \sum_{n=-N}^N -J'_n(kr_\delta) \exp(in(\theta_\delta - \theta_\omega + \pi/2)) + A_n^\delta H'_n(kr_\delta) \exp(in\theta_\delta) + \\ & \left(\sum_{\mu=1}^{\delta-1} + \sum_{\mu=\delta+1}^{\Delta} \right) \sum_{m=-N}^N A_m^\mu H_{n+m}(kr_{\delta\mu}) J'_m(kr_\delta) \exp(im(\theta_{\delta\mu} - \theta_\delta)) \exp(in\theta_{\mu\delta}) \end{aligned} \right\} \quad (13)$$

and

$$\bar{u}_\theta^\delta = \frac{-\cosh ks}{kr \sinh kd} \left\{ \begin{aligned} & \sum_{n=-N}^N -n J_n(kr_\delta) \exp(in(\theta_\delta - \theta_\omega + \pi/2)) + n A_n^\delta H_n(kr_\delta) \exp(in\theta_\delta) + \\ & \left(\sum_{\mu=1}^{\delta-1} + \sum_{\mu=\delta+1}^{\Delta} \right) \sum_{m=-N}^N A_m^\mu (-m) H_{n+m}(kr_{\delta\mu}) J_m(kr_\delta) \exp(im(\theta_{\delta\mu} - \theta_\delta)) \exp(in\theta_{\mu\delta}) \end{aligned} \right\} \quad (14)$$

It can be shown that for a two cylinder case, the total number of images $N=7$ provides sufficient accuracy (up to 4 significant digits) for forces. For symmetric two caisson/ one pile configuration

at right angles to the flow, the last two terms in the radial velocity expression u_r^6 should provide equal values at the pile. This provides a check on the numerical computation. Thus the transverse force will be absent in this case as one would expect.

NUMERICAL RESULTS

In order to show the effect of a single large caisson on the forces on a pile, numerical values on the forces on the pile are computed with and without the presence of the caisson. For this comparison the values of the hydrodynamic coefficients are taken as $C_M=2.0$ and $C_D=1.0$. The water depth to the caisson radius is taken as 1.0 and the forces are computed at the still water surface. The pile diameter to the wave height ratio is considered to be 0.25. In deep water this corresponds to a Keulegan-Carpenter value of about 12. Three different diffraction parameter values ka are chosen: $ka=1.0, 2.0, 3.0$. The pile is placed at different distances from the center of the caisson at 0, 90, and 180 degree orientation. Note that 0 degree corresponds to the pile placed behind the caisson with respect to the wave direction, 180 degrees places it in front of the caisson while 90 degrees is transverse to the flow.

The results for ka values of 1.0, 2.0 and 3.0 are shown in Figs. 3-5. The x-axis corresponds to the nondimensional distance r/a where r is the distance between the centers of the caisson and the pile and a is the caisson radius. The y-axis represents nondimensional force amplitudes on the pile. The quantities FX and FZ show forces in the presence of the caisson while FXA is the force in its absence. For the 0 and 180 degree cases only the x forces (FX) are presented as one would expect. However, for the 90 degree case, there is a force component in the z direction (FZ) as well.

The 0 degree case shows the shielding effect. When the pile is very close to the caisson the x force on the pile is small compared to the single pile case. As the pile is moved away from the caisson in the 0 degree direction, the x force on the pile increases and approaches in value to the single pile forces. This increase is slow and the forces are close to each other at a distance of six radius away.

When the pile is in front of the caisson facing the wave, the force on the pile is affected by the oscillating nature of the wave as the pile is moved away. The effect of the caisson here is high and is felt by the pile for a long time. Interestingly, the diffracted wave being out of phase with the incident wave, the forces experienced by the pile as it is moved away, fluctuates in magnitude, sometimes re-inforcing and sometimes canceling the single pile forces. This oscillation frequency corresponds to the wave length of the incident (and diffracted) wave.

When the pile is transverse to the caisson with respect to the wave direction, the wave load on the pile is considerably higher than the pile alone case due to closeness of the caisson. As in the 180 degrees case, the load fluctuates about the pile-alone force as the caisson is moved along the 90 degree line. The load approaches the pile-alone force with increasing distance. In fact, at a distance of about five times the radius, the forces are almost identical. This orientation also experiences a transverse load whose magnitude is as much as 25 percent of the single pile load.

The transverse load is small in the close proximity of the caisson and grows steadily with distance reaching maximum quickly near a distance of two radii.

As the diffraction parameter is increased in value (equivalent to higher wave frequency), the oscillation frequencies at 90 and 180 deg. increase. The normalized forces, however, are higher at the lower ka values.

A second numerical example shown here is the load on a pile in the presence of two large caissons symmetrically placed around the pile (Fig. 6). In this case the pile is always assumed to be in the center while the distance of the caissons from the pile is varied symmetrically. The normalized x and z loads on the pile are plotted in Fig. 7 for a ka value of 2.0. The loads at still water surface as before are shown and the values of C_M and C_D are taken as 2.0 and 1.0 respectively. The other values are the same as before. In this case, the transverse force is zero due to the symmetric configuration since the forces produced by the caisson no. 1 will be equal and opposite to the forces generated due to the presence of caisson no. 2. On the other hand, the x -force is considerably higher than the single pile force due to the re-inforcement caused by the caisson pair. For example, close to the caissons (r/a near 1.0), the force on the pile is more than twice that of the single pile.

CONCLUDING REMARKS

Analytical expressions have been derived on forces on piles in the presence of caissons. The theory is derived for a pile near a single caisson as well as near multiple caissons. Numerical values are given for several examples, including pile near a single caisson, and pile in the center of a caisson pair. Results show that the force is influenced by the presence of the caisson for $r/a < 2.0$. A transverse force is generated for a single caisson case at 90 deg. due to diffraction of waves. Multiple caisson interaction with the pile is more pronounced. Many offshore and coastal structures include the geometry presented in the above examples, e.g., Maureen Gravity Platform, Risers on Tension Leg Platforms, etc. where this interaction may be important.

REFERENCES

- Chakrabarti, S.K., "Wave Forces on Multiple Vertical Cylinders", Journal of the Waterway, Port, Coastal and Ocean Division, ASCE, Vol. 104, May, 1978, pp. 147-161.
- MacCamy, R.C. and Fuchs, R.A., "Wave Forces on Piles: A Diffraction Theory", Tech Memo No. 69, U.S. Army Corps of Engineers, Beach Erosion Board, 1957.
- Molin, B. "Second-Order Diffraction Loads upon Three-Dimensional Bodies", Applied Ocean Research, Vol. 1, No. 4, 1979, pp. 197-202.
- Ohkusu, M., "Ship Motions in Vicinity of a Structure", Proceedings of International Conference on the Behavior of Offshore Structure, Norwegian Institute of Technology, Trondheim, Norway, Vol. 1, 1976, pp. 284-306.

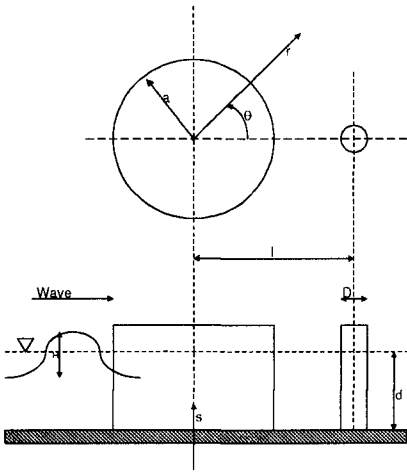


Fig. 1 Definition Sketch for Single Caisson

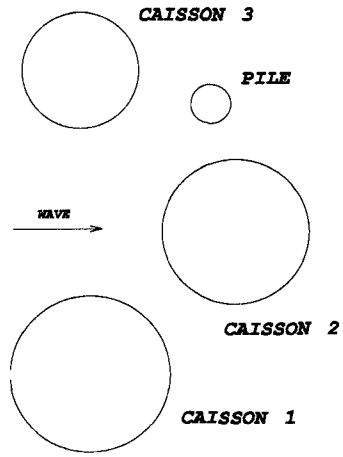


Fig. 2 Definition Sketch for Multiple caisson

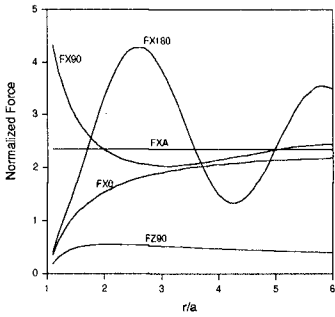


Fig. 3 Forces on Pile with and without Single Caisson -- $ka=1.0$

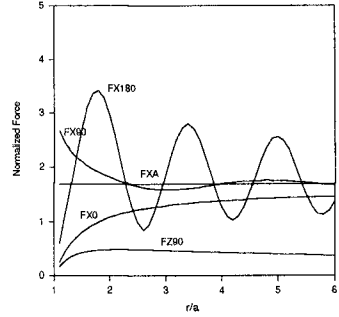


Fig. 4 Forces on Pile with and without Single Caisson -- $ka=2.0$

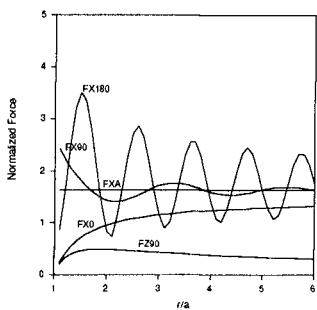


Fig. 5 Forces on Pile with and without Single Caisson -- $ka=3.0$

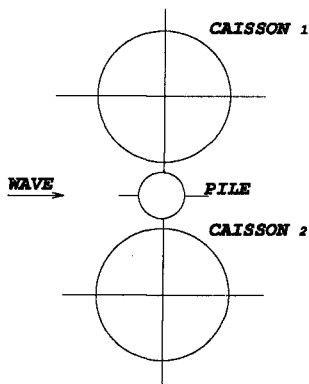


Fig. 6 Example Problem -- Pile in the Center of Two Caissons

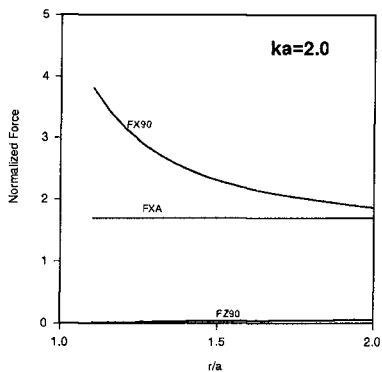


Fig. 7 Forces on Pile with and without Two Caissons -- $ka=2.0$

CHAPTER 31

WAVE DYNAMICS AT COASTAL STRUCTURES: DEVELOPMENT OF A NUMERICAL MODEL FOR FREE SURFACE FLOW

Zoheir A. Sabeur⁽¹⁾, N William H.Allsop⁽²⁾, Robert G.Beale⁽³⁾, John M.Dennis⁽⁴⁾

Abstract

The development of third generation wave models is needed for a detailed study of wave dynamics and impact at coastal structures. This would require the modelling of wave flows with high distortion of the free surface at confined boundaries. In our opinion, the Volume of fluid method, which uses concepts of local advection of fluid in free surface flow modelling, is the prime candidate for simulating realistic flows at sea defences and walls. In this paper, the numerical techniques for the simulation of waves with highly distorted water/air interfaces at a slope, using the volume of fluid method, are considered

Introduction

The volume of fluid method (VOF), originally developed by Hirt and Nichols [1], can be used for the study of transient waves within confined structures. The possibility for simulating the interaction (or interactions) of waves at structures with complex geometry leads to a more realistic modelling of wave impact at breakwaters and coastal defences. Furthermore, a stable numerical simulation of such wave dynamics can provide important information on impact pressures, jets and wave flows at specified locations of the coastal structure.

-
- 1) Principal Modeller, BMT Marine Information Systems Ltd, Grove House, Meridians Cross, 7 Ocean Way, Ocean Village, Southampton, SO14 3TJ, UK.
 - 2) Coastal Structures Manager, HR Wallingford Ltd, Oxfordshire OX10 8BA, UK.
 - 3) Senior Lecturer, Oxford Brookes University, Civil Engineering Division, Oxford, OX3 0BP, UK.
 - 4) Principal Lecturer, Oxford Brookes University, Civil Engineering Division, Oxford, OX3 0BP, UK.
-

Thus, the numerical approach based on the VOF technique for the simulation of transient waves can lead to a good design for the construction of sea defences that sustain wave forces encountered during severe ocean, sea and atmospheric conditions.

In previous years, two dimensional depth integrated models have been widely used in the study of wave action at vertical walls and slopes [2]. However they are limited by the fact that the free surface is assumed to remain a single valued function of space in all flow cases. Vertical fluid accelerations which are large in magnitude and short in duration, during wave impact, cannot be modelled and the free surface is implicitly maintained as a simply connected function of space. These first generation type of models are well established in coastal engineering. They can provide solutions to problems involving wave propagation at structures with simple geometry and in flow cases where breaking and overturning waves do not take place. They are also important for the study of solitary waves and can be used in the development of the next generation wave models. [3], [4]

The speed and storage memory of modern computers have allowed scientists to develop the second and third generation wave models, and despite the task for a large amount of numerical operations, driven by new mathematical algorithms, the total CPU time used by such computers can be optimised and lead to an efficient study of wave dynamics at coastal structures.

Second generation wave models based on Boundary Integral Methods (BIM) which were developed by Peregrine *et al* , and others [5], raised important questions on the physics of impact pressures at vertical walls. Peregrine showed the existence of large magnitude vertical accelerations of a wave front at impact and the possible mechanisms by which air bubble entrapment could be governed. The existence of short timed (~ 1 msec) oscillatory impact pressure peaks at specific locations of the vertical wall suggests the existence of several types of wave interactions with the wall. Therefore, a detailed numerical investigation needs to be carried out.

As a result, the third generation wave models which describe the dynamics of waves before, at and after impact have been developed, and recent simulations of breaking and overturning waves at vertical walls and slopes have been completed.[6].

Mathematical formulation

The general equations for fluid motion under transient conditions are given by the Navier-Stokes equations (NS). They incorporate fluid mass and momentum conservation and take into account of the external forces that are applied on the fluid body.

In two dimensional cartesian coordinates, the NS equations are given by the following differential equations:

Conservation of mass:

$$\frac{\partial \rho}{\partial t} + \frac{\partial(\rho u)}{\partial x} + \frac{\partial(\rho v)}{\partial y} = 0 \quad (1)$$

Conservation of momentum:

$$\frac{\partial(\rho u)}{\partial t} + \frac{\partial(\rho u^2)}{\partial x} + \frac{\partial(\rho uv)}{\partial y} = \rho F_x + \sum_{r=x,y} \frac{\partial \sigma_{xr}}{\partial r} \quad (2)$$

and

$$\frac{\partial(\rho v)}{\partial t} + \frac{\partial(\rho uv)}{\partial x} + \frac{\partial(\rho v^2)}{\partial y} = \rho F_y + \sum_{r=x,y} \frac{\partial \sigma_{yr}}{\partial r} \quad (3)$$

F_x and F_y represent the components of the resultant external force applied on the fluid in the x (horizontal) and y (vertical) directions respectively. σ is the stress tensor and ρ is the density of the fluid. u and v are the velocity field components in the x and y directions respectively. t is the time variable.

In the case of a Newtonian incompressible fluid the density ρ is constant in time and the stress tensor σ is assumed to vary linearly with the fluid deformation rate.

Thus:

$$\frac{1}{\rho} \begin{bmatrix} \sigma_{xx} & \sigma_{xy} \\ \sigma_{yx} & \sigma_{yy} \end{bmatrix} = \begin{bmatrix} -p & 0 \\ 0 & -p \end{bmatrix} + \gamma \begin{bmatrix} 2 \frac{\partial u}{\partial x} & \frac{\partial u}{\partial y} + \frac{\partial v}{\partial x} \\ \frac{\partial u}{\partial y} + \frac{\partial v}{\partial x} & 2 \frac{\partial v}{\partial y} \end{bmatrix} \quad (4)$$

where p is the reduced pressure and γ is the kinematic viscosity. (All variables are used in (SI) units.). As a result, equations (1), (2) and (3) simplify and can be written in a compact vectorial form:

$$\operatorname{div}U = 0 \quad (5)$$

$$\text{and} \quad \frac{\partial U}{\partial t} + (U \cdot \operatorname{grad})U = F - \operatorname{grad}(p) + \gamma \nabla^2 U \quad (6)$$

U and F are the velocity and external force vector fields respectively.

Numerical Model

Sabeur *et al* developed a new VOF based model in recent years [7]; this model discretises the NS equations in both time and space by means of finite difference techniques. Equations (5) and (6) can be written as follows:

$$\operatorname{div}U^{n+1} = 0 \quad (7)$$

and

$$\frac{U^{n+1} - U^n}{\delta t} + \operatorname{grad}(p^{n+1}) = Q^n \quad (8)$$

δt is the time step and Q^n involves the finite difference advective terms and the external force F of the NS equations:

$$Q = -(U \cdot \operatorname{grad})U + \gamma \nabla^2 U + F \quad (9)$$

Various finite difference schemes can be implemented in the spatial discretisation of Q . As far as numerical stability and accuracy are concerned, each of the schemes have their advantages and drawbacks. The choice of the finite difference scheme greatly depends on the computing task required for the wave modelling case. ie, Number of wave propagation periods, wave length, boundary geometrical complexity.

When combined, equations (7) and (8) lead to the Poisson equation (PE) for the pressures:

$$\nabla^2 p^{n+1} = \operatorname{div}\left(\frac{U^n}{\delta t} + Q^n\right) \quad (10)$$

The volume of fluid method

The study of wave motion with a highly distorted free surface needs the implementation of the VOF method which tracks the fluid locally in space. For a specified rectangular grid and time step, fluid fluxes are computed at each cell face. The fractional amount of fluid per cell is then determined by the net flux of fluid advected in both vertical and horizontal directions.

The flux calculation leads to the update of the F function in time. That is the fractional volume of fluid at each cell centre point. Thus, a zero value of F in a cell means that it is empty while a unit value of F corresponds to a cell full of fluid. An intermediate value of F between zero and one normally represents a free surface cell, or indeed a trapped bubble. In strict numerical modelling terms, however, a true free surface cell is a cell that has at least one empty neighbouring cell. In figure 1 for example, the cell where $F= 0.99$ is not considered as a free surface cell because its four nearest neighbour cells are not empty. Therefore the PE is applied for such type of cell as if it was a full cell.

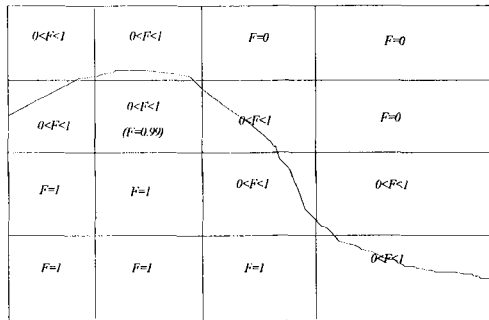


Figure 1. Illustration on the type of fluid and void cells considered by the VOF wave model.

In addition to the above, a numerical correction is performed on the F function values at the end of each computational cycle because, usually, a unit value of the F function (or, indeed a zero value) cannot be reached accurately by computational means. Instead, it is rounded to one (or zero) if it reaches a value of $1 \pm \epsilon$. (or $\pm \epsilon$). In practice, and for an efficient modelling of the fluid interface, ϵ should be no bigger than 0.00001.

Boundary conditions

In the VOF method, pressure and velocity equations must be specified.

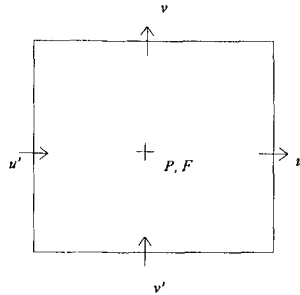


Figure 2. A typical 2D VOF cell with six dynamic variables

Figure 2 shows the location of the six variables used in a staggered finite difference grid and computed for each time level n . In the case of a full cell located inside the flow (meaning, that the cell is totally surrounded by full cells), equations (8) and (10) are used to compute the velocities and pressures at time level $n+1$ respectively. Then, the F function value in the cell can be updated and the fluid advected in time. However, in the case of boundary cells, the computation of the pressures, the velocities and function F becomes tedious and time consuming.

Boundary cells can be classified as follows:

- Ordinary free surface cell
- Non-ordinary free surface cell
- Inflow cell
- Full cell at a vertical/horizontal/sloped rigid boundary

For each boundary cell, apart from the free surface cells, pseudo Poisson equations can be implemented by setting fluid mass conservation and virtual velocities inside local boundaries [8]. For example, rigid free-slip (or no slip) boundary conditions can be established for solid boundaries. The normal velocities to the boundaries and the gradient of the tangential velocities are set to zero. Parallel (or anti-parallel) and equal in magnitude virtual velocities are set for rigid free-slip (or no-slip) boundary conditions.

Free surface cells are provided with different pressure equations which involve the orientation and curvature of the interface, the nearest pressure inside the fluid, the local atmospheric pressure at the free surface and surface tension. The continuity of normal and tangential shear stresses is also enforced. A typical pressure equation at the free surface is given by:

$$-p + 2\gamma \frac{\partial U_n}{\partial r_n} = -p_{Air} \frac{\rho_{Air}}{\rho} + \frac{2\phi\psi}{\rho} \quad (11)$$

supplemented with a condition on stresses at the interface:

$$\gamma \left(\frac{\partial U_n}{\partial r_t} + \frac{\partial U_t}{\partial r_n} \right) = 0 \quad (12)$$

ϕ and ψ are the free surface tension and curvature respectively. p_{Air} and ρ_{Air} are the reduced pressure and density of air respectively. U_n and U_t are the normal and tangential velocities to the free surface. The reduced pressure at the interface, p , is interpolated (or extrapolated) from the nearest dynamic pressure inside the fluid and normal to the interface. It can be located from the orientation of the free surface. Hence, the nearest interpolation dynamic pressure can be found either below or above the fluid interface, or can be located to the left or to the right of the interface. The orientation and curvature of the interface are computed by the F function local gradients corresponding to nearest neighbouring cells to the free surface.

This approach for setting the boundary conditions at the free surface is used by most VOF methods, however the boundary conditions for cells which intercept the slope are not straightforward.

In the new VOF wave model, the conditions on the orientation of the interface, given by the local gradients of F , are slightly modified at air/water/slope boundary cells. Virtual values of F , inside the sloped structures, are given *a priori*. Then, a stable air/water/slope interface can be modelled.

Further numerical development of air/water/slope boundary conditions is needed. Applications of flows with the VOF method can be then extended to more complicated type of interface. For instance, in cases of floating and moving objects in fluids.

The simulation of progressive waves at sloped structures can be generated by a weakly reflective inflow boundary condition (WRIB). [6], [8]. Continuity of flow is enforced at the boundary and the free surface is assumed horizontal at all time. The velocity vector field U and water elevation η at the inflow boundary must satisfy the following conditions:

$$\frac{\partial U}{\partial t} - C \frac{\partial U}{\partial x} = \frac{\partial U_{in}}{\partial t} - C \frac{\partial U_{in}}{\partial x} \quad (13)$$

and

$$\frac{\partial \eta}{\partial t} - C \frac{\partial \eta}{\partial x} = \frac{\partial \eta_{in}}{\partial t} - C \frac{\partial \eta_{in}}{\partial x} \quad (14)$$

C is the wave celerity. U_{in} and η_{in} are the inflow velocity field and water elevation (above or below still water level) respectively. For example, they take the following sinusoidal forms:

$$U_{in}(x, y, t) = \frac{H\omega}{2 \sinh(kh)} [\cosh(ky) \sin(\omega t) + j \sinh(ky) \cos(\omega t + kx)] \quad (15)$$

and

$$\eta_{in}(x, t) = \frac{H}{2} \sin(kx - \omega t) \quad (16)$$

h is the still water level (SWL), ω the angular wave frequency, k the wave number and H the total wave amplitude. ($j = \sqrt{-1}$.)*

**(The use of imaginary complex j in equation (15) should not be confused with grid cell coordinate j .)*

Equations (13) and (14) are discretised forward in time and solved one time step earlier than the pressure and velocity equations. In this manner, the velocity field U and elevation η , can be provided for the computation of term Q , which appears in equation (8) at time level n . Water elevation η enables the computation of F at the inflow boundary free surface cell. At the free surface, F is given by:

$$F = \eta + h - \sum_{j=1}^{j=N} F_{ij} \delta y_{ij} \quad (17)$$

N values of F_{ij} are found strictly equal to unity in a water column, j , which is adjacent to the inflow boundary column. δy_{ij} is the height of cell ij .

The combination of PE, the pseudo Poisson equations at the boundaries, and the free surface pressure equations leads to a system of M equations with M unknowns. M is the number of grid cells occupied by the fluid where F is greater than zero. Once the pressure equations are computed at a specified time level, the new velocity field is calculated, the F function is updated and the fluid advanced accordingly. The updated values of F provide the new value of M .

In an early simulation of a dam-break flow by the VOF method, the Gauss-Seidel (GS) iterative scheme was used to solve the pressure equations. The GS algorithm requires a computational time that is proportional to M^2 . For M smaller than ~ 10000 , the algorithm converged after approximately 1200 iterations.

Numerical simulations, results and discussion

The speed of the pressure solver can be improved by adapting successive over-relaxation techniques (SOR) to the GS algorithm. However, as M gets larger with high resolution grids, or when diagonal dominance of the PE deteriorates, the SOR algorithm slows down and does not successfully converge. Powerful methods such as the Conjugate gradient (CG) or Lanczos (LZ), should be used to overcome this problem. The pressure field should be therefore represented in vectorial form and the structure of the corresponding Poisson matrix updated at each time step. Preliminary attempts to the matrix formulation, using parallel processors, [9] have been carried out and adapted to the VOF wave model. The simulation of a Dam-break flow showed similar results to the early calculations with the GS method.

The simulation of progressive waves at a slope, using the WRIB condition, has been completed. The stability of the VOF model over several wave periods and for two cases of slopes, in a 4m deep and 35m long rectangular tank, has been achieved. The computation of the pressure equations was performed on a uniform 150x80 rectangular grid and the minimum time set to 0.001 sec. In this early simulation, surface tension was not included and the pressure at the interface was set to zero. (void representation). The wave characteristics for each cases of slopes are given in the table below:

Wave parameters	T (sec)	H(m)	SWL(m)	Slope	Surf ξ
1st case	2.8	1.	1.5	1:3	0.3
2nd case	2.8	1.	1.5	1:4	0.2

Table 1. Wave characteristics used for model tests.

According to Battjes theory on breakers[10], the first and second wave test cases correspond to flows with spilling breakers. Spilling breakers occur with a surf similarity coefficient ξ smaller than 0.5, which is the case in our study. Large magnitude impact pressures are not encountered in such flows but distortions of the free surface with large velocity jets at air/water/slope boundaries do take place. In the first wave test case, shown in figure 3 for example, air entrapment at the slope region occurs at $t=11.65$ sec. Maximum velocity jets reaching approximately 5 m/s at the wave crest are calculated. The wave then spills along the slope, as shown in figure 4, and the front of the spill changes direction due to gravity. This change in the direction of motion causes the top of the wave to break and overturn, as shown in figure 5 at $t=13.60$ sec. Additional air bubbles are then trapped inside the fluid and lead to the formation of velocity jets that are parallel to the slope plane and persist in time. (Figure 6.) The kinetic energy of the wave flow region driven by the jets, decreases gradually in time and causes the collapse of part of the wave crest back onto the slope, as shown in figure 7. This feature of the model clearly illustrates the potential modelling of transient waves by the VOF technique. Similar observations to the above equally apply to the second wave test case. They are shown in figures 8-12.

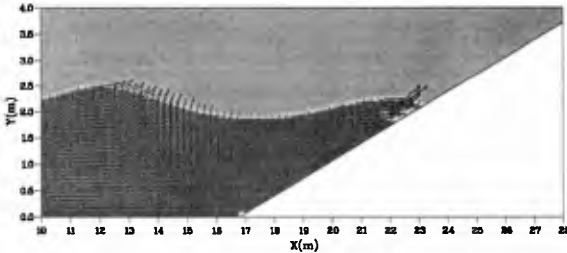


Figure 3. $t=11.65$ sec, slope=1:3

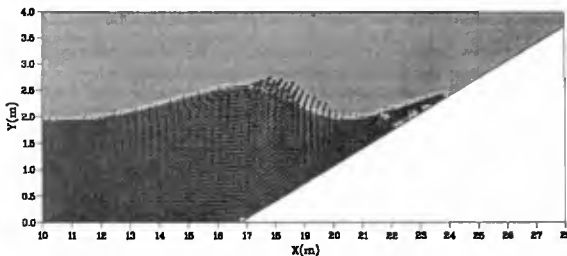


Figure 4. $t=12.70$ sec, slope=1:3

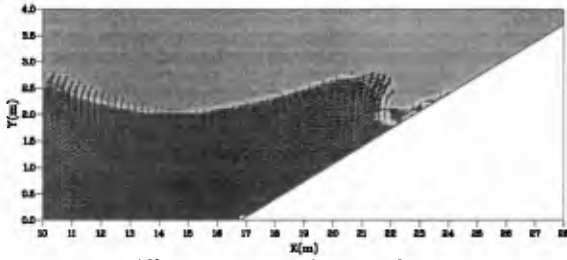


Figure 5. $t=13.60$ sec, slope=1:3

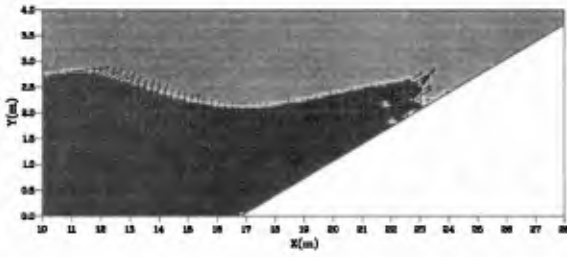


Figure 6. $t=14.19$ sec, slope=1:3

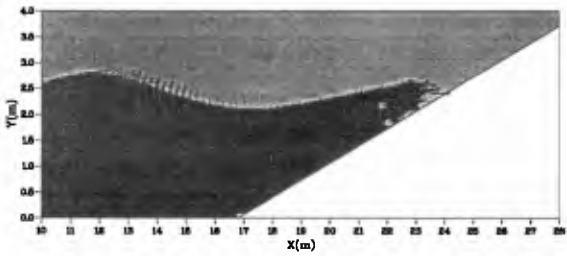


Figure 7. $t=14.30$ sec, slope=1:3

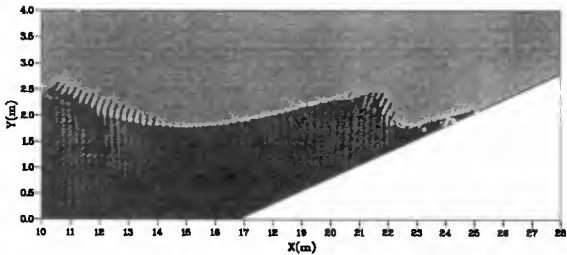


Figure 8. $t=11.09$ sec, slope=1:4

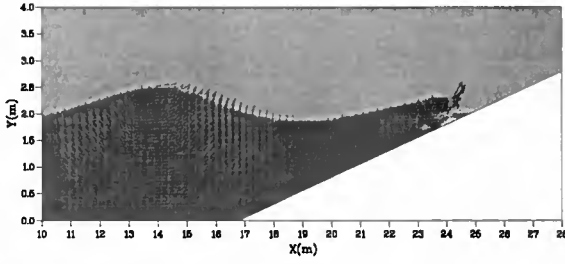


Figure 9. $t=12.10$ sec, slope=1:4

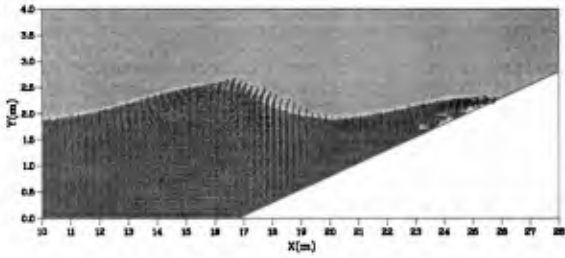


Figure 10. $t=12.40$ sec, slope=1:4

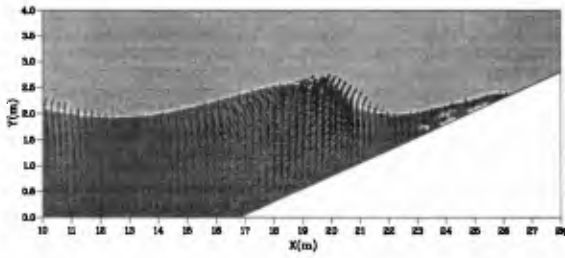


Figure 11. $t=13.30$ sec, slope=1:4

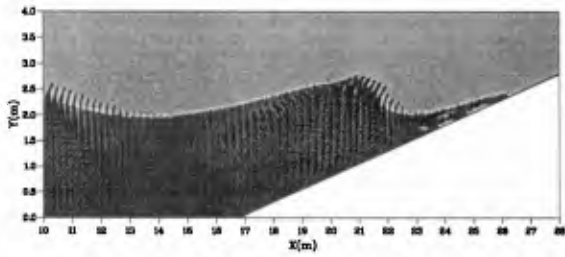


Figure 12. $t=13.60$ sec, slope=1:4

Conclusion and recommendations

This work clearly demonstrates the potential of the VOF implementation to the NS equation for the study of wave dynamics within confined domains, i.e. coastal structures. The newly developed model is capable of simulating the full process of wave interaction with structures. Wave impact generated from collapsing and plunging breakers can be equally modelled and dynamic pressures and jets predicted at specified locations of the structure. The model also provides more understanding in wave dynamics at coastal structures which in turn helps to promote improved design methods.

In order to realise the full potential of VOF based wave models in coastal engineering, the following research and development is recommended:

- Implementation of the Conjugate gradient or Lanczos algorithms in the pressure solver.
- Development of boundary conditions at water/porous medium interfaces.
- Implementation of the compressible NS equations for air entrapment dynamics study.
- Extension of the theory to 3D for a better understanding of wave interactions.
- Calibration and validation of numerical data with laboratory results.
- Comparison of numerical predictions of wave dynamics with field data.

Acknowledgements

This work was originally funded by Oxford Brookes University (OBU) and the UK Department of the Environment (Contract no. CI 39/5/86). The authors are grateful to A.J.Cooper and W.Roberts (HR Wallingford) for useful discussions during early development of the model. Z.A.Sabeur is thankful to A.E.P.Veldman of the University of Groningen, the Netherlands, for guidance on free surface modelling and impact dynamics at boundaries, L.Zieleznik (OBU), for processing the wave model data by AVS/Gsharp graphics, and the technical staff of BMT Marine Information Systems Ltd for support in the visualisation and transfer of .cgm files into Word 6. documents. The authors also thank A.Bracci-Laudiero of the University of Naples, Italy, for assistance in the preparation of the conference presentation, and V.Bovolin of the University of Salerno, Italy, for research collaboration. X.He (OBU) and M.Waller (HR Wallingford) are also thanked for the progress made in the implementation of the SOR technique to the pressure solver.

References

- [1] Hirt, C.W. & Nichols, B.D. (1981). Volume of fluid method for the dynamics of free boundaries. *Journal of Computational Physics*, 39/1, 201-225.
- [2] Allsop, N.W.H *et al.* (1988). Development and application of a mathematical model on wave action on steep slopes. Proc. 21st ICCE/ 88, Malaga. publ. ASCE. New York
- [3] McConnell, K.J *et al.* (1995). Wave dynamics at near port and coastal structures. Hydraulics Report IT422 HR Wallingford, UK.
- [4] Sabeur, Z.A and Dennis, J.M. (1995). Wave Dynamics at Coastal Structures: Numerical Methods for the Simulation of flows with moving interfaces. Hydraulics Report IT428, HR Wallingford, UK .
- [5] Cooker, M.J. and Peregrine, D.H. (1995). Pressure impulse theory for liquid impact problems. *Journal of Fluid Mechanics*, 297, 193-214.
(Also, Peregrine, D.H. (1994). *Pressure on breakwaters: A forward look. University of Bristol Mathematics research report, AM-93-17, Bristol, UK.*)
- [6] van der Meer, *et al.* (1992). Numerical simulation on and in coastal structures, Proc. 23rd ICCE/ 92, 1448-1460, Venice. publ. ASCE, New York.
- [7] Sabeur, Z.A., *et al.* (1995). Development and use of an advanced numerical model using the volume of fluid method for the design of coastal structures. In *Numerical methods for fluid dynamics V.* (Ed K.W.Morton & M.J.Baines), Oxford University Press, UK, 565-573.
- [8] Sabeur, Z.A., *et al.* (1996). A full numerical simulation of wave dynamics at coastal structure with the VOF method. In, *Hydraulic Software VI, Computational Mechanics Publications.* (Ed W.R.Blain), Southampton, UK, 395-404.
- [9] Sabeur, Z.A. (1995). A parallel computation of the Navier-Stokes equations for the simulation of free surface flows with the volume of fluid method. In, *Applied Parallel Computing*, (Ed J.Dongara & J.Wasniewski), Lecture Notes in Computer Science no 1041, Springer-Verlag, Denmark, 483-492.
- [10] Battjes, J.A. (1974). Surf similarity, Proc. 14th ICCE/74., 466-480, Copenhagen. publ. ASCE, New York.

CHAPTER 32

Scale Effects in Oxygenation in the Breaker Zone of Coastal Structures

V.K. Tsoukala¹ and C.I. Moutzouris²

Abstract

The significance of oxygen transfer across the air-water interface with its associated impact on water quality and environmental pollution control in coastal zones has become a matter of concern for coastal engineers. In the present paper experimental data on oxygen transfer obtained in the large scale facility of Delft Hydraulics have been presented. The obtained oxygen transfer coefficients have been compared to existing models for gas transfer under breaking and non breaking waves. Scale effects are found to be an important factor which needs to be considered when laboratory results are translated to field conditions.

Introduction

Oxygen transfer across the air-water interface with its associated impact on water quality and environmental pollution control in coastal zones has become increasingly important for coastal engineers. Systematic studies of the oxygenation of water systems commenced with the emergence of water pollution problems associated with river systems (Streeter and Phelps, 1925). Years later these studies were augmented to incorporate lakes and oceans.

Understanding of the parameters influencing air-sea gas exchange has increased considerably in recent years, although little is known about the exact mechanisms that control the process. Recent research has also begun to investigate the penetration of other gases in water, including nitrogen oxide, N_2O , carbon dioxide, CO_2 , helium, He, and sulfur hexafluoride, SF_6 (Keeling, 1993, Woolf, 1991, Wanninkhof, 1992, Wanninkhof et al., 1995). However, available data for the evaluation of the different gas exchange models is still limited.

¹Research Associate, ²Professor

Laboratory of Harbour Works, Civil Engineering Department, National Technical University of Athens, 5 Iroon Polytechniou Str., Zografou, 157 73 Athens, Greece

Experimental results indicate that wave action increases the penetration of gases into the water (Jähne, 1985, 1987, Hosoi, 1977, Hasse and Liss, 1980). It is therefore considered that waves have a positive effect on the oxygenation of water bodies. Breaking waves enhance the aeration process by entraining air bubbles and increasing turbulent mixing. Field, laboratory and theoretical studies have been performed to study this phenomenon in detail. The presence of air bubbles increases the air-water interface area available for gas exchange. The formation of bubbles and increased turbulence that result from the action of breaking waves contribute to the increase of dissolved oxygen (DO) in water. Hosoi and Murakami (1986) assumed that oxygenation due to non-breaking waves in their experiments was negligible and that the whole water body is oxygenated through the wave breaking zone. Wallace and Wirick (1992) observed that breaking waves can increase the rate of aeration by up to 200 times due to the entrainment of bubbles.

The role of coastal structures in water oxygenation has recently come under investigation (Moutzouris and Daniil, 1994b, Hosoi et al., 1977), as wave breaking results in high oxygenation rates and therefore in improvement of water quality in the vicinity of coastal structures. For oceans the transfer coefficient is usually correlated to the wind velocity (Wanninkhof, 1992, Wanninkhof et al., 1993). It should be noted though that laboratory and field data give significantly different correlations possibly (Liss, 1983) due to scale effects.

A research program has been initiated at the Laboratory of Harbour Works (LHW), National Technical University of Athens, to investigate and model air penetration in the wave breaker zone of inclined coastal structures. Initial experimental results from a small wave flume at LHW (Daniil and Moutzouris, 1993) indicated that scale effects should be investigated for application to field conditions. In order to quantify these effects and to compare to earlier results, further experiments were conducted in a larger facility. Measurements were carried out in the large wave flume of Delft Hydraulics (DH), the Netherlands, financed by the European Community, as part of the Large Installations Program (LIP): "Training and Mobility of Researchers- Access to Large Scale Facilities".

This paper presents the preliminary results from this research program, which indicate that the scale of the phenomenon has a considerable influence on the transfer mechanisms. Oxygen transfer velocities determined from the large scale experimental result are compared in this paper to the models of Daniil and Gulliver (1991) for non-breaking waves and Daniil and Moutzouris (1994, 1995) for breaking waves, derived and verified from measurements in small scale facilities.

Experimental Procedure

Large scale oxygenation experiments under breaking waves were performed at the Wind Wave Flume of Delft Hydraulics (DH) as a part of the European Program: "Training and Mobility of Researchers - Access to Large -Scale Facilities".

The wave flume of Delft Hydraulics is "T" shaped with a total length of 100m and 8m width while the last 9 m are 25m wide. The outline of the flume is shown in Figure 1. The flume is equipped with a hydraulic dual piston wave maker for the generation of mechanical waves. Waves are generated by a computer-controlled wave board with adjustable rotation and translation. Waves with frequencies between 0.65-0.90 Hz and heights between 8.5-20.5 cm were produced.

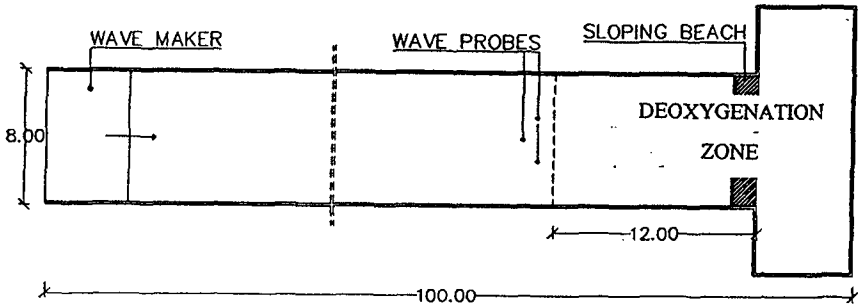
A concrete structure with a uniform slope of 1:2.3 was placed at one end of the flume in order to model a sloping beach and initiate wave breaking. The structure was watertight and no water exchange between the front and the back of the sloping beach was possible. The water depth was 0.72m for all experiments.

Three capacitance wave gauges were used for recording the wave characteristics (Figure 1). The experimental procedure consisted of two distinct phases. During the first set of experiments, the water was deoxygenated using sodium sulfite (Na_2SO_3) and cobalt chloride (CoCl_2). About 8 kg of Na_2SO_3 and 0.55 Kg of $\text{CoCl}_2 \cdot 6\text{H}_2\text{O}$ were required for every experiment and these were sufficient to deoxygenate an area of 12m length and 8m width.

In the second set of experiments the water was deoxygenated using the nitrogen stripping method. Long elastic tubes with small pores were connected to nitrogen cylinders equipped with regulating pressure valves. The elastic tubes were placed in a 12m long area of the flume which was isolated during the deoxygenation process from the rest of the flume by a movable divider. Approximately 60-70 m^3 of nitrogen were needed for each experiment. For the deoxygenation process approximately 10 hours were required.

The concentration of DO in the water body was monitored over time by a portable oxygen meter type OXI-96, at 21 sampling locations along the flume (see Figure 1). In order to verify the accuracy of readings obtained with the oxygen meter, water samples were also taken and analyzed using the azide modification of the Iodometric Winkler titration method for D.O. determination. The measurements of the dissolved oxygen concentration commenced immediately upon wave generation and continued until the DO value reached 80% of the estimated saturation level for the specific conditions of temperature and atmospheric pressure.

OUTLINE OF THE FLUME



DEOXYGENATED AREA

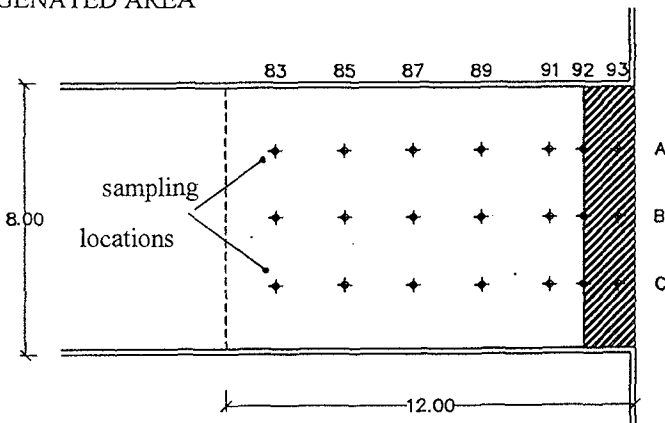


Figure 1. Schematic layout of the wave flume of the laboratory of Delft Hydraulics.

The transfer of oxygen between the air-water interface is a term of source or sink in the mass transfer equation. In the experiments performed the only source considered is oxygen transfer through the water surface. The oxygenation is characterized by the oxygenation coefficient K_2 (sec^{-1}) or the oxygen transfer coefficient (or oxygen transfer velocity) K_L (m/sec).

Data analysis

For all sampling locations the change in DO concentration under wave action was monitored and DO-time histories were obtained. A comparison of DO-time histories for experiments in the large and small scale facilities with waves of about the same period and height, illustrating that the transfer velocity is lower for the large scale facility is shown in Figure 2.

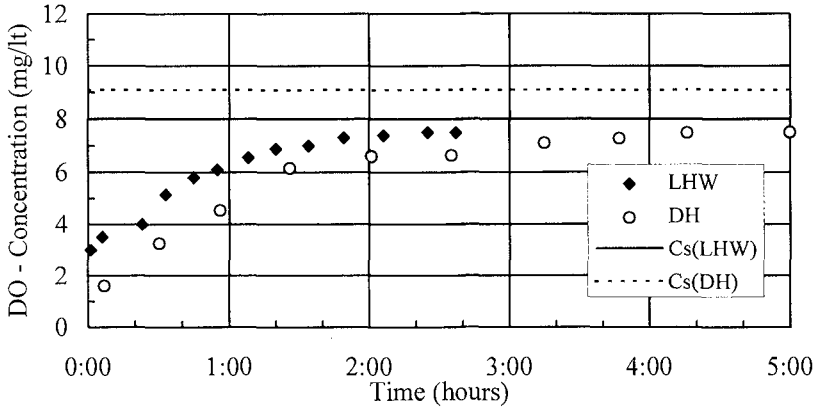


Figure 2. Comparison of DO-time histories at the wave breaking point for experiments in different scale facilities with approximately the same wave characteristics ($T=1.55$ sec $H=18.3$ cm).

The transfer coefficient K_L is determined from the one dimensional transport equation, using linear regression and the measured DO concentration time history from a location where the horizontal transport can be assumed negligible:

$$\ln (C_s - C) = - K_L (A/V)t + \ln (C_s - C_0) \quad (1)$$

where C is the concentration of DO (mg/l), C_0 is the initial concentration (mg/l), C_s is the saturation concentration (mg/l), K_L is the oxygen transfer coefficient (m/sec), A is the projected free surface area (m^2), and V is the aerated volume (m^3). It is assumed that the saturation concentration is steady and for the initial time $t=0$ the concentration is $C=C_0$.

Exp No	T (sec)	H (cm)	L (m)	θ ($^{\circ}$ C)	P (mmHg)	Sc	$K_{L,20} * 10^5$	$K_{L,20} * 10^5$
<i>Breaking Waves</i>								
D ₁	1.55	20.3	3.30	19.4	757.5	563	8.02	8.15
D ₂	1.55	18.26	3.30	19.3	760.0	566	6.91	7.04
D ₄	1.55	9.21	3.30	18.5	764.0	590	2.12	2.20
D ₅	1.30	12.52	2.50	18.6	757.5	587	6.02	6.24
D ₆	1.30	9.68	2.50	18.6	754.5	587	3.51	3.64
D ₇	1.30	10,30	2.50	18.6	751.0	587	4.82	5.00
D ₈	1.10	8,75	1.86	18.3	752.5	597	2.43	2.54
D ₉	1.10	10,92	1.86	18.0	759.0	606	3.49	3.68
<i>Non Breaking Waves</i>								
D ₁₀	1.10	10.92	1.86	17.9	759.0	609	4.8	5.1
D ₁₁	1.55	20.32	3.30	17.9	759.0	609	6.2	6.5
D ₁₂	1.55	12.52	2.50	17.9	751.1	609	3.0	3.1
A ₄	1.90	28.27	4.37	12.7	762.5	809	3.4	4.2
A ₅	1.90	21.14	4.37	13.2	761.0	785	3.5	4.2
A ₇	1.55	20.18	3.30	13.9	766.5	756	3.9	4.6

Table 1. Experimental data from Delft Hydraulics wind wave flume for breaking and non-breaking waves.

In order to compare experimental data, it is necessary to transform the coefficients obtained to their values at 20^o C, using the equation given by Daniil and Gulliver (1988):

$$(K_{L,20}/K_L) = (Sc/Sc_{20})^{1/2} = (v/v_{20}) [293/(\theta+273)]^{1/2} (\rho/\rho_{20})^{1/2} \quad (2)$$

where $Sc = \nu/D$ is the Schmidt number, ν is the kinematic viscosity of water, D is the molecular diffusivity, θ is the water temperature in degrees Celsius, and ρ is the water density. The water density and the kinematic viscosity were determined by the relations given by Heggen (1983).

The transfer coefficients K_L at the wave breaking area and the transformed coefficients to 20 °C are presented in Table 1.

Comparison of results with existing gas transfer models

Various models have been proposed for the prediction of the oxygen transfer coefficient. The most commonly used is the surface renewal model, first developed by Dankwerts (1951). In this model the transfer coefficient is expressed as a function of the surface renewal rate:

$$K_L \propto \sqrt{Dr} \quad \text{or} \quad K_L Sc^{1/2} \propto \sqrt{v r} \quad (3)$$

where K_L is the oxygen transfer coefficient (LT^{-1}), and r is the average surface renewal rate (T^{-1}).

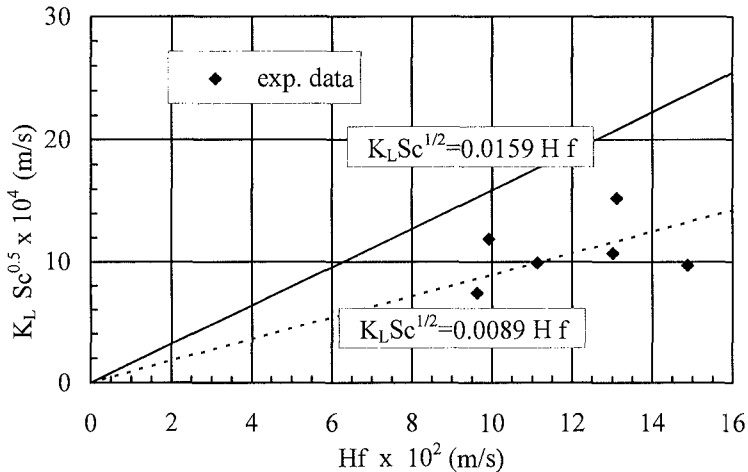


Figure 3. Comparison of large scale experiments to Daniil and Gulliver (1991) model for non-breaking waves.

Non Breaking waves

Based on this surface renewal model Daniil and Gulliver (1991) expressed the renewal rate as a function of a wave Reynolds number, and proposed the

following equation for the determination of the oxygen transfer coefficient, under non-breaking waves:

$$K_L = a H f S c^{-1/2} \quad (4)$$

The gas transfer coefficient is thus shown to be proportional to the vertical wave velocity at the water surface. Equation (4) provided the best comparison to the wave maker data and to data from other small scale flumes. Using data from the small scale facility of St. Antony Falls Hydraulic Laboratory the coefficient a was determined equal to 0.0159.

Experimental data from the large scale facility of Delft Hydraulic are compared to equation (4) in Figure 3. The experimental data are considerably lower than the predictive equation. Correlating experimental data from Delft Hydraulics, the constant of proportionality a for equation (4) is equal to 0.0089 which is approximately 0.60 of the predicted values of the model of Daniil and Gulliver (1991).

Breaking waves

For gas transfer under breaking waves, two models have been developed recently by Daniil and Moutzouris (1994, 1995). The constants were determined from experimental results in small scale facilities.

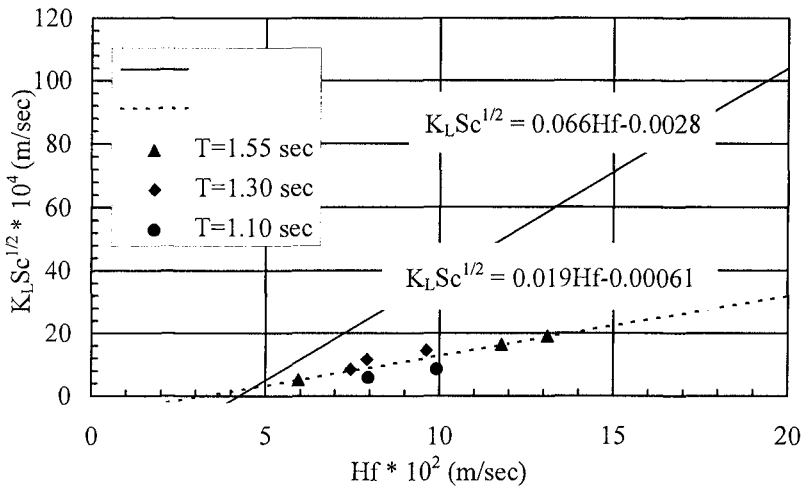


Figure 4. Comparison of large scale experiments to Daniil and Moutzouris, (1994) model for breaking waves.

Daniil and Moutzouris (1994), relate the transfer coefficient for breaking waves to the vertical wave velocity at the water surface with a qualitatively similar equation to Daniil and Gulliver (1991) equation as follows:

$$K_L Sc^{1/2} = a H f - b \quad (5)$$

where H is the wave height, f is the wave frequency, $a = 0.066$ and $b = 0.0028$ m/sec. Data from experiments in Delft Hydraulics are compared to equation (5) in Fig. 4. Fitting equation (5) to data from Delft Hydraulics yields $a = 0.019$ and $b = 0.0006$ m/sec.

Daniil and Moutzouris (1995) proposed the vorticity based model for gas transfer under breaking waves, where the renewal rate was expressed as a function of the wave vorticity at the water surface and the term L/d that express the influence of relative depth:

$$K_L Sc^{1/2} = a (L/d) (v\omega)^{1/2} + b \quad (6)$$

where L is the wave length, d is the water depth, v is the water viscosity, ω is the wave vorticity at the water surface. Daniil and Moutzouris (1995) give $a = 2.86$ and $b = -0.00246$ m/sec for breaking waves on a uniformly sloping beach based on a number of 9 experiments in the wave flume of LHW and mention that this model gives considerably better correlations, as compared to correlation with the vertical wave velocity and wave slope presented previously.

In Fig. 5 data from DH are compared to equation (6). Fitting equation (6) to data from DH give $a = 0.91$ and $b = -0.0004$ m/sec.

Although data for breaking waves from the large scale facility of DH are lower, approximately 30% of the corresponding coefficients obtained from small scale facilities for the same wave characteristics, the correlation of the data to the wave parameters of the existing models is good. This indicates that the existing models include the important wave parameters, but an attenuation coefficient expressing the effect of length scale should also be included.

Conclusions

Experimental data on oxygen transfer obtained in the large scale facility of Delft Hydraulics, as a part of the European program "Training and mobility of Researchers-Access to Large Scale Facilities", have been presented. The obtained

oxygen transfer coefficients have been compared to existing models for gas transfer under breaking and non breaking waves.

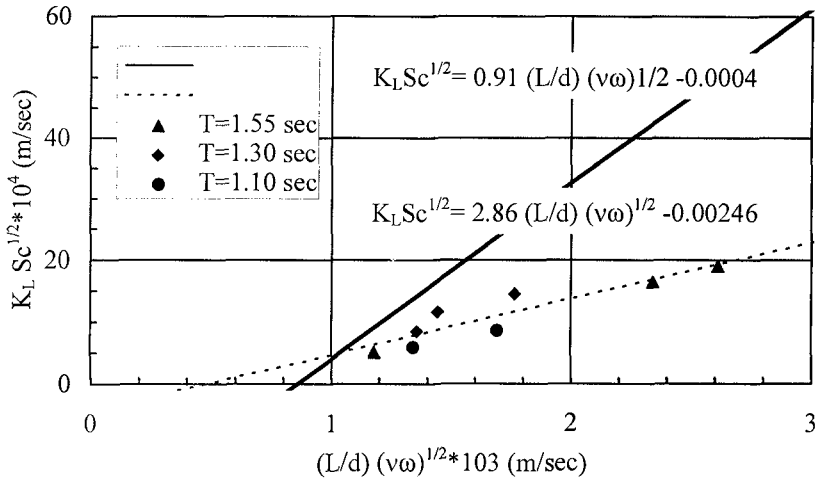


Figure 5. Comparison of large scale experiments to Daniil and Moutzouris model, (1995) for breaking waves.

In all cases the coefficients were considerably lower than the corresponding coefficients obtained from small scale facilities for the same wave characteristics. This could be possibly due to the minimized effect of solid boundaries in the large scale facility. Using the same wave parameters new constants were determined to the large scale experimental data with high correlation coefficients. For non breaking waves the coefficients obtained in the large scale facility were 60% of those obtained in the small wave facility for the same wave characteristics whereas for breaking waves the measured coefficients were 30% of those obtained in the small wave facility.

Finally it is concluded that the effect of scale is pronounced and should be taken into account when small scale laboratory results are translated to field conditions. The above comparisons and analysis indicate that the coefficients of the existing models should be expressed as a function of the length scale of the phenomenon.

Acknowledgments

The authors wish to thank Dr. E.I. Daniil for continuous assistance during the program.

References

- Danckwerts, P. V., (1951). "Significance of liquid-film coefficients in gas adsorption." *Ind. Engrg. Chem.*, 46(6), 1460 - 1467.
- Daniil, E. I. and Gulliver, J. S., (1991). "The Influence of Waves on Air-Water Gas Transfer." *J. Environmental Eng.*, ASCE, 117(5), 522 - 540.
- Daniil, E. I. and Gulliver, J. S., (1988). "Temperature dependence of the liquid film coefficient for gas transfer." *J. Environmental Eng.*, ASCE, 114(5), 1224 - 1229.
- Daniil, E.I. and Moutzouris, C.I., (1995). "A vorticity - based model for gas transfer under breaking waves." *Annales Geophysicae*, EGS, 13, 1039-1046.
- Daniil, E.I. and Moutzouris, C.I. (1994). "Gas Transfer Experiments with Breaking Waves." , "The Air - Sea Interface," M.A. Donelan, W.H. Hui and W.J. Plant, eds, The University of Toronto Press, Toronto, 487-492.
- Daniil, E.I. and Moutzouris, C.I. (1993). "Oxygenation Experiments in the Wave Breaking Zone." *Hydraulic Engineering '93*, H.W. Shen, S.T. Su , F. Wen (eds), ASCE, 2008-2013.
- Hase, L. and Liss, P.S. (1980) "Gas exchange across the air - sea interface" *Tellus*, 32, 470-481.
- Heggen, R. J. (1983). "Thermal Dependent Physical Properties of Water." *Jour. of Hydraulic Eng.*, ASCE, 109(2), 298 - 302.
- Hosoi, M. A., Ishida, A., and Imoto, K. (1977). "Study on reaeration by waves." *Coastal Engineering in Japan*, 20, 121 - 127.
- Hosoi, Y. and Murakami, H. (1986). "Effect of waves on dissolved oxygen and organic matter." *20th Coastal Eng. Conference*, Proc. CERC, ASCE, Taipei, 2498 - 2512.
- Hosoi, Y., Murakami, H., and Mitsui, H. (1990). "Reaeration due to wave breaking at coastal structures." *Coastal Engineering in Japan*, 33(1), 89 - 100.
- Jähne, B., Münnich, K.O., Börsinger, R., Dutzi, A., Huber W., and Libner, P. (1987). "On the parameters influencing air-water gas exchange." *Jour. Geophys. Res.*, 92(C2), 1937 - 1949, 1987.
- Jähne, B., Wais, T., Mémerly, L., Cauliez, G., Merlivat, L., Münnich K.O., and Coantic, M. (1985). "He and Rn Gas Exchange Experiments in the Large Wind - Wave Facility of IMST." *J. Geoph. Research*, 90(C6), 11989 - 11997.

Keeling, R. F. (1993). "On the role of large bubbles in air-sea gas exchange and supersaturation in the ocean." *J. Mar. Res.*, 51, 237 - 271.

Liss, P. S. (1983) 'Gas Transfer: Experiments and Geochemical Implication.' In *Air-Sea Exchange of Gases and Particles*, P. S. Liss and W. G. N. Slinn (eds.), 241 - 298.

Moutzouris, C.I., and Daniil, E.I. (1994b). "Oxygenation in the Vicinity of Coastal Structures." *24th International Conference on Coastal Engineering*, ICCE 94, ASCE, CERC, Proceedings, 3167-3177.

Streeter, H.W., and Phelps, E. B. (1925). "A Study of the Pollution and Natural Purification of the Ohio River.", *Public Health Bulletin*, Washington, U.S. Public Health Service, 146, 75p., 1925.

Wallace, D. W. R., and Wirick, C. D. (1992). "Dissolved O₂ time-series records large air-sea gas fluxes associated with breaking wavcs." *Nature*, 356, 694 - 696,.

Wanninkhof, R. (1992). "Relationship between wind speed and gas exchange over the ocean." *J. Geoph. Res.*, 97(C5), 7373 - 7382.

Wanninkhof, R., Asher, W., Monahan, E., (1995). "The Influence of Bubbles on Air-Water Gas Exchange Results from Gas Transfer Experiments during Wabex-93." *Air Water Gas Transfer*, Selected Papers from the Third International Symposium on Air-Water Gas Transfer, Germany, 239-254.

Wanninkhof, R., Asher, W., Weppernig, R., Chen, H., Schlosser, P., Langdon, C., and Sambrotto, R. (1993) "Gas Transfer Experiment on Georges Bank Using Two Volatile Deliberate Tracers." *J. Geophys. Research*, 98(C11), 20237 - 20248.

Woolf, D. K. and Thorpe, S. A. (1991). "Bubbles and the air- sea exchange of gases in near - supersaturation conditions." *J. Mar. Res.*, 49, 435 - 466.

CHAPTER 33

WAVE ACTIONS ON A VERTICAL CYLINDER IN MULTI-DIRECTIONAL RANDOM WAVES

Yu-xiu Yu*, Ning-chuan Zhang** and Qun Zhao***

Abstract

The wave actions on a vertical cylinder in multi-directional random waves are experimentally studied in this paper. The two-dimensional (2-D) wave method is extended to calculate the three-dimensional (3-D) wave forces. The variation of various hydrodynamic coefficients with KC number and wave directional spreading are investigated. The three-dimensional wave forces are compared with that of two-dimensional waves.

1. INTRODUCTION

The sea waves are three-dimensional (multi-directional) and irregular. So the effects of irregularity and directional spreading of waves should be included in the prediction method of the wave actions on cylinder. The wave actions on a slender rigid cylinder consist of in-line forces and lift forces (transverse forces) and both forces are nonlinear. Moreover, in multi-directional random waves, the in-line forces and the lift forces are mixed each other, it makes the problem more complex. At present the physical model test and the field observation are usually conducted to study it. But these study are rare owing to the complex of technique and the huge expense. Aage et al (1989), Chaplin et al (1993) and Hogedal et al (1994) studied the effects of spectral shape and the directional spreading on the 3-D wave action on a vertical cylinder, and no effect of spectral shape was found. Comparing with that of 2-D waves, for the 3-D waves, the in-line forces were smaller and the transverse forces were much larger. Moreover, the effect of directional spreading on the drag force is more than that on the inertial force and these effects were specially obvious at the place near and above the still water level. But they only gave a few data points of the ratio between the forces of 3-D waves and 2-D waves. Koterayama and Nakamura (1992) and Chaplin et al. (1993) measured the 3-D wave forces on a platform and in laboratory respectively. They measured the wave forces on cylinder and the orbital velocity of waves simultaneously and found that the 3-D wave forces could be simplified as a 2-D problem and calculated with Morison Equation.

* Professor, Department of Civil Engineering, Dalian University of Technology (DUT), Dalian 116024
** Associate Professor, Department of Civil Engineering, DUT, Dalian 116024, China
*** Master, Department of Civil Engineering, DUT, Dalian 116024, China

In this paper, the effects of wave directional spreading and KC number on the wave forces and the hydrodynamic coefficients are emphasized. Moreover the 3-D wave forces are compared with 2-D one.

2. THEORETICAL CONSIDER AND ANALYSIS METHOD

2.1 Sea wave spectrum

The Sea wave is a complex 3-D random process. It is commonly described by the directional spectrum in frequency domain, which is generally expressed as the product of the frequency spectrum, $S(f)$ and the directional spreading function, $G(f, \theta)$, i. e.

$$\left. \begin{aligned} S(f, \theta) &= S(f) \cdot G(f, \theta) \\ \int_{-\pi}^{\pi} G(f, \theta) d\theta &= 1 \end{aligned} \right\} \quad (1)$$

There were many studies on the frequency spectrum and many formulas of spectrum have been proposed (Yu, 1992). The effects of the shape of frequency spectrum on wave force coefficients on cylinder in both 2-D and 3-D wave field can be negligible from Yu and Zhang (1989) and Hogedal (1994) respectively. Therefore, only the JONSWAP spectrum ($\gamma=3.3$) is used in test due to its popular application in the world. Concerning the directional spreading function there is not a generally recognized formular, and a simplified Mitsuyasu-type spreading,

$$\left. \begin{aligned} G(\theta) &= G_0(s) \left| \cos \frac{\theta}{2} \right|^{2s} \\ G_0(s) &= \left[\int_{\theta_{\min}}^{\theta_{\max}} \cos^{2s} \frac{\theta}{2} d\theta \right]^{-1} \end{aligned} \right\} \quad (2)$$

is used. In Eq. (2), the spreading parameter, s is independent on frequency. In this test, s is varied to change the directional spreading, and $s=\infty$ means an unidirectional irregular wave.

2.2 Effects of directional spreading on wave forces

The unidirectional wave forces on a cylinder consist of in-line forces and transverse forces. According to Morison Equation, the in-line forces consist of drag forces and inertial forces. The transverse forces are equal to lift forces (Yu and Miao, 1989). In the multi-directional irregular waves, the wave actions on a cylinder are rather complex. The waves may be coming from all directions and the in-line force induced by a component wave in a certain direction can be mixed with the lift force induced by the component wave in the perpendicular direction. In this paper, the multi-directional wave forces on a cylinder are still divided into the in-line forces, F_x , and the transverse forces, F_y , paralleled and perpendicular to the main wave direction respectively. There are two methods for calculating these forces:

(1) Extend the calculation method from 2-D wave forces to 3-D wave forces. The 3-D wave surface measured at the position of cylinder is treated as a unidirectional wave with the main wave direction. Then the in-line force can be calculated with Morison Equation, and the transverse force is calculated with lift force equation, but the effects of directional spreading on forces are included in the hydrodynamic coefficients. According to the field observation by Koterayama et al (1992) and the experimental study by Chaplin et al (1993), this approximate treatment was acceptable. Because the effects of directional spreading on drag force are different from that on inertial force and the ratio between drag force and inertial force is

dependent on KC number. So the applicability of this method will be further examined and the variation of hydrodynamic coefficients with the directional spreading parameter and KC number will be investigated in this paper.

KC number is usually defined as $KC = U_m \cdot T/D$, where T is the wave period; U_m the maximum horizontal orbital velocity, D the diameter of the cylinder. For irregular waves, the height and period of each wave in a wave train are varied. Here regardless of the directional spreading, the parameters of the significant wave and its maximum horizontal orbital velocity at the wave surface are chosen to define KC number, hereafter referred to as $(KC)_{\frac{1}{3}}$ or KC, and it is in agreement with the engineering practice.

(2) The multi-directional wave surface is decomposed into a set of wave components of definite amplitudes, frequencies, directions of propagation and initial phases. Using the decomposed wave components, more accurate prediction of wave kinematics can be made. Then the directional wave forces on a cylinder can be calculated with Morison Equation in vectorial form. In this way, the characteristics of the 3-D irregular wave forces can be better described. We will discuss it in the near future.

2.3 Forces calculation and force coefficients

(1) The total in-line wave forces acting on a whole cylinder can be calculated with Morison Equation and the drag coefficient, C_D and inertia coefficient, C_M can be determined by the method of least squares in time domain from test data (Yu and Zhang, 1989).

(2) There are some limitation for the application of Morison Equation to 3-D wave forces. So the single force coefficient method is also used to calculate the in-line forces, F_x , transverse forces F_y and their resultant forces, F_R .

$$\left. \begin{aligned} (F_x)_p &= \frac{1}{2} (C_{F_x})_p \rho D \int_0^d u_p^2 dz \\ (F_y)_p &= \frac{1}{2} (C_{F_y})_p \rho D \int_0^d u_p^2 dz \\ (F_R)_p &= \frac{1}{2} (C_{F_R})_p \rho D \int_0^d u_p^2 dz \end{aligned} \right\} \quad (3)$$

where C_{F_x} , C_{F_y} and C_{F_R} are the coefficients of in-line forces, transverse forces and resultant forces respectively. The subscript p is the index of the statistical characteristics. For example, when $p = \frac{1}{10}$, $(F_x)_{\frac{1}{10}}$, $(F_y)_{\frac{1}{10}}$ and $(F_R)_{\frac{1}{10}}$ are the average peak values of the highest one tenth in-line forces, transverse forces and resultant forces respectively. $U_{\frac{1}{10}}$ is the maximum horizontal orbital velocity of wave which height is $H_{\frac{1}{10}}$. The coefficients $(C_{F_x})_p$, $(C_{F_y})_p$ and $(C_{F_R})_p$ can be determined from measured wave forces with Eq. (3). With this method, only the characteristic value of the wave forces can be calculated.

2.4 Orbital velocity of waves

For calculating the wave forces on the cylinder, the orbital velocity and the acceleration should be known. It is difficult to measure the horizontal velocities along the water depth simultaneously, so they are usually calculated from wave surface with a suitable wave theory. For the multi-directional irregular waves there is not a generally recognized available wave theory. In the field observation ($d = 15m$, $H_{\frac{1}{3}}/$

$d \leq 0.19$) from Koterayama et al(1992) and the model test with multi-directional irregular waves ($d=2.0\text{m}$, $H_{\frac{1}{3}}/d \leq 0.15$) by Chaplin et al(1993), the wave surfaces and the orbital velocities were measured simultaneously. It is found that the measured horizontal orbital velocities in 3-D waves conform to that directly calculated from the wave surface with the 2-D linear wave theory. In our experimental study on the unidirectional wave action on pile array (Yu and Shi 1994, $d=1.0\text{m}$, $H_{\frac{1}{3}}/d \leq 0.34$), the linear wave theory and the Stokes wave theory of second order were used and compared each other. It was found that the results obtained with linear theory are better than another. Moreover, it is considered that the linear wave theory is suitable for the simulation of orbital velocity, acceleration and the wave forces on pile in irregular waves with linear summation method. So the linear wave theory is used in this test ($H_{\frac{1}{3}}/d \leq 0.297$).

3. EXPERIMENT

The experiments were conducted in the State Key Laboratory of Coastal and Offshore Engineering, Dalian University of Technology, China. The wave basin is 55m long, 34m wide and 1.3m deep. The multi-directional wavemaker consists of 30 independent segments of 0.8m wide. The wave absorbers were placed along the basin walls to prevent wave reflection from the walls.

DS-30 multi-point wave gages were used to measure the wave height. The top of the model cylinder was fixed onto a supporting frame, so the cylinder model worked as a cantilever beam under the wave action and the force meter was set between the cylinder and the support frame. The force meters were used to measure both the total in-line forces and the total transverse forces simultaneously. The sensitivity, linearity and stability of this meter are very good. The natural frequencies of the meter system in both directions in still water are 7.3~8.2Hz. A VAX-II computer was used for controlling wavemaker. Both the data acquisition and processing of wave surfaces and wave forces were conducted with a computer IBM-386.

The water depth was kept at 0.5m. The JONSWAP spectrum ($\gamma=3.3$) and the simplified Mitsuyasu type directional spreading, $E_q(2)$ were used to simulate the multi-directional waves with spreading indices from $s = \infty$, unidirectional wave, to $s=2\sim 5$ and the main wave direction is $\theta=0^\circ$. For each group of s , there were several wave heights and periods. Each of cylinder models with diameters of 2, 4 and 6cm was placed at the center line of basin and was 7m away from the wavemaker.

The single direction per frequency model (Yu et al, 1991) was used to generate the directional waves. The wave gage array consisted of four gages was used to measure the directional spectra. The wave surface measured with gage No. 5 was used to approximately represent that at the place of cylinder. The sampling of data was done at the interval of 0.05sec, and the data length was 204.8sec., 4096 points. The datum signals were lowpass filtered with a cut-off frequency of 4HZ.

There are several methods for evaluating directional spectrum, of which the Bayesian approach (Hashimoto et al. 1987) is better from our primary comparison (Liu and Yu, 1993) and therefore it is used in this paper.

4. RESULTS AND ANALYSES

4.1 Waves

The measured wave parameters are shown in Table 1. The surface variation of the multi-directional irregular waves is more complex than that of the unidirectional waves. The distributions of the instantaneous values of wave surface are close to normal distribution but there is a little trend of skewness in wave profiles, with an excess of high crest points and lack of low trough points. The distribution of wave height is close to Rayleigh distribution and is close to Gluhoviski distribution along with the relative water depth decreasing.

4.2 Characteristics of wave forces in time domain

Fig. 1 and Fig. 2 are the examples of the simultaneous histories of measured wave surface, total in-line wave forces, total transverse wave forces and total resultant wave forces. It is found that in the same condition of wave parameter and cylinder diameter, the in-line wave force decreases with s decreasing, but its frequency is basically the same as wave's. For the transverse forces, the effects of spreading parameter, s are more obvious. In Figs. 1 and 2, the KC numbers are not large. The transverse force of unidirectional wave, $s = \infty$, is pure lift force, whose value is small and frequency is higher. For the directional waves with $s = 15$, the transverse forces maybe consist of the components of in-line forces induced by oblique waves and the lift forces, and the former rapid increases with s decreasing. Its frequency is larger than wave's. The variation in resultant force is similar with that in in-line forces.

The experimental data and fitting curves of the variation of the ratios between transverse and in-line forces, resultant and in-line forces along with KC number show that even if the data points are scattered to some extent, but the variation law is clear and they are synthesized in Fig. 3. Along with s decreasing, the vortex shedding behind cylinder is changed by the gradually increased oblique waves, it makes lift forces decreasing and the oblique wave force increasing. Therefore, the transverse force changes from lift force dominating to component of in-line forces dominating. As $s = 15 \sim 25$, the value of transverse force can be up to more than half of in-line force, when $s = 2 \sim 5$, it can be up to 74% of in-line force. But the peak values of in-line forces and transverse forces are not of usual occurrence simultaneously, so the resultant forces increase slowly with s decreasing.

4.3 Wave force coefficients

The drag coefficient C_D and inertia coefficient C_M are varied with KC number and directional spreading parameter s as shown in Fig. 4. Both coefficients decrease with s decreasing.

The single force coefficients C_{F_x} , C_{F_y} and C_{F_r} can be determined with Eq. (3) from measured wave force data and they are also varied with KC and s , but their test datum points are less scattered. It can be noticed from Fig. 5 that the in-line forces and the resultant forces decrease and the transverse forces increase with s decreasing. Concerning the transverse forces, the lift forces induced by unidirectional waves ($s = \infty$) vary with KC along a wave type curve, but along with s decreasing it gradually becomes to a progressively decreasing curve similar to that of in-line forces.

4.4 3-D wave forces compare with 2-D wave forces

In Fig. 5, for a given KC number one can get a set of force coefficients from different curves of s , then divides each coefficient by that of $s = \infty$ to get the ratio

Table 1 Measured characteristic value of waves

Wave type	S	m_0 (cm ²)	H	H _{1/3}	H _{1/10}	H _{max}	H/H _{1/3}	H _{1/10} /H _{1/3}	H _{max} /H _{1/3}	T	T _p	T _{H1/3}	T _{H1/10}	T _{Hmax}	T _{H1/3} /T	T _{H1/10} /T	T _{Hmax} /T	N	
Uni.	4003	∞	3.4	4.61	7.45	9.74	2.82	0.62	1.31	1.72	0.88	0.98	0.93	1.00	0.93	1.06	1.06	1.14	231
	4007	∞	6.9	6.76	10.46	13.45	17.38	0.64	1.29	1.65	1.03	1.18	1.10	1.11	1.08	1.07	1.08	1.05	197
	4001	∞	11.3	8.46	12.94	15.45	17.85	0.65	1.19	1.36	1.25	1.46	1.39	1.39	1.45	1.12	1.12	1.16	161
Directional	5002	60	2.2	3.14	5.47	7.28	8.85	0.57	1.33	1.62	0.90	1.23	0.98	0.97	0.93	1.16	1.14	1.09	239
	5000	45	5.4	5.03	8.83	11.26	14.24	0.57	1.28	1.61	0.89	1.23	1.09	1.11	1.15	1.15	1.17	1.21	214
	5005	35	13.7	8.36	14.21	17.27	19.46	0.59	1.22	1.37	1.15	1.51	1.38	1.34	1.35	1.22	1.19	1.19	180
Directional	6003	40	9.4	6.89	11.78	14.86	17.85	0.58	1.26	1.52	1.11	1.51	1.34	1.34	1.34	1.20	1.20	1.20	180
	6002	20	2.9	3.93	6.58	8.32	11.47	0.60	1.26	1.74	0.81	1.03	1.06	1.08	1.04	1.18	1.20	1.16	225
	6003	25	5.5	5.39	9.29	11.69	13.80	0.58	1.26	1.49	0.93	1.23	1.06	1.11	1.00	1.19	1.25	1.12	227
Directional	6005	15	10.2	7.32	12.04	14.78	18.15	0.61	1.23	1.51	1.09	1.48	1.36	1.35	1.38	1.18	1.17	1.20	176
	6006	15	15.6	9.03	14.82	17.74	19.75	0.61	1.20	1.33	1.16	1.51	1.38	1.37	1.39	1.24	1.23	1.25	183
	3002	5	4.1	4.81	8.05	10.05	12.46	0.60	1.25	1.55	0.85	1.02	0.92	0.94	0.89	1.14	1.16	1.10	251
Directional	3004	5	9.4	6.92	11.78	14.41	18.23	0.59	1.22	1.55	0.95	1.20	1.11	1.09	1.09	1.19	1.17	1.17	218
	3005	4	14.4	8.85	14.29	17.47	21.83	0.60	1.22	1.53	1.13	1.48	1.36	1.35	1.50	1.25	1.24	1.38	186
	3006	2	20.5	9.82	16.59	19.57	23.18	0.59	1.18	1.40	1.12	1.48	1.38	1.35	1.38	1.19	1.16	1.19	176

Note: The unit of wave height is cm, period is second.

N — Number of waves.

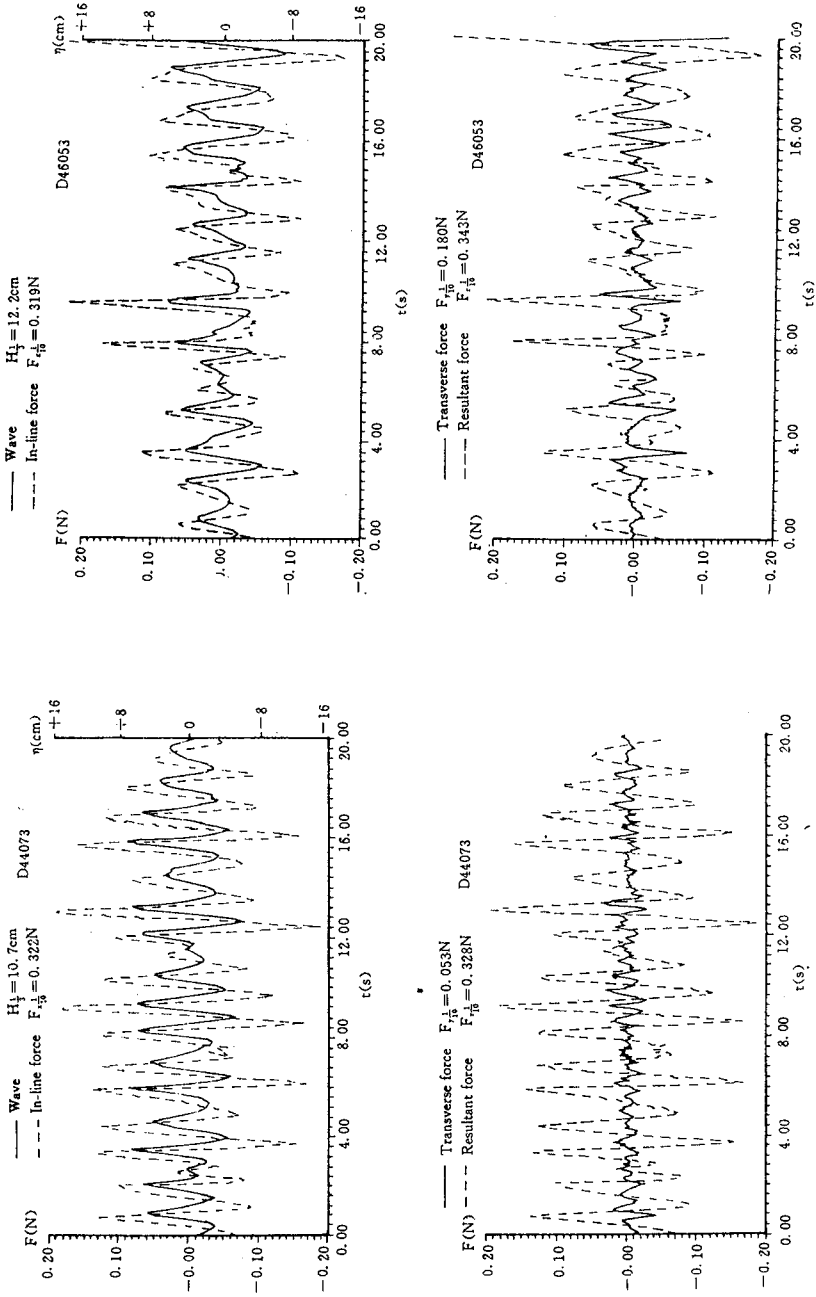


Fig. 1 Measured wave surface and wave force histories $H_{1/3} = 10.7$ cm, $T_{H1/3} = 1.09$ s, $D = 4$ cm, $(KC)_{1/3} = 8.9$ Unidirectional wave ($s = \infty$)

Fig. 2 Measured wave surface and wave force histories $H_{1/3} = 12.2$ cm, $T_{H1/3} = 1.26$ s, $D = 4$ cm, $(KC)_{1/3} = 11.5$ Directional wave ($s = 15$)

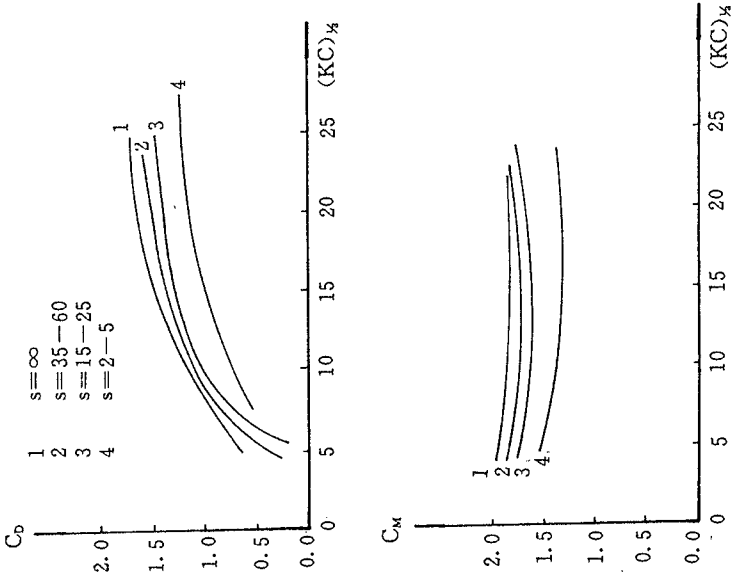


Fig. 4 Variation of C_D and C_M with KC and s

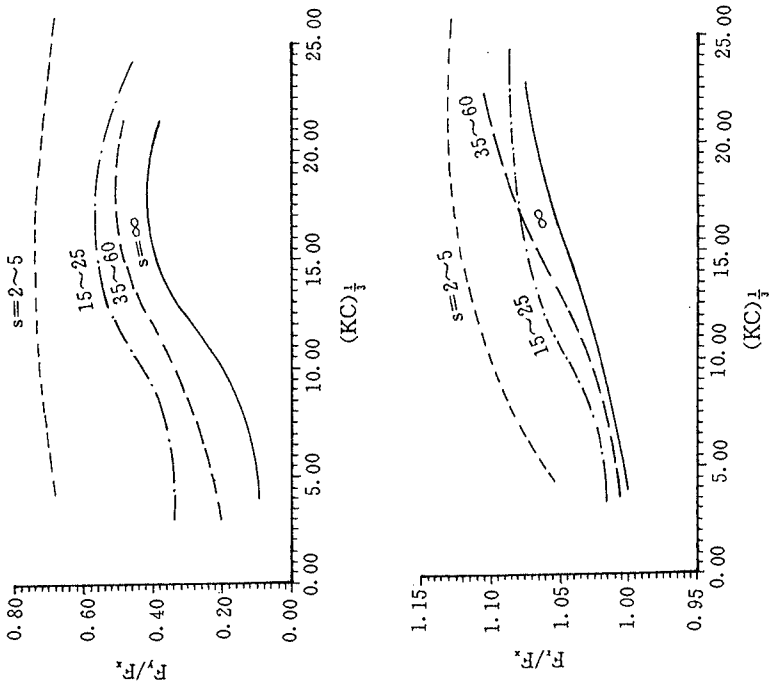


Fig. 3 F_y/F_x , F_r/F_x versus KC number and s

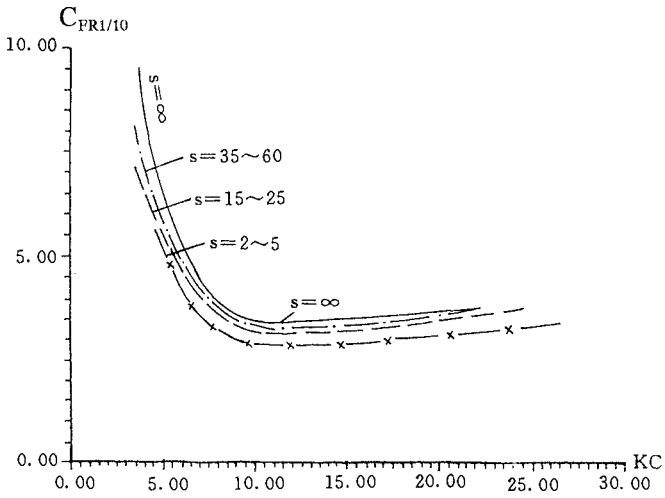
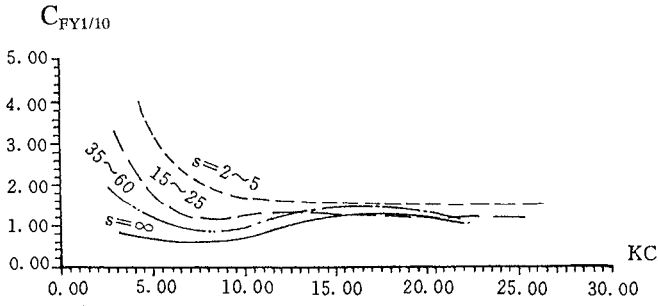
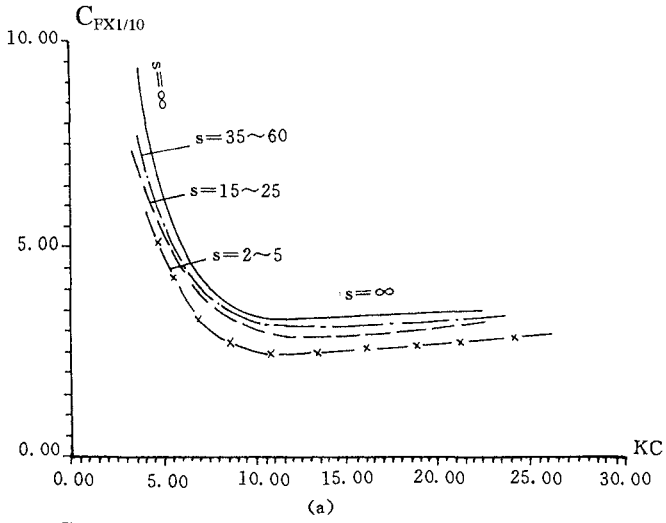


Fig. 5 Single forces coefficient versus KC and s

between 3-D wave force and 2-D one as shown in Table 2. Because the test runs are limited and the test data are scattered to some extent, so these results are preliminary and should be further examined and improved.

Table 2 Ratio between 3-D wave force and 2-D wave force

	$(KC)^{\frac{1}{3}}$	5	10	15	20
	s				
In-line wave forces	35-60	0.92	0.92	0.91	0.91
	15-25	0.88	0.88	0.82	0.89
	2-5	0.80	0.73	0.74	0.77
Transverse wave forces	35-60	1.82	1.48	1.21	1.09
	15-25	2.90	2.03	1.09	1.02
	2-5	5.24	2.58	1.30	1.28
Resultant wave forces	35-60	0.89	0.96	0.96	0.96
	15-25	0.83	0.93	0.92	0.94
	2-5	0.80	0.83	0.80	0.83

4.5 Characteristics of wave forces in frequency domain

Fig. 6 shows two examples of wave spectrum and wave force spectrum. The spectral shapes of in-line force and resultant force basically conform to that of wave spectrum. But for unidirectional wave the transverse force spectrum is exactly the lift force spectrum and its peak frequently appears at the twice peak frequency of wave. When s is small, the transverse force spectrum have not a twice frequency peak but it is different in shape from wave spectrum.

5. EXAMINATION AND DISCUSSION

(1) For examining the feasibility of Morison Equation to calculate the in-line wave forces on cylinder, the values of C_D and C_M obtained from Fig. 4 are substituted into Morison Eq. to calculate the in-line wave force history with measured wave surface history. Then the calculated wave force history is compared with the measured one as Fig. 7 shows. For the unidirectional wave, two histories are conformable. Along with s decreasing the degree of conformability decreases to some extent, but two histories are basically conformable. It means that the in-line force of directional waves can be calculated with present method.

(2) Concerning the wave fore coefficients, there are rare data for directional waves. The experimental data obtained by Chaplin et al(1993) are very scattered. Koterayama et al gave the variation of C_D , C_M with KC from field observation, but the value of s is not clear. Their curve of C_D is basically within the range of curves in Fig. 4 and the curve of C_M is close to that of $s=15\sim 25$ in Fig. 4.

(3) Ratio between 3-D and 2-D wave forces

Some researchers studied the 3-D wave forces on cylinder mainly by experiments and gave some data concerning the ratio between 3-D and 2-D wave forces, which are collected in Table 3. These data are in comparison with present results. It turns out that the existing data are in the range of present results except the ratio of transverse forces, but in this paper, the variation of ratios with KC and s are given. About the transverse force, it is found from tests that when KC is small, the transverse forces induced by unidirectional wave are very small, but under the

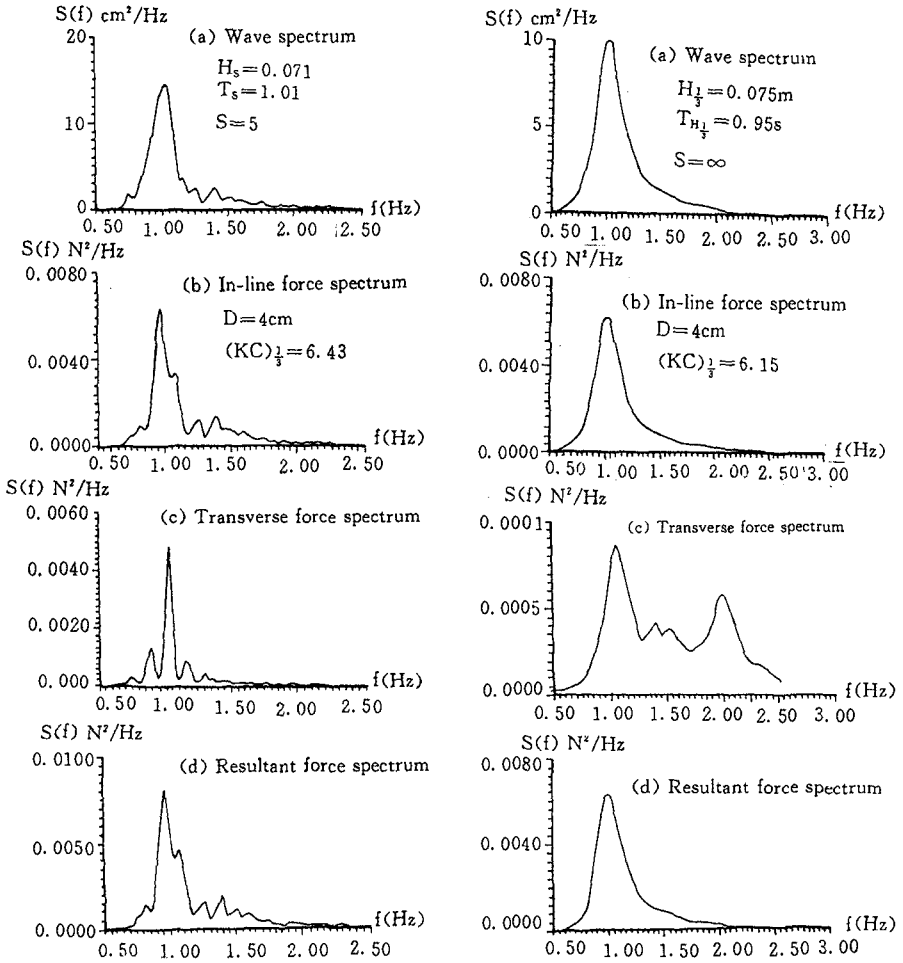


Fig. 6 Measured wave spectrum and force spectra

actions of directional waves with small s , the transverse forces induced by oblique waves are large. Therefore, the ratio of transverse force can be up to about 5.0. It is reasonable.

6 CONCLUSIONS

1 The effects of directional spreading of waves on wave forces acting on a cylinder are obvious and the level of effect is dependent on $(KC)_{1/3}$ and s . Within

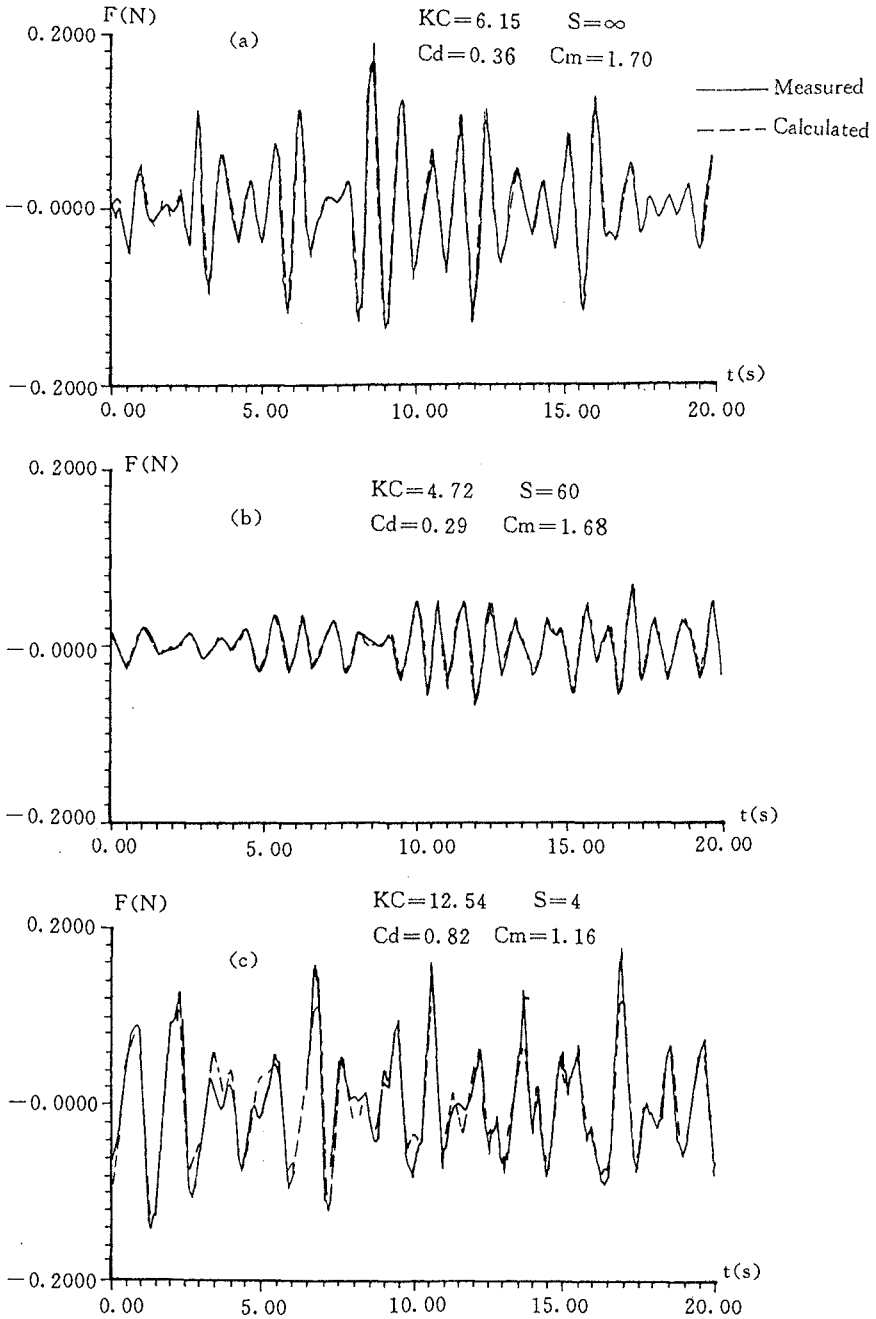


Fig. 7 Comparison between calculated and measured in-line wave force histories

Table 3 The ratios between 3-D and 2-D wave forces

Authors	Directional spreading	KC	Inline forces	Transverse forces	Resultant forces
Nwogu and Isaacson (1989)	$\sigma_\theta = 32^\circ$ $\sigma_\theta = 43^\circ$ $\sigma_\theta = 65^\circ$				0.95 0.911 0.816
Aage et. al (1989)	North Sea spreading and $\sigma_\theta = 29^\circ$	≈ 20	0.82~0.87	1.4~1.8	
Chaplin et. al (1993)	$n=2, \sigma_\theta = 26.5^\circ$ $n=8, \sigma_\theta \cong 15^\circ$	2~9	0.77 0.88		
Hogedal et. al (1994)	North Sea spreading $\sigma_\theta = 30^\circ$ $\sigma_\theta = 43^\circ$	8.8~12.6* 4.22~6.52* 4.22~8.86*	0.875 0.865 0.765	~1.62	0.916 0.874 0.798
This paper (1996) $G(f, \theta) = G_0(s) \cos^2 \frac{\theta}{2}$	$s=35\sim 60$ $(\sigma_\theta = 13.6\sim 10.4^\circ)$	3.0~20	0.92~0.91	1.82~1.09	0.96~0.89
	$s=15\sim 25$ $(\sigma_\theta = 20.6\sim 16^\circ)$	3.9~20	0.89~0.82	2.90~1.02	0.93~0.83
	$s=2\sim 5$ $(\sigma_\theta = 43^\circ\sim 33.6^\circ)$	3.9~20	0.80~0.73	5.24~1.28	0.83~0.80

Note: (1) σ_θ is the standrad deviation of directional spreading function.
(2) * KC number is defined with peak frequency period , T_p and $H_{\frac{1}{3}}$.

the extent of this experiment, the in-line forces of multi-directional waves can decrease to 73—92% of that of unidirectional waves, and the transverse forces can increase to 200% or more.

2 Multi-directional wave forces exerting on a vertical cylinder can be predicated with the methods used for unidirectional wave except $s=2-5$, but the effects of directional spreading must be included in their force coefficients.

3 All wave force coefficients of C_D , C_M , C_{F_x} , C_{F_y} and C_{F_R} are varied with $(KC)_{1/3}$ and s . Among them, the scatters of the coefficients C_{F_x} , C_{F_y} and C_{F_R} are relatively small.

4 For unidirectional waves ($s=\infty$), the transverse force acting on cylinder is the pure lift force and its main frequency is frequently double or three times the wave frequency. Along with s dreasing the transverse component forces induced by the oblique waves increase. As the test results show, when $s=15-25$, the transverse component forces of oblique waves have been dominant.

Acknowledgements-This research was supported by the Science Foundation of National Commttee of Education, China.

REFERENCE

Aage, C. , Jorgensen P. , Andersen L. W. , Dahl C. and Klinting P. (1989), Wave loads on a cylinder in 2-D and 3-D deep water waves, Proc. of 8th Int.

- Conf. on Offshore Mechanics and Arctic Engineering, II, 175—181
- Chaplin J. R. , Subbiah K. and Irani M. , (1993). Effects of wave directionality on the in-line loading of a vertical cylinder, Proc. of 3rd Int. Offshore and Polar Engineering Conf. III, 116—121
- Hogedal M. , Skourup J. and Burcharth H. F. (1994). Wave forces on a vertical smooth cylinder in directional waves, Proc. of 4th Int. Offshore and Polar Engineering Conf. III, 218—224
- Koterayama W. and Nakamura M. (1992). Drag and inertia force coefficients derived from field tests. Inter. J. Offshore and Polar Engineering, 2(3), 161—167
- Nwogu, O. and Isaacson, M (1989), Force distribution due to short-crested waves, Proc. Inter, Association for Hydraulic Research XXIII Congress, c-33—c-40, Ottawa, Canada.
- Yu, Y. X. and Miao S. (1989a). Transverse forces on vertical cylinder in regular and irregular waves, China Ocean Engineering, 3(1), 71—86.
- Yu, Y. X. and Zhang, N. C. (1989b), Inline forces on vertical cylinder in irregular waves, Acta Oceanologica Sinica, 8(4), 565—576.
- Yu. Y. X. Liu, S. X. and Li, L. (1991) Numerical simulation of multi-directional random seas, China Ocean Engineering, 5(3), 311—320.
- Yu, Y. X. (1992) Random waves and its engineering application, The Press of Dalian University of Technology, (in Chinese).
- Yu. Y. X. and Shi, X. H. (1994), Hydrodynamic coefficients of grouping cylinders under the action of irregular waves, China Ocean Engineering, 8(2), 123—134.

CHAPTER 34

WIND/WAVE RELATION AND THE PRESSURE GRADIENT EFFECT

Spiros M. Gouloumis ¹

Abstract

The S.M.B. prediction model is used worldwide to hindcast sea wave characteristics using wind data. Even though wave parameters showed that qualitative similarities are present between ocean and small basin waves, major weather factors such as the wind speed and barometer pressure gradients in relation with the topography should be considered as calibration factors.

Introduction

The Laboratory of Harbour Works, National Technical University of Athens (N.T.U.A.), is conducting a Wave Measurement Project aiming at developing a wave prediction model adjusted to Greek Seas, especially in the Aegean Sea, well-known for its particular wind and wave conditions. Nowadays, the L.H.W. has installed the Wave Measurement, Transmission and Analysis network (in Greek: KYMATA) in the Aegean Sea and Cyprus using five Waverider buoys.

The Heraklio Wave Measurement Program was conducted in the South Aegean Sea for one year, using a Waverider buoy. In the present paper, the wind/wave interrelations and the S.M.B. prediction model are examined, taking into account the topography and the pressure systems affecting the East Mediterranean region.

The wind velocity gradient and the pressure jump are major factors in waves' development. The S.M.B. prediction model seems not always to be adequate in fully describing the development of the waves, in the Aegean Sea. A special model should be applied, distinguishing at least the most critical differences (North from South winds and storm from squall events).

¹ Civil Engineer, Research Associate, Post-graduate student
Laboratory of Harbour Works, Civil Engineering Department, National Technical
University of Athens, 5, Iroon Polytechniou Str., 157 73 Zografou, Greece

Wave Measurements

The South Aegean Basin is about 130 km long from North to South and 300 km wide from West to East, while the whole Aegean basin, being a little narrower, is nearly 610 km long. Due to the orientation of the measurements' field and the dominant weather conditions in the Aegean Sea, the winds of interest are those blowing from the North during the winter season, when several storms occur. (See Fig. 1)



Fig. 1 Geomorphologic map of the Greek Archipelagos and the Aegean Sea region.

A Waverider buoy was moored about a mile off Heraklio shore North of Crete Island, at a water depth of about 22 m. Wave characteristics were recorded from of October 1, 1992 until September 22, 1993.

An accelerometer on board the buoy estimated the vertical acceleration. Water surface elevation time series of 20-min. duration was

recorded every second hour or continuously in cases where the wave was higher than a threshold defined height (2.5 m). Considering the quality of raw data, the measurements conducted are highly accurate.

A total of 5014 records were processed, examining the relationship between the wave characteristic parameters, as well as the wave energy density spectrum characteristics. The wave parameters investigated showed that qualitative similarities exist between ocean and small basin waves, and also that quantitative differences do exist (Gouloumis and Moutzouris, 1995).

Wind/Wave Interrelation

Significant wave heights were related to the corresponding wind speed blowing from the North and recorded onshore, considering several storm events of developing sea. The data plotted in Fig. 2 refer to rather high wind speeds, being proportional to the wave heights as it is widely accepted and supported from both theory and field measurements (Bretschneider, 1958; Pierson and Moshowitz, 1964; Hogben N., 1988). Further on, the spectral peak periods T_p of the waves vs. the corresponding wind speed seem to be in some agreement with the JONSWAP result (Fig. 3)

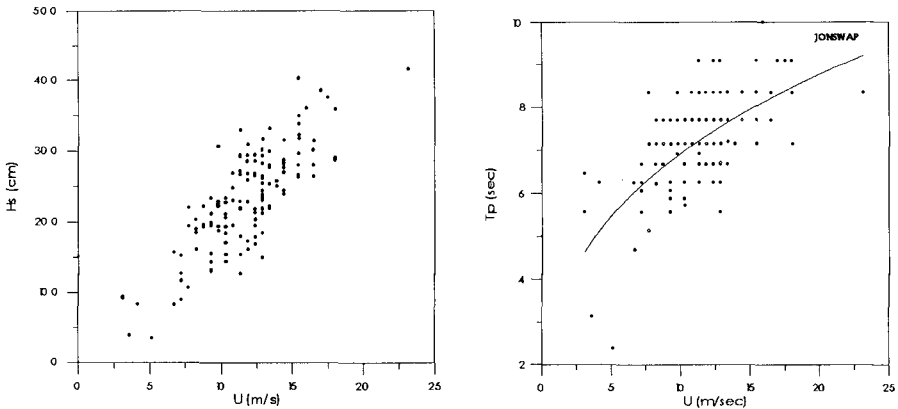


Fig. 2, 3 Significant wave heights and spectral peak periods vs. the wind speeds blowing three hours before the wave measurements

An interesting feature also is that the relation between the non-dimensional expressions of the characteristic wave heights H_s and the spectral peak periods T_p plotted in Fig. 4, is found to be almost identical to the result found if the deepwater fetch-limited equations for wave height and wave period in the Shore Protection Manual (SPM) (1984) are combined, and to the TMA equations for deep water (Hughes S., 1984), the only

difference being a coefficient of 0.01096 instead of 0.0105 and 1.0112 respectively. Thus, it can be supposed that waves have similar characteristic parameters both in the ocean and in the small Aegean basin examined.

Three wind records have been used from the Heraklio and Thira Island weather stations, corresponding to winds that were blowing simultaneously and 3 hours before the wave measurements. Thira is located at the North of the basin we examine. The Heraklio weather station seems to give the most appropriate wind data.

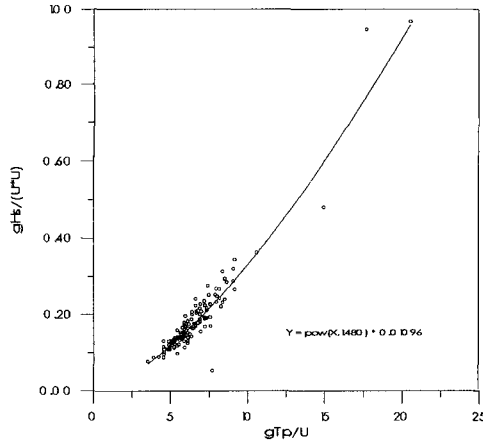


Fig. 4 The nondimensional expressions of the characteristic wave height H_s and the spectral peak period T_p .

An evaluation was carried out using the SMB method of predicting wave conditions from wind data, since "...the best equations to use in a simple wind/wave hindcast model are the SMB equations of SPM '77" (Parle P., Burrows R., 1989) and it is a widely used method in the design of most marine works. The SPM '77 simplified wave prediction equations using the SMB method are as follows:

$$gH_s/U^2 = 0.283 \tanh(0.0125 F^{0.42})$$

$$gT_z/U = 1.20 \tanh(0.077 (gF/U^2)^{0.25}), \text{ where } F = gX/U^2 \text{ is the fetch coefficient}$$

The data plotted refer only to the North wind records which is the dominant wind direction, in order that better correlation is achieved. In Fig. 5 the dimensionless wave height equation has been plotted vs. the fetch coefficient, where the effective fetch for the North direction is calculated to be 150.6 km.

The data plotted using the Thira wind records seem not to be suitable enough to describe weather conditions at Heraklio area, probably due to the location of the station (the island's airport on a plateau). Further more, it is not yet understood what is the effect of the numerous islands lying in the central Aegean Sea to the wind field and the wave generation conditions.

It should be noted that although a lot of data points are gathered near the values estimated by the SMB model, many other measurements are well out of the predicted values, scattered over a large area of Fig. 5.

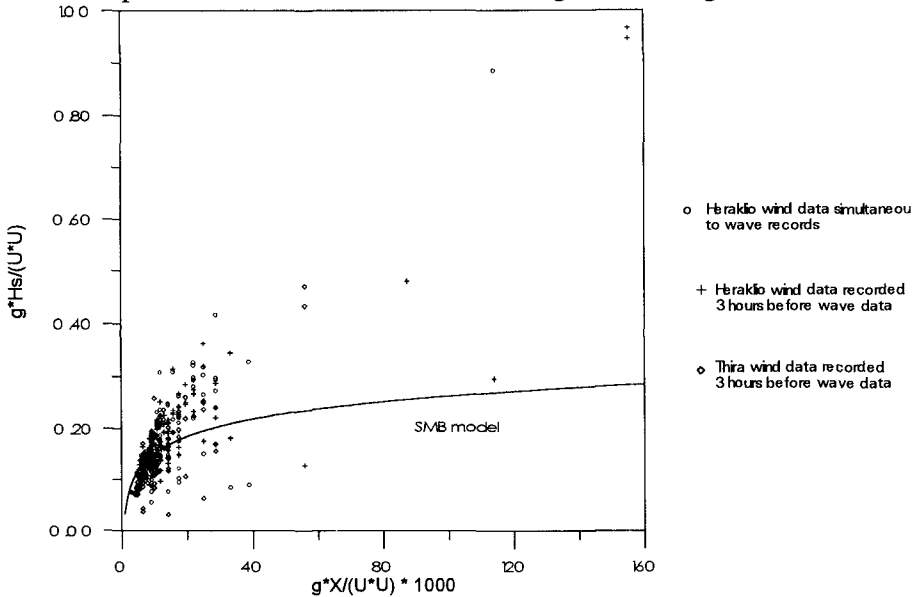


Fig. 5 The dimensionless significant wave heights vs. the fetch coefficient.

The S.M.B. prediction model seems not always to be adequate in fully describing the development of the waves, in the Aegean Sea. A major reason could be that the wind field over the Aegean Sea is not uniform due to the topography forming a long, from North to South, rather narrow basin containing the Archipelagos Islands causing strong orographic effect.

The Pressure Jump Effect

In order to further investigate the situation, six representative storm events of developing sea were selected. The wind was always blowing from the 48 degrees north sector. In Fig. 6 the dimensionless wave heights have been plotted versus the fetch coefficient. The data clearly represent two different sea-states, one of which is characterized by sudden occurring high waves, corresponding to relatively low wind speeds.

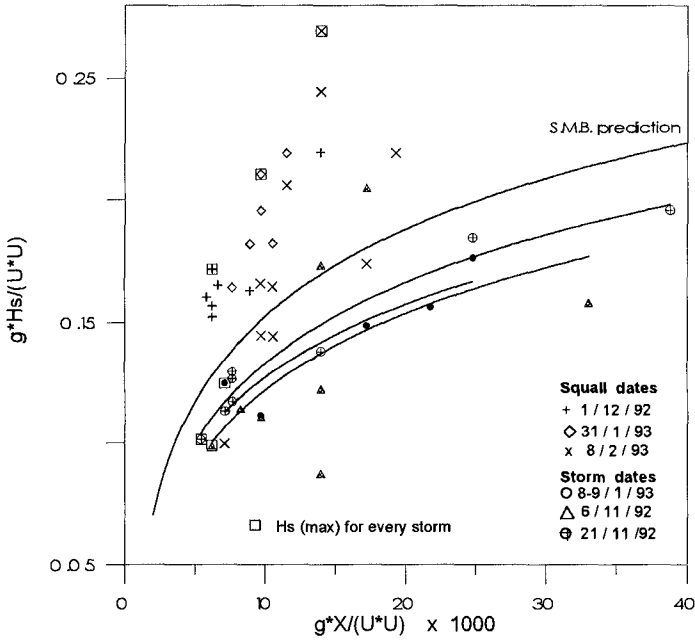


Fig. 6 The six storm events forming two groups with different characteristics (Heraklio wind data recorded 3 hours before wave measurements)

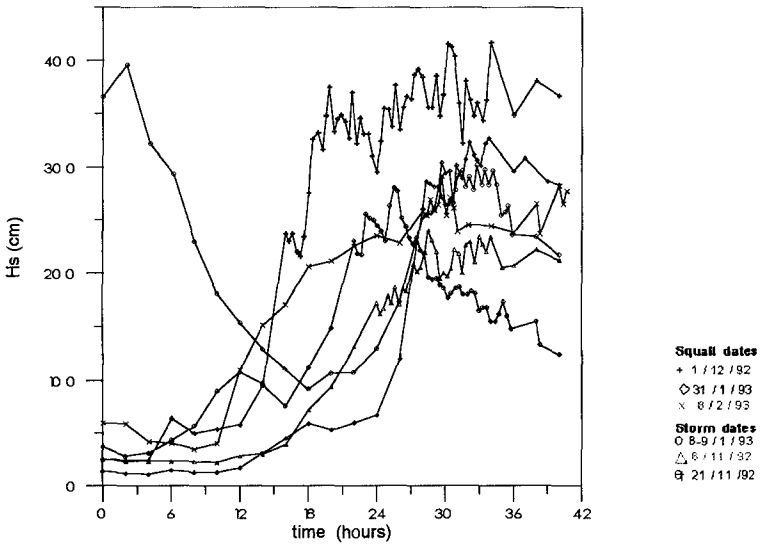


Fig. 7 Significant wave heights' time series of six storm events.

The time series of measured significant wave heights (H_s) plotted in Fig. 7 show that three of the curves corresponding to the storm events of December 1st, 1992, January 31st and February 8th, 1993, are characterized by rapidly growing waves, being fully developed in just 3 to 6 hours, indicating the occurrence of squall storms and fast arising sea.

Examining the weather systems experienced at the time of the wave measurements, we can distinguish a certain combination of pressure systems over East Europe, similar for all three cases of fast arising sea not complying with the S.M.B. prediction model (Fig. 8 of the Appendix). Waves rise much faster during squall storms where intense winds, suddenly blowing, sweep over the Aegean Sea. Winds are triggered by the intense barometric gradient in South East Europe, caused by the combination of an East Europe High pressure field and the Low pressure systems passing over East Mediterranean, in the region of the island of Cyprus.

Medium velocity winds blowing over the Black Sea are canalized into the Aegean Sea through the mountain ranges of mainland Greece on the west and Asia Minor on the east, becoming very intense because of the Bernoulli phenomenon. Furthermore, simultaneously to the maximum wind gust, a major barometric pressure jump is noticed at all three episodes where wave development does not follow the S.M.B. prediction model, as it can be clearly seen in Fig. 9 of the Appendix.

In all other cases examined, where the measured wave heights were close to the predicted ones rarely exceeding them, the High pressure system lies at the west over central Europe and the pressure gradient is mild causing winds of normally arising speed (Fig. 10)

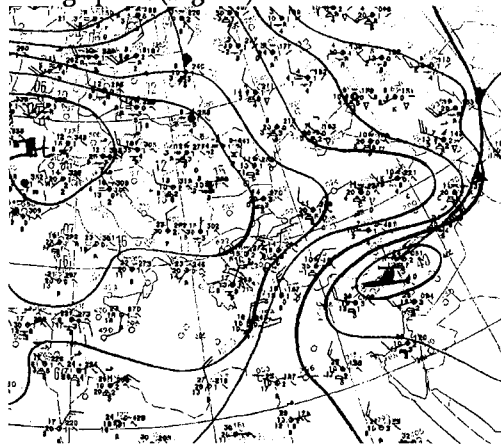


Fig. 10 Weather map dated on November 6th 1992, at 12:00 UTC. When the High pressure system lies at the west the pressure gradient is mild.

While the frontal systems pass over the measurements' region, the pressure jumps up to 9 milibars in total and on the order of 1 Mb per hour. In all three cases, the wave still rises following the pressure jump, even though the wind speed decreases. The relative isobar maps in Fig. 11 show clearly that a pressure front moves from north to south over the Aegean Sea, causing a forced wave which seems to reinforce the wind generated wave while interaction between them should be present, as well. Examining the barometric pressure records as well as the isobar maps of the events, we can estimate the speed of the pressure front propagation to be in the order of $U=51$ km per hour as the 610 km long Aegean basin was swept from north to south in about 12 hours. A resonant wave is therefore possible to be produced, since the face velocity at the specific depth of 22 m at the buoy location is $C=\sqrt{gh} = 52.2$ km/hour $\approx U$, indicating the possible presence of a squall line surge (Thieke R., Dean R., GARCIA A., 1994).

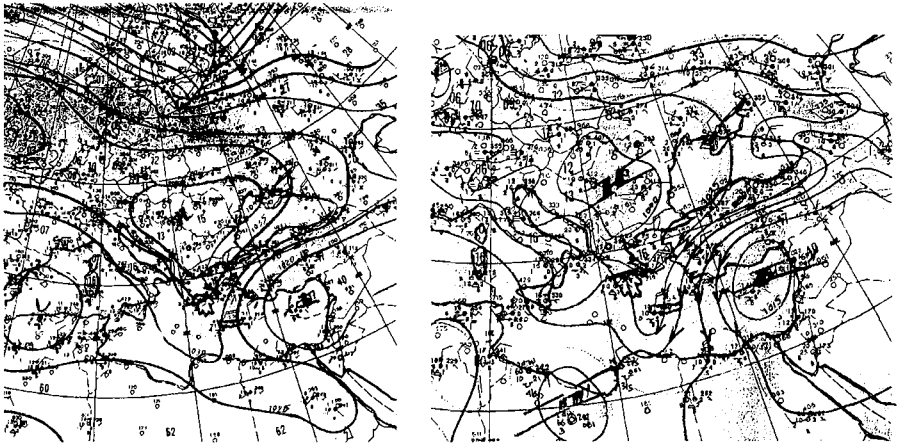


Fig. 11 Weather map dated on February 8th 1993, at 06:00 and 12:00 UTC. The High pressures propagate from north to south over the Aegean Sea.

Focusing on Fig. 6, it can be noted that during the three storm events where the wind is increasing in a normal way and there is no severe change in the barometric pressure, the wave development is generally over-estimated by the S.M.B. model. The dimensionless maximum wave heights appear close to the predicted values and they are all gathered together showing the maximum possible wave developed at this area under normal weather conditions.

On the other hand, considering the cases not complying with the SMB model, the dimensionless maximum wave height expressions show a tendency that unusually high significant waves can appear corresponding to relatively low wind speeds the fetch being constant, depend obviously on the pressure gradient propagation experienced. The corresponding characteristic wave periods of these cases are higher than the periods corresponding to the "normal" conditions, indicating long wave existence mentioned before (Fig. 12). Attention should also be paid to the characteristic periods of the maximum significant waves measured during the abnormal storms, being linear proportional to the wind speed.

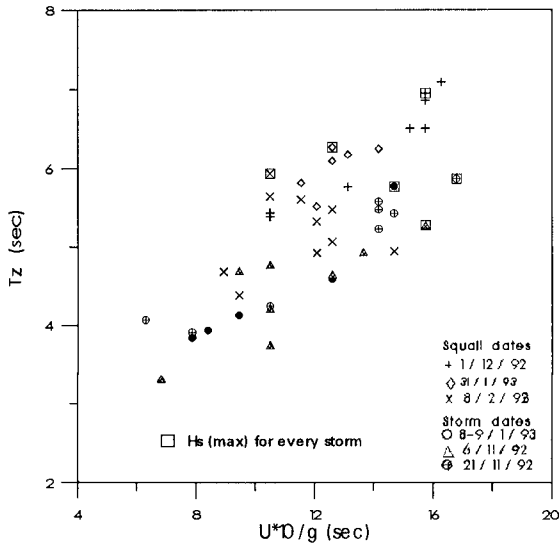


Fig. 12 Characteristic wave periods versus wind speed transformed to period

The theory analyzed above in order to explain high waves measured corresponding to relatively low wind speeds at fetch limited conditions, is further supported by the storm episode of November 21, 1992. Even though it has the characteristics of the "abnormal" cases, it is well described by the S.M.B. model. Besides the fact that the wind speed rises very quickly and the pressure jump is intense (Fig. 13), the measured wave heights follow the S.M.B. model supporting even further the previous conclusion since the pressure front propagates from west to east as it seen in Fig. 14, not reinforcing the north wind generated waves as the buoy's location is sheltered from the west.

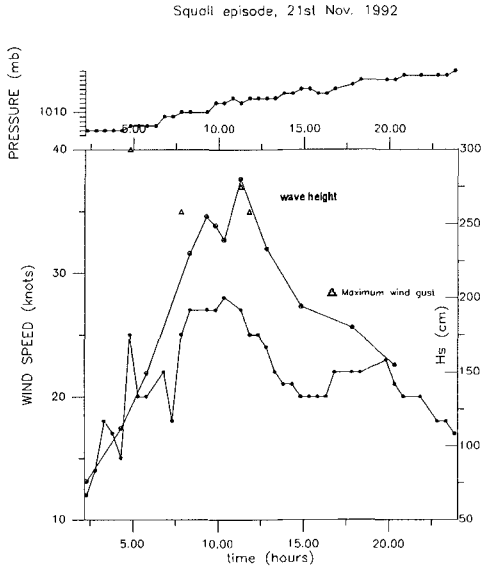


Fig. Wind speed, significant wave height and barometric time series of the storm episode dated November 21, 1992.

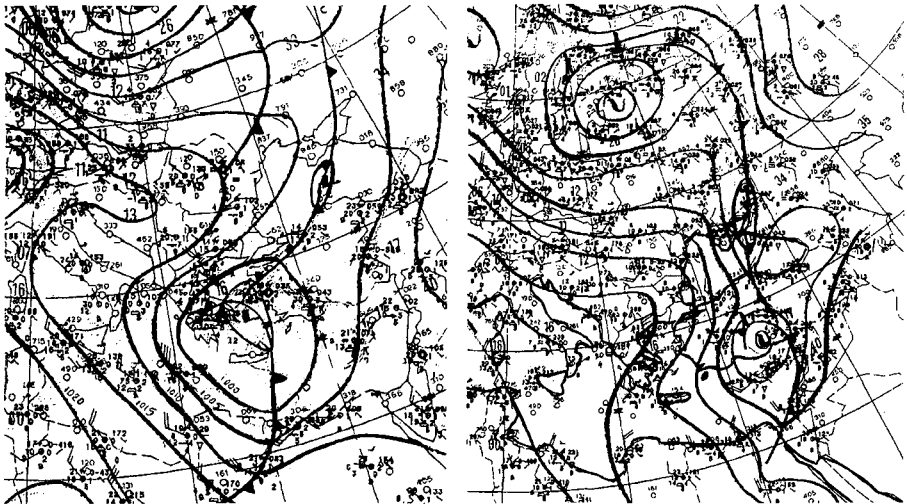


Fig. Weather maps of November 20th and 21st 1992, at 12:00 UTC. The Low pressure system travels from west to east not reinforcing the north wind generated waves.

Conclusions

Even though waves seem to have similar characteristic parameters both in the ocean and in the small Aegean basin examined, the S.M.B. prediction model is proved to be insufficient to fully predict wave climate in the Aegean Sea, where strong orographic effects and peculiar weather conditions are present.

It is necessary to consider all the meteorological factors involved to successfully predict wave heights under different weather conditions.

The wind velocity gradient and the pressure jump, when propagates to the same direction of the wind blowing, are major factors in describing the development of the waves. The possible effect of the Cyclades islands lying in the middle of the Aegean basin on the wave development and propagation has also to be assessed.

Large amount of measurements expected to derive from the Wave Measurement KYMATA network will hopefully give insight into the situation, now that a new perspective is applied.

The S.M.B. prediction model seems not always to be adequate in fully describing the development of the waves, in the Aegean Sea. A special model should be applied, distinguishing at least the most critical differences (North from South winds and storm from squall events).

Acknowledgments

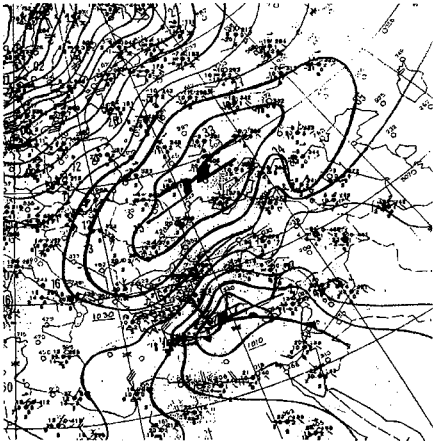
Wind data and weather maps were obtained from the Greek National Meteorological Service. The contribution of the meteorologists Mrs. Petrou and Mr. Ziakopoulos to interpret the weather systems is highly appreciated.

Professors C. I. Moutzouris (N.T.U.A.) and M. S. Bruno (Stevens Institute of Technology) have substantially encourage the present work.

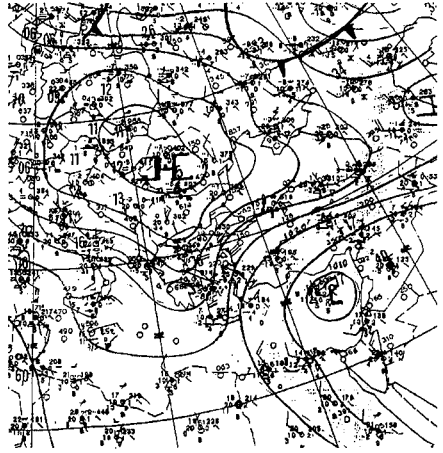
APPENDIX

References

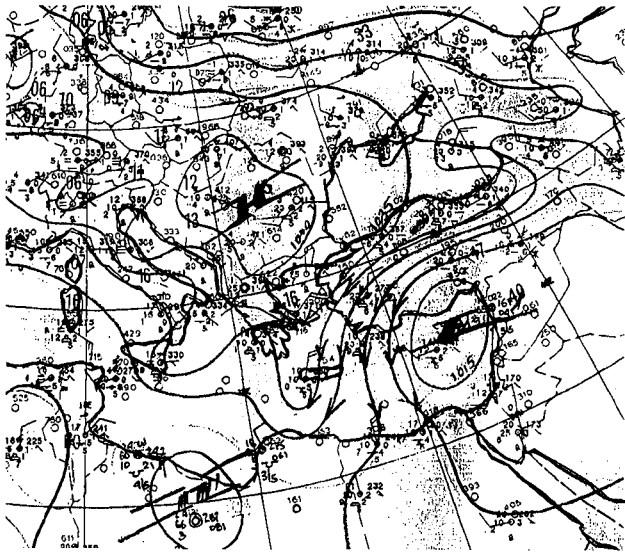
- Bretschneider C. I. (1958): "Revisions in wave forecasting deep and shallow water", Proc. 6th Conf. on Coastal Engineering, New York.
- Gouloumis S. M. and Moutzouris C. I. (1996): The Greek Wave Measurement and Analysis Network (KYMATA), First International Conference on EuroGOOS, The Hague, The Netherlands.
- Gouloumis S. M., Moutzouris C. I. (1995): "Wave measurements under fetch- and duration- limited conditions in the South Aegean Sea, Greece", Proc. 4th Int. Conf. on Coastal & Port Engin. in Developing Countries, RJ, Brazil.
- Hughes S. A. (1984): "The TMA shallow-water spectrum description and applications", Technical Report CERC-84-7, US Army Corps of Engineers.
- Parle P., Burrows R. (1989): "Comparison of simplified wave prediction methods as recommended in the S.P.M.", BHRA, The Fluid Engineering Center, Ch. 24.
- Pierson W. J. and Moskowitz I. (1964): "A proposed spectral form for fully developed wind seas on the similarity theory of S. A. Kitaigorodskii", J. geophys. Res.
- Thieke R., Dean R., Garcia A. (1994): The Daytona beach "Large Wave" event of 3 July 1992, Proc. of the 2nd Int. Symp. on Ocean Wave Measurements and Analysis, pp.45-60, Publ. by ASCE, NY, USA.



December 1st 1992 at 12:00 UTC



January 31st 1993 at 12:00 UTC



February 8th 1993 at 12:00 UTC

Fig. 8 Weather maps over the East Mediterranean Sea and Europe

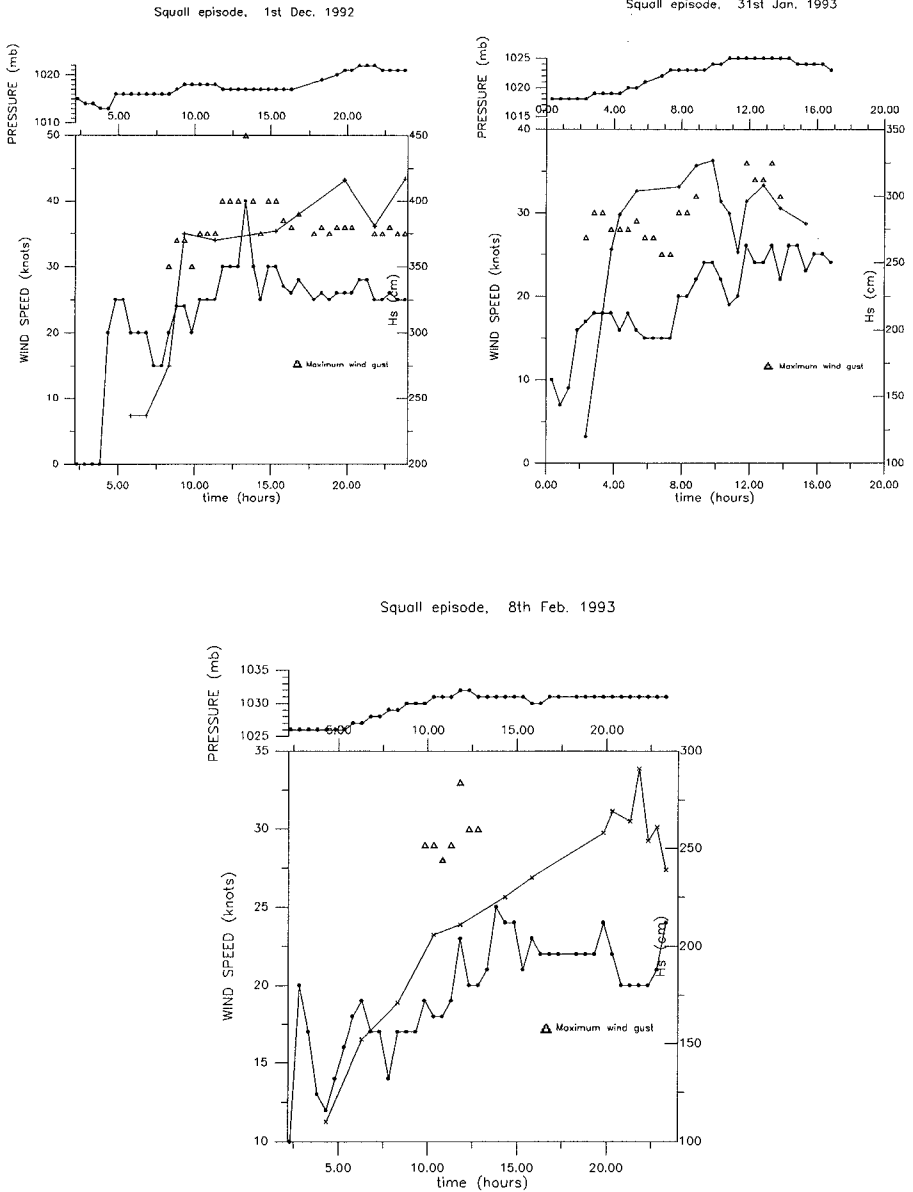


Fig. 9 Wind speed, significant wave height and barometric pressure time series of the storm episodes not complying with the SMB model.

CHAPTER 35

NON-REFLECTED MULTI DIRECTIONAL WAVE MAKER THEORY AND EXPERIMENTS OF VERIFICATION

Kazunori ITO¹ , Hidehiro KATSUI², Masashi MOCHIZUKI³, Masahiko ISOBE⁴

ABSTRACT

In the hydraulic model test in a wave basin, reflected waves from models of structures and walls of the basin reflect again at the wave maker. The re-reflected waves disturb wave field in the basin and consequently reduce the accuracy of experiments. We developed a non-reflected multi directional wave maker theory. By taking into account both current and past water elevation data in front of the wave paddles, the theory makes the wave makers possible to absorb reflected multi directional waves. Numerical simulations and experiments show that this theory is superior to the conventional theory in its efficiency of the absorption.

1. INTRODUCTION

In general, multi directional wave experiments using wave makers placed in a line have the following problems: an experiment area with a uniform wave field is small, and reflected waves from a model and/or a wave basin cannot be absorbed efficiently. In order to create a larger experiment area, reflecting walls are installed at the end of multi directional wave makers placed in a line[1], or wave makers are set in the J-shape[2]. These methods are very effective to enlarge an experiment area. However, when a model is surrounded by wave makers and/or a reflecting wall, re-reflected waves from these wave makers and/or a reflecting wall exert a large effect on the model; thus, it becomes important to absorb reflected waves. The method proposed by Kawaguchi[3], which uses the data on water surface elevation at the wave paddle front, has been put to a practical use for absorbing uni- directional reflected waves. Hiraguchi et al.[4] carried out experiments by applying this method to multi-directional wave makers to absorb multi-directional waves. However, as only an orthogonal wave direction against a wave paddle is taken into account in Kawaguchi's method, the absorptivity decreases when the incidence angle of reflected waves is oblique. Ikeya et al.[5] proposed the method

¹ M.Eng, Taisei Corporation, Wakasu-Nai, Koto-Ku, Tokyo, Japan 136

² Dr.Eng, Manager, Hydraulic Section, Technology Research Center, Taisei Corporation
Nase-machi 344-1, Totsuka-Ku, Yokohama-City, Kanagawa, Japan 245

³ Deputy Section Chief, Akishima Eng. Dept., Advanced Machines And Systems, Div., Mitsui
Engineering and Ship Building Co., LTD
Tsutsujigaoka1-1-50, Akishima-City Tokyo, Japan 196

⁴ Professor, Dr.Eng, Dept. of Civil Engineering, University of Tokyo
Hongo-7-3-1, Bunkyo-Ku, Tokyo, Japan 113

for absorbing oblique waves using the data on water surface elevation at the front of two or more wave paddles. However, the absorptivity in this method also decreased due to the errors in computing reflected waves, as evanescent waves are not taken into account. Their theory does not have a wide application, because it stands on the assumption that a wave basin has side walls. Besides, as the above two methods take only a representative frequency into account, the absorptivity decreases when a wave has dominant frequency dispersion.

This paper aims to establish a non-reflected wave maker theory for multi-directional waves in consideration of directional dispersion, frequency dispersion and evanescent waves[6], and to report the results of the basic experiments on oblique regular waves to verify the theory[7].

2. FORMULATION OF NON-REFLECTED WAVE MAKER THEORY

Fig. 1 shows the coordinates used in the analysis: x- and y-axes in the horizontal direction, and z-axis in the vertical upward direction.

Wave paddles are set along the x-axis. Here, let us take a piston-type wave maker by way of example to develop the theory.

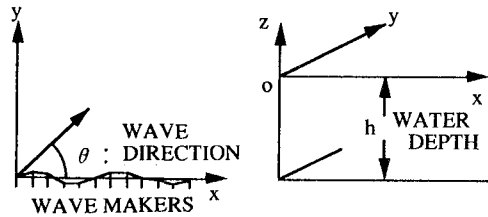


Fig.1 Definition of coordinate

2.1. WAVE MAKER THEORY

The fluid treated here is inviscid and unconsolidated. When a small amplitude wave theory can be applied to the wave and the amplitude of a wave paddle is small enough, the problems of wave making with the constant water depth are governed by the following equations:

$$\frac{\partial^2 \Phi}{\partial x^2} + \frac{\partial^2 \Phi}{\partial y^2} + \frac{\partial^2 \Phi}{\partial z^2} = 0 \tag{1}$$

$$\frac{\partial \Phi}{\partial t} + g\eta = 0 \tag{2}$$

: z = 0

$$\frac{\partial \eta}{\partial t} - \frac{\partial \Phi}{\partial z} = 0 \tag{3}$$

: z = 0

$$\frac{\partial \Phi}{\partial n} = \frac{\partial X}{\partial t} \tag{4}$$

: y = 0

$$\frac{\partial \Phi}{\partial z} = 0 \tag{5}$$

: z = -h

where, $\Phi(x,y,z,t)$: velocity potential, $\eta(x,y,t)$: water surface elevation, g : gravity acceleration, h : water depth, n : normal direction, X : displacement of a wave paddle.

Now, the theory is developed for regular waves. By separating a variable Φ , Eq.(6) can be obtained from Eq.(1) and (5).

$$\Phi(x,y,z,t) = \sum_{n=0}^{\infty} \phi_n(x,y) \frac{\cosh[k_n(z+h)]}{\cosh k_n h} e^{-i\omega t} \tag{6}$$

When $n=0$, angular frequency ω and a wave number kn in Eq.(6) satisfy the

dispersion relation Eq.(7) of a progressive wave component; when $n=1$ to ∞ , they satisfy the dispersion relation Eq.(8) of an evanescent wave component. Here, k_n is an imaginary number when $n=1$ to ∞ , and \hat{k}_n is the imaginary part of k_n .

$$\omega^2 = gk_n \tanh k_n h \tag{7}$$

$$\omega^2 = -g\hat{k}_n \tan \hat{k}_n h \tag{8}$$

Next, use Eq.(4) as follows:

$$\left. \frac{\partial \Phi}{\partial n} \right|_{y=0} = \frac{\partial \Phi}{\partial y} = U(x,y)F(z)e^{-i\omega t} \tag{9}$$

where, $U(x,y)$: amplitude of wave paddle velocity $F(z)$: function of wave paddle motion ($F(z)$ of a piston-type wave maker = 1)

By substituting Eq.(6) into Eq.(9) and integrating in the vertical direction using orthogonality, Eq.(10) can be obtained as follows:

$$U = \frac{D_n}{G_n} \frac{\partial \phi_n}{\partial y} \tag{10}$$

In the case of a piston-type wave maker, D_n and G_n can be obtained as follows, respectively.

$$D_n = \frac{\tanh k_n h}{2k_n} \left[1 + \frac{2k_n h}{\sinh 2k_n h} \right] : n = 0 \quad , \quad = \frac{\tan \hat{k}_n h}{2\hat{k}_n} \left[1 + \frac{2\hat{k}_n h}{\sin 2\hat{k}_n h} \right] : n = 1, 2, 3, \dots \tag{11}$$

$$G_n = \frac{\tanh k_n h}{k_n} : n = 0 \quad = \frac{\tan \hat{k}_n h}{\hat{k}_n} : n = 1, 2, 3, \dots \tag{12}$$

If water surface elevation η_p of a progressive wave component is given as Eq.(13), U which is necessary for making a progressive wave can be determined as Eq.(14) from Eq.(10) with $y=0$.

$$\eta_p = a e^{i\{k_0(x \cos \theta + y \sin \theta) - \omega t\}} \tag{13}$$

$$U(x,0) = \frac{D_0}{G_0} \frac{g a k_0}{\omega} \sin \theta e^{i\{k_0(x \cos \theta)\}} \tag{14}$$

where, the subscript 0 represents a progressive wave, and a represents a complex amplitude of component waves.

ϕ_n of an evanescent wave is the solution of Eq.(15) and the boundary condition $\lim_{y \rightarrow \infty} \phi_n = 0$; then, from the relation in Eq.(10), Eq.(16) can be obtained.

$$\frac{\partial^2 \phi_n}{\partial x^2} + \frac{\partial^2 \phi_n}{\partial y^2} - \hat{k}_n^2 \phi_n = 0 \tag{15}$$

$$\phi_n = -\frac{D_n G_n}{D_n G_0} \frac{g a k_0 \sin \theta}{\omega \sqrt{\hat{k}_n^2 + k_0^2 \cos^2 \theta}} e^{i k_0 x \cos \theta - y \sqrt{\hat{k}_n^2 + k_0^2 \cos^2 \theta}} \tag{16}$$

Therefore, when making a regular wave, the water surface elevation η_e of an

evanescent wave component at the wave paddle front ($y=0$) can be described as follows:

$$\eta_e(x, 0, t) = -\frac{D_0 G_n}{D_n G_0} \frac{ik_0 \sin \theta}{\sqrt{\hat{k}_n^2 + k_0^2 \cos^2 \theta}} e^{ik_0 x \cos \theta - i\omega t} \quad (17)$$

Thus, the water surface elevation at the wave paddle front can be obtained by adding the water surface elevation of a progressive wave component and that of an evanescent wave component as in Eq.(18):

$$\eta(x, 0, t) = \left[1 - \frac{D_0 G_n}{D_n G_0} \frac{ik_0 \sin \theta}{\sqrt{\hat{k}_n^2 + k_0^2 \cos^2 \theta}} \right] a e^{ik_0 x \cos \theta - i\omega t} \quad (18)$$

Multi-directional waves can be described as superposition of component waves. Therefore, the wave paddle velocity $A^{(i)}(x, y=0, t)$ and the water surface elevation at the wave paddle front $\eta^{(i)}$ are obtained in Eq.(19) and (20), respectively.

$$\left. \frac{\partial \Phi}{\partial n} \right|_{y=0} = A^{(i)} = \sum_{j=1}^{\infty} \frac{D_{j0}}{G_{j0}} \frac{g a_j k_{j0}}{\omega_j} \sin \theta_j e^{i\{k_{j0}(x \cos \theta_j) - \omega_j t\}} \quad (19)$$

$$\eta^{(i)}(x, 0, t) = \sum_{j=1}^{\infty} \left[1 - \sum_{n=1}^{\infty} \frac{G_{jn} D_{j0}}{G_{j0} D_{jn}} \frac{ik_{j0} \sin \theta_j}{\sqrt{\hat{k}_{jn}^2 + k_{j0}^2 \cos^2 \theta_j}} \right] \times a_j e^{i(k_{j0} x \cos \theta_j - \omega_j t)} \quad (20)$$

Both the actual wave paddle velocity and water surface elevation are real variables, thereby becoming the real parts in Eq.(19) and (20). Hereafter, a symbol $\tilde{\sim}$ in this paper stands for a real variable.

2.2. ABSORPTION THEORY

The conventional non-reflected wave maker theory[3],[5], where the water surface elevation measured at the wave paddle front is converted into a wave making signal, is based on a so-called feedback control. This method has a great advantage in the aspect of practical control. This paper develops a new non-reflected wave maker theory using the data on water surface elevation at the wave paddle front.

In the case of non-reflected wave making, the water surface elevation at the wave paddle front ($\tilde{\eta}^{(m)}$) is the sum of the water surface elevation of a progressive wave which is a target wave ($\tilde{\eta}_p^{(i)}$), the water surface elevation of an evanescent wave which is created due to wave making ($\tilde{\eta}_e^{(i)}$), the water surface elevation of a progressive wave component of a reflected wave ($\tilde{\eta}_p^{(r)}$), and the water surface elevation of an evanescent wave which is created due to the motion of wave paddle to absorb a reflected wave ($\tilde{\eta}_e^{(r)}$); that is, ($\tilde{\eta}^{(m)} = \tilde{\eta}_p^{(i)} + \tilde{\eta}_e^{(i)} + \tilde{\eta}_p^{(r)} + \tilde{\eta}_e^{(r)}$). As $\tilde{\eta}^{(i)}$ ($= \tilde{\eta}_p^{(i)} + \tilde{\eta}_e^{(i)}$) can be calculated by Eq.(20), a reflected wave $\tilde{\eta}^{(r)}$ ($= \tilde{\eta}_p^{(r)} + \tilde{\eta}_e^{(r)}$) can be obtained as $\tilde{\eta}^{(r)} = \tilde{\eta}^{(m)} - (\tilde{\eta}_p^{(i)} + \tilde{\eta}_e^{(i)})$, where no re-reflection occurs from the wave paddle since reflected waves are absorbed.

The relation between the water surface elevation $\tilde{\eta}^{(r)}$ at the wave paddle

front which includes an evanescent wave and the wave paddle velocity $\tilde{A}^{(r)}$ is defined by transfer function $H_{pe}(\omega, \theta)$ as $\tilde{A}^{(r)}(x, 0, t) = H_{pe}(\omega, \theta) \tilde{\eta}^{(r)}(x, 0, t)$ in the case of a regular wave. The concrete form of $H_{pe}(\omega, \theta)$ is described in the following equation, which uses the real parts in Eq.(19).

$$H_{pe}(\omega, \theta) = \frac{D_0}{G_0} \frac{gk_0}{\omega} \sin \theta \times \left\{ 1 + \left(\sum_{n=1}^{\infty} \frac{D_n G_n}{D_n G_0} \frac{k_0 \sin \theta}{\sqrt{\hat{k}_n^2 + k_0^2 \cos^2 \theta}} \right)^2 \right\}^{-\frac{1}{2}} \quad (21)$$

Assuming that a reflected wave $\tilde{\eta}^{(r)}$ is in a narrow band spectrum of frequency and wave direction, Eq.(22) and (23) can be obtained as follows:

$$\tilde{\eta}^{(r)}(x, y, t) = \sum_{m=1}^{\infty} \tilde{a}_m \cos \varphi_m \quad (22)$$

$$\varphi_m = (\bar{k} + \Delta k_m) \left[x \cos(\bar{\theta} + \Delta \theta_m) - y \sin(\bar{\theta} + \Delta \theta_m) \right] - (\bar{\omega} + \Delta \omega_m) t + \varepsilon_m \quad (23)$$

where, ε_m is a phase number.

When $H_{pe}(\omega, \theta)$ can be expanded around a representative frequency $\bar{\omega}$ and a representative wave direction $\bar{\theta}$ using Taylor expansion in consideration of the first order quantity, the motion velocity of a wave paddle which absorbs reflected waves can be obtained in Eq.(24).

$$\tilde{A}^{(r)}(x, 0, t) = \bar{H}_{pe} \sum_{m=1}^{\infty} \tilde{a}_m \cos \varphi_m + \frac{\partial \bar{H}_{pe}}{\partial \omega} \times \sum_{m=1}^{\infty} \Delta \omega_m \tilde{a}_m \cos \varphi_m + \frac{\partial \bar{H}_{pe}}{\partial \theta} \sum_{m=1}^{\infty} \Delta \theta_m \tilde{a}_m \cos \varphi_m \quad (24)$$

Then, by obtaining a series of the second and third terms in the right side of Eq.(24) using simultaneous equations of $\tilde{\eta}^{(r)}$, $\partial^2 \tilde{\eta}^{(r)} / \partial t^2$ and $\partial^2 \tilde{\eta}^{(r)} / \partial x \partial t$ in consideration of the first order quantity, the motion velocity of a wave paddle can be expressed as follows:

$$\begin{aligned} \tilde{A}^{(r)} = & \bar{H}_{pe} \tilde{\eta}^{(r)} + \frac{\partial H_{pe}}{\partial \omega} \left\{ \frac{1}{2\bar{\omega}} \left(-\bar{\omega}^2 \tilde{\eta}^{(r)} - \frac{\partial^2 \tilde{\eta}^{(r)}}{\partial t^2} \right) \right\} \\ & + \frac{\partial H_{pe}}{\partial \theta} \left\{ \frac{1}{2} \left(1 - \frac{\bar{c}}{\bar{c}_g} \right) \cot \bar{\theta} \tilde{\eta}^{(r)} - \frac{1}{2\bar{\omega}^2} \left(1 + \frac{\bar{c}}{\bar{c}_g} \right) \right. \\ & \left. \times \cot \bar{\theta} \frac{\partial^2 \tilde{\eta}^{(r)}}{\partial t^2} - \frac{1}{\bar{k} \bar{\omega} \sin \bar{\theta}} \frac{\partial^2 \tilde{\eta}^{(r)}}{\partial x \partial t} \right\} \end{aligned} \quad (25)$$

where, \bar{k} : wave number of a progressive wave against $\bar{\omega}$
 \bar{c} : phase velocity of a progressive wave against $\bar{\omega}$
 \bar{c}_g : group velocity of a progressive wave against $\bar{\omega}$
 \bar{H}_{pe} : transfer function regarding a representative value

The second term in the right side of Eq.(25) is a correction term for frequency dispersion, and the third term is a correction term for directional dispersion.

From the above equations, the wave paddle velocity $\tilde{A}^{(r)}$ for absorbing can be calculated from a reflected wave; then, by subtracting $\tilde{A}^{(r)}$ from the wave paddle velocity $\tilde{A}^{(i)}$ for making a target wave, a wave paddle can be controlled. Thus, non-reflected wave making becomes possible.

3. DISCUSSION ON THE THEORY THROUGH NUMERICAL CALCULATION

3.1. DISCUSSION ON AN EVANESCENT WAVE

An evanescent wave occurs due to the difference between the wave paddle motion and a vertical distribution of horizontal water particle velocity of the target wave. The amplitude of an evanescent wave becomes largest at the wave paddle front, and decreases in accordance with the distance from a wave paddle.

Fig. 2 shows the ratio of progressive wave amplitude and evanescent wave amplitude, when a regular wave is created using a piston-type wave maker. From the figure, it is clear that when a piston-type wave maker creates a deep-sea wave with the large ratio of wavelength and water depth kh , an evanescent wave is more likely to occur; while, as the wave direction is tilted, it occurs less frequently.

Therefore, in the control method where a reflected wave is detected by using the water surface elevation at the wave paddle front, an evanescent wave must not be neglected. By taking into account of this wave, the absorption of a reflected wave is expected to be improved.

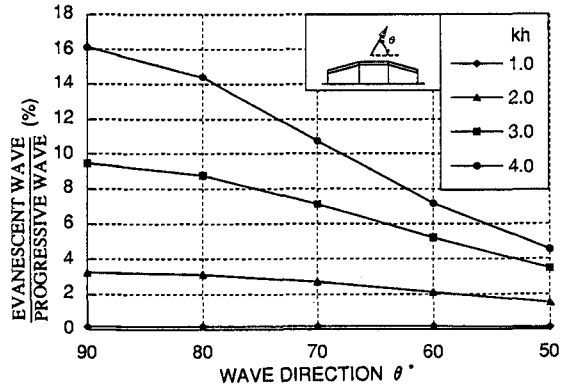


Fig.2 The ratio of progressive wave amplitude and evanescent wave amplitude

3.2. DISCUSSION ON NON-REFLECTED CONTROL

In a practical use of a reflected wave absorption control, a reflected wave is detected by a wave gauge installed on the wave paddle front as in conventional methods. Therefore, the differential of the theoretical equation(25) is necessarily approximated with finite- differential. Besides, it is not easy to give a representative wave direction in advance. For some structural models, a representative wave direction of a reflected wave is particularly difficult to predict. In the case of a floating model, wave direction of a reflected wave reaching a wave paddle varies from hour to hour according to the motion of the model. Here, a practical calculation method is adopted; as for a representative frequency, a representative value of the wave to be created is given in advance, and a representative wave direction is approximated using Eq.(26) and (27).

$$\theta(t) = \cos^{-1} \left[-\bar{c} \frac{\partial \tilde{\eta}^{(r)} / \partial x}{\partial \tilde{\eta}^{(r)} / \partial t} \right] \tag{26}$$

$$\bar{\theta}(t) = \frac{1}{N} \left[(N-1) \bar{\theta}(t - \Delta t) + \theta(t) \right] \tag{27}$$

where, $\theta(t)$: wave direction at the time t
 $\bar{\theta}(t)$: a representative wave direction

N is the value obtained by dividing the elapsed time of absorption control of reflected waves by the intervals of sampling of water surface elevation (Δt), that is, the number of times of sampling. $\partial/\partial x$ is the mean finite-differential of the second order, which is calculated from the data on water surface elevation at the front of two or more wave paddles. When $\partial/\partial t$ is defined as the unilateral finite-differential of the second order and $\partial^2/\partial t^2$ is as the unilateral finite-differential of the first order, they can be calculated from the data on water surface elevation measured in the past using a water gauge. As shown above, the characteristic of absorption control in this theory is the use

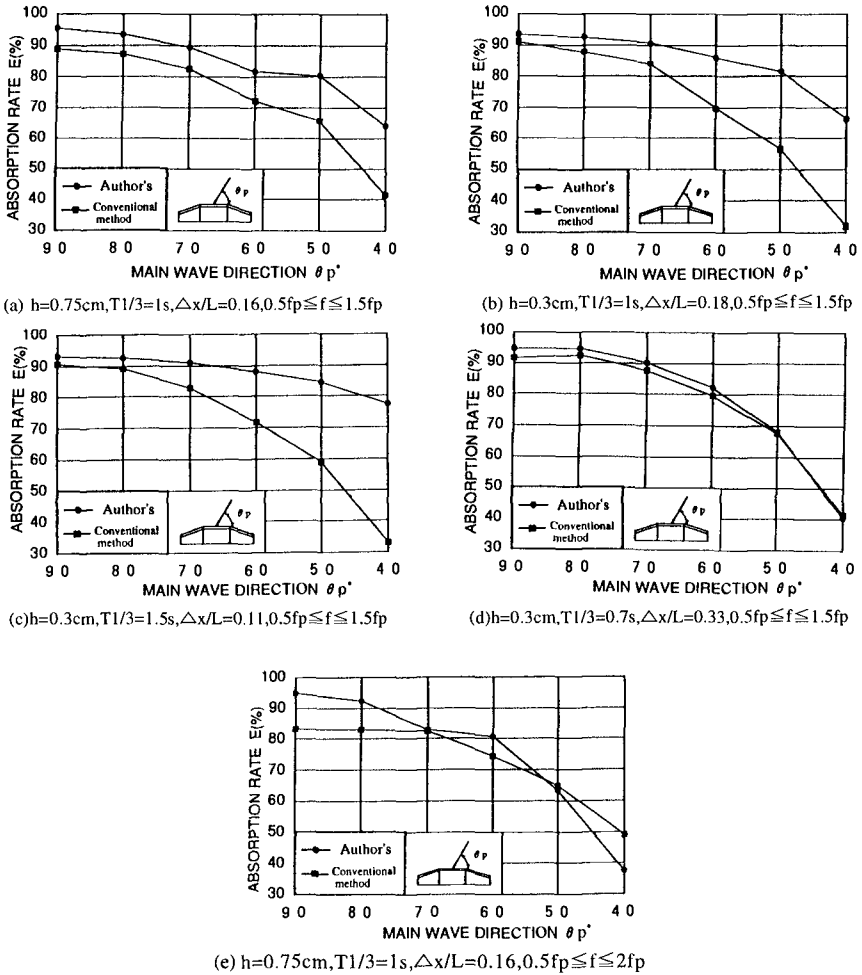


Fig.3 The comparison of the absorption rate between Author's method and Conventional method

of data on water surface elevation at the wave paddle front and the past data. As a result of numerical calculation without approximating the derivation in Eq.(25), this theory was proved valid regardless of a wave direction or water depth. Next, by approximating the derivation in Eq.(25), numerical calculation was conducted. The conditions of a reflected wave include Bretschneider-Mitsuyasu spectrum, Mitsuyasu-type directional function ($S_{max}=10$), significant wave height 3cm, significant wave period 0.7s, 1.0s, 1.5s, and the water depth 0.3m, 0.75m. Wave direction against the peak wave direction is in the range of $\pm 30^\circ$. The frequency range is 0.5 to 1.5 times and 0.5 to 2.0 times as large as the peak frequency f_p . The intervals of wave gauges (Δx) is 0.25m, and Δt is given as 0.01s. Using these, it is quantitatively examined using the absorption rate E which is defined by Eq.(28).

$$E = \left[1 - \frac{\sqrt{\left(\int_0^T (\tilde{A}_r(x,0,t) - \tilde{A}_n(x,0,t))^2 dt \right)}}{\left(\int_0^T \tilde{A}_r(x,0,t)^2 dt \right)} \right] \times 100 \% \tag{28}$$

where, $\tilde{A}_r(x,0,t)$: the wave paddle velocity in Eq.(19)

$\tilde{A}_n(x,0,t)$: the wave paddle velocity in Eq.(25)

For comparison, the results of conventional method are also shown: in the conventional method, there are no second and third terms in the right side of Eq.(25); $\sin \theta$ in the right side of transfer function equation(21) is 1; and the total series is 0.

Fig.3 shows the comparison of the absorption rate when the peak frequency of a reflected wave, water depth and the frequency range are varied. From (a) and (b), it is clear that when the peak frequency is 1s, this theory is superior to the conventional method in terms of absorptivity, regardless of the water depth. When frequency becomes 1.5s as in (c), the ratio of the wave gauge space and the wavelength ($\Delta x/L$) becomes smaller and the approximation becomes more accurate, thereby improving the absorptivity. On the other hand, in (d) where frequency is 0.7s and the water depth is 0.3m, the accuracy of approximation decreases, showing no significant difference from the conventional method. Therefore, when the frequency range of reflected waves is about 0.5 to 1.5 times as large as f_p , this theory is significant on condition that $\Delta x/L$ is 0.33 or smaller. In (e) where the frequency range is larger (0.5 to 2.0 times as large as f_p), this theory exceeds the conventional method on condition that the wave direction is around 90° ; however, as the wave direction is tilted, there becomes no difference from the conventional method. This is caused by the limit in assuming a narrow band spectrum and the error in approximation.

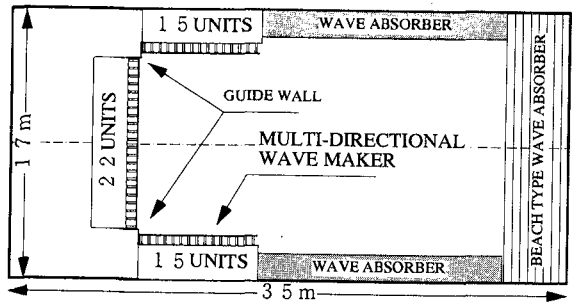


Fig.4 The C-shape multi directional wave makers

4. EXPERIMENTS ON REFLECTED WAVE ABSORPTION

4.1. EXPERIMENTAL EQUIPMENT AND METHOD

(1) EXPERIMENTAL EQUIPMENT

A multi-directional wave maker is a multiplex piston-type wave maker, consisting of 52 wave makers. Two capacitance-type wave gauges were installed with a space of 25cm on a 50cm-wide wave paddle: one at the front of a driving shaft, the other in the middle of two driving shafts. As shown in Fig.4, multi-directional wave makers were arranged in the C-shape within a wave basin (35×24m). The number of wave makers on each side was 15, 22, and 15, respectively. The L-shape installation is also possible: 30 wave makers on the long side and 22 on the short side of the wave basin. Cut-off walls called guide walls were installed at each corner of the C-shape. The neutral point of each wave paddle can be shifted arbitrarily within the range of $\pm 40\text{cm}$ stroke. The power of each driving shaft can also be adjusted arbitrarily.

(2) EXPERIMENTAL METHOD

The experiment was carried out by making waves from WAVE MAKER 1 and 2 shown in Fig.5, with the WAVE MAKER 3 serving as absorption control as in Eq.(25). Following the method proposed by Toida et al.[8], the power of five driving shafts installed at the ends of the wave makers 1 and 2 (C, F) was controlled to be 100% to 0%, in order to decrease the effect of diffraction waves from the ends. In addition, in order to decrease the effect of diffraction waves from the corner, the method of shifting the neutral point of wave paddles[7] was adopted. In absorption control in Eq.(25), both ends were controlled for the purpose of decreasing diffraction waves.

The water surface elevation at the front of WAVE MAKER 3 was measured at the lattice points (24×15) with a 30cm-space, as described by hatching in Fig.5.

4.2. DISCUSSION ON AN EVANESCENT WAVE

Regular waves were made in the vertical direction from the wave makers 2 in Fig.5, then both the water surface elevation at the wave paddle front and an evanescent wave were measured. The measurement conditions were: frequency changing from 0.7s to 1.0s and 1.5s, water depth from 50cm to 60cm, 70cm and 80cm, and wave height from 0.5cm to 0.8cm.

Fig.6 shows the relation of the ratio of wavelength and water depth kh and the amplitude

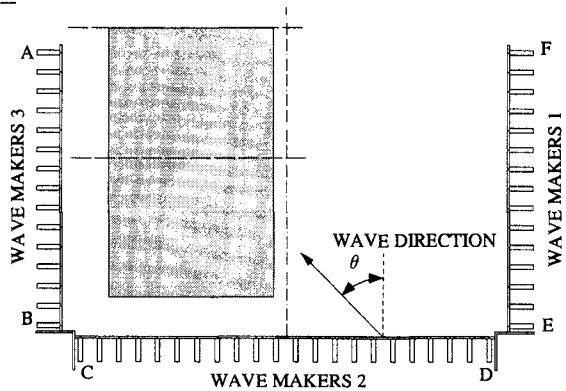


Fig.5 Measurement area and definition of wave direction

Fig.6 shows the relation of the ratio of wavelength and water depth kh and the amplitude

The water surface elevation at the front of WAVE MAKER 3 was measured at the lattice points (24×15) with a 30cm-space, as described by hatching in Fig.5.

4.2. DISCUSSION ON AN EVANESCENT WAVE

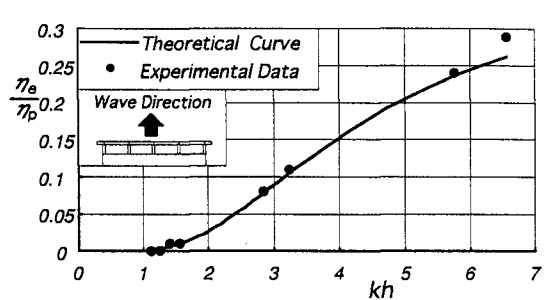


Fig.6 The comparison between theoretical evanescent wave and experimental one

absorption control was conducted using Eq.(25), the wave height distribution showed uniformity. However, around A, at the end of the wave makers, showed a tendency to form a standing wave field.

Fig.8 shows the similar results, when frequency was given as 1.5s. The absorptivity by Eq.(25) was high.

(Regular wave: $T=1s, H=5cm, \theta=45^\circ$) Fig.9 shows the results when the wave direction was 60° . Though the pattern of isolines was slightly different, there was no significant difference in the region where a standing wave field was formed and in the isoline

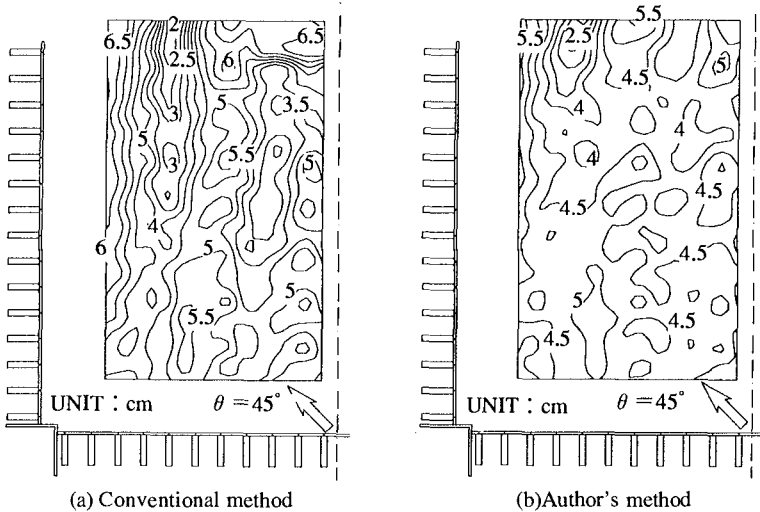


Fig.8 The contour of the wave heights
Regular wave: $T=1.5s, H=5cm, \theta=45^\circ$)

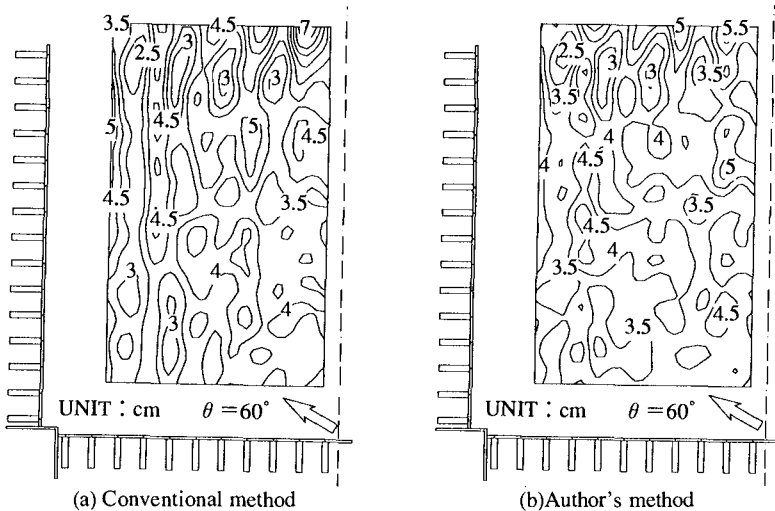


Fig.7 The contour of the wave heights
Regular wave: $T=1.5s, H=5cm, \theta=60^\circ$)

values. Thus, it is judged that both absorption controls had the same degree of absorptivity.

4.4 CAPABILITY OF NON-REFLECTED WAVE MAKER THEORY FOR MULTI DIRECTIONAL WAVES

The experiments were carried out to investigate capability of absorption for multi directional waves. WAVE MAKER1 and WAVE MAKER 2 generated multi directional waves and WAVE MAKER 3 absorbed waves propagating toward WAVE MAKER 3. WAVE MAKER 3 was driven by using author's method or conventional method for the sake of comparison. Furthermore WAVE MAKER 3 was controlled as the reflecting wall. The water elevations were measured by STAR ARRAY that was located in front of WAVE MAKER 3 (Fig.5). Directional spectrum were calculated by using Expanded Maximum Entropy Principle Method(EMEP). Since EMEP can not estimate the phase interaction of incident and reflected waves, STAR ARRAY was set over one wave length (2.7 m) distant away from WAVE MAKER 3.

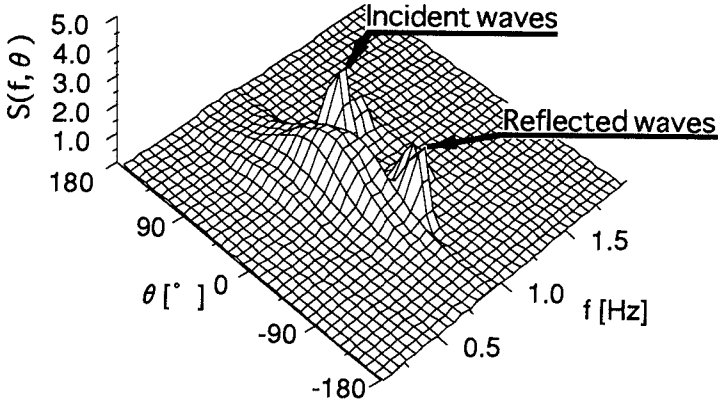
In the experiments, the wave generated by WAVE MAKER1 and 2 had Bretschneider-Mitsuyasu spectrum, Mitsuyasu type directional function ; $S_{max}=10,70$, $H_{1/3}=5\text{cm}$, $T_{1/3}=1\text{s}$ and $\theta_p=45^\circ$. S_{max} is spreading parameter, $H_{1/3}$ significant wave height, $T_{1/3}$ significant wave period, θ_p is principal wave direction.

Fig.10 shows the directional spectrum in the case of $S_{max}=70$. In the case of WAVE MAKER 3 being the reflecting wall (Fig.10 (a)), three peak frequency appear at around 0° , -45° and 45° . The wave direction of incident component waves appears at about 45° . Reflected component waves corresponding to the incident component waves propagate to the direction of -45° . The component wave of which frequency is about 0.9Hz can be understood as the component waves that propagate crosswise between WAVE MAKER 1 and 2. On the other hand, the reflected component waves less than 1.3Hz can not be seen in the case of author's method (Fig.10 (b)). This figure indicates that the author's method can absorb multi directional waves effectively. And the directional spectrum analysis showed the similar results for $S_{max}=10$ and $S_{max}=70$.

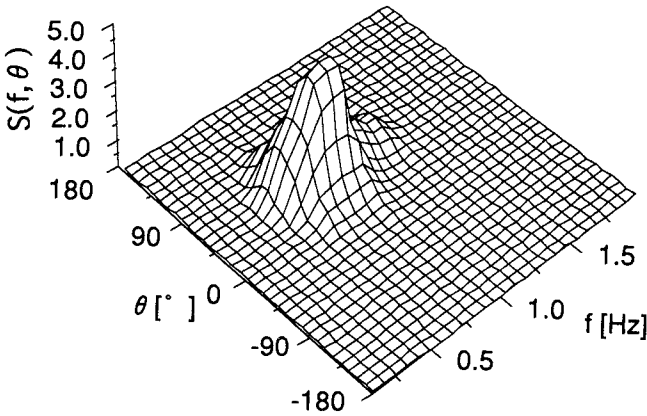
But, the results of directional spectrum analysis did not indicate the remarkable difference between author's method and conventional one.

The conventional method can effectively absorb the wave trains which propagate toward the wave paddles only at a right angle. But this can not absorb the wave trains coming obliquely to the wave paddles. Thus reflected waves should remain in the basin. Now we try to explain the reason why the directional spectrum could not show the remarkable difference between the author's method and the conventional one. In the calculation of directional spectrum, cross-spectrum must have presumption error and smoothing operation is indispensable for cross-spectrum analysis. Consequently, it is judged that the influence of the reflected waves vanished in the process of the calculation.

Fig.11 shows significant wave heights($h_1 \sim h_4$) at STAR ARRAY. Legends(●, ○, ■) indicate the difference of the control method of WAVE MAKER 3; ● for standstill as a wall, ○ for control by the author's method, ■ for control by the conventional one. As shown in figure($S_{max}=70$), each significant wave height does not show the large difference between the author's method and the conventional one and distribution of $H_{1/3}$ is uniform. But, for $S_{max}=10$, the significant wave heights of the conventional method is not specially uniform. This attributes to the disturbance caused by the reflected waves from WAVE MAKER 3. Therefore, we may conclude that as an angle between wave direction and wave paddle is large, the conventional method can not absorb oblique wave groups with such wave direction.



(a) Reflecting wall



(b) Author's method

Fig.10 The comparison of the directional spectrum($S_{max}=70$)

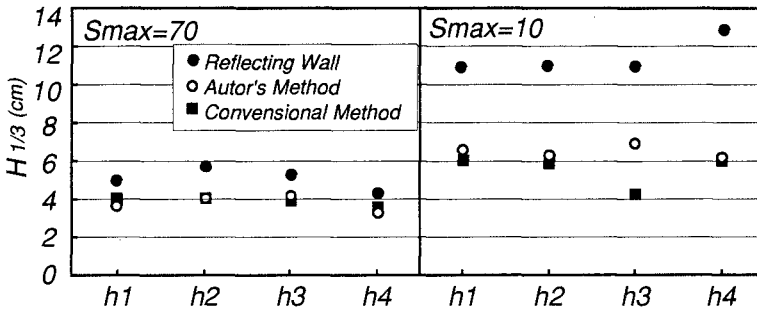


Fig. 11 The comparison of the wave heights at STAR ARRAY

5. CONCLUSION

This paper established a non-reflected wave maker theory for multi-directional waves considering evanescent waves as well, using the data on water surface elevation at the front of two or more wave paddles and the past data. From the results of numerical calculation and experiments, this theory was proved to have higher absorptivity than the conventional method.

Acknowledgments

The authors also wish to thank Professor Masaru Mizuguchi at Chuo University for his helpful suggestions. The authors would like to express his gratitude to Mr. Takamitsu Noguchi, Mr. Masaki Anzai, and Mr. Hiroyuki Kishi of Taisei Service, Inc. for their cooperation.

References

- [1] T. Hiraishi (1991): Experimental Study on the Effective Test Area for Directional Waves by a Serpent-Type Wave Generator., Proc. of the Coastal Engineering, Vol.38, pp.126-130.(In Japanese).
- [2] T. Hiraishi (1990): Report on Wave Makers in Canada - Reclamation and Dredge, No.156, pp.30-38. (In Japanese).
- [3] T. Kawaguchi (1986): Absorbing Wave Making System with Wave Sensor and Velocity Control, Mitsui Zousen Technical Review., No.128, pp.20-24. (In Japanese).
- [4] H. Hiraguchi, R. Kajima, H. Tanaka, T. Ishii (1990): Wave Absorption of a Directional Wave Maker, Proc. of the Coastal Engineering, Vol.38, pp.121-125.(In Japanese).
- [5] T. Ikeya, Y. Akiyama, K. Imai (1992): Wave Absorption Theory for Multi-directional Waves, Proc. of the Coastal Engineering, Vol.39, pp.81-85.(In Japanese).
- [6] K. Ito, M. Isobe, H. Katsui (1994): Directional wavemaker theory that can absorb reflected waves, Proc. of the Coastal Engineering, Vol.41, pp.101-105.(In Japanese).
- [7] K. Ito, H. Katsui, M. Mochizuki, M. Isobe (1995): Experiment of Non-reflected Multi directional Wave Maker Disposed in to C-shape, Proc. of the Coastal Engineering (now being printed), Vol.42. (In Japanese).
- [8] H. Toida, Masaru M., Y. Moriya (1994): End Control Method for Making a Uniform Wave Field Using Multi-directional Wave Makers, Proc. of the Coastal Engineering, Vol.41, pp.106-109. (In Japanese).

CHAPTER 36

Fifty Years of Wave Growth Curves¹

Paul C. Liu²

Abstract

It has been over fifty years since the public release of the well-known monograph of Navy H.O. 601, prepared by Sverdrup and Munk (1947) during World War II. In celebrating 50th anniversary of the International Coastal Engineering Conference that was started in 1948, it is of interest to revisit the wave growth curves developed in H.O. 601 and compare them with a recent study on wave growth curves (Donelan et al. 1992). It is clear that while significant progress has been made over the last 50 years, Sverdrup and Munk's original idea still prevails in light of modern developments.

Introduction

The mid years of the decade of 1990s observe many 50th anniversaries of events that relate to the end of World War II. The end of the war marks the start of two important events that are of interest to coastal and ocean engineers: the public release of the well-known monograph of the Navy H.O. 601 by Sverdrup and Munk (1947) and the beginning of the International Coastal Engineering Conference. These two events practically ushered in the modern era of wind wave studies, and on this Silver Conference of ICCE it is interesting to pay a return visit to Sverdrup and Munk's wave growth curves given in H.O. 601 and to compare them with the

¹GLERL Contribution No. 1034

²NOAA Great Lakes Environmental Research Laboratory, Ann Arbor, MI 48105-1593. Email: liu@glер1.noaa.gov

recent study of wave growth curves given by Donelan et al. (1992). This paper summarizes the essentials of the development of the two growth curves 50 years apart to show the differences in general approaches and the significance of the conceptual basis of H.O. 601 that prevails over time and still appears refreshing in light of modern achievements.

The Wave Growth Curves According to Sverdrup and Munk

When Sverdrup and Munk set out to develop techniques for wave forecasting in the early 1940's in support of U.S. amphibious operations during World War II, the state of knowledge at the time was based mainly on empirical relationships. Notable results such as that maximum wave heights are proportional to the square root of the fetch and that wave height is proportional to the wind speed or the square of the wind speed, all dependent on dimensional constants.

Sverdrup and Munk started the initial efforts to realistically model the wind waves by examining the growth of waves on the basis of energy considerations. They formulated the fetch equation as

$$\frac{c}{2} \frac{dE}{dx} + \frac{E}{2} \frac{dc}{dx} = R_t + R_v$$

where E is the mean energy per unit surface area, c is the wave phase speed, and R_t and R_v are the energy transferred to the waves at the sea surface due to the tangential stress and normal pressure of wind, respectively.

By formulating the physical considerations of R_t and R_v , incorporating measured information available at the time, and normalizing significant wave height, H , wave phase speed, c , and fetch, x , with wind speed, U , and gravitation acceleration, g , they were able to derive analytical expressions for dimensionless wave height, gH/U^2 , and dimensionless wave speed, c/U , (the wave age,) as functions of dimensionless fetch, gx/U^2 .

In essence they focused on the two basic parameters, the wave age $\beta = c/U$ and the wave steepness $\delta = H/L$, L is the wave length, where empirical functional relationships between the two can be deduced from the above fetch equation. They then derived three separate expressions for gx/U^2 in terms of β and δ over three divided ranges of β . Wave height relations were then obtained in the dimensionless form from linear theory as

$$\frac{gH}{U^2} = 2\pi\delta\beta^2 = f\left(\frac{gx}{U^2}\right).$$

Following these developments, the final analytical expressions given in H.O. 601 also included no less than 17 empirical constants. These growth curves are plotted in Figure 1 as thin solid lines along with the historical data originally used.

The developments of Sverdrup and Munk clearly set the stage for modern wind wave prediction and study. Their innovative introduction of the concept of *significant waves* based on statistical considerations is still the most basic and effective parameter used in characterizing wave field parameters. One might conclude that is also part of Sverdrup and Munk's innovations. However, the use of dimensionless parameters was actually suggested to Sverdrup and Munk by Morrough P. O'Brien based on intuitive understanding of fluid mechanics and knowledge of similitude and model laws² (Wiegel and Saville, 1996.) The practice of correlating dimensionless parameters gH/U^2 and c/U with respect to gx/U^2 is still widely used today as part of the basic analysis of wind and wave measurement.

²The author is indebted to Prof. Wiegel for pointing out this important historical fact to him.

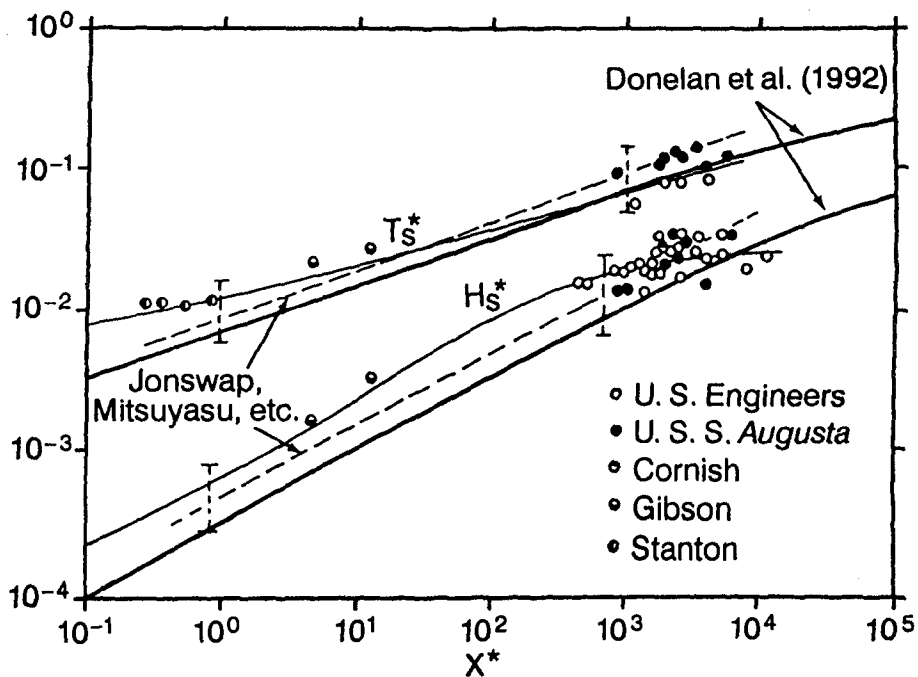


Figure 1. H.O. 601 growth curves and data as compared with later and more recent developments. The original H.O. 601 curves are shown as thin solid lines. The results of JONSWAP, Mitsuyasu, and others are summarized in dashed lines as given in Hasselmann (1982). The results of Donelan et al. (1992) are shown as the thick solid curves. Nondimensional significant wave height, H_s^* , and wave period, T_s^* , are plotted as functions of nondimensional fetch, X^* .

An Ode to H.O. 601

Sverdrup and Munk prepared the H.O. 601 that established the physical foundations for wind wave predictions and subsequent wave studies. Bretschneider (1952) made further analysis with additional data and developed practical curves that became the widely used SMB (Sverdrup-Munk-Bretschneider) method of wave forecasting. With the advance of spectrum analysis in the 1950's and increasing use of computers in the 1960's, along with new instrumentation and measurement techniques, new approaches have subsequently evolved. But the basic principles implemented in H.O. 601 have been continuously practiced, some maybe unwittingly, by most of the later wind wave analysis and model developments.

Hasselmann (1984) in an article that pays tribute to Walter Munk's 65th birthday, entitled "An Ode to H.O. 601," presented a comparison of the H.O. 601 growth curves with modern data of JONSWAP program (Hasselmann et al., 1973) and Mitsuyasu (1969) as shown in Figure 1. He commended the legacy of H.O. 601 and concluded that "The progress in measurement techniques has clearly been commensurate with the progress in wave modeling." More recent modeling developments (Komen et al., 1994) appear to substantiate this effect.

The Wave Growth Curves of Donelan et al.

The work of Donelan et al. (1992) provides an interesting account of the current state of the art of the wave growth curve studies. They explored the fetch-limited wind wave growths, using the wind and wave measurements from a linear array of five towers located along the prevailing wind direction on the eastern shore of Lake St. Clair, and found the differential growth of spectral wave energy between the towers, $\Delta E / \Delta x$, to be a linear function of local wave age, U / c_p , where U is the wind speed, and c_p the phase speed of the waves at the spectral peak as:

$$\frac{c_p^2}{2gE} \frac{\Delta E}{\Delta x} = 0.78 \times 10^{-4} \left(\frac{U}{c_p} - 0.83 \right).$$

Note that the right-hand side vanishes at $U/c_p = 0.83$, which is the well-established condition for a fully development wave field (Pierson and Moskowitz 1964.) Now combining the differential equation with that of the well-known empirical relation between nondimensional energy, $\varepsilon = g^2 E / U^4$, and wave age substantiated by most of the measurements made from many parts of the world:

$$\varepsilon = 0.0023 \left(\frac{U}{c_p} \right)^{-3.2},$$

readily yields the following fetch relations:

$$X^* = 4.0946 \times 10^4 \ln \left[\frac{1}{1 - 5.5414 \varepsilon^{\frac{1}{3.2}}} \right] - 2.2690 \times 10^5 \left[1 + 2.7707 \varepsilon^{\frac{1}{3.2}} \right] \varepsilon^{\frac{1}{3.2}},$$

and

$$X^* = 4.0946 \times 10^4 \ln \left[\frac{\frac{U}{c_p}}{\frac{U}{c_p} - 0.8302} \right] - 3.3992 \times 10^5 \left[\frac{U}{c_p} + 0.4151 \right] \left[\frac{c_p}{U} \right]^2.$$

where X^* is the nondimensional fetch gx/U^2 . The corresponding results of these two equations are also plotted as the thick solid lines in Figure 1 in which $H_s^* = 4g\sqrt{\varepsilon}/U^2$ and $T_s^* = c_p/U$ are used to facilitate the comparison with original H.O. 601 curves. An examination of Figure 1 indicates that the results of Donelan et al. (1992) are lower than the H.O. 601 curves, but reach the fully developed stage much later.

In general, however, while data measurement and analytic modeling have made significant progress over the past 50 years, the ingenuity of Sverdrup and Munk's original development with very limited available data not only helped the Allied forces during the North Africa operations that led to WW II victory, but also remained reasonably close to the modern and latest measurements.

Concluding Remarks

For the most part, the wave growth curve developments of Sverdrup and Munk and that of Donelan et al. (1992) are basically similar. Both are basically started on available measured results followed by analytical derivations. With limited data Sverdrup and Munk's development required 17 constants for the operation. Donelan et al., however, with much more and better established data and analysis relied on four empirical constants. The current state of the art of wind wave modeling as given in the comprehensive book by Komen (1994) cautioned that "Despite the progress, we still are not able to make wave predictions that always fall within the error bands of the observations." It appears that after 50 years development and progress on wave modeling and wind wave studies, while wave modeling techniques have made significant progress for practical applications, there is ample room of further progress and enhancement remain to be explored.

References

Bretschneider, C. L. (1952), Revised wave forecasting relationships, Proc., 2nd Conf. Coastal Eng, Council Wave Research, Engineering Foundation, Berkeley, CA, 1-5.

Donelan, M. A. et al. (1992), On the growth rate of wind-generated waves, Atmosphere-Ocean, **30**, 457-478.

Hasselmann, K. (1984), The science and art of wave prediction - An ode to HO 601, in A Celebration in Geophysics and Oceanography - 1982, Scripps Institution of Oceanography Reference Series **84-5**, 31-37.

Hasselmann, K. et al. (1973), Measurements of wind-wave growth and swell decay during the Joint North Sea Project (JONSWAP), Deutsche Hydrogr. Z., **12**.

Komen, G. J. et al. (1994), Dynamics and Modelling of Ocean Waves, Cambridge University Press, 532p.

Mitsuyasu, H. (1968/1969), On the growth of the spectrum of wind-generated waves, Rep. Res. Inst. Appl. Mech., Kyushu Univ., **16/17**.

Pierson, W. J. and L. Moskowitz (1964), A proposed spectrum form for fully developed wind seas based on similarity theory of S. A. Kitaigorodskii, J. Geophys. Res., **69**, 5181-5190.

Sverdrup, H. U. and W. H. Munk (1947), Wind, Sea and Swell: Theory of relations for forecasting, U. S. Navy Hydrographic Office, H. O. Publ. No. **601**.

CHAPTER 37

DEVELOPMENT OF A THIRD GENERATION SHALLOW-WATER WAVE MODEL WITH UNSTRUCTURED SPATIAL MESHING

Michel BENOIT ¹, Frédéric MARCOS ¹, Françoise BECQ ²

Abstract

A numerical third-generation wave model dedicated both to deep water and near-shore applications is presented and applied to several test-cases to highlight its capabilities. Among its main features, this model uses a finite-elements technique for the discretization of the modelled area, which makes it suitable to represent complex bottom topographies and irregular shorelines. Furthermore, the piece-wise ray method used for wave propagation allows to use rather large time-steps, which in turn allows to keep the computational time at a very moderate level. The implementation of shallow-water physics in the model is also described, in particular with respect to depth-induced breaking. Several applications of the model are presented and compared to field or laboratory data for their validation. Finally, the main research and development items are mentioned and discussed.

1. INTRODUCTION

Although originally developed for deep water applications and meteorological purpose (e.g. WAMDI Group, 1988), spectral “phase-averaged” wave models are presently being extended towards the near-shore and coastal domains. This extension implies first to improve the physics of the numerical models so that they become able to reproduce shallow-water effects. Several efforts have already been attempted in this way by developing numerical formulations for bottom friction, depth-induced breaking and non-linear interactions between triplets of waves (the so-called “triad-interactions”) (e.g. Ris *et al.*, 1994 ; Van Vledder *et al.*, 1994).

A second point to consider is the ability of the model to deal with the complex bottom topography of coastal and near-shore areas. Compared to oceanic applications, these shallow-water domains usually need a finer spatial discretization to properly represent bathymetric gradients and irregular shorelines. This requires a number of properties from the numerics of the wave model (discretization techniques, integration schemes) which are usually not encountered in present third-generation wave models. For instance, if one wishes to apply the WAM model to local areas, the size of the finite-difference spatial grid has to be decreased over the whole domain, which highly increases the number of computational points and

¹ Research Engineer — Maritime Group

² PhD Student — Maritime Group

EDF - Laboratoire National d'Hydraulique, 6, quai Watier 78400 CHATOU, FRANCE

often leads to use nested grids. Furthermore, the explicit scheme for wave propagation in WAM will then imply a strong decrease of the time-step in order to ensure that the Courant Number remains lower than 1. This, in turn, will cause a significant increase of the computational time, so that the computation will likely become unrealistic at an operational stage.

This paper deals with the development of a third generation spectral wave code applicable to deep water oceans, but also dedicated to shallow-water domains. This model, named TOMAWAC (which stands for "TELEMAC-based Operational Model Addressing Wave Action Computation"), is included in the TELEMAC modelling package developed by LNH, which contains numerous finite elements modules covering a wide range of maritime hydrodynamics applications.

The TOMAWAC model is presented in Section 2. Special attention to the implementation and validation of depth-induced breaking is paid in Section 3. Section 4 presents the application of the model on a test-case of waves propagating on a current whirl. In Section 5, the model is applied to the simulation of an actual storm in the North-eastern part of the Atlantic Ocean and in the Channel. Finally, present and future research items are presented and discussed in Section 6.

2. PRESENTATION OF TOMAWAC WAVE MODEL

2.1 Main modelling equations of TOMAWAC

TOMAWAC solves the wave action conservation equation (or wave action balance equation) in spherical or Cartesian co-ordinates for infinite or finite water depth. The wave action density N is defined as the ratio of directional variance density F to relative (or intrinsic) angular frequency σ : $N = F / \sigma$.

The directional variance density $F(f, \theta)$ corresponds to the "classical" directional spectrum of waves and models the way the wave energy (or variance) spreads over frequency f and direction θ .

In the presence of a current field \vec{U} , the action density is conserved (Bretherton and Garret, 1968). This leads to the following equation for the variance density $F(x, y, f_r, \theta, t)$, expressed in TOMAWAC as a function of time t , spatial Cartesian co-ordinates x and y , direction of propagation θ and relative frequency f_r :

$$\frac{\partial(B.\tilde{F})}{\partial t} + C_x \frac{\partial(B.\tilde{F})}{\partial x} + C_y \frac{\partial(B.\tilde{F})}{\partial y} + C_\theta \frac{\partial(B.\tilde{F})}{\partial \theta} + C_{f_r} \frac{\partial(B.\tilde{F})}{\partial f_r} = B.Q \quad (1)$$

$$\text{with : } F(f, \theta) = \frac{C_g}{C_g + \vec{U} \cdot \vec{k} / k} \tilde{F}(f_r, \theta)$$

The absolute angular frequency $\omega = 2\pi.f$ (as observed in a fixed frame of reference) is related to the relative angular frequency $\sigma = 2\pi.f_r$ (as observed in a frame moving with the speed \vec{U}) by the Doppler equation: $\omega = \sigma + \vec{k} \cdot \vec{U}$, where \vec{k} is the wave-number vector, as given by the dispersion relation for linear waves as a function of water depth d : $\sigma^2 = g k \tanh(k.d)$

The transfer rates in space, direction and relative frequency are computed according to the linear wave theory :

$$\begin{aligned} C_x &= C_g \cdot \sin \theta + U_x & C_\theta &= -\frac{1}{k} \frac{\partial \sigma}{\partial d} \frac{\partial d}{\partial \vec{n}} - \frac{\vec{k}}{k} \cdot \frac{\partial \vec{U}}{\partial \vec{n}} \\ C_y &= C_g \cdot \cos \theta + U_y & C_{f_r} &= \frac{1}{2\pi} \left(\frac{\partial \sigma}{\partial d} \left(\frac{\partial d}{\partial t} + \vec{U} \cdot \text{grad } d \right) - C_g \vec{k} \cdot \frac{\partial \vec{U}}{\partial \vec{s}} \right) \end{aligned}$$

\vec{n} is the direction perpendicular to wave propagation direction and \vec{s} corresponds to the direction of propagation (given by θ). The coefficient B results from the fact that the conservation equation must be basically written for the action density expressed as a function of wave number : $B = C.C_g / (2\pi \sigma^2)$.

$C = \sigma / k$ and $C_g = \partial \sigma / \partial k$ are the phase and group speeds respectively.

The TOMAWAC model is unsteady (variable wind forcing conditions usually given by the wind-speed 10 m above the sea surface), but the current field U is assumed to be steady in version 1.2 of the code, as well as the water depth.

2.2 Modelisation of source and sink terms in TOMAWAC

In the Q term at the right-hand side of the balance equation (1), TOMAWAC 1.2 operationally includes the following physical processes : generation by wind (Q_{in}), dissipation by white-capping (Q_{wc}), bottom friction (Q_{bf}) and depth-induced breaking (Q_{br}), non-linear interactions between quadruplets of frequencies (Q_{nl4}). For each of these processes, several state-of-the-art formulations, calibrated against data from experimental campaigns in the field, are available in TOMAWAC and summarized in Table 1. The presentation of all the formulations is clearly out of the scope of this paper and can be found in the mentioned references. However, a more detailed presentation of depth-induced breaking is given in Section 3. In addition to these processes, a term modelling the non-linear transfers between triads of waves in shallow water (Eldeberky and Battjes, 1995) is presently under development and will be soon operational for use.

	<i>Formulation 1</i>	<i>Formulation 2</i>	<i>Formulation 3</i>
Q_{in} wind input	Janssen (1991)	Snyder <i>et al.</i> (1981) + u^* from drag law	Snyder <i>et al.</i> (1981) + u^* from Charnock
Q_{wc} white-capping	Komen <i>et al.</i> (1984)	Janssen (1991)	
Q_{nl4} quadruplets	Hasselmann <i>et al.</i> (1985)	Webb (1978) (<i>under development</i>)	
Q_{bf} bot. friction	Bouws and Komen (1983) + JONSWAP	Madsen <i>et al.</i> (1988)	Christoffersen and Jonsson (1985)
Q_{br} surf-breaking	Battjes and Janssen (1978)	Thornton and Guza (1983)	Roelvink (1993)

Table 1 : Review of source and sink terms available in TOMAWAC 1.2.

2.3 Numerical aspects of TOMAWAC

2.3.1 Spatial and spectral discretizations

Finite elements spatial discretization

Spectral wave models usually use finite differences grids for spatial meshing. This may however become a limitation for nearshore applications, where complex bathymetry and irregular shoreline often require a refined resolution. As already mentioned in the introduction, the first solution to this problem is to use nested grids, but this implies an heavy management of input/output files, complicates programming and significantly increases the computational effort.

The finite elements technique used in TOMAWAC (and in all the models of the TELEMAC system as well) overcomes this problem quite elegantly because the user can determine locally the size of the mesh and then optimize the number of nodes according to the accuracy expected in the various parts of the computational domain. The maritime area to be modelled is then discretized in a number of triangular elements whose size may be varied according to the desired resolution. This unique feature allows for instance to have on a same grid large oceanic areas (with mesh size in the order of several hundreds of kilometres) and nearshore areas (with mesh size in the order of one kilometre or less). Examples of spatial grids used by TOMAWAC are given in the following sections of this paper dealing with applications and validation test-cases.

Directional-spectral discretization

The range $[0 ; 2\pi]$ of wave directions is discretized in a number of equally spaced directions. This number of directions usually lies between 12 ($\Delta\theta = 30^\circ$) and 72 ($\Delta\theta = 5^\circ$). The discretized frequencies follow a logarithmic distribution ($f_{i+1} = (1+\epsilon).f_i$). The number of frequencies usually lies between 15 and 30. This results in a directional-spectral grid for the directional wave spectrum which is regular over directions and logarithmic over frequencies.

2.3.2 Numerical schemes

The wave action balance equation is solved in TOMAWAC by a fractional step method, including :

- a convection step (left-hand side of the balance equation (1)) :

$$\frac{\partial(B \cdot \tilde{F})}{\partial t} + \vec{V} \cdot \overrightarrow{\text{grad}}(B \cdot \tilde{F}) = 0 \quad \text{with : } \vec{V} = (C_x; C_y; C_\theta; C_{fr})$$

- and a source terms integration step (right-hand side of the equation (1)) :

$$\frac{\partial(B \cdot \tilde{F})}{\partial t} = B \cdot Q \quad \text{which reduces to : } \frac{\partial \tilde{F}}{\partial t} = Q \quad \text{as B is independent of time.}$$

Propagation step :

The convection step is treated by a piece-wise ray method or method of characteristics. Due to the fact that the convective field is stationary, the characteristics curve have to be computed only once, at the beginning of computation. The results are stored in computer memory. At each time step, the convection step is thus reduced to an interpolation, which allows to save a good amount of computing time.

Source terms step

The source terms integration is carried out through a weighted implicit scheme :

$$\frac{\tilde{F}^{n+1} - \tilde{F}^*}{\Delta t_s} = \alpha \cdot Q^* + (1-\alpha) \cdot Q^{n+1}$$

where \tilde{F}^* is the value of the variance spectrum after the propagation step and Q^* represent the value of source-terms based on \tilde{F}^* .

Choosing $\alpha = 0$ ($\alpha = 1$) makes the scheme fully implicit (explicit). In one selects $\alpha = 0.5$, this scheme reduces to the semi-implicit scheme used in the WAM model (WAMDI Group, 1988).

2.3.3 Vectorization

TOMAWAC is fully vectorized and may be run either on super-computers or on workstations, depending on the size of the computational domain.

3. IMPLEMENTATION OF DEPTH-INDUCED BREAKING IN TOMAWAC

The modelling in TOMAWAC of energy dissipation due to depth-induced breaking is achieved by solving two successive problems : (i) estimation of the total energy dissipation due to breaking for the whole directional wave spectrum and (ii) distribution of this total dissipation over both frequencies and directions.

(i) Total dissipation of wave energy due to breaking:

The transformation of statistical parameters of an incident random wave train across the surf zone can be basically treated by two classes of models both based on the wave energy balance. The “probabilistic models” are based on a wave-by-wave approach (e.g. Dally, 1992) and offer a detailed description of the transformation of wave height distribution. This type of models was however not selected in TOMAWAC because of their important computational cost. The second class of models, the so-called “parametric models”, assumes that the wave height distribution $p(H)$ and the breaking probability conform to distributions whose shapes are *a priori* known all along the bathymetric profile. By combining these distributions with a dissipation rate per breaking wave, the total dissipation term \bar{D} is obtained as a function of local wave and bathymetric parameters. As mentioned in Table 1, three such parametric models together with a model based on turbulence considerations for monochromatic waves have been implemented in TOMAWAC :

- Battjes and Janssen (1978) model (BJ78) : The authors assume that the local depth limits the wave heights in the distribution to a maximum height H_m which is a function of water depth and incident conditions (Miche criterion). So the wave height distribution follows a Rayleigh distribution clipped at $H=H_m$. All the waves having a wave height of H_m are assumed to break. The dissipation rate per unit area for a breaking wave is evaluated by using the analogy with an hydraulic jump. As the breaking wave height H_m is assumed to be in the order of water depth, the combination with the fraction of breaking waves Q_b leads, after algebraic manipulations, to the formulation for the breaking dissipation rate:

$$\bar{D} = \frac{\alpha}{4} f_p \rho g H_m^2 Q_b \quad \text{with } \alpha = 1$$

H_m is given by : $H_m = \frac{0.88}{k} \tanh\left(\gamma \frac{k \cdot d}{0.88}\right)$ with $0.5 < \gamma < 0.8$

Note that in shallow-water the above criterion reduces to : $H_m = \gamma \cdot d$.

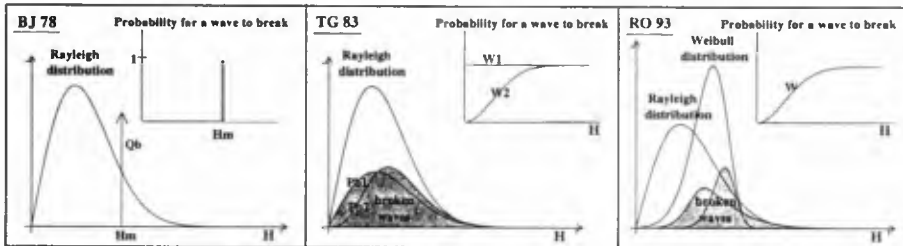


Figure 1 : Schematic diagram of parametric surf-breaking models.

- Thornton and Guza (1983) model (TG83) : Based on field observations, the authors assume a Rayleigh distribution for the wave heights even in the surf zone, but propose two different formulations for the breaking probability. The first one assumes that all waves may break with the same probability, so the repartition of breaking waves, $p_{b1}(H)=W_1(H) \cdot p(H)$ is directly proportional to the Rayleigh distribution (figure 1.b). As, in general however, the largest waves of the

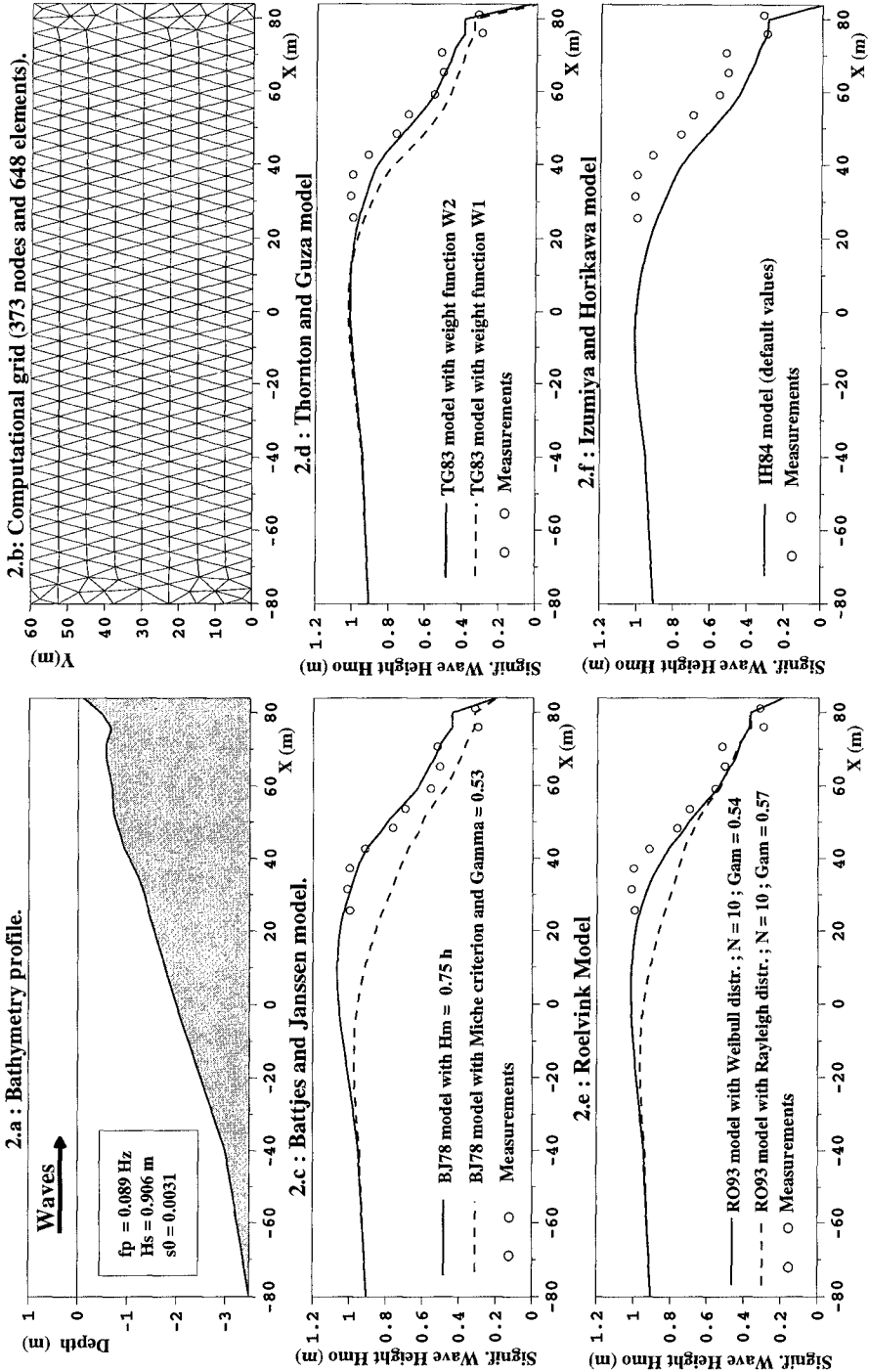


Figure 2 : Application of TOMAWAC wave model to case DUCK 41510 - Validation of surf-breaking models

distribution are more likely to break, another formulation W_2 (leading to $pb_2(H)$) is formulated. The average dissipation rates are obtained by combining $p_b(H)$ with a dissipation rate per breaking wave (based on bore theory) :

$$\bar{D}_1 = \frac{3\sqrt{\pi}}{16} B^3 \rho g f_p \frac{H_{rms}^7}{H_m^4 h} \quad \text{and} \quad \bar{D}_2 = \frac{3\sqrt{\pi}}{16} B^3 \rho g f_p \frac{H_{rms}^5}{H_m h} \left[1 - \left(1 + \left(\frac{H_{rms}}{H_m} \right)^2 \right)^{-5/2} \right]$$

• Roelvink (1993) model : The originality of this model lies in the use of two different functions for the distribution of wave heights, namely a Rayleigh and a Weibull distributions. The breaking probability is close to the second formulation of the TG83 model where the H_{rms} dependence is suppressed. The average dissipation terms \bar{D} then read (m and A depend on local wave parameters) :

$$\bar{D}_{Weibull} = \frac{\alpha}{2} \rho g f_p m A H_{rms} \int_0^{\infty} \left(\frac{H}{H_{rms}} \right)^{2m+1} \exp \left[-A \left(\frac{H}{H_{rms}} \right)^{2m} \right] \left[1 - \exp \left(- \left(\frac{H}{\gamma h} \right)^n \right) \right] dH$$

$$\bar{D}_{Rayleigh} = \frac{\alpha}{2} \rho g f_p H_{rms} \int_0^{\infty} \left(\frac{H}{H_{rms}} \right)^3 \exp \left(- \left(\frac{H}{H_{rms}} \right)^2 \right) \left[1 - \exp \left(- \left(\frac{H}{\gamma h} \right)^n \right) \right] dH$$

• Izumiya and Horikawa (1984) model (IH84) : this model is based on the Reynolds equations and was developed for monochromatic waves propagating over a bathymetry profile. The breaking dissipation term is expressed as a function of wave energy E :

$$D = -\beta_0 \left(\frac{Cg}{C} \frac{E}{\rho g h^2} - M_{*s}^2 \right)^{1/2} \frac{E^{3/2}}{\rho^{1/2} d^{3/2}} \left(\frac{2Cg}{C} - 1 \right)^{1/2}$$

where M_{*s}^2 is a stable wave criterion (about $0.9 \cdot 10^{-2}$) and $\beta_0 = 1.8$.

(ii) Distribution of total dissipation over both frequencies and directions :

No directional dependence has been demonstrated until now, so the discussion will be restricted to the frequency dependence. Vincent *et al.* (1994) have analyzed laboratory data for the evolution of single-peaked spectra along a monotonic bathymetry profile. The normalised energy loss was found to be quite independent of frequency allowing the assumption that the spectral distribution of energy dissipation is directly proportional to the energy density, so that :

$$Q_{br}(f, \theta) = -\bar{D}(m_0, f_p, d) \frac{F(f, \theta)}{m_0} \quad \text{with} \quad m_0 = \int_0^{\infty} \int_0^{2\pi} F(f, \theta) df d\theta$$

Experiments from Beji and Battjes (1993) for waves propagating over a bar also indicate the same trend, leading to the above state-of-the-art method currently used in other wave models (Ris *et al.*, 1994 ; Van Vledder *et al.*, 1994).

On the other hand, Mase and Kirby (1992) observed in their laboratory experiments a frequency dependence of the breaking dissipation. They proposed to add a quadratic dependence on frequency, so that :

$$Q_{br}(f, \theta) = -(a_0 + f^2 a_1) \cdot F(f, \theta) \quad \text{with} \quad \bar{D}(m_0, f_p, d) = \int_0^{\infty} \int_0^{2\pi} (a_0 + f^2 a_1) \cdot F(f, \theta) df d\theta$$

As, from the observations, a linear dependence on frequency could not be excluded, both the quadratic and linear dependences have been implemented in TOMAWAC (in addition to the above classical approach neglecting any frequency dependence). The inclusion of the frequency dependence for the breaking sink term does not significantly modify the evolution of the significant wave height along the

profile. As expected however, the mean frequency is found to decrease when a quadratic dependence of frequency is activated. Indeed the higher frequencies of the spectrum are more concerned by breaking dissipation, shifting the spectral shape towards the lower frequencies. However, such a behaviour can not be validated solely, but must be analysed in conjunction with (in particular) triad interactions, which play a central role in the energy flux between the spectral components in shallow water.

(iii) Example of validation of depth-induced breaking in TOMAWAC model :

A field experiment was conducted on September 4-6, 1985, at the Field Research Facility of the U.S. Army Coastal Engineering Research Center (CERC) in Duck, North California (Ebersole and Hughes, 1987). The case presented below was recorded on September 4, 15:10 hrs (41510). The wave conditions imposed at the seaward boundary for the application of TOMAWAC are summarized on figure 2.a. The numerical simulations were carried out for the bathymetry profile shown on figure 2.a with a computational grid of approximately constant mesh (figure 2.b). The surf-breaking dissipative term was assumed to be frequency independent.

The TOMAWAC results (figures 2-c to 2-f) show that all breaking models are able to correctly reproduce the significant wave height variations along the bathymetry profile. BJ78 model was used in a first run with a value of γ determined from the Battjes and Stive (1984) formulation ($\gamma=0.53$) and with the Miche criterion for the computation of H_m (Figure 2.c). This results in an overestimation of the dissipation. In fact, Battjes and Stive formulation is not efficient for low values of steepness s_0 . This test-case requires to increase γ up to 0.75, which gives quite good results. The use of the weighting function W_2 in TG83 model gives better results on this experiment than W_1 (figure 2.d), even if it does not well reproduce the wave height enhancement observed before breaking. RO93 model gives too much dissipation with the Rayleigh distribution (figure 2.e), but the use of the Weibull distribution improves the results. The IH84 model is also too much dissipative (figure 2.f), but partly reproduces the wave height enhancement before breaking.

4. WAVES PROPAGATING OVER A CURRENT WHIRL

This computation has to show the capability of TOMAWAC to represent wave-current interactions on a realistic (although schematic) case of a current eddy. This case was proposed by Mathiesen (1987) as fairly representative of the whirls sometimes occurring in the nearshore zone.

4.1 Description of the test case

The spatial domain is a square of 80 km (figure 3). We consider an idealised circular whirl, centered on the origin :

- The tangential current velocity increases linearly from zero at the center of the whirl : $u(r) = u_1 \frac{r}{r_1}$ for $r \leq r_1 < r_0$

- Further away from the whirl center, the current follows a gaussian profile :

$$u(r) = u_{\max} \exp \left[- \left(\frac{r - r_0}{b r_0} \right)^2 \right] \text{ for } r > r_1$$

For this run, $u_{\max} = 1$ m/s, $r_0 = 10$ km and $b = 0.3$, which leads to $r_1 = 9.5277$ km.

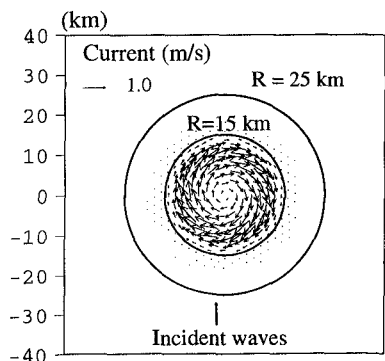


Figure 3 : Definition sketch and current field for the whirl test-case.

Mathiesen (1987) developed a semi-analytical model for this refraction problem using a ray tracing technique. This technique can be carried out upward or backward. Mathiesen used the backward ray method to determine the point (x,y,f,θ) where the energy originates to reach the point of interest. Such computations were performed for different wave frequencies and directions in order to build a complete wave spectrum. Therefore, his results can be compared with those of TOMAWAC.

The input offshore directional wave spectrum, chosen by Mathiesen (1987), is written in the form : $F(f,\theta) = S(f).D(f,\theta)$ where $S(f)$ is the frequency spectrum and $D(f,\theta)$ is the directional spreading function. The frequency spectrum is a classical JONSWAP spectrum with a peak frequency f_p equal to 0.1 Hz. $D(f,\theta)$ is based a Gaussian-shaped directional distribution :

$$D(f,\theta) = \frac{1}{\sqrt{2\pi}\sigma_0} \exp\left(-\frac{(\theta - \theta_m)^2}{2\sigma_0^2}\right)$$

θ_m is the mean incident wave direction (here $\theta_m = 0$) and σ_0 is the circular standard deviation given by the following expression :

$$\sigma_0 = \sigma_{0p} \left(\frac{f}{f_p}\right)^{-2.03} \quad \text{if } f < f_p$$

$$\sigma_0 = \sigma_{0p} \left(\frac{f}{f_p}\right)^{1.04} \quad \text{if } f \geq f_p$$

where $\sigma_{0p} = \sigma_0(f_p) = 25^\circ$

The water depth is supposed to be constant at 200 m. The computation is achieved with Cartesian co-ordinates, without any source term ($Q=0$). The mesh used consists of 1876 points and 3590 elements of about 2 km on one side.

4.2 Results and discussion

Several computations were performed with TOMAWAC, using different time-steps and different directional resolutions. Only the results obtained with a time-step of 1200 s and a directional resolution of 7.5° will be presented below. The 25 discretized frequencies range from 0.04 Hz to 0.4 Hz (geometrical factor 1.1). The computed normalised significant wave height is given on figure 4. We can clearly see two zones where wave heights are enhanced separated by a zone where they are decreased. The greatest increase in wave height is obtained when waves propagate against the current while the greatest decrease is observed when they go the same way. The variations of significant wave height remain in the range $\pm 30\%$.

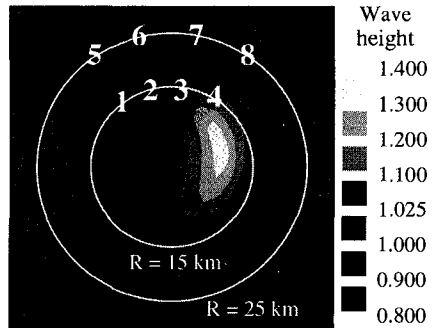


Figure 4 : Map of normalised significant wave height

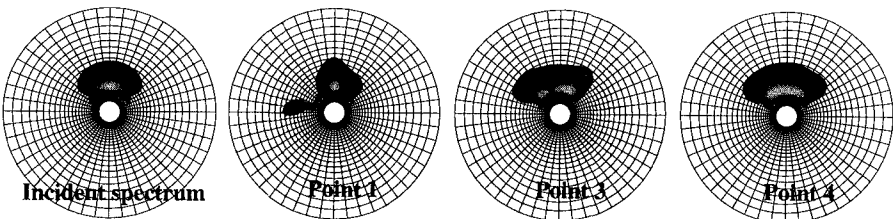


Figure 5 : Computed directional wave spectra at various locations

Figure 5 shows the wave spectra computed at various locations. We can see the presence of crossing seas, with several directional peaks in the spectrum, especially at points n°1 and 3. The directional distribution of wave energy is very inhomogeneous on this test-case. On figure 6, the directional spectra at $f = 0.1$ Hz are plotted for the eight points presented in figure 4. Mathiesen (1987) gives similar results with his model whose directional discretization (2.5°) was finer than ours. The TOMAWAC results compare very satisfactorily with the semi-analytical solution. The model thus appears to be able to reproduce the main features of the directional spectra, although they have a quite complex shape at several locations.

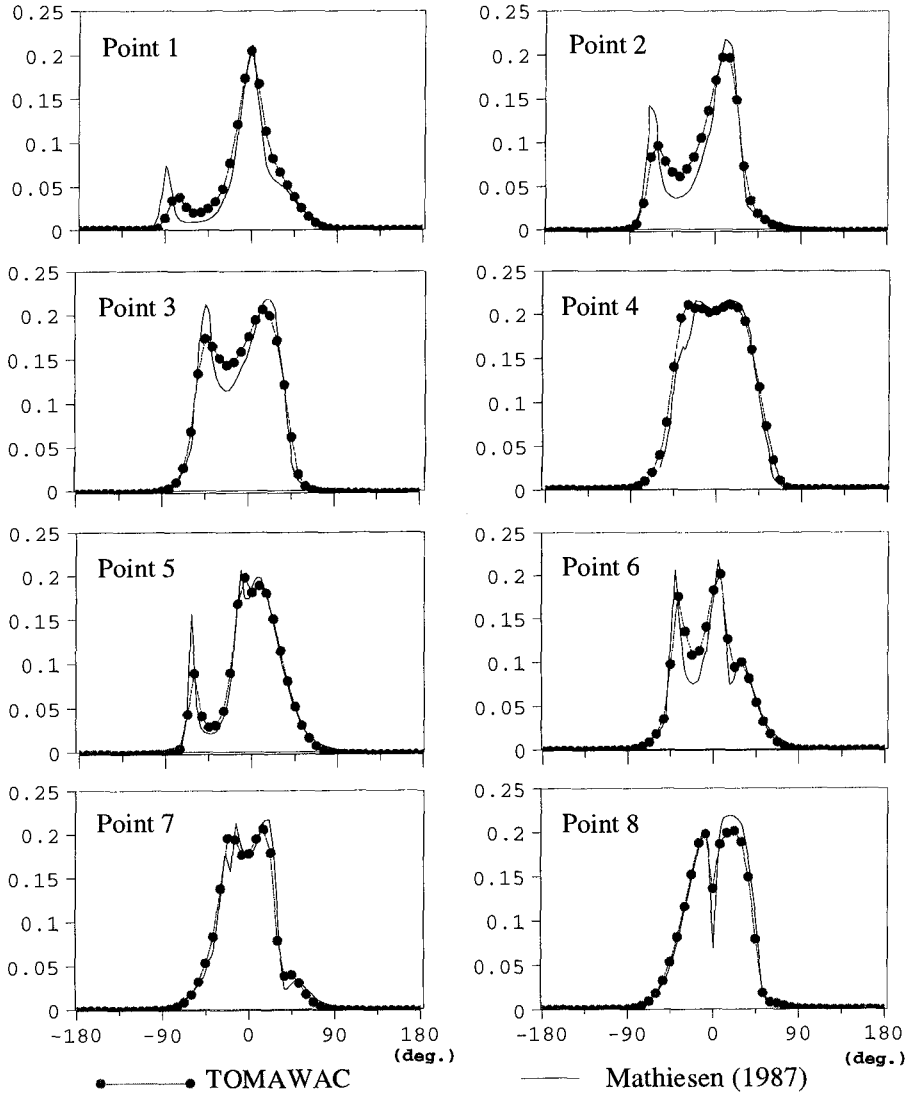


Figure 6 : Directional spectra at $f = \text{fp} = 0.1$ Hz - Comparison with Mathiesen (1987) model

5. SIMULATION OF THE STORM OF JANUARY 25, 1990 IN THE CHANNEL

Of all the storms to hit the Atlantic coast of France during the winter of 1989-1990, the one on January 25, 1990 was one of the most violent, with winds of force 9 to 11 (on the Beaufort scale) over French Brittany. On this particular day, the strongest gust of wind recorded at the Hague signal station was measured at 46 m/s (166 km/h). The winds blew continuously from the West, which was particularly conducive to the formation of strong waves to the West of Cotentin, and on that day, the buoys located at Ouessant registered wave heights of over 16 metres !

The period chosen for computer simulation with TOMAWAC runs from January 16 to 30, 1990, with a time-step of 5 minutes. The computational mesh consists of 6 205 nodes and 11 444 triangular elements (figure 7). The broadest meshes cover approximately 40 km on the grid boundaries, whereas the most refined ones cover less than 5 km in the English Channel. The directional wave energy spectrum has been discretized into 25 frequencies and 12 directions. The windfields (two horizontal components of the 10 m wind-speed) were provided every 6 hours from the French meteorological model results. Boundary conditions were provided by a previous simulation performed on a coarser grid covering the Northern part of the Atlantic Ocean. All source terms, including surf-breaking, were activated for this computation. The simulation was carried out without taking tidal effects into account. It required less than two hours of computing time on a Cray C98 computer for modelling an actual duration of 14 days.

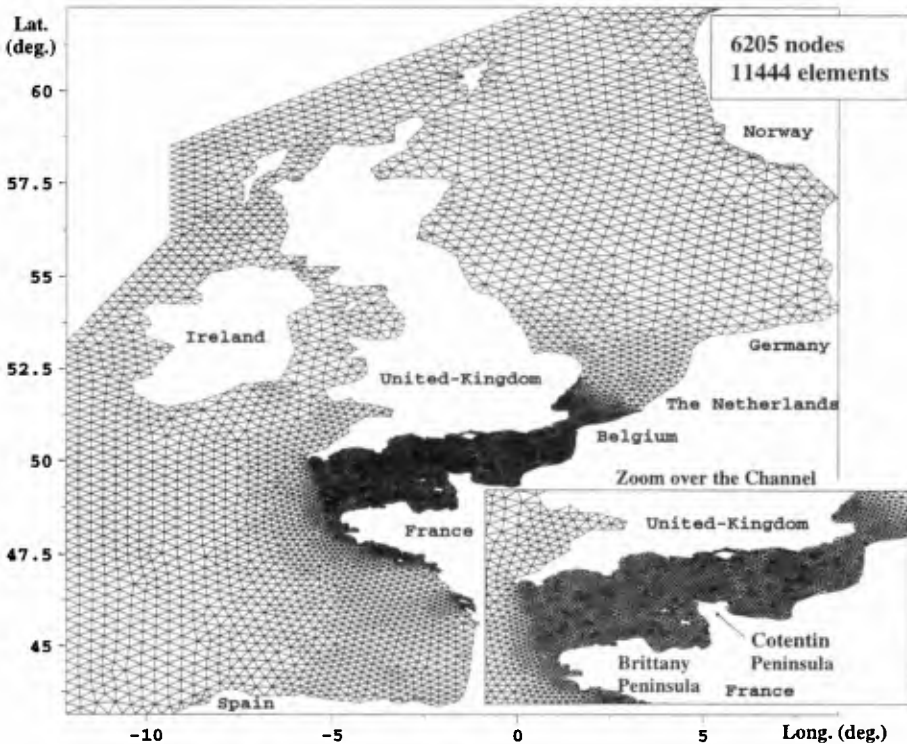


Figure 7 : Grid used for the simulation of the storm of January 25, 1990.

Figure 8 shows a chart of significant wave heights computed at the paroxysm of the storm, along with the energy spectra at the same moment at various points in the Channel. We can see that the storm's maximum intensity occurs close to the West Brittany. The further we move into the Channel, the smaller the wave heights, even though heights still manage to reach 5.5 m to the West of Cotentin (Flamanville). To validate the simulation, computational results are compared with the buoy measurements at Ouessant and Flamanville on figure 9. On both places, numerical results compare quite satisfactorily to buoy data. Furthermore, it appears from figure 8 that wave breaking significantly contributes to decrease the wave heights along the coasts of the French Brittany Peninsula.

The TOMAWAC model thus gave a good overall account of itself as far as reproducing the height of the waves was concerned, even though it slightly underestimated the January 25, 1990 peak at Ouessant. The mean periods are also fairly well reproduced, despite being generally rather overestimated by the code.

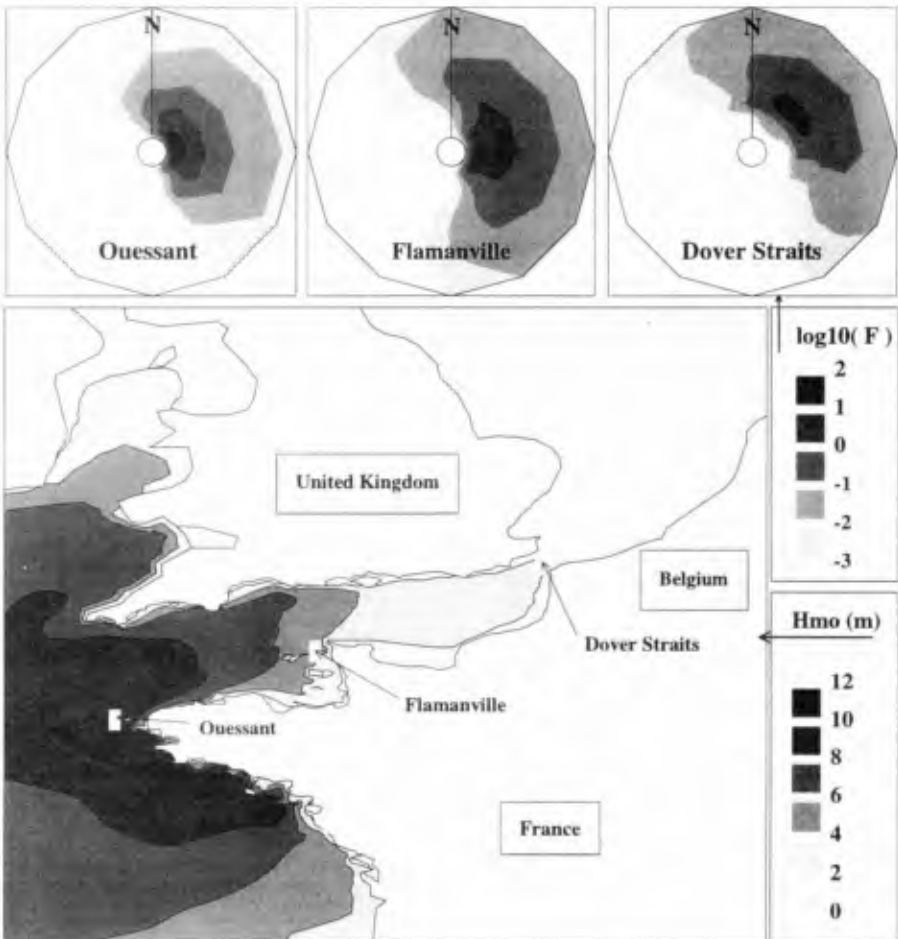


Figure 8 : Results of TOMAWAC at the peak of the storm of January 25, 1990. (Upper plots : directional spectra ; Lower plot : map of significant wave height)

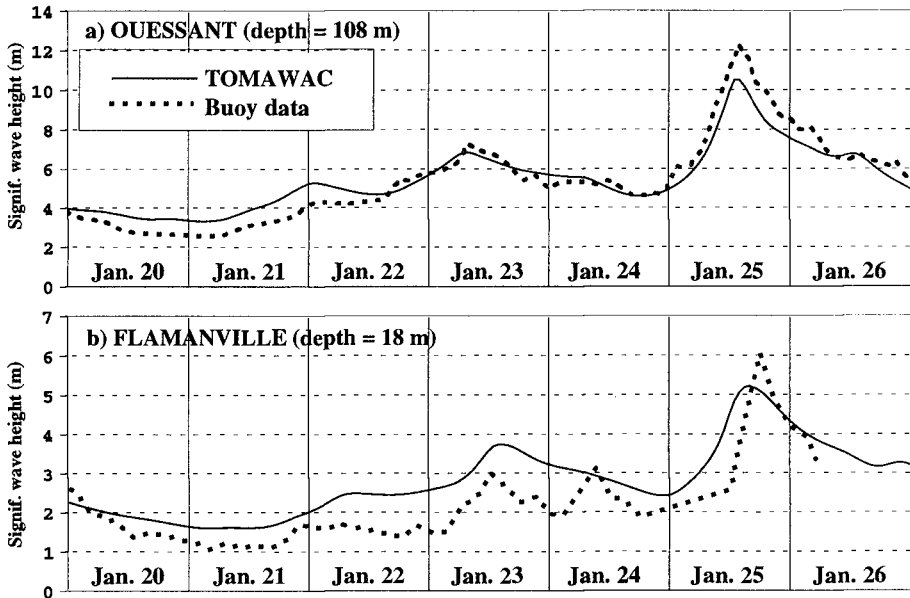


Figure 9 : Comparison of TOMAWAC results with buoy data at two locations.

6. CONCLUSIONS — FUTURE WORK

The applications presented in the previous sections show some of the capabilities of the TOMAWAC wave model, in particular for the simulation of storm waves for both offshore and nearshore areas. These cases are however only samples from the numerous test-cases performed during the validation step of the model. As a part of the TELEMAC modelling system, TOMAWAC indeed follows the Insurance Quality Procedure of EDF-LNH, with precise development rules and a complete documentation.

The inclusion of shallow-water effects such as bottom friction and depth-induced breaking has allowed to further extend the range of validity of the model towards the nearshore zone. In addition, the numerical background for spatial discretization (unstructured “finite elements” grid) and propagation scheme (piecewise ray method) make the model very attractive for the modelling of shelf seas and shallow-water domains.

Present development efforts are dedicated to the extension of the TOMAWAC model towards the very shallow water depth, in particular by considering the non-linear interactions between triads of waves. The possibility to deal with unsteady currents and water levels is also a field of present research, in order to study the interactions between waves, storm-surges and tides.

7. ACKNOWLEDGEMENTS

This study is a joint research program between EDF-Laboratoire National d'Hydraulique and the French Ministry of the Sea (Service Technique de la Navigation Maritime et des Transmissions de l'Équipement — STNMTE).

8. REFERENCES

- BATTJES J.A., JANSSEN P.A.E.M. (1978) : Energy loss and set-up due to breaking of random waves. *Proc. 16th Int. Conf. on Coastal Eng., Vol 1, pp 569-587*
- BATTJES J.A., STIVE M.J.F. (1984) : Calibration and verification of a dissipation model for random breaking waves. *Proc. 19th Int. Conf on Coastal Eng., Vol. 1, pp 649-660*
- BEJI S., BATTJES J.A. (1993) : Experimental investigation of wave propagation over a bar. *Coastal Eng., Vol. 19, pp 151-162*
- BOUWS E., KOMEN G. J. (1983) : On the balance between growth and dissipation in an extreme depth-limited wind-sea in the southern North-Sea. *J. Phys. Oceanogr., Vol 13, pp 1653-1658.*
- BRETHERTON F.P., GARRET C.J.R. (1968) : Wavetrains in inhomogeneous moving media. *Proc. Roy. Soc. A. 302, pp 529-554.*
- CHRISTOFFERSEN J.B., JONSSON I.G. (1985) : Bed friction in a combined current and wave motion. *Ocean Eng., Vol 12, pp 387-423.*
- DALLY W.R. (1992) : Random breaking waves : Field verification of a wave-by-wave algorithm for engineering applications. *Coastal Eng., Vol. 16, pp 369-397.*
- EBERSOLE B.A., HUGHES S.A. (1987) : DUCK85 photopole experiment. *US Army Waterways Experiment Station, Misc. paper CEREC-87-18, Vicksburg , MS.*
- ELDEBERKY Y., BATTJES J.A. (1995) : Parameterisation of triad interactions in wave energy models. *Proc. Int. Conf. Coastal Dynamics'95, pp 140-148.*
- HASSELMANN S., HASSELMANN K., ALLENDER J.H., BARNETT T.P. (1985) : Computations and parameterizations of the nonlinear energy transfer in gravity-wave spectrum. Part II : Parameterizations of the nonlinear energy transfer for application in wave models. *J. Phys. Oceanogr., Vol 15, pp 1378-1391.*
- IZUMIYA T., HORIKAWA K. (1984) : Wave energy equation applicable in and outside the surf zone. *Coastal Engineering in Japan, Vol. 27, pp 119-137*
- JANSSEN P.A.E.M. (1991) : Quasi-linear theory of wind-wave generation applied to wave forecasting. *J. Phys. Oceanogr., Vol 21, pp 1631-1642.*
- KOMEN G.J., HASSELMANN S., HASSELMANN K. (1984) : On the existence of a fully developed windsea spectrum. *J. Phys. Oceanogr., Vol 14, pp 1271-1285.*
- MADSEN O.S., POON Y.K., GRABER H.C. (1988) : Spectral wave attenuation by bottom friction : theory. *Proc. 21st Int. Conf. on Coastal Eng., pp 492-504.*
- MASE H., KIRBY J.T. (1992) : Hybrid frequency-domain KdV equation for random wave transformation. *Proc. 23rd Int. Conf on Coastal Eng., pp 474-487.*
- MATHIESEN M. (1987) : Wave refraction by a current whirl. *J. Geophys. Res., Vol 92, n° C4, pp 3905-3912.*
- RIS R.C., HOLTHUIJSEN L.H., BOOIJ N. (1994) : A spectral wave model for waves in the near shore zone. *Proc. 24th Int. Conf on Coastal Eng., pp 68-78.*
- ROELVINK J.A. (1993) : Dissipation in random wave groups incident on a beach. *Coastal Eng., Vol. 19, pp 127-150.*
- SNYDER R.L., DOBSON F.W., ELLIOT J.A., LONG R.B. (1981) : Array measurements of atmospheric pressure fluctuations above surface gravity waves. *J. Fluid. Mech., Vol 102, pp 1-59.*
- THORNTON E.B., GUZA R.T. (1983) : Transformation of wave height distribution. *J. Geophys. Res., Vol. 88, N° C10, pp 5925-5938*
- VAN VLEDDER G.P., DE RONDE J. G., STIVE M.J.F. (1994) : Performance of a spectral wind-wave model in shallow water. *Proc. 24th Int. Conf. on Coastal Eng., p 761.*
- VINCENT C.L., SMITH J.M., DAVIS J. (1994) : Parametrization of wave breaking in models. *Proc. Int. Symposium "Waves : Physical and numerical modelling", Vancouver (Canada), pp 753-762*
- WAMDI Group (1988) : The WAM Model - A third generation ocean wave prediction model. *J. Phys. Oceanogr., Vol 18, N°12, p 1775-1810.*
- WEBB D.J. (1978) : Non-linear transfer between sea waves. *Deep Sea Research, vol 25, pp 279-298.*

CHAPTER 38

New Optimization Method for Paddle Motion of Multi-Directional Wavemaker

Akira Matsumoto ¹ and Minoru Hanzawa ²

Abstract

Uniformity of monochromatic oblique waves in a wave basin is investigated. A new method, using non-linear least square formulation, to determine individual wave paddle motions of multi-directional wavemaker to improve uniformity, is proposed. The possibilities and limitations of the method are discussed. Trial computations and comparisons with experiments demonstrate the validity and usefulness of the method.

Introduction

It is of prime importance to reproduce the desired oblique planar wave train in a wave basin. If an accurate and simple method were available for this purpose, directional random waves could also be reproduced through superposition of various oblique waves for constituent elements. Up to now, however, monochromatic oblique waves generated by a multi-directional wavemaker using the conventional snake principle (Biesel, 1954) have shown considerable spatial variations in wave height and wave propagating direction due to the finite length of the entire wavemaker and the finite width of each paddle (Takayama, 1982).

To reduce these spatial variations, Dalrymple (1989) presented a theory which utilizes reflection from the sidewall. Although his method is widely employed, if a reflective structure is to be tested using it, significant re-reflection will occur from the sidewall and the resultant wave field will become contaminated. In this context, a method which does not use sidewall reflection is quite promising. This kind of approach was first proposed by Ishida and Watanabe

¹Researcher, Applied Hydraulics Laboratory, TETRA Co., Ltd., 2-7 Higashi Nakanuki, Tsuchiura, Ibaraki, 300, Japan.

²Senior Researcher, Ditto.

(1984) for a discrete-type multi-directional wavemaker under the condition of normal incidence. They showed that such spatial variations can be suppressed by controlling the amplitude of some of the wave paddles at both ends of the wavemaker without using the sidewall reflection. Mizuguchi (1993,1994) established a theory for continuous-type multi-directional wavemaker and proposed a general method to produce a uniform wave field for waves of oblique incidence. Toita *et al.* (1994) validated his method experimentally. The method employs linear decrease of paddle amplitude at both ends of the wavemaker while the conventional method uses a constant paddle amplitude. Although this method is very successful, the total length of the wave board to be controlled must be equal to one wavelength for the best result. The method is thought to be somewhat empirical. It cannot specify the target area in the basin, and the experimental work does not refer to uniformity of the wave propagating direction. Hanzawa *et al.* (1994) applied an electromagnetic wave theory for the generation of oblique waves. The applicability of this was investigated numerically using the boundary element method presented by Isaacson (1989). They suggested that the Dolph-Chebyshev distribution (Dolph, 1946), which was originally derived to determine the current distribution feeding to broadside antenna array and is optimum to minimize the beam width when a side lobe level is specified, showed possibility to improve the uniformity of an oblique water wave field.

In this paper, a new optimization method is proposed to determine each wave paddle motion to improve the uniformity of the monochromatic oblique wave field without using sidewall reflection. First, the amplitude of each wave paddle is determined using a non-linear least square method instead of the intuitive linear decrease proposed by Mizuguchi. Second, the wave heights and water particle motions are computed to investigate the generated wave fields. Finally, the method is validated by comparing computed and experimental wave fields. In comparison to Mizuguchi's method, the proposed method improves the uniformities of both the wave propagating direction and wave height, and the method can specify the location of the target area in the basin arbitrarily.

Formulation of the Problem

A wavemaker of continuous piston type is assumed to be installed in constant depth in a very wide wave basin with negligible sidewall reflection. In the following linear wave analysis, $2N$ is the total number of driving rods, a_i is the amplitude of the i -th rod, M is the total number of reference points distributed within the reference area, and A_j is the wave amplitude at the j -th reference point. Within the reference area, the uniformity of the wave field is improved. In this study, the magnitude of a_i is determined as the optimum value while the phase difference between adjacent paddles is simply decided in accordance with the conventional snake principle. Fig.1 gives a schematic view of the formulation.

The Hankel function gives a unit solution of the Helmholtz equation, expressing waves spreading from a point source over a horizontal bottom. Lin-

earity of the equation permits an arbitrary superposition of such unit solutions for multiple sources distributed along the wave paddles. A particular solution is obtained by determining the alignment of the point sources so that the resultant oblique wave field has a uniform wave height distribution within a given area in the basin. Fig.2 shows the coordinate system and waves emitting from a point source on the wave board.

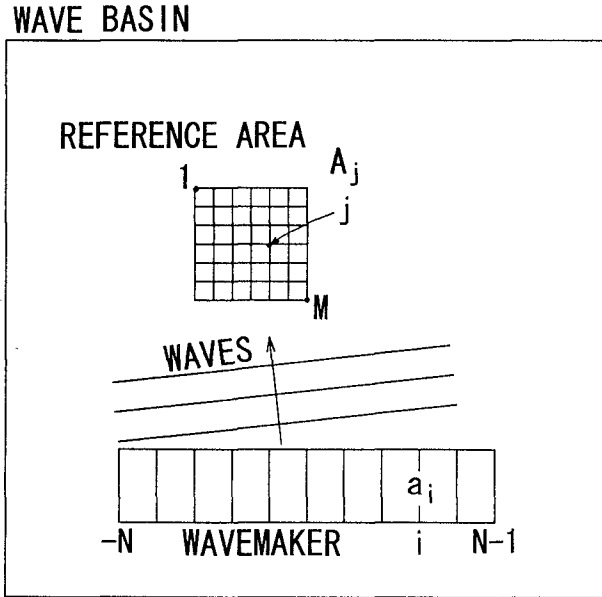


Figure 1: Schematic view of the formulation.

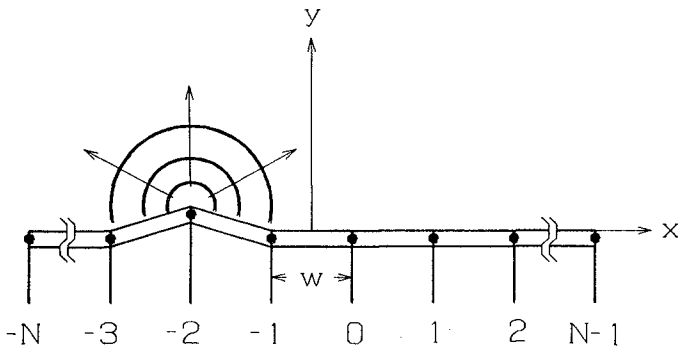


Figure 2: Coordinate system.

Neglecting the evanescent mode waves, the water surface profile at the j -th reference point (x_j, y_j) can be written as follows (Mizuguchi, 1993).

$$\eta_j = \alpha \sqrt{E_s^2 + E_c^2} \cos \left\{ \arctan \left(\frac{E_s}{E_c} \right) - \sigma t \right\} \quad (1)$$

The wave amplitude at the j -th reference point normalized by the representative amplitude of the driving rod, b_0 , is thus expressed as

$$A_j = \frac{\alpha}{b_0} \sqrt{E_s^2 + E_c^2} \quad (2)$$

where

$$\alpha = \frac{2 \sinh^2 kd}{\sinh 2kd + 2kd} \quad (3)$$

and

$$E_s = \sum_{i=-N}^{N-1} a_i \cos \beta \{ N_{ij} \cos (ikw \sin \beta) - J_{ij} \sin (ikw \sin \beta) \} \quad (4)$$

$$E_c = \sum_{i=-N}^{N-1} a_i \cos \beta \{ N_{ij} \sin (ikw \sin \beta) + J_{ij} \cos (ikw \sin \beta) \} \quad (5)$$

$$N_{ij} = \int_{-kw}^{kw} \left(1 - \frac{|q|}{kw} \right) N_0 \left(\sqrt{\left(k \left(x_j - iw - \frac{w}{2} \right) - q \right)^2 + (ky_j)^2} \right) dq \quad (6)$$

$$J_{ij} = \int_{-kw}^{kw} \left(1 - \frac{|q|}{kw} \right) J_0 \left(\sqrt{\left(k \left(x_j - iw - \frac{w}{2} \right) - q \right)^2 + (ky_j)^2} \right) dq \quad (7)$$

in which, t is the time, σ is the angular frequency, k is the wave number, d is the water depth, β is the wave propagating direction measured counterclockwise from the y -axis indicated in Fig.2, w is the width of a wave paddle, and N_0 and J_0 denote the Bessel and Neumann functions of zeroth-order. In Eq.(6) and (7), when $i=-N$ or $i=N-1$, the integration is performed in the range of $[0, kw]$ or $[-kw, 0]$ respectively.

Denoting the target wave amplitude normalized by the representative amplitude of the driving rod, b_0 , by A_c , the total residual squared is given by

$$r^2 = \sum_{j=1}^M [A_c - A_j]^2 \quad (8)$$

The problem can then be regarded as a non-linear least square problem. The optimum amplitude of each rod is obtained by finding the values of a_i which

minimize r^2 . In this study, as expressed in Eq.(9), A_c is taken to be 1/2 of the wave generating efficiency of a two dimensional piston type wavemaker.

$$A_c = \frac{2(\cosh 2kd - 1)}{\sinh 2kd + 2kd} \quad (9)$$

Marquardt's method is suitably employed to solve Eq.(8) because of its stability in computation. Since this type of approach allows arbitrary collocation of reference points, it makes experiments more flexible.

Optimum Distribution of Driving Rod Amplitude

The general description of the least square problem is to find a set of N unknown parameters

$$(x_1, x_2, \dots, x_N) \quad (10)$$

which minimizes the value of

$$r^2(\mathbf{x}) = \sum_{j=1}^M f_j^2(\mathbf{x}) \quad (11)$$

where $f_j(x_1, x_2, \dots, x_N)$ ($j = 1, \dots, M$) are arbitrary functions of \mathbf{x} .

When $r^2(\mathbf{x})$ depends nonlinearly on a set of N unknown parameters x_i , ($i = 1, \dots, N$), the minimization must proceed iteratively. From the given initial trial values for the parameters, the calculation proceeds in a way that improves the trial solution. Such a procedure is then repeated until $r^2(\mathbf{x})$ reaches an equilibrium (Press *et al.*, 1992).

Table 1 and Fig.3 summarize the conditions and the setup for computation and experiments in this study. The wave basin was 50m long, 40m wide, 1.5m high. Wave absorbers placed along the side wall and the onshore slope were used to prevent waves from reflecting from the wall. The number of driving rods was 28 (the number of wave paddles was 27) and the width of a wave paddle was 0.9m.

Table 1: Experimental conditions.

Case	Water depth (m)	Wave period (s)	Wave direction (°)	Reference area
1	0.6	1.8	0.0	A
2	0.6	1.8	22.5	B
3	0.6	1.8	22.5	A

The reference area of the uniform wave field is the rectangular region of $x=-4$ to 4m, $y=4$ to 12m (Area A) and $x=-9$ to -1m, $y=4$ to 12m (Area B).

Within this area, 81 reference points are collocated at every 1m grid point. A uniform distribution of the driving rod amplitude is used for the initial values and the iteration count of the minimization procedure is one. Computation to calculate the wave amplitude at the j -th reference point in Eq.(8) is made in the manner presented by Mizuguchi under the assumption of small amplitude wave theory.

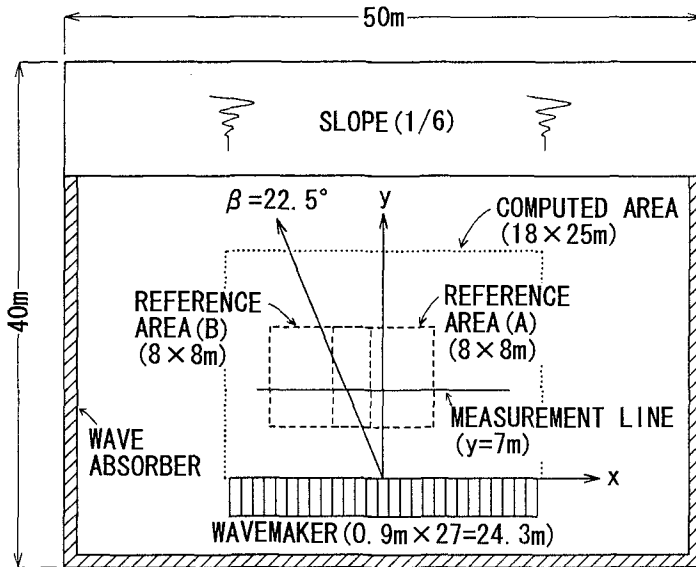


Figure 3: Wave basin.

Fig.4 gives the computed distributions of the rod amplitude for Case 1 and Case 2. This figure shows that the present method yields the distribution of the rod amplitude with high peaks at both ends of the wavemaker. The conventional method uses constant rod amplitude, while Mizuguchi proposed a linear decrease at both ends. These peaks, representing singularities at both ends, produce an improved uniformity of the wave field in the reference area. Such a non-uniform distribution of the point source intensities was correctly suggested by Nishimura *et al.* (1994) for the continuation condition at the artificial boundary of a wave field calculation.

The relationship between the iteration count of the minimization procedure and the values of residual squared for Case 1 is illustrated in Fig.5. This figure shows that only one time of iteration can reduce the value of residual squared up to approximately 1/100 of the original value. A preliminary investigation demonstrates that the uniformity of the wave field can be well improved by the distribution of the rod amplitude obtained by only one time of iteration. It is worth noting that not only the uniformity of the wave field in the reference area, but also that in its peripheral region can be widely improved to coincide

with its target value because of the continuity of the fluid, and the fact that too much iteration count narrows the area of such a peripheral region. As this study stresses the development of the new method and the examination of properties of generated wave fields, hereafter the number of iteration counts will be fixed to one.

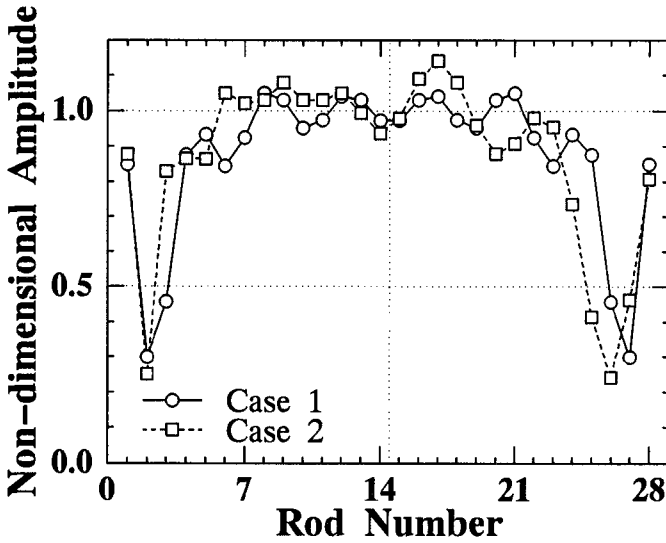


Figure 4: Computed distribution of the driving rod amplitude.

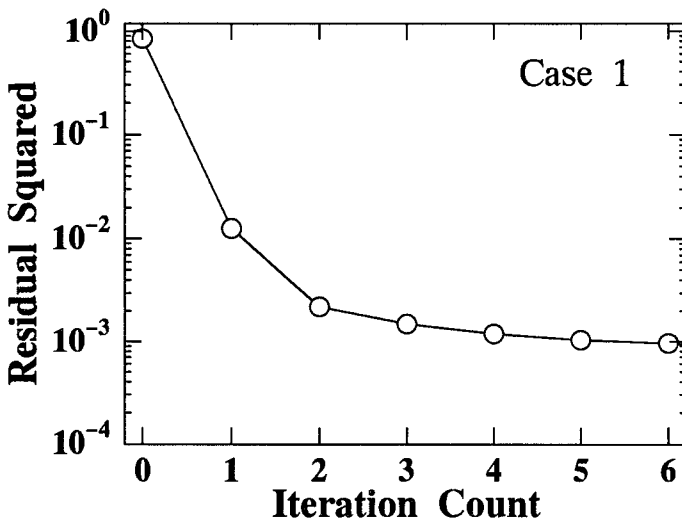


Figure 5: Changes of the residual squared.

Properties of Generated Waves

A series of computations on wave height, wave propagating direction and flatness of the hodograph of two component horizontal composed velocities were conducted to investigate the properties of oblique waves generated by the proposed method. Computations were carried out at every 50cm grid point over the area indicated in Fig.3

Fig.6 shows definitions of the wave propagating direction and the flatness of the hodograph. Because of the phase difference between one velocity component and the other, the path of the water particle does not follow a straight line but it forms an ellipse (Takayama, 1982). The wave direction is defined by the direction of longer radius. It should be noted that this definition gives a mean value of the wave direction because the wave direction at a fixed location varies from time to time. The flatness of the hodograph χ , is defined by using a longer and shorter radius as follows:

$$\chi = r_2/r_1 \quad (12)$$

where, r_1 is the longer radius and r_2 is the shorter one. The flatness of the hodograph indicates the magnitude of fluctuation of the wave propagating direction and is equal to zero if the wave field has complete uniformity.

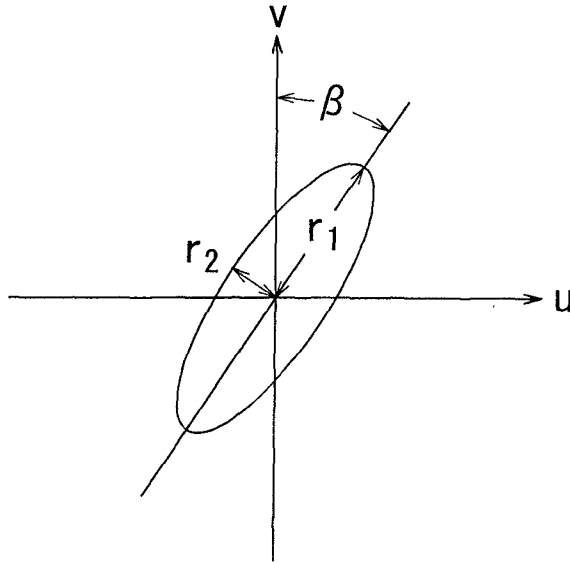


Figure 6: Trajectory of a water particle.

Fig.7 shows the computed distributions of the normalized wave height, the deviation of the wave propagating direction, and the flatness of the hodograph for Case 2. These results were obtained by the conventional method, Mizuguchi's method, and the proposed method. The normalized wave height was defined as the ratio of generated wave height to twice the amplitude of the driving rod. The target value is 0.97 according to the water depth and wave period used. The dark areas indicate that the normalized wave height is between 0.9 and 1.1, deviations of the wave propagating direction is between -2.5° and 2.5° , and the flatness of the hodograph is less than 0.05 respectively.

The wave fields computed by the conventional method display wavy features of considerable variations around 30% in the normalized wave height and the wave propagating direction differs by nearly 10° from the target values over a large area. Furthermore, the flatness of the hodograph shows the maximum value to be over 0.15. These wavy features are considered to be largely related to the phenomenon that the wave energy of the oblique uni-directional random waves have directional spreading and the multi-directional random waves show a spatial variation of the directional spectrum.

As shown in the figure, the proposed method reduced these wavy features to produce a wave field in which the error in the normalized wave height was less than 10%, the error in the wave propagating direction less than 2.5° , and the error in flatness of the hodograph less than 0.05. It is interesting to note that although the design procedure for paddle amplitude was, as was described above, derived from the viewpoint of wave height, not only the uniformity of the wave height but also the uniformities of both the wave propagating direction and flatness of the hodograph were significantly improved simultaneously. This may be explained by using the transfer function between the time series of the water particle velocities and the water surface elevation. The uniformity of the wave field for Case 1 produced by the proposed method is also improved with favorable results. See Matsumoto *et al.* (1995) for the reference.

Mizuguchi's method also reduced the wavy features. However, it produced some spots of unacceptable errors. These may be ascribed to the fact that his method modifies only a few wave paddles at both the generator ends empirically while the proposed method controls all the paddle amplitudes as an optimum distribution.

The normalized wave height computed by the proposed method for Case 3 is indicated in Fig.8. In this case, the wave ray from the center of the whole wave paddle did not go through the center of the reference area. The figure demonstrates that, even in such a case, the uniformity of the wave field can be improved by the proposed method. This supports the idea that the proposed method has a high possibility to reproduce a desired directional random wave field, which does not show any spatial variation of directional spectrum, by the superposition of oblique waves.

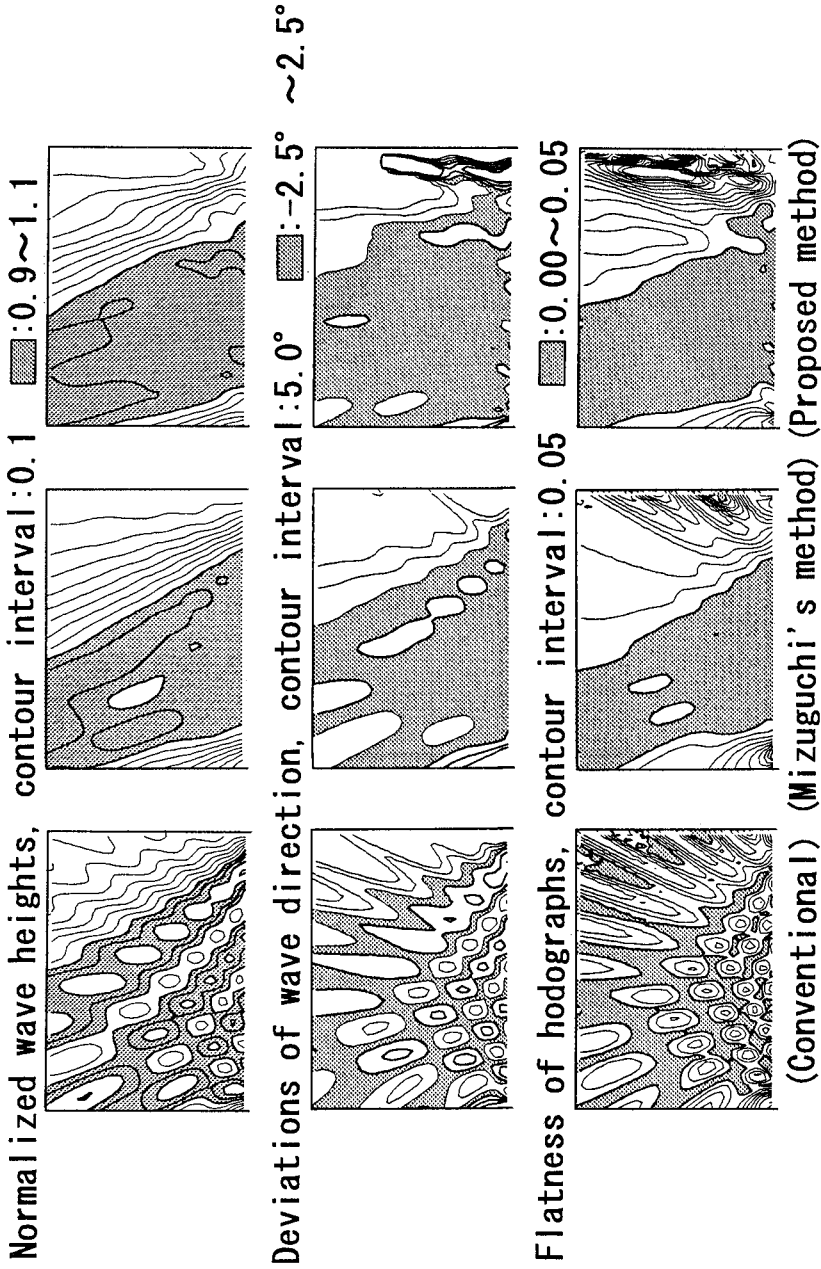



Figure 7: Computed wave fields (Case2).

contour interval:0.1  :0.9~1.1

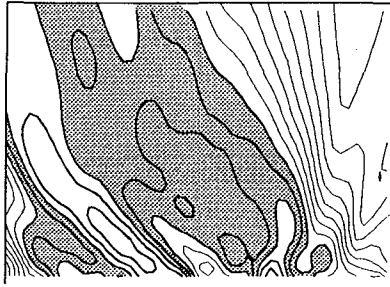


Figure 8: Computed normalized wave height (Case3).

Comparison with Experiments

Experiments were carried out to provide the wave height distribution and the water particle velocity to examine the performance of the proposed method. Equipment and experimental conditions are summarized in Fig.3 and Table 1. The representative amplitude of the driving rod was 3.7cm. Both the water surface elevation and two component horizontal water particle velocities were measured using capacitance type wave gauges and electromagnetic velocimeters along the measurement line ($y=7.0\text{m}$) as indicated in Fig.3. In the analysis, time series of the water surface elevation and water particle velocity before reaching the reflected waves from the sidewall were used.

Figs.9 and 10 compare the measured and computed distributions of the relative wave heights normalized with the target wave height for Case 1 and Case 2. In these figures, the loss of wave generating efficiency due to leakage of energy through the spacing between the wave board and the bottom of the wave basin, which was measured in the preliminary experiment, are taken into account. The agreement is good for both the proposed and conventional methods. A comparison of the measured and computed wave heights for Case 3 was also conducted. The measured wave heights agree well with those computed. This confirms the validity of the proposed method and the linear analysis of the wave field.

Figs.11 and 12 present the measured and computed hodographs of normalized horizontal velocities for Case 2 obtained at the location $x=2.25\text{m}$, $y=7.00\text{m}$, $z=-0.15\text{m}$. The diagonal dotted line shows the specified wave direction. The measured values follow computed ones quite well for both the conventional and proposed method. The water particle motions are also found to be reproduced well. Fig.12 indicates that the wave propagating direction coincides with its target direction. Moreover, the orbital curve becomes thinner, i.e., the magnitude of fluctuation of the wave direction decreases. These results confirm the validity of the proposed method from the viewpoint of the uniformity of wave direction.

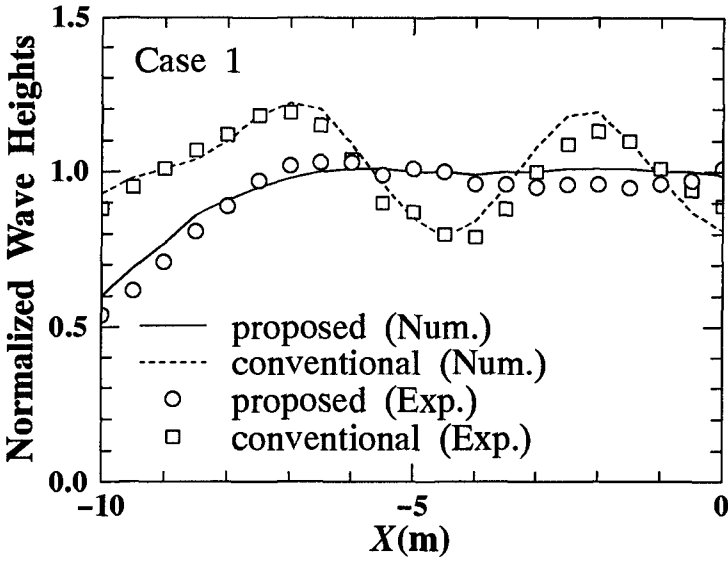


Figure 9: Measured and computed normalized wave heights (Case 1).

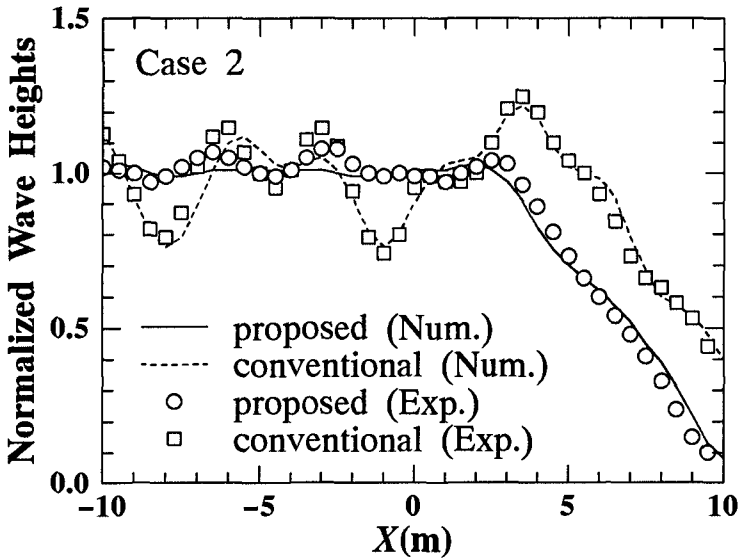


Figure 10: Measured and computed normalized wave heights (Case 2).

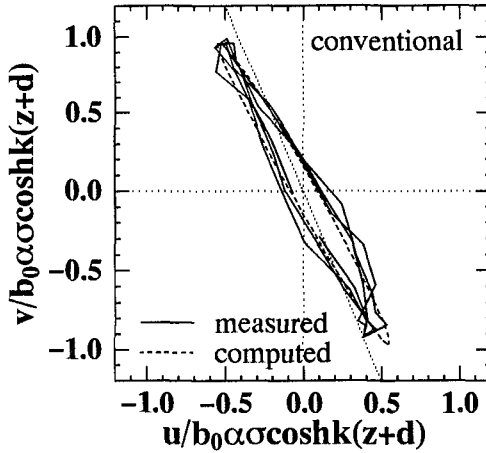


Figure 11: Hodographs of composed velocities (Case 2, Conventional method).

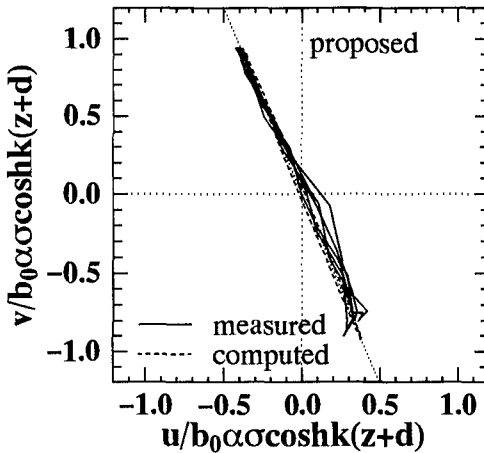


Figure 12: Hodographs of composed velocities (Case 2, Proposed method).

Concluding Remarks

Throughout this study, it was clarified that the method as presented actually improves the uniformity of both wave height and wave propagating direction. Since the method can specify the target area in the basin arbitrarily, it should prove very useful for applying to multi-directional random wave fields. As the method is formulated by using an inverse problem, it is applicable independent of the type of wavemaker and boundary conditions in the wave basin.

Acknowledgment

The authors wish to express their gratitude to Prof. Nobuhisa Kobayashi, Associate Director, Center for Applied Coastal Research, University of Delaware, for his valuable advice and encouragement in this study.

References

- Biesel, F.(1954): Wave Machines, Proc. of 1st Conference on Ships and Waves, pp.288-304.
- Dalrymple R.A.(1989): Directional wavemaker theory with sidewall reflection, Journal of Hydraulic Research, Vol.27, No.1, pp.23-34.
- Dolph C.L.(1946): A Current Distribution for Broadside Arrays Which Optimizes the Relationship between Beam Width and Side-Lobe Level, Proc. of IRE and Waves and Electrons, pp.335-348.
- Hanzawa, M., A. Matsumoto and T. Bunyu(1994): An Application of Antenna Theory to the Oblique Wave Generation, Proc. of 49th Annual Conference of the JSCE, Vol.2-(B), pp666-667. (in Japanese)
- Isaacson, M.(1989): Prediction of Directional Waves Due to a Segmented Wave Generator, Proc. of 23rd IAHR Congress, Vol.C, pp.435-442.
- Ishida, S. and I. Watanabe(1984): Properties of Oblique Waves Generated by Snake Motion of Segmented Wavemaker, Trans. of the West Japan Society of Naval Architects, No.69, pp135-141. (in Japanese)
- Matsumoto, A., M. Hanzawa and M. Noguchi(1995): Design Principles for the Paddle Motion of a Multi-Directional Wave Maker, Proc. of 42nd Japanese Conference on Coastal Engineering, pp.141-145. (in Japanese)
- Mizuguchi, M.(1993): Wave Maker Theory for Continuous-type Multi-directional Wave Maker and its Application to Generating Uniform Wave Field, Bulletin of the Faculty of Science and Engineering Chuo university, Vol.36, pp.21-37. (in Japanese)
- Mizuguchi, M.(1994): Uniformity of Wave Field Produced by Multi-Directional Wave Maker, Abstract of 24th International Conference on Coastal Engineering, pp.98-99.
- Nishimura, H., M. Matsuoka and A. Matsumoto(1994): A Generalized Green-Function Method for Wave Field Analysis, Proc. of 24th International Conference on Coastal Engineering, pp.442-454.
- Press, W., S. Teukolsky, W. Vetterling and B. Flannery(1992): Numerical Recipes in FORTRAN, 2nd Ed., Cambridge University Press, 963p.
- Takayama, T.(1982): Theoretical Properties of Oblique Waves Generated by Serpent-Type Wavemakers, Report of the Port and Harbour Research Institute, Vol.21, No.2, pp.3-48.
- Toita, H., M. Mizuguchi and Y. Moriya(1994): End Control Method for Multi-Directional Wave Maker to Produce Uniform Wave Field, Proc. of 41st Japanese Conference on Coastal Engineering, pp.106-109. (in Japanese)

CHAPTER 39

GENERATION OF SECOND-ORDER LONG WAVES BY A WAVE GROUP IN A LABORATORY FLUME AND ITS CONTROL

M. Mizuguchi and H. Toita

ABSTRACT

Generation of second-order long waves at a wave maker by non-periodic wave group is analyzed in time series by Mizuguchi(1995). The analysis, which include a way to control the long wave generation, is briefly described. Then confirmation by using a single wave packet is successfully undertaken both in numerical simulation by Boussinesq equation and in laboratory experiment.

1. INTRODUCTION

Long period waves (infra-gravity waves) are of typical time scale a few minutes. Recent studies on field waves in the nearshore zone reveals that these long waves are quite significant and cannot be neglected even for engineering purposes.

Reproduction of a field phenomenon in laboratory experiments is a way to understand it if tried or a proof of understanding if successfully done. Here we deal with a method of correct reproduction of the long waves coexisting with grouping short-period waves. Ottesen Hansen et al.(1980) presented a theoretical analysis of the bound second-order long waves in the frequency space. The long waves are calculated as the second-order difference waves of the two primary waves with slightly different frequencies in Stokes-type nonlinear analysis. They also give discussions both on the production of spurious free long waves at a wave maker and on a method to suppress them. Kostense(1984) successfully applied the method to bichromatic waves. However this approach in frequency space cannot be applied to non-periodic wave

Dept. Civil Eng., Chuo Univ., Kasuga 1-13-27, Bunkyo-ku,
Tokyo JAPAN

groups such as the initial growth stage of the wave generation and a single wave packet.

On the other hand, Longuet-Higgins and Stewart(1962) show a way to describe these long waves by applying linear long wave equation with a forcing term given by second-order quantity (radiation stress) of the short period waves. Mizuguchi(1995) follows their approach to study the behavior of the second-order long waves produced at the wave maker when grouping waves are generated in a laboratory flume. He also shows a way to control them in time domain. Here we report their experimental confirmation both numerically and physically.

2. TIME SERIES ANALYSIS OF SECOND-ORDER LONG WAVE GENERATION

Radiation stress approach employed by Mizuguchi(1995) is briefly described below. He assumes one dimensional case with a constant depth h . Then basic conservation equations are

$$\text{mass:} \quad \eta_t + (hu)_x = 0 \quad (1)$$

$$\text{momentum:} \quad u_t + g\eta_x = -(S_{xx}/\rho)_x/h \quad (2)$$

where η and u are surface elevation and onshore velocity for long waves. S_{xx} is a radiation stress component. Here the long waves are assumed to be of small amplitude. Eliminating u in Eqs.(1) and (2), we have the linear long wave equation with a forcing term.

$$\eta_{ct} - g(h\eta_x)_x = (S_{xx}/\rho)_{xx} \quad (3)$$

For a wave group, which propagates in a steady form on a constant depth, Longuet-Higgins and Stewart(1962) shows Eq.(3) has the following particular solution (the bound long waves) η_* ,

$$\eta_* = -S_{xx}(x - c_g t)/\rho(c^2 - c_g^2) \quad \text{where } c^2 = gh. \quad (4)$$

For the long waves under short wave groups in a laboratory flume, the general solution for $x > 0$ (wave maker at $x=0$) is written as

$$\eta(x, t) = f(x - ct) + \eta_*(x - c_g t) \quad (5)$$

where $f(x - ct)$ is a general solution of Eq.(3), which propagates in the positive direction. Uniqueness exclude other general solution, which propagates in the negative direction. Functional form of f should be determined by either initial conditions or boundary conditions. In

other words the general solution $f(x-ct)$ is needed to satisfy conditions which reflect a real situation.

When generating either grouping waves or irregular waves, we normally neglect the existence of the second-order long waves. Then this natural boundary condition at the wave maker is written as

$$u=0 \quad \text{at } x=0. \quad (6)$$

Surface elevation η of Eq.(5) gives the following horizontal velocity u ,

$$u(x,t)=(c/h)f(x-ct)+(c_g/h)\eta_*(x-c_g t) \quad (7)$$

For a boundary condition where $u(0,t)$ is specified, Eq.(7) yields

$$f=-n\eta_*(h/c)u|_{x=0} \quad (8)$$

where $n=c_g/c$. For the natural boundary condition described by Eq.(6), we have the following solution

$$\eta(x,t)=\eta_*(x-c_g t)-n\eta_*[n(x-ct)]. \quad (9)$$

In addition to the bounded long waves $\eta_*(x-c_g t)$, free long waves, whose magnitude is $-n$ times of the bound one, are generated and propagate with the phase speed \sqrt{gh} .

To control the free long waves, in particular, to suppress the free long waves, one put $f=0$ in Eq.(8) so that the following extra board motion is added to the motion for the group of primary waves.

$$u|_{x=0}=(c_g/h)\eta_* \quad (10)$$

To introduce arbitrary free long waves $f(x-ct)$ at the wave maker, one should further add

$$u|_{x=0}=(c/h)f. \quad (11)$$

Generation of free long waves for an initial value problem is also discussed in Mizuguchi(1995).

3. NUMERICAL AND EXPERIMENTAL CONFIRMATION

Numerical as well as physical experiments are conducted to confirm the theoretical analysis.

For numerical simulation, Boussinesq equation is employed. Boussinesq equation can describe weakly nonlinear and weakly dispersive waves and is known to be able to simulate well the water waves in shallow water up to the second-order phenomena. We follow the normal procedure in the numerical coding, that is, the staggered

mesh in space and the leap-frog method in the time stepping. One advantage of the numerical simulation is that the boundary condition at the wave maker is exactly specified by the horizontal velocity as is done in the analysis.

Laboratory experiment is conducted in a flume of 40m long, 30 cm wide with a piston-type wave maker. The displacement of the wave maker board is calculated by numerically integrating the corresponding velocity at $x=0$. The displacement of the wave maker board is assumed to be negligibly small.

A group of waves are generated by introducing the velocity

$$u_p = A(t) \cos(2\pi t/T) \quad (12)$$

at $x=0$, where u_p is the vertically uniform horizontal velocity. $A(t)$ is a slowly-varying amplitude function and is given by

$$A(t) = (a_{\max}/2) [1 - \cos(2\pi t/T_g)] \quad 0 < t < T_g \text{ otherwise } A=0. \quad (13)$$

Here T the period of the primary waves, T_g the duration of the wave group, and a_{\max} is the maximum amplitude of primary waves. In the experiments, T , T_g and a_{\max} are chosen to be 1.0 s, 8.0 s and 0.5 cm respectively. The small value of the amplitude a_{\max} assures the small amplitude assumption for the primary waves and also justify the way to convert the velocity to the motion of a wave maker. Water depth is 10 cm so that Boussinesq equation is applicable.

First we generate the group of waves in a traditional way, or without any consideration on second-order phenomena. Figure 1 shows comparison of the surface profiles among measured, simulated and of analysis. Overall agreement is very good. The amplitudes measured in the physical experiment show a little decay while propagating. Linear modulation of the wave group, which is not long enough, might be responsible for the decay, although frictional loss may not be negligible. Figure 2 shows long waves obtained by low-pass filtering the data in Fig. 1. All three envelopes agree very well, revealing the separation process of the free long wave, generated at the wave maker, from the bound long wave. Near the wave maker they almost cancel each other to give zero velocity at the wave maker. Some distance from the wave maker the free long wave, which is a positive hump in this case, starts to emerge as it leads the bound long waves with faster phase velocity. The free and bound long waves may be completely separated after travelling long distance, though nonlinear effects may come in to play non-negligible role there.

Next we generate a group of waves with the extra velocity of Eq.(10) or the corresponding paddle motion, which is shown in Fig. 3. Figure 4 shows comparison of the three envelope profiles. As is in Fig. 1, they show good agreement. The measured maximum amplitude in the laboratory experiment is a little smaller than 0.5 cm even very near the wave maker. This may be caused by some mechanical loss and/or the displacement of the paddle to account for Eq.(10). It is noted that there is little difference between the data plotted in Fig. 1 and in Fig. 4.

Fig. 5 shows long waves obtained from the data in Fig. 3. Again three profiles are in good agreement, though they are quite different from those in Fig. 2. The analytical result in Fig. 5 is the Longuet-Higgins and Stewart solution (hereafter abbreviated LHS solution) or Eq.(4). This shows that one can realize the LHS solution by introducing the velocity of bound waves

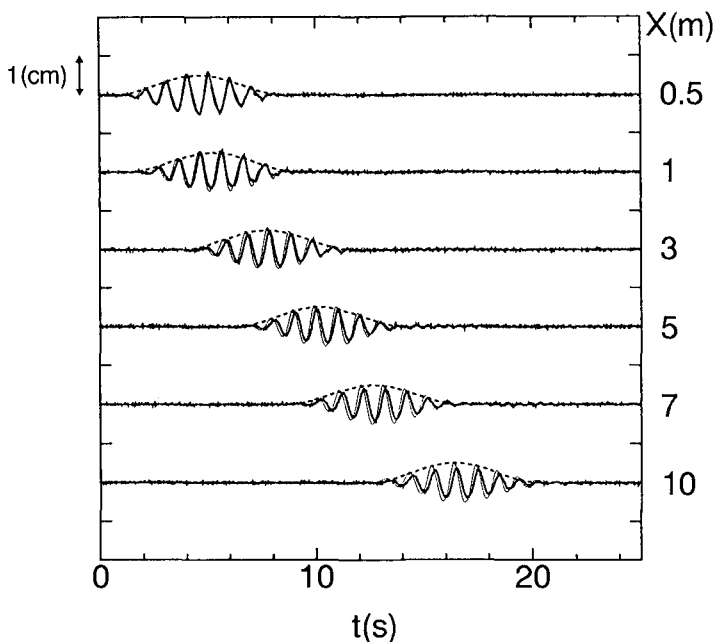


Fig. 1 Surface profiles of normally generated grouping waves

Thick solid lines : laboratory experiment

Thin lines : numerical simulation (Boussinesq equation)

Broken lines : theory (a permanent wave group)

to the wave making. The long waves measured in the physical experiment decrease their magnitude while propagating, as the amplitude of the primary waves also decrease their amplitude. The long waves in Boussinesq model also show a slightly larger difference from the analytical one than those in Fig. 2. The difference may result from the fact that modulation of the wave group is more significant when the free long waves are suppressed. The total magnitude of long waves is larger than that with the free waves and resultant modulation stronger.

It is worthwhile to be stated here that the LHS solution is correct as a solution of the problem and can be realized in an ideal situation. However free long waves, generated at the wave making process as shown in Fig. 2 and/or free long waves generated while wave groups shoals on a sloping bottom as discussed in Nagase and Mizuguchi(1996), contribute to canceling the LHS bound waves which tend to be infinitely large in the very shallow water.

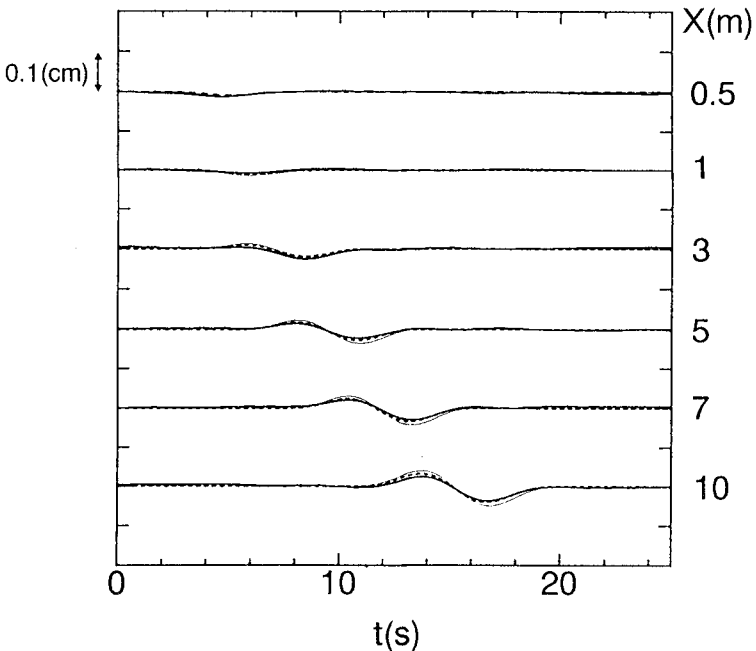


Fig. 2 Long waves obtained by low-pass filtering the data in Fig. 1. Vertical scale is ten-times larger than that in Fig. 1.

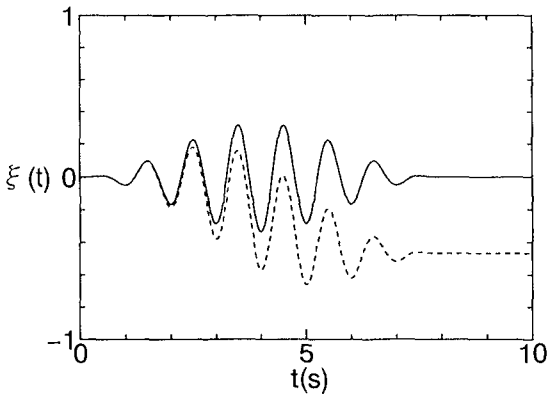


Fig. 3 Displacement of the wave paddle
 Solid line ... traditional
 Broken line ... free long waves suppressed

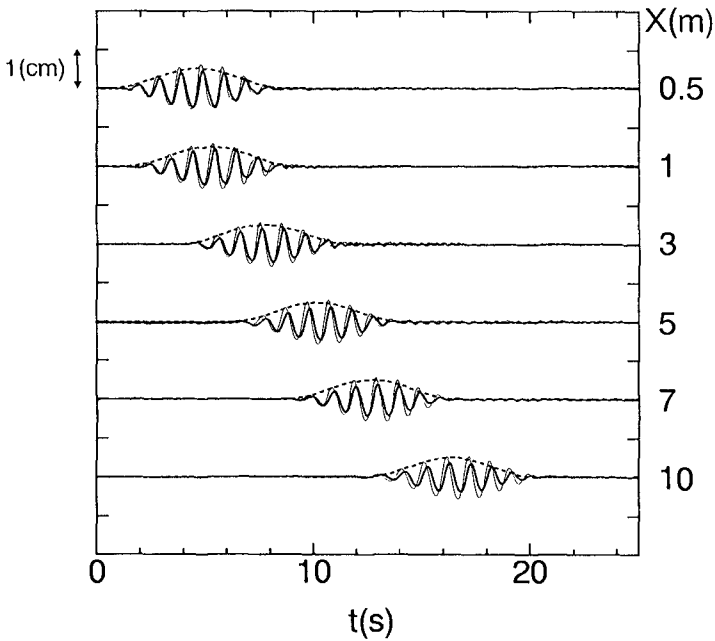


Fig. 4 Surface profiles of grouping waves with no free long waves

4. CONCLUSIONS

From the results stated above, we can conclude

1) A time-domain analysis to understand the generation of second-order long waves in a laboratory flume is presented.

2) Analytical results are successfully confirmed both numerically and experimentally, showing a way to control the generation of second-order long waves for non-periodic wave group.

3) Even in very shallow water bounded long waves is described by the solution of Longuet-Higgins and Stewart(1962). However the observed long waves may not be so large as predicted by the LHS solution as accompanying free long waves nearly cancels it in reality.

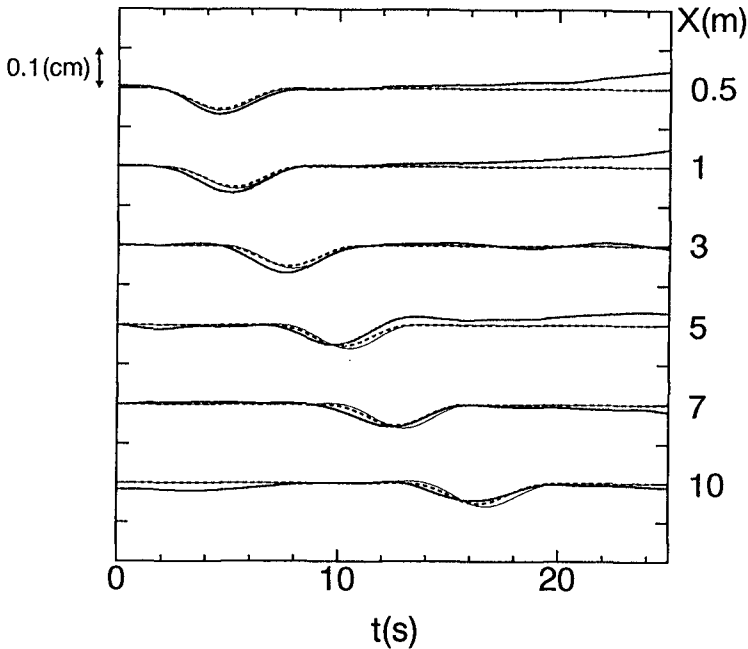


Fig. 5 Bound long waves in the data shown in Fig. 4 (Longuet-Higgins and Stewart solution)

REFERENCES

- Kostense, J.K.(1984), Measurement of surf beat and set-down beneath wave groups, Proc. 19th ICCE, Houston, 724-740.
- Longuet-Higgins, M.S. and R.W. Stewart(1962), Radiation stress and mass transport in gravity waves, with application to "surf beat", JFM, Vol. 13, 481-504.
- Mizuguchi, M.(1995), Radiation stress approach to generation of long waves by a wave group in a flume, Coastal Eng. in Japan, Vol. 38, No. 1, 1-4.
- Nagase, S. and M. Mizuguchi(1996), Laboratory experiment on long wave generation by time-varying breakpoint, Proc. 25th ICCE, Orlando. (in press)
- Ottesen Hansen, N.E., S.E. Sand, H. Lundgren, T. Sorensen and H. Gravesen(1980), Correct reproduction of group-induced long waves, Proc. 17th ICCE, Sydney, 784-800.

CHAPTER 40

Kinematic Predictions in Large Shallow Water Waves.

Susan Smith¹ & Christopher Swan².

Abstract.

The present paper concerns the description of extreme waves in shallow water, and in particular contrasts the success of two recently developed wave theories (Sobey, 1992 and Baldock and Swan, 1994) to model the maximum water particle velocities arising beneath a highly nonlinear and transient (or unsteady) wave event. To achieve these comparisons exact numerical calculations were undertaken using the time-stepping procedure outlined by Dold and Peregrine (1984). Comparisons between this numerical “data” and the kinematics models confirm the importance of both the non-linearity and the unsteadiness, and further suggest that the nature of the wave-wave interactions has important implications for the accuracy of the kinematics predictions. In particular, the local Fourier series solution (Sobey, 1992) is shown to be unable to model the global wave frequency-difference terms, and therefore tends to over-predict the fluid velocities beneath the still water level. In contrast, the double Fourier series solution (Baldock and Swan, 1994) explicitly incorporates both the nonlinearity and the unsteadiness of the wave, and typically provides a good description of the flow field beneath the still water level. However, this solution is limited in terms of the total number of Fourier components included, and consequently the largest velocities arising close to the water surface are typically under-predicted in the largest wave events. Nevertheless, both kinematics models provide a significant improvement over the existing design solutions.

Introduction.

Within both coastal and offshore engineering the identification of an appropriate wave climate represents a fundamental input into the design process. If,

¹Research student & ²lecturer, Department of Civil Engineering, Imperial College, London, SW7 2BU. United Kingdom.

as is usually the case, design calculations are required to assess the applied fluid loading, the stability and transport of bed material, or the potential for over topping, a second and equally important aspect of the design involves the prediction of the water particle kinematics. In respect of this latter point current design procedures are either based upon a non-linear steady wave theory, or an unsteady linear theory. In the first of these cases the wave model incorporates the non-linearity of the wave motion, but neglects the unsteadiness or the transient nature of the sea state. Indeed, within this category the most commonly applied model is based upon a fifth-order Stokes' solution (Fenton, 1985). In this case a large wave is characterised by a representative wave height (H) and a wave period (T), and it is assumed that the wave forms part of a regular wave train which propagates without change of form. Alternatively, a higher-order stream function solution (Dean, 1965) may also be applied in which the wave profile is either specified in terms of H and T , or the series solution is matched to a measured surface profile, $\eta(t)$, using some form of constrained minimisation. However, in both applications of the stream function solution the wave is assumed to propagate without change of form, and thus the dispersive properties are neglected.

In contrast, a linear random wave theory recognises the fact that a realistic sea state comprises a large number of wave components, many of which may be described as free waves and thus travel at a phase velocity (c) which is only dependent upon the wave period (T) and the water depth (d). Solutions of this type fall into the second category (noted above) in that they partially incorporate the unsteadiness of the sea state, but are restricted in the sense that they neglect the nonlinearity. Indeed, in solutions of this type all terms of order a^2k^2 and above (where a is the wave amplitude and k is the wave number) are neglected. As a result, such solutions make no attempt to model the nonlinear wave harmonics which include both the higher-order Stokes' terms and the nonlinear wave-wave interactions arising between two or more frequency components (Longuet-Higgins and Stewart, 1960).

Unfortunately, it is now widely recognised that the largest waves within a sea state are both nonlinear and unsteady. As such, they do not arise as part of a regular wave train, but occur as individual events within a random, or irregular, sea state. If one considers a typical broad-banded spectrum in deep water, frequency dispersion provides a plausible explanation for the evolution of the largest wave events. In this case the extreme events are produced by constructive interference when a large number of wave crests arise at one point in space and time. Indeed, recent field measurements undertaken at the Tern Platform (Rozario et al, 1993) have confirmed the validity of this argument, and have demonstrated that the most probable shape of the largest wave is closely related to the auto correlation function of the underlying wave spectra (Tromans et al, 1991).

However in intermediate and shallow water depths the evolution of the largest waves is perhaps more complicated. For example, although frequency

dispersion provides an effective method of focusing wave energy in all but the shallowest water depths ($kd < 0.4$), large waves may also be related to changes in the local bathymetry (Peregrine, 1983); the interaction with uniform and depth-varying currents (Swan, 1990, 1992); or the occurrence of side-band instabilities (Benjamin and Feir, 1969). Although these effects are entirely separate, they will each produce extreme events which are both highly non-linear and unsteady. As a result, it is clear that the present design solutions do not model the fundamental characteristics of the largest wave events. Indeed, previous work presented by Baldock and Swan (1994) and Baldock, Swan and Taylor (1996) has considered large deep water waves, and has demonstrated that the underlying kinematics can only be predicted if both the nonlinearity and the unsteadiness is taken into account. However, the relative importance of these effects in shallow water remains unclear. For example, recent experimental observations (Baldock and Swan, 1996) have shown that the transfer of energy to the nonlinear harmonics is strongly dependent upon the water depth. However, these results are primarily concerned with intermediate water depths, and only contrast the measured data with one fully nonlinear unsteady wave model. The present paper will address this point, and will consider the extent to which recently developed wave theories are able to model extreme shallow water waves. In particular, exact numerical calculations based on the time-stepping procedure outlined by Dold and Peregrine (1984) will be used to contrast the kinematic models presented by Sobey (1992) and Baldock and Swan (1994).

Kinematics Models.

In recent years the possible inadequacy of the existing design solutions has been recognised, and in particular two alternative wave models have been proposed. In both cases these models are based upon a time-history of the water surface elevation measured at one spatial location, $\eta(t)$, and are thus appropriate to design calculations. In particular, they represent a significant improvement over the existing design solutions in that they attempt to incorporate both the nonlinearity and the unsteadiness of the wave motion. The first model, proposed by Sobey (1992) is based upon a local Fourier series approximation originally outlined by Fenton (1992). Within this solution the time-history of the water surface elevation, $\eta(t)$, is subdivided into a large number of local windows within which the surface profile is assumed to be locally steady. This does not imply that the entire wave form propagates without change of form, merely that a small section of the wave profile is locally steady during the time interval that it passes the measuring point. If (x, z) represent the usual Cartesian co-ordinates in which $z=0$ corresponds to the still water level, and $z=-d$ represents the bottom boundary, a velocity potential ϕ may be defined within each window such that:

$$\phi(x, z, y) = C_E x + \sum_{j=1}^J A_j \frac{\cosh(jk(d+z))}{\sinh(jkd)} \sin(jkx - j\omega t) \quad (1)$$

where C_E is the co-flowing Eulerian current, ω is the fundamental wave frequency (or $2\pi/T$, where T is the corresponding wave period) and k is the fundamental wave number (or $2\pi/\lambda$, where λ is the wave length). The constant coefficients A_j (for $j = 1$ to J) thus represent the amplitudes of the individual harmonics which are determined by minimising the errors in the free surface boundary conditions. Within this solution the input parameters correspond to the upper limit of the series expansion (or the truncation order J), the local window length (τ), and the time interval between adjacent data describing the surface profile (Δt). Although the minimisation procedure is somewhat involved, and the outcome strongly dependent upon the input parameters, the scheme is computationally efficient, and suitable for use on a standard personal computer.

In contrast, the wave solution proposed by Baldock and Swan (1994) explicitly includes both time and space dependence. This solution is based upon a double Fourier series solution first proposed by Lambrakos (1981), and adopts a velocity potential defined by:

$$\phi(x, z, t) = \sum_{m=1}^M \sum_{n=1}^N \cosh k(z+d) [A_{nm} \cos(k_n x - \omega_m t) + B_{nm} \sin(k_n x - \omega_m t)] \quad (2)$$

In this case the proposed solution incorporates a total of M wave numbers each with M frequency components (where typically $N = M$), such that a total of $2NM$ wave harmonics are included within the overall solution. If T_1 defines some large fundamental period, over which the solution is assumed periodic, the fundamental wave frequency is defined by $\omega_1 = 2\pi/T_1$, and the corresponding wave number (k_1) is calculated using the linear dispersion equation. Having identified these values the solution matrix (k_n, ω_m) is assembled from wave numbers and frequency components which are integer multiples of the fundamental:

$$k_n = nk_1, \quad \omega_m = m\omega_1 \quad (3)$$

The final solution is again based upon a time-history of the water surface elevation measured at one spatial location (i.e. $\xi(t)$ at $x = 0$). In effect the unknown coefficients A_{nm} and B_{nm} , together with the unknown surface profiles at all other spatial locations (i.e. $\eta(t)$ at $x \neq 0$), are determined by a minimisation of the error in the nonlinear free surface boundary conditions arising at all points in space and time. Provided the fundamental period is sufficiently large relative to the dominant (or peak) wave period, an appropriate mix of free waves and bound waves are generated. As a result, the final wave solution deforms in both space and time, and has to date been shown to provide a good description of the wave-induced water particle kinematics arising in deep water (Baldock and Swan, 1994).

To assess the effectiveness of these solutions in intermediate and shallow water depths, we have sought to compare the predicted water particle velocities with

exact numerical calculations based upon the time-stepping procedure outlined by Dold and Peregrine (1984). Previous studies (Johannessen and Swan, 1996) have shown that these and other time-stepping procedures (notably Longuet-Higgins and Cokelet (1976), Fenton and Rienecker (1980) and Craig and Sulem (1993)) are in near-perfect agreement with laboratory data, and thus provide an excellent benchmark with which to test potential design solutions. At this stage it should be noted that these time-stepping solutions, although exact, are not appropriate for typical design calculations since they are based upon initial conditions which require a spatial representation of both the water surface elevation and the velocity potential at the water surface (i.e. $\eta(x)$ and $\phi(x)$ at $z=\eta$). This information is seldom available in a laboratory study, and never available from field data.

Test Conditions.

To assess the effectiveness of the wave solutions three test cases were considered in which an extreme wave group was produced in a water depth of $d=0.7\text{m}$, 0.3m , and 0.15m respectively. In each case the underlying frequency spectrum was broad-banded (at a laboratory scale), and consists of a total of 29 frequency components which were each of equal amplitude and equally spaced within the period range $0.6 \leq T \leq 1.4\text{s}$. Expressed in terms of an energy spectrum within the frequency domain this distribution of wave components has a peak frequency at approximately 0.71Hz , and decays according to ω^{-4} . In each of the three test cases the initial conditions used to commence the time-stepping procedure were such that the wave energy was fully dispersed within the spatial domain. On this basis a linear wave theory was used to provide both the surface elevation $\eta(x)$ and the magnitude of the velocity potential at the surface ($\phi(x)$ at $z=\eta(x)$). However, the relative phasing of the wave components was such that after a large number of time-steps (typically larger than 100) frequency dispersion produced a focusing of wave energy such that a large highly nonlinear wave event was generated at one point in space and time. The numerically predicted horizontal velocities, $u(z)$, arising beneath this large wave event were chosen as an appropriate yard-stick with which to judge the success of the kinematics models discussed previously.

Discussion of Results.

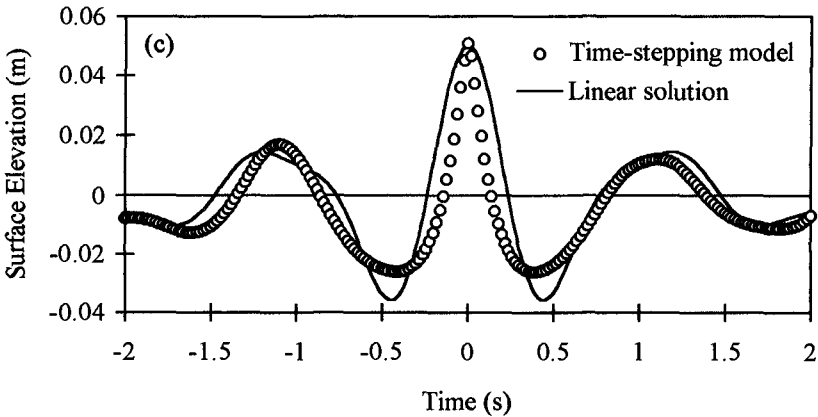
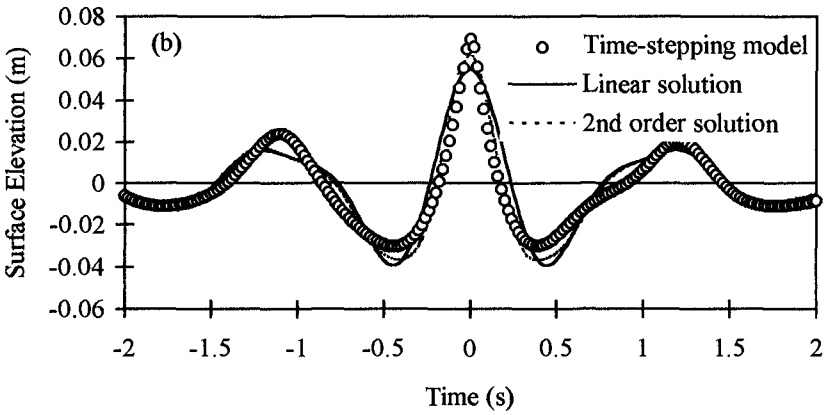
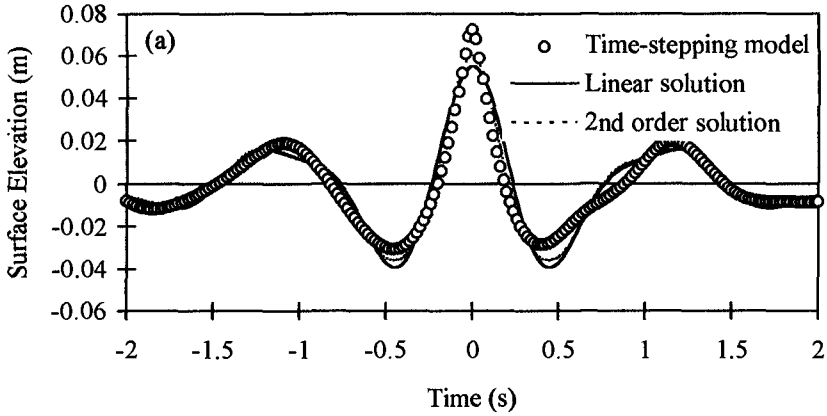
Figures 1a-1c concern the broad-banded spectrum ($0.6\text{s} \geq T \geq 1.4\text{s}$) in the three different water depths ($d = 0.7\text{m}$, 0.3m , and 0.15m respectively), and describes the time-history of the water surface elevation, $\eta(t)$, predicted at the spatial location at which the maximum crest elevation arises. In each of these cases the exact numerical calculations (following Dold and Peregrine, 1984) are compared to both a linear wave solution and a second-order approximation based upon the sum of the interactions identified by the Longuet-Higgins and Stewart (1960). These latter two

models are based upon the twenty nine free waves which were initially implemented within the time-stepping procedure, and are thus very different to either a linear random wave theory or a hybrid second-order solution (Stansberg, 1993) based upon a Fourier analysis of the measured water surface elevation. To facilitate comparisons of this type the time base on the horizontal axis has been shifted such that (for each wave solution) the maximum crest elevation arises at $t=0$. Comparisons of this type, and in particular the difference between the exact numerical calculations and the linearly predicted results, demonstrate the importance of the nonlinear wave-wave interactions. For example, in deep water conditions ($d=0.7\text{m}$) figure 1a suggests that a linear solution underestimates the maximum crest elevation by approximately 25%; while the inclusion of the second-order terms only accounts for approximately 30% of the total nonlinear effects. These results are consistent with deep water data presented by Baldock and Swan (1994).

However, comparisons with figures 1b and 1c clearly suggest that the nature of the nonlinear contribution differs significantly with the water depth. For example, in figure 1b (corresponding to a water depth of 0.3m) the nonlinear increase in the maximum crest elevation is reduced to approximately 20%; while the second-order interactions account for approximately 50% of this increase. Furthermore, if one considers the shallow water depth ($d=0.15\text{m}$ in figure 1c) there is almost no nonlinear increase in the maximum crest elevation when compared to a linear theory based upon the component free waves. However, the maximum crest elevation (relative to linear theory) does not alone provide an appropriate measure of the nonlinearity of a wave form. Indeed, if one considers the steepness of the wave profiles outlined in figures 1a-1c, there is almost no change depending on the water depth.

An explanation for this effect lies in the nature of the nonlinear wave-wave interactions and, as will be indicated below, these also have implications for the ability of the nonlinear wave models to accurately predict the water particle kinematics. If one considers the second-order solution originally outlined by Longuet-Higgins and Stewart (1960), the nonlinear wave-wave interactions may be subdivided into two categories. Firstly, there are the so-called frequency-sum terms which correspond to a transfer of energy into the short wave or high frequency components. These may be interpreted as representing local nonlinear wave-wave interactions, and are responsible for increases in the local energy density as well as the increase in the maximum crest elevation. In contrast, the second category of interactions are represented by the so-called frequency-difference terms. These correspond to a transfer of energy into the long wave, or low frequency, wave components. These interactions may be interpreted as representing the global changes which are, in particular, responsible for the set-down beneath the wave group.

Before considering the relative magnitude of these varying nonlinear wave-wave interactions, we will first contrast the ability of the nonlinear kinematics models discussed previously (namely Sobey, 1992 and Baldock and Swan, 1994) to

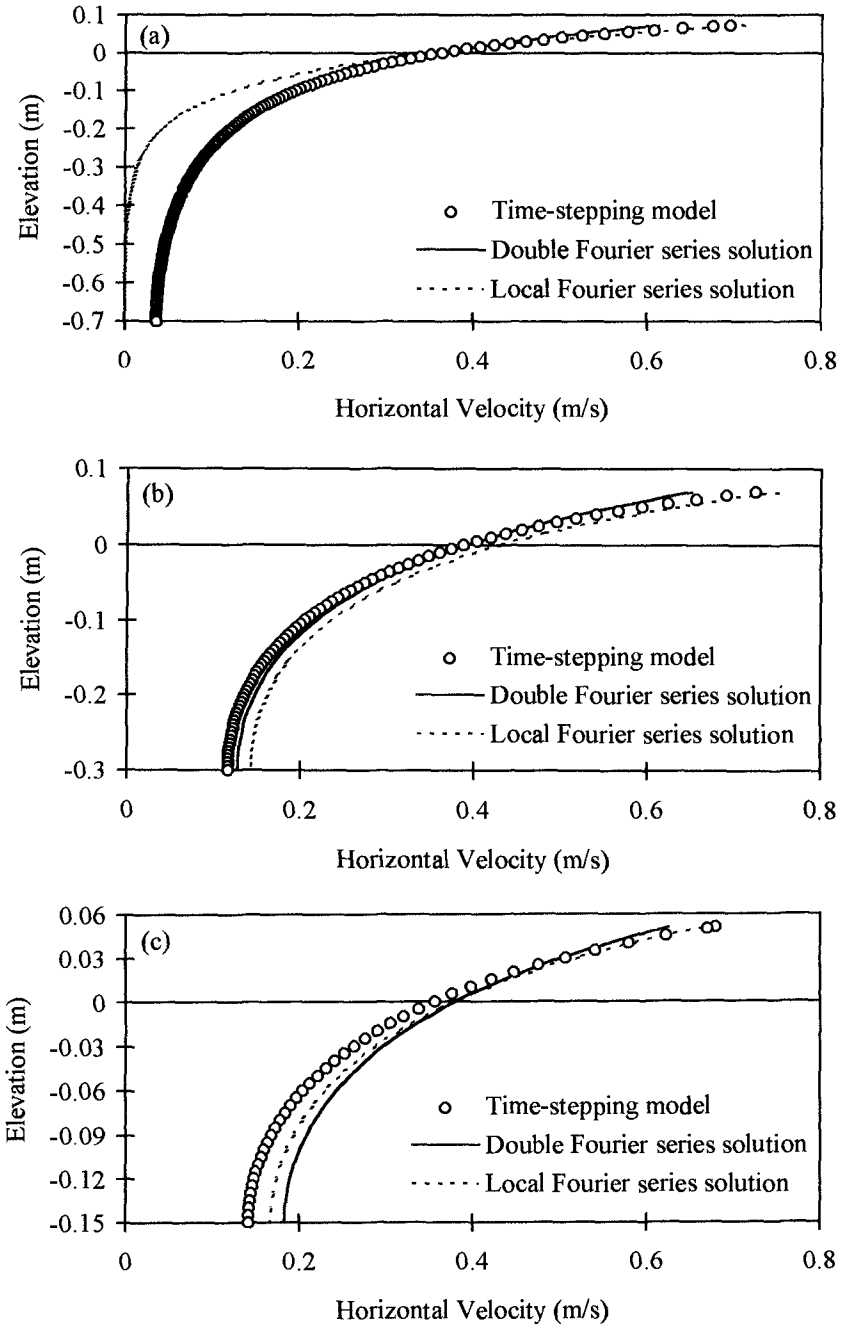


Figures 1a-1c. Time-histories of the water surface elevation, $\eta(t)$.
 (a) Deep water: $d=0.7\text{m}$ (b) intermediate water: $d=0.3\text{m}$ (c) shallow water: $d=0.15\text{m}$.

reproduce the exact numerical calculations provided by Dold and Peregrine (1984). Figures 2a-2c again relate to the broad-banded spectrum in three different water depths, and describe the depth variation in the maximum horizontal velocity, $u(z)$, arising beneath the largest wave crest (i.e. $t=0$ in figures 1a-1c). Since the kinematics models are both based upon a least squares fit to the predicted nonlinear surface profile, it may be assumed that in all cases the surface profile, $\eta(t)$, is well represented by these models. Indeed, if this were not the case the underlying kinematics could not be confidently predicted. However, despite near-perfect agreement with the surface profile, the predicted kinematics show considerable variation. For example, in the deep water case ($d=0.7\text{m}$ on figure 2a) the double Fourier series solution (Baldock and Swan, 1994) provides a very good description of the nonlinear kinematics up to the still water level, but slightly underestimates the maximum velocities within the vicinity of the water surface. In contrast, the local Fourier series solution (Sobey, 1992) provides an excellent description of the kinematics within the wave crest, but wildly underestimates the horizontal velocities beneath the still water level.

The reasons for these discrepancies are clear. Firstly, the double Fourier series solution is based upon a fifteenth order approximation (or $N=M=15$ in equation 2), and thus incorporate a total of 225 harmonics. However, since the peak of the input spectrum arises at $N=M=3$, the accuracy of the solution is approximately equivalent to a fifth-order Stokes' solution. Since the wave events under consideration are extremely steep (within 5% of their breaking limit), it is not at all surprising that this level of approximation underestimates the near-surface crest kinematics. Unfortunately, the nature of this solution is such that small increases in the order of the approximation (i.e. $N=M=18$) provides little by way of increased accuracy, but has a large effect upon the computational requirements. Indeed, significant increases in the order of the approximation become practically unrealistic. In contrast, the local Fourier series solution is only fitted to a small section of the wave profile in any one window, and in the vicinity of the largest crest the curvature of the surface profile is such that the solution locates a large proportion of the wave energy in the high frequency range. As a result, it obtains a good description of the surface profile and the near-surface kinematics, but the predicted velocities decay too rapidly with depth (as is consistent with high frequency wave components), and the solution thus underestimates the kinematics at all points beneath the still water level.

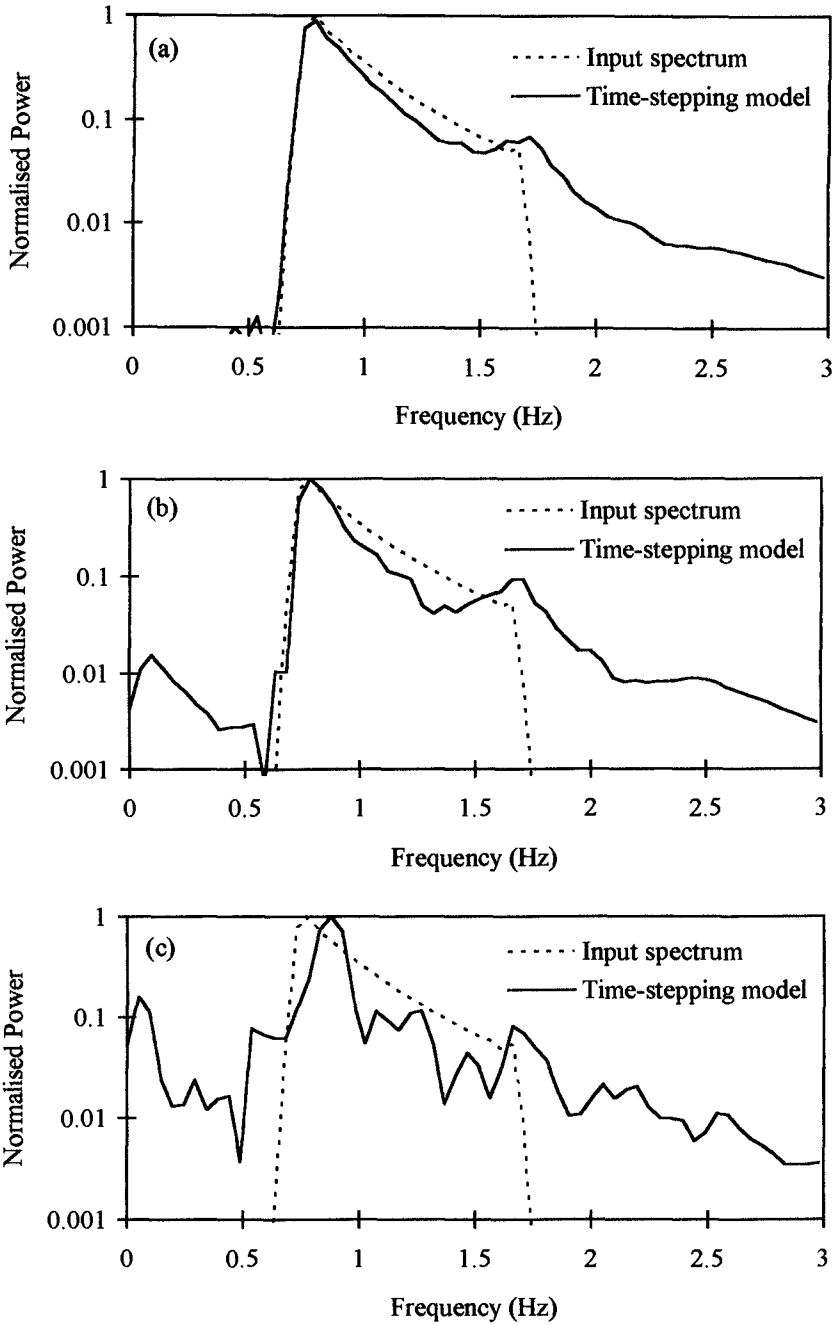
A similar pattern of results is also presented in figures 2b and 2c corresponding to water depths of $d=0.3\text{m}$ and 0.15m respectively. In each of these cases (and indeed many other cases which have also been investigated) the local Fourier series solution provides a good description of the maximum horizontal velocities arising close to the water surface. However, with increasing depth beneath the surface, the description becomes poor. In contrast, the double Fourier series solution provides reasonable agreement over most of the water column, but consistently under-predicts the largest velocities arising close to the water surface.



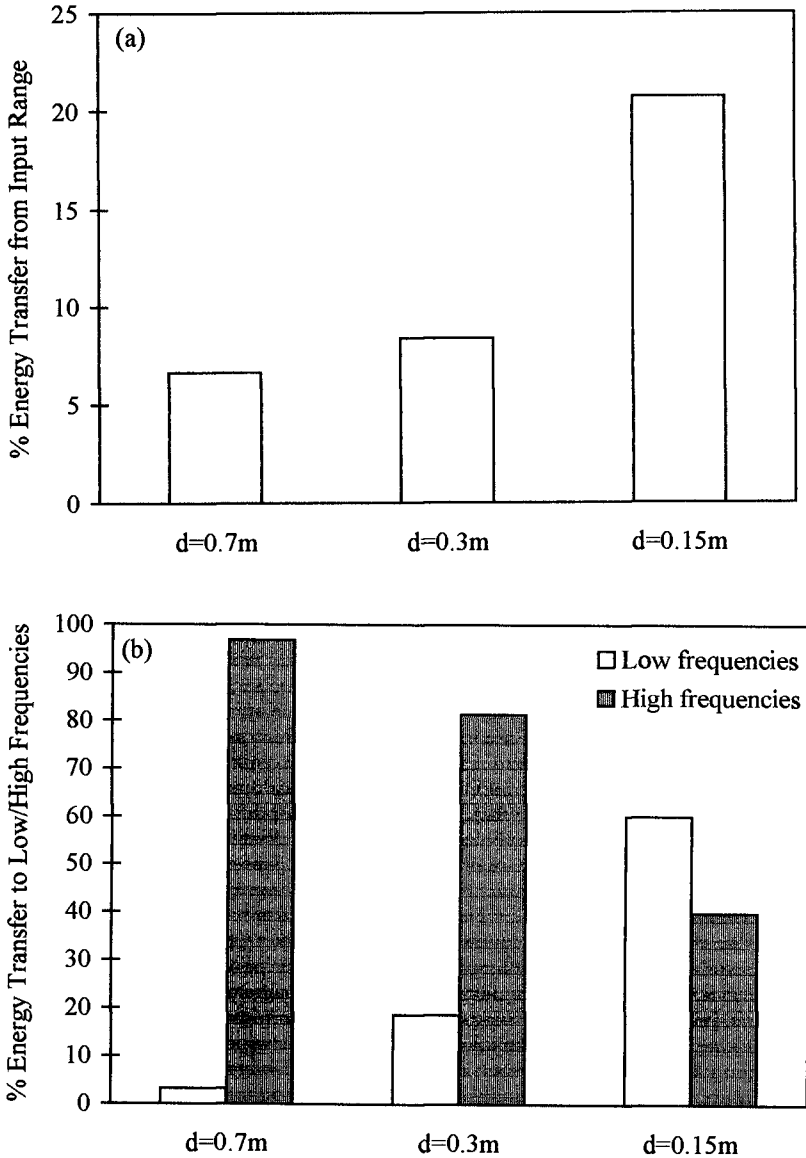
Figures 2a-2c. Horizontal velocities beneath the wave crest, $u(z)$.
(a) Deep water: $d=0.7\text{m}$ (b) intermediate water: $d=0.3\text{m}$ (c) shallow water: $d=0.15\text{m}$.

To explain the varying success of these solutions, and in particular its dependence on the water depth, the normalised power spectra derived from a Fourier transform of the numerically predicted water surface elevations are presented on figures 3a-3c. In the deep water case (figure 3a) it is clear that the dominant nonlinear interactions generate high frequency or frequency-sum terms which in turn produce a large increase in the local energy density in the vicinity of the large wave crest. This is consistent with the experimental study presented by Baldock, Swan and Taylor (1996), and explains the large local increase in the maximum water surface elevation. However, as the water depth reduces it becomes apparent that there is a larger transfer of energy into the low frequency, or frequency-difference, terms. These results are consistent with the analysis of measured wave records presented by Mansard et al (1988), and with recent laboratory data presented by Baldock and Swan (1996). The relative importance of the total nonlinearity within the numerically calculated wave profiles is further considered in figure 4a. Within this figure each water depth has been considered separately, and the total transfer of energy out of the input range (ie. $0.6 \leq T \leq 1.4$ or $4.5 \leq \omega \leq 10.5$) has been determined from the wave spectra given in figures 3a-3c. At first sight these results are perhaps unexpected since it suggests that the shallow water case ($d=0.15\text{m}$) represents the most nonlinear wave form, at least defined in terms of energy transfers, despite the fact that the maximum crest elevation in this case shows no significant increase above the linearly predicted value (figure 1c). However, the reasons for this are clarified in figure 4b where the relative importance of the local and global nonlinearity is addressed. In this case the transfer of energy into the high and low frequencies are expressed as a percentage of the total energy transferred out of the input range for each water depth. These results clearly suggest that in deep water the local nonlinearity is dominant; while a reduction in the water depth leads to an increase in the importance of the frequency-difference terms, and a reduction in the importance of the frequency-sum terms. As a result, in the shallow water case ($d=0.15\text{m}$) the transfer of energy into the frequency-difference terms (or global interactions) is larger than the transfer of energy into the frequency-sum terms (or local interactions).

This variation in the nature of the nonlinearity explains the success (or otherwise) of the kinematics models. For example, the double Fourier series solution is based upon a best fit to a measured (or in this case predicted) time-history of the water surface elevation which includes several complete wave forms. As such, it is able to resolve both the local and the global nonlinearity, and is only restricted in the sense that the total number of harmonics is small when compared to the peak of the wave spectrum. As a result, this solution will give satisfactory results provided the transfer of energy to either the high frequencies or the low frequencies is not too large. For example, if the local nonlinearity is very strong the double Fourier series solution will typically underestimate the maximum horizontal velocity arising close to the water surface (figure 2a); while if the global nonlinearity is excessive, this solution will typically underestimate the set-down beneath the wave group, and will therefore tend to overestimate the horizontal velocities arising close to the bottom boundary (figure 2c). In contrast, the local Fourier series solution is fitted to a small section of



Figures 3a-3c. Normalised power spectra based on predicted $\eta(t)$.
 (a) Deep water: $d=0.7\text{m}$ (b) intermediate water: $d=0.3\text{m}$ (c) shallow water: $d=0.15\text{m}$.



Figures 4a-4b. Energy transfers arising due to nonlinear wave-wave interactions. (a) Energy transferred out of the input range. (b) Relative importance of the high and low frequencies.

the water surface profile within an individual window. As a result, it can successfully model the high frequency, or local nonlinearity, since this will determine the local curvature of the surface profile. However, given the input in any one window, it is unable to resolve the global nonlinearity, since the window length is significantly shorter than the length-scale appropriate to the set-down beneath the wave group. As a result, in those cases where the global nonlinearity is important, one would typically expect the local Fourier series solution to overestimate the velocities beneath the still water level (figures 2b and 2c).

Concluding Remarks.

The present paper has considered the description of highly nonlinear and unsteady (or transient) wave events, and has demonstrated that the nature of the nonlinear wave-wave interactions is strongly dependent upon the water depth. In particular, in deep water the exact numerical calculations indicate that the local nonlinear wave-wave interactions, corresponding to the frequency-sum terms, are dominant. However, as the water depth reduces the global nonlinearity, represented by the frequency-difference terms, become progressively more important. This result has important implications for the prediction of the underlying kinematics. For example, a double Fourier series solution (Baldock and Swan, 1994) is limited in respect of the total number of Fourier components which can practically be included; while the local Fourier series solution is unable to model the global non-linearity and thus becomes less effective in shallow water. However, despite these reservations, it should be stressed that these models will typically provide an improved description of the water particle kinematics when compared to the existing design solutions which either ignore the unsteadiness of the wave form, or the nonlinearity. In particular, the double Fourier series solution can accurately incorporate both the increased crest-trough asymmetry due to the local nonlinearity, and the set-down beneath the wave group due to the global nonlinearity, provided the extreme wave event is not too close to its breaking limit.

Acknowledgements

The authors gratefully acknowledge the assistance provided by Professors Peregrine and Sobey for allowing access to their respective numerical codes, and for the financial support provided by the UK Engineering and Physical Sciences Research Council (EPSRC) via the Marine Technology Directorate Ltd.

References.

Baldock, T.E. and Swan, C. 1994. Numerical calculations of large transient water waves. *Applied Ocean Research*, **16**: 101-112.

- Baldock, T.E. and Swan, C. 1996. Extreme waves in shallow and intermediate water depths. *Coastal Engineering*, **27**: 21-46.
- Baldock, T.E., Swan, C. and Taylor, P.H. 1996. A laboratory study of non-linear surface waves on water. *Philos. Trans. Royal Society, London. Ser. A*, **354**: 1-28.
- Benjamin, T.B. and Feir, J.E. 1967. The disintegration of wavetrains on deep water. Part 1. Theory. *J. Fluid Mech.*, **27**: 417-430.
- Craig, W., and Sulem, C. 1993. Numerical simulation of gravity waves. *J. Comp. Phys.* **108**: 73-83.
- Dean, R.G. 1965. Stream function representation of non-linear ocean waves. *J. Geophys. Research*, **70**: 4561-72.
- Dold, J.W. and Peregrine, D.H. 1984. Steep unsteady waves: an efficient computational scheme. *Proc. 19th Int. Conf. on Coastal Engineering*, ASCE, **1**: 955-67.
- Fenton, J.D. 1985. A fifth order Stokes' theory for steady waves. *J. Waterways Port Coastal & Ocean Engineering*, ASCE, **111**: 216-234.
- Fenton, J.D. 1992. Polynomial approximations and water waves. Proc. 23rd. Inter. Conf. Coastal Eng. **1**: 193-207. Venice 1992.
- Fenton, J.D. and Rienecker, M.M. 1982. A Fourier method for solving nonlinear water wave problems: applications to solitary wave interactions. *J. Fluid Mech.*, **118**: 411-443.
- Johannessen, T.B. & Swan, C. 1996. Numerical calculations of large unsteady water waves. Part 1: Comparisons with laboratory data. Submitted to Appl. Ocean Res.
- Lambrakos, K.F. 1981. Extended velocity potential wave kinematics. *J. Waterways Port Coastal & Ocean Engineering*, ASCE, **107**: 159-174.
- Longuet-Higgins, M.S. and Stewart, R.W. 1960. Changes in the form of short gravity waves on long waves and tidal currents. *J. Fluid Mechanics*, **8**: 565-583.
- Longuet-Higgins, M.S. and Cokelet, E.D. 1976. The deformation of steep surface waves on water. A numerical method of computation. *Proc. Roy. Soc. Ser. A*. **350**: 1-26.
- Mansard, E.P.D., Sand, S.E. and Klinting, P. 1988. Sub and super-harmonics in natural waves. *J. Offshore Mechanics and Arctic Engineering*, **110**: 270-217.
- Peregrine, D.H., 1983. Wave jumps and caustics in the propagation of finite-amplitude water waves. *J. Fluid Mechanics*, **136**: 435-452.
- Rozario, J.B., Tromans, P.S., Taylor, P.H. and Efthymiou, M. 1993. Comparisons of loads predicted using NewWave and other wave models with measurements on the Tern structure. *Advances in underwater tech., ocean sci., & offshore engng.* **29**: 143-58.
- Sobey, R.J. 1992. A local Fourier approximation method for irregular wave kinematics. *Applied Ocean Research*, **14**: 93-105.
- Stansberg, C.T. 1993. Second-order numerical reconstruction of laboratory generated random waves. Proc. 12th. OMAE conf., Glasgow, Scotland. **2**:143-51.
- Swan, C. 1990. An experimental study of waves on a strongly sheared current profile. Proc. 22nd Inter. Conf. Coastal Eng. **1**: 489-502. Delft. 1990.
- Swan, C. 1992. A stream function solution for waves on a strongly sheared current. Proc. 23rd. Inter. Conf. Coastal Eng. **1**: 684-697. Venice 1992.
- Tromans, P.S., Anaturk, A. and Hagemeijer, P. 1991. A new model for the kinematics of large ocean waves - application as a design wave. *Proc. 1st Int. Offshore & Polar Engng. Conf.* ISOPE.

CHAPTER 41

FETCH LIMITED SPECTRAL EVOLUTION IN FINITE DEPTH WATER

I.R. Young¹
L.A. Verhagen²

ABSTRACT

The results of a field experiment aimed at investigating the evolution of fetch limited waves in water of finite depth are presented. In particular, non-dimensional growth curves, the parametric form of the one dimensional spectrum and the directional spreading of the spectrum are investigated.

INTRODUCTION

Commencing with the cornerstone JONSWAP experiment (Hasselmann et al., 1973), the investigation of the evolution of deep water wind generated ocean waves has been a common theme. Although this case represents a very idealized situation, the resulting evolution provides valuable insight into the complex physics of wind wave evolution. In addition, the resulting non-dimensional growth curves and parametric spectral forms have proved a valuable aid to preliminary engineering design and for use in the validation of comprehensive spectral models.

The limitation of such studies to deep water is restrictive, particularly when it is considered that a significant percentage of coastal engineering works are in areas where finite water depth will influence the resulting wave field. Despite the obvious requirement, there exists no comprehensive counterpart to JONSWAP (Hasselmann et al., 1973) in finite depth water.

This paper presents the results of such an experiment. The evolution of the wave spectrum has been measured at a number of points along a shallow lake. The relatively simple geometry and bathymetry of the lake and the absence of contaminating swell results in a near ideal test basin in which to investigate fetch limited growth in finite depth water.

¹School of Civil Engineering, University College, UNSW, Canberra, ACT 2600, Australia

²Fugro-Inpark, P.O. Box 3000, 2260 DA Leidschendam, The Netherlands

The paper investigates three basic areas of finite depth fetch limited evolution: the development of non-dimensional energy and non-dimensional peak frequency with fetch, the one dimensional spectral form and directional spreading.

DESCRIPTION OF EXPERIMENT

The site chosen for the present experiment was Lake George (see Figure 1). The lake is approximately 20 km long by 10 km wide and has a relatively uniform bathymetry with an approximate water depth of 2 m. A series of 8 measurement stations were established along the long North-South axis of the lake as shown in Figure 1. With the exception of Station 6, the sites consisted of minimum blockage space frame towers, designed to provide minimum contamination to either wind or wave measurements made from the towers. The central site, Station 6, consisted of a large platform with temporary accommodation for the research team. Each of the sites was instrumented with a surface piercing Zwarts poles. In addition, cup anemometers at a reference height of 10 m were located at Stations 2, 4, 6, 7 and 8. Air temperature and relative humidity and water temperature were also measured at Stations 2, 6 and 8. A spatial array consisting of 7 Zwarts poles was established adjacent to the platform at Station 6 to provide high resolution measurements of the directional wave spectrum.

NON-DIMENSIONAL GROWTH CURVES

It is convenient to represent the data in terms of the non-dimensional variables: non-dimensional energy, $\epsilon = g^2 E / U_{10}^4$, non-dimensional frequency, $\nu = f_p U_{10} / g$, non-dimensional fetch $\chi = gx / U_{10}^2$ and non-dimensional depth $\delta = gd / U_{10}^2$ where g is gravitational acceleration, E is the total wave energy or variance of the wave record, f_p is the frequency of the spectral peak, d is the water depth, x is the fetch and U_{10} is wind velocity.

Figures 2 and 3 show scatter plots of ϵ (Figure 2) and ν (Figure 3) verses χ . The data have been partitioned into discrete intervals of δ . Figures 2 and 3 show data in the range $\delta = 0.2 - 0.3$. A preliminary investigation of the north/south data indicated that the data which conformed to deep water conditions was consistent with previous deep water growth law formulations. In particular, ϵ was well modeled by the JONSWAP relationship (Hasselmann et al., 1973), $\epsilon = 1.6 \times 10^{-7} \chi$ and ν by the Kahma and Calkoen (1992) form, $\nu = 2.18 \chi^{-0.27}$.

Noting these deep water asymptotic limits to the data, a nonlinear least squares analysis of the data yielded the model

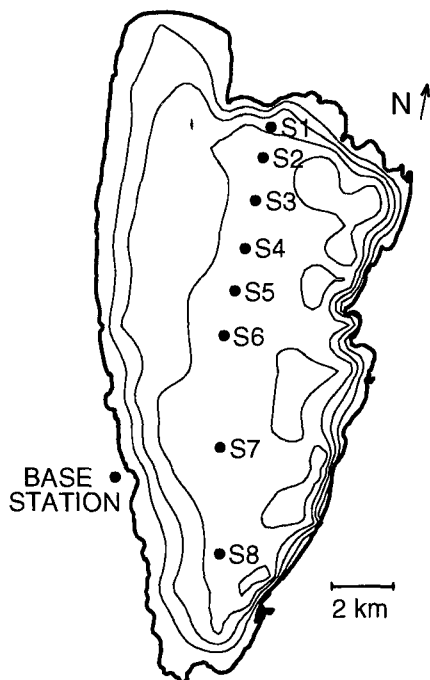


Figure 1: Map of the Lake George experimental site. The measurement locations are labelled S1 to S8. Data were transmitted to the Base Station on the western shore of the lake where it was logged under computer control. The contour interval is 0.5 m, with the maximum contour value 2 m.

$$\varepsilon = 3.64 \times 10^{-3} \left\{ \tanh A_1 \tanh \left[\frac{B_1}{\tanh A_1} \right] \right\}^{1.74} \quad (1)$$

where

$$A_1 = 0.493\delta^{0.75} \quad (2)$$

$$B_1 = 3.13 \times 10^{-3} \chi^{0.57} \quad (3)$$

and

$$\nu = 0.133 \left\{ \tanh A_2 \tanh \left[\frac{B_2}{\tanh A_2} \right] \right\}^{-0.37} \quad (4)$$

where

$$A_2 = 0.331\delta^{1.01} \quad (5)$$

$$B_2 = 5.215 \times 10^{-4} \chi^{0.73} \quad (6)$$

Equations (1) and (4) are shown in Figures 2 and 3 respectively. As these figures contains data for a finite range of δ (ie. $\delta = 0.2 - 0.3$), two curves are shown, one for each of the extremes of δ for that figure. Generally, the proposed

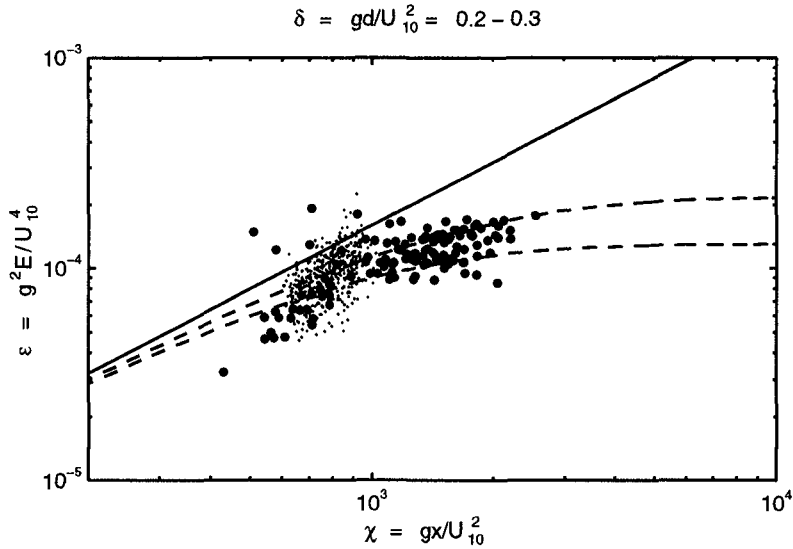


Figure 2: A scatter plot of non-dimensional energy, ϵ against non-dimensional fetch, χ . Only data with values of non-dimensional depth, δ between 0.2 and 0.3 are shown. The north/south data are shown as the large dots and the lower quality east/west data as the small dots. Equation (1) is shown for the two extremes of δ (ie. 0.2 and 0.3) by the two dashed lines. The deep water asymptotic form of Equation (1) is shown as the solid line.

relationships [(1) and (4)] approximate the data well. As with all previous field measurements of this type there is some data scatter.

At short non-dimensional fetch the waves are in deep water and approach the deep water asymptotic limits which are consistent with the numerous previous deep water data sets. As the non-dimensional fetch increases, the effects of the finite water depth become more pronounced and the data progressively deviate from the deep water limit. At relatively large values of non-dimensional fetch, further spectral development ceases as shown by the “plateau” regions of the curves in Figures 2 and 3. Rather than there being a single universal growth curve, there are a family of curves, one for each value of non-dimensional depth.

Lake George is approximately twice as long as it is wide and whether this aspect ratio limits the wave development along the north/south fetch must be addressed. To investigate this point, cases for which the wind direction was approximately perpendicular to the long east and west boundaries of the lake were extracted from the full data set. As there are no measurements of wind speed

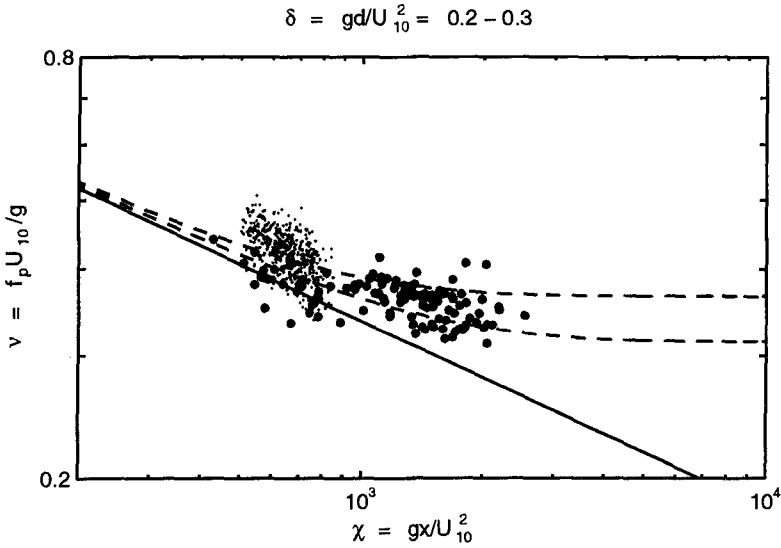


Figure 3: A scatter plot of non-dimensional peak frequency, ν against non-dimensional fetch, χ . Only data with values of non-dimensional depth, δ between 0.2 and 0.3 are shown. The north/south data are shown as the large dots and the lower quality east/west data as the small dots. Equation (4) is shown for the two extremes of δ (ie. 0.2 and 0.3) by the two dashed lines. The deep water asymptotic form of Equation (4) is shown as the solid line.

along the fetch for these cases, only data from Station 6, where the wind was always measured have been considered. As these east/west events are common, we can be very selective with the data, retaining only those cases for which the wind direction is within $\pm 10^\circ$ of normal to the respective shore lines. This east/west data set is also shown in Figures 2 and 3. Since there is no detailed information to determine the development of the wind field with fetch for these cases and since there is moderately elevated land to the east and west of the lake (compared with north/south which is quite flat) the east/west data set is considered to be of inferior quality to the north/south data set. Nevertheless, the east/west data set is consistent with the north/south data, confirming that the lake geometry has no significant influence on the results. It should be noted that there is only a relatively small range of values of χ for each selected range of δ for the east/west data, since all data is obtained from only a single dimensional fetch of approximately 5 km. Also, since the east/west data is believed to be of lesser quality than the north/south data, it was not used in the nonlinear least squares curve fit used to develop (1) and (4).

SPECTRAL EVOLUTION

Bouws et al. (1985) proposed the TMA spectral form for the representation of wind generated waves in water of finite depth

$$E(f) = \alpha g^2 (2\pi)^{-4} f^{-5} \exp \left[\frac{-5}{4} \left(\frac{f}{f_p} \right)^{-4} \right] \cdot \gamma \exp \left[\frac{-(f-f_p)^2}{2\sigma^2 f_p^2} \right] \cdot \Phi \quad (7)$$

and

$$\Phi = \left\{ \frac{[k(f, d)]^{-3} \frac{\partial k(f, d)}{\partial f}}{[k(f, \infty)]^{-3} \frac{\partial k(f, \infty)}{\partial f}} \right\} \quad (8)$$

Based on the wavenumber scaling arguments implicit in the TMA spectral form, Bouws et al. (1985, 1987) speculated that the spectral parameters should be functions of the non-dimensional wavenumber, $\kappa = U_{10}^2 k_p / g$, where k_p is the wavenumber of the spectral peak. To investigate this dependence with the present data set, the spectral parameters of α , γ and σ are presented as functions of κ in Figures 4, 5 and 6, respectively. As with previous studies of spectral evolution, there is significant scatter in the data.

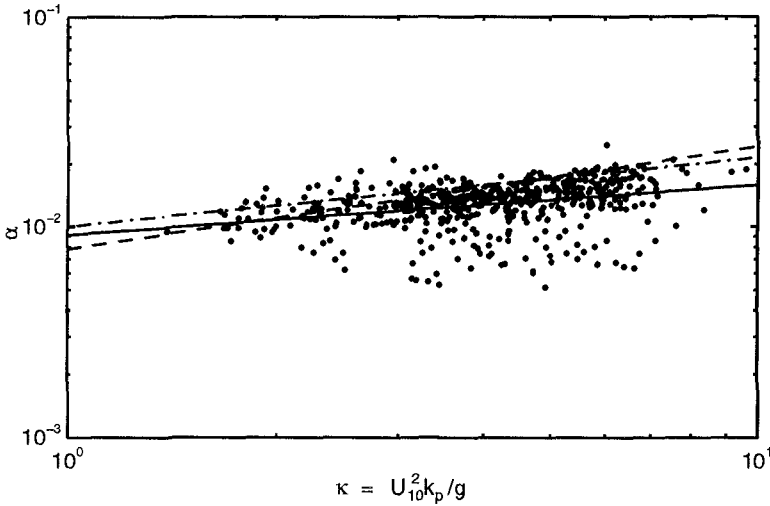


Figure 4: Values of the parameter α as a function of non-dimensional wavenumber, κ . The solid line is a least squares fit to the data [Equation (9)]. The TMA result is shown by the dashed line and the JONSWAP form, transformed from frequency to wavenumber space, by the dash-dot line.

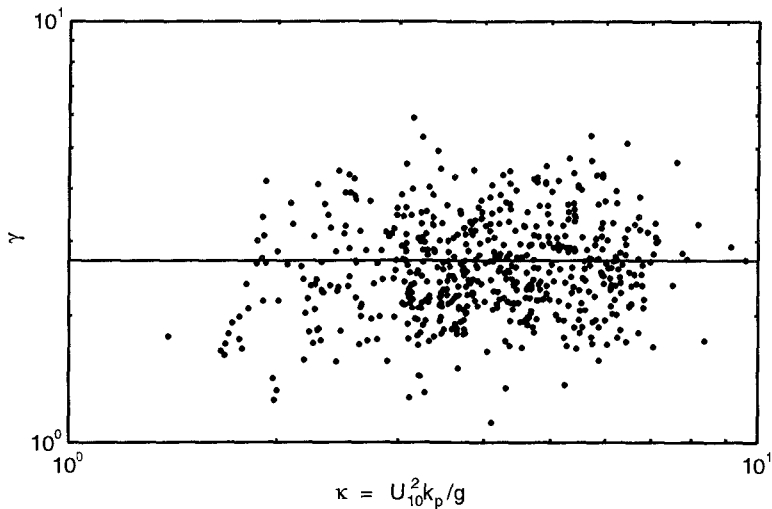


Figure 5: Values of the peak enhancement parameter, γ as a function of non-dimensional wavenumber, κ . The horizontal line represents the data mean.

Within the data scatter, a relationship between α and κ is clear, with α an increasing function of κ (see Figure 4). A least squares fit to the data yields the power law relationship

$$\alpha = 0.0091\kappa^{0.24} \quad (9)$$

Equation (9) is shown on Figure 4, together with the TMA result, $\alpha_{TMA} = 0.0078\kappa^{0.49}$. Both (9) and the TMA form are consistent with the data. In deep water the general TMA form reverts to that of JONSWAP. The deep water JONSWAP result scales α in terms of the non-dimensional frequency, ν , $\alpha_{JONSWAP} = 0.033\nu^{0.67}$. Assuming a deep water linear dispersion relationship, this result can be converted to wavenumber space, $\alpha_{JONSWAP} = 0.01\kappa^{0.33}$. This JONSWAP result is also shown in Figure 4 and is broadly consistent with the finite depth formulations.

All results are comparable and confirm that the trend towards decreasing values of α with increasing maturity of the waves, already observed in deep water, also holds in finite depth situations.

In contrast to the observable trend in α with κ , no similar result is apparent for either γ or σ . This result is consistent with both TMA (Bouws et al., 1985, 1987) and JONSWAP (Hasselmann et al., 1973). There is, however, significant sampling variability associated with these parameters. The mean values of the

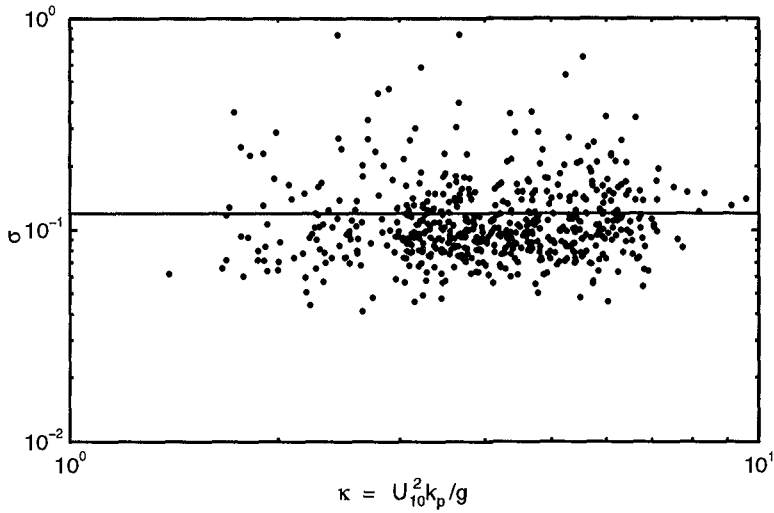


Figure 6: Values of the spectral parameter, σ as a function of non-dimensional wavenumber, κ . The horizontal line represents the data mean.

data set yield $\gamma_{mean} = 2.70$ and $\sigma_{mean} = 0.12$.

DIRECTIONAL SPREADING

Two common models have been proposed to represent the directional spreading of wind waves: $\cos^{2s} \theta/2$ and $\text{sech}^2 \beta \theta$. A number of different techniques have been reported for the fitting of such analytical forms to the data. Mitsuyasu et al. (1975) and Hasselmann et al. (1980) analyzed their buoy data using the Fourier Expansion Method (Longuet-Higgins et al., 1963; Young, 1994) and determined the value of s from the first 2 components of the Fourier expansion. Donelan et al. (1985) compared this approach with one in which the directional form was matched to the half-power points of the measured spreading function. It was argued that matching the half-power points was more meaningful since interest is concentrated on the energetic region of the directional distribution. This technique appeared to reduce the scatter in the data.

In addition to these techniques, application of a nonlinear least squares fit [Levenberg-Marquardt method, Press et al. (1986)] was also investigated with the present data. This least squares approach, was adopted here, together with a Maximum Likelihood Method analysis of the data from the directional array.

Both formulations of the spreading function yield qualitatively similar results,

indicating the spectrum is narrowest at the spectral peak frequency and broadens at frequencies both larger and smaller than the peak value. The $\cos^{2s} \theta/2$ formulation exhibited marginally less scatter than the $\text{sech}^2 \beta \theta$ form and was adopted for further analysis.

A least squares analysis of the directional data yields the following form for the present finite depth data

$$s = \begin{cases} 11 \left(\frac{f}{f_p}\right)^{2.7} & f < f_p \\ 11 \left(\frac{f}{f_p}\right)^{-2.4} & f \geq f_p \end{cases} \quad (10)$$

Equation (10) has been constrained to yield narrowest spreading at $f/f_p = 1$. The scatter in the data is such that the actual point of narrowest spreading cannot be determined with great accuracy. It is clearly, however, in the vicinity of the spectral peak frequency.

Equation (10) is shown in Figure 7 together with the deep water results of Mitsuyasu et al. (1975), Hasselmann et al. (1980) and Donelan et al. (1985). As the results of Mitsuyasu et al. (1975) and Hasselmann et al. (1980) are both wave age dependent, mean values typical of their respective data sets have been used to construct Figure 7 (Mitsuyasu et al., 1975 - $U_{10}/C_p = 1.1$; Hasselmann et al., 1980 - $U_{10}/C_p = 1.4$). As Donelan et al. (1985) provide no functional form expressed in terms of s , the result in Figure 7 was obtained from digitizing the result given in their Figure 30.

The present results are marginally narrower (higher s) than those of both Mitsuyasu et al. (1975) and Hasselmann et al. (1980), they are however significantly broader than the high resolution results of Donelan et al. (1985). As shown by Donelan et al. (1985), the results of both Mitsuyasu et al. (1975) and Hasselmann et al. (1980) are excessively broad due to the instrumentation and analysis technique utilized. The present result [Equation (10)] should have comparable resolving power to the result of Donelan et al. (1985). The inference is that finite depth wind wave spectra are broader than their deep water counterparts. Due to the relatively narrow range of $k_p d$ spanned by the present data set a more emphatic statement cannot be made. At present it is necessary to rely on these two independent data sets (Donelan et al., 1985 - deep water; Lake George - finite depth). There is always some possibility that, in addition to water depth, there are other unknown influences responsible for the different spreading.

CONCLUSIONS

The data set presented in this paper represents the first comprehensive field study of the evolution of fetch limited waves in water of finite depth. The data set is sufficiently comprehensive to fully define non-dimensional growth curves for both energy and peak frequency. In contrast to deep water results, a single growth relationship does not exist for each quantity. Rather, a family of curves result,

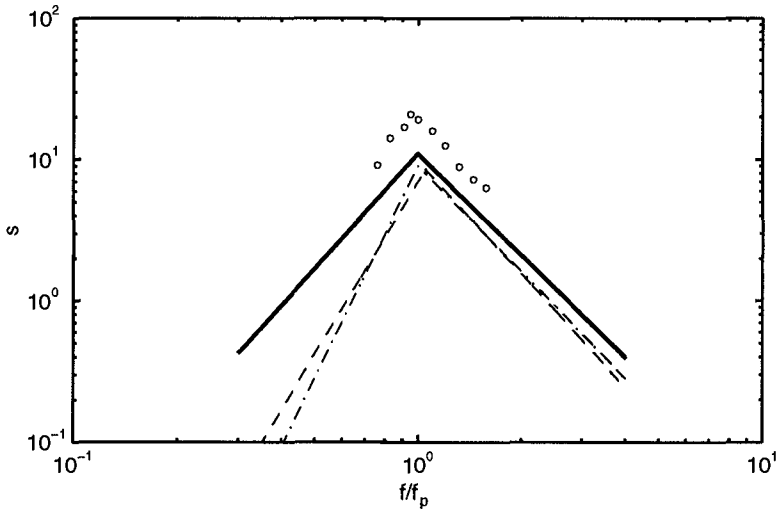


Figure 7: The dependence of the directional exponent s for the present finite depth data as a function of f/f_p [Equation (10)] (thick solid line). Also shown for comparative purposes are previous deep water data sets: Mitsuyasu et al. (1975) - 'dash dot line'; Hasselmann et al. (1980) - 'dashed line'; Donelan et al. (1985) - 'open circles'.

depending on the non-dimensional depth.

The one-dimensional spectrum has been shown to conform to the TMA form. The spectral parameter α is shown to be a function of the non-dimensional peak wavenumber, κ .

The directional spreading is qualitatively similar to deep water results. The spectra are narrowest at the spectral peak frequency and broaden at frequencies both above and below the peak. Compared with deep water results, finite depth spectra appear to exhibit broader spreading. This is possibly due to the different nonlinear coupling which will exist in finite depth cases.

The present data set is significantly more comprehensive than previous finite depth studies. The results of these previous studies are, however, consistent with the present results. This occurs, despite the fact that a wide range of bed materials exist for the various data sets. As a result, it can be speculated that bed material has little influence on spectral evolution under fetch limited conditions. This is markedly different to other finite depth cases, such as swell attenuation, where the rate of decay is very sensitive to the bed material.

REFERENCES

- Bouws, E., Günther, H., Rosenthal, W. and Vincent, C.L., 1985. Similarity of the wind wave spectrum in finite depth water, 1. Spectral form. *J. Geophys. Res.*, 90: 975-986.
- Bouws, E., Günther, H., Rosenthal, W. and Vincent, C.L., 1987. Similarity of the wind wave spectrum in finite depth water, 2. Statistical relationships between shape and growth stage parameters. *Dtsch. Hydrogh. Z.*, 40: 1-24.
- Donelan, M.A., Hamilton, J. and Hui, W.H., 1985. Directional spectra of wind-generated waves. *Phil. Trans. R. Soc. Lond.*, A 315: 509-562.
- Hasselmann, K. et al., 1973. Measurements of wind-wave growth and swell decay during the Joint North Sea Wave Project (JONSWAP). *Dtsch. Hydrogh. Z., Suppl. A*, 8, 12, 95pp.
- Hasselmann, D.E., Dunckel, M. and Ewing, J.A., 1980. Directional wave spectra observed during JONSWAP 1973. *J. Phys. Oceanogr.*, 10, 8: 1264-1280.
- Kahma, K.K. and Calkoen, C.J., 1992. Reconciling discrepancies in the observed growth of wind-generated waves. *J. Phys. Oceanogr.*, 22: 1389-1405.
- Longuet-Higgins, M.S., Cartwright, D.E. and Smith, N.D., 1963. Observations of the directional spectrum of sea waves using the motions of a floating buoy. in 'Ocean wave spectra', Englewood Cliffs, Prentice Hall, Inc.: 111-136.
- Mitsuyasu, H., Tasai, F., Suhara, T., Mizuno, S., Onkusu, M., Honda, T. and Rukiiski, K., 1975. Observations of the directional spectrum of ocean waves using a cloverleaf buoy. *J. Phys. Oceanogr.*, 5: 751-761.
- Press, W.H., Flannery, B.P., Teukolsky, S.A. and Vetterling, W.T., 1986. *Numerical Recipes*. Cambridge University Press, 818pp.
- Young, I.R., 1994. On the Measurement of Directional Wave Spectra. *Applied Ocean Research*, 16: 283-294.

CHAPTER 42

Measurement of Breaking Waves Using Particle Image Velocimetry

Kuang-An Chang ¹ and Philip L.-F. Liu ²

1. Introduction

The water wave breaking problem has been studied for many years. The most popular experimental methods for studying this problem include the flow visualization method and the Laser Doppler Velocimetry (LDV). However, the first method lacks quantitative description and the second method, in general, needs hundreds of measurements to form a flow field. Instantaneous quantitative flow field information is nearly impossible, if these two methods are used. In recent years, the Particle Image Velocimetry (PIV) has been proven to be a powerful tool for two-dimensional instantaneous velocity measurement. Tens to hundreds of velocity measurements using the LDV can be done in only one single measurement using the PIV.

The LDV is the most common tool for non-intrusive velocity measurements. By using the LDV and the phase average method, Mizuguchi (1986) and Okayasu et al. (1986) measured hundreds of points under a plunging breaker on sloping beaches. The flow fields of the mean and turbulence velocity were formed and the vorticity was calculated. In addition, Nadaoka et al. (1989) studied turbulent structures in surf zone using either the phase-averaged method or the moving-averaged method and demonstrated the differences between these two methods. In their work, the strain rate and its principal axes, Reynolds stress and momentum transport were obtained. More recently, a series of papers published by Ting and Kirby (1994, 1995, 1996) attempted to describe the turbulence structure under plunging and spilling breaking waves. In their works, turbulence transport under trough level was studied based on the turbulent kinetic energy equation. All the work mentioned above are based on either the phase or the moving average in turbulence measurements. In other words, experimental studies of wave breaking contain, in general, instantaneous and/or phase-averaged velocity information. As far as the authors know, the ensemble-averaged velocity field is rare for the unsteady problems such as breaking waves. However, the wave period in the

¹Graduate Student, ²Professor, School of Civil and Environmental Engineering, Cornell University, Ithaca, NY 14853

surf zone is not quite constant even for the monochromatically generated waves. The effect of the questionable “phase average” is not yet known.

Beside the LDV technique, the PIV has been used to measure velocity field in recent years. A good review of the PIV technique can be found in Adrian (1991). However, the PIV is still a quite new tool in water-wave related studies. A detailed description of the PIV used in a coastal engineering laboratory is given by Greated et al. (1992). By using PIV, Quinn (1995) studied near-breaking and broken waves on different slopes and compared the results with those of Boussinesq models. Skyner (1996) studied near-breaking plunging waves and compared PIV results with a boundary element model. The instantaneous flow field and the evolution of a quasi-steady breaking wave generated by a submerged airfoil was studied by Lin and Rockwell (1994, 1995). Hornung et al. (1995) measured velocity field and calculated vorticity under a hydraulic jump and used the results to confirm a control-volume prediction. Perlin et al. (1996) studied a plunging breaker in deep water and found the largest particle velocity is about 30% greater than the phase speed. In all the work mentioned above either the instantaneous flow field information or the quasi-steady breaker such as hydraulic jump was reported. No turbulence properties have been obtained.

In this study, deep-water spilling breaking waves are investigated by applying the PIV technique. By repeating the initial and boundary conditions carefully, the mean velocity and turbulence intensity are obtained from ensemble average.

2. Experimental Set-up

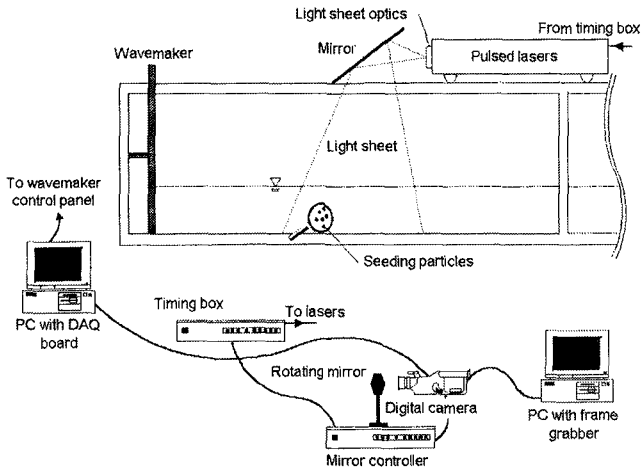


Figure 1: Experimental Set-up

The experiments were conducted in a 30m long, 0.6m wide and 0.9m deep wave tank. Waves are generated by a piston-type wavemaker controlled by a Pentium PC. Monochromatic waves were generated by moving the wave board periodically as fol-

lows: $\xi(t) = -A \cos(2\pi ft)$ in which $A = 7.0$ cm and $f = 1.0$ Hz. The error of the wave board motion is less than 0.5% of the stroke if the same motion is repeated. The PC also sent out pulses to trigger a camera so that the time interval between starting wavemaker and triggering camera can be well controlled. The breaking point, defined as the front face of wave becomes vertical, is about 1/3 of the wavelength away from the wave board at $x = 38$ cm with $x = 0$ representing the center of wave board trajectory. The wavelength, calculated from linear theory, is 1.2m. A wave gauge placed close to breaking point at $x = 35$ cm showed that the wave height is 14.5cm. The water depth was kept at 20cm. A light sheet about 1mm in thickness at the center of tank was created by frequency-doubled dual Nd:YAG lasers with a -12.7mm cylindrical lens combined with a 2000mm spherical lens. The lasers have a 200mJ/pulse maximum output energy and 10ns pulse duration in 532nm wavelength. A high resolution digital CCD camera (1316×1034 pixels) connected to a Pentium PC with a frame grabber in it was used to perform the so-called "on line" PIV. The camera equipped with a 60mm focus lens set at f/4.0 was located 2.7m in front of the light sheet. The field of view (FOV) is 40cm which is 1/3 of the wavelength and the resolution is 0.3mm/pixel. The time interval between two laser pulses was 2ms with error less than 1 μ s. In order to resolve the directional ambiguity, a rotating mirror was used (Adrian 1986). The lasers were located on top of the tank. The light sheet was redirected by a mirror to the test section. A black tape was stuck on the bottom of tank to reduce the reflection. The seeding particles were conifer pollen which has mean diameter 54 μ m and their specific weight are close to that of water. The conifer pollen has been proven to be good seeding particles for large scale PIV experiments (Greated et al. 1992). Velocity fields of three areas were measured. The first area is centered at $x = 40$ cm where the wave starts to break. The second and the third area are centered at $x = 70$ cm and $x = 97$ cm, respectively, which are about 1/4 and 1/2 wavelength behind the breaking point. Only the results from the first and third measuring areas are shown here. The ensemble-averaged velocity was obtained by repeating 24 runs at the third measuring area for studying the turbulence generated by broken waves. See figure 1 for the sketch of experimental set-up.

After the image was captured, it was then analyzed by first applying the threshold to remove the noise and then performing the auto-correlation (Lourenco and Krothapalli 1994). The interrogation area for velocity calculation was 64×64 pixels. The timing was calibrated to have an uncertainty less than 1ms. Following the same procedure as the experiments were done, the error in velocity measurement is 1 cm/s which was obtained from the standard deviation of the stationary flow.

3. Results and Discussion

It is known that the particle velocity exceeds phase speed when a wave starts to break. This can be seen from figure 2 and 3. Figure 2 shows the velocity field under the second crest (first one doesn't break) just before breaking. The maximum velocity is 1.08 m/s which is 90% of the phase speed. Figure 3 shows the same wave crest just passing its breaking point. It has maximum velocity 1.52 m/s which is 25% greater than phase speed. Therefore it is expected that the particle velocity will be at least 25% higher than the phase speed during breaking.

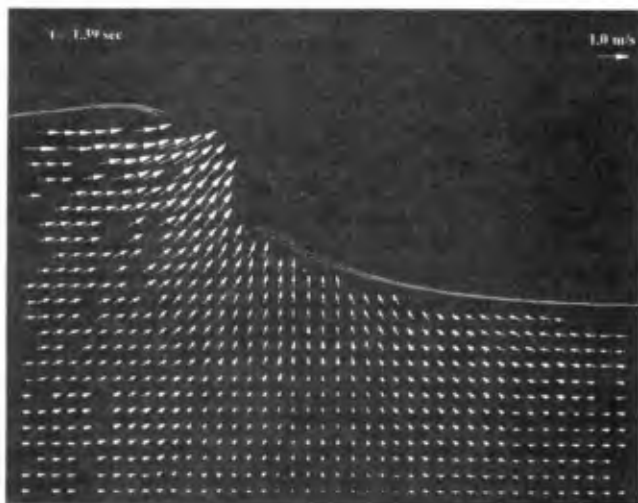


Figure 2: The first breaking wave reaching the breaking point at $t = 1.39$ sec with FOV from $x = 21$ to 61 cm and $z = -17.4$ to 14.4 cm (the first measuring area).

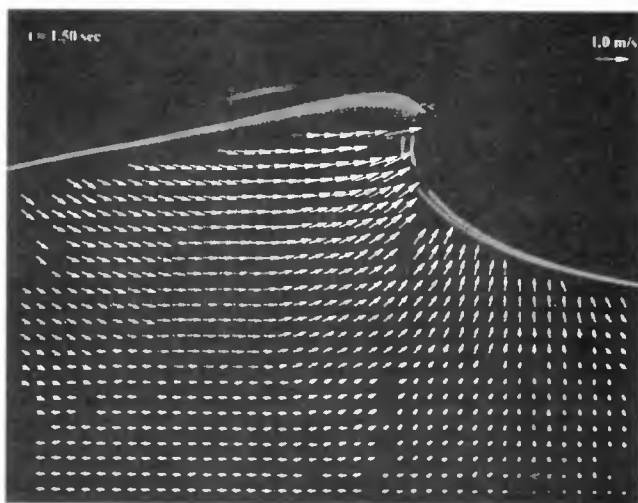


Figure 3: The first breaking wave passing the breaking point at $t = 1.50$ sec with the same FOV as figure 2.

Once the wave breaks, it generates lots of air bubbles near the surface which make the measurement very difficult. Due to this reason, we only show velocity field at one particular moment—broken wave crest just passes the third measuring area. At this moment the area has the strongest turbulence and the measurements are not affected by air bubbles. In order to obtain turbulence intensity, 24 measurements with same boundary and initial conditions were taken. Figure 4(a) shows the instantaneous

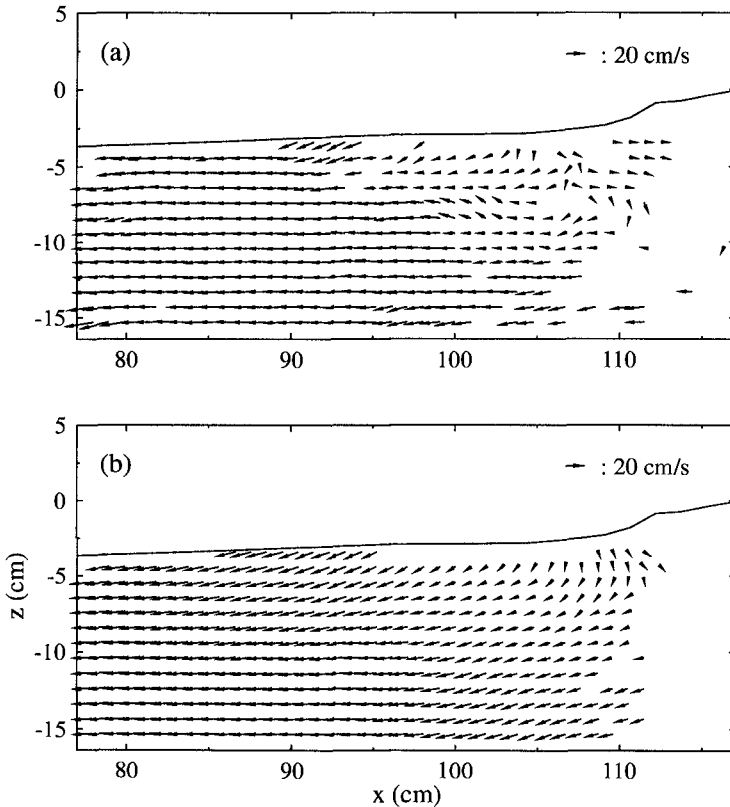


Figure 4: (a) Instantaneous velocity field (b) ensemble-averaged mean velocity field at $t = 3.39$ sec with FOV from $x = 77$ to 117 cm and $z = -16.4$ to 15.4 cm (the third measuring area).

velocity field of one of the 24 measurements at the third measuring area centered at $x = 97$ cm which is about $1/2$ wavelength behind the breaking point. Figure 4(b) shows the ensemble-averaged mean velocity from all 24 measurements. From the figure one

can see that some velocity data are missing near the right side. This is due to the residue air bubbles from the just-passed breaking waves. The linear kriging method (see Agterberg 1970) was used to interpolate and extrapolate the missing data. The

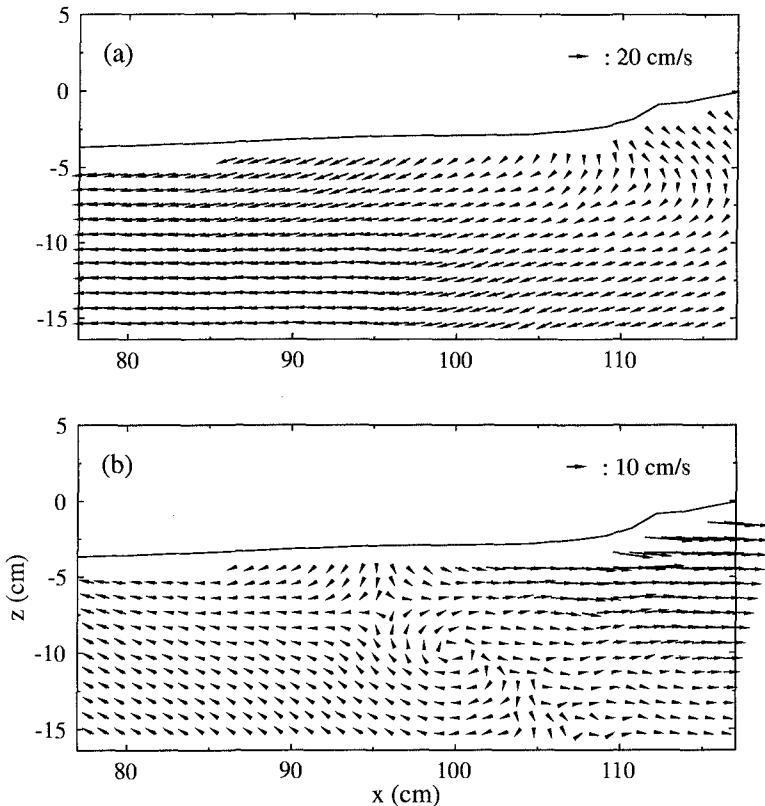


Figure 5: Linear kriging interpolated mean velocity field of figure 4(b) at (a) fixed frame (b) moving with $(-0.2, -0.05)\text{m/s}$.

interpolated velocity field is shown in figure 5(a). Figure 5(b) shows the same velocity field but from a moving frame $(-0.2, -0.05)\text{m/s}$. A clockwise vortex near the center of figure 5(b) can be clearly seen. This vortex is also shown in the later vorticity plot. Figure 6 shows the mean velocity contour in the horizontal and vertical directions. The vorticity of mean flow calculated by applying central finite difference is plotted in figure 7. One can find that the vorticity is negative in most of the area with the order of magnitude in a couple sec^{-1} . Figure 8 shows the turbulence intensity

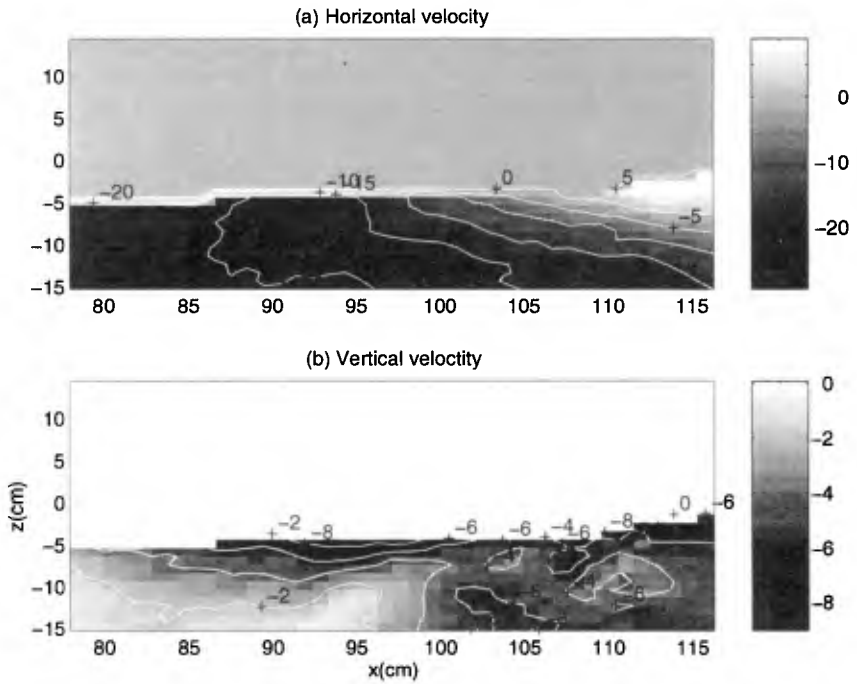


Figure 6: (a) Horizontal (b) vertical velocity (cm/s) of mean flow in the third measuring area.

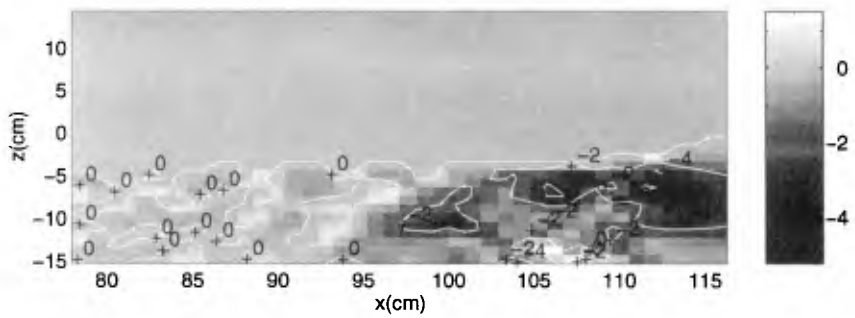


Figure 7: Vorticity (1/s) of mean flow in the third measuring area.

calculated from the ensemble average. Since the ensemble average is based on large number of samples, the ensemble-averaged turbulence intensity from different number of measurements were compared. It is found, from the contour plot, that the result from 15 measurements or more is close to that from 24 measurements. This may not mean 15 measurements are enough in performing ensemble average, but simply mean that the result from 15 measurements is quite close to that from 24 measurements and 15 measurements may be the minimum requirement. In other words, since it is difficult to obtain many measurements for calculating ensemble average in such kind of unsteady flow, at least 15 or more measurements may be necessary for performing the ensemble average. From figure 8 one can see the distribution of the turbulence

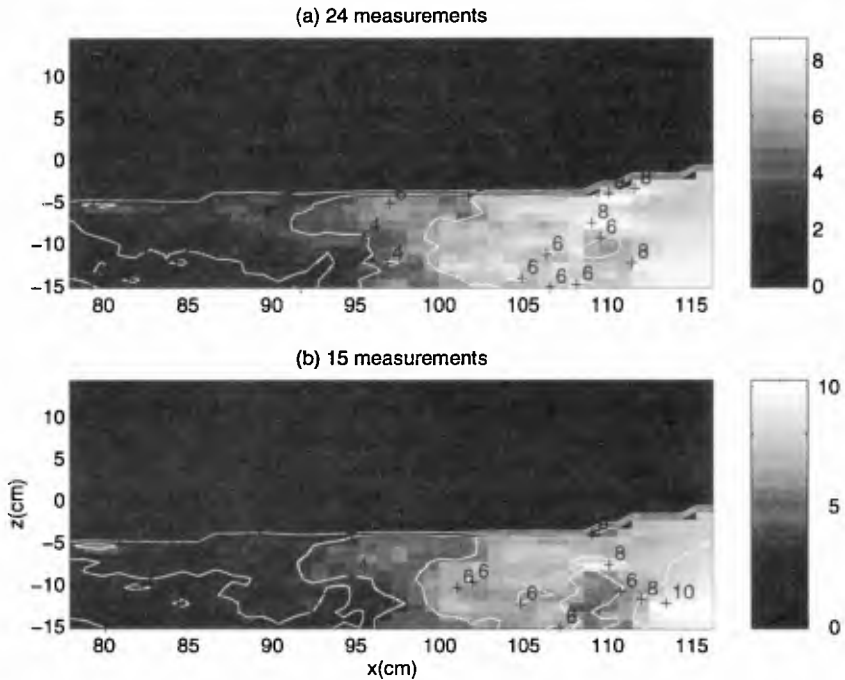


Figure 8: Turbulence intensity (cm/s) calculated from (a) 24 measurements (b) 15 measurements in the third measuring area.

intensity is quite uniform in the vertical direction. The maximum turbulence intensity in figure 8 is 10 cm/s. However, the maximum local mean velocity is only about 30 cm/s. This means that the turbulence intensity is almost the same order of magnitude as the local mean velocity, especially in the region close to the crest.

4. Conclusion

The PIV technique is proved to be a powerful tool in flow velocity measurement. The velocity field of non-breaking and near-breaking waves can be obtained without much difficulty. The maximum particle velocity of the deep-water spilling breaker is close to its phase speed at the breaking point and at least 25% greater than its phase speed during breaking. For broken waves, the mean velocity and turbulence intensity can be obtained from the ensemble average by repeating the same initial and boundary conditions. The turbulence intensity is about the same order of magnitude as the local mean velocity in the region the broken crest just passing through it. However, for the region which has highly concentrated air bubbles, more effort is needed in the future.

Acknowledgement

This research was supported by a grant from the National Science Foundation (CTS-9302203) to Cornell University.

References

- Adrian, R. J. 1986 "Image shifting technique to resolve directional ambiguity in double-pulsed velocimetry." *Appl. Opt.*, **25**(21), 3855-3858.
- Adrian, R. J. 1991 "Particle-imaging techniques for experimental fluid mechanics." *Annu. Rev. Fluid Mech.*, **23**, 261-304.
- Agterberg, F. P. 1970 "Autocorrelation functions in geology." *Geostatistics*, Merriam, D.F. (ed.), 113-141.
- Greated, C. A., Skyner, D. J. & Bruce, T. 1992 "Particle image velocimetry (PIV) in the coastal engineering laboratory." *Proc. 23th Int. Conf. Coastal Engrg.*, 212-225.
- Hornung, H. G., Willert, C. & Turner, S. 1995 "The flow field downstream of a hydraulic jump." *J. Fluid Mech.*, **287**, 299-316.
- Lin, J.-C. & Rockwell, D. 1994 "Instantaneous structure of a breaking wave." *Phys. Fluids*, **6**(9), 2877-2879.
- Lin, J.-C. & Rockwell, D. 1995 "Evolution of a quasi-steady breaking wave." *J. Fluid Mech.*, **302**, 29-44.
- Lourenco, L. & Krothapalli, A. 1994 "On the accuracy of velocity and vorticity measurements with PIV." *Experiments in Fluids*, **18**, 421-428.
- Mizuguchi, M. 1986 "Experimental study on kinematics and dynamics of wave breaking." *Proc. Int. Conf. Coastal Engrg.*, 589-603.
- Nadaoka, K., Hino, M. & Koyano, Y. 1989 "Structure of the turbulent flow field under breaking waves in the surf zone." *J. Fluid Mech.*, **204**, 359-387.
- Okayasu, A., Shibayama, T. & Mimura, N. 1986 "Velocity field under plunging waves." *Proc. Int. Conf. Coastal Engrg.*, 660-674.
- Perlin, M., He, J. & Bernal, L. P. 1996 "An experimental study of deep water plunging breakers." *Phys. Fluids*, **8**(9), 2365-2374.
- Quinn, P. A. 1995 *Breaking Waves on Beaches*. PhD thesis, University of Edinburgh.

- Skyner, D. 1996 "A comparison of numerical predictions and experimental measurements of the internal kinematics of a deep-water plunging wave." *J. Fluid Mech.*, **315**, 51-64.
- Skyner, D. J., Gray, C. & Greated, C. A. 1990 "A comparison of time-stepping numerical predictions with whole-field flow measurement in breaking waves." *Water Wave Kinematics*, eds. A. Torum and O.T. Gudmestad, 491-508.
- Ting, F.C.K. & Kirby, J. T. 1994 "Observation of undertow and turbulence in a laboratory surf zone." *Coastal Engineering*, **24**, 51-80.
- Ting, F.C.K. & Kirby, J. T. 1995 "Dynamics of surf-zone turbulence in a strong plunging breaker." *Coastal Engineering*, **24**, 177-204.
- Ting, F.C.K. & Kirby, J. T. 1996 "Dynamics of surf-zone turbulence in a strong spilling breaker." *Coastal Engineering*, **27**, 131-160.

CHAPTER 43

Computation of the near-bottom kinematics of shoaling waves

Luc Hamm¹

Abstract

Two practical formulations from Isobe and Horikawa (1982) and Swart and Crowley (1988) are tested against laboratory measurements: seven cases with monochromatic waves and two cases with random waves. It appears that the Isobe and Horikawa formulation can be used with confidence over a large range of wave conditions except in the surf zone when monochromatic waves are considered. The covocoidal theory from Swart and Crowley provides a more comprehensive description of wave properties but abnormal results have been noticed in a few cases. The use of one representative wave height and period in random waves may lead to an underestimation of velocity moments with low steepness waves.

1. Introduction

Shoaling waves (i.e. waves normally transforming over a sloping bottom) exhibit a more or less pronounced vertical asymmetry of the free surface elevation and orbital velocity when approaching the breaking point. Classical wave theories developed by assuming a flat bottom are able to predict the horizontal asymmetry of the waves in deep and intermediate water depths but not such a vertical asymmetry (Soulsby et al, 1993).

In this paper, we shall focus mainly on the prediction of near-bottom (i.e. outside the bottom boundary layer) kinematics of shoaling waves which is of special interest for the computation of sediment transport on the shereface and in the nearshore zone.

¹ Chief Engineer, Sogreah Ingénierie, BP 172, F-38042 Grenoble Cedex 9 - France

Firstly, the main results obtained from published experimental investigations in laboratory will be reviewed. Secondly, two existing practical formulations able to predict the near-bottom orbital velocities of shoaling waves will be briefly described. Their ability and accuracy will be then assessed against laboratory measurements in the third part of this paper.

2. A review of laboratory experiments

a) Monochromatic waves

A summary of the published laboratory studies reviewed for this paper is presented in table 1. Historically, many studies have focused on the prediction of the horizontal velocity under the crest which is one of the most important quantities used for design purposes (Dean and Perlin, 1986; Kirkgöz, 1986). The main result of interest is that **near the bottom**, the linear theory gives the best overall adjustment for flat and sloping beds up to the breaking point and within the surf-zone. It should be pointing out that this very flattering comparison cannot be extrapolated to the overall velocity profile (Hattori, 1986). In particular, the observed skewness of velocities (Nadaoka and Kondoh, 1982) cannot be predicted.

Table 1 Measurements of near bottom orbital velocities in laboratory (regular waves)

Authors	beach slope	n° of tests	type of measurements	measur. in surfzone
Iwagaki & Sakai (1970)	flat	22	profiles at crest and time series near bottom	No
Tsuchiya & Yamaguchi (1972)	1/100	3	at crest and trough above mid-depth	No
Stive (1984)	1/40	2	profiles at crest and trough	Yes
Flick et al. (1981)	1/35	2	time series near bottom	Yes
Isobe & Horikawa (1982)	1/10 & 1/20	21	time series near bottom	Yes
Nadaoka & Kondoh (1982)	1/20	12	near-bottom mean velocity and velocity skewness	Yes
Hattori (1986)	1/20	15	profiles at crest and trough	No
Sato et al. (1988)	1/20	3	time series near bottom (+ random waves)	Yes
Kirkgöz (1986)	1/4.45 to 1/12	17	profiles at crest	No

This skewness is peaking at the breaking point and tends to decrease significantly in the surfzone except for steep waves. It is a relevant indicator of the development of asymmetries observed in shoaling waves which are of two kinds.

The horizontal asymmetry includes an increase of the velocity speed under the crest (u_c) which could become twice the velocity speed under the trough (u_t). This increase is accompanied by a shortening of the crest duration T_c (i.e. the duration of time when the velocity is in the direction of the wave propagation).

This is explained by the development of higher harmonics which are locked to the primary (sinusoidal) wave. The ratio u_c/u_t was found to be maximum at the breaking point and then to decrease significantly in the surf zone (Stive, 1984).

The vertical asymmetry includes a steepening of the velocity (temporal) profile between a trough and the following crest producing a higher acceleration than between the crest and the following trough. This is explained by the development of phase differences between the harmonics and the primary wave (Flick et al., 1981) induced by the slope of the bottom and producing a sawtooth shape.

b) Random waves

When randomness of waves is considered, the situation becomes complicated by presence of bounded and free low frequency waves. In intermediate depths, bounded second-order wave velocities can be computed from second-order random theories (Dean and Perlin, 1986).

In the nearshore zone, partially standing long-waves are often present. Guza and Thornton (1985) have analysed velocities measured at Torrey Pines beach including the surfzone. They have shown that low frequency velocity variance increases monotonically as depth decreases. Cross-shore high frequency velocity moments appear to be near gaussian offshore, reach a maximum deviation from gaussian near the mean breaker location and trend back to gaussian as the shoreline is approached. Such an evolution cannot be predicted by a monochromatic or a linear gaussian model.

Roelvink and Stive (1989) carried out detailed near-bottom velocity measurements in a laboratory flume and also found that high frequency velocity moments were very significant in the nearshore region. They used a non-linear wave theory to successfully predict these moments.

3. Practical formulations tested

Existing formulations have been reviewed by Soulsby et al. (1993). Two of them have been chosen for the validation tests presented hereafter.

a) Isobe and Horikawa

Isobe and Horikawa (1982) proposed two series of empirical corrections of the linear velocity profile. As a first step, an estimation of the ratio $u_c/(u_c + u_t)$ is obtained for their equations (13) to (23). From these expressions, u_t could be predicted assuming that u_c is accurately computed with the linear theory.

Similarly, the ratio T_c/T could be computed. Two sinusoidal profiles could then be adjusted to simulate the velocity profile under the crest and under the trough.

In a second step, the vertical asymmetry is accounted for by introducing two time lags in the above profile with the equations (24) to (28). To apply these expressions, one should correct the following typing errors:

- 1) The right side of equation (23) should read $0.5 - 0.018(T\sqrt{g}/d)$.
- 2) In the second right side of equation (28), π is outside the brackets.

Please also note that in equation (28), the origin of time is at $0.5(T - T_c)$ following figure 9 of Isobe and Horikawa.

b) The covocoïdal theory

In order to provide a simple and accurate tool for engineering purposes, Swart and Loubster(1978) have presented a numerical method and a parametrized solution of the problem valid at any water depth for a flat bottom. They called it the vocoïdal theory (vocoïdal stands for **V**ariable **O**rders **C**osinus **O**idal function). It is based on basic assumptions concerning the form of the free-surface elevation, the orbital velocity and the celerity which are expressed as:

$$\eta(t) = H(\cos^{2P}(\pi \frac{t}{T}) - \eta_{*t}) \quad (1)$$

$$\frac{u(z,t)}{C} = k\eta \frac{\cosh(M(X)kz)}{\sinh(M(X)k(h+\eta))} \quad (2)$$

$$\frac{C^2}{gh} = \frac{1}{kh} \tanh(Nkh) \quad (3)$$

t is time, H and T are the wave height and period, $X = t/T$, P is the wave profile parameter, η_{*t} is the non-dimensional wave trough, k is the wave number, C the celerity, z the vertical coordinate, $M(X)$ is the orbital velocity function and N is the wave celerity parameter. Equations (1) and (3) have been originally proposed by Van Hijum (1972) and equation (2) by Mejlhede(1975). A numerical method to solve this simplified problem has been established by Swart(1978).

Then, a parametrized form of this solution has been derived empirically from numerous computations in order to provide analytical equations very easy to use. The comprehensive derivation and validation of the method could be found in Swart (1978) and Swart and Loubster(1979).

This theory was then extended by Swart and Crowley(1988) to the case of a sloping bottom by modifying equations (1) and (2) in order to introduce a parametrized form of the vertical asymmetry. This new theory has been called the Covocoidal theory. The same numerical approach has been used and an analytical parametrized form of the solution was also given. This parametrization has then been slightly modified by Swart and Crowley(1989). This is this parametrized solution which has been tested here.

c) An unsuccessful test

Finally, it should be noted that Hattori and Katsurakawa (1990) followed the idea of Flick and al (1981) by proposing empirical formulae of phase lags. Such a method could be easily used with numerical wave models based on Fourier developments. Unfortunately, we have not been able to recompute the results presented in their paper (i.e. figure 5 of their paper from their equation (5)).

4. Validation tests

The two formulations have been tested against several laboratory data with monochromatic and random waves.

a) Monochromatic wave tests

As a first test, two velocity time-series of near-breaking shoaling waves measured by Isobe and Horikawa (1982) on a fixed slope of 1 in 20 have been used. The first one has been obtained with a deep-water steep wave ($H/L_0 = 0.059$) and the second with a low-steepness wave ($H_0/L_0 = 0.0067$). The measured and computed velocity profiles are shown on figure 1. For both cases the agreement is excellent with Isobe and Harikawa's formulation and reasonable with the covocoïdal theory. It is worth to note that in the first case, the ratio H/h is 0.88 far over the limiting value on a flat bottom. It means that very accurate high order Fourier wave theories cannot provide any result here.

A second test made use of the measurements of the skewness of the velocity from Nadaoka and Kondoh (1982) along a 1 in 20 slope. Two typical cases including as previously high and low steepness waves have been simulated. Figure 2 presents the results obtained. In order to perform the computations of the velocity, the wave height transformation has been computed with a finite amplitude wave model including the surfzone.

Outside the surfzone negative abnormal values are obtained with the covocoïdal theory in the first case. Furthermore, the skewness is peaking too much offshore in the second case. On the other hand, the Isobe and Horikawa formulation is providing smoother results in reasonable agreement with the measurements. In the surfzone, no formulation is able to predict the decrease of the skewness.

Because the covocoïdal theory provides a comprehensive wave description, further tests considering the free surface elevation profile have also been performed. Measurements of wave crests and troughs on a 1 in 12 slope reported by Bowen et al (1968) have been simulated. The results are shown in figure 3. The agreement is quite good in the outer shoaling region. Further inshore the wave crest elevation is rather overestimated and the trough underestimated. This deviation from the measurements increases in the surfzone.

Finally, a last test concerning the shape factor (B_o defined as the ratio of the standard deviation of the surface elevation over the wave height) has been carried out using the data from Stive (1984). A good prediction of this factor is essential in surfzone models in order to accurately compute the radiation stresses and the set-up. Figure 4-up indicates that before the breakpoint, the use of the covocoïdal theory can improve the computation of B_o compared to a classical second-order cnoidal theory. This is no more the case in the surfzone. Results are even worse in the case of a low-steepness wave (figure 4-down).

b) Random wave tests

Results obtained with monochromatic waves show that both approaches can be used before the breaking point but not in the surfzone. If we now consider random waves which generate wider surfzones, it implies that a probabilistic approach considering the joint distribution of wave heights and periods to compute the velocity distribution will not work properly in the nearshore. This is the reason why an alternative approach to estimate the velocity moments in random waves is considered here. It consists of applying the two formulations with a representative wave height and period. Flume data at prototype scale collected in the Delta flume in the Netherlands (Arcilla et al., 1994) have been used to test that approach. Figure 5 presents the computation of the second order and the third order velocity moments (high frequency part only) obtained by using the root-mean-square wave height and the peak period of the waves. In the first case (test 2A) the bottom slope is monotonic but in the second (test 1C) a bar has developed which explains the presence of two peaks. Furthermore, the low steepness of the waves in the second case makes it a more difficult case to simulate: a significant underestimation of the third order velocity moment is clearly visible in figure 5-down.

5. Conclusions

The validation tests of the two formulations indicate that the Isobe and Horikawa (1982) formulation can be used with confidence in a large range of wave conditions except inside the surfzone when monochromatic waves are considered. The covocoïdal theory provides a more comprehensive description of the waves properties but abnormal results have been noticed in a few cases. This is probably due to the limitations of the parametrization which is rather complex and should be carefully checked at both limits: « deep »-water and breaking point. The accuracy of the prediction is generally reasonable. More tests with random waves are needed to confirm the choice of the root-mean-square wave height as the most suitable input.

Acknowledgements

The present research work is part of the MAST2 G8 Coastal Morphodynamics and MAST3 SAFE research programs. It is partly funded by the Service Technique Central des Ports Maritimes et des Voies Navigables (France), Ministère de l'Équipement, des Transports et du Tourisme and by the Commission of the European Communities, Directorate General for Science, Research and Development, under contracts no MAS2-CT92-0027 and no MAS3-CT95-0004. Many thanks to Marianela Fornerino (Laboratoire d'Hydraulique de France - Grenoble - France) who has written the first version of the simulation software known as CINEMA.

References

- Arcilla, A.S., J.A. Roelvink, B.A. O'Connor, A. Reniers and J.AJimenez (1994). The Delta Flume '93 experiment. Proc. Int. Conf. on the role of large scale experiments in coastal research, ASCE, 488-502.
- Bowen, A.J., D.L. Inman and V.P. Simons (1968). Wave set-down and set-up. J. of Geophysical Research, Vol. 73, 2569-2577.
- Dean R.G. and M. Perlin(1986). Intercomparison of near-bottom kinematics by several wave theories and field and laboratory data. Coastal Engineering, 9, 399-437
- Fenton, J.A. (1986). Polynomial approximations and water waves. Proc. 20th Int. conf. on Coastal Engng., Taipei, ASCE, 193-207.
- Fenton, J.D. (1990). Nonlinear wave theories. In: B. Le Méhauté and D.M. Hanes (Editors), The Sea, Vol.9, Part A. Wiley Intersciences, New-York, pp.3-25

Flick, R.E., R.T. Guza and D.L. Inman (1981). Elevation and velocity measurements of laboratory shoaling waves. *J. of Geophys. Res.*, Vol. 86, no. C5, 4149-4160.

Guza R.T. and E.B. Thornton (1985). Velocity moments in nearshore. *J. of Waterways, Port, Coastal and Ocean Eng.*, Vol. 111, no. 2, ASCE, 235-256.

Hattori M.(1986). Experimental study on the validity range of various wave theories. *Proc. Int. Conf. on Coastal Eng.*, ASCE,232-246

Hattori M. and T. Katsurakawa (1990). Improved calculation of the shoaling wave fields. *Proc. Int. Conf. on Coastal Eng.*, ASCE 396-409.

Isobe M. and K. Horikawa(1982). Study on water particle velocities of shoaling and breaking waves. *Coastal Eng. in Japan*,Vol.25,109-123

Iwagaki, Y. and T. Sakai (1970). Horizontal water particle velocity of finite amplitude waves. *Proc. Int. Conf. on Coastal Engng.*, ASCE, 309-325.

Iwagaki, Y. and T. Sakai (1972). Shoaling of finite amplitude long waves on a beach of constant slope. *Proc. Int. Conf. on Coastal Eng.*,ASCE,347-364

Kirkgöz M.S.(1986). Particle velocity prediction at the transformation point of plunging breakers. *Coastal Engineering*,10, 139-147.

Mejlhede, N. (1975). Cnoïdal waves on arbitrary depth. *Prog. Report 36, Inst. Hydrodyn. and Hydraulic Engng, Techn. Univ. Denmark*, 11-20.

Nadaoka K. and T. Kondoh(1982). Laboratory measurements of velocity field structure in the surf-zone by LDV. *Coastal Eng. in Japan*, Vol.25,125-145.

Roelvink, J.A. and M.J.F. Stive (1989). Bar-generating cross-shore flows mechanisms on a beach. *J. of Geophysical Res.*, vol.94, n°C4, 4785-4800 .

Sato S., M. Fukuhama and K. Horikawa (1988). Measurements of near-bottom velocities in random waves on a constant slope. *Coastal Engineering in Japan*, Vol. 31, no. 2, 219-229.

Soulsby, R.L., L. Hamm, G. Klopman, D. Myrhaug, R.R. Simons and G.P. Thomas (1993). Wave-current interaction within and outside the bottom boundary layer. *Coastal Engineering*, 21: 41-69.

Stive, M.J.F. (1984). Energy dissipation in waves breaking on a gentle slope. *Coastal Engineering*, 8, 99-127.

Swart D.H.(1978). Vocoidal water wave theory. Volume 1: Derivation. CSIR Research Report 357.

Swart D.H. and C.C. Loubster(1978). Vocoidal theory for all non-breaking waves. Proc. Int. Conf. on Coastal Eng.,ASCE, 467-486

Swart D.H. and C.C. Loubster(1979). Vocoidal water wave theory Volume 2: Verification. CSIR Research Report 360

Swart D.H. and J.B. Crowley(1988). Generalized wave theory for a sloping bed. Proc. Int. Conf. on Coastal Eng.,ASCE, 181-203

Swart D.H. and J.B. Crowley(1989). Approximate solution for water waves on a sloping bottom. CSIR Research Report 641.

Tsuchiya Y. and M. Yamaguchi (1972). Some considerations on water particle velocities of finite amplitude wave theories. Coastal Engineering in Japan, Vol. 15, 43-57.

Van Hijum E. (1972). P-golf. internal report. Delft Hydraulics

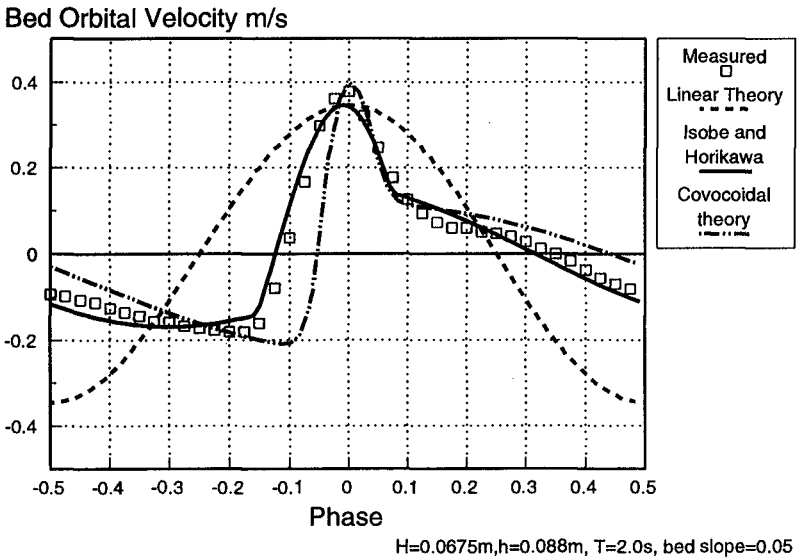
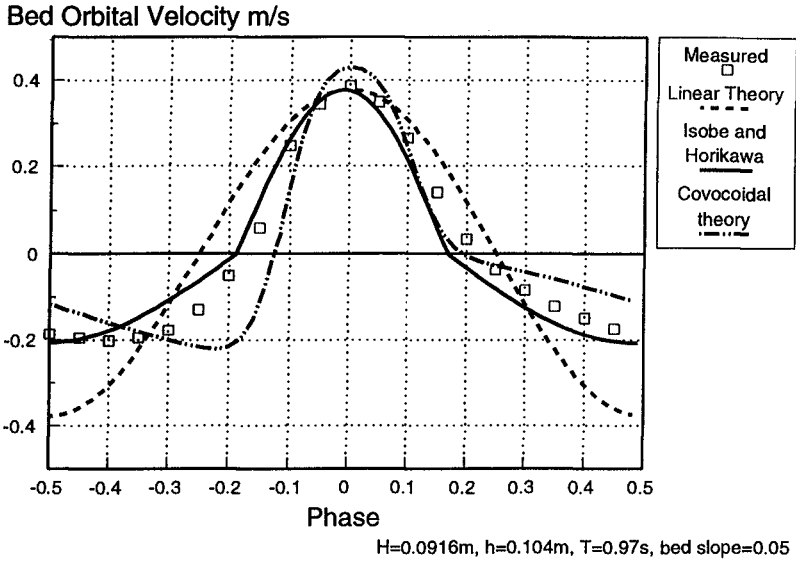


Figure 1. Validation test against bottom velocity measurements of Isobe and Horikawa (1982)

up: $H = 0.0916\text{ m}, T = 0.97\text{ s}, h = 0.104\text{ m}, \text{bed slope} = 0.05$

down: $H = 0.0675\text{ m}, T = 2.0\text{ s}, h = 0.088\text{ m}, \text{bed slope} = 0.05$

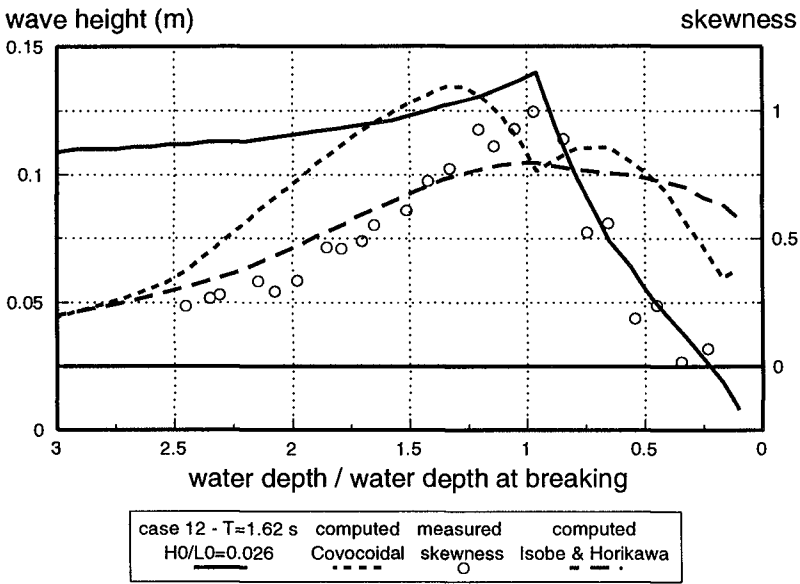
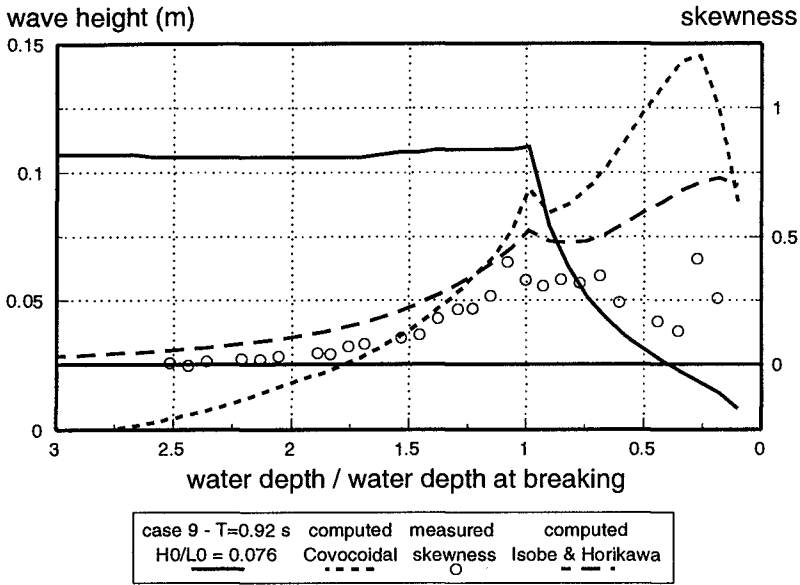
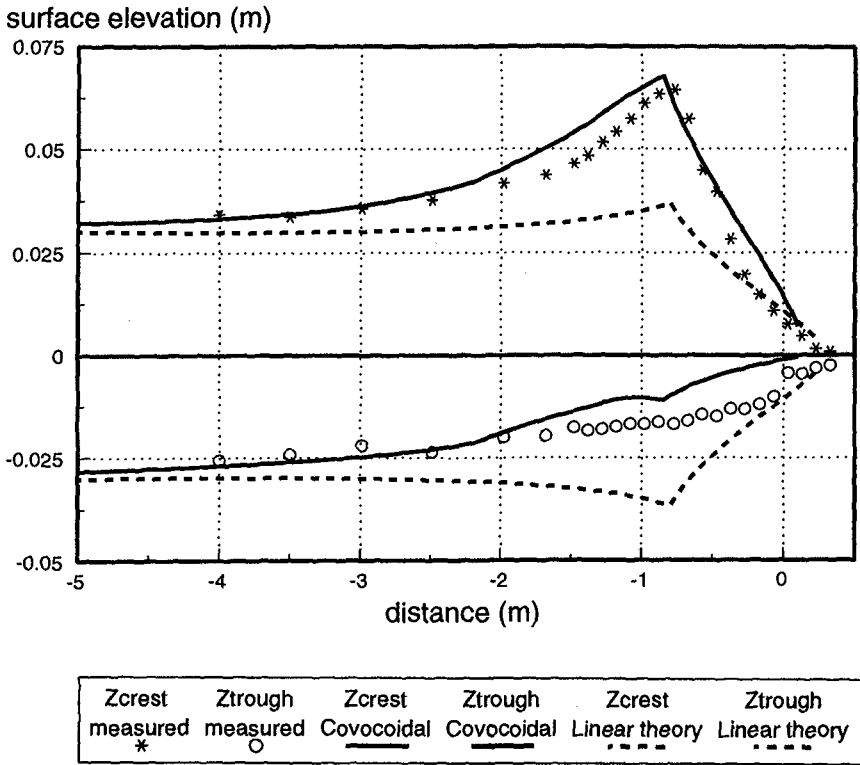


Figure 2. Validation test against bottom velocity skewness measurements of Nadaoka and Kondoh (1982)

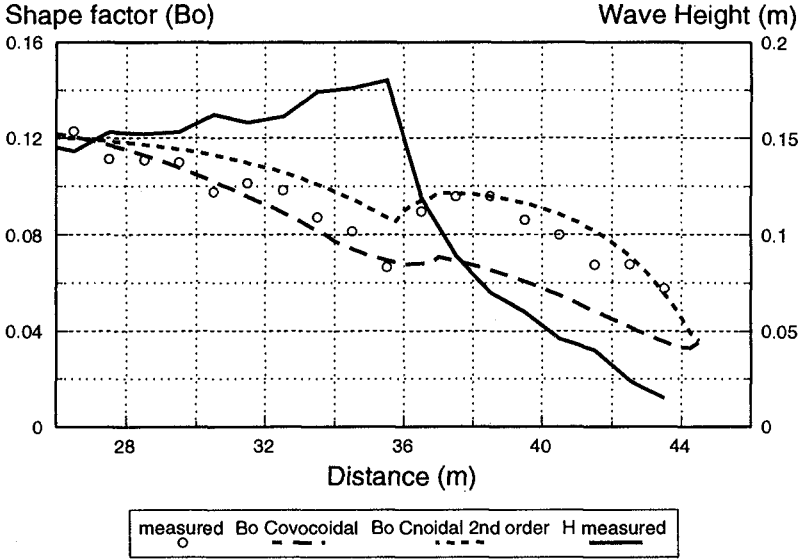
up: case 9 - $H_0 = 0.10$ m, $T = 0.92$ s, bed slope = 0.05
 down: case 12 - $H_0 = 0.108$ m, $T = 1.62$ s, bed slope = 0.05



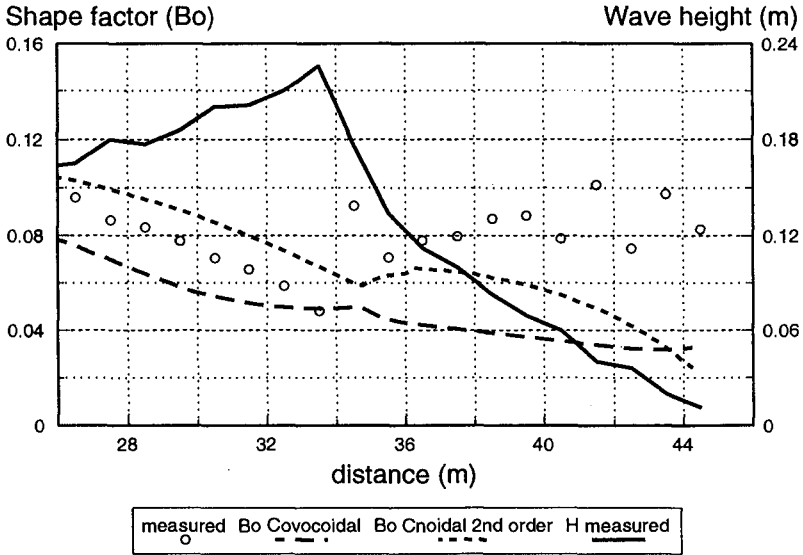
test 51/6 - $T = 1.14s$, $H = 0.064 m$

Figure 3. Validation test against surface elevation measurements of Bowen et al (1968)

test 51/6 - $H_{inc} = 0.0645 m$, $T = 1.14 s$, bed slope = 0.083



test 1 - $T=1.79$ s, $H=0.145$ m



test 2 - $T=3.0$ s, $H_{inc}=0.145$ m

Figure 4. Validation test against surface elevation shape factor measurements of Stive (1984)

up: test 1 - $H_{inc} = 0.145$ m, $T = 1.79$ s, bed slope = 0.025

down: test 2 - $H_{inc} = 0.145$ m, $T = 3.0$ s, bed slope = 0.025

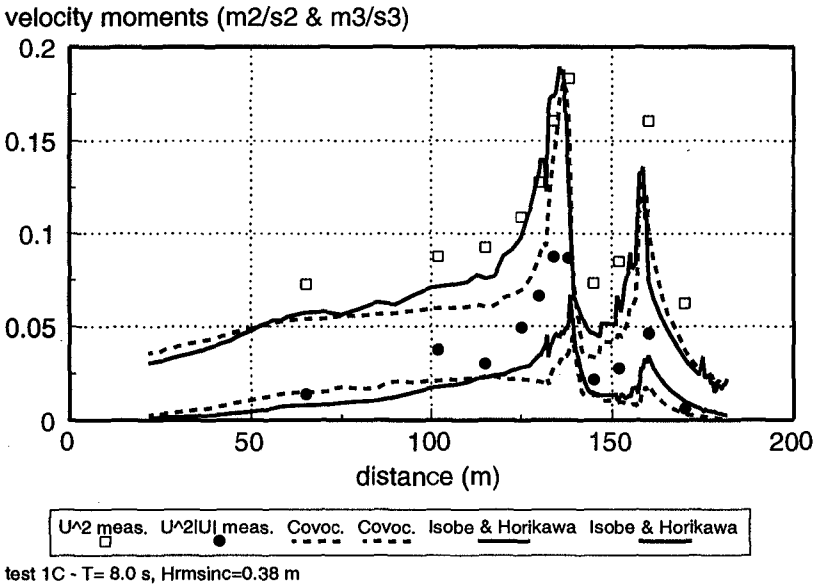
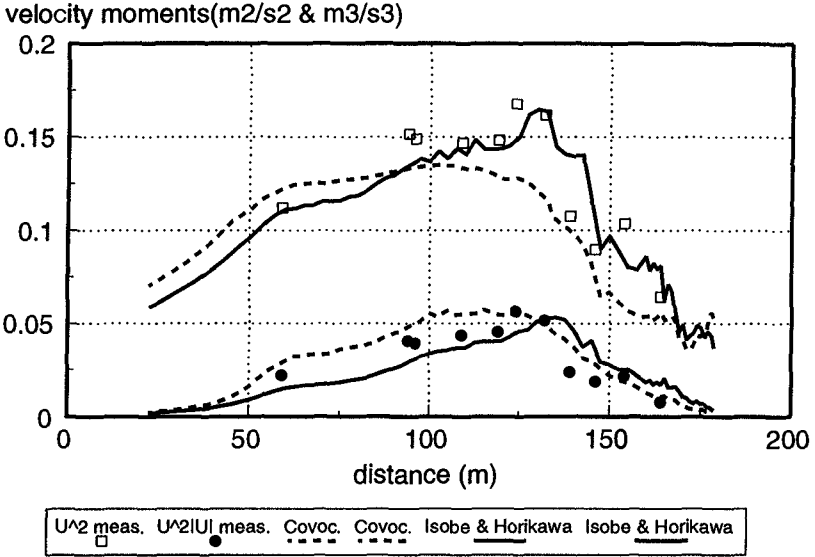


Figure 5. Validation test with random waves against Delta-Flume '93 experiments (Arcilla et al., 1994)

up: test 2A - $H_{sinc} = 0.87m$, $T_p = 5s$, mean bed slope = 0.018
 down: test 1C - $H_{sinc} = 0.60m$, $T_p = 8s$, barred beach profile

CHAPTER 44

FORMULATION AND VALIDATION OF VERTICALLY 2-D SHALLOW-WATER WAVE MODEL

Bradley D. Johnson¹, Nobuhisa Kobayashi², and Daniel T. Cox³

Abstract

A numerical model is developed to predict the time-dependent, two-dimensional velocity field under normally incident breaking waves on beaches and coastal structures. Use is made of the depth-integrated continuity and horizontal momentum equations, where the momentum equation includes the momentum flux correction due to the vertical variation of the horizontal velocity. The third equation for the momentum flux correction is derived from the depth-integrated wave energy equation together with a cubic horizontal velocity profile. The three equations are solved using the MacCormack finite difference method. The quasi two-dimensional model is compared with two laboratory data sets and is found to predict the vertical variation of the horizontal velocity measured below the trough reasonably well. However, the energy dissipation in the model is primarily numerical for breaking waves on gentle slopes despite the explicitly modeled energy dissipation due to wave breaking.

Introduction

The quantitative prediction of detailed sediment transport on beaches and armor stability on coastal structures requires a numerical model that can predict the time-dependent, vertically two-dimensional velocity field of breaking waves on slopes with sufficient accuracy and reasonable computation time.

Available time-dependent, one-dimensional and other numerical models for breaking and nonbreaking waves on inclined structures and beaches (e.g., Kobayashi and Wurjanto 1989) are relatively simple and robust. Generally, these models predict the free surface elevation fairly accurately, within about 20% errors. The comparisons of a one-dimensional model with the experiment for regular waves spilling on a rough, impermeable 1:35 slope conducted by Cox *et al.* (1995) indicated that the horizontal velocity measured below the wave trough level was represented by the computed depth-averaged velocity reasonably well. The temporal variation of the bottom shear stress was predicted poorly because errors in the computed horizontal velocity were magnified in the computed bottom shear stress and because the bottom friction factor was not really constant. These limited comparisons suggest that a vertically

¹Ph.D. Student, Center for Applied Coastal Research, University of Delaware, Newark, DE 19716.

²Professor and Associate Director, Center for Applied Coastal Research, University of Delaware, Newark, DE 19716.

³Assistant Professor, Department of Civil Engineering, Texas A&M University, College Station, TX 77843-3136.

two-dimensional model will be required to predict the detailed vertical variations of the fluid velocities and shear stress which are essential for predicting cross-shore sediment transport on beaches and hydrodynamic forces acting on armor units on coastal structures.

A simplified two-dimensional model called VBREAK has been developed assuming a cubic horizontal velocity profile outside of the wave boundary layer. The vertically two-dimensional problem is then reduced to a depth-integrated one-dimensional problem in which three time-dependent, one-dimensional differential equations can be solved numerically for the water depth h , depth-averaged horizontal velocity U , and near-bottom horizontal velocity u_b . The simplified two-dimensional model is computationally as efficient as the previous one-dimensional models. As a result, the new model can be applied easily and routinely using workstations. This paper summarizes the numerical model VBREAK described in detail by Kobayashi and Johnson (1995) and the comparisons of the model to available data presented in Johnson *et al.* (1996).

Mathematical Formulation

The approximate governing equations adopted in the numerical model named VBREAK are derived from the two-dimensional continuity and Reynolds equations

$$\frac{\partial u'_j}{\partial x'_j} = 0 \quad (1)$$

$$\frac{\partial u'_i}{\partial t'} + u'_j \frac{\partial u'_i}{\partial x'_j} = -\frac{1}{\rho} \frac{\partial p'}{\partial x'_i} - g\delta_{i2} + \frac{1}{\rho} \frac{\partial \tau'_{ij}}{\partial x'_j} \quad (2)$$

in which the prime indicates the physical variables and the summation convention is used with respect to repeated indexes. The symbols used in (1) and (2) are depicted in Fig. 1 where t' = time; x'_1 = horizontal coordinate taken to be positive landward; x'_2 = vertical coordinate taken to be positive upward with $x'_2 = 0$ at the still water level (SWL); u'_1 = horizontal velocity; u'_2 = vertical velocity; ρ = fluid density which is assumed constant; p' = pressure; g = gravitational acceleration; δ_{i2} = Kronecker delta; and τ'_{ij} = sum of turbulent and viscous stresses. Assuming that the viscous stresses are negligible, τ'_{ij} may be expressed as (e.g., Rodi 1980)

$$\tau'_{ij} = \rho \left[\nu'_t \left(\frac{\partial u'_i}{\partial x'_j} + \frac{\partial u'_j}{\partial x'_i} \right) - \frac{2}{3} k' \delta_{ij} \right] \quad (3)$$

in which ν'_t = turbulent eddy viscosity; and k' = turbulent kinetic energy per unit mass.

To simplify (1) and (2) with (3) in shallow water, the dimensional variables may be normalized as

$$t = \frac{t'}{T'} ; \quad x_1 = \frac{x'_1}{T' \sqrt{gH'}} ; \quad x_2 = \frac{x'_2}{H'} ; \quad p = \frac{p'}{\rho g H'} \quad (4)$$

$$u_1 = \frac{u'_1}{\sqrt{gH'}} ; \quad u_2 = \frac{u'_2}{H'/T'} ; \quad \nu_t = \frac{\nu'_t}{H'^2/T'} ; \quad k = \frac{k'}{\sqrt{gH'} H'/T'} \quad (5)$$

$$\sigma = T' \sqrt{\frac{g}{H'}} ; \quad \eta = \frac{\eta'}{H'} ; \quad z_b = \frac{z'_b}{H'} ; \quad h = \frac{h'}{H'} \quad (6)$$

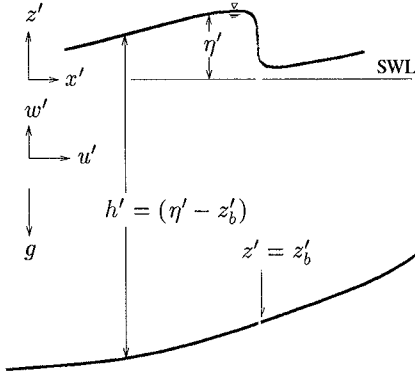


Figure 1: Definition sketch
 terms of the order of σ^{-2} are neglected in the normalized equations corresponding to (1) and (2).

The conventional notations of $x = x_1$, $z = x_2$, $u = u_1$ and $w = u_2$ are used in the following. The simplified depth-integrated continuity and horizontal momentum equations under the assumption of $\sigma^2 \gg 1$ are expressed as

$$\frac{\partial h}{\partial t} + \frac{\partial q}{\partial x} = 0 \quad (7)$$

$$\frac{\partial q}{\partial t} + \frac{\partial}{\partial x} \left(qU + m + \frac{1}{2}h^2 \right) = -\theta h - \tau_b \quad (8)$$

with

$$m = \int_{z_b}^{\eta} (u - U)^2 dz \quad (9)$$

where h = water depth given by $h = (\eta - z_b)$; q = volume flux per unit width; U = depth-averaged horizontal velocity defined as $U = q/h$; θ = normalized bottom slope defined as $\theta = dz_b/dx$; τ_b = bottom shear stress; and m = momentum flux correction due to the vertical variation of the horizontal velocity u . The vertical momentum equation yields essentially hydrostatic pressure for shallow water.

To include energy dissipation due to wave breaking in Boussinesq equations, Zelt (1991) and Schäffer *et al.* (1992) added a term corresponding to the term for the momentum flux correction m in (8). Zelt (1991) expressed this additional term in the form of horizontal momentum diffusion with an artificial viscosity. The artificial viscosity was calibrated for breaking solitary waves where the diffusion term was activated using a semi-empirical criterion for solitary wave breaking. On the other hand, Schäffer *et al.* (1992) expressed the additional momentum flux using a simple approach based on a surface roller that represented a passive bulk of water riding on the front of a breaking wave. An empirical geometric method was used to determine the shape and location of the surface rollers during the computation. Unlike the present model, these models do not predict the vertical variations of the fluid velocities.

The equation for the momentum flux correction m is derived from the depth-integrated instantaneous wave energy equation (Kobayashi and Wurjanto 1992)

$$\frac{\partial E}{\partial t} + \frac{\partial}{\partial x} (E_F) = -D \quad (10)$$

in which T' and H' are the reference wave period and height used for the normalization. The parameter σ defined in (6) is the ratio between the horizontal and vertical length scales and is assumed to be much larger than unity.

The normalized variables in (4) and (5) are assumed to be on the order of unity in shallow water. The normalization of ν'_i and k' in (5) is based on the turbulence measurements in a wave flume by Cox *et al.* (1994) which have indicated that ν'_i and k are on the order of unity or less inside and immediately outside the surf zone, respectively. The

The specific energy E defined as the sum of kinetic and potential energy per unit horizontal area is given by

$$E = \frac{1}{2} (qU + m + \eta^2) \quad \text{for } z_b < 0 \quad (11)$$

$$E = \frac{1}{2} (qU + m + \eta^2 - z_b^2) \quad \text{for } z_b > 0 \quad (12)$$

in which the potential energy is taken to be relative to the potential energy in the absence of wave action with SWL at $z = 0$. The energy flux E_F per unit width is expressed as

$$E_F = \eta q + \frac{1}{2} (qU^2 + 3mU + m_3) \quad (13)$$

with

$$m_3 = \int_{z_b}^{\eta} (u - U)^3 dz \quad (14)$$

in which m_3 = kinetic energy flux correction due to the third moment of the velocity deviation $(u - U)$ over the depth. The energy dissipation rate D per unit horizontal area in (10) is given by

$$D = \int_{z_b}^{\eta} \tau \frac{\partial u}{\partial z} dz \quad (15)$$

where use is made of the no slip condition $u = 0$ at $z = z_b$.

The energy dissipation rate D may be expressed as the sum of dissipation due to bottom friction, D_f , and dissipation due to wave breaking outside of the wave boundary layer, D_B . The wave boundary layer is not analyzed explicitly in this numerical model. The energy dissipation rate D_f inside the wave boundary layer may be estimated by (Jonsson and Carlsen 1976)

$$D_f = \tau_b u_b; \quad \tau_b = f_w |u_b| u_b; \quad f_w = \frac{1}{2} \sigma f'_w \quad (16)$$

where u_b = near-bottom horizontal velocity immediately outside the wave boundary layer and f'_w = friction factor (Jonsson 1966). Assuming that the thickness of the wave boundary layer is much smaller than the water depth, D_B may be estimated as

$$D_B = \int_{z_b}^{\eta} \nu_t \left(\frac{\partial u}{\partial z} \right)^2 dz \quad \text{outside boundary layer} \quad (17)$$

Rearranging the instantaneous wave energy equation (10), the equation for the momentum flux correction m is derived

$$\frac{\partial m}{\partial t} + \frac{\partial}{\partial x} (3mU + m_3) = 2U \frac{\partial m}{\partial x} - 2(\tau_b \tilde{u}_b + D_B) \quad (18)$$

in which $\tilde{u}_b = u_b - U$ = near-bottom horizontal velocity correction due to the vertical variation of the horizontal velocity u outside the wave boundary layer.

In order to express m , m_3 , and D_B in terms of \tilde{u}_b , the horizontal velocity u outside the wave boundary layer is assumed to be expressible in the form

$$u(t, x, z) = U(t, x) + \tilde{u}_b(t, x) F(\zeta) \quad (19)$$

with

$$\zeta = [z - z_b(x)]/h(t, x) \quad \text{for } 0 \leq \zeta \leq 1 \tag{20}$$

in which F = normalized function expressing the vertical variation of the velocity deviation ($u - U$) from $\zeta = 0$ immediately outside the wave boundary layer to $\zeta = 1$ at the free surface. Substitution of (19) into the normalized continuity equation corresponding to (1) yields the vertical velocity $w(t, x, z)$ where $w = 0$ at $z = z_b$. The dimensional turbulent eddy viscosity ν'_t outside the wave boundary layer is assumed to be given by

$$\nu'_t = (C_\ell h')^2 \left| \frac{\partial u'}{\partial z'} \right| \tag{21}$$

in which C_ℓ = mixing length parameter. The turbulence measurements inside the surf zone by Cox *et al.* (1994) have indicated that (21) is a reasonable first approximation outside the wave boundary layer and that C_ℓ is on the order of 0.1 ($C_\ell = 0.1$ is used herein). The corresponding normalized turbulent eddy viscosity ν_t defined in (5) is expressed as

$$\nu_t = C_\ell^2 \sigma h^2 \left| \frac{\partial u}{\partial z} \right| \tag{22}$$

Substitution of (19) with (22) into (9), (14), and (17) yields

$$m = C_2 h \tilde{u}_b^2 \quad ; \quad C_2 = \int_0^1 F^2 d\zeta \tag{23}$$

$$m_3 = C_3 h \tilde{u}_b^3 \quad ; \quad C_3 = \int_0^1 F^3 d\zeta \tag{24}$$

$$D_B = C_B C_\ell^2 \sigma |\tilde{u}_b|^3 \quad ; \quad C_B = \int_0^1 \left| \frac{dF}{d\zeta} \right|^3 d\zeta \tag{25}$$

Madsen and Svendsen (1983) and Svendsen and Madsen (1984) assumed a cubic velocity profile for their analyses of a hydraulic jump and a turbulent bore on a beach. Accordingly, the function F in (23) – (25) outside the wave boundary layer is assumed to be cubic and expressed as

$$F = 1 - (3 + 0.75a)\zeta^2 + a\zeta^3 \quad \text{for } 0 \leq \zeta \leq 1 \tag{26}$$

in which a = cubic velocity profile parameter. The shear stress τ should drop to zero at the free surface. To satisfy $\frac{\partial u}{\partial z} = 0$ at the free surface, $a = 4$. The assumed form (26) results in $\tau = 0$ at $\zeta = 0$ immediately outside the wave boundary layer in contradiction with the turbulence measurements inside the surf zone by Cox *et al.* (1994). The cubic profile assumed by Svendsen and Madsen (1984) suggests that the parameter a is approximately 3 and the range of $a = 3-4$ is considered in the following. Substitution of (26) into (23) – (25) yields C_2 , C_3 , and C_B as a function of a .

Fig. 2 shows the cubic velocity profile function F given by (26) as a function of ζ for $a = 3.0, 3.5,$ and 4.0 . The abscissa in Fig. 2 is the value of $-F$ because \tilde{u}_b is expected to be negative under the wave crest. Fig. 2 hence depicts the normalized vertical variation of the horizontal velocity deviation ($u - U$) under the wave crest. The assumed cubic profile is not sensitive to the parameter a in the range of $a = 3-4$ except in the vicinity of the free surface where no velocity data is available inside the surf zone. Fig. 3 shows the parameters C_2 , C_3 and C_B as a function of the cubic

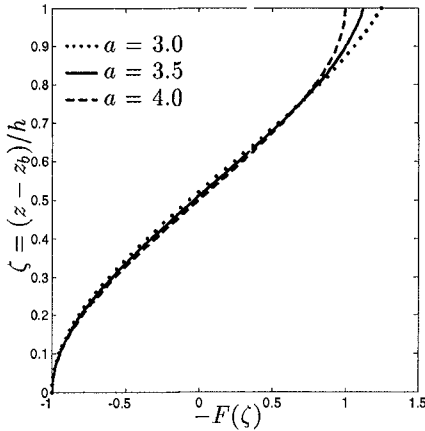


Figure 2: Cubic velocity profile function $-F$ as a function of ζ

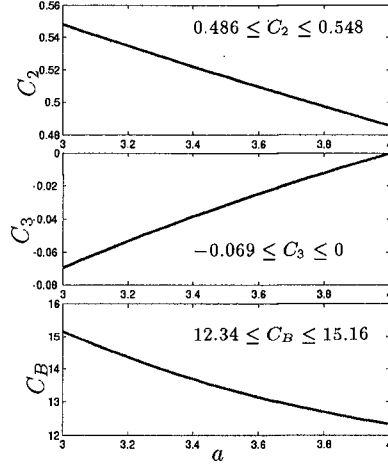


Figure 3: C_2 , C_3 , and C_B vs. a

profile parameter a . These parameters vary little for $a = 3-4$. Fig. 3 indicates that $C_2 \simeq 0.5$, $C_3 \simeq -0.03$ and $C_B \simeq 13$. The computed results are also found to be insensitive to a and in this paper $a = 3$ for most comparisons with data.

To obtain \tilde{u}_b for the computed h and m , it is assumed that

$$\tilde{u}_b = -\left(\frac{m}{C_2 h}\right)^{1/2} \quad \text{for } U \geq 0 \tag{27}$$

$$\tilde{u}_b = \left(\frac{m}{C_2 h}\right)^{1/2} \quad \text{for } U < 0 \tag{28}$$

which ensures that $|u_b| \leq |U|$ with $u_b = (U + \tilde{u}_b)$.

To examine the degree of numerical dissipation hidden in the computed results, the instantaneous energy equation (10) is averaged over time. The time averaged energy balance is

$$\frac{d}{dx} (\overline{E_F}) = -\overline{D_f} - \overline{D_B} - \overline{D_n} \tag{29}$$

Where the overbar denotes time averaging and E_F , D_f , and D_B are given by (13), (16), and (25) respectively. The time-averaged numerical dissipation rate $\overline{D_n}$ is added in (29) so that $\overline{D_n}$ can be estimated for the computed $\overline{E_F}$, $\overline{D_f}$, and $\overline{D_B}$.

Numerical Method

To solve (7), (8) and (18) for h , q , and m , these equations are combined in the following vector form:

$$\frac{\partial \mathbf{U}}{\partial t} + \frac{\partial \mathbf{F}}{\partial x} + \mathbf{G} = 0 \tag{30}$$

with

$$\mathbf{U} = \begin{bmatrix} h \\ q \\ m \end{bmatrix} ; \quad \mathbf{F} = \begin{bmatrix} q \\ F_2 \\ F_3 \end{bmatrix} ; \quad \mathbf{G} = \begin{bmatrix} 0 \\ G_2 \\ G_3 \end{bmatrix} \tag{31}$$

and

$$F_2 = qU + m + \frac{1}{2}h^2 \quad ; \quad G_2 = \theta h + \tau_b \quad (32)$$

$$F_3 = 3mU + m_3 \quad ; \quad G_3 = 2 \left(\tau_b \tilde{u}_b + D_B - U \frac{\partial m}{\partial x} \right) \quad (33)$$

Eq. (30) is solved numerically using the MacCormack method (MacCormack 1969) which is a simplified variation of the two-step Lax-Wendroff method (e.g., Anderson *et al.* 1984) and has been applied successfully for the computation of unsteady open channel flows with hydraulic jumps (e.g., Chaudhry 1993). The use of the Lax-Wendroff method for (30) would be very difficult because this method requires the Jacobian of \mathbf{F} with respect to \mathbf{U} .

The values of \mathbf{U}_j at the node j with $j = 1, 2, \dots, s$ and at the present time t are known in the following, where $s =$ the most landward node. Computation is initiated at time $t = 0$ with no wave action in the computational domain, thus $h = q = m = 0$. The unknown values of \mathbf{U}_j^* at the node j and at the next time level $t^* = (t + \Delta t)$ are denoted by the superscript asterisk. The predictor, corrector and final steps of the MacCormack method are expressed as

$$\dot{\mathbf{U}}_j = \mathbf{U}_j - \frac{\Delta t}{\Delta x} (\mathbf{F}_{j+1} - \mathbf{F}_j) - \Delta t \mathbf{G}_j \quad \text{for } j = 1, 2, \dots, s-1 \quad (34)$$

$$\ddot{\mathbf{U}}_j = \dot{\mathbf{U}}_j - \frac{\Delta t}{\Delta x} (\dot{\mathbf{F}}_j - \dot{\mathbf{F}}_{j-1}) - \Delta t \dot{\mathbf{G}}_j \quad \text{for } j = 2, 3, \dots, s-1 \quad (35)$$

$$\mathbf{U}_j^* = \frac{1}{2} (\mathbf{U}_j + \ddot{\mathbf{U}}_j) \quad \text{for } j = 2, 3, \dots, s-1 \quad (36)$$

The variable time step Δt is calculated by the following approximate expression

$$\Delta t = \frac{C_n \Delta x}{\max(|U_j| + \sqrt{h_j})} \quad \text{for } j = 1, 2, \dots, s \quad (37)$$

in which C_n is the Courant number and the denominator in (37) is the maximum value of $(|U_j| + \sqrt{h_j})$ at all the wet nodes.

Use of the MacCormack method results in numerical high-frequency oscillations which tend to appear at the rear of a breaking wave, especially on a gentle slope. For open-channel flows, Chaudhry (1993) summarized a procedure to smooth these high-frequency oscillations. To apply this procedure for breaking waves on slopes excluding the boundary points, the computed water depth h_j^* at the node j and at the next time level t^* is used to calculate the parameter ν_j at the node j defined as

$$\nu_j = \frac{|h_{j+1}^* - 2h_j^* + h_{j-1}^*|}{|h_{j+1}^*| + 2|h_j^*| + |h_{j-1}^*|} \quad \text{for } j = 2, 3, \dots, (s^* - 1) \quad (38)$$

The parameter $\epsilon_{j+0.5}$ at the midpoint of the nodes j and $(j+1)$ is given by

$$\epsilon_{j+0.5} = \kappa \left(\frac{h_j^* + h_{j+1}^*}{2} \right)^{0.5} \max(\nu_j, \nu_{j+1}) \quad \text{for } j = 2, 3, \dots, (s^* - 2) \quad (39)$$

in which κ = numerical damping coefficient for regulating the amount of damping of the high-frequency oscillations. The computed water depth h_j^* is modified as

$$h_j^* = h_j^* + \epsilon_{j+0.5} (h_{j+1}^* - h_j^*) - \epsilon_{j-0.5} (h_j^* - h_{j-1}^*) \quad \text{for } j = 3, 4, \dots, (s^* - 2) \quad (40)$$

Likewise, U_j^* and m_j^* are smoothed using (40) with h_j^* being replaced by U_j^* and m_j^* , respectively, where $\epsilon_{j+0.5}$ is the same. The smoothed h_j^* and U_j^* are used to calculate $q_j^* = h_j^* U_j^*$. Chaudhry (1993) suggested expressions of ν_j at the boundary points for open-channel flows. However, the addition of these expressions in (39) and (40) is found to produce spurious fluid motions even in the absence of waves on slopes. As a result, the smoothing at the end points is not recommended for breaking waves on slopes. For breaking waves on gentle beach slopes, $\kappa = 1$ has been used to damp the high-frequency oscillations. For waves surging on steep slopes of coastal structures, $\kappa = 0.1$ appears to be sufficient. However, the smoothing procedure based on (38) tends to cause more damping near the shoreline where the water depth h is very small. To remedy this uneven damping, the factor $[(h_j^* + h_{j+1}^*)/2]^{0.5}$ is included in (39) to reduce the damping near the shoreline.

The landward boundary is located at the moving shoreline on the slope where the water depth is essentially zero and the landward boundary algorithm is a minor extension of the previous one-dimensional algorithm. The seaward boundary conditions on h and q utilizes the method of characteristics in basically the same way as the previous models (e.g., Kobayashi and Wurjanto 1989) with the inclusion of the momentum flux correction, m . However, the value of m at the seaward boundary needs to be found using (18). The value of m at $x = 0$ might be taken as $m = 0$ at $x = 0$ if the seaward boundary is located outside the surf zone. This is because the vertical variation of the horizontal velocity assumed in (18) is caused by wave breaking in this numerical model for shallow water waves. However, the boundary condition of $m = 0$ at $x = 0$ will yield $m = 0$ for $t > 0$ and $x > 0$ because $m = 0$ is a trivial solution of (18). It is hence required to introduce $m \geq 0$ at $x = 0$ so that $m \geq 0$ for $t > 0$ and $x > 0$. One option is to rewrite (18) in terms of \tilde{u}_b as

$$\frac{\partial \tilde{u}_b}{\partial t} + \frac{\partial}{\partial x} (U \tilde{u}_b) = -\frac{C_3 \tilde{u}_b}{2C_2} \left(\frac{\tilde{u}_b}{h} \frac{\partial h}{\partial x} + 3 \frac{\partial \tilde{u}_b}{\partial x} \right) - \frac{\tau_b + C_{B\ell} |\tilde{u}_b| \tilde{u}_b}{C_2 h} \quad (41)$$

where $C_{B\ell} = C_B C_\ell^2 \sigma$. Note that $\tilde{u}_b = 0$ is not a trivial solution of (41). The value of $m = C_2 h \tilde{u}_b^2$ at $x = 0$ may then be obtained using the value of \tilde{u}_b at $x = 0$ computed using (41) which is approximated by an explicit first-order finite difference.

Comparison of Previous 1-D and Present Models

To demonstrate the effectiveness of the MacCormack method, the present model VBREAK is reduced to a one-dimensional model and compared with the previous one-dimensional model IBREAK of Kobayashi and Wurjanto (1989). The quasi one-dimensional model uses an explicit first order finite difference of (41) to obtain the value of $(\tilde{u}_b)_1^*$ and thus m_1^* , the momentum correction factor at the next time level at the seaward boundary. However, when the value of m_1^* is set to zero at all times, the computed values of m_j^* at any node are zero for all times everywhere inside the computational domain. Thus the computed horizontal velocity has no vertical variation through the specification of zero vertical variation at the seaward boundary.

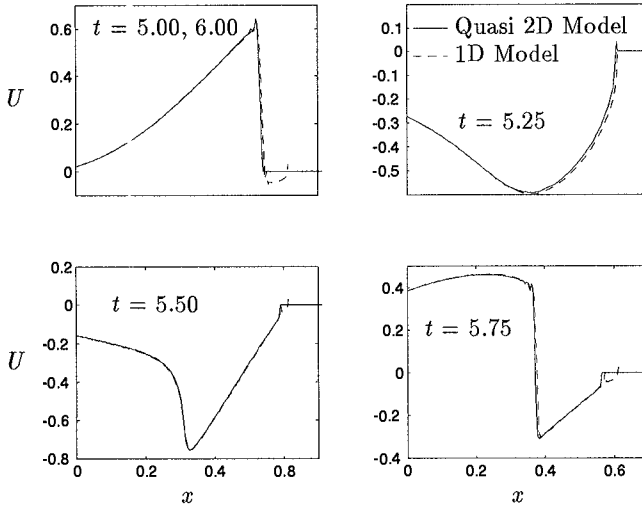


Figure 4: Cross-shore variations of computed depth-averaged velocity U

The only difference, then, between VBREAK and IBREAK is the different numerical methods employed to solve the same governing equations where IBREAK is based on the dissipative Lax-Wendroff method. Use is made of the 1:2.5 riprap revetment test conducted by Ahrens (1975) for the comparison. The computed free surface elevations turn out to be essentially identical while the computed depth-averaged velocities U display minor differences near the shoreline as shown in Fig. 4. The cross-shore variation of the depth-averaged velocity is depicted at 5 times throughout the final wave period. The computed velocities for each model are identical at $t = 5$ and 6 due to wave periodicity in Fig. 4.

Comparison with Data of Stive (1980)

The model is compared with the comprehensive measurements of test 1 presented by Stive (1980) and Stive and Wind (1982). Because the numerical model predicts the vertical variations of the horizontal velocity, the comparison of the measured and computed velocities can be made without any ambiguity. In Stive's test 1, the incident regular waves with period $T' = 1.79$ s broke as spilling breakers on the 1:40 concrete beach. The seaward boundary for the computation is taken to be at the location of still water depth $d'_i = 0.2375$ m, where the near-breaking wave profile was shown to be similar to the cnoidal wave profile as explained by Kobayashi *et al.* (1989). The measured wave height at the seaward boundary was $H' = 0.172$ m. The friction factor of 0.05 is used as in the previous computation by Kobayashi *et al.* (1989). A Courant number of 0.3 is adopted for the stable computation.

The measured and computed temporal variations of the free surface are compared at $x = 0, 1.29, 2.15,$ and 3.01 in Fig. 5. The variation of the free surface from the mean water level $\bar{\eta}$ for the last wave from $t = 29.0$ to $t = 30.0$ is shown in each panel. The crest of the computed wave form has been matched by hand with the measured crest;

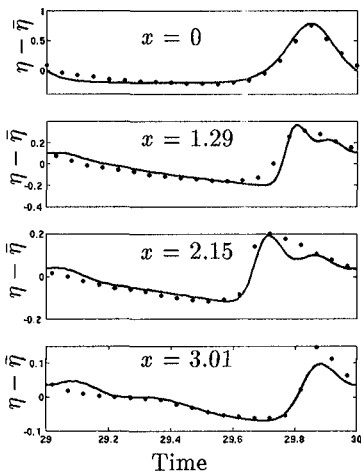


Figure 5: Measured and computed wave profiles.

• Data - - - Computed u — Computed U

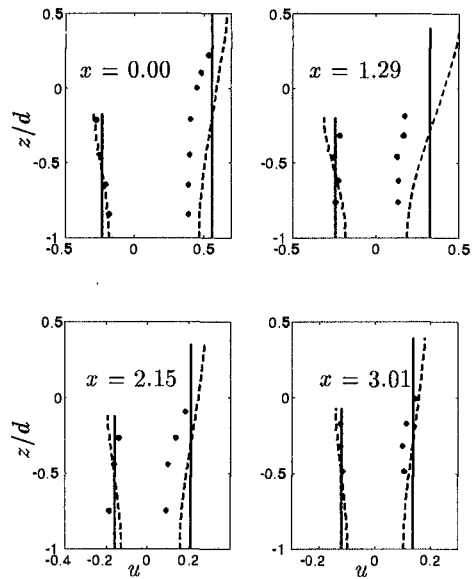


Figure 6: Measured and computed maximum and minimum normalized horizontal velocities

therefore, Fig. 5 should indicate only the comparison of the predicted and measured wave shapes. The first panel shows that the specified incident cnoidal wave at $x = 0$ agrees well with the measured profile. The high frequency oscillations following the wave crest are apparent in Fig. 5.

The maximum and minimum horizontal velocities at $x = 0, 1.29, 2.15,$ and 3.01 are depicted in Fig. 6. In each panel the dashed line represents the computed horizontal velocity u and the solid line is the computed depth averaged velocity U . The vertical axis is the ratio of z/d where z is the vertical coordinate and d is the water depth below SWL. The maximum and minimum values in Fig. 6 are obtained at each elevation z without regard to the vertical phase differences. Panel one indicates that although the specified and measured free surface elevations match at the seaward boundary well, the maximum horizontal velocity is considerably overpredicted. Likewise, at locations $x = 1.29, 2.15,$ and 3.01 the maximum velocity is overpredicted. The greatest computed variation of the velocity over the depth occurs after breaking, at $x = 1.29$. This, however, does not correspond well to the velocity measured below the trough level that displays virtually no variation with depth at $x = 1.29$.

Comparison with Data of Cox *et al.* (1995)

Comparison is also made with the data collected by Cox *et al.* (1995) that included detailed velocity profiles inside the surf zone. The experiment was performed in a wave flume with a 1:35 beach constructed of Plexiglas with a layer of sand glued to the surface to increase the bottom roughness. At each measuring line, water velocity measurements were taken at approximately twenty elevations. The free surface and

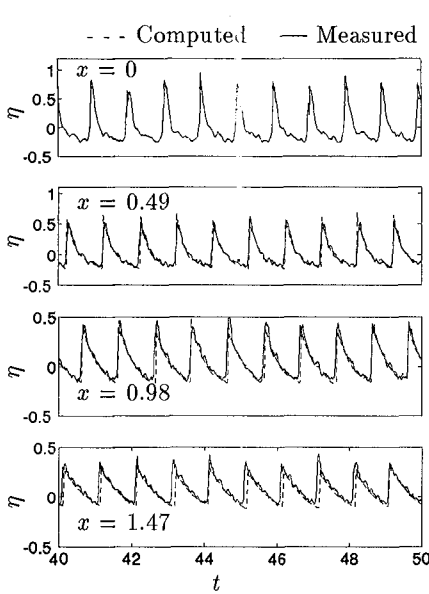


Figure 7: Measured and computed free surface

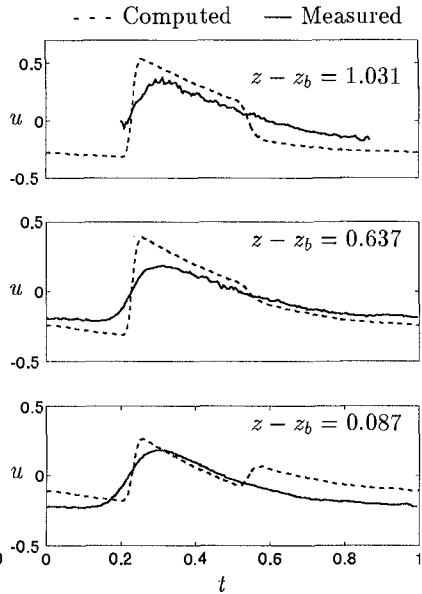


Figure 8: Normalized phase-averaged horizontal velocity u at three elevations at L4

velocities were measured for the duration of the last 50 waves out of 300 at each line. The numerical model is run with 300 waves of 2.2 s period in order to be consistent with the experimental procedure. The phase averaging is based on the last 50 waves in the same way as the measured data.

The friction factor $f'_w = 0.05$ is used. A Courant number of 0.4 maintained numerical stability in the following comparison. The seaward boundary is located landward of the break point, at measuring line L3 as defined by Cox *et al.* (1995). The height of the incident regular waves at L3 was $H' = 12.71$ cm and the corresponding still water depth was 17.71 cm.

Fig. 7 depicts the free surface at $x = 0.0, 0.49, 0.98,$ and 1.47 in the surf zone at L3, L4, L5, and L6 where L denotes the measuring line. The free surface prediction is quite good despite a lagging phase error seen most prominently at $x = 1.47$.

Fig. 8 shows the predicted and measured phase-averaged horizontal velocities at three elevations at L4 as a typical example. The first panel shows the velocities near the wave trough level. The solid line represents the measured values excluding dropouts in the data near the free surface. The second panel is a comparison at approximately mid-depth. The near bottom (1.1 cm above the bottom) velocities are plotted in the last panel. The unrealistic kink seen in panels one and three are due to the adopted relations (27) and (28) where the abrupt change in the velocity correction \tilde{u}_b is assumed to occur with the sign change in the depth averaged velocity, U .

The measured and computed horizontal and vertical velocity profiles are compared at six equally-spaced phases over one wave period for L5 in Fig. 9. The first panel depicts the computed and measured horizontal velocity as a function of the normalized

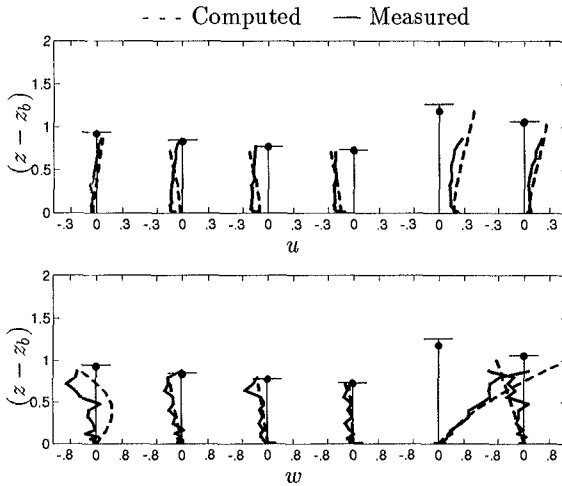


Figure 9: Vertical variations of horizontal and vertical velocities at six phases at L5

vertical distance $(z - z_b)$ above the bottom. The computed and measured free surfaces are shown as a black dot and as a horizontal line, respectively. The second panel depicts the comparison of the measured and computed vertical velocities at the same six phases. The discrepancy between the measured and computed vertical variations are caused, in part, by the aforementioned phase mismatch. As a whole, the agreement is reasonable in spite of the assumed simple vertical velocity profile (26). This is probably because the comparison is limited to below the wave trough level.

The normalized energy quantities involved in (29) are shown in Fig. 10. The numerical dissipation rate \overline{D}_n dominates over the dissipation rate due to bottom friction, \overline{D}_f , and the dissipation rate due to wave breaking, \overline{D}_B . This clearly indicates the shortcoming of the assumed velocity profile (26) which may be reasonable below the trough level but can not account for the much larger dissipation occurring above the trough level. Velocity data above the trough would be required to improve (26).

Conclusions

A numerical model is developed to predict the cross-shore and temporal variations of the free surface elevation η , the depth-averaged horizontal velocity U , and the near-bottom horizontal velocity correction \tilde{u}_b associated with the momentum flux correction m due to the vertical variation of the horizontal velocity u under the action of normally incident breaking waves. The three governing equations required for the three unknown variables are the depth-integrated continuity and horizontal momentum equations together with the new equation for the momentum flux correction m derived from the depth-integrated wave energy equation.

The normalized vertical profile of the horizontal velocity u outside the thin wave boundary layer is assumed to be cubic on the basis of limited available data. The turbulent shear stress outside the wave boundary layer is assumed to be expressed using the turbulent eddy viscosity whose mixing length is proportional to the instantaneous water depth. Although two additional empirical parameters are introduced in rela-

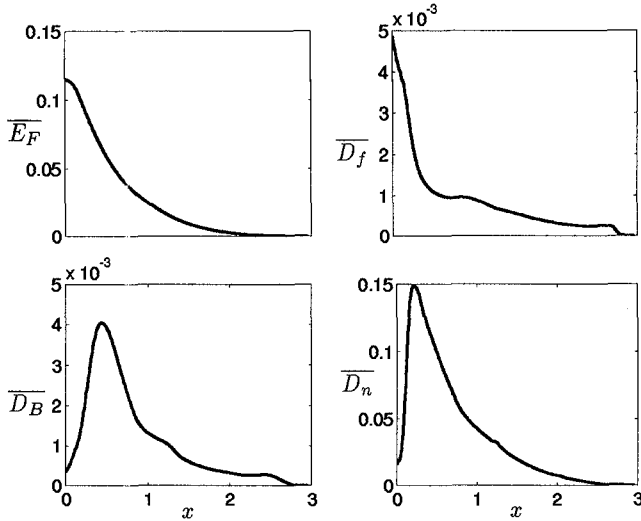


Figure 10: Computed cross-shore variation of normalized energy flux, bottom dissipation, breaking dissipation, and numerical dissipation.

tion to these assumptions, the computed vertical profiles of the horizontal velocity are found to be fairly insensitive to these empirical parameters in their ranges expected from limited available data.

The numerical model is reduced to a one-dimensional model and compared to the previous one-dimensional model. With appropriate simplification of the seaward boundary condition, the momentum flux correction equals zero identically throughout the computation domain for all times. The results are essentially the same for both models. This comparison demonstrates the efficiency and accuracy of the MacCormack method in the solution of the finite-amplitude shallow-water equations. The model is compared with the laboratory data presented by Stive (1980) and Stive and Wind (1982). The free surface elevations are predicted fairly accurately, while the maximum horizontal velocities are consistently overpredicted. The model is compared with the detailed fluid velocity measurements of Cox *et al.* (1995). Again, the free surface elevations are predicted fairly well. The horizontal velocity prediction is satisfactory apart from some phase mismatch and the unrealistic discontinuity in the velocity accompanying the sign change in U . As a whole, the agreement is reasonable considering the assumed simple vertical velocity profile. However, the model does not offer significant advantages over the previous one-dimensional models.

Acknowledgments

This work was sponsored by the US Army Research Office, University Research Initiative under contract No. DAAL03-92-G-0116 and by the National Science Foundation under grant No. CTS-9407827.

References

- Ahrens, J.P., 1975. "Large wave tank tests of riprap stability." *Technical Memo No. 51*, U.S. Army Coastal Engineering Research Center, Ft. Belvoir, VA

- Anderson, D.A., Tannehill, J.C., and Pletcher, R.H., 1984. *Computational fluid mechanics and heat transfer*. Hemisphere, New York, NY.
- Chaudhry, M.H., 1993. *Open-channel flow*. Prentice Hall, Englewood Cliffs, NJ.
- Cox, D.T., Kobayashi, N., and Okayasu, A., 1994. "Vertical variations of fluid velocities and shear stress in surf zones." *Proc. 23rd Coast. Engrg. Conf.*, ASCE, 98-112.
- Cox, D.T., Kobayashi, N., and Okayasu, A., 1995. "Experimental and numerical modeling of surf zone hydrodynamics." *Res. Rept. No. CACR-95-07*, Ctr. for Applied Coast. Res., Univ. of Delaware, Newark, DE.
- Johnson, B.D., Kobayashi, N., and Cox, D.T., 1996. "Formulation and validation of vertically two-dimensional shallow-water wave model." *Res. Rept. No. CACR-96-05*, Ctr. for Applied Coast. Res., Univ. of Delaware, Newark, DE.
- Jonsson, I.G., 1966. "Wave boundary layers and friction factors." *Proc. 10th Coast. Engrg. Conf.*, ASCE, 1, 127-148.
- Jonsson, I.G., and Carlsen, N.A., 1976. "Experimental and theoretical investigations in an oscillatory turbulent boundary layer." *J. Hydraul. Res.*, 14, 45-60.
- Kobayashi, N., DeSilva, G.S., and Watson, K.D., 1989. "Wave transformation and swash oscillation on gentle and steep slopes." *J. Geophys. Res.*, 94(C1), 951-966.
- Kobayashi, N., and Johnson, B.D., 1995. "Numerical model VBREAK for vertically two-dimensional breaking waves on impermeable slopes" *Res. Rept. No. CACR-95-06*, Ctr. for Applied Coast. Res., Univ. of Delaware, Newark, DE.
- Kobayashi, N., and Wurjanto, A., 1989. "Numerical model for design of impermeable coastal structures." *Res. Rept. No. CE-89-75*, Ctr. for Applied Coast. Res., Univ. of Delaware, Newark, DE.
- Kobayashi, N., and Wurjanto, A., 1992. "Irregular wave setup and run-up on beaches." *J. Wtrwy. Port, Coast. and Oc. Engrg.*, ASCE, 118(4), 368-386.
- MacCormack, R.W., 1969. "The effect of viscosity in hypervelocity impact cratering." *Paper 69-354*, Am. Inst. of Aeronaut. and Astronaut., New York.
- Madsen, P.A., and Svendsen, I.A., 1983. "Turbulent bores and hydraulic jumps." *J. Fluid Mech.*, 129, 1-25.
- Rodi, W., 1980. *Turbulence models and their application in hydraulics*. Intl. Assoc. Hydraul. Res., Delft, the Netherlands.
- Schäffer, H.A., Deigaard, R., and Madsen, P., 1992. "A two-dimensional surf zone model based on the Boussinesq equations." *Proc. 23rd Coast. Engrg. Conf.*, ASCE, 1, 576-589
- Stive, M.J.F., 1980. "Velocity and pressure field of spilling breakers." *Proc. 17th Coast. Engrg. Conf.*, ASCE, 547-566.
- Stive, M.J.F., and Wind, H.G., 1982. "A study of radiation stress and set-up in the nearshore region." *J. Coast. Engrg.*, 6, 1-25.
- Svendsen, I.A., and Madsen, P.A., 1984. "A turbulent bore on a beach." *J. Fluid Mech.*, 148, 73-96.
- Zelt, J.A., 1991. "The run-up of nonbreaking and breaking solitary waves." *J. Coast. Engrg.*, 15, 205-246.

CHAPTER 45

Particle Velocity Distribution in Surface Waves

Geir Moe¹ and Øivind A. Arntsen²

Abstract

In offshore and ocean engineering it is often of interest to be able to model particle velocities in the so-called splash zone, in which during a wave cycle, a given point is sometimes submerged, sometimes in air. (Emergence effects.) This paper applies the so-called Gerstner wave theory, extends it to narrow banded irregular waves, and presents it in an Eulerian description to second order in wave amplitude, so that the results may be compared with measurements made at fixed positions in the fluid. Mean horizontal velocities have been determined, and shown to compare excellently to laboratory measurements, both for regular and irregular waves. At this point in time, it can not be said whether the fit will be equally good in real ocean waves.

Introduction

The design of structures in an ocean environment is often governed by wave loading, requiring the determination of water particle kinematics. However, real ocean waves are irregular and nonlinear, and no universally accepted theory is available for predictions of such flows, especially not in the splash zone. This is unfortunate, since rather large contributions to the total loading may originate in the splash zone. The most important statistical properties of particle kinematics at fully submerged points for mildly nonlinear, irregular waves have been successfully determined by Longuet-Higgins (1963). The term "particle kinematics" is here used to denote particle velocities as well as accelerations. When emergence effects in the splash zone are to be included, most of the available models are of an approximate, "engineering" type, such as Wheeler stretching or similar, e.g. the models associated with the names of Chakrabarti, Gudmestad or

¹ Professor, Department of Structural Eng., Norwegian University of Science and Technology, N-7034 Trondheim, Norway.

² Associated Professor, Department of Structural Eng., Norwegian University of Science and Technology, N-7034 Trondheim, Norway.

Heideman, see e.g. Skjelbreia et al. (1991) for full references. A different type of approach was introduced by Tung (1975). He used Airy wave theory, but modified the results by checking whether a splash zone point at a given instant was submerged, or in air, by comparing the vertical coordinate to the instantaneous location of the wave profile, again predicted by Airy theory. Technically this was done by multiplication with a step function, constructed such that the flow velocity became zero when the considered point was in air. Cieslikiewicz & Gudmestad (1993) used a similar approach in conjunction with the previously mentioned higher order wave approach of Longuet-Higgins. However, their results compared only moderately well to Laser Doppler measurements of particle velocities made by Skjelbreia et al. (1989).

In the present paper an alternative theory will be explored, which gives quite good predictions of the mean of the measured horizontal particle velocity. Good agreement were found for several cases tested, in irregular as well as regular waves. The idea underlying this model is quite simple: it is assumed that the particle paths are circles which are traversed at constant velocity. This assumption leads to a deep water wave theory commonly denoted as the Gerstner wave, which will be presented in the next section. A word of caution may be appropriate at this point: The comparison is made between a Gerstner wave and experimental results from a closed wave tank in which waves were generated into quiescent water. The measurements cover only the initial phases after the wave generator had been turned on, the flow field will change if the wave generator is left on for a long time, see Mei (1972). Real ocean waves may have different characteristics from this, since there the waves have been generated in a different manner, viz. over vast areas and during long times, and by different mechanisms of generation. Even so, it is suggested that studies of waves under carefully controlled conditions in test basins may shed considerable light on the general wave kinematics problem.

Basic Equations

The derivation of Airy wave theory is well known and will not be repeated here. It is normally developed in an Eulerian frame of reference, the key point being that the boundary condition at the free surface is applied at the still water level, and that quadratic velocity terms are dropped from the surface boundary condition. Its justification rests on a number of assumptions, notably that the wave amplitude is vanishingly small compared to the wavelength. However in engineering practice linear theory is routinely applied to situations where the amplitude typically is 0.01 to 0.05 of the wavelength, and experience indicates that acceptable accuracy will usually be obtained for most of the physical quantities involved, provided the observation point stays submerged at all times. One major advantage to the Airy theory is that it is linear, and that therefore the principle of superposition applies. The Gerstner wave is also linear, (Kinsman, 1965). It satisfies continuity and the surface conditions exactly, but the flow is rotational. The Gerstner wave will now be described in the usual coordinate system with the x -axis in the direction of wave propagation and z vertically upwards, and the origin at the still water level.

Assuming deep water waves of wave period $T = 2\pi/\omega$ and wave length $\lambda = 2\pi/k$, the location of the particle $x(x_0, z_0, t)$, $z(x_0, z_0, t)$ at time t is given by:

$$x = x_0 - ae^{kz_0} \cos(\omega t - kx_0), \tag{1}$$

$$z = z_0 + ae^{kz_0} \sin(\omega t - kx_0). \tag{2}$$

This is in fact a Lagrangian description of particle motions. It easily seen that for fixed values of x_0, z_0 , and varying t , the coordinates (x, z) describe a circle about the point (x_0, z_0) , whose radius is a at the surface (i.e. at $z_0 = 0$), and decays exponentially with the distance below the surface. The shape of the free surface $\eta(x,t)$ follows by setting $z_0 = 0$:

$$\eta(x,t) = a \sin(\omega t - kx_0(x,t)) \tag{3}$$

When t is kept constant, the equation defines the surface profile, as a function of x . This represents a trochoid³ as depicted in Fig. 1 for fixed time $t = 0$.

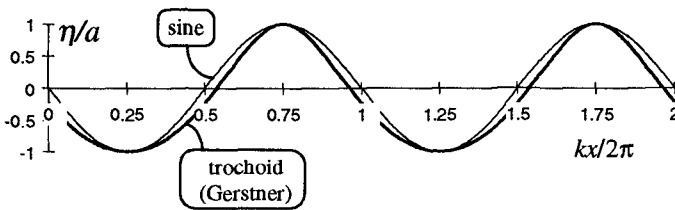


Figure 1. Free surface variation of a Gerstner wave.
 Data as for wave case R15b. (Skjelbreia et al., 1989)
 $H = 0.13$ m, $T = 1.5$ s, $\lambda = 3.5$ m, $d = 1.3$ m.

The phase velocity $c = \lambda/T$ is as for the Airy wave, and a close inspection of the free surface condition would reveal that it will be satisfied exactly, provided the deep water dispersion relation is satisfied, see e.g. Kinsman (1965) or Lamb (1932):

$$c = \omega / k \tag{3B}$$

$$k = \omega^2 / g \tag{3C}$$

It is now necessary to convert to a description in terms of fixed coordinates (x, z) , in order to describe the particle velocities at a given point, i.e. an Eulerian description is required. Without loss of generality one may consider the point $(x = 0, z)$.

³ trochoid: the curve generated by a point somewhere on the radius line (centre distance a) of a circle (radius $r = \lambda/2\pi$) as the circle circumference rolls on a fixed straight line.

This is convenient because then (kx_0) represents a small parameter, of order (ka) , so that a low order Taylor expansion may be used for functions of (kx_0) . In the final expressions the equations will be expanded to second order in (ka) . From (1) with $x = 0$ initially to first order one has

$$x_0^{(1)} = ae^{kz} \cos(\omega t) , \tag{4}$$

$$\zeta^{(1)} = z - z_0 = ae^{kz} \sin \omega t . \tag{5}$$

The second order expression for x_0 may be found by substitution of the above first order approx. into (1),

$$\begin{aligned} x_0 &= a \exp(kz - k\zeta^{(1)}) \cos(\omega t - kx_0^{(1)}) \\ &= ae^{kz} (1 - k\zeta^{(1)}) (\cos \omega t + kx_0^{(1)} \sin \omega t) \\ &= ae^{kz} \cos \omega t . \end{aligned} \tag{6}$$

Similarly for z one has

$$\begin{aligned} \zeta &= z - z_0 \\ &= ae^{kz} (1 - k\zeta^{(1)}) (\sin \omega t - kx_0^{(1)} \cos \omega t) \\ &= ae^{kz} \sin \omega t - ka^2 e^{2kz} . \end{aligned} \tag{7}$$

Thus for a point at the surface $z_0 = 0$, and $z(0,0, t)$ represents the surface elevation $\eta(0, t)$ as shown in Fig. 2. At a crest $z = a$ and $\sin \omega t = 1$ and from (7) follows that $\zeta = a$, while at a trough $\zeta = -a$, both accurate to second order in a . Zero crossing occurs at $\sin \omega t = ka$, i.e. at $\omega t = ka$ or $\omega t = \pi - ka$. Thus the crests are sharper and the troughs more rounded than for a pure sine wave. This was to be expected, since the formulae represents the trochoid.

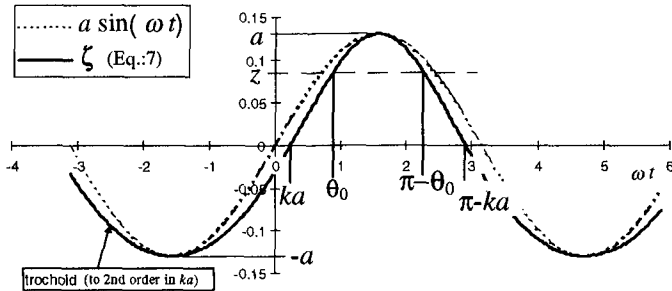


Figure 2. The surface variation of the trochoid correct to second order in ka .
Data as in Fig. 1.

In the same manner one may find the horizontal and vertical velocity components at $(x = 0, z)$ as

$$u = a\omega e^{kz_0} \sin(\omega t - kx_0) = a\omega e^{kz} \sin \omega t - a^2 k\omega e^{2kz}, \quad (8)$$

$$w = a\omega e^{kz} \cos \omega t. \quad (9)$$

Mean particle velocity, regular waves

The above are expressions for regular deep water (Gerstner) waves of amplitude a and period $T = 2\pi/\omega$ and wave length $\lambda = 2\pi/k$. The particles moves in closed circles, hence the mean velocity when following a particle is zero. (Laplacian description). For a stationary observer (Eulerian description) the picture is different, however, and that is the relevant viewpoint when comparing to measurements taken at a fixed point. From (9) is seen that the vertical mean velocity is zero,

$$\bar{w} = 0. \quad (10)$$

For points that are always submerged, the mean horizontal velocity can similarly be determined from (8)

$$\bar{u} = -a^2 \omega k e^{2kz}. \quad (11)$$

For points in the splash zone, $-a < z < a$, emergence effects must be considered. The considered point will be in air for $z_0 > 0$ or, using $z_0 = z - \zeta$ and (7), the point will be in water, provided

$$z_0 = z + ka^2(1 + 2kz) - a(1 + kz)\sin \omega t < 0. \quad (12)$$

Solving and retaining terms to second order in amplitude a in the numerator and denominator, (and remembering that in the splash zone z is of order a .) one obtains

$$\Rightarrow \sin \omega t \geq \sin \theta_0 = \frac{z + ka^2}{a(1 + ka)}. \quad (13)$$

Thus the limiting phase angle is $(\omega t)_0 = \theta_0$ (cf. Fig. 2), and the mean value of horizontal particle velocity in the splash zone becomes

$$\begin{aligned} \overline{u(0, z)} &= \frac{1}{\pi} \int_{\theta_0}^{\pi/2} u(0, z, t(\theta)) d\theta \\ &= \frac{a\omega}{\pi} [e^{kz} \cos \theta_0 - ake^{2kz} (\frac{\pi}{2} - \theta_0)]. \end{aligned} \quad (14)$$

The considered contribution represents the value of the integral in the phase angle range $(-\pi/2 < \theta < \pi/2)$, which in view of symmetry yields the average over a full cycle. The result is shown in Fig. 3, which also includes the experimental points from a project conducted at SINTEF NHL, Trondheim, under the supervision of Dr. Skjelbreia (Skjelbreia et al., 1989). The experimental data points have been read off from a figure presented in Cieslikiewicz & Gudmestad (1992).

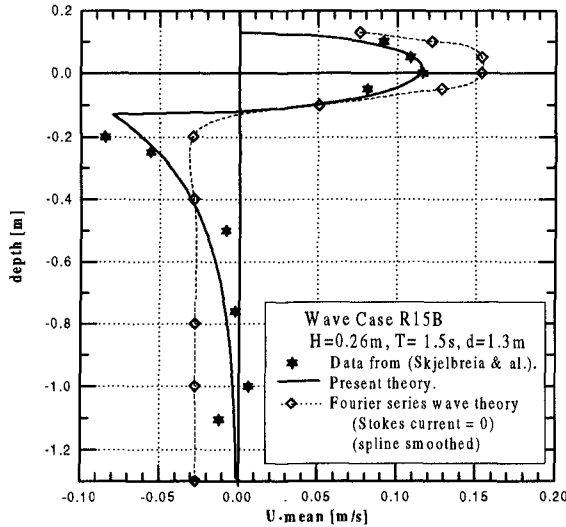


Figure 3. $E[u]$ vs depth. Regular wave case.

Irregular waves

Typically the variance spectrum, $S_{\eta}(\omega)$, of the sea surface is known. Let us for simplicity assume that the particle kinematics represent ergodic and narrow band processes, and further that h , u and w are Gaussian, so that their peaks are Rayleigh distributed. The choice of a frequency, that can be considered to be the most representative for the narrow process $u(x, z, t)$, is not straight forward. In the splash zone one might think that the zero crossing frequency of u (which is ω_{42}) would be the best choice, however the surface shape is dictated by the zero crossing frequency of η (ω_{20}), and this would also govern the frequency of the horizontal particle velocity. The shape of the variance spectrum of the horizontal particle velocity will change with depth, since the wave components of higher frequencies attenuate more rapidly with depth, than those of the lower frequencies. The frequency of the depth averaged horizontal particle velocity turns out to be ω_{20} which therefore is chosen as the representative frequency for the narrow band process used herein.

$$\omega_{20} = (M_2 / M_0)^{1/2}, \quad (15)$$

$$\omega_{42} = (M_4 / M_2)^{1/2}, \quad (16)$$

$$M_j = \int_0^{\infty} \omega^j S_{\eta}(\omega) d\omega. \quad (17)$$

The expected value of u in an irregular seastate depends on the wave amplitude, which is a slowly varying envelope for η , and is as such Rayleigh distributed with parameter σ_{η} , viz.

$$f_A(a) = \frac{a}{\sigma_{\eta}^2} \exp\left(-\frac{a^2}{2\sigma_{\eta}^2}\right); a \geq 0, \quad (18)$$

in which $f_A(a)$ is the probability density of a . Then the expectation of u is given by

$$E[u] = \int_0^{\infty} f_A(a) E[ua] da. \quad (19)$$

Equation (19) states that for a given amplitude, the result depends on the expectations of u , summed over all amplitudes, and weighting according to their frequency of occurrence. The ergodicity theorem implies that the calculation of (19) may be done as a time average. Since the wave spectrum is narrow-banded, the components in (19) represent almost harmonic waves occurring sequentially rather than superposition of components that occur simultaneously. Hence the decision whether the point is in air can be made on a wave by wave basis for each value of the amplitude. Then the expectations in (11) and (14) represent $E[ua]$ for points that are submerged or in the splash zone respectively. For a given depth, z , the decision whether the point is submerged or not depends on the amplitude a . Hence (19) must be split in two integrals, one for $(-z) > a$ which can be evaluated analytically, and another in which the lower integration limit must first be determined according to (13), and the integral in (19) then must be evaluated numerically. The results are shown in Fig. 4 together with points representing the results of the measurements made by Skjelbreia and his team. The experimental values have been read off from a figure, this time the figure is taken from Cieslikiewicz & Gudmestad (1993). It is seen that the fit between experiments and theory is very good.

Discussion

The Gerstner theory used herein shows results that correspond very well to the Skjelbreia experiments. In contrast, application of linear (Airy) wave theory resulted in considerable discrepancies between experiments and theory. In the results presented in the two papers by Cieslikiewicz and Gudmestad, the discrepancy relative to maximum of the mean velocity as calculated from the measurements, amounted to about 25% through much of the splash zone and up to 40% in the zone of total submergence. This was the case both for the regular and the irregular wave case. The regular wave case R15b was also modeled using an eighteen Fourier component method (ACES107). As

recommended in the guide the integrated Stokes flow in a wave flume should be equal to zero and set accordingly in the Fourier-series model. The results are presented in Fig. 3. We see that this model fit the observations much less than the Gerstner approach.

It must be emphasized very strongly that the case considered herein is laboratory measurements, and hence different from real ocean waves in many ways. The Airy wave can be made equal to the Gerstner wave, provided a so-called Stokes drift is added. Stokes drift is a steady current that decays exponentially with depth, and is in fact equal and opposite to the current determined herein for the totally submerged case, as given by (11). Integrated over the whole depth this yields a total flow of water in the direction of wave propagation and per unit width of the wave crest, equal to ωa^2 . Under the conditions at which the experiments were conducted, such a flux can not take place, since it violates continuity both at the wavemaker and at the wave front. This can hardly be remedied by superposition of another irrotational flow. Therefore it may not be too surprising that the Gerstner wave is in better agreement with measurements, even though it has the unusual character of being rotational. Another rotational solution to this problem has been presented by Kyoizuka (1995). One possibility is that the required rotation is generated from shear along the boundaries of the fluid region. It is not known how well the two theories discussed herein will compare to measurements in real ocean waves.

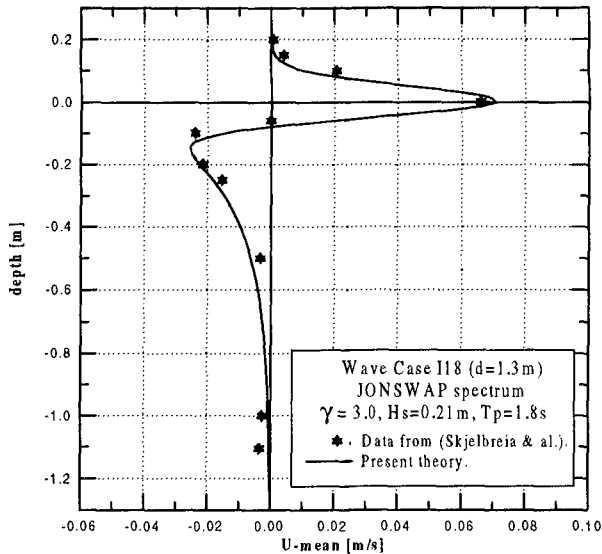


Figure 4. $E[u]$ vs depth. Irregular wave case.

Conclusions

- The Gerstner wave has been presented in an Eulerian description, to second order in the wave amplitude.
- Mean particle velocities have been computed for the regular and irregular case.
- The results have been compared to laboratory measurements, exhibiting an excellent fit, see Fig. 3 and Fig. 4.
- No statements can at this time be made on how the predictions from the present theory would compare to measurements in the ocean.

References

- ACES107: "Automated Coastal Engineering System: The Wave Theory Functional Area/Fourier Series Wave Theory", User's guide and technical reference. Version 1.07D, October 1993. Coastal Engineering Research Center, Waterways Experiment Station, 3909 Halls Ferry Road, Vicksburg, Mississippi 39180-6199
- Cieslikiewicz, W., Gudmestad, O.T.: "Stochastic characteristics of orbital velocities of random water waves", *J. Fluid Mech.*(1993), Vol 255, pp.275-299.
- Cieslikiewicz, W., Gudmestad, O.T.: "Mass transport within the free surface zone of water waves", *Wave Motion*, Aug 1992
- Lamb, H.: *Hydrodynamics*, Sixth edition, Cambridge University Press, 1932.
- Kinsman, B.: *Wind Waves*, Prentice-Hall, Inc., Englewood Cliffs, New Jersey, USA, 1965.
- Kyozuka, Y.: "Mass transport in two-dimensional tanks", preliminary version of paper, private communication, 1995.
- Longuet-Higgins, M.S.: "The effects of nonlinearities on statistical distributions in the theory of sea waves", *J. Fluid Mech.* (1963), Vol 17, pp.459-480.
- Mei, C.C., (1972): *Mass transport in Water Waves*, dept. of Civil Engineering, Massachusetts Institute of Technology, Research report R72-15., 287p.
- Skjelbreia, J., Tørum, A., Berek, E., Gudmestad, O.T., Heideman, J., Spidsøe, N.: "Laboratory measurements of regular and irregular wave kinematics", *Proceedings E & P Forum Workshop, Paris, 25-26 Oct, 1989*
- Skjelbreia, J., Berek, E., Bolen, Z., Gudmestad, O.T., Heideman, J., Ohmart, R.D., Spidsøe, N., Tørum, A.: "Wave kinematics in irregular waves", *OMAE proceedings, Vol 1A, pp 223-228, 1991.*
- Tung, C.C.: "Statistical properties of the kinematics and dynamics of a random gravity wave field. *J. Fluid Mech.* (1975), Vol 70, pp. 251-255.

CHAPTER 46

A comparison of analysis methods for wave pressure data

Murray Townsend¹ and John D. Fenton²

ABSTRACT

A comparison of a range of wave pressure analysis methods has been conducted using both numerical data generated by a Fourier steady wave method and experimental data gathered in a wave flume. The results show that the local methods (local sinusoid approximations and local polynomial approximations) are more accurate than the traditional global linear spectral method. A new local polynomial approximation method shows improvement compared to similar methods developed previously.

INTRODUCTION

Pressure transducers have been used for many years by coastal engineers for measuring the wave climate at a site of interest. These instruments are well suited to this purpose, being unobtrusive and robust. Problems do occur, however, when the surface elevation is inferred from the pressure data. The problem is fundamentally a poorly posed one, the subsurface pressure data being an attenuated representation of the flow conditions. In addition, the nonlinearity of waves in the coastal zone means that the traditional linear analysis methods may be inaccurate for such an application. The aim of the present study is to evaluate existing analysis techniques and if possible to improve the accuracy and robustness of those that are more suitable. Both numerical and experimental data was used in the analysis.

The methods examined include one global method and several local methods. The global method is the linear spectral method, described at length by Bishop and

¹Research Student, Australian Maritime Engineering Cooperative Research Centre (AMECRC), Department of Mechanical Engineering, Monash University, Clayton, Victoria, 3168, Australia.

²ARC Senior Research Fellow, Department of Mechanical Engineering, Monash University, Clayton, Victoria, 3168, Australia.

Donelan (1987). The local methods are the first order Local Sinusoidal Approximation (LSA) method, the empirical LSA method (Nielsen, 1989), the fully nonlinear Local Polynomial Approximation (full LPA) method (Fenton, 1986) and the simple LPA method (Fenton and Christian, 1989). A new method, using LPA, is presented and tested - the nonlinearly optimised LPA (NOLPA). There is a new local Fourier approximation method (Barker and Sobey, 1996) based upon the surface method of Sobey (1991), which is being published in these proceedings.

ANALYSIS METHODS

Linear spectral method

The most common analysis technique used in this area is the linear spectral method, which has been presented and comprehensively discussed by Bishop and Donelan (1987). Briefly, the spectrum of the water surface elevation, $S_s(\omega)$ is related to the spectrum of the dynamic pressure at the pressure transducer, $S_p(\omega)$ by:

$$S_s(\omega) = \left[\frac{N(\omega)}{K_p(\omega)} \right]^2 S_p(\omega), \quad (1)$$

where ω is the angular frequency of each Fourier component, $N(\omega)$ is an empirical correction factor and $K_p(\omega)$ is the pressure response factor defined as:

$$K_p(\omega) = \frac{\cosh k(\omega)y_p}{\cosh k(\omega)D}, \quad (2)$$

where D is the mean water level (MWL) and y_p is the height of the pressure transducer from the sea bed.

The authors have, for the purpose of this paper set $N(\omega)$ to 1 for all ω . Bishop and Donelan consider the presence of $N(\omega)$ as an attempt to compensate for poor measurements, instruments and/or analysis methods. As the authors are using 'exact' nonlinear waves and pressure traces to conduct these tests none of the above need be considered and only potential inadequacies in the linear spectral method will be highlighted.

It was necessary to determine a maximum ω above which the pressure response factor was not applied, as doing so would cause the method to 'blow-up' when $K_p(\omega)$ became small. To determine this limit, the ratio of the spectral amplitude to $K_p(\omega)$ was determined at each ω . When this ratio began to increase at frequencies above the spectral peak the method had started to 'blow-up'.

Local sinusoidal approximation methods

The first of the computer-based local methods to emerge were the two developed simultaneously by Nielsen (1989). Both are known as LSA methods in which a sine curve is passed through three points from the pressure data which are adjacent or with a small number of intermediate points between them. This sine curve is used to determine the 'local' frequency. The water surface elevation at the instant in time of the central point can then be calculated by one of two methods. One method applies a transfer function derived from stretched linear theory (the first order LSA), the other applies a semi-empirical transfer function.

First order local sinusoidal approximation

This transfer function is expressed:

$$\hat{\eta}_n = \frac{p_n}{\rho g} \frac{\cosh k_n \left(D + \frac{p_n}{\rho g} \right)}{\cosh k_n z}, \quad (3)$$

where $\hat{\eta}_n$ is the water surface elevation corresponding to the n th central pressure reading, p_n is the n th central pressure reading, k_n is the n th wave number derived from the local frequency calculated from the three pressure readings and ρ is the water density.

The local frequency is determined by:

$$\hat{\omega}_n^2 = \frac{-p_{n-M} + 2p_n - p_{n+M}}{p_n (M\delta)^2}, \quad (4)$$

which is an estimate corrected by:

$$\omega_n^2 = \hat{\omega}_n^2 \left[1 + \frac{1}{12} (\hat{\omega}\delta)^2 \right]. \quad (5)$$

Empirical local sinusoidal approximation

Nielsen derived this transfer function from Dean (1974):

$$\hat{\eta}_n = \frac{p_n}{\rho g} \left[A \left(\frac{y_p}{D} \right) \frac{-p_{n-M} + 2p_n - p_{n+M}}{p_n g (M\delta)^2} \left(D + \frac{p_n}{\rho g} - y_p \right) \right] \quad (6)$$

where M is a positive integer the value of which can be estimated by $M \approx \sqrt{D/g}/\delta$ and is a multiplier which smoothes noisy data by selecting more widely spaced points instead of adjacent ones in the frequency calculation, δ is the sampling period of the data, and $A(y_p/D) = 0.67 + 0.34 y_p/D$ and accounts for the height of the pressure transducer above the sea bed.

Both the above are extremely simple to apply with little computational effort required. In this study M was set to 1 when used with numerically generated data as no noise was present in the input and the authors felt that this gave a better indication of the method's robustness. With real data M was calculated by the above equation.

Local polynomial approximations

The other two local methods are LPA techniques and were developed by Fenton (1986) and Fenton and Christian (1989). Both utilise the principle of low-degree polynomial approximation, partly based on least-squares approximation methods and partly on solving locally the full nonlinear equations of motion.

Fully nonlinear local polynomial approximation

The approach followed for the full LPA (Fenton, 1986) was to approximate the complex velocity potential as follows:

$$w(x, y, t) = \phi(x - ct, y) + i\psi(x - ct, y) \\ = c_e(z - ct) + \sum_{j=0}^J \frac{a_j}{j+1} (z - ct)^{j+1}, \quad (7)$$

where $z = x + iy$, c_e is the Eulerian current and the surface elevation is given by

$$\eta(x, t) = \sum_{j=0}^J b_j (x - ct)^j. \quad (8)$$

From equation (7) ϕ satisfies Laplace's equation identically throughout the flow and the bottom boundary condition ($v(x, 0, t) = 0$) is satisfied if the coefficients a_j and b_j are real.

To satisfy the necessary boundary conditions on the free surface the steady kinematic equation is invoked such that:

$$\psi(x - ct, \eta(x - ct)) = -Q, \quad (9)$$

where Q is a constant, and the steady Bernoulli equation:

$$R = \frac{1}{2} \left| \frac{dw}{d(z-ct)} \right|_s^2 + \eta, \quad (10)$$

where R is the Bernoulli constant and s denotes the surface $y=\eta$.

Bernoulli's equation is also written about the position $(0, y_p)$, the position of the pressure transducer, expressed as a Taylor series in $x-ct$:

$$p(0, y_p, t) = R - \frac{1}{2} \left| \frac{dw}{d(z-ct)} \right|_{y_p}^2 - y_p = \sum_{j=0}^J p_j (-ct)^j. \quad (11)$$

The p_j are calculated using a least squares fit across K data points where K is an odd integer greater than or equal to $J + 3$ with $(K - 1)/2$ data points each side of the point of interest. For the above method $K = 21$ was found to give good results for both smooth and noisy data and is the value used in these tests. $J = 4$ was found to be the optimum degree of approximation.

By manipulation of equations (7), (8), (9), (10) and (11) and isolating powers of $(x-ct)$, a system of nonlinear equations in terms of the unknown a_j and b_j is obtained. The solution of these equations is performed for each point in the pressure series using direct iteration to achieve convergence. The surface elevation data obtained was then passed through a simple 3-point smoothing routine. Space does not permit explanation of the details regarding the solution of these equations for the a_j and b_j coefficients.

Simple local polynomial approximation

The simple LPA (Fenton and Christian, 1989) is somewhat simpler in that a point value is used to describe each value of η at $t = 0$ as opposed to the polynomial expansion across the window in the former method. The resulting solution is much simplified with the extraction of a system of quite manageable nonlinear equations. Unfortunately, there are only 6 equations in that set with a total of seven unknowns. It was necessary to introduce more equations to be able to find a solution. The first assumption required is that the wave speed c is given by long wave theory:

$$c = \sqrt{g\eta}, \quad (12)$$

and the second is that the main fluid velocity component a_0 is given by:

$$a_0 = -c. \quad (13)$$

For the results that follow the value of K was set to 17.

Nonlinearly optimised local polynomial approximation

This method (NOLPA) was developed using some of the ideas mentioned in the two sections above. The same basic idea of approximating the velocity potential by a low degree polynomial over a small window of data remains, but the method of solving this nonlinear problem is quite different.

The velocity potential ϕ is represented by equation (7) and substituted into Bernoulli's equation at the pressure transducer

$$\frac{P}{\rho}(x, y_p, t) = R - \frac{1}{2}(u_p^2 + v_p^2) - gy_p, \quad (14)$$

where u_p and v_p are the horizontal and vertical velocities ($\partial\phi/\partial x$ and $\partial\phi/\partial y$ respectively) at the pressure transducer ($y=y_p$). Neglecting the kinematic boundary condition, this equation can be solved across K pressure points (K is an odd integer greater than or equal to $J+3$) using a nonlinear least squares solver such as the Levenberg-Marquardt method (Grace, 1994). The actual function to be optimised by this method is written

$$F = \sum_{k=1}^K \left[R - \frac{1}{2}u_{pk}^2 - \frac{1}{2}v_{pk}^2 - gy_p - \frac{P_k}{\rho} \right]^2. \quad (15)$$

The initial estimates of the unknowns R/gD , c/\sqrt{gd} , $a_0 - a_J$ were set to the still water values $\{1.5, 1, -1, 0, 0, 0, 0\}$ and the time vector t_k (embedded in the velocity equations) was scaled such that the temporal length of the window was between -1 and +1. This, along with the appropriate rescaling if the system on equations approximates orthogonality in the velocity potential (Fenton, 1994), a property not held by the polynomial chosen.

Once this solution has been obtained, the location of the surface can be calculated. Bernoulli's equation at the unknown surface η

$$F_{\eta} = R - \frac{1}{2}u_{\eta}^2 - \frac{1}{2}v_{\eta}^2 - g\eta, \quad (16)$$

is a nonlinear equation in one unknown and can be solved at any time within -1 and +1. In the results that follow the surface estimates shown were calculated in the middle of the window ($t = 0$).

When dealing with experimental data each window was smoothed using an equally weighted moving average filter which was made larger or smaller depending upon the quality of the pressure data used. $K = 11$ was used for numerically generated smooth data while $K = 17$ was used for real data. As with the other LPA method it was found to be unnecessary to use a degree of approximation greater than $J = 4$.

It was sometimes required, when analysing extreme waves, such as in Figure 4, that the length of the window be made a smaller proportion of the wavelength than was normally used to allow convergence of the least squares routine. To give an adequate number of data points in the smaller window, the number of points actually used in the solution was increased by cubic spline interpolation, adding data points in between the originally sampled data, in a similar manner to Sobey (1991) with his surface based local Fourier method.

Methodology

The methods described above were tested with data from a Fourier method for generating steady waves (Fenton, 1988) and with experimental data obtained in a wave flume. The input from the Fourier method was generated for three different wavelengths, $\lambda/D=6.31, 10$ and 19.95 all with 64 data points per wavelength plus 5 extra points at each end of the data. The waves shown are extreme with a height/depth ratio (H/D) of 0.6. The gathering of the experimental data is described below.

Experimental Procedure

Experiments were performed in the large wave flume in the Department of Mechanical Engineering at Monash University. The facility is 52m long, 2.5 m wide with two working sections of 4m and 2.5m connected by a ramp. The shallower working section was modified for a working depth of 1.5m with a false floor. It is capable of generating both regular and irregular waves using a feedback system to obtain the desired sea state. There is a wave absorbing beach at the far end which allows less than 10% reflection across the range of working frequencies.

Four pressure transducers were set into a false wall in the flume at y_p/D ratios from 0 to 0.5. Two more transducers were mounted further 'downstream' at y_p/D of 0 and 0.5 to obtain phase data if required. The surface elevation above the first column of transducers was measured using a capacitance wave probe.

Results

Numerically generated data

Figure 1 shows results for a short wave with $\lambda/D = 6.31$, $H/D = 0.6$ with the pressure measured on the bed ($y_p/D = 0$). It seems that LPA methods should not be used for waves shorter than this, the full LPA and the NOLPA underestimating the crest. The traditional linear spectral method and the simple LPA do not perform at all well. Considering the considerably attenuated signal that occurs with such a short wave it is significant that the two LSA methods are almost identical and predict the wave height well although the wave shape is poor. Note the failure of the LSA methods on the wave "shoulder".

Figure 2 shows a longer wave with $\lambda/D = 10$ and all other properties the same as the previous figure. At this wavelength/depth ratio, the level attenuation of the pressure signal is much less and the quality of the output from all methods is higher. Only the simple LPA underestimates the crest while the full LPA and the NOLPA perform extremely well. The LSA methods perform in a similar manner to the previous figure and the linear spectral method does not describe the trough of the wave very well.

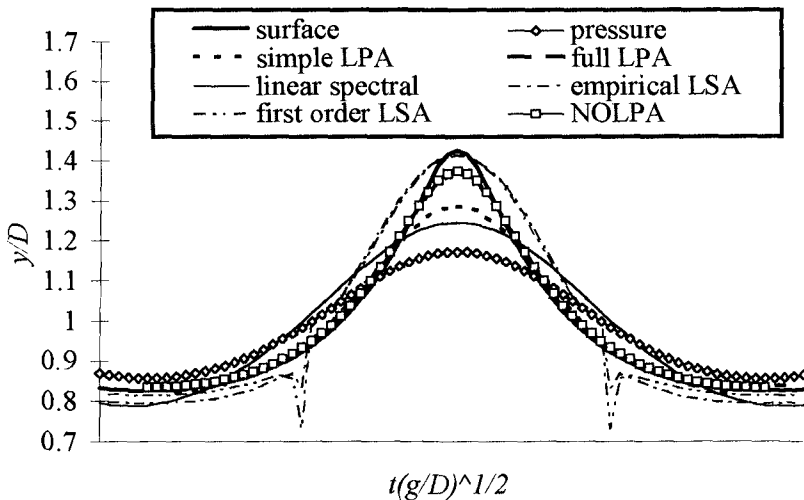


Figure 1: $\lambda/D = 6.31$, $H/D = 0.6$, $y_p/D = 0$

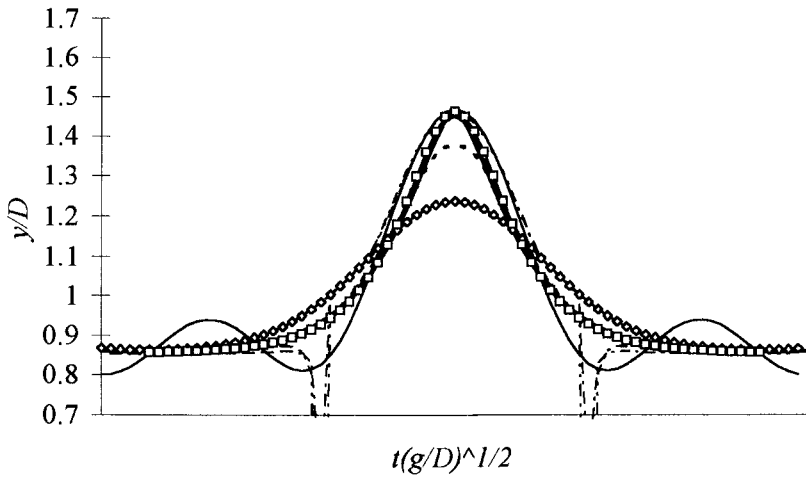


Figure 2: $\lambda/D = 10.0$, $H/D = 0.6$, $y_p/D = 0$

The wave in Figure 3 is identical to that in the previous figure, the difference being that the pressure was sampled higher in the water column, at $y_p/D = 0.5$. The most noticeable improvement is the result from the linear spectral method, the higher measurement position detecting the higher frequency components required to describe the trough of the wave. The performance of the simple LPA is much improved, while all other methods are similar in their performance to Figure 2.

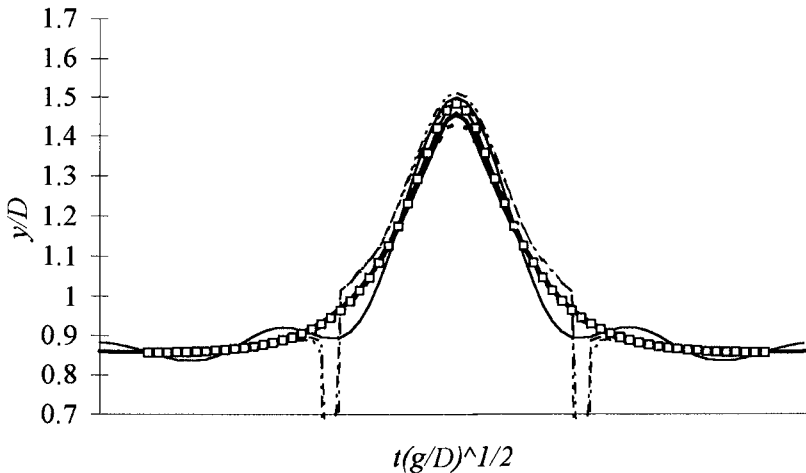


Figure 3: $\lambda/D = 10.0$, $H/D = 0.6$, $y_p/D = 0.5$

Figure 4 is a longer wave again, with $\lambda/D = 19.95$ but with the pressure, once again measured at the bottom. Once again the linear spectral method cannot describe both the sharp crest of the wave and the long flat trough, as the high frequency components attenuate completely before reaching the sea bed. The LSA methods predict both the profile and the height well, with a slight overprediction of the crest, as does the NOLPA. The simple LPA underpredicts the crest, as could be expected, while the full LPA performs very well.

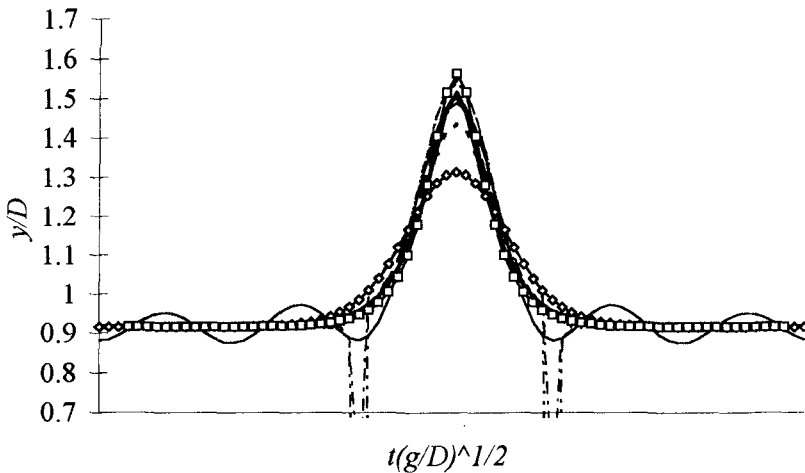


Figure 4: $\lambda/D = 19.95$, $H/D = 0.6$, $y_p/D = 0$

Experimental data

The irregular wave results shown in this section were generated from a JONSWAP spectrum with the properties: peak frequency, $f_0 = 0.4$ Hz, $D = 1.55$ m, Stokes current, $c_s = 0$, and a sampling rate of 20 Hz. The exception is Figure 7 where there is an Eulerian current, $c_e = 0.134$ m/s in the direction of wave propagation. This peak frequency corresponds to a λ/D ratio of approximately 6 in this water depth, a condition where the LPA methods are not expected to perform at their best. Unfortunately the flume is not capable of generating irregular waves with a lower peak frequency.

The full LPA method is not shown in these results. This method was shown to be extremely sensitive to noisy data in an earlier, numerical comparison (Townsend and Fenton, 1995), where convergence appeared to be case dependent with regard to the number of data points per window.

The almost identical performance of the two LSA methods was shown in the previous section and due to the more cluttered appearance of the experimental results, the first order LSA has not been included. The empirical LSA has also proved to be more robust when dealing with noisy data.

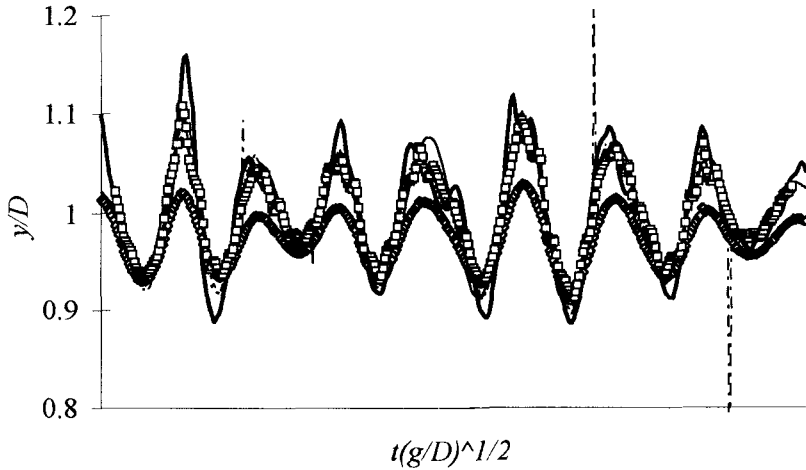


Figure 5: $y_p/D = 0$, $c_s = 0$

Figure 5 shows a zero Stokes current condition with the pressure measured at the floor of the flume. The effect of the noise in the pressure signal is evident, with the linear spectral method providing the smoothest output due to its inherent low pass filtering. The empirical LSA performs well, with the exception of the expected occasional failure, while the simple LPA and the NOLPA perform almost identically, which is well considering the shortness of the waves.

The wave trace shown in Figure 6 is the same as in Figure 5 except that the pressure data was measured almost halfway up the water column ($y_p/D = 0.484$). All methods exhibited an improvement with this data, with the signal to noise ratio being more favourable.

Figure 7 shows a wave train with a superimposed Eulerian current of 0.134 m/s. In this case the first order LSA differs from the empirical LSA in that, like the linear spectral method, it can be modified to account for the current. The linear spectral method and the first order LSA were modified by including the current in the wave number calculation. The LPA methods already had the current included in the expression for ϕ (equation 7). Surprisingly the differences between the first order LSA and the empirical LSA are quite small. The current level is the highest that can be generated in the wave flume but it seems that it is not high enough to have a

significant effect on the wave properties. All other methods performed in a manner similar to the other irregular wave traces

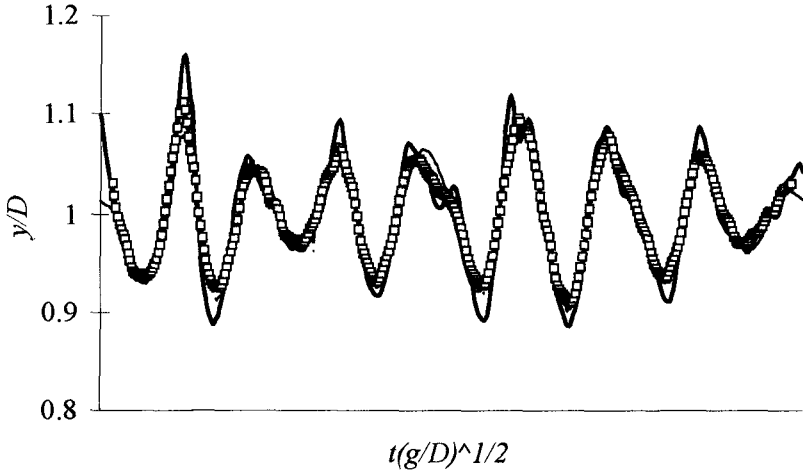


Figure 6: $y_p/D = 0.484$, $c_s = 0$

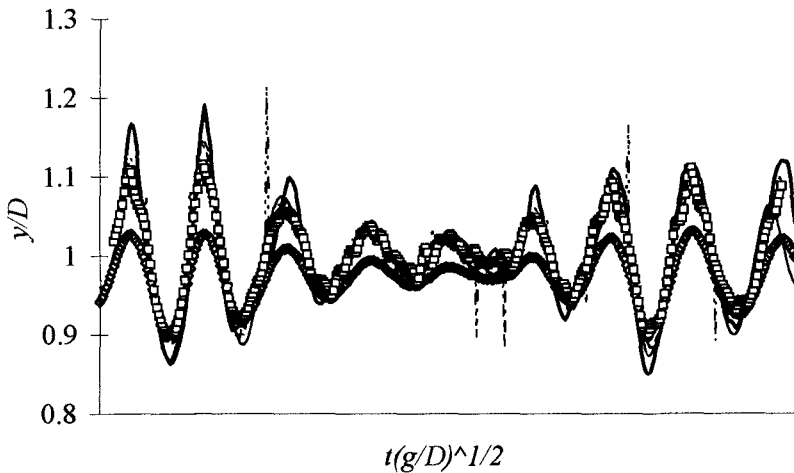


Figure 7: $y_p/D = 0$, $c_e = 0.134$ m/s

Figure 8 shows a moderately long regular wave with wave period, $T = 4.1$ s and zero Stokes current. This gives a λ/D ratio of approximately 12 in the wave flume. All methods perform well with this moderately long and high wave, although it can be seen that the empirical LSA is affected by the noise in the pressure signal.

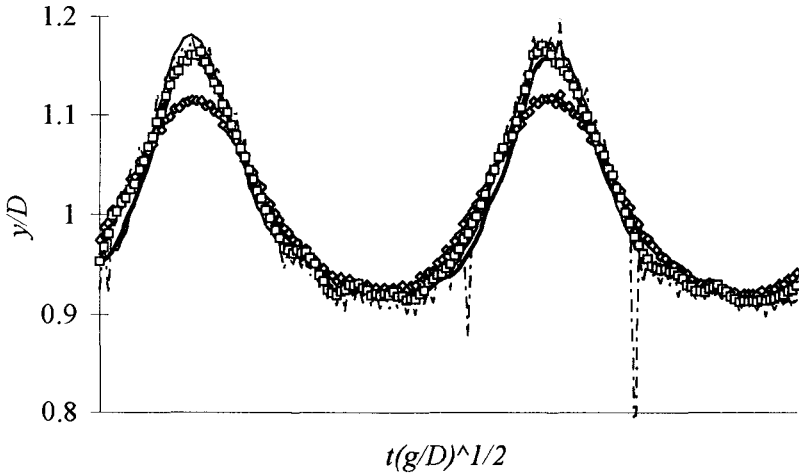


Figure 8: regular wave, $T = 4.1\text{s}$, $y_p/D = 0$, $c_s = 0$, $\lambda/D \approx 12$

Conclusions

A comprehensive comparison of a variety of global and local wave analysis methods has been conducted. The aim was to compare the accuracy of these methods for determining wave surface elevation data from sub-surface pressure readings. Overall the local methods are more effective in dealing with highly nonlinear steady waves than is the global linear spectral method. Unsurprisingly, all methods provided better results with pressure readings taken higher up in the water column.

The linear spectral method performed better for moderate waves but behaved poorly when the waves were steep and y_p/D was small. Both the LSA methods behaved similarly, generally predicting wave heights well. These methods were affected by noise although a post analysis smoothing routine would result in fairly smooth curves. Of the two, the empirical LSA is the simpler to apply, without sacrificing any accuracy compared to the first order method. However a disadvantage of the LSA methods is the failure just above the trough or the 'shoulder' of the wave.

The simple LPA method does not perform as well as the LSA methods when predicting wave heights from pressure readings at low y_p/D values but generally describe the wave profile with greater accuracy and is reasonably accurate when y_p/D is high. It is able to deal with noise in a satisfactory manner, better in fact than the full LPA method. In addition to this, the simple LPA is much easier to derive and program than the full LPA. The fragility of the full LPA method is unfortunate as its accuracy is higher than all other methods if no noise is present.

Many of these shortcomings have been addressed by the nonlinearly optimised local polynomial approximation. Accuracy is comparable to the full LPA, it is simple to develop the theory and it is possible to deal with noise in a relatively simple manner. As with all the LPA methods, it performs better when dealing with longer waves, due to the polynomial form of the velocity potential. As a rational nonlinear method these results are promising and there is potential for further development to determine the full wave kinematics.

REFERENCES

- Barker, C. H. and Sobey, R.J. (1996), "Irregular wave kinematics from a pressure record", *Proceedings, 25th International Conference on Coastal Engineering*, Orlando, Florida.
- Bishop, C.T. and Donelan, M.A. (1987), "Measuring waves with pressure transducers", *Coastal Engineering*, 11, pp. 309-328.
- Dean, R.G. (1974), "Evaluation and development of water wave theories for engineering application", *Special Report No. 1*, U.S. Army Corps of Engineers, Coastal Engineering Research Center.
- Fenton, J.D. (1986), "Polynomial approximation and water waves", *Proc. 20th International Conference on Coastal Engineering*, Taipei, pp. 193 - 207.
- Fenton, J.D. (1988), The numerical solution of steady water wave problems, *Computers & Geosciences*, Vol. 14, No. 3, pp. 357-368.
- Fenton, J.D. and Christian, C.D. (1989), "Inferring wave properties from sub surface pressure data", *Proc. 9th Aust. Conference on Coastal and Ocean Engineering*, Adelaide, Australia, pp. 380 - 384.
- Fenton, J.D. (1994), "Interpolation and numerical differentiation in civil engineering problems", *Aust. Civil Engng Trans.*, Vol. CE36, No. 4, the Institution of Engineers, Australia, pp. 331 - 337.
- Nielsen, P. (1989), "Analysis of natural waves by local approximations", *ASCE Journal of Waterway, Port, Coastal, and Ocean Engineering*, Vol. 115, No. 3, May, pp. 384-397.
- Sobey, R.J. (1991), "A local Fourier approximation method for irregular wave kinematics", *Applied Ocean Research*, No. 14, pp. 93-105.
- Townsend, M and Fenton, J.D. (1995), "Numerical comparisons of wave analysis methods", *Proceedings 12th Australasian Conference on Coastal and Ocean Engineering*, Melbourne, pp. 169-173.

CHAPTER 47

A Nonlinear Model for Wave Propagation

Ting-Kuei Tsay¹ Philip L.-F. Liu² Nan-Jing Wu³

Abstract

Employing the Hamiltonian theory, the canonical equations of water waves is used to derive a nonlinear model. In this paper, a unified nonlinear model for water wave propagation is presented. This model can be simplified to the mild-slope equation in the linear case. It is consistent with Stokes wave theory when water depth is deep and reduces to an equation of Boussinesq's type in shallow waters. Results of numerical computations of nonlinear water waves propagating over a submerged bar and a rectangular step are also presented in one-dimensional case. Nonlinear behaviors of water waves are captured, but further works are needed.

Introduction

A unified mathematical model for wave propagation from deep sea into the coastal waters has been long in pursuit. In early seventies, the mild-slope equation was first derived independently by Berkhoff (1972) and Smith & Sprinks (1975). The mild-slope equation reduces to the Helmholtz equation in deep waters and constant water depth. It reduces to shallow water wave equation when water depth becomes shallow. Because of depth integration, the mild-slope equation has simplified the three-dimensional problem into a two-dimensional one on the horizontal plane. Although the original equation is derived for monochromatic waves, it has been used for the entire spectrum of wave frequency. Based on the mild-slope equation, several numerical models have been developed to describe the combined wave refraction and diffraction successfully (Bettess and Zienkiewicz, 1977; Tsay and Liu, 1983).

In order to take other physical mechanisms, such as absorbing boundary, energy dissipation and fast-varying water depth, etc, into accounts, a variety of model equations has been employed to develop numerical mod-

¹ Professor, Department of Civil Engineering, National Taiwan University, Taipei, 10617 TAIWAN

² Professor, School of Civil & Environmental Engineering, Cornell University, Ithaca, 14853 U.S.A.

³ Graduate Student, Department of Civil Engineering, National Taiwan University, Taipei, 10617 TAIWAN

els for computation of wave scattering (Chen, 1986; Kirby, 1986; Tsay et al., 1989). However, all of the model equations are limited to linear waves. The nonlinear effects can not be ignored for waves of finite amplitude or when linear waves propagate into the shallow water regions. For weakly nonlinear waves over varying topography, mathematical models have been proposed either using Stokes' approach or employing Boussinesq equations (Liu & Tsay, 1984; Witting, 1984; Liu, et al., 1985; Nwogu, 1993; Liu, 1993). These models are limited to different water depth regimes. A unified model to describe wave transformation when it propagates from deep sea into coastal shallow water is strongly desired (Witting, 1984; Nwogu, 1993; Liu, 1993).

The governing equations for weakly nonlinear water waves can be obtained by employing the Hamiltonian theory in variational calculus (Broer, 1974). Radder and Dingmans (1985) had shown that the canonical equations of the Hamiltonian theory can be reduced to Stokes' wave form in deep waters and reduced to a Boussinesq-type equation in shallow waters. However, Radder and Dingmans did not derive an explicit, nonlinear equation for wave propagation. In this paper, employing Taylor's series expansion of free surface displacement and keeping the terms up to the third-order, we derive a unified nonlinear model equation for wave propagation. Validity of present nonlinear model is demonstrated theoretically by comparing model equations for different regimes of applications. Present nonlinear model is applied to calculate waves propagating over a submerged bar and a rectangular step in the third section. Discussions of present nonlinear wave model are followed.

Mathematical Formulation

For self-completeness of this paper, we give a brief derivation following Broer (1974), and Radder and Dingmans (1985).

For water body defined between bottom, $z = -h$, and free surface ζ , the canonical equations of Hamiltonian theory can be expressed as:

$$\frac{\delta H}{\delta \phi} = \frac{\partial \zeta}{\partial t} \quad (1)$$

$$\frac{\delta H}{\delta \zeta} = -\frac{\partial \phi}{\partial t} \quad (2)$$

where ϕ is the free surface velocity potential, and ζ is the free surface displacement. H is a functional and represents the total energy of water body.

$$H = \iint H_0 dx dy \quad (3)$$

where H_0 is the energy density function and can be written as:

$$H_0 = \frac{1}{2}g\zeta^2 + \frac{1}{2} \int_{-h}^{\zeta} [(\nabla\Phi)^2 + \left(\frac{\partial\Phi}{\partial z}\right)^2] dz \quad (4)$$

where the velocity potential at any point, Φ , is related to the velocity potential at the free surface by a distribution function in z -direction.

$$\Phi = f(z)\phi \tag{5}$$

with

$$f(z) = \frac{\cosh k(z+h)}{\cosh k(\zeta+h)} \tag{6}$$

It is noted that $f(\zeta) = 1$ and k is a characteristic value. When ζ is dropped from the equation, the distribution function reduces to the same one as linear cases and the characteristic value k represents wave number.

Assuming that change rates of water depth and characteristic value are negligible when slope of water bottom is mild, eqs.(1) and (2) after integrating from the bottom to the free surface can be expressed as:

$$\begin{aligned} \frac{\partial \zeta}{\partial t} = & (D + E\zeta)\nabla\phi \cdot \nabla\zeta + (F + G\zeta + H\zeta^2)\phi + I\phi(\nabla\zeta)^2 \\ & - \nabla \cdot [(A + B\zeta + C\zeta^2)\nabla\phi + (D + E\zeta)\phi\nabla\phi] + O(\zeta^4) \end{aligned} \tag{7}$$

$$\begin{aligned} \frac{\partial \phi}{\partial t} = & -[g\zeta + \frac{1}{2}(\nabla\phi)^2(B + 2C\zeta) + E\phi\nabla\phi \cdot \nabla\zeta + \frac{1}{2}\phi^2(G + 2H\zeta)] \\ & + \nabla \cdot [(D + E\zeta)\phi\nabla\phi + I\phi^2\nabla\zeta] + O(\zeta^4) \end{aligned} \tag{8}$$

where

$$\begin{aligned} A &= k \tanh kh \\ B &= k(k - k \tanh^2 kh) \\ C &= \frac{2kh + \sinh 2kh}{4k \cosh^2 kh} \\ D &= \frac{\cosh kh - kh \sinh kh}{\cosh^3 kh} \\ E &= \frac{-4kh + 2kh \cosh 2kh - 3 \sinh 2kh}{4k \cosh^4 kh} \\ F &= \frac{k(-2kh + \sinh 2kh)}{4 \cosh^2 kh} \\ G &= \frac{k^3 h \tanh kh}{\cosh^2 kh} \\ H &= \frac{k^3(4kh - 2kh \cosh 2kh + \sinh 2kh)}{4 \cosh^4 kh} \end{aligned} \tag{9}$$

The free surface, ζ , is related to the velocity potential, ϕ ,

$$\begin{aligned} \zeta = & -\frac{1}{g} \frac{\partial \phi}{\partial t} - \frac{1}{2g} [(B - \frac{2C}{g} \frac{\partial \phi}{\partial t})(\nabla\phi)^2 - \frac{2E}{g} \phi \nabla(\frac{\partial \phi}{\partial t}) \cdot \nabla\phi + (G - \frac{2H}{g} \frac{\partial \phi}{\partial t})\phi^2] \\ & - \frac{1}{g} \nabla \cdot [(-D + \frac{E}{g} \frac{\partial \phi}{\partial t})\phi\nabla\phi + \frac{I}{g} \phi^2 \nabla(\frac{\partial \phi}{\partial t})] + O(\zeta^4) \end{aligned} \tag{10}$$

Combining eqs.(7) and (8), a nonlinear equation of velocity potential can be obtained as:

$$\begin{aligned}
& \frac{1}{g} \frac{\partial^2 \phi}{\partial t^2} + \frac{1}{2g} \frac{\partial}{\partial t} \left[\left(B - \frac{2C}{g} \frac{\partial \phi}{\partial t} \right) (\nabla \phi)^2 - \frac{2E}{g} \phi \nabla \left(\frac{\partial \phi}{\partial t} \right) \cdot \nabla \phi + \left(G - \frac{2H}{g} \frac{\partial \phi}{\partial t} \right) \phi^2 \right] \\
& + \frac{1}{g} \frac{\partial}{\partial t} \nabla \cdot \left\{ \left[-D + \frac{E}{g} \frac{\partial \phi}{\partial t} \right] \phi \nabla \phi + \frac{I}{g} \phi^2 \nabla \left(\frac{\partial \phi}{\partial t} \right) \right\} \\
& = \frac{-1}{g} \left[-D - \frac{E}{g} \frac{\partial \phi}{\partial t} \right] \nabla \left(\frac{\partial \phi}{\partial t} \right) \cdot \nabla \phi - \left\{ \frac{I}{g^2} \left[\nabla \left(\frac{\partial \phi}{\partial t} \right) \right]^2 + F - \frac{G}{g} \frac{\partial \phi}{\partial t} - \frac{GB}{2g} (\nabla \phi)^2 \right. \\
& \quad \left. - \frac{G^2}{2g} \phi^2 - \frac{G}{g} \nabla \cdot (D \phi \nabla \phi) + \frac{H}{g^2} \left(\frac{\partial \phi}{\partial t} \right)^2 \right\} \phi + \nabla \cdot \left\{ \left[A - \frac{B}{g} \frac{\partial \phi}{\partial t} - \frac{B^2}{2g} (\nabla \phi)^2 - \frac{GB}{2g} \phi^2 \right. \right. \\
& \quad \left. \left. + \frac{B}{g} \nabla \cdot (D \phi \nabla \phi) + \frac{C}{g^2} \left(\frac{\partial \phi}{\partial t} \right)^2 \right] \nabla \phi - \frac{1}{g} \left[-D + \frac{E}{g} \frac{\partial \phi}{\partial t} \right] \phi \nabla \left(\frac{\partial \phi}{\partial t} \right) \right\} + O(\zeta^4) \quad (11)
\end{aligned}$$

In shallow water, where the parameter of $kh = \mu$ is small, we expand the coefficients of A, B, C, D, E, F, G, H and I in eq.(9) up to the accuracy of $O(\mu^3)$ of Taylor series. For one-dimensional cases, when normalized variables, $\varepsilon = a/h$ (a : amplitude), $x' = kx, t' = k\sqrt{gh} t, \zeta' = \zeta/a, \phi' = k\phi/\varepsilon\sqrt{gh}$ are introduced, and ε and μ^2 are assumed in the same order of magnitude, eq.(11) can be reduced to:

$$\phi'_{t't'} + \varepsilon(2\phi'_{x't'}\phi'_{x't'} + \phi'_{t'}\phi'_{x't'}) - \phi'_{x't'} = O(\varepsilon^2, \mu^3) \quad (12)$$

This is a nonlinear equation of Boussinesq type for waves propagating over shallow water depths.

Using Stokes expansion,

$$\begin{aligned}
\zeta &= a_1 \cos \theta + (a_{20} + a_{21}) \cos 2\theta + a_3 \cos 3\theta \\
\phi &= b_1 \sin \theta + b_2 \sin 2\theta + b_3 \sin 3\theta + O(a_1^4) \quad (13)
\end{aligned}$$

where $\theta = kx - \omega t$, ω is the radian frequency, we obtain the following coefficients in terms of amplitude, a_1 , up to the accuracy of $O(a_1^4)$:

$$\begin{aligned}
a_{20} &= -\frac{ka_1^2}{2 \sinh 2kh} \\
a_{21} &= \frac{8kh - 4kh \cosh 2kh + 12 \sinh 2kh + \sinh 4kh}{4(-2kh + \sinh 2kh) \sinh 2kh} ka_1^2 \\
b_1 &= \frac{g}{\omega} \left[a_1 + \frac{k^2(66 \cosh kh - 3 \cosh 3kh + \cosh 5kh - 52kh \sinh kh - 4kh \sinh 3kh)}{16(-2kh + \sinh 2kh) \sinh 2kh \cosh kh} a_1^3 \right] \\
b_2 &= \frac{g}{\omega} \frac{k(7 \cosh kh + \cosh 3kh - 4kh \sinh kh)}{4(-2kh + \sinh 2kh) \cosh kh} a_1^2 \\
a_3 &= k^2 a_1^3 (932kh \cosh kh - 246kh \cosh 3kh - 30 \cosh 5kh \\
& \quad + 541 \sinh kh - 264k^2 h^2 \sinh kh + 616 \sinh 3kh + 72k^2 h^2 \sinh 3kh \\
& \quad + 78 \sinh 5kh + 3 \sinh 7kh) / [128(-2kh + \sinh 2kh)^2 \sinh kh \cosh^2 kh] \quad (14)
\end{aligned}$$

with the nonlinear dispersion relation:

$$\begin{aligned}
\frac{\omega^2}{g} &= k \tanh kh \left[1 \right. \\
& \quad \left. + \frac{32kh - 16kh \cosh 2kh - 4kh \cosh 4kh + 31 \sinh 2kh + 4 \sinh 4kh + \sinh 6kh}{8(-2kh + \sinh 2kh) \sinh 2kh^2} k^2 a_1^2 \right] \quad (15)
\end{aligned}$$

The quantity of a_{20} represents change of lower mean water level under nonlinear wave action and is the same as that derived by Bowen (1968) for wave set down.

When kh approaches infinity for deep water depth, those coefficients in eqs. (14), and nonlinear dispersion relation, eq.(15) reduces to:

$$\begin{aligned} a_{20} &= 0 \\ a_{21} &= \frac{1}{2}ka_1^2 \\ a_3 &= \frac{3}{8}k^2a_1^3 \\ \frac{\omega^2}{g} &= k(1 + k^2a_1^2) \end{aligned} \quad (16)$$

These results are identical to those in the Stokes wave theory.

When all the nonlinear terms are dropped and monochromatic waves are assumed, eq.(11) can be easily simplified to the mild-slope equation (Berkhoff, 1972) with linear dispersion relation of the characteristic value, k , defined as wave number.

The model equation, eq.(11), therefore unifies propagation of nonlinear waves from deep to shallow water depths which is accurate up to the third order of incident wave amplitude. We plausibly use eq.(11) to simulate nonlinear wave propagation.

Numerical Computations

Due to the complexity of the model equation and difficulty of determining the characteristic value for nonlinear waves of third order, we employ Stokes expansion for second order nonlinear monochromatic waves.

$$\zeta = Re\{\zeta_0 + \zeta_1e^{-i\omega t} + \zeta_2e^{-2i\omega t}\} + O(|\zeta_1|^3) \quad (17)$$

$$\phi = Re\{\phi_0 + \phi_1e^{-i\omega t} + \phi_2e^{-2i\omega t}\} + O(|\phi_1|^3) \quad (18)$$

The model equations for different orders can be written as:

$$\left(\frac{\omega^2}{g} - F\right)\phi_1 + \nabla \cdot (A\nabla\phi_1) = 0 \quad (19)$$

$$\zeta_1 = \frac{i\omega}{g}\phi_1 \quad (20)$$

$$\zeta_0 = \frac{-B}{4g}|\phi_1|^2(\nabla S_{\phi_1})^2 - \frac{G}{4g}|\phi_1|^2 \quad (21)$$

$$\begin{aligned} \left(\frac{4\omega^2}{g} - F\right)\phi_2 + \nabla \cdot (A\nabla\phi_2) &= \frac{D}{2}\nabla\phi_1 \cdot \nabla\zeta_1 + \frac{G}{2}\phi_1\zeta_1 - \nabla \cdot \left(\frac{B}{2}\zeta_1\nabla\phi_1 + \frac{D}{2}\phi_1\zeta_1\right) \\ &+ \frac{2i\omega}{g}\left[-\frac{B}{4}(\nabla\phi_1)^2 - \frac{G}{2}\phi_1^2 + \nabla \cdot \left(\frac{D}{2}\phi_1\nabla\phi_1\right)\right] \end{aligned} \quad (22)$$

$$\zeta_2 = \frac{2i\omega}{g}\Phi_2 - \frac{B}{4g}(\nabla\phi_1)^2 - \frac{G}{4g}\Phi_1^2 + \frac{1}{g}\nabla \cdot \left(\frac{D}{2}\Phi_1\nabla\phi_1\right) \quad (23)$$

where S is the phase function and the characteristic value, k , determined by the dispersion relation of

$$\frac{\omega^2}{g} = k \tanh kh \quad (24)$$

Wave field can be calculated by using eqs.(19), (20), (21), (22), and (23) for each component. The free surface displacement is obtained by employing eq.(17). For the case of nonlinear waves propagating over a submerged bar (Beji and Battjes, 1994), Fig. 1, incident waves with wave height 2cm , period 2sec . propagate from left to right. The constant depth before the bar is 0.40m and the Ursell number, ($U_r = (a/h)/(kh)^2$), is 0.054 . In the computational domain of 12m , 481 nodal points are used. For numerical calculations, eqs.(19) and (22) are discretized into finite difference equations. Radiation conditions of outgoing wave components are applied to both ends of the computational domain. The sloping bottom on the right hand side is assumed to absorb all of the wave energy. In experiments (Beji and Battjes, 1993), gage 1 indicated incident waves. We compare the numerical solutions with experimental results for waves over the submerged bar (Figs. 2, 3, 4, 5, 6 and 7). The numerical solutions are obtained by calculating amplitude distribution in space of each component and reconstructing the time history of free surface at each point. It can be observed that there is a significant difference between linear and nonlinear waves. The nonlinear behavior of waves due to change of water depth is captured by present nonlinear model quite nicely. However, discrepancy between numerical solutions and experimental results at wave troughs seems quite persistent.

We further extend present nonlinear model to calculate waves over a step, Fig.8 (Kittitanasuan et al., 1993). Although the slope at the step violate mild-slope assumption, waves evolve nonlinearly after the step. The depths before and after the step are 0.376cm and 0.113cm , respectively. Incident wave height is 1.63cm and period 1.85sec . The Ursell number in this case is 0.042 . Total nodal points of 601 are used in a 12m computational domain. The step is simulated by a sudden change of water depth between two nodes with a slope of 6.575 . Present numerical time histories of free surface at points after the step of 1m and 2m are compared with experimental results, Figs.9 and 10 (Kittitanasuan et al., 1993). Good agreement is observed except profiles at wave troughs. We also calculate free surface profile in space and compare with that of Kittitanasuan et al (1993). The step is located at the origin of x-axis. Waves behaves almost linearly before the step and evolve nonlinearly further away from the step. Present nonlinear model is in good agreement with theory of Kittitanasuan et al (1993).

Discussions and Conclusions

In this paper, we present a derivation of nonlinear model in the accuracy of $O(\zeta^4)$ for water wave propagation. It unifies nonlinear wave models for different depth regimes. Present nonlinear model reduces to the mild-slope equation in the linear case. It is shown that present model can be simplified to a Boussinesq equation for shallow water and Stokes waves when water

depth is deep. However, due the complexity of the governing equation and the difficulty in determining the characteristic value of dispersion relation, we calculate nonlinear waves up to the second order and compare present numerical solutions with experimental results in two one-dimensional cases. Good agreement is obtained. Discrepancy between present numerical solutions and experimental results of free surface profiles at wave troughs remains for future study.

Acknowledgement

The financial support of National Science Council under research project, NSC-85-2621-002-035, is acknowledged. The second author was a Visiting Professor at National Taiwan University in 1995.

References

1. Berkhoff, J.C.W. (1972), "Computation of combined refraction- diffraction," Proc. 13th Conf. Coastal Engrg., ASCE, Vancouver, 471-490.
2. Beji, S. & Battjes, J. A. (1993), "Experimental investigation of wave propagation over a bar," Coastal Eng. Vol. 19, pp. 151-162.
3. Bettess, P. and Zienkiewicz, O.C. (1977), "Diffraction and refraction of surface waves using finite and infinite element," Int. J. Numer. Meth. for Engrg., 11:1271-1290.
4. Bowen, L. J., Inman, D. L., and Simmons, V. P.,(1968), "Wave set down and set up," J. Geophys. Res. 73:2569-2577.
5. Broer, L.J.F. (1974), "On the Hamiltonian theory of surface waves," Appl. Sci. Res., 29:430-446.
6. Chen, H.S. (1986), "Effects of bottom friction and boundary absorption on water wave scattering," Appl. Ocean Res., 8:99-104.
7. Kirby, J.T. (1986), "A general wave equation for waves over rippled beds," J. Fluid Mech., 162:171-186.
8. Kittitanasuan, W., Goda, Y., and Shiobara, T.,(1993), "Deformation of nonlinear waves on a rectangular step," Coastal Eng. in Japan, Vol.36, No.2, pp.133-153.
9. Liu, P.L.-F. and Tsay, T.K. (1984), "Refraction-diffraction model for weakly nonlinear water waves," J. Fluid Mech., 141:265-274.
10. Liu, P.L.-F., Yoon, S.B., and Kirby, J.T. (1985), "Nonlinear refraction- diffraction of waves in shallow water," J. Fluid Mech., 153: 185-201.
11. Liu, P.L.-F. (1993), *Model equations for wave propagation from deep to shallowwater*, Res. Rep. CACR-93-09, Univ. of Delaware.
12. Nwogu, O. (1993), "Alternative form of Boussinesq equations for nearshore wave propagation," J. Waterways, Port, Coast. and Ocean

Engrg., ASCE, 119:618-638.

13. Radder, A.C. and Dingmans, M.W. (1985), "Canonical equations for almost periodic, weakly nonlinear waves," *Wave Motion*, 7:473-485.
14. Smith R. and Sprinks, Y. (1975), "Scattering of surface waves by a conical island," *J. Fluid Mech.*, 72, pp.373-384.
15. Tsay, T.K. and Liu, P.L.-F. (1983), "A finite element model for wave refraction and diffraction," *Appl. Ocean Res.*, 5, pp.30-37.
16. Tsay, T.K., Zhu, W., and Liu, P.L.-F. (1989), "A finite element model for wave refraction, diffraction, reflection and dissipation," *Appl. Ocean Res.*, 11(1), pp.33-38.
17. Witting, J.M., (1984), "A unified model for the evolution of nonlinear water waves," *J. Computational Phys.*, 56, pp.203-236.

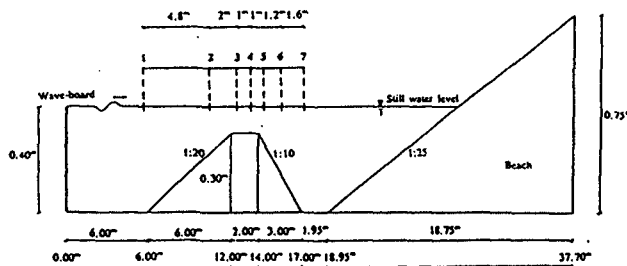


Fig. 1 Experimental set-up for waves over a submerged bar
(Beji and Battjes, 1993)

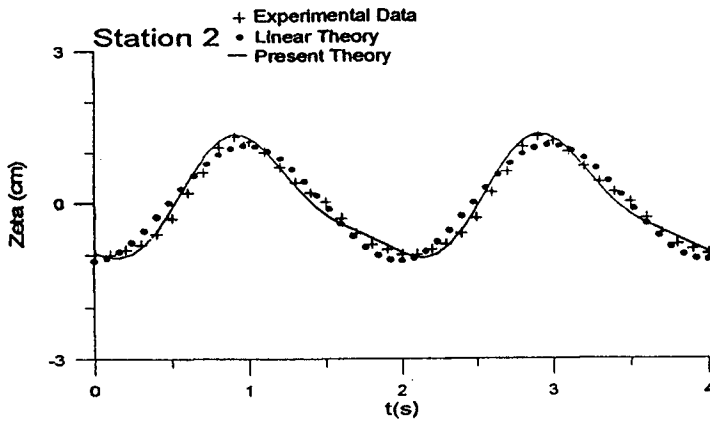


Fig. 2 Comparison of present numerical solutions with experimental results (Beji and Battjes, 1993), station 2

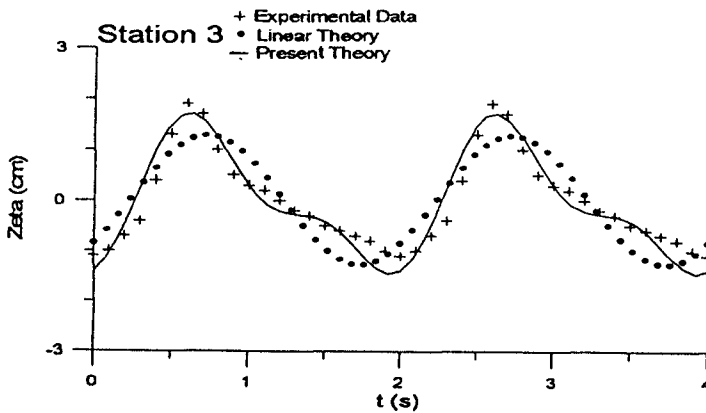


Fig. 3 Comparison of present numerical solutions with experimental results (Beji and Battjes, 1993), station 3

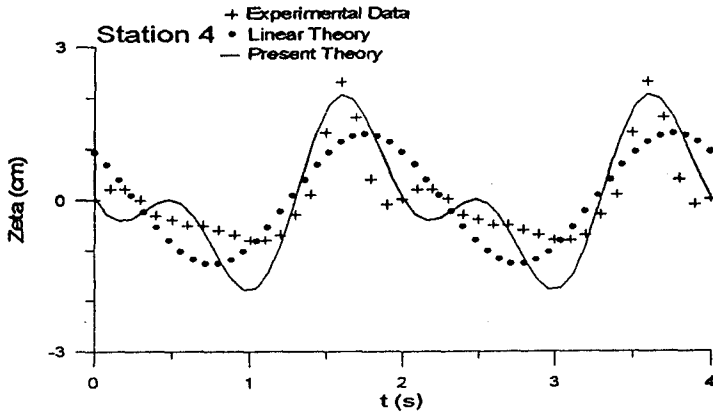


Fig. 4 Comparison of present numerical solutions with experimental results (Beji and Battjes, 1993), station 4

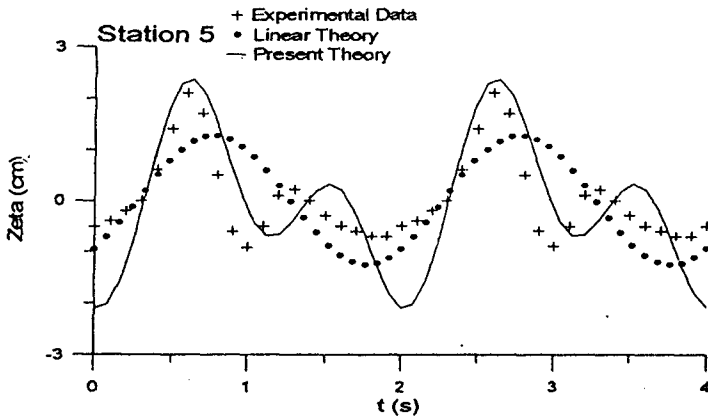


Fig. 5 Comparison of present numerical solutions with experimental results (Beji and Battjes, 1993), station 5

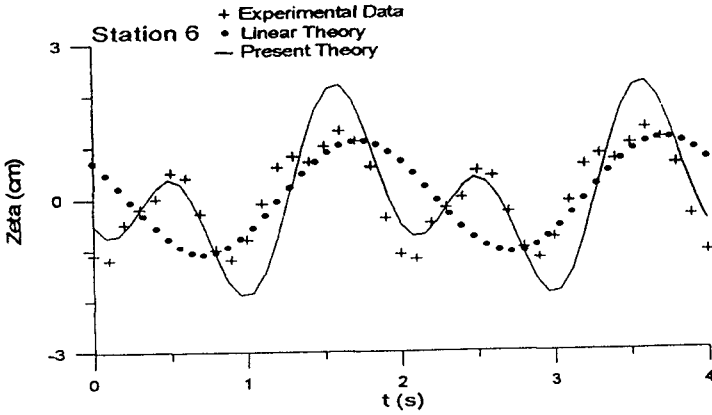


Fig. 6 Comparison of present numerical solutions with experimental results (Beji and Battjes, 1993), station 6

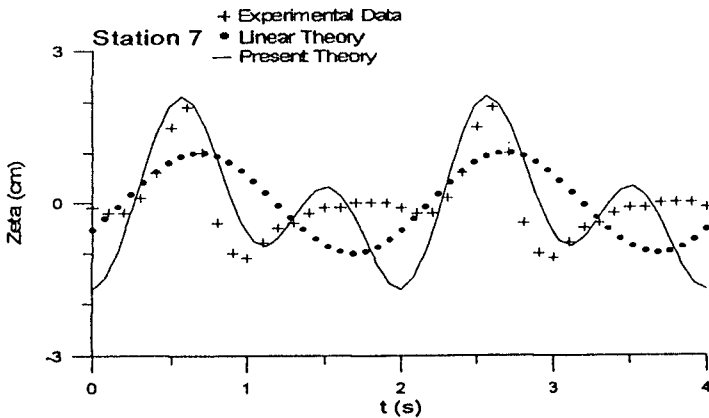


Fig. 7 Comparison of present numerical solutions with experimental results (Beji and Battjes, 1993), station 7

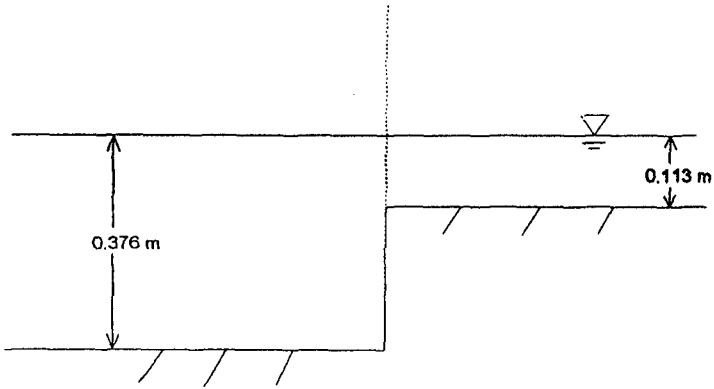


Fig. 8 Experimental set-up for waves over a rectangular step (Kittitanasau et al.,1993)

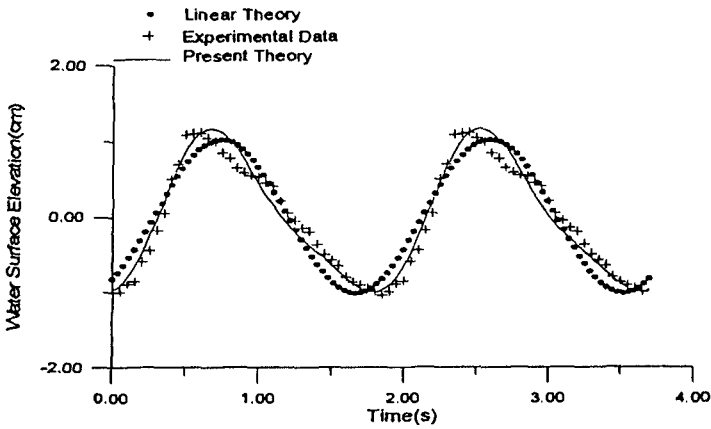


Fig. 9 Comparison between present numerical solutions and experimental results (Kittitanasuan et al., 1993) at 1m after the step

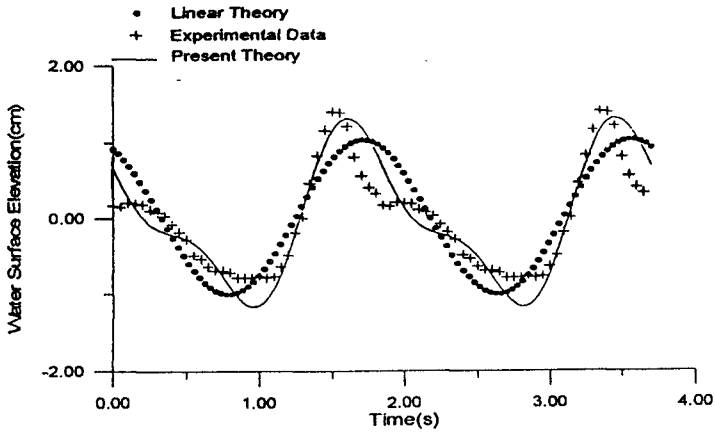


Fig. 10 Comparison between present numerical solutions and experimental results (Kittatanasuan et al., 1993) at 2m after the step

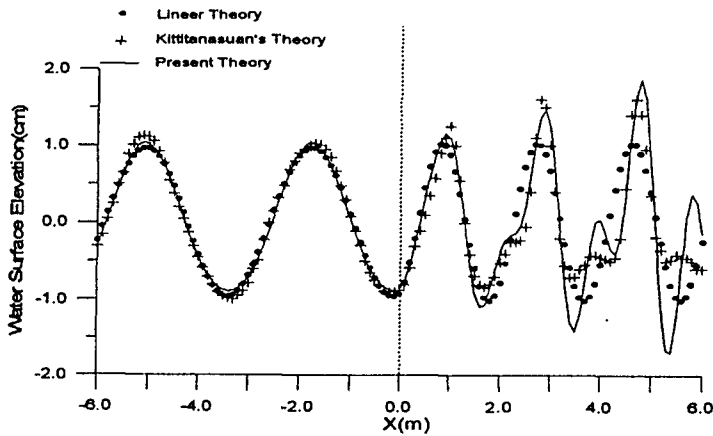


Fig. 11 Comparison of free surface profile in space between present model and Kittatanasuan et al., (1993).

CHAPTER 48

APPLICATION OF A DIGITAL PARTICLE IMAGE VELOCIMETRY (DPIV) SYSTEM TO BREAKING WAVES IN THE SURF ZONE

Kenneth R. Craig II¹ and Robert J. Thieke²

BACKGROUND

The modeling of cross-shore and longshore currents in the nearshore region has improved greatly over the past twenty years with accompanying advances in an understanding of the relevant physical processes in shallow water and the surf zone. The empirical guidance provided by numerous laboratory and field experiments has been an essential element in sustaining these advances. However good experimental data are still largely lacking for aspects of these flows, the most notable being the flow in waves following breaking, which coincidentally represents the single most important physical process in the nearshore region.

For the two-dimensional case of waves normally incident on a beach, a variety of techniques have recorded velocities in surf zone flows. Wang, et al. (1982) used tracer techniques incorporating particles and film to provide significant qualitative information, but it generally suffers from poor spatial resolution and generally provides lagrangian information where an eulerian perspective is desirable. The air entrainment associated with the free surface instability of breaking waves also inhibits these methods, particularly near the water surface. Jansen (1986) used fluorescent tracers and ultraviolet light to view particle trajectories in the aerated region of breaking waves, yet these measurements still suffer from the other previously mentioned shortcomings. More recently several investigators have employed velocity measurement using Laser Doppler Anemometry (LDA). Stive (1980) and Nadaokah and Kondoh (1982) have contributed some of the early significant data sets using this technique in the surf zone. LDA offers very high precision and spatial resolution but the time it requires generally precludes any truly synoptic measurements of the flow

¹ Engineer, Taylor Engineering, Inc., 9086 Cypress Green Drive, Jacksonville, FL 32256, U.S.A. (formerly Graduate Assistant, Department of Coastal and Oceanographic Engineering, University of Florida).

² Assistant Professor, Department of Coastal and Oceanographic Engineering, University of Florida, Gainesville, FL 32611, U.S.A.

field. However, the most significant drawback to LDA techniques is that the high levels of air entrainment typical of the upper surf zone cause such significant signal drop-out as to completely degrade the fidelity of the measurements in this region. For example, although Nadaoka and Kondoh (1982) provide measurements of the vertical distribution of cross-shore velocity at several stations through the surf zone, they do not provide measurements above the level of the wave trough, and aeration affects the velocity profiles below the trough in the inner reaches of the surf zone significantly. As a result even averaged quantities such as the shoreward directed mass flux (due to contributions above the wave trough level) are not measured directly but only inferred by integration of the corresponding below-trough velocity measurements. These restrictions inhibit the development of a complete picture of the vertical flow structure in this region.

DPIV THEORY

Willert and Gharib (1991) describe a system that digitally performs a process similar to the opto-mechanical method employed in particle image velocimetry. Neutrally buoyant particles are introduced into a fluid flow and video images are recorded and digitized. Sequential digital images (each frame capturing a single instance in time) are analyzed using frequency domain techniques. After digitizing, small sections of each image, called areas of interest (AOIs), are compared. The AOIs represent identical locations on each consecutive image.

Willert and Gharib used the mathematical definition of cross-correlation in the frequency domain

$$\Phi_{fg}(u,v) = F^*(u,v) \times G(u,v) \quad (1)$$

where F^* is the complex conjugate of the Fourier transform of $f(m,n)$ and $G(u,v)$ is the Fourier transform of $g(m,n)$. They employed fast Fourier transforms (FFT) to reduce processing time. After finding Φ , they performed an inverse FFT to return the data to the spatial domain.

Essentially the process tries to match the pattern found in the first AOI with that in the second after the pattern has shifted. The location of the peak value of the cross-correlation function represents the point that best correlates the particle positions in each AOI. The shape of the peak value depends on the noise level. Large amounts of noise tend to broaden the peak. Smaller peaks also occur due to some correlation between incorrect particle pairings. However, the maximum value found in Φ_{fg} indicates the best correlated displacement over the AOI. Particles generate noise as they move out of the AOI laterally, vertically or normal to the plane of view. Assumably the AOI is large enough to allow a majority of the particles in the first AOI to appear in the second. Figure 1 shows a typical example resulting from the application of the correlation technique for particles settling in the +y direction.

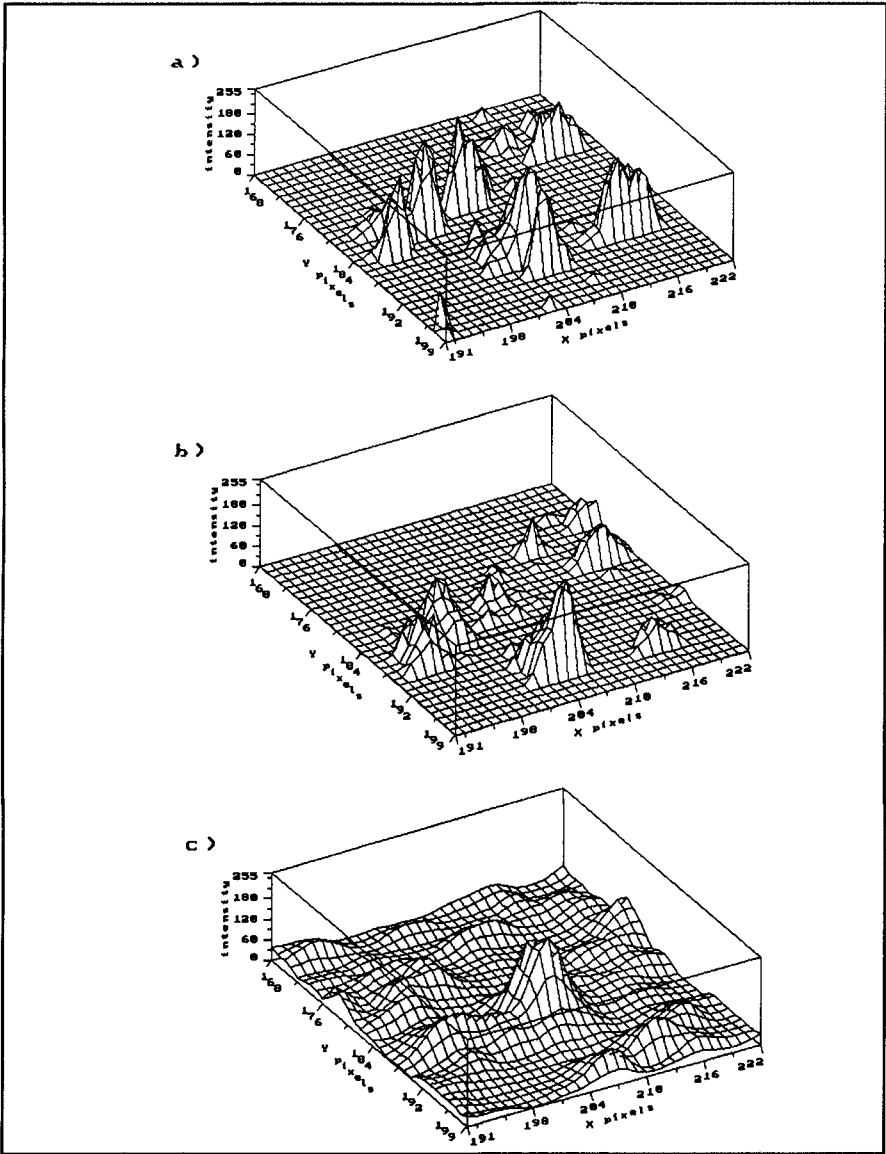


Figure 1 Graphical representation of pixel intensities within an area of interest in a) image 1 and b) image 2 and c) the inverse transformed correlation peak in the spatial domain. The maximum peak in c) indicates a displacement of approximately 4 pixels in the +y direction (downward).

Two different centroiding techniques may then be employed to examine the peak. A center of mass method (Kimura and Takamori, 1986) provides one pixel accuracy but depends on the threshold value used to determine the limits of the peak. The method Willert and Gharib suggest provides sub-pixel accuracy. In controlled experiments, they found a minimum uncertainty value of 0.01 pixels. However, in practice the uncertainty may reach an order of magnitude higher. The peak and each of the two neighboring data points are fitted with parabolic curves in both the vertical and horizontal directions. The distances from the origin to the location of the maxima of these parabolas determine the displacement vector to sub-pixel accuracy. Dividing the displacement vector by the known time difference between frames provides the velocity vector.

EXPERIMENTAL SETUP

All experiments were carried out by the authors at the University of Florida's Coastal and Oceanographic Engineering Laboratory in Gainesville, Florida, USA. Waves were generated in the multifunctional wave flume equipped with plate glass panels running the entire length on both sides providing flexible access to camera and lighting positions. Wave data were collected using a capacitance type wave gauge. Six separate tests were run: tests 1, 2, and 3 in approximately 30 centimeters of water and tests 4, 5, and 6 in approximately 23 centimeters of water. For each test series at a specific water depth, the wave periods varied from 0.85 to 2.13 seconds. The video tape and wave data were then analyzed to determine velocity fields, mean water level set-up and wave height distributions.

All video imaging employed gray scales rather than color because gray scales provide a higher spatial resolution and tangibly greater light sensitivity. Gray scale video equipment also costs substantially less than similar quality color equipment. The advantage of gray scale imaging is realized during processing because DPIV relies on pixel intensity values to distinguish particles. Color does not offer any advantage over gray scale for this process.

Mulifunctional Wave Flume

The internal wave flume—approximately 28 meters long, 58 centimeters wide and 1.4 meters deep—is equipped with both a flap type and piston type wave maker. The smaller Seasim RSP 60-20 Modular Piston Wave maker used during the experiments is computer controlled through a central electronic system with feedback loops to minimize reflections and generation of free second harmonics. The wave maker produced monochromatic waves propagating towards a fixed beach with slope 1 on 20. The horizontal bottom portion of the flume extends 15 meters from the wave maker. The fixed beach slope then extends for another 10 meters. The flume also comes with a remotely controlled carriage capable of transiting its entire length. A capacitance type wave gauge was attached to the movable carriage and cabled to a data acquisition computer.

Video equipment used at the experiment site included a Panasonic WV-5470 high resolution gray scale video monitor, a Panasonic AG-1970 super-VHS recording

VCR, and a Vicon VC2400 high resolution gray scale CCD video camera with variable shutter speed. The camera provides 570 lines of horizontal resolution (which is actually above super-VHS quality) and requires only 0.2 lux minimum illumination. Shutter speeds range from continuously open to 1/10,000 of a second. A shutter speed of 1/1,000th of a second minimized blurring of the particles and still allowed sufficient light to pass through the camera lens for adequate videotaping. Both zoom and wide angle lenses were available for use. Lens magnification depended upon the wave characteristics at each particular camera location. The goal was to fill the view with as much of the flow field as possible to maximize resolution during processing. Ambient light was controlled by placing a light shield made of flexible polyurethane coated nylon fabric around the position of the video camera and flume. The light shield covered three panes of glass and could be positioned anywhere along the flume. Removable side panels on the light shield provided access to the camera when necessary. All video was recorded on master quality double coated super-VHS video tapes.

The moveable chassis was equipped with the following items: a light source, a cylindrical focusing lens and a dispenser for the neutrally buoyant particles. The light source was a 500 watt electric bulb enclosed in a wooden box with a slit approximately 2 millimeters wide cut in the bottom. The slit was aligned with the long axis of the flume (i.e., direction of wave propagation) and allowed only a portion of the light from the bulb to escape the box as a quickly dispersing plane (see Figure 2 for a schematic of the experimental apparatus).

The light then passed through the cylindrical lens and focused into a tight plane perpendicular to the bottom of the flume. With the lens approximately 1 meter above the flume bottom, the focused light diffused to a width of 1 centimeter at the flume bottom. Notably the light only remained on for periods of a few minutes to minimize the chance of overheating caused by the high power consumption of the light source and the wooden box. Despite this safety precaution, the inside bottom of the box was charred by the end of the experiment. The use of a nonflammable material to construct the light box for future applications is recommended.

Pliolite, a granular material used as a road paint strengthening ingredient with a specific gravity of 1.04 was used for the neutrally buoyant particles. Bright white, Pliolite is readily visible under the lighting conditions used during the experiments. Pliolite's highly irregular shape traps a proportionately large amount of air, causing the Pliolite to remain on the water surface when first introduced. Therefore, the pliolite was first washed in liquid soap and stored under water to facilitate breaking the surface tension when the particles were introduced to the flume. Separating the fines from the pliolite left particles ranging in size from 0.5 to 2 millimeters.

The pliolite dispenser, located next to the light source, was designed to work like a hopper. A board was fixed diagonally across the inside of the dispenser to act as a chute for the released pliolite. A second hinged board was installed so that it would form a "V" with the fixed board. Two elastic bands maintained tension on the hinged board. The pliolite was placed along the intersection of these two boards and held there until being dispensed. The chute was positioned to distribute the particles

linearly near the intersection of the light plane and the water surface. The pliolite release mechanism, designed to overcome the tension of the elastic bands, was connected to the outside of the flume. Water from an elevated container located above the chassis was fed along the top of the fixed board by plastic tubing and released through a series of small holes directed down the chute. This water washed any pliolite out of the dispenser that gravity had not removed during the initial opening.

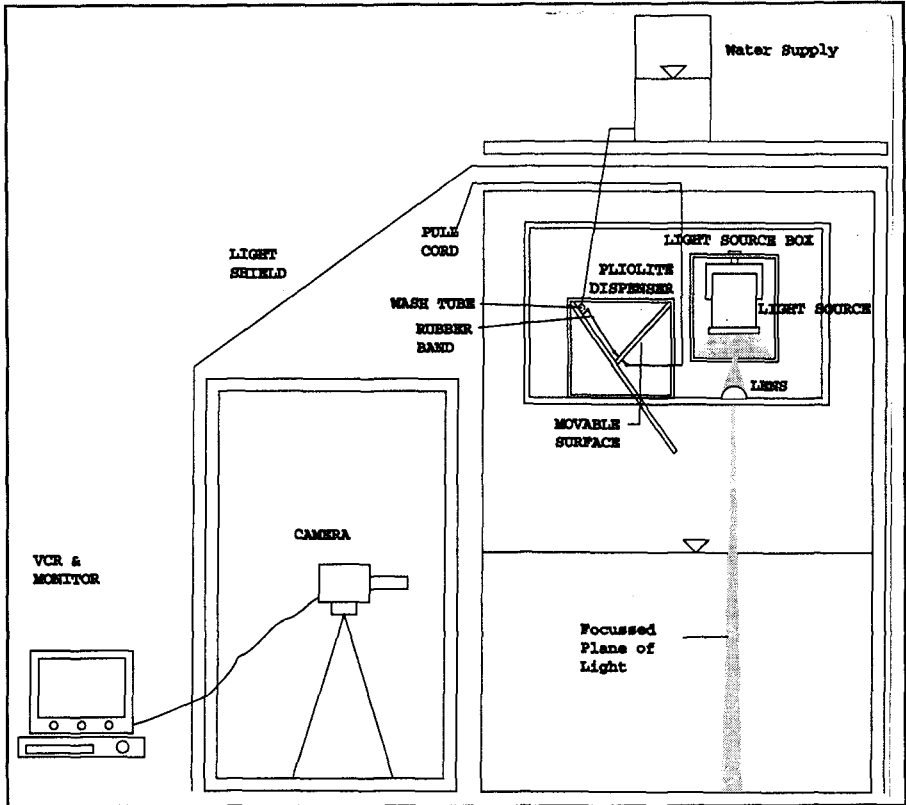


Figure 2 Experimental apparatus including video equipment location and movable chassis arrangement (cross section, long axis of tank).

To calibrate the video, a grid of 2 centimeter by 2 centimeter squares etched in clear Plexiglas was used to compensate for the magnification effects of filming through three types of media, namely air, glass, and water. Video of this grid was used to determine the number of pixels per centimeter as recorded by the camera. The bottom of the grid, tapered to the beach and held firmly to the slope, allowed the grid lines to be read vertically and horizontally.

Experiments began once the wave flume was filled to the appropriate water level and allowed to settle, after which a water depth reading was recorded from the flat portion of the flume. The wave maker then generated waves at the designated frequency. These waves were observed to determine the break point position and initial camera location. Wave gauge data were recorded along the flat portion for a deep water reading, at the beginning of the slope for initial shoaling data, and any appropriate locations outside and within the surf zone for setup and shoaling data.

The number of camera positions required for each test depended upon the field of view that could be achieved. The area from just outside the breakpoint to inside of the transition point was the focus of these experiments. The camera was placed inside the light shield at the proper location and the position of the center of the field of view along the flume was recorded. Next, the calibration grid was placed along the long axis of the flume in the field of view. The light source without the focusing lens illuminated the grid. This allowed filming the grid and minimizing any shadows the grid produced. It was found that the cylindrical lens created shadows too intense to provide any readings from the grid. The grid also allowed the camera to be focused to the proper location at the tank centerline. The pliolite was loaded into the dispenser and the flushing water source was connected to the dispenser and the focusing lens was replaced. At this point, the VCR began recording, the pliolite was released into the flume, and the light source was turned on. To produce an adequate ensemble average of flow characteristics required a minimum 30 cycles for each wave so taping lasted about two minutes for each test, at which point the light was shut off and the recording stopped. The camera was then moved to a location partially overlapping the field of view of the previous position and the process repeated until the transition point had been recorded.

When the taping ended the wave maker was stopped and the flume water level allowed to settle in order to eliminate any residual low frequency activity. Wave gauge data for still water levels were recorded for each station previously investigated. A second water level reading was taken in the flat portion of the flume to determine if any water was lost during the testing. The entire process was repeated for the next wave frequency.

DATA PROCESSING

All image digitization was carried out on a personal computer equipped with a 80486/66 MHz DX2 CPU. Computer peripheries included an EditLink 2200/TCG VCR controller card and a one megabyte frame grabber board as accessories. An image processing software package with macro language capabilities digitized and filtered the images. Several C language programs were written to control the VCR through the VCR controller card. The same super-VHS recording VCR and high resolution monitor were used during the digitization process.

The EditLink 2200/TCG can stripe a video tape with longitudinal Society of Motion Picture and Television Engineers (SMPTE) time code on one or both audio tracks. This was done after initial taping; however striping the tape before taping reduces the possibility of erasure. The EditLink manufacturers claim that the time

code can be used to locate any position on the video tape to an accuracy of +/- 1 frame. Trials of various positions on the tape confirmed this. Actually, each trial resulted in the EditLink finding the exact frame searched.

Macro files were written to automate the process of digitizing the video images by the frame grabber board. The images were processed in batches of 50. First, an image is digitized at a resolution of 640 columns by 480 lines. The 480 lines is the maximum allowable vertical resolution of the frame grabber card. A compiled C program called from the macro instructs the VCR controller card to advance the tape one frame. The next image is digitized and the process repeated. After 50 images have been digitized, a C program stops the VCR. This circumvents the automatic shut-off feature of the Panasonic AG-1970. This feature will shut the VCR off if it detects no "activity" for roughly three consecutive minutes. Unfortunately, it does not recognize frame advance as "activity." This 50 image limit actually provides an amount of data, about 15 megabytes, that most current hard disk drives can reasonably handle.

Next, the fifty images were filtered. The filtering process is based on a histogram analysis of the pixel values in each image. All pixel values lower than the 90th percentile are set to black or 0. All remaining pixels from the 90th to 99th percentile are linearly scaled from black to white (0 to 255). These filtered images were stored for later processing. A C program then directs the EditLink to find the next frame and digitizing continues.

The filtering process produced one of the most important advances in this research. Air bubbles entrained in the flow due to the breaking wave's impinging jet can be filtered out of the image. Given the lighting conditions used in the experiment, the bubbles have lower gray scale pixel intensities than do the pliolite. By visual inspection of the filtered images, the authors determined the histogram percentile range for the air bubbles and pliolite.

A Sun SPARC-LX workstation processed most of the velocity fields. The 486 microcomputer can process the velocity fields about 33% slower than the Sun workstation, so it was used to process only a small portion of the velocity fields. *Matlab*® by the Math Works, a matrix manipulation software package (also with macro language capabilities), was used to process the images on both the 486 microcomputer and the Sun workstation. All analysis of the velocity fields was done on the 486 microcomputer using this software package.

The filtered images were transferred to the Sun (or occasionally the 486) for DPIV processing. A series of M files (*Matlab*® macro language) were written to fully automate the process of analyzing the images and returning velocity fields. All data (i.e., filtered images and velocity field files) were stored on a high capacity magneto-optical (MO) disk in compressed format. The MO disk can store over 600 megabytes of data and currently contains over 200 MB of compressed velocity field data and over 300 MB of compressed filtered images.

A concern exists regarding the extent to which aeration of a broken wave crest, combined with the filtering process, may affect the velocity field determination in DPIV. The bubbles produced during wave breaking may distort the perceived

location of particles due to refraction/diffraction of the reflected light. To determine the net effect of this phenomenon, a mesh grid containing particles glued to fixed positions was videotaped in the highly aerated section of flow centered on the transition region. Velocity fields were then found for this video. In theory, particles held stationary should produce zero motion in the velocity fields. Analysis of the calculated velocity fields indicated that the distortional effects of the bubbles create a mean error of 1.0 pixels in the horizontal direction and 0.8 pixels in the vertical direction. A typical scaling scenario in the test conducted results in a converted 0.5 millimeter error in the calculated displacements.

VELOCITY FIELD RESULTS

Velocity field processing began by determining the calibration values used to convert pixels to centimeters for each camera position. This rather primitive method consisted of analyzing several frames from the grid video. Unfortunately, the grid lines were very difficult to observe in the still video frame. However, the outer edges of the grid—surrounded by an opaque paper coating—provided a known distance of 12 centimeters. The pixel columns values corresponding to the left and right edges were determined using a screen pointer and mouse. The difference of these two values divided by the 12 centimeter distance yields the horizontal calibration for that camera position. The vertical calibration was determined by multiplying the horizontal calibration by the pixel aspect ratio. Several frames were compared to evaluate the accuracy of the results. Each test showed slight variation from frame to frame due to slight grid movements on the order of one pixel. An average calibration value was selected after analyzing several frames.

All velocity field processing was done without converting from pixel displacements to actual centimeters per second velocity values. Doing so reduced the multiplicative error effects produced from numerous calculations using the less accurate length conversion from pixels to centimeters. Instantaneous displacement vectors were found in pixel units—final ensemble averages were then converted back to centimeters per second values using the calibrations taken from the recorded grid frames. Vertical and horizontal displacements were saved separately for each image pair processed. Mean flow velocity and turbulence intensities were the two principle derived quantities.

The raw velocity field data resulting from the DPIV method was analyzed using ensemble averaging techniques in an effort to separate the wave and turbulent parts of the motion. Consequently, the corresponding number of video frames per period for monochromatic waves had to be determined. Table 1 shows a summary of the values for the various tests and the relevant measured wave characteristics.

To calculate ensemble values for both mean flow and turbulence requires an appropriate value for the number of frames per cycle (i.e., wave period). Standard video records at 60 frames per second. Multiplying this value and the period and rounding to the nearest whole number yields the frames per cycle. Taking an ensemble average over all of the cycles corresponding to that point in the period then

Table 1 Experimental wave and frame data.

Test Number	Period (sec)	H _b (cm)	h _b (cm)	h _o (cm)	Frames/cycle	Total Frames Processed 30 cycles	Total Frames Processed 50 cycles
1B	0.85	4.85	4.7	31.2	51	N/A	2560
2C	1.42	6.52	4.2	30.7	85	2560	4266
3C	2.13	6.42	4.5	31.2	128	3840	N/A
4C	0.85	N/A	N/A	N/A	51	1536	2560
6A	2.13	8.86	8.4	23.2	128	3840	N/A

yields the mean velocities at each 1/60th of a second interval of the wave period. For example, to process a one second wave (corresponding to 60 frames per cycle) requires the average of frame 1, frame 61, frame 121... However, due to the limiting effect of the Nyquist frequency criterion in the DPIV method, certain sections of each velocity field are sometimes left without a value. In short, holes may exist in the data. This can occur if the area of interest contains a displacement greater than 1/3 its length. This is accounted for by keeping a running total of the number of valid values for each position in the velocity fields during the ensemble averaging. Therefore, to ensemble average 50 cycles requires independent totals for each position in the resulting velocity field. This improves the flawed values near free surfaces where small variations in the wave height produce a physical velocity value during only a few of the cycles. Care must be taken when analyzing the data near boundaries so as not to overstate the effect there. This method ensures that values within the main part of the flow are not understated as they would be if the summed values for, say, 48 cycles were actually averaged over 50 cycles. Both of the above effects become more pronounced for the longer period waves processed using only 30 cycles.

The time averaging analysis consisted of summing the ensemble averaged velocities over the entire period. Absent data are accounted for in the same manner as above. Time averaging the ensemble averaged velocity fields yields the mean flow velocities.

Turbulence was found using the ensemble averaged data for each point during the period. These values are subtracted from the instantaneous values of each velocity field used to find the ensemble average. These differences are squared and summed. Dividing the sum by a running total similar to that described above accounts for the nonexistent data. The turbulence values are then time averaged similar to the mean flow. Turbulence values are returned as squared values, their same form in the momentum conservation equations.

APPLICATION OF RESULTS

A total of 21,162 velocity fields were incorporated in the ensemble averaging during all of the tests. Actually, only 17,066 of these fields are completely independent because the fields found during the 30 cycle ensemble averaging in tests 2C and 4C were used as the first 30 cycles of the 50 cycle ensemble averaging. This allows a comparison of the effectiveness of increasing the number of cycles included in the ensemble averaging.

With the required number of digitized images known, digitization began. On average, images were digitized and fully filtered within 15 seconds. The filtered images were stored in compressed format on a magneto-optical disk and transferred to the workstation for processing. Given a sufficient data storage capacity available at the processing computer, one large data exchange will yield instantaneous velocities from the DPIV image processing method. This generally did not occur. Data transfer usually entailed transferring 200 images to the workstation while removing the previously processed velocity field files for the preceding 200 images. An example of a typical instantaneous velocity field is shown in Figure 3 (recall 1 cm is approximately 16 pixels).

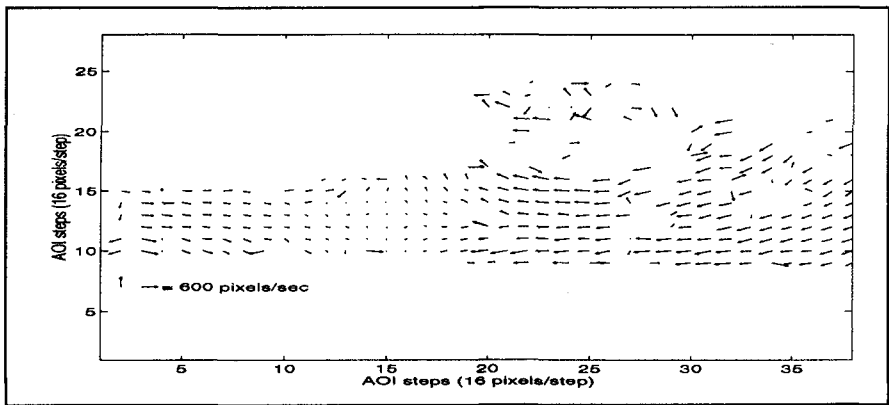


Figure 3 Instantaneous velocity field from DPIV (Test 6C, Field 536)

After acquiring all of the required instantaneous velocity fields, ensemble averaging was performed according to criteria in Table 1. As described earlier, an ensemble average of the corresponding velocity fields for each 1/60th of a second interval in the period is determined and saved. These ensemble averages, when time averaged over the period, yield results similar to Figure 4. The first image in Figure 4 shows the resultant ensemble average velocity fields of the entire field of view, including “velocities” outside the flow. A digital stopwatch superimposed on the lower portion of the screen during videotaping accounts for most of the extraneous velocities. The data in the bottom portion of the field shows the correlated motion of the stopwatch numerals. Some spurious data are also present above the flow possibly due to splashing that occurs when the jet impinges the front face of the breaking wave. Instrument noise associated with the video equipment that occurs during digitization may provide another source of non-flow velocities. All data other than the desired flow data has been removed from the second image.

Figure 5 represents an enlarged section of the middle view for the 50 cycle case in test 4C. Profiles represent typical examples of the expected flow—for the first time measurements are included above and below the wave trough elevation. In

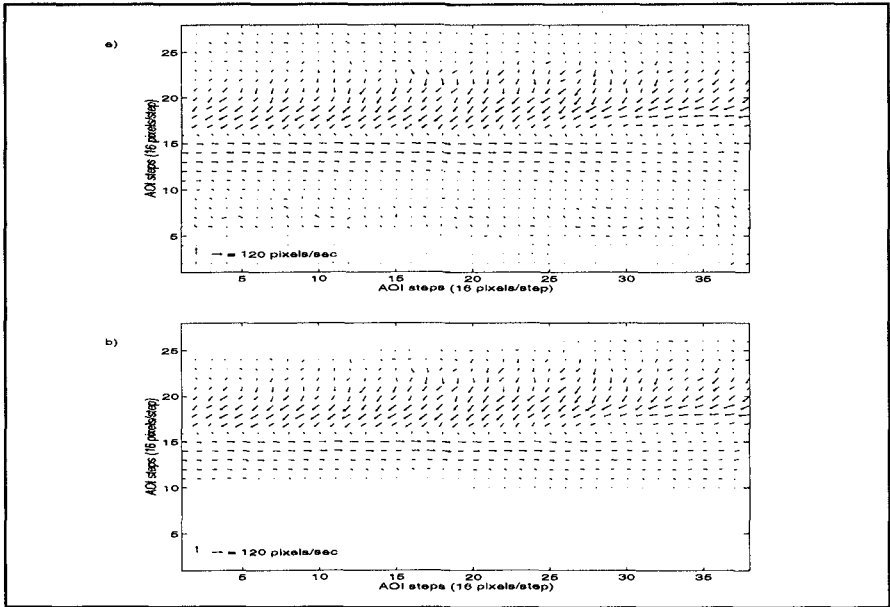


Figure 4 Ensemble time averaged velocity field with a) all non-flow data included and b) only flow related data included.

principle, mass (volume) should be conserved across any given vertical section (column) in this flow. Figure 5 indicates that mass is largely conserved in the measurements.

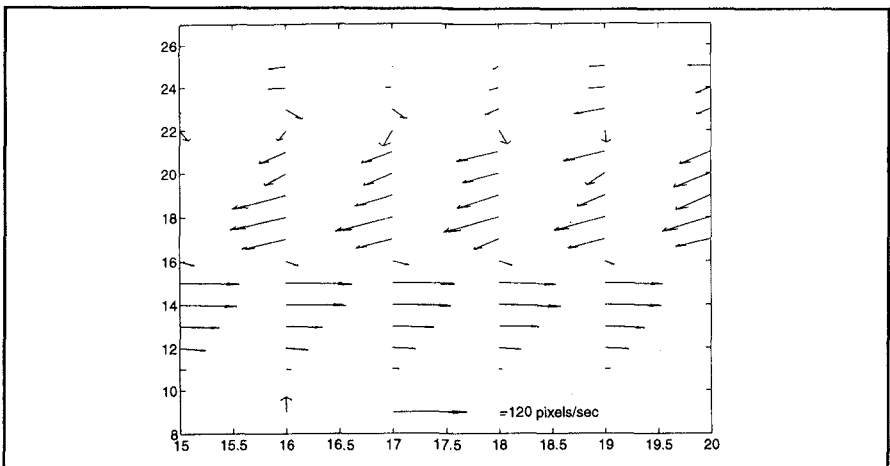


Figure 5 Columns 15-20 of ensemble, time-averaged velocity field from 50 cycle Test 6C indicating conservation of mass.

Ensemble turbulent r.m.s. velocity fluctuations are then calculated as described earlier. Observing the original video record determined the location of the relatively abrupt break in wave height change that signals the end of the transition region (or the location of the transition point). Albeit a somewhat subjective process, this technique provides greater accuracy than wave gauge data given the five centimeter gap between wave gauge stations. After determining the general location of the transition point, the average of each row in the three columns of horizontal turbulent velocity data on the offshore side of the transition point (toward the breakpoint) developed a depth varying profile of horizontal turbulent velocity fluctuations. Three column averaging thus provides two advantages: first, it further minimizes any effects that missing data may have on the ensemble averages and, second, increases the likelihood that the data represent values not only near the transition point but within the transition region. Figure 6 presents the depth varying values of the r.m.s. horizontal turbulent fluctuations (normalized by the local wave speed).

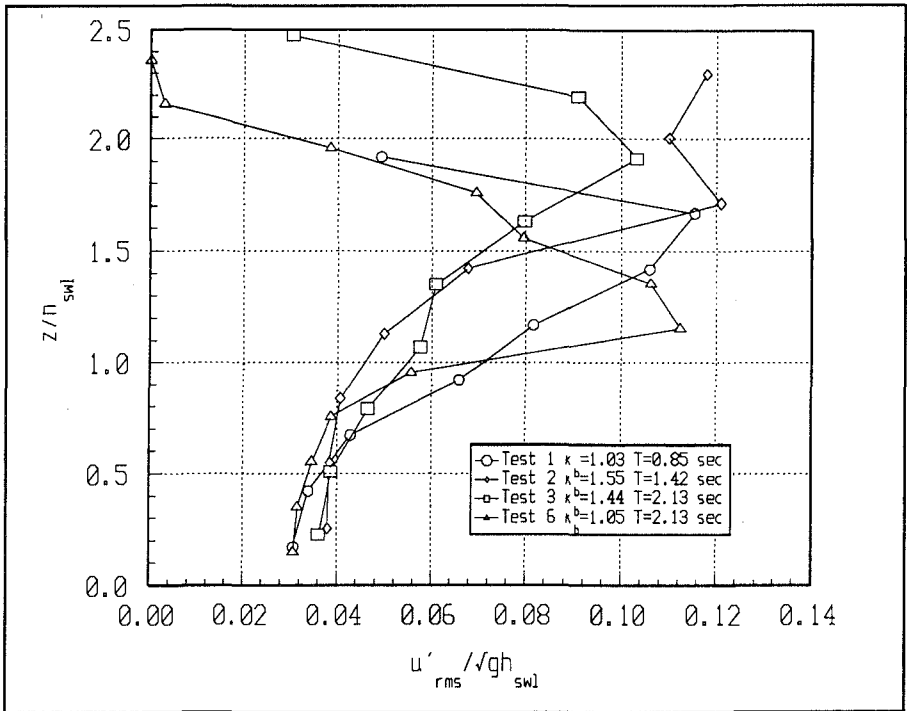


Figure 6 Dimensionless $u'_{r.m.s.}$ versus depth at the transition point.

Figure 6 shows that the below still water level (SWL) values of $u'_{r.m.s.}$ are fairly consistent within each test as well as between tests. For each test, the waves at the transition point are highly asymmetric about the SWL. This results in a majority of the crest appearing above the SWL. Mean values of the horizontal turbulent velocity

results above SWL were found and then normalized by the known breakpoint conditions.

CONCLUSION

The work presented here suggests the following:

1) Velocity measurements are now possible in the aerated crest of a broken wave within the transition region through the use of digital imaging and application of appropriate filtering techniques. The distortional characteristics of the bubbles produced during wave breaking somewhat affect the spatial resolution of these velocities. However, the errors introduced are on the order of one millimeter per frame and, considering the fairly coarse resolution of the velocities found with DPIV, are negligible.

2) Digital particle image velocimetry provides an effective alternative to standard PIV techniques and should improve as video technology and processing speeds advance.

3) The use of video for examination of large temporal data sets by ensemble averaging provides the most efficient and economical method currently available for applications in which the temporal and spatial resolution provided by video imaging are adequate.

4) DPIV can resolve turbulent velocity fluctuations over the entire water column. However to maintain accuracy requires a high particle seeding density in the crest region.

REFERENCES

- Jansen, P.C.M. (1986). Laboratory observations of the kinematics in the aerated region of breaking waves. *Coastal Engineering*, **9**, 453-477.
- Nadaoka, K. and Kondoh, T. (1982). Laboratory measurement of velocity field structure in the surf zone by LDV. *Coastal Engineering in Japan*, **25**, 125-145.
- Okayasu, A., Shibayama, T. and Mimura, N. (1986). Velocity field under plunging waves. *Proceedings 20th Coastal Engineering Conference*, vol. 1, 660-674.
- Stive, M.J.F. (1980). Velocity and pressure field under spilling breakers. *Proceedings 17th Coastal Engineering Conference*, vol. 1, 547-566.
- Wang, H., Sunamura, T. and Hwang, P.A. (1982). Drift velocity at the wave breaking point. *Coastal Engineering*, **6**, 121-150.
- Willert, C.E. and Gharib, M. (1991). Digital particle image velocimetry. *Experiments in Fluids*, **10**, 181-193.

CHAPTER 49

Wave Gauging Networks Worldwide — An Overview

J. Michael Hemsley¹
PE, MASCE

Abstract

Throughout the history of society's attempts to build on the beach, waves have been the principal antagonist. Engineers soon learned that to be successful, they had to understand the nature of the waves that attacked their structures. That understanding has led to many efforts to measure or estimate waves to develop a climatology useful in coastal design.

Over the past 25 years, our ability to accurately and cost-effectively measure waves has improved considerably. This has resulted in an increasing number of gauging networks worldwide. This paper is a summary of many of those networks. Information on the networks will include, where available, the type gauges used, locations of stations, additional data collected, and data distribution means.

Introduction

Because many wave gauging programs are locally installed and operated, they are known only to their operators. Only a few of the networks are associated with the World Meteorological Organization (WMO) and have their data distributed worldwide on the Global Telecommunications System (GTS). Information about the networks operated by the U.S. National Data Buoy Center (NDBC), Canadian Atmospheric Environment Service (AES), and the United Kingdom Meteorological Office was relatively easy to acquire. The smaller networks have been a challenge. That challenge has been offset, though, by the willingness of most network operators, once identified, to share information.

To most coastal scientists and engineers, the small networks are the most interesting. The large networks, often funded by the country's weather service, are well known. But most network operators — or potential operators — must operate on a much smaller scale, so there is often much more to learn from others who manage data collection efforts within similarly restrictive budgets.

¹ Chief, Program Management Division, National Data Buoy Center, Building 1100, Stennis Space Center, MS 39529-6000, U.S.A.

Networks

In all, information has been received or obtained about wave measurement networks in 19 countries. Information has come from personal communications, papers or other publications, and, in several cases, from a "Guide to Moored Buoys and Other Ocean Data Acquisition Systems" (Data Buoy Cooperation Panel, in publication). Programs are likely to exist in countries other than those reported in this paper, particularly in countries such as Germany, The Netherlands, People's Republic of China, Portugal, and Sweden. Unfortunately, time ran out before all leads could be followed and information produced. It is hoped that this information will be useful to anyone who operates a wave gauging network or even a single station by providing information about the alternative hardware, techniques, and approaches available. A presentation of these alternatives should also help those who are interested in collecting wave data for research or engineering purposes.

Of the information that has been received, several networks stand out. Two particular examples of those that deserve mention are the efforts by Spain to establish their national network and the international effort to define the wave climate along the coasts of the Black Sea. The Clima Maritimo is the research and development department of the Puertos del Estado, which is responsible for coordinating the activities of 27 of Spain's ports. To provide data critical to their mission, they have installed and are operating a network of 20 nondirectional and 4 directional wave buoys. In the future, they will add three more directional wave buoys, five coastal wave radars, and six to nine oceanographic buoys that will report atmospheric information, current data, and temperature and salinity profiles, as well as wave data.

The international effort on the Black Sea, called NATO-TU WAVES, is supported by Russia, Turkey, the Ukraine, Bulgaria, and Rumania. Four nondirectional and six directional stations are being established to provide data needed for wave modeling and forecasting around the perimeter of the Black Sea.

The collection of wave data is important to coastal engineers and scientists. This overview is intended to be a minor reference for use when new networks are being planned or existing networks are updated. While an attempt has been made to ensure that the stations are currently in service, it is possible that some information may no longer be current. A consistent set of symbols will be used and will follow the key provided below. For simplicity, the only symbols used on the figures will be for directional and nondirectional systems. Where the information is available, the type of gauge will be mentioned in the discussion. The presentation to follow is organized alphabetically by country, except for the network in the Black Sea, which will be listed as NATO-TU WAVES because of its international nature.

Australia

Gauging networks in Australia are operated, primarily, by the states. This decentralization made identification of networks a bit more difficult than for countries with centralized control of their programs.

Three programs have been identified, those of Queensland, New South Wales, and Western Australia. In Queensland, wave data are collected at 13 locations (Figure 1). Nondirectional data are collected using Datawell Waverider buoys and from InterOcean S4 current meters, while directional data are collected from Datawell Directional Waverider buoys. All stations in the Queensland network are shown on Figure 1 as nondirectional, although several are likely to collect directional data. Data from the Waverider buoys are transmitted to shore via radio.

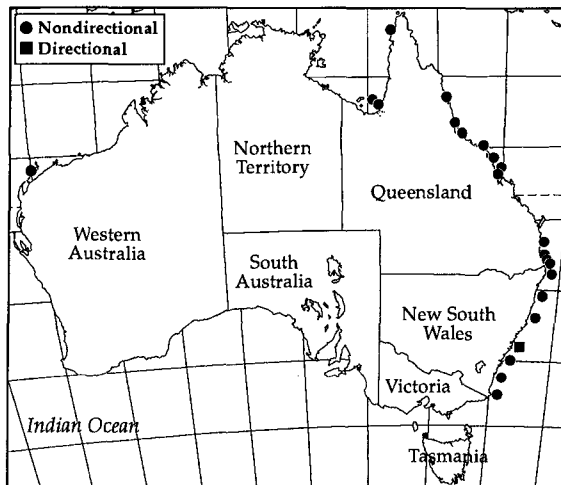


Figure 1. Australian Wave Gauging Networks

The wave data network in New South Wales presently consists of seven stations, one of which collects directional data (Figure 1). The oldest station in this network was installed in 1974; all stations have been operational since 1987. Datawell Waverider buoys are used at every station, and the data are transmitted to a shore station by radio.

There is one station in Western Australia for the past 4 years (Figure 1). A Datawell Waverider buoy is used to collect nondirectional data that are transmitted to shore by radio every 20 minutes. These data are used for "real" time ship operations.

Canada

There are two wave gauging networks in Canada. The first, and more traditional, is operated by the AES and has stations in the Atlantic and Pacific Oceans and in the Great Lakes and other major inland waters (Figure 2). The other network is operated in Quebec Province as a part of the James Bay Hydroelectric Project by the Societe d'Énergie de la Baie

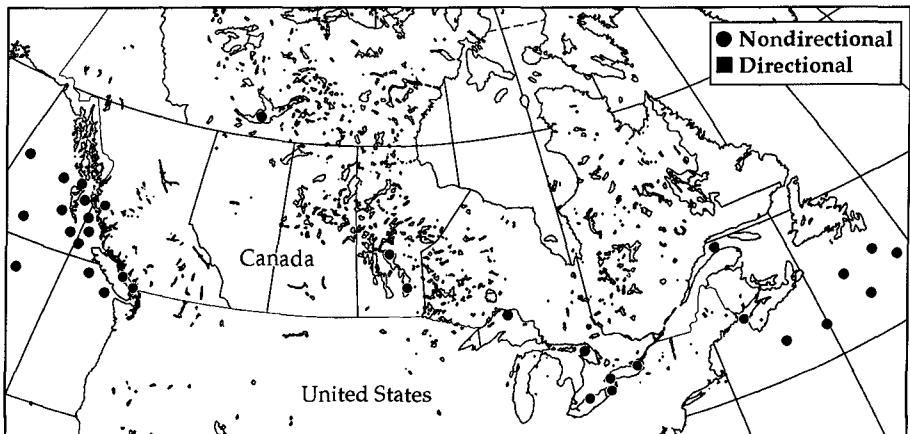


Figure 2. Canadian AES Buoy Network

James (Figure 3). The AES operates a total of 33 buoy stations, 8 in the Atlantic, 9 in the Great Lakes region, and 16 in the Pacific. The buoys in the Atlantic and Pacific consist of fifteen 3-m-diameter discus buoys in the nearshore areas and nine 6-m boat-shaped buoys offshore. In the Great Lakes region, two of the stations are occupied by 12-m-diameter discus buoys. All stations collect nondirectional wave spectral data as well as meteorological data such as wind speed and direction, pressure, and temperature. All data are transmitted hourly via the Geostationary Operational Environmental Satellite (GOES) and are available on the GTS.

In Quebec, four Endeco WaveTrack 1156 buoys are used to collect data from eight stations in the James Bay area. These buoys collect directional wave data that are transmitted hourly via an RF radio link to a base station. The buoys are deployed in a most unusual manner — by helicopter.

France

Meteo-France operates one buoy station in cooperation with the United Kingdom Meteorological Service. The buoy was developed and used by the UK Met Service and is operated by them. The station is located 300 km off the Brittany coast in 2,000 m of water. Additional information on the buoy used can be found in the section on the United Kingdom. Meteo-France plans to operate another buoy in the Bay of Biscay soon. Another plan to operate four additional stations, two in the Mediterranean Sea and two in the West Indies, is currently under study. Two directional Datawell Waverider buoys are currently deployed in the West Indies as a part of the Oceanilles project. The French Aids-to-Navigation Service (STNMTE), which operates its own network of ten wave buoys along the coast of France, assisted Meteo-France in the establishment of the stations in the West Indies (Data Buoy Cooperation Panel, in publication).

Iceland

The Icelandic Lighthouse and Harbour Authority operates a network of stations within the Information System on Weather and Seastate for Seafarers, an automated call-up voice information system (Figure 4). Among the stations are seven Datawell Waverider buoys reporting nondirectional wave data and nine harbor installations that report wave and

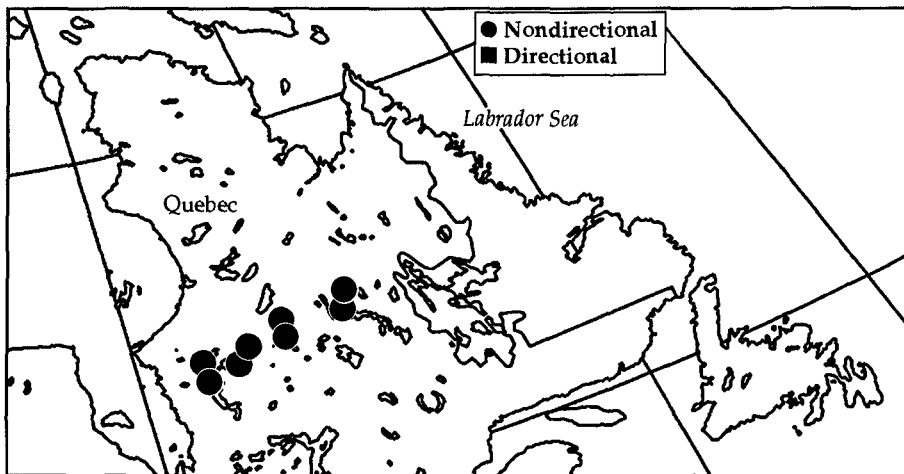


Figure 3. James Bay Hydroelectric Project Wave Gauging Network

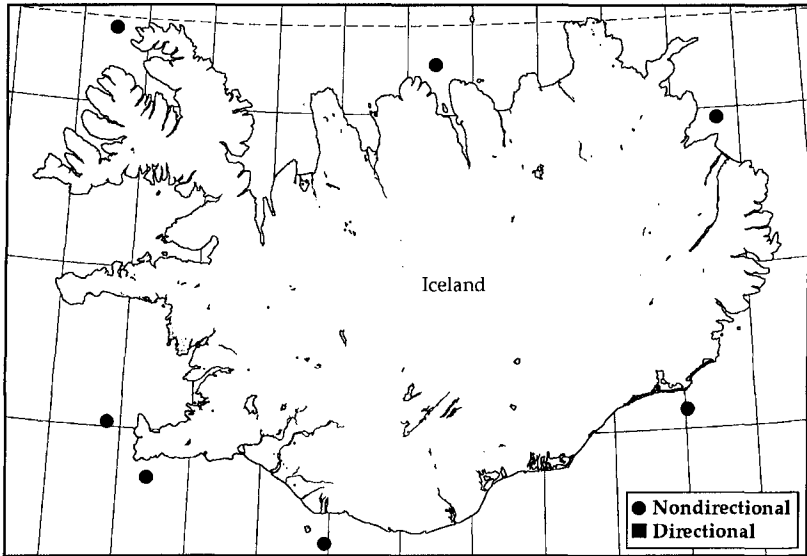


Figure 4. Icelandic Data Buoy Network

meteorological information. Another 12 automated weather stations are located on lighthouses. Waverider data are transmitted via radio link to a shore station (Data Buoy Cooperation Panel, in publication).

Israel

The Israel Meteorological Service operates a small network of directional Datawell Waverider buoys. The Waverider buoys are deployed in Haifa Bay and the ports of Asdod and Hadera. Data are received by direct radio link to a shore station (Data Buoy Cooperation Panel, in publication).

Italy

In an article in *History and Heritage of Coastal Engineering*, Professor Leopoldo Franco reports that there have been nearly 100 wave gauging stations on the Italian coast since 1974 (Franco, 1996) (Figure 5). Currently, there are 13 permanent stations. Eight of these are operated as a part of the National Wave Measurement Network. These stations are directional Datawell Wavec buoys reporting their data via polar orbiting satellites. The network is managed by the Italian Hydrographic and Tidal Service and has accomplished an average data acquisition rate of more than 90 percent since the network was established in 1989.

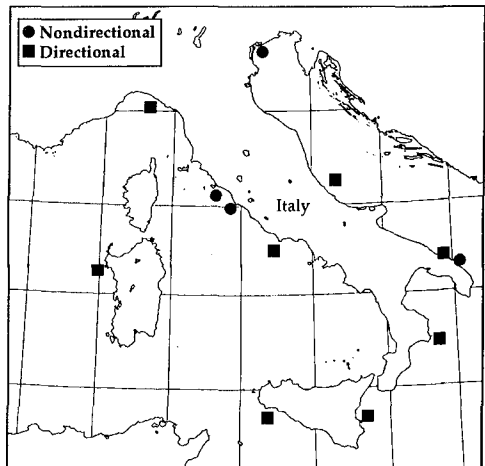


Figure 5. Permanent Wave Gauging Stations in Italy

Japan

For years, the Japanese have been leaders in coastal engineering research. Various agencies and research institutions have, therefore, operated networks of wave gauging stations. The diversity of organizations that have been involved in wave measurements has made the identification of all stations a bit difficult. Those stations that have been identified are reported here.

Japan's ocean data buoy program was initiated by the Japanese Meteorological Agency (JMA) in 1968. A total of seven 10-m-diameter discus buoys was eventually constructed. Four of these buoys remain in service, rotating among three stations (Figure 6). These buoys report data hourly via the JMA Geostationary Meteorological Satellite. Nondirectional wave data, as well as considerable meteorological data, are collected and reported. These data are published annually on CD-ROM in a report entitled "Data Report of Oceanographic Observations" available from JMA headquarters (Data Buoy Cooperation Panel, in publication).

A much more extensive network is operated and maintained by the Ports and Harbours Bureau of the Ministry of Transport. In particular, the Port and Harbour Research Institute (PHRI) operates a 42-station network of wave measurement stations called Nationwide Ocean Wave information network for Ports and HARbourS, or NOWPHAS (Figure 6). The network includes a variety of sensor types, some quite innovative. PHRI has deployed directional arrays, nondirectional buoys, measurements from towers, two acoustic meters, and a new Doppler-type wave directional meter. The Doppler meter is installed at three existing stations and one new research station.

NOWPHAS and JMA data are provided to a semi-governmental agency and from there to users. The Coastal Development Institute of Technology operates the Coastal Wave Information Center.

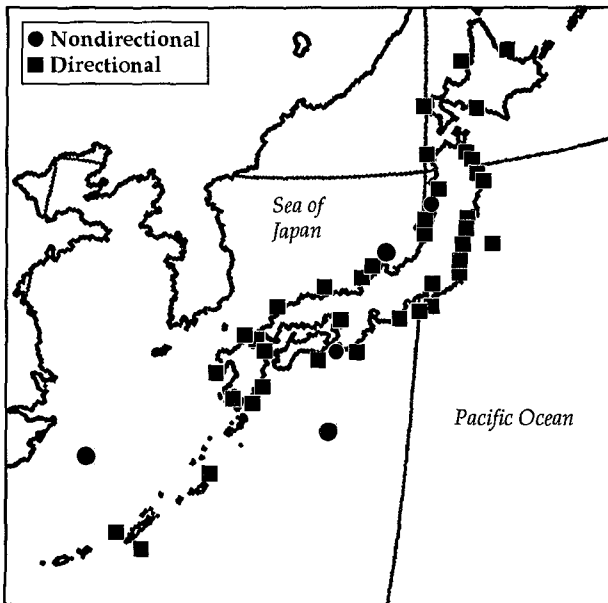


Figure 6. NOWPHAS and JMA Wave Measurement Stations

Korea

The Korean Meteorological Agency (KMA) and the Korean Maritime and Port Administration, the latter together with the PHRI in Japan, are cooperating in the establishment of a wave gauging network around the Korean peninsula. So far, the KMA has one buoy on station in the Yellow Sea—it is the northernmost buoy shown in Figure 7. The other stations are operated by the Maritime and Port Administration and include seven directional Datawell Waverider buoys and one directional pressure sensor and electromagnetic current meter (PUV) gauge—the northernmost station in the Sea of Japan. This PUV gauge is temporary and will be replaced by one of the Doppler meters being developed by the PHRI.

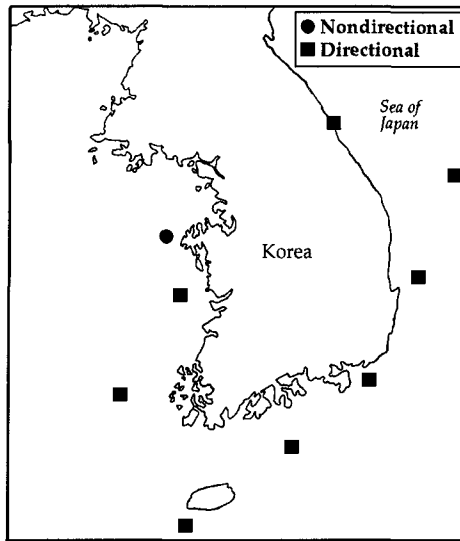


Figure 7. Korean Wave Gauging Networks

Kuwait

One directional wave station is maintained by the Hydraulics and Coastal Engineering Department of the Kuwait Institute for Scientific Research. Data are received by radio from the Endeco 1156 buoy located 6 km off the Fintas Coast in the Persian Gulf. The purpose of the station is to study deep-water waves in Kuwait's territorial waters.

NATO-TU WAVES

Bulgaria, Rumania, Russia, Turkey, and the Ukraine are cooperating in a program to better understand the wave climate affecting the Black Sea coastline and the Turkish coastline of the Mediterranean Sea. Partially funded by NATO, the program is being executed by four collaborating Turkish organizations and four institutes in the other Black Sea countries. A total of ten stations are collecting data, including six collecting directional wave data from directional Datawell Waverider buoys and four others from a Ukrainian-built wave staff that measure nondirectional waves (Figures 8 and 9). All buoy data are transmitted to shore using radio frequencies (Ozhan and Abdalla, 1993).

There is one additional station located in Turkish waters. A PUV gauge installed in conjunction with the Japanese International Corporation Agency — an installation supervised by the PHRI — is reporting directional wave data from a station at Filyos near Zongldak.

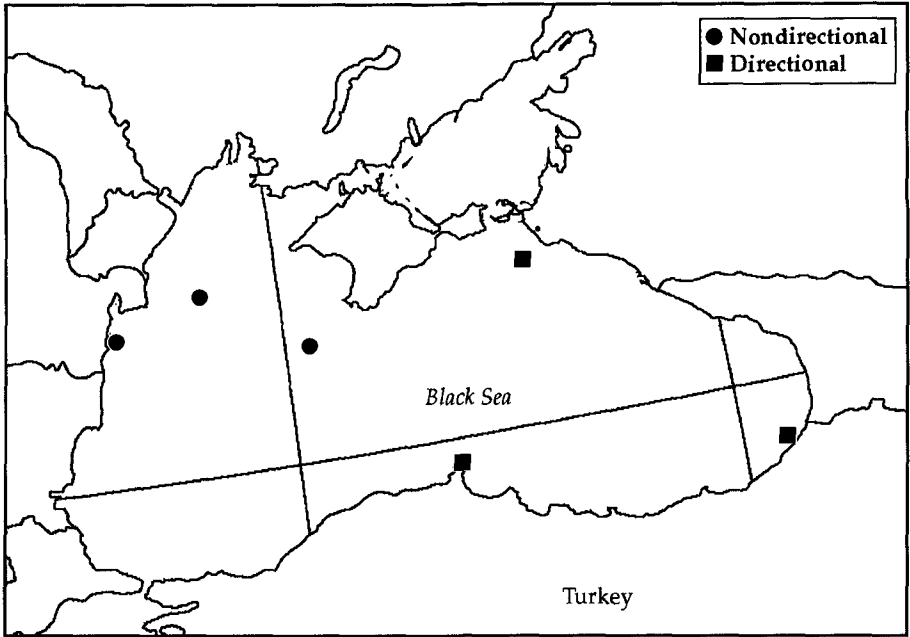


Figure 8. NATO-TU WAVES Black Sea Network

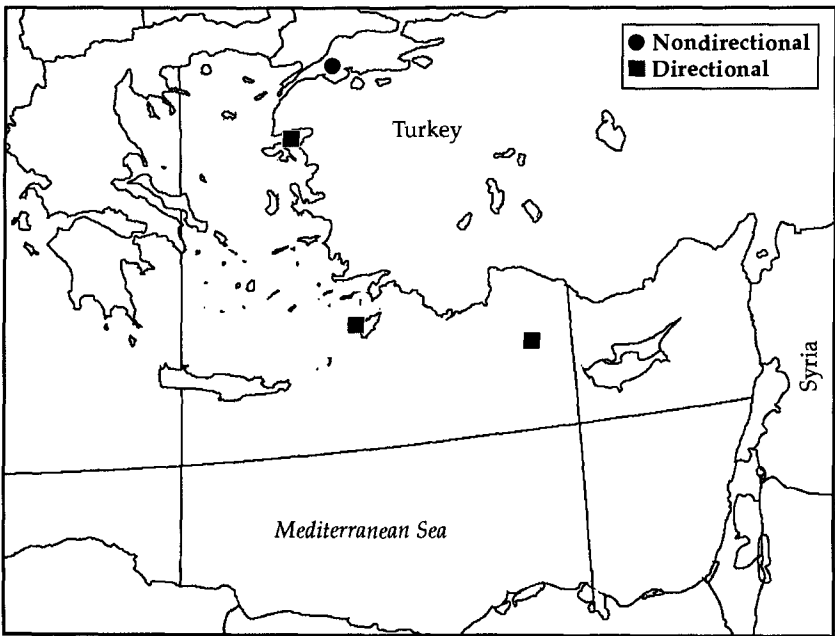


Figure 9. NATO-TU WAVES Mediterranean Sea Network

Spain

Clima Maritimo, the research department of the Puertos del Estado, is in the process of installing 21 nondirectional and 4 directional wave buoys (Figures 10 and 11). An additional four nondirectional stations are operated by other organizations. The scalar buoys are Datawell Waveriders, while the directional buoys are Seatex WaveScans. The data are collected to support the operation of Spain's harbors. Additional directional buoy stations and shore-based wave radars are planned for the future (Ruiz de Elvira, et al., date unknown).

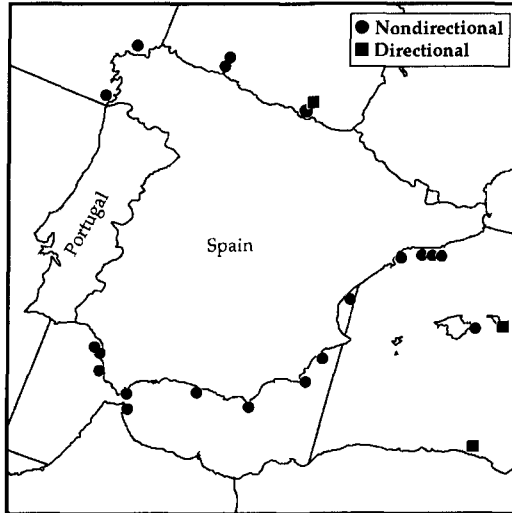


Figure 10. Spain's Coastal Wave Gauging Network

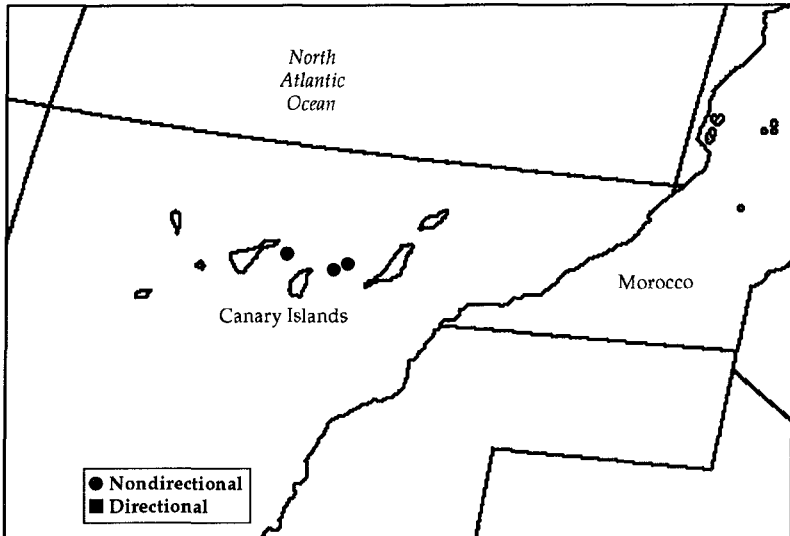


Figure 11. Spanish Wave Data Collection in the Canary Islands

Sri Lanka

An Endeco directional wave buoy has been operating offshore Galle on Sri Lanka's southwestern coast for 8 years. It was installed by the Sri Lanka Hydraulic Institute for the Coast Conservation Department.

Republic of China

A network of four directional stations is being established by the Central Weather Bureau around Taiwan. At least two, and probably all, of the stations are now in place. The current plan is to have Endeco 1156 WaveTrack buoys measuring directional waves at Bytougau at the northern tip of the island, Tonchiyu in the middle of the Taiwan Strait, Shaoliucho off Kaohsiung Harbor, and Chengkung on the southeastern coast facing the Pacific Ocean. Each of these stations reports by UHF to shore. Ultimately, the plan is to have a network of more than 20 stations ringing the island, including underwater ultrasonic wave gauges, shallow-water observation piles, buoys, and shore-based radars.

United Kingdom

The United Kingdom Meteorology Office has established a network of nondirectional data buoys off the British Isles in both relatively shallow water and in deep water off the continental shelf (Figure 12). Two types of buoys are used. Nearshore, a 2.5-m-diameter toroidal buoy transmits data via a VHF radio link to shore. Offshore, a new purpose-built buoy of less than 3-m-diameter (so it can be transported over public roads without special precautions) has been installed at four of the open-ocean locations. These buoys report via METEOSAT or GOES, and the data are distributed on the GTS (Bentley and Jones, 1993).

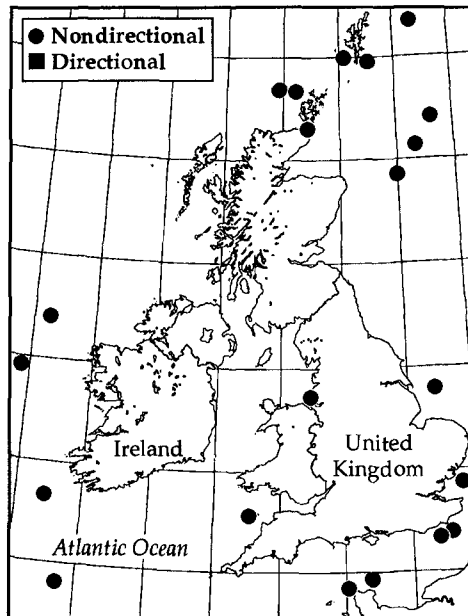


Figure 12. Wave Data Collection Off the British Isles

United States

Two agencies operate extensive networks of wave data collection stations in the United States, NDBC of the National Weather Service (NWS) and the U.S. Army Waterways Experiment Station Coastal Engineering Research Center (CERC). While buoys are the primary means of wave data collection for NDBC, laser wave systems are used on several Atlantic offshore platforms in the Coastal-Marine Automated Network. Buoys used by NDBC include the large 10- and 12-m discus buoys, 6-m boat-shaped hulls, 3-m-diameter discus buoys, and, on occasion, 2.4-m discus buoys. All NDBC's discus buoys are capable of collecting directional wave data, although those data are only collected at special locations. NWS sponsors many of the stations, but CERC, the Minerals Management Service, and the National Aeronautics and Space Administration fund a number of stations operated by NDBC as well. CERC is the primary sponsor of directional wave data from this network. In addition to wave data, NDBC buoys collect a full range of meteorological data and, occasionally, oceanographic data as well. All data are transmitted hourly from the buoys via GOES to the NWS Telecommunications Gateway and are distributed worldwide on the GTS (Figure 13).

While CERC operates wave gauging stations primarily in support of coastal projects, and therefore for short periods of time, they do fund or operate a network of relatively permanent stations (Figure 14). The principal operator of many of these stations is the Scripps Institution of Oceanography, University of California at San Diego. The Prototype Measurement and Analysis Branch of CERC operates the others. Their nondirectional stations are most often Waverider buoys; directional stations can be either PUV gauges or multiple pressure sensor arrays, including a linear array at the CERC Field Research Facility in Duck, NC. These data are usually either transmitted to shore by radio or cable where they are collected periodically by telephone connection (U.S. Army Corps of Engineers, Waterways Experiment Station, July 1996).

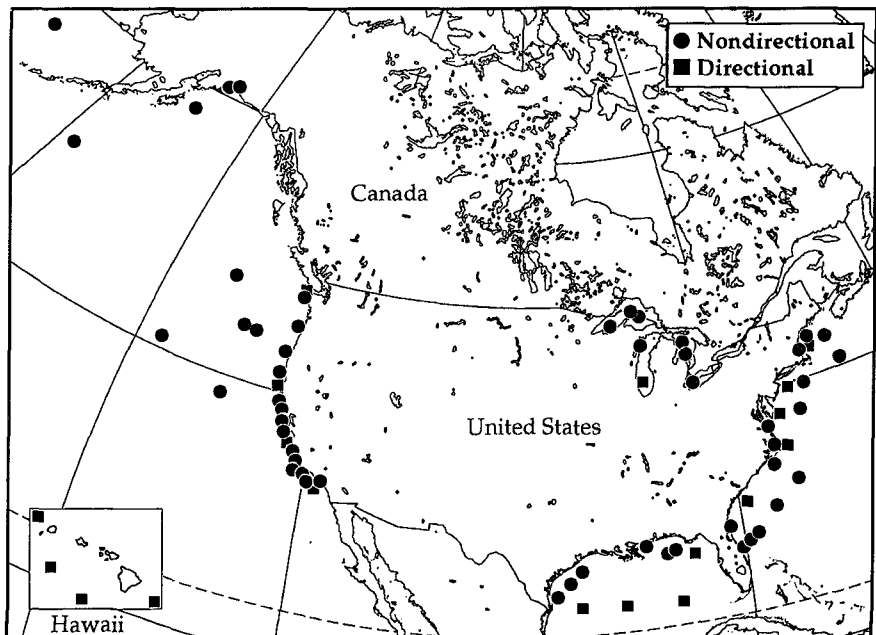


Figure 13. NDBC Wave Gauging Network

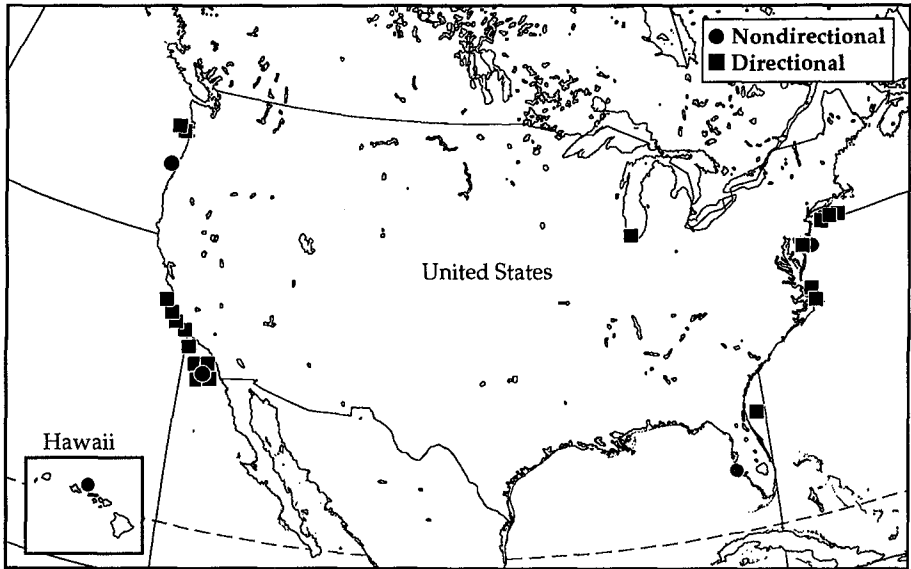


Figure 14. CERC Wave Gauging Network

Archival

Unfortunately, much of the wave data collected around the world is not archived outside the organizations that collect them. In the United States, for example, the National Oceanographic Data Center accepts all quality-controlled wave data collected, if they are sent to them. All NDBC data are archived in this way, but data collected in other agencies' programs are not always archived. So, someone searching for wave data often has to seek out a variety of sources. Internationally, there is no organization that exists to archive wave data from around the world. With proper coordination and cooperation, it is possible that this state could be corrected. The Intergovernmental Oceanographic Commission (IOC) and the WMO worked together to establish the Marine Environmental Data Service (MEDS) in Canada as the Responsible National Oceanographic Data Centre (RNODC) for drifting buoy data. All drifting buoy data transmitted on the GTS are archived by MEDS and are available to anyone who needs them. Possibly the same thing could be done for wave data and an RNODC established for them. It would seem that the IOC and WMO would have an interest in such a center.

Conclusion

Wave data are being collected by at least 19 countries around the world. This paper has attempted to summarize the programs the author could discover. Too many may have gone undetected. This is an indication that the results of many wave gauging efforts go unrecognized by others in the field, and valuable data lie unused after their initial purpose is served. These data do not decrease in value with time. It appears that the time has come for an international effort to provide an archive for wave data.

Acknowledgments

The author acknowledges the critical assistance he has received from those who provided the information that appears in this paper. Without the enthusiastic support of those who responded to requests for information, this paper could not have been successfully completed.

References

- BENTLEY, A.N., and JONES, D.W., "Development of the UK Meteorological Office's Open-Ocean Data Buoy," *Proceedings of the 2nd Data Collection System Users' Conference*, Athens, Greece, 14-17, September, 1993.
- DATA BUOY COOPERATION PANEL, "Guide to Moored Buoys and Other Ocean Data Acquisition Systems," Data Buoy Cooperation Panel Technical Document No. 8, IOC (of UNESCO) and WMO, Geneva, in publication.
- FRANCO, L., "History of Coastal Engineering in Italy," *History and Heritage of Coastal Engineering*, edited by Nicholas C. Kraus, American Society of Civil Engineers, NY, 1996.
- OZHAN, E., and ABDALLA, S., "Wave Climatology of the Turkish Coast: NATO TU-WAVES Project," *Proceedings of the First International Conference on the Mediterranean Coastal Environment*, Antalya, Turkey, November 1993.
- RUIZ DE ELVIRA, A., NISTAL, A., PEREZ, B., HUERTA, M., RUIZ, M.I., NIETO, J.C., and SERRANO, O., "Wave and Oceanographic Data Bases at Clima Maritimo," Puertos del Estado, Spain, date unknown.
- U.S. ARMY CORPS OF ENGINEERS, WATERWAYS EXPERIMENT STATION, "Compendium of U.S. Wave Data Summary Statistics July 1996," Vicksburg, MS, July 1996.

CHAPTER 50

Improvement of Submerged Doppler-Type Directional Wave Meter and its Application to Field Observations

Noriaki Hashimoto¹, Masao Mitsui², Yoshimi Goda³,
Toshihiko Nagai⁴, and Tomoharu Takahashi⁵

Abstract

This paper presents an improved submerged Doppler-type directional wave meter which has the capability of measuring water surface elevations and multiple current velocity components. These components are determined from Doppler frequency shifts of ultrasonic waves in water. The improved system has proven to be capable of successfully obtaining tide, current and directional wave data. In addition, this directional wave meter has accurately estimated directional wave spectra in severe sea conditions with the use of some techniques introduced in this paper.

1. Introduction

Field studies in coastal areas are indispensable not only for scientific research but also for pre- and post-construction monitoring of the effects of engineering projects. Particularly for the latter cases, field surveys often require not only a long observation period but also require the measurement of many parameters such as waves, currents, and tides to clarify the mutual interaction between those natural conditions and human activities. Many types of observational devices have been developed and improved on over the years. Most of them, however, were designed to measure specific parameters separately using their own techniques. To obtain meaningful results, it is necessary to measure the sea conditions comprehensively, i.e., the measurement of

¹ Chief, Hydrodynamics Lab., Marine Environment Div., Port and Harbour Research Institute (PHRI), Ministry of Transport, 1-1-3 Nagase, Yokosuka 239, Japan.

² Member, Research and Development Division, Kaijyo Corporation, 3-1-5 Sakae-cho, Hamura Tokyo 205, Japan.

³ Professor, Department of Civil Engineering, Yokohama National University, Hodogaya-ku, Yokohama 240, Japan.

⁴ Chief, Marine Observation Lab., Hydraulic Engineering Div., PHRI.

⁵ Managing Director, Japan Marine Surveyors Association, 14-12 Kodenma-cho, Nihonbashi, Chuo-ku, Tokyo 103, Japan.

many parameters at the same time and at the same location, because each item is mutually and closely interrelated.

Until recently, a simple instrument for directional seas has not yet been developed. In Japan, the commonly used wave meter is a submerged ultrasonic-type wave gage (USW) which can be installed in maximum water depths of 50m. A submerged ultrasonic-type current meter (CWD) has also been developed for measuring directional seas but it is limited to applications with maximum water depths of about 30m because of the decay of water particle velocities due to depth. For these reasons, the development of a well-combined measurement system has been anticipated in Japan.

With this background, we developed the submerged Doppler-type directional wave meter and introduced it at ICCE '94 in Kobe. This system, known as the DWM, is extremely convenient since it is a single instrument that can be used to obtain accurate observations of directional seas. It is considered to be one of the most useful measuring systems for investigating directional seas.

Since ICCE '94, further improvements have been made to the DWM and additional field experiments have been conducted to enhance the performance of the DWM from many aspects. In this paper, we introduce new features of the DWM-II (the improved DWM is hereafter called the DWM-II) with its validity and applicability demonstrated with experimental results. Some techniques for improving the performance of the DWM-II are also presented along with the results of field experiments.

2. System Description

An improved "submerged Doppler-type directional wave meter", the DWM-II, possesses the multiple functions of a wave meter, current meter and tide gage. The main components of the system are a submerged transducer, measurement section, and computation unit. The transducer is supported with gimbals and has oscillators which operate four acoustic beams. One beam is vertically directed and operates at a frequency of 200 kHz. The other three acoustic Doppler current profiler (ADCP) beams operate at a frequency of 500 kHz, each of which has an inclination of 30 degrees to the vertical.

To measure the water surface elevation, the transducer transmits upward-directed ultrasonic waves and receives that portion of the energy which is reflected off of the water surface. The water surface elevation is estimated by using the ultrasonic wave propagation time based on the known propagation speed in water.

By also transmitting ultrasonic waves upward in three directions, separated by an inclination of 30 degrees, current velocity components, $U_1(t)$, $U_2(t)$, $U_3(t)$, can be measured by receiving the acoustic waves reflected back from selected layers of water. The water particle velocity of each layer is estimated from the frequency shift caused

by the Doppler effect between the transmitted waves and the reflected waves. Using a time sharing system, all measurements are made every 0.125 seconds or at a sampling frequency of 8 Hz.

In addition, the DWM-II is equipped with a pressure sensor, compass and inclinometer in the transducer. These are used to monitor the conditions of the DWM-II itself and to check the quality of the measured data.

3. Field Testing

Field testing was carried out from August 1993 to March 1995 off the entrance of Kamaishi Port, as shown in **Figure 1**, where the conventional ultrasonic wave meter (USW) has been operational since 1983. The transducer of the DWM-II was positioned about 100m away from the USW at a height of 1.5m above the seabed where the water depth is 48m. The time series data consisted of water surface elevation and current velocity components that were measured at three different water depths of 10m, 23m and 38m below the water surface. These data were recorded on an optical magnetic disk at a sampling rate of 2 Hz for 20 minutes every two hours. Some statistical parameters, including the directional spectrum, were computed immediately after each observation and were recorded on the optical magnetic disk. In addition, a rotor-type current meter (RCM) was moored to a float and positioned 100m away to examine the validity of the DWM-II by comparing the results of both meters.

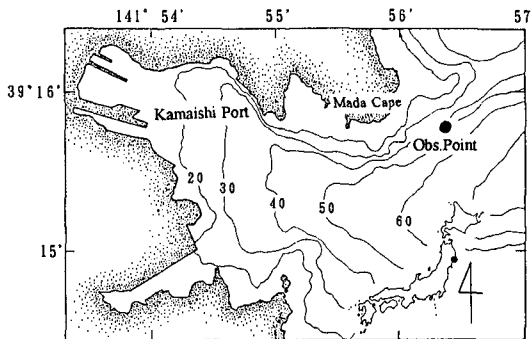


Figure 1 Field Observation Locations

4. Examples of Observational Results

Figure 2 shows some examples of the DWM-II time series of wave parameters such as significant wave height $H_{1/3}$, significant wave period $T_{1/3}$, mean wave direction $\bar{\theta}$, peak wave direction θ_p , mean spreading angle θ_N , and long-crestedness parameter γ .

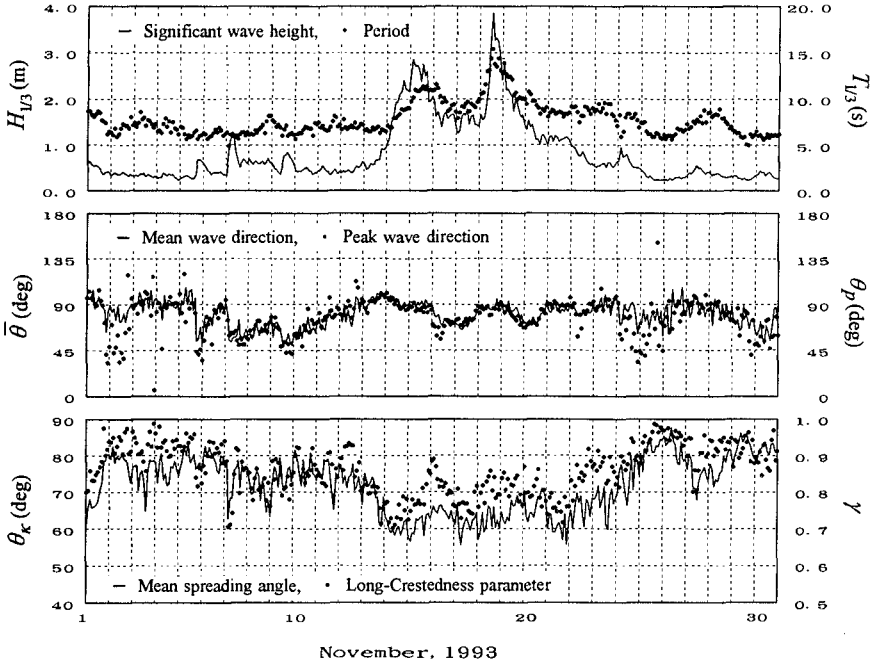


Figure 2 Time Series of Wave Parameters

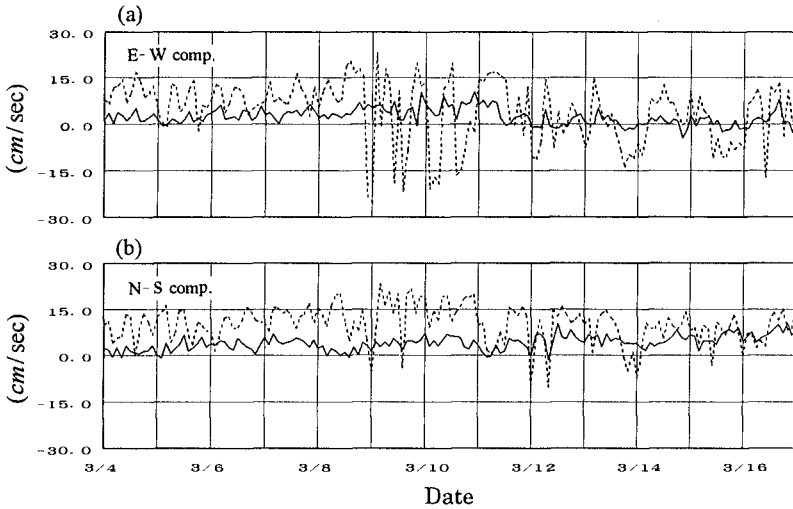


Figure 3 Time Series of the East-West and North-South Current Velocity Components by the DWM- II (solid line) and the RCM(dashed line)

Results have shown that wave parameters, such as significant wave height and period, measured by the DWM-II, show good agreement with those obtained by the USW. The current velocities, however, measured by the DWM-II, are very different than those obtained by the RCM as shown in **Figure 3**. It is important to note that the RCM is very vulnerable to the current induced by waves and, in fact, moves following the wave motions. This is demonstrated in **Figure 4**. The existing reports on the currents around the observation site show that the currents there are weak, i.e., 10 cm/s or less, which is consistent with the results of the DWM-II which are also shown in **Figure 4**. **Figure 5** shows the spectra of the currents of the east-west and north-south components measured by the DWM-II at the upper layer 10m below the mean free surface. As shown in **Figure 5**, two predominant tidal periods can be seen at the diurnal and the semi-diurnal frequencies. These predominant peaks were not observed in the spectra obtained by the RCM due to the limitations already discussed. Therefore, the DWM-II has an advantage over the RCM of measuring intrinsic current fields since it is relatively unaffected by waves.

Figures 6 (a) and (b) show the comparison of the tide level measurements obtained by a tide gage and estimates from the ultrasonic wave data and pressure data of the DWM-II, respectively. Three minute long ultrasonic measurements were made of the mean free surface every two hours at a sampling frequency of 2 Hz. The tide level was obtained by averaging each record. Pressure samples were obtained with the same sampling scheme. Corrections, with respect to the atmospheric pressure measured about 30km away from the observation site, were made to the tide level estimated by the pressure data. Both figures show high correlation.

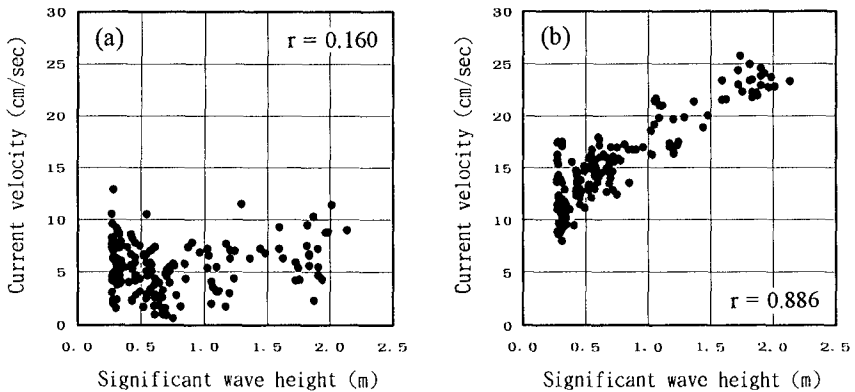


Figure 4 Significant Wave Height and Current Velocity Correlation Measured by the DWM- II (a) and the RCM (b)

Furthermore, **Figure 7** shows the relationship between the atmospheric pressure obtained from a barometer 30km away and the estimated atmospheric pressure from the DWM-II. Since the DWM-II pressure sensor measures the combined atmospheric pressure and hydrostatic pressure, the atmospheric pressure can be obtained by taking the difference between ultrasonic tide level data (hydrostatic pressure) and total pressure data. As seen in this figure, there was considerably high correlation. The fact that the atmospheric pressure can be estimated by the DWM-II, with a high degree of accuracy, further demonstrates the high quality of water surface elevation and water pressure data obtained by the DWM-II.

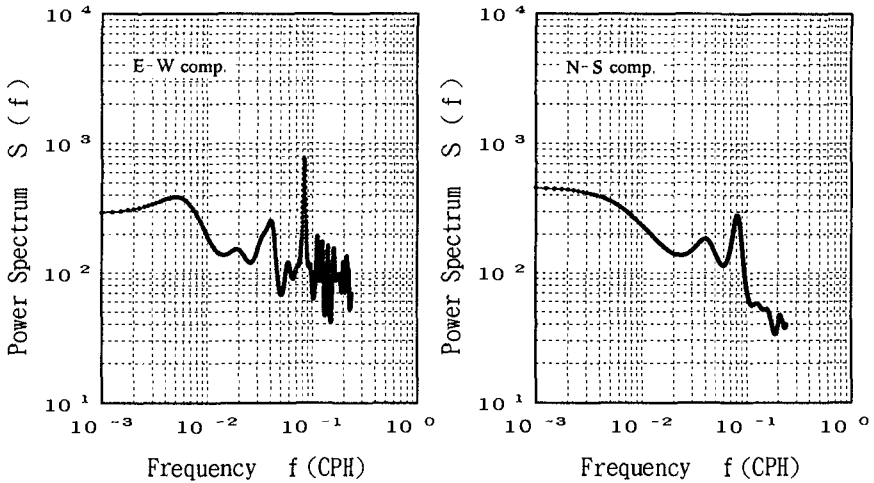


Figure 5 Spectra of the East-West and North-South Current Velocity Components measured by the DWM-II

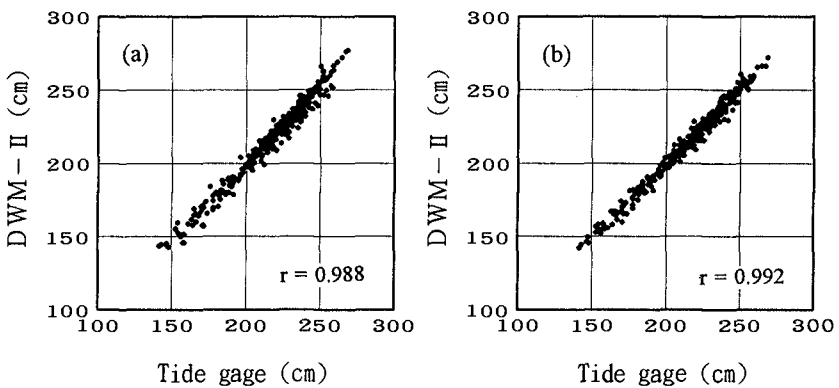


Figure 6 Comparison of Tide Level Measurements

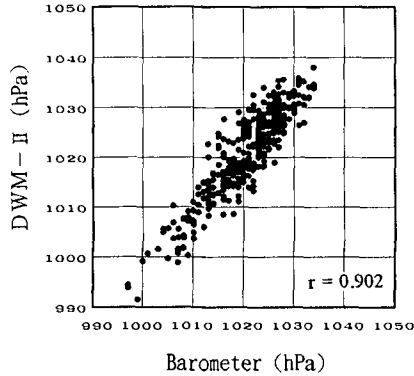


Figure 7 Comparison of Atmospheric Pressure Measurements

5. Proposed Techniques for Improving the Performance of the DWM-II

During this study to enhance the performance of the DWM-II, some new techniques have been introduced to mitigate some of its shortcomings. These techniques are presented in the following three sections.

5.1 Estimation of the Principal Wave Direction With Covariances

A disadvantage of measuring directional seas using wave arrays is that waves with lengths L less than two times the minimum separation distance, D_{\min} , of the array can not be analyzed to produce a directional spectrum. That is, if we wish to analyze waves of length L , the requirement of $2D_{\min} \leq L$ must be satisfied. However, if we measure x - and y -components such as (u, v) or (η_x, η_y) related to random wave motions in the same location, we can estimate the representative wave direction using the covariance method described below without being subjected to the above restriction on array spacing.

Longuet-Higgins defined the principal wave direction θ_p as the direction along which the root-mean-square (RMS) wave number is the largest or the wave crests are the densest. This can be expressed by the following relationship:

$$\theta_p = \frac{1}{2} \tan^{-1} \frac{2M_{11}}{M_{20} - M_{02}} \quad (1)$$

where the spectral moment M_{pq} of equation (1) can be evaluated by the following equation:

$$M_{pq} = \int_0^\infty \int_{-\pi}^\pi S(f, \theta) k^{p+q} \cos^p(\theta) \sin^q(\theta) d\theta df \quad (2)$$

The spectral moment defined by equation (2) can be alternatively evaluated with the covariance between the time series of several wave motion parameters (Goda, 1982).

By using covariances such as $\overline{u^2}$, $\overline{v^2}$, and \overline{uv} , the principal wave direction can be defined by:

$$\theta_p = \frac{1}{2} \tan^{-1} \frac{2\overline{uv}}{\overline{u^2} - \overline{v^2}} \tag{3}$$

The i -th water particle velocity component U_i measured by the DWM-II is expressed by:

$$U_i = a_i u + b_i v + c_i w \tag{4}$$

where u , v , and w are the orthogonal components of the water particle velocities at the measuring location U_i and a_i , b_i and c_i are the coefficients expressed by the following equations:

$$\left. \begin{aligned} a_i &= \sin \alpha_i \cos \beta_i \\ b_i &= \sin \alpha_i \sin \beta_i \\ c_i &= \cos \alpha_i \end{aligned} \right\} \tag{5}$$

where α_i , and β_i are the angles shown in **Figure 8**. Then the covariance of U_i is expressed by:

$$\overline{U_i^2} = a_i^2 \overline{u^2} + b_i^2 \overline{v^2} + c_i^2 \overline{w^2} + 2a_i b_i \overline{uv} + 2b_i c_i \overline{vw} + 2a_i c_i \overline{uw} \tag{6}$$

That is, the covariance $\overline{U_i^2}$ is expressed by the six independent covariances such as $\overline{u^2}$, $\overline{v^2}$, \dots , \overline{uw} . From the linear wave theory, however,

$$\overline{uw} = \overline{vw} = 0 \tag{7}$$

Therefore, Equation (6) reduces to;

$$\overline{U_i^2} = a_i^2 \overline{u^2} + b_i^2 \overline{v^2} + c_i^2 \overline{w^2} + 2a_i b_i \overline{uv} \tag{8}$$

In addition to equation (8), since the DWM-II measures free surface displacement $\eta(t)$, the covariances $\overline{w^2}$ can be estimated with the linear wave theory by the following equation:

$$\overline{w^2} = \int_0^\infty S_w(f) df = \int_0^\infty |H_w(f)|^2 S_\eta(f) df \tag{9}$$

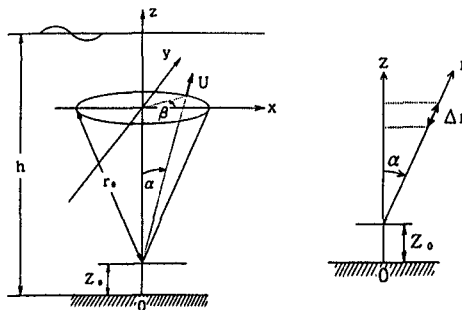


Figure 8 Definition of Coordinate System

where $S_w(f)$ is the power spectrum of the vertical component of water particle velocity $w(t)$, $S_\eta(f)$ is the power spectrum of the free surface displacement $\eta(t)$ and $H_w(f)$ is the transfer function from $w(t)$ to $\eta(t)$.

Finally, the following simultaneous equations, with respect to the unknown values $\overline{u^2}$, $\overline{v^2}$ and \overline{uv} can be obtained:

$$\begin{pmatrix} a_1^2 & b_1^2 & 2a_1b_1 \\ a_2^2 & b_2^2 & 2a_2b_2 \\ a_3^2 & b_3^2 & 2a_3b_3 \end{pmatrix} \begin{pmatrix} \overline{u^2} \\ \overline{v^2} \\ \overline{uv} \end{pmatrix} = \begin{pmatrix} \overline{U_1^2 - c_1^2 w^2} \\ \overline{U_2^2 - c_2^2 w^2} \\ \overline{U_3^2 - c_3^2 w^2} \end{pmatrix} \tag{10}$$

By solving this set of simultaneous linear equations, the principal wave direction can be determined from the definition of Equation (3).

By using these techniques and measuring the water particle velocities, the DWM-II can estimate the principal wave direction, θ_p , even in calm sea conditions.

This means that even in short wave environments the principal wave direction can be estimated without being restricted by the minimum array spacing requirement. **Figure 9** shows examples of the comparison of the estimated principal wave directions (solid vertical line) and the directional spectra. It can be seen that the estimated principal wave directions compare favorably with the peak energy direction of the directional spectra.

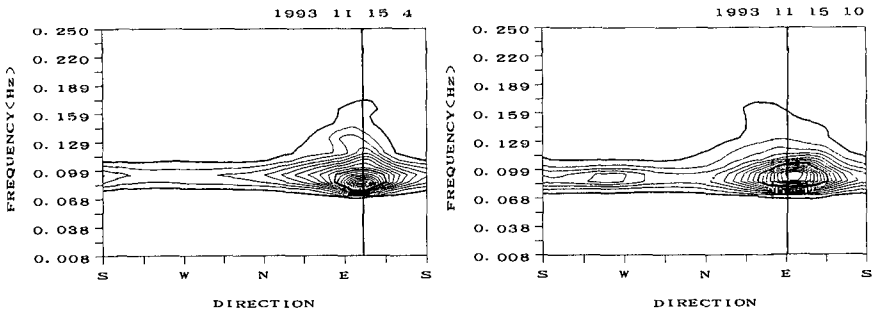


Figure 9 Principal Wave Direction (solid line) and the Directional Spectrum Measured by the DWM- II

5.2 Surface wave Recovery From Subsurface Pressure Records

A disadvantage of utilizing ultrasonic waves in water is that they are severely scattered and absorbed by bubbles when the free surface is disturbed by strong winds or breaking waves. To overcome this limitation, the DWM-II measures pressure as an auxiliary parameter. A proper transformation can be performed to obtain surface wave information from subsurface pressure records. Although many researchers have

gone to great lengths to investigate the possibility of generating surface wave information from subsurface pressure records, and many methods have been proposed to date, almost all of the existing methods are supplemented with various empirical corrections.

Recently, we investigated the relationship between surface waves and subsurface pressure records in detail on the basis of weakly nonlinear directional wave theory. From this investigation we were able to propose a practical method to recover surface wave information by utilizing the shape of the subsurface pressure records. The use of directional spectra information is not required for this new method. This method can be applied for the recovery of surface waves by the DWM-II. The details of these techniques will appear in a paper soon to be published but an outline of this research and methods is presented below.

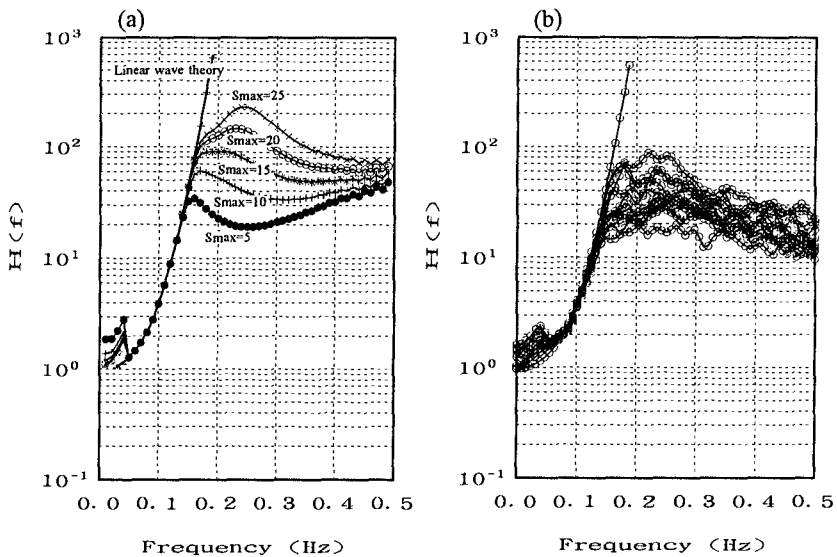


Figure 10 Examples of Theoretical (a) and Observed (b) Transfer Functions $H(f)$ in Water Depth of 50 Meters

Figures 10 (a) and (b) show examples of theoretical and observed transfer functions, $H(f)$, respectively, given by the square root of the ratio $S_{\eta}(f)/S_p(f)$ where $S_{\eta}(f)$ is the power spectrum of the water surface elevation and $S_p(f)$ is that of the subsurface pressure. Note the favorable comparison between the theoretical and observed transfer functions. The Bretschneider-Mitsuyasu type power spectrum and Mitsuyasu type directional spreading function are assumed for the directional spectrum of linear waves. As seen in the figures, the transfer function shows peculiarity in its lower and higher frequency ranges. The characteristics of the transfer functions in those ranges are dependent on the angular spreading parameter,

S_{\max} , of the directional spectrum and can be successfully explained on the basis of weakly nonlinear directional wave theory. This is due to the fact that k is a vector and ω is a scalar. That is to say, the second order nonlinear effect is a function of the wave propagation direction of each linear component wave. Therefore, accurate surface wave recovery, including the high frequency range, requires information of the directional spectrum. The wider the angular spreading function becomes, the greater the difference between the transfer function of the linear wave theory and that of the weakly nonlinear directional wave theory. However, by properly analyzing the shape of the subsurface pressure spectrum, sufficient information can be obtained to accurately recover the surface waves without obtaining the surface directional spectrum.

The proposed method is quite reliable for estimating a wide range of wave heights and periods for both calm and severe sea states.

5.3 Surface Wave Recovery from Current Velocity Component Records

In addition to recovering surface waves from subsurface pressure records, the DWM-II is capable of measuring surface waves, without obtaining information about the free surface displacement, $\eta(t)$, by properly transforming current velocities at several layers. This is useful since quite frequently, the ultrasonic waves used for measuring $\eta(t)$ are scattered and absorbed by bubbles at the surface.

The DWM-II can estimate the directional spreading function, $G(\theta|f)$, from a set of three current velocities, $U_1(t)$, $U_2(t)$ and $U_3(t)$ without information about the free surface displacement, $\eta(t)$.

$$G(\theta|f) = \frac{\kappa}{H^* \Phi^{-1} H} \quad (11)$$

where κ is a proportionality constant ensuring that $G(\theta|f)$ satisfies

$$\int_{-\pi}^{\pi} G(\theta|f) d\theta = 1 \quad (12)$$

H is the matrix comprised of the transfer functions from the i -th current velocity, $U_i(t)$, to the free surface displacement, $\eta(t)$, and is given by:

$$H_{U_i} = \frac{-i\omega \exp(-i\omega\Delta t)}{\Delta r k \sinh kh} \left[\cosh\{k(r \cos\alpha_i + z_0)\} \right. \\ \left. \times \exp\{ikr \sin\alpha_i \cos(\theta - \beta_i)\} \right]_{r_0 - \Delta r/2}^{r_0 + \Delta r/2} \quad (13)$$

Here α_i , β_i , and r_0 are the coordinates of the i -th current velocity from the coordinate system (α, β, r) shown in **Figure 8** and Δr is the "thickness" of the water volume shown in **Figure 8**. The DWM-II detects the current velocity, $U_i(t)$, by taking the average velocity of the water volume defined by α_i , β_i , and Δr . The water depth, wave number, angular frequency, wave propagation direction, and height at which the meter is situated above the seabed are represented by h , k , ω , θ and z_0 , respectively.

The time lag between the measurement of each velocity component and that of the water surface elevation is designated by Δt . Φ^{-1} is the inverse matrix of Φ consisting of the cross-spectra between each current velocity, $U_i(t)$;

$$\Phi = \begin{pmatrix} \phi_{U_1U_1} & \phi_{U_1U_2} & \phi_{U_1U_3} \\ \phi_{U_2U_1} & \phi_{U_2U_2} & \phi_{U_2U_3} \\ \phi_{U_3U_1} & \phi_{U_3U_2} & \phi_{U_3U_3} \end{pmatrix} \tag{14}$$

Equation (11) is the formula used to estimate the directional spreading by the Extended Maximum Likelihood Method (EMLM-Isobe, et al., 1984). Other methods such as the Bayesian Directional spectrum estimation Method (BDM-Hashimoto and Kobune, 1987) and the Extended Maximum Entropy Principle (EMEP-Hashimoto, et al., 1994) can also be applied to estimate the directional spreading function $G(\theta|f)$.

Using $G(\theta|f)$ as estimated by Equation (11), the power spectrum $S_\eta(f)$ of the free surface displacement, $\eta(t)$, can be estimated by:

$$S_\eta(f) = \Phi_{U_iU_j}(f) / \int_{-\pi}^{\pi} H_{U_i} H_{U_j} G(\theta|f) d\theta \quad (i = 1, 2, 3) \tag{15}$$

Multiplying $G(\theta|f)$ and $S_\eta(f)$ yields the directional spectrum $S(f, \theta)$,

$$S(f, \theta) = S_\eta(f) G(\theta|f) \tag{16}$$

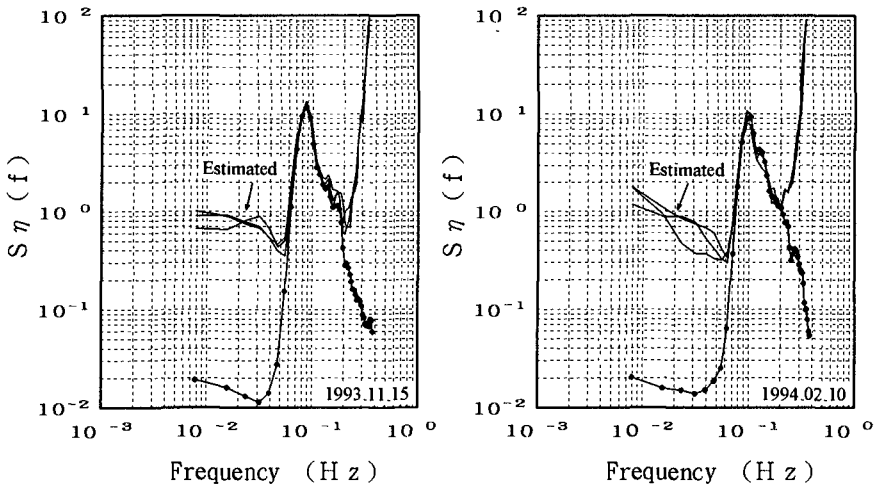


Figure 11 Power Spectra of Free Surface Displacement

Figure 11 shows a comparison between the surface elevation power spectrum measured directly by the ultrasonic waves (indicated by a dotted line) and that obtained from the multiple current velocity components using Equation (15) (indicated by the three thin lines).

Although three power spectra can be estimated from Equation (15), by using $i=1,2,3$, all of the estimated power spectra show good agreement with the power spectrum measured by the ultrasonic waves around the spectral energy peak.

Figure 12 (a) shows a typical directional spectrum estimated by the EMLM where all of the measured quantities, $\eta(t)$, $U_1(t)$, $U_2(t)$, $U_3(t)$ were used to estimate the directional spectrum. **Figure 12 (b)** shows the directional spectrum for the same sea conditions estimated from the three current velocities, $U_1(t)$, $U_2(t)$, $U_3(t)$, using the present method without knowledge of the free surface displacement, $\eta(t)$. It can be seen that the two spectra compare favorably. The entrance of the experimental observation site faces East and the results clearly show that the waves propagate from the appropriate direction.

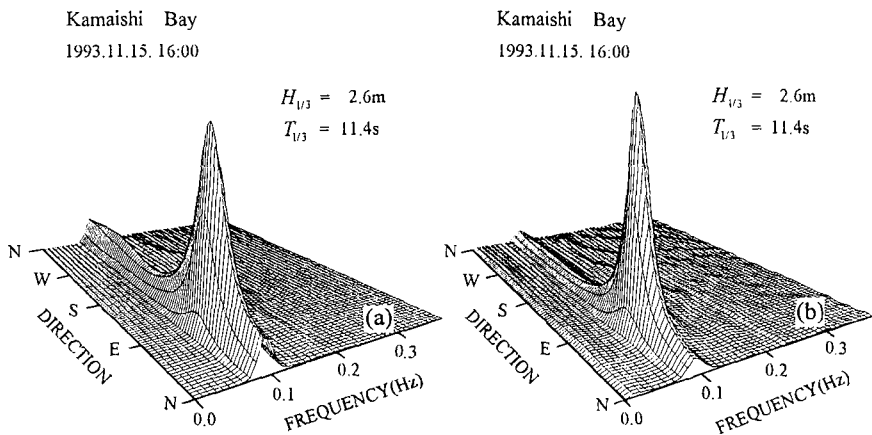


Figure 12 Estimated Directional Wave Spectra

Conclusions

Adequate knowledge of sea conditions is essential for clarifying various coastal engineering problems. Difficulties in measuring actual sea conditions, however, have resulted in a lack of critical information. Since the DWM-II can be employed to provide accurate information on directional waves, as well as currents and tides, with only one instrument, it is considered to be one of the most useful measuring systems for conducting research on actual sea conditions. By using techniques introduced in this paper, the auxiliary parameters of the DWM-II can be used to improve its performance. The DWM-II will contribute to increasing the reliability of long-term observations, especially in severe sea states, and will, therefore, lead to the enrichment of our knowledge of realistic sea conditions.

Acknowledgments

This research was jointly carried out by the Port and Harbour Research Institute, Ministry of Transport, and Japan Marine Surveyors Association under the direction of the Committee for the Development of a Submerged Doppler-Type Directional Wave Meter (Chairman, Professor Y. Goda, Yokohama National University) organized by Japan Marine Surveyors Association. The analyzed field wave data were contributed by the Second Port Construction Bureau, Ministry of Transport. Sincere gratitude is extended to all those involved in this study. We also wish to thank Sidney W. Thurston III, National Sea Grant Fellow of NOAA, who kindly gave us many valuable comments on this research work.

References

- Goda, Y., K. Miura and K.Kato (1982): On-Board analysis of mean wave direction with discus buoy, Int. Conf. Wave and Wind Directionality, Paris, Editions Technip, pp.339-359.
- Hashimoto, N. and K. Kobune (1988): Directional spectrum estimation from a Bayesian approach, Proc. 21st ICCE, Spain, Vol. 1, pp. 62—76.
- Hashimoto, N, T. Nagai, K. Sugahara, T. Asai and K. S. Bahk (1993): Surface wave recovery from subsurface pressure record on the basis of weakly nonlinear directional wave theory, Rept. of the Port and Harbour Res. Inst., Vol. 31, No.1, pp.27-51 (in Japanese).
- Hashimoto, N., T. Nagai, and T. Asai (1994): Extension of the maximum entropy principle method for directional wave spectrum estimation, Proc. 24th ICCE, Kobe, Vol. 1, pp. 232—246.
- Isobe, M., K. Kondo and K. Horikawa (1984): Extension of MLM for estimating directional wave spectrum, Proc. Symp. on Description and Modeling of Directional Seas, Paper No. A-6, 15 p.
- Takayama, T., N. Hashimoto, T. Nagai, T. Takahashi, H. Sasaki and Y. Ito (1994): Development of a submerged Doppler-type directional wave meter, Proc. 24th ICCE, Kobe, Vol. 1, pp. 624—634.

CHAPTER 51

COMPARISON OF DIRECTIONAL WAVE DATA QUALITY FROM TWO DIFFERENT MONITORING SYSTEMS

Lihwa Lin¹, Sidney Schofield², and Hsiang Wang³

ABSTRACT

A simple criterion was derived for evaluation and comparison of directional wave data quality from two underwater measuring systems – a point gage system consisting of a pressure transducer and a bi-axial current meter (PUV gage), and a slope array consisting of four pressure transducers. By using this criterion to the measured field data, it was demonstrated that directional wave data analyzed from PUV gage contain absolutely better quality than those from pressure array gages. Further examination of the pressure array data alone showed that the resolved directional wave quality was worse for long waves than short waves. However, the flaw of directional wave data quality from pressure array gages can be mended by forcing simple linear corrections on the analyzed directional data with a maximal tolerance to the criterion introduced in the present study.

1. INTRODUCTION

Directional wave data have been used widely in many coastal planning, designing, and operating projects. The data can be obtained from several sources: (1) measured directly in the coastal water, (2) measured at ocean and carried in numerically to the coastal area, (3) hindcast data, and (4) imitated data by numerical simulation. With no doubt, the measured directional data should be more representable to the real sea waves than the data from other sources. However, the usefulness of the measured directional data relies primarily on the quality and accuracy of the data being collected and analyzed.

Three basic types of measuring systems have been utilized today in finding directional wave information. They are: (1) a point gage system which will either measure the temporal changes of water surface slope in two horizontal principle directions, e.g., a pitch/roll buoy, or those of underwater horizontal wave orbital

1) Research Scientist, 2) Associate Engineer, 3) Professor, Dept. of Coastal and Oceanographic Engineering, University of Florida, Gainesville, FL 32611, USA.

velocity vectors, e.g., a biaxial current meter, (2) a slope array which measures the spacial changes of water surface elevations in several cross directions, and (3) casting images by remote sensing. In general, the first two systems are more applicable in the offshore area while the last one is useful in the nearshore area. In terms of the analysis, a directional wave spectrum is usually estimated based on a truncated Fourier series solved from the measured data. Nonetheless, this estimated directional spectrum presents only a limited directional information since a true spectrum shall include an infinite long Fourier series.

Comparison of directional wave data collected from different measuring systems is essential in order to know if the data quality is influenced by a particular instrumental system. Carrying out this comparison, however, can be difficult without clear criteria or standards to evaluate the data. A recent study by Corson and McKinney (1991), who compared the analyzed directional spectra from three different monitoring systems including a PUV gage, a slope array, and an ocean buoy, has addressed the difficulty of comparing the measured spectra without knowing the true spectrum.

The present study evaluates and compares the quality of directional wave data analyzed from two underwater measuring systems – a point gage consisting of a pressure transducer and a bi-axial current meter (PUV gage), and a slope array consisting of four pressure transducers. Evaluating directional wave data quality was carried out by examining the Fourier coefficients which are used to estimating a directional spectrum rather than a simple inspection of the spectrum itself.

2. BACKGROUND THEORY

A general but unique expression of directional spectrum, $E(f, \phi)$, is

$$E(f, \phi) = E(f)H(f, \phi), \quad (f = \text{frequency}, \phi = \text{direction})$$

where $E(f)$, the one-dimensional frequency spectrum, and $H(f, \phi)$, a directional distribution function, satisfy the following conditions:

$$E(f) = \int_0^{2\pi} E(f, \phi) d\phi; \quad \int_0^{2\pi} H(f, \phi) d\phi = 1, \quad \text{and} \quad H(f, \phi) \geq 0.$$

In terms of a Fourier Series,

$$H(f, \phi) = \frac{1}{\pi} \left[\frac{1}{2} + \sum_{n=1}^{\infty} a_n(f) \cos n\phi + \sum_{n=1}^{\infty} b_n(f) \sin n\phi \right],$$

where $a_n(f) = \int_0^{2\pi} H(f, \phi) \cos n\phi d\phi$, $b_n(f) = \int_0^{2\pi} H(f, \phi) \sin n\phi d\phi$

define the dimensionless, frequency-dependent Fourier coefficients.

It can be easily proved that $|a_n(f)| \leq 1$ and $|b_n(f)| \leq 1$ by using the facts of $|\cos n\phi| \leq 1$, $|\sin n\phi| \leq 1$, and integrating the quantities of $H(f, \phi) \cos n\phi$ and $H(f, \phi) \sin n\phi$, respectively, over the entire directional domain of $|\phi| \leq \pi$. However, a more rigid constraint on $a_n(f)$ and $b_n(f)$ also exists as a consequence of that $a_n(f)$ is related to $b_n(f)$ through the extant of $H(f, \phi)$. Since $(\cos n\phi \pm \sin n\phi)^2 = 1 \pm \sin 2n\phi \leq 2$, or $|\cos n\phi \pm \sin n\phi| \leq \sqrt{2}$, it can be shown by first multiplying $H(f, \phi)$ to both sides and then integrating over entire ϕ domain that

$$(i) \quad |a_n(f) \pm b_n(f)| \leq \sqrt{2}.$$

Now, for any real numbers of a and b , there is a binomial inequality:

$$-(a - b)^2 \leq 4ab \leq (a + b)^2.$$

Let $a = a_n(f)$, $b = b_n(f)$, and use the result from (i), it is further shown that

$$(ii) \quad |a_n(f)b_n(f)| \leq \frac{1}{2}.$$

Combining the results in (i) and (ii), and using the fact that $a_n(f)$ and $b_n(f)$ are resemblant in functional form, yields

$$(iii) \quad a_n^2(f) + b_n^2(f) \leq 1.$$

3. EVALUATION OF $a_n(f)$ AND $b_n(f)$ COEFFICIENTS

The methods used in evaluating $a_n(f)$ and $b_n(f)$ coefficients are different for the data collected by the PUV gage system and pressure array gages. Since these methods have been well developed and documented in the past, only the results from these methods are summarized here.

3.1 Submerged PUV Gage(1 pressure transducer and 1 biaxial currentmeter)Data

Based on a standard stochastic approach, only the first 2 pairs of $a_n(f)$ and $b_n(f)$ can be determined from the PUV data (Cartwright, 1963; Long, 1980):

$$a_1(f) = \frac{R_{pu}(f)}{\sqrt{R_{pp}(f)[R_{uu}(f) + R_{vv}(f)]}}, \quad b_1(f) = \frac{R_{pv}(f)}{\sqrt{R_{pp}(f)[R_{uu}(f) + R_{vv}(f)]}},$$

$$a_2(f) = \frac{R_{uu}(f) - R_{vv}(f)}{R_{uu}(f) + R_{vv}(f)}, \quad b_2(f) = \frac{2 R_{uv}(f)}{R_{uu}(f) + R_{vv}(f)},$$

where $R_{xy}(f)$ is the measured cospectrum of the random variables of $X(t)$ and $Y(t)$. The subscripts p , u , and v are corresponding to the measurements of underwater dynamic pressure, and two orthogonal horizontal wave orbital velocity components, respectively.

3.2 Submerged Pressure Transducer Array Data

By means of a standard stochastic approach, the cross spectrum of simultaneous measurements of water surface elevation from two horizontally spaced gages can be expressed as (Borgman, 1969)

$$\begin{aligned} E_{1,2}(f) &= R_{1,2}(f) + iQ_{1,2}(f) = \int_0^{2\pi} E(f, \phi) \exp[ikD_{1,2} \cos(\phi - \beta_{1,2})] d\phi \\ &= E(f) \{ J_0(kD_{1,2}) + 2 \sum_{n=1}^{\infty} [a_n(f) \cos n\beta_{1,2} + b_n(f) \sin n\beta_{1,2}] (i)^n J_n(kD_{1,2}) \}, \end{aligned}$$

where $i = \sqrt{-1}$ denotes the imaginary unit, k is the wave number, $Q_{1,2}(f)$ is the quadrature spectrum presenting the imaginary part of $E_{1,2}$, $D_{1,2}$ is the distance between two gages 1 and 2, $\beta_{1,2}$ is the angle of the vector from Gages 1 to 2, and

$$J_n(z) = \frac{1}{\pi(i)^n} \int_0^\pi \exp[iz \cos \phi] \cos n\phi d\phi$$

is the Bessel function of the first kind of order n . For N gages, a total of $2(N, 2) = N(N-1)$ equations are available for evaluation of $a_n(f)$ and $b_n(f)$ coefficients. These equations are

$$\begin{aligned} \frac{R_{jm}}{E(f)} &= J_0(kD_{jm}) + 2 \sum_{n=1}^M (-1)^n J_{2n}(kD_{jm}) [a_{2n}(f) \cos 2n\beta_{jm} + b_{2n}(f) \sin 2n\beta_{jm}], \\ \frac{Q_{jm}}{E(f)} &= 2 \sum_{n=1}^M (-1)^{n-1} J_{2n-1}(kD_{jm}) [a_{2n-1}(f) \cos(2n-1)\beta_{jm} + b_{2n-1}(f) \sin(2n-1)\beta_{jm}], \end{aligned}$$

where $j, m = 1, 2, \dots, N$, $j \neq m$ and $M = N(N-1)/4$. Here, M is the total number of pairs or harmonics of $a_n(f)$ and $b_n(f)$ existing in the above equations. This method of evaluating $a_n(f)$ and $b_n(f)$ is also valid on the source data from submerged pressure measurements instead of water surface elevations by calculating the cross spectrum and one-dimensional frequency spectrum from the measured pressure data.

In practice, it is preferable to solve $a_n(f)$ and $b_n(f)$ less than M harmonics. This is because that solving a finite number of $a_n(f)$ and $b_n(f)$ from a set of cross spectrum equations can be contaminated by the possible existence of directional wavelets higher than M harmonics. The contamination is deemed to be more severe to $a_n(f)$ and $b_n(f)$ with higher harmonics than lower harmonics being solved from the cross spectrum equations. Now, to solve for a less number of $a_n(f)$ and $b_n(f)$ than M harmonics, a least squared method can be used. This is the case of solving $\{x\}$ in the matrix system of $[A]_{m \times n} \cdot \{x\}_{n \times 1} = \{y\}_{m \times 1}$, with $m > n$ (more equations than unknowns). Utilization of a least squared method, which minimizes the quantity of $\|[A]\{x\} - \{y\}\|^2$, leads to the solution:

$$\{x\} = ([A]^T[A])^{-1} \cdot ([A]^T\{y\}), \text{ where } [A]^T = \text{the transpose of } [A].$$

Table 1: Coastal wave monitoring stations (1995).

Station	Depth(m)	Gage Type	Operating Period
Cape Canaveral	8.5	PUV P-array	Oct.,Nov. Feb.-Apr.
Palm Beach	3.5	PUV	Apr.-Jun.
Miami	6.5	PUV P-array	May-Jun. Jan.,Feb.,Apr. Nov.-Dec.

4. FIELD EXPERIMENTS

Wave data for use in the present study were measured from a number of PUV gages and pressure transducer arrays deployed in three coastal stations at Cape Canaveral, Palm Beach, and Miami Beach, Florida, in 1995. The data were collected four times daily, each containing a 20-minutes of measurements with a sampling rate of 1 Hz. The employed PUV gage is a submerged point gage system consisting of a pressure transducer and a bi-axial current meter. The slope array consists of four pressure transducers fixed by an aluminum tripod anchored on the sea floor. The geometry of the slope array is an equilateral triangle with one pressure transducer located at the center and three others at each corner of the triangle. This slope array setup is known as the star array geometry using four pressure transducers. The distances between the center and side transducers, and between any two side transducers, are 2m and 3.4m, respectively (Figure 1). Figure 2 shows the locations of wave monitoring stations and Table 1 lists the water depth, type of gage, and operating period of the stations.

5. COMPARISON OF DIRECTIONAL WAVE QUALITY

Directional wave data quality from both PUV and slope array data measurements was evaluated by examining $a_n(f)$ and $b_n(f)$ which are used in the estimation of directional spectrum rather than a simple inspection of the spectrum itself. The comparison of directional data quality is carried out for $a_1(f)$, $b_1(f)$, $a_2(f)$, and $b_2(f)$, based on the criterion of $a_n^2(f) + b_n^2(f) \leq 1$ shown earlier in Condition (iii). Table 2 presents a summary of the result of evaluation and comparison of these data. It is seen that directional data obtained from a PUV gage have absolutely better quality than those from a slope array. The worse quality of the latter is caused by the aliasing of higher directional wave modes to a finite number of $a_n(f)$ and $b_n(f)$ solved based on the slope array data. Figure 3 shows the histograms of directional data quality, based on the data satisfying the criterions of $a_1^2(f) + b_1^2(f) \leq 1$ and $a_2^2(f) + b_2^2(f) \leq 1$ over the frequency domain of $0 \leq f \leq 0.32$ Hz, for all the slope array data collected from Cape Canaveral and

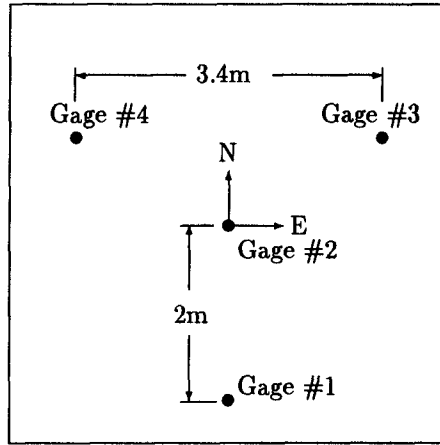


Figure 1: The star array geometry of 4 pressure gages.

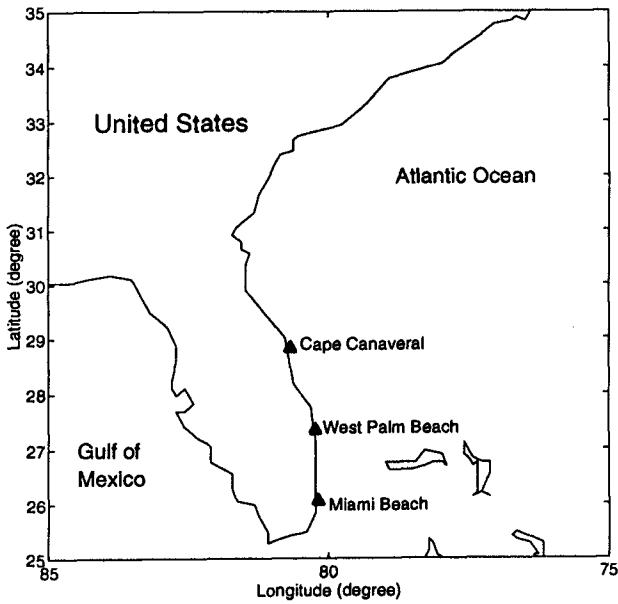


Figure 2: Location of field wave monitoring stations.

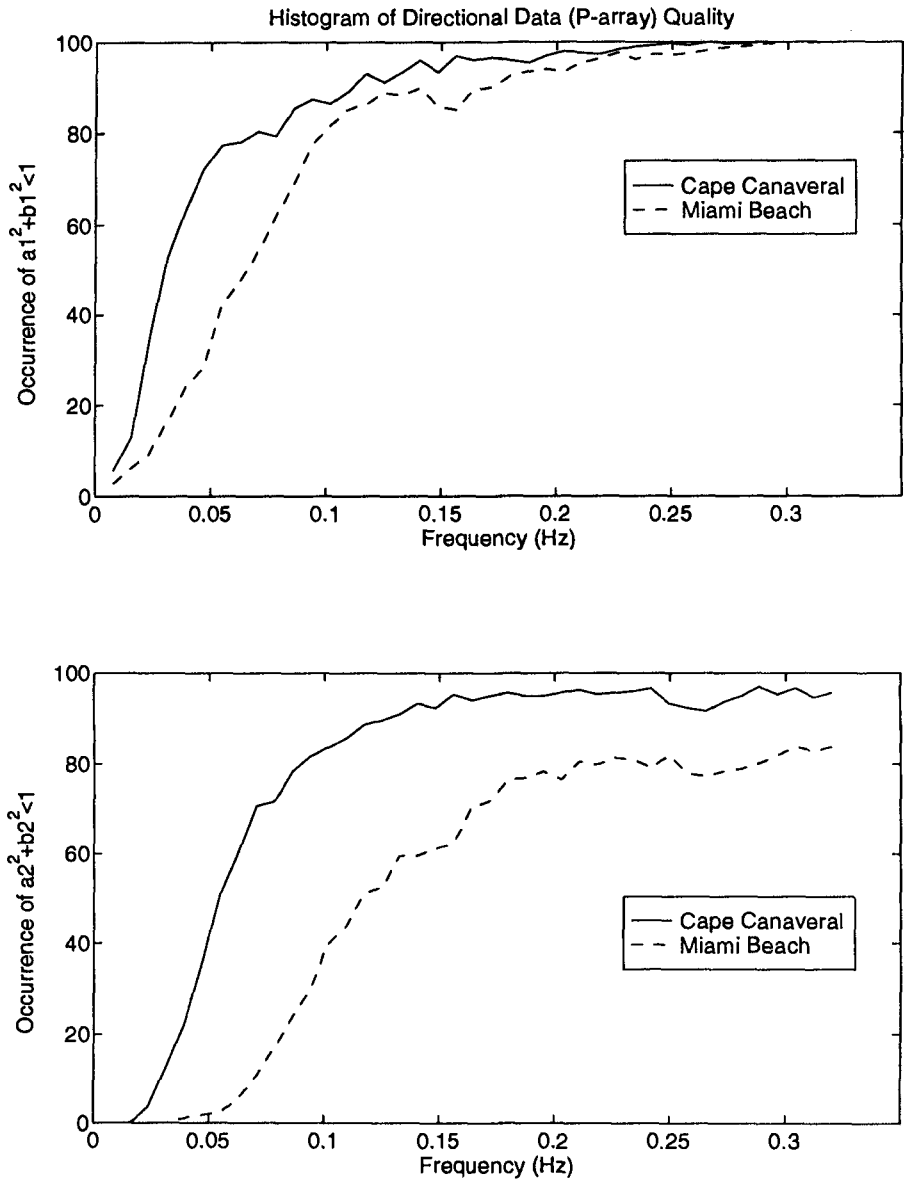


Figure 3: Histograms of directional wave data quality versus frequency.

Table 2: Comparison of directional data quality based on $a_n^2(f) + b_n^2(f) \leq 1, n = 1, 2.$

Month (1995)	Percent of Data Passing Criterion				
	Cape Canaveral		Palm Beach	Miami Beach	
	P-Array	PUV	PUV	P-Array	PUV
Jan.				58 %	
Feb.	87 %			52 %	
Mar.	88 %				
Apr.	86 %		100 %	83 %	
May			100 %		100 %
Jun.			100 %		100 %
Oct.		100 %			
Nov.		100 %		64 %	
Dec.				51 %	
Summary	87 %	100 %	100 %	62 %	100 %

Miami Beach stations. The analyzed results of slope array data show that $a_2(f)$ and $b_2(f)$ have much worse quality than $a_1(f)$ and $b_1(f)$. The results further indicate that all of these coefficients, regardless of $a_1(f)$, $b_1(f)$ or $a_2(f)$, $b_2(f)$, show overall worse quality for longer waves than shorter waves. Therefore, directional wave data quality measured from slope array gages is expected to be worse in shallow water than in deep water.

In fact, the quality of directional data measured from a slope array depends also on the total number of pressure gages employed and displacement geometry of the gages in the array. However, the degree of improvement of directional wave quality from the use of more gages in a slope array will always be affected by the finite number of $a_n(f)$ and $b_n(f)$ solved from the data.

Although the slope array measurements are seen to yield less satisfactory directional data quality, the analyzed data can be modified according to the criterion of $a_n^2(f) + b_n^2(f) \leq 1$ when the criterion is violated. A simple modification is proposed in the present study to multiply a common factor of γ to both $a_n(f)$ and $b_n(f)$ such that

$$(iv) \quad (a_n)' = \beta a_n, \quad (b_n)' = \beta b_n, \quad \beta = \frac{\gamma}{\sqrt{a_n^2 + b_n^2}},$$

where γ has a magnitude between 0 and 1. Again, without knowing the true directional spectrum, it is not possible to find γ . However, it is clear that γ approaching to 1 indicates a narrower directional band while γ approaching to 0

implies a broader directional distribution. Therefore, when Condition (iii) is violated, the sea is likely to have a quite narrower distribution of directional waves and the correction factor of γ shall have a value close to its upper limit of 1. A constant value of $\gamma = 0.99$ has been adopted in the present study for modifying the less perfect directional data quality from the pressure transducer arrays.

An example is presented here comparing the directional spectra analyzed for the data collected at midnight of 95/04/12 by a PUV gage from West Palm Beach station and a pressure transducer array system from Cape Canaveral station. At this particular time, waves may have reached to an equilibrated state under relatively strong winds with consistent magnitude and direction within the interval of ± 12 hrs (Figure 4). Figures 5 and 6 present the computed one-dimensional frequency spectra and Fourier coefficients of $a_1(f)$, $b_1(f)$, $a_2(f)$, $b_2(f)$ from the measured data. It is seen that all of these Fourier coefficients computed from PUV gage data satisfy Criterion (iii) whereas those from pressure transducer array can violate the same criterion. In order to compute the directional spectrum, the coefficients of $a_1(f)$, $b_1(f)$, $a_2(f)$, $b_2(f)$ determined based on the pressure transducer array data were modified according to the equations presented in (iv) if they violate Condition (iii). The computation of directional spectrum is, based on a Maximum Entropy approach (Kim *et al.*, 1993),

$$E(f, \phi) = E(f) \cdot \exp[-\lambda_0 - \lambda_1 \cos \phi - \lambda_2 \sin \phi - \lambda_3 \cos 2\phi - \lambda_4 \sin 2\phi],$$

where λ_i , the Lagrange's multipliers, can be approximated by

$$\lambda_1 = 2a_1a_2 + 2b_1b_2 - 2a_1(1 + a_1^2 + b_1^2 + a_2^2 + b_2^2),$$

$$\lambda_2 = 2a_1b_2 - 2b_1a_2 - 2b_1(1 + a_1^2 + b_1^2 + a_2^2 + b_2^2),$$

$$\lambda_3 = a_1^2 - b_1^2 - 2a_2(1 + a_1^2 + b_1^2 + a_2^2 + b_2^2),$$

$$\lambda_4 = 2a_1b_1 - 2b_2(1 + a_1^2 + b_1^2 + a_2^2 + b_2^2),$$

and

$$\lambda_0 = \ln \left[\int_{-\pi}^{\pi} \exp(-\lambda_1 \cos \phi - \lambda_2 \sin \phi - \lambda_3 \cos 2\phi - \lambda_4 \sin 2\phi) d\phi \right].$$

Figure 7 compares the directional spectra computed based on the PUV and pressure transducer array data. The computed spectra show that the associated wave systems are mainly moving westward against the coastal shore. The comparison shows that the two computed spectra are very similar in size and shape except that the one measured from Cape Canaveral station has the spectral tail twisted more towards NW direction than the spectrum from West Palm Beach station. This twisting in spectral direction is due to the effect of wave refraction in shallow water. The refraction effect is stronger for the spectrum measured at West Palm Beach station where the water depth is much shallower than Miami station.

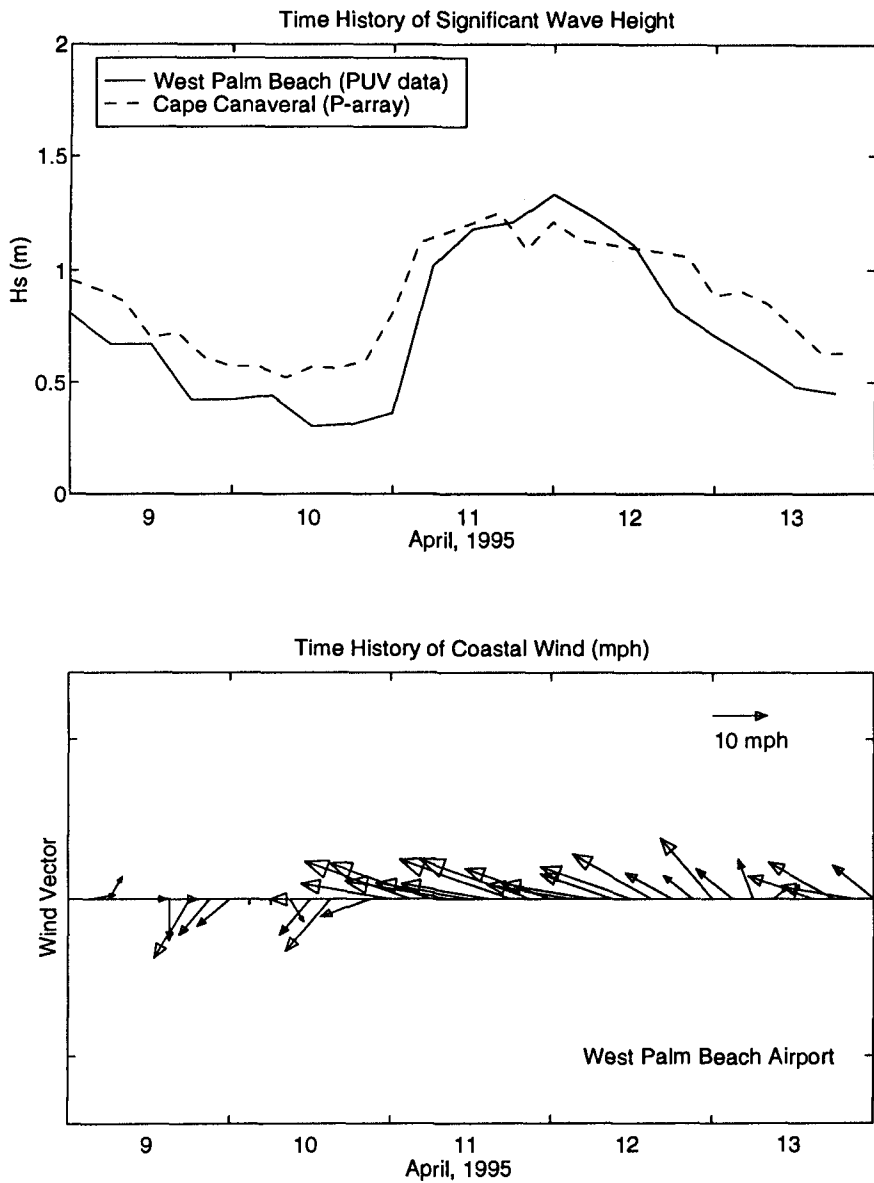


Figure 4: Measured significant wave heights and surface winds.

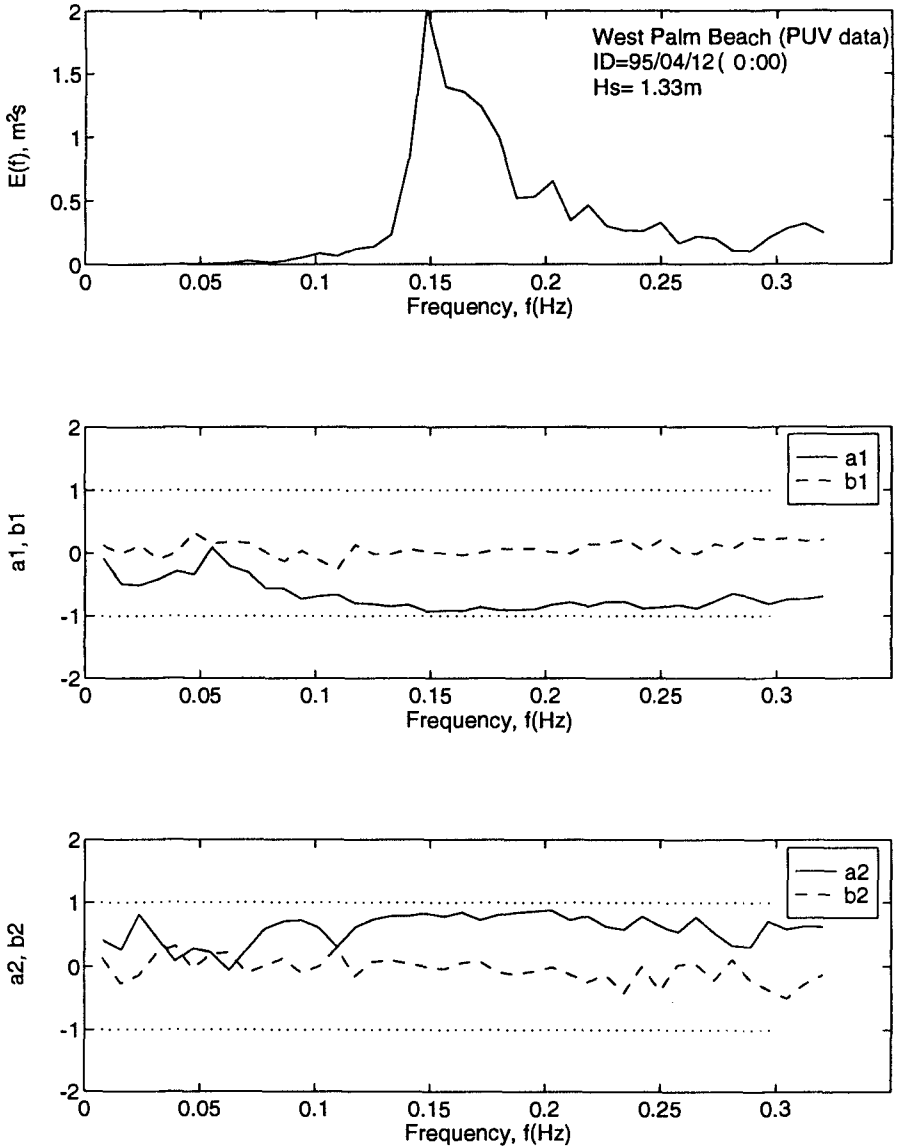


Figure 5: Wave information analyzed from West Palm Beach gage data.

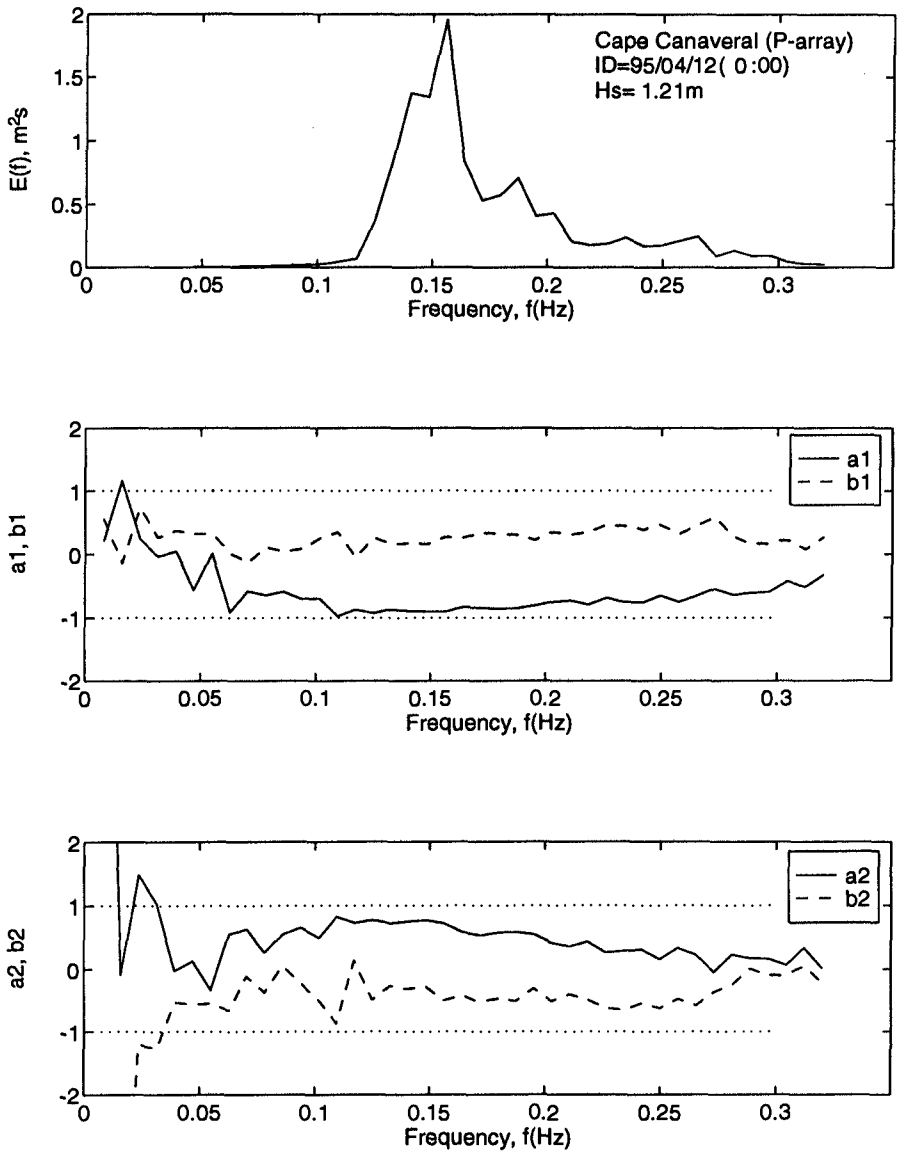


Figure 6: Wave information analyzed from Cape Canaveral gage data.

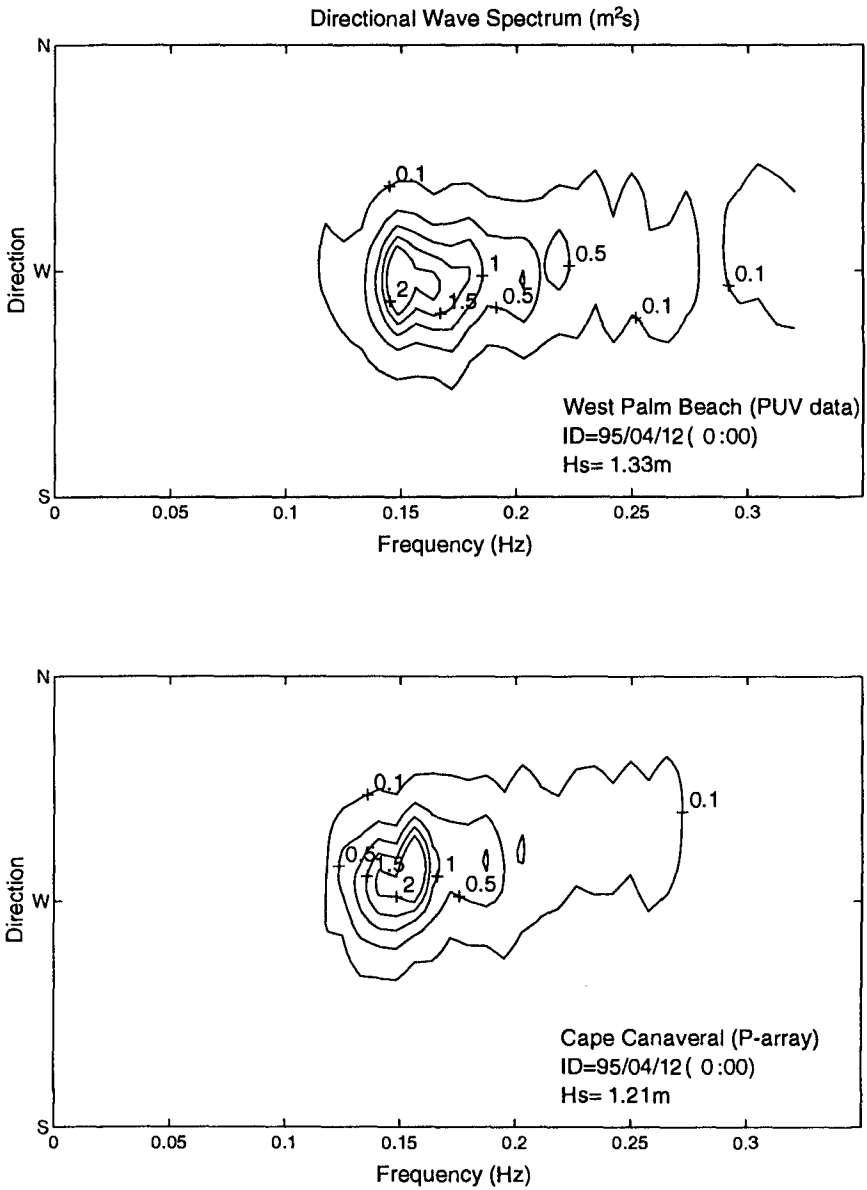


Figure 7: Comparison of analyzed directional wave spectra.

6. CONCLUSION

The conclusion drawn from this study is summarized as follows:

(1) Directional sea wave data need to satisfy the condition:

$$a_n^2(f) + b_n^2(f) \leq 1.$$

(2) The analyzed directional wave data based on PUV measurements show absolutely better quality than those based on P-array data (100% vs 75%), according to the criterion presented in (iii).

(3) The analyzed pressure gage array data show that the coefficients of a_2 , b_2 have much worse quality than a_1 , b_1 . Nevertheless, all of these coefficients show worse quality for longer waves in the range of shallow water condition.

(4) Corrections to the slope array directional wave data from

$$(a_n)' = \beta a_n, \quad (b_n)' = \beta b_n, \quad \text{with } \beta = \frac{\gamma}{\sqrt{a_n^2 + b_n^2}}, \quad \gamma = 0.99$$

have shown to yield directional spectra similar to those from PUV gage data.

REFERENCES

1. Borgman, L.D. 1969. 'Directional Spectra Models for Design Use,' Technical Report, HEL 1-12. Hydraulic Engineering Laboratory, University of California, Berkeley, California.
2. Cartwright, D.E., 1963. 'The Use of Directional Spectra in Studying Output of a Wave Recorder on a Moving Ship,' Ocean Wave Spectra, Proceedings of a Conference, pp.203-218.
3. Corson, W.D., and J.P. McKinney. 1991. 'Summary of Directional Wave Data from 3 Different Monitoring Systems Deployed Offshore of St. Mary's Entrance, Georgia,' Biological and Physical Aspects of Dredging, Kings Bay, Georgia. Seventh Symposium on Coastal and Ocean Management, ASCE, Long Beach, California. pp.132-142.
4. Kim, T, L. Lin, and H. Wang, 1993. 'Comparisons of Directional Wave Analysis Methods,' Waves'93 Ocean Wave Measurement and Analysis, Proceedings of the 2nd International Symposium, New Orleans, Louisiana. pp.554-568.
5. Long, R.B., 1980. 'The Statistical Evaluation of Directional Spectrum Estimates Derived from Pitch/Roll Buoy Data,' Journal of Physical Oceanography, Vol. 10. pp.944-952.

CHAPTER 52

THE DIGITAL SIMULATION OF NON-LINEAR RANDOM WAVES

Kyungmo Ahn *

Abstract

This paper presents the method for the digital simulation of the second-order nonlinear random waves including strongly nonlinear shallow water waves and near breaking waves, which can be considered to be non-Gaussian random process. The method generates time series of the second order nonlinear random waves from the given energy spectrum and bispectrum obtained from the wave records. Numerical examples indicate that the procedure is basically worked well and generated time series of waves having the similar target spectral density function and probability distribution function. The proposed method has a wide range of applicability to problems involving the second-order nonlinear systems where outputs have strongly nonlinear and non-Gaussian characteristics.

Introduction

The time series simulation of nonlinear random waves has many practical applications in many engineering problems. For example, the simulated waves can be used for the analysis of the response of offshore structures excited by irregular waves (Duncan and Drake, 1995) and also can be used as wave-board control signals to generate nonlinear random waves (Klopman and Leeuwen 1990; Yasuda et al. 1994).

For the realistic reproduction of coastal waves, it is necessary to include the effects of the second-order nonlinear waves associated with the sum and difference frequency

* Assistant Professor, School of Construction and Environmental Engineering,
Handong University, 3 Namsong-ri, Pohang, Kyungbuk, 791-940, Korea

components of linear waves. For weakly nonlinear waves, the second-order random wave theory derived from the perturbation method using potential theory can be used to derive formulas for the generation of second-order random waves (Sharma and Dean, 1979; Klopman and Leeuwen 1990). However, the method cannot be used to generate strongly nonlinear waves in shallow water.

Recently, Ochi and Ahn (1994) developed a method to separate bound harmonic wave components from free linear wave components by applying the concept of the bicoherence spectrum. When various spectral components interact with one another due to nonlinearities, the resulting components are phase coherent with the primary components. Therefore, those components are not considered to be statistically independent. The bispectrum, which measures the statistical dependence of three spectral components whose sum frequency is zero, may therefore be a useful tool to investigate the nonlinearities of random waves especially in shallow water waves. By applying the concept of a bicoherent spectrum, it is possible to separate the linear free wave spectral component from the spectrum obtained from the measured wave profile record. Then, by using the separated linear spectrum and bispectrum, we can digitally simulate the strongly non-linear random waves which have the similar stochastic characteristic of the target waves.

Digital Generation of Second-Order Nonlinear Random Waves.

In this paper, a method is presented to generate time series of strongly nonlinear waves from the linear energy spectrum and bispectrum of surface elevation obtained from the wave record. For this, we first write surface profile of second-order random waves in finite water depth as follows:

$$y(t) = \text{Re} \sum_{k=1}^N c_k e^{i(2\pi f_k t + \varepsilon_k)} + \text{Re} \sum_{k=1}^N \sum_{l=1}^N c_k c_l \left[q_{kl} e^{\{2\pi(f_k + f_l)t + (\varepsilon_k + \varepsilon_l)\}} + r_{kl} e^{\{2\pi(f_k - f_l)t + (\varepsilon_k - \varepsilon_l)\}} \right] \quad (1)$$

where f = frequency, ε = phase lag, q_{kl} = wave-wave sum interaction coefficient associated with $f_k + f_l$, and r_{kl} = wave-wave difference interaction coefficient associated with $f_k - f_l$.

According to Ahn (1993), wave-wave interaction coefficients q_{kl} and r_{kl} can be

represented as follows:

$$q_{kl} \approx \frac{m}{s_k^2 s_l^2} B_s(f_k, f_l) \tag{2}$$

$$r_{kl} \approx \frac{m}{s_k^2 s_l^2} \{B(f_l, f_k - f_l) - B_s(f_k, f_l)\} \tag{3}$$

where $m = 1$ for $k \neq l$, $m = 2$ for $k = l$, $s_k^2 = c_k^2 / 2$, $s_l^2 = c_l^2 / 2$ represent the discrete linear spectral wave energy components at frequencies f_k and f_l , respectively. $B(f_k, f_l)$ denotes the bispectrum which is formally defined as the Fourier transform of the second-order covariance function (Hasselmann et al., 1963). The bispectrum can also be expressed in terms of Fourier coefficients (Kim and Powers, 1979) as follows:

$$B(f_k, f_l) = E[Y(f_k)Y(f_l)Y^*(f_k + f_l)] \tag{4}$$

where $y(f_k)$ is the complex Fourier coefficient for frequency f_k and the asterisk denotes the complex conjugate. $B_s(f_k, f_l)$ represents the portion of the bispectrum which is due to wave-wave interactions of sum frequency components.

From Equations (1) through (3) we can generate the time series of nonlinear random waves for given linear energy spectrum and bispectrum.

Numerical Example Problem

To verify the method proposed, a numerical example is given. We generated 64 records of test waves which involve three primary linear wave components at frequencies f_1, f_2 and f_3 and non-linear wave components generated from interactions of components at frequencies f_1, f_2 and f_3 .

Let's consider a test waves such that

$$\begin{aligned} y(t) &= \operatorname{Re} \sum_{k=1}^3 c_k e^{i(2\pi f_k t + \varepsilon_k)} + \operatorname{Re} \sum_{\kappa=1}^2 \sum_{l=1}^2 c_\kappa c_l [q_{\kappa l} e^{i\{(2\pi f_\kappa + 2\pi f_l)t + (\varepsilon_\kappa + \varepsilon_l)\}} + r_{\kappa l} e^{i\{(2\pi f_\kappa + 2\pi f_l)t + (\varepsilon_\kappa - \varepsilon_l)\}}] \\ &= c_1 \cos(2\pi f_1 t + \varepsilon_1) + c_2 \cos(2\pi f_2 t + \varepsilon_2) \\ &\quad + c_1^2 r_{11} \cos(4\pi f_1 t + 2\varepsilon_1) + c_2^2 r_{22} \cos(4\pi f_2 t + 2\varepsilon_2) \\ &\quad + 2c_1 c_2 r_{12} \cos((2\pi f_1 + 2\pi f_2)t + (\varepsilon_1 + \varepsilon_2)) \\ &\quad + 2c_1 c_2 q_{12} \cos((2\pi f_1 - 2\pi f_2)t + (\varepsilon_1 - \varepsilon_2)) \end{aligned} \tag{5}$$

where $f_3 = f_1 + f_2$. The phases of each wave were independently taken from a set of uniformly distributed random numbers between 0 and 2π . Fig.1 shows the energy spectrum of test waves $y(t)$. The wave energy in the spectrum corresponds to frequencies from the lowest to the highest frequency $f_2 - f_1$, $f_1, f_2, 2f_1, f_3 = f_1 - f_2$, and $2f_2$ respectively. The wave energy at $2f_1, 2f_2$ and $f_2 - f_1$ is entirely due to self-interactions of f_1 and f_2 and difference interactions of f_1 and f_2 . A portion of the energy at $f_3 = f_1 + f_2$ is due to the sum interaction of waves at f_1 and f_2 and the rest of the energy at f_3 is due to the free linear wave component.

The wave-wave difference interaction coefficient r_{ke} in Eq(3), can be obtained from the bispectrum and corresponding linear energy spectral components. In evaluating the interaction at the frequency $f_1 - f_2$, it is assumed that the spectral energy density at frequencies smaller than the minimum frequency f_s is entirely due to the nonlinear interactions associated with the difference between various combinations of the two frequency component at f_1 and f_2 . Furthermore, noting that $Y(f_k) = Y^*(-f_k)$ for real $y(t)$, it can be shown that the bispectrum has the following symmetry relations:

$$\begin{aligned} B(f_1, f_2) &= B(f_2, f_1) = B(f_1, -f_1 - f_2) \\ &= B(f_1, -f_1 - f_2) = B(f_2, -f_1 - f_2) = B(-f_1, -f_2, f_2) \end{aligned} \quad (6)$$

By the above symmetry relations and definition of f_s , the difference interaction coefficient r_{ke} , can be obtained in the unique bifrequency space, $B - B_s$ as shown in Fig 2. Fig.3 shows the real part of the bispectrum obtained for $y(t)$ by using MATLAB, higher order spectral analysis toolbox.

The analytically computed bispectral values for $y(t)$ are also shown as follows:

$$\mathbf{B}(f_1, f_1) = E[Y(f_1)Y(f_1)Y^*(2f_1)] = \frac{c_1^4 r_{11}}{8} \quad (7a)$$

$$\mathbf{B}(f_2, f_2) = E[Y(f_2)Y(f_2)Y^*(2f_2)] = \frac{c_2^4 r_{22}}{8} \quad (7b)$$

$$\mathbf{B}(f_1, f_2) = E[Y(f_1)Y(f_2)Y^*(f_1 + f_2)] = \frac{c_1^2 c_2^2 r_{12}}{4} \quad (7c)$$

$$\mathbf{B}(f_2, f_1 - f_2) = E[Y(f_2)Y(f_1 - f_2)Y^*(f_1)] = \frac{c_1^2 c_2^2 q_{12}}{4} \quad (7d)$$

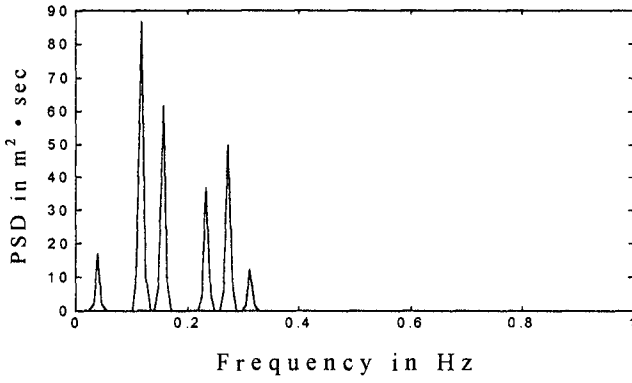


Fig.1 The energy spectrum of $y(t)$

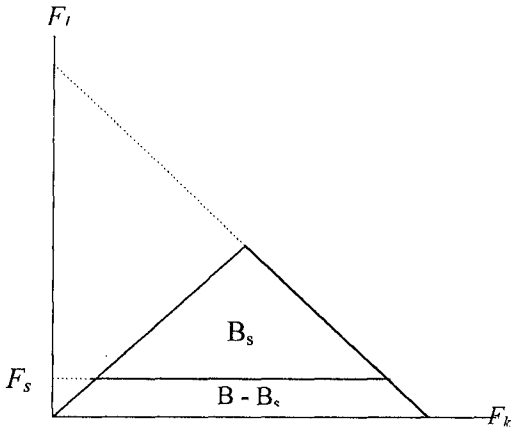


Fig.2 Domains for computing $B(f_k, f_l)$ and $B(f_l, f_k - f_l)$

$$\mathbf{B}(f_1 + f_2, f_1 - f_2) = E[Y(f_1 + f_2)Y(f_1 - f_2)Y^*(2f_1)] = \frac{c_1^4 c_2^2 r_{11} r_{12} q_{12}}{2} \quad (7e)$$

$$\mathbf{B}(2f_2, f_1 - f_2) = E[Y(2f_2)Y(f_1 - f_2)Y^*(f_1 + f_2)] = \frac{c_1^2 c_2^4 r_{22} r_{12} q_{12}}{2} \quad (7f)$$

The plan view of the bispectrum is drawn in Fig.4 to identify the bispectrum in the unique bifrequency space. As can be seen in the figure and from Eq.(7d), the difference interaction coefficient q_{12} is obtained from $\mathbf{B}(f_2, f_1 - f_2)$. Since bispectral values $\mathbf{B}(f_1 + f_2, f_1 - f_2)$ and $\mathbf{B}(2f_2, f_1 - f_2)$ in Eq.(7a,b) are order of magnitude smaller than $\mathbf{B}(f_2, f_1 - f_2)$, we may neglect the terms in evaluating difference interaction coefficient.

The energy spectral component at frequency f_3 is due to free linear wave component $c_3 \cos(2\pi f_3 t + \varepsilon_3)$ as well as the nonlinear sum interaction of waves at f_1 and f_2 . The separation of the nonlinear energy from the total spectrum can be achieved approximately by applying the method proposed by Kim and Power(1979) and Ahn(1993) as following:

$$S(f_m) = S_L(f_m) + \sum_{f_m=f_k+f_l} b^2(f_k, f_l) S(f_m) \quad (8)$$

where the bicoherence squared spectrum is defined as

$$b^2(f_k, f_l) = \frac{|B(f_k, f_l)|^2}{E[|Y(f_k)Y(f_l)|^2] E[|Y(f_m)|^2]} \quad (9)$$

Fig.5 shows the bicoherence squared spectrum. The computed bicoherence for the sum interaction is $b^2(f_1, f_2) = 0.14$ which implies that only 14% of the energy at f_3 is due to the nonlinear sum interaction of the waves at f_1 and f_2 . The computed bicoherences for the self interactions and difference interaction are $b^2(f_1, f_1) = 0.9969$, $b^2(f_2, f_2) = 0.9989$ and $b^2(f_2, f_1 - f_2) = 0.9980$, respectively, which implies that the energy at $2f_1$, $2f_2$ and $f_1 - f_2$ are entirely due to the nonlinear interactions.

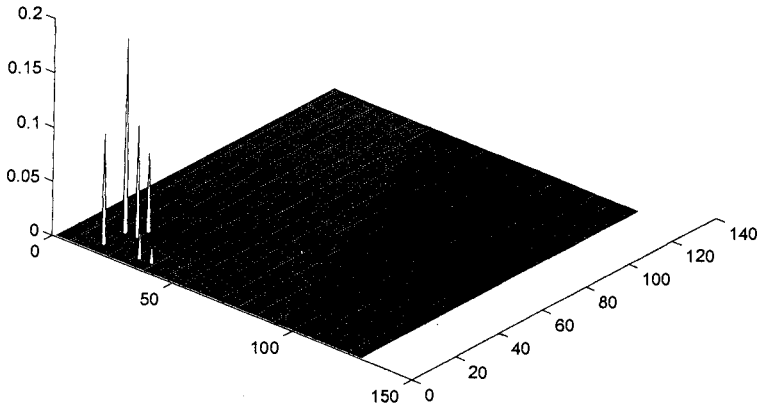


Fig.3 Real part of bispectrum

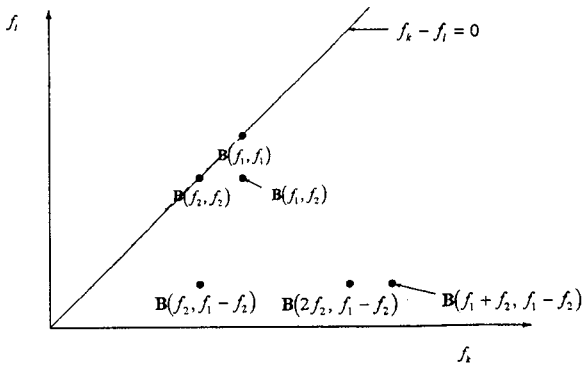


Fig.4 Plan view of bispectrum

Digital simulation of non-linear waves

The time series and the histogram of $y(t)$ in Eq.(4) are shown in Fig.6 and Fig.7, respectively. In these figures, the wave profile shows a definite excess of high crests and shallow troughs, which is a typical feature of nonlinear waves (non-Gaussian random process). In the previous section, we computed the linear energy spectrum and bispectrum of $y(t)$. We now demonstrate the simulation of time series of the second-order random waves from the given linear energy spectrum and bispectrum. The digitally simulated waves should have similar stochastic characteristics such as the spectral density function and the probability distributions. Fig.8, shows the digitally simulated waves by the method proposed. Fig.9 and Fig.10 show the energy spectral density and the histogram of the simulated waves. The digitally simulated waves have good agreement with the target spectral density function and the probability density function of $y(t)$ (compare Fig.9 and Fig.10 with Fig.1 and Fig.6). Therefore the simulated waves is proved to satisfy both the target spectral density and probability distribution function. The following table shows the statistical values of the target time series and the simulated time series of waves. The agreement between them is satisfactory.

	Target time series $y(t)$	Simulated time series
Variance	2.48	2.83
Skewness	1.11	1.05
Kurtosis	4.17	3.71

Conclusions

A method to digitally generate the time series of second-order nonlinear random waves applicable to strongly nonlinear shallow water waves is developed. For the given bispectrum and the bicoherence spectrum, the linear spectrum is separated from the measured spectrum. Then, the wave-wave interaction coefficients associated with various pairs of sum and difference frequency components can be evaluated from the bispectrum. Time series of the second-order nonlinear waves are then digitally simulated using linear spectral components and wave-wave interaction coefficients derived from the bispectrum. The simulated waves have the similar spectral density function and probability distribution

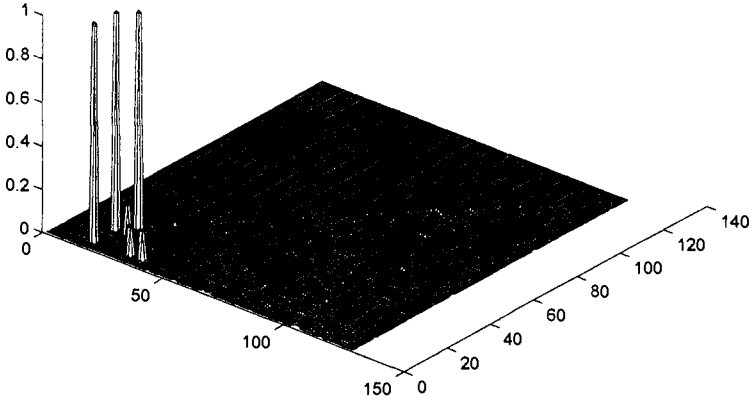


Fig.5 Bicoherence squared spectrum

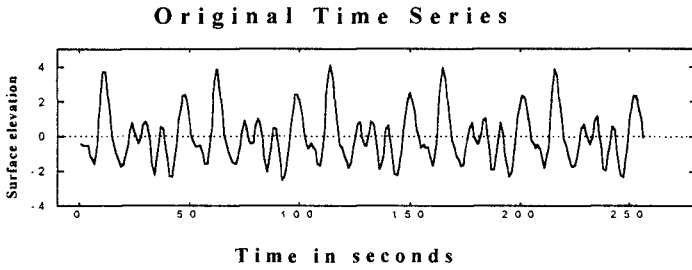


Fig.6 Portion of the test wave record $y(t)$

Histogram of wave displacement

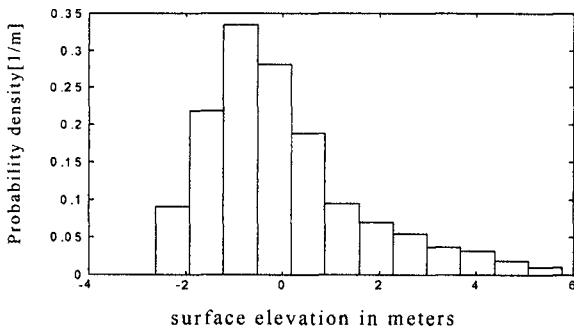


Fig.7 Histogram constructed from test waves $y(t)$

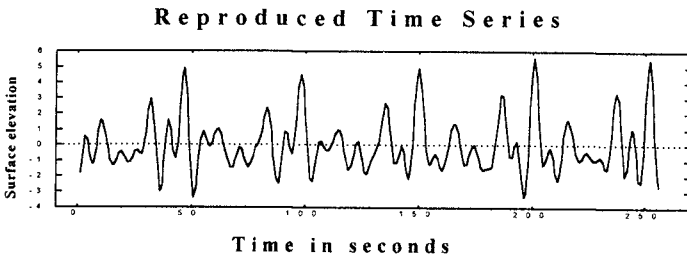


Fig.8 Portion of the time series of simulated waves

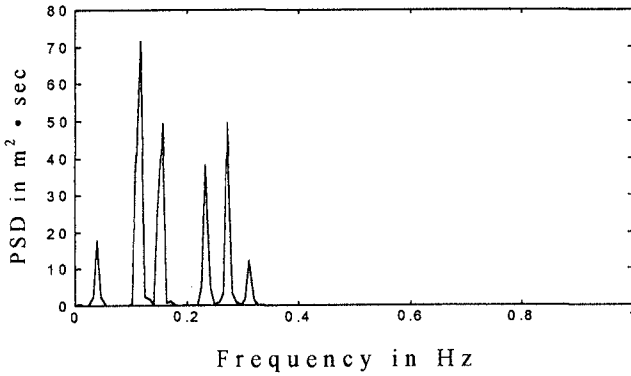


Fig.9 The energy spectrum of the simulated waves

Histogram of wave displacement

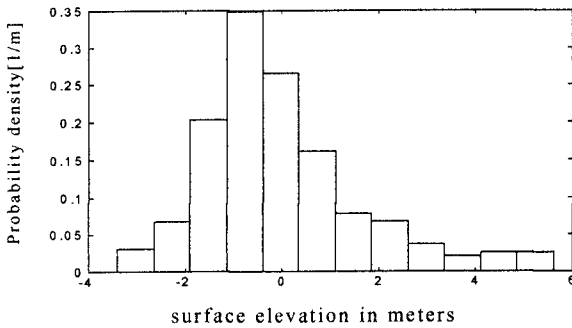


Fig.10 Histogram constructed from the simulated waves

function. A numerical example is used to verify the method developed. The simulated time series of waves closely reproduce the target spectral density function and probability distribution function. It is noted that the proposed method can be applied to wide range of outputs produced by the quadratic nonlinear system. The method could be applied to many practical engineering fields.

References

- Ahn, K. (1993), "Nonlinear Analysis of Waves in Finite Water Depth", Ph.D. Dissertation, University of Florida, Gainesville, FL., U.S.A.
- Duncan, P.E. and K.R. Drake (1995), "A note on the Simulation and Analysis of Irregular Non-linear Waves", *Appl. Ocean Res.*, 17(1), pp.1-8.
- Hasselmann, K., Munk, W.H., and MacDonald, G.J.F., (1963) "Bispectra of Ocean Waves" in *Time Series Analysis.*, M. Rosenblatt, Ed. New York: Wiley, P.125.
- Kim, Y.C. and Power, E.,J., 1979, *Digital Bispectral Analysis and its Applications to Nonlinear Wave Interactions*, IEEE Trans, Plasma Science, Vol. PS-7, No. 2, pp.120-131.
- Klopman, G. and P.J. Leeuwen (1990), "An Efficient Method for the Reproduction of Non-linear Random waves", *Proc. 2nd Int. Conf. on Coastal Eng.*, pp.479-488.
- Ochi, M.K. and K. Ahn (1994), "Probability Distribution Applicable to Non-Gaussian Random Process", *Prob. Eng. Mech.*, 9(4), pp.255-264.
- Sharma, J.N. and Dean, R.G. (1981), "Second-Order Directional Seas and Associated Wave Forces", *Society of Petroleum Engineers Journal*, Feb. pp.129-140.
- Yasuda, T., Shinoda, S. and Hattori, T. (1994), "Solution-Mode Wavemaker Theory and System for Coastal Waves", *Proc. 24th Int. Conf. on Coastal Eng.*, pp704-718.

CHAPTER 53

THE "SWAN" WAVE MODEL FOR SHALLOW WATER

N. Booij¹, L.H. Holthuijsen¹ and R.C. Ris¹

ABSTRACT

The numerical model SWAN (Simulating WAves Nearshore) for the computation of wave conditions in shallow water with ambient currents is briefly described. The model is based on a fully spectral representation of the action balance equation with all physical processes modelled explicitly. No a priori limitations are imposed on the spectral evolution. This makes the model a third-generation model. In Holthuijsen et al. (1993) and Ris et al. (1994) test cases for propagation, generation and dissipation have been shown without currents. Current effects have now been added and academic cases are shown here. The model is also applied in a fairly academic case of a shallow lake (Lake George, Australia) and in a complex, realistic case of an inter-tidal area with currents (Friesche Zeegat, the Netherlands). The results are compared with observations. A new development to formulate the model on a curvi-linear grid to accommodate linkage to hydro-dynamic circulation models is presented and a first test is shown.

INTRODUCTION

Over the last decade, the traditional wave ray models in coastal engineering to compute waves in nearshore conditions are being replaced by models that formulate the wave evolution in terms of a spectral energy balance on a regular grid (or the action balance in the presence of ambient currents). In third-generation versions of such models the wave spectrum is allowed to evolve free of any a priori limitations and all relevant physical processes are represented explicitly in a discrete spectral formulation. Such a wave model (the SWAN model), with the inclusion of ambient currents is described here. Conceptually it is an extension of deep water third-generation wave models but the physical processes and the numerical techniques involved are more complicated. The SWAN wave model has been conceived to be a computationally feasible third-generation spectral wave model for waves in shallow water (including the surf zone) with ambient currents in a consulting environment with return times of less than 30 min on a desk top computer.

¹ Delft University of Technology, Department of Civil Engineering, P.O. Box 5048, 2600 GA Delft, Netherlands.

THE SWAN WAVE MODEL

The SWAN wave model (Ris et al., 1994) is a fully discrete spectral model based on the action balance equation which implicitly takes into account the interaction between waves and currents through radiation stresses (e.g., Phillips, 1977):

$$\frac{\partial}{\partial t} N(\sigma, \theta) + \nabla_{x,y} \cdot [c_{x,y} N(\sigma, \theta)] + \frac{\partial}{\partial \sigma} [c_{\sigma} N(\sigma, \theta)] + \frac{\partial}{\partial \theta} [c_{\theta} N(\sigma, \theta)] = \frac{S(\sigma, \theta)}{\sigma}$$

The first term in the left-hand side is the rate of change of action density in time, the second term is the rectilinear propagation of action in geographical x -, y -space. The third term describes the shifting of the relative frequency due to currents and time-varying depths with propagation velocity c_{σ} in σ -space. The fourth term represents the propagation in θ -space (depth- and current-induced refraction) with propagation velocity c_{θ} . The term $S(\sigma, \theta)$ at the right hand side of the action balance equation is the source term representing the growth by wind, the wave-wave interactions and the decay by bottom friction, whitecapping and depth-induced wave breaking.

To reduce computer time, we remove time from the action balance equation (i.e., $\partial/\partial t = 0$). This is acceptable for most coastal conditions since the residence time of the waves is usually far less than the time scale of variations of the wave boundary conditions, the ambient current, wind or the tide. For cases in which the time scale of these variations becomes important, i.e., variable incoming waves at the boundary, or variable winds or currents, a quasi-stationary approach can be taken by repeating the computations for predefined time intervals.

The formulations for the generation, the dissipation and the quadruplet wave-wave interactions are taken from the WAM model (WAM Cycle 3, WAMDI group, 1988 and optionally WAM Cycle 4, Komen et al., 1994 as presently operational at the European Centre for Medium Range Weather Forecasting). For the present study the formulations from WAM Cycle 3 are used. These are supplemented with a spectral version of the dissipation model for depth-induced breaking of Battjes and Janssen (1978) (with the maximum wave height to depth ratio from Nelson, 1987) and a recently formulated discrete interaction approximation for the triad wave-wave interactions (Eldeberly and Battjes, 1995).

Fully implicit numerical schemes are used in the SWAN model for propagation in both geographic space and spectral space (an iterative, forward-marching, four-sweep technique, Ris et al., 1994). This scheme is unconditionally stable in contrast with the explicit schemes of conventional spectral wave models which are only conditionally stable and which require therefore very small time steps in shallow water (typically 10 s for 100 m resolution in water depth of 10 m where in the SWAN model the time increment may be as large as 15 min). The formulation is basically in terms of finite differences on a regular, rectangular grid. This is inconvenient in regions with highly variable scales such as tidal inlets, tidal flats and

estuaries. Nesting of grids with decreasing resolution is the conventional approach in such cases but it requires extra computations. A variable resolution grid would avoid such extra computations, in particular if the grid would conform to the topography of the region. It would also accommodate the linkage with hydrodynamic circulation models which are often formulated on such grids. Such a curvilinear approach is implemented in the SWAN model by considering in the numerical scheme of each spatial grid point, two separate, non-equidistant finite up-wind differences in each of two orthogonal directions. For the x -direction this is for grid point i, j (the grid points are ordered in x, y -space):

$$\frac{\partial C_x N}{\partial x} \approx \left[\frac{[c_x N]_{i,j} - [c_x N]_{i-1,j}}{\Delta \bar{x}_1} \right] + \left[\frac{[c_x N]_{i,j} - [c_x N]_{i,j-1}}{\Delta \bar{x}_2} \right]$$

where $\Delta \bar{x}_1 = \Delta x_1 - (\Delta y_1 / \Delta y_2) \Delta x_2$, $\Delta \bar{x}_2 = \Delta x_2 - (\Delta y_2 / \Delta y_1) \Delta x_1$. The increments are $\Delta x_1 = x_{i,j} - x_{i-1,j}$, $\Delta x_2 = x_{i,j} - x_{i,j-1}$, $\Delta y_1 = y_{i,j} - y_{i-1,j}$ and $\Delta y_2 = y_{i,j} - y_{i,j-1}$.

PROPAGATION TESTS

In Holthuijsen et al. (1993) the excellent agreement for academic cases is shown between computed wave propagation and analytical solutions and wave ray solutions of the linear wave theory without ambient currents. A similar good agreement with ambient currents added is shown here. For this, consider current-induced refraction in deep water, of monochromatic, long-crested waves with a (significant) wave height of 1 m and a (peak) frequency of 0.1 Hz. In the SWAN computation these waves are simulated with a Gaussian-shaped frequency spectrum with 0.01 Hz standard deviation and a $\cos^{500}(\theta)$ -directional distribution. Consider first these waves propagating from a uniform up-wave boundary over a distance of 4000 m in a following or opposing current of which the speed increases from 0 m/s to 2 m/s in the down-wave direction (current direction 0° or 180° direction relative to the mean wave direction). Only whitecapping is activated in the computations (although its effect is marginal). The computational results in terms of (significant) wave height for this current-induced shoaling test are shown in Fig. 1. The agreement for these cases with linear theory is excellent as the computational errors are less than 0.5% for the significant wave height and less than 0.1° for the mean wave direction (both differences hardly noticeable in Fig. 1). Consider next the same waves slanting across a 4000 m wide current field of which the current speed increases from 0 m/s to 2 m/s across the width and the current direction is constant and parallel to the straight current field boundaries. The wave direction is either $+30^\circ$ or -30° relative to the current direction. The results for the significant wave height and the wave direction are also shown in Fig. 1. The agreement for these cases with linear theory is as good as in the current-induced shoaling test.

The propagation with the curvilinear formulation is tested here by comparing the computational results on a rectangular grid with those on a curvilinear grid near

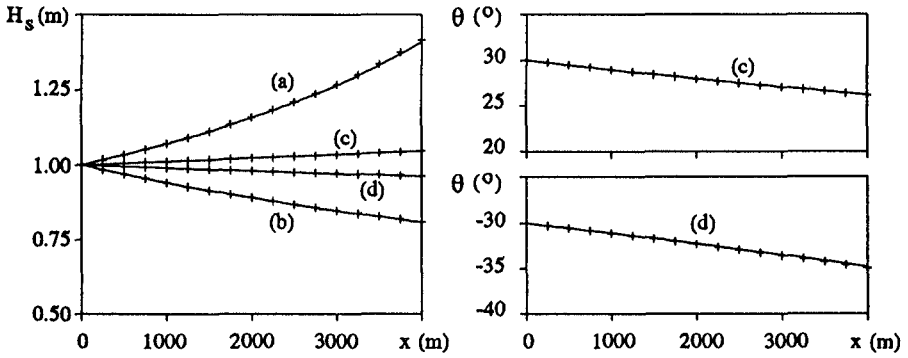


Fig. 1 Current-induced shoaling and refraction for monochromatic, long-crested waves for travelling against an opposing current (line a), a following current (line b) and a slanting current with incident wave direction $\theta_o=30^\circ$ (line c) and $\theta_o=-30^\circ$ (line d). Left panel: significant wave height H_s (m). Right panel: mean wave direction θ ($^\circ$), (—) analytical solutions and (+ + +) results from the SWAN model.

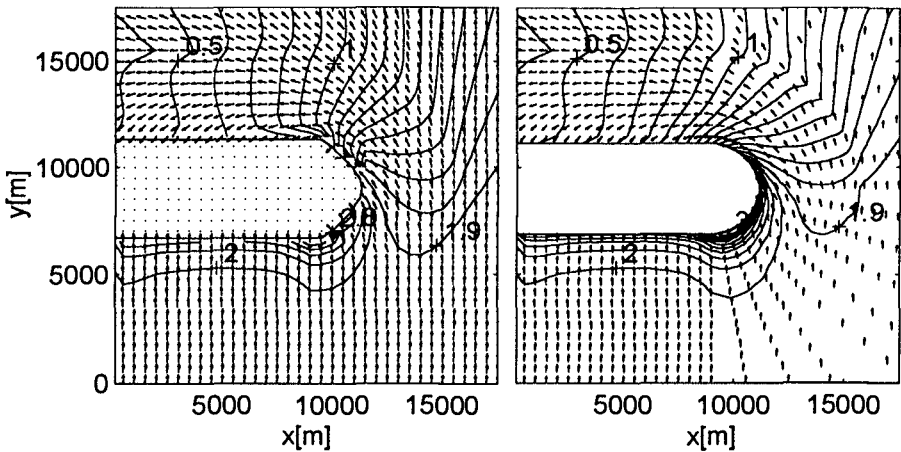


Fig. 2 The propagation of a short-crested wave field around a barrier island; significant wave height with contour line interval of 0.1 m and mean wave direction. The depth increases from the shore line over a distance of 4500 m to a constant water depth of 10 m. Left panel: computational results on a rectangular grid. Right panel: computational results on a curvi-linear grid (grid points at start of each vector).

a hypothetical barrier island (Fig. 2). All source terms are de-activated in these computations. The incoming waves are characterized with a JONSWAP spectrum with a $\cos^4(\theta)$ -directional distribution. The significant wave height and the mean wave period are 2.0 m and 6.0 s, respectively. The results of the computation on the curvi-linear grid agrees well with the results on the rectangular grid (Fig. 2).

WIND-WAVE GENERATION IN SHALLOW WATER

The observations of Young and Verhagen (1996) in the shallow Lake George (Australia) provide an excellent opportunity to test the generation of waves in the SWAN model in shallow water. These observations were carried out at eight wave stations in the lake, the bathymetry of which is fairly flat with an average depth of 2m (Fig. 3).

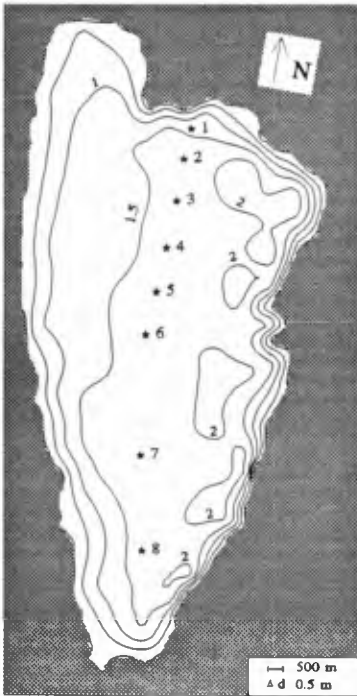


Fig. 3 Bathymetry of Lake George and the locations of the eight wave stations. Isolines represent depth contours (interval 0.5 m).

One case with a relatively high wind speed of $U_{10}=15.2$ m/s (at station 6 on 02-11-1992 at 16:00 local time) from northerly directions is chosen to demonstrate the performance of the SWAN model. From wind measurements at other stations it was found that the wind speed varied slightly along the north-south axis of the lake. This variation is calculated with the simple expression of Tayler and Lee (1984) proposed for these cases by Young and Verhagen (1996). As the up-wave coast line was not very well defined in this case (due to a very gentle bottom slope) the up-wind boundary condition was taken to be the observed wave spectrum at station 1. Fig. 4 shows the good agreement between the observed

significant wave height and peak frequency (I.R. Young and L.A. Verhagen, private communication, 1996) and the computational results. The inclusion of depth-induced wave breaking in modelling such conditions is unusual. Its effect is determined here by repeating the computation with this process de-activated in the model. The effect is significant only at the down-wind end of the lake (Fig. 4) and only for these high wind speeds (computations with wind speeds less than 10 m/s do not show this effect).

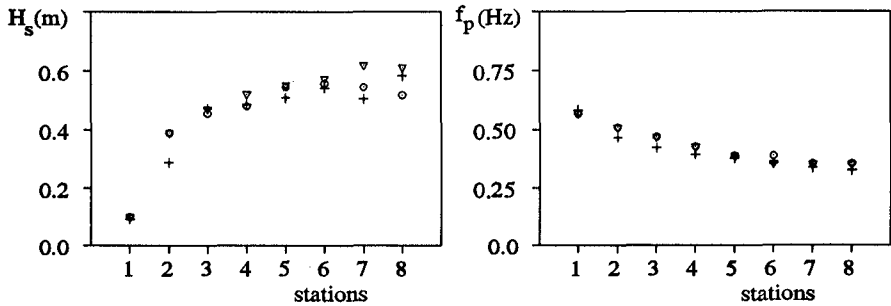


Fig. 4 Model results and observations of the significant wave height (left panel) and peak frequency (right panel) at the observation stations in Lake George for $U_{10}=15.2$ m/s. (+) measurements, (o) SWAN results, (v) SWAN results with depth-induced wave breaking de-activated.

APPLICATION

The performance of the SWAN model is shown here for a field case with wind and complex bottom and current patterns and 95% reduction in wave energy. It is a case in the Friesche Zeegat (the Netherlands) where a system of narrow channels (10 km length scale) runs from the North Sea into an area of tidal flats (the Wadden Sea, Fig. 5, the two main channels are about 10 m and 14 m deep). The waves were measured with one WAVEC pitch-and-roll buoy (station 1) at the deep water boundary of the area and five Waverider buoys (stations 2 to 6) located along the two channels (see Fig. 5). The observations that have been selected from the extensive data set for this verification are a flood current case which occurred on 09-10-1992 at 05:00 UTC (J.G. de Ronde and J.H. Andorka Gal, private communication, 1996). The reasons for this selection are that (a) at this time relatively high waves were observed (significant wave height about 2.5 m) which were generated by a storm in the northern North Sea, (b) during the period of observation the wind speed and direction were nearly constant, (c) the frequency spectrum was uni-modal and (d) tidal currents and water levels were measured. The wind velocity of $U_{10}=11.5$ m/s and direction of 320° are assumed to be uniform over the Friesche Zeegat area. The corresponding currents and water levels in the area were computed with a shallow water circulation model, resulting in a maximum current speed of about 1 m/s.

The spectrum at the up-wave boundary in deep water for the computations is taken equal to the frequency spectrum observed by the WAVEC buoy at station 1. It is taken uniform along a straight line through the location of the WAVEC buoy and roughly parallel with the 20 m depth contour. The observed significant wave height is $H_s = 2.24$ m and the mean wave period is $T_{m01} = 5.6$ s. The observed overall mean wave direction is 328° (nautical convention) and the overall directional width of the waves is 31° . The directional distribution is correspondingly

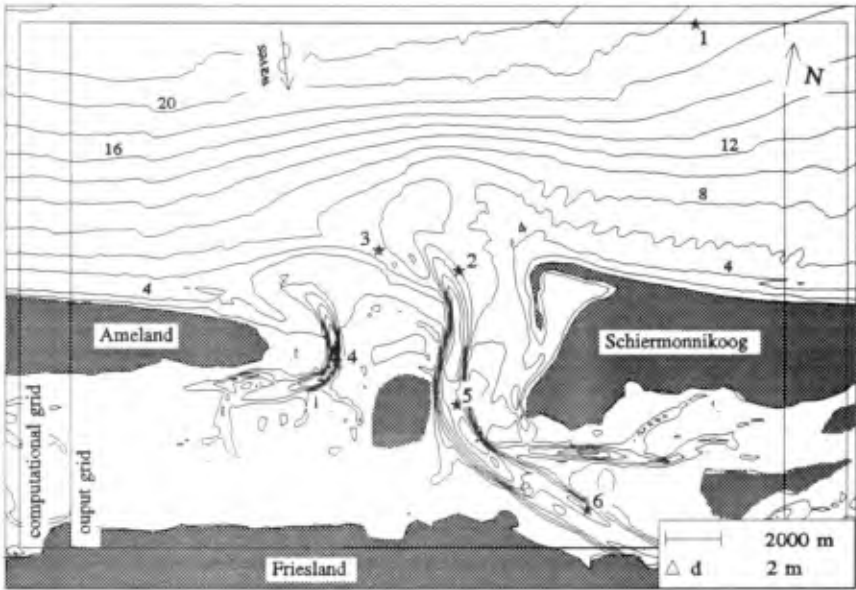


Fig. 5 The bathymetry of the Friesche Zeegat with the locations of the six stations. The isolines represent depth contours (interval 2 m). All water depths are in m.

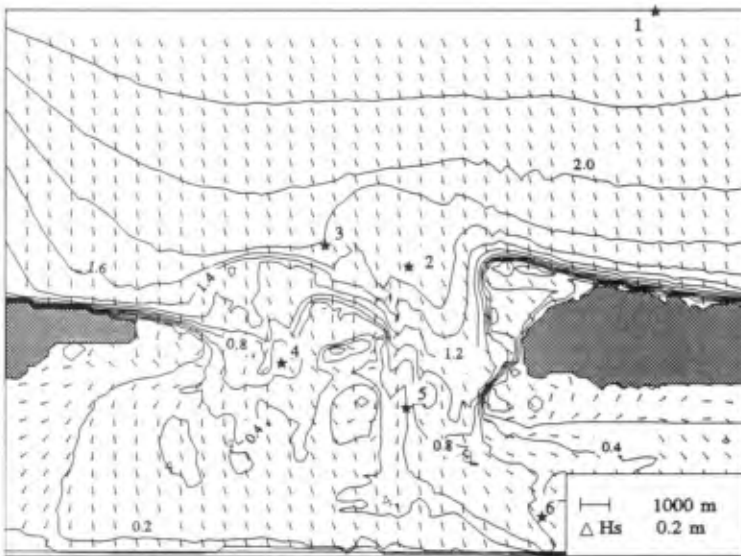


Fig. 6 Computed wave height pattern and mean wave direction (denoted with vectors) for a flood current case in the Friesche Zeegat. The isolines represent wave height contours (interval 0.2 m).

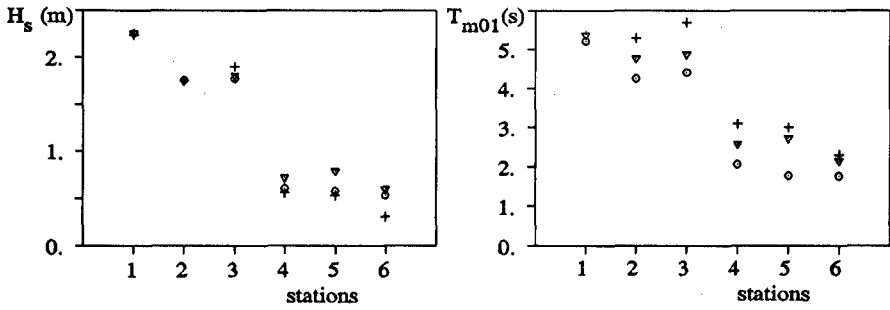


Fig. 7 Computed and observed significant wave height (left panel) and mean wave period (right panel) at the observation stations for the flood current case in the Friesche Zeegat: (+) observations, (o) SWAN results, (v) SWAN results without currents.

approximated with a $\cos^{2.1}(\theta)$ -directional distribution at all frequencies. The computed pattern of the significant wave height is shown in Fig. 6. This pattern is consistent with the pattern of the observations: the wave height gradually decreases between the deep water boundary and the entrance of the tidal inlet. Due to depth effects, more wave energy penetrates into the deeper eastern entrance than into the shallower western entrance of the tidal inlet (roughly 20 % lower wave height near station 4 than in the other entrance). As the waves penetrate through the tidal gap into the inlet they refract laterally to the shallower parts of the tidal inlet. They completely reverse direction behind the two barrier islands. The mean wave period (not shown here) follows roughly the same pattern. The effect of currents is shown with results of computations without currents (Fig. 7). This effect is evident but generally not very important in this case.

The calculated significant wave heights and mean wave periods at the six observation stations are given in Fig. 7. The agreement with the observations is fairly reasonable although the model tends to underestimate the mean wave period.

CONCLUSIONS

The SWAN wave model, which has been conceived as a computationally feasible third-generation spectral wave model for waves in shallow water (including the surf zone) with ambient currents for engineering consultancy has been implemented. It accounts for all relevant processes of propagation, generation, dissipation and nonlinear wave-wave interactions (except diffraction but including depth-induced wave breaking, triad wave-wave interactions and the effects of currents). Tests so far in academic conditions and in realistic field conditions show good agreement between computational results and observations although the present version of the model tends to slightly underestimate the mean wave period.

The present computation time is 6×10^{-5} s per grid point in x -, y -, σ -, θ -space per iteration on a HP 9000/735 work station (without currents; three times more than this when currents are included). A typical engineering application (without currents) of 100×100 geographic (water covered) grid points, 24 frequencies and 36 directions with 3 to 5 iterations will therefore take typically between 30 and 45 min computation time. With the expected performance of desk-top computers presently entering the market this will reduce to less than 15 - 30 min within the next few years. The operational goal has therefore been achieved. Future versions of the SWAN model (presently under development) will be non-stationary, formulated on a curvi-linear grid, and optionally formulated in spherical coordinates with a higher-accuracy propagation scheme and possibly include the effects of diffraction and reflections.

ACKNOWLEDGEMENTS

We gratefully acknowledge the generosity of I.R. Young and L.A. Verhagen of the University of New South Wales in Australia and of J.G. de Ronde, J.H. Andorka Gal and their colleagues from the Ministry of Transport and Public Works in the Netherlands in sharing their data from Lake George and the Friesche Zeegat, respectively. We are equally grateful to B.A.J. Les from the Delft University of Technology who (at the Ministry of Transport and Public Works) carried out the calculations for the currents and water levels in the Friesche Zeegat.

REFERENCES

- Battjes, J.A. and J.P.F.M. Janssen, 1978, Energy loss and set-up due to breaking of random waves, 16th Int. Conf. Coastal Engineering, ASCE: 569 - 587
- Eldeberky, Y. and J.A. Battjes, 1995, Parameterization of triad interactions in wave energy models, Coastal Dynamics '95, W.R. Dally and R.B. Zeidler (Eds.), ASCE: 140-148
- Holthuijsen, L.H., N. Booij and R.C. Ris, 1993, A spectral wave model for the coastal zone, 2nd International Symposium on Ocean Wave Measurement and Analysis, New Orleans, Louisiana, July 25-28, 1993, New York, pp. 630-641
- Komen, G.J., L. Cavaleri, M. Donelan, K. Hasselmann, S. Hasselmann and P.A.E.M. Janssen, 1994, Dynamics and Modelling of Ocean Waves, Cambr. Univ. Press, 532 p.
- Nelson, R.C., 1987, Design wave heights on very mild slopes, Civil Eng. Trans., Inst. Eng. Aust., 29, 157-161
- Ris, R.C., L.H. Holthuijsen and N. Booij, 1994, A spectral model for waves in the near shore zone, 24th Int. Conf. Coastal Engng, Kobe, Oct. 1994, pp. 68-78
- WAMDI group: S. Hasselmann, K. Hasselmann, E. Bauer, P.A.E.M. Janssen, G.J. Komen, L. Bertotti, P. Lionello, A. Guillaume, V.C. Cardone, J.A. Greenwood, M. Reistad, L. Zambresky and J.A. Ewing, 1988, The WAM model - a third generation ocean wave prediction model, J. Phys. Oceanogr., Vol. 18: 1775-1810
- Young, I.R. and L.A. Verhagen, 1996: The growth of fetch limited waves in water of finite depth. Part I: Total Energy and peak frequency, Coastal Engineering, Vol. 29, pp. 47-78
- Taylor, P.A. and R.J. Lee, 1984: Simple guidelines for estimating wind speed variations due to small-scale topographic features, Climatol. Bull., 18, 3-32

CHAPTER 54

Generation Depths from Water Wave Data

J. Ernest Breeding, Jr.¹

Abstract

It is shown that by determining wave group back tracks for recorded data it is possible to determine whether the waves were generated in deep, intermediate, or shallow water depths. The general movement of a storm can be tracked if a storm moves through water of intermediate depths. For the examples shown reasonable results were obtained by approximating the geometric group velocity by the conventional group velocity.

Introduction

When water waves are generated the depth of the water where the waves begin becomes a characteristic trait of the waves. Through the use of simple refraction concepts it is possible to determine from recorded data whether the waves originated in deep, intermediate, or shallow water depths. If the waves were generated in intermediate water depths the actual water depths can be determined.

It is assumed that initially the wave groups and the individual waves within the groups have the same direction where the waves are generated. In shoaling water, refraction causes the groups and the individual waves to have different directions because of their differing velocities. This difference is used to determine the water depths where the waves are generated, i.e., the generation depths. The method is based on determining back tracks from the measurement site to the source of wave generation.

Breeding (1978, 1986) found that the paths of wave groups are determined

¹Research Physicist, Code 7183, Naval Research Laboratory, Stennis Space Center, MS 39529-5004

according to Snell's law with the geometric group velocity. The geometric group speed G is defined

$$G = U \cos \phi \quad (1)$$

$$U = d\omega/dk \quad (2)$$

$$\phi = \theta - \gamma \quad (3)$$

where U is the conventional group speed, ω is the angular frequency, k is the wave number, θ is the wave group direction, and γ is the direction that the individual waves move within the group. The direction γ is given by Snell's law with phase velocity.

This concept can be used to explain a number of physical processes in coastal waters that cannot be explained on the basis of a single refraction law. For example, when both refraction laws are used together it is possible to show (Breeding, 1981b) that the widely occurring sinuous shoreline is part of an equilibrium beach form.

The primary objective in this paper is to determine the generation depths of recorded waves. A second objective is to demonstrate that under certain conditions good results can be obtained if the conventional group velocity is used as an approximation to the geometric group velocity. This approach can be highly desirable for many practical applications since it greatly simplifies the ray equations and the complexity of the computer program for ray tracing.

Wave Group Directions and Trajectories from Wave Data

The directions obtained in a directional-power spectral analysis of wave measurements are those of the individual waves. It is necessary to compute the corresponding wave group directions. If the water depth contours are parallel the wave group directions can be determined through the use of Snell's laws. For the wave group Snell's law can be stated

$$(\sin \theta_m)/G_m = (\sin \theta_g)/G_g \quad (4)$$

where the subscript m denotes the measurement site and the subscript g refers to the place of wave generation. Snell's law for the individual waves is given by

$$(\sin \gamma_m)/v_m = (\sin \gamma_g)/v_g \quad (5)$$

where $v = \omega/k$ is the phase speed. It is assumed that $\theta_g = \gamma_g$. When (4) and (5) are combined it is found that

$$\tan \theta_m = (J \sin 2\gamma_m) / [2(1 - J \sin^2 \gamma_m)] \quad (6)$$

$$J = (v_g / U_g) (U_m / v_m) \quad (7)$$

The ratio of U_m/v_m is determined by the water depth at the measurement site for a given wave period. So θ_m is a function of γ_m and the ratio of U_g/v_g . For a given wave period the latter ratio depends on the water depth of wave generation. If this depth is known the wave group directions are readily determined. If the water depth where the waves are generated is not known, then this depth and the wave group directions can be determined together by trial and error for a range of wave periods.

The best way to illustrate how the method works is to consider some simulated examples. It will be assumed that water waves have been generated at a distant location where the water depth is 200 m. The directions of the individual waves are presumed to have been determined with high accuracy for a range of wave periods from data obtained at a water depth of 15 m near shore. The water depth contours are parallel. Now assume that the water depth where the waves were generated is unknown. The objective is to work backwards using the measured individual wave directions to determine the corresponding wave group directions and the water depth of wave generation. Equations (6) and (7) are used to calculate wave group directions at the measurement site for a range of wave periods and for trial values of water depths of wave generation. Back tracks produced from the measurement site will determine which trial value of water depth of wave generation is consistent with the wave source. In Figure 1a wave group back tracks are shown for wave periods of 7.7, 8.3, 9.1, 10.0, 11.1, 12.5, and 13.3 s for an assumed depth of wave generation of 50 m. Since the rays are seen to diverge and not go back together to a common source the trial value of generation depth must be incorrect. In Figure 1b the wave group directions at the measurement site were determined on the assumption that the waves were generated in water of 100 m depth. Although the results are better than in the previous example, they are not entirely consistent. The correct answer is obtained in Figure 1c where the assumed depth of wave generation is 200 m. The wave group back tracks are seen to go back together to a common source and to be parallel at the 200 m water depth. The wave group directions determined for this example using (6) and (7) also have to be correct.

Determination of Water Depths of Wave Generation from Field Data

Two field data sets will be used to further illustrate the theory and methodology for determining water depths of wave generation and wave group

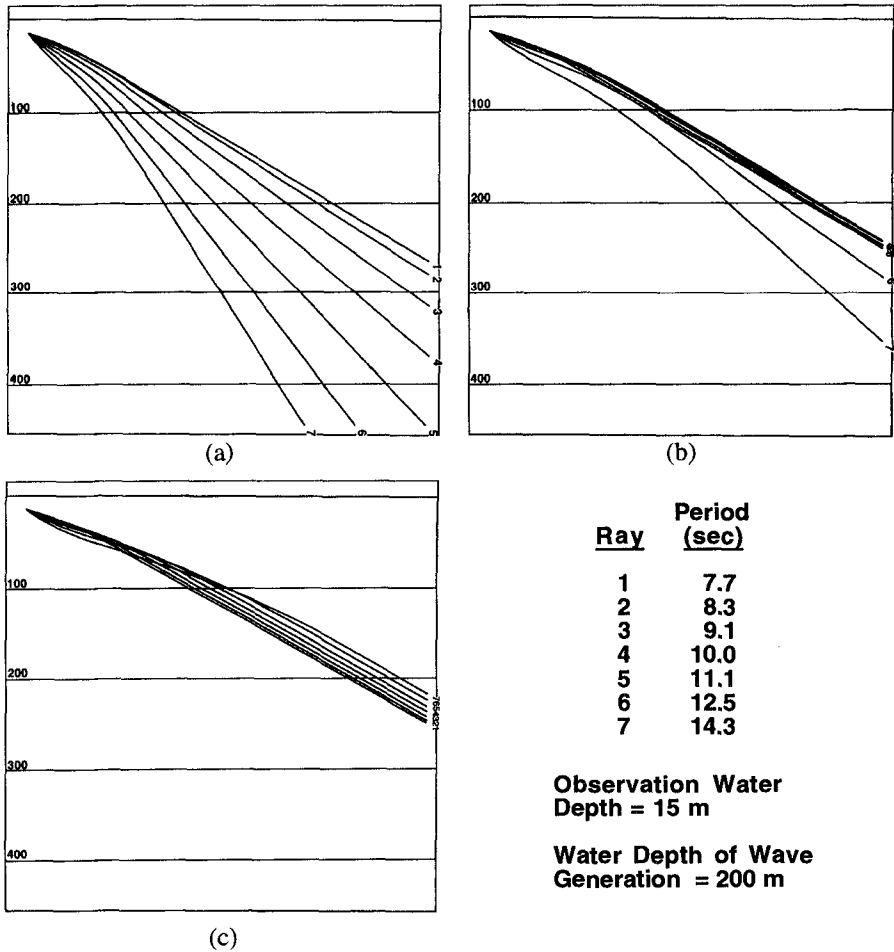


Figure 1. Wave group back tracks for assumed water depths of wave generation of (a) 50 m, (b) 100 m, and (c) 200 m. Soundings in meters.

trajectories. In both cases the waves were measured (Bennett, et al, 1964; Breeding, 1972) with an array of up to six pressure sensors on the sea floor in 31.7 m of water 17.7 km from shore near Panama City, Florida. In the array a pressure sensor was located at each corner of a pentagon of side 35.8 m, and these sensors were located 30.5 m from a sensor at the center of the array. Directional power spectra with 60 degrees of freedom were computed for time series records about 30 minutes in length by Bennett (1972) based on the method of Munk, et al (1963).

The water depth contours for the region of interest are shown in Figure 5. Over much of the region the water depth contours are approximately parallel. Accordingly, in determining wave group back tracks two approximations are made in the calculations. Firstly, the wave group directions at the measurement site are determined on the assumption that the water depth contours are parallel. And secondly, the conventional group velocity is used as an approximation to the geometric group velocity. The latter approximation can be made since Breeding (1981a) has shown for parallel water depth contours that G does not differ from U by more than 14%. The difference is usually much less. When G is replaced by U and the Snell's law equations are combined it is found that

$$\sin \theta_m = J \sin \gamma_m \quad (8)$$

This equation is used as an approximation to (6).

The wave group back tracks for the field data examples are determined using a ray curvature expression for nonparallel water depth contours based on the conventional group velocity U . Details are given in Breeding (1972). The approximations noted above greatly simplify the analysis.

Summer Storm

In the first example, waves measured on June 1, 1965 are considered. The directional power spectra computed from the waves are presented in Figure 2. This "3-D" representation is due to Bennett (1968). The bottom of each arrow gives both the frequency and bearing of the waves. Note that the frequency increases in the form of concentric circles moving outward from the center. The direction north (N) represents magnetic north. To obtain true north one adds 3 degrees. The tip of each arrow indicates the log power density of the waves at the depth of measurement. In this example the waves have small amplitudes.

In Figure 2 it can be seen that the directional power spectra near 0.1 Hz varies in a smooth fashion indicating that the waves are due to a common source.

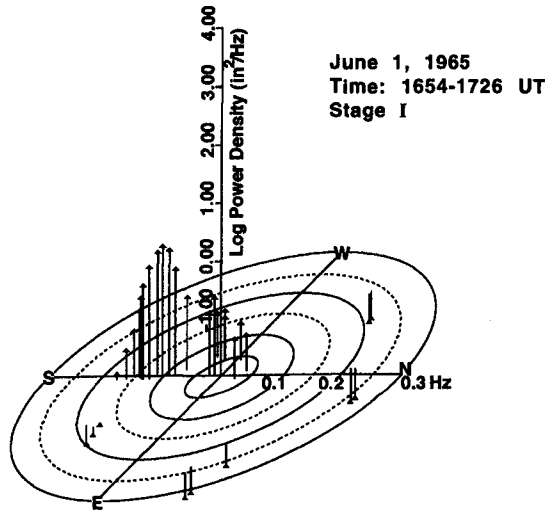


Figure 2. Directional power spectral for summer storm.

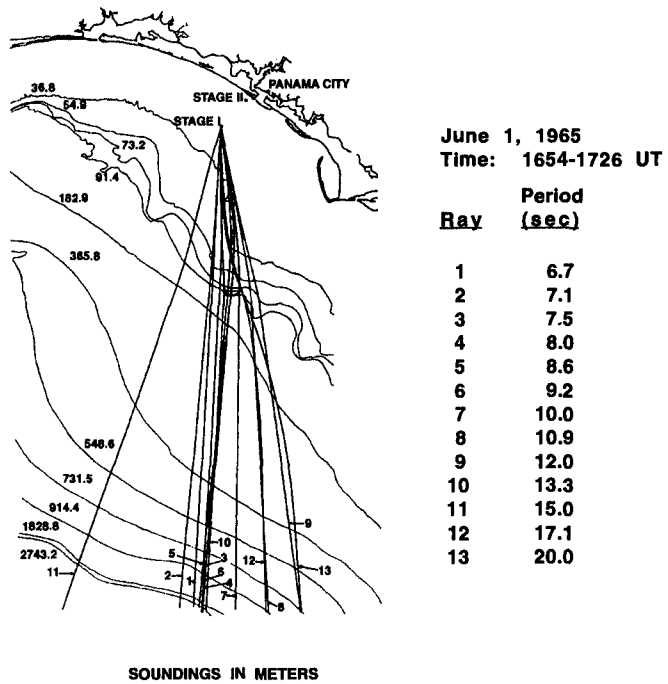


Figure 3. Wave group back tracks for summer storm.

The wave periods which are too short to be affected by refraction indicate the waves come from near south. Back tracks were produced for wave groups assuming that the waves had a deep water source and using (8) to determine the wave group directions at the measurement site. The resulting back tracks, which are shown in Figure 3, are generally consistent with a common source in the Caribbean Sea. All but two of the group rays go back through the Yucatan Channel, and only one misses badly.

Hurricane Betsy

In the second example, an investigation is made of waves measured in September 1965 due to Hurricane Betsy. The storm crossed the tip of South Florida and entered the Gulf of Mexico at about 1500 UT (Greenwich mean time) on September 8. After making a curved path the hurricane entered land at the Mississippi Delta near New Orleans, Louisiana at about 0400 UT on September 10. Over much of the storm path water waves were generated in intermediate water depths.

Figure 4 is an example of the directional power spectra (Bennett, 1972) for September 9 for the time period 1359 - 1430 UT. This is an example of a very energetic source.

The wave group back tracks and water depths of wave generation have to be determined by trial and error for each wave period. The general procedure is as follows. A water depth of wave generation is assumed as a trial value, the initial direction of the back track is calculated, and the ray traced. If the ray does not take a path which crosses water of the depth assumed the depth assumption must be rejected. If the location of the storm is known from meteorological records the range of possible depths is readily restricted. Once a few depths have been tried it is usually easy to decide which values to try next. Further, the answer found for one wave period must be consistent with the results found for other wave periods. After ray trajectories are drawn for the various wave periods a final check is made by comparing travel times computed along the paths to the region of wave generation. The computed travel times should agree with the known movement of the storm.

Equation (8) was used to determine the wave group directions at the measurement site. The corresponding back tracks and the water depths of wave generation are shown in Figure 5. The rays emanate from the measurement site, and they are continued until they reach either shore or a boundary of the water depth grid. Tick marks have been placed on the rays at five hour intervals of travel time. The course of Hurricane Betsy is indicated along the bottom of the illustration. The back tracks appear reasonable when viewed with respect to the hurricane path.

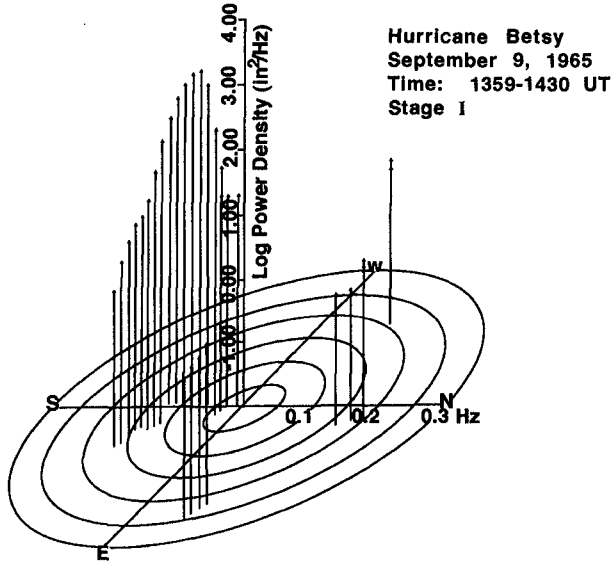


Figure 4. Directional power spectra for Hurricane Betsy.

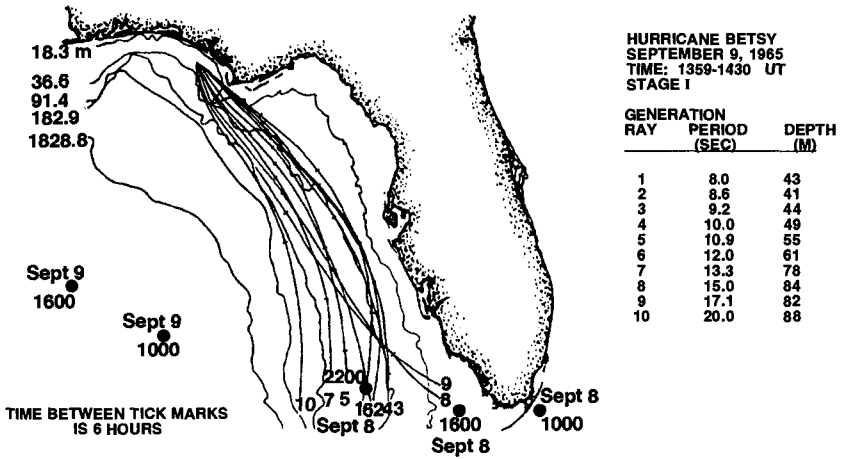


Figure 5. Wave group back tracks for Hurricane Betsy.

Consider, for example, ray number five which has a wave period of 10.9 s. Back tracking along this ray for fifteen hours gives water depths near the determined generation depth of 55 m. Timewise this corresponds to September 8 at 2300 UT. This time and location compare favorably with the record of the storm and its counterclockwise wind pattern.

It can be observed that portions of the wave group trajectories in Figure 5 are nearly parallel with the water depth contours. Although this would not be possible for monochromatic trajectories, it is not unusual for wave group trajectories. For wave group trajectories Breeding (1981a, 1986) has shown that the ray curvature goes to zero for rays parallel as well as perpendicular to the water depth contours.

Water depths of wave generation and wave group back tracks were also determined for the time periods 0800 - 0829 and 1816 - 1847 UT on September 9. The water depths of wave generation for the three wave measurement periods are presented in Table 1. For the first measurement period the waves were generated close to the Florida coast and were in the initial stages of development. For the second and third measurement periods the waves had become quite large. Note that for a given measurement time the water depths of wave generation generally increase with wave period. This result is what one would expect for dispersed gravity water waves due to a storm moving toward deeper water, as was the case. Observe further that for a given wave period the generation depths generally increase with the measurement recording time. This is clearly in agreement with the meteorological record.

Table 1. Water Depths of Wave Generation, 9 September 1965

Period (sec)	Time UT, Generation Depths in m		
	<u>0800 - 0829</u>	<u>1359 - 1430</u>	<u>1816 - 1847</u>
8.0	44	43	depth > 50
8.6	44	41	depth > 58
9.2	46	44	depth > 66
10.0	47	49	67
10.9	47	55	72
12.0	47	61	82
13.3	50	78	93
15.0	50	84	88
17.4	48	82	85
20.0	---	88	111

Monochromatic Trajectories

Monochromatic back tracks are presented in Figure 6 for comparison with the wave group back tracks shown in Figure 3 for the summer storm. The same individual wave directions were used to produce both results. The monochromatic rays were determined using the numerical method for nonparallel water depth contours developed by Wilson (1965). These back tracks are not at all consistent with a common wave source.

In Figure 7 monochromatic back tracks are shown for the same individual wave directions used to determine the wave group back tracks presented in Figure 5 for Hurricane Betsy. The Wilson (1965) program was used to determine the rays. It is seen that the monochromatic rays are in poor agreement with the path of the storm.

Conclusions

If the directions of the individual waves of a group are determined from wave data as a function of wave period, and if some simple refraction concepts are used for parallel water depth contours, it is possible to determine: (1) the wave group directions at the measurement site, (2) the wave group back tracks to their sources, and (3) the depths of water where the waves were generated. A wave example was presented where the apparent source of the waves was in deep water. Waves due to Hurricane Betsy (September 1965) were analyzed, and by determining the wave group back tracks and the corresponding water depths of wave generation, it was possible to track the general movement of the storm as it passed through intermediate water depths. For the cases considered reasonable results were obtained using the conventional group velocity as an approximation to the geometric group velocity. Finally, monochromatic wave back tracks are not consistent with the wave sources for the examples considered.

Acknowledgments

The data were collected and the spectral analysis was done at the Naval Coastal Systems Center, Panama City, Florida by George B. Austin and Carl M. Bennett, respectively. I thank them for their help and suggestions. I was particularly indebted to the late Franklyn C. W. Olson for many hours of constructive criticism. I also thank Donald R. Del Balzo, Christopher T. Mullins, Sheryl L. Goynes, Leslie M. Tarter, and Christy Vise for their help in the preparation of this paper. The research was supported by the Office of Naval Research.

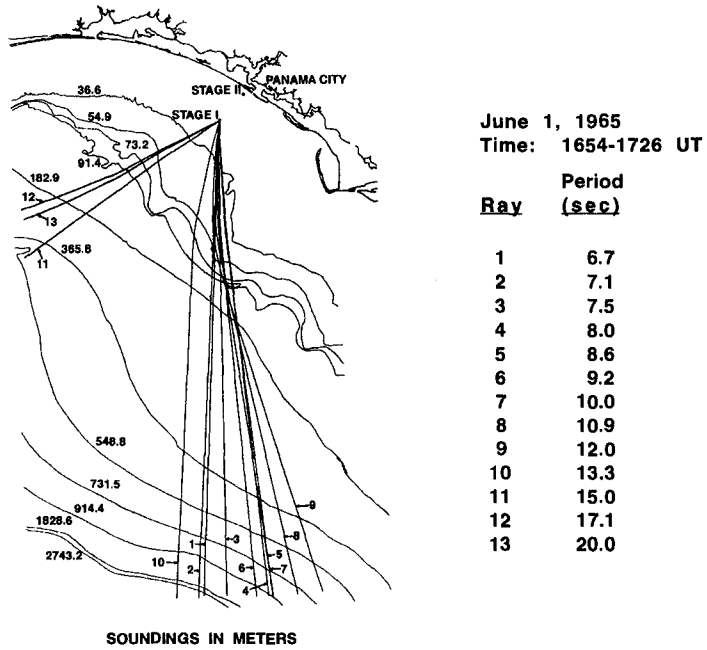


Figure 6. Monochromatic back tracks for summer storm.

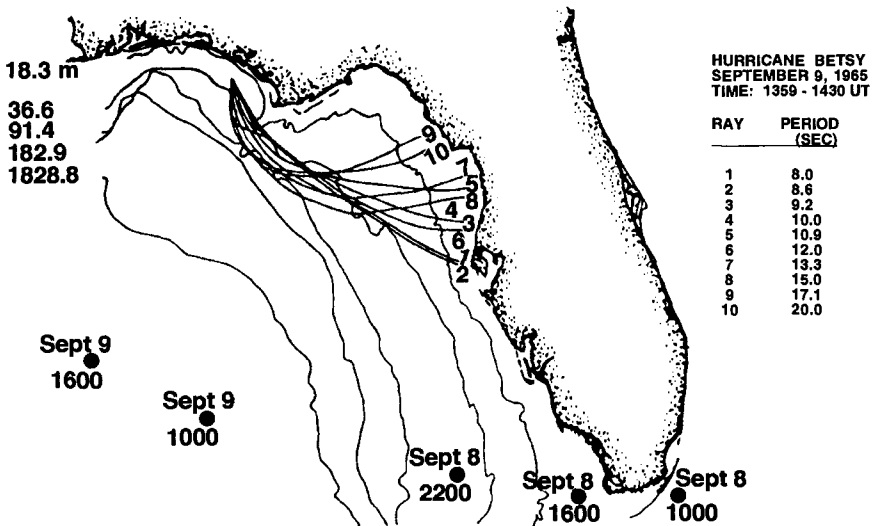


Figure 7. Monochromatic back tracks for Hurricane Betsy.

References

- Bennett, C.M. (1968). A directional analysis of sea waves from bottom pressure measurements, *Transactions: Symposium on Ocean Sciences and Engineering of the Atlantic Shelf*, Marine Tech. Soc., Washington, D.C.
- Bennett, C.M. (1972). The directional analysis of ocean waves: an introductory discussion, 2nd ed., *Naval Coastal Systems Center Report No. 144-72*, Panama City, Florida.
- Bennett, C.M., Pittman, E.P., and Austin, G.B. (1964). A data processing system for multiple time series analysis of ocean wave induced bottom pressure fluctuations, *Proceedings of the First U.S. Navy Symposium on Military Oceanography*, Vol. 1, U.S. Naval Oceanographic Office, Stennis Space Center, Mississippi.
- Breeding, J.E., Jr. (1972). *Refraction of gravity water waves*, Thesis (Ph.D.), Columbia Univ., New York, New York.
- Breeding, J.E., Jr. (1978). Velocities and refraction laws of wave groups: a verification. *J. Geophys. Res.*, Vol. 83, No. C6, pp. 2970-2976.
- Breeding, J.E., Jr. (1981a). Ray curvature and refraction of wave packets. *Proc 17th Coastal Eng. Conf.*, Am. Soc. Civil Eng., New York, pp. 82-100.
- Breeding, J.E., Jr. (1981b). Hydrons and alongshore migrating undulating beach forms. *J. Geology*, Vol. 89, pp. 260-265.
- Breeding, J.E., Jr. (1986). Velocities, refraction, and particle aspects of water waves. *Am. J. Phys.*, Vol. 54, No. 5, pp. 406-411.
- Munk, W.H., Miller, G.R., Snodgrass, F.E., and Barber, N.F. (1963). Directional recording of swell from distant storms. *Phil. Trans. Roy. Soc. of London, Series A*, Vol. 255, No. 1062, pp. 505-584.
- Wilson, W.S. (1965). A method for calculating and plotting surface wave rays, *Coastal Eng. Res. Center Tech. Memo. No. 17*, Vicksburg, Mississippi.

CHAPTER 55

WAVE CLIMATE ASSESSMENT IN THE SOUTH AEGEAN SHELF

Spiros Christopoulos¹, Christos Solomonidis²

Abstract

Wave climate parameters are estimated in a coastal area in the South Aegean Sea with the use of wave hindcast, wave transformation and spectral transformation models. The relative performance of these models is judged with the aid of a field measurements campaign. It is shown that most models can give the correct prediction in the intermediate depth waters, whereas only models taking into account nonlinear phenomena can match the measurements in the very shallow water area.

Intoduction

The correct estimation of the wave climate parameters such as wave height and period both in deep waters and in the coastal zone, is of paramount importance for the design of offshore and coastal works, safe navigation and the operation of marine systems such as fisheries.

For the determination of the wave conditions in deep and intermediate depth waters, a series of hindcast models have been developed and validated by many researchers. Second generation hindcast models are already used by various meteorological centres, as is the UK Met. Office, for daily prediction of the wave conditions, usually updated every 6 hours. Even third generation hindcast models, like the WAM, are used for hindcasts in European waters. The use of third generation models for operational purposes has been explored extensively (Komen et al., 1994).

Numerical models for wave transformation in the nearshore area have been used for many years for research and for coastal engineering design purposes as well. A large number of monochromatic wave models, based either on Berkoff's Mild Slope Equation (Berkhoff, 1976) or on geometrical physics (ray tracing) are widely used in applications. Spectral models based

-
- 1) Dr. Eng., Aristotle University of Thessaloniki, Department of Civil Engineering, Division of Hydraulics & Environmental Engineering, 540 06 Thessaloniki, Greece.
 - 2) Dr. Eng., Marine Technology Development Company S.A., 2nd Merarchias 16, 185 35 Piraeus, Greece.

on the energy balance equation are also used, whereas spectral models, which solve Boussineq type equations, including non-linear energy dissipation processes (Madsen et al., 1991) are gaining popularity recently. Research is under way for the refinement of these models in order to include the non-linear interaction of spectral ordinates (Komen et al., 1994).

Despite the variety of numerical wave models, not much work has been done for their calibration with simultaneous wave measurements, and even less in the direction of assimilating the measurements in the models themselves. The recent abundance of satellite imagery is facilitating though this task.

In the work which is presented in this paper, the wave climate in an area of the South Aegean Sea (North Coast of Crete), is assessed with the aid of wave hindcast and numerical wave transformation models as well as semi-analytical (spectral transformation) methods, in conjunction with in situ wave measurements.

Wave Measurements

A field campaign of wave measurements was conducted in the context of MAST2-WAVEMOD project at a site near Rethymno, in the North coast of Crete, Greece. The field

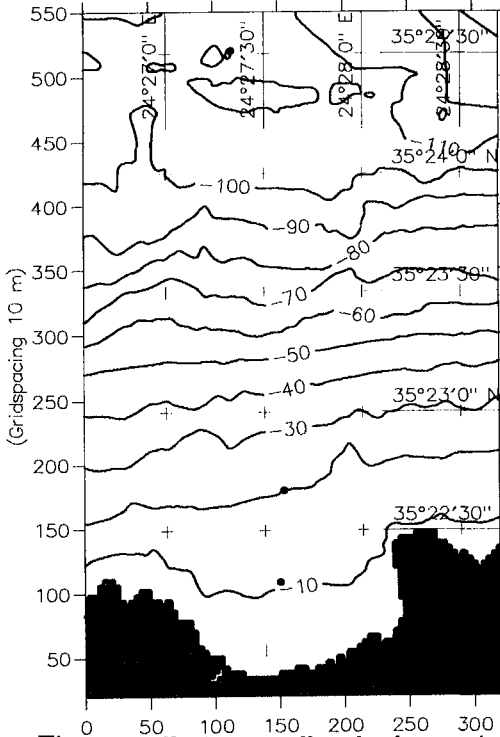


Figure 1. Rethymno Bay bathymetric grid and locations of the wave riders

campaign was conducted by the French Insitute IFREMER, subcontracting to METEOMER, with the collaboration of MARTEDEC and the Institute of Marine Biology of Crete. Two directional and one non-directional wave riders (all by Datawell) were used for the wave measurements, deployed along the predominant direction of wave attack, at three locations of different depths (100m and 10m for the directional waveriders, 20m for the non-directional). The campaign lasted for a period of 10 months, in particular from the 1st of February to the 28th November 1994. Next to each waverider, a current meter was deployed; two AANDERA RCM 7 were used at the 100 and 20 m locations, and a S4DW current and wave measuring instrument, by InterOcean, was used at the 10 m location (Solomonidis 1995, Paillard 1995).

At the same time, a fully equipped land based station was installed in a public building and overlooking the area of the experiment. The raw data (timeseries of heave and N-S & E-W translation), as well as spectral data processed on board the wave riders, were continuously transmitted via VHF to the land based station. The sampling rate for the directional buoys was 1.28 Hz, recording for 20 min every 30 min, and 2.56 Hz for the non-directional buoy, recording for 20 min every 20 min. The bathymetry of the area as well as the locations of the instruments is shown in Figure 1.

Intense climatic incidences were recorded during February (11-13), March (5-6, 10-14), October (10-16) and November (15-16, 20-24), with significant wave heights H_s from 3 - 6 m, peak periods T_p from 9 to 10 sec and predominant directions North to North West. In Figure 2 the significant wave heights H_s recorded at the location of the offshore buoy are shown.

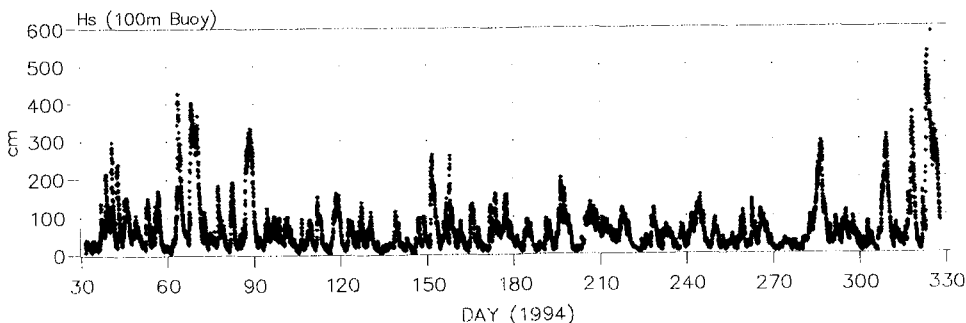


Figure 2. Time history of H_s from the 100m wave rider.

Wave Hindcast Model

The wave climate in the broader area is assessed with the aid of a second generation wave model (Christopoulos & Koutitas, 1991). The model AUT simulates the wave energy balance equation, which for deep water is written as

$$\frac{\partial F}{\partial t} + c_g \cos \theta \frac{\partial F}{\partial x} + c_g \sin \theta \frac{\partial F}{\partial y} = S_{in} + S_{nl} + S_{ds} \quad (1)$$

where $F(f,\theta;x,y;t)$ is the spectral energy density of the wave component (f,θ) at location (x,y) and time t , c_g the group velocity, S_{in} the wind input, S_{nl} the nonlinear wave energy transfer and S_{ds} the wave dissipation due to white capping.

The equation is solved using the fractional step method, where for the advection a first order upwind scheme is adopted. For the wind input the Bight of Abaco result is used, while the wave dissipation is represented by means of Komen's et al. (1984) explicit formula. The nonlinear energy transfer between the various wave components is estimated implicitly through the redistribution of the wave energy, after the above steps, according to a Jonswap spectrum having the same wave energy.

The model is implemented in the whole area of Aegean Sea with grid resolution of 1/6 of a degree. For the wind data, the ECMWF data from analysis results are used. The model output is compared with the results from

the deep buoy for the storm of March 1994 (Figure 3). As it can be seen, there is a good agreement for the characteristic wave parameters of the significant wave height and the mean wave period.

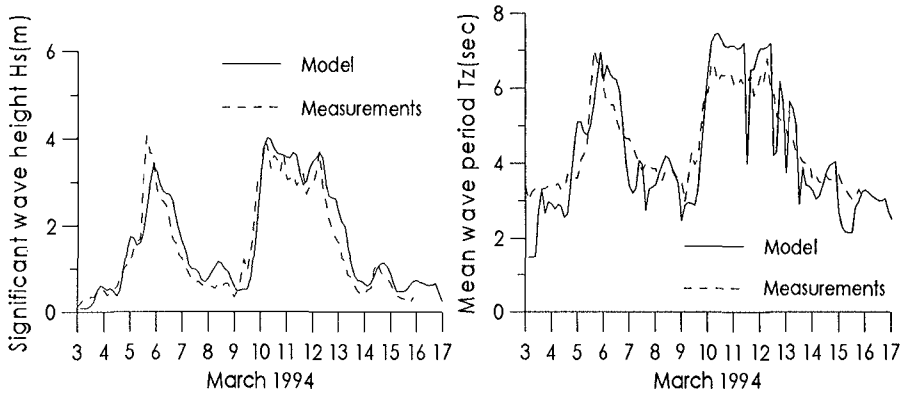


Figure 3. AUT model results for 3-17 March 1994

Numerical Wave Transformation Models

The offshore wave climate is specified either from the deep water wave hindcast model results or from the offshore wave buoy data. From the offshore location the deep water waves propagating to the coastal zone, are transformed to the shallow water waves through various physical processes like refraction, shoaling, diffraction, wave breaking, bottom friction and nonlinear energy transfer. For the simulation of these transformation processes three different numerical models are used, a shallow spectral model, an elliptic mild slope model and a Boussinesq wave model. The spectral model is a version of the AUT hindcast wave model, while the other two are belonging to DHI's suite of programs MIKE 21, namely MIKE 21 EMS (Elliptic Mild Slope) and MIKE 21 BW (Boussinesq).

The results of the models in the vicinity of the two inner buoys locations are compared with the corresponding measurements of the buoys. A short description of the numerical wave transformation models, as well as the way in which they are used in the present work, will be given in the following paragraphs.

Shallow Spectral Model

The shallow spectral model SAUT is a modified version of the AUT deep water wave model. The governing equation is

$$\frac{\partial F}{\partial t} + c_g \cos \theta \frac{\partial F}{\partial x} + c_g \sin \theta \frac{\partial F}{\partial y} + \partial \{ (c_g \cdot \nabla \theta) F \} / \partial \theta = S_{bf} + S_{ds} \quad (2)$$

where the refraction term is added on the left-hand side of the equation, while the processes of the bottom friction and wave dissipation are taken into account on the right-hand side.

The refraction term is based on Snell's law and after some manipulations is solved through

$$c_g \cdot \nabla \theta = -\frac{1}{k} \left(\frac{\partial H}{\partial x} \sin \theta - \frac{\partial H}{\partial y} \cos \theta \right) \left(\frac{-k^2 \operatorname{sech}^2 kH}{\tanh kH + kH \operatorname{sech}^2 kH} \right) \quad (3)$$

where k is the wave number and H the water depth. For the full refraction term the upstream difference in θ is expressed in flux form with the upstream direction determined by the sign of $c_g \cdot \nabla \theta$. The resulting difference for a single component may be written (Golding, 1983)

$$\begin{aligned} [\Delta F]_\theta &= -\frac{\partial}{\partial \theta} \{ (c_g \cdot \nabla \theta) F \} \Delta t \\ &= \left\{ \left[\min \begin{pmatrix} c_g \cdot \nabla \theta \\ 0 \end{pmatrix} \cdot F \right]_{\theta+\Delta\theta} + \left[\max \begin{pmatrix} c_g \cdot \nabla \theta \\ 0 \end{pmatrix} \cdot F \right]_{\theta-\Delta\theta} - [(c_g \cdot \nabla \theta) F]_\theta \right\} \frac{\Delta t}{\Delta \theta} \quad (4) \end{aligned}$$

The bottom friction is calculated using the Collins formula, while the calculated wave heights are checked using the following wave breaking criterion (Battjes & Janssen, 1978)

$$H_m = 0.88 k^{-1} \tanh(0.78 kH / 0.88) \quad (5)$$

The model is implemented on the area of Rethymno Bay with space step of 200m and time step of 15 sec. Results for the episode of March 1994 - date 03052300 (MMDDhhmm) are shown in Figure 4.

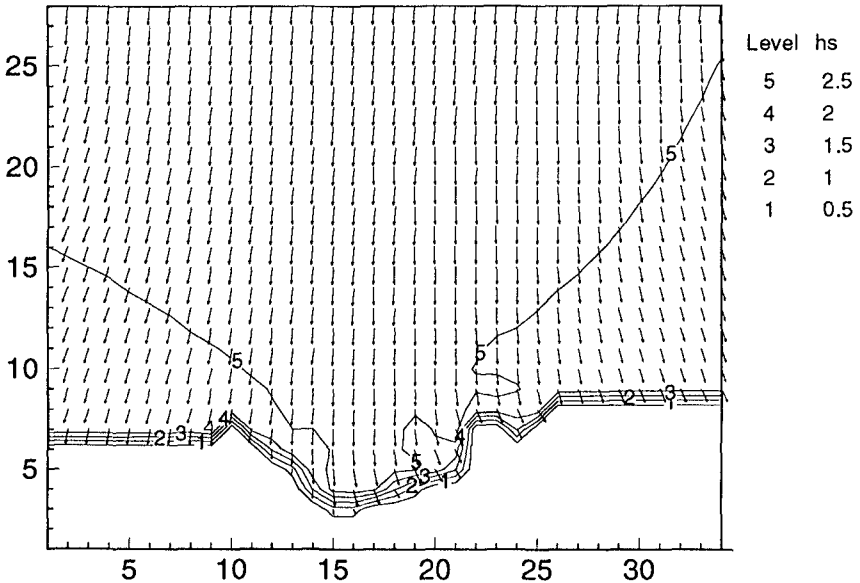


Figure 4. SAUT simulation, input $H_s=2.98\text{m}$, $T_z=6.3\text{sec}$, $\theta=185^\circ$

Elliptic Mild Slope Model

This program simulates the propagation of monochromatic waves over a gently sloping bathymetry. It basically solves numerically the Elliptic

Mild Slope equations (Berkhoff, 1976) which take into account the combined effects of shoaling, refraction, diffraction and back-scattering. The equations have been generalised in order to include the internal generation of waves, absorption by sponge layers, partial reflection by breakwaters or other structures, and energy dissipation due to bed friction and wave breaking.

The basic set of equations which are numerically solved in this model (MIKE 21 EMS manual) are the following:

$$\begin{aligned} \lambda_1 \frac{\partial S}{\partial x} + \lambda_2 S + \frac{\partial P}{\partial x} + \frac{\partial Q}{\partial y} &= SS \\ \lambda_1 \frac{\partial P}{\partial x} + \lambda_3 P + c_g^2 \frac{\partial S}{\partial x} &= 0 \\ \lambda_1 \frac{\partial Q}{\partial y} + \lambda_3 Q + c_g^2 \frac{\partial S}{\partial y} &= 0 \end{aligned} \quad (6)$$

where S, P and Q are complex variables of x , y , t expressing surface elevation and flux densities (in x and y directions) respectively, SS is the source magnitude per unit horizontal area, whereas the λ coefficients are terms which include frictions due to porous structures and sponge layers, and energy dissipation effects.

These equations are solved by implicit finite difference techniques. The double sweep algorithm is utilised, which is a form of the Gauss elimination.

The bathymetric grid which was used for the model extends to the line of -50m, which is sufficient so as to be considered as deep water conditions. A number of sponge layers is introduced in order to absorb wave energy.

Two parameters in the model set-up can be used for calibration purposes. One is the *bed friction*. For Rayleigh distributed wave heights, the energy dissipation is (MIKE21 EMS manual):

$$\frac{dE}{dt} = \frac{-1}{8\pi^{1/2}} \frac{f_e/2}{g} \left(\frac{\omega H_{rms}}{\sinh(kd)} \right)^3 \quad (7)$$

where H_{rms} is the rms value of wave height. The energy loss factor f_e is a function of the Nikuradse roughness parameter, k_N .

The other calibration factor are the friction coefficients which are used in the model to specify the partial reflection from breakwaters or from the surrounding area (in our case it is the later). The simulations showed that there is a sensitivity in the variation of these friction coefficients which specify the reflections from the rocks surrounding the area of interest.

A series of simulations were performed. Wave breaking was included in all of the simulations. The energy dissipation due to wave breaking is calculated by the Battjes and Janssen formulation.

The program calculates the maximum wave height at all grid points. In Figure 5, contour plots of the maximum wave heights are shown. In this simulation spectral parameters recorded at the 100m buoy location at 03052317 (MMDDhhmm) were used as input to the model ($H_s=3.65m$,

$T_p=9.09\text{sec}$, $\theta=359\text{ deg}$). The reflection coefficients which were used are 0.20, 0.10,0.25.

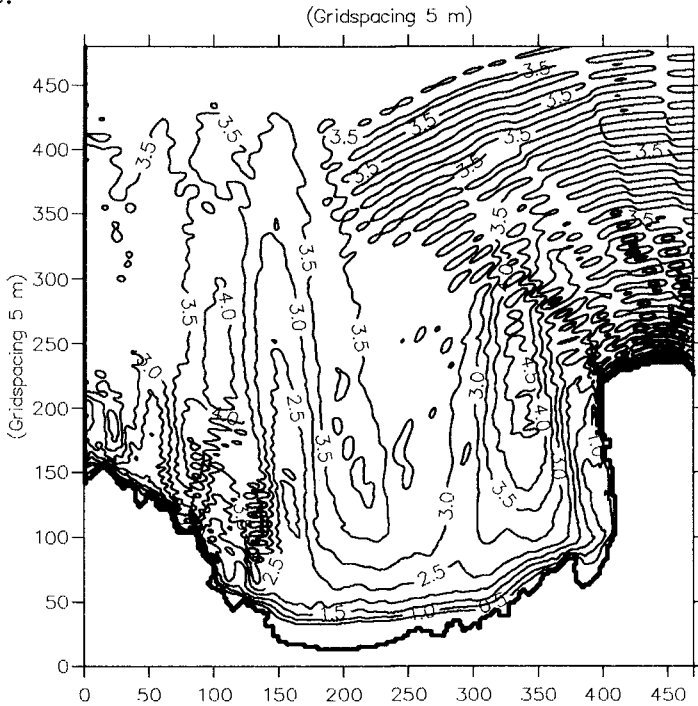


Figure 5. EMS simulation, contours of maxH, input $H=3.65\text{m}$, $T=9.09\text{sec}$, $\theta=359^\circ$.

Boussinesq Wave Model

This model is based on the numerical solution of the two-dimensional Boussinesq equations. These equations include non-linearity and frequency dispersion. In the classical form of the Boussinesq equations there is a very restrictive limitation on the maximum water depth in the simulation area ($\max d/L_0 = 0.22$). In the new forms of the equations, which are used in DHI's MIKE21 BW model, this ratio can go up to $d/L_0=0.5$ (Madsen et al., 1991).

Most wave transformation processes are taken into account in this model shoaling, refraction, diffraction and partial reflection from breakwaters and structures. Bed friction can also be included in the simulation. The only shortcoming of this model is wave breaking, which is not included in the energy dissipation processes. The basic equations, which are solved, are the continuity, the x -Momentum and the y - Momentum (Mike21 BW User Guide & Manual):

$$nS_t + P_x + Q_y = 0 \quad (8)$$

$$nP_t + \left(\frac{P^2}{h}\right)_x + \left(\frac{PQ}{h}\right)_y + n^2ghS_x + n^2P \left[\alpha + \beta \frac{\sqrt{P^2 + Q^2}}{h} \right] + \frac{gP\sqrt{P^2 + Q^2}}{C^2h^2} + n\Psi_1 = 0$$

$$nQ_t + \left(\frac{Q^2}{h}\right)_y + \left(\frac{PQ}{h}\right)_x + n^2ghS_y + n^2Q \left[\alpha + \beta \frac{\sqrt{P^2 + Q^2}}{h} \right] + \frac{gQ\sqrt{P^2 + Q^2}}{C^2h^2} + n\Psi_2 = 0$$

where S , P , Q are surface elevation, and flux density in x -direction and flux density in y -direction respectively; subscripts denote partial differentiation, h is total depth, resistance coeffs, porosity, etc are included, whereas the non-linear Boussinesq terms Ψ_1 and Ψ_2 are cross terms of derivatives of fluxes and elevation. The equations are solved by implicit finite difference techniques, with variables defined on a space staggered rectangular grid.

Due to restrictions which are imposed by the model, the bathymetry which is used in BW simulations is modified: by choosing as a minimum wave period (cut-off frequency of the spectrum) $T_{\min} = 6.02\text{sec}$, the maximum depth which can be allowed in the modelled area (assumption $d/L_0 = 0.60$, including deep water correction terms) is $d_{\max} = 34$ m, whereas with the given grid spacing $\Delta x = 5$ m and the assumption $L/\Delta x = 7$, the minimum water depth d_{\min} is 4 m. The time step Δt which is used in the simulations is chosen on the basis of the resolution and the *Courant* criteria and is set as $\Delta t = 0.18\text{sec}$.

Bed Resistance is included in the model by means of a uniform number for the whole area of simulation (Chezy number C). Sponge layers all along the coastline were introduced in the BW simulations, in order to compensate for the energy absorption due to wave breaking, which cannot be modelled here.

Storm cases from March and November were chosen to demonstrate BW modelling. As input to the models (boundary conditions) time series of flux densities generated from the spectra of the heave time series recorded at the deep water (100m) buoy were used. The spectra were truncated at $T_{\min} = 6.02\text{sec}$ or $f_{\text{cut}} = 0.17\text{Hz}$.

The output of these simulations are time series of wave elevation at all grid points of the modelled area. Contours of the significant wave heights, calculated as the RMS of the elevation time series for the whole period of simulation can also be drawn. In Figure 6 contour maps of significant wave heights H_s are plotted for the case date = 03052317, $H_s = 3.65\text{m}$, $T_p = 9.09\text{sec}$.

Spectral Transformation Methods

Spectral transformation techniques which focus on saturation, shoaling and refraction processes are also assessed by means of utilising them for the transformation of wave spectra recorded at the offshore location (100m) and comparing the resulting shallow water spectra with the ones measured at the two inner locations, for corresponding instances. Two methods are used, the TMA spectrum and the spectral slicing and reconstruction.

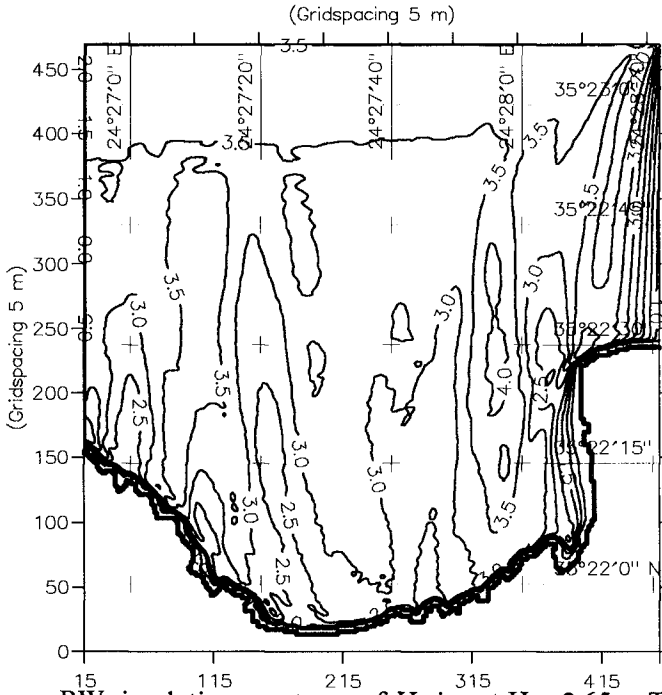


Figure 6. BW simulation, contours of H_s , input $H_s = 3.65\text{m}$, $T_p = 9.09\text{sec}$, $\theta = 359^\circ$

TMA spectrum

The TMA spectrum yields an extension of the shelf-similar JONSWAP shape to finite water depth using the expression (Bouws et al., 1983)

$$E_{TMA}(f, H) = E_j(f) \Phi_{\kappa}(\omega_H) \tag{9}$$

where $E_j(f)$ is the well known JONSWAP spectrum and $\Phi_{\kappa}(\omega_H)$ is a transformation factor calculated through the relation

$$\Phi = \tanh^2(kH) \left\{ 1 + \frac{2kH}{\sinh(2kH)} \right\}^{-1} \tag{10}$$

For a given spectrum, ie an output of the hindcast wave model or a measured spectrum at the offshore location, a JONSWAP spectrum with equivalent wave energy is estimated following the procedure, which is given in details elsewhere (Müller, 1976). Then the transformation factor for a specific depth is calculated and thus we obtain the TMA spectrum at a specific shallow site.

Spectral slicing and reconstruction

The incident wave energy spectrum, corresponding to a measurement at the outer location, is sliced to a number of discrete frequencies f_1, f_2, \dots, f_n , so that the total incident wave energy is given as:

$$m_0 = \int_0^\infty S(f)df = \sum_{i=1}^n S(f_i)\Delta f_i = E_1 + E_2 + \dots + E_n \tag{11}$$

Each component is introduced to a linear numerical wave transformation model as a monochromatic wave with the frequency of this component. The relative wave height k_i or wave disturbance coefficient for every frequency f_i is calculated at every grid point in the studied area, and the resulting wave disturbance coefficient (of the pseudo-random wave) is consequently calculated by the formula:

$$k_{res} = \sqrt{\sum_{i=1}^n \alpha_i k_i^2} \tag{12}$$

where $\alpha_i = E_i/m_0$ is the percentage of wave energy which belongs to this particular discrete frequency f_i . The coefficients k_i are weighted either by the percentage of the total wave energy on this frequency (Equal Frequency method), or by the width of the frequency band it represents (Equal Energy), and then are superimposed.

Finally, the whole spectrum at a particular location P in the shallow area can be reconstructed, using the relation:

$$S(f_i, p) = |H(f_i, p)|^2 S(f_i) = k^2_{pi} \cdot S(f_i) \text{ or } S(f_i, p) = \frac{E_i}{df_i} k^2_{pi} \tag{13}$$

where k_{pi} is the disturbance coefficient for component frequency i . In Figure 7 comparisons are shown between a measured spectrum in shallow water, a reconstructed with the equal frequency slicing method spectrum, and a TMA spectrum. We can observe that for the 20m location the agreement is good, although the slicing method cannot reconstruct the tail of the spectrum (which is expected since only a limited number of frequencies were included).

At the 10m location, the TMA grossly underestimates the spectral peak

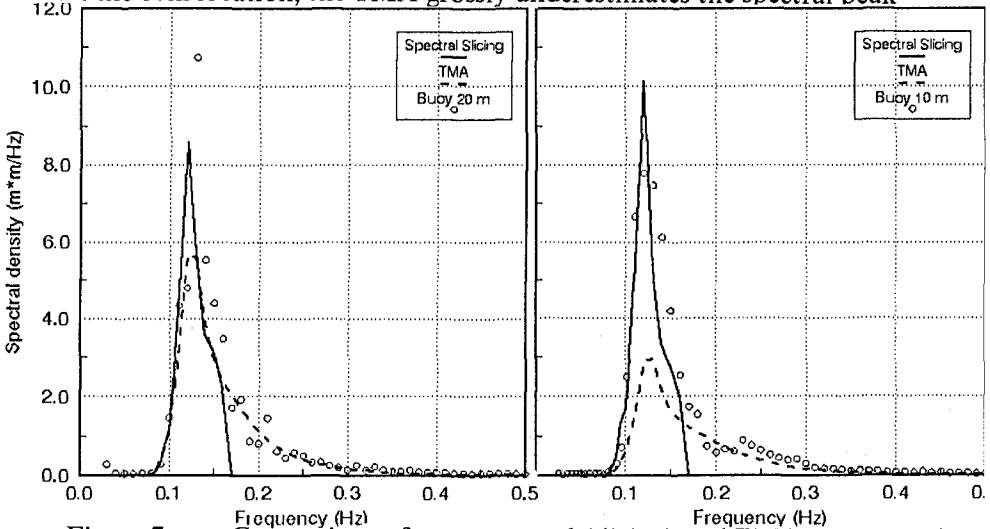
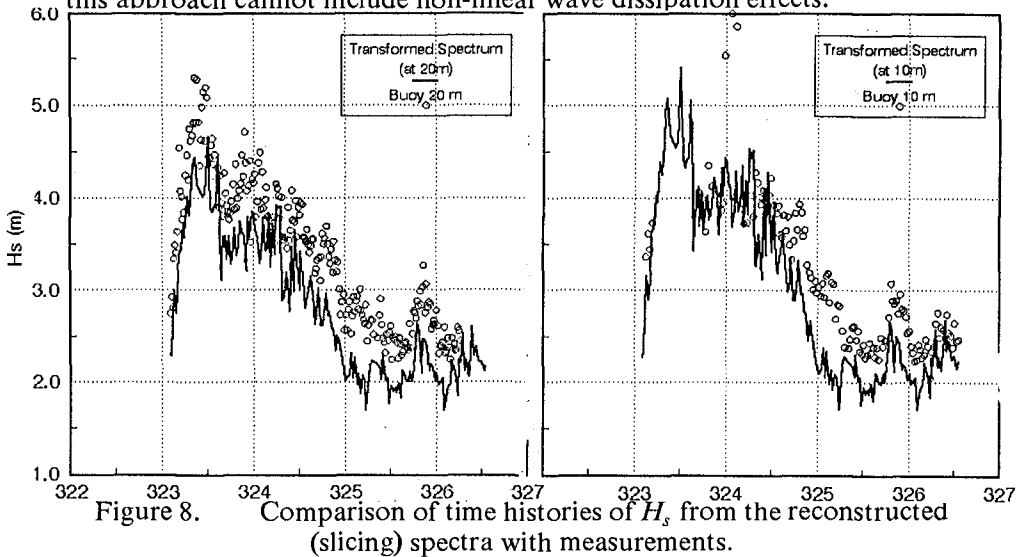


Figure 7. Comparison of reconstructed (slicing) and TMA spectra with measurements.

In Figure 8 the H_s calculated from the zero-th moment of the spectrum (slicing and reconstruction method) as $H_s=4*m_0^{1/2}$ is compared with the H_s of the measured spectrum, for a number of recordings in November 1994, for both the 20m and the 10m locations. We can see that the agreement is in general good, with some discrepancies appearing in the 10m location, since this approach cannot include non-linear wave dissipation effects.



Comparison of the methods

The methods which were employed in this work for the estimation of some of the nearshore wave climate parameters, are comparatively assessed in this section. In particular, the calculated wave heights, as they result from the numerical modelling are compared with the two inner buoys (20m and 10m) measured parameters. Transects, cutting perpendicularly to the coast are drawn on the contour maps of the solutions, whereas the corresponding measured parameters are marked on the same graphs.

In Figure 9 the case of date= 03052317, $H_s=3.65\text{m}$, $T_p=9.09\text{sec}$ and $\theta=359$ deg is presented; the results which are superimposed on the same graph are from the following simulations:

- EMS simulation with input parameters measured at the offshore location.
- BW simulation with input parameters measured at the offshore location.
- AUT shallow water simulation with input parameters calculated from the AUT hindcast model at the offshore location.
- BW simulation with input parameters calculated from the AUT hindcast model at the offshore location

It can be seen that whereas at the 20 m location most methods predict correctly the wave height, for the 10 m they overestimate it, which can be explained by the fact that they cannot include energy dissipation due to wave breaking. The BW simulation gives a better approximation, as it takes into account modal interactions. The SAUT model gives lower values overall due to initial underestimation at the offshore location.

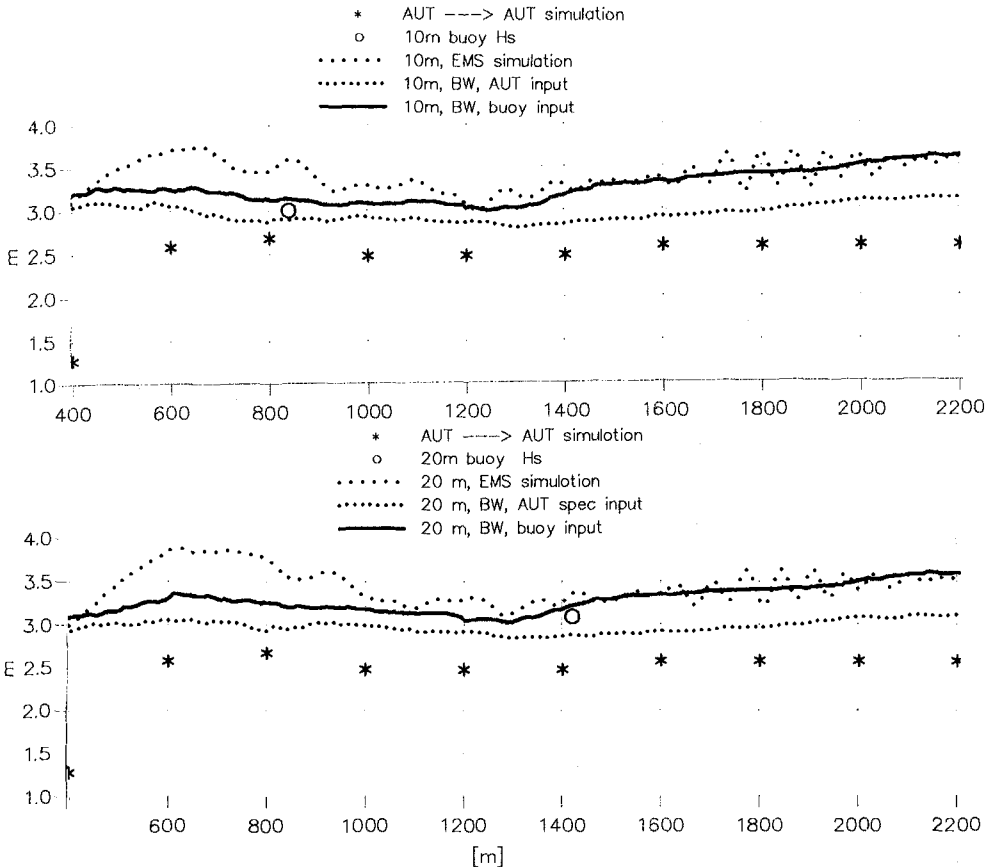


Figure 9. Comparison of estimated wave heights from various methods with measurements

In Figure 10 a comparison of the calculated disturbance coefficients for the case of date= 11201512, $H_s=4.54\text{m}$, $T_p=9.09\text{sec}$ and $\theta=0$ deg. is presented. The results which are superimposed on the same graph are from the following simulations:

- EMS simulation with input parameters measured at the offshore location.
- BW simulation with input parameters measured at the offshore location
- The Pseudo-random simulation (slicing and reconstruction)

It can be seen that whereas for the 20 m location the prediction is correct from all methods, for the 10m location the pseudo-random method is grossly overshooting, which can again be attributed to the omission of both wave breaking and the interaction between modes.

Conclusions

Wave hindcast, numerical wave transformations and spectral transformation methods are employed for the assessment of the wave climate in a coastal area. The models are calibrated with the use of 10 month's duration of in situ wave measurements.

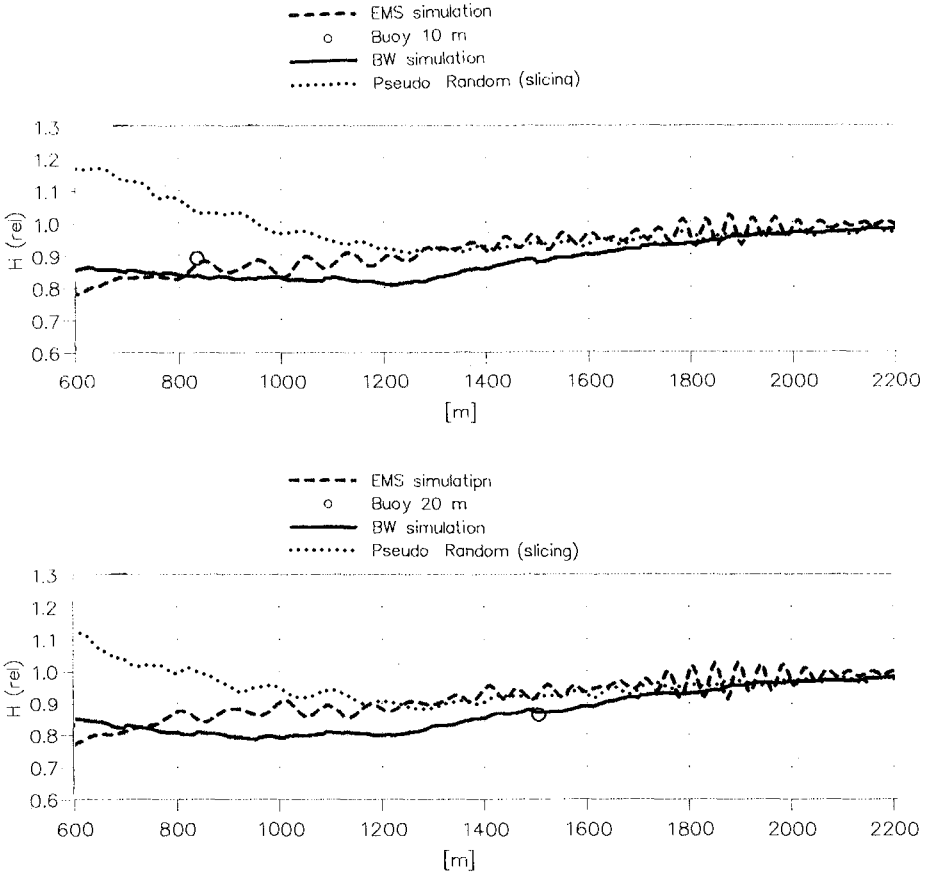


Figure 10. Comparison of estimated wave disturbance coeffs from various methods with measurements

The results of the deep water wave hindcast model compare well with the measured parameters. The results of the numerical wave transformation models match the measurements at the 20m and 10m buoys. It was found that, particularly for the monochromatic model (EMS), there is a sensitivity in the reflections from the area bordering the water. Despite the difference in scale (Δx and Δt) between the AUT shallow water model, and the BW and EMS models, they all predict correctly the wave parameters, as juxtaposed to the measurements.

Spectral transformation methods (TMA and slicing) seem to work well for the intermediate depth but not so well for the very shallow water. This is attributed to the lack of modelling both wave dissipation effects (breaking) and non-linear interactions. Great computational efficiency can be achieved though by using these methods.

Acknowledgements

The field campaign as well as part of the work of the second author has been carried out in the MAST II WAVEMOD project, in part funded by the EU contract no MAST2-CT92-0025. Part of the work of the first author was also funded by the MAST III SAFE project contract no. MAS3-CT95-0057.

References

- Battjes J.A. and Janssen J.P.F.M., 1978.
Energy loss and set-up due to breaking of random waves, Proc. 16th ICCE, ASCE, pp. 569-588.
- Berkhoff, J.C.W., 1976.
Mathematical Models for Simple Harmonic Linear Water Waves, Wave Diffraction and Refraction, Publication 163, Delft Hydraulics Laboratory, Delft, The Netherlands, pp 109.
- Bouws E., Günther H., Rosenthal W. and Vincent C.L., 1985.
Similarity of the wind wave spectrum in finite depth water, 1. Spectral form, J. of Geoph. Research, 90, C1, pp. 975-996.
- Christopoulos S. and Koutitas C., 1991.
Wave modelling in the North Aegean Sea, Ann. Geophysicae, 9, pp. 91-101.
- Golding B.W., 1983.
A wave prediction system for real-time sea state forecasting, Quart. J. R. Met. Soc., 109, pp. 393-416.
- Komen G.J., Hasselmann S. and Hasselmann K., 1984.
On the existence of a fully developed wind-sea spectrum, J. of Phys. Oceanography, 14, August, pp. 1271-1285.
- Komen G.J., Cavaleri L., Donelan M., Hasselmann K., Hasselmann S. and Janssen P.A.E.M., 1994.
Dynamics and Modelling of Ocean Waves, Cambridge University Press, pp. 532.
- Madsen P, Murray R. and Sorensen O., 1991.
A new form of the Boussinesq equations with improved linear dispersion characteristics, Coastal Engineering, 15, pp. 371-368.
- MIKE 21 EMS & BW Wave Modules, 1994.
User Guide and Reference Manuals, Rel. 2.4, DHI.
- Müller P., 1976.
Parametrization of one-dimensional wind wave spectra and their dependence on the state of development, Heft 31, Hamburger Geophysikalische Einzelschriften, pp. 177.
- Paillard M., 1995.
The Greek Field Experiment in the MAST 2- WAVEMOD- Project, IFREMER, MAST - WAVEMOD, TEC-1.3-02, March.
- Solomonidis C., 1995.
Logistical Aspects of the Greek Site experiment, MARTEDEC, MAST - WAVEMOD Project, TEC -1.3 - 05, March.

CHAPTER 56

SEA STATE PARAMETERISATION USING EMPIRICAL ORTHOGONAL FUNCTIONS

Witold Cieřlikiewicz¹ and Jerzy Graff¹

Abstract

In this paper the development of a parametric transformation linking the meteorological conditions with the sea response for the Irish Sea and the southern North Sea regions is presented. The method of *empirical orthogonal functions* and *system identification* procedures are used to develop the parameterisation. The reference data sets used in the investigation consist of high quality hindcast data (41 storm events) and field measurements (13 years) covering meteorological and sea state parameters. The method of empirical orthogonal functions is applied to the wind velocity field and it is shown that the wind field time history can be adequately represented by the first few principal components. These wind field principal components together with atmospheric pressure parameters are used to synthesise the meteorological input for system identification. The system identification procedures are then applied to develop a new efficient form of parametric model linking spatial meteorological data with sea state response.

1. Introduction

This study is a part of the NEPTUNE project (see Graff & Cieřlikiewicz 1996, and Graff *et al.* 1995) under the EU MASTII framework. It is concerned with the requirement to develop a fast and efficient scheme to predict the sea state response during extreme storms using wind field and atmospheric pressure field data. The project methodology involves a cause-effect process chain, the first part of which links the storm meteorological variables field \mathbf{M}_t and the offshore sea state variables \mathbf{X}_t . In the project a relatively long data set is available for meteorological variables \mathbf{M}_t . This is the *Norwegian Meteorological Institute—DNMI* 6-hourly gridded pressure field \mathbf{p}_t and wind field \mathbf{W}_t for the North Sea – NE Atlantic covering the period 1955–1993. In order to create long time series of offshore variables \mathbf{X}_t the parametric transformation $\mathcal{F} : \mathbf{M}_t \rightarrow \mathbf{X}_t$ has to be developed. In this paper we present a new approach to derive the parametric transformation models \mathcal{F} .

There are many classic methods for prediction of sea state determined by local winds under prescribed conditions of fetch and wind duration. The simplest assume a uniform and steady wind blowing over a limited fetch or over an unlimited ocean for time t after a sudden onset. These are cases of fetch-limited and duration-limited waves, respectively. Those methods provide a very useful first look at the wave field,

¹ British Maritime Technology Limited, 7 Ocean Way, Ocean Village, Southampton SO14 3TJ, England

but the assumption of a uniform wind field is generally unrealistic and is often a source of considerable error. Examination of regional wind fields over relatively small areas, e.g. the Irish Sea, during hurricane type storms shows that the wind field is not uniform. The variation of both the magnitude and the direction of wind velocity vector, which influences the wave field, is small but significant. The spatial pattern of the wind velocity field reflects the circulation of the air in the cyclonic direction around the centre of a moving pressure depression (see Fig. 1). Over the larger areas, the non-uniformity of the wind field is much more pronounced and the sea state wave forecasts based on fetch-limited or duration-limited algorithms cannot be usually accepted. A further limitation of these methods is their difficulty in reflecting the *dynamic* features of the metocean system, i.e., the fact that the current sea state depends not only on the current meteorological conditions but also on their history.

In this study we seek a fast and efficient prediction scheme as an alternative to conventional numerical modelling. The scheme must be capable of taking into account the non-uniformity of the wind field and should incorporate the most characteristic features of its spatial distribution concerning storm track history. Moreover it should also reflect the dynamic features of the metocean system.

When long historical time series of metocean parameters are available it becomes possible to apply *system identification* (SI) techniques to investigate the required types of prediction schemes. In this study, the available data consist of the DNMI 6-hourly gridded meteorological data \mathbf{W}_t , \mathbf{p}_t and the offshore variables \mathbf{X}_t describing the sea state in terms of both hindcast data (41 storm event periods) and 3-hourly field measurements extending over 13 years 1979–1991 at five monitoring stations near the Dutch coast (provided by the *National Institute for Coastal and Marine Management of Rijkswaterstaat—RIKZ*). The parameters selected from the RIKZ data set consist of time series of significant wave height $H_S(t)$, mean wave period $T_z(t)$, principal wave direction $\theta_0(t)$, astronomical tide and the observed still water level. The difference between the latter two was taken as the surge level $S(t)$.

The application of the SI technique in sea response modelling, when the non-uniform wind field over selected area is taken as the input data, will lead to very large model dimensions and to enormous amounts of data involved. For example, in this study for the southern part of the North Sea the area covered by a sector of 221 DNMI grid points was selected. This leads to 442 time series of wind components, each 37984 data points long. This amount of input information which has to be processed in the

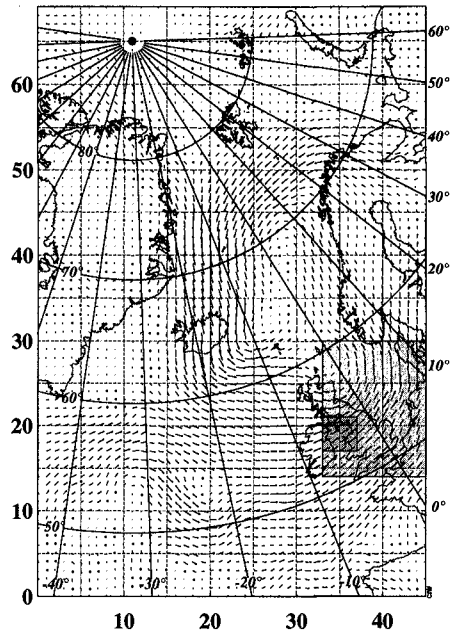


Fig. 1. DNMI wind field at elevation 10 m at 0:00h on 12 Nov 1977. DNMI grid coordinates and study areas.

SI modelling may be well beyond the capabilities of most desktop computer systems available nowadays. However, the question arise: is all that input information equally important? Certainly not. It will contain noise and, moreover, it is possible that part of that information is in a some way redundant. In order to reduce the volume of input wind data and still preserve its salient features, while filtering out most of the noise and redundant information, the *empirical orthogonal functions* (EOF) analysis is used. EOF analysis in time domain, has been variously used in meteorological, environmental, and oceanographic studies for some two decades (see e.g. Prandle & Matthews 1990, Ng 1993). It is applied here to analyse and decompose the DNMI wind field time series over two selected areas, namely the Irish Sea and the southern North Sea.

In the EOF analysis, the temporal and spatial variation of the wind field is partitioned into orthogonal spatial patterns, so called EOF modes \mathbf{e}_m , which are constant in time domain and principal components $P_m(t)$ (corresponding to each EOF mode). Each principal component $P_m(t)$ is given as a time series describing the time evolution of the corresponding EOF mode. The importance to this study is the fact that the wind field time history can be determined with sufficient accuracy by a few principal components only. Those few principal components and not the wind time series itself, are taken as the SI stimuli and are used to build the parametric models linking the meteorological parameters field \mathbf{M}_t with the offshore sea state variables \mathbf{X}_t .

We assume that input-output variables are related by a *linear dynamic system* and we use SI models in multi-input, single-output version, i.e. each component of the offshore parameters vector \mathbf{X}_t is modelled one by one. The estimated models $\mathcal{F}_{\mathcal{L}}^X : \mathbf{Q}_t^X \rightarrow X_{\mathcal{L}}$ link the meteorological input \mathbf{Q}_t^X with the output $X_{\mathcal{L}}$ which is one of the sea state parameters: $H_S(t)$, $T_z(t)$, $\theta_0(t)$ or $S(t)$ at offshore monitoring station indicated by the location index \mathcal{L} . The input \mathbf{Q}_t^X is composed using the first few wind field components $P_m(t)$ and the atmospheric pressures p_i in the selected grid points indexed by i . We use superscript X to emphasise the fact that the model input may be prepared differently for different output variables. For example, when the surge is modelled we use atmospheric pressure, which is however not the case for the wind wave variables.

Summarising, there are two important elements in this study: The EOF analysis, and SI procedure. Both are schematically depicted on Fig. 2. The EOF prepares the input data by reducing the amount of input information, i.e., by extracting only that information which is most significant. Then, the SI deals with the actual problem of building a mathematical model of a dynamical metocean system in which the sea response is stimulated by the meteorological conditions.

2. EOF analysis of wind field

2.1 Basics

Let \mathbf{W}_t denote the complex state vector formed by the M complex functions of time $W_m(t)$

$$W_m(t) = U_m(t) - \langle U_m \rangle + i(V_m(t) - \langle V_m \rangle) \quad (1)$$

where $U_m(t)$, $V_m(t)$ are the wind velocity components in m th of M locations and $\langle \cdot \rangle$ denotes the expected value of a quantity enclosed in the angle brackets. As the covariance matrix \mathbf{H}

$$\mathbf{H} = \langle \mathbf{W}_t \mathbf{W}_t^+ \rangle \quad (2)$$

is Hermitian (the cross denotes the transpose complex conjugate) it has M real eigenvalues λ_m and complex unitary eigenvectors \mathbf{e}_m which are called EOF modes and may be normalised: $\mathbf{e}_m^+ \mathbf{e}_n = \delta_{mn}$

The EOF modes \mathbf{e}_m , as eigenvectors, form a complete and orthonormal basis for \mathbf{W}_t . Thus the original wind field state vector \mathbf{W}_t may then be expanded in terms of the EOF modes

$$\mathbf{W}_t = \sum_n P_n(t) \mathbf{e}_n \quad (3)$$

The so called principal components $P_n(t)$ are obtained as

$$P_n(t) = \mathbf{e}_n^+ \mathbf{W}_t \quad (4)$$

It can be shown that the principal components compose a set of orthogonal vectors satisfying the relation $\sum_{\nu=1}^N P_{\nu\mu}^* P_{\nu\lambda} = N \lambda_n \delta_{nm}$ which shows the principal components corresponding to different

modes are uncorrelated in time and that $\lambda_m = (\sum_{\nu=1}^N |P_{\nu m}|^2)/N$ is the mean energy contained in the EOF mode \mathbf{e}_m . The fraction χ_m of the total variance (total in the sense that this is the local variance of wind velocity summed over all locations, i.e. $\text{Tr}(\mathbf{H})$) corresponding to the EOF mode \mathbf{e}_m , with the eigenvalue λ_m , is given by

$$\chi_m = \lambda_m / \text{Tr}(\mathbf{H}) \quad (5)$$

We shall assume henceforth that EOF modes are ranked in descending order according to that fraction.

Concluding, the EOF analysis separates the space-time variation of the wind field state vector into the space variation of the EOF modes which are constant in time and uncorrelated over space and the time variation of the principal components that do not depend on location in space and are uncorrelated in time. The time evolution of each EOF mode \mathbf{e}_m is described by a time series of the principal component $P_m(t)$ defined in (4). The observed wind field pattern at a given time in the study region is given by the sum of the mean wind velocity vector and EOF modes, each being modulated by the complex value of the corresponding principal component at that time. It is assumed in this study that those EOF modes that account for small fractions of total variance are not important for the physical process which is modelled. In that sense the EOF technique provides an effective way to reduce, or compress, the data and filter out most of the noise whilst retaining the most relevant information to be incorporated into the analysis.

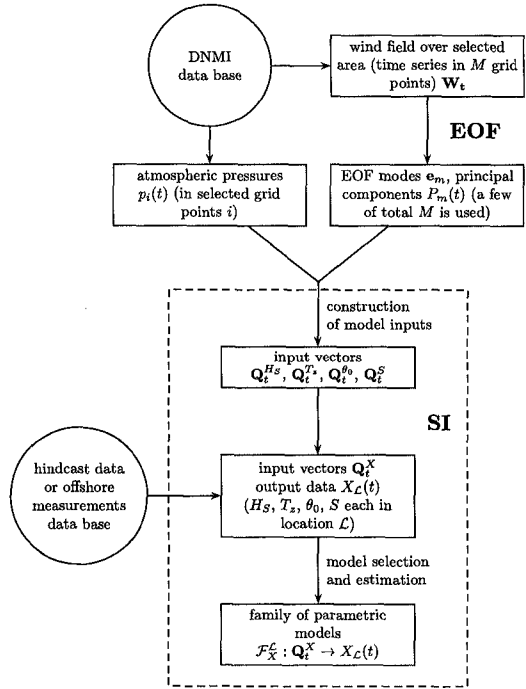


Fig. 2. Methodology for the study.

2.2 Application of EOF analysis

The DNMI 6-hourly gridded pressure field and wind field data which cover the North Sea and NE Atlantic are given in a rectangular grid on a polar stereographic projection with grid size 75 km at 60° N. The area covered by the DNMI data base and the grid used are presented on Fig. 1. In the project NEPTUNE two distinct demonstrator zones were established, one on the west coast of Great Britain and the other on the Dutch coast. The EOF analysis of wind field data was applied for both demonstrator zones. In both cases the rectangular areas for EOF analysis were selected. They are marked on Fig. 1. The area covering the Irish Sea consists of 5×5 grid points, i.e., $M = 25$. In the case of the Dutch zone, because of the open character of North Sea, much more wind time series have been subjected to the EOF analysis. The area selected for the Dutch zone consists 13×17 grid points resulting in $M = 221$.

In this section, as an example, the result of EOF analysis performed for two storm events and for two whole years over the Irish Sea is presented. Over the southern North Sea the results of EOF analysis performed for the 13 year period are described in greater detail. In Table 1 the fractions χ_m of the total variance corresponding to the first four EOF modes for the Irish Sea area are presented.

Table 1. First four EOF modes of the wind velocity field over the Irish Sea.

Mode	Percent of total variance			
	1977		1983	
	7 Nov – 17 Nov	whole year	25 Jan – 6 Feb	whole year
1	93.88	90.08	93.07	92.71
2	2.69	4.10	4.32	3.55
3	2.26	3.37	2.07	3.10
4	0.42	0.58	0.23	0.28

On Fig. 3 (a) the mean wind velocity field during the storm period 7–17 November, 1977 is shown. Fig. 3 (b) presents the associated first two modes. The most important first EOF mode containing 94% of total variance appeared to be almost uniform with characteristic “cyclonic twist” clearly visible. On Fig. 3 (c) the time histories of the first two principal component vectors during the storm are shown. The orientation of vectors is related to DNMI grid co-ordinates.

It was found that the EOF analysis performed for each of the whole year periods results in spatial patterns very similar to those obtained for the storm event only. Of course, the mean wind field over the whole year differs significantly from that calculated for storms only. The first EOF mode still consists about 90% of the total variance (see Table 1), which suggests possible usage of the EOF technique for describing the continuous time history of the wind field over the longer period covered by DNMI data set. In the case of the southern North Sea the first four EOF modes for 6 year and 13 year periods were calculated and compared. They proved very similar and it was decided to utilise the result of EOF analysis for 13 year period in further SI work.

The period 1979–1991 covered by RIKZ offshore parameters data base was selected. To adjust the 6-hourly wind velocity time series to the 3-hourly RIKZ measurements the interpolation suitable for SI analysis was performed first. Because of the greater number of the wind time series taken into the analysis ($M = 221$) and the wider area

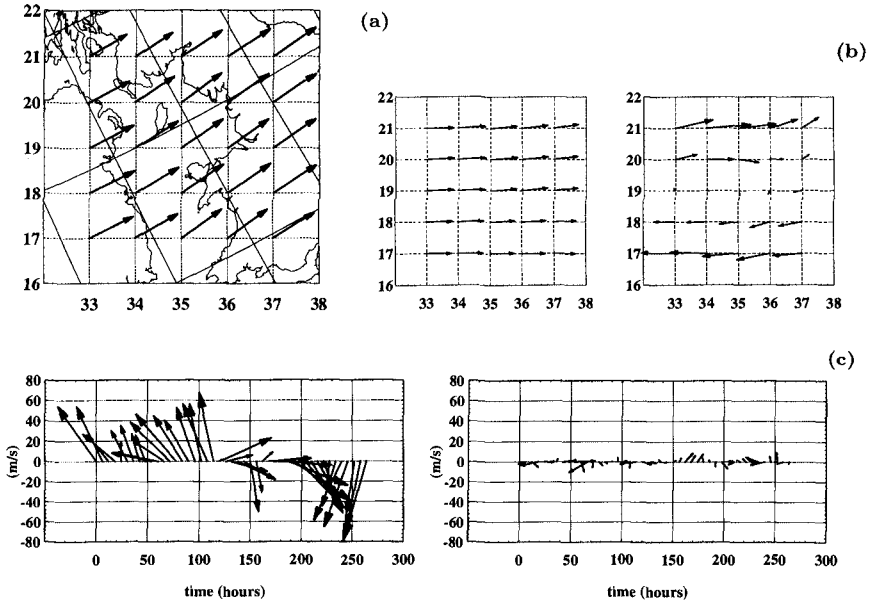


Fig. 3. EOF analysis of wind velocity field over the Irish Sea during the storm period 7 Nov – 17 Nov, 1977; (a) mean wind velocity field, scale: upper-left vector has length 10.70 m/s; (b) first (left) and second (right) EOF modes, scale: upper-left vector in the first mode has the length 0.20 (vectors of EOF modes are dimensionless); (c) evolution of first (left) and second (right) principal components, scale: left-hand side vector in the first component has the length 66.29 m/s. Time is counted starting from 0:00h of first day of storm period.

covered, the 90% of the total variance is distributed over the first eight EOF modes. The numerical values for the first eight EOF modes are given in Table 2. On Fig. 4(a) the mean wind velocity field over the area covering the 221 DNMI grid points used for the EOF analysis over 13 years is presented. Fig. 4(b) shows the first four EOF modes. Similar to the Irish Sea area case, the first mode shows the cyclonic twist characteristic for storm events determined by the depressions situated North of the Dutch coast. Also the second EOF mode is similar to the second mode of the Irish Sea case. It becomes clear that the EOF modes reflect certain characteristic features of the storm climate of both the Irish Sea and the southern North Sea areas. This is demonstrated for short storm periods and for longer one year periods as well as for the relatively long 13 year period.

Table 2. First eight EOF modes of the wind field over the southern North Sea.

Mode	1	2	3	4	5	6	7	8
Percent of total variance	59.50	15.15	9.68	3.55	2.22	1.57	1.34	1.01

On Fig. 4(c) the time series of the first four EOF principal components for one of the extreme storms selected within the study for Dutch demonstrator zone are presented for illustration.

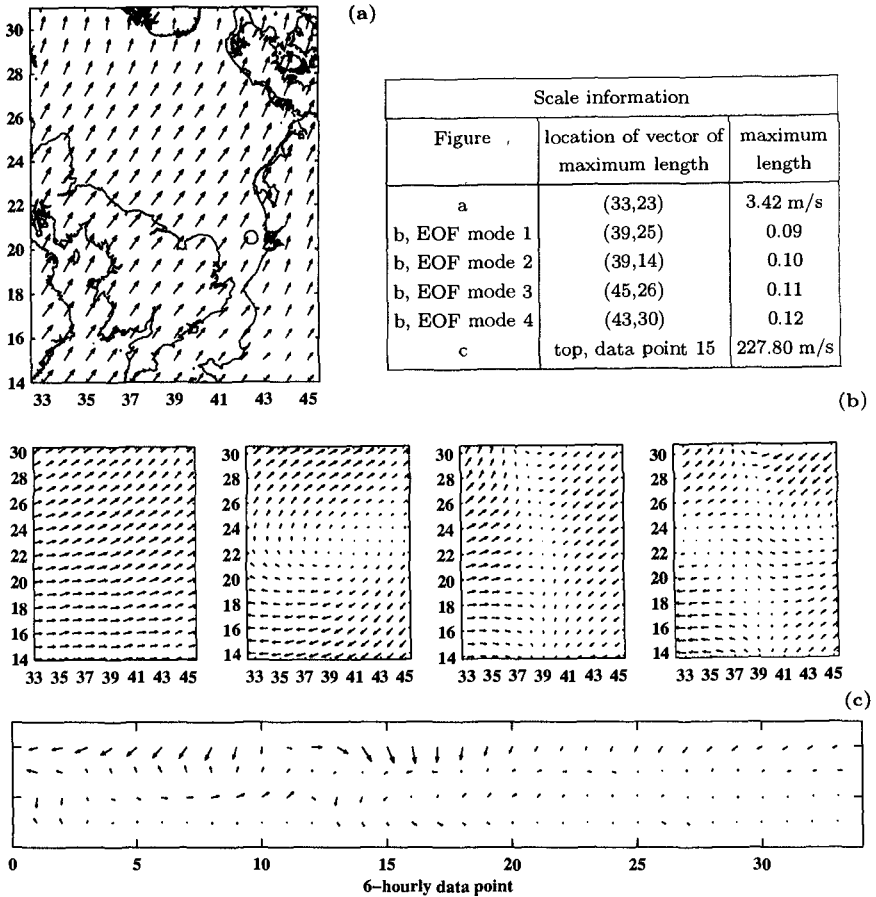


Fig. 4. EOF analysis of wind velocity field over 13 years 1979–1991 for the southern North Sea; (a) mean wind velocity field. Location of station EUR is marked with \circ ; (b) first four EOF modes (from left to right); (c) 8 days (storm No 9, Table 3) extracted from 13 year long 6-hourly time series of first four principal components (first at the top to fourth at the bottom).

In order to verify the results of EOF analysis the comparison of original wind field data \mathbf{W}_t with the wind field reproduced, according to equation (3), by the first four and eight EOF modes and principal components was performed. Examples of this comparison are shown on Figs. 5 (a) and (b). Fig. 5 (a) shows the comparison of time histories of the wind velocity at a selected grid point while Fig. 5 (b) shows the comparison of spatial distribution of the wind velocity field at a selected time instant. It can be seen that reasonably good agreement exists when the first four EOF modes are utilised and becomes very good when the first eight EOF modes are taken into account. The remarkably good agreement reflects the fact that the first eight EOF modes contain 95% of the total variance of analysed wind velocity time series, i.e., total variance calculated using reproduced wind will be equal to 95% of total variance

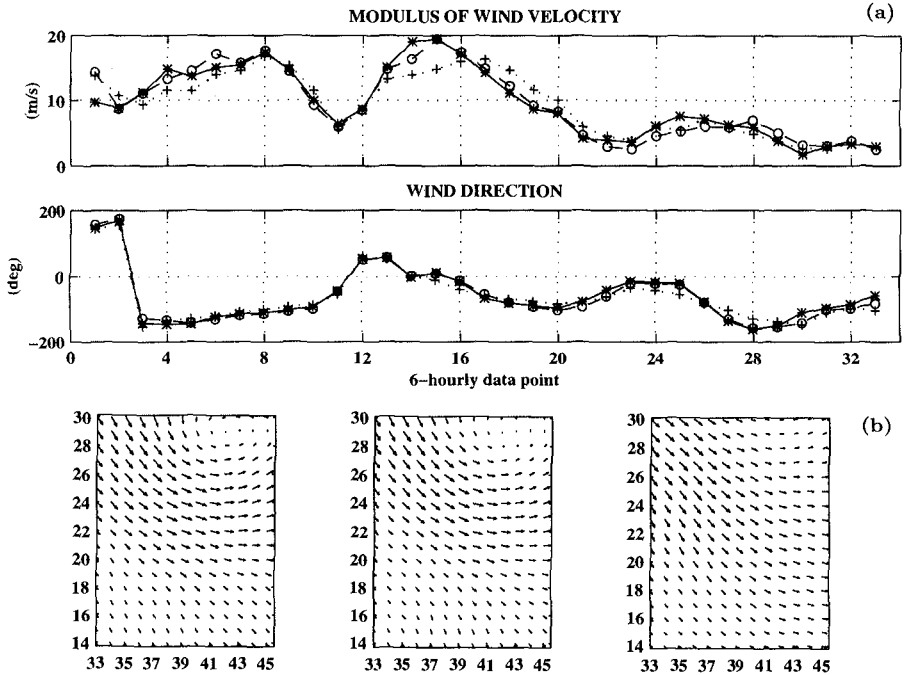


Fig. 5. Results of EOF analysis of wind data over the southern North Sea; (a) comparison of original DNMI wind velocity time series (*) with those recalculated via EOF method using first four (+) and first eight (o) principal components. Time series extending over 8 days (storm No 9, Table 3) are given in grid point (43, 24); (b) spatial distribution of DNMI wind velocity field at 12h on 12 Dec, 1990 (peak of the storm, data point 15); original distribution (to left), and recalculated using first eight principal components (in the middle) and first four (to right).

of the original wind field. This also indicates the scale of reduction in the volume of data that should be handled in further SI procedures. Namely, it shows that using 8 of the 221 EOF modes and 8 of the 221 principal components, one is able to reproduce the information contained in the original data base to a reasonably high level. In other words, using only 3.6% of the whole data set we are still able to retrieve most of the information contained within it.

3. System identification

3.1 Background

The metocean system and basic input-output configuration may be symbolically depicted as in Fig. 6. The output data $X(t)$ across the locations \mathcal{L} are the offshore sea state parameters. The principal components of wind field and atmospheric pressures compose the input data vectors Q_t of N_Q dimension. There is also some unmeasurable random disturbance \mathcal{N}_t that influences the output. We shall include that disturbance as an additive filtered white-noise \mathcal{E}_t .

We assume in this study that the metocean system can be described by a linear time-invariant model which is specified by the sequence of impulse response series

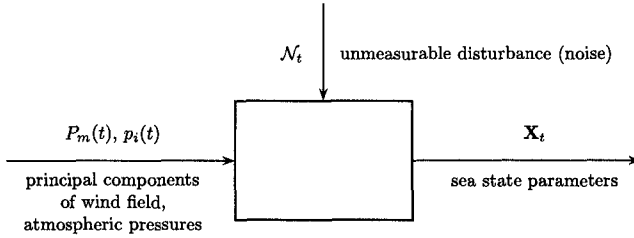


Fig. 6. Basic input-output configuration of metocean system being modelled.

$g_q(k)$, $q = 1, \dots, N_Q$ and the weighting function $h(k)$ of random additive disturbance, $k = 0, 1, \dots, \infty$, and, possibly, the probability density function of the white-noise \mathcal{E}_t .

It is worth noting, that despite the assumption of linear model we are still able to incorporate in a system the nonlinearities that have the character of a static nonlinearity at the input side, while dynamics itself is linear. In case the nonlinearity is known, say as function F , the input can be transformed as $Y(t) = F(X(t))$ and the system can be treated as linear. We have such a situation in this study were the moduli of the wind field principal components are taken as stimuli rather than the principal components themselves.

A complete model is given by the following relationship (see e.g. Ljung 1987)

$$X(t) = \mathbf{G}(f)\mathbf{Q}(t) + \mathcal{N}(t) \quad (6)$$

in which f is the forward shift operator, \mathbf{G} is the transfer function of the system and $\mathbf{G}(f)\mathbf{Q}(t)$ is short for

$$\sum_{q=1}^{N_Q} G_q(f)Q_q(t) = \sum_{k=0}^{\infty} \sum_{q=1}^{N_Q} g_q(k)Q_q(t-k) \quad (7)$$

and for any $q = 1, 2, \dots, N_q$

$$G_q(f) = \sum_{k=0}^{\infty} g_q(k)f^{-k}; \quad f^{-1}Q_q(t) = Q_q(t-1) \quad (8)$$

As mentioned above, we assume that the disturbance \mathcal{N} can be described as filtered white-noise, so

$$\mathcal{N}(t) = H(f)\mathcal{E}(t) \quad (9)$$

where

$$H(f) = 1 + \sum_{k=1}^{\infty} h(k)f^{-k} \quad (10)$$

Within SI we work with the structures that permit the specification of \mathbf{G} and H in terms of a finite number of numerical values. As it is common, we assume that $\mathcal{E}(t)$ is Gaussian, in which case the PDF is specified by the first and second moments. Thus, a particular model (6) is entirely determined in terms of a number of numerical

coefficients which are included as parameters to be determined. The purpose of SI is to determine the values of those parameters. If we denote the parameters in question by the vector θ , and if we take into account equation (9), the basic description for the modelled system becomes

$$X(t) = \mathbf{G}(f, \theta)\mathbf{Q}(t) + H(f, \theta)\mathcal{E}(t) \quad (11)$$

$p_{\mathcal{E}}(\cdot, \theta)$, the PDF of $\mathcal{E}(t)$; $\mathcal{E}(t)$ white-noise

which is a set of models, each of them associated with a parameter value θ .

One of a commonly used way of parameterising G_q and H is to represent them as rational functions of f^{-1} and specify the numerator and denominator coefficient in some way (see e.g. Ljung 1987). Such model structures, which are known as *black-box models*, were utilised in this study. A few different model structures were tested. However, in the limited frame of the present paper we are not able to present the modelling results for all of them. The examples demonstrating the results of SI with the simplest ARX model structures for the significant wave height and surge will be presented. Those models were estimates using *least-squares methods*.

ARX model structure

If in (11) we assume

$$G_q(f, \theta) = \frac{B_q(f)}{A(f)} \quad \text{for } q = 1, \dots, N_Q, \quad H(f, \theta) = \frac{1}{A(f)} \quad (12)$$

where

$$A(f) = 1 + a_1 f^{-1} + \dots + a_{N_A} f^{-N_A} \quad (13)$$

and for $q = 1, 2, \dots, N_Q$

$$B_q(f) = b_0^q + b_1^q f^{-1} + b_2^q f^{-2} + \dots + b_{N_{B_q}}^q f^{-N_{B_q}} \quad (14)$$

we obtain one of the simplest model structures, i.e., the autoregressive with extra input model (ARX). If (11) is rewritten as $A(f)X(t) = \mathbf{B}(f)\mathbf{Q}(t) + \mathcal{E}(t)$, $A(f)X(t)$ is the autoregressive part while $\mathbf{B}(f)\mathbf{Q}(t)$ is the extra input of the ARX model.

The vectorial parameter θ to be determined is in this case

$$\theta = [a_1, a_2, \dots, a_{N_A}, b_0^1, b_1^1, \dots, b_{N_{B_1}}^1, b_0^2, b_1^2, \dots, b_{N_{B_2}}^2, \dots, b_0^{N_Q}, b_1^{N_Q}, \dots, b_{N_{B_{N_Q}}}^{N_Q}] \quad (15)$$

where $N_A, N_{B_1}, N_{B_2}, \dots, N_{B_{N_Q}}$ are the orders of the multi-input ARX model.

By substituting (12) into (11) the following input-output relationship is obtained

$$X(t) + a_1 X(t-1) + \dots + a_{N_A} X(t-N_A) = b_0^1 Q_1(t) + b_1^1 Q_1(t-1) + \dots + b_{N_{B_1}}^1 Q_1(t-N_{B_1}) + \dots + b_0^{N_Q} Q_{N_Q}(t) + b_1^{N_Q} Q_{N_Q}(t-1) + \dots + b_{N_{B_{N_Q}}}^{N_Q} Q_{N_Q}(t-N_{B_{N_Q}}) + \mathcal{E}(t) \quad (16)$$

which is the *linear difference equation*. The ARX model represented by (16) is sometimes called an *equation error model* because of the way in which the white-noise term $\mathcal{E}(t)$ enters the difference equation (16).

3.2 Application in modelling of significant wave height and surge

As mentioned in the introduction, we use the RIKZ measurements as the output data for the purpose of SI. Those 3-hourly measurements covering the 13 year period 1979–1991 were recorded at five offshore monitoring stations.

In this paper, as examples demonstrating the SI carried out within the study, the modelling of significant wave height $H_S(t)$ and surge $S(t)$ in the location of the station EUR are presented. The position of the EUR station is marked on Fig. 4 (a).

Table 3. Selected extreme storms.

Storm no.	Year	Start (00:00 hrs)	End (24:00 hrs)
1	1981	21 Nov	28 Nov
2	1982	13 Dec	18 Dec
3	1983	15 Jan	22 Jan
4	1983	29 Jan	5 Feb
5	1984	11 Jan	18 Jan
6	1989	11 Feb	18 Feb
7	1990	22 Jan	29 Jan
8	1990	23 Feb	2 Feb
9	1990	9 Dec	16 Dec

Within the NEPTUNE project 41 storms over the Irish Sea and the southern North Sea were selected in order to study in a very extensive way the historical extreme coastal events. 9 of the 20 storms selected for the southern North Sea region overlap the 13 year period of the Dutch measurements. They are listed in Table 3. We use those 9 storms to present the results of SI. Namely, both the synthetic data produced by the estimated models and the measured data are plotted and the standard deviations of differences between measured and modelled values are given for the 9 storms listed in Table 3.

In order to select the structure of the model, i.e., to set up the input-vectors and decide about the combination of model orders, a *cross-validation* procedure was utilised. Namely, the data series covering the 13 year period were split into independent *working* and *validation* data sets. The working data (covering 7 years) were used for the estimation while the validation data (covering 6 years) were used to evaluate an estimated model's properties. That evaluation was done mainly by comparison of the simulated and measured output time series, and computing of the sum of squared prediction errors. The model structure resulting in the smallest sum was selected and then estimated again using the whole 13 year long data set. The synthetic data produced by those re-estimated models, for the 9 storms listed in Table 3, are shown in Figs. 7 and 8.

Below we describe the construction of the input-vectors used in SI procedures applied in the modelling of the significant wave height $H_S(t)$ and surge $S(t)$.

Significant wave height

In the modelling of significant wave height H_S the principal components of the wind velocity field for the 13 year period were taken as the only system stimuli. The units of the wind velocity field principal components P_m are, as in the case of wind velocity itself, m/s (EOF modes e_m are dimensionless). The dimensional analysis applied to the significant wave height H_S and principal components P_m suggests that the squares of the latter should be used as input in SI. However, slightly better results were obtained when $|P_m|$ to the first power were also incorporated.

The analysis of equation (3) together with the examination of the spatial patterns shown by the first and second EOF modes with reference to the geographical features of the southern North Sea led to the conclusion that the first EOF mode should have

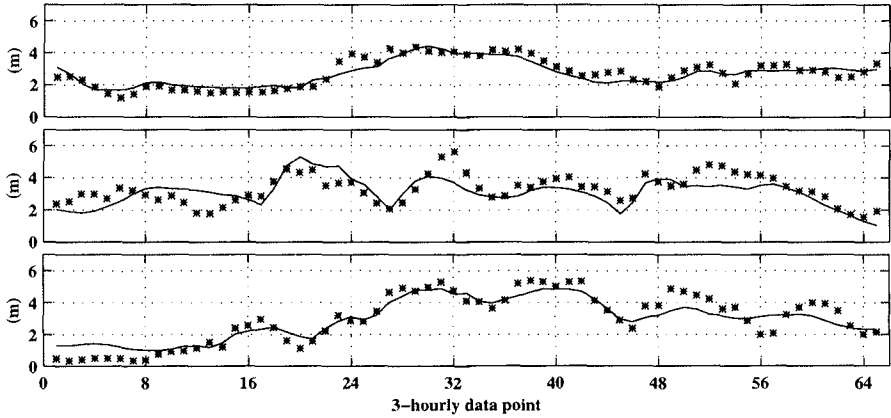


Fig. 7. Comparison between modelled (solid line) and recorded (stars) time series of significant wave height $H_S(t)$ for 3 of the 9 storms listed in Table 3: storms No 1, 5 and 8 (from top to the bottom).

greatest influence when it is rotated by an angle of about $\alpha_1 = -70^\circ$ and also $\beta_1 = 45^\circ$, while for the second EOF mode, the rotation angle of about $\alpha_2 = -80^\circ$ was selected. As a result, the projections of the first principal component P_1 on α_1 and β_1 , and the second principal component P_2 on α_2 were used in the construction of the input-vector rather than their arguments. The projection directions were then subjected to the cross-validation procedure (by varying the projection angles over the ranges around the initially selected values) which confirmed the goodness of the initial guess. In addition, the cross-validation procedure showed it was useful to introduce the second projection also for the second principal component P_2 , namely $\beta_2 = 35^\circ$.

Interestingly, it was found by cross-validation, with the projections of P_1 and P_2 taken into account, that there was no improvement arising from the greater number of components involved in the input-data vector. However, by taking the higher model orders, the modelling was improved, namely, when 7 past input values were taken into account. This suggests that the most important input information in the modelling of the sea response is involved in the first two principal components, despite the fact that they compose only about 75% of the total variance. However, longer history of the dynamic metocean system (21 hours in our case) should be taken into account.

Finally, the following input-vector \mathbf{Q}^{H_S} was selected to model the significant wave height:

$$Q_q^{H_S} = \begin{cases} |P_q| & \text{for } q = 1, 2 \\ |P_{q-2}|^2 & \text{for } q = 3, 4 \\ \Re(P_{q-4} \exp(-i\alpha_{q-4})) & \text{for } q = 5, 6 \\ \Re(P_{q-6} \exp(-i\beta_{q-6})) & \text{for } q = 7, 8 \end{cases} \quad (17)$$

in which $\Re(\cdot)$ denotes the real part of a complex number enclosed in the brackets, with the orders:

$$N_A = 0; \quad N_{B_1} = N_{B_2} = \dots = N_{B_8} = 7 \quad (18)$$

Fig. 7 demonstrates the result of ARX modelling with the structure given by (17) and (18). The standard deviation of the differences between the synthetic and measured significant wave heights are listed in Table 4.

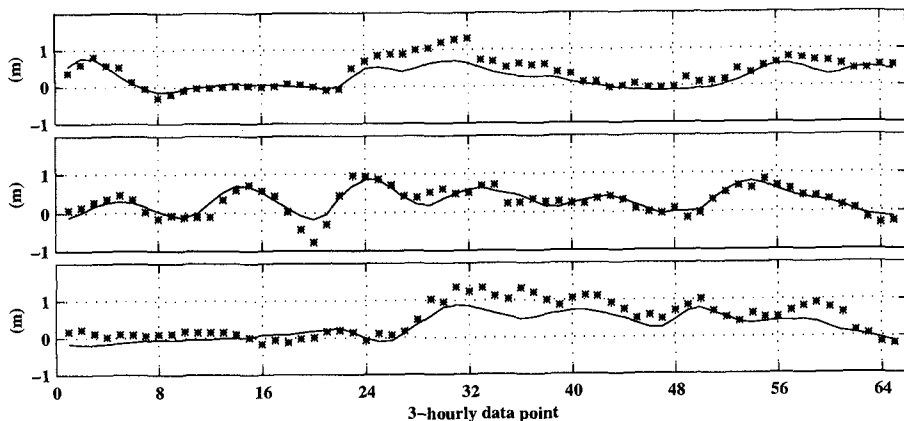


Fig. 8. Comparison between modelled (solid line) and recorded (stars) time series of surge $S(t)$ for 3 of the 9 storms listed in Table 3: storms No 1, 5 and 8 (from top to the bottom).

Surge

In its simplest form the SI can be considered to take the form of regression techniques applied in past years to examine and estimate storm surges (see e.g. Ovadia 1980 and Amin 1982). In this section the results of surge modelling using the ARX structure with the principal components of wind velocity field and local atmospheric pressure taken as the system stimuli are presented. The dimensional analysis applied to the surge S , principal components P_m and local pressure p suggests to use the squares of principal components and the atmospheric pressure to the first power. The input-

Table 4. Standard deviations of differences between modelled and recorded time series.

Calculated for	Variable and model used	
	H_S	S
	ARX (17) & (18)	ARX (19) & (20)
Storm 1	0.37	0.19
Storm 2	0.45	0.13
Storm 3	0.52	0.16
Storm 4	0.51	0.24
Storm 5	0.69	0.16
Storm 6	0.48	0.28
Storm 7	0.55	0.14
Storm 8	0.60	0.22
Storm 9	0.66	0.29
Average of 9 storms	0.54	0.20
13 years: 1979–1991	0.46	0.12

vector \mathbf{Q}^S was selected in the same manner as for significant wave height H_S (with the first two principal component projections) with additional component being the local atmospheric pressure. However, in this case, contrary to H_S case, the cross-validation analysis suggested not to take into account the first powers of the principal component moduli. Finally, the input-data vector \mathbf{Q}^S was constructed as

$$Q_q^{H_S} = \begin{cases} |P_q|^2 & \text{for } q = 1, 2 \\ \Re(P_{q-2} \exp(-i\alpha_{q-2})) & \text{for } q = 3, 4 \\ \Re(P_{q-4} \exp(-i\beta_{q-4})) & \text{for } q = 5, 6 \\ p & \text{for } q = 7 \end{cases} \quad (19)$$

with the orders:

$$N_A = 0; \quad N_{B_1} = N_{B_2} = \dots = N_{B_7} = 7 \quad (20)$$

The local pressure p was computed from the DNMI pressure data base by bi-linear interpolation of the time series taken from the four neighbour DNMI grid points.

The surge time series created by the ARX model with the structure given in (19) and (20) are demonstrated in Fig. 8. The standard deviations of errors are listed in Table 4.

4. Conclusions

Comparison between the modelled and observed time series of both significant wave height and surge level present a sufficiently good agreement to prove effectiveness of the new approach. In the case of significant wave height for 9 storms examined, the standard deviations of differences between the predicted and observed values appeared to be of the same order as those found for the second generation numerical wave forecasting model utilised within the project. Extreme values are found to be underestimated which may be due to possible inconsistency between the input and output data, i.e., the DNMI synthetic wind field and the Dutch field measurements. Further research is being directed to improve the modelling of individual extremes.

This study was carried out as a part of the NEPTUNE project funded by the Commission of the European Communities, Directorate General for Science, Research, and Development under MAST contract No. MAS2-CT94-0081. The Royal Norwegian Meteorological Institute and the National Institute for Coastal and Marine Management (RIKZ) provided data utilised in this study. We are especially grateful to Dr John de Ronde of RIKZ for his permission to access the Dutch offshore station data.

References

- Amin, M. 1982. On analysis and forecasting of surges on the west coast of Great Britain. *Geophys. J. R. astr. Soc.*, **68**, 79–94.
- Graff, J. & Cieřlikiewicz, W. 1996. Determining NW European coastal extremes within the NEPTUNE project. *Proc. 25th Coastal Engng Conf., ICCE'96*, Orlando, Florida.
- Graff, J., Cieřlikiewicz, W., de Haan, L., de Ronde, J., Holt, T., Hurdle, D., Rosenthal, W., & Tawn, J. 1995. NEPTUNE—An integrated approach to determining NW European coastal extremes. *Proc. Second MAST Days and EUROMAR Market*, Sorrento, **1**, 685–700.
- Ljung, L. 1987. *System identification: theory for the user*. Prentice-Hall, Inc., Englewood Cliffs, New Jersey.
- Ng, B. 1993. Tidal current predictions using rotary empirical orthogonal functions. *J. Atmos. Oceanic Technol.*, **10**, No. 6, 868–879.
- Ovadia, D. C. 1980. A regression model for the statistical prediction of extreme sea levels at Liverpool. *Rep. No. 102*, Institute of Oceanographic Sciences (unpublished manuscript).
- Prandle, D. & Matthews, J. 1990. The dynamics of nearshore surface currents generated by tides, wind and horizontal density gradients. *Contin. Shelf Res.*, **10**, 665–681.

CHAPTER 57

Fully Nonlinear Properties of Periodic Waves Shoaling over Slopes

Stéphan T. Grilli¹, M. ASCE, and Juan Horrillo²

ABSTRACT : Shoaling of finite amplitude periodic waves over a sloping bottom is calculated in a *numerical wave tank* which combines : (i) a Boundary Element Model to solve Fully Nonlinear Potential Flow (FNPF) equations; (ii) an exact generation of *zero-mass-flux Streamfunction Waves* at the deeper water extremity; and (iii) an *Absorbing Beach* (AB) at the far end of the tank, which features both free surface absorption (through applying an external pressure) and lateral active absorption (using a piston-like condition). A feedback mechanism adaptively calibrates the beach absorption coefficient, as a function of time, to absorb the period-averaged energy of incident waves.

Shoaling of periodic waves of various heights and periods is modeled over 1:35, 1:50, and 1:70 slopes (both plane and natural), up to very close to the breaking point. Due to the low reflection from both the slope and the AB, a quasi-steady state is soon reached in the tank for which local and integral properties of shoaling waves are calculated ($K_s, c, H/h, kh, \eta_m, S_{xx}, \dots$). Comparisons are made with classical wave theories and observed differences are discussed. Parameters providing an almost one-to-one relationship with relative depth kh in the shoaling region are identified. These could be used to solve the so-called *depth-inversion problem*.

INTRODUCTION

In the coastal region, incident ocean waves propagating towards the shore (in direction x ; Fig. 1) increasingly feel the effects of the reducing depth $h(x)$, due to the sloping ocean bottom. These effects induce significant changes in wave shape, height H , length L , and phase celerity c , while the wave period T stays closely constant. Predicting such changes (usually referred to as *wave shoaling*) up to the point waves become unstable and break (breaking point; BP) is one of the important tasks of coastal

¹Distinguished Assoc. Professor, Dept. of Ocean Engng., University of Rhode Island, Narragansett-RI 02882, USA, email: grilli@oce.uri.edu, <http://www.oce.uri.edu/~grilli>

²Graduate Student, same address

engineering. Characteristics of waves at the BP indeed are used to design coastal structures and predict littoral sediment transport; detailed wave kinematics at the BP is also needed for surfzone models which are increasingly used in coastal engineering research and design. In the more specific problem referred to as *depth inversion*, one seeks to predict the nearshore bottom topography based on observed characteristics of shoaling waves (e.g., through remote sensing). Hence, simple relationships between these and $h(x)$ are sought after.

In most wave transformation models used so far, shoaling of deep water waves is calculated based on linear or weakly nonlinear theories (e.g., modified Boussinesq eqs.) and using semi-empirical breaking criteria to locate the BP. Such theories, however, despite their satisfactory predictions in deep and intermediate water, may not be sufficiently accurate close to the BP where wave height reaches a significant fraction of the depth. Highly nonlinear waves have been modeled using a higher-order Fourier steady-wave theory (FSWT), e.g., by Sobey and Bando³ (1991). In the latter work, up to three conservation equations for mass, momentum, and energy flux, are expressed to propagate incident waves over a mildly sloping bottom. In such an approach, however, the bottom slope is replaced by a cascade of horizontal steps and, hence, wave profiles do not take the characteristic skewed shape observed in experiments before breaking occurs. As a result, wave kinematics and dynamics cannot be well represented close to the BP⁴. Finally, in this approach, breaking corresponds to the highest wave which is stable over constant depth. This is quite unrealistic since, as we will see, skewness and unsteadiness allow waves to reach a larger height before they break.

To accurately predict wave properties close to the BP, we will show that, in addition to full nonlinearity, even for mild slopes, the influence of bottom topography on wave shape must be included in shoaling models. Time dependent models based on fully nonlinear potential flow (FNPF) theory have this capability, provided proper wave generation and absorption methods are implemented (e.g., 2D : Klopman, 1988; Grilli *et al.*, 1989; Cointe, 1990, Cooker, 1990; Ohyama and Nadaoka, 1991; 3D : Romate, 1989; Broeze, 1993). Hence, with such models, a "numerically exact" solution can be obtained for waves shoaling over an arbitrary bottom geometry, for which no approximation other than potential flow theory is made.

NUMERICAL MODEL

The two-dimensional FNPF model by Grilli, *et al.* (1989, 1990, 1996) will be used to compute characteristics of periodic waves shoaling over both plane and natural slopes, up to a very high fraction of the breaking height (Fig. 1). FNPF computations can

³Also see their detailed review of other similar works. Note, Johnson and Arneborg (1995) followed a similar approach using a fourth-order perturbation method.

⁴The authors nevertheless assume that integral properties should be insensitive to such details and are thus well predicted by a FSWT. The latter assumption is quite questionable, since radiation stresses, for instance, are strongly influenced by wave skewness.

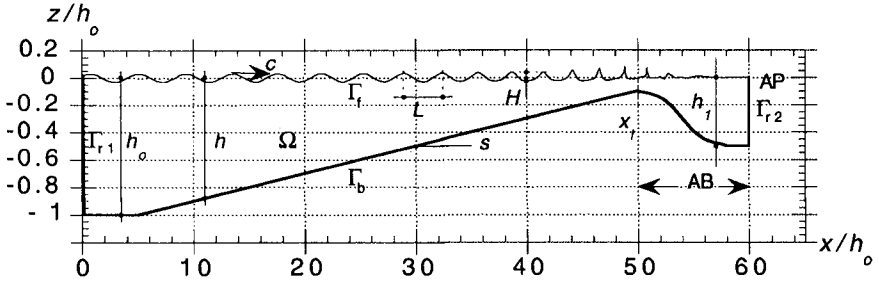


Figure 1: Sketch for FNPF computations of a periodic wave shoaling over a plane slope s , in a “numerical wave tank”.

model overturning waves but, by nature, are limited to prior to the time touch-down of a breaker jet first occurs. This does not pose problems when solitary waves are used in the analysis, as it has often been the case in the past⁵. For periodic or irregular waves, however, an *absorbing beach* (AB) must be used to absorb the energy of incident waves, hence eliminating reflection and preventing these from breaking at the top of the slope.

Grilli and Horrillo (1996) implemented such an AB in the model over a shallower region located in the upper part of the slope whose geometry was specified somewhat similar to natural bars on beaches⁶ (Fig. 1). Energy absorption combined both free surface and lateral absorption with an adaptive calibration of the absorption coefficient : (i) an exterior counteracting pressure is specified on the AB free surface, proportional to the normal particle velocity (Cointe, 1990; Cao *et al.*, 1993), to create a negative work against incident waves; this is shown to absorb high frequency wave energy well; (ii) a piston-like (active) absorbing boundary condition is specified at the tank extremity Γ_{r2} (“absorbing piston”, AP), which is shown to absorb low frequency wave energy well (Clément, 1996); (iii) the AB’s absorption coefficient is adaptively calibrated in time to absorb the period-averaged energy of incident waves entering the beach at $x = x_l$. Grilli and Horrillo developed and tested this AB and showed that wave reflection could be reduced to a few percent only. Hence, in a “numerical wave tank” such as sketched in Fig. 1, computations for periodic waves can reach a quasi-steady state for which properties of shoaling waves can be calculated, up to very close to the BP, and compared to results of other shoaling methods (theory or models), which usually assume there is no reflection from the slope or beach. [In the present method, reflection from the slope still occurs as it does in nature.]

Incident waves can be arbitrary in the model but, for sake of comparison with other wave theories, permanent form wave solutions of the FNPF problem are generated on the leftward boundary (Γ_{r1} , Fig. 1). These are so-called streamfunction waves

⁵In such cases, FNPF calculations can predict characteristics of breaking solitary waves within 2% of experimental measurements (Grilli *et al.*, 1994, 1997)

⁶In this case, gradual deshoaling of waves occurs in the AB which helps absorbing wave energy.

(SFW; Dalrymple 1974; Dean and Dalrymple 1984) which, unlike finite amplitude waves produced by a wavemaker, do not exhibit the generation of higher harmonics and the beat phenomenon observed in wave tanks as they propagate over constant depth (e.g., Chapalain *et al.*, 1996). Since SFW's have a non-zero mass flux, they are generated in the model together with a mean current, equal and opposite to their period-averaged mass transport velocity (Grilli and Horrillo, 1996). Hence, volume stays constant within the "numerical wave tank" as it would on a beach for which the undertow current balances the incident mass flux at some distance from the shore.

Details of model equations, numerical methods and validation applications can be found in the above-referenced papers. It will just be mentioned that Laplace's equation is solved in the model, over domain Ω , based on a higher-order Boundary Element Method (BEM) derived from Green's 2nd identity. Boundaries are discretized using N nodes and M higher-order elements are specified to interpolate in between the nodes. Quadratic isoparametric elements are used on lateral and bottom boundaries (Γ_{r1} , Γ_{r2} , Γ_b) and cubic elements ensuring continuity of the slope are used on the free surface boundary Γ_f (Grilli and Subramanya 1996). The nonlinear free surface kinematic and dynamic boundary conditions are time integrated using second-order Taylor series expansions expressed in terms of a time step Δt and of the Lagrangian time derivative. Numerical errors are kept to a very small value by adaptively selecting the time step based on a mesh Courant number $C_o(t)$ (Grilli and Svendsen, 1990; Grilli and Subramanya 1996). In shoaling computations, as waves become increasingly steep towards the top of the slope, discretization nodes may get quite close to each other and create quasi-singular values for the BEM integrals, leading to poor accuracy. Hence, the adaptive regridding method developed by Grilli and Subramanya (1996) is used to automatically regrid nodes three by three when the distance between two nodes is either more than 4 times or less than 0.25 times the distance between the previous two nodes. In the following applications, a minimum of 20 nodes per wavelength is maintained throughout shoaling.

APPLICATIONS

Figure 1 illustrates a typical set-up for shoaling computations : (i) incident zero-mass-flux SFW's are generated on Γ_{r1} (in depth h_o , with height H_o and period T ; o-indices denote deep water values); (ii) waves propagate up the sloping bottom and are absorbed in the AB/AP; (iii) since reflection is very small from both the sloping bottom and the beach, computations soon reach a quasi-steady state for which successive waves undertake similar transformations (see Grilli and Horrillo, 1996, for a detailed discussion of numerical parameters and results); (iv) model parameters are tuned-up to let incident waves shoal up to impending overturning before they are absorbed in the AB. Numerical "wave gages" are specified at several fixed locations, $x = x_g$, over the slope where wave characteristics are calculated, both on the free surface (e.g., elevation $\eta(x_g, t)$) and as a function of depth z (e.g., velocity $u(x_g, z, t)$, dynamic pressure $p_D(x_g, z, t)$).

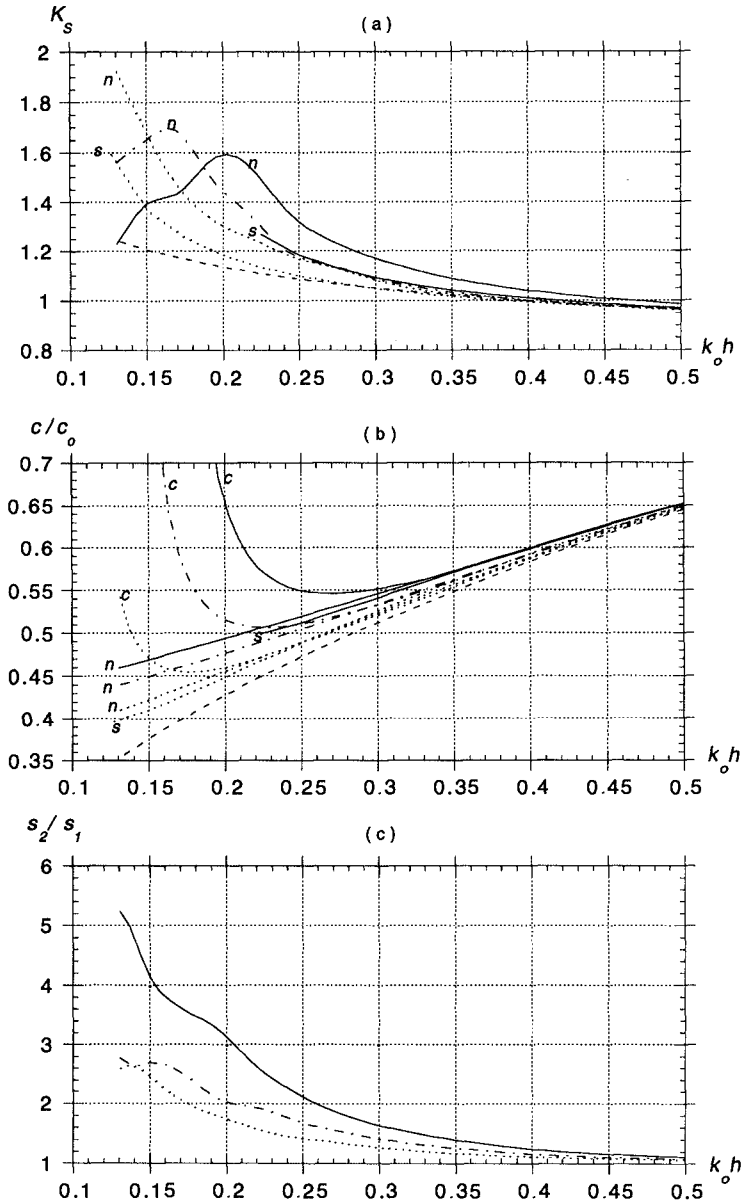


Figure 2: (a) shoaling coefficient $K_s = H/H_0$; (b) celerity c ; and (c) left/right asymmetry s_2/s_1 , for periodic waves shoaling over a 1:50 slope, with $H'_0 = H_0/h_0 =$ (- - -) 0.04, (- - -) 0.06, and (—) 0.08, and $T' = T\sqrt{g/h_0} = 5.5$: (n) FNP results; (s) Sobey and Bando's (1991) FSWT results; (---) LWT results; (c) CWT results. $c_0 = gT/(2\pi)$ is the (linear) deep water celerity.

Local wave properties

After quasi-steady state is reached, successive incident waves are identified and tracked in the results : (i) envelopes of crest and trough elevations are calculated, from which wave height $H(x)$ and shoaling coefficient $K_s(x) = H/H_o$ are obtained; (ii) phase velocity $c(x)$ is calculated from the time derivative of crest trajectories; (iii) to quantify wave skewness, forward and backward normalized wave slopes are calculated as, $s_2(x) = H_2/(s_o L_2)$ and, $s_1(x) = H_1/(s_o L_1)$, respectively, in which (L_1, L_2) and (H_1, H_2) denote horizontal and vertical distances from a crest to the previous and next troughs, respectively, and $s_o = 2H_o/L_o = k_o H_o/\pi$. Results show that these quantities are quite well reproduced as a function of x , for successive incident waves (Grilli and Horrillo, 1996); in the applications, however, to eliminate small variations, ensemble averages of these quantities for each x are calculated over at least 4 successive waves.

In the model, waves are found to shoal up the slope, qualitatively, as expected from linear wave theory (Fig. 1) : (i) both wavelength L and celerity $c = L/T$ continuously decrease; (ii) deshoaling first occurs, with a reduction in wave height, followed by shoaling and an increase in wave height up to the top of the slope where waves almost reach overturning before entering the AB and decaying.

More specifically, in Fig. 2, K_s , c , and s_2/s_1 have been plotted as a function of normalized depth $k_o h$, for a bottom slope $s = 1:50$ and three incident waves of normalized incident height $H'_o = H_o/h_o = 0.04, 0.06, \text{ and } 0.08$, and normalized period $T' = T\sqrt{g/h_o} = 5.5$ ($k_o = (2\pi)^2/(gT^2)$ is the (linear) deep water wavenumber). Results of linear (LWT) and cubic (CWT) Stokes wave theories are also indicated. For $k_o h < 0.5$, significant differences are observed between FNPF results and the wave theories; this also corresponds to $kh = 2\pi h/L < 0.77$ (or $H/h > 0.10$; see Fig. 4b). For diminishing depths, due to increased nonlinearity, both K_s and c become significantly larger than predicted by LWT (Figs. 2a and 2b) and, as could be expected, increasingly so with the incident wave height. CWT predicts celerity better for shallower depths but diverges in very shallow water. The more accurate FSWT performs reasonably well for predicting celerities (Fig. 2b) but does quite poorly for wave heights (Fig. 2a). This is likely due to the lack of skewness in modeled waves whereas FNPF results for s_2/s_1 (Fig. 2c) show that waves are significantly skewed—i.e., forward tilted, left/right asymmetric—for very shallow water (see also Fig. 1 for spatial wave profiles).

The significant differences observed in Fig. 2 between FSWT and FNPF results show that, even for a very mild slope, the influence of actual bottom shape on local wave properties is important. Fig. 3 now investigates how this influence varies with bottom slope. An incident wave with $H'_o = 0.06$ and $T' = 5.5$ is shoaled up three plane beaches of slopes $s = 1:35, 1:50, \text{ and } 1:70$, and a “natural beach” geometry with an average slope of 1:50. The natural beach has a depth variation defined according to Dean’s equilibrium beach profile, $h = A(x^* - x)^{2/3}$, with x^* denoting a constant, function of the location of the toe of the slope in depth h_o , and A depending on the

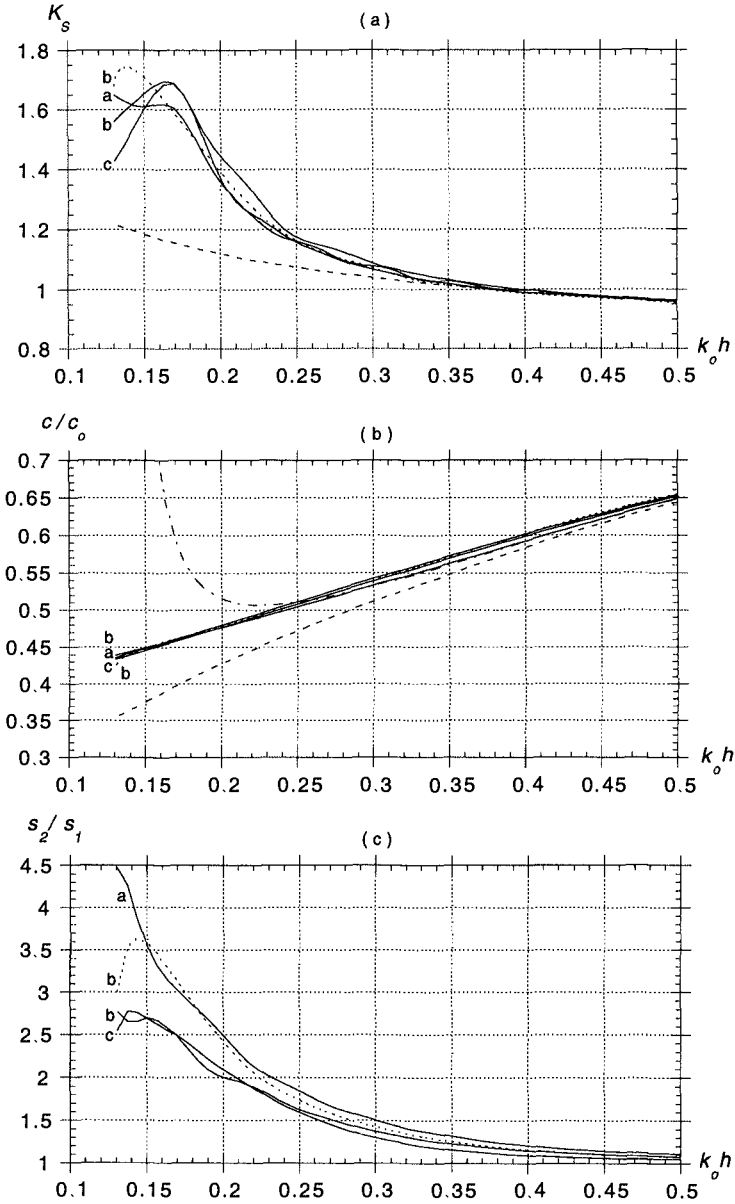


Figure 3: FNPF results for : (a) shoaling coefficient; (b) celerity; and (c) left/right asymmetry, for periodic waves with $H'_o = 0.06$ and $T' = 5.5$, on : 1:35 (curve a); 1:50 (curve b); 1:70 (curve c), plane (—) or natural (----) beaches. (---) LWT results; (- - -) CWT results.

specified average slope. This “natural beach”, hence, has a milder slope in deeper water and a steeper slope in shallower water. For the wave height and celerity, Figs. 3a and 3b show fairly small differences between results calculated for the same depth on various slopes, for most of the shoaling region. The wave left/right asymmetry— s_2/s_1 , shown in Fig. 3c—seems to be more sensitive to bottom slope, becoming larger for the shallower parts of the (steeper) 1:35 slope and the “natural beach”. Overall, however, no major differences are observed provided wave properties are compared for the same normalized depth.

Results in Fig. 3 imply that, for a given depth, local wave properties vary little for the same wave propagating over a range of mild slopes from 1:35 to 1:70. Hence, a broader parametric study will be carried out on a 1:50 slopes only, for 9 waves combining heights, $H'_o = 0.04, 0.06, \text{ and } 0.08$ and period, $T' = 5.5, 6.5, \text{ and } 7.5$. Results for each wave are given in Fig. 4 as a function, this time (due to the varying wave period), of the relative local depth kh . First, in Fig. 4a, we see that, for the phase celerity normalized by the linear wave celerity, $c_l = c_o \tanh kh$, the larger the incident wave height and the smaller the period (or similarly the larger $k_o H_o$) then, for a given kh , the larger the celerity increase with respect to c_l . Such results illustrate the well known amplitude dispersion effects due to increasing wave steepness⁷ kH which, for the studied cases in shallow water ($kh < \pi/10$), lead to a 40 to 85% maximum increase in celerity with respect to linear wave theory. In Fig. 4b, we see that, in all cases, the wave height to depth ratios H/h reach $\mathcal{O}(1)$ values in the shallow water region, confirming the very strong nonlinearities. A similar analysis of shoaling coefficients would show that linear wave theory significantly underpredicts wave height for depths corresponding to $H/h > 0.2$ (which also corresponds to the region where celerity is significantly underpredicted in Fig. 4a); for the studied cases this underprediction of K_s is up to 55%. With regard to these results, it is anticipated that the quantity, $kH/(k_o H_o) = K_s/(c/c_o)$, i.e., the local wave steepness normalized by the deep water steepness, should exhibit somewhat less variations (i.e., overprediction) with respect to linear wave results, since underprediction of wave height and celerity should compensate each other to some extent. This is confirmed in Fig. 4c where we see, first of all, that all FPNF results follow quite a similar increase as a function of kh , up to maximum steepness, and that results of LWT (i.e., $K_s/\tanh kh$) are a better predictor of normalized wave steepness, with a maximum underprediction of only 11%, than for the other wave properties discussed above. Considering the many differences in wave shape, height and length, and kinematics, observed between FPNF and LWT results, the latter result is somewhat unexpected.

Integral wave properties

These are the mean water level η_m , the mean undertow current U_m , the energy flux E_f , and the radiation stress S_{xx} . In the model, integral properties are computed at

⁷Such effects are predicted at third-order by Stokes theory (CWT).

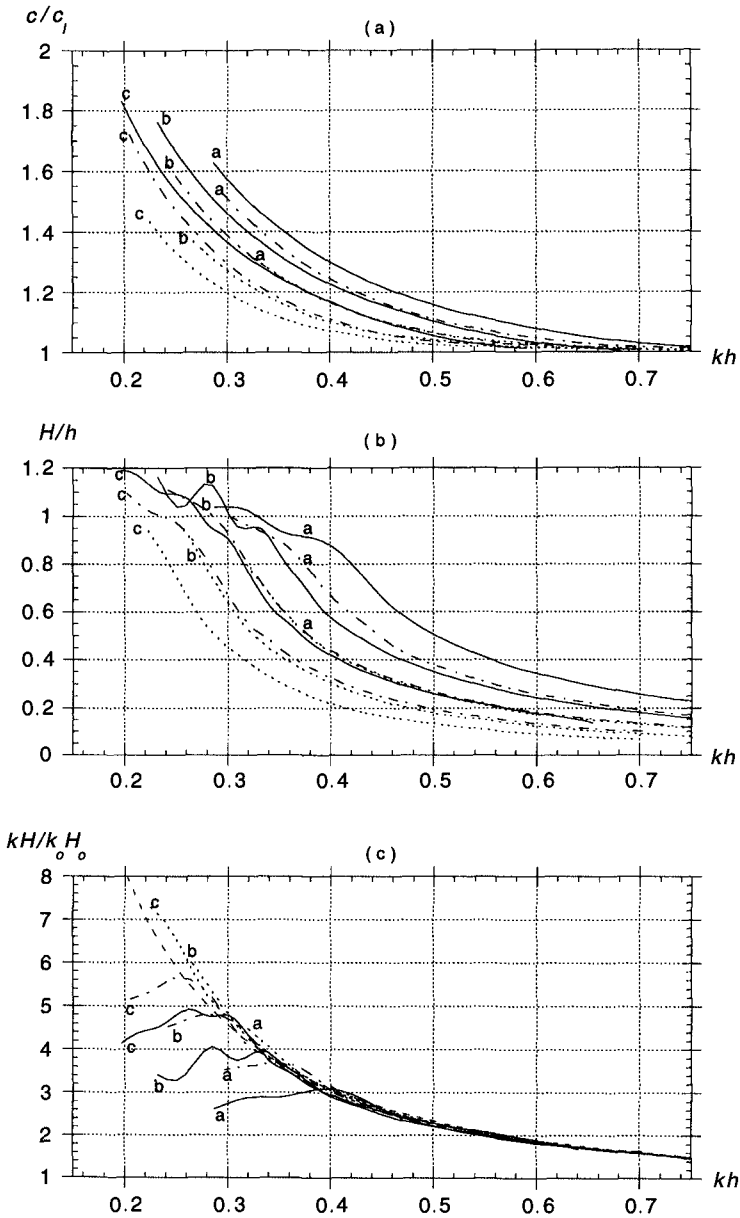


Figure 4: Periodic waves shoaling over a 1:50 slope. $H'_o = (- - -)$ 0.04, $(- \cdot - \cdot)$ 0.06, and (—) 0.08, and $T' = : 5.5$ (curves a); 6.5 (curves b); 7.5 (curves c). $(- - -)$ LWT results; $c_l = c_o \tanh kh$, is the linear wave celerity.

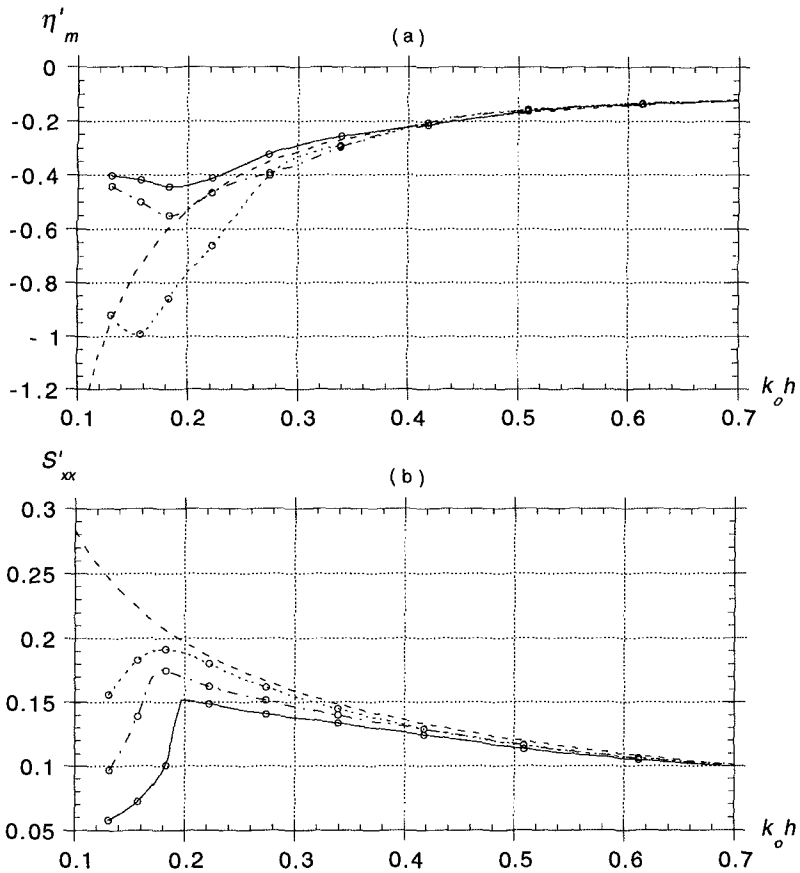


Figure 5: Normalized (a) mean water level $\eta'_m = \eta_m/h_o H_o'^2$; and (b) radiation stress $S'_{xx} = S_{xx}/\rho g H_o'^2$ (with ρ the fluid density), for three periodic waves shoaling over a 1:50 slope. Symbols and definitions are as in Fig. 2. Results have been averaged over $3T$ in the quasi-steady regime. Symbols (\circ) denote locations $x = x_g$ of "numerical gages". Corrections, $\Delta\eta'_{mo} = -0.0274$ and $\Delta S'_{xxo} = h'_o(\Delta\eta'_{mo}) + (\Delta\eta'_{mo})^2/2$, have been applied to the linear results for η'_m and S'_{xx} , respectively, to account for the actual mean water level in depth h_o in the FNPF results.

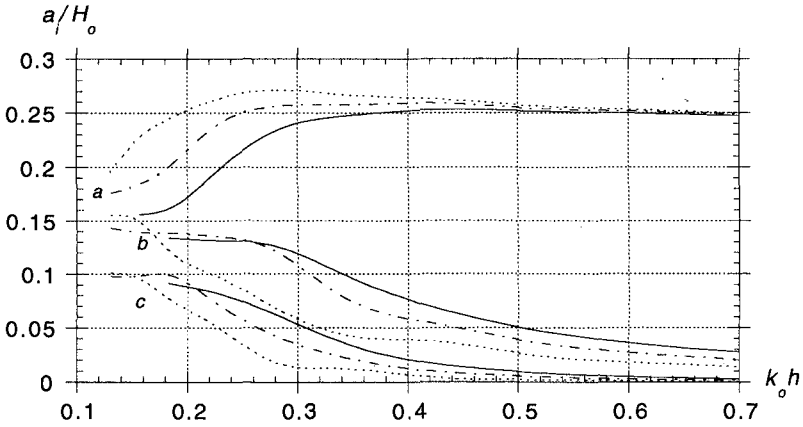


Figure 6: Normalized amplitudes of first three harmonics (a,b,c), a_i ($i = 1,2,3$), for three periodic waves shoaling over a 1:50 slope. Definitions are as in Fig. 2.

“numerical gages” located at $x = x_g$ above the sloping bottom using classical equations, i.e., through depth integrations and wave period-averaging involving, $\eta(x_g, t)$, $\mathbf{u}(x_g, z, t)$ and $p_D(x_g, z, t)$. To account for the non-zero mean Eulerian velocity in the model (resulting from specifying zero-mass-flux incident waves at boundary Γ_{r1}), and for the set-down η_m , expressions of integral properties are corrected following Klopman (1990) and Jonsson and Arneborg (1995). In the model, time averaging is performed at time t , for the results calculated from time $t - T$ to t . Time series of integral properties are thus obtained for each gage location x_g . When computations reach a quasi-steady state, integral properties stabilize to fairly constant values in time for each gage location. To eliminate small time fluctuations and oscillations of integral properties with respect to these constant values, averages are calculated over $3T$, before results are analyzed.

In all cases, the energy flux is found to be very close to constant at the gages located in the region where wave height increases (e.g., over the shoaling parts of curves in Figs. 2a and 3a). This indicates that reflection is small from both the sloping bottom and from the AB. As depth decreases, the mean undertow current increases roughly proportionally to $1/h$, as expected from the period-averaged continuity equation, and then decreases when wave height starts decreasing.

Mean water level and radiation stress results are given in Fig. 5, for the same three waves as in Fig. 2, shoaling over a 1:50 slope. As expected, the normalized η_m in Fig. 5a follows a trend opposite to S_{xx} in Fig. 5b, first setting-down over the slope and then stabilizing towards the top of the slope and increasing in the AB due to wave height reduction. In shallow water, the set-down becomes relatively larger, the smaller the incident wave, as a result of the steeper drop in radiation stresses for the larger waves. Results obtained from a first-order nonlinear perturbation of LWT

(FNLT; Dean and Dalrymple, 1984) and adjusted to match the initial FNPF set-down in depth h_o , show reasonable agreement with FNPF results. In the shallower region at the top of the slope, however, FNLT results do not capture the leveling-up of η_m . Radiation stresses in Fig. 5b gradually increase while wave height increases and depth decreases, following the expected pattern from FNLT, which predicts results quite well in the deeper water region. At some stage, however, FNPF results become smaller than FNLT results, and more so, for a given depth, the larger the incident wave height. A more detailed analysis of these results would show that this decrease in S_{xx} is strongly correlated with the increase in "skewness index" s_2/s_1 , shown earlier in Fig. 2c for $k_o h < 0.45$; this confirms that radiation stresses are quite sensitive to wave shape.

Fourier analysis

Another way of analyzing how wave shape changes during shoaling is to calculate Fourier transforms of wave surface elevations $\eta(x_g, t)$ obtained at fixed gages at $x = x_g$. Harmonic amplitudes can then be plotted as a function of x_g . This was done in Fig. 6 which shows normalized amplitudes of the first three harmonics a_i ($i = 1, 2, 3$), for the same three waves as in Fig. 2 shoaling over a 1:50 slope. In all cases, in the shoaling region where wave height increases (Fig. 2a), after a slight initial increase, a_1 decreases while a_2 and a_3 continuously increase. This indicates that, in shoaling periodic waves, energy is being continuously transferred to higher-order harmonics, as a result of nonlinear interactions. As could be expected, for a given depth, this nonlinear energy exchange is stronger, the larger the incident wave height, and the energy transfer to the higher-order harmonics thus starts occurring in deeper water. Not surprisingly, variations of the "skewness index" s_2/s_1 in Fig. 2c are strongly correlated with variations of a_2 and (particularly) of a_3 in Fig. 6.

Conclusions

A numerical wave tank was used to model finite amplitude periodic waves shoaling over a sloping bottom. Periodic waves of various heights and periods, covering the range $k_o H_o = [0.028, 0.105]$, were modeled over 1:35, 1:50, and 1:70 slopes (both plane and natural), up to very close to the breaking point. Due to the low reflection from the slope and the AB, a quasi-steady state was soon reached in the tank for which both local and integral properties of fully nonlinear shoaling waves were calculated (K_s , c , s_2/s_1 (left/right asymmetry), H/h , kH , η_m , S_{xx}).

For a shallow enough normalized depth ($k_o h < 0.5$ or $kh < 0.77$), significant differences are observed between FNPF results and 1st (LWT), 3rd (CWT), and higher-order steady wave (FSWT) theories. For the first two theories, low-order nonlinearity is clearly the main reason for the observed differences in a region where $H/h = \mathcal{O}(1)$; in the latter theory, the lack of wave skewness and the representation of the bottom by horizontal steps likely explain the observed differences.

Despite the significant effects of actual bottom shape on the results, for the range of tested mild slopes, FNPF results are found fairly similar for the same wave taken at the same normalized depth ($k_o h$ or kh). This, hence, allows us to use kh as the *unique parameter* describing a mild bottom variation and to compute additional results on a unique mild slope (1:50). In these results, for the range of tested waves, the normalized wave steepness, $kH/k_o H_o$, shows an almost one-to-one relationship with kh in the shoaling region. Steepness thus could be used to solve the so-called *depth-inversion problem*. Quite surprisingly, due to a partial compensation of nonlinear effects for the wave height and celerity, LWT is found quite a good predictor of this parameter (maximum difference is 11%), whereas discrepancies for H and c reach 55 and 85%, respectively.

For the tested waves, set-down is quite well predicted by the first-order perturbation of LWT, except in the shallower region, where it is smaller, following the steep drop in radiation stresses. [This could also be partly due to the mean undertow current. More work remains to be done about this.]. Radiation stresses are overpredicted by the first-order theory in the region where wave left/right asymmetry s_2/s_1 (i.e., skewness) becomes large, confirming the sensitivity of this parameter to wave shape. Otherwise, agreement with the theory is quite good. A Fourier analysis of surface profiles $\eta(x_g, t)$ calculated for gages located at $x = x_g$ shows a continuous transfer of energy from the fundamental to higher-order harmonics in the shoaling region, illustrating nonlinear interactions in the shoaling wave field. The 3rd-harmonic amplitude a_3 is strongly correlated with s_2/s_1 .

Acknowledgments

This publication is the result of research sponsored by the US Naval Research Laboratory, Stennis Space Center, grants N-00014-95-1-G607 and N-00014-96-C012, from the Remote Sensing Division (code 7240). The kind assistance of Dr. Peter Smith is gratefully acknowledged.

References

- [1] Broeze, J., *Numerical Modelling of Nonlinear Free Surface Waves With a 3D Panel Method*. Ph.D. Dissertation, Enschede, The Netherland, 1993.
- [2] Cao, Y., Beck, R.F. and Schultz, W.W., An Absorbing Beach for Numerical Simulations of Nonlinear Waves in a Wave Tank. *Proc. 8th Intl. Workshop Water Waves and Floating Bodies* (St. John's, 5/93) pps. 17-20, 1993.
- [3] Chapalain, G., Cointe, R. and Temperville, A., Observed and Modeled Resonantly Interacting Progressive Water-waves. *Coastal Engng.*, **16**, 267-300, 1996.
- [4] Clément, A., Coupling of Two Absorbing Boundary Conditions for 2D Time-domain Simulations of Free Surface Gravity Waves. *J. Comp. Phys.*, **126**, 139-151, 1996.

- [5] Cointe, R., Numerical Simulation of a Wave Channel. *Engng. Analysis with Boundary Elements*, **7** (4), 167-177, 1990.
- [6] Cooker, M.J., A Boundary-integral Method for Water Wave Motion over Irregular Bed. *Engng. Analysis with Boundary Elements*, **7** (4), 205-213, 1990.
- [7] Dalrymple, R.A., 1974, A Finite Amplitude Wave on a Linear Shear Current, *J. Geophys. Res.*, **79**(30), 4498-4504.
- [8] Dean, R.G. and Dalrymple R.A., *Water Wave Mechanics for Engineers and Scientists* Prentice-Hall, 1984.
- [9] Grilli, S.T., and J., Horrillo, Numerical Generation and Absorption of Fully Nonlinear Periodic Waves. *J. Engng. Mech.* (accepted), 1996.
- [10] Grilli, S., Skourup, J., and Svendsen, I.A., An Efficient Boundary Element Method for Nonlinear Water Waves, *Engng. Analysis with Boundary Elements*, **6**(2), 97-107, 1989.
- [11] Grilli, S.T. and Subramanya, R., Numerical Modeling of Wave Breaking Induced by Fixed or Moving Boundaries. *Computational Mech.*, **17**, 374-391, 1996.
- [12] Grilli, S.T., Subramanya, R., Svendsen, I.A. and Veeramony, J., Shoaling of Solitary Waves on Plane Beaches. *J. Waterway Port Coastal and Ocean Engng.*, **120** (6), 609-628, 1994.
- [13] Grilli, S. and Svendsen, I.A., Corner Problems and Global Accuracy in the Boundary Element Solution of Nonlinear Wave Flows, *Engng. Analysis with Boundary Elements*, **7**(4), 178-195, 1990.
- [14] Grilli, S.T., Svendsen, I.A. and Subramanya, R., Breaking Criterion and Characteristics for Solitary Waves on Plane Beaches. *J. Waterway Port Coastal and Ocean Engng.*, **123** (3) (in press), 1997.
- [15] Jonsson, I.G. and Arneborg, L., Energy Properties and Shoaling of Higher-order Stokes Waves on a Current. *Ocean Engng.*, **22** (8), 819-857, 1995.
- [16] Klopman, G., Numerical Simulation of Gravity Wave Motion on Steep slopes. *Delft Hydraulics Report No. H195*, 1988.
- [17] Klopman, G., A Note on Integral Properties of Periodic Gravity Waves in the Case of a Non-zero Mean Eulerian Velocity. *J. Fluid Mech.* **211**, 609-615, 1990.
- [18] Ohyama, T. and Nadaoka, K., Development of a Numerical Wave Tank for Analysis of Nonlinear and Irregular Wave Fields. *Fluid Dyn. Res.* **8**, 231-251, 1991.
- [19] Romate, J.E., The Numerical Simulation of Nonlinear Gravity Waves in Three Dimensions using a Higher Order Panel Method. *Ph.D. Dissertation. Department of Applied Mathematics, University of Twente, The Netherland*, 1989.

CHAPTER 58

WATER WAVE FLUCTUATIONS INDUCED BY IRREGULAR BATHYMETRY

Lulin Guo¹ and Robert A. Dalrymple²

Abstract: Small irregular water depth variations may cause relatively large variations of the wave field, which may affect the results of various water wave models. Statistical properties of depth variation are obtained from real bathymetry and idealized water depths are generated to study this influence on wave fields. An angular spectral model and a parabolic model are examined for their sensitivity to depth variations. It is shown that diffraction and nonlinear effects are dominant to the wave energy scattering. Correlation functions, especially correlation lengths, play an important role in the wave field variation.

INTRODUCTION

In shallow water, waves are strongly affected by depth variations, yet the water depth near a site of interest is often not well known and may vary rapidly in time and space. Slight depth variations can cause relatively large variations of the wave properties particularly after significant propagation distance. Recent studies showed that some models are very sensitive to bathymetry variation; fluctuations of depth can lead to chaotic patterns in the wave field (Brown *et al.* 1991; ray tracing model).

An important input to numerical wave models is a bathymetric grid, containing digitized water depths. These digitized depths may contain errors caused by sounding errors, errors in digitizing the chart, unknown variation in depth between survey points and bottom variation since the sounding. These errors can be regarded as random depth variations. The influence of the random variations can be fairly large depending on the model, the initial wave field, the systematic bottom bathymetry, and the statistical properties of the random bottom variation. The statistical properties can be described by distribution function and correlation functions.

A variety of numerical models, which differ in their underlying theories and their numerical implementations, are used to simulate wave fields. Results exist for a wave ray model, mild-slope equation, Boussinesq equations, an Eulerian

¹Graduate student, Center for Applied Coastal Research, University of Delaware, Newark, DE 19716, USA.

²Professor and Director, Center for Applied Coastal Research, University of Delaware, Newark, DE 19716, USA.

model, which is a stationary model based on the action balance of short-crested waves (Holthuijsen *et al.*, 1989), and some other models. The traditional ray tracing model does not consider diffraction and nonlinearity effects. It is not applicable for the study on wave fluctuations when these effects are important to be neglected. Other models contain effects of refraction, diffraction and nonlinearity, and their sensitivity to the random bottom variation are different. Numerical methods include finite element, spectral, pseudo-spectral and parabolic methods. The WANGLE model (Dalrymple *et al.* 1989) is an angular spectrum model to solve the modified mild-slope equation. It permits wide wave propagation angles which could appear in the situations when the refraction and diffraction of the waves are strong. The nonlinearity is included through the nonlinear dispersion relationship. The REF/DIF model (Kirby and Dalrymple, 1992) is a parabolic model originating from the mild-slope equation with the influence of current added. The sensitivity of these two models are examined.

Some studies of the influence of bottom variation have been done recently. Brown *et al.* (1991) showed that a ray tracing model is very sensitive to the bottom perturbations. When the bottom fluctuations are 20% of the mean water depth, the wave field can become chaotic. Holthuijsen and Booij studied the effects of the water depth variations using HISWA (Holthuijsen and Booij, 1989), a predictive model for stationary, short-crested waves in shallow water, in 1994. Their results showed that the bottom-induced fluctuation may be a serious problem and the effects of bottom variations on long-crested waves was more dominant than on short-crested waves. Reeve (1992) applied an analytical method and Monte Carlo simulations. Some quantitative results were obtained with the help of the angular spectrum of the bathymetry variation.

In this paper, we examine the influence of the random variability of the ocean bottom on waves in shallow water and the sensitivity of various numerical models to these depth variations. Some idealized bathymetries and the measured bathymetry near Duck, North Carolina is used for the numerical simulation. The REF/DIF and WANGLE models are examined. Statistical analyses of the bathymetry will be done. Bathymetries with the same statistical properties will be used to obtain the average wave properties and the fluctuations of the wave field. Results are compared with that of the traditional wave ray model. The relationship between the fluctuation in the wave field and the randomness of water depth is obtained.

GENERATION of WATER DEPTH

As an exact complete measurement of real bathymetry is almost impossible, a statistical analysis of the properties of bathymetry, such as the distribution of the depths and the correlation length scales in different directions, are needed. For the numerical study, different water depth profiles with different statistical properties are needed to study the wave field response.

The depth variation can be described statistically by its distribution and its correlation function. First we generated depth variations with uniform distribution, whose correlation function is the Dirac delta function (white noise) on a rectangular horizontal grid. The standard deviation is controlled to be some ratio of the mean water depth. Such variations are not related to the horizontal distance as the depths are taken firstly to be uncorrelated, and they lead unfortunately to rapid changes of water depth between grid points. As the grid size is reduced, larger depth gradients occur.

We also generated depth variations with Gaussian distributions and smooth correlation functions. Figure 1.a shows the generated correlation function in a 2-dimensional case. Its form is roughly similar to that of the bathymetry in Duck, NC. Correlation length is defined by the length at which the correlation function has the value around 0.6. It describes the relationships among the randomly varied depths. We will compare the correlation length to wave length to determine if there is an effect (such as Bragg scattering) when they are similar. The following formulae are used to calculate the generated depth variations.

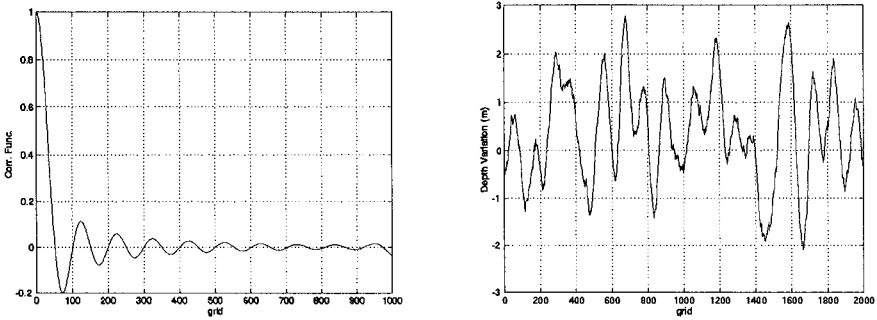


Figure 1: A sampled correlation function and a generated water depth variations for 2-D case. a). Correlation function; b). Water depth variation. The correlation length is about 30 grid sizes.

$$h(x) = \sum_{i=1}^N A_i \sin(i\Delta kx + \epsilon_i)$$

$$A_i = \sqrt{2F(c)_i}; \Delta k = 2\pi/L$$

where N is the number of grids, the correlation function $c(x_1-x_2) = \langle h'(x_1)h'(x_2) \rangle$ is the ensemble average of $h'(x_1)h'(x_2)$ and it is assumed a function of $x_1 - x_2$, where h' is the depth variation and x_1 and x_2 are two locations, $F(c)$ is the Fourier transform of c , L is the length of the domain, and $\epsilon \in [0, 2\pi]$ is an uniformly distributed which serves as the random phase. Using different ϵ , we can obtain different results of the same probability properties. Figure 1.b shows one of the results.

The 3D case is similar to that of 2D. A correlation function is used to generate the depth variation. Note that the correlation function has two arguments x and y , and there are two correlation lengths, in x and y direction. We are going to compare these two lengths to the incident water wave length separately to see which one is more important. Figure 2 shows the results. The formulae used are

$$h(x, y) = \sum_m \sum_n A_{mn} \cos(k_{mx}x + k_{ny}y + \epsilon_{mn})$$

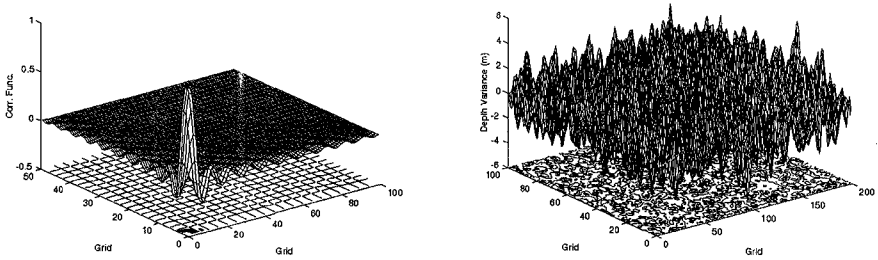


Figure 2: A sampled correlation function and a generated water depth variations for 3-D case. a). Correlation function; b). Water depth variation. The correlation lengths in the two directions are about 3 and 4.5 grid sizes, respectively.

$$A_{mn} = \sqrt{F(c)_{mn}}; kmx = \Delta k_x \cdot m; kny = \Delta k_y \cdot n; \epsilon_{mn} \in [0, 2\pi]$$

where $\Delta k_x = 2\pi/L_x$, $\Delta k_y = 2\pi/L_y$ and L_x and L_y are the size of the domain in x and y directions, respectively. The correlation function is $c(x_1 - x_2, y_1 - y_2) = \langle h'(x_1, y_1)h'(x_2, y_2) \rangle$.

NUMERICAL EXPERIMENTS AND RESULTS

Both REF/DIF and WANGLE models involve the effects of refraction, diffraction and shoaling. Weak nonlinearity can also be included. We examined the sensitivity of the two models, and then we studied the fluctuations of wave field response to different bottom changes. To demonstrate the importance of refraction and diffraction, we did two cases, one of which included only shoaling effects and the other included refraction, diffraction and shoaling effects. To study the model sensitivity, we compared Holthuijsen and Booij's results with our results obtained by REF/DIF and WANGLE models. Their results showed quantitatively that long-crested waves were affected more than short-crested waves by the bottom variation. In our cases, we only used plane waves for the comparison.

To study water wave fluctuations induced by the bottom randomness, we did some numerical experiments using the generated water depth and the measured bathymetry in Duck, NC.

Figure 3 shows the comparison of shoaling effect and the combination of refraction, diffraction and shoaling effects. We used the bathymetry in Duck, NC measured in August, 1994. (Thanks to Casey Church who supplied the data to us) In Fig. 3.a, the normalized amplitude variation calculated from the alongshore-averaged bathymetry by the REF/DIF model is shown. The incident wave is normal to the shoreline, so only shoaling effect is involved. The wave amplitude increases from 1 to about 1.09, a 9% increase. In Fig 3.b, we used the real bathymetry, with its alongshore variation. Now the fluctuation of the wave amplitude is much larger than that with shoaling effect only. The largest amplitude increase is about 55%, over 6 times larger larger than the shoaling-only case.

When water waves propagate in shallow water toward the shoreline, the water depth variation in the propagation direction causes the waves to shoal, while the variation in the transverse direction causes refraction and diffraction. It is the transverse variations that cause the variation of wave direction scattering and wave focusing. The transverse variation, rather than the onshore variation, is more important to the wave scattering.

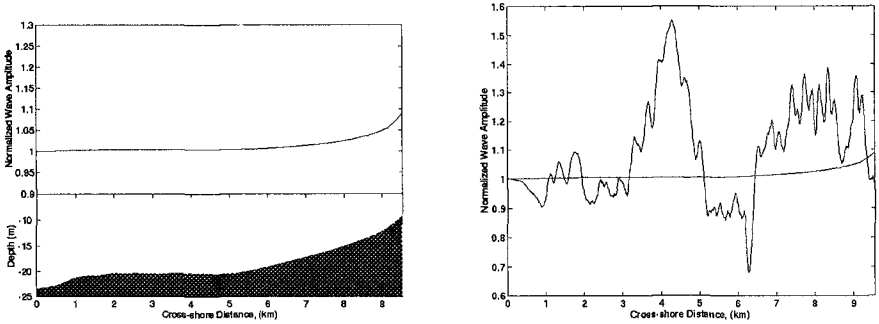


Figure 3: REF/DIF model, nonlinear version. Wave period = 10 sec. a). Upper: Normalized wave amplitude; Lower: Alongshore-averaged water depth (Duck, NC); b). Comparison of shoaling effect and refraction, diffraction and effects. Real bathymetry

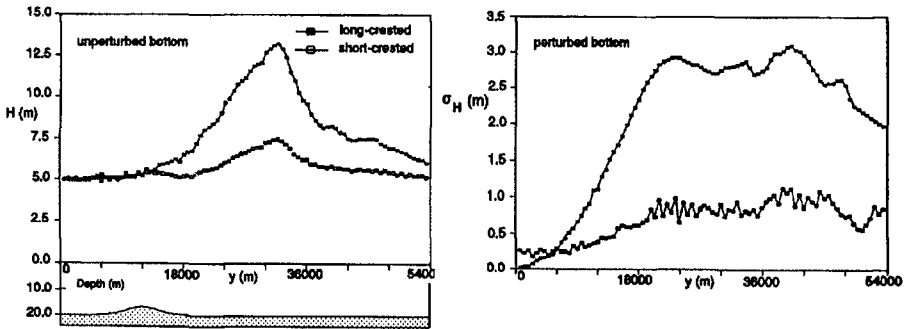


Figure 4: Results obtained by the HISWA model (Holthuijsen and Booij, 1994.) for the circular shoal. a). Wave heights along centerline profile for circular shoal with unperturbed bottom; b). The standard deviations of the wave height for the perturbed bottom.

Holthuijsen and Booij studied an idealized case numerically using the HISWA model. The bathymetry is a isotropic Gaussian-shaped shoal superimposed on

an otherwise flat horizontal bottom. The ambient depth is 20 m and the minimum depth over the shoal is 17 m. The width of the shoal is 6 km. The presence of the shoal causes the waves to focus behind it. For the cases when the bottom is perturbed, the superimposed variation on the bathymetric grid points is Gaussian uncorrelated noise of 0.5 m standard deviation, 2.9% of the minimum depth. The wave height of the incident wave is 5 m and the wave period is 10 sec. Holthuijsen and Booij considered both long- and short-crested incident waves. Only long-crested waves were simulated in our experiments. Their results are shown in Figure 4. Fig. 4.a shows the results of unperturbed bottom, the bathymetry profile and the wave amplitude profiles of long- and short-crested incident waves along the centerline which is parallel to the initial wave propagation direction and crosses the top of the shoal. Fig. 4.b shows the depth perturbation induced wave height standard deviations on the centerline, averaged by the results of 25 cases.

We can see both long- and short- waves focus at the same position, about 20,000 m behind the shoal. The wave height at the focusing point is 12.5 m for long-crested wave, 2.5 times larger than the initial wave height of 5 m. The standard deviation of the wave height is 2.5 m, half as the initial waves. But for short-crested waves, the focusing wave height and the wave fluctuation are much smaller.

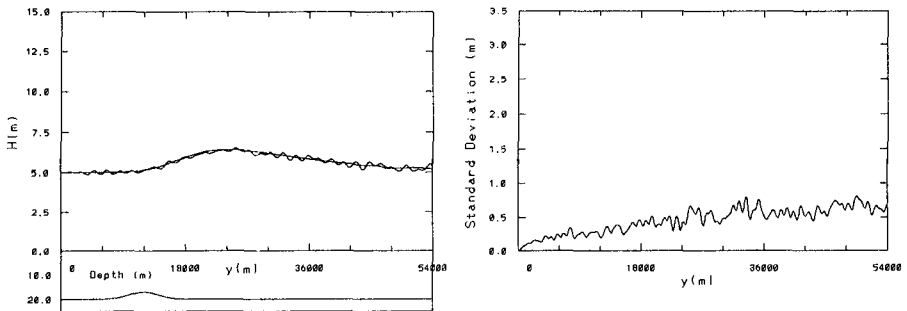


Figure 5: Results obtained by the nonlinear version of the REF/DIF model for the circular shoal. a). Wave height along the centerline with unperturbed bottom and the average of the results of 25 perturbed bottoms; b). The standard deviation of the wave height for the perturbed bottom.

Using the REF/DIF and WANGLE models, both the linear and nonlinear versions, we replicated the same case. We obtained the wave field with an unperturbed bottom for each model and version. Then 25 cases were run with different perturbed bottoms to get the ensemble-averaged water wave height and standard deviation. The ensemble-averaged wave height was calculated by averaging the 25 cases. The ensemble-averaged standard deviation was calculated by computing the standard deviation for each of the 25 cases, as compared to the unperturbed case, and then averaging the results.

Results obtained by the nonlinear version of the REF/DIF model are shown in Fig. 5. The wave height at the focusing point is 6.3 m, 26% larger than that

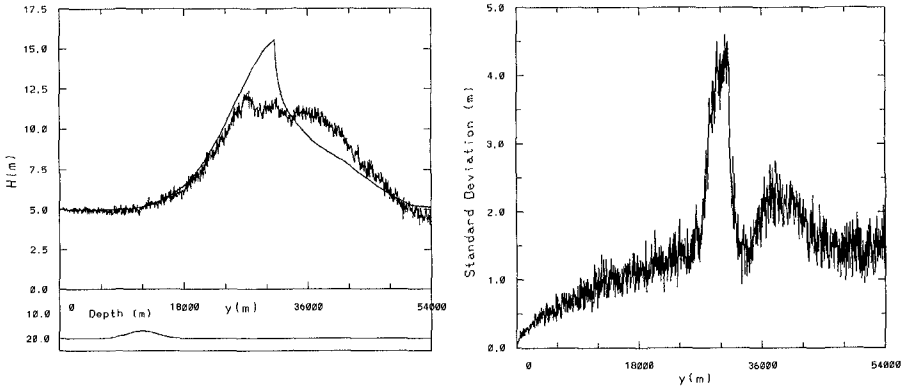


Figure 6: Results obtained by the nonlinear version of the REF/DIF model for the circular shoal. Same conditions as that for Fig. 5.

of the incident wave. The maximum standard deviation is about 0.8 m, 16% of the initial wave height. It is even smaller than the result of HISWA model of the short-crested waves. The focusing happens earlier due to diffraction and nonlinear effects. These effects help to transfer wave energy to different locations and smooth down the roughness of the wave field.

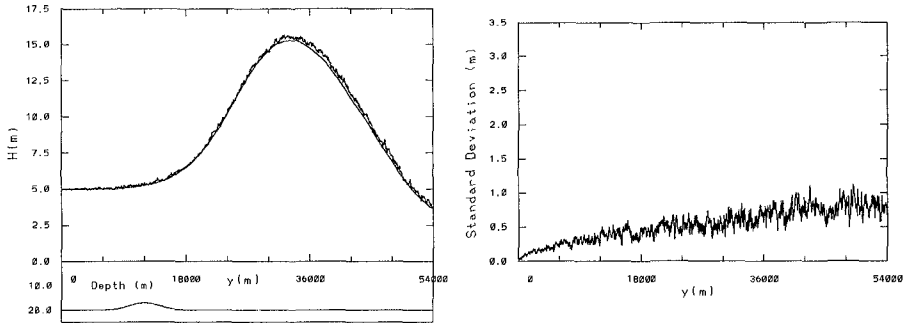


Figure 7: Results obtained by the nonlinear version of the WANGLE model for the circular shoal. Same conditions as that for Fig. 5.

Fig. 6 shows the results obtained by the linear version of the REF/DIF model. For the unperturbed bottom, there seems to be wave breaking when waves are focusing behind the shoal. But there is no wave breaking with the perturbed bottom. The reason is that the random depth variations make wave refract and diffract before focusing behind the shoal. Wave energy is scattered to other directions and eventually the wave height at the focusing position is reduced, avoiding breaking. The breaking position is further behind the shoal than the focusing position obtained by the nonlinear version model. The only

difference between the two experiments is that nonlinear effect is not involved here. Nonlinearity can smooth down the amplitude variation, transfer wave energy to the area right behind the shoal, and make results more reasonable. The standard deviation shown in Fig. 6.b is very large around the breaking area due to the big difference between breaking and non-breaking waves.

We also studied the same case with WANGLE model. Fig.7 and Fig. 8 show the results of WANGLE model of nonlinear and linear versions, respectively.

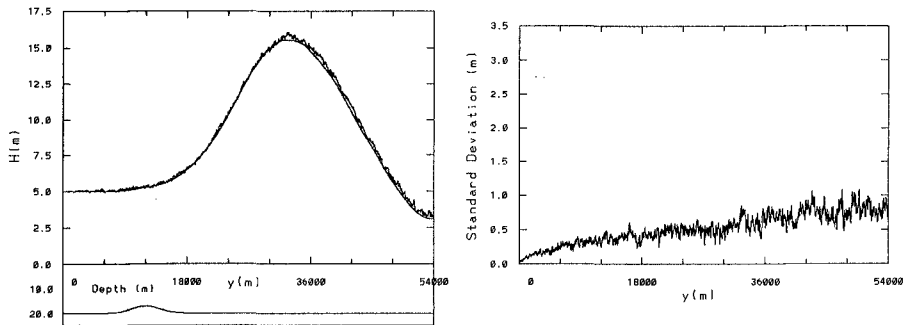


Figure 8: Results obtained by the nonlinear version of the WANGLE model for the circular shoal. Same conditions as that for Fig. 5.

We can see the focusing is still very large, about 15m here, larger than than of HISWA model. However, the standard deviation is smaller even than that obtained by REF/DIF model. For these cases, WANGLE is not very sensitive to bottom perturbation, so it does not suffer as much from bathymetry errors. Results of the linear and the nonlinear versions are not quite different. WANGLE model is an angular spectrum model that is supposed to be applicable to those cases where the wave direction varies widely. It emphasizes diffraction and refraction effects.

As mentioned above, we generated two kinds of water depth variations to superimpose on flat bottoms: uniformly distributed uncorrelated variations and Gaussian distributed correlated variations. Using the generated water depth and the nonlinear REF/DIF model, we did some numerical studies on depth variation influence. Fig. 9 and Fig. 10 are the results of the first kind of variations. They are the normalized standard deviations of wave height for bottom perturbations of different orders and different gradients, respectively. We choose bottom perturbations as 1%, 5% and 10% related to the mean depth. The corresponding normalized amplitude standard deviations are 10%, 30% and 50% of the incident wave, respectively. It is not surprising to see the larger the perturbation is, the larger the amplitude fluctuation is. But the ratio between amplitude variation and bottom perturbation becomes smaller as the perturbation increases. The reason is that as the bottom variation increases, the diffraction and nonlinearity effects becomes larger and they scatter and transfer wave energy, hence reduce the relative wave height fluctuation. To get the results in Fig. 10, we used the same water depth but different grid sizes, 5m, 2.5m and 1.25m, decreasing by half. The grid sizes are much smaller than the wave length. After waves propa-

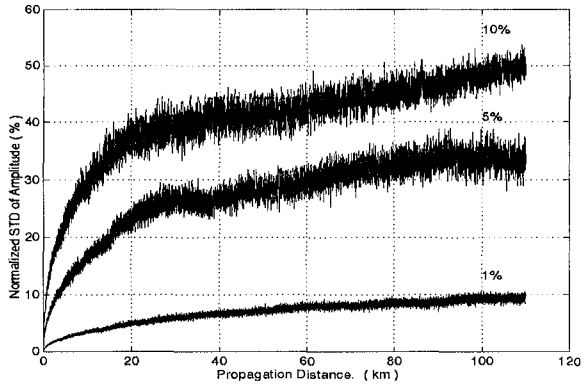


Figure 9: Amplitude standard deviations for different depth perturbations on a flat bottom, 1%, 5% and 10% of the mean water depth, respectively. Wave period = 5 sec. Mean water depth = 5 m. Grid size = 5 m. Incident wave amplitude = 0.5 m. REF/DIF, nonlinear version.

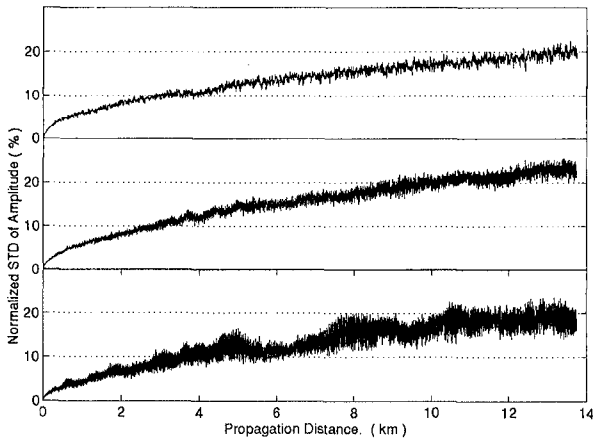


Figure 10: Amplitude standard deviations for different grid sizes, 5m, 2.5m and 1.25m, respectively. Wave period = 5 sec. Mean water depth = 5 m. Incident wave amplitude = 0.5 m. Depth perturbation = 5% of the mean depth. REF/DIF, nonlinear version.

gate over a very long distance, about 300 wave lengths, the amplitude variations approach roughly the same value. For large gradients, or rougher bottom surface, there are more grid points in one wave length and the wave field is more sensitive.

Results of the normal distributed and correlated water depth variations are shown in Fig. 11. The figures show the amplitude profiles in sections perpendicular to the initial wave direction. A normally distributed water depth can be described by its correlation function. We used water depths with different correlation lengths in different directions and examined how the wave field responds when the wave length (L) is similar to the correlation lengths in the wave propagation and the transverse directions (L_x and L_y). In Fig. 11.a, we fixed L_y and varied L_x ; in Fig. 11b, L_x was fixed and L_y was varied. The results of wave focusing of the three cases shown in Fig. 11a are not very different and bottom variation correlation length in wave direction does not affect the wave field much. Fig. 11.b shows that when L_y is much longer than wave length, the focusing is relatively small. When the two lengths are the same, focusing is large. So correlation length in the direction perpendicular to wave propagation is an important factor to the wave field. When the correlation length is much shorter than the wave length, the focusing is also fairly dominant. This is because for this case, the bottom is rougher, as there are more grid points in one wave length, and the wave fields are sensitive to this in short wave propagation distance.

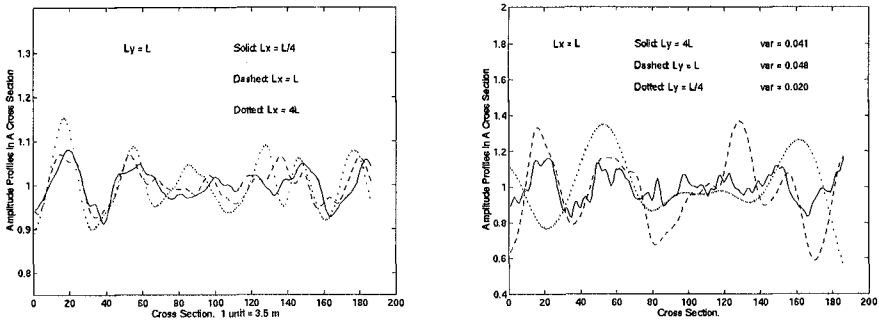


Figure 11: Cross-section amplitude profiles obtained by the REF/DIF model, nonlinear version. L : water wave length, L_x and L_y : water depth correlation lengths in wave propagation and transverse directions, respectively. Wave period = 5 sec, Mean water depth = 5 m. Standard deviation of water depth = 0.5 m. Distance from where waves start: 700 m.

We also used the bathymetry in Duck, NC to study the influence of bottom randomness of different statistical properties. The correlation length is about 150 m in both alongshore and cross-shore directions. We used waves of different wave length for numerical studies. The results are similar to what we got from the generated water depth. When correlation length and wave length are similar, the effects on wave field is dominant. This can be observed quantitatively by the amplitude standard deviations. After waves propagate for certain distances (1

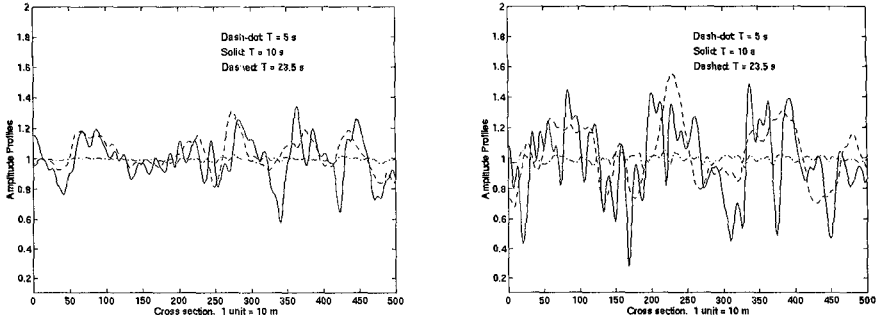


Figure 12: Cross-section amplitude profiles obtained by the REF/DIF model, nonlinear version, for incident waves of different wave periods T . Bathymetry in Duck, NC is applied. Distance from the incident waves, left figure: 1 km; right figure: 2 km.

km and 2 km), the amplitude standard deviations are 0.0323, 4.4, 2.5 and 0.0982, 13.2, 8.6 for waves with time periods of 5sec, 10sec and 23.5sec, respectively. When the two lengths are the the most similar, the standard deviation is the largest.

DISCUSSION AND CONCLUSIONS

We have shown that small water depth perturbation can cause large wave fluctuations based on the wave model used. Different numerical models are sensitive to depth variation in different ways, and models involving nonlinearity, refraction and diffraction effects can be applied to study the effects of random bottom variations, such as the REF/DIF and the WANGLE models. Large and rapid water depth variations cause large wave field fluctuations, and with the same variance, different statistical water depths have different effects on wave field. The effects of a Gaussian distributed bottom variation on wave field depends on its variance and correlation function. The numerical results show that correlation length in the direction perpendicular to water waves direction is important to the wave fluctuations. When it is similar to the incident wave length, the wave fluctuation becomes larger.

ACKNOWLEDGMENTS

This work was sponsored by the U.S. Army Research Office, University Research Initiative under Contract No. DAAL03-92-G-0116.

REFERENCE

- Brown, M. G., Tappert, F. D. and Sundaram, S. E., Chaos in Small-Amplitude Surface Gravity Waves Over Slowly Varying Bathymetry, *J. Fluid Mech.*, vol. 227, pp.35-46, 1991.
- Dalrymple, R. A., Suh, K. D., Kirby, J. T., and Chae, J. W., Models for Very Wind-Angle Water Waves and Wave Diffraction. Part 2. Irregular Bathymetry, *J. Fluid Mech.*, 201, 299-322, 1989.

- Holthuijsen, L. H. and Booij, N., Bottom Induced Scintillation of Long- and Short-crest Waves, *Proc. the Intl. Symp.: Waves-Physical and Numerical Modeling*, Vancouver, Canada, 1994.
- Kirby, J.T. and Dalrymple, R.A., Combined Refraction/Diffraction Model-REF/DIF 1, Version 2.4, Documentation and User's Manual, Center for Applied Coastal Research, Res. Rpt. CACR-92-04, 1992.
- Reeve, D. E., Bathymetric Generation of an Angular Wave Spectrum, *Wave Motion*, 16, 217-228, 1992.

CHAPTER 59

INTEGRAL CONTROL DATA ASSIMILATION IN WAVE PREDICTIONS

L.H. Holthuijsen¹, N.Booij¹, M. van Endt¹, S. Caires², C. Guedes Soares²

ABSTRACT

In the present study a technique for assimilating observed wave data in numerical wave predictions is developed that exploits (a) the efficiency of a limited number of integral control variables and (b) the effectiveness of variational (model-consistent) assimilation. The formal procedure is independent of the type of control variables and of the wave model. The integral control variables in this study are chosen to represent large-scale errors in the driving wind fields and uncertainties in the wave model. The assimilation technique is validated with observations of the ERS-1 satellite altimeter and two waverider buoys in two consecutive storms in the Norwegian Sea. The assimilation of the observations reduced the errors in the predicted significant wave height at the buoy locations typically from 25% to 15%. The technique is also demonstrated with an simulation of swell prediction in the Indian Ocean based on simulated buoy data and satellite data.

INTRODUCTION

Good quality wave forecasts are often required for estimating the workability for coastal and offshore activities. The quality of these forecasts, which are usually based on numerical wave models can be improved by assimilating wave observations (Komen et al., 1994). In simple assimilation techniques (sequential techniques), observed waves are used to correct the model wind and waves locally and instantaneously. The effect is short-lived as the corrections are quickly lost in the uncorrected wind and waves elsewhere in the model. In the more advanced variational assimilation techniques the observed waves are used to correct the entire space-time structure of the wind in detail, which is more effective. This requires very large computer capacity. However, this detail in the corrections is not required for two reasons. First, the wind errors that affect the waves are highly correlated in space and time and second, the waves are an integral effect of the wind in which

¹ Delft University of Technology, Department of Civil Engineering, P.O. Box 5048, 2600 GA Delft, Netherlands.

² Lisbon University of Technology, Av. Rovisco Pais, 1096 Lisbon, Portugal

details of the wind are lost. In the present study a variational technique is developed that exploits this correlated and integral character of wind and waves by using integral control variables. It is efficient and seems therefore operationally feasible (e.g., all experiments of the present study were carried out on a personal computer). The technique is validated with an application in the Norwegian Sea and it is demonstrated with simulated data in the Indian Ocean.

TECHNIQUE

The essence of data assimilation in wave forecasting is that wave observations just prior to the forecast are used to obtain wind fields and wave fields that are as consistent as possible with both the first-guess wind field and the observed waves. The forecast system, including the driving wind fields, thus continuously adapts to the wave observations.

Assimilation techniques for wave forecasting are commonly divided into sequential techniques and variational techniques (e.g., Komen et al., 1994). In the sequential techniques the wave observations are used to correct the wind and the waves at each time level of the model without regard for the previous states of the model. Since the space-time structure of the modelled wave field is not taken into account, the results are not consistent with the dynamics of the wave model. The variational techniques do take the dynamics of the wave model into account. Since the generation, dissipation and propagation of the waves in the entire geographic model domain is thus accounted for, the effect of these techniques is expected to be of longer duration. The most advanced of these techniques is the adjoint technique which determines a very large number of local corrections (in fact, every single wind vector in space and time, e.g., de las Heras, 1994). The variational technique presented here combines (a) the effectiveness of the variational techniques by correcting the driving wind field (consistency with the model dynamics) and (b) the efficiency of the sequential techniques using a relatively small number of corrections (compared with the conventional adjoint techniques). In the present study the chosen control variables are: (1) a shift in time and space of the wind field and (2) a common correction to all wind vectors and (3) a model coefficient representing wave dissipation. These control variables are taken to be constant in time and space during the assimilation period. To improve the subsequent forecast, the assimilated values of the control variables are extrapolated into the forecast.

The assimilation technique optimizes the driving wind field and the corresponding wave field taking into account (a) the differences between the observed and computed waves and (b) the confidence in the driving wind fields and the wave model itself. These aspects are quantified in a cost function J :

$$J = J^x + J^y \quad (1)$$

where J^x represents the differences (that need to be minimized) between the observed and the modelled waves and J^y represents the corrections (that will be

penalized) that are needed in the wind field and the wave model. These differences and corrections are quantified as follows.

- (i) In the following the observed wave field is represented by a set of observed wave parameters such as significant wave height, mean wave frequency etc. Each of these may be observed at different locations and times. They are indicated as χ_i^o where subscript i is the realization index. The modelled waves are similarly represented by the same set of wave parameters χ_i at the same locations and times as χ_i^o . The penalty is expressed as

$$J^x = \sum_i \sigma_{\chi_i}^{-2} (\chi_i^o - \chi_i)^2 \quad (2)$$

where σ_{χ_i} is the standard deviation of the error of the wave parameter χ_i .

- (ii) The corrections that are required in the driving wind fields and in the wave model can be represented as corrections of a set of control variables such as a shift in the location of a storm or a coefficient in the wave model. Each such control variable is indicated as ψ_j . Its value prior to the assimilation is indicated as its first-guess value ψ_j^f . Confidence in these values is expressed by penalizing the corrections that are needed in the assimilation, again with a quadratic measure with the variance of the errors in the control variables as weights:

$$J^\psi = \sum_j \sigma_{\psi_j}^{-2} (\psi_j - \psi_j^f)^2 \quad (3)$$

where σ_{ψ_j} is the standard deviation of the error of the control variable ψ_j (representing the confidence in the control variable).

The assimilation consists essentially of minimizing the cost function J which can be interpreted as adjusting the driving wind field and the wave model with a certain penalty, to produce the best-fit wave field. This minimum is estimated with one small perturbation per control variable in the driving wind field and in the wave model. The optimum values of the control variables thus obtained are used to carry out the fully assimilated wave forecast. Details of the method are given in Holthuijsen et al. (1996).

The assimilation is carried out with the original wave model (no adaptations). The computer storage capacity for this technique is therefore equal to that required for one conventional model run. It follows from the above that the number of model runs with the wave model is equal to the number of control variables plus one. The technique is therefore efficient only when a limited number of control variables is considered. This condition is fulfilled if only a few integral control variables are used.

VALIDATION

The technique is validated in two storms in the Norwegian Sea (1 - 10 March, 1993). For the data assimilation and the verification, observations of the significant wave height (values of up to 7.5 m) from two waverider buoys and from the altimeter of the ERS-1 satellite are used (Fig. 1). The wave model is the second-generation model DOLPHIN-B of Holthuijsen and de Boer (1988). The integral control variables that were chosen for this validation experiment, are the ones mentioned above. They were taken to be constant in time and space (extrapolated into the forecast).

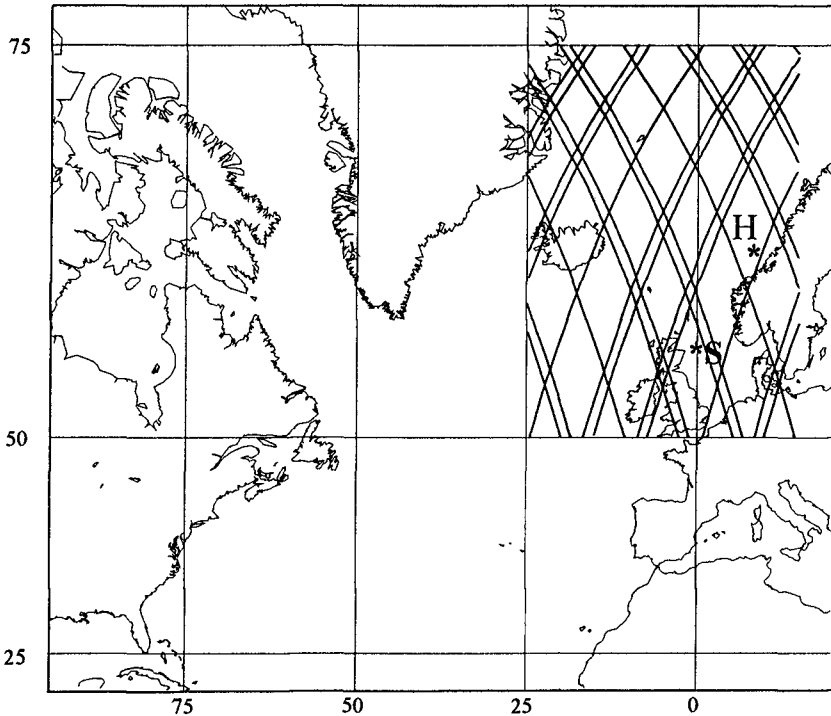


Fig. 1 The area covered by the wave model with the locations SCOTT (S) and HALTENBANKEN (H) and the ERS-1 tracks that were used in this study during the assimilation period 3 - 8 March, 1993.

Several combinations of the buoy and satellite data have been used. The effect is evaluated by comparing the computed significant wave height (before and after assimilation) with the observed significant wave height both in the assimilation period and in the forecast (e.g. Fig. 2 for the HALTENBANKEN location). Table 1 presents some of the results in terms of the scatter index (rms-difference normalized with the mean observed significant wave height). Day 1 - 3 were used as spin-up of the wave model. Day 4 - 8 is the assimilation period. Day 9 - 10 is the forecast period. It is obvious that the agreement between computed and observed

waves improves considerably both in the assimilation period and in the forecast, in particular in the forecast at location SCOTT where the scatter index drops from 37.2% to 12.4% (buoy assimilated) or 17.1% (buoy and satellite assimilated).

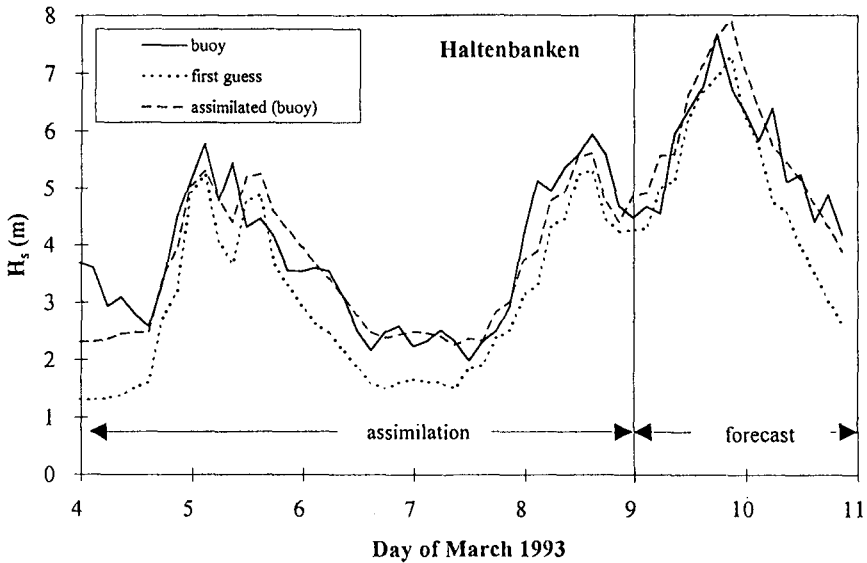


Fig. 2 The observed significant wave height at HALTENBANKEN (waverider buoy) with the first-guess significant wave height and the assimilated significant wave height (HALTENBANK buoy only) in the assimilation period and in the forecast period.

DEMONSTRATION

The assimilation technique is demonstrated in the Indian Ocean with a simulated swell forecast at a near-shore location (10 km offshore) off Kerala (southern India, Fig. 3). All wave information in this demonstration has been simulated with the wave model. A period has been selected with a storm south of Madagascar that produced high swell conditions off Kerala in July of 1995 (Fig. 3). The aim of the assimilation is to improve the forecast of crossing the 1 m threshold of the swell wave height at the near-shore location. The observed swell wave height (defined as $H_{swell} = 4 m_{0.1}^{1/2}$ where $m_{0.1}$ is the variance of frequencies less than 0.1 Hz) is simulated with actual (not simulated) 12-hour wind forecasts of the European Centre for Medium Range Weather Forecasts (ECMWF, Reading, England). The "observed" swell wave heights at the near-shore location are given in Fig. 4. Two cases are considered. In the first case, simulated wave data from one buoy, located 200 km south-west off Kerala are used. In the second case, simulated wave data from the ERS-1 satellite are used. For the assimilation the same control variables are used as in the validation experiment, except the wave dissipation coefficient which is not included (wave physics cannot be inferred from simulated wave data; the value of this coefficient is set at the value obtained in the above validation experiment).

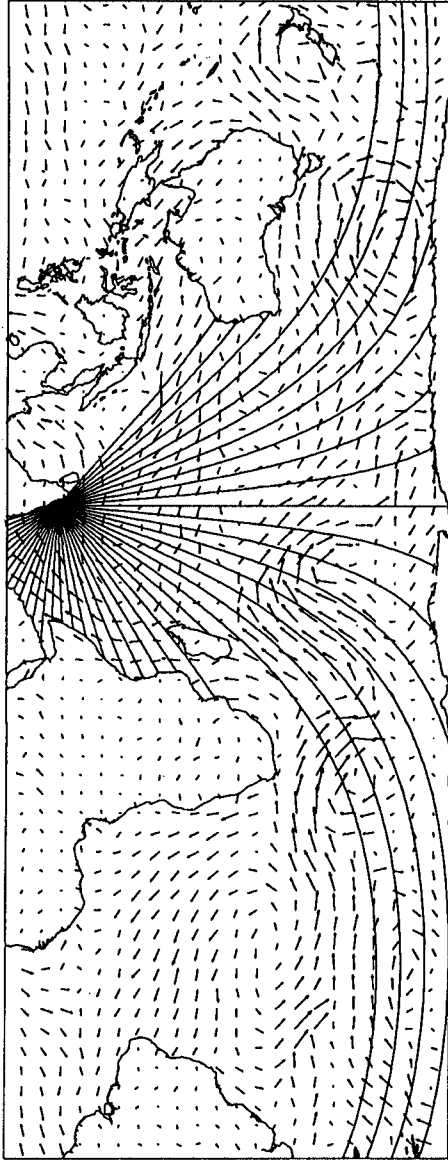


Fig. 3 The area covered by the wave model in the Indian Ocean with the wind field analysis of ECMWF showing the storm south of Madagascar that generated the high swell conditions at Kerala (India). The wave rays indicate great circles along which swell can propagate towards Kerala (the ones shown here are used in the wave model). Note the coinciding directions of wind and swell rays in the storm.

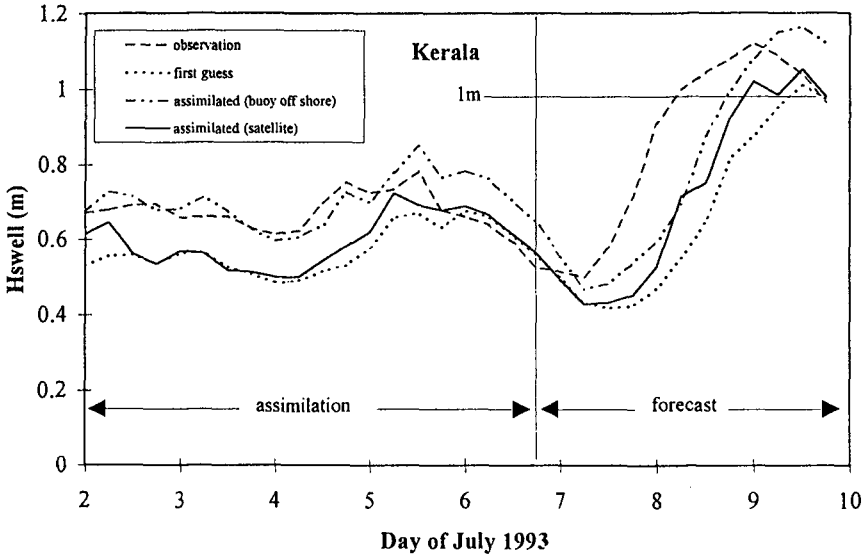


Fig. 4 The "observed" (simulated) swell wave height at the near-shore location off Kerala with the first-guess swell wave height and the assimilated swell wave height (off-shore buoy and satellite) in the assimilation period and in the forecast period.

The first-guess swell wave height (including the first-guess forecast) at the near-shore location is simulated with the wind analyses of ECMWF (to obtain wave fields that are somewhat different from the "observed" wave fields). It is obvious from Fig. 4 that this first-guess, at July 7, 00:00 UTC, predicts the crossing of the 1 m threshold on July 9th more than 24 hours too late. The result of assimilating the off-shore buoy data over a period of 5 days (sampled at 6 hour interval) is to predict the time of threshold-crossing only 9 hours late. This is an improvement of 17 hours. The scatter index of the swell wave height at the near-shore location reduces significantly e.g. in the forecast from 30.9% to 19.2% (Table 2). The satellite data were simulated at the actual tracks of the ERS-1 over a period of 23 days (15 days spin-up, 5 days assimilation and 3 days forecast) with the same wind fields but sampled every 30 min when the satellite was (a) over the Indian Ocean and (b) the observation was on a great circle through the near-shore location off Kerala (so that swell could potentially affect the Kerala location). This resulted in about 6 observations per day, or 88 in total during the 15 day assimilation period (Fig. 5). The effect of assimilating these data on predicting the threshold-crossing is somewhat uncertain as the corrected swell wave height fluctuates around this level (Fig. 4). In terms of the scatter index, the effect is small in the assimilation period but reasonable in the forecast period (Table 2). It is speculated that the poor performance in the assimilation period is due to the fact that 6 observations per day

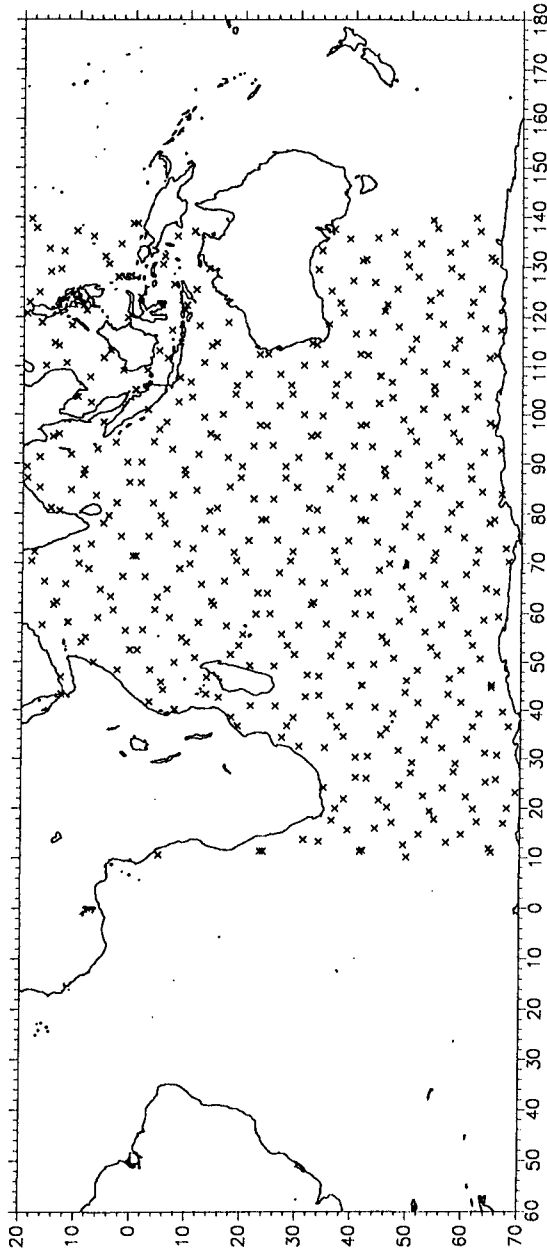


Fig. 5 Locations at which the wave data from the ERS-1 satellite were simulated for the demonstration in the Indian Ocean. The locations are at 30 min interval and on great circles centered at the near-shore location off Kerala (potentially affecting the waves there).

over such a large area is not sufficient to detect and correct rather local (on the scale of the Indian Ocean) errors in the wind field (the timing or location of the storm south of Madagascar that generated the swell).

CONCLUSIONS

A variational data assimilation technique has been developed based on the notion of integral control variables. It has been shown to be rather effective and efficient in the sense that the forecasts of the significant wave height in the validation experiment improved considerably with only a small fraction of the computer effort that is normally involved in variational techniques. Adding satellite data to the (buoy) assimilation in this validation experiment did not improve the forecasts at the buoy locations. This is possibly due to the fact that the satellite data contribute to the overall improvement of the wave field rather than to the improvement at one particular (buoy) location. The demonstration of the assimilation technique for swell forecasting in the Indian Ocean showed that for satellite data to be effective, more than only a few satellite observations per day are required over such extensive areas as the Indian Ocean.

ACKNOWLEDGEMENTS

We are grateful to DELFT HYDRAULICS, in particular H. Wensink for providing us with the buoy data at SCOTT and for obtaining the permission from the owners (Heeremac V.O.F.) to use the data. We are similarly indebted to S. Barstow of OCEANOR A/S who provided us with the buoy data of HALTENBANKEN. These data were collected in the framework of the SEAWATCH Europe project and put at our disposal under the terms of reference of the WAVEMOD project that was funded by the European Commission in the MAST-II programme under contract N°. CT92/0025. For permission to use these data we are indebted to OCEANOR A/S. The altimeter data were provided by the Faculty of Aerospace Engineering of the Delft University of Technology with the support and assistance of E. Wisse, R. Scharroo and M. Naeije who we sincerely thank for this. We also thank S. Kruisinga of the Royal Netherlands Meteorological Institute (KNMI) for providing us with the wind fields of ECMWF (the European Centre for Medium Range Weather Forecasts). Permission from KNMI to use these wind fields is gratefully acknowledged. This study was partly funded by the WAVEMOD project that was funded by the European Commission in the MAST-II programme under contract N°. CT92/0025.

scatter index in %	location of forecast	data sets in assimilation	March 1993	
			significant wave height	
			assimilation period	forecast period
ERS-1		<u>first-guess</u>	24.7	26.4
		<u>assimilated</u>	18.3	25.5
		altimeter altimeter + buoys	18.3	25.4
SCOTT		<u>first-guess</u>	22.0	37.2
		<u>assimilated</u>	16.3	12.4
		SCOTT buoy	16.0	17.1
		SCOTT buoy + altimeter HALTENBANKEN buoy	22.8	28.0
HALTENBANKEN		<u>first-guess</u>	27.5	17.1
		<u>assimilated</u>	14.5	10.1
		HALTENBANKEN buoy	19.0	10.0
		HALTENBANKEN buoy + altimeter SCOTT buoy	15.2	13.5

Table 1. Scatter index (= normalized rms-error, see text) between computed and observed significant wave height for the ERS-1 altimeter and two waverider buoys in the Norwegian Sea and the North Sea in the validation experiment.

scatter index in %	location of forecast	data sets in assimilation	July 1995	
			swell wave height	
			assimilation period	forecast period
near-shore		<u>first-guess</u>	18.4	30.9
		<u>assimilated</u>	9.9	19.2
		off-shore buoy ERS-1 satellite	15.4	23.1

Table 2. Scatter index (= normalized rms-error, see text) between computed and "observed" (simulated) swell wave height at the near-shore location off Kerala (India) using simulated wave data from either an off-shore buoy or the ERS-1 satellite.

REFERENCES

- Heras, M.M. de las, G.J.H. Burgers and P.A.E.M. Janssen, 1994, Variational data assimilation in a third generation wave model, *J. Atmos. Ocean. Techn.*, 11, 5, pp. 1350 -1369
- Holthuijsen, L.H. and S. de Boer, 1988, Wave forecasting for moving and stationary targets, in *Computer modelling in ocean engineering*, Eds. B.Y. Schrefler and O.C. Zienkiewicz, Balkema, Rotterdam, pp. 231-234
- Holthuijsen, L.H., N. Booij, M. van Endt, S. Caires, and C. Guedes Soares, 1996, Assimilation of buoy and satellite data in wave forecasts with integral control variables, *Journal of Marine Systems*, in press
- Komen, G.J., L. Cavaleri, M. Donelan, K. Hasselmann, S. Hasselmann and P.A.E.M. Janssen, 1994, *Dynamics and modelling of ocean waves*, Cambridge, 300 p.

CHAPTER 60

TWO-DIMENSIONAL ANALYSIS OF WAVE TRANSFORMATION BY RATIONAL-APPROXIMATION-BASED, TIME-DEPENDENT MILD-SLOPE EQUATION FOR RANDOM WAVES

Toshimasa Ishii¹, Masahiko Isobe² and Akira Watanabe²

ABSTRACT

The method for determining coefficients in the rational approximation is improved and a numerical method is developed for application of time-dependent mild-slope equation for random waves to two-dimensional wave fields. The validity of the method is verified through comparisons with analytical solutions in typical situations and an experimental result of wave transformation around a man-made island on a uniform slope.

1. INTRODUCTION

Time-dependent mild-slope equations for random waves were derived from Berkhoff's mild-slope equation by approximating frequency-independent expressions to frequency-dependent coefficients (Kubo *et al.*, 1992; Kotake *et al.*, 1992; Isobe, 1994). It can be used to simulate directly the time evolution of irregular waves. The approximation by a rational function (Padé approximation) has a high accuracy to the coefficient over a wide frequency range (Isobe, 1994). However, the method for determining the coefficients in the rational function and the numerical calculation method for applying to two-dimensional problems were not established. In this paper, a method was developed to apply the time-dependent mild-slope equation for random waves to practical problems. The results of calculations are compared with analytical solutions in typical situations and an experimental result of wave transformation around a man-made island on a uniform slope.

¹Tokyo Electric Power Co., Ltd., Tsurumi-ku, Yokohama, 230, Japan

²Dept. of Civil Eng., Univ. of Tokyo, Bunkyo-ku, Tokyo, 113, Japan

2. A TIME-DEPENDENT MILD-SLOPE EQUATION FOR RANDOM WAVES BASED ON RATIONAL APPROXIMATION

The governing equation is as follows:

$$\nabla^2 \tilde{\phi} - ia_1 \nabla^2 \left(\frac{\partial \tilde{\phi}}{\partial t} \right) + (b_0 + ic_0) \tilde{\phi} + i(b_1 + ic_1) \frac{\partial \tilde{\phi}}{\partial t} - b_2 \frac{\partial^2 \tilde{\phi}}{\partial t^2} = 0 \tag{1}$$

where t is the time, ∇ the differential operator in the horizontal two directions, i the imaginary unit and $\tilde{\phi}$ the unknown variable which is related to complex amplitude $\hat{\phi}$ as follows.

$$\tilde{\phi} = \hat{\phi} e^{-i\omega' t}, \quad \omega' = \omega - \bar{\omega} \tag{2}$$

where $\bar{\omega}$ is a representative angular frequency, ω and ω' the angular frequency and its deviation from $\bar{\omega}$, a_1, b_0, b_1 and b_2 the coefficients in the rational function in (4) which is approximated to k^2 (k : wave number) in a Helmholtz equation (3) (Radder, 1979), and c_0 and c_1 the energy dissipation term to model the wave breaking.

$$\nabla^2 \tilde{\phi} + k^2 \tilde{\phi} = 0 \tag{3}$$

$$k^2 = \frac{b_0 + b_1 \omega' + b_2 \omega'^2}{1 - a_1 \omega'} \tag{4}$$

3. IMPROVEMENT OF METHOD FOR DETERMINING COEFFICIENTS

3. 1. Condition of numerical stability

For monochromatic progressive waves, $\tilde{\phi}$ is expressed as

$$\tilde{\phi} = a e^{i(kx \cos \theta + ky \sin \theta - \omega' t)} \tag{5}$$

Then, equation(1) becomes

$$-k^2 + a_1 k^2 \omega' + (b_0 + ic_0) + (b_1 + ic_1) \omega' + b_2 (\omega')^2 = 0 \tag{6}$$

Equation(6) can be solved for ω' as

$$\omega' = \left\{ -(a_1 k^2 + b_1 + ic_1) \pm \sqrt{(a_1 k^2 + b_1 + ic_1)^2 - 4b_2(-k^2 + b_0 + ic_0)} \right\} / (2b_2) \tag{7}$$

To avoid numerical divergence, $Im\{\omega'\} \leq 0$. This requires that the magnitude of the imaginary part for $\sqrt{\quad}$ should not exceed c_1 . Let the real and imaginary parts in the $\sqrt{\quad}$ be denoted by X and Y , respectively, then the condition is written as

$$X \geq 0 \quad (c_1 = 0) \quad (8)$$

$$X \geq (Y/2c_1)^2 - c_1^2 \quad (c_1 > 0) \quad (9)$$

The above condition should be satisfied for an arbitrary k , which yields

$$b_1^2 - 4b_0b_2 \leq 0, \quad c_0 = 0 \quad (c_1 = 0) \quad (10)$$

$$\left(\frac{c_0}{c_1}\right)^2 - \left(\frac{b_1}{b_2}\right)\left(\frac{c_0}{c_1}\right) + \left(\frac{b_0}{b_2}\right) \leq 0 \quad (c_1 > 0) \quad (11)$$

In a previous study (Isobe, 1994), equal signs were taken for the sake of convenience within the above restrictions. Then,

$$b_2 = b_1^2/(4b_0) \quad (12)$$

$$c_1 = (2b_2/b_1)c_0 \quad (13)$$

However, numerical divergence occurs due to round-off error if the coefficients are determined by the above equations. An example is in the calculation of wave propagation over a submerged circular shoal. In the present study, the conditions were modified to avoid the numerical instability as follows:

$$b_1^2 - 6b_0b_2 \leq 0, \quad c_0 = 0 \quad (c_1 = 0) \quad (14)$$

$$\left(\frac{c_0}{c_1}\right)^2 - \left(\frac{b_1}{b_2}\right)\left(\frac{c_0}{c_1}\right) + \frac{3}{2}\left(\frac{b_0}{b_2}\right) \leq 0 \quad (c_1 > 0) \quad (15)$$

Within the above restrictions, we take equal signs. Then,

$$b_2 = b_1^2/(6b_0) \quad (16)$$

$$c_1 = (2b_2/b_1)c_0 \quad (17)$$

By considering the above two equations, independent parameters are a_1 , b_0 , b_1 and c_0 .

3. 2. Determination of coefficients

The coefficients a_1 , b_0 , b_1 and b_2 can be determined from three sets of ω' and k which satisfy the dispersion relation exactly and equation(16) which is the condition to avoid numerical divergence. In the previous method (Isobe, 1994),

equation(4) was applied piece by piece to three intervals of frequency range to approximate dispersion relation accurately, but it required extensive computational time for calculation of two-dimensional wave transformation of random waves. In the present study, equation(4) is applied for the whole range of frequency and the coefficients are determined by using three sets of ω' and k which satisfy the dispersion relation exactly on $f/f_p = 0.76, 1.22, 1.92$, where f is frequency, f_p the peak frequency. Figure 1 shows the dispersion relation which was obtained by applying equation (4). The relative error due to the method is at most 10 % in the range of $f/f_p = 0.68 \sim 2.07$ which occupies the major portion of wave energy in frequency spectrum.

When we determine the values of coefficients a_1, b_0, b_1 and b_2 , we compensate for the error included in the finite difference form of the equation in the ADI method of which the detail is given later. The finite difference expressions for each term in equation(1) are related with the corresponding derivatives as

$$\left. \frac{\partial^2 \tilde{\phi}}{\partial x^2} \right|_{\text{F.D.}} = \left(\frac{\sin(\frac{1}{2}k\Delta x \cos \theta)}{\frac{1}{2}k\Delta x \cos \theta} \right)^2 \left(\cos(\frac{1}{2}\omega'\Delta t) \right)^2 \frac{\partial^2 \tilde{\phi}}{\partial x^2} \quad (18)$$

$$\left. \frac{\partial^2 \tilde{\phi}}{\partial y^2} \right|_{\text{F.D.}} = \left(\frac{\sin(\frac{1}{2}k\Delta y \sin \theta)}{\frac{1}{2}k\Delta y \sin \theta} \right)^2 \left(\cos(\frac{1}{2}\omega'\Delta t) \right)^2 \frac{\partial^2 \tilde{\phi}}{\partial y^2} \quad (19)$$

$$\left. \frac{\partial^3 \tilde{\phi}}{\partial x^2 \partial t} \right|_{\text{F.D.}} = \left(\frac{\sin(\frac{1}{2}k\Delta x \cos \theta)}{\frac{1}{2}k\Delta x \cos \theta} \right)^2 \frac{\sin(\frac{1}{2}\omega'\Delta t)}{\frac{1}{2}\omega'\Delta t} \frac{\partial^3 \tilde{\phi}}{\partial x^2 \partial t} \quad (20)$$

$$\left. \frac{\partial^3 \tilde{\phi}}{\partial y^2 \partial t} \right|_{\text{F.D.}} = \left(\frac{\sin(\frac{1}{2}k\Delta y \sin \theta)}{\frac{1}{2}k\Delta y \sin \theta} \right)^2 \frac{\sin(\frac{1}{2}\omega'\Delta t)}{\frac{1}{2}\omega'\Delta t} \frac{\partial^3 \tilde{\phi}}{\partial y^2 \partial t} \quad (21)$$

$$\left. \tilde{\phi} \right|_{\text{F.D.}} = \left(\frac{2}{3} \cos \omega'\Delta t + \frac{1}{3} \right) \tilde{\phi} = \beta_0 \tilde{\phi} \quad (22)$$

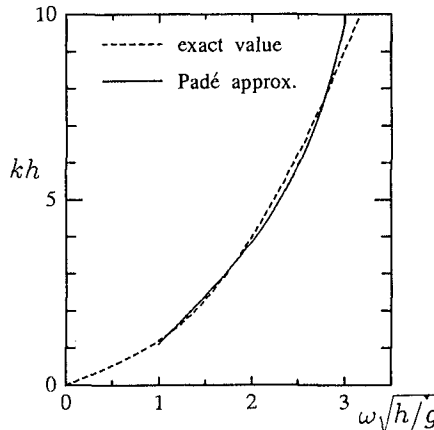


Figure 1: Accuracy of Padé approximation to kh

$$\left. \frac{\partial \tilde{\phi}}{\partial t} \right|_{\text{F.D.}} = \frac{\sin \omega' \Delta t}{\omega' \Delta t} \frac{\partial \tilde{\phi}}{\partial t} = \beta_1 \frac{\partial \tilde{\phi}}{\partial t} \tag{23}$$

$$\left. \frac{\partial^2 \tilde{\phi}}{\partial t^2} \right|_{\text{F.D.}} = \left(\frac{\sin(\frac{1}{2} \omega' \Delta t)}{\frac{1}{2} \omega' \Delta t} \right)^2 \frac{\partial^2 \tilde{\phi}}{\partial t^2} = \beta_2 \frac{\partial^2 \tilde{\phi}}{\partial t^2} \tag{24}$$

where |_{F.D.} denotes the finite difference expressions. The wave directions θ at calculation grid points are assumed as 45°, which makes the values of correction factors the same for x - and y -directions and closer to unity. Under the condition that $\Delta x = \Delta y = \Delta l$, the finite difference expressions and correction factors are as follows:

$$\left. \begin{aligned} \left. \frac{\partial^2 \tilde{\phi}}{\partial x^2} \right|_{\text{F.D.}} = \alpha_1 \frac{\partial^2 \tilde{\phi}}{\partial x^2}, \quad \left. \frac{\partial^2 \tilde{\phi}}{\partial y^2} \right|_{\text{F.D.}} = \alpha_1 \frac{\partial^2 \tilde{\phi}}{\partial y^2} \\ \left. \frac{\partial^3 \tilde{\phi}}{\partial x^2 \partial t} \right|_{\text{F.D.}} = \alpha_2 \frac{\partial^3 \tilde{\phi}}{\partial x^2 \partial t}, \quad \left. \frac{\partial^3 \tilde{\phi}}{\partial y^2 \partial t} \right|_{\text{F.D.}} = \alpha_2 \frac{\partial^3 \tilde{\phi}}{\partial y^2 \partial t} \end{aligned} \right\} \tag{25}$$

$$\alpha_1 = \left(\frac{\sin(\frac{1}{2\sqrt{2}} k \Delta l)}{\frac{1}{2\sqrt{2}} k \Delta l} \right)^2 \left(\cos(\frac{1}{2} \omega' \Delta t) \right)^2, \quad \alpha_2 = \left(\frac{\sin(\frac{1}{2\sqrt{2}} k \Delta l)}{\frac{1}{2\sqrt{2}} k \Delta l} \right)^2 \frac{\sin(\frac{1}{2} \omega' \Delta t)}{\frac{1}{2} \omega' \Delta t} \tag{26}$$

Then, instead of equation (6), the finite difference equation for equation(1) implies

$$- \alpha_1 k^2 + a_1 \alpha_2 k^2 \omega' + b_0 \beta_0 + b_1 \beta_1 \omega' + b_2 \beta_2 \omega'^2 = 0 \tag{27}$$

for $c_0 = c_1 = 0$. By rearranging the equation with $b_2 = b_1^2/6b_0$, the equation is written

$$- b^* \alpha_1 k^2 + a^* \alpha_2 k^2 \omega' + \beta_0 + \xi \beta_1 \omega' + \frac{1}{6} \beta_2 \xi^2 \omega'^2 = 0 \tag{28}$$

where

$$b^* = 1/b_0, \quad \xi = b_1/b_0, \quad a^* = a_1/b_0 \tag{29}$$

Three independent parameters can be determined from three set of exact values.

Since equation (29) is linear in a^* and b^* , these parameters can be eliminated to yield a parabolic equation in terms of ξ . After solving for ξ , we can determine a_1, b_0, b_1 and b_2 by equations (16) and (29).

4. METHOD OF NUMERICAL CALCULATION

The ADI method is employed in the numerical calculation to achieve high accuracy in a reasonable computational time. The calculation is carried out alternately in the x - and y -direction. In the discretization by the ADI method, the term $\nabla^2 \tilde{\phi}$ cannot be ensured a second-order accuracy in time. In the present study, the term is averaged over time to ensure the accuracy. The finite difference equations of the equation (1) in the x - and y -directions are written

(t+1 time step : x -direction)

$$\begin{aligned}
 & \frac{1}{2} \left(\frac{\tilde{\phi}_{i-1,j}^{t+1} - 2\tilde{\phi}_{i,j}^{t+1} + \tilde{\phi}_{i+1,j}^{t+1}}{(\Delta x)^2} + \frac{\tilde{\phi}_{i-1,j}^t - 2\tilde{\phi}_{i,j}^t + \tilde{\phi}_{i+1,j}^t}{(\Delta x)^2} \right) \\
 & - ia_1 \frac{(\tilde{\phi}_{i-1,j}^{t+1} - 2\tilde{\phi}_{i,j}^{t+1} + \tilde{\phi}_{i+1,j}^{t+1}) - (\tilde{\phi}_{i-1,j}^t - 2\tilde{\phi}_{i,j}^t + \tilde{\phi}_{i+1,j}^t)}{(\Delta x)^2 \Delta t} \\
 & + \frac{1}{2} \left(\frac{\tilde{\phi}_{i,j-1}^t - 2\tilde{\phi}_{i,j}^t + \tilde{\phi}_{i,j+1}^t}{(\Delta y)^2} + \frac{\tilde{\phi}_{i,j-1}^{t-1} - 2\tilde{\phi}_{i,j}^{t-1} + \tilde{\phi}_{i,j+1}^{t-1}}{(\Delta y)^2} \right) \\
 & - ia_1 \frac{(\tilde{\phi}_{i,j-1}^t - 2\tilde{\phi}_{i,j}^t + \tilde{\phi}_{i,j+1}^t) - (\tilde{\phi}_{i,j-1}^{t-1} - 2\tilde{\phi}_{i,j}^{t-1} + \tilde{\phi}_{i,j+1}^{t-1})}{(\Delta y)^2 \Delta t} \\
 & + (b_0 + ic_0) \frac{\tilde{\phi}_{i,j}^{t+1} + \tilde{\phi}_{i,j}^t + \tilde{\phi}_{i,j}^{t-1}}{3} + i(b_1 + ic_1) \frac{\tilde{\phi}_{i,j}^{t+1} - \tilde{\phi}_{i,j}^{t-1}}{2\Delta t} \\
 & - b_2 \frac{\tilde{\phi}_{i,j}^{t+1} - 2\tilde{\phi}_{i,j}^t + \tilde{\phi}_{i,j}^{t-1}}{(\Delta t)^2} = 0
 \end{aligned} \tag{30}$$

(t+2 time step : y-direction)

$$\begin{aligned}
 & \frac{1}{2} \left(\frac{\tilde{\phi}_{i-1,j}^{t+1} - 2\tilde{\phi}_{i,j}^{t+1} + \tilde{\phi}_{i+1,j}^{t+1}}{(\Delta x)^2} + \frac{\tilde{\phi}_{i-1,j}^t - 2\tilde{\phi}_{i,j}^t + \tilde{\phi}_{i+1,j}^t}{(\Delta x)^2} \right) \\
 & - ia_1 \frac{(\tilde{\phi}_{i-1,j}^{t+1} - 2\tilde{\phi}_{i,j}^{t+1} + \tilde{\phi}_{i+1,j}^{t+1}) - (\tilde{\phi}_{i-1,j}^t - 2\tilde{\phi}_{i,j}^t + \tilde{\phi}_{i+1,j}^t)}{(\Delta x)^2 \Delta t} \\
 & + \frac{1}{2} \left(\frac{\tilde{\phi}_{i,j-1}^{t+2} - 2\tilde{\phi}_{i,j}^{t+2} + \tilde{\phi}_{i,j+1}^{t+2}}{(\Delta y)^2} + \frac{\tilde{\phi}_{i,j-1}^{t+1} - 2\tilde{\phi}_{i,j}^{t+1} + \tilde{\phi}_{i,j+1}^{t+1}}{(\Delta y)^2} \right) \\
 & - ia_1 \frac{(\tilde{\phi}_{i,j-1}^{t+2} - 2\tilde{\phi}_{i,j}^{t+2} + \tilde{\phi}_{i,j+1}^{t+2}) - (\tilde{\phi}_{i,j-1}^{t+1} - 2\tilde{\phi}_{i,j}^{t+1} + \tilde{\phi}_{i,j+1}^{t+1})}{(\Delta y)^2 \Delta t} \\
 & + (b_0 + ic_0) \frac{\tilde{\phi}_{i,j}^{t+2} + \tilde{\phi}_{i,j}^{t+1} + \tilde{\phi}_{i,j}^t}{3} + i(b_1 + ic_1) \frac{\tilde{\phi}_{i,j}^{t+2} - \tilde{\phi}_{i,j}^t}{2\Delta t} \\
 & - b_2 \frac{\tilde{\phi}_{i,j}^{t+2} - 2\tilde{\phi}_{i,j}^{t+1} + \tilde{\phi}_{i,j}^t}{(\Delta t)^2} = 0
 \end{aligned} \tag{31}$$

where (i, j) is the grid number in the (x, y) coordinate system, t the time, Δx and Δy the grid size in x - and y -direction, respectively.

5. NUMERICAL RESULTS

As for the frequency spectrum and the directional spreading function, the Bretschneider-Mitsuyasu-type and the Mitsuyasu-type were employed. The incident waves consisted of 1000 components and were given by the single summation method.

5. 1. Refraction

The present method was applied to the calculation of refraction of multi-directional irregular waves on 1/50 slopes. The significant deepwater wave height and period are 1.0m and 8.0s. The principal wave direction is normal to the shoreline (0°). The maximum directional concentration parameter, S_{max} , is 10 in deepwater. In this case, the analytical solution can be obtained by means of linear superposition of the spectral components by Snell's law. Figure 2 and 3 compare the two-dimensional and cross-shore distributions of the significant wave height, respectively. Dashed lines show analytical solution and solid lines represent the results of numerical calculation. Good agreement is observed.

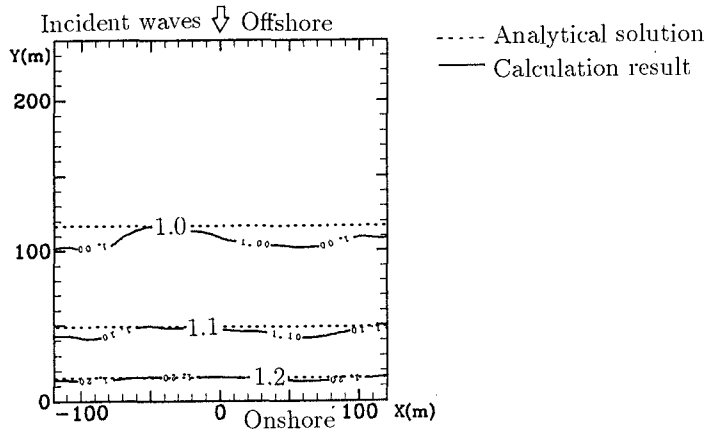


Figure 2: Significant wave height distribution due to refraction

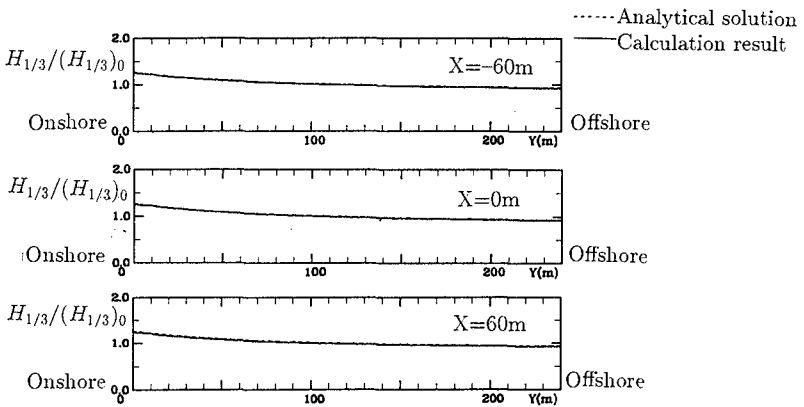


Figure 3: Significant wave height cross-shore distribution due to refraction

5. 2. Diffraction

Diffraction coefficients of multi-directional irregular waves for a semi-infinite breakwaters and through a breakwater gap have been calculated by Goda *et al.* (1978) by superposing analytical solutions. In the calculation, Bretschneider-Mitsuyasu-type frequency spectrum and Mitsuyasu-type directional distribution function are used. Dashed lines in Figures 4 and 5 show the results with the maximum directional concentration parameter, $S_{max} = 10$. In Figure 4, L denotes the wavelength corresponding to the significant wave period. In Figure 5, B denotes the gap width and this figure shows the case of $B/L=8$. Solid lines represent the results of the present method. These lines agree well with the dashed lines.

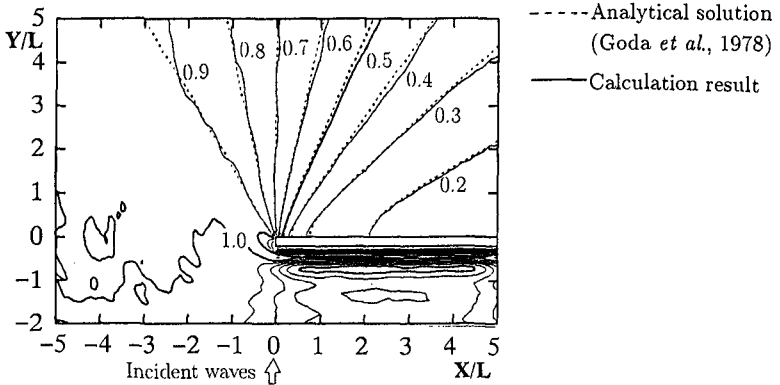


Figure 4: Diffraction coefficient around a semi-infinite breakwater for irregular waves

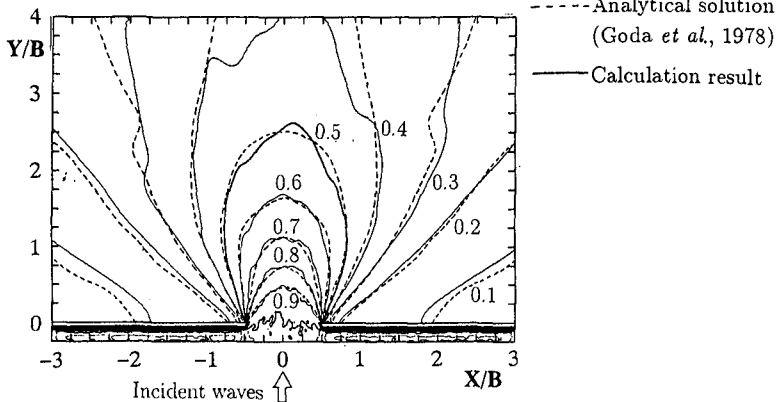


Figure 5: Diffraction coefficient around a breakwater gap for irregular waves (A gap width of 8 significant wavelength)

5. 3. Submerged circular shoal on a constant bottom

When waves propagate over a submerged circular shoal, the phenomenon of combined refraction-diffraction of waves occurs. To illustrate the capability of the present numerical model for the phenomenon, we compared the present results with that obtained by using the parabolic equation for a submerged circular shoal (Serizawa *et al.*, 1990). Figure 6 shows a submerged circular shoal on a constant depth. The constant water depth is 15m, the water depth at the peak of the circular shoal with radius 160m is 5m. Serizawa *et al.* (1990) calculated for this case. The significant wave height and period are 1.0m and 5.1s. The principal wave direction is in the positive y -axis (0°). The maximum value S_{\max} of the parameter S in the Mitsuyasu-type directional spreading function was 10. Significant wave height distributions are presented in Figures 7 and 8, to compare with the previous numerical result. Good agreement is observed.

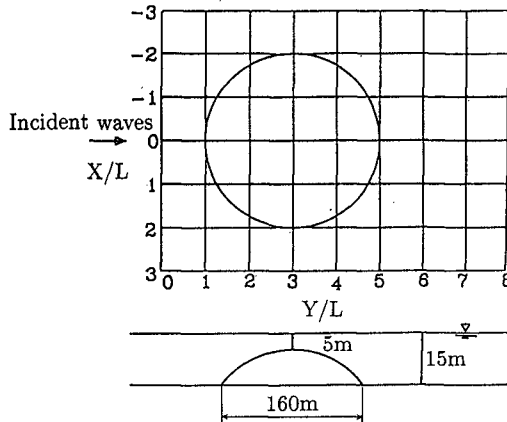


Figure 6: Sketch of submerged circular shoal on a constant bottom

5. 4. Wave breaking

Breaking wave model used is the same as Isobe (1987). The calculation of wave breaking was carried out in the cross-shore wave transformation problem for uni-directional irregular waves. The slope is 1/50. The significant wave period is 8.0s. The significant deepwater wave heights are 2.0m and 4.0m. In Figure 9, dashed lines show the results of calculation and solid lines show the results by Goda (1975). In the figure, H_0 is the significant wave height in deep water and h the water depth. The effect of wave nonlinearity and wave setup in shallow water is neglected in the present method. By considering this, the results seems to be in reasonable agreement with the results by Goda.

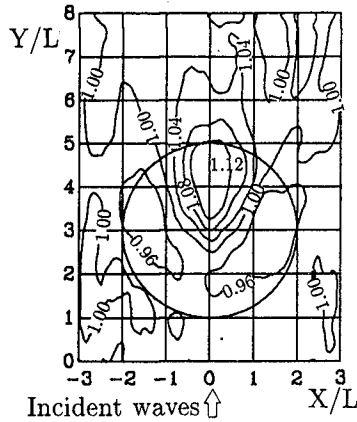


Figure 7: Present result for a submerged circular shoal on a constant bottom (the ratio of significant wave height to incident wave height)

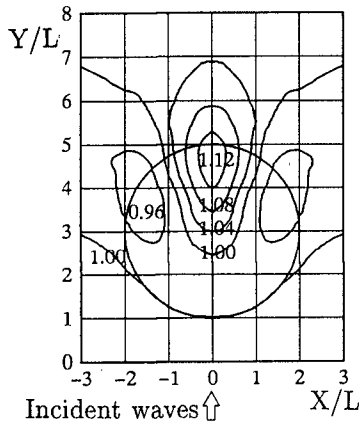


Figure 8: Previous result for a submerged circular shoal on a constant bottom (The ratio of significant wave height to incident wave height)

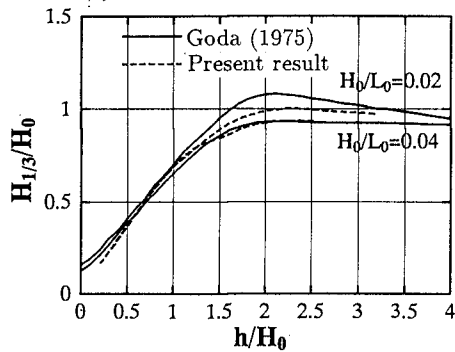


Figure 9: Significant wave height change of uni-directional irregular waves due to shoaling and breaking

6. WAVE HEIGHT DISTRIBUTION AROUND A MAN-MADE ISLAND

Numerical calculation of wave transformation around a rectangular man-made island on 1:50 slope is performed. It is an island of 1km long in the alongshore direction and 0.5km wide, and located about 1km from the coastal line. Hydraulic model tests with a multi-directional wave maker were carried out by Central Research Institute of the Electric Power Industry, Japan (Ikeno *et al.*, 1995) to investigate effects of the irregularity and directional spreading of waves behind the man-made island. The model is 1/150 in scale and the island is 6.6m long and 3.3m wide. The water depth at the man-made island is 20m at prototype scale which corresponds to 15cm at model scale. Side walls in the laboratory basin are installed on the slope along both edges of the wave maker, preventing waves from being diffracted.

Numerical calculation is performed under the same condition as that of the experiment. The offshore significant wave height and period are 9.2m and 14.3s. As for the frequency spectrum and the directional spreading function, the Bretschneider-Mitsuyasu-type and the Mitsuyasu-type were employed. The maximum values S_{\max} of the parameter S in the Mitsuyasu-type directional spreading function were 25. The incident waves consisted of 512 components and were given by the single summation method, whereas input signal to each segment of wave maker was computed by superposing component waves with 512 frequencies and 90 directions by the double summation method.

Figure 10 and 11, respectively, depict the numerical result and the experimental result (Ikeno *et al.*, 1995) for significant wave height distribution. Figure 12 compares the longshore distributions of the significant wave height. The validity of the numerical model is verified through comparison with the experimental result.

7. CONCLUSION

We have proposed a method for determining coefficients in the rational approximation and an efficient numerical calculation method for applying the time-dependent mild-slope equation for random waves to two-dimensional problems. The results of numerical calculations were compared with analytical and experimental results, which confirmed the validity of the present method.

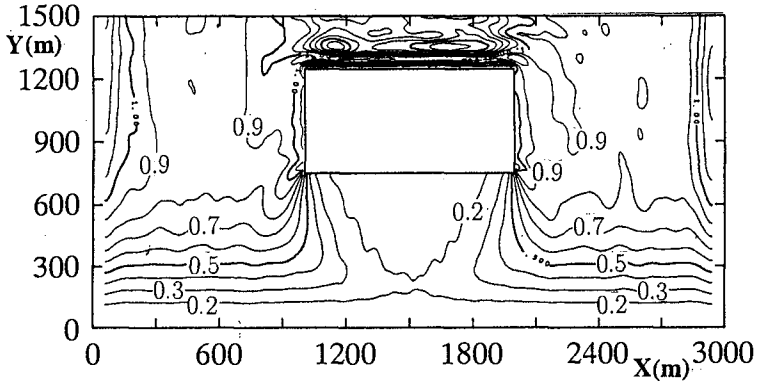


Figure 10: Calculation result (The ratio of significant wave height to incident wave height, $(H_{1/3})_0 = 9.2\text{m}$, $T_{1/3} = 14.3\text{s}$, $S_{\text{max}} = 25$, $\theta_p = 0^\circ$)

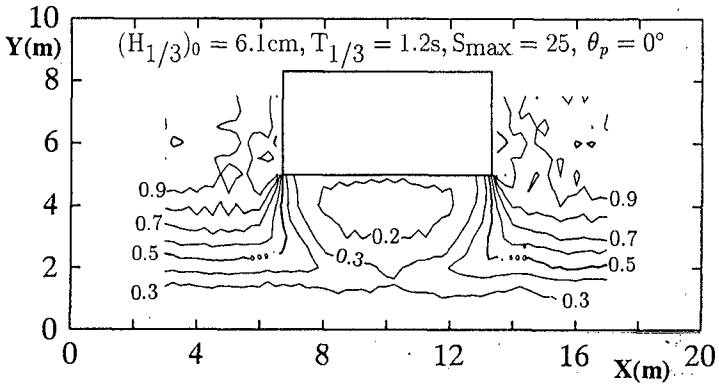


Figure 11: Experimental result (The ratio of significant wave height to incident wave height, 1/150 model)

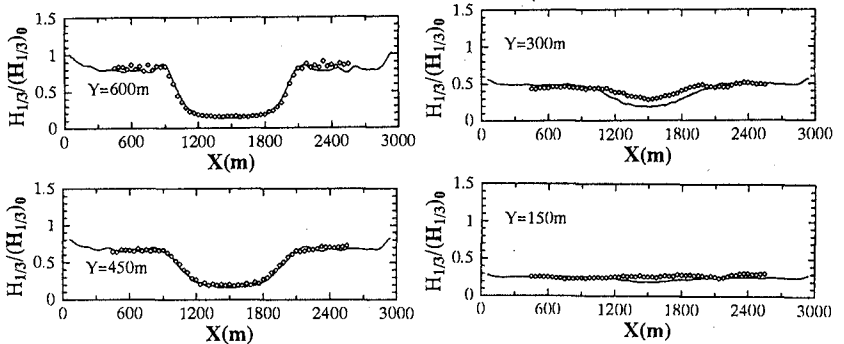


Figure 12: Comparison of the calculated and measured alongshore distribution of the wave height

ACKNOWLEDGMENTS

The experimental results were provided by Central Research Institute of Electric Power Industry. This experiment was carried out as part of "Studies on advanced siting civil engineering technology for nuclear power plants". It was supported by nine Japanese power companies and the Japan Atomic Power Company.

REFERENCES

- Berkhoff, J. C. W. (1972): Computation of combined refraction-diffraction, Proc. 13th Int. Conf. on Coastal Eng., ASCE, pp. 471-490.
- Goda, Y. (1975): Irregular wave deformation in the surf zone, Coastal Eng. in Japan, Vol. 18, pp.13-26.
- Goda, Y., T. Takayama and Y. Suzuki (1978): Diffraction diagrams for directional random waves, Proc. 16th Coastal Eng. Conf., ASCE, 1978, pp. 628-690.
- Ikeno, M., R. Kajima, M. Matsuyama and T. Sakakiyama (1995): Characteristics of Short-Crested Waves and Currents Behind Offshore Man-Made Island Type Power Plant, Proc. 5th Int. Offshore and Polar Eng. Conf., pp. 168-175.
- Ishii, T., M. Isobe and A. Watanabe (1994): Improved boundary conditions to a time-dependent mild-slope equation for random waves, Proc. 24th Int. Conf. on Coastal Eng., ASCE, pp. 272-284.
- Isobe, M. (1987): A parabolic equation model for transformation of irregular waves due to refraction, diffraction and breaking, Coastal Eng. in Japan, Vol. 30, pp. 33-47.
- Isobe, M. (1994): Time-dependent mild slope equations for random waves, Proc. 24th Int. Conf. on Coastal Eng., ASCE, pp. 285-299.
- Kubo, Y., Y. Kotake, M. Isobe and A. Watanabe (1992): Time-dependent mild slope equation for random waves, Proc. 23rd Int. Conf. on Coastal Eng., ASCE, pp. 419-431.
- Kotake, Y., M. Isobe and A. Watanabe (1992): On the high-order time-dependent mild slope equation for irregular waves, Proc. 39th Japanese Conf. on Coastal Eng., pp. 91-95 (in Japanese).
- Radder, A. C. (1979): On the parabolic equation method for water-wave propagation, J. Fluid Mech., Vol. 95, pp. 159-176.
- Serizawa, M., K. Ozawa, S. Mifune and M. Isobe (1990): Application of the parabolic equation for irregular waves to practical problems, Proc. 37th Japanese Conf. on Coastal Eng., pp. 26-30 (in Japanese).

CHAPTER 61

NONLINEAR WAVE TRANSFORMATION DUE TO A SUBMERGED BREAKWATER

Masahiko Isobe¹, Akira Watanabe¹ and Shogo Yamamoto²

Abstract

A nonlinear model of wave transformation due to a submerged breakwater is developed on the basis of the nonlinear mild-slope equations. Numerical computation shows that significant amount of wave energy can be transferred from the fundamental component to higher harmonics by adjusting configuration of the submerged breakwater. In case of oblique incidence, wave direction as well as wave period changes due to the breakwater. These results implies the possibility to control wave period and direction as well as wave height.

1 Introduction

When waves propagate in a region of rapidly changing depth such as over a submerged breakwater, higher harmonic components are generated due to nonlinear effect. Various numerical simulations have been carried out for nonlinear wave transformation due to a submerged breakwater (Ohyama and Nadaoka, 1992, 1994; Tsubota *et al.*, 1994). This implies that submerged breakwaters can change and control characteristics of waves such as wave height, period and direction, which can be utilized in coastal engineering. Since floating breakwaters are, in general, effective for controlling only short period waves, combination of submerged and floating breakwaters may become an efficient breakwater system. Change of frequency spectrum over an offshore bar is an essential factor in predicting wave field and resultant wave-induced nearshore current. These indicate the importance to study wave transformation due to a submerged breakwater.

Since generation of higher harmonics is a strongly nonlinear phenomenon, it cannot be reproduced by linear or weakly nonlinear wave theories. Isobe (1994) derived a set of nonlinear mild-slope equations which includes full nonlinearity and full dispersion. In the present study, numerical simulations are performed based on the nonlinear mild-slope equations to examine the function of a submerged breakwater to control not only wave height but also wave period and direction.

2 Basic Equations and Boundary Conditions

2.1 Nonlinear mild-slope equation

Fully nonlinear and fully dispersive wave theories have been developed by Nadaoka *et al.* (1994), Nochino (1994) and Isobe (1994) among which the nonlinear mild-slope equations derived by Isobe (1994) is employed in the following numerical simulation.

¹Dept. of Civil Eng., Univ. of Tokyo, 7-3-1 Hongo, Bunkyo-ku, Tokyo 113, Japan.

²Penta-Ocean Construction Inst. of Tech., Nishinasuno-machi, Nasu-gun, Tochigi 329-27, Japan.

In deriving the nonlinear mild-slope equations, the velocity potential, ϕ , is expanded into a series in terms of a set of vertical distribution functions, Z_α , which are given a priori:

$$\phi(\mathbf{x}, z, t) = \sum_{\alpha=1}^N Z_\alpha(z; h(\mathbf{x})) f_\alpha(\mathbf{x}, t) \equiv Z_\alpha f_\alpha \quad (1)$$

where h is the water depth, $\mathbf{x} = (x, y)$ the horizontal coordinates, z the vertical coordinate, t the time, and N the total number of terms.

By substituting the above expression into the Lagrangian defined by Luke (1967), applying the variational principle, and neglecting terms of the second order in bottom slope, the following equations can be obtained:

$$g\eta + Z_\beta^\eta \frac{\partial f_\beta}{\partial t} + \frac{1}{2} Z_\gamma^\eta Z_\beta^\eta \nabla f_\gamma \nabla f_\beta + \frac{1}{2} \frac{\partial Z_\gamma^\eta}{\partial z} \frac{\partial Z_\beta^\eta}{\partial z} f_\gamma f_\beta + \frac{\partial Z_\gamma^\eta}{\partial h} Z_\beta^\eta f_\gamma \nabla f_\beta \nabla h = 0 \quad (2)$$

$$Z_\alpha^\eta \frac{\partial \eta}{\partial t} + \nabla(A_{\alpha\beta} \nabla f_\beta) - B_{\alpha\beta} f_\beta + (C_{\beta\alpha} - C_{\alpha\beta}) \nabla f_\beta \nabla h + \frac{\partial Z_\beta^\eta}{\partial h} Z_\alpha^\eta f_\beta \nabla \eta \nabla h = 0 \quad (3)$$

where η is the water surface elevation, g the gravitational acceleration and

$$Z_\alpha^\eta = Z_\alpha|_{z=\eta} \quad (4)$$

$$A_{\alpha\beta} = \int_{-h}^{\eta} Z_\alpha Z_\beta dz \quad (5)$$

$$B_{\alpha\beta} = \int_{-h}^{\eta} \frac{\partial Z_\alpha}{\partial z} \frac{\partial Z_\beta}{\partial z} dz \quad (6)$$

$$C_{\alpha\beta} = \int_{-h}^{\eta} \frac{\partial Z_\alpha}{\partial h} Z_\beta dz \quad (7)$$

Unknown functions in Eqs. (2) and (3) are f_α ($\alpha = 1$ to N) and η which yield $N + 1$ unknowns, whereas the total number of equations is also $N + 1$. No assumptions other than expanding the velocity potential into a series are made in deriving the equations. Therefore, the nonlinear mild-slope equations can be used to simulate even strongly nonlinear and strongly dispersive wave transformation.

2.2 Vertical distribution functions

Since the present study deals with wave transformation in shallow water, even-order polynomial functions are chosen as vertical distribution functions:

$$Z_\alpha = \left(\frac{h+z}{h} \right)^{2(\alpha-1)} \quad (8)$$

Then, Eqs. (4) to (7) become

$$Z_\alpha^\eta = \zeta^{2(\alpha-1)} \quad (9)$$

$$A_{\alpha\beta} = h \frac{\zeta^{2(\alpha+\beta)-3}}{2(\alpha+\beta)-3} \quad (10)$$

$$B_{\alpha\beta} = \frac{4(\alpha-1)(\beta-1)}{h} \frac{\zeta^{2(\alpha+\beta)-5}}{2(\alpha+\beta)-5} \quad (11)$$

$$C_{\alpha\beta} = 2(\alpha - 1) \left[\frac{\zeta^{2(\alpha+\beta)-4}}{2(\alpha + \beta) - 4} - \frac{\zeta^{2(\alpha+\beta)-3}}{2(\alpha + \beta) - 3} \right] \quad (12)$$

where

$$\zeta = \frac{h + \eta}{h} \quad (13)$$

In the following calculation, the series is truncated at the second term ($N=2$) as

$$\phi(x, y, z) = f_1(x, y, t) + \left(1 + \frac{z}{h}\right)^2 f_2(x, y, t) \quad (14)$$

so that Eqs. (2) and (3) are rewritten in more specific forms:

$$g\eta + \frac{\partial f_1}{\partial t} + \frac{(h + \eta)^2}{h^2} \frac{\partial f_2}{\partial t} + \frac{1}{2} \left[\nabla f_1 + \frac{(h + \eta)^2}{h^2} \nabla f_2 \right]^2 + \frac{1}{2} \left[\frac{2(h + \eta)}{h^2} f_2 \right]^2 - \frac{2\eta(h + \eta)}{h^3} f_2 \left[\nabla f_1 + \frac{(h + \eta)^2}{h^2} \nabla f_2 \right] \nabla h = 0 \quad (15)$$

$$\frac{\partial \eta}{\partial t} + \nabla \left[(h + \eta) \nabla f_1 + \frac{(h + \eta)^3}{3h^2} \nabla f_2 \right] + \frac{(h + \eta)^2(h - 2\eta)}{3h^3} \nabla f_2 \nabla h - \frac{2(h + \eta)\eta}{h^3} f_2 \nabla \eta \nabla h = 0 \quad (16)$$

$$\frac{(h + \eta)^2}{h^2} \frac{\partial \eta}{\partial t} + \nabla \left[\frac{(h + \eta)^3}{3h^2} \nabla f_1 + \frac{(h + \eta)^5}{5h^4} \nabla f_2 \right] - \frac{4(h + \eta)^3}{3h^4} f_2 - \frac{(h + \eta)^2(h - 2\eta)}{3h^3} \nabla f_1 \nabla h - \frac{2(h + \eta)^3}{h^5} f_2 \nabla \eta \nabla h = 0 \quad (17)$$

2.3 Boundary condition

We first consider one-dimensional (on-offshore) wave transformation. At the onshore boundary, waves propagate only shoreward (i.e., positive x direction) with wave celerity, C so that for any independent variable, Φ ($= \eta, f_1$ or f_2),

$$\Phi = \Phi(x - Ct) \quad (18)$$

At the offshore boundary, waves consist of incident and reflected waves denoted by Φ_{in} and Φ_r , respectively:

$$\Phi = \Phi_{in}(x - Ct) + \Phi_r(x + Ct) \quad (19)$$

where the incident waves are given and the reflected waves are unknown.

Differentiating the above two equations with respect to x and t , we obtain the following boundary conditions:

$$\frac{\partial \Phi}{\partial t} + C \frac{\partial \Phi}{\partial x} = 0 \quad (\text{at onshore boundary}) \quad (20)$$

$$\frac{\partial \Phi}{\partial t} - C \frac{\partial \Phi}{\partial x} - 2 \frac{\partial \Phi_{in}}{\partial t} = 0 \quad (\text{at offshore boundary}) \quad (21)$$

The water surface elevation, η_{in} , due to the incident waves can be given from an appropriate progressive wave theory from given water depth h , wave period T , and wave height H . The functions, f_{1in} and f_{2in} , should also be able to be given from the same wave theory, but an explicit expression is not available in any wave theory. However, since nonlinearity is normally negligible at the offshore boundary, linear relationships between η_{in} , and f_{1in} and f_{2in} are derived as follows.

One-dimensional linearized forms of Eqs. (15) to (17) for a constant depth are written as follows:

$$g\eta + \frac{\partial f_1}{\partial t} + \frac{\partial f_2}{\partial t} = 0 \quad (22)$$

$$\frac{\partial \eta}{\partial t} + h \frac{\partial^2 f_1}{\partial x^2} + \frac{h}{3} \frac{\partial^2 f_2}{\partial x^2} = 0 \quad (23)$$

$$\frac{\partial \eta}{\partial t} + \frac{h}{3} \frac{\partial^2 f_1}{\partial x^2} + \frac{h}{5} \frac{\partial^2 f_2}{\partial x^2} - \frac{4}{3h} f_2 = 0 \quad (24)$$

which result in an eigenvalue problem for η , f_1 and f_2 . To solve the problem, we seek for a non-trivial solution of the following forms:

$$\eta = a e^{i(kx - \omega t)} \quad (25)$$

$$f_1 = a_1 e^{i(kx - \omega t)} \quad (26)$$

$$f_2 = a_2 e^{i(kx - \omega t)} \quad (27)$$

where ω ($= 2\pi/T$) is the angular frequency to be given, k the wave number to be determined from the eigen value, and a , a_1 and a_2 are the amplitudes.

By differentiating Eq. (22) with respect to t and substituting it into Eqs. (23) and (24), η can be eliminated:

$$-\frac{1}{g} \left(\frac{\partial^2 f_1}{\partial t^2} + \frac{\partial^2 f_2}{\partial t^2} \right) + h \frac{\partial^2 f_1}{\partial x^2} + \frac{h}{3} \frac{\partial^2 f_2}{\partial x^2} = 0 \quad (28)$$

$$-\frac{1}{g} \left(\frac{\partial^2 f_1}{\partial t^2} + \frac{\partial^2 f_2}{\partial t^2} \right) + \frac{h}{3} \frac{\partial^2 f_1}{\partial x^2} + \frac{h}{5} \frac{\partial^2 f_2}{\partial x^2} - \frac{4}{3h} f_2 = 0 \quad (29)$$

Then substitution of Eqs. (26) and (27) into the above two equations yield the following two equations:

$$\frac{\omega^2}{g} (a_1 + a_2) - hk^2 a_1 - \frac{hk^2}{3} a_2 = 0 \quad (30)$$

$$\frac{\omega^2}{g} (a_1 + a_2) - \frac{hk^2}{3} a_1 - \frac{hk^2}{5} a_2 - \frac{4}{3h} a_2 = 0 \quad (31)$$

To obtain a non-trivial solution, the determinant of the above simultaneous equations should vanish, from which we can determine the wave number as

$$k^2 = \frac{6h^2\omega^2 - 15gh \pm \sqrt{(6h^2\omega^2 - 15gh)^2 + 60gh^3\omega^2}}{2gh^3} \quad (32)$$

in which positive sign should be selected because positive and negative signs, respectively, yield positive and negative values of k^2 corresponding to progressive and evanescent waves. Then the normalized eigenvector, (r_1, r_2) , becomes

$$r_1 = \frac{a_1}{a_1 + a_2} = \frac{3\omega^2}{2ghk^2} - \frac{1}{2} \quad (33)$$

$$r_2 = \frac{a_2}{a_1 + a_2} = \frac{3}{2} - \frac{3\omega^2}{2ghk^2} \quad (34)$$

By considering Eqs. (22), (25) to (27), (33) and (34), we finally obtain the following relationships:

$$f_{1in} = \frac{g}{i\omega} \left(\frac{3\omega^2}{2ghk^2} - \frac{1}{2} \right) \eta_{in} \quad (35)$$

$$f_{2in} = \frac{g}{i\omega} \left(\frac{3}{2} - \frac{3\omega^2}{2ghk^2} \right) \eta_{in} \quad (36)$$

The above relationships will be used even when a nonlinear wave theory such as Stokes or cnoidal wave theory is employed to give incident waves because nonlinearity is normally not so strong at the offshore boundary.

3 Computational Method and Condition

Eqs. (15) to (17) are solved numerically by an implicit finite difference scheme. The initial condition is still water and the time evolution of η , f_1 and f_2 is calculated by these equations as well as the boundary conditions (20) and (21). Spatial derivatives are evaluated at the center of the old and new time steps. This necessitates an iteration procedure, for which the Newton-Raphson method is employed in the present study.

The computational domain is 500m long including a submerged breakwater or a step. The grid size is 1/64 of the wavelength, and the time increment is 1/64 of the wave period. This fine grid size assures the accuracy of the numerical solution for the nonlinear mild-slope equations.

To give incident waves, a third-order Stokes wave theory and a second-order cnoidal wave theory (Isobe and Kraus, 1983a, b) are employed depending on the Ursell parameter. Stokes wave theory is employed when the Ursell parameter is less than 25, and cnoidal wave theory is employed otherwise.

The incident wave conditions for close examination of the numerical result are shown in **Table 1**.

Table 1 Incident wave condition for numerical experiment

	wave period (s)	wave height (m)	water depth (m)
Case 1	7.1	1.0	10.0
Case 2	7.1	2.0	10.0

Two types of bottom configuration are employed: step type and submerged breakwater type. Samples are shown in **Figure 1** and detailed dimensions used are shown in **Table 2**.

Table 2 Bottom configuration

step		
slope of step	$\tan \theta$	1/3, 1/5, 1/10, 1/20
relative depth on step	h_s/h	0.2, 0.3, 0.4, 0.5, 0.6, 0.7
submerged breakwater		
relative crown depth	h_s/h	0.2, 0.3, 0.4, 0.5, 0.6, 0.7
relative crown width	b/h	2, 4, 6, 8, 10, 12, 14, 16, 20, 22

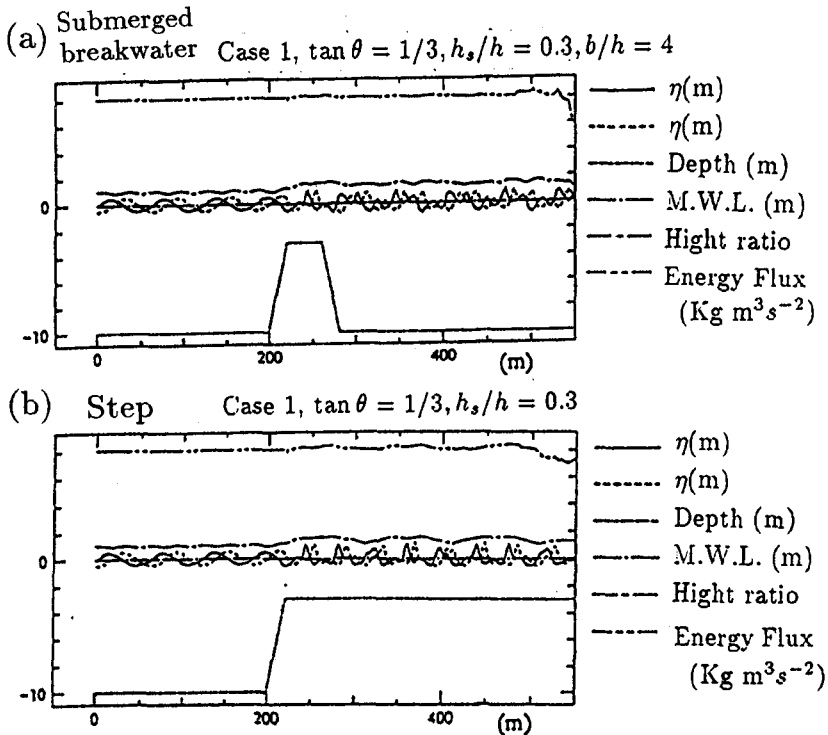


Figure 1 Examples of calculated distribution of the water surface elevation, wave height, mean water level, and energy flux.

4 Result for 1-D Calculation

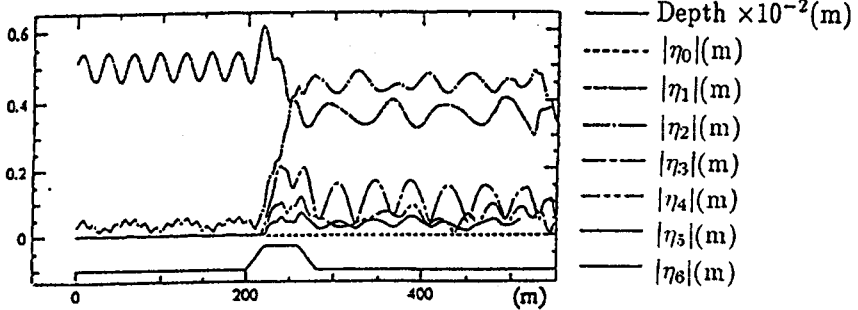
Figure 1 shows examples of calculated distribution of the water surface elevation at two different time steps, wave height, mean water level, and energy flux. Waves are incident from left to right. (a) is for a submerged breakwater, and (b) is for a step. The energy flux is kept constant except for a small fluctuation which may have resulted from the error due to insufficient number of terms in the series expansion of the velocity potential. As can be seen from the water surface elevation, wave disintegration on the breakwater or step is significant.

To examine the nonlinear wave disintegration, the temporal change of water surface elevation is transformed into a Fourier series at every point. Figure 2 shows the distribution of amplitude of the first six components. Spatial change of amplitudes on the step are periodic.

The spacing between two adjacent peaks of the second harmonics is derived theoret-

(a) Submerged

breakwater Case 1, $\tan \theta = 1/3, h_s/h = 0.3, b/h = 4$



(b) Step

Case 1, $\tan \theta = 1/3, h_s/h = 0.3$

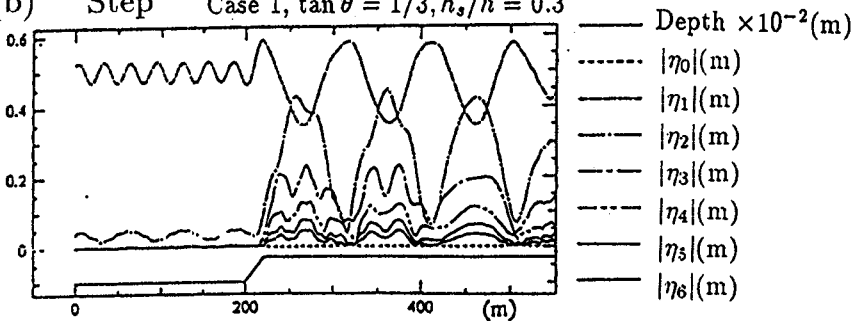


Figure 2 Distribution of amplitude of various harmonics.

ically as (Massel, 1983)

$$\lambda_2 = 2\pi/(k_2 - 2k_1) \quad (37)$$

where k_1 and k_2 are the wave numbers corresponding to the linear dispersion relation for ω and 2ω , respectively:

$$\omega^2 = gk_1 \tanh k_1 h \quad (38)$$

$$4\omega^2 = gk_2 \tanh k_2 h \quad (39)$$

The present result agrees well with the above theory, which implies the return spacing is predicted theoretically. However, the amplitude cannot be predicted accurately especially for strongly nonlinear cases. Thus, it is examined in the present study in detail.

Figure 3 shows the relation between the maximum amplitudes, $|\eta_n|$ ($n = 1$ to 3), of the first three harmonics, and the slope, $\tan \theta$, of the offshoreward face of a step. The maximum amplitude of higher harmonics increases with increasing slope. The effect of the water depth on a step is shown in **Figure 4**. In the figure, h_s/h is the ratio between the water depth, h_s , on the step and that, h , in the offshore region. Results are plotted for non-breaking cases for which $h_s/h \geq 0.3$ for Case 1 and $h_s/h \geq 0.5$ for Case 2. The maximum amplitudes of higher harmonics increase with decreasing water depth on the step.

As can be expected from the periodicity of the amplitude of higher harmonics on the step which is shown in **Figure 2(b)**, the amplitudes of various harmonics behind a submerged breakwater oscillate significantly with the width. **Figure 5** shows the average amplitudes of the first three harmonics behind a submerged breakwater. (a) is for the incident waves of Case 1 and $h_s/h = 0.3$, (b) for Case 1 and $h_s/h = 0.5$, and (c) for Case 2 and $h_s/h = 0.5$. For each figure, the return spacing, λ_2 , of the second harmonics agrees well with that predicted by Eq. (37). The amplitude behind the breakwater becomes maximum for $b = m\lambda_2$ ($m = 1, 2, \dots$), and minimum for $b = (m - 1/2)\lambda_2$, and the difference between the maximum and minimum values increases with

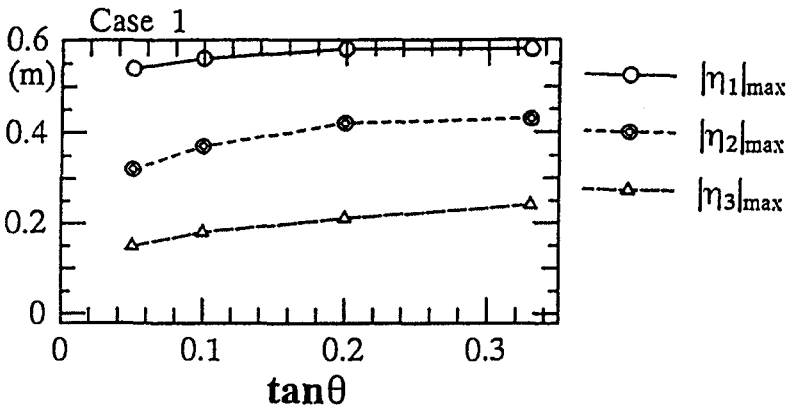


Figure 3 Relation between the maximum amplitude of various harmonics and the slope of the offshoreward face of a step.

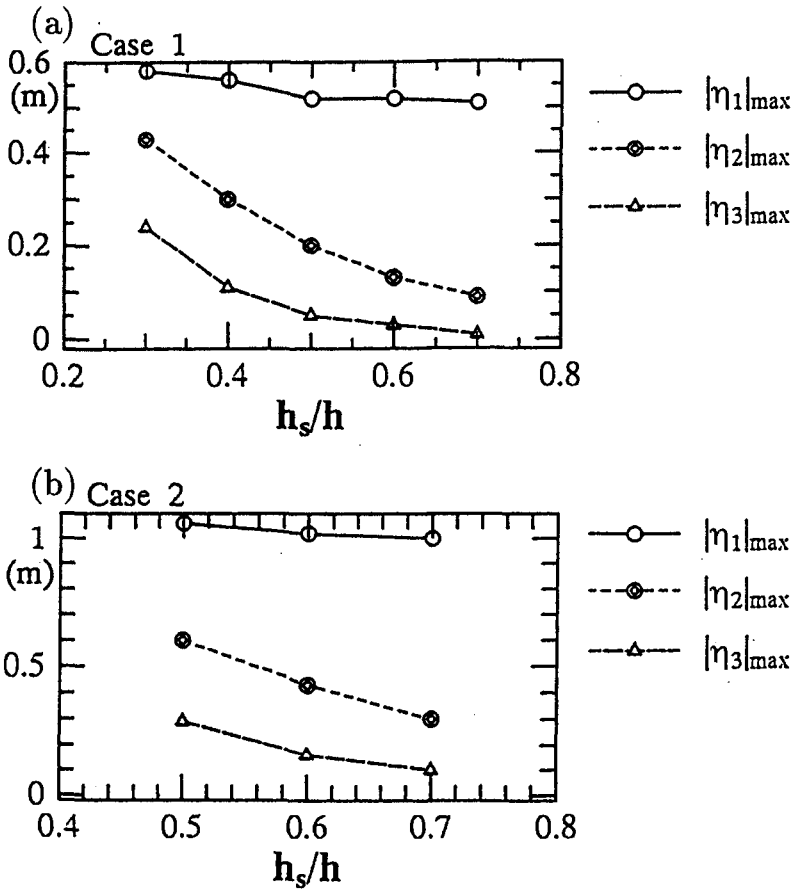


Figure 4 Relation between the maximum amplitude of various harmonics and the water depth on a step.

decreasing crown water depth. By comparing between (b) and (c), it is understood that the ratios of amplitudes of higher harmonics to the first harmonics grow larger for larger incident wave steepness.

The above results imply that significant amount of wave energy is transferred from the fundamental component to higher harmonics and the amplitude of the second harmonics can become comparable or larger than that of the first harmonics behind a submerged breakwater by adjusting its configuration.

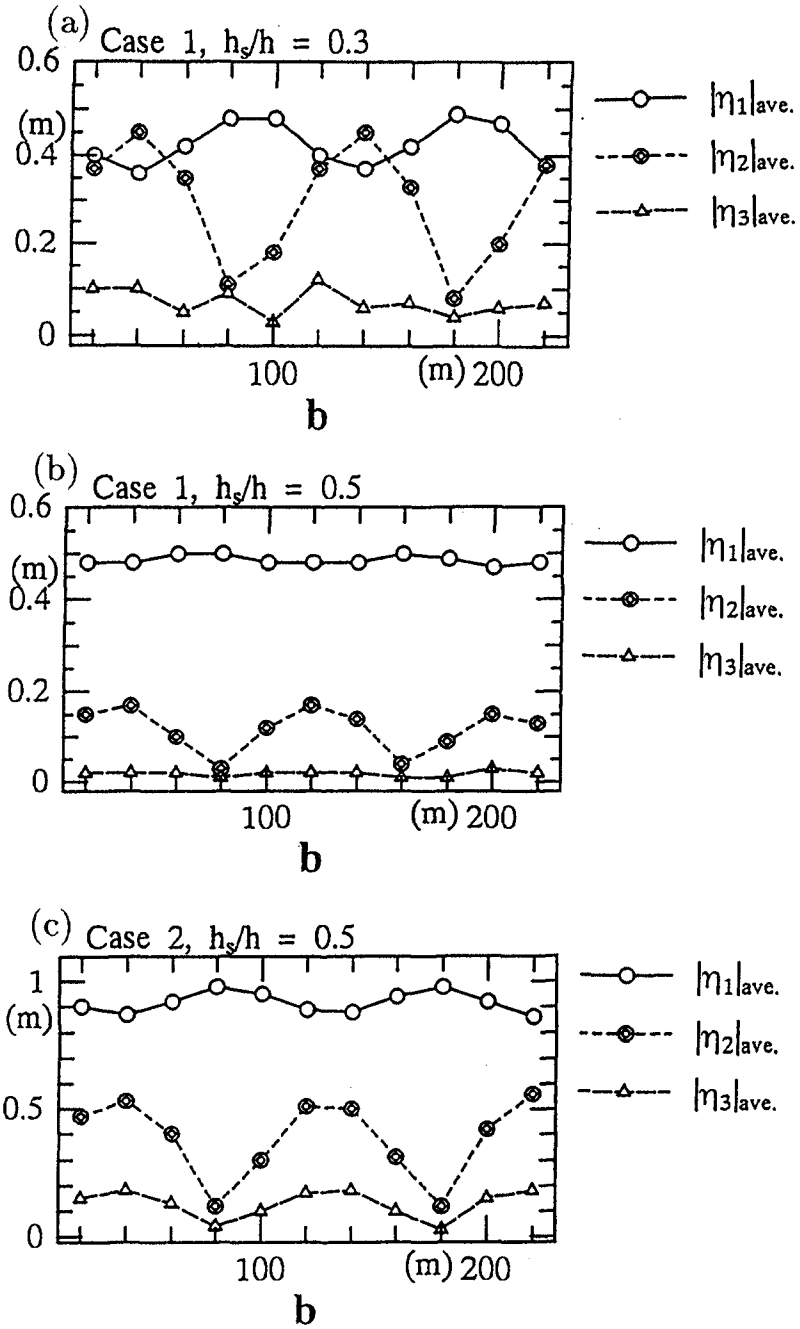


Figure 5 Relation between the average amplitude of various harmonics and the crown width of a submerged breakwater.

5 Basic Equations for Obliquely-Incident Waves

When waves are incident obliquely to a region with parallel depth contours, the celerity, C_y , in the alongshore direction, y , becomes constant throughout the depth. The quantity C_y is evaluated at the offshore boundary as

$$C_y = \frac{C_o}{\sin \theta_o} \quad (40)$$

where C_o and θ_o are the wave celerity and direction at the offshore boundary. Then the derivative with respect to y is converted to that with respect to t :

$$\frac{\partial}{\partial y} = \frac{1}{C_y} \frac{\partial}{\partial t} \quad (41)$$

If Eq. (41) is substituted into Eqs. (15) to (17), independent variables become only x and t . However, numerical solution could not be obtained due to numerical instability because the equations include the second-order derivatives with respect to t . Therefore, by considering the linear relationships (35) and (36), the following equations are used to eliminate the second-order derivatives:

$$\frac{\partial^2 f_1}{\partial t^2} = -gr_1 \frac{\partial \eta}{\partial t} \quad (42)$$

$$\frac{\partial^2 f_2}{\partial t^2} = -gr_2 \frac{\partial \eta}{\partial t} \quad (43)$$

Then Eqs. (15) to (17) become

$$g\eta + \frac{\partial f_1}{\partial t} + \frac{(h+\eta)^2}{h^2} \frac{\partial f_2}{\partial t} + \frac{1}{2} \left[\frac{\partial f_1}{\partial x} + \frac{(h+\eta)^2}{h^2} \frac{\partial f_2}{\partial x} \right]^2 + \frac{1}{2} \frac{1}{C_y^2} \left[\frac{\partial f_1}{\partial t} + \frac{(h+\eta)^2}{h^2} \frac{\partial f_2}{\partial t} \right]^2 + \frac{1}{2} \left[\frac{2(h+\eta)}{h^2} f_2 \right]^2 - \frac{2\eta(h+\eta)}{h^3} f_2 \left[\frac{\partial f_1}{\partial x} + \frac{(h+\eta)^2}{h^2} \frac{\partial f_2}{\partial x} \right] \frac{\partial h}{\partial x} = 0 \quad (44)$$

$$\begin{aligned} & \frac{\partial \eta}{\partial t} + \frac{\partial}{\partial x} \left[(h+\eta) \frac{\partial f_1}{\partial x} + \frac{(h+\eta)^3}{3h^2} \frac{\partial f_2}{\partial x} \right] \\ & + \frac{1}{C_y^2} \left[\left\{ \frac{\partial f_1}{\partial t} + \frac{(h+\eta)^2}{h^2} \frac{\partial f_2}{\partial t} - gr_1(h+\eta) - gr_2 \frac{(h+\eta)^3}{3h^2} \right\} \frac{\partial \eta}{\partial t} \right] \\ & + \frac{(h+\eta)^2(h-2\eta)}{3h^3} \frac{\partial f_2}{\partial x} \frac{\partial h}{\partial x} - \frac{2(h+\eta)\eta}{h^3} f_2 \frac{\partial \eta}{\partial x} \frac{\partial h}{\partial x} = 0 \end{aligned} \quad (45)$$

$$\begin{aligned} & \frac{(h+\eta)^2}{h^2} \frac{\partial \eta}{\partial t} + \frac{\partial}{\partial x} \left[\frac{(h+\eta)^3}{3h^2} \frac{\partial f_1}{\partial x} + \frac{(h+\eta)^5}{5h^4} \frac{\partial f_2}{\partial x} \right] \\ & + \frac{1}{C_y^2} \left[\left\{ \frac{(h+\eta)^2}{h^2} \frac{\partial f_1}{\partial t} + \frac{(h+\eta)^4}{h^4} \frac{\partial f_2}{\partial t} - gr_1 \frac{(h+\eta)^3}{3h^2} - gr_2 \frac{(h+\eta)^5}{5h^4} \right\} \frac{\partial \eta}{\partial t} \right] \\ & - \frac{4(h+\eta)^3}{3h^4} f_2 - \frac{(h+\eta)^2(h-2\eta)}{3h^3} \frac{\partial f_1}{\partial x} \frac{\partial h}{\partial x} - \frac{2(h+\eta)^3\eta}{h^5} f_2 \frac{\partial \eta}{\partial x} \frac{\partial h}{\partial x} = 0 \end{aligned} \quad (46)$$

The numerical solution method for the above equations is the same as that for normal incidence previously described.

6 Result for Obliquely-Incident Waves

Once a numerical solution is obtained in terms of x and t as $\Phi(x, t)$, the solution in terms of x , y and t is written as $\Phi(x, t - y/C_y)$. **Figure 6** shows the pattern of wave crests near an infinitely-long submerged breakwater with a trapezoidal cross section. Waves are incident obliquely from the lower boundary.

For **Figure 6(a)**, wave direction changes on the breakwater due to refraction, and secondary crests appear due to the nonlinear effect, but the secondary crests disappear behind the breakwater and the wave direction turns back to that of the incident waves. However, for **Figure 6(b)** in which the amplitude of the second harmonics grows larger than that of the first harmonics, secondary crests remain behind the breakwater and the wave direction is different from that of incident waves. The reason is as follows. Since celerities of all component waves must be the same in the y direction, higher harmonics, of which the wave celerities are smaller than that of fundamental component, should propagate in the direction closer to the shore-normal. Therefore, the predominant direction changes when higher harmonic components dominate behind the breakwater.

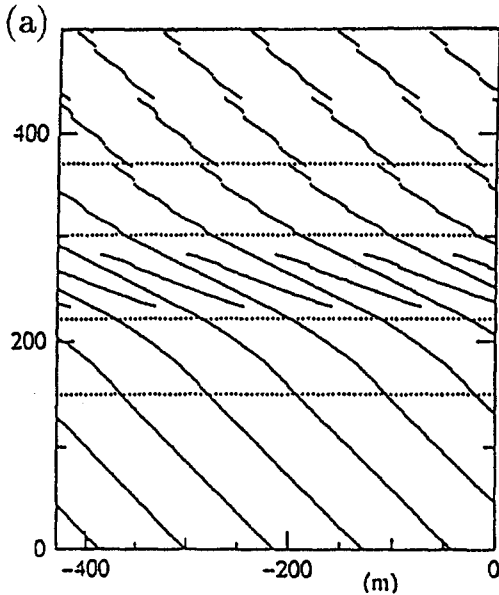
7 Conclusion

Numerical scheme for the nonlinear mild-slope equations is developed to examine wave transformation due to a submerged breakwater for normal and oblique incidence.

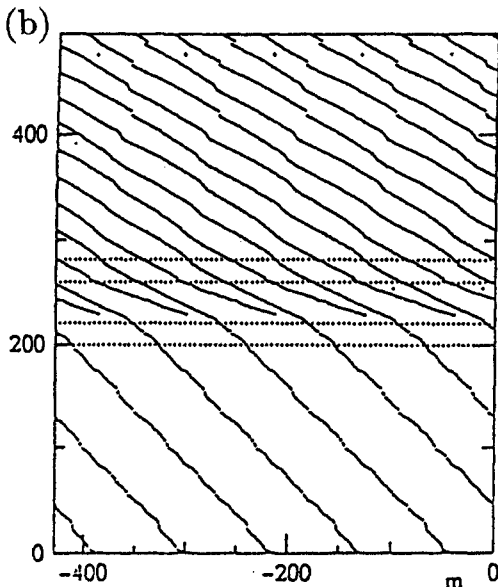
Generation of higher harmonics for normal incidence to a step and a submerged breakwater is first examined. The amplitudes of higher harmonics on a submerged breakwater are larger for steeper offshoreward slope and for smaller crown water depth. The amplitudes of higher harmonics behind a submerged breakwater become maximum for $b = m\lambda_2$ ($m = 1, 2, \dots$), and minimum for $b = (m - 1/2)\lambda_2$. When the nonlinearity of incident waves is stronger, higher harmonics grow larger.

Higher harmonics appear also for obliquely incident waves. When higher harmonics dominate behind the submerged breakwater, predominant wave direction changes to keep the alongshore celerity constant.

These results imply that, utilizing a submerged breakwater, we can control wave period and direction as well as wave height.



Case 1, $\theta_0 = 45$, $\tan \theta = 1/10$, $h_s/h = 0.3$, $b/h = 8$



Case 1, $\theta_0 = 45$, $\tan \theta = 1/3$, $h_s/h = 0.3$, $b/h = 4$

Figure 6 Change of crest lines due to a submerged breakwater.

References

- [1] Isobe, M. (1994): Time-dependent mild-slope equations for random waves, Proc. 24th Int. Conf. on Coastal Eng., ASCE, pp. 285-299.
- [2] Isobe, M. and N. C. Kraus (1983): Derivation of a third-order Stokes wave theory, Hydraulics Lab. Rep., Dept. of Civil Eng., Yokohama Nat. Univ., No. YNU-HY-83-1, 32p.
- [3] Isobe, M. and N. C. Kraus (1983): Derivation of a second-order cnoidal wave theory, Hydraulics Lab. Rep., Dept. of Civil Eng., Yokohama Nat. Univ., No. YNU-HY-83-2, 43p.
- [4] Luke, J. C. (1967): A variational principle for a fluid with a free surface, J. Fluid Mech., Vol. 27, pp. 395-397.
- [5] Massel, S. R. (1983): Harmonic generation by waves propagating over a submerged step, Coastal Eng., Vol. 7, pp. 357-380.
- [6] Nadaoka, K., S. Beji and Y. Nakagawa (1994): A fully-dispersive nonlinear wave model and its numerical solution, Proc. 24th Int. Conf. on Coastal Eng., ASCE, pp. 427-441.
- [7] Nochino, M. (1994): Fully-nonlinear coupled vibration equations for irregular water waves and their basic characteristics, Proc. 41st Japanese Conf. on Coastal Eng., JSCE, pp. 16-20(inJapanese).
- [8] Ohyama, T. and K. Nadaoka (1992): Modeling the transformation of nonlinear waves passing over a submerged dike, Proc. 23rd Int. Conf. on Coastal Eng., ASCE, pp. 526-539.
- [9] Ohyama, T. and K. Nadaoka (1994): Transformation of a nonlinear wave train passing over a submerged shelf without breaking, Coastal Eng., Vol. 24, No. 1-2, pp. 1-22.
- [10] Tsubota, H., M. Isobe and A. Watanabe (1994): Study on wave control by submerged breakwater, Proc. Coastal Eng., JSCE, Vol. 41, pp. 641-645.

CHAPTER 62

Observed and Modeled Wave Results From Near-Stationary Hurricanes

Charles L. Vincent, PhD¹ and Robert E. Jensen, PhD²

Abstract

Wave conditions in hurricanes have been difficult to study because of a lack of high-quality wave data and poor descriptions of the wind field. In the 1994 and 1995 hurricane seasons, two Category 1 hurricanes (Gordon and Felix) approached the North Carolina coast and stalled for a period of about 2 days. Although the storms were minimal hurricanes they produced large swell that persisted for several days. A wave gauging network of two to five directional instruments in water depths ranging from 8 to 50 m operated throughout the storms. Because of their proximity to land, both storms were extensively observed by radar and aircraft so that the wind fields are well described. The data set offers an opportunity to evaluate two prediction methods to examine the wave field during these most unusual hurricanes.

Introduction

In 1994 and 1995, Hurricanes Gordon and Felix approached the U. S. Army Engineer Waterways Experiment Station's Field Research Facility (FRF) at Duck, NC (Figure 1), stalled, and then eventually moved away. Of the two, Felix was by traditional meteorological measures the stronger (Categories 1 and 2) on the Saffir-Simpson scale but produced lower wave heights in the vicinity of the FRF than Gordon (tropical storm to brief Category 1) which produced some of the largest wave heights recorded at National Data Buoy Center (NDBC) Buoy 44014 located 90 km to the northeast of the FRF.

¹Senior Scientist, USAE Waterways Experiment Station, Coastal and Hydraulics Laboratory, 3909 Halls Ferry Rd., Vicksburg, MS 39180-6199.

²Res. Hyd. Eng., USAE Waterways Experiment Station, Coastal and Hydraulics Laboratory, 3909 Halls Ferry Rd., Vicksburg, MS 39180-6199.

This paper investigates the wave fields in the two storms by comparing simple and complex simulation models of the wind and wave fields to observations in order to determine if the wave field in Gordon was indeed anomalous. Most engineering models of hurricane wind fields assume a symmetric vortex that is uniformly propagated at a forward speed, so that when a vector is added to the vortex, the asymmetric wind field of a moving storm is produced. Thus, when hurricanes became nearly stationary, they would be expected to be similar to the simple vortex. Observations provide an opportunity to understand how well the simulation technology can estimate the stationary case, as well as the approaching and receding storm cases. Waves in each storm were estimated by (1) using the procedure described in the *Shore Protection Manual* (1984) termed SPM84, and (2) simulation with Cycle 4 of the wave model WAM (Komen et al. 1995) driven by an analyzed wind field provided by Oceanweather, Inc.

The concept of the paper is to apply two types of simulation approaches to wave estimation in the two storms using routine approaches for obtaining input meteorologic information. These are used with fairly standard wave estimation procedures to obtain an estimate of the waves. In this study the wind and wave models were not iteratively run to obtain a best estimate of the wave field by providing feedback corrections to the wind field model. The goal is to understand results obtained using routine approaches, because this is closer to a case where extensive wave data would not be available for hindcast or forecast, which is typical of many design situations.

Wave Observations

Locations of the wave buoys and arrays used in the study are shown in Figure 1. All except the Waverider buoy and Linear Array at the FRF are NDBC buoys emplaced for routine measurements or in the case of Gordon for the DUCK94 experiment (e.g. Birkemeier 1994, Jensen 1994). Table 1 provides a summary of the location and water depths of the buoys and gauges. The height, period, direction, and spectral data used in the study were produced by the routine analysis procedures of NDBC (Steele et al. 1992) or the FRF reported in Leffler et al. (1993) and Long and Oltman-Shay (1991).

Wind-Field Simulations

The wind field required for SPM84 is an internal element of the wave field parameterization of the wave estimates and requires central pressure,

Table 1. Measurement Sites for 3GWAM Comparisons

BUOY #	GORDON	FELIX	LONGITUDE	LATITUDE	DEP.
41001	X	X	72° 39' 46"	34° 42' 06"	4444
41002	X		75° 14' 26"	32° 17' 42"	3658
44004	X	X	70° 43' 16"	38° 32' 14"	3231
44009		X	74° 42' 07"	38° 27' 49"	28
44014	X	X	74° 50' 01"	36° 34' 59"	48
44006	X		75° 30' 00"	36° 16' 00"	30
44019	X		75° 10' 00"	36° 25' 00"	40
44010	X		74° 59' 00"	36° 01' 00"	52
FRF-WR	X	X	75° 41' 59"	36° 10' 05"	18
FRR-LA	X	X	75° 44' 43"	36° 11' 16"	8.5

which the wave model equations are integrated. The method used by Oceanweather, Inc. (e.g. Cardone, Greenwood, and Greenwood 1992; Cox et al. 1994) assumes that the hurricane wind field can be simulated by a vortex embedded in an overall large-scale pressure gradient field. The wind field is estimated from the gradient wind approximations. An interactive optimal kinematic analysis (IOKA) procedure is then applied to modify the estimated winds so that they better match observed winds in the vicinity of the wave field. This solution was obtained at snapshots of the storm's history and then interpolated in time and space to give the required input to the wave model. For these simulations, the snapshots were taken every 3 hours (interpolated to 1 hour using a moving center algorithm preserving the storm's center), and data were output on a 0.5-deg grid. The NDBC buoys and FRF have wind field records for the storms. However these data have been used in the IOKA as an essential ingredient of the windfield analysis. Since they cannot provide independent validation of the wind field, they will not be presented here.

SPM84 Procedure

The method for producing hurricane wave estimates in deep water is relatively straightforward. The method has an equation of significant wave height H_s and period T_s

$$H_s = 5.03 \exp(R\Delta p/4700) [1 + 0.29 \alpha V_r / (U_R)^{0.5}]$$

$$T_s = 8.6 \exp(R\Delta p/9400) [1 + 0.145 \alpha V_F / U_R^{0.5}]$$

where R is radius of maximum winds (km), Δp is the pressure drop, α is the forward speed coefficient (about 1 for a slow-moving storm), V_F is the forward speed (m/s), and U_R is the maximum sustained wind speed at the 10-m elevation. Once these values are obtained, the SPM84 provides a generalized nomogram (in terms of r/R : radius of the local r relative to the eye over the radius to maximum winds) that displays the wave height pattern in reference to the eye and the direction of movement.

WAM Model Set-up

WAM Cycle 4 was set up on a 0.25-deg grid for the entire region shown in Figure 1 using 25 frequencies ($f_{i+1} = 1.1 \cdot f_i$) and 24 directions (15 degree bins). The refraction and shoaling routines were turned on. The model received wind input every hour and was interpolated to the 0.25-deg grid in space and 600 s in time (WAM propagation time-step). Both hurricane fields were generated 3 days prior to the test period for spin-up of the wave model domain.

Hurricane Gordon

Gordon formed in the Caribbean and moved into the Gulf of Mexico across Florida into the Atlantic. Our analysis begins with the movement of the storm into the Atlantic near Cape Canaveral, FL at which point it was a tropical storm. The tropical storm moved northeastward from November 17, 1994, until early on the 18th when it slowed its movement and began to drift to the west approximately 200 km to the south of Cape Hatteras. As the storm was blocked from further northward movement, it intensified to a minimal hurricane for about 1 day, and then rapidly moved southward towards the Bahamas and lost strength.

SPM Method: The SPM84 calculations were made at a point when the storm was nearly stationary and had peak winds of 35-38 m/s. In the region of maximum winds, SPM84 (Table 2) indicates a maximum wave height of 7.7 m with a period of 12 s. The height and period at buoy 41002 - just north of the eye of the storm (r/R of 1.6) were estimated to be 5.7 m at 12 s compared to a buoy observation of 5-5.7 m and 10-12 s for the times bracketing the analysis (eight buoy observations are missing). At buoy 41001 at an r/R of 2.4 northeast of the eye, the estimate via SPM84 is a height of 5.7 m with a period of 12 s. The buoy observations are significantly larger, 11 m and 13 s.

Table 2. Wave Height Results, SPM84 and WAM

STORM	LOC	SPM84	WAM	NDBC Obs.
GORDON	Max. Wind	7.7m / 12s*	10m / 13s*	---
	41001	5.7m / 12s*	7m / 11s*	11m / 13s
	41002	5.7m / 12s*	6.9m / 11s*	5m / 11s
	44014	3.8m / 12s*	6m / 12s*	9m / 15s
FELIX	Max. Wind	9m / 12s*	10m / 13s*	---
	44004	5.4m / 12s* 7.2m / 12s**	6.0m / 12s* 5m / 12s**	6.0m / 12s* 8.0m / 12s**
	44009	3.6m / 12s*	4.0m / 12s	3.8m / 12s*
	44014	5.4m / 12s* 7.6m / 12s**	4.0m / 12s* 6.2m / 14s**	4.0m / 12s* 6.8m / 15s**
	41001	6.3m / 12s* 7m / 12s**	5.2m / 9s* 8.0m / 14s**	5.8m / 9s* 7.8m / 15s**

* Stationary

** Closest Approach

At buoy 44014, 90 km northeast of the FRF and at an r/R of 5.4, the estimate was 3.8 m with a 12-s period, compared to the buoy observations of 9 m and 15 s.

Thus the SPM84 provided an estimate consistent with the observations near the center of the storm if the missing observations were similar to the ones bracketing it. However, the SPM84 technique dramatically missed the wave heights at 41001 and 44014, which were more to the east and northeast of 41002 and much further from the storm. Orientation of the nomogram was varied relative to the storm motion, but no significant improvement was obtained. The only way to achieve the size answers at 41001 and 44014, given the SPM84 method, would be to greatly increase the wind speed (and pressure drop) which was unsupported by the meteorological estimates.

WAM Simulations: The WAM simulations provide a detailed history of the waves over the entire region with hourly output. The input wind field has far more detail and asymmetry than is possible with the SPM approach. Figure 2 provides the wave height traces for 41002, 41001, and 44014. Results at the peak times are also provided in Table 2. Estimated peak wave conditions for the storm on the 18th were 10 m with a peak period of 13 s - substantially larger than the SPM84 estimate. The trace at 41002 indicates that the simulation and observations were fairly close on the 17th and the latter half of the 18th. On the morning of the 18th, the simulation suggests waves of 7 m, but the buoy failed

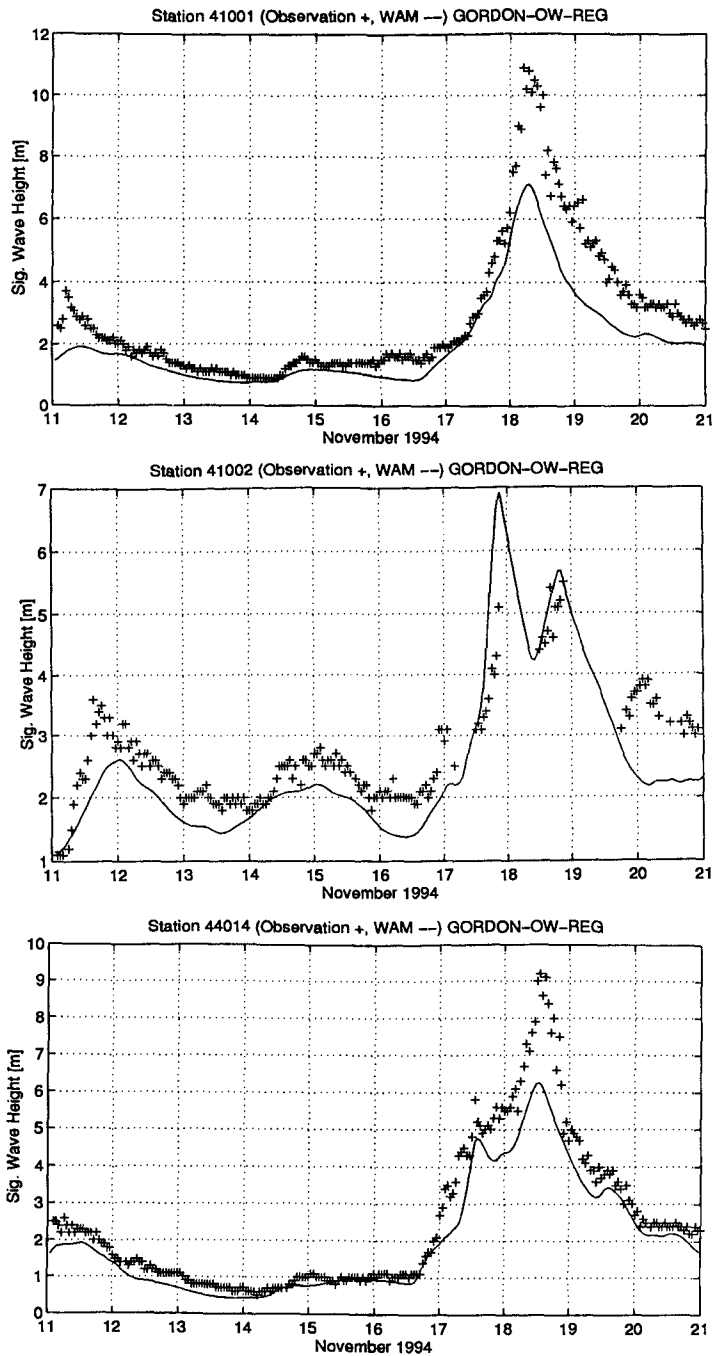


Figure 2. Comparison of WAM (solid line) versus measurements (+) at Buoys 41001 (top), 41002 (middle), and 44014 (bottom).

to collect data. At 41001, the simulation trace is fairly close to the observations until the morning of the 18th, at which time the model peaks at 7 m, but the observations continue to climb to 11 m and 13 s. The trace comparison at 44014 is fairly similar in that the simulation significantly underestimates the peak wave conditions (6 m predicted versus 9 m observed).

The WAM simulations provide larger wave heights than the SPM84 simulations, but it is clear that although the observations near the center of the storm (41002) are not poorly predicted, those to the east and northeast were badly underpredicted. If just the observations at 41002 and 41001 are compared (the buoys are about 150 km apart), the waves at 1200 on the 18th are about 4.5 m at 41002 versus 11 m at 41001. So there is a very rapid variation in conditions depending upon location with respect to the eye (both radial distance and quadrant), as is generalized in SPM84.

Hurricane Felix

Felix originated in the eastern Atlantic and moved steadily towards the United States. Our interest begins on the August 13, 1995 as the storm enters the computational grid some 4 days before closest approach to Cape Hatteras, NC. The storm moved steadily to the northwest towards Cape Hatteras as a Category 2-3 hurricane. By the 17th, the storm's northwest movement has been greatly reduced and the storm moves slowly to the north, then recurves to the east, looping on the 19th and 20th offshore of the Outer Banks of NC. Finally, on the 21st, the storm moves rapidly to the northeast as it becomes a tropical storm. In the region of Cape Hatteras, the storm remained a medium Category 1.

SPM Method: The SPM84 was applied several times. The first was when the storm was nearly stationary, and additional estimates were made when the storm was at closest approach 41001 and 44014 to the buoy (Table 2). The estimated maximum wave was 9 m at 12 s for the stationary case. SPM84 and buoy observations were fairly close - normally within a meter. Wave periods were low for the closest approaches at 41001 and 44014. Based on this very simple approach, the SPM method appeared to give a satisfactory estimate for this storm.

WAM Simulations: Results of the WAM simulations are given in Table 2. The simulated wave heights and periods based on stationary and closest approach times compare favorably with the observations. Comparisons of the wave height traces to the observations provides more mixed results (Figures 3 and 4). At 41001 (Figure 3), where the hurricane passed right over, the simulations are quite reasonable until 1200 on the 16th. After that time the observed heights fall more quickly than the simulated. From the 18th on, the simulations are 1-2 m

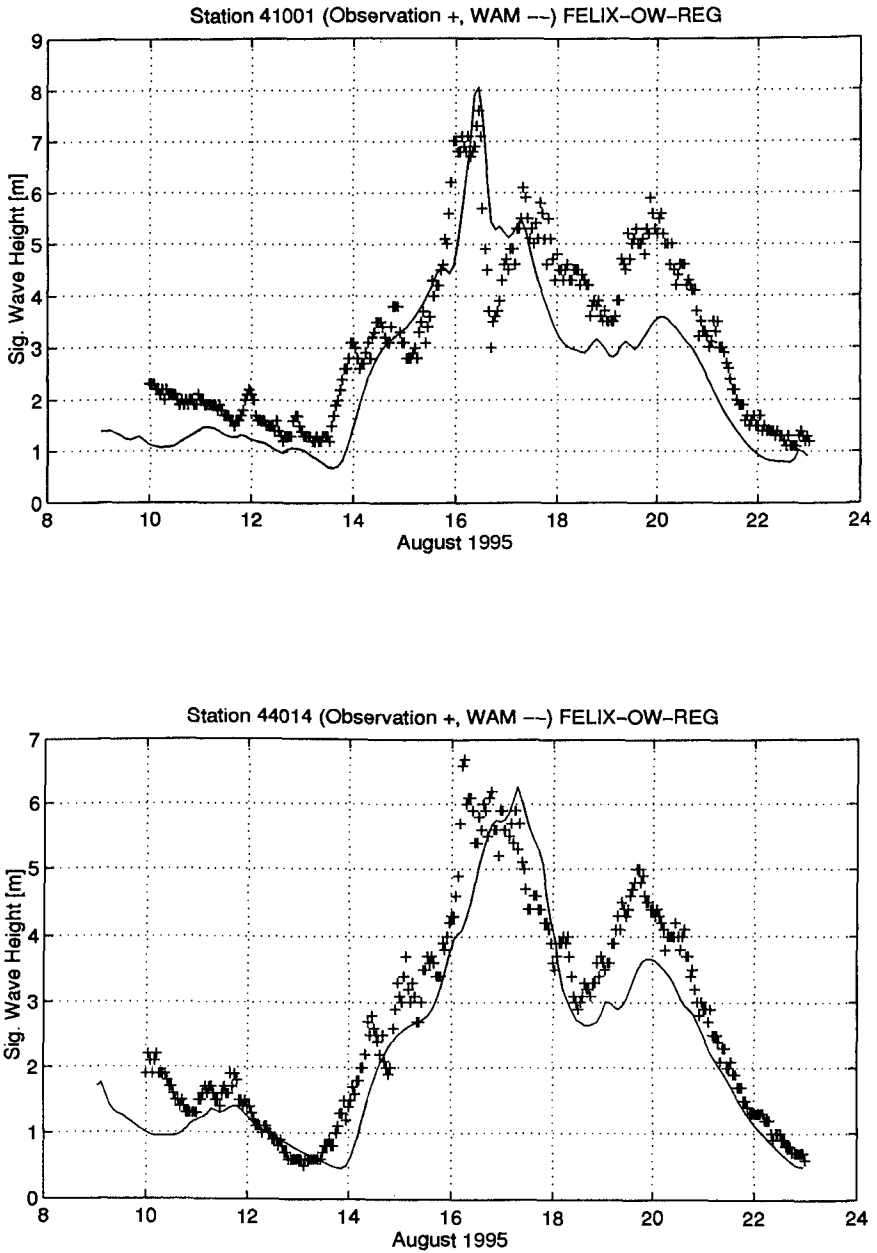


Figure 3. Comparison of WAM (solid line), and measurements (+), at 41001 (top), and 44014 (bottom) panel.

lower than the observed. At this time, the hurricane is in the looping process. At 44014 (Figure 3), the pattern is fairly similar. The simulations produce a similar peak height though the largest waves appear to arrive earlier than indicated by the simulation. The simulated decay of the storm is excellent until the 18th, when the observations rise more than the simulated values with a difference of 1 to 2 m seen. At 44009 (Figure 4), which lies in fairly shallow water off of Delaware bay, the pattern is similar to 44014, although the waves do not get as large as at 44014. Comparison of the simulation results to observations at 44004 (Figure 4), which is several hundred kilometers off of Delaware Bay and just to the north of the storm path, is by far the worst. The simulations completely underestimate large waves on the 16th and underestimate waves by nearly 3 m on the 18th-21st. Ship observations near 44004 recorded during the time of Felix were on the order of 2 to 4 m lower than the buoy wave heights. This suggests the potential of other factors such as the Gulf Stream influencing the measurements at 44004.

Thus, even though comparison of the WAM and SPM84 results to the observations at closest approach and when the storm was stationary are fairly good, comparison of the simulated history of wave heights shows that the WAM results underestimated (as much as 4 m) the storm when it was in the looping phase.

Discussion

Objectives of this paper were to understand (1) if Gordon was in some sense anomalous, and (2) how well two wave estimation approaches (one very simple, one very complex) performed with the typical level of information available for many forecasts and hindcasts. In judging the prediction approaches, it must be stated that any error is an integrated error for both wind field specification/modeling and wave model physics and numerics.

In considering Hurricane Gordon, it is best to contrast results to Hurricane Felix. In Felix application of both prediction methods gave fairly satisfactory results for peak quantities in the storm at most locations. Felix had consistently stronger winds and a somewhat smaller physical size. Felix at most produced 8 m waves at the buoys it passed by. Gordon, although generally weaker, produced waves larger than Felix by 3 m at 41001 and 2 m at 44014. At 41002, the simulation results from WAM and the observations were in reasonable agreement. Thus, although some systematic error in WAM or SPM84 cannot be ruled out, the authors hypothesize that Gordon must have been highly asymmetric with a region of larger winds to the east of the storm that is not caught in the current meteorological specification of the storm.

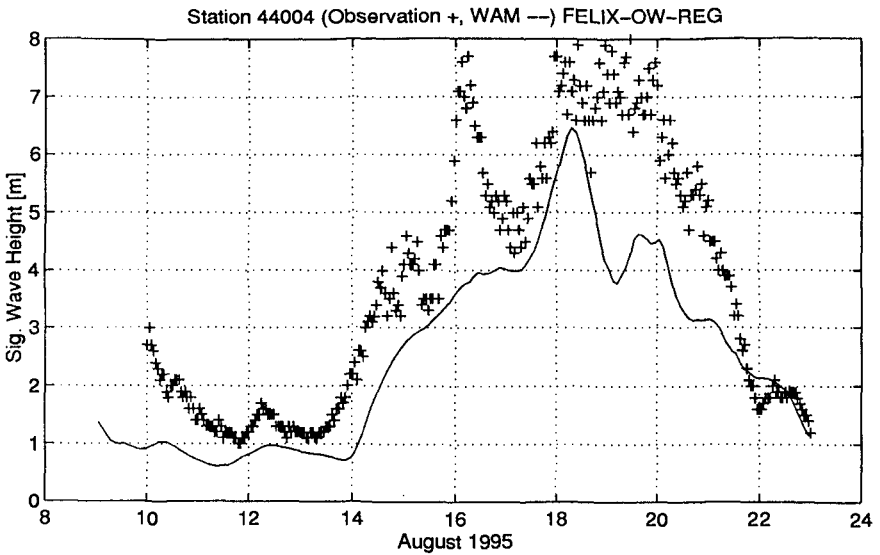
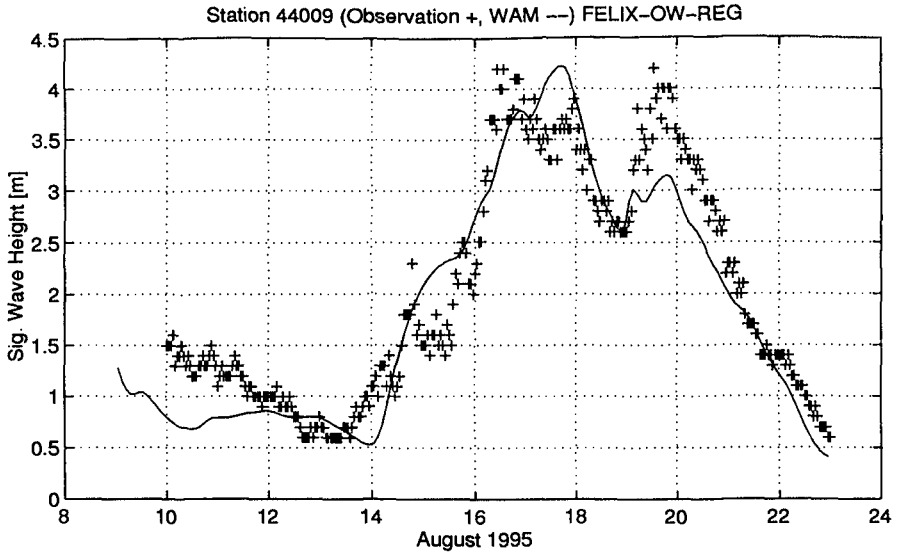


Figure 4. Comparison of WAM (solid line), and measurements (+), at 44009 (top) and 44004 (bottom) panel.

With regard to Felix, it appears that simulation methods do reasonably well when the storm is moving in a more or less straight line, but that the combination in wind field and WAM does not replicate what happened in the turning and looping situation. One can postulate two reasons for the problem. First, the simple vortex model approach may not be adequate when the storm is wobbling in a loop. Second, the ability of a model such as WAM to handle such radically turning winds and mixed sea-swell conditions has never been proven.

The principal lesson learned of engineering consequence is that fairly weak-appearing storms can produce unexpected high wave heights if the storm stalls or loops, with the error for a weak hurricane/strong tropical storm approaching 3-4 m in significant wave height. Moreover, forecast/hindcast of the wave height trace in the stalling/looping storms may produce errors of 1-2 m.

Acknowledgements

The research conducted here was performed under the Navigation Hydrodynamics Research and Development Program, Modelling the Evolution of Wave Spectra in Shallow Water work unit. The authors acknowledge Headquarters, U.S. Army Corps of Engineers, for authorizing publication of this paper. Special thanks are extended to Ms. Claudette Doiron for compiling, and Ms. Janean Shirley for editing this manuscript.

References

- Birkemeier, W.A. (1994). "The DUCK94 nearshore field experiment." U.S. Army Engrs. Wtrwy. Experiment Station, Vicksburg, Miss.
- Cardone, V.J., Greenwood, C.V., and Greenwood, J.A. (1992). "Unified program for the specification of hurricane boundary layer winds over surfaces of specified roughness." *Contract Rep. CERC-92-1*, U.S. Army Engrs. Wtrwy. Experiment Station, Vicksburg, Miss.
- Cox, A.T., Greenwood, J.A., Cardone, V.J., and Swail, V.R. (1994). "An interactive objective kinematic analysis system." *Proc. 4th Inter. Workshop on Wave Hindcasting and Forecasting*, Banff, Alberta, CANADA, 109-118.
- Jensen, R.E. (1994). "An evaluation of two extreme storms events in the mid-Atlantic coastal waters: measurements and 3GWAM assessment." kinematic analysis system." *Proc. 4th Inter. Workshop on Wave Hindcasting and Forecasting*, Banff, Alberta CANADA, 235-249.

Komen, G.J., Cavaleri, L., Donelan, M., Hasselmann, K., Hasselmann, S., and Janssen, P.A.E.M. (1994). *Dynamics and Modelling of Ocean Waves*, Cambridge Press.

Leffler, M.W., Baron, D.F., Scarborough, B.L., and Hathaway, K.K. (1993). "Annual data summary for 1991, CERC Field Research Facility." *Tech. Rep. CERC-93-9*, U.S. Army Engrs. Wtrwy. Experiment Station, Vicksburg, Miss.

Long, C.E. and Oltman-Shay, J.M. (1991). "Directional characteristics of waves in shallow water." *Tech. Rep. CERC-91-1*, U.S. Army Engrs. Wtrwy. Experiment Station, Vicksburg, Miss.

Shore Protection Manual (1984). 4th ed., 2 Vol, U.S. Army Engrs. Wtrwy. Experiment Station, U.S. Government Printing Office, Washington, DC.

CHAPTER 63

Estimation of Persistence Statistics of the Waves Observed on Japanese Coast in the Light of Recent Studies

Hajime Kato¹, Hisamichi Nobuoka²

Abstract

The NMI method proposed by Kuwashima and Hogben (1986) for estimating the wave persistence statistics and Mathiesen's Model (1994) which was expected to develop the NMI method were applied to the wave data observed at four sites at Japanese coast to investigate the validity of the models. Mathiesen's model was found not to be superior to NMI method. We show the modification of the NMI parameters based on the data improve the accuracy of the estimated persistence statistics.

1. Introduction

The estimation of wave height duration statistics is needed in various engineering fields such as planning and execution of maritime construction works as well as oil industry operations. For the case when continuous data sequences are not available Graham (1982) proposed an approximate method based on the probability distribution of significant wave height. Kuwashima and Hogben (1986) generalized the method using mainly North Sea wave data, and proposed an empirical method which they called the NMI method. Recently Mathiesen (1994) proposed a theoretically founded parametric model for the estimation of duration statistics for wave height. Although he suggested that his study established a theoretical basis for the development of NMI method, the fact was not confirmed.

In this study we estimate the wave persistence statistics from the wave data observed at the coasts of Japan using both NMI and Mathiesen's method. We pay attention to the local differences of persistence statistics examining the applicability of the two methods to the present wave data of Japanese area.

¹Professor and ²Research Associate, Department of Urban and Civil Engineering, Ibaraki University, 4-12-1 Nakanarusawa, Hitachi, Ibaraki, 316 Japan

2. Data and method of analysis

2.1 Wave data used

We used the wave data observed at the four sites in the Japanese coast. Fig.1 shows the locations of the four sites. Hitachinaka and Kashima are at the coast of Ibaraki facing to the Pacific Ocean, and Sakata and Wajima are in the Sea of Japan. They are hereafter abbreviated as HI, KA, SA and WA. The name of Ibaraki will also be used to denote both HI and KA. Those data are measured every two hours and the time spans are 13 years for HI and 8 or 9 for other sites.

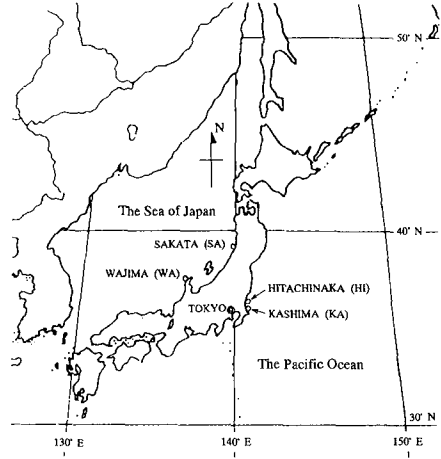


Fig.1 Map of the sites of the wave data used in this study.

2.2 Estimation of wave height persistence statistics by the NMI method

In the NMI method, the input data used are cumulative probability distributions of significant wave height H_s which is written for the case of height exceedance as $Q(\geq H_s)$. The mean duration of exceedance waves $\bar{\tau}_g$ for a threshold height H_s' are expressed as:

$$\bar{\tau}_g = A[-\ln Q(\geq H_s')]^{-\beta} \tag{1}$$

where A and β are constants and Q is cumulative probability distribution for a threshold H_s' . The equation (1) was originally proposed by Graham (1982) with constants $A=20.0$ and $1/\beta = 1.3$ for the North Sea wave data.

Kuwashima and Hogben (1986) allowed variations in the parameters A and β by deriving empirical relations (based on exceedance data) between the parameters and a shape parameter γ for the input distribution defined in terms of a 2 parameter Weibull distribution. At first the distribution is written in terms of the normalized significant wave height defined by $H_n = \bar{H}_s / H_s$ as:

$$Q(\geq H_n) = \exp(-B H_n^\gamma) \tag{2}$$

where the parameter B and γ are related by

$$B = [\Gamma(1+1/\gamma)]^\gamma \tag{3}$$

and Γ is a gamma function. Then the relevant relations of A and β with γ have been obtained from many data sets as follows:

$$A=35 \gamma^{-0.5}, \quad \beta=0.6 \gamma^{0.287} \tag{4a,b}$$

Although Eqs.(4a,b) are empirical formulas, they are expected applicable to any world wide sites since the wave statistics is well represented by the

parameter γ . When $\bar{\tau}_g$ is obtained from Eq.(1), then the mean duration of non-exceedance waves $\bar{\tau}_l$ is obtained as

$$\bar{\tau}_l = \bar{\tau}_g [1 - Q(\geq H_s')] / Q(\geq H_s') \quad (5)$$

The cumulative distribution of duration for exceedance and non-exceedance waves are also expressed in terms of a 2-parameter Weibull distribution. Writing $x = \tau / \bar{\tau}$ where $\bar{\tau}$ is the mean duration, the distribution is written as:

$$Q_g(\tau / \bar{\tau}_g) = Q_g(\geq x_g) = \exp[-C_g x_g^{\alpha_g}] \quad (6a)$$

$$Q_l(\tau / \bar{\tau}_l) = Q_l(\geq x_l) = \exp[-C_l x_l^{\alpha_l}] \quad (6b)$$

The shape parameters α_g and α_l of the above equations are also given in the following empirical forms:

$$\alpha_g = 0.267 \gamma (H_s' / \bar{H}_s)^{0.4} \quad (7a)$$

$$\alpha_l = 0.267 \gamma (H_s' / \bar{H}_s)^{-0.4} \quad (7b)$$

C_g and C_l of Eq.(6) are related to α_g and α_l as :

$$C_g = [\Gamma(1+1/\alpha_g)]^{\alpha_g} \quad (8a)$$

$$C_l = [\Gamma(1+1/\alpha_l)]^{\alpha_l} \quad (8b)$$

If we know the probability distribution of wave height for a certain area, then from the cumulative probability distribution $Q(\geq H_s')$ and the shape parameter γ of a 2-parameter Weibull distribution, we can estimate the mean duration $\bar{\tau}_g$ (or $\bar{\tau}_l$) and the cumulative probability of duration Q_g (or Q_l) of exceedance (or non-exceedance) wave for a threshold wave height by using the equations stated above.

2.3 Mathiesen's model

Mathiesen (1994) assumed that the time variation of significant wave height is a continuous stationary process and applied a level crossing theory for water waves to the time series of wave heights. In this section we write a significant wave height H_s simply as H and a threshold wave height H_s' as H_c .

The average number of exceedances or level-upcrossings per unit time $\nu(H)$ is given by:

$$\nu(H) = (1/2) \int_{-\infty}^{\infty} |H'| |p(H, H')| dH' \quad (9)$$

where $H' = dH/dt$ and $p(H, H')$ is the joint probability of H and H' . Then Mathiesen obtained the relation:

$$\nu(H) = (1/2) f(H) S(H) \tag{10}$$

where $f(H)$ is the probability density function for H , and $S(H)$ the average absolute rate of change of significant wave height H . That is, he showed that the duration statistics depended not only on $f(H)$ but also $S(H)$, the average absolute rate of change of H . Considering the equation of mean duration of exceedance $\bar{\tau}_g$:

$$\bar{\tau}_g = T Q(\geq H_c) / N \tag{11}$$

where N is the number of up-crossing for the total time length T , then $\bar{\tau}_g$ is given as :

$$\bar{\tau}_g = 2 Q(\geq H_c) / [f(H) S(H)] \tag{12}$$

$f(H)$ and $Q(H)$ are evaluated in the 3-parameter Weibull form as follows:

$$f(H) = (\gamma' / X_0) ((H-a) / X_0)^{\gamma'-1} \exp[- ((H-a) / X_0)^{\gamma'}] \tag{13}$$

$$Q(H) = \exp[- ((H-a) / X_0)^{\gamma'}] \tag{14}$$

where γ' is the shape parameter, a the local parameter which was set as zero in practice and X_0 the scale parameter.

Mathiesen (1994) found that $S(H)$ could be expressed as

$$S = q (H/H_0)^R, \quad (H_0=1.0m) \tag{15}$$

where q and R are constants different between the locations.

From Eqs.(11) to (15) and Eq.(3), the NMI parameters A and β are found to become to A_M and β_M in the following equations:

$$A_M = 2 / [\gamma' (X_0 / H_0)^{R-1} (q / H_0)] \tag{16}$$

$$\beta_M = (\gamma' + R - 1) / \gamma' \tag{17}$$

It is seen that the parameters A_M and β_M depend on both the shape of the distribution $Q(H)$ and the average absolute rate of change $S(H)$ in Mathiesen's model.

3. Applicability of the NMI method to the present wave data

In this study we used the measured wave data for calculating the wave height persistence statistics in three ways; (a) data sets of each year, (b) seasonally divided data sets for four years, and (c) monthly divided for 9 (KA and HI) or 8 (SA and WA) years. For testing the reliability of the NMI method Kuwashima and Hogben (1986) showed comparisons of the estimated persistence statistics with those directly derived from measured data in cumulative distribution form. We made the same comparisons for the test of

applicability of the NMI method to the present wave data. Figure 2 is one of the results which are calculated for a 4-year data set of HI (Hitachinaka). The upper one is for exceedance waves and the lower one non-exceedance. As seen from these figures the NMI method yielded moderately good but slightly deviated results. More or less, this was the case for most of other data sets.

This may be due to the fact that the parameters A , β , α , etc. given by Eqs.(4) and (7) does not sufficiently fit to the present wave data. So following Kuwashima and Hogben (1986) we tried to obtain more suitable expressions from the measured data in stead of Eqs.(4) and (7). To complete this, we calculated A , β , α_M (value of α for $H_s' = \bar{H}_s$) from the measured wave data and plotted them against the parameter γ as Fig.3 in which the original values of NMI method are shown with dotted lines. Although there are considerable

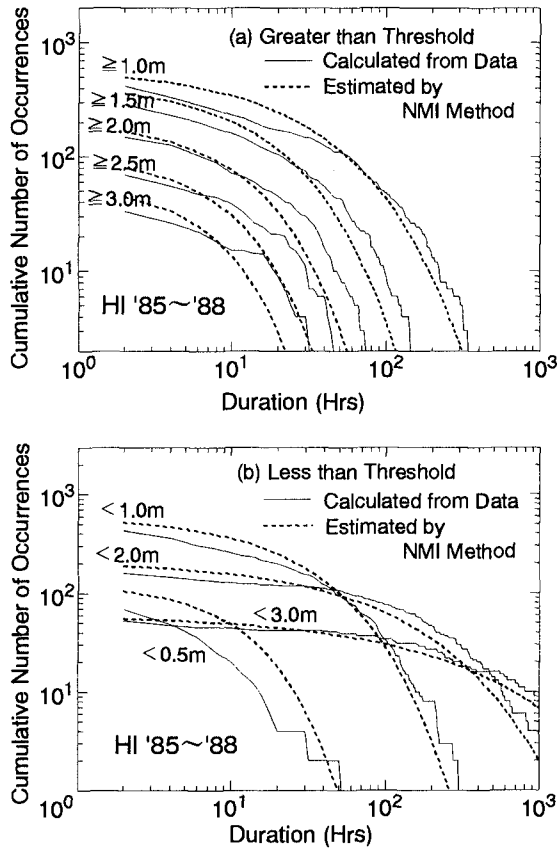


Fig. 2 Comparison of the estimated persistence statistics by NMI method with those directly derived from the measured wave data.

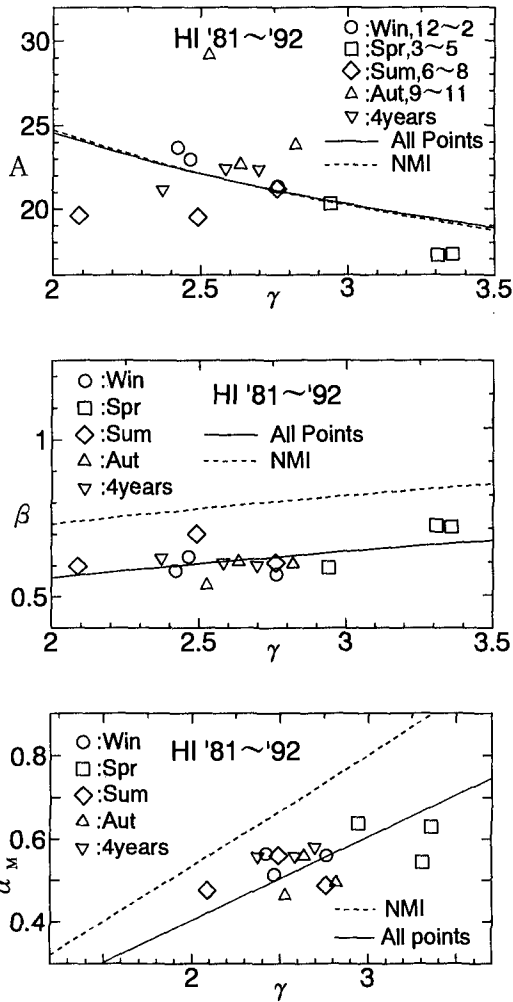


Fig. 3 Plots of NMI parameters A , β , α_M against γ
 Seasonal dataset of HI for 4 years were used.

scatter, we obtained the empirical relations instead of Eqs.(4). For example the relations for HI are as follows:

$$A=32.3 \gamma^{-0.464}, \quad \beta=0.552 \gamma^{0.100} \tag{18a,b}$$

$$\alpha_M = 0.202 \gamma \tag{19}$$

The relation of A is almost the same as that of NMI. However the values of β are smaller than those of NMI about by 2.0 and α_M is as small as nearly 3/4

of NMI values.

Figure 4 shows the variations of α_g and α_l of HI normalized by α_M against various threshold height H_s' in the form of Eqs.(7a,b). From the results of these figures we can obtain the following relations:

$$\alpha_g = 0.202 \gamma (H_s' / \bar{H}_s)^{0.318}, \tag{20a}$$

$$\alpha_l = 0.202 \gamma (H_s' / \bar{H}_s)^{-0.044} \tag{20b}$$

When we used Eqs.(18) and (19) in estimating persistence statistics for HI we found that the agreement of the estimated values with those calculated from the measured data increased in most cases. Figure 5 shows the results corresponding to the previous figure 2 and it is seen that the modification of coefficients such as Eqs.(18) to (19) yields better agreements.

We conducted the similar procedures for the monthly divided data sets. Figure 6 shows the calculated values of A , β , α_M for KA and HI, the location of which are the Pacific Ocean side. Since no different tendency was found between the values of HI and KA, both quantities are plotted together and the

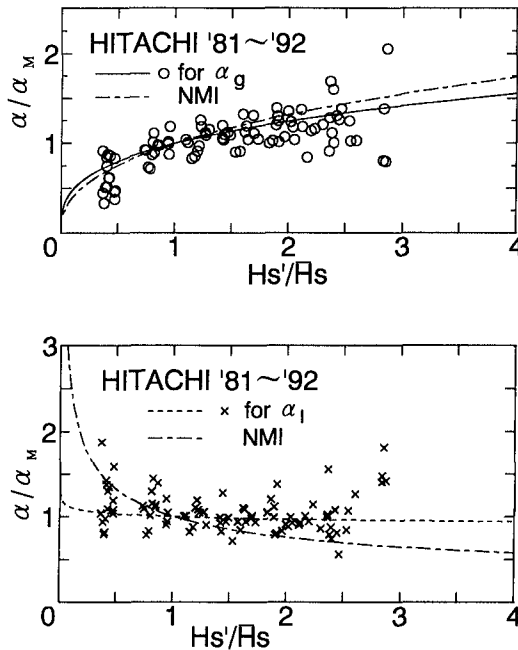


Fig. 4 Plots of α_g and α_l against threshold wave heights.

relations common to the two sites were obtained. Figure 7 shows the variation of α normalized by α_M for HI and KA. From these monthly data we obtained the following relations:

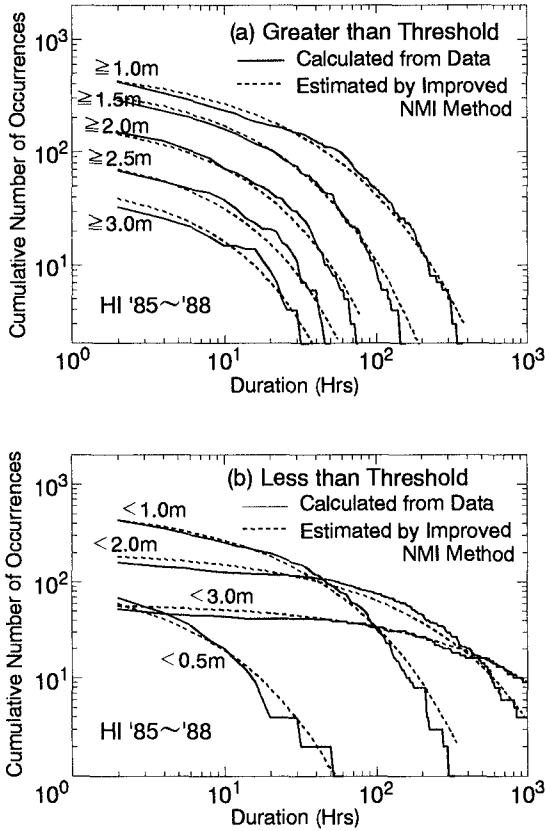


Fig. 5 Comparison of the estimates by the improved NMI formula with those directly derived from the measured wave data.

$$A=32.5 \gamma^{-0.439}, \quad \beta = 0.618 \gamma^{0.0052} \quad (21a,b)$$

$$\alpha_M = 0.195 \gamma \quad (22)$$

$$\alpha_g = 0.195 \gamma (H_s' / \bar{H}_s)^{0.163} \quad (23a)$$

$$\alpha_l = 0.195 \gamma (H_s' / \bar{H}_s)^{-0.150} \quad (23b)$$

Optimum parameter formula for SA and WA

When we applied the NMI method for the wave data of SA and WA in the coast of the Sea of Japan, good agreements were not found similarly to HI and

KA in the coast of the Pacific Ocean. Therefore in the similar way as HI and KA, we tried to obtain the optimum relations for SA and WA. The results of A , β , α_M calculated from the measured data are plotted in Fig.7. Concerning A and β we may take the common formula, that is

$$A=31.1 \gamma^{-0.451}, \quad \beta=1.05 \gamma^{-0.453} \quad (24a,b)$$

Since, however, the magnitude of α_M are slightly but distinctly different between SA and WA, the different relations may be obtained as:

$$\alpha_M = 0.398 \gamma \quad (\text{SA}) \quad (25)$$

$$\alpha_M = 0.355 \gamma \quad (\text{WA}) \quad (26)$$

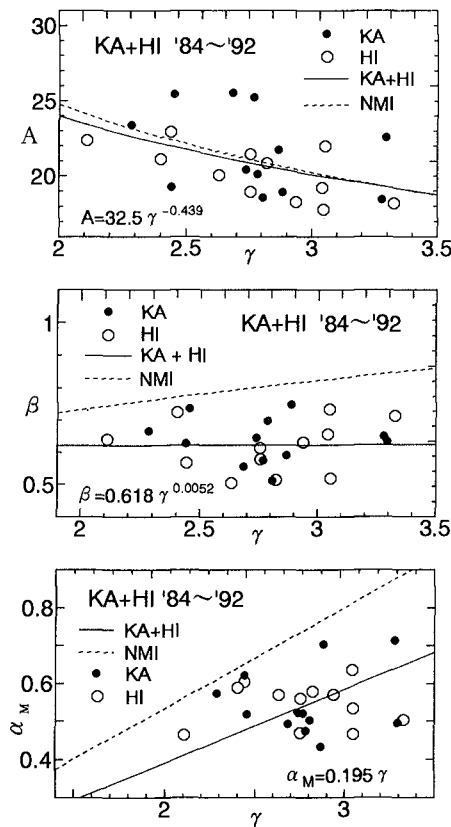


Fig. 6 Plots of A , β , α_M against γ . Monthly data of HI and KA.

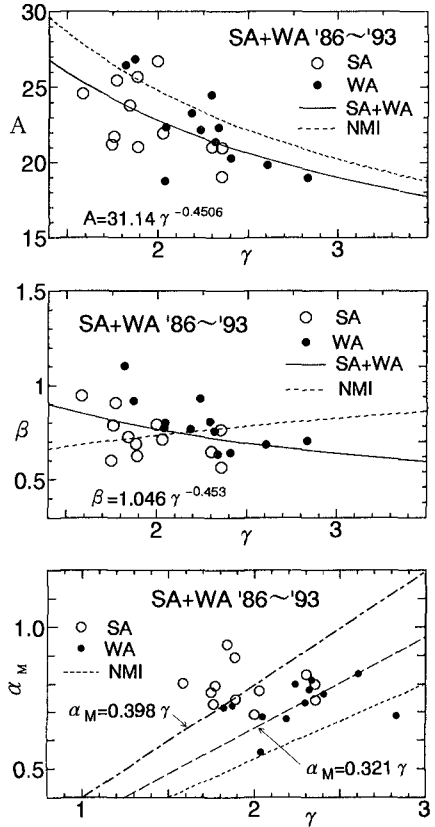


Fig.7 Plots of A , β , α_M against γ . Monthly data of SA and WA.

For reference we show α_g and α_l for SA and WA:

$$\alpha_g = 0.398 \gamma (H_s' / \bar{H}_s)^{0.185} \quad (\text{SA}) \quad (27a)$$

$$\alpha_l = 0.396 \gamma (H_s' / \bar{H}_s)^{-0.137} \quad (\text{SA}) \quad (27b)$$

$$\alpha_g = 0.355 \gamma (H_s' / \bar{H}_s)^{0.176} \quad (\text{WA}) \quad (28a)$$

$$\alpha_l = 0.355 \gamma (H_s' / \bar{H}_s)^{-0.232} \quad (\text{WA}) \quad (28b)$$

It is noted that the magnitude of α_M in the Pacific coast is smaller than that of the NMI method, while it is larger in the Sea of Japan coast as seen from the bottom ones in Figs. 6 and 7. The variability of the estimates by the NMI method are discussed further in the later section.

4. Applicability of Mathiesen's model

Mathiesen (1994) found that the average absolute rate of change of significant wave height S could be expressed by Eq.(15). Figure 8 shows an example of $S(H)$ calculated from the wave data of HI. We can see that the relation of Eq.(15) holds well. Although for the same site the constants q and R in Eq.(15) slightly vary month to month, we neglected the monthly changes similarly to Mathiesen. The mean values of q and R for each location are shown in Table - 1.

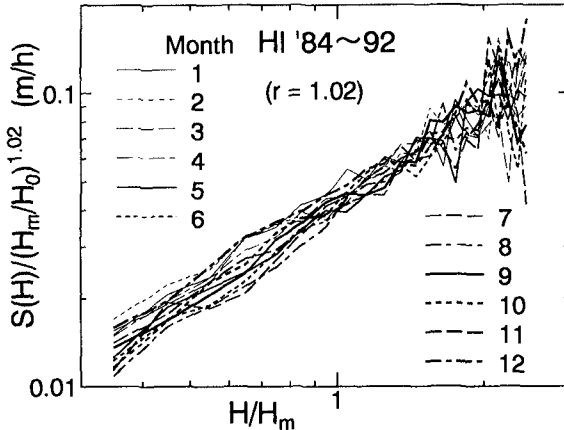


Fig.8 Average absolute rate of change of significant wave height at HI.

The values of A and β calculated from Mathiesen's Eqs.(16) and (17) are compared with those of the NMI method and its improved (data-fitted) equation in Fig.9 (HI:upper, SA:lower) in which the monthly average

significant wave heights H_m are also shown. The suffix M and NMI denote Mathiesen's and NMI method, respectively and no suffix the improved equation method. It is noted that A_M are in general different from A_{NMI} and A , and especially too small in summer.

Some examples of the estimated mean durations by the three methods for

Table-1 Constants in Eq.(7)

Station	q	r
HI	0.045 m/h	1.02
KA	0.045	0.98
SA	0.062	0.85
WA	0.055	0.89

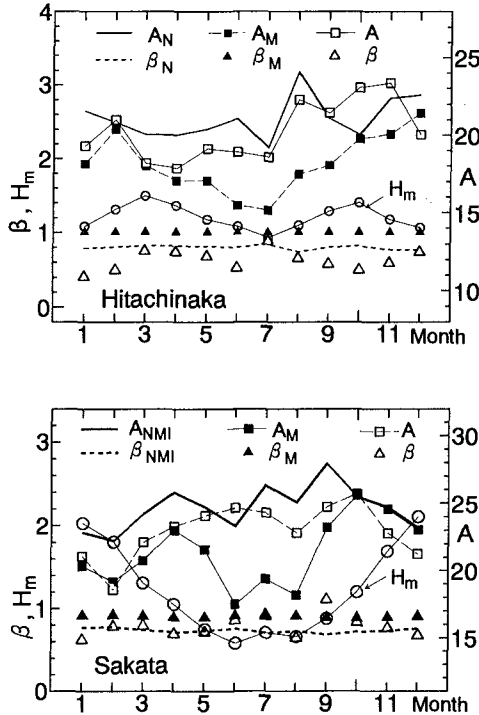


Fig.9 A and β for three method; NMI, improved NMI and Mathiesen at HI (upper) and SA (lower). Suffix N or NMI: NMI method, M: Mathiesen's, no suffix: Improved NMI.

exceedance (GE) and non-exceedance (LT) waves are shown together with those calculated directly from the measured data in Fig.10.

Contrary to our expectation Mathiesen's method generally did not show the better agreement with the measured data than NMI method. Improved NMI method which utilized the relations like Eq.(4) yielded the best agreement.

We tried to find the reason why Mathiesen's model showed rather worse results than the NMI method. The relation of Eq.(9), which Mathiesen used

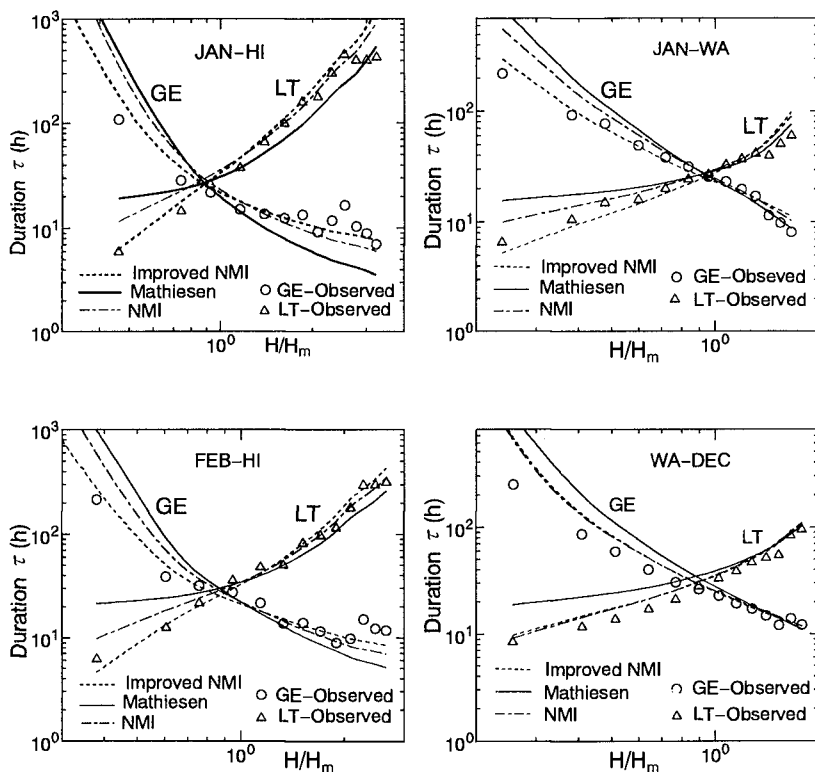


Fig. 10 Comparison of estimates by Mathiesen’s method with NMI and improved NMI method. (Mean duration for exceedance and non-exceedance waves for HI and WA.)

as the foundation of his model, is originally valid to the time series of surface displacement of water waves and $\nu(0)$ coincides with a reciprocal of the zero up-cross wave period. With regard to the time series of wave eight which we used, it was found that the validity of Eq.(9) became poor at the wave height apart from the mean height. It was also found that the degree of accuracy of Eq. (10) was reduced depending on the month.

5. Discussion

Figure 11 shows the monthly values of γ for 4 sites analyzed in this study. As seen from this figure, the values of γ for the two sites (SA and WA) in the Sea of Japan are, except the months in winter, smaller than those of the two sites (HI and KA) in the coast of Pacific Ocean.

In the figures 3, 6 and 7, etc. from which the expressions of A and β were

obtained in terms of γ , the point were scattered considerably. So it may give an impression that the estimates by NMI method or improved NMI method include a great deal of errors. The figure such as Figs. 2 and 5 is not suitable to grasp the general degree of agreement. In order to see the accuracy of the estimated values compared with the observed values, we prepared Fig.12. It shows the cumulative frequency (times/month) of the non-exceedance waves ($H \leq 1.0\text{m}$) and exceedance waves ($H \geq 1.5\text{m}$) for durations of 24 and 72 hours for HI in the Pacific coast and WA in the Sea of Japan. Triangle points

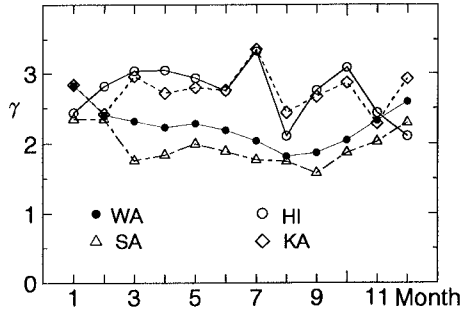


Fig. 11 Monthly variations of γ for 4 stations.

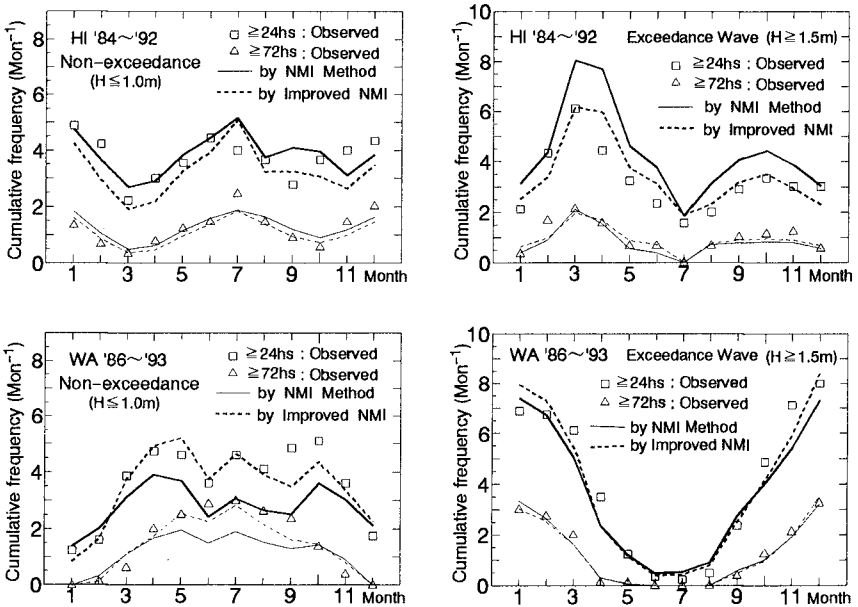


Fig.12 Estimates of wave persistence by NMI and improved NMI method in comparison with observed data at HI (upper) and WA (lower).

represent the observed values for 24 hours and square points 72 hours. Solid and dotted lines denote the estimates by NMI and improved NMI method, respectively.

From these figures it is seen that the increasing or decreasing tendencies of the estimated results are in good agreement with those of the observed values, and it may indicate the excellent feature of the NMI method in which the estimates of wave height persistence statistics are obtained from cumulative probability distributions of significant wave height $Q(\geq H_s)$ and a single parameter γ .

6. Conclusions

The NMI method was found to give reasonably good estimates, though it yielded slightly deviated result for each site. Modification like Eqs.(4) and (7) was effective. Although considerable scatters were found in evaluating the optimum NMI parameters for the different data sets, it was found from the monthly data analysis that the NMI method yielded good tendencies of variations of wave persistence statistics in comparison with the real values calculated directly from the measured wave data.

It was found contrary to our expectations that Mathiesen's model did not give any better estimates than the NMI method for the mean durations of both exceedance and non-exceedance waves. Some possible reasons were discussed. .

References

- Graham,C.(1982): The parameterisation and prediction of wave height and wind speed persistence statistics for oil industry operational planning purposes, Coastal Engg., Vol.6, pp.303-329.
- Kuwashima,S. and Hogben,N.(1984): The estimation of persistence statistics from cumulative probabilities of wave height, Report of N.M.I., London, No.R183, 72p.
- Kuwashima,S. and Hogben,N.(1986): The estimation of wave height and wind speed persistence statistics from cumulative probability distributions, Coastal Engg., Vol.9, pp.563-590.
- Mathiesen,M. (1994): Estimation of wave height duration statistics, Coastal Engg., Vol.23, pp.167-181.

CHAPTER 64

PROBABILISTIC MODELING OF LONG-TERM WAVE CLIMATE

V.M. Leyden¹ and W.R. Dally²

Abstract

Utilizing eight years of wave measurements from the U.S. Army Corps of Engineers Field Research Facility (FRF), this study develops a long-term probabilistic model for the energy-based significant wave height (H_{m0}) based on the shifted gamma distribution. The method of moments is used in best-fit model parameter estimation. Shifted gamma distributions are developed for the entire eight years of H_{m0} data, as well as for the individual years in the data set. The shifted gamma distribution represents the FRF H_{m0} data for both the total and yearly data sets. Further, the distribution which represents the total, or long-term, data also effectively models the yearly data, indicating that the shifted gamma distribution is a useful engineering tool for predicting long-term wave climate.

Introduction

In order to obtain the most accurate and reliable information on ocean waves, wave climate needs to be studied over the long-term. Hogben (1990) defines long-term statistics as those which describe sea conditions over time spans of years, and it is in this definition that one discovers the problem; not many data sets exist which have time scales on this order. Isaacson and MacKenzie (1981) note in their review of long-term distributions of ocean waves that design wave estimates based on 100 years of data differ by a factor of 3 when compared to estimates considering only two successive years. Furthermore, Soares (1988) found that predictions of significant wave height varied between 9.02 and 14.11

¹Graduate Research Assistant and ²Associate Professor, Ocean Engineering Program, Florida Institute of Technology, 150 W. University Blvd., Melbourne, FL, 32901 USA.

meters when based on data sets that were one year long, whereas the significant wave height only varied between 10.49 and 12.79 meters when based on data sets which were 10 years in length. It is clear that an adequate data base is crucial to the value of any long-term wave climate study.

Although the long-term wave climate is a basic element of many coastal engineering issues, few probabilistic models for long-term statistics have been developed. Of those available, e.g., the modified exponential distribution for significant wave height presented in the Shore Protection Manual (1984), estimation of best-fit model parameters has been hampered by a lack of suitable long-term data. There are several means available for acquiring long-term wave data: visual observations, remotely sensed wave data, hindcast results, and in situ measurements. Of these, in situ measurements are regarded as the most accurate and reliable form of wave data. Because of measurement programs initiated in the early 1980's, such in situ data sets are now becoming available. For instance, Teng, Timpe, and Palao (1994) use thirteen years of buoy data from the National Data Buoy Center (NDBC) to estimate design wave heights, and Soares and Henriques (1994) use seven years of data collected from an oil platform in the North Sea to examine model parameter estimation. This study will develop generic, long-term wave climate statistical models utilizing a similar measurement program.

Description of Field Data

One of the best long-term data sets of nearshore wave climate has been collected by the U.S. Army Corps of Engineers Field Research Facility (FRF), located in Duck, North Carolina. The wave data used in this study were collected from a pressure gage located at a nominal water depth of 8 m. These time series consist of 34 minute records collected once every six hours. The sampling rate of the gages was 2 Hz (U.S. Army, 1993). Both the energy-based significant wave height, H_{m0} , and the peak wave period, T_p , are computed from the pressure gage time series and reported in monthly data summaries. H_{m0} is equal to four times the square root of the area under the wave energy spectrum, and T_p is the wave period associated with the maximum wave energy in the spectrum. The FRF data used in this study were collected from May 1987 to April 1995 - almost 11,400 entries in all.

Constructing histograms, along with finding some of the basic statistical properties of the data, provides an immediate indication of the range of the data, its most frequently occurring values, and how the data is dispersed about the typical value. A bivariate histogram of H_{m0} and T_p (Figure 1) illustrates the entire range of wave heights and periods the FRF experiences. The histograms of H_{m0} and T_p are also useful in the visualization of the wave climate at the FRF. Figures 2 and 3 show these histograms respectively.

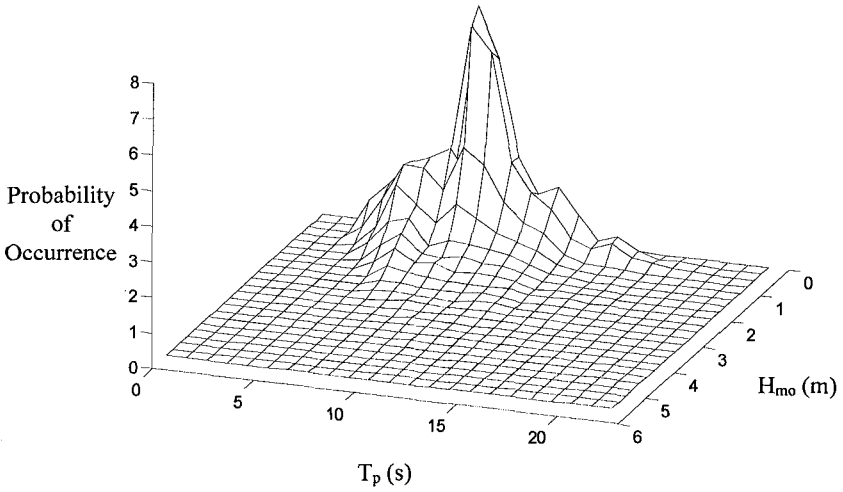


Figure 1. U.S. Army Field Research Facility (FRF) Bivariate histogram of significant wave height (H_{mo}) and peak period (T_p) for May 1987 - April 1995

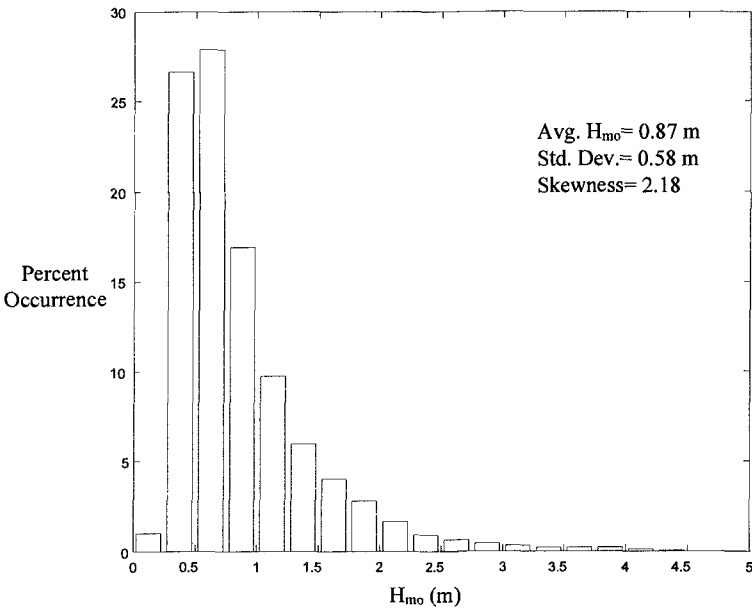


Figure 2. Histogram of H_{mo} Data from FRF (May 1987 - April 1995)

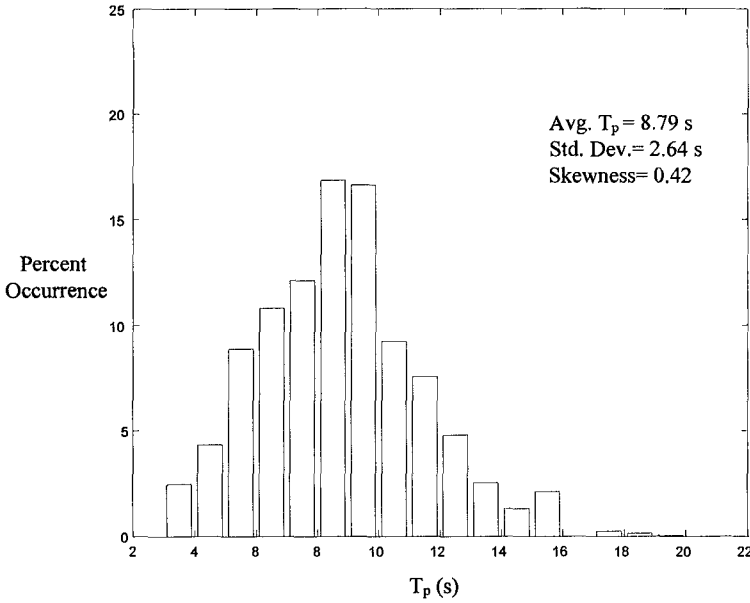


Figure 3. Histogram of T_p Data from FRF (May 1987 - April 1995)

The Shifted Gamma Model

Past research efforts have found several probability distributions which successfully model long-term distributions of wave height. For instance, using between one and seven years of data from 18 sites around the British Isles, Burrows and Salih (1986) concluded that even though the Weibull distribution did not fit the lowermost regions of the significant wave height (H_s) histograms as well as the lognormal distribution, it provided a better overall fit. On the other hand, Soares, Lopes, and Costa (1988) took four years of waverider buoy data collected off the coast of Portugal and found that the lognormal distribution provided the best fit for H_s .

After considering several probability distributions, the present study found that the shifted gamma distribution best represented the FRF H_{mo} data set (see e.g., Benjamin & Cornell, 1970):

$$pdf(H_{mo}) = \frac{\lambda}{\Gamma(k)} [\lambda(H_{mo} - H_*)]^{k-1} e^{-\lambda(H_{mo} - H_*)} \quad H_{mo} \geq H_* \quad (1)$$

In this model H_* is a shifting parameter, λ is a scaling parameter, k is a shape parameter, and $\Gamma(k)$ is the gamma function. The method of moments was used to

determine the best-fit parameters. This method utilizes the mean (\bar{H}_{mo}), the standard deviation (σ), and the skewness (s) of the FRF H_{mo} data set to estimate the model parameters. Using this method, equations (2), (3), and (4) are solved simultaneously:

$$\bar{H}_{mo} = H_* + \frac{k}{\lambda} \quad (2)$$

$$\sigma = \frac{\sqrt{k}}{\lambda} \quad (3)$$

$$s = \frac{2}{\sqrt{k}} \quad (4)$$

One property of the shifted gamma model should be noted; i.e. if $k \leq 1$, then the shifted gamma distribution reduces to an exponential-like function, which does not represent the basic shape of the H_{mo} histogram (see Figure 2). Because the shape parameter (k) is determined strictly from the skewness of the data set [refer to equation (4)], s must be less than two. In order to overcome this problem, the H_{mo} data set was edited by removing all wave heights above 3.0 meters. As the focus of this study is on long-term wave climate, and not on extreme storm events, the removal of the largest values is not detrimental.

H_{mo} Data Editing and Statistics

Once H_{mo} values above 3.0 meters were removed from the FRF data, the edited data could be modeled successfully using the shifted gamma distribution. Table 1 presents some of the basic statistical properties of the raw data, and how these properties fared once wave heights above 3.0 meters were removed. For the entire eight years of FRF H_{mo} data (11385 observations) a total of 139 observations above 3.0 meters were trimmed. Although the mean and the standard deviation do not change significantly, the skewness undergoes the greatest change. For instance, the mean of the raw and trimmed data sets for the entire eight years are 0.87 and 0.84 meters, respectively. There is a slightly larger change in the standard deviation which drops from 0.58 meters in the raw data set to 0.49 meters in the trimmed set. The skewness undergoes the greatest change. It drops from 2.18 for the raw data to 1.52 for the trimmed data.

Comparisons between the raw and trimmed data statistics for the individual years are similar to those of the entire data set. Out of the eight years of data, the period from 1987-1988 had the fewest observations trimmed (seven observations). Although the mean and the standard deviation do not change significantly, the

skewness drops from 2.44 to 1.75. In contrast, the greatest number of observations trimmed was during 1992-1993, when 39 values were found to be above 3.0 meters. Once again, there is little change in the mean and standard deviation, whereas the skewness value drops from 1.89 to 1.40.

Table 1. Basic Statistics of Raw and Trimmed FRF H_{mo} Data

Year (s)	Raw Data Set				Trimmed Data Set				
	# of Obs.	Mean (m)	Std. dev. (m)	Skewness	# of Obs.	# Trimmed	Mean (m)	Std. dev. (m)	Skewness
1987-1995	11385	0.87	0.58	2.18	11246	139	0.84	0.49	1.52
1987-1988	1423	0.82	0.50	2.44	1416	7	0.81	0.45	1.75
1988-1989	1406	0.89	0.58	2.15	1386	20	0.85	0.48	1.33
1989-1990	1423	0.85	0.57	2.40	1410	13	0.82	0.49	1.65
1990-1991	1423	0.88	0.51	1.84	1414	9	0.86	0.47	1.28
1991-1992	1446	0.87	0.62	2.39	1421	25	0.82	0.49	1.55
1992-1993	1440	0.99	0.69	1.89	1401	39	0.92	0.55	1.40
1993-1994	1435	0.80	0.52	2.04	1425	10	0.78	0.48	1.66
1994-1995	1389	0.88	0.60	1.96	1373	16	0.84	0.53	1.50

Best-fit Model Parameters

The best-fit model parameters for the shifted gamma distribution were found using the method of moments as dictated by equations (2), (3), and (4). Table 2 illustrates the values of the shifting parameter (H_*), the shape parameter (k), and the scaling parameter (λ) for the entire eight years of FRF H_{mo} data, as well as for the yearly data sets. Table 2 also includes the maximum and minimum values of each model parameter (the bold numbers in each column), and the mean and standard deviation of the model parameters from the eight individual years of data.

The first row in Table 2 contains the values of the best-fit parameters for the entire eight years of H_{mo} data from the FRF. These values ($H_*=0.19$ m, $k=1.72$, and $\lambda=2.66$ m⁻¹) are comparable to the mean values computed from the eight individual years of data. Beginning in the second row of Table 2, the model parameters for the eight individual years of data are presented. The minimum and maximum values of H_* are 0.13 (1988-89 and 1990-91) and 0.29 meters (1987-1988), respectively. The mean value of the shifting parameter is 0.18 meters and its standard deviation is 0.06 meters. The second column contains the values for the shape parameter, k . Its minimum value occurred during the year 1987-1988 (1.31) and its maximum value occurred during 1990-1991 (2.44). The mean of the shape parameter for the eight years is 1.80 and the standard deviation is 0.40. Finally,

column three of Table 2 contains the values of the scaling parameter, λ . The minimum value for the scaling parameter is 2.49 m^{-1} , which is associated with the data from 1989-1990. The maximum value for λ is 3.33 m^{-1} (1990-1991). The mean and the standard deviation of λ from the eight individual years of data are 2.72 m^{-1} and 0.32 m^{-1} , respectively.

It is interesting to note that the maximum values for k and λ and the minimum value for H_s all occur during the year 1990-1991. For an explanation one need look no further than the skewness values for both the raw and trimmed data during this time period. In both instances, 1.84 for the raw data and 1.28 for the trimmed data, the skewness values are the lowest of all eight years. As the method of moments begins with solving equation (4), it is easy to see how the skewness of the data set can have such an impact on the rest of the model parameters.

Table 2. Best-fit Model Parameters for the Trimmed Data Sets of H_{m0}

Year(s)	H_s (m)	k	λ (m^{-1})
1987-1995	0.19	1.72	2.66
1987-1988	0.29	1.31	2.53
1988-1989	0.13	2.25	3.14
1989-1990	0.23	1.47	2.49
1990-1991	0.13	2.44	3.33
1991-1992	0.18	1.66	2.62
1992-1993	0.14	2.02	2.59
1993-1994	0.21	1.46	2.54
1994-1995	0.14	1.78	2.53
<i>Mean</i>	0.18	1.80	2.72
<i>Std. Dev.</i>	0.06	0.40	0.32

Model Comparison to Long-Term Wave Climate

Figure 5 illustrates the ability of the shifted gamma distribution to model the long-term (entire eight years) FRF H_{m0} data. In Figure 5 the circles represent the percent occurrences of the data, whereas the shifted gamma model is represented by the solid line. Although the model under-predicts the most frequently occurring wave heights (in the 0.60 meter range) by 3%, it correctly predicts that H_{m0} values in the 0.40 meter range occur 26% of the time. Overall, the shifted gamma distribution is in good agreement with the data.

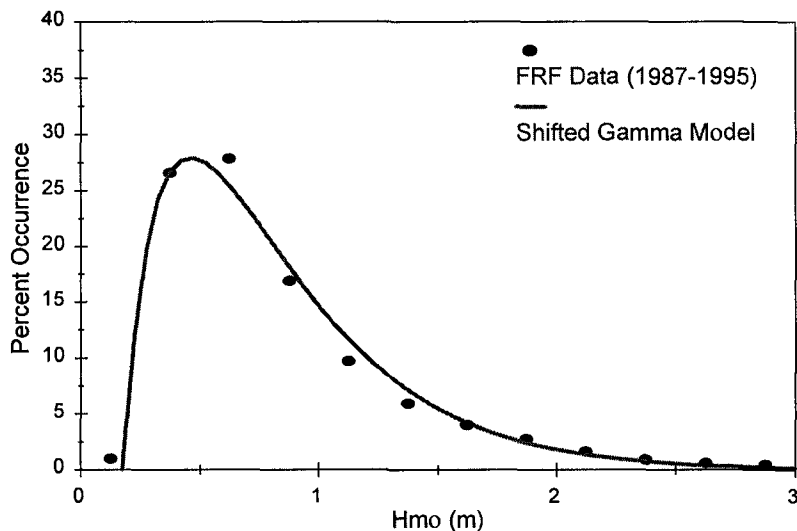


Figure 4. FRF H_{m0} Model Comparison -- 1987-1995

Model Comparisons to Yearly Data Sets

Figures 5-12 show how the shifted gamma distribution compares to the FRF H_{m0} data on a yearly basis. Beginning with the year 1987-1988 (Figure 5) and ending with the year 1994-1995 (Figure 12), the shifted gamma distribution shows good agreement with the data. These figures also illustrate how the long-term shifted gamma model (the dashed line) performs when plotted on top of the yearly H_{m0} histograms. In Figures 6, 8, 9, and 12 the long-term model does as well, or better, than the model developed from only that one year of data. In three of the years (Figures 6, 8, and 12) the long-term model more accurately captures the peak of the distribution. However, there are also several cases where the long-term model fails to provide as accurate a fit as that provided by the yearly model. In

Figures 5, 7, and 11 the long-term model noticeably under-estimates the percent occurrence of the most commonly occurring wave heights. It is interesting to note, however, that these three years of data have the highest skewness values. And for two of the years, 1987-1988 (Figure 5) and 1989-1990 (Figure 7), even the yearly model failed to capture the peak percent occurrence.

Figure 10 presents the only case in which the long-term model noticeably over-predicts the most commonly occurring wave heights. This time period, (1992-1993), is unique from any other because the H_{m0} histogram lacks a well-defined peak. This year of data had the highest mean and standard deviation values, as well as the third-smallest skewness (see Table 1).

Conclusions

The problem hampering the development of long-term wave climate models, i.e. a lack of suitable data, is gradually being overcome as monitoring programs such as that from the FRF continue. Utilizing data sets such as these, best-fit model parameters can be estimated with more confidence than in the past.

Utilizing eight years of data from the FRF (May 1987 to April 1995) and the method of moments, best-fit model parameters were found for the shifted gamma distribution. This probabilistic model appears to represent the FRF H_{m0} data for the entire eight years of data, as well as on a yearly basis. Furthermore, although it sometimes fell short of capturing the peak percent occurrence, the long-term distribution modeled the yearly H_{m0} histograms to a reasonable degree. Therefore, the shifted gamma distribution should be considered when developing long-term wave climate models.

Acknowledgments

The data used in this study were provided by the Field Research Facility of the U.S. Army Engineer Waterways Experiment Station's Coastal Engineering Research Center. The authors would particularly like to thank Dr. Charles E. Long for his numerous suggestions and comments regarding the use of this data. The financial support of the Sebastian Inlet Tax District is also gratefully acknowledged.

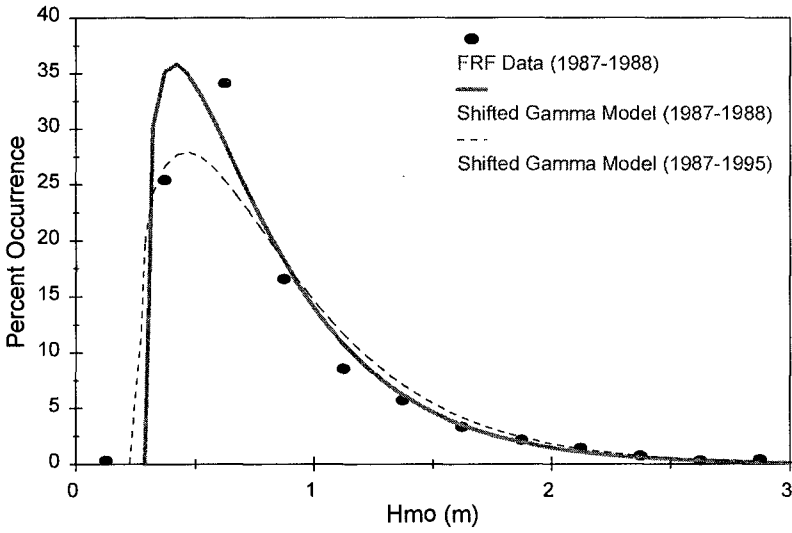


Figure 5. FRF H_{mo} Model Comparison -- 1987-1988

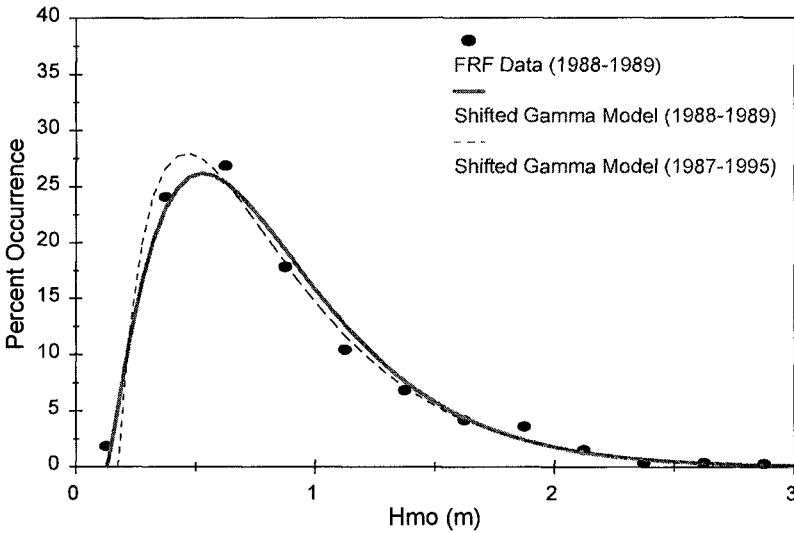


Figure 6. FRF H_{mo} Model Comparison -- 1988-1989

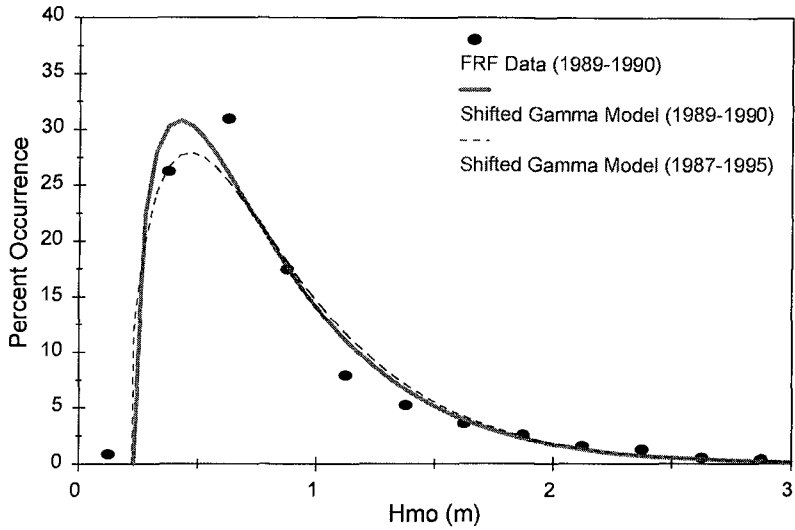


Figure 7. FRF H_{mo} Model Comparison -- 1989-1990

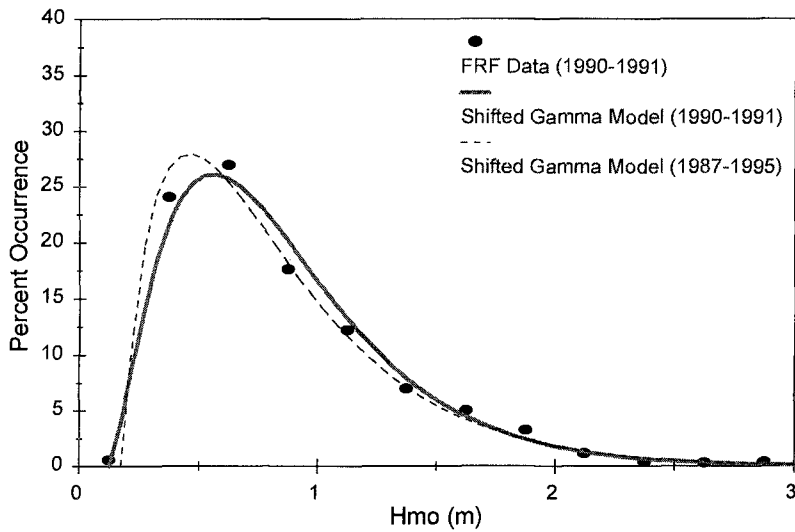


Figure 8. FRF H_{mo} Model Comparison -- 1990-1991

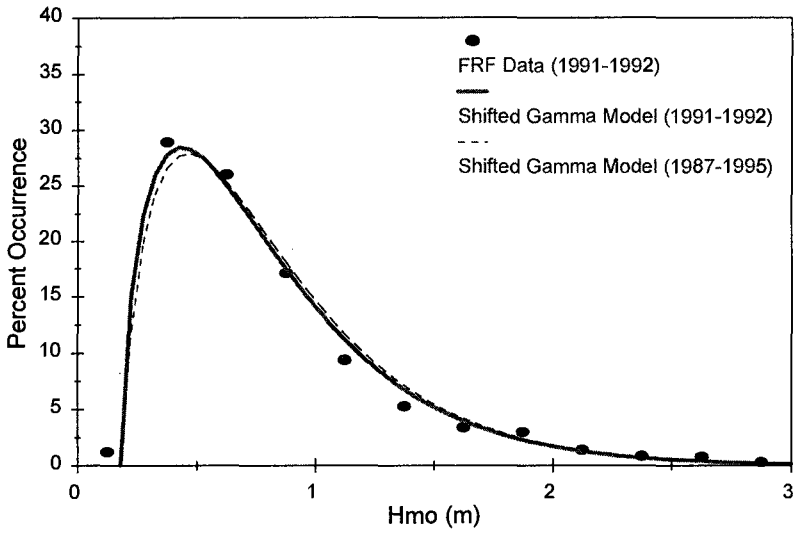


Figure 9. FRF H_{mo} Model Comparison -- 1991-1992

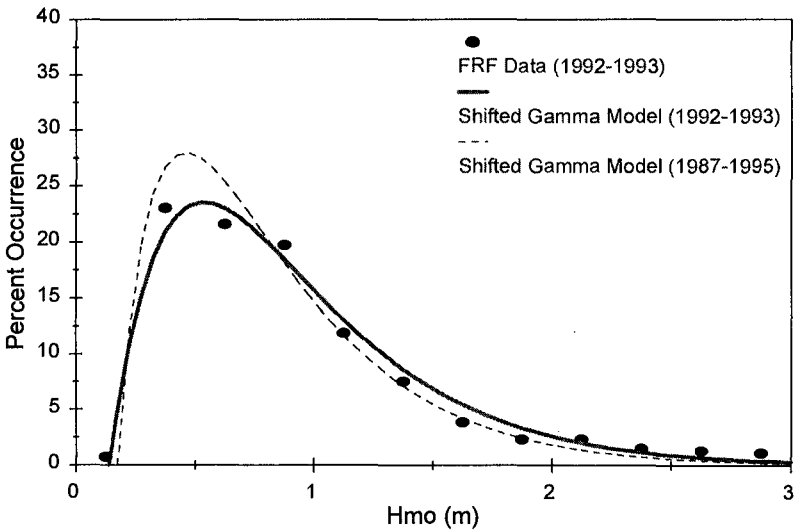


Figure 10. FRF H_{mo} Model Comparison -- 1992-1993

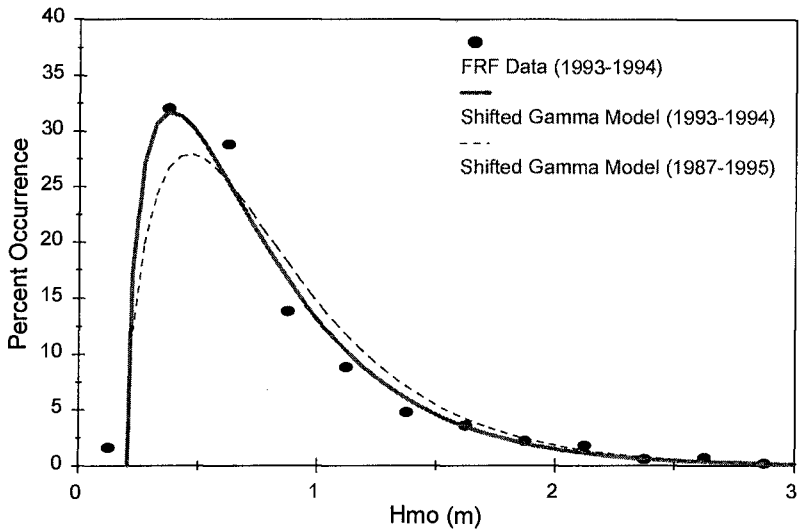


Figure 11. FRF H_{mo} Model Comparison -- 1993-1994

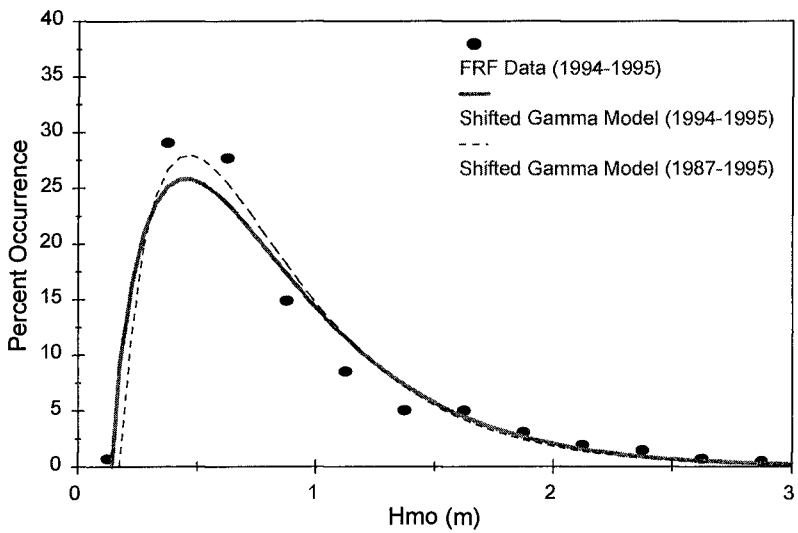


Figure 12. FRF H_{mo} Model Comparison -- 1994-1995

References

- Benjamin, J.R., and Cornell, C.A., Probability, Statistics and Decision for Civil Engineers, McGraw-Hill, New York, 1970.
- Burrows, R. and Salih, B.A., “Statistical Modelling of Long-Term Wave Climates”, *Proceedings of the Twentieth International Conference on Coastal Engineering*, Taipei, Taiwan, pp. 42-56, 1986.
- Hogben, N., “Long-Term Wave Statistics”, *Ocean Engineering Science*, Vol. 9, Part A-The Sea, ed. by B. Le Mehaute and D. Hanes, John Wiley and Sons, Inc., New York, pp. 293-334, 1990.
- Isaacson, M., and MacKenzie, N., “Long-term Distributions of Ocean Waves: A Review”, *J. of Waterway, Port, Coastal, and Ocean Engineering*, Vol. 7, No. WW2, pp. 93-109, 1981.
- Soares, C.G., “Bayesian Prediction of Design Wave Heights”, *Reliability and Optimization of Structural Systems*, ed. by P. Thoft-Christensen, Vol. II, pp. 67-75, 1988
- Soares, C.G., Lopes, L.C., and Costa, L.C., “Wave Climate Modelling for Engineering Purposes”, Computer Modelling in Ocean Engineering, B.A. Schrefler and O.C. Zienkiewicz (Eds.), A.A. Balkema Pub., Rotterdam, pp. 165-175, 1988.
- Soares, C.G., and Henriques, A.C., “On the Statistical Uncertainty in Long-Term Predictions of Significant Wave Height”, *Proceedings of the 13th International Conference on Offshore Mechanics and Ocean Engineering*, Vol. 2, pp. 67-75, 1994.
- Teng, C.C., Timpe, G., and Palao, I.M., “The Development of Design Waves and Wave Spectra for Use in Ocean Structure Design”, *SNAME Transactions*, Vol. 102, pp. 475-499, 1994.
- U.S. ARMY, CORPS OF ENGINEERS, (July 1993). *Preliminary Data Summary*, Field Research Facility, Coastal Engineering Research Center, U.S. Army Engineer Waterways Experiment Station, Kitty Hawk NC.
- U.S. ARMY, CORPS OF ENGINEERS, (1984). Shore Protection Manual, Volumes I and II, p.4-40, Coastal Engineering Research Center, Washington DC.

CHAPTER 65

MONTE CARLO SIMULATION FOR NEARSHORE WAVE STATISTICS IN SOUTHERN CALIFORNIA

Chia-Chi Lu¹, Member, ASCE and R. Rea Strange III²

ABSTRACT

To develop the nearshore wave condition in Southern California, six meteorological weather patterns including extratropical cyclones of the northern hemisphere, northwest winds in the outer coastal waters, west to northwest local sea, pre-frontal local sea, tropical storm swell and extratropical cyclones of the southern hemisphere were identified and classified. Wave characteristics in deep water, corresponding to the categorized weather patterns, were computed and then transferred to the nearshore target sites via a spectral back-refraction transformation model. A Monte Carlo simulation technique was applied to generate a synoptic atlas of the nearshore wave climate in this region.

INTRODUCTION

Waves, currents and water levels are the dominant oceanographic forces that control the movement of sediment and determine, in part, the potential for coastal flood damage exposure. Waves that impinge on the shoreline perhaps more than any other oceanographic factor, determine the fate of sediment movement and the associated impacts to coastal development. An understanding of the temporal and spatial variation of waves is critical to the formulation of effective shoreline erosion management plans. Although wave hindcast and measurement data are currently available in Southern California, existing databases are sparse and lack sufficient detail of important information. For example, wave direction data, important in the understanding of sediment transport processes, are limited; and most of the hindcast wave data exclude waves generated in the southern hemisphere ocean (southerly swell). This study was therefore performed to address data gaps and to develop a practical database that can characterize the wave climate for the Orange County shoreline in Southern California.

¹ Coastal Engineer, Ph.D., P.E., Noble Consultants Inc., 2001 Dupont Dr., Suite 620 Irvine, California, USA

² President, Pacific Weather Analysis, 648 Ladera Lane, Santa Barbara, California, USA

METHODOLOGY

The technical approach taken in this study is unique and represents a significant departure from previous wave studies within Southern California. In general, the following procedures were adopted.

1. Local, regional and hemispheric meteorological weather systems which influence the wave climate within this region were identified. In this manner, the local and distant origins of ocean wave generation patterns and their recurrence frequencies were defined.
2. A state-of-art spectral transformation numerical model was applied to characterize how the offshore waves will change in height and angle of shoreline approach as they propagate into the nearshore water area.
3. A synthetic nearshore wave database was compiled by using a Monte Carlo simulation technique based on the probable sequential and combined occurrences of different meteorological events and their associated wave generation patterns.

Pattern Identification

Waves that impact the Southern California coastline, as shown in Figure 1, are generated by any one or more of the following meteorological patterns:

- I. Extratropical cyclones of the northern hemisphere (northwest to west-southwest swell);
- II. Northwest winds in the outer coastal waters (wind swell);
- III. West to northwest local sea (west sea);
- IV. Pre-frontal local sea (southeast sea);
- V. Tropical storm swell ;
- VI. Extratropical cyclones of the southern hemisphere (southerly swell).

Low pressure centers which develop along the polar front are the source of the predominant wave action along the Southern California coast during the winter half of the year. Storm swell is generated at some distance from the Southern California coastline in the North Pacific. Most commonly these storms will traverse the mid-Pacific before turning northeastward toward the Gulf of Alaska with swell decaying on the average of 2,400 kilometers to the coast of Southern California. However, under some meteorological conditions, storms can move in much closer to the coast; and on rare occasion these storms may move directly across Southern California, following either a northeast, east or southeast trajectory. In general, the modal deep water approach directions range between 275° and 285°. However, these North Pacific low pressure systems exhibit great variations from year to year such that wave approach directions and amplitudes will show a corresponding degree of variation. Years when the storm centers follow a more northerly route in the eastern Pacific will result in extremely quiet conditions in Southern California, whereas more southerly storm tracks through the mid and/or eastern Pacific will result in frequent periods of high wave conditions.

The predominant swell along the Southern California coast in spring and summer is generated by the prevailing northwest winds north and west of this area. Wave heights are usually low, less than one meter, but on occasion, with superposition of a strong surface high and an upper level trough, the northwesterlies increase, becoming very strong from north of Point Conception to San Nicolas Island. Waves traveling at a variance to the mean wind direction reach Southern California with periods on the order of 6 to 10 seconds. Moderate northwesters will produce breaker heights of one to two meters, while strong events can give two to 3 meters.

Seas generated by westerly winds can be divided into two types: 1) temperature-induced sea breezes, and 2) gradient winds. The strong sea breezes occur during the late spring and summer months, while the lightest winds are during December and January. The sea breezes usually set in during the morning and peaks in the mid-afternoon. Gradient winds are confined largely to the months of November through May with the peak in March and early April.

Pre-frontal winds blow strongly from the southeast along the coast but turn toward the south to southwest a short distance offshore. Significant wave heights are generally in the range of one to 2.5 meters. Westerly swells tend to follow the frontal passage, when southeast seas are well on the way down, but on occasion the two wave trains overlap.

Tropical cyclones form regularly along the intertropical convergence zone west of Mexico from early July to early October. On the average, about 15 of them are to be expected each year. Most of them take a westerly track, and swells generated by these storms will have little or no effect on Southern California. Some, however, take a more northerly track and swells off Southern California may reach 2 to 4 meters.

Southerly swells occur primarily between April and October and to a lesser extent the remainder of the year. Large South Pacific storm systems traversing the ocean between 40° and 60° south from Australia to South America send swells northward to the west coast of Central and North American. Great circle approach directions off Southern California range from about 215° for storms near New Zealand to 170° for South American storm system. The decay distance ranges from 7,200 to 11,200 kilometers. Swells in deep water off Southern California are generally about one meter, but breaker height may be 3 to 4 meters or more.

To better distinguish the wave conditions generated from the aforementioned meteorological patterns, each weather type was further classified according to wind speed, effective fetch, decay distance and storm duration. Table 1 tabulates the meteorological criteria for the classified categories within each generated wave pattern. The destructive storms of March 2, 1983 and January 17, 1988 are examples of the storm swells of Category 4a.

Pattern Recurrence

The meteorological characteristics, which produce various wave generation patterns, change seasonally. Four meteorological seasons were defined according to weather characteristics instead of the traditional calendar seasons. The discrete meteorological seasons have a two-month spring (April and May), a three-month summer (June to August) and fall (September to November), and a four-month winter (December to March). Observed storm swells or seas between 1974 to 1993 were reviewed from the Pacific Weather Analysis' daily logged data bank. Seasonal recurrence of the classified wave generation patterns was then derived to characterize the probability of occurrence for each classified category. Table 2 shows the resultant seasonal occurrence for each wave generation pattern. For example, the occurrence of northwest to west swells (Pattern I) has its peak frequency in winter, while observations of long-period southerly swells (Pattern VI) have a summer peak.

The possible wave approach directions generated from all six weather patterns were also evaluated from the historical data between 1974 to 1993. Wave directions with a 5-degree increment were discretized for the northwest or west storm swells (Pattern I). Table 3 lists the discretized ranges of deep water wave approach directions and their probability of occurrence for each category. Three discretized wave directions were designated for the tropical storm (Pattern V) and the southerly swell (Pattern VI). Tables 4 and 5 show the directional occurrence probability for the tropical storm and the southerly swell respectively. The prevailing deep ocean approach direction is from west (270°) for both the wind swell and west to northwest local sea, and southeast (160°) for pre-frontal local sea (southeast sea).

Deep Water Wave Characteristics

Based on the aforesaid meteorological parameters such as wind speed, effective fetch, decay distance and storm duration, the deep water wave characteristics were computed from a PWA wave generation model. The PWA hindcast method is based on the principles set forth by Pierson, Newmann, and James (1955) wherein the energy in each frequency band of the wave spectrum, propagating at group velocity with angular spreading, is generated and recombined with other frequency bands at the hindcast point to give the predicted spectrum.

The PWA model, which is proprietary, has been developed through analysis of wave data taken from several locations along the California coast. The hindcasted spectral form is quite wide during the early stages of development; but as the wind speed, fetch or duration increases the spectrum narrows, with the front face becoming steeper. The wind speed is the most critical as compared to the effect due to the fetch. The spectral area does increase as the fetch increases, and the peak energy shifts toward longer periods but at a decreasing rate. Although there is no fully developed absolute condition for this spectrum, the spectral curves flatten out to such an extent at low frequencies that maximum periods have been assigned as the criterion for the "fully developed" sea. The approximate areas where the hindcast deep water wave characteristics were performed are indicated in Figure 1.

Nearshore Wave Transformation

The wave characteristics derived from the meteorological weather patterns, described in the last section, all represent deep water environments. To determine the wave conditions within the Southern California coast, it is necessary to transform the predicted deep water wave conditions to the nearshore water area. The transformation process consists of adjusting deep water wave heights and approach directions due to the effects of island sheltering, shoaling, refraction and diffraction. In this study, a spectral back-refraction model (O'Reilly & Guza, 1991) was selected as the tool to transfer the deep water wave environments into the nearshore water area.

O'Reilly's spectral back-refraction model performs a linear spectral refraction transformation in which the transferred spectrum is established from the incident wave spectrum by back-refracting rays from the target site. The model accounts for island blocking, wave refraction, and wave shoaling. It is typically used to model waves with periods between 8 and 25 seconds. The model includes deep ocean swell directions ranging from 150 to 335 degrees. Unlike more traditional forward ray refraction methods, O'Reilly's model back-refracts wave rays from the site of interest, therefore eliminating caustics which plague forward ray tracing schemes. As a result, the spectral transformations are robust (finite solutions are always obtained), easily interpreted, and more realistic than those obtained using forward ray tracing and the assumption of unidirectional, monochromatic deep ocean waves.

For a known deep water wave condition including both energy and directional spectra, the transformation is performed by :1) decomposing the deep water energy spectrum and the deep water directional spectrum into 1-second and 1-degree increments, respectively; 2) obtaining the transformed energy at the target point for each component from the transformed and normalized coefficients; 3) assembling the transformed wave components to form an energy spectrum and a directional spectrum at the target point; and 4) determining the significant wave height, the wave period and the approach direction from the transferred spectra.

In this study, the nearshore wave conditions transformed from the hindcasted deep water wave characteristics in spectrum form were computed every three hours to describe the temporal variability of the wave condition. The significant wave height was determined from the spectrum computed every three hours; and the significant wave period and the predominant wave direction correspond to the period and the direction at the peak wave energy component. Approximately, 5,800 wave event data sets were computed and cataloged, including all classified categories and different wave approach directions for each nearshore site of interest. This wave information provides the data bank necessary for the characterization of long-term wave statistics.

Monte Carlo Simulation

A Monte Carlo simulation technique was applied to generate a synthetic practical data base to characterize the Orange County nearshore wave climate. This technique

recreates a stochastic process to solve a problem which can not be easily evaluated by a direct analytic or a standard numerical analysis procedure. In this study, a computer code was written in accordance with the probability occurrence scenarios derived from the 20-year daily recorded weather patterns, as previously described.

In addition to the individual seasonal probability distribution related to each wave pattern, the 20-year statistics of the recorded wave patterns also provide a basis for assessing the coupling (coincident events) and the likely sequential order among different wave patterns. A few principles were derived and implemented in the computer code. These are:

1. The recurrence for each weather pattern varies seasonally in accordance with the derived probabilities of occurrence.
2. The occurrence of southerly swells and tropical storms were treated independently since their meteorological characteristics are not related to the remaining weather patterns. Also, there is no intercorrelation between southerly swells and tropical storms.
3. There is a 30% chance in which the coupling between two northwest to west-southwest extratropical storm swells occurs in winter. The occurrence distribution for each storm category is listed in Table 6.
4. After a west local sea, there is a 50% chance that a wind swell follows for all seasons.
5. After a southeast local sea, there is a 30% chance that a category 4 northwest to west storm swell or a 30% chance of a west sea follows in winter.
6. A background noise is selected if no wave event occurs in each simulated day. The noise can be either a weak northwesterly swell, a light wind swell, a slight southerly swell or a sea breeze only occurring in the afternoon.

In the Monte Carlo simulation, numbers between 1 and 100 were randomly generated. The model performed the wave event selection in accordance with the sequence of the random numbers. For example, if the first random number implies a storm event is evident, the following random numbers would determine the wave pattern, intensity category and incoming direction. The model then determines if another wave pattern occurs simultaneously. After the end of all possible coincident or subsequent events which may be a few simulated days later, the model reselects a random number and repeats the same procedure. On the other hand, if the random number implies a no-storm event, the model would generate a background noise for the particular simulated day and selects a new random number the next day to proceed the simulation. The simulated daily nearshore wave environment may be composed of a single, multiple wave events or no event with a background noise only.

RESULTS

The recurrence probability of the identified weather patterns was compiled on a season-by-season basis. Therefore, the simulation can be used to statistically characterize the seasonal and annual nearshore wave environments. Figure 2 illustrates one of the simulated wave environments for a winter month at San Clemente, where a California Data Information Program (CDIP) gage station is located. For a multiple-wave-event selection, the significant wave height was computed from the superposition of all the wave energy spectra, and its associated wave period and approach direction was defined as the period and direction of the peak energy component.

In order to be statistically significant, it was necessary to perform replicate simulations so that the statistical moments such as the mean and deviation can be derived. The trial and error process was conducted to determine the required number of simulations to yield a valid record of data for one year. It was found that approximately 10 simulations were adequate to provide a statistical significance of the results. Figure 3 presents the average annual statistics of significant wave height and period at the San Clement gage station obtained from the Monte Carlo simulation compared to the average field measurements recorded over 6 years (US Army and State of California, 1984, 1985, 1986, 1987, 1992 and 1993). It is noted that no complete annual wave measurements were collected at the San Clemente gage from 1988 to 1991.

As seen in Figure 3, the majority of observed wave heights (about 88% of time) ranges from 0.4 to 1.3 meters, while an occurrence of about 73 % was estimated from the simulated results. The model overpredicts the occurrence of lowest significant wave height (16% for $H_s < 0.4$ meter). The difference may be attributed to the following reasons.

1. In the field condition, the background noise is always present. This noise would contribute additional wave energy to the total spectrum, thereby increasing the resultant significant wave height. However, in the model simulation, no background noise was introduced as long as a wave event was selected. A test simulation was conducted to incorporate the background noise on a daily basis. The resultant statistics shows the reduced occurrence of low wave events ($H_s < 0.4$ meter) and more frequent recurrence of high wave event ($H_s > 1.6$ meters). This implies that incorporated background noise combined with the selected wave patterns will overmagnify the storm events. The model result can be improved with the development of an improved background noise incorporated in the simulation.
2. The El Nino effect, which occurs every 3 to 7 years, was not implemented in the model simulation. Approximately two to three El Nino scenarios of different severities (Seymour et al, 1984) may occur over 10 simulations (10-year span). During an El Nino year, the frequency of storm events occurring in winter may increase, which would result in occurrence of more intermediate wave events ($0.4 \text{ meter} < H_s < 1.3 \text{ meters}$) and a reduction in the average percentage of occurrence for low wave events ($H_s < 0.4 \text{ meter}$).

In the statistical representation, the wave period selected only represents a peak energy component of the combined wave trains. Other components are not included in the statistical count. For example, if two wave trains with different significant periods of 11 and 15 seconds are simulated and the wave energy for the 11-second wave train is slightly higher, the statistics only count for the period of 11 seconds. The wave train with a 15-second significant wave period is as important, but is not counted in the annual statistics. Thus, comparisons of significant wave period, based solely on the peak energy period without further evaluating the combined wave trains, may be somewhat misleading. The discrepancy of annual statistics for wave period may not be as significant as that for wave height.

CONCLUSIONS

The Monte Carlo simulation method presented in this study provides an alternative to characterize a long-term (annually or seasonally) synoptic nearshore wave climate within Southern California. For each simulated daily wave environment, the influencing weather patterns originating from distant or local areas can easily be identified. Also, the spatial variation of wave climate can be evaluated as the simulation is applicable to any selected nearshore location. Further studies in better quantifying the specified background noise and including the El Nino effect are suggested.

REFERENCES

- U.S. Army and State of California. "Coastal Data Information Program (CDIP) Annual Report, 1984 to 1993 ", A Cooperative Program by Coastal Engineering Research Center, Corps of Engineers and Department of Boating and Waterways, State of California.
- O'Reilly, W.C., and Guza, R.T., 1991. "Modeling Surface Gravity Waves in the Southern California Bight", SIO Reference Series No, 91-25.
- Pierson, W.J. Jr., Newmann, G. and James, R.W., 1955. "Practical Methods for Observing and Forecasting Ocean Waves by Means of Wave Spectra and Statistics", U.S. Navy Hydrographic Office, Publication No. 603.
- Seymour, R.J., Strange, R.R. III, Cayan, D.R. and Nathan, R.A., 1984. " Influence of El Ninos on California's Wave Climate", Coastal Engineering 1984 Proceedings, Vol. I, pp577-592.

ACKNOWLEDGMENTS

This study was prepared in partial fulfillment of the Coast of California Storm and Tidal Waves Study, Orange County, California. The authors wish to express their gratitude to Corps of Engineers, County of Orange, Cities of Huntington Beach, Newport Beach and Laguna Beach for their sponsoring the study. Specific thanks extend to Drs. W. C. O'Reilly and N. Graham for their assistance in wave transformation computation, and Mr. J. T. Moore for his valuable suggestions during this study.

Table 1: Classification of Meteorological Patterns

Weather Pattern	Category	Decay Distance (kilometer)	Duration (days)	Wave Direction (degrees)	Sub-Category	Wind Speed (m/sec)
Extratropical Cyclone of Northern Hemisphere	1	>2,880	4	265-305	a	24.7
					b	21.6
					c	18.5
	2	1,920-2,880	3	260-305	a	24.7
					b	21.6
					c	18.5
	3	960-1,920	3	240-305	a	24.7
					b	21.6
					c	18.5
					d	16.5
	4	<960	2	185-305	e	14.4
					a	24.7
b					21.6	
c					18.5	
Northwest Winds in Outer Coastal Waters	1	192	1	270	-	15.5
	2	192	2	270	-	15.5
	3	192	2	270	-	16.5
	4	192	3	270	-	15.5
	5	192	3	270	-	16.5
	6	192	3	270	-	17.5
	7	192	4	270	-	17.5
	8	192	5	270	-	16.5
	9	192	6	270	-	17.5
West to Northwest Local Sea	1	0	1	270	-	11.6
	2	0	1.5	270	-	14.2
	3	0	2	270	-	18.0
Pre-frontal Local Sea	1	0	1	160	-	11.6
	2	0	2	160	-	14.2
	3	0	3	160	-	18
Tropical Storm	1	1,440	2.5	165-190	-	25.8
	2	1,120	2.5	165-190	-	25.8
	3	800	2.5	165-190	-	25.8
Extratropical Cyclones of Southern Hemisphere	1	8,000	5	180-210	-	20.6
	2	8,000	5	180-210	-	23.2
	3	8,000	5	180-210	-	25.8

Table 2: Occurrence Probability of Wave Patterns

METEOROLOGICAL SEASON	PROBABILITY OF OCCURRENCE (%)					
	PATTERN					
	I	II	III	IV	V	VI
Spring	5.2	11	5.7	0.5	0	8.0
Summer	0.3	6.7	1.7	0.1	2.7	10.0
Fall	8.5	6.3	2.5	1.0	1.5	5.8
Winter	18.5	7.8	5.0	3.9	0	0.9

Table 3: Directional occurrence Probability of Northwest or West Storm Swell

Direction (degs.)	METEOROLOGICAL SEASON															
	SPRING				SUMMER				FALL				WINTER			
	PERCENTAGE OF OCCURRENCE															
	Category				Category				Category				Category			
	1	2	3	4	1	2	3	4	1	2	3	4	1	2	3	4
180																
185																6.7
190																
195																
200																1.3
205																
210																2.7
215																
220				20								7.1				
225												7.1				4
230																1.3
235																1.3
240															0.8	
245																
250															2.3	4
255												7.1			2.3	8
260												7.1			1.5	3.1
265			4.5						2.5		4		0.83	3.1	4.7	9.3
270			13.6	20						4	14.3		1.7	11.4	13.3	13.3
275		11.5	9.1	20	5	5	5	5	2.5	2	7.8	21.3	9.2	13.7	17.2	13.3
280		3.8	18.2		10	10	10	10	10	5.9	7.8	7.1	23.3	24.4	14.0	8
285	9.1	19.2	22.7		15	15	15	15	17.5	19.6	13.7		25	16.8	14.0	5.3
290	36.4	26.9	9.1		25	25	25	25	25	31.4	25.5	7.1	21.7	13	12.5	5.3
295	45.5	26.9	9.1		20	20	20	20	30	21.6	13.7		12.5	9.2	8.6	2.7
300	9.0	11.5	9.1		15	15	15	15	7.5	13.7	11.8	21.4	2.5	5.3	4.7	2.7
305			4.5	40	10	10	10	10	5	6	11.9		3.3	1.5	2.4	5.2

Table 4: Directional Occurrence Probability of Tropical Storm Swell

DIRECTION (deg.)	PERCENTAGE OF OCCURRENCE		
	Category 1	Category 2	Category 3
165	70	78	87
175	20	15	10
190	10	7	3

Note: Probability distribution applies to all seasons.

Table 5: Directional Occurrence Probability of Southerly Swell

DIRECTION (deg.)	PERCENTAGE OF OCCURRENCE		
	Category 1	Category 2	Category 3
185	50	50	50
195	35	35	35
210	15	15	15

Note: Probability distribution applies to all seasons.

Table 6: Coupling Probability Distribution by Category for Northwest or West Storm Swell

CATEGORY	PERCENTAGE OF COUPLING PROBABILITY DISTRIBUTION			
	1	2	3	4
1	30	40	20	10
2	18	36	28	18
3	15	30	30	25
4	25	25	25	25

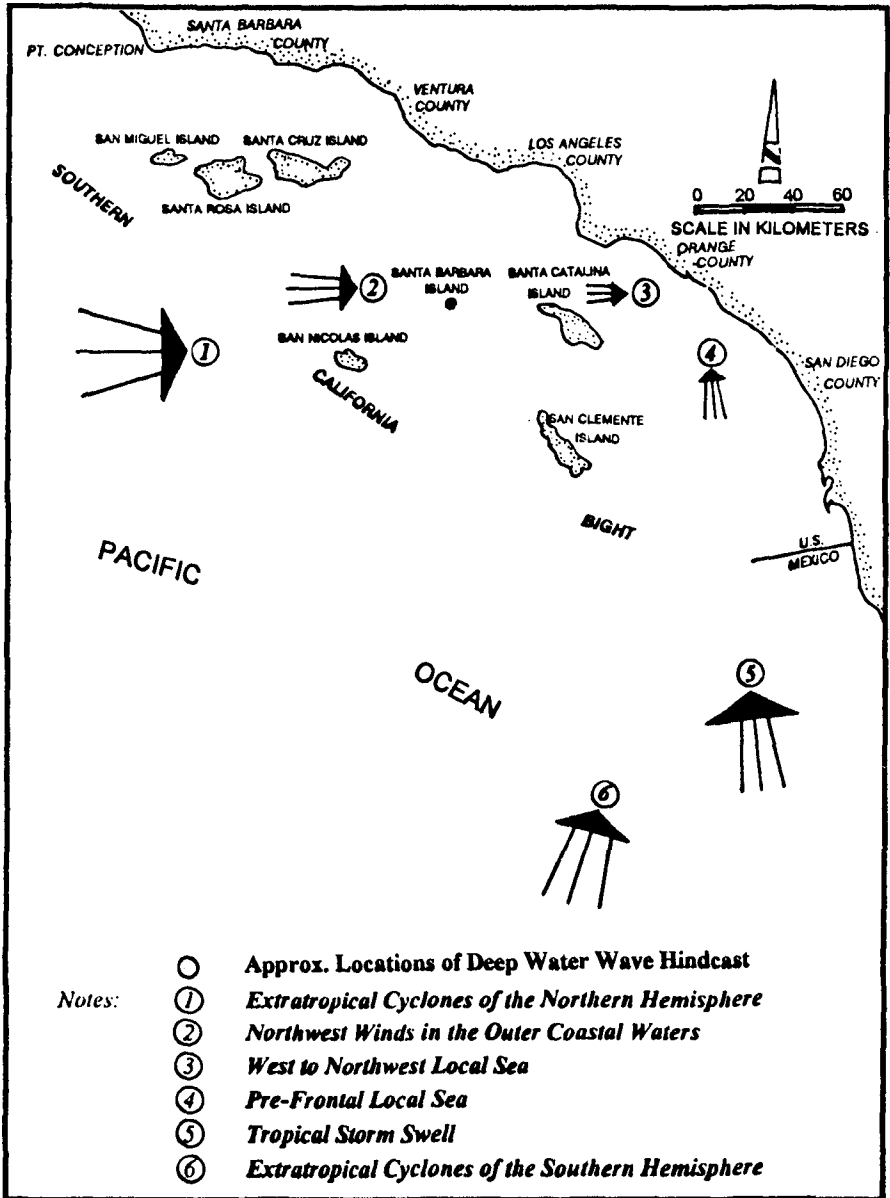


Figure 1: Study Area

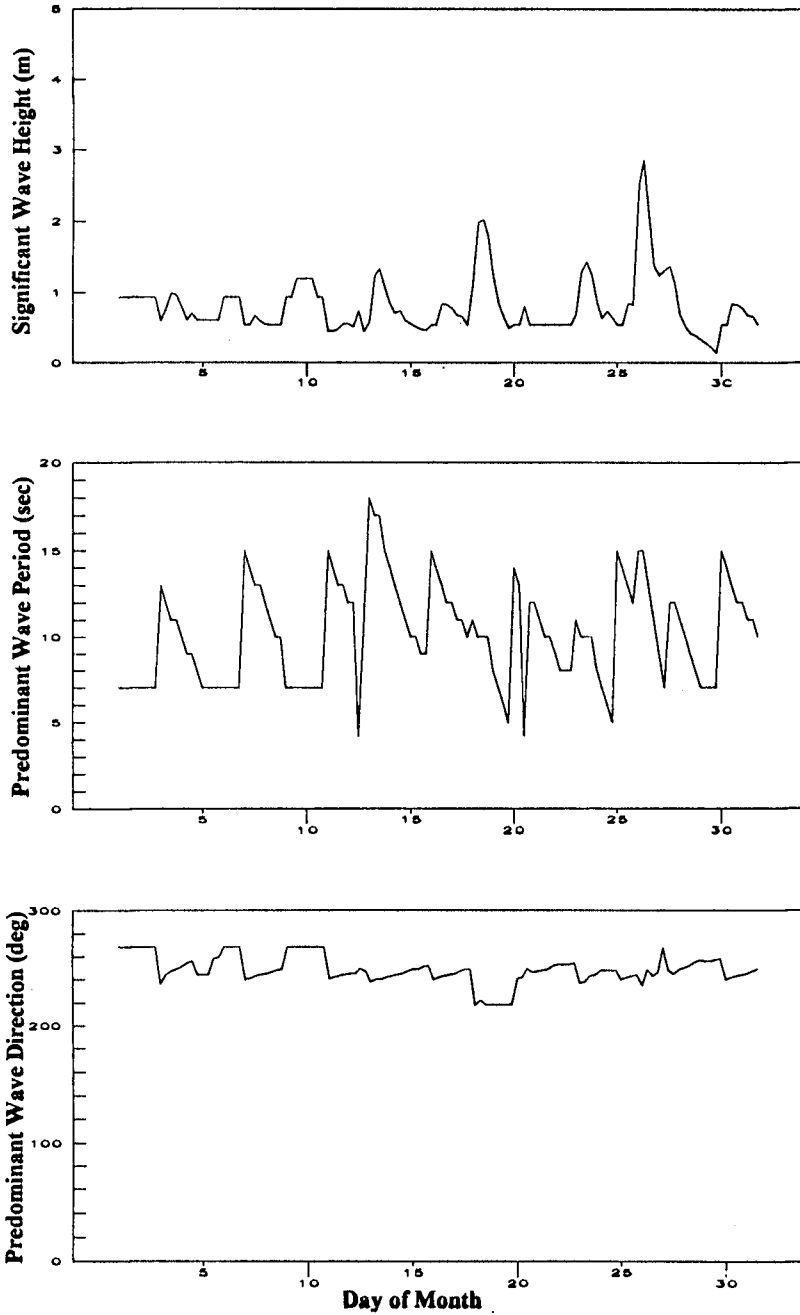


Figure 2: Simulated Daily Wave Climate for Winter Month

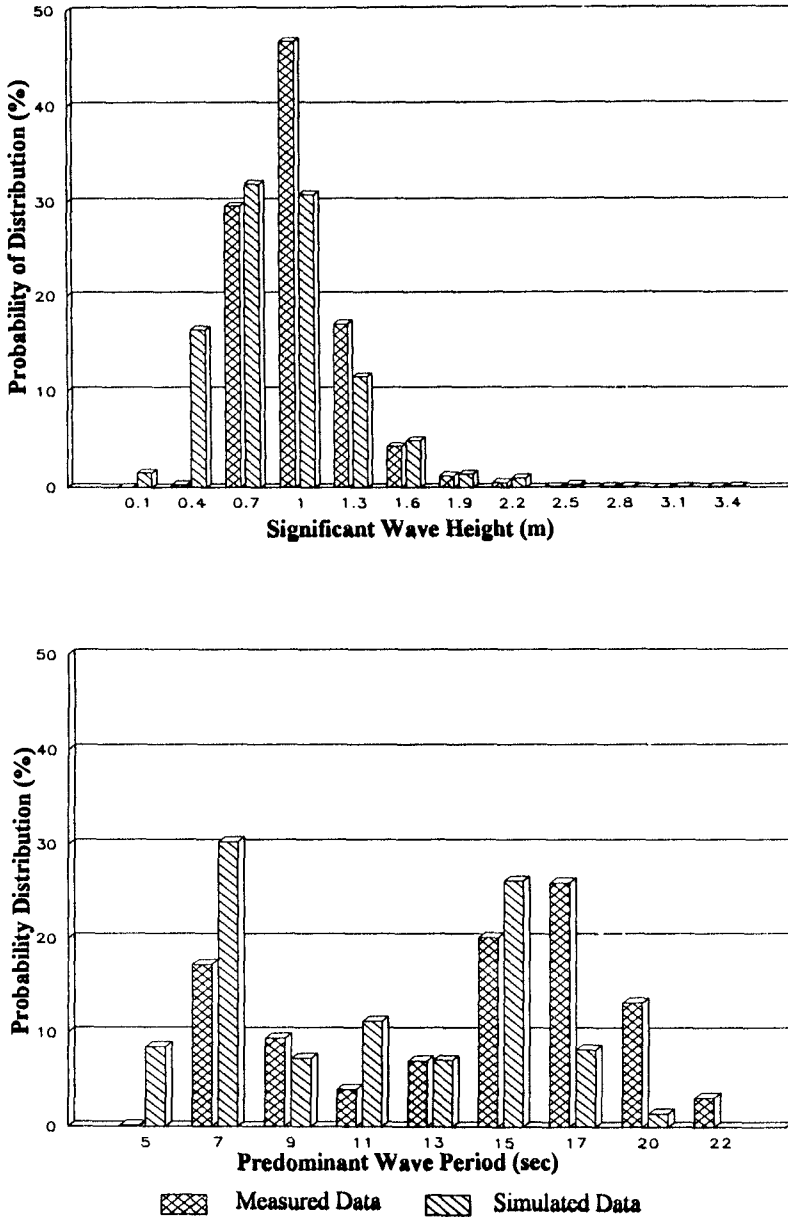


Figure 3: Comparison of Annual Wave Statistics at San Clemente Gage Station

CHAPTER 66

BOTTOM FRICTION DISSIPATION IN THE BELGIAN COASTAL REGIONS

Weimin Luo¹, Jaak Monbaliu², Jean Berlamont²

Abstract

The effect of bottom friction dissipation and of the different formulations used for this term on the wave evolution has been investigated in the Belgian coastal regions. Two eddy viscosity models for the bottom friction dissipation, the Madsen *et al.* (1988) model and Weber's (1991a) model have been implemented in the Cycle 4 version of the third generation WAM model (Günther *et al.*, 1992). The wave conditions for the area of the southern North Sea were hindcasted for the February 1993 storm. The results are compared with buoy data. It is found that the net effect of bottom friction dissipation on the significant wave height hindcast is quite big, in the order of 80% (of the wave height when the bottom friction dissipation is taken into account) along the Belgian coast. Different formulations for the bottom friction dissipation have a quite significant effect on wave evolution in storm conditions. The use of equivalent dissipation coefficients (Luo *et al.*, 1994) results in nearly identical wave hindcasts.

Introduction

Accurate knowledge of wave conditions in coastal areas is very important for the design of harbours or of coastal protection works. Very often these data are not available from measurements and one has to rely on wave models. For example, in Belgium, a wave prediction model is a very useful tool for the navigation of large sea vessels through the shallow entrance channels towards the harbours of Antwerp and Zeebrugge. In general, deep water wave hindcasts are fairly reliable. In shallower areas energy dissipation due to bottom friction can become

¹ Postdoctoral fellow, Proudman Oceanographic Lab., Birkenhead, UK.

² Professor, Lab. of Hydraulics, K.U.Leuven, de Croylaan 2, 3001 Heverlee, Belgium.

important. The Belgian coastal area is characterised by a sandy bottom and the bottom friction contributes significantly to the energy dissipation. A good representation of this source term is necessary.

In the last decades several different bottom friction dissipation formulations have been developed, including an empirical expression based on the JONSWAP experiment (Hasselmann *et al.*, 1973), two drag-law models (Hasselmann and Collins, 1968; Collins, 1972) and two eddy viscosity models (Madsen *et al.*, 1988; Weber, 1991a). These formulations have widely been used in many operational wave models. The effects of different bottom friction formulations on the energy balance were quantitatively investigated by Luo and Monbaliu (1994). They found that these formulations for the bottom friction source terms result in quite different growth curves for the total energy and the peak frequency for depth-limited wind generated waves. For a water depth of $15m$ and a wind friction velocity of $0.71m/s$ (the corresponding U_{10} equal to $16.5m/s$) a difference as big as 70% for the total energy was reported. Moreover, the required CPU time for different formulations is quite different. The empirical formulation is the simplest one and needs the least amount of computing time. The eddy viscosity model is the most complicated one, and costs the most computing time owing to the extra determination of the friction factor and the bottom friction velocity. Later on Luo *et al.* (1994) proposed the equivalent dissipation coefficients so that different bottom friction dissipation formulations produce the same or nearly the same levels for the total energy and the peak frequency for fetch-limited shallow water conditions.

In this study, the effect of different bottom friction dissipation models on wave evolution in the Belgian coastal regions is investigated. Three different models for the bottom friction dissipation, the empirical expression (Hasselmann *et al.*, 1973) and two eddy viscosity models (Madsen *et al.*, 1988; Weber, 1991a), have been implemented in the Cycle 4 version of the third generation WAM model (Günther *et al.*, 1992). Hindcasts are made for February 1993 in the Belgian coastal area as to study the effect of different bottom friction dissipation formulations on wave evolution and to test the validity of using equivalent coefficients for different formulations in operational circumstances. The results are compared with buoy data at different measurement stations.

THE WAVE MODEL

The wave model used for the present study is the Cycle 4 version of the WAM model (Günther *et al.*, 1992) with a choice for the bottom friction dissipation term. The WAM model is a third generation wave

model which solves the wave transport equation explicitly without any ad hoc assumption on the shape of the wave spectrum. It contains today's knowledge of the physics for the wave evolution of a two dimensional wave spectrum. The basic energy transport equation for a spherical latitude-longitude (ϕ, λ) co-ordinate system, in the absence of currents, can be expressed as,

$$\frac{\partial F}{\partial t} + \frac{1}{\cos\phi} \frac{\partial}{\partial\phi}(c_\phi \cos\phi F) + \frac{\partial}{\partial\lambda}(c_\lambda F) + \frac{\partial}{\partial\omega}(c_\omega F) + \frac{\partial}{\partial\theta}(c_\theta F) = S_{in} + S_{nl} + S_{ds} + S_{bf}$$

where F is the wave energy spectrum, t is the time, ϕ is the latitude, λ is the longitude, ω is the angular frequency, θ is the wave direction measured clockwise from the true north, c_ϕ , c_λ , c_ω and c_θ are the rate of change of the position and propagation direction of a wave packet travelling along a great circle path. The left hand side of the above equation represents the local rate of change of wave energy density, propagation along great circles, shifting of frequency due to time variation in depth (note that currents are not included in this study), and refraction. The right hand side represents all effects of generation and dissipation of the waves. They include wind input S_{in} , whitecapping dissipation S_{ds} , non-linear quadruplet wave-wave interactions S_{nl} and bottom friction dissipation S_{bf} . The detailed description of these source terms, except the bottom friction dissipation, can be found in Günther et al. (1992).

Models for bottom friction dissipation

The wave energy dissipation due to the bottom friction in the wave boundary layer equals the work done by the turbulent bottom stress on the free stream orbital bottom velocity. There are different models to parametrize the bottom stress. The ones implemented in this study is are an empirical expression, and some variations on the eddy viscosity model, which relates the bottom shear stress to the vertical gradient of the velocity through an eddy viscosity coefficient.

An empirical expression

The simplest form for the bottom friction dissipation was proposed by Hasselmann et al. (1973) who applied the Hasselmann and Collins (1968) theory to measure the decay of swell in the JONSWAP experiment (Hasselmann et al., 1973). It can be expressed as

$$S_{bf}(f, \theta) = -\frac{2c}{g} \frac{k}{\sinh 2kh} F(f, \theta)$$

with $S_{bf}(f, \theta)$ the bottom friction dissipation spectrum, c an empirical coefficient, g the acceleration of gravity, k the wave number, and h the

water depth. In the JONSWAP experiment, the empirical coefficient c was found to vary over two orders of magnitude, with a mean value for c of $0.038m^2s^3$. This empirical dissipation formulation with the mean value for c has been used in wave models by WAMDI (1988) and performed well.

Two eddy viscosity models

Based on the linearized form of the boundary layer equations and a simple eddy viscosity formulation of shear stress, Madsen *et al.* (1988) derived a formulation for bottom friction dissipation

$$S_{bf}(f, \theta) = -f_w u_{br} \frac{k}{\sinh 2kh} F(f, \theta)$$

with

$$u_{br}^2 = 2 \iint \frac{\omega^2}{\sinh^2 kh} F(f, \theta) df d\theta$$

where f_w is the friction factor, u_{br} is the representative near bottom velocity, and ω is the angular frequency. The friction factor f_w in the Madsen *et al.* model is a function of the bottom roughness height and parameters characterised by the wave conditions. It can be estimated using the formulation of Jonsson (1966):

$$\frac{1}{4\sqrt{f_w}} + \log_{10} \frac{1}{4\sqrt{f_w}} = m_f + \log_{10} \frac{a_{br}}{K_N}$$

where m_f is a constant. A value of -0.08 for m_f was determined experimentally by Jonsson and Carlsen (1976). The bottom roughness height K_N depends on the flow field and the sediment properties. The near-bottom excursion amplitude a_{br} is formulated as:

$$a_{br}^2 = 2 \iint \frac{1}{\sinh^2 kh} F(f, \theta) df d\theta$$

This dissipation formulation was implemented in a parametric windsea model for finite water depths by Graber and Madsen (1988), and in a third-generation model for wind waves in combined wave-current flow by Tolman (1991). Graber and Madsen (1988) incorporated the bottom dissipation using a tuned constant friction factor. Tolman (1991) reported that a constant bottom roughness height ranging between $2cm$ and $5cm$ produced a good agreement between numerical results and measurements for the nondimensional wave height and period.

With a one-layer eddy viscosity model, based on the random turbulent wave boundary layer and using perturbation theory, Weber (1991a) derived another eddy viscosity model, which results in a frequency-dependent representative bottom friction velocity.

$$S_{bf}(f, \theta) = -u_{a^*} (T_{\bar{k}}(\zeta_0) + \tilde{T}_{\bar{k}}(\zeta_0)) \frac{k}{\sinh 2kh} F(f, \theta)$$

where u_{a^*} is the wave boundary layer friction velocity and can be determined as a function of wave number, wave spectrum, bottom boundary layer thickness and bottom roughness height. $T_{\bar{k}}$ is a dimensionless function and $\tilde{T}_{\bar{k}}(\zeta_0)$ is its complex conjugate. When the bottom roughness height is given, the values for u_{a^*} , $T_{\bar{k}}$ and $\tilde{T}_{\bar{k}}(\zeta_0)$ can be worked out iteratively with an initial u_{a^*} .

This formulation was implemented in a regional third generation WAM model for the Texel storm hindcast case, and a value of $4cm$ for the bottom roughness height was selected according to the flow conditions in the southern North Sea (Weber, 1991b). Because of the better prediction of the significant wave height for that storm it was suggested that the eddy viscosity formulation with a bottom roughness height of $4cm$ is to be preferred upon the empirical JONSWAP expression with the mean value for c of $0.038 m^2 s^{-3}$.

In fact, the study of Luo and Monbaliu (1994) and Luo et al. (1994) showed that the bottom roughness height of $4cm$ in Weber's formulation is not equivalent to the mean value for c of $0.038 m^2 s^{-3}$ of the empirical JONSWAP expression in terms of the resulting total energy and peak frequency growth curve levels for an idealised fetch-limited shallow water case. In order to produce the same or nearly the same growth curves levels, a c value of $0.067 m^2 s^{-3}$ for the empirical JONSWAP formulation is equivalent to the bottom roughness height of $4cm$. A bottom roughness height of $0.69cm$ in the Weber model and a bottom roughness height of $0.35cm$ in the Madsen et al. model are equivalent to the mean value $0.038 m^2 s^{-3}$ for c of the empirical JONSWAP expression.

Model Area

The model implementation was made on two grids. In order to intercept swell generated far away, but which may travel to the Belgian coast, a coarse grid was used. A fine grid was used to cover the southern North Sea, including the Belgian coastal area, with a spatial resolution of $10km \times 10km$. This grid is nested in the coarse grid with a resolution of $50km \times 50km$ covering the whole North Sea from $48^\circ N$ to $70^\circ N$ latitude and $7^\circ W$ to $12^\circ E$ longitude. We used a stereographic projection for the grid description running the model with the Cartesian co-ordinate option. Fig. 1 shows the fine grid model bathymetry and also the indication of the two Belgian buoy stations: A2-buoy (A2B) and Westhinder (WEH). It is

clear that the water depths are quite limited and vary from less than 5m to about 47m in this area. The water depth at A2B is about 8m and at WEH it is about 25m.

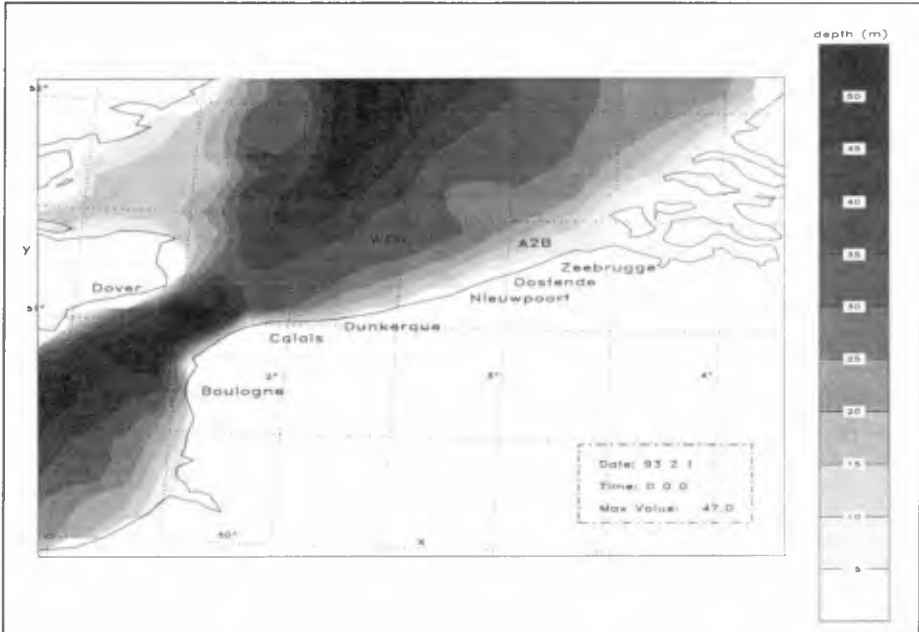


Fig. 1 The bathymetry of the southern North sea and locations of two Belgian buoy stations.

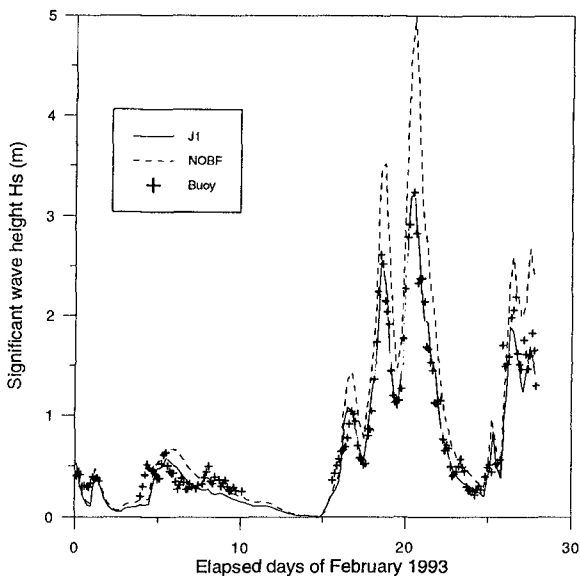
Hindcast Study

One month period running from the 1st to the 28th of February 1993 is hindcasted by the WAM model. From the 19 to the 21 February, there happened a strong storm in the southern North Sea. The model wind was provided by the United Kingdom Meteorological Office (UKMO) in GRIB (GRIdded Binary) and decoded by the Management Unit of the North Sea Mathematical Models (M.U.M.M.). These winds were compared with ERS-1 satellite data and with buoy data. The comparison showed that the wind forcing used to drive the wave model is of good quality (Ovidio *et al.*, 1994).

Effect of bottom friction dissipation

In order to see the effect of the net bottom friction dissipation on the wave evolution, this term was simply switched on and off in the model. Runs were carried out, and they are denoted by J1 when the empirical JONSWAP expression ($c=0.038m^2s^{-3}$) was used as bottom

friction formulation and by NOBF for cases when no bottom friction dissipation term was used. Figures 2 (a) and (b) show the hindcasted significant wave heights from the runs J1 and NOBF and the wave buoy measurements at A2B and WEH, respectively. The maximum net effect of the bottom friction dissipation on the hindcasted H_s values is in the order of 53% (of the wave height from the J1 run) at A2B and only 12% at WEH. (a)



(b)

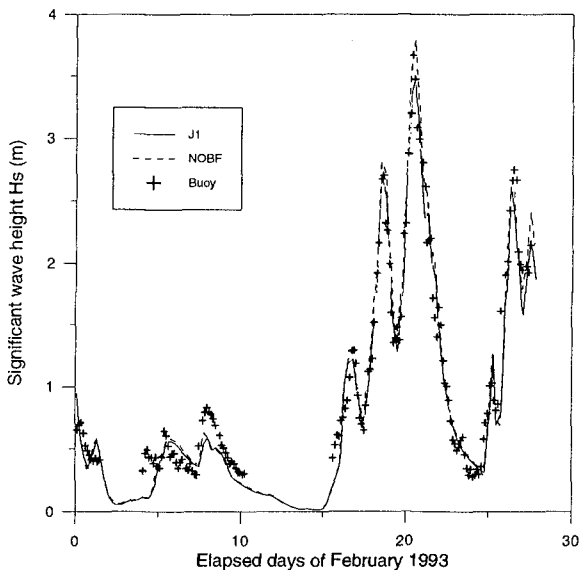


Fig. 2 Time series of the significant wave height from the runs J1 and NOBF and observations: (a) at A2 Buoy (A2B); (b) at Westhinder (WEH).

A2B is located in water with a depth of about $8m$, i.e. at a much shallower position than WEH where the water depth is about $25m$. At A2B, the model results agree very well with the observations when the bottom friction dissipation is included.

A global view of the net effect of the bottom friction dissipation on the significant wave height hindcast in the southern North Sea is displayed in Fig. 3 on February 21, 1993 at 12h GMT. Fig. 4 shows the prediction of the wave height from the run J1 (empirical formulation) to calculate the bottom friction dissipation in the model. It is clear that the bottom friction dissipation has to some extent an effect on the wave evolution in the whole southern North Sea. The effect is particularly strong in front of the Belgian and Dutch coast and in the south-east coastal area of the United Kingdom. Differences for the significant wave height prediction in the storm conditions can be as large as 80% (of the wave height from the J1 run) along the Belgian coast.

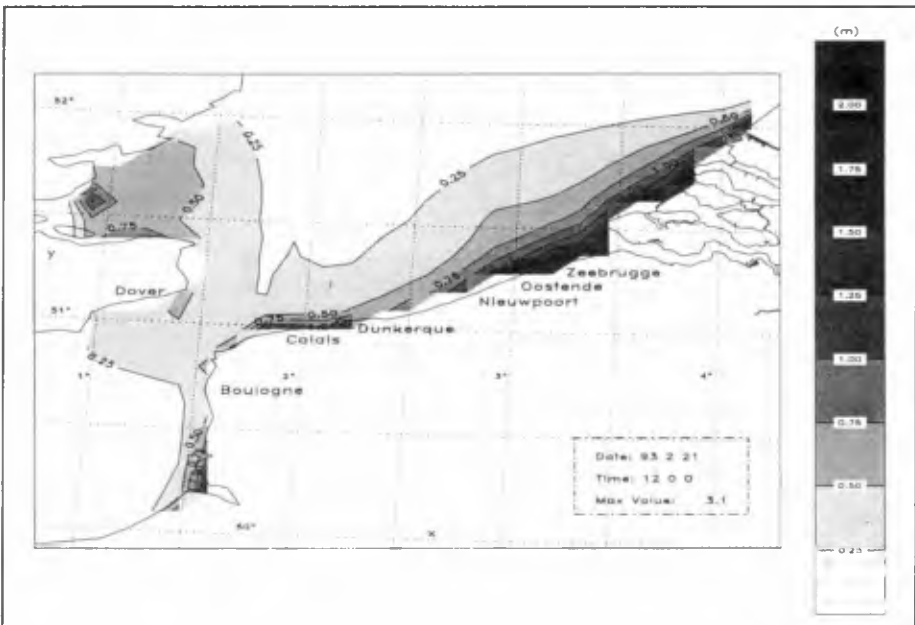


Fig. 3 The net effect of the bottom dissipation on the significant wave height hindcast at 12h GMT 21 February 1993

Effect of different formulations

Runs were also carried out with the two eddy viscosity models implemented for this study. They are denoted by M1 for the Madsen et al. (1988) model and W1 for Weber's model (1991a). The bottom roughness

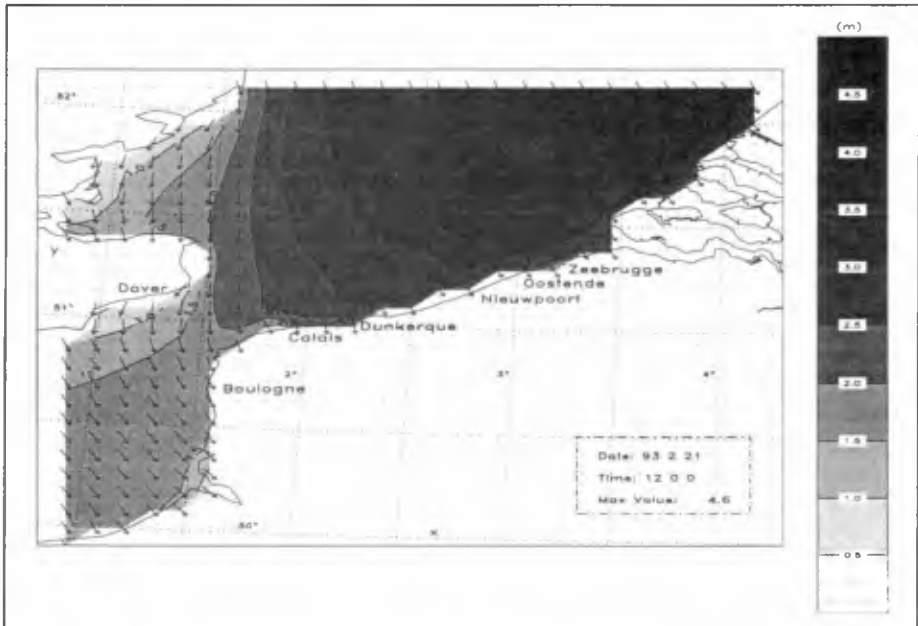


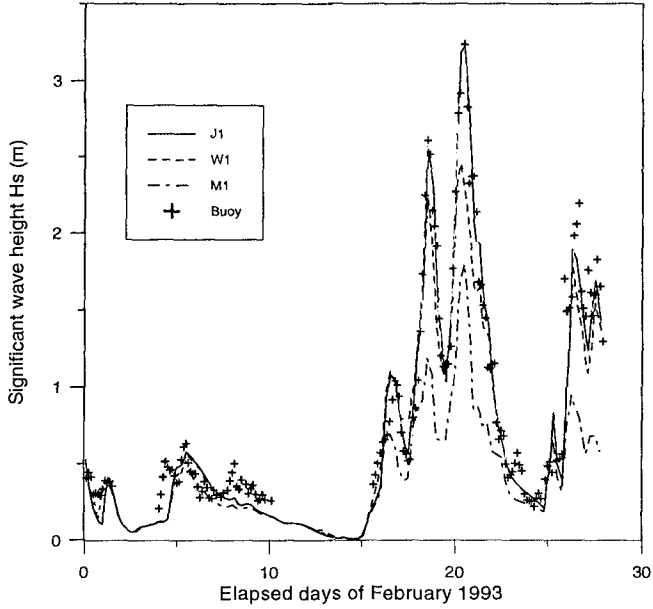
Fig. 4 The significant wave height predicted by the WAM Cycle 4 with the empirical formulation for bottom friction dissipation at 12h GMT 21 February 1993.

height in these two runs was kept the same as the original value ($K_n=4cm$) suggested by Weber (1991b) for the southern North sea areas. In Fig. 5 (a) and (b) the hindcasted results for the significant wave height from the runs J1, M1 and W1 are displayed with the measured data for stations A2B and WEH, respectively. The resultant effect on the hindcasted H_s values of using different bottom friction dissipation models with their original coefficients can be as big as 47% for station A2B and 15% for station WEH. The J1 run with the empirical formulation predicts significant wave height very close to the buoy measurement. The eddy viscosity model from Madsen et al. (1988, denoted by M1) underestimates the H_s value with about 1.5m (47% of the J1 H_s peak value in storm conditions) at A2B. The W1 run with Weber's (1991a,) model also underestimates the H_s with about 1.0m (30% of the J1 H_s peak value in storm conditions). Both eddy viscosity models with the bottom roughness height at 4cm predict too much bottom friction dissipation for this storm.

A global view at 12h GMT February 21, 1993 of the significant wave height difference between the run J1 with the empirical bottom friction dissipation formulation and the run M1 with the Madsen model is shown in Fig. 6. The maximum difference for the significant wave height

was found in front of the Belgian coast zone, in the order of $1.5m$ (about 47% of the significant wave height from the J1 run).

(a)



(b)

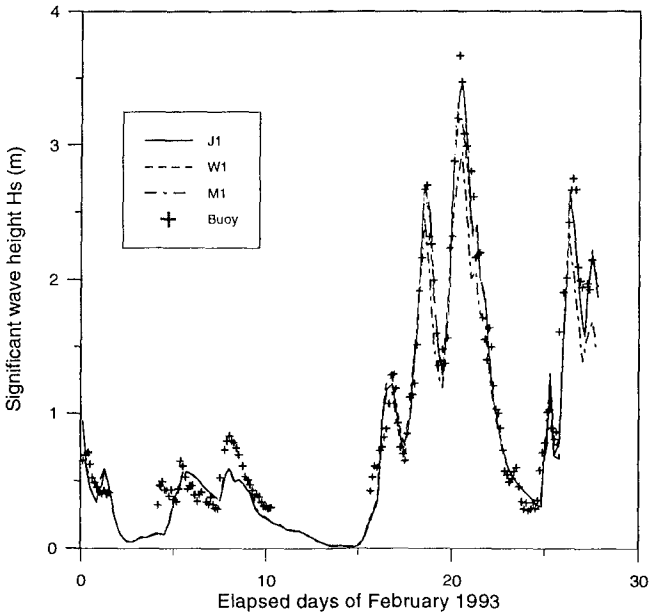


Fig. 5 Time series of significant wave height using three different bottom friction formulations for February 1993: (a) A2B; (b) WEH.

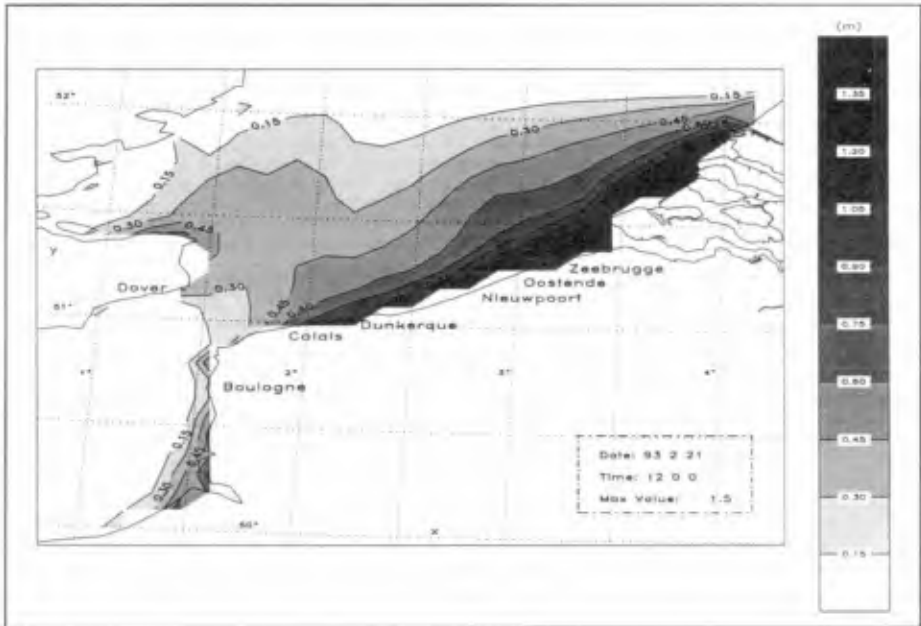


Fig. 6 The significant wave height difference between J1 and m1 runs at 12h GMT 21 February 1993.

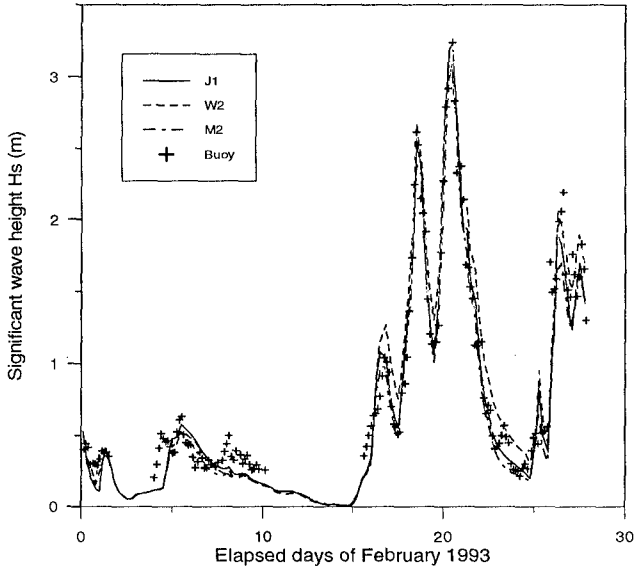
Test of Equivalent Coefficients

As we discussed in the introduction, the study of Luo *et al.* (1994) proposed to use equivalent dissipation coefficients for different models of bottom friction dissipation in order to produce the same or nearly the same fetch-limited growth curves levels. For example, a bottom roughness height of 0.69cm in the Weber model and a bottom roughness height of 0.35cm in the Madsen *et al.* model are equivalent to the mean value of c of $0.038\text{ m}^2\text{s}^{-3}$ in the empirical JONSWAP expression. The questioned remained whether these so-called equivalent dissipation coefficients are still valid for the real circumstances. These equivalent coefficients were tested for the February 1993 storm. Different model runs were carried out with the equivalent coefficients, denoted by M2 for the Madsen model with a bottom roughness height of 0.35cm , and W2 for Weber's model with a bottom roughness height of 0.69cm .

Figures 7 (a) and (b) show time series of the significant wave height for the runs J1, M2 and W2 for the stations A2B and WEH, respectively. The obtained H_s values from the different bottom friction dissipation models with equivalent coefficients are nearly identical, and very close to the wave observations. A global view of the significant wave height difference at 12h GMT 21st of February 1993 between the

empirical formulation and the eddy viscosity Madsen et al. model but using equivalent dissipation coefficients is presented in Fig. 8. Compared with Fig. 6, it is found that the wave height difference resulting from

(a)



(b)

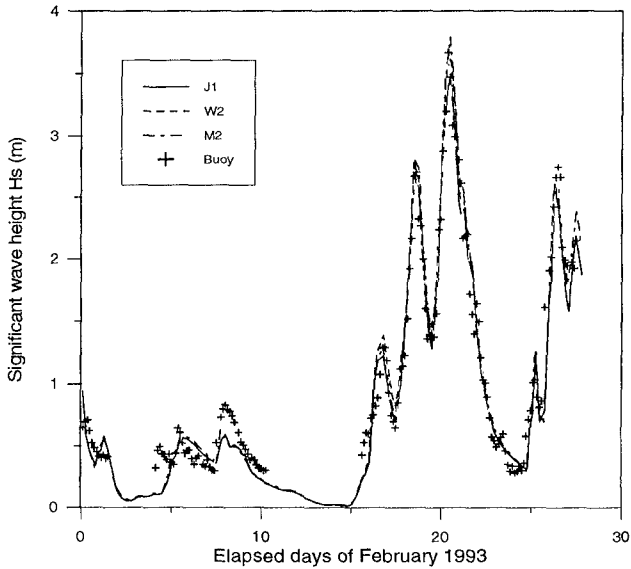


Fig. 7 Time series of significant wave height from three different bottom friction formulations with the equivalent dissipation coefficients for the February 1993: (a) A2B; (b) WEH.

different bottom friction formulations has been dramatically reduced (from more than $1.5m$ to only $0.2m$) along the Belgian coast .

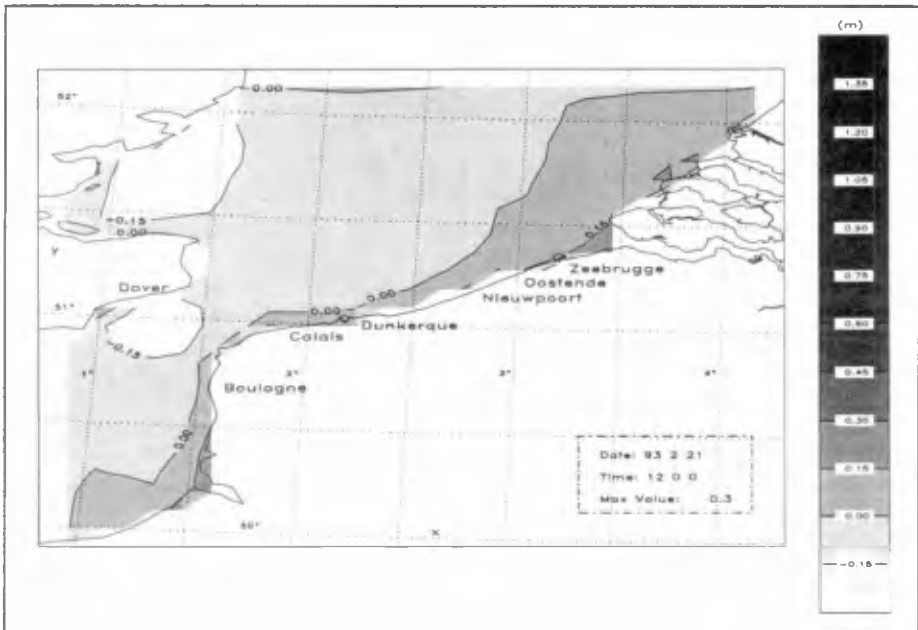


Fig. 8 The significant wave height difference between J1 and M2 runs at 12h GMT 21 February 1993.

Conclusions

A wave hindcast in the Belgian coastal region was made by using the 3G WAM Cycle 4 with three different bottom dissipation models. The results were intercompared and also compared to buoy data. It is found that the net effect of bottom friction dissipation on the significant wave height hindcast is quite big, in the order of 80% along the Belgian coast. The hindcasted wave conditions are sensitive to the use (including the choice of coefficient) of the bottom friction dissipation model, specially in storm conditions. The use of equivalent dissipation coefficients results in the same or nearly the same effect on the wave evolution and improves wave hindcast results.

Acknowledgement

This work is partly supported by the Human Capital Mobility Program of the European Commission (contract No ERB CHB GC7 920230) and by the MAST III Program: PROMISE (contract No MAS3 CT 950025). We thank the *Afdeling Waterwegen Kust* for providing the buoy data.

References

- Collins J.I. (1972), Prediction of shallow water spectra, *J. Geophys. Res.*, **93** (C1), 491-508.
- Günther, H., S. Hasselmann and P.A.E.M. Janssen (1992), The WAM model Cycle 4, Report No. 4, Hamburg.
- Graber, H.C. and O.S. Madsen (1988), A finite-depth wind wave model, Part 1: Model description, *J. Phys. Oceanogr.*, **18**, 1465-1483.
- Hasselmann, K. and J.I. Collins (1968), Spectral dissipation of finite depth gravity waves due to turbulent bottom friction, *J. Mar. Res.*, **26**, 1-12.
- Hasselmann, K., T.P. Barnett, E. Bouws, H. Carlson, D.E. Cartwright, K. Enke, J.I. Ewing, H. Gienapp, D.E. Hasselmann, P. Kruseman, A. Meerbrug, P. Müller, D.J. Olbers, K. Richter, W. Sell and H. Walden (1973), Measurements of wind-wave growth and swell decay during the Joint North Sea Wave Project (JONSWAP), *Dtsch. Hydrogr. Z.*, **A8**, 95p.
- Jonssen, I.G. and N.A. Carlsen (1976), Experimental and theoretical investigations in an oscillatory turbulent boundary layer, *J. Hydr. Res.*, **14**, 45-60.
- Komen, G.J., L. Cavaleri, M. Donelan, K. Hasselmann, S. Hasselmann, P.A.E.M. Janssen (1994), Dynamics and Modelling of Ocean Waves, Cambridge University Press, Cambridge, 532p.
- Luo, W. and J. Monbaliu (1994), Effects of bottom friction dissipation formulation on the energy balance for gravity waves in shallow water, *J. Geophys. Res.*, **99** (C9), 18,501-18,511.
- Luo, W., J. Monbaliu and J. Berlamont (1994), Equivalent dissipation coefficients for different bottom friction dissipation models in depth limited wind generated waves, Proc. of int. Symp. Waves - Phys. and Num. Modelling, Canada, 743-752.
- Madsen O. S., Y.-K. Poon and H.C. Graber (1988b), Spectral wave attenuation by bottom friction: theory, Proc. 21st Int. Conf. Coastal Eng., Malaga, 492-504.
- Ovidio, F., J.-R. Bidlot and D. Van den Eynde (1994), Validation and improvement of the quality of the operational wave model mu-WAVE by the use of ERS-1 satellite data, Report M.U.M.M./T3/AR02, 87p, Gulledele 100, B-1200 Brussels, Belgium
- Tolman, H.L. (1991), Effects of tides and storm surges on North Sea wind waves, *J. Phys. Oceanogr.*, **21**, 766-781
- WAMDI Group (1988), The WAM model - a third generation ocean wave prediction model, *J. Phys. Oceanogr.*, **18**, 1775-1810.
- Weber, S.L. (1991a), Eddy viscosity and drag law models for random ocean wave dissipation, *J. Fluid Mech.*, **232**, 73-98.
- Weber, S.L. (1991b), Bottom friction for wind sea and swell in extreme depth limited situations, *J. Phys. Oceanogr.*, **21**, 149-172.

CHAPTER 67

Weakly non-Gaussian model of wave height distribution for nonlinear random waves

Nobuhito MORI * and Takashi YASUDA †

ABSTRACT

The wave height distribution with Edgeworth's form of a cumulative expansion of probability density function(PDF) of surface elevation are investigated. The results show that a non-Gaussian model of wave height distribution reasonably agrees with experimental data. It is discussed that the fourth order moment(kurtosis) of water surface elevation corresponds to the first order nonlinear correction of wave heights and is related with wave grouping.

INTRODUCTION

Wave height statistics(*e.g.* wave height distribution, run length and etc) of random waves play important roles in designing coastal and ocean structures. The Rayleigh distribution is regarded as the distribution of wave heights in stochastic processes with a linear and narrow banded spectrum. Over a few decades, a considerable number of studies have been made on the validity of the Rayleigh distribution. It is commonly known that large wave heights in field do not necessarily obey the Rayleigh distribution. For example, Haring(1976) shows that large wave heights observed in storms are on the order of 10 percent less than those predicted by the Rayleigh distribution. After that, Forristall(1984), and Myrhaug and Kjeldsen(1987) also reported that occurrence probabilities of large wave heights in field are smaller than the predicted value of the Rayleigh distribution.

On the contrary, Yasuda *et al.*(1992,1994) numerically investigated that the third order nonlinear interactions have significant effects on the statistical

*Hydraulics Dept., Abiko Research Laboratory, Central Research Institute of Electric Power Industry(CRIEPI), Abiko 1646, Chiba 270-11, JAPAN (mori@criepi.denken.or.jp)

†Dept. of Civil Eng., Gifu University, Yanagido 1-1, Gifu 501-11, JAPAN
(coyasuda@cc.gifu-u.ac.jp)

properties of random wave train. That is, the third order nonlinear solution in deep water increases the occurrence probabilities of large wave heights more than the linear and second order one do. Stansburg(1993) also found the same results in his experimental work. However, there is no theoretical distribution which agrees with the data, although many studies have attempted to establish the wave height distribution without a linear or narrow banded spectrum assumption.

The Rayleigh distribution is put to practical use under the assumption that water surface elevations are regarded as independent stochastic processes, since the nonlinear wave-wave interactions are weak in deep water. Thus, the probability density function of the surface elevation had been assumed to be the Gaussian on the basis of the central-limit theorem. For the statistical point of view, the fourth order moment of the surface elevation is directly related to the third order nonlinear interaction(Longuet-Higgins 1963). It is therefore necessary to include the effects of the fourth order moment of the surface elevation for the wave height distribution to consider the influences of the third order nonlinear interaction.

In this study, a wave height theory is extended for a weakly nonlinear random waves with cumulative expansion of surface elevation including the fourth order moment and then its validity is checked with experimental data.

PDF OF WAVE HEIGHTS

Probability density function of surface elevation

According to statistical theory, the probability density function(PDF) $p^{(l)}(x)dx$ of the l -independent variables x_i $\{i \in Z\}$ (subscript i is dropped hereafter for simplicity) can be described as

$$p^{(l)}(x)dx = \sum_{r=0}^{\infty} c_r H_r(x) G(x) dx, \quad (r \in Z) \quad (1)$$

$$G(x) = \frac{1}{\sqrt{2\pi}} \exp\left(-\frac{x^2}{2}\right), \quad (2)$$

where $H_r(x)$ is the Chebyshev-Hermite polynomial, $G(x)$ the Gaussian and c_r the r th order coefficient of the Gram-Charlier expansion. The convergence of the Gram-Charlier expansion is not monotonic with the order r (e.g. $c_4=O(l^{-1})$, $c_5=O(l^{-3/2})$), although the convergence of the r th order cumulant $\kappa_r^{(l)}$ is independent of l . We hence choose the Edgeworth asymptotic expansion to describe the PDF of surface elevation.

Introducing the characteristic function and collecting the terms for l , the Edgeworth expansion of type A is formally given by (e.g. Kendall and Stuart

1963)

$$p^{(l)}(x)dx = G(x) \left\{ 1 + \frac{1}{\sqrt{l}} \frac{\kappa_3}{6} H_3(x) + \frac{1}{l} \left[\frac{\kappa_4}{24} H_4(x) + \frac{\kappa_3^2}{72} H_6(x) \right] + \frac{1}{l\sqrt{l}} \left[\frac{\kappa_5}{120} H_5(x) + \frac{\kappa_3 \kappa_4}{144} H_7(x) \right] + \dots \right\} dx, \tag{3}$$

where κ_r is the r th order cumulant. The r th order cumulant has the relationship to the r th order moment μ_r :

$$\left. \begin{aligned} \kappa_1 &= 0 \\ \kappa_2 &= 1 \\ \kappa_3 &= \mu_3 \\ \kappa_4 &= \mu_4 - 3 \\ \kappa_5 &= \mu_5 - 10\mu_3 \\ \kappa_6 &= \mu_6 - 15\mu_4 - 10\mu_3^2 + 30 \\ \kappa_7 &= \mu_7 - 21\mu_2\mu_5 - 35\mu_3\mu_4 + 210\mu_2^2\mu_3 \end{aligned} \right\}. \tag{4}$$

We set the mean value μ_1 so as equal to zero and normalize all the variables by the standard deviation. Therefore, μ_3 is skewness and μ_4 is kurtosis. Each component within the bracket $[\cdot]$ of eq.(3) has monotonic convergence for l (the typical notation for l is dropped hereafter for simplicity).

It must be noted that an asymptotic expansion does not have monotonic convergence for higher order corrections, although it sometimes gives good agreement for a first few terms. Moreover, higher order moments and cumulants are influenced by sampling frequencies of data. We, therefore, use first three terms of eq.(3) to describe the PDF of the surface elevation. The influences of truncation of eq.(3) are already discussed in detail by Mori(1996). We truncate here higher than $1/l\sqrt{l}$ terms of eq.(3) following Mori(1996). This truncation gives the following relationship to the moments

$$\kappa_5 = \mu_5 - 10\mu_3 = 0, \tag{5}$$

$$\kappa_6 = \mu_6 - 15\mu_4 + 30 = 0. \tag{6}$$

The validity of these assumptions will be examined in next section.

Distribution of wave height

We assume that waves to be analyzed here are unidirectional with narrow banded spectrum and satisfy the stationarity and ergodic hypothesis. The surface elevation hence can be evaluated by the characteristic frequency $\bar{\omega}$:

$$I_c(t) = \sum_{n=1}^{\infty} a_n \cos[(\omega_n - \bar{\omega})t + \varepsilon_n] \tag{7a}$$

$$I_s(t) = \sum_{n=1}^{\infty} a_n \sin[(\omega_n - \bar{\omega})t + \varepsilon_n] \tag{7b}$$

where a_n is the amplitude of the n th mode, ω_n the angular frequency and ε_n the phase function. If ε_n is distributed uniformly and is a temporally independent variables, eq.(7) give a linear random wave field. The surface elevation $\eta(t)$ is rewritten into the amplitude of wave envelope $R(t)$ and phase angle $\theta(t)$ with I_c and I_s :

$$\eta(t) = R(t) \cos[\bar{\omega}t + \theta(t)] \quad (8a)$$

$$R(t) = \sqrt{I_c^2 + I_s^2} \quad (8b)$$

$$\theta(t) = \tan^{-1} \left[\frac{I_s(t)}{I_c(t)} \right] \quad (8c)$$

Under the assumption that the PDF of I_c and I_s are described by eq.(3) up to $1/l$ terms, I_c and I_s are independent statistical variables. Integration of $\theta(t)$ over the range from 0 to 2π results in the following PDF of wave amplitude

$$p(R) dR = \frac{1}{2\pi} \exp \left(-\frac{R^2}{2} \right) \left[1 + \sum_{i,j} \alpha_{i,j} A_{i,j}(R) \right] dR, \quad (9)$$

where $\sum_{i,j}$ is a special double summation for $i, j (i=4,6 \text{ and } j=i/2)$, $A_{i,j}(R)$ is polynomial for R (see Appendix) and $\alpha_{i,j}$ is the coefficient with μ_3 and μ_4 :

$$\left. \begin{aligned} \alpha_{4,1} &= \frac{1}{2^5}(\mu_4 - 3) \\ \alpha_{4,2} &= \frac{1}{2^{13} \times 3}(\mu_4 - 3)^2 \\ \alpha_{6,1} &= \frac{5}{2^6 \times 3^2} \mu_3^2 \\ \alpha_{6,2} &= \frac{1}{2^{13} \times 3^2} \mu_3^2 (\mu_4 - 3) \\ \alpha_{6,3} &= \frac{5}{2^{16} \times 3^4} \mu_3^4 \end{aligned} \right\} \quad (10)$$

The assumption that I_c and I_s are mutually independent is inadequate for strong nonlinear waves ($\mu_3 \geq 0.30$, see Mori 1996), but we should keep this assumption in this study.

By assuming a narrow banded spectrum for a wave field, a wave height H is regarded by two times of its amplitude A ($H=2A$). This assumption is inadequate when the vertical asymmetry of surface profile is not negligible (*i.e.* $\mu_3 \rightarrow$ large). Therefore, eq.(10) is valid for a weakly narrow banded process ($\mu_3 \ll 1$).

The assumptions of a weakly nonlinear and narrow banded spectrum give the wave height distribution as

$$p(H) dH = \frac{H}{4} \exp \left(-\frac{H^2}{8} \right) \left[1 + \sum_{i,j} \beta_{i,j} B_{i,j}(H) \right] dH, \quad (11)$$

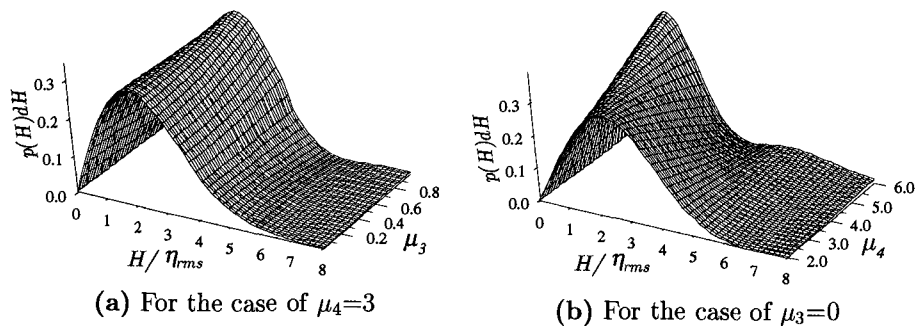


Figure 1 The variation of PDF of wave heights for the fixed value of μ_3 and μ_4 .

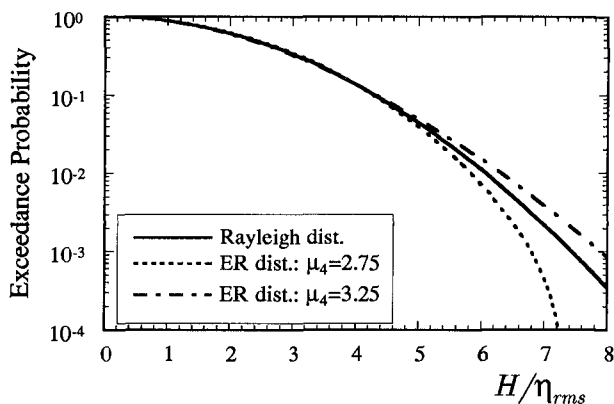


Figure 2 The exceedance probability of wave heights for $\mu_4=2.75$ and 3.25 with $\mu_3=0$.

where,

$$\left. \begin{aligned}
 \beta_{41} &= \frac{1}{2^9} (\mu_4 - 3) \\
 \beta_{42} &= \frac{1}{3 \times 2^{21}} (\mu_4 - 3)^2 \\
 \beta_{61} &= \frac{5}{2^{12} \times 3^2} \mu_3^2 \\
 \beta_{62} &= \frac{1}{2^{23} \times 3^2} \mu_3^2 (\mu_4 - 3) \\
 \beta_{63} &= \frac{5}{2^{28} \times 3^4} \mu_3^4
 \end{aligned} \right\}, \tag{12}$$

and $B_{i,j}(H)$ is polynomial for H (see Appendix).

The exceedance probability of wave heights is given by integrating eq.(11)

Table 1 Wave statistics of typical two cases.

Case	m	$k_p a_{1/3}$ at P1	breaking ratio
1	10	0.10	0%
2	10	0.20	10%

between $[H, \infty)$ as

$$P(H) = \exp\left(-\frac{H^2}{8}\right) \left[1 + \sum_{i,j} \beta_{i,j} E_{i,j}(H)\right], \quad (13)$$

where $E_{i,j}(H)$ is polynomial for H (see Appendix).

The first point to be noticed is that the additional terms within brackets $[\cdot]$ in eqs.(9), (11) and (13), which are related to non-Gaussian properties of the PDF of surface elevation, are equal to zero when $\mu_3=0$ and $\mu_4=3$ (*i.e.* Gaussian). Therefore eqs.(9) and (11) with $\mu_3=0$ and $\mu_4=3$ are the same the Rayleigh distribution. We shall, hence, call with distribution of this type as the Edgeworth-Rayleigh distribution. The second important point to be noted is that the first order correction to the wave amplitudes or wave heights is kurtosis ($\alpha_{4,j}$ or $\beta_{4,j}$).

Figure 1 show the variation of the PDF of the wave heights on the values of μ_3 and μ_4 . For the case of $\mu_4=3$ case, Fig.1(a), the shape of the PDF of the wave heights is not varied as increasing the value of μ_3 . However, Fig.1(b) shows that the peak of the PDF is shifted to gently as increasing of μ_4 , because μ_4 is the first order correction of the wave height distribution. Figure 2 shows the exceedance probability of the wave heights for the case of $\mu_4=2.75$ and 3.25 with $\mu_3=0$. The occurrence probability of the larger wave heights exceeds that of the Rayleigh distribution is increased when the value of μ_4 is larger than 3. We can summarize that the value of kurtosis is dominated parameter for the PDF of wave heights.

RESULTS

The laboratory experiment was conducted in the glass channel and is 65m long, 1m wide, 2m high and was filled to a depth of about 1.0m. Waves were generated by a computer-controlled piston type wave paddle. Water surface displacements were measured with twelve capacitance type wave gages. The measurements with a sampling frequency of 32Hz were performed for over 330s. No corrections were applied for filter response of the wire.

The initial spectra were given using the Wallops type spectra with band widths of $m=5, 10, 30, 60$ and 100 , and peak frequency of $f_p=1$ Hz which gives a spectral peak wavenumber $k_p=4.072\text{m}^{-1}$ and a characteristic water depth of

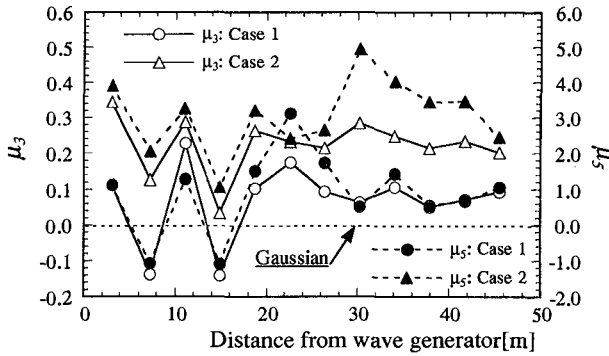
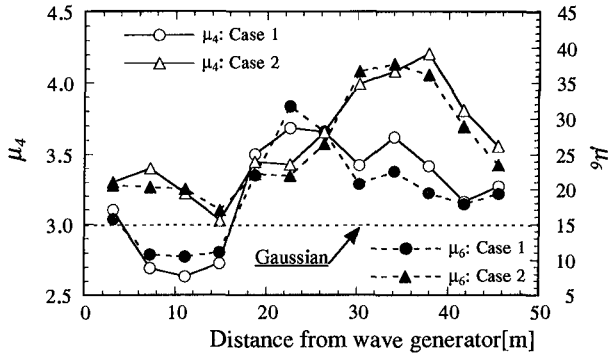
(a) Spatial variation of μ_3 and μ_5 (b) Spatial variation of μ_4 and μ_6

Figure 3 The spatial variations of the higher order moments of surface elevations of the case 1 and 2.

$k_p h = 3.99$, so that the waves were deep water waves. Here, h is the water depth. The number of waves were about 350-450. The maximum frequency of generated waves were 2Hz. Therefore, higher frequency components of generated waves were generated by nonlinear interaction. Initial phases of the waves were given by uniformly distributed random numbers. The initial characteristic wave steepnesses $k_p a_{1/3}$ were set about 0.1 to 0.25. Here, $a_{1/3}$ is a half of the significant wave height. Breaking waves were observed for higher waves with the steepness that the value of $k_p a_{1/3}$ is larger than 0.13. For example, the visually observed breaking ratio is about 10% for waves with the initial steepness of $k_p a_{1/3} = 0.20$ and 20% for 0.14. Consequently, waves of 24 cases were generated under the combination of the spectrum bandwidth parameter m and the wave steepness.

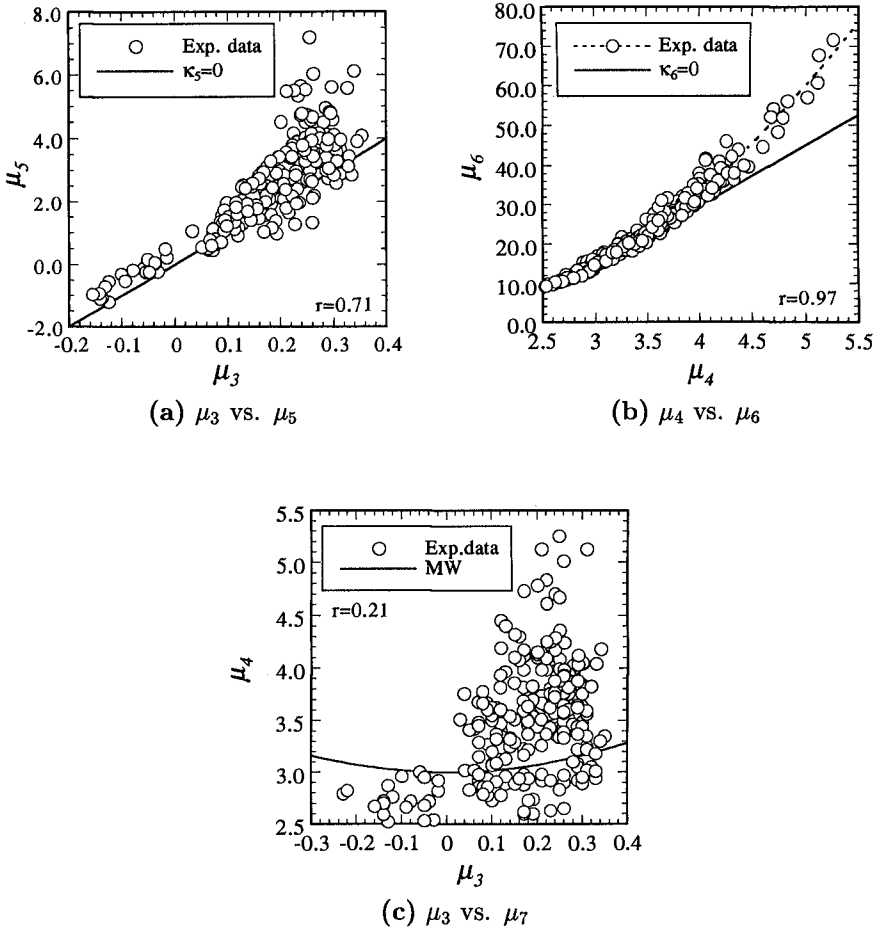


Figure 4 Relationships among the higher order moments, μ_3 , μ_4 , μ_5 , μ_6 and μ_7 .

Typical measured two cases are shown in Table 1 for breaking and non-breaking cases. The spatial variations of higher order moments for case 1 and 2 are shown in Fig.3. These show that the higher order moments are fluctuated until the location 20m distant from the wave generator(that is about 13 wave lengths of peak frequency). There are marked increase in the moments more than 20m away from the wave generator. All of the higher order moments are not equal to the Gaussian, more and less. The odd order moments μ_3 and μ_5 seem to level out 20m away from wave generator, although the even order moments μ_4 and μ_6 are still increased. The higher order moments are generally influenced

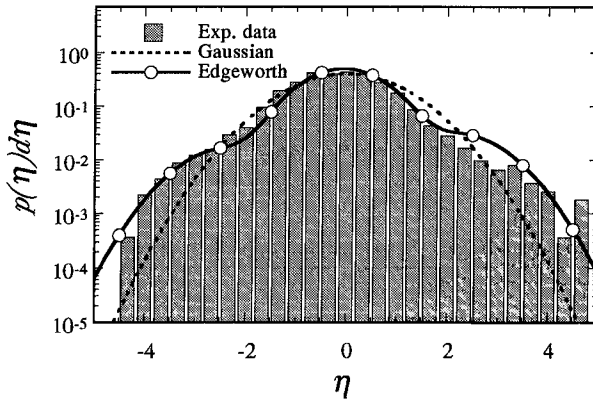


Figure 5 PDF of the surface elevation of experimental data of case 1 at location 8.

by the sampling frequency, but these trends do not depend on the sampling of data in our experiments. In addition, the spatial variations of μ_5 and μ_6 are similar to those of μ_3 and μ_4 , respectively. These indicates the non-Gaussian properties of surface elevations.

The experimental data show that the higher order moments are not constant. It should be examined the relationship between the higher order moments. The $(n+2)$ th order cumulant is related to the n th order cumulant at the lowest order correction. Hence, the higher order cumulants than the 5th one are assumed zero to formulate the Edgeworth-Rayleigh distribution:

$$\begin{aligned} \kappa_5 &= \mu_5 - 10\mu_3 = 0 \\ \kappa_6 &= \mu_6 - 15\mu_4 + 30 = 0 \end{aligned}$$

In order to check the validity of these assumptions, the relationships between μ_3 and μ_5 , μ_4 and μ_6 , and μ_3 and μ_4 are examined, respectively and are shown in Fig.4. Circles denote experimental data and solid lines in Fig.4(a) and Fig.4(b) are given by the eq.(5) and eq.(6), respectively. The correlation coefficient between μ_5 and μ_3 is 0.71, and therefore μ_5 could be regarded as a linear dependent variable on μ_3 . μ_6 is also strongly related with μ_4 (the correlation coefficient is 0.97). The experimental data show quite good agreement with eq.(6) in which the value of μ_4 is less than 4. Marthinsen and Winterstein(1992) derived the relationship between μ_3 and μ_4 from the second order kernel functions:

$$\mu_4 = 3 + \left(\frac{4}{3}\mu_3\right)^2 \tag{14}$$

The solid line in Fig.4(c) indicates eq.(14). However, there is no obvious relation between μ_3 and μ_4 from the data(the correlation coefficient is 0.21). Conse-

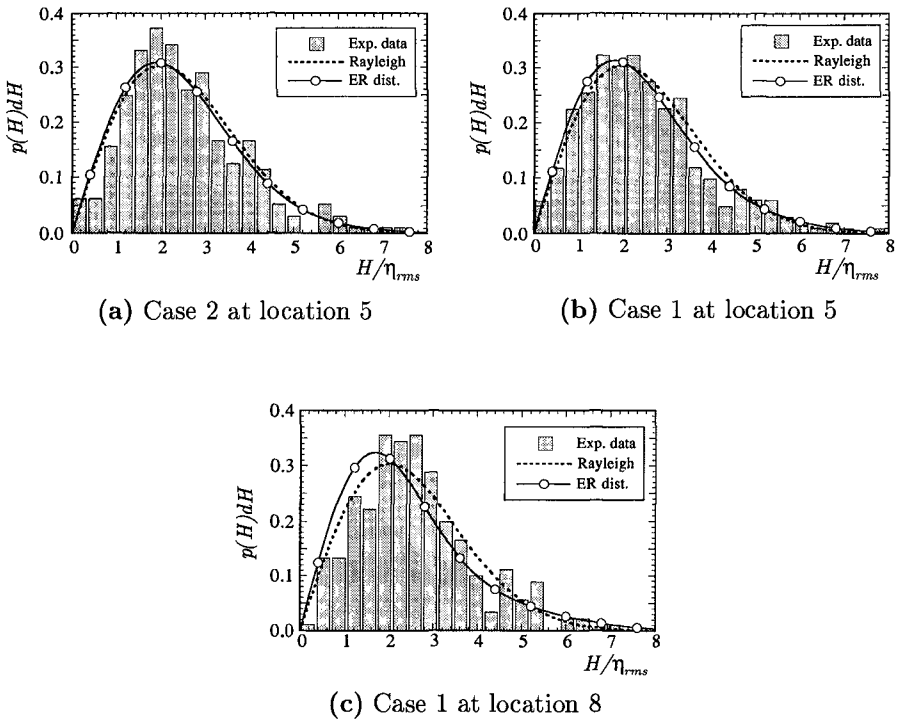
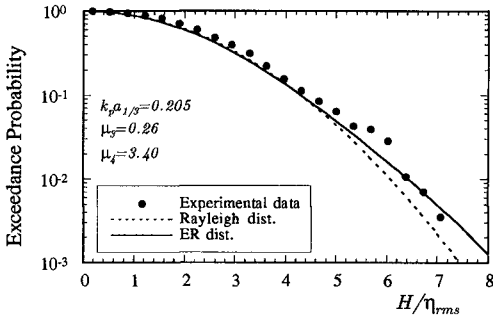


Figure 6 The PDF of wave heights at several locations.

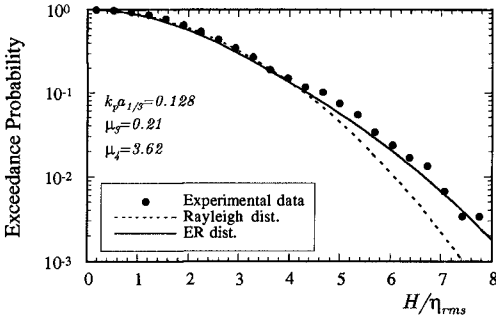
quently, it follows from what has been said that the 5th and 6th order cumulants can be regarded as zero (*i.e.* eqs.(5) and (6) are valid), if the value of μ_3 is smaller than 0.3 and μ_4 is smaller than 4. And the value of μ_4 is independent on μ_3 .

The PDF of surface elevation of case 1 at location 8 is shown in Fig.5. The histogram is experimental data, dotted line is the Gaussian and solid line with circle is eq.(3) up to $1/l$ terms. The Edgeworth expansion shows agreement with experimental data in comparison with the Gaussian.

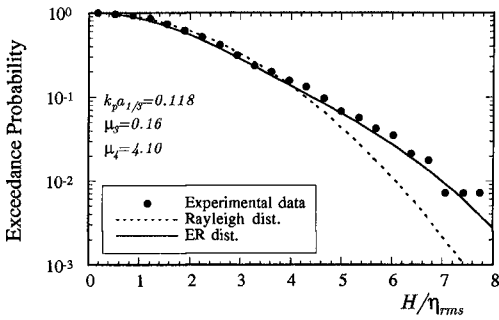
The PDF and exceedance probability of wave heights are shown in Figs.6 and 7, respectively. The histogram and filled circles \bullet denotes experimental data, dotted line the Rayleigh distribution and solid line the Edgeworth-Rayleigh distribution. There are no significant difference between the Rayleigh and the Edgeworth-Rayleigh distribution for the PDF of wave heights. However, the Edgeworth-Rayleigh distribution for the exceedance probability of wave heights show good agreement with the experimental data in comparison with the



(a) Case 2 at location 5



(b) Case 1 at location 5



(c) Case 1 at location 8

Figure 7 The exceedance probability of wave heights at several cases and locations.

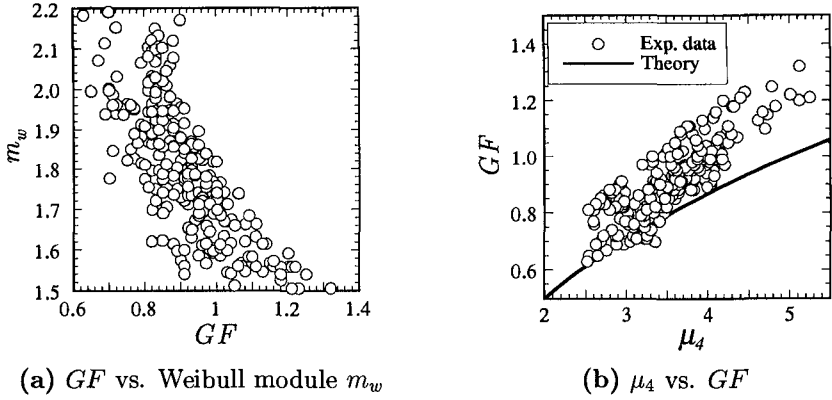


Figure 8 Relationships between μ_4 , GF and the Weibull modulus m_w , and GF and μ_4 .

Rayleigh distribution. The number of waves decrease as wave heights getting larger, so the number of waves are quite few in the range $H/\eta_{rms} \geq 5$ in Fig.7. The Edgeworth-Rayleigh distribution agrees with the experimental data, even if the number of waves are not so many. Moreover, the Edgeworth-Rayleigh distribution agrees with the experimental data for larger value of μ_4 ($\mu_4 \geq 4$), such as Fig.7(c).

RELATIONSHIP BETWEEN WAVE HEIGHT AND WAVE GROUPING

Before move to conclusion, it should be added that the relationship between the PDF of wave heights and wave grouping. Mase(1989) investigated an empirical relationship between the groupiness factor(GF) and the PDF of wave height with the Weibull modulus m_w of single parameter of the Weibull distribution.

GF is defined as

$$GF = \sqrt{\frac{1}{T_0} \int_0^{T_0} [E(t) - \bar{E}]^2 dt / \bar{E}}, \tag{15}$$

$$E(t) = \int_{-T_p}^{T_p} \eta^2(t + \tau)(1 - |\tau|/T_p)d\tau, \tag{16}$$

where $E(t)$ is SIWEH, \bar{E} a mean value of $E(t)$, T_0 an observation period and T_p the spectral peak period. If we substitute the delta function $\delta(t - \tau)$ into the numerical trigonometric filter $1 - |\tau|/T_p$ of eq.(16), we obtain the following simple relation

$$GF' = \sqrt{\mu_4 - 1}. \tag{17}$$

This means that if we do not use the numerical filter to calculate GF , there is a direct relation between GF and kurtosis μ_4 . We already know that kurtosis μ_4 is the parameter which controls the wave height distribution. That is, both the parameters the Weibull modulus and μ_4 govern the wave height distribution. Therefore, there is an obvious relation between kurtosis and GF . That is the reason why the Weibull modulus m_w governing the wave height distribution depends on GF . The relationship between GF and the Weibull modulus, and GF and μ_4 are shown in Fig.8. These relations can be summarized as

$$GF \sim \mu_4 \sim m_w. \quad (18)$$

The relationship between the Weibull modulus and GF has not a physical meaning so that we suggest to use kurtosis instead of GF to represent the wave grouping. Moreover, GF suffers from the influence of the numerical filter to obtain SIWEH. Therefore, the value of GF is influenced by two characteristics of random waves as a shape of wave height distribution and a spectrum band width. In other words, GF is insufficient as the fundamental statistical parameter to represent properties of the random wave.

CONCLUSION

A weakly non-Gaussian model of wave height distribution referred here as to the Edgeworth-Rayleigh distribution is suggested for waves with narrow banded spectra. It is found that the first order correction of the wave height distribution is equal to the fourth order moment of the surface elevation. It is also made clear that the occurrence probability of larger wave heights increases with the increasing of the value of kurtosis. The experimental data show good agreement with the Edgeworth-Rayleigh distribution within $\mu_3 \ll 1$ and $\mu_4 \leq 4$.

ACKNOWLEDGMENT

The authors are grateful to Dr. Tada at Technical Research & Development Institute of Nishimatsu Construction Co., Ltd. for his cooperation.

APPENDIX

$$\left. \begin{aligned} A_{4,1}(R) &= R^4 - 8R^2 + 8 \\ A_{4,2}(R) &= R^8 - 32R^6 + 288R^4 - 768R^2 + 384 \\ A_{6,1}(R) &= R^6 - 18R^4 + 72R^2 - 48 \\ A_{6,2}(R) &= R^{10} - 50R^8 + 800R^6 - 4800R^4 + 9600R^2 - 3840 \\ A_{6,3}(R) &= R^{12} - 72R^{10} + 1800R^8 - 19200R^6 + 86400R^4 \\ &\quad - 138240R^2 + 46080 \end{aligned} \right\} \quad (19)$$

$$\left. \begin{aligned}
 B_{4,1}(H) &= H^4 - 32H^2 + 128 \\
 B_{4,2}(H) &= H^8 - 128H^6 + 4608H^4 - 49152H^2 + 98304 \\
 B_{6,1}(H) &= H^6 - 72H^4 + 115H^2 - 48 \\
 B_{6,2}(H) &= H^{10} - 200H^8 + 12800H^6 - 307200H^4 + 2457600H^2 \\
 &\quad - 3932160 \\
 B_{6,3}(H) &= H^{12} - 288H^{10} + 28800H^8 - 1228800H^6 \\
 &\quad + 2211840H^4 - 141557760H^2 + 188743680
 \end{aligned} \right\} \quad (20)$$

$$\left. \begin{aligned}
 E_{4,1}(H) &= H^2(H^2 - 16) \\
 E_{4,2}(H) &= H^2(H^6 - 96H^4 + 2304H^2 - 12288) \\
 E_{6,1}(H) &= H^2(H^4 - 48H^2 + 384) \\
 E_{6,2}(H) &= H^2(H^8 - 160H^6 + 7680H^4 - 1228800H^2 + 4915200) \\
 E_{6,3}(H) &= H^2(H^{10} - 240H^8 + 19200H^6 - 614400H^4 \\
 &\quad + 7372800H^2 + 23592960)
 \end{aligned} \right\} \quad (21)$$

REFERENCES

- Forristall, G. (1984). The distribution of measured and simulated wave heights as a function of spectral shape. *J. Geophys. Res.* 89(C6), 10, pp.547-552.
- Haring, R., A. Osborne, and L. Spencer (1976). Extreme wave parameters based on continental shelf storm wave records. *Proc. 15th Conf. on Coastal Engg.* 1, pp.151-170.
- Kendall, M. and A. Stuart (1963). *The advanced theory of statistics* (4th ed.), Chapter 3 and 6. London: Charles Griffin.
- Longuet-Higgins, M. (1963). The effect of non-linearities on statistical distributions in the theory of sea waves. *J. Fluid Mech.* 17, pp.459-480.
- Marthinsen, T. and S. Winterstein (1992). On the skewness of random surface waves. In *Proc. of the 2th Int. Offshore and Polar Eng. Conf.*, Volume 3, San Francisco, pp.472-478.
- Mase, H. (1989). Groupiness factor and wave height distribution. *JWPCO* 114(1), pp.105-121.
- Mori, N. (1996). *Influences of nonlinear interactions on random wave trains*. Ph. D. thesis, Gifu University.
- Myrhaug, D. and S. Kjeldsen (1987). Prediction of occurrences of steep and high waves in deep water. *JWPCO* 113(2), pp.122-138.
- Stansberg, C. (1993). Propagation-dependent spatial variations observed in wave-trains generated in a long wave tank. Technical Report 490030.01, MARINTEK Data Report.
- Yasuda, T. and N. Mori (1994). High order nonlinear effects on deep-water random wave trains. In *International Symposium: Waves-Physical and Numerical Modelling*, Volume 2, Vancouver, pp.823-332.
- Yasuda, T., N. Mori, and K. Ito (1992). Freak waves in a unidirectional wave train and their kinematics. *Proc. 23th Conf. on Coastal Engg.*, 1, Venice, pp.751-764.

CHAPTER 68

An attempt at applying the chaos theory to wave forecasting

Takao Ohta¹ and Akira Kimura²

Abstract

In this paper, a prediction method based on the chaos theory is applied to wave forecasting. First, it is investigated whether a time series data of the significant wave is chaotic. The correlation integral and the Lyapunov exponent are calculated for this purpose. In the second part of the paper, the prediction for the time series of the significant wave is attempted on the basis of the chaos theory.

1. Introduction

Wave forecasting information is required to secure port and harbor works. Classifying roughly, two methods have been used for wave forecasting. One is the deterministic method using the energy balance equation. The other is the statistical method using meteorological data - atmospheric pressure and wind speed. However, the former has a problem that the meteorological knowledge, a lot of cost and time are needed. The latter requires much labor to prepare the meteorological data. Recently, a new method based on the chaos theory (deterministic nonlinear prediction method) has been developed. This methodology has been applied to the prediction of stock prices, electricity demand and water supply. An outline of the method is that ; if a time series data has chaotic characteristics, the system which generates the time series can be considered deterministic and nonlinear. The dynamical rule of the system is estimated conversely from

1 Research associate, Dept. of Social Systems Eng.,
Tottori Univ., 4-101 Koyama Minami, Tottori 680, JAPAN

2 Professor, Dept. of Social Systems Eng.,
Tottori Univ., 4-101 Koyama Minami, Tottori 680, JAPAN

the time series data. Once the hypothetical dynamical rule has been estimated, the near future of the time series is predicted using the assumed dynamical rule. Two attractive features of this method are that only time series data is needed and there is a possibility of prediction with high accuracy. In this study, it is investigated whether the obtained time series data of the significant wave height has chaotic characteristics. Furthermore the deterministic nonlinear prediction method is applied to the prediction of the significant wave height.

2. Chaotic characteristics of the obtained data

The data of the significant wave height were obtained at the Tottori, Fukui and Miyazaki port in Japan. These data are part of NOWPHAS 1991-1994. Location of the observation points is shown in Figure 1. Length and acquirement rate of the data are indicated in Table 1. Linear interpolation is used for lack of data which is less than continuous 10 times. First of all, it is necessary to verify the chaotic characteristics of the significant wave height data. The method of trajectory reconstruction by delay coordinates (Takens(1981)) is used for that purpose. A set of m-dimensional vectors X_i are made of the time series $\{x_i\}$.

$$\begin{aligned} X_1 &= \left(x_1, x_{1+r}, \dots, x_{1+(m-1)r} \right) \\ X_2 &= \left(x_2, x_{2+r}, \dots, x_{2+(m-1)r} \right) \\ &\quad \vdots \\ X_n &= \left(x_n, x_{n+r}, \dots, x_{n+(m-1)r} \right) \end{aligned} \quad (1)$$

where, r is delay time. These vectors represent points in the m-dimensional phase space and a trajectory is constructed by connecting these points. Figure 2 illustrates making of 3-dimensional vectors from a time series schematically. Figure 3 is a schematic diagram of a trajectory that is reconstructed in the 3-dimensional phase space. Two methods are proposed to investigate whether a time series is chaotic. One is based on geometric characteristic of the trajectory, and the other is related to dynamical characteristic of it. In this study, the geometric characteristic of the trajectory is examined using the correlation integral method described in 2.1. The dynamical characteristic is examined using the Lyapunov exponent described in 2.2.

2.1 Correlation integral method

If a trajectory reconstructed from a time series

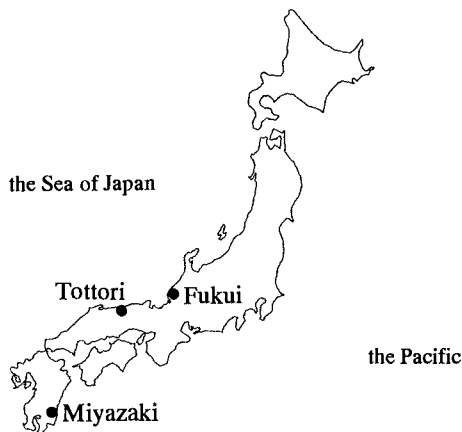


Figure 1. Location of the observation points

Table 1. Length and acquirement rate of the data

point	period	number of data	acquirement rate
Tottori	Jan.'91 ~ Jul.'92 (19 months)	6868	96.8 %
Fukui	Apr.'91 ~ Apr.'94 (37 months)	13512	99.4
Miyazaki	Jan.'92 ~ Nov.'94 (35 months)	12780	98.8

data has fractal structure, there is a possibility that the time series is chaotic. Grassberger and Procaccia(1983) proposed a method to calculate fractal dimension of the trajectory by the correlation integral. The correlation integral is defined by Eq.(2).

$$C^m(\varepsilon) = \frac{1}{N^2} \sum_{i,j=1}^N H\left(\varepsilon - |X_i - X_j|\right) \quad (2)$$

where, $H(t)$ is the Heaviside function, $|X_i - X_j|$ represents distance between vector X_i and X_j . The correlation integral is calculated for variable ε respectively. If a part of plotted $(\log \varepsilon, \log C^m(\varepsilon))$ is approximately on a straight line,

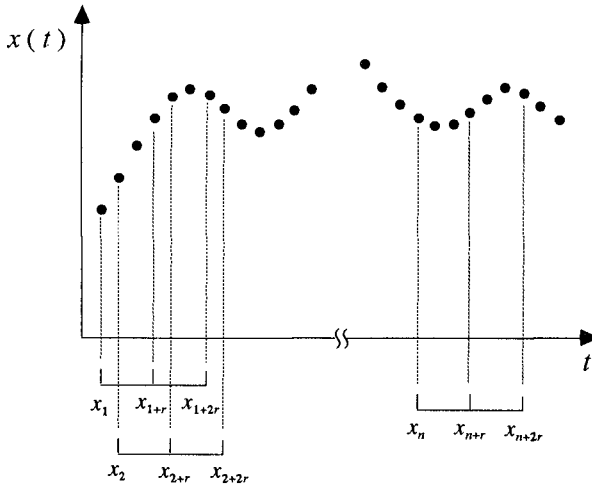


Figure 2. Making of vectors from a time series

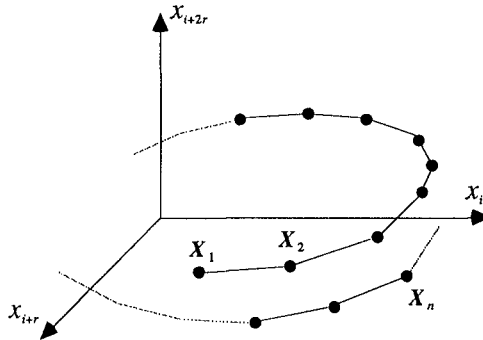


Figure 3. Reconstructed trajectory

the slope is defined as the correlation exponent $\nu(m)$. Furthermore, if the correlation exponent converges to a certain value D_c following the increase of the phase space dimension m , D_c represents the fractal dimension of the reconstructed trajectory. That is, the time series was generated by a deterministic nonlinear system, and it is estimated that the degree of freedom for this system is more than D_c . In this study, the correlation integral is calculated under the following conditions; $r=10, 20, 30$ and 40 hours, $m=5, 6, 7, 8, 9, 10, 12, 14, 16, 18, 20, 22, 24, 26, 28, 30$

and 35. Figure 4.(a), (b) and (c) illustrate the results of the correlation integral. These are the cases for the significant wave height data of Tottori, Fukui and Miyazaki respectively. Figure 5.(a),(b) and (c) show the correlation exponents which were obtained from Figure 4. In the cases of Tottori (Figure 5.(a)) and Miyazaki(Figure 5.(c)), the correlation exponent tends to converge. Therefore, there is a possibility that the significant wave height data of Tottori and Miyazaki are chaotic. In the case of Fukui(Figure 5.(b)), the tendency shown in the others is not distinct. The possibility that the data of Fukui is chaotic can not be found from this result.

2.2 Lyapunov exponent

Trajectory instability is a dynamical characteristic of chaos. It means that a distance between a point on the reconstructed trajectory and its near neighboring point increases exponentially with time development. The Lyapunov exponent is an index to represent change rate of the distance. If the Lyapunov exponent is a positive value, the distance is extended exponentially. Therefore, the trajectory is considered to be unstable. Sano and Sawada(1985) proposed a method to compute the Lyapunov exponent using a time series data. The procedure for this method is as follows. First, a point on the reconstructed trajectory is denoted with X_i , and its near neighbors X_{ki} ($i=1, \dots, M$) are looked for. Displacement vectors between X_{ki} and X_i are given as ;

$$y_i = X_{ki} - X_i \quad (3)$$

The center point X_i moves to $X_{i+\tau}$ and the points X_{ki} shift to $X_{ki+\tau}$ after the time τ . The displacement vectors z_i are as follows:

$$z_i = X_{ki+\tau} - X_{i+\tau} \quad (4)$$

If the absolute values of y_i and z_i are small sufficiently, z_i can be expressed by Eq.(5).

$$z_i = A_i y_i \quad (5)$$

The matrix A_i is given as;

$$A_i V = C$$

$$v_{kl} = \frac{1}{M} \sum_{i=1}^M y_{ik} y_{il} \quad , \quad c_{kl} = \frac{1}{M} \sum_{i=1}^M z_{ik} y_{il} \quad (6)$$

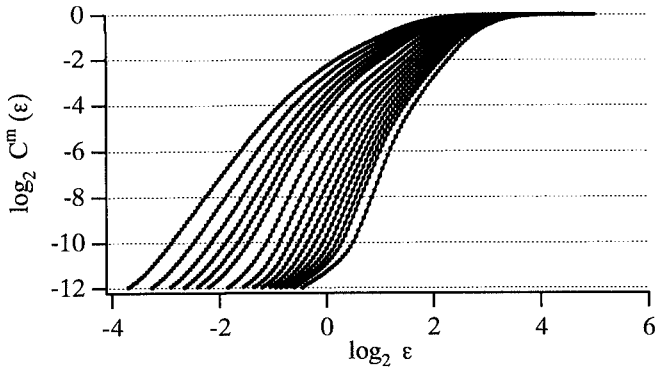
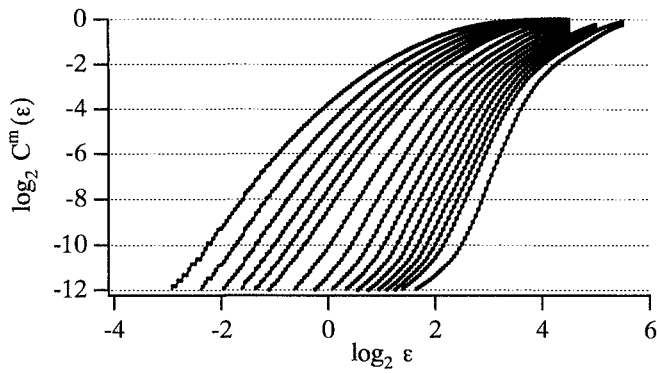
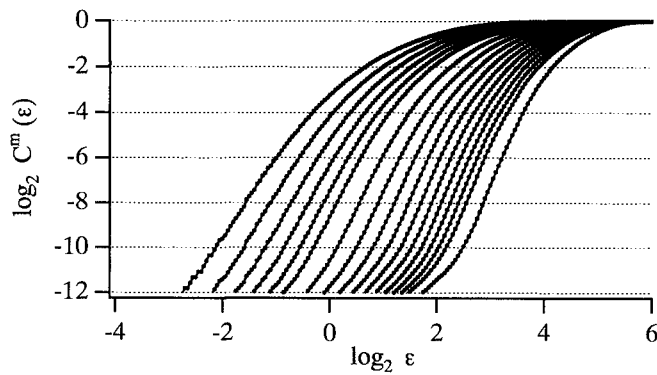
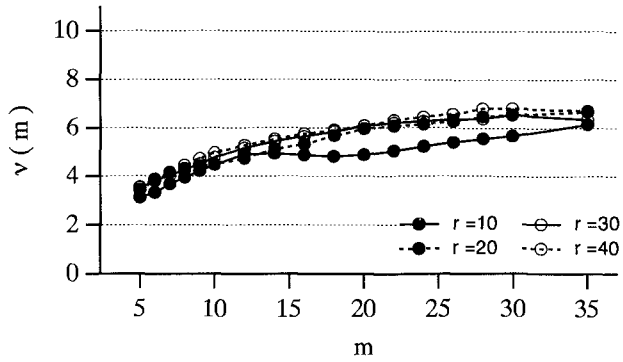
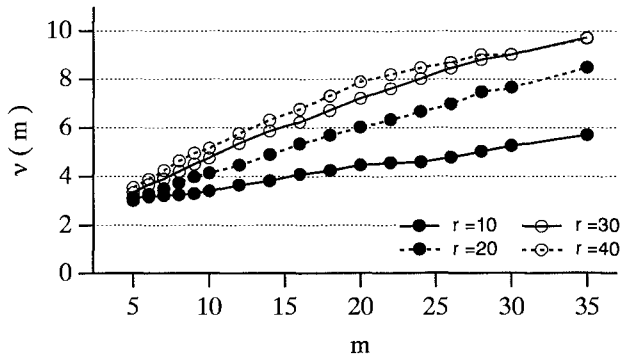
(a) Tottori ($r=10$)(b) Fukui ($r=10$)(c) Miyazaki ($r=10$)

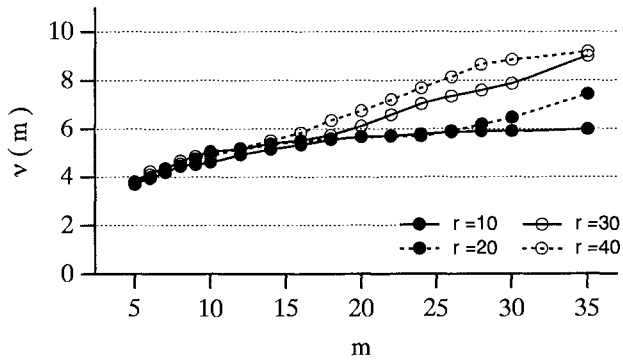
Figure 4. Results of correlation integral



(a) Tottori



(b) Fukui



(c) Miyazaki

Figure 5. Change of correlation exponent

where, y_{ik} :k-th component of y_i , z_{ik} :k-th component of z_i . The matrix A_i is used for computing the Lyapunov exponent. A set of orthonormal system $\{u_i(t)\}$ ($i=1, \dots, m$) is given as an initial condition, and the matrix A_i operates on the orthonormal system. Eq.(7) represents this operation.

$$e_i(t+\tau) = A_i u_i(t) \quad (7)$$

Furthermore, $e_i(t+\tau)$ is orthonormalized by the Gram-Schmidt method (e.g., Shimada and Nagashima(1979));

$$e_i'(t+\tau) = e_i(t+\tau) - \sum_{j=1}^{i-1} \langle e_i(t+\tau), u_j(t+\tau) \rangle u_j(t+\tau) \quad (8)$$

$$u_i(t+\tau) = \frac{e_i'(t+\tau)}{|e_i'(t+\tau)|} \quad (9)$$

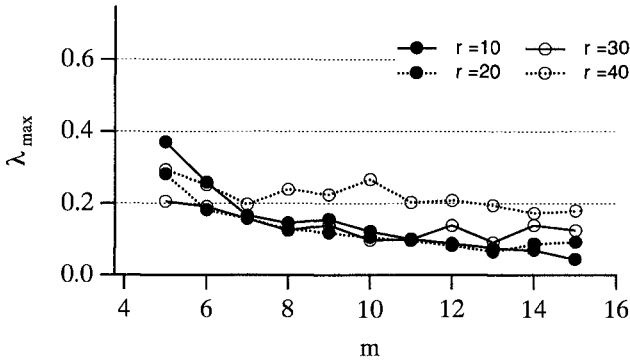
where, \langle, \rangle denotes the inner product. In the next step, $A_{t+\tau}$, $e_i(t+2\tau)$, $e_i'(t+2\tau)$ and $u_i(t+2\tau)$ are computed. $\{e_i'(t)\}$, which expresses a set of e_i' , is obtained by repeating this procedure. The Lyapunov exponent λ_i ($i=1, \dots, m$) is given by Eq.(10).

$$\lambda_i = \lim_{N \rightarrow \infty} \frac{1}{N} \sum_{i=0}^{N-1} \log \left| \left\{ e_i'(t) \right\} \right| \quad (10)$$

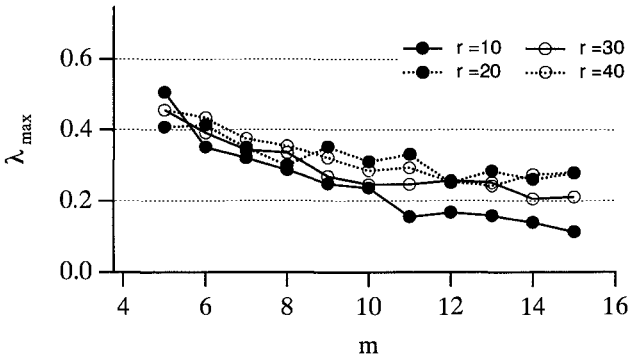
Figure 6.(a), (b) and (c) show the maximum Lyapunov exponent, which is calculated under the following conditions: delay time τ is 10, 20, 30 and 40 hours, phase space dimension m is from 5 to 15 and number of iteration N is 200. Because all of the maximum Lyapunov exponents are positive, the significant wave height data are considered to be chaotic.

3. Deterministic nonlinear prediction method

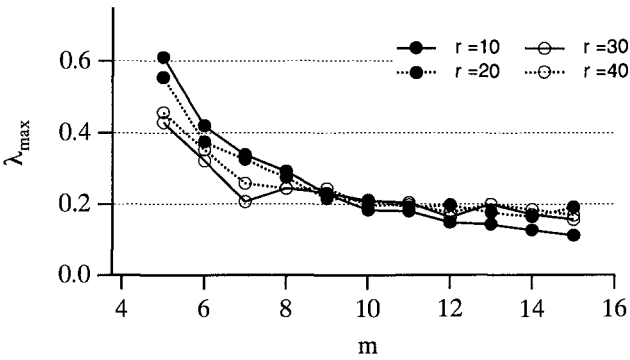
If a time series data is chaotic, the time series is considered to be generated by a deterministic nonlinear dynamical system. However, the dynamical rule of this system is unknown. It is necessary to estimate the dynamical rule conversely from the obtained time series data. In this paper, the reconstructed trajectory is divided into small sections, and a local dynamical rule is estimated for each section. The conception of Farmer and Sidorowich(1987) and the above-mentioned procedure of Sano and Sawada is applied to estimation of the local dynamical rule. In other words, the matrix A_i given by Eq.(6) is an approximation of the local dynamical rule.



(a) Tottori



(b) Fukui



(c) Miyazaki

Figure 6. Maximum Lyapunov exponent

The procedure to predict near future of a time series is as follows:

1) Take the vector which contains the latest data as X_t in Eq.(3). 2) Look for X_{k_i} ($i=1,2,\dots,M+1$), which are the close vectors to X_t . 3) Permute X_{k_i} in the order of increasing distance to X_t . Therefore, X_{k_1} is the nearest vector. 4) Set the displacement vectors $y_i = X_{k_i} - X_{k_1}$ ($i=2,\dots,M+1$) and $y_p = X_t - X_{k_1}$. 5) Obtain the displacement vectors $z_i = X_{k_{i+r}} - X_{k_{1+r}}$ ($i=2,\dots,M+1$). 6) Compute the matrix A_i by Eq.(6). 7) Calculate $z_p = A_i y_p$ and $X_{t+r} = X_{k_{1+r}} + z_p$.

The m -th component of X_{t+r} is the predicted value of the time series. In the prediction of the significant wave height, the following steps are taken furthermore; With changing M in the range of $[m+2, 2m+30]$, compute X_{t+r} for each M . From first to $(m-1)$ th (or $(m-2)$ th) component of the predicted X_{t+r} corresponds to the observed time series datum. Pick up five X_{t+r} whose sum of the square errors between the components and the observed data are small. Define the mean of m -th components as the predicted value of the significant wave height. When all X_{t+r} include negative component in the above range of M , the prediction is considered to be impossible.

4. Prediction of the significant wave height

The significant wave height is predicted by the procedure described in the section 3. The conditions under which the prediction is performed are as follows:

Tottori; The delay time r is 20 and 30 hours, the phase space dimension m is 10 and 12.
Fukui and Miyazaki; r is 10 hours and m is 10.
The prediction value is computed every 6 hours, that is, at 0,6,12 and 18 o'clock every day. The following two criteria are used to evaluate the accuracy of the prediction: Criterion I (Goto et.al.(1993));

$$\begin{cases} |H_p - H_o| \leq 0.3 (m) & (H_o \leq 1.0 (m)) \\ |H_p - H_o| / H_o \leq 0.3 & (H_o \geq 1.0 (m)) \end{cases} \quad (11)$$

where H_o is the observed significant wave height and H_p is the predicted one. The fitting rate is defined as N_r/N_t . N_r is the number of the predicted values which are in the range of Eq.(11), and N_t is the total number of the prediction.

Criterion II; Both the observed and predicted significant wave height are more or less than a set standard wave height of 1 meter.

The results of the prediction are as follows.

Table 2. Fitting rate (Tottori)

		r = 20 hours		r = 30 hours	
		m = 10	m = 12	m = 10	m = 12
Fitting rate I	Jan. '92	42.7 %	42.7 %	42.7 %	33.1 %
	Apr.	56.7	55.8	38.3	42.5
Fitting rate II	Jan. '92	71.0 %	71.0 %	70.2 %	56.5 %
	Apr.	80.0	86.7	60.8	64.2

Table 3. Fitting rate

		Tottori			Fukui			Miyazaki	
		6-hour	12-hour		6-hour	12-hour		6-hour	12-hour
Fitting rate I	Jan. '92	58.1 %	42.7 %	Jul. '93	79.8 %	66.9 %	Jan. '94	76.6 %	61.3 %
	Apr.	63.3	55.8	Oct.	70.9	48.7	Apr.	80.0	60.8
	Jul.	71.3	55.9	Jan. '94	67.7	40.7	Jul.	78.9	69.1
	-	-	-	Apr.	71.2	56.7	Oct.	79.0	61.3
Fitting rate II	Jan. '92	75.8 %	71.0 %	Jul. '93	85.5 %	80.6 %	Jan. '94	80.6 %	72.6 %
	Apr.	82.5	86.7	Oct.	83.8	72.6	Apr.	84.2	78.3
	Jul.	85.1	89.2	Jan. '94	84.7	70.2	Jul.	81.3	75.6
	-	-	-	Apr.	85.8	79.2	Oct.	85.5	79.8

Tottori: First, the 12-hour prediction for January and April 1992 was performed to compare the accuracy under the conditions of $r=20,30$ and $m=10,12$. Table 2 shows the fitting rate I and II, which are based on the criterion I and II respectively. The difference between $r=20$ and $r=30$ can be seen, however, the difference between $m=10$ and $m=12$ in the case of $r=20$ is not distinct. The 12-hour prediction for July 1992 and the 6-hour prediction for January, April and July 1992 were obtained under the conditions of $r=20$ and $m=12$. The fitting rates are shown in Table 3.

Fukui and Miyazaki: The 6-hour and 12-hour prediction was performed under the conditions of $r=10$ and $m=10$. The objects of the prediction are July, October 1993, January and April 1994 in Fukui, and January, April, July and October 1994 in Miyazaki. The data of the past 2 years was used for the prediction. The fitting rates are shown in Table 3.

Figure 7.(a),(b) and (c) illustrate a part of the results, in which the solid line is the observed value and the dotted line with closed circles is the predicted value. In the cases of the 6-hour prediction, the predicted

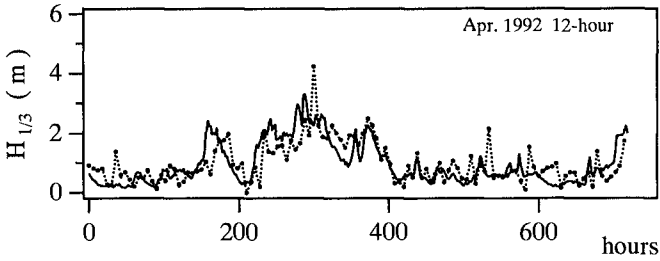
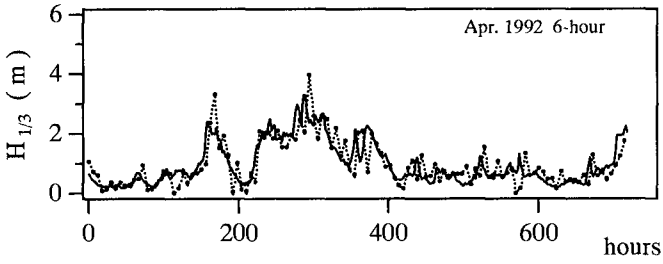


Figure 7.(a) Results of prediction (Tottori)

— ; observed , ...●... ; predicted

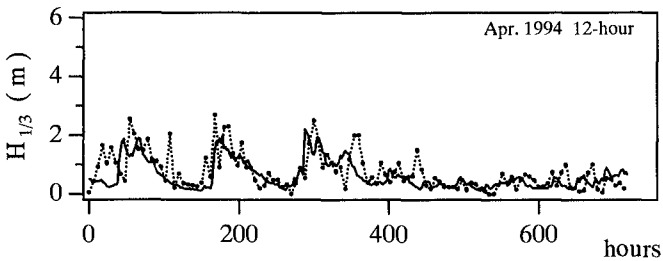
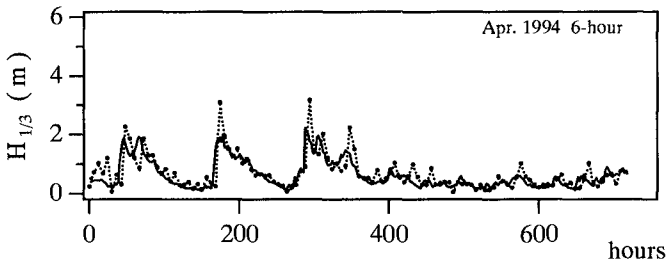


Figure 7.(b) Results of prediction (Fukui)

— ; observed , ...●... ; predicted

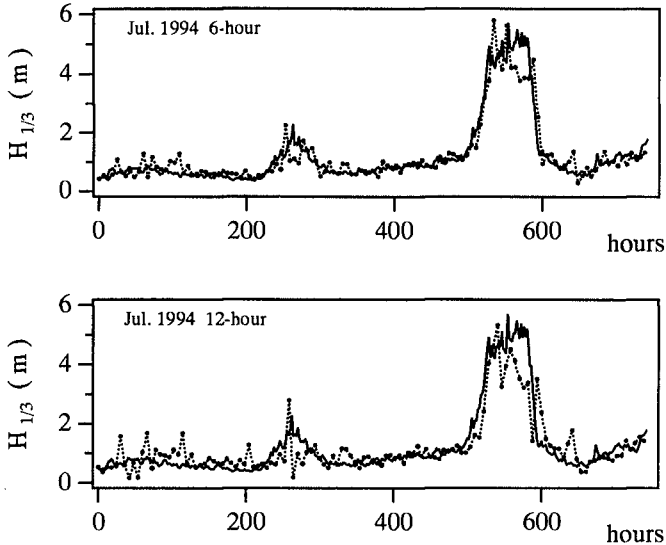


Figure 7.(c) Results of prediction (Miyazaki)

— ; observed, ...●... ; predicted

agree comparatively with the observed. However, time lags and fluctuations of the predicted become large in the cases of the 12-hour prediction.

5. Conclusion

In this study, the prediction method based on the chaos theory (deterministic nonlinear prediction method) was applied to the significant wave height data. The data whose length were from 19 months to 37 months were used for the prediction, and a certain of the applicability was found. However, it is necessary to improve the prediction accuracy. To increase the number of the data and to improve the estimation method of the local dynamical rule are mentioned for that purpose.

References

Farmer, J.D. and Sidorowich, J.J.(1987): Predicting Chaotic Time Series, Physical Review Letters, Vol.59, No.8, pp.845-848.

- Goto, C., Shibaki, H., Aono, T. and Katayama, T.(1993): Multiple Regression Models Described in Physical Parameters for the Purpose of Wave Forecasting, Proc. of JSCE, No.473/||-24, pp.45-53. (in Japanese)
- Grassberger, P. and Procaccia, I.(1983): Characterization of Strange Attractors, Physical Review Letters, Vol.50, No.5, pp.346-349.
- NOWPHAS 1991-1994, Coastal Development Institute of Technology, Ports and Harbours Bureau of the Ministry of Transport.
- Sano, M. and Sawada, Y.(1985): Measurement of the Lyapunov Spectrum from a Chaotic Time Series, Physical Review Letters, Vol.55, No.10, pp.1082-1085.
- Shimada, I. and Nagashima, T.(1979): A Numerical Approach to Ergodic Problem of Dissipative Dynamical Systems, Prog. Theor. Phys., 61, 6, pp.1605-1616.
- Takens, F.(1981): Detecting Strange Attractors in Turbulence, in Dynamical Systems and Turbulence, Lecture Notes in Mathematics, 898, pp.366-381, Springer-Verlag.

CHAPTER 69

TRANSITION OF STOCHASTIC CHARACTERISTICS OF WAVES IN THE NEARSHORE ZONE

David J. Robillard¹ and Michel K. Ochi²

Abstract

The purpose of this paper is twofold. The first is to clarify the transition of stochastic characteristics of waves; in particular, the transition from a Gaussian to non-Gaussian random process in the nearshore zone as a function of water depth and sea severity, and the second is to develop a method to estimate the non-Gaussian properties of waves at a specified water depth in the nearshore zone from knowledge of the sea severity in deep water. The probability density function applicable to non-Gaussian waves in finite water depth is applied to more than 1,000 samples of wave data obtained by the Coastal Engineering Research Center, U.S. Army, during the ARSLOE Project. From analysis of the data, the limiting water depth is defined below which wind-generated waves can no longer be considered Gaussian for a given sea severity. Furthermore, by presenting the parameters of the probability density function as a function of water depth and sea severity, it is possible to estimate the sea condition at a specified water depth in the nearshore zone from knowledge of sea severity in deep water.

Introduction

It has been known that the probability distribution of the displacement of waves in the deep ocean obeys the normal probability distribution and hence waves are considered to be a Gaussian random process. As waves propagate from deep to shallow water, however, a significant change is evident in the wave profile and this results in waves in shallow water being usually categorized as a non-Gaussian random process. It is noted, however, that transformation of wave characteristics

¹ Lieutenant, US Navy, Engineering Officer, Naval Coastal Systems Station, Panama City Beach, Florida, 32407, USA.

² Professor, Department of Coastal & Oceanographic Engineering, University of Florida, Gainesville, Florida, 32611, USA.

from a Gaussian to non-Gaussian random process may not always occur when waves propagate from deep to shallow water. If the sea severity is very mild, waves in shallow water are still a Gaussian random process. In other words, the non-Gaussian characteristics of waves in finite water depth depend on the water depth and sea severity.

One of the purposes of this study is to clarify the transition of wave characteristics from a Gaussian to a non-Gaussian random process as a function of water depth and sea severity. Another purpose is to develop a method to estimate the non-Gaussian characteristics at a specified water depth in the nearshore zone from knowledge of the sea severity in deep water, which is an extremely significant subject in practice.

Throughout the present study, the probability density function applicable to non-Gaussian waves in finite water depths is applied and analyses are carried out on more than 1,000 wave records obtained by the Coastal Engineering Research Center, U.S. Army, during the ARSLOE Project at Duck, North Carolina. The probability density function was developed based on the concept that stochastic characteristics of waves in finite water depth may be considered to be the same as the output of a nonlinear system (Ochi and Ahn 1994).

A broad range of sea conditions and water depths are examined to ensure the probability density function well represents the histograms of wave displacement data over various conditions. With the applicability verified, the probability density function is used to define criteria for the boundary where the wave field can no longer be considered Gaussian. Furthermore, analyses are carried out on parameters involved in the probability density function to present them as a function of water depth and sea severity. From the results of these analyses it is possible to estimate the sea condition, including the probability density function, at a specified water depth in the nearshore zone from knowledge of the sea severity (significant wave height) in deep water, although applicability of the results may be limited to a water depth of 25 meters where wave data were acquired and analyzed.

Probability Distribution Representing Non-Gaussian Waves

For evaluating the transformation of Gaussian to non-Gaussian characteristics of nearshore waves, the following probability density function developed based on the concept of the stochastic response of a nonlinear mechanical system (Ochi and Ahn 1994) is considered throughout the analysis in this paper:

$$f(y) = \frac{1}{\sqrt{2\pi} \sigma_*} \exp \left\{ -\frac{1}{2(\gamma a \sigma_*)^2} (1 - \gamma a \mu_* - e^{-\gamma a y})^2 - \gamma a y \right\} \quad (1)$$

where y = wave displacement from the mean, $\gamma = 12.8$ for $y \geq 0$ and 3.00 for $y < 0$.

The probability density function carries three parameters, a , μ_* and σ_* . In particular, the parameter 'a' controls the nonlinearity; the severity of nonlinear characteristics increases with increase in the magnitude of 'a'. The magnitude of 'a' becomes zero for Gaussian random waves.

It may be well to show that the above probability density function provides a good representation of the histogram of wave displacement constructed from data obtained in deep as well as in shallow water during a storm. Comparisons between the non-Gaussian probability density function given in Eq.(1) (solid line), the Gaussian distribution (broken line) and the histogram constructed from data obtained during the ARSLOE Project are shown in Figures 1(a) through 1(e). Included also in each figure is a portion of the wave data obtained at each location. The water depth, D , rms-value, σ , evaluated from data and the ratio between them, σ/D are tabulated in Table 1. The water depth is that at the time of measurement including the effect of tide as well as storm surge.

As can be seen in Figure 1(a), the histogram of wave displacement obtained at a water depth of 24.7 meters obeys the Gaussian probability distribution, while all other histograms obtained at shallower water depths deviate from the normal distribution but are well represented by the non-Gaussian probability distribution given in Eq.(1). Table 1 shows that the magnitude of σ/D increases as waves propagate from deep to shallow water, and hence the ratio σ/D may be used as a criterion indicating the limiting condition for the transformation from Gaussian to non-Gaussian random waves. Although only five examples of comparisons between the non-Gaussian distribution and histogram are shown here, about 100 comparisons for various water depths and sea severities all show excellent agreement.

Since Eq.(1) represents well the probability distribution of displacement of waves in the nearshore area, over 1,000 wave data obtained during a storm encountered at the ARSLOE Project (October 23-25, 1980) are reduced for evaluating parameters of the probability distribution function. Then, further analysis is carried out to represent these parameters as a function of water depth and sea severity.

Limiting Water Depth and Sea Severity of Gaussian Waves

The non-Gaussian property of waves in the nearshore zone depends on water depth and sea severity. Analysis of wave records obtained in shallow water shows clearly that they are still a Gaussian random process if sea severity is mild. Table 1 indicates that the transition from Gaussian to non-Gaussian waves occurs for σ/D values between 0.042 and 0.086. From analysis of about 100 samples of wave data with σ/D between 0.045 to 0.080, it is found that $\sigma/D = 0.060$ is the limiting condition below which waves can be considered as a Gaussian random process. As an example of the analysis results, Figure 2(a) shows a comparison between the Gaussian (broken line) and non-Gaussian (solid line) probability density functions of wave displacement data for $\sigma/D = 0.071$. In this case, the χ^2 -test with level of significance of 0.05 shows that the measured data cannot be considered to

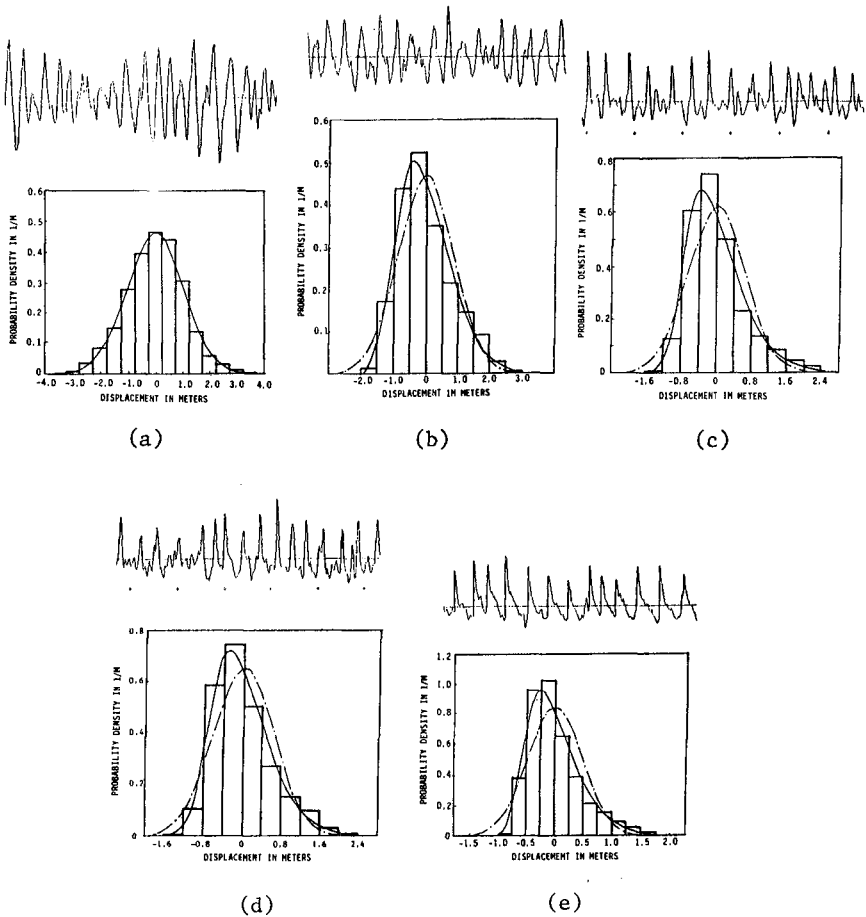


Figure 1 Comparison between probability density function and histogram of wave displacement

Table 1 Water depth and rms-value of data shown in Figure 1

WAVE DATA SHOWN IN FIG. 1	WATER DEPTH D (m)	RMS-VALUE σ (m)	σ/D
(a)	24.70	1.034	0.042
(b)	10.04	0.858	0.086
(c)	6.52	0.650	0.100
(d)	4.66	0.612	0.131
(e)	2.23	0.480	0.215

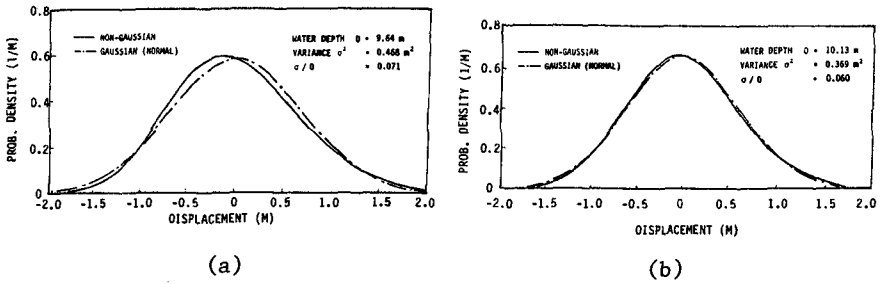


Figure 2 Comparison between Gaussian (broken line) and non-Gaussian (solid line) probability density functions of wave displacement data

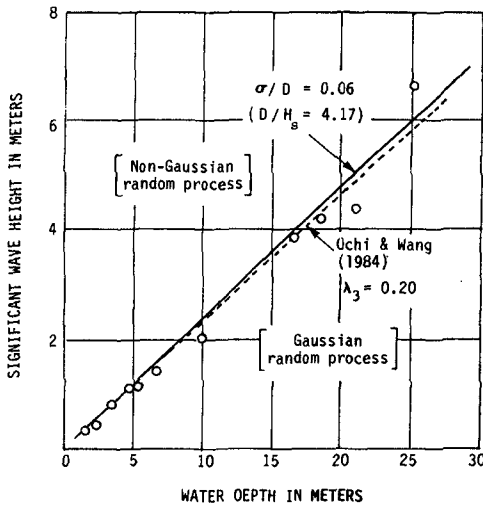


Figure 3 Limiting water depth for non-Gaussian waves as a function of significant wave height

be a Gaussian random process. On the other hand, Figure 2(b) shows a comparison for $\sigma/D = 0.060$. As seen, the non-Gaussian probability distribution computed from data is virtually the normal probability distribution. It was found that all probability distributions of wave displacement obey the normal probability distribution and/or pass the χ^2 -test (using a normal distribution as the hypothesized distribution) when the ratio σ/D is less than 0.06. Assuming that waves are narrow-banded, $\sigma/D = 0.06$ is equivalent to $D/H_s = 4.17$, where $H_s =$ significant wave height.

Based on the findings presented above, Figure 3 shows the limiting water depth below which wind-generated waves are considered to be a non-Gaussian random process for a specified significant wave height. The criterion $\sigma/D = 0.06$ for the limit of Gaussian waves is given as the solid line in the figure. It is noted that the parameter 'a' of the probability density function given in Eq.(1) is zero for

Gaussian waves, which can certainly be used as another criterion for evaluating the limiting Gaussian random process. Hence, the sea severities (significant wave heights) for which the computed a-values of the density function is zero or near zero are evaluated at various water depths and plotted as the open circles in the figure. Finally, a criterion for limiting Gaussian random waves was developed from analysis using the Gram-Charlier series probability distribution with skewness $\lambda_3 = 0.2$ (Ochi and Wang 1984). This criterion is given as the dotted line in the figure.

The results obtained from the above mentioned three different analyses for evaluating limiting conditions of Gaussian waves as a function of significant wave height, H_s , and water depth show good agreements; therefore, it may be concluded that the water depth in a given sea severity for which $\sigma/D = 0.06$ (or $D = 4.17 H_s$) is the limiting depth below which waves may be considered to be a non-Gaussian random process. This criterion, however, is valid only for water depths not exceeding 25 meters where the data were acquired and analyzed.

Parameters of the probability Distribution

In this section, the functional relationship between parameters of the non-Gaussian probability density function given in Eq.(1) will be discussed and presented as a function of water depth and sea severity. Since the three parameters, a , μ_* and σ_* carry different dimensions, these parameters are expressed in dimensionless forms, $a\sigma$, μ_*/σ and σ_*/σ , respectively, where σ is the rms-value of waves at a specified location.

Figure 4 shows the functional relationship between σ_*/σ and $a\sigma$. In this figure, the relationship obtained from data at three locations (calm water depth of 1.35 m, 5.5 m and 8.8 m) are given, but data obtained at other water depths fall within the upper and lower bounds drawn in the figure. The vertical scale range is very small; from 1.00 to 1.05. Therefore, the difference between the formula given in the figure and the upper and lower bounds of data is within one per cent. That is, we can evaluate σ_*/σ as a function of $a\sigma$ within one per cent as follows:

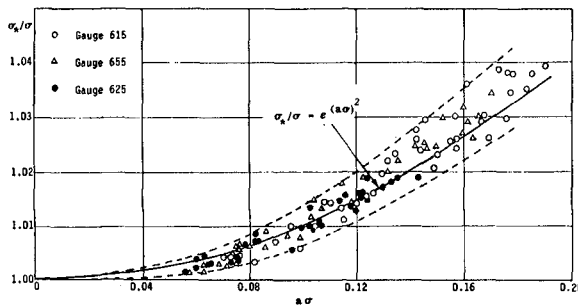


Figure 4 Functional relationship between σ_*/σ and $a\sigma$

$$\sigma_* / \sigma = \exp\{(\alpha\sigma)^2\} \tag{2}$$

Figure 5 shows the functional relationship between μ_* / σ and $\alpha\sigma$. Again, the figure shows the results obtained at the three locations shown in Figure 5, but all data obtained at other water depths fall within the range of scatter shown in the figure. By drawing the average line, μ_* / σ can be presented as a function of $\alpha\sigma$ as follows:

$$\mu_* / \sigma = -1.55(\alpha\sigma)^{1.20} \tag{3}$$

Figure 6 shows the dimensionless parameter $\alpha\sigma$ as a function of the sea severity-water depth ratio σ/D . As seen, $\alpha\sigma$ is zero for $\sigma/D = 0.06$ as mentioned

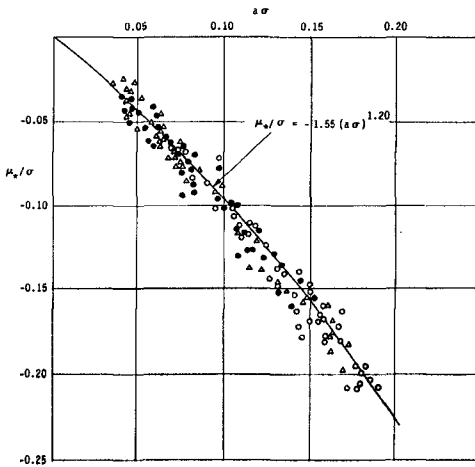


Figure 5
Functional relationship
between μ_* / σ and $\alpha\sigma$

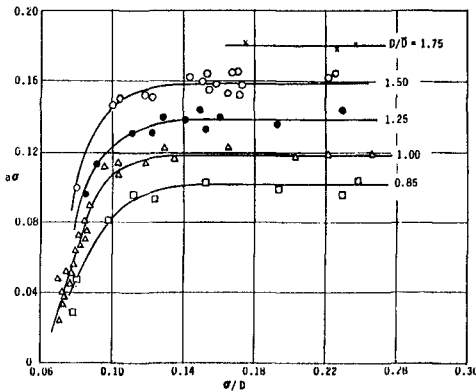


Figure 6
Relationship between $\alpha\sigma$
and σ/D as a function of
dimensionless water depth
 D/\bar{D}

earlier, and $a\sigma$ depends to a great extent on the water depth. In order to present the results as a function of water depth, the dimensionless water depth D/\bar{D} is used where \bar{D} is the calm water depth at each location where data were obtained. The water depth in the shallow water area, in general, increases to 1.5 (or greater) times the calm water level. Points for D/\bar{D} greater than 1.5 and σ/D greater than 0.12 in the figure are those in shallow water, on the order of less than 4 meters depth in calm water. As seen in the figure, for a specified D/\bar{D} , the value of $a\sigma$ increases rapidly for σ/D between 0.06 and 0.12 beyond which it remains constant. That is, for σ/D greater than 0.12, the parameter $a\sigma$, representing the severity of the nonlinear property of waves may be represented approximately by

$$a\sigma = 0.032 + 0.085(D/\bar{D}) \quad (4)$$

Estimation of Sea Condition in the Nearshore Zone

It may be of considerable interest to estimate the sea condition in the nearshore zone from knowledge of the sea severity (significant wave height) in the offshore area. For this, it is assumed that the sea condition remains constant in the offshore area where the water depth is greater than $4.17 H_s$; the relationship obtained in Figure 3. This water depth is denoted by D_0 in Figure 7. Next, let the variance of non-Gaussian random waves at an arbitrary location in the nearshore zone be σ^2 where the water depth is D . Figure 8 presents the sea severity-water depth ratio, σ/D , evaluated from analysis of data obtained at various locations in the nearshore zone as a function of dimensionless water depth D/D_0 . The solid circles represent high tide condition, while the open circles are for low tide. The triangular marks are indicative of the water depth during the storm being almost equal to the still water level at the various locations. By drawing the average line in the figure, the functional relationship between σ/D and D/D_0 can be obtained from the figure as

$$\sigma / D = 0.06(D / D_0)^{-0.58} \quad (5)$$

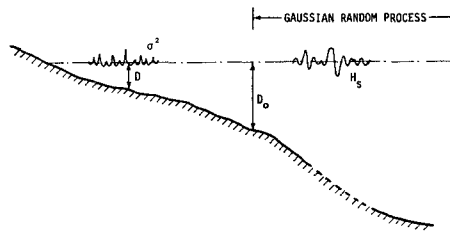


Figure 7 Sketch indicating the estimated transition of sea severity due to water depth variation in the nearshore zone

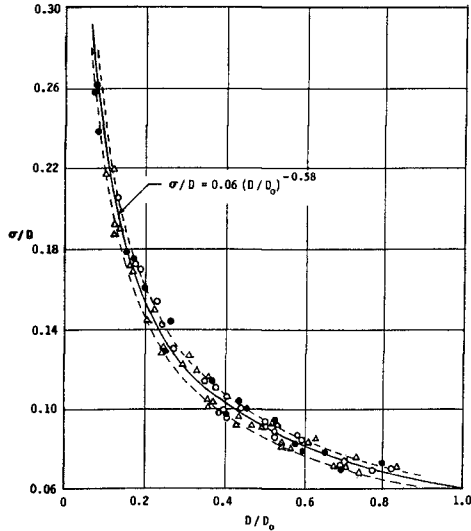


Figure 8 Relationship between σ/D and dimensionless water depth D/D_0

The two lines in Figure 8 are $\pm 5\%$ lines of the mathematical formulation which cover all data. Thus, upon estimating the water depth D at a specific location including the effect of tide and storm surge, the sea condition in the nearshore zone can be predicted by Eq.(5) from knowledge of the significant wave height in deep water. The parameters of the probability distribution of non-Gaussian waves applicable to that location can then be estimated from Eqs.(2) through (4) with information on the water depth in calm water.

As an example, Figure 9 shows the application of this approach for predicting the sea condition in the nearshore zone from knowledge of significant wave height in the offshore area, the sea condition at Duck, North Carolina at noon on October 25th, 1980 is estimated. The records show the tide was high at this time. The horizontal scale in Figure 9 is the distance from the shoreline given in logarithmic scale. The significant wave height at a distance 12 Km offshore was 4.28 meters where the water depth was 24.7 meters. It is assumed that the sea severity remains constant in areas deeper than $D_0 = 17.5$ m, which is equal to 4.17 times the significant wave height and that waves are non-Gaussian in areas shallower than D_0 . The values of σ/D are estimated at various water depths from Figure 8, and compared with measured data which are given by the square-marks in the figure. The variances, σ^2 , are then computed and compared with measured data given by the open circles. Furthermore, the dimensionless parameters $a\sigma$ are estimated at various water depths from Figure 6 (or by Eq. 4 for $\sigma/D > 0.12$) and are plotted in the figure. Good agreement between estimated and computed values from measured data is obtained in this example.

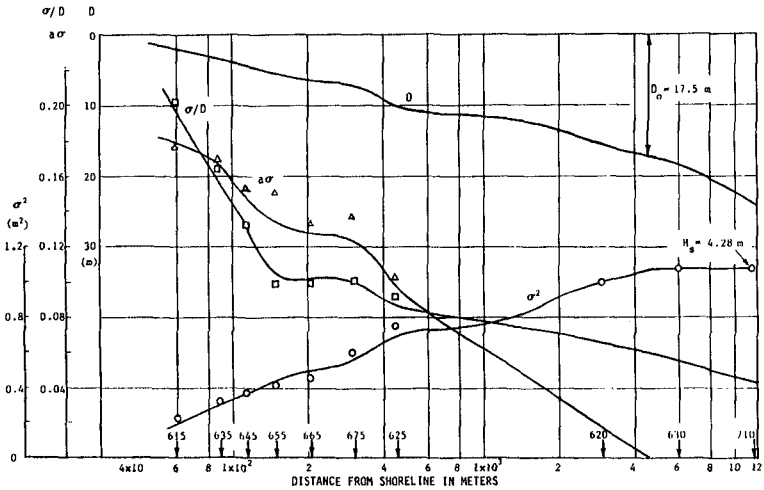


Figure 9 Comparison between estimated σ/D , σ^2 , $a\sigma$ and those computed from measured data at various locations in the nearshore zone

Conclusions

This paper presents the results of a study to clarify the transition characteristics of waves from a Gaussian to non-Gaussian random process in the nearshore zone and presents them as a function of water depth and sea severity. From analysis of more than 1,000 samples of wave data obtained by the Coastal Engineering Research Center, U.S. Army, during the ARSLOE Project, it is found that for a given sea severity a water depth of 4.17 times the significant wave height is the limiting depth for which waves may be considered to be a non-Gaussian random process. Furthermore, the parameters of the probability density function representing non-Gaussian waves are presented as a function of water depth and sea severity. By applying the results of this analysis, a method is developed to estimate the sea condition at a specified water depth in the nearshore zone from knowledge of sea severity (significant wave height) in deep water.

Acknowledgments

The authors express their appreciation to Dr. Ahn for his valuable contribution in evaluating the limiting water depth associated with non-Gaussian waves. They are also grateful to Ms. Laura Dickinson for typing the manuscript.

References

- Ochi, M.K. and Wang, D.W.C. (1984), Non-Gaussian Characteristics of Coastal Waves, Proc. 19th Coastal Eng. Conf., Vol.1, pp.516-531.
- Ochi, M.K. and Ahn, K. (1994), Non-Gaussian Probability Distribution of Coastal Waves, Proc. 24th Coastal Eng. Conf., Vol.1, pp.482-496.

CHAPTER 70

MONITORING AND MODELLING ON SHALLOW WATER WAVE PROPAGATIONS IN “EL SALER” BEACH

José C. Santás¹, Jose M. de la Peña², José Lozano³,
Studies Center of Harbors and Coast, CEDEX,
Ministry of Public Works, Spain⁴

ABSTRACT

Physical modelling with 3-D basins have mainly been used in relation with wind wave propagation, which input are irregular and multidirectional trains obtained from a directional system in the prototype, to test harbour structures . Very few applications are been developed to test the spectral propagation over a beach from deep waters to surf zone neither to study the relationship between spectral directional characteristic of time series obtained in prototype and in the basin. The aim of this study has been the study of the propagation of real data obtained in El Saler beach along the beach slope towards the bar and compare these results with real data, employing the 3-D basin , with the real beach profile. These data have been obtained from the Monitoring Campaign developed by CEDEX, partially sponsored by the contract MAST2, CT92-0027, G8M project, on El Saler Beach.

1.-INTRODUCTION

The general aims of the “El Saler” Project were the monitoring of the beach as well as the wind waves to study the beach evolution and the waves propagation. For that two systems to obtain wave climate data were installed at medium deep waters , 50 meters depth, and on the submerged beach, firstly located at 10 meters deep before bars, to be moved after 1 year, towards a surf position, between the bar and the swash zone of the beach.

¹Marine Sc.Ph.D.&Physicist; Field Adv. Measurements. Prog.;Jose.C.Santas@cedex.es

²Civil Eng.,Head of Littoral Studies Division; e-mail: Jose.M.Pena@cedex.es

³Civil Eng.,Head of Physical Models Divison; e-mail : Jose.Lozano@cedex.es

⁴Antonio López 81, 28026-Madrid; Spain. Tel.: 34-1-3357700,Fax: 34-1-3357622

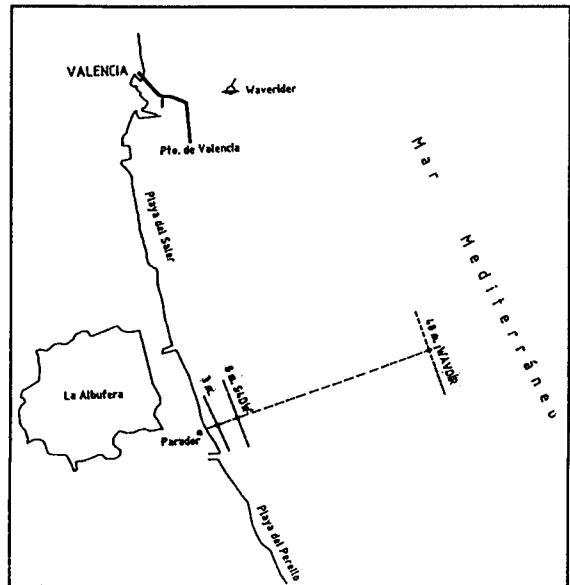
The first work developed with the obtained information was the propagation of selected trains by mean two numerical models: a lineal one and a Boussinesq standard model, which results were compared each other. The relationship allowed between them and also taking into account the field data, were not as good as we hoped in the previous step, specially if we compare the longshore variations oh the significant wave with the field data, and also the second order peaks that appeared on the field spectra. Otherwise the relation between shoaling coefficients was so big.

Taking into account the 3-D Basin facilities, a physical model was planned to be used as a final step of this work. The aim of this paper is to show the characteristic of the physical model phase as well as its results .

2.-FIELD DATA AND SPECTRAL ASSIMILATION

The monitoring of "El Saler" beach, located in the Mediterranean spanish coast, incorporated a wide knowledge of the directional waves for no very rough conditions and the bathymetric data.

The field data acquisition survey was developed from February-93 till June-95, with 3 systems located along a perpendicular line to the coast, from 47 meters depth till 3.5, beyond the bar. Yearly bathymetric surveys have been made to study area evolution, from dune (+5 meters) to submerged beach till 10 meters deep. Special focusing was employed on three control profiles, over wich the systems were installed, with 12 surveys profiles, in front of Luis Vives Parador. An idealized profile was obtained as mean profile to get the propagation by mean the physical model as we can see later. The picture 1 shows the study area
Figure 1: Studied zone with locations of measurement systems.



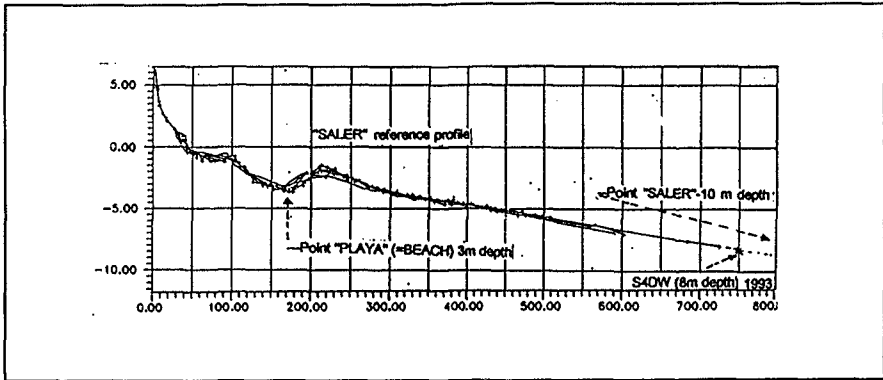


Figure 2: Studied profile with the EMCM installation points

The basic equipment used into this project has been composed by :

-A **Datowell Waverider Directional buoy** (which will be called WavDir in this report) deployed in depth water (50 meters), linked to the shore station , composed by a receiver , a PC and a recording system, by RF . The buoy location has been kept watch on by the Argos System . (@Argos CLS.)

-Two **Interocean Electro-Magnetic Current-Meters**, S4ADW, instrumented with a high resolution pressure cell. These systems were located on the control profile, 0.8 meters over the bottom, in points of 8 and 3 meters deep respectively, with a special rig to sink to maintain the equipment near the bottom. These systems provided data concerning the characterization of the Waves Sea Climate in the Inshore Zone as well as near the bar , figure 2 .

The Waves Data acquisition was made attending the following items:

-Time series duration: approximately 20 minutes (wav-Dir) and 35 for S4DW,

-Sampling period of 0.78(Dir.-Wav) and 0.5 sec. (S4DW)

-Repetition period of 3 hours.

-Time series length: 1560 data points for Waverider Directional buoy and 4200 for EMCM's.

Characteristics of the Raw Data Process

The spectral process has been made with 6 blocks of 256 points and averaging the 6 spectra obtained (degrees of freedom : dof=12) for the Wav-Dir data and using 16 blocks of 128 points to obtain (dof= 32) EMCM's prototype spectra. The process allow us to obtain statistical and spectral usual results for heave (according the IAHR recommendations) as well as directional parameters for directional distribution functions.

As the EMCM Raw Data are absolute pressures and velocities in N-S direction and E-W direction, they have to be transformed to instantaneous water column height. The mean level which is eliminated in the spectral process, is taken to calculate the hydrodynamic attenuation. Also a correction taking into account non linear terms is used (proposed by Grace, 1977). Some calculations has been made in order to evaluate the effect of different possible incoming directions for waves and currents. The relative error for $u = .25$, $T_z < 2s$ and $d = 3m$ (limiting conditions in these deployments) is less that 5% .

Data sets selection and Spectral parametrization

A set of data records was chosen to fit their $S(f)$ and $G(f,\theta)$ spectral forms to parametric Jonswap Spectrum and Gaussian Distribution Functions. Four sea states were selected in order to study the propagation with the 3-D basin. The employed criteria were:

- Existence of simultaneous data in the three systems,
- Medium sea climate conditions,
- Narrow One-Peak spectral form and low directional dispersion.

A bigger number of sea states were employed for the propagations made by numerical modelling, because its ease for change initial conditions.

The parameters used to generate the waves were:

- Jonswap data : f_p , γ , H_s , σ
- Directional distribution function: Th_{Tp} , $\sigma(Th_{Tp})$ for $f=f_p$ and $f=1.5f_p$.

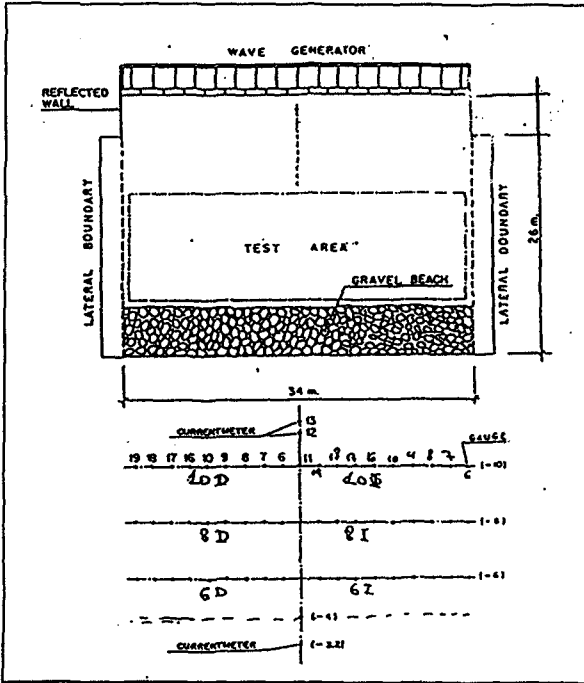
As the s-Misuyatsu parameter is used to generate the wave train, the relation $\sigma^2(Th_{Tp}, f_p) = 2/(s+0.5)$ was used.

3.-PHYSICAL MODEL CHARACTERISTICS

The Multidirectional Wave Tank of CEDEX, Cepyc, is 34 x 26 x 1.6 m.. The generator is endowed with 72 independent piston paddles (1.3x0.4 meters) with a total front of 28.8 meters. It is managed by modular computers controlled and connected to a VAX computer by an Ethernet network. The 3-D basin uses the GEDAP software, Hyd. Inst, NRC of Canada(3) to generate and analyze the waves. The duration of every test was 30 minutes taking 16400 data points. The method used for the generation is single summation method.

The modelled area reproduces, with a undistorted scale 1:50, the El Saler beach from coast to 30 meters depth, with an averaged profile obtained from field data. A regularization zone between the -30.0m to paddles existed. The employed measurement equipment was:

- 2 six wave-probes platforms and 2 EMCM as directional systems, located



alternatively along the test points: the perpendicular line to coast at 10,8,6,4 and 3.5 (beyond the bar) meters depth plus a platform always located at 30 m in front of the paddles system.

-Also 19+19 test points along parallel lines to coast were employed with 19 probes at same depths, figure 3.

The layout of the modelled profile is shown in the figure 4. The characteristics of the modelled sea states were specified on the Table. Figure 3 : layout of physical model

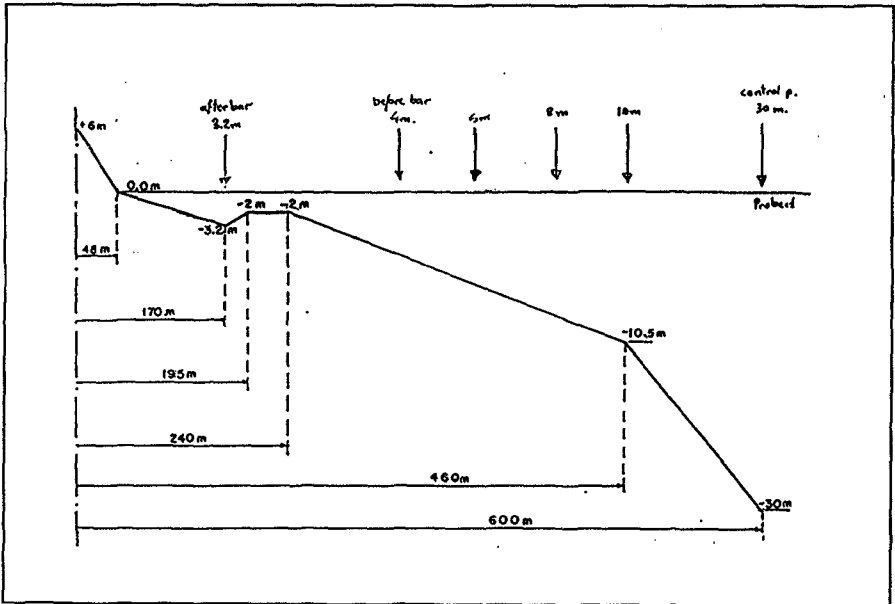


Figure 4: Profile used along the axis of the model.

TABLE I

Test number	Hm0 (50)	Hm0 (30)	Tp	γ	θ (aver)	$\sigma(\theta)$	s	α	ϕ
15	1.82	1.63	12.5	2.61	67	12	10	-3	18
17	1.40	1.32	11.1	1.86	67	13	9	-3	20
21a	1.20	0.70	7.7	1.44	68.5	21	5	-1.5	35
21b	0.52	0.47	7.7	1.44	68.5	21	5	-1.5	35

As the buoy was installed in 47 meters depth, and the deepest point of the physical model was 30, a previous lineal propagation by numerical model was employed, and the Hs(30)meters was obtained . These both data appear in the table.

The Peak period and Gamma were deduced from the fitting. The Incoming Direction θ , and its spreading were deduced from the data. The angle α is the difference between the normal to coast and θ .The angle ϕ is the propagation angle.

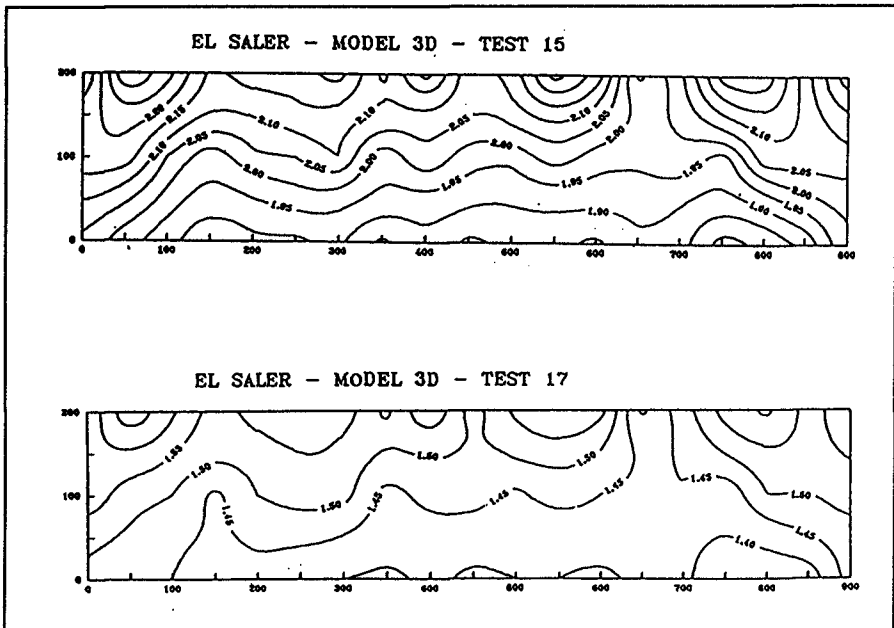


Figure5 : long shore variation of Hs, test 15th and 17th : Edge waves

4.-DATA OBTAINED FROM THE MODEL

The Directional distribution functions for $f=f_p$, $f=1.5 f_p$, mean direction and its spreading versus frequency were obtained. From the EMC system also the current spectra (longshore and cross shore) were taken. Only the scalar spectra were recorded for the measurement points with wavestaff

Every test was ran 6 times and the spectral characteristics were compared between them, also between the different tests, and between 3-D results and prototype. The directional spectra were obtained only along the model axis and the heave spectra for all the test points. Obtained results, statistics and spectral, have been studied to characterize wave propagation and its evolution as the depth decrease and for both sides from the axis. The more relevant items founded are:

4.1.-Significant wave height variations in parallel lines

In relation with the local variability of H_s along the measurement area, it was obtained a pattern with the H_s contour line that was compared with field data. A modulation appeared that could be produced by edge waves. The aspect of that is shown in the picture 5.

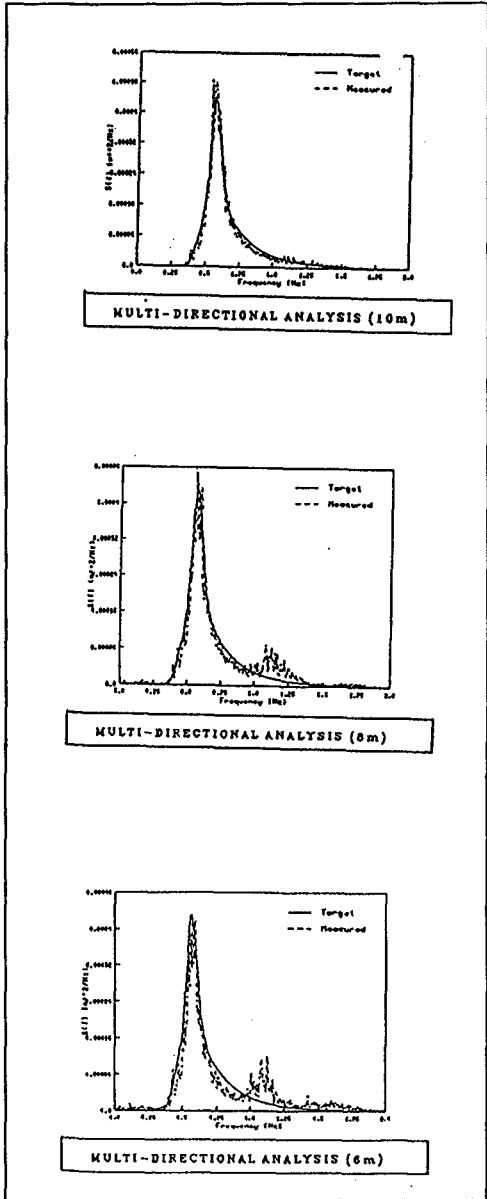


Figure 6: Wave spectra along the axis of the model: 2nd order peaks.

A modulation appeared that could be produced by edge waves. The aspect of that is shown in the picture 5.

4.2.-Peaks from the 2nd order interactions

La interaction between bands produces 2nd order peaks, as for short frequencies (Long Wave band), named as f_{-} , as in high frequencies (Short Wave band), named as f_{+} . This last peak grows up as the depth decreases, and it disappears after the breaking point, figure 6.

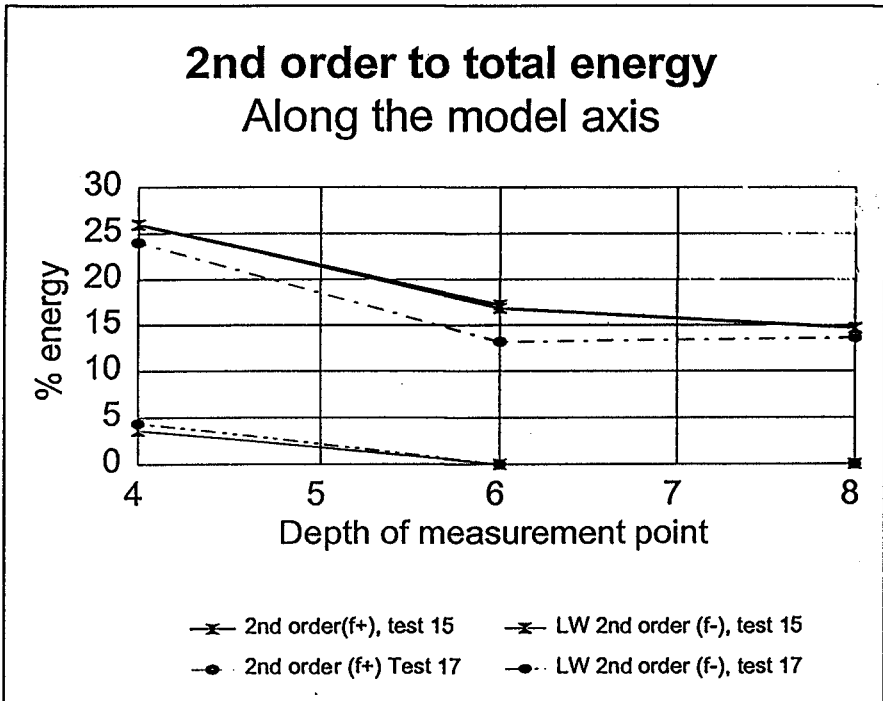


Figure 7

The central frequency of these 2nd order bands are approximately double and half, respectively, of the primary spectra, f_p .

The relationship between the energies of these 2nd order peaks and the first order peak, m_0 , have been calculated for the shallow waters between 8 to 4 meters depth, figure 7.

4.3.-Currents spectra

The directions X and Y have been chosen in the way that OX is the coast line and OY is normal towards sea. The spectra obtained from the central line, at 8

and 4 meters are shown in the figure 8.

The peaks of the f_+ band (short wave), only appears in the cross shore spectra. The opposite appends with the f_- , Long Wave band, that only appears in the long shore spectra. This could be seen by comparison between the same kind of spectra, V_y or V_x , in function of deep.

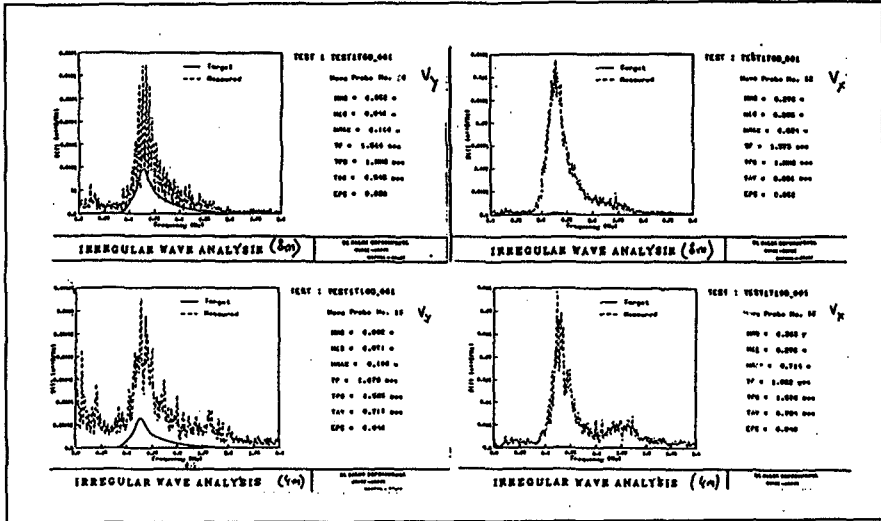


Figure 8 : Cross shore spectra (V_y) and Long shore spectra (V_x).

5.-CONCLUSIONS

The employed methodology reproduces quite well the evolution that has been obtained in the prototype, better than the numerical model before used (2). The test points located along the axis show the appearance of 2 second order peaks as well as for higher frequencies (double that the primary peak f_p) as for lower frequencies, long wave band, approximately at $f_p/2$. This effect was detected into the prototype.

The energy of these 2nd order peaks increases as the depth decreases. Also a modulation along the coast line is found with a length of wave function of the characteristics of the incoming wave train. This effect was not reproduced by the used numerical models (2)

The currents spectra near the bar show that the contribution of the long wave band is more important in cross shore direction, while the long shore has an important contribution of the short wave spectra.

The spectra of waves look like 'pink' noise after the bar, instead of the direction keeps incoming wave characteristics showing a few wider spreading.

Acknowledgements:

This work has been undertaken by CEDEX, as a part of a contract MAST-G8M "Coastal Morphodynamics Research Programme" with the European Community, with reference MAST-2 CT92-0027. We thank the collaboration of the Direccion General de Costas of the Ministry of Environment and the "Jefatura de Costas" of Valencia. In the project have collaborated Dr. Prf. Joseph R. Medina and his equipment, U.P. Valencia, and the staff of CEPYC, in special María J. Martín and Cristina Benito.

REFERENCES:

- Cedex-Cepyc**, 1993; "Seguimiento de la Playa de El Saler" , Technical Report made by Muñoz, F., and Jose C Santás
- Cedex-Cepyc**, 1995; "Data Sets for Coastal Aresa Modeling at el Saler beach", Technical Report made by Moreno, Luis.
- Grassa Garrido, José M.**; "Directional Random Wave Propagations on beaches", 1990; Proc. of 23th Int Conference on Coastal Eng., Delft , Netherland.
- Lechuga A.**; 1993 ;"Profile Measurements on the El Saler beach: Main characteristics and some results"; MAST2-G8M Overall Workshop, Grenoble.
- Madsen P.A.** , J.Larsen; "An efficient finite difference approach to the mild slope equation"; 1987, Coastal Engineering , 11, pp 329-351
- Medina-Villaverde, J. María**; "Modelling of the beach profile Dynamics"; MAST2-G8M meeting ,Gregynoc-Sept.-1994.
- Nwogu, Okey** "Maximum Entropy Method Estimation of Directional Wave Spectra from an Array of Wave Probes"; App. Oc. Res., Vol II, No 4, 1989
- Peña, Jose M. de la, and José C. Santás**, 1995, "Comparación de datos de oleaje en modelo y Naturaleza, en la Playa de El Saler, Valencia, 1ª fase", Rev. Ing. Civil, 97, 51-57
- Peregrine D H.**; 1976; "Interactions of Water Waves and Currents", Adv. Appl. Mech., 16, 9-117.
- Stig E. Sand, A.E Mynett**; "Directional Wave Generation and Analysis"; IAHR Seminar on Wave Analysis and Generation in Laboratory Basins; Lausanne , 1987
- Santás, José C.**; "Simultaneous Waves Measurements in the Saler Beach"; 1994, Gregynog (Wales), Overall Workshop G8 Coastal Morphodynamics ,
- Santás , Jose C., J.M. de la Peña**; "Wave Propagation in Shallow Waters: Modelling and Real Data"; Int. Conf. on Coastal Dynamics, Gdansk, 1995

DEFINITIONS OF THE USED SYMBOLS:

η : heave

(u, v) : velocity components , N-S and E-W respectively.

T_p : peak period of spectral estimation, (integrated all the directions).

H_s or H_{m0} : Significant Wave Height =4 times the squared root of m_0 ,

Th or θ : incoming direction of waves

Th_{Tp} or θ_p : Peak period band direction

$D_s(T_p)$ or $\sigma(Th_{Tp})$: Standard gaussian dispersion for the peak period band

γ, σ : Jonswap peakness parameter

$S(f, \theta)$: spectral densities for the prototype directional spectrum ,

$S(f)$: spectral densities for the scalar spectrum ; $S'(f)$: JONSWAP fitted spectrum

$G(f, \theta)$: Normalized Directional Spreading distribution for $S(f, Th)$,

dof : number of freedom degrees

d: depth

CHAPTER 71

Intercomparison of Parameter Estimation Methods in Extremal Wave Analysis

Masataka Yamaguchi¹

Abstract

Based on statistical analysis of extreme wave height data generated with a Monte-Carlo simulation technique for the prescribed parent probability distributions, a preferable method for the parameter estimation was determined for each of 8 distributions. It is also verified that a jackknife method is applicable to the correction of bias and the estimation of variance irrespective of parameter estimation method in most parent distributions, and that the information matrix methods inherent to the maximum likelihood method give generally satisfactory results in the estimation of variance of return wave height for samples of size greater than around 50.

1. Introduction

In the statistical analysis of extreme wave height data, several kinds of theoretical probability distributions and fitting methods for the parameter estimation have been employed, because the population distribution is not known a priori. Many attempts (for instance, Goda et al., 1993) have been made to find what kind of fitting method is preferable for the parameter estimation of each probability distribution to obtain a reliable estimate of return wave height and how the sampling variability could be evaluated, but the answer is still uncertain, because the class of parent distribution and the parameter condition investigated are limited.

This study uses 8 kinds of probability distributions including the Gumbel and Weibull distributions and 4

1 Prof. of Civil and Environmental Eng., Ehime Univ.
Bunkyocho 3, Matsuyama 790, Ehime Pref., Japan

kinds of parameter estimation methods. Based on the statistical analysis with use of the 4 methods for data generated by a Monte-Carlo simulation technique, in which case the parent probability distribution is taken from one of the 8 distributions, the advantage of a parameter estimation method over the other methods is investigated from the view points of bias and variance of return wave height. Also, applicability of a jackknife method to the correction of bias and the estimation of variance of return wave height, and that of information matrix methods usable in the maximum likelihood method to the estimation of variance of return wave height are discussed.

2. Parent Distributions and Estimation Methods of Parameter and Variance

2. 1 Parent distributions

The probability distributions investigated are the Gumbel, Weibull, GEV, Lognormal, Gamma, Loggamma, Hypergamma (Generalized Gamma) and Poisson-square root exponential-type maximum (SQRT) distributions. These distributions except for the Gumbel and SQRT distributions have three parameters respectively. Each probability distribution $F(x)$ is written as follows.

(a) Gumbel distribution (Greenwood et al., 1979; Goda, 1988)

$$F(x) = \exp[-\exp\{-(x-B)/A\}] ; -\infty < x < \infty \quad (1)$$

where x is the random variable, A the scale parameter and B the location parameter.

(b) Weibull distribution (Greenwood et al., 1979; Goda, 1988)

$$F(x) = 1 - \exp[-\{(x-B)/A\}^k] ; B < x < \infty \quad (2)$$

where k is the shape parameter.

(c) GEV distribution (Fisher-Tippett type II (FT-II) distribution for $k > 0$) (Hosking et al., 1985; Phien and Emma, 1989; Goda, 1990)

$$F(x) = \exp[-\{1 + (x-B)/kA\}^{-k}] ; \begin{array}{l} B - kA < x < \infty, k > 0 \\ -\infty < x < B - kA, k < 0 \end{array} \quad (3)$$

(d) 3-parameter Lognormal distribution (Takeuchi and Tsuchiya, 1988)

$$F(x) = (1/\sqrt{\pi}) \int_{-\infty}^y \exp(-y^2) dy$$

$$\begin{array}{l} y = k \cdot \log\{(x-B)/A\} ; B < x < \infty, C_S > 0 \\ y = k \cdot \log\{A/(B-x)\} ; -\infty < x < B, C_S < 0 \end{array} \quad (4)$$

where C_s is the skewness coefficient.

(e) 3-parameter Gamma distribution (Bobée, 1975; Takeuchi and Tsuchiya, 1988)

$$\begin{aligned} F(x) &= \gamma\{k, (x-B)/A\} / \Gamma(k) & ; B < x < \infty, A > 0 \\ F(x) &= 1 - \gamma\{k, (x-B)/A\} / \Gamma(k) & ; -\infty < x < B, A < 0 \end{aligned} \quad (5)$$

where $\Gamma(k)$ is the gamma function and $\gamma(k, x)$ the incomplete gamma function of the first kind defined by

$$\gamma(k, x) = \int_0^x \exp(-t) t^{k-1} dt \quad (6)$$

(f) 3-parameter Loggamma distribution (Condie, 1977)

$$\begin{aligned} F(x) &= \gamma\{k, (\log x - B)/A\} / \Gamma(k) & ; B < \log x < \infty, A > 0 \\ F(x) &= 1 - \gamma\{k, (\log x - B)/A\} / \Gamma(k) & ; -\infty < \log x < B, A < 0 \end{aligned} \quad (7)$$

(g) 3-parameter Hypergamma distribution (Suzuki, 1964)

$$\begin{aligned} F(x) &= \gamma(k, t) / \Gamma(k), \quad t = (x/A)^C & ; 0 < x < \infty, C > 0 \\ F(x) &= 1 - \gamma(k, t) / \Gamma(k) & ; 0 < x < \infty, C < 0 \end{aligned} \quad (8)$$

(h) SQRT distribution (Etoh et al., 1986)

$$F(x) = \exp\{-k(1 + \sqrt{x/A}) \exp(-\sqrt{x/A})\} ; 0 < x < \infty \quad (9)$$

This is one of the compound distributions, and k signifies yearly-averaged occurrence rate of event rather than shape property of the distribution.

2. 2 Parameter estimation methods

The parameter estimation methods used in this study are the moment method (MOM), the probability weighted moment (PWM) method and the maximum likelihood method (MLM) and the least square method (Goda, 1988, 1990) (LSM). Sample mean, unbiased variance and skewness are used in the moment method. In the parameter estimation with the moment method for the Loggamma distribution, two methods based on mean, unbiased variance and skewness of log-transformed sample data (MOM1) and cumulants of sample data (MOM2) are applied. PWM solutions are not derived in the cases of Lognormal distribution for negative skewness, Loggamma distribution, Hypergamma distribution and SQRT distribution. The parameter estimation for SQRT distribution is only derived from the maximum likelihood method.

The least square method is based on the model by Goda (1988, 1990). A set of candidate distributions is the Gumbel and Weibull distribution whose shape parameter is either of 0.75, 1.0, 1.4 or 2.0. The other set consists of the Gumbel and FT-11 type distribution whose

shape parameter is either of 2.5, 3.33, 5.0 or 10.0. A distribution with the largest correlation coefficient between the ordered data of sample and its reduced variate is selected as the best fitting distribution.

2. 3 Index of goodness of fit

The SLSC (Takasao et al., 1986) is used as an index of goodness of fit. It is defined by

$$SLSC = \left\{ \sum_{i=1}^N (x_i - s_i)^2 / N \right\}^{1/2} / |s_{0.99} - s_{0.01}| \tag{10}$$

where N is the sample size, x_i the ordered data, s_i the variate which is calculated from a theoretical probability distribution for designated probability such as 0.99 or 0.01. The Weibull plotting position formula is used as a standard formula to estimate non-exceedance probability F(x) of sample data, but in the least square method, the distribution-dependent plotting position formula is applied. The least square method eventually gives smaller SLSC than the other methods owing to its definition.

2. 4 Methods of bias correction and variance estimation

A jackknife method (Miller, 1974) is applied for bias correction and variance estimation of return wave height estimated using either method of MOM, PWM or MLM. The formulas are given by

$$H_J = N\hat{H} - (N-1)\hat{H}_*, \quad \hat{H}_* = \sum_{i=1}^N H_{*i} / N, \quad \sigma_J^2 = (N-1) \sum_{i=1}^N (H_{*i} - \hat{H}_*)^2 / N \tag{11}$$

where \hat{H} is the estimate of return wave height, H_{*i} the estimate of return wave height based on N-1 data excluding x_i , H_J the bias-corrected estimate of return wave height and σ_J^2 the jackknife estimate of variance indicated by σ_{JM}^2 for MOM, σ_{JP}^2 for PWM and σ_{JY}^2 for MLM.

In the application of the maximum likelihood method for the parameter estimation of the probability distributions except for SQRT distribution, the methods based on variance-covariance matrix of the maximum likelihood estimator (Suzuki, 1964; Phien and Emma, 1989) can be used for the asymptotic evaluation of variance of return wave height. It is defined as

$$A_{ij} = -E \left\{ \frac{\partial^2 L(X; \theta_1, \dots, \theta_r)}{\partial \theta_i \partial \theta_j} \right\} ; i, j = 1, 2, \dots, r \tag{12}$$

where E means the expected value operator, L the log-transformed maximum likelihood and θ_i the parameter of a probability distribution. A_{ij} is called the Fisher

information matrix, and if the expected value operator is dropped in eq. (12), it is called the observed information matrix. The variances estimated with both methods are indicated by σ_{FM}^2 and σ_{OM}^2 respectively.

In the case of the least square method, the standard deviation of return wave height σ_{LSM} is estimated with the empirical formula derived from numerical experiments by Goda (1988, 1990).

3. Monte-Carlo Simulation

As the inverse forms of the Gumbel, Weibull, GEV and lognormal distributions are known analytically, a sample of extreme wave height data is simulated sequentially by giving uniformly-distributed numbers between 0 and 1 generated by computer as input. In the cases of the other distributions such as the Gamma distribution, a sample of wave height is made with use of a numerical table given as the relation between equally-divided non-exceedance probability $F(x)$ and random variable x . The number of samples is 5,000 and sample size in each sampling N ranges from 10 to 1000, i.e. 10, 20, 30, 40, 50, 70, 100, 200, 500 and 1000. Value of SLSC, the parameters and the resulting 5 return wave heights $H(n)$ from 50 to 1000 years ($n=50, 100, 200, 500$ and 1000) and their variances are estimated with the above-mentioned methods from each sample. By averaging the results of 5000 simulations for each data size, mean values for SLSC, return wave height $H(n)$, jackknife-corrected return wave height $H_J(n)$, variances ($\sigma_{JM}^2, \sigma_{JP}^2, \sigma_{JY}^2, \sigma_{FM}^2, \sigma_{OM}^2$) and standard deviation σ_{LSM} , and variance of 5000 return wave height data $Var(n)$ are obtained. Then two kinds of bias $\Delta H(n)$ and $\Delta H_J(n)$ are respectively as

$$\Delta H(n) = \overline{H(n)} - H_{tr}(n), \quad \Delta H_J(n) = \overline{H_J(n)} - H_{tr}(n) \quad (13)$$

where $H_{tr}(n)$ is the true return wave height corresponding to n years, $\Delta H_J(n)$ the residual bias after jackknife correction, and ' $\bar{}$ ' means the average value. These quantities are called error statistics. Error statistics $\Delta H(n)$, $\Delta H_J(n)$, $Var^{1/2}(n)$ are normalized with use of the true return wave height $H_{tr}(n)$, and square root mean variances and mean standard deviation are divided by $Var^{1/2}(n)$. The normalized error statistics are expressed with the notation ' \sim ' and the figures are shown in the case of return period of 100 years.

4. Consideration of Results

A set of parameters is given to every parent dis-

tribution as input condition in the simulation study to find the advantage of one parameter estimation method over the other methods. Four shape parameters with the other parameters fixed are used in the simulation study to investigate the effect of shape of the distribution on the bias and variance estimated with the optimum parameter estimation method for each parent distribution.

Fig. 1 shows the relation between normalized error statistics and sample size N in the case of the Gumbel distribution, in which simulation is conducted under the condition of $A=1.39$ m and $B=4.5$ m, and the bias by the LSM given in both figures of ΔH and ΔH_j is the same one. It can be seen that bias of each, especially bias after jackknife correction by any methods is small and that the jackknife method and the information matrix methods give proper estimates of variance. Although the MLM with the jackknife correction is the optimum method for samples of size greater than about 30 from view-points of bias and variance, the PWM method is more proper from general view-points, when goodness of fit is taken into account. The LSM naturally produces the smallest SLSC, but gives greater bias and variance than the other methods. Also, the LSM yields poor estimate of standard deviation. This may be due to the fact that the empirical formula for the estimation of standard deviation is

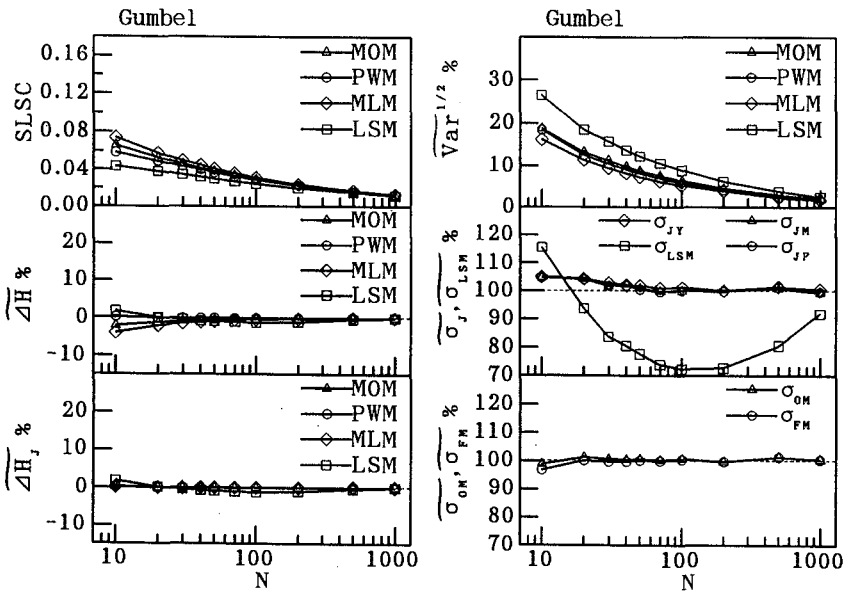


Fig. 1 Relation between error statistics and sample size (Gumbel distribution).

derived on the basis of numerical simulation for a fixed shape parameter, without taking a procedure of selecting the best fitting distribution. Similar tendencies are observed for the Weibull and FT-II type distributions.

Fig. 2 describes the relation between error statistics and sample size for the Weibull distribution. Simulation corresponding to the upper figures is conducted for the condition of $k=1.8$, $A=4.0$ m and $B=1.0$ m to find a preferable parameter estimation method, and simulations corresponding to the lower figures are made by giving either of $k=0.75, 1.0, 1.4$ or 2.0 under the fixed values of

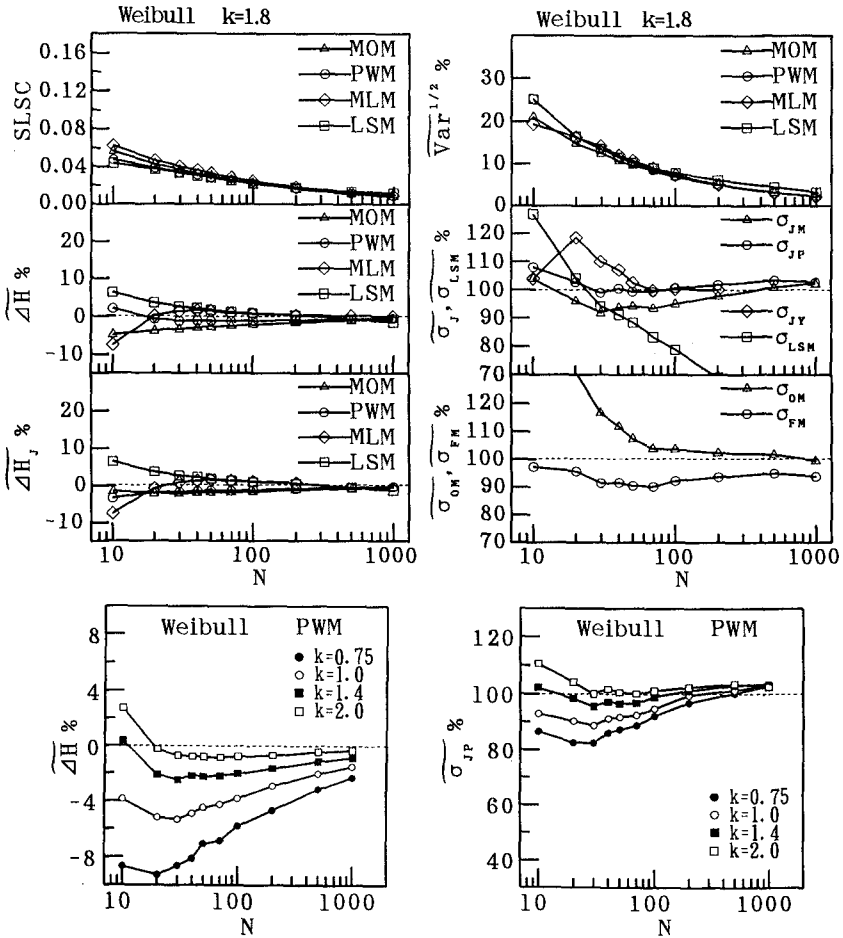


Fig. 2 Relation between error statistics and sample size (Weibull distribution).

$A=4.0$ m and $B=1.0$ m to investigate the effect of shape parameter on the error statistics. The PWM method is seen to be the optimum method from a view point of bias, although it yields a slightly larger estimate of variance than the MOM. In the PWM method, the jackknife method does not always work effectively for the bias correction, but it gives close estimate of variance. The MLM is a recommendable method in the case of sample size greater than 50 or 70. It is seen that the use of the observed information matrix method (OIMM) to the estimation of variance is possible for sample data greater than 30, if overestimation less than 10 % is allowed and that the Fisher information matrix method (FlMM) is applicable with underestimation less than 10 %. The OIMM usually gives greater estimate of variance than the FlMM. The effects of shape parameter on bias and estimate of variance are not negligible. Negative bias and degree of underestimation of variance increase with decrease of shape parameter. These reflect the widening of the Weibull distribution with decrease of shape parameter. Therefore, the application of the PWM method is preferably restricted for the case of shape parameter less than 1.0 to properly estimate return wave height and its variance.

Results for the GEV distribution are shown in Fig. 3. Conditions of simulation for finding a preferable parameter estimation method and for investigating the effect of shape parameter are $k=5.0$, $A=1.0$ m, $B=4.0$ m, and either value of $k=2.5$, 3.33, 5.0 or 10.0 for the fixed values of $A=1.0$ m and $B=4.0$ m respectively. The PWM method with the jackknife method produces excellent estimates of return wave height and its variance. Small bias is also brought about by the LSM which uses the adjusted plotting position formula, but the accuracy of estimation of variance is not so high for the reason mentioned above. The MLM with the jackknife correction gives small bias, but it does not yield good results on variance for small sample size. The information matrix methods are applicable for sample of size greater than about 50 or 70. According to the results of the lower figures, bias based on the PWM method is small except for $k=2.5$, distribution of which is widest in the investigated distributions, and the jackknife method gives fairly proper estimate of variance.

Fig. 4 illustrates the results for the Lognormal distribution. Parameter conditions in the simulation are taken as $k=3.4$, $A=8.0$ m, $B=-2.9$ m and $k=1.5$, 2.0, 2.5, 3.0, $A=3.5$ m, $B=-2.5$ m for each purpose mentioned above. The MOM is a more preferable method than the other methods from view points of bias and variance, and the jackknife method gives proper correction to bias and good

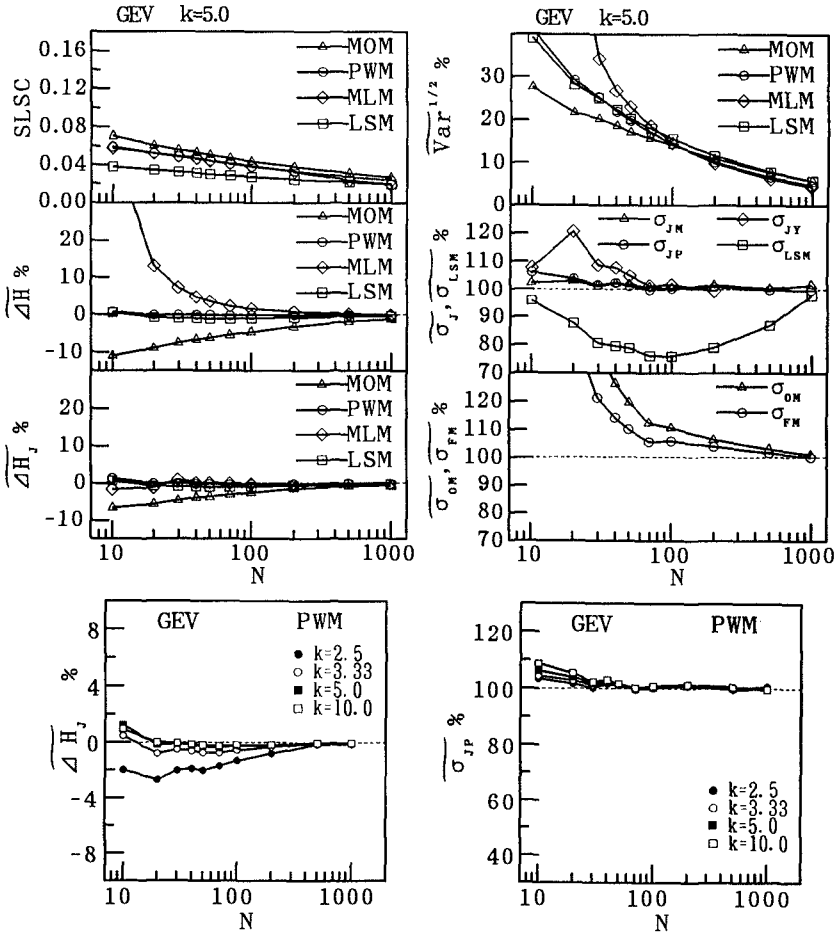


Fig. 3 Relation between error statistics and sample size (GEV distribution).

estimate of variance. Also, the MLM is a preferable method, in particular, for sample of size greater than 50 or 70. The influence of shape parameter on error statistics is seen in a diagram of bias. Even if bias-correction with the jackknife method is made, negative bias for small shape parameters is still at significant level. On the other hand, the jackknife method yields proper estimate of variance irrespective of the value of shape parameter.

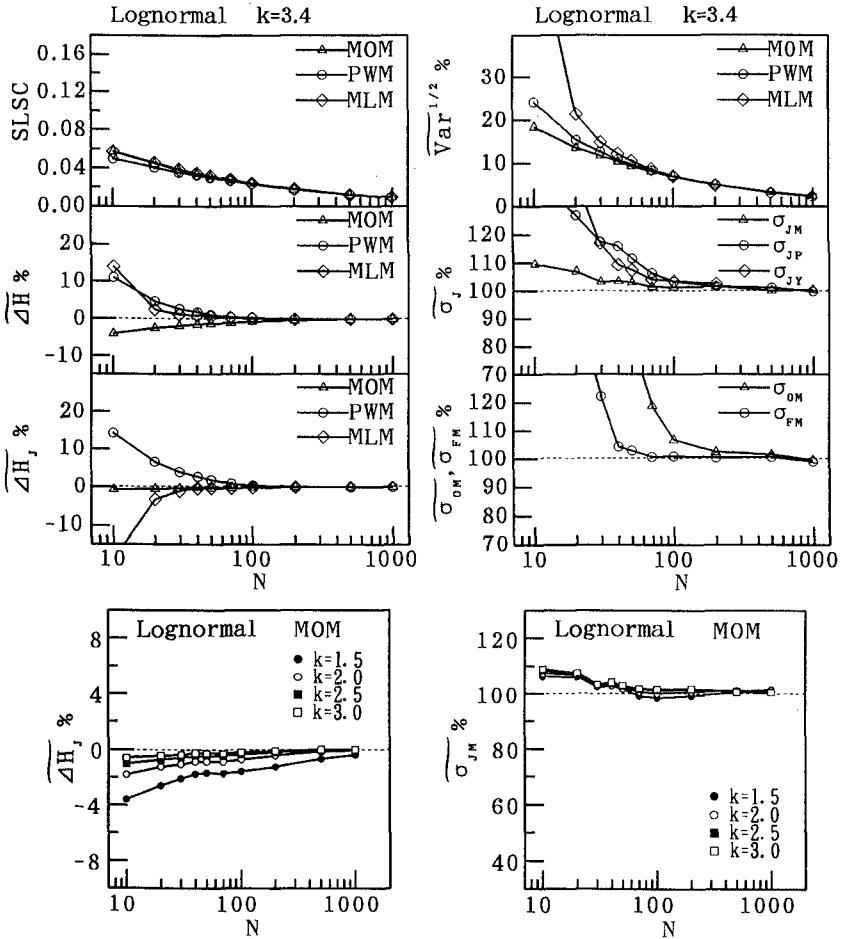


Fig. 4 Relation between error statistics and sample size (Lognormal distribution).

It can be said from similar investigation that the optimum parameter estimation method is the PWM method for the Gamma distribution, the MOM2 for the Loggamma distribution and the MOM for the Hypergamma distributions. Fig. 5 illustrates the effect of shape parameter on bias and estimate of variance in the cases of Gamma ($A=1.0$ m, $B=4.5$ m), Loggamma ($A=-0.1$ m, $B=3.5$ m) and Hypergamma ($A=0.447$ m, $C=2.0$) distributions. The shape parameters used are indicated in the corresponding figure. In the case of the Gamma distribution, even the PWM method which was judged to be the optimum method of the three methods pro-

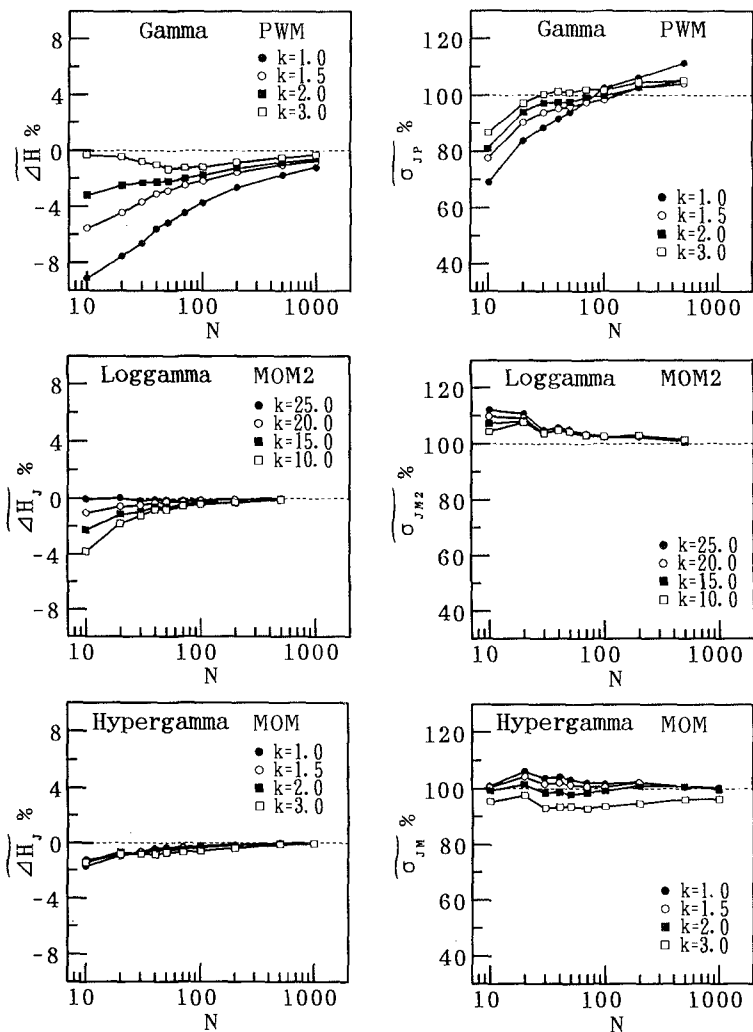


Fig. 5 Effect of shape parameter on error statistics (Gamma, Loggamma and Hypergamma distributions).

duces negative bias increasing with decrease of shape parameter, and the jackknife method does not work efficiently on the bias correction and the variance estimation. In the cases of the Loggamma and Hypergamma distribution, the jackknife method is effective for the correction to bias and the estimation of variance, although deviation from the true value slightly increases for wider distribution.

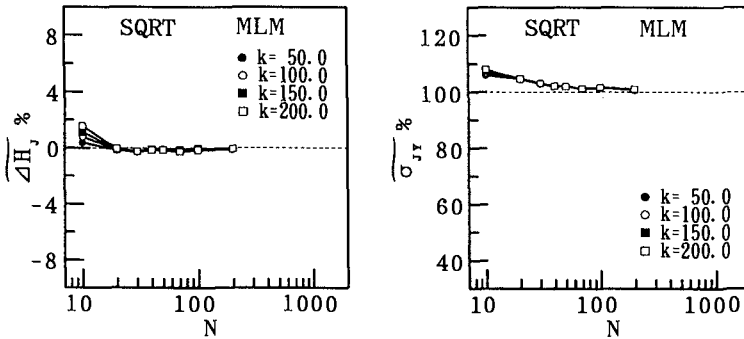


Fig. 6 Effect of shape parameter on error statistics (SQR distribution).

Finally, Fig. 6 shows the effect of shape parameter on bias and estimate of variance in the case of the SQR distribution. The scale parameter λ is fixed as $1/13$ m and the shape parameter k is either of 50, 100, 150 or 200. At present, the only method applicable to the parameter estimation is the MLM. As mentioned above, the parameter k means yearly-averaged occurrence rate of event. Change of shape parameter k in this case brings shift of a peak position of the distribution rather than variation of shape of the distribution. In the usage of the MLM, the jackknife method yields excellent correction to bias and proper estimate of variance for the given cases.

5. Conclusions

Conclusions in this study are summarized as follows.

- (1) A jackknife method is applicable to the correction of bias and the estimation of variance irrespective of parameter estimation methods in most parent probability distributions.
- (2) A preferable method to the parameter estimation in each distribution is determined as

Gumbel distribution	: PWM with jackknife correction
Weibull distribution	: PWM without jackknife correction
GEV distribution	: PWM with jackknife correction
Lognormal distribution	: MOM with jackknife correction
Gamma distribution	: PWM without jackknife correction
Loggamma distribution	: MOM2 with jackknife correction
Hypergamma distribution	: MOM with jackknife correction
SQR distribution	: MLM with jackknife correction

- (3) The LSM proposed by Goda is a preferable method from the view points of bias and goodness of fit.
- (4) The MLM with the jackknife method usually gives satisfactory estimates of return wave height and its variance for samples of size greater than about 50.
- (5) The information matrix methods are effective as variance estimators in the MLM for samples of size greater than about 50.

References

- Bobée, B.(1975): The log Pearson type 3 distribution and its application in hydrology, Water Resour. Res., Vol. 11, No. 5, pp.681-689.
- Condie R.(1977): The log Pearson type 3 distribution: the T-year event and its asymptotic standard error by maximum likelihood theory, Water Resour. Res., Vol. 13, No. 6, pp.987-991.
- Etoh, T. et al.(1986): Frequency of record-breaking large precipitation, Proc. JSCE, No. 369/11-5, pp.165-174 (in Japanese).
- Goda, Y.(1988): Numerical investigations on plotting formulas and confidence intervals of return values in extreme statistics, Rept. of the Port and Harb. Res. Inst., Vol. 27, No. 1, pp.31-91 (in Japanese).
- Goda, Y. and M. Onozawa(1990): Characteristics of the Fisher-Tippett type 11 distribution and their confidence intervals, Proc. JSCE, No. 417/11-13(note), pp.289-292 (in Japanese).
- Goda, Y. et al.(1993): Intercomparison of extremal wave analysis methods using numerically simulated data: a comparative analysis, Proc. WAVES'93 Conf., pp.963-977.
- Greenwood, J. A. et al.(1979): Probability weighted moments: definition and relation to parameters of several distributions expressible in inverse form, Water Resour. Res., Vol. 15, No. 5, pp.1049-1054.
- Hosking, J. R. M. et al. (1985): Estimation of the generalized extreme-value distribution by the method of probability-weighted moments, Technometrics, Vol.27, No. 3, pp.251-261.
- Miller, R. G.(1974): The jackknife - review, Biometrika, Vol. 61, No. 1, pp.1-15.

Phien, H. N. and F. T. Emma(1989): Maximum likelihood estimation on the parameters and quantiles of the general extreme-value distribution from censored sample, Jour. Hydrol., Vol.105, pp.139-155.

Suzuki, E.(1964): Hypergamma distribution and its fitting to rainfall data, Papers in Meteorol. and Geophy., Vol. 15, pp.31-51.

Takasao, T. et al.(1986): A basic study on frequency analysis of hydrologic data in the Lake Biwa basin, Annual Rept. of Disas. Prev. Res. Inst., Kyoto Univ., No. 29 B-2, pp.157-171 (in Japanese).

Takeuchi, K. and K. Tsuchiya(1988): PWM solutions to normal, lognormal and Pearson-III distributions, Proc. of JSCE, Vol. 393/II-9, pp.95-112 (in Japanese).

CHAPTER 72

INFLUENCES OF SPECTRAL SHAPES ON THE STATISTICAL PROPERTIES OF SIMULATED RANDOM WAVES

John Z. Yim¹ & M.-Y. Lai²

Abstract

Random wave fields were generated both numerically using a computer algorithm, and mechanically through a computer-controlled irregular wave generator. Statistical properties of these synthesized random waves are then compared with measured field results. It is shown that, irrespective of the methodology used, wave heights obtained from simulation always have a Rayleigh distribution, and surface elevations are approximately normally distributed, measured field data can, however, show other trend for the former with a large percentage of possibility.

Introduction

Random wave simulations provide a convenient tool for coastal engineers to study the stochastic properties associated with a wave field. Simulation can be carried out either numerically on a digital computer (Hudspeth & Borgman, 1979; Hudspeth & Chen, 1979), or physically through a computer-controlled wave generating device (Svendsen, 1985; Takayama, 1990). Tuah & Hudspeth (1982) compared the numerical methods then available, and a review was given recently by Hughes (1993). Depending upon the desired characteristics to be modeled, simulations can be carried out either in frequency (Hudspeth & Chen, 1979), or in time domain (Mo, 1993). In frequency domain, a white noise spectrum from certain pseudo-random number generator algorithm is filtered through a target spectrum. Surface elevations are then obtained by inverse Fourier transforming the simulated spectral densities.

¹Associate Professor, Dept. Harbour & River Engng., National Taiwan Ocean University, 2, Bee-Ning Road, 20224 Keelung, Taiwan, Rep. China.

²Graduate Student, Dept. Harbour & River Engng. National Taiwan Ocean University, 2, Bee-Ning Road, 20224 Keelung, Taiwan Rep. China.

For laboratory experiments, a (nonlinear) transfer function connecting the actual strokes of the wave generating device and simulated results must be further implemented.

Although not stated explicitly, it is often assumed that waves thus generated have all the characteristics that are in close agreement with those of actual wave fields (Kimura, 1981; Sobey, 1992). Deterministic properties obtained through analyzing simulated surface elevations are then used to verify theoretical predictions. Kimura (1981), for example, used a two-dimensional Weibull distribution to model the joint distribution of wave heights and periods of mechanically generated random waves. He found that the so-called shape parameter for the marginal distribution of wave heights has a value close to 2. Sobey (1992) studied the distributions of zero-crossing wave heights and periods of numerically simulated random wave fields, and concluded that, wave heights "*differ little from Rayleigh distribution.*" It should be noted that since Rayleigh distribution is a special case of the Weibull distribution with a shape parameter equals to 2, the findings of these two researchers, therefore, all indicate to the same fact that, simulated random waves have heights that are Rayleigh distributed.

It is well known that Longuet-Higgins (1952) derived the Rayleigh model based upon the assumptions of narrow-banded wave fields and normality of the surface fluctuations. Even though this model was often shown to overpredict larger wave heights (Chakrabarti & Cooley, 1977), most researchers, however, do find it rather satisfactory (Dattatri et al., 1979).

For the majority of studies concerning random wave simulations, a theoretical and/or empirical spectrum is often used as target spectrum. Spectra carrying the names such as Bretschneider-Mitsuyasu, Pierson-Moskowitz [P-M], or JONSWAP are the most frequently used ones. Among these spectra, the first two are often considered to represent fully developed seas and can be categorically termed as broad-banded, while the JONSWAP spectral shape is designated for growing wind-seas, and is thus narrow-banded.

Even if simulated random wave fields may have spectral shapes that have close resemblance with targets, it would be justifiable to ask whether other deterministic properties of the simulated wave fields, such as the probability distributions of wave heights and periods, would also bear the same affinity with reality. This assumption can be questioned when one considers that measured spectra are sometimes wider and flatter, and sometimes more energetic and narrower than theoretical predictions. Under these circumstances, it is not clear how close the deterministic statistical properties obtained from simulated random waves would match those of measured ones. Direct comparisons with field data are, as far as the authors are aware of, rather limited. This problem is addressed here in some detail.

In the following, the remaining of this paper is further divided into three parts. In section II a short description of the methodologies applied will be given. Section III presents some of the experimental results, and with a discussion in section IV we conclude this paper.

The methodology

Waves were also generated mechanically in a large wave flume of the Department of Harbour and River Engineering in National Taiwan Ocean University. The wave flume has a dimension of $100 \times 3.0 \times 3.0$ (length \times width \times height, in meters). Two series of experiments were conducted. For the first series of experiments only five wave gauges were installed. As the results of these experiments were not quite satisfactory, a second series of experiments with eight wave gauges was carried out. Variations of surface elevations along the flume were measured by capacitance wave gauges. Locations of the measuring stations are: 3.0, 12, 22, 32, and 42 meters for the first series of experiment, and 3.0, 12.0, 32.0, 42.0, 71.5, 73.4, 75.0, and 76.1 meters for the second series, away from the piston wave generator. Figure 1 shows the experimental setups for the first series of experiments.

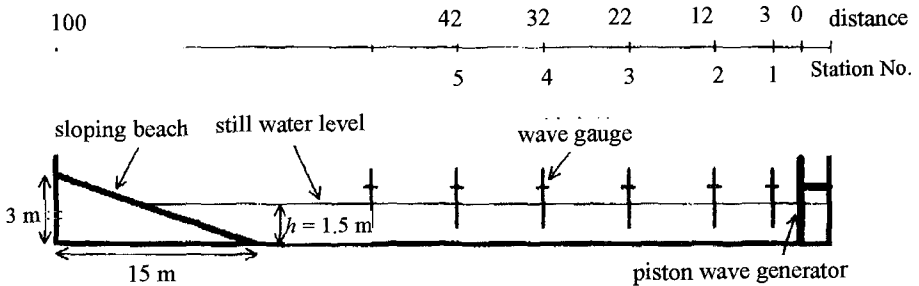


Fig. 1 Schematic representation of wave generation facilities.

Throughout the experiments, water depth was kept constant at 1.5 meter. As target spectrum, the theoretical five-parameter JONSWAP spectrum is used. Experimental conditions were varied by changing values of the parameters of the target spectrum. A recording time of 330 seconds (5.5 minutes) was used for all experiments so that statistical equilibrium in the wave flume was always achieved. Surface elevations measured by wave gauges and the amplified analog signals were then digitized by an A/D converter of type TEAC DR-F1. The sampling frequency is 50 Hz, so that each data set contains a total of 16,500 sampling points. Table 1 summarizes all the experimental conditions used.

During spectral analyses, wave records were further divided into segments, each containing 1024 data points. The degrees of freedom for the spectral density es-

timates are 32, with a frequency resolution equal to 0.048828. A total of 71 for the first, and 66 for the second, series of experiments were conducted.

Table 1 Experimental conditions (Symbols for f_p : a = 0.3; b = 0.5, c = 0.6, d = 0.8, and e = 1.0 Hz)

f_p	a, b, c, e	e	a, b, c, d, e	e	a, b, c, d, e	a, b, c, d, e	a, b, c, e	a, b, c, d	a, b, c, d, e	a, b, c, e
γ	1.0	1.0	3.0	3.0	3.3	3.3	3.3	3.3	3.3	3.3
σ_a	0.07	0.07	0.07	0.07	0.07	0.07	0.07	0.15	0.15	0.15
σ_b	0.09	0.3	0.09	1.0	0.09	0.3	1.0	0.09	0.3	1.0
f_p	a, b, c, d, e	a, b, c, d, e	a, b, c, d, e	a, b, c, d	e	a, b, c, d	e	a, b, c, d	e	--
γ	3.3	3.3	3.3	5.0	5.0	7.0	7.0	9.0	9	--
σ_a	1.0	1.0	1.0	0.07	0.15	0.07	0.15	0.07	0.15	--
σ_b	0.09	0.3	1.0	0.09	0.09	0.09	0.3	0.09	1.0	--

Field data were recorded with a pressure gauge in a two hour interval from October 1991 to October 1993 in northern Taiwan. The measuring station is located 800 m away from coastline where the mean water depth is 16 m. Total length of the data is 10 minutes with a sampling rate of 2.0 Hz. The field records were first divided into segments each containing 256 points. A cosine squared taper function was used to eliminate the discontinuities at the beginning and end of each record. The FFT calculated spectral densities were then smoothed with a Hanning window. The degrees of freedom and the frequency resolution are, 24 and 0.0078, respectively.

Numerical simulations were carried out using the two algorithms originally proposed by Tuah & Hudspeth (1982), with an extra term representing nonlinear correction as given by Duncan & Drake (1995). As target spectra, both measured and theoretical spectra were used. Every target spectrum was simulated 205 times and all the parameters obtained were averaged to account for statistical variability. All analyses were carried out on an IBM 586 compatible personal computer.

Traditional zero-crossing methods were applied for all "wave records." Characteristics of numerical simulations are compared with those obtained from measurements, either from laboratory, or field. Since the program for generating measured spectra in wave flume still needs some adjustments, only field spectra with shapes that can be fitted into the standard JONSWAP form were used for comparison. Probability distributions of wave heights, and surface elevations from all these three sources were compared with each other. Three models, namely, the Rayleigh,

the Gaussian, and the two-parameter Weibull, were used to test the distribution of wave heights. Surface elevations were fitted using a Gaussian and a Gram-Charlier series expansion.

The results

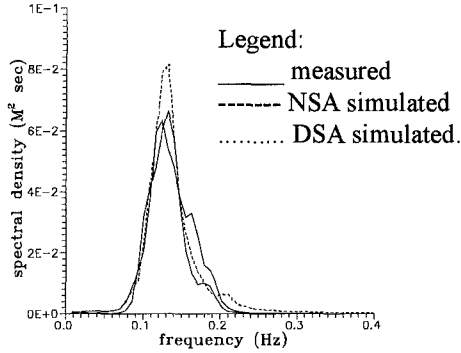


Fig. 2 Comparison of measured and simulated spectral densities: _____ measured; ----- NSA simulated and DSA simulated. Field data taken at 17.00, on February 4, 1992.

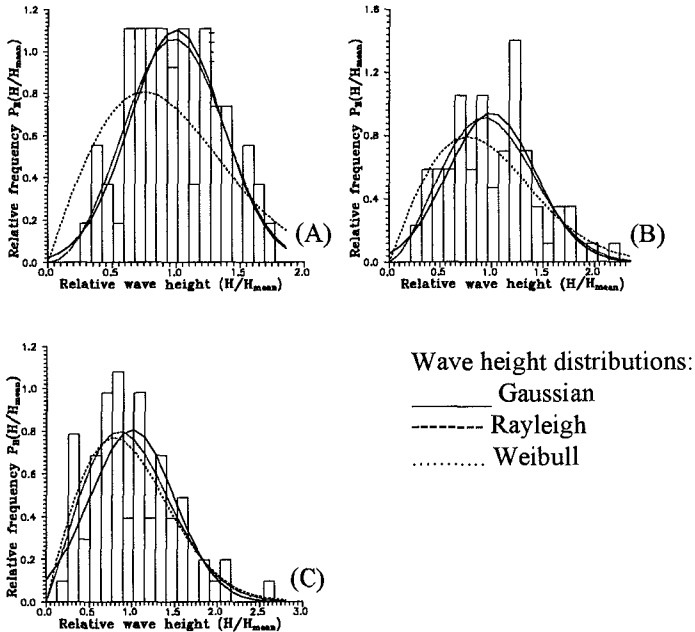


Fig. 3 Wave height distributions from measured (Fig. 3A), NSA simulated (Fig. 3B) and DSA simulated (Fig. 3C). Actual data source same as Fig. 2.

Even though spectral densities of target spectra can be modelled rather satisfactorily through the present algorithms, deterministic properties of a wave field can not be reproduced truthfully. Figure 3 compares measured wave height distribution with the 100th numerically simulated results. It should be mentioned that this choice is purely arbitrary. Three curves, representing, respectively, the Gaussian, the Rayleigh, and the Weibull distributions, were also plotted along with the histograms for comparison. As can be seen, simulated wave heights have distributions that are very close to the theoretical Rayleigh (Figs. 3B & 3C), whereas that of measured results can be approximated with Gaussian or the Weibull distribution (Fig. 3A), either one can fit the data better than the Rayleigh.

Distributions of measured and simulated surface elevations were plotted in Figure 4 for comparison. Also shown in the figure are the theoretical curves representing, respectively, normal distributions (solid lines) and the Edgeworth's form of the type A Gram-Charlier series (dotted lines). As can be seen from Figure 4, all surface elevations have probability distributions that are approximately Gaussian. Except causing small deviations from normality (Figs. 4B & 4C), nonlinear correction does not seem to a profound influence on the simulated results. In the following, since results concerning distributions of surface elevations are rather similar for all the cases studied, figures concerning this topic will not be presented for space reasons.

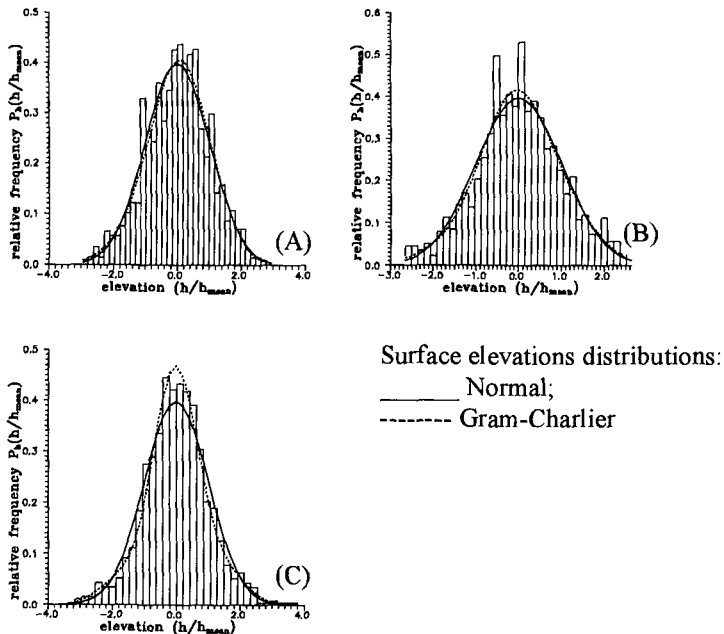


Fig. 4 Comparison of measured and simulated probability distributions for surface elevations. Original data source same as Figure 2.

As mentioned before, experiments were conducted by varying the parameters of the typical five-parameter JONSWAP spectrum. Figure 5 shows the development of the spectra along the wave flume for the first four measuring stations. Conditions used for this example is: peak frequency $f_p = 0.5$ Hz, peak enhancement factor $\gamma = 1.0$, with all other parameters equal to the standard JONSWAP spectrum. Nondimensionalized theoretical spectra are also shown in every figure for comparison. It is seen that, except for the irregularities occurred at approximately 0.75 Hz, the target spectra are reproduced quite satisfactorily.

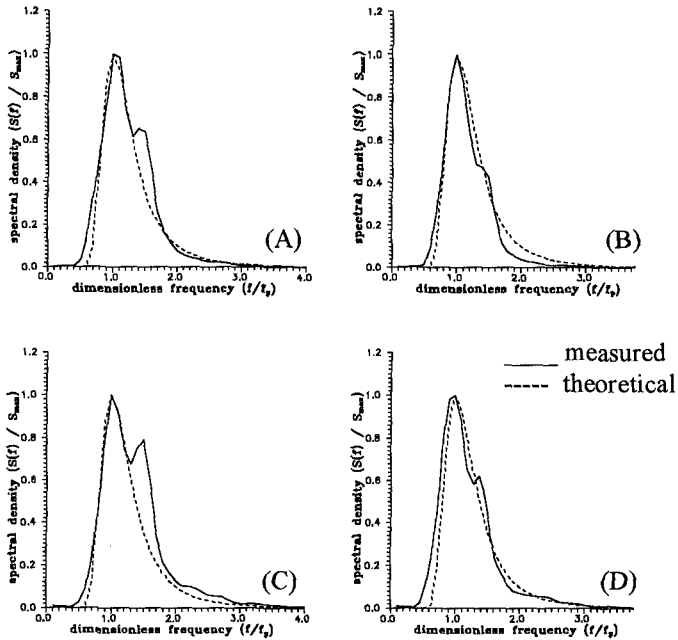


Fig. 5 Measured and theoretical spectra. Experimental conditions: $f_p = 0.5$ Hz, peak enhancement factor $\gamma = 1.0$.

Figure 6 shows the distributions of wave heights along the wave flume. As is seen from this figure, all the three models used seem can be used quite satisfactorily. In fact, judging from the χ^2 goodness-of-fit test results (Table 2), no definite conclusion can be drawn as which one of the models applied is more appropriate for this case. As can be seen from Table 2, based upon the χ^2 test results, the Gaussian model should sometimes be rejected. However, the numbers of misfits are too small to be conclusive.

Results shown in Figure 6 are not inconsistent with theoretical predictions. As is well known, Longuet-Higgins (1952) derived the Rayleigh distribution for wave heights based upon the assumptions of narrow-bandedness and Gaussianity of the

surface elevations. With $\gamma = 1$ of the JONSWAP spectrum, the case shown in Figures 5 & 6 represents, however, Pierson-Moskowitz spectrum for a fully-developed wind-sea. A fully-developed wave field has energies more widely spread over low- and high-frequency component waves, as compared with the case for growing sea. Wave heights for a typical P-M spectrum should, therefore, differ from those for JONSWAP.

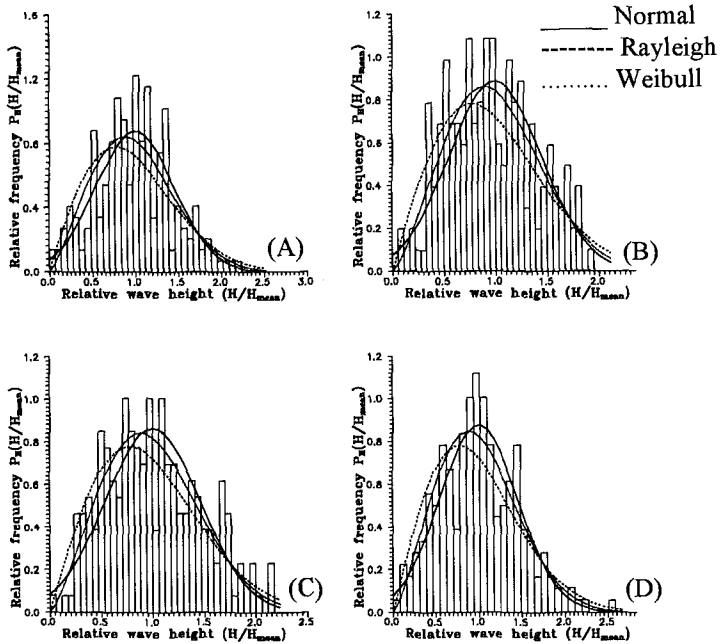


Fig. 6 Distributions of wave heights for the first four stations along the wave flume. Experimental conditions same as Fig. 5.

Table 2 shows values of the χ^2 goodness-of-fit test results for the second series of experiments. For every peak frequency considered, there are occasions where the χ^2 test results of the fitted normal distribution are too large for the theoretical values of the χ^2 distribution based on a 90% confidence interval. This is called misfit here in this paper and the total count of misfits for every peak frequency is shown in the square parentheses in the table. Since for the other two models, namely Rayleigh and Weibull distributions, no misfits occurred, it seems that the normal distribution is probably not a good model for simulated wave heights in a wave flume. However, it seems worth mentioning that the maximum count of misfits is limited to 3, for peak frequency $f_p = 1.0$ Hz at station 3. Considering the total number of experiments for this series, namely 66, it seems also safe to say that this model can not be totally rejected as well. It should, however, be remembered that among other available tests, the χ^2 goodness-of-fit test is not a very stringent one and perhaps other tests should be used before any definite conclusion can be drawn.

Table 2 Statistical properties of χ^2 goodness-of-fit test results for wave height distributions. Figures shown are mean values, figures in the parentheses represent standard deviations, and figures in the square parentheses are number of misfits, i.e., the model should be rejected.

frequency (f_p) [Hz]		0.5	0.8	1.0
χ^2 test results				
Normal	Station 1	5.47 (6.02) [0]	4.05 (1.68) [2]	5.66 (4.35) [1]
	Station 2	3.22 (0.96) [1]	4.94 (4.47) [1]	5.48 (3.35) [1]
	Station 3	3.13 (0.98) [0]	5.46 (4.36) [1]	6.50 (4.01) [3]
	Station 4	5.81 (4.81) [2]	4.19 (1.85) [1]	6.65 (5.58) [1]
Rayleigh	Station 1	3.68 (1.09) [0]	3.28 (0.83) [0]	3.12 (0.90) [0]
	Station 2	3.24 (0.80) [0]	2.39 (0.60) [0]	2.99 (0.67) [0]
	Station 3	4.79 (1.17) [0]	3.18 (0.75) [0]	2.91 (0.85) [0]
	Station 4	3.39 (0.94) [0]	2.87 (0.64) [0]	3.17 (0.58) [0]
Weibull	Station 1	3.40 (1.60) [0]	2.71 (0.87) [0]	3.15 (2.07) [0]
	Station 2	3.16 (0.99) [0]	2.41 (1.34) [0]	3.33 (2.73) [0]
	Station 3	2.90 (0.85) [0]	3.01 (1.02) [0]	4.31 (4.41) [0]
	Station 4	4.65 (5.03) [0]	2.71 (1.09) [0]	3.26 (1.28) [0]

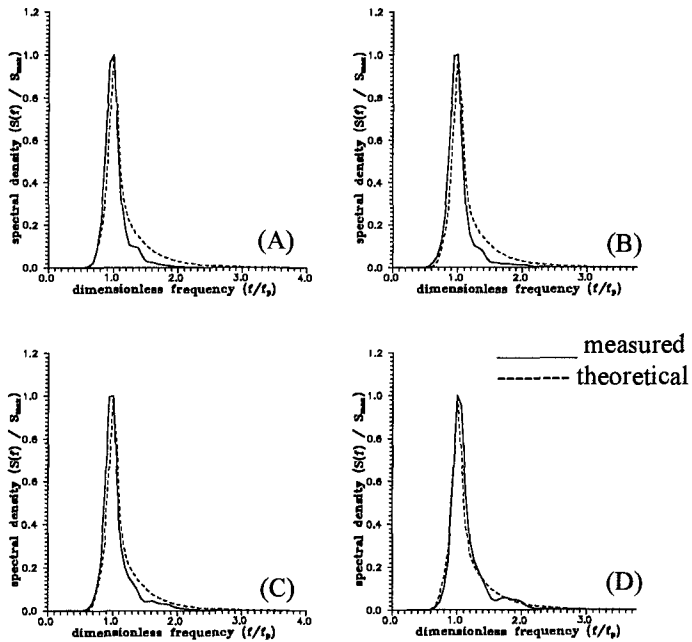


Fig. 7 Development of spectral densities of simulated JONSWAP spectrum along the wave flume. Experimental conditions: $f_p = 0.8$ Hz, $\gamma = 3.3$. Figs. (A)-(D): Measuring stations 1-4.

For the case with narrower band width, Figure 7 shows measured spectra along the flume. It is seen that high frequency components are missing at the first three stations, as compared with theoretical predictions. Whether this will affect the deterministic properties of simulated wave fields is not known at present, but is believed to be small. This is because wave heights from other experiments (not shown here) all have probability distributions that are not markedly different to those shown in Fig. 8. Wave heights for this experiments are rather scattered. Judging by eye examination, strictly speaking, all of the three models applied are not suitable for describing the probability distribution of wave heights in the flume. However, based upon the χ^2 test results, none of these models can also be rejected. It should be stressed that, wave heights shown in this figure are rather special, because in analyzing our experimental results, it is found that wave heights are mostly Rayleigh distributed. This fact is also reflected in Table 2, where all the χ^2 test results of the Rayleigh distribution are smaller than those for the other two models.

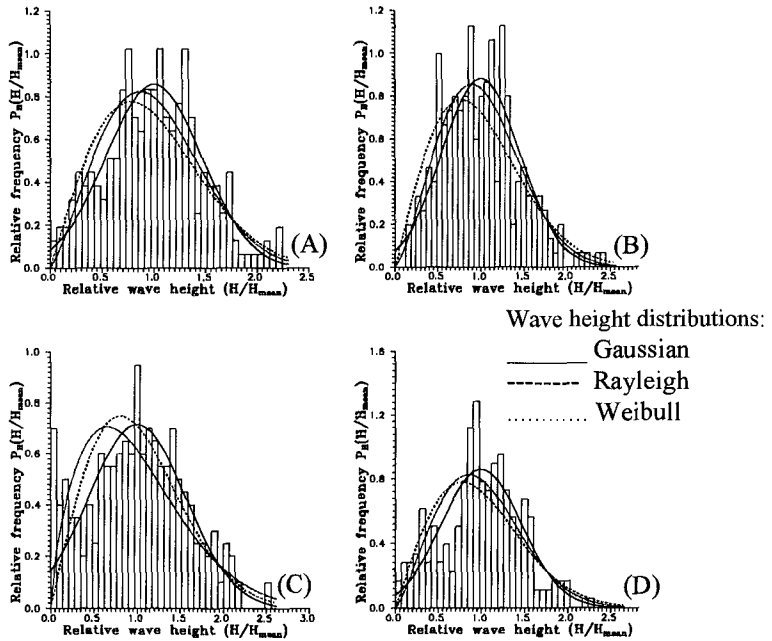


Fig. 8 Distributions of wave heights along the flume. Experimental conditions same as Fig. 7.

Discussions and Conclusions

When the energy of a random wave field is concentrated within a few components (narrow-bandedness), and when the phases of these waves are randomly distributed, then as shown by Longuet-Higgins (1952), wave heights should have a

Rayleigh distribution. Almost all (linear) random wave simulation techniques presently available, utilize these two basic assumptions. Even though a (nonlinear) transfer function is involved in wave flume experiments, present study indicates that the results have little difference as compared with numerical simulations.

In the experiments the JONSWAP spectrum is used. This can be written as:

$$S(f) = \frac{\alpha g^2}{(2\pi)^4 f^5} \exp\left[-\frac{5}{4}\left(\frac{f}{f_p}\right)^{-4}\right] \gamma^a \quad \dots (1)$$

where

f_p = the peak frequency;

α = the "Phillips constant" with a mean value of 0.0081;

γ = the peak enhancement factor, having a mean value of 3.3; with

$$a = \exp\left[-\frac{(f - f_p)^2}{2 \sigma^2 f_p^2}\right] \quad \dots (2)$$

and

$$\sigma = \begin{cases} \sigma_a = 0.07 & \text{for } f \leq f_p \\ \sigma_b = 0.09 & \text{for } f > f_p \end{cases} \quad \dots (3)$$

where the parameters σ_a and σ_b denote deviations from the peak frequency to, respectively, the left and right side of the corresponding Pierson-Moskowitz (P-M) spectrum. As can be seen from Eq. (1), the P-M spectrum is recovered with the peak enhancement factor $\gamma = 1$. It is generally believed that the JONSWAP spectrum represents the case of active wave generation by wind, where energies are concentrated; and the P-M spectrum represents fully developed wind-sea, where energies of the wave field are spread more or less widely over frequency bands.

During second series of the physical experiments, three values, $\gamma = 1.0, 3.3,$ and $7.0,$ of the peak enhancement factor were chosen. It is considered that in this way the results should cover all the possible conditions encountered in the reality, i.e., from extremely narrow- to broad-bandedness. Effects of spectral width on wave height distribution have been studied theoretically by Longuet-Higgins (1980), and experimentally by Larsen (1981). They all concluded that spectral width affects the distribution more profoundly than nonlinearity. Our present results indicate, however, no noticeable effects can be found in simulated random wave fields, at least with the present algorithms.

Simulations were also carried out numerically using spectra from measured field data. The results indicate that, irrespective of the underlying target spectral shapes, wave heights obtained from synthesized wave records always have a distribution that is better to be approximated by a Rayleigh than the other two models used. With the inclusion of a term representing nonlinearity in the algorithms, it is found that only the probability distributions of surface elevations is slightly improved, whereas wave heights may still have distributions that deviate largely from reality. In conclusion, it is plausible to say, even though simulated waves may have spectral densities similar to that of the targets, this does not necessarily mean that other characteristics of the wave field are also successfully modelled automatically. Possible modifications of the applied methodologies are needed and are presently under study.

Acknowledgments: This work is supported by the National Science Council of the Rep. China. Contract No. NSC 83-0209-E-019-004

References

- Chakrabarti, S. K. & Cooley, R. P. (1977). "Ocean wave statistics for 1961 North Atlantic storm" *J. Waterway Port Coastal & Ocean Div. ASCE*, 103, 433-448.
- Dattatri, J., H. Raman & N. J. Shankar (1979) "Height and period distribution for waves off Mangalore Harbour - West coast" *J. Geophys. Res.*, C84, 3767-3772.
- Duncan, P. E. & K. R. Drake (1995) "A note on the simulation and analysis of irregular non-linear waves" *Appl. Ocean Res.*, 17, 1-8.
- Hudspeth, R. T. & L. E. Borgman (1979) "Efficient FFT simulation of digital time sequences" *J. Engineering Mech. Div. ASCE*, 105, 223-235.
- Hudspeth, R. T. & M.-C. Chen (1979) "Digital simulation of nonlinear random waves" *J. Waterway, Port, Coastal and Ocean Div.*, ASCE, 105, 67-85
- Hughes, S. A. (1993) "*Physical models and laboratory techniques in coastal engineering*" World Scientific Pub. Co. Singapore, 392-427.
- Kimura, A. (1981) "Joint distribution of the wave heights and periods of random sea waves" *Coastal Eng. Japan*, 24, 77-92.
- Larsen, L.H. (1981). "The influence of bandwidth of the distribution of heights of sea waves" *J. Geophys. Res.*, C86, 4299-4301.
- Longuet-Higgins, M. S. (1952) "On the statistical distribution of the heights of sea waves" *J. Marine Res.*, 9, 245-266.
- Longuet-Higgins, M.S. (1980). "On the distribution of the heights of sea waves: some effects of nonlinearity and finite band width" *J. Geophys. Res.*, 85, 1519-1523.
- Mo. K. (1993) "An efficient method for simulation of wave elevation and wave drift force in the time domain" *Appl. Ocean Res.*, 15, 57-59.
- Sobey, R. J. (1992) "The distribution of zero-crossing wave heights and periods in a stationary sea state" *Ocean Engng.*, 19, 101-118.

- Svendsen, I. A. 1985 "*Physical modelling of water waves*" in Dalrymple, R. A. (ed.) "*Physical modelling in coastal engineering*" Balkema Rotterdam, 13-48.
- Tuah, H. & R. T. Hudspeth 1982 "Comparisons of numerical random sea simulations" *J. Waterway, Port, Coastal & Ocean Eng.*, ASCE, 108, 569-584.
- Takayama, T. (1990) "Laboratory wave generation" in "*The sea*" Vol. 9 "*Ocean Engineering Science*" Le Mehaute, B. & D. M. Hanes (eds.), Part B, Wiley-Interscience Pub., 1007-1032.

CHAPTER 73

SECOND-ORDER INTERACTION BETWEEN RANDOM WAVE AND SUBMERGED OBSTACLE

Akinori Yoshida¹, Keisuke Murakami,²
Masaru Yamashiro³, Haruyuki Kojima⁴

Abstract

A numerical method to solve the second-order interaction between a multi-component random wave and a submerged obstacle is presented by using Stokes' wave expansion and Green's second identity. The wave is unidirectional random wave, but nonlinear interaction up to the second-order is strictly considered. Laboratory experiments with several multicomponent random waves for several different wave powers are conducted. The transmitted wave spectra obtained both in the experiment and in the numerical calculation are compared. The effects of wave breaking on the obstacle to the transmitted wave spectra are also investigated.

Introduction

When propagating waves encounter a submerged obstacle, comparably large amplitude of higher order waves (free waves) could be generated because of the abruptly decreased water depth and nonlinear free-surface boundary condition. This free wave generation is called near-resonant interaction (e.g., Bryand, 1973). Several numerical method applicable to solve this nonlinear wave-structure interaction have been presented: for example, Massel(1983) solved the second-order interaction for a submerged step using the method of matched eigenfunction expansions; Ohyama and Nadaoka (1992) investigated nonlinear interaction for a submerged dike using time domain boundary integral

¹Associate Professor, Dept. of Civil Eng., Kyushu Univ., Hakozaki, Higashi-ku, Fukuoka 812, Japan

²Research Associate, ditto

³Graduate student, ditto

⁴Professor, Dept. of Civil Eng., Kyushu Kyoritsu Univ., Yahatanishi-ku, Kitakyushu, 807, Japan

equation method; Kojima et al.(1994) clarified the second-order interaction for a submerged horizontal plate using the collocation method of matched eigenfunction expansions; Yoshida. et al.(1994) solved the second-order interaction between bichromatic wave and submerged structure using a frequency domain boundary integral equation method.

These solutions however deal mostly with interaction of a single frequency component wave. Since in real sea state waves generally consist of a multicomponent wave of different frequency, second-order interactions between different frequency components also occur, and lower and higher harmonics at the difference and the sum frequencies of the primary component waves are generated. The knowledge of this energy transfer between frequencies caused by nonlinear wave-structure interactions seems to be lacking.

Main aim of this study is to obtain a theoretical method to solve interaction problems between a random wave train of arbitrary spectrum and a submerged obstacle in relatively deep water depth. The wave is an unidirectional random wave, but nonlinear interaction up to the second-order is strictly considered. A solution to a multicomponent random wave is first derived using frequency domain boundary integral equation method, then Laboratory experiments with several multicomponent random waves are conducted as well as numerical calculations. Transmitted wave spectra obtained in the experiment are compared to those obtained with the present method. The effect of wave breaking on the obstacle to the free-wave generation is also investigated.

Theoretical Formulation

Basic assumptions and free surface boundary condition

As shown in figure-1, a N component random wave is incident on a submerged obstacle from the positive x -direction. The water depth h is constant, and the angular frequency of each component wave is designated with σ_p , ($p = 1, \dots, N$). Fluid motion is assumed to be incompressible, inviscid wave motion, and the velocity potential $\Phi(x, z, t)$ exists. We consider the waves are Stokes' waves, and the velocity potential $\Phi(x, z, t)$, water surface variation $\zeta(x, t)$, Bernoulli's constant $Q(t)$ can be expanded with small parameter $\epsilon (= k\zeta_0)$ as follows:

$$\Phi(x, z, t) = \frac{g\zeta_0}{\sigma} \left\{ \epsilon\varphi^{(1)}(x, z, t) + \epsilon^2\varphi^{(2)}(x, z, t) + \dots \right\} \quad (1)$$

$$\zeta(x, t) = \zeta_0 \left\{ \zeta^{(1)}(x, t) + \epsilon\zeta^{(2)}(x, t) + \dots \right\} \quad (2)$$

$$Q(t) = g\zeta_0 \left\{ Q^{(1)}(t) + \epsilon Q^{(2)}(t) + \dots \right\} \quad (3)$$

in which k , σ , ζ_0 mean the wave number, the angular frequency and the wave amplitude, respectively, of a characteristic wave in the multicomponent random wave.

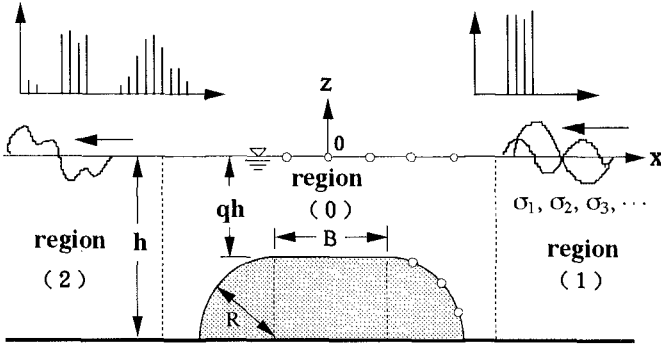


Figure 1: Definition sketch

From Stokes' wave theory, the free surface boundary condition for the second-order velocity potential $\varphi^{(2)}$ can be expressed in terms of the first-order velocity potential $\varphi^{(1)}$ as (e.g. Newman,1977)

$$\frac{\partial\varphi^{(2)}}{\partial z} + \frac{1}{g} \frac{\partial^2\varphi^{(2)}}{\partial t^2} = -\frac{1}{k\sigma} \frac{\partial}{\partial t} \left\{ \left(\frac{\partial\varphi^{(1)}}{\partial x} \right)^2 + \left(\frac{\partial\varphi^{(1)}}{\partial z} \right)^2 \right\} - \frac{1}{kg\sigma} \frac{\partial\varphi^{(1)}}{\partial t} \frac{\partial}{\partial z} \left\{ \frac{\partial^2\varphi^{(1)}}{\partial t^2} + g \frac{\partial\varphi^{(1)}}{\partial z} \right\} + \frac{\sigma}{g} \frac{\partial Q^{(2)}(t)}{\partial t} \tag{4}$$

The first-order velocity potential $\varphi^{(1)}(x, z, t)$ can be expressed as

$$\varphi^{(1)}(x, z, t) = Re \left[\sum_{p=1}^N \phi_p(x, z) e^{i\sigma_p t} \right] \tag{5}$$

where $\phi_p(x, z)$ is a non-dimensional complex function.

Substituting equation (5) into equation (4), we have

$$\frac{\partial\varphi^{(2)}}{\partial z} + \frac{1}{g} \frac{\partial^2\varphi^{(2)}}{\partial t^2} - \frac{\sigma}{g} \frac{\partial Q^{(2)}}{\partial t} = Re \left[\sum_{p=1}^N \left\{ \Omega_{pp}(x) e^{i\sigma_p t} + \Pi_{pp}(x) \right\} + \sum_{p=1}^N \sum_{q=p+1}^N \left\{ \Omega_{pq}(x) e^{i\sigma_{pq} t} + \bar{\Omega}_{pq}(x) e^{i\bar{\sigma}_{pq} t} \right\} \right] \tag{6}$$

where $\Omega_{pp}(x)$, $\Omega_{pq}(x)$, $\bar{\Omega}_{pq}(x)$ and $\Pi_{pp}(x)$ are given by

$$\Omega_{pp}(x) = -\frac{i}{2k} \left[\frac{\sigma_{pp}}{\sigma} \left\{ \left(\frac{\partial\phi_p}{\partial x} \right)^2 + \left(\frac{\partial\phi_p}{\partial z} \right)^2 \right\} + \frac{\sigma_p}{\sigma} \phi_p \left\{ \frac{\sigma_p^2}{g} \frac{\partial\phi_p}{\partial z} - \frac{\partial^2\phi_p}{\partial z^2} \right\} \right]_{z=0} \tag{7}$$

$$\Omega_{pq}(x) = -\frac{i}{2k} \left[2 \frac{\sigma_{pq}}{\sigma} \left\{ \frac{\partial \phi_p}{\partial x} \frac{\partial \phi_q}{\partial x} + \frac{\partial \phi_p}{\partial z} \frac{\partial \phi_q}{\partial z} \right\} + \frac{\sigma_p}{\sigma} \phi_p \left\{ \frac{\sigma_q^2}{g} \frac{\partial \phi_q}{\partial z} - \frac{\partial^2 \phi_q}{\partial z^2} \right\} + \frac{\sigma_q}{\sigma} \phi_q \left\{ \frac{\sigma_p^2}{g} \frac{\partial \phi_p}{\partial z} - \frac{\partial^2 \phi_p}{\partial z^2} \right\} \right]_{z=0} \quad (8)$$

$$\bar{\Omega}_{pq}(x) = -\frac{i}{2k} \left[2 \frac{\bar{\sigma}_{pq}}{\sigma} \left\{ \frac{\partial \phi_p}{\partial x} \frac{\partial \bar{\phi}_q}{\partial x} + \frac{\partial \phi_p}{\partial z} \frac{\partial \bar{\phi}_q}{\partial z} \right\} + \frac{\sigma_p}{\sigma} \phi_p \left\{ \frac{\sigma_q^2}{g} \frac{\partial \bar{\phi}_q}{\partial z} - \frac{\partial^2 \bar{\phi}_q}{\partial z^2} \right\} - \frac{\sigma_q}{\sigma} \bar{\phi}_q \left\{ \frac{\sigma_p^2}{g} \frac{\partial \phi_p}{\partial z} - \frac{\partial^2 \phi_p}{\partial z^2} \right\} \right]_{z=0} \quad (9)$$

$$\Pi_{pp}(x) = -\frac{i}{2k} \left[\frac{\sigma_p}{\sigma} \phi_p \left\{ \frac{\sigma_p^2}{g} \frac{\partial \bar{\phi}_p}{\partial z} - \frac{\partial^2 \bar{\phi}_p}{\partial z^2} \right\} \right]_{z=0} \quad (10)$$

in which $\bar{\phi}_q, \partial \bar{\phi}_p / \partial z, \dots$ mean complex conjugate of $\phi_q, \partial \phi_p / \partial z, \dots$, and $\sigma_{pp}, \sigma_{pq}, \bar{\sigma}_{pq}$ mean angular frequencies defined by $\sigma_{pp} = 2\sigma_p, \sigma_{pq} = \sigma_p + \sigma_q, \bar{\sigma}_{pq} = \sigma_p - \sigma_q$

Equation (6) implies the second-order potential $\varphi^{(2)}$ takes the form as

$$\varphi^{(2)}(x, z, t) = Re \left[\sum_{p=1}^N \left\{ \phi_{0pp}^{(2)}(x, z) + \phi_{pp}^{(2)}(x, z) e^{i\sigma_{pp}t} \right\} + \sum_{p=1}^N \sum_{q=p+1}^N \left\{ \phi_{pq}^{(2)}(x, z) e^{i\sigma_{pq}t} + \phi_{pq*}^{(2)}(x, z) e^{i\bar{\sigma}_{pq}t} \right\} \right] \quad (11)$$

where $\phi_{0pp}^{(2)}(x, z), \phi_{pp}^{(2)}(x, z), \dots$ are non-dimensional complex functions; the stationary component $\phi_{0pp}^{(2)}(x, z)$ does not contribute to the estimation of the second-order water surface variation and the pressure of the fluid motion, thus it will be neglected in the theoretical formulation from now on.

Then from equation (11) and equation (6), the free surface boundary conditions for $\phi_{pp}^{(2)}, \phi_{pq}^{(2)}$ and $\phi_{pq*}^{(2)}$ are obtained, for example, for $\phi_{pp}^{(2)}$ as

$$\frac{\partial \phi_{pp}^{(2)}}{\partial z} - \frac{\sigma_{pp}^2}{g} \phi_{pp}^{(2)} = \Omega_{pp}(x) \quad (12)$$

Exact solutions in the open regions (1) and (2)

The first-order potential functions ϕ_p in the open region (1) and (2) are found in any textbook and they can be expressed as:

$$\phi_p(x, z) = \begin{cases} \{ a_p e^{ik_p x} + A_p e^{-ik_p x} \} Z(k_p, z) & \text{(region(1))} \\ \{ B_p e^{ik_p x} \} Z(k_p, z) & \text{(region(2))} \end{cases} \quad (13)$$

in which $Z(k_p, z) = \cosh k_p(z + h) / \cosh k_p h$ and k_p is the wave number given by the dispersion equation, $\sigma_p^2/g = k_p \tanh k_p h$.

The complex coefficient a_p denotes the wave amplitude and phase of each component of the incident wave, with angular frequency σ_p ; the complex coefficients A_p and B_p , the wave amplitude and phase of each component of the reflected and transmitted waves, respectively.

Substitution of the first-order potential into equations (7), (8) and (9) yields

$$\Omega_{pp}(x) = \begin{cases} -i\beta_1 \{ a_p^2 e^{ik_{pp}x} + A_p^2 e^{-ik_{pp}x} \} - i\beta_2 a_p A_p & \text{(region(1))} \\ -i\beta_1 B_p e^{ik_{pp}x} & \text{(region(2))} \end{cases} \tag{14}$$

$$\Omega_{pq}(x) = \begin{cases} -i\beta_3 \{ a_p a_q e^{ik_{pq}x} + A_p A_q e^{-ik_{pq}x} \} \\ \quad -i\beta_4 \{ a_p A_q e^{i\bar{k}_{pq}x} + a_q A_p e^{-i\bar{k}_{pq}x} \} & \text{(region(1))} \\ -i\beta_3 B_p B_q e^{ik_{pq}x} & \text{(region(2))} \end{cases} \tag{15}$$

$$\bar{\Omega}_{pq}(x) = \begin{cases} -i\beta_5 \{ a_p \bar{a}_q e^{i\bar{k}_{pq}x} + A_p \bar{A}_q e^{-i\bar{k}_{pq}x} \} \\ \quad -i\beta_6 \{ a_p \bar{A}_q e^{ik_{pq}x} + \bar{a}_q A_p e^{-ik_{pq}x} \} & \text{(region(1))} \\ -i\beta_5 B_p \bar{B}_q e^{i\bar{k}_{pq}x} & \text{(region(2))} \end{cases} \tag{16}$$

in which $k_{pp} = k_p + k_p$, $k_{pq} = k_p + k_q$, $\bar{k}_{pq} = |k_p - k_q|$, $\Gamma_p = \sigma_p^2/g$ and β_1, β_2, \dots are

$$\left. \begin{aligned} \beta_1 &= \frac{3}{2k} \frac{\sigma_p}{\sigma} \{ \Gamma_p^2 - k_p^2 \}, & \beta_2 &= \frac{1}{k} \frac{\sigma_p}{\sigma} \{ 3\Gamma_p^2 + k_p^2 \} \\ \beta_3 &= \frac{1}{2k} \left[2 \frac{\sigma_{pq}}{\sigma} \{ \Gamma_p \Gamma_q - k_p k_q \} + \frac{\sigma_p}{\sigma} \{ \Gamma_q^2 - k_q^2 \} + \frac{\sigma_q}{\sigma} \{ \Gamma_p^2 - k_p^2 \} \right] \\ \beta_4 &= \frac{1}{2k} \left[2 \frac{\sigma_{pq}}{\sigma} \{ \Gamma_p \Gamma_q + k_p k_q \} + \frac{\sigma_p}{\sigma} \{ \Gamma_q^2 - k_q^2 \} + \frac{\sigma_q}{\sigma} \{ \Gamma_p^2 - k_p^2 \} \right] \\ \beta_5 &= \frac{1}{2k} \left[2 \frac{\bar{\sigma}_{pq}}{\sigma} \{ \Gamma_p \Gamma_q + k_p k_q \} + \frac{\sigma_p}{\sigma} \{ \Gamma_q^2 - k_q^2 \} - \frac{\sigma_q}{\sigma} \{ \Gamma_p^2 - k_p^2 \} \right] \\ \beta_6 &= \frac{1}{2k} \left[2 \frac{\bar{\sigma}_{pq}}{\sigma} \{ \Gamma_p \Gamma_q - k_p k_q \} + \frac{\sigma_p}{\sigma} \{ \Gamma_q^2 - k_q^2 \} - \frac{\sigma_q}{\sigma} \{ \Gamma_p^2 - k_p^2 \} \right] \end{aligned} \right\}$$

Now we can derive a general solution of the second-order potential function in the open region (1) and (2). The equations, for example, governing $\phi_{pp}^{(2)}$ can be given by

$$\frac{\partial^2 \phi_{pp}^{(2)}}{\partial x^2} + \frac{\partial^2 \phi_{pp}^{(2)}}{\partial z^2} = 0 \quad (-h \leq z \leq 0) \tag{17}$$

$$\frac{\partial \phi_{pp}^{(2)}}{\partial z} = 0 \quad (z = -h) \tag{18}$$

$$\frac{\partial \phi_{pp}^{(2)}}{\partial z} - \frac{\sigma_{pp}^2}{g} \phi_{pp}^{(2)} = -i\beta_1 \left\{ a_p^2 e^{ik_{pp}x} + A_p^2 e^{-ik_{pp}x} \right\} - i\beta_2 a_p A_p \quad (z = 0) \tag{19}$$

The general solution $\phi_{pp}^{(2)}$ can be obtained by the sum of a homogeneous solution which satisfies homogeneous surface boundary condition given by replacing the right-hand side of equation (19) by zero and a special solution which satisfies equation (19), and it can be obtained, after some calculations, as

$$\left. \begin{aligned} \phi_{pp}^{(2)}(x, z) = & A_{pp}^{(2)} Z(k_{pp}^{(2)}, z) e^{-ik_{pp}^{(2)}x} + i b_{s1} a_p A_p \\ & + i a_{s1} \left\{ a_p^2 e^{ik_{pp}x} + A_p^2 e^{-ik_{pp}x} \right\} Z(k_{pp}, z) \end{aligned} \right\} \tag{20}$$

and similarly $\phi_{pq}^{(2)}$ and $\phi_{pq*}^{(2)}$ are also obtained as:

$$\left. \begin{aligned} \phi_{pq}^{(2)}(x, z) = & A_{pq}^{(2)} Z(k_{pq}^{(2)}, z) e^{-ik_{pq}^{(2)}x} \\ & + i c_{s1} \left\{ a_p a_q e^{ik_{pq}x} + A_p A_q e^{-ik_{pq}x} \right\} Z(k_{pq}, z) \\ & + i d_{s1} \left\{ a_p A_q e^{i\bar{k}_{pq}x} + A_p a_q e^{-i\bar{k}_{pq}x} \right\} Z(\bar{k}_{pq}, z) \end{aligned} \right\} \tag{21}$$

$$\left. \begin{aligned} \phi_{pq*}^{(2)}(x, z) = & A_{pq*}^{(2)} Z(k_{pq*}^{(2)}, z) e^{-ik_{pq*}^{(2)}x} \\ & + i d_{s2} \left\{ a_p \bar{a}_q e^{i\bar{k}_{pq}x} + A_p \bar{A}_q e^{-i\bar{k}_{pq}x} \right\} Z(\bar{k}_{pq}, z) \\ & + i c_{s2} \left\{ a_p \bar{A}_q e^{ik_{pq}x} + A_p \bar{a}_q e^{-ik_{pq}x} \right\} Z(k_{pq}, z) \end{aligned} \right\} \tag{22}$$

in which $k_{pp}^{(2)}$, $k_{pq}^{(2)}$ and $k_{pq*}^{(2)}$ are the wave numbers given by the dispersion equations to angular frequencies, σ_{pp} , σ_{pq} and $\bar{\sigma}_{pq}$, respectively. The coefficients a_{s1} , b_{s1} , \dots are

$$\left. \begin{aligned} a_{s1} = & \frac{-\beta_1}{k_{pp} \tanh k_{pp} h - \Gamma_{pp}}, & b_{s1} = & \frac{\beta_2}{\Gamma_{pp}} \\ c_{s1} = & \frac{-\beta_3}{k_{pq} \tanh k_{pq} h - \Gamma_{pq}}, & c_{s2} = & \frac{-\beta_6}{k_{pq} \tanh k_{pq} h - \bar{\Gamma}_{pq}} \\ d_{s1} = & \frac{-\beta_4}{\bar{k}_{pq} \tanh \bar{k}_{pq} h - \Gamma_{pq}}, & d_{s2} = & \frac{-\beta_5}{\bar{k}_{pq} \tanh \bar{k}_{pq} h - \bar{\Gamma}_{pq}} \end{aligned} \right\}$$

where $\Gamma_{pp} = \sigma_{pp}^2/g$, $\Gamma_{pq} = \sigma_{pq}^2/g$, $\bar{\Gamma}_{pq} = \bar{\sigma}_{pq}^2/g$.

The general solutions, $\phi_{pp}^{(2)}$, $\phi_{pq}^{(2)}$ and $\phi_{pq*}^{(2)}$ in the transmitted wave region (2) are also obtained as follows:

$$\phi_{pp}^{(2)}(x, z) = B_{pp}^{(2)} Z(k_{pp}^{(2)}, z) e^{ik_{pp}^{(2)}x} + ia_{s1} \left\{ B_p^2 e^{ik_{pp}x} \right\} Z(k_{pp}, z) \tag{23}$$

$$\phi_{pq}^{(2)}(x, z) = B_{pq}^{(2)} Z(k_{pq}^{(2)}, z) e^{ik_{pq}^{(2)}x} + ic_{s1} \left\{ B_p B_q e^{ik_{pq}x} \right\} Z(k_{pq}, z) \tag{24}$$

$$\phi_{pq*}^{(2)}(x, z) = B_{pq*}^{(2)} Z(k_{pq*}^{(2)}, z) e^{ik_{pq*}^{(2)}x} + id_{s2} \left\{ B_p \bar{B}_q e^{i\bar{k}_{pq}x} \right\} Z(\bar{k}_{pq}, z) \tag{25}$$

Green's second identity and linear equations

Potential theory shows harmonic function in a closed domain, $\phi(X)$, which is a solution of Laplace equation, can be expressed with Green's second identity

$$\phi(X) = \frac{1}{\alpha} \int_D \left\{ \phi(X_b) \frac{\partial}{\partial \nu} G(r) - G(r) \frac{\partial}{\partial \nu} \phi(X_b) \right\} ds \tag{26}$$

where $G(r) = \log r + \log r^*$, and r is the length between an arbitrary point $X = (x, z)$ in the domain and a point $X_b = (x_b, z_b)$ on the boundary, r^* is the length between the point X and its mirror image X_b^* with respect to the uniform bottom boundary. α is defined to take π when X is on the boundary, and to take 2π when X is inside the boundary. ν denotes outward normal to the boundary of the region (0), and the direction of the integral is taken counterclockwise along the boundary $D (= S_1 + S_2 + S_3 + S_4)$.

By dividing the boundary D into N number of small elements, ΔS_j ($j = 1, 2, \dots, N$), and by assuming that the potential ϕ is uniform on each element, the integral equation (26) can be discretized as

$$\left. \begin{aligned} \sum_{j=1}^N \left\{ (\bar{E}_{ij} - \delta_{ij}) \phi(j) - E_{ij} \frac{\partial \phi(j)}{\partial \nu} \right\} = 0 \\ (i = 1, 2, \dots, N) \end{aligned} \right\} \tag{27}$$

where

$$\left. \begin{aligned} E_{ij} &= \frac{1}{\alpha} \int_{\Delta S_j} G(r_{ij}) ds, & \bar{E}_{ij} &= \frac{1}{\alpha} \int_{\Delta S_j} \frac{\partial G(r_{ij})}{\partial \nu} ds \\ r_{ij} &= \sqrt{(x_j - x_i)^2 + (z_j - z_i)^2}, & r_{ij}^* &= \sqrt{(x_j - x_i)^2 + (z_j + 2h + z_i)^2} \end{aligned} \right\} \tag{28}$$

Substituting all the boundary conditions along the closed region (0) into equation (27), we have a set of linear equations, for the second-order as well as the first-order problems, in terms of the velocity potentials on the boundary elements and unknown coefficients $A_p, B_p, A_{pp}, B_{pp}, \dots$. The boundary conditions on the imaginary boundaries are given through the exact solutions

for $\phi_{pp}^{(2)}$, $\phi_{pq}^{(2)}$, $\phi_{pq*}^{(2)}$ in the open regions (1) and (2). Thus we solve at first the linear interaction problem (e.g., Yeoung,1975) for every component wave of angular frequency σ_p , then for every combination of the first-order solutions with frequency components σ_p and σ_q , the linear equations for the second-order potentials $\phi_{pp}^{(2)}$, $\phi_{pq}^{(2)}$, $\phi_{pq*}^{(2)}$ are solved, respectively.

Energy flux correction

The solutions have to be corrected to balance wave energy fluxes between the incident, reflected and transmitted waves, because in perturbation analysis up to the second-order the balance of wave energy flux is satisfied in the first-order; the generated second-order free waves produce excessive wave energy. The effect of this excessive energy may be negligible for a single incident wave, but for multicomponent incident wave the number of generated free waves increases in proportion to the square of the number of the incident wave components, and numerical results may become unrealistic.

To correct the numerical results so as to satisfy the conservation of the incident wave energy flux, the incident wave energy flux F_I , the reflected wave energy flux F_R and the transmitted wave energy flux F_T are calculated with numerical results of the first-order and the second-order potentials; F_R and F_T include in them the excessive wave energy flux of the generated free-waves, and thus F_I is always less than $F_R + F_T$. The correction factor β is defined as $\sqrt{F_I/(F_R + F_T)}$, and all the reflected and the transmitted wave components are multiplied by β . The effects of this energy flux correction are verified by comparing the corrected numerical results against the experimental results.

Numerical and Experimental Results

Laboratory experiments were conducted with a submerged structure as shown in figure-1 with $B/h=2.0$, $q=0.3$, $R/h=0.7$, and the water depth $h=0.37m$. Multicomponent random waves used in the experiment are shown in Table-1. For each multicomponent random wave, ten different phase combinations were used, and the results were averaged. The wave amplitudes of the component waves were set approximately the same, and for each multicomponent random wave, several different wave amplitudes ranging from small amplitude to large amplitude that intense wave breaking occurs on the structure were used to investigate the effects of wave breaking on the generation of the second-order free waves. In addition to the above multicomponent random waves, twenty component random wave, modeled from Bretschneider-Mitsuyasu spectra, was also used.

The wave tank is 0.3m wide, 0.5m deep and 28m long, and it is equipped at one end with a random wave generator having a function of wave absorption, and at the other end with a wave absorber. The reflection coefficients of the

wave absorber were measured for several frequencies ranging $kh=0.5 \sim kh=3.0$, and they are around 0.05 for waves kh greater than 1.0 (frequency 0.7_{Hz}). Thus the lowest frequency in the multicomponent random waves was chosen to be greater than $kh=1.0$ to minimize the contamination by the reflected waves from the wave absorber.

Before setting the model of the submerged obstacle in the wave tank, every multicomponent random wave was generated and it was measured by capacity-type wave gauges with sampling interval 10_{Hz} for the number of sampled data 8192, and from the data the incident wave spectra were obtained using First-Fourier-Transform(FFT). Then setting the model structure midway of the wave tank, transmitted waves were measured 3.0m behind the center of the structure, and the transmitted wave spectra were also calculated by FFT. The wave spectra for ten different phase combinations were averaged for every multicomponent random wave.

f (Hz)	kh	number of component			
		2	3	5	10
0.772	1.139			●	●
0.809	1.215		●	●	●
0.844	1.286	●	●	●	●
0.879	1.369	●	●	●	●
0.915	1.453			●	●
0.953	1.545				●
0.993	1.651				●
1.038	1.774				●
1.089	1.922				●
1.145	2.101				●

Table 1: Frequencies of multicomponent random waves

In the numerical calculations, the location of the right-hand side and the left-hand side imaginary boundaries are taken both $6h$ apart from the center of the obstacle. The length of the boundary element is taken $0.05h$ for all the elements. Incident wave amplitudes of component waves in the numerical calculation were obtained by integrating the power spectra of the incident multicomponent random waves in the experiment. The phases of the component waves are given by generating random number numerically, and thus the numerical calculation were also carried out for ten phase combinations as in the experiment for every multicomponent random wave. Water surface variations at the same location where transmitted waves were measured in the experiment were computed and their wave spectra were also obtained by using FFT with the same sampling interval and data length as in the experiment.

Figure-2 shows power spectra of the transmitted wave $S_T(f)$ for two component incident wave. \bar{S} means component averaged power of the incident wave,

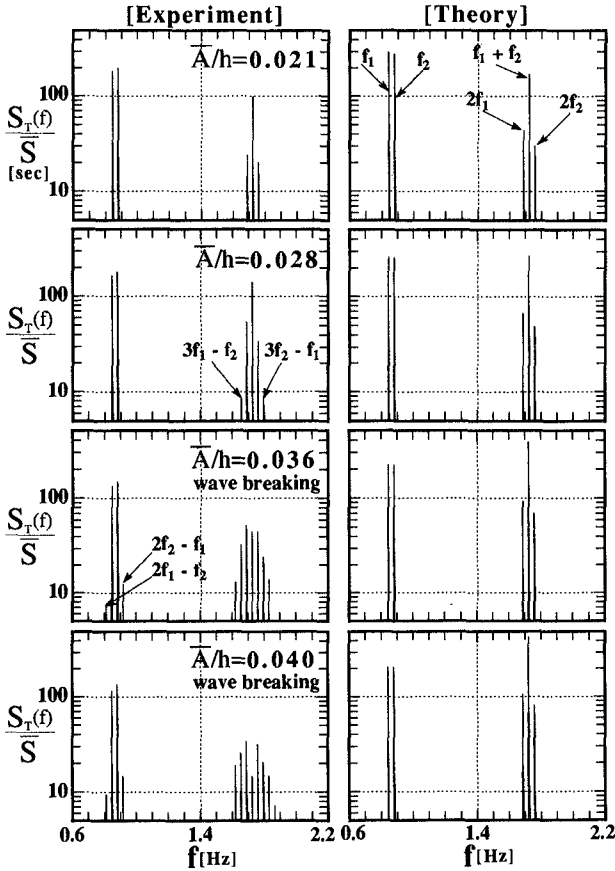


Figure 2: Comparison of the numerical results against the experimental results in terms of transmitted wave spectra $S_T(f)$ for two component wave ($f_1 = 0.772_{Hz}$, $f_2 = 0.809_{Hz}$); \bar{S} is component averaged power of incident wave: from the top, figures show spectral change resulting from increase of incident wave amplitude.

which is given by dividing the power of the incident wave by its number of component. \bar{A} means wave amplitude which has the same power as \bar{S} . Since the amplitudes of the component wave in a multicomponent random wave were made almost the same each other, \bar{A} is approximately the same as the amplitude of the component wave in the experiment. In the figure-2, when the averaged wave amplitude \bar{A}/h is 0.036 and 0.040, wave breakings occur on the structure, and especially when $\bar{A}/h = 0.040$ the wave breaking is very intense. The power of the second-order difference frequency waves and the power of the higher order waves generated around the third-order sum frequencies are negli-

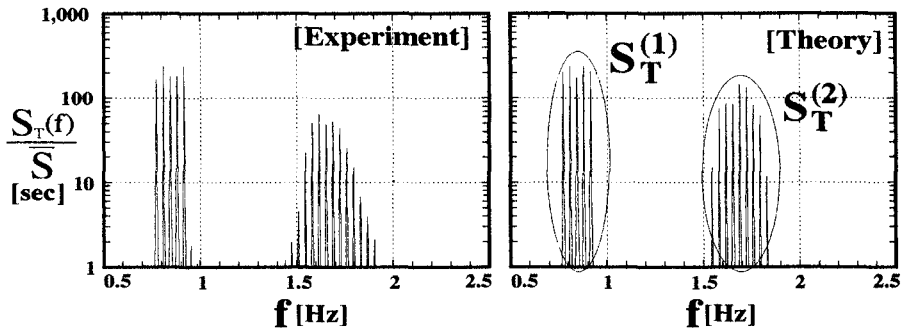


Figure 3: Comparison of the numerical results against the experimental results in terms of transmitted wave spectra $S_T(f)$ for five component incident wave: $\bar{A}/h = 0.015$.

gibly small compared to the powers of the second-order sum frequency waves, and thus results are shown for the first-order frequency and the second-order sum frequency ranges.

It can be seen that as \bar{A} increases more higher order waves are observed around the second-order sum frequencies, though their powers are very small, even before wave breaking occurs. Once wave breaking occurs on the obstacle, more power is transformed to higher order waves around the incident wave frequencies (f_1, f_2) as well as around the second-order sum frequencies, and the power of the second-order sum frequency components ($2f_1, f_1 + f_2, 2f_2$) decrease drastically. On the contrary in the numerical results, the amplitudes of the second-order sum frequency waves increase unrealistically even after wave breaking occurs.

The figure-3 shows the comparison for five component wave. The averaged wave amplitude \bar{A}/h is 0.015 and wave breaking occurs on the obstacle intermittently. Since the energy dissipation caused by vortices and wave breaking are not considered in the present method, the numerical results gives smaller power spectra, but it can be however said that the numerical calculation gives good estimation for the spectral structure of the transmitted waves.

In order to compare the numerical results against the experimental ones more quantitatively, the power along the incident wave frequency range $S_T^{(1)}$ and the power of the second-order sum frequency range $S_T^{(2)}$ were obtained by integrating the transmitted wave spectra as illustrated in figure-3. The square root of their ratios to the power of the incident wave spectra, $\sqrt{S_T^{(1)}/S_I}$ and $\sqrt{S_T^{(2)}/S_I}$, are computed and they are shown in figure-4 for five and ten component waves. The broken lines in the figures show the numerical results without energy flux correction. The numerical results always underestimate the exper-

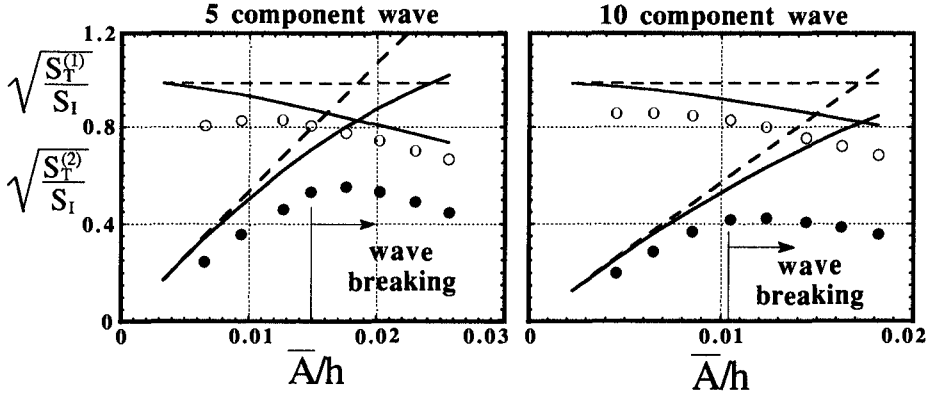


Figure 4: Comparison of the numerical results against the experimental results in terms of power $S_T^{(1)}$ obtained by integrating transmitted wave spectra along the first-order frequency range and Power $S_T^{(2)}$ for the second-order sum frequency range, which are normalized by power of incident wave S_I : ● ○ experimental results, — numerical results with energy flux correction, - - - numerical result without energy flux correction.

imental results even before wave breaking occurs, due to the energy dissipation by vortices caused around the structure, and thus the numerical results gradually deviate from the experimental results as the incident wave amplitude increases. Once however wave breaking begins to occur on the structure, even it is not so intense, numerical results for the second-order waves largely underestimate the experimental results. It however should be noted that the power of the first-order frequency range $\sqrt{S_T^{(1)}/S_I}$ well estimated by the present method even after wave breaking occurs. This may imply that the energy lost by wave breaking is approximately equal to the energy which should have been transferred to the second-order free-waves in potential theory.

To show more clearly the effect of wave breaking, the ratios of $\sqrt{S_T^{(2)}/S_T^{(1)}}$ are calculated and the results are shown in figure-5. These show that the present method can well estimate the rate of wave energy transferred to the generated second-order waves as far as no wave breaking occurs on the structure.

Figure-6 shows transmitted wave spectra for twenty component incident wave, modeled of Bretschneider-Mitsuyasu spectra with significant wave height $H_{1/3} = 4.0cm$ ($H/h = 0.11$) and significant wave period $T_{1/3} = 1.25sec$ ($kh = 1.16$). No wave breaking observed in this case. Because of the energy dissipation due to vortices around the structure the numerical results underestimate the experimental ones, but overall structure of the transmitted wave spectra is well estimated.

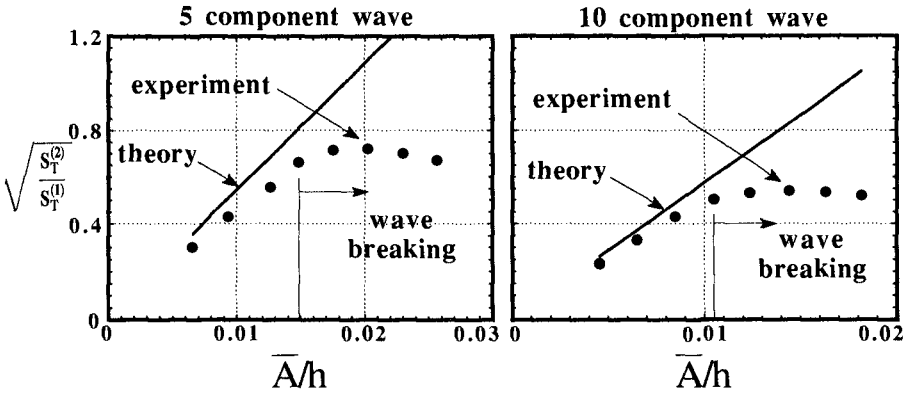


Figure 5: Comparison of the numerical results against the experimental results in terms of ratio $\sqrt{S_T^{(2)}/S_T^{(1)}}$: ——— numerical results, ● experimental results.

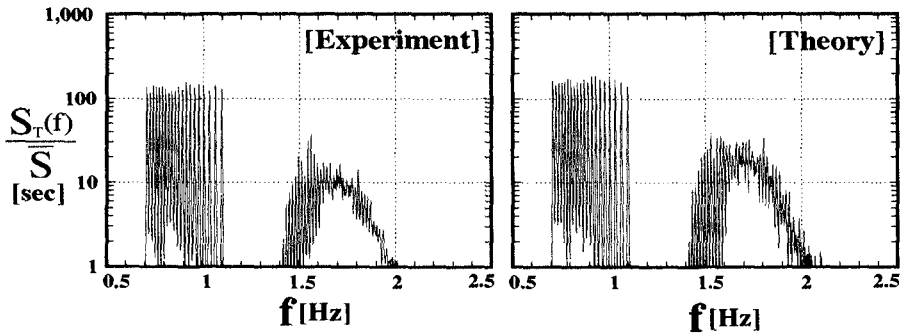


Figure 6: Comparison of the numerical results against the experimental results in terms of transmitted wave spectra for incident random wave modeled from Bretschneider-Mitsuyasu spectra ($H_{1/3} = 4\text{cm}$, $T_{1/3} = 1.25\text{sec}$); low frequency side ($f < 0.7\text{Hz}$) and high frequency side ($f > 1.1\text{Hz}$) are cut off in the incident wave to avoid contamination by reflected waves from wave absorber and to avoid overlap of incident wave and generated second-order sum frequency waves.

Conclusions

A numerical method to solve the second-order interactions between multicomponent random wave and submerged obstacle is presented. Numerical results give good estimation of the transformation of the incident wave spec-

tra, caused by the second-order wave structure interactions, as long as no wave breaking occurs on the obstacle. Once however wave breaking occurs (even if it is not so intense), the generation of the second-order free waves is greatly suppressed, and numerical results largely underestimate the experimental results. The energy flux correction of the numerical results is particularly effective, even after wave breaking occurs, for accurate estimation of the first-order transmitted waves.

References

- Bryant, P. J.(1973): Periodic waves in shallow water, *J. Fluid Mech.* 59, part4, pp.625-644.
- Kojim, H., A. Yoshida and T. Ijima(1994): Second-order interactions between water waves and a submerged horizontal plate, *Coastal Engineering in Japan*, vol.37, No.2, pp.153-172.
- Massel, S. R.(1983): Harmonic generation by waves propagating over a submerged step, *Coastal Engineering*, Vol.7, pp.357-380.
- Mei, C. C.(1983): *The applied dynamics of ocean surface waves*, A Wiley-Interscience Publication.
- Newman, J. N.(1977): *Marine Hydrodynamics*, The MIT Press
- Ohyama, T. and K. Nadaoka(1992): Modeling the transformation of nonlinear waves passing over a submerged dike, *Proc. 23rd Coastal Eng. Conf.*,pp.526-539.
- Yeung, R. W.(1975): A hybrid integral-equation method for time-harmonic free-surface flow, *Proc. First Int. Conf. on Numerical Ship Hydrodynamics*, pp.581-605.
- Yoshida, A., K. Murakami and T. Takahira(1994): Nonlinear interaction between two component Stokes' waves and structures, *Proc. of the 41th Japanese Conf. on Coastal Eng.*, pp.736-740.(in Japanese)

CHAPTER 74

A uniform mild-slope model for waves over varying bottom

Libang Zhang¹ and Billy L. Edge²

Abstract

A time-dependent mild-slope equation is derived, based on the formal derivation of Smith & Sprinks (1975), from which the higher-order dispersion relation for waves over uneven bottom is obtained. If only linear dispersion is used for steady waves, the equation (2.12) of Chamberlain & Porter (1995), referred as the modified mild-slope equation (MMSE), is recovered from this equation. To the leading-order solution, it is found that the modified curvature terms of the MMSE have significant effects, while the slope square terms are negligible in accordance with mild-slope assumption. Therefore, retaining all the modified curvature terms neglected in the MSE, the uniform model is developed.

A numerical model using the finite element method (FEM) is developed to predict wave scattering by a varying bottom. In general, the uniform model can predict salient features of waves over various sea beds, such as sinusoidal beds and man-made bars. For sinusoidal beds, the results of the uniform model are in closer agreement with the experimental data than other established models. For man-made bars, the results of both the MMSE and uniform model are in closer agreement with the experimental data than the results of Kirby (1986). An important result of the FEM model is application to transformation of waves over arbitrarily-varying bathymetry.

Introduction

Surface wave scattering by rippled seabeds has been studied by many researchers during the past decade. Rippled seabed are used to represent both regular and irregular ocean bottoms. Davies & Heathershaw (1984) provided solutions to the linear problem and verified their solutions experimentally. Mei (1985) concentrated his studies on the process close to the Bragg resonance condition. Dalrymple & Kirby (1986) studied a single sinusoidal bed for both resonant and non-resonant cases, using a boundary integral equation method. The step-approximation model (Guazzelli et al. 1992), or the successive-application matrix (O'Hare & Davies 1993), in which the bed is divided into a series of very small horizontal shelves, was also developed to model the wave scattering by the rippled bed. Edge & Zhang (1996) first predicted random wave scattering by berms using P-M spectrum.

Alternative methods related to the mild-slope equation (MSE), such as the modified mild-slope equation (MMSE), have been investigated extensively since it was derived by Berkhoff (1972) and Smith & Sprinks (1975). Kirby (1986) developed the equations to predict wave propagation over rapidly varying to-

¹Research Assistant, Ocean Engineering Program, Department of Civil Engineering, Texas A & M University, College Station, TX 77843-3136

²W.H. Bauer Professor of Dredging Engineering and Head, Ocean Engineering Program, Department of Civil Engineering, Texas A & M University, College Station, TX 77843-3136

pography, which is based on the concept of expanding the rapidly varying component on a very mild-slope bottom. Massel (1993) extended the mild-slope equation by using a Galerkin-eigenfunction method. Recently, Chamberlain & Porter (1995) presented several modified versions of the MSE (or MMSE) by using both variational and Galerkin methods.

Kirby's model (1986) is limited to a rapidly-varying topography. The deficiency of the Kirby's model in prediction of the higher- and sub-harmonic resonance peaks was found by Guazzelli et al. (1992) and O'Hare & Davies (1993). Two of Chamberlain & Porter's models, i.e. Eqs.(3.2) and (3.3) of Chamberlain & Porter (1995), were shown to be ineffective in predicting some resonance peaks (see Fig.3 of Chamberlain & Porter, 1995). In other words, these models break down at some frequencies, similar to the MSE's breaking down as described by Kirby (1986). It means that the approximations of these models are not uniform, but are frequency-dependent. Therefore, to overcome the deficiency of the models mentioned above, the uniform model is developed to predict wave scattering by both slowly-varying and rapidly-varying components of beds uniformly.

The first part of this paper presents the three-dimensional wave model based on Green's identity method for general topography. Secondly, the paper presents a numerical implementation for the finite element method (FEM). Thirdly, the uniform model is verified and the results for sinusoidal beds are given. Finally, numerical results of the uniform models for waves over the man-made bars are presented and compared with the experimental data and other numerical solutions.

Governing equations for general topography

For a small-amplitude wave with angular frequency ω , it is assumed that the flow is incompressible and irrotational and that the pressure is constant at the free surface. The rectilinear coordinates (x, y, z) are fixed in space and $z=0$ is located at the calm water level. The wave potential $\Phi(x, y, z)$ satisfies the equations:

$$\nabla^2 \Phi + \Phi_{zz} = 0, \quad (-h \leq z \leq 0), \quad (1)$$

$$\Phi_{tt} + g\Phi_z = 0, \quad \text{at } z = 0, \quad (2)$$

Since the sea bottom is fixed at $z = -h(x, y)$, the normal velocity vanishes; this implies

$$\Phi_z + \nabla h \cdot \nabla \Phi = 0, \quad \text{at } z = -h, \quad (3)$$

where ∇ denotes the horizontal gradient operator, i.e. $\nabla = \{\partial/\partial x, \partial/\partial y\}$.

By utilizing the Green's identity method, Equations (1)-(3) can be combined to obtain the time-dependent equation governing the velocity potential $\phi(x, y)$ and the wave number $k(x, y)$:

$$\phi_{tt} - \nabla \cdot (CC_g \nabla \phi) + (\omega^2 - k^2 CC_g) \phi - gF\phi = 0 \quad (4)$$

where

$$\omega^2 = gk \tanh kh, \quad (5)$$

is leading-order dispersion relation, and

$$F = \alpha_1(\nabla h \cdot \nabla h)k + \alpha_2 \nabla^2 h + \alpha_3 \nabla k \cdot \nabla h/k + \alpha_4 \nabla^2 k/k^2 + \alpha_5(\nabla k \cdot \nabla k)/k^3. \quad (6)$$

$C(x, y) = \omega/k$ and $C_g(x, y) = \partial\omega/\partial k$ are the wave celerity and the group velocity, respectively. The dimensionless parameters of α_i ($i = 1, 5$) become

$$\alpha_1 = -\sigma(1 - \sigma^2)(1 - \sigma q) \quad (7)$$

$$\alpha_2 = -\sigma q(1 - \sigma^2)/2 \quad (8)$$

$$\alpha_3 = q(1 - \sigma^2)(2q\sigma^2 - 5\sigma/2 - q/2) \quad (9)$$

$$\alpha_4 = q(1 - \sigma^2)(1 - 2\sigma q)/4 - \sigma/4 \quad (10)$$

$$\alpha_5 = q(1 - \sigma^2)(4\sigma^2 q^2 - 4q^2/3 - 2\sigma q - 1)/4 + \sigma/4 \quad (11)$$

Throughout this paper, the notations $q = kh$, $Q = k(z+h)$, and $\sigma = \tanh kh$ are used for convenience. The detailed derivation of Eq.(4) is given in the Appendix.

Higher-order dispersion relation

The time-dependent MMSE can be further decomposed into the real and imaginary parts, which are corresponding to the dispersion relation and wave action conservation, respectively. Let

$$\phi = Ae^{i\theta}$$

where A is the potential amplitude and θ is the phase and is defined by

$$\nabla\theta = \hat{k} \quad \theta_t = -\hat{\omega}$$

Separating the time-dependent equation into real and imaginary parts, the higher-order dispersion relation is obtained:

$$\hat{\omega}^2 = \omega^2 + CC_g(\hat{k}^2 - k^2) + \frac{A_{tt}}{A} - CC_g \frac{\nabla^2 A}{A} - \frac{\nabla(CC_g) \cdot \nabla A}{A} - gF, \quad (12)$$

where ω is defined in Eq.(5). If the frequency is fixed and temporal variation of amplitude is not considered, the effective wave number for the MMSE is

$$\hat{k}^2 = k^2 + \frac{\nabla^2 A}{A} + \frac{\nabla(CC_g) \cdot \nabla A}{CC_g A} + \frac{gF}{CC_g}. \quad (13)$$

Discarding the last terms, the effective wave number for the MSE (Liu, 1990, p35)

$$\hat{k}^2 = k^2 + \frac{\nabla^2 A}{A} + \frac{\nabla(CC_g) \cdot \nabla A}{CC_g A} \quad (14)$$

is recovered. It is clear that the last terms in general MMSE will directly affect the wave phase prediction if they are comparable with the original terms in the MSE.

Correspondence to previous models

For the monochromatic and steady waves, the general MMSE becomes:

$$\nabla \cdot (CC_g \nabla \phi) + k^2 CC_g \phi + gF\phi = 0 \tag{15}$$

by using

$$\phi_{tt} = -\phi\omega^2. \tag{16}$$

The relations of the wavenumber slope and curvature with those of bottom, can be obtained from $\nabla\omega = 0$, i.e.

$$\frac{\nabla k}{k} = \beta_1 \frac{\nabla h}{h}, \tag{17}$$

and

$$\frac{\nabla^2 k}{k} = \beta_1 \frac{\nabla^2 h}{h} + \beta_2 \frac{(\nabla h \cdot \nabla h)}{h^2}, \tag{18}$$

where

$$\beta_1 = -q(1 - \sigma^2)/\gamma, \tag{19}$$

$$\beta_2 = 2q^2(1 - \sigma^2)(\gamma - \alpha_1)/\gamma^3, \tag{20}$$

$$\gamma = \sigma + q(1 - \sigma^2). \tag{21}$$

Thus the MMSE in specific case reads

$$\nabla \cdot (CC_g \nabla \phi) + k^2 CC_g \phi + g [f_c \nabla^2 h + k f_s (\nabla h \cdot \nabla h)] \phi = 0 \tag{22}$$

where

$$f_c(kh) = \alpha_2 + \alpha_4 \beta_1 / q, \tag{23}$$

$$f_s(kh) = \alpha_1 + \alpha_3 \beta_1 / q + \alpha_4 \beta_2 / q^2 + \alpha_5 \beta_1^2 / q^2. \tag{24}$$

Using the notations of Massel(1993) and Chamberlain & Porter(1995), the following relations are found:

$$R_{00}^1 = 2qf_s, \quad R_{00}^2 = 2q\sigma f_c, \tag{25}$$

$$u_1 = f_c, \quad u_2 = kf_s. \tag{26}$$

Therefore, both Equation (34) of Massel(1993) and Equation (2.12) of Chamberlain & Porter(1995) can be recovered from Eq.(4). Obviously, Eq.(4) for the MMSE is more general. The plots of R_{00}^1 and R_{00}^2 have been done for checking with Massel (1993).

However, if the water depth is constant but k is still arbitrary due to the variation of wave amplitude, the general equation is reduced to:

$$\phi_{tt} - \nabla \cdot (CC_g \nabla \phi) + (\omega^2 - k^2 CC_g) \phi - g \{ \alpha_4 \nabla^2 k / k^2 + \alpha_5 (\nabla k \cdot \nabla k) / k^3 \} \phi = 0 \tag{27}$$

In this case the equations of Massel(1993) and Chamberlain & Porter(1995) fail to consider the variation of wavenumber k . Obviously, the equation (4) in this paper is more general.

Uniform model equation

To exam errors induced by omitting the last terms, which consist of either curvature or slope terms, we compare the ratio of modified terms to the original term of the conventional MSE by using Eqs.(17), (18) and

$$CC_g = g\gamma/(2k), \tag{28}$$

i.e.

$$\frac{gF\phi}{k^2CC_g\phi} = R_c \frac{\nabla^2 h}{k} + R_s(\nabla h \cdot \nabla h) \tag{29}$$

where

$$R_c(kh) = 2(\alpha_2 + \alpha_4\beta_1/q)/\gamma, \tag{30}$$

and

$$R_s(kh) = 2(\alpha_1 + \alpha_3\beta_1/q + \alpha_4\beta_2/q^2 + \alpha_5\beta_1^2/q^2)/\gamma, \tag{31}$$

are functions of only kh . The plots of R_c and R_s are presented in Fig. 1. It is found that approximately $max|R_c, R_s| < 0.2$ in Fig. 1. Nevertheless, from Eq.(29) it is clear that the relative errors still depend on both

$$\frac{\nabla^2 h}{k}, \quad \text{and} \quad (\nabla h \cdot \nabla h).$$

It is well known that the MSE was derived by neglecting all the modified terms based on the assumption that

$$\frac{\nabla h}{kh} \ll 1.$$

In the following we will show that the slope square terms are negligible, but the mild-slope assumption does not mean that the terms proportional to bottom curvature (i. e. $\nabla^2 h$) can also be neglected. For example, Massel (1993, p109) mentioned an example that the curvature terms are quite significant even for small mean bottom slope for a sinusoidal bed:

$$|\nabla h| = 0.1\pi \approx 0.3 \quad |\nabla^2 h| = 0.2\pi^2 \approx 2.$$

Instead of using $|\nabla^2 h|$, dimensionless $|\nabla^2 h|/k$ is used in this paper. It can be proved that the slope square terms are higher order than the curvature terms, if the ratio of bed wave number to surface wave number is of unity order. For simplicity, let the sinusoidal bed be defined by

$$h(x) = h_0 - b\sin Kx, \tag{32}$$

where h_0 is mean depth, K is bed wave number, and b is bed amplitude. It is easily found that

$$\frac{|\nabla^2 h|}{k} = \frac{K}{k} |\nabla h|$$

for sinusoidal bed case. It indicates that curvature terms depend not only on bed slope but also the ratio of bed wave number to surface wave number. Since

the modified terms are omitted in the MSE, the errors induced by the MSE will be significant in the lower frequency ranges.

Moreover, the ratio of slope square terms to curvature terms in Eq.(22) can be found from Eq.(32):

$$\frac{f_s k(\nabla h \cdot \nabla h)}{f_c \nabla^2 h} = \frac{f_s}{f_c}(kb) \cot Kx = O(kb) \tag{33}$$

From Eqs.(23) and (24) it is seen that the ratio of f_s to f_c is of $O(1)$. It means that the magnitude of Eq.(33) depends on surface wave number k and bottom amplitude b . Generally, kb is small value, except for very high frequency waves. Thus based on this ratio of Eq.(33), it is clear that slope square terms are only comparable to curvature terms for very large k , i.e. in the very high frequency ranges. According to Guazzelli et al. (1992), the high-frequency waves are hardly scattered by bottom undulation. Therefore, if the mild-slope assumption

$$\frac{\nabla h}{kh} \ll 1,$$

is applied, only slope square terms can be omitted, i.e.

$$\nabla \cdot (CC_g \nabla \phi) + k^2 CC_g \phi + gf_c \nabla^2 h \phi = 0 \tag{34}$$

The conventional mild-slope equation (MSE)

$$\nabla \cdot (CC_g \nabla \phi) + k^2 CC_g \phi = 0 \tag{35}$$

is recovered, if the modified term (last term) in Eq.(34) is neglected. Since the magnitude of neglected terms (curvature terms) is depend on the ratio of bed wave number to surface wave number (K/k), the error induced by the MSE is frequency-dependent.

On the other hand, Kirby's equation (1986) is originally derived for a rapidly-varying bottom. For the fixed bottom, the surface wave number k should be smaller than bed wave number K . It means that the solutions of Kirby's model are also frequency-dependent, which have been confirmed by other numerical methods and experimental data. The error of the model based on Eq.(34) is more uniform over a large frequency range than other models, thus it is called uniform mild-slope model.

Finite element method based on a weak form

For simplicity, we limit the remaining parts to the problem of two dimensional wave problems. For steady waves, the MMSE reads:

$$(CC_g \phi_x)_x + p\phi = 0 \tag{36}$$

where

$$p = k^2 CC_g + gF \tag{37}$$

The boundary conditions for a patch of rippled beds are

$$\phi_x = -ik(\phi - 2\phi_I) \quad (x_1 \leq 0) \tag{38}$$

$$\phi_x = ik\phi \quad (x_2 \geq L) \tag{39}$$

where $\phi_I = e^{ikx}$ is the incident wave of unit amplitude, x_1 and x_2 represent the upwave and downwave limits of the computational grid, and L is the length of computation domain. These boundary conditions have been given previously by Kirby (1986).

Considering potential applications in the three dimensional wave, a FEM model is developed for general topography. It seems that the numerical model in Chamberlain & Porter (1995) is suitable for periodic topography. The FEM model has advantages in the three dimensional problems with complex geometries, where it is desirable to use irregular meshes.

Multiplying the entire left hand side of equation (36) with a weight function w , and integrating over the domain $(0,L)$ gives the weighted-residual statement:

$$\int_0^L \{(CC_g\phi_x)_x + p\phi\}w dx = 0 \tag{40}$$

Mathematically, the above equation is a statement that the numerical error is needed to be zero in the weighted-integral sense. The trading of differentiability from ϕ to w provides the weak form

$$\int_0^L (CC_g\phi_x w_x - p\phi w) dx - [CC_g w \phi_x] \Big|_0^L = 0 \tag{41}$$

The trading of differentiability from ϕ to w can only be performed if it leads to boundary terms that are physically meaningful. The choice of the approximation ϕ for weight function gives the boundary terms $CC_g(\phi)_x\phi$, which has physical meaning of energy flux through a section. It is easy to find that the primary variable and the secondary variable are ϕ and $(\phi)_x$ respectively. Thus $[\phi_x] \Big|_0^L$ is the natural boundary condition. Using the notations of Reddy (1993), we have

$$B(w, \phi) - l(w) = 0$$

where

$$B(w, \phi) = \int_0^L (\phi_x w_x - p\phi w) dx - [ikCC_g w \phi_x] \Big|_0^L,$$

and

$$l(w) = -[2ikCC_g w \phi_I] \Big|_{x=0}$$

are bilinear and linear forms, respectively. For a typical element, ϕ is approximated by

$$\phi = \sum_{j=1}^4 \phi_j N_j$$

where N_j are cubic shape functions and ϕ_j are unknowns at the nodes. The water depth $h(x)$, slope and curvature of both h and k at each element in the FEM scheme can readily be evaluated as

$$h = \sum_{j=1}^4 h_j N_j, \quad k = \sum_{j=1}^4 k_j N_j$$

$$h_x = \sum_{j=1}^4 h_j \frac{\partial N_j}{\partial x}, \quad k_x = \sum_{j=1}^4 k_j \frac{\partial N_j}{\partial x}$$

$$h_{xx} = \sum_{j=1}^4 h_j \frac{\partial^2 N_j}{\partial x^2}, \quad \text{and} \quad k_{xx} = \sum_{j=1}^4 k_j \frac{\partial^2 N_j}{\partial x^2}.$$

The FEM schemes based on weak forms for the MSE, EMSE and UMSE are similar but much more simple. Bubnov-Galerkin method is adopted, thus the solution shape functions are used as weighting function.

It is worthy to note that most FEM models for water wave problems are established based on the functional formulation. For example, the hybrid element method of Mei (1983) and the modified hybrid element method of Zhang (1991,1996) are all based on variation of a functional. As noted in Reddy (1993), not all differential equations admit the functional formulation, and in order for the functional to exist, the bilinear form must be symmetric in its arguments. Since the weak form statement is equivalent to the differential equation and the specified natural boundary condition of the problem, the weak form FEM is used in this paper. Substituting the assumed approximate solution into the weak form (42), and following the procedure in Reddy (1993), the FEM is developed. Considering the fact that the coefficients of the FEM are high order functions of space, cubic shape functions are used here.

Verification of numerical model

In this section, the numerical solutions for sinusoidal beds and man-made bars are presented in *Figs.2 ~ 4*, and compared with experimental data.

For the case of the bottom having only one sinusoidal component, there are two resonant peaks of reflection coefficients, which were shown numerically by Dalrymple & Kirby (1986) by solving the 2-D Laplace equation. Later it was confirmed by Davies et al. (1989) and O'Hare & Davies (1993). Consider the case of sinusoidal bed $n = 2$, $b/h_0 = 0.32$, where h_0 is mean water depth, b is amplitude of bed undulation, and n is the number of sinusoidal bars. The numerical results of the MMSE, uniform and Kirby's model are presented in *Fig.2*, respectively, to compare with experimental data of Davies & Heathershaw (1984).

In *Fig.2*, it is seen that Kirby's model does not predict the second resonance peaks, while results of MMSE and uniform models are in good agreement with experimental data. Also it noted that the uniform model predicts the second peak better than the MMSE model.

Consider now the case of a doubly-sinusoidal bed (chosen here to be of equal amplitude b). The inclusion of a more rapid component makes the

bottom slope relatively larger, so the difference between the uniform model and the model of Chamberlain & Porter (1995) becomes significant. As indicated in *Fig.3*, Chamberlain & Porter (1995) overpredict reflection coefficients at higher-harmonic resonant peaks, if compared with experimental data (Guazzelli et al. 1992).

Numerical solutions and experimental results for the artificial bar field (Kirby & Anton 1990) are also studied. The bar field is periodic over intervals of width L , and can be conveniently represented by the Fourier series. The man-made bars have many sinusoidal components (Kirby & Anton 1990), some of which have shorter wavelengths than the surface wavelength, not belonging to rapidly-varying case. Since Kirby's model is valid only for rapidly-varying components, the slowly-varying components are not properly modeled. Therefore the overall reflections predicted by Kirby's model have larger discrepancy with experimental data than these predicted by the uniform model and MMSE as indicated in *Fig.4*.

The convergence of the numerical model is confirmed by checking the energy relation $R^2 + T^2 = 1$, where R and T are reflection and transmission coefficients, respectively. The maximum error is less than 10^{-5} .

Conclusions

To overcome the limitations of Kirby's model, the uniform model for wave transformation over an arbitrary-varying topography has been developed. Several cases of sinusoidal bed configuration have been studied and presented to confirm the numerical models. Based on the comparison between the numerical results and experimental data, it is clear that Kirby's method is frequency-dependent.

For sinusoidal beds, the numerical results of the MMSE, uniform and Kirby's model are all in good agreement with the experimental data of Davies & Heathershaw (1984), except at the second resonance peak ($2k/K \sim 2$), the uniform model predicts a reflection coefficient closer to the laboratory data than the other numerical results. For man-made bar case, it is shown that both the MMSE and uniform model give excellent comparison with experiments. Since Kirby's equation is originally derived for a rapidly-varying bottom, it becomes less accurate as ripple-bed undulations become slower (i.e. $2k/K$ becomes larger). The uniform model is capable of modeling not only the slowly-varying components but also rapidly-varying of sea beds.

The success of the uniform model in model tests and better agreement with experimental data than other models, suggest that the uniform model is more efficient and accurate tool for the prediction of wave transformation over general sea bed. An important result of the uniform model is application to reflection of wave energy from offshore bars and dredged material dump sites. In addition, the uniform wave model can be extended to further the work of Kirby (1984).

Appendix: Derivation of the time-dependent wave equation

The depth-integrated wave equation for monochromatic, linear waves propagating over ripple beds may be formulated following the Green's identity method of Smith & Sprinks (1975). The solution to Equation (1)-(3) may be expressed as

$$\Phi(x, y, z, t) = f(q, Q)\phi(x, y, t) + (\text{non-propagating modes}) \quad (\text{A1})$$

where

$$f = \cosh Q / \cosh q \quad (\text{A2})$$

is a function of z , k , and h . The propagation of waves is associated with only the propagating mode, thus extracting this mode component and applying Green's identity to f and Φ :

$$\int_{-h}^0 (f\Phi_{zz} - \Phi f_{zz}) dz = [f\Phi_z - \Phi f_z]_{-h}^0$$

or

$$\int_{-h}^0 (f\nabla^2\Phi + \Phi f_{zz}) dz = -[f\Phi_z - \Phi f_z]_{-h}^0 \quad (\text{A3})$$

Using (A1) and (A2)

$$\begin{aligned} f_{zz} &= k^2 f \\ \nabla\Phi &= f\nabla\phi + \phi\nabla f \\ \nabla^2\Phi &= f\nabla^2\phi + 2\nabla\phi \cdot \nabla f + \phi\nabla^2 f \\ \Phi_z|_{z=-h} &= -\nabla h \cdot (f\nabla\phi + \phi\nabla f) \end{aligned} \quad (\text{A4})$$

Inserting (A4) into (A3)

$$\int_{-h}^0 (\phi k^2 f^2 + \nabla^2\phi f^2 + 2f\nabla\phi \cdot \nabla f + \phi f\nabla^2 f) dz = (\phi_{tt} + \omega^2\phi)/g|_{z=0} + \Phi_z f|_{z=-h} \quad (\text{A5})$$

Based on (A2), every term in (A5) is evaluated using the following

$$\nabla f = f_h \nabla h + f_k \nabla k$$

$$\nabla^2 f = f_{hh}(\nabla h \cdot \nabla h) + f_h \nabla^2 h + 2f_{hk} \nabla h \cdot \nabla k + f_k \nabla^2 k + f_{kk}(\nabla k \cdot \nabla k)$$

where $f_h = \frac{\partial f}{\partial h}$, $f_k = \frac{\partial f}{\partial k}$, $f_{hh} = \frac{\partial^2 f}{\partial h^2}$, $f_{hk} = \frac{\partial^2 f}{\partial h \partial k}$, $f_{kk} = \frac{\partial^2 f}{\partial k^2}$, and derived in the following:

$$\begin{aligned} f_h &= k(\sinh Q - \sigma \cosh Q) / \cosh q \\ f_k &= (Q \sinh Q - q\sigma \cosh Q) / (k \cosh q) \\ f_{hh} &= 2\sigma k^2(\sigma \cosh Q - \sinh Q) / \cosh q \\ f_{kk} &= \{Q^2 \cosh Q - 2\sigma q Q \sinh Q - q^2(1 - 2\sigma^2) \cosh Q\} / (k^2 \cosh q) \\ f_{hk} &= \{(2q\sigma^2 - \sigma - q) \cosh Q + (1 - q\sigma) \sinh Q + Q \cosh Q - Q\sigma \sinh Q\} / \cosh q \end{aligned} \quad (\text{A6})$$

Applying Leibniz's rule,

$$\int_{-h}^0 (\nabla^2 \phi f^2 + 2f \nabla \phi \cdot \nabla f) dz + f^2 \nabla h \cdot \nabla \phi|_{z=-h} = \nabla \cdot (CC_g \nabla \phi) / g \quad (A7)$$

Using the following integrations

$$g \int_{-h}^0 k^2 \phi f^2 dz = k^2 CC_g \phi$$

$$2k \int_{-h}^0 \sinh Q \cosh Q dz = \sigma^2 / (1 - \sigma^2)$$

$$4k \int_{-h}^0 Q \sinh Q \cosh Q dz = \{q(1 + \sigma^2) - \sigma\} / (1 - \sigma^2)$$

$$4k \int_{-h}^0 Q \cosh Q \cosh Q dz = \{q^2(1 - \sigma^2) + 2q\sigma - \sigma^2\} / (1 - \sigma^2)$$

$$4k \int_{-h}^0 Q^2 \cosh Q \cosh Q dz = \{2q^3(1 - \sigma^2) + 2q^2\sigma - q(1 + \sigma^2) + \sigma\} / (1 - \sigma^2)$$

and substituting (A6) and (A7) into (A5), finally the time-dependent Eq.(4) is obtained.

It may be worth remarking that the terms in (A5) involving

$$f_k = \frac{\partial f}{\partial k}, \quad f_{hk} = \frac{\partial^2 f}{\partial h \partial k}, \quad f_{kk} = \frac{\partial^2 f}{\partial k^2},$$

were mistakenly omitted by Smith & Sprinks (1975). Furthermore, Smith & Sprinks (1975) obtained the conversional mild-slope equation (MSE) by neglecting all the so-called 'forcing' terms, which are assumed to be of higher order. The validity of this assumption of higher order about the forcing terms must, however, be questioned. In the absence of current, similar treatment was made by Kirby (1984) (see Eq.17 of Kirby, 1984).

Acknowledgement

The authors would like to thank Drs. A. G. Davies and T. J. O'Hare for providing experimental data, and Drs. M. H. Kim and Jun Zhang for their helpful discussions.

References

- Berkhoff, J. C. W. 1972. Computation of combined refraction-diffraction. *Proc. 13th Int. Conf. on Coastal Eng.* ASCE pp471-90
- Chamberlain, P. G. and Porter, D. 1995. The modified mild-slope equation. *J. Fluid Mech.* **291**: 393-407.
- Davies, A. G., Heathershaw, A. D. 1984. Surface wave propagation over sinusoidally varying topography. *J. Fluid Mech.* **144**: 419-43
- Davies, A. G., Guazzelli, E., & Belzons, M., 1989. The propagation of long waves over an undulating bed. *Phys. Fluids A1(8)*: 1331-1340.
- Dalrymple, R. A. and Kirby, J. T. 1986. Water waves over ripples. *J. Waterway Port Coast. Ocean Eng.* **112** 309
- Edge, B. L. & Zhang, L. 1996 Transformation of waves over shallow open-water disposal sites, *Proc. WEDA XVII Tech. Conf.*, pp405-419, New Orleans, Louisiana, June, 1996.
- Guazzelli, E., Rey, V. & Belzons, M., 1992 Higher-order Bragg reflection of gravity surface waves by periodic beds. *J. Fluid Mech.* **245**: 301-17.
- Kirby, J. T. 1986 A general wave equation for waves over rippled beds *J. Fluid Mech.* **162**: 171-86
- Kirby, J. T. 1984 A note on linear surface wave-current interaction over slowly varying topography, *J. of Geophysical Research*, Vol. 89, No. C1:745-747.
- Kirby, J. T. & Anton, J. P. 1990 Bragg reflection of waves by artificial bars, *Proc. 22nd ICCE*, ASCE, 757-68
- Liu, Philip L.-F. 1990 Wave transformation, *The Sea, Ocean Eng. Science* Eds. B. LeMehaute & D. M. Hanes, A Wiley-Interscience Publication New York
- Massel, S. R. 1993 Extended refraction-diffraction equation for surface waves *Coastal Engrg.* **19**: 97-126
- Mei, C. C. 1983 *The applied dynamics of ocean surface waves*. New York: Wiley-Interscience
- Mei, C. C. 1985. Resonant reflection of surface water waves by periodic sand-bars. *J. Fluid Mech.* **152**: 315-35
- O'Hare, T. J. & Davies, A. G., 1993, A comparison of two models for surface-wave propagation over rapidly varying topography. *Appl. Ocean Res.* **15**: 1-11
- Reddy, J. N. 1993. *An introduction to the finite element method*, 2nd edition, McGraw-Hill, Inc.
- Smith, R. & Sprinks, T., 1975. Scattering of waves by a conical island. *J. Fluid Mech.* **72**: 373-84.
- Tsay, T. K. Zhu, W. & Liu, P.L.-F. 1989. A finite element model for wave refraction, diffraction, reflection and dissipation. *Appl. Ocean Res.* **15**: 33-38.
- Zhang, L. 1991 Numerical analysis of wave forces on arbitrarily shaped multi-pillars over varying topography. *China Ocean Eng.* Vol.5, No.4: 465-471.
- Zhang, L. 1996 A modified hybrid element model for combined diffraction-reflection-reflection-dissipation waves over large regions. *Chinese J. of Oceanology and Limnology*, Vol.14, No.1: 68-78.

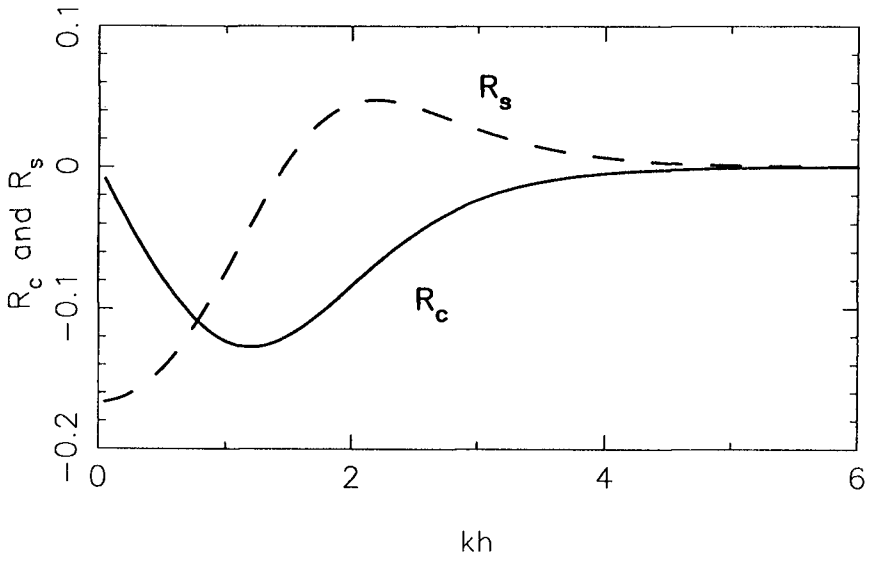


Fig.1 Curvature and Slope Functions(R_c , R_s)

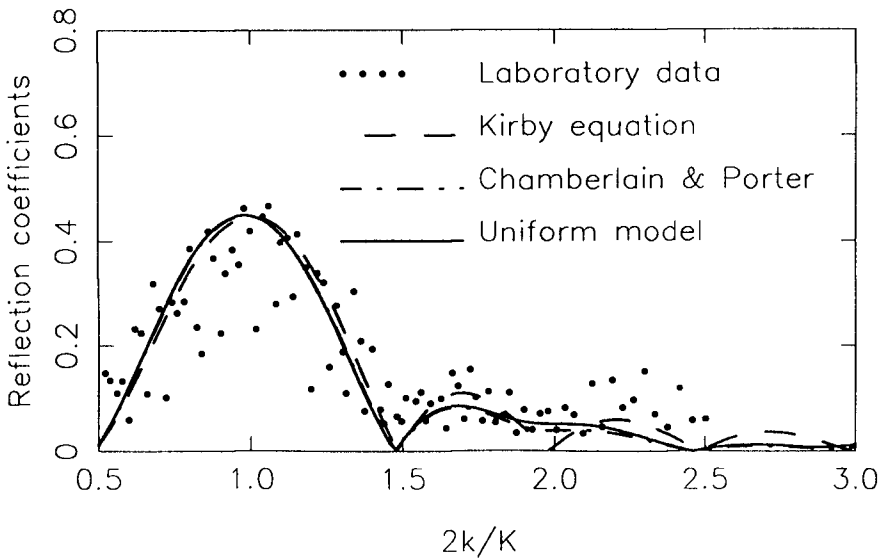


Fig.2 Singly-sinusoidal bed, $n=2$, $b/h_0=0.32$

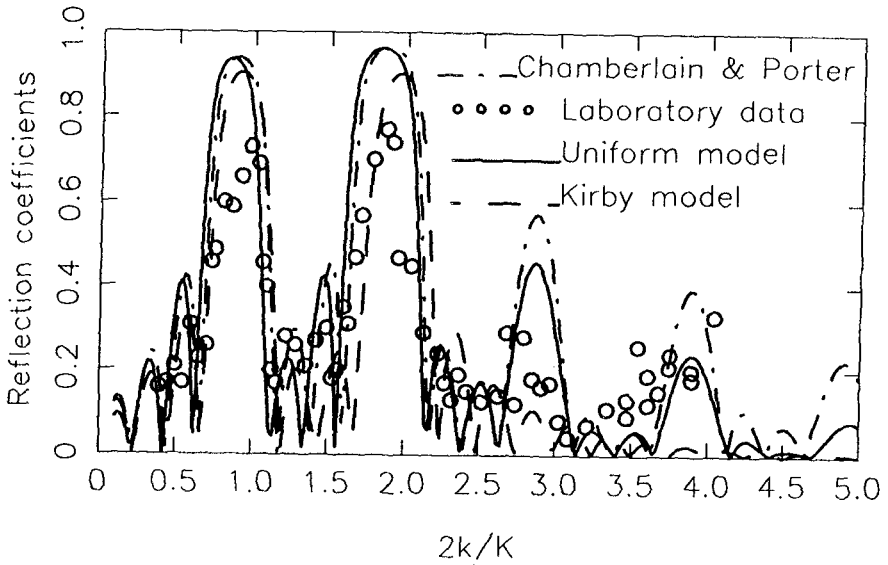


Fig.3 Doubly-sinusoidal bed, $n=4, m=2, b/h_0=0.4$

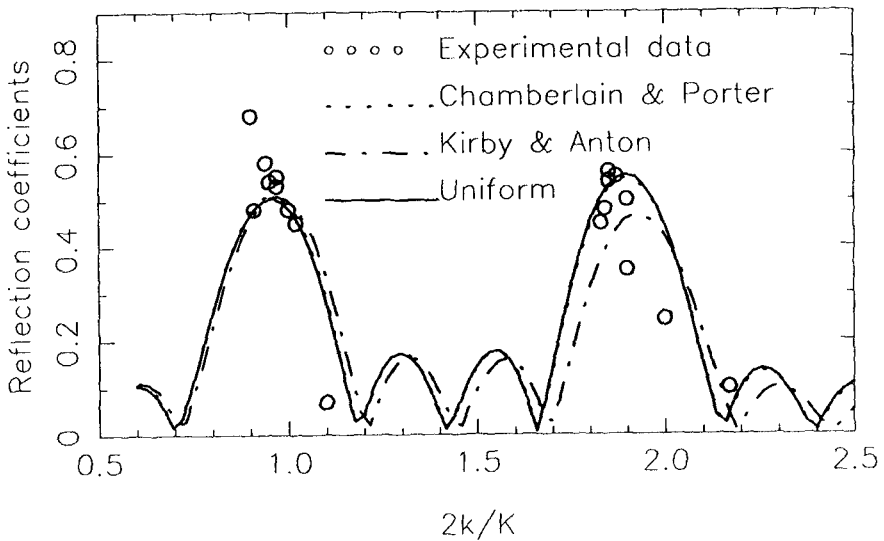


Fig.4 Four man-made bars (bar spacing=120cm)

CHAPTER 75

Bragg Reflection of Shallow-Water Waves on a Sloping Beach

Yong-Sik Cho¹ · Jong-In Lee² · Jong-Kyu Lee³

Abstract

In this study a set of governing equations describing the evolution of modulated shallow-water waves over a sinusoidally varying topography on a sloping beach is derived. The governing equations include the nonlinear interactions among different wave components as well as the shoaling effect over a slowly varying topography. It has been shown that the incident waves could be resonantly reflected by the interaction with the rippled seabed under the Bragg reflection condition. The magnitude of the resonantly reflected wave is almost equal to those of the incident and the transmitted waves.

1. Introduction

Water waves, approaching the coastline from deep water, undergo many physical phenomena caused by combined effects of bottom topographical variations, interference with man-made structures and nonlinear interactions among different wave components. One fascinating but challenging feature among these phenomena is so called the Bragg reflection occurring when the wave number of incident wave is a half of that of the sinusoidally varying topography. The Bragg reflection is believed to play an important role in the formation of submerged offshore sandbars frequently observed in Danish coast, the Great Lakes, Japanese coast and many other open coasts. In general, typical offshore multiple sandbars exist on beaches milder than 5 per 1000 and the number of sandbars varies 3 to 17 with a spacing of 10 m to 480 m between two adjacent bars (Mei and Liu, 1993).

¹Assistant Professor, Dept. of Civil Engineering, Sejong University, Seoul, 143-747, KOREA

²Research Assistant, ³Professor, Dept. of Civil Engineering, Hanyang University, Seoul, 133-791, KOREA

A lot of experimental and theoretical investigations have been performed to explain the possible formation mechanism of these sandbars as well as the effects of offshore sandbars on the change of the coastal morphology and the wave characteristics (Davies and Heathershaw, 1984; Mei, 1985; Yoon and Liu, 1987; Hara and Mei, 1987; Kirby and Vengayil, 1988; Liu and Cho, 1993). Through the laboratory experiment Carter et al. (1973) found that the formation of offshore sandbars is probably triggered by mass transport velocity near the seabed under partially reflected waves. They also pointed out that the incipient reflection coefficient for the sandbar formation is about 0.414. According to Mei and Liu (1993), a special bottom topography can reflect a significant amount of wave energy, and therefore can protect the beach from the possible erosion and deposit, that is, the strong reflection of incident waves could be the cause and the effect of offshore multiple sandbars.

Yoon and Liu (1987) investigated the near resonant reflection of periodic waves in shallow water over a sinusoidally varying topography. Since they were interested in near resonant reflection, only self-product terms of propagating wave components were considered. In this paper, we extend Yoon and Liu's study to examine the effects of the cross-product terms of oppositely propagating wave components and the number of seabed ripples. Thus, Yoon and Liu's study can be viewed as a limiting case of the present study. We also investigate the effect of a sloping beach on the reflection. Since the domain is fixed in shallow water, the Boussinesq equations are adequate to describe wave fields. The resonant reflection of incident periodic waves from a sinusoidally varying seabed laid on a sloping beach will be examined by solving a set of coupled nonlinear, ordinary differential equations. The effects of nonlinear interactions among different harmonics will also be examined for different numbers of seabed ripples.

In the following section, a set of governing equations describing modulation of shallow-water waves is first derived. These governing equations include effects of nonlinearity, dispersion, shoaling and interactions among different wave components. In section 3, two coupled ordinary differential equations are derived to describe evolution of water waves over a slowly varying topography. Numerical examples are given in section 4. Finally, concluding remarks are made in section 5.

2. Modulation Equations

By using a_0' as the characteristic wave amplitude, h_0' as the water depth and k' as the wave number, we introduce the following nondimensional variables:

$$\begin{aligned} (x, y) &= k'(x', y'), & z &= \frac{z'}{h_0'}, & h &= \frac{h'}{h_0'}, \\ t &= k' \sqrt{gh_0'} t', & \zeta &= \frac{\zeta'}{a_0'}, & \mathbf{u} &= \frac{h_0'}{a_0' (gh_0')^{1/2}} \mathbf{u}'. \end{aligned} \quad (1)$$

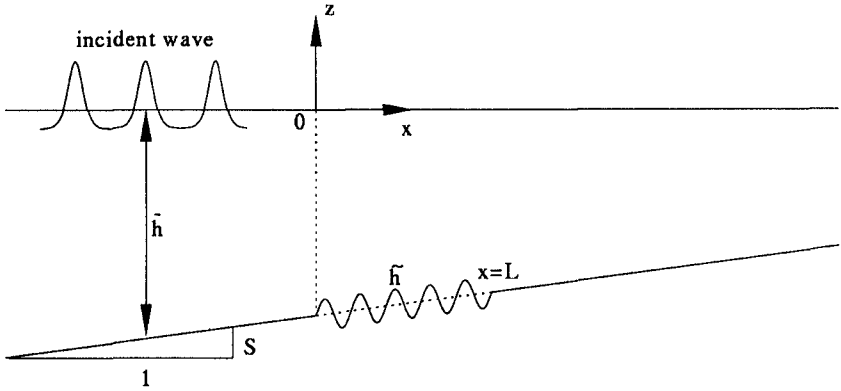


Figure 1. Definition sketch of the seabed and incident waves.

in which ζ' represents the free surface displacement and \mathbf{u}' does the depth-averaged horizontal velocity vector. We also introduce following two parameters:

$$\varepsilon = \frac{a_0'}{h_0'}, \quad \mu^2 = (k' h_0')^2 \quad (2)$$

in which ε and μ^2 represent the nonlinearity and the frequency dispersion, respectively. In the Boussinesq equations, orders of magnitude of both parameters are assumed to be equal and small enough. Using nondimensional variables the Boussinesq equations can be written in the following form (Yoon and Liu, 1987; Liu and Cho, 1993):

$$\frac{\partial \zeta}{\partial t} + \nabla \cdot [(h + \varepsilon \zeta) \mathbf{u}] = 0, \quad (3)$$

$$\frac{\partial \mathbf{u}}{\partial t} + \varepsilon \mathbf{u} \cdot \nabla \mathbf{u} + \nabla \zeta = \mu^2 \left\{ \frac{1}{2} h \frac{\partial}{\partial t} \nabla [\nabla \cdot (h \mathbf{u})] - \frac{1}{6} h^2 \frac{\partial}{\partial t} \nabla (\nabla \cdot \mathbf{u}) \right\}. \quad (4)$$

It is noted that equation (3) is an exact expression, while equation (4) is truncated at the order of $O(\varepsilon^2, \varepsilon \mu^2, \mu^4)$.

To investigate resonant reflection and shoaling of incident waves over a slowly varying topography the water depth is defined as (see figure 1):

$$h(x, y) = \bar{h}(x, y) + \hat{h}(x, y) \quad (5)$$

in which

$$\bar{h}(x, y) \sim O(1), \quad \hat{h}(x, y) \sim O(\mu^2) \quad (6)$$

and

$$|\nabla \bar{h}| \sim O(\mu^2), \quad |\nabla \hat{h}| \sim O(\mu^2). \quad (7)$$

Following Yoon and Liu (1987) the free surface displacement and the velocity can be expressed in Fourier series. That is,

$$\zeta(x, y, t) = \frac{1}{2} \sum_n \zeta_n(x, y) e^{-int}, \tag{8}$$

$$u(x, y, t) = \frac{1}{2} \sum_n U_n(x, y) e^{-int} \tag{9}$$

in which a periodic motion in time has been assumed and $n=0, \pm 1, \pm 2, \dots$. In equations (8) and (9), ζ_{-n} and U_{-n} are the complex conjugates of ζ_n and U_n , respectively. For simplicity, the symbols of $O(\varepsilon)$ and $O(\varepsilon^2)$ will be used to represent $O(\varepsilon, \mu^2)$ and $O(\varepsilon^2, \varepsilon\mu^2, \mu^4)$, respectively throughout the study.

By substituting equations (5)-(9) into equations (3) and (4), the following continuity and momentum equations are obtained for the n th Fourier components:

$$-in\zeta_n + \nabla \cdot (h U_n) + \frac{1}{2} \varepsilon \sum_s \nabla \cdot (\zeta_s U_{n-s}) = 0, \tag{10}$$

$$\begin{aligned} -in U_n + \frac{1}{2} \varepsilon \sum_s U_s \cdot \nabla U_{n-s} + \nabla \zeta_n \\ = -\frac{1}{3} in\mu^2 \bar{h}^2 \nabla (\nabla \cdot U_n) = O(\varepsilon^2), \end{aligned} \tag{11}$$

in which $s=0, \pm 1, \pm 2, \dots$. The leading order terms of equations (10) and (11) give

$$\zeta_n = -\frac{i}{n} \bar{h} \nabla \cdot U_n + O(\varepsilon), \tag{12}$$

$$U_n = -\frac{i}{n} \nabla \zeta_n + O(\varepsilon) \tag{13}$$

for $n \neq 0$ and

$$U_0 = -\frac{\varepsilon}{2\bar{h}} \sum_s \zeta_s U_{-s} + O(\varepsilon^2), \tag{14}$$

$$\zeta_0 = -\frac{1}{4} \varepsilon \sum_s U_s \cdot U_{-s} + O(\varepsilon^2) \tag{15}$$

for $n=0$. Equations (14) and (15) represent steady components which have no contribution to other harmonics up to $O(\varepsilon)$. Thus, the steady components are excluded in this study. By eliminating the velocity vector from equations (10) and (11) and using equations (5), (12) and (13), we can obtain the following combined equation:

$$\begin{aligned} n^2 \zeta_n + \nabla \cdot (h \nabla \zeta_n) - \varepsilon \frac{\bar{h}}{2} \sum_{s \neq 0, n} \frac{1}{s(n-s)} \nabla \cdot [(\nabla \zeta_s \cdot \nabla) \nabla \zeta_{n-s}] \\ + \frac{1}{3} \mu^2 \bar{h}^3 \nabla^4 \zeta_n + \varepsilon \frac{n}{2} \sum_{s \neq 0, n} \frac{1}{n-s} \nabla \cdot (\zeta_s \nabla \zeta_{n-s}) = O(\varepsilon^2). \end{aligned} \tag{16}$$

The leading orders of equation (16) yield

$$\nabla^2 \zeta_n = -\frac{n^2}{\bar{h}} \zeta_n. \tag{17}$$

By substituting equation (17) into equation (16), we also obtain

$$\begin{aligned} & \bar{h} \nabla^2 \zeta_n + \nabla(\bar{h} + \hat{h}) \cdot \nabla \zeta_n + n^2 \left[1 - \frac{\hat{h}}{h} - \frac{1}{3} \mu^2 \bar{h} n^2 \right] \zeta_n \\ &= \varepsilon \sum_{s \neq 0, n} \left\{ \frac{\bar{h}}{2s(n-s)} \nabla \cdot [(\nabla \zeta_s \cdot \nabla) \nabla \zeta_{n-s}] - \frac{n}{2(n-s)} \nabla \cdot (\zeta_s \nabla \zeta_{n-s}) \right\} \end{aligned} \quad (18)$$

where $|\partial \zeta / \partial y|^2 \sim O(\varepsilon, \mu^2)$ has been assumed.

3. Evolution Equations

In this section we derive a set of coupled ordinary differential equations to describe evolution of waves over a slowly varying topography. After omitting y -direction components equation (18) can be rewritten as:

$$\begin{aligned} & \bar{h} \frac{d^2 \zeta_n}{dx^2} + \frac{d\bar{h}}{dx} \frac{d\zeta_n}{dx} + n^2 \left(1 - \frac{\hat{h}}{h} + \frac{1}{3} \mu^2 \bar{h} n^2 \right) \zeta_n \\ &= \frac{\varepsilon}{2\bar{h}} \sum_{s \neq 0, n} (n^2 - s^2) \zeta_s \zeta_{n-s} - \frac{\varepsilon}{2} \sum_{s \neq 0, n} \frac{n+s}{n-s} \frac{d\zeta_s}{dx} \frac{d\zeta_{n-s}}{dx} + O(\varepsilon^2). \end{aligned} \quad (19)$$

The homogeneous leading order of equation (19) is the long wave equation and implies that wave components propagate both in $+x$ and $-x$ directions. Thus, the wave field can be split into the right- and the left-going components as (Liu and Cho, 1993):

$$\zeta_n = \zeta_n^+ + \zeta_n^- \quad (20)$$

where ζ_n^+ and ζ_n^- represent the right- and the left-going wave components, respectively. Then, the following coupled relationships can be obtained (Liu and Cho, 1993):

$$\frac{d\zeta_n^+}{dx} = \frac{in}{h} \zeta_n^+ + F_n, \quad \frac{d\zeta_n^-}{dx} = -\frac{in}{h} \zeta_n^- - F_n \quad (21)$$

in which F_n is an unknown coupling term. By substituting equations (20) and (21) into equation (19) and after lengthy algebra, the coupling term F_n is determined as:

$$\begin{aligned} F_n = & -\frac{1}{2\bar{h}} \left(\frac{1}{2} \frac{d\bar{h}}{dx} + \frac{d\hat{h}}{dx} \right) (\zeta_n^+ - \zeta_n^-) + \frac{in}{2h} \left(-\frac{\hat{h}}{h} + \frac{1}{3} \mu^2 n^2 \bar{h} \right) (\zeta_n^+ + \zeta_n^-) \\ & - \frac{i\varepsilon}{4h\bar{h}} \sum_{s \neq 0, n} (n+s) \left[(\zeta_s^+ \zeta_{n-s}^+ + \zeta_s^- \zeta_{n-s}^-) + \frac{n-2s}{n} (\zeta_s^- \zeta_{n-s}^+ + \zeta_s^+ \zeta_{n-s}^-) \right]. \end{aligned} \quad (22)$$

By assuming a periodic motion in space the wave components can be expressed as:

$$\zeta_n^+ = A_n(x) e^{in\theta}, \quad \zeta_n^- = B_n(x) e^{-in\theta} \quad (23)$$

in which $A_n(x)$ and $B_n(x)$ are complex amplitude functions for the right- and the left-going waves, respectively and the following definition is used:

$$\theta = \int \frac{dx}{h}$$

Substituting equations (22) and (23) into equation (21), a set of coupled nonlinear ordinary differential equations can be obtained:

$$\begin{aligned}
& \frac{dA_n}{dx} + \left[\frac{in\tilde{h}}{2h\sqrt{h}} + \frac{1}{4} \frac{d}{dx} (\ln \bar{h}) + \frac{1}{2h} \frac{d\tilde{h}}{dx} - \frac{i}{6} \mu^2 n^3 \sqrt{\bar{h}} \right] A_n \\
& - \left[-\frac{in\tilde{h}}{2h\sqrt{h}} + \frac{1}{4} \frac{d}{dx} (\ln \bar{h}) + \frac{1}{2h} \frac{d\tilde{h}}{dx} + \frac{i}{6} \mu^2 n^3 \sqrt{\bar{h}} \right] B_n e^{-2in\theta} \\
& = \text{NLT}_r + O(\varepsilon^2)
\end{aligned} \tag{24a}$$

where

$$\begin{aligned}
\text{NLT}_r = & -\frac{i\varepsilon}{4h\sqrt{h}} \sum_{s \neq 0, n} (n+s) \left[(A_s A_{n-s} + \frac{n-2s}{n} B_s A_{n-s} e^{-2is\theta}) \right] \\
& - \frac{i\varepsilon}{4h\sqrt{h}} \left[\sum_{s \neq 0, n} (n+s) (B_s B_{n-s} + \frac{n-2s}{n} A_s B_{n-s} e^{2is\theta}) \right] e^{-2in\theta}
\end{aligned}$$

for right-going waves,

$$\begin{aligned}
& \frac{dB_n}{dx} + \left[-\frac{in\tilde{h}}{2h\sqrt{h}} + \frac{1}{4} \frac{d}{dx} (\ln \bar{h}) + \frac{1}{2h} \frac{d\tilde{h}}{dx} + \frac{i}{6} \mu^2 n^3 \sqrt{\bar{h}} \right] B_n \\
& - \left[\frac{in\tilde{h}}{2h\sqrt{h}} + \frac{1}{4} \frac{d}{dx} (\ln \bar{h}) + \frac{1}{2h} \frac{d\tilde{h}}{dx} - \frac{i}{6} \mu^2 n^3 \sqrt{\bar{h}} \right] A_n e^{2in\theta} \\
& = \text{NLT}_l + O(\varepsilon^2)
\end{aligned} \tag{24b}$$

where

$$\begin{aligned}
\text{NLT}_l = & \frac{i\varepsilon}{4h\sqrt{h}} \sum_{s \neq 0, n} (n+s) \left[(B_s B_{n-s} + \frac{n-2s}{n} A_s B_{n-s} e^{2is\theta}) \right] \\
& + \frac{i\varepsilon}{4h\sqrt{h}} \left[\sum_{s \neq 0, n} (n+s) (A_s A_{n-s} + \frac{n-2s}{n} B_s A_{n-s} e^{-2is\theta}) \right] e^{2in\theta}
\end{aligned}$$

for left-going waves. Equations (24a) and (24b) are evolution equations for waves propagating over a slowly varying topography.

In summary, equations (24a) and (24b) are the governing equations for shallow-water waves forced by self- and cross-product wave components. In equation (24) the terms multiplied by the exponential function and $d\tilde{h}/dx$ are mathematically fast varying, whereas the other terms are slowly varying. The effects of the fast varying terms are generally insignificant, while they are significant if a phase is properly matched. Therefore, the present study is more general than Yoon and Liu's (1987) in which all fast varying terms are ignored. The role of fast varying terms will be discussed in detail in the following section. After solving equation (24) the free surface profile of wave can be recovered as

$$\zeta(x, t) = \frac{1}{2} \sum_n [A_n e^{in\theta} + B_n e^{-in\theta}] e^{-int}. \tag{25}$$

The corresponding velocity up to the leading order can also be obtained by substituting equation (25) into equations (9) and (13).

4. Numerical Example

An iterative scheme is employed to solve coupled equations (24a) and

(24b) with prescribed initial conditions of A_n . In the iterative scheme the transmitted wave field is first solved without considering the reflected wave field. The reflected wave field is then estimated with the calculated transmitted wave. The transmitted wave field is finally updated with the newly obtained reflected wave field. The procedure is repeated until the converged solutions are obtained. More detailed description of the iterative scheme and the convergence condition are given in Liu and Cho (1993).

Now we examine the resonant reflection of incident periodic waves over a finite length of the rippled seabed. Although the shoaling effect is included in equation (25), we first focus on the Bragg reflection. Then, the shoaling effect over a sloping beach will also be examined later. In this study the nondimensional water depth is given as:

$$\begin{aligned} h &= 1 - Sx, & x \leq 0, \quad x \geq L \\ h &= 1 - Sx - \rho \sin(\delta x), & 0 \leq x \leq L \end{aligned} \quad (26)$$

in which ρ is the amplitude, S is the beach slope and δ is the wave number of the sinusoidally varying seabed. As mentioned in section 2, the orders of magnitudes of ρ and δ are $O(\mu^2)$ and $O(1)$, respectively. Figure 1 briefly illustrates the bottom topography consisting of sinusoidal ripples and a sloping beach as defined in equation (26).

In the first numerical example, we investigate the Bragg reflection of a train of cnoidal waves over a sinusoidally varying topography. Following Yoon and Liu (1987), the initial conditions for incident cnoidal waves are given as:

$$A_1 = 0.8923, \quad A_2 = 0.4198, \quad A_3 = 0.1568, \quad A_4 = 0.0522, \quad A_5 = 0.0163.$$

The number of harmonics is fixed at 5 throughout the study. Figure 2 shows the free surface profile of a train of cnoidal waves obtained by using 5 harmonics given above.

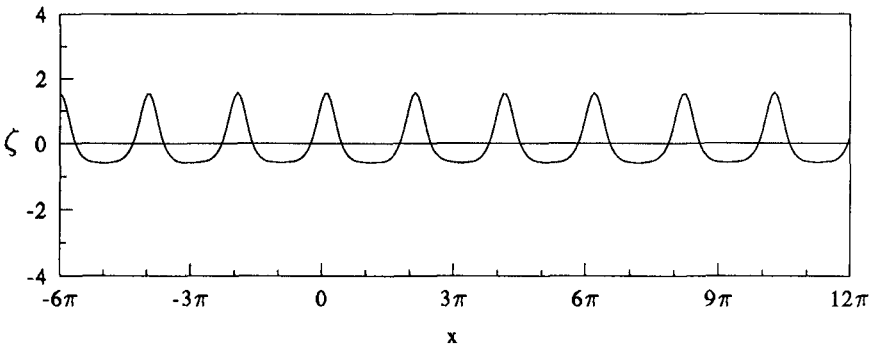


Figure 2. Free surface profile of the incident cnoidal waves at $t=0$.

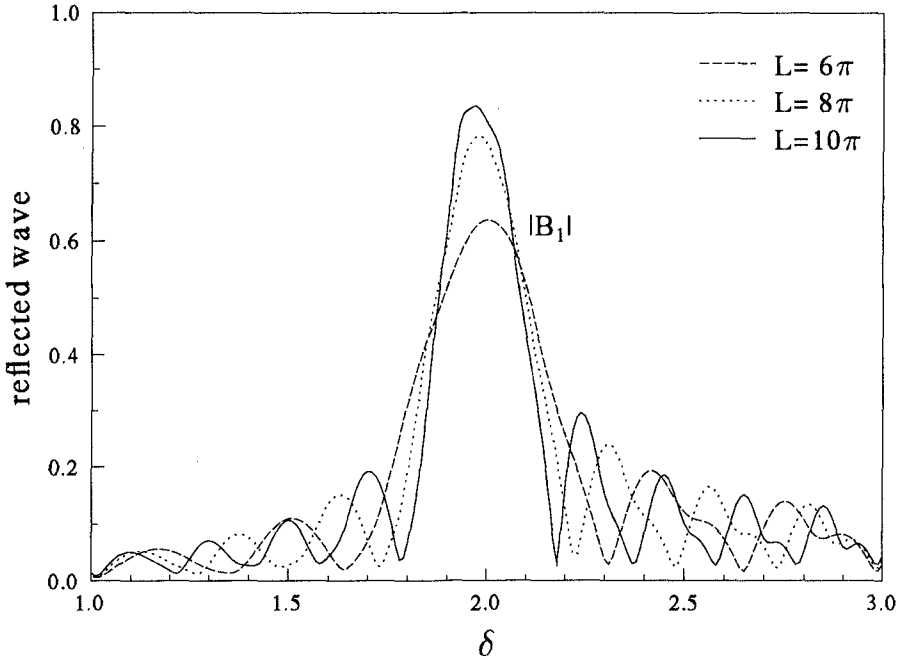


Figure 3. Reflected amplitude $|B_1|$ of cnoidal wave for $n = 5, \epsilon = 0.0881, \mu^2 = 0.1067, \rho = 0.15$.

To examine the effect of ripples on the reflection we calculate the reflected waves for three different numbers of ripples, that is, $m = 6, 8$ and 10 with m being the number of sinusoidal ripples. The reflection becomes stronger as the number of ripples increases as shown in figure 3. Therefore, the strongest reflection occurs when $m = 10$. We briefly explain the mathematics involved in the Bragg reflection. From equation (26)

$$\begin{aligned} \frac{d\tilde{h}}{dx} &= \frac{d\tilde{h}}{dx} = -\rho\delta \cos(\delta x) \\ &= -\rho\delta \frac{e^{i\delta x} + e^{-i\delta x}}{2} \end{aligned} \tag{27}$$

By substituting equation (27) into equation (24b) the third term in the second parenthesis becomes

$$\begin{aligned} &\frac{1}{2\tilde{h}} \frac{d\tilde{h}}{dx} e^{2in\theta} \\ &= -\frac{\rho\delta}{4} [e^{i(\delta+2n)x} + e^{i(-\delta+2n)x}] \end{aligned} \tag{28}$$

We can see that the second term of equation (28) becomes the unity if $\delta = 2n$. The second term of equation (28) varies slowly, whereas the first term does fast. Since the first harmonic dominates the incident wave system (Yoon and Liu, 1987), the forcing term of equation (24b) becomes largest

when $\delta=2$, that is, the wave number of the ripple is twice that of the first harmonic of incident wave. As plotted in figure 3, the maximum reflection occurs at $\delta \approx 2$. The reflection coefficient is greater than 0.414 even for $m=6$.

The reflected waves for the first and the second harmonics are plotted with $L=6\pi$ and $L=10\pi$ in figures 4 and 5, respectively. The amplitude of the seabed ripple is fixed as $\rho=0.1$ for both cases. The reflected waves without considering fast varying terms are slightly larger than those with considering fast varying terms. As stated previously, the magnitude of the first harmonic component is much larger than that of the second harmonic component. The difference between without considering and with considering fast varying terms is not surprising but appreciable. The beach slope is not considered both in figures 4 and 5.

In figure 6, the reflected waves for the first harmonic are plotted for $L=10\pi$ and $\rho=0.1$ with three different nonlinear effects. The strength of reflection is rapidly decreasing as the nonlinearity increases. This is because wave energy transfers more actively as the nonlinearity increases. That is, more wave energy transfers to higher harmonic components. The peak is also moving leftward as the nonlinearity increases.

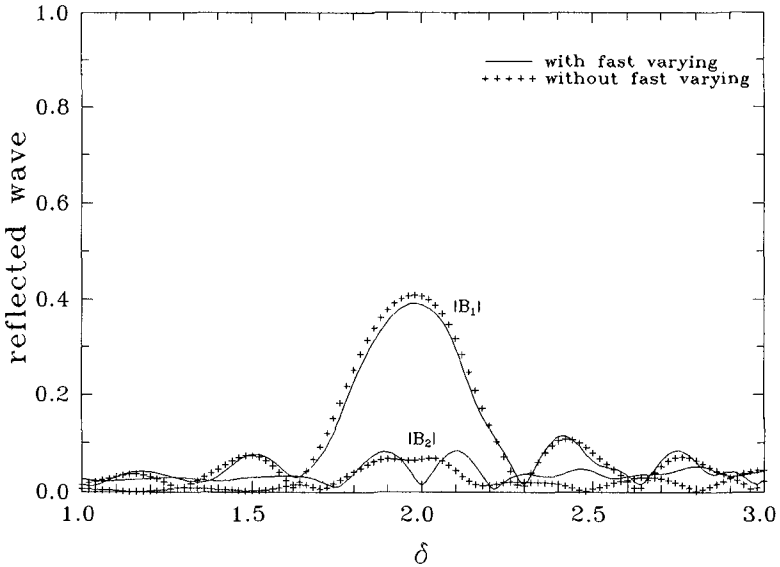


Figure 4. Reflected amplitudes of cnoidal wave for $L=6\pi$, $S=0.0$, $\epsilon=0.10$, $\mu^2=0.1067$, $\rho=0.10$.

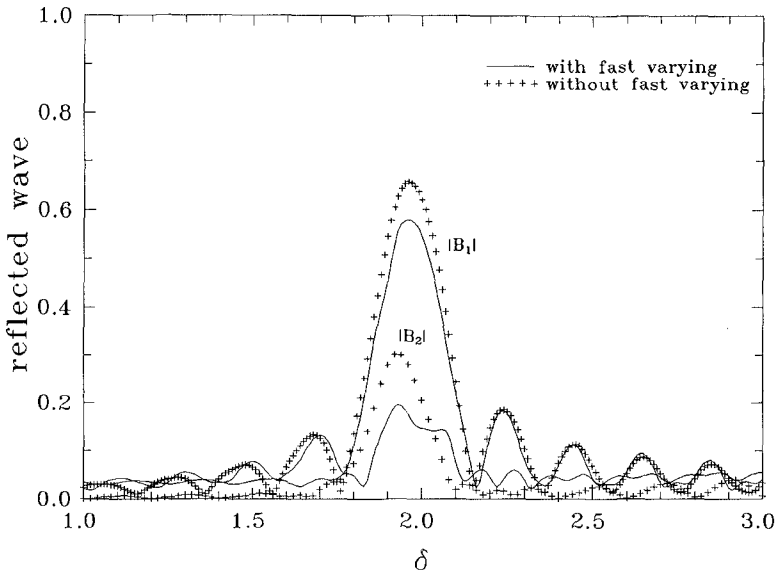


Figure 5. Reflected amplitudes of cnoidal wave for $L=10\pi$, $S=0.0$, $\epsilon=0.10$, $\mu^2=0.1067$, $\rho=0.10$.

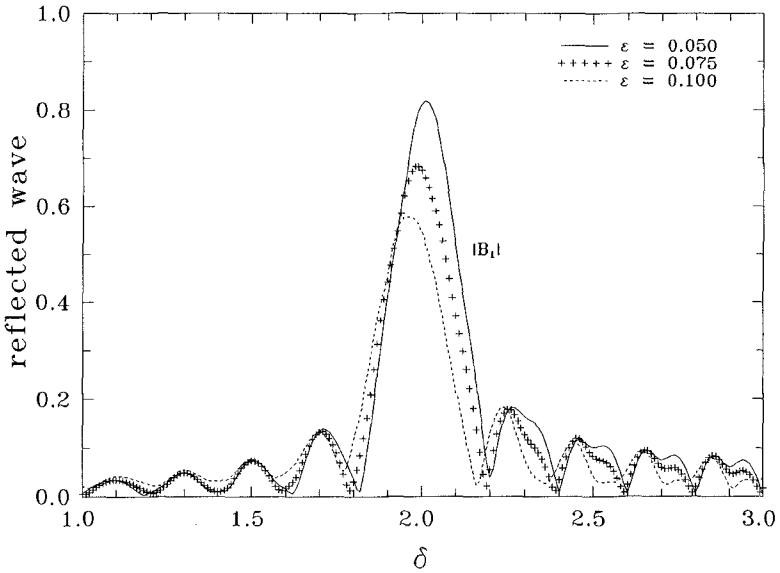


Figure 6. Effects of nonlinearity for $L=10\pi$, $S=0.0$, $\mu^2=0.1067$, $\rho=0.10$.

Finally, the first harmonic components of reflected waves are plotted in figures 7 and 8 for $L=6\pi$ and $L=10\pi$ with two different beach slopes, $S=0$ and $S=0.005$. The amplitude of the seabed ripple is also fixed as $\rho=0.1$. The magnitudes of reflected waves remain almost the same in figures 7 and 8, respectively. This is because the beach slope $S=0.005$ is too mild to affect to the magnitude of the reflected wave. As discussed in section 2, the order of magnitude of a beach slope is assumed to be $O(\mu^2)$ in this study. However, the slope used in figures 7 and 8 is 0.005 much smaller than $O(\mu^2)$. The peak moves slightly leftward as the beach slope increases.

5. Concluding Remarks

In this study a set of governing equations is derived from the Boussinesq equations to examine the evolution of periodic waves over a sinusoidally varying topography laid on a sloping beach. The derived governing equations are used to study the evolution of cnoidal waves over a slowly varying topography. It has been shown that reflected waves can be resonantly amplified under the Bragg reflection condition..

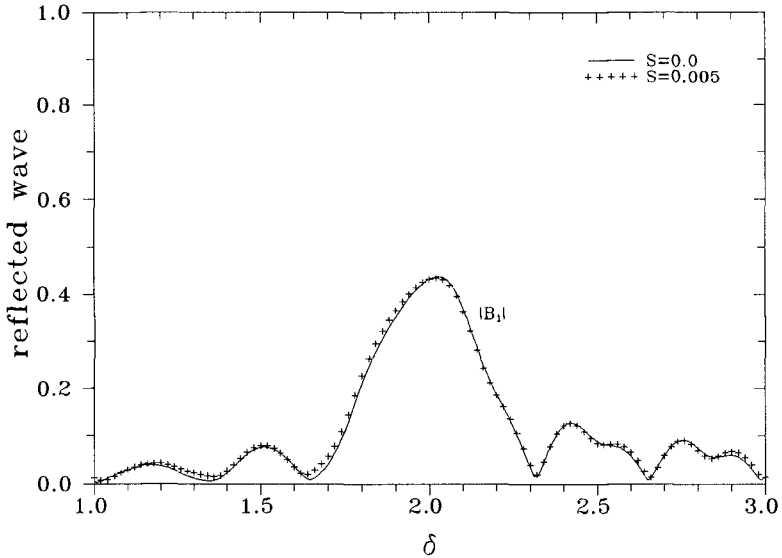


Figure 7. Comparison of reflected amplitudes for $L=6\pi$, $\varepsilon=0.075$, $\mu^2=0.10$, $\rho=0.10$.

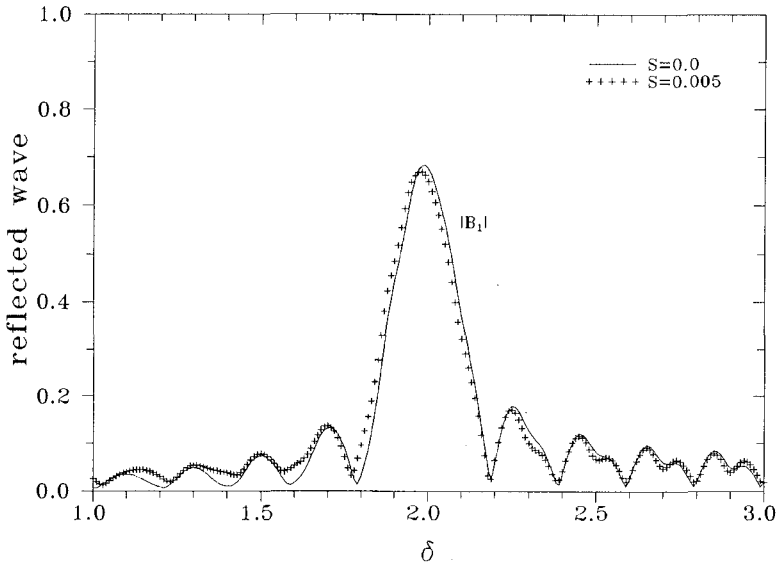


Figure 8. Comparison of reflected amplitudes for $L=10\pi$, $\varepsilon=0.075$, $\mu^2=0.10$, $\rho=0.10$.

In very shallow water the nonlinear effect may dominate the entire wave system. Especially, just before the breaking point waves might be highly nonlinear. Furthermore, the bottom friction becomes increasingly important as the water depth decreases. An extension with inclusion of highly nonlinear terms and the bottom friction is now progressing. The result will be reported in future.

Acknowledgment

This research was, in part, supported by the Korean Science and Engineering Foundation.

References

- Carter, T.G., Liu, P.L.-F., and Mei, C.C.(1973). "Mass transport by waves and offshore sand bedforms." *J. Waterway, Port, Coastal and Ocean Eng.*, ASCE, Vol. 99, pp. 165-184.
- Davies, A.G. and Heathershaw, A.D.(1984). "Surface wave propagation over sinusoidally varying topography." *J. Fluid Mech.*, Vol. 144, pp. 419-443.
- Hara, T. and Mei, C.C.(1987). "Bragg reflection of surface waves by periodic bars: Theory and experiment." *J. Fluid Mech.*, Vol. 178, pp. 221-241.
- Kirby, J.T and Vengayil, P.(1988). "Nonresonant and resonant reflection of long waves in varying channels." *J. Geophys. Res.*, Vol. 93, pp. 10,782-10,796.

- Liu, P.L.-F. and Cho, Y.-S.(1993). "Bragg reflection of infragravity waves by sandbars." *J. Geophys. Res.*, Vol. 98, pp. 22,733-22,741.
- Mei, C.C.(1985). "Resonant reflection of surface water waves by periodic bars." *J. Fluid Mech.*, Vol. 152, pp. 315-335.
- Mei, C.C. and Liu, P.L.-F.(1993). "Surface waves and coastal dynamics." *Annu. Rev. Fluid Mech.*, Vol. 25, pp. 215-240.
- Yoon, S.B. and Liu, P.L.-F.(1987). "Resonant reflection of shallow-water waves due to corrugated boundaries." *J. Fluid Mech.*, Vol. 180, pp. 451-469.

CHAPTER 76

Reflection Analysis with Separation of Cross Modes

John Grønbech*, Thomas Jensen** and Henning Andersen**

Abstract

During physical model tests in a wave flume an accurate determination of the incident waves is crucial. Normally, the determination of the incident waves is conducted by a traditional reflection analysis and in this case the influence of any cross modes is ignored. The present paper concerns the advantage of including the possible presence of cross modal activity in the reflection analysis when determining the incident waves. It is shown both analytically and numerically how the cross modes affect the results of a traditional reflection analysis, and that ignoring cross modal activity can lead to an inaccurate determination of the incident waves. A new method is introduced where the cross modes are separated in the reflection analysis. This method requires at least three wave probes while a traditional reflection analyses only requires two wave probes. The applicability of the method is verified both numerically and by physical flume tests at the Hydraulic Laboratory of Aalborg University, Denmark. In both cases the new method seems to give very good results.

1 Introduction

One of the most important tasks in physical model studies is the determination of incident waves. The determination of the incident waves is often carried out using some kind of reflection analysis capable of separating the incident and reflected wave components mathematically.

* Department of Civil Engineering, Aalborg University, Sohngaardsholmsvej 57, DK-9000 Aalborg, Denmark.

** Danish Hydraulic Institute, Agern Allé 5, DK-2970 Hørsholm, Denmark.

Goda and Suzuki (1976) presented a method capable of separating the incident and reflected waves on the basis of wave measurements at two known positions on a line parallel to the direction of wave propagation. Mansard and Funke (1980) improved this method by applying three wave gauges instead of only two. This enabled an optimization of the determination of the incident and reflected waves by the use of a least squares technique. Zelt and Skjelbreia (1992) improved this optimization procedure further by applying an arbitrary number of wave probes.

However, all these commonly used methods of reflection analysis are based on the assumption that the waves measured in the flume are composed of only two wave components; The incident and reflected components. If the measured waves contain other components, for instance cross modes, which is a well-known phenomenon in flume tests, the reflection analysis can produce inaccurate results.

In this paper, a new method of reflection analysis is presented. This method, which also uses an arbitrary number of wave probes, assumes that the measured waves are composed of three components; The usual incident and reflected wave components *and* a component representing any cross modal activity present in the wave flume. Before presenting the new method of reflection analysis, the influence of cross modes on the results of a traditional reflection analysis is addressed. This is done using the method of Zelt and Skjelbreia (1992).

2 Influence of Cross Modal Activity

The presence of cross modal activity affects the composite wave field measured in the flume. Depending on the phase differences between the cross modes and the longitudinal waves, the ordinary wave heights measured at each wave probe either increase or decrease. In case of regular waves, the influence of the cross modes is verified analytically by decomposing the measured Fourier coefficients into a primary term representing the longitudinal waves and secondary term representing the cross modes. The analytical approach is supported by numerical simulations using the method of Zelt and Skjelbreia (1992) with 5 wave probes on simulated time series with and without cross modes. In case of irregular waves, the influence of cross modes is investigated by comparing the incident and reflected wave spectra with and without cross modes contained in the simulated time series.

2.1 Analytical Verification of the Influence of Cross Modes

To investigate the influence of cross modes in traditional methods of reflection analysis analytically, the method of Zelt and Skjelbreia (1992) has been used. The method is explained very briefly in the following.

Using standard Fourier analysis techniques the surface elevation (η_p) measured at wave probe p (see Figure 1) can be expressed as:

$$\eta_p(t) = \sum_{n=0}^{N-1} A_{n,p} e^{i\omega_n t} \quad ; \quad A_{n,p} = a_{n,p} - ib_{n,p} \tag{1}$$

where $a_{n,p}$ and $b_{n,p}$ are the Fourier coefficients corresponding to frequency component n and wave probe p . ω_n is the n th cyclic frequency. Assuming linear wave theory, no frequency modulation due to the reflection process, and a composite wave field composed of incident waves and reflected waves only, the theoretical surface elevation at wave probe p (see Figure 1) can be written as:

$$\eta(x_p, t) = \sum_{n=0}^{N-1} (a_{I,n} e^{-ik_n x_p} + a_{R,n} e^{ik_n x_p}) e^{i\omega_n t} \tag{2}$$

where $a_{I,n}$ and $a_{R,n}$ are complex numbers containing the Fourier coefficients of the n th frequency component of the incident waves and reflected waves. k_n is the wave number of the n th frequency component and x_p is the position of wave probe p .

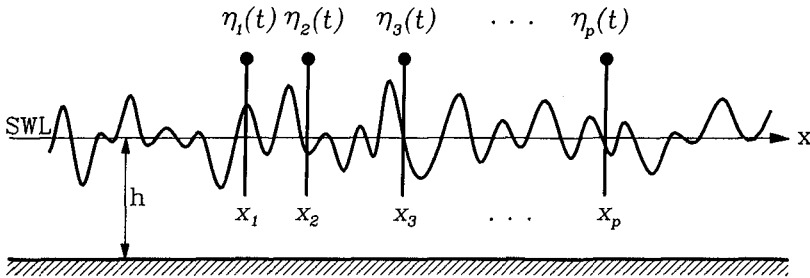


Figure 1 - Measuring composite wave fields at P wave probes.

Combining Equations (1) and (2) a complex equation for each wave probe p and frequency component n is obtained:

$$A_{n,p} = a_{I,n} e^{-ik_n x_p} + a_{R,n} e^{ik_n x_p} \tag{3}$$

The unknowns of this equation ($a_{I,n}$ and $a_{R,n}$) are the same for each wave probe. If only two wave probes are applied, Equation (3) is solved exactly but singularities at certain frequencies will occur (Goda and Suzuki, 1976). If more than two wave probes are applied the overdetermined system of equations is solved by introducing an error $\epsilon_{n,p}$ to the decomposed wave field:

$$\varepsilon_{n,p} = a_{L,n} e^{-ik_n x_p} + a_{R,n} e^{ik_n x_p} - A_{n,p} \tag{4}$$

$a_{L,n}$, and $a_{R,n}$ are then determined by minimizing a weighted sum of the squares of the error $\varepsilon_{n,p}$ (for details please refer to Zelt and Skjelbreia, 1992). The explicit solution is given by:

$$a_{L,n} = \left[S_n \sum_{p=1}^P W_{n,p} A_{n,p} e^{i\Delta\phi_{n,p}} - \sum_{p=1}^P W_{n,p} A_{n,p} e^{-i\Delta\phi_{n,p}} \sum_{p=1}^P W_{n,p} e^{2i\Delta\phi_{n,p}} \right] \frac{e^{i\phi_{n,1}}}{D_n} \tag{5}$$

$$a_{R,n} = \left[S_n \sum_{p=1}^P W_{n,p} A_{n,p} e^{-i\Delta\phi_{n,p}} - \sum_{p=1}^P W_{n,p} A_{n,p} e^{i\Delta\phi_{n,p}} \sum_{p=1}^P W_{n,p} e^{-2i\Delta\phi_{n,p}} \right] \frac{e^{-i\phi_{n,1}}}{D_n} \tag{6}$$

where:

$$S_n = \sum_{p=1}^P W_{n,p} \quad ; \quad \Delta\phi_{n,p} = \phi_{n,p} - \phi_{n,1} = k_n (x_p - x_1) \tag{7}$$

$$D_n = S_n^2 - \sum_{p=1}^P W_{n,p} e^{2i\Delta\phi_{n,p}} \sum_{q=1}^P W_{n,q} e^{-2i\Delta\phi_{n,q}} \tag{8}$$

$W_{n,p}$ is a weight coefficient determined for each wave probe and frequency component as introduced by Zelt and Skjelbreia (1992).

If cross modes are present in the flume their influence can be investigated by decomposing the measured Fourier coefficients ($A_{n,p}$) into one part representing the longitudinal waves ($A_{L,n,p}$) and one part representing the cross modes ($A_{C,n}$), which is independent of the probe number.

$$A_{n,p} = A_{L,n,p} + A_{C,n} \tag{9}$$

Equations (5) and (6) can now be rewritten as:

$$a_{L,n} = a_{L,L,n} + A_{C,n} B_n \tag{10}$$

$$a_{R,n} = a_{L,R,n} + A_{C,n} B_n^* \tag{11}$$

where:

$$B_n = \left[S_n \sum_{p=1}^P W_{n,p} e^{i\Delta\phi_{n,p}} - \sum_{p=1}^P W_{n,p} e^{-i\Delta\phi_{n,p}} \sum_{p=1}^P W_{n,p} e^{2i\Delta\phi_{n,p}} \right] \frac{e^{i\phi_{n,1}}}{D_n} \tag{12}$$

and B_n^* is the complex conjugate of B_n , $a_{L,L,n}$ and $a_{L,R,n}$ in Equation (10) and (11)

represent the solution without cross modes, whereas the last terms represent the cross mode contribution, consisting of one part representing the Fourier coefficients ($A_{c,n}$) and one pure geometrical part depending on the probe spacings (B_n and B_n^*).

The influence of the cross modes is not determined by the amplitude only, also the phase of the cross modes affects the incident and reflected Fourier coefficients as it appears from Equations (10) and (11). Due to the fact that B_n appears as the complex conjugate in Equation (11) the presence of cross modes does not affect the determination of the incident and reflected waves equally. Essentially, this means that no constant ratio of the deviations between the estimated incident and reflected wave heights and their true values exists. Furthermore, it is seen that depending on the amount of reflection, the relative deviation of the reflected amplitudes is larger than the relative deviation of the incident amplitudes.

2.2 Numerical Verification of the Influence of Cross Modes

To investigate the influence of cross modes numerically, the cross modal activity has been introduced to the longitudinal wave train by adding a secondary wave train propagating perpendicular to the ordinary direction of wave propagation. This secondary wave train is assumed to have similar spectral properties as the primary wave train but with a different phase spectrum. For regular waves the amount of cross modes in the simulated wave trains is denoted by the ratio of the amplitudes of the cross modes to the amplitude of the incident waves. For irregular waves a JONSWAP spectrum was synthesized and the ratio of the significant cross mode wave height ($H_{m0,c}$) to the incident significant wave height ($H_{m0,i}$) has been used to describe the amount of cross modal activity.

It is of course possible that natural cross modal activity would possess different spectral distributions with the spectral density concentrated at the natural frequencies of the flume. However, it seems reasonable to investigate the case where the noise in each spectral band is proportional to the energy in this band. This was also used by Mansard and Funke (1987).

Analytically, it was shown that the influence of cross modes is affected by the phase of the cross modes, but the significance of the influence has not been shown. For regular waves the influence is illustrated by varying the phase from 0 to 2π . In Figure 2, the relative deviation between the calculated wave height and the simulated wave height is shown as a function of the phase difference between the cross mode and the incident wave ($\Phi_c - \Phi_i$). A positive deviation corresponds to an overestimation of the incident or reflected wave height (H_i and H_R).

The relative deviations shown in Figure 2 are calculated on the basis of 10% and 20% cross modes. The simulated incident wave height is $H_i=0.5$ m, the period is $T=1.86$ s and the reflection coefficient is $C_r=0.25$. The phase of the incident

waves is zero, essentially meaning that the phases in Figure 2 correspond to the phase of the cross mode. However, from Equations (10) and (11) it is seen that the phase of the reflected waves also affects the results. This is also seen in Figure 2 since a constant ratio of -0.25 between the deviations of the incident and reflected wave heights exists when shifting the phase difference approximately $\pi/10$ between the two curves. Of course, the absolute value of this ratio corresponds to the ratio between the theoretical reflected and the incident wave heights.

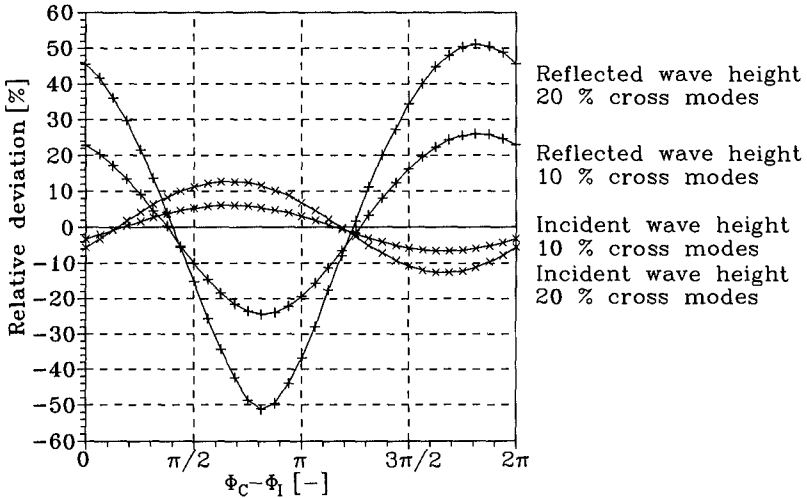


Figure 2 - Dependency of phase difference ($\Phi_C - \Phi_I$). $H_I=0.50$ m, $H_R=0.125$ m.

It appears from Figure 2 that the relative deviations are strongly dependent on the phase of the cross mode (Φ_C), the phase of the incident wave (Φ_I), and the phase of the reflected wave (Φ_R). For 10% cross modes, the relative deviation of the reflected wave height varies from zero to approximately 25%, whereas the relative deviation of the incident wave height does not exceed 7%.

Equations (10) and (11) explain the fact that the deviation in the determination of the incident and reflected waves is in almost opposite phase because of the appearance of B_n as the complex conjugate in Equation (11). If the deviations should be in exactly opposite phases, it can be seen from Equations (10) and (11) that the cross mode contribution must be zero.

As experienced through the analysis with regular waves, the appearance of cross modes do affect the individual frequency components, which is also seen for irregular waves in Figures 3 and 4, where 25 % cross modes have been introduced. Again, the cross modes affect the determination of the reflected spectrum more significantly than the determination of incident spectrum. However, the deviations are small and they can be reduced by further smoothing of the of the wave spectra.

Thus, the sensitivity to cross modes for irregular waves must be evaluated in terms of the applied smoothing of the spectra. Keeping in mind that the wave heights of the incident and reflected waves are determined as H_{m0} -values, the deviations in Figure 3 do not represent the real picture of the deviations, which is seen from the listed parameters in Figure 3. In case of regular waves it was seen from Figure 2 that if the incident wave height was overestimated, the reflected wave heights was underestimated for most phase differences. For irregular waves the deviations will be the mean value of the curves shown in Figure 2.

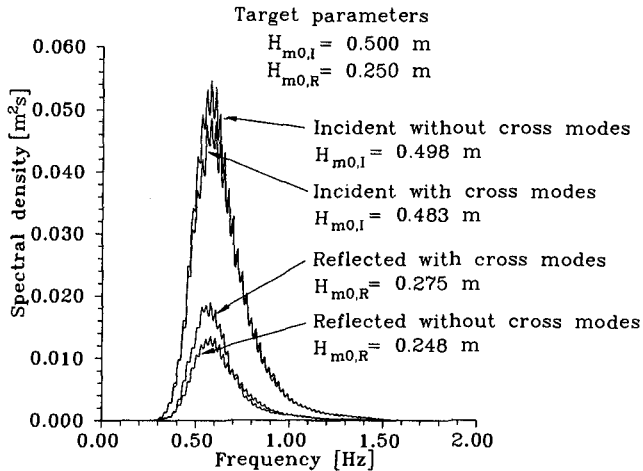


**Figure 3 - The influence of cross modes on irregular waves. $DOF=64$.
 Bandwidth=0.156 Hz.**

It is seen from Figure 2* that for irregular waves the incident wave height is underestimated in general (mean value < 0), whereas the reflected wave height is overestimated (mean value > 0). This is also seen from the irregular test shown in Figure 3.

As regards the reflection coefficient spectrum (Figure 4), the presence of cross modes causes a relative deviation of approximately 30% in the vicinity of the peak frequency, that is, a 30% overestimation of the reflection coefficient at the peak frequency. However, as it appears from Figure 4, the reflection coefficient is both overestimated and underestimated (depending on the frequency), which obviously can be reduced by further smoothing of the spectra.

* However, this implies that the cross mode phases, the phases of the incident waves and the phases of the reflected waves are independent and uniformly distributed between 0 and 2π . Normally, this assumption is not fulfilled for "real" waves. For instance, the phases of the incident and the reflected waves are correlated.

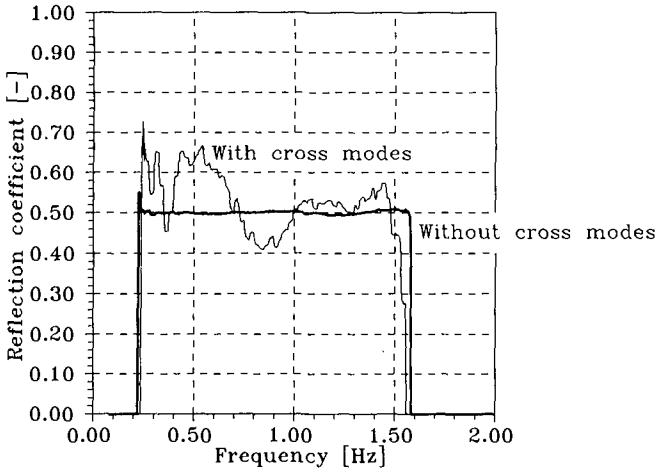


Figure 4 - The influence of cross modes on irregular waves. $DOF=64$.
Bandwidth=0.156 Hz.

3 Reflection Analysis with Cross Mode Separation

It has been shown above that the presence of cross modes can cause inaccurate estimations of the incident and reflected waves when using traditional reflection analysis methods. In this section a new method of reflection analysis will be presented, capable of taking the cross modal activity into account and thereby improving the estimation of the incident and reflected waves. First, the mathematical formulation of the reflection analysis with separation of cross modes is developed. Secondly, results from reflection analysis with separation of cross modes based on simulated data are presented. Finally, the result of a flume test carried out at the Hydraulics Laboratory of Aalborg University, Denmark is presented.

3.1 Mathematical Formulation

The cross modes are characterized by an oscillating signal which is the same at all probe locations. Obviously, this implies that the probes are placed on a straight line in the direction of wave propagation. Expanding Equation (2) the new composite wave field at wave probe p can be written as:

$$\eta(x_p, t) = \sum_{n=0}^{N-1} (a_{I,n} e^{-i\phi_{n,p}} + a_{R,n} e^{i\phi_{n,p}} + a_{C,n}) e^{i\omega_n t} \quad (13)$$

where $a_{C,n}$ is the Fourier coefficients of the cross modes.

The measured wave field is still given by Equation (1) and equating the coefficients in Equations (1) and (13) yields:

$$A_{n,p} = a_{I,n} e^{-i\phi_{n,p}} + a_{R,n} e^{i\phi_{n,p}} + a_{C,n} \quad ; \quad p = 1, 2, \dots, P \quad (14)$$

A complex equation for each wave probe with three unknowns (as opposed to two unknowns in Equation (3)), which are the same for all wave probes for each frequency has now been obtained. Therefore, an exact solution to Equation (14) requires at least three wave probes. However, using only three wave probes will cause singularities at certain frequencies, similar to those for two wave probes in the traditional methods (Andersen et al., 1995). For more than three wave probes, Equation (14) is solved by a least squares minimization procedure similar to the one described in Section 2.1 (please refer to Andersen et al. (1995) for further details). The solution is given implicitly by Equation (15).

$$\begin{aligned} a_{I,n} \sum_{p=1}^P W_{n,p} e^{-2i\phi_{n,p}} + a_{R,n} S_n + a_{C,n} \sum_{p=1}^P W_{n,p} e^{-i\phi_{n,p}} &= \sum_{p=1}^P W_{n,p} A_{n,p} e^{-i\phi_{n,p}} \\ a_{I,n} S_n + a_{R,n} \sum_{p=1}^P W_{n,p} e^{2i\phi_{n,p}} + a_{C,n} \sum_{p=1}^P W_{n,p} e^{i\phi_{n,p}} &= \sum_{p=1}^P W_{n,p} A_{n,p} e^{i\phi_{n,p}} \\ a_{I,n} \sum_{p=1}^P W_{n,p} e^{-i\phi_{n,p}} + a_{R,n} \sum_{p=1}^P W_{n,p} e^{i\phi_{n,p}} + a_{C,n} S_n &= \sum_{p=1}^P W_{n,p} A_{n,p} \end{aligned} \quad (15)$$

The explicit solution for the three complex unknowns has not been derived. Because the unknowns are complex numbers, Equation (15) is solved as six linear equations with six unknowns using standard procedures. In the present study the weight function ($W_{n,p}$) introduced by Zelt and Skjelbreia (1992) has been set equal to one (see Andersen et al., 1995).

3.2 Results

In the following the results of reflection analysis with cross mode separation are shown. These results are presented in terms of spectra and wave heights for a simulated irregular composite wave field. The composite wave field is based on the same geometry and spectral characteristics as used in Section 2. Again $H_{m0,I} = 0.50$ m, and $C_r = 0.50$ for all frequencies and finally 25 % cross modes have been added to the signal i.e., $H_{m0,C} = 0.125$ m. The peak period is 1.86 s.

In Figure 5 the incident, the reflected and the cross mode spectra are shown. It is seen that the calculated wave heights correspond to the target parameters within acceptable accuracy.

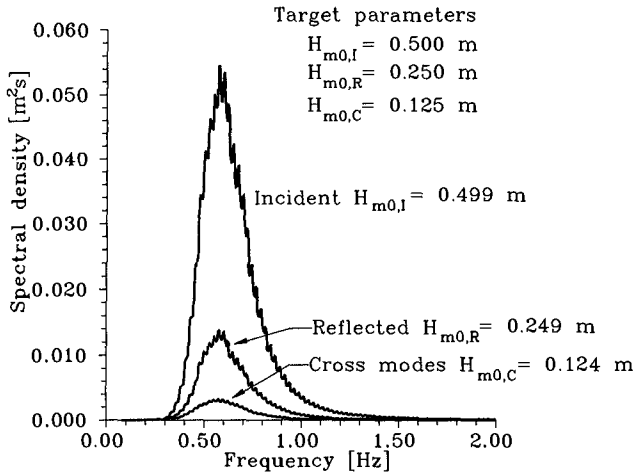


Figure 5 - Incident, reflected and cross mode spectra. Irregular waves. $DOF=64$, $bandwidth=0.156$ Hz.

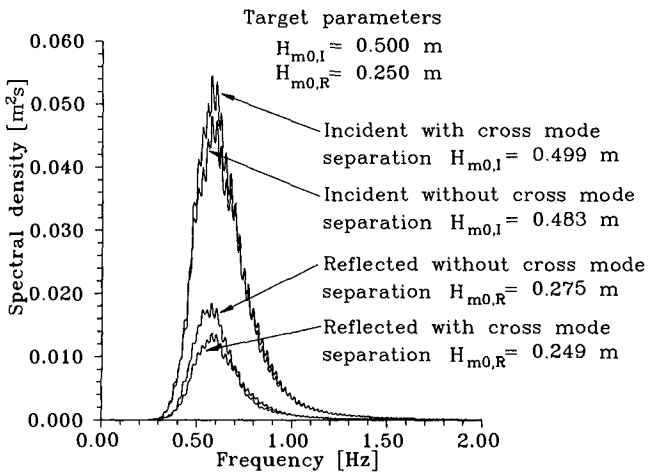


Figure 6 - Spectra with and without cross mode separation. $DOF=64$, $bandwidth=0.156$ Hz.

In Figure 6 the spectra from the reflection analysis with cross mode separation and the spectra from the analysis without cross mode separation are shown. It is seen that the incident spectrum determined with cross mode separation has larger spectral densities than the spectrum determined without cross mode separation. Particularly near the peak this is significant. This is also seen from the wave heights where the former corresponds to the simulated while the latter is 3.5 % too small. Regarding the reflected spectra the opposite is seen and the deviations are more significant, since the wave height from the analysis without cross mode separation is 8.8 % too large. These contrasts were explained in connection to Figures 2 and 3. The difference between the two spectra would be even larger if less smoothing of the wave spectra was applied. Therefore, in the case of the presence of cross modal activity the separation of cross modes is important when determining the incident wave train by inverse Fourier transformation because too much smoothing should be avoided. The deviations between the two incident spectra and the two reflected spectra are of course also seen on the reflection coefficient spectra in Figure 7.

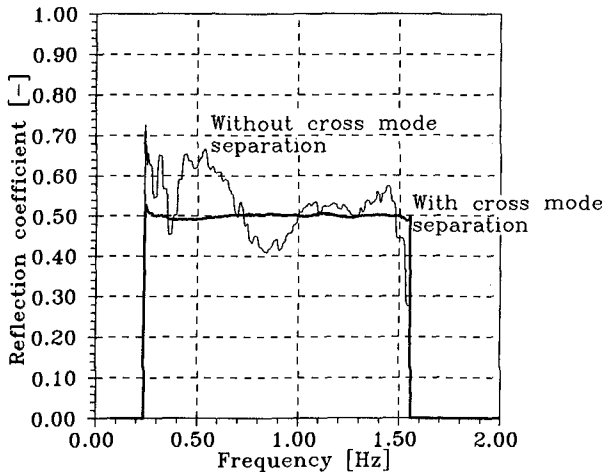


Figure 7 - Reflection coefficient spectra with and without cross mode separation.
DOF=64, bandwidth=0.156 Hz.

In Figure 8, the results of a flume test carried out in the Hydraulics Laboratory at Aalborg University, Denmark are shown. The irregular waves had a peak period of 1.00 s, corresponding to the 2nd natural frequency of the flume. It appears that the cross mode spectrum has a significant peak at the 2nd natural frequency of the flume ($f=1.00$ Hz). The two minor peaks (at $f=1.44$ Hz and $f=2.28$ Hz) correspond to the 4th and the 10th eigenmode, respectively. The deviation between the incident and reflected significant wave heights determined with and without cross mode separation is about 2 % in the present case.

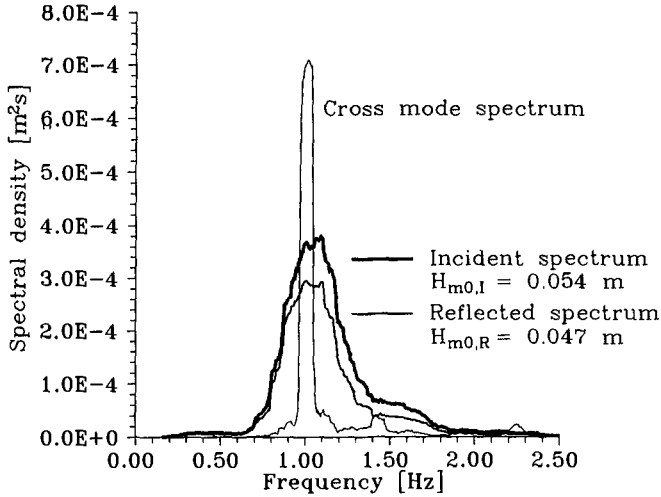


Figure 8 - Incident, reflected and cross mode spectra from flume test with irregular waves. $DOF=128$ and $bandwidth=0.31$ Hz for the incident and reflected spectra. $DOF=32$ and $bandwidth=0.078$ Hz for the cross mode spectrum.

4 Conclusions

It has been shown that if the waves measured during a flume test contain cross modal activity, it can lead to an inaccurate determination of the incident and reflected waves if ordinary methods of reflection analysis are applied. For regular waves it was shown that an error of 7 % can occur in the estimation of the incident wave height for 10 % cross modes. It was also found that the error on the reflected wave height was generally higher than the error on the incident wave height. For irregular described by their H_{m0} -value only, the error is of course smaller due to averaging.

To obtain a better estimation of the incident and reflected waves in case of cross modal activity in the flume, a new method was developed. Instead of only assuming a composite wave field composed of the incident and reflected wave components, the new method assumes that the composite wave field also contains a cross mode component. Whereas the traditional methods of reflection analysis requires at least two wave probes in order to separate the incident and reflected wave components, the new method requires at least three wave probes. To avoid singularities and to obtain more reliable solutions it is however recommended to use a least 5 wave probes.

The performance of the new reflection analysis with cross mode separation was tested both numerically and physically. It was shown that the method is capable of

separating the cross mode spectrum and thereby obtain a more accurate determination of the incident and reflected waves.

Acknowledgements

This study was carried out as a part of the authors MSc. Thesis at Aalborg University, Denmark. The use of laboratory equipment and the many useful discussions with staff at the Hydraulics Laboratory at Aalborg University are gratefully acknowledged.

References

- Andersen, H., Grønbech, J. and Jensen, T. (1995): *Determination of Incident Waves Using Reflection Analysis*. Part of MSc. Thesis at the Department of Civil Engineering, Aalborg University, Denmark.
- Goda, Y. and Suzuki, Y. (1976): *Estimation of Incident and Reflected Waves in Random Wave Experiments*. Proc. 15th ICCE, Vol.1, pp. 828-845, Honolulu, USA.
- Mansard, E.P.D. and Funke, E.R. (1980): *The Measurement of Incident and Reflected Spectra Using a Least Squares Method*. Proc. 17th ICCE, Vol.1, pp. 154-172, Sydney, Australia.
- Mansard, E.P.D. and Funke, E.R. (1987): *On the Reflection of Irregular Waves*. Technical Report TR-HY-017, NRCC No. 27522. National Research Council of Canada, Ottawa, Canada.
- Zelt, J.A. and Skjelbreia, J. (1992): *Estimating Incident and Reflected Wave Fields Using an Arbitrary Number of Wave Gauges*. Proc. 23th ICCE, Vol.1, pp. 777-789, Venice, Italy.

CHAPTER 77

Wave Runup on Beaches

John P. Ahrens¹ and William N. Seelig²

Abstract

Runup on beaches is an important topic in coastal engineering because it defines the upper limit of direct wave influence on land. It is also a phenomenon that has proved very difficult to analyze and characterize in a quantitative manner. The reason for this difficulty is the more general problem of understanding the response of beaches to waves. This paper develops formulas to estimate the approximate upper limit of wave runup on sand and gravel beaches. The relationship between these formulas and recent progress in quantifying beach profile response to waves and the morphodynamics of beaches is discussed. It was found that estimates of wave runup on sand beaches could be improved if sediment sizes in both swash zone and surf zone are known.

Introduction

This paper develops equations to predict the approximate upper limit of wave runup on sand and gravel beaches and shows the connection between runup and beach morphology. Runup on beaches is an important topic in coastal engineering because it defines the limit of direct wave influence on land. Specifically, these concerns relate to beach and dune erosion and coastal flooding.

1) Specialist, Coastal Processes; NOAA, Sea Grant, 1315 East-West Highway, Silver Spring, Maryland 20910

2) Engineer; Naval Facilities Engineering Command NFESC ECDDET, Washington Navy Yard, Washington DC 20374-5063

Background and Approach

A logical starting point for the analysis of wave runup is Hunt's (1959) formula, i.e.\

$$R/H = C[\tan\theta/\sqrt{(H/L_o)}] = C\xi \quad \text{Eq. 1}$$

where R is the vertical limit of wave uprush above the still water level, H is the incident wave height, L_o is the deep water wave length, $\tan\theta$ is the tangent of the slope of the structure or beach, C is a dimensionless coefficient, ξ is the Iribarron Number (Battjes 1974) and R/H is referred to as relative runup. Hunt found that Eq.1 worked very well for monochromatic breaking wave conditions on plane, smooth slopes. Subsequent research has confirmed the usefulness of Eq.1 for irregular wave conditions and rough slopes (van der Meer and Stam 1992).

Eq. 1 presents some problems for use with beaches. It is not clear if the submerged beach slope that the wave is propagating over or the beach face slope should be used in Eq. 1. The submerged slope presents the additional problem of being dynamic and not being plane, even in an approximate way. To circumvent the problem, beach slope can be treated as a dependent variable and Eq. 1 can be rewritten as:

$$R_2/\sqrt{(H_{so}L_o)} = f(X_1, X_2, \text{etc.}) \quad \text{Eq. 2}$$

where R_2 is the elevation above the still water level exceeded by two percent of the runups and H_{so} is the deep water significant wave height. The left hand side of Eq. 2 is referred to as the runup intensity and the equation indicates that it is a function of one or possibly more variables that act approximately as surrogates for beach slope. Recent research, including this study, suggests some possible simple variables for predicting beach slope, they are:

$$N_o = H_{so}/wT \text{ -----> beach face slope, Kriebel, et al. (1991), and}$$

$$F_o = w/\sqrt{(gH_{so})} \text{ -----> beach slope in surf zone, Dean (1991) and appendix,}$$

where T is a characteristic wave period, g is the acceleration of gravity and w is the sediment fall velocity. H_{so}/wT is a fall speed parameter sometimes referred to as the Dean Number and $w/\sqrt{(gH_{so})}$ is a surf zone Froude-type number, Kraus, et. al (1991). Equations developed in this study are formulated in terms of deep water wave conditions because of the wider range of applicability and utility for users.

The approach sketched out above converges with findings from a very extensive study of beach profiles and beach evolution that show erosion/accretion profiles, bar size, bar depth, and bar movement are all

functions of wave steepness and the fall speed parameter, Larson and Kraus (1989, 1992). There is also convergence with research on beach morphology by Wright and Short (1984). Wright et al. (1985) shows that reflective beaches are associated with small values of the fall speed parameter, dissipative beaches are associated with large values and beaches with a variety of bar and trough configurations are associated with intermediate values. Wright also notes that runup is high on reflective beaches and low on dissipative beaches.

Sources of Data

Data on the height of the berm crest of gravel beaches was collected in the laboratory by van Hijum and Pilarczyk (1982) and Ward and Ahrens (1992). The primary source of the two percent runup was Nielsen and Hanslow (1991), collected on six sand beaches in New South Wales, Australia. Additional two percent runup data was collected on the sand beach at the Field Research Facility of the Corps of Engineers at Duck, North Carolina, Holman (1986) and Douglass (1990).

Analysis and Development of Equations

Swash Zone Fall Speed Parameter

Fig. 1 shows the runup intensity versus fall speed parameter calculated using the fall speed for sediment in the swash zone. The data shown is from the two laboratory studies of gravel beaches, van Hijum and Pilarczyk (1982) and Ward and Ahrens (1992), and the six sand beaches in New South Wales, Nielsen and Hanslow (1991). From a morphological perspective the gravel beaches can be regarded as adsorbitive beaches and the sand beaches fall into the reflective, dissipative, or intermediate categories of Wright and Short (1984). For the gravel beaches the two percent runup has been assumed to be equal to the berm crest height. This assumption is supported by laboratory and field research of Powell (1988), who found the berm crest formed after 3000 waves was overtopped by less than 3% of the waves, with a mean probability of being overtopped of 0.015 ± 0.011 . A data trend curve is shown which is given by the equation

$$R_2/\sqrt{H_{s0}L_0} = 0.27\exp[-0.26(H_{s0}/d)]/(1.0+6.3\exp[-5.6/N_0]) \quad \text{Eq. 3}$$

where, d , is the depth of water at the toe of the gravel beach. The trend curve in Fig. 1 does not fit the gravel beach data well, i.e. $N_0 < 1$, because the figure does not account for the influence of relative wave height which is assumed to be zero, i.e. $H_{s0}/d = 0$, for plotting in Fig. 1.

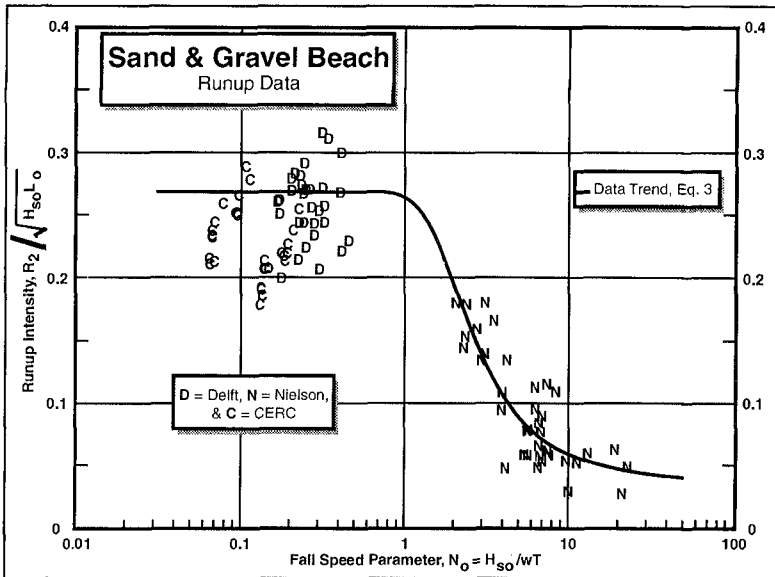


Fig. 1 Runup intensity as a function of the swash zone fall speed parameter, for three studies.

Fig. 2 shows the runup intensity versus the relative wave height for just the gravel beach data. The figure shows that runup intensity decreases as relative wave height increases. This trend is interpreted as being due to the truncation of the wave height distribution in shallow water; it is the larger waves which build and maintain the berm crest. Eq. 3 follows this trend reasonably well, which is more pronounced for CERC data, Ward and Ahrens (1992), because of the relatively shallow water at the toe of the gravel beach in that study as compared to the Delft data, van Hijum and Pilarczyk (1982).

Eq. 3 approaches a limit of 0.27 for runup intensity on gravel beaches which appears logical from Fig. 2, albeit there is considerable data scatter. For dissipative beaches the limiting value of Eq. 3 for runup intensity is 0.037 which seems reasonable from Fig. 1 and is consistent with a limiting value of 0.035 found by Yamamoto, et al. (1994). The analysis based on the swash zone fall speed parameter and relative wave height worked moderately well, but has at least two limitations for sand beaches: 1.) It is not clear what is the meaning of the water depth, d , (possibly the depth over a bar ?) and 2.) The lack of information about the surf zone. In order to predict runup on a sand beach in terms of deep water wave conditions, clearly some information about what is going on between the two locations is required.

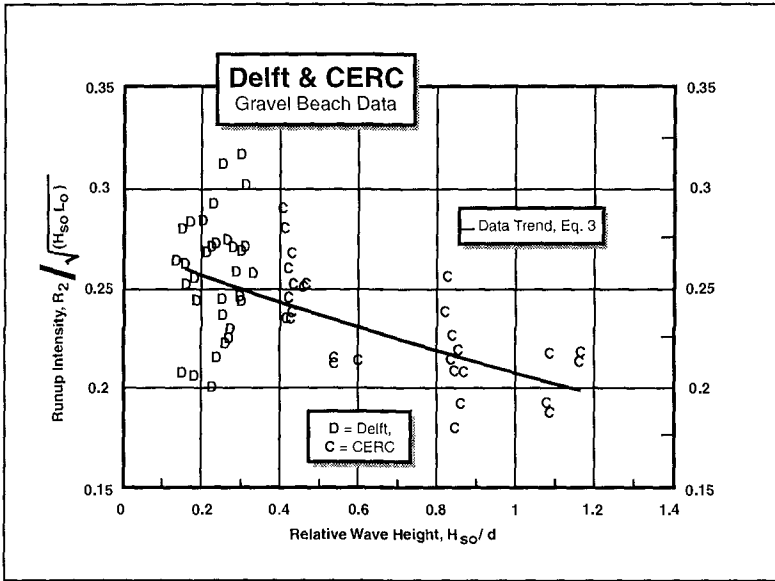


Fig. 2 Runup intensity as a function of relative wave height, for gravel beaches.

Surf Zone Froude Number

At the beginning of this study the authors did not know the sediment characteristics in the surf zone of the New South Wales beaches, Nielsen and Hanslow (1991). After receiving this information (Nielsen 1996) the authors realized that information about the surf zone was probably more important for predicting sand beach runup than swash zone data. The gravel beach studies (van Hijum and Pilarczyk 1982, Ward and Ahrens 1992) were collected in the laboratory with fixed beds offshore so no surf zone analysis was conducted with this data.

The surf zone Froude Number, F_o , addresses limitations noted in the above section in using the swash zone fall speed parameter to predict wave runup on sand beaches. Fig. 3 shows there is a surprisingly strong linear relationship between runup intensity and F_o on sand beaches, Nielsen and Hanslow (1991). Regression analysis was used to quantify the data trend shown in Fig. 3, i.e.,

$$R_2 / \sqrt{(H_{s0} L_0)} = 11.6 [w_{sr} / \sqrt{(g H_{s0})}] = 11.6 F_o \quad \text{Eq. 4}$$

As shown in the appendix F_o is proportional to the submerged beach slope in the surf zone. An attempt was made to use the information given in Nielsen and Hanslow to classify beaches using categories proposed by Wright and Short (1984) and shown by symbols in Fig. 3.

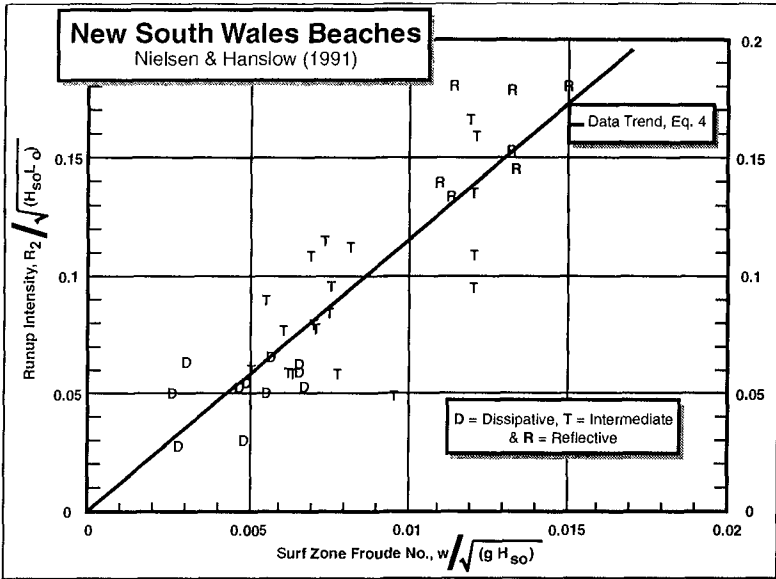


Fig. 3 Runup intensity as a function of surf zone Froude Number, for sand beaches in New South Wales.

Beach Diversity Correction

In examining the New South Wales data (Nielsen and Hanslow 1991) it was observed that there was a tendency for runup intensity to increase with increasing diversity in the sediment sizes on the beach profile. Beach diversity is defined as the ratio of median sediment size in the swash zone, d_{sw} , to median size in the surf zone, d_{sr} . Typically this ratio is greater than one and for the New South Wales beaches it was in the range, $1.0 \leq d_{sw}/d_{sr} \leq 1.6$.

Considering the influence of the surf zone Froude No. and beach diversity on runup intensity, regression analysis was used to help develop the following prediction equation for sand beaches:

$$R_2/\sqrt{(H_{s0}L_0)} = 10.4\sqrt{(d_{sw}/d_{sr})}[w_{sr}/\sqrt{(gH_{s0})}] \tag{Eq. 5}$$

The right hand side of Eq. 5 can be thought of as the $C[\tan\theta]$ terms in Hunt's Eq., Eq. 1, in the sense of a compound slope approach to predicting beach runup. Median diameter of the swash zone is used in Eq. 5 rather than fall speed of the sediment because beach permeability is so strongly dependent on sediment size. Permeability and wave conditions are the most important variables influencing the slope of the beach face. Therefore, the form of Eq. 5 helps identify the physical processes influencing runup even though it may seem anomalous to use sediment size and fall speed in the same equation. Eq. 5 explains 77.3 %

of the variance in the dependent variable compared to 74.6 % for Eq. 4.

For wave runup the value of a prediction method can best be judged by how well it predicts the dimensional runup rather than a dimensionless runup parameter. Fig. 4 shows the predicted two percent runup using Eq. 5 versus the observed two percent runup. Eq. 5 explains about 80% of the variance in the data.

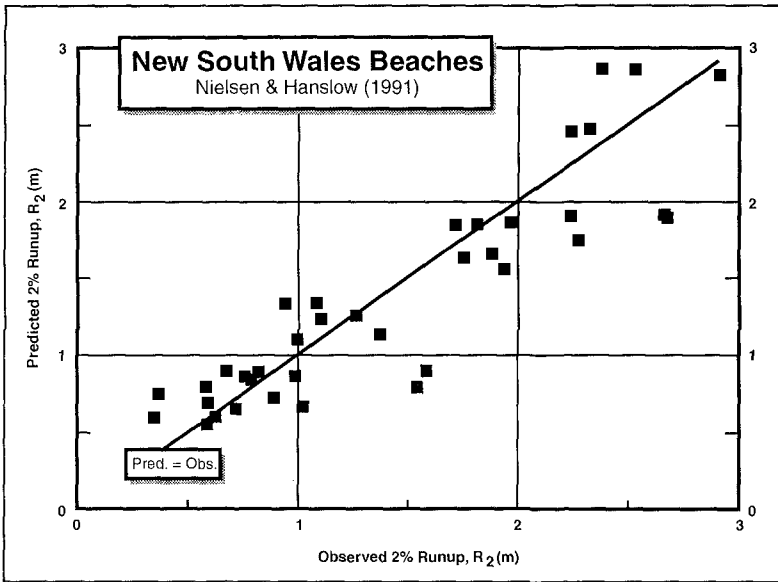


Fig. 4 Predicted two percent runup versus the observed two percent runup for sand beaches in New South Wales.

Thought Experiment

It is useful to use a thought experiment approach to illustrate the implications of Eq. 5. Imagine two beaches both having fine sand in the surf zone but one also having fine sand in the swash zone, i.e. a uniform beach, and the other having coarse sand in the swash zone, i.e. a diverse beach. Consider the response of the two beaches to both mild and storm wave conditions. For the same wave conditions the runup intensity is always greater on the beach with coarse sand in the swash zone. In going from mild to storm wave conditions runup intensity decreases on both beaches because the slope of the surf zone gets flatter or the surf zone gets wider. Interestingly, the difference in runup intensity between the two beaches is less during storm conditions because the increased width of the surf zone has made runup intensity less sensitive to conditions on the beach face, see thought experiment sketch, Fig. 5. The effects noted in the experiment seem consistent with current understanding of runup on beaches.

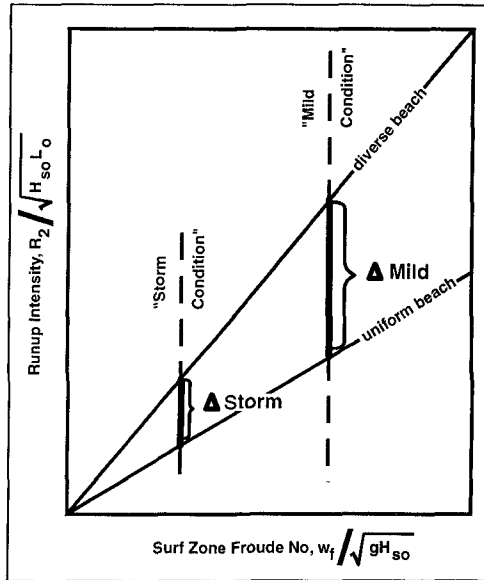


Fig. 5 Thought experiment figure to illustrate implications of runup equation, Eq. 5.

Duck 1982 Data

During the initial stages of the analysis the runup data from the beach at Duck, N.C. seemed to be anomalously high (Holman 1986 and Douglass 1990). However, after seeing the influence of sediment diversity the Duck data looked more logical. The beach at Duck has sediment with a median diameter of about 0.75mm in the swash zone and about 0.20mm in the surf zone (Mason et al. 1984) for a diversity ratio of 3.75, much higher than any of the New South Wales beaches.

Fig. 6 shows the predicted two percent runup versus the observed two percent runup for the data collected on the beach at Duck, N.C. Some data has been omitted to eliminate bimodal spectra using the approach of Resio (1987). Eq. 5 explains about 51% of the variance in the data.

There is relatively high alongshore variability in runup on the beach at Duck. This is what would be expected based on the morphological categorization of Wright and Short (1984) which puts the beach in intermediated categories that are dominated by a variety of offshore bars and troughs. Normally some of these features are three dimensional. There is one particularly long subset of data from Duck that shows runup variability along 500m of beach for storm wave conditions. For 13 stations the mean two percent runup was 2.163m with

a standard deviation of 0.215m or a mean percent deviation of about 10%. Conditions were unusual for an East Coast storm with $H_{s0} = 2.51\text{m}$ and $T_p = 12.2\text{sec}$. Eq. 5 gives a predicted $R_2 = 2.26\text{m}$ which is somewhat higher than the observed mean value of the two percent runup but well within one standard deviation of the mean.

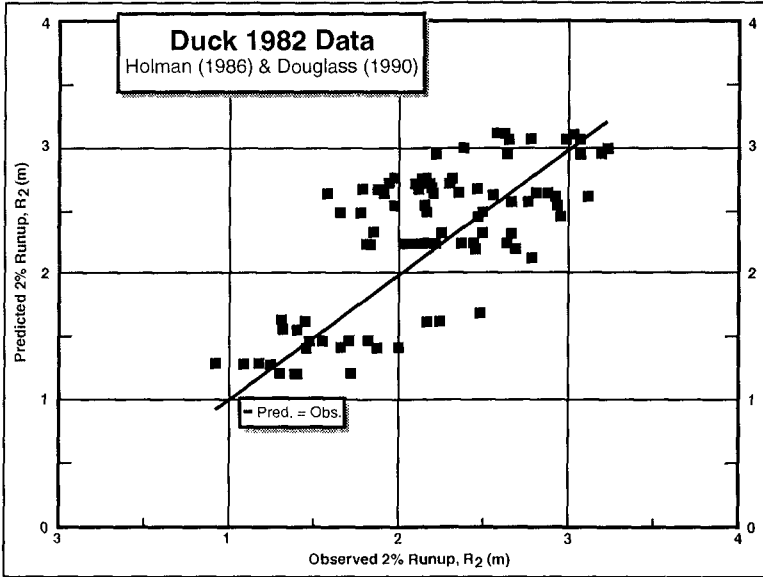


Fig. 6 Predicted two percent runup versus the observed two percent runup for the sand beach at Duck, N.C.

Surf Zone Fall Speed Parameter and Morphological Connection

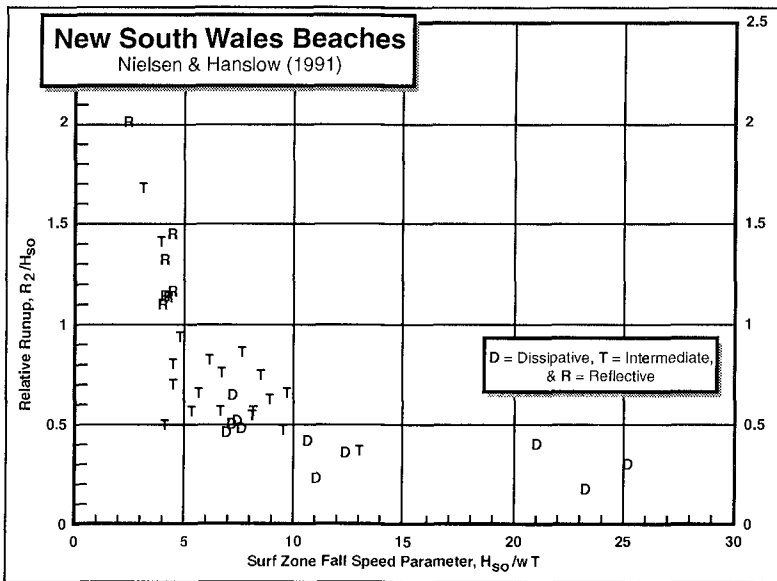
Surprisingly, Eq. 5 can be rewritten in a form which helps suggest the processes involved and using the surf zone fall speed parameter provides a connection to beach morphology, i.e.

$$\begin{aligned}
 R_2/H_{s0} &= C[\tan\theta]/\sqrt{(H_{s0}/L_0)} \\
 &= 10.4\sqrt{(d_{sw}/d_{sr})}[w_{sr}\sqrt{(gH_{s0})}]/\sqrt{(H_{s0}/L_0)} \\
 &\quad \begin{array}{c} <-----> <-----> <-----> \\ \text{swash} & \text{surf} & \text{deep-water} \end{array} \\
 &= \{10.4/\sqrt{(2\pi)}\}\sqrt{(d_{sw}/d_{sr})}/N_0 = 4.1\sqrt{(d_{sw}/d_{sr})}/N_0
 \end{aligned}
 \tag{Eq. 6}$$

The fall speed parameter, N_o , used in the final line of Eq. 6 is similar to the parameter used by Wright and Short (1984) to categorize the morphology of beaches. The difference between the parameters is that Wright and Short used the breaker height while the deep water significant height is used in this study.

Eq. 6 also provides a link to the beach profile study of Kraus, et al. (1991) who found that erosional or accretionary profiles could be predicted using $w_{sr}/\sqrt{(gH_{s0})}$ and H_{s0}/L_0 . Since these two variables can be used to form a surrogate for the surf similarity parameter or Iribarron No., i.e. $\xi \approx 3.4 [w_{sr}/\sqrt{(gH_{s0})}] / \sqrt{(H_{s0}/L_0)} = 1.3/N_o$, they should be able to predict breaker characteristics near the shoreline.

In Fig. 7 the relative runup is shown as a function of the surf zone fall speed parameter, as suggested by Eq. 6. Data points are shown in Fig. 7 using letters to distinguish morphopological conditions of dissipative, reflective, or intermediate beaches as defined by Wright and Short (1984). The figure shows that both relative runup and beach morphology are strongly correlated to the surf zone fall velocity parameter.



Surf Beat and Edge Waves

A variety of oscillations are present in the surf zone at periods greater than the period of incident wind waves. These long waves tend to modulate the conspicuous runup oscillations occurring at approximately the period of wind waves. Trapped edge waves at periods twice the incident wind waves are responsible for cusp formations on reflective beaches, Guza and Inman (1975). As morphological conditions change from reflective to dissipative beaches there is a corresponding attenuation of trapped edge waves and amplification of surf beat. Surf beat periods typically are in the range of one to three minutes.

Summary, Conclusions and Recommendations

Starting with Hunt's (1959) equation and replacing the beach slope with functional relationships, which provide an equivalent compound slope that includes both the slope of the beach in the surf zone and the slope of the beach face, produces an equation, Eq. 6, to calculate the approximate upper limit of runup on a beach. Eq. 6 makes reasonably good estimates of runup for a variety of beach and wave conditions and helps to show the connection between beach morphology and wave runup.

It was found that when estimating runup in terms of deep water wave conditions that the slope of the beach in the surf zone or the width of the surf zone, was generally more important than the slope of the beach face. In Eq.6 the beach face or swash zone characteristics are treated as a correction to the basic runup equation, Eq. 4. This correction is important when there is a big difference between the sediment size in the surf and swash zone.

This research shows that studies of beach morphology and beach runup should be coordinated. Data requirements include, but are not limited to: knowledge of the sediment size across the beach profile, reliable estimates of deep water wave conditions, the three dimensional characteristics of the submerged beach, and the alongshore variation in runup. In addition, a time history of beach states and wave characteristics as discussed by Wright et al. (1985) would almost certainly help make better estimates of beach runup.

Acknowledgments

The senior author acknowledges the support of NOAA's National Sea Grant Office. The junior author acknowledges the support of the Naval Facilities Engineering Service Center.

Appendix: Slope of Beach in Surf Zone

A standard beach equilibrium profile is given by:

$$h = Ax^{2/3} \text{ or } x = (h/A)^{3/2}, \quad \text{Dean (1991)}$$

therefore the tangent of the submerged slope from the still water line out to some depth, h , is given by $\tan\theta = h/x = A^{3/2}/\sqrt[3]{h}$,

and since $A = 2.25(w_f^2/g)^{1/3}$, good in the range $1.0 \leq w_f \leq 10$ cm/sec. and temperatures around 20°C, Kriebel, Kraus & Larson (1991), then

$$\tan\theta = 3.375w_f/\sqrt[3]{gh},$$

and if h is set equal to H_{s0} as suggested for biplaner slopes or composite slope analysis, de Waal and van der Meer (1992), then

$$\tan\theta = 3.375w_f/\sqrt[3]{gH_{s0}} = 3.375F_o.$$

References

- Battjes, J.A. (1974). "Surf Similarity," Proc. 14th Coastal Eng. Conf., ASCE, Vol., 466-480.
- Dean, R.G. (1991). "Equilibrium Beach Profiles: Characteristics and Applications", *J. of Coastal Research* 7(1).
- Douglass, S.L. (1990). "Estimating Runup on Beaches: A Review of the State of the Art," U.S. Army, Waterways Experiment Station Report CERC-90-3, Vicksburg, MS.
- Guza, R.T., and Inman, D.L. (1975). "Edge Waves and Beach Cusps", *J. of Geophysical Res.*, Vol. 80, No. 21, 2997-3012.
- van Hijum, E. and Pilarczyk, K.W. (1982). "Gravel Beaches: Equilibrium Profile and Longshore Transport of coarse Material under Regular and Irregular Wave Attack", Delft Hydraulic Laboratory Pub. No. 272, Delft, the Netherlands.
- Holman, R.A. (1986). "Extreme Value Statistics for Wave Run-up on a Natural Beach", *Coastal Engineering* 9, 527-544.
- Hunt, I.A.(1959), "Design of Seawall and Breakwaters", ASCE Journal Waterways and Harbors, Vol. 85, No. WW3, paper 2172.
- Kraus, N.C., Larson, M., and Kriebel, D.L. (1991), "Evaluation of Beach Erosion and Accretion Predictors," Proceedings Coastal Sediments '91, Seattle, WA, pp 572-587.
- Kriebel, D.L., Kraus, N.C., and Larson, M. (1991), "Engineering Methods for Predicting Beach Profile Response," Proceedings Coastal Sediments '91, Seattle, WA, pp 557-571.

Larson, M., and Kraus, N.C.(1989). "SBEACH: Numerical Model for Simulating Storm-Induced Beach Change, Report 1, Empirical Foundation and Model Development," U.S. Corps of Engineers, Waterways Experiment Station, Technical Report CERC-89-9, Vicksburg, MS.

Larson, M. and Kraus, N.C.(1992),"Analysis of Cross-Shore Movement of Natural Longshore Bars and Natural Placed to Create Longshore Bars", U.S. Corps of Engineers, Waterways Experiment Station, Technical Report DRP-92-5, Vicksburg, MS.

Mason, C., Sallenger, A.H., Holman, R.A., and Birkmeier, W.A. (1984). "Duck 82 - A Coastal Storm Processes Experiment", Proc. 19th Conf. On Coastal Engr. ASCE, 1913-1928.

van der Meer, J.W. and Stam, C-J M. (1992). "Wave Runup on Smooth and Rock Slopes of Coastal Structures" *J. Waterway, Port, Coastal and Ocean Eng.*, ASCE 118(5), 534-550.

Nielsen, P. and Hanslow, D.J. (1991). "Wave Runup Distributions on Natural Beaches", *J. of Coastal Research* 7(4), 1139-1152.

Nielsen, P. (1995). personal communication.

Powell, K.A. (1988). "The Dynamic Response of Shingle Beaches to Random Waves", Proc. 21st Conf. Coastal Engr., ASCE, 1763-1773.

Resio, D.T. (1987). "Extreme Runup Statistics on Natural Beaches", U.S. Army Corps of Engineers, Waterways Experiment Station, Misc. Paper CERC-87-11, Vicksburg, MS.

de Waal, J.P. and van der Meer, J.W. (1992). "Wave Runup and Overtopping on Coastal Structures", Proc. 23th Conf. on Coastal Engr.,ASCE, 1758-1771.

Ward, D.L. and Ahrens, J.P.(1992). "Laboratory Study of a Dynamic Berm Revetment", U.S. Army Corps of Engineers, Waterways Experiment Station, Technical Report CERC-92-1, Vicksburg, MS.

Wright, L.D. and Short, A.D. (1984). "Morphodynamic Variability of Surf Zones and Beaches: A Synthesis", *Marine Geology*, Vol. 56, 93-118.

Wright, L.D., Short, A.D., and Green, M.O.(1985), "Short-Term Changes in the Morphodynamic States of Beaches and Surf Zones: An Empirical Predictive Model", *Marine Geology*, Vol. 62, pp 339-364.

Yamamoto, Y., Tanimoto, K., and Harshinie, K.G. (1994). "Run-up of Irregular Waves on Gently Sloping Beach", Proc. 24th Conf. On Coastal Engr., ASCE, 689-703.

CHAPTER 78

FIELD STUDY ON WAVE RUN-UP ON SEADYKES

Joachim Grüne ¹

Abstract

This paper deals with a comprehensive field research program on wave run-up, which is ongoing at different locations at the landside borders of the wadden sea (tidal flats) and the tidal estuaries of the German Bight since 1991. The field measurement equipment is described and an overview about first results is given.

Introduction

Due to the increasing of storm surges and the supposed long-term rising of water levels at the coastlines of the North Sea, for safety analysis of existing dykes in field a more exact knowledge is needed on wave run-up and overtopping process, especially with respect to non-uniform dyke cross-sections and to real sea state conditions. Air entrainment and wave climate characteristics under real sea state conditions play an important role on wave run-up process. Thus boundary effects and scale effects have to be minimized by using field data or large scale laboratory test data.

Field measuring program and equipment

The ongoing research program is focussed on the influence not only of real sea state wave climate but also of complex non-uniform dyke cross-sections on wave run-up. The investigations have been doing for recent years at four different locations at the coast of Dithmarschen and at the Elbe river estuary (Fig. 1) in cooperation with the Regional State Board for Water Management (ALW Heide, supervision Dipl.-Ing. J. Gärtner) of the State of Schleswig-Holstein. At two locations (Heringsand and Stinteck) the measurements have started in 1991,

¹ Dipl.-Ing., Senior researcher, Operation Manager of Joint Central Institution " Coastal Research Center (F Z K) " of University Hannover and of Technical University Braunschweig, GWK, Merkurstrasse 11, 30419 Hannover, Germany

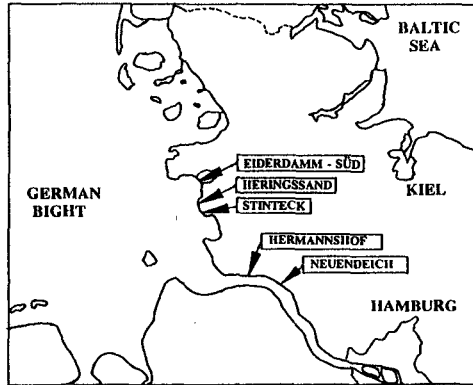


Fig. 1 Measuring locations at German Bight

at the two other locations in 1993. At another location (Eiderdamm-Süd) measurements already had been done during previous programs (Grüne, 1982).

Each of these locations represents one specific type with respect as well to different characteristics of morphologic boundary conditions, which generally occur in wadden seas and estuaries as to different existing non-uniform types of dyke cross-sections. Fig. 2 shows a scheme of the installed sensors at each location. The incoming wave climate has been measuring with a pressure cell for evaluation of surface elevation and with a two-component velocity meter for evaluation of the wave approach direction at the outermost seawards position. At two locations additional pressure cells were installed between the outermost position and the dyke. The wave run-up has been measured with a 70-step gauge. The aim of the program is to generalize all the measured relations between wave climate (in dependence of the morphologic boundary conditions) and wave run-up (in dependence of dyke cross-sections). The generalized results shall be used for safety analysis with extrapolated storm surge level conditions.

At the locations Heringsand and Stinteck (Fig. 3) occur a distinct wadden sea wave climate. At Heringsand location there are less wave energy parts dissipating from the closedby tidal gully compared to Stinteck. Furthermore at Heringsand the wave climate in front of the dyke is strongly influenced by the wave damping effect of the higher green foreland, which has a mean level of NN + 2.0 m and a width of roughly 500 m.

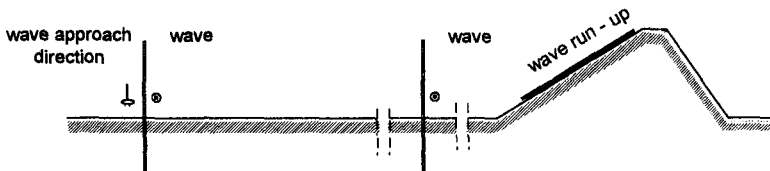


Fig. 2 Scheme of installed sensors at each location.



Fig. 3 Measuring locations Heringsand and Stinteck

The cross-section of the dyke at Heringsand is plotted in Fig. 4. Due to the relatively less intensive wave climate the dyke surface is covered totally with grass on clay and has a relatively gentle slope of roughly 1:10 in the lower part. In all cross-sections in Fig. 4 the dotted lines give the geodetic reference level (Normalnull). The upper waterlevels are the highest ones ever been recorded (HHThw), the lower ones are the Mean High Tide levels (MThw) and the water levels between HHThw and MThw are the highest ones, used for measurements within this program till today. The supports of the installed run-up step gauges (which are described in detail by Grüne, 1982) are marked with a solid line parallel on the dyke surface. The 70 steps of the gauge have different distances between each other in dependence of the slope. But all steps are calibrated in such way, that the signal is linear to the vertical component of the watertongue running up and down on dyke surface.

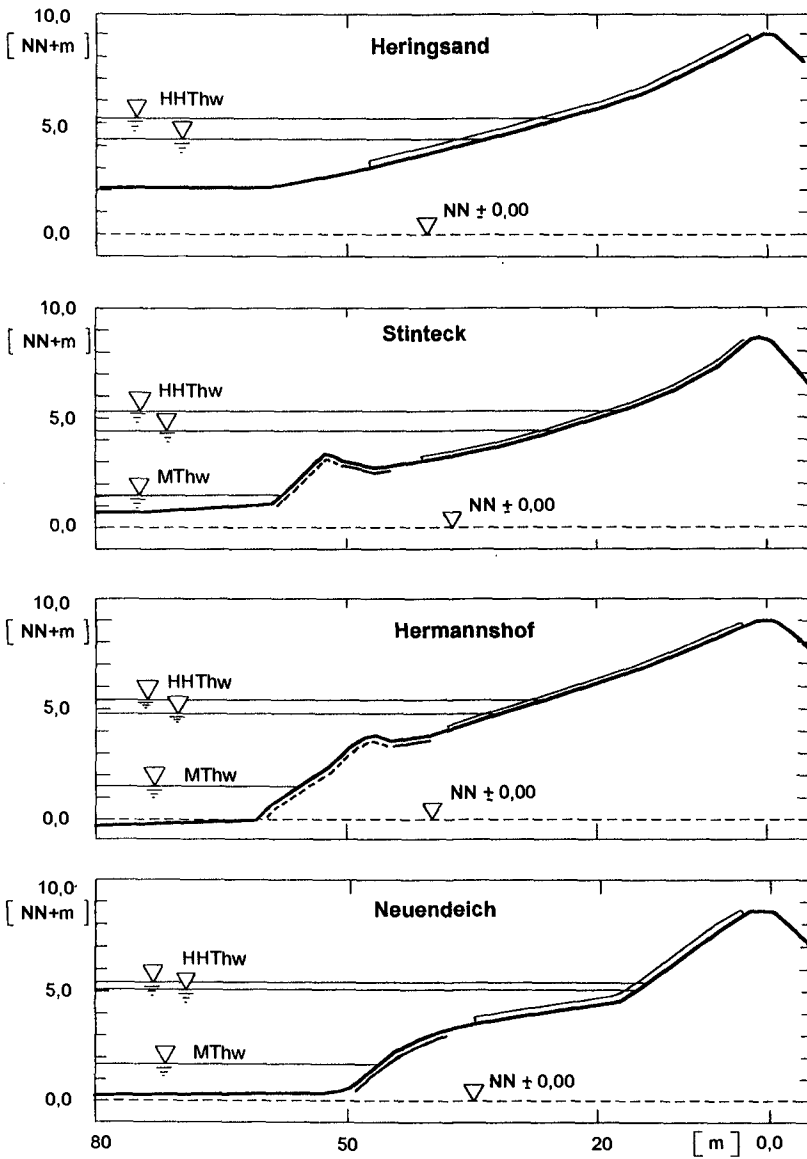


Fig. 4 Cross - sections of the dykes used for field measurements

The Mean High Tide level MThw at Heringsand lies roughly 0.5 m below the green foreland. Wave climate at Heringsand is measuring at three positions: 1040 m, 470 m and 50 m in front of the dykefoot. The vertical distances of the 70 run-up steps at Heringsand vary from 5 cm on the lower gentle slope to 12 cm on the higher steeper slope.

The dyke at Stinteck location has a berm made with natural stones, which are placed irregular (marked in Fig. 4 with a dotted line under the dyke surface). The top of the berm partly is covered with smooth artificial concrete stones and is used as a working road (marked with a solid line under the surface). This area also has an inner slope partly, which creates an extended water basin for water levels around the berm top level. The dyke surface above this area is covered with grass. The wave climate is measuring 700 m and 50 m in front of the dykefoot. The run-up steps have vertical distances from 4 cm on the lower gentle slope to 12 cm on the higher steeper slope. An impression of waves acting on the dyke at Stinteck is given in Fig. 7. The photo was taken during a stormsurge with a water level roughly 2.0 m above Mean High Tide, where all waves break on top of the berm.

The wave climate at the locations Hermannshof (Fig. 5) and Neuendeich (Fig. 6) are influenced as well by the deepwater conditions in the Elbe river estuary as by the restricted depths due to flats in front of the dykes. But these flats only have a width of roughly 200 meters at Hermannshof and of roughly 400 meters at Neuendeich, respectively.

The berm of the dyke at Hermannshof (Fig. 4) is covered in the same way as at Stinteck with stones up to the top, but the top of the berm is smaller and has an outer slope, which is covered with asphalt concrete. The grass covered surface above the berm has a nearly uniform slope. Wave climate at Hermannshof only is measuring 50 m in front of the dyke. The vertical distances of the 70 run-up steps vary from 5 cm at the lower levels up to 9 cm at the higher levels.



Fig. 5 Measuring location Hermannshof



Fig. 6 Measuring location Neuendeich



Fig. 7 Waves acting on the dyke at Stintek location during a storm surge

The dyke profile at Neuendeich (Fig. 4) has an extended berm. The outer steep berm slope is covered with artificial smooth concrete stones (in Fig. 4 marked with a solid line under surface). The surface on the berm and on the higher steep slope is covered with grass. Wave climate is measuring also only at the positions 50 m in front of the dykefoot. The run-up steps have vertical distances between 3 cm on the lower gentle slopes and 11 cm on the higher steeper slope.

At all locations the sensors are connected by cables with a computer-controlled recording system in a shelter box at the backside of the dykes. Data recording is starting automatically in dependance of desired storm surge waterlevels (usually 1.5 m above MThw).

Data analysing

The wave parameters of the surface elevation were evaluated from the recorded pressure signals. Linear theory was used for transformation, modified with correctionfactors. These factors depend on relative depth of sensor and were found from laboratory and field experiments. Analysis has been done in time domain (modified Zerodowncrossing method) and in frequency domain.

Analyzing run-up records from field can be rather complicate, because characteristics of run-up signals may be strongly influenced by two main effects:

- Firstly by the physical breaking process on gentle slopes and on berms.
- Secondly by the kind of gauge with a relatively long distance on the slope between the steps for gentle slopes.

The first effect can be demonstrated in Fig. 8, where in the lefthand plot a short time history is given as an example of synchronous signals of waves and run - ups, recorded at Stinteck location. One won't find any direct linkage between both signals, as one may expect it from the literature according to small scale model tests with regular or irregular PM-spectra waves on uniform steep slopes. This effect comes out clearly, if one look on the cross-section in Fig. 4 with the extremely broad berm and on Fig. 7, where one can see the waves breaking in front of or on the berm, which create reduced and longperioded run-ups after passing the distance to the upper dyke surface. Furthermore the run-downs mostly stay above stillwaterlevel, which is a typical result of gentle slopes.

With other boundary conditions the run-up records may have other characteristics. Such an example from Neuendeich location is given in the righthand plot of Fig. 8 with same time scale as in lefthand plot. Due to a very high water level for these data the waves break mainly at the higher steep slope. Thus these run-ups are neighter affected by breaking of waves before they reach the dyke surface nor by breaking on gentle slopes. In the timeexpanded part of the righthand plot the different linkage behaviour between the run-up signals from these both locations comes out evident.

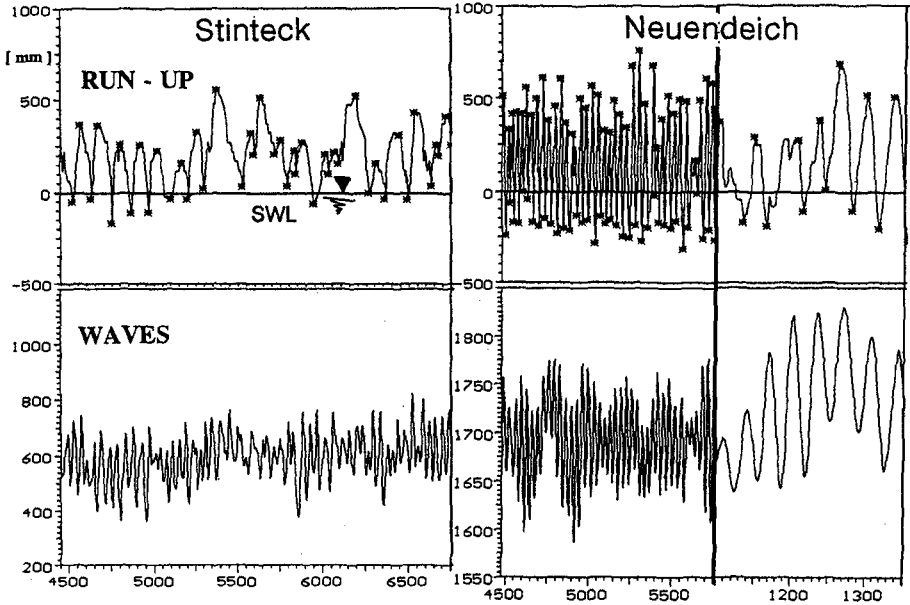


Fig. 8 Time histories of synchronously measured waves and run-ups

The second effect, mentioned before is caused by the kind of gauge. A step gauge on gentle slopes necessarily has long distances between the single steps. Together with longperioded and damped run-ups thus leads to signals, which are shown schematically in Fig. 9. Such signals may be processed with step identification and smoothing modes.

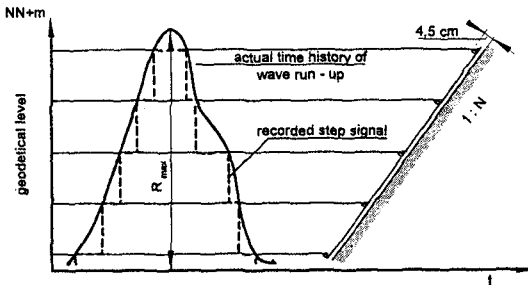


Fig. 9
Scheme of signals
from a step gauge

Furthermore a definition mode far from the zerocrossing mode is necessary, due to the fact, that the run-down mostly stay above stillwaterlevel. An overview about the definitions and analysing modes used in this paper for the run-ups R_u , run-downs R_d (R_{dR} is used) and periods T_R is given in Fig. 10. The mode for separating single run-up events from a sequence is shown schematically in Fig. 11. Separated run-ups were analyzed, if the relation a/b don't exceed the threshold value G within a certain time window. The used treshold value is in the order of magnitude of 10 to 20. As conclusion it must be stated that run-up records from field measurements have to be analysed very carefully and seriously.

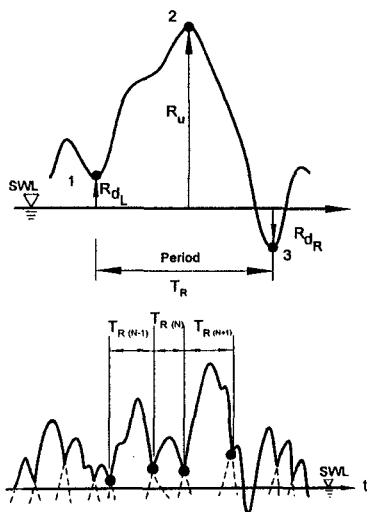


Fig. 10 Definition of run-up and run-down parameters

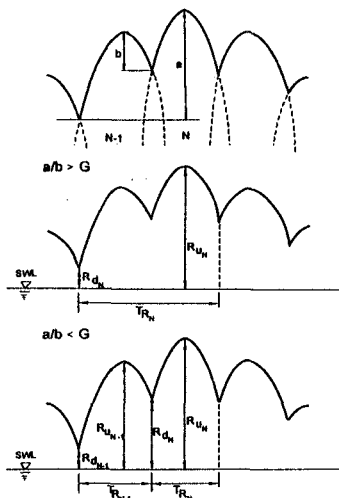


Fig. 11 Mode for separating of single run-up events

First results

Data were recorded during strong wind and storm surge conditions. A part of the data were measured at the different locations during same storm surge events. A comparison of the first data from all different types of cross-sections show distinct differences, which are both influenced by the different wave climates and by the different shapes of cross-sections. Due to restricted space in this paper only an overview of some first results can be given. More detailed results will be published in following papers.

The maximum run-up and run-down values, measured at all four locations, are shown in Fig. 12. The values are added on the stillwaterlevel *SWL* and are plotted versus the stillwaterlevel *SWL*, which is referred to geodetic level Normal Null. The full line represents the stillwaterlevel, the dotted line shows the geodetic level of the lowest step of the run-up gauge. Obvious are the small run-down values (except for higher waterlevels at Neuendeich), mostly around the stillwaterlevel, which is caused by the gentle slopes mainly, as already mentioned before.

In Fig. 13 the run-ups R_{98u} and run-down R_{98d} are related to significant waveheights $H_{1/3}$ and are again plotted versus the stillwaterlevel *SWL*. No run-up data are presented for Hermannshof location, because a part of those were measured without recording wave climate due to sensor defects. The data from Heringssand and Neuendeich have a trend of higher values for smaller waterdepths. This is contrary to that, which could be expected, but has simple reasons, which will be explained later.

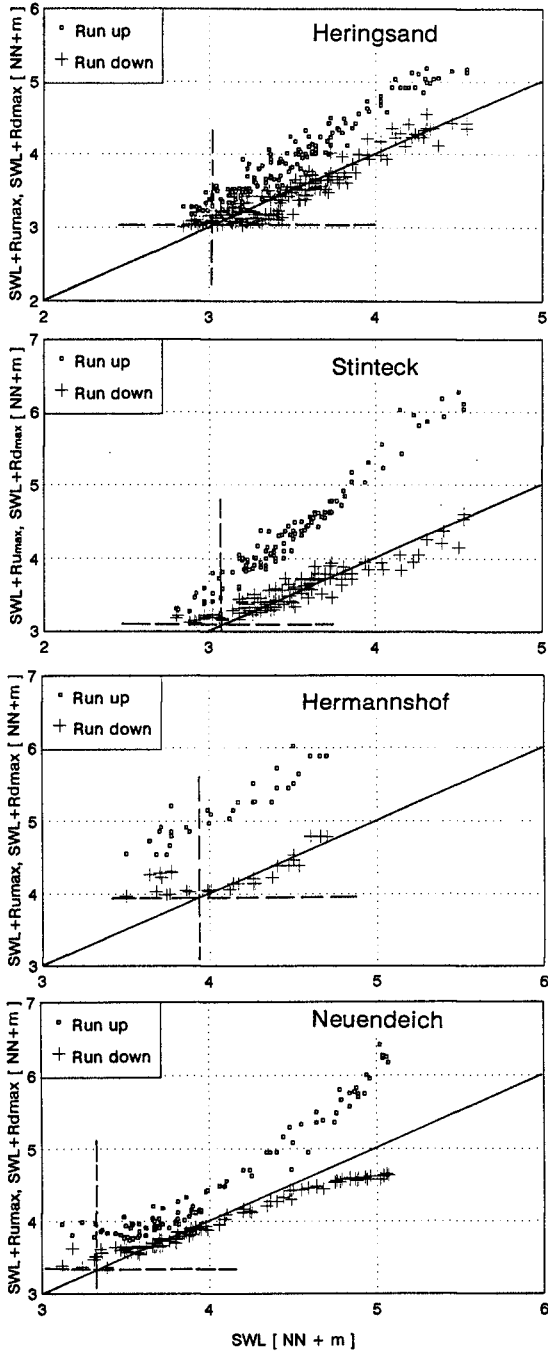


Fig. 12 Maximum run-up and run-down levels versus stillwaterlevels

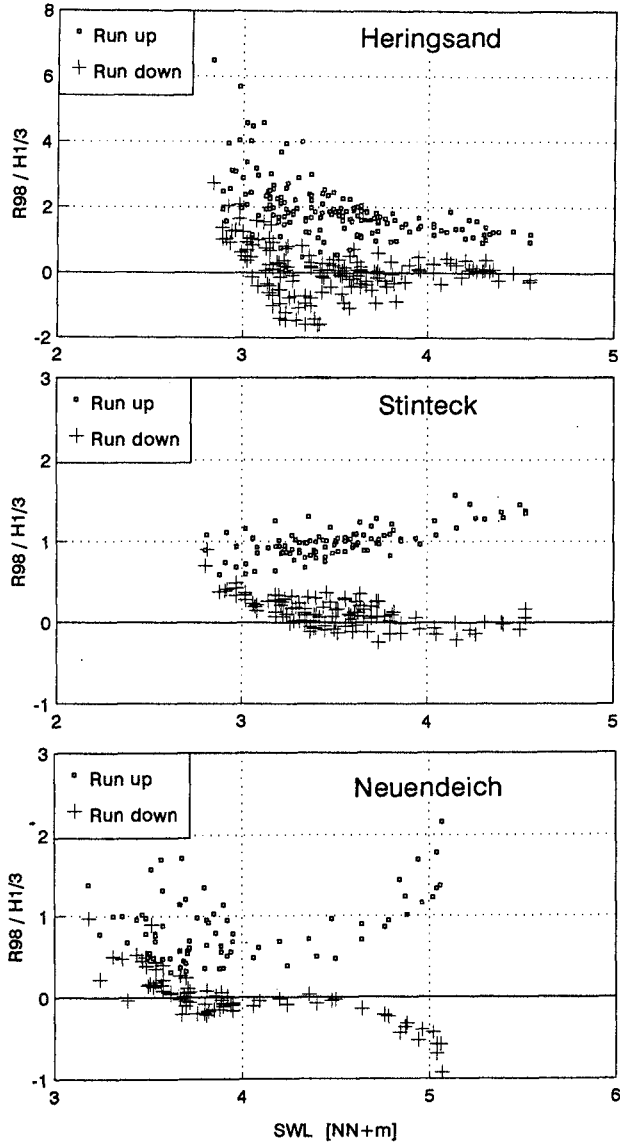


Fig. 13 $R_{98} / H_{1/3}$ versus stillwaterlevel SWL

Similar confusions come out from Fig. 14, where the relations between the mean wave periods T_{Hm} and the mean run-up periods T_{Rm} are plotted versus the stillwaterlevel SWL . Considerable differences are obvious between the different locations. Whereas at Heringsand location with higher stillwaterlevels above $NN + 4.0$ m only 20% of the waves create a run-up, at Stinteck there are 40% and at Neuendeich up to 100% of the waves, which create a run-up.

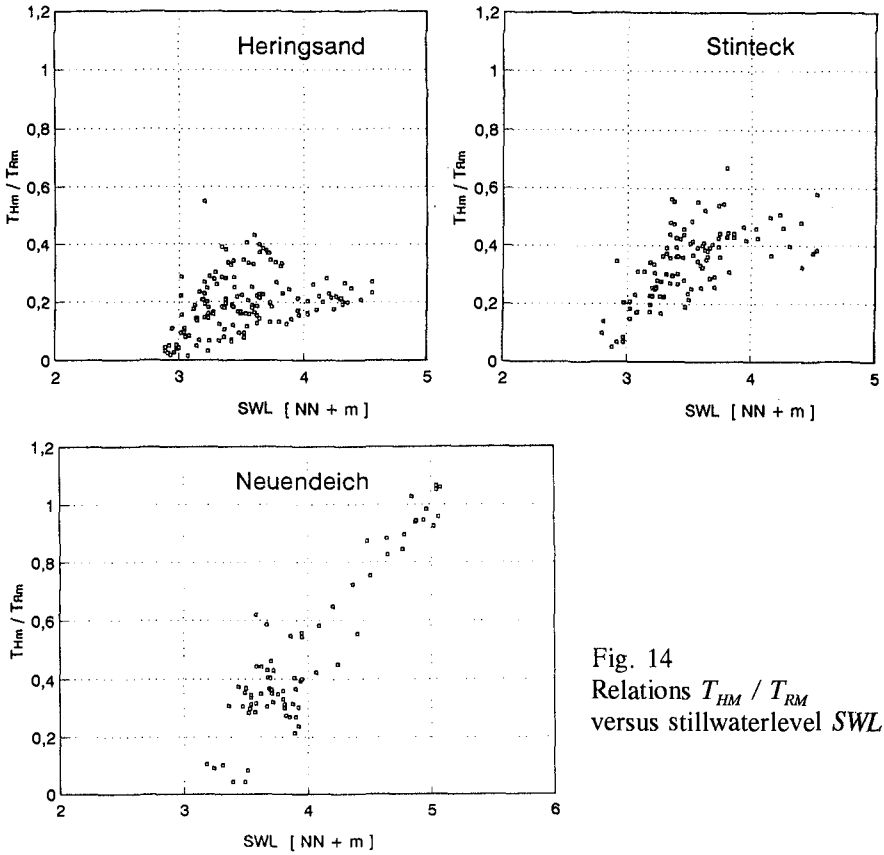


Fig. 14
Relations T_{HM} / T_{RM}
versus stillwaterlevel SWL

Other results with confusing different trends for the different locations occur for other parameters and relations, as shown in Fig. 15, where all data $R_{98} / H_{1/3}$ are plotted versus the breakerindices ξ . But all these trends can be explained by the different boundary conditions at the different locations. The boundary conditions also are changing in dependence of the stillwaterlevel SWL . One example is the occurrence of relatively high values $R_{98} / H_{1/3}$ up to 6 at Heringsand (upper plot in Fig. 15). From detailed analysis it was found, that the relative higher run-ups are created by longperioded parts of the surface elevations, which are eliminated for wave analysis, but have amplitudes up to roughly 0.3 m.

Another example can be demonstrated by the results, found for Neuendeich location and plotted in the lower parts of Figs. 13 and 15. In both plots one can distinguish the data into two groups, each with a more or less distinct trend. In Fig. 16 the appertaining mean waterdepths on the berm $d_{BE} / H_{1/3}$ (related to $H_{1/3}$) of these data are plotted versus stillwater level SWL and breakerindex ξ , respectively. From this figure and comparison with Figs. 13 and 15 the separation comes

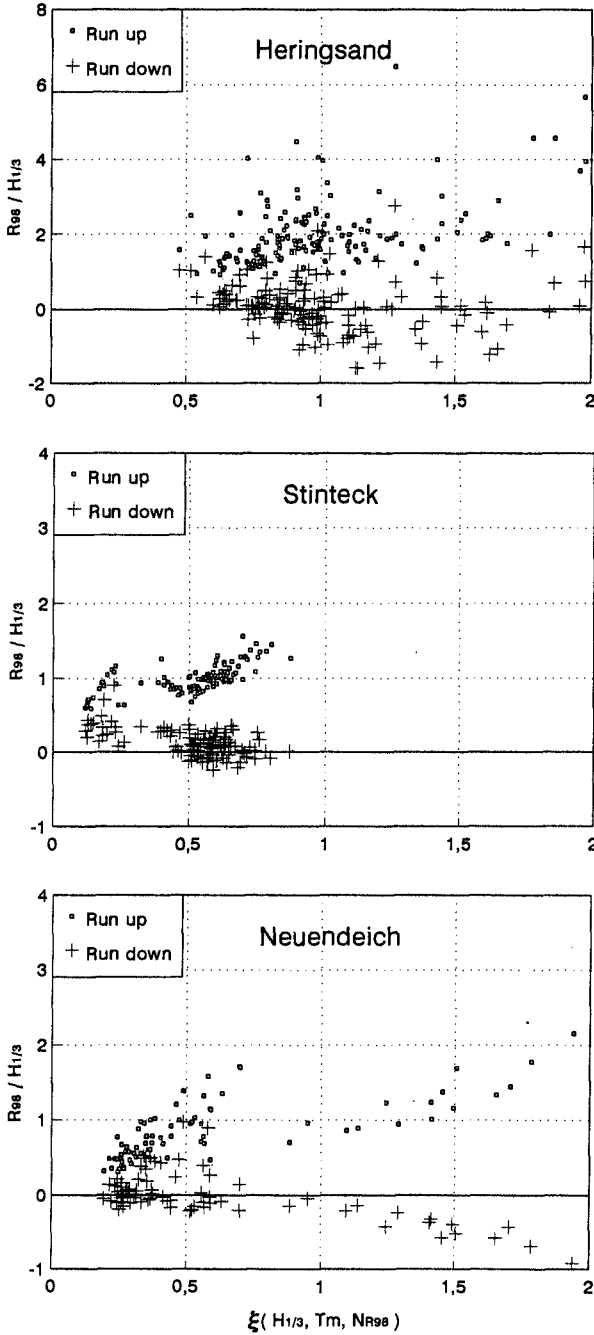


Fig. 15 $R_{98} / H_{1/3}$ versus breakerindex ξ

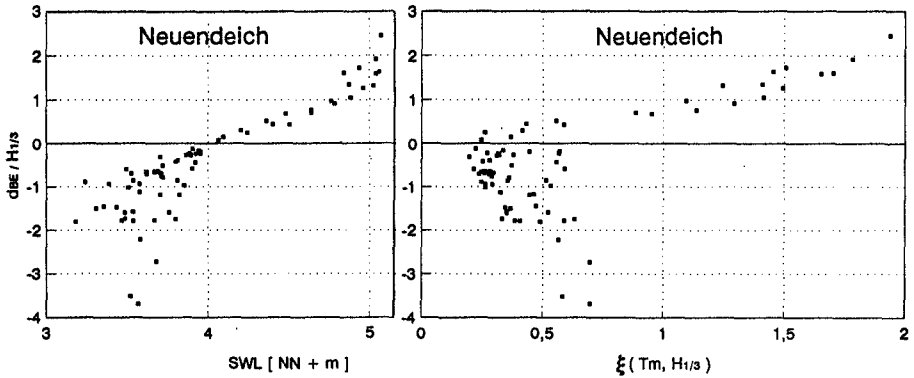


Fig. 16 $d_{BE} / H_{1/3}$ versus SWL (lefthand) and breakerindex ξ (righthand)

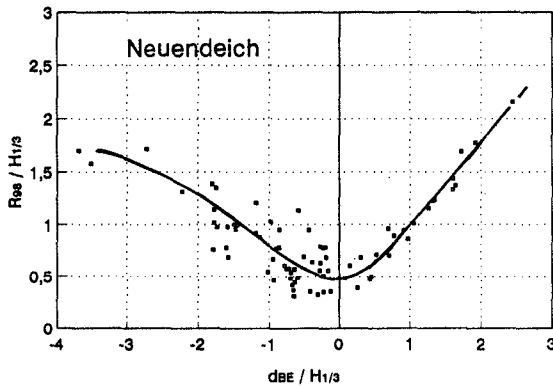


Fig. 17 $R_{98} / H_{1/3}$ versus $d_{BE} / H_{1/3}$

out clearly: one group with waterlevels below and one group with such above mean berm level. It can be stated that $R_{98} / H_{1/3}$ increase with increasing distance $d_{BE} / H_{1/3}$ as well for SWL below as for SWL above the mean berm level, which is shown distinctly in Fig. 17. The data in this plot confirm the well-known effect, that run-up reduction is most effective for waterlevels around the berm level.

Conclusion

Analyzing of run-up measured in field and on complex cross-sections can be complicate, therefore the analysis has to be done very carefully and seriously. All the different influences have to be separated and quantified in detail.

Reference

Grüne, J. : Wave run-up caused by natural storm surge waves. Proc. 18th Intern. Conf. on Coast. Eng., Kapstadt, 1982

CHAPTER 79

WAVE RUN-UP ON REVETMENTS WITH COMPOSITE SLOPES

Zeya Wang¹ and Joachim Grüne²

Abstract

The paper deals with wave run-up on revetments and seadykes with composite slopes. The presented data were obtained from large scale laboratory tests with different wave climate characteristics in the " Large Wave Channel " (GWK) at Hannover, Germany. The results are discussed with respect to slope angle transformation mode to be used in the well-known HUNT-formula.

Introduction

Safety analysis of existing coastal protection works becomes again more important due to the world wide increasing of storm surges and the supposed long-term rising of water levels at the coastlines. Within such a safety analysis wave run-up and overtopping is the most important load factor.

Previous investigations on wave run-up have shown different results using different verifications of formulae to fit the boundary conditions with complex cross-sections and with real sea state wave conditions. Thus a research program has been established, which is focussed on the effects of non-uniform cross-sections and of real sea state wave characteristics. A part of this research program deals with cross-sections, which are composed from different uniform slopes. Results from investigations on run-up with such composed cross-sections are presented in the following.

¹ M.-Ing., Researcher,

² Dipl.-Ing., Senior researcher, Operation Manager of Joint Central Institution " Coastal Research Center (FZK) " of University Hannover and of Technical University Braunschweig, GWK, Merkurstrasse 11, 30419 Hannover, Germany

The most convenient formula for calculating wave run-up on gentle smooth slopes like seadykes and revetments normally have, is the well-known one derived by HUNT (1959). Although originally derived for regular waves on a uniform slope the tendency of the HUNT-formula also agrees quite well with irregular data.

Usually the HUNT-formula is written in dependence of the breakerindex ξ in the following form:

$$R / H = C_{\xi} \cdot \xi, \quad \text{with} \quad \xi = \frac{\tan \alpha}{\sqrt{\frac{2\pi H}{g \cdot T^2}}}$$

and with R = run-up
 C = coefficient
 H = waveheight
 T = wave period
 α = slope angle ($\tan \alpha = 1 : N$, with N = slope value)

For using this formula in a savety analysis of dykes and revetments in field this general form has to be verified as well with respect to the irregular waveheight and wave period parameters of the real sea state conditions (see BATTJES, 1974) as with respect to the non-uniformly sloped seadyke cross-sections, which mostly occur in prototype. These verifications lead to different values C_{ξ} in dependence of used irregular wave parameters and/or the mode of slope angle α transformation for non-uniform cross-sections. In a lot of previous papers such verifications of the HUNT-formula have been reported, among them a few with data from field and/or from large scale laboratory tests. For example are those from GRÜNE (1982), FÜHRBÖTER et. al. (1989), SPARBOOM et. al. (1990), v. d. MEER & STAM (1992), d. WAAL & v. d. MEER (1992), WANG & GRÜNE (1995). The results shown in this paper will be discussed mainly with respect to the mode of slope angle transformation for composed slopes.

Only a few suggestions exist for slope angle α transformation approaches for slopes of composed cross-sections. SAVILLE (1958) proposed an equivalent gradient method, where the equivalent slope is defined by the linear interpolation between the breakerpoint and the maximum wave run-up on the non-uniform slope. But this mode is not necessarily representative for all types of non-uniform slopes, the method was not tested by SAVILLE (1958) with measurements on convex slopes. Some field data for composite slopes (1:4 and 1:6) have been reported by GRÜNE (1982), who found that the influence of slopes occur roughly in the range between $1.0 H_{1/3}$ below and $2.0 H_{1/3}$ above stillwaterlevel. A similar suggestion for an average slope was given by d. WAAL & v. d. MEER (1992) with a linear interpolation between the points $1.0 H_{1/3}$ below and $1.0 H_{1/3}$ above stillwaterlevel on the dyke surface.

Test equipment

The data, presented in this paper, are from large scale laboratory tests, which have been done in the Large Wave Channel (GWK) at Hannover (GRÜNE & FÜHRBÖTER, 1976). The GWK is a facility of the recently founded Coastal Research Center "Forschungszentrum Küste (FZK)", which is a joint institution both of the University Hannover and the Technical University Braunschweig.

The cross-sections of the revetment used for the tests in the GWK are shown in Fig. 1. It has a sand core and is covered with asphalt-concrete. The composed slope consist of two different uniform slopes: a slope of 1:6 in the upper part and a slope of 1:3 in the lower part. The lower slope 1:3 was varied twice: for one testseries the slope junction level of both uniform slopes was 3.3 m above bottom, for the other testseries the slope junction level was 4.5 m above bottom.

Wave run-up was measured with a run-up step gauge (GRÜNE, 1982), which was installed on the upper slope 1:6 for the testseries with the slope junction level 3.3 m above bottom and on both slopes for the other testseries. The steps of the run-up gauge had vertical distances of 6.5 cm on the slope 1:6. The waves in front of the revetment were measured with some wire gauges. The wire gauges had roughly constant distances between each other and reflexion effects had been minimized by using the data of four of these gauges. The analog signals from waves gauges and run-up step gauge were continuously digitized with 100 Hz and stored by the main processing computer.

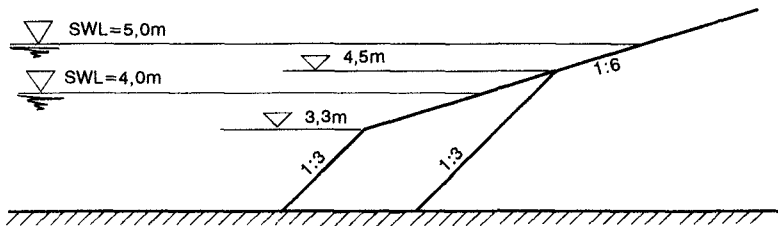


Fig. 1 : Cross-section of the revetment used for large scale tests in the GWK

All tests were conducted with two different water levels (4.0 m and 5.0 m above bottom), this results in altogether four different testseries with respect to the vertical distance D_c between still water level SWL and slope junction level ($D_c = 1.7$ m, 0.7 m, 0.5 m and - 0.5 m). Three different types of wave characteristics were generated: Regular waves, PM - spectra (narrow banded) and field spectra (wide banded). The generated field spectra had been measured in front of similar dyke cross-sections at the german coast during high storm surges. For each testseries roughly 15 single tests with each of these three different wave climate types were run. Fig. 2 gives an impression of wave acting on the revetment during a large scale test in the GWK.



Fig. 2 : Wave action on the revetment during a test in the GWK

Results

The results presented in this paper will be focussed on the approach of slope angle transformation with respect to HUNT-formula. All data are referred to the mean period T_m from the time domain analysis. In a previous report on the results from the tests with the berm (WANG, GRÜNE, 1995), it was demonstrated, that the correlation using T_m is quite better than using the peak period T_p . This is due to the fact, that the estimation of a peak period from the spectral density distribution of real sea state shallow water waves is of problematic nature and can create confusion.

The first results to be discussed are from the testseries with regular waves, where the still water level *SWL* was 1.7 m above, 0.5 m above and 0.5 m below the junction level of the two slopes ($D_c = +1.7$ m, $+0.5$ m, and -0.5 m).

The measured run-up data R_{98} are related to the mean regular wave height and are plotted in Fig. 4 versus the breakerindex ξ , which is related to three different slopes separately (slopes of upper part of 1:6, lower part of 1:3 and average slope $1:N_{av}$). The average slope N_{av} has been evaluated according to the mode, given by d. WAAL & v. d. MEER (1992), and is defined in Fig. 3 (left hand). It is clear that due to the mode the data for N_{av} with $D_c = +1.7$ m (waterdepth of 1.7 m above junction level) are identical with those of the upper slope 1:6. This means, that the lower slope 1:3 has more or less no influence.

It must be remarked, that the average slope approach by de WAAL and v. d. MEER was evaluated for irregular waves, but there is no functional difference for regular waves. On the other hand, because the HUNT formula was originally evaluated from regular wave run-up data, thus fundamental trends may be demonstrated firstly with regular wave run-up data.

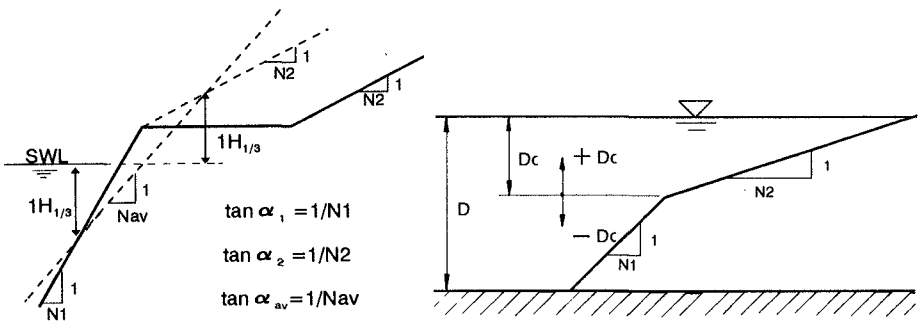


Fig. 3 : Definition of average slope N_{av} by de WAAL and v. d. MEER (left hand) and Definition of slope junction D_c (right hand)

In the middle plot of Fig. 4 the data with $D_c = +0.5$ m (SWL only 0.5 m above the junction level) show similar trends and only small differences between the average slope N_{av} related data and those for the uniform upper slope 1:6, which means, that the lower slope 1:3 has only a small influence. Greater differences occur for the data with $D_c = -0.5$ m (SWL 0.5 m below the junction level). The average slope data agree much more to the 1:3 slope, but they all are far away from a linear dependence with identical gradients.

A new mode for slope angle transformation of two composed uniform slopes is based on the rather old approach, derived by DROGOSZ-WAWRZY尼亚K (1965) as follows with the definitions shown in Fig. 3 (right hand):

$$\frac{1}{N} = \frac{1}{N_1} + 2 \cdot \frac{D_c}{L_o} * \left(\frac{1}{N_2} - \frac{1}{N_1} \right)$$

This formula was modified by the authors in the following manner: the original factor $2 * D_c / L_o$, which is a function of position of junction level D_c and

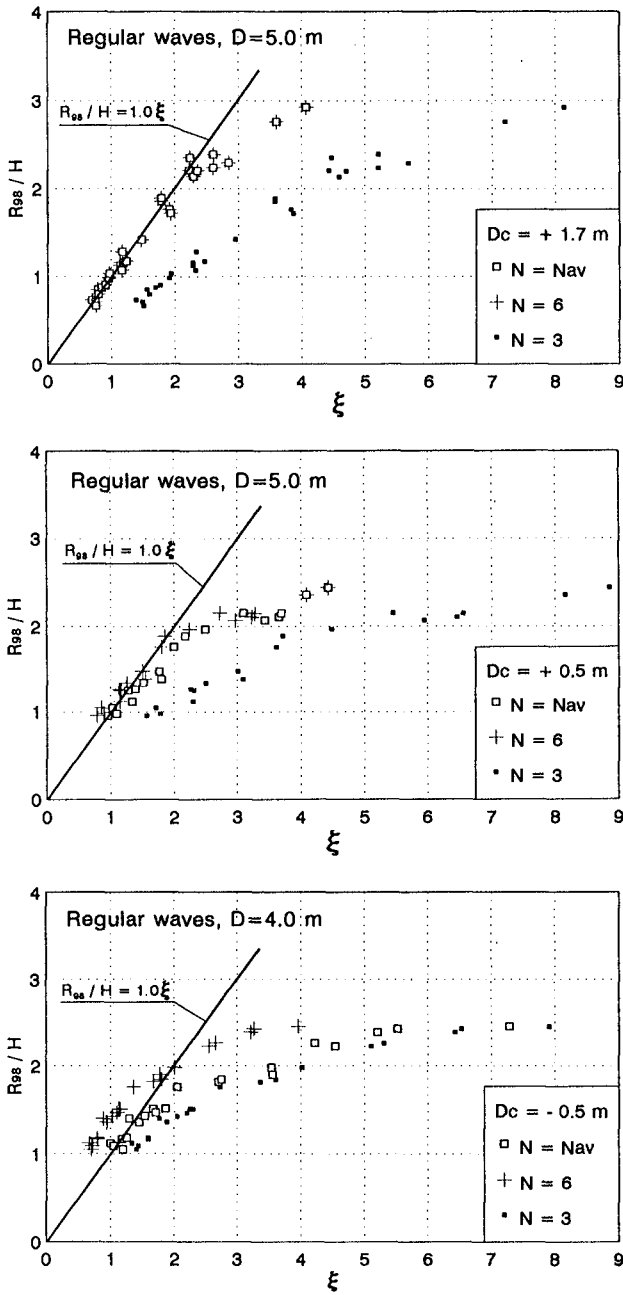


Fig. 4 : R_{98}/H versus breakerindex ξ for tests with regular waves

wavelength L_o , has been extended, so that the new factor is a function of the dyke geometry in terms of the depth related position of junction level D_c / D and the deepwater wave steepness H / L_o or the wave period, respectively. Compared to the average slope approach of d. WAAL and v. d. MEER, this slope approach has been extended by the wave period:

$$2 * \frac{D_c}{L_o} \Rightarrow f \left(\frac{D_c}{D}, \frac{H}{L_o} \right)$$

Thus the modified formula is written:

$$\frac{1}{N_{su}} = \frac{1}{N_2} + f \left(\frac{D_c}{D}, \frac{H}{L_o} \right) * \left(\frac{1}{N_1} - \frac{1}{N_2} \right)$$

with the following factors
for regular wave climate:

$$f \left(\frac{D_c}{D}, \frac{H}{L_o} \right) = \left(\frac{1}{2} - \frac{D_c}{D} \right) * \left(7 * \left(\frac{H}{L_o} \right)^{0.1} - 4.43 - \frac{D_c}{D} \right)$$

for irregular wave climate:

$$f \left(\frac{D_c}{D}, \frac{H_{1/3}}{L_o} \right) = 2 * e^{-\frac{D_c}{D}} * \left(3 * \left(\frac{H_{1/3}}{L_o} \right)^{0.2} - 1 \right)$$

with D_c = distance between stillwaterlevel and junction level
 D = waterdepth
 H = waveheight
 L_o = deepwater wave length = $g * T_m^2 / 2\pi$

The high accuracy of this slope angle transformation may be demonstrated in the best way by the plots in Fig. 5, where the results for waveheight related run-up data are plotted versus the deepwater steepnesses H / L_o for the testseries with regular waves and $D_c = +0.5$ m (upper plot) and $D_c = -0.5$ m (lower plot). The full line in Fig. 5 represents the HUNT-formula, using the new approach for slope angle transformation with $1:N = 1:N_{su}$. It is obvious, that the differences to the measured values are rather small. The two dotted straight lines, marked with $N = 3$ and $N = 6$, represents the original HUNT-formula, using one of the uniform slopes $N = 3$ or $N = 6$ respectively. If one of these slope angle approaches would be correct, all measured data should fit one of these dotted lines. The irregular dotted line, marked with $N = N_{av}$, which lies between the two others straight ones, represents the HUNT-formula, using the average slope N_{av} according to de WAAL & v. d. MEER. Whereas the agreement for higher wave steepnesses is quite well, there are considerable differences for lower steepnesses.

The accuracy of the new slope angle transformation also comes out clearly in Fig. 6, where the measured data are plotted versus the breakerindex ξ . The upper plot again is for the data with $D_c = +0.5$ m and the lower plot for the data with $D_c = -0.5$ m. It must be stated, that the measured data agree quite well with

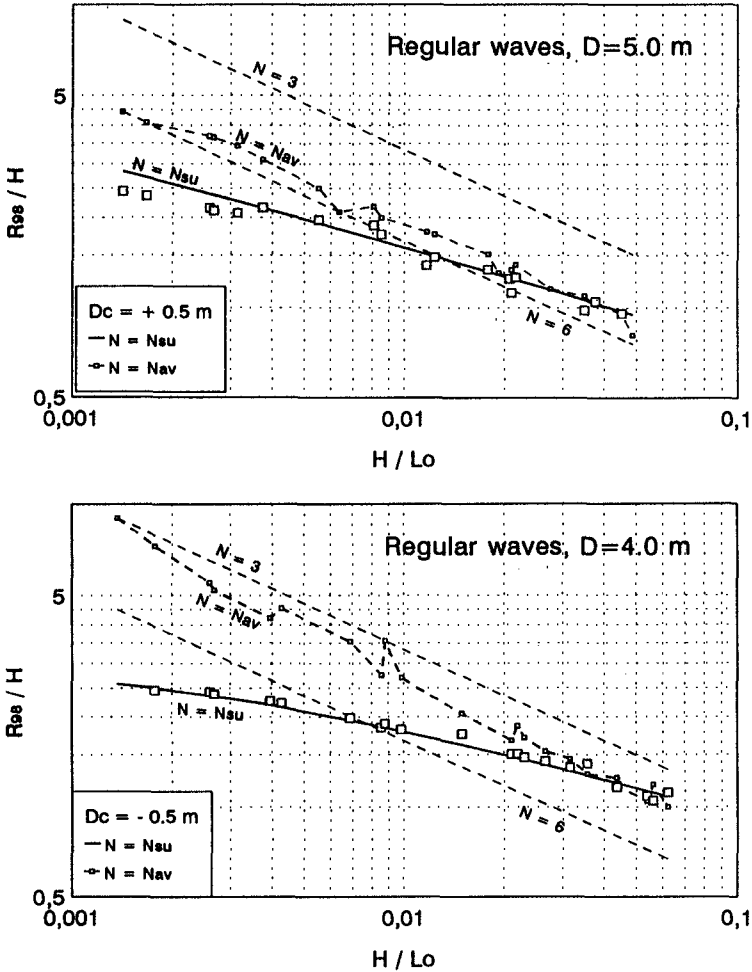


Fig. 5 : R_{98} / H versus steepness H / L_0 for tests with regular waves

the HUNT-formula with the new mode of slope angle transformation, especially no range with a constant value has to be defined as it is necessary with previous slope angle transformation modes.

Similar relations were found for the data from the testseries with PM-spectra and field spectra, using the slope angle transformation mode $N = N_{su}$ in the HUNT-formula. The measured run-up data $R_{98} / H_{1/3}$ from the testseries with PM-spectra are plotted versus the significant waveheight related deepwater steepnesses $H_{1/3} / L_0$ in Fig. 7 for the testseries with $D_c = +0.5 \text{ m}$ and with $D_c = -0.5 \text{ m}$. The notations for N are the same as used in Fig. 5.

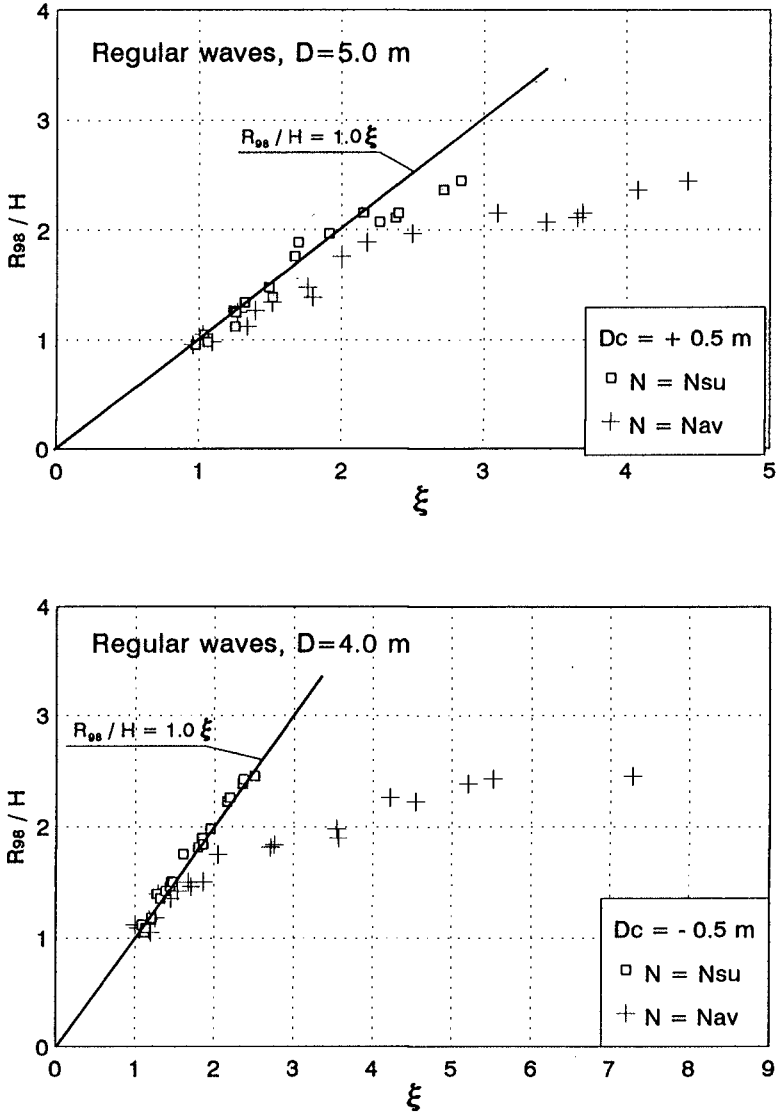


Fig. 6 : R_{98} / H versus breakerindex ξ for tests with regular waves

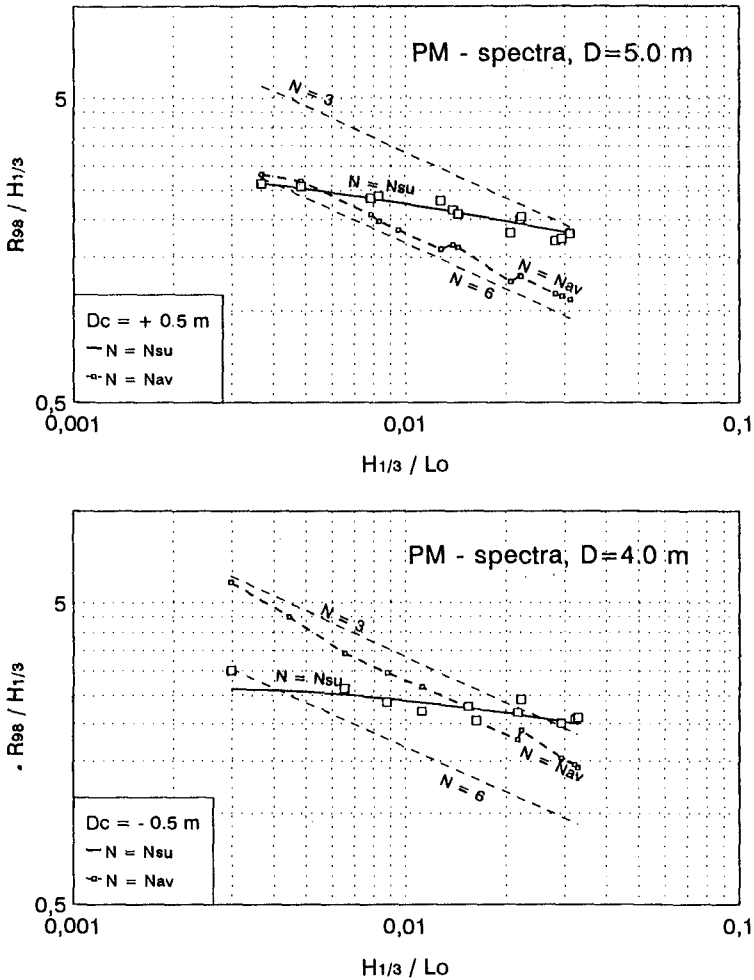


Fig. 7 : $R_{98} / H_{1/3}$ versus steepness $H_{1/3} / L_0$ for tests with PM-spectra

The data from the testseries with field spectra in Fig. 8 indicate similar relations, but they have a much smaller range of deepwater steepnesses, which is normal for a wadden sea wave climate.

The same data from Fig. 7 and 8 are plotted versus the breakerindex ξ in Fig. 9 (PM-spectra) and 10 (field spectra), respectively. As well as for tests with regular waves the linear correlation of the test data with irregular waves is much stronger (PM- and field spectra), using the new slope approach $N = N_{su}$, in comparison with using the average slope approach. The field spectra in Fig. 10 data scatter a little bit more, but without any distinct trend.

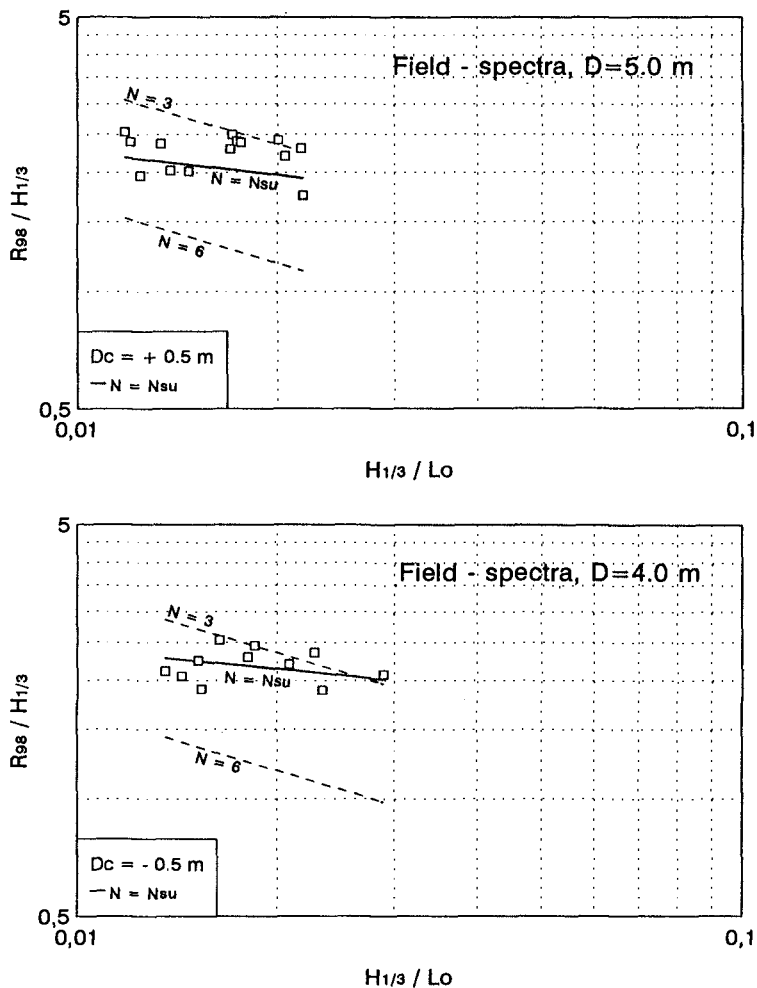


Fig. 8 : $R_{98} / H_{1/3}$ versus steepness $H_{1/3} / L_0$ for tests with field-spectra

Conclusion

The HUNT-formula has been verified with respect to slope angle transformation. Data from large scale laboratory tests with regular waves and irregular waves (PM-spectra and field spectra) were used. The wave run-up data on revetments with composite slopes are well presented with the HUNT-formula, using a new slope angle transformation, which takes not only the depth related position of junction point D_c / D but also the wave steepnesses H / L_0 into account.

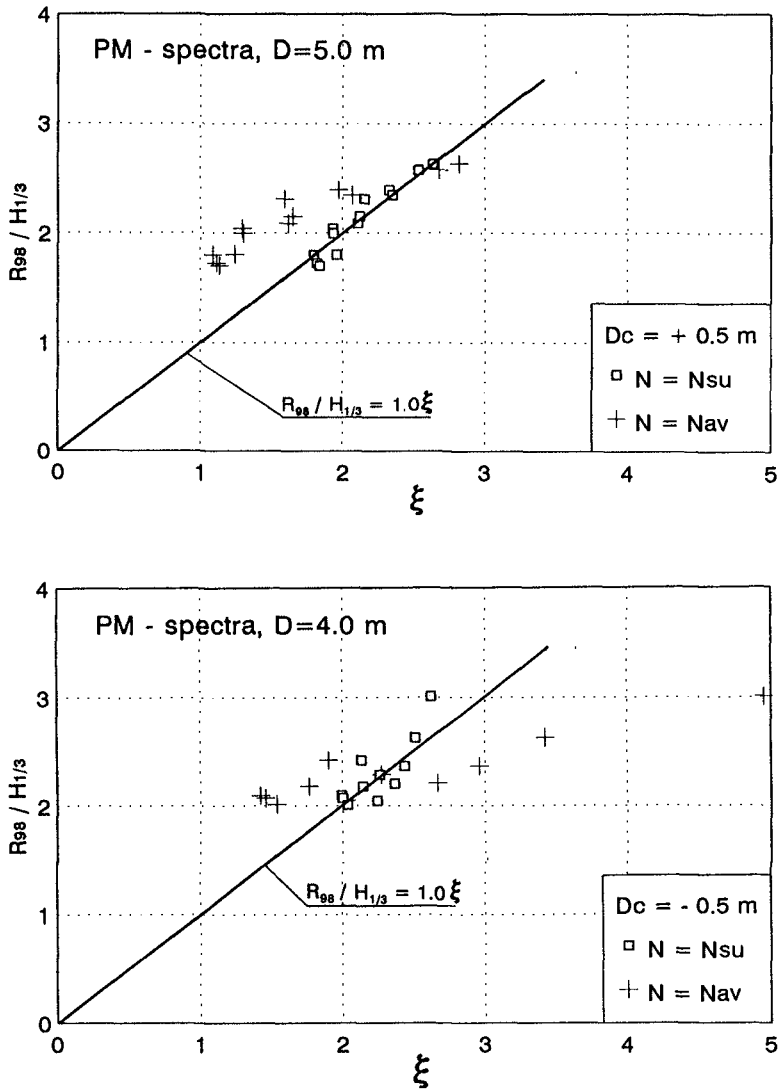


Fig. 9 : $R_{98} / H_{1/3}$ versus breakerindex ξ for tests with PM-spectra

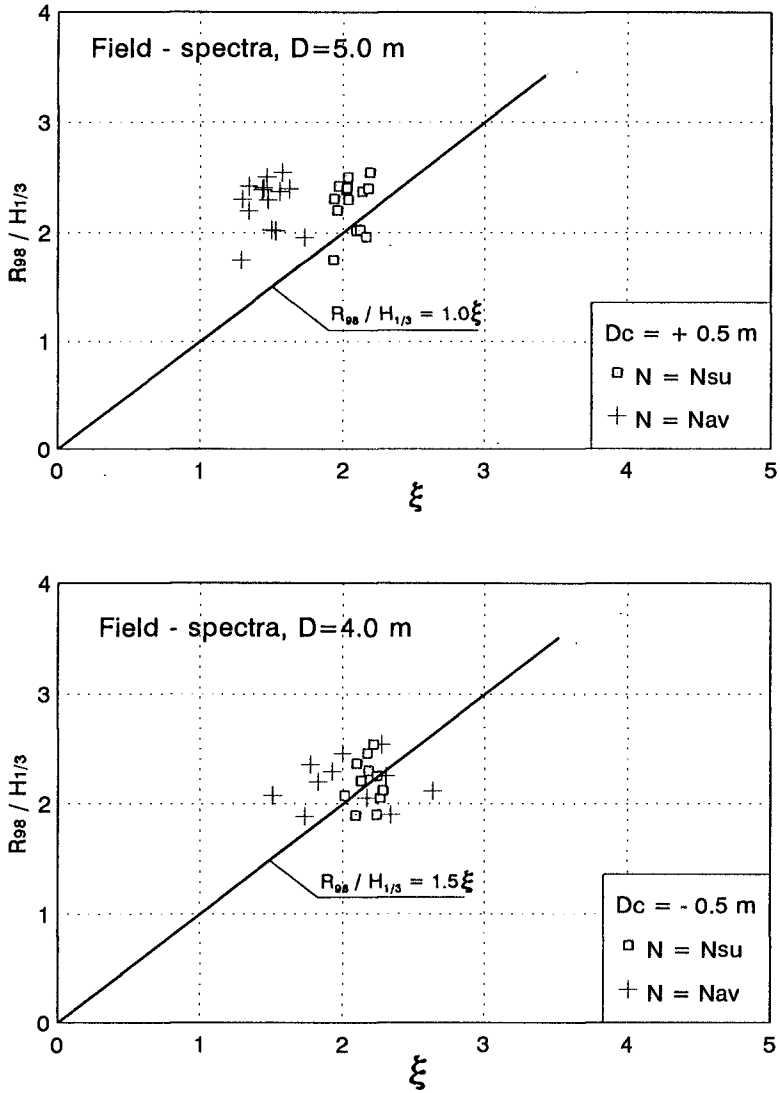


Fig. 10 : $R_{98} / H_{1/3}$ versus breakerindex ξ for tests with field-spectra

Acknowledgements

The research work was granted by the German Ministry for Research and Technology (BMFT) within the research project " Bemessung auf Seegang " of the KURATORIUM FÜR FORSCHUNG IM KÜSTENINGENIEURWESEN (KFKI). The authors would like to give their severe thanks for using the data from the research program of SONDERFORSCHUNGSBEREICH 205 / A1 (supervision Prof. Dr.-Ing. A. Führböter, Dr.-Ing. Dette), which was supported by the GERMAN RESEARCH FOUNDATION (DFG).

References

- BATTJES, J.A. : Computation of set-up, longshore currents, run-up and overtopping due to wind-generated waves, Dept. of Civil Engineering, Delft University of Technology, Report Nr. 74-2, 1974
- DE WAAL, J.P.; VAN DER MEER, J.W. : Wave run-up and overtopping on coastal structures. Proc. 23rd Intern. Conf. on Coast. Eng., Venice, 1992
- DROGOSZ-WAWRZYNIAK, L.: in "Wave run-up and overtopping", Technical advisory committee on protection against inundation, Government publishing office - The Hague 1974, Holland
- FÜHRBÖTER, A.; SPARBOOM, U.; WITTE, H.-H. : Großer Wellenkanal Hannover: Versuchsergebnisse über den Wellenaufbau auf glatten und rauhen Deichböschungen mit der Neigung 1:6. Die Küste, Heft 50, 1989 (in German)
- GRÜNE, J. : Wave run-up caused by natural storm surge waves. Proc. 18th Intern. Conf. on Coast. Eng., Kapstadt, 1982
- GRÜNE, J.; FÜHRBÖTER, A. : Large Wave Channel for "full-scale modelling" of wave dynamics in surf zones. Proc. of Symp. on Modelling Techniques, San Francisco, 1976
- HUNT, I.A.jr. : Design of seawalls and breakwaters. Journal of the Waterways and Harbors Division, Proc. ASCE, Vol. 85, WW3, 1959
- SAVILLE, T. jr. : Wave run-up on composite slopes. Proc. 6th Conf. on Coast. Eng., 1958
- SPARBOOM, U.; GRÜNE, J.; GROSCHE, S.; HAIDEKKER, M. : Full-scale measurements of wave run-up at sea dykes. Proc. 22nd Intern. Conf. on Coast. Eng., Delft, 1990
- VAN DER MEER, J.W.; STAM, C.J.M. : Wave run-up on smooth and rock slopes of coastal structures. Journal of Waterways, Ports, Coastal and Ocean Engineering, Proc. ASCE, Vol. 118, WW4, 1992
- WANG, Z.Y.; GRÜNE, J. : Influence of berms on wave run-up on sloping seadykes, Proc. 4th Intern. Conf. on Coast. and Port Eng. in developing countries (COPEDEC IV), Rio de Janeiro, Brazil, 1995

CHAPTER 80

Landward Transport of Spray Generated from a Wave Absorbing Sea Wall

Misao Hashida¹, Nobuhiro Matsunaga² and Isao Irie³

Abstract

A landward transport process of spray generated from a wave absorbing sea wall under a strong wind has been investigated experimentally. Near the wall, the concentration of spray decays exponentially both in the leeward direction and in the upward direction. The profiles are determined by the equilibrium between the advection of spray and the sedimentation. The characteristic quantities on the profiles have been related to the experimental parameters.

1. Introduction

Extending from August to October every year, Japan often suffers severe damages due to typhoons. In winter, a strong seasonal wind from the northwest blows against coastal areas fronting the Japan Sea. Moreover, Japanese coastal line is exposed to the danger of tsunami disasters because Japanese Archipelago is one of the world's most seismologically active areas. Therefore, most of Japanese coastal engineers and researchers have devoted their energies to the prevention against the coastal disasters due to big waves, storm surges, tsunamis and so on. Various types of wave absorbing works have been developed to protect the coastal areas and have made remarkable achievements.

1 Professor, Dept. of Civil Engineering, Nippon Bunri University, Oita 870-03, Japan.

2 Associate Professor, Dept. of Earth System Science and Technology, Kyushu University, Kasuga 816, Japan.

3 Professor, Dept. of Civil Engineering, Kyushu University, Fukuoka 812, Japan.

Wave absorbing sea wall construction is one of them. In a storm, however, a wave absorbing sea wall generates a large amount of spray in compensation for the effective dissipation of wave energy. If it is transported landward, salt damages are given to the agricultural products or the infrastructural system in the coastal zone. Recently, the human life zone is expanding rapidly in the seaward direction. It also requires that the generation of sea water spray should be reduced from the standpoint of the preservation of atmospheric environments. Several studies have been already made on the generation of water spray and the transport of sea-salt particles. Hayami & Toba (1958) and Toba (1959) observed the generation of spray in the bursting process of air bubbles floating on the water surface, and concluded that the process is essential as a source of sea-salt particles in the atmosphere. Toba & Tanaka (1963) and Toba (1965 a, b) measured sea-salt particles in the atmosphere and demonstrated a good agreement to be seen between the observed results and the theoretical ones. Matsunaga et al (1994) investigated a transport process of spray generated from breaking waves by using a wave tank equipped with a wind tunnel. They showed that a large amount of spray is separated from the crests of breaking waves and the concentration of spray decreases exponentially in the vertical direction.

However, no studies have been made on the generation of spray from coastal structures in a storm and its landward transport process. In this study, how spray occurring from a wave absorbing sea wall is transported landward has been investigated experimentally.

2. Experimental methods

Experiments were carried out by using a wave tank, which is equipped with an inhalation-type wind tunnel (see figure 1). The tank

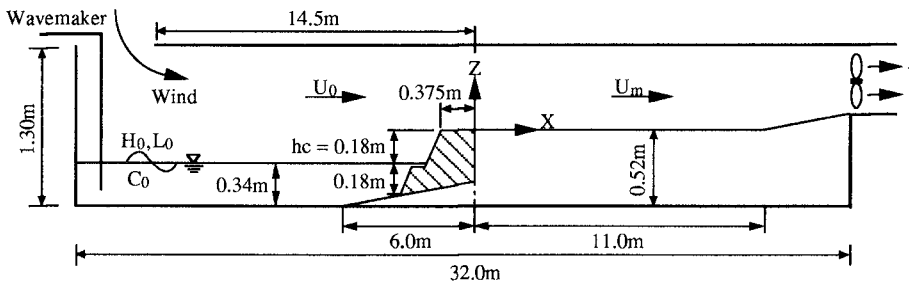


Fig. 1 Schematic diagram of experimental set-up.

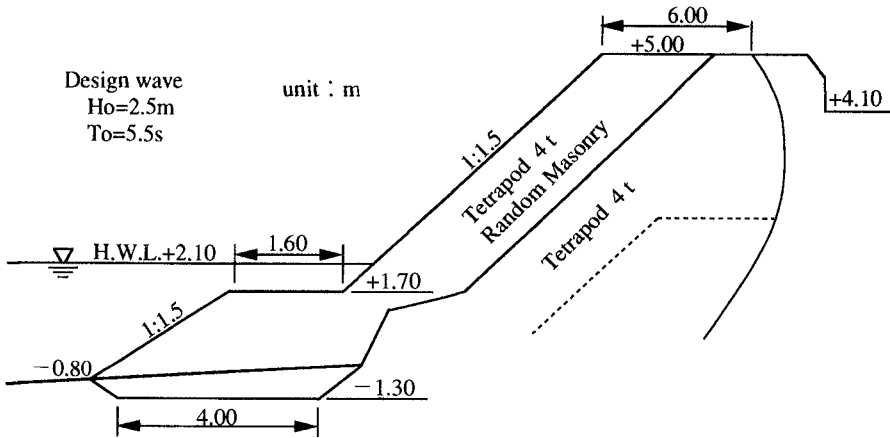


Fig. 2 Cross section of wave absorbing sea wall.

Table 1 Experimental parameters and characteristic quantities of spray concentration profiles.

Experimental Parameters									
Run	T(s)	H ₀ (cm)	L ₀ (cm)	C ₀ (m/s)	U ₀ (m/s)	U _m (m/s)	H ₀ /L ₀	U ₀ /C ₀	hc/H ₀
1	1.38	14.3	295	2.14	9.43	11.9	0.048	4.41	1.27
2	1.38	14.3	295	2.14	13.1	16.6	0.048	6.12	1.27
3	1.38	14.3	295	2.14	15.1	19.1	0.048	7.06	1.27
4	1.20	11.7	225	1.88	13.1	16.6	0.052	6.97	1.55
5	1.20	11.7	225	1.88	15.1	19.1	0.052	8.03	1.55

Characteristic Quantities				
Run	\bar{l} (cm)	\bar{l}/hc	C(0,0)	w ₀ /U _m
1	7.52	0.42	9.03E-5	1.37E-1
2	5.48	0.30	8.58E-4	9.37E-2
3	5.28	0.29	1.08E-3	8.03E-2
4	6.69	0.37	6.01E-4	1.26E-1
5	5.96	0.33	1.00E-3	9.83E-2

was 32 m long, 0.6 m wide and 1.30 m high. A wave absorbing sea wall, which is constructed at Beppu Port in Oita Prefecture, Japan, was used as a model. Figure 2 shows its cross-section and dimensions. The sea wall is covered with randomly piled 4 t-Tetrapod blocks. The gradient of the wall surface was 1 : 1.5. In the experiments, the scale of the wall was reduced to 1/16. The mean water depth was set at 0.34 m. The crown height h_c was 0.18 m. As a model of land, a 11 m

solid bed was attached horizontally to the back of the wall model. Five tests were made by varying wave parameters and wind velocity (see table 1). Two types of regular waves were made by a wavemaker. Their periods T were 1.38 s and 1.20 s. The wave heights in deep water H_0 were 14.3 cm and 11.7 cm. The wave parameters L_0 and C_0 are the wavelength and the wave velocity in deep water, respectively. U_0 is the cross-sectionally averaged wind velocity above the water surface and U_m is the one above the horizontal bed. The values of U_0 were varied from 9.43 to 15.1 m/s. The coordinate axes x and z were taken leeward and vertically upward from the back of the wall model, respectively. Water spray was captured by using cylindrical containers filled with cotton. They were 3.0 cm in diameter and 5.0 cm in depth. The vertical profiles of spray quantity were obtained by setting the containers at 5.0 cm vertical intervals. The measurements were made at 1.0 m horizontal intervals in the range of $x=0$ m to 11 m. The descriptions about the characteristic quantities l , $C(0, 0)$ and w_0/U_m shown in table 1 will be given in the next section.

3. Results and discussion

Figures 3 (a) to (e) show how the vertical profiles of spray concentration C vary in the leeward direction. The values of C are calculated from $C = q / \rho U_m$, where q is the mass of spray transported per unit area and time, and ρ the density of water. The concentration decreases exponentially with the increase of z and approaches to a constant value. As spray is transported in the leeward direction, the concentration decreases rapidly near the bed surface and the vertical profiles become uniform. It means that relatively large spray distributing at the back of the sea wall precipitates rapidly during the advection. On the other hand, very small spray remains to be suspended in a region far away from the wall. Therefore, the equilibrium between the advection of spray and the sedimentation may be essential near the wall and the advection-diffusion equilibrium may determine the concentration profiles far away from the wall. A typical profile of spray concentration is drawn schematically in figure 4, and the characteristic quantities are defined. The spray concentration at $z=0$, i.e., $C(x, 0)$, is estimated by extrapolating from the data in the exponentially decaying region. The characteristic length scale l is defined as a height at which the spray concentration takes the value of $C(x, 0)/e$. C^* is defined as a spray concentration at a large value of z and z^* is the height where C becomes nearly equal to C^* . It is unsuitable to examine experimentally the spray concentration in the

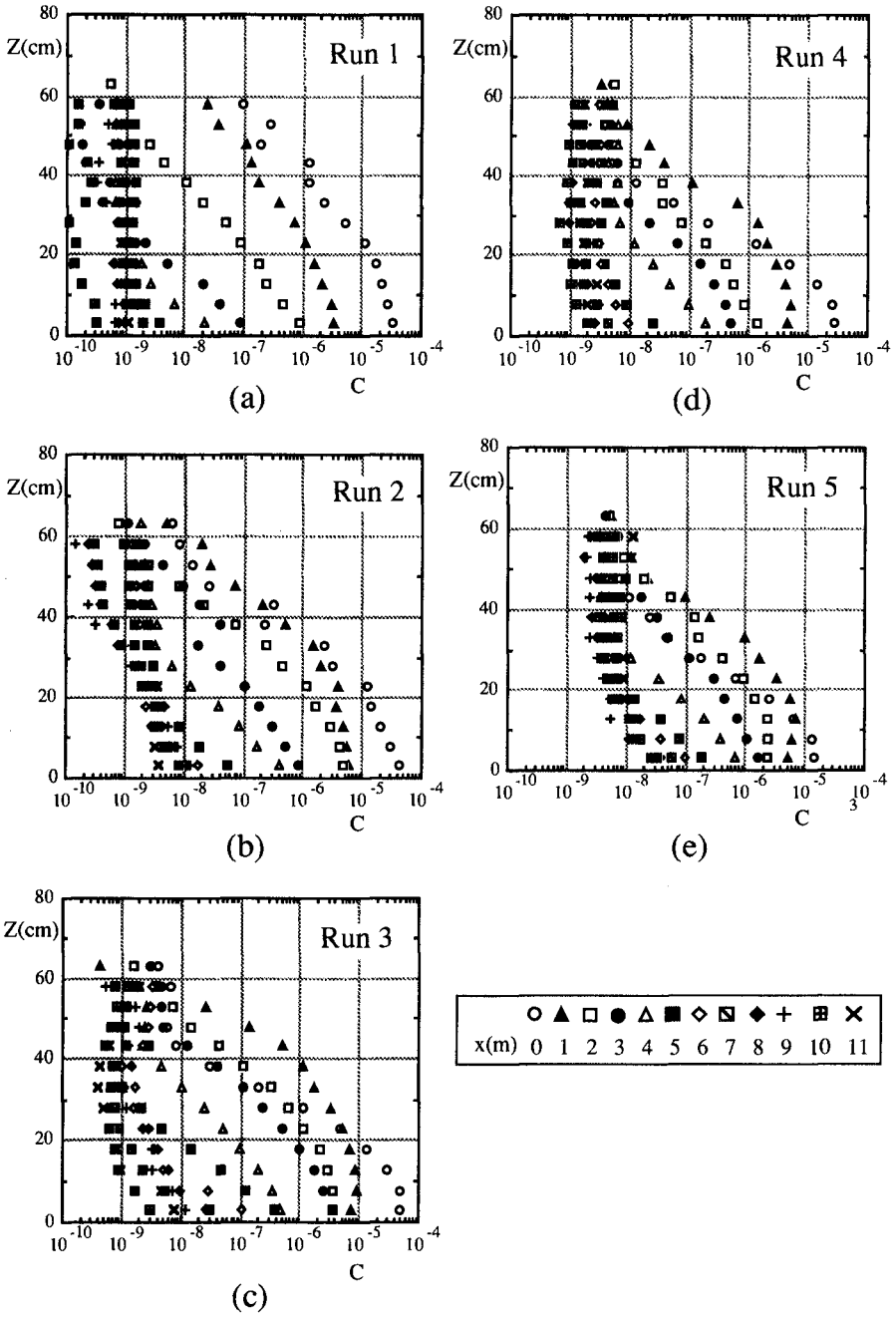


Fig. 3 Leeward variation of vertical profiles of spray concentration.

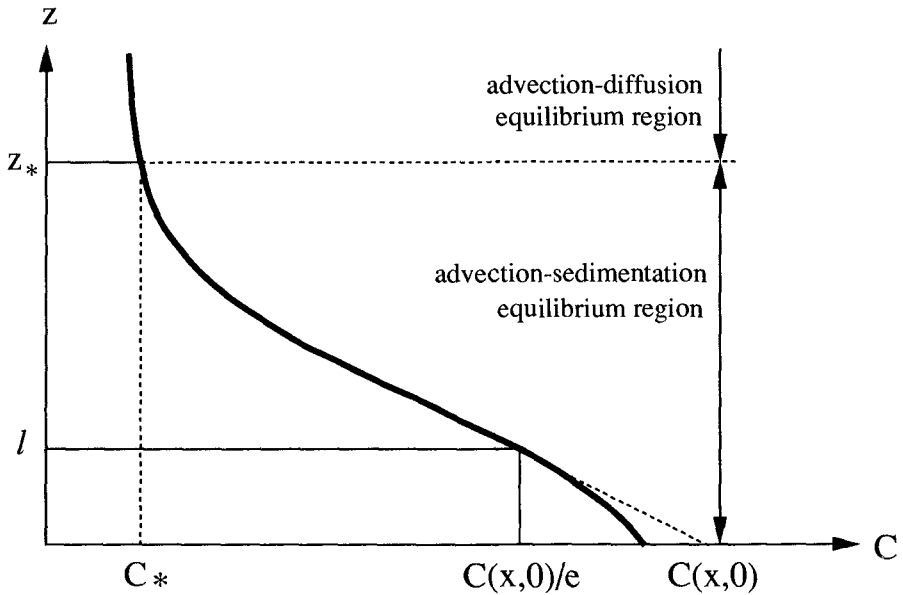


Fig. 4 Typical vertical profile of spray concentration and definition of characteristic quantities.

advection-diffusion equilibrium region because the concentration depends strongly on the height of the wind tunnel. Therefore, the characteristic quantities of C^* and z^* are not discussed here. In the advection-sedimentation equilibrium region, the equation of the spray concentration is given by

$$U_m \frac{\partial C}{\partial x} - w_o \frac{\partial C}{\partial z} = 0. \tag{1}$$

Here, it is assumed that the distribution of the spray concentration is steady and the settling velocity of spray w_o is constant. By assuming

$$C(x, z) = C(x, 0) \exp\left(-\frac{z}{l}\right), \tag{2}$$

we obtain

$$C(x, 0) = C(0, 0) \exp\left(-\frac{w_o}{U_m} \frac{x}{l}\right) \tag{3}$$

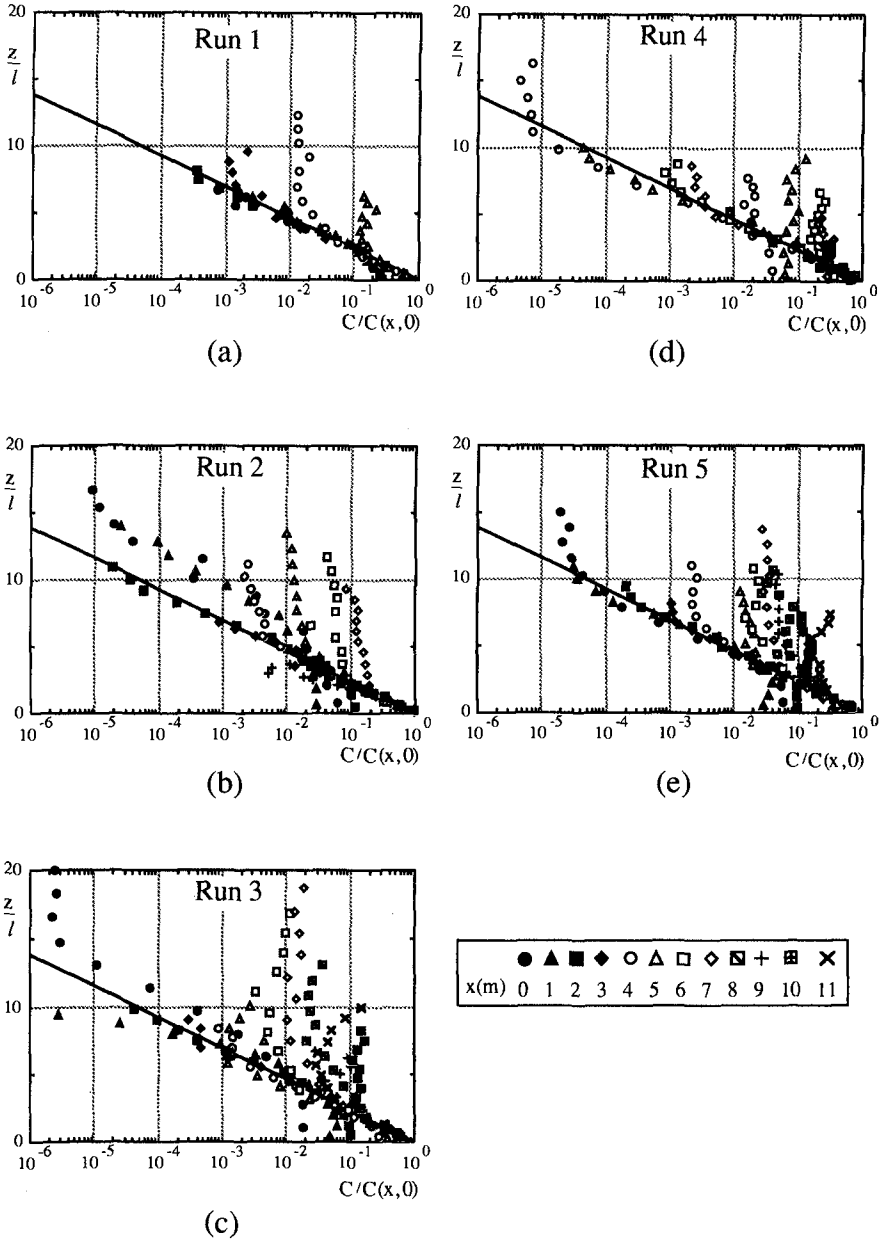


Fig. 5 Normalized profiles of spray concentration.

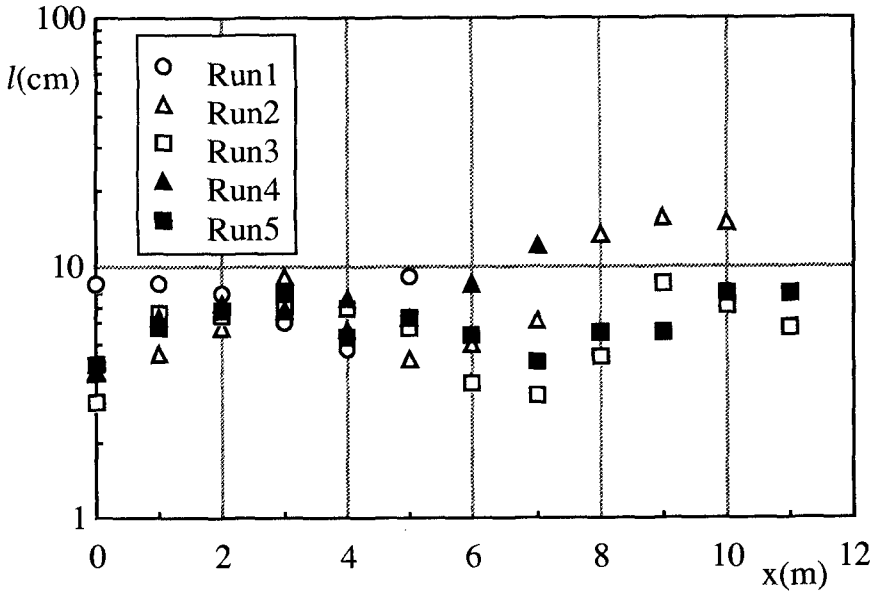


Fig. 6 Dependence of l on x .

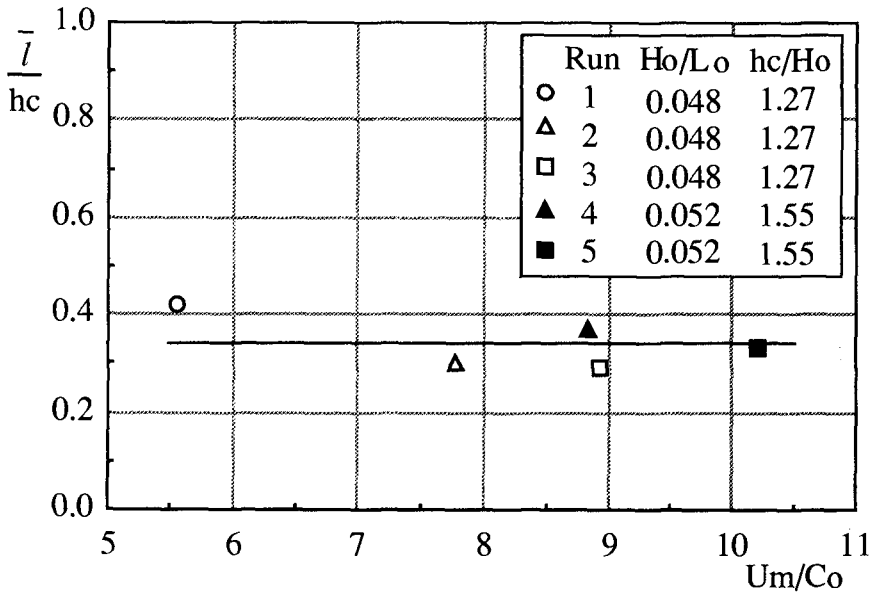


Fig. 7 Relationship between \bar{l} / hc and U_m/C_o .

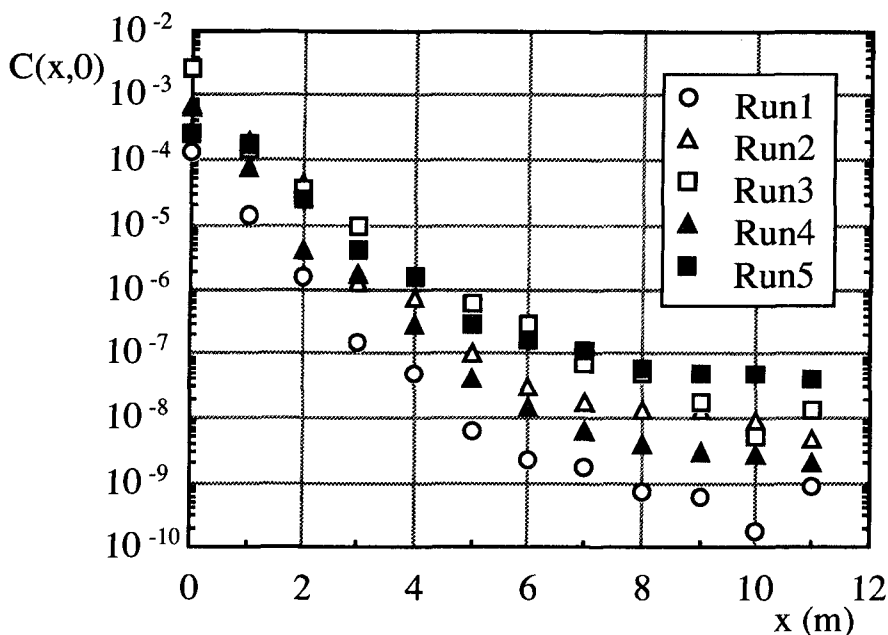


Fig. 8 Dependence of $C(x, 0)$ on x .

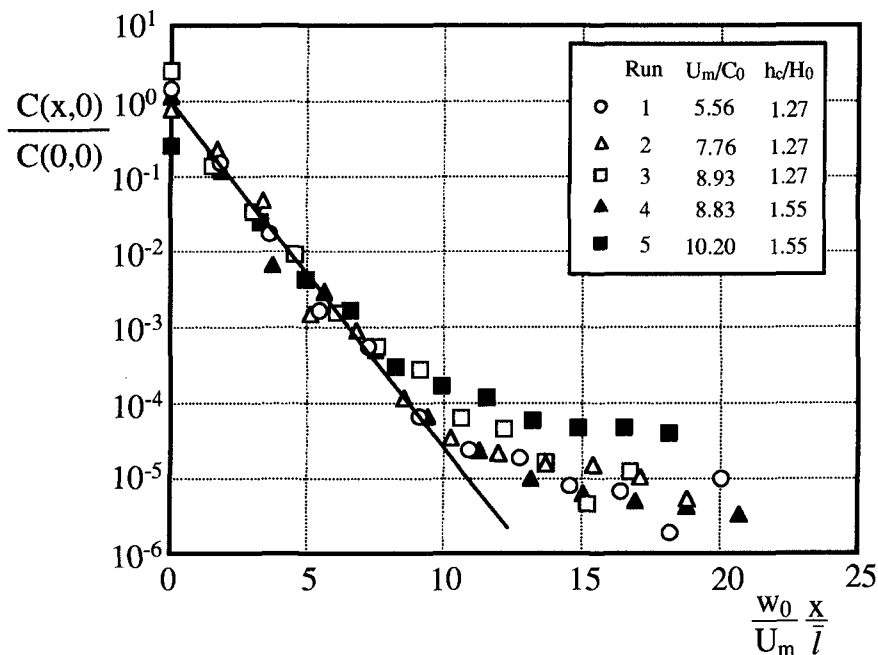


Fig. 9 Normalized profiles of $C(x, 0)$.

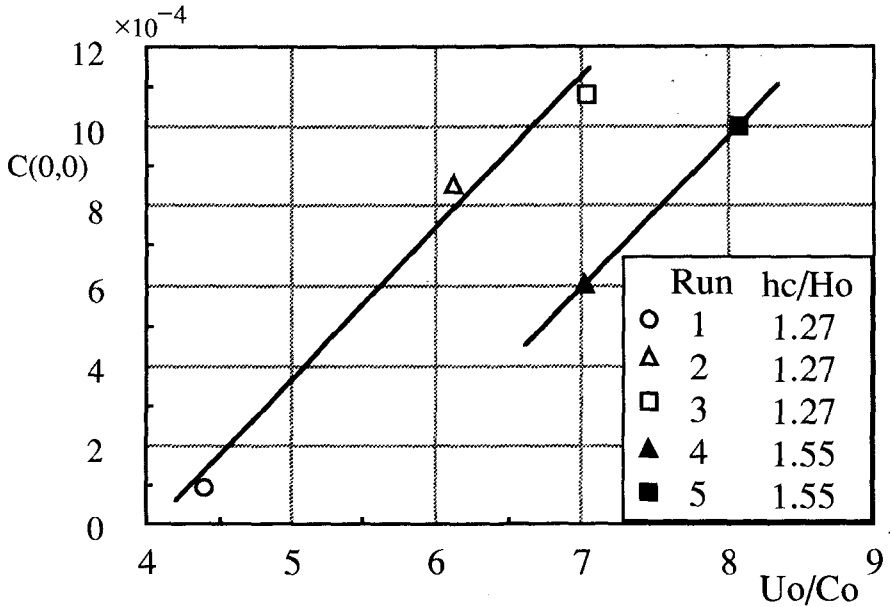


Fig. 10 Relationship between $C(0, 0)$ and U_o/C_o .

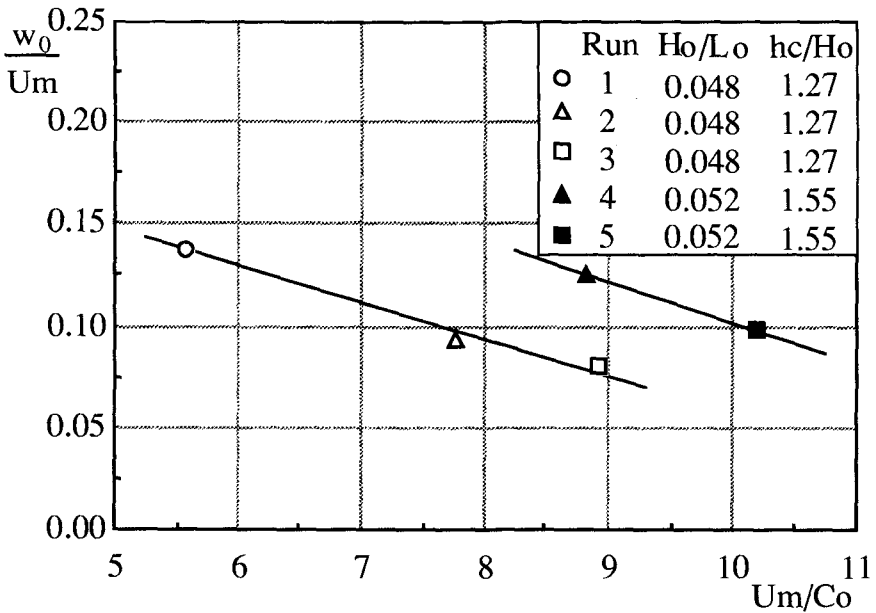


Fig. 11 Relationship between w_o/U_m and U_m/C_o .

The values of $C(x, 0)$ and l can be estimated by fitting equation (2) to the experimental data shown in figures 3 (a) to (e). In figures 5 (a) to (e), the data are normalized by using the obtained values. The data plotted above the solid lines are relatively uniform in the vertical direction and belong to the advection-diffusion equilibrium region. It is seen that the exponentially decaying region becomes narrow as the increase of x .

Figure 6 shows the dependence of l on x . Though some variation is seen, it is very small in comparison with the 11 m horizontal advection. Therefore, the values averaged in the leeward direction \bar{l} are given in table 1. The values of \bar{l} / h_c are plotted against U_m / C_0 in figure 7. The values of \bar{l} are approximately given by $0.35 h_c$.

The relationship between $C(x, 0)$ and x is shown in figure 8. Near the sea wall, $C(x, 0)$ decreases exponentially in the leeward direction. It is seen, therefore, that the relationship given by equation (3) is compatible with the data. The decreasing rate becomes small with the increase of the wind velocity. On the other hand, $C(x, 0)$ takes large values with the increase of the wind velocity. The values of $C(x, 0)$ approach to constant values in the region far away from the sea wall. We can estimate the values of $C(0, 0)$ and w_0 / U_m by fitting equation (3) to the data and using the values of \bar{l} . The obtained values are given in table 1. Figure 9 shows the profiles normalized by using $C(0, 0)$ and $w_0 / U_m \bar{l}$. It is seen that $C(x, 0)$ decreases exponentially in the range of $\frac{w_0}{U_m} \frac{x}{\bar{l}} \leq 10$.

Figure 10 shows the relationship between $C(0, 0)$ and U_0 / C_0 . The values of $C(0, 0)$ increase with the increase of U_0 / C_0 . In the case when the relative crown height h_c / H_0 is large, it is seen that $C(0, 0)$ takes small values. Figure 11 shows the dependence of w_0 / U_m on U_m / C_0 . The tendency is seen that w_0 / U_m decreases with the increase of U_m / C_0 and large spray is transported as the wave steepness increases.

4. Conclusions

In this study, the quantity of spray generated from a wave absorbing sea wall under a storm and its landward transport process were investigated experimentally. The obtained main points are as follows.

- 1) Near the sea wall, the spray concentration is determined by the equilibrium between the advection of spray and the sedimentation.

- 2) The spray concentration near the sea wall decreases exponentially both in the vertically upward direction and in the leeward direction.
- 3) The spray concentration on the horizontal bed decreases exponentially in the region of $\frac{w_0}{U_m} \frac{x}{l} \leq 10$.

The authors are grateful to Mr H. Kawakami and Ms Y. Arizumi for their help. A grant from the Ministry of Education, Science and Culture is also acknowledged.

References

- Hayami, S. and Toba, Y. (1958) Drop production by bursting of air bubbles on the sea surface (1): Experiments at still sea water surface, *J. Oceanogr. Soc. Japan*, **14**, 145-150.
- Matsunaga, N., Hashida, M., Mizui, H. and Sugihara, Y. (1994) Quantity of spray transported by a strong wind over breaking waves, *Proc. 24 th Int. Conf. Coastal Eng., ASCE*, 219-231.
- Toba, Y. (1959) Drop production by bursting of air bubbles on the sea surface (II): Theoretical study on the shape of floating bubbles, *J. Oceanogr. Soc. Japan*, **15**, 121-130.
- Toba, Y. and Tanaka, M. (1963) Study on dry fallout and its distribution of giant sea-salt nuclei in Japan, *J. Meteor. Soc. Japan*, **41**, 135-144.
- Toba, Y. (1965 a) On the giant sea-salt particles in the atmosphere I: General features on the distribution, *Tellus*, **17**, 131-145.

CHAPTER 81

Irregular Wave Kinematics from a Pressure Record

Christopher H. Barker¹ and Rodney J. Sobey²

Abstract:

A local Fourier approximation method is presented for the prediction of the complete kinematics of irregular waves from a submerged pressure trace. The method seeks a potential function and local water surface elevation that fit the pressure record and the full nonlinear free surface boundary conditions very closely in a small window in time. The result is a complete prediction of the kinematics of the waves throughout the water column that satisfies the complete nonlinear equations for irrotational gravity waves. Comparisons with the predictions of steady wave theory are excellent.

Introduction

A knowledge of wave kinematics is necessary for most aspects of coastal engineering. Fluid velocities and accelerations are necessary for the study of the wave loading of structures through the use of the O'Brien-Morison equation. Knowledge of the kinematics near the sea bed are necessary for studies of sediment transport processes. High order steady wave theories are quite successful at the prediction of the kinematics of steady waves, but are not directly applicable to the irregular waves usually found in the field.

Subsurface pressure transducers are a commonly used method for the measurement of waves in the near-shore zone, as they are relatively easy to deploy. They are frequently used in shallow and transitional depth water. Most methods currently in use for the interpretation of these measurements rely on linear wave

¹Doctoral Candidate, Dept. Civil and Environmental Engineering, 412 O'Brien Hall, University of California, Berkeley, CA 94720 USA

²Professor, Dept. Civil and Environmental Engineering, 412 O'Brien Hall, University of California, Berkeley, CA 94720 USA

theory. Linear theory is appealing in that solutions are readily available and can easily be applied to a variety of situations. Unfortunately, linear theory is based on the assumption that wave amplitudes are small. It is also a Stokes theory, with optimum theoretical applicability in deep water. In fact, the cases of most interest in the interpretation of pressure measurements are for large waves in shallow water, exactly the conditions in which linear theory is least adequate.

In this paper, a method is presented for the interpretation of a measured point pressure time history that preserves the full non-linearity of the process, and can be applied to an irregular sea in any depth of water.

Global and Local Approximations

Methods used for the interpretation of irregular wave records fall into two general categories, global and local approximations. Global methods are those that seek a solution that matches an entire measured record, or a single complete measured wave, from trough to following trough, or zero crossing to zero crossing. These methods apply the same frequency and wave number for all z (vertical variation) and t (time).

Local methods seek an approximation to each small local segment of a measured record. In these methods, the frequency and wave number vary, providing a separate solution for each small window in time.

Global Methods

The most commonly used global method for the analysis of irregular waves is spectral analysis, coupled with superposition of linear waves. This method has a number of shortcomings, including the high frequency contamination of the kinematics above the crest (Forristall, 1985; Sobey, 1992). Fundamentally, the difficulties arise from the approximations made by linear wave theory to the free surface boundary conditions. If the full nonlinear free surface boundary conditions are not satisfied, one can expect that the resulting predictions will be inaccurate, particularly near the free surface. Empirical modifications to linear theory have been adopted eg. (Wheeler, 1969), but these no longer conserve mass (Sobey, 1992).

Other global methods rely on zero crossing analysis to identify particular waves that are then analyzed by using steady wave theory for a wave of the same height and period. This approach can provide an order of magnitude estimate for the kinematics, but does not take into account the detail of the record. Dean (Dean, 1965) extended his stream function method to irregular waves, seeking a Fourier expansion for the stream function that fit a water surface record from trough to following trough. While taking into account the detail of the record, the assumption that the wave is globally steady is a major compromise.

Baldock and Swan (Baldock and Swan, 1994) presented a method for the

analysis of a point water surface record that includes unsteady motion. Their method employs a potential function in the form of a double Fourier expansion in time and space. The coefficients of the expansion are found by minimizing the errors in the full non-linear free surface boundary conditions over a grid of nodes in time and space. While comparisons of their results with laboratory data were quite good, the method involves a huge matrix of unknown coefficients and must solve for the water surface far from the actual measurement location. While making no assumptions about the steadiness of the wave field, the method requires an assumed periodicity (usually the length of the record). In order to obtain a good fit to the measured record, a substantial weighting function must be applied to assure that the errors in the boundary conditions are small at the measured location. This need for a weighting function suggests that a local solution may be advantageous.

Local Methods

The Nielsen method (Nielsen, 1986; Nielsen, 1989) uses a local frequency and linear wave theory to find the location of the water surface from a pressure record. Best results were achieved from a stretching method, similar to Wheeler's (Wheeler, 1969), or a semi-empirical transfer function derived from Fourier steady wave theory. In either case, the method does not supply the complete kinematics, and does not satisfy the governing equations.

Fenton (Fenton, 1986) employed a local polynomial approximation to the complex potential function. In this method, the potential function is represented by a separate polynomial in each small window in time. Coefficients of the polynomial are sought that fit the measured pressure record, and the full nonlinear free surface boundary conditions. This approach provides the complete kinematics and satisfies the full governing equations. Based on a polynomial variation with depth, it should work well in shallow water, but may have difficulty in transitional or deep water.

Sobey's Locally Steady Fourier Method (LSFI) (Sobey, 1992) employs a potential function represented by a low order Fourier expansion in a small window in time. It is a method derived for the analysis of a point water surface trace. Local frequency, wave number, and Fourier coefficients are sought that fit the measured record and the full free surface boundary conditions. This method provides the complete kinematics, satisfies the full governing equations, and is successful in all depths of water. The method presented in this paper is an adaptation of Sobey's method to the analysis of a measured pressure trace.

Governing Equations

The formulation of the problem of uni-directional irregular waves is similar to that for classical steady wave theory. The flow is taken to be incompressible

and irrotational. The kinematics can therefore be represented by a potential function, ϕ , where

$$u = \frac{\partial\phi}{\partial x} \qquad w = \frac{\partial\phi}{\partial z} \qquad (1)$$

where u and w are the horizontal and vertical velocities, respectively. Mass conservation then becomes the Laplace equation:

$$\nabla^2\phi = \frac{\partial^2\phi}{\partial x^2} + \frac{\partial^2\phi}{\partial z^2} = 0 \qquad (2)$$

The boundary conditions are the bottom boundary condition (BBC),

$$w = \frac{\partial\phi}{\partial z} = 0 \qquad \text{at} \qquad z = -h \qquad (3)$$

the kinematic free surface boundary condition (KFSBC),

$$w - \frac{\partial\eta}{\partial t} - u \frac{\partial\eta}{\partial x} = 0 \qquad \text{at} \qquad z = \eta \qquad (4)$$

and the dynamic free surface boundary condition (DFSBC),

$$\frac{\partial\phi}{\partial t} + \frac{1}{2}u^2 + \frac{1}{2}w^2 + g\eta - \bar{B} = 0 \qquad \text{at} \qquad z = \eta \qquad (5)$$

where η is the location of the free surface and \bar{B} is the Bernoulli constant.

In steady wave theory, periodic lateral boundary conditions are imposed, forcing the solution to be periodic in space and time. With irregular waves, there is no periodicity. Rather, a solution is sought that fits a local segment of the record, the Laplace equation, bottom boundary condition, and both nonlinear free surface boundary conditions.

A form for the potential function in each window is motivated by Fourier steady wave theory. This is the same form as that used by Sobey (Sobey, 1992).

$$\phi(x, z, t) = U_E x + \sum_{j=1}^J A_j \frac{\cosh jk(h+z)}{\cosh jkh} \sin j(kx - \omega t) \qquad (6)$$

U_E and h are the known depth uniform Eulerian current and water depth, J is the truncation order of the Fourier series, A_j are the local Fourier coefficients, and ω and k are the local fundamental frequency and wave number. This form exactly satisfies mass conservation and the BBC. A different set of parameters is found for each segment of the pressure record. While this form for the potential function is periodic, the periodicity is not defined a priori, but found to fit the record, defining a local frequency and wave number.

Fitting to a Pressure Record

While the potential function provides the complete kinematics, the dynamics are found through the unsteady Bernoulli equation:

$$\frac{\partial \phi}{\partial t} + \frac{1}{2}(u^2 + w^2) + \frac{P_d}{\rho} - \bar{B} = 0 \quad (7)$$

where P_d is the dynamic pressure ($P_d = P - \rho g z$). In steady wave theory, the Bernoulli constant is (Longuet-Higgins, 1975):

$$\bar{B} = g\bar{\eta} + \frac{1}{2}u_b^2 \quad (8)$$

where u_b is the velocity at the bed, and the over-bars indicate time averaging. In this case, it will be different in each window. With z defined to be zero at the mean water level, and Eqn. 6 as the potential function, \bar{B} becomes (Sobey, 1992):

$$\bar{B} = \frac{1}{2}U_E^2 + \frac{1}{4} \sum_j \left(\frac{jkA_j}{\cosh jkh} \right)^2 \quad (9)$$

thus all the terms in Eqn. 7 are defined by the potential function except the dynamic pressure, which is given by the measured record.

Eqns. 6 and 7 apply to many periodic flows. There might be any number of these flows that could produce a given pressure record at a single location. It is the free surface boundary conditions (Eqn. 4 and 5) that identify a potential flow as a surface gravity wave. As the solution sought is a gravity wave, these boundary conditions must be included in the formulation. To include the free surface boundary conditions, the location of the water surface, together with the potential function, become the unknowns in each window.

Locating the water surface

The water surface is defined at N surface nodes in each window ($\eta(t_n), n = 1 \dots N$). The elevation of these nodes is unknown, and will be sought as part of the solution. Eqn. 5 is directly applied at each node. In order to apply Eqn. 4 at the surface, the time gradient is estimated by cubic spline interpolation among these nodes. This provides a smooth and consistent estimate at all locations within the window. The spatial gradient can be computed from the time gradient by assuming that the water surface is locally steady. This assumption follows from the steady form of the potential function, and is the same assumption used by Sobey.

$$\frac{\partial \eta}{\partial x} = -\frac{k}{\omega} \frac{\partial \eta}{\partial t} \tag{10}$$

Including the water surface nodes as part of the sought solution introduces N additional unknowns for a total of $3 + J + N$ unknowns in each window $(k, kx, \omega, A_j, \eta_n)$. Eqn. 4 is applied at the locations between the water surface nodes. Eqn. 5 is applied at each of the nodes, yielding $2N - 1$ additional equations. Eqn. 7 is applied at I nodes on the pressure record $(P_d(t_i), i = 1 \dots I)$ within the local window (see Fig. 1).

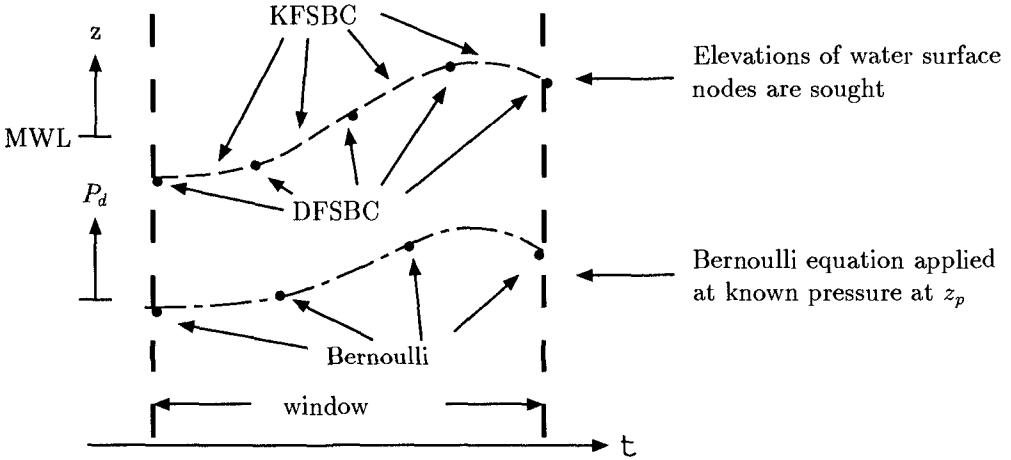


Figure 1: Schematic of system of equations in a window

The problem is uniquely specified for $I + N = 4 + J$ and overspecified for $I + N > 4 + J$. If overspecified, the solution is that which results in the minimum error in all equations, in the least squared sense. Overspecification, with additional nodes on the pressure record, is likely to be advantageous for an actual record to minimize the effect of unavoidable measurement noise.

Computation Methods

Non-dimensionalization

The comparisons of errors of different dimensional quantities would be meaningless. All parameters and variables are scaled by factors computed from physically identifiable parameters. These are the mass density of water, acceleration of gravity, and the mean zero crossing frequency. The characteristic length scale

is g/ω_z^2 , time scale is $1/\omega_z$ and the mass scale is $\rho g^3/\omega_z^6$ where ω_z is the mean zero crossing frequency of the record. The familiar dimensional forms of the equations have been presented in this paper to aid in readability. The unknown parameter, x , appears in the equations only when coupled with the parameter, k . It is simpler to solve for the non-dimensional parameter, kx , essentially a phase parameter in the potential function.

Initial Estimate

The primary process in this LSFI-P method is nonlinear optimization to find the minimum error in a system of nonlinear algebraic equations typically involving 14 equations in 12 unknown parameters. A system as complex as this is likely to have a number of local minima that result in spurious physical solutions. The best way to avoid these solutions, as well as to allow for efficient optimization, is to start with a good estimate for the unknowns in the system, and to have a basic set of criteria for identifying spurious solutions.

The first step in each window is to establish an initial estimate for the optimization procedure. Linear wave theory can be used to produce estimates for the parameters of approximately correct magnitudes.

Nielsen (Nielsen, 1986; Nielsen, 1989) established a method for determining the parameters of a local linear approximation to waves from a pressure record. A similar method is used here. Frequency of a sinusoidal signal of the form $P_d = a \cos(kx - \omega t)$ is available from the second derivative:

$$\omega^2 = -\frac{\partial^2 P_d / \partial t^2}{P_d} \quad \text{or} \quad \omega = \sqrt{-\frac{\partial^2 P_d / \partial t^2}{P_d}} \quad (11)$$

Once the frequency is known, the amplitude and phase of a particular segment of record can be found by rearranging the equation as a linear least squares problem by separating the cosine and sine components:

$$P_d = a \cos(kx - \omega t) = b_1 \cos \omega t + b_2 \sin \omega t \quad (12)$$

The linear terms (a and kx) are a function of ω , reducing the nonlinear problem to one variable (Lawton and Sylvestre, 1971). The estimates for ω , a , and kx are refined by optimizing for the frequency that results in the least error throughout the current window, using Eqn. 11 as a first estimate.

Once the optimum frequency is found, the wave number is estimated from the linear dispersion relation, and the first estimate for the Fourier amplitudes are assigned as follows:

$$A_1 = \frac{a}{\rho \omega \cosh k(h+z) / \cosh kh} \quad A_2 = \alpha A_1 \quad A_j = \alpha A_{j-1} \quad (13)$$

$\alpha = 0.1$ was found to be satisfactory. The location of the water surface is estimated from the linear pressure response function with stretching (Nielsen, 1986).

$$\eta = \frac{P_d \cosh k(h + (P_d/\rho g))}{\rho g \cosh k(h + z)} \quad (14)$$

An estimate for the values of the second time derivative of the record in each window is required. This is accomplished by a least squares fit of a third order polynomial to the record in each window. The derivatives can then be computed from this polynomial. This approach was very successful in the analysis of artificially generated noisy records, resulting in reasonable estimates for the value at the middle of the window, as well as both derivatives at that point.

Optimization

Once there is a reasonable first guess for all the parameters, nonlinear optimization routines can be applied to this system. For the results in this paper, the Levenburg-Marquart algorithm was used as implemented by the Matlab Optimization Toolbox. If the optimization routine successfully finds a minimum, the solution is checked to see if a clearly spurious solution is found. Spurious solutions can be identified by the following criteria: very large or highly variable errors, first order amplitude smaller than higher order amplitudes, unrealistically large or small frequency or wave number. It is unusual for the routine to converge to a spurious solution. It is far more common for the routine not to converge at all.

If no solution or a spurious solution is found, it is necessary to revise the parameters of the solution to make another attempt. For the next attempt, the window width is increased by a factor of 1.5, and the procedure is repeated. If this is not successful, the window width is increased once more to twice the standard width. When increasing the window width is not successful, the order of the potential function is decreased until a solution is found. If none of these adjustments result in a reasonable solution, the window is skipped, and future analysis must be interpolated through that point. These adjustments are most likely to be needed in the long, flat trough of a shallow water wave, where the window needs to be expanded to include some curvature to indicate the frequency. There can also be difficulties near zero crossings, where there is little curvature in the record, and the effects of amplitude and frequency are not independent. Widening the window to include more of the surrounding record is generally successful in this situation as well.

Another complication can be a record that is symmetric about the crest of a wave. In this case, the equations on either side of the crest are not independent. This situation is unlikely to arise in a field record, and can easily be accommodated by using an asymmetric distribution of points in that window.

Results

In order to remove complications from measurement error in the initial testing of the method, pressure records generated by Fourier Steady wave theory (Sobey, 1989) were used. This also has the advantage of providing a solution with the complete kinematics, to compare with results from the LSFI-P method. High order Fourier wave theory is essentially an exact solution for irrotational steady waves that can be applied at any depth (Rienecker and Fenton, 1981; Sobey, 1989). Fig. 2 presents the results after the first guess, before optimization. This is a window near the crest of a steep, shallow water wave generated by 18th order Fourier theory. The predictions for the dynamic pressure are approximately correct, and the water surface estimate is in the vicinity of the actual water surface. Note that the location of the actual surface is given in the plot, but it is not available to help determine the solution. These points were all generated by the method outlined in the previous section, with only the pressure record as a guide. The third plot shows the non-dimensional errors in the Bernoulli equation and the free surface boundary conditions. The errors are of order .03 and show a systematic pattern, particularly in the Bernoulli equation. It is clear from these plots that a better solution can be found.

The results after optimization are given in Fig. 3. At this point the prediction for the dynamic pressure is essentially exact. This is virtually always the case, as the pressure record is available, and the parameters are found to fit that record. The predictions for the water surface are also extremely close. This is an impressive achievement, as location of the water surface was found only by minimizing the errors in the free surface boundary conditions. In this case, the LSFI-P method was able to accurately capture the crest of a steep shallow water wave.

Fig. 4 shows the results of the method for the complete wave. The parameters of the wave are: 5m water depth, 3m wave height, and 10s period, with the pressure record measured on the bottom. The LSFI-P method finds the water surface and the kinematics on the surface essentially exactly. While these results show the complete wave, it is important to keep in mind that each of the indicated points is in the center of a separate window, and was computed completely independently of the other windows. In this case, the standard window width was 2s, with a sixth order potential function and seven water surface nodes. The 2s window width is one fifth of the period of the wave, and is a reasonable length of time to extend the locally steady approximation. It is not expected that the standard window width will exceed about one fifth of the zero crossing period of a record, nor the solution to be of order higher than six.

The dotted lines on the plot are the water surface and horizontal velocity at the surface as predicted by the linear wave theory pressure response function. It is clear that this method completely misses the high, sharp crest, and the large velocities at the crest.

Fig. 5 shows the results of the LSFI-P method for an entire deep water wave.

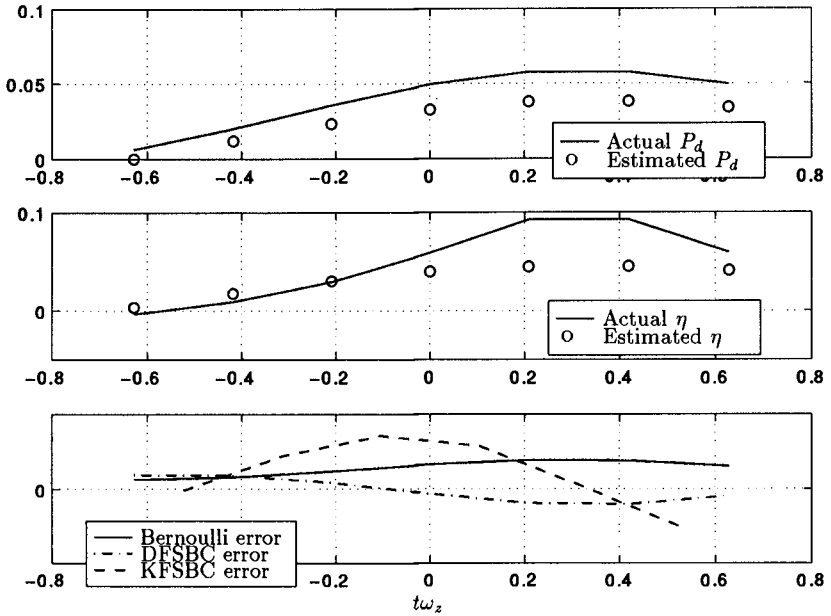


Figure 2: Results in a window after first estimate

The wave was generated by 12th order Fourier wave Theory, with parameters: 100m water depth, 10m wave height, and 10s period, with the pressure record measured 10m below the mean water level. Standard window width is 1s, with a fourth order potential function and five water surface nodes. Once again the LSF1-P solution matches the actual solution exactly. In the case of deep water, linear wave theory performs fairly well on steady waves, but is not applicable to irregular records, as there is no clearly defined single frequency or wave number.

Conclusions

While the given results are on artificially generated steady wave records, they show the potential for the method for a variety of conditions. In the case of steady waves, the LSF1-P method accurately computed the detail of the wave, using only data from a small window in time. In particular, the method was able to capture the pronounced sharp crest of a steep, shallow water wave. It is expected that it will perform well on segments of an irregular record.

The analysis of regular waves provides guidelines for the parameters to be

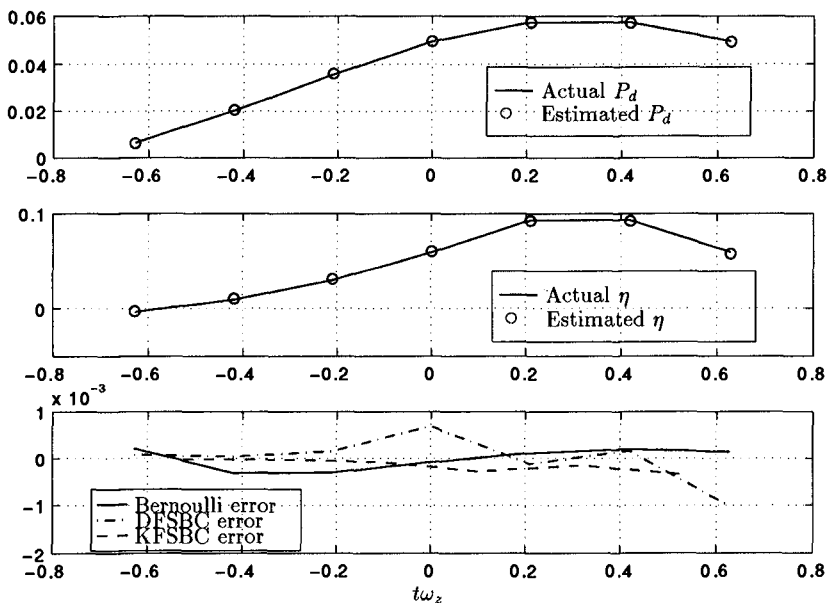


Figure 3: Final results in a window

used in the analysis of irregular waves. Higher order solutions and wider windows must be used in shallow water than in deep. Window widths of one fifth of the zero crossing period and a sixth order potential function are adequate for the shallowest waves, and window widths as small as one tenth of the zero crossing period and a third order potential function are adequate for deep water.

The Locally Steady Fourier approximation for irregular waves is an effective method for the computation of the kinematics of irregular waves from a point pressure record. The method results in a complete description of the water surface and kinematics of the waves that fit the given pressure record and the full free surface boundary conditions very closely in a small window in time. Comparisons with the predictions of steady wave theory are excellent.

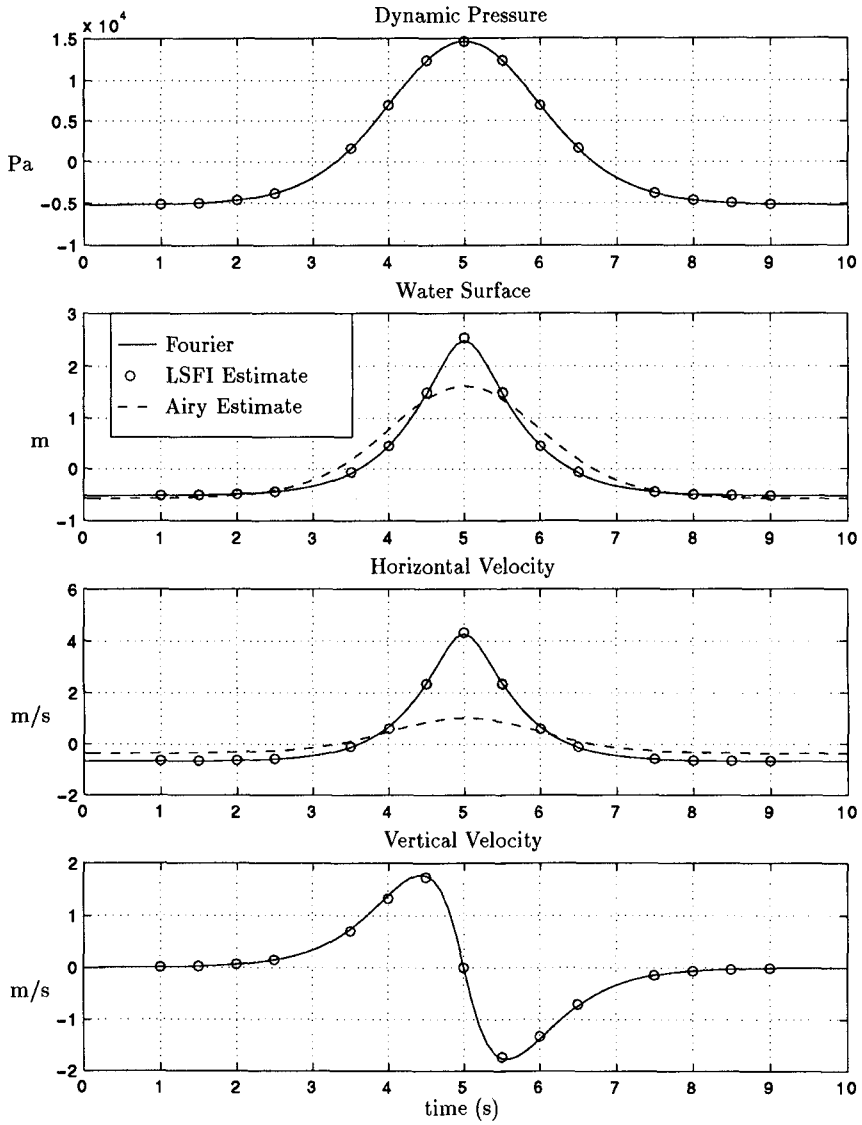


Figure 4: Results for a shallow water wave

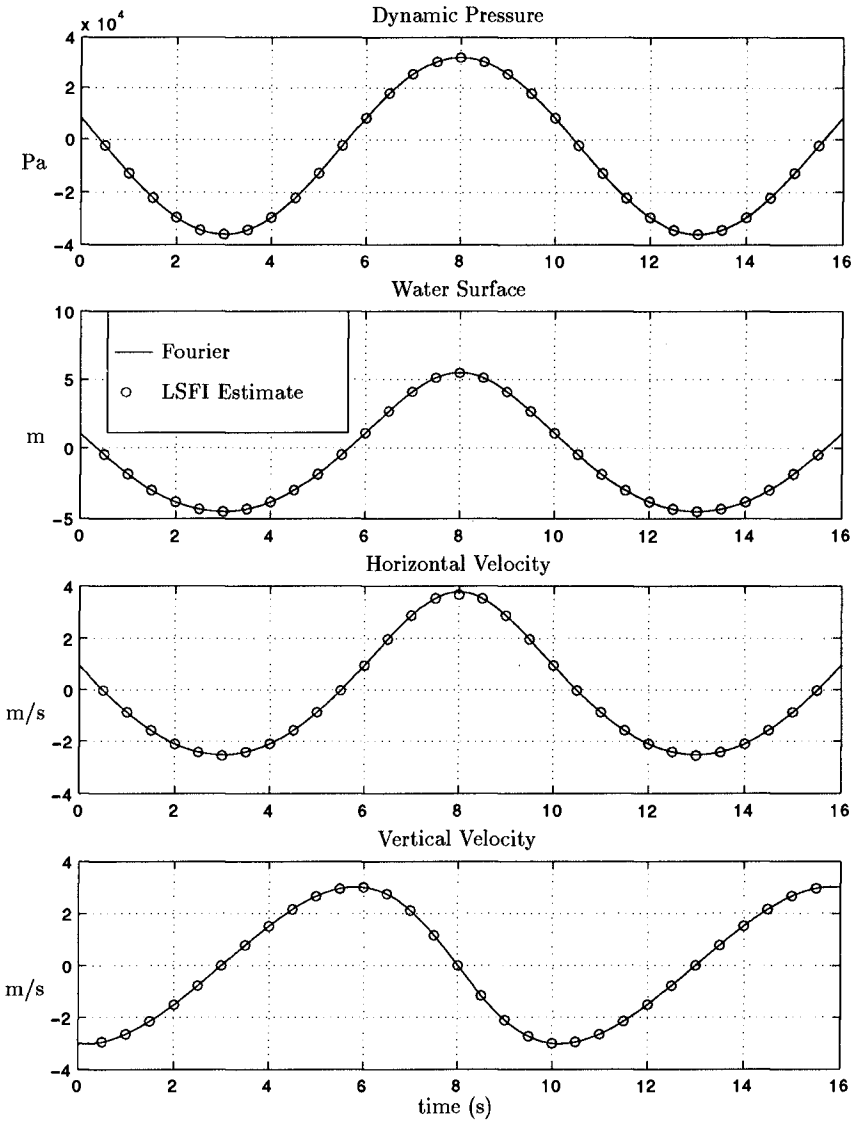


Figure 5: Results for a deep water wave

Acknowledgements

The work described and the results presented herein, unless otherwise noted, were obtained from research funded by the Scour Holes at Inlet Structures work unit of the U.S. Army Corps of Engineers, Coastal Engineering Research Center. Permission was granted by the Chief of Engineers to publish this information.

References

- Baldock, T. E. and Swan, C. (1994). Numerical calculations of large transient water waves. *Applied Ocean Research*, 16:101–112.
- Dean, R. G. (1965). Stream function representation of nonlinear ocean waves. *Journal of Geophysical Research*, 70:4561–4572.
- Fenton, J. D. (1986). Polynomial approximation and water waves. In *Proceedings of the International Conference on Coastal Engineering*, pages 384–396. ASCE.
- Forristall, G. Z. (1985). Irregular wave kinematics from a kinematic boundary condition fit. *Applied Ocean Research*, 7:202–212.
- Lawton, W. H. and Sylvestre, E. A. (1971). Elimination of linear parameters in nonlinear regression. *Technometrics*, 13(3):461–467.
- Longuet-Higgins, M. S. (1975). Integral properties of periodic gravity waves of finite amplitude. *Proceedings of the Royal Society of London, Series A*, 342:157–174.
- Nielsen, P. (1986). Local approximations: A new way of dealing with irregular waves. In *Proceedings of the International Conference on Coastal Engineering*, volume 115, pages 384–396.
- Nielsen, P. (1989). Analysis of natural waves by local approximations. *Journal of Waterway, Port, Coastal and Ocean Engineering*, 115:384–396.
- Rienecker, M. and Fenton, J. (1981). A Fourier approximation for steady water waves. *Journal of Fluid Mechanics*, 135:301–321.
- Sobey, R. J. (1989). Variations on Fourier wave theory. *International Journal for Numerical Methods in Fluids*, 9:1453–1467.
- Sobey, R. J. (1992). A local Fourier approximation for irregular wave kinematics. *Applied Ocean Research*, 14:93–105.
- Wheeler, J. D. (1969). Method for calculating forces produced by irregular waves. In *Offshore Technology Conference*, pages 71–82.

CHAPTER 82

Nonlinear Refraction-Diffraction of Surface Waves over Arbitrary Depths

Serdar Beji¹ and Kazuo Nadaoka²

Abstract

A nonlinear dispersive wave model recently introduced by the authors is used for sample simulations of directional wave transformations over gently varying depths. Various forms of the generic equation are presented first, and the dispersion and nonlinear characteristics of the model are investigated analytically. Following the numerical descriptions, the experimental data for linear wave propagation over a circular shoal and for nonlinear wave propagation over a topographical lens are compared to the model predictions with satisfactory agreements. Finally, as a demonstration of the unified character of the model, the unidirectional version of the wave equation is implemented for simulating the gradual transformation of an initially second-order Stokes wave train over decreasing depth into a cnoidal wave train.

Introduction

The mean wave-number of a wave field propagating from deep to shallow water changes gradually and, when subject to spatial non-uniformities and non-linearity, causes quite profound modifications in the overall wave pattern. For an accurate description of such phenomena it is essential that a good wave model accommodates the relevant physical mechanisms. One such a model is Berkhoff's (1972) mild-slope equation, which has been used successfully in the last two and half decades. The model however has a few shortcomings, notably its restriction to linear, monochromatic waves. The time-dependent form of this equation (Smith and Sprinks, 1975) performs better in representing a narrow-banded wave field but cannot account for nonlinear effects which are quite appreciable for waves propagating on shallow waters or over sand-bars (Freilich and Guza 1984, Byrne 1969, Young 1989). In the nearshore zone the Boussinesq-type models are probably the best choice; however, their weak

¹ Assoc. Prof., Department of Naval Architecture and Ocean Engineering, Istanbul Technical University, Maslak 80626, Istanbul, Turkey

² Professor, Graduate School of Information Science and Engineering, Tokyo Institute of Technology, 2-12-1 O-okayama, Meguro-ku, Tokyo 152, Japan

dispersion characteristics imposes limits on the applicable range of these equations. Despite the successful reports of extending their validity range (Witting 1984, Madsen *et al.* 1991, Nwogu 1993, Beji and Nadaoka, 1996), due to the certain assumptions introduced in their derivation, they remain finite-depth equations. The existing wave models then provide only partial representations of the observed effects: the mild-slope type equations are usable only for linear, narrow-banded waves while the Boussinesq equations are restricted by their applicable depth.

In order to overcome the drawbacks of the available wave models; namely, the linearity, narrow-bandedness, and depth-limitation, Nadaoka *et al.* (1994, 1997) advanced a new approach which was termed as the *multiterm-coupling technique*. They expressed the velocity field as a sum, each term comprising a hyperbolic vertical-dependence function and a corresponding velocity vector independent of depth. This expression was then used in nonlinear forms of the depth-integrated continuity and momentum equations in conjunction with the Galerkin procedure which ensured the solvability. The result was a set of wave equations that could describe the evolutions of a broad-banded nonlinear wave field propagating over arbitrary depths. These general equations have been shown to produce the aforementioned well-known wave models as degenerate cases besides generating the second-order Stokes waves on deep water. Here, the single-component (*i.e.*, a single-term expansion of the velocity field) equations in combined form as given by Beji and Nadaoka (1997) is used.

Wave Model and Its Various Forms

Nadaoka *et al.* (1997) give the following continuity and momentum equations as the single-component wave model, correct to the second-order in non-linearity:

$$\eta_t + \nabla \cdot \left[\left(\frac{C_p^2}{g} + \eta \right) \mathbf{u} \right] = 0, \quad (1)$$

$$\begin{aligned} & C_p C_g \mathbf{u}_t + C_p^2 \nabla \left[g\eta + \eta w_t + \frac{1}{2} (\mathbf{u} \cdot \mathbf{u} + w^2) \right] \\ &= \frac{C_p(C_p - C_g)}{k^2} \nabla (\nabla \cdot \mathbf{u}_t) + \nabla \left[\frac{C_p(C_p - C_g)}{k^2} \right] (\nabla \cdot \mathbf{u}_t), \end{aligned} \quad (2)$$

where η is the free surface displacement, $\mathbf{u}(u, v)$ the two-dimensional horizontal velocity vector and w the vertical component of the velocity both at the still water level $z = 0$. C_p , C_g , and k are respectively the phase and group velocities, and wave-number computed according to linear theory for a prescribed incident frequency ω and a local depth h . g is the gravitational acceleration, ∇ stands for the horizontal gradient operator with components $(\partial/\partial x, \partial/\partial y)$, and subscript t indicates partial differentiation with respect to time. Note that (1) and (2) are formulated for varying depth and therefore C_p , C_g , and k are in general spatially varying quantities. The above single-component equations may be considered as evolution equations that can simulate weakly-nonlinear, narrow-banded wave transformations over arbitrary depths. Compared with the Boussinesq-type equations, these equations are superior in the sense that they may be used without any restriction on the depth.

Eliminating \mathbf{u} from (1) and (2) to obtain a wave equation for the surface displacement η results in (Beji and Nadaoka, 1997):

$$C_g \eta_{tt} - C_p^3 \nabla^2 \eta - \frac{(C_p - C_g)}{k^2} \nabla^2 \eta_{tt} - C_p \nabla(C_p C_g) \cdot \nabla \eta - \frac{3}{2} g C_p \left(3 - 2 \frac{C_g}{C_p} - \frac{k^2 C_p^4}{g^2} \right) \nabla^2 (\eta^2) = 0. \quad (3)$$

Equation (3), named as the *time-dependent nonlinear mild-slope equation*, is the wave model adopted in this work. For a prescribed wave frequency and a definite water depth the wave number and the phase and group celerities are determined according to the relations given by linear theory.

Instead of eliminating the velocity field, invoking the existence of a two-dimensional potential function at the still water level $z = 0$ such that $\mathbf{u} = \nabla \phi$ and eliminating the surface elevation from (1) and (2), one obtains

$$C_g \phi_{tt} - C_p^3 \nabla^2 \phi - \frac{(C_p - C_g)}{k^2} \nabla^2 \phi_{tt} - C_p \nabla(C_p C_g) \cdot \nabla \phi + \frac{3}{2} C_p \left(1 - \frac{k^2 C_p^4}{g^2} \right) [(\nabla \phi)^2]_t = 0, \quad (4)$$

where the obvious approximation $(\nabla \phi)^2 \simeq -k^2 \phi^2$ in the nonlinear term is intentionally avoided since ϕ itself is not a directly measurable physical quantity and cannot be specified uniquely in the computations. Note also that for infinitely deep water waves $C_p^2 = g/k$ hence the coefficient of the nonlinear term in (4) vanishes, indicating a linear velocity potential for the second-order waves as in the Stokes second-order theory. The surface displacement on the other hand remains nonlinear regardless of the relative depth.

The linearized form of (3) or (4) is comparable with the time-dependent mild-slope equation of Smith and Sprinks (1975) but equation (3) can simulate a relatively broader wave spectrum as shown by Beji and Nadaoka (1997).

It is possible to extract from (3) a wave equation describing only the one-dimensional, right-going waves (Beji and Nadaoka, 1997):

$$C_g \eta_t + \frac{1}{2} C_p (C_p + C_g) \eta_x - \frac{(C_p - C_g)}{k^2} \eta_{xxt} - \frac{C_p (C_p - C_g)}{2k^2} \eta_{xxx} + \frac{1}{2} [C_p (C_g)_x + (C_p - C_g) (C_p)_x] \eta + \frac{3}{4} g \left(3 - 2 \frac{C_g}{C_p} - \frac{k^2 C_p^4}{g^2} \right) (\eta^2)_x = 0, \quad (5)$$

which may be shown to include the KdV equation as a special case as well as admitting the second-order Stokes waves as solution in deep water.

The counterpart of (5) in terms of the one-dimensional potential is

$$C_g \phi_t + \frac{1}{2} C_p (C_p + C_g) \phi_x - \frac{(C_p - C_g)}{k^2} \phi_{xxt} - \frac{C_p (C_p - C_g)}{2k^2} \phi_{xxx} + \frac{1}{2} [C_p (C_g)_x + (C_p - C_g) (C_p)_x] \phi + \frac{3}{4} C_p \left(1 - \frac{k^2 C_p^4}{g^2} \right) (\phi_x)^2 = 0. \quad (6)$$

It should be remarked that the linear dispersion characteristics of (5) and (6) are better than those of (3) and (4). More specifically, (5) and (6) can simulate waves with broader spectral width than the generic equations (3) and (4). The details on the subject will be reported separately.

Solitary and Stokes Second-Order Waves

It has already been indicated that the wave model provides a unified approach in describing the nonlinear waves at arbitrary water depths. Simple analytical investigations are now presented to clarify the nonlinear characteristics of the model regarding the solitary and Stokes second-order waves. We begin with the solitary waves.

Let us seek a solution of the form $\eta = H \cosh^{-2}[(x \pm C_s t)/l_s]$, where H is the prescribed wave height, l_s and C_s are respectively the length scale and the phase speed of the solitary wave which are yet unknown quantities to be determined from the wave equation (3). The form adopted is the lowest-order solution, the general expression is an infinite sum of hyperbolic cosine functions of higher powers (see Fenton, 1972); for the present purposes however it will suffice. Substituting this expression in (3) and solving for l_s and C_s give

$$l_s = \left[\frac{6(C_p - C_g)(C_p^2 + \frac{2}{3}\beta H)}{\beta k^2 C_g H} \right]^{1/2}, \quad C_s = \left[\frac{C_p}{C_g} \left(C_p^2 + \frac{2}{3}\beta H \right) \right]^{1/2} \quad (7)$$

where $\beta = \frac{3}{2}g \left(3 - 2\frac{C_g}{C_p} - \frac{k^2 C_p^4}{g^2} \right)$ is the coefficient of the nonlinear term in (3) divided by C_p . A matter of historic interest is obvious from the form of l_s . It becomes zero for $C_p = C_g$; that is, nonlinear-nondispersive waves cannot maintain a permanent form simply because there exists no dispersivity to counterbalance the steepening action of nonlinearity. However, allowing the lowest-order dispersion by letting $C_p \simeq (gh)^{1/2}(1 - k^2 h^2/6)$ and $C_g \simeq (gh)^{1/2}(1 - k^2 h^2/2)$, as in the Boussinesq theory, is sufficient to obtain a permanent form. If these approximate forms are used in (7) and the higher-order dispersion contributions are dropped,

$$l_s \simeq \left[\frac{4h^3(1 + H/h)}{3H} \right]^{1/2}, \quad C_s \simeq [g(h + H)]^{1/2}, \quad (8)$$

which are in complete agreement with the classical expressions (Miles, 1980). l_s is the same as Rayleigh's (1876) result and for small H/h it may be replaced with $(4h^3/3H)^{1/2}$, which is the well-known expression.

Assuming that the wave equation (3) admits the second-order Stokes waves as solution we let $\eta = a \cos(k_s x \pm \omega t) + b \cos 2(k_s x \pm \omega t)$ and substitute this expression into (3) to determine the unknown wave number k_s and the second-harmonic amplitude b . The primary wave amplitude a and the frequency ω are taken to be known. Equating the zeroth- and first-order terms to zero gives

$$k_s^2 = k^2, \quad b = \frac{\beta a^2}{6C_p(C_p - C_g)}, \quad (9)$$

where the interaction of the primary wave with the second-harmonic is excluded in the above analysis to be consistent with the perturbation approach of Stokes. Note, for deep water waves $C_p = (g/k)^{1/2}$, $C_g = C_p/2$, and $\beta = \frac{3}{2}g$ hence $b = \frac{1}{2}ka^2$, which is the same as the second-order Stokes theory predicts.

Equation (3) is an evolution equation and therefore, unlike a sharply truncated perturbation solution, produces higher-order nonlinear dispersion effects which are partially correct. If the term produced through the interaction of the primary wave with the second-harmonic is retained, k_s becomes

$$k_s^2 = k^2 \left(1 + \frac{\beta b}{C_p C_g} \right)^{-1}, \quad (10)$$

where b is as given in (9). For infinitely deep water waves equation (10) may be approximately written as $k_s \simeq (1 - \frac{3}{4}k^2 a^2)k$, which is slightly at variance with the Stokes' third-order result $k_s \simeq (1 - k^2 a^2)k$ (approximated for small ka). We may then conclude that the partially correct third-order nonlinear effects produced by essentially second-order wave equation (3) is a good approximation to the Stokes third-order theory. This point has been verified through numerical simulations as well (Beji and Nadaoka, 1997).

Numerical Modeling

Equation (3) is first manipulated into the following form:

$$\begin{aligned} n\eta_{tt} - C_p^2 \nabla^2 \eta - \frac{C_p^2(1-n)}{\omega^2} \nabla^2 \eta_{tt} - \nabla(nC_p^2) \cdot \nabla \eta \\ - \frac{3}{2}g \left(3 - 2n - \frac{\omega^2 C_p^2}{g^2} \right) \nabla^2 (\eta^2) = 0, \end{aligned} \quad (11)$$

where ω is the prescribed dominant wave frequency and $n = C_g/C_p$. Compared with (3) equation (11) is computationally preferable as it requires the storage of only n and C_p (or C_p^2) over the computational domain instead of k , C_p , C_g . Three-time-level centered finite difference approximations were used for the discretization of (11) which resulted in implicit schemes both in x - and y -directions. The three-point-averaging formulation of Zabusky and Kruskal (1965) was used in evaluating the spatial derivatives of the nonlinear terms, as it improved the robustness of the scheme. For computational efficiency an iterative approach was adopted and the domain was swept in the x - and y -directions separately, treating the crosswise new time level variables known by using the last available values. Giving only the time derivatives in discretized form, the x -sweep equation is

$$\begin{aligned} n \frac{(\eta^{k+1} - 2\eta^k + \eta^{k-1}))}{\Delta t^2} - \frac{C_p^2(1-n)}{\omega^2} \frac{(\eta_{xx}^{k+1} - 2\eta_{xx}^k + \eta_{xx}^{k-1}))}{\Delta t^2} \\ = \frac{C_p^2(1-n)}{\omega^2} \frac{(\eta_{yy}^{k+1} - 2\eta_{yy}^k + \eta_{yy}^{k-1}))}{\Delta t^2} + C_p^2 (\eta_{xx}^k + \eta_{yy}^k) \\ + (nC_p^2)_x \eta_x^k + (nC_p^2)_y \eta_y^k + \frac{3}{2}g \left(3 - 2n - \frac{\omega^2 C_p^2}{g^2} \right) [(\bar{\eta}^k \bar{\eta}^k)_{xx} + (\bar{\eta}^k \bar{\eta}^k)_{yy}], \end{aligned} \quad (12)$$

in which the superscript k denotes the time level and $\bar{\eta}^k = (\eta_{i+1,j}^k + \eta_{i,j}^k + \eta_{i-1,j}^k)/3$ with i and j denoting the spatial nodes in the x and y - directions, respectively. The new time level values η_{yy}^{k+1} 's appearing on the right-hand side of (12) are treated as known by using the last computed values so that η^{k+1} and η_{xx}^{k+1} 's appearing on the left-hand side are the only unknowns. The resulting matrix equation is tridiagonal and can be solved quite efficiently.

Similarly, the y -sweep equation is

$$\begin{aligned} & n \frac{(\eta^{k+1} - 2\eta^k + \eta^{k-1})}{\Delta t^2} - \frac{C_p^2(1-n)}{\omega^2} \frac{(\eta_{yy}^{k+1} - 2\eta_{yy}^k + \eta_{yy}^{k-1})}{\Delta t^2} \\ & = \frac{C_p^2(1-n)}{\omega^2} \frac{(\eta_{xx}^{k+1} - 2\eta_{xx}^k + \eta_{xx}^{k-1})}{\Delta t^2} + C_p^2 (\eta_{xx}^k + \eta_{yy}^k) \\ & + (nC_p^2)_x \eta_x^k + (nC_p^2)_y \eta_y^k + \frac{3}{2}g \left(3 - 2n - \frac{\omega^2 C_p^2}{g^2} \right) [(\bar{\eta}^k \bar{\eta}^k)_{xx} + (\bar{\eta}^k \bar{\eta}^k)_{yy}], \end{aligned} \tag{13}$$

in which $\bar{\eta}^k = (\eta_{i,j+1}^k + \eta_{i,j}^k + \eta_{i,j-1}^k)/3$. η^{k+1} and η_{yy}^{k+1} 's appearing on the left-hand side are the only unknowns. The η^{k+1} 's obtained from (12) are only the first estimates, which are used on the right-hand side of (13) for improved computations. Since the x -direction is taken as the main wave propagation direction, equation (12) is solved once more using the updated new time values obtained from (13). In all the computational tests presented later further iterations brought no improvements so it was concluded that three sweeps (x , y , and x again) would be enough for most problems.

Equation (5) may likewise be manipulated into a computationally efficient form

$$\begin{aligned} & n\eta_t + \frac{1}{2}C_p(1+n)\eta_x - \frac{C_p^2}{\omega^2}(1-n)\eta_{xxt} - \frac{C_p^3}{2\omega^2}(1-n)\eta_{xxx} \\ & + \frac{1}{2} [(C_p)_x + C_p n_x] \eta + \frac{3}{4} \frac{g}{C_p} \left(3 - 2n - \frac{\omega^2 C_p^2}{g^2} \right) (\eta^2)_x = 0, \end{aligned} \tag{14}$$

where n and C_p are the only variables to be stored. Equation (14) yields an implicit scheme when three-time-level finite difference approximations are used for replacing the derivatives:

$$\begin{aligned} & n \frac{(\eta^{k+1} - \eta^{k-1})}{2\Delta t} - \frac{C_p^2}{\omega^2}(1-n) \frac{(\eta_{xx}^{k+1} - \eta_{xx}^{k-1})}{2\Delta t} \\ & = \frac{1}{2}C_p(1+n)\eta_x^k - \frac{C_p^3}{2\omega^2}(1-n)\eta_{xxx}^k + \frac{1}{2} [(C_p)_x + C_p n_x] \eta^k \\ & + \frac{3}{4} \frac{g}{C_p} \left(3 - 2n - \frac{\omega^2 C_p^2}{g^2} \right) (\bar{\eta}^k \bar{\eta}^k)_x. \end{aligned} \tag{15}$$

Sample Simulations

The first simulation is linear wave propagation over a circular shoal. This experiment was designed and carried out by Ito and Tanimoto (1972) to test their numerical wave model. The shoal was constructed as concentric circles whose centers were located three wavelengths away from the incoming boundary. The width of the wave flume was $6L_o = 2.4$ m, where $L_o = 0.4$ m is the incident wavelength. Analytically, the water depth h may be expressed as

$$\begin{aligned} h &= h_c + e_o r^2 & \text{for } r < R \\ h &= h_o & \text{for } r \geq R \end{aligned}$$

where

$$\begin{aligned} r^2 &= (x - x_c)^2 + (y - y_c)^2, \\ e_o &= (h_o - h_c)/R^2. \end{aligned} \quad (16)$$

Here, $R = 2L_o$ is the shoal radius, $h_o = 0.15$ m the water depth outside the shoal, $h_c = 0.05$ m the water depth at the center of the shoal located at $(x_c = 3L_o, y_c = 3L_o)$. Thus, the depth to the wavelength ratio at the incoming boundary was $h_o/L_o = 0.375$, which reduced to $h_c/L_o = 0.125$ at the shoal center.

Ito and Tanimoto (1972) performed their experiments for three different incident wave height to wavelength ratios $H_o/L_o = 0.016, 0.026, \text{ and } 0.035$. In the computations however, the selected wave height was immaterial because the linearized form of (11) was used. The computations were done with $\Delta x = L_o/10$, $\Delta y = L_o/6$, and $\Delta t = T/10$. Higher resolutions were found to be unnecessary as the results changed very little. An equally important point is the computational time which for this case was no more than a few minutes on a personal computer. This computational efficiency applied to nonlinear cases as well since the inclusion of nonlinearity amounts to only quasi-linear additions appearing on the right-hand sides of equations (12) and (13). A perspective view of the fully-developed wave field is depicted in figure 1, after 20 wave periods elapsed from the commencement of the computation.

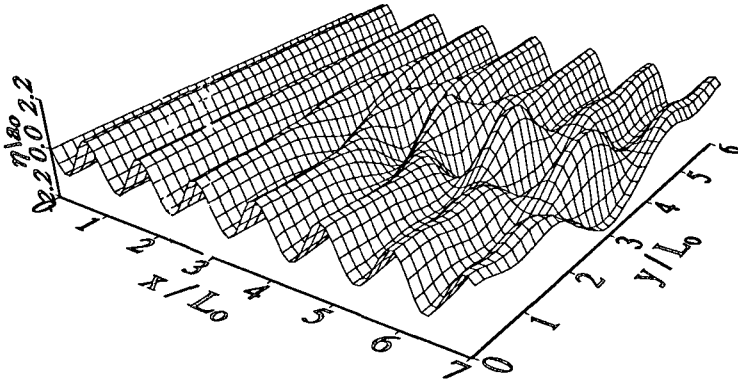
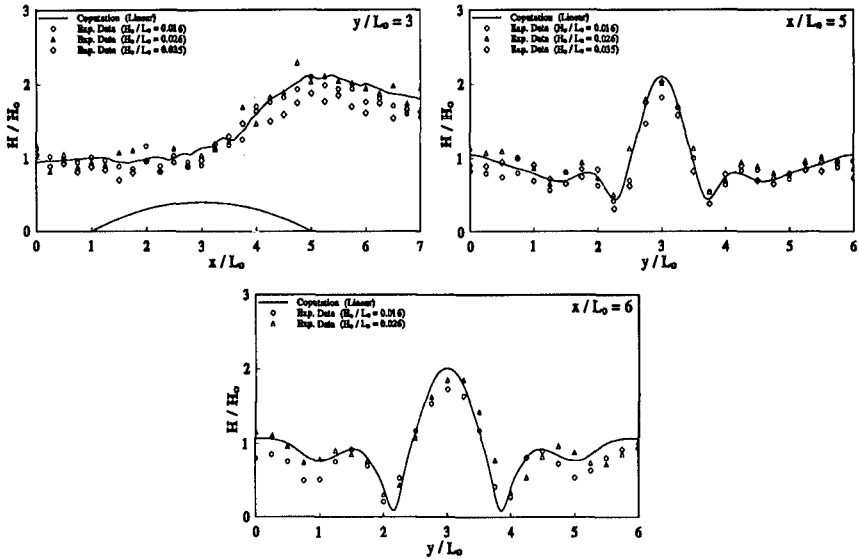


Figure 1: Perspective view of the fully developed wave field over a circular shoal.

In figures 2a, 2b, and 2c, the nondimensional wave height variations along the centerline and across the wave tank are compared with the measurements. As it is seen, the computational results agree remarkably well with the measurements.

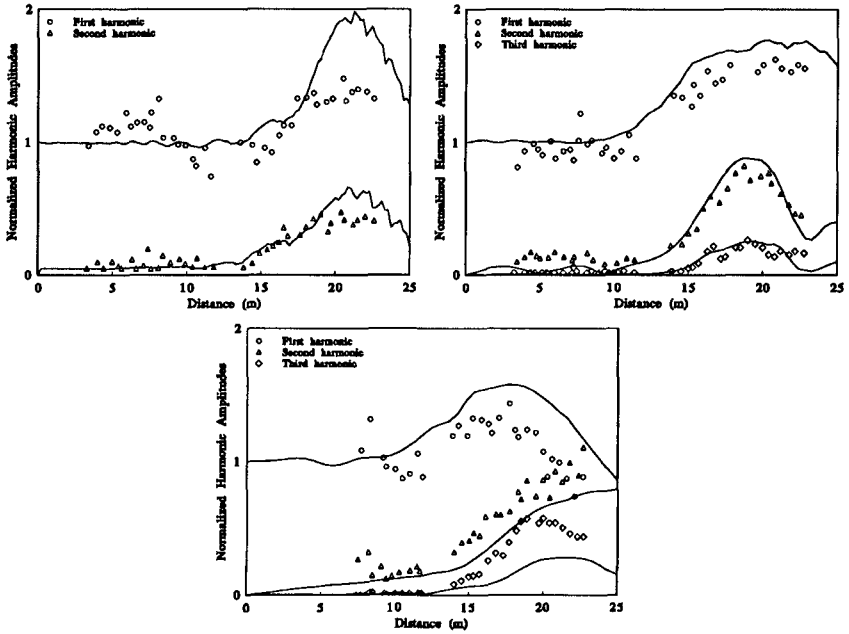


Figures 2a, b, c: Comparisons of the measured and computed wave-height variations along the centerline $y/L_0 = 3$, across the wave tank at $x/L_0 = 7$ and at $x/L_0 = 6$.

The second case is the computation of wave convergence over a bottom topography that acts as a focusing lens (Whalin, 1972). The wave tank used in the experiments was 25.6 m long and 6.096 m wide. In the middle portion of the tank eleven semicircular steps were evenly spaced to form a topographical lens. The equations describing the topography are given in Whalin (1972).

Three sets of experiments were conducted by generating waves with periods $T = 1, 2,$ and 3 seconds and the harmonic amplitudes along the centerline of the wave tank were measured at various stations. For all three cases the computations were performed with a span-wise resolution Δy of $1/10$ of the wave tank width. Since the bathymetry is symmetric with respect to the centerline, only one-half of the tank is discretized. The no-flux boundary conditions are used along the centerline and the side-wall. Figure 3a compares the computed harmonic amplitudes with the measured data for the incident wave period $T = 1$ second and the wave amplitude $a_0 = 1.95$ cm. The time-step and the x -direction resolution were $\Delta t = T/25$ and $\Delta x = L_m/25$ with L_m denoting the mean wavelength computed as the average of the deep-water and shallow-water wavelengths. In figure 3b the case for $T = 2$ seconds and $a_0 = 0.75$ cm is shown, the resolutions were $\Delta t = T/30$ and $\Delta x = L_m/30$. Figure 3c gives the comparisons for $T = 3$ second waves with the deep water wave amplitude $a_0 = 0.68$ cm. Since the harmonic amplitudes were comparable with the primary wave amplitude, it was necessary to adopt somewhat higher resolutions and therefore $\Delta t = T/35$ and $\Delta x = L_m/35$ for this last case.

Figures 3a, b, and c show that the agreements of the computations with the measurements are not as good as the previous case; nonetheless the overall model predictions appear to be acceptable. For nonlinear directional waves, a better numerical approach is expected to yield better results, as the present numerical scheme has been observed to be sensitive (unlike the linear case) to the adopted resolution when the waves were nonlinear.



Figures 3a, b, c: Comparisons of the measured (scatter) and computed (solid line) harmonic amplitude variations along the centerline of the wave tank for $T = 1$ s (top left), $T = 2$ s (top right), and $T = 3$ s (bottom) waves.

To give an idea about the wave patterns, a perspective view of the fully-developed wave field is given in figure 4 for $T = 2$ second waves.

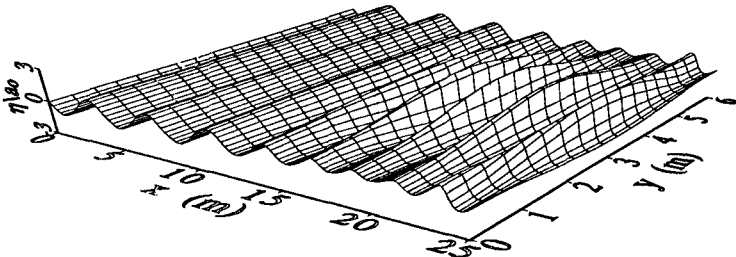
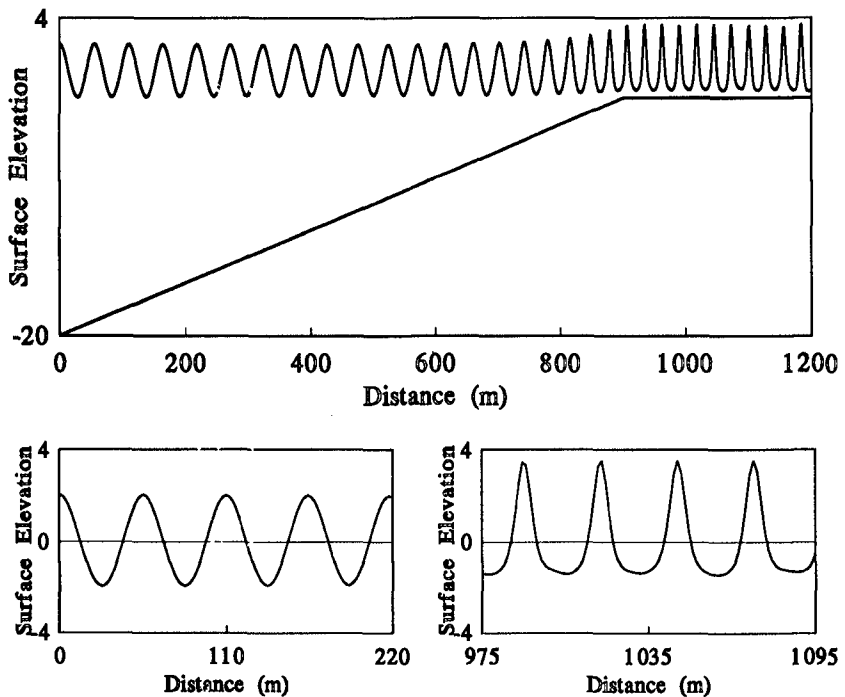


Figure 4: Perspective view of the fully-developed nonlinear wave field over a topographical lens ($T = 2$ s waves).

In order to demonstrate the wide applicable range of the proposed wave model we shall now consider the transformation of an initially second-order Stokes wave train into a cnoidal wave train over uniformly decreasing depth with a constant slope of 1:50. The water depth in the deep section is 20 m and after a distance of 900 m it reduces to 2 m. The incident wave is a second-order Stokes wave with $T = 6$ s and $kH_0 = 0.1$. The initial steepness was chosen small so that an unacceptably large wave steepness in the shallowest region could be prevented.

The computations were done with $\Delta t = T/40$ and $\Delta x = L/40$. Figure 5a shows the spatial variation of the initially second-order Stokes wave as it propagates over the slope. In the deeper region the wave train does not yet feel the bottom so it travels without change of form for more than 500 m. Then, the finite-depth effect begins to steepen the waves. Finally, when the waves reach the shallowest region they are much steeper $H/h = 0.55$ and resemble to the cnoidal waves rather than the Stokes waves, as it can clearly be seen from the closer views given in the figures 5b and 5c. Indeed, the computations with the Stokes theory yields a very unacceptable wave form for this shallow depth as the theory virtually breaks down. Unlike the Stokes theory, the coefficients of the wave model adjusts properly according to the local depth hence enable the model simulate the proper wave form for the depth concerned.



Figures 5a, b, c: Transformation of an initially second-order Stokes wave train into a cnoidal wave train over a uniformly decreasing water depth. The two closer views show respectively the deep and shallow water regions. (Vertical scale is arbitrary.)

Concluding Remarks

Various forms of a recently proposed nonlinear refraction-diffraction model have been presented along with analytical investigations examining its nonlinear and dispersion characteristics. Sample simulations using the time-dependent nonlinear mild-slope equation and its unidirectional form have been performed. The proposed equations do not have any depth restriction and accommodate exact linear shoaling characteristics over mild-slopes so long as the incident wave frequency coincides with the specified dominant frequency of the wave model. The equations also include all the second-order nonlinear contributions and therefore can simulate the cnoidal waves and the Stokes waves with equal accuracy. The proposed equations may thus be regarded models for the combined nonlinear refraction-diffraction of waves over arbitrary depths. It is also worthwhile to emphasize that the applicability of the model equations is not limited to periodic waves; narrow-banded random waves may as well be simulated accurately.

Acknowledgment

The first author would like to acknowledge the grant received from Tokyo Institute of Technology during the major part of this work.

References

- Beji, S. and K. Nadaoka, 1997. A time dependent nonlinear mild-slope equation for water waves. *Proc. Roy. Soc. Lond. A*, **454**.
- Beji, S. and K. Nadaoka, 1996. A formal derivation and numerical modelling of the improved Boussinesq equations for varying depth. *Ocean Engng.*, **23-8**: 691-704.
- Berkhoff, J.C.W., 1972. Computation of combined refraction-diffraction. *Proc. 13th Int. Conf. Coast. Engng.*, **1**: 471-490.
- Byrne, R.J., 1969. Field occurrences of induced multiple gravity waves. *J. Geophys. Res.*, **74-10**: 2590-2596.
- Fenton, J., 1972. A ninth-order solution for the solitary wave. *J. Fluid Mech.*, **53**: 257-271.
- Freilich, M.H. and R.T. Guza, 1984. Nonlinear effects on shoaling surface gravity waves. *Philos. Trans. R. Soc. Lond. A*, **311**: 1-41.
- Ito, Y. and K. Tanimoto, 1972. A method of numerical analysis of wave propagation-Application to wave diffraction and refraction. *Proc. 13th Int. Conf. Coast. Engng.*, **1**: 503-522.
- Madsen, P.A., R. Murray and O.R. Sørensen, 1991. A new form of the Boussinesq equations with improved linear dispersion characteristics. *Coastal Engng.*, **15**: 371-388.
- Miles, J.W., 1980. Solitary waves. *Ann. Rev. Fluid Mech.*, **12**: 11-43.
- Nadaoka, K., Beji, S. and Nakagawa, Y. 1994. A fully-dispersive nonlinear wave model and its numerical solutions. *Proc. 24th Int. Conf. Coast. Engng.*, **1**: 427-441.
- Nadaoka, K., Beji, S. and Nakagawa, Y. 1997. A fully-dispersive weakly-nonlinear model for water waves. *Proc. Roy. Soc. Lond. A*, **453**: 1-16.

- Nwogu, O., 1993. Alternative form of Boussinesq equations for nearshore wave propagation. *J. Waterway, Port, Coastal, and Ocean Engng.*, **119-6**: 618-638.
- Rayleigh, Lord, 1876. On waves. *Phil. Mag.*, **1**: 257-279.
- Smith, R. and T. Sprinks, 1975. Scattering of surface waves by a conical island. *J. Fluid Mech.*, **72**: 373-384.
- Young, I.R., 1989. Wave transformation over coral reefs. *J. Geophys. Res.*, **94**: 9779-9789.
- Whalin, R.W., 1972. Wave refraction theory in a convergence zone. *Proc. 13th Int. Conf. Coast. Engng.*, **1**: 451-470.
- Witting, J.M., 1984. A unified model for the evolution of nonlinear water waves. *J. Comp. Phys.*, **56**: 203-236.
- Zabusky, N.J. and M.D. Kruskal, 1965. Interaction of solitons in a collisionless plasma and recurrence of initial states. *Phy. Rev. Lett.*, **15**: 240.

CHAPTER 83

BOUSSINESQ EQUATIONS WITH IMPROVED DOPPLER SHIFT AND DISPERSION FOR WAVE/CURRENT INTERACTION

Qin Chen¹, Per A. Madsen², Ole R. Sørensen² and David R. Basco³

Abstract

Boussinesq-type equations with improved dispersion characteristics for the combined motion of waves and currents are introduced. The ambient current is assumed to be uniform over depth and to have a magnitude as large as the shallow water wave celerity, allowing for the consideration of wave blocking of fairly long waves. The temporal variation of the current is ignored, while the spatial variation is assumed to vary on a larger scale than the wave-length scale. Boussinesq-type equations are derived by explicit use of four scales v , δ , ϵ and μ representing the particle velocity and the surface elevation of the total wave-current motion, as well as the wave-nonlinearity and the wave-dispersion, respectively. Firstly, equations are derived in terms of the depth-averaged velocity to obtain a generalization of the equations of Yoon & Liu (1989) to allow for stronger currents. Secondly, these equations are formulated in terms of the velocity variable at an arbitrary z -location resulting in an improved dispersion relation which corresponds to a Padé [2,2] expansion in the wave number of the squared intrinsic celerity for the fully dispersive linear theory. For vanishing currents, these equations reduce to the equations of Nwogu (1993). Finally, this formulation is enhanced to achieve Padé [4,4] dispersion characteristics. Model results for monochromatic and bichromatic waves being fully or partly blocked by opposing currents are given and the results are shown to be in reasonable agreement with theoretical calculations based on the wave-action principle.

1. Introduction

Various forms of lower-order Boussinesq equations are reported in the literature and they may be classified into three groups as follows: (1) the classical Boussinesq equations for wave motion (e.g. Peregrine, 1967); (2) the Boussinesq-type equations with improved linear dispersion properties (e.g. Madsen et al., 1991; Nwogu, 1993; Schäffer and Madsen, 1995); (3) the Boussinesq equations derived for the combined motion of waves and ambient currents (e.g. Yoon & Liu, 1989 and Prüzer & Zielke, 1990). As shown by Chen et al. (1996), only the equations in the third group incorporate a correct form of Doppler shift in connection with wave-current interaction. Their dispersion relation, however, suffers the same inaccuracy as the classical Boussinesq equations for higher wave numbers. In case of opposing

¹ Joint Graduate Research Assistant at ICCH and ODU where the acronyms stand for the following institutes.

² International Research Center for Computational Hydrodynamics (ICCH), Agern Allé 5, DK-2970, Hørsholm, Denmark.

³ Coastal Engineering Center, Dept. of Civil & Environmental Engineering, Old Dominion University (ODU), Norfolk, VA 23529-0241, USA.

currents this limitation quickly becomes critical for the applicability of the equations as wave numbers increase with the current speed. It is therefore desirable to improve the equations to achieve Padé-type expansions of the dispersion relation similar to what has been achieved by e.g. Madsen et al. (1991) and Schäffer & Madsen (1995) for the case of pure wave motion. First attempts in this direction were made by Kristensen (1995).

This paper focuses on the derivation and analysis of Boussinesq-type equations with Padé [4,4] dispersion characteristics for coupled wave-current motion. A one-dimensional version of the new equations is solved by the finite-difference method and simulation results of waves blocked by a strong, opposing current are presented.

2. Scaling Assumptions and Governing Equations

As a starting point we consider the combined motion of waves and ambient currents and split the velocity variable into two parts, a wave orbital velocity, u^w and a current velocity, u^c , which is assumed to be uniform over depth. This splitting is only made for scaling purposes and it does not appear in the final equations. A Cartesian coordinate system with the x' -axis and y' -axis located at the still water level (SWL) and the z' -axis pointing vertically upwards is employed. The free surface is defined by $z' = \eta'(x', y', t')$ while the sea bed is defined by $z' = -h'(x', y')$. Non-dimensional variables are used as follows:

$$x = x'/l'_0, \quad y = y'/l'_0, \quad z = z'/h'_0, \quad t = t' \sqrt{(gh'_0)/l'_0} \quad (2.1)$$

where prime denotes dimensional variables and h'_0 and l'_0 denote a characteristic water depth and wave length, respectively. In the following discussion of scales of waves and currents in shallow water we respectively utilize the linear and nonlinear version of the shallow water equations (SWE). The discussion is kept brief and detailed analyses can be found in the work by Chen et al. (1996).

In connection with pure wave motion in shallow water we introduce the classical measures of nonlinearity and frequency dispersion by

$$\epsilon = a'_0/h'_0, \quad \mu = h'_0/l'_0 \quad (2.2)$$

where a'_0 denotes a characteristic wave amplitude. As in conventional Boussinesq theory we shall assume that $\epsilon = O(\mu^2)$ and $\epsilon \ll 1$. Linear long-wave theory can be employed to estimate the order of magnitude of the wave particle velocities (u'^w, w'^w), the free surface elevation (η'^w) and the pressure (p'^w) as well as their temporal and spatial variation.

For pure current motion, the temporal variation of the current is ignored as it is assumed to be several orders of magnitude slower than that of the wind waves. The spatial variation of the current is closely related to the variation of the bottom bathymetry and we generally assume this to vary on a larger spatial scale than the wave-length scale. This can be expressed by $u'^c = u'^c(\sigma x, \sigma y)$, $\eta'^c = \eta'^c(\sigma x, \sigma y)$ and $h' = h'(\sigma x, \sigma y)$, where σ denotes the slow scale, which is yet to be chosen. Coastal currents are typically stronger than the wave particle velocity and weaker than the wave celerity, but in the derivation we use the shallow water wave celerity as the scale of the current speed in order to be able to consider wave-blocking in shallow water. Consequently, we express the order of magnitude of the current velocity by $u'^c = O(v) \sqrt{(gh'_0)}$ in which $\epsilon \leq v \leq 1$. The corresponding surface elevation due to the current is expressed by $\eta'^c = O(\delta) h'_0$ where $\delta = O(v^2)$ as analysed in Chen et al. (1996)'s work. In comparison, Yoon & Liu (1989) used $v = \mu$ and $\delta = \mu^2$ so that wave-

blocking in shallow water was not allowable under their assumptions. By the use of σ , ν , δ and μ we can also determine the order of magnitude of the temporal and spatial variation of the variables.

On the basis of the scaling analyses for pure wave and pure current motion, the scaling of variables in case of coupled wave-current motion becomes

$$u' = O(\epsilon, \nu) \sqrt{(gh'_0)}; \quad w' = O(\epsilon\mu, \sigma\nu\mu) \sqrt{(gh'_0)} \quad (2.3)$$

$$\eta'_t = O(\epsilon, \nu^2) h'_0; \quad p' = O(\epsilon, \nu^2) (\rho gh'_0) \quad (2.4)$$

The order of magnitude of the leading terms in the continuity equation of the SWE becomes

$$\eta'_{t'} = O(\epsilon\mu) \sqrt{(gh'_0)}; \quad h' u'_{x'} = O(\epsilon\mu, \sigma\nu\mu) \sqrt{(gh'_0)}; \quad u' h'_{x'} = O(\epsilon\mu, \sigma\nu\mu) \sqrt{(gh'_0)} \quad (2.5)$$

The order of magnitude of the terms in the momentum equation of the SWE becomes

$$u'_{t'} = O(\epsilon\mu) g; \quad g\eta'_{x'} = O(\epsilon\mu, \sigma\nu^2\mu) g; \quad u' u'_{x'} = O(\epsilon^2\mu, \sigma\nu^2\mu) g \quad (2.6)$$

The spatial variation of the current and the bathymetry was defined by σ which is rather arbitrary. We adopt the assumption in Madsen & Schäffer's (1996) work specifying $h' u'_{x'} = O(h' u'_{x'})$. This assumption in combination with the expression in (2.5) yields

$$\sigma = O(\epsilon/\nu) \quad (2.7)$$

This means that strong currents (with $\nu = O(1)$) can be treated only in connection with weakly varying bathymetries, while weak currents (with e.g. $\nu = O(\epsilon)$) do not imply any restrictions on the bathymetric variations. The condition expressed by (2.7) is basically in agreement with the assumptions by Yoon & Liu (1989) and Dingemans (1994), who used $\epsilon = \mu^2$, $\nu = \mu$ and $\sigma = \mu$.

The governing equations serving as our starting point of derivation are the depth-integrated conservation laws for mass and momentum with the dimensionless variables as defined by

$$\mathbf{u} = \frac{\mathbf{u}'}{\sqrt{gh'_0}}, \quad w = \frac{w'}{\mu\sqrt{gh'_0}}, \quad p = \frac{p'}{\rho gh'_0}, \quad \eta = \frac{\eta'}{h'_0} \quad (2.8)$$

where $\mathbf{u} = (u, v)$ is the horizontal velocity vector; w is the vertical velocity; p is the pressure and η is the free surface elevation of the combined wave and current motion. The actual magnitude of each term appearing in the derivation will be explicitly determined by the use of the scaling assumptions (2.3)-(2.7).

In terms of the dimensionless variables defined by (2.1) and (2.8) we express the depth-integrated mass equation as

$$\eta_t + \nabla \cdot \int_{-h}^{\eta} \mathbf{u} dz = 0 \quad (2.9)$$

where $\nabla = (\partial/\partial x, \partial/\partial y)$ is the horizontal gradient operator, and the depth-integrated horizontal momentum equations as

$$\frac{\partial}{\partial t} \int_{-h}^{\eta} u dz + \frac{\partial}{\partial x} \int_{-h}^{\eta} u^2 dz + \frac{\partial}{\partial y} \int_{-h}^{\eta} uv dz + \frac{\partial}{\partial x} \int_{-h}^{\eta} p dz - p|_{z=-h} h_x = 0 \quad (2.10a)$$

$$\frac{\partial}{\partial t} \int_{-h}^{\eta} v dz + \frac{\partial}{\partial x} \int_{-h}^{\eta} uv dz + \frac{\partial}{\partial y} \int_{-h}^{\eta} v^2 dz + \frac{\partial}{\partial y} \int_{-h}^{\eta} p dz - p|_{z=-h} h_y = 0 \quad (2.10b)$$

while the pressure field reads

$$p(x, y, z, t) = (\eta - z) + \mu^2 \left\{ \frac{\partial}{\partial t} \int_z^\eta w dz + \nabla \cdot \int_z^\eta \mathbf{u} w dz - w^2 \right\} \tag{2.11}$$

The vertical velocity w is evaluated by the vertical integration of the continuity equation from the sea bed to z and the use of the bottom boundary condition, which yields

$$w = - \nabla \cdot \int_{-h}^z \mathbf{u} dz \tag{2.12}$$

The above depth-integrated equations are as exact as their original continuity equation and the Euler equations of motion and the detailed derivation procedure can be found in the literature (e.g. Phillips, 1977). The closure of the equations (2.9)-(2.12) consists of determining the vertical distribution of the horizontal velocity vector \mathbf{u} by the use of the vorticity equations of the fluid. As in Yoon & Liu (1989)'s work, the current field is allowed to be horizontally sheared while the vertical shear is limited. Hence, the vorticity equations read

$$u_z - \mu^2 \nabla w = O(\mu^4) \tag{2.13}$$

$$u_y - v_x = O(1) \tag{2.14}$$

3. Derivation of a Generalized Version of the Equations by Yoon & Liu (1989)

In the previous section the governing equations were listed in non-dimensional form using μ as the only explicit scaling parameter. In the following derivation of the horizontal and vertical particle velocities, the dynamic pressure and the resulting mass and momentum equations we introduce the parameters ϵ , ν , δ and σ as explicit measures of the order of magnitude of each term in the equations. As defined in Section 2 we take $\sigma = \epsilon/\nu$ and $\delta = O(\epsilon, \nu^2)$. Further specifying $\epsilon \leq \nu \leq 1$ ensures that the equations will be also valid in the limit of vanishing currents. Generally, the order of magnitude of the different terms is determined as the maximum of all possible combinations of wave and current components and in this process the difference in horizontal scaling of current and wave components is taken into account. As a key step of the development of Boussinesq-type equations, we must determine the depth-dependence of the horizontal velocity field which can be expanded as a Taylor series with respect to the velocities $\hat{\mathbf{u}} = \mathbf{u}(x, y, 0, t)$ at the still water level.

$$\mathbf{u}(x, y, z, t) = \mathbf{u}(x, y, 0, t) + z \mathbf{u}_z(x, y, 0, t) + \frac{1}{2} z^2 \mathbf{u}_{zz}(x, y, 0, t) + \dots \tag{3.1}$$

We make use of the vorticity equations (2.13) and the local continuity equation to evaluate \mathbf{u}_z and \mathbf{u}_{zz} in (3.1). By the use of the definition of the depth-integrated velocity, \bar{U} and algebraic manipulation (see Chen et al., 1996 for details) we obtain

$$\begin{aligned} \mathbf{u} = & \bar{U} + \frac{\epsilon}{\nu} \mu^2 \left\{ \left(\frac{h^2}{6} - \frac{z^2}{2} \right) \nabla(\nabla \cdot \bar{U}) - \left(z + \frac{h}{2} \right) \nabla[\nabla \cdot (h \bar{U})] \right\} \\ & - \delta \frac{\epsilon}{\nu} \mu^2 \eta \left\{ \frac{1}{6} h \nabla(\nabla \cdot \bar{U}) - \frac{1}{2} h \nabla[\nabla \cdot (h \bar{U})] \right\} + \delta^2 \frac{\epsilon}{\nu} \mu^2 \frac{1}{6} \eta^2 \nabla(\nabla \cdot \bar{U}) + O\left(\frac{\epsilon}{\nu} \mu^4\right) \end{aligned} \tag{3.2}$$

Substitution of (3.2) into (2.12) gives the vertical velocity in terms of \bar{U}

$$w = -\nabla \cdot [(z+h)U] + O(\mu^2) \quad (3.3)$$

By inserting (3.2) and (3.3) into (2.11) and determining the ordering, the pressure field may be expressed as

$$\begin{aligned} p = & \left(\eta - \frac{z}{\delta} \right) + \frac{\epsilon}{\delta} \mu^2 \left[z \nabla \cdot (hU_t) + \frac{z^2}{2} \nabla \cdot U_t \right] \\ & - \epsilon \mu^2 \left\{ \frac{1}{2} \delta \eta^2 \nabla \cdot U_t + \eta \nabla \cdot (hU_t) \right\} \\ & + \frac{\nu \epsilon}{\delta} \mu^2 \left\{ z U \cdot \nabla [(\nabla \cdot (hU))] + \frac{z^2}{2} U \cdot \nabla (\nabla \cdot U) \right\} \\ & - \nu \epsilon \mu^2 \left\{ \frac{1}{2} \delta \eta^2 U \cdot \nabla (\nabla \cdot U) + \eta U \cdot \nabla [\nabla \cdot (hU)] \right\} + O\left(\frac{\epsilon^2}{\delta} \mu^2, \frac{\epsilon}{\delta} \mu^4\right) \end{aligned} \quad (3.4)$$

Use of the definition of depth-averaged velocity in (2.9) and substitution of (3.2) and (3.4) into the depth-integrated equations (2.10) lead to a modified version of the equations by Yoon & Liu (1989) for wave/current interaction in shallow water as follows,

$$\eta_t + \nabla \cdot (hU) + \delta \eta \nabla \cdot U + \nu U \cdot \nabla \eta = 0 \quad (3.5)$$

and

$$\begin{aligned} U_t + \nu(U \cdot \nabla)U + \nabla \eta \\ + \mu^2 [\Lambda_0^I + \nu \Lambda_1^I + \delta(\Lambda_2^I + \nu \Lambda_3^I) + \delta^2(\Lambda_4^I + \nu \Lambda_5^I)] = O(\epsilon \mu^2, \mu^4) \end{aligned} \quad (3.6)$$

where

$$\Lambda_0^I = h\Gamma_t^I; \quad \Lambda_1^I = (U \cdot \nabla)(h\Gamma^I) \quad (3.7a)$$

$$\Lambda_2^I = -\eta \{ \Gamma_t^I + \nabla [\nabla \cdot (hU)] \}; \quad \Lambda_3^I = -\eta (U \cdot \nabla) \{ \Gamma^I + \nabla [\nabla \cdot (hU)] \} \quad (3.7b)$$

$$\Lambda_4^I = -\frac{1}{3} \eta^2 \nabla (\nabla \cdot U_t); \quad \Lambda_5^I = -\frac{1}{3} \eta^2 (U \cdot \nabla) [\nabla (\nabla \cdot U)] \quad (3.7c)$$

where

$$\Gamma^I = \frac{h}{6} \nabla (\nabla \cdot U) - \frac{1}{2} \nabla [\nabla \cdot (hU)] \quad (3.7f)$$

In comparison with the original Yoon & Liu's equations, the new scaling assumptions result in additional terms Λ_2^I , Λ_3^I , Λ_4^I and Λ_5^I . These terms take into account the change in the mean water level due to an ambient current and should be included if we consider $\nu = O(1)$. The Doppler shift properties of both sets of equations however, remain identical and correspond to the Padé [0,2] expansion of the linear dispersion relation of fully dispersive waves. When the speed of an ambient current becomes as weak as the wave particle velocity, all μ^2 -terms in the momentum equation except for Λ_0^I will become negligible in the lower-order Boussinesq-type equations. Then this set of equations reduces to the equations by Peregrine (1967).

4. Equations with Padé [2/2] Characteristics for Wave-Current Interaction

It is desirable to improve the dispersion accuracy of the modified equations we obtained in the last section. For pure wave motion, Nwogu (1993) introduced an alternative to the Madsen & Sørensen (1992)'s equations with improved linear dispersion properties. Nwogu's equations are formulated in terms of the velocity at an arbitrary level instead of depth-integrated or depth-averaged velocities. As shown by Chen et al. (1996), the equations by Nwogu (1993) are not applicable to coupled wave/current motion due to the lack of accuracy in Doppler shift. We shall start our derivation from the generalized version of the equations by Yoon & Liu (1989) (i.e. (3.5) & (3.6)) and consistently replace the depth-averaged velocities by the velocities at an arbitrary elevation by keeping the same scaling assumptions as discussed in Section 2. This also demonstrates an alternative approach to obtaining Nwogu's equations directly from the equations by Peregrine (1967).

As shown in Chen et al. (1996)'s work, the relation between the depth-averaged velocity, \mathbf{U} and the velocity at an arbitrary level, \mathbf{u}_α may be expressed by

$$\begin{aligned} \mathbf{U} = \mathbf{u}_\alpha + \frac{\epsilon}{\nu} \mu^2 \left\{ \left(z_\alpha + \frac{h}{2} \right) \nabla [\nabla \cdot (h \mathbf{u}_\alpha)] + \left(\frac{z_\alpha^2}{2} - \frac{h^2}{6} \right) \nabla (\nabla \cdot \mathbf{u}_\alpha) \right\} \\ - \frac{\delta \epsilon}{\nu} \mu^2 \eta \left\{ \frac{1}{2} \nabla [\nabla \cdot (h \mathbf{u}_\alpha)] - \frac{h}{6} \nabla (\nabla \cdot \mathbf{u}_\alpha) \right\} - \frac{\delta^2 \epsilon}{\nu} \mu^2 \frac{1}{6} \eta^2 \nabla (\nabla \cdot \mathbf{u}_\alpha) + O \left(\frac{\epsilon}{\nu} \mu^4 \right) \end{aligned} \quad (4.1)$$

Substitution of (4.1) into the continuity equations (3.5) and the momentum equations (3.6) leads to a set of equations formulated in terms of the velocities at an arbitrary elevation as follows

$$\begin{aligned} \eta_t + \nabla \cdot (h \mathbf{u}_\alpha) + \delta \eta \nabla \cdot \mathbf{u}_\alpha + \nu \mathbf{u}_\alpha \cdot \nabla \eta \\ + \mu^2 (\Pi'_{\alpha 0} + \delta \Pi'_{\alpha 1} + \delta^2 \Pi'_{\alpha 2} + \delta^3 \Pi'_{\alpha 3}) = O(\epsilon \mu^2, \mu^4) \end{aligned} \quad (4.2)$$

where

$$\Pi'_{\alpha 0} = \nabla \cdot h \Gamma'_\alpha - \nabla \cdot \left\{ \frac{h^3}{6} \nabla (\nabla \cdot \mathbf{u}_\alpha) - \frac{h^2}{2} \nabla [\nabla \cdot (h \mathbf{u}_\alpha)] \right\}; \quad \Pi'_{\alpha 1} = \eta \nabla \cdot \Gamma'_\alpha \quad (4.3a)$$

$$\Pi'_{\alpha 2} = -\frac{\eta^2}{2} \nabla \cdot \{ \nabla [\nabla \cdot (h \mathbf{u}_\alpha)] \}; \quad \Pi'_{\alpha 3} = -\frac{\eta^3}{6} \nabla \cdot [\nabla (\nabla \cdot \mathbf{u}_\alpha)] \quad (4.3b)$$

in which

$$\Gamma'_\alpha = \frac{z_\alpha^2}{2} \nabla (\nabla \cdot \mathbf{u}_\alpha) + z_\alpha \nabla [\nabla \cdot (h \mathbf{u}_\alpha)] \quad (4.3c)$$

and

$$\begin{aligned} \mathbf{u}_{\alpha t} + \nu (\mathbf{u}_\alpha \cdot \nabla) \mathbf{u}_\alpha + \nabla \eta \\ + \mu^2 [\Lambda'_{\alpha 0} + \nu \Lambda'_{\alpha 1} + \delta (\Lambda'_{\alpha 2} + \nu \Lambda'_{\alpha 3}) + \delta^2 (\Lambda'_{\alpha 4} + \nu \Lambda'_{\alpha 5})] = O(\epsilon \mu^2, \mu^4) \end{aligned} \quad (4.4)$$

where

$$\Lambda_{\alpha 0}^I = \Gamma_{\alpha}^I ; \quad \Lambda_{\alpha 1}^I = (\mathbf{u}_{\alpha} \cdot \nabla) \Gamma_{\alpha}^I \quad (4.5a)$$

$$\Lambda_{\alpha 2}^I = -\eta \nabla [\nabla \cdot (h \mathbf{u}_{\alpha})] ; \quad \Lambda_{\alpha 3}^I = -\eta (\mathbf{u}_{\alpha} \cdot \nabla) \nabla [\nabla \cdot (h \mathbf{u}_{\alpha})] \quad (4.5b)$$

$$\Lambda_{\alpha 4}^I = -\frac{1}{2} \eta^2 \nabla (\nabla \cdot \mathbf{u}_{\alpha}) ; \quad \Lambda_{\alpha 5}^I = -\frac{1}{2} \eta^2 (\mathbf{u}_{\alpha} \cdot \nabla) [\nabla (\nabla \cdot \mathbf{u}_{\alpha})] \quad (4.5c)$$

equations (4.2) to (4.5) form a new set of equations with the improved Doppler shift corresponding to the Padé [2,2] expansion of the linear dispersion relation given by the first order Stokes theory by choosing the appropriate z_{α} as suggested by Nwogu (1993). We shall analyse the dispersion properties in Section 6. When the speed of an ambient current becomes as weak as the wave particle velocity, those terms $\Pi_{\alpha i}^I$ ($i=1, 2, 3$) in (4.3) and $\Lambda_{\alpha i}^I$ ($i=1, 2, 3, 4, 5$) in (4.5) will become negligible in the lower-order Boussinesq-type equations. Then this set of equations reduces to the equations by Nwogu (1993) for pure wave propagation in nearshore regions.

5. Further Enhancement of the Dispersion Accuracy

It is possible to improve the Doppler shift accuracy of the equations we obtained in the last section even further. Starting from (4.2) to (4.5), we shall formulate another set of Boussinesq-type equations by consistent incorporation of the Padé [4,4] expansion of the Doppler shift relation predicted by the first order Stokes theory for waves on uniform ambient currents. Following Schäffer & Madsen (1995), we introduce four free parameters ($\beta_1, \beta_2, \gamma_1, \gamma_2$) which are less than or equal to $O(1)$. Use of each of the operators $-\beta_1 \mu^2 \nabla \cdot (h^2 \nabla)$ and $\beta_2 \mu^2 \nabla \cdot \nabla (h^2)$ on the continuity equation (4.2) leads to

$$-\beta_1 \mu^2 \{ \nabla \cdot (h^2 \nabla \eta_t) + \nabla \cdot [h^2 \nabla [\nabla \cdot (h \mathbf{u}_{\alpha})]] \} \\ + \delta \eta \nabla \cdot [h^2 \nabla (\nabla \cdot \mathbf{u}_{\alpha})] + \nu \mathbf{u}_{\alpha} \cdot \nabla (h^2 \nabla^2 \eta) \} = O(\epsilon \mu^2, \mu^4) \quad (5.1)$$

and

$$\beta_2 \mu^2 \{ \nabla \cdot [\nabla (h^2 \eta_t)] + \nabla \cdot \{ \nabla [h^2 \nabla \cdot (h \mathbf{u}_{\alpha})] \} \} \\ + \delta \eta \nabla \cdot [\nabla (h^2 \nabla \cdot \mathbf{u}_{\alpha})] + \nu \mathbf{u}_{\alpha} \cdot \nabla [\nabla \cdot (h^2 \nabla \eta)] \} = O(\epsilon \mu^2, \mu^4) \quad (5.2)$$

Similarly, employing each of the operators $-\gamma_1 \mu^2 h^2 \nabla (\nabla \cdot)$ and $\gamma_2 \mu^2 h \nabla (\nabla \cdot h)$ on the momentum equations (4.4) yields

$$-\gamma_1 \mu^2 h^2 [\nabla (\nabla \cdot \mathbf{u}_{\alpha}) + \nabla (\nabla \cdot \nabla \eta)] \\ - \gamma_1 \nu \mu^2 h^2 (\mathbf{u}_{\alpha} \cdot \nabla) [\nabla (\nabla \cdot \mathbf{u}_{\alpha})] = O(\epsilon \mu^2, \mu^4) \quad (5.3)$$

and

$$\gamma_2 \mu^2 h \{ \nabla [\nabla \cdot (h \mathbf{u}_{\alpha})] + \nabla [\nabla \cdot (h \nabla \eta)] \} \\ + \gamma_2 \nu \mu^2 h (\mathbf{u}_{\alpha} \cdot \nabla) [\nabla (\nabla \cdot h \mathbf{u}_{\alpha})] = O(\epsilon \mu^2, \mu^4) \quad (5.4)$$

Adding (5.1) and (5.2) to (4.2), we obtain a new continuity equation

$$\eta_t + \nabla \cdot (h \mathbf{u}_\alpha) + \delta \eta \nabla \cdot \mathbf{u}_\alpha + \nu \mathbf{u}_\alpha \cdot \nabla \eta + \mu^2 (\Pi''_{\alpha 0} + \nu \Pi''_{\alpha 1} + \delta \Pi''_{\alpha 2} + \delta^2 \Pi''_{\alpha 3} + \delta^3 \Pi''_{\alpha 4}) = O(\epsilon \mu^2, \mu^4) \quad (5.5)$$

where

$$\Pi''_{\alpha 0} = \Pi'_{\alpha 0} + \nabla \cdot \left\{ \beta_2 \nabla [h^2 \nabla \cdot (h \mathbf{u}_\alpha)] - \beta_1 h^2 \nabla [\nabla \cdot (h \mathbf{u}_\alpha)] \right\} + \nabla \cdot \left\{ \beta_2 \nabla (h^2 \eta_t) - \beta_1 h^2 \nabla \eta_t \right\} \quad (5.6a)$$

$$\Pi''_{\alpha 1} = \mathbf{u}_\alpha \cdot \nabla [\beta_2 \nabla \cdot (h^2 \nabla \eta) - \beta_1 \nabla (h^2 \nabla^2 \eta)] \quad (5.6b)$$

$$\Pi''_{\alpha 2} = \Pi'_{\alpha 1} + \eta \nabla \cdot [\beta_2 \nabla (h^2 \nabla \cdot \mathbf{u}_\alpha) - \beta_1 h^2 \nabla (\nabla \cdot \mathbf{u}_\alpha)] \quad (5.6c)$$

while $\Pi''_{\alpha 3} = \Pi'_{\alpha 2}$, $\Pi''_{\alpha 4} = \Pi'_{\alpha 3}$, $\Gamma''_\alpha = \Gamma'_\alpha$ as defined by (4.3b-c). Similarly, adding (5.3) and (5.4) to (4.4) leads to new momentum equations

$$\mathbf{u}_{\alpha t} + \nu (\mathbf{u}_\alpha \cdot \nabla) \mathbf{u}_\alpha + \nabla \eta + \mu^2 [\Lambda''_{\alpha 0} + \nu \Lambda''_{\alpha 1} + \delta (\Lambda''_{\alpha 2} + \nu \Lambda''_{\alpha 3}) + \delta^2 (\Lambda''_{\alpha 4} + \nu \Lambda''_{\alpha 5})] = O(\epsilon \mu^2, \mu^4) \quad (5.7)$$

where

$$\Lambda''_{\alpha 0} = \Gamma''_{\alpha t} - \gamma_1 h^2 \nabla (\nabla \cdot \mathbf{u}_{\alpha t}) + \gamma_2 h \nabla [\nabla \cdot (h \mathbf{u}_{\alpha t})] - \gamma_1 h^2 \nabla (\nabla \cdot \nabla \eta) + \gamma_2 h \nabla [\nabla \cdot (h \nabla \eta)] \quad (5.8a)$$

$$\Lambda''_{\alpha 1} = (\mathbf{u}_\alpha \cdot \nabla) \Gamma''_\alpha - \gamma_1 h^2 (\mathbf{u}_\alpha \cdot \nabla) [\nabla (\nabla \cdot \mathbf{u}_\alpha)] + \gamma_2 h (\mathbf{u}_\alpha \cdot \nabla) [\nabla (\nabla \cdot h \mathbf{u}_\alpha)] \quad (5.8b)$$

while $\Lambda''_{\alpha 2} = \Lambda'_{\alpha 2}$, $\Lambda''_{\alpha 3} = \Lambda'_{\alpha 3}$, $\Lambda''_{\alpha 4} = \Lambda'_{\alpha 4}$, $\Lambda''_{\alpha 5} = \Lambda'_{\alpha 5}$, $\Gamma''_\alpha = \Gamma'_\alpha$ as defined by (4.5b-c) and (4.3c). Equations (5.5)-(5.8) form a new set of Boussinesq-type equations for wave/current interaction applicable up to even shorter waves for a suitable choice of the free parameters (β_1 , β_2 , γ_1 , γ_2) and z_α as analysed by Schäffer and Madsen (1995) for pure wave motion. In the following section, we shall analyse the Doppler shift behaviour of this new set of equations in comparison with the Stokes theory.

6. Analysis of Linear Dispersion Characteristics

We shall use dimensional form in this chapter and drop primes for convenience. The one-dimensional version of (5.5) and (5.7) with constant water depth can be expressed as

$$\eta_t + h u_{\alpha x} + (u_\alpha \eta)_x - \beta h^2 (\eta_{xxt} + u_\alpha \eta_{xxx}) + \left[\left(\alpha - \beta + \frac{1}{3} \right) h^3 + (\alpha - \beta) h^2 \eta - \frac{1}{2} h \eta^2 - \frac{1}{6} \eta^3 \right] u_{\alpha xxx} \quad (6.1a)$$

and

$$u_{\alpha\alpha} + g\eta_x + u_\alpha u_{\alpha\alpha} - \gamma gh^2 \eta_{xxx} + \left[(\alpha - \gamma)h^2 - \eta h - \frac{1}{2}\eta^2 \right] (u_{\alpha\alpha x} - u_\alpha u_{\alpha\alpha x}) = 0 \quad (6.1b)$$

where $\alpha \equiv z_\alpha/h + 0.5(z_\alpha/h)^2$, $\beta \equiv \beta_1 - \beta_2$, $\gamma \equiv \gamma_1 - \gamma_2$. By the use of Fourier analysis we obtain the linear dispersion relation of the new equations (5.5) to (5.8) as

$$(\omega - u^c k)^2 = \frac{\left[1 - \left(\alpha - \beta + \frac{1}{3} \right) (kh)^2 \right] [1 + \gamma (kh)^2] k^2 gh}{[1 + \beta (kh)^2] [1 - (\alpha - \gamma) (kh)^2]} \quad (6.2)$$

Different choices of the parameters in (6.2) result in different Doppler shift accuracy. For example, $(\alpha, \beta, \gamma) = (-2/5, 0, 0)$ gives

$$(\omega - u^c k)^2 = \frac{\left(1 + \frac{1}{15} k^2 h^2 \right) k^2 gh}{1 + \frac{2}{5} k^2 h^2} \quad (6.3)$$

This is the Padé [2,2] approximation of the linear dispersion relation given by the first-order Stokes theory. It turns out that (6.3) is also the linear dispersion relation of (4.2) to (4.5). Choosing $(\alpha, \beta, \gamma) = (-1/3, 0, 0)$ yields

$$(\omega - u^c k)^2 = \frac{k^2 gh}{1 + \frac{1}{3} k^2 h^2} \quad (6.4)$$

which corresponds to the linear dispersion relation of the original and generalized versions of the equations by Yoon & Liu (1989) using the depth-averaged velocities as variables.

Schäffer and Madsen (1995) obtained four sets of coefficients. Each of them leads to the highly accurate linear dispersion relation

$$(\omega - u^c k)^2 = \frac{\left(1 + \frac{1}{9} k^2 h^2 + \frac{1}{945} k^4 h^4 \right) k^2 gh}{1 + \frac{4}{9} k^2 h^2 + \frac{1}{63} k^4 h^4} \quad (6.5)$$

which is correct to fourth-order in $(kh)^2$ in comparison with the first-order Stokes' solution. Linear shoaling analyses by Schäffer & Madsen (1995) show that these four sets of parameters all give accurate linear shoaling behaviour. The influence of these four sets of parameters on the nonlinearity of the new equations can be analysed by examination of the transfer functions for sub-harmonics and super-harmonics as discussed in Madsen & Schäffer's (1996) work. The best set of parameters can therefore be chosen based on accuracy in the nonlinear properties. We adopt the one recommended by Madsen & Schäffer (1996) as follows.

$$\left. \begin{aligned} \left(\alpha, \frac{z_\alpha}{h} \right) &= (-0.39476, -0.54122) \\ (\beta, \beta_1, \beta_2) &= (0.03917, -0.12919, -0.16836) \\ (\gamma, \gamma_1, \gamma_2) &= (0.01052, -0.07327, -0.08379) \end{aligned} \right\} \quad (6.6)$$

With this set of parameters, equations (5.5) to (5.8) are applicable to deeper water for waves on ambient currents. For waves on following currents, the currents increase the wave length, thus the application range of the new equations exceeds that of the corresponding equations for pure wave motion. For waves on opposing currents, the currents reduce the wave length so that the applicable area depends on the ambient current speed. We use the linear dispersion properties of the first-order Stokes theory to estimate the applicable range of various forms of the Boussinesq-type equations for wave/current interaction. Solving the linear dispersion relations (6.4) & (6.5) gives two sets of curves corresponding to the dimensionless wave number (kh), relative water depth (h/L_0) and Froude number $F_r = U^c / \sqrt{gh}$. Figs. 7.1a-b illustrate the applicable areas of the new equations (5.5) & (5.7) and the equations by Yoon & Liu (1989) in case of opposing currents, respectively. The 5% error contour for kh as compared with the first-order Stokes' solution is also shown. Obviously, the new form of the equations gives a much larger applicable range than those of Yoon & Liu's equations.

It deserves to be mentioned that Madsen & Schäffer (1996) recently derived equations with equivalent properties for wave-current interaction by following a different line of derivation: In their work Boussinesq-type equations were derived on the basis of the two wave scales μ and ϵ , while the ambient current was not explicitly considered during the derivation procedure. In contrast to the present work, however, Madsen & Schäffer allowed $\epsilon = O(1)$ rather than $\epsilon = O(\mu^2)$ and retained all nonlinear terms to the particular order of dispersion. In retrospect this is the reason why their equations could account also for the case of ambient currents, as it turns out that the equations derived in this paper appear as a subset of the former equations by Madsen & Schäffer (1996). Since the extra nonlinear dispersive terms included by Madsen & Schäffer (1996) are expected to be minor in the present applications, the code developed for their equations is adapted for the following numerical experiments.

7. Numerical Solutions for Wave-Current Interaction

A one-dimensional version of the equations (5.5) to (5.8) is solved by the finite-difference method. The equations are discretized on a space staggered grid by means of fourth-order central differencing for first derivative terms in space and second-order central differencing for second and third spacial derivatives. The time-integration of the governing equations consists of the third-order Adams-Bashforth predictor and fourth-order Adams-Moulton corrector schemes. This numerical method was utilized in the work by Wei et al. (1995) and Banijamali (1997) and essentially designed to eliminate the truncation errors which mathematically have the same form as the Boussinesq-type terms due to the use of conventional second-order schemes for pure wave motion. It can be adapted for modelling fully coupled wave/current motion. For the case of strong ambient currents with significant nonlinear advection a smaller convergence criterion for the iterating corrector step

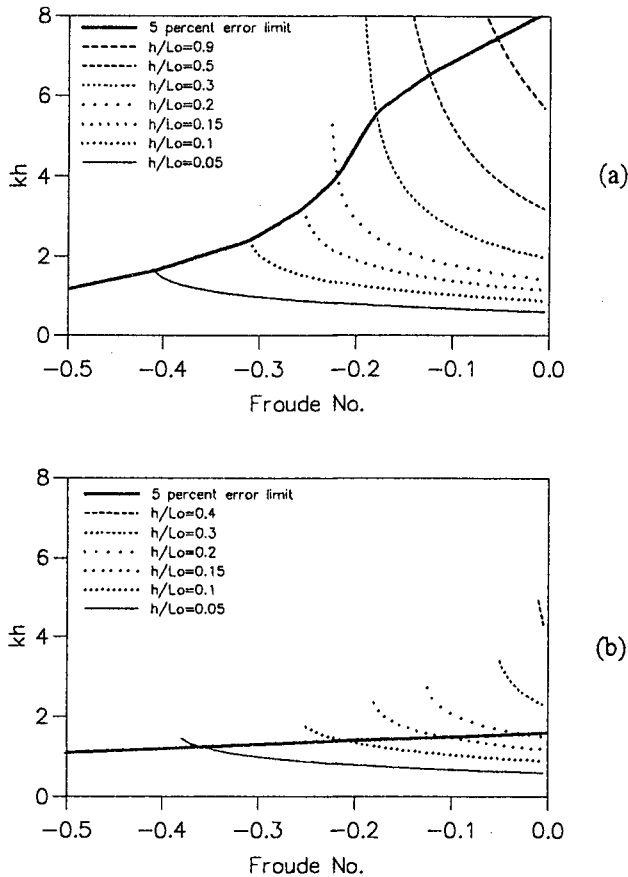


Fig. 7.1 Illustration of the applicable ranges of the equations with (a) the Padè [4,4] expansion (i.e.(5.5) & (5.7)) and (b) the Padè [0,2] expansion (i.e.(3.5) & (3.6)). The area below the 5% kh -error limit predicts the applicable regime.

is required, which leads to more iterations. A prototype of the numerical model for pure wave motion developed by Banijamali (1997) is adopted in the present work. We incorporate the model with non-reflective boundary conditions for fully coupled wave/current motion. The sponge layer technique (Larsen & Dancy, 1983) applicable to absorption of short waves is combined with the Sommerfeld radiation condition for radiating long waves or currents. We shall present some model results in connection with waves blocked by strong opposing currents.

The first test case considers monochromatic waves propagating against a current in a channel with a submerged bar. A sketch of the bathymetry is shown in Fig 7.1a. The channel is 60m long, 0.8m deep on both sides of the bar and 0.2m deep on top of the bar. The western and eastern slopes of the bar are 1/50 and 1/20, respectively. Bed friction is modelled by the use of the Chezy friction law, using a

Chezy coefficient of $300 \text{ m}^{1/2}/\text{s}$ in the sections $0 < x < 37\text{m}$ and $55\text{m} < x < 60\text{m}$, and a coefficient of $30 \text{ m}^{1/2}/\text{s}$ in the section $37\text{m} < x < 55\text{m}$. The relatively strong friction in the latter section serves as a stabilizing factor for the flow simulation. Initially we impose a constant velocity of -0.17 m/s at the eastern boundary and a radiating condition at the western boundary. This leads to an increase in the surface elevation at the western boundary of approximately 0.05m . Fig 8.1b shows the computed spatial variation of the velocity, which is found to be in fairly good agreement with conventional theory neglecting the vertical accelerations of the flow.

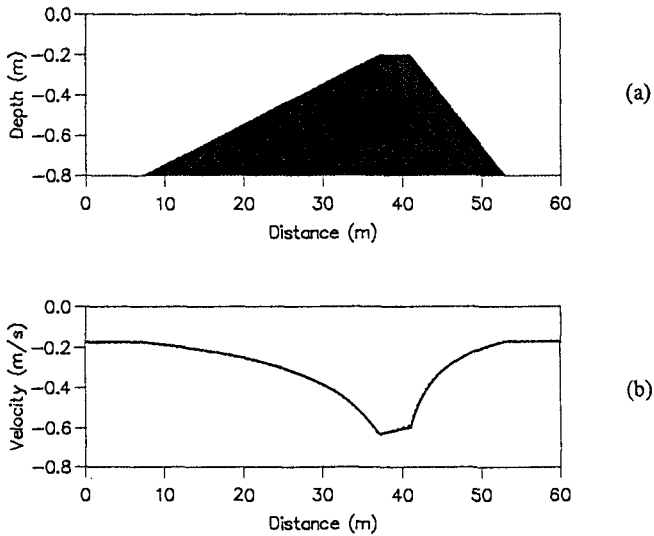


Fig. 8.1 Steady open channel flow predicted by the model (dotted line) and the nonlinear shallow water equations (solid line). a) Submerged bar topography; b) Particle velocity.

As the next step we impose a sinusoidal wave train on top of the steady current field. This is done by specifying a velocity condition at the western boundary including the local current obtained in the previous calculation. At the eastern boundary we use a sponge layer which absorbs the short waves while allowing the current to pass through. The incoming wave has a period of 1.2s and an initial height of 0.02m . The grid size and the time step are chosen to be 0.02m and 0.005s , respectively. Fig 8.2 shows the computed surface elevation for the combined wave-current motion. We notice that the oscillatory motion is stopped at the position $x=33.5\text{m}$ where wave blocking occurs because the local current velocity exceeds the local group velocity of the wave. The dotted line in Fig 8.2 indicates the theoretical solution obtained by the principle of wave action and we notice a good agreement with the computations with respect to amplitude amplification as well as the position of the blocking point.

The theory of wave action based on linear progressive wave motion obviously fails close to the blocking point as it predicts the wave height to go to infinity, which does not happen in reality (nor in the model). As suggested by Smith (1975), Stiassnie & Dagan (1979) and Shyu & Phillips (1990) the wave action is

eventually reflected at the blocking point and energy is transferred to much higher wave numbers. Furthermore, the wave numbers of the reflected waves will decrease rapidly with the distance from the blocking point due to the decreasing current.

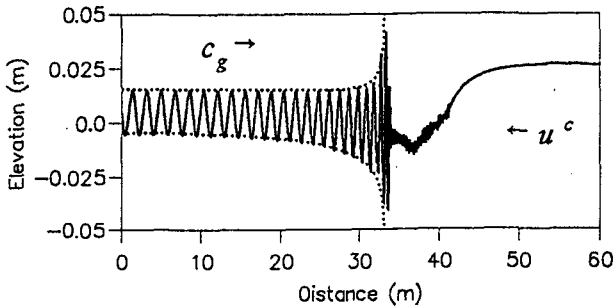


Fig. 8.2 Monochromatic wave propagation on a spatially-varying, opposing current.

In Fig. 8.3, a bichromatic wave train on a spatially-varying current is simulated. The same bathymetry, steady current field, grid size and time step as in the simulation of the monochromatic wave are employed. The bichromatic waves consist of a 1.2s wave and a 3.0s wave. Both of them have the same wave height of 0.02m. The model predicts that the shorter wave of 1.2s is blocked by the opposing current at the position $x=33.5\text{m}$ (as before) while the longer wave of 3.0s propagates through the blocking point and reaches the eastern boundary where a sponge layer efficiently absorbs the wave energy. The wave profile in Fig. 8.3 with bichromatic and regular wave forms before and after blocking, respectively, illustrates the blocking of the shorter wave in the bichromatic wave train.

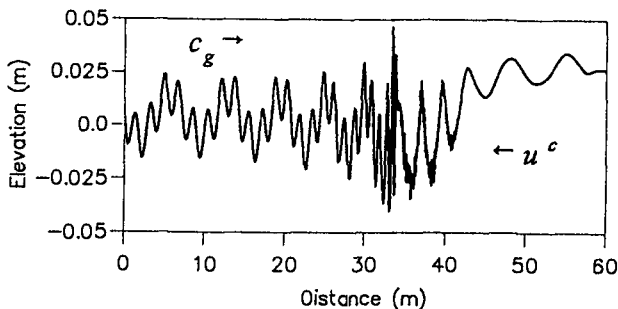


Fig. 8.3 A bichromatic wave train propagating on a spatially-varying, opposing current.

9. Conclusions

This paper deals with the derivation and application of Boussinesq-type equations with Padé [4,4] dispersion characteristics for the combined motion of waves and currents in nearshore areas. The waves are assumed to be weakly nonlinear and

the ambient current is assumed to be uniform over depth. In order to allow for the treatment of wave blocking in shallow water we assume the magnitude of the current to be as large as the shallow water celerity. A one-dimensional numerical model has been implemented on the basis of the new equations and as demonstrated it can simulate the complicated phenomenon of monochromatic and bichromatic waves being fully or partly blocked by opposing currents. Further verification of the model against measurements is obviously required, but the results obtained so far are promising and show that the new equations make it possible to simulate a range of complicated phenomena related to the interaction of waves and depth-uniform currents in coastal regions.

Acknowledgements

This work has been financed by the Danish National Research Foundation. QC and DRB's work at the early stage of the project was also partly financed by USAE WES Coastal Engineering Research Centre through Contract DACW39-95-M-3275. Their supports are greatly appreciated. We also acknowledge Mette K. Kristensen who influenced the early stage of this project during her MsC study.

References

- Banijamali, B., 1997. A study of enhanced Boussinesq equations and their numerical modelling. Ph.D thesis, International Research Centre for Computational Hydrodynamics (ICCH), Danish Hydraulic Institute and Aalborg University, Denmark.
- Chen, Q., Madsen, P.A., Schäffer, H.A. and Basco, D.R., 1996. Wave-current Interaction based on an enhanced Boussinesq approach. Submitted to Coastal Eng.
- Dingemans, M.W., 1994. Water Wave Propagation Over Uneven Bottom. Ph.D thesis, Delft University of Tech., The Netherlands.
- Kristensen, M.K., 1995. Boussinesq equations and wave-current interaction. MsC. thesis, International Research Centre for Computational Hydrodynamics (ICCH), Danish Hydraulic Institute and ISVA, Technical University of Denmark.
- Largen, J. and Dancy, H., 1983. Open boundaries in short-wave simulations-A new approach. Coastal Eng. 7(3): 285-297.
- Madsen, P.A., Murray, R. and Sørensen, O.R., 1991. A new form of the Boussinesq equations with improved linear dispersion characteristics (part 1). Coastal Eng., 15: 371-388.
- Madsen, P.A. and Sørensen, O.R., 1992. A new form of the Boussinesq equations with improved linear dispersion characteristics, part 2: a slowly-varying bathymetry. Coastal Eng., 18: 183-205.
- Madsen, P.A. and Schäffer, H.A., 1996. Higher order Boussinesq-type equations: derivation and analysis. Submitted to Phil. Trans. Roy. Soc. London.
- Nwogu, O., 1993. Alternative form of Boussinesq equations for nearshore wave propagation. J. of Waterway Port Coastal Ocean Eng., ASCE, 119(6): 618-638.
- Peregrine, D.H., 1967. Long waves on a beach. J. Fluid Mech., 27(4): 815-827.
- Phillips, O.M., 1977. The Dynamics of the Upper Ocean. 2nd edition. Cambridge University Press, London.
- Prüser, H.H. and Zielke, W., 1990. Irregular waves on a current. In: Proc. 22nd Int. Conf. Coastal Eng., Delft, The Netherlands. ASCE, New York, Vol. 1, pp. 1088-1101.
- Schäffer, H.A. and Madsen, P.A., 1995. Further enhancements of Boussinesq-type equations. Coastal Eng., 26: 1-14.
- Shyu, J.H. and Phillips, O.M., 1990. The blockage of gravity and capillary waves by longer waves and currents. J. Fluid Mech., 217: 115-141.
- Smith, R., 1975. The reflection of short gravity waves on a non-uniform current. Math. Proc. Camb. Phil. Soc. 78:517-525.
- Stiassnie, M. and Dagan, G., 1979. Partial reflexion of water waves by non-uniform advection currents. J. Fluid Mech., 92 (1): 119-129.
- Wei, G. Kirby, J.T., Grilli, S.T. and Subramanya, R., 1995. A fully nonlinear Boussinesq model for surface waves. part 1. highly nonlinear unsteady waves. J. Fluid Mech., 294: 71-92.
- Yoon, S.B. and Liu, P.L.F., 1989. Interaction of currents and weakly nonlinear water waves in shallow water. J. Fluid Mech., 205: 397-419.

CHAPTER 84

The Propagation of Water Waves in Prismatic Channels

Li Li¹, Robert A. Dalrymple² and Jeffrey M. Mlynarski³

Abstract:

Short waves in a channel can present navigational problems and may excite harbor oscillations. Channel sidewalls may reduce much of this wave energy, if they are sufficiently porous or they are sloped. Previously we presented a model for wave propagation in prismatic channels of arbitrary cross-section utilizing a numerical eigenfunction expansion. Here a series of small scale laboratory experiments were conducted to verify the numerical model. Comparisons of the numerical model to the experimental data are made for water surface profile and for eigenfunctions. The possibility of resonance between the edge wave and the second harmonic of the incident wave is also studied.

1 Introduction

Water waves encountering entrance channels present an interesting problem as the waves undergo reflection, refraction, diffraction and shoaling due to shorelines, shoals, jetties, tidal currents, and channels with varying depths. Long waves within channels have served as the impetus for the study of waves. Kelland (1839, as cited in Lamb, 1945) provided a wave equation for waves in triangular channels with the sidewalls inclined at 45°. Scott Russell (1844) provided evidence for the presence of solitary waves in channels. More recently, Peregrine (1968, 1969) examined nonlinear long waves in narrow channel. Golinko (1987) studied the reflection of a long wave from the vertical walls of a channel with a parabolic cross-section. Mathew and Akylas

¹Graduate Student, Center for Applied Coastal Research, Department of Civil and Environment Engineering, University of Delaware, Newark, DE 19716, USA.

²Professor, Department of Civil and Environment Engineering, Center for Applied Coastal Research, University of Delaware, Newark, DE 19716, USA

³Student, Department of Civil and Environment Engineering, University of Delaware, Newark, DE 19716, USA

(1990) conducted research on the wide channel case, noting the three-dimensional nature of the waves. Teng and Wu (1994) studied nonlinear long wave in convergent and divergent channels.

However, short waves in a channel also can present navigational problems and may excite harbor oscillations, and less work has been done on short waves. Kelland (1839) and Macdonald (1894) (all cited in Lamb, 1945) obtained analytical solutions for triangular channels with the sidewalls inclined at 45° and 60° to the vertical. Recently, Isaacson (1978) studied wave decay along the center line of a trapezoidal channel with rubble sidewalls in a laboratory experiment. Melo and Guza (1991a, 1991b), through field and numerical means, showed that a tidal inlet comprised of rubblemound jetties absorbed a considerable amount of the wave energy entering the inlet from the ocean into the porous inlet sidewalls. Dalrymple (1992) developed a simple model to explain this behavior using a simple eigenfunction expansion of the waves in the channel (assuming a rectangular channel cross-section) and an impedance boundary condition at the sidewalls. It was assumed that the waves at the mouth of the inlet had a constant amplitude and phase; that is, they were planar and normally incident. One consequence of this assumption and the impedance boundary condition was a fictitious amplification of the waves occurring within one wavelength of the channel mouth. Dalrymple and Martin (1996) have reduced this amplification by including the effect of the scattering of waves into the ocean. Kirby, Dalrymple, Kaku (1994) used parabolic model to study conformal coordinate system. Dalrymple, Kirby, Martin (1994) used spectral model to study conformally-mapped channel, including the diverging channels and circular channels.

Dalrymple, Kirby and Li (1994) using an eigenfunction expansion, studied an arbitrary cross-section channel. The basis of the eigenfunction expansion model is that the wave motion can be viewed as a summation of simple eigenmodes (Y_n) in the cross-channel direction. The amplitudes of the eigenmodes (A_n) are determined at the mouth of the channel. The wave motion (in an assumed ideal fluid) is governed by the following equation:

$$\Phi(x, y, z, t) = \hat{\phi}(x, y) \frac{\cosh k(h+z)}{\cosh kh} e^{-i\omega t}$$

$$\hat{\phi}(x, y) = \sum_{n=0}^{\infty} A_n e^{i\sqrt{K^2 - \lambda_n^2}x} Y_n(y)$$

$$\frac{d^2 Y}{dy^2} + (\lambda^2 - \overline{K^2} \nu(y)) Y = 0$$

where x is the propagation direction, y is the direction across the channel, z is the direction vertically upwards from the still water level, k is the local wavenumber, g is gravity; C and C_g are the phase and group velocity, corresponding the dispersion relationship, $\omega^2 = gk \tanh kh$.

Channels with symmetric and antisymmetric cross section were studied. With the numerical model, showed that channels with sloping sidewalls give rise to the presence of edge waves, excited by the incident wave field, while the incident wave propagate in the center of channel. The edge wave length is shorter than the incident wave

length. The edge wave amplitude, represented by the zeroth mode eigenfunction, is much higher than the magnitude of the incident wave.

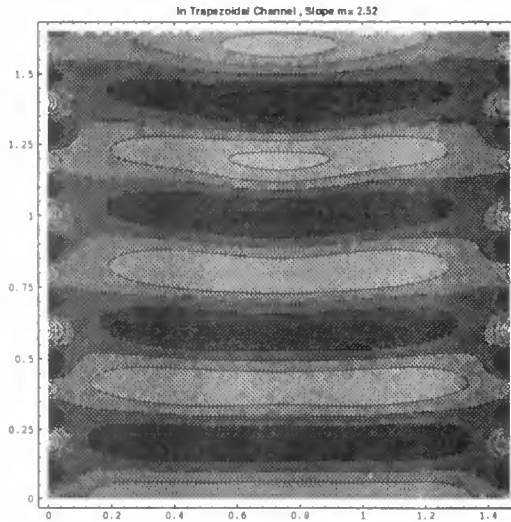


Figure 1: Plane View of Instantaneous Water Surface Elevation in Trapezoidal Channel Case 2; Ocean at the Bottom of Figure, Harbor to the Top. Edgewaves are excited at both the left and the right sides of the channel.

In this paper, a series of small scale laboratory experiments were conducted to verify the theoretical model. We studied the wave motion in triangular and trapezoidal channels with smooth sidewalls. Measurements of the free surface profile at different locations for several cross sections were obtained. The eigenfunctions were obtained from the wave displacement data by using Empirical Orthogonal Eigenfunction (EOF) method and were compared to those obtained from the numerical model.

2 Experiment Set-up

The wave experiments were conducted in a small tank at the Center of Applied Coastal Research at the University of Delaware. This section describes the experimental setup for the wave propagating in the channel and data acquisition procedure.

The tank was 236.0cm long, 122.5cm wide and 20.0cm deep. Waves were generated by a flap wavemaker at one end. Figures 2 and 3 show the experimental setup and tank. Two pieces of glass were used in the tank in order to form a triangular channel. Each piece of glass was 60.0cm wide, 165.0cm long and 0.64cm thick. Each glass panel was supported by two pieces of wood, allowing for the ability to vary the slopes of the sidewalls of the channel and to avoid any major deflection caused by bending. In order to diminish wave reflection, a gravel beach was located at the end of the tank. Four capacitance wave gages were used to measure the variations in the free surface.

Figure 3 shows the setup of the gages. Three gages were mounted on a movable fiberglass boom allowing for measurement at any particular position along the channel. The gages were numbered 1 through 4. Gage 4 in particular was placed parallel to the sloping side of channel and was used to measure the edge waves. Since the channel was symmetric in cross-section, gages were placed on only one side of the channel. In Figure 3, we define y as the horizontal coordinate taken to be positive landward, and $y = 0$ at the location of the midpoint of the channel cross-section.

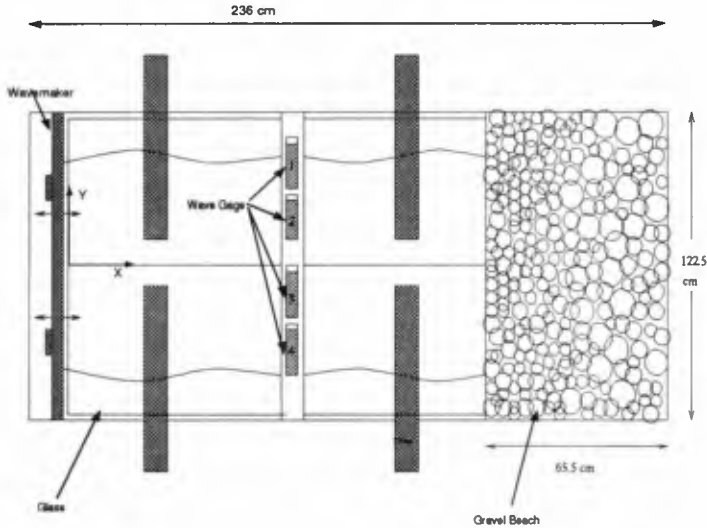


Figure 2: Experimental Setup (Top View)

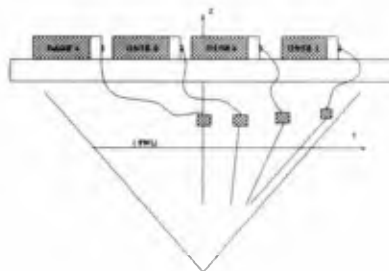


Figure 3: Layout of Wave Gages across Triangular Channel (Side View)

2.1 Analysis of Wave Data

Four tests, exploring the effect of varying channel slopes and varying wave frequencies for triangular channels, were conducted, as listed in Table 1.

Table 1: List of Experiments with Triangular Channel

Test	Slope	Wave Period (s)	Water Depth (m)	Measurement Locations			
				Along Channel Distance from Wavemaker d_x (m)		Across Channel Distance from Center point d_y (m)	
S1F1	1:2.9	0.700	0.0705	0.950		0.030 0.070 0.120 0.195	
S1F2	1:2.9	0.800	0.0705	0.985		0.030 0.070 0.120 0.195	
S2F1	1:3.1	0.680	0.0650	0.985		0.015 0.050 0.100 0.190	
S2F2	1:3.1	0.725	0.0650	0.950		0.015 0.050 0.100 0.190	

Two additional tests were also performed for trapezoidal channel, varying the wave frequencies; as listed in Table 2.

Table 2: List of Experiments with Trapezoidal Channel

Test	Slope	Wave Period (s)	Water Depth (m)	Measurement Locations			
				Along Channel Distance from Wavemaker d_x (m)		Across Channel Distance from Center point d_y (m)	
S3P1	1:2.5	0.570	0.0675	0.680		0.120 0.245 0.367 0.450	
S3P2	1:2.5	0.570	0.0675	1.095		0.120 0.245 0.367 0.450	
						0.512 0.565 0.625 0.730	

In order to test the repeatability of the experiments, each test was repeated six times. Test data from the six cases, including the time series and the amplitudes of the free surface waves were used for the data analysis. The eigenfunctions of the wave form across the channel were computed by the EOF method and later compared to the numerical model solution. The contour plots of the instantaneous wave field for the triangular and trapezoidal channels are also shown later.

3 Experimental Results

3.1 Comparison of Numerical Model To Experimental Data for Surface Profile

The amplitude of the propagating wave measured by each gage was used to create a surface profile along channel cross section. The amplitude η^i is defined by the mean maximum magnitude of time series for each gage:

$$\eta^i = \overline{\max(\eta^i(t))}$$

The surface profiles for the numerical solution and the experimental data are shown in Figures 4 through 9 (by symmetry, only half of the channel is shown; solid line indicates results of the numerical solution and the dot marks mean experimental data). The group of dots on the far right, are the experimental data obtained from the measure point close to the shoreline, representing the maximum magnitudes of the edge wave. The group of dots on the far left, are the experimental data obtained from the measuring point near the center line of channel, which represents the maximum magnitudes of the incident wave. The measuring error along y distance is $\pm 0.0018m$. As shown in these figures, there is a good agreement between the experimental data and numerical solution. The edge wave amplitude, represented by the zeroth mode eigenfunction, is much higher than the magnitude of the incident wave.

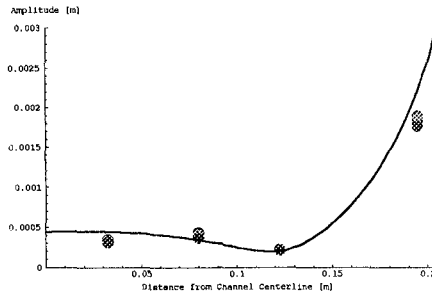


Figure 4: Comparison between the Cross-Channel Free Surface Profile for Case S1F1 and Numerical Solution, $T=0.700$ s, 0.950 m from Wavemaker

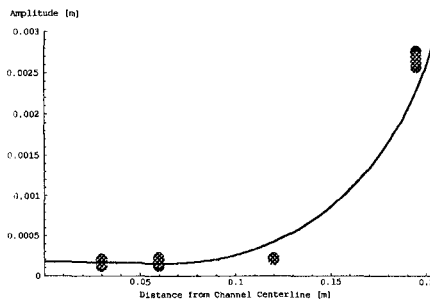


Figure 5: Comparison between the Cross-Channel Free Surface Profile for Case S1F2 and Numerical Solution, $T=0.800$ s, 0.985 m from Wavemaker

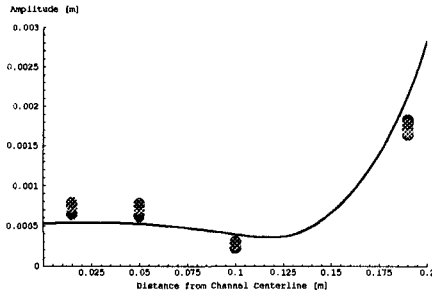


Figure 6: Comparison between the Cross-Channel Free Surface Profile for Case S2F1 and Numerical Solution, $T=0.680$ s, 0.985 m from Wavemaker

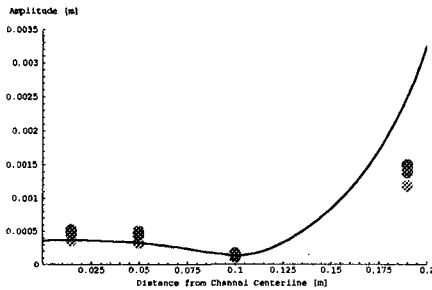


Figure 7: Comparison between the Cross-Channel Free Surface Profile for Case S2F2 and Numerical Solution, $T=0.725$ s, 0.950 m from Wavemaker

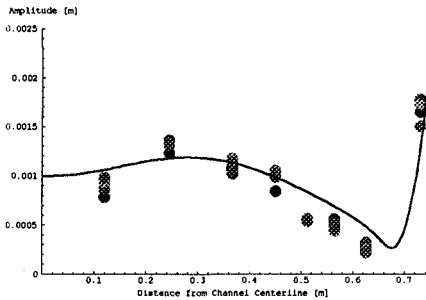


Figure 8: Comparison between the Cross-Channel Free Surface Profile for Case S3P1 and Numerical Solution, 0.680 m from Wavemaker

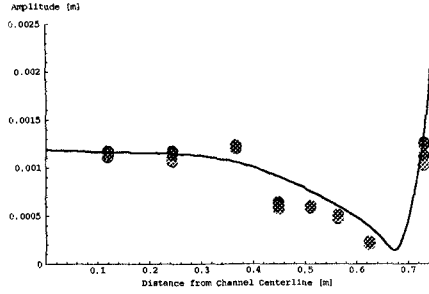


Figure 9: Comparison between the Cross-Channel Free Surface Profile for Case S3P2 and Numerical Solution, 1.095 m from Wavemaker

3.2 Comparison of Eigenfunction from Numerical Model and Experiment

3.2.1 The EOF method

The surface profile is assumed to be a superposition of eigenfunctions. Eigenfunctions can be obtained from the experimental data by using EOF(Empirical Orthogonal Eigenfunction) method.

The EOF method is a widely-used statistical tool which has been used for a number of analyses, including beach profile analysis. For the surface wave profile, the theoretical basis of the EOF method is the same as that for beach profile. The first eigenfunction is selected so that it accounts for the greatest possible amount of the data variance (the variance is defined as the mean square of the free surface displacement). The successive eigenfunctions each in turn are selected such that they represent the greatest possible amount of the remaining variance, Winant, Inman and Nordstrom (1975, as cited in Dean and Dalrymple, 1995).

The free surface displacement time series are recorded at the same time at the I locations across the channel width. Assume that there are K data points in one free surface displacement time series. These measured elevation are denoted as η_{ik} .

$$\eta_{ik} = \sum_{n=1}^N C_{nk} e_{ni}$$

for each I positions. Here, e_{ni} represents the n^{th} empirical eigenfunction evaluated at the i^{th} location across the channel width; and the constant C_{nk} represents a coefficient for the k^{th} recorded data and the n^{th} eigenfunction.

One property of the eigenfunctions is that they are independent of each other and orthogonal; that is,

$$\sum_{i=1}^I e_{ni} e_{mi} = \delta_{nm}$$

where $\delta_{nm} = 1$ if $n = m$, and it is zero otherwise. To obtain the value of the unknown C_{nk} , the error is minimized in the fit of η_{ik} by the eigenfunction. The minimization is carried out in the least squares sense by

$$2 \sum_{i=1}^I (\eta_{ik} - \sum_{n=1}^N C_{nk} e_{ni}) e_{mi} = 0$$

Using the orthogonality relationship,

$$C_{mk} = \sum_{i=1}^I \eta_{ik} e_{mi}$$

Parseval's theorem is then applied: the sum of the squares of the coefficients is equal to the square of the variance. To find each eigenfunction, its contribution to the variance will be maximized. Finally, by using the Lagrange Multiplier approach, the following equation can be obtained

$$a_{im} = \frac{1}{IK} \sum_{k=1}^K \eta_{ik} \eta_{mk}$$

and the symmetric matrix equation

$$\sum_{i=1}^I a_{im} e_{ni} = \lambda e_{nm} \quad (1)$$

Equation 1 is an eigenvalue matrix equation, consisting of a symmetric real coefficient matrix. By solving this matrix equation, eigenfunctions are obtained as many as measured locations I in the cross-section of channel. The eigenfunctions obtained by EOF method from experimental free surface displacement time series are discussed in next section.

3.2.2 Comparison of Eigenfunction from Numerical Model and Experiment

The zeroth mode eigenfunction for the trapezoidal channel obtained from the experiment by the EOF method is compared to that obtained from numerical solution, as shown in Figures 10 through 13. From the numerical model, amplitude of the zeroth mode edge wave is normalized to unity. The next eigenmode has a magnitude of 0.32. The third mode has an amplitude of only 0.18. From the experiment by the EOF method, the maximum amplitude of the zeroth mode eigenfunction is 1.0. The next eigenmode has the maximum magnitude of 0.067. The third mode has an amplitude of only 0.037. From both methods, it is clearly seen that the wave motion can be viewed as a summation of simple eigenfunctions, and the zeroth mode eigenfunction is the dominant one.

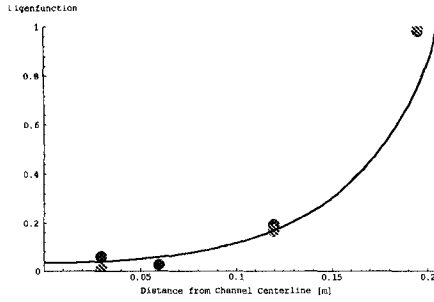


Figure 10: Comparison between the Zeroth Mode Eigenfunction for Case S1F2 and Numerical Solution, slope=1:2.9, T=0.800 s, h=0.0705 m, 0.985 m from Wavemaker

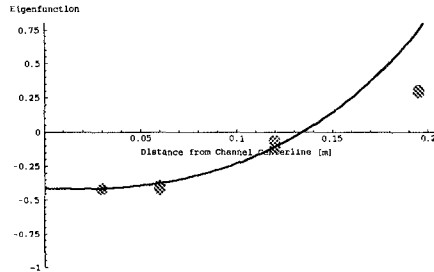


Figure 11: Comparison between the First Mode Eigenfunction for Case S1F2 and Numerical Solution

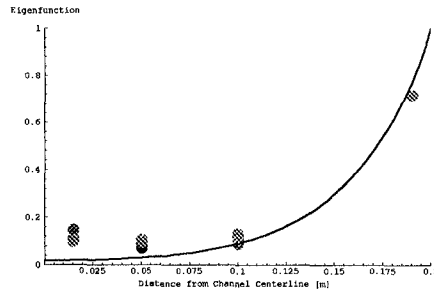


Figure 12: Comparison between the Zeroth Mode Eigenfunction for Case S2F2 and Numerical Solution, slope=1:3.1, T=0.725 s, h=0.0650 m, 0.950 m from Wavemaker

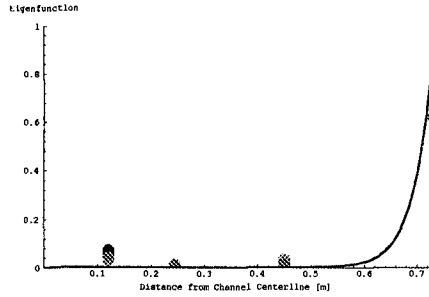


Figure 13: Comparison between the Zeroth Mode Eigenfunction for Trapezoidal Channel and Numerical Solution, slope=1:2.5, $T=0.570$ s, $h=0.0675$ m, 0.680 m from Wave-maker

3.3 Resonance ?

Figure 1 shows the instantaneous wave field obtained by the numerical model for the trapezoidal channel used in the test. It shows that zeroth mode edge wave has a wave length half of the incident wave length. From the nonlinear wave theory, the second harmonic wave over a flat bottom has a wave length equal to half of that of the incident wave. The issue whether there is any relationship between the zero mode edge wave and the second harmonic wave will be discussed here. Typical wave spectra in the experiments for trapezoidal channel are shown in Figures 14 and 15, which indicate the second harmonic wave frequency is twice of the first harmonic wave frequency.

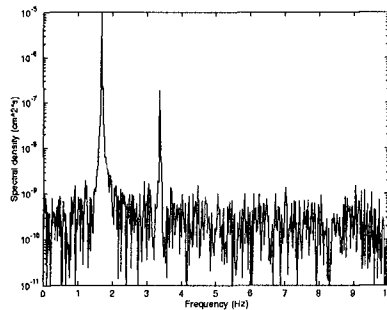


Figure 14: Wave Spectrum from Wave Data at Point: 0.410 m from Wavemaker, 0.425 m from Channel Center Line

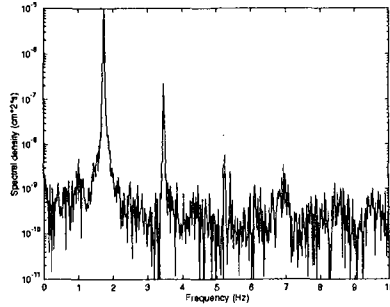


Figure 15: Wave Spectrum from Wave Data at Point: 0.820 m from Wavemaker, 0.425 m from Channel Center Line

Figure 16 shows the amplitude of the first three harmonics down the trapezoidal channel along the center line of the half-channel width, and Figure 17 shows the amplitude of the first three harmonics down the trapezoidal channel along the shoreline of the channel. It is seen that the second harmonics does not increase as might be expected by nonlinear interactions with the wave in the channel providing the forcing for edge wave growth (as indicated before). So the edge wave does not exhibit any resonance with the second harmonic of the incident wave.

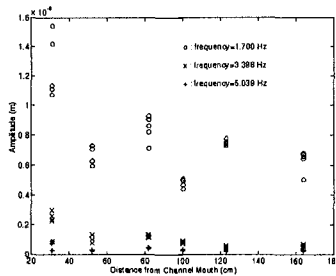


Figure 16: The Amplitudes of The First Three Harmonics Down the Channel; Channel Mouth to the Left, Channel End to the Right

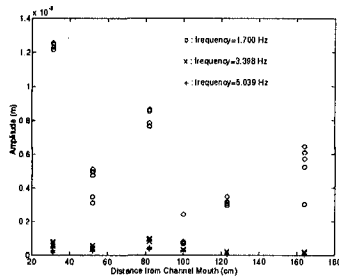


Figure 17: The Amplitudes of The First Three Harmonics Down the Channel along the Sidewall

4 Conclusion

A series of small scale laboratory experiments for triangular channel and trapezoidal channel were conducted to provide substance to the theoretical argument. It shows the experimental data exhibit good agreement with the numerical solutions. The results from the experiments and the numerical model show that channels with sloping sidewalls give rise to the presence of edge waves, excited by the incident wave field, while the incident wave propagate in the center of channel. The edge wave length is shorter than the incident wave length. The edge wave amplitude, represented by the zeroth mode eigenfunction, is much higher than the magnitude of the incident wave. According to the weight of each eigenfunction, the edge wave modes are the dominant ones in the wave motion. Because the amplitudes of higher harmonics do not increase, the edge wave does not exhibit any resonance with the second harmonic of the incident wave.

Reference

- Dalrymple, R.A. (1989), "Water Waves Past Abrupt Channel Transitions," *Applied Ocean Research*, v. 11, n. 4, pp 170-175.
- Dalrymple, R.A. (1992), "Water Wave Propagation in Jettied Channels," *Proc. 23rd Intl. Conference on Coastal Engineering*, pp 3040-3053 .
- Dalrymple, R.A. and J.T. Kirby (1988), "Models for Very Wide Angle Water Waves and Wave Diffraction," *Journal of Fluid Mechanics*, v. 192, pp 33-50.
- Dalrymple, R.A. and J.T. Kirby (1992), "Angular Spectrum Modelling of Water Waves," *Reviews in Aquatic Sciences*, CRC Press, 6, Iss. 5 and 6, pp 383-404.

- Dalrymple, R.A., J.T. Kirby and P.A. Martin (1994), "Spectral Methods for Forward-Propagating Water Waves in Conformally-Mapped Channels," *Applied Ocean Research*, v. 16, pp 249-266.
- Dalrymple, R.A., J.T. Kirby and L. Li (1994), "The Propagation of Water Waves in Channels," *Proc. Intl. Symp. on Waves*, IAHR, Vancouver, pp 570-579.
- Dalrymple, R.A. and P.A. Martin (1996), "Water Waves Incident on an Infinitely Long Rectangular Inlet," *Applied Ocean Research*, v. 18, pp 1-11.
- Dean, R.G. and R.A. Dalrymple (1995), **Coastal Processes with Engineering Applications**, manuscript.
- Golinko, V.I. (1987), "Interaction Between a Vertical Wall and a Wave Propagating in a Channel of Parabolic Cross Section", *Fluid Dyn.*, v. 22, n. 1, pp 87-90.
- Isaacson, M. de St.Q. (1978), "Wave Damping Due to Rubblemound Breakwater," *J. Waterways, Port, Coastal and Ocean Division*, v. 104, WW4, pp 391-405.
- Lamb, H. (1945), **Hydrodynamics**, 6th ed., New York, Dover Press, 1945.
- Mathew, J. and T.R. Akylas (1990), "On Three-Dimensional Long Water Waves in a Channel with Sloping Sidewalls", *J. Fluid Mech.*, v. 215, pp 289-307.
- Melo, E. and R.T. Guza (1991a), "Wave Propagation in a Jettied Entrance Channel, I: Models," *J. Waterways, Port, Coastal and Ocean Engrg.*, v. 117, n. 5, pp 471-492.
- Melo, E. and R.T. Guza (1991b), "Wave Propagation in a Jettied Entrance Channel, II: Observations," *J. Waterways, Port, Coastal and Ocean Engrg.*, v. 117, n. 5, pp 493-510.
- Peregrine, D.H. (1968), "Long Waves in a Uniform Channel of Arbitrary Cross-Section", *J. Fluid Mechanics*, v. 32, pp 353-365.
- Peregrine, D.H. (1969), "Solitary Waves in Trapezoidal Channel", *J. Fluid Mechanics*, v. 35, pp 1-6.
- Teng, M.H. and T.Y. Wu (1994), "Evolution of Long Water Waves in Variable Channels", *Journal of Fluid Mechanics*, v. 266, pp 303-317.
- Winant, C.D., D.L. Inman and C.E. Nordstrom (1975), "Description of Seasonal Beach Changes using Empirical Eigenfunction," *J. Geophys. Res.*, 80, 15, pp 1976-1986.

CHAPTER 85

A Statistical Approach for Modeling Triad Interactions in Dispersive Waves

Y. Eldeberky^{1,*}, V. Polnikov^{2,+}, and J.A. Battjes³

Abstract

The feasibility of a statistical approach to model the effect of triad interactions on the evolution of wave spectrum is investigated. The approach is based on the Zakharov kinetic integral for resonant triad interactions in capillary gravity waves. For application to dispersive gravity waves, the kinetic integral is modified by inclusion of a spectral filter (smeared delta function), to allow for the cross-spectral energy transfers in dispersive wavefields, with bandwidth to be determined empirically. Numerical investigation of the resulting expression indicates that the energy flux from the spectral peak region toward higher harmonics increases with decreasing water depth.

The interaction integral has been cast into an energy source/sink term and implemented in an energy balance equation that describes the evolution of a unidirectional energy spectrum in shoaling regions. The evolution model is investigated using observations of harmonic generation. Qualitatively the comparisons have shown the ability of the model to generate higher harmonics and a consequent upward shift in the mean frequency. However, quantitatively the model performance needs improvement.

1. Introduction

The evolution of wave spectra in shallow water is significantly affected by the cross-spectral energy transfers between various wave components due to triad

¹ Former Research Fellow, ² Visiting Researcher, ³ Professor at Delft University of Technology, Department of Civil Eng., P.O. Box 5048, 2600 GA Delft, The Netherlands.

* Presently Post-Doc at International Research Centre for Computational Hydrodynamics (ICCH), Danish Hydraulic Institute, Agern Allé 5, 2970 Hørsholm, Denmark.

+ Permanent at Marine Hydrophysical Institute of National Ukrainian Academy of Sciences, Kapitanskaya 2, Sevastopol 335000, Ukraine.

interactions. Boussinesq equations have been used to establish evolution equations for the complex amplitudes of waves propagating over slowly varying topography, simulating harmonic generation (Madsen and Sørensen, 1993).

For computational efficiency in practical applications, phase-averaged energy-based models are preferred. Abreu et al. (1992) have presented a statistical model for the nonlinear evolution of the frequency-directional spectrum, suitable as a source term in a spectral energy balance equation. The model is based on the nondispersive, nonlinear shallow-water equations and an asymptotic closure (Newell and Aucoin, 1971) for directionally spread nondispersive waves. The restriction to nondispersive waves is easily violated in practical application. The consequence of this is an unwanted behavior of the high-frequency part of the spectrum (dispersive waves).

The purpose of this paper is to investigate the feasibility of a statistical approach to model the average effects of triad interactions in dispersive surface gravity waves. The arrangement of this paper is as follows. In section 2, the kinetic integral for triad wave interactions in gravity waves is presented. The kinetic integral is numerically investigated and the results are analyzed in section 3. In section 4, the kinetic integral is used as an energy source/sink term in a spectral evolution model for investigation against observations of harmonic generation. Finally a discussion and conclusions are given in section 5.

2. Kinetic integral for triad interactions in surface gravity waves

The nonlinear triad interactions in surface gravity waves are treated mathematically using the Zakharov kinetic integral (Zakharov, 1968). The evolution equation of the spectral "energy" density n_k due to the triad interaction between (\mathbf{k}, ω) , (\mathbf{k}_1, ω_1) and (\mathbf{k}_2, ω_2) , where \mathbf{k} and ω are the wavenumber vector and the angular frequency respectively, is

$$\frac{dn_k}{dt} = 4 \iint d\mathbf{k}_1 d\mathbf{k}_2 [V_{k12}^2 N_{k12} \mu_{k-1-2} \delta_{k-1-2} - 2V_{1k2}^2 N_{1k2} \mu_{k-1+2} \delta_{k-1+2}] \quad (1)$$

Here V is the interaction coefficient and

$$N_{k12} = n_1 n_2 - n_k (n_1 + n_2) \quad (2)$$

in which the density n_k is related to the surface elevation wavenumber energy spectrum $E(\mathbf{k})$ by

$$n(\mathbf{k}) = \frac{(2\pi)^2 g}{\omega(\mathbf{k})} E(\mathbf{k}) \quad (3)$$

The factor μ_{k-1-2} in (1) is defined as

$$\mu_{k-1-2} = \frac{\Omega}{(\omega_k - \omega_1 - \omega_2)^2 + \Omega^2} \tag{4}$$

Ω is an auxiliary frequency parameter which is small compared to the spectral peak frequency ($\Omega \ll \omega_p$). The factor μ functions as a frequency filter. It is useful to gain insight in its behavior. Using the shorthand notation $\Delta\omega = \omega_k - \omega_1 - \omega_2$ and μ for μ_{k-1-2} , Fig. 1 shows μ (in Hz^{-1}) plotted versus $\Delta\omega$ (in Hz) for various values of Ω . The plot indicates that the filter becomes narrower and more spiky by decreasing the value of Ω , but the integral always equals π independent of Ω .

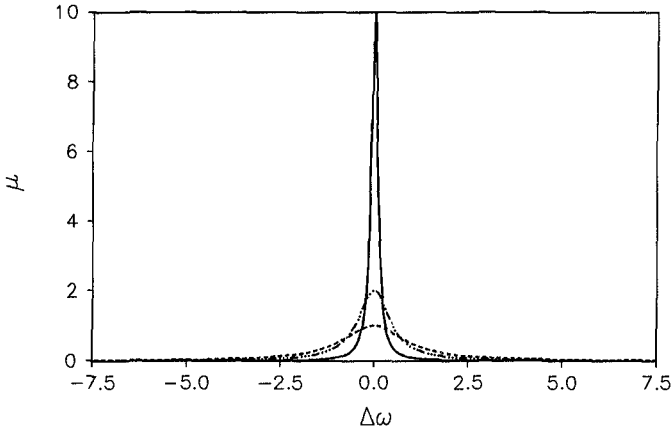


Fig. 1 μ plotted versus $\Delta\omega$ for various values of Ω . Dashed line: $\Omega=1.0$; Dot-dashed line: $\Omega=0.5$; Solid line: $\Omega=0.1$.

In the limit of $\Omega \rightarrow 0$, the filter becomes a dirac delta function and $\mu_{k-1-2} = \pi\delta(\omega_k - \omega_1 - \omega_2)$. Zakharov et al. (1992) use this limit, which upon substitution in (1) results in the kinetic integral for resonant three-wave interactions. The kinetic integral for resonant interactions gives nonzero contributions only for waves satisfying the resonance conditions

$$\omega(k) - \omega(k_1) - \omega(k_2) = 0 \tag{5}$$

$$k - k_1 - k_2 = 0$$

Exact resonance cannot be satisfied for surface gravity waves in water of arbitrary depth (Phillips, 1960; Hasselmann, 1962) with the following frequency dispersion

$$\omega^2 = gk \tanh(kh) \tag{6}$$

Thus for practical applications in intermediate depth, a formulation which allows for a degree of phase mismatch between the interacting waves is required to model

the cross-spectral energy transfers.

For the problem of off-resonant energetic triad interaction, Holloway (1980) suggested to use (4) for μ_{k12} with a small but finite value of Ω instead of its limit for $\Omega \rightarrow 0$. Thus instead of replacing equation (4) by a dirac delta function we use a smeared delta function (finite value of Ω) to allow for spectral energy transfers in dispersive wavefields. Here we treat Ω as a constant to be determined empirically. The feasibility of this approach will be investigated in the following.

Substituting equation (4) into equation (1) and integrating in k space yield the time evolution of the spectral "energy" density n_k due to triad interaction between components k , k_1 and k_2

$$\frac{dn_k}{dt} = 4 \int dk_1 \left\{ V_{k12}^2 N_{k12} \frac{\Omega}{(\omega_k - \omega_1 - \omega_2)^2 + \Omega^2} - 2 V_{1k2}^2 N_{1k2} \frac{\Omega}{(\omega_k - \omega_1 + \omega_2)^2 + \Omega^2} \right\} \quad (7)$$

This is the final equation describing the slow time evolution of the wave spectrum due to triad interactions. Assuming that the spectral energy is of second-order in nonlinearity: $n(k) \sim \epsilon^2$, one can define the time scale $t_1 = t_p \epsilon^{-2}$ for the slow variation of the wave spectrum. An appropriate value for the filter band-width Ω should be of the order $\Omega \cong t_1^{-1} = \epsilon^2 \omega_p$.

In application to spectral wave models based on the energy (or action) balance equation, source/sink terms are normally expressed in terms of energy (or action) density function $E(\omega, \theta)$ of the sea surface elevation. The relation between the wavenumber spectrum $E(k)$ and the frequency-directional spectrum $E(\omega, \theta)$ is

$$E(k) = \frac{c c_g}{\omega} E(\omega, \theta) \quad (8)$$

The evolution equation of the frequency-directional energy spectrum $E(\omega, \theta)$ can be found by substitution of (8) into (7) and rearranging

$$\frac{dE(\omega_k, \theta_k)}{dt} = 16 \pi^2 g \int_0^{2\pi} \int_0^\infty d\omega_1 d\theta_1 \frac{c_2 c_{g2}}{\omega_1 \omega_2^2} (T_{k12}^+ - 2T_{1k2}^-) \quad (9)$$

Here

$$T_{k12}^+ = V_{k12}^2 \left[\frac{\omega_k^2}{c_k c_{g,k}} E_1 E_2 - \frac{\omega_2^2}{c_2 c_{g2}} E_k E_1 - \frac{\omega_1^2}{c_1 c_{g1}} E_k E_2 \right] \frac{\Omega}{(\omega_k - \omega_1 - \omega_2)^2 + \Omega^2} \quad (10)$$

$$T_{1k2}^- = V_{1k2}^2 \left[\frac{\omega_1^2}{c_1 c_{g1}} E_k E_2 - \frac{\omega_2^2}{c_2 c_{g2}} E_k E_1 - \frac{\omega_k^2}{c_k c_{g,k}} E_1 E_2 \right] \frac{\Omega}{(\omega_k - \omega_1 + \omega_2)^2 + \Omega^2} \quad (11)$$

Note that the units of $E(\omega, \theta)$ is $m^2/\text{Hz}/\text{rad}$. The interaction coefficient V is given by

$$V_{k12} = \frac{g^{1/2}}{8\pi\sqrt{2}} \left\{ [k \cdot k_1 - (\omega_k \omega_1 / g)^2] (\omega_2 / \omega_k \omega_1)^{1/2} \right. \\ + [k \cdot k_2 - (\omega_k \omega_2 / g)^2] (\omega_1 / \omega_k \omega_2)^{1/2} \\ \left. + [k_1 \cdot k_2 + (\omega_1 \omega_2 / g)^2] (\omega_k / \omega_1 \omega_2)^{1/2} \right\} \quad (12)$$

Equations (9-11) describe the time evolution of wave energy spectrum $E(\omega, \theta)$ due to triad interactions. The first term of the integrand T_{k12}^+ represents the sum interaction ($k=k_1+k_2$), the second T_{k12}^- the difference interaction ($k=k_1-k_2$). The present formulation is directionally coupled and thus allows for both colinear and noncolinear interactions. Note that the resonance condition (5) does not necessarily have to be fulfilled in (7).

3. Numerical investigation of energy transfer rate

Aim and method of discretization

The general purpose of the investigations is to study the characteristics of the kinetic integral and the dependence of the nonlinear rate (NLR) of energy transfer on the filter bandwidth Ω and relative depth kh . The Jonswap spectrum is used to describe the frequency distribution of the wave energy and a \cos^2 -distribution is used for the directional spreading. The kinetic integral is calculated by means of simplest trapezium method of integration.

For a sufficiently fine grid (ω, θ) resolution, the values obtained for the kinetic integral do not significantly depend on the choice of grid. This choice is important from the point of view of good resolution of spectral form $E(\omega, \theta)$ and covering a proper interval of frequencies and directions for the output rate dE/dt . After some test calculations, we used a logarithmic frequency distribution with 48 discrete frequencies in the range $0.265 \leq \omega/\omega_p \leq 4$, and a uniform directional grid with 24 discrete components.

Results of calculations and analysis

The calculations of the kinetic integral have been carried out for a range of relative depths $k_p h = 3, 1.2, 0.6$, and 0.3 . Two values for the nondimensional parameter Ω/ω_p are considered, these are 0.01 and 0.1 .

Fig. 2 shows NLR for Jonswap spectrum for $k_p h = 0.3$ and $\Omega/\omega_p = 0.01$. The results are given in one-dimensional form, i.e., integrated over directions. The results show an energy flux from the region near the primary peak toward the higher harmonics. The behavior of the NLR indicates the following two features. First the maximum of the positive lobe occurs at $f/f_p = 1.9$ (less than the location of the first harmonic $2f_p$). This is due to the fact that a triad of waves is considered such that two wave components (ω_1, k_1) and (ω_2, k_2) can force a motion at the vector sum or

difference wavenumber $k=k_1 \pm k_2$ and frequency $\omega(k)$. This consideration implies that the first harmonic appears in the wavenumber spectrum at $2k_p$, which corresponds to a peak in the frequency spectrum at $\omega < 2\omega_p$ (in intermediate water). The second feature is that the area under the positive lobe is smaller than the area under the negative lobe, implying attenuation in the total energy.

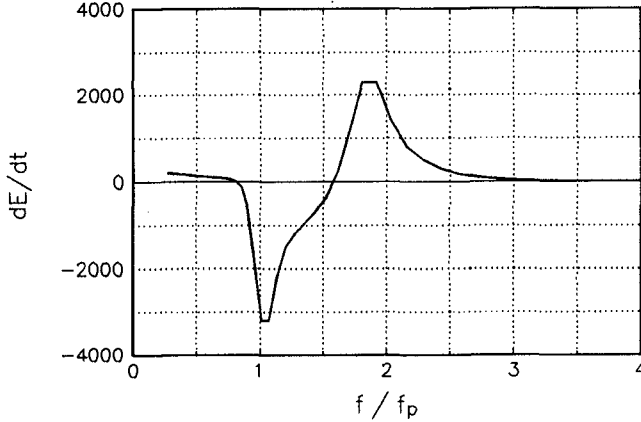


Fig. 2 Nondimensional rate of energy transfer in Jonswap spectrum, $\Omega/\omega_p=0.01$, $k_p h=0.3$, directional spreading; \cos^2 -distribution.

For quantitative analysis of the calculations we used the following characteristics:

- maximum value of positive lobe of two-dimensional NLR: MT^+ ;
- maximum absolute value of negative lobe of two-dimensional NLR: MT^- ;
- ratio of total NLR (two-dimensional NLR integrated over frequency and direction) to the absolute value of the total negative part of NLR: D

Table 1 summarizes the results for various relative depths and Ω -values. Note that the parameter D is a measure of energy conservation within the system. Positive values of D indicate energy gain and negative values indicate energy attenuation. Table 1 indicates that NLR is roughly proportional to the value of Ω .

Table 1 *Statistics of nonlinear rate (NLR) of energy transfer for Jonswap spectrum with direction spreading of \cos^2 -distribution*

$k_p h$	3		1.2		0.6		0.3	
Ω/ω_p	0.01	0.1	0.01	0.1	0.01	0.1	0.01	0.1
MT^+	0.1	1.1	1.1	10.7	48	401	2,031	11,071
MT^-	-0.6	-6.1	-1.9	-18.4	-64	-548	-2,566	-17,646
D	-0.48	-0.48	-0.26	-0.32	+0.16	-0.13	+0.12	-0.07

The parameter D measures the percentage of energy gain/loss from the total energy flux across the spectrum. In deep water D reaches large values but there the energy transfers are weak, so that the nonconservation of energy is weak also. As the water depth decreases in shallow water, the NLR increases strongly. In shallow water, although the values of D decrease, the energy attenuation becomes significant because of the strong increase in the NLR values. In fact for $\Omega/\omega_p=0.01$, D indicates an energy gain in shallow water ($k_p h=0.6, 0.3$).

The preceding analysis permits to state the following characteristics of NLR of energy transfers due to off-resonant triad interactions:

1. NLR strongly depends on the relative depth $k_p h$. With decreasing $k_p h$, the intensity of NLR increases.
2. NLR has a non-conservativity feature. Generally it results in an energy attenuation in intermediate and shallow water depths.
3. The intensity of NLR varies in proportion to Ω .

4. Spectral evolution

4.1 Model formulation and implementation

Assessment of the characteristics of the kinetic integral for triad interactions requires verification with observations. For simulation of the spectral evolution, we need to develop a spatial evolution model for the energy spectrum with a source/sink term representing the effect of triad wave interactions. Since the observations used here are measured in flume experiments that are characterized by long-crested waves, the following one-dimensional energy balance equation is used

$$\frac{d}{dx} [c_{g,k} E(\omega_k)] = S_k \quad (13)$$

Here $E(\omega_k)$ is the frequency energy density, $c_{g,k}$ is the one-dimensional group velocity and S_k is the net source/sink term. To implement the effect of triad wave interactions in equation (13), the kinetic integral (9-11) is cast in an energy source/sink term for unidirectional waves as follows:

$$S_{tr}(\omega_k) = 16\pi^2 g \int_0^\infty d\omega_1 \frac{c_2 c_{g2}}{\omega_1 \omega_2^2} (T_{k12}^+ - 2T_{1k2}^-) \quad (14)$$

$$T_{k12}^+ = V^2(\omega_k, \omega_1) \left[\frac{\omega_k^2}{c_k c_{g,k}} E_1 E_2 - \frac{\omega_2^2}{c_2 c_{g2}} E_k E_1 - \frac{\omega_1^2}{c_1 c_{g1}} E_k E_2 \right] \frac{\Omega}{(\omega_k - \omega_1 - \omega_2)^2 + \Omega^2}$$

$$T_{1k2}^- = V^2(\omega_1, \omega_k) \left[\frac{\omega_1^2}{c_1 c_{g1}} E_k E_2 - \frac{\omega_2^2}{c_2 c_{g2}} E_k E_1 - \frac{\omega_k^2}{c_k c_{g,k}} E_1 E_2 \right] \frac{\Omega}{(\omega_k - \omega_1 + \omega_2)^2 + \Omega^2}$$

The energy source/sink term given in (14), for the effect of triad wave interactions, represents a (positive/negative) contribution to the temporal rate of change of spectral density. The energy balance equation (13) comprises a set of first-order ordinary differential equations that describe the evolution of the energy spectrum $E(\omega)$. Giving the initial energy spectrum at the upwave boundary, equation (13) has been numerically integrated using a fourth-order Runge-Kutta method.

4.2 Simulation of spectral evolution

In this section, the evolution model (13) together with the triad source term (14) is investigated using observations for harmonic generation in random waves propagating over a shallow bar (Beji and Battjes, 1993) as well as over a beach profile (Arcilla et al., 1994).

The investigation of the nonlinear rate (NLR) of energy transfers presented in section (3) has shown that the present formulation is not conservative. To ensure energy conservation in the simulation of spectral evolution the following *ad hoc* method is used. First the NLR of energy transfer is estimated as a first guess using the present formulation. Next the integral (of NLR) over the spectrum which represents the total energy gain/loss I is computed. The NLR of energy transfer is then rescaled by adding (or subtracting) the quantity I . If I is negative, implying energy loss, then the area of negative lobe is reduced with I in proportion to the values of the NLR. On the other hand if I is positive, implying energy gain, then the area of positive lobe is reduced with I in proportion to the values of the NLR.

To simulate energy dissipation due to wave breaking over a beach profile, the energy balance equation (13) is supplemented with a source term for depth induced wave breaking after Eldeberky and Battjes (1996), in which the total energy dissipation due to breaking in random waves is calculated according to Battjes and Janssen (1978) and spectrally distributed in proportion to the spectral levels.

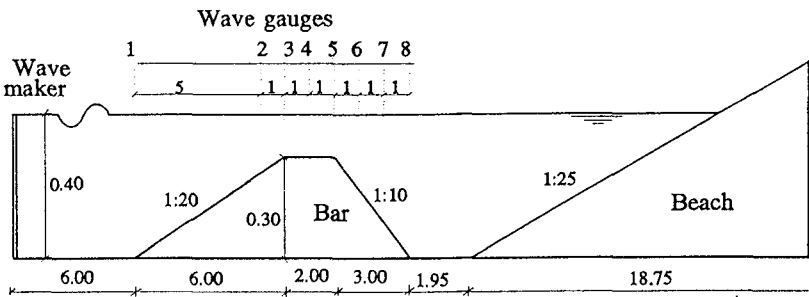


Fig. 3 Layout for the experimental setup of Beji and Battjes (1993). All lengths are expressed in meters.

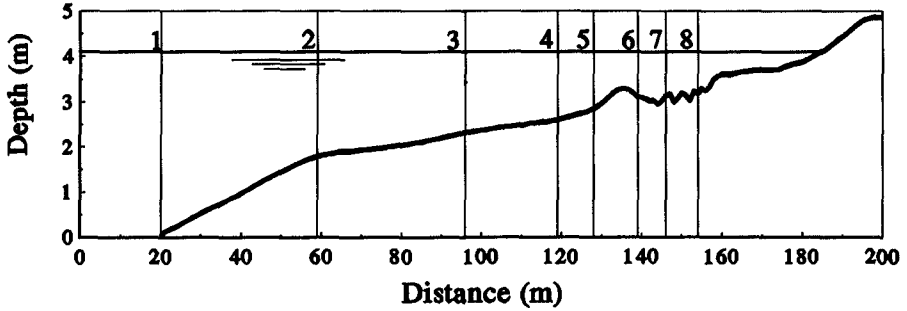


Fig. 4 Bed profile and locations of wave gauges (Arcilla et al., 1994)

To examine the sensitivity of the spectral evolution to the choice of Ω , two values are used in the computations: $\Omega/\omega_p=0.01$ and 0.1 . The computed spectra are compared to the measured ones in nonbreaking waves propagating over a bar (Fig. 3) and breaking waves over a beach profile (Fig. 4). The results are given in Figs. 5 and 6 respectively. The comparisons indicate the following characteristics of the triad source term:

1. The intensity of energy transfers from the primary spectral peak to the higher frequencies is mainly controlled by the choice of Ω -value. Increasing Ω -value results in stronger energy transfers, extended to higher frequencies.
2. The energy transfers to higher harmonics are underestimated when $\Omega/\omega_p=0.01$, and overestimated when $\Omega/\omega_p=0.1$. The latter results in an unwanted behavior for the energy spectrum at the high frequency range (spectral tail).
3. The second spectral peak (in frequency-domain) is shifted to a lower frequency compared with observation. It appears at a frequency less than two times the primary peak. This is ascribed to the fact that triads are considered such that $k=k_1+k_2$, which results in $\omega_k < \omega_1 + \omega_2$ in intermediate water depths.

4.3 Sensitivity to the filter bandwidth

The previous results for the computed spectral evolution have shown dependence of the NLR of energy transfer on the choice of the filter bandwidth Ω . Additional numerical simulations for wave propagation over a shallow bar and beach profile have been carried out with different values of Ω . To evaluate the variation in the spectral evolution for various values of Ω , the variations in the mean frequency of the spectrum are computed. The mean frequency of the energy spectrum is defined as

$$f_m = \frac{\int \omega E(\omega) d\omega}{2\pi \int E(\omega) d\omega} \quad (15)$$

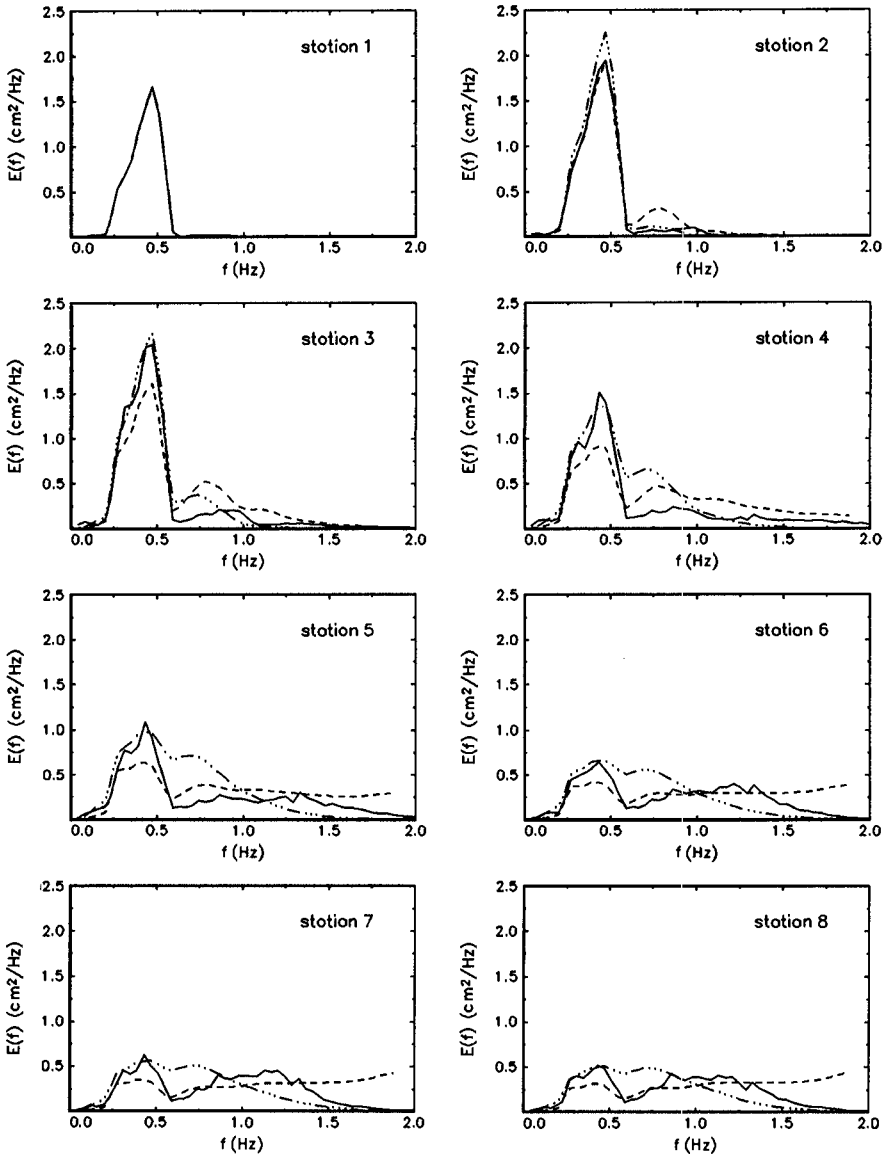


Fig. 5 Energy spectra from experiments (solid lines) and from the evolution model: with $\Omega/\omega_p=0.01$ (dashed lines) and $\Omega/\omega_p=0.1$ (dot-dashed lines) for waves propagating over a shallow bar.

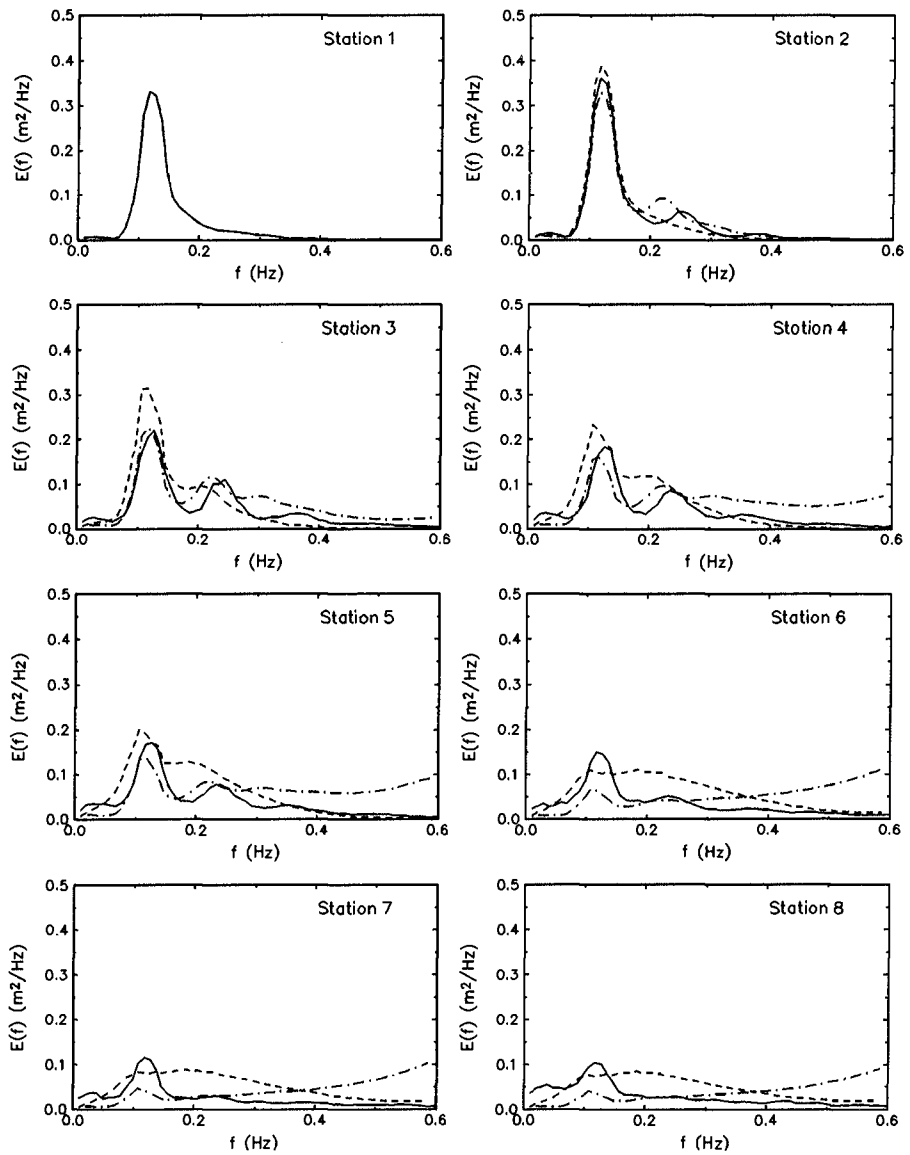


Fig. 6 Energy spectra from experiments (solid lines) and from the evolution model: with $\Omega/\omega_p=0.01$ (dashed lines) and $\Omega/\omega_p=0.1$ (dot-dashed lines) for waves propagating over a beach profile.

Fig. 7 shows the observed variations in the mean frequency in waves passing over a shallow bar and those computed by the evolution model with different values of Ω/ω_p . The observed variation in the mean frequency shows a rapid increase (from 0.43 Hz to 0.85 Hz) over the upslope side and the horizontal part of the bar, which is ascribed to generation of higher harmonics. Beyond the bar crest, the mean frequency remains at a high level without significant change. The computed variations in the mean frequency using the evolution model show a strong dependence on the value of the parameter Ω . The larger the value of Ω/ω_p , the stronger the energy transfers and hence the shift in the mean frequency to higher harmonics. From the results one can see that the best choice for the parameter Ω/ω_p , for best simulation of the observed shift in the mean frequency, in this case is between 0.01 and 0.03.

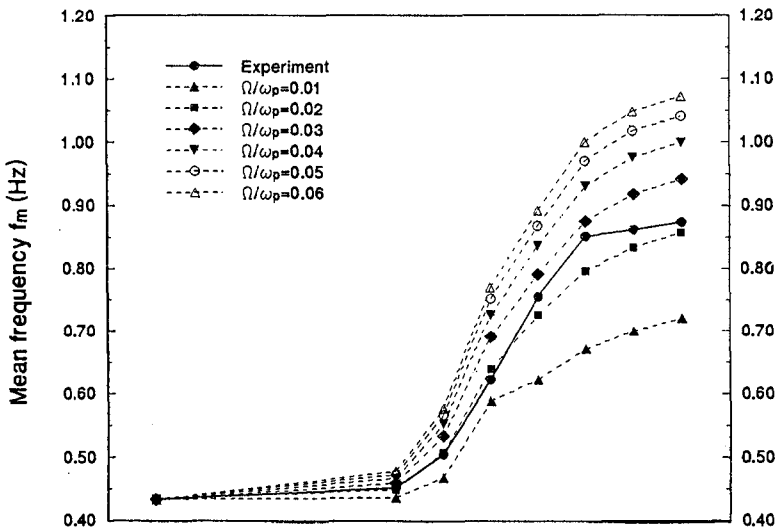


Fig. 7 Spatial variation of mean frequency f_m in waves propagating over a shallow bar. Solid line: experiment; Dashed lines: evolution model using different values for Ω/ω_p

Fig. 8 shows the observed variations in the mean frequency in waves propagating over a beach profile and those computed by the evolution model with different values of Ω . The observed variation in the mean frequency shows a rapid increase in intermediate water from 0.14 Hz to 0.21 Hz due to harmonic generation. In very shallow water, the mean frequency nearly attains a constant level. The computed variations in the mean frequency using the evolution model show a strong dependence on the value of Ω . In intermediate water depths (between stations 1 and 3) computations with $\Omega/\omega_p=0.04$ and 0.05 seem to best match the observed shift in the mean frequency. In shallow water, all computations with different values of Ω result in a trend which differs strongly from the observed one, significantly overestimating the mean frequency.

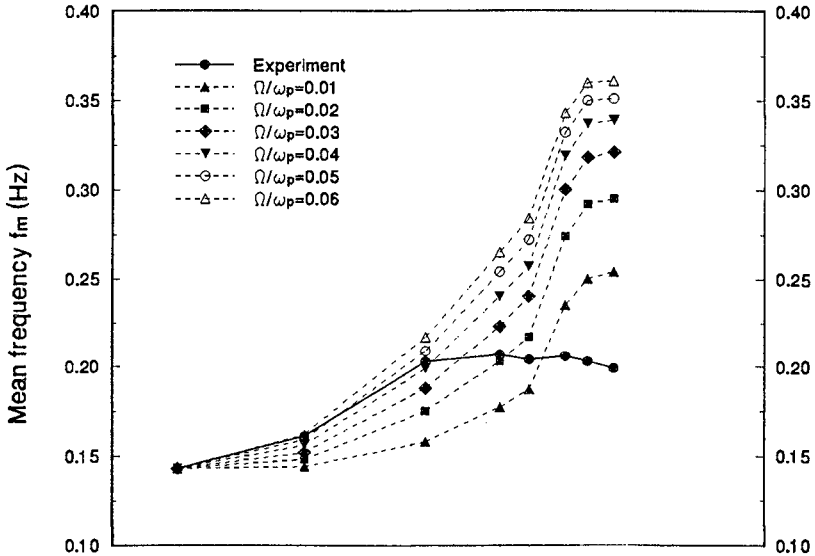


Fig. 8 Spatial variation of mean frequency f_m in waves propagating over a beach profile. Solid line: experiment; Dashed lines: evolution model using different values for Ω/ω_p

5. Discussion and conclusions

The feasibility of a statistical approach to model the average effects of triad interactions on the evolution of wave spectrum is investigated. The approach is based on the Zakharov kinetic integral for resonant triad interactions in capillary gravity waves. For application to surface gravity dispersive waves, the kinetic integral is supplemented with a frequency filter to allow for the off-resonant energetic interactions. The filter bandwidth Ω is of small but finite value resulting in a smeared delta function. Ω is treated as a constant to be determined empirically. The interactions integral is used as a source term in an evolution model to simulate observations of harmonic generation in waves propagating over a shallow bar as well as over a beach profile. In general the comparisons have shown the ability of the model to generate higher harmonics and a consequent upward shift in the mean frequency.

The consequences of treating the filter bandwidth Ω as a constant have resulted in an energy attenuation and unguaranteed spectral evolution in some cases. Holloway (1980) proposed to treat Ω as a prognostic variable with magnitude related to the rate of interaction of the three components involved in the interaction and increases with increasing nonlinearity. In Holloway's approach, the magnitude of Ω for the interaction between l , m , and n needs to be determined first by solving three equations representing the interaction rates of the three components. These three equations for each possible triad together with the spectral evolution equations

represent a closed set of equations guiding the evolution of the energy density spectrum.

In principle the approach of Holloway (1980) sketched above may be applied to provide an estimate for the parameter Ω . This may achieve a better prediction of the evolution of the energy spectrum. On the other hand the extensive computational efforts required to resolve the closed set of equations are a concern. For computational efficiency in practical applications, we recommend a parametrized source term for triad wave interactions (Eldeberky, 1996, Chapter 7 and Eldeberky and Battjes, 1997)

Acknowledgements

The work presented here is part of a project sponsored by the Dutch Department of Public Works (RWS). V. Polnikov was supported by a grant from the Burgers Centrum, The Netherlands. This manuscript is prepared while Y. Eldeberky is supported by the Danish National Research Foundation.

References

- Abreu, M., A. Larraza, and E.B. Thornton, 1992, Nonlinear transformation of directional wave spectra in shallow water, *J. Geophys. Res.*, 97, pp. 15579-15589.
- Arcilla, A.S., J.A. Roelvink, B.A. O'Connor, A.J.H.M. Reniers, and J.A. Jimenez, 1994, The Delta flume '93 experiment, *Proc. Coastal Dynamics Conf. '94*, Barcelona, Spain, pp. 488-502.
- Battjes, J.A., and J.P.F.M. Janssen, 1978, Energy loss and set-up due to breaking of random waves, *Proc. Coastal Eng. Conf.*, 16th, pp. 569-587.
- Beji, S., and J.A. Battjes, 1993, Experimental investigation of wave propagation over a bar, *Coastal Eng.*, 19, pp. 151-162.
- Eldeberky, Y., and J.A. Battjes, 1996, Spectral modeling of wave breaking: Application to Boussinesq equations, *J. Geophys. Res.*, 101(C1), pp. 1253-1264.
- Eldeberky, Y., 1996, Nonlinear transformation of wave spectra in the nearshore zone, *Ph.D. thesis*, Delft University of Technology, The Netherlands.
- Eldeberky, Y., and J.A. Battjes, 1997, Parameterized energy formulation for triad wave interactions, In preparation.
- Hasselmann, K., 1962, On the non-linear energy transfer in a gravity wave spectrum, Part 1. General theory, *J. Fluid Mech.*, 12, pp. 481-500.
- Holloway, G., 1980, Oceanic internal waves are not weak waves, *J. Physical Ocean.*, 10(6), pp. 906-914.
- Madsen, P.A., and O.R. Sørensen, 1993, Bound waves and triad interactions in shallow water, *J. Ocean Engng.*, 20(4), pp. 359-388.
- Newell, A.C., and P.J. Aucoin, 1971, Semidispersive wave systems, *J. Fluid Mech.*, 49(3), pp. 593-609.
- Phillips, O.M., 1960, On the dynamics of unsteady gravity waves of finite amplitude. Part 1, *J. Fluid Mech.*, 9, pp. 193-217.
- Zakharov, V.E., 1968, Stability of periodic waves of finite amplitude on the surface of a deep water, Engl. trans. *Soviet Physics, J. Appl. Mech. Tech. Phys.*, 4, pp. 86-94.
- Zakharov, V.E., V.S. L'vov, and G. Falkovich, 1992, *Kolmogorov spectra of turbulence, I. Wave Turbulence*, Springer verlag.

CHAPTER 86

A Fully Nonlinear 3D Method for the Computation of Wave Propagation

Andrew B. Kennedy¹ and John D. Fenton¹

Introduction

The computational capabilities for calculating nonbreaking wave evolution have advanced a great deal in recent years. For fully nonlinear models, the adoption of multi-subdomain techniques (Wang et al., 1995, de Haas et al., 1996) has provided much greater efficiency while still allowing the calculation of wave transformation up to overturning. Still, computational times remain great enough that the application of these methods to three dimensional domains remains somewhat limited. The variable depth Boussinesq equations were originally developed with the twin assumptions of mild nonlinearity and frequency dispersion (Peregrine, 1967), but recently, beginning with Witting (1984), there have been concerted efforts to increase their range of applicability. Papers of particular note include Madsen and Sørensen (1992), Nwogu (1993), Wei et al. (1994), Schäffer and Madsen (1995), and Gobbi and Kirby (1996) (GK). Of these, all but GK assume a flow field that varies quadratically in the vertical coordinate y , while GK derive their equations for a quartic vertical variation in the velocity potential. All of these methods have at least one free parameter which is invariably used to calibrate model linear phase speed, linear shoaling, second order transfer functions, or some combination of the three, to known analytic results over a level bed or small slope. For these special conditions, the accuracy of the various Boussinesq equations may be greatly improved and, in fact, the above papers have shown that accuracy is also improved for conditions which differ significantly from the idealised situations used for tuning. However, it is not possible to place confidence in velocities, pressures, and higher order free surface nonlinearities calculated by any of these methods except in reasonably shallow depths. The one exception to this are the GK higher order Boussinesq equations, which are quite complex.

In Kennedy and Fenton (1995) a method was developed to calculate wave evolution over varying topography for one dimension in plan. The flow field was locally represented by a polynomial of arbitrary degree which analytically satisfied Laplace's

¹ Dept. of Mech. Eng., Monash University, Clayton, Vic. Australia 3168

equation. By applying continuity conditions between subdomains, an overall solution to the boundary value problem was obtained and highly accurate time stepping solutions could be obtained. A summary of this, plus another related method appears in Fenton and Kennedy (1996).

In this paper, a method is developed which uses some of the same ideas but is valid for three dimensional fluid motion (two dimensions in plan). Again, the velocity potential is represented in the vertical by a polynomial of arbitrary degree but here, a set of differential equations results for a local polynomial approximation (LPA) to the exact solution. This is shown to provide excellent linear and nonlinear results for a wide range of waves. The degree of polynomial may also be easily changed to give the level of accuracy desired for a particular problem.

Solution of Laplace's Equation

For nonbreaking wave motion, the flow field is usually represented by a velocity potential, $\phi(x, z, y, t)$, and fluid velocities are thus $(u, w, v) = (\partial\phi/\partial x, \partial\phi/\partial z, \partial\phi/\partial y)$, where x and z are the horizontal coordinates and y is the vertical coordinate. The continuity equation for fluid flow to be satisfied at every point in the domain then becomes

$$\frac{\partial^2\phi}{\partial x^2} + \frac{\partial^2\phi}{\partial y^2} + \frac{\partial^2\phi}{\partial z^2} = 0, \quad (1)$$

which is simply Laplace's equation in three dimensions. At any time t_0 this velocity potential is subject to the boundary conditions

$$\phi = \phi_s \quad \text{on } y = \eta, \quad (2)$$

and

$$\frac{\partial\phi}{\partial y} - \frac{\partial\phi}{\partial x} \frac{\partial h}{\partial x} - \frac{\partial\phi}{\partial z} \frac{\partial h}{\partial z} = 0 \quad \text{on } y = h, \quad (3)$$

where $h(x, z)$ is the bed elevation, and the free surface elevation $\eta(x, z, t)$ and velocity potential $\phi_s(x, z, t)$ are both known at time t_0 . With the addition of appropriate conditions on the horizontal boundaries, these two conditions (2) and (3), along with the field equation (1) completely specify the problem and may be used to solve for the flow field.

The velocity potential function used here assumes a polynomial variation in the vertical coordinate such that

$$\phi(x, z, y, t) = \sum_{j=0}^r A_j(x, z, t) y^j, \quad (4)$$

where $r \geq 2$, and the A_j coefficients are independent and may vary in time.

From here, there are many directions that could be taken. The Boussinesq approach would be to create a Taylor series expansion about some point in the water column which satisfies the bottom boundary condition (3) to the order of accuracy desired, and proceed from there. However, it is desired here to use an approximation which

distributes error more evenly than is possible with a Taylor series, where error quickly increases away from the expansion point. The obvious approach would now be some sort of finite element method, but this would involve volume integrals, which are slow to compute. Furthermore, unless higher order elements were used, convergence would be slow, and introducing them would increase computational costs significantly.

Therefore, a different approach is used, which is simple in concept, and distributes the error in (1) over the water column. First, constraints are imposed so that the velocity potential satisfies (2) and (3). Next, the average and first $r - 2$ weighted averages of (1) over the water column are set to zero, such that

$$\int_h^\eta y^l \left(\frac{\partial^2 \phi}{\partial x^2} + \frac{\partial^2 \phi}{\partial y^2} + \frac{\partial^2 \phi}{\partial z^2} \right) dy = 0, \quad l = 0, \dots, r - 2. \quad (5)$$

The appropriate global horizontal boundary conditions finish the specification of the problem and a set of linear equations results, which may be solved as desired.

Once the flow field is known, the free surface elevations and velocity potentials may be updated in time using the evolution equations

$$\frac{\partial \eta}{\partial t} = \frac{\partial \phi}{\partial y} - \frac{\partial \eta}{\partial x} \frac{\partial \phi}{\partial x} - \frac{\partial \eta}{\partial z} \frac{\partial \phi}{\partial z} \quad \text{on } y = \eta, \quad (6)$$

and

$$\frac{\partial \phi_s}{\partial t} = C - g\eta - \frac{1}{2} \left(\frac{\partial \phi^2}{\partial x} + \frac{\partial \phi^2}{\partial z} + \frac{\partial \phi^2}{\partial y} \right) + \frac{\partial \phi}{\partial y} \frac{\partial \eta}{\partial t} \quad \text{on } y = \eta. \quad (7)$$

Alternate Formulations for the Velocity Potential

It is possible to rearrange the form of the velocity potential given in (4) so that it has fewer parameters at each computational point. The velocity potential

$$\begin{aligned} \phi(x, z, y, t) = & \phi_s \left(\frac{y-h}{\eta-h} \right)^2 + A_B \left[(y-\eta) + \frac{f_2 (y-\eta)(y-h)}{f_1 (\eta-h)} \right] \\ & + \frac{\partial A_B}{\partial x} \frac{\partial h}{\partial x} \frac{(y-\eta)(y-h)}{f_1} \\ & + \frac{\partial A_B}{\partial z} \frac{\partial h}{\partial z} \frac{(y-\eta)(y-h)}{f_1} + A_3 (y-h)^2 (y-\eta) \\ & + A_4 (y-h)^2 (y-\eta)^2 + \dots \\ & + A_r (y-h)^2 (y-\eta)^{r-2}, \end{aligned} \quad (8)$$

where

$$f_1 = 1 + \frac{\partial h^2}{\partial x} + \frac{\partial h^2}{\partial z},$$

and

$$f_2 = 1 + \frac{\partial h}{\partial x} \frac{\partial \eta}{\partial x} + \frac{\partial h}{\partial z} \frac{\partial \eta}{\partial z},$$

analytically satisfies both (2) and (3). If made to satisfy (5), the resulting velocity potential will be identical to that described in the previous section. Furthermore, since

two fewer coefficients are defined at each point, computational speed should increase significantly. However, it is obvious that coding will be much more complex and, due to time constraints, and because the main thrust of this paper is to determine the accuracy of this LPA method, the velocity potential formulation of (8) was not used.

Linear Properties

Phase Speed

Using linearised versions of the free surface conditions (6) and (7), analytic LPA solutions for a given level of approximation, r , may be found for a plane progressive wave train. For the level of approximation $r = 2$ (y^2 terms included in ϕ), the phase velocity c is

$$\frac{c^2}{gd} = \frac{1}{1 + \frac{1}{3} (kd)^2}, \tag{9}$$

where g is the gravitational acceleration, d is the fluid depth, and k is the wavenumber. For the level of approximation $r = 3$ (y^3 terms in ϕ), the relationship is

$$\frac{c^2}{gd} = \frac{1 + \frac{1}{10} (kd)^2}{1 + \frac{13}{30} (kd)^2 + \frac{1}{80} (kd)^4}, \tag{10}$$

and using $r = 4$ (y^4 terms in ϕ), the phase velocity is

$$\frac{c^2}{gd} = \frac{1 + \frac{13}{105} (kd)^2 + \frac{1}{420} (kd)^4}{1 + \frac{16}{35} (kd)^2 + \frac{3}{140} (kd)^4 + \frac{1}{6300} (kd)^6}. \tag{11}$$

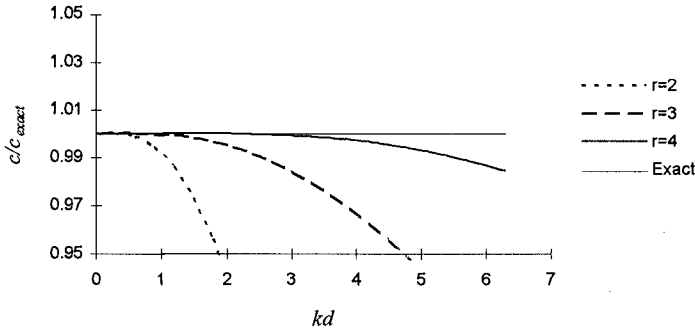


Figure 1. Small amplitude phase velocity

These expressions are identical to those obtained for Green-Naghdi shallow water Theories I, II, and III respectively (Shields and Webster, 1988). All of these are approximations to the exact small amplitude relationship

$$\frac{c_{exact}^2}{gd} = \frac{\tanh(kd)}{kd}. \tag{12}$$

In both (9) and (10) errors are of $O((kd)^4)$, while (11) contains errors of $O((kd)^8)$. Figure 1 compares LPA and exact phase speeds. Using the LPA level $r = 2$, phase speeds are found to be quite reasonable until a dimensionless wavenumber of $kd = 1.25$ ($L/d = 5$) is reached, while with $r = 3$, phase speeds are adequate up until the nominal deep water limit of $kd = \pi$ ($L/d = 2$). The level of approximation $r = 4$ gives very good results well into deep water and is usable even for a wave with $kd = 2\pi$ ($L/d = 1$) which is a very pleasing result.

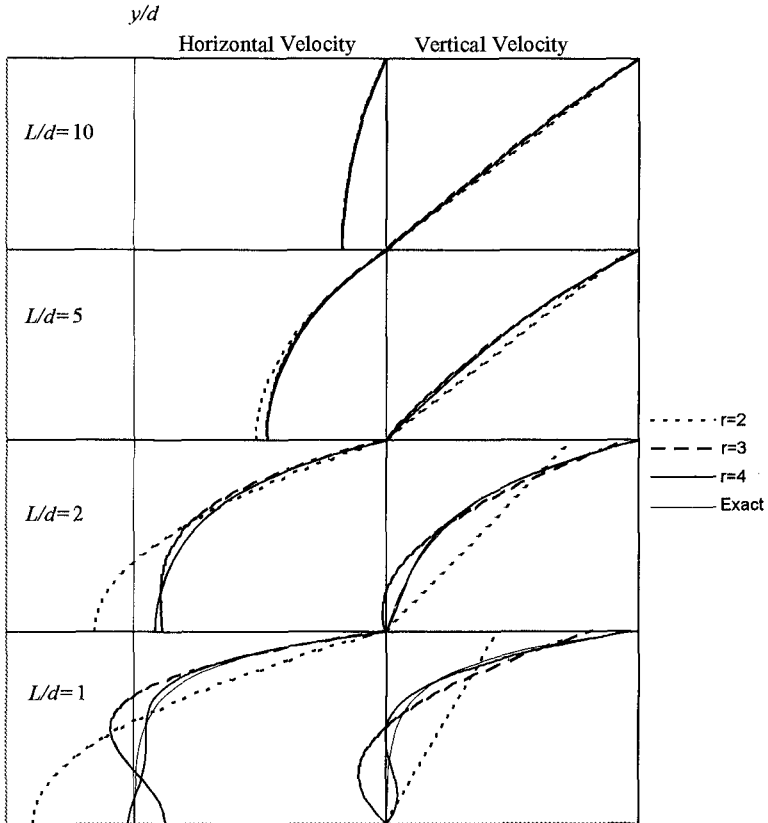


Figure 2. Normalised fluid velocities under a small amplitude wave

Fluid Velocities and Pressures

Small amplitude LPA solutions for ϕ may also be used to compare internal fluid velocities and pressures with Stokes first order results. Figure 2 shows the variation of the horizontal and vertical velocities, u and v , over the water column. For a wave with length $kd = \pi/5$ ($L/d = 10$), all levels of LPA approximation give a good result,

although the level $r = 2$ shows slight differences, with the vertical velocity looking least accurate. Decreasing the wavelength to $kd = 2\pi/5$ ($L/d = 5$) increases error for the level $r = 2$, although all other levels predict velocities well. At the nominal deep water limit of $kd = \pi$ ($L/d = 2$), LPA levels $r = 2$ and $r = 3$ have significant errors in velocity, while with $r = 4$, the velocity is still modeled well. For a wave with length $kd = 2\pi$ ($L/d = 1$), all levels of approximation show error, although a convergence toward the exact solution is evident. Results for the dynamic pressure response factor $f(y)$, which gives the ratio of dynamic pressure at any elevation to the dynamic pressure just below the still water level, are identical to the results for relative horizontal velocity.

General Comments

With an overall view of the linear properties, some judgements may now be made. The first is that the level of LPA approximation $r = 2$ is only suitable for waves in shallow and mildly intermediate depths. For all other waves, the assumed structure of the velocity potential is inadequate to describe the vertical variation of the fluid flow. For these reasons, and since other levels are much more accurate, the level $r = 2$ will be discarded. The LPA level $r = 3$ gives significantly better results through to near the nominal deep water limit of $L/d = 2$, both for phase speed and fluid velocities. The level of approximation $r = 4$ has very accurate linear properties into quite deep water, and an increase to an LPA level to greater than this does not appear to be justified at the present time.

It is quite easy to introduce tuning parameters into the solution. By replacing (5) with the more general

$$\int_h^n w_l(y) \left(\frac{\partial^2 \phi}{\partial x^2} + \frac{\partial^2 \phi}{\partial y^2} + \frac{\partial^2 \phi}{\partial z^2} \right) dy = 0, \quad l = 0, \dots, r - 2 \quad (13)$$

where $w_l(y)$ is some weighting function, sets $\{w_l\}$ were easily found which gave more accurate phase velocities for the LPA levels $r = 3, 4$. However, any increase in accuracy of phase velocity was invariably coupled with a decrease in accuracy of some other quantity of interest. For example, a set $\{w_l\}$ was found where the approximation of (11) for the LPA level $r = 4$ had errors decrease from $O((kd)^8)$ to $O((kd)^{10})$. However, errors in the horizontal velocity at the bed, which could be taken as another measure of accuracy, increased from $O((kd)^8)$ to $O((kd)^6)$. Because of results like this, and because the set of weighting functions $\{1, y, y^2, \dots\}$ is very general, no attempt was made to tune the model for any particular quantity.

Nonlinear Properties

The nonlinear properties implied by the LPA set of governing equations were investigated by comparing their solutions for steady nonlinear waves with numerically exact solutions of the full potential flow equations. Numerically exact waves were generated using the Fourier method of Fenton (1988), while the fully nonlinear LPA solutions were found using the same general idea adapted to LPA.

Figure 3 compares LPA and numerically exact profiles for three highly nonlinear waves. The first wave generated is long, with a length to depth ratio of $L/d = 20$ ($kd = \pi/10$), and a height of $H/d = 0.6$. Both LPA levels $r = 3$ and $r = 4$ predict the profile very well. The second wave has length $L/d = 5$ ($kd = 2\pi/5$) and height $H/d = 0.4$. Once again, both LPA levels tested predict the nonlinear wave profile very accurately. The final wave in Figure 3 is at the nominal deep water limit, with a length to depth ratio of $L/d = 2$ ($kd = \pi$), and a height $H/d = 0.2$. For this wave, the LPA level of approximation $r = 3$ shows small errors, although the overall wave form is predicted well. However, the level $r = 4$ once again provides a solution which is indistinguishable by eye from the numerically exact profile.

Nonlinear phase speeds may also be compared with exact solutions. Figure 4 plots LPA and exact speeds for waves with length $L/d = 20, 5,$ and 2 . Circles, triangles and squares show the highest wave computed for the levels $r = 3, r = 4,$ and numerically exact solutions, respectively. These do *not* represent the limiting waves, but instead describe a failure of the solution method to solve the system of nonlinear equations past these points.

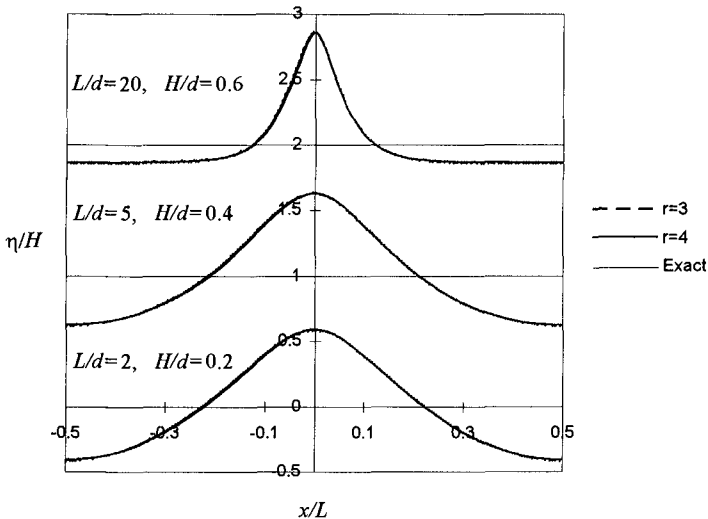


Figure 3. Nonlinear wave profiles

Both LPA levels $r = 3$ and $r = 4$ give a very good estimate of phase speed up to the highest waves tested, with the only significant differences occurring using $r = 3$ with a wave of length $L/d = 2$. However, even here the trend is followed quite well. The results for the level $r = 4$ and the wave with length $L/d = 5$ are especially noteworthy. Here, LPA solutions were found close to the limiting height which predicted the maximum and subsequent decrease in wave speed shown by

Cokelet (1977). This good representation of highly nonlinear waves gives additional confidence in the accuracy of the 3D LPA method.

Time Stepping Solutions

Time stepping solutions of the governing equations may be divided into two main tasks: the LPA solution of Laplace's equation, and the advance of the solution to the next time step. Of the two, the second is the most straightforward, as (6) and (7) were used with either a second order leapfrog or third order Adams-Bashforth technique to update the free surface elevations and velocity potentials. As neither of these methods are self starting, a fourth order Runge-Kutta technique was used for the first few time steps.

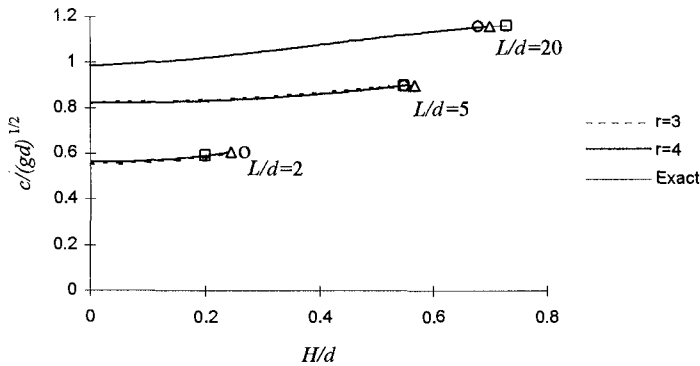


Figure 4. Nonlinear wave speeds

To solve Laplace's equation, all coefficients were represented using fifth degree two dimensional B-splines (see de Boor, 1978), which are simply the product of one dimensional B-splines in x and z which have the same centre. Solutions were also computed using third degree B-splines, but convergence was found to be poorer than desired. The sparse system of linear equations which results from the B-spline representation was solved using a line by line successive under-relaxation technique. Using this representation, errors in the LPA solution are theoretically proportional to $(\Delta l)^4$, where Δl is mesh size. This was tested by computing the maximum relative error in vertical velocity at the free surface for a flow field with a flat bed and surface, and free surface velocity potential $\phi_s = \cos(kx)$, where $kd = \pi/10$ ($L/d = 20$). Figure 5 shows the relative error, plotted alongside $(L/\Delta l)^4$ for comparison. Convergence is seen to follow the theoretical behaviour closely. Furthermore, even for a very coarse representation of $\Delta l/L = 1/6$ (6 points/wavelength), relative errors are still only two parts in a thousand, which allows confidence to be placed in computations with relatively coarse resolution.

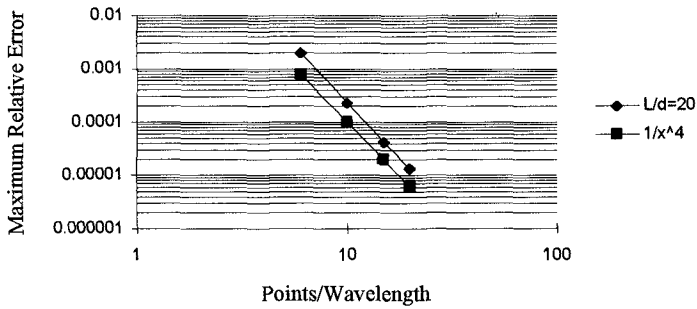


Figure 5. Convergence of the numerical scheme

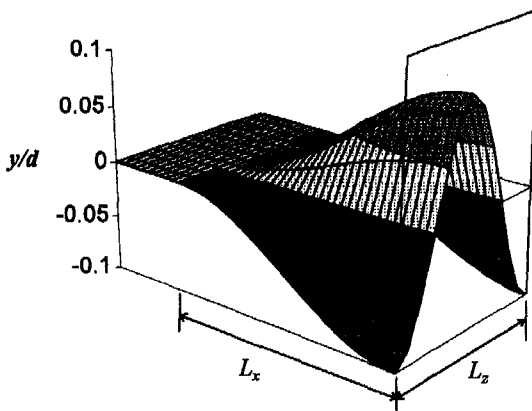


Figure 6. Bottom topography for solitary wave reflection

The Runup of a Focused Solitary Wave on a Vertical Wall

For a first test, a solitary wave of height $H/d = 0.2$ was propagated over topography which tended to focus the wave, which was then reflected by a vertical wall. Computations were performed using the LPA level $r = 4$. Figure 6 shows the focusing topography which consisted of a flat bed followed by a double cosine variation in the x and z directions with an amplitude of $0.1d$. However, for all x , the average bed elevation still remained $y = 0$. Different scales L_x and L_z as marked would focus the wave to different degrees, leading to a varying runup on the vertical wall. This numerical experiment could be thought of as representing the effect on solitary wave runup of small variations in topography about a mean. Figure 7 shows a snapshot of the wave's surface profile slightly after maximum runup. The three dimensional effects can clearly be seen.

Figure 8 shows the maximum runup of the wave for varying L_x and L_z . The computed

runup for a level bed and predicted runup for a wave propagated onto an infinite two dimensional shoal of depth $d_s/d_0 = 0.9$ are also shown. The latter result was predicted using the KdV results of Johnson (1973) and the solitary wave runup formula of Su and Mirie (1980). For small spatial scales, the topography has very little effect on runup but, as the scale increases, runup also increases significantly. Although the maximum value for the focused runup is only slightly greater than the predicted result for an infinite shoal, it is by no means clear that the limiting runup has been reached, and a further increase in L_x and L_z might well give significantly higher values.

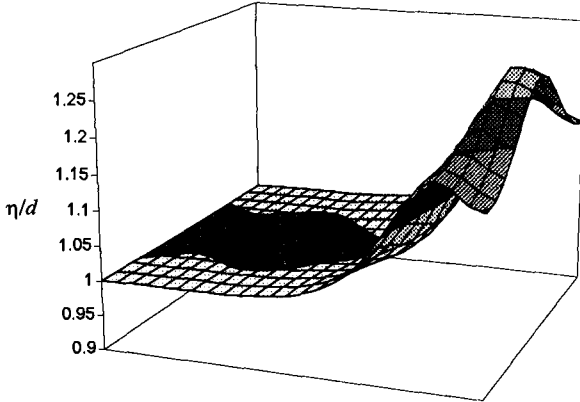


Figure 7. The reflection of a focused solitary wave by a vertical wall

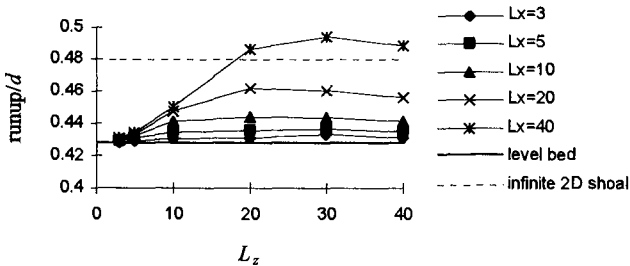


Figure 8. Maximum runup of a focused solitary wave

Since all of the above computations were performed in an enclosed space with no dissipation, conservation of energy could be used as an independent check on accuracy. For all tests, the maximum fluctuation in total energy at any point in time relative to the initial value was less than 2×10^{-4} .

The propagation of regular waves over Whalin’s topography

For a final test of the LPA method, the propagation of regular waves over Whalin’s

topography was computed. In a series of experiments, Whalin (1971) propagated waves over a semicircular shoal which tended to focus waves on the flat behind the shoal. Many investigators have since performed computations over the same topography.

In these computations, regular waves were generated from one boundary using as input the time series of velocity from the fully nonlinear LPA wave forms. Odd derivatives of surface elevation were also specified at the boundary. On the transmitting boundary, a small amplitude boundary condition was combined with a zone where the evolution equations (6) and (7) gradually changed to become the advection equations

$$\frac{\partial}{\partial t} \left(\frac{\partial \eta}{\partial x} \right) = -c \frac{\partial}{\partial x} \left(\frac{\partial \eta}{\partial x} \right) \quad (14)$$

and

$$\frac{\partial}{\partial t} \left(\frac{\partial \phi_s}{\partial x} \right) = -c \frac{\partial}{\partial x} \left(\frac{\partial \phi_s}{\partial x} \right) \quad (15)$$

where c is some characteristic phase velocity on the shelf. These equations were solved in finite difference form using an upwinding scheme. This type of area around the boundary makes it very difficult for errors due to an imperfect boundary condition to propagate back into the domain, as they are continuously pushed out by the advection equations. All computations shown use the level of approximation $r = 3$.

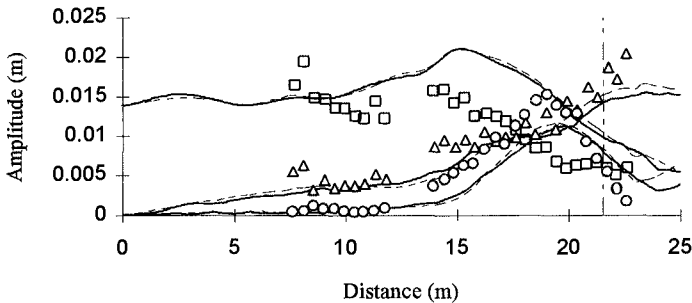


Figure 9(a). Harmonic Amplitudes along centreline of Whalin's topography, $T = 3$ s, $A_1 = 0.0146$ m. Solid lines indicate present results; dashed lines show results of Rygg (1988); symbols are experimental results of Whalin (1971). Chain-dashed line shows beginning of dissipating beach, which was not reproduced in computations.

Figure 9 shows the experimental and computational harmonic amplitudes along the centreline for the highest waves with experimental periods $T = 1$ s, 2s, 3s. Also included are the results of Madsen and Sørensen (1992) using their extended Boussinesq equations for the $T = 1$ s case and the results of Rygg (1988) using the Boussinesq equations of Peregrine (1967) for $T = 2$ s, 3s.

For the longest wave, with $T = 3\text{s}$, both computational methods severely overpredict the amplitude of the first harmonic and moderately underpredict the amplitude of the second and third harmonics. Although the LPA results for $r = 3$ are shown, increasing the level to $r = 4$ (not shown here) provides no real change. This is somewhat distressing, as both LPA models and the extended Boussinesq equations should operate best in this range. However, the experimental topography used by Whalin was made up of a series of steps and only approximated the smooth topography used in the computations. Consequently, dissipation, neglected in computations, was significant in the experiments, especially for high, long waves. This is speculated to be the major source of discrepancies for this wave.

For the next wave, with $T = 2\text{s}$, computations agree somewhat better with experimental data. Once again, the first harmonic is overpredicted and so, to some degree, is the second harmonic, while the third harmonic is predicted relatively well. Both LPA and Boussinesq computations predict similar features, although there are differences. One strange feature of this wave is that the initial amplitude of the first harmonic used to calculate the incoming waves, which is given as $A_1 = 0.0149\text{m}$, appears to be too high. In actual fact, it appears to be approximately $A_1 = 0.0135\text{m}$. Figure 9(c) shows LPA results for a wave with this initial amplitude, and agreement is much better. The final wave tested had a period of $T = 1\text{s}$, which gave it an initial length to depth ratio of $L/d = 3.27$. Of all waves, this was the best predicted. The computational values of the first harmonic are still slightly high on the final shoal but, aside from some numerical noise near the wave generator, the second harmonic is extremely well predicted. In contrast, the extended Boussinesq equations tend to somewhat underpredict the amplitude of the second harmonic.

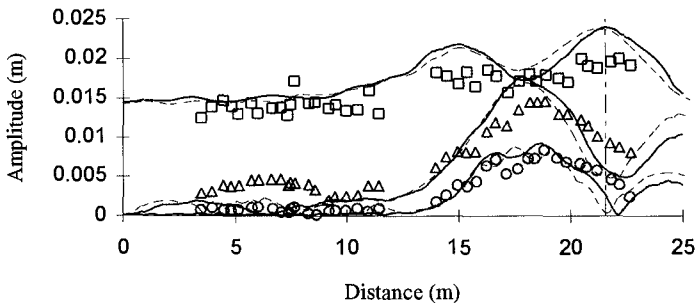


Figure 9(b). $T = 2\text{s}$, $A_1 = 0.0149\text{m}$. Dashed lines here are the Boussinesq results of Rygg (1988)

Overall, agreement between experiment and computations is not as good as would be hoped, possibly because of the neglect of dissipation in computations. It is worthwhile to note that for the cases $T = 2\text{s}$, 3s , where computations and experiments differed, both computational models behaved similarly. Therefore, it is believed that the dis-

crepancies result from something other than an inaccurate solution of the potential flow problem.

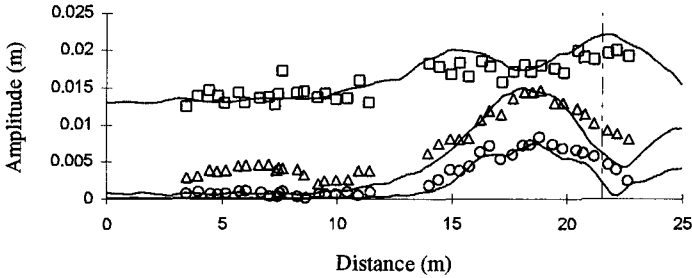


Figure 9(c). Experimental results from Whalin (1971) $T = 2\text{s}$, $A_1 = 0.0149\text{m}$. Computational results $T = 2\text{s}$, $A_1 = 0.0135\text{m}$.

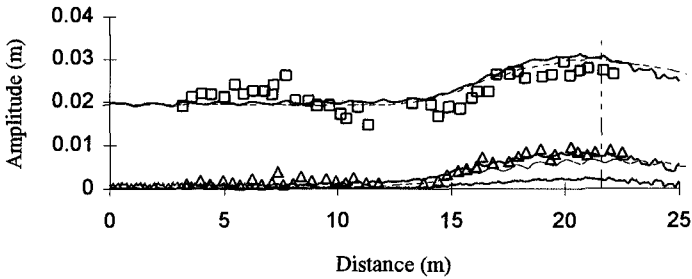


Figure 9(d). $T = 1\text{s}$, $A_1 = 0.0195\text{m}$. Dashed line shows extended Boussinesq results of Madsen and Sørensen (1992).

Conclusions

The local polynomial approximation method developed here has excellent linear and nonlinear properties for a wide range of waves. The simplicity of its formulation makes it an easy task to change the level of approximation, and thus the accuracy, of the method. Computations over varying topography show good accuracy for highly unsteady, nonlinear cases. For accurate potential flow computations in three dimensions, the LPA method is therefore an excellent choice for the numerical modeler.

References

- Cokelet, E. D. (1977), Steep gravity waves in water of arbitrary uniform depth, *Phil. Trans Roy. Soc. London A* **286**, 183–230.

- de Boor, C. (1978), *A practical guide to splines*. Springer-Verlag, New York, third edition.
- de Haas, P., Dingemans, M., and Klopman, G. (1996), Simulation of free long-wave generation due to uneven bottoms, In *Proc. 25th Int. Conf. on Coastal Eng.*
- Fenton, J. D. (1988), The numerical solution of steady water wave problems, *Computers and Geosciences* **14**, 357–368.
- Fenton, J. D. and Kennedy, A. B. (1996), Fast methods for shoaling waves, In *Proc. 25th Int. Conf. Coastal Eng., Orlando*.
- Gobbi, M. F. and Kirby, J. T. (1996), A fourth order fully nonlinear Boussinesq wave model, In *Proc. 25th Int. Conf. on Coastal Eng.*
- Johnson, R. S. (1973), On the development of a solitary wave moving over an uneven bottom, *Proc. Camb. Phil. Soc.* **73**, 183–203.
- Madsen, P. A. and Sørensen, O. R. (1992), A new form of the Boussinesq equations with improved linear dispersion characteristics. Part 2. A slowly-varying bathymetry, *Coastal Engng* **18**, 183–204.
- Nwogu, O. (1993), An alternative form of the Boussinesq equations for nearshore wave propagation, *J. Waterway Port Coastal and Ocean Engng* **119**, 618–638.
- Peregrine, D. (1967), Long waves on a beach, *J. Fluid Mech.* **27**(4), 815–827.
- Rygg, O. B. (1988), Nonlinear refraction-diffraction of surface waves in intermediate and shallow depths, *Coastal Eng.* **12**, 191–211.
- Schäffer, H. A. and Madsen, P. A. (1995), Further enhancements of Boussinesq-type equations, *Coastal Eng.* **26**, 1–14.
- Shields, J. J. and Webster, W. C. (1988), On direct methods in water wave theory, *J. Fluid Mech.* **197**, 171–199.
- Su, C. and Mirie, R. (1980), On head-on collisions between two solitary waves, *J. Fluid Mech.* **98**, 509–525.
- Wang, P., Yao, Y., and Tulin, M. (1995), An efficient numerical tank for nonlinear water waves, based on the multi-subdomain approach with BEM, *Int. J. Numer. Meth. Fluids* **20**, 1315–1336.
- Wei, G., Kirby, J., Grilli, S., and Subramanya, R. (1994), A fully nonlinear Boussinesq model for surface waves. 1. Highly nonlinear waves, Res. Rpt. CACR-94-15, Center for Applied Coastal Research, University of Delaware.
- Witting, J. (1984), A unified model for the evolution of nonlinear water waves, *J. Comp. Phys* **56**, 203–236.

CHAPTER 87

A Fourth Order Boussinesq-Type Wave Model

Maurício F. Gobbi ¹ and James T. Kirby ²

Abstract

A fully nonlinear Boussinesq-type model with dispersion accurate to $O((kh)^4)$ is derived. As an extension to the second order extended model proposed by Nwogu (1993), a new dependent variable is defined as a weighted average between the velocity potential at two distinct water depths to force the model to have a (4,4) Padé approximation of the exact dispersion relationship. The present model is similar to the fully nonlinear extension of Nwogu's model proposed by Wei et al (1995), except that the dependent variable is expanded in a fourth (rather than second) order polynomial in the vertical coordinate.

Introduction

Important progress has been made in variable-depth Boussinesq-type models since the development of the more-or-less standard model of Peregrine (1967). Madsen et al (1991) introduced higher order dispersive terms into the governing equations to improve linear dispersion properties. By redefining the dependent variable, Nwogu (1993) achieved the same improvement without the need to add such terms to the equations. Wei et al (1995, referred to as WKGS) used the approach of Nwogu to derive a Boussinesq-type model which retains full nonlinearity. Numerical computations show that the WKGS model agrees well with solutions of the full potential problem over the range of relevant water depths, except for some discrepancies in the vertical profile of horizontal velocity in nearly-breaking waves. These inaccuracies in the prediction of vertical profiles in existing Boussinesq-type models are due to the fact that they assume the velocity profiles to be second order polynomials in the vertical coordinate z . In this paper, we derive a fourth order Boussinesq model in which the velocity potential is approximated by a fourth order polynomial in z . A new dependent variable is defined to be the weighted average of the velocity potential at 2 different elevations in the water column, and the weight and positions are chosen to give a (4,4) Padé approximant of the exact linear dispersion relationship.

¹Graduate student, Center for Applied Coastal Research, Department of Civil and Environmental Engineering, University of Delaware, Newark, DE 19716, USA.

²Professor, Center for Applied Coastal Research, Department of Civil and Environmental Engineering, University of Delaware, Newark, DE 19716, USA.

Derivation of New Model

The full boundary value problem for potential flow is given in terms of nondimensional variables by

$$\phi_{zz} + \mu^2 \nabla^2 \phi = 0; \quad -h \leq z \leq \delta\eta \quad (1)$$

$$\phi_z + \mu^2 \nabla h \cdot \nabla \phi = 0; \quad z = -h \quad (2)$$

$$\eta + \phi_t + \frac{\delta}{2} \left[(\nabla \phi)^2 + \frac{1}{\mu^2} (\phi_z)^2 \right] = 0; \quad z = \delta\eta \quad (3)$$

$$\eta_t + \delta \nabla \phi \cdot \nabla \eta - \frac{1}{\mu^2} \phi_z = 0; \quad z = \delta\eta \quad (4)$$

Here, x and y are the horizontal coordinates scaled by a representative wave number $k_0 = 2\pi/L_0$, z is the vertical coordinate starting at the still water level and pointing upwards and h is the water depth, both scaled by a typical depth h_0 . η is the water surface displacement and scaled by a representative amplitude a . Two dimensionless parameters are apparent; $\delta = a/h_0$ and $\mu^2 = (k_0 h_0)^2$. Time t is scaled by $(k_0(g h_0)^{1/2})^{-1}$, and ϕ , the velocity potential, is scaled by $\delta h_0 (g h_0)^{1/2}$. We integrate (1) over the water column and use (2) and (4) to obtain a mass conservation equation

$$\eta_t + \nabla \cdot \mathbf{M} = 0; \quad \mathbf{M} = \int_{-h}^{\delta\eta} \nabla \phi dz. \quad (5)$$

For simplicity, we assume a constant depth h_0 ; the variable depth model can be derived in straightforward manner and is presented in Gobbi et al (1996). We assume a fourth order polynomial approximation for ϕ and choose the coefficients to satisfy the bottom boundary condition (2) and Laplace's equation (1), retaining terms up $O(\mu^4)$. The approximate potential is given by (Mei, 1989)

$$\phi = \phi_0 - \frac{\mu^2(1+z)^2}{2} \nabla^2 \phi_0 + \frac{\mu^4(1+z)^4}{24} \nabla^2 \nabla^2 \phi_0 + O(\mu^6) \quad (6)$$

where ϕ_0 is the velocity potential at the bottom. Commensurate with the extension of the velocity potential to $O(\mu^4)$, we seek to derive a set of model equations having a corresponding dispersion relation in the form of a (4,4) Padé approximant, given by

$$\frac{\tanh \mu}{\mu} = \frac{1 + (1/9)\mu^2 + (1/945)\mu^4}{1 + (4/9)\mu^2 + (1/63)\mu^4} + O(\mu^6) \quad (7)$$

For the case of approximations retaining terms to $O(\mu^2)$, the goal of obtaining the corresponding (2,2) Padé approximant is achieved by redefining the velocity potential in terms of the value of the potential at an elevation $z_\alpha = h[(1+2\alpha)^{1/2} - 1]$; $\alpha = -2/5$ and using the resulting reference value ϕ_α as the dependent variable; see Nwogu (1993), Chen and Liu (1995) and Kirby (1996). This procedure is not adequate in the present context. Instead, we define a new dependent variable

$$\tilde{\phi} = \beta \phi_a + (1 - \beta) \phi_b \quad (8)$$

where ϕ_a and ϕ_b are the velocity potentials at elevations $z = z_a$ and $z = z_b$, and β is a weight parameter. $\tilde{\phi}$ may be written in terms of ϕ_0 using (6) to obtain

$$\tilde{\phi} = \phi_0 - \frac{\mu^2}{2} B \nabla^2 \phi_0 + \frac{\mu^4}{2} D \nabla^2 \nabla^2 \phi_0 + O(\mu^6) \quad (9)$$

where

$$\begin{aligned} B &= \beta(1+z_a)^2 + (1-\beta)(1+z_b)^2 \\ D &= \beta(1+z_a)^4 + (1-\beta)(1+z_b)^4 \end{aligned} \quad (10)$$

Inverting (9) gives a formula for ϕ_0 in terms of $\tilde{\phi}$ which is substituted into (6) to get an approximation to the full velocity potential in terms of $\tilde{\phi}$:

$$\begin{aligned} \phi &= \tilde{\phi} + \frac{\mu^2}{2} \left\{ B - (1+z)^2 \right\} \nabla^2 \tilde{\phi} \\ &+ \frac{\mu^4}{4} \left\{ B^2 - B(1+z)^2 - \frac{D}{6} + \frac{(1+z)^4}{6} \right\} \nabla^2 \nabla^2 \tilde{\phi} + O(\mu^6). \end{aligned} \quad (11)$$

Defining the total depth $H = 1 + \delta\eta$, and substituting (11) into (5) gives a mass flux conservation equation for $\tilde{\phi}$ and η :

$$\begin{aligned} \eta_t + \nabla \cdot \left\{ H \left[\nabla \tilde{\phi} + \frac{\mu^2}{2} \left(B - \frac{H^2}{3} \right) \nabla (\nabla^2 \tilde{\phi}) \right. \right. \\ \left. \left. + \frac{\mu^4}{4} \left(B^2 - B \frac{H^2}{3} - \frac{B}{6} + \frac{H^4}{30} \right) \nabla (\nabla^2 \nabla^2 \tilde{\phi}) \right] \right\} = O(\mu^6). \end{aligned} \quad (12)$$

Next we substitute (11) into (3) to obtain an approximate Bernoulli equation, given by

$$\begin{aligned} \eta + \tilde{\phi}_t + \frac{\mu^2}{2} \left\{ B - H^2 \right\} \nabla^2 \tilde{\phi}_t + \frac{\mu^4}{4} \left\{ B^2 - BH^2 - \frac{B}{6} + \frac{H^4}{6} \right\} \nabla^2 \nabla^2 \tilde{\phi}_t \\ + \frac{\delta}{2} \left[(\nabla \tilde{\phi})^2 + \mu^2 \left\{ B - H^2 \right\} \nabla \tilde{\phi} \cdot \nabla (\nabla^2 \tilde{\phi}) + \mu^2 H^2 (\nabla^2 \tilde{\phi})^2 \right. \\ + \frac{\mu^4}{2} \left\{ B^2 - BH^2 - \frac{B}{6} + \frac{H^4}{6} \right\} \nabla \tilde{\phi} \cdot \nabla (\nabla^2 \nabla^2 \tilde{\phi}) \\ + \frac{\mu^4}{4} \left\{ B^2 - 2BH^2 + H^4 \right\} \left\{ \nabla (\nabla^2 \tilde{\phi}) \right\}^2 \\ \left. + \mu^4 \left\{ BH^2 - \frac{H^4}{3} \right\} (\nabla^2 \tilde{\phi})(\nabla^2 \nabla^2 \tilde{\phi}) \right] = O(\mu^6). \end{aligned} \quad (13)$$

If we neglect μ^4 terms from (12) and (13) and set $\beta = 1$, we recover the WKGS model with Nwogu's α being related to B by

$$B = 2\alpha + 1 \quad (14)$$

If, in addition, we neglect products $\delta\mu^2$ or higher, we recover Nwogu's model in the velocity potential form given by Chen and Liu (1995).

Linear Dispersion Properties

Neglecting all terms containing δ in (12) and (13), we obtain the following linear equations for mass flux conservation,

$$\begin{aligned} \eta_t + \nabla^2 \tilde{\phi} + \frac{\mu^2}{2} \left(B - \frac{1}{3} \right) \nabla^2 \nabla^2 \tilde{\phi} \\ + \frac{\mu^4}{4} \left(B^2 - \frac{B}{3} - \frac{D}{6} + \frac{1}{30} \right) \nabla^2 \nabla^2 \nabla^2 \tilde{\phi} = 0 \end{aligned} \quad (15)$$

and an approximate Bernoulli equation,

$$\begin{aligned} \eta + \tilde{\phi}_t + \frac{\mu^2}{2} (B - 1) \nabla^2 \tilde{\phi}_t \\ + \frac{\mu^4}{4} \left(B^2 - B - \frac{D}{6} + \frac{1}{6} \right) \nabla^2 \nabla^2 \tilde{\phi}_t = 0 \end{aligned} \quad (16)$$

To analyse the dispersion properties of these equations, we assume the following general solution to the equations:

$$\eta = a e^{i(\mathbf{x} - \omega t)} \quad \tilde{\phi} = b e^{i(\mathbf{x} - \omega t)} \quad (17)$$

where ω in the angular frequency nondimensionalized by $k_0 (gh_0)^{1/2}$, a and b are amplitudes, and $i = \sqrt{-1}$. Substituting (17) into (15) and (16) we obtain the linear dispersion relationship for the model:

$$\omega^2 = \frac{1 - \frac{1}{2} \left(B - \frac{1}{3} \right) \mu^2 + \frac{1}{4} \left(B^2 - \frac{B}{3} - \frac{D}{6} + \frac{1}{30} \right) \mu^4}{1 - \frac{1}{2} (B - 1) \mu^2 + \frac{1}{4} \left(B^2 - B - \frac{D}{6} + \frac{1}{6} \right) \mu^4} \quad (18)$$

The expression (18) is the (4,4) Padé approximant to the exact linear dispersion relationship $\omega^2 = \tanh \mu / \mu$ if we set $B = 1/9$ and $D = 5/189$. The parameters β , z_a , and z_b are chosen in order to obtain these values. Since we have 3 unknowns and 2 equations, there are an infinite number of solutions that give the desired values of B and D . However, an arbitrary choice of β can give imaginary values of z_a or z_b or values lying outside of the fluid domain, making these parameters lack physical significance. It can easily be shown that values of β between 0.018 and 0.467 will give both z_a and z_b to be real values lying inside the water column. In the present paper we arbitrarily choose $\beta = 0.2$, and solve for z_a and z_b to give us the (4,4) Padé approximant to the exact linear dispersion relationship.

Figure (1) shows the ratio of modelled phase speed with Airy's exact linear solution for the standard Boussinesq theory based on depth-averaged velocity, the (2,2) Padé approximant formulation (referred to as Nwogu's formulation for simplicity), and the (4,4) Padé approximant dispersion relationship (referred to as the present formulation). It is clear that the present model has improved linear dispersion properties over Nwogu's already accurate Nwogu's model, and closely reproduces the exact solution through intermediate to deep water. Similarly, the linear group velocity, defined as $C_g = \partial \omega / \partial k$ is shown in figure (2) and the improvement in the present model over Nwogu's model is even more evident.

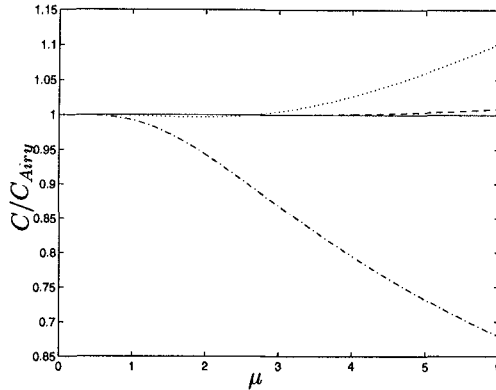


Figure 1: Ratio of model phase speed and Airy's exact linear solution. Standard Boussinesq (dash-dotted), Nwogu's (2,2) Padé approximant(dotted), Present (4,4) Padé approximant(dashed).

Nwogu (1993) found that the range and accuracy of the (2,2) Padé formulation could be extended by adjusting the model coefficients using an error minimization procedure. In the present case, the authors found that the error surface in the neighborhood of the (4,4) Padé approximant is sufficiently flat so that further adjustment of the model parameters is unwarranted.

Internal Kinematics

The internal kinematics of the present model can be obtained from (11). We define a function $f_1(z)$ as the the velocity potential normalized by its value at position $z = 0$:

$$f_1(z) = \frac{1 - \frac{\mu^2}{2} [B - (1+z)^2] + \frac{\mu^4}{4} [B^2 - B(1+z)^2 - \frac{D}{6} + \frac{(1+z)^4}{6}]}{1 - \frac{\mu^2}{2} [B - 1] + \frac{\mu^4}{4} [B^2 - B - \frac{D}{6} + \frac{1}{6}]} \quad (19)$$

The vertical velocity component w can be obtained by differentiating (11) with respect to z . Similarly to f_1 , a vertical velocity profile function can be obtained by defining $f_2(z) = w(z)/w(0)$:

$$f_2(z) = \frac{\mu^2 [(1+z)] + \frac{\mu^4}{2} [-B(1+z) + \frac{(1+z)^3}{3}]}{\mu^2 + \frac{\mu^4}{2} [-B + \frac{1}{3}]} \quad (20)$$

The corresponding f_2 from the exact linear theory is $\sinh[\mu(1+z)]/\sinh[\mu]$.

Figure (3) shows comparisons of $f_1(z)$ between the exact linear solution $\cosh[\mu(1+z)]/\cosh[\mu]$, Nwogu's model and the present model, for various values of μ . For moderately shallow water, the two models reproduce the exact solution quite well. As μ increases, Nwogu's model starts to deviate strongly, while the present model remains very accurate until quite deep water.

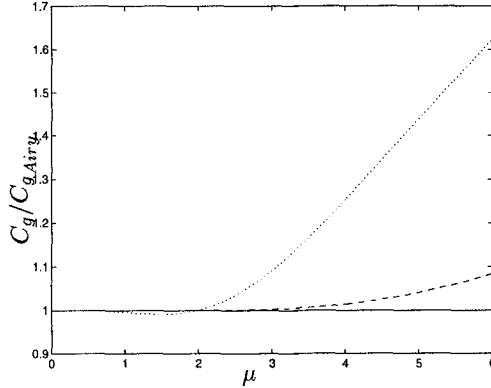


Figure 2: Ratio of model group velocity and Airy's exact linear solution. Nwogu (dotted), Present (dashed)

Figure (4) shows plots similar to figure (3) for f_2 . Notice that Nwogu's model has a linear vertical profile for w , a poor representation in intermediate to deep water. The present model stays close to the exact solution for a wide range of μ . Finally, figure (5) shows the ratio to the exact linear solution $\tanh(\mu)$ of the ratio between vertical and horizontal velocities w/u at $z = 0$, $f_3(\mu)$, for the present model and Nwogu's model. The approximate expression for f_3 is:

$$f_3(\mu) = \frac{w(z=0)}{u(z=0)} = \frac{\mu + \frac{\mu^3}{2} \left[-B + \frac{1}{3} \right]}{1 - \frac{\mu^2}{2} [B - 1] + \frac{\mu^4}{4} \left[B^2 - B - \frac{D}{6} + \frac{1}{6} \right]} \quad (21)$$

The present model agrees better with the exact linear solution than Nwogu's model for a wide depth range.

Second Order Nonlinear Interactions

In the previous sections we have seen that the proposed model has excellent linear dispersion properties as well as a greatly improved representation of the internal flow kinematics. It is useful to analyse some of the nonlinear properties of the model by using analytical tools such as Stokes' type asymptotic expansions and multiple scales expansions. Since these types of analysis have been extensively applied and studied for the full boundary value potential problem, we can obtain an idea of how well the nonlinear version of the present model would perform by comparing some of its nonlinear properties with those of the full problem, and also with WKGS and Nwogu's model, keeping in mind that a numerical implementation of WKGS model has already been tested and compared to data with success. We will now look at the generation of super- and subharmonics by second order Stokes-type interactions. It is well known that in intermediate and deep water the first nonlinear correction of a linear wave solution is a set of bound waves called the superharmonics (resulting from sum-wave

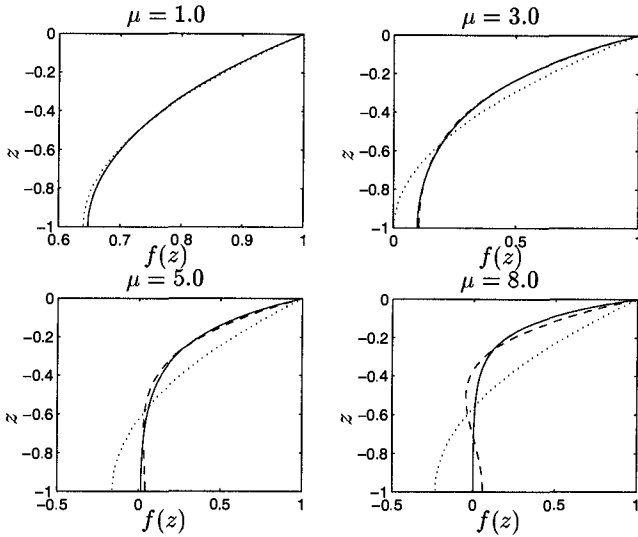


Figure 3: Normalized vertical profile of linear horizontal kinematics for (a) $\mu = 1$, (b) $\mu = 3$, (c) $\mu = 5$, (d) $\mu = 8$. Exact (solid), Nwogu (dotted), Present (dash)

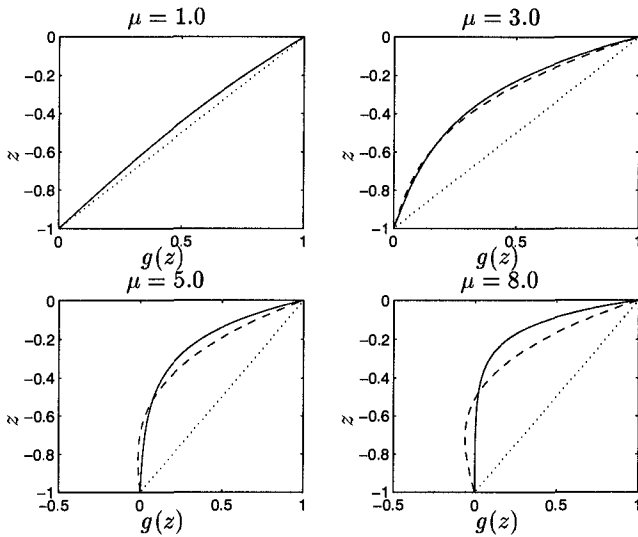


Figure 4: Normalized vertical profile of linear vertical velocity for (a) $\mu = 1$, (b) $\mu = 3$, (c) $\mu = 5$, (d) $\mu = 8$. Exact (solid), Nwogu (dotted), Present (dash)

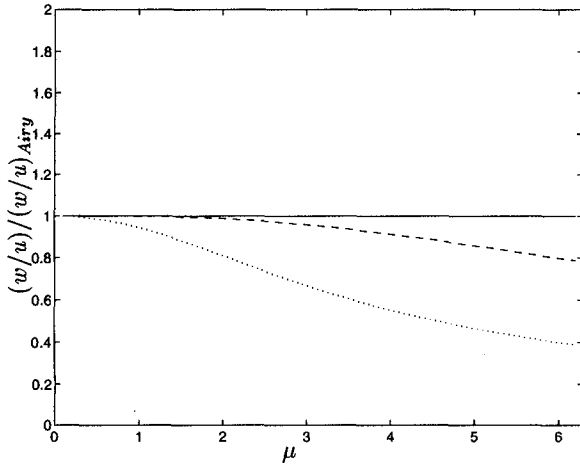


Figure 5: Ratio of approximate results for $w(0)/u(0)$ to the exact linear solution. Nwogu and WKGS (dotted), Present solution (dash).

interactions) and corresponding subharmonics (resulting from difference-wave interactions) (Hasselmann, 1962). These bound waves are proportional to products of the amplitudes of solutions to the linear equations. The constants of proportionality (which are functions of the local depth) will be referred to as transfer coefficients. Nwogu (1993) has investigated the generation of these bound waves in his extended Boussinesq model and found qualitatively reasonable agreement with Stokes' theory. Madsen and Sørensen (1993) have found similar results. Kirby and Wei (1994) extended Nwogu's model to full nonlinearity and found that the retention of terms proportional to $\delta\mu^2$ (which are neglected in Nwogu's model and the standard Boussinesq model by assumption) is essential for a prediction of the transfer coefficients to the level of accuracy implied by the order of retained dispersive terms in the original model equations. Here, we derive the transfer coefficients for the present model and compare to results from previous models.

We investigate nonlinear properties of the present model by introducing the perturbation expansion:

$$\begin{aligned}\eta &= \eta_0 + \delta\eta_1 + \delta^2\eta_2 \\ \tilde{\phi} &= \phi_0 + \delta\phi_1 + \delta^2\phi_2\end{aligned}\tag{22}$$

into (12) and (13), and order the equations in powers of δ . At each order $O(\delta^n)$ we obtain:

$$\begin{aligned}\eta_{nt} + L_1\phi_n &= F_n \\ \eta_n + L_2\phi_{nt} &= G_n\end{aligned}\tag{23}$$

where L_1 and L_2 are the linear operators:

$$L_1 = \nabla^2 + \frac{\mu^2}{2} \left(B - \frac{1}{3} \right) \nabla^2 \nabla^2 + \frac{\mu^4}{4} \left(B^2 - \frac{B}{3} - \frac{D}{6} + \frac{1}{30} \right) \nabla^2 \nabla^2 \nabla^2 \tag{24}$$

$$L_2 = 1 + \frac{\mu^2}{2} (B - 1) \nabla^2 + \frac{\mu^4}{4} \left(B^2 - B - \frac{D}{6} + \frac{1}{6} \right) \nabla^2 \nabla^2 \tag{25}$$

and the forcing terms for the first 2 orders are given by:

$$F_0 \equiv 0$$

$$G_0 \equiv 0$$

$$F_1 \equiv -\nabla \cdot (\eta_0 \nabla \phi_0) - \frac{\mu^2}{2} (B - 1) \nabla \cdot \left\{ \eta_0 \nabla (\nabla^2 \phi_0) \right\} - \frac{\mu^4}{4} \left(B^2 - B - \frac{D}{6} + \frac{1}{6} \right) \nabla \cdot \left\{ \eta_0 \nabla (\nabla^2 \nabla^2 \phi_0) \right\} \tag{26}$$

$$G_1 \equiv -\frac{1}{2} (\nabla \phi_0)^2 + \frac{\mu^2}{2} \left\{ 2\eta_0 \nabla^2 \phi_{0t} - (B - 1) \nabla \phi_0 \cdot \nabla (\nabla^2 \phi_0) + (\nabla^2 \phi_0)^2 \right\} - \frac{\mu^4}{4} \left\{ \left(\frac{2}{3} - 2B \right) \eta_0 \nabla^2 \nabla^2 \eta_{0t} + \left(B^2 - B - \frac{D}{6} + \frac{1}{6} \right) \nabla \phi_0 \cdot \nabla (\nabla^2 \nabla^2 \eta_0) + \frac{1}{2} (B - 1)^2 \nabla (\nabla^2 \phi_0) \cdot \nabla (\nabla^2 \phi_0) + 2 \left(B - \frac{1}{3} \right) (\nabla^2 \phi_0) (\nabla^2 \nabla^2 \phi_0) \right\} \tag{27}$$

We assume the following random linear sea as the solution to the $O(1)$ problem:

$$\eta_0 = \sum_n a_n \cos \psi_n; \quad \phi_0 = \sum_n b_n \sin \psi_n; \tag{28}$$

where a_n and b_n are nondimensional amplitudes of the functions η_0 and ϕ_0 , $\psi_n = \mathbf{k}_n \cdot \mathbf{x} - \omega_n t - \theta_n$, \mathbf{k}_n is the n -component wavenumber vector nondimensionalized by k_0 , \mathbf{x} is the horizontal coordinates vector nondimensionalized by $1/k_0$, ω_n is the n -component angular frequency nondimensionalized by $k_0(g h_0)^{1/2}$. Substitution of (28) into the $O(1)$ set of equations (23) with $n = 0$ gives a set of n relationships between ω_n and $k_n = |\mathbf{k}_n|$; each of them is the same as (18). We also find a relationship between a_n and b_n given by:

$$b_n = \frac{\omega_n}{k_n K_n} a_n; \quad K_n = k_n \left\{ 1 - \frac{\mu^2}{2} k_n^2 \left(B - \frac{1}{3} \right) + \frac{\mu^4}{4} k_n^4 \left(B^2 - \frac{B}{3} - \frac{D}{6} + \frac{1}{30} \right) \right\} \tag{29}$$

Following the standard perturbation technique, we substitute the $O(1)$ solution (28) into the right-hand-side of the $O(\delta)$ equations (23) to find the forcing of the $O(\delta)$ problem. The forcings F and G in the mass and dynamic equations (23) respectively are:

$$F = \frac{1}{4} \sum_l \sum_m a_m a_l \left\{ \mathcal{F}_{ml}^+ \sin(\psi_l + \psi_m) + \mathcal{F}_{ml}^- \sin(\psi_l - \psi_m) \right\}$$

$$G = \frac{1}{4} \sum_l \sum_m a_m a_l \left\{ \mathcal{G}_{ml}^+ \cos(\psi_l + \psi_m) + \mathcal{G}_{ml}^- \cos(\psi_l - \psi_m) \right\} \tag{30}$$

where

$$\mathcal{F}_{ml}^{\pm} = \frac{\omega_m k_l^2 \pm \omega_l k_m^2 + (\omega_l \pm \omega_m)(\mathbf{k}_l \cdot \mathbf{k}_m)}{\omega_l \omega_m} \quad (31)$$

$$\begin{aligned} \mathcal{G}_{ml}^{\pm} = & \frac{1}{k_l k_m K_l K_m} \left[-\omega_l \omega_m (\mathbf{k}_l \cdot \mathbf{k}_m) + \mu^2 \left\{ \omega_m^2 k_m^2 k_l K_l \right. \right. \\ & + \omega_l^2 k_l^2 k_m K_m + \frac{1}{2} (B-1) \omega_l \omega_m (k_l^2 + k_m^2) (\mathbf{k}_l \cdot \mathbf{k}_m) \pm \omega_l \omega_m k_l^2 k_m^2 \left. \left. \right\} \right. \\ & + \mu^4 \left\{ -\frac{1}{2} \left(B - \frac{1}{3} \right) \left(\omega_l^2 k_l^4 k_m K_m + \omega_m^2 k_m^4 k_l K_l \right) \right. \\ & - \frac{1}{4} \left(B^2 - B - \frac{D}{6} + \frac{1}{6} \right) (\mathbf{k}_l \cdot \mathbf{k}_m) \omega_l \omega_m (k_l^4 + k_m^4) \\ & \left. \left. - \frac{1}{4} (B-1)^2 \omega_l \omega_m k_l^2 k_m^2 (\mathbf{k}_l \cdot \mathbf{k}_m) \mp \frac{1}{2} \left(B - \frac{1}{3} \right) \omega_m \omega_l k_m^2 k_l^2 (k_m^2 + k_l^2) \right\} \right] \quad (32) \end{aligned}$$

Equation (31) is identical to the full Stokes' theory result, except for the approximate dispersion relationship. Equation (32) can be rearranged within the level of approximation of the present model to:

$$\mathcal{G}_{ml}^{\pm} = \frac{-\mathbf{k}_l \cdot \mathbf{k}_m + \mu^2 \{ \omega_l \omega_m (\omega_l^2 + \omega_m^2) \pm \omega_l^2 \omega_m^2 \}}{\omega_l \omega_m} + O(\mu^6) \quad (33)$$

which is, again, formally the same as the full Stokes' theory result but with an approximate dispersion relationship.

The forced solution for η_1 can be obtained by solving (23) and is given by

$$\eta_1 = \sum_l \sum_m a_m a_l \left\{ \mathcal{H}_{ml}^+ \cos(\psi_l + \psi_m) + \mathcal{H}_{ml}^- \cos(\psi_l - \psi_m) \right\} \quad (34)$$

where

$$\mathcal{H}_{ml}^{\pm} = \frac{\omega_m^{\pm} \mathcal{F}_{ml}^{\pm} - k_{ml}^{\pm} \mathcal{G}_{ml}^{\pm} T_{ml}^{\pm}}{4(\omega_{ml}^{\pm})^2 - k_{ml}^{\pm} T_{ml}^{\pm}}, \quad (35)$$

$$T_{ml}^{\pm} \equiv k_{ml}^{\pm} \frac{1 - \frac{\mu^2}{2} \left(B - \frac{1}{3} \right) (k_{ml}^{\pm})^2 + \frac{\mu^4}{4} \left(B^2 - \frac{B}{3} - \frac{D}{6} + \frac{1}{30} \right) (k_{ml}^{\pm})^4}{1 - \frac{\mu^2}{2} (B-1) (k_{ml}^{\pm})^2 + \frac{\mu^4}{4} \left(B^2 - B - \frac{D}{6} + \frac{1}{6} \right) (k_{ml}^{\pm})^4},$$

$$k_{ml}^{\pm} = |\mathbf{k}_l \pm \mathbf{k}_m|, \quad \omega_{ml}^{\pm} = \omega_l \pm \omega_m$$

\mathcal{H}_{ml}^+ , \mathcal{H}_{ml}^- are respectively the super- and subharmonic transfer coefficients of the interaction between the (l, m) pair of waves. Figures (6) and (7) show comparisons of the ratio of approximate \mathcal{H}_{ml}^{\pm} to Stokes' solution, for Nwogu's model, WKGS model, and the present model. Note that the poor representation of these coefficients at small μ in Nwogu's model is due to the assumption of weak nonlinearity, as discussed by Kirby and Wei (1994). The present model predicts superharmonic amplitudes very accurately over a wide range of water depths. The asymptotic representation of subharmonic amplitudes is also more accurate than in previous models. However, the new solution deviates more rapidly from the exact solution than do the previous results.

Third Order Nonlinear Interactions

We now extend our analysis to third order interactions. We will focus on obtaining the amplitude dispersion of a simple unidirectional monochromatic wave train. It is well known that at this order, it is necessary to introduce a "slow" time scale into the problem, since resonant interactions take place and the perturbation problem becomes singular. We will concentrate on plane waves traveling in the x direction. The "stretched" time scale is given by:

$$t = t' + \delta t' + \delta^2 t' = t' + T_1 + T_2 \tag{36}$$

We then substitute (36) and (22) into (12) and (13), and order the equations up to $O(\delta^2)$. We assume the solution to each order to be of the form

$$\begin{aligned} \eta_n &= \sum_{m=-(n+1)}^{n+1} \eta_{nm}(T_1, T_2) e^{im(x'-\omega t')} \\ \phi_n &= \sum_{m=-(n+1)}^{n+1} \phi_{nm}(T_1, T_2) e^{im(x'-\omega t')} \end{aligned} \tag{37}$$

We then seek an equation for the $O(1)$ wave amplitude, in T_1 by relating the coefficients (amplitudes) in (37) of each order to the ones of the previous order. After some algebra, the following equation for the wave amplitude $A = \eta_{01}$ is found after we neglect current components (terms involving ϕ_{10}):

$$A_{T_2} + i\sigma_1 |A|^2 A = 0 \tag{38}$$

where, for the present model:

$$\begin{aligned} \sigma_1 &= \frac{-P_{22}}{\omega Q_1 Q_2} \left[4 + 16C_1 \mu^2 - \omega^{-2} (1 + 4C_3 \mu^2 + 16C_4 \mu^4) \right] \\ &- \frac{\omega}{2Q_1} (E_{20} + E_{22}) (\mu + C_1 \mu^3 - \omega^{-2} \mu^{-1} Q_1) \\ &+ \frac{P_{22}}{4\mu^2 \omega^3 Q_1^2 Q_2} \left[1 + (2 + 5C_3) \mu^2 + (10C_1 + 17C_4 + 4C_3^2) \mu^4 \right] \\ &- \frac{3}{16Q_1} \left[1 + C_3 \mu^2 - \omega^{-2} (1 + C_1 \mu^2) \right] \\ &+ \frac{1}{\omega Q_1^2} \left[4 + (8C_3 + 1/6) \mu^2 \right] \end{aligned} \tag{39}$$

and

$$\begin{aligned} C_1 &= -\frac{1}{2} \left(B - \frac{1}{3} \right); & C_2 &= \frac{1}{4} \left(B^2 - \frac{B}{3} - \frac{D}{6} + \frac{1}{30} \right) \\ C_3 &= -\frac{1}{2} (B - 1); & C_4 &= \frac{1}{4} \left(B^2 - B - \frac{D}{6} + \frac{1}{6} \right) \end{aligned} \tag{40}$$

and where $E_{20}, E_{22}, P_{22}, Q_1$ and Q_2 are complicated functions of μ which may be found in Gobbi et al (1996). The corresponding σ_1 for the full boundary value problem is given by:

$$\sigma_{1Full} = \frac{\cosh 4\mu + 8 - 2 \tanh^2 \mu}{16 \sinh^4 \mu} \tag{41}$$

Equation (38) can be integrated to give:

$$A = a_0 e^{-i(\sigma_1 a_0^2 T_2)} \quad (42)$$

where $a_0 = |A|$. The leading order solution of η is, then:

$$\eta_1 = a_0 \cos(kx - \omega_1 t) \quad (43)$$

where

$$\omega_1 = \omega + (\delta\mu)^2 \sigma_1 a_0^2 \quad (44)$$

The coefficient σ_1 characterizes the amplitude dispersion occurring at leading order due to third order wave-wave interactions. Figure (8) shows comparison of the ratio σ_1 from the present model and from WKGS model to the Stokes' solution to the full problem. The present model appears to have a better asymptotic approximation to the full problem, with excellent agreement in shallower water and acceptable agreement in intermediate to deep water.

Conclusions

A Boussinesq-type model with $O(1)$ nonlinearity and $O(\mu^4)$ dispersion has been proposed. By defining one the dependent variables as the weighted average of the velocity potential at two distinct water depths, it is possible to achieve an extremely accurate (4,4) Padé approximant for the linear dispersion relationship. A major improvement over the existing second order models has been found in the prediction of the internal flow kinematics. A perturbation approach was carried out to analyse random wave second order nonlinear interactions and it has been shown that the present model predicts the transfer coefficients of super and subharmonics generation very well over a wide range of water depths. Finally, the present model predicts well the amplitude dispersion due to third order nonlinear wave-wave interactions. The authors are now preparing a more thorough paper, and are working on the direct solution of the proposed equations by numerical techniques.

Acknowledgements

This work was supported by the Army Research Office through University Research Initiative Grant DAAL 03-92-G-0116, and by the Brazilian agency Fundação Capes.

Appendix: References

- Chen, Y. and Liu, P. L.-F., 1995, "Modified Boussinesq equations and associated parabolic models for water wave propagation", *J. Fluid Mech.*, 288, 351-381.
- Gobbi, M. F., Kirby, J. T. and Wei, G., 1996, "A fully nonlinear Boussinesq model for surface waves. II. Extension to $O(kh)^4$ ", manuscript.
- Hasselmann, K., 1962, "On the nonlinear energy transfer in a gravity wave spectrum", *J. Fluid Mech.*, 12, 481-500.

- Kirby, J. T. and Wei, G., 1994, "Derivation and properties of a fully nonlinear model for weakly dispersive waves", *Proc. Intl. Symp. on Wave - Physical and Numerical Modelling*, Vancouver, August 21-24, 386-395.
- Kirby, J. T., 1996, "Nonlinear, dispersive long waves in water of variable depth", in *Gravity waves on water of variable depth*, J. N. Hunt (ed), Computational Mechanics Publications, in press.
- Madsen, P. A., Murray, R. and Sørensen, O. R., 1991, "A new form of Boussinesq equations with improved linear dispersion characteristics. Part 1.", *Coastal Engineering*, 15, 371-388.
- Madsen, P. A., and Sørensen, O. R., 1993, "Bound waves and triad interactions in shallow water", *Ocean Engineering*, 20, 359-388.
- Nwogu, O., 1993, "An alternative form of the Boussinesq equations for nearshore wave propagation", *J. Waterway, Port, Coast. Ocean Engng*, 119(6), 618-638.
- Peregrine, D. H., 1967, "Long waves on a beach", *J. Fluid Mech.*, 27, 815-827.
- Wei, G., Kirby, J. T., Grilli, S. T., and Subramanya, R., 1995, "A fully nonlinear Boussinesq model for surface waves. Part 1. Highly nonlinear unsteady waves", *J. Fluid Mech.*, 294, 71-92.

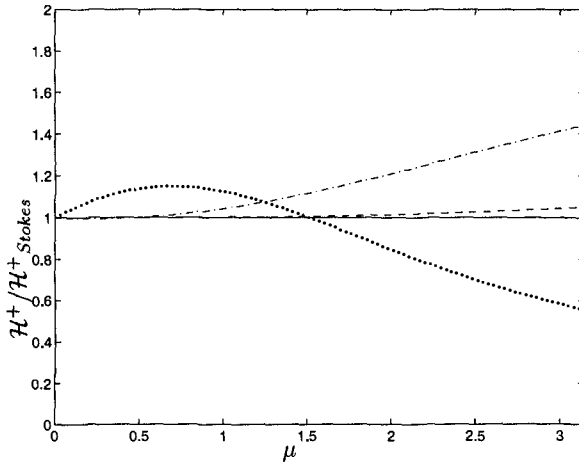


Figure 6: Ratio of approximate superharmonic transfer coefficients to Stokes' solution. Stokes' theory (solid), Nwogu (dotted), WKGS (dash-dot), Present (dashed), Present rearranged (thin dot)

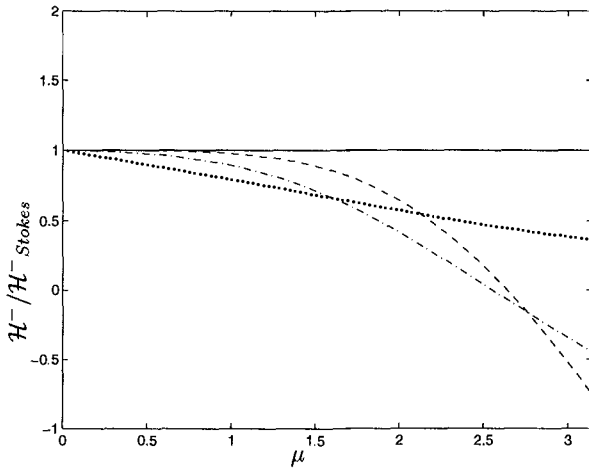


Figure 7: Ratio of approximate subharmonic transfer coefficients to Stokes' solution. Stokes' theory (solid), Nwogu (dotted), WKGS (dash-dot), Present (dash), Present rearranged (thin dot)

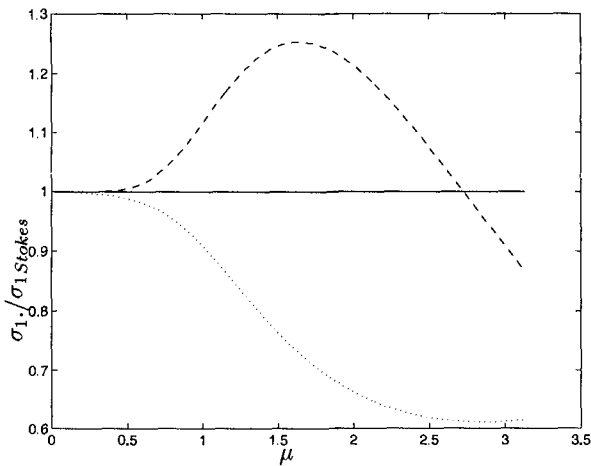


Figure 8: Ratio of Schrodinger equation's cubic term coefficient to full problem's Stokes solution. Wave-wave interaction contribution. Full boundary value problem (solid), WKGS (dotted), Present (dash)

CHAPTER 88

Fast methods for computing the shoaling of nonlinear waves

J. D. Fenton¹ and A. B. Kennedy¹

Abstract

Accurate nonlinear numerical methods for wave propagation have existed for some years. Most of these are very demanding of computer resources as they use global means of approximation which usually requires the costly solution of a full matrix equation at each time step. It is the aim of the present paper to describe and to compare the features of two new methods for the two-dimensional propagation of nonlinear waves over varying topography. A method based on local polynomial approximation is presented, which was found to be efficient, cheap and accurate. A novel boundary integral method is also presented, which was capable of good accuracy even for waves which overturned. For practical purposes, the local polynomial approximation method is to be preferred and may have some useful contributions to make.

Introduction

In computing nonlinear wave evolution over topography, there has always been a trade-off between accuracy and efficiency. On one hand, boundary integral equation methods (BIEM) have been able to perform accurate potential flow calculations past the point of overturning, but their computational expense has traditionally been very high. On the other hand, Boussinesq-type methods have had a much smaller computational cost, especially for large domains, but are limited to mildly nonlinear, mildly dispersive waves. Recently, there have been many attempts both to increase the efficiency of BIEM (Wang *et al.*, 1995, de Haas *et al.*, 1996) and to increase the accuracy of Boussinesq-type approximations (Madsen and Sørensen, 1992, Nwogu, 1993, Wei *et al.*, 1994) However, much room still remains for fast methods which can accurately predict wave evolution.

This paper presents details of and results from two new potential flow methods which have not yet been widely published, but combine excellent accuracy with a reasonable

¹ Dept of Mechanical Engng, Monash University, Clayton, Vic., Australia 3168

computational cost. The first is a finite depth technique which assumes that the flow field is represented locally by polynomial variation. Two variants are presented: one has excellent accuracy for highly nonlinear waves, while the other has greater efficiency at the cost of some accuracy for nonlinear waves. Both variants have a computational cost which is linearly proportional to the number of computational points, which makes them suitable for computations over large domains. The second method presented here is a BIEM which is formulated differently from those currently in use. This new form is simpler, potentially more accurate, and allows for the use of faster solution techniques than are currently standard. It is not as robust as the local polynomial approximation (LPA) method presented and does take longer to run, but unlike that method it can describe wave overturning. As with all boundary integral techniques, accuracy remains good up to overturning.

Governing Equations

For irrotational flow a velocity potential $\phi(x, y, t)$ exists such that the fluid velocity vector $(u, v) = (\partial\phi/\partial x, \partial\phi/\partial y)$, restricting consideration here to two dimensions. If the fluid is incompressible, the potential satisfies Laplace's equation

$$\frac{\partial^2 \phi}{\partial x^2} + \frac{\partial^2 \phi}{\partial y^2} = 0. \quad (1)$$

At any time t , this elliptic equation is governed by the conditions on the domain boundary. At all points along the free surface specified by $y = \eta(x, t)$:

$$\phi = \phi_s(x, t), \quad (2)$$

where ϕ_s is known. The kinematic boundary condition on the bed is

$$\frac{\partial \phi}{\partial y} - \frac{\partial h}{\partial x} \frac{\partial \phi}{\partial x} = 0 \quad \text{on} \quad y = h, \quad (3)$$

where $h(x)$ is the bed elevation. Along the left and right boundaries, the horizontal velocity is set to

$$\frac{\partial \phi}{\partial x} = f(y). \quad (4)$$

These equations completely specify the velocity potential, and (1) may then be used to solve for the flow field. To advance the solution in time, the free surface kinematic boundary condition is used to advance the free surface elevation:

$$\frac{\partial \eta}{\partial t} = \frac{\partial \phi}{\partial y} - \frac{\partial \eta}{\partial x} \frac{\partial \phi}{\partial x} \quad \text{on} \quad y = \eta, \quad (5)$$

and the unsteady form of Bernoulli's equation, modified here to compute the rate of change of ϕ_s at a surface point, is used to advance the free surface velocity potential ϕ_s :

$$\frac{\partial \phi_s}{\partial t} = C - g\eta - \frac{1}{2} \left(\left(\frac{\partial \phi}{\partial x} \right)^2 + \left(\frac{\partial \phi}{\partial y} \right)^2 \right) + \frac{\partial \phi}{\partial y} \frac{\partial \eta}{\partial t} \quad \text{on} \quad y = \eta, \quad (6)$$

where $C(t)$ is constant throughout space.

Slightly different versions of these equations are generally used for BIEM which do not assume a single valued free surface, and use Lagrangian methods to track moving surface particles.

Local Polynomial Approximation Methods

In finite depths, the representation of a velocity potential locally by a polynomial can provide an excellent approximation to the flow field. Local polynomial approximation (LPA) methods for one dimension in plan use this principle to model wave evolution over varying topography, with very good results. A preliminary version has been given by Kennedy and Fenton (1995). Two main variants are summarised here: a fully nonlinear model which can provide highly accurate results, and an model which uses Taylor expansions about the undisturbed surface to increase speed, but which sacrifices some accuracy for high waves. For both methods, the expense of solution at each time step is directly proportional to the number of computational subdomains, which allows wave evolution to be computed over relatively large regions with a reasonable computational cost.

Solution of Laplace's Equation

For both the fully nonlinear and expansion LPA methods for one dimension in plan, the basic method of solution for Laplace's equation is very similar. As shown in Figure 1, the computational domain is divided into subdomains extending vertically from the free surface to the bed. In any typical subdomain, m , the velocity potential ϕ_m at any point (x_m, y) is represented by the polynomial

$$\phi_m(x_m, y, t) = \left[A_{0R} + \text{Re} \left(\left(\sum_{j=1}^{n-1} (A_{jR} + iA_{jI}) (x_m + iy)^j \right) + (x_m + iy)^n \begin{cases} A_{nR}, & n \text{ odd} \\ iA_{nI}, & n \text{ even} \end{cases} \right) \right]_m \quad (7)$$

where n is an integer ≥ 3 which controls the level of approximation, $i = \sqrt{-1}$, $\text{Re}(\dots)$ means taking the real part. The A coefficients are functions of time. For any given n , it is these A coefficients which must be chosen to best satisfy the boundary value problem. Because of the complex formulation used, Equation (1) is identically satisfied. With the introduction of subdomains, two additional constraints are introduced: the velocity potential, ϕ , and its normal derivative, $\partial\phi/\partial x$, must be continuous across subdomain boundaries.

The velocity potential ϕ may be made analytically continuous across subdomain boundaries through a transformation of basis functions which, in addition, almost halves the number of independent coefficients. However, $\partial\phi/\partial x$ will still be discontinuous across boundaries. (Details of the transformation may be found in Kennedy and Fenton, 1995.) In a domain with M subdomains, the revised basis functions may now be thought of as having n independent coefficients defined at each internal boundary between subdomains, plus n coefficients at each of the left and right global

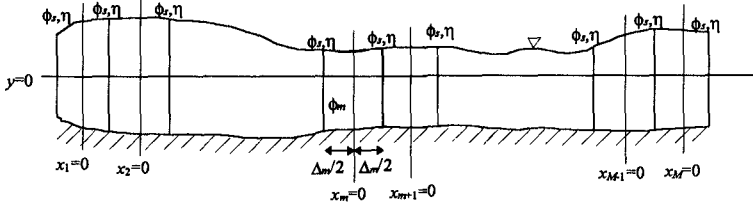


Figure 1: Definition sketch for local polynomial approximation boundaries, for a total of $(M - 1)n + 2n = (M + 1)n$ independent coefficients. The constraints on these are as follows. At each internal boundary between subdomains, the free surface velocity potential is set to the specified value, satisfying (2). Next, the bottom boundary condition (3) is imposed, using the average value of $\partial\phi/\partial x$ across the boundary. The remaining $n - 2$ constraints at each internal boundary match the horizontal velocity, $\partial\phi/\partial x$, across the boundary at $n - 2$ discrete points. For overall continuity, these collocation points are here set to the Gauss-Legendre points for level $N = n - 2$, using the free surface (or still water level for the expansion method) and bed as limits. At each of the left and right global boundaries, (2) is also specified at the surface and (3) at the bed. However, instead of a velocity match as with the internal boundaries, the horizontal velocity at the boundary, $\partial\phi/\partial x$, is instead set to the known value at $n - 2$ collocation points, satisfying (4).

All of these constraints result in a set of block banded linear equations. These may be solved using any banded or block banded matrix solver, both of which have a computational cost which is directly proportional to the number of subdomains, M . This allows for the computation of wave evolution over reasonably large areas without great expense. Traditional methods which use global approximation usually have a computational cost proportional to the second or third power of the number of computational points.

Linear Dispersion Characteristics

Here, as a test of the ability of polynomials to describe the flow field, we consider what results they give for the linear phase speed, compared with traditional approximation by periodic functions in x and hyperbolic functions in y . As subdomain lengths go to zero, a set of differential equations for the velocity potential results, which may be easily solved for the case of small amplitude waves over a level bed. Figure 2 shows the LPA small amplitude phase speed relative to the exact relationship for the levels $n = 3, 4, 5, 7$, with collocation points set to the Gauss-Legendre points for $N = n - 2$. Accuracy for the level of approximation $n = 3$ is poor in anything other than shallow water but increasing to $n = 4$ gives usable small amplitude results past the nominal deep water limit of $kd = \pi$ ($L/d = 2$). The level of approximation $n = 5$ (usually used with the LPA expansion method) has good dispersion characteristics even for

very short waves with $kd = 2\pi$ ($L/d = 1$), while with $n = 7$, phase speeds remain excellent past a dimensionless wavenumber of $kd = 3\pi$ ($L/d = 2/3$).

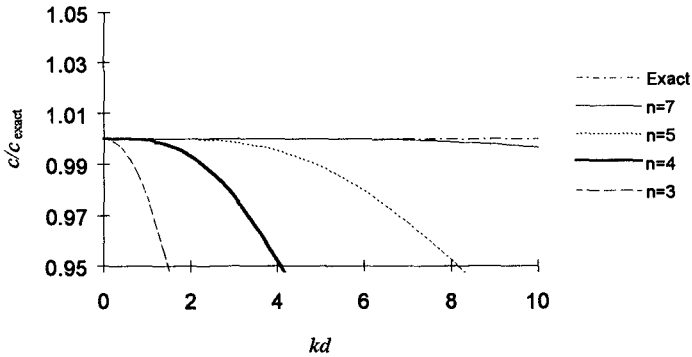


Figure 2: LPA linear phase speed

Fully Nonlinear LPA

The fully nonlinear version of LPA can provide excellent accuracy for finite depth potential flow calculations. There are two main steps: Laplace's equation is solved exactly as described earlier, and a time stepping method (here usually third or fourth order Adams-Bashforth) is then used to solve the evolution equations (5) and (6) to advance the solution to the next time step. If the Gauss-Legendre points of level $N = n - 2$ are used as collocation points, then the first $n - 3$ weighted moments of flow will be conserved between subdomains, as well as having velocity matches at the collocation points. For an accurate potential flow method, computations are also quite efficient. For a very large computational run with 900 subdomains and 4000 time steps, total run time for the level $n = 7$ would be about 3.5 hours on a Pentium 150 personal computer. Figure 3 shows the shoaling of a solitary wave of initial height $H/d = 0.15$ as it propagates onto a shelf of depth $0.5d$. The classical fissioning into multiple solitons is clearly evident, with the leading wave reaching a final dimensionless height on the shelf of 0.507. As an independent estimate of computational accuracy, relative energy fluctuations were less than 2×10^{-4} .

LPA Free Surface Expansion Method

The free surface expansion method is somewhat more complex, with two major differences from the fully nonlinear version. The first difference is that, instead of solving Laplace's equation using the free surface and the bed as limits, it is instead solved between the still water level and the bed. The mode coupling free surface expansion of Dommermuth and Yue (1987) is then used to relate the value of ϕ at the free surface to the value of ϕ at the still water level. The order of expansion may be easily changed to accommodate the level of nonlinearity of the problem considered.

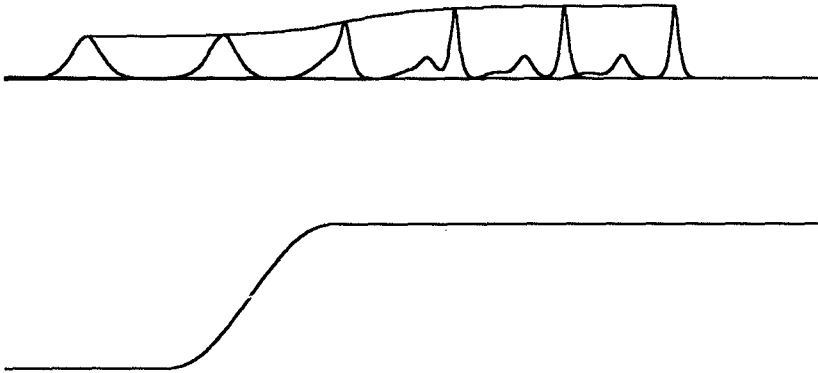


Figure 3: Results from the LPA method for the propagation of a wave over a shelf of depth 50%

Accuracy is still, of course, less than the fully nonlinear version for higher waves, but there is one major advantage: since the upper limit of the computational domain remains constant through time, a matrix equation must only be filled and decomposed once, rather than at each time step as with fully nonlinear LPA. This decomposed matrix is then solved with different right hand sides at each time step, which is much faster.

It is worthwhile to implement the second major change only if the computational domain is invariant with time, as is the case here. This involves another change of basis functions, so that there is only one independent variable per computational point. Details of this transformation may be found in Kennedy (1997). With the new basis functions, all conditions but (2) are automatically satisfied, so this constraint is used at every computational point to generate a new set of linear matrix equations for the LPA solution to Laplace's equation. The new matrix is purely banded and has both fewer variables and a smaller bandwidth than with the previous basis functions. Computational speeds are therefore further increased. A reasonable analogy may be made between the new basis functions and B-splines, as both are piecewise continuous polynomials which use a set of interpolation conditions to reduce the number of independent computational variables to one per computational point. These new basis functions could also be computed for the fully nonlinear version, but to retain full accuracy, they would have to be recomputed at each time step as the free surface moves. This would slow down computations, which is why they were not used.

The two parameters which control the accuracy of the LPA expansion method are the degree of the polynomials, n , and the order of free surface expansion, Q . While the fully nonlinear LPA was developed to calculate potential flow problems with very high accuracy, the LPA expansion method is viewed as a tool for more practical problems. To give reasonable nonlinear accuracy, which is mostly controlled by the order of free surface expansion, Q , and good frequency dispersion, which is only affected by the LPA level, n , the parameters $Q = 3$ and $n = 5$ were generally used.

For an example of the capabilities of the method, computations here will be compared with the experimental results of Beji and Battjes (1993) as reported by Ohyama *et al.* (1994). In this experiment regular waves were propagated over a two dimensional bar-trough setup and time series of surface elevations were taken at various points. Two wave trains were considered – both were initially of reasonably small amplitude in intermediate depths, but became significantly nonlinear over the bar.

The first wave train had an initial height of $H_0/d = 0.05$ and a period of $T\sqrt{g/d} = 9.903$. Figure 4 shows a comparison between computed and experimental values at Stations 1, 3, 5 and 7, which are, respectively, just before the bar, on the bar crest, on the downslope and in the trough. Agreement is quite good, with the LPA expansion model accurately predicting the steepening of the wave as it progresses up and sheds secondary waves on the bar, and its decomposition into higher harmonics on the downslope. As the wave progresses, computations begin to overestimate wave heights slightly due to the lack of dissipation in the model, and a small phase difference appears. However, similar differences were also noted in the fully nonlinear boundary element computations of Ohyama *et al.* (1994).

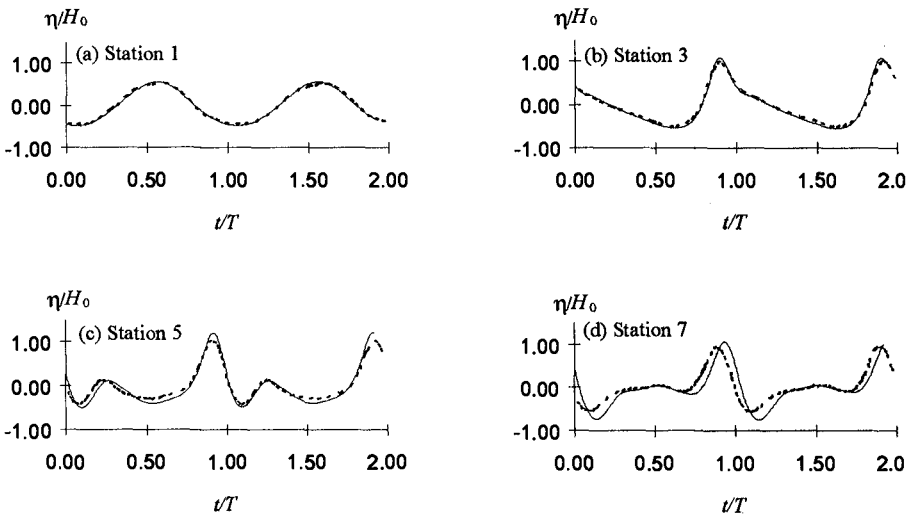


Figure 4: Measured and computed time series, $H_0/d = 0.05$, $T\sqrt{g/d} = 9.903$.

Figure 5 shows results for the second wave train which was shorter, with a period of $T\sqrt{g/d} = 6.189$ and an initial height of $H_0/d = 0.0625$. Due to its shorter length, this wave did not evolve as much passing over the bar, but the model still predicts the features of its evolution well. A small phase lag is visible at the last station. The fully nonlinear results of Ohyama *et al.* (1994) were similar to those here, although the phase lag at Station 7 was somewhat smaller. Overall, the expansion model predicts wave evolution quite well, and may be relied on to provide a good estimate of nonlinear wave evolution for a wide range of waves.

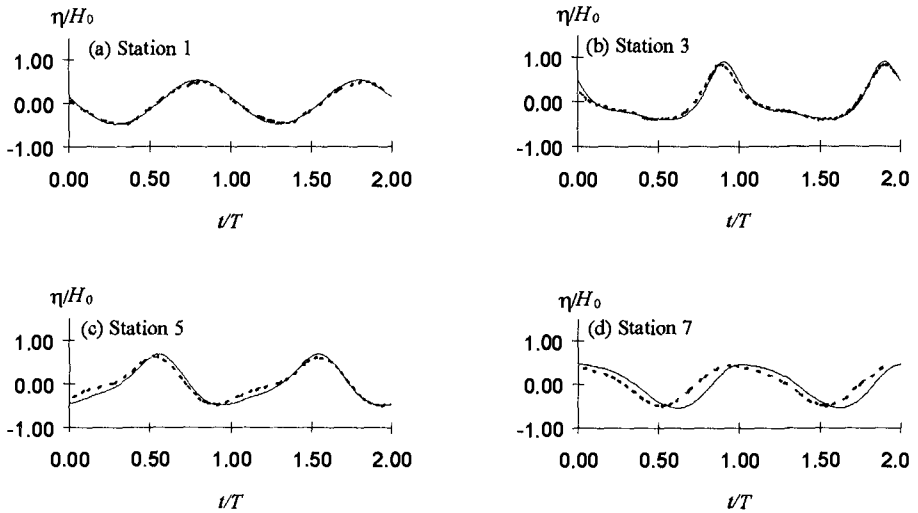


Figure 5: Measured and computed time series, $H/d = 0.0625$, $T\sqrt{g/d} = 6.189$. Solid lines – computations, dashed lines – experiment

Computations with the expansion method are quite fast. For example a computation with 900 subdomains and 4000 time steps would have a total run time on a Pentium 150 personal computer of about 10 minutes for the LPA level $n = 5$ and expansion level $Q = 3$, compared with 3.5 hours for the fully nonlinear version using $n = 7$.

A new boundary integral equation method

Introduction

The approach of using boundary integral equations for the study of waves in deep water was initiated by Longuet-Higgins and Cokelet (1976), who set up and solved a boundary integral equation with a logarithmic kernel. A different approach was introduced by Vinje and Brevig (1981), who used the Cauchy integral theorem in terms of a complex potential function. A number of powerful results have been

obtained in recent years for waves over topography, including Dold & Peregrine (1985), Grilli *et al.* (1989, 1994), and Subramanya & Grilli (1994). A brief history of various attempts using BIEM is described by Liu *et al.* (1992).

A quicker but less accurate approach was introduced by Leitão and Fernandes (1992), who took as the upper surface of the computational domain the undisturbed water surface, and used a second-order Taylor expansion there. As with the LPA expansion method described above, their computational domain was constant, and they only had to solve a matrix equation once rather than at each time step.

Fenton (1992 & 1996) has developed a method for the solution of Laplace's equation in two dimensions which has some advantages over traditional methods: it is simpler in theory and implementation, yet is more accurate. Of particular importance to the problem of shoaling waves, is that it allows the use of iterative methods for solution which are rapidly convergent because of the nature of the equations and because information from previous time steps can be incorporated. A preliminary study applying that method to shoaling waves has been published (Fenton, 1993), but in that work it was concluded that the method advocated, despite its high accuracy for fixed domains, was somewhat fragile for shoaling. Here, the method will be briefly described and the results of rather more robust computations will be described.

Theory

Consider a two-dimensional region such as that shown in Figure 1 containing an incompressible fluid which flows irrotationally, in which case a scalar potential function ϕ exists and satisfies Laplace's equation: $\nabla^2\phi = 0$. As ϕ is an harmonic function, another function ψ exists, related to ϕ by the Cauchy-Riemann equations: $\partial\phi/\partial x = \partial\psi/\partial y$ and $\partial\phi/\partial y = -\partial\psi/\partial x$. It can be shown that if these relations are satisfied, then the complex function $w = \phi + i\psi$, where $i = \sqrt{-1}$, has a unique derivative with respect to the complex variable $z = x + iy$, satisfies the integral equation

$$\oint \frac{w(z) - w(z_m)}{z - z_m} dz = 0, \quad (8)$$

for a reference point m . In this equation, unlike other formulations, the integrand is everywhere continuous, even at $z = z_m$, and its numerical approximation should be simpler and potentially more accurate. It will be shown below that using this form leads to a system of algebraic equations which are all nearly diagonally dominant, giving desirable numerical properties.

Boundary conditions: On the sea bed, assumed impermeable here, the condition that flow does not cross the boundary is $\psi = 0$. On the free surface, denoted by $y = \eta(x, t)$, the governing equations are nonlinear, partly because the location of the free surface also appears in them. There are two equations: one is the kinematic condition that the velocity of a particle on the surface is equal to the fluid velocity at that point. These have been described above. A slight difference here is that a Lagrangian description is used, like other BIEM, such that surface particles are followed and it is necessary to update the ϕ on the surface. This necessitates the

computation of the material derivative which can be shown to become

$$\frac{D\phi_m}{Dt} = -g\eta_m + \frac{1}{2} \left| \frac{dw}{dz} \right|_m^2, \quad (9)$$

a differential equation for ϕ_m at the free surface particle. This gives us a way of calculating ϕ as time evolves so that at any instant it is known at all points on the free surface, while we know that $\psi = 0$ on the sea bed. Hence we have enough boundary information to obtain a solution of equation (8) at each time step, namely to obtain the values of ϕ on the bottom and ψ on the free surface, so that $\omega = \phi + i\psi$ is known at all points, dw/dz can be calculated, the solution advanced, and so on.

Numerical scheme using periodicity around the contour

Around the boundary all variation is periodic, for in a second circumnavigation of the boundary the integrand is the same as in the first, and so on. This suggests the use of methods that exploit periodicity to gain handsomely in accuracy. A continuous co-ordinate j is introduced here, which is 0 at some reference point on the boundary, and after a complete circumnavigation of the boundary has a value N , which will be taken to be an integer. The integral in equation (8) can be written

$$\int_0^N \frac{w(z(j)) - w(z_m) dz}{z(j) - z_m} \frac{dz}{dj} dj = 0. \quad (10)$$

Now a numerical approximation is introduced to transform the integral equation into an algebraic one in terms of point values. The integral in equation (10) is replaced by the trapezoidal rule approximation:

$$\sum_{j=0}^{N-1} \frac{w(z_j) - w(z_m)}{z_j - z_m} z'_j = 0, \quad (11)$$

where $z_j = z(j)$ and $z'_j = dz(j)/dj$, but in which after the differentiation, j takes on only integer values. In this case the trapezoidal rule has reduced to the simple sum as the end contributions are from the same point, $z_0 = z_N$ because of the periodicity. This is a particularly simple scheme when compared with some such as Gaussian formulae which have been used to approximate boundary integrals. Where the integrand is periodic, as it is here, the trapezoidal rule is capable of very high accuracy indeed, a fact which is relatively little-known.

In the form of equation (11), the expression is not yet useful, as the point $j = m$ has to be considered. It is easily shown that in this limit, the integrand (and hence the summand) becomes $dw(m)/dm$, and extracting this term from the sum gives the expression with a "punctured sum" $j \neq m$:

$$\frac{dw}{dm}(m) + \sum_{j=0, j \neq m}^{N-1} \frac{w_j - w_m}{z_j - z_m} z'_j = 0, \quad (12)$$

for $m = 0, 1, 2, \dots, N - 1$, and where the obvious notation $w_j = w(j)$ etc. has been introduced. The notation $dw(m)/dm$ means differentiation with respect to the continuous variable m , evaluated at integer value m . It is convenient here to introduce the symbol Ω_{mj} for the geometric coefficients:

$$\Omega_{mj} = \alpha_{mj} + i\beta_{mj} = \frac{z'_j}{z_j - z_m}, \quad (13)$$

whose real and imaginary parts are the coefficients α_{mj} and β_{mj} . One is free to use either the real or imaginary part of the integral equation and of the sum which approximates it, equation (12). The two parts can be extracted to give

$$\frac{d\phi}{dm}(m) + \sum_{j=0, j \neq m}^{N-1} [\alpha_{mj}(\phi_j - \phi_m) - \beta_{mj}(\psi_j - \psi_m)] = 0 \quad (14)$$

and

$$\frac{d\psi}{dm}(m) + \sum_{j=0, j \neq m}^{N-1} [\alpha_{mj}(\psi_j - \psi_m) + \beta_{mj}(\phi_j - \phi_m)] = 0. \quad (15)$$

One of these equations can be used at each of the N computational points, provided either $d\phi/dm$ or $d\psi/dm$ is known that point, which can be done from the boundary conditions as described above. Each equation is written in terms of the $2N$ values of ϕ_j and ψ_j . If N of these are known, specified as boundary conditions, then there are enough linear algebraic equations and it should be possible to solve for all the remaining unknowns.

As equation (14) can be used on the free surface where $d\phi/dm$ can be evaluated and where ψ_m is the unknown and (15) on the sea bed where $d\psi/dm = 0$, and where ϕ_m is unknown, examination of the coefficients shows that the system of equations is nearly diagonally dominant, which suggests a certain computational robustness, and the possibility of iterative solution.

Distribution of computational points: The linear algebraic equations approximating the integral equations have been expressed relatively simply in terms of the coordinates of the computational points z_j and the derivative around the boundary, z'_j . The accuracy of the method depends on how continuous the latter are, and in Fenton (1992, 1996) some effort was spent in ensuring continuity across corners of the boundary. In fact it was found that even if no special spacing was used, the accuracy was still surprisingly high.

Numerical computation of coefficients: In problems of wave shoaling, the boundary of the computational region, including the sea bed and the free surface, is quite irregular. The periodicity around the boundary may be exploited to give a simple scheme for computing the necessary derivatives around the boundary. The main problem is to compute values of the z'_j . Also, it is convenient to be able to use a means of interpolation between the computational points for plotting purposes which

has the same accuracy as the underlying numerical method. Both can be accomplished simply and economically using Fourier approximation, once again exploiting periodicity as the boundary is traversed. If fast Fourier transform programs are available, the z'_j may be computed easily and accurately in $O(N \log N)$ operations, where there are N boundary points.

Set-up and solution of system of equations: When the z'_j have been obtained, the coefficients $\Omega_{mj} = \alpha_{mj} + i\beta_{mj}$ can be calculated and used in expressions (14) and (15), one for each point at which an unknown exists. As the equations are nearly diagonally dominant, however, it should be possible to exploit the simple Gauss-Seidel iterative procedure, particularly for timestepping problems such as those for wave propagation, and in practice this was found to work very well indeed. The computational effort is $O(N^2)$ per iteration, and the happy result was found in the present work, that as all boundary points are interpreted as Lagrangian particles, and carry the geometry of the problem with them, then the coefficients are very slowly varying, and a forward extrapolation of previous results gave such an accurate initial estimate that typically only five iterations were necessary each time step. Much programming detail can be avoided if the step of assembling into a matrix is bypassed. In this case, equations (14) and (15) may simply be rewritten: for points on the free surface to give an equation for ψ_m , and for points on the sea bed an equation for ϕ_m .

In practice, a procedure of over-relaxation can be adopted to give faster convergence. It was found convenient in the present work where the coefficients changed slowly, not to store all the coefficients α_{mj} etc., as this requires storage of $O(N^2)$, but to generate the coefficients necessary for each equation every time it had to be evaluated such that the storage was $O(N)$, and large numbers of points could be used. Overall, the implementation of the scheme in the form described here was particularly simple.

Results

The only results reported here are for a wave height $H/d = 0.25$ and a length 25 times that of the depth, rather higher than that used in Figure 3 above. The initial conditions were computed using an accurate Fourier method. The wave was allowed to propagate across a shelf with a cosine profile, which shoaled to $1/4$ the depth in a distance of roughly half the horizontal length scale of the wave, a rather more abrupt case than Figure 3, and corresponding to the shoaling of a wave on a coral reef. Results are shown in Figure 6, and they show some of the interesting phenomena associated with this nonlinear problem. After the wave travelled almost right across the shelf, quite quickly it started to grow in height, travelling over water of constant shallower depth, and the large feature of a shelf developed behind the wave, which seemed to be in the process of separating from the main wave and possibly becoming part of an oscillatory tail. At the final stage a sharp crest began to form, which turned over as shown, the surface particles in this latter stage experiencing very large accelerations.

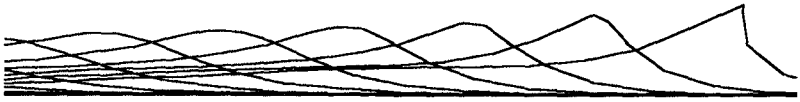


Figure 6: High wave on a steeply-shelving beach showing overturning

Conclusions

The local polynomial methods were found to be robust, accurate, and efficient, and may provide a useful practical means of computing nonlinear wave propagation over extended regions and times. The boundary integral method can be used to simulate shoaling considerably faster than other similar methods, and it has the potential to be more accurate than them. It can describe wave overturning with relatively few points, but for some problems it was found to be not as robust as had been hoped. Its most appropriate application might be to methods such as those of Leitão and Fernandes (1992) which use such a fixed domain with approximate boundary conditions.

References

- Beji, S. and Battjes, J. A. (1993), Experimental investigation of wave propagation over a bar, *Coastal Engng* **19**, 151–162.
- de Haas, P., Dingemans, M., and Klopman, G. (1996), Simulation of free long-wave generation due to uneven bottoms, In *Proc. 25th Int. Conf on Coastal Eng.*
- Dold, J. W. and Peregrine, D. H. (1985), An efficient boundary-integral method for steep unsteady water waves, In *Proc. Conf. Numerical Methods for Fluid Dynamics*, Reading. Inst. Maths. Applics.
- Dommermuth, D. G. and Yue, D. K. P. (1987), A high-order spectral method for the study of nonlinear gravity waves, *J. Fluid Mech.* **184**, 267–288.
- Fenton, J. D. (1992), Exploiting periodicity in boundary integral equations, In *Proc. 11th Australasian Fluid Mech. Conf., Hobart*, 667–670.
- Fenton, J. D. (1993), Simulating wave shoaling with boundary integral equations, In *Proc. 11th Australasian Conference on Coastal and Ocean Engng, Townsville*, 71–76.
- Fenton, J. D. (1996), Exploiting periodicity in boundary integral equations, In Easton, A. K. and Steiner, J. M., editors, *The Role of Mathematics in Modern Engineering*, Proc. 1st Biennial Engng Mathematics Conference, Melbourne, 565–576. Studentlitteratur, Lund.
- Grilli, S. T., Skourup, J., and Svendsen, I. A. (1989), An efficient boundary element

- method for nonlinear water waves, *Engng Analysis with Boundary Elements* **6**, 97–107.
- Grilli, S. T., Subramanya, R., Kirby, J. T., and Wei, G. (1994), Comparison of modified Boussinesq and fully nonlinear potential models for shoaling solitary waves, In *Proc. Int. Symp. on Waves - Physical and Numerical Modelling, Vancouver*, 524–533.
- Kennedy, A. B. (1997), *The propagation of water waves over varying topography*, PhD thesis, Monash University.
- Kennedy, A. B. and Fenton, J. D. (1995), Simulation of the propagation of surface gravity waves using local polynomial approximation, In *Proc. 12th Australasian Coastal and Ocean Engng Conference, Melbourne*, 287–292.
- Leitão, J. C. and Fernandes, J. L. M. (1992), On a model to propagate surface waves - a second order approach, *Coastal Engng* **18**, 315–332.
- Liu, P. L.-F., Hsu, H.-W., and Lean, M. H. (1992), Applications of boundary integral equation methods for two-dimensional non-linear water wave problems, *Int. J. Numer. Meth. Fluid Mech.* **15**, 1119–1141.
- Longuet-Higgins, M. S. and Cokelet, E. D. (1976), The deformation of steep surface waves on water, I. A numerical method of computation, *Proc. Roy. Soc. Lond. A* **350**, 1–26.
- Madsen, P. A. and Sørensen, O. R. (1992), A new form of the Boussinesq equations with improved linear dispersion characteristics. Part 2. A slowly-varying bathymetry, *Coastal Engng* **18**, 183–204.
- Nwogu, O. (1993), An alternative form of the Boussinesq equations for nearshore wave propagation, *J. Waterway Port Coastal and Ocean Engng* **119**, 618–638.
- Ohyama, T., Beji, S., Nadaoka, K., and Battjes, J. (1994), Experimental verification of numerical model for nonlinear wave evolutions, *J. Waterway Port Coastal and Ocean Engng* **120**(6), 637–644.
- Subramanya, R. and Grilli, S. T. (1994), Kinematics and properties of fully nonlinear waves shoaling and breaking over a gentle slope, In *Proc. Int. Symp. on Waves - Physical and Numerical Modelling, Vancouver*, 1106–1115.
- Vinje, T. and Brevig, P. (1981), Numerical calculations of forces from breaking waves, In *Proc. Int. Symp. Hydrodynamics in Ocean Engng, Trondheim, Norway*.
- Wang, P., Yao, Y., and Tulin, M. (1995), An efficient numerical tank for nonlinear water waves, based on the multi-subdomain approach with BEM, *Int. J. Numer. Meth. Fluids* **20**, 1315–1336.
- Wei, G., Kirby, J., Grilli, S., and Subramanya, R. (1994), A fully nonlinear Boussinesq model for surface waves. 1. Highly nonlinear waves, Res. Rpt. CACR-94-15, Center for Applied Coastal Research, University of Delaware.

CHAPTER 89

STRUCTURE OF FREQUENCY DOMAIN MODELS FOR RANDOM WAVE BREAKING

James T. Kirby¹ and James M. Kaihatu²

Abstract

We consider the form of a breaking wave dissipation term for use in spectral or stochastic wave evolution models. A time-domain Boussinesq model is tested for accuracy in modelling evolution of second and third moment statistics in shoaling and breaking waves. The structure of the dissipation term in the time domain is then used to infer the corresponding structure of the term in the frequency domain. In general, we find that the dissipation coefficient is distributed like $1/S_\eta(f)$, where $S_\eta(f)$ is the spectral density of the surface displacement η . This implies an f^2 dependence for the coefficient in the inner surfzone, as opposed to a constant distribution over frequency as suggested by Eldeberky and Battjes (1996).

Introduction

Recently, there have been several suggestions on how to structure the breaking wave dissipation term in spectral or stochastic wave evolution models, with the principle question being how to structure the dissipation coefficient as a function of frequency. As an example, Mase and Kirby (1992) developed evolution equations for the shoreward (x direction) evolution of component amplitudes $A_n(x)$, where the A_n are related to surface displacement η according to

$$\eta = \sum_{n=1}^{\infty} \frac{A_n(x)}{2} e^{i \int k_n(x) dx - \omega_n t} + c.c. \quad (1)$$

where k_n is related to ω_n through a suitable wave dispersion relation. Index n is the analog in the discrete spectral representation to a continuous dependence on frequency f in the continuous spectrum representation, and the two representations will be used interchangeably below. Restricting our attention here to wave breaking effects, the evolution equations may be written as

$$A_{n,x} = -\alpha_n A_n + \dots \quad (2)$$

¹Professor, Center for Applied Coastal Research, University of Delaware, Newark, DE 19716, USA. kirby@coastal.udel.edu

²Oceanographer, Oceanography Division (Code 7322), Naval Research Laboratory, Stennis Space Center, MS 39529-5004

where the omitted terms are related to shoaling and nonlinear interaction effects. Mase and Kirby (1992) proposed a form for α_n given by

$$\alpha_n = \alpha_0 + (f_n/\bar{f})^2 \alpha_1 \tag{3}$$

with

$$\alpha_0 = F\beta \tag{4}$$

$$\alpha_1 = (1 - F)\beta \frac{\bar{f}^2 \sum_n |A_n|^2}{\sum_n f_n^2 |A_n|^2} \tag{5}$$

and where β is determined from a bulk dissipation model such as the one of Thornton and Guza (1983). Based on analysis of laboratory data and numerical results, Mase and Kirby chose to set $F = 0.5$, indicating a dissipation term with a partial dependence on the square of the frequency. They also found that choosing $F = 0.0$, corresponding to an f^2 dependence for the entire dissipation term, destroyed the tail of the computed power spectrum in very shallow water but had little impact on the evolution of spectral shape away from the shallowest measuring gages.

Eldeberky and Battjes (1996) have suggested that a similar formulation corresponding to the choice $F = 1.0$, spreading the dissipation term uniformly over all frequencies, should be utilized, and showed that an adequate description of power spectrum evolution was obtained in several simulations of field data. Eldeberky and Battjes did not consider the effect of this choice on the evolution of higher statistical moments. More recently, Chen et al (1996; referred to as CGE) have examined a number of laboratory and field cases. They have shown that the estimates of power spectrum evolution are relatively insensitive to the choice of F , with error-minimizing F values occupying the entire range $0 \leq F \leq 1$ for various field and laboratory cases. Aside from the Mase and Kirby case, error measures changed by as little as 20% over the entire range of values. In contrast, all data sets support the choice of $F = 0.0$ when error measures based on third-moment statistics are introduced, with the exception of the Mase-Kirby data set. (This last discrepancy is fairly weak, however). There is a clear trend towards increasing error with increasing F in most data sets.

In this talk, the problem of determining the form of the spectral dissipation term is approached from a different direction. Instead of considering a bulk energy decay and an arbitrary distribution of dissipation over f , we instead consider the structure of the dissipation term in a time-dependent Boussinesq model setting, and consider the contribution of the term to energy loss and the structure of that loss in the frequency domain. This loss is then related to the spectral evolution equations, and the form of the dissipation term is deduced. We find that, in general, the dissipation coefficient is distributed more or less as $S_\eta(f)^{-1}$, where $S_\eta(f)$ is the power spectrum of the surface displacement η . For the case of a smooth spectrum, this result indicates an f^2 dependence in the dissipation coefficient in the surfzone, consistent with CGE's results with $F = 0.0$. The conclusions here are based on an examination of the Mase and Kirby (1992) data set, which is well modelled by the chosen time-domain breaking wave model.

Time-Domain Model for Wave Breaking

The literature includes examples of a number of formulations for computing wave breaking in the context of Boussinesq wave models. Three examples include an eddy viscosity model (Zelt, 1991), a surface roller model with an assumed two-layer velocity profile (Schäffer et al, 1993), and a surface roller model with a computed horizontal profile (Svendsen et al, 1996). Schematically, the eddy viscosity model may be written as

$$u_t + uu_x + g\eta_x + \text{dispersive terms} - (\nu_b u_x)_x = 0 \quad (6)$$

The simple roller model of Schäffer et al (1993) is written in the context of a model for total volume flux, and may be written schematically as

$$P_t + \left(P^2/H\right)_x + gH\eta_x + \text{dispersive terms} + R_x = 0 \quad (7)$$

where

$$R = \int_{-h}^{\eta} \left(u_{\text{rot}}^2 - u_{\text{irrot}}^2\right) dz \quad (8)$$

and

$$H = h + \eta \quad (9)$$

The more complex roller model of Svendsen et al (1996) is essentially of the same form. While these models differ in both form and theoretical intent, it may be shown that the numerical representations of each dissipative term are similar. In particular, the contribution of each dissipation term is highly localized in space and time, since it is concentrated on the front face of the breaking wave. Further, the contribution of each dissipation term is about the same size, since each successfully calibrated model must extract the same amount of energy. An illustration of this fact is given by Figure 9 of Svendsen et al (1996).

Since our primary goal below is to examine the spectral signature of the wave energy decay, we can conclude that, due to the structural similarity of the various breaking models in the time domain, it should not matter which of the existing models is used to perform the analysis. The analysis will be based on the eddy viscosity model of Zelt (1991) for two reasons: it is already incorporated in an existing time-domain Boussinesq model (Wei and Kirby, 1996), and it is simple to interpret the terms in the eddy viscosity model in terms of measured sea surface elevations, as described below.

Leading-Order Energy Balance

Let $r = R/H$ or $-\nu_b u_x$ represent the breaking-induced momentum deficit per unit depth. Then, each of the models above may be written in the form

$$u_t + uu_x + g\eta_x + \text{dispersive terms} + r_x = 0 \quad (10)$$

Neglecting nonlinear and dispersive effects, we have

$$u_t + g\eta_x + r_x = 0 \quad (11)$$

$$\eta_t + (hu)_x = 0 \quad (12)$$

Multiplying (11) by ρhu , (12) by $\rho g\eta$ and adding then gives

$$E_t + F_x = -\epsilon_b \tag{13}$$

where

$$E = \frac{1}{2}\rho g\eta^2 + \frac{1}{2}\rho hu^2 \tag{14}$$

is the local energy density/unit surface area,

$$F = \rho gh u\eta \tag{15}$$

is the flux of energy in the x direction, and

$$\epsilon_b = \rho h u r_x \tag{16}$$

is the local rate of energy decay. Each of these quantities may be averaged in time, yielding (for a stationary wave process)

$$\langle F \rangle_x = -\langle \epsilon_b \rangle \tag{17}$$

The average or bulk energy decay (ϵ_b) can be specified according to models such as the one of Thornton and Guza (1983), which models the data set considered below quite well. Each of the quantities in (17) may be thought of as the sum of contributions from each frequency to the total value; i.e.,

$$\langle F \rangle = \sum_n F_n; \quad \langle \epsilon_b \rangle = \sum_n \epsilon_{bn} \tag{18}$$

We will attach a meaning to each of these component terms in the analysis below.

In order to proceed further, we need to choose a model to evaluate ϵ_b . This will be done using the Zelt (1991) eddy viscosity model.

Eddy Viscosity Model

The eddy viscosity appearing in (6) is written by Zelt (1991) as

$$\nu_b = -\ell^2 u_x; \quad \ell = B\gamma (h + \eta) \tag{19}$$

where $\gamma = 2$ is a mixing length parameter determined by Heitner & Housner (1970) and chosen so that the resulting model correctly predicts the width of a hydraulic jump. The factor B is given by

$$B = \begin{cases} 1 & ; \quad u_x \leq 2u_x^* \\ u_x/u_x^* - 1 & ; \quad 2u_x^* < u_x \leq u_x^* \\ 0 & ; \quad u_x > u_x^* \end{cases} \tag{20}$$

and provides a somewhat smoothed onset of breaking dissipation when the local breaking criterion is exceeded. The breaking criterion is given in terms of a critical velocity divergence, chosen to be

$$u_x^* = -0.3\sqrt{g/h} \tag{21}$$

The accuracy of this formulation in modelling breaking random waves will be illustrated below. The model is particularly useful to us in the present context because the terms in the model may be evaluated (to leading order) using time derivatives of the surface elevation. Using $u_x \approx -\eta_t/h$, we get

$$\nu_b = B\gamma^2 h^2 u_x \approx B\gamma^2 h \eta_t \quad (22)$$

$$B = \begin{cases} 1 & ; \eta_t \geq 2\eta_t^* \\ \eta_t/\eta_t^* - 1 & ; \eta_t^* \leq \eta_t < 2\eta_t^* \\ 0 & ; \eta_t < \eta_t^* \end{cases} \quad (23)$$

$$\eta_t^* = 0.3\sqrt{gh} \quad (24)$$

Finally, the instantaneous energy dissipation may be written as

$$\epsilon_b = -\rho h u (\nu_b u_x)_x \approx -\rho \left(\frac{\eta}{h} \right) (\nu_b \eta_t)_t \quad (25)$$

The advantage of this formulation is clear in the context of evaluating experimental results, since the energy loss term that would be predicted by the numerical model may be deduced directly from the measured data. Thus, in order to evaluate dissipation effects, we may proceed without actually running the model in the majority of cases, provided that the model as formulated is known to be an accurate predictor of the wave field in sample representative cases.

Laboratory Data

The experimental data considered here is taken from Run 2 of Mase and Kirby (1992). The present results have been reproduced for a number of other data sets, and a more comprehensive view of the study will be published elsewhere. The single case shown here suffices as an indication of the results for a wide range of conditions studied to date.

Figure 1 shows a schematic of the experimental facility. The experimental wave conditions correspond to a Pierson-Moskowitz spectrum generated in 47cm of water, with a peak frequency $\bar{f} = 1Hz$ and a significant wave height of 6cm. Waves were measured using capacitance wave gages at twelve stations across the 1:20 beach profile. Data for the analysis below is taken from the measurement at the $h = 10cm$ depth. This depth corresponds to a point where the probability of breaking is increasing rapidly but the saturated inner surfzone has not yet been established.

A sample of 20 seconds of measured and computed time series of surface elevations at $h = 10cm$ is shown in Figure 2, which indicates an accurate reproduction of wave heights and phases in the numerical model. Computations were performed using the extended fully-nonlinear Boussinesq model code of Wei et al (1995), which is capable of propagating waves in the large water depths used in this experiment. Second and third moment statistics were computed based on the entire experimental run, covering about 800 wave periods. Figure 3 shows the evolution of significant wave height up the beach slope and through the surfzone, while Figure 4 shows the evolution of skewness and asymmetry. Reproduction of measured values by the numerical model is good in both cases.

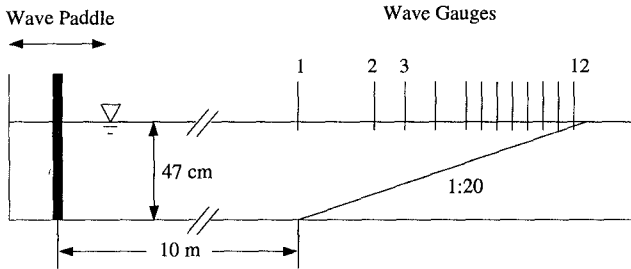


Figure 1: Bottom configuration and wave gage locations for experiments of Mase and Kirby (1992).

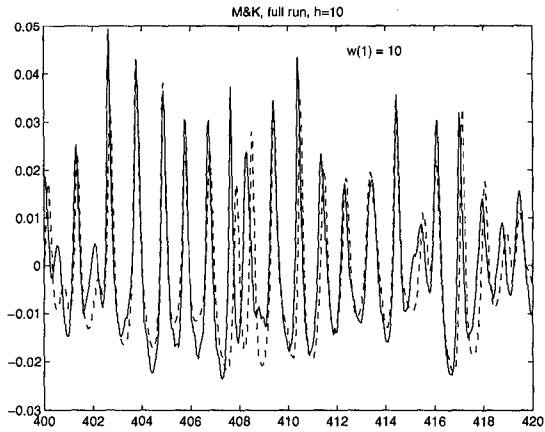


Figure 2: Sample of measured (solid) and predicted (dashed) time series of elevation η for Run 2 of Mase and Kirby (1992). Measurements at $h = 10\text{cm}$, corresponding to analysis of dissipation rates below.

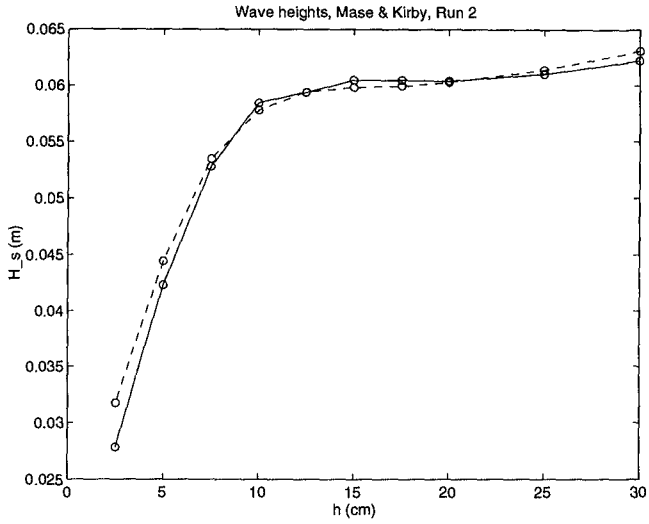


Figure 3: Measured (solid) and predicted (dash) significant wave heights for Run 2 of Mase and Kirby (1992).

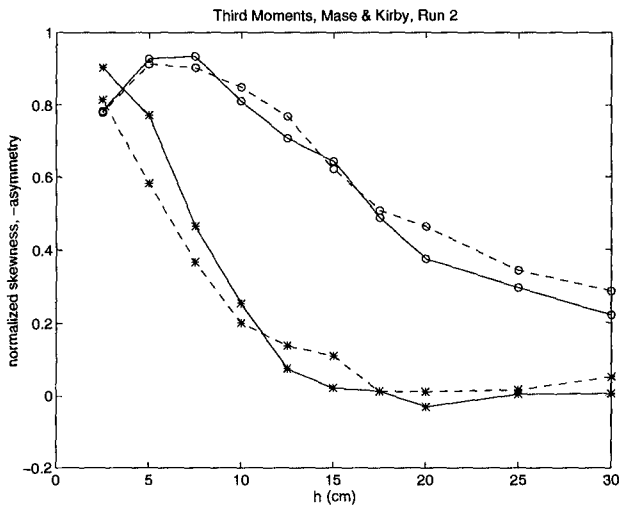


Figure 4: Measured (solid) and predicted (dash) skewness (circles) and asymmetry (stars) for Run 2 of Mase and Kirby (1992).

Analysis of Data

Having verified that the numerical model is capable of correct reproduction of second and third moment statistics in the evolution of a shoaling and breaking random wave train, we may now examine the results for energy dissipation in the model based on a direct analysis of the laboratory data. Figure 5 shows a short segment of the record of surface displacement $\eta(t)$ and dissipation $\epsilon_b(t)$ at $h = 10\text{cm}$. Dissipation $\epsilon_b(t)$ is computed directly from the measured data using (25). We compute the smoothed power spectrum of each of these quantities for the entire data run, according to the definitions

$$S_\eta(n) = \frac{\langle |A_n|^2 \rangle}{2\Delta f} \tag{26}$$

$$S_{\epsilon_b}(n) = \frac{\langle |\hat{\epsilon}_{bn}|^2 \rangle}{2\Delta f} \tag{27}$$

where $\hat{\epsilon}_{bn}$ is the Fourier transform of the dissipation term and where brackets here indicate ensemble averaging. Results for the Run 2 data at $h = 10\text{cm}$ are shown in Figure 6.

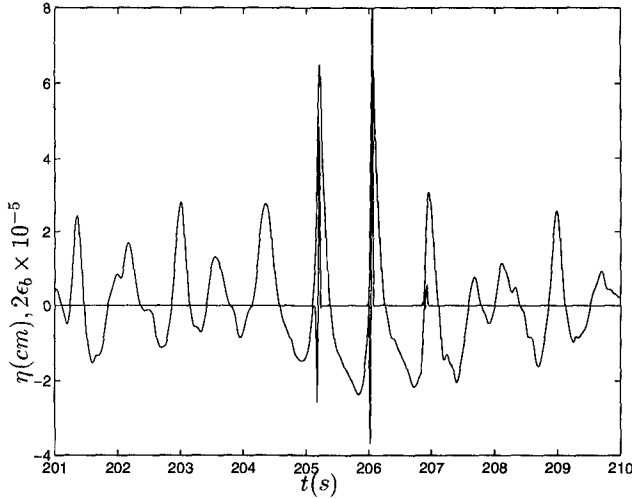


Figure 5: Time history of surface elevation and computed loss $\epsilon_b(t)$ for 9 seconds of Run 2, showing two strong breaking events at a 10cm depth.

Returning to the schematic frequency domain model, we may rearrange the original model equation

$$A_{n,x} + \dots = -\alpha_n A_n \tag{28}$$

into the form of an energy equation

$$\left\{ \frac{1}{2} \rho g |A_n|^2 \sqrt{gh} \right\}_x = -2\sqrt{gh} \alpha_n \left(\frac{1}{2} \rho g |A_n|^2 \right) \tag{29}$$

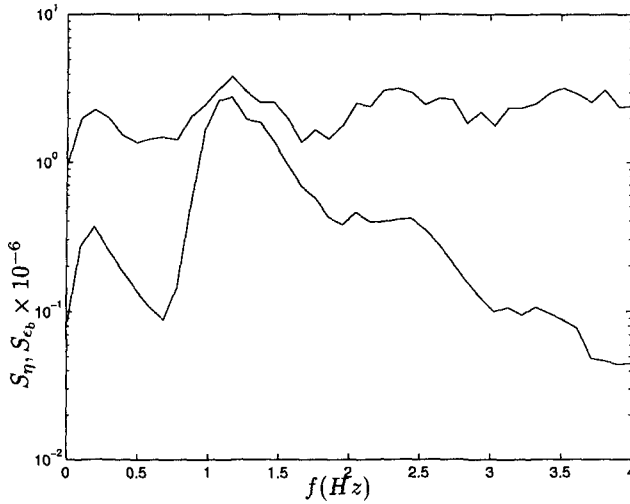


Figure 6: Power spectrum $S_\eta(f)$ of surface displacement (lower trace) and $S_\epsilon(f)$ of energy loss (upper trace) for Mase and Kirby (1992) Run 2 data.

The quantity in brackets on the left hand side of (29) represents the contribution to the wave energy flux from the n 'th frequency component, or F_n . The quantity on the right is the contribution to the loss of wave energy at that frequency, or ϵ_{bn} . Using the definitions of power spectral densities (26) and (27), we may write the dissipation coefficient in the form

$$\alpha_n = \frac{1}{\rho g \sqrt{gh}} \frac{1}{\sqrt{2\Delta f}} \frac{[S_{\epsilon_b}(n)]^{1/2}}{S_\eta(n)} \quad (30)$$

Results similar to those presented in Figure 6 may now be utilized to determine the form of α_n . Analysis of a number of data sets has indicated that the spectral tail of $S_\eta(f)$ tends to have an f^{-2} dependence on frequency after breaking is established. This is consistent with the notion that the wave form tends towards a sawtooth shape, with a vertical front face and a linear back slope. We note that this is somewhat simplistic representation of the waves, as it implies that the wavefield would have significant asymmetry and zero skewness, whereas the measured data exhibits a balance between skewness and asymmetry in the inner surfzone. Nevertheless, the f^{-2} dependence seems to characterize several of the data sets which have been examined extremely well.

In contrast, Figure 6 shows that the dependence of $S_{\epsilon_b}(f)$ on f is relatively weak, so that this quantity can be taken to be constant. This is consistent with the notion that the dissipation term has the character of a sequence of isolated, spike-like processes. Taken together, these results indicate that the dominant frequency dependence of α_n is given by

$$\alpha_n \propto S_\eta(n)^{-1} \quad (31)$$

and we may further infer that this dependence translates into a dependence on f^2 in the inner surfzone. Figure 7 shows a sample distribution of $\alpha(f)$ as calculated from (30), together with a best quadratic fit to the calculated distribution. The fit is centered fairly close to the frequency of the spectral peak at $1Hz$, and the dependence of α on f is clearly quadratic towards higher frequencies.

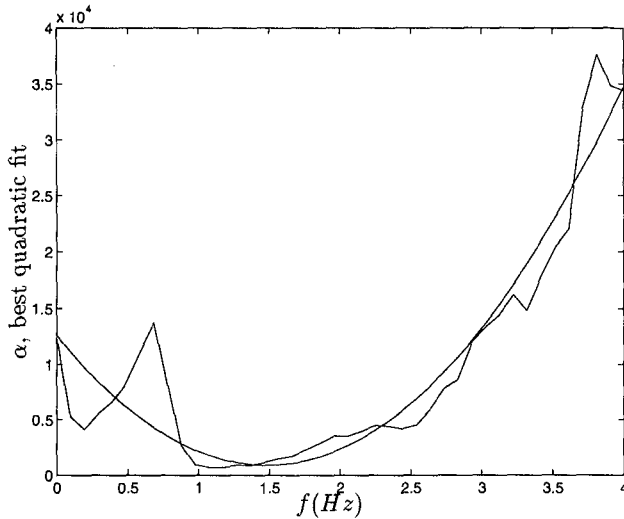


Figure 7: Sample $\alpha(f)$ deduced from data (according to (30)) together with a best quadratic fit.

Effect of Choice $F = 1$ on Modelled Waves

The results of the previous section strongly imply that a value of $F = 0$ should be chosen in the model (3)-(5). CGE have shown that the choice of F does not introduce a strong bias in the prediction of evolving power spectra. It appears that there is a preferred spectral shape that is obtained in shallow water, for which the reasons are still unclear. The effect of redistributing the loss differently across the spectrum serves mainly to enhance or suppress the nonlinear transfer of energy needed to maintain the target spectral shape.

In particular, the choice $F = 1$ implies that the rate of energy loss is the same in all spectral components, which accounts for the entire pattern of overall energy loss in evolving waves (Mase and Kirby, 1992; Eldeberky and Battjes, 1996). However, if the dissipation term is chosen to account for all changes in spectral energy density, there is necessarily a parallel suppression of all nonlinear energy transfer across the spectrum during the breaking process. This loss of an active transfer should suppress the imaginary part of the bispectrum, and would be evidenced by a loss of front-to-back asymmetry in the wave form, or a loss of statistical asymmetry. CGE have shown the consequence of choosing $F = 1$ on the prediction of third moment statistics, which

are severely damaged. A more graphic example is provided by Liu (1990, see pages 55-57), who modelled the breaking decay of a periodic wave using a dissipation coefficient which was uniform across the modelled spectrum. The resulting wave crests in the surfzone clearly lose their asymmetry, which provides direct evidence that nonlinear energy transfer across the spectrum has been suppressed.

In contrast, the choice $F = 0$ strongly concentrates dissipation at higher frequencies. As a result, there is necessarily a high rate of nonlinear transfer of energy across the spectrum from low to high frequencies, in order to maintain the tail of the spectrum. This accounts for the presence of a strong, negative asymmetry. This choice is much more sensible in light of our understanding of the nonlinear processes going on in this region, and agrees with a direct analysis of the behavior of a well-tested time domain model of the breaking process.

Conclusions

The results of this study indicate that dissipation due to wave breaking should be biased strongly towards higher frequencies in spectral calculations, and that an f^2 dependence in the dissipation coefficient comes closest to matching the desired structure of the breaking terms using a simple functional dependence. This result supports the conclusions of Chen et al (1996) and is obtained by an entirely different route, being based on an analysis of the frequency structure of the dissipation term in a time-domain wave evolution model.

A much more comprehensive description of the results of this study is currently being prepared, and will consider the form of the dissipation coefficient in the outer surfzone as well as in the established inner surfzone. In particular, there is some indication that, in regions where the breaking events are infrequent, that there is a tendency for α_n to be slightly negative at frequencies below the wind wave peak. This result could be thought of as the effect of distributing a set of localized momentum sources in the domain. Each breaking wave event would impart a kick to the water column in the manner described by Rapp and Melville (1990). The irregular, widely-spaced-in-time nature of these kicks translates into a wave generating mechanism at low frequency, and could contribute to the growth of the low-frequency wave climate in the surfzone.

Acknowledgements. This work was supported by the Army Research Office through Grant DAAL-03-92-G-0116, the National Science Foundation through Grant OCE-9203277, and the Office of Naval Research, Coastal Sciences Program through Grant N00014-94-1-0214. We thank Yongze Chen for sharing the manuscript of Chen et al (1996) with us prior to publication.

References

- Chen, Y., Guza, R. T. and Elgar, S., 1996, "Modelling breaking surface waves in shallow water", *J. Geophys. Res.*, submitted.
- Eldeberky, Y. and Battjes, J. A., 1996, "Spectral modeling of wave breaking: Application to Boussinesq equations", *J. Geophys. Res.*, **102**, 1253-1264.

- Heitner, K. L. and Housner, G. W., 1970, "Numerical model for tsunami runup", *J. Waterway, Port, Coast. and Ocean Engrng.*, **96**, 701-719.
- Liu, P. L.-F., 1990, "Wave transformation", in *The Sea. Ocean Engineering Science*, **9**, (eds. B. Le Mehaute and D. M. Hanes), Part A, 27-63. Wiley-Interscience.
- Mase, H. and Kirby, J. T., 1992, "Hybrid frequency-domain KdV equation for random wave transformation", *Proc. 23rd Intl. Conf. Coast. Engrng.*, Venice, 474-487.
- Rapp, R. J. and Melville, W. K., 1990, "Laboratory measurements of deep-water breaking waves", *Phil. Trans. Roy. Soc. London A*, **331**, 735-800.
- Schäffer, H. A., Madsen, P. A. and Deigaard, R., 1993, "A Boussinesq model for waves breaking in shallow water", *Coastal Engrng.*, **20**, 185-202.
- Svendsen, I. A., Yu, K. and Veeromony, J., 1996, "A Boussinesq type breaking wave model with vorticity", *Proc. 25th Intl. Conf. Coastal Engrng.*, this volume.
- Thornton, E. B. and Guza, R. T., 1983, "Transformation of wave height distribution", *J. Geophys. Res.*, **88**, 5925-5938.
- Wei, G., Kirby, J. T., Grilli, S. T. and Subramanya, R., 1995, "A fully nonlinear Boussinesq model for surface waves. Part 1. Highly nonlinear unsteady waves", *J. Fluid Mech.*, **294**, 71-92.
- Wei, G. and Kirby, J. T., 1996, "A coastal processes model based on time-domain Boussinesq equations", Res. Report CACR-96-01, Center for Applied Coastal Research, University of Delaware. Paper presented at *Coastal Dynamics '95*, Gdansk, Sept. 1995.
- Zelt, J. A., 1991, "The runup of nonbreaking and breaking solitary waves", *Coastal Engrng.* **15**, 205-246.

CHAPTER 90

A HAMILTONIAN MODEL FOR NONLINEAR WATER WAVES AND ITS APPLICATIONS

A.K. Otta¹, M.W. Dingemans², A.C. Radder³

Abstract

Evolution equations for nonlinear long waves are considered from an approximation to the exact Hamiltonian (total energy) for the water waves. The approximation which is used here has two distinct advantages over many other formulations which are commonly used for the same purpose. Further, a variation of these evolution equations is considered in order to incorporate higher-order nonlinearity. Numerical solutions of the evolution equations have been carried out for both the systems. Application of these models is illustrated in some practical cases. Comparisons between experimental measurements and computed results show that the model can be used for satisfactory prediction of nonlinear transformation of non-breaking waves over varying depth. Two features for further investigation are: (i) inclusion of both short-wave and long-wave nonlinearity so that the model can be used with uniform validity from deep to shallow water and (ii) modifications of the evolution equations so that they can be applied to propagation of breaking waves in a robust way.

Introduction

Commonly used nonlinear equations for propagation of water waves can be categorised into two main groups: Stokes-type valid in deep water and Boussinesq-type valid for fairly long waves. Several modifications to classical Boussinesq equations have been presented in an attempt to increase the validity of the model equations with respect to frequency dispersion and varying depth (e.g., Madsen *et al.*, 1991; Dingemans & Merckelbach, 1996). In this article, we discuss an alternative approach based on an explicit Hamiltonian formulation (Radder, 1992) for modelling of nonlinear waves over varying depth. The explicit expression for

¹[Formerly at Delft Hydraulics], ICCH, Agern Alle 5, DK-2970 Hørsholm, Denmark

²Senior Researcher and corresponding author, Delft Hydraulics, P.O. Box 152, 8300 AD Emmeloord, The Netherlands

³Senior Researcher, Rijkswaterstaat-RIKZ, P.O. Box 20907, 2500 EX The Hague, The Netherlands

the kinetic energy in the form of a surface integral involving the free surface potential φ and the surface elevation ζ is derived by using a conformal mapping in the complex plane. Therefore, the formulations are limited in a strict sense to unidirectional problems in the horizontal space.

Formulations

We use the symbols $\zeta(x, t)$ and $\varphi(x, t) = \Phi \{x, \zeta(x, t), t\}$ to denote respectively the free surface elevation and potential where Φ is the usual velocity potential. The evolution equations for ζ and φ follow the Hamiltonian structure (see, for example, Benjamin and Olver, 1982):

$$\frac{\partial \zeta}{\partial t} = \frac{\delta \mathcal{H}}{\delta \varphi} \quad , \quad \frac{\partial \varphi}{\partial t} = -\frac{\delta \mathcal{H}}{\delta \zeta} \tag{1}$$

where \mathcal{H} is the total energy (sum of potential and kinetic energy) of the water mass which reads as

$$\begin{aligned} \mathcal{H} &= \frac{1}{2} \rho g \int_{-\infty}^{\infty} \zeta^2 dx + \frac{1}{2} \rho \int_{-\infty}^{\infty} dx \int_{-h}^{\zeta} (\nabla \Phi \cdot \nabla \Phi) dz \\ &= \int_{-\infty}^{\infty} \frac{1}{2} \rho g \zeta^2 dx + \frac{1}{2} \rho \int_{-\infty}^{\infty} dx \sqrt{1 + (\zeta_x)^2} \varphi \Phi_n . \end{aligned} \tag{2}$$

The essential difficulty in deriving explicit evolution equations from (1) and (2) lies in the vertical integral or the Neumann operator of the potential Φ in the expression for kinetic energy density. This is where different procedures differ in the way that the simplifications are made. Several of the more commonly known weakly nonlinear formulations (either of the Stokes or Boussinesq-like approximations) correspond to some of these variations. Recently, Craig and Groves (1994) have presented a comprehensive discussion of these variations.

The basis for our approach is an explicit formulation of the Hamiltonian for two-dimensional water wave problems (unidirectional propagation) presented by Radder (1992). All details of the derivations are not included here. These may be found in Radder (1992), Otta and Dingemans (1994a) and Dingemans and Otta (1996). Radder has shown that an exact expression for the kinetic energy \mathcal{T} as a function of the free-surface variables ζ and φ can be obtained in an explicit form using a conformal mapping, namely the Woods' transformation from the physical space (horizontal and vertical coordinates x and z) to $(-\infty < \chi < \infty, 0 \leq \xi \leq 1)$. This expression for the kinetic energy in the χ space along the free surface ($\xi = 1$) is given by

$$\mathcal{T} = -\frac{\rho}{2\pi} \int_{-\infty}^{\infty} d\chi \frac{\partial \varphi}{\partial \chi} \int_{-\infty}^{\infty} d\chi' \frac{\partial \varphi}{\partial \chi'} \log \tanh \frac{\pi}{4} |\chi - \chi'| \tag{3}$$

where \log is the natural logarithm and the variable χ is related to x along the free surface through

$$\frac{dx}{d\chi} = \left(\frac{d/d\chi}{\tan d/d\chi} \right) \zeta(\chi) + \left(\frac{d/d\chi}{\sin d/d\chi} \right) h(\chi) . \tag{4}$$

The mapping (4) is valid exactly for arbitrary variation of depth h and surface elevation ζ .

We need to inverse the Jacobian, given by (4), in order to express \mathcal{T} in the physical space. It is, however, difficult to obtain an exact inversion. Consequently, we shall use an approximation to the exact Jacobian leading to an approximation of the Hamiltonian (\mathcal{H}^a) in the physical space. A notable distinction of the method is that the positive definiteness of the kinetic energy density can be ensured for each approximation if one selects the inversion such that $\frac{dx}{d\chi} > 0$.

The simplest approximation which accounts for long-wave nonlinearity (it is assumed that $kh \cdot ka$ is small) for moderately high waves is arrived at by $dx/d\chi \approx \eta$ where η is the total water depth ($h + \zeta$). The resulting Hamiltonian \mathcal{H}^a is

$$\frac{\mathcal{H}^a}{\rho} = \frac{1}{2} \int_{-\infty}^{\infty} dx g \zeta^2 - \frac{1}{2\pi} \int_{-\infty}^{\infty} dx \int_{-\infty}^{\infty} dx' \phi_x \phi_{x'} \log \tanh \frac{\pi}{4} \left| \int_x^{x'} \frac{dx''}{\eta} \right|. \quad (5)$$

With regards to the approximate inversion we introduce the variable p such that

$$\frac{dx}{dp} = h + \zeta \quad (6)$$

and the resulting evolution equations are

$$\frac{\partial \zeta}{\partial t} = \frac{1}{\pi} \frac{\partial}{\partial x} \int_{-\infty}^{\infty} dx' \varphi_{x'} \log \tanh \frac{\pi}{4} \left| \int_x^{x'} \frac{dr}{\eta} \right| \quad (7)$$

$$\frac{\partial \varphi}{\partial t} = -g\zeta - \frac{1}{2\eta^2} \int_{-\infty}^x dx' \int_x^{\infty} dx'' \frac{\varphi_{x'} \varphi_{x''}}{\sinh \left(\frac{\pi}{2} \int_{x'}^{x''} \frac{dr}{\eta} \right)}. \quad (8)$$

We note that for this approximation, positive definiteness is maintained as long as the total water depth ($h + \zeta$) remains greater than zero. This feature of positive definiteness is not guaranteed in the entire wave spectrum in many other approximate Hamiltonian system. Another significant advantage is that in the limiting case of infinitesimal waves the dispersion relationship of the evolution equations derived from (5) is identical to that from the classical linear wave theory over uniform depth. This has the positive consequence that linear propagation and shoaling are properly predicted for all free components over the entire wave spectrum in transferring from deep to shallow water although nonlinear interactions of the short-wave type may suffer from the same limitation as when Boussinesq formulations are used.

Higher-order Description

The approximation (5) and the evolution equations derived therefrom do very well in reproducing long-wave nonlinearity as will be shown later. However, for better description of the form near the crests during wave steepening and propagation of higher waves, higher-order nonlinearity needs to be incorporated in the evolution

equations. Both short-wave and long-wave nonlinearity can be accounted for in the approximate Hamiltonian in a hierarchical way by seeking higher-order inversion to (4) than used in (6). This is, however, not very straightforward. Instead, we choose an intermediate approach where the evolution equation for the surface elevation is obtained by replacing χ by p in the exact expression for the kinetic energy; *i.e.*,

$$\frac{\partial m}{\partial t} = \frac{1}{\pi} \int_{-\infty}^{\infty} dp \varphi_{p'} \log \tanh \frac{\pi}{4} |p - p'| \tag{9}$$

with $\zeta(x, t) = \partial m / \partial x$ in combination with the dynamic free surface boundary condition used directly for the free surface potential, *i.e.*

$$\frac{\partial \varphi}{\partial t} = -g\zeta - \frac{1}{2} \varphi_x^2 + \frac{1}{2} \frac{(\zeta_t + \varphi_x \zeta_x)^2}{1 + (\zeta_x)^2}. \tag{10}$$

Numerical Solution

The evolution equations (7) and (8) are not convenient for direct numerical treatment due to the singular kernels and the double integral in the latter. The integrands are first regularised to make them more amenable for numerical solution. The modified equations (Otta & Dingemans, 1994a) are presented in the following:

$$\zeta_t = \frac{1}{\pi} \frac{d}{dx} \left[-\pi v \eta + \int_{-\infty}^{\infty} dx' \lambda(x', x) \log \tanh \frac{\pi}{4} \left| \int_x^{x'} \frac{dx''}{\eta} \right| \right] \tag{11}$$

$$v_t = -g\zeta_x + \frac{d}{dx} \left[\frac{1}{\eta^2} \int_{-\infty}^x dx' v \eta \zeta_t \right] \tag{12}$$

where

$$v = \varphi_x, \quad \lambda(x', x) = v(x') - \frac{\eta(x)}{\eta(x')} v(x). \tag{13}$$

The equations, given by (11) and (12), are numerically solved using an predictor-corrector scheme, namely the Adams-Bashforth-Moulton method. The spatial discretization of the right hand sides of the equations is carried out using the **sinc**-series approximation (Lund & Bowers, 1992). More about the characteristics and advantages of using the **sinc**-series and the high order of accuracy of the numerical scheme used is described in a separate article under preparation.

Certain advantages are gained by carrying out the numerical evaluation of the evolution equations, given by (9) and (10), in a uniformly spaced p -space. Using the sinc approximation to express $\mathcal{V}(p')$ ($\mathcal{V} = \varphi_p$), *i.e.*,

$$\mathcal{V}(p') = \sum_{l=-\infty}^{\infty} \mathcal{V}_l \operatorname{sinc} \frac{p' - pl}{\Delta p} \tag{14}$$

with l denoting the grid index and Δp the uniform interval between two consecutive grids in the p -space we obtain the discretised form of the evolution equation (9):

$$\left. \frac{\partial m}{\partial t} \right|_j = \sum_l \nu_l I(|l-j|; \Delta p) \quad (15)$$

where

$$I(|l-j|; \Delta p) = -\frac{1}{\pi} \int_{-\infty}^{\infty} dp' \operatorname{sinc} \frac{p' - p_l}{\Delta p} \log \tanh \frac{\pi}{4} |p_j - p'|. \quad (16)$$

For a time-invariant value of Δp , the terms $I(|l-j|; \Delta p)$'s remain constant and need to be evaluated only once. We note, however, that the x -coordinates corresponding to the fixed values of p grids are time-variant. The local evolution rates $[\zeta_t(x, t), \varphi_t(x, t)]$ then need to be transferred to the constant p -grids through the relation

$$\begin{aligned} \frac{d\psi}{dt}(x^p, t) &= \frac{\partial \psi}{\partial t} + \frac{dx^p}{dt} \frac{\partial \psi}{\partial x} \\ &= \frac{\partial \psi}{\partial t} + \frac{dx^p}{dt} \frac{\partial p}{\partial x} \frac{\partial \psi}{\partial p} \end{aligned} \quad (17)$$

where ψ is used to denote either ζ or φ and x^p denotes the x -coordinate of a constant p -value. The value of x^p itself is updated with time.

Boundary Conditions

The evolution equations (with the exception of (10)) described so far include an integral over the infinite span. This has its origin to our deliberate choice of excluding the lateral boundary from the formulations in order that the Hamiltonian can be expressed as a function of ζ and φ . With no further modifications, these evolution equations can be used to study an initial value problem. This means that the span in the x -interval for the numerical solution has to be much longer than the physical interval of interest with the consequence that the required computational time increases tremendously. This is, however, not necessary.

Consider for example the evolution equation (9). We rewrite this equation as

$$\begin{aligned} \frac{\partial m}{\partial t} &= \frac{1}{\pi} \int_{-\infty}^{p_0} dp \varphi_{p'} \log \tanh \frac{\pi}{4} |p - p'| + \frac{1}{\pi} \int_{p_0}^{p_n} dp \varphi_{p'} \log \tanh \frac{\pi}{4} |p - p'| \\ &\quad + \frac{1}{\pi} \int_{p_n}^{\infty} dp \varphi_{p'} \log \tanh \frac{\pi}{4} |p - p'| \end{aligned} \quad (18)$$

where p_0 and p_n denote respectively the begin and end point of the computation interval. Though the intervals of the first and third integrals in (18) outside the computational interval are semi-infinite, the rapid decay of the function $\log \tanh()$ appearing in the kernel of the integral allows reduction of the interval to usually a few (local) water depths without any loss of accuracy. We assume for simplicity

that the bottom stretches uniformly to the left of p_0 and the right of p_n . For generating incoming waves in the computational interval, we use an appropriate theory to translate the time record of surface elevation $\zeta(t)$ at a given location (say p_0) to a space and time record for both ζ and φ outside of the computational interval. In the simplest way this is done by using linear theory to specify the incident field in the offshore side. On the shallower part a sponge layer can be introduced to absorb the radiating waves. For this purpose the evolution equations are modified; *i.e.*,

$$\zeta_t = R_\zeta(\zeta, \varphi) - \mu(x)\zeta \quad (19)$$

where $R_\zeta(\zeta, \varphi)$ represents the unmodified part of the equation and $\mu(x)$ a damping coefficient. In many cases, the introduction of a sponge layer over a reasonable length of the computational domain allows absorption of the radiating waves such that the third integral in (18) becomes non-significant. In a more general approach, a combination of the sponge layer and a Sommerfeld type of radiation condition can be implemented to specify the space and time record of ζ and φ outside of p_n to compute the third integral in (18). Details of the types of boundary conditions and the procedures are described in Otta & Dingemans (1994b) and Dingemans & Otta (1996).

Examples of Applications

In this section we discuss the application of the models to some critical cases. An illustrative example is the study of the propagation of a solitary wave over a bottom of constant depth. The initial surface profile $\zeta(x, t = 0)$ and the potential $\varphi(x, t = 0)$ are specified from Tanaka's (1986) solution which may be considered exact. Fig. 1 shows that this profile changes considerably with a decrease in the crest height and the formation of a dispersive tail during the propagation according to (7) and (8). The change in crest height and the dispersive tail is much less prominent when the set of evolution equations with the higher order of nonlinearity is used.

An example of practical interest is the propagation of waves over varying depth. To test the validity of our two models for such cases we consider an experimental setup (Fig. 2) as described in Luth *et al.* (1994) and used in Dingemans (1994). Transformation of an incident train of periodic waves is shown at different locations along the bar in Fig. 3. The incident waves are of mild amplitude such that they do not break over the bar. The computed profiles shown here are obtained by using (9) and (10). The nonlinear interactions on top of the bar (at location $x = 13.5$ m) and the propagation of the free waves behind the bar (location $x = 19$ m) are reproduced in a satisfactory manner. Though not shown here, results obtained from (7) and (8) for this case have been found to be nearly as good with only slightly differences near the crest. In a previous study (Dingemans, 1994), the model based on (7) and (8) has been found to yield better agreement with experimental measurements than many Boussinesq-like models.

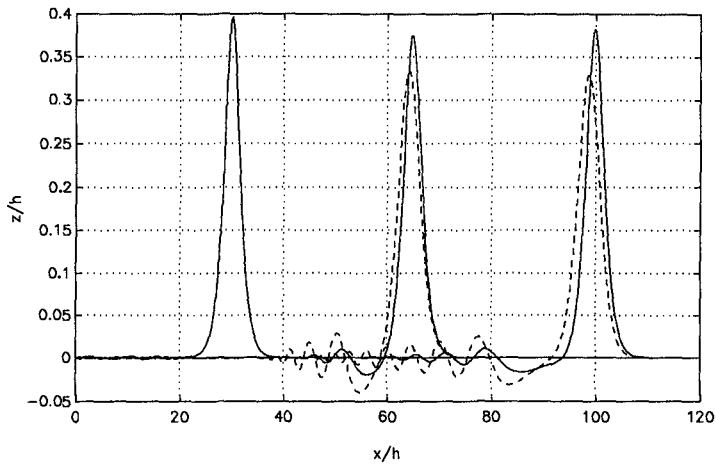


Figure 1: Computed profiles of a solitary wave (initial height/depth= 0.4) during propagation over a bottom of constant depth. Solid line: based on (9) and (10); dashed line: based on (7) and (8).

Wave Breaking

The evolution equations, given by (7) and (8) or by (9) and (10), are valid for waves which do not break. Wave-breaking is, however, of great practical significance in coastal areas. In field conditions, wave breaking in shallow water is identified by overturning of the water surface and plunging on to itself (plunging breaker) or the formation of a thin jet near the crest that spills over (spilling breaker). There are several difficulties, both physical and numerical, in modelling this process of breaking reasonably. Although a proper description of the water motion in the neighbourhood of breaking is essential for some purposes, it is sufficient to incorporate the main effects of breaking in the post-breaking behaviour of wave propagations for many a problem. To incorporate this effect in weakly nonlinear equations two steps are essential. Since either overturning of the surface and the spilling jet may not be manifested in the model behaviour or the numerical limitations of an adopted scheme may not permit computations advancing to the desired point, a criterion has to be used to indicate the incipience of breaking. Secondly, the evolution equations (derived originally for non-breaking waves) have to be modified so that the effects of wave-breaking (*e.g.*, energy dissipation) are incorporated within the framework.

Several criteria have been used in different models for the definition of the onset of breaking. For example, Schäffer *et al.* (1993) found it necessary to use a

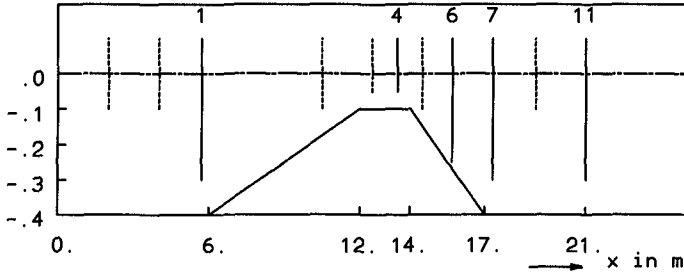


Figure 2: Geometry of the experimental setup.

criterion of the maximum of the local surface slope reaching a value of 20° in their time-domain Boussinesq model to a mark the onset of breaking. We consider here a criterion which is based on the idea of the Jacobian of the conformal mapping $d\chi/dx$ becoming zero. This condition has been mentioned for horizontal bottom by Dingemans and Radder (1991) using a first-order expression for the Jacobian including both short-wave and long-wave nonlinearity. For varying depth, the criterion reads as

$$\eta(p) + \int_0^\infty \frac{d[\zeta(p+q) + \zeta(p-q)]}{\exp(\pi q) - 1} - \int_0^\infty \frac{d[h(p+q) + h(p-q)]}{\exp(\pi q) + 1} = 0. \quad (20)$$

The criterion (20) has been found to be a good indicator of the onset of breaking for waves of symmetric permanent form and some cases of asymmetric forms before plunging (Radder, 1995; personal communication) although a comprehensive analysis of the criterion for the onset of breaking in dynamical situations is still very much needed.

During numerical experimentations with the model equations (7) and (8) we have observed that the condition (20) was never reached in the computed surface form while breaking did occur in reality. Though this observation is not completely surprising, it was difficult to predict *a priori*. It is our conjecture that this is caused by the inadequacy in the representation of nonlinearity in the equations (7) and (8). This conjecture is in fact the primary motivation behind the set-up for a higher-order description. On application of the model, based on (9) and (10), the breaking criterion is met in several cases followed by numerical instabilities. An example of such a computation is shown in Fig. 4 where a train of periodic waves is allowed to propagate onshore over a sea-bed profile near Egmond on the Dutch coast. In a preliminary approach to model post-breaking behaviour, we have considered modifying the surface elevation at each evolution step following two criteria: (a) the surface form remains within the limit of the breaker criterion and (b) the modification does not lead to a change in the mass balance. The effect is to reduce the crest height and the surface steepness with an associated dissipation of energy. This approach has shown some qualitative success in a limited number of cases, *e.g.*, during the propagation of a solitary wave

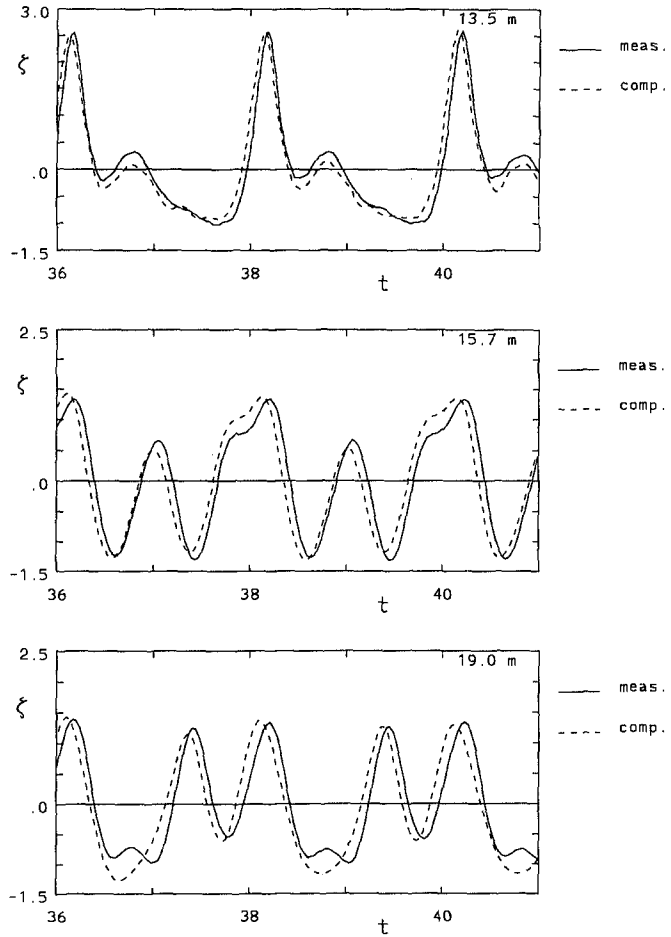


Figure 3: Transformation of a train of periodic sine waves due to propagation over a bar (Fig. 2), Water depth= 40 cm (offshore), 10 cm (over the bar); Incident wave height= 2 cm, period= 2.02 s.

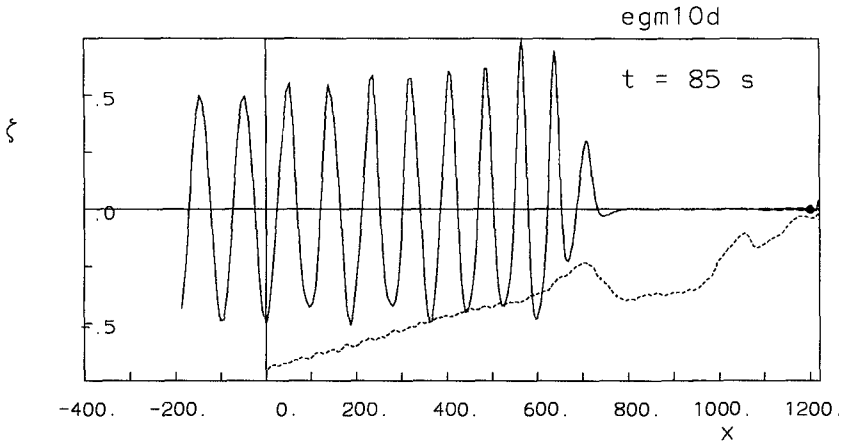


Figure 4: Propagation of a regular wave train towards the shore over the barred bathymetry near Egmond. Incident wave height= 1 m, period= 10 s. The bed profile is not shown to scale. Still-water depth at $x = 0$ is 11.4 m.

on a slope. However, much remains to be done in the formulation of a proper breaking mechanism in the model and making the model practically applicable to breaking waves.

Summary

In the present article, we have discussed two sets of evolution equations. One set of evolution equations, given by (7) and (8), is derived from an approximate Hamiltonian with two important properties: the kinetic-energy density is guaranteed to be positive definite for all wave heights across the entire wave spectrum as long as the local water depth is greater than zero and secondly the dispersion relationship in the limiting case of infinitesimal amplitude is exactly identical to that obtained from the classical linear theory of water waves. These two features are of great practical significance in ensuring stability of the model equations during propagations of an irregular train or of the generated higher harmonics and in representation of proper phase speed of all components. Numerical experiments with some critical test cases show that the model describes the nonlinear transformation during propagation of non-breaking waves over a varying depth satisfactorily. The performance of the model has been found to be superior to that of many Boussinesq-like models during an intercomparison study completed recently. We have experimented with including a higher-order nonlinear representation in the model equations. The experiments indicate that higher-order nonlinearity can improve the result of the Boussinesq-like approximations of fairly long, fairly low waves especially near the breaking point. However, a more systematic approach is necessary than what has been here presented in order to

ensure stability and conservation of energy of the system.

Acknowledgements

This work was commissioned by the National Institute for Coastal and Marine Management/RIKZ of the Dutch Public Works Department. The work done by the first author as reported here was completed during his employment in Delft Hydraulics of the Netherlands.

References

- Benjamin, T.B. & P.J. Olver (1982)**. Hamiltonian structure, symmetries and conservation laws for water waves, *J. Fluid Mech.*, 125: 137-185.
- Craig, W. & M.D. Groves (1994)**. Hamiltonian long-wave approximations to the water-wave problem, *Wave Motion*, 19: 367-389.
- Dingemans, M.W. (1994)**. Comparison of computations with Boussinesq-like models and laboratory measurements, MAST G8-M Note, H1684, 32 pp.
- Dingemans, M.W. and A.C. Radder (1991)**. Use of Hamiltonian techniques in water wave propagation problems. In: *Nonlinear Water Waves Workshop*, University of Bristol, ed. D.H. Peregrine, pp 24-31.
- Dingemans, M.W. & L.M. Merckelbach (1996)**. Boussinesq-like equations with higher-order frequency dispersion, in preparation.
- Dingemans, M.W. & A.K. Otta (1996)**. Hamiltonian formulation of water waves: higher-order description, wave breaking formulation and numerical implementations. Report H782, Part 3, *Delft Hydraulics*, 69 pp.
- Lund, J. and K.L. Bowers (1992)**. *Sinc Methods for Quadrature and Differential Equations*, SIAM, Philadelphia, 304 pp.
- Luth, H.R., G. Klopman and N. Kitou (1994)**. Project 13G: Kinematics of waves breaking partially on an offshore bar; LDV measurements for waves with and without a net onshore current, Report H1573, *Delft Hydraulics*, 40 pp.
- Madsen, P.A., R. Murray and O.R. Sorensen (1991)**. A new form of the Boussinesq equations with improved linear dispersion characteristics, *Coastal Engineering*, 15: 371-388.
- Otta, A.K. and M.W. Dingemans (1994a)**. Hamiltonian formulation of water waves: 1D-formulation, numerical evaluations and examples. Report H782, *Delft Hydraulics*, 63pp.
- Otta, A.K. and M.W. Dingemans (1994b)**. Hamiltonian formulation of water waves: formulation for weakly-reflecting boundary conditions, Report H782, part 2, *Delft Hydraulics*, 18pp.
- Radder, A.C. (1992)**. An explicit Hamiltonian formulation of surface waves in water of finite depth, *J. Fluid Mech.*, 237: 435-455.
- Radder, A.C. (1993)**. An integral criterion for wave breaking in deep and shallow water, *Personal note*, 5 pp.
- Schäffer, H.A., P.A. Madsen and R. Deigaard (1993)**. A Boussinesq

model for waves breaking in shallow water, *Coastal Engineering*, 20: 185-202.

Tanaka, M. (1986). The stability of solitary waves, *Physics of Fluids*, 29: 650-655.

CHAPTER 91

THE ROLE OF WAVE-INDUCED SHEAR STRESSES IN THE MOMENTUM BALANCE EQUATIONS

Francisco J. Rivero and Agustín S.-Arcilla*, M. ASCE

ABSTRACT

The wave-induced shear stresses, which result from the correlation between horizontal and vertical components of the oscillatory velocity after time-averaging the horizontal momentum balance equations, are shown in this paper to play an important role in vertical circulation analysis, having the same order of magnitude than other wave-induced (normal) stresses. The model of Rivero and Arcilla (1995) to calculate the wave-induced shear stress for a 2DV situation, based on a mathematical identity that relates this stress to the wave-induced normal stresses and the oscillatory vorticity, is now extended to a general 3D flow. The consequences of neglecting the wave-induced shear stresses are shown to be an overprediction of the waves effect on the description of the vertical profiles of the mean (current) velocity. Theoretical examples of such effects are presented and discussed for some simplified situations (the undertow and longshore current vertical profiles).

1. INTRODUCTION

The correlations between horizontal (\tilde{u}_i) and vertical (\tilde{w}) components of the oscillatory (wave) motion, which appear explicitly in the time-averaged momentum balance equations as wave-induced (effective) shear stresses, have been shown to play an important role in the analysis of the vertical distribution

* Associate professor and professor, Maritime Engineering Laboratory (LIM), Catalonia University of Technology (UPC), Campus Nord (módul D-1), Gran Capitá s/n, 08034 Barcelona, Spain

of wave-induced currents (see e.g. Deigaard and Fredsøe (1989), De Vriend and Kitou (1990), Stive and De Vriend (1994), and Rivero and Arcilla (1995), to mention some recent references). However, most circulation models have, until very recently, neglected the $\langle \tilde{u}_i \tilde{w} \rangle$ -contribution ($\langle \rangle$ denotes the time-averaging operator over a wave period) by simply arguing that the two wave velocity components, \tilde{u}_i and \tilde{w} , are 90° out of phase. This result, which corresponds to periodic waves of permanent form, is not valid for real waves propagating over a sloping bottom and/or with energy dissipation (be it in the bottom boundary layer or in the free surface area for the roller of breaking waves).

The purpose of this paper is to present new formulations to calculate the wave-induced shear stresses $\langle \tilde{u}_i \tilde{w} \rangle$, based on mathematical identities that relate these stresses to other wave stresses ($\langle \tilde{u}_i \tilde{u}_j \rangle$ and $\langle \tilde{w}^2 \rangle$), easier to calculate by any given wave theory (e.g. linear theory), and the vorticity of the oscillatory velocity, and to investigate the relevance of these stresses in vertical circulation analysis.

The outline of the paper is as follows. Section 2 gives an overview of the model of Rivero and Arcilla (1995) to calculate the wave-induced shear stress $\langle \tilde{u} \tilde{w} \rangle$ in a 2DV situation. This model is extended in section 3 to a general 3D flow, and its implication in the horizontal momentum balance equations are discussed in section 4. Theoretical examples on the role of wave-induced shear stresses in the description of the vertical circulation for some simplified situations are given in sections 5 (undertow profiles) and 6 (longshore current profiles). Finally, section 7 presents the summary and conclusions.

2. WAVE-INDUCED SHEAR STRESS IN A 2DV FLOW

For a 2DV situation (as that encountered in a wave flume), in which waves propagate along the x-direction and the z-axis is directed vertically upwards (Fig. 1), Rivero and Arcilla (1995) derived a mathematical identity which relates the wave-induced shear stress $\langle \tilde{u} \tilde{w} \rangle$ to other wave-induced stresses ($\langle \tilde{u}^2 \rangle$ and $\langle \tilde{w}^2 \rangle$) and to the (scalar) vorticity of the oscillatory flow $\tilde{\omega} = \frac{\partial \tilde{u}}{\partial z} - \frac{\partial \tilde{w}}{\partial x}$:

$$\frac{\partial}{\partial z} \langle \tilde{u} \tilde{w} \rangle = \langle \tilde{w} \tilde{\omega} \rangle - \frac{1}{2} \left[\frac{\partial}{\partial x} \left(\langle \tilde{u}^2 \rangle - \langle \tilde{w}^2 \rangle \right) \right] \quad (1)$$

where the oscillatory components of the velocity (\tilde{u} and \tilde{w}) are defined such that $\langle \tilde{u} \rangle = \langle \tilde{w} \rangle = 0$, and hence, $\langle \tilde{\omega} \rangle = 0$.

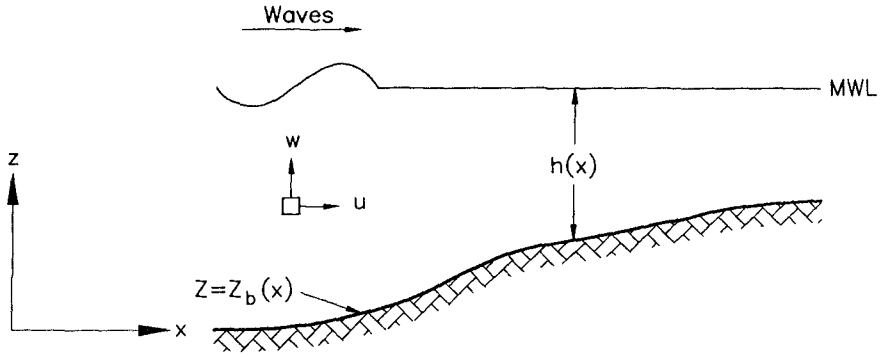


Figure 1. Domain definition sketch -2DV situation- (after Rivero and Arcilla, 1995).

Assuming irrotational flow ($\tilde{\omega} = 0$) and invoking linear wave theory to evaluate $\langle \tilde{u}^2 \rangle$, $\langle \tilde{w}^2 \rangle$ and the near-bed value of $\langle \tilde{u}\tilde{w} \rangle$, which is given by the kinematic boundary condition at the bottom $z = z_b$ (Putrevu and Svendsen, 1993) —see Fig. 2—, the vertical distribution of $\langle \tilde{u}\tilde{w} \rangle$, after integration of Eq. (1), is found to be linear over depth:

$$\langle \tilde{u}\tilde{w} \rangle = -G \left(\frac{E}{\rho h} \right) \frac{\partial d}{\partial x} - \left[\frac{\partial}{\partial x} \left(\frac{1}{2} G \frac{E}{\rho h} \right) \right] (z - z_b) \quad (2)$$

where d is the still-water depth, h is the mean water depth, E is the wave energy density, ρ is the fluid density, and $G = 2kh / \sinh(2kh)$.

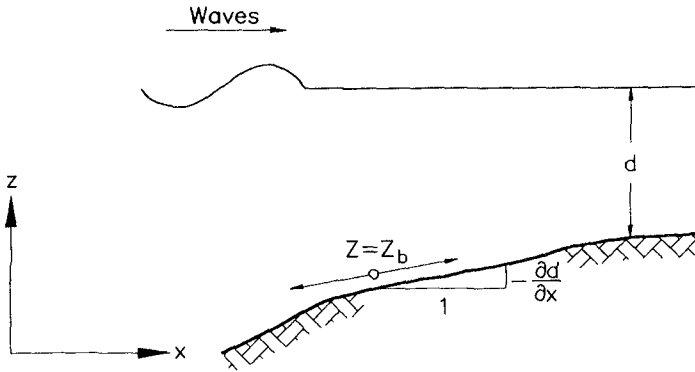


Figure 2. Simplified model for the oscillatory wave motion near the bed. (after Rivero and Arcilla, 1995)

This general expression (2), using linear wave theory, has been applied to simplified situations and has been shown to coincide or degenerate into other existing formulations with comparable simplifying assumptions, viz. irrotational waves over a sloping bottom in the shallow-water approximation (De Vriend and Kitou, 1990), and surf-zone breaking waves over a horizontal bottom (Deigaard and Fredsøe, 1989).

Expression (2) has also been compared (Rivero and Arcilla, 1997) with experimental results for the vertical distribution of the wave-induced shear stress $\langle \tilde{u}\tilde{w} \rangle$ in shoaling waves within the framework of a research project (*Dynamics of Beaches*) funded by the EU —see Prinos et al. (1994) for details. Simultaneous time series of horizontal and vertical velocity components, and free surface elevation were measured at several stations along the wave flume and at several points within each station. Various regular and irregular wave conditions were generated with and without a submerged breakwater on a 1:15 sloping beach (Rivero et al, 1996). The experimental results presented here correspond to the test without submerged breakwater under irregular wave action (Test E: Jonswap-type spectrum with $\gamma = 3.3$, peak period $T_p=2.50$ s and significant wave height $H_s=0.25$ m in the deeper part of the wave flume, with water depth $h=3.06$ m). Fig. 3 shows the measured values of $\langle \tilde{u}\tilde{w} \rangle$ at 3 stations located in the shoaling zone, and the predicted $\langle \tilde{u}\tilde{w} \rangle$ -distribution with expression (2). As can be seen from this figure, both the sign (positive) and the trend (decreasing upwards) of the vertical distribution of $\langle \tilde{u}\tilde{w} \rangle$ is correctly predicted by the authors' model, as well as quantitatively.

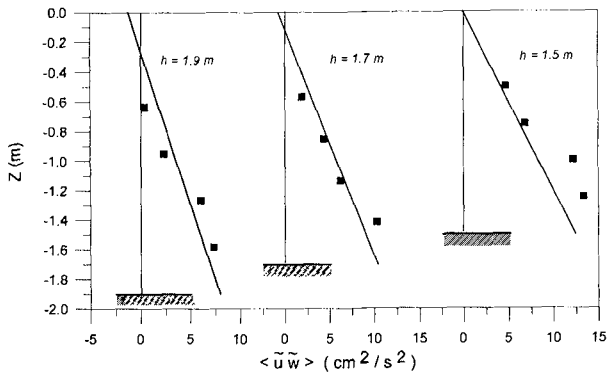


Figure 3. Comparison between experimental data (squares) and this model (Eq. 2) for the vertical distribution of the wave-induced shear stress $\langle \tilde{u}\tilde{w} \rangle$.

Test E: irregular waves, Jonswap-type, $H_s=0.25$ m, $T_p=2.5$ s.

(after Rivero and Arcilla, 1997)

3. WAVE-INDUCED SHEAR STRESSES IN A 3D FLOW

Explicit expressions for the vertical distribution of the wave-induced shear stresses ($\langle \tilde{u}\tilde{w} \rangle$, $\langle \tilde{v}\tilde{w} \rangle$) in a 3D situation may be found from (2) in a horizontally rotated frame of reference, after assuming that the (irrotational) flow is essentially two-dimensional in the direction of wave propagation x' (see Fig. 4), and neglecting the curvature of wave rays:

$$\begin{aligned} \langle \tilde{u}\tilde{w} \rangle = & -2\mathcal{A} \left(\frac{\partial d}{\partial x} \cos^2 \alpha + \frac{\partial d}{\partial y} \sin \alpha \cos \alpha \right) - \\ & - \left(\frac{\partial \mathcal{A}}{\partial x} \cos^2 \alpha + \frac{\partial \mathcal{A}}{\partial y} \sin \alpha \cos \alpha \right) (z - z_b) \end{aligned} \quad (3a)$$

$$\begin{aligned} \langle \tilde{v}\tilde{w} \rangle = & -2\mathcal{A} \left(\frac{\partial d}{\partial x} \sin \alpha \cos \alpha + \frac{\partial d}{\partial y} \sin^2 \alpha \right) - \\ & - \left(\frac{\partial \mathcal{A}}{\partial x} \sin \alpha \cos \alpha + \frac{\partial \mathcal{A}}{\partial y} \sin^2 \alpha \right) (z - z_b) \end{aligned} \quad (3b)$$

where $\mathcal{A} = \frac{1}{2}G \left(\frac{E}{\rho h} \right)$ is an energy-like magnitude.

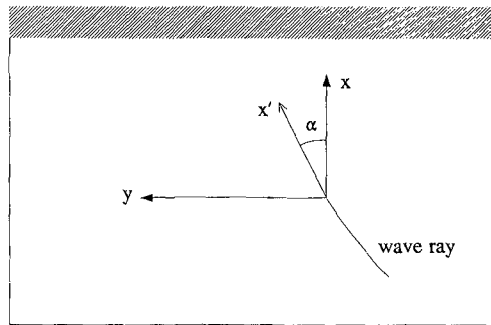


Figure 4. Domain definition sketch -3D situation- (after Rivero and Arcilla, 1997).

A more general (differential) expression for $\langle \tilde{u}\tilde{w} \rangle$ and $\langle \tilde{v}\tilde{w} \rangle$, from which their implication in the time-averaged momentum balance equations may be easily assessed, is given by the following straightforward mathematical identities that involve the oscillatory vorticity components,

$$\tilde{\omega}_x = \frac{\partial \tilde{w}}{\partial y} - \frac{\partial \tilde{v}}{\partial z} \qquad \tilde{\omega}_y = \frac{\partial \tilde{u}}{\partial z} - \frac{\partial \tilde{w}}{\partial x}$$

and the continuity equation for the oscillatory velocity components,

$$\frac{\partial \tilde{u}}{\partial x} + \frac{\partial \tilde{v}}{\partial y} + \frac{\partial \tilde{w}}{\partial z} = 0 \quad :$$

$$\frac{\partial}{\partial z} \langle \tilde{u}\tilde{w} \rangle = \langle \tilde{w}\tilde{\omega}_y \rangle - \frac{1}{2} \left[\frac{\partial}{\partial x} \left(\langle \tilde{u}^2 \rangle - \langle \tilde{w}^2 \rangle \right) \right] - \langle \tilde{u} \frac{\partial \tilde{v}}{\partial y} \rangle \quad (4a)$$

$$\frac{\partial}{\partial z} \langle \tilde{v}\tilde{w} \rangle = - \langle \tilde{w}\tilde{\omega}_x \rangle - \frac{1}{2} \left[\frac{\partial}{\partial y} \left(\langle \tilde{v}^2 \rangle - \langle \tilde{w}^2 \rangle \right) \right] - \langle \tilde{v} \frac{\partial \tilde{u}}{\partial x} \rangle \quad (4b)$$

For an irrotational flow ($\tilde{\omega}_x = \tilde{\omega}_y = 0$), these mathematical identities read:

$$\frac{\partial}{\partial z} \langle \tilde{u}\tilde{w} \rangle = -\frac{1}{2} \left[\frac{\partial}{\partial x} \left(\langle \tilde{u}^2 \rangle - \langle \tilde{w}^2 \rangle \right) \right] - \langle \tilde{u} \frac{\partial \tilde{v}}{\partial y} \rangle \quad (5a)$$

$$\frac{\partial}{\partial z} \langle \tilde{v}\tilde{w} \rangle = -\frac{1}{2} \left[\frac{\partial}{\partial y} \left(\langle \tilde{v}^2 \rangle - \langle \tilde{w}^2 \rangle \right) \right] - \langle \tilde{v} \frac{\partial \tilde{u}}{\partial x} \rangle \quad (5b)$$

4. WAVE-INDUCED STRESSES IN THE HORIZONTAL MOMENTUM BALANCE EQUATIONS

The "conventional" wave-induced stresses appearing in the time-averaged horizontal momentum balance equations (see e.g. Svendsen and Lorenz, 1989):

$$\text{X-direction} \quad \frac{\partial}{\partial x} \left(\langle \tilde{u}^2 \rangle - \langle \tilde{w}^2 \rangle \right) + \frac{\partial}{\partial y} \langle \tilde{u}\tilde{v} \rangle + \frac{\partial}{\partial z} \langle \tilde{u}\tilde{w} \rangle \quad (6a)$$

$$\text{Y-direction} \quad \frac{\partial}{\partial y} \left(\langle \tilde{v}^2 \rangle - \langle \tilde{w}^2 \rangle \right) + \frac{\partial}{\partial x} \langle \tilde{u}\tilde{v} \rangle + \frac{\partial}{\partial z} \langle \tilde{v}\tilde{w} \rangle \quad (6b)$$

would read, after invoking identities (4a-b):

$$\text{X-direction} \quad \langle \tilde{w}\tilde{\omega}_y \rangle + \frac{1}{2} \frac{\partial}{\partial x} \left(\langle \tilde{u}^2 \rangle - \langle \tilde{w}^2 \rangle \right) + \langle \tilde{v} \frac{\partial \tilde{u}}{\partial y} \rangle \quad (7a)$$

$$\text{Y-direction} \quad - \langle \tilde{w}\tilde{\omega}_x \rangle + \frac{1}{2} \frac{\partial}{\partial y} \left(\langle \tilde{v}^2 \rangle - \langle \tilde{w}^2 \rangle \right) + \langle \tilde{u} \frac{\partial \tilde{v}}{\partial x} \rangle \quad (7b)$$

and assuming irrotational flow ($\tilde{\omega}_x = \tilde{\omega}_y = 0$):

$$\text{X-direction} \quad \frac{1}{2} \frac{\partial}{\partial x} \left(\langle \tilde{u}^2 \rangle - \langle \tilde{w}^2 \rangle \right) + \langle \tilde{v} \frac{\partial \tilde{u}}{\partial y} \rangle \quad (8a)$$

$$\text{Y-direction} \quad \frac{1}{2} \frac{\partial}{\partial y} \left(\langle \tilde{v}^2 \rangle - \langle \tilde{w}^2 \rangle \right) + \langle \tilde{u} \frac{\partial \tilde{v}}{\partial x} \rangle \quad (8b)$$

The implication of taking into account the wave-induced shear stresses, $\langle \tilde{u}\tilde{w} \rangle$ and $\langle \tilde{v}\tilde{w} \rangle$, as given by Eqs.(7a-b), or equivalently, Eqs.(8a-b) for an irrotational flow, with respect to the case in which those stresses are neglected from the conventional form of the time-averaged horizontal momentum balance equations (Eqs. 6a-b), are discussed in the following sections for some idealized situations.

5. UNDERTOW VELOCITY PROFILES

For normally incident waves ($\alpha=0$) on a cylindrical beach ($\partial d/\partial y=0$), the vertical distribution of mean shear stress $\langle \tau_{xz} \rangle$ (associated with viscous and/or turbulent effects) can be found from the time-averaged horizontal momentum balance equation in the cross-shore direction after assuming a given mean pressure distribution (usually, $\langle p \rangle = \langle p_h \rangle - \rho \langle \tilde{w}^2 \rangle$, where $\langle p_h \rangle$ is the mean hydrostatic pressure) —see e.g. (Svendensen, 1984) for the assumptions and motivation of this equation—:

$$\frac{\partial}{\partial z} \left(\frac{\langle \tau_{xz} \rangle}{\rho} \right) = \frac{\partial U^2}{\partial x} + g \frac{\partial \langle \eta \rangle}{\partial x} + \frac{\partial}{\partial x} \left(\langle \tilde{u}^2 \rangle - \langle \tilde{w}^2 \rangle \right) + \frac{\partial}{\partial z} \langle \tilde{u}\tilde{w} \rangle \quad (9)$$

where $U(x, z)$ is the (undertow) mean velocity and $\langle \eta \rangle (x)$ is the mean water level (set-up/set-down). Eq. (9) shows the vertical variation of the mean shear stress $\langle \tau_{xz} \rangle$ in the $\{x, z\}$ vertical plane.

As already mentioned before, the $\langle \tilde{u}\tilde{w} \rangle$ contribution has been, until very recently, neglected throughout the water column except in the bottom boundary layer, in which it led to the streaming solution (Longuet-Higgins, 1953). The relevance of the $\langle \tilde{u}\tilde{w} \rangle$ contribution in the vertical distribution of $\langle \tau_{xz} \rangle$ can be easily assessed after substitution of identity (1) into Eq. (9):

$$\frac{\partial}{\partial z} \left(\frac{\langle \tau_{xz} \rangle}{\rho} \right) = \frac{\partial U^2}{\partial x} + g \frac{\partial \langle \eta \rangle}{\partial x} + \frac{1}{2} \left[\frac{\partial}{\partial x} \left(\langle \tilde{u}^2 \rangle - \langle \tilde{w}^2 \rangle \right) \right] + \langle \tilde{w}\tilde{\omega} \rangle \quad (10)$$

Since the $\langle \tilde{w}\tilde{\omega} \rangle$ term will be, in general, unknown—it depends on the vertical distribution of the current velocity—it may be set to zero as a first approximation, in which case Eq. (10) would read:

$$\frac{\partial}{\partial z} \left(\frac{\langle \tau_{xz} \rangle}{\rho} \right) = \frac{\partial U^2}{\partial x} + g \frac{\partial \langle \eta \rangle}{\partial x} + \frac{1}{2} \left[\frac{\partial}{\partial x} \left(\langle \tilde{u}^2 \rangle - \langle \tilde{w}^2 \rangle \right) \right] \quad (11)$$

It may be, thus, seen that the $\langle \tilde{u}\tilde{w} \rangle$ -term first effect is to halve the normal wave stress contribution to $\langle \tau_{xz} \rangle$. This would mean that unrealistic closure submodels for $\langle \tau_{xz} \rangle$ (i.e. eddy viscosity coefficient ν_t values) must be used to fit measured undertow profiles if the $\langle \tilde{u}\tilde{w} \rangle$ term is neglected in the momentum balance equation (9). It should be noticed that, although wave stress gradients are usually small compared to $g \frac{\partial \langle \eta \rangle}{\partial x}$ inside the surf zone (Svendsen and Lorenz, 1989), that is not necessarily the case outside the breaker region or in the transition zone (Putrevu and Svendsen, 1993). This means that the $\langle \tilde{u}\tilde{w} \rangle$ contribution, and therefore the need to calculate it, is expected to be more significant in areas in which mean water level gradients do not dominate the momentum balance equation.

6. LONGSHORE CURRENT VELOCITY PROFILES

For obliquely incident waves ($\alpha \neq 0$) on a cylindrical beach ($\partial d/\partial y=0$), the vertical distribution of the mean shear stress $\langle \tau_{yz} \rangle$, which may be related to the vertical gradients of the longshore current velocity $V(x, z)$, can be found from the time-averaged horizontal momentum balance equation in the alongshore direction—see e.g. (Svendsen and Putrevu, 1994)—:

$$\frac{\partial}{\partial z} \left(\frac{\langle \tau_{yz} \rangle}{\rho} \right) = \frac{\partial UV}{\partial x} + \frac{\partial}{\partial x} \langle \tilde{u}\tilde{v} \rangle + \frac{\partial}{\partial z} \langle \tilde{v}\tilde{w} \rangle \quad (12)$$

Upon substitution of identity (4b) with the assumption of alongshore uniformity ($\partial/\partial y=0$), Eq. (12) may be written as

$$\frac{\partial}{\partial z} \left(\frac{\langle \tau_{yz} \rangle}{\rho} \right) = \frac{\partial UV}{\partial x} - \langle \tilde{w}\tilde{\omega}_x \rangle + \langle \tilde{u} \frac{\partial \tilde{v}}{\partial x} \rangle \quad (13)$$

If, as in the preceding section, the term involving the vorticity is disregarded, the governing equation for the vertical distribution of $\langle \tau_{yz} \rangle$ (13) would read

$$\frac{\partial}{\partial z} \left(\frac{\langle \tau_{yz} \rangle}{\rho} \right) = \frac{\partial UV}{\partial x} + \langle \tilde{u} \frac{\partial \tilde{v}}{\partial x} \rangle \quad (14)$$

In this situation wave stresses are, in the absence of alongshore mean water level gradients, the dominant factors governing the vertical distribution of $\langle \tau_{yz} \rangle$. Again, it may be noticed that the primary effect of the $\langle \tilde{v}\tilde{w} \rangle$ term, as given by Eq. (14), is to reduce (approximately, to halve) the contribution of wave stresses ($\langle \tilde{u} \frac{\partial \tilde{v}}{\partial x} \rangle$ versus $\frac{\partial}{\partial x} \langle \tilde{u}\tilde{v} \rangle$) in the vertical distribution of $\langle \tau_{yz} \rangle$, with respect to the case in which the $\langle \tilde{v}\tilde{w} \rangle$ term is neglected in the original equation (12). This fact indicates that, for a given closure submodel of $\langle \tau_{yz} \rangle$, the predicted curvature of the vertical profiles of longshore currents taking into account the $\langle \tilde{v}\tilde{w} \rangle$ term (Eq. 14) is smaller than the one predicted neglecting the $\langle \tilde{v}\tilde{w} \rangle$ term (in Eq. 12), which may help explaining the good fit of logarithmic functions to field measurements of the longshore current vertical profiles (see e.g. Thornton et al, 1995).

7. CONCLUSIONS

The following general conclusions may be drawn from the theoretical derivations presented in this paper:

- New mathematical identities (4a-b) have been derived which express the wave-induced shear stresses ($\langle \tilde{u}\tilde{w} \rangle$ and $\langle \tilde{v}\tilde{w} \rangle$) in a 3D flow in terms of other wave-induced stresses ($\langle \tilde{u}^2 \rangle$, $\langle \tilde{v}^2 \rangle$, $\langle \tilde{w}^2 \rangle$ and $\langle \tilde{u}\tilde{v} \rangle$), easier to calculate by any given wave theory, and the oscillatory vorticity ($\vec{\omega}$).
- In general, the implication of the wave-induced shear stresses ($\langle \tilde{u}\tilde{w} \rangle$ and $\langle \tilde{v}\tilde{w} \rangle$) in the horizontal momentum balance equations is to approximately halve the contribution of other wave-induced stresses ($\langle \tilde{u}^2 \rangle$, $\langle \tilde{v}^2 \rangle$, $\langle \tilde{w}^2 \rangle$ and $\langle \tilde{u}\tilde{v} \rangle$) with respect to the case where horizontal-vertical correlations are neglected, which has been an otherwise common procedure in vertical circulation analysis.

ACKNOWLEDGEMENTS

The authors would like to acknowledge financial support for research underpinning this work from the CICYT-*Programa Nacional de Ciencia y Tecnología Marinas* (Ref: MAR95-1915). The experimental data were obtained within the "Dynamics of Beaches" project, funded by the *Human Capital and Mobility* programme of the EU under contract no. CHRX-CT93-0392. Figures are reprinted from *Coastal Engineering* with kind permission of Elsevier Science - NL, Sara Burgerhartstraat 25, 1055 KV Amsterdam, The Netherlands.

REFERENCES

- Deigaard, R. and Fredsøe, J. (1989). Shear stress distribution in dissipative water waves. *Coastal Engineering*, 13, pp. 357-378.
- De Vriend, H.J. and Kitou, N. (1990). Incorporation of wave effects in a 3D hydrostatic mean current model. Delft Hydraulics Report H-1295.
- Longuet-Higgins, M.S. (1953). Mass transport in water waves. *Phil. Trans. Royal Soc. London, Series A*, No. 903, pp.535-581.
- Prinos, P., Arcilla, A.S.-, Christiansen, N., van de Graaff, J., Høgedal, M., Lewis, A., O'Connor, B.A., Rivero, F.J. and de Rouck, J. (1995). The "Dynamics of Beaches" project. *Proc. of the Coastal Dynamics'95 Conference*, Gdansk, Poland, pp. 571-582.
- Putrevu, U. and Svendsen, I.A. (1993). Vertical structure of the undertow outside the surf zone. *Journal of Geophysical Research*, Vol. 98, no. C12, pp. 22,707-22,716.
- Rivero, F.J. and Arcilla, A.S.- (1995). On the vertical distribution of $\langle \tilde{u} \rangle$. *Coastal Engineering*, 25, pp. 137-152.
- Rivero, F.J., Arcilla, A.S.-, Gironella, X. and Corrons, F.A. (1996). The "Dynamics of Beaches" project: Database Catalogue (Part I). Report for the European Commission (DG-XII), Barcelona, Spain, 48 p.
- Rivero, F.J. and Arcilla, A.S.- (1997). On the vertical distribution of $\langle \tilde{u} \rangle$: reply to the comments of Z.-J. You. *Coastal Engineering* (in press).
- Stive, M.J.F. and De Vriend, H.J. (1994). Shear stresses and mean flow in shoaling and breaking waves. *Proc. of the 24th Int. Con. on Coastal Engineering*, Kobe, Japan, pp. 594-608.
- Svendsen, I.A. (1984). Mass flux and undertow in a surf zone. *Coastal Engineering*, 8, pp. 347-365.
- Svendsen, I.A. and Lorenz, R.S. (1989). Velocities in combined undertow and longshore currents. *Coastal Engineering*, 13, pp. 55-79.
- Svendsen, I.A. and Putrevu, U. (1994). Nearshore mixing and dispersion. *Proc. Royal Soc. London, Series A*, No. 445, pp.561-576.
- Thornton, E.B., Soares, C.M.C.V. and Stanton, T.P. (1995). Vertical profiles of longshore currents and bed shear stress. *Proc. of the Coastal Dynamics'95 Conference*, Gdansk, Poland, pp. 449-459.

CHAPTER 92

NONLINEAR WAVE DYNAMICS IN THE SURF ZONE

O. R. Sørensen¹, P. A. Madsen¹ and H. A. Schäffer¹

Abstract

In this paper we shall study and model various nonlinear interaction processes in the surf zone on the basis of a two-dimensional time-domain depth-integrated Boussinesq type model, which features the possibility of wave breaking and a moving boundary at the shoreline. Phenomena to be studied include breaking and runup of bicromatic wave groups on gentle slopes with emphasis on the evolution of surface elevations, the shoreline motion and the low frequency waves generated and released in the surf zone. The model results are compared with laboratory experiments by Mase (1994), and the agreement is generally found to be very good. Special details in the surf beats are investigated, e.g. the motion of the breaker line and of the shoreline, change of wave group modulation through the surf zone, and the sensitivity of surf beats to group frequency, modulation rate and bottom slope.

1. Introduction

Shoaling, breaking and runup of irregular wave trains in shallow water is a nonlinear process involving a number of complicated details. Triad interactions between harmonics in shallow water lead to substantial cross spectral energy transfer in relatively short distances, and during shoaling still more energy will be transferred into bound sub-harmonics and super-harmonics, which will travel phase locked to the primary wave train.

In a number of situations, however, part of the energy may be released as free harmonics, e.g. during the passage over submerged bars or during the process of breaking. When wave breaking occurs, the primary waves and their super-

¹International Research Centre for Computational Hydrodynamics (ICCH). Located at the Danish Hydraulic Institute, Agern Allé 5, DK-2970 Hørsholm, Denmark

harmonics will start dissipating, and this will allow for a gradual release of the bound sub-harmonics and result in free long waves moving towards the shoreline from which they will be almost fully reflected.

To some extent bound long waves will persist in the surf zone depending on the degree of groupiness in this region. The groupiness of the incident waves will generally be partially transmitted into the surf zone, and it may even be reversed if the higher waves in a wave group decay sufficiently during breaking to appear as the lower waves further inshore.

The individual waves in a wave group will break at different depths, which will result in a horizontal oscillation of the breakpoint. The excursion of the breakpoint will depend on the groupiness of the incident waves, and while a linear sinusoidal motion can be expected for a weakly modulated bichromatic group, this is somewhat modified for a fully modulated group where the shoreward extreme of the breakpoint will in principle be at the shoreline. The motion of the breakpoint will result in large time-varying radiation stress gradients in the region of incipient breaking, and this will act as a local forcing of free long waves at the group frequency and its higher harmonics (Symonds et al (1982)). These will propagate in the onshore as well as in the offshore direction. Since the breakpoint forced long waves are basically due to variations of the starting point for the setup, the phenomenon is sometimes referred to as dynamic setup.

The present paper concentrates on the investigations of nonlinear interaction processes in the surf zone using a time-domain Boussinesq type model, which resolves the primary wave motion as well as the long waves. A detailed description of the model can be found in Madsen et al. (1996), while a short description of the model is given in Chapter 2. In Chapter 3 the numerical model is verified with respect to the evolution of surface elevation and shoreline motion due to incident bichromatic wave trains. In Chapter 4 special details of the surf beat mechanism are investigated.

2. Model Description

The numerical model is based on a special type of depth-integrated equations derived by Madsen et al. (1991) and Madsen and Sørensen (1992) and incorporates enhanced linear dispersion characteristics and shoaling properties, which are important for an accurate representation of the nonlinear energy transfer (Madsen and Sørensen, 1993).

The inclusion of wave breaking is based on the surface roller concept for spilling breakers following the formulation by Schäffer et al. (1993). The effect of the roller on the wave motion is taken into account by excess momentum terms originating from a non-uniform velocity profile due to the presence of the roller. The excess momentum terms are a function of the roller thickness and the roller celerity. The instantaneous roller thickness at each point is determined based on a further development of the heuristic, geometrical approach by Deigaard (1989). Breaking is predicted to occur when the local slope of the surface elevation

exceeds an initial critical value, $\tan\phi_B$, using $\phi_B = 20$ deg. During the transition from initial breaking to a bore-like stage in the inner surf zone, the critical angle is assumed to gradually change from ϕ_B to a smaller terminal angle, ϕ_0 which is taken to be 10 deg. The roller thickness is determined as the water above the tangent of slope $\tan\phi$ and the resulting thickness is multiplied by a shape factor which is taken to 1.5. The roller celerity is determined interactively from the instantaneous wave field. The basic approximation is that the waves can locally be assumed to be regular and progressive.

The moving boundary at the shoreline is treated numerically by replacing the solid beach by a permeable beach characterized by an extremely small porosity. This allows for the determination of wave motion in the swash zone and it provides a shoreline condition which like a natural beach tends to be reflective for waves of small steepness viz. the low frequency waves. Radiation of short and long period waves from the offshore boundary is allowed by use of absorbing sponge layers.

Bottom friction is described by the classical quadratic friction law with a friction coefficient f_w of 0.01.

3. Evolution of Surface Elevations and Shoreline Motion

In recent publications Mase (1994,1995) presented experimental results for shoaling, breaking and runup of various types of bichromatic wave trains on a gentle slope. Fig. 1 illustrates the experimental setup. The flume consists of a 10 m horizontal section with a water depth of 0.47 m and a 12 m section with a constant impermeable 1/20 slope. Twelve wave gauges of capacitance type are installed at still water depths of 47, 35, 30, 25, 20, 17.5, 15, 12.5, 10, 7.5, 5 and 2.5 cm, and they are denoted WG1 to WG12. Furthermore, a runup meter is placed at the shoreline. Mase considered a range of wave conditions. Here we shall concentrate on the case with the two primary frequencies $f_1 = 0.95f_m$ and $f_2 = 1.05f_m$, where the mean frequency, f_m was taken as 0.3, 0.4, 0.5, 0.6, 0.8, 1.0 and 1.2 hz, and with the amplitudes $a_1 = a_2 = 0.025$ m.

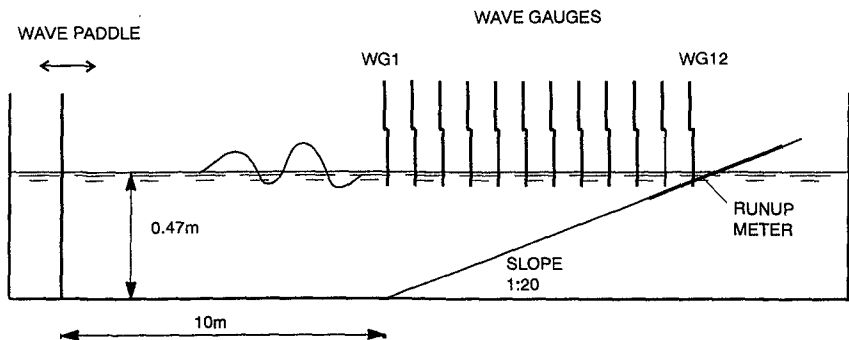


Fig. 1 Sketch of physical wave flume (Mase, 1994)

The variation in mean frequency from 1.2 hz to 0.3 hz represents a significant change in wave conditions, which are listed in Table 1 in terms of h/L_0 , H_0/L_0 , and ζ , where L_0 is the deep water wave length based on the mean frequency, H_0 is an estimate of the deep water wave height and h is the water depth taken at the toe of the slope. ζ is the surf similarity parameter defined as the beach slope divided by the square root of the deep water wave steepness. Based on Galvin's (1968) classification of wave breaking, Battjes (1974) found that spilling breakers would occur for $\zeta < 0.5$, while plunging would occur for $0.5 < \zeta < 3.3$. Hence, the test cases considered by Mase (1994) cover both regimes, and this will lead to rather different spatial evolutions of wave energy during the shoaling and breaking process. A further analysis of the measurements shows that for decreasing values of the mean frequency, there is a gradual increase in the motion at the group frequency and a pronounced increase in the primary wave motion at the shoreline.

Mean frequency (hz)	h/L_0	H_0/L_0	ζ	Breaker type
1.2	0.43	0.046	0.23	Spilling
1.0	0.30	0.032	0.28	Spilling
0.8	0.19	0.021	0.35	Spilling
0.6	0.11	0.012	0.47	Spilling
0.5	0.075	0.008	0.56	Plunging
0.4	0.048	0.005	0.70	Plunging
0.3	0.027	0.003	0.93	Plunging

Table 1 Wave characteristics of test cases by Mase (1994)

The wavemaker was controlled by a signal generated off-line using linear theory. Thus, advanced features as compensation for generation of spurious sub-harmonics and super-harmonics as well as active absorption of free waves reflected from the slope were not included. Furthermore, the measured frequencies and amplitudes deviated slightly from the target. Altogether, this prevents us from modelling the exact experimental setup and consequently we have chosen to place the numerical model boundary at the position of the first wave gauge (WG1) i.e. at the toe of the sloping beach. The energy of the primary frequencies and their super-harmonics propagates mainly onshore while sub-harmonic energy will propagate offshore as well as onshore. Neglecting the low frequency part of the incident waves, we use the following procedure: The measured signal at WG1 is analysed by FFT, the low frequency motion is removed and the remaining signal is converted into a flux boundary condition using linear theory. At the position of WG1 the waves are generated internally and re-reflection from this boundary is avoided by using a 1 m wide sponge layer offshore from the line of generation. In order to resolve the super-harmonics in shallow water a grid size of 0.02 m and

a time step of 0.01 s is used in the simulations. Numerical simulations have been performed for mean frequencies in the interval between 0.3 and 1.0 Hz. The computed evolution of surface profiles and the resulting shoreline motion agree quite closely with the measurements, indicating that phenomena like dispersion, wave-wave interaction and dissipation due to breaking are well represented by the present model. As an illustration of this Fig. 2 shows for the case of $f_m = 0.3$ Hz the measured and computed time series of water surface elevations at locations WG8, WG10 and WG12 as well as the motion of the shoreline converted into vertical displacement. For clarity the measurements are shifted relative to the computational results by 0.08 m in the figure. All cases were simulated with the same set of standard model parameters, and the quality of the agreement is very good for all values of f_m . This is actually a bit surprising, considering the fact that the roller concept used in the breaker model is primarily suited for spilling type of wave breaking.

The transient shoreline motion is shown in Fig. 3 for the mean frequency $f_m = 0.3, 0.6$ and 1.0 Hz. Again, the agreement between the present model and the measurements is very good. The different wave conditions, ranging from plunging type to spilling type wave breaking, can be seen clearly in the shoreline motion: For the lower mean frequencies the swash of the individual primary waves is quite distinct at the shoreline, while in the case of higher mean frequencies the group induced subharmonic motion dominates the swash oscillations.

It appears that the type of shoreline motion is governed by the type of wave breaking and consequently the surf zone similarity parameter, ζ can be used as an indicator. Hence we can conclude that ζ can be used to characterize the type of shoreline motion, and that plunging/surging breakers result in individual swash, while spilling breakers result in low-frequency dominated shoreline motion.

4. Investigations of Surf Beat

Release of incident bound long waves as well as long-wave generation by a time-varying breakpoint result in a long wave emitted from the surf zone. The amplitude of this wave is a measure of the surf beat activity and it was studied in a series of laboratory experiments by Kostense (1994). The numerical model has been verified against the experimental data by Kostense and the comparison was most satisfactory. For more details see Madsen et al. (1996). Here we shall concentrate on special details of the surf beat mechanism. The following topics are addressed: Trajectories of surface rollers; the motion of the breaker line and of the shoreline; the change of wave group modulation through the surf zone; the sensitivity of surf beats to group frequency, modulation rate and bottom slope.

For this investigation we shall concentrate on incident bichromatic wave groups which are effectively linear at the seaward boundary. This has the advantage that the determination of the amplitude of the outgoing free long waves due to the surf beat can be determined very accurately by simple means. The

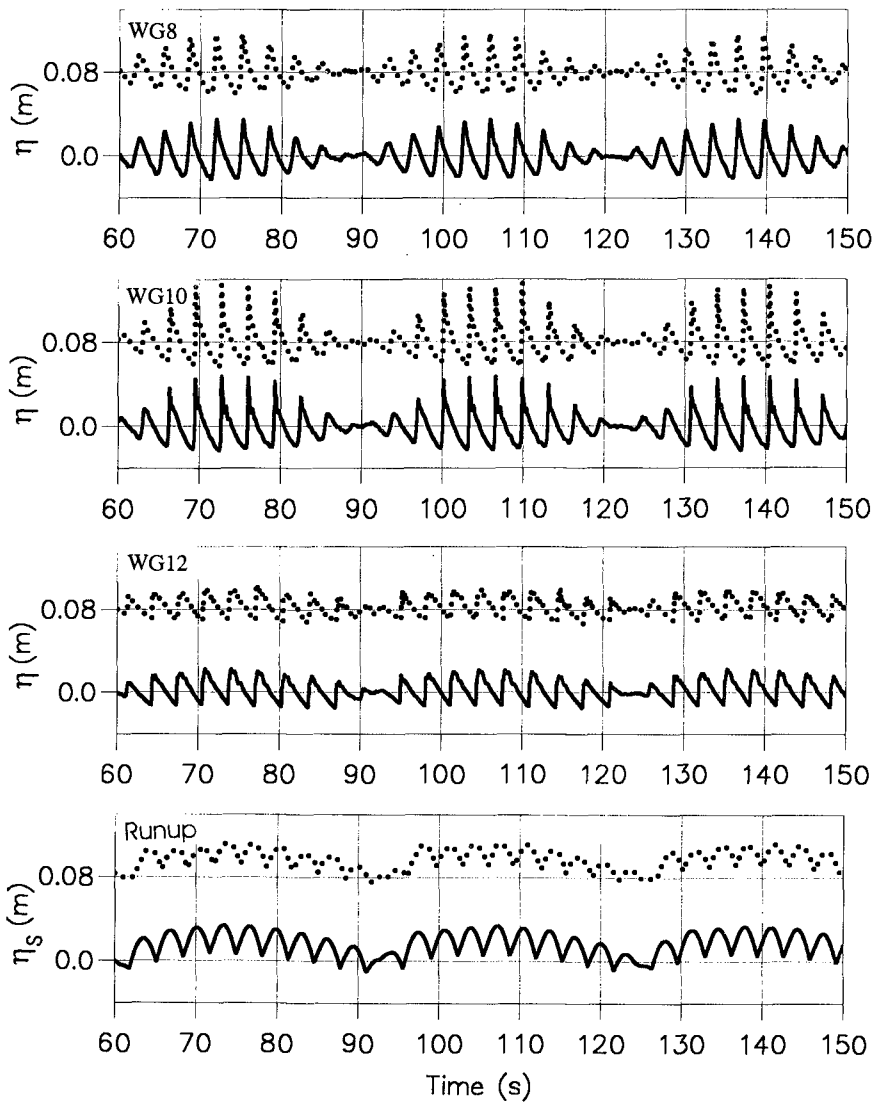


Fig. 2 Surface elevation (η) and swash oscillation (η_s , vertical displacement).
 Case: WP2, $f_m=0.3$ hz i.e. $f_1=0.285$ hz and $f_2=0.315$ hz.
 — Present model
 Experimental data by Mase (1994), shifted relative to computed results by 0.08m.

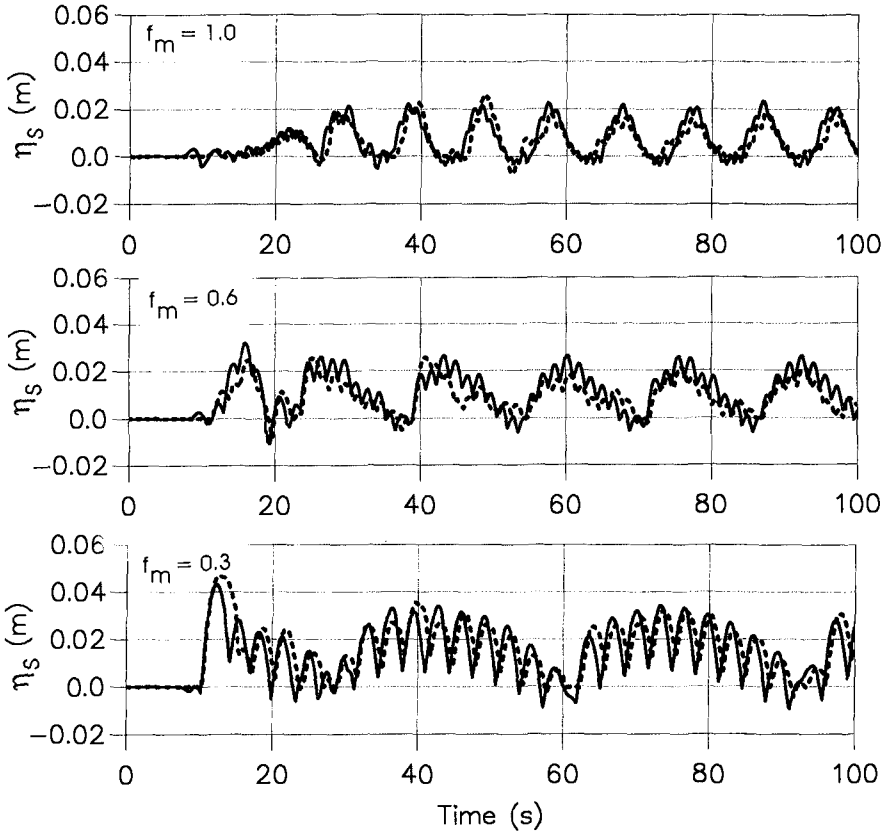


Fig 3 Transient Shoreline motion (η_s , vertical displacement).
 Case WP2: $f_m=0.3$ hz, 0.6 hz and 1.0 hz.
 — Present model
 Experimental data by Mase (1994)

bathymetry used for this study consists of a horizontal part of 10 m with a depth of 1.2 m and a part with a constant sloping beach (various slopes are considered).

The grid size, the time step and other model parameters are identical to those used in Chapter 3. Again, bichromatic wave trains are considered. The two primary frequencies are given by $f_1 = f_m + \Delta f/2$ and $f_2 = f_m - \Delta f/2$, where the mean frequency $f_m = 0.60$ hz and the group frequency, Δf is varied in the range 0.02-0.15 hz. The sum of the amplitudes is fixed ($a_1 + a_2 = 0.08$ m) and two different initial modulation rates, $\sigma (= a_2/a_1)$ are considered. In all tests waves are generated inside the model domain and re-reflection from the offshore boundary is avoided by using a sponge layer seawards of the point of generation.

In the first test case the beach slope is $h_x=1/40$, the still water shoreline is at $x=58\text{m}$, while two wave groups with $\sigma=0.2$ and $\sigma=1.0$ are considered. As mentioned above, the sum of a_1 and a_2 at the point of wave generation is constant which implies that the highest waves in each of the two wave groups are of equal size. Hence, we may expect that the outermost breakpoint position, $x_{B,outer}$ will be almost the same for the two wave groups, while the innermost breakpoint, $x_{B,inner}$ will be quite different as it is determined from the smallest waves in the wave group. This is confirmed by Figs 4a-b, which show the computed trajectories of

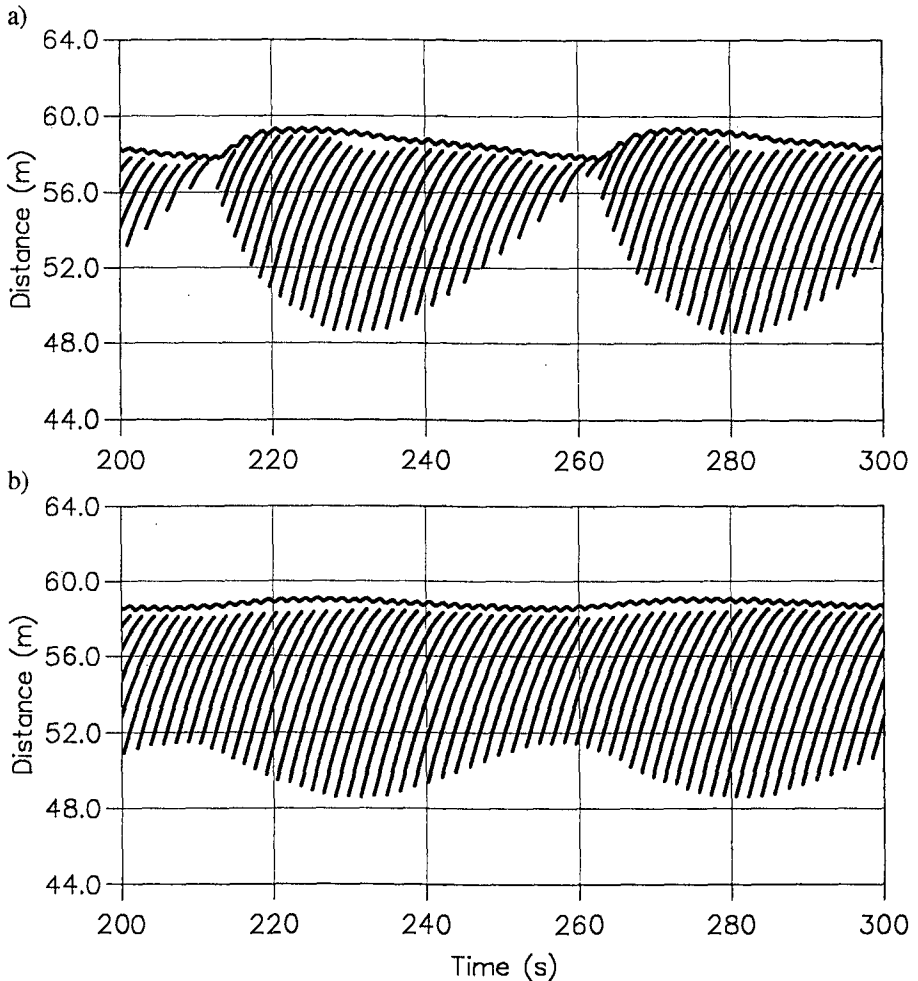


Fig. 4

Trajectories of surface rollers and shoreline motion.

Group frequency, $\Delta f=0.02$ hz. Bottom slope= $1/40$, $f_m=0.60$ hz, $f_1=f_m+\Delta f/2$, $f_2=f_m-\Delta f/2$; $a_1+a_2=0.080\text{m}$; a) Modulation rate, $a_2/a_1=1.0$ b) Modulation rate, $a_2/a_1=0.2$

the surface rollers and the shoreline motion for a group frequency $\Delta f = 0.02 \text{ Hz}$ in which case the group motion is resolved by 30 mean periods. We notice that $x_{B,outer}$ is practically identical for the two modulation rates, while $x_{B,inner}$ strongly depends on σ . The breakpoint excursion between these two limits is seen to be well resolved by the number of rollers being detected and traced. The almost sinusoidal time-variation of x_B for $\sigma = 0.2$ is significantly distorted as the modulation is increased to $\sigma = 1.0$, the reason being that $x_B(t_2) = x_{B,inner}$ is delayed relative to $x_B(t_1) = x_{B,outer}$ with half a group period *plus* the travelling time

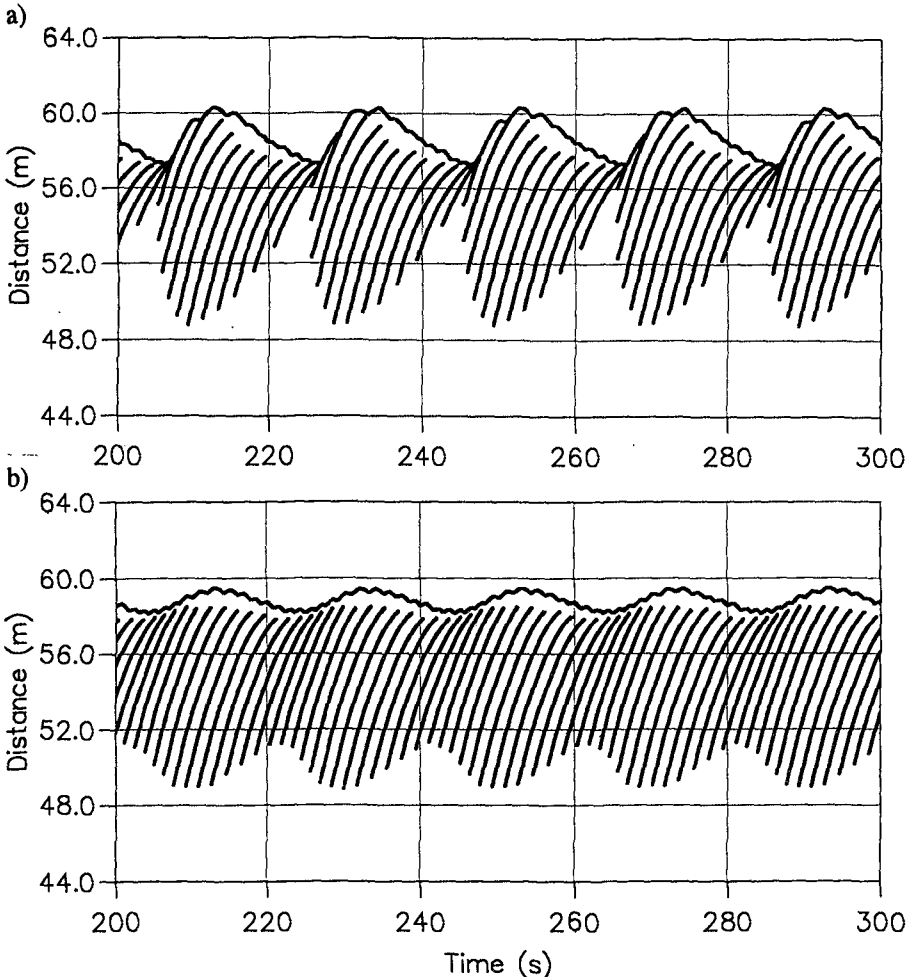


Fig 5 Trajectories of surface rollers and shoreline motion.
 Group frequency, $\Delta f = 0.05 \text{ Hz}$. Otherwise as Fig 4.
 a) Modulation rate, $a_2/a_1 = 1.0$ b) Modulation rate, $a_2/a_1 = 0.2$

necessary for the lowest waves to cover the distance from $x_{B,outer}$ to $x_{B,inner}$. This delay was also discussed by Symonds et al. (1982). In Figs. 5a-b the group frequency is increased to $\Delta f=0.05\text{hz}$. Apparently, this leads to a small shoreward shift of $x_{B,outer}$ and a seaward shift of $x_{B,inner}$ leading to a minor reduction in the breakpoint excursion for both modulation rates. It turns out that this trend is amplified for increasing ratios of the group frequency to the mean frequency ($\Delta f/f_m$) and when this number is larger than say $1/3$ the effective excursion produced by the model almost vanishes.

The shoreline excursion in Figs 4 and 5 is seen to be dominated by low frequency motion while the individual bores almost vanish. The fully modulated case obviously results in the strongest motion, as would be expected from both second order theory for bound waves and from the theory of the generating mechanism due to breakpoint oscillations. The non-sinusoidal variation of the breakpoint position is also found in the breakpoint forcing and thereby in the surf beat motion. Thus, (in Figs 4a and 5a) the shape of the resulting shoreline motion indicates substantial energy on harmonics of the group frequency i.e. $2\Delta f$ etc.

The modulation of the wave groups changes slightly during the processes of shoaling and nonlinear interactions, but much more rapid variations can be expected in the surf zone. In numerical modelling this obviously depends on the type of breaker model applied and as an example the classical assumption of a saturated surf zone (with wave amplitudes proportional to the local water depth) leads to a vanishing modulation. Schäffer (1993), on the other hand, discussed the possibility of a reversion of modulation and such a reversion is indeed possible in the present model, because of the difference between the initial limiting breaker angle for non-breaking waves (20 deg) and the final breaker angle (10 deg) for waves already breaking.

Fig. 6 shows high-pass filtered timeseries of computed surface elevations at three locations for the case of $\sigma=0.2$ and $\Delta f=0.05$ hz. The high-pass filtering ($f > 2\Delta f$) makes it easier to spot the modulation of the primary waves without the influence of the low frequency motion. At $x=49$ m the highest waves have just started breaking and the modulation is similar to the input wave train. At $x=50.8$ m the former highest waves (indicated by I) have been reduced by breaking and are now approximately of the same size as the former lowest waves (indicated by II). Hence the modulation has almost vanished at this location. At $x=52$ m a relatively strong reversion of modulation has occurred and the former highest waves are now the lowest waves in the wave group. A similar trend can actually be observed in Mase's (1994) fully modulated experimental data. We can therefore conclude that the reversion is not just an artifact of the numerical model.

We shall now turn to an investigation of the surf beat sensitivity to group frequency, modulation rate and bottom slope. Emphasis is put on the amplitude of the resulting outgoing free long waves determined on the horizontal section seawards from the surf zone. Figs. 7 and 8 show the computed amplitudes versus the group frequency. In Fig. 7 the amplitude is shown for the bottom slope $h_x = 1/40$ and for the two modulation rates $\sigma = 0.2$ and 1.0 . Fig. 8 shows the amplitude for the case of full modulation ($\sigma=1.0$) and for the three bottom slopes

$h_x = 1/20, 1/30$ and $1/40$. The curves are seen to oscillate with the group frequency, a trend which is in qualitative agreement with the theory of Symonds et al. (1982), who showed the importance of the relative phase between the long waves reflected from the shoreline and the long waves directly generated in the seaward direction by the moving breakpoint mechanism. The computed values of Δf , for which minimum response occurs, are much larger than the values predicted by Symonds et al. This trend is, on the other hand, supported by Kostense's (1984) measurements as well as by Schäffer's (1993) analytical work.

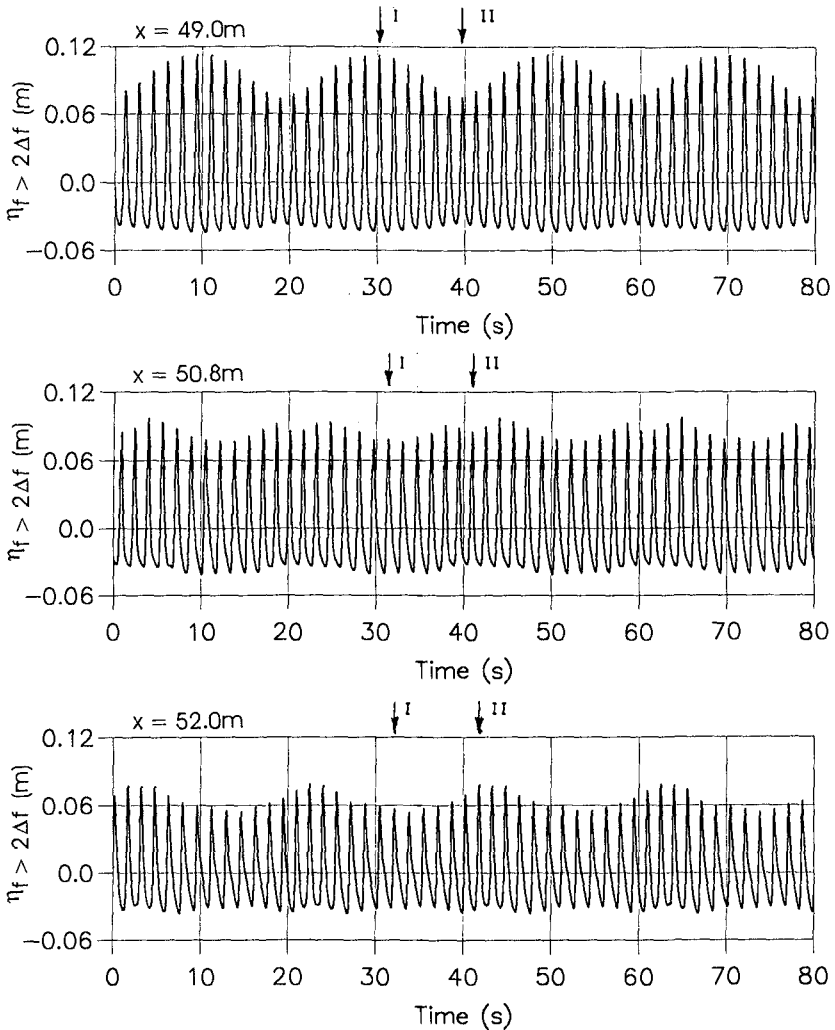


Fig 6 Time series of computed high-pass filtered ($f > 2\Delta f$) surface elevations at three locations. $\Delta f = 0.05$ hz, $a_2/a_1 = 0.2$. Otherwise as Fig 4.

It is therefore likely that the deviation from the prediction of Symonds et al. is due to their omission of the incident bound long waves. Fig. 8 shows that the values of Δf , for which the amplitude of the outgoing long wave is minimum, increases for increasing values of the slope. The effect of the modulation rate is small. Fig. 7 shows that when σ is increased from 0.2 to 1.0 the local minima occur for slightly higher values of Δf .

From Figs 7 and 8 it is seen that the maximum amplitude of the outgoing free long wave increases significantly for increasing modulation rate while there only is a small increase of the amplitude for increasing values of the slope. The main reason for this trend can be related to the incoming bound long waves. Second order theory (valid on a horizontal bottom) predicts that the long waves bound to the incoming wave groups will be proportional to the product of a_1 and a_2 , which indicates a scaling of $\sigma/(1+\sigma)^2$ i.e. they will be almost twice as large with $\sigma=1.0$ as compared to $\sigma=0.2$. Another obvious trend is that the local maxima decrease for increasing group frequencies. This is connected with the overall decrease in thereflection from the shoreline. When $f_m/\Delta f$ is decreased one will expect that the individual rollers connected with the short waves will have a dissipative effect on the long waves. However, the numerical treatment at the shoreline can also be shown to be increasingly dissipative for higher group frequencies. Further investigation is needed in order to quantify the reliability of the numerical model in this regime. A more detailed discussion of these results is given by Madsen et al (1996).

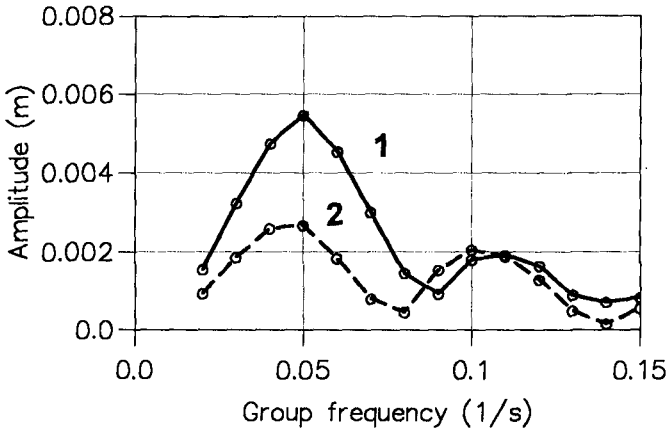


Fig 7

Amplitude of outgoing free long wave as a function of modulation and group frequency. Bottom slope, $h_x=1/40$.

1: $a_2/a_1=1.0$; 2: $a_2/a_1=0.2$

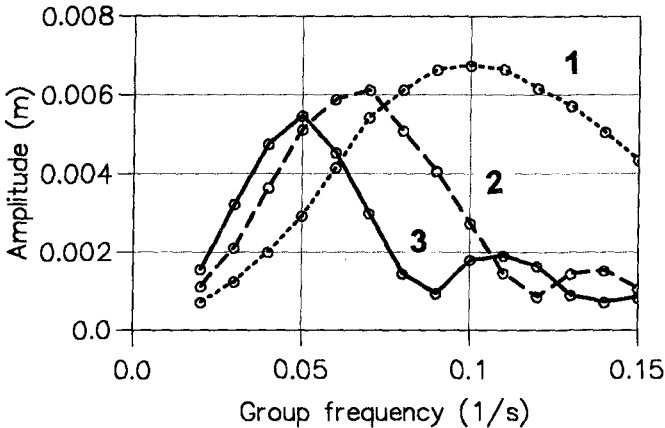


Fig 8 Amplitude of outgoing free long wave as a function of group frequency. Full modulation ($a_2/a_1=1.0$).
 1: $h_x=1/20$; 2: $h_x=1/30$; 3: $h_x=1/40$

Related and future research

This work is part of an extensive research effort at ICCH within the field of Boussinesq-type modelling. Concurrently with the present applications to strictly cross-shore motion, the investigation of situations in two horizontal dimensions as presented at the 24th ICCE (Sørensen et al. 1994) is continued. Improvements, e.g. with regard to the celerity of the surface roller as well as comparison with laboratory experiments on nearshore circulations are in progress. For applications in one as well as in two horizontal dimensions the main discrepancy between measurements and computation of e.g. the wave height variation appears to be the nonlinear shoaling close to the breakpoint rather than the following decay in the surf zone. This is one of the reasons for pursuing a higher order Boussinesq model as also presented at this conference (Madsen et al. 1996). In the near future the breaking model will be coupled with this higher order model. This will provide a tool for studying waves and current in a region extending from quite deep water and all the way to the shoreline. Related developments accounting explicitly for waves on ambient currents is also documented at this conference (Chen et al. 1996).

Acknowledgement

Many thanks are due to Dr. Hajime Mase from Kyoto University for making his raw experimental data for swash oscillations available to us.

This work has been financed by the Danish National Research Foundation and their support is greatly appreciated.

References

Battjes, J.A. (1974), "Surf Similarity", In Proc. of the 14th Coastal Eng. Conf., ASCE, pp 466-480.

Deigaard, R. (1989), "Mathematical modelling of waves in the surf zone", Prog. Report 69, ISVA, Technical University, Lyngby, Denmark, pp 47-59.

Galvin, C.J. Jr. (1968), "Breaker Type Classification on three Laboratory Beaches", Journal of Geophysical Research, Vol. 73, No. 12, pp 3651-3659.

Kostense, J.K. (1984), "Measurements of surf beat and set-down beneath wave groups", In Proc. of the 19th Coastal Eng. Conf., pp 724-740.

Madsen, P.A., R. Murray and O.R. Sørensen (1991), "A new form of the Boussinesq equations with improved linear dispersion characteristics. Part 1", Coastal Engineering, Vol 15, pp 371-388.

Madsen, P.A. and O.R. Sørensen (1992), "A new form of the Boussinesq equations with improved linear dispersion characteristics. Part 2: A slowly varying bathymetry", Coastal Engineering, Vol 18, pp 183-204.

Madsen, P.A. and O.R. Sørensen (1993), "Bound waves and triad interactions in shallow water", Ocean Engineering, Vol 20, pp 359-388.

Madsen, P.A., H.A. Schäffer and O.R. Sørensen (1996), "Surf zone dynamics simulated by a Boussinesq type model. Part 1: Model description and cross-shore motion of regular waves", Submitted to Journal of Geophysical Research.

Madsen, P.A., O.R. Sørensen and H.A. Schäffer (1996), "Surf zone dynamics simulated by a Boussinesq type model. Part 2: Irregular waves and surf beat", Submitted to Journal of Geophysical Research.

Mase, H. (1994), "Uprush-backrush interaction dominated and long wave dominated swash oscillations", In Proc. of Int. Symposium: Waves - Physical and Numerical Modelling, Vancouver, Canada, pp 316-325.

Mase, H. (1995), "Frequency down-shift of swash oscillations compared to incident waves", Journal of Hydraulic Research, Vol 33, No 3, pp 397-411.

Schäffer, H.A. (1993), "Infragravity waves induced by short-wave groups", J. Fluid Mech. (1993), Vol. 247, pp. 551-588.

Schäffer, H.A., P.A. Madsen and R. Deigaard (1993), "A Boussinesq model for waves breaking in shallow water", Coastal Engineering, Vol 20, pp 185-202.

Symonds, G., G.A. Huntley and A. J. Bowen (1982), "Two dimensional surf beat: Long wave generation by a time-varying break point", J. Geophys. Res, 87, C1, pp 492-498.

Sørensen, O.R., H.A. Schäffer, P.A. Madsen and R. Deigaard (1994), "Wave breaking and induced nearshore circulations", In Proc. 24th Coastal Eng. Conf., Kobe, Japan, pp. 2583-2594.

CHAPTER 93

A Boussinesq breaking wave model with vorticity

I. A. Svendsen, Ke Yu, and J. Veeramony¹

ABSTRACT: The paper describes a breaking wave model based on the classical assumptions for long, moderately nonlinear Boussinesq waves. It is shown that wave breaking can be described by accounting for the effect of vorticity generated by the breaking process. This leads to two additional terms in the momentum equation, both of which represent the enhancement of the momentum flux associated with the extra particle velocities found at and around the turbulent front of the breaking waves. In addition to the wave height decay and profile deformation predicted by earlier breaker models, the present model also provides information about particle velocity profiles including the undertow. Comparisons are made to measurements for these quantities. The similarities and differences between various breaker models are also examined and explained.

1. Introduction

The present paper presents a Boussinesq wave model that includes the effects of wave breaking in the equation of continuity and momentum.

The process of wave breaking has been widely studied during particularly the past two decades. For a long time, almost all detailed information came from experimental investigations but the success of the Boussinesq approach in modelling nearshore wave motion has also lead to Boussinesq models that, by various means, create the decrease in wave height and the transformation of the wave shape observed during breaking in the surf-zone on a gently sloping beach.

Since breaking involves strong energy dissipation, it was natural as a first approach to heuristically add a “dissipation term”, usually taking the form of the double derivative of the unknown variable to the momentum equation. Early examples are Zelt (1991), Karambas et al (1992) and more have followed. If the coefficient for the dissipation term is chosen carefully as in Wei et al (1995), such models can give breaker like wave development. The reason for this will be discussed later.

However, the Boussinesq wave models are developed from the fundamental equations of hydrodynamics. In the case of wave breaking this would mean the

¹Center for Applied Coastal Research, Ocean Engineering Lab, University of Delaware, Newark, DE 19716, USA. Correspondence e-mail: ias@coastal.udel.edu

Reynolds equations, in which the Reynolds stresses represent the only signature of the turbulence generated by breaking. Following the usual procedure, one finds (if the Reynolds stresses, as a reasonable approach, are modelled by means of an eddy viscosity) that the “dissipation term” of the assumed $\partial^2/\partial x^2$ -form originates from the turbulent normal stresses, which are small (see eg. Stive and Wind, 1982) and are very far from modelling the dramatic changes in the momentum flux typical of wave breaking.

An approach closer to meet that goal was used by Brocchini et al (1992) and, in more explicit form, by Schäffer et al (1992, 1993). They observed the importance the roller of a mature breaking wave has in enhancing the momentum flux of the wave. The roller essentially is the volume of recirculating water flow carried forward in the turbulent front at the speed c of the wave. The concept was first used by Svendsen (1984a,b) in the wave averaged equations to calculate wave height decay, set-up and undertow. The two above mentioned models essentially introduced that concept into the Boussinesq equations, and, though there are limitations, the results are remarkably convincing, as they should be because the models give an approximate representation of the actual physics. In addition, such models only represent a moderate extension of the computational work relative to Boussinesq models for non-breaking waves.

Because of the heuristically assumed form of the velocity profiles, these models cannot be expected to provide detailed information about the particle motion in the breaking wave motion, including the undertow. The model presented in the following is aiming at including such information by avoiding apriori assumptions about the velocity profiles. This means it is necessary to include in the model the vorticity generated by the breaking, which is an important feature of breaking waves: the motion is not irrotational as assumed in traditional Boussinesq theory.

The model is therefore formulated in terms of a stream function and the vorticity is an additional unknown which is determined separately by solving the vorticity transport equation. The model equations are outlined in section 2 and section 3 gives additional discussion about particularly the boundary conditions for the vorticity. In section 4 we show a comparison with measurements including particle velocities and undertow. The last section gives a comparison with previous models mentioned above which explains why all these models seem equally successful in predicting the wave height and wave profile development.

2. Outline of model equations

The governing equations are derived from the basic equations for conservation of mass and momentum. Only a brief outline is given here, for more details see Yu & Svendsen, 1995. We consider a breaking wave propagating over a gently sloping bottom topography of depth $h_0(x)$. Fig 1 shows the definitions of all geometrical quantities used. Then the depth integrated equations of continuity and momentum becomes

$$\frac{\partial \zeta}{\partial t} + \frac{\partial Q}{\partial x} = 0 \quad (1)$$

where

$$Q = \int_{-h_0}^{\zeta} u dz \quad (2)$$

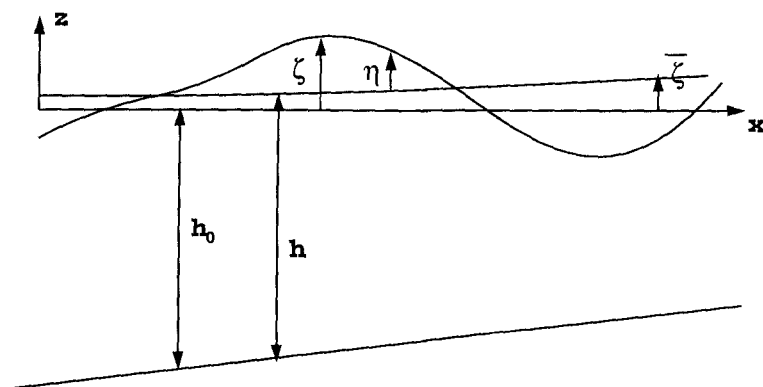


Figure 1: Definition sketch showing the geometrical quantities.

and

$$\begin{aligned} \frac{\partial Q}{\partial t} + \frac{\partial}{\partial x} \int_{-h_0}^{\zeta} u^2 dz - (h_0 + \zeta) \frac{\partial \zeta}{\partial x} - \int_{-h_0}^{\zeta} \frac{\partial^3}{\partial x^2 \partial t} \int_z^{\zeta} \int_{-h_0}^z u dz dz dz \\ - \int_{-h_0}^{\zeta} \frac{\partial^2}{\partial x^2} \int_z^{\zeta} u \frac{\partial}{\partial x} \int_{-h_0}^z u dz dz dz + \frac{\tau_b - \tau_s}{\rho} = 0 \end{aligned} \quad (3)$$

where τ_b and τ_s are the bottom and surface stresses, respectively. In (3) the pressure term has been eliminated using the depth integrated vertical component of the momentum equation.

To evaluate the integrals in (3) the velocity u must be determined. In breaking waves the flow cannot be assumed irrotational. However the stream function ψ for the flow satisfies the equation

$$\nabla^2 \psi = \omega \quad (4)$$

where ω is the vorticity which must be determined separately. Equation (4) is solved by introducing the usual assumptions of Boussinesq wave theory that the water depth to wave length ratio μ and wave amplitude to water depth ratio δ are small and δ/μ^2 are $O(1)$. The stream function ψ can then be expanded in a power series

$$\psi = \sum_{n=0}^{\infty} (z + h_0)^n \psi_n(x, t) \quad (5)$$

Substituting this into (4) and solving it turns out to be convenient to distinguish between the rotational and the irrotational part of the solution. Hence for the velocity we define u_r and u_p respectively and find

$$u_p = u_0 - \mu^2 (z + h_0) (2h_x u_{0x} + h_{xx} u_0) - \frac{\mu^2}{2} (z + h_0)^2 u_{0xx} + O(\mu^4) \quad (6)$$

$$u_r = \int_{-h_0}^z \omega dz - \mu^2 \int_{-h_0}^z \int_{-h_0}^z \int_{-h_0}^z \omega_{xx} dz dz dz + O(\mu^4, \mu^2 h_x, u^2 h_{xx}) \quad (7)$$

Though ω is assumed large, the ω_{xx} terms in (7) turn out to contribute little to the solution. The u_r -terms represent the additional terms generated by the presence of vorticity. We further define the discharge Q_r as

$$Q_r = \int_{-h_0}^{\zeta} u_r dz \quad (8)$$

which implies that $Q = Q_p + Q_r$.

When these results are substituted into the integrals of (3) these integrals can be written

$$\int_{-h_0}^{\zeta} u^2 dz = \frac{Q^2}{d} + \Delta M \quad (9)$$

$$\int_{-h_0}^{\zeta} \frac{\partial^3}{\partial x^2 \partial t} \int_z^{\zeta} \int_{-h_0}^z u dz dz dz = \frac{h^3}{6} \left(\frac{Q}{h} \right)_{xxt} - \frac{h^2}{2} Q_{xxt} + \Delta P_{xxt} \quad (10)$$

where $d = h_0 + \zeta$ and again the ΔM and ΔP_{xxt} represent the contributions caused by the breaking. For ΔM and ΔP_{xxt} we get

$$\Delta M = \int_{-h_0}^{\zeta} u_r^2 dz - \frac{Q_r^2}{d} + O(\mu^4) \quad (11)$$

$$\Delta P = - \int_{-h}^{\bar{\zeta}} \int_z^{\bar{\zeta}} \int_{-h}^z u_r dz dz dz + \frac{(h + \bar{\zeta})^2}{3} Q_r + O(\delta, \mu^2, h_x) \quad (12)$$

The Boussinesq equations for the breaking waves therefore become

$$\zeta_t + Q_x = 0 \quad (13)$$

$$Q_t + g(h_0 + \zeta) \zeta_x + \left(\frac{Q^2}{h} \right)_x + \Delta M_x + \frac{h^3}{6} \left(\frac{Q}{h} \right)_{xxt} - \frac{h^2}{2} Q_{xxt} + \Delta P_{xxt} = 0 \quad (14)$$

The two unknowns in these equations are the surface variation ζ and the total instantaneous volume flux Q in the waves. The vorticity ω is determined from the vorticity transport equation, which to the same order of approximation as (14) reads

$$\omega_t = [\nu_t \omega_z]_z + O(\mu^2, \delta) \quad (15)$$

where ν_t is the eddy viscosity. This is solved using the boundary conditions

$$\omega(-h) = 0 \quad (16)$$

$$\omega(\bar{\zeta}) = \omega_s \quad (17)$$

Here ω_s is the maximum value of ω generated near the surface due to the wave breaking.

3. Discussion of boundary conditions for the vorticity

The bottom boundary condition of zero vorticity is consistent with the general neglect of the bottom friction in the model.

At the free surface we can expect that the vorticity will be zero along the part of the surface which is outside the roller area.

In the roller region, the free surface vorticity will also be near zero. However, strong vorticity is generated inside the recirculating roller flow. Measurements in that region of breaking are not yet available for surf-zone conditions, but measurements have been made in weak hydraulic jumps (see Lin & Rockwell, 1994). The flow patterns in all such jumps will of course differ somewhat from breaking waves, in particular far away from the turbulent roller region. Around the roller region, however, the flows in a hydraulic jump and a surf-zone wave are very similar indeed with the same local mechanisms dominating. Hence the measurements around the roller in a hydraulic jump can be expected to model the equivalent conditions in a surf-zone wave well.

There are a number of flow features that play an important role in assessing the vorticity in this region. Considering a vertical section through a point in the roller, one of the dominating features observed in such measurements is the increase in vorticity to a maximum which always occurs at or below the so called dividing streamline, which is the streamline limiting the roller. Above that streamline, the average flow recirculates, below it continues to the downstream. At the toe of the turbulent region, the dividing streamline joins the surface streamline ahead of the jump.

In this region, we can approximate the vorticity ω by

$$\omega \sim \frac{\partial u}{\partial z} \quad (18)$$

and hence we notice that

$$\nu_t \omega \sim \frac{\tau_{zx}}{\rho} \quad (19)$$

Hence the specification of ν_t and ω_s is equivalent to the specification of the shear stress at the lower edge of the dividing streamline used in some breaker models (see eg. Brocchini et al, 1991 or Schäffer et al, 1992). The advantage of the present method, however is that through the solution of the vorticity transport equation, it explicitly models the mechanisms for the effect such a shear stress has on the entire flow, a problem previous models do not address at all.

In spite of the limited knowledge we have about the value of ω and ν_t , there are some very specific bounds on how these parameters vary. One such bound is given by (19). Fig 2 shows an analysis of the maximum shear stress which occurs at or just below the dividing streamline in three different hydraulic jumps with Froude numbers $F = 1.28, 1.44,$ and 1.60 . Here l_r is the length of the roller. We see that in all three cases, $\tau/\rho u_0^2$ (where u_0 is the inflow velocity) varies the same way over the length of the roller.

Another set of bounds for ω near the surface are related to the flow conditions at the toe of the roller. As indicated in Fig 3 in the immediate neighborhood of the toe, the free surface and the dividing streamline can both be approximated by straight lines so that the roller height e in that region increases linearly with distance x_t from the toe ($x_t = x - x_{toe}$). Since the particle velocity in the wave

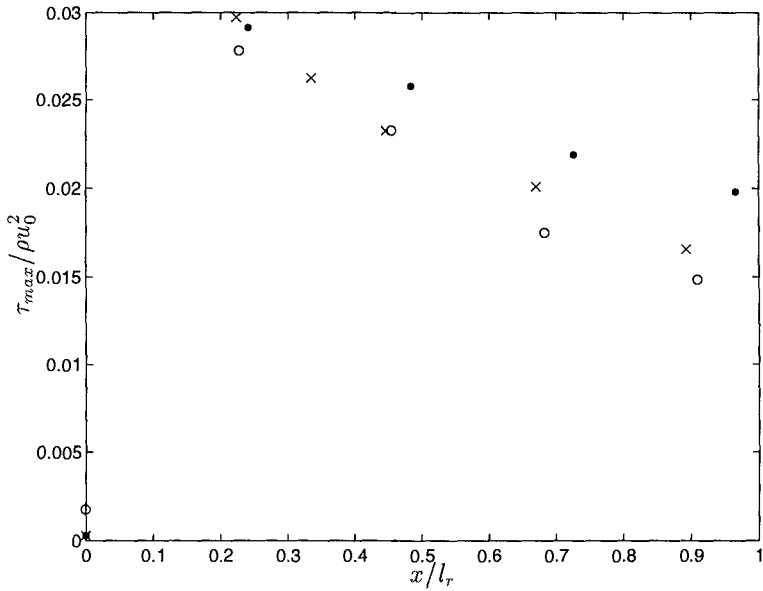


Figure 2: Variation of the maximum shear stress normalized by the square of the inflow mean velocity for three different hydraulic jumps with Froude numbers of 1.28 ('o'), 1.44 ('•') and 1.60 ('x').

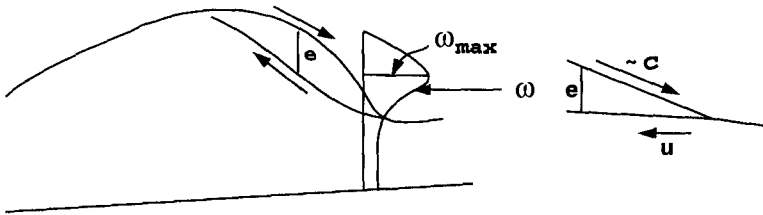


Figure 3: Schematic diagram showing the distribution of vorticity and the approximation at the toe of the roller.

at the surface of the roller is $\sim c$ and at the dividing streamline is $u \ll c$ (where u is close to the velocity in the wave trough) the vorticity ω must vary as

$$\omega \approx \frac{c+u}{e} \quad (20)$$

For dynamic reasons, however, we must also have in that region

$$\tau \propto \rho g e \propto x_t \quad (21)$$

which according to (19) implies that near the toe

$$\nu_t \approx \frac{\tau}{\rho \omega} \propto e^2 \approx x_t^2 \quad (22)$$

Based on the geometry, combined with (19) and measurements of τ and e , we find that ν_t rapidly increases to a maximum value and then decays slowly to near zero before the next breaker arrives.

Based on this information we are able to construct a realistic variation of ν_t and ω_s . We have used

$$\omega_s = A \left(1 - \frac{x_t}{l_r}\right)^2 \quad 0 < x_t < l_r \quad (23)$$

where l_r is the horizontal length of the roller from the toe to the wave crest, which for dynamic reason must be the rear edge of the roller². For ν_t the relationship is

$$\nu_t = Ch \sqrt{ghe}^{-\beta x_t^2} \tanh^2(\alpha x_t) \quad (24)$$

Though the formulation used in the computations shown in the following are slightly more complicated, the expressions above are similar in effect to those used.

When the boundary condition (17) is applied at $z = \bar{\zeta}$ we get the ω variation shown in Fig 4. Between the $z = \bar{\zeta}$ and the instantaneous MWS it is assumed that ω varies linearly from ω_s to zero at the surface. The hydraulic jump measurements indicate that this is a good approximation to the actual variation.

4. Comparison with experiments

Examples of comparisons with experimental results are shown in the following. The experiments used were obtained by Okayasu and analyzed by Cox et al (1995). Waves were generated in the Precision Wave Tank (PWT) at the Center for Applied Coastal Research at a depth of 0.40m and propagated onto a 1 : 35 sloping beach. The measurements were taken at 6 different locations of which some were in the surf-zone. Because a laser-doppler velocimeter was used to measure the velocities, the measurements could only be taken up to a point slightly above the trough level of these waves. Inside the surf-zone, bubble entrainment due to breaking also restricted the measurements.

Figure 5 shows a picture of the model simulations of the waves in the tank at two fixed times. The full line shows the solution of (13) and (14), the dotted line shows the wave transformation without the breaker terms in the equations.

²The rapid fluctuations of the toe position imply that at the turbulent averaged mean position of the toe it has a small but finite thickness (Brocchini and Peregrine, 1996). This justifies the finite value of ω_s at the toe in (23)

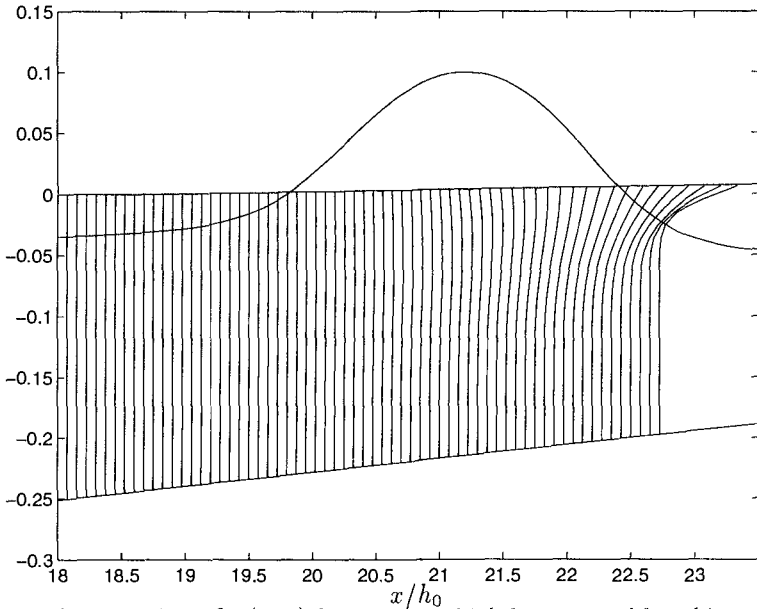


Figure 4: The variation of $\omega(x, z)$ for a wave which has started breaking. Above the MWL, ω varies linearly from the value at the MWL to zero at the MWS.

A comparison with the measured and computed wave heights during the experiment is shown in Fig 6. This figure also shows the measuring positions of the experiment. It turns out that the increase in wave height due to shoaling is slightly underpredicted by the model. In the shown calculation, this has been adjusted for by increasing the input wave height at the left boundary so that the breaker height in this comparison is the same as the measurements. This makes the comparison of the model performance in the surf-zone more relevant.

The underprediction of the shoaling process turns out to be a common feature of the $\zeta - Q$ version of the Boussinesq equations used as the basic Boussinesq model. For comparison we find that if a Boussinesq model based on the depth averaged particle velocity is used, the shoaling is overpredicted slightly. The reason for these inaccuracies and for the difference between the two types of Boussinesq models is that they are both lowest order Boussinesq methods in which terms $O(\delta^2, \delta^3, \dots)$ have been omitted. When waves approach breaking, these terms become large enough to influence the solution. The difference between the two model versions appear because the neglected higher-order terms are different in the two versions. Hence, these deficiencies can be eliminated by use of a higher order Boussinesq model (see Wei et al, 1995).

Figure 7 shows a comparison between measured and computed velocity profiles at position L5 which is well into the surf-zone. We see that the agreement is generally acceptable, though it is evident that the lack of measurements near the wave crest makes this comparison less valuable.

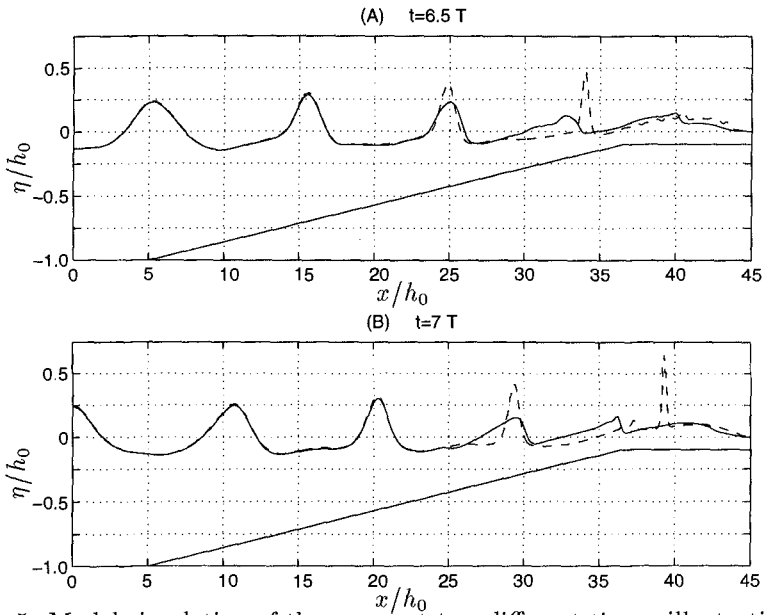


Figure 5: Model simulation of the waves at two different times, illustrating the difference between the non-breaking model (-) and the breaking model (—).

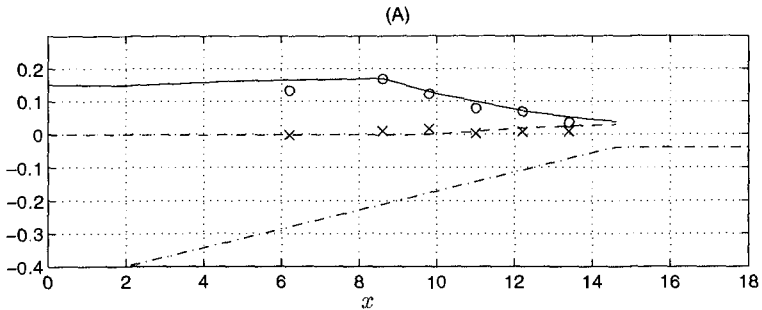


Figure 6: Comparison between the measured wave heights ('o') and the computed wave heights (—) for the experiment described in Cox et al (1995).

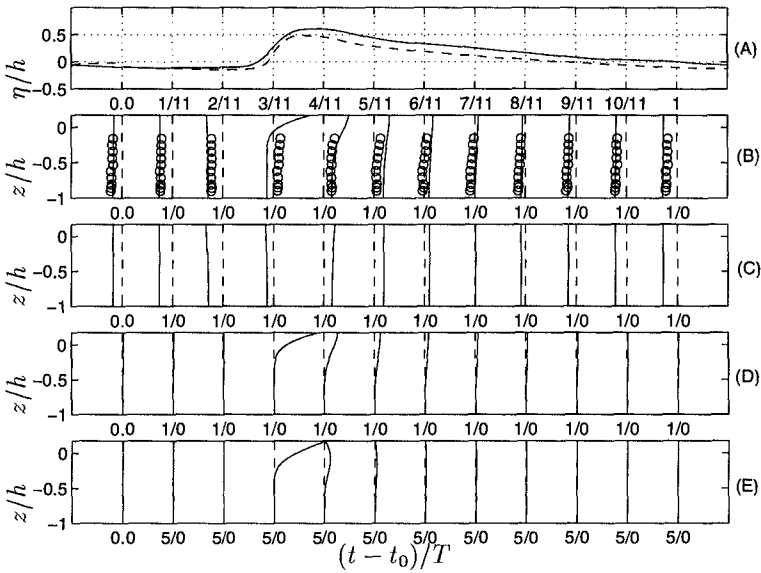


Figure 7: Vertical variations at L5 of: (B) u/c (Solid - Model, Circle - Data), (C) u_p/c , (D) u_r/c and (E) $\omega/(c/h)$ at different phases marked on (A) the surface elevation (solid - Model results, dashed - Data). $t_0 = 7.773 T$.

Since the effects of turbulence generated by the breaking is included in the model predictions, the average velocity over a wave period should also predict the undertow profiles, which represent a balance in which the shear stresses play a role. Figure 8 shows a comparison between the computed and measured undertow velocities at the 6 measurement positions. Again the agreement is quite good. It is interesting to notice that both measurements and model predictions pick up the principal difference between the undertow under non-breaking waves (parts (A) and (B) in the figure) and breaking waves (parts C-F). Since we have neglected the bottom shear stress, the model predicts a slip velocity at the bottom. It is clear that in the measurements, the effect of the bottom boundary layer is also limited to very close to the bottom.

5. Discussion and comparison with other models

In (13) and (14) the breaker terms are relatively small and it is of interest to see how the strong process of breaking can be properly modelled by adding such seemingly weak modifications.

When solving (13) and (14) the values obtained for Q are actually changed quite substantially. To see this we note that over most of the surf-zone the waves are only changing very slowly. Hence for a given value of ζ we have

$$Q \approx c\zeta \quad (25)$$

which is valid for waves of permanent form with no net mass flux, whether the waves are breaking or not. Therefore, when the wave shape ζ is modified due to

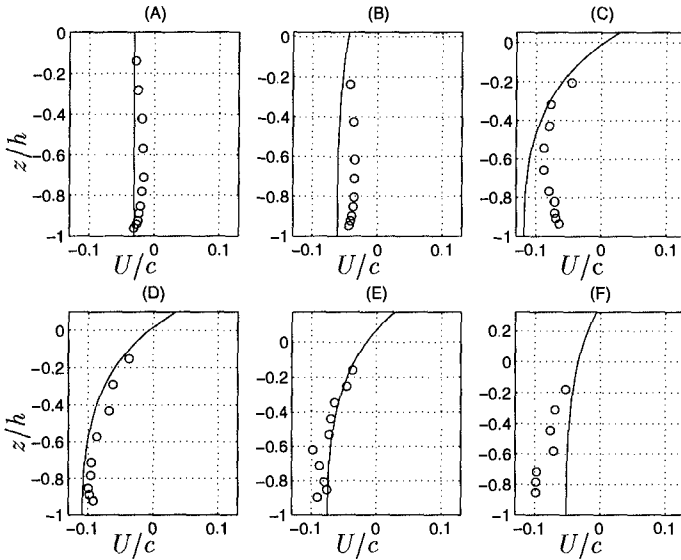


Figure 8: Nondimensional undertow profiles at L1 (A), L2 (B), L3 (C), L4 (D), L5 (E) and L6 (F). (solid) - Model results. (circle) - Data.

the breaking, so is Q .

Even more pronounced is the change in velocity profiles caused by the breaking process. Since Q_r represents a substantial increase in volume flux which is mainly concentrated near the surface it appears that for a given Q the velocity near the bottom must be similarly reduced. This is probably the most significant effect the wave breaking has on the bottom conditions and as the above arguments illustrate, it occurs for simple kinematic reasons³.

It is also illustrative to examine why several, seemingly quite different, Boussinesq models for breaking waves appear to be comparably good at predicting the wave height decay and surface profile development of breaking waves. In particular, three models show the reduction in wave height and change in skewness of the wave profile towards a sawtooth shape that are typical features of mature surf-zone breakers. The three models in question are the model by Wei & Kirby (1995) which is based on a dissipative term with an eddy viscosity, the model by Schäffer et al (1992) in which the breaking effect is generated by including a surface roller in the model and the present model in which breaking is modelled by taking into account the rotational part of the water motion.

To understand why three so different approaches apparently produce similar effects on the wave profiles, we only need to realize that in the Boussinesq

³Another effect of the breaking is the change in the wave profile shape and hence the temporal variation of the pressure gradient and velocities. A third is the added turbulence level even at the bottom.

momentum equation the three models produce almost identical signature of the breaking: the present model and Schäffer et al's model both include two and one terms, respectively, that represent enhancement of the momentum flux. In both models, the (x, t) variation of these terms are approximately the same as shown in Fig 9 (a) and (b). It turns out that, in particular, the position of this momentum enhancement relative to the wave crest is crucial for obtaining the breaking effect. It furthermore appears that in the Wei & Kirby model, the variation of the eddy viscosity has, on a heuristic basis, been chosen so that the "dissipative-term" it creates, in spite of its lack of physical justification, gives an almost identical contribution to the momentum equation. In other words: the Boussinesq equations respond equally to terms that represent the appropriate momentum enhancement, no matter which method are used to determine their variation and magnitude.

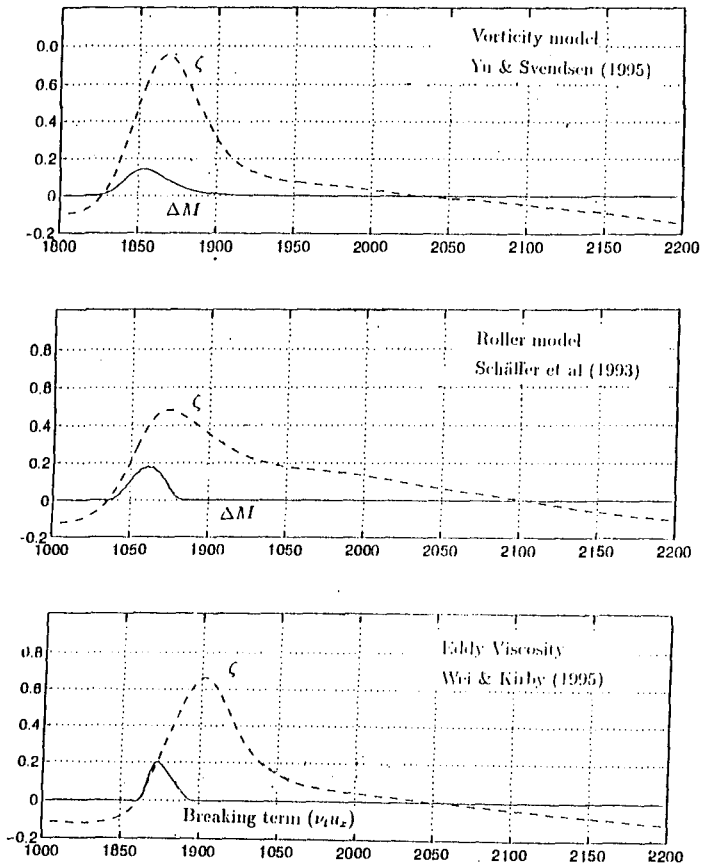


Figure 9: The variation of the terms in the momentum equation which induces breaking, for the three different models discussed in section 5.

6. Conclusions.

The Boussinesq model represents breaking by including the vorticity generated by the breaking. This gives rise to additional terms in the momentum equation which represent the enhanced momentum flux associated with the very large particle velocities at and near the turbulent front of the breaker. The model is based entirely on the Reynold's equations and no artificial dissipation terms are included. It also predicts particle velocities including undertow quite accurately.

Acknowledgment

This study was sponsored by the National Science Foundation under the grant OCE-9203277 and by the US Army Research Office, University Research initiative under contract No. DAAL 03-92-G-0016. The United States Government is authorized to produce and distribute reprints for government purposes notwithstanding any copyright notation that may appear herein.

References

- Brocchini, M. and Peregrine, D.H., (1996). "Integral flow properties of the swash zone and averaging" *J. Fluid Mech.*, 317, pp.241-273
- Brocchini, M., Cherubini, P. and Iovenitti, L., (1991). "An extension of Boussinesq type model to the surf zone." *Computer Modelling in Ocean Engineering 91*, Rotterdam, The Netherlands. pp. 349-359.
- Karambas, Th. K. and Koutitas, C., (1992). "A breaking wave propagation model based on the Boussinesq equations." *Coastal Engrg.*, Vol. 18, pp. 1-19.
- Lin, J. C. and Rockwell, D., (1994). "Instantaneous structure of a breaking wave." *Phys. Fluids*. Vol 6(9), pp. 2877-2879.
- Madsen, P. A. and Svendsen, I. A., (1984). "Turbulent bores and hydraulic jumps.", *J. Fluid Mech.*, Vol. 129, pp. 1-25.
- Schäffer, H. A., Deigaard, R. and Madsen, P., (1992). "A two-dimensional surf zone model based on the Boussinesq equations." *Proc. 23rd Int. Coast. Engrg. Conf.*, ASCE, pp. 576-589.
- Schäffer, H. A., Madsen, P. and Deigaard, R., (1993). "A Boussinesq model for wave breaking in shallow water." *Coastal Engineering*, Vol 20, pp185-202.
- Stive, M.J.F. and H.G. Wind (1982). A study of radiation stress and set-up in the nearshore region. *Coastal Engineering*, 6, pp. 1-26.
- Svendsen, I.A. (1984a). Wave heights and set-up in a surf-zone. *Coastal Engineering*, 8, pp. 303-329.
- Svendsen, I.A. (1984b). Mass flux and undertow in a surf-zone. *Coastal Engineering*, 8, pp. 347-365.
- Svendsen, I. A. and Madsen, P. A., (1984). "A turbulent bore on a beach." *J. Fluid Mech.*, Vol. 148, pp. 73-96.
- Zelt, J.A., (1991). "The run-up of nonbreaking and breaking solitary waves." *Coastal Engrg.*, Vol. 15, pp. 205-246.

CHAPTER 94

ROLLER CONTRIBUTIONS AS INFERRED FROM INVERSE MODELLING TECHNIQUES

¹D.J.R. Walstra, G.P. Mocke, F. Smit

Environmentek, CSIR, PO Box 320, Stellenbosch 7600, South Africa

ABSTRACT

Two independent approaches are discussed whereby inverse modelling is employed as a means of better quantifying roller contributions in the near shore. A so-called integral approach utilizes a coupling between the extended wave energy and momentum balance equations to make inferences regarding roller properties based on wave height and set up measurements. In a somewhat more indirect inverse modelling approach, as first discussed in Mocke et al. (1994), the roller properties are obtained from predicted vertical distributions of internal flow properties such as turbulent kinetic energy, suspended sediment concentrations and undertow velocities which are optimally fitted against measured profiles. An intercomparison between the two approaches is made to get an indication of the validity of the applied theories and inverse modelling techniques. The integral approach further serves to evaluate a new conceptual model for dissipation due to wave breaking

1. INTRODUCTION

Nearshore circulation modelling in wave-dominated environments requires accurate quantification of both wave height and mean water levels across the surf zone. Although attempts at modelling wave height have been relatively successful (Battjes and Janssen, 1978) little progress has been achieved in arriving at a reliable prediction of mean water levels across the surf zone. This is particularly the case for the so-called transition zone immediately following breaking, an area characterized by significant wave height decay whereas the water level remains more or less constant. The observation (Nadaoka and Kondoh, 1982) that the seawards directed return flow or undertow, the primary mechanism for cross-shore sediment transport, attains maximum strength some distance landwards of the breakpoint reinforces the necessity to better quantify this lag effect.

¹ Present address: Delft Hydraulics, P O Box 177, 2600 MH Delft, The Netherlands.

Svendsen(1984) incorporated additional contributions of mass and momentum to account for the presence of the aerated water body or “roller” at the water surface in the surf zone. It was however only with later models such as those of Roelvink and Stive(1989) and Nairn et al(1990) that attempts were made to model the extent of the transition zone and the spatial evolution of the roller. These models incorporated a lag between the production and dissipation of turbulent kinetic energy (TKE) arising from the breaking process. More recently, Dally and Brown(1995) propose an empirical roller model wherein the transition zone arises from the interval in time required for roller creation.

2. INVERSE MODELLING APPROACHES

2.1 System of Equations

Integral Properties

The wave energy balance according to Battjes and Janssen (1978) is used to describe the wave height distribution across the surf zone. Only waves travelling perpendicular towards the coast are considered. The wave energy balance is written as:

$$\frac{\partial F_x}{\partial x} = -D_w \quad (1)$$

Where F_x is the onshore energy flux per unit width and D_w is the time averaged energy dissipation in a breaking wave (LeMehaute, 1962).

With the assumption that breaking waves are modelled as bores travelling towards the coast with the wave celerity (c). Nairn et al. (1990) propose the following equation:

$$\frac{\partial E_w c_g}{\partial x} + \frac{\partial E_R c}{\partial x} + \tau_s c = 0 \quad (2)$$

where E_R denotes the kinetic energy of the roller and τ_s is the shearstress in the nearsurface. The result given in Deigaard and Fredsoe (1989) that the dissipation originates from the work done by the shear stress due to the roller acting on the fluid right below it is included in the third term of Equation 2 (i.e. $D_R = \tau_s c$).

The properties of the roller are described according to Svendsen (1984):

$$E_R = \frac{\frac{1}{2} m_r c^2}{L} = \rho A \frac{c^2}{2L} = \frac{\rho A c}{2T} \quad (3)$$

For the derivation of the dissipation in the roller, D_R , the findings of Deigaard and Fredsoe (1989) are used again to relate the shear stress exerted by the roller onto the underlying wave to this dissipation. The shear stress is derived under the assumption that the position of the roller does not change relative to the underlying wave. This implies that the shear stress induced by the roller should balance the downward force exerted on the roller due to gravity. D_R is then written as:

$$D_R = \tau_s c = \beta \rho g \frac{A}{L} c = \beta \rho g \frac{A}{T} \tag{4}$$

In which A is the cross-sectional area of the roller, T is the wave period, β is the slope of the wave front, and L is the wave length.

Incorporating a contribution due to the wave roller the time averaged momentum equation reads:

$$\left(2 \frac{c_g}{c} - \frac{1}{2} \right) \frac{\partial E_w}{\partial x} + M_r + \rho g h \frac{\partial \eta}{\partial x} = 0 \tag{5}$$

De Vriend and Kitou (1990) presented an analysis in which for the case of spatially varying waves on a sloping bottom the orbital velocity moments were derived. Based on these results Stive and De Vriend (1994) derived an expression for the vertical shear stress distribution in case of a sloping bottom and wave breaking dissipation. At the water surface this expression reads:

$$\tau_t = -\frac{1}{c} \frac{\partial E_w c_g}{\partial x} - M_R \tag{6}$$

The second term on the right-hand side has to be interpreted as the time averaged gradient of momentum in the roller. Using the roller concept (Equations 3 and 4) M_R can be written in terms of the kinetic energy of the roller which yields:

$$M_R = 2 \frac{\partial E_R}{\partial x} \tag{7}$$

By inserting Equation 7 into Equation 6 the energy balance obtained from the momentum balance results:

$$\frac{\partial E_w c_g}{\partial x} + 2 \frac{\partial E_R c}{\partial x} + \tau_s c = 0 \tag{8}$$

The wave celerity c has been included in the gradient of the energy flux of the roller, which is acceptable if it is assumed that the spatial variations in wave celerity are small relative to those in E_R .

Comparing Equations 8 and 2 an apparent inconsistency is visible; there is a factor 2 difference in the term in which E_R appears. This inconsistency was clarified by Deigaard (1993), as discussed in Stive and De Vriend (1994). Deigaard (1993) found that the inconsistency arises from the complicated situation that occurs when the volume of the roller is changing in the wave propagation direction. Besides the shear layer between the roller and the wave there is a net transfer of water from the wave to the roller as the volume of the roller increases, and vice versa if the volume of the roller decreases. This implies that an additional momentum exchange between the roller and the underlying wave is present. The corrections that these considerations give to the shear stress and to the energy balance remove the inconsistency resulting

in an energy balance with the factor 2 included.

Flow Properties

According to 2DV momentum balance considerations, equilibrium between the depth-integrated wave induced momentum flux (i.e. the radiation stress and the set-up gradient) yields a depth-mean zero flow. However, due to the fact that mass and momentum fluxes need not be in balance at any point through the depth a secondary return flow known as the undertow may result.

The undertow equation, which follows from a combination of the local and horizontal momentum balances, has the form (assuming a wave-averaged eddy viscosity for approximation of the Reynolds stresses):

$$\frac{\partial}{\partial z} \left(\nu_t \frac{\partial U}{\partial z} \right) = \frac{\partial}{\partial x} (\overline{u^2} - \overline{w^2}) + \frac{\partial}{\partial x} g\overline{\eta}_x + \frac{\partial}{\partial z} (\overline{uw}) \quad (11)$$

where U is the wave-averaged return flow or undertow, η_x is the mean water level set-up, and u and w are the horizontal and vertical wave-orbital velocities.

For the considered wave-averaged situation the above equation is presumed to be valid from the bottom boundary to the vicinity of the surface.

As discussed by Stive and De Vriend (1994), wave averaged shear stresses are solely due to wave amplitude variations associated with shoaling, and dissipation due to boundary layer shear and/or breaking waves. From a quantification of the wave-related terms, the depth variation of eddy viscosity, the mean mass flux above wave trough level and the shear stress at mean water level may be resolved the undertow variation over depth.

The roller effects of the near surface layer (NSL) are manifested through a shear stress τ_s acting at the mean water level. Hence the upper boundary condition corresponds to:

$$\nu_t \frac{\partial U}{\partial z} = \frac{\tau_s}{\rho} \text{ at } z = z_s \quad (12)$$

A no slip condition applies at the bottom boundary:

$$U = 0 \text{ at } z = 0 \quad (13)$$

According to mass balance considerations the total mass flux (M) in the lower layers balances that in the NSL, from which can be derived the set-up gradient. The assumption is made that the wave terms (orbital velocity movements) can be derived independently from the mean flow. Based on a derivation by Bijker (1974), Stive and De Vriend (1994) proposed approximations for the time-averaged values of the wave terms defined in Equation 11. These are incorporated in the present model. For the determination of the depth dependant eddy viscosity (ν_t) use is made of a two

equation (k - ϵ) turbulence model wherein the dissipation due to wave breaking is the primary forcing term (Mocke and Smith, 1992).

The time-mean vertical distribution of suspended sediment is described by the classical equation describing a balance between an upward flux due to eddy-diffusion and a downward settling component:

$$0 = D_c \frac{\partial C}{\partial z} + w_s C \tag{14}$$

where C is the suspended sediment concentration, w_s the sediment fall velocity and D_c the sediment diffusion or mixing coefficient. The diffusion coefficient is generally assumed proportional to the eddy viscosity.

2.2 Inverse Modelling Procedures

Integral Properties

The inverse modelling procedure using integral properties is illustrated in the flow chart shown in Figure 1. The initial step entails use of the extended momentum equation (Equation 6). Since the wave height and set up are known from measurements the term M_R can be determined directly (inverse model results have a subscript “inv”, and the measured results are extended with the subscript “meas”):

$$M_{R_{inv}} = -\rho g \left(\left(\frac{1}{4} \frac{c_g}{c} - \frac{1}{16} \right) \frac{\partial H_{meas}^2}{\partial x} + h_{meas} \frac{\partial \eta_{meas}}{\partial x} \right) \tag{13}$$

Integrating Equation 8 results in the kinetic energy present in the roller:

$$E_{R_{inv}}(x) = \frac{1}{2} \int_{x=x_b}^x M_{R_{inv}} dx + E_{R_{inv}}(x=x_b) \tag{14}$$

in which the second term on the right hand-side is zero by definition.

The dissipation in the roller, D_R , can be calculated from the energy balance in which the term $M_{R_{inv}}$ obtained from the momentum equation is used to determine the gradient of the energy flux in the roller:

$$D_{R_{inv}} = -\frac{1}{8} \rho g \frac{\partial (H_{meas}^2 c_g)}{\partial x} - c M_{R_{inv}} \tag{15}$$

Note the fact that in the equation above the assumption that the spatial variations of c are small compared to those of $E_{R_{inv}}$ is used.

With the inverse model it is now possible to determine the dissipation in the roller D_R directly from the momentum equation. The only assumption that has to be made is Equation 7 which gives the connection between the momentum and energy balance. The assumption that the spatial variation of the wave celerity can be neglected

compared to the variation of the energy in the roller is not expected to influence the results dramatically.

Having determined E_r using the momentum equation and D_r using the wave energy balance, an inverse modelled β can be found applying the roller approach

according to Svendsen (1984):

$$\beta = \frac{D_r c}{2gE_r} \tag{16}$$

A number of studies have concluded that a constant value of 0.1 gives the best set up results (e.g. Roelvink, 1993).

Following a spline smoothing interpolation of wave height and set up measurements, the procedure outlined above is followed and the cross shore distribution of E_r , D_r , and β are calculated.

Flow Properties

As the most readily available and reliable set of flow measurements, the inverse modelling analysis is carried out principally on undertow data. Limited investigation has however also been carried out using TKE and sediment concentration measurements. The analysis procedure for undertow measurements is illustrated in the flowchart shown in Figure 2. A first estimate of D_r is made using the transition zone model of Nairn et al(1990), however the exercise could also conceivably start with D_w as a first estimate of D_r . With D_r and the wave induced mass flux the independant variables, an optimal combination having least rms error between measured and computed velocities is determined.

The analysis procedures for TKE and concentrations is somewhat simpler in that the sole variable is D_r , the source of TKE production at the surface boundary.

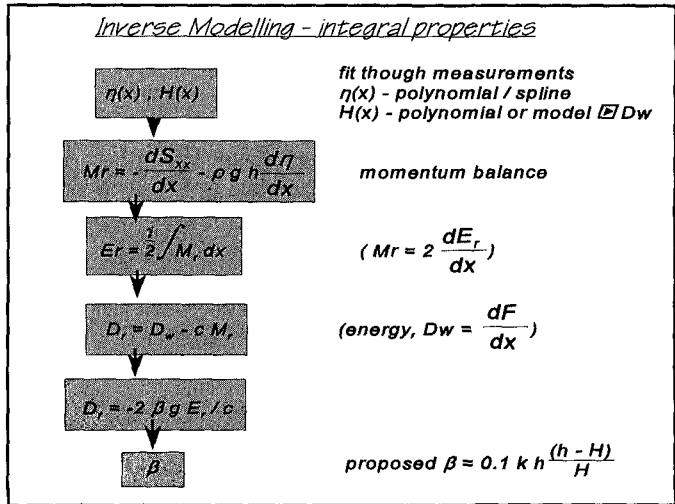


Figure 1 Inverse modelling procedure

3. RESULTS

Integral Properties

Presented in Figure 3 is a step-by-step illustration of an application of the inverse integral modelling approach. Depicted in Figures 3(a) and (b) are measured wave heights(H) and mean water levels(η) for test 1 of Stive(1983). This case corresponds to a monochromatic spilling type wave ($Ho=0.16m, T=1.8s$) with breaking induced on a plane 1:40 beach slope. Using a polynomial fitting procedure a continuous representation of the cross-shore distribution of wave heights and mean water levels is obtained.

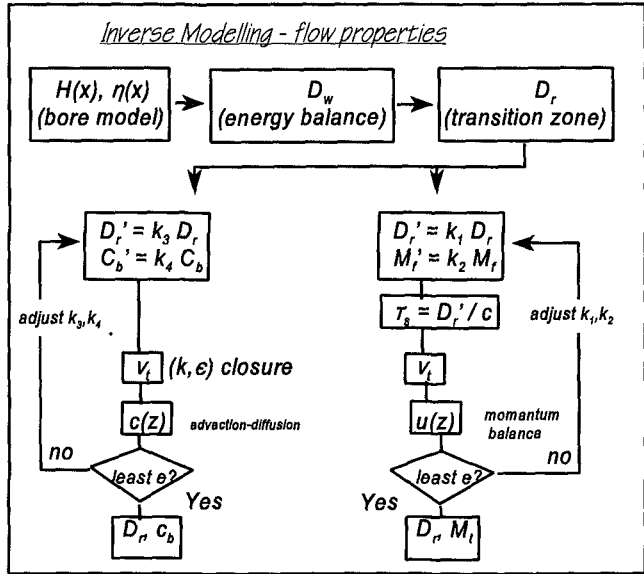


Figure 2 Analysis procedure for undertow measurements

The corresponding cross-shore distribution of wave energy dissipation(D_w), calculated from Equation 1 using linear, 2nd order cnoidal and covocoidal theory, is shown in Figure 3(c).These distributions demonstrate a prominent peak in D_w , immediately following the break point, reflecting the observed rapid attenuation in wave height after breaking.

The fitted wave heights are subsequently used to compute the radiation stress distribution. As illustrated in Figure 3(d) these estimates are highly dependant on the wave theory employed. Also plotted in this figure are measurements of radiation stress made by Stive (1983). The generally accepted tendency for linear theory to significantly overestimate radiation stress in the vicinity of the breaking point is clearly demonstrated. It may further be remarked that although the covocoidal theory provides improved estimates in this region, linear theory is in close correspondence with radiation stress measurements made in the inner surf zone.

Figure 3(e) presents the results of the following step, whereby the cross-shore radiation stress and mean water level distributions are introduced in Equation 16 to solve for M_{riv} . In much the same manner as for D_w , the M_r distribution demonstrates a prominent peak immediately post-breaking. This is consistent with a transfer of momentum to this roller storage term through the initial transition zone. M_r

subsequently attains negative magnitudes in the inner surf zone where excess momentum is transferred from the roller into the underlying flow.

The roller energy E_r distribution is obtained from M_r , using Equation 17. As depicted in Figure 3(f) this parameter has a peak significantly shorewards of the breaking point. This feature is consistent with physical reality, whereby the wave roller is only fully established at the limit of the transition zone.

Using Equation 18 the wave roller dissipation can subsequently be obtained from energy balance. As illustrated in Figure 3(g) this parameter shows a landwards shift in peak value as had been observed for E_r . The D_r distribution can further be seen to be very much different from that previously found for D_w .

From Equation 19 relating D_r to the roller geometry and E_r , the cross-shore distribution of the roller slope may be resolved. For the case under consideration it may be seen from Figure 3(h) that a constant value of the order 0.1 as proposed by Nairn et

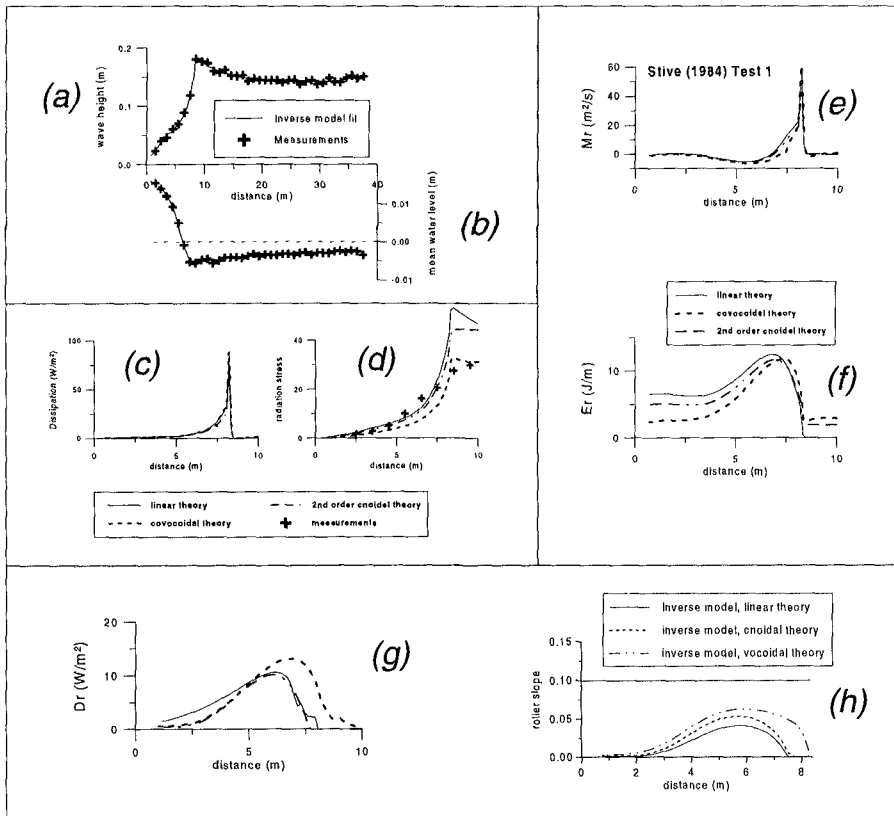


Figure 3 Step-by-step illustration of an application of the inverse integral modelling approach

al(1990) is inappropriate.

For the case of random waves principal reference is made to the LIP11D measurements made in the large scale Delta Flume. For a description of these tests reference should be made to Arcilla et al(1993).

In Figure 4 is shown the fitted H_{rms} and η distributions for measurements made mid-way through test 1A. For the H_{rms} measurements a Battjes and Janssen(1978) type bore model is run until an optimal fit is obtained whilst a spline curve is used for the water level. Using a similar procedure to that described previously for the monochromatic wave case, Figure 5 shows the constituent terms of the momentum balance equation. An initial increase in M_r , coincident with increased wave breaking, is followed by rapid decrease to negative values as both the radiation stress and set-up term increase. Figure 6 depicts cross-shore distributions of D_w and D_r , under linear and cocircular wave theories, for the same case. Although the two wave theories result in very different D_w distributions the inverse modelled D_r distributions are in reasonably good accordance. Although linear theory does not attain the same peak value at around $X=148m$ both theories show a distinct landwards shift from the D_w distribution.

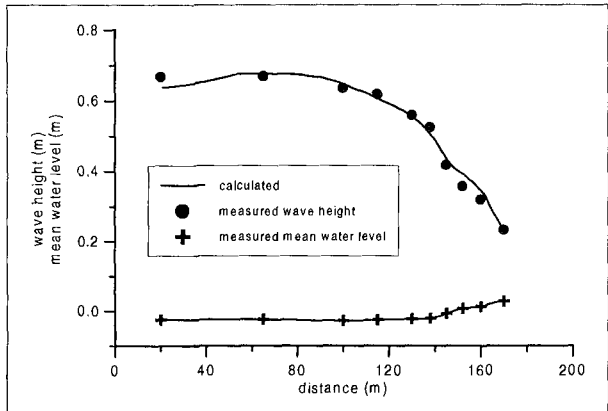


Figure 4 Fitted H_{rms} and eta distributions for measurements of LIP test 1A.

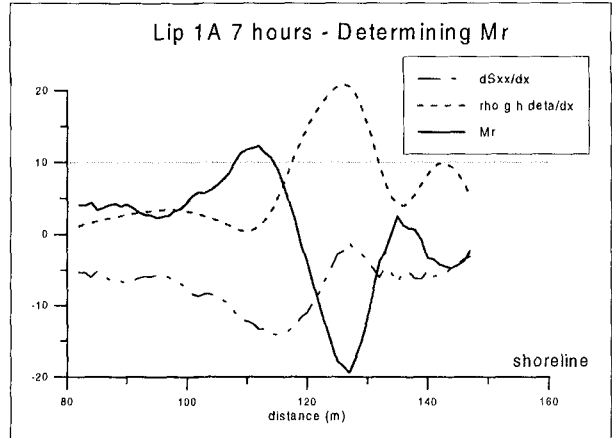


Figure 5 Constituent terms of the momentum balance equation

Model sensitivity

The sensitivity of the inverse modelling procedure to measured mean water levels is illustrated in Figure 7. Depicted in Figure 7(a) are spline fits of the mean water level as recorded on four occasions during Test 1A. Figure 7(b) shows the corresponding D_r distributions for each of the 4 measuring instances. Although water levels do not change by more than about 1cm there are distinct differences between the modelled D_r distributions. This is particularly the case for the situation after 7 hours where a dip in the water level near $X=120m$ results in a D_r peak not evident for other times. On the whole however the principal features of the cross-shore distribution of D_r appear to be consistent.

Slope of wavefront

A principle finding is that β is not constant for all the investigated theories. A new β will be defined which is derived for linear wave theory. The old definition of β being the slope of the wave front is extended with an additional factor that takes the internal dissipation of roller energy into account. Attention is primarily focussed on predicting β in the area where the external roller dissipation is non-zero or relatively large for respectively mono-chromatic and random waves.

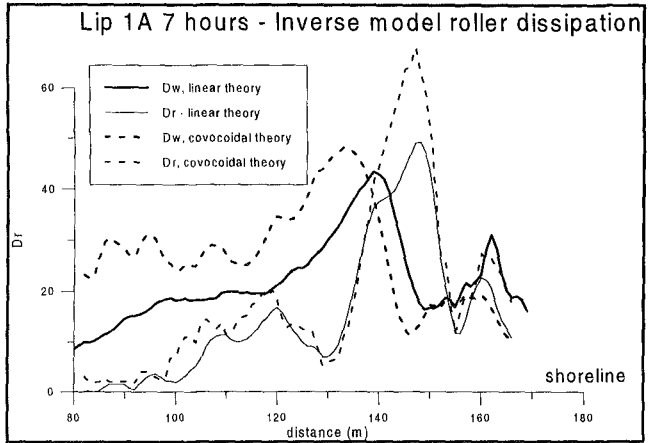


Figure 6 Cross-shore distributions of D_w and D_r under linear and covocoidal wave theories for Lip Test 1A

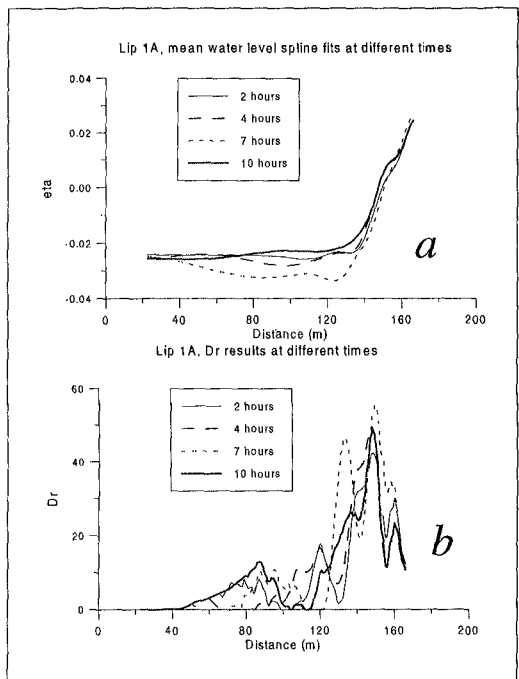


Figure 7 Sensitivity of the inverse modelling procedure to measured mean water levels

An extensive statistical analysis of waveflume experiments (Stive, 1983, Buhr Hansen and Svendsen, 1984, Arcilla et al, 1993) resulted in the following expression for β :

$$\beta = 0.1kh \frac{h - H}{H} \wedge < 0.1 \tag{17}$$

in which k is the wave number, H is the wave height, and h is the water depth.

In Figure 8a the inverse β and the approximation given by Equation 20 are compared for the Stive tests. It is clear from all tests that the proposed simple expression does give a surprising good result. Although β should be zero pre-breaking it also shown for that region so as to indicate the performance of the suggested expression. Even the location at which the dissipation of kinetic energy is initiated is well approximated for most of the tests as the minimum value of the proposed expression for β gives a reasonably accurate indication of this position. Figure 8b the performance of the proposed expression for beta is shown for a number of sets from LIP11D test 2B. Although the variation of the inverse modelled beta are considerable a distinct trend is visible which is represented reasonably by the proposed expression for beta.

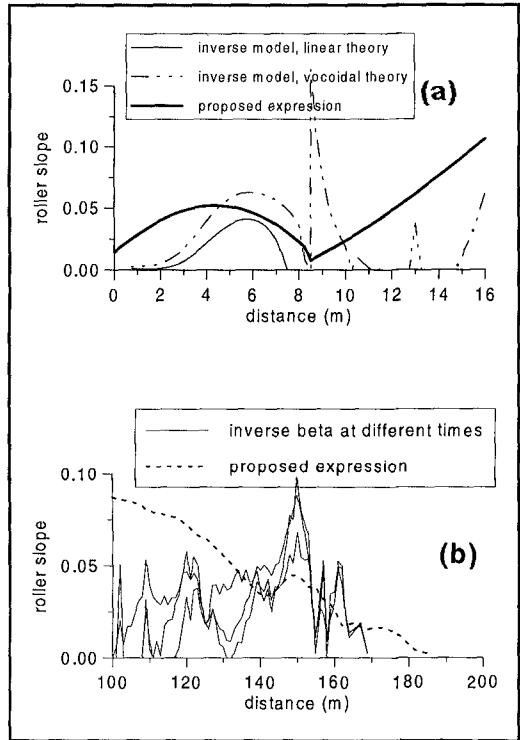


Figure 8 Inverse roller slope and slope expression for (a) Stive test 1 and (b) LIP 1A

Flow Properties

The predicted vertical distributions of TKE shown in Figure 8 are obtained by adjusting Dr so as to minimize the rms error between measurements and predictions. Although the model tends to demonstrate slightly more vertical variability than the measurements of Stive(1983) it is likely that the measurements in the upper part of the water column have been contaminated somewhat due to aeration associated with the breaking process.

Figure 9 depicts the optimal undertow fit for the same test case of Stive(1983). In this inverse modelling procedure both D_r and the wave induced mass flux contribution are adjusted independantly until the rms error is minimized. The precision of this exercise is limited however by the existence of measurements over only part of the depth.

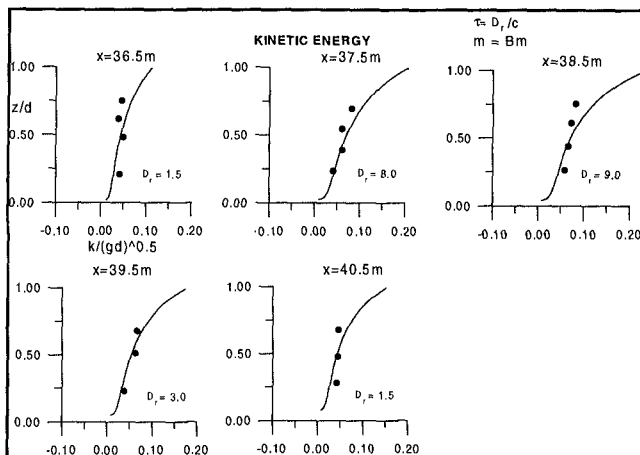


Figure 9 Predicted vertical distributions of TKE for Stive Case 1

As can be seen in Figure 10 the optimal correspondance between measurements and predictions for the LIP11D cases was in most cases very good, with rms errors generally less than 5%.

Intercomparisons

The inverse modelled D_r distributions using the integral approach have been found to differ markedly from those for D_w . Figure 11 compares estimates of D_r as determined by the integral approach and the inverse fits of TKE and undertow measurements for Stive Test 1.

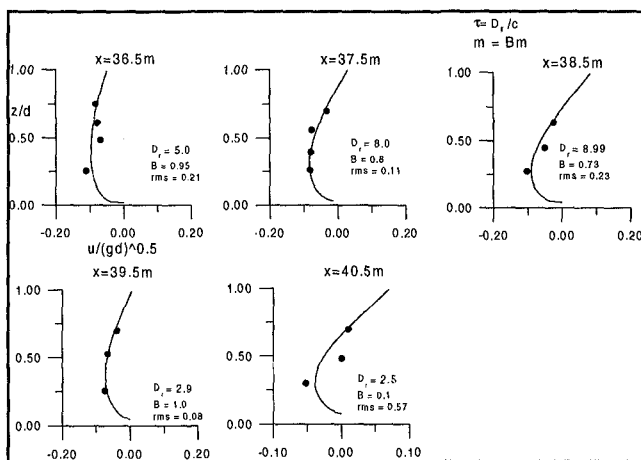


Figure 10 Optimal undertow fit for the Stive case 1

Both inverse approaches show a similar cross-shore distribution and suggest a peak in D_r some 3m landwards of the break point. As previously observed this lag has important implications for localizing the point of maxima for cross-shore and longshore currents and sediment suspension and transport.

Figure 12 compares Dw and inverse modelled Dr distributions for LIP(t=7hrs) case 1A. In general the independent inverse modelling approaches are in good correspondence, with a noticeable landwards shift in the position of Dr peaks relative to Dw. For the cases under consideration such shifts are far from negligible, generally exceeding 10m. Also plotted in Figure 12 are the predicted Dr distributions using both a constant and variable beta value. Although these distributions are in generally close accord to that found by inverse modelling, the lag effect is somewhat underestimated.

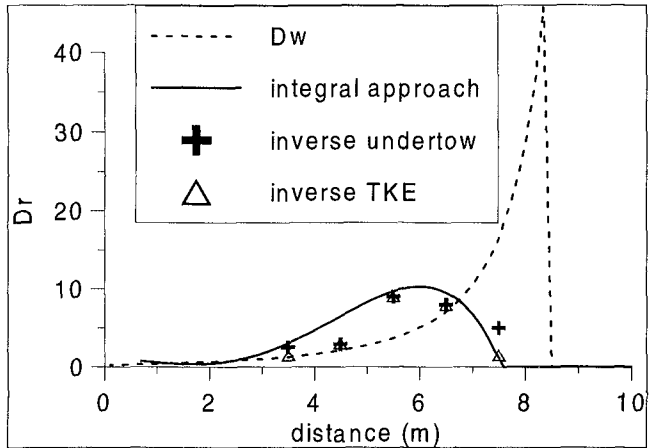


Figure 12 Estimates of Dr for Stive Test 1

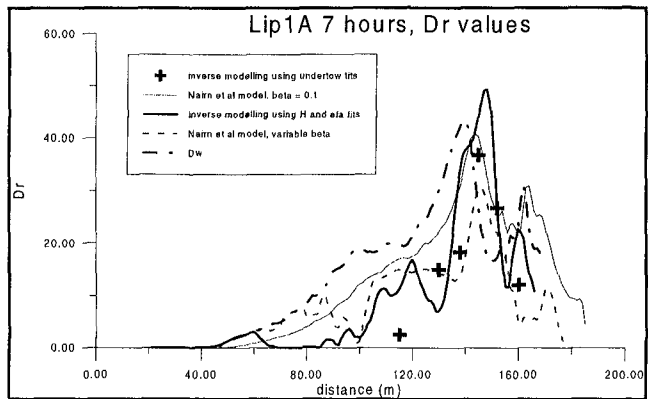


Figure 11 Comparison between Dw and inverse modelled Dr distributions for LIP(t=7hrs) case 1A

4. CONCLUSIONS

Due to the good agreement between both inverse modelling techniques a strong indication of the validity of both approaches and applied theories is obtained. The two independent inverse modelling techniques clearly indicate a landward shift of the maximum roller energy dissipation compared to the wave dissipation. This suggests that the apparent landwards shift for maxima of TKE, undertow and suspended sediment concentrations and consequently cross-shore and longshore sediment transport rates can only be obtained by accurately predicting the cross-shore distribution of wave heights and especially the mean waterlevel. Although the integral approach is sensitive to the accuracy of wave and water level measurements it can provide continuous cross-shore distributions of roller properties. Recent experiments

provide additional types of data such as the measurement of the roller slope (e.g. Boers, 1996) which can be used to verify the roller expressions proposed by Svendsen (e.g. area of the roller and slope of wave front) and improve the proposed expression for beta.

REFERENCES

- Arcilla, A.S., Roelvink, J.A., O'Connor, B.A., Reniers, A., Jiménez, J.A., 1994. The Delta flume '93 Experiment. *Proc. Coastal Dynamics Conf.*
- Battjes, J.A., Janssen, J.P.F.M., 1978. Energy loss and Setup due to breaking of random waves. *Proc. 16th Coastal Eng. Conf.*
- Bijker, E.W. 1974. Mass transport of gravity waves on a sloping bottom. *Proc. 14th Coastal Eng. Conf.*
- Boers, M., 1996. Simulation of a Surfzone with a Barred Beach. Report 1: Wave Heights and Wave Breaking. *Communications on Hydraulic and Geotechnical Engineering Report no 96-5*, Delft University of Technology.
- Buhr Hansen, J. and Svendsen, I.A., 1984. A theoretical and experimental study of undertow. *Proc. 19th Coastal Eng. Conf.*
- Dally, W.R. and Brown, C.A., 1995. A modelling investigation of the breaking wave roller with application to cross-shore currents. *J Geophys Res.*, 100, C12.
- Deigaard, R., 1993. A note on the three-dimensional shear stress distribution in a surf zone. *Coastal Eng.*, **20**, 157-171.
- Deigaard, R. and Fredsoe, J., 1989. Shear stress distribution in dissipative water waves. *Coastal Eng.*, **13**, 357-378.
- De Vriend, H.J. and Kitou, N., 1990. Incorporation of wave effects in a 3D hydrostatic mean current model, *Proc. 22nd Coastal Eng. Conf.*
- Le Mehauté, B., 1962. On non-saturated breakers and the wave run-up. *Proc. 8th Coastal Eng. Conf.*
- Mocke, G.P., Reniers, A., Smith, G.G., 1994. A surf zone parameter sensitivity analysis on LIP11D suspended sediment and return flow measurements. *Proc. Coastal Dynamics Conf.*
- Mocke, G.P., Smith, G.G., 1992. Wave breaker turbulence as a mechanism for sediment suspension, *Proc. 23rd Coastal Eng. Conf.*
- Nadaoko, K. and Kondoh, T. (1982). Laboratory Measurements of Velocity Field Structure in the Surf Zone by LDV. *Coastal Engineering in Japan*, **25**, 125-145.
- Nairn, R.B., Roelvink, J.A., Southgate, H.N., 1990. Transition zone width and implications for modelling surf zone dynamics. *Proc 22nd Coastal Eng. Conf.*
- Okayasu, A., 1989. Characteristics of turbulence structure and undertow in the surf zone. *Ph.D. thesis*, Yokohama Nat. Univ.
- Roelvink, J.A., 1993. Surface roller effect in a surfbeat model. *G8 Coastal Morphodynamics*, Grenoble Overall Workshop.
- Stive, M.J.F., De Vriend, H.J., 1994. Shear stresses and mean flow in shoaling and breaking waves. *Proc. 24th Coastal Eng. Conf.*
- Stive, M.J.F., 1983. Two dimensional breaking of waves on a beach. *Delft Hydraulics report M1585*.
- Svendsen, I.A. 1984. Mass flux and undertow in the surf zone. *Coastal Eng.*, **8**(4).

CHAPTER 95

Wave-Current Interaction in Inlets

Michael J. Briggs¹, Zeki Demirbilek¹, and Debra R. Green²

ABSTRACT

Laboratory experiments were conducted in a flume to study wave-current interaction at the entrance to an inlet. Regular and irregular waves were studied with and without ebb and flood currents. These data are being used to develop a parameterization of the wave breaking criterion in the presence of currents in inlets, provide guidance to the field on the effects of currents on waves, and improve the predictive capability of numerical models for enhancing navigation in inlets.

INTRODUCTION

The coastal zone involves interactions between winds, waves, currents, structures and sediment. To develop a sound coastal management plan for shoreline stabilization and protection near inlets and improve navigation safety, it is essential to have a better understanding of the complicated physics which occur between waves and currents in coastal waters. In the vicinity of tidal inlets and river mouths, currents can significantly modify wave amplitudes, form, and directions. Although wave-current interaction has been studied extensively, little design guidance exists for its effect on wave breaking.

In 1993 the U.S. Army Engineer Waterways Experiment Station's Coastal Engineering Research Center began a large research program entitled the Coastal Inlets Research Program (CIRP). One of the goals of this program is to better understand wave-current interaction in the vicinity of coastal inlets and to develop a wave model that will be an integral part of an Inlet Modeling System (IMS) for numerically modeling waves, currents, and sediment transport over relatively short temporal and spatial scales. Part of this effort involves conducting laboratory studies of wave-current interaction to develop an empirical wave

¹Research Hydraulic Engineer, Coastal and Hydraulics Laboratory, USAE Waterways Experiment Station, 3909 Halls Ferry Rd., Vicksburg, MS 39180-6199.

²Computer Specialist, Coastal and Hydraulics Laboratory, USAE Waterways Experiment Station, 3909 Halls Ferry Rd., Vicksburg, MS 39180-6199.

breaking criterion for waves in the presence of ebb and flood currents.

This paper presents an overview of a CIRP flume experiments and results from an initial analysis of some of the ebb current data. The first section gives a brief summary of some previous flume and basin experiments involving wave-current interaction. The next section gives a comprehensive description of the flume experiments including model setup, wavemaker, current system, instrumentation, and experimental program. The final section presents and discusses some of the preliminary analyses of the flume data for eight representative, wave-ebb current cases.

BACKGROUND

Sakai and Saeki (1984) measured the effect of opposing currents on wave height transformation over a 1:30 sloping beach for a range of wave periods and steepness. They found an increase in wave height and decay rate in the presence of the opposing current. Lai et al. (1989) conducted flume experiments on the kinematics of wave-current interactions for strong interactions with waves propagating with and against a current. They found the influence of the waves on the mean current profiles was small, although opposing waves would give a slightly lower current. They also observed a drastic change in the spectral shape, especially the higher harmonics, following wave breaking in the presence of opposing currents. Their experiments confirmed that blockage of waves by a current (when the wave group velocity equals the opposing current velocity) occurs when the ratio of depth-averaged current velocity to wave celerity without currents approaches 0.25.

Yucheng et al. (1991) and Yucheng and Guohai (1993) noted that breaker indices for finite water depth for regular and irregular waves in the presence of opposing currents can be classified by geometric, kinematic, and dynamic criteria. Typical geometric stability criteria include McCowan's critical crest angle $\beta = 120$ deg, Longuet-Higgin's limiting wave surface slope of about 30.4 deg, McCowan's wave breaking index $\kappa = 0.78$, Miche's limiting wave steepness value $H_b/L_b = 0.142 \tanh kh$, and Goda's limiting relative wave height H_b/h_b as a function of relative water depth h/L_0 and bottom slope m . The kinematic stability parameter is based on the concept that the horizontal water particle velocity u is equal to the wave celerity C at breaking. The dynamic stability criterion relates the vertical acceleration of the water particles in the crest at breaking to a limiting value. They found that the two geometric criteria of limiting wave steepness H_b/L_b and limiting relative wave height H_b/h_b are consistent and stable with values of $H_b/L_b = 0.129$ for irregular spilling breakers with and without currents on a gentle slope.

Briggs and Liu (1993) conducted laboratory experiments of the interaction of ebb currents with regular waves on a 1:30 beach and entrance channel. Good agreement was obtained between these data and numerical model predictions. They found little effect on wave period, but significant increases in wave height and nonlinearity. Raichlen (1993) conducted a laboratory investigation on the propagation of regular waves on an adverse three-dimensional jet. He found increases in incident wave height by a factor of two or more for ebb current to wave celerity (i.e., U/C) values as small as 10 percent.

Suh et al. (1994) developed an equation for the equilibrium-range spectrum of waves propagating on an opposing current in finite depth water. Comparison with experimental data agreed reasonably well with the change in high-frequency energy in the wave spectrum.

Klopman (1994) conducted a series of flume experiments to study flow kinematics of regular and irregular waves in the presence of ebb and flood currents. He found that waves opposing the current increase the horizontal velocity in the upper half of the water column and that this change depends mainly on wave energy and less on the shape of the wave spectrum.

EXPERIMENTAL DESIGN

Model Setup

A 1.5-m-wide, 1.5-m-deep, 64-m-long flume (Figure 1) was used to simulate a three-dimensional flow environment by partitioning the down-wave end of the flume with a temporary vertical wall into an 18-cm-wide, 7.2-m-long channel. Turbulence (due to the ebb currents transitioning from the full width of the flume into the narrower channel) was minimized by a 2.8-m-long, convex-shaped transition zone on the landward side of the channel. Water depth in the flat-bottomed flume was 50 cm. A 14.6-m-long glass window allowed observation in the study area.

The x-axis extended longitudinally down the centerline of the channel from the seaward end of the partition wall or channel entrance at $x=0$. The y-axis origin was at the channel centerline and extended laterally towards the wide part of the flume.

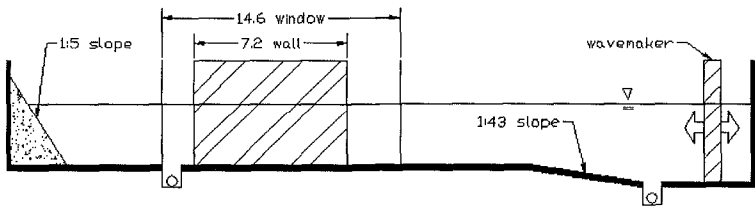


Figure 1. Layout of wave-current flume.

Wavemaker

The hydraulic wavemaker was located 39.6 m from the origin at the channel entrance. It has an 86 cm maximum stroke and is driven in translational motion (i.e., piston mode) by a Digital MicroVax minicomputer. It is submerged 46 cm lower than the floor of the flume, separated by a 20.4-m-long, 1:43 slope. Wave absorption was provided by a 1:5 rock beach on the back wall of the flume and a 1:6 rock beach and several rolls of horsehair on the seaward side of the channel partition.

Current System

Ebb and flood currents were generated with a circulation system consisting of two inflow/outflow boxes, a pump, a pipe manifold, flow meter, and return pipe. The inflow/outflow boxes were separated a distance of 48.1 m and located below floor level at each end of the flume. Each box had a total volume of 0.89 m^3 , measuring 1.07 m long, 1.37 m wide, and 0.61 m deep. A 20-cm-diameter manifold pipe was suspended across the width of the flume in each box to distribute the flow evenly while minimizing wave disturbance and

flow turbulence. Radial cuts extending ± 70 deg from the bottom of the pipe, rather than perforations, were used to increase the cross-sectional area of the manifold to reduce vertical flow velocities to less than 3 cm/s.

The pump and pipe manifold were located midway between the inflow/outflow boxes to minimize flow resistance. A Goulds horizontal split-case centrifugal pump, with a maximum discharge of 126 l/s, was at the center of the manifold. The manifold consisted of 25.4-cm-diameter PVC pipe and ball valves to reverse the flow from ebb to flood. Flow discharge was controlled by an electrically actuated butterfly valve and measured by a Dynasonics clamp-on ultrasonic transit time flowmeter. Typical accuracy of this meter is 1 percent. The return pipe on either side of the manifold was also 25.4-cm-diameter PVC pipe.

Instrumentation

Wave gages. Surface elevations were measured by twenty capacitance wave gages in a 10-m by 0.7-m measurement area, bounded by the channel centerline and the origin at the channel entrance. Eleven of the twenty gages were located along the channel centerline in Row 1. The remaining gages were located on two parallel cross-shore transects: six in Row 2 and three in Row 3. Gage spacing was 91 cm in the x-direction and 37 cm in the y-direction. These spacings corresponded to normalized channel widths of 5 x/w and 2 y/w , respectively, where w is the channel width. Table 1 lists gage locations and normalized distances.

Current meters. Seven acoustic Doppler current meters were used to calibrate ebb and flood currents and quantify the wave-current interaction effect. These current meters are manufactured by Sontek. The system consists of a measurement probe and stem, signal conditioning and processing modules, and a 486 PC.

Incident ebb current flows were measured by two meters positioned inside the channel along the centerline. The meter at the channel entrance was the primary meter, with the interior meter serving in a backup role. Because it was not physically possible to co-locate current meters and wave gages, they were positioned between wave gages along all three

Gage	x, m	y, m	x/w	y/w
W1	0.91	0	5	0
W2	1.83	0	10	0
W3	2.74	0	15	0
W4	3.66	0	20	0
W5	4.57	0	25	0
W6	5.49	0	30	0
W7	6.40	0	35	0
W8	7.32	0	40	0
W9	8.23	0	45	0
W10	9.14	0	50	0
W11	10.06	0	55	0
W12	1.83	0.37	10	2
W13	2.74	0.37	15	2
W14	3.66	0.37	20	2
W15	4.57	0.37	25	2
W16	5.49	0.37	30	2
W17	9.14	0.37	50	2
W18	2.74	0.73	15	4
W19	4.57	0.73	25	4
W20	5.49	0.73	30	4

transects: two on each of the first two transects and one on the third transect. Table 2 lists meter positions and normalized x/w and y/w distances.

Measurements were made at a depth equal to 0.4 times the depth from the bottom of the flume. This depth corresponds approximately (0.37 factor) to a logarithmic profile for the depth-averaged velocity. This depth was a compromise to ensure that the current meter remained submerged for all wave troughs while providing clearance for the largest wave crests.

Positive u - and v -velocities were oriented in the positive x - and y -axis directions, respectively. Five of the meters measured u -, v -, and w -velocities. However, only those in the horizontal plane were analyzed for this study.

Experimental Program

Wave and current conditions. A total of over 160 cases, representative of wave and current conditions in a typical inlet, were studied. Cases consisted of 12 irregular waves, 6 regular waves, 3 ebb current, 3 flood current, and 96 wave-current combinations. Only the irregular wave and ebb current results are presented in this paper. Table 3 lists corresponding model and prototype values for water depth, and wave and current parameters, based on a model-to-prototype scale of 1 to 20.

Wave calibration. The target frequency spectrum for the model waves was based on the Texel Marsden Arsloe (TMA) spectrum (Bouws et al. 1985). The TMA spectrum is a function of five parameters: peak frequency, Phillip's constant, peak enhancement factor, lower and upper spectral width parameters σ_1 and σ_u , and water depth h . Although identical to the JONSWAP spectrum in deep water, the TMA is modified by a depth-correction factor in shallow water. Peak enhancement factors of 2 and 10 were chosen to simulate sea and swell frequency spreading, respectively. Values of $\sigma_1=0.07$ and $\sigma_u=0.09$ were used for all irregular waves. The Phillip's

Meter	x , m	y , m	x/w	y/w
C1	-1.83	0.00	-10.0	0
C2	0.00	0.00	0.0	0
C3	2.29	0.00	12.5	0
C4	3.20	0.00	17.5	0
C5	2.29	0.37	12.5	2
C6	3.20	0.37	17.5	2
C7	3.66	0.73	20.0	4

Quantity	Model	Prototype
Water depth	50 cm	10 m
Wave Period	1.57 s	7 s
	2.24 s	10 s
	3.35 s	15 s
Wave Height	5 cm	1 m
	10 cm	2 m
	15 cm	3 m
Ebb Current	11.2 cm/s	0.5 m/s
	22.4 cm/s	1.0 m/s
	44.7 cm/s	2.0 m/s

Case	Target, cm	Gages 1-11, cm	% Dev	Gages 1-20, cm	% Dev
1	5	5.00	0.00	4.97	0.60
2	10	10.12	1.20	10.04	0.40
3	15	14.94	0.40	14.82	1.20
4	5	4.96	0.80	4.94	1.20
5	10	9.88	1.20	9.82	1.80
6	15	15.08	0.53	14.98	0.13
7	5	5.00	0.00	4.98	0.40
8	10	9.99	0.10	9.96	0.40
9	15	14.93	0.47	14.88	0.80
A	5	5.02	0.40	4.97	0.60
B	10	10.04	0.40	9.96	0.40
C	15	14.94	0.40	14.86	0.93

constant was calculated based on the target zero-moment wave height H_{m0} .

Control signal durations of 2,000 s were created for each wave case. Data were collected for 1,000 s at a sampling rate of 10 Hz after a waiting time of 60 s to allow the slowest traveling wave to reach the farthest wave gage (W1).

Single channel frequency spectral analysis was used for the data analysis. Data records of 1,000 s were zero-meaned, tapered by a 10% cosine bell window, Fourier transformed, and band averaged, yielding a frequency resolution of 0.05 Hz with 100 degrees of freedom. Values for H_{m0} were computed for all cases.

Two or three iterations were required for each wave case to obtain target values. In general, the agreement between measured and target wave period, wave height, and spectral shape was very good. Table 4 compares measured and target H_{m0} for the 12 irregular wave cases for the average of the 11 gages on the centerline and all 20 gages. The percent deviation between measured and target values is also listed. Overall agreement is excellent for all cases, with a maximum variation of 1.2 percent for the centerline gages and 1.8 percent for all gages.

Current calibration. Software on the PC allowed real-time observation of the current time series and magnitudes. Current data were also collected for 1,000 s, but at a sampling rate of 25 Hz.

Prior to sampling, water was circulated for approximately 30 min to allow the current to reach a steady-state condition. This time is equivalent to 3-5 cycles of the slowest current traveling between inflow/outflow boxes. Seeding was added to the water and mixed to improve the signal-to-noise ratio of the current meters to acceptable levels. Initial calibration of each current condition required an iterative procedure of adjusting the flow control valve and waiting to re-establish steady-state conditions before continuing. After successfully matching the target velocity, the settings of the valve were recorded for future runs.

A current-only case was run first each day. Then, the 12 wave-current combinations for that current were run sequentially with approximately 5 min between each run for the flume to reach steady-state conditions prior to the next run. At the end of each day, the current-only run was repeated as a check on the current stability. The current repeatability was very good during a day's runs.

RESULTS AND ANALYSES

In this section, discussions of the current distribution, current-modified wave parameters, wave amplification, and spectral evolution are presented for eight representative cases. These cases consist of two wave periods ($T=1.57$ and 2.24 s), two wave heights ($H=5$ and 15 cm), and two ebb currents ($U=11.2$ and 44.7 cm/s). They correspond to prototype wave and current conditions of $T=7$ and 10 s, $H=1$ and 3 m, and $U=0.5$ and 2.0 m/s, respectively. Only wave gage and current meter data from the channel centerline are considered in this paper.

Current Distribution

As the ebb current exits the channel it decreases in magnitude and spreads out laterally within the confines of the flume side walls. Figure 2 shows the measured ebb current along the channel centerline for each of the eight wave-current cases. The value for U is plotted versus normalized distance x/w (i.e., equivalent number of channel widths w) seaward of the channel entrance for the $T=1.57$ s cases in the top panel and $T=2.24$ s cases in the bottom panel. All current values are interpolated or extrapolated from the three current measurement locations on the channel centerline.

The stronger ebb currents are felt by the waves at a larger x/w distance from the channel entrance. At this distance, the wave celerity effectively overpowers the current and it

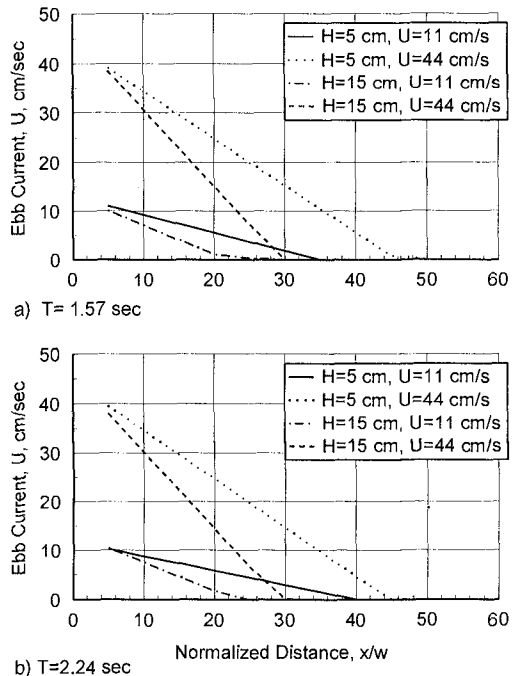


Figure 2. Current distribution.

vanishes. Waves with larger wave heights reduce the current closer to the mouth of the channel, effectively changing the current field.

Wave Parameters

Wave parameters are modified by the presence of a steady, uniform ebb current U . The apparent or absolute wave frequency σ_a and celerity C_a of the wave traveling on the current are reduced relative to their intrinsic or calm water values (i.e. σ_i and C_i) when an ebb current is not present. The wavelength L and wavenumber k remain fixed, however. These relationships are given by

$$\sigma_a = \sigma_i + kU \cos \theta \quad (1)$$

$$C_a = C_i - U \quad (2)$$

where θ = the angle between the direction of wave propagation and that of the ebb current, which is 180 deg in our case. Thus, the absolute wave period $T_a (=2\pi/\sigma_a)$ for waves on an ebb or opposing current is increased or stretched relative to the intrinsic period $T_i (=2\pi/\sigma_i)$. Also, the wave height H and wave steepness H/L are increased. Table 5 lists intrinsic values for the eight cases, based on linear wave theory. The first digit in the "Case" ID corresponds to the wave case from Table 4 and the second digit to the current magnitude.

The numerical wave model REFDIF, a combined refraction-diffraction, parabolic approximation model, was used for computing changes in wave parameters due to ebb and flood currents (Kirby and Dalrymple 1994). Using the flume geometry and measured current data, current-modified wave parameters were calculated with this model. Irregular waves

Case ID	T_i , s	H , cm	U , cm/s	C_i , cm/s	U/C_i	H/L
11	1.57	5	11.2	191	0.06	0.005
13			44.7		0.23	0.005
31	1.57	15	11.2		0.06	0.050
33			44.7		0.23	0.050
41	2.24	5	11.2	207	0.05	0.011
43			44.7		0.22	0.011
61	2.24	15	11.2		0.05	0.032
63			44.7		0.22	0.032

were modeled as equivalent regular waves corresponding to the peak period with $H_{rms} = H_{m0} / \sqrt{2}$.

The change in H/L as a function of U/C_n for each of the eight cases is shown in Figure 3. Values for H/L are calculated by dividing the measured wave height by the predicted wavelength from the REFDIF wave model. The U/C_n values correspond to the different gage locations along the channel centerline. Wave steepness increases by a factor of two for all the cases, and as much as an order of magnitude for case 11 (i.e., $T=1.57$ s, $H=5$ cm, $U=11.2$ cm/s).

Wave Amplification

Figure 4 shows wave amplification H/H_i versus normalized distance x/w for the eight cases. Measured wave height H was divided by incident wave height H_i for the wave-only condition at each location for each case to obtain values of H/H_i .

The largest amplification occurred for the $T=1.57$ s cases (top panel), and for the largest ebb current for both wave periods. Wave height increased by almost a factor of two for case 13 with the larger current. Maximum amplification was somewhat smaller for the $T=2.24$ s cases shown in the bottom panel, on the order of 1.5.

Spectral Transformation

As waves propagate toward the channel entrance, they are affected by the ebb current more strongly. This is manifested in the growth of the higher frequency components. The wave may initially experience gentle or occasional breaking due to blockage of these higher frequency waves, with correspondingly increased wave steepness. The higher frequency components are reduced relative to those previously present. The total energy in the spectrum, however, does not decrease appreciably. According to Lai et al. (1989), the peak frequency may be Doppler shifted to a lower value. Suh et al. (1994), however, did not observe this phenomenon in their experiments.

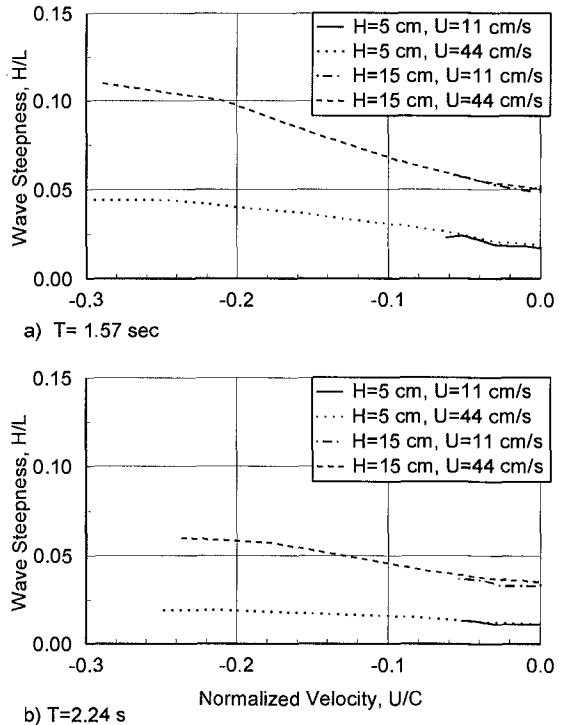


Figure 3. Current effect on wave steepness

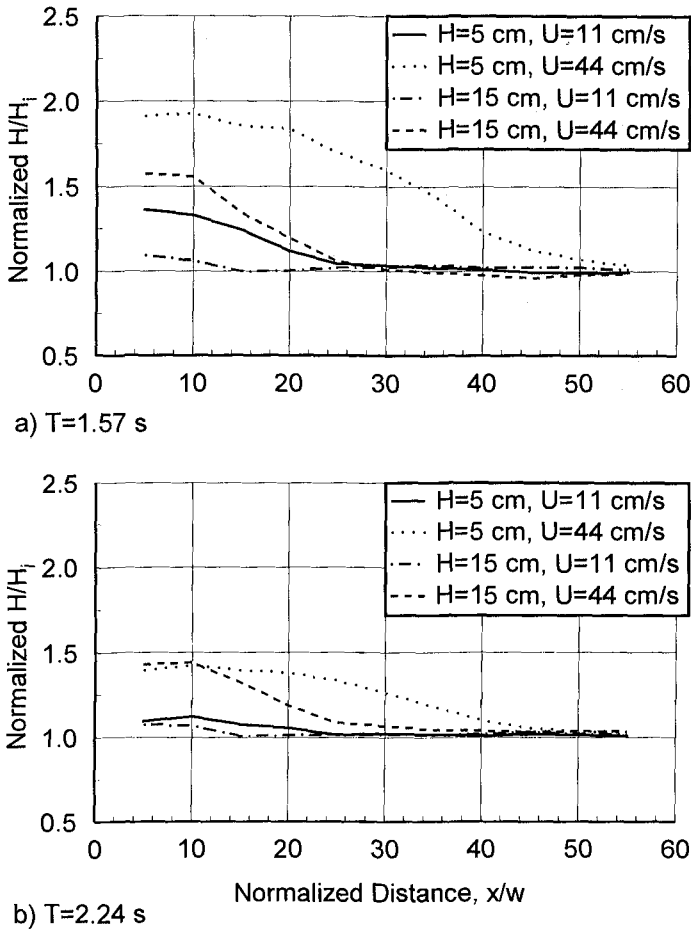


Figure 4. Wave amplification effect.

In a severe breaking environment, however, the spectral shape may change appreciably. The higher frequency components of the spectrum are often completely blocked, resulting in violent breaking and drastic change in the spectral shape. The high-frequency half of the spectrum above the spectral peak may be reduced an order of magnitude relative to its wave-only condition. The peak frequency may be reduced as well.

Figures 5 and 6 are semi-log plots of the measured frequency spectra for wave-only and wave-current conditions for wave periods of $T=1.57$ and $T=2.24$ s, respectively. Gage positions 1 through 6 are shown for x/w equivalent to (a) 5, (b) 10, (c) 15, (d) 20, (e) 25, and (f) 30. The incident wave height is $H=15$ cm in all plots. In each plot, the dotted line corresponds to the wave-only condition at $x/w=55$ (i.e., gage 11), the solid line to the wave-current condition with $U=11.2$ cm/s current, and the dot-dash line to the $U=44.7$ cm/s case.

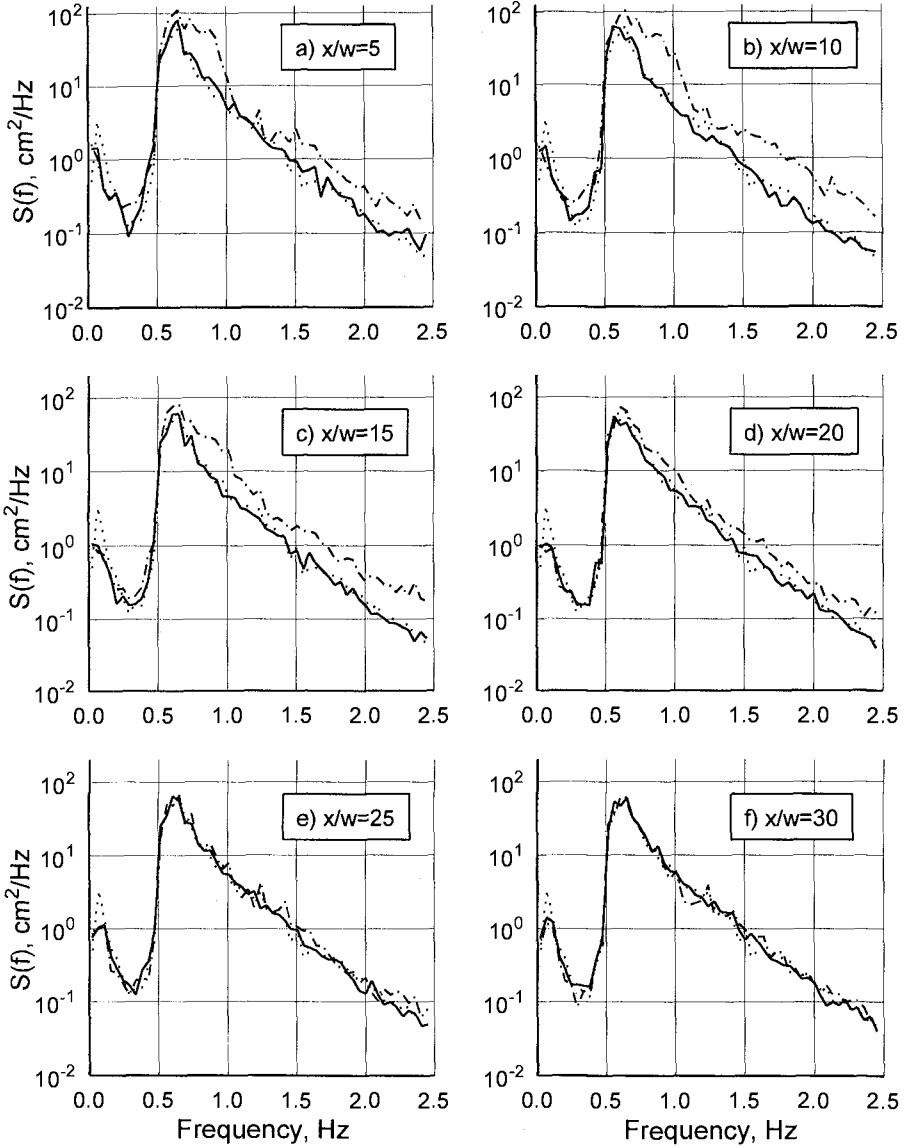


Figure 5. Spectral evolution for $T=1.57$ s, $H=15$ cm cases for $x/w=5$ to 30. Dotted line is wave-only, solid line is $U=11$ cm/s, and dot-dash line is $U=44$ cm/s.

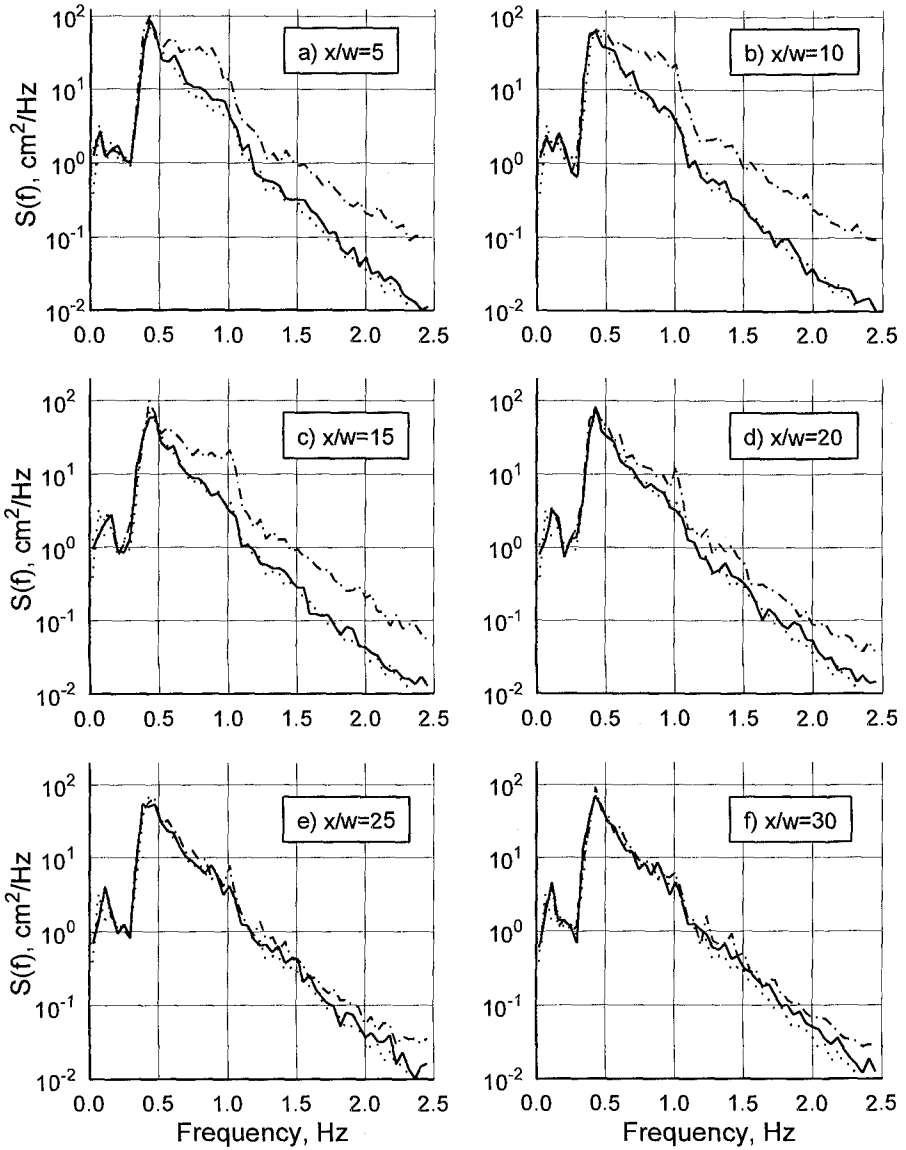


Figure 6. Spectral evolution for $T=2.24$ s, $H=15$ cm cases for $x/w=5$ to 30. Dotted line is wave-only, solid line is $U=11$ cm/s, and dot-dash line is $U=44$ cm/s.

For the $T=1.57$ s cases, the $U=11.2$ cm/s ebb current has little effect on the spectral shape. The wave celerity is much stronger than the current velocity, on the order of $U/C_a=-0.06$ (see Table 5 and Figure 3). The larger current ($U/C_a=-0.23$), however, does have an effect on this wave. Initially, there is little effect, but at $x/w=20$ the higher frequency components increase, reaching a maximum at $x/w=10$. Gentle breaking then occurs between $x/w=5$ and 10, as evidenced by the decrease in the higher frequency components. This is in agreement with the H/L and U/C_a values predicted by the numerical model and the observations of Lai et al. (1989) that the wave blockage limit is approximately $U/C_a \leq -0.25$. There does not appear to be any obvious frequency shifting in the peak frequency, however.

For the $T=2.24$ s cases, again there is no significant effect of the current on the wave spectrum. The U/C_a ratio is on the same order as before. The larger current $U=44.7$ cm/s case causes a growth of higher frequency components, much like the previous case. The decrease in this frequency range is less than before with the most significant decrease occurring between 1.25 and 1.50 Hz. Occasional breaking was observed in this case between $x/w=5$ and $x/w=15$.

These increases in the higher-frequency components of the wave spectra are much like what was observed by Briggs and Smith (1990) and Smith and Vincent (1992) due to shoaling alone. The ebb current appears to enhance this nonlinear growth of the higher harmonics.

CONCLUSIONS

Laboratory experiments were conducted in a flume to study wave-current interaction at the entrance to an inlet. Regular and irregular waves were studied with and without ebb and flood currents. This paper presents an overview of the experiments and results from an initial analysis of some of the ebb current data. Gentle or occasional wave breaking was observed in the larger wave height cases. A numerical wave model was used to predict the effect of the current on the wave parameters. The agreement with these predictions and model measurements with previous experiments was very good. Ebb currents tend to enhance the nonlinear growth of higher-harmonic components, much like shoaling on a beach. Additional research with this data is in progress to develop a current-induced wave breaking criterion, provide guidance to the field on the effects of currents on waves, and improve the predictive capability of numerical models for enhancing navigation in inlets.

ACKNOWLEDGMENTS

The authors wish to acknowledge Headquarters, U.S. Army Corps of Engineers, for authorizing publication of this paper. It was prepared as part of the "Modeling Waves at Inlets" work unit in the Coastal Inlets Research Program. We would like to thank Messrs. Dave Dailey, Jeremy Mucha, and John Evans for their help during this project.

REFERENCES

- Bouws, E, Gunther, H, Rosenthal, W, and Vincent, C (1985). "Similarity of the Wind Wave Spectrum in Finite Depth Water," *J Geophys Res*, Vol 90, No C1, pp 975-986.
- Briggs, MJ, and Smith, JM (1990). "The Effect of Wave Directionality on Nearshore Waves," *Proc 22nd ICCE Conference*, Delft, The Netherlands, 2-6 Jul, pp 267-280.

Briggs, MJ, and Liu, PLF (1993). "Experimental Study of Monochromatic Wave-Ebb Current Interaction," *Proc Waves '93 Conference*, New Orleans, LA, Jul, pp 474-488.

Kirby, JT, and Dalrymple, RA (1994). "Combined Refraction/Diffraction Model REFDIF 1," *CACR Report No. 94-22*, Cntr for Appl Coastal Res, Univ Delaware, pp 77.

Klopman, G (1994). "Vertical Structure of the Flow Due to Waves and Currents," *Progress Report H 840.30, Part II*, Delft Hydraulics, The Netherlands, Feb, pp 1-38.

Lai, RJ, Long, SR, and Huang, NE (1989). "Laboratory Studies of Wave-Current Interaction: Kinematics of the Strong Interaction," *J Geophysical Research*, Vol 94, No C11, November, pp 16,201-16,214.

Raichlen, F (1993). "Waves Propagating on an Adverse Jet," *Proc Waves '93 Conference*, New Orleans, LA, Jul, pp 657-670.

Sakai, S, and Saeki, H (1984). "Effects of Opposing Current on Wave Transformation on a Sloping Bed," *Proc 19th Conf. on Coastal Engineering*, ASCE, Vol 1, pp 1132-1148.

Smith, JM, and Vincent, CL (1992). "Shoaling and Decay of Two Wave Trains on Beach," *J Waterway, Port, Coastal, and Ocean Engineering*, ASCE, Vol 118, No 5, Sep/Oct, pp 517-533.

Suh, KD, Kim, YY, and Lee, DY (1994). "Equilibrium Range Spectrum of Waves Propagating on Currents," *J Waterway, Port, Coastal, and Ocean Engineering*, ASCE, Vol 120, No 5, Sep/Oct, pp 434-450.

Yucheng, L., Guohai, D., and Bin, T. (1991). "Wave Breaker Indices in Finite Water Depth," *China Ocean Engineering*, Vol 5, No 1, pp 51-64.

Yucheng, L. and Guohai, D. (1993). "Wave Breaking Phenomena of Irregular Waves Combined with Opposing Current," *China Ocean Engineering*, Vol 7, No 2, pp 197-206.

CHAPTER 96

Wave Climate of Large Reservoirs and a Revised Wave Hindcast Formula

Pierre Dupuis¹, Jean-Pierre Tournier¹, Octave Caron²

Abstract

Since impounding of the various reservoirs of the La Grande Complex in northern Québec, the riprap of several dams and dykes has suffered some damage during the fifteen-year period that followed. A mandate was given to the Société d'énergie de la Baie James (SEBJ) in January 1992 to review the riprap design and evaluate the necessary repairs. This paper focuses on the revaluation of the design wave with revised wave hindcast formulas based on the large amount of wind and wave data collected.

Introduction

Damage was observed to the riprap of some of the 215 embankment dams and dykes during the fifteen years since impoundment for the various reservoirs of the La Grande Hydroelectric Complex in northern Quebec. In January 1992, La Société d'énergie de la Baie James (SEBJ) was mandated by Hydro-Québec to review the riprap design and performance and to evaluate the necessary repairs. To fulfill its mandate, SEBJ conducted extensive field studies, including wind and wave measurements from four reservoirs and large scale model testing of repair schemes with irregular waves. Model testing is described by Mansard et al. (1996) while riprap repairs and design are presented by Tournier et al. (1996).

Wind and Wave Data Acquisition

Extensive field measurements were made from 1992 to 1995 (SEBJ, 1996a) to establish the wave climate on four large reservoirs of the La Grande Complex that are located within the area delimited by 52 to 55°N of latitude and 67 to 79°W of longitude (figure 1). Wind speed and direction, wind gust and air temperature were monitored continuously and logged every five minutes at three nearby airports and six small islands on the reservoirs by Aanderaa weather stations.

¹ La Société d'Énergie de la Baie James, 500 Boul. René-Lévesque Ouest, Montréal, Québec, Canada, H2Z 1Z9

² Hydro-Québec, 800 Boul. De Maisonneuve Est, Montréal, Québec, Canada, H2L 4M8

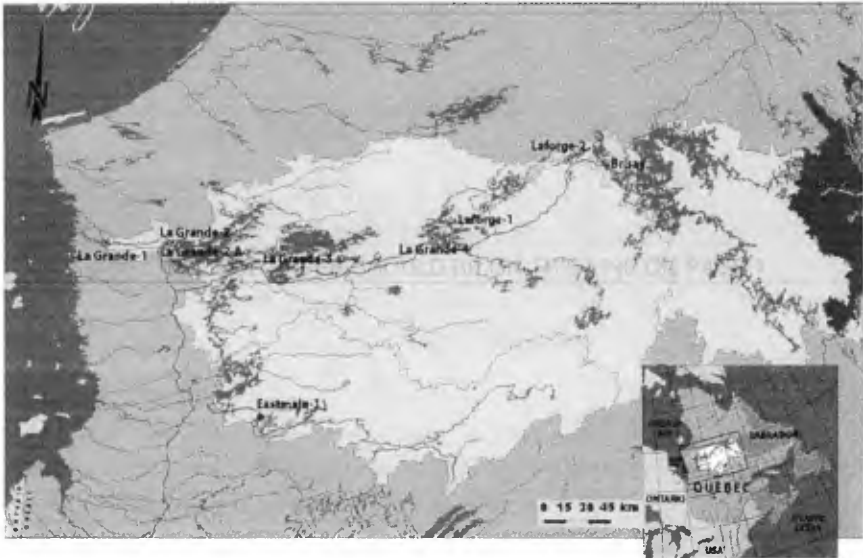


Figure 1. La Grande Hydroelectric Complex

WaveTrack buoys (0,9m diameter sphere) recorded wave trains for 17 minutes at the start of every hour at a sampling frequency of 2 Hz (figure 2). Raw data from the buoy accelerometer and tilt sensors were sent ashore via telemetry to a computer and archived for later processing. Over the four years, 9 different wave sites were monitored. In all, over 38 000 wave records were obtained for the ice free period that lasts from mid-June to the end of October.

This paper focuses on the dyke TA-13 mooring site, in the northern part of the LG-3 reservoir, for which over 9000 records cover all four years and where the most energetic episodes were recorded ($H_{mo} = 2,4$ m in September, 1992). The buoy was moored a few kilometers south of the dyke in order to monitor various fetch length conditions. A weather station was erected nearby on a flat island to record the overwater wind. The wave acceleration record values are processed in the frequency domain to yield the significant wave height (H_{mo}) and the mean period (T_{02}), as defined in IAHR/PIANC (1986). They form the basic set of variables used in further analysis. This is acceptable since evaluation of wave height ratios (figure 3) indicate good agreement with the



Figure 2 WaveTrack buoy

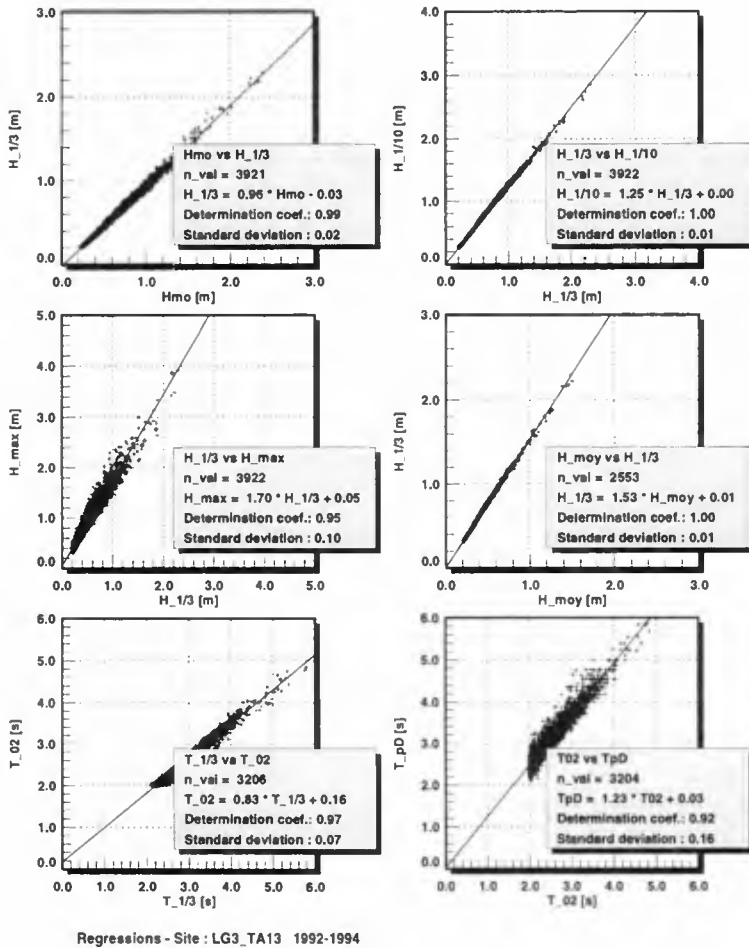
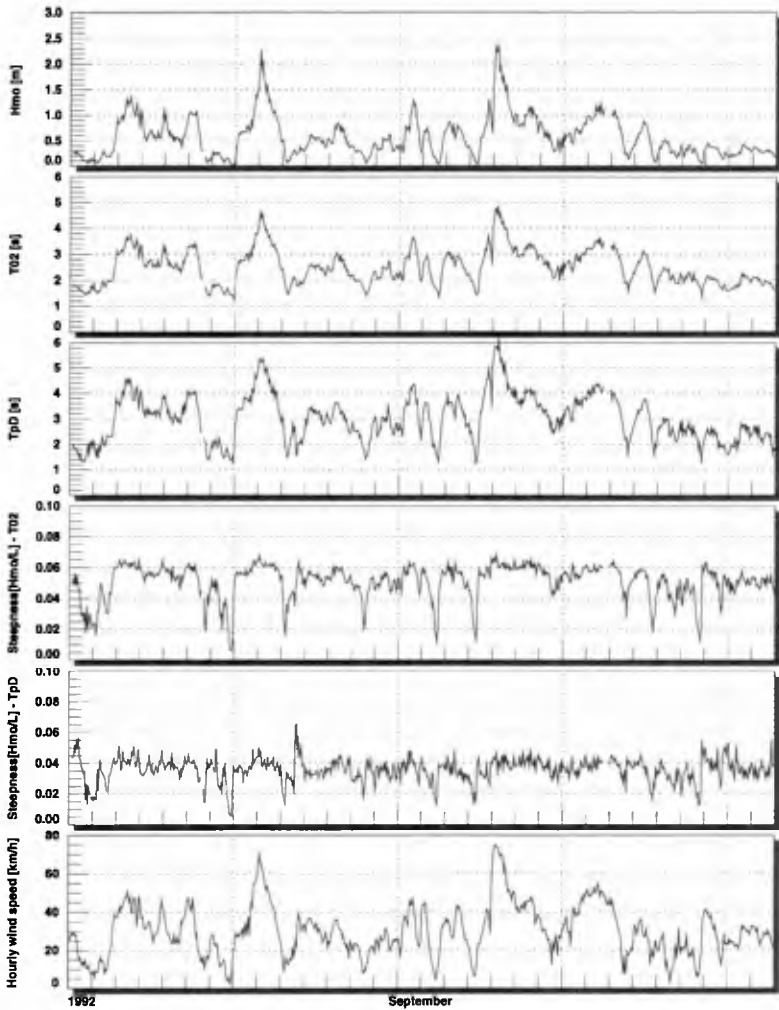


Figure 3. Wave parameter ratios for site TA-13.

Rayleigh distribution. These results are satisfactory for design purposes.

As shown on figure 4, similarity between wind speed and wave height response signals is evident, and similar results are obtained for all sites. This is indicative of the quick response of the body of water to the wind input. It can be noted that the wave steepness attains a limiting value in the vicinity of 0,06 for quite different wave conditions when T_{02} is used. This indicates that the wave energy growth or decay, due to the wind is such that the ratio of wave height to wave length remains the same, when limiting conditions exists. This is very important since it will be used in determining the correct set of values for the various dimensional parameters.



Wave data - La Grande 3 reservoir - Digue TA13
 Wind data - La Grande 3 reservoir - Ile TA13
 Campaign of - September 1992

Figure 4. Typical measurements

Dimensional analysis

Based on dimensional considerations, Bretschneider (1965) derives these relations:

$$\frac{gH}{U^2} = \psi_1 \left[\frac{gF}{U^2}, \frac{gt}{U} \right] \quad [1]$$

$$\frac{C}{U} = \psi_2 \left[\frac{gF}{U^2}, \frac{gt}{U} \right] \text{ or equivalently } \frac{gT}{U} = \psi_3 \left[\frac{gF}{U^2}, \frac{gt}{U} \right] \quad [2]$$

With H the wave height, T the period, F the fetch length, U the wind speed and t the duration. ψ_1 and ψ_2 are functional relations that must be determined using wave data. Different editions of the Shore Protection Manual (CERC, 1977, 1984), noted SPM77 and SPM84, suggest the following:

SPM 77	$\frac{gH}{U^2} = 0,00354 \left(\frac{gF}{U^2} \right)^{0,42}$	$\frac{gT}{U} = 0,581 \left(\frac{gF}{U^2} \right)^{0,25}$	[3]
SPM 84	$\frac{gH}{U_a^2} = 0,00160 \left(\frac{gF}{U_a^2} \right)^{0,50}$	$\frac{gT}{U_a} = 0,286 \left(\frac{gF}{U_a^2} \right)^{0,333}$	[4]

where the hyperbolic functions found in the SPM84 are linearized in order to help to compare values from both editions and U_a is the wind stress factor as defined in SPM84. Use of these formulas, however, results in poor hindcast, with over prediction of small wave heights and under prediction of large wave height events, when compared with measured waves in the La Grande Complex reservoirs. An in depth analysis was undertaken to eventually correct the formulas, with the objective being to accurately hindcast the wave hourly time series with locally measured wind data. The general form of the above equations is:

$$\frac{gH}{U_a^2} = \alpha_H \left(\frac{gF}{U_a^2} \right)^{\beta_H} \quad \frac{gT}{U_a} = \alpha_T \left(\frac{gF}{U_a^2} \right)^{\beta_T} \quad [5]$$

with a power law assumed valid and therefore linear regression in the log-log domain of the dimensional variables yields the coefficient and exponent values for these equations. Duration is considered by establishing the celerity of the wave group in deep water, as follows:

$$\frac{C_g}{U_a} = \frac{1}{2} \left[\frac{\alpha_T}{2\pi} \left(\frac{gF}{U_a^2} \right)^{\beta_T} \right] \Rightarrow C_g = \frac{\alpha_T}{4\pi} g^{\beta_T} U_a^{1-2\beta_T} F^{1-\beta_T} \quad [6]$$

$$\int_0^t dt = \int_0^F \frac{dF}{C_g} = \frac{4\pi}{\alpha_T g^{\beta_T} U_a^{1-2\beta_T}} \int_0^F \frac{dF}{F^{\beta_T}} \quad [7]$$

$$\frac{gt}{U_a} = \frac{4\pi}{\alpha_T} \left(\frac{1}{1-\beta_T} \right) \left(\frac{gF}{U_a^2} \right)^{1-\beta_T} \quad [8]$$

Note that equation 8 is defined when α_T and β_T are found.

Regression analysis is performed as an iterative process (figures 5a and 5b) which starts by first specifying starting values for α and β in equation [5]. Equation [8] is then evaluated. Hourly time series are used and time duration is considered to evaluate the dimensional variables. Duration seldom extends beyond 3 hours due to the reservoir size and then only for mild wind states. Only peaks of events are retained when performing the regression. Results give a new set of coefficients and exponent values that affect the relation between duration and fetch length (equation 8). This iterative process converges to specific values of α and β . In parallel with this approach, multivariate analysis is performed to check the validity of the dimensional relations above. By expressing [5] in terms of H , one gets a relation in the form of [9] for which there is an additional constraint on exponent c which must equal: 2-2b.

Multivariate analysis performed on the data set gives exponent values for F and U that do not obey the above constraint (SEBJ, 1996b). In fact exponent "c" of U is found to be 1,21 for the dike TA-13 data set, which is quite close to the wind stress factor exponent (equation 10) given in SPM84. Based on this finding, all subsequent analyses are made with this wind stress factor:

$$H = \alpha_H g^{\beta_H - 1} F^{\beta_H} U^{2-2\beta_H} = aF^b U^c \tag{9}$$

$$U_a = 0,71 U^{1,23} \tag{10}$$

The fact that the wave steepness has a limiting value found to be in the vicinity of 0,06 for different fetch lengths and wind speed, implies that the exponent β_H must be twice the value of the exponent β_T .

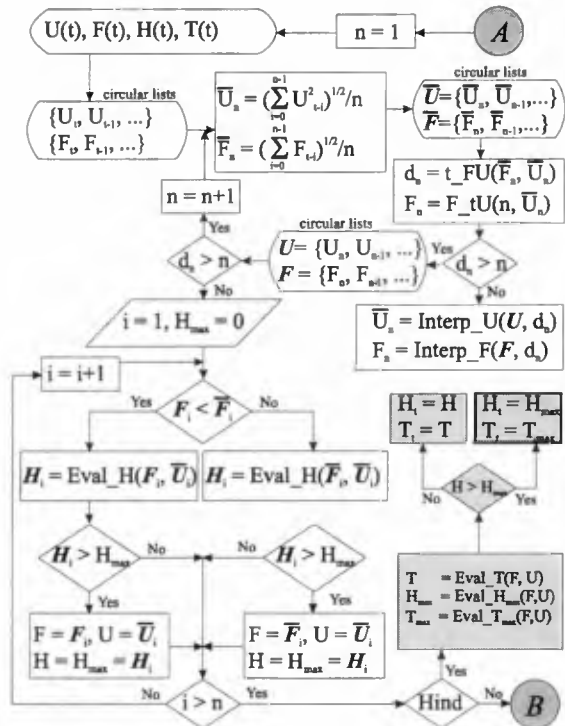


Figure 5a. Flowchart for dimensional analysis

$$S = \frac{H}{L} = \frac{H}{\left(\frac{gT^2}{2\pi}\right)} = \frac{H}{\frac{1}{2\pi} \left[\frac{gT}{U_a}\right]^2} = \frac{2\pi\alpha_H \left(\frac{gF}{U_a^2}\right)^{\beta_H}}{a_T^2 \left(\frac{gF}{U_a^2}\right)^{2\beta_T}} \Rightarrow \frac{2\pi\alpha_H}{\alpha_T^2} \quad \text{if } \beta_H = 2\beta_T \quad [11]$$

This comes, from the definition for wave steepness(see equation 11) , that for S to be constant, F has to vanish, meaning $\beta_H = 2\beta_T$. The maximum wave steepness attainable is found to be theoretically equal to $2\pi\alpha_H / \alpha_T^2$.

Dimensional analysis of site TA-13 data

Analysis is performed with a data set of over 9000 hourly values measured at the TA-13 mooring site. Figure 6 illustrates the body of water (in gray) along with the fetch evaluated following three different approaches (SPM77, SPM84 and the one proposed herein). Testing of different sector apertures were conducted (from 20 to 180 degrees), along with different weighting schemes (\cos^2 , \cos , unity). The use of a 180 degree sector with a \cos^2 weighting scheme, which is a Saville like fetch function, gave the best results for both regular and irregular shoreline cases. The fetch function is defined by the following equation:

$$F(\theta) = \frac{\sum_{\gamma=-90}^{90} R(\theta + \gamma) \cos^2(\gamma)}{\sum_{\gamma=-90}^{90} \cos(\gamma)} \quad [12]$$

- with $R(\theta)$ Length of radial of heading θ [m]
- $F(\theta)$ Length of fetch of heading θ . [m]
- γ Angle formed by the radial and the central radial of the sector. [°]

A wave height of 0,5 m is chosen, as a lower threshold, in order to eliminate the influence of the buoy on the measurement of small waves. Analysis is first

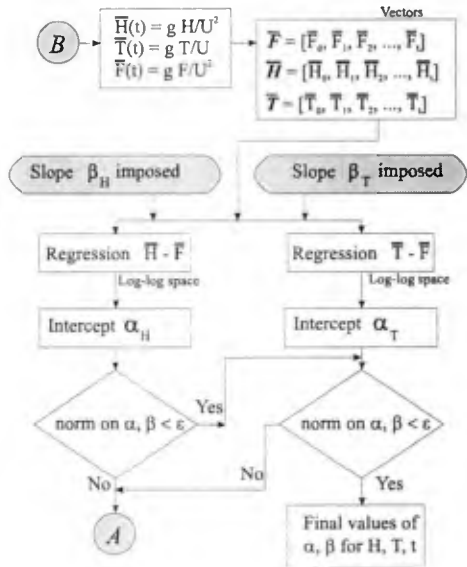


Figure 5b. Flowchart for dimensional analysis

The fetch function is defined by the following equation:

performed according to the procedures given in SPM77 and SPM84 (Table 1). The slope (m_H, m_T) and intercept values (b_H, b_T) of the scatter graph of predicted values against measured values are also listed (figure 7). For the SPM77, the wind speed U is used. When the exponents are forced to the values proposed in the SPM, the difference in α_H are insignificant when compared to equations 3 and 4. This indicates that the wave climate of the reservoir is a short crested wave regime, no different then elsewhere, except for the mean period which is lower.

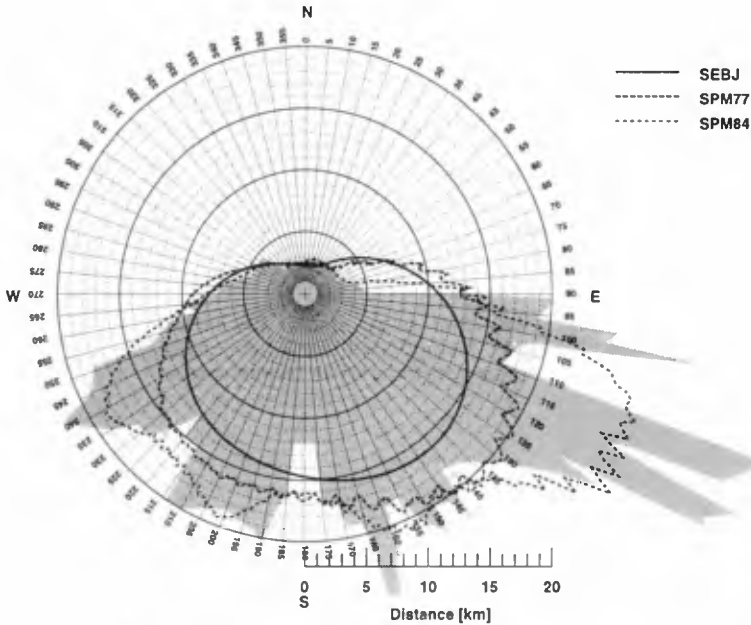
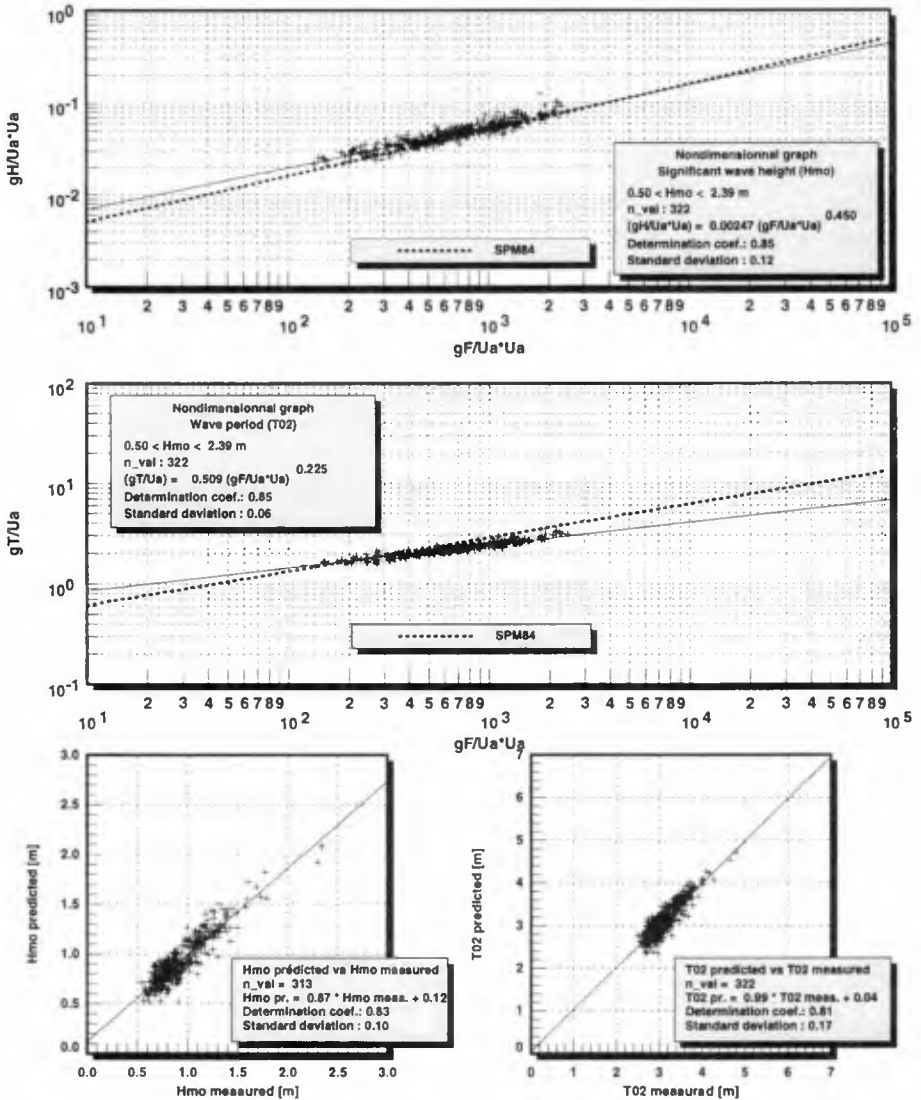


Figure 6. Fetch evaluation at mooring site TA-13

Table 1. Dimensional analysis results from dyke TA-13 data

Method	β_H	β_T	α_H	α_T	m_H	b_H	m_T	b_T
SPM77	0,42 ¹	0,25 ¹	0,00363	0,462	0,73	0,24	0,78	0,7
SPM84	0,50 ¹	0,33 ¹	0,00161	0,240	0,84	0,16	0,78	0,7
SPM77	0,369	0,214	0,00521	0,602	0,79	0,19	0,90	0,3
SPM84	0,374	0,187	0,00374	0,628	1,02	-0,01	1,14	-0,42
SEBJ	0,45 ¹	0,225 ¹	0,00247	0,509	0,87	0,12	0,99	0,04
SEBJ	0,467	0,238	0,00225	0,467	0,85	0,14	0,95	0,15

¹ Exponent value forced



Nondimensionnel graph - Digue TA13 (LG3)
Method SEBJ - Fetch : from 0 to 40 km - With correction for duration
Exponents of H and T forced and Ua = 0.71 U^{1.23}

Figure 7. Example of dimensional analysis for mooring site TA-13

When exponents are let free to adjust, results are quite different, with lower values for the exponent and higher values for the coefficient. The maximum wave steepness, according to equation 11, are 0,084 and 0,074 respectively, which is high. The slopes from the scatter graphs indicate a tendency to under evaluate large

wave episodes and over evaluate small wave episodes. Results from the analysis of dyke TA-13 yield exponent values of 0,467 and 0,238 respectively for which the ratio of exponent is near 1,96. The resulting wave steepness is found to be 0,065 which is a bit high but acceptable when compared with the values ranging from [0,06-0,065] obtained from measured data (figure 4). Since use of a common variable (U_a) raised to a given power can have adverse effects on the quality of the regression (Kenney, 1993), the right set of parameters is chosen from a subset of results obtained by imposing the regression slope. Table 2 shows the results obtained, when the analysis is performed for different values of β_H imposed with the constraint that β_H is twice the value of β_T . In fact, by forcing the exponent to a given value, better prediction is obtained for H_{mo} when β_H is in the range [0,40-0,45] as it is shown on figure 8.

Table 2. Dimensional analysis results from dyke TA-13 data - β forced

β_H	β_T	α_H	α_T	m_H	b_H	m_T	b_T
0,40	0,200	0,00341	0,598	0,94	0,06	1,05	-0,17
0,43	0,215	0,00281	0,543	0,90	0,10	1,02	-0,04
0,45	0,225	0,00247	0,509	0,87	0,12	0,99	0,04
0,47	0,235	0,00217	0,477	0,84	0,14	0,96	0,12
0,50	0,250	0,00179	0,433	0,80	0,18	0,92	0,17

SEBJ uses exponents of 0,45 and 0,225 which yield good prediction for waves in the range of the large measured wave episodes for both regular and irregular shorelines. The maximum wave steepness value is 0,06 which is the expected value.

Hindcast procedure

Hindcast follows the same process used for dimensional analysis and shown in figure 5a, to evaluate wave height and period for a given hour. Figure 8 illustrates how hindcasted waves from overwater wind compare with measured waves at the buoy site. Both hindcasted and measured signals appear in the upper left. Shown in the upper right is the scatter graph and in the lower right is the ratio between computed and measured values as a function of direction. A perfect fit would mean that all values should lie on the unit circle. During the first year of measurements, influence of trees located in a particular sector of the island, at a greater distance than the recommended 10 times the height of the taller obstacle, was obvious, as the ratio went up. It is thus very important to locate wind stations far away from any obstacles, on flat land. Much of the scatter can be explained by time lag between signals due to the fast response of the water surface to quick change in wind state or to rapidly varying fetch length. This is one of the reason why a fetch defined by a large sector give a better results for a large variety of reservoir shoreline geometry. Notice that some short extreme wave episodes can be missed since the mean hourly wind speed is used and that the significant wave height value can change by more

than 10% within an hour. Any event that lasts is fairly well reproduced. All hourly values are retained for regression in the scatter graph, which was not the case in dimensional analysis, where only peak values were considered. Hindcast at eight other sites gives similar results.

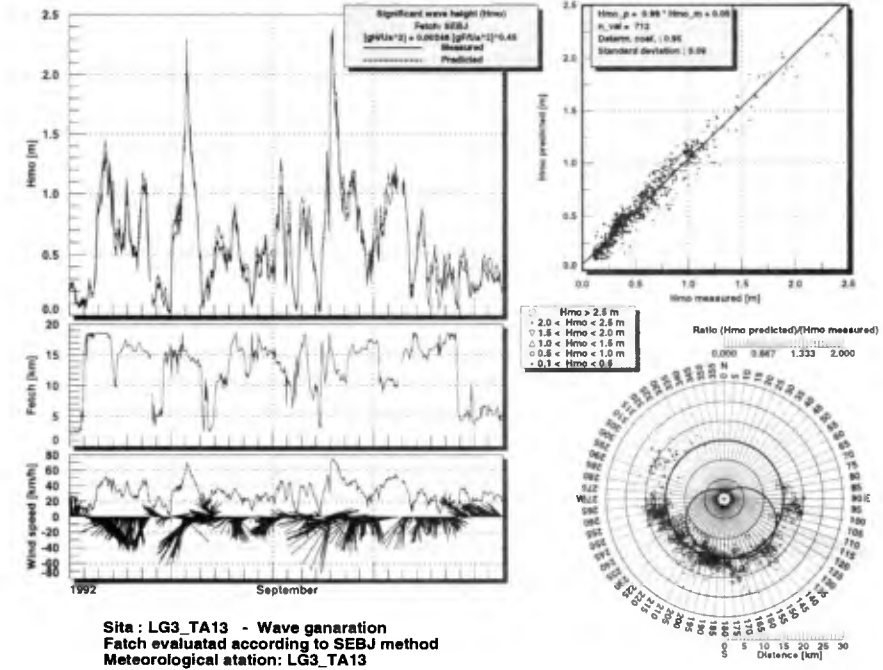


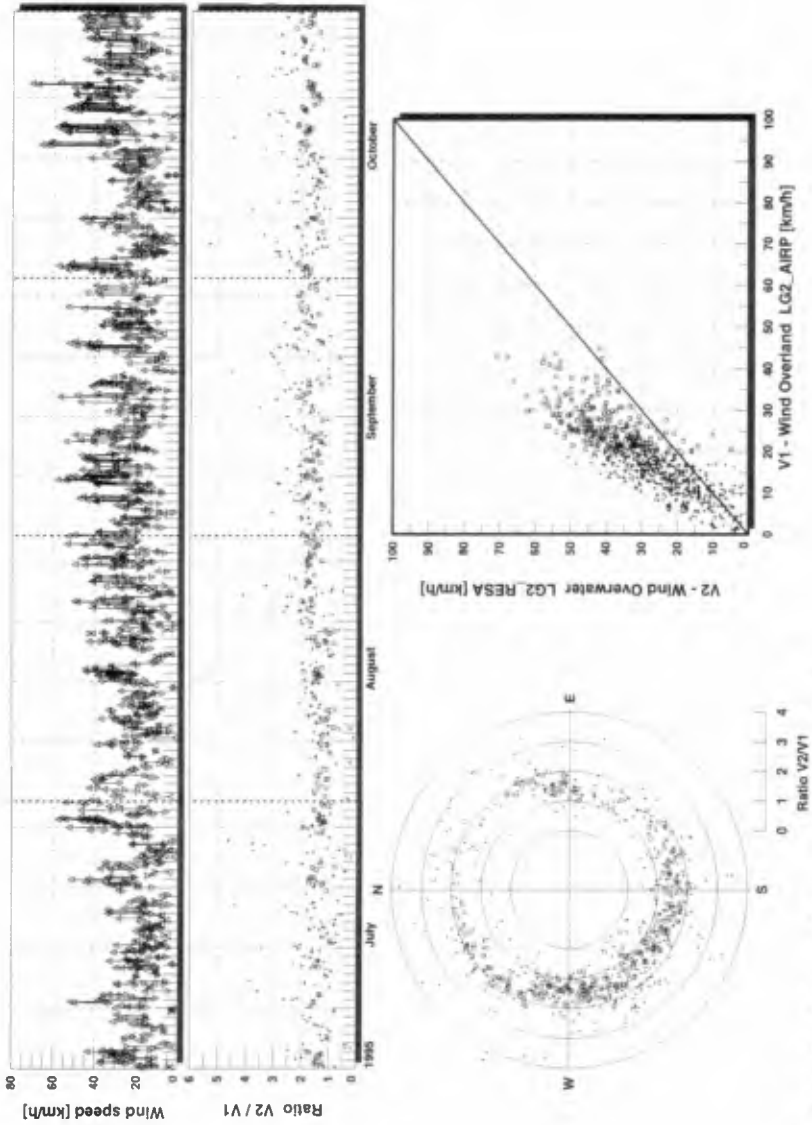
Figure 8. Example of wave hindcast from overwater wind data

Wind overland and wind overwater

Hindcast for lengthy periods of time can be achieved only with airport meteorological stations. The weather stations (figure 9) were used to better define the transfer function between wind measured overland and wind measured overwater, three of which were located at nearby airports.



Figure 9. Retrieval of weather station in November



Comparison between wind overland and wind overwater
Sites: LG2 Airport [V1] - Kanaupscow confluency [V2]
From July to October 1995

Figure 10. Wind overland and wind overwater

Records from both overland and overwater sites are visually inspected and punctual events are associated, to allow for the time lag between the two sites. All selected pairs are then plotted for further analysis. Figure 10 shows the results for one ice-free season. The scatter graph indicates that the wind overwater is larger but rarely exceeds the wind overland by more than 30 km/h. The way these points are distributed on the graph indicates that the ratio should decrease toward unity as the wind speed increases. Since there are only scarce measures for overland wind speed over 50 km/h, the relation can only be assumed for large values of wind speed. For design purposes and until sufficient data covering the upper region is obtained, the following relations are used to hindcast wave conditions from airport wind data:

$$U_w = 1,5 U_l \quad \text{for } U_l \leq 50 \text{ km/h}$$

$$U_w = 0,643 U_l + 42,9 \quad \text{for } 50 < U_l < 120 \text{ km/h}$$

$$U_w = U_l \quad \text{for } U_l \geq 120 \text{ km/h}$$

where U_l and U_w are respectively the wind overland and wind overwater in km/h.

Hindcast with overland wind

Although this empirical relation needs more data for strong wind events, it has the advantage of being easy to implement and should yield a proper annual extreme event since most years will have events with extreme wind overland speed in the vicinity of 50 km/h. In this region, a ratio value of 1,5 yields the envelope curve of measured data. Quality of such procedure is checked using data from the La Grande Airport located 130 km west of site TA-13 for which waves were measured from 1992 to 1995. Results are shown in Table 3. Except for 1994, all differences are within 10%, which is satisfactory.

Table 3. Site TA-13. Measure and hindcast of annual extreme wave event.

Year	Measure [m]	Hindcast [m]
1992	2,39	2,25
1993	1,79	1,80
1994	1,17	1,34
1995	1,69	1,75

Conclusion

Measurement of winds and waves in large reservoirs give good insight into wave generation by wind since the wave field is not contaminated by swell. The fast response of the reservoir is illustrated by the striking similarity between the wind speed and the significant wave height time series signals. Coefficients and exponents cannot be blindly evaluated from regression analysis in the log-log domain since use of a common variable raised to a given power can lead to false

correlation. The fact that wave steepness, using T_{02} , has been measured to be a maximum value around 0,06 enables a relationship between α_H and β_H to be derived and narrows the set of valid values from which to choose the correct pairs. The exponent of the dimensional wave height must be twice the value of the exponent for the mean wave period. For these conditions, it is possible to hindcast wave time series accurately with a model based on dimensional analysis, provided good quality overwater winds are used. Good quality wind hindcast for overland wind is then possible for long periods of time giving an effective tool for dam and dyke riprap design.

Acknowledgements

The authors wish to thank La Société d'Énergie de la Baie James for permitting publication of this paper and Hydro-Québec for use of the information acquired during the mandate.

References

- Bretschneider C.L., 1964. *Generation of waves by wind. State of the art*. International Summer Course, Lunteren, The Netherlands, National Engineering Science Company, NESCO Report SN-134-6, Washington DC, September 1964, 96 p.
- Caron O., P. Dupuis, T. Tran Van, 1993. *The Hydraulics of Riprap Design Applied to the Repairs of Dams and Dykes of the La Grande Hydroelectric Project*. Proceedings of the 5th Canadian Dam Safety Conference, St. John's, Nfld, September 1993.
- CERC, 1977. *Shore Protection Manual*. U.S. Army Corps of Engineers, Coastal Engineering Research Center, Fort Belvoir, Virginia, 3 volumes, 1977 edition.
- CERC, 1984. *Shore Protection Manual*. U.S. Army Corps of Engineers, Coastal Engineering Research Center, Fort Belvoir, Virginia, 3 volumes, 1984 edition.
- IARH/PIANC, 1986. *List of Sea State Parameters*. PIANC Supplement to Bulletin no 52, Brussels, Belgium.
- Kenney B.C., 1993. *On the validity of empirical power laws*, Stochastic Hydrology and Hydraulics, 7, pp. 179-194. Springer-Verlag.
- Mansard E., M.H. Davies, O. Caron, 1996. *Model Study of Reservoir Riprap Stability*. 25th International Conference on Coastal Engineering, CERC-ASCE, Orlando, Florida, U.S.A, Book of abstracts, Paper no 94, September 1996.
- SEBJ, 1996a *Mesures des vagues et du vent. Campagnes 1992-1995*. Rapport technique interne, Juin 1996, 56 p.
- SEBJ, 1996b *Génération des vagues par le vent*. Rapport technique interne, Janvier 1996.
- Tournier J.P., P. Dupuis, R. Arès, 1996. *An Improved Design Method for the Riprap of Earthfill Dams of Large Reservoirs*. 25th International Conference on Coastal Engineering, CERC-ASCE, Orlando, Florida, USA, Book of abstracts, Paper no 95, September 1996.

CHAPTER 97

SPECTRAL MODELLING OF CURRENT INDUCED WAVE-BLOCKING

R.C. Ris¹ and L.H. Holthuijsen¹

ABSTRACT

Waves travelling against an increasing opposing current tend to dissipate energy and part of the energy reflects back (in blocking conditions). The kinematic behaviour of these waves can be approximated with the linear theory for surface gravity waves. This theory has been implemented for random, short-crested waves in the third-generation wave model SWAN with numerical schemes that are fully implicit. Ad hoc assumptions that are made in other, similar models for blocking conditions are therefore not required and the model is consistent with the underlying theory. To represent the dissipation of the breaking waves in these blocking conditions, the pulse-based model of Hasselmann (1974) as adapted by Komen et al. (1984) has been chosen. Computations have been compared with the flume observations of Lai et al. (1989) in which random waves are blocked with violent breaking by an increasing counter current in relatively deep water. The computations underestimate the dissipation considerably but the addition of the bore-based model of Battjes and Janssen (1978) for steep, breaking waves in deep water improves the agreement with the observations significantly although some discrepancy remains.

INTRODUCTION

Field and laboratory observations of random waves in an opposing current show that the wave spectrum changes considerably, often accompanied with (current-induced) wave breaking. These changes take place rapidly at the moment that waves are blocked by the current. The third-generation spectral SWAN wave model (Holthuijsen et al., 1993; Ris et al., 1994; Holthuijsen et al., 1996) can be used to simulate these wave-blocking conditions in a linear approach as it is fully consistent with the linear wave theory for surface gravity waves. The model includes the third-generation formulation for deep-water wave breaking of Hasselmann (1974) as adapted by Komen et al. (1984). The flume experiments of Lai et al. (1989) offer an excellent opportunity to test this formulation against observations.

¹ Delft University of Technology, Department of Civil Engineering, P.O. Box 5048, 2600 GA Delft, Netherlands.

WAVE-BLOCKING

The evolution of monochromatic surface gravity waves and surface tension waves in an opposing current in blocking conditions has been described by Shyu and Phillips (1990) and Trulsen and Mei (1993). In the linear approach for a stationary ambient current a wave component that travels against a (spatially) increasing opposing current, increases its intrinsic frequency. It therefore shortens its wave length and decreases its relative propagation speed in geographic space (i.e. group velocity relative to the current). Its absolute frequency obviously remains constant. If, at some location, the relative propagation speed has reduced to be equal (but opposite) to the current velocity, the wave component is blocked. However, its intrinsic frequency continues to decrease and the wave component reflects at this point. After this reflection it continues to travel down-current while it continues to increase its intrinsic frequency. When this frequency enters the capillary range, the relative propagation speed (still directed against the current) increases and a second reflection may occur that sends the wave components up-current again. This capillary effect is ignored here because dissipation will have reduced the energy levels of these components to insignificant values.

This evolution can be readily interpreted for random waves by considering the wave component to travel through geographic and spectral space simultaneously. The evolution of the intrinsic frequency can thus be presented as propagation of energy (or action) over the intrinsic frequencies. If the wave direction is slanting across the current, the resulting refraction can similarly be modelled by propagation over the spectral directions. For a monochromatic wave, the wave height would go to infinity at the blocking point. For random waves this effect is reduced because of the distribution of the wave energy over the continuum of frequencies below the blocking frequency (analogous to reducing the effect of a caustic in geographic space). This does not imply that wave energy (in the gravity range) does not exist in the spectrum above the blocking frequency. Such energy has been generated at some location up-current from the blocking location and travels down-current.

THE WAVE MODEL

In presently operating third-generation wave models, wave-current interactions are commonly computed with explicit numerical schemes (e.g., Komen et al., 1994 and Tolman, 1991) and wave energy beyond the blocking frequency is simply removed in these models. This is an ad-hoc approach that solves a number of operational problems but it is not consistent with the basic equations underlying the models. For instance, energy at these frequencies can still travel down-current. In the SWAN model, all propagation schemes are fully implicit so that the model is always stable and the ad hoc measure of arbitrarily removing energy at these frequencies is avoided. By this, wave energy is propagated in the SWAN model through spectral space in a manner that is consistent with the linear theory for surface gravity waves. The proper kinematics are retained: wave energy travelling against the current can propagate to the blocking frequency where it is reflected in geographic space. Wave energy that is travelling down-current above the blocking

frequency is present in the model and can propagate through the blocking frequency to lower frequencies. Wave-current interactions through radiation-stresses are taken into account by formulating the wave evolution in terms of the action balance equation rather than the energy balance equation (e.g. Hasselmann et al., 1973):

$$\frac{\partial}{\partial t} N + \frac{\partial}{\partial x} c_x N + \frac{\partial}{\partial y} c_y N + \frac{\partial}{\partial \sigma} c_\sigma N + \frac{\partial}{\partial \theta} c_\theta N = \frac{F}{\sigma} \quad (1)$$

where $N = N(\sigma, \theta)$ is the action density with σ as intrinsic frequency, θ as wave direction, x and y as cartesian geographical coordinates and t as time. The first term in the left-hand side of this equation represents the rate of change of action in time, the second and third term represent propagation of action in geographical space (with propagation velocities c_x and c_y respectively). The fourth term represents propagation through the intrinsic frequency domain due to variations in depths and currents (with propagation velocity c_σ). The fifth term represents propagation in directional space due to depth and current induced refraction (with propagation velocity c_θ). These velocities are all taken from the linear theory of surface gravity waves. The term $F (= F(\sigma, \theta))$ at the right hand side of the action balance equation is the source term in terms of energy density $E (= E(\sigma, \theta))$ representing the effects of generation, wave-wave interactions and dissipation. This spectral action balance equation is the basic equation of the SWAN model.

To investigate the effect of current-induced breaking in blocking conditions, a third-generation formulation for whitecapping is used. It is the *pulse-based model* of Hasselmann (1974) as adapted by Komen et al. (1984):

$$F_{br}(\sigma, \theta) = -\Gamma \bar{\sigma} \frac{k}{\bar{k}} E(\sigma, \theta) \quad (2)$$

where $\bar{\sigma}$ is an average frequency, k is the wave number, \bar{k} is an average wave number and

$$\Gamma = \Gamma_k = \alpha_1 \left[\frac{s}{s_{PM}} \right]^4 \quad (3)$$

where s is an overall wave steepness and s_{PM} is the value of s for the Pierson-Moskowitz (1964) spectrum (so that s/s_{PM} is a normalized overall steepness). Details of the model are given in Komen et al. (1984).

The proportionality coefficient α_1 has been calibrated by Komen et al. (1984) to attain the Pierson-Moskowitz (1964) limit situation of fully developed seas in deep water. This formulation has been implemented in the third-generation WAM model (Cycle 3, WAMDI group, 1988) to compute whitecapping. With the same coefficient and with the same formulations for the wind generation and the quadruplet interactions as in the WAM model, the SWAN model also attains the Pierson-Moskowitz limit (as interpreted by Komen et al., 1984, Fig. 1). It also reproduces well the evolution of the wave energy and the peak frequency in the

idealized deep water case of a constant wind blowing perpendicularly off a straight upwind coast (no ambient current). This is evident from the agreement shown in Fig. 1 with the compilation of several data sets by Wilson (1965) and Kahma and Calkoen (1992; derived for $5 \cdot 10^4 < X^* < 4 \cdot 10^6$, E^* is the total wave energy, f_p^* is the peak frequency and X^* is the fetch, all normalized with gravitational acceleration and wind friction velocity, assuming $u_* = U_{10}/24$? for the Wilson data).

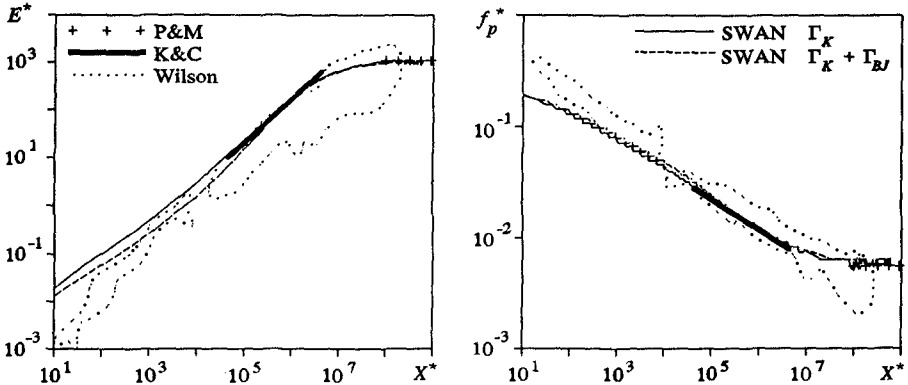


Fig. 1 The evolution of the dimensionless wave energy and the dimensionless peak frequency as function of the dimensionless fetch in the idealized deep water case according to the compilation of Kahma and Calkoen (1992; *K & C*) and of Wilson (1965, envelope), Pierson-Moskowitz (1964; *P & M*, as interpreted by Komen et al., 1984) and as computed by the SWAN model with the dissipation model of Komen et al. (1984; Γ_K), with and without the supplementing model of Battjes and Janssen (1978; Γ_{BJ}).

THE EXPERIMENT

A well documented experiment with waves travelling against a current in blocking conditions with violent breaking has been carried out in a laboratory flume by Lai et al. (1989). The waves with incident significant wave height $H_s = 0.019$ m and a mean wave period $T_{m01} = 0.51$ s are blocked in the flume by an opposing current that increases in down-wave direction ($U_{max} = -0.22$ m/s). This variation in the current speed was obtained with an elevated bottom over part of the flume in relatively deep water, see Fig. 2. The wave conditions have been computed with the SWAN model with a very narrow directional distribution of the wave energy (directional standard deviation 2.5°) and with all formulations for generation, dissipation and wave-wave interactions disabled except the above described whitcapping formulation.

In Fig. 2 the observed and computed evolution of the significant wave height along the flume are shown. It is obvious that the computed wave height reduction is considerably underestimated. In fact, the significant wave height increases some distance down the flume where the observations show a decrease. The whitewater formulation of Komen et al. (1984) apparently permits a wave steepness that is considerably larger than observed. As noted above, the coefficient α_1 in this formulation has been calibrated for deep water wave generation where the wave steepness is rather limited. In the present experiment it is apparently used for higher

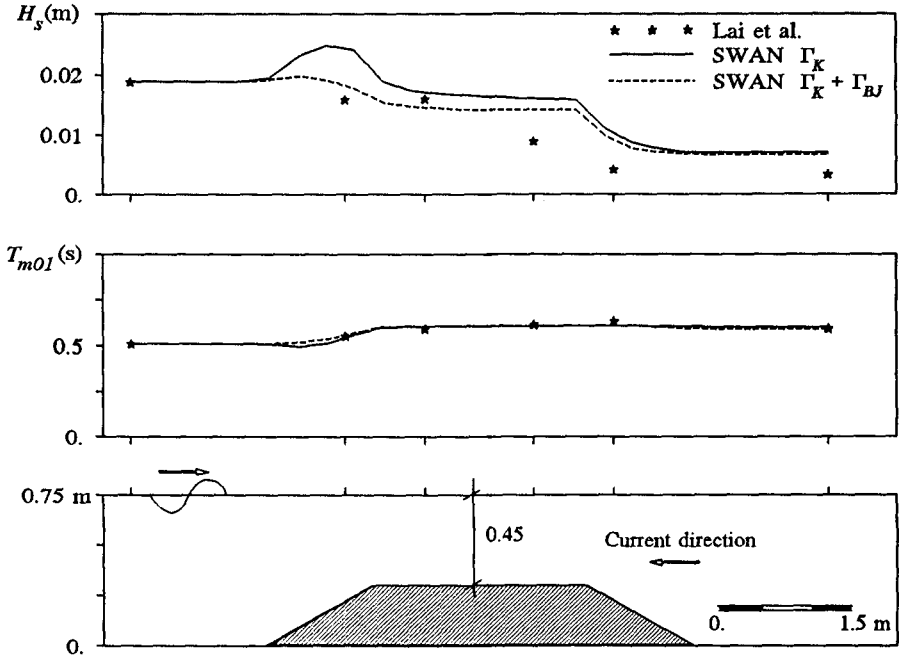


Fig. 2 The observed evolution of the significant wave height and the mean wave period in the opposing current experiment of Lai et al. (1989) and the computational results of the SWAN model with the dissipation model of Komen et al. (1984; Γ_K), with and without the supplementing model of Battjes and Janssen (1978; Γ_{BJ}).

values of the wave steepness. It therefore seems that either another value for the coefficient is needed for higher wave steepness or that another formulation is required. We speculate that the total dissipation of the steeper waves can be better modelled with the *bore-based model* of Battjes and Janssen (1978). If this total dissipation is distributed over spectral space as in the pulse-based model, then the formulation of Γ becomes:

$$\Gamma = \Gamma_{BJ} = \alpha_2 Q_b \left(\frac{s_{\max}}{s} \right)^2 \quad (4)$$

in which Q_b is the fraction of breaking waves and s_{\max} is the maximum steepness of an individual breaker (so that s_{\max}/s is a normalized maximum steepness of an individual breaker). The maximum steepness is set at $s_{\max} = 0.14$ and the value of α_2 is taken from Battjes and Janssen (1978). The fraction of breakers Q_b increases very quickly as function of the overall steepness s above $s = 0.08$ so that the dissipation is relatively large for steep waves. This is shown in Fig. 3 with Γ_K and Γ_{BJ} as a function of overall steepness s . In the SWAN model this bore dissipation of Battjes and Janssen (1978) is added to the whitecapping dissipation of Komen et al. (1984).

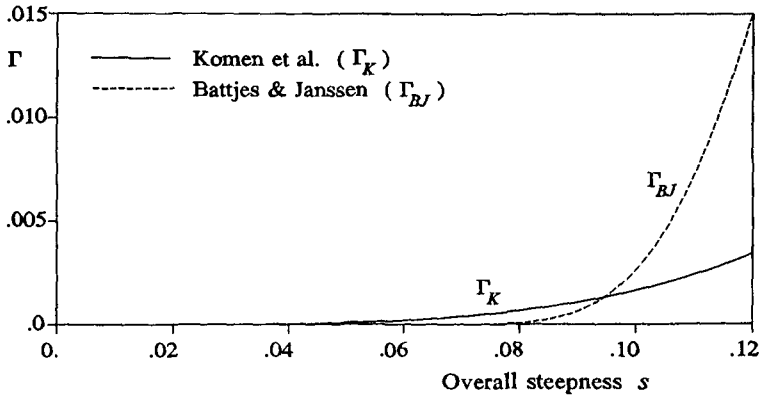


Fig. 3 The coefficient of whitecapping as a function of overall wave steepness according to Komen et al. (1984) and the expression of the present study that is based on Battjes and Janssen (1978).

The evolution of the waves in the idealized fetch-limited conditions is hardly affected by this addition of the bore-based model except for very short fetches where the SWAN results now agree slightly better with the compilation of Wilson (1965) for $X^* < 10^4$ (Fig. 1; not considered by Kahma and Calhoun, 1992). In the experiment of Lai et al. (1989) the agreement between the computed and observed evolution of the waves has improved (see Fig. 2) but the observed continued reduction in wave height up-current from the location where the current speed attains a constant speed (at the down-current end of the elevated bottom), is not reproduced. This continued reduction is unexpected since the wave steepness decreases to rather low values and breaking is expected to be insignificant. This continued dissipation needs further investigation.

CONCLUSIONS

The numerical schemes in the third-generation spectral wave model SWAN allow a treatment of the kinematic characteristics of wave-blocking and wave reflections against an opposing current that is consistent with the linear theory for surface gravity waves without any ad hoc assumptions. Numerical simulations of wave-

blocking experiments in a flume show that the pulse-based whitecapping formulation of Hasselmann (1974), adapted by Komen et al. (1984) is not adequate in representing the process of energy dissipation in the blocking situation that was considered. Supplementing this formulation with the bore-based model of Battjes and Janssen (1978) shows an improvement but the observed continued reduction in wave height in the region of constant current has not been resolved.

ACKNOWLEDGEMENTS

We gratefully acknowledge receiving additional information on the flume experiment from Steven R. Long of NASA, Wallops Flight Facility (USA).

REFERENCES

- Battjes, J.A. and J.P.F.M. Janssen, 1978, Energy loss and set-up due to breaking of random waves, Proc. 16th Int. Conf. Coastal Engineering, ASCE, pp. 569 - 587
- Hasselmann, K., 1974, On the spectral dissipation of ocean waves due to whitecapping, Boundary - Layer Meteorology, Vol. 6, No. 1-2, pp. 107-127
- Hasselmann, K., T.P. Barnett, E. Bouws, H. Carlson, D.E. Cartwright, K. Enke, J.A. Ewing, H. Gienapp, D.E. Hasselmann, P. Kruseman, A. Meerburg, P. Müller, D.J. Olbers, K. Richter, W. Sell and H. Walden, 1973, Measurements of wind-wave growth and swell decay during the Joint North Sea Wave Project (JONSWAP), Dtsch. Hydrogr. Z. Suppl., A8(12), 95p.
- Holthuijsen, L.H., N. Booij and R.C. Ris, 1993, A spectral wave model for the coastal zone, Proc. 2nd International Symposium on Ocean Wave Measurement and Analysis, New Orleans, Louisiana, July 25-28, 1993, New York, pp. 630-641
- Holthuijsen, L.H., R.C. Ris and N. Booij, 1996, A third-generation model for near-shore waves with ambient currents, 25th Int. Conf. Coastal Engineering., Orlando, accepted for presentation
- Kahma, K.K. and C.J. Calkoen, 1992, Reconciling discrepancies in the observed growth of wind-generated waves, J. Phys. Oceanogr., Vol. 22, pp. 1389-1405
- Komen, G.J., S. Hasselmann, and K. Hasselmann, 1984, On the existence of a fully developed wind - sea spectrum, J. Phys. Oceanogr., Vol. 14, pp. 1271-1285
- Komen, G.J., L. Cavaleri, M. Donelan, K. Hasselmann, S. Hasselmann and P.A.E.M. Janssen, 1994, Dynamics and modelling of ocean waves, Cambridge, 300 p.
- Lai, R., S.R. Long and N.E. Huang, 1989, Laboratory studies of wave-current interactions: kinematics of the strong interaction, J. Geophys. Res., 94, No. C11, 16201-16214
- Pierson, W.J. and L. Moskowitz, 1964, A proposed spectral form for fully developed wind seas based on the similarity theory of S.A. Kitaigorodskii, J. Geophysical Res., Vol. 69, No. 24, pp. 5181-5190
- Ris, R .C., L.H. Holthuijsen and N. Booij, 1994, A spectral model for waves in the near shore zone, Proc. 24th Int. Conf. Coastal Engineering, Kobe, Oct. 1994, Japan, pp. 68-78

- Shyu, J.-H. and O.M. Phillips, 1990, The blockage of gravity and capillary waves by longer waves and currents, *J. Fluid Mech.*, Vol. 217, pp. 115-141
- Tolman, H.L., 1991, A third-generation model for wind waves on slowly varying, unsteady, and inhomogeneous depths and currents, *J. Phys. Oceanogr.*, Vol. 21, No. 6, pp. 782 -797
- Trulsen, K. and C.C. Mei, 1993, Double reflection of capillary/gravity waves by a non uniform current: a boundary-layer theory, *J. Fluid Mech.*, Vol. 251, pp. 239-271
- WAMDI group: S. Hasselmann, K. Hasselmann, E. Bauer, P.A.E.M. Janssen, G.J. Komen, L. Bertotti, P. Lionello, A. Guillaume, V.C. Cardone, J.A. Greenwood, M. Reistad, L. Zambresky and J.A. Ewing, 1988, The WAM model - a third generation ocean wave prediction model, *J. Phys. Oceanogr.*, Vol. 18, pp. 1775-1810
- Wilson, B.W., 1965, Numerical prediction of ocean waves in the North Atlantic for December 1959, *Deutsche Hydrographische Zeitschrift*, Vol. 18, No. 3, pp. 114-130

SUBJECT INDEX

Page number refers to the first page of paper

- Abrasives, 2166
Absorption, 55
Accretion, 2955, 4038
Accuracy, 2, 4770
Acoustic measurement, 275
Advection, 4024
Aeolian sands, 4214
Aerial surveys, 1944
Aging, 1888
Alaska, 1293
Algorithms, 914
Analytical techniques, 575, 1762, 1985
Anchorage, 1631
Anemometers, 602
Aquatic habitats, 4300
Armor units, 1542, 1583, 1617, 1640, 1665, 1679, 1721, 1735, 1748, 1789, 1803, 1862, 1944, 2377, 2418, 2522, 3006, 3791, 4228
Artificial islands, 754, 1862, 2298
Asymmetry, 3183, 3467
Australia, 4200, 4390
- Backfills, 3231, 4261
Baltic Sea, 2142
Barrier beaches, 247, 2732, 3391, 3546
Barrier islands, 2128, 2732, 2756, 2897, 4621
Barriers, 2087, 2352, 2470, 4505, 4601
Bars, 3680, 4289
Bars, riverine, 2884, 2897, 3546, 3588, 3600, 3666, 4491
Bathymetry, 731, 3521, 4376
- Bays, 4242, 4531
Beach erosion, 1349, 1985, 2352, 2666, 2691, 2705, 2718, 2732, 2756, 2770, 2820, 2857, 2871, 2884, 2911, 2918, 2955, 2982, 3115, 3295, 3378, 3442, 3521, 3874, 3976, 3986, 4038, 4583, 4613, 4650, 4717, 4744, 4756
Beach nourishment, 2746, 2770, 2857, 2897, 2911, 2918, 2927, 2941, 2955, 2982, 3115, 3642, 3708, 3722, 4014, 4390, 4440, 4613, 4621, 4650, 4730, 4756
Beaches, 151, 233, 261, 275, 602, 616, 717, 889, 955, 981, 1130, 2036, 2050, 2128, 2142, 2152, 2284, 2612, 2640, 2654, 2677, 2779, 2829, 2843, 2969, 2994, 3006, 3020, 3062, 3090, 3104, 3169, 3349, 3405, 3442, 3560, 3666, 3680, 3736, 3750, 3770, 3888, 3921, 3948, 3962, 3986, 4000, 4079, 4088, 4120, 4161, 4188, 4228, 4353, 4376, 4477
Bed load, 3467, 3913
Bed load movement, 3614
Bed movements, 3495
Bed ripples, 3129, 3183, 4079
Bed roughness, 3143
Bedforms, 3129, 3169, 3391, 3784
Belgium, 836
Benefit cost ratios, 2927, 4717
Berms, 1528, 1542, 1617, 1693, 1735, 1826, 1930, 2192, 2897, 2982, 3708, 3722, 4636
Blocks, 1888

Volume 1 1-1254, Volume 2 1255-2572, Volume 3 2573-3804, Volume 4 3805-4832

- Boundary conditions, 3770, 4120, 4134
- Boundary element method, 165, 1516, 2377, 2548
- Boundary layer, 3194, 3207, 3818
- Boundary layer flow, 3183, 3219, 4779
- Boussinesq equations, 95, 109, 123, 493, 589, 955, 1060, 1116, 1144, 1178, 1192, 1491, 3048, 3349, 4807
- Breaking, 1876
- Breaking waves, 2, 109, 151, 186, 200, 214, 233, 247, 261, 275, 286, 403, 527, 551, 602, 657, 754, 1144, 1156, 1178, 1192, 1219, 1321, 1403, 1803, 1826, 2216, 2244, 2298, 2338, 2366, 2442, 2456, 2484, 2598, 3104, 3194, 3588, 3805, 4228, 4793, 4807
- Breakwaters, 137, 186, 300, 767, 1280, 1528, 1542, 1589, 1640, 1652, 1665, 1693, 1707, 1721, 1735, 1789, 1803, 1816, 1826, 1852, 1930, 1998, 2008, 2022, 2036, 2050, 2063, 2178, 2192, 2216, 2312, 2324, 2352, 2366, 2377, 2391, 2404, 2428, 2470, 2494, 2508, 2522, 2534, 2584, 2770, 2871, 3830, 3976, 3986, 4664, 4676, 4689, 4744
- Bridges, piers, 2230
- Buoyant jets, 4325, 4569
- Buoys, 616, 743, 2087
- Caissons, 1516, 1902, 2008, 2584, 4583
- Calibration, 247, 1102, 3614
- California, 4214, 4636
- Canada, 2230
- Case reports, 1293, 2404, 2732, 3986, 4717
- Channel flow, 4491
- Channel improvements, 3323
- Channels, waterways, 1074, 4531, 4703
- Chaos, 864
- China, People's Republic of, 354
- Climatic changes, 314, 1349, 4364
- Climatic data, 81
- Closed form solutions, 3244
- Cnoidal waves, 2598
- Coastal engineering, 2, 67, 109, 286, 314, 328, 340, 354, 457, 465, 616, 1034, 1465, 1707, 2114, 3652, 3680, 4431
- Coastal environment, 314, 689, 794, 836, 1022, 1478, 2244, 3270, 3363, 3962, 4300, 4807
- Coastal management, 864, 1008, 1375, 2666, 2677, 2793, 2820, 2884, 2911, 2927, 3020, 3431, 4000, 4014, 4253, 4339, 4418, 4440, 4636, 4703, 4744
- Coastal morphology, 1349, 1417, 2770, 2806, 2829, 2897, 2955, 3048, 3090, 3391, 3521, 3534, 3560, 3574, 3600, 3750, 3762, 3830, 3913, 4024, 4038, 4079, 4477, 4517
- Coastal processes, 214, 2022, 2036, 2691, 2779, 2871, 3295, 3378, 3481, 3495, 3600, 3614, 3642, 3666, 3708, 3750, 3805, 3874, 3888, 4052, 4200, 4364, 4464, 4477, 4545, 4583, 4703, 4821
- Coastal structures, 43, 55, 214, 221, 314, 380, 389, 403, 616, 743, 981, 1452, 1569, 1735, 1852, 1862, 1876, 1957, 1971, 2008, 2114, 2128, 2142, 2152, 2166, 2178,

- 2206, 2216, 2258, 2272, 2284,
2338, 2352, 2391, 2404, 2418,
2456, 2560, 2573, 2718, 2918,
2969, 3507, 4397, 4440, 4531
- Coefficients, 1516
- Cohesive sediment, 3337
- Cold weather construction, 4397
- Colorado River, 3309
- Composite structures, 1707
- Computation, 537, 1102, 1130
- Computer aided design, 4650
- Computer aided drafting (CAD),
4650
- Computer networks, 1443
- Concrete blocks, 1652, 1665
- Concrete structures, 1556
- Configuration, 1735, 1816, 3155,
4636
- Construction, 4689
- Control, 493, 1998
- Control systems, 55
- Convection, 3784, 4098
- Coral reefs, 3143, 4261
- Core, 1735
- Corrosion, 2166
- Cost effectiveness, 2114, 4583
- Costs, 1735
- Cracks, 4411
- Crossflow, 175, 3378, 3405, 3666
- Currents, 30, 67, 95, 354, 629, 1060,
1219, 1247, 2391, 3363, 3431,
4066, 4079, 4569, 4730, 4807,
4821
- Curtain walls, 2470, 2484
- Cylinders, 380, 415
- Damage, 1233, 1789, 2969, 4261,
4676
- Damping, 2298, 2626, 3143, 4174
- Dams, 1233
- Dams, earth, 2101
- Data banks, 3652
- Data collection, 81, 137, 368, 629,
643, 677, 1916, 3722, 4200
- Data processing, 4770
- Databases, 81, 2418
- Decay, 300
- Decks, 2573
- Deep water, 2494
- Deflection, 2456
- Deformation, 261, 2338, 3062, 4411
- Deltas, 2806, 2820, 3270, 3284,
3976, 4505, 4545
- Denmark, 2927, 4703
- Density stratification, 4557
- Design, 314, 616, 1280, 1403, 1617,
1631, 1640, 1665, 1748, 1776,
1826, 1971, 2036, 2114, 2128,
2508, 2584, 2897, 2927, 3034,
3628, 4261, 4440, 4451, 4689,
4717
- Design criteria, 221, 354, 2352,
2534, 4397, 4431, 4591
- Design improvements, 2101
- Design waves, 328, 1233, 2494,
2560
- Dewatering, 2677
- Diffusers, 4325
- Diffusion, 3784, 4098
- Digital techniques, 657
- Dikes, 994, 1008, 1233, 1876, 1888,
2746, 2820
- Discharge, 3309
- Docks, 1293
- Documentation, 1443
- Dolos, 4664
- Doppler systems, 527, 629, 1060
- Drag, 3846
- Drag coefficient, 3363
- Drainage, 3507
- Drainage systems, 2640, 2654
- Drains, 2666, 2677
- Dredge spoil, 3708

- Dredging, 3284, 3708, 4274, 4289, 4390
 Ducts, 3913
 Dunes, 2793, 2884, 2955, 2969, 3034, 3115, 4148
 Dynamic response, 2456, 2584
 Dynamic stability, 1930, 2534
 Dynamics, 1178, 2955, 3560, 3805, 3846, 3921, 4052, 4364, 4601

 Earthfill, 2101
 Earthquakes, 1478
 Ecology, 4274
 Eddy viscosity, 200, 3194, 3419
 Education, 1443, 4431
 Effluents, 4325
 Egypt, 3976
 Eigenvalues, 1074, 2470
 Eigenvectors, 2829, 4730
 Embankments, 1707, 4188
 Energy conversion, 4591
 Energy dissipation, 261, 836, 1088, 1192, 1247, 2626, 3062
 Engineers, 4431
 Entropy, 643
 Environmental impact statements, 4274
 Equations of motion, 3846
 Equipment, 4591
 Erosion, 214, 1693, 2230, 2404, 3034, 4052, 4148, 4353, 4397, 4451, 4557, 4621, 4703
 Erosion control, 2666, 2677, 2820, 4038
 Estimates, 328, 3453
 Estimating, 16, 43, 2508
 Estimation, 30, 689, 794, 900, 981, 1389, 1503
 Estuaries, 2691, 4289, 4491, 4557
 Europe, 1375
 Evaluation, 340, 2036, 2677, 2857, 3652

 Experimentation, 443, 479, 516, 1617, 1840, 2640, 2746
 Extraction procedures, 4583

 Failure modes, 1902
 Failures, 1542, 1589
 Fatigue, 4664
 Feasibility studies, 4591
 Field investigations, 137, 994, 1652, 1876, 3600, 3901, 4000, 4491
 Field tests, 516, 689, 2077, 2612, 2654, 3257, 3323, 3962, 4052, 4111, 4591
 Finite element method, 2548
 Finite elements, 465
 Fisheries, 4253
 Floating breakwaters, 1631
 Floating structures, 2548
 Flood control, 2820, 4253, 4339, 4505
 Flood plain insurance, 4339
 Flooding, 1349, 2244, 2746, 4314, 4339, 4418
 Floods, 2258, 2705, 3284, 4491
 Florida, 2312, 3323, 3642, 4242, 4613
 Flow characteristics, 67
 Flow patterns, 4134
 Fluid flow, 3546
 Fluidizing, 4161
 Flumes, 300, 493, 575, 968, 1542, 1816, 1826, 1902, 2428, 3076, 3442
 Forecasting, 340, 743, 864
 Foundation performance, 3507
 Fourier analysis, 968, 1034
 Fourier transform, 3762
 Fractures, 4411
 Free surfaces, 389
 Frequency analysis, 123, 1144
 Frequency distribution, 16

- Friction, 836
Friction factor, 3143, 3495
- Gaging stations, 1465
Geographic information systems, 4650
Geometry, 1280
Georgia, 4314
Geotextiles, 1902, 2114
Germany, 2128, 3534, 4621
Gradient, 4161
Grain size, 4756, 4779
Gravel, 981
Gravity, 2640, 2654
Gravity waves, 1335
Great Lakes, 2705, 4289
Groins, structures, 2128, 2142, 2770, 3976, 4024, 4517, 4744
Ground water, 2152, 2654, 4120, 4601
Ground-water flow, 2640
Guidelines, 1748, 4188, 4253
Gulf of Mexico, 4770
- Harbors, 864, 889, 1256, 1268, 1280, 1491, 1816, 3284, 3986, 4014, 4451, 4744
Head loss, 1776
History, 457
Human factors, 275
Hurricanes, 781, 2756, 2982
Hydraulic design, 4314
Hydraulic models, 221, 443, 3169
Hydraulic performance, 1721
Hydraulic roughness, 3143
Hydraulics, 1679, 4531, 4545
Hydrodynamics, 109, 415, 668, 3419, 3546, 3680, 3948, 4289, 4491
Hydrology, 4274
- Ice forces, 4397
Ice loads, 4397
Ice sheets, 4411
Impact, 1640, 2022, 2442, 2573, 2779
Impact forces, 2456
Impact loads, 2508, 2522, 2534, 2584
Incipient motion, 1803
Indonesia, 1443
Infiltration, 2654
Inlets, waterways, 1219, 2258, 2779, 3270, 3284, 3295, 3323, 3642, 4464, 4477, 4517, 4531
Installation, 1631
Interactions, 1060, 1219, 2377, 2548, 3694, 4120, 4821
Ireland, 4557
Islands, 1452
Italy, 2404
- Japan, 137, 794, 1349, 1389, 1465, 1491, 4000, 4038, 4545, 4676
Jets, 4451
Jetties, 1852, 2573, 3295, 3309, 4531
- Kinematics, 502, 537, 565, 1034, 1247, 1776, 2442, 3481
- Laboratory tests, 43, 493, 927, 1022, 1307, 1321, 1583, 1631, 2077, 2626, 2746, 3295, 3628
Lagrangian functions, 4569
Landslides, 1293, 1478
Large structures, 380
Lasers, 527, 602
Leakage, 1556
Limit analysis, 3874
Liquefaction, 1902, 3860
Littoral currents, 175, 233, 602, 1361, 3391, 3419, 3481, 3560, 3628, 3666, 3860

- Littoral deposits, 2779
Littoral drift, 1998, 2871, 2897,
3270, 3309, 3628, 3652, 3830,
4390, 4464, 4545
Loading, 3507
Long waves, 151, 493, 1307, 1321,
1431, 1452, 1478, 3076, 3090
Louisiana, 2756
- Maintenance, 1852, 2770
Maintenance costs, 2969
Mass transport, 4174
Mathematical models, 589, 2941,
3104
Measurement, 286, 1762, 1916,
3129, 3169, 3391, 3431, 3588,
4079, 4098, 4161, 4569
Measuring instruments, 643
Mechanics, 4300
Membranes, 2087
Meteorology, 703, 822, 4200
Mixing, 175, 3419, 4098, 4325, 4569
Model studies, 1748, 4242
Model tests, 1431, 1528, 1693, 1971,
2428, 2484, 2534, 4689
Model verification, 2806, 4730
Modeling, 109, 186, 286, 565, 889,
1205, 1247, 1375, 2036, 2230,
2857, 2982, 2994, 3805, 3913,
4120, 4464, 4477, 4621, 4821
Models, 2, 81, 123, 165, 247, 403,
429, 502, 703, 767, 781, 794,
1048, 1060, 1116, 1144, 1168,
1192, 1307, 1335, 1417, 1589,
2008, 2022, 2178, 2298, 2456,
2494, 3062, 3115, 3207, 3257,
3405, 3419, 3467, 3574, 3784,
3935, 4066, 4214, 4569, 4756,
4770, 4779
Momentum transfer, 175
Monitoring, 889, 1944, 2312, 2871,
4014, 4664, 4689, 4730
- Monte Carlo method, 822, 900, 1665
Morphology, 3231
Movable bed models, 1998, 2258,
2428, 3169, 3295, 3495, 3628
Mud, 3337, 4174
- Navier-Stokes equations, 200
Navigation, 1074, 3231, 3284, 3323,
4390, 4531
Nearshore circulation, 808, 822, 878,
1205, 1335, 1361, 1417, 2391,
2843, 3020, 3694, 3722, 3830,
4000, 4052, 4242
Netherlands, 1876, 3600
Networks, 616
New Zealand, 3284
Noise measurement, 275
Nomographs, 781
Nonlinear analysis, 165, 589
Nonlinear response, 95, 717, 731,
767, 850, 927, 955, 1034, 1048,
1088, 1130, 1156, 1178
Nonlinear systems, 657, 1491
North Carolina, 3521, 3588, 3666,
4517
Numerical analysis, 575, 754, 927,
1130, 1361, 1516, 2548
Numerical models, 30, 95, 137, 200,
233, 300, 340, 389, 465, 551, 668,
941, 1074, 1219, 1256, 1268,
1876, 1930, 2050, 2324, 2338,
2666, 2746, 2770, 2969, 3614,
3722, 3736, 3818, 3830, 3888,
3962, 4174, 4289, 4601, 4807
- Ocean engineering, 457, 565
Ocean waves, 16, 1465, 1789
Oceanography, 3090
Offshore structures, 1603
Optimal design, 1589
Optimization, 479
Oregon, 2718

- Oscillations, 1268, 1491, 2884
Oscillatory flow, 3183, 3244, 3495,
4353, 4779
Outfall sewers, 4228
Outflows, 4120
Outwash, 4148
Overtopping, 1721, 1816, 1840,
1862, 2178, 2192, 2206, 2216,
2598
Oxygen transfer, 403
- Parks, 4274
Particle motion, 3846
Peak values, 900, 2484
Performance, 1852, 4636
Performance evaluation, 2087
Permeability, 2142
Photogrammetry, 3750, 4664
Piers, 2573
Piles, 2142
Pipelines, 3231, 4228
Planning, 3986
Plunging flow, 2442
Polynomials, 1130
Ponding, 2312
Pore pressure, 1916, 3219, 3860
Porosity, 2366
Porous materials, 2063
Porous media, 2377
Ports, 1707, 4376, 4676
Predictions, 123, 314, 429, 502, 703,
743, 864, 878, 941, 1321, 1417,
2077, 2230, 2338, 2806, 2941,
3231, 3378, 3405, 3574, 3652,
4650, 4807, 4821
Pressure measurement, 429, 1034
Pressures, 4161
Probabilistic methods, 2793, 4717
Probabilistic models, 808
Probability, 2560, 4418, 4440
Probability density functions, 368,
850, 4793
- Probability distribution, 328, 2272
Professional development, 4431
Profiles, 2829, 2982, 2994, 3006,
3020, 3048, 3104, 3169, 3194,
3349, 3405, 3442, 3736, 3750,
3784, 3901, 3921, 4052, 4650,
4756
Programs, 4613
Progressive waves, 3183
Projects, 1375, 2941
Propellers, 4451
Protective structures, 1403
Prototypes, 1762
Public land, 4418
Public opinion, 4253
Pumps, 4591
- Quality control, 643
Quays, 4451
- Radioactive tracers, 3901
Random waves, 2, 16, 30, 43, 261,
415, 537, 657, 754, 850, 914, 927,
1144, 1247, 2272, 3006, 3034,
3076, 3442
Ratings, 1852
Rayleigh waves, 914, 2272
Reaeration, 403
Recirculation, 3628
Recreational facilities, 2770
Reefs, 2298
Regulation, 2391
Reliability, 1589
Remote sensing, 1944
Repairing, 4689
Research, 286, 994, 1375, 1876,
1888, 3481
Reservoirs, 1233, 1748, 2101, 2918
Resonance, 1583
Resonators, 1280
Restoration, 4261

- Revetments, 1008, 1556, 1583, 1888,
2206, 2718
- Reynolds stress, 200, 4079
- Rheological properties, 4174
- Rip currents, 1361, 2142, 3391,
3680, 3694, 4000
- Riprap, 1233, 1748, 2101
- Risk analysis, 4339, 4440, 4717
- River flow, 4505
- River systems, 2244
- Rivers, 1349, 4545, 4557
- Rock structures, 2077
- Rocks, 1957
- Rotational flow, 2178
- Roughness, 3129, 3495
- Rubble-mound breakwaters, 1516,
1569, 1589, 1603, 1617, 1679,
1776, 1916, 1944, 1957, 1971,
2418
- Russia, 2918
- Salt water, 1022
- Salt water intrusion, 4601
- Sand, 981, 1876, 2050, 2166, 2927,
3034, 3219, 3600, 3642, 3770,
3874, 3888, 3962, 4353, 4390,
4505, 4613
- Sand transport, 137, 2284, 2829,
2871, 2911, 2994, 3708, 3736,
3784, 3791, 3846, 3948, 4111,
4148, 4188, 4214, 4464, 4779
- Sand waves, 3183, 3521, 3574, 4024
- Satellite mapping, 81
- Satellite photography, 3762
- Scale effect, 403, 1762, 2152, 2192,
2522
- Scale models, 1762, 1888, 2101,
2152, 2941
- Scattering, 941
- Scour, 2152, 2230, 2258, 4397, 4517
- Scouring, 1652, 4451, 4676
- Screens, 1762
- Sea cliffs, 2793
- Sea floor, 941, 955, 2230, 3129,
3155, 3207, 3378, 3507, 3860,
4376
- Sea level, 1349, 1503, 3860, 4364,
4418, 4583
- Sea state, 703
- Sea walls, 1022, 1403, 1840, 1862,
1902, 1985, 2192, 2216, 2442,
2456, 2508, 2612, 2718, 4621
- Sea water, 354
- Sediment, 2152, 2732, 4161
- Sediment concentration, 3901, 3935,
4088
- Sediment deposits, 4200, 4214
- Sediment transport, 214, 1321, 2022,
2612, 2691, 2756, 2843, 2941,
2994, 3006, 3048, 3062, 3076,
3104, 3115, 3155, 3194, 3231,
3309, 3337, 3349, 3363, 3378,
3405, 3467, 3534, 3546, 3560,
3614, 3628, 3642, 3652, 3736,
3770, 3791, 3805, 3818, 3860,
3888, 3901, 3913, 3921, 4014,
4289, 4300, 4376, 4545, 4744,
4793
- Sediment yield, 2391
- Sedimentation, 3231
- Sedimentology, 2050
- Sensitivity analysis, 2746
- Sensors, 3453
- Settlement analysis, 1902
- Sewage disposal, 4325
- Shallow water, 95, 109, 123, 221,
465, 502, 551, 589, 602, 668, 878,
889, 955, 1088, 1452, 1930, 2192
- Shape, 1957
- Shear, 175, 3207
- Shear stress, 1168, 3155, 3194, 3337,
3467, 3481, 3913, 4325
- Shellfish, 4300, 4353
- Ship motion, 1268

- Ships, 4261
Shoaling, 2, 95, 151, 247, 537, 717,
754, 955, 1130, 3295, 4517
Shore protection, 2063, 2114, 2128,
2206, 2312, 2352, 2391, 2404,
2418, 2428, 2470, 2640, 2654,
2705, 2718, 2911, 2918, 3034,
3976, 4440
Shoreline changes, 1985, 2404, 2732,
2756, 2779, 2820, 2829, 2843,
2857, 2884, 2927, 3405, 3521,
3588, 3750, 3770, 3874, 3921,
4000, 4024, 4038, 4364, 4376,
4464, 4613, 4744
Simulation, 16, 389, 657, 900, 914,
1431, 1789, 3442, 3560, 3818,
3976, 4024, 4242
Simulation models, 67, 731, 2806
Slope stability, 1556, 1603
Slopes, 941, 3913
Small structures, 380
Soil mechanics, 1603
Soil-structure interaction, 3507
Solitary wave, 1156
Sonar, 1944
South Africa, 340
Spain, 1816, 2806, 2871, 4014, 4418,
4730, 4744
Spectral analysis, 43, 175
Spraying, 994, 1022, 1840
Sri Lanka, 4200
Stability, 1583, 1617, 1640, 1652,
1665, 1679, 1721, 1748, 1776,
1789, 1803, 1826, 1862, 1888,
1957, 1971, 3534, 4161, 4228,
4664, 4756
Stabilization, 2640, 2654, 2718,
2829, 3986
Standing waves, 151, 3090
Statistical analysis, 900, 914, 1985,
2560
Statistical models, 1088
Statistics, 123, 794, 808, 822, 1375,
1503
Steel pipe piles, 2166
Stochastic models, 1389, 4300
Stochastic processes, 878
Stones, 1583, 1640, 1693
Storm surges, 822, 994, 1268, 1389,
1403, 1417, 4397
Storms, 703, 743, 781, 1789, 2982,
3034, 3115, 3257, 3874, 3921,
4300, 4339, 4703
Stratified flow, 4557
Streams, 3183
Stress, 3453
Stress analysis, 4274
Structural elements, 4261
Structural response, 1617
Submerged flow, 927
Surf zone, 109, 151, 200, 214, 233,
286, 537, 551, 602, 1178, 1321,
1361, 1431, 3048, 3076, 3104,
3431, 3453, 3694, 3805, 3901,
4066, 4088, 4098, 4111, 4228,
4793
Surface dynamics, 389
Surface waves, 565, 1048, 3244,
3935
Surveys, 2114, 3020
Suspended sediments, 2612, 3076,
3207, 3257, 3736, 3784, 3791,
3888, 3935, 3948, 3962, 4088,
4098, 4111, 4793
Tests, 30, 221, 286, 968, 1542, 1816,
3442, 3680
Texas, 3736
Theories, 443, 864, 3962
Three-dimensional analysis, 1102
Three-dimensional models, 233,
2843
Tidal currents, 2691, 3722, 4491
Tidal effects, 2994, 3090, 3574

- Tidal energy, 1478
Tidal flats, 994
Tidal waters, 3270, 3284, 3295,
3323, 3534, 3948, 4242, 4314,
4477, 4491
Tides, 629, 1603, 1707, 3431, 3442
Time studies, 1307
Toe aprons, 1971
Topography, 1349, 1417, 1452, 1998,
3534, 3560, 3762, 4545
Transducers, 3129
Trenches, 3231, 4188
Tributaries, 4289
Tsunamis, 1443, 1465, 1478, 1707,
4676
Turbidity, 4088
Turbulence, 186, 200, 214, 3207,
3818, 3935, 4111, 4228, 4325
Turbulent boundary layers, 3244
Turbulent diffusion, 4066
Turbulent flow, 200, 3453
Two-dimensional models, 3846
Typhoons, 1389, 1417, 1491

Uncertainty analysis, 1256, 2560
Undertow, 3006, 3048, 3062, 3194,
3419, 3830
Underwater structures, 380, 927,
1998, 2312, 2324
Uniformity, 479
United Kingdom, 286, 3614, 4253,
4339
United States, 3020, 3708
Uplift pressure, 2008

Validation, 551, 794, 1256, 3574
Vegetation, 2626, 3935, 4188
Velocity, 629, 677, 1116, 1168, 1803,
2666, 3244, 3431, 3453, 3818,
4066, 4353, 4793
Velocity distribution, 565, 1569
Velocity profile, 109, 527, 551

Vietnam, 2820
Virginia, 1985
Viscosity, 2178
Vortices, 186, 1168, 3183, 3888,
3935, 4111, 4821

Waste disposal, 4274
Water depth, 516, 677, 878, 1116,
2324, 3257
Water levels, 1205, 1826, 2244,
2793, 4148
Water pressure, 1603, 3155
Water quality, 403, 2677, 4557
Water surface, 850
Water surface profiles, 629
Water table, 3860, 4120, 4601
Water waves, 55, 81, 186, 275, 340,
457, 465, 502, 516, 527, 589, 657,
677, 717, 731, 878, 889, 1022,
1034, 1074, 1088, 1156, 1168,
1205, 1219, 1256, 1268, 1280,
1375, 1417, 1478, 1528, 1542,
1776, 1862, 2063, 2087, 2166,
2178, 2192, 2377, 2470, 2573,
3020, 3155, 3363, 4174, 4353,
4411
Wave action, 137, 175, 221, 380,
389, 415, 1603, 1679, 1693, 1930,
3048, 3337, 3507, 3784, 3791,
3948, 4038, 4088
Wave attenuation, 1022, 1916, 3349
Wave climatology, 314, 328, 575,
689, 808, 864, 1008, 1233, 1503,
1789, 2022, 2312, 4464, 4517,
4621
Wave diffraction, 2, 731, 754, 1048,
1862, 2063, 2366
Wave dispersion, 95, 300, 668, 767,
836, 941, 1048, 1060, 1116, 1144,
1631, 1652, 1665, 1840, 2077,
2298

- Wave energy, 261, 731, 767, 836,
1156, 1205, 2484, 2598, 2626,
3270, 4583, 4591
- Wave equations, 1452, 2324, 2366
- Wave forces, 415, 1168, 1528, 2008,
2050, 2377, 2494, 2508, 2522,
2534, 2548, 2573, 2584, 3129,
3155, 3467, 3481, 3495, 3507,
3694, 4676
- Wave generation, 55, 165, 443, 479,
493, 668, 677, 1293, 1307, 1321,
1335, 2338
- Wave groups, 151, 165, 493, 677,
1178, 1307, 1335, 1491, 1503,
3006, 3143, 3257, 3546
- Wave height, 67, 221, 247, 261, 300,
328, 368, 537, 689, 717, 743, 767,
794, 808, 850, 900, 1192, 1205,
1389, 1431, 1583, 1679, 2272,
2298, 2560, 2640, 2705, 3270,
4770
- Wave measurement, 354, 368, 429,
527, 537, 565, 616, 629, 643, 689,
703, 781, 1034, 1465, 4636, 4770
- Wave pressure, 575, 1403, 1556,
1762, 2442, 2484, 2522
- Wave propagation, 123, 165, 457,
589, 668, 878, 889, 1074, 1102,
1130, 1156, 1335, 1569, 1998,
2626, 3244, 4134, 4411, 4807
- Wave reflection, 43, 55, 443, 955,
968, 1516, 2077, 2284, 2338,
2366, 2418, 2470, 2598, 2612
- Wave refraction, 2, 754, 1048, 2324,
2366, 2691, 3762, 4505
- Wave runup, 233, 551, 981, 994,
1008, 1431, 1452, 1556, 1916,
2206, 2244, 2793, 3104, 3349,
3770, 4120, 4134, 4601
- Wave spectra, 16, 30, 43, 175, 368,
516, 629, 643, 689, 781, 822, 914,
927, 968, 1247, 2272, 3762
- Wave tanks, 479, 717, 1840, 2428,
3034, 3219, 3680, 3830
- Wave velocity, 502, 1569, 1776
- Waves, 3207, 3219, 3378, 3560,
3722, 4066, 4079, 4148, 4569,
4821
- Weibull density functions, 2272
- Weirs, 3309
- Wetlands, 4314
- Wildlife habitats, 4314
- Wind, 354, 1233
- Wind forces, 781, 2206, 2216, 3363,
4188, 4200, 4214, 4364
- Wind speed, 429, 4770
- Wind velocity, 2705
- Wind waves, 30, 429, 1088, 3363
- Yield strength, 3337

AUTHOR INDEX

Page number refers to the first page of paper

- Ahn, Kyungmo, 657
Ahn, Sung Mo., 1516
Ahrens, John P., 981, 3378
Akedo, Sadamitsu, 4353
Akiyama, Yoshinobu, 3860
Alikhani, A., 1528
Alikhani, Amir, 1693
Allsop, N. W. H., 2508, 2522
Allsop, N. William H., 389
Aminti, P., 1542
Andersen, Henning, 968, 1679
Anglin, C. D., 2230
Annandale, G. W., 2230
Aono, Toshio, 2298
Appleton, William S., 4664
Araki, Hideo, 275
Archetti, Renata, 1693
Arès, Raymond, 2101
Arntsen, Øivind A., 565
Asano, Toshiyuki, 3770
Axe, Philip, 2036
Azarmsa, Seyed Ali, 2442
- Baird, Andrew J., 4120
Bakker, Willem T., 1876, 2857
Baldock, Thomas E., 3006, 4161
Bando, Kozo, 3860
Banijamali, B., 95
Barker, Christopher H., 1034
Barnes, T. C. D., 186, 214
Bartels, A., 4689
Basco, David R., 1060, 1985, 2969
Bascom, Willard N., 3020
Battalio, Robert T., P.E., 2691
Battjes, J. A., 109, 1088, 3337
Battjes, Jurjen A., 175
Bauer, Bernard O., 4214
- Bazhenov, Yuri, 2918
Beach, R. A., 2793, 3207
Beachler, Kim E., P.E., 4613
Beale, Robert G., 389
Beccq, Françoise, 465
Bedford, Keith W., 4289
Beji, Serdar, 1048
Benoit, Michel, 465, 1617
Berlamont, Jean, 836
Bian, J., 354
Bird, Paul A. D., 2077
Birkemeier, William A., 3874, 4052
Black, Kerry, 3284
Boczar-Karakiewicz, B., 3546
Bodge, Kevin R., P.E., 4261
Bollmann, Chad A., 2470
Bona, J. L., 3546
Booij, N., 668, 743
Bos, K. J., 2022
Bosboom, J., 109
Bosma, Kirk F., 2829
Bowen, A. J., 3207
Breeding, J. Ernest, Jr., 677
Breteler, M. Klein, 1556
Breteler, Mark Klein, 1888
Briggs, Michael, 1631
Briggs, Michael J., 1219
Brocchini, M., 186, 4134
Brodie, R. P. (Jock), 4390
Brøker, I., 3048, 4703
Brøker, Ida, 2927, 3805
Browder, Albert E., 2312
Brunone, Bruno, 1569
Bullock, Geoff N., 2077
Bullock, Geoffrey N., 2584
Burcharth, H. F., 1589, 1640

- Burcharth, Hans F., 2560
Burger, G., 1957
- Cadevall, Cristina, 1816
Caires, S., 743
Camfield, Fred E., 1583
Capobianco, Michele, 2884
Caron, Octave, 1233, 1748
Castañeda, A. M., 4014
Chadwick, Andrew, 2036
Chae, J. W., 1268
Chakrabarti, Subrata K., 380
Chakrabarti, Sumita, 380
Chan, Ray T. C., 3006
Chang, Kuang-An, 527
Chawla, Arun, 2
Chen, Qin, 1060
Chen, Renjie, 2312
Cho, Yong-Sik, 955
Christiani, E., 1589
Christopoulos, Spiros, 689
Cialone, Mary A., 3921, 4531
Cieślíkiewicz, Witold, 703, 1375
Cinotto, Charles M., 2206
Claessen, Edward W. M., 2428
Clark, Stephen, 3784
Coates, L. E., 3257
Collins, Michael B., 3948
Cook, Benjamin, 1443
Cornett, A. M., 2230
Cox, Daniel T., 551, 3194
Craig, Kenneth R., II, 602
Creed, Christopher G., 4464
Cruz, Eric C., 2298
Curtis, William R., 2677
- Dally, W. R., 808
Dally, William R., 3419
Dalrymple, Robert A., 731, 1074,
2829
Damgaard, Jesper S., 3614, 3913
d'Angremond, Kees, 1971, 2418
- Davidson, Mark A., 2077
Davies, Michael H., 1679, 1748,
3507
Davies, P., 214
Davis, J. P., 2522
Davis, Jack E., 2677
Davis, Justin, 4242
Davis, Richard A., Jr., 2982
de Haas, Paul, 165
de Jong, Rutger J., 2418
de la Peña, Jose M., 889
de Lange, Willem, 3284
de Looff, A. P., 2770
de Looff, Harry, 2746
de Rouck, Julien, 1603, 1916, 1944
de Somer, Mare, 1916
de Vries, J. M., 4274
de Waal, Johannes P., 2216
Dean, Robert G., 2312, 3115, 3680
Deguchi, Ichiro, 3349, 3888
Deigaard, R., 3048
Deigaard, Rolf, 3805
Demirbilek, Zeki, 1219, 1256
Dennis, John M., 389
Dennis, William A., 4517
Dette, Hans-H., 3442
Diaz Rato, J. L., 1762
Dibajnia, Mohammad, 3104, 3791
DiCastro, Dan, 4376
Dingemans, M. W., 1156, 2022, 4821
Dingemans, Maarten, 165
Dombrowski, Michael R., 3270
Dong, Lifen, 2324
Dong, Ping, 4717
Donnars, Philippe, 1617
Douglass, Scott L., 3708
Dubi, Alfonse, 2626
Dunaszegi, L., 2230
Dupuis, Pierre, 1233, 2101
Duy, Nguyen The, 200

- Ebersole, Bruce A., 2779
Edge, B. L., 2087
Edge, Billy L., 941, 3309
Elbahrawy, Ali, 3976
Eldeberky, Y., 1088
Elfiky, Abd-Elfattah, 3976
Elfrink, Berry, 3805
Elgar, Steve, 3666
Elmongy, Abd-Elmohsen, 3976
Elsaeed, Gamal, 3976
Elwany, M. Hany S., 314
Escartfn, F. Javier, 4014, 4744
- Falqués, Albert, 3560
Faria, A. F. Garcez, 3391
Feddersen, Falk, 3666
Fenton, J. D., 1130
Fenton, John D., 575, 1102
Fernández, A. J., 4418
Fisher, John S., 3750
Fisher, Paul R., 2994
Fleming, Chris, 4339
Fontijn, Henri L., 4228
Foster, D. L., 3207
Fowler, Jimmy, 1631
Fowler, Jimmy E., 3628
Franco, Claudio, 2008
Franco, Leopoldo, 2008
Fredsoe, Jørgen, 3231
Frigaard, P., 1640
Fujiwara, Ryuichi, 16, 1516
Fukumoto, Tadashi, 300
Fukunaga, Masahiko, 2666
Fukushima, Tadahiro, 2666
- Gadd, Peter E., 4397
Galofré, J., 4730
Galofré, Jordi, 4744
García, Cristina, 1816
Gares, Paul A., 4214
Gelfenbaum, Guy, 3453
Glodenis, Marina, 2918
- Gobbi, Maurício F., 1116
Goda, Yoshimi, 261, 629
Golan, Arik, 4376
Goldenbogen, Roland, 3534
Golik, Abraham, 4376
Gomyoh, Michio, 1652
Göricke, Frank, 2142
Gotoh, Hitoshi, 3155, 4300
Gouloumis, Spiros M., 429
Gracia, Vicente, 4098
Graff, Jerzy, 703, 1375
Grant, Geoffrey T., 2152
Gravens, Mark B., 4477
Greated, C. A., 214
Green, Debra R., 1219
Greenwood, B., 3546
Grilli, Stéphan T., 717
Groenewoud, Martin D., 2428, 2857
Grønbech, John, 968, 1679
Grüne, Joachim, 994, 1008
Guillen, Jorge, 2884
Guo, Lulin, 731
Guza, R. T., 3666
- Haines, John W., 3453
Hald, T., 1640
Hallermeier, Robert J., 2705, 3874
Hamill, G. A., 4451, 4557
Hamilton, David G., 3628
Hamm, Luc, 537
Hands, Edward B., 3378
Hanes, Daniel M., 3129, 3846
Hann, D. B., 214
Hansen, Erik Asp, 3805
Hansen, Mark E., 2756
Hanslow, David J., 2244
Hanson, Hans, 4024
Hanzawa, Minoru, 479, 1665
Harari, Pinkhas, 4376
Harcastle, P. J., 3257
Hasegawa, Iwao, 2640
Hashida, Misao, 1022, 3363

- Hashimoto, Noriaki, 30, 629, 1465
Hatada, Yoshio, 1389
Hathaway, Kent K., 4052
Hattori, Masatato, 2456
Haydon, T. R., 214
Healy, Terry, 3284
Hearon, G. E., 2718
Heilman, Daniel J., 3309
Hemsley, J. Michael, P.E., 616
Herbers, T. H. C., 3666
Herbich, John B., 3976
Hewson, Peter J., 2584
Hibbert, Kevin, 2244
Hinata, Hirofumi, 3431
Hoekstra, P., 2897
Holman, R. A., 3207
Holman, Rob, 3521
Holman, Rob A., 3588
Holmes, Patrick, 3006, 4161
Holthuijsen, L. H., 668, 743, 1247
Horikawa, Kiyoshi, 3405, 4188
Horn, Diane P., 4120
Horrrillo, Juan, 717
Hosoi, Yoshihiko, 275
Hotta, Shintaro, 4188
Housley, John G., P.E., 2911
Houwman, K. T., 2897
Houwman, Klaas T., 4793
Howarth, M. W., 2522
Howell, Gary L., 3323
Hsu, John R. C., 3986
Huan, Nguyen Ngoc, 2820
Hubertz, Jon M., 4770
Hughes, Steven A., 2258
Hulscher, S. J. M. H., 3574
Humphery, J. D., 3257
Huntley, David A., 2077, 2612, 3090
Hwang, Ching-Her, 4088
Hwang, K. S., 3219
Hwung, H. H., 3219
Ikeno, Masaaki, 3076
Ilic, Suzana, 2036
Inman, Douglas L., 314
Iranzo, Vicente, 3560
Irie, I., 1840
Irie, Isao, 1022, 1998, 2391
Irish, Jennifer L., 3736
Ishii, Toshimasa, 754
Ishikawa, Motoyasu, 3860
Isobe, Masahiko, 16, 43, 443, 754, 767, 2324
Itabashi, Naoki, 137
Ito, Kazunori, 443
Ito, Shinichi, 2166
Itoh, Sadahiko, 275
Ivanova, Nadya, 2918
Iwata, Koichiro, 2338
Izumiyama, Koh, 4411
Jackson, Derek W. T., 4214
Jaffe, Bruce E., 2756
Jakobsen, Per Roed, 4703
Janssen, C. Marjolein, 4779
Jenkins, Scott A., 314
Jensen, Jacob Hjelmager, 3231
Jensen, Robert E., 781
Jensen, Thomas, 968, 1679
Jeong, W. M., 1268
Jervis, M., 2192
Jetté, Christopher D., 3129
Jeuken, Claire, 4491
Jiang, Qin, 4174
Jiménez, José A., 2806, 4098
Johanson, Hans, 1888
Johnson, Bradley D., 551
Johnston, H. T., 4557
Jones, Bryan N., 1985
Jones, R. J., 2522
Juang, Jea Tzyy, 3762
Juhl, J., 1528
Juhl, Jørgen, 1693

- Jung, K. T., 1268
Justesen, Peter, 3805
- Kaczmarek, Jarka, 4364
Kaczmarek, Leszek M., 3467
Kaihatu, James M., 123, 1144
Kaiser, Ralf, 4621
Kajima, R., 1862
Kakuno, Shohachi, 1516
Kamikubo, Y., 1840
Kamphuis, J. William, 221, 1431, 2258
Kana, Timothy W., 2732, 4314, 4756
Kanada, Shigeo, 4411
Kanazawa, Hiroshi, 2640
Kang, Hong-Yoon, 4601
Kânog'lu, Utku, 1452
Kant, G., 2770, 2820
Kariyazono, Yoshihisa, 2166
Karjadi, Entin A., 233
Karlsson, Robert I., 2152
Kaskevitch, Liya, 2918
Katmarian, R. Eric, 4314
Kato, Hajime, 794, 2391
Katoh, Kazumasa, 2640, 2654
Katori, Sadakazu, 3818
Katsui, Hidehiro, 443, 3183
Kawaguchi, Eiichi, 1349
Kawakami, Hiroshi, 3363
Kawamori, Akira, 1707
Kawanakajima, Y., 4000
Kawasaki, Koji, 2338
Kee, S. T., 2087
Kendall, Thomas, 4664
Kennedy, A. B., 1130
Kennedy, Andrew B., 1102
Khabidov, Alexander, 2918
Kim, Do-Sam, 2338
Kim, M. H., 2087
Kim, Taerim, 3830
Kimura, Akira, 864, 1776, 2272, 2366
Kimura, Katsutoshi, 4676
Kimura, Yoshiaki, 1707
Kioka, Wataru, 1491
Kirby, James T., 2, 123, 1116, 1144, 1361
Kitamura, Fujio, 1465
Klammer, P., 2534
Klopman, G., 109
Klopman, Gert, 165
Knaack, Heiko, 4621
Kobayashi, N., 1721, 1803
Kobayashi, Nobuhisa, 233, 551, 3194, 4148
Kojima, Haruyuki, 927
Komar, P. D., 2718, 2793
Kondo, Hideo, 1707, 4583, 4591
Konicki, Kathryn M., 3588
Kortenhaus, A., 1403, 2534
Kos'yan, R. D., 4111
Koyabu, Tsuyoshi, 275
Kraak, Arie W., 2746
Kranenburg, C., 3337
Kraus, Nicholas C., 3020, 3034, 4024
Krecic, Michael R., 3846
Kriebel, David L., 2470
Kroon, A., 2897
Krylenko, M. V., 4111
Kudale, M. D., 1721
Kumagai, Takahiro, 2843
Kunz, H., 4111
Kunz, Hans, 2128, 3534
Kurata, Katsuhiko, 1516
Kuriyama, Yoshiaki, 247
Kuwabara, Shinji, 1707
Kuznetsov, S. Yu., 4111
Kwan, K. H., 4569
Kweon, Hyuck-Min, 261
- Lai, M.-Y., 914
Lamberti, A., 1542
Lamberti, Alberto, 2352

- Larson, Magnus, 3244
Lastrup, Christian, 2857, 2927
Lee, B. H., 3219
Lee, Jiin Jen, 1293
Lee, Jiin-Jen, 2178, 4325
Lee, Jong-In, 955
Lee, Jong-Kyu, 955
Leidersdorf, Craig B., 4397
Lesnik, John, 1852
Leyden, V. M., 808
Li, Li, 1074
Liaw, S.-R., 2494
Lillycrop, W. Jeff, 3736
Lin, Lihwa, 643, 3295
Lin, Paul C.-P., P.E., 3642
Lin, Po-Ching, 4088
Lissev, Nikolay, 1735
List, Jeffrey H., 2756
Liu, Paul C., 457
Liu, Philip L.-F., 527, 589
Liu, Xiaodong, 2548, 4411
Liu, Zhou, 2560
Long, Charles E., 4052
Losada, I. J., 4418
Losada, M. A., 1762
Loveless, John H., 2152
Lozano, José, 889
Lu, Chia-Chi, 822
Luo, Weimin, 836
Lupón, Nuria, 4014, 4744
- MacIver, Ruairi D., 3481
Maddrell, Roger, 4339
Madsen, Holger Toxvig, 2927
Madsen, P. A., 95, 1178, 3048
Madsen, Per A., 1060
Maeno, Yoshihiko, 3860
Mancinelli, Alessandro, 2352
Mann, Douglas W., P.E., 4613
Mano, Akira, 4505
Mansard, Etienne P. D., 1679, 1748
Manzenrieder, H. A., 4274
- Marcos, Frédéric, 465
Marinski, Jordan, 2484
Martens, Jean-Pierre, 1916
Martin, F. L., 1762
Mase, Hajime, 2366
Mason, Travis, 3948
Mason, Travis E., 4120
Masselink, Gerhard, 4200
Mathew, Joseph, 3284
Matsukawa, Fumihiko, 2640
Matsumi, Yoshiharu, 1776
Matsumoto, Akira, 479
Matsumoto, Teruki, 1321
Matsunaga, Hiroshi, 1516
Matsunaga, Nobuhiro, 1022, 3363
Matsuoka, Gaku, 2166, 4353
McClarty, A., 4689
McDougal, W. G., 2377, 2718, 2793
McGarvey, J. A., 4451
McKee, Philip A., 4314
McKenna, J. E., 2508
Medina, Josep R., 328, 1789, 2871
Medina, R., 4418, 4730
Mehta, Ashish J., 3270
Melby, J. A., 1803
Melby, Jeffrey A., 4664
Méndez, F., 4418
Mesa, Chuck, 4636
Miles, Jonathon R., 2612
Miller, C., 1403
Miller, Herman C., 4517
Mimura, Nobuo, 1349, 2391
Mitsui, Masao, 629
Mizuguchi, M., 493
Mizuguchi, Masaru, 1307, 2598, 3818
Mizuno, Yuzo, 4591, 4676
Mizutani, N., 2377
Mlynarski, Jeffrey M., 1074
Mochizuki, Hitoshi, 1280
Mochizuki, Masashi, 443
Mocke, G. P., 1205

- Moe, Geir, 565
Mohan, Ram K., P.E., 4756
Mohan, Ram Krishna, P.E., 2732
Monbaliu, Jaak, 836
Monsó, José Luis, 1816
Montoto, Amadeu, 3560
Montoya, F. J., 4730
Moore, S. P., 3257
Mori, Nobuhito, 850
Morita, Satoshi, 1280
Moriya, Yoichi, 2598
Mostafa, A. M., 2377
Mounsey, Chris, 4339
Moutzouris, C. I., 403, 1826
Murakami, Hitoshi, 275
Murakami, Keisuke, 927, 1840
Murray, Russell J., 4390
Mutsuda, Hidemi, 300, 2442
- Nadaoka, Kazuo, 1048, 3183, 3431
Nagai, Toshihiko, 629, 1465
Nagase, Satoru, 1307
Nairn, R. B., 2230
Nakagawa, Yasuyuki, 30, 4676
Nakamura, Satoshi, 1503
Nakamura, Takayuki, 1280
Nelson, Raymond C., 3143
Neshaei, M. Ahmad L., 3006
Newe, Jürgen, 3442
Nicholls, Robert J., 3874
Nielsen, Peter, 2244, 3495, 3784,
4066, 4601
Niemeyer, Hanz D., 4621
Nishi, Ryuichiro, 2666, 3034
Nobuoka, Hisamichi, 794, 2391
Nolten, R., 2770
Nwogu, Okey George, 4807
- Ochi, Michel K., 878
O'Donoghue, Tom, 2284
Oh, Tae-Myoung, 3680
Ohara, S., 4000
- O'Hare, Tim J., 2994, 3090
Ohno, Kenichi, 1776
Ohta, Takao, 864, 2272
Okayasu, Akio, 200, 1321
Oliver, John, 1852
O'Neil, Sean, 4289
Ono, Masanobu, 3349, 3888
Osanai, Senji, 4591
Osiecki, Daniel A., 3419
Ostrowski, Rafaxl, 3467
Otay, Emre N., 3722
Otta, A. K., 1156
Oumeraci, H., 1403, 2534
Overton, Margery F., 3750
Owczarczyk, Andrzej, 3901
Oya, Atsushi, 300
Özkan-Haller, H. Tuba, 2, 1361
- Palao, Ian M., 368
Panchang, Vijay, 1256
Panchang, Vijay G., 81
Park, W. S., 1268
Parson, Larry E., 3736
Pattiaratchi, Charitha, 4200
Péchon, Philippe, 2050
Peregrine, D. H., 186, 2192, 2573,
4134
Peters, Karsten, 3442
Petroff, Catherine, 1293, 1443
Phelp, D., 340, 4689
Pilarczyk, K. W., 1556
Pilarczyk, Krystian W., 2114
Pirie, Douglas, 1852
Plant, Nathaniel, 3521
Plotkin, Don, 1852
Pluijm, M., 2770
Podber, David P., 4289
Pollock, Cheryl, 1631
Polnikov, V., 1088
Porter, Mark, 4390
Pruszek, Z., 2820
Pruszek, Zbigniew, 3901

- Purnell, Reg, 4253
Pykhov, N. V., 4111
- Radder, A. C., 1156, 4821
Raichlen, Fredric, 1293
Rakha, K. A., 3048
Raudkivi, Arved J., 2142
Reniers, Ad, 175
Resio, Donald, 1631
Resio, Donald T., 3378
Ribberink, Jan S., 4779
Riddell, Keith J., 4717
Ris, R. C., 668, 1247
Rivero, Francisco J., 1168, 4098
Robillard, David J., 878
Robinson, David A., 4390
Rodríguez, Andrés, 4098
Roelvink, J. A., 109, 2022, 2897
Rogers, W. Erick, 2941
Romańczyk, W., 3546
Rønberg, J. K., 3048
Rosati, Julie D., 3628
Rosati, Julie Dean, 2779
Rose, C. P., 3257
Rosen, Dov S., 4376
Rossouw, Jan, 328
Rossouw, M., 340
Róz'yński, Grzegorz, 4364
Ruessink, B. G., 2897
Ruessink, Gerben, 4793
Ruggiero, P., 2793
Russell, Paul E., 2612
Ryan, Joseph A., P.E., 4650
Rybak, Oleg, 2918
- Sabeur, Zoheir A., 389
Saeki, Hiroshi, 2166
Saito, K., 4000
Sakai, Kazuhiko, 1652
Sakai, Shigeki, 2548, 4411
Sakai, Tetsuo, 3155, 4300
Sakakibara, Hiroshi, 2366
- Sakakiyama, T., 1862
Saleh, Wameidh M., 3481
Sallenger, Asbury H., Jr., 2756
Sánchez-Arcilla, Agustín, 2806, 4098
Sancho, F. E., 1335
Santás, José C., 889
S.-Arcilla, Agustín, 1168
Sasamoto, Makoto, 4411
Sasso, R. Harvey, P.E., 3642
Sato, Hirokazu, 1665
Sato, Koichi, 2166
Sato, Michio, 2666
Savkin, Valery, 2918
Sawamoto, Masaki, 4505
Sawaragi, Toru, 3349, 3888
Schäffer, H. A., 95, 1178
Schäffer, Hemming A., 55
Scheffner, Norman W., 4440
Schiereck, Gerrit J., 1971, 4228
Schofield, Sidney, 643
Schoonees, J. S., 3652
Schroeder, Ernst, 3534
Seabergh, William C., 4531
Seaman, Roy C., 2284
Seelig, William N., 981
Serra, José, 2871
Shah, Adam M., 1431
Shak, Arthur T., P.E., 4650
Sharma, Jagat N., 354
Sheng, Y. Peter, 4242
Shepherd, Ian E., 3169
Sherman, Douglas J., 4214
Shibayama, Tomoya, 200, 3062
Shimizu, Kazuyoshi, 1465
Shimizu, Takao, 3076
Shimizu, Takuzo, 2843
Shimosako, Kenichiro, 1665
Shimosako, Ken-ichiro, 1902
Shin, Cheol S., 2969
Shoshany, Maxim, 4376
Siddabathula, M., 81
Sigurdarson, Sigurdur, 1640

- Silvester, Richard, 3986
Simmonds, David J., 3090
Simons, Richard R., 3481
Skaja, Marek, 4364
Skourup, Jesper, 55
Sloth, Peter, 1693
Smit, F., 1205
Smith, Jane M., 3628
Smith, Susan, 502
Soares, C. Guedes, 743
Sobey, Rodney J., 67, 1034
Solomonidis, Christos, 689
Somers, Christel, 1876
Sørensen, J. Dalsgaard, 1589
Sørensen, O. R., 95, 1178
Sørensen, Ole R., 1060
Sørensen, Per, 2927
Soulsby, Richard L., 3614, 3913
Southgate, Howard N., 286
Spanhoff, R., 2897
Spanhoff, Ruud, 2857
Stansby, P. K., 186
Stanton, T. P., 3391
Stanton, Timothy P., 4079
Stauble, Donald K., 3921, 4531
Steetzel, Henk J., 2746
Stelling, Guus S., 1876
Stive, Marcel J. F., 2884
Stoutjesdijk, Theo, 1888
Strange, R. Rea, III, 822
Stripling, Stuart, 286
Suriamihardja, D. A., 3694
Suzuki, Kojiro, 1652, 1902
Suzuki, Yasuyuki, 1321
Svendsen, I. A., 151, 1192, 1335
Swan, C., 4569
Swan, Christopher, 502
Synolakis, Costas Emmanuel, 1452,
1478

Tada, Akihide, 300
Tadepalli, Srinivas, 1478

Takahashi, Atsushi, 4545
Takahashi, Fumihiko, 4545
Takahashi, Shigeo, 1652, 1665, 1902
Takahashi, Tomoharu, 629
Takayama, Tomotsuka, 1665
Takayama, Tomotuka, 1652
Takewaka, Satoshi, 1998
Tanaka, Hitoshi, 4545
Tanimoto, Katsutoshi, 1665, 3405
Tega, Yukiko, 4148
Teisson, Charles, 2050
Teng, Chung-Chu, 368
Theron, A. K., 3652
Thevenot, Michelle M., 4024
Thieke, Robert J., 602
Thompson, Edward F., 4440
Thorne, P. D., 3257
Thornton, E. B., 3391
Thornton, Edward B., 4079
Togashi, Hiroyoshi, 2063
Toita, H., 493
Tokubuchi, Katsumasa, 1902
Tomasicchio, G. R., 1528
Tomasicchio, Giuseppe R., 1569
Tomasicchio, Ugo, 2404
Tönjes, Patrick, 2216
Tørum, Alf, 1735, 2626
Toue, Takao, 3183
Tournier, Jean-Pierre, 1233, 2101
Townsend, Murray, 575
Trampenau, Thomas, 2142
Trivedi, Dilip, P.E., 2691
Trizno, Anatoly, 2918
Troch, Peter, 1916
Tryggestad, S., 354
Tsai, Chin-Chi, 4088
Tsai, Li-Hung, 4088
Tsay, Ting-Kuei, 589
Tsoukala, V. K., 403
Tsuchiya, Yoshito, 3694, 4038
Tsujiimoto, Gozo, 3935
Tsujioka, Nobuaki, 2456

- Tsuruya, Hiroichi, 30, 4676
Turner, Ian L., 2677
Turnham, J., 2230
Tutuarima, W. H., 1957
Tzang, S.-Y., 2494
- Uchida, K., 4000
Uda, T., 4000
Uda, Takaaki, 137
Uittenbogaard, R. E., 4821
- van Damme, Luc, 1603, 1916, 1944
van de Graaff, Jan, 2428, 2857
van der Biezen, Stephan C., 2428
van der Meer, Jentsje W., 1957,
2008, 2216, 2418
van der Meulen, Ton, 1971
Van Dongeren, A. R., 1335
van Endt, M., 743
van Gent, Marcel R. A., 1930
van Hove, Conan, 1916
van Kessel, Thijs, 3337
van Kester, J. A. Th. M., 4821
van Kuik, Christine, 1876
Vann, A. M., 2522
Vaudrey, Kennon D., 4397
Veeramony, J., 151, 1192
Verhagen, Henk Jan, 4431
Verhagen, L. A., 516
Vermeir, Dierik, 1916
Vicinanza, D., 2508
Vidal, C., 1762
Vidaor, Alfonso, 1816, 4014, 4744
Vincent, Charles L., 781
Vinh, Ton That, 2820
Voulgaris, George, 3948
- Wada, Akira, 4353
Walkden, Michael J. A., 2584
Walker, S. A., 4557
Walstra, D. J. R., 1205
Wang, Hsiang, 643, 3295, 3830
- Wang, Ping, 2982
Wang, Xu, 3295
Wang, Zeya, 1008
Ward, Donald L., 2206
Watabe, Tomiji, 4591
Watanabe, Akira, 754, 767, 2324,
2843, 3104, 3791, 3818, 4174
Watson, Gary, 1417
Watts, Philip, 1293
West, J. R., 3257
White, Thomas E., 3962
Whitehouse, Richard J. S., 3913
Whittaker, T. T. J., 2508
Wibner, Christopher G., 2206
Wiegel, Robert L., 3020
Wierzchnicki, Ryszard, 3901
Wijnberg, Kathelijne M., 3600
Williams, J. J., 3257
Wilson, D. J., 3257
Winyu, Rattanapitikon, 3062
Wood, D. J., 2573
Work, Paul A., 2941, 3722
Wu, Ji, 3762
Wu, Lilun, 4325
Wu, Nan-Jing, 589
Wutkowski, Michael, 4440
Wutkowski, Michael J., 4517
- Xu, Bingyi, 1256
Xu, Jianlu, 67
- Yabe, Kouichi, 3860
Yagi, Hiroshi, 3431
Yamaguchi, Masataka, 900, 1389
Yamaji, Kosuke, 137
Yamamoto, Shogo, 767
Yamamoto, Yoshimichi, 137, 3405
Yamashiro, Masaru, 927
Yamashita, Takao, 1417
Yamashita, Toshihiko, 2166, 4353
Yanagishima, Shin-ichi, 2654
Yano, Kenji, 4353

- Yasuda, Takashi, 300, 850, 2442
Yedapin, Veniamin, 2918
Yim, John Z., 914
Yokoki, Hiromune, 43
Yokota, K., 4000
Yoshida, Akinori, 927
You, Zai-Jin, 3495, 4066
Young, I. R., 516
Yu, Ke, 1192
Yu, Xiping, 2063
Yu, Yu-xiu, 415
Zawadzka, Elz'bieta, 2955
Zeidler, Ryszard B., 3901, 4364
Zelensky, Grigory, 2918
Zhang, Jun, 2206
Zhang, L., 2087
Zhang, Libang, 941
Zhang, Ning-chuan, 415
Zhao, Qun, 415
Zheng, Jie, 3115
Zhuang, Fei, 2178
Zyserman, J. A., 4703

Volume 2

Coastal Engineering 1996

Proceedings of the
twenty-fifth international conference

September 2-6, 1996
The Peabody Hotel
Orlando, Florida

Held under the auspices of the
Coastal Engineering Research Council of the
American Society of Civil Engineers

Edited by Billy L. Edge

Published by the

ASCE *American Society
of Civil Engineers*

345 East 47th Street
New York, New York 10017-2398

Abstract:

This proceedings contains over 370 papers presented at the 25th International Conference on Coastal Engineering which was held in Orlando, Florida, 2-6 September, 1996. The book is divided into six parts: 1) Characteristics of coastal waves and currents; 2) long waves and storm surges; 3) coastal structures; 4) coastal processes and sediment transport; 5) coastal, estuarine and environmental problems; and 6) case studies. The individual papers include such topics as the effects of wind, waves, storms and currents as well as the study of sedimentation, erosion and beach nourishment. Special emphasis is given to case studies of completed engineering projects. With the inclusion of both theoretical and practical information, these papers provide the civil engineer and professionals in related fields with a broad range of information on coastal engineering.

Library of Congress Cataloging-in-Publication Data

Coastal engineering 1996 : proceedings of the twenty-fifth international conference, September 2-6, 1996, The Peabody Hotel, Orlando, Florida / edited by Billy L. Edge.

p. cm.

“Held under the auspices of the Coastal Engineering Research Council of the American Society of Civil Engineers.”

ISBN 0-7844-0242-6

1. Coastal engineering--Congresses. 2. Ocean waves--Congresses. I. Edge, Billy L. II. Coastal Engineering Research Council (U.S.) III. International Conference on Coastal Engineering (25th : 1996 : Orlando, Fla.)

TC203.5.C6184 1997

97-10664

627'.58--dc21

CIP

The Society is not responsible for any statements made or opinions expressed in its publications.

Photocopies. Authorization to photocopy material for internal or personal use under circumstances not falling within the fair use provisions of the Copyright Act is granted by ASCE to libraries and other users registered with the Copyright Clearance Center (CCC) Transactional Reporting Service, provided that the base fee of \$4.00 per article plus \$.25 per page is paid directly to CCC, 222 Rosewood, Drive, Danvers, MA 01923. The identification for ASCE Books is 0-7844-0242-6/97/\$4.00 + \$.25 per copy. Requests for special permission or bulk copying should be addressed to Permissions & Copyright Dept., ASCE.

Copyright © 1997 by the American Society of Civil Engineers,
All Rights Reserved.

Library of Congress Catalog Card No: 97-10664

ISBN 0-7844-0242-6

Manufactured in the United States of America.

Cover: One year after nourishment at Palm Beach, Florida. Photo courtesy of Applied Technology & Management, Inc. and Aerial Photography, Inc.

CONTENTS

Part I Characteristics of Coastal Waves and Currents

CHAPTER 1	
Experimental Study of Breaking Waves over a Shoal	2
<i>Arun Chawla, H. Tuba Ozkan-Haller, James T. Kirby</i>	
CHAPTER 2	
A Method for Estimating Standardized Bimodal Directional Spectra	16
<i>Ryuichi Fujiwara, Masahiko Isobe</i>	
CHAPTER 3	
The Effects of Currents on Estimations of Directional Wave Spectra	30
<i>Yasuyuki Nakagawa, Hiroichi Tsuruya, Noriaki Hashimoto</i>	
CHAPTER 4	
A Method for Estimating Directional Spectra in a Field of Incident and Reflected Waves	43
<i>Hiromune Yokoki, Masahiko Isobe</i>	
CHAPTER 5	
Active Absorption of Multidirectional Waves	55
<i>Hemming A. Schaffer, Jesper Skourup</i>	
CHAPTER 6	
Time-Averaged Wave Field Evolution in Coastal Zone	67
<i>Jianlu Xu, Rodney J. Sobey</i>	
CHAPTER 7	
Quality Control of GEOSAT Wave Data for Engineering Applications	81
<i>M. Siddabathula, Vijay G. Panchang</i>	
CHAPTER 8	
Boussinesq Type Equations with High Accuracy in Dispersion and Nonlinearity	95
<i>P.A. Madsen, B. Banijamali, H.A. Schaffer, O.R. Sorensen</i>	
CHAPTER 9	
Wave Kinematics Computations Using Boussinesq Models	109
<i>J. Bosboom, G. Klopman, J.A. Roelvink, J.A. Battjes</i>	
CHAPTER 10	
Effects of Mode Truncation and Dissipation on Predictions of Higher Order Statistics ..	123
<i>James M. Kaihatu, James T. Kirby</i>	
CHAPTER 11	
Field Observation of Movement of Sand Body Due to Waves and Verification of Its Mechanism by Numerical Model	137
<i>Takaaki Uda, Yoshimichi Yamamoto, Naoki Itabashi, Kosuke Yamaji</i>	

CHAPTER 12	
Wave Groups in the Surf-Zone: Model & Experiments	151
<i>J. Veeramony, I. A. Svendsen</i>	
CHAPTER 13	
Simulation of Propagating Nonlinear Wave Groups	165
<i>Paul de Haas, Maarten Dingemans, Gert Klopmann</i>	
CHAPTER 14	
Cross-Shore Momentum Flux Due to Shear Instabilities	175
<i>Ad Reniers, Jurjen A. Battjes</i>	
CHAPTER 15	
Modelling Post-Wave Breaking Turbulence and Vorticity	186
<i>T.C.D. Barnes, M. Brocchini, D.H. Peregrine, P.K. Stansby</i>	
CHAPTER 16	
A Turbulent Flow Model for Breaking Waves	200
<i>Nguyen The Duy, Tomoya Shibayama, Akio Okayasu</i>	
CHAPTER 17	
Turbulence Structures in the Surf Zone	214
<i>T.R. Haydon, D.B. Hann, P. Davies, C.A. Greated, T.C.D. Barnes</i>	
CHAPTER 18	
Experiments on Design Wave Height in Shallow Water	221
<i>J. William Kamphuis</i>	
CHAPTER 19	
Time-Dependent Quasi-3D Modeling of Breaking Waves on Beaches	233
<i>Entin A. Karjadi, Nobuhisa Kobayashi</i>	
CHAPTER 20	
Models of Wave Height and Fraction of Breaking Waves on a Barred Beach	247
<i>Yoshiaki Kuriyama</i>	
CHAPTER 21	
A Parametric Model for Random Wave Deformation by Breaking on Arbitrary Beach Profiles	261
<i>Hyuck-Min Kweon, Yoshimi Goda</i>	
CHAPTER 22	
Generation Characteristics of Wave Sounds as a Factor of Beach Amenity	275
<i>Hitoshi Murakami, Sadahiko Itoh, Yoshihiko Hosoi, Hideo Araki and Tsuyoshi Koyabu</i>	
CHAPTER 23	
Measurements of Wave Breaking in the UK Coastal Research Facility	286
<i>Howard N. Southgate, Stuart Stripling</i>	
CHAPTER 24	
A New Type Breaker Forming a Giant Jet and Its Decaying Properties	300

CHAPTER 25	
Wave Climate Cycles and Coastal Engineering Practice	314
<i>Douglas L. Inman, Scott A. Jenkins, M. Hany S. Elwany</i>	
CHAPTER 26	
Stability of Design Wave Estimates	328
<i>Jan Rossouw, Josep R. Medina</i>	
CHAPTER 27	
An Evaluation of Two Wave Forecast Models for the South African Region	340
<i>M. Rossouw, D. Phelp</i>	
CHAPTER 28	
A Comprehensive Wind, Wave, and Current Measurement Program in the South China Sea	354
<i>Jagat N. Sharma, S. Tryggestad, J. Bian</i>	
CHAPTER 29	
Wave Height and Period Distributions from Long-Term Wave Measurement	368
<i>Chung-Chu Teng, Ian M. Palao</i>	
CHAPTER 30	
Interference of Small Structures in the Vicinity of Large Structures	380
<i>Subrata K. Chakrabarti, Sumita Chakrabarti</i>	
CHAPTER 31	
Wave Dynamics at Coastal Structures: Development of a Numerical Model for Free Surface Flow	389
<i>Zoheir A. Sabeur, N. William H. Allsop, Robert G. Beale, John M. Dennis</i>	
CHAPTER 32	
Scale Effects in Oxygenation in the Breaker Zone of Coastal Structures	403
<i>V.K. Tsoukala, C.I. Moutzouris</i>	
CHAPTER 33	
Wave Actions on a Vertical Cylinder in Multi-Directional Random Waves	415
<i>Yu-xiu Yu, Ning-chuan Zhang, Qun Zhao</i>	
CHAPTER 34	
Wind/Wave Relation and the Pressure Gradient Effect	429
<i>Spiros M. Gouloumis</i>	
CHAPTER 35	
Non-Reflected Multi Directional Wave Maker Theory and Experiments of Verification ..	443
<i>Kazumori Ito, Hidehiro Katsui, Masashi Mochizuki, Masahiko Isobe</i>	
CHAPTER 36	
Fifty Years of Wave Growth Curves	457
<i>Paul C. Liu</i>	

CHAPTER 37	
Development of a Third Generation Shallow-Water Wave Model with Unstructured Spatial Meshing	465
<i>Michel Benoit, Frederic Marcos, Francoise Becq</i>	
CHAPTER 38	
New Optimization Method for Paddle Motion of Multi-Directional Wavemaker	479
<i>Akira Matsumoto, Minoru Hanzawa</i>	
CHAPTER 39	
Generation of Second-Order Long Waves by a Wave Group in a Laboratory Flume and Its Control	493
<i>M. Mizuguchi, H. Toita</i>	
CHAPTER 40	
Kinematic Predictions in Large Shallow Water Waves	502
<i>Susan Smith, Christopher Swan</i>	
CHAPTER 41	
Fetch Limited Spectral Evolution in Finite Depth Water	516
<i>I.R. Young, L.A. Verhagen</i>	
CHAPTER 42	
Measurement of Breaking Waves Using Particle Image Velocimetry	527
<i>Kuang-An Chang, Philip L.-F. Liu</i>	
CHAPTER 43	
Computation of the Near-Bottom Kinematics of Shoaling Waves	537
<i>Luc Hamm</i>	
CHAPTER 44	
Formulation and Validation of Vertically 2-D Shallow-Water Wave Model	551
<i>Bradley D. Johnson, Nobuhisa Kobayashi, Daniel T. Cox</i>	
CHAPTER 45	
Particle Velocity Distribution in Surface Waves	565
<i>Geir Moe, Oivind A. Arntsen</i>	
CHAPTER 46	
A Comparison of Analysis Methods for Wave Pressure Data	575
<i>Murray Townsend, John D. Fenton</i>	
CHAPTER 47	
A Nonlinear Model for Wave Propagation	589
<i>Ting-Kuei Tsay, Philip L.-F. Liu, Nan-Jing Wu</i>	
CHAPTER 48	
Application of a Digital Particle Image Velocimetry (DPIV) System to Breaking Waves in the Surf Zone	602
<i>Kenneth R. Craig, Robert J. Thieke</i>	

CHAPTER 49	
Wave Gauging Networks Worldwide - An Overview616
<i>J. Michael Hemsley</i>	
CHAPTER 50	
Improvement of Submerged Doppler-Type Directional Wave Meter and its Application to Field Observations629
<i>Noriaki Hashimoto, Masao Mitsui, Yoshimi Goda, Toshihiko Nagai, Tomoharu Takahashi</i>	
CHAPTER 51	
Comparison of Directional Wave Data Quality from Two Different Monitoring Systems643
<i>Lihwa Lin, Sidney Schofield, Hsiang Wang</i>	
CHAPTER 52	
The Digital Simulation of Non-Linear Random Waves657
<i>Kyungmo Ahn</i>	
CHAPTER 53	
The “SWAN” Wave Model for Shallow Water668
<i>N. Booij, L.H. Holthuijsen, R.C. Ris</i>	
CHAPTER 54	
Generation Depths from Water Wave Data677
<i>J. Ernest Breeding, Jr.</i>	
CHAPTER 55	
Wave Climate Assessment in the South Aegean Shelf689
<i>Spiros Christopoulos, Christos Solomonidis</i>	
CHAPTER 56	
Sea State Parameterisation Using Empirical Orthogonal Functions703
<i>Witold Cieslikiewicz, Jerzy Graff</i>	
CHAPTER 57	
Fully Nonlinear Properties of Periodic Waves Shoaling over Slopes717
<i>Stephan T. Grilli, Juan Horrillo</i>	
CHAPTER 58	
Water Wave Fluctuations Induced by Irregular Bathymetry731
<i>Lulin Guo, Robert A. Dalrymple</i>	
CHAPTER 59	
Integral Control Data Assimilation in Wave Predictions743
<i>L.H. Holthuijsen, N. Booij, M. van Endt, S. Caires, C. Guedes Soares</i>	
CHAPTER 60	
Two-Dimensional Analysis of Wave Transformation by Rational-Approximation-Based, Time-Dependent Mild-Slope Equation for Random Waves754
<i>Toshimasa Ishii, Masahiko Isobe, Akira Watanabe</i>	

CHAPTER 61	
Nonlinear Wave Transformation Due to a Submerged Breakwater767
<i>Masahiko Isobe, Akira Watanabe, Shogo Yamamoto</i>	
CHAPTER 62	
Observed and Modeled Wave Results from Near-Stationary Hurricanes781
<i>Charles L. Vincent, Robert E. Jensen</i>	
CHAPTER 63	
Estimation of Persistence Statistics of the Waves Observed on Japanese Coast in the Light of Recent Studies794
<i>Hajime Kato, Hisamichi Nobuoka</i>	
CHAPTER 64	
Probabilistic Modeling of Long-Term Wave Climate808
<i>V.M. Leyden, W.R. Dally</i>	
CHAPTER 65	
Monte Carlo Simulation for Nearshore Wave Statistics in Southern California822
<i>Chia-Chi Lu, R. Rea Strange III</i>	
CHAPTER 66	
Bottom Friction Dissipation in the Belgian Coastal Regions836
<i>Weimin Luo, Jaak Monbaliu, Jean Berlamont</i>	
CHAPTER 67	
Weakly non-Gaussian Model of Wave Height Distribution for Nonlinear Random Waves .	.850
<i>Nobuhito Mori, Takashi Yasuda</i>	
CHAPTER 68	
An Attempt at Applying the Chaos Theory to Wave Forecasting864
<i>Takao Ohta, Akira Kimura</i>	
CHAPTER 69	
Transition of Stochastic Characteristics of Waves in the Nearshore Zone878
<i>David J. Robillard, Michel K. Ochi</i>	
CHAPTER 70	
Monitoring and Modelling on Shallow Water Wave Propagations in “El Saler” Beach ..	.889
<i>Jose C. Santos, Jose M. de la Pena, Jose Lozano</i>	
CHAPTER 71	
Intercomparison of Parameter Estimation Methods in Extremal Wave Analysis900
<i>Masataka Yamaguchi</i>	
CHAPTER 72	
Influences of Spectral Shapes on the Statistical Properties of Simulated Random Waves .	.914
<i>John Z. Yim, M.-Y. Lai</i>	
CHAPTER 73	
Second-Order Interaction between Random Wave and Submerged Obstacle927

CHAPTER 74	
A Uniform Mild-Slope Model for Waves over Varying Bottom941
<i>Libang Zhang, Billy L. Edge</i>	
CHAPTER 75	
Bragg Reflection of Shallow-Water Waves on a Sloping Beach955
<i>Yong-Sik Cho, Jong-In Lee, Jong-Kyu Lee</i>	
CHAPTER 76	
Reflection Analysis with Separation of Cross Modes968
<i>John Gronbech, Thomas Jensen, Henning Andersen</i>	
CHAPTER 77	
Wave Runup on Beaches981
<i>John P. Ahrens, William N. Seelig</i>	
CHAPTER 78	
Field Study on Wave Run-Up on Seadykes994
<i>Joachim Grune</i>	
CHAPTER 79	
Wave Run-Up on Revetments with Composite Slopes1008
<i>Zeya Wang, Joachim Grune</i>	
CHAPTER 80	
Landward Transport of Spray Generated from a Wave Absorbing Sea Wall1022
<i>Misao Hashida, Nobuhiro Matsunaga, Isao Irie</i>	
CHAPTER 81	
Irregular Wave Kinematics from a Pressure Record1034
<i>Christopher H. Barker, Rodney J. Sobey</i>	
CHAPTER 82	
Nonlinear Refraction-Diffraction of Surface Waves over Arbitrary Depths1048
<i>Serdar Beji, Kazuo Nadaoka</i>	
CHAPTER 83	
Boussinesq Equations with Improved Doppler Shift and Dispersion for Wave/Current Interaction1060
<i>Qin Chen, Per A. Madsen, Ole R. Sorensen, David R. Basco</i>	
CHAPTER 84	
The Propagation of Water Waves in Prismatic Channels1074
<i>Li Li, Robert A. Dalrymple, Jeffrey M. Mlynarski</i>	
CHAPTER 85	
A Statistical Approach for Modeling Triad Interactions in Dispersive Waves1088
<i>Y. Eldeberky, V. Polnikov, J. A. Battjes</i>	

CHAPTER 86	
A Fully Nonlinear 3D Method for the Computation of Wave Propagation	1102
<i>Andrew B. Kennedy, John D. Fenton</i>	
CHAPTER 87	
A Fourth Order Boussinesq-Type Wave Model	1116
<i>Mauricio F. Gobbi, James T. Kirby</i>	
CHAPTER 88	
Fast Methods for Computing the Shoaling of Nonlinear Waves	1130
<i>J.D. Fenton, A.B. Kennedy</i>	
CHAPTER 89	
Structure of Frequency Domain Models for Random Wave Breaking	1144
<i>James T. Kirby, James M. Kaihatu</i>	
CHAPTER 90	
A Hamiltonian Model for Nonlinear Water Waves and Its Applications	1156
<i>A.K. Otta, M.W. Dingemans, A.C. Radder</i>	
CHAPTER 91	
The Role of Wave-Induced Shear Stresses in the Momentum Balance Equations	1168
<i>Francisco J. Rivero, Agustin S.-Arcilla</i>	
CHAPTER 92	
Nonlinear Wave Dynamics in the Surf Zone	1178
<i>O.R. Sorensen, P.A. Madsen, H.A. Schaffer</i>	
CHAPTER 93	
A Boussinesq Breaking Wave Model with Vorticity	1192
<i>I.A. Svendsen, Ke Yu, J. Veeramony</i>	
CHAPTER 94	
Roller Contributions as Inferred from Inverse Modelling Techniques	1205
<i>D.J.R. Walstra, G.P. Mocke, F. Smit</i>	
CHAPTER 95	
Wave-Current Interaction in Inlets	1219
<i>Michael J. Briggs, Zeki Demirbilek, Debra R. Green</i>	
CHAPTER 96	
Wave Climate of Large Reservoirs and a Revised Wave Hindcast Formula	1233
<i>Pierre Dupuis, Jean-Pierre Tournier, Octave Caron</i>	
CHAPTER 97	
Spectral Modelling of Current Induced Wave-Blocking	1247
<i>R.C. Ris, L.H. Holthuijsen</i>	

Part II Long Period Waves, Storm Surges and Wave Groups

CHAPTER 98	
Uncertainties in the Validation of Harbor Wave Models	1256
<i>Zeki Demirbilek, Bingyi Xu, Vijay Panchang</i>	
CHAPTER 99	
Field Measurements and Numerical Modeling of Harbor Oscillations During Storm Waves	1268
<i>W.M. Jeong, J.W. Chae, W.S. Park, K.T. Jung</i>	
CHAPTER 100	
Performance of a Resonator Designed by the Wave Filter Theory - Applicability to a Harbor	1280
<i>Takayuki Nakamura, Hitoshi Mochizuki, Satoshi Morita</i>	
CHAPTER 101	
The Generation of Waves by a Landslide: Skagway, Alaska - A Case Study	1293
<i>Fredric Raichlen, Jiin Jen Lee, Catherine Petroff, Philip Watts</i>	
CHAPTER 102	
Laboratory Experiment on Long Wave Generation by Time-Varying Breakpoint	1307
<i>Satoru Nagase, Masaru Mizuguchi</i>	
CHAPTER 103	
Laboratory Experiments on Generation of Long Waves in the Surf Zone	1321
<i>Akio Okayasu, Teruki Matsumoto, Yasuyuki Suzuki</i>	
CHAPTER 104	
Generation of Infragravity Waves	1335
<i>A. R. van Dongeren, I.A. Svendsen, F.E. Sancho</i>	
CHAPTER 105	
Responses of Coastal Topography to Sea-Level Rise	1349
<i>Nobuo Mimura, Eiichi Kawaguchi</i>	
CHAPTER 106	
Numerical Study of Low Frequency Surf Zone Motions	1361
<i>H. Tuba Ozkan-Haller, James T. Kirby</i>	
CHAPTER 107	
Neptune - An Integrated Approach to Determining NW European Coastal Extremes ...	1375
<i>Jerzy Graff, Witold Cieslikiewicz</i>	
CHAPTER 108	
A Stochastic Typhoon Model and Its Application to the Estimation of Extremes of Storm Surge and Wave Height	1389
<i>Yoshio Hatada, Masataka Yamaguchi</i>	

CHAPTER 109	
Design of Vertical Walls Against Storm Surge	1403
<i>A. Kortenhaus, C. Miller, H. Oumeraci</i>	
CHAPTER 110	
Nearshore, Wave and Topographic Effects in Storm Surges	1417
<i>Gary Watson, Takao Yamashita</i>	
CHAPTER 111	
The Swash Zone: A Focus on Low Frequency Motion	1431
<i>Adam M. Shah, J. William Kamphuis</i>	
CHAPTER 112	
The Development of an On-Line, Interactive, Tsunami-Information Resource	1443
<i>Benjamin Cook, Catherine Petroff</i>	
CHAPTER 113	
Long Wave Runup on Coastal Structures	1452
<i>Utku Kanoglu, Costas Emmanuel Synolakis</i>	
CHAPTER 114	
Offshore Tsunami Profiles Observed at the Coastal Wave Stations	1465
<i>Toshihiko Nagai, Noriaki Hashimoto, Kazuyoshi Shimizu, Fujio Kitamura</i>	
CHAPTER 115	
A Realistic Model for the 1992-96 Tidal Waves	1478
<i>Srinivas Tadepalli, Costas Emmanuel Synolakis</i>	
CHAPTER 116	
Long-Period Oscillations in a Harbour Caused by Typhoon	1491
<i>Wataru Kioka</i>	
CHAPTER 117	
Estimation of Wave Groups Parameter from Wave Climate Statistics	1503
<i>Satoshi Nakamura</i>	

Part III Coastal Structures

CHAPTER 118	
Reflection Coefficients of the Step-Shaped Slit Caisson on the Rubble Mound	1516
<i>Sung Mo Ahn, Ryuichi Fujiwara, Hiroshi Matsunaga, Katsuhiko Kurata, Shohachi Kakuno</i>	
CHAPTER 119	
Berm Breakwater Trunk Exposed to Oblique Waves	1528
<i>A. Alikhani, G.R. Tomasicchio, J. Juhl</i>	
CHAPTER 120	
Interaction Between Main Armour and Toe Berm Damage	1542
<i>P. Aminti, A. Lamberti</i>	

CHAPTER 121	
Stability of Artificial Roughness Elements and Run-Up Reduction	1556
<i>M. Klein Breteler, K.W. Pilarczyk</i>	
CHAPTER 122	
Wave Induced Velocities at a Rubble Mound Breakwater	1569
<i>Bruno Brunone, Giuseppe R. Tomasicchio</i>	
CHAPTER 123	
Natural Periods of Armor Stones	1583
<i>Fred E. Camfield</i>	
CHAPTER 124	
Reliability Based Optimal Design of Vertical Breakwaters Modelled as a Series System of Failure	1589
<i>E. Christiani, H.F. Burcharth, J. Dalsgaard Sorensen</i>	
CHAPTER 125	
Overall Slope Stability Analysis of Rubble Mound Breakwaters	1603
<i>Julien De Rouck, Luc Van Damme</i>	
CHAPTER 126	
Interactions in the Stability of Toe-Berm and Main-Armour for Rubble-Mound Breakwaters: An Experimental Study	1617
<i>Philippe Donnars, Michel Benoit</i>	
CHAPTER 127	
Potential Uses for the Rapidly Installed Breakwater System	1631
<i>Jimmy Fowler, Donald Resio, Michael Briggs, Cheryl Pollock</i>	
CHAPTER 128	
Stability of Reshaping Breakwaters with Special Reference to Stone Durability	1640
<i>P. Frigaard, T. Hald, H.F. Burcharth, Sigurdur Sigurdarson</i>	
CHAPTER 129	
Field Investigations on Wave-Dissipating Concrete Blocks Covering Vertical Wall Breakwater	1652
<i>Michio Gomyoh, Kazuhiko Sakai, Tomotuka Takayama, Kojiro Suzuki, Shigeo Takahashi</i>	
CHAPTER 130	
New Stability Formula for Wave-Dissipating Concrete Blocks Covering Horizontally Composite Breakwaters	1665
<i>Minoru Hanzawa, Hirokazu Sato, Shigeo Takahashi, Kenichiro Shimosako, Tomotsuka Takayama, Katsutoshi Tanimoto</i>	
CHAPTER 131	
Breakwater Stability under Regular and Irregular Wave Attack	1679
<i>Thomas Jensen, Henning Andersen, John Gronbech, Etienne P.D. Mansard, Michael H. Davies</i>	
CHAPTER 132	
Roundhead Stability of Berm Breakwaters	1693

CHAPTER 133	
Improvement of Composite Breakwater on Solid Bottom Against Severe Tsunamis	1707
<i>Yoshiaki Kimura, Hideo Kondo, Shinji Kuwabara, Akira Kawamori</i>	
CHAPTER 134	
Hydraulic Stability Analysis of Leaside Slopes of Overtopped Breakwaters	1721
<i>M.D. Kudale, N. Kobayashi</i>	
CHAPTER 135	
Influence of the Core Configuration on the Stability of Berm Breakwaters	1735
<i>Nikolay Lissev, Alf Torum</i>	
CHAPTER 136	
Model Study of Reservoir Riprap Stability	1748
<i>Etienne P. D. Mansard, Michael H. Davies, Octave Caron</i>	
CHAPTER 137	
Prototype Measurements of Wave Pressures on a Wave Screen: Comparison to Physical and Analytical Models	1762
<i>F.L. Martin, M. A. Losada, C. Vidal, J.L. Diaz Rato</i>	
CHAPTER 138	
Velocity Field Measurements over Breakwater Heads under 3D Waves	1776
<i>Yoshiharu Matsumi, Akira Kimura, Kenichi Ohno</i>	
CHAPTER 139	
Wave Climate Simulation and Breakwater Stability	1789
<i>Josep R. Medina</i>	
CHAPTER 140	
Incipient Motion of Breakwater Armor Units	1803
<i>J. A. Melby, N. Kobayashi</i>	
CHAPTER 141	
Overtopping Reduction in Crownwall Design	1816
<i>Jose Luis Monso, Alfonso Vidoar, Cristina Cadevall, Cristina Garcia</i>	
CHAPTER 142	
Stable Profiles of Reshaping Breakwaters with a Berm Below the Water Level	1826
<i>C.I. Moutzouris</i>	
CHAPTER 143	
Experiments on a Non-Wave Overtopping Type Seawall	1840
<i>Keisuke Murakami, I. Irie, Y. Kamikubo</i>	
CHAPTER 144	
A Condition and Performance Rating System for Breakwaters and Jetties	1852
<i>John Oliver, Don Plotkin, John Lesnik, Douglas Pirie</i>	

CHAPTER 145
Wave Overtopping and Stability of Armor Units under Multidirectional Waves1862
T. Sakakiyama, R. Kajima

CHAPTER 146
Numerical Modeling of Breach Growth in a Sanddike1876
Guus S. Stelling, Willem T. Bakker, Christine van Kuik, Christel Somers

CHAPTER 147
Aging and Stability of Placed Block Revetments1888
Theo Stoutjesdijk, Hans Johanson, Mark Klein Breteler

CHAPTER 148
Experimental Analysis of the Settlement Failure Mechanism Shown by Caisson-Type Seawalls1902
Shigeo Takahashi, Kojiro Suzuki, Katsumasa Tokubuchi, Ken-ichiro Shimosako

CHAPTER 149
Full Scale Measurements of Wave Attenuation Inside a Rubble Mound Breakwater ...1916
Peter Troch, Marc De Somer, Julien De Rouck, Luc van Damme, Dierik Vermeir, Jean-Pierre Martens, Conan van Hove

CHAPTER 150
Numerical Modelling of Wave Interaction with Dynamically Stable Structures1930
Marcel R.A. van Gent

CHAPTER 151
Monitoring of Zeebrugge Breakwaters1944
Luc van Damme, Julien de Rouck

CHAPTER 152
Influence of Rock Shape and Grading on Stability of Low-Crested Structures1957
Jentsje W. van der Meer, W.H. Tutuarima, G. Burger

CHAPTER 153
Toe Stability of Rubble Mound Breakwaters1971
Ton van der Meulen, Gerrit J. Schiereck, Kees d'Angremond

CHAPTER 154
Seawall Effects on Historically Receding Shorelines1985
Bryan N. Jones, David R. Basco

CHAPTER 155
Control of Wave Propagation Angle by Tapered-Submerged Breakwater1998
Satoshi Takewaka, Isao Irie

CHAPTER 156
Multidirectional Wave Loads on Vertical Breakwaters2008
Claudio Franco, Jentsje W. Van der Meer, Leopoldo Franco

CHAPTER 157	
Modelling the Impact of Detached Breakwaters on the Coast	2022
<i>K.J. Bos, J.A. Roelvink, M.W. Dingemans</i>	
CHAPTER 158	
Evaluation of Beach Modelling Techniques Behind Detached Breakwaters	2036
<i>Philip Axe, Suzana Ilic, Andrew Chadwick</i>	
CHAPTER 159	
Numerical Modelling of Bed Evolution Behind a Detached Breakwater	2050
<i>Philippe Pechon, Charles Teisson</i>	
CHAPTER 160	
Combined Diffraction and Transmission of Water Waves around a Porous Breakwater	
Gap	2063
<i>Xiping Yu, Hiroyoshi Togashi</i>	
CHAPTER 161	
Prediction of Wave Reflection from Rock Structures: An Integration of	
Field & Laboratory Data	2077
<i>Mark A. Davidson, Paul A.D. Bird, David A. Huntley, Geoff N. Bullock</i>	
CHAPTER 162	
Performance Evaluation of Buoy-Membrane Wave Barriers	2087
<i>M.H. Kim, B. L. Edge, S.T. Kee, L. Zhang</i>	
CHAPTER 163	
An Improved Design Method for the Riprap of Earthfill Dams of Large Reservoirs ...	2101
<i>Jean-Pierre Tournier, Pierre Dupuis, Raymond Ares</i>	
CHAPTER 164	
Geotextile Systems in Coastal Engineering - An Overview -	2114
<i>Krystian W. Pilarczyk</i>	
CHAPTER 165	
Groynes on the East Frisian Islands: History and Experiences	2128
<i>Hans Kunz</i>	
CHAPTER 166	
Permeable Pile Groins	2142
<i>Thomas Trampenau, Frank Goricke, Arved J. Raudkivi</i>	
CHAPTER 167	
The Effect of Groundwater on Scour Near Structures	2152
<i>John H. Loveless, Geoffrey T. Grant, Robert I. Karlsson</i>	
CHAPTER 168	
Abrasion of Steel Pipe Piles by Sediment Motion in Coastal Zones	2166
<i>Gaku Matsuoka, Shinichi Ito, Toshihiko Yamashita, Hiroshi Saeki, Yoshihisa Kariyazono, Koichi Sato</i>	

CHAPTER 169	
A Viscous Rotational Model for Wave Overtopping over Marine Structure	2178
<i>Fei Zhuang, Jiin-Jen Lee</i>	
CHAPTER 170	
Overtopping of Waves at a Wall: A Theoretical Approach	2192
<i>M. Jervis, D.H. Peregrine</i>	
CHAPTER 171	
Wind Effects on Runup and Overtopping of Coastal Structures	2206
<i>Donald L. Ward, Jun Zhang, Christopher G. Wibner, Charles M. Cinotto</i>	
CHAPTER 172	
Wave Overtopping of Vertical Structures Including Wind Effect	2216
<i>Johannes P. de Waal, Patrick Tonjes, Jentsje W. van der Meer</i>	
CHAPTER 173	
Bridge Pier Scour Assessment for the Northumberland Strait Crossing	2230
<i>C.D. Anglin, R.B. Nairn, A.M. Cornett, L. Dunaszegi, J. Turnham, G.W. Annandale</i>	
CHAPTER 174	
Wave Setup at River Entrances	2244
<i>David J. Hanslow, Peter Nielsen, Kevin Hibbert</i>	
CHAPTER 175	
Scour at Coastal Inlet Structures	2258
<i>Steven A. Hughes, J. William Kamphuis</i>	
CHAPTER 176	
Probability Distribution of the Maximum Wave Height along a Sea Wall with Finite Width	2272
<i>Akira Kimura, Takao Ohta</i>	
CHAPTER 177	
Beach Response in Front of Wave-Reflecting Structures	2284
<i>Roy C. Seaman, Tom O'Donoghue</i>	
CHAPTER 178	
Fundamental Characteristics of Wave Transformation around Artificial Reefs	2298
<i>Toshio Aono, Eric C. Cruz</i>	
CHAPTER 179	
Performance of a Submerged Breakwater for Shore Protection	2312
<i>Albert E. Browder, Robert G. Dean, Renjie Chen</i>	
CHAPTER 180	
Nonlinear Wave Transformation over a Submerged Triangular Breakwater	2324
<i>Lifen Dong, Akira Watanabe, Masahiko Isobe</i>	
CHAPTER 181	
Breaking Limit, Breaking and Post-Breaking Wave Deformation Due to Submerged	

Structures	2338
<i>Koichiro Iwata, Koji Kawasaki, Do-Sam Kim</i>	
CHAPTER 182	
Italian Experience on Submerged Barriers as Beach Defence Structures	2352
<i>Alberto Lamberti, Alessandro Mancinelli</i>	
CHAPTER 183	
Resonant Reflection and Refraction-Diffraction of Surface Waves Due to Porous Submerged Breakwaters	2366
<i>Hajime Mase, Akira Kimura, Hiroshi Sakakibara</i>	
CHAPTER 184	
BEM-FEM Combined Analysis of Nonlinear Interaction between Wave and Submerged Breakwater	2377
<i>N. Mizutani, W.G. McDougal, A.M. Mostafa</i>	
CHAPTER 185	
Regulation of Nearshore Circulation by Submerged Breakwater for Shore Protection .	2391
<i>Hisamichi Nobuoka, Isao Irie, Hajime Kato, Nobuo Mimura</i>	
CHAPTER 186	
Submerged Breakwaters for the Defence of the Shoreline at Ostia - Field Experiences, Comparison	2404
<i>Ugo Tomasicchio</i>	
CHAPTER 187	
Wave Transmission of Low-Crested Structures	2418
<i>Kees d'Angremond, Jentsje W. van der Meer, Rutger J. De Jong</i>	
CHAPTER 188	
Effect of Submerged Breakwater on Profile Development	2428
<i>Martin D. Groenewoud, Jan van de Graaff, Edward W.M. Claessen, Stephan C. van der Biezen</i>	
CHAPTER 189	
Cause and Characteristics of Impact Pressure Exerted by Spilling and Plunging Breakers on a Vertical Wall	2442
<i>Seyed Ali Azarmsa, Takashi Yasuda, Hidemi Mutsuda</i>	
CHAPTER 190	
Dynamic Response of Vertical Elastic Walls to Breaking Wave Impact	2456
<i>Masatato Hattori, Nobuaki Tsujioka</i>	
CHAPTER 191	
Wave Transmission Past Vertical Wave Barriers	2470
<i>David L. Kriebel, Chad A. Bollmann</i>	
CHAPTER 192	
Physical Study of the Nature of High Peak Wave Pressures	2484
<i>Jordan Marinski</i>	

CHAPTER 193	
A Design Short-Crested Wave Force Model for Vertical Deep-Water Breakwaters2494
	<i>S.-Y. Tzang, S.-R. Liaw</i>
CHAPTER 194	
New Design Methods for Wave Impact Loadings on Vertical Breakwaters and Seawalls . .	.2508
	<i>N.W.H. Allsop, J.E. McKenna, D. Vicinanza, T.T.J. Whittaker</i>
CHAPTER 195	
Scale Effects of Wave Impact Pressures on Cob Armour Units2522
	<i>M.W. Howarth, N.W.H. Allsop, A.M. Vann, R.J. Jones, J.P. Davis</i>
CHAPTER 196	
Wave Impact Loading of Vertical Face Structures for Dynamic Stability	
Analysis - Prediction Formulae -2534
	<i>P. Klammer, A. Kortenhaus, H. Oumeraci</i>
CHAPTER 197	
Analysis on the Interaction of Waves with Flexible Floating Structure	
by BE-FE Combined Method2548
	<i>Xiaodong Liu, Shigeki Sakai</i>
CHAPTER 198	
Design Wave Height Related to Structure Lifetime2560
	<i>Zhou Liu, Hans F. Burcharth</i>
CHAPTER 199	
Wave Impact Beneath a Horizontal Surface2573
	<i>D.J. Wood, D.H. Peregrine</i>
CHAPTER 200	
Wave Impulse Prediction for Caisson Design2584
	<i>Michael J.A. Walkden, Peter J. Hewson, Geoffrey N. Bullock</i>
CHAPTER 201	
Wave Overtopping Rate and Reflection Coefficient for Obliquely Incident Waves2598
	<i>Yoichi Moriya, Masaru Mizuguchi</i>
CHAPTER 202	
Sediment Transport and Wave Reflection near a Seawall2612
	<i>Jonathon R. Miles, Paul E. Russell, David A. Huntley</i>

Part IV Coastal Processes and Sediment Transport

CHAPTER 203	
Wave Energy Dissipation in Kelp Vegetation2626
	<i>Alfonse Dubi, Alf Torum</i>
CHAPTER 204	
Experimental Study on the Effect of Gravity Drainage System on Beach Stabilization . .	.2640
	<i>Hiroshi Kanazawa, Fumihiko Matsukawa, Kazumasa Katoh, Iwao Hasegawa</i>

CHAPTER 205
Field Experiment on the Effect of Gravity Drainage System on Beach Stabilization ...2654
Kazumasa Katoh, Shin-ichi Yanagishima

CHAPTER 206
On the Change of Velocity Field in Nearshore Zone Due to Coastal Drain and the Consequent Beach Transformation2666
Michio Sato, Tadahiro Fukushima, Ryuichiro Nishi, Masahiko Fukunaga

CHAPTER 207
Evaluation of a Beach Dewatering System: Nantucket, USA2677
William R. Curtis, Jack E. Davis, Ian L. Turner

CHAPTER 208
Sediment Transport Processes at Ocean Beach, San Francisco, California2691
Robert T. Battalio, Dilip Trivedi

CHAPTER 209
Two Treatments of Shore Erosion in Extreme Floods on U.S. Great Lakes2705
Robert J. Hallermeier

CHAPTER 210
Long-Term Beach Response to Shore Stabilization Structures on the Oregon Coast ...2718
G.E. Hearon, W.G. McDougal, P.D. Komar

CHAPTER 211
Profile Volumes as a Measure of Erosion Vulnerability2732
Timothy W. Kana, Ram Krishna Mohan

CHAPTER 212
Breach Growth: Experiments and Modelling2746
Harry de Looff, Henk J. Steetzel, Arie W. Kraak

CHAPTER 213
The Impact of an Extreme Event on the Sediment Budget: Hurricane Andrew in the Louisiana Barrier Islands2756
Jeffrey H. List, Mark E. Hansen, Asbury H. Sallenger, Jr., Bruce E. Jaffe

CHAPTER 214
Beach Maintenance Strategies, a Comparison for a Recreational Beach2770
M. Pluijm, G. Kant, R. Nolten, A.P. de Looff

CHAPTER 215
Littoral Impact of Ocean City Inlet, Maryland, USA2779
Julie Dean Rosati, Bruce A. Ebersole

CHAPTER 216
Extreme Water Levels, Wave Runup and Coastal Erosion2793
P. Ruggiero, P.D. Komar, W.G. McDougal, R.A. Beach

CHAPTER 217	
A Morphological “Mixed-Type” Model for the Ebro Delta Coast	2806
<i>Agustin Sanchez-Arcilla, Jose A. Jimenez</i>	
CHAPTER 218	
Sea Dike Erosion and Coastal Retreat at Nam Ha Province, Vietnam	2820
<i>Ton That Vinh, G. Kant, Nguyen Ngoc Huan, Z. Pruszek</i>	
CHAPTER 219	
Beach Profile Analysis around Indian River Inlet, Delaware, U.S.A	2829
<i>Kirk F. Bosma, Robert A. Dalrymple</i>	
CHAPTER 220	
Improved 3-D Beach Evolution Model Coupled with the Shoreline Model (3D-SHORE)	2843
<i>Takuzo Shimizu, Takahiro Kumagai, Akira Watanabe</i>	
CHAPTER 221	
Evaluation of Shoreface Nourishments by Line Modelling	2857
<i>Martin D. Groenewoud, Willem T. Bakker, Jan van de Graaff, Ruud Spanhoff, Christian Laustrup</i>	
CHAPTER 222	
Beach Monitoring Program of Valencia (Spain)	2871
<i>Jose Serra, Josep R. Medina</i>	
CHAPTER 223	
Bar Migration and Duneface Oscillation on Decadal Scales	2884
<i>Marcel J.F. Stive, Jorge Guillen, Michele Capobianco</i>	
CHAPTER 224	
Morphological Development of the Terschelling Shoreface Nourishment in Response to Hydrodynamic and Sediment Transport Processes	2897
<i>P. Hoekstra, K.T. Houwman, A. Kroon, B.G. Ruessink, J.A. Roelvink, R. Spanhoff</i>	
CHAPTER 225	
Justification for Beach Nourishment	2911
<i>John G. Housley</i>	
CHAPTER 226	
Beach Nourishment Versus Shore Protection Structures	2918
<i>Alexander Khabidov, Yuri Bazhenov, Marina Glodenis, Nadya Ivanova, Liya Kaskevitch, Oleg Rybak, Valery Savkin, Anatoly Trizno, Grigory Zelensky, Veniamin Yedapin</i>	
CHAPTER 227	
Comparison of Beach and Shoreface Nourishment Torsminde Tange, Denmark	2927
<i>Christian Laustrup, Holger Toxvig Madsen, Per Sorensen, Ida Broker</i>	
CHAPTER 228	
Mathematical and Physical Modeling of Beach Nourishment Projects	2941
<i>W. Eric Rogers, Paul A. Work</i>	

CHAPTER 229	
Coastal Zone Dynamics during Artificial Nourishment	2955
<i>Elzbieta Zawadzka</i>	
CHAPTER 230	
Dune Damage Curves and Their Use to Estimate Dune Maintenance Costs	2969
<i>David R. Basco, Cheol S. Shin</i>	
CHAPTER 231	
Hurricane Opal Induced Changes on Natural and Nourished Beaches, West-Central Florida	2982
<i>Richard A. Davis, Jr., Ping Wang</i>	
CHAPTER 232	
Modelling Sand Transport and Profile Evolution on Macrotidal Beaches	2994
<i>Paul R. Fisher, Tim J. O'Hare</i>	
CHAPTER 233	
Beach Evolution Under Random Waves	3006
<i>Patrick Holmes, Thomas E. Baldock, Ray T.C. Chan, M. Ahmad L. Neshaei</i>	
CHAPTER 234	
Beach Profile Surveys Along the U.S. Pacific Coast 1945-1947	3020
<i>Nicholas C. Kraus, Robert L. Wiegel, Willard N. Bascom</i>	
CHAPTER 235	
Mechanism and Calculation of Sand Dune Erosion by Storms	3034
<i>Ryuichiro Nishi, Nicholas C. Kraus</i>	
CHAPTER 236	
Simulation of Coastal Profile Development Using a Boussinesq Wave Model	3048
<i>K.A. Rakha, R. Deigaard, P.A. Madsen, I. Broker, J.K. Ronberg</i>	
CHAPTER 237	
Cross-shore Sediment Transport and Beach Deformation Model	3062
<i>RattanapitikonWinyu , Tomoya Shibayama</i>	
CHAPTER 238	
Experimental Study on Sediment Transport in Surf and Swash Zones Using Large Wave Flume	3076
<i>Takao Shimizu, Masaaki Ikeno</i>	
CHAPTER 239	
The Influence of Long Waves on Macrotidal Beach Morphology	3090
<i>David J. Simmonds, Tim J. O'Hare, David A. Huntley</i>	
CHAPTER 240	
Mathematical Models for Waves and Beach Profiles in Surf and Swash Zones	3104
<i>Akira Watanabe, Mohammad Dibajnia</i>	

CHAPTER 241
Comparisons of Erosion Models for Storms at Ocean City, Maryland3115
Jie Zheng, Robert G. Dean

CHAPTER 242
Measurements of Wave Generated Bedforms3129
Christopher D. Jette, Daniel M. Hanes

CHAPTER 243
Field Measurement of Bed Roughness for Waves on an Offshore Reef3143
Raymond C. Nelson

CHAPTER 244
Effect of Wave-Induced-Pressure on Seabed Configuration3155
Tetsuo Sakai, Hitoshi Gotoh

CHAPTER 245
The Measurement of Bed Form Shapes in Hydraulic Models3169
Ian E. Shepherd

CHAPTER 246
Asymmetric Boundary Layer Flow above Sand Ripples under Progressive Waves3183
Takao Toue, Kazuo Nadaoka, Hidehiro Katsui

CHAPTER 247
Undertow Profiles in the Bottom Boundary Layer under Breaking Waves3194
Daniel T. Cox, Nobuhisa Kobayashi

CHAPTER 248
A Comparison of Field Observations and Quasi-Steady Linear Shear Instabilities of the Wave Bottom Boundary Layer3207
D.L. Foster, A.J. Bowen, R.A. Beach, R.A. Holman

CHAPTER 249
Wave Boundary Layer Flows and Pore Pressures in Permeable Beds3219
H.H. Hwang, K.S. Hwang, B.H. Lee

CHAPTER 250
Backfilling of Trenches Exposed to Waves3231
Jacob Hjelmager Jensen, Jorgen Fredsoe

CHAPTER 251
A Closed-Form Solution for Turbulent Wave Boundary Layers3244
Magnus Larson

CHAPTER 252
Observed Suspended Sediments in Storm Conditions3257
J.J. Williams, C.P. Rose, P.D. Thorne, L.E. Coates, J.R. West, P.J. Harcastle, J.D. Humphery, S.P. Moores, D.J. Wilson

CHAPTER 253	
Ebb Tidal Delta Evolution of Coastal Inlets	3270
<i>Michael R. Dombrowski, Ashish J. Mehta</i>	
CHAPTER 254	
Adjustments toward Equilibrium of a Large Flood -Tidal Delta after a Major Dredging Program, Tauranga Harbour, New Zealand	3284
<i>Terry Healy, Joseph Mathew, Willem de Lange, Kerry Black</i>	
CHAPTER 255	
Laboratory Mobile Bed Model Studies on Ebb Tidal Shoal Evolution	3295
<i>Xu Wang, Lihwa Lin, Hsiang Wang</i>	
CHAPTER 256	
Interaction of the Colorado River Project, Texas, with Longshore Sediment Transport ..	3309
<i>Daniel J. Heilman, Billy L. Edge</i>	
CHAPTER 257	
A Comprehensive Field Study of Tidal Inlet Processes at Ponce de Leon Inlet, Florida ..	3323
<i>Gary L. Howell</i>	
CHAPTER 258	
Transport of Fluid Mud Generated by Waves on Inclined Beds	3337
<i>Thijs van Kessel, C. Kranenburg, J.A. Battjes</i>	
CHAPTER 259	
Wave on Pebble Beach and Deformation of Pebble Beach	3349
<i>Ichiro Deguchi, Masanobu Ono, Toru Sawaragi</i>	
CHAPTER 260	
Wind-Induced Waves and Currents in a Nearshore Zone	3363
<i>Nobuhiro Matsunaga, Misao Hashida, Hiroshi Kawakami</i>	
CHAPTER 261	
Predicting Large-Scale, Cross-Shore Sediment Movement from Orbital Speeds	3378
<i>Edward B. Hands, John P. Ahrens, Donald T. Resio</i>	
CHAPTER 262	
Small-scale Morphology Related to Wave and Current Parameters Over a Barred Beach	3391
<i>A.F. Garcez Faria, E.B. Thornton, T.P. Stanton</i>	
CHAPTER 263	
Prediction of Shoreline Change Considering Cross-Shore Sediment Transport	3405
<i>Yoshimichi Yamamoto, Kiyoshi Horikawa, Katsutoshi Tanimoto</i>	
CHAPTER 264	
The Influence of Rollers on Longshore Currents	3419
<i>Daniel A. Osiecki, William R. Dally</i>	

CHAPTER 265	
Velocity Field Measurements in a “Coastal Buffer Zone”	3431
<i>Hiroshi Yagi, Hirofumi Hinata, Kazuo Nadaoka</i>	
CHAPTER 266	
Development of Underwater Beach Profile by Monochromatic and Random Waves ...	3442
<i>Karsten Peters, Jurgen Newe, Hans-H. Dette</i>	
CHAPTER 267	
Turbulent Stresses in the Surf-Zone: Which Way Is Up?	3453
<i>John W. Haines, Guy Gelfenbaum</i>	
CHAPTER 268	
Asymmetric and Irregular Wave Effects on Bedload: Theory Versus Laboratory and Field Experiments	3467
<i>Leszek M. Kaczmarek, Rafal Ostrowski</i>	
CHAPTER 269	
Kinematics and Shear Stresses from Combined Waves and Longshore Currents in the UK Coastal Research Facility	3481
<i>Richard R. Simons, Ruairi D. MacIver, Wameidh M. Saleh</i>	
CHAPTER 270	
Movable Bed Roughness in the Flow of Irregular Waves and Currents Over Movable Beds	3495
<i>Zai-Jin You, Peter Nielsen</i>	
CHAPTER 271	
Seabed and Foundation Response to Wave Loading	3507
<i>Michael H. Davies</i>	
CHAPTER 272	
Interannual Shoreline Variations at Duck, NC, USA	3521
<i>Nathaniel Plant, Rob Holman</i>	
CHAPTER 273	
Long Term Behaviour of the Sediment Volume inside a Tidal Basin after Poldering ...	3534
<i>Ernst Schroeder, Roland Goldenbogen, Hans Kunz</i>	
CHAPTER 274	
Wave Groups in a Barred Nearshore	3546
<i>B. Boczar-Karakiewicz, W. Romanczyk, J.L. Bona, B. Greenwood</i>	
CHAPTER 275	
Coastal Morphodynamic Instabilities	3560
<i>Albert Falques, Amadeu Montoto, Vicente Iranzo</i>	
CHAPTER 276	
On Validation of a Sand Waves and Sand Banks Model	3574
<i>Suzanne J.M.H. Hulscher</i>	

CHAPTER 277	
Transverse Bars in Duck, North Carolina	3588
<i>Kathryn M. Konicki, Rob A. Holman</i>	
CHAPTER 278	
On the Systematic Offshore Decay of Breaker Bars	3600
<i>Kathelijne M. Wijnberg</i>	
CHAPTER 279	
Longshore Bed-Load Transport	3614
<i>Jesper S. Damgaard, Richard L. Soulsby</i>	
CHAPTER 280	
Design Capacity of a Longshore Current Recirculation System for a Longshore Sediment Transport Laboratory Facility	3628
<i>David G. Hamilton, Julie D. Rosati, Jimmy E. Fowler, Jane M. Smith</i>	
CHAPTER 281	
Influence of Nearshore Hardbottom on Regional Sediment Transport	3642
<i>Paul C.-P. Lin, R. Harvey Sasso</i>	
CHAPTER 282	
Improvement of the Most Accurate Longshore Transport Formula	3652
<i>J.S. Schoonees, A.K. Theron</i>	
CHAPTER 283	
Cross-shore Structure of Longshore Currents during Duck94	3666
<i>Falk Feddersen, R.T. Guza, Steve Elgar, T.H.C. Herbers</i>	
CHAPTER 284	
Three-Dimensional Hydrodynamics on a Barred Beach	3680
<i>Tae-Myoung Oh, Robert G. Dean</i>	
CHAPTER 285	
Rip Current Generation on a Plane Beach	3694
<i>D.A. Suriamihardja, Yoshito Tsuchiya</i>	
CHAPTER 286	
Nearshore Placement of Sand	3708
<i>Scott L. Douglass</i>	
CHAPTER 287	
Influence of Nearshore Berm on Beach Nourishment	3722
<i>Paul A. Work, Emre N. Otay</i>	
CHAPTER 288	
Accuracy of Sand Volumes as a Function of Survey Density	3736
<i>Jennifer L. Irish, W. Jeff Lillycrop, Larry E. Parson</i>	
CHAPTER 289	
Shoreline Analysis Using Digital Photogrammetry	3750

CHAPTER 290	
Application of Satellite Images to the Detection of Coastal Topography	3762
<i>Ji Wu, Jea Tzyy Juang</i>	
CHAPTER 291	
Sediment Transport in Swash Zone under Obliquely Incident Waves	3770
<i>Toshiyuki Asano</i>	
CHAPTER 292	
Sheet Flow Modelled As Pure Convection	3784
<i>Stephen Clark, Peter Nielsen</i>	
CHAPTER 293	
A Transport Rate Formula for Mixed-Size Sands	3791
<i>Mohammad Dibajnia, Akira Watanabe</i>	
CHAPTER 294	
Modelling of 3D Sediment Transport in the Surf Zone	3805
<i>Berry Elfrink, Ida Broker, Rolf Deigaard, Erik Asp Hansen, Peter Justesen</i>	
CHAPTER 295	
A Numerical Model of Sheet Flow Sediment Transport	3818
<i>Sadakazu Katori, Masaru Mizuguchi, Akira Watanabe</i>	
CHAPTER 296	
Numerical Modeling of Nearshore Morphological Changes under a Current-Wave Field	3830
<i>Taerim Kim, Hsiang Wang</i>	
CHAPTER 297	
An Analysis of Particle Saltation Dynamics	3846
<i>Michael R. Krecic, Daniel M. Hanes</i>	
CHAPTER 298	
Sediment Movement and Stress Condition in Sea Bed	3860
<i>Yoshihiko Maeno, Motoyasu Ishikawa, Kozo Bando, Yoshinobu Akiyama, Kouichi Yabe</i>	
CHAPTER 299	
Application of the Depth of Closure Concept	3874
<i>Robert J. Nicholls, William A. Birkemeier, Robert J. Hallermeier</i>	
CHAPTER 300	
Numerical Modeling of Sediment Transport for Various Mode	3888
<i>Masanobu Ono, Ichiro Deguchi, Toru Sawaragi</i>	
CHAPTER 301	
Nearbed Sediment Concentration from Tracer Studies	3901
<i>Zbigniew Pruszek, Ryszard Wierchnicki, Andrzej Owczarczyk, Ryszard B. Zeidler</i>	

CHAPTER 302	
A Sloping Duct for the Study of Sediment Transport	3913
<i>Jesper S. Damgaard, Richard J.S. Whitehouse, Richard L. Soulsby</i>	
CHAPTER 303	
Sediment Dynamics and Profile Interactions: DUCK94	3921
<i>Donald K. Stauble, Mary A. Cialone</i>	
CHAPTER 304	
A Study on Flow Structure and Suspended Sediment Concentration over Seaweed Bed .	3935
<i>Gozo Tsujimoto</i>	
CHAPTER 305	
An Energetics Approach for Suspended Sand Transport on Macrotidal Ridge and Runnel Beaches	3948
<i>George Voulgaris, Travis Mason, Michael B. Collins</i>	
CHAPTER 306	
Field Tests of Suspended-Load Transport Theories Used in Numerical Models	3962
<i>Thomas E. White</i>	
CHAPTER 307	
Shore Protection Studies for Ras-Elbar Area, Egypt	3976
<i>John B. Herbich, Abd-Elfattah Elfiky, Abd-Elmohsen Elmongy; Ali Elbahrawy, Gamal Elsaeed</i>	
CHAPTER 308	
Stabilizing Beaches Downcoast of Harbor Extensions	3986
<i>John R.C. Hsu, Richard Silvester</i>	
CHAPTER 309	
Observation of Nearshore Currents and Beach Changes around Headlands Built on the Kashimanada Coast, Japan	4000
<i>K. Saito, T. Uda, K. Yokota, S. Ohara, Y. Kawanakajima, K. Uchida</i>	
CHAPTER 310	
Nourished Beach Control Between Balis and Arenys Harbours (Spain)	4014
<i>F. Javier Escartin, Alfonso Vidoar; A.M. Castaneda, Nuria Lupon</i>	
CHAPTER 311	
Numerical Simulation of Shoreline Change with Longshore Sand Waves at Groins	4024
<i>Hans Hanson, Michelle M. Thevenot, Nicholas C. Kraus</i>	
CHAPTER 312	
Erosive Waves in Shoreline Change Due to the Reduction of a River Delta	4038
<i>Yoshito Tsuchiya</i>	
CHAPTER 313	
DELILAH, DUCK94 & SandyDuck: Three Nearshore Field Experiments	4052
<i>William A. Birkemeier, Charles E. Long, Kent K. Hathaway</i>	

CHAPTER 314	
Eulerian Mean Velocities under Non-Breaking Waves on Horizontal Bottoms	4066
<i>Peter Nielsen, Zai-Jin You</i>	
CHAPTER 315	
Reynolds Stress and Small-Scale Morphology Measurements during DUCK94	4079
<i>Timothy P. Stanton, Edward B. Thornton</i>	
CHAPTER 316	
Studies on the Suspended Concentration in the Surf Zone	4088
<i>Ching-Her Hwang, Li-Hung Tsai, Po-Ching Lin, Chin-Chi Tsai</i>	
CHAPTER 317	
Suspended Sediment Mixing in the Surf Zone	4098
<i>Jose A. Jimenez, Francisco J. Rivero, Agustin Sanchez-Arcilla, Vicente Gracia, Andres Rodriguez</i>	
CHAPTER 318	
Sand Suspension Events and Intermittence of Turbulence in the Surf Zone	4111
<i>R.D. Kos'yan, H. Kunz, S.Yu. Kuznetsov, N.V. Pykhov, M.V. Krylenko</i>	
CHAPTER 319	
Mechanisms of Beach Ground Water and Swash Interaction	4120
<i>Andrew J. Baird, Travis E. Mason, Diane P. Horn</i>	
CHAPTER 320	
The Equations for Integral and Mean Flow Properties in the Swash Zone	4134
<i>M. Brocchini, D.H. Peregrine</i>	
CHAPTER 321	
Wave Overwash of Subaerial Dunes	4148
<i>Yukiko Tega, Nobuhisa Kobayashi</i>	
CHAPTER 322	
Pressure Gradients Within Sediment Beds	4161
<i>Thomas E. Baldock, Patrick Holmes</i>	
CHAPTER 323	
Analysis of Mud Mass Transport under Waves Using an Empirical Rheological Model . .	4174
<i>Qin Jiang, Akira Watanabe</i>	
CHAPTER 324	
Countermeasures Against Wind-Blown Sand on Beaches	4188
<i>Shintaro Hotta, Kiyoshi Horikawa</i>	
CHAPTER 325	
Sea Breeze Effects on Nearshore Coastal Processes	4200
<i>Charitha Pattiaratchi, Gerhard Masselink</i>	
CHAPTER 326	
Wind Blown Sand at Castroville, California	4214
<i>Douglas J. Sherman, Bernard O. Bauer, Paul A. Gares, Derek W.T. Jackson</i>	

Part V Coastal, Estuarine and Environmental Problems

CHAPTER 327	
Pipeline Protection in the Surf Zone	4228
<i>Gerrit J. Schiereck, Henri L. Fontijn</i>	
CHAPTER 328	
Modeling Tidal Circulation in Florida Bay	4242
<i>Y. Peter Sheng, Justin Davis</i>	
CHAPTER 329	
Recent Developments in Coastal Defence Policy and Guidance in England	4253
<i>Reg Purnell</i>	
CHAPTER 330	
Structural Restoration of Coral Reefs Damaged by Vessel Groundings	4261
<i>Kevin R. Bodge</i>	
CHAPTER 331	
Dredging and Disposal within the Limits of a National Park	4274
<i>H. A. Manzenrieder, J.M. de Vries</i>	
CHAPTER 332	
Storm-Derived Bar/Sill Dynamics in a Dredged Channel	4289
<i>Sean O'Neil, Keith W. Bedford, David P. Podber</i>	
CHAPTER 333	
Bivalve Habitat Based on Sediment-Transport Mechanics	4300
<i>Hitoshi Gotoh, Tetsuo Sakai</i>	
CHAPTER 334	
Hydraulic Controls on Tidal Wetlands	4314
<i>R. Eric Katmarian, Philip A. McKee, Timothy W. Kana</i>	
CHAPTER 335	
Enhanced Mixing Through Perforated Discs on Round Buoyant Jet	4325
<i>Lilun Wu, Jiin-Jen Lee</i>	
CHAPTER 336	
Assessing Coastal Flood Risks	4339
<i>Roger Maddrell, Chris Fleming, Chris Mounsey</i>	
CHAPTER 337	
Experimental Study on the Behavior of Bivalves by Oscillatory Flow	4353
<i>Toshihiko Yamashita, Akira Wada, Gaku Matsuoka, Kenji Yano, Sadamitsu Akeda</i>	
CHAPTER 338	
Wind- and Sea Level-Induced Shore Evolution in Poland	4364
<i>Ryszard B. Zeidler, Marek Skaja, Grzegorz Rozynski, Jarka Kaczmarek</i>	

CHAPTER 339	
Ashdod Port's Effect on the Shoreline, Seabed and Sediment	4376
<i>Abraham Golik, Dov S. Rosen, Arik Golan, Maxim Shoshany Dan DiCastro, Pinkhas Harari</i>	
CHAPTER 340	
Tweed River Sand Bypass: Concepts and Progress	4390
<i>Russell J. Murray, R.P. (Jock) Brodie, Mark Porter, David A. Robinson</i>	
CHAPTER 341	
Design Considerations for Coastal Projects in Cold Regions	4397
<i>Craig B. Leidersdorf, Peter E. Gadd, Kennon D. Vaudrey</i>	
CHAPTER 342	
Experimental Study on Deformation and Fracture of Ice Sheet by Propagating Water Wave	4411
<i>Shigeki Sakai, Xiaodong Liu, Makoto Sasamoto, Shigeo Kanada and Koh Izumiyama</i>	
CHAPTER 343	
An Attempt to Determine the Spanish Public Domain Border	4418
<i>R. Medina, I.J. Losada, F. Mendez, A.J. Fernandez</i>	
CHAPTER 344	
Education of Coastal Engineers for the 50th ICCE	4431
<i>Henk Jan Verhagen</i>	
CHAPTER 345	
Risk-Based Analysis of Coastal Projects	4440
<i>Edward F. Thompson, Michael Wutkowski, Norman W. Scheffner</i>	
CHAPTER 346	
Designing for Propeller Action in Harbours	4451
<i>G.A. Hamill, J.A. McGarvey</i>	
CHAPTER 347	
Modeling Inlet Sand Bypassing	4464
<i>Christopher G. Creed</i>	
CHAPTER 348	
An Approach to Modeling Inlet and Beach Evolution	4477
<i>Mark B. Gravens</i>	
CHAPTER 349	
Hydrodynamics of a Bar in a Flood Channel - the Westerschelde Estuary	4491
<i>Claire Jeuken</i>	
CHAPTER 350	
Interactions between a Sand Barrier and Flood Terrace at the Abukuma River Mouth ..	4505
<i>Akira Mano, Masaki Sawamoto</i>	
CHAPTER 351	
A Unique Look at Oregon Inlet, NC USA	4517

CHAPTER 352	
Impacts of Inlet Structures on Channel Location	4531
<i>William C. Seabergh, Mary A. Cialone, Donald K. Stauble</i>	
CHAPTER 353	
Complete Closure of the Nanakita River Mouth in 1994	4545
<i>Hitoshi Tanaka, Fumihiko Takahashi, Atsushi Takahashi</i>	
CHAPTER 354	
The Erosion of a Salt Wedge Trapped Behind a Barrage Across An Estuary	4557
<i>S.A. Walker, G.A. Hamill, H.T. Johnston</i>	
CHAPTER 355	
Near-Field Measurements of a Buoyant Jet in Waves and Currents	4569
<i>K.H. Kwan, C. Swan</i>	
CHAPTER 356	
Cost Effectiveness of Wave Power Extraction at Erosive Coasts	4583
<i>Hideo Kondo</i>	
CHAPTER 357	
Feasibility Tests of New Pendular-Type Wave Energy Conversion Apparatus	4591
<i>Senji Osanai, Hideo Kondo, Yuzo Mizuno and Tomiji Watabe</i>	
CHAPTER 358	
Watertable Dynamics in Coastal Areas	4601
<i>Hong-Yoon Kang, Peter Nielsen</i>	
CHAPTER 359	
Long Range Positive Effects of the Delray Beach Nourishment Program	4613
<i>Kim E. Beachler, Douglas W. Mann</i>	
CHAPTER 360	
Effectiveness of a Combined Beach and Shoreface Nourishment on the Island of Norderney/East Frisia, Germany	4621
<i>Hanz D. Niemeyer, Ralf Kaiser, Heiko Knaack</i>	

Part VI Case Studies

CHAPTER 361	
Nearshore Berm Performance at Newport Beach, California, USA	4636
<i>Chuck Mesa</i>	
CHAPTER 362	
San Gabriel River to Newport Bay Erosion Control Project, Orange County, California—30 Years of Periodic Beach Replenishment	4650
<i>Arthur T. Shak, Joseph A. Ryan</i>	

CHAPTER 363	
A Ten-Year History of Dolos Monitoring at Crescent City	4664
<i>William S. Appleton, Thomas Kendall, Jeffrey A. Melby</i>	
CHAPTER 364	
Breakwater Damage in Okushiri Port Due to the Hokkaido Nansei-oki Earthquake Tsunami	4676
<i>Katsutoshi Kimura, Yuzo Mizuno, Hiroichi Tsuruya, Yasuyuki Nakagawa</i>	
CHAPTER 365	
Richards Bay North Breakwater - Repair of a Roundhead: Monitoring, Model Testing, Design and Construction	4689
<i>D. Phelp, A. McClarty, A. Bartels</i>	
CHAPTER 366	
Thyboron Coastal Investigations 1995: New Lessons from an Old Coastal Problem ...	4703
<i>I. Broker, J.A. Zyserman, Per Roed Jakobsen</i>	
CHAPTER 367	
Probabilistic Risk Assessment of Beach Erosion at Pevensy Bay in England	4717
<i>Ping Dong, Keith J. Riddell</i>	
CHAPTER 368	
Beach Nourishment in Altafulla, Spain: Verification of Theoretical Models	4730
<i>J. Galofre, F.J. Montoya, R. Medina</i>	
CHAPTER 369	
Alternatives to Beach Stabilization: Cambrils Coast Case Study (Spain)	4744
<i>Nuria Lupon, Alfonso Vidaor, Jordi Galofre, F. Javier Escartin</i>	
CHAPTER 370	
The Effect of Grain Sorting on Profile Stability of Nourished Beaches	4756
<i>Ram K. Mohan, Timothy W. Kana</i>	
CHAPTER 371	
The Use of Data Assimilation to Improve Wave Hindcast Results	4770
<i>Jon M. Hubertz</i>	
CHAPTER 372	
Grain-Size Influence on Sand Transport in Oscillatory Sheet Flow	4779
<i>C. Marjolein Janssen and Jan S. Ribberink</i>	
CHAPTER 373	
Cross-Shore Sediment Transport Mechanisms in the Surfzone on a Timescale of Month to Years	4793
<i>Klaas T. Houwman and Gerben Ruessink</i>	
CHAPTER 374	
Numerical Prediction of Breaking Waves and Currents with a Boussinesq Model	4807
<i>Okey George Nwogu</i>	

CHAPTER 375
The Effect of the CL-Vortex Force in 3D Wave-Current Interaction4821
M. W. Dingemans, J. A. Th. M. van Kester, A. C. Radder and R. E. Uittenbogaard

Subject Index4833

Author Index4847

PART II

Long Period Waves, Storm Surges and Wave Groups



Martin County shoreline, Florida. Photo courtesy of Applied Technology & Management, Inc. and Aerial Photography, Inc.

CHAPTER 98

Uncertainties in the Validation of Harbor Wave Models

Zeki Demirbilek¹, Bingyi Xu & Vijay Panchang²

Abstract

Various sources of uncertainties contributing to the difficulties in the validation of harbor wave models with field measurements are discussed in this paper. Some aspects of a new theoretical formulation for removing these uncertainties for estimates of waves in harbors are presented. Implementation of the new formulation is illustrated for waves incident on a planar beach by comparing numerical model predictions to the closed-form analytical solution for normal incident waves and to the results from an one-dimensional Helmholtz equation for oblique waves.

Introduction

Reliable modelling of coastal hydraulic phenomena is vital for commercial and military activities, including harbor design, shoreline evolution, navigation, ship motion during loading/unloading operations, dredging, design of structures, harbor wave agitation, contaminant transport, just a few to name. Military coastal hydraulics deals with amphibious operations, mooring forces, mine movement, and others. Computer models presently play an important role in the ever-increasing coastal activities in some countries, and in the past two decades, industrial activity in the coastal and offshore environment worldwide has witnessed a phenomenal growth. Many nations have quite liberal policies to promote the development of new ports and harbors to meet the need for growing exploration and transport of petro-products, aquaculture, and commerce by shipping. Ongoing and future investment by governments, international participants, and the private sector will further accelerate the use of numerical wave prediction models for coastal projects and design studies.

Although a number of mathematical models have been successfully developed

¹U.S. Army Engineer Waterways Experiment Station, Coastal and Hydraulics Laboratory, 3909 Halls Ferry Road, Vicksburg, MS 39180-6199

²Department of Civil and Environmental Engineering, University of Maine, Orono, ME 04469-5706

worldwide for coastal hydraulics, wave modelling confronts us with numerous complexities in the physics and the numerics. Many available models have been developed in a somewhat ad-hoc manner with the immediate needs of a project in mind, and time and budgetary constraints have often taken priority over rigorous model evaluation and systematic development. In fact, many model solutions are perforce accepted at face value, even though model sensitivity to grid resolution, open boundary conditions, parameters associated with various mechanisms, model assumptions, etc. are almost never tested.

This paper addresses a general discussion of some of the key uncertainties in the validation of harbor wave models. Using a state-of-the-art wave model called "CGWAVE", model uncertainties are discussed for a simple application, waves transforming over a plane sloping beach. The CGWAVE model is developed by the US Army Corps of Engineers and the US Navy in collaboration with the University of Maine, for civil and military applications. CGWAVE is a comprehensive and sophisticated finite-element nearshore wave prediction model that can be used for predicting wave climate either in open-coast type applications or in harbors of irregular bathymetry which are surrounded by complex land boundaries and protective structures such as jetties, breakwaters, or islands.

The model CGWAVE is based on the elliptic mild-slope wave equation and can simultaneously simulate the effects of refraction, diffraction, reflections by bathymetry and structures, dissipation due to friction and breaking, and nonlinear amplitude dispersion. The computational capabilities of CGWAVE model permit the modeling of large coastal regions. The model has been compared to several academic test-cases and laboratory data for complex bathymetries (e.g. Panchang et al. 1990, 1991, 1996; Xu and Panchang 1993; Panchang et al. 1993; Panchang & Xu 1995; Xu et al. 1996). The governing equations of CGWAVE pass, in the limit, to the deep and shallow water equations, making this model applicable to a wide range of frequencies, including short wind waves, swell, and infra-gravity waves.

Harbor Models and Applications

The three most widely-known elliptic wave models are HARBD (Chen and Mei 1974; Mei 1983; Chen & Houston 1987), PHAROS (Kostense et al. 1986), and CGWAVE (Panchang et al. 1991; Xu, Panchang & Demirbilek 1996). These steady-state models may either use finite-element or finite-difference schemes for solving the governing equations and associated boundary conditions for calculating the linear wave oscillations in harbors of arbitrary configuration and variable bathymetry. Effects of bottom friction and boundary absorption (reflection) are included. Boundary reflection is based on a formulation similar to the impedance condition in acoustics, expressed as a function of the wavenumber and reflection coefficient.

For modeling waves over an arbitrary depth, these models divide the water domain into near- and far-regions. The near-region, also known as the model domain

(Fig. 1), that includes the actual harbor, is bounded by an offshore boundary, in the form of a semi-circle for HARBD and PHAROS models, and a semi-circle or rectangular-box boundary for CGWAVE. The offshore boundary is a mathematical artifice and typically is located some distance offshore of the harbor entrance. The near-region encompasses the entire harbor area and all its protective marine structures, and part or all of the entrance and approach navigation channels. Water depth in the near-region is generally variable, overlaid with a finite-element triangular-mesh whose grid resolution is determined by the project-specific design wave conditions. Element attributes such as water depth and bottom friction are specified at the centroid of each element. For those elements along the solid boundaries (land or structure), a reflection coefficient is assigned to each element.

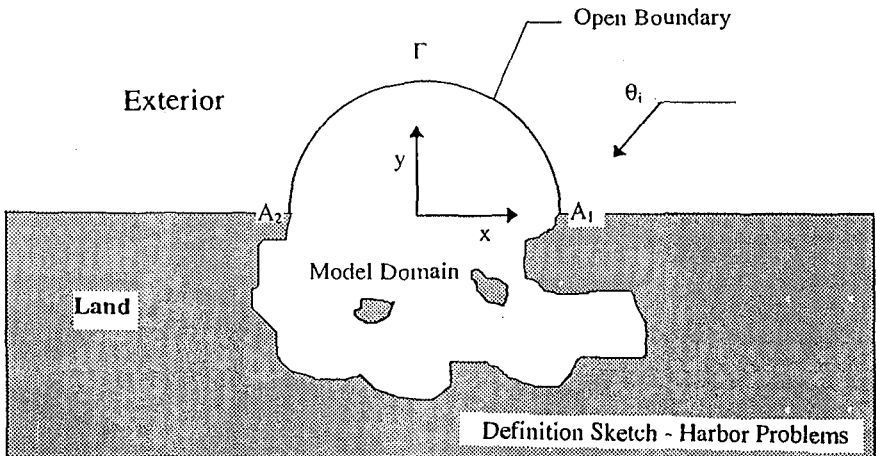


Figure 1. Near- and Far-regions (Model & Exterior Domain) & Open Boundary, Γ .

The far-region, also known as the exterior domain (Fig. 1), of the elliptic wave models covers the domain outside the offshore boundary of the near-region, and is bounded by the coastline and deepwaters of the sea, extending to infinity (Fig. 2). Water depth in the far-region is assumed to be constant for HARBD and PHAROS models, whereas it is treated as variable depth in the CGWAVE model (Fig. 3). Bottom friction and reflection are neglected in the far-region. The constancy of water depth in the far-region for HARBD and PHAROS models permits a simpler analytical solution of waves at the expense of introducing some undesirable depth-discontinuities at the interface between the near-region and the coastlines on either side of the harbor entrance. These discontinuities are one of the major source of difficulties in the validation of elliptic wave models. CGWAVE avoids this problem by considering the water depth in the far-region to be piece-wise continuous by allowing the water depth to change in the cross-shore direction as waves approach the coastlines and the harbor. This is one of the major differences between CGWAVE

and all other existing elliptic models. In CGWAVE, the wave field in the far- and near-regions is obtained by solving the one- and two-dimensional Helmholtz equations, respectively. These two solutions are mathematically coupled along the offshore boundary of the modeling domain to obtain the complete wave field estimates in the combined regions.

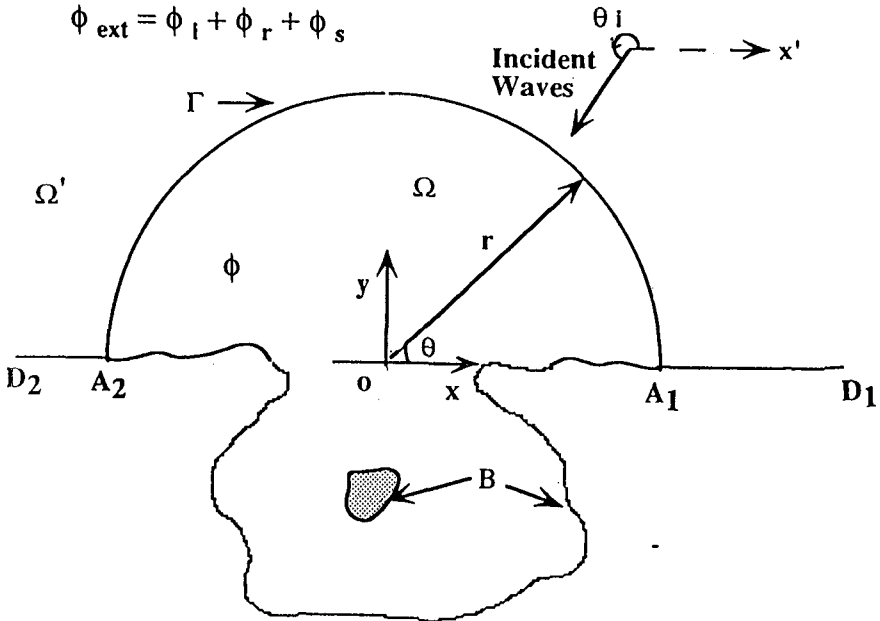


Figure 2. Collinear and Fully-reflective Exterior Coastlines.

Elliptic wave models require a wave period and direction as input, as well as the three-dimensional coordinates for the near-region finite-element mesh. For CGWAVE, grid coordinates for the far-region are also required. In addition, models may require certain parameters for their numerical solvers, which vary from model to model depending on the specific numerical algorithms used to solve the linear system of equations. CGWAVE model uses a Galerkin formulation for discretizing its equations. The resulting matrix equations are solved iteratively using the so-called conjugate gradient method (CGM). The CGM (Panchang et al. 1991; Li 1994) is a powerful, iterative scheme for solving system of equations without any matrix inversion. The iterative solution scheme of CGWAVE significantly improves our wave modelling capabilities in the nearshore when large domains have to be modelled using highly refined grids. While the basic model developed so far incorporates all the nearshore wave transformation mechanisms noted earlier and also includes a graphical user interface, a number of important questions remain. These remaining issues introduce uncertainties into the predictions of models as described in the following sections of this paper.

Uncertainties due to Model Assumptions

Traditional elliptic harbor wave models such as HARBD and PHAROS are based on the assumptions that the exterior sea region outside the computational finite-element grid is of constant depth and that exterior coastlines are collinear and fully reflecting (Figs. 2 & 3). These assumptions are generally not true for most practical applications and their effects on model predictions are substantial (Xu, Panchang, and Demirebilek 1996), resulting in unreliable simulations. This is not surprising since the exterior geometry varies arbitrarily, and the unrealistic bathymetric representation used by modelers should invariably have an adverse influence on model predictions.

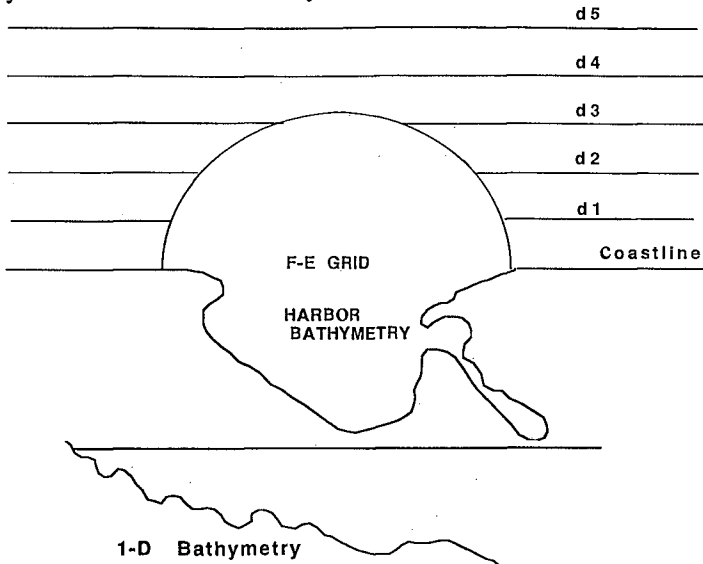


Figure 3. Exterior Domain Bathymetry Representation for CGWAVE model.

A solution to this problem has been to extend the near-region as far as possible to minimize the effects of these assumptions. But, this practice in turn introduces some prohibitive computational resource demands that are difficult to meet. An alternative solution has been developed (Xu, Panchang, and Demirebilek 1996) that eliminates such demands by invoking the use of parabolic approximation as the open boundary condition for the scattered waves. Theoretical details and implementation of this innovative method are omitted here since several illustrations of its practical applications have been presented in that paper.

The requirement that exterior coastlines are fully reflecting is particularly troublesome, almost always giving rise to extremely large wave amplitude estimates and rapidly varying wave patterns in the exterior region of the modeling domain. This has been illustrated by the authors (see Fig. 2 in Xu, Panchang, and Demirebilek 1996), in which CGWAVE predictions for Toothacher Bay, Maine were obtained by forcing CGWAVE to mimic a HARBD-like solution. In this application, using full

reflection from exterior coastlines of low reflectivity did clearly lead to erroneous model results, and made the said assumption very problematic. The parabolic approximation treatment of the scattered waves developed by Xu, Panchang, and Demirbilek (1996) does in deed overcome this requirement and allows the modeler much greater flexibility for tackling realistic applications.

In fact, there are a number of sources that give rise to uncertainties in the predictions of elliptic models, including:

- model set-up/open boundary location
- coastal reflectivity
- grid resolution
- parameters (dissipation, etc.)
- forcing (input)

These uncertainties make the validation and comparison of models to field measurements difficult. A brief discussion of the role played by the open boundary in these uncertainties is presented next.

Uncertainties due to Open Boundary

Figure 2 depicts the open boundary Γ , shown as a semi-circular boundary that separates the near-region Ω from the far-region Ω' . The solution of problem, expressed in term of the velocity potential Φ , in the far-region (exterior region) consists of the incident (Φ_i), reflected (Φ_r), and scattered (Φ_s) components, respectively. Both HARBD and PHAROS make use of the Bessel-Fourier series for representation of Φ_s . This traditional approach for determining Φ_s requires (1) depths in the exterior-region Ω' be constant, (2) exterior coastlines A_1D_1 and A_2D_2 be fully-reflecting, and (3) exterior coastlines A_1D_1 and A_2D_2 be collinear. All three requirements which are unrealistic for practical applications, can be avoided using the parabolic representation of Φ_s (Xu, Panchang, and Demirbilek 1996). Advantages of this new approach are that it eliminates requirements (2) and (3). A novel approach for eliminating requirement (1) has also been developed by the same authors and was presented in the ICCE'96. Their proposed solution for eliminating the requirement #1 was to represent the bathymetry in the far-region by a piece-wise continuous one-dimensional (1-D) bathymetry (Fig. 3) to solve the 1-D Helmholtz equation for $\Phi_0 = \Phi_i + \Phi_r$ in the exterior domain. This 1-D solution for Φ_0 and the parabolic solution of Φ_s are then used along the open boundary Γ for coupling of the solutions of the near- and far-regions. Figure 4 presents an illustration of this method for predicting waves on a 3-km long planar beach with a slope of about 1:50 and offshore depth of 54 m. CGWAVE predictions for this problem are next discussed for different incident wave conditions, for both normal incident and oblique waves, and model predictions are compared to the closed-form analytical J_0 -solution (Mei 1983) of this problem.

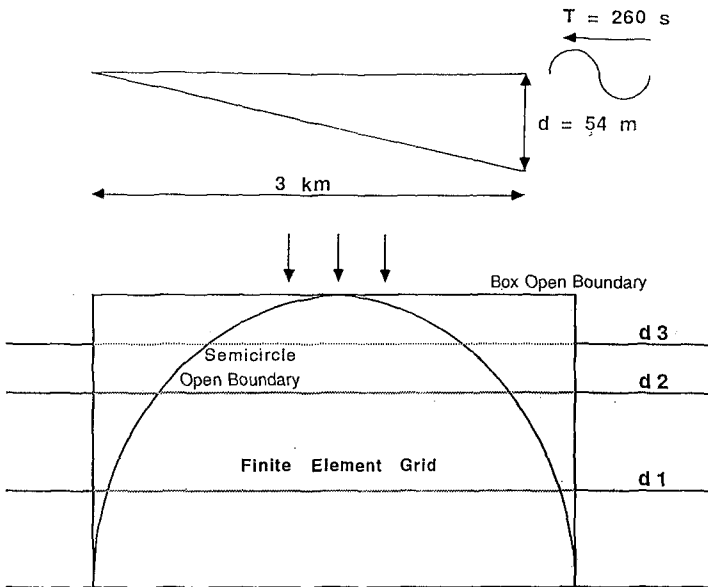


Figure 4. CGWAVE Model Setup for a Planar Beach of About 1:50 Slope.

Discussion of Waves on a Sloping Beach

In the comparison of CGWAVE to the analytical solution, we examine the performance our model CGWAVE for different sizes of the semi-circle and the cross-shore extent of the exterior domain. Due to space limitations, model results will only be presented at three on-offshore cross-sections. We choose cross-sections 1 and 3 at 500 m from the left- and right-edge of the semi-circle, respectively, and cross-section 2 at the center of the semi-circle. Since the open-boundary related effects manifest themselves mainly near that boundary, the greatest differences between the model predictions and the analytical solution should occur at cross-sections 1 and 3, and the least difference at cross-section 2. In addition, as the size of the semi-circle decreases, the effect of the boundary should become more dominating throughout the entire domain. Conversely, for a larger semi-circle, these effects should be localized in the vicinity of the open boundary.

Figures 5 and 6 represent model versus the analytical solution results for a 3-km domain (i.e. diameter of the semi-circle is 3 km) for normal and oblique incident waves, respectively, of 260 sec period. The agreement between the model and J_0 solution in all three cross-sections is excellent for both normal and oblique incident waves. Since the J_0 -solution is for normal incident waves, we provide in Figure 6 a true comparison of the CGWAVE model estimates to the solution from a one-dimensional Helmholtz equation, the exact solution of this problem for 30-degrees

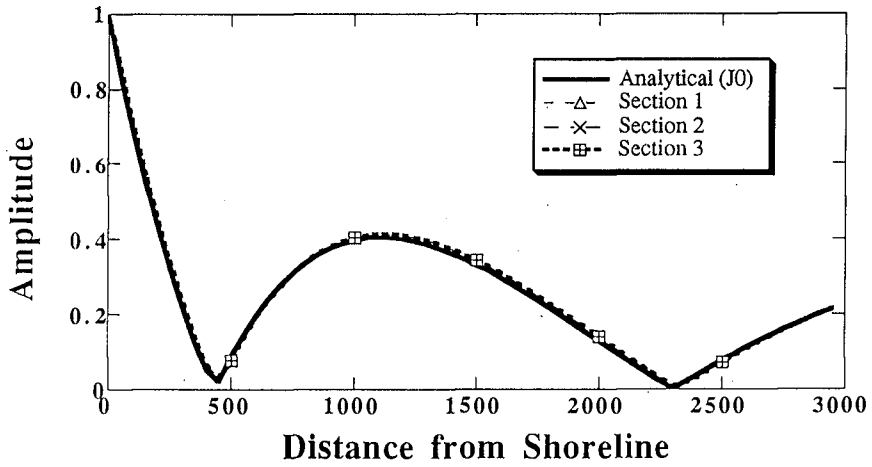


Figure 5. Comparison of CGWAVE Model Predictions versus Analytical Solution at Three Cross-sections for a 3-km Planar Beach (Normal Incident).

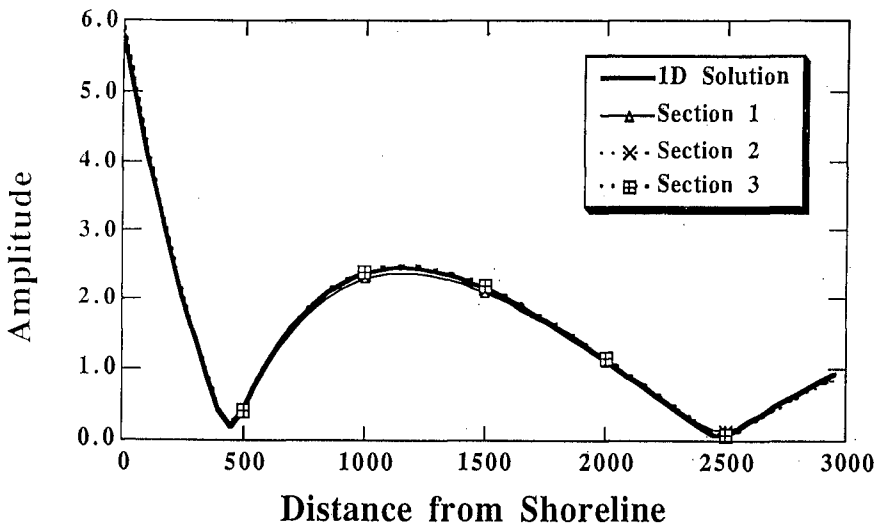


Figure 6. Comparison of CGWAVE Model Predictions versus 1-D Solution (Helmholtz Equation) at Three Cross-sections for a 3-km Planar Beach (Oblique Incident).

oblique waves from left of the normal to the boundary. Model compares extremely well to this solution also at all three sections.

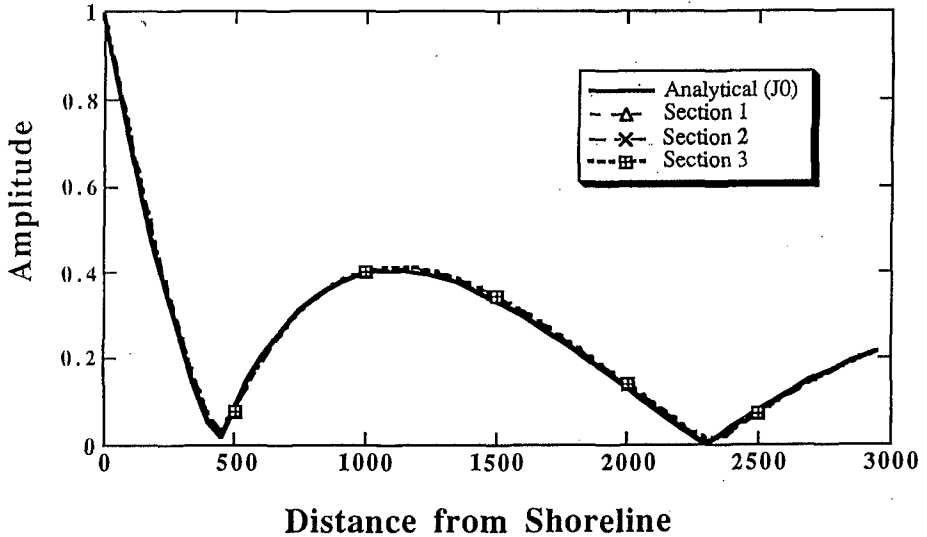


Figure 7. Comparison of CGWAVE Model Predictions versus Analytical Solution at Three Cross-sections for a 2-km Planar Beach (Normal Incident).

The results of CGWAVE model for a 2-km domain are presented in Figs. 7 and 8. For this smaller domain, model estimates still compare exceptionally well to the predictions from the J_0 -solution and 1-D Helmholtz equation even though the modeling domain has been reduced by 30 percent. This shows that CGWAVE results are robust and do not vary as the domain size varies.

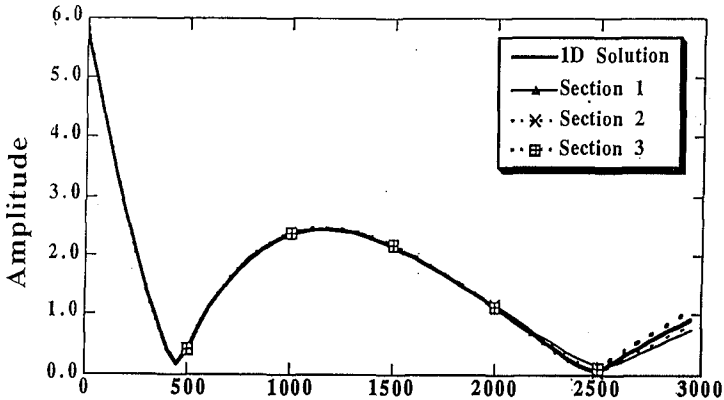


Figure 8. Comparison of CGWAVE Model Predictions versus 1-D Solution (Helmholtz Equation) at Three Cross-sections for a 2-km Planar Beach (Oblique Incident).

Lastly, model results at cross-section 1 are shown for a domain size ranging from 1.5 to 6 km in Fig. 9. We can clearly see a slight change in the model results when the domain size is varied four-fold, but overall, CGWAVE predictions do not show any strong dependence to the size of the modeling domain.

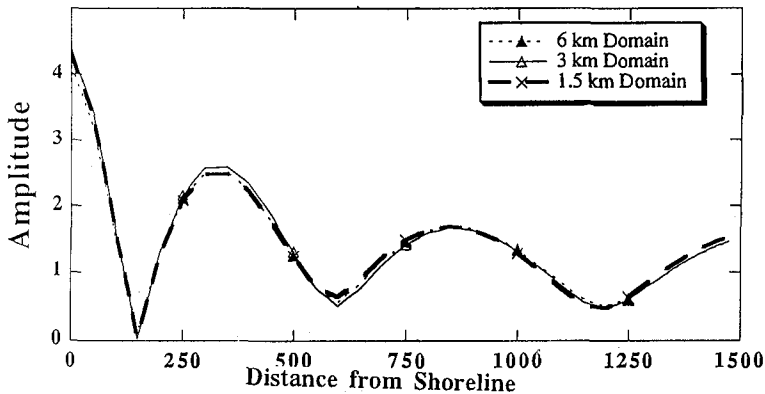


Figure 9. Comparison of CGWAVE Model Predictions versus Analytical Solution at Cross-section 1 for Varying Widths of Beach (Normal Incident).

Conclusions

Elliptic wave models that use the traditional mathematical formulation for wave estimates in the offshore and inside the harbors impose some unrealistic demands as described earlier in this paper. Exterior depth variations in the outside areas of the harbor neglected by these models and the position of the semi-circular open boundary become rather problematic in the field application of these models. Presented here is a discussion of some solutions for eliminating the effects of these undesirable demands. We have demonstrated here the implementation of the proposed solutions for waves on a plane sloping beach by providing a comparison of the model predictions and analytical and approximate solutions.

Our proposed solutions are compromises between an account of the effects of the field bathymetry and radiation boundary condition. The presented model results show that the proposed solutions work very well and that a negligible contamination occurs due to relaxation of the open boundary condition. The suggested solutions eliminate the need to select a constant depth in the exterior region. Our new formulation of the scattered waves greatly reduces the sensitivity of model predictions to the position of the open boundary. Efforts are underway now to evaluate these new ideas implemented in the CGWAVE model for Kahului, Barbers Point, and Oceanside harbors using field measurements.

This work was carried out under the Coastal Research Program of Civil Works Research and Development. The Office of the Chief of Engineers, U.S. Army Corps of Engineers is acknowledged for authorizing publication of this paper.

References

- Chen, H.S., and Mei, C.C. (1974) "Oscillations and Wave Forces in an Offshore Harbors," Rep. 190, Massachusetts of Technology, Cambridge, MA.
- Chen, H.S., and Houston, J.R. (1987) "Calculation of Water Oscillation in an Coastal Harbors: HARBS and HARBD User's Manual," Rep. CERC-87-2, U.S. Army Engineer Waterways Experiment Station, Vicksburg, MS.
- Kostense, J.K., Meijer, K.L., Dingemans, M.W., Mynett, A.E., and Bosch, P. (1986). "Dissipation in Arbitrarily Shaped Harbors of Variable Depth," Proc. 20th Internat. Conf. Coastal Engr., 2002-2016.
- Li, B. (1994). "A Generalized Conjugate Gradient Model for the Mild Slope Equation," Coastal Engr., 23, 215-225.
- Mei, C. C. (1983). *The Applied Dynamics of Ocean Surface Waves*, Wiley, New York.
- Panchang, V. G., W. Ge, B. R. Pearce, and Briggs, M. J. (1990). "Numerical Simulation of Irregular Wave Propagation over a Shoal," J. Waterway, Port, Coastal and Ocean Engg, vol. 116, No.3, 324-340.
- Panchang, V. G. , B. R. Pearce, W. Ge, and Cushman-Roisin, B. (1991). "Solution to the Mild-Slope Wave Problem by Iteration," Applied Ocean Research, 13, No. 4, pp 187-199.
- Panchang, V. G., B. Xu and Cushman-Roisin, B. (1993). "Bathymetric Variations in the Exterior Domain of a Harbor Wave Model," Proc. Internat. Conf. Hydroscience & Engg, Washington DC. Ed. S. Wang. 1555-1562.
- Panchang, V. G. and Xu, B. (1995). "CGWAVE: A Coastal Wave Transformation Model for Arbitrary Domains," Tech. Report, Dept. of Civil and Environmental Engineering, University of Maine, Oct. 1995.
- Panchang, V.G., B. Xu, and Demirebilek, Z. (1996). "Wave Models for Coastal Wave Prediction; A Review," Handbook of Coastal Engineering, Ed. J. Herbich (in print).
- Tsay, T.-K., and Liu, P. L.-F. (1983). "A Finite Element Model for Wave Refraction and Diffraction," Applied Ocean Research, 5, No.1, 30-37.
- Xu, B. and Panchang, V. G. (1993). "Outgoing Boundary Conditions for Finite-Difference Elliptic Water-Wave Models," Proceedings, The Royal Society of London, Series A. v441, 575-588.

Xu, B., V. G. Panchang and Demirebilek, Z. (1996). "Exterior Reflections in Elliptic Harbor Wave Models," *Journal of Waterway, Port, Coastal, and Ocean Engr.*, Vol.122, 118-126.

CHAPTER 99

FIELD MEASUREMENTS AND NUMERICAL MODELING OF HARBOR OSCILLATIONS DURING STORM WAVES

W. M. Jeong¹, J. W. Chae², W. S. Park¹, and K. T. Jung²

Abstract

A series of simultaneous field measurements for long and short-period waves under storm and calm wave conditions were made to understand harbor resonances in a partially enclosed harbor. During storm condition the frequency spectra show peaks of considerable magnitude around the wave period of 1 ~ 5 minutes, which are bounded long waves and their harmonics. They are strongly related with storm waves but longer period (free long) waves are not in the harbor. Numerical tests were also carried out by using the hybrid element model including entrance separation losses in a simple rectangular harbor to validate the model for a mostly constricted entrance case. Further the model was used to simulate the long period oscillation in Muko harbor. Comparisons were made between field data and numerical results to discuss the effect of storm waves on the long period oscillations. Tests demonstrate the effect of input parameters on model results and proper choice of them are stressed.

INTRODUCTION

Long-period wave oscillations in a harbor could create unacceptable vessel motions, excessive mooring forces and fender reactions leading to the breaking of mooring lines and fender system. The typical natural periods of a reasonable sized harbor or a moored vessel are of the order of magnitudes of minutes (Nagai *et al.*, 1994). One of the sources that generate the long-period waves of 2 ~ 3 minutes in the offshore side is the wave set-down travelling with the wave groups. In a partially enclosed harbor attacked by short waves through the narrow entrance, free long waves can be generated, and the waves further resonate the natural modes of the harbor basin (Mei and Agnon, 1989; Wu and Liu, 1990). Recently Girolamo (1996), and Okihiro and Guza (1996) showed that irregular short waves generate bounded long waves and free long waves which excite harbor resonance with extensive analyses of experimental and field measured data, respectively.

¹Senior Research Scientist, Coastal Engineering Division, Korea Ocean Research & Development Institute, Ansan P.O. Box 29, Seoul 425-600, KOREA

²Principal Research Scientist

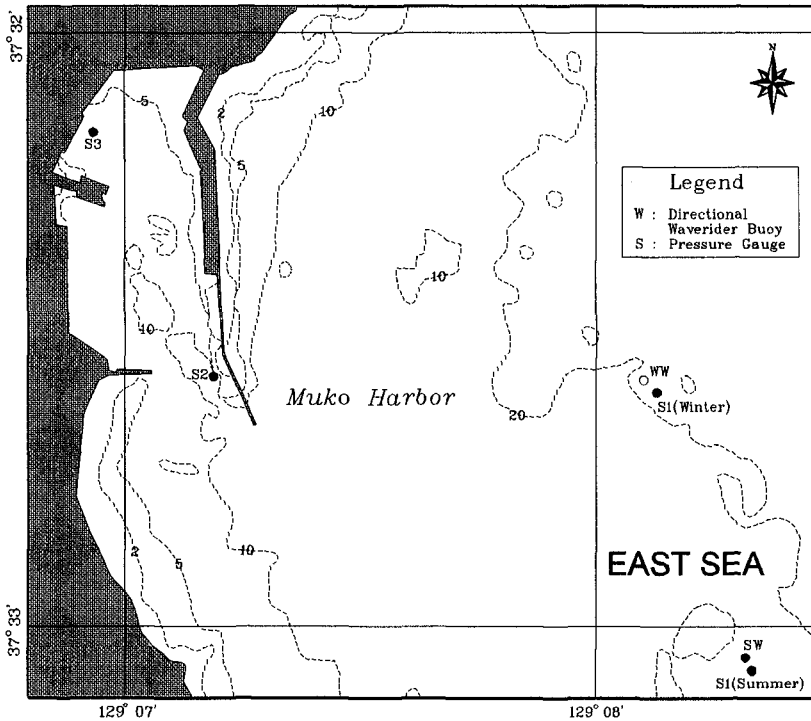


Figure 1: Location map for field measurements around Muko harbor.

Most of previous studies are restricted to theoretical analysis with limited number of narrow frequency waves, and a few experimental and field measurement works taking into account irregular frequency-directional waves during storm conditions. As actual wind waves do not lie in a narrow frequency band, the resonance process is different. In order to investigate the effect of storm short waves to long-period harbor oscillations, a series of field measurements were conducted for both random sea waves and long-period waves inside and outside a small harbor. Harbor amplifications were calculated using HARBD linear model (Chen, 1986) including entrance loss and directional effects (Sand, 1982).

FIELD MEASUREMENTS AND ANALYSIS

Such phenomena of long-period oscillations were observed in the Muko harbor located at the east coast of Korea where north-eastern storm waves are dominant in winter season. The harbor is of a partially-enclosed rectangular shape with dimensions of 1 km long, 410 m wide, and entrance width of 250 m as shown in figure 1. The averaged water depth in the harbor is about 8.5 m.

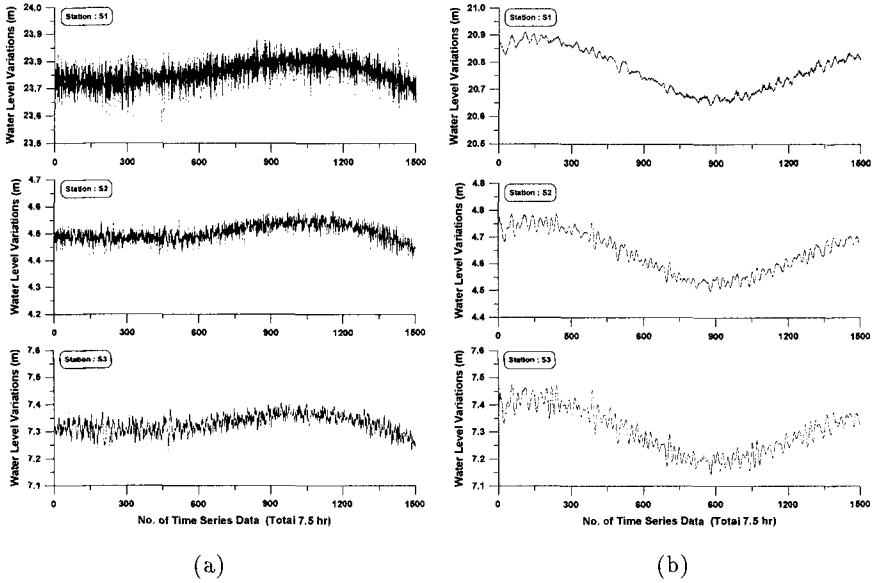


Figure 2: Time series of water level variations measured around Muko harbor; (a) Storm sea; (b) Calm sea.

Table 1: Characteristics of short- and long-period waves.

Data set no.	Starting time of measurement period in 1993	Periods of seiche at each station (min.)			Characteristics of measured short-period waves		
		S1	S2	S3	$\overline{H}_{1/3}$ (m)	$\overline{T}_{H_{1/3}}$ (sec)	Mean direction
1	03/18 15:10	23.1~28.2	11.1~28.2, 4.5, 3.6	11.1~12.2, 4.6, 3.4~3.6, 1.5~1.9	1.67	9.0	N55 ° E
2	03/20 01:18	28.2	13.4	13.4, 3.3~3.7	0.77	8.0	N56 ° E
3	07/07 15:00	18.0~27.8	12.3~20.4 (14.6)	11.4~14.6 (12.3)	0.35	4.0	N83 ° E
4	07/09 01:08	18.0~27.8	13.3~14.6, 5.8	13.3	0.43	4.4	N19 ° E
5	07/10 11:16	20.4~27.8	20.4, 13.3	11.4~13.3	0.37	5.2	N54 ° E

* Each record length is 34.1 hr.

** Shaded numeral denotes peak period corresponding to peak spectral density.

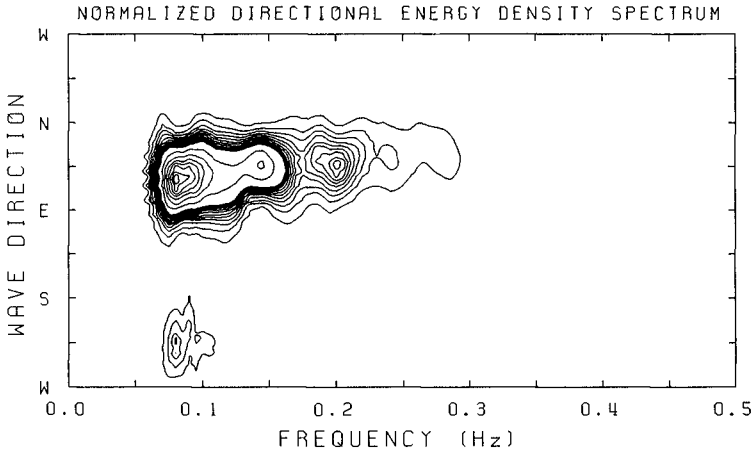
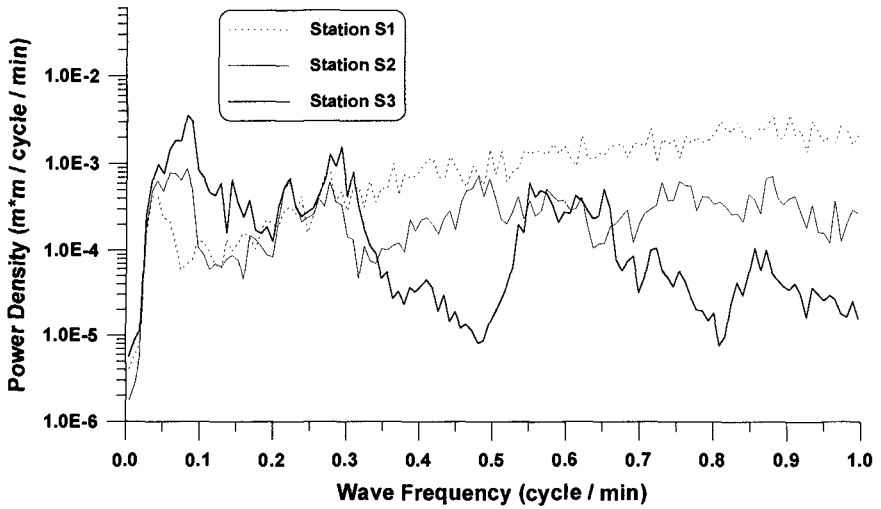


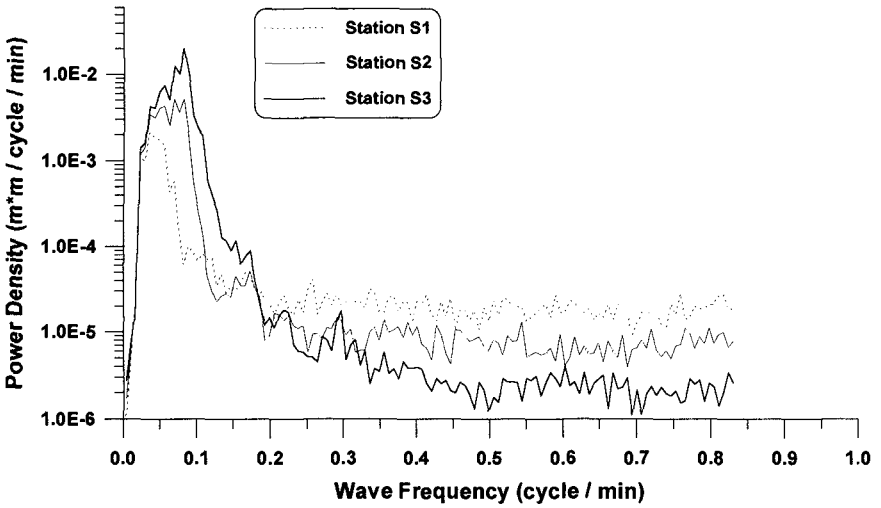
Figure 3: Typical directional spectrum of a short-period wave condition.

To investigate the relationship of short-period storm waves and long-period waves in a harbor, field measurements were performed at three reference stations as shown in figure 1. Using a Datawell directional waverider buoy short-period waves were measured at offshore stations WW and SW for 26.7 minutes at every hour in the interval of 0.78125 second. The frequency of the waves is in the range from 0.04 Hz (25 sec) to 0.25 Hz (4 sec). Using pressure-type wave gauges long-period waves were simultaneously measured at three stations S1, S2 and S3 (figure 1) for March 18 ~ 21 and July 7 ~ 12, 1993. Five sets of data (Table 1) were chosen for the analysis which show typical storm and calm wave conditions. Each set was recorded at 5 second intervals and recording length is approximately 34 hours. Typical time series of measured long-period waves for storm and calm sea conditions are presented in figure 2. It can be clearly found that the long period waves are amplified in a harbor and modulated with tide.

Directional-frequency spectra were obtained from the short-period wave analyses using Maximum Entropy Method (Kobune and Hashimoto, 1986), which show spreading of wave energy in both frequency and directional bands (figure 3). They are different from the narrow frequency banded waves used in the theoretical analysis. After filtering low-frequency waves from long-period wave signals using Butterworth high-pass filter in MATLAB, spectral analyses were made for each record of 4096 data points (at 30 second intervals averaged over 6 raw data). Standard spectral analysis based on FFT provides wave parameters and frequency spectrum that was herein obtained averaging over 16 raw harmonics. Two typical frequency spectra of storm and calm seas corresponding to time series of figure 2 in 128 frequency bands are shown in figure 4. Several peak frequency bands can be found around the wave period of 1 ~ 5 minutes in the frequency spectrum for the storm wave condition, which may be resulted from group-bounded long waves and their harmonics resonated in the harbor (refer to Girolamo, 1996).



(a)



(b)

Figure 4: Power spectra measured around Muko harbor; (a) Storm sea; (b) Calm sea.

LONG-PERIOD WAVES AND HARBOR RESONANCE

Several resonant peaks are clearly seen in the frequency spectrum of long-period waves in the harbor when the storm waves occurred outside the harbor (figure 4(a)). However, only primary resonant peak can be seen in the calm sea condition (figure 4(b)). The observations reveal that long-period waves in the harbor are excited due to the nonlinear resonance by the groups of short waves.

On the basis of case studies of Wu and Liu (1990), it is possible to analyse approximately the characteristics of the oscillations. A little difference in the bounded long waves across the harbor mouth could generate free long waves of small amplitude in the neighbourhood of the first mode. But bounded long waves could be dominant at frequencies beyond the first mode because the harbor entrance is relatively large in comparison with the dimension of the harbor basin. The bounded long waves are mainly affected by short waves (swell) and resonated in the small harbor, but the first resonant mode and free long waves are not dependant on them. It may be because of nonlinear energy dissipation in the harbor entrance even with the increase of the bounded long wave energy.

NUMERICAL MODELING

Mild slope equation of Berkhoff (1972) was adopted for simulating the harbor oscillations. There are three major energy dissipating processes in harbor resonance problem, i.e., bottom friction, energy absorption at solid boundaries, and entrance separation. Chen (1986) considered first two terms in his hybrid element model by introducing frictional loss parameter in governing equation and partial absorbing boundary condition. The governing equation and boundary conditions of Chen's model are summarized in figure 5. In the figure, ϕ is the complex-valued velocity potential in finite element region; ϕ^s is the velocity potential for scattered waves in the far field region; λ is the frictional parameter; α is a coefficient related to the wave reflection characteristics on solid boundaries; and C and C_g are celerity and group velocity, respectively.

Harbor Entrance Energy Loss

In this study, entrance separation losses were considered by introducing two matching conditions at the harbor mouth depicted as a dashed line in figure 6 as follows.

Continuity equation:

$$u_1 = u_2 = u_e \quad (1)$$

Dynamic equation:

$$\frac{p_1}{\rho} = \frac{p_2}{\rho} + \frac{1}{2} f_e u_e |u_e| + l \frac{\partial u_e}{\partial t} \quad (2)$$

in which u_1 and u_2 are water particle velocities in open sea region, A_1 and inner harbor region, A_2 , respectively; u_e is the velocity of water particle at harbor entrance; f_e is loss coefficient; and l is the length of the jet flowing through the harbor mouth.

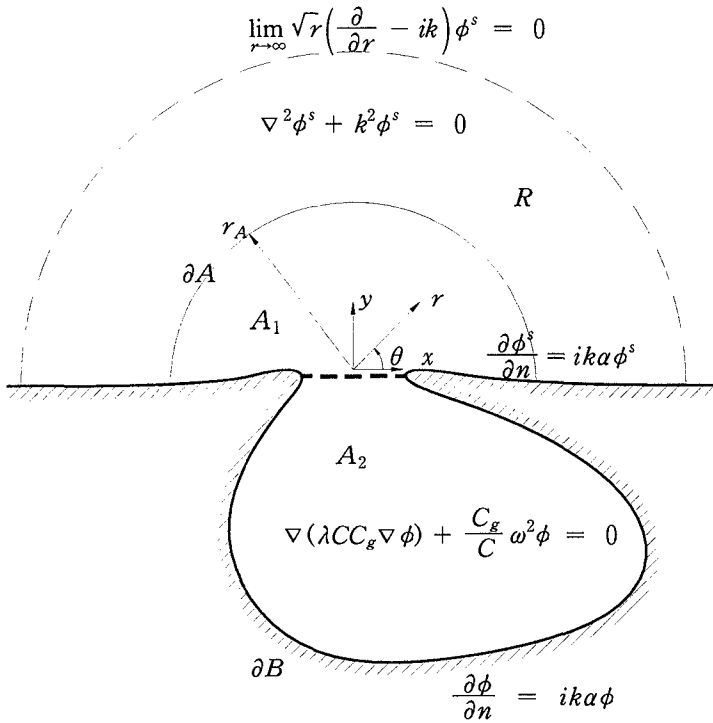


Figure 5: Hybrid element model, HARBD (Chen, 1986).

The second term of right hand side of equation (2) is generally nonlinear. To solve the boundary value problem efficiently in frequency domain, it should be linearized. Using Lorentz's transformation and averaging power along the water depth, it can be linearized as

$$\frac{1}{2} f_e u_e |u_e| \approx \gamma u_e \tag{3}$$

in which γ is the linearized loss coefficient including amplitude of water particle velocity at the interface of A_1 and A_2 , which is given by

$$\gamma = \frac{4}{3\pi} f_e \bar{u}_e \frac{\sinh kh}{\cosh kh} \frac{2(5 + \cosh 2kh)}{3(2kh + \sinh 2kh)} \tag{4}$$

in which \bar{u}_e is the amplitude of u_e ; k is the incident wave number; and h is the depth of water.

Using complex valued velocity potential, the linearized matching conditions can be rewritten as

$$\frac{\partial \phi_1}{\partial n} = - \frac{\partial \phi_2}{\partial n} \tag{5}$$

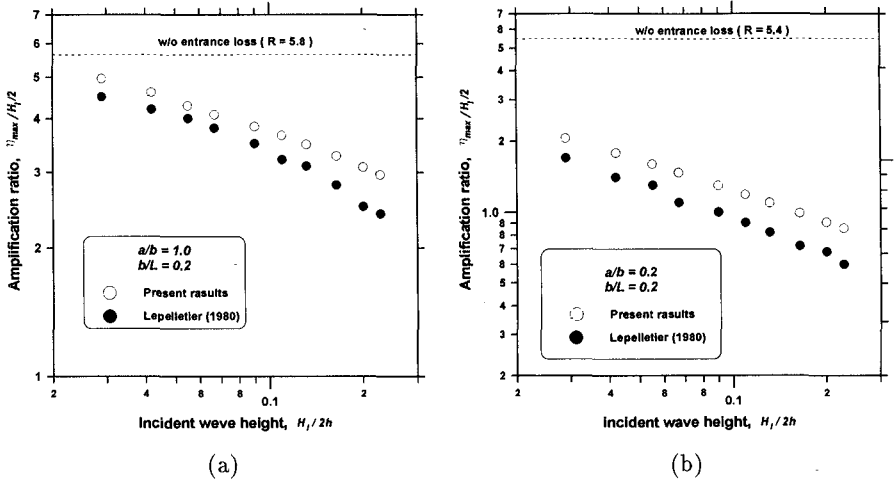


Figure 6: Variation of amplifications varying with incident wave heights; (a) fully opened case; (b) partially opened case.

$$\phi_1 = \phi_2 + \left(\frac{i\gamma}{\omega} + l \right) \frac{\partial \phi_2}{\partial n} \tag{6}$$

The entrance loss coefficient, f_e , are determined from the empirical formulation developed by Lepelletier (1980) given by

$$f_e = \begin{cases} CS & \text{for } S \leq 1 \\ C & \text{for } S \geq 1 \end{cases} \tag{7}$$

in which S is Stroul number ($=u_e/a\omega$); C is empirical coefficient, 0.8 for fully opened harbor ($a/b = 1.0$) and 1.15 for partially opened harbor ($a/b \leq 0.8$); a is the width of entrance; and b is the width of harbor.

Comparison with Experimental Data

With reference to Lepelletier's (1980) laboratory tests a simple rectangular harbor was chosen for numerical calculation of amplification factors. The harbor bottom is flat and widths of the entrance gap are 0.2 (partially open) and 1.0 (fully open) times the harbor width. Using the values of K_r and β (discussed in Thompson et al., 1993), the modified Chen's model was run for the two cases (figure 6). The amplification factor is half as big as Lee's (1969). As shown in the figures the amplification factors taking into account of harbor entrance loss effects are reasonably in good agreement with the data for the most constricted entrance case (figure 6(b)). It can be said that the linear model (HARBD) with linearization of nonlinear dissipation term due to flow separation in the harbor entrance will be a good tool for the estimation of the amplification of a restricted harbor. In case of Muko harbor the entrance energy loss may be not significant because the harbor is relatively wide opened.

No. of Nodes = 7,408
 No. of Elements = 14,379

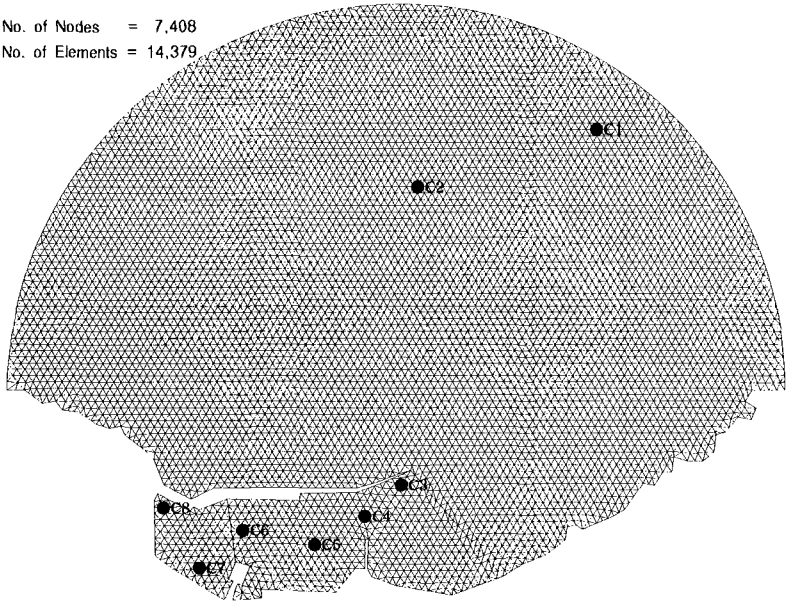


Figure 7: Finite element mesh for Muko harbor.

Model Application

The modified model was applied to calculate the harbor amplification due to group bounded and free long waves generated during the storm wave condition and resonated in the Muko harbor. Model boundary was taken large enough to cover offshore measurement station S1 as shown in figure 7. The water depth of far field area (analytic solution region in HARBD model) is assumed to be constant. Reflection coefficients vary from 0.95 (natural beach) to 0.99 (vertical sea wall) and also vary depending on the magnitude of frequency (i.e., from 0.4 for 15 sec to 0.98 for 180 sec waves at energy absorbing boundary). The numbers of triangular elements are 14379 and its size is small in order to resolve 30 sec period wave in water of 8.5 m depth. Numerical computation has been made for the 54 component waves of period range from 60 sec to 1400 sec. Some comparison was made with experimental data. The amplification ratio is $\sqrt{S_i(f)/S(f)}$, where $S_i(f)$ is spectral density at the i -th point in the domain and $S(f)$ at offshore station. Figure 8 shows the amplification ratio at C7 (measurement station S3), and computation results are in reasonably good agreement with measured data, where water depth is chosen as mean depth of 17.2m. The water depth effects are dominant on the waves around the first resonant peak. The incident wave direction is also very important on the estimation of harbor amplification especially in high frequency range below 350 sec in Muko harbor (figure 9). Those wave periods are related with bounded long waves. Upon the test results of partial wave reflection (figure 10) the coefficient should vary depending on the wave length up to a certain wave period. With proper choice of parameters the modified numerical model performs reasonably well in relation to field data.

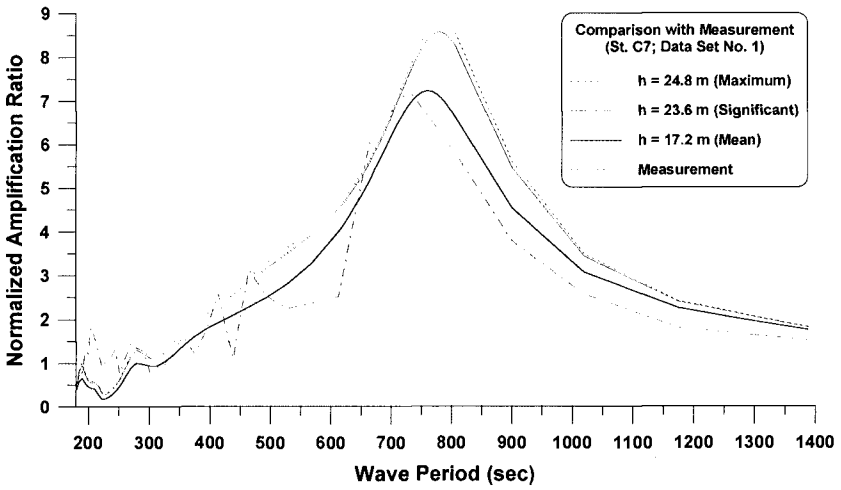


Figure 8: Comparison of normalized amplification ratios obtained by measurements and numerical calculation with various water depths in far field region.

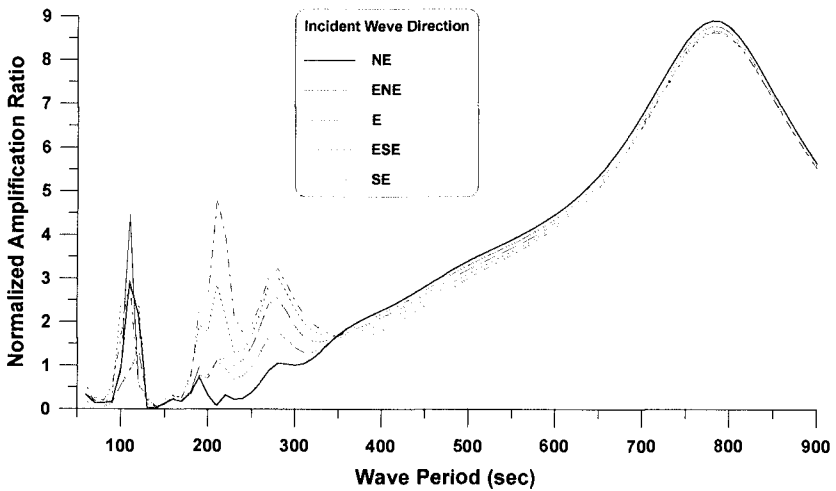


Figure 9: Variation of normalized amplifications with incident wave directions.

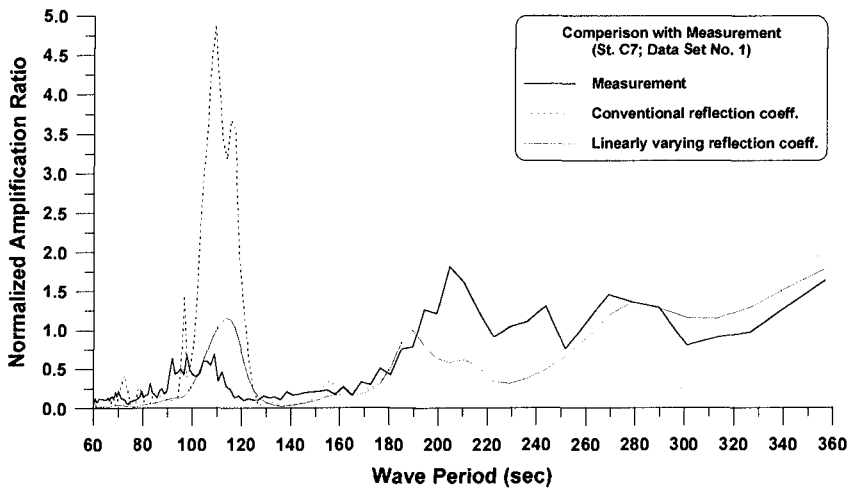


Figure 10: Comparison of normalized amplification ratios obtained by measurement and numerical calculation with different reflection coefficients.

CONCLUSIONS

Field measurements of short- and long-period waves were made to understand long-period oscillations generated by storm waves in a partially enclosed harbor. In a storm wave condition the frequency spectrum shows several resonant peaks, which are free long waves in the neighbourhood of the first mode, and bounded long waves and harmonics in the other modes. The bounded long waves are strongly dependent on short wind waves but the longer waves may be not. Chen's linear model was modified to cope with entrance energy losses due to flow separation. The model provided a good approximation to the harbor amplification of major resonant modes in the Muko harbor.

ACKNOWLEDGEMENTS

This work has been financially supported by the Korea Ministry of Science and Technology under the Project Nos. BSPN00192 and BSPN00323. The authors are grateful to their colleagues for collecting the field data.

REFERENCES

- Bowers, E. C. (1977). Harbor resonance due to set-down beneath wave groups. *J. Fluid Mech.*, **70**, 71-92.
- Berkhoff, J. C. W. (1972). Computation of combined refraction and diffraction. *Proc., 13th Coast. Engrg. Conf.*, ASCE, New York, 471-490.

- Chen, H. S. (1986). Effects of bottom friction and boundary absorption on water wave scattering. *Applied Ocean Research*, **8**(2), 99-104.
- Girolamo, P. D. (1996). An experiment on harbor resonance induced by incident regular waves and irregular short waves. *Coastal Engrg.*, **27**, 47-66.
- Kobune, K. and N. Hashimoto. (1996). Estimation of directional spectra from the maximum entropy principle. *Proc. 5th Int. Offshore Mech. and Arctic Engrg. Symp.*, ASME, **1**, 80-85.
- Lee, J. J. (1969). Wave induced oscillations in harbors of arbitrary shape. *Report No. KH-R-20*, W. M. Keck Lab. of Hydraulics and Water Resources, Calif. Inst. of Technology, Pasadena, CA.
- Lepelletier, T. G. (1980). Tsunamis-harbor oscillations induced by nonlinear transient long waves. *Report No. KH-R-41*, W. M. Keck Lab. of Hydraulics and Water Resources, Calif. Inst. of Technology, Pasadena, CA.
- Mei, C. C. and Y. Agnon. (1989). Long-period oscillations in a harbor induced by incident short waves. *J. Fluid Mech.*, **208**, 595-608.
- Nagai, T., N. Hashimoto, T. Asai, I. Tobiki, K. Ito, T. Toue, A. Kobayashi, and T. Shibata. (1994). Investigation of the harbor tranquility based on wavegroup characteristics. *HYDRO-PORT'94*, 203-215.
- Okiihiro, M. and R. T. Guza. (1996). Observations of seich forcing and amplification in three small harbors. *J. Wtrwy., Harb., Coast., Engrg., Div.*, ASCE, **122**(5), 232-238.
- Sand, S. E. (1982). Long waves in directional seas. *Coastal Engrg.*, **6**, 195-208.
- Thompson, E. F. (1993). Numerical modeling of waves in harbors. *Waves'93*, 590-601.
- Wu, J. K. and P. L.-F. Liu. (1990). Harbor excitations by incident wave groups. *J. Fluid Mech.*, **217**, 595-613.

CHAPTER 100

PERFORMANCE OF A RESONATOR DESIGNED BY THE WAVE FILTER THEORY – APPLICABILITY TO A HARBOR

Takayuki Nakamura¹, Hitoshi Mochizuki² and Satoshi Morita³

ABSTRACT

A wave resonator, which has a comparatively wide opening and still keeps effectiveness for a wider range of wave frequency, is newly developed based on the Wave Filter Theory. Applying this resonator both to a long channel and a harbor entrance, the sheltering effect for incoming waves was examined by the numerical and physical experiments. It was confirmed that the Wave Filter theory is very effective to design a wave resonator for required conditions, such as an effective band width of wave frequency.

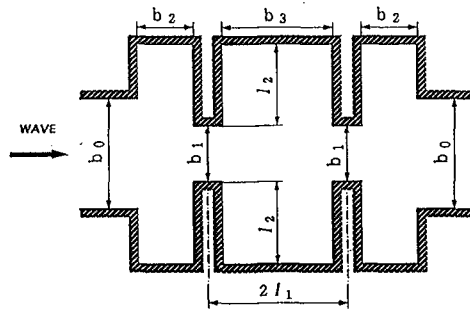
INTRODUCTION

In the 1950s, Valembouis(1953) has already presented an idea of resonators to reduce incoming waves to harbors and canals by installing resonators at the entrance. In this attempt, the shape of a resonant basin is fixed to the definite one; the ratio of a length to a width of the resonant basin is 2:1. It was reported that the effective range of a wave frequency is comparatively narrow. In order to expand the effective range, he has proposed a series of resonators with different dimensions instead of a single resonator. However, in his study, the influence of an opening length between the two facing resonators on the sheltering effect has not been clarified. Consequently, it may be very hard to out find the total geometry of a resonator-type breakwater.

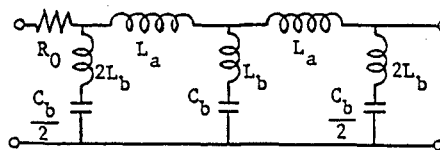
-
- 1) Associate Professor, Department of Civil and Ocean Engineering, Ehime University, 3 Bunkyo-cho, Matsuyama City, Ehime 790, Japan
 - 2) Professor, Department of Electronic Engineering, Meisei University, Japan
 - 3) Researcher, Technical Research Institute, Kumagai-gumi, Japan

Recently, Mochizuki et al.(1990) have developed a new method to design a resonator that is effective for wider frequency range based on the electric filter theory, which is called the Wave Filter Theory. Nakamura et al.(1994) may be very hard to out find the total geometry of a resonator-type have conducted a series of experiments on a resonator designed by the theory in a long wave flume. However, applicability of the resonator to a fully three-dimensional wave field, such as harbor tranquility problems, has not been verified sufficiently.

In this study, using the Wave Filter Theory, a resonator that is effective for a wider range of wave frequency is first obtained. Especially, intending the resonator at harbor entrances, a resonator with a wider opening is presumed for passing ships. Experimental verification of this resonator was carried out in a long wave channel to check the principal validity of the Wave Filter Theory. Finally, for protecting a harbor from incoming waves of wider frequency range, the designed resonator is installed at the entrance. Numerical experiments on the wave height distributions in the harbor were carried out to examine the effectiveness of the resonator. Some additional case studies were also given to compare with the result of a resonator case.



(a) Wave resonators in series.



(b) Equivalent electric circuit to the wave resonators.

Fig.1 Analogy between the wave resonators and the electric filter.

RESONATOR DESIGNED BY THE WAVE FILTER THEORY

Mochizuki et al. (1990) have presented a rational way to determine a geometrical shape of the resonator that is effective for a specified wave frequency range. The basic idea is to consider the analogy between a wave resonator and its equivalent electric filter. In the field of an electric filter, filter actions of various electric filters are well known. Consequently, considering the corresponding parts between the resonator and its equivalent electric filter, we can easily find out the geometrical shape of the resonator.

In the theory, a resonator model as shown in Fig.1(a) is assumed. The corresponding electric filter to the resonator is given in Fig.1(b). In the latter figure, L_a and L_b =inductance, R_0 =resistance, and C_b =capacitance. This equivalent electric circuit is known as a derived m-type low-pass filter. By considering the analogy between the two models and also the frequency characteristics of the electric filter, we can derive design equations of a wave resonator for required conditions.

Here, we made some simplifications for convenience of practical designs. At first, we assume that the long wave approximation can be used. Secondly, a longitudinal length of the first and third resonant basin in Fig.1(a) is equal to a half of that of the center one, i.e., $b_2=b_3/2$. By use of these assumptions, the following equations are given (Mochizuki et al. 1990)

$$\left. \begin{aligned} b_3 &= \frac{m b_0}{\sqrt{2(1-m^2)}} \\ l_2 &= \frac{1}{\pi f_c} \sqrt{\frac{gh(1-m^2)}{2}} \\ \frac{l_1}{b_1} &= \frac{m\sqrt{gh}}{2\pi f_c b_0} \end{aligned} \right\} \quad (1)$$

where g =gravitational acceleration, h =water depth, and m is a function of the critical frequency f_c and the pole frequency f_∞ of an effective frequency band ($f_c < f < f_\infty$) of a wave resonator and is defined by

$$m = \sqrt{1 - \left(\frac{f_c}{f_\infty}\right)^2} \quad (2)$$

The pole frequency f_∞ is a frequency at which wave transmissions through a resonator become the lowest.

Fig.2 shows a typical result by use of Eq.(1), which is designed under the required conditions given in Table 1: In the figure, however, only the center part of a series of resonators is adopted. Nakamura et al.(1994) have reported that such a single resonator has similar filter actions to a series of resonators as seen in Fig.1(a). They also pointed out that the aligned resonators have a sharper cutoff feature of filtering actions than the single resonator. For economical and practical designs, it might be said that a single resonator is much more acceptable than the aligned resonators. Therefore, in the followings, we will use the single resonator as shown in Fig.2 as a model.

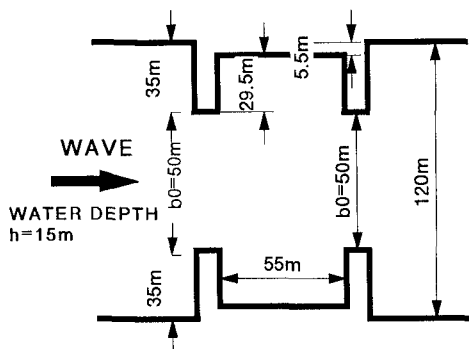


Table 1 Design conditions for a resonator

Critical frequency f_c	1/20 Hz
Pole frequency f_p	1/11 Hz
Opening length b_0	50 m
Water depth h	15 m

Fig.2 A resonator designed by the Wave Filter Theory.

EXPERIMENTAL RESULTS IN A CHANNEL

Experimental setup

In order to check the validity of the Wave Filter Theory, we carried out a model test in a long channel with a width of 1m, a height of 1.2m and a length of 26m. Using the 1/60 model of the resonator shown in Fig.2, wave transmission and reflection characteristics were examined. In the experiment, as shown in Fig.3, we built a half of the single resonator in the channel. There are two different types of model structures with the same dimensions, but having different reflection characteristics. One model is made of plywood and shows a high reflective nature. The other model is made of steel nets and pebbles and shows a low reflective nature.

Considering the mirror image effect of side walls of a channel, the wave field in the channel described above is equivalent to the one around an infinite array of identical resonators. In the above case, an allocation pitch length λ of arrayed structures is equal to double of a channel width.

According to the recent studies (Darlymple et al. 1990; Nakamura 1994), it has become known that the wave pattern around an arrayed bodies is short-crested, especially under the condition in which a wave length L is less

than a pitch length λ of the array. This is due to the generation of obliquely transmitted and reflected wave trains about the arrayed bodies in addition to the usual scattered waves as seen in a vertical two-dimensional wave field.

In order to be able to analyze the short-crested wave pattern in the channel, we set a linear array of five wave gauges in the transverse direction to measure transmitted waves through a resonator. Wave conditions used in the experiment are as follows; a wave period T_m ranges from 0.9 sec to 2.6sec (in prototype scale $T=7\sim 20$ sec) and a wave height H_m is fixed at about 4cm (in prototype scale $H=2.4$ m). Above conditions of a wave period T_m correspond to the dimensionless parameter λ/L being from 0.5 to 1.8.

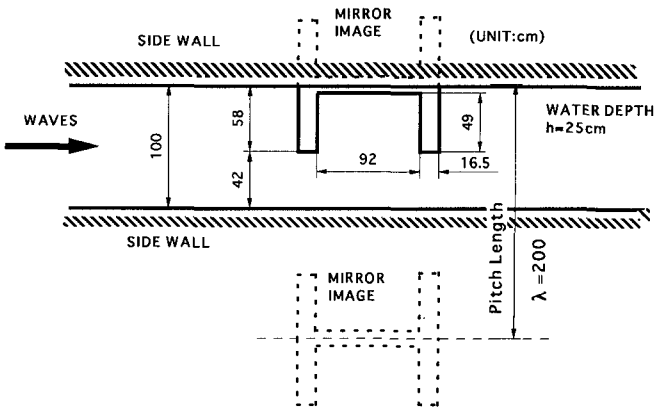


Fig.3 Experimental setup (model scale 1/60).

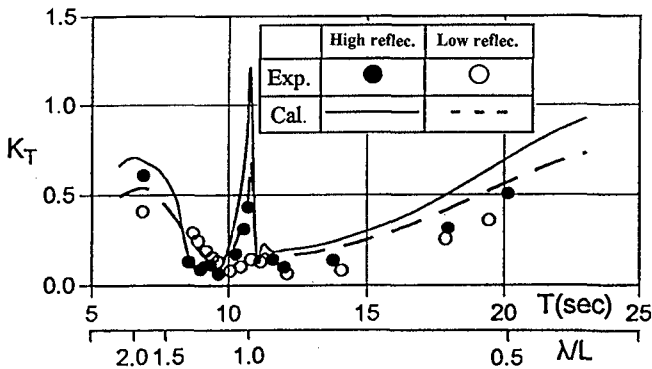


Fig.4 Ratio of a RMS transmitted wave height to an incident wave height.

Wave transmission characteristics

Fig.4 shows typical results, where the dimensionless transmitted wave height K_T is plotted as a function of a wave period T in the prototype scale. A parameter λ/L is also specified as the second horizontal axis.

Where K_T is defined by

$$K_T = (H_T)_{rms} / H \quad (3)$$

$(H_T)_{rms}$ is a root-mean-square(RMS) value of transmitted wave height along the array direction, which is consistent with the transverse direction of a channel. The RMS value is necessary to account for the short-crested wave pattern in the transmission side of the channel, especially under the condition $\lambda/L > 1$. In other condition where $\lambda/L < 1$, the definition of K_T coincides with that of a well known transmission coefficient.

In the figure, two different experimental results are shown. One is for the resonator consisting of high-reflective walls. Other is for dissipative walls made of steel nets and pebbles. Further, in the figure, the calculated result by the Green's function method is also plotted. Nakamura(1992) has developed a method of numerical analysis to analyze wave transformations about an infinite array of vertical bodies by the wave source distribution method.

From this figure, we can see reasonable agreements between the calculated and experimental results, except near the condition $\lambda/L = 1$. The spike-like variation of K_T is caused by the wave resonance in the transverse direction. It is seen that there is little influence of the different wall types on the wave transmission. As an important point, we can say that the Wave Filter Theory is useful to design a resonator for required conditions, such as a target band width of wave frequency ($f_c < f < f_\infty$) and a necessary opening length. A small discrepancy of the pole frequency f_∞ between the Wave Filter Theory and the calculated and experimental results may be due to the assumption of the long wave approximation as described in the Wave Filter Theory.

Wave height variations in a resonator

Figs.5 and 6 show typical measurement results of wave height distributions in a resonator, in which the wave height is normalized by the incident wave height. These two figures correspond to the two different wall-type cases, i.e., a high-reflective wall case and a low-reflective wall case, respectively. The condition of a wave period T used in these figures is approximately consistent with that where K_T becomes minimum as seen in Fig.4.

From these figures, we can see that K_T becomes comparatively small when a node of two-dimensional standing waves appears at the transmission-side mouth of a resonator. It is also seen that the maximum wave height in

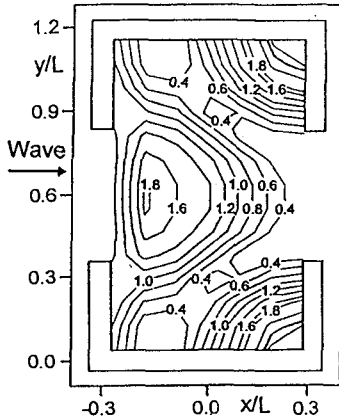


Fig.5 Wave height distributions in a resonator of high-reflective walls .

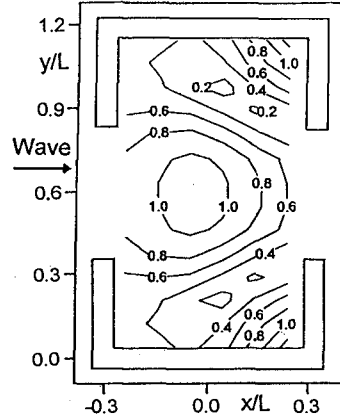


Fig.6 Wave height distributions in a resonator of low-reflective walls .

the resonator becomes about two times as high as the incident wave height when the wall-type is high reflective. By changing the wall-type of a resonator to the low reflective one, it is possible to reduce the maximum wave height effectively, say by one half. For the practical use of a wave resonator at a harbor entrance, it may be required to reduce the maximum wave height in a resonant basin to the order of an incident wave height for safety operation of ships. Therefore, a resonator consisting of low-reflective walls is highly recommended, especially for the use at a harbor entrance.

NUMERICAL EXPERIMENT ON THE HARBOR TRANQUILITY

Numerical method

In order to check the applicability of the resonator described above to a harbor, numerical experiments were carried out for a harbor with a typical shape in Japan. The vertical line source Green's function method developed by Isaacson (1978) was mainly adopted. Nakamura et al. (1985) precisely examined singular functions included in the wave source function and modified the numerical method so that a thin-walled structure can be treated as compared to a wave length. In the numerical analysis, reflection characteristics from harbor boundaries can be treated generally by using

partially absorbing boundary conditions (Engquist et al. 1977) instead of well-known no-flux conditions.

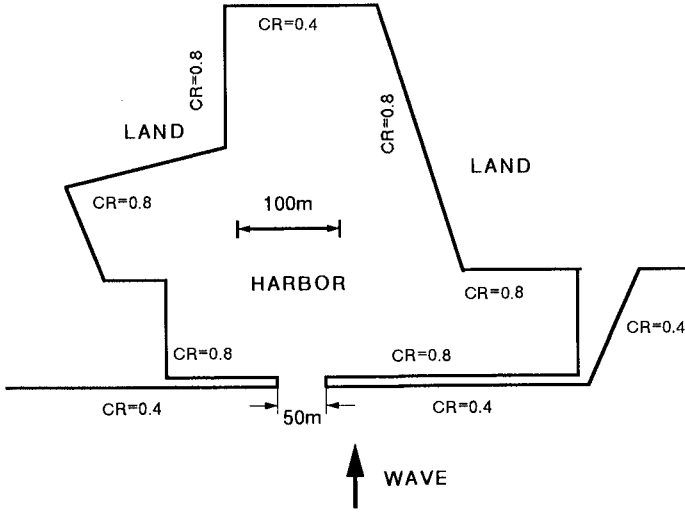


Fig.7 Layout of a harbor and wave reflection characteristics of the boundary.

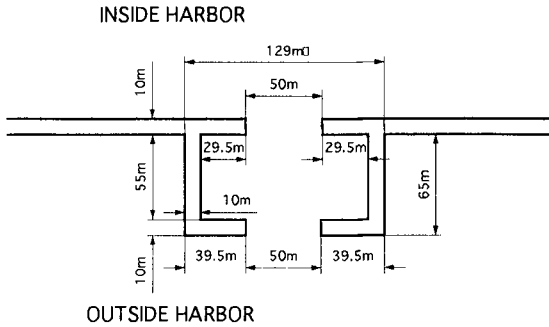


Fig.8 A harbor entrance with a resonator.

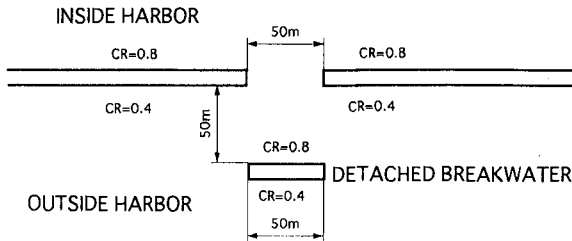


Fig.9 A harbor entrance with a detached breakwater.

Model harbors

Fig.7 shows a layout of an original harbor used in the numerical experiment. It is assumed that a water depth h inside and outside a harbor is constant and equal to 15m. Reflection characteristics of harbor boundaries are specified in the figure by using reflection coefficients C_R . We presume that the boundary outside the harbor of $C_R=0.4$ is covered with dissipative concrete blocks. Further, the boundary inside the harbor with the same

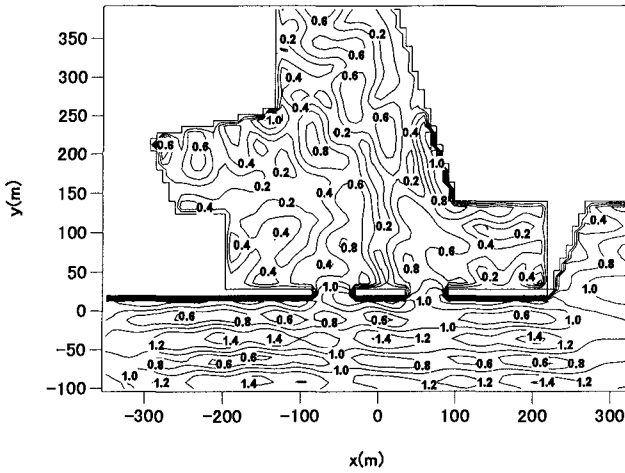


Fig.10 Wave height distributions around the original harbor ($T=9\text{sec}$).

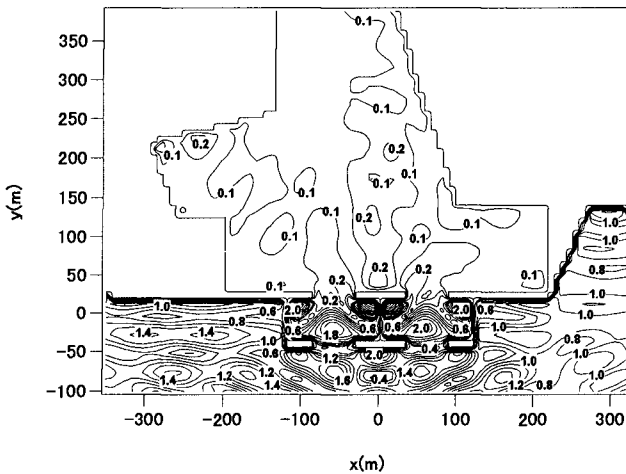


Fig.11 Wave height distributions around the harbor with a resonator of high-reflective walls ($T=9\text{sec}$).

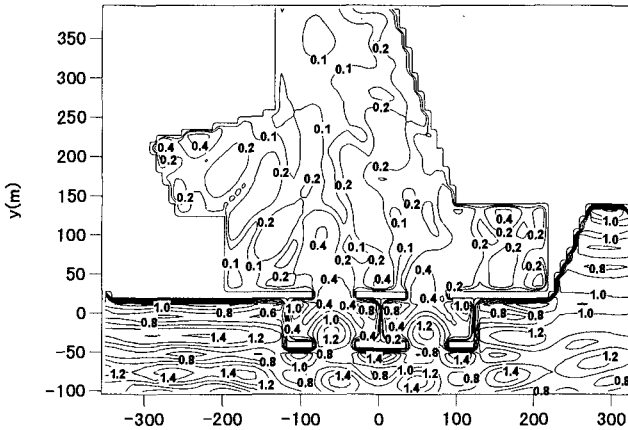


Fig.12 Wave height distributions around the harbor with a resonator of low-reflective walls($T=9$ sec).

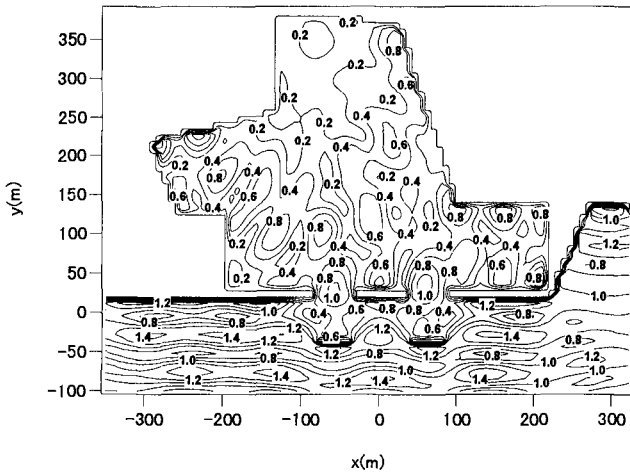


Fig.13 Wave height distributions around the harbor with a detached breakwater($T=9$ sec).

C_R is an inclined quay. Other boundaries of $C_R=0.8$ are vertical sea walls. In the experiment, three different models are examined; an original harbor as shown in Fig.7, a harbor with resonators at harbor entrances (Fig.8) and a harbor with detached breakwaters outside harbor entrances (Fig.9). Regarding the resonator case, we have adopted the same shape specified in Fig.2. Two different reflection characteristics from inside walls of a resonator are again used, a high reflective wall case of $C_R=1.0$ and a low

reflective wall case of $C_R=0.6$, respectively. In all cases, an opening length of each harbor entrance is fixed at 50m.

Inter-comparisons of wave height distributions among different cases described above are shown in Figs.10 to 13 by the use of normalized wave height contours. A normal incidence of plane waves to harbor entrances is presumed. Further, the wave period T is fixed at 9sec, which corresponds to the condition of minimum wave transmission for the case of arrayed resonators as shown in Fig.4.

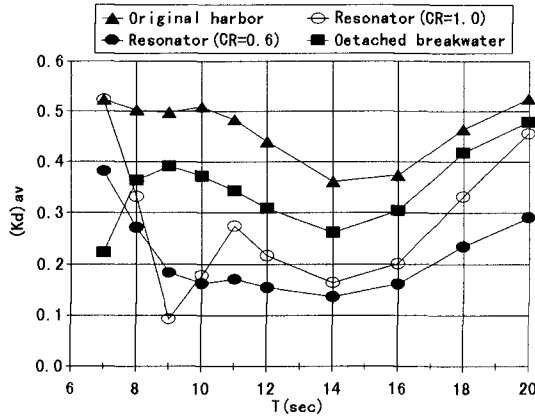


Fig. 14 Averaged wave height ratio in a harbor for various types of breakwaters.

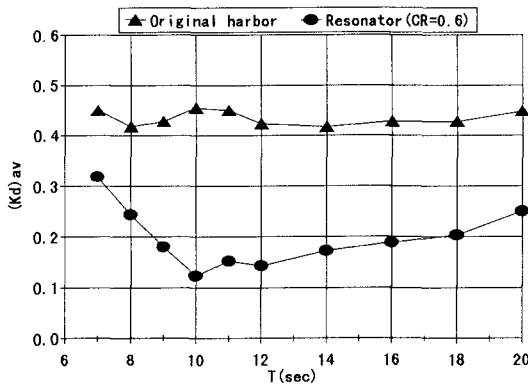


Fig. 15 Averaged wave height ratio in a harbor for obliquely incident waves; 60-degree incidence.

We can see that the resonator with high-reflective walls is the most effective breakwater to reduce wave heights in the harbor. The resonator with low-reflective walls is also very useful as compared to the detached breakwater case. However, it must be noted that the maximum wave height in a resonant basin reaches more than twice as high as an incident wave height for the resonator case with high-reflective walls. Therefore, it is again confirmed that a resonator with low-reflective walls is highly recommended. In this case, the maximum wave height in a resonant basin is reduced to the order of an incident wave height.

Fig. 14 shows the variation of a representative wave height ratio $(K_d)_{av}$ in a harbor with a wave period T for each case described above. Where $(K_d)_{av}$ is a spatially averaged wave height ratio in a harbor. It can be seen that a resonator designed by the Wave Filter Theory is very effective to reduce incoming waves for a comparatively wide range of wave period. It is also seen that the resonator with low-reflective walls has a wider effective range of wave period than the one with high-reflective walls, especially for longer waves.

Fig. 15 also shows the variation of $(K_d)_{av}$ with T , but under the condition of obliquely incident waves (incident angle of waves is 60-degree from the x axis). From this figure, it is confirmed that the resonator is still effective for obliquely incident waves to harbor entrances. The reduction of a wave height in a harbor is almost the same for the case of normally incident waves as shown in Fig. 14.

CONCLUSIONS

The Wave Filter Theory is very useful to design a resonator for required conditions, such as an effective range of wave frequency ($f_c < f < f_w$) and a necessary opening length. It was confirmed that the resonator designed by the Wave Filter Theory plays an effective protector for reducing incoming waves to harbors and canals.

A resonator consisting of low-reflective walls is highly recommended for the use at a harbor entrance because of safety operations of ships. It is also possible to expand the effective range of wave frequency of a resonator by the use of low-reflective walls.

REFERENCES

Dalrymple, R.A. and Martin, P.A. (1990) : Wave diffraction through offshore breakwaters. *Journal of the Waterway, Port, Coastal and Ocean Engineering Division, ASCE*, Vol.116, No.6, pp.727-741.

Engquist, B. and Majda, A. (1977) : Absorbing boundary conditions for the numerical simulation of waves, *Mathematics of Computation*, Vol.31,

No.139, pp.629-651.

Valembois, J. (1953) : Investigation of the effect of resonant structures on wave propagation, Proc. of Minnesota International Hydraulics Convention, pp 193-199.

Isaacson, M.Q. (1978) : Vertical cylinders of arbitrary section in waves. Journal of the Waterway, Port, Coastal and Ocean Engineering Division, ASCE, Vol.104, No.WW4, pp.309-324.

Mochizuki, H. and Mitsuhashi, W. (1990) : A frequency filter for ocean waves, Proc. Inter. Symp. Techno-Ocean '90, pp.398-406.

Nakamura, T. and Oku, Y. (1985) : A method of numerical analysis on wave diffractions about a vertical structure of arbitrary section, Proc. of 32nd Japanese Conf. on Coastal Eng., pp.594-598.

Nakamura, T, Mochizuki, H and Nakako, T. (1994) : Performance of an array of resonator-type breakwaters based on the Wave Filter Theory, Proc. of 41st Japanese Conf. on Coastal Eng., pp.621-625.

Nakamura, T. (1994) : Wave directional change by an array of breakwaters, Proc. of Inter. Symp. Waves - Physical and Numerical Modeling, pp.1069-1078.

CHAPTER 101

The Generation of Waves by a Landslide: Skagway, Alaska—A Case Study

Fredric Raichlen¹, Jiin Jen Lee², Catherine Petroff³, and Philip Watts⁴

1. Introduction

On November 3, 1994, at about 7:10 p.m. Alaska time, a combined aerial and sub-aerial landslide, which was not seismically induced, occurred at a railway dock on the eastern side of the harbor at Skagway, Alaska. A small portion of the landslide, consisting in part of rip-rap, was initially above water. The submerged landslide material was composed of loose alluvium accumulated along the eastern side of the harbor on an underwater slope with an average angle between 0 deg. and 30 deg. Witnesses reported waves 30 ft to 36 ft high at the eastern side of the harbor. The slide and the generated water waves claimed the life of one construction worker and caused an estimated \$21 million damage. A map of the Skagway Harbor is presented in Fig. 1 showing the location of the landslide and the surrounding area including the Taiya Inlet which is an arm of the much longer Lynn Canal.

A floating dock used as an Alaska state ferry terminal is located in the middle of the harbor at the end of a 660 ft long jetty, and a small boat harbor is located near the east side of the harbor. The chains which moored the floating dock were broken during the event.

At the time of the landslide the tide elevation was at about -4 ft MLLW; the tide range at Skagway varies from about 9.8 ft to about 24.6 ft over a month. The record from a tide gage located at a dock on the west side of the harbor is presented in Fig. 2 showing the waves generated by the landslide. The tide gage trace is truncated for extremely low water surface elevations because, for those readings, the travel of the gage recording pen was stopped by the chart paper guide.

The purpose of the study reported in this paper was to more fully understand the wave events which could have taken place in Skagway Harbor after the landslide. The interest is not in precisely modeling the landslide, but in defining the response of the harbor and of the moored floating ferry dock to waves generated by a moving boundary which is used as an analogy to the landslide for purposes of wave generation.

¹Prof. C.E., Calif. Inst. of Tech., Pasadena, CA 91125; ²Prof. C.E., Univ. of So. Calif., Los Angeles, CA 90089; ³Asst. Prof. C.E., Univ. of Wash., Seattle, WA 98195; ⁴Grad. Stud., Calif. Inst. of Tech., Pasadena, CA 91125

Three aspects of the problem will be investigated and will be discussed in subsequent sections. The first deals with the dynamics of a gas-purged nitrogen bubbler tide gage which was of the same type as used in Skagway. The dynamics of the tide gage were determined experimentally in the laboratory, and the response is presented in this discussion. The second aspect is the response of Skagway Harbor to the waves generated by the transient motion of a section of the harbor boundary. This was investigated primarily to simplify the problem of the generation mechanism for landslide induced waves. The transient waves generated by the moving boundary have a similar ability to induce oscillations in the harbor as waves generated by an aerial and a sub-aerial landslide. With the harbor connected to a large open region, i.e., the Taiya Inlet, the questions are how energy generated by a moving boundary (representing the landslide) propagates across the harbor and into the inlet and what is the frequency content of this energy at various locations within Skagway Harbor. The third portion of the overall problem deals with the failure of the floating ferry dock mooring chains. An analytical model was developed for the response of the moored-floating dock to incident waves, and combined with wave spectra determined from the harbor response model, the parting of the mooring chains which was observed at Skagway was investigated qualitatively.

2. The Landslide Event

In this section the characteristics of the landslide and the generated waves will be discussed along with some observations made by witnesses of the event (see Watts and Petroff (1995)). There were four major docks in Skagway Harbor prior to the landslide: an Ore Loading Dock situated adjacent to a jetty that forms the west side of the harbor and is the site of the tide gage location; the Ferry Terminal Floating Dock located in the middle of the harbor at the end of a 660 ft long landfill jetty; the Broadway Dock immediately west of the Ferry Terminal Dock and jetty; and the White Pass Company Railway Dock located along 1312 ft of the eastern shore of the harbor and immediately south of the small boat harbor. (These can be seen in the map presented as Fig. 1.)

The underwater landslide on November 3, 1994 destroyed the southern 984 ft of the White Pass Company Railway Dock. Construction work was underway at the White Pass Company Railway Dock, and the northern quarter (328 ft) of the dock had been cut away from the southern three quarters (984 ft) to replace wooden piles with steel sheet pile cells. Several construction workers standing on the northern quarter of the dock watched the landslide and the southern part of the dock disappear into the water. The job superintendent estimated the total time from the beginning of the slide to the total loss of ground at between 15 to 20 seconds. The wave generated by the landslide was described as a "wall of water" by the survivor who escaped from one of the sheet pile cells that disappeared in the landslide. At about the same time it was observed by two of the three witnesses that a barge alongside the White Pass Company Railway Dock appeared to be level with the remaining northern portion of the dock, providing evidence of a positive wave generated by the landslide and/or a wave reflecting off the shoreline.

The Ferry Terminal Dock located at the center of the Skagway Harbor was moored with thirteen chains each with a scope such that it would allow for the relatively large vertical movement of the dock caused by the tide range. The chains consisted of both 1.5 in. diameter and 2.5 in. diameter chain links (a submerged unit weight of about 48 lbs/ft), and links were broken on all thirteen chains as a result of the dock movement. Observers reported that the dock was not overtopped

by waves. However, tall lamp posts located on the dock were all buckled at the base with the poles bent westward indicating that there must have been either a significant eastward acceleration of the dock or large westward deceleration.

3. The Tide Gage Response

The tide record shown in Fig. 2 was measured using a gas-purged nitrogen bubbler gage (see Young, 1977). The gage records the change in water level by sensing the change in hydrostatic pressure at the open end of a gas filled tube, termed the orifice chamber, which is secured beneath the still water level. For the case of a steady water surface the pressure of the gas throughout the tube is approximately equal to the pressure of the water at the gas-water interface at the end of the tube. For example, as the pressure increases with the rising tide, the gas in the tube compresses to reach equilibrium and shifts the gas-water interface. By supplying a regulated flow of gas the interface is kept at the end of the tube throughout the tidal range. The other end of the tube is connected to a bellows and through a mechanical linkage to a pen recorder. A needle valve located between the end of the tube and the bellows can be adjusted to damp out pressure fluctuations due to normal short period wave activity. The adjustment is subjective and is determined on-site by the gage operator depending on the ambient wave conditions. Thus, as the pressure at the open end of the tube changes the bellows expands or contracts thereby providing a tide record or marigram. The tube length for the Skagway bubbler tide gage was about 150 ft. Due to effects of compressibility, the bellows arrangement, the linkages, and especially the setting of the damping valve this type of transducer has a dynamic response which varies as a function of the frequency of the pressure fluctuation at the open end. To correctly interpret the tide gage record presented in Fig. 2 for waves with periods much shorter than the tide, it was necessary to independently calibrate the bubbler tide gage.

A calibration system was designed to determine the dynamic response of the nitrogen bubbler tide gage to an imposed sinusoidal pressure. The orifice chamber was immersed in a partially water-filled pressure chamber which could have a time-varying air pressure impressed above the water surface. The air pressure was varied sinusoidally with an adjustable period from 10 sec to about 1200 sec. The dynamic response of the gage obtained with this calibration system is presented in Fig. 3. The ratio of the maximum wave amplitude indicated on the chart to the imposed wave is the ordinate and the period of the oscillation is the abscissa. Based on information that the ambient wave condition on the day of the landslide was 3 to 4 foot waves of 10 sec, the gage was adjusted so that the response from this wave condition was barely observable. This corresponded to a needle valve opening of $3/4$ turns. Additionally, the responses at other valve positions were tested including $1/2$ and $3/8$ turns as suggested by NOAA field personnel. For excitation periods greater than about 1,000 sec (16 min) the response is nearly unity, but as the excitation frequency increases, i.e. the wave period decreases, the signal is damped dramatically. For example, at a period of about 3 min, the response, a/a_0 , varies from 40 % to 75 % depending on the needle valve setting. At a wave period of approximately 20 to 30 sec the response is between 5 % and 25 %.

4. A Numerical Model for Harbor Response

A finite element model based on the depth averaged equations of motion was developed to determine the wave response of Skagway Harbor to a moving section of the boundary corresponding to the region of the observed landslide. This

somewhat simplified numerical model was chosen, since it was believed that the important elements of the landslide-induced waves could be generated in this manner. Indeed the object of this study was to investigate the wave motions induced by a transient disturbance in this harbor and to develop wave spectra at various locations. These results will help to explain how the floating ferry dock mooring system was damaged.

As a guide to the concept of using a boundary motion to represent a material landslide, simple experiments were conducted in a laboratory channel (with depth $h = 28.2$ cm) by a two-dimensional triangular solid block (with horizontal and vertical edges 12.4 cm long) moving on a 45° slope. The horizontal face was initially 3 cm above and submerged 3 cm below the still water surface. The water-surface time histories recorded at the toe of the slope are presented in Fig. 4 with the nondimensional wave amplitude plotted as a function of nondimensional time. Offshore of the generation region, a lead positive wave is followed by a negative wave with the part-aerial landslide producing a larger positive wave than the sub-aerial one. The positive wave is generated by the forward advancing vertical front face of the block while the negative wave is generated by the downward moving horizontal face. For both model landslides the wave has some similarity to one cycle of a sinusoid. Therefore, in the numerical model, a boundary motion was chosen that would generate a similar wave near the source.

Three motions were considered for a 984 ft section of the east boundary of Skagway Harbor corresponding in length to the section of the White Pass railway dock's foundation which failed. The motions were: a combined positive and negative motion with a period of 20 sec and an amplitude of 20 ft/sec, and separately, a positive motion and a negative motion alone each with a maximum amplitude of 20 ft/sec and a duration of 10 sec. The maximum velocity was based on the both the estimated time of the landslide event and the thickness of the slide. Since the equation of motion was depth averaged, the boundary generator moved as a piston.

The governing equations used for the present finite element model are similar to those used by Leendertse (1967). (Leendertse (1967) used a finite difference method for his solution.) The equations of motion used in the two propagation directions are as follow:

$$\text{for the x-direction: } \frac{Du}{Dt} = -g \frac{\partial \eta}{\partial x} + 2\Omega(\sin \Phi)v - \frac{\tau_{bx}}{\rho(h+\eta)} \quad (1)$$

$$\text{and for the y-direction: } \frac{Dv}{Dt} = -g \frac{\partial \eta}{\partial y} + 2\Omega(\sin \Phi)u - \frac{\tau_{by}}{\rho(h+\eta)} \quad (2)$$

where u and v are the velocity components in the x and y directions, g is the acceleration of gravity, η is the amplitude of the wave, Ω is the earth's rotational speed, Φ is the latitude, τ_b is the bottom shear stress with direction indicated by the subscript, and ρ is the fluid density. The second term on the right in Eqs. 1 and 2 is termed the Coriolis acceleration. The last term is the bottom friction expressed in terms of the shear stress along the bottom. The continuity equation for a long wave in the x and y directions is:

$$\frac{\partial \eta}{\partial t} + \frac{\partial}{\partial x} [(h+\eta)u] + \frac{\partial}{\partial y} [(h+\eta)v] = 0 \quad (3)$$

These equations have been solved using a finite element technique with finite difference in time. The grid used is shown in Fig. 5. For this model, the shoreline is considered perfectly reflecting. The portion of the shoreline which was impulsively moved to represent the landslide is shown. Along the region of the model denoted as ABCDE the boundary of the numerical model is non-reflecting and represents the so-called "open sea". Wave energy can pass through this boundary but will not be reflected back to the harbor. However, at the limit of the modeled Skagway Harbor, due to the change in width of the harbor entrance compared to the width of the outer region, reflection occurs. This "mis-matching" at the entrance is one reason for the "ringing" which was seen in the tidal record presented in Fig. 2. An open harbor entrance acts to some extent like a leaky closed boundary allowing energy to escape and some to be reflected back into the harbor; this is the basis for resonance. Although the model is three-dimensional the velocities are depth-averaged. Thus, it is expected that the information obtained from the model may be more qualitative than would be obtained from a more general set of equations developed from the equations of motion incorporating a moving sediment mass. A velocity time history imposed along a section of the grid which corresponds to the location of the moving boundary was used as the forcing function for the model.

In Fig. 6 water surface contours corresponding to the ratio of the wave amplitude to the boundary motion are shown in the harbor at two different times after generation by the combined positive and negative boundary motion. An outline of the planform of Skagway Harbor is incorporated so that one can better appreciate the general outward spreading of the wave from the generation source; the ordinate is oriented north-south and the abscissa east-west. The upper plot corresponds to the time of the completion of the boundary motion. It is seen that the waves generally propagate toward the north-northwest as a spreading cylindrical wave. The positive maximum wave can be seen propagating toward the site of the Floating Ferry Dock while the negative wave is still relatively close to the generation boundary. As the wave spreads the wave amplitude decreases. The lower portion of the Fig. 6 corresponds to 40 seconds after motion begins. Toward the western side of the harbor, near the site of the tide gage, the waves propagate into the Ore Dock slip moving generally northward. Near the entrance to Skagway Harbor the wave amplitudes become very small; wave energy will propagate north and south in the inlet reducing further the wave energy which may reach the far shore of Taiya Inlet.

Three water surface time histories corresponding to three locations are presented in Fig. 7: at the Tide Gage (Location 8), at the Floating Ferry Dock (Location 6), and at the head (landward end) of the Ore Dock slip (Location 2). At Location 6, both the wave amplitude and the wave frequency are larger than at either Locations 2 or 8. Apparently at the head of the Ore Dock slip the impulsive wave generated excites a mode of oscillation with a frequency much smaller than at Location 6. This also appears near the site of the Tide Gage (Location 8). The proximity of Location 6 to the boundaries must influence the frequency of the waves. Skagway Harbor does not reach steady state due to the leakage of energy past the entrance. The difference between the tide gage record presented in Figs. 2 and 7 is probably due to several factors. First, the boundary motion used in this model is a highly simplified; some features are reasonably represented while others are not. In addition, during the movement of the slide, the bathymetry within the

harbor changes and the numerical model does not incorporate these time-varying changes. Finally, and perhaps most important, the numerical model is depth averaged, and although some aspects of the waves are well represented by shallow water wave theory others are not. Therefore, the results from this model can only be considered an approximate representation of the events observed on November 3, 1994. It is believed that they do show the frequency characteristics of the waves in the harbor.

The energy spectra obtained at Locations 2, 6, and 8 are presented in Fig. 8 with frequency as the abscissa, and the energy normalized by the area under the spectrum is the ordinate. At each location, spectra corresponding to each of the three different boundary motions are presented. At the head of the Ore Dock slip and at the location of the Tide Gage, Locations 2 and 8, respectively, the major component is at about 0.007 Hz (wave period of 143 sec). It is recalled from Fig. 3 that the dynamics of the nitrogen bubbler tide gage will attenuate most high frequency energy so that only low frequencies will be present in the tide gage record. The most important feature of Fig. 8 is that in the vicinity of the floating ferry dock the predominant frequency is much larger than that observed at either Location 2 or 8. The frequency of the peak energy is about 0.045 Hz (a period of 22 sec). This change in frequency as a function of location will be shown to be important with regard to the excitation of the floating dock.

5. The Response Of The Floating Ferry Dock

A schematic is presented in Fig. 9 showing the Floating Ferry Dock moored by chains, each with a submerged weight of approximately 48 lbs/ft. As shown in the lower portion of Fig. 9 these chains are arranged so the dock can rise and fall with the tide. The dock and the chains form a dynamic system with the chains and their catenary shape defining the restraining and restoring force associated with dock motion. As the chain lifts up from the seabed or is laid down the changing weight and resultant tension in the suspended portion of the chain provide a non-linear restoring force. This is shown in Fig. 10 for one typical chain. The abscissa is the horizontal displacement of the mooring point on the barge, and the ordinate is the restraining force associated with this displacement.

A simplified analytical model of the moored Floating Ferry Dock was developed primarily to determine the important range of frequencies for the excitation of the dock. These could then be compared to the spectrum corresponding to Location 6 in Fig. 8 to assist in inferring the cause of the observed chain failure. The method used to develop the equation of motion of the dock was presented by Raichlen (1965). The floating body was excited by a volume averaged acceleration and velocity, i.e. the average over the displaced volume of the dock of the acceleration and velocity in a small amplitude long wave. It was assumed that viscous damping and wave damping were small and could be neglected, and that dock motion was controlled primarily by inertial forces. Resistance to motion was due to the varying weight of the mooring chains. Although waves approach the barge obliquely in the harbor model, for the motion analysis, it was assumed that waves approach from an easterly direction and that the barge's motion would then be east-west and defined as the x-direction. Considering the shape of the curve of restoring force vs. displacement, the simplified equation of motion in the absence of damping is as follows:

$$\frac{d^2x}{dt^2} + \alpha x + \beta x^3 = \frac{dU}{dt} \quad (4)$$

The constants α and β in Eq. 4 which define the restoring force are based on a total of five chains acting simultaneously. The volume averaged acceleration dU/dt is determined from small amplitude wave theory as:

$$\frac{dU}{dt} = \frac{ag}{kLD} \left[\frac{\sinh kh - \sinh ks}{\cosh kh} \right] \sin kL \cos \sigma t \quad (5)$$

where a is the amplitude of the wave, k is the wave number, L is the length of the barge in the direction of wave propagation, i.e. 120 feet, D is the draft, h is the depth, s is the distance from the bottom to the keel of the barge, and σ is a circular wave frequency. For long waves Eqs. 4 and 5 become:

$$\frac{d^2x}{dt^2} + \alpha x + \beta x^3 \approx a \sqrt{\frac{g}{h}} \sigma \cos \sigma t \quad (6)$$

This equation has the form of the Duffings equation with the exception that the forcing function is linearly proportional to the circular frequency, σ . This equation is evaluated by assuming a motion for the horizontal displacement of the vessel from the at-rest-position of:

$$x = X \cos \sigma t \quad (7)$$

as discussed by Stoker (1963). Although this may be a significant simplification, the assumption of Eq. 7 leads to the development of the response curves to show the important forcing frequencies for this problem.

The response curves for this non-linearly moored body obtained in this manner are presented in Fig. 11 where the amplitude of motion of the dock is plotted as a function of excitation frequency for given wave amplitudes. A so called "backbone" curve represents a zero wave amplitude. The response to the right of this curve is out-of-phase with the excitation and to the left it is in-phase. Referring to Fig. 8, the important wave frequency present at Location 6 (the location of the floating ferry dock) is approximately 0.045 Hz ($\sigma = 0.283$ rad/sec), i.e., a wave period of 22.2 sec. The response curve in Fig. 11 shows that this excitation frequency is near the resonant frequency of the moored dock. For a wave amplitude of one foot and a circular frequency of 0.283 rad/sec, the response of the barge is approximately four times the forcing function. Perhaps more important, as the wave height increases from zero at this frequency the motion increases until a minimum of the response curve is reached for the given excitation amplitude. The motion will jump to the higher branch of the curve changing suddenly from out-of-phase to in-phase. This can create significant dynamic chain stresses. Thus, it is believed that although the observed wave periods at the tide gage were relatively large, because of the influence of the geometry and the proximity of the dock to the harbor boundaries, the higher frequency which is observed at the site of the floating ferry dock might have led to the mooring line and lampost failures.

An example of the motion time history of the dock is shown in Fig. 12 for an excitation based on the spectrum presented in Fig. 8 using Eq. 6 to represent the excitation spectrum by the superposition of forcing functions :

$$\frac{d^2x}{dt^2} + \alpha x + \beta x^3 \approx \sum_{i=1}^N \left[a_i \sqrt{\frac{g}{h}} \sigma_i \cos \sigma_i t \right] \quad (8)$$

where i is the frequency component of the forcing function varying from $i = 1$ to N , and the phase angles have been arbitrarily set equal to zero. The frequencies and the amplitudes of the components are shown in the table accompanying the figure. Significant motions approaching amplitudes of ± 10 ft can be seen for the assumed waves. This corresponds to an amplification factor, i.e., the ratio of the amplitude of the horizontal dock motion to the average of the amplitudes of the wave components, of approximately fifteen. Thus, the dynamics of the mooring system could have been a major contributor to the failure of the mooring chains at Skagway.

5. Conclusions

The following major conclusions can be drawn from this study:

1. The gas-purged pressure recording (bubbler) tide gage with normal operating settings has a response (measured amplitude/actual amplitude) of 40 % to 75 % for waves with periods of 3 min and 5 % to 25 % for waves with periods of 20 sec.
2. An impulsive wave generated in Skagway Harbor by the simple motion of a section of the coast can induce groups of complex waves composed of a wide range of frequencies.
3. The frequency content of the transient waves generated by the boundary motion is strongly dependent on location.
4. Different forms of the boundary motion tend to generate similar spectral energy distributions at the same location in the harbor.
5. The damage to the floating ferry dock observed at Skagway may have occurred due to the combined effect of the mooring dynamics of the dock and the frequency content of the waves at that location.

6. Acknowledgments

Authors FR and PW appreciate the support of the National Science Foundation Grant CMS-9115422 during this study.

7. References

- Leedertsee, J.J., "Aspects of a Computational Model for Long-Period Water Wave Propagation", Memo KM-5294-PR RAND Corp., Santa Monica, CA, 1967.
- Raichlen, F., "Wave-Induced Oscillations of Small Moored Vessels", W.M.Keck Laboratory of Hydraulics and Water Resources, California Institute of Technology, Report No. KH-R-10, 1965.
- Stoker, J.J., "Nonlinear Vibrations", Interscience Publishers, Inc., 1963.
- Watts, P. and Petroff, C.M., Report of Visit to Skagway, Alaska, December 1994", Tsunami Bulletin Board, January 1995.
- Young, S.A., "User's Guide for the Gas-Purged Pressure Recording (Bubbler) Tide Gage", NOS, NOAA, 1977.

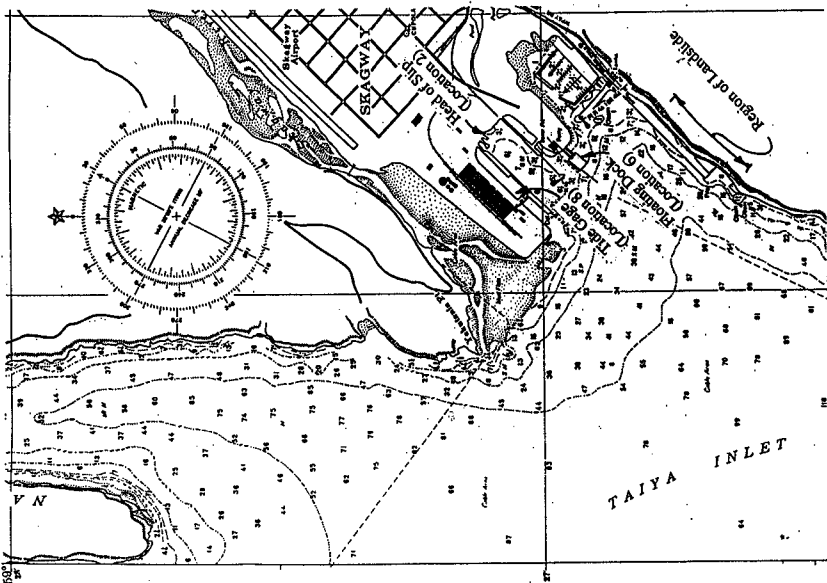


Figure 1 Map of Skagway Harbor

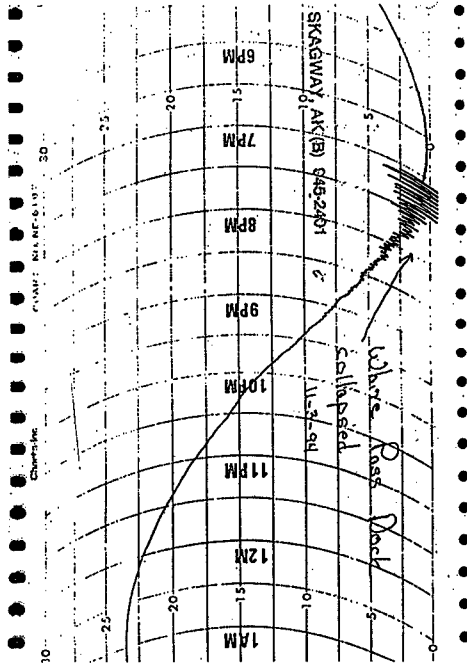


Figure 2 Tide gauge record for November 3, 1994

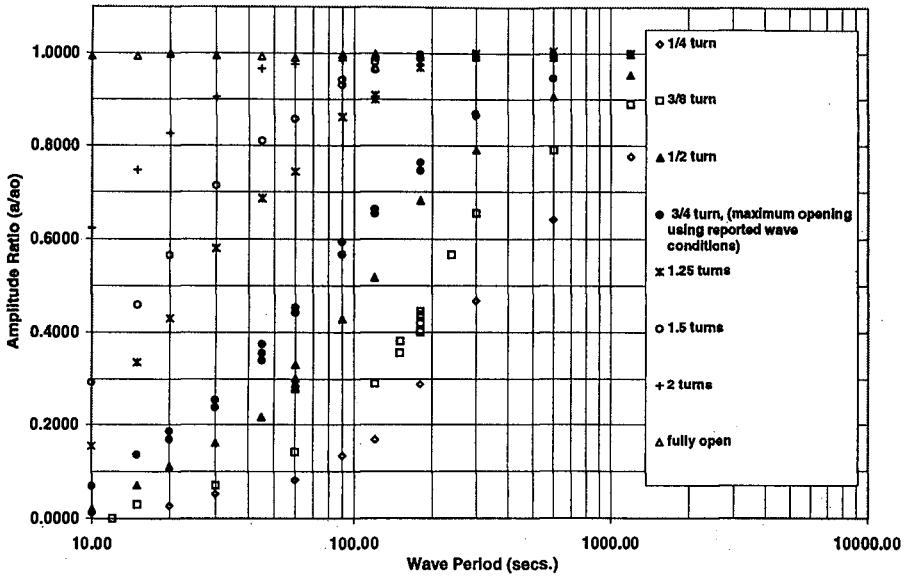


Figure 3 Measured tide gage response

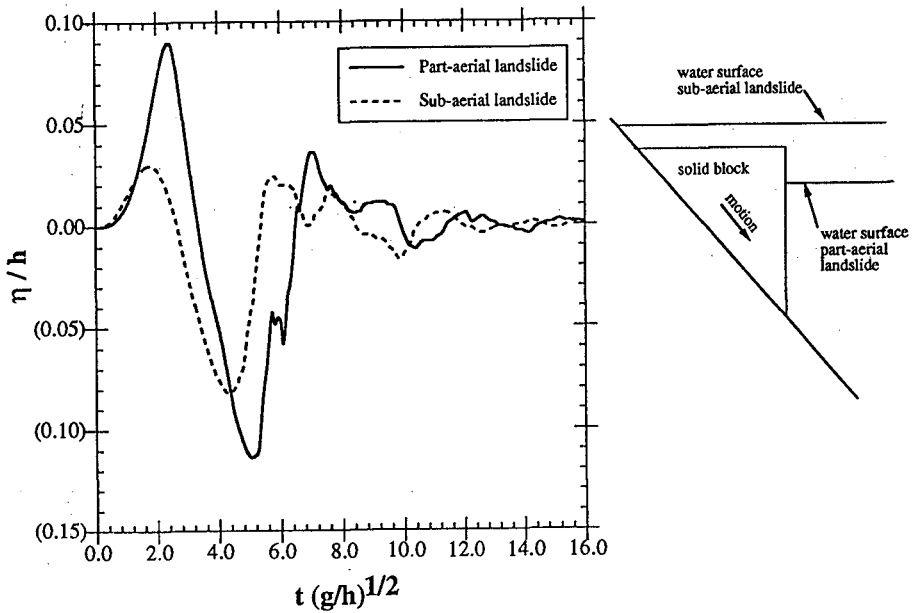


Figure 4 Water waves generated by a simple laboratory model of a part-aerial and sub-aerial landslide

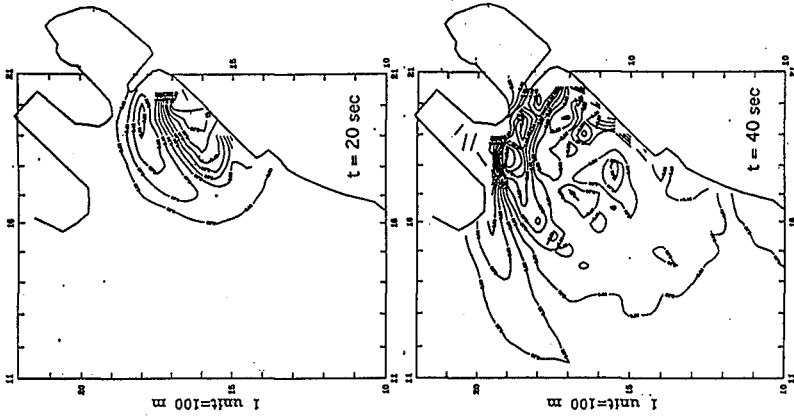


Figure 6 Normalized water surface contours at the end of wave generation ($t = 20$ sec) and at $t = 40$ sec.

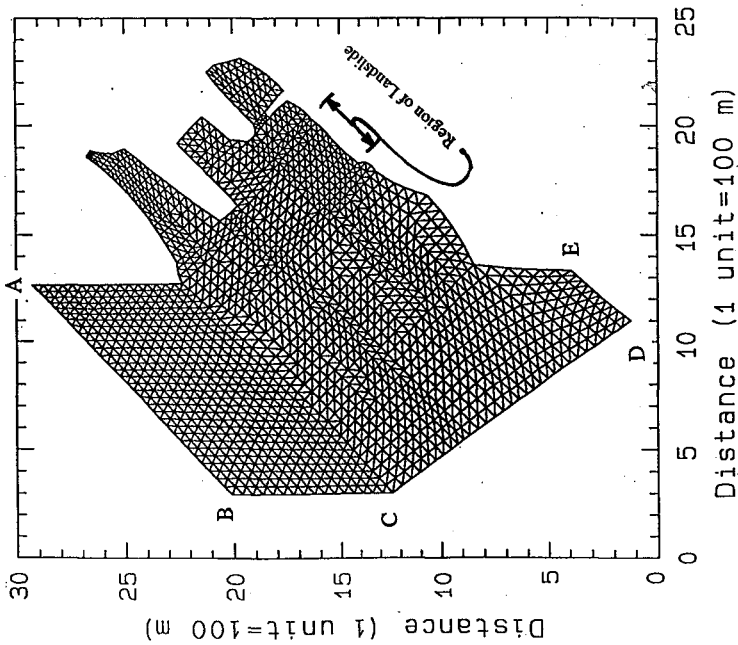


Figure 5 Grid for a finite element model of wave propagation in Skagway Harbor

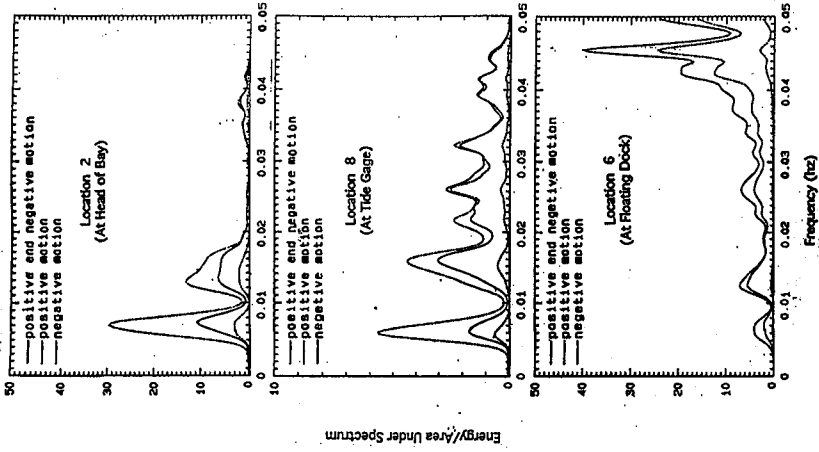


Figure 8 Wave spectra at three locations in Skagway Harbor for three boundary motions

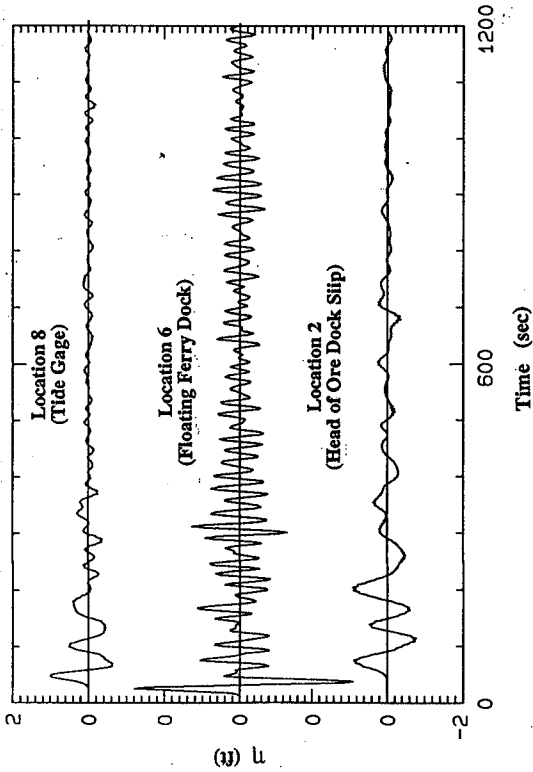


Figure 7 Water surface-time histories at three locations in Skagway Harbor

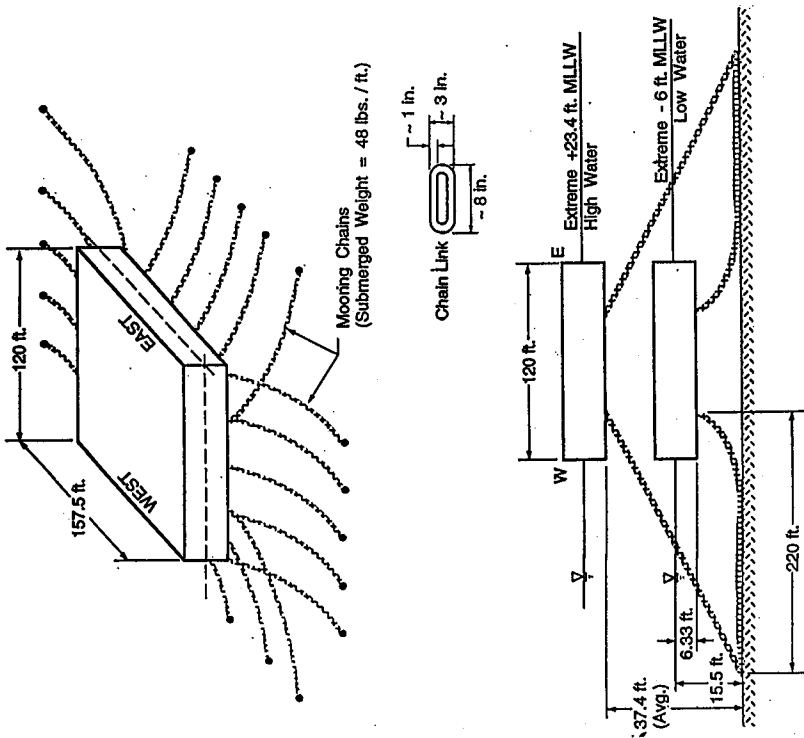


Figure 9 Sketch of mooring configuration for Floating Ferry Dock

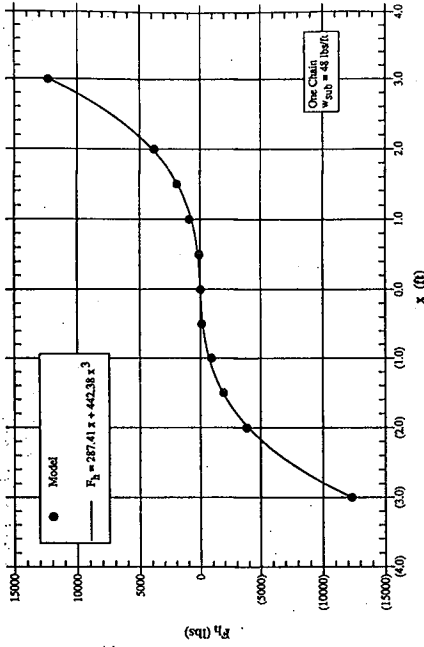


Figure 10 The variation of the restoring force as a function of horizontal displacement for one chain

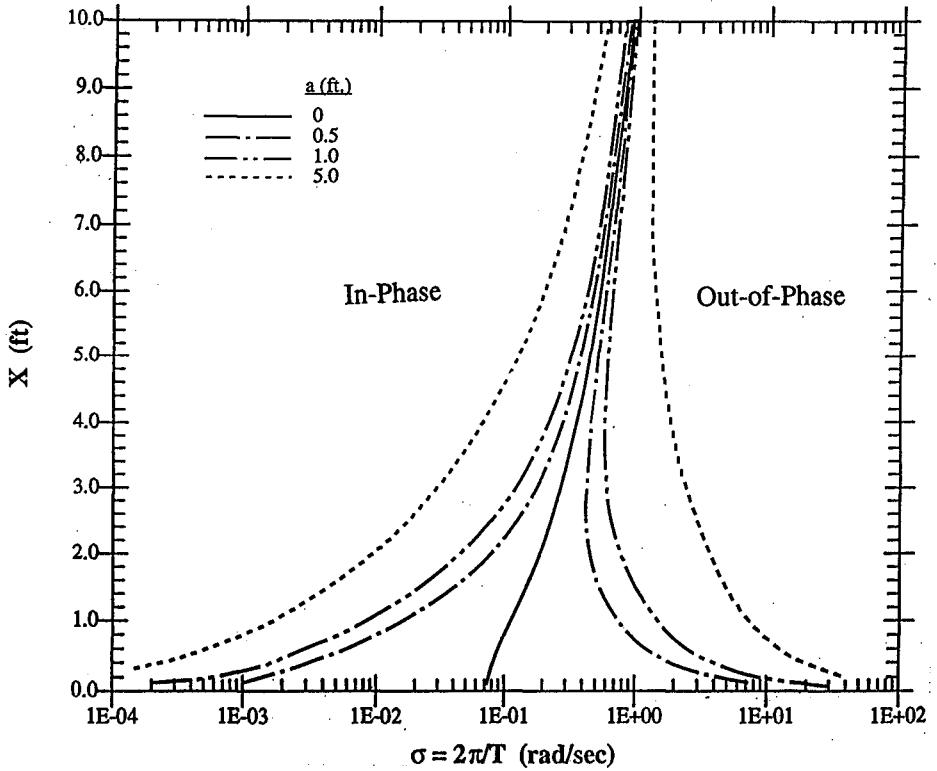


Figure 11 Response of moored Floating Ferry Dock as a function of wave amplitude and circular frequency

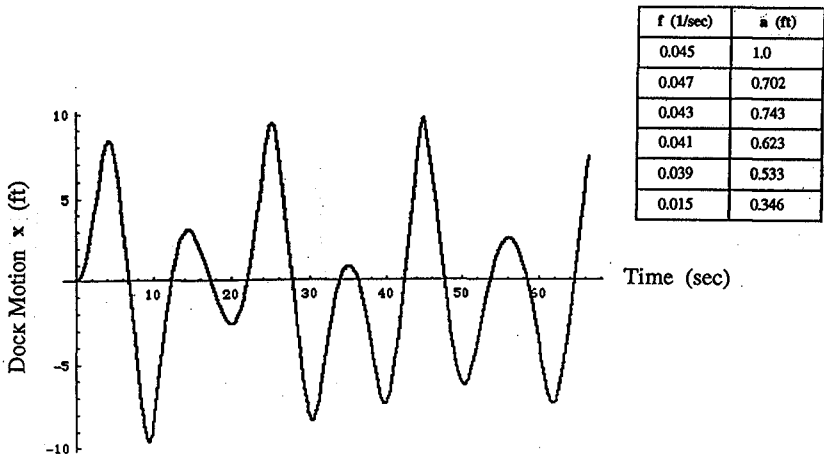


Figure 12 Horizontal motion time history for moored Floating Ferry Dock for a given wave input

CHAPTER 102

Laboratory experiment on long wave generation by time-varying breakpoint

Satoru Nagase¹ and Masaru Mizuguchi²

Abstract

Laboratory experiment is conducted to investigate the long waves generated by time-varying breakpoint. We focus our attention on the variation of plunging point as well as the variation of breaking point. The results show that free long waves (BFLW) are really generated by the variation of the starting point of wave set-up which coincide with the plunging point and that the BFLW observed can be quantitatively evaluated by Mizuguchi(1995) model, which is more direct and realistic model. The generation mechanisms of long waves of other origins, such as bound long waves to wave groups and free long waves generated during shoaling process of wave groups, are also discussed.

1. Introduction

Some lively discussions have been going on concerning the origins of the free long waves (of typical time scale 1 to 3 minutes) observed in the nearshore zone. It is well known that the generation of long waves is closely related with wave groups. However the characteristics of long waves, which may be free or bound, are still not well understood because of the difficulty of detailed measurements. One of the possible mechanism for the generation of free long waves is that the breaking of wave groups generates free long waves.

Longuet-Higgins and Stewart (1962) suggested that the bound long wave to a positive wave group is freed as a set-down wave when the wave group disappears by wave breaking. This concept has been used

¹Engineer; Taisei corp., Nishi Shinjuku Shinjuku-ku, Tokyo 163-06, JAPAN (Formerly graduate student, Chuo Univ.)

²Professor; Dept. of Civil Eng., Chuo Univ., Kasuga, Bunkyo-ku, Tokyo 112, JAPAN

for a long time without any physical or mathematical explanation. In fact, little is known about the behavior of the bound long waves when the primary waves break. Symonds et al.(1982) showed theoretically that time-varying breakpoint generates free long waves by playing a role of time-varying forcing term in the long wave equation. Schaffer(1993) extended their approach by including both the effect of bound long waves to wave groups and the behavior of wave groups in the surf zone. This topic has been studied mainly in a theoretical manner. Most studies have concluded that the model of Symonds et al.(1982) is in qualitative agreement with experimental results. For example, Kostense(1984) in laboratory experiment, Nakamura and Katoh(1992) in field observation. However they have neither measured the variation of breaking point nor the behavior of long waves around the breaker zone. More direct experimental measurements are needed to support or to reject the theoretical modeling.

Here we report a carefully conducted experiment, where the long waves generated by time-varying breakpoint can be quantitatively estimated. Based on the experimental results, we show that the modeling proposed by Symonds et al.(1982) is really valid and the analytical solution for bound long waves by Longuet-Higgins and Stewart (1962) is still correct even in shallow water. Then we show another treatment applicable to non-periodic wave group for the generation of free long waves in the nearshore zone, proposing a simple formula to estimate the magnitude of the free long waves generated by time-varying breakpoint.

2. Experiment

Figure 1 shows our laboratory flume. The wave flume is 20m long and

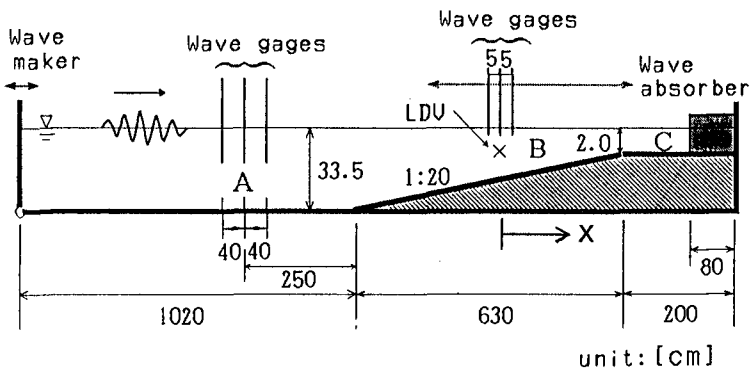


Fig.1 Experimental setup and the origin of x coordinate
The location of water depth 13.5cm is taken to be the origin of x coordinate.

30cm wide. It is equipped with a flap-type wave maker controlled by a personal computer. The slope of 1/20 with a constant depth area in the shoreward is set in a wave flume so that all waves can break on a uniformly sloping beach and then reform on a constant depth area in the shoreward. The wave absorber is installed at the end of the wave flume in order to dissipate the energy of reformed waves. Incomplete absorption of reformed waves at the shore end may cause unstable breakpoint variations due to wave reflection. The water depths at location A in the offshore, location B on a sloping beach and location C on a constant depth area in the shore are 33.5cm, 10.0cm and 2.0cm, respectively. The wave gages and current meter are moved in the nearshore zone so that detailed measurements of the process of long wave generation may be possible.

In order to investigate the simplest case of long wave generation in as much detail as possible, a single hump-type grouping waves are selected. A single wave height variation signal is given by Eq.(1).

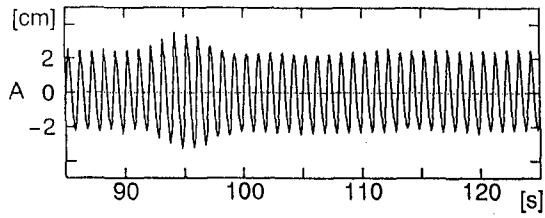
$$H(t) = \begin{cases} H_M(1 + \beta(1 - \cos(2\pi(t-t_0)/T_g))) & t_0 \leq t \leq t_0 + T_g \\ H_M & t < t_0, t_0 + T_g < t \end{cases} \quad (1)$$

where H_M is the steady wave height, T_g is the wave group period and β is the wave height ratio. The experiments are conducted on the following conditions. Both $T=1.0s$ for the wave period of the primary waves and $T_g=8.0s$ are fixed in all cases. The steady wave height at location A in Fig. 1, $H_M=5.5cm, 4.5cm, 4.2cm, 3.7cm, 2.8cm$ and the wave height ratio, $\beta=0.2, 0.1, -0.2, -0.1$, which introduce the variation of breaking point, are varied. Total of experimental cases are fourteen.

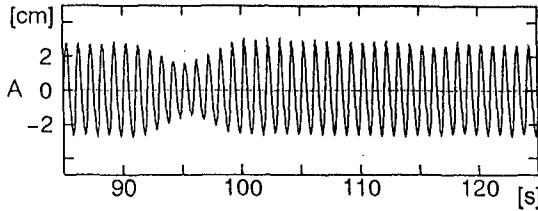
Figure 2 shows examples of a single hump-type grouping waves, a positive wave group and a negative wave group. For generating stable grouping waves, first, the amplitude of the wave maker board is increased very slowly, then the steady uniform waves are maintained for a while (about 40s) and finally a single hump-type grouping waves are added. However, we did not apply the control method either to suppress the generation of the second-order free long waves or to absorb free long waves coming back from the shore. At each location, waves are measured during 180s from the start of wave making with a sampling time of 0.02s.

3. Experimental results

Figure 3 shows the wave height variation of individual waves when a positive single hump-type grouping waves are incident into the surf zone. In this study, individual waves are defined by applying the zero-down crossing method. The breaking point clearly moves offshoreward



(a) A positive wave group ($H_M=4.5\text{cm}$, $\beta=-0.2$)



(b) A negative wave group ($H_M=5.5\text{cm}$, $\beta=-0.2$)

Fig.2 A single hump-type grouping waves (measured at location A)

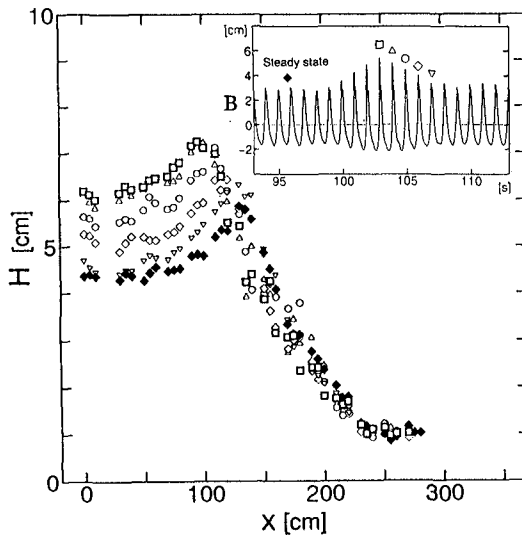


Fig.3 Wave height variation of individual waves in the positive wave group shown in Fig.2(a)

as the wave height increases gradually. As a wave starts to break, its height decreases very rapidly while maintaining an approximately constant ratio of wave height to water depth, in other words, the wave group tends to disappear in the surf zone.

The time variation of the breaking position of individual waves is visually measured using a high-speed video camera. The solid squares in Fig.4 denote the measured variation of breaking position. The variation shows good correspondence with the wave height variation measured outside the breaking zone. Spilling breakers are observed in all cases.

Figure 5 shows the measured wave group structure and the generated long waves for a positive wave group. The long wave components are obtained by applying a numerical filter, by which the short-period components less than 4 second are removed perfectly. The wave group shows stable propagation up to the breaking zone and then disappears or shows slightly negative wave group during the breaking process (between $x=90$ to 130 cm). Low-pass filtered long waves show that the set-down wave propagates at the group velocity of primary waves without significant amplification with a slight delay to the wave group up to the breaking point. Since the wave maker is not controlled to suppress the generation of the second-order free long waves, a free wave (a positive single hump) generated at the wave maker travels just ahead. See the data at location A. As the wave group disappears while breaking, a set-up wave is formed in the surf zone and propagates in the shoreward direction. A set-down wave also appears to be generated and

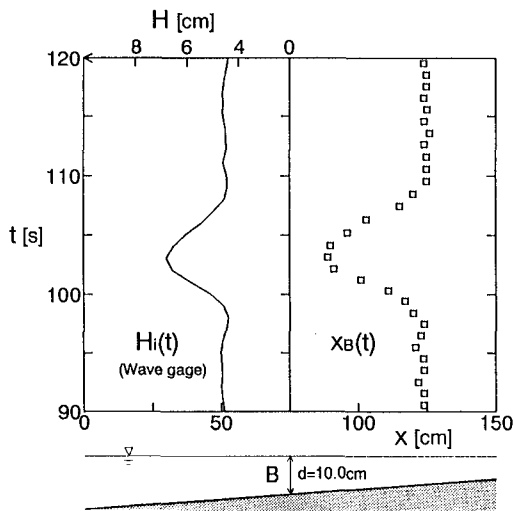


Fig.4 Time variation of breaking position of individual waves in the positive wave group

travel offshoreward outside the breaking zone.

When a negative single hump-type grouping waves is generated, the bound long wave as a set-up wave is observed in the offshore shown in Fig.6. When the primary waves in a negative wave group break, a set-down wave is observed in the surf zone and propagates in the shoreward direction.

These two experimental results are just opposite in the phase of the long waves as are expected. This shows the reliability of the experiment.

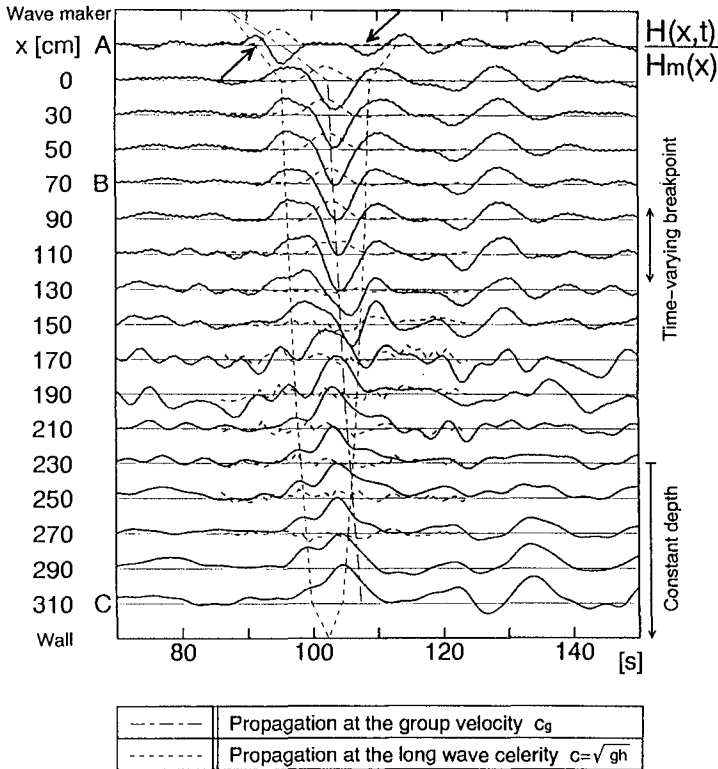


Fig.5 Low pass filtered data (solid line) and time history of wave height (broken line) in the positive wave group

Reference level for long waves is the mean water level of steady state at each location. Wave heights are nondimensionalized by mean wave height of steady state at each location. Scales of vertical axis for long waves and nondimensionalized wave heights are 0.2cm and 1.0, respectively, for an interval of two horizontal lines.

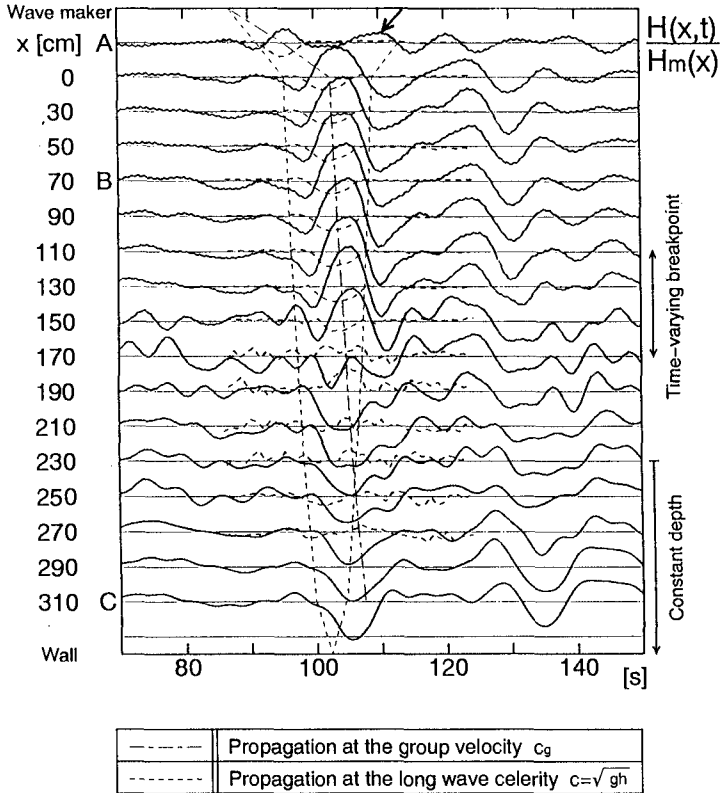


Fig.6 Low pass filtered data (solid line) and time history of wave height (broken line) in the negative wave group shown in Fig.2(b). (See Fig. 5 for explanation.)

4. Discussion

4.1 Generation of long waves

The generation mechanism of long waves in the laboratory experiment may be illustrated schematically as shown in Fig.7.

Long waves in this experiment consist of, ① free long waves generated at the wave maker, ② bound long waves to wave group, ②' bound long waves being freed at the breaking point, ③ free long waves generated during the shoaling process of wave group and ④ time-varying breakpoint forced (free) long waves (BFLW). Wave groups are assumed to disappear after their breaking.

Free waves generated at the wave maker (①) can be identified as the leading positive hump on a sloping beach. Then a point to be noted is

that the transforming wave group due to wave shoaling does accompany free long waves (③) in addition to the bound long waves (②). Any change of wave group may result in the generation of free long waves, simply because the new bounded solution is different from the old one and free waves are needed to satisfy the old condition. This free waves have the opposite sign to the bound waves and travel only a little faster as schematically illustrated in Fig.7(b). This is the reason why in shallow water the long waves appear to lag behind the wave group, as is also pointed out by List(1992) and Van Leewen(1992), and why its magnitude is not so large as the analytical solution by Longuet-Higgins and Stewart (1962).

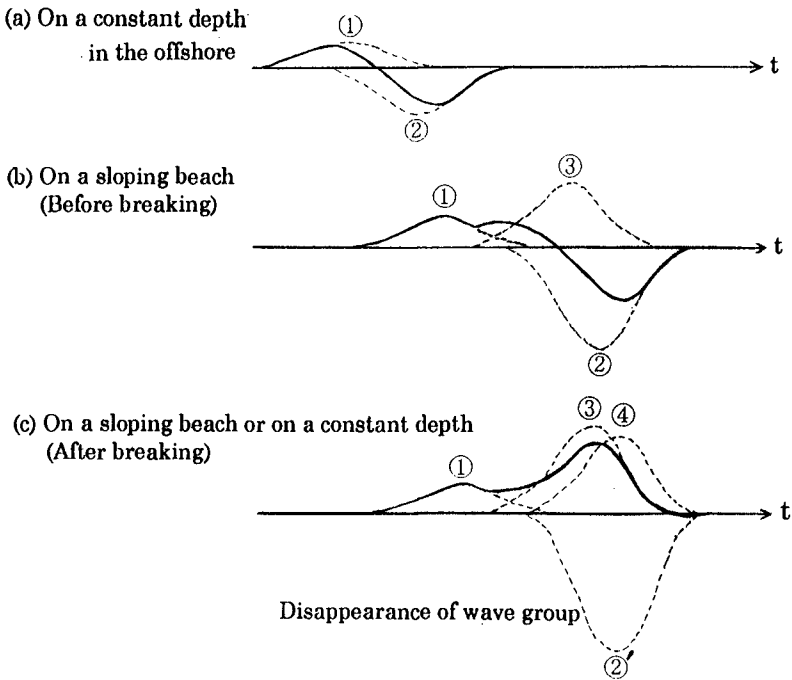


Fig.7 Schematic illustration of generation and propagation of long waves(time profile) in the positive wave group
 Solid lines denote the observed long waves, which can be resolved into,
 ① Free long waves generated at the wave maker
 ② Bound long waves to wave group
 ②' Bound long waves being freed at the breaking point
 ③ Free long waves generated during the shoaling process of wave group
 ④ Time-varying breakpoint forced (free) long waves (BFLW)

It has been quoted in various studies that the LHS solution predict unreasonably large wave heights in shallow water and cannot be applied in the nearshore. The fact is that the LHS solution is a particular solution and the physical situation must include general solutions, which nearly cancel the particular solution. For more detailed discussion, see Mizuguchi and Toita(1996). In addition to these long waves, free outgoing long waves (set-down waves) generated by time-varying breakpoint may have an effect on both the phase and the magnitude of long waves observed in the offshore. However this free waves were difficult to evaluate separately and are neglected in Fig.7.

At the breaking point, bound long wave (②') to a positive wave group is freed as a set-down wave due to sudden disappearance of the wave group, and the free wave generated while shoaling (③) continues to propagate as a free wave. In addition to these waves, the BFLW is generated. The shoreward propagating BFLW has the same phase with the wave group, that is, a positive wave group produces a set-up wave.

4.2 Magnitude of the BFLW

We discuss the generation mechanism of the BFLW, trying to evaluate its magnitude. First, in Fig.8 we plot the change of mean water level of individual waves in the nearshore zone when the positive wave group is generated. Figure 8 shows the starting points of the rise of mean water level, that is, the plunging points of individual waves move offshoreward corresponding to the offshoreward movement of the breaking points. The mean water level rises in the shoreward region with approximately constant gradient. This is what the generation of the BFLW really is. Thus the variation of the plunging point is essential. In Fig.8 the theoretical results (Bowen et al.,1968) on wave set-down and wave set-up for regular waves are also shown. The value of the wave height to water depth ratio, γ , is typically taken to be 0.8. Here the gradients of mean water level of individual waves in the transition region between the breaking point and the plunging point are neglected. The gradient of the measured set-up shows good agreement with the predicted value. As mentioned later, the vertical difference shown in Fig.8 is taken to be the magnitude of the BFLW traveling shoreward measured just after breaking.

Symonds et al.(1982) first proposed the model for the long waves generated by time-varying breakpoint. Figure 8 supports their modeling. However their approach assumes the periodicity in time of the breaking point variation and cannot be applied to a single hump-type grouping waves employed with this experiment. Recently, Mizuguchi(1995) shows more direct and realistic modeling with much simpler solution in the time domain. The modeling may be illustrated as shown in Fig.9.

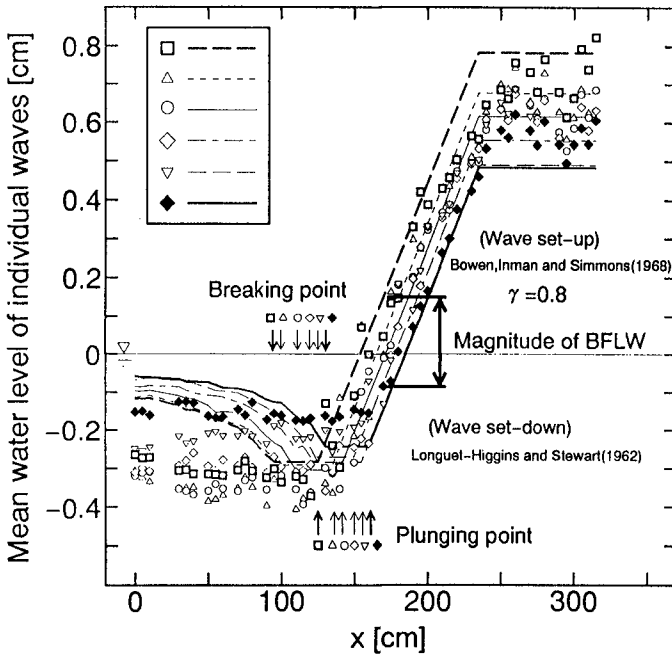


Fig.8 Change of mean water level of individual waves in the positive wave group

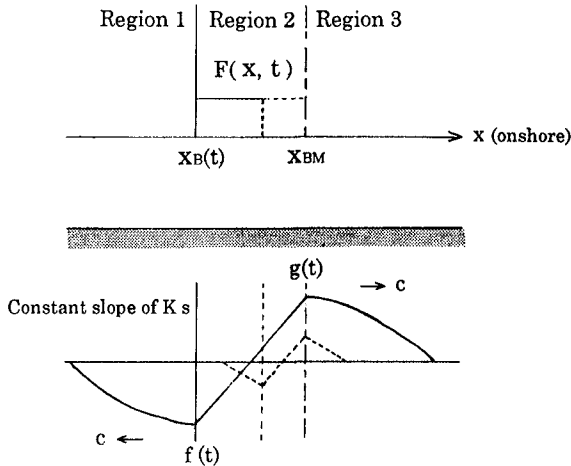


Fig.9 Schematic illustration of forcing term (top) and local profiles of long waves (bottom) after Mizuguchi(1995)

The well-known linear long wave equation with a forcing term is solved analytically on the following assumptions. First, the water depth around the breaking point is taken to be constant as far as the long waves are concerned. Second, a bounded solution for region 2 may be given by the steady version of the momentum equation, as is observed in this experiment.

The solutions obtained are so simple as shown in Eq.(2).

$$\begin{aligned} g(t) &= K s(x_{BM} - x_B(t)) / 2 \\ f(t) &= -K s(x_{BM} - x_B(t)) / 2 \end{aligned} \quad \text{at } x = x_{BM} \quad (2)$$

where $g(t)$ and $f(t)$ are the functional form of the long waves propagating toward the shore and that propagating toward the offshore, respectively, $x_B(t)$ is the time-varying breaking point, x_{BM} is the mean (or steady) breaking point, K is the constant given by γ , wave height-water depth ratio in the surf zone (Bowen et al., 1968) and s is the local bottom slope around the breaking point. Therefore, the magnitude of the BFLW, which radiate both shoreward and offshoreward, can be expressed as follows.

$$\Delta \bar{\eta} = K s \Delta x_B / 2 \quad (3)$$

where Δx_B is the width of breaking variation.

In order to evaluate the magnitude of the BFLW with Eq.(3), it is necessary to estimate the variation of breaking points. Here a very crude model for the variation of breaking points is employed. That is, by assuming that the structure of wave group incident on a shallow water region can be expressed by Eq.(1), and by applying Green's formula for shoaling up to wave breaking, Δx_B , is simply given by Eq.(4).

$$\Delta x_B = 1.6 \beta h_{BM} / s \quad (4)$$

where h_{BM} is the mean (or steady) breaking depth. In Eq.(4) $\beta \ll 1$ is assumed.

Figure 10 shows the comparison of the width of breaking point variation predicted by Eq.(4) with that measured. In spite of a crude approximation, the model predicts the width of breaking point variation reasonably well. The measured width of plunging point variation are also compared in Fig.11. The measured values show surprisingly good agreement with the predicted ones.

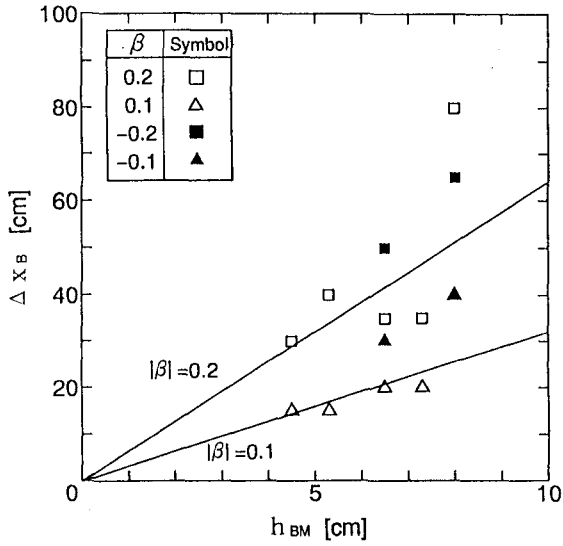


Fig.10 Comparison of width of breaking point variation predicted with that measured

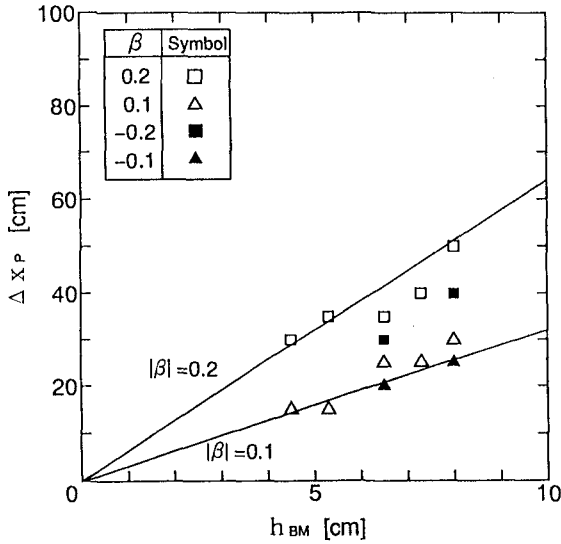


Fig.11 Comparison of width of plunging point variation predicted with that measured

As was already discussed using illustration in Fig.7, one needs care to evaluate the BFLW separately. Here, as marked in Fig.8, the maximum height of long waves measured just after breaking is simply assumed to correspond to the magnitude of the BFLW. Because, around the breaking zone, the new free waves due to wave shoaling(③) and the new bound waves being freed(②') may cancel each other and may not exceed the old bound waves in the offshore(②), which may be negligible compared to the BFLW, as shown in Fig.7. Thus evaluated magnitude of the long waves traveling shoreward is plotted in Fig.12 with solid lines which denote Mizuguchi(1995) model. Good quantitative agreement between the experimental values and theoretical ones is observed. The experimental values show linear dependency on the mean breaking depth, h_{BM} , and the wave height ratio, β , as is also predicted by the model.

The quantitative discussions on free long waves in the offshore direction is rather difficult as the separation between the incoming bound waves and the outgoing free waves was not possible in the nearshore area. However the data at location A in Fig.5 and 6 shows long period motion with the opposite sign for the first motion of reflected mode, supporting the results in Eq.(2) at least qualitatively.

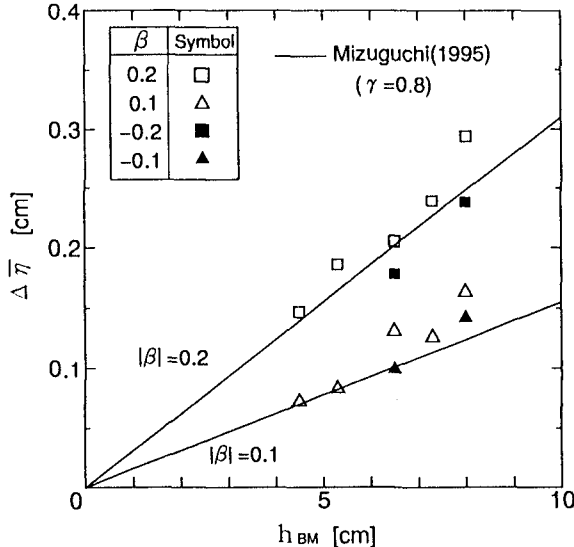


Fig.12 Magnitude of the BFLW traveling shoreward

5. Conclusions

In this study the main conclusions are as follows.

- (1) Careful experiments with both detailed measurements and elaborate data analysis reveal that free long waves, which radiate both shoreward and offshoreward, are really generated by time varying breakpoint.
- (2) The generation of the BFLW result from the variation of the starting point of wave set-up which coincide with the plunging point.
- (3) The BFLW observed in this experiments can be quantitatively evaluated by Mizuguchi(1995) model, although the measured data may be contaminated with long waves of other origins.

References

- Bowen, A. J. , D. L. Inman and V. P. Simmons (1968), Wave set-down and set-up, JGR, Vol.73, 8, pp.2569-2577.
- Kostense, J. K. (1984), Measurements of surf beat and set-down beneath wave groups, Proc.19th ICCE, Houston, pp.724-740.
- List, J. H. (1992), A model for the generation of two-dimensional surf beat, JGR, Vol.97, C4, pp.5623-5635.
- Longuet-Higgins, M.S. and R.W. Stewart (1962), Radiation stress and mass transport in gravity waves, with application to " surf beat ", JFM, Vol.13, pp.481-504.
- Mizuguchi, M. (1995), A simple analysis of long wave generation by time-varying breakpoint, Coastal Eng. In Japan, JSCE, Vol.38, pp.105-109.
- Mizuguchi, M. and Toita, H. (1996), Generation of second-order long waves by a wave group in a laboratory flume and its control, Proc.25rd ICCE, Orlando (in press)
- Nakamura, S. and K. Katoh (1992), Generation of infragravity waves in breaking process of wave groups, Proc.23rd ICCE, Venice, pp.990-1003.
- Schaffer, H. A. (1993), Infragravity waves induced by short-wave groups, JFM, Vol.247, pp.551-588.
- Symonds, G. , D, A. Huntley and A. J. Bowen (1982), Two-dimentional surf beat : long wave generation by a Time-varying breakpoint, JGR, Vol.87, C1, pp.492-498.
- Van Leeuwen, P. J. (1992), Low-frequency wave generation due to breaking wind waves, Communications on hydraulic and geotechnical engineering, Delft University of Technology, 151pp.

CHAPTER 103

LABORATORY EXPERIMENTS ON GENERATION OF LONG WAVES IN THE SURF ZONE

Akio Okayasu¹, Teruki Matsumoto² and Yasuyuki Suzuki³

Abstract

Laboratory experiments were performed to investigate generation of long waves in the surf zone. Amplitude of long waves generated by time-varying breaking points was found to be nearly same as that of incoming bounded long wave. The generated long waves showed phase difference with the incoming long waves. The difference of the phases reached to $3/4 \pi$ through π at the shoreline.

1. Introduction

In order to predict the sediment transport in the nearshore area, the mechanism of generation and propagation of long period waves in the surf zone must be clarified. Long waves observed in the surf zone consist of three major components. The first component is free long wave (FLW) coming from outside of the surf zone which includes both of wave group bounded long wave (BLW) released at the breakpoint and free long waves generated by the wave maker. The second component is breakpoint forced long wave (BFLW) which is generated by moving breakpoint due to wave group. The third one is outgoing long wave which is formed by reflection of the former two components at the shoreline.

Long wave outside the surf zone can be basically explained by the mechanism proposed by Longuet-Higgins and Stewart (1962) (see *e.g.* Sato *et al.*, 1989, Nagase and Mizuguchi, 1996). Long wave generated by moving breakpoint was also theoretically investigated by Symonds *et al.* (1982), Schäffer (1993) and others. On the qualitative description of long wave sources in the surf zone, Mizuguchi (1982) wrote that the long wave coming from outside of the surf zone

¹Associate Professor, Department of Civil Engineering, Yokohama National University, 79-5 Tokiwadai, Hodogaya, Yokohama 240, Japan. E-mail: okayasu@cvg.ynu.ac.jp.

²Tokyu Construction Co.Ltd., Tokyo, Japan.

³Graduate Student, Department of Civil Engineering, Yokohama National University.

was predominant among observed onshore propagating long waves in the surf zone. On the other hand, Nakamura and Katoh (1992) considered that BFLW should be predominant.

Nagase and Mizuguchi (1996) observed BFLW by putting a single packet of wave group into stable regular wave field in a wave flume. However, quantitative analysis for generation of BFLW should be difficult by the single packet experiment. Shibayama *et al.* (1992) pointed out that phase relation between wave group and long waves in the surf zone is important for suspended sediment movement due to low-frequency velocity change. Statistic analysis of phase shift also requires the measurement under usual random wave condition in the surf zone.

In the present study, generation and propagation of long waves in the surf zone are investigated on a step, 1/30, 1/20 and 1/10 uniform beaches in a flume under irregular wave conditions. Amplitude and phase variation of the long waves in the surf zone are quantitatively investigated. The experimental results are compared with a theory proposed by Mizuguchi (1995).

2. Experimental Procedures

2.1 Experimental setup and condition

The experiments were performed in a wave flume which was 17 m long and 0.5 m wide. A random wave generator with absorption control for reflected waves was equipped at one end of the flume. Beach topography were a step, 1/30, 1/20 and 1/10 uniform beaches. The step beach consisted of the first 2 m of 1/10, the next 1 m of 1/20, 6 m of flat bed and the last 2 m of 1/10 slopes. The 1/30 and 1/20 slopes had an 1 m of 1/10 slope at the toe. The beaches were made of 15-mm-thick plywood on stainless steel base.

Surface elevation and cross-shore velocity were measured by wave gages and a optic-fiber laser Doppler velocimeter (FLV). A wave gage was set 3 m onshore of the wave paddle in the offshore constant depth region. Seven (step and 1/30) or eleven (1/20 and 1/10) measuring stations were located from the offshore side of the breaking point to the shoreline. The elevation of the velocity measuring point was 1 cm from the local bottom of the slope. Figure 1 shows the setup of the flume with the step and 1/30 beaches. The x -axis was set to be onshoreward from the shoreline at the still water level.

The experiments were performed for total 14 wave conditions. Random incident waves were designed to have the Bretshneider-Mitsuyasu spectrum. The experimental conditions are listed in Table 1. In the table, h_i is the still water depth in the offshore region, h_s the still water depth on the step, $H_{1/3}$ is the significant wave height offshore, $T_{1/3}$ is the significant wave period. $H_{1/3}$ and $T_{1/3}$ were obtained by using the zero-down cross method. The "breaking point" in the table shows the mean location of wave breaking denoted by the measuring station (St.) numbers. The positions on the x -axis of the measuring stations are listed in Table 2.

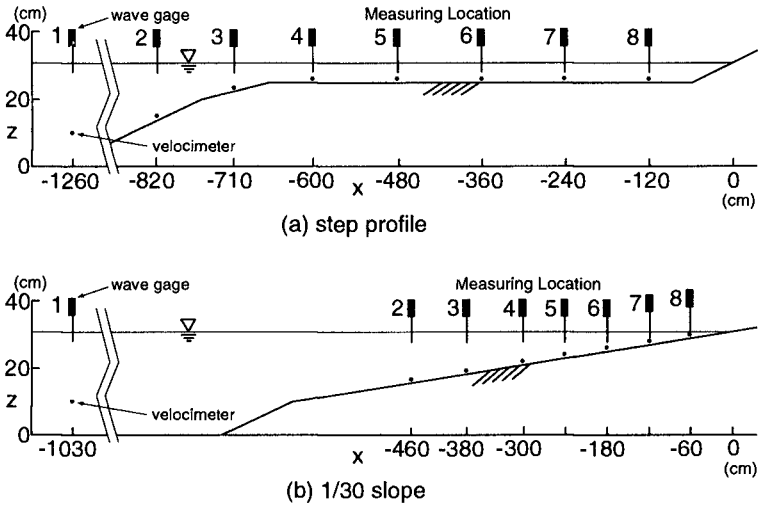


Figure 1: Experimental setup in wave flume

Table 1: Experimental Conditions

case	beach type	h_i (cm)	h_s (cm)	$H_{1/3}$ (cm)	$T_{1/3}$ (s)	breaking point
1-1	step	31.0	6.0	5.81	1.03	St.3
1-2				4.87	0.88	St.3
1-5		29.0	4.0	5.69	1.03	St.3
1-6				4.69	0.89	St.3
2-1	1/30	31.0	-	3.98	1.01	St.5 - St.6
2-2				3.32	0.86	St.5 - St.6
2-5		29.0	-	3.91	1.01	St.5 - St.6
2-6				3.25	0.86	St.5 - St.6
3-1	1/20	40.0	-	6.20	0.90	St.9 - St.10
3-2				7.88	1.03	St.8 - St.9
3-3				9.11	1.05	St.8 - St.9
4-1	1/10	40.0	-	6.19	0.89	St.8 - St.9
4-2				7.92	1.03	St.7 - St.8
4-3				9.28	1.03	St.6 - St.7

Table 2: Location of Measuring Stations

case	measuring location on x -axis (cm)											
	St.1	St.2	St.3	St.4	St.5	St.6	St.7	St.8	St.9	St.10	St.11	St.12
1-1 & 2	-1260	-820	-710	-600	-480	-360	-240	-120	-	-	-	-
1-5 & 6	-1240	-800	-690	-580	-460	-340	-220	-100	-	-	-	-
2-1 & 2	-1030	-460	-380	-300	-240	-180	-120	-60	-	-	-	-
2-5 & 6	-970	-400	-320	-240	-180	-120	-60	0	-	-	-	-
Series 3	-1100	-440	-400	-360	-320	-280	-240	-200	-160	-120	-80	-40
Series 4	-1260	-240	-200	-180	-160	-140	-120	-100	-80	-60	-40	-20

2.2 Data acquisition

Since only one FLV was used, the velocity measurement was repeatedly done for each measuring station with the same incident wave signal. Wave generation was started with still water condition at each time. Preparatory generation of wave was done for 600 seconds which was considered to make the wave field enough stable. Measurements of velocity and water surface elevation were conducted after this moment.

The wave profile data were sampled at the rate of 20 Hz and were stored in a digital data recorder. The velocity signal was also acquired more than 20 valid data per second. Since the time intervals of velocity records are not equal, the data were resampled every 50 ms. 300 seconds of cross-shore velocity and water surface elevation data were used for analysis.

3. Experimental Results

3.1 Extract of BFLW

Long wave components of velocity and water surface elevation of long waves were extracted by a numerical filter with the cut-off frequency of 0.25 Hz. Then the long wave components were separated into incident and reflected low frequency components by using the water surface elevation and velocity after Mizuguchi (1991).

Figure 2 shows a result of incident and reflected wave separation on the step beach for Case 1-2. In the figure, t is the time-axis, the origin of which was the start of data acquisition, and η is water surface elevation change around the mean water level. The incident component is given by the solid line and the reflected component is shown by the dotted line. The chain and the chain with 2 dots lines respectively show paths of incident and reflected free long wave calculated by the shallow water wave theory. The separation of incident and reflected long waves are found to be fairly good on the step part.

In Case 1-2, the breaking point was around St. 3 ($x = -710$ cm). By following a prominence along the incident wave path in Fig. 2, significant change

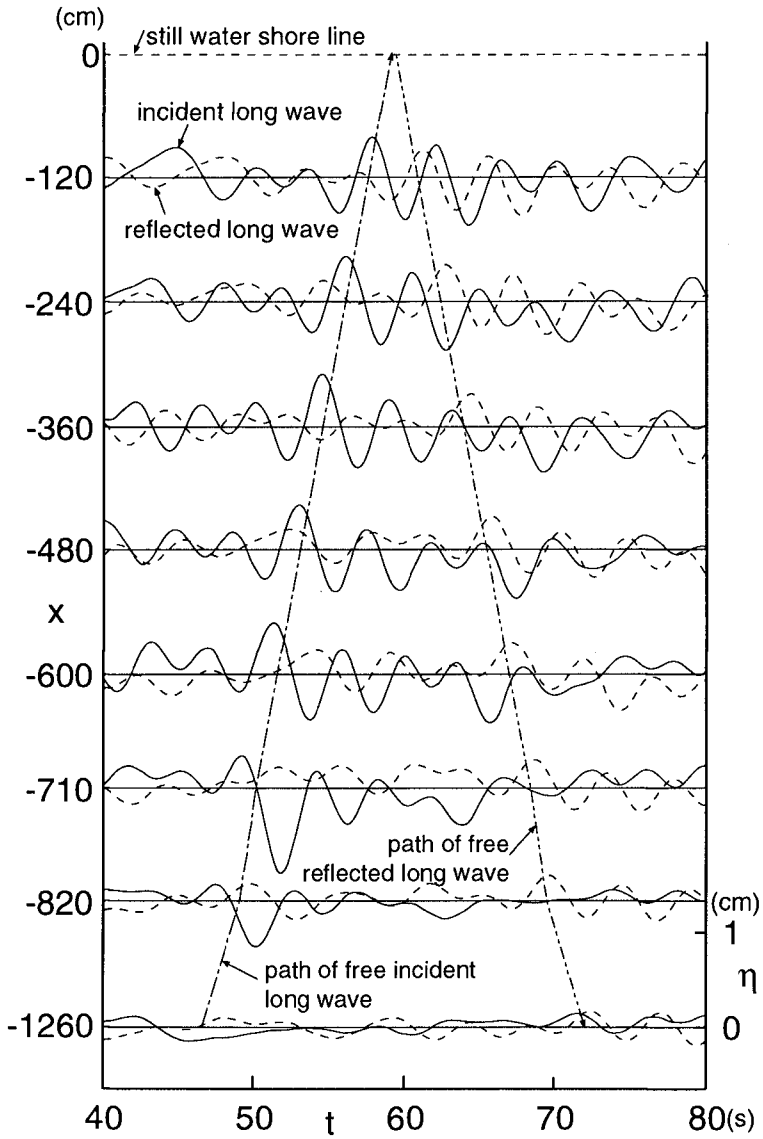


Figure 2: Incident and reflected long waves in the surf zone (chain line: path of free incident long wave, chain with 2 dots line: path of free reflected long wave)

of the amplitude and phase of the incident long wave can be seen between St. 2 and St. 4. This should be caused by generation of free long wave due to moving breakpoint.

In the present study, incoming long wave is given at a measuring station just offshore the breaking point after the separation of onshore propagating component. Onshore propagating free long wave in the surf zone can be calculated by using the shallow water wave theory from the coming long wave from the offshore-side of the boundary, the breaking point. In the present study, this calculated onshore propagating FLW is termed as "predicted free long wave (in the surf zone)". It can be considered that the deviation of observed onshore propagating FLW from this "predicted FLW" is caused by long wave generated at the breaking point. Therefore, the "measured BFLW" was obtained by "observed onshore propagating FLW" - "predicted FLW".

The dotted line in Fig. 3 shows predicted FLW for Case 1-2. This free long wave is calculated from the observed incoming long wave at St. 2. The solid line gives BFLW evaluated by subtracting the predicted FLW (dotted lines in the figure) from the observed onshore propagating long wave at each station (solid lines in Fig. 2).

The random wave field in a flume is not the same as that on the natural beach, because the seiche and multi-reflection of long waves at the flume ends as well as the unexpected free long wave generated by the wave maker affects the wave field. However, all incoming long waves from outside into the surf zone can be considered as free long waves at the breaking point. On the other hand, BFLW should be essentially the same as that on the natural beach, if the incident short wave component can be regarded as the same. Therefore, by excluding the incoming free long waves (with any origin) from the onshore propagating free long waves observed in the surf zone, the breakpoint generated long wave can be extracted with basically the same condition in the field.

The figure shows generation of relatively large long wave between St. 2 and St. 4. This generated long wave propagates onshoreward on the step as free long wave. The form of it doesn't change so much after St. 4.

3.2 Estimation of BFLW amplitude

The amplitude of BFLW was investigated quantitatively with a model proposed by Mizuguchi (1995). The displacement of water surface $\Delta\eta$ caused by onshore propagating long wave generated by the moving breakpoint is given by

$$\Delta\eta = -Ks[x_b(t) - x_{bm}]/2 \quad (1)$$

in the model. K is a constant and given by 0.194 with wave height to water depth ratio at breaking point = 0.8. s is the mean bottom slope around the breakpoint and $[x_b(t) - x_{bm}]$ the moving distance of breakpoint.

By giving $0.8\delta(1 - \kappa)h_{bm}/s$ for the moving distance of breakpoint after

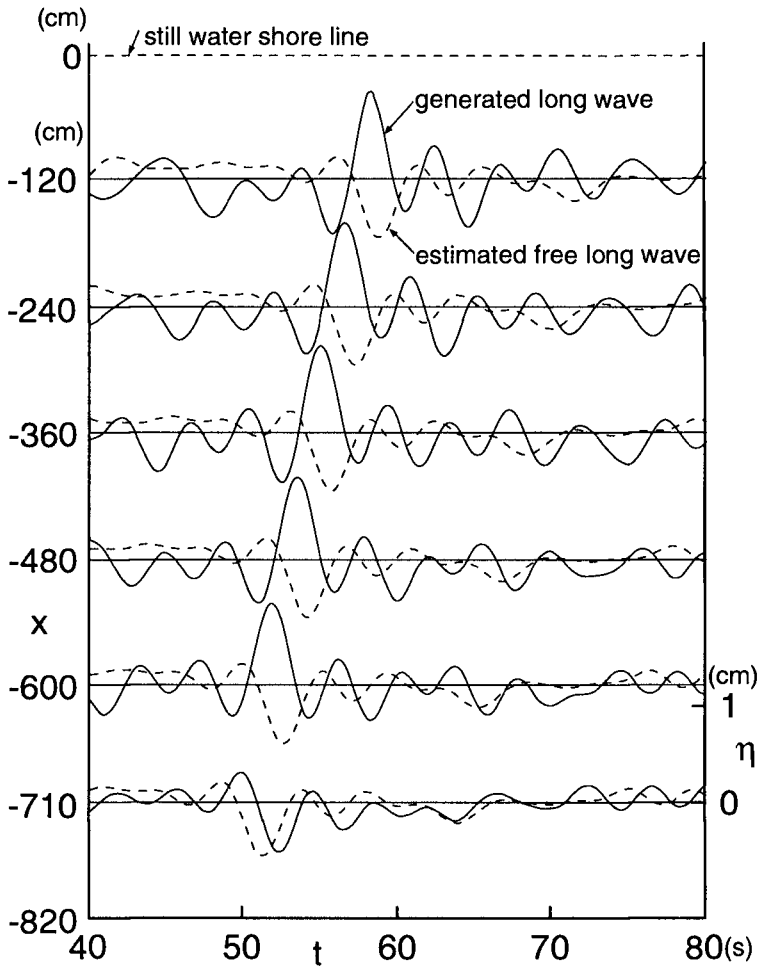


Figure 3: Predicted free long wave and generated long wave which obtained from the difference between the predicted and observed long waves

Table 3: Observed r.m.s. values of BFLW and those predicted by Mizuguchi (1995)

case	bottom slope s	breakpoint water depth h_{bm} (cm)	estimated r.m.s. value η_{crms} (cm)	measured r.m.s. value η_{mrms} (cm)	measured r.m.s. for incident wave η_{irms} (cm)
1-1	1/20	8.30	0.228	0.283	0.205
1-2		6.96	0.191	0.215	0.172
1-5		8.13	0.223	0.317	0.179
1-6		6.70	0.184	0.216	0.192
2-1	1/30	5.69	0.156	0.188	0.224
2-2		4.74	0.130	0.149	0.169
2-5		5.59	0.153	0.196	0.256
2-6		4.64	0.127	0.154	0.160
3-1	1/20	8.86	0.243	0.276	0.299
3-2		11.3	0.309	0.328	0.370
3-3		13.0	0.357	0.346	0.395
4-1	1/10	8.84	0.243	0.260	0.267
4-2		11.3	0.310	0.509	0.343
4-3		13.3	0.364	0.392	0.359

Mizuguchi (1994), Eq. 1 is obtained as

$$\Delta\eta = 0.8K\delta(1 - \kappa)h_{bm} \quad (2)$$

where δ is modulation parameter for the short waves and κ the degree of transmission of short wave grouping which are taken to be here as 0.5 and 0, respectively. h_{bm} is the mean water depth at breaking point which is approximately given by $H_{1/3}/0.7$ in the present study.

Amplitude of BFLW was calculated with above described conditions. Root-mean-square (r.m.s.) value of variation is $1/\sqrt{2}$ of the amplitude, if sinusoidal change can be assumed. Comparison between $1/\sqrt{2}$ of the calculated BFLW amplitude and observed r.m.s. value of BFLW are listed in Table 3 together with measured r.m.s. values of onshore propagating FLW (including BFLW) in the surf zone. The observed value in the table shows the mean value through the surf zone. The value 1/20 of s in Series 1 is the local bottom slope at St. 3 which was the breakpoint for the cases.

The calculated values for BFLW shown in the table are slightly smaller than the measured values. However, it can be considered that the Mizuguchi's model can predict the BFLW variation fairly well. The table also shows that the amplitude of BFLW is comparable to that of FLW coming from outside the surf zone.

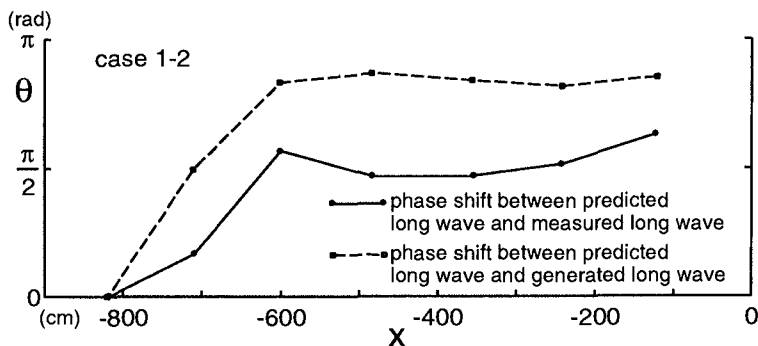


Figure 4: Phase delay of observed and generated long waves from predicted free long wave for Case 1-2

3.3 Phase shift between BFLW and incoming FLW

Cross-shore variations of phase shifts between the long wave components in the surf zone for Case 1-2 are shown in Fig. 4. θ in the figure is the phase delay from the predicted FLW (dotted line in Fig. 3) in the surf zone. The solid line in the figure gives phase delay of the observed onshore propagating long wave (solid line in Fig. 2). The broken line shows phase delay of the observed BFLW (solid line in Fig. 3).

The phase shifts were defined as mean value of Fourier components around the frequency of 0.1 Hz in spectrum analysis. The right end of the figure shows the shoreline on the beach. The phase of the observed long wave delays $\pi/2$ on the step and that of the generated long wave reaches to π . The result supports the theoretical value of phase shift π given by Mizuguchi (1995). The figure shows that the phase shifts change between St. 2 and St. 4 and quite stable on the flat bed.

Figure 5 shows phase shifts between the observed BFLW and the predicted FLW for other 3 cases on the step beach. The phase shifts are stable on the step and take values around π in all cases.

Figure 6 shows phase shifts between the observed onshore propagating long wave from the predicted FLW for Series 2, 3 and 4 which were the measurements on 1/30, 1/20 and 1/10 constant slopes. The horizontal axis in the figure is non-dimensionalized by the surf zone width x_b . The straight bold broken line in the figure shows $\theta = 0.4\pi x/|x_b|$. Although the deviation of the phase shifts near the shoreline is large, this bold broken line shows good agreement with the phase shift variations in the surf zone for all cases.

Figure 7 shows phase shifts between the observed BFLW from the predicted FLW on 1/30, 1/20 and 1/10 constant slopes. The phase shift just onshore the

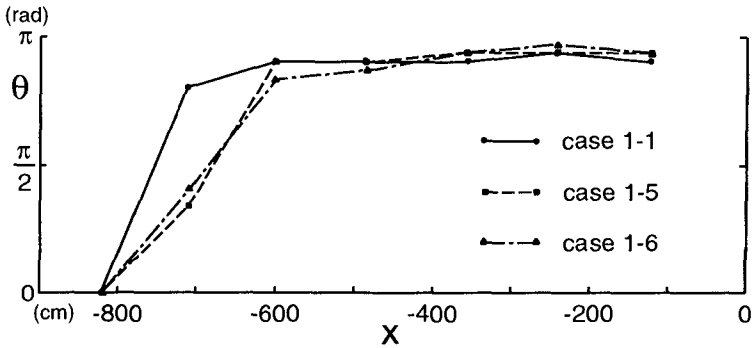


Figure 5: Phase delay of generated long waves from predicted free long waves on the step beach

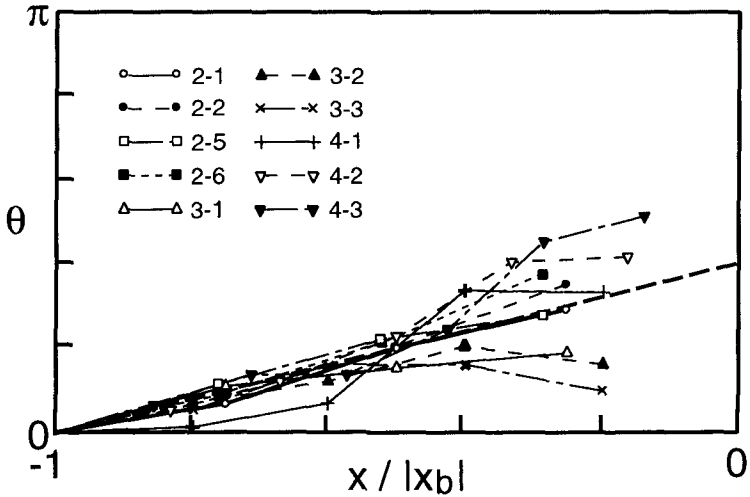


Figure 6: Phase delay of observed long waves from predicted long waves on the constant slope bottoms

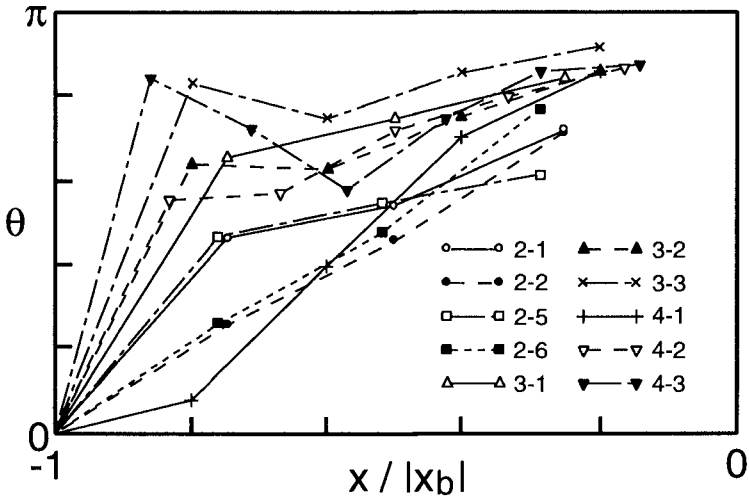


Figure 7: Phase delay of generated long waves from predicted long waves on the constant slope bottoms

breaking point takes various value. However, the value near the shoreline is within the range of $0.6 - 0.9 \pi$. The average is around $3/4\pi$.

As mentioned before in this section, the theoretical phase shift between BFLW and bounded long wave at the breaking point which should be transferred to free long wave in the surf zone is π (Mizuguchi, 1995). Near the breaking point, the measured values in the figure show wide variation and is far smaller than π . In the case of large short wave modulation, the generated long wave (BFLW) is relatively small near the mean breakpoint. This causes poor separation of generated long wave, then results in a large error in the phase calculation. Since the generated long wave becomes enough large, the stable phase shift close to π can be obtained near the shoreline. On the step, where the generation of BFLW is almost finished, the phase shifts show values close to π as seen in Fig. 5.

4. Calculation of BFLW by a Numerical Wave Model

It is considered that BFLW can be numerically simulated by presenting momentum flux change due to wave breaking in time and space. The concept is basically the same as Symonds *et al.* (1982) or Mizuguchi (1995) did in their theoretical models.

Watson *et al.* (1994) numerically simulated propagation and run-up of BFLW caused by a single wave group with a non-linear shallow water equation. In the

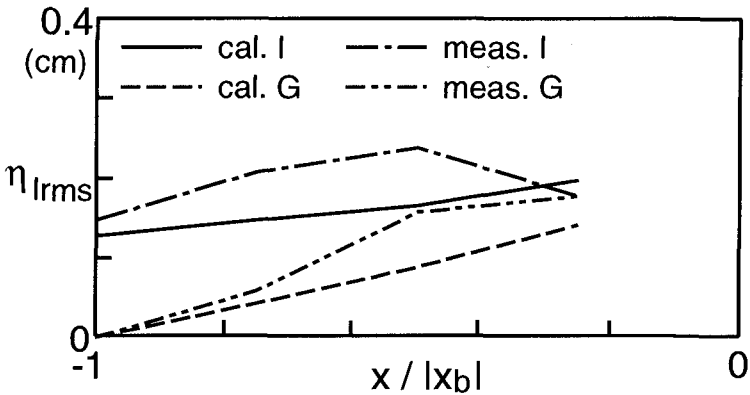


Figure 8: Comparison of r.m.s. values of calculated and measured long waves in the surf zone (Case 2-1)

present study, numerically simulated long waves in the surf zone were compared with the observed waves under random short wave conditions. Information on phase shifts can be examined with the random waves.

Boussinesq-type nonlinear dispersive wave model was used for the numerical simulation. Wave energy dissipation was expressed by a surface roller model which had been proposed by Deigaard (1989). Advantages for using the surface roller model in the simulation is: 1) Breakpoints are determined for individual short waves. Characteristics of wave groupiness can be reflected in the numerical calculation. 2) Momentum flux of surface rollers is included in the calculation. 3) Since the surface roller area is determined from the surface geometry, catching up of a wave crest to the previous wave crest can be simulated in the calculation, *etc.*

An example of the results of numerical simulations is shown in Fig. 8. Comparisons of r.m.s. values of the simulated and measured long waves for Case 2-1 are given. The solid line in the figure shows calculated onshore propagating long wave and the chain line gives measured onshore propagating long wave. The broken line is calculated BFLW and the chain with 2 dots line is measured BFLW. The calculated values at the shoreline show good agreement with measured values.

Figure 9 gives calculated and measured phase shifts between onshore propagating long wave and BFLW for Case 2-2. The solid line in the figure is calculated phase delay of onshore propagating long wave (including BFLW) from incoming long wave. The broken line is calculated phase delay of BFLW from incoming long wave. The chain line shows observed phase delay of onshore

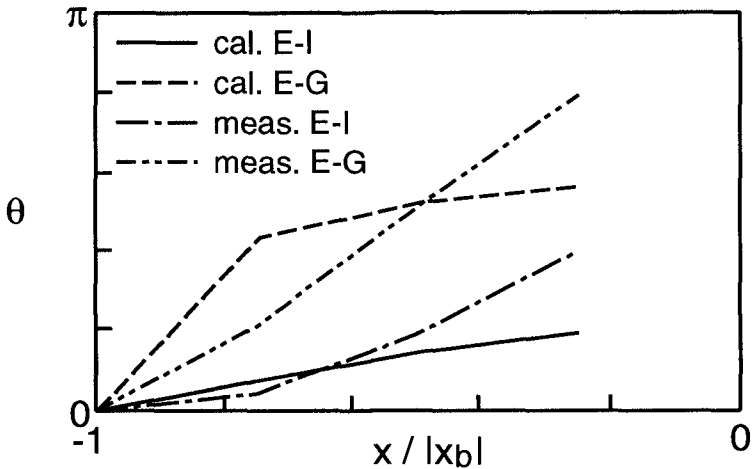


Figure 9: Comparison of phase shifts of calculated and measured long waves in the surf zone (Case 2-2)

propagating long wave and the chain with 2 dots line is observed phase delay of BFLW. Calculated phase shifts near the shoreline are slightly smaller than the observed values. However, it is considered that the numerical simulation can be used for evaluation of BFLW with phase information.

5. Conclusions

In the present study, laboratory experiments were performed for long waves observed in the surf zone under random incident wave conditions. Breakpoint forced long wave (BFLW) was evaluated from the measured cross-shore velocity and surface water elevation. Phase relation between incoming long wave and BFLW was also investigated for various wave conditions and beach topography.

The conclusions of this study are as follows:

1. With propagation of random waves onshore in a flume, long wave generated near the breaking point was observed in the surf zone. This long wave is considered to be generated by time-varying breakpoint.
2. Root-mean-square value of the generated long wave was comparable to that of incoming long wave propagating from outside of surf zone. Predicted amplitude of generated long wave calculated after Mizuguchi (1995) showed good agreement with the observed value.
3. Phase shift was found between the observed long wave in the surf zone and predicted free long wave which was calculated by using shallow water approximation. The phase delay of the onshore propagating long wave was roughly

evaluated by $\theta = 0.4\pi x/|x_b|$. Phase delay of the generated long wave from that of the incoming free long waves was around $3/4 \pi$ (for constant slopes) through π (for step-type beach) at the shoreline.

4. Boussinesq-type nonlinear dispersive wave model with the surface roller model can quantitatively simulate BFLW. The phase information can be also evaluated by the numerical model.

References

- Deigaard R. (1989): Mathematical modelling of waves in the surf zone, Prog. Rep. No. 69, Inst. of Hydrodyn. and Hydraulics Eng., Tech. Univ. of Denmark, pp. 47-60.
- Longuet-Higgins, M. S. and R. W. Stewart (1962): Radiation stress and mass transport in gravity waves, with application to "surf beat", J. Fluid Mech., Vol. 13, pp. 481-504.
- Mizuguchi, M. (1982): A field observation of wave kinematics in the surf zone, Coastal Eng. in Japan, Vol. 25, pp. 91-107.
- Mizuguchi, M. (1991): Separation of incident and reflected waves in shallow water, Proc. of Coastal Eng., JSCE, Vol. 38, pp. 31-35 (in Japanese).
- Mizuguchi, M. (1995): A simple analysis of long wave generation by time-varying breakpoint, Coastal Eng. in Japan, Vol. 38, pp. 105-109.
- Nagase, S. and M. Mizuguchi (1996): Laboratory experiment on long wave generation by time-varying breakpoint 25th Int. Conf. on Coastal Eng., ASCE (in press).
- Nakamura, S. and K. Katoh (1992): Generation of infragravity waves in breaking process of wave group, 23rd Int. Conf. on Coastal Eng., ASCE, pp. 990-1003.
- Sato S., T. Isayama and T. Shibayama (1989): Long-wave component in near-bottom velocities under random waves on a gentle slope, Coastal Eng. in Japan, Vol. 32, No. 2, pp. 149-159.
- Schäffer, H. A. (1993): Infragravity waves induced by short-wave groups, J. Fluid Mech., Vol. 247, pp. 551-588.
- Shibayama T., A. Okayasu and M. Kashiwagi (1992) : Long period wave and suspended sand transport in the surf zone, 23rd Int. Conf. on Coastal Eng., ASCE, pp. 2438-2449.
- Symonds, G., D. A. Huntley and A. J. Bowen (1982): Two-dimensional surf beat: long wave generation by a time-varying breakpoint, J. Geophys. Res., Vol. 87, C1, pp. 492-498.
- Watson, G., T. C. D. Barnes and D. H. Peregrine (1994): The generation of low-frequency waves by a single wave group incident on a beach, 24th Int. Conf. on Coastal Eng., ASCE, pp. 776-790.

CHAPTER 104

Generation of Infragravity Waves

A.R. Van Dongeren, I.A. Svendsen and F.E. Sancho¹

ABSTRACT: In this paper the depth-integrated, short wave-averaged nearshore circulation model SHORECIRC is used to study the generation of infragravity waves due to normally incident short wave groups on a plane beach. After linear separation of the incident and reflected long waves, it is shown that the incoming long wave shoals faster than Green's Law predicts for free waves. This indicates that energy is transferred from the short wave groups to the long wave. However, it does not shoal as quickly as Longuet-Higgins & Stewart's (1962) steady state theory for bound waves suggests. The outgoing long wave deshoals according to Green's Law but it is shown that energy is traded back and forth with the incoming short wave groups. Different shoaling and deshoaling curves can be found for different parameter choices. The work term in the long wave energy equation is used to explain these differences and ratio of the number of short wave groups to the surf zone width is confirmed to be an important parameter. As a consequence, the energy of the outgoing long wave can be larger or smaller than that of the incoming long wave, depending on the value of that parameter. Finally, the nonlinear version of the model shows the importance of the mean set-up on the generation of long waves, in particular very close to the shoreline.

INTRODUCTION

It is well-known that a forced long wave propagates with short wave groups at the group speed (Longuet-Higgins & Stewart, 1962) [LHS62 in the remainder]. When these groups propagate onto a beach, the short waves shoal and break. In the shoaling process the incoming, bound long wave gains energy and is released from the groups. The incoming long wave propagates shoreward, interacts with the breaking process, eventually reflects off the beach and propagates seaward as a free wave. The principle of this process is generally agreed upon, but the precise mechanisms by which energy is transferred to the long (or infragravity) waves are not.

For the case of normally incident waves, two different infragravity wave generation mechanisms have been proposed for the interaction with the breaking. Symonds *et al.* (1982) assumed that the groupiness which existed outside the

¹Center for Applied Coastal Research, Ocean Engineering Lab, University of Delaware, Newark, DE 19716, USA. Correspondence e-mail: apper@coastal.udel.edu

breaker zone is destroyed by the breaking and that the short waves inside the surf zone will decay with a saturated wave height. This implies a time-varying break point which generates long waves while no long wave generation takes place inside the surf zone.

Schäffer & Svendsen (1988) [SS88] examined the other extreme where all short waves regardless of their height are assumed to break at a fixed break point. This means that the groupiness outside the surf zone is transmitted into the surf zone where long wave generation can take place.

It is likely that neither mechanism is exclusively responsible for long wave generation but that it is due to a combination of both effects. Therefore Schäffer (1993) [S93] merged the two extreme mechanisms into one hybrid analytical solution and showed the effects of parameter variations.

Some field studies suggest that there is more energy in the free (outgoing or trapped) waves than in the incoming bound waves (Munk, 1949; Tucker, 1950; Elgar *et al.*, 1992; Herbers *et al.*, 1995 to name a few). This indicates that in the nearshore region energy has been transferred from the short waves to the long waves. However, other observations (Guza & Thornton, 1985; Kostense, 1984) show that the energies of the in- and outgoing long waves are about equal, which means that no net long wave energy was gained.

In this paper the nearshore circulation model SHORECIRC (Van Dongeren *et al.*, 1994) is applied to study the generation of infragravity waves on a plane beach with normally incident short wave groups. In the next section, the general governing equations of nearshore circulation are stated. Then, the linearized version of the model is used to study the growth of the amplitude of the incoming and outgoing long waves for different parameter choices. The linear long wave energy equation is used to explain the characteristics of the shoaling and deshoaling curves. It is shown that net energy can either be gained or lost depending on the values of certain parameters. Finally, the nonlinear version of the model reveals the importance of the nonlinear terms, in particular the mean set-up of the surface elevation.

GOVERNING EQUATIONS

The depth-integrated, time-averaged mass and momentum equations read (Van Dongeren *et al.*, 1994; Svendsen & Putrevu, 1996):

$$\frac{\partial \bar{\zeta}}{\partial t} + \frac{\partial}{\partial x_\alpha} \left(\int_{-h_0}^{\bar{\zeta}} V_\alpha dz + Q_{w\alpha} \right) = 0 \quad (1)$$

$$\begin{aligned} \frac{\partial \bar{Q}_\beta}{\partial t} + \frac{\partial}{\partial x_\alpha} \left(\frac{\bar{Q}_\alpha \bar{Q}_\beta}{h} \right) + \frac{\partial}{\partial x_\alpha} \int_{-h_0}^{\bar{\zeta}} V_{1\alpha} V_{1\beta} dz + \frac{\partial}{\partial x_\alpha} \int_{\zeta t}^{\bar{\zeta}} \overline{u_{w\alpha} V_{1\beta} + u_{w\beta} V_{1\alpha}} dz \\ + g(h_0 + \bar{\zeta}) \frac{\partial \bar{\zeta}}{\partial x_\beta} + \frac{1}{\rho} \frac{\partial}{\partial x_\alpha} \left(S_{\alpha\beta} - \int_{-h_0}^{\bar{\zeta}} \tau_{\alpha\beta} dz \right) - \frac{\tau_\beta^S}{\rho} + \frac{\tau_\beta^B}{\rho} = 0 \end{aligned} \quad (2)$$

where the total current has been split into depth uniform and depth varying components:

$$V_\alpha = \frac{\bar{Q}_\alpha}{h_0 + \bar{\zeta}} + V_{1\alpha}(x, y, z, t) \quad (3)$$

which implies

$$\int_{h_o}^{\bar{\zeta}} V_{1\alpha} dz = -Q_{w\alpha} \quad (4)$$

It turns out that in this formulation the radiation stress $S_{\alpha\beta}$ is defined as by Mei (1983). For a discussion of the details see Svendsen & Putrevu (1996).

In (1) and (2), V_α and $\bar{\zeta}$ represent the horizontal current velocity and the mean surface elevation, respectively. u_w is the short wave velocity defined so that $\bar{u}_w = 0$ below through level, \bar{Q}_α represents the total volume flux and $Q_{w\alpha}$ is the volume flux due to the short wave motion. ζ_t is the elevation of the wave trough, $\tau_{\alpha\beta}$ is the Reynolds stress, h_o is the still water depth, while τ_β^S and τ_β^B represent the surface and the bottom shear stress, respectively. The overbar denotes short wave averaging and the subscripts α and β denote the directions in a Cartesian coordinate system. Fig. 1 shows the definitions.

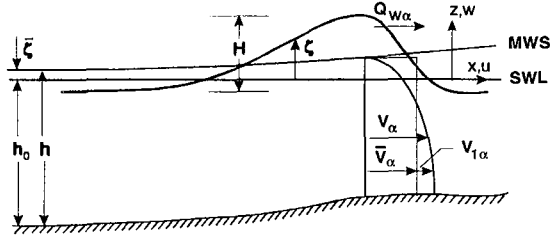


Figure 1: Definition sketch.

For the present purpose we will consider depth-uniform long waves in the shore-normal x -direction, which reduces the set of equations to:

$$\frac{\partial \bar{\zeta}}{\partial t} + \frac{\partial \bar{Q}}{\partial x} = 0 \quad (5)$$

$$\frac{\partial \bar{Q}}{\partial t} + \frac{\partial}{\partial x} \left(\frac{\bar{Q}^2}{h} \right) + g(h_o + \bar{\zeta}) \frac{\partial \bar{\zeta}}{\partial x} + \frac{1}{\rho} \frac{\partial S_{xx}}{\partial x} + \frac{\tau_x^B}{\rho} = 0 \quad (6)$$

These equations correspond to the forced nonlinear shallow water equations where the radiation stress gradient provides the forcing on the long waves. The equations are solved by finite differences using a second-order predictor-corrector method for time and horizontal space on a fixed rectangular grid. On the seaward side we specify an absorbing-generating boundary condition as derived by Van Dongeren & Svendsen (1996). In the linear version of the model a no-flux boundary condition is specified at the still water line while in the nonlinear version a moving shoreline condition is used (Van Dongeren *et al.*, 1995).

LINEAR ANALYSIS

The simplest possible case to analyze is a plane beach with a shelf and forcing generated by a bichromatic short wave group while using the linearized version of the model. This case provides valuable insights into the long wave generation mechanisms.

Following SS88 and S93 we can write the radiation stress forcing as:

$$S_{xx} = \frac{1}{2} \rho g \left(2n - \frac{1}{2} \right) \begin{cases} a_1^2 \left(1 + 2\delta \cos \left(f \frac{\Delta\omega}{c_g} dx - \Delta\omega t \right) \right), & h \geq h_b \\ \gamma^2 h_o^2 \left(1 + 2\delta(1 - \kappa) \cos \left(f \frac{\Delta\omega}{c_g} dx - \Delta\omega t \right) \right), & h \leq h_b \end{cases} \quad (7)$$

where κ is the parameter controlling the generation mechanism: $\kappa = 0$ corresponds to the case of a fixed break point, while $\kappa = 1$ represents the time-varying break point case. $n = c_g/c$ where c_g is the group speed. a_1 is the amplitude of the primary short wave in the group while the groupiness $\delta = a_2/a_1$ is the ratio of the amplitude of the secondary wave and the primary wave. $\Delta\omega = \omega_1 - \omega_2$ is the difference frequency between the two short waves which is also the long wave frequency. $\gamma = 2a_1/h$ is the saturated wave height over water depth ratio. h_b is the breaking depth. It is important to notice that the forcing consists of a steady part - which causes a steady set-up - and a time-varying part which forces a long wave. In our analysis we are only interested in the latter and in the rest of the paper we show only the time varying part of the solution.

It is assumed that the shelf is wide enough so that at the toe of the beach the incoming long wave corresponds to the equilibrium bound long wave for the flat shelf:

$$\bar{\zeta}_i = -\frac{1}{\rho} \frac{S_{xx}^{(1)}}{g h_s - c_{gs}^2} \quad (8)$$

where the subscript s corresponds to conditions on the shelf and $S_{xx}^{(1)}$ is the time-varying part of the forcing of (7). The outgoing wave is absorbed using the absorbing-generating boundary condition referenced above.

Case 1: fixed breakpoint

The first case considered is that of a fixed breakpoint ($\kappa = 0$) corresponding to the mechanism proposed by SS88. In the example studied, the following parameter values are used: forcing frequency $\Delta\omega = 0.422 \text{ s}^{-1}$, primary wave amplitude $a_{1,s} = 0.4415 \text{ m}$ on the shelf, groupiness $\delta = 0.1$, saturated breaking parameter $\gamma = 0.7$, beach slope $h_x = 1/30$ and shelf depth $h_s = 3 \text{ m}$.

The solid line in Fig. 2a shows the envelope of the long wave versus the depth, nondimensionalized by the shelf depth. The surface elevations are normalized by $a_{1,s}^2 \delta / h_s$, so that the incoming bound long wave of (8) is $O(1)$ at the offshore boundary. In the Figure, the still water line is on the left-hand side while the toe of the beach is on the right-hand side. Notice the agreement of the model with the dashed line which corresponds to the analytical solution by SS88. The break point is located at $h/h_s = 0.45$ and is indicated in the Figure.

The long wave can be separated into an incoming and an outgoing long wave

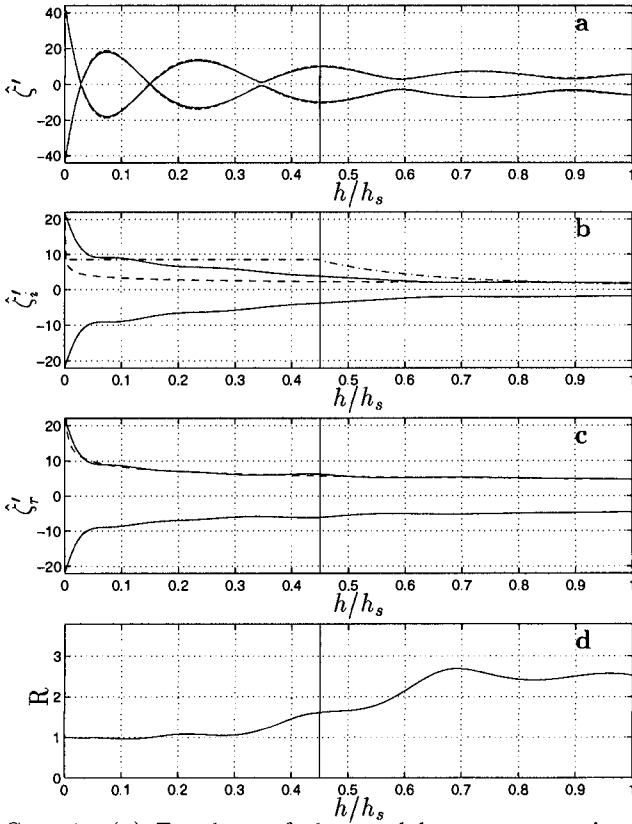


Figure 2: Case 1: (a) Envelope of the total long wave motion vs. depth : present model (—) and analytical solution (- -); (b) Envelope of the incoming long wave: present model (—), Green's Law (- -) and LHS62's steady state solution (-·-); (c) Envelope of the outgoing long wave: present model (—) and Green's Law (- -); (d) Reflection coefficient.

using linear superposition of the surface elevation and the flux

$$\bar{\zeta} = \bar{\zeta} + \bar{\zeta}_i + \bar{\zeta}_r \quad \text{and} \quad \bar{Q} = \bar{Q}_i + \bar{Q}_r \quad (9)$$

where $\bar{\zeta}$ is the steady set-up, subscript i denotes the incoming wave and subscript r denotes the outgoing wave. Also, we know the following relationships between the surface elevation and the flux of the incoming and outgoing wave, respectively:

$$\bar{Q}_i = c_g \bar{\zeta}_i \quad \text{and} \quad \bar{Q}_r = -\sqrt{g h_o} \bar{\zeta}_r \quad (10)$$

which implies that the incoming wave essentially propagates with group speed c_g and the free outgoing wave propagates with the shallow water wave speed.

This is confirmed by the computations. Solving for $\bar{\zeta}_i$ and $\bar{\zeta}_r$ from these four equations yields

$$\bar{\zeta}_i = \frac{\sqrt{g h_o} (\bar{\zeta} - \bar{\zeta}) + \bar{Q}}{c_g + \sqrt{g h_o}} \quad \text{and} \quad \bar{\zeta}_r = \frac{c_g (\bar{\zeta} - \bar{\zeta}) - \bar{Q}}{c_g + \sqrt{g h_o}} \quad (11)$$

The solid line in Fig. 2b shows the envelope of the *incoming* long wave. Note that the long wave shoals faster than as predicted by Green's Law ($\hat{\zeta} \propto h^{-1/4}$, the dashed line), which means that energy must have been transferred to the long wave. Also shown is the shoaling curve according to LHS62's steady state theory, Eq. (8) (the dash-dotted line, $\hat{\zeta} \propto h^{-5/2}$ outside the surf zone), which grows much faster than the actual wave. This indicates that on a sloping beach the bound long wave does not have "time" to attain local equilibrium but that it depends on its history. Therefore, on the slope the forced long wave does not increase with depth as $h^{-5/2}$ as is assumed in the analysis of field data in some papers (e.g., Elgar *et al.*, 1992; Herbers *et al.*, 1995).

In Fig. 2c the outgoing long wave (solid line) closely follows Green's Law (dashed line) which indicates that this wave is a free long wave. There are some oscillations noticeable around the dashed line because energy is traded back and forth with the incoming short wave group, as will be explained below.

Figure 2d shows the ratio of the amplitude of the outgoing wave and the incoming wave (the "reflection coefficient"). This ratio is by definition equal to unity at the shore. For the chosen parameter values, the ratio is larger than unity everywhere else, meaning that there is more energy in the outgoing wave than in the incoming wave, which indicates that energy has been transferred from the short waves to the long waves.

As a tool to study this energy transfer in more detail we can use the linear long wave energy equation

$$\frac{\partial E}{\partial t} + \frac{\partial E_f}{\partial x} + \frac{\bar{Q}}{h_o} \frac{\partial S_{xx}}{\partial x} = 0 \quad (12)$$

where E is the long wave energy, $E_f = \rho g \bar{\zeta} \bar{Q}$ is the energy flux and the third term represents the work the short waves do on the long wave through the radiation stress. Averaging over the IG-wave period (denoted by the double overbar) eliminates the temporal variation and yields a balance between the energy flux and the work

$$\frac{\partial \overline{\overline{E_f}}}{\partial x} + \frac{\overline{\overline{Q}}}{h_o} \frac{\partial \overline{\overline{S_{xx}}}}{\partial x} = 0 \quad (13)$$

The two terms can be each split into an incoming and outgoing part

$$\frac{\partial \overline{\overline{E_{f,i}}}}{\partial x} + \frac{\partial \overline{\overline{E_{f,r}}}}{\partial x} + \frac{\overline{\overline{Q_i}}}{h_o} \frac{\partial \overline{\overline{S_{xx}}}}{\partial x} + \frac{\overline{\overline{Q_r}}}{h_o} \frac{\partial \overline{\overline{S_{xx}}}}{\partial x} = 0 \quad (14)$$

Figure 3a shows the balance between the energy flux term (dashed line) and the work term (solid line) in (13) across the domain for the same parameter

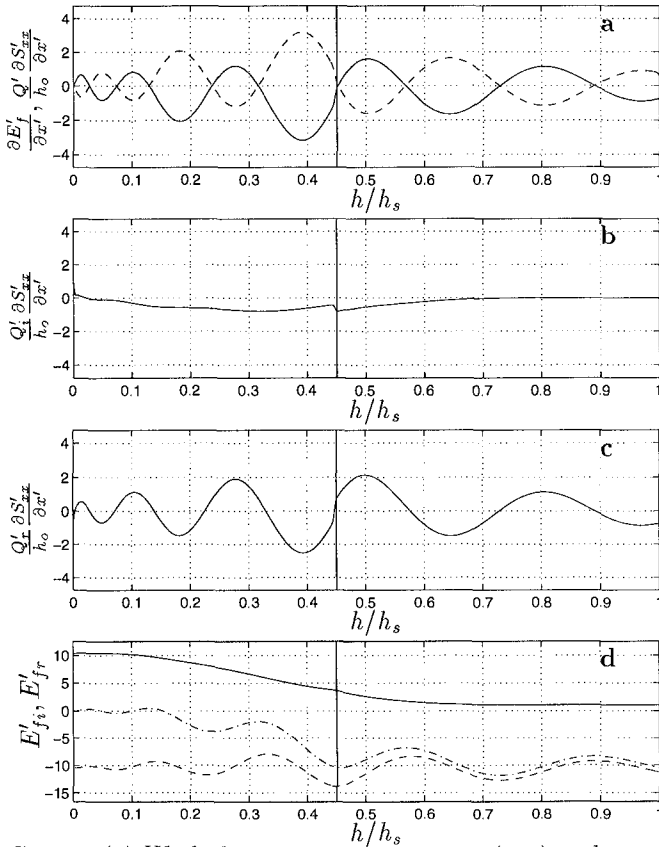


Figure 3: Case 1: (a) Work done on total long wave (—) and energy flux (- -); (b) Work on incoming long wave; (c) Work on outgoing long wave; (d) Energy flux of incoming wave (—), energy flux of outgoing wave (- -), and energy flux of total long wave (- .).

values as in Fig. 2. Both terms are normalized by $\rho g \sqrt{gh_s} \delta^2 a_{1,s}^4 / h_s^3$. Figure 3b shows the work done on the incoming wave which is the third term in (14). It is negative across the whole domain, which means that energy flux is gained. This is consistent with the finding of Fig. 2 that the incoming long wave increases faster in amplitude than a free long wave. Conversely, Fig. 3c reveals that the work done by the short waves on the outgoing long wave oscillates around zero, which means that energy is traded back and forth but that over the whole domain the long wave loses or gains very little energy. It essentially deshoals as a free long wave as was already seen in Fig. 2c.

In Fig. 3d the energy fluxes of the incoming, the outgoing and the total long wave motion are shown, normalized by $\rho g \sqrt{gh_s} \delta^2 a_{1,s}^4 / h_s^2$. Notice that the incoming wave already gains about 30% of energy flux seaward of the break point. The incoming long wave reaches its maximum energy flux at the shore-

line where it is fully reflected. The outgoing wave shows an oscillating energy flux. The total energy flux therefore becomes increasingly negative seawards as a consequence of the net transfer of energy from the short waves to the long wave.

Case 2a: moving breakpoint

The second case considered is that of a moving breakpoint ($\kappa = 1$) corresponding to the mechanism proposed by Symonds *et al.* (1982). The same parameter values as in case 1 are used.

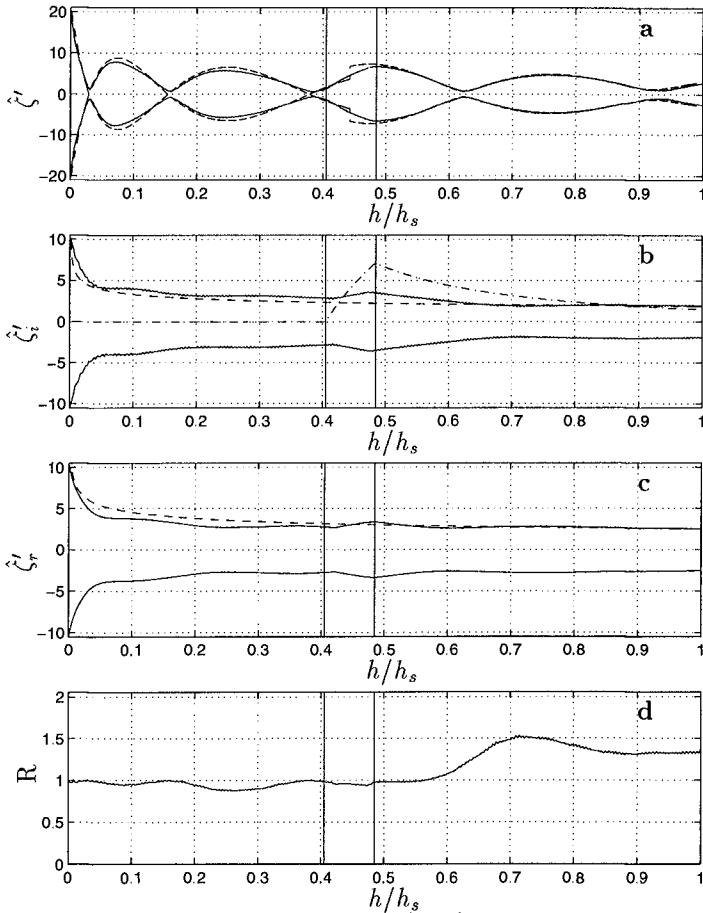


Figure 4: Case 2a: labels as Fig. 2. The breaking region is indicated by the vertical lines.

Figure 4a shows the comparison of the long wave envelope as predicted by the model and the analytical solution by S93. The differences are due to the fact that in the analytical solution the breaking region (ranging from $0.41 \leq h/h_s \leq 0.48$) is contracted into a point at $h/h_s = 0.45$ whereas the model is capable of reproducing the breaking region itself.

Up to the point where breaking starts, the incoming long wave in Fig. 4b gains energy flux as before. Over the breaking region, however, the energy flux is now decreasing, a feature which is investigated in more detail below. Inside the surf zone ($h/h_s \leq 0.41$) a standing long wave occurs due to the absence of forcing in that region, see Figs. 4b and c. Figure 4c shows that outside the surf zone the long wave again deshoals according to Green's Law.

Finally, the ratio of the amplitudes of the outgoing wave and the incoming wave is shown in Fig. 4d. Though the long wave energy is reduced through the breaking region the amplitude of the outgoing wave is still about equal to or larger than that of the incoming wave.

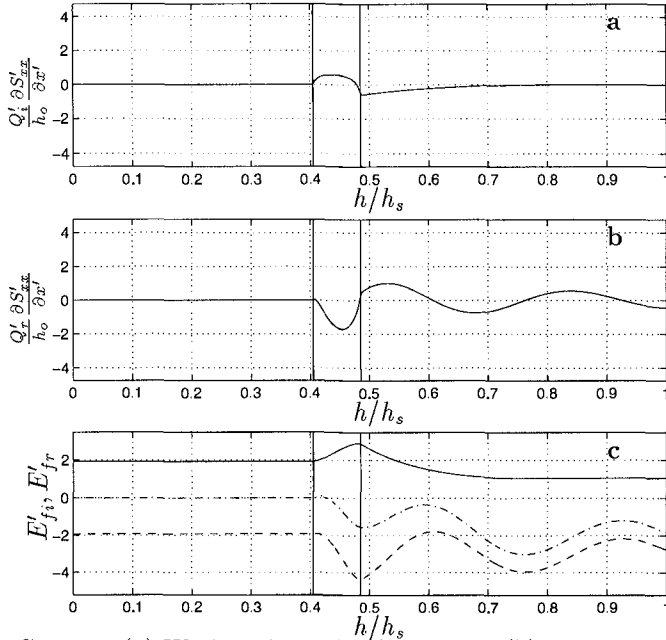


Figure 5: Case 2a: (a) Work on incoming long wave; (b) Work on outgoing long wave; (c) Energy flux of incoming wave (—), energy flux of outgoing wave (---) and energy flux of total long wave (-.-); The breaking region is indicated by the vertical lines.

This is further illustrated by the direct analysis of the energy transfer in Fig. 5. Panel (a) shows that in case 2a the work done on the incoming wave by the short waves in the breaking region itself is positive, which indicates an energy flux loss. This is consistent with the loss of amplitude shown in Fig. 4b. Inside the surf zone no forcing occurs, so the work is zero.

Fig. 5b shows that through the breaking region the work done on the outgoing wave is negative so that energy flux is *gained* (in magnitude) when the wave propagates out. Seaward of breaking the work is oscillating around zero as in case 1. The according energy fluxes of the incoming, outgoing and total wave are plotted in Fig. 5c.

Case 2b: moving breakpoint with halved forcing frequency

The results of case 2a are valid only for the chosen set of parameters. It turns out that a profound change occurs when the forcing frequency or the beach slope are varied. Either of these parameters control the number of wave groups in the surf zone, which is an important parameter, as will be shown below.

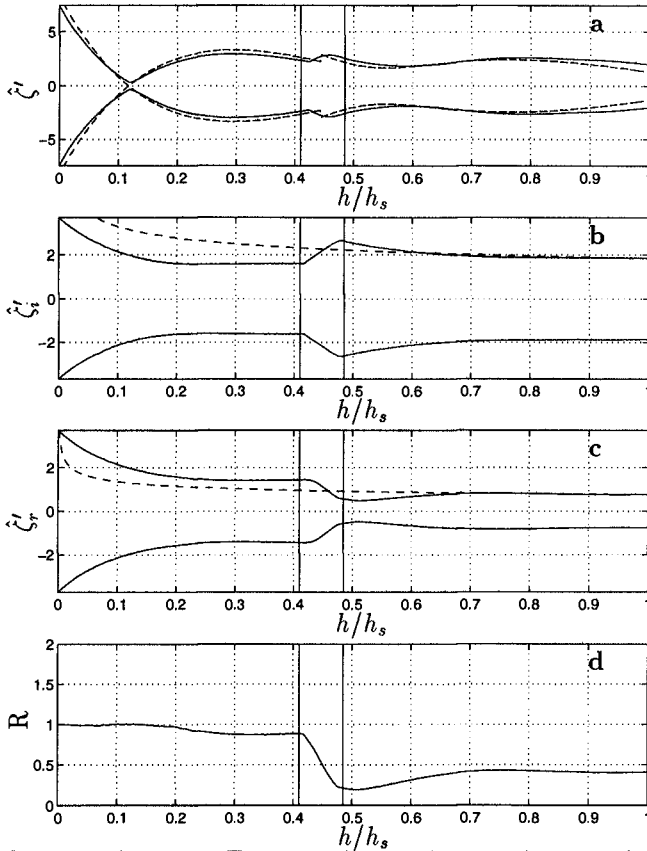


Figure 6: Case 2b: labels as Fig. 2. The breaking region is indicated by the vertical lines.

The conditions of case 2a are repeated except that the forcing frequency is halved, $\Delta\omega = 0.211 \text{ s}^{-1}$. Again the deviation between the model and the slightly simpler analytical solution is negligible (Fig. 6a). Fig. 6b shows that the amplitude of the incoming wave increases outside of the breaking region and decreases in the breaking region itself, similar to the previous case. Inside the surf zone forcing is absent and a standing wave occurs, see Figs. 6b and c. In this case, however, the outgoing long wave *loses* amplitude when propagating out through the breaking region (Fig. 6c). This results in a reflection coefficient less than unity outside the surf zone, i.e. the long waves have *lost* energy in the breaking process (Fig. 6d).

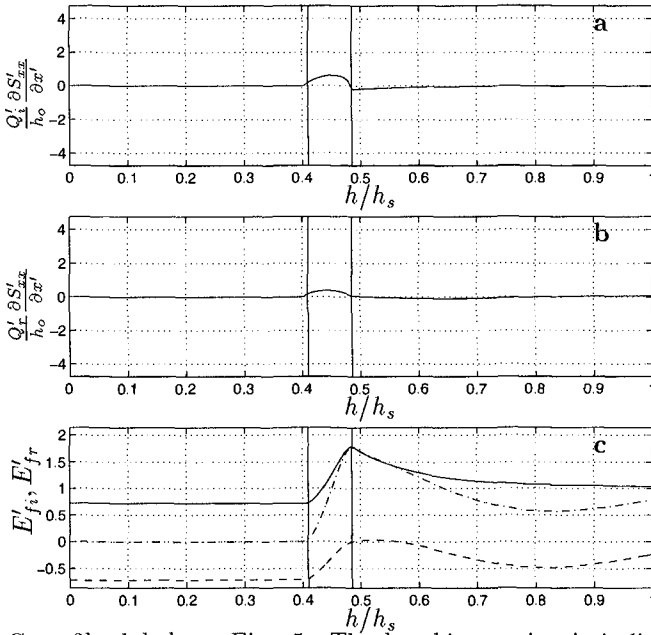


Figure 7: Case 2b: labels as Fig. 5. The breaking region is indicated by the vertical lines.

Analysis of the energy transfer using the terms in (14) confirms this result. Figure 7a is similar to Fig. 5a, but Fig. 7b shows that contrary to the previous case the work the short waves do on the outgoing long wave is now positive, which means that the energy flux decreases in magnitude as the long wave propagates out through the breaking region.

The reason for this different behavior is the phase difference between the short wave groups and the incoming and outgoing long waves. As the short waves propagate onto the beach, the phase shift between the associated incoming long wave and the groups grows from 0.5π to about 0.6π . This phase shift causes the work (which is the time-averaged product of the radiation stress gradient and the incoming long wave) to be negative so energy is transferred to the long waves. In the breaking region the forcing is varying in time (when the short waves in the group are smaller and break closer to shore) or constant (when the waves are larger and break further offshore). This causes the long wave-averaged work done on the incoming long wave to be positive in the breaking region. This behavior is independent of the period of the incoming wave groups.

With the destruction of the wave groups by the varying break point, the long wave is released in the breaking region and propagates shoreward as a free wave, where it is reflected and propagates seaward. The sign of the work that the short waves do on the outgoing wave is then dependent on the relative phase between them, which is a function of the time it takes the long wave to propagate through the surf zone and back. For a plane beach this time lag can be calculated as

twice the propagation time from the shore to the mean break point h_b :

$$\Delta T = 2 \int_0^{h_b} \frac{dh}{h_x \sqrt{gh}} = \frac{4}{h_x} \sqrt{\frac{h_b}{g}} \quad (15)$$

where $\Delta T = 44.5$ s in the cases considered here. In case 2a the ratio of the time lag ΔT to the group period $T_g = 2\pi/\Delta\omega$ is

$$\frac{\Delta T}{T_g} = \frac{2}{h_x} \sqrt{\frac{2a_b}{\gamma g}} \frac{\Delta\omega}{\pi} = 3 \quad (16)$$

This integer value means that the outgoing long wave is "in phase" with the incoming long wave in the breaking region (which is short relative to the long wave length). Because these waves propagate in opposite directions, the signs of the work terms are opposite as well. In case 2b the ratio $\Delta T/T_g$ is 1.5, which means the incoming and outgoing waves are in "anti-phase", which causes the work on the incoming and outgoing waves to have the same sign. The ratio $\Delta T/T_g$ essentially specifies the number of wave groups in the surf zone. As can be seen from (16) it depends on the forcing frequency, the beach slope and on the short wave amplitude at breaking. Instead of changing the forcing frequency, an equivalent variation of the beach slope would yield the same result.

This ratio is equivalent to the parameter \mathcal{X} which was already found by Symonds et al. (1982) and the slope parameter $S_b = h_x L_b/h_b$ used by SS88 where L_b is the length of the surf zone and h_b is the depth at breaking. Rewriting those parameters yields

$$\mathcal{X} \equiv \frac{\Delta\omega^2 h_b}{g h_x^2} = \frac{\pi^2}{4} \left(\frac{\Delta T}{T_g} \right)^2 = 4\pi^2 S_b^{-2} \quad (17)$$

IMPORTANCE OF NONLINEAR TERMS

To investigate the importance of nonlinearities on the results, the model is rerun with the parameters of case 2a but now using the nonlinear Equations (5) and (6). In this case it is impossible to linearly separate the incoming and outgoing long waves. Therefore, we will examine the terms in the nonlinear long wave equation, averaged over the IG-wave period

$$\frac{\partial}{\partial x} \overline{\left(\frac{1}{2} \rho \frac{Q^3}{h^2} + \rho g \zeta Q \right)} + \frac{\overline{Q}}{h} \frac{\partial \overline{S_{xx}}}{\partial x} + \overline{U \tau_{b,x}} = 0 \quad (18)$$

which is the nonlinear extension of (13). The work that the bottom friction is small and is neglected in the following. The energy flux and the work balance each other, as can be seen in Fig. 8a. It turns out that for the particular set of parameter values used here the same case run with the linearized equations (Fig. 8b) shows a change of sign of the terms. This is due to the fact that in the nonlinear version of the model the travel time ΔT is dependent on the still water depth h_o as well as the set-up $\bar{\zeta}$. In short, the set-up effectively changes the beach slope in the surf zone experienced by the long waves. Artificially including the mean set-up $\bar{\zeta}$ in the linear model reverses the sign of the terms, see Fig. 8c. In fact, it can be seen that Figs. 8a and c agree well, which indicates that the mean set-up is the most important nonlinear term.

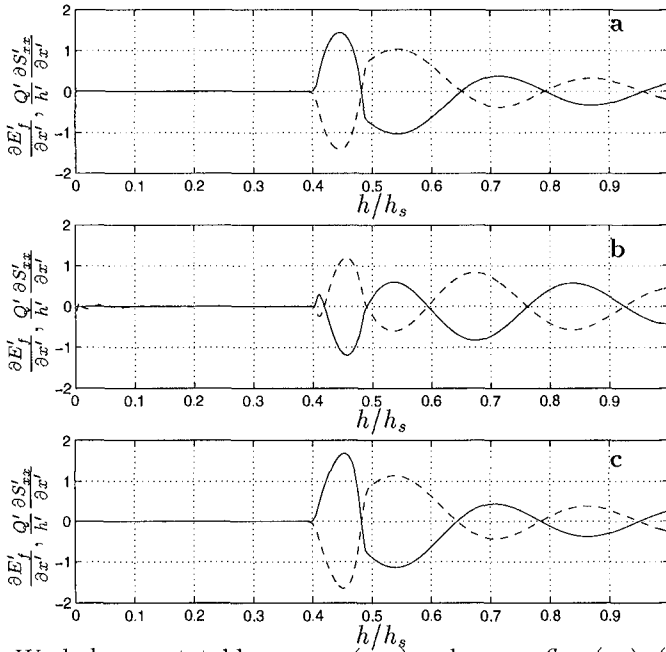


Figure 8: Work done on total long wave (—) and energy flux (- -): (a) Nonlinear version; (b) Linear version; (c) Linear version with mean set-up included in the depth.

CONCLUSIONS

The SHORECIRC model has been used to study infragravity wave generation. In the linear version of the model, the incoming and outgoing long waves can be separated. As expected, the incoming long wave already gains energy flux outside the surf zone due to the changing forcing but not nearly as fast as the local value of the LHS62 steady state theory for bound waves suggests. In the case of a fixed break point the energy flux gain continues inside surf zone, whereas in the case of a moving break point, it is found that the incoming wave loses energy flux in the varying break point region.

In the case of a fixed break point the outgoing long wave is seen to exchange energy flux with the short waves with very little net gain over the domain, so that it essentially deshoals according to Green’s Law. When the breakpoint is allowed to move, however, the outgoing wave either gains or loses flux depending on the phase between the short wave forcing and the outgoing wave. This gain or loss is dependent on a parameter which represents the number of wave groups in the surf zone. This result may explain the variation in the ratio of outgoing to ingoing wave energy found in field data.

Extending the model to include the nonlinear terms shows the importance of the steady set-up over the other nonlinear terms.

ACKNOWLEDGMENTS

Dr. H.A. Schäffer is gratefully acknowledged for making available his surf-beat computer code. This work is a result of research sponsored by NOAA Office of Sea Grant, Department of Commerce, under Award No. NA 56 RG 0147 (Project No. R/OE-17), by the U.S. Army Research Office, University Research Initiative under Contract No. DAAL03-92-G-0116 and Office of Naval Research (contract no. N00014-95-1-0075). The U.S. Government is authorized to produce and distribute reprints for government purposes notwithstanding any copyright notation that may appear herein.

REFERENCES

- Elgar, S., T.H.C. Herbers, M. Okihiro, J. Oltman-Shay and R. T. Guza (1992). Observations of infragravity waves. *Journal of Geophysical Research*, 97, pp. 15,573-15,577.
- Guza, R.T. and E.B. Thornton (1985). Observations of surf beat. *Journal of Geophysical Research*, 90, C2, pp. 3161-3171.
- Herbers, T.H.C., S. Elgar, R.T. Guza and W.C. O'Reilley (1995). Infragravity-Frequency (0.005-0.05 Hz) motions on the shelf. Part II: Free waves. *J. Phys. Oceanogr.*, 25, pp. 1063-1079.
- Kostense, J.K. (1984). Measurements of surf beat and set-down beneath wave groups. *Proc. of the 19th ICCE*, pp. 724-740.
- Longuet-Higgins, M.S. and R.W. Stewart (1962). Radiation stress and mass transport in gravity waves with application to 'surf-beats'. *J. of Fluid Mech.*, 8, pp. 565-583.
- Mei, C.C. (1983). The applied dynamics of ocean surface waves. John Wiley and Sons, New York, 740 pp.
- Munk, W.H. (1949). The solitary wave theory and its application to surf problems. *Annals of the New York Academy of Sciences*, 51, pp. 376-424.
- Schäffer, H.A. (1993). Infragravity waves induced by short-wave groups. *J. Fluid Mech.*, 247, pp. 551-588.
- Schäffer, H.A. and I.A. Svendsen (1988). Surf beat generation on a mild slope beach. *Proc. of the 21st ICCE*, pp. 1058-1072.
- Svendsen, I.A. and U. Putrevu (1996). Surf zone hydrodynamics. In *Advances in Coastal and Ocean Engineering*, Vol. 2, World Scientific Publ., pp. 1-78.
- Symonds, G., D.A. Huntley and A.J. Bowen (1982). Two dimensional surf-beat: Long wave generation by a time-varying break point. *J. of Geoph. Res.*, 87, C1, pp. 492-498.
- Tucker, M.J. (1950). Surf beats: sea waves of 1 to 5 minute period. *Proceedings of the Royal Society of London, A*, 202, pp. 565-573.
- Van Dongeren, A.R., F.E. Sancho, I.A. Svendsen and U. Putrevu (1994). SHORECIRC: A quasi 3-D nearshore model. *Proc. of the 24th ICCE*, pp. 2741-2754.
- Van Dongeren, A.R., I.A. Svendsen and F.E. Sancho (1995). Application of the Q-3D SHORECIRC model to surfbeat. *Proc. Coastal Dynamics*, pp. 233-244.
- Van Dongeren, A.R. and I.A. Svendsen (1996). An absorbing-generating boundary condition for shallow water models. Submitted to *J. of Wat., Port, Coastal and Ocean Eng.*

CHAPTER 105

RESPONSES OF COASTAL TOPOGRAPHY TO SEA-LEVEL RISE

Nobuo Mimura¹, Member ASCE and Eiichi Kawaguchi²

ABSTRACT

The impacts of sea-level rise induced by global warming on sandy beaches and sediment deposition around the river mouth are assessed. The exacerbated erosion by sea-level rise is evaluated in a national scale for Japan, on the basis of the Bruun Rule assuming the existence of the equilibrium beach profile. The eroded area reaches 56.6, 81.7, and 90.3% of the total area of the existing beaches for the sea-level rises of 30, 65, and 100cm, respectively. The effects on sandy beaches is extremely large, since such erosion superposes on the already existing erosion. The effect of sea-level rise on the river mouth is also examined by a numerical model. The place of sand deposition changes from the river mouth to the upper reaches along the river as the mean sea level rises higher. Higher risk of flooding is anticipated because of the rise of river floor and the backwater effect of sea-level rise.

INTRODUCTION

It is anticipated that global warming will bring about accelerated sea-level rise through thermal expansion of ocean water and melting of land-based glaciers, and climate change such as changes in precipitation and tropical cyclones. IPCC(1990) projected that the mean sea level would rise 65cm by the year 2100, with an uncertain range of 30 to 110cm in its first report. The best estimate for the sea-level rise has been revised to 50cm by 2100 in the second assessment report(IPCC, 1996), as shown in Fig.1. If climate change and sea-level rise occur in future as estimated, they can impose a variety of impacts on the natural environment and human society in the coastal zones. Since most coasts in the world consist of natural geographic features, such as sandy beach, dune,

¹ Professor and ² Graduate student, Department of Urban and Civil Engineering, Ibaraki University, 4-12-1 Nakanarusawa, Hitachi, Ibaraki 316, Japan

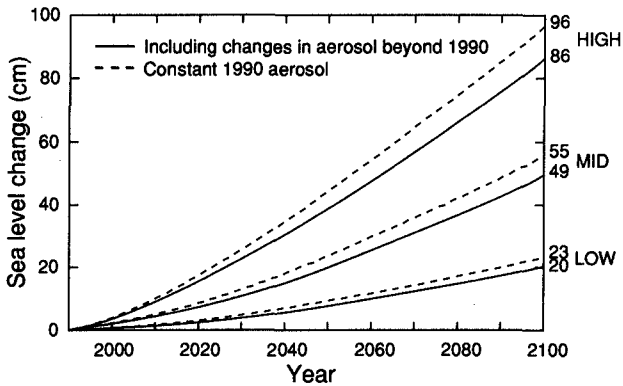


Fig.1 Projections of global sea level(IPCC, 1996)

delta and river mouth, wetlands and coral reef, a concern has arisen about what and how serious the impacts of sea-level rise and climate change on them will be. As the natural geographic features show particular adaptive responses to the changes in external conditions, it is necessary to estimate such responses of the coastal topography in order to evaluate the impacts of sea-level rise and climate change. This paper is an attempt toward this direction focusing on sandy beaches and river mouth.

IMPACTS ON SANDY BEACHES

Outline of the predictive model

Topographic changes of sandy beaches are caused by cross-shore and longshore sediment transport. Sea-level rise due to global warming acts uniformly on the world coasts, though the amount of the rise relative to the land differs place to place because of the uneven distributions of sea temperature rise, plate movement, and local land subsidence, etc. Therefore, it is assumed, as the first step of assessment, that local factors for the beach topographic change, such as sources of sediment supply and the longshore transport, can be neglected. Under such assumption, the response of sandy beaches to the sea-level rise is considered to take place only in the cross-shore direction, i.e. as beach profile change.

A sandy beach is eroded by sea-level rise more than simple inundation. If there is an equilibrium form of the beach profile, the sandy beach changes toward forming a new equilibrium profile for the increased sea level, as shown in Fig.2. This concept is known as the Bruun Rule (Bruun, 1962), and a number of predictive models have been developed on its basis. The Bruun Rule-based models has been calibrated by Mimura et al.(1995) by correlating the land subsidence due to pumping up ground water, i.e. relative sea-level rise, and the resultant retreats of the shoreline in Niigata, Japan. Equation (1) is often

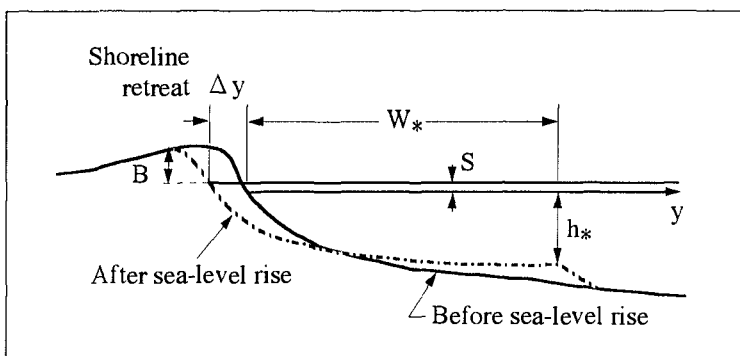


Fig.2 Response of the beach profile to sea-level rise

used to represent the equilibrium beach profile.

$$h = Ay^{2/3} \quad (1)$$

where, h is water depth at an offshore distance y from the shoreline, and A is a shape coefficient determined for the individual beach. The amount of shoreline retreat, Δy , can be calculated by balancing the sediment volumes eroded in the foreshore and transported offshore (Dean, 1991; Mimura et al., 1993). The formula derived by Dean is as follows.

$$\Delta y + \frac{3}{5} \frac{h_* W_*}{B} \left(1 + \frac{\Delta y}{W_*}\right)^{5/3} = \frac{3}{5} \frac{h_* W_*}{B} - \left(\frac{S}{B} W_*\right) \quad (2)$$

Mimura et al. (1993) took into account the foreshore slope in the calculation, whereas Dean (1991) assumed that the foreshore above the mean sea level was vertical. However, as there were no significant difference in the shoreline retreat calculated by the two formulas, Eq. (2) was used in this study.

Data and Calculation

In order to apply the Bruun Rule-based model, it is necessary to know the height of berm, B , critical depth of sediment movement in the offshore region, h_* , and the median diameter of sand to determine A . The first two parameters, i.e. B and h_* , can be estimated by the existing studies such as Takeda and Sunamura (1983) and Hallermeier (1981) if the wave conditions and the average slope of the beach are given. Therefore, the necessary data for the calculation are at least the dimensions of incident waves, the sediment diameter and the average beach slope.

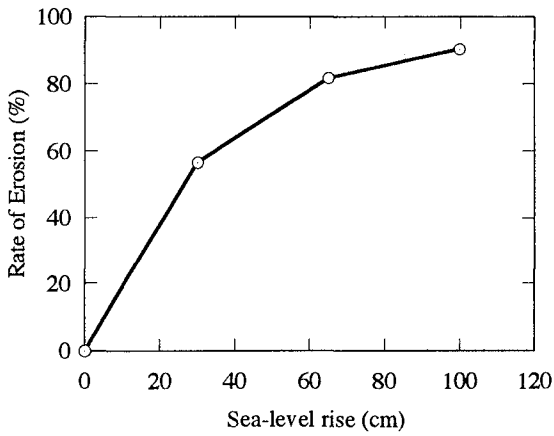


Fig.3 Nation-wide average of erosion rate with sea-level rise

Table 1 Present situation of Japanese coasts and impacts of sea-level rise

Total coastline	34,386 km
Sandy beaches	
Length	5,508 km
Area	191 km ²
Ave. Width	35 m
Sandy beaches eroded (past 70 yrs)	125 km ²
Impact of SLR	
0.3 m	108 km ²
0.65 m	156 km ²
1 m	173 km ²

The Japanese coastline of about 34,000 km in length is divided into 9,688 segments for the purpose of management by four governmental ministries and agency. About one sixth of the total length is occupied by sandy beaches as indicated in Table 1. It was fortunate for us to be able to use the results of a national coastal survey carried out by the related ministries in 1993. The coastal survey covered the length, width and average slope of the beach. The data of incident waves were collected from this survey, Sugahara et al.(1986), and field measurements where available. These data were used to determine the height of berm, B , the critical depth of sediment movement, h_c , and the shape-factor, A . Then the amounts of shoreline retreat, Δy , was calculated for each sandy beach using Eq.(2).

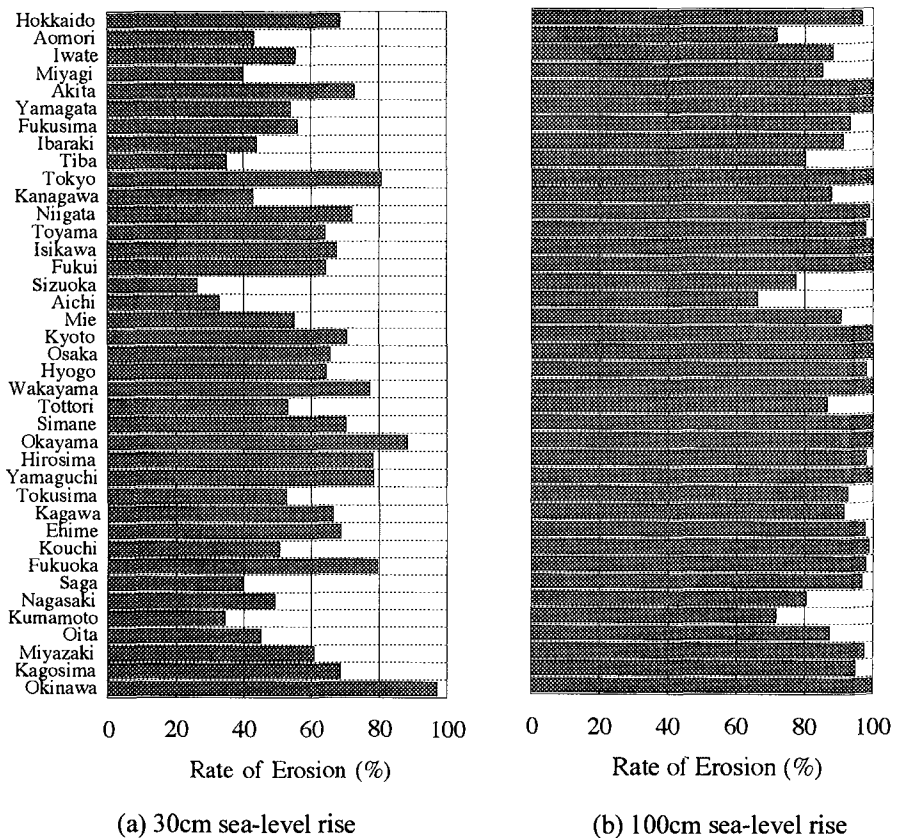


Fig.4 Distribution of erosion rate with prefectures

Regarding the sea-level rise, three scenarios of 30, 65, and 110cm rise were used according to IPCC(1990). The best estimate of sea-level rise by the year 2100 has been revised from 65 cm in IPCC(1990) to 50cm in IPCC(1996) as mentioned above. However, the scenarios used in this study are still useful to examine the possible range of the impacts.

Sea level rise-induced erosion estimated for the Japanese beaches

The results of the estimation for the area of erosion are shown in Fig. 3 and 4. Figure 3 shows the national summary of the percentage of eroded area, which is called the erosion rate here. A 30 cm sea-level rise would erode 11,775 ha or 56.6% of the present sandy beaches in Japan. The total area eroded for the past about seventy years was 12,880 ha, which was estimated by the comparison between old and the present topographic maps by Tanaka et al. (1993). Therefore, the area to be eroded by a 30 cm sea-level rise is comparable to that occurred for the past several tens years. It is surprising that even a 30cm rise of mean sea level would cause such severe erosion. If the sea-level rise becomes 65cm and 100cm, 81.7% and 90.3% of the present sandy beaches will disappear by erosion, respectively. Table 1 shows a summary of the present situation of the Japanese coasts and the estimated impacts.

In Fig. 4, the distributions of the estimated erosion rate are shown with coastal prefectures which are thirty-nine out of forty-seven prefectures in total. The areas eroded by 30cm sea-level rise range from 24 to 95% of the existing beaches. If the sea-level rise reaches 1 m, most prefectures would lose more than 90% of their beaches. Large differences in the erosion rate can be seen among prefectures in Fig. 4. Figures 5 and 6 show the relationships between the erosion rate, and the significant wave height of the incident waves and beach width of the coastal segments. There is no apparent correlation between the erosion rate and the significant wave height, while it decreases clearly with the beach width. Such tendencies indicate that there are no large differences in the amount of the shoreline retreat among beaches for the same sea-level rise, and that narrow beaches tend to disappear early as the sea-level rise proceeds.

It is quite natural that beach erosion due to sea-level rise will superpose on those by other mechanisms such as lack of sediment supply and imbalance of the longshore transport. Therefore, the role of sea-level rise is to exacerbate the present trend of beach erosion.

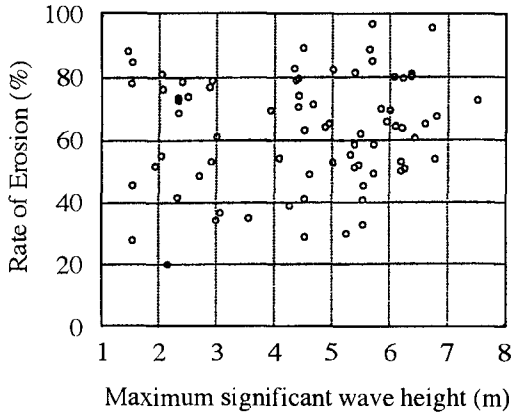


Fig.5 Relationship of erosion rate and incident wave height

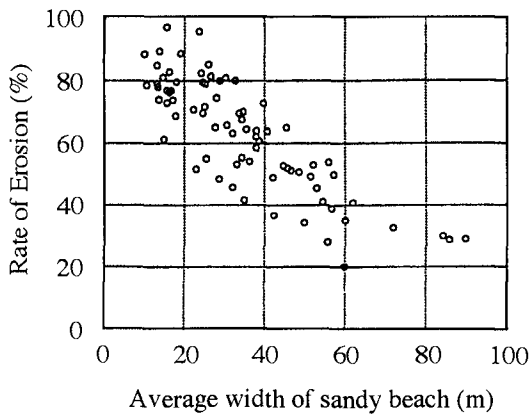


Fig.6 Relationship of erosion rate and beach width

IMPACTS ON RIVER MOUTH

Applied model

The topographic change of river mouth consists of complicated interactions of river and marine forces, and topography, so the response to sea-level rise must vary widely from place to place. Therefore, it seems more appropriate to take a simple case to study the basic phenomena related to the sea-level rise. In this study, a small-scaled and simplified model of the river mouth was studied on a basis of the numerical simulation.

The numerical model developed by Sawai et al.(1993) was used, since it has been verified to simulate the results of laboratory experiments well. The model consists of two sub-models; one is to calculate the flow field based on the equations of continuity and momentum, and the other the sediment transport and topographic changes. The equations are as follows.

1) Flow field

$$\frac{\partial \zeta}{\partial t} + \frac{\partial}{\partial x} [(\zeta + h)u] + \frac{\partial}{\partial y} [(\zeta + h)v] = 0 \quad (3)$$

$$\frac{\partial u}{\partial t} + u \frac{\partial u}{\partial x} + v \frac{\partial u}{\partial y} - fv + g \frac{\partial \zeta}{\partial x} - A_h \left(\frac{\partial^2 u}{\partial x^2} + \frac{\partial^2 u}{\partial y^2} \right) + \frac{gu\sqrt{u^2 + v^2}}{(\zeta + h)C^2} = 0 \quad (4)$$

$$\frac{\partial v}{\partial t} + u \frac{\partial v}{\partial x} + v \frac{\partial v}{\partial y} + fu + g \frac{\partial \zeta}{\partial y} - A_h \left(\frac{\partial^2 v}{\partial x^2} + \frac{\partial^2 v}{\partial y^2} \right) + \frac{gv\sqrt{u^2 + v^2}}{(\zeta + h)C^2} = 0 \quad (5)$$

where, ζ is elevation of water surface, u and v components of velocity, h local water depth, f the Coriolis factor, A_h vertical eddy viscosity, C Cezy's coefficient of friction, and g the gravitational acceleration.

2) Topographic change

$$\frac{\partial z}{\partial t} + \frac{1}{1-\lambda} \left(\frac{\partial q_x}{\partial x} + \frac{\partial q_y}{\partial y} \right) = 0 \quad (6)$$

where, q_x and q_y are sediment transport rates, and λ is the void ratio of the sand layer.

Regarding the sediment transport rate, the longitudinal and transverse components are given separately for bed and suspended loads. In the calculation of topographic change by bed load, the effect of gravity was taken into account to prevent the slope of the local topography from becoming too steep.

The model of river mouth consists of a straight river and rectangular sea as shown in Fig. 7. The conditions of flow rate and sediment discharge were given at the uppermost boundary of the river, and were kept constant for all the calculations. Three scenarios of sea-level rise were assumed as shown in Fig. 8, i.e. no sea-level rise, slow and fast rise scenarios.

Results of calculations

The calculated profiles along the river channel are indicated in Fig. 9 (a)~(c), while three-dimensional pictures of the results are shown in Fig. 10. Figure 9 (a) is for the case

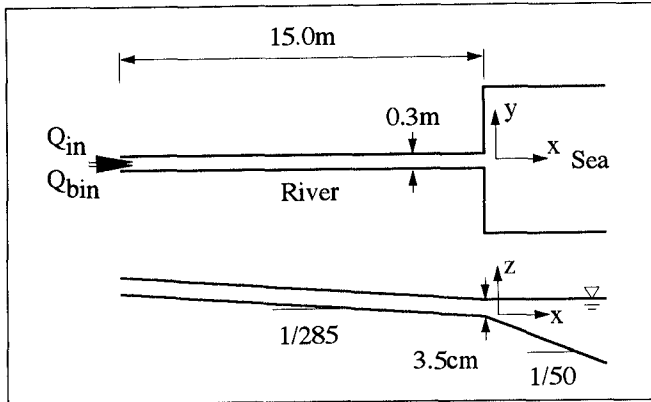


Fig.7 Model of river mouth

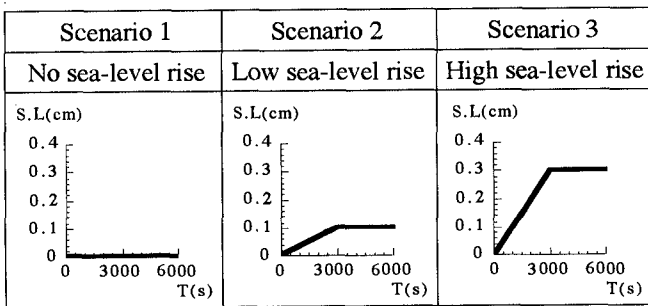
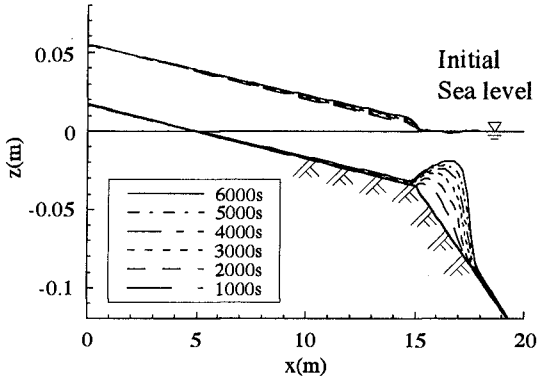


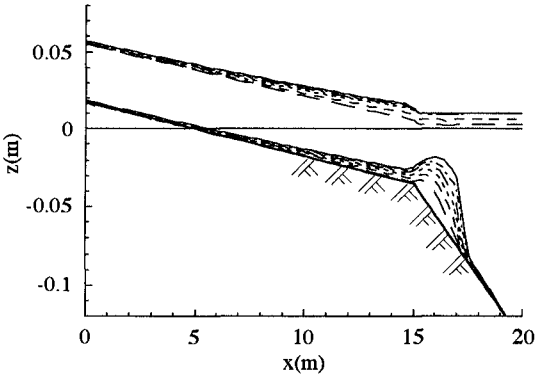
Fig.8 Assumed scenarios of sea-level rise

case of no sea-level rise, showing that a terrace is forming around the river mouth as time proceeds. After the terrace reached some length in the cross-shore direction, it stopped growing in that direction and started to expand in the longshore direction. In the case of no sea-level rise, little deposition of sand takes place on the river floor.

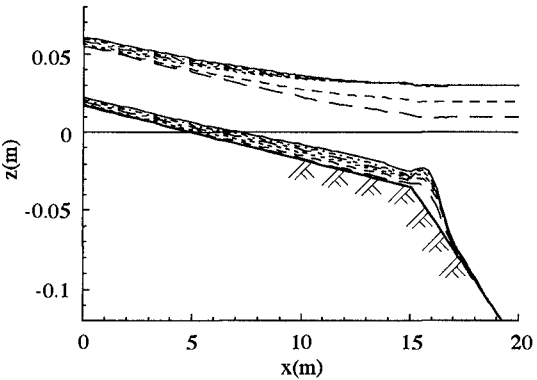
Figures 9(b) and (c) show the results for the cases of slow and fast sea-level rise. The water surface of the river tends to increase due to the backwater effect as the sea level rises. The significant feature of these cases is that the deposition of sediment occur along the river channel with the increase of river water surface, even in the upper reach. As the deposition on the river floor takes place, the terrace to be formed around the river mouth stay small compared with the no sea-level rise case. When the elevation of river floor is increased by sand deposition, this makes the river surface higher in addition to the backwater effect. According to such feedback mechanism, the area of sediment deposition moves further upstream.



(a) Scenario 1 (No sea-level rise)

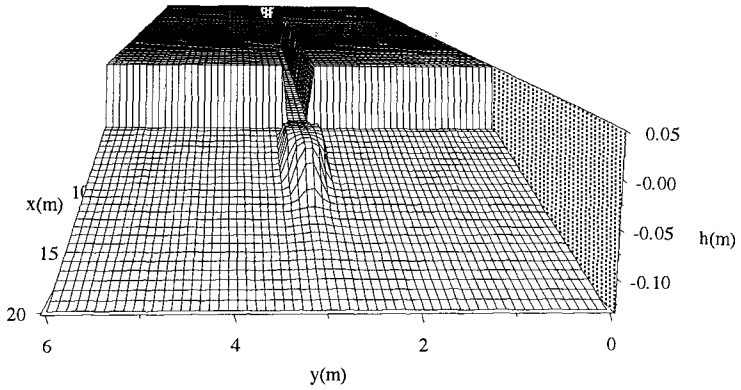


(b) Scenario 2 (Low sea-level rise)

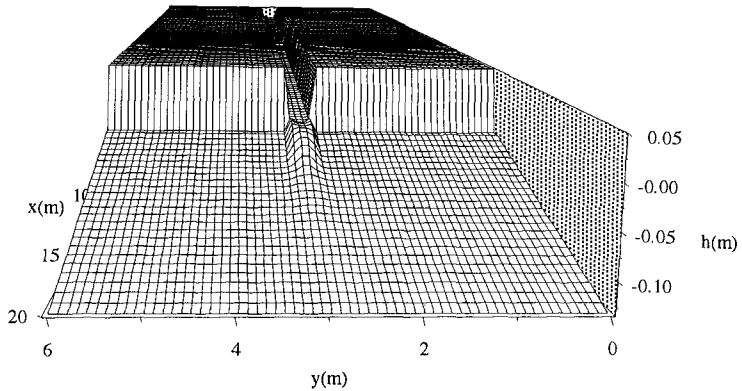


(c) Scenario 3 (High sea-level rise)

Fig.9 Topographic changes of river mouth with different sea-level rise scenarios



(a) No sea-level rise



(b) High sea-level rise

Fig.10 Three-dimensional picture of the topographic changes around river mouth

The combined effects of sea-level rise and sand deposition along the river floor exacerbate the potential danger of river flood. Attention has to be paid to this phenomena, as a possible impact of sea-level rise.

CONCLUSIONS

In the present paper, responses of coastal topography to sea-level rise and related impacts have been examined. Regarding the beach erosion, the nation-wide assessment revealed that the effect of sea-level rise is extremely large; even a 30 cm sea-level rise may cause beach erosion comparable with that took place for the past 70 years. Keeping

such fact in mind that the sea level rise-induced erosion superposes on the existing erosion, it is necessary to pay careful attention to the future trend of sea-level rise.

Regarding the impacts on the river mouth, sea-level rise has two effects; one is the backwater effect to increase the water level along the river, the other the changes in the place of sediment deposition. If the scale of sea-level rise is large, the deposition of sand transported by rivers will move upstream. Both effects act to increase the water level along the river, suggesting that the risk of river flooding would increase. Since the analyses performed in this study were rather simple, further studies are needed to evaluate the impacts of sea-level rise on the complicated situation of real river mouths.

The authors wish to thank the Ministries of Transport, Public Works, and Agriculture and Prof. Yamaguchi of Ehime University for providing the coastal data, and Prof. Sawai of Setsunan University for giving advice on the calculation of river mouth topography.

REFERENCES

- Bruun, P.(1962): Sea-level rise as a cause of shore erosion, *Jour. Waterways and Harbors Division, ASCE*, 88(WW1), pp.117-130.
- Dean, R.G.(1991): Equilibrium beach profiles: characteristics and applications, *Jour. Coastal Research*, 7(1), pp.53-84.
- Hallermeir, R.J.(1981): A profile zonation for seasonal sand beaches from wave climate, *Coastal Engineering*, 4, pp.253-277.
- IPCC(1990): *Climate Change-The IPCC Scientific Assessment*, Cambridge University Press, 365p.
- IPCC(1996): *Climate Change 1995-The Science of Climate Change*, Cambridge University Press, 572p.
- Mimura, N., M. Kiyohashi and K.Inoue (1993): Impacts of sea-level rise on sandy beaches, *Proc. Coastal Engineering, JSCE*, 40, pp.1046-1050 (in Japanese).
- Mimura, N. and H. Nobuoka(1996): Verification of the Bruun Rule for the estimation of shoreline retreat caused by sea-level rise, *Coastal Dynamics '95, ASCE*, pp.607-616.
- Sawai, K. and J. Sheng(1993): Study on the deposition control around the river mouth by tidal reservoir, *Jour. Hydro-science and Hydraulic Engineering, JSCE*, 37, pp.729-736 (in Japanese).
- Sugahara, K. et al.(1986): *Wave Statistics with 15-year Data in the Coastal Wave Observation Network*, Technical Note No.554, The Port and Harbor Research Institute, Ministry of Transport, 872p (in Japanese).
- Tanaka, S., M. Koarai and M. Fukazawa(1993): Coastal changes in Japan measured by comparison of topographic maps, *Proc. Coastal Engineering, JSCE*, 40,pp.416-420(in Japanese).
- Takeda, I. and T. Sunamura (1983): Topographic evolution of sandy beaches in the accretion process, *Proc.30th Japanese Conference on Coastal Engineering, JSCE*, pp.254-258 (in Japanese).

CHAPTER 106

Numerical Study of Low Frequency Surf Zone Motions

H. Tuba Özkan-Haller¹ and James T. Kirby²

Abstract

This paper describes the application of a model of the two dimensional shallow water equations to the growth of instabilities of the longshore current at SUPERDUCK on October 18th. Simulations are carried out using two initial current profiles. In the first case the initial longshore current profile results from a balance between bottom friction, the radiation stress gradient and lateral mixing due to turbulence. In the second case lateral mixing is neglected. The shear wave climates resulting from both simulations are analyzed and compared to data. In the first case the energy in the shear wave band is underpredicted whereas in the second case, it is overpredicted. In both cases, the initial longshore current profile changes due to lateral mixing induced by the shear instabilities. The resulting longshore current profile after shear instabilities have reached finite amplitude is found to be very similar for both cases.

Introduction

Surf zone current measurements from experiments such as SUPERDUCK, Delilah, NSTS at Leadbetter beach, and others show that a variety of low frequency motions, such as edge waves, leaky waves, surf beat, rip currents and shear waves exist in the surf zone. These motions coexist and interact with each other as well as the short wave climate. Among these low frequency motions shear waves have been identified most recently. They were seen in current data from the SUPERDUCK experiment by Oltman-Shay *et al.* (1989) as a meandering of the longshore current over time scales up to $O(1000\text{ s})$. During the SUPERDUCK experiment a longshore array of current meters was positioned in the surf zone of a predominantly north-south tending beach at Duck, NC. A storm hit Duck on the 15th of October and caused a fairly stationary short wave field from the north quadrant through the 18th of October. During this four day period the shear wave climate was very energetic.

Time series of current measurements from one of the current meters in the surf zone for the 18th of October clearly show the meandering character of the

¹Graduate Student, Center for Applied Coastal Research, University of Delaware, Newark, DE 19716, USA. E-mail: ozkan@coastal.udel.edu

²Professor, Center for Applied Coastal Research, University of Delaware, Newark, DE 19716, USA.

longshore current (Figure 1). Using five current meters from the longshore surf zone array, frequency-longshore wavenumber spectra can be computed. Such a spectrum for the longshore current velocities on the 18th of October is shown in Figure 2. Shear waves are readily distinguishable from edge waves due to the low range of frequencies they occupy as well as their nearly nondispersive character.

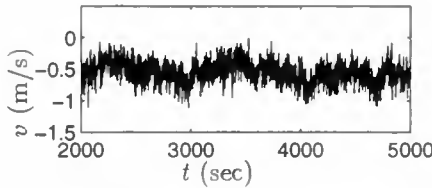


Figure 1: Time series of longshore velocity from gage LS07, SUPERDUCK field experiment, October 18th.

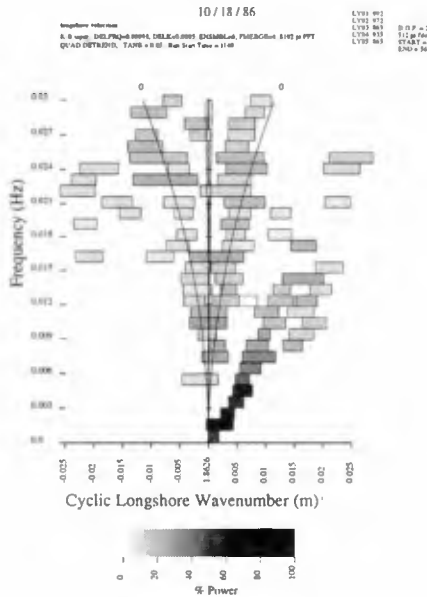


Figure 2: Frequency-longshore wavenumber spectrum for longshore velocity, SUPERDUCK field experiment, October 18th.

Bowen and Holman (1989) attributed these disturbances to instabilities of the longshore current. Analytical and numerical linear instability analyses were carried out by various investigators such as Dodd and Thornton (1990), Dodd *et al.* (1992), Dodd (1994), Putrevu and Svendsen (1992) and Falqués and Iranzo (1994). In these studies an initial current over a given bottom bathymetry is analyzed. Results show that longshore currents are unstable to longshore periodic perturbation in many cases.

In order to study these disturbances as they reach finite amplitude, a non-linear analysis needs to be employed. Such analyses were, to date, carried out by Dodd and Thornton (1992), Falqués *et al.* (1994), Özkan and Kirby (1995) and Allen *et al.* (1996). In these studies the spirit of a linear instability analysis is preserved since an initial current is generated and subsequently the temporal growth of the instabilities to finite amplitude is observed. In addition, Deigaard *et al.* (1994) performed a study where the longshore current was generated by ramping the short wave forcing. In their study the strengthening of the longshore current and the spatial growth of the instabilities were observed simultaneously.

In this study, we seek to find out whether or not instabilities of the longshore current are the source of the low frequency energy observed during the SUPER-DUCK experiment and to assess the importance of lateral mixing caused by shear instabilities. For this purpose we choose to simulate the low frequency climate on October 18th. Linear instability calculations for this day were previously carried out by Dodd *et al.* (1992) assuming straight and parallel bottom contours and a stationary wave field. Their results showed good agreement between the range of linearly unstable wavenumbers with observation as well as agreement between the linear prediction for the speed of propagation of the disturbances with observation.

Here, the analysis by Dodd *et al.* (1992) is taken one step further by carrying out a similar analysis using nonlinear computations. The assumption of straight and parallel bottom contours is retained, and it is also assumed that a stationary wave field forces an initial longshore current profile that subsequently becomes unstable. The instabilities are observed to grow to a finite amplitude and comparisons to data are made.

In the following, the governing equations of the model and their solution technique are discussed briefly. The generation of the initial longshore current profile is also documented along with results for the shear wave calculations and comparisons to data. For a detailed description of the numerical methods employed the reader is referred to Özkan-Haller and Kirby (1996a) where the application of the model to subharmonic edge waves is also documented.

Governing Equations

The governing equations are the nonlinear shallow water equations with added short wave forcing and bottom friction terms.

$$\begin{aligned}
 \frac{\partial \eta}{\partial t} + \frac{\partial}{\partial x}[u(h + \eta)] + \frac{\partial}{\partial y}[v(h + \eta)] &= 0 \\
 \frac{\partial u}{\partial t} + u \frac{\partial u}{\partial x} + v \frac{\partial u}{\partial y} &= -g \frac{\partial \eta}{\partial x} - \tau_{bx} \\
 \frac{\partial v}{\partial t} + u \frac{\partial v}{\partial x} + v \frac{\partial v}{\partial y} &= -g \frac{\partial \eta}{\partial y} + \tau_y - \tau_{vy}.
 \end{aligned} \tag{1}$$

Here, η is the water surface elevation above the mean water level, h is the depth with respect to the mean water level, u and v are the depth-averaged current velocities in the x and y directions, respectively, where x points offshore and y points in the longshore direction. The parameter τ_y represents the effect of the

short wave forcing in the y direction. The bottom friction is modeled using a linear representation assuming a small angle of wave incidence and weak mean longshore currents in relation to the horizontal wave orbital velocities, such that τ_{bx} and τ_{by} are given by

$$\tau_{bx} = \frac{\mu}{h + \eta} u, \quad \tau_{by} = \frac{\mu}{h + \eta} v, \quad (2)$$

where

$$\mu = \frac{2}{\pi} c_f u_0. \quad (3)$$

Here, u_0 is the horizontal orbital velocity of the short waves and can be expressed in terms of the wave height (Dodd *et al.*, 1992).

In order to estimate the term τ_y the short wave climate has to be considered. The bottom bathymetry at SUPERDUCK on October 18th is depicted in Figure 3a. It is characterized by a steep foreshore slope, a sand bar about 60 m offshore, and a milder offshore slope. The bathymetry on this day was fairly uniform in the longshore direction (Dodd *et al.*, 1992). The incident wave field measured at 8 m water depth consisted of waves from the north quadrant at about 15° to the beach inducing a southward longshore current. The root-mean-square (rms) wave height was about 1 m with a peak period around 5 sec.

In order to simulate the transformation of these random waves into shallow water, the wave height transformation model by Whitford (1988) which is based on Thornton and Guza (1983) is used. This model assumes random waves with Rayleigh distributed wave heights as well as wave stationarity and straight and parallel contours. The applicability of these assumptions to the SUPERDUCK experiment is discussed in Whitford (1988). The results of this model for the conditions on October 18th are given in Figure 3b. The waves are predicted to break at the seaward side of the bar, the breaking process stops at the shoreward side and strong breaking occurs on the foreshore slope.

Model Setup

The radiation stress gradient resulting from the short wave motion can now be computed. In the presence of this steady forcing and in the absence of any fluctuating motions a steady longshore current $V(x)$ would result, representing a balance between the radiation stress gradient, bottom shear stress, and lateral momentum mixing. The simplest formulation of the longshore balance neglects turbulent momentum exchange and incorporates a linearized bottom stress. The longshore current profile that would result from such a balance will have two peaks, one around the location of the bar crest and another close to the shoreline. This is due to the prediction that waves break as they approach the crest of the bar, cease to break as they travel into the trough region of the bar and break again on the shore. This mechanism causes two distinct areas of radiation stress forcing, hence the two peaks in the current which can be seen in Figure 3c.

In reality, however, significant currents are observed in the trough regions of barred profiles. A mixing mechanism is required to model such a case. The mixing can be due to many factors such as turbulent momentum mixing (Battjes,

1975), the contribution to the radiation stress by the rollers of breaking waves (Lippman *et al.*, 1995) and effects of depth variations of the nearshore currents (Svendsen and Putrevu, 1994). All of these mechanisms have the tendency to smooth the longshore current profile. As a simple but representative case of the effect of such mechanisms on the shape of the longshore current profile, turbulent momentum mixing is considered. The addition of a lateral mixing term (Battjes, 1975) into the mean longshore current balance decreases the magnitude of both peaks and introduces a significant current in the bar trough region. The current profile resulting from choosing a mixing coefficient of unity is depicted in Figure 3c and represents a good agreement with the current maximum as dictated by measurements. It should be noted that the amount of turbulent momentum mixing introduced here is unrealistically high, but it is anticipated that total mixing induced by the Taylor mixing process described by Svendsen and Putrevu (1994) added to a realistic treatment of turbulence and wave rollers is of comparable magnitude. A detailed discussion of the model and parameters used in obtaining these results can be found in Özkan-Haller and Kirby (1996b).

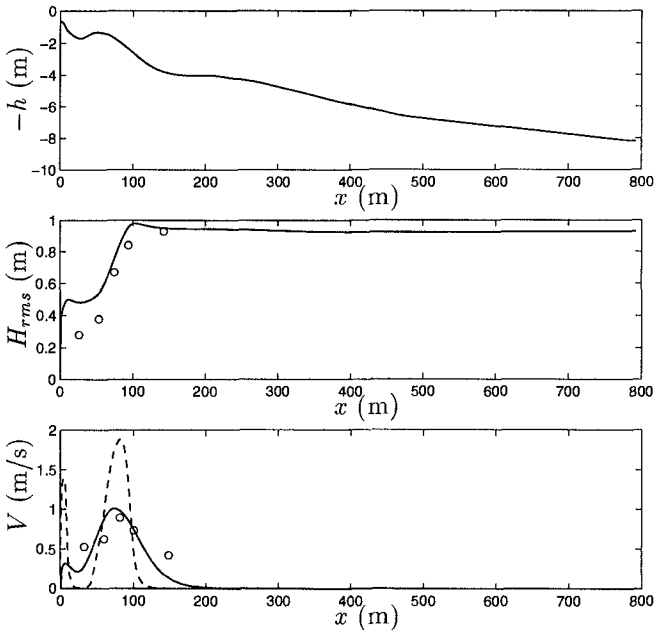


Figure 3: (a) Bottom bathymetry, (b) Wave height transformation, computed (solid) and measurements (o) and (c) Current profiles for October 18th, Case 1 (solid), Case 2 (dashed) and measurements (o).

The short wave forcing term in the y -momentum equation can now be expressed as

$$\tau_y = \frac{\mu}{h + \eta} V(x) \quad (4)$$

since the profile $V(x)$ is computed such that it is balanced with the steady

radiation stress gradient and the lateral mixing. Simulations with this forcing function result in the generation of the current $V(x)$ initially. It subsequently becomes unstable and finite amplitude shear instabilities develop.

In the following, two distinct initial current profiles will be used. The first case, hereafter referred to as Case 1, involves the initial current profile $V(x)$ depicted by the solid line in Figure 3c. In the second case, hereafter referred to as Case 2, any momentum mixing in the surf zone is neglected in the short wave forcing terms resulting in a $V(x)$ profile with two distinct peaks seen in Figure 3c (dashed line).

The shear wave climate for both of these forcing functions is computed for a given friction coefficient of $c_f=0.004$. This value has previously been used by Dodd *et al.* (1992). Linear instability analysis gives the wavenumber corresponding to the maximum growth rate in Case 1 as 0.0315 rad/m. The length of the modeling domain in the longshore direction L_y is chosen to be 16 times the wavelength that corresponds to this wavenumber. This longshore length scale is used in both cases since the most unstable wavenumber for Case 2 occurs at higher wavenumbers due to the presence of the highly unstable shoreline jet. The modeling domain extends 400 m offshore. An absorbing boundary condition is used at the offshore boundary (Özkan-Haller and Kirby, 1996a). Periodicity is assumed in the longshore direction. The current profile $V(x)$ corresponding to the each case is specified as an initial condition.

Results for Case 1

The simulation for the forcing profile including the effects of additional mixing is presented first. Time series taken in the trough region of the bar (about 35 m offshore) are shown in Figure 4. The longshore averaged longshore velocity is also shown and is defined as

$$\bar{v}(x, t) = \frac{1}{L_y} \int_0^{L_y} v(x, y, t) dy. \quad (5)$$

It can be observed that the instabilities gain energy about one hour into the simulation, the time series display an intermittent character where periods of higher frequency oscillations are followed by periods of low frequency oscillations. A mean longshore current already exists in the trough region; it is seen to increase slightly after the shear instabilities reach finite amplitude.

The intermittent character of the motion is also evidenced by plots of the potential vorticity defined as

$$q = \frac{v_x - u_y}{h + \eta}. \quad (6)$$

The patterns of potential vorticity shown in Figure 5 are propagating in the $+y$ direction and show that features with longer longshore scales are followed by packets of features with shorter longshore scales.

To aid the interpretation of the potential vorticity a plot of the circulation pattern in a portion of the domain depicted in Figure 5 is shown in Figure 6a. The shear instabilities can be observed to cause flow across the bar crest which is located about 60 m offshore. Also of interest are the offshore directed velocities

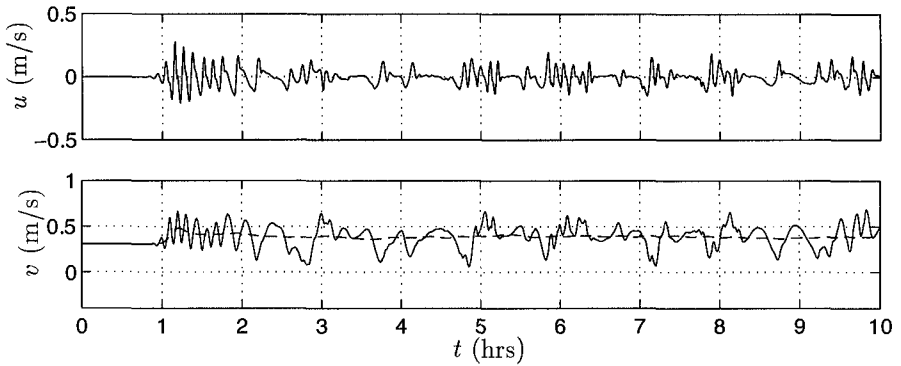


Figure 4: **Case 1** Time series of u and v in the bar trough region (solid) and longshore averaged longshore velocity \bar{v} (dashed).

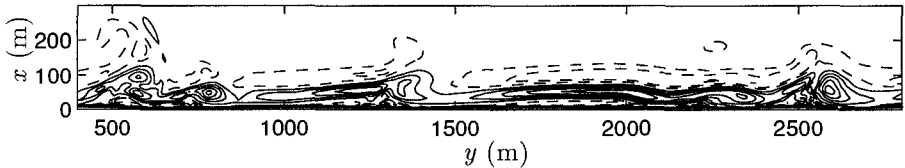


Figure 5: **Case 1** Contour plot of potential vorticity (solid for $q > 0$, dashed for $q < 0$) at $t=10$ hrs.

occurring further offshore. These features can be seen to be active up to about 250 m offshore corresponding to about 3 times the surf zone width.

The change in the mean longshore current profile that occurs as the shear instabilities reach finite amplitude is documented in Figure 7a where the initial current profile is shown along with the mean current profile after the instabilities develop. It can be noted that the value of the current maximum as well as the value of its slope on the seaward side have decreased. Multiplying the longshore momentum equation (1) by the total water depth, longshore averaging, and assuming stationarity of the mean quantities identifies the dominant terms and leads to a balance between lateral mixing induced by the shear instabilities and the change in the mean longshore current profile given by

$$\overline{(Duv)_x} = -\mu(\bar{v} - V), \quad (7)$$

where subscripts denote differentiation and $D = h + \eta$ is the total water depth. The initial current profile is denoted by V and \bar{v} is the current profile after the development of the shear instabilities. Any change in the longshore current profile is, therefore, directly due to lateral momentum mixing induced by the shear instabilities.

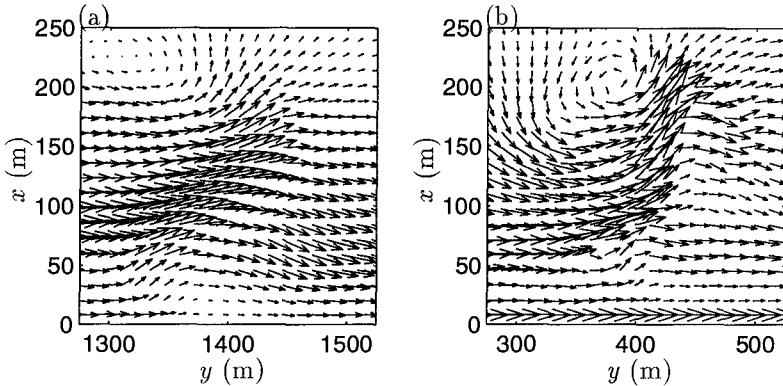


Figure 6: Circulation pattern at $t=10$ hrs (a) Case 1 (b) Case 2.

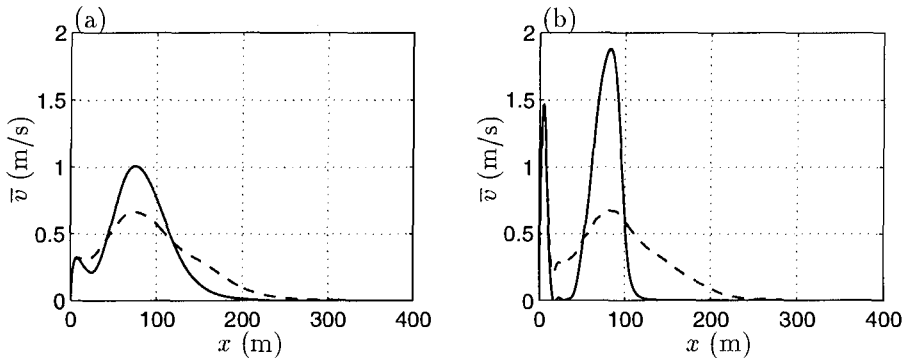


Figure 7: Initial (solid) and final (dashed) mean current profiles (a) Case 1 (b) Case 2.

Results for Case 2

Results for the simulation involving the forcing function with no mixing involved are discussed next. Time series for the velocity components (see Figure 8) show that the instabilities reach finite amplitude in a shorter amount of time than in Case 1. Higher frequency oscillations are evident but there is no evidence of intermittent behavior. It can be noted that there is no mean current at this location initially but a mean current of about the same magnitude as in Case 1 is created after the instabilities reach finite amplitude. The oscillations also appear to be more energetic in this case.

A contour plot of the potential vorticity at the end of the simulation (see Figure 9) shows that the organized layers of positive and negative potential vorticity are being mixed. Features with positive and negative potential vorticity can be seen to pair up. Some pairs that have previously been released are seen about 300 m offshore. The resulting pattern is similar to results obtained by

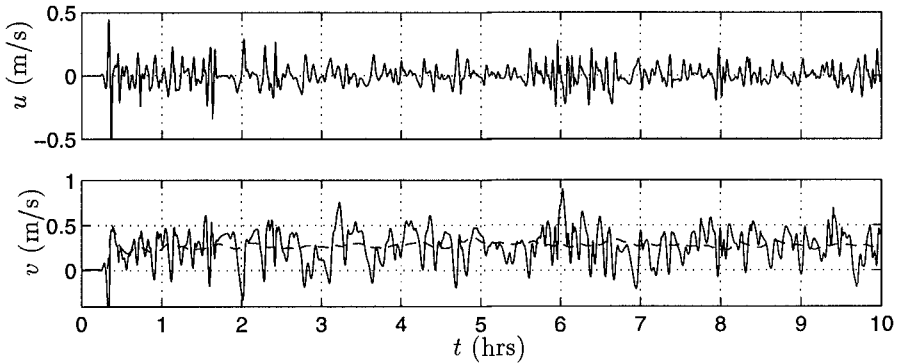


Figure 8: **Case 2** Time series of u and v in the bar trough region (solid) and longshore averaged longshore velocity \bar{v} (dashed).

Slinn *et al.* (1995) for a generic barred beach in a regime they called “eddy formation”.

An interesting feature can be seen in Figure 9 around $y = 400$ m. It resembles a “rip-head”. A plot of the circulation pattern associated with this feature is given in Figure 6b and exhibits strong offshore directed velocities across the bar crest extending offshore, much like a rip current. Flow across the bar trough is also evident.

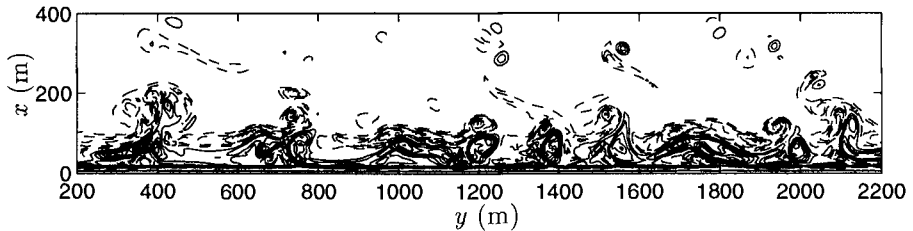


Figure 9: **Case 2** Contour plot of potential vorticity (solid for $q > 0$, dashed for $q < 0$) at $t=10$ hrs

The change in the mean longshore current profile due to the shear instabilities can be observed in Figure 7b. The peak longshore current has decreased significantly due to the presence of the shear waves. In addition, an appreciable current is introduced in the trough region of the bar.

Comparisons with data

The predictions for the final mean longshore current for the two cases are plotted in Figure 10 along with data points from sequential measurements from a measurement sled that was pulled onshore during an experimental run, collecting data for 35 minutes at each stop. It should be noted that the current profiles

resulting from the two cases are remarkably similar. They exhibit similar maximum current values, the seaward slope of the current profiles are also similar. However, the current profile resulting from simulations for Case 2 shows a strong shoreline jet. The maximum longshore current is underpredicted by about 20 %. However, caution should be used in interpreting the data to model agreement in this case since the measurements were carried out sequentially and sled data and model data are based on very different averaging periods.

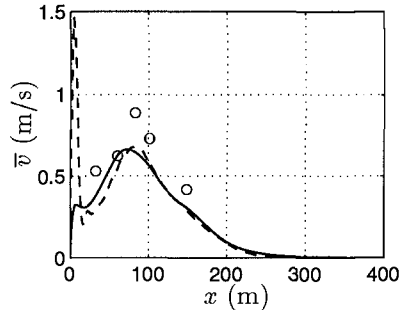


Figure 10: Final mean current profiles for Case 1 (solid) and Case 2 (dashed), measurements (o)

Time series obtained from the model can be compared to velocity measurements from one of the current meters located in the surf zone. Three hour segments of computations for the two cases as well as measurements of cross-shore and longshore velocities are shown in Figure 11. The time scales involved in Case 1 are much longer than what is seen in the data. The intermittent character is also not repeated in the data. In turn, simulations for Case 2 exhibit more high frequency activity than Case 1, but the fluctuations have higher amplitudes than the fluctuations seen in the data.

Frequency spectra for the longshore velocities confirm that the energy in high frequencies is underpredicted in Case 1 (see Figure 12a). The shape of the spectrum in Case 2 (see Figure 12b) is similar to that of data but the energy in the motions is overpredicted. The same trend can be seen in frequency spectra of the cross-shore velocities shown in Figure 13.

In order to determine if the propagation speeds of these motions are predicted well, comparisons of frequency-longshore wavenumber spectra for the longshore velocities are made. Frequency-longshore wavenumber spectra are obtained using the high resolution Iterative Maximum Likelihood Estimator (IMLE) utilizing time series from five sensors in the surf zone (Oltman-Shay *et al.*, 1989) (see Figure 14a). Since model computations are carried out with high resolution in both space and time a direct Fourier Transform in both space and time is used to obtain the two-dimensional spectra from the computed time series (see Figure 14b and c).

Results for Case 1 show that the wavenumber range in which shear instabilities are present is underpredicted as is expected after analyzing frequency spectra. The predicted spectra displays a nondispersive character. The two-dimensional spectra for Case 2 predicts a wider range of wavenumbers where

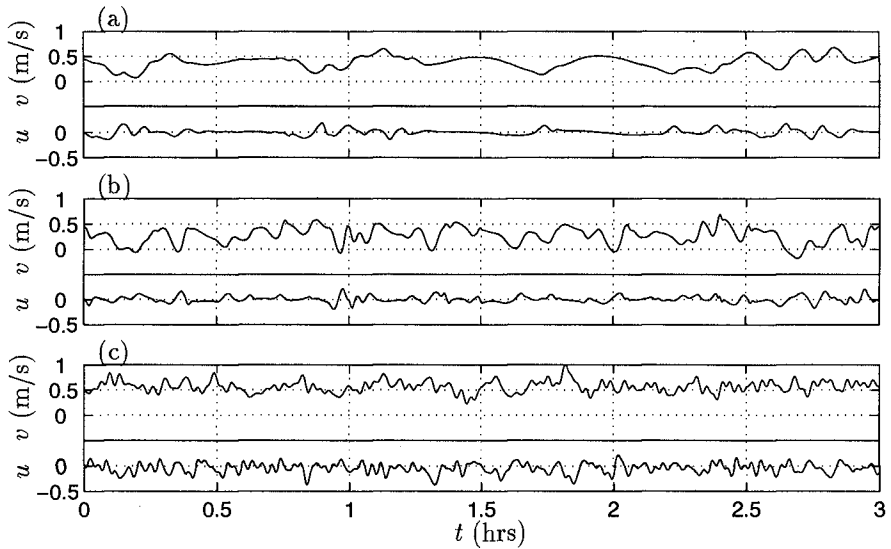


Figure 11: Three hour segments of time series (a) Case 1 (b) Case 2 (c) Data from gage LS07 at SUPERDUCK, October 18th.

shear instabilities are present. The slight increase in the speeds with increasing frequency is also reproduced. The propagation speeds are similar in both cases and correspond to an underprediction of the propagation speed seen in the data by about 20 %. This is likely to be a direct consequence of the fact that the peak mean longshore current velocity is underpredicted by about 20 %, since the shear instabilities propagate at a fraction of the maximum mean longshore current velocity (Bowen and Holman, 1989).

Summary and Conclusions

In this study, a comprehensive model of low frequency motions has been used to study the shear wave climate on October 18th at SUPERDUCK. Two cases including and neglecting a simple lateral mixing mechanism, respectively, are simulated. Time series, frequency spectra, frequency-longshore wavenumber spectra and time variations of the mean longshore current profiles are analyzed for both cases, the results are compared to measurements where possible.

It is seen that when intensive mixing is considered in the forcing function (Case 1) the mean current profile only changes slightly, therefore the lateral mixing caused by the shear instabilities is small. The resulting shear wave climate is not very energetic, underpredicting what is seen in data. In turn, if mixing due to mechanisms related to the short wave climate and turbulence is neglected entirely in the forcing function (Case 2), the initial profile undergoes drastic changes, therefore lateral mixing induced by the shear instabilities is appreciable and the shear wave climate is very energetic, overpredicting what is seen in data. The final longshore current profiles resulting from the simulations

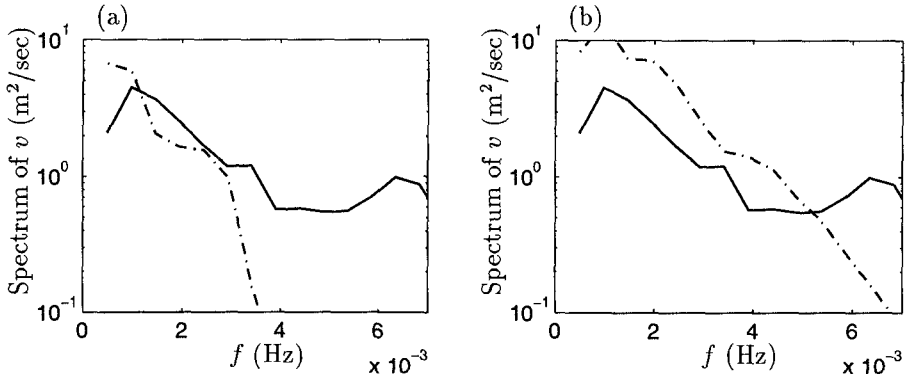


Figure 12: Frequency spectra for v , measured (solid), computed (dashed-dotted) (a) Case 1 (b) Case 2.

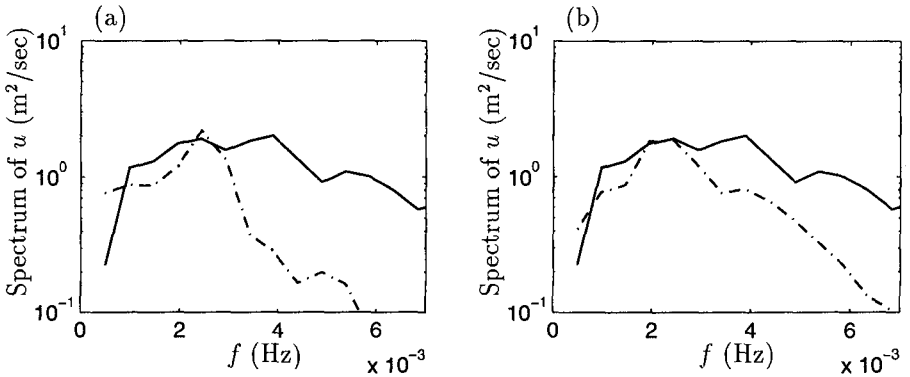


Figure 13: Frequency spectra for u , measured (solid), computed (dashed-dotted) (a) Case 1 (b) Case 2.

are remarkably similar regardless of the shape of the initial current profile. If the short wave forcing is far removed from producing this final current profile, shear instabilities arise, causing enough lateral mixing to redistribute the momentum in the surf zone.

In conclusion, the results of this study suggest that in this model the final mean longshore current profile is not a function of how much lateral mixing is initially included into the model, but only a function of the friction factor. If no (intensive) mixing due to the turbulence or Taylor dispersion is initially considered, the shear wave climate responds by creating intensive (minimal) mixing. Therefore, in this model the amount of energy in the shear wave band is a function of how much lateral mixing due to other considerations is already present in the initial forcing function. Hence, it is anticipated that the accurate prediction of the amount of energy present in the shear wave band in data is strongly linked to an accurate representation of the mixing processes due to turbulence, depth variations in the current or additional physics in the breaking process.

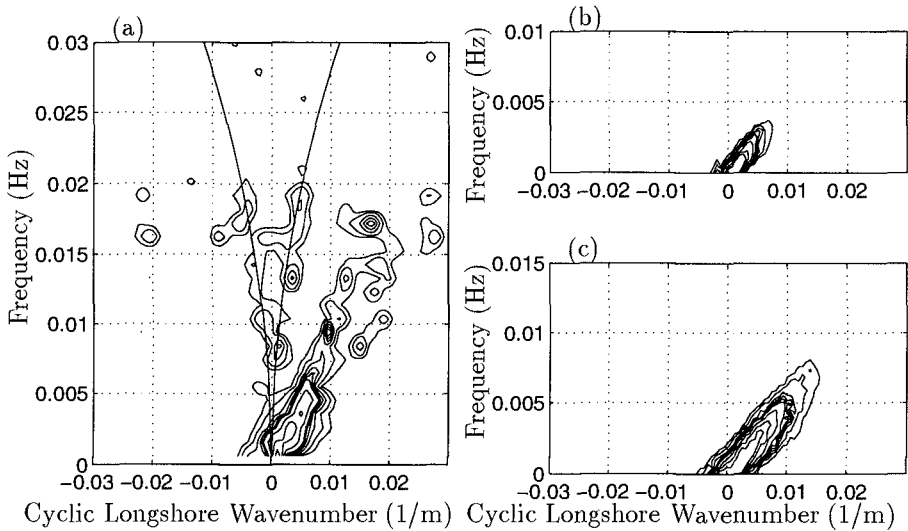


Figure 14: Frequency-longshore wavenumber spectrum for the longshore velocity v (a) Data for October 18th (b) Case 1 (c) Case 2.

Acknowledgments. The authors thank Dr. U. Putrevu for providing the software used to carry out linear instability calculations. Thanks are also due to Dr. J. Oltman-Shay for providing the SUPERDUCK data as well as the software to obtain estimates for two-dimensional spectra of the data. Thanks also to Dr. N. Dodd for providing the measured depth profiles used herein. This research has been sponsored by the Office of Naval Research, Coastal Sciences Program.

References

- Allen, J., P.A. Newberger and R.A. Holman (1996). "Nonlinear shear instabilities of alongshore currents on plane beaches." *J. Fluid Mech.*, 310, 181-213.
- Battjes, J. (1975). "Modeling of turbulence in the surf zone." *Proc. Symposium on Modeling Techniques*, San Francisco, 1050-1061.
- Bowen, A.J. and R.A. Holman (1989). "Shear instabilities of the mean longshore current. 1. Theory." *J. Geophys. Res.*, 94, 18023-18030.
- Deigaard, R., E.D. Christensen, J.S. Damgaard and J. Fredsøe (1994). "Numerical simulation of finite amplitude shear waves and sediment transport." *Proc. 24th Intl. Conf. Coastal Eng.*, Kobe, 1919-1933.
- Dodd, N. (1994). "On the destabilization of a longshore current on a plane beach: Bottom shear stress, critical conditions, and onset of stability." *J. Geophys. Res.*, 99, 811-824.

- Dodd, N., and E.B. Thornton (1990). "Growth and energetics of shear waves in the nearshore." *J. Geophys. Res.*, 95, 16075-16083.
- Dodd, N. and E.B. Thornton (1992). "Longshore current instabilities: Growth to finite amplitude." *Proc. 23rd Intl. Conf. Coastal Eng.*, Venice, 2655-2668.
- Dodd, N., J. Oltman-Shay and E.B. Thornton (1992). "Shear instabilities in the longshore current: A comparison of observation and theory." *J. Phys. Oceanog.*, 22, 1, 62-82.
- Falqués, A. and V. Iranzo (1994). "Numerical simulation of vorticity waves in the nearshore." *J. Geophys. Res.*, 99, 825-841.
- Falqués, A., V. Iranzo and M. Caballería (1994). "Shear instability of longshore currents: Effects of dissipation and nonlinearity." *Proc. 24th Intl. Conf. Coastal Eng.*, Kobe, 1983-1997.
- Lippman, T.C., E.B. Thornton and A.J.H.M. Reniers (1995). "Wave stress and longshore current on barred profiles." *Proceedings of Coastal Dynamics 1995*, Gdansk, Poland, 401-412.
- Oltman-Shay, J., P.A. Howd and W.A. Birkemeier (1989). "Shear instabilities of the mean longshore current. 2. Field Observation." *J. Geophys. Res.*, 94, 18031-18042.
- Özkan, H.T. and J.T. Kirby (1995). "Finite amplitude shear wave instabilities." *Proceedings of Coastal Dynamics 1995*, Gdansk, Poland, 465-476.
- Özkan-Haller, H.T. and J.T. Kirby (1996a). "A Fourier-Chebyshev collocation method for the shallow water equations including shoreline runup." *Appl. Ocean Res.*, in press.
- Özkan-Haller, H.T. and J.T. Kirby (1996b). "Shear instabilities of the longshore current on a barred beach: A comparison of observation and nonlinear computations." in preparation.
- Putrevu, U. and I.A. Svendsen (1992). "Shear instability of longshore currents: A numerical study." *J. Geophys. Res.*, 97, 7283-7303.
- Slinn, D.N., J.S. Allen and R.A. Holman (1995). "Nonlinear shear instabilities of alongshore currents over barred beaches." *AGU Fall Meeting, 1995*, San Francisco, CA.
- Svendsen, I.A. and U. Putrevu (1994). "Nearshore mixing and dispersion." *Proc. Roy. Soc. Lond. A*, 445, 561-576.
- Thornton, E.B. and R.T. Guza (1983). "Transformation of wave height distribution." *J. Geophys. Res.*, 88, 5925-5938.
- Whitford, D.J. (1988). "Wind and wave forcing of longshore currents across a barred beach." Ph.D. Dissertation, Naval Postgraduate School, pp. 202.

CHAPTER 107

NEPTUNE—AN INTEGRATED APPROACH TO DETERMINING NW EUROPEAN COASTAL EXTREMES

Jerzy Graff^{1) 2)} and Witold Cieřlikiewicz¹⁾

Abstract

NEPTUNE is an EU-research project under the MASTII framework. It involves seven partners: British Maritime Technology, Delft Hydraulics, Department of Mathematics & Statistics, University of Lancaster, Climate Research Unit, University of East Anglia, Econometrics Institute, Erasmus University, National Institute for Coastal and Marine Management of Rijkswaterstaat (RIKZ), and Forschungszentrum Geesthacht GmbH (GKSS). The purpose is to investigate *a new integrated approach for modelling the statistics of NW European coastal extremes* by first characterising the coastal impact and then *linking it through a process model chain with the causative storm involved*. The project methodology recognises that the North-European storm climate is made of several different storm types which impact on the coastline in different ways. The project strategy is described and some of the main results are presented.

1. Introduction

Information requirements for modern coastal management and engineering design need a statistical characterisation of the impact of storms on the shoreline or coastal structure. The impact is related to the combined influence of waves, tides and surges which are the hydraulic parameter inputs into functional relationships that describe the loading and response of the structure. The relationships describe the *limit-state* conditions that provide for the *design formulae* which are the basis of the modern approach to structural design and risk analysis (CUR/TAW 1990). Traditionally, estimates of the frequency distribution of extreme sea levels are based on analysis of historical tide gauge measurements of still water levels. These data are always site-specific and cover historical periods which are rarely consistent from site-to-site. The principal extreme value methods used to compute the *return periods* are the *annual maxima method* (Wemelsfelder 1961, Lennon 1963 a, Suthons 1963, Führböter 1976, Graff 1981) and the *joint probability method* (Pugh and Vassie 1980, Walden *et al.* 1982, Tawn 1992). Although the statistical methods have been extensively developed over recent years (de Valk 1991, Smith 1994, Coles and Tawn 1994) they are applied only to sea state observations without consideration to the influence and variability of the causative storm events involved.

The NEPTUNE project originated from the conviction that an integrated approach allowing for storm climate influence is called for. Changes in global weather climate

¹⁾ British Maritime Technology Limited, 7 Ocean Way, Ocean Village, Southampton SO14 3TJ, England

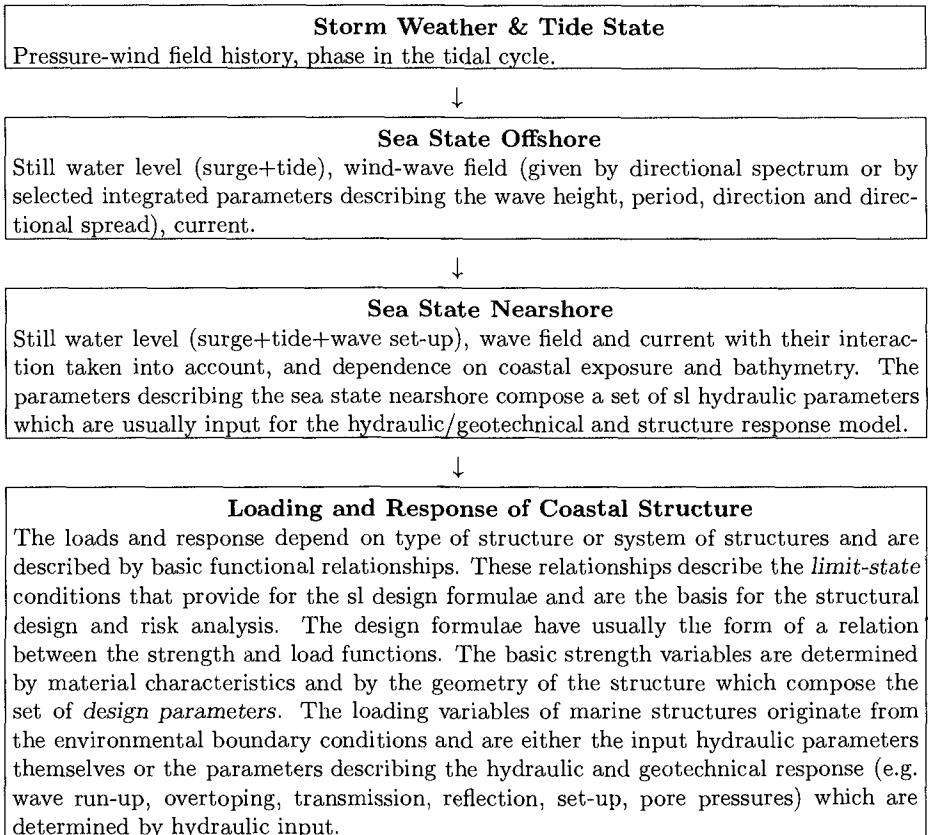
²⁾ Project Co-ordinator

will naturally influence storm climate which will induce consequential changes in the severity and frequency of regional coastal extremes. This may help explain the historical time variation in the probability of extreme sea levels around Great Britain and along the German coast identified independently by Graff (1978, 79) and Führböter (1976, 78) in the late 1970's. Ultimately, a stochastic description of the regional storm climate could form the common basis for the required joint statistics of coastal extremes, in which a combination of numerical models is used to parameterise the transformation from storm climate to local statistics. Such a description can serve as a solid basis for assessment of the consequences of changes in storm climate. Recently this same philosophy has been adopted by a number of other European research project groups (WASA, IMPACT) which will no doubt help to accelerate progress and development.

2. Project Methodology

The methodology seeks to develop an integrated approach for modelling the statistics of coastal extremes by first characterising the coastal impact and then linking it through a process model chain with the causative storm involved which in turn is attributed a statistical form within the global climate of storms.

The cause-consequence process chain linking the causative storm with impact on a coastal structure can be summarised in the following diagram:



The cause-consequence chain is represented as follows:

$$\mathbf{W}_t \xrightarrow{\mathcal{F}_1} \mathbf{X}_t \xrightarrow{\mathcal{F}_2} \mathbf{Y}_t \xrightarrow{\mathcal{F}_3} D_t \quad (1)$$

where \mathbf{W}_t , \mathbf{X}_t , \mathbf{Y}_t and D_t denote the random wind field, offshore variables, nearshore variables and design variable respectively, each indexed by time t . \mathcal{F}_1 is the superposition of the offshore tide-surge model and numerical wave generation model run on deep water up to 20 m depth. \mathcal{F}_2 is the superposition of the tide-surge model and wave model that transforms the offshore variables to the nearshore environmental variables (hydraulic parameters). Finally, \mathcal{F}_3 is a function of the nearshore variables which gives the design parameter D_t , assumed to be scalar. The function \mathcal{F}_3 (design formula) is usually determined by a *boundary function* of a failure region defined as a sub-set of \mathbf{Y}_t space. In order to develop a statistical model integrating the \mathbf{W}_t , \mathbf{X}_t , \mathbf{Y}_t and D_t variables the simplified versions of \mathcal{F}_1 and \mathcal{F}_2 need to be developed; in the case of \mathcal{F}_3 we assume that it is a known function. These are simple parametric models $\tilde{\mathcal{F}}_1 : \mathbf{W}_t \rightarrow \mathbf{X}_t$ and $\tilde{\mathcal{F}}_2 : \mathbf{X}_t \rightarrow \mathbf{Y}_t$. The parametric models $\tilde{\mathcal{F}}_1$ and $\tilde{\mathcal{F}}_2$ are designed and calibrated based on the data hindcast for the storms selected for both demonstrator zones.

NEPTUNE assumes that, on a European coastal cell scale, the extreme water levels generated at the shoreline are due to the impact of a particular type of storm. These storm types may vary for different coastal cell regions. Because wave effects play a critical role in maximising the water level at the shoreline it is obvious that storm directionality is important. It is assumed that the different coastal storm types which arise can be characterised into sub-classes of the overall climate of European storms.

Two distinct demonstrator zones were established, one on the west coast of Great Britain and the other on the north coast of Holland as shown in Fig. 1. Each zone has a particular type of region-specific storm climate associated with the generation of extreme coastal impact events and each is characterised by different physiography which would be used to investigate the relative influence of regional features affecting the storm-wave transformation to shore. In each demonstrator zone a review was made of the historical coastal flood events within the period 1955–1993 and the worst 20 events were selected independently for each region. The period 1955–1993 was chosen because high quality gridded digital meteorological data covering the NE Atlantic were available from DNMI—Norwegian Meteorological Institute. The DNMI data would provide a consistent set of boundary conditions both for analysing the storm weather directly and for modelling the sea state processes \mathcal{F}_1 and \mathcal{F}_2 associated with each of the 40 storm events.

3. Structure of Project

The project objectives span four main task areas of which three cover detailed research and investigation namely:

T100 Identify and analyse extreme sea state data

Establish a database of field measurements and information describing coastal physiography and sea state associated with historical coastal flood events in two selected coastal zones. One demonstrator zone was chosen on the west coast of Great Britain and the other on the Dutch coast. The extreme flood events in each zone are characterised by different types of storm.

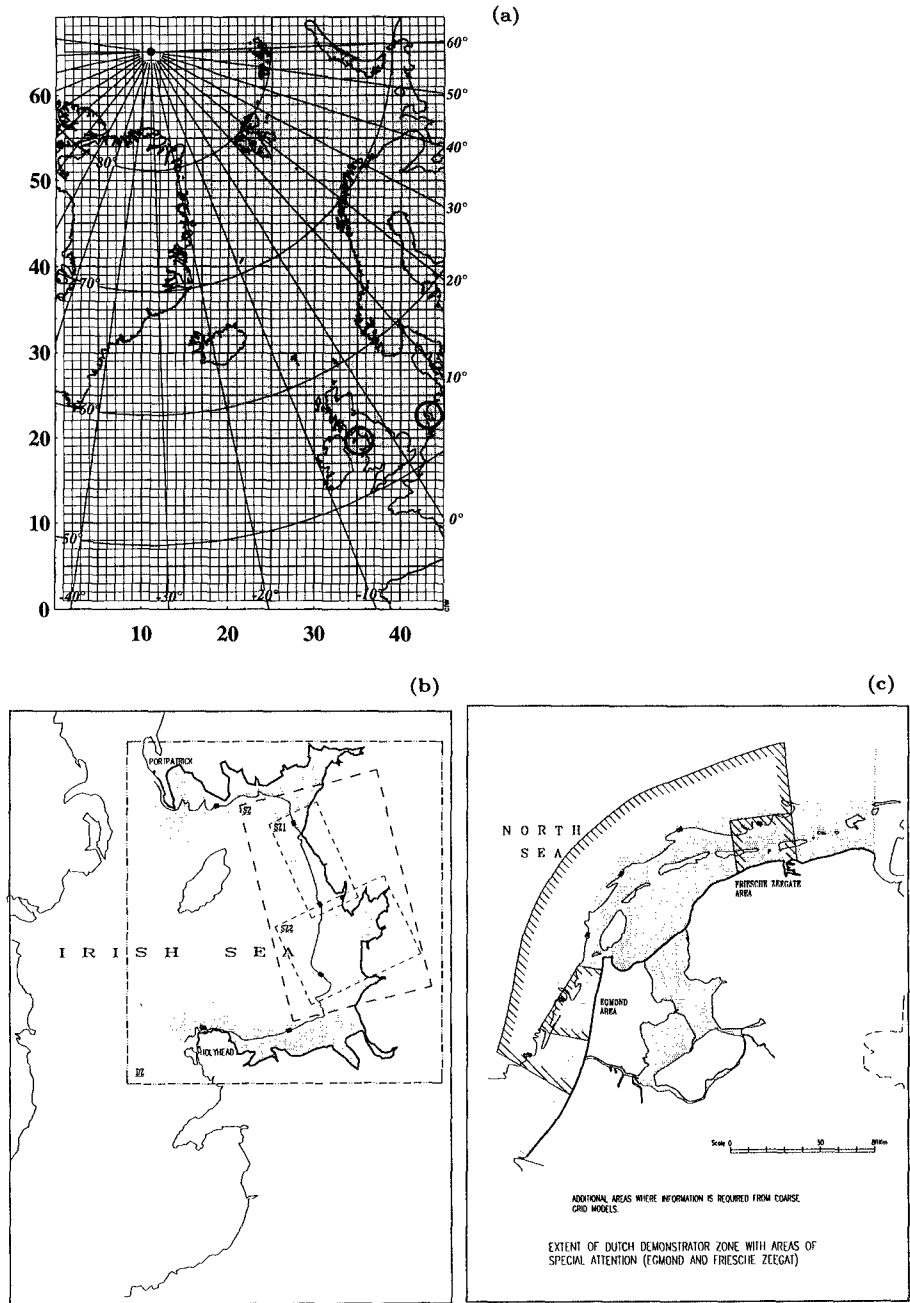


Fig. 1. (a) DNMI grid co-ordinates and study demonstrator zones; (b) UK demonstrator zone; (c) Dutch demonstrator zone.

T200 Identify and analyse storm weather data

Investigate the local and regional storm climate associated with generation of extreme coastal impact in respective demonstrator zones. The aim is to develop a parametric representation of the storm weather for input to sea state models and evaluate trends in storm character and frequencies of occurrence of different types of storms.

T300 Simulate extreme sea state processes and coastal impact

Use established operational hydrodynamic models to simulate the storm generated sea states offshore and their transformation to shore and investigate ways to parameterise the model responses and assess modelling uncertainties.

T400 Develop methods for determining joint statistics

The main goal is to develop, using the results from the two different demonstrator zones, a generic framework and associated multivariate models for describing joint statistics of coastal extremes allowing for relationships between storm climate and coastal response.

4. Key Features and Results

T100 Identify and analyse extreme sea state data

For each demonstrator zone the criteria for individual storm selection differed between the UK and Holland. The UK events were selected on the basis of regional coastal tide gauge records and documented public reports of the flood impact whereas the Dutch coast selection was made directly from available full scale measurements of winds, waves and tides monitored at a number of offshore platforms. The Dutch storm selection procedure is described in Dunsbergen (1994) and is based on metocean measurements recorded near Den Helder which was selected as representative location for the Dutch demonstrator zone. Many of the UK Irish Sea storm-surge events have been extensively studied and modelled at the Institute of Oceanographic Sciences (IOS), Bidston Observatory—now Proudman Oceanographic Laboratory (POL) (e.g. Amin 1982, and Heaps 1983) however, supporting wave measurement were rarely available.

T200 Identify and analyse storm weather data

Storm weather data

The primary data set used is the North Sea – NE Atlantic gridded pressure and wind data prepared by the DNMI covering the period 1955–1993. The coverage is shown in Fig. 1 (a) and represents a rectangular grid on a polar stereographic projection with grid size 75km at 60° N. These data were processed to provide coverage for all storm events in the study and were also used as common boundary data to model both the storm surge and storm wave simulation.

Storm classification and parameterisation

A key objective of NEPTUNE is to identify, characterise and classify storms affecting the two different demonstrator zone and seek to develop a parametric link between the causative storm features and the resulting hydraulic response (waves, tides and surges) at the shoreline. In part, this requires a need to parameterise the storms in order to exploit the digital DNMI database. The approach adopted was based on the recent work of Ferrier *et al.* (1993) which assumes that the storm pressure field (affecting

the Dutch coast) can be represented as a Gaussian bell of elliptical cross section whose geometry and motion are determined by a set of 11 parameters. The DNMI gridded data were processed to produce colour contoured pressure field maps at 6hrly intervals extending over a 20 day period for each of the 40 selected storms. These maps were used to study and classify the storms and to determine the parameters required for their characterisation and modelling. Preliminary analysis of the storms suggests that they can be divided into three classes each characterised by specific features associated with track and form of isobar distribution and dynamics. The assumption of a generic form of elliptic bell shaped storm structure proves to be an oversimplification. The findings reaffirm the view that UK west coast extremes are associated with a particular type of storm first identified by Lennon (1963 b) and that the great 1953 storm does in fact characterise the worst-case storms affecting the Dutch coast. The contrasting structure of the two types of storm at moment of maximum coastal impact are shown in Fig. 2.

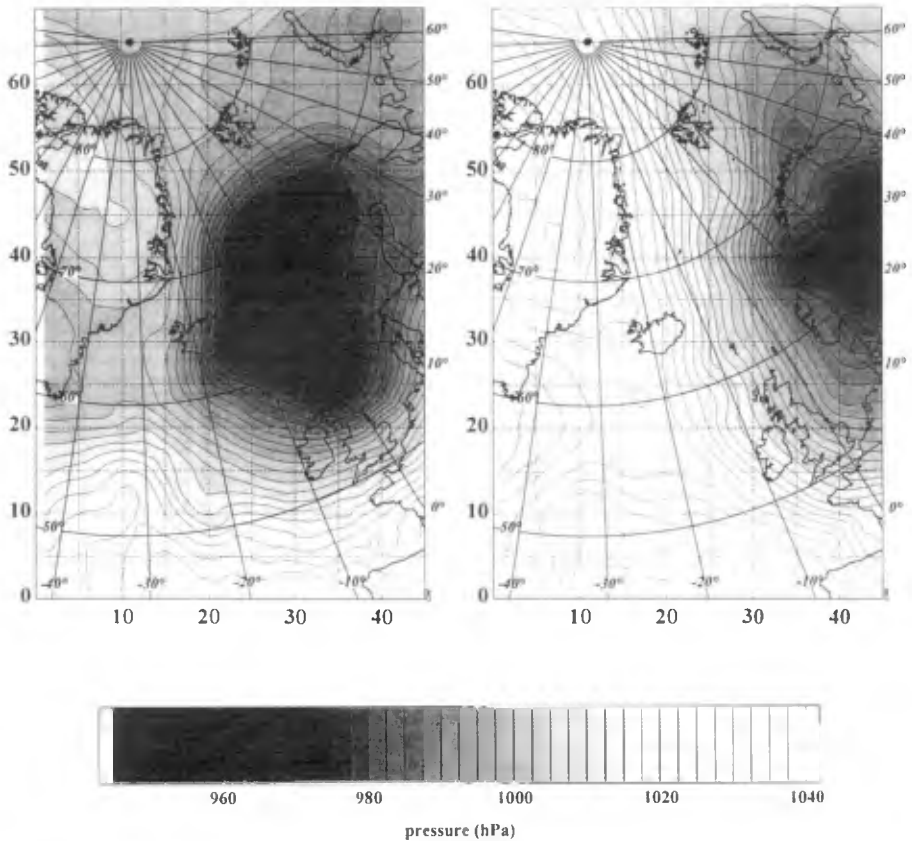


Fig. 2. Pressure distribution at time of coastal extreme for two contrasting storm types; Irish Sea extreme at 0:00h on 12/11/77 (left) and Dutch coast extreme at 6:00h on 13/02/62 (right).

T300 Simulate extreme sea state processes

Simulate offshore extremes

A conventional hybrid scheme involving the separate modelling of tide-surge and wave-current interaction processes was used to simulate the offshore storm induced sea state in each demonstrator zone. The DNMI gridded data were used to provide the boundary conditions associated with the forty storms selected. Storm surge levels were computed by POL using their CSX model and the associated wind-wave field was computed by GKSS using their hybrid parametrical surface wave prediction model (HYPA) in a nested model chain. The POL CSX model has a uniform grid resolution of $1/3^\circ$ latitude by $1/2^\circ$ longitude (approximately 36km) whereas the GKSS HYPA model chain coupled grid resolutions of 150km, 30km and 10km. HYPA (Günther *et al.* 1979) is a second-generation wave forecasting model that includes parametric prediction of the one-dimensional wind-sea spectrum with the mean wave direction as an additional prediction parameter. At each grid point the model generates the directional wave spectra as well as a set of 24 integrated spectral parameters.

Verification of hindcast wave and still water levels has been performed in detail for nine severe storm events using the independent field measurements available at five Dutch zone monitoring stations. The results were extremely good and an example of surge and wave comparison for a Dutch zone station is shown on Fig. 3.

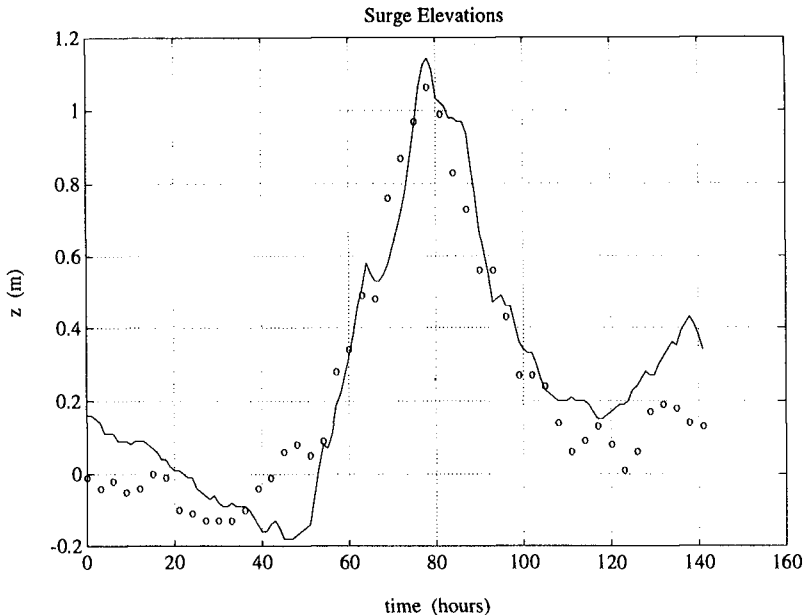


Fig. 3. Comparison of surge hindcast (solid line) and observed (circles) at SON, 21–28 Nov, 1981. Time is counted from 00h of first day of storm period.

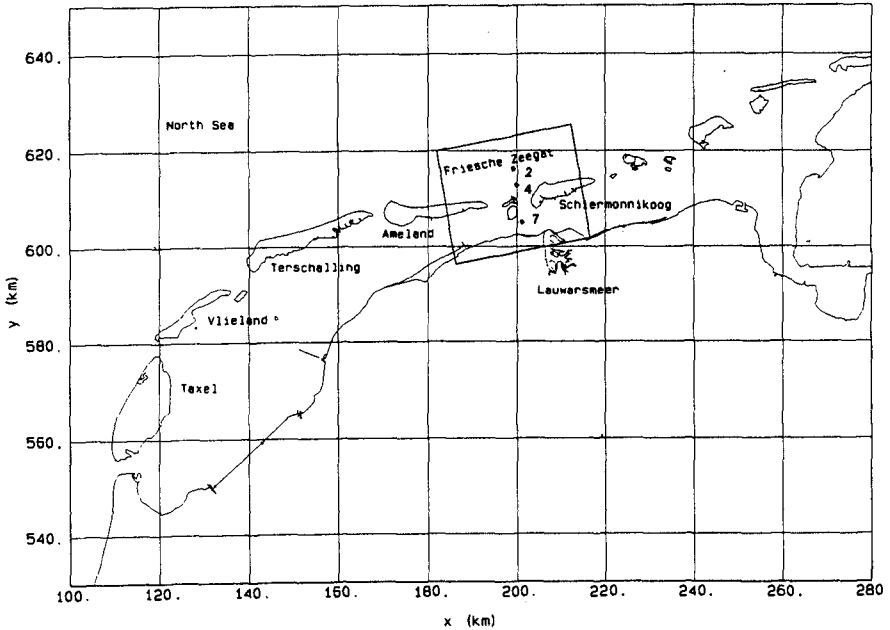


Fig. 4. Friesche Zeegat modelling area (ref. Spaan *et al.* 1996).

Transfer offshore extremes to shore

The transfer of offshore extremes to shore represents a strategic task since it forms the basis for developing the parametric relationships \tilde{F}_2 between physical parameters which are required to develop appropriate statistical models for the transfer of statistics to shore.

The Friesche Zeegat area in the Dutch demonstrator zone shown in Fig. 4 was used to undertake a number of detailed simulations and sensitivity studies involving different state-of-the-art models. The area is a special focus for ongoing coastal research modelling trials and associated field measurement experiments. The two principal models were HISWA (Holthuijsen *et al.* 1989) a 2nd generation stationary wave model and SWAN (Holthuijsen *et al.* 1993, 1994) another stationary but fully spectral 3rd generation wave model. Additionally the more advanced 3rd generation non-stationary wave model PHIDIAS (van Vledder *et al.* 1994) which is still under development was also used. The models were configured to provide grid cell resolution over various scales down to 100m. The results (Dunsbergen 1995, Otta 1995, van Vledder 1994, van Endt 1996) show that in complex coastal regions such as Friesche Zeegat it becomes necessary to employ the very latest advances in shallow water wave modelling in order to approach the degree of reality needed to correctly simulate wave transfer processes.

In association with the HYDRA project a special study was performed (Booij *et al.* 1996) to investigate in detail the nearshore wave conditions in the Friesche Zeegat during

a suprestorm. The superstorm (Bijl 1995) was an adapted version of the parameterised 1953 storm. The wave simulation was carried out using two models. First the SWAN model was used to compute the wave conditions at the height of the storm when the highest still water levels occurred in the central part of the Friesche Zeegat. The PHIDIAS model was then used to compute the time variation of the wave conditions over a period of 8 hours around the peak of the storm. The results show that the wave field along the Friesche Zeegat shoreline is mainly determined by local winds and by depth limitation on the tidal flats in the Waddensea. The offshore storm wave boundary conditions have little or no effect on the nearshore wave effects. Figs. 5 (a)–(c) show the storm wave spectra computed at the three locations marked on Fig. 4. The results clearly illustrate the form of double-peak spectra which may be associated with shallow water non-linear wave interaction.

Parameterisation of the modelling response

It has been assumed that full scale modelling of the process chain described in section 2 may lead to relatively simple parametric relationships linking \mathbf{W}_t , \mathbf{X}_t , \mathbf{Y}_t and design variables D_t . The objective is to represent the model responses \mathcal{F}_1 , \mathcal{F}_2 in simplified form $\tilde{\mathcal{F}}_1$, $\tilde{\mathcal{F}}_2$ to allow transformation not only of input data but also of statistics.

For the $\mathbf{W}_t \rightarrow \mathbf{X}_t$ link a parametrisation scheme has been developed (Cieřlikiewicz and Graff 1996) which can effectively relate the NE Atlantic wind and pressure field with the consequential NW European coastal surge and wave climate response. The novel approach involves use of empirical orthogonal functions (EOF) to transform the DNMI based NE Atlantic wind field into principal components targeting the UK and Dutch demonstrator zones and system identification techniques (SI) to develop the wave and surge field response. The scheme which involves linear system simulation techniques such as ARX and ARMAX has been trialed successfully for the Dutch demonstrator zone where 13 years of offshore metocean measurements are available in addition to the hindcast modelled data. Some results showing EOF wind field transformation and subsequent wave climate simulated using the SI technique are presented in Figs. 6 and 7. The scheme provides a potentially powerful tool for fast and efficient simulation of sea state parameters in response to weather field input.

A simple parameterisation scheme for the $\mathbf{X}_t \rightarrow \mathbf{Y}_t$ link specific to the Pettemer Zeewering shoreline was also developed. In this case available wave measurements were used to develop a parametric transformation matrix linking offshore storm waves with their shoreline response. The wave transform relationship needed to develop the multi-regression based matrix was determined using the 1-D version of the HISWA model. The transform matrix was then used to synthesise multivariate hydraulic parameters and associated statistics required to develop the $\mathbf{X}_t \rightarrow \mathbf{Y}_t$ association. Subsequently a family of seventy storms consisting of 22 historical storms and 48 fictitious conditions were used to compute $\mathbf{X}_t \rightarrow \mathbf{Y}_t$ wave transforms in the Friesche Zeegat region (Spaan *et al.* 1996) as a basis for the transfer of hydraulic parameter statistics.

T400 Determining joint statistics of extremes

The project methodology has been already outlined in section 2 and relations between the fields of random variables \mathbf{W}_t , \mathbf{X}_t , \mathbf{Y}_t and design variable D_t were discussed. The integration of a suitable multivariate extreme value model is dependent on the success of developing simple parametric models $\tilde{\mathcal{F}}_1$ and $\tilde{\mathcal{F}}_2$ of low dimension.

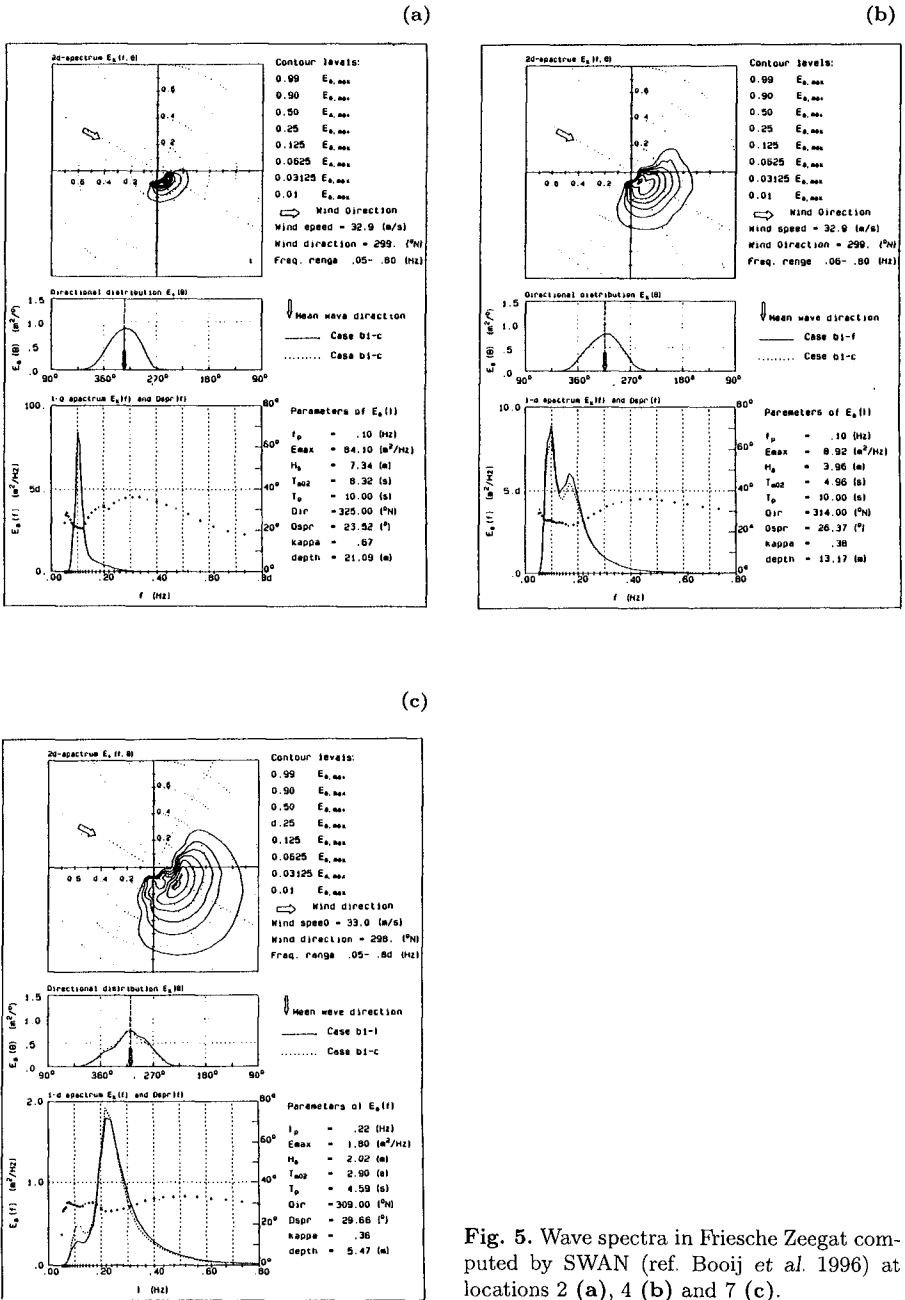


Fig. 5. Wave spectra in Friesche Zeegat computed by SWAN (ref. Booij et al. 1996) at locations 2 (a), 4 (b) and 7 (c).

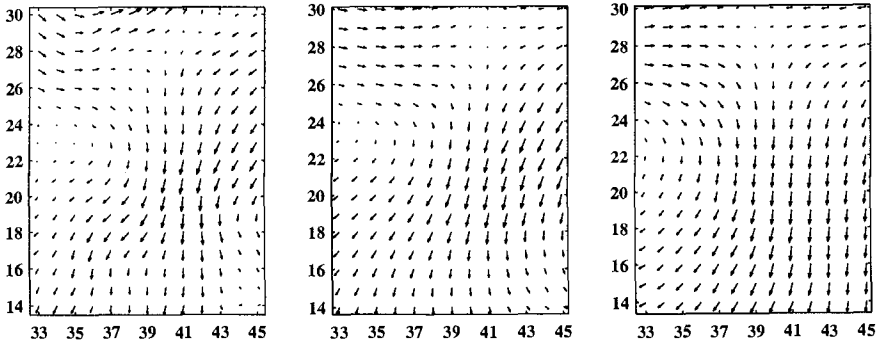


Fig. 6. Comparison between spatial distribution of DNMI wind velocity field at 12h on 16 May, 1988 and wind obtained via EOF analysis; original distribution (to left), and recalculated using first eight principal components (in the middle) and first four (to right).

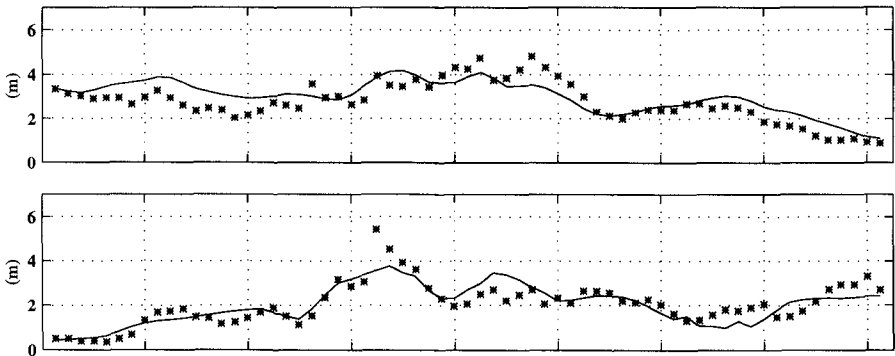


Fig. 7. Comparison between modelled (solid line) and recorded at EUR station (stars) time series of significant wave height for storm periods 15–22 Jan, 1983 (top) and 11–18 Feb, 1989 (bottom).

The hydraulic parameters $Y_{1,t}, Y_{2,t}, \dots, Y_{d,t}$, which compose the d -dimensional random vector \mathbf{Y}_t , determine the design variable D_t through \mathcal{F}_3

$$\mathbf{Y}_t = [Y_{1,t}, Y_{2,t}, \dots, Y_{d,t}] \xrightarrow{\mathcal{F}_3} D_t \quad (2)$$

If we assume that the marginal distributions of $Y_{1,t}, Y_{2,t}, \dots, Y_{d,t}$ are known then we can analyse the joint dependent structure of the multivariate data $[Y_{1,t}, Y_{2,t}, \dots, Y_{d,t}]$ and extrapolate, or create a structure variable D_t through $\mathcal{F}_3(\mathbf{Y}_t)$ and study the univariate structure data. One aim of the project has been to compare the accuracy of

joint probability models (analysis of \mathbf{Y}_t) to the structure variable approach (analysis of D_t) in estimating the return level for given probabilities of failure for D_t .

Considerable progress has been made in advancing both theoretical and practical aspects of the alternative approaches namely, the structured variable approach favoured by the Dutch research partners de Valk (1995, 1996) and Draisma and de Haan (1995, 1996) and the joint probability method favoured by the UK research partners Ledford and Tawn (1996 a, b) and Bruun and Tawn (1996). Issues examined cover multivariate dependency between the different parameters, temporal behaviour of the joint distributions and spatial dependency.

A practical case study application of the Structure Variable approach was developed and trialed by de Valk (1996) for a seawall dyke structure at Pettemer Zeewering in Holland. Only one failure mechanism was considered namely, wave overtopping of the crest of the seawall. Based on the expression for the 2 percent run-up level $z_{2\%}$ from Van der Meer (1993) a reliability function z was defined as the difference between the crest level z_{crest} and $z_{2\%}$; $z = z_{\text{crest}} - z_{2\%}$. If z is positive the overtopping is acceptable, whereas if z is negative, the structure fails. Contours of the reliability function involving nearshore wave height and period for two different still water levels are shown in Fig. 8.

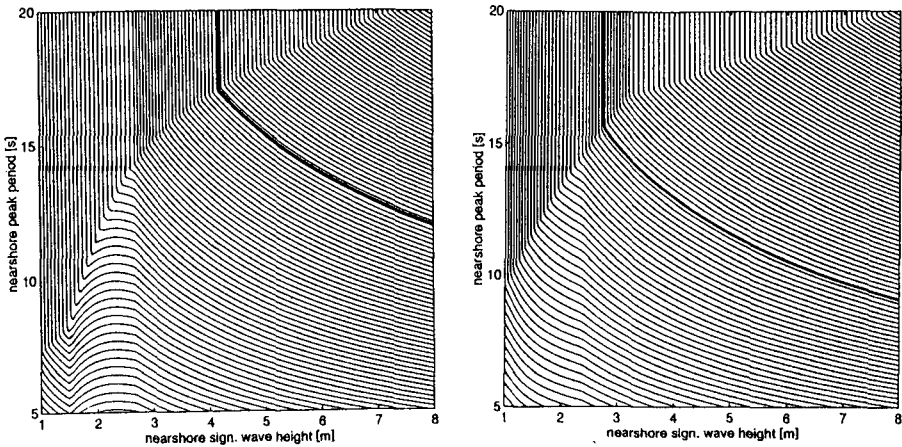


Fig. 8. Contours of run-up reliability function z as function of nearshore significant wave height and nearshore peak wave period for sea level 3.0 m (left) and 5.0 m (right) at Pettemer Zeewering (ref. de Valk 1996).

5. Acknowledgement

The research on which this paper is based has been supported by the Commission of the European Communities, Directorate General for Science, Research, and Development under MAST contract No. MAS2-CT94-0081. Data and information central to the project have been provided by the Proudman Oceanographic Laboratory, the Royal Norwegian Meteorological Institute and National Institute for Coastal and Marine Management—RIKZ. The authors acknowledge that this paper represents

the combined efforts of all the project partners.

References

- Amin, M. 1982. On analysis and forecasting of surges on the west coast of Great Britain. *Geophys. J. R. astr. Soc.*, **68**, 79–94.
- Bijl, W. 1995. Impact of a wind climate change on the surge in the southern part of the North sea. Rijkswaard voor Kust en Zee/RIKZ, Rep. No. 95.016.
- Booij, N., Ris, R. C. and Holthuijsen, L. H. 1994. A spectral model for waves in the near shore zone. *Proc. 24th Coastal Engng Conf.*, Kobe, Japan, 68–78.
- Booij, N., Holthuijsen, L. H., Ris, R. C. and van Vledder, G. Ph. 1994. Spectra in an estuary during a superstorm. Delft Hydraulics, Rep. H2368.
- Bruun, J. T. and Tawn, J. A. 1996. Comparison of approaches for estimating the probability of coastal flooding. *J. R. Statist. Soc. B.* (in press).
- Cieřlikiewicz, W. and Graff, J. 1995. Sea state parameterisation using empirical orthogonal functions. *Proc. 25th Coastal Engng Conf.*, Orlando, Florida.
- Coles, S. G. and Tawn, J. A. 1994. Statistical Methods for Multivariate Extremes: an Application to Structural Design. *J. Roy. Statist. Soc., B*, **43**, 1–48.
- CRU-TAW, 1990. Probabilistic design of flood defences. Centre for Civil Engineering Research and Codes (CUR), Technical Advisory Committee on water defences (TAW), Rep. No. 141.
- de Valk, C. 1991. Definition of joint extreme condition statistics of hydraulic parameters off the coast of Netherlands. Delft Hydraulics, Rep. H957.
- de Valk, C. 1995. Correction of wave height marginals for the temporal variability in storm intensity. Delft Hydraulics, Rep. H1931.
- de Valk, C. F. 1996. Estimation of frequencies of failure of coastal structures from offshore data of environmental loads. Delft Hydraulics, Rep. H2240.
- Draisma, G. and de Haan, L. 1995. Estimating bivariate extremes. Erasmus University, NEPTUNE technical report.
- Draisma, G. and de Haan, L. 1996. Estimating trivariate extremes. Erasmus University, NEPTUNE technical report.
- Dunsbergen, D. W. 1994. Identification of storms 1953–1993 (Den Helder). Rijkswaard voor Kust en Zee/RIKZ, NEPTUNE technical report.
- Dunsbergen, D. 1995. Validation of SWAN 20.51 against field measurements in the Friesche Zeegat. Rijkswaard voor Kust en Zee/RIKZ, Rep. No. 95.051.
- Ferier, P., Holthuijsen, L., Eldeberky, Y. and Booij, N. 1993. Extreme parametric storms for waves in the southern North Sea. Technical University of Delft, Rep. No. 8-93.
- Führbötter, A. 1976. Time variation in the probability of extreme storm tides on the German north sea coast. *Mitteilungen-Leichtweiss Institut für Wasserbau der Technischen Universität Braunschweig*, **51**, 1–93, BL translation RTS 11592.
- Führbötter, A. 1979. Frequencies and probabilities of extreme storm surges. *Proc. 16th Coastal Engng Conf.*, Hamburg, ASCE, 949–967.
- Graff, J. and Blackman, D. L. 1978. Analysis of maximum sea levels in southern England. *Proc. 16th Int. Conf. Coast. Engng*, Hamburg, ASCE, 931–948.
- Graff, J. 1979. Concerning the recurrence of abnormal sea levels. *Coastal Engineering*, **2**, 177–187.
- Graff, J. 1981. An investigation of the frequency distributions of annual sea level maxima at ports around Great Britain. *Estuarine Coastal Shelf Sci.*, **12**, 389–449.
- Günther, H., Rosenthal, W., Weare, T. J., Worthington, B. A., Hasselman, K. and Ewing, J. A. 1979. A hybrid parametric wave prediction model. *J. Geophys. Res.*, **84**, No. C9, 5727–5738.
- Heaps, N. 1983. Storm surges 1967–1982. *Geophys. J. R. astr. Soc.*, **74**, 331–376.
- Holthuijsen, L. H., Booij, N. and Herbets, T. H. C. 1989. A prediction model for stationary, short-crested waves in shallow water with ambient currents. *Coastal Engng*, **13**, 23–54.
- Holthuijsen, L. H., Booij, N. and Ris, R. C. 1993. A spectral wave model for the coastal zone. *Proc. 2nd. Symposium on Ocean Waves Measurement and Analysis*, New Orleans, 630–641.

- Ledford, A. W. and Tawn, J. A. 1996 a. Statistics for near independence in multivariate extreme values. *Biometrika*, **83**, 169-187.
- Ledford, A. W. and Tawn, J. A. 1996 b. Modelling dependence within joint tail regions. *J. R. Statist. Soc. B.*, (in press).
- Lennon, G. W. 1963 a. A frequency investigation of abnormally high tidal levels at certain west coast ports. *Proc. Instn. Civ. Engrs.*, **25**, 451-483.
- Lennon, G. W. 1963 b. The identification of weather conditions associated with the generation of major storm surges along the west coast of the British Isles. *Quart. J. Roy. Met. Soc.*, **89**, No. 381, 381-394.
- Otta, A., et al. 1995. Validation of SWAN against field and experimental data. Delft Hydraulics, Rep. H2117.
- Pugh, D. T. and Vassie J. M. 1980. Applications of the joint probability method for extreme sea level computations. *Proc. Instn. Civ. Engrs.*, Part 2, **69**, 959-975.
- Smith, R. L. 1994. Multivariate threshold methods. In *Extreme Value Theory and Applications*, 249-268.
- Spaan, G. B. H., van Vledder, G. Ph. and Hurdle, D. P. 1996. Seventy storms in the Friesche Zeegat. Delft Hydraulics, Rep. H3020.
- Suthons, C. T. 1963. Frequency of occurrence of abnormally high sea levels on the east and south coasts of England. *Proc. Instn. Civ. Engrs.*, **25**, 433-450.
- Tawn, J. A. 1992. Estimating probabilities of extreme sea levels. *Appl. Statist.*, **41**, 77-93.
- van der Meer, J. W. 1993. Goloploop en golfoverslag bij dijken. Delft Hydraulics, Rep. H638, (in Dutch).
- van Endt, M. 1996. Comparison of SWAN and HISWA in the Friesche Zeegat. Rijksinstituut voor Kust en Zee/RIKZ, Rep. No. 096.129.
- van Vledder, G. Ph., Stive, M. J. F. and de Ronde, J. G. 1994. Performance of a spectral wind-wave model in shallow water. *Proc. 24th Coastal Engng Conf.*, Kobe, Japan, 761-774.
- van Vledder, G. Ph. 1994. Verification of PHIDIAS against shallow water wave data. Delft Hydraulics, Rep. H1914.
- Walden, A. T., Prescott, P. and Webber, N. B. 1982. An alternative approach to the joint probability method for extreme sea level computations. *Coastal Engineering*, **6**, 71-82.
- Wemelsfelder, P. J. 1961. On the use of frequency curves of storm floods. *Proc. 7th Coastal Engng Conf.*, The Hague, ASCE, 617-632.

CHAPTER 108

A Stochastic Typhoon Model and its Application to the Estimation of Extremes of Storm Surge and Wave Height

Yoshio Hatada¹ and Masataka Yamaguchi²

Abstract

This paper presents a system for estimating extremes of storm surge height and wave height associated with typhoons, which consists of a Monte-Carlo simulation model for probabilistic generation of typhoon characteristics, termed a stochastic typhoon model, a parametric typhoon model for wind estimation, numerical models for the computation of storm surges or waves and an extreme analysis model for estimation of their return values. The system is applied to the estimation of 50 to 1000-year return values and their confidence intervals based on the computations over a period of 1000 years for storm surge heights in Ise Bay connecting to the Pacific Ocean, and for wave heights at some representative locations around the Pacific coast of Japan.

1. Introduction

Japanese coasts facing the Pacific Ocean and the East China Sea have frequently been hit by powerful typhoons and consequently have suffered severe damage by typhoon-generated storm surges and high waves. Design heights of sea water level and waves in the area are conventionally estimated based on statistical analysis of their extreme data hindcasted for typhoons which occurred in the past several decades. Extremes of typhoon-generated storm surges and waves are strongly dependent on the strength and track of a typhoon, because the severe wind

1 Research Associate of Civil and Environmental Eng., Ehime Univ., Bunkyocho 3, Matsuyama 790, Japan.

2 Professor of Civil and Environmental Eng., Ehime Univ., Bunkyocho 3, Matsuyama 790, Japan.

area in a typhoon is limited, the radius being usually less than about 200 km and typhoon-generated winds greatly vary in space and time. Thus, the problem is whether the above-mentioned method could properly evaluate great variability of storm surge height and wave height associated with the contingency of typhoon characteristics. As an alternative and complementary method, this paper presents a system for estimating extremes of storm surge height and wave height around the concerned sea area, which consists of a stochastic typhoon model, a parametric typhoon model, numerical models for the computation of storm surges or waves and an extreme analysis model for the evaluation of their return values and confidence intervals.

2. Estimation System for Extremes of Storm Surge and Wave Height

(1) Stochastic typhoon model

Atmospheric pressure distribution in a typhoon is approximated with the Meyers formula such as

$$p = p_{\infty} - (p_{\infty} - p_c) \exp(-R/R_a)$$

$$R^2 = (X - X_c)^2 + (Y - Y_c)^2 \quad (1)$$

where p_c (hPa) is the central pressure, p_{∞} (=1013 hPa) the pressure of the far field, (X_c, Y_c) the position of the typhoon center in km unit and R_a (km) the typhoon radius. The stochastic typhoon model is a Monte-Carlo simulation model for probabilistic generation of typhoon parameters which are represented with the position of the typhoon center, the central pressure and the typhoon radius.

Data of typhoon parameters used in the modeling were gathered every 6 hours for 320 typhoons which passed through the Northwestern Pacific Ocean area during the period of 1951 to 1991 and had a central pressure of less than 980 hPa in the area, with 15 typhoons generated within the area being excluded in the modeling due to data scarcity. The data set consists of 7 parameters such as X_c , Y_c , p_c , their incremental change rates dX_c , dY_c , dp_c , and R_a . Fig. 1 shows the domain covered with the north latitude of about 23° to 44° and the east longitude of about 120° to 149° , which is divided into a grid system of 34 by 35 with a grid distance of 80 km.

The basic idea in the modeling is that each typhoon parameter may be represented by the sum of its mean value and the deviation from the mean value. Mean variation of each typhoon parameter along the boundary is approximated with use of a one-dimensional weighted spline function,

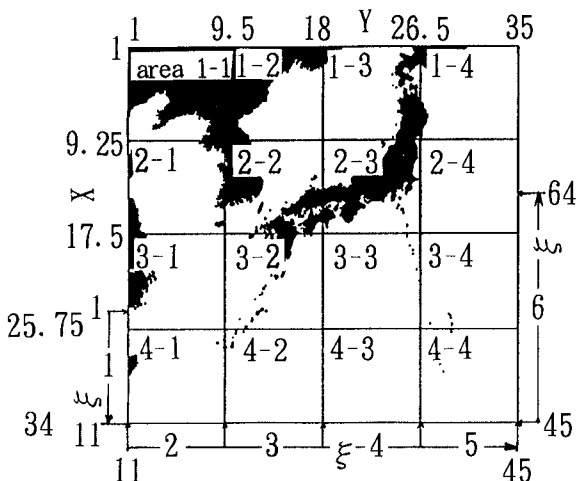


Fig. 1 The Pacific Ocean area where modeling of stochastic typhoons is made.

and correlations between typhoon parameters in the area as well as those between incremental change rates of typhoon parameter are taken into account with use of linear regression equations. Deviations from averaged typhoon parameters along the boundary and in the area are represented with empirical probability distribution functions obtained by data analysis. In order to improve reproducibility of the stochastic typhoon model, regression equations and empirical distribution functions are separately constructed at 6 sub-divided boundaries and in 16 sub-divided areas shown in Fig. 1.

Modeling of stochastic typhoon and Monte-Carlo simulation are conducted according to the following procedure.

(a) The annual occurrence rate of typhoons is fairly well approximated with the Poisson distribution for a mean value of 7.8, as shown in Fig. 2. So, it is determined with use of a computer-generated Poisson-type random number.

(b) The position where a typhoon generates is defined as the position where the typhoon crosses the boundary. Data of typhoon occurrence position and the other typhoon parameters are obtained from linear interpolation between the data before and after crossing the boundary. In order to describe the typhoon occurrence position on the boundary, a one-dimensional co-ordinate system ξ which is taken from the west boundary to the east boundary through the south boundary is introduced as indicated in Fig. 1. Fig. 3 shows the cumulative distribution of typhoon occurrence position. In the simulation, the occur-

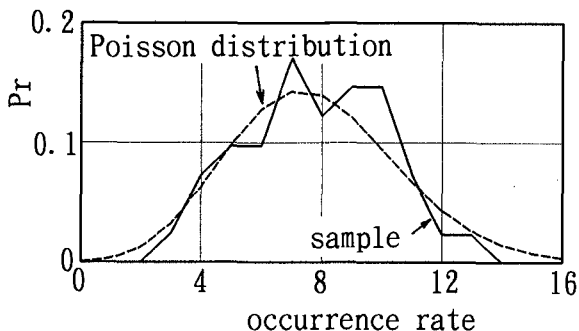


Fig. 2 Annual occurrence rate of typhoons and approximation with Poisson distribution.

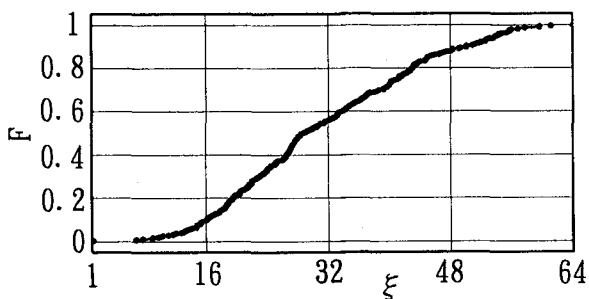


Fig. 3 Cumulative distribution of typhoon occurrence positions on the boundary.

rence position of a typhoon is obtained from the linear interpolation for cumulative distribution curve by giving a uniformly-distributed random number between 0 and 1 generated by computer.

(c) Mean variation of incremental change rate of typhoon position dX_{c0} along the boundary is approximated with a one-dimensional weighted spline function and then the deviation of individual data from the mean variation is separately expressed in the form of a cumulative distribution every sub-divided boundary. Fig. 4 illustrates the smoothing effect for scattered data by use of a one-dimensional spline function and an example of the cumulative distribution. Similar figures are prepared for the typhoon parameters such as dY_{c0} , p_{c0} and dp_{c0} .

In the formulation of typhoon radius, correlation with central pressure of the typhoon is taken into account using the regression equation such as

$$R_{a0} = a \cdot p_{c0}^n + b \quad (2)$$

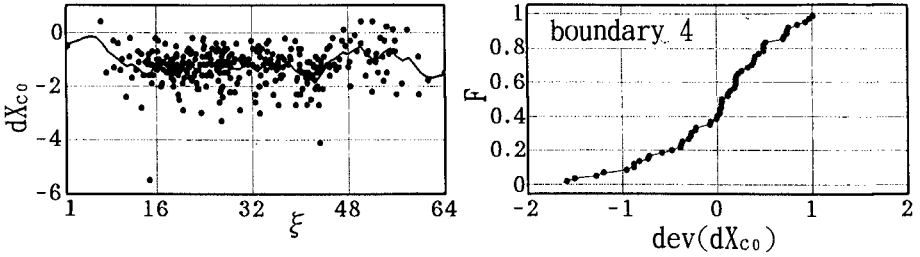


Fig. 4 Smoothing of dX_{c0} data along the boundary with spline function and cumulative distribution of deviation from mean variation.

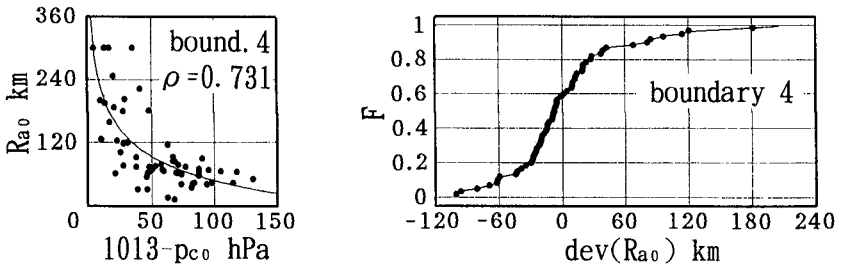


Fig. 5 Regression equation for R_{a0} and cumulative distribution of deviation from mean value in a sub-boundary.

where a , b and n are the coefficients to be determined by the least square method. Typhoon radius is expressed as the sum of mean value obtained from the above regression equation and its deviation from mean value for each sub-boundary. Fig. 5 indicates an example of the correlation diagram and the cumulative distribution.

Now typhoon parameters on the boundary X_{c0} , Y_{c0} , dX_{c0} , dY_{c0} , P_{c0} , dP_{c0} and R_{a0} can be successively simulated by using the regression equations and the cumulative distribution diagrams for each of which uniformly-distributed random number is given as input, and then position and central pressure of the typhoon at the next step can be determined from the relations such as

$$\begin{aligned}
 X_{c1} &= X_{c0} + dX_{c0}, & Y_{c1} &= Y_{c0} + dY_{c0} \\
 P_{c1} &= P_{c0} + dP_{c0} & & (3)
 \end{aligned}$$

Some restraint conditions are imposed on the generated typhoon parameters, and simulation is repeated until the conditions are satisfied.

(d) Regression equations are used to describe change of typhoon parameters every 6 hours associated with the typhoon movement in the simulation area. These are written as

$$\begin{aligned}
 X_{ci+1} &= a \cdot X_{ci} + b, & Y_{ci+1} &= c \cdot Y_{ci} + d \\
 P_{ci+1} &= e \cdot P_{ci} + f
 \end{aligned}
 \tag{4}$$

where i is the time step and a to f are the regression coefficients to be determined by the least square method. Change of typhoon radius is formulated with the following multiple regression equation including the effect of central pressure of the typhoon.

$$R_{ai+1} = a \cdot R_{ai} + b \cdot P_{ci+1} + c
 \tag{5}$$

Variability of each typhoon parameter is taken into account with use of the cumulative distribution for the deviation from mean value obtained from the regression equation as before. Regression equations and cumulative distribution diagrams are separately constructed for 16 sub-areas shown in Fig. 1. Examples of the correlation diagram and the cumulative distribution of the deviation from mean value for X_c , and those for R_a in the sub-

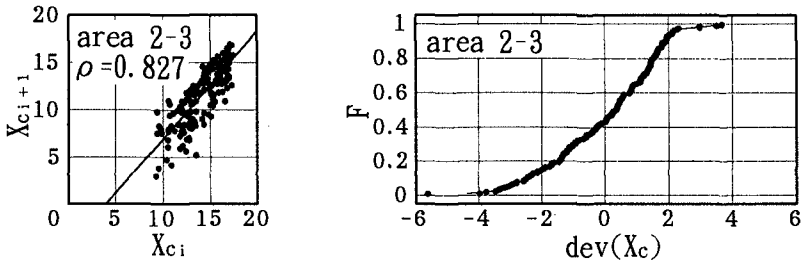


Fig. 6 Regression equation for X_c and cumulative distribution of deviation from mean value in a sub-area.

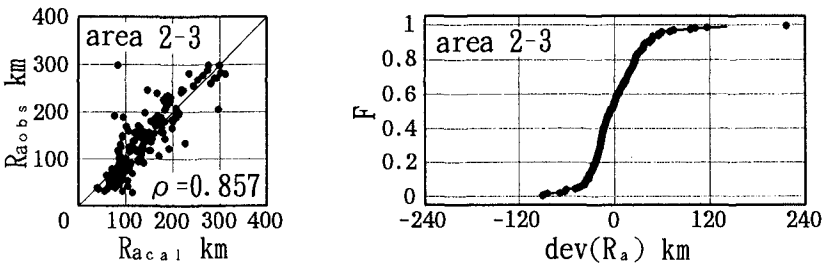


Fig. 7 Correlation diagram for R_a and cumulative distribution of deviation from mean value in a sub-area.

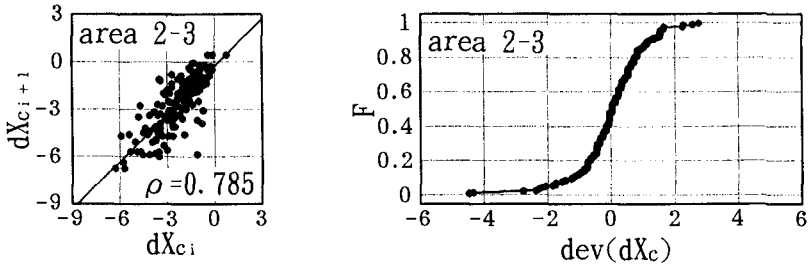


Fig. 8 Regression equation for dX_C and cumulative distribution of deviation from mean value in a sub-area.

area 2-3 are given in Fig. 6 and Fig. 7. Only eq.(5) is used to generate data of typhoon radius in the simulation area, because inclusion of the deviation gives rise to rapid and unnatural change of the typhoon radius with typhoon movement. Another reason is that correlation between data of typhoon radius and data calculated with eq. (5) is usually high to the extent that addition of the deviation is not required.

(e) Incremental change rates of the typhoon parameters dX_C , dY_C and dp_C are formulated in the same way as before. The regression equations are written as

$$\begin{aligned} dX_{Ci}^+ &= a \cdot dX_{Ci}^- + b, & dY_{Ci}^+ &= c \cdot dY_{Ci}^- + d \\ dp_{Ci}^+ &= e \cdot dp_{Ci}^- + f \end{aligned} \quad (6)$$

where

$$\begin{aligned} dX_{Ci}^+ &= X_{Ci+1} - X_{Ci}, & dX_{Ci}^- &= X_{Ci} - X_{Ci-1} \\ dY_{Ci}^+ &= Y_{Ci+1} - Y_{Ci}, & dY_{Ci}^- &= Y_{Ci} - Y_{Ci-1} \\ dp_{Ci}^+ &= p_{Ci+1} - p_{Ci}, & dp_{Ci}^- &= p_{Ci} - p_{Ci-1} \end{aligned} \quad (7)$$

Superscripts '+' and '-' mean change of typhoon parameter occurring from i step to $i+1$ step and from $i-1$ step to i step respectively. Both are defined at i step. Fig. 8 indicates the correlation diagram for dX_C and the cumulative distribution of the deviation from mean value based on the regression equation in the sub-area. Critical values of incremental change rates are used to restrict excess change over one time step of simulated typhoon parameters. Each critical value is calculated as the sum of the mean values obtained from the regression equation and deviation corresponding to 3% or 97% non-exceedance probability of the cumulative distribution. No restriction on typhoon radius is imposed because the

regression equation gives high correlation with the original data of typhoon radius.

(f) Monte-Carlo simulation of typhoon parameters for a typhoon is continued until the typhoon center moves out of the simulation area or the center pressure rises more than 1008 hPa. Simulation is repeated by the annual occurrence rate of typhoons and then by the number of years arbitrarily given as input condition.

(2) Parametric typhoon model

The estimation of typhoon-generated winds relies on the application of a simple parametric model. The model computes the spatial distribution of wind speed and wind direction in a typhoon by composing axisymmetrical gradient wind components and wind components related to the movement of the typhoon. Eq. (1) is assumed for the pressure distribution in a typhoon. Correction factor to wind speed at the height of 10 m is generally taken as 0.6, but some adjustment is made to improve the reproductiveness of storm surge computation.

(3) Storm surge model

Storm surge computation is based on a finite difference model for the vertically-integrated momentum and continuity equations, in which constant bottom friction factor and wind speed-dependent surface drag coefficient are used. Astronomical tides are not included in the storm surge computation because there is no way to determine phase relation between astronomical tides and storm surges associated with simulated typhoons. The domain of Ise Bay whose location is given in Fig. 9 is divided into a grid system of 38 by 34 with a grid size of 2.5 km. The time steps in wind and storm surge computations are 15 min and 45 s respectively. Although the topographical resolution is not sufficient for the storm surge computation in this area, the present grid system is necessary in order to save enormous computer processing time required for the computations of storm surges associated with more than 2300 typhoons.

(4) Wave model

Wave computation is performed with a shallow water wave model (Yamaguchi et al., 1987) which belongs to a decoupled propagation model, tracing the change of directional spectrum along a refracted ray of each component focused on a prescribed point. The usage of a nesting grid system with high topographical resolution results in a reasonable estimate of waves in coastal sea water. Fig. 9 shows a nesting grid system composed of the Northwestern Pacific Ocean area divided with a grid size of 5 km and a small sea area off Shikoku Island divided with a grid size of 0.5 km. The figure includes

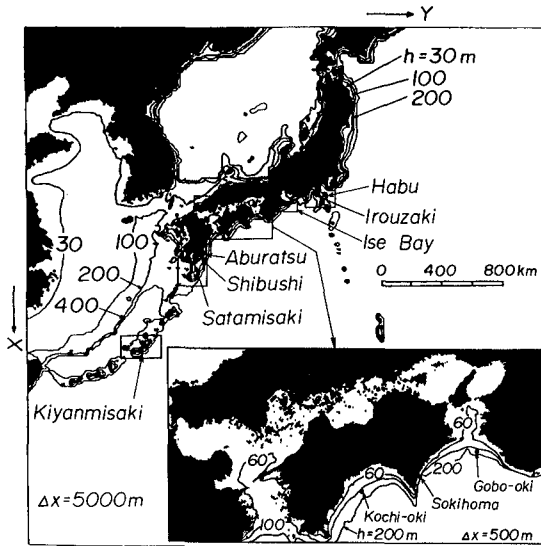


Fig. 9 Nesting grid used in wave computation, location of wave computation points and contour plot of water depth.

the location of Ise Bay where storm surge computation is conducted, the location of 9 wave computation points along the Pacific coast of Japan and contour plot of water depth. The numbers of frequency and direction data are 23 and 19 respectively, and the time step in wind and wave computations is 1 hour.

(5) Extreme analysis model

Return storm surge height and its standard deviation are evaluated applying the extreme analysis model based on the least square method (Goda, 1988) to data of its peak value during a typhoon. The optimum distribution is chosen among the Gumbel distribution and the Weibull distributions, shape parameters of which are 0.75, 1.0, 1.4, and 2.0, based on the largest correlation coefficient between the ordered data and its reduced variate.

Return wave height and its standard deviation are estimated with the extreme analysis model based on the PWM method (Yamaguchi et al., 1995), which was found from a numerical simulation study by the authors to be an excellent parameter estimation method. A sample of data is obtained from peak wave height during a typhoon in the case of simulated data and from typhoon-generated annual maximum wave height in the cases of observed and hindcasted data. Candidate distributions are the Gumbel and 3-parameter Weibull distributions, and choice of the

optimum distribution is due to a criterion of the correlation coefficient. A jackknife method is applied to estimate the standard deviation of return wave height.

3. Reproductiveness of Stochastic Typhoon Model, Storm Surge Model and Wave Model

Table 1 shows an example of the comparison between mean values and standard deviations of simulated typhoon parameters and those of observed typhoon parameters for each sub-area, and Fig. 10 illustrates the courses and radius of simulated typhoons in a representative year.

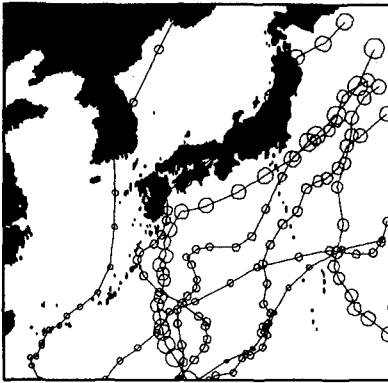


Fig. 10 Tracks and radius of simulated typhoons in a representative year.

Table 1 Comparison between simulation and observation for mean value and standard deviation of typhoon parameters.

typhoon parameters	area 2-3	
	mean	dev.
p_c obs.	981.0	14.8
(hPa) cal.	981.7	13.3
R_a obs.	139.0	72.1
(km) cal.	151.7	43.3
velocity obs.	42.6	20.9
(km/h) cal.	38.2	12.5
direction obs.	37.2	31.9
(°) cal.	35.5	27.7

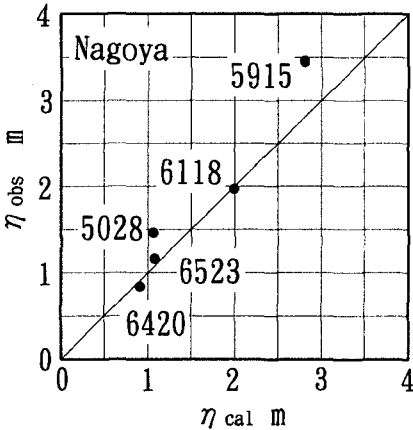


Fig. 11 Comparison of hindcast and observation for maximum storm surge height during a typhoon.

The stochastic typhoon model reasonably reproduces not only overall properties of typhoon characteristics but also their space-time variation associated with northward movement. It is natural that the model underestimates the standard deviation of typhoon radius because the effect of the deviation from mean value on the typhoon radius is neglected in the simulation.

Examples of the comparison between hindcasts and observations for typhoon-generated maximum

storm surge height in Nagoya Harbor and for maximum significant wave height at 4 wave observation points are indicated in Fig. 11 and Fig. 12 respectively. Applicability of the storm surge model and wave model are verified by satisfactory agreement between computation and observation for many typhoon cases.

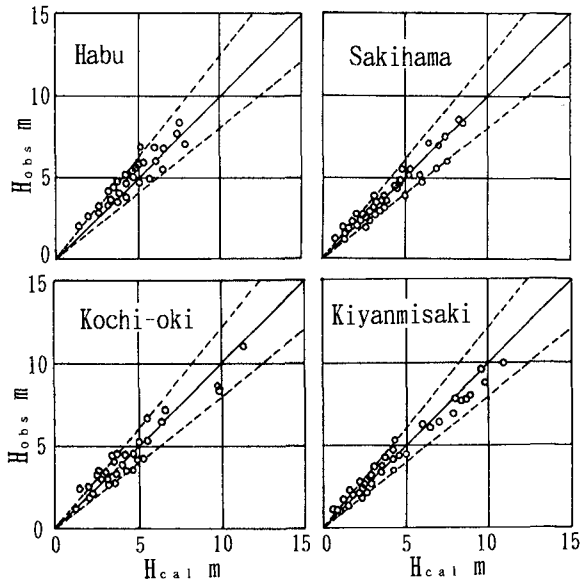


Fig. 12 Comparison of hindcast and observation for maximum wave height during a typhoon.

4. Estimation of Extremes of Storm Surge in Ise Bay

A Monte-Carlo simulation for the generation of typhoon parameters is carried out over a period of 1000 years. The number of typhoons generated is about 7800. The associated storm surges in Ise Bay are computed for 2347 influential typhoon cases.

Fig. 13 shows the relation between return storm surge height with standard deviation at Nagoya Harbor and return period, where they are estimated based on the simulated data and the observed data over a period of 42 years from 1950 to 1991. It should be noted that the standard deviation estimated using the observed data for a shorter period becomes increasingly larger than that based on the simulated data for a longer return period. It can be said that estimates of return storm surge heights for return periods of less than 100 years by this system are close to those evaluated from the observed data, and that even for longer return periods, the re-

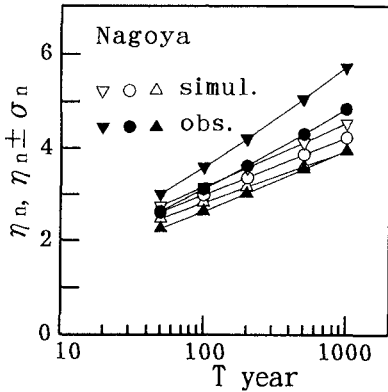


Fig. 13 Relation between return storm surge height with standard deviation and return period.

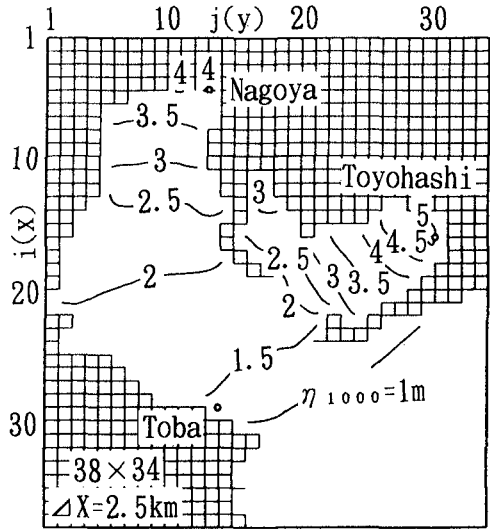


Fig. 14 Distribution of 1000-year return storm surge height in Ise Bay.

sults correspond well with each other, when their standard deviations are taken into account.

Spatial distribution of the 1000-year return storm surge height in Ise bay is given in Fig. 14, where the standard deviation ranges from 2.4 to 4.0 % of the return value and the maximum is 0.2 m. Return storm surge height rapidly increases from the entrance of the bay toward the inner most areas, in which case the maximum value exceeds 4 m at Nagoya Harbor and 5 m at Toyohashi point.

5. Estimation of Extremes of Wave height at the Pacific Coast of Japan

Two types of Monte-Carlo simulation are conducted. One is the simulation over a period of 1000 years as well as the case of storm surge computation, and the other is 100 times reiteration of the simulation over a period of 50 years. This is done for the purpose of directly computing standard deviation of each return wave height and investigating the applicability of a jackknife method to the evaluation of standard deviation based on the comparison between both estimates. Wave heights are calculated for about 3000 influential typhoon cases at 9 wave observation points indicated in Fig. 9.

Fig. 15 illustrates the effect of the number of iterations on mean and standard deviation of return wave height, in which statistically stable results can be seen for more than 50 iterations. Table 2 is the results of extreme analysis, in which standard deviations with a jackknife method agree well with those by direct calculation.

Fig. 16 shows longshore variation of the 1000-year return wave height and its standard deviation (68 % confidence interval) estimated using two kinds of simulation data, hindcasted data and observed data. Wave hind-casting is conducted for more than 150 intense typhoons which occurred during 45 years from 1948 to 1992, and period of wave observation ranges from 10 years to 21 years up to 1993. The return wave heights estimated from 4 kinds of extreme wave height data are in general agreement in spite of a great difference between computation period and observation period, when their standard devi-

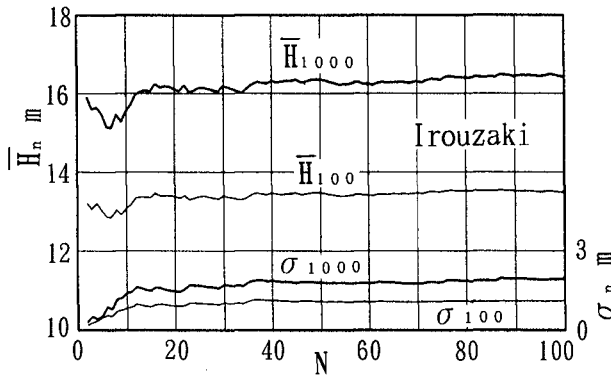


Fig. 15 Effect of iteration number of simulation on return wave height and standard deviation.

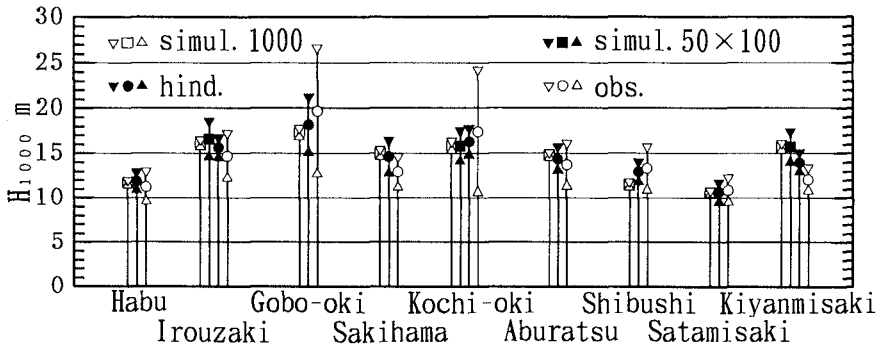


Fig. 16 Variation of 1000-year return wave height with standard deviation around the Pacific coast.

Table 2 Applicability of jackknife method in estimation of standard deviation.

location (depth m)	data	N _y (years)	H _n ± σ _n (m)	
			100 years	1000 years
Irouzaki (50)	simul.	50×100	13.5±1.1	16.6±2.0
	jack.		1.1	1.9
Kochi-oki (120)	simul.	50×100	12.9±1.0	15.8±1.7
	jack.		1.1	1.9
Kiyamisaki (51)	simul.	50×100	13.2±1.0	15.7±1.7
	jack.		0.9	1.6

ations are taken into account, but the confidence intervals are much wider in the estimates based on observation data.

6. Conclusions

It should be emphasized that the system proposed in this study is very useful to estimate extremes of storm surge height and wave height for return periods of more than several hundred years and their confidence intervals around the Pacific coast and the East China Sea coast of Japan.

7. Acknowledgements

A part of this study was accomplished with the support of the Science Research Fund (No. 06680431) of the Ministry of Education, for which the authors express their appreciation. Thanks are due to Messrs. Y. Nakamura and Y. Ohki, former master course students of Civil and Ocean Engineering, Ehime University for their sincere assistance during the study.

References

- Goda, Y. (1988): Numerical investigation on plotting formulas and confidence intervals of return values in extreme statistics, Rep. of the Port and Harbor Res. Inst., Vol. 27, No. 1, pp.31-92 (in Japanese).
- Yamaguchi, M. et al. (1987): A shallow water prediction model at a single location and its applicability, Proc. JSCE, No. 381/11-7, pp.151-160 (in Japanese).
- Yamaguchi, M. et al. (1995): Comparison of parameter estimation methods in extreme wave analysis, Proc. Coastal Eng., in Japan, Vol. 42, pp.231-235 (in Japanese).

CHAPTER 109

DESIGN OF VERTICAL WALLS AGAINST STORM SURGE

A. Kortenhaus¹, C. Miller², H. Oumeraci³

ABSTRACT

A concept for the design of high water protection (HWP) walls under storm surge conditions has been developed and is applied to the geometry found in the harbour of Hamburg, Germany. However, the design methods used have been generalized so that they may be used for a wide range of cases with similar geometries. Many gaps in standard design formulae have been filled by developing engineering approaches or formulae as reflection by steep berms, new breaker criterion, design formulae for impact breakers, reduction of loads by overtopping and soil pressure distribution in front of the wall.

INTRODUCTION

Interest in protective structures against storm surges is expected to largely increase in the near future, mainly due to the increased rate of storminess in the last decades. In order to be able to react more rapidly and to better protect the coastal estuary zones of high economic, social and environmental value, the performance of existing structures and their design must be reconsidered. Especially in areas with limited space, where the construction of "classic" high water protection (HWP walls) is impossible, the HWP walls as commonly found for instance in Hamburg are very suitable protective structures. Such a study has recently been conducted for the city of Hamburg, reconsidering the safety margin of all vertical wall structures within the harbour area. The motivation for this study was the change of the wave climate and of the rising water level assessments in the Hamburg harbour. To date, no general formulae have been developed to account for (i) the complicated foreland geometries in the harbour area, (ii) the different processes of wave transformation on these types of foreland, (iii) breaking of waves on the foreland and

¹Dipl.-Ing., Leichtweiß-Institut, TU Braunschweig, Beethovenstr. 51a, 38106 Braunschweig, Germany, e-mail: a.kortenhaus@tu-bs.de

²Dr.-Ing., Wirtschaftsbehörde Strom- und Hafenbau, Hamburg, Dalmannstr. 1, 20457 Hamburg, Germany

³Prof. Dr.-Ing., Leichtweiß-Institut, TU Braunschweig, Beethovenstr. 51a, 38106 Braunschweig, Germany, e-mail: h.oumeraci@tu-bs.de

(iv) different breaker types occurring at the protective structures. The design of HWP walls is very often considered to be much simpler than other more classical protection works. The relatively small heights of the HWP walls and their "simplicity" constitute the main reason, why this research field was neglected in the past. In fact there are many important peculiarities showing the need to develop this research field. Among the peculiarities there is for instance the size of the areas to be protected by the HWP walls which often extend over considerable lengths (e.g. more than 100 km in Hamburg harbour). Further reasons showing the need for more research will be addressed below.

In the Hamburg harbour area four typical foreland geometries can be identified (Fig. 1) which illustrate the large variety of harbour protection works. Due to these different types, a general design procedure is necessary which (i) accounts for different foreland geometries, (ii) is suitable for engineering practice and therefore must be easy to use and (iii) takes into account the large differences in water levels during a tidal cycle.

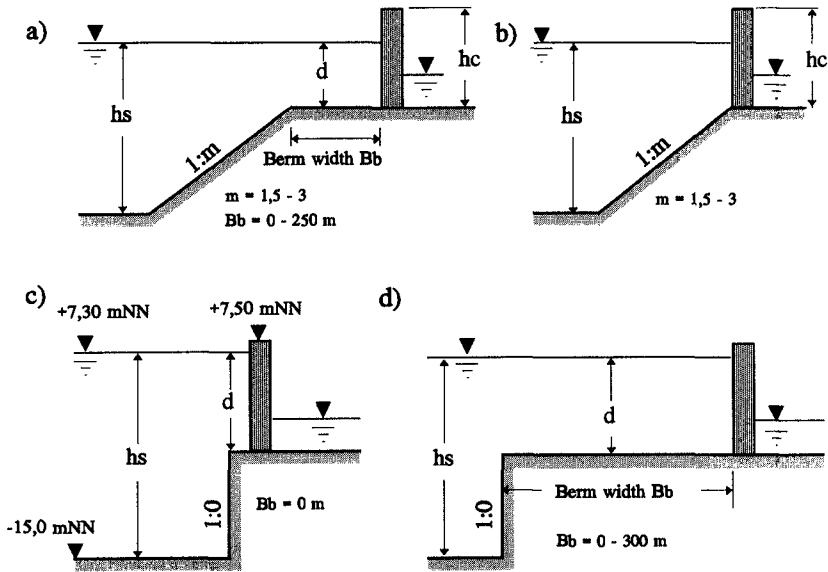


Fig. 1: Typical foreland geometries in the Hamburg harbour area

It is the main purpose of this paper to suggest a new design philosophy for protection works consisting of a variable foreland geometry with a vertical wall on top. In particular, a method is described to evaluate the wave transformation on the foreland and to calculate the most critical forces and moments on the vertical wall with respect to the critical water level and breaker type.

DESIGN STRATEGY

A set of five parameters is defined which describes all typical wall and foreshore geometries in the harbour area (Fig. 1). The walls are built as sheet walls or concrete wall structures with free heights of up to three meters. The design strategy for these conditions can be principally summarized in Fig. 2. The variable water level in this figure requires an iteration procedure until the design water level is reached which yields the most critical load at the wall. Breaking wave criteria, wave overtopping and wave load forces are evaluated by using the most updated design formulae/diagrams. It can be seen from Fig. 2 that three different loading cases may be distinguished:

- Standing waves: standing waves are very rare under prototype conditions for irregular wave trains but may occur during high water levels. A modification of the MICHE-RUNDGREN procedure for standing or almost standing waves was found to give reasonable results (*SPM, 1984*).
- Broken waves: broken waves at the wall represent the most frequent loads in the harbour area and may carry floating bodies (empty containers) hitting the wall. The standard CERC procedure for broken waves will be used to predict these loads (*SPM, 1984*).
- Plunging breakers: plunging breakers are relatively rare and will only occur under particular storm surge conditions but represent the most dangerous situation for the protection works since breaking waves cause very high impact loads. Results of hydraulic model tests which have been performed under the Marine Science and Technology Programme (MAST III) of the European Communities and formulae most recently developed to account for these type of loads (*Klammer et al., 1996*) will be used.

The variety and complexity of the foreland geometry makes it more difficult to define the design wave in front of the wall. The reason for this is that there are no reliable tools to describe the wave transformation and breaking criteria for most of the conditions shown in Fig. 1. The same reason is also valid for the lack of general design formulae to calculate the wave load and overtopping under these conditions.

The problem becomes more difficult by the complexity of the dynamic interaction of the "wave-structure-soil"-system under the impact load of breaking waves. Very often it is impossible to simplify the problem so that a static design method can be used. Moreover, the design water levels, wave parameters, loading and overtopping conditions do vary along the structure implying that there is not the same safety along the HWP walls at equal wall height.

The four design steps shown in Fig. 2 may be briefly described in the following sections.

(a) Step 1: Determination of Input Parameters

First, all important input parameters have to be defined or determined, respectively. The relevant water levels and the geometry of the foreland as well as the construction can be summarized by five parameters: water depth at the toe of the berm h_s , slope of the berm m , width of the berm B_b , water depth at the wall d and the free wall height h_c (Fig. 1).

The significant wave height $H_0 = H_s$, the peak-period T_p and the wave direction θ are needed as deep water input parameters. These parameters can be determined from

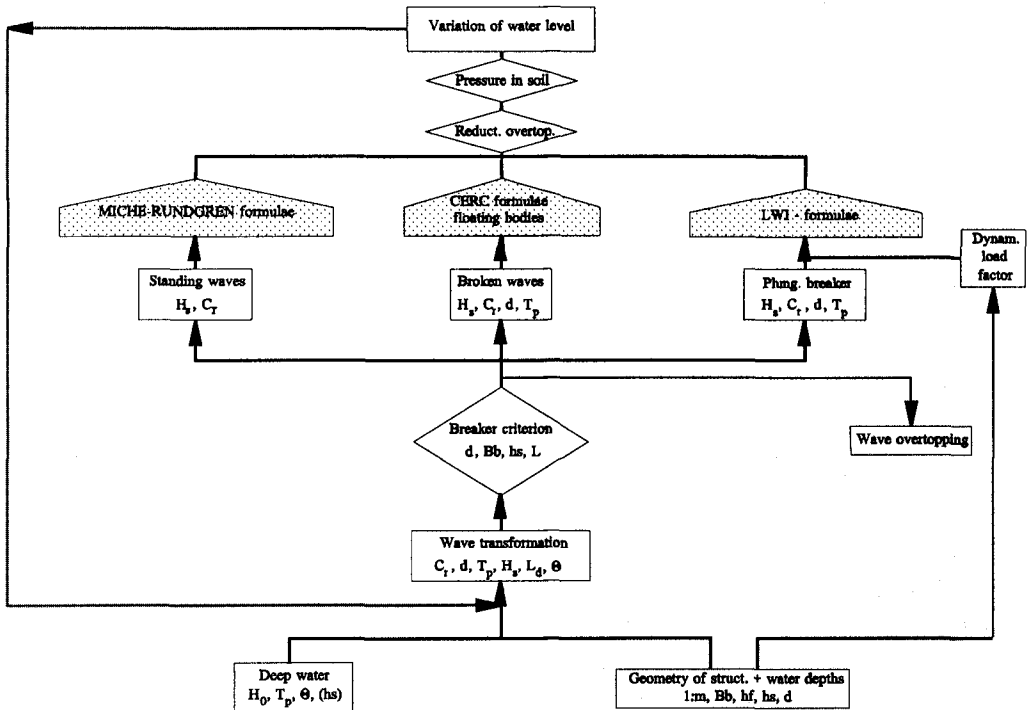


Fig. 2: Design procedure for high water protection works

measurements or by numerical wave forecast (*van Vledder, 1995*). Furthermore, particular boundary conditions provided by harbour authorities must also be taken into account. In Hamburg "Strom- und Hafengebäude" is responsible for the protection works used to provide shelter against high storm surges. These authorities generally provide information regarding the design of the load by floating bodies (empty containers etc.) as well as detailed data about the geometry of the HWP wall segments and their alignment relative to the wind direction. The latter is important as the design of HWP walls on the lee side can be performed by considering only the highest possible hydrostatic pressure (water level at the top of the wall); i.e. without any wave load (*Kortenhaus and Oumeraci, 1996*).

(b) Step 2: Wave Transformation and Breaker Criteria

Incident waves approaching from deep water will be transformed on the berm by shoaling, refraction and reflection; i.e. the wave height H_d in the water depth d (at the wall) can be derived by:

$$H_d = \kappa_s \cdot \kappa_R \cdot \kappa_X \cdot H_{\max} \quad (1)$$

H_{\max} is the maximum wave height in deep water (Rayleigh distribution) which can be derived from $H_{\max} = 1.86 H_s$ (H_s from step 1).

κ_s , κ_R and k_x are the shoaling, the refraction and the reflection factor, respectively (determined by linear wave theory). The shoaling factor κ_s and the refraction factor κ_R can be calculated as follows:

$$\kappa_s = \frac{k_{s,W}}{k_{s,0}} \quad (2)$$

$$\kappa_R = \frac{k_{R,W}}{k_{R,0}} \quad (3)$$

where $k_{s,0}$ and $k_{s,W}$ are the shoaling coefficients in deep water (subscript 0) and at the wall (subscript W) and $k_{R,0}$ and $k_{R,W}$ are the refraction coefficients. The reflection factor k_x describes the reduction of wave energy by the reflection due to the steep berm and can be calculated as follows:

$$k_x = \sqrt{1 - \kappa_B^2} \quad (4)$$

The total reflection coefficient of the wall-berm-system κ_B can be estimated as follows:

$$\kappa_B = \sqrt{\frac{E_{01}}{E_0} \cdot \kappa_{01}^2} \quad (5)$$

where κ_{01} is the reflection coefficient at the berm, E_0 is the wave energy in deep water calculated from linear wave theory and E_{01} is the part of the wave energy in front of the berm which can also be estimated by linear wave theory. The reflection coefficient at the berm κ_{01} can be estimated as follows (ξ is the Iribarren number):

$$\kappa_{01} = 1 - \exp\left(-\frac{1}{7} \xi^2\right) \quad (6)$$

Fig. 3 shows the reflection factor k_x plotted against the relative water depth d/L_0 according to Eqs. (4)-(6). It can be seen that changes in effective reflection coefficients up to 25% may result for design water levels ($d \approx 2$ m; $L_0 \approx 20$ -25 m) in the Hamburg harbour area.

To determine the relevant loading case under storm surge conditions breaking criteria are needed which account for the reflection properties of the HWP wall and for the foreland geometry.

Assuming the reflection coefficient to be 0.9 for vertical HWP walls (Kondo *et al.*, 1986) the wave height of the breaking wave H_b can be determined by the following formula (Oumeraci *et al.*, 1993):

$$H_b \approx 0.10 L_0 \left[\tanh \left(2\pi \frac{d}{L_b} \right) \right]^2 \quad (7)$$

L_0 is the wave length in deep water and L_b is the wave length at the breaking point (water depth d) which can be calculated from linear wave theory as follows:

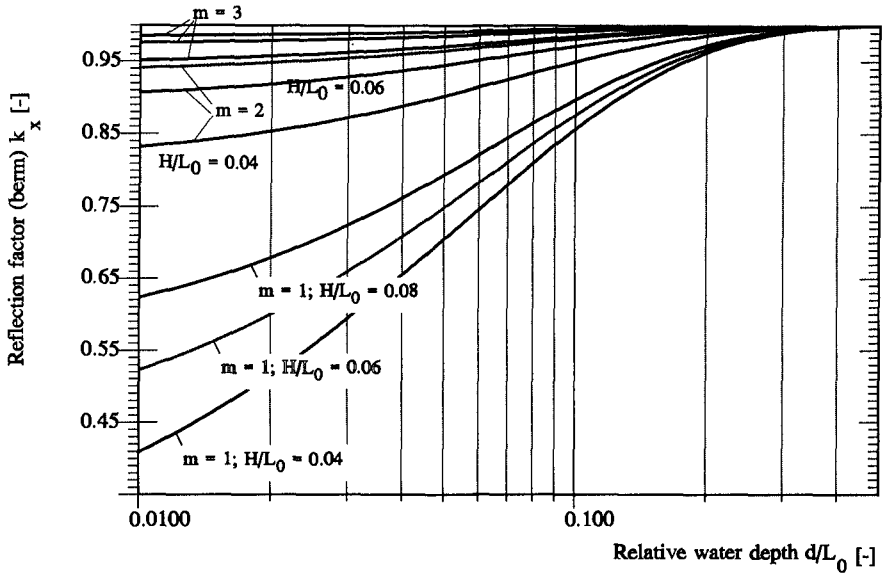


Fig. 3: Reflection nomogram for a vertical wall with a foreshore sloping berm

$$L_b \approx L_0 \left[\tanh \left(2\pi \frac{d}{L_0} \right)^{3/4} \right]^{2/3} \tag{8}$$

The comparison of the breaking wave height H_b from Eq. (7) and the wave height H_d from Eq. (1) allows a first distinction into two loading cases. If H_b is smaller than H_d the waves will not break and the 'Standing wave' loading case can be applied.

If H_b is larger than H_d loading cases 'plunging breaker' or 'broken wave' can be applied. To check for 'plunging breaker' conditions a 'breaker type nomogram' in Fig. 4 has been developed on the basis of existing experimental data (Takahashi *et al.*, 1993). Comparison to results obtained in large-scale model tests showed that these breaking criteria give acceptable results (Oumeraci and Kortenhaus, 1996). A further comparison to another method recently published by Allsop *et al.* (1996) shows only slight differences. The relative berm width Bb/L_b , the relative berm height $h_r = (hs - d)/hs$ and the relative wave height H_d/d are needed as input parameters for the nomogram.

The 'plunging breaker' loading case occurs when the point is inside the corresponding H_d/d area. If the point is outside the loading case "Broken Wave" can be assumed. Two examples in Fig. 4 demonstrate the use of the breaker type nomogram.

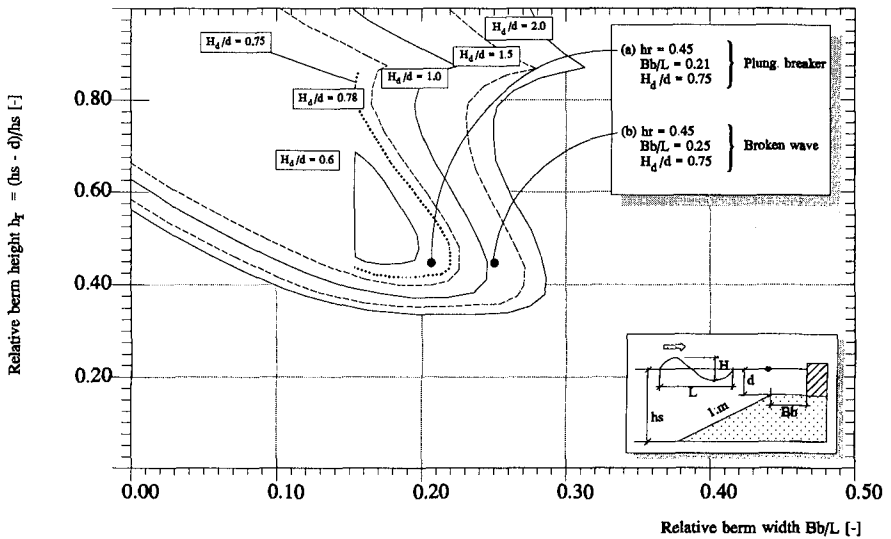


Fig. 4: Nomogram for identification of loading case 'plunging breaker'

(c) Step 3: Calculation of Loading Cases

The wave pressure distribution at the wall, wave forces and moments for each of the loading cases described before have to be determined. For all cases a load reduction due to overtopping and the pressure distribution in the soil in front of the wall will be given. These calculations are described below in the third section of this paper.

(d) Step 4: Variation of Water Level

During storm surge conditions the water level will vary significantly in front of the wall. Therefore it is necessary to perform step 3 for a stepwise reduction of the water level (down to $d = 0$). As a result a critical water level and a corresponding load for each section of the wall along the HWP line are obtained.

This procedure can be used for the identification of the most critical spots along the HWP walls in the harbour area where impact loading may occur under particular water level and sea state conditions.

DETERMINATION OF LOADING CASES

This chapter summarizes the methods to estimate the pressure distributions, forces and moments due to the wave action in front of the structure for the three loading cases shown in Fig. 2. Due to the limited space for this paper, related references will be given in all cases where standard procedures have been used.

(a) Standing Waves

For the loading induced by standing waves the method of *Sainflou (1928)*, the method by *Rundgren (1958)*, modified by Miche and summarized in *SPM (1984)* and a more recent method based on a crest elevation proposed by *Goda (1985)* have been compared. As a result the method of Miche-Rundgren has been selected for the design, because of its simplicity in engineering use and because it accounts for both terms of higher order as well as for the reflection coefficient of the HWP wall (see design diagrams in *SPM, 1984*).

It is proposed to use a constant reflection coefficient for the Miche-Rundgren method. It is well known that a reflection coefficient of 1.0 is too conservative but to be on the safe side a constant reflection coefficient of $C_r = 0.9$ is proposed. In applying the method to the harbour of Hamburg this value was used.

(b) Broken Waves

This loading case is assumed to be the predominant loading case for HWP walls under storm surge conditions and geometric boundary conditions as for instance found in Hamburg harbour. The fast change from deep water conditions in front of the berm to shallow water conditions in front of the wall will induce wave breaking. A plunging breaker at the wall will occur under very special geometric conditions (relative berm height and width) as already shown in Fig. 4. Therefore broken waves are more likely to be expected. The design for this loading case may be combined with a load induced by floating bodies as it is most likely that floating bodies will be transported by broken waves. For the assessment of design load, the method by *CERC (SPM, 1984)* is proposed.

The input parameters for the SPM method are:

- the wave depth at the wall d
- the wave height of the breaking wave H_b according to Eq. (7)

(c) Plunging Breakers

For plunging breakers at the wall a new method was developed to calculate pressure distribution and forces at the vertical wall (*Klammer et al., 1996*). The latter formula takes into account the total duration and the rise time of the load.

From experiments on a large-scale breakwater model the following formula for the impact force has been derived for the design of the HWP walls in Hamburg:

$$F_{h,\max} = 8.0 \cdot \rho g H_b^2 \quad (9)$$

$F_{h,\max}$ is the maximum horizontal wave force, H_b is the height of the breaking wave in front of the structure and ρ is the density of the water. From statistical analysis it has been found that the non exceedance probability of the relative horizontal force $F_{h,\max}/\rho g H_b^2$ in Eq. (9) is about 10 to 15%. The point of application of the force is close to the height of the design water level. The pressure distribution at the time of the maximum horizontal force and further design details can be taken from *Klammer et al., 1996*.

To account for the dynamic behaviour of the system the load has to be multiplied by a dynamic load factor D . Dynamic load factors for caisson structures were principally investigated by *Oumeraci and Kortenhaus (1994)*. In the example case of the Hamburg harbour dynamic load factors were determined from prototype measurements at the protection walls in the Hamburg harbour area where D was found to be in the range from 0.85

to 1.2 (Kruppe, 1996). A conservative value for D of 1.5 can be used for each section along the HWP walls where no detailed information on the dynamic characteristics of the structure-soil-system are available. The force increased by the dynamic load factor has to be used for a static design approach instead of the values calculated by the method described before:

$$F_h = D \cdot \left(8,0 \cdot \rho g H_b^2 \right) \tag{10}$$

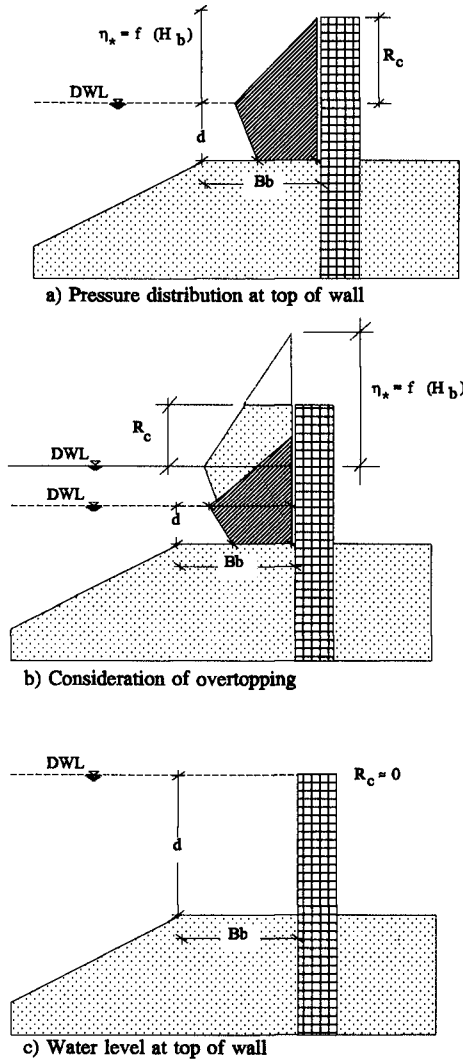


Fig. 5: Comparison of pressure distributions with and without overtopping

Reduction of wave impact at the wall due to oblique wave attack and short-crestedness may also be taken into account by using the results of extensive 3D hydraulic model tests (Franco et al., 1995). For short-crested waves almost no reduction of horizontal forces can be found whereas for long-crested waves, reductions in horizontal forces can be found only for higher wave obliquity.

OVERTOPPING

Overtopping will lead to a reduction of the horizontal loading. This phenomenon has not yet been addressed in detail in the literature. Generally, in the case of overtopping the pressure figure is cut at the top of the wall (Fig. 5b). The pressure ordinate at the top of the wall is then calculated by an interpolation between the ordinate at the height of the design water level (DWL) and the point above the water level where the pressure would be zero if the wall were high enough. However, this method particularly fails for higher DWL. Therefore an additional approach is suggested below.

In Fig. 5a the wave and the pressure distribution just reach the top of the wall whereas in Fig. 5c the design water level

(DWL) has reached the top of the wall. In the latter case the dynamic pressure induced by wave motion is relatively small as compared to the hydrostatic head. Hence, the governing load is the hydrostatic head related to the water depth at the wall.

Therefore the reduction of the loading on the wall due to overtopping is about zero at the top of the wall. Especially for impact loading this is not the case when the pressure distribution is simply cut off at the top of the wall. Contrarily this procedure would result in a significantly high pressure at the top of the wall.

Hence, a factor k_{Fh} has been introduced to reduce the loading by more than a simple 'cutting' of the pressure distribution. This factor accounts for the fact that the pressure distribution and the force in Fig. 5c has to be zero ($R_c \approx 0$) and has its maximum for an infinitely high wall (Fig. 5a):

$$F_{h,ov} = k_{F,h} \cdot F_h \tag{11}$$

with

$$k_{F,h} = 1 \quad \text{für } \eta_* \leq R_c$$

$$k_{F,h} = \sqrt[3]{\frac{R_c}{\eta_*}} \quad \text{für } \eta_* > R_c \tag{12}$$

$F_{h,ov}$ is the reduced force, F_h is the horizontal force according to the method valid for each loading case, η_* is the distance of the highest point of the pressure distribution to the design water level and R_c is the freeboard of the wall. Applying this procedure for the three loading cases shown will result in the lower curve related to the respective loading case in Fig. 6.

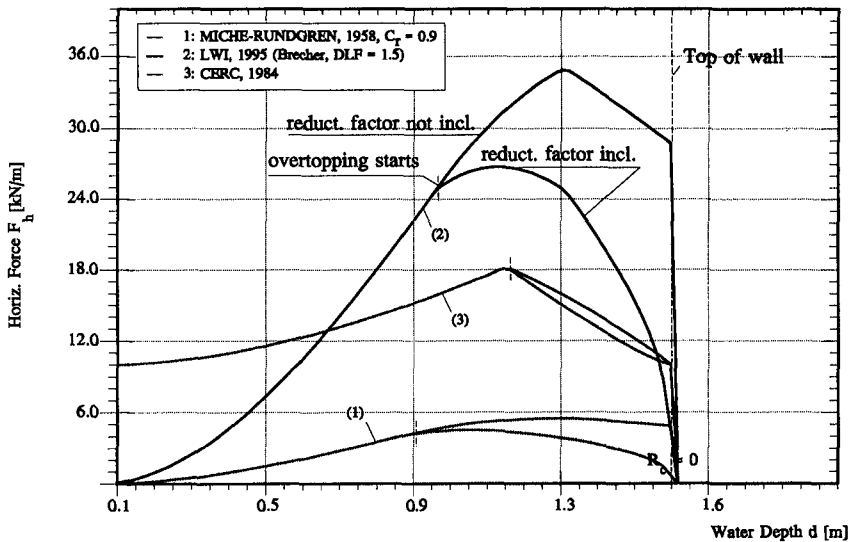


Fig. 6: Reduction of horizontal force by reduction factor k_{Fh}

SOIL PRESSURE IN FRONT OF THE WALL

(a) Standing Waves

For standing waves where the loading changes with the wave period T_p the pressure in the height of the berm p_s for a water depth d can be calculated by:

$$p_s = \rho_w g \left(1 + C_r\right) \frac{H}{2} \frac{1}{\cosh \frac{2\pi d}{L}} \quad (13)$$

For a berm made of *rubble material* it can be assumed that the decrease of pressure $p(z)$ in the soil still can be described by linear theory. Increasing depth in the soil z will result in:

$$p(z) = p_s \frac{\cosh \left[2\pi (t_B + z) \right]}{\cosh \left(\frac{2\pi d_b}{L} \right)} \quad (14)$$

For a berm made of *finer soil material* like sand the method of *Moshagen and Tørum (1975)* can be used. For $k_x = k_z$ (same permeability in horizontal and vertical direction) the method of *Moshagen and Tørum (1975)* can be simplified to:

$$p(z) = p_s \frac{\cosh \left[\mu (z + t_B) \right]}{\cosh \left[\mu t_B \right]} \quad (15)$$

n is the porosity of the soil material ($n \approx 0,4$); k_x is the permeability of the soil material in horizontal direction ($k_x \approx 10^{-4}$ m/s for sand); T is the wave period in s; L is the wave length in the water depth d in m and μ can be given by:

$$\mu = \left[\left(\frac{2\pi}{L} \right)^4 + \left(\frac{\frac{2\pi}{T} n \rho_w g}{k_x E_F} \right)^2 \right] \frac{1}{4} \quad (16)$$

Since *Moshagen and Tørum (1975)* assumed a total saturation of the soil E_F is set equal to E_{water} . This is not completely true as air and water will fill the pores of the soil. Therefore the following approach for E_F will be used in Eq. (16):

$$E_F = \frac{1}{\beta'} \quad (17)$$

In this β' is the compressibility of the pore fluid which can be calculated from:

$$\beta' = \beta + \frac{1-s}{p_a} \quad \text{für } (1-s) \ll 1 \quad (18)$$

β is the compressibility of the water ($\beta = 4.2 \cdot 10^{-7}$ m²/kN); s is the saturation of the soil; p_a is given by $p_a = p_{\text{atm}} + p_{\text{hydrostat}}$; p_{atm} is equal to 101.325 kN/m² and p_{hyd} is the hydrostatic pressure which is given by $p_{\text{hyd}} = \rho_w g d$.

The application of Eq. (18) to three typical water depths in the Hamburg harbour area is given in Tab. 1.

Tab. 1: Compressibility β' of the pore fluid as a function of the saturation of the soil s and the water depth d

Saturation s [-]	Compressibility of the pore fluid β' [m^2/kN]		
	$d = 0.5 \text{ m}$	$d = 1.0 \text{ m}$	$d = 2.0 \text{ m}$
1.00	$\beta' = \beta = 4.2 \cdot 10^{-7}$		
0.999	$9.83 \cdot 10^{-6}$	$9.42 \cdot 10^{-6}$	$8.96 \cdot 10^{-6}$
0.99	$9.45 \cdot 10^{-5}$	$9.04 \cdot 10^{-5}$	$8.31 \cdot 10^{-5}$
0.98	$1.89 \cdot 10^{-4}$	$1.80 \cdot 10^{-4}$	$1.66 \cdot 10^{-4}$
...
0.95	$4.71 \cdot 10^{-4}$	$4.50 \cdot 10^{-4}$	$4.14 \cdot 10^{-4}$

(b) Broken Waves and Impact Breakers

For impact loads and broken waves no method is yet available to assess the damping in fine soil material. For rubble material the respective pressure distribution can be extended in the soil. For fine soil materials (sand) it is proposed to neglect the pressure distribution in the soil due to the strong damping (highly frequent loading).

CONCLUDING REMARKS AND FUTURE RESEARCH WORK

A concept for the design of high water protection (HWP) walls under storm surge conditions has been developed. The concept was initially developed for the harbour of Hamburg (Germany) but the design methods have been generalized so that they may be used for a wide range of cases with similar geometries.

In the future however a more elaborated concept for the safe and economic design of this kind of protective structures is needed which requires both an integrative procedure by accounting for hydraulic, structural and soil mechanical aspects as well as for all possible failure modes and their probability of occurrence. Therefore it is necessary to use dynamic and probabilistic design methods where the 3D-character of the problem has to be taken into consideration.

This task has been undertaken in the "Marine Science and Technology"-programme (MAST III) of the European Union. This research project of 23 European institutes out of different disciplines (hydrodynamics, coastal engineering, soil mechanics, structural mechanics, applied mathematics, etc.) is coordinated by Leichtweiss-Institut, Braunschweig (Oumeraci, 1995) and is aiming for providing a basis for the design of vertical breakwaters under probabilistic aspects.

ACKNOWLEDGEMENTS

This study has been supported by the Hamburg harbour authority "Strom- und Hafengebäude". The support of basic research studies by the German Research Council (DFG) on monolithic breakwaters and by the European Union (contract no. MAS2-CT95-0041) on

vertical structures is also gratefully acknowledged. Without the latter basic research studies the results described in this paper would not have been achieved.

REFERENCES

- ALLSOP, N.W.H.; VICINANZA, D.; CALABRESE, M.; MCKENNA, J.E. (1996): Wave forces on vertical and composite breakwaters. *Strategic Research Report. Hydraulics Research Station, Wallingford, SR 443, Wallingford, U.K.*, 94 pp.
- FRANCO, L.; DE GERLONI, M.; VAN DER MEER, J.W. (1995): Wave overtopping on vertical and composite breakwaters. In: *Final Proceedings, MAST II, MCS-Project: Monolithic (Vertical) Coastal Structures*, Paper 4.10, 16 pp.
- GODA, Y. (1985): Random seas and design of maritime structures. Tokyo: University of Tokyo Press, 323 pp.
- KLAMMER, P.; KORTENHAUS, A.; OUMERACI, H. (1996): Wave impact loading of vertical face structures for dynamic stability analysis - prediction formulae. *Proceedings International Conference Coastal Engineering (ICCE)*, ASCE, Orlando, Florida, USA, vol. 25. In these Proceedings.
- KONDO, K.; AKAMA, M.; ISOBE, M. (1986): Measurement of reflection coefficient of seawall in Omura Bay. *Proceedings International Conference Coastal Engineering (ICCE)*, ASCE, Taipei, Taiwan, vol. 20, Part 2, Chapter 146, pp. 1987-2001.
- KORTENHAUS, A.; OUMERACI, H. (1996): Hochwasserschutzwände im Hamburger Hafen - Lastansätze für Wellendruck. *HTG-Sprechtage "Hochwasserschutz in Häfen / neue Bemessungsansätze"*, Oktober 1996, HtG, Hamburg, Germany, 21 S. In German.
- KRUPPE, J. (1996): Berücksichtigung dynamischer Einflußfaktoren bei Wellendruckschlag. *HTG-Sprechtage "Hochwasserschutz in Häfen / neue Bemessungsansätze"*, Oktober 1996, HtG, Hamburg, Germany, 9 S. In German.
- MOSHAGEN, H.; TORUM, A. (1975): Wave induced pressures in permeable seabeds. *Journal of Waterways, Harbors and Coastal Engineering Division*, ASCE, vol. 101, no. WW1, pp. 49-57.
- OUMERACI, H.; KLAMMER, P.; PARTENSKY, H.-W. (1993): Classification of breaking wave loads on vertical structures. *Journal of Waterway, Port, Coastal and Ocean Engineering*, ASCE, vol. 119, no. WW4, pp. 381-397.
- OUMERACI, H.; KORTENHAUS, A. (1994): Analysis of dynamic response of caisson breakwaters. *Coastal Engineering, Special Issue on 'Vertical Breakwaters'*, Oumeraci, H. et al., Amsterdam, The Netherlands: Elsevier Science Publishers B.V., vol. 22, nos. 1/2, pp. 159-183.
- OUMERACI, H. (1995): Multi-disciplinary research experience on vertical breakwaters: the MCS-Project. In: Commission of the European Communities (ed.): *MAST Days and EUROMAR Market. Project Reports.*, Sorrento, Italy, 26 pp.
- OUMERACI, H.; KORTENHAUS, A. (1996): Bemessung von Hochwasserschutzwänden im Hamburger Hafen. *Berichte Leichtweiß-Institut für Wasserbau, Technische Universität Braunschweig, LWI, Braunschweig, Germany, Nr. 799, 44 S.; 9 Teilberichte*. In German.

- RUNDGREN, L. (1958): Water wave forces - a theoretical and laboratory study. *Kungliga Tekniska Hoegskolans handlingar*, Stockholm, Sweden, no. 122, 123 pp.
- SAINFLOU, G. (1928): Essai sur les diques maritimes verticales. *Annales des Ponts et Chaussées*, vol. 98, no. 4, pp. 5-48. In French.
- SPM (1984): Shore protection manual. Chapters 6 through 8; appendices A through D, Vicksburg, Mississippi, USA, 4th edition, 800 pp.
- TAKAHASHI, S.; TANIMOTO, K.; SHIMOSAKO, K.-I. (1993): Experimental study of impulsive pressures on composite breakwaters. *Report. Port and Harbour Research Institute (PHRI)*, Tokyo, Japan, vol. 31, no. 5, pp. 33-72.
- VAN VLEDDER, G.PH. (1996): Wave climate during the design storm surge. *HTG-Sprechtage "Hochwasserschutz in Häfen / neue Bemessungsansätze"*, Oktober 1996, HtG, Hamburg, Germany, 9 pp., 4 figs. In German.

CHAPTER 110

NEARSHORE, WAVE AND TOPOGRAPHIC EFFECTS IN STORM SURGES

Gary Watson¹ and Takao Yamashita²

Abstract

Some ideas for improving the accuracy of storm surge prediction models are discussed. A detailed coastal flooding model is applied to the flooding of Chittagong in the April 1991 disaster, but results are only illustrative due to the lack of good topography data. The influence of waves on wind stress forcing and bottom friction is discussed. Some recent results from a coastal observation tower taken during a typhoon show enhanced stress compared with values from empirical formulae in the literature. A new model for improving the representation of typhoon wind fields in areas surrounded by mountains is presented. Its applicability for storm surge computation is demonstrated using observations of a typhoon and surge in Osaka Bay.

Introduction

Storm surges, abnormal rises in sea level caused by strong onshore winds, pose one of the most severe natural hazards in many coastal areas. As recently as 1991, 150,000 people died in Bangladesh, mostly by drowning in coastal floods caused by a severe cyclone and surge. Effective action to minimize the impact of such disasters depends on advance knowledge of the threat to any particular location. A number of numerical models have been developed for predicting surges, and in some countries they are used operationally for making surge warnings. However, there remains scope for improving the representation of a number of phenomena in the models and this paper describes some recent investigations. These include new work on modelling coastal flooding; modelling of the wave field and its effects

¹Cooperative Foreign Researcher, Disaster Prevention Research Institute, Kyoto University, Gokasho, Uji, Kyoto 611, Japan

²Associate Professor, same address.

on wind stress, bottom friction and coastal set-up; and the effect of mountains on the wind field.

Surge models commonly use some form of the non-linear shallow-water equations for mass and momentum conservation, with appropriate forcing terms. Here we use the following:

$$\frac{\partial \zeta}{\partial t} + \frac{\partial(ud)}{\partial x} + \frac{\partial(vd)}{\partial y} = 0 \quad (1)$$

$$\frac{\partial u}{\partial t} + u \frac{\partial u}{\partial x} + v \frac{\partial u}{\partial y} = f v - g \frac{\partial \zeta}{\partial x} - \frac{1}{\rho} \frac{\partial p_a}{\partial x} + \frac{1}{\rho d} \tau_{sx} - \frac{1}{\rho d} \tau_{bx} + A \nabla^2 u \quad (2)$$

$$\frac{\partial v}{\partial t} + u \frac{\partial v}{\partial x} + v \frac{\partial v}{\partial y} = -f u - g \frac{\partial \zeta}{\partial y} - \frac{1}{\rho} \frac{\partial p_a}{\partial y} + \frac{1}{\rho d} \tau_{sy} - \frac{1}{\rho d} \tau_{by} + A \nabla^2 v \quad (3)$$

where ζ is surface elevation, d is total water depth, and (u, v) is depth-averaged velocity. The terms on the right of the momentum equations (2) and (3) are due respectively to Coriolis force, surface slope, atmospheric pressure gradient, surface wind stress $\vec{\tau}_s = (\tau_{sx}, \tau_{sy})$, bottom friction stress $\vec{\tau}_b = (\tau_{bx}, \tau_{by})$, and eddy viscosity. A is an eddy viscosity coefficient.

If the wind field is reasonably well approximated, the storm surge predicted by models based on these equations is generally good enough to be useful. In principle however, it is possible to make improvements to the methods currently used. In the case of surges generated by tropical storms, the main limitation is the accuracy of storm forecasts. Prediction of the storm's track and speed are especially important, because landfall point and timing relative to local high tide strongly affect the location and depth of flooding (Flather, 1994). Storm intensity is also a primary factor determining surge height and this too is difficult to forecast, as it can change unexpectedly. Any progress in these respects would improve the surge forecasts.

Besides this, there are other improvements which could be made. Figure 1 illustrates some phenomena that occur during storm surges, which are not normally included in the models. Those discussed briefly in this paper are the flooding of rivers and low-lying coastal land, including the possibility of bore formation; the effect of waves on the wind stress, bottom stress and coastal set-up; and the effect of mountains on the wind field. Others that are not discussed here include coastal wave hazard, the drag effects of terrain, vegetation and buildings on flooding, changes in river levels (especially when in flood), and morphodynamic changes due to sediment transport during the surge. Ideally, all of these effects should be incorporated into future operational surge models.

Flooding of Rivers and Low-Lying Coastal Land

The most dangerous threat during a storm surge is the sudden flooding of inhabited areas on land near the coast. It is thus highly desirable to be able to model and predict such events in as much detail as possible. A standard surge model with a fixed boundary is able to make a reasonable prediction of the

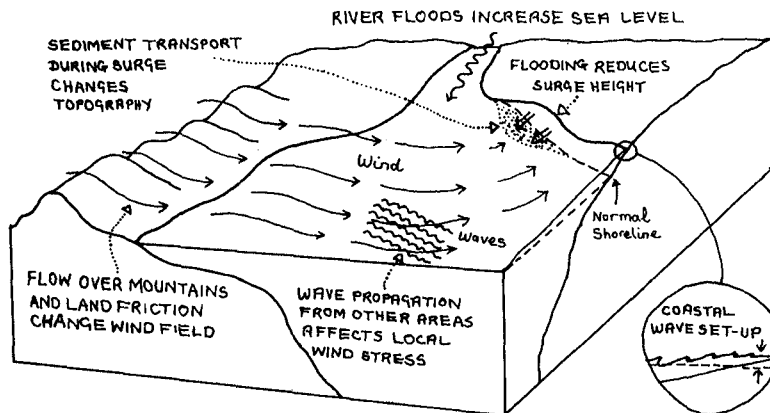


Figure 1: Some phenomena that occur during storm surges.

increase in coastal sea level, but this does not tell us the extent of flooding to be expected in any particular area. For example, if there is a river or an extensive area of low-lying land, the flooding will reach further inland and pose a more severe hazard. For flooding studies, we can use a local model with a fine grid covering the area of interest. Here we present some preliminary results from a model which is under development, simulating the flooding of Chittagong during the April 1991 disaster in Bangladesh.

A number of reports have said that surges in the Bay of Bengal are sometimes observed as “walls of water”, suggesting that they may steepen and break in the same way as a tidal bore. Tides and tsunamis are well known for steepening into breaking bores in suitably-shaped estuaries and rivers. It is likely that this may also sometimes happen with storm surges. The sudden increase in water level and associated turbulence would increase the resulting danger, and it is thus important to understand and be able to predict the circumstances under which bore formation can occur.

We thus use a model for coastal flooding that is able to represent bore formation. It is based on the nonlinear shallow-water equations and uses a numerical method which accurately handles the formation of discontinuities (representing bores) in the solution. It is an extension into two horizontal dimensions of an earlier model used for waves on beaches (Watson et al., 1994). The boundary condition at the moving shoreline is satisfied, allowing flooding to be simulated properly. The model includes a bottom friction term but for these preliminary studies, the drag coefficient was set to zero. The model is applied to a detailed local area using a fine grid, with offshore boundary conditions provided by a surge model of a wider area including the continental shelf.

Here we show results from a simulation of the flooding of Chittagong in the

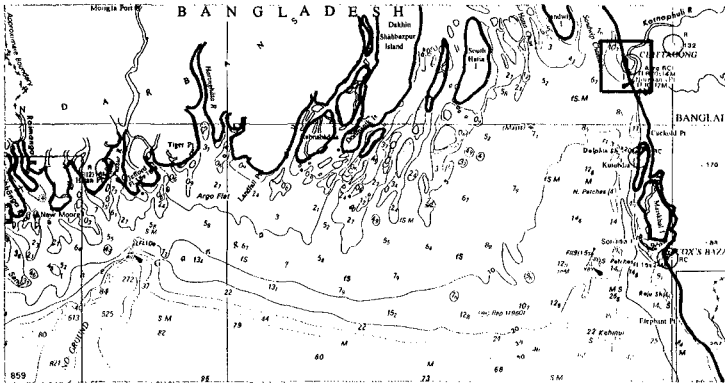


Figure 2: Map of the area showing the boundaries of the large-scale storm surge model and the small-scale flooding model.

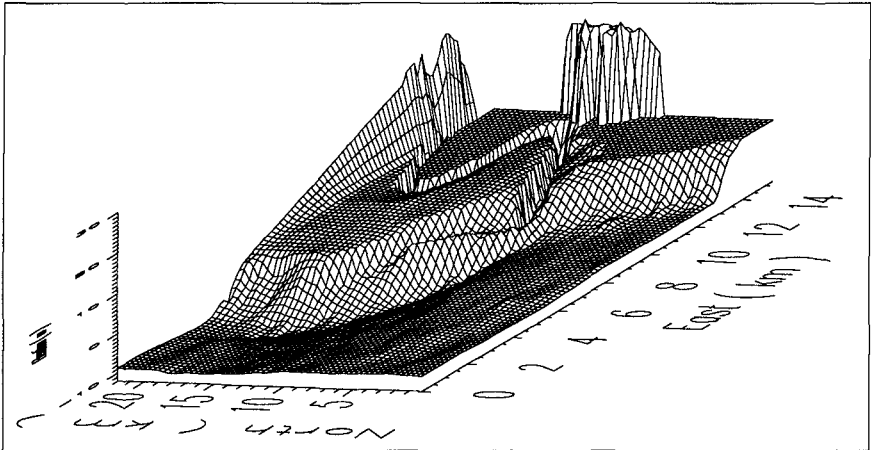


Figure 3: The topography of Chittagong and the Karnaphuli River.

April 1991 cyclone disaster in Bangladesh. A surge model of the northern Bay of Bengal (grid size $1,700 \text{ m} \times 1,726 \text{ m}$) was run using idealized pressure and wind fields based on available data for the cyclone intensity and track (Katsura et al., 1992). A fine-grid model (grid size $0.1' = 170 \text{ m} \times 185 \text{ m}$) was then constructed for a small area around Chittagong including the Karnaphuli River, solving the nonlinear shallow-water equations. The areas covered by the two models are shown in Figure 2. A time series of water level from the surge model at the point closest to Chittagong was applied to the western boundary of the local model.

The bathymetry and topography of the local model are plotted in Figure 3.

Bathymetry data were read and interpolated manually from British Admiralty chart No. 84. It has not been possible to obtain good elevation data for the city of Chittagong, so for this preliminary study a very approximate topography was constructed. East and south of the Karnaphuli River, heights were interpolated between the water and the 25 m contour on the Admiralty chart. To the north, the 20 m contour on the Chittagong Guide Map (Govt. of Bangladesh, 1976) was used. Between coast and river, Chittagong airport was set to its elevation of 3 m. North of the airport, data were invented. This is of course an important limitation on these results, which should be taken only as an illustration of the method. An example of the results from this simulation is shown in Figure 4. Extensive flooding of Chittagong is seen, but according to Katsura et al. (1992), the flooding was not quite as extensive as is shown here.

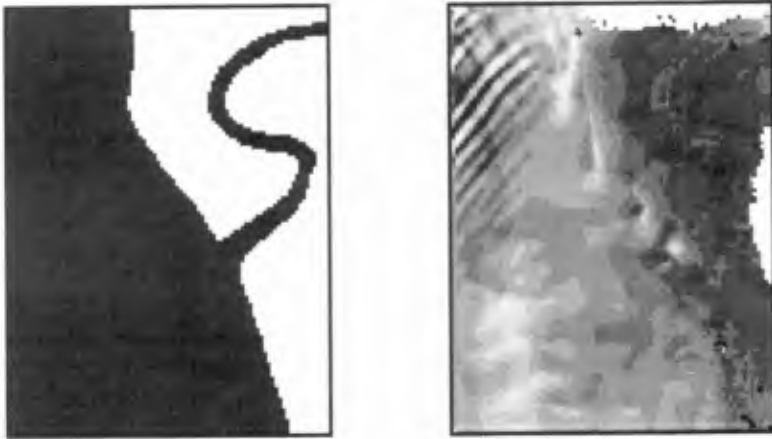


Figure 4: Preliminary results of the model showing flooding of Chittagong. *N.B. This calculation uses inaccurate topography and the result is only illustrative of the method. This result is not considered to be a good representation of the flood which actually occurred, nor of possible future floods.* On the left, the initial undisturbed state. On the right, during the storm surge flooding. Land is white and higher water levels are lighter shades.

No bore occurred in the Karnaphuli River. This is not surprising since the river has no V-shaped estuary to concentrate the wave energy, as is common in rivers which have tidal bores. A tidal bore exists in the Meghna estuary, which was also affected by the 1991 surge, but it has so far not been possible to run the model there because of a lack of bathymetric data.

The combined model shows potential for making detailed flooding and bore formation predictions, but uncertainties remain such as how to treat buildings and different types of terrain. Unfortunately, no precise observations for testing the predictions are available. Accuracy is also limited by a lack of good topo-

graphic data for the sites of interest. Thus, it is not yet possible to apply the results with confidence to particular localities.

Wave Effects

For storm surge modelling, the most important forcing terms are the atmospheric pressure, surface wind stress and bottom friction stress. The former is of course theoretically well-defined and depends only on a reasonably accurate knowledge of the relevant time-dependent pressure field.

The stress terms represent the exchange of momentum between atmosphere and ocean, and between ocean and sea bed. Air-sea momentum exchange is a complex process involving turbulent boundary-layer flow over a changing rough surface, wave generation, non-linear energy transfer between wave components, and wave breaking. Waves also affect the bottom stress, by increasing bottom boundary layer turbulence and eddy viscosity, and hence momentum transfer. These processes are not very well understood theoretically, especially in strong winds and high waves, and so are not incorporated into the models. If they can be better understood, then in principle the accuracy of the corresponding forcing terms in the models could be improved.

Dependence of Surface Wind Stress on Wave Conditions

The mean force acting on the surface of a body of water due to wind stress is usually approximated as

$$\vec{\tau}_s = \rho_a C_{D10} \vec{U}_{10} |\vec{U}_{10}| \quad (4)$$

where $\vec{\tau}_s$ is the wind stress at the surface (the horizontal force per unit area acting on the surface), ρ_a the air density, \vec{U}_{10} the mean wind at 10 m and C_{D10} the drag coefficient for wind at 10 m. To represent the fact that surface roughness increases with windspeed, this coefficient is normally specified as a function of the windspeed at 10 m, $C_{D10}(U_{10})$. An example is the empirical relationship of Smith et al. (1992), which is based on data from the HEXOS experiment. This is a linear relationship given by $C_{D10} = (0.66 + 0.072U_{10}) \times 10^{-3}$. A number of similar relationships have been proposed, based on different data sets. Although the data are scattered, these empirical functions are all quite similar. This approach is a useful first approximation, and produces acceptable results in many circumstances. Note however that it applies only to well-developed seas in which the waves are approximately in equilibrium with the local wind, in deep water, and also mainly for wind speeds greater than about 5 ms^{-1} .

There may be important cases where this is inaccurate, especially if the wind is rapidly changing (such as in tropical storms), or near the coast where the water is shallow and the waves fetch-limited, or where the wave spectrum has more than one significant component. Higher values of C_D are found both in growing waves, such as during the onset of a storm, and in shallow water. Both of these conditions are necessary for the development of a storm surge, so the effect is po-

tentially important. An important parameter here is the ratio of dominant wave phase speed to wind speed, known as the wave age c_p/U , which is an indication of whether or not the wind and waves have reached equilibrium. However, what field data exist are hard to interpret because the effect is comparable in size with measurement errors, and therefore cannot be determined very accurately. It has not so far been possible to derive any empirical formulae based on the data, and so this effect is not usually incorporated into surge models. Such cases could potentially be more accurately represented by a theory which correctly accounts for momentum transfer between wind and waves, and between waves and the mean current, such as that of P. Janssen (1992). Note however that there is currently much debate on this subject, for example J. Janssen (1995) recently argued that the HEXOS data show no statistically significant dependence of wind stress on sea state.

Wind and Wave Data from the Observation Tower

This section discusses drag coefficient estimates made from observations taken by the Kyoto University DPRI Tanabe-Nakajima Storm Surge Observation Tower. The tower is located about 2 km offshore from the town of Tanabe in southern Honshu, mainland Japan. It stands at the mouth of Tanabe Bay, on a plateau about 10 m in depth, about 100 m in diameter, in an area where the depth is predominantly about 30 m. It is possible that this plateau will have some local influence on the waves, but this is difficult to determine. The tower measures wave elevation (using a downward-looking ultrasonic sea-surface height gauge), current (using an electromagnetic current meter at a depth of 10 m) and wind (using a 3-component ultrasonic anemometer at a height of 20 m). Data are recorded at 20 Hz for 20 minutes during each hour. This section discusses some drag coefficient estimates made from these data.

Because the largest surges are generated by storms, priority was given to the analysis of data from Typhoon 9426, which passed very close to the tower on 29 Sept. 1994. The lowest recorded pressure was 965 hPa at about 19:00, and the central pressure was estimated as about 950 hPa. The track was slightly south of the tower, so that the wind direction changed rapidly from east to west, also at about 19:00. Maximum recorded wind speed was 24 ms^{-1} at about 21:00. Wave height peaked at around 5 m near 17:00 and the wave period reduced from 13 s to 7 s as the typhoon passed. Direct measurements of wave direction are not available. These observations are reported in more detail by Yoshioka et al. (1995).

Following Yelland et al. (1994), wind stress was estimated from the anemometer data using the turbulent (or inertial) dissipation method. This is based on the assumption that the energy spectrum of the down-wind component is governed by the rate of dissipation of energy by high-frequency turbulence. In this case,

the spectrum is assumed to have the form:

$$S(f) = K \epsilon^{2/3} f^{-5/3} \left(\frac{U}{2\pi} \right)^{2/3} \tag{5}$$

where $S(f)$ is the power spectrum of the down-wind component, K is the 1-D Kolmogorov constant, taken as 0.55, and ϵ is the high-frequency turbulent dissipation rate. If the measured spectrum is found to obey the $f^{-5/3}$ law reasonably well, then an average value of $S(f)f^{5/3}$ over an appropriate frequency range may be used in (5) to estimate ϵ . The wind stress τ is then estimated from

$$\tau = \rho_a (k_\nu \epsilon z)^{2/3} \tag{6}$$

where k_ν is the von Kármán constant (taken as 0.4), and z is the measurement height (20 m). The drag coefficient is then obtained from (4) after correcting the observed mean wind to an estimated value at 10 m using the relation for a logarithmic boundary layer,

$$\frac{U(z)}{U(10)} = \frac{\ln(z/z_0)}{\ln(10/z_0)} \tag{7}$$

where z_0 is the roughness length $z_0 = ze^{-k_\nu/\sqrt{C_D}}$. Note that (5) applies to neutral atmospheric stability. A correction is possible for non-neutral conditions, but was found to be small in this case.

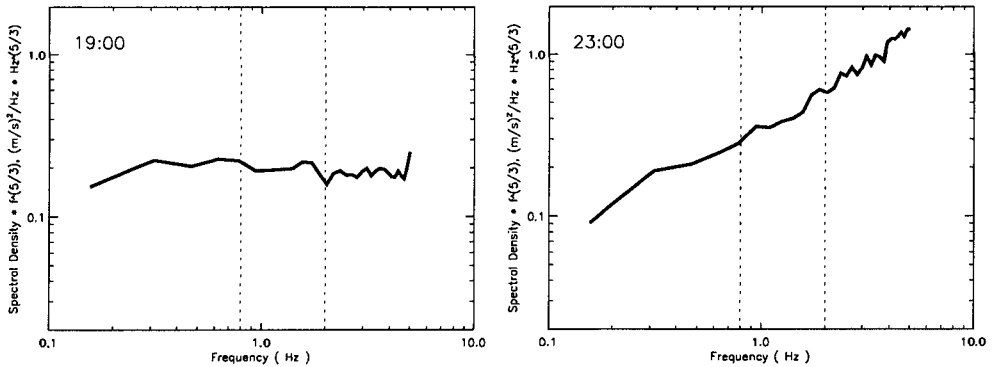


Figure 5: Wind Spectra $S(f)f^{5/3}$ at 19:00 and 23:00, 29 Sep 94 (T9426)

Figure 5 shows $S(f)f^{5/3}$ for two samples during the typhoon, at 19:00 (close to the point of closest approach) and 23:00 (a few hours after the typhoon centre passed). The plot for 19:00 is typical of those before 21:00, and the spectrum is almost constant over the frequency range used for the average (0.8–2.0 Hz, dotted

lines). This permits Eq. 5 to be used with some confidence. At 23:00 however, the spectrum exhibits a distinct slope throughout the frequency range, indicating that the $f^{-5/3}$ power law does not apply, and that (5) should not be used. Such data must be excluded from the analysis. This is unfortunate, since results just after a rapid change of wind direction are of particular interest. The reason for the different spectral slope (these data have much more high-frequency content) are not clear but may be caused by interference of the anemometer structure with the flow. One must also be aware that mean flow distortion around the tower will change the observed value of the mean wind, introducing an unknown error into the estimated drag coefficient.

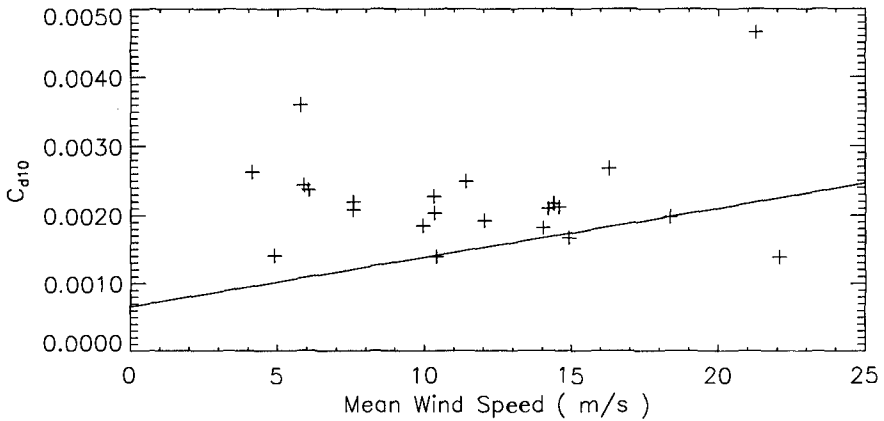


Figure 6: Drag coefficient estimates against wind speed during the typhoon.

The final estimates of stress for this day, excluding the data from 22:00 and 23:00, are plotted against mean wind speed in Figure 6 and compared with the empirical relation of Smith et al. (1992). Particularly at intermediate wind speeds, the data lie well above this curve. There is no obvious trend with wind speed, and as with other such data, they are rather scattered. If anything, a constant drag coefficient of about 2.2×10^{-3} may be appropriate in this instance. These limited data appear to be an example of departure from the standard formulae, although the whole data set should be examined before drawing firm conclusions.

Dependence of Bottom Stress on Wave Conditions

Another effect of waves which may sometimes be important is their influence on the bottom stress. In shallow water, waves affect momentum exchange with the sea bed. The wave-induced oscillatory flow near the bottom produces

turbulence when flowing over the rough bed. This increases the rate of vertical transfer of horizontal momentum, and hence the mean drag force between the water and the sea bed. Theoretically, this is represented as an increase in eddy viscosity.

In models, the mean retarding force acting on a body of water due to bottom friction is usually approximated as

$$\bar{\tau}_b = \rho_w C_{Db} \bar{u} |\bar{u}| \quad (8)$$

where $\bar{\tau}_b$ is the bottom stress, ρ the water density, \bar{u} the wave-averaged bottom current and C_{Db} a bottom drag coefficient. For many applications, it is found good enough to use a constant value for C_{Db} .

The effect of wave-induced turbulence is to increase the effective value of C_{Db} . Mastenbroek (1992) estimated the size of this effect on surges in the North Sea using the relationship between drag coefficient and significant wave height, $C_{Db}(H_s)$, in Figure 3 of his paper. He found that in some shallow areas it could significantly affect the predicted surge, more so than the effect of a wave-dependent wind drag coefficient. However, the size of this effect is similar to that of geographical variations in C_{Db} due to variations in bed roughness. This makes practical implementation difficult because of the lack of sufficiently detailed data on bed roughness.

Wave Set-Up

For completeness, we also point out that another effect of waves on local water level at the coast is that of wave set-up. This may be evaluated using forcing by the gradient of radiation stresses of shoaling and breaking waves. The effect is significant in storm surges occurring on coastlines facing the open sea. Depending on the beach topography and wave conditions, this can be about 10% of the incident wave height or even more, sometimes up to about 1 m. Although not the subject of this paper, it is an effect that should also be taken into account when considering the flood risk during storms and surges.

Incorporation of Wave Effects into Surge Models

The next stage of this work, in addition to further analysis of the wind stress data, will be to incorporate wave effects into a surge model. The first step will be to use an ocean wave model suitable for the region in question, which for storm surges will usually mean shallow shelf regions with strong winds. After predicting the time-dependent wave field during the storm, the next step will be to use the results for wave height to modify the surface and bottom drag coefficients in the surge model, as outlined above. In this way, the size of wave effects on the surge prediction will be assessed.

Influence of Mountains on the Wind Field

In coastal areas with mountains, the simple formulae which are often used to

represent the wind field in tropical storms may become quite inaccurate and thus affect surge predictions. Both the shape of the mountains, and surface roughness have an effect. This is particularly so in a number of bays in Japan, such as Osaka Bay and Ise Bay, where storm surges pose a threat to low-lying urban areas. In order to reproduce the wind fields of typhoons in such places, empirical attenuation parameters have been used to decrease both the moving wind and the gradient wind, in a rough attempt to include the effects of land topography and surface roughness. However, the values have to be adjusted in each case to give results which best fit the observed wind - the best values are different for each typhoon and cannot be predicted in advance. This is unsatisfactory because it is impossible to make credible predictions for hypothetical typhoons, as for example would be desirable when planning coastal defences.

Here we improve the situation using Schloemer's equation for the typhoon pressure field, Yoshizumi's formula for the variation of wind with height in the friction layer, and a finite-difference model for air flow over topography based on mass conservation, called 'MASCON'. This model is based on Sasaki's (1970) theory and is similar to one developed by Sherman (1978), for interpolating wind vectors in complicated topography from limited wind observations.

The model works as follows. First, the equation of Schloemer (1954) is used for the atmospheric pressure as a function of distance r from the cyclone centre:

$$p = p_c + \Delta p e^{-r_m/r}. \quad (9)$$

The model of Yoshizumi (1968) is then used to evaluate the three-dimensional wind field which this would produce over a flat surface, considering the effects of surface friction (the Eckman spiral) and storm movement. This is the initial wind field for the MASCON model. The wind field is then corrected so as to satisfy the conservation of mass for an incompressible fluid, using the calculus of variations. The error of adjustment is expressed as,

$$E(u, v, w, \lambda) = \int_V \left[\alpha_1^2 (u - u_0)^2 + \alpha_1^2 (v - v_0)^2 + \alpha_2^2 (w - w_0)^2 + \lambda \left(\frac{\partial u}{\partial x} + \frac{\partial v}{\partial y} + \frac{\partial w}{\partial z} \right) \right] dx dy dz \quad (10)$$

where (u, v, w) is the corrected wind field, λ is Lagrange's indeterminate coefficient and α_1, α_2 are Gauss precision moduli. Euler-Lagrange's equations have a solution minimizing (10) which can be written as,

$$u = u_0 + \frac{1}{2\alpha_1^2} \frac{\partial \lambda}{\partial x} \quad (11)$$

$$v = v_0 + \frac{1}{2\alpha_1^2} \frac{\partial \lambda}{\partial y} \quad (12)$$

$$w = w_0 + \frac{1}{2\alpha_2^2} \frac{\partial \lambda}{\partial z} \quad (13)$$

Differentiating with respect to x, y, z respectively, and substituting into the mass conservation equation gives the following Poisson-type partial differential equation:

$$\frac{\partial^2 \lambda}{\partial x^2} + \frac{\partial^2 \lambda}{\partial y^2} + \left(\frac{\alpha_1}{\alpha_2}\right)^2 \frac{\partial^2 \lambda}{\partial z^2} = -2\alpha_1^2 \left(\frac{\partial u_0}{\partial x} + \frac{\partial v_0}{\partial y} + \frac{\partial w_0}{\partial z}\right) \quad (14)$$

This is solved for $\lambda(x, y, z)$ subject to the boundary condition

$$\frac{\partial \lambda}{\partial n} = 0 \quad (15)$$

at the boundary, where n is the coordinate normal to the boundary (for the lower boundary, this is the shape of the mountains). The solution is obtained numerically using a successive over-relaxation method.

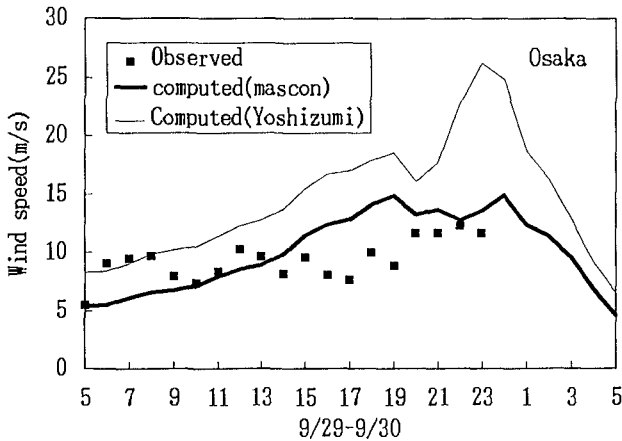


Figure 7: Observed and predicted wind speed, with and without MASCON. (Osaka, Typhoon 9426).

Wind speed and surge calculations with and without MASCON are compared with data from Typhoon 9426 in Osaka Bay (the same typhoon as in the previous section) in Figures 7 and 8. Figure 7 shows that MASCON does not so greatly overestimate the wind speed as does Yoshizumi's model, although there is still some disagreement. Figure 8 shows that although still overpredicted, the surge result from MASCON agrees better with the measured surge. The 20 cm shift of data relative to the model results is presumed to be a temporary increase in sea level due to some event in the coastal ocean dynamics, such as a change in the Kuroshio current. Similar improvements were found when this model was applied to other historical typhoons and surges in Japan.

Conclusions

The modelling of coastal flooding during storm surges may be achieved using a local model with a fine grid. This could be useful in the Bay of Bengal where the

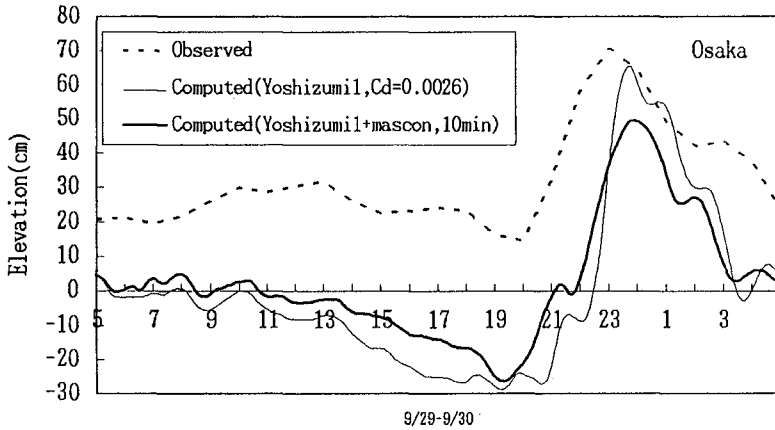


Figure 8: Observed and predicted surge, with and without MASCON. (Osaka, Typhoon 9426).

land is low, coastal defences against flooding are weak, and precise predictions of danger areas could in principle save many lives. A test case was performed for the city of Chittagong, but the results are only indicative since good land topography data were not available.

The wave field in a storm surge influences both the surface drag and, in shallow water, the bottom friction coefficients. These effects are likely to influence the size of a storm surge in some circumstances, but are not normally included in surge models. There is room for improving our understanding of the physics of these processes, especially under what circumstances they are likely to be significant. For wind stress, this should come from further collection and analysis of comprehensive and accurate field measurements of wind stress in a range of wind and wave conditions. Having done so, the effects may in principle be incorporated into surge models using results from an ocean wave model. Waves may also produce a measurable set-up at the coast.

Data taken during storms are particularly important for the storm surge problem. One such dataset, from a new tower, shows enhanced stress during a typhoon, in comparison with empirical formulae from the literature. Data from this tower add to those currently in existence and should be thoroughly analyzed as they become available. Eventually, a more accurate formulation of wave effects in surge models should be possible.

If there are high mountains near the coast, the resulting distortion of the wind field may have a measurable effect on the predicted surge. Using Yoshizumi's Model and the MASCON Model, a typhoon model in which the effects of both land topography and surface roughness are introduced has been developed. Hindcasts of the wind field have been made for various typhoons. These show

that even without using empirical attenuation parameters, it is possible to estimate the wind field in areas surrounded by mountains, such as Osaka Bay and Kii Channel. The predicted storm surges, although sometimes still over-predicted, also agree better with the data than the predictions of models with empirical attenuation parameters.

Acknowledgments

Thanks are due to Dr. H. Nakagawa of DPRI for providing the Chittagong bathymetry data; Dr. H. Yoshioka of DPRI for discussion and help with analysis of the tower data; Prof. S. Nakamura of Kyoto University's Shirahama Oceanographic Observatory for making the wind data available; Ms. M. Yelland of Southampton Oceanography Centre for advice on the inertial dissipation method and Dr. S. Smith of Bedford Institute of Oceanography for advice on the eddy-correlation method.

References

- Flather, R.A. A storm surge prediction model for the northern Bay of Bengal with application to the cyclone disaster in April 1991. *J. Phys. Oceanogr.* **24**, 172-190, 1994.
- Janssen, J.A.M. Does wind stress depend on sea-state or not? A statistical error analysis of HEXMAX data. *KNMI preprint*, Dec. 1995.
- Janssen, P.A.E.M. Quasi-linear theory of wind wave generation applied to wave forecasting. *J. Phys. Oceanogr.* **21**, 1631-1642, 1992.
- Katsura, J. et al., Storm surge and severe wind disasters caused by the 1991 cyclone in Bangladesh. *Japanese Group for the Study of Natural Disaster Science, Report No. B-2*, 101 pp., 1992.
- Mastenbroek, C., The effect of waves on surges in the North Sea. *Proc. 23rd Int. Conf. Coastal Eng.*, ASCE, 1992, 874-882.
- Sherman, C.A., A mass-consistent model for wind fields over complex terrain. *J. Appl. Meteor.* **17**, 312-319, 1978.
- Smith, S.D. et al., Sea surface wind stress and drag coefficients: the HEXOS results. *Boundary-Layer Meteorology* **60**, 109-142, 1992.
- Watson, G., Barnes, T.C.D. and Peregrine, D.H., The generation of low-frequency waves by a single wave group incident on a beach. *Coastal Engineering 1994, Proc. 24th Int. Conf. Coastal Eng.*, 776-790, 1994.
- Yelland, M.J. et al., The use of the inertial dissipation technique for shipboard wind stress determination. *J. Atmos. Oceanic Technology*, **11**, 1093-1108, 1994.
- Yoshioka, H. et al., The storm surge induced by Typhoon 9426. (in Japanese). *Ann. Disast. Prev. Res. Inst., Kyoto Univ.*, **38**, B-2, 581-598, 1995.
- Yoshizumi, S., On the asymmetry of wind distribution in the lower layer in typhoon. *J. Met. Soc. Japan*, **46**, 153-159, 1968.

CHAPTER 111

THE SWASH ZONE: A FOCUS ON LOW FREQUENCY MOTION

Adam M. Shah¹ and J. William Kamphuis²

ABSTRACT

This paper presents an analysis of physical model tests of the swash zone. A mild, impermeable slope was used to create a wide swash zone. Bichromatic and irregular waves with varying wave heights, wave periods and wave grouping were tested. The experiments showed the swash zone to be dominated by low frequency motions, which were closely related to the incident wave groups. The incident waves were still grouped in the surf and swash zones.

An empirical relationship was determined, relating the long wave height at the shoreline to the deep water wave parameters. The long waves were found to be partially reflected from the swash zone and this partial reflection was successfully simulated by the superposition of an absorbed and a reflected long wave. The generation of spurious long waves and the seiche at the natural frequency of the equipment were also investigated.

INTRODUCTION

The swash zone extends from the limit of run-down to the limit of run-up. Although the very shallow water and the low incident wave energy levels in the swash zone might suggest it to be of minor importance, Kraus *et al.* (1981) and Kamphuis (1991) have shown that it contains a peak in sediment transport rate. Thus the swash zone plays an important role in shaping natural beaches. Since very little is known about flow in the swash zone, all the numerical models of beach morphology use drastic simplifications within the swash zone. The goal of this paper is, therefore, to improve the understanding of swash zone flow so that eventually the computation of beach morphology can be improved.

Wave energy in the swash zone is concentrated in the infra-gravity band, at frequencies about one order lower than the incident waves. These low frequency motions are initially generated offshore by the distribution of wave

¹ MSc, Research Assistant, Dept. of Civil Engineering, Queen's University, Kingston, Ontario, Canada, K7L 3N6.

² Professor of Civil Engineering, Queen's University, Kingston, Ontario, Canada, K7L 3N6, kamphuis@civil.queensu.ca.

heights within wave groups. A Bound Long Wave travels with the incident waves at their group velocity and with its trough located under the highest waves in the group (Longuet-Higgins and Stewart, 1964).

Inshore of the break-point, the behaviour of the long waves and their interaction with individual breakers is not fully understood. One theory states that the bound long wave shoals as it travels inshore. Upon reaching the breakpoint it becomes a free long wave which is reflected seaward once it reaches the shore (Longuet-Higgins and Stewart, 1964). Another theory suggests that the amplitude of long waves decreases from the break-point and if the breaking is gentle all of the long wave energy is absorbed along with the short wave energy (Ottesen - Hansen *et al.*, 1980). Symonds *et al.* (1980) present a completely different mechanism for long waves within the surf zone. They state that the long wave motion inside the breaker zone is driven by the spatial variation of the breakpoint. As the breakpoint location varies with the group frequency it generates a long wave at that frequency. The experimental results in this paper favour a modified Longuet-Higgins and Stewart (1964) approach.

The long waves inside the breaking zone are difficult to study in the field. But they are also difficult to study in the laboratory, where studies of long waves are plagued by undesired low frequency motions resulting from spurious long waves coming off the wave generator and from seiche. Most wave generators are driven by a signal that only generates the grouped short waves and does not generate the bound long wave that accompanies the wave groups. Since the bound long wave will physically accompany the short waves anyway, this simplistic wave generation procedure amounts to generation of a spurious, free long wave equal and opposite to the bound long wave, travelling at the shallow water wave speed. Seiche (an oscillation at the natural frequency of the laboratory flume) results from transfer of wave energy into the natural frequency band of the wave flume. Such an oscillation increases with time and may eventually dominate the low frequency motion, contaminating measurements. Since the predominant mode of oscillation for the natural frequency has an antinode at the shoreline, seiche has the greatest significance in shallow water. Flick and Guza (1980) developed an expression for the natural frequency of the first mode of oscillation for a composite section, consisting of a slope and a horizontal section:

$$\sigma_n = \frac{1}{4} \pi \frac{(g\beta x_s)^{1/2}}{x_L + x_s} \quad (1)$$

where β is the slope, x_s is the length of the slope and x_L is the total length of the flume.

In view of the confusion and lack of understanding of long wave motion and the difficulties in studying long waves in the field and in the laboratory, this study (described in more detail in Shah, 1996) has the following objectives:

1. To relate the long wave at the shoreline to the offshore wave climate by a simple expression,
2. To study the development of the long wave from the breakpoint to the swash zone,
3. To study the contamination of long wave measurements by incorrect wave generation and seiche.

EXPERIMENTAL PROCEDURE

Laboratory tests were conducted at the Queen's University Coastal Engineering Research Laboratory (QUCERL) and the National Research Council of Canada (NRCC). An impermeable 0.6 m wide ramp with a 1:50 slope was installed in a 2.1 m wide wave flume at QUCERL. The mean water depth at the wave generator was 0.7 m, 26.2 m from the still water line (Figure 1). The tests at NRCC were conducted in a larger facility and made use of their more sophisticated generators. The ramp in Figure 1 was extended by 5 m, at NRCC, increasing the test depth to 0.80 m. The distance from the wave generator to the toe of the ramp was also increased from 1.2 m to 5 m.

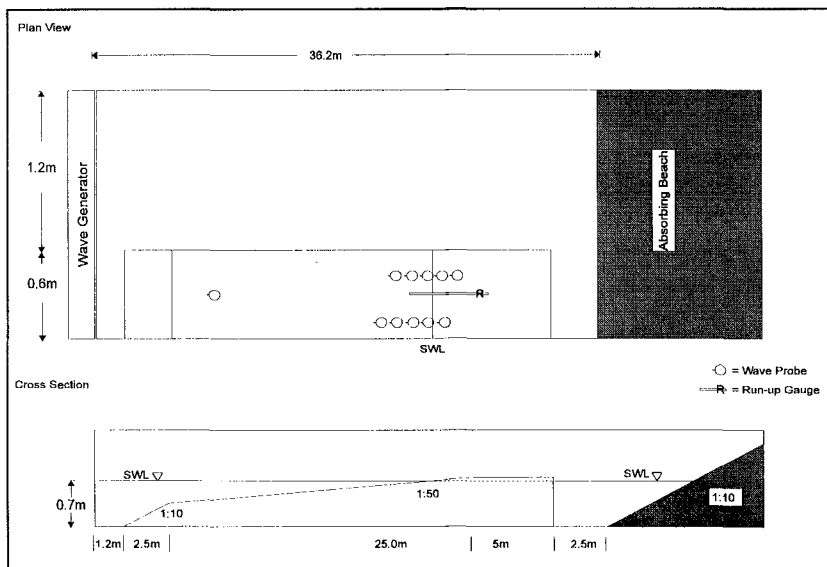


Figure 1 Experimental Setup at QUCERL

Table 1 summarizes the test series. For the irregular waves, H_s is the offshore significant wave height, T_p the peak period, and GF the groupiness factor (Funke and Mansard, 1979). For the bichromatic waves, H_1 and H_2 are the wave heights of the two components, T_{av} , the average period and T_g the group period.

Table 1 Wave Parameters Tested

Irregular Waves 19 tests at QUCERL 16 tests at NRCC			Bichromatic Waves 24 tests at NRCC			
H_s	T_p	GF	H_1	H_2	T_g	$T_{av.}$
.08 to .175 m	0.83 to 2.0 s	0.5 to 1.0	.05 to .25 m	.015 to .10 m	14 to 38 s	1.7 to 1.9 s

The effect on swash flow was measured at QUCERL by 11 capacitance wave gauges placed between 1.7 m offshore of the still water line and 0.5 m inshore. As well, a continuous run-up gauge was placed in the swash zone. At NRCC, 12 probes were placed between the breakpoint and the shoreline, to detect shoaling of the long waves and decay of the breakers through the surf zone.

The principal tool for data reduction was spectral analysis. Since all of the wave spectra showed a minimum spectral density at about one half the incident peak frequency, this was used to separate the high frequency and low frequency components. Wave heights were calculated as the zero spectral moment H_{moh} , for the high frequency ($f \geq f_p/2$) and H_{mol} , for the low frequency ($f < f_p/2$) components.

RESULTS

Swash Zone Wave Measurements

The QUCERL experiments provided high resolution measurements of water surface elevation within the swash zone. Figure 2 presents the first 50 seconds of sampling for four of the wave signals from an irregular wave test in which the initial conditions were $T_p=1.00$ s, $H_0=0.116$ m, $GF=0.94$. The heavy line is a low pass filtered signal to identify the long wave action. The low pass cut-off frequency was $f_p/2 = 0.50$ Hz. The importance of the low frequency motion ranges from minor at the offshore probe to near-total domination at the still water line.

The first panel shows the unbroken wave train for the furthest probe offshore. The groupiness of the wave train is clearly visible. In the second panel, Probe 1 was located 1.7 m offshore of the still water line, in the inner surf zone, and the wave train shows the saw-tooth profile indicative of broken waves. Though the waves are well inshore of the breakpoint they are still highly grouped and a high proportion of the incident waves are still intact. The final two panels show waves within the swash zone and present the final stages of wave decay. There are substantially fewer individual waves in the swash zone than there are incident waves as breakers coalesce into less frequent, more energetic uprush surges. The rate of decay is not the same for all the breakers. The waves that arrive at the swash zone during a strong downrush, characterized by a steep drop in water level, decay rapidly. For example, those waves arriving between 27 and 34 seconds at Probe 1 never reach Probe 2, which is only 1.2 m closer to the

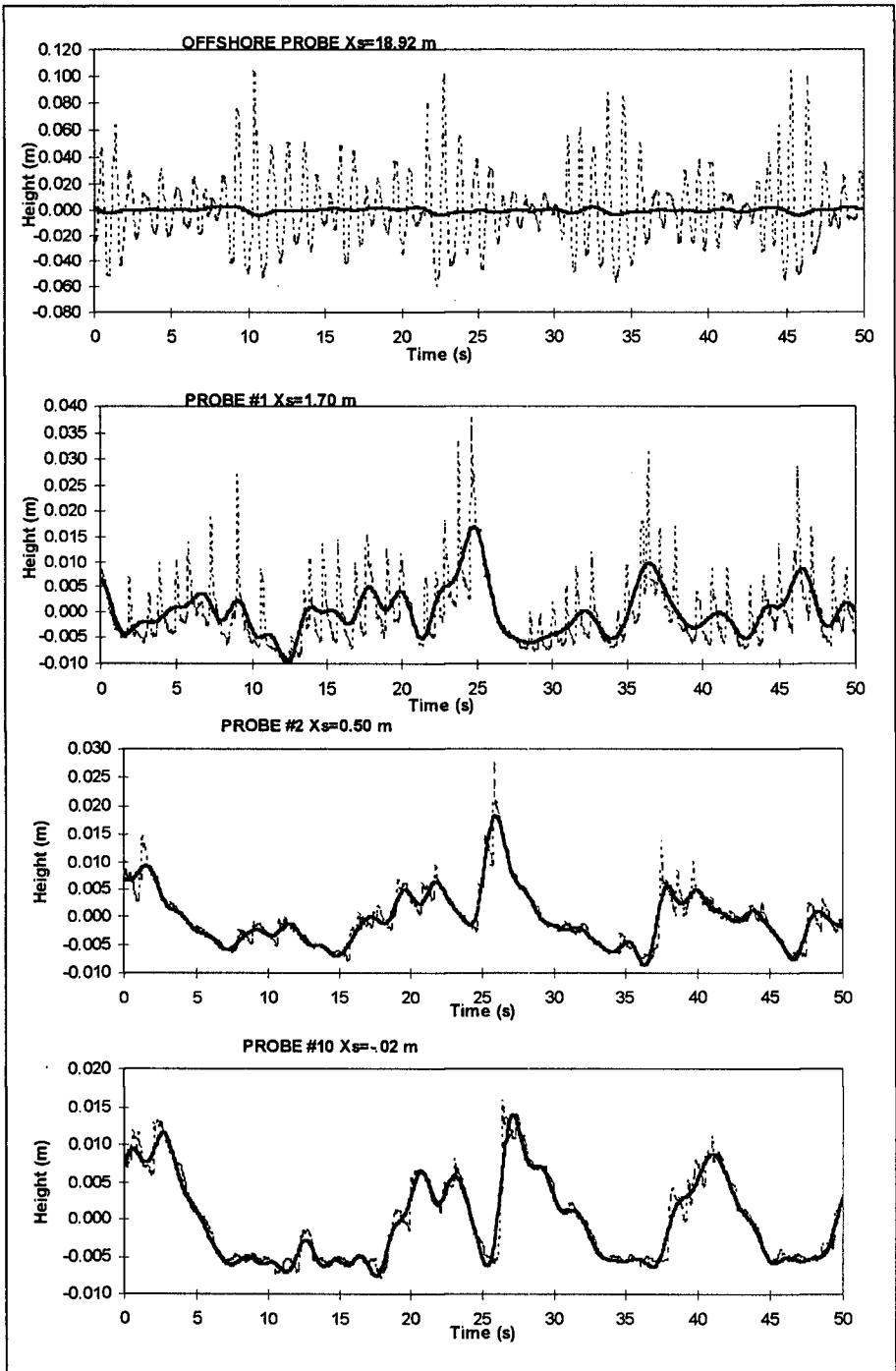


Figure 2 Example Wave Trains with Low-Pass Filtering

shoreline. Waves that arrive during an uprush cycle, for example from 20 to 25 s at Probe 1, progress with much less energy dissipation and eventually correspond to the extreme uprushes.

In addition to the increase in amplitude of the low frequency motion, the phase of the low frequency motion relative to the wave groups shifts 180° as the waves approach shore. At the offshore probe, the troughs of the low frequency motion occur under the highest waves in the group, at 2, 10 and 45 s. But at the probes inshore of the breakpoint, the highest waves in the group are on the crest of the long waves. This phase shift of the low frequency motion relative to the incident wave groups is undoubtedly complicated and no satisfactory explanation or theory has yet been proposed.

Spurious Long Waves and Seiche

Some of the tests at NRCC were specifically aimed at studying the effect of undesirable, spurious long waves resulting from not generating the bound long wave in the wave generation process. Such spurious long waves were found to be negligible for the tests conducted at NRCC due to a relatively large water depth at the wave generator and the longer wave period (Ottensen-Hansen *et al.*, 1980). For the tests at QUCERL such waves were calculated to contribute 10-15% to the total measured long wave energy.

Seiche was measured by recording water levels after the wave generator was shut down. The natural period of the NRCC flume was found to be 55 s, which is somewhat larger than the value of 40 s calculated from Equation (1). The difference can be attributed to run-up. Equation (1) predicts the resonant period based on the still water dimensions of the flume, as if vertical walls existed at the generator and the still water line. In the experiments, run-up excursions of 2.5 m or more were typical and the time required for the long wave to travel this distance is significant, since the speed of propagation is very small in very shallow water. The travel time required from the original still water line to the limit of run-up and back may be approximated using an expression developed by Wilson (1966) for the natural frequency of a triangular basin:

$$t = 1.64 \frac{2L}{\sqrt{gh}} \quad (2)$$

For a typical wave set-up of 20 mm at the shoreline and a run-up excursion of 2.5 m, the additional time is 19 s and when this is added to the value calculated by Equation (1) the total of 59 s, is close to the measured value of 55 s.

Contamination by the seiche was evaluated from the energy at the natural frequency and its harmonics. Bichromatic waves excited seiche, even during short duration testing. When the group frequency approached the natural frequency, energy leaked into the natural frequency band of the flume. Figure 3 shows the energy leakage for a bichromatic test with $H_1=0.10$ m, $H_2=0.05$ m, $T_g=38$ s. The offshore spectral peak, at $X_s = 9.8$ m, is at the group frequency of 0.026 Hz while

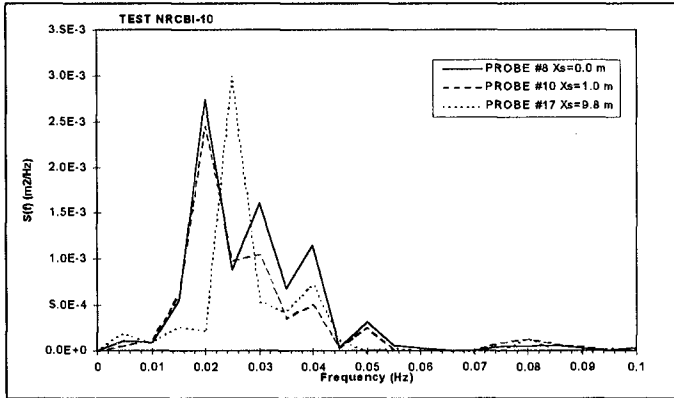


Figure 3 Energy Leakage from Group to Natural Frequency

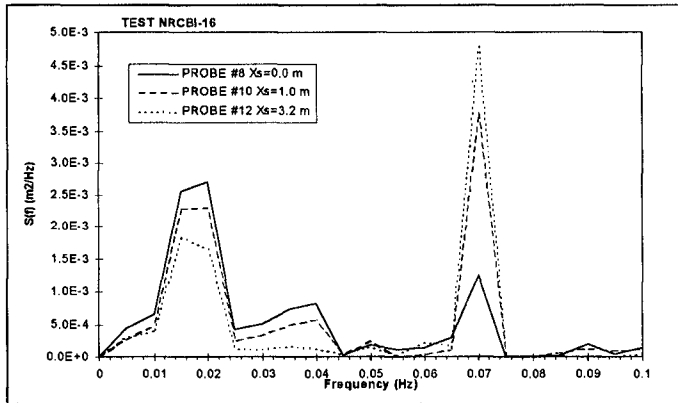


Figure 4 Subharmonic Excitement of the Natural Frequency

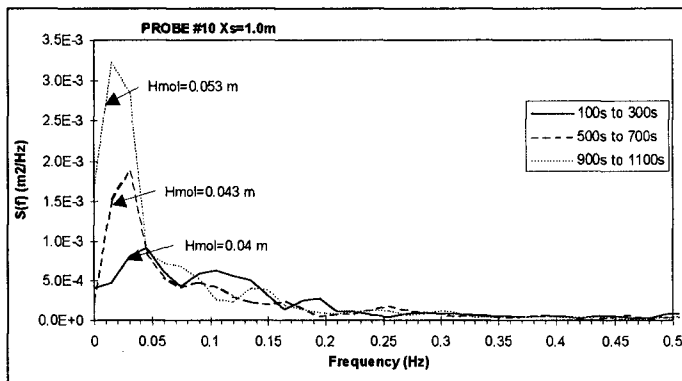


Figure 5 Build-up of Seiche Energy for Irregular Wave Testing

in the vicinity of the shoreline the spectral peak has shifted to the natural frequency of 0.018 Hz. Obviously the long wave measurements in this test were severely contaminated by seiche. Seiche was also generated when the group frequency matched a superharmonic of the natural frequency. Figure 4 shows a bichromatic wave test with $H_1=0.075$ m, $H_2=0.015$ m, $T_g=14$ s. The peak, at 0.07 Hz, is at the group frequency, the peak near 0.04 Hz is the first subharmonic and the peak near 0.018 Hz is the second subharmonic, which is also the natural frequency of the flume.

Irregular wave tests built up energy at the natural frequency over a longer duration; short duration tests did not excite appreciable seiche. Irregular waves have a broad band of group frequencies and can excite the natural frequency by a first-order interaction between any two incident group frequencies. Figure 5 presents three long wave spectra calculated at different times for the same irregular wave test with $H_o=0.175$ m, $f_p=0.5$ Hz, $f_g=0.05$ Hz. While the energy levels at and above the group frequency of 0.05 Hz were relatively constant, energy levels near the natural frequency of .02 Hz increased by a factor of six. This resulted in an incorrect increase of the calculated long wave H_{mo} from 0.04 m to 0.053 m.

Swash Zone Long Wave Height

The long wave height at the shoreline, $H_{mol,s}$ is a function of the beach slope and the deep water zero moment wave height, H_o , wave length, L_o , and Groupiness Factor. The effect of beach slope was not tested. One dimensionless expression that was found to satisfy the necessary conditions is:

$$\frac{H_{mol,s}}{L_o} = 0.078 \left(\frac{H_o}{L_o} \right)^{0.7} \quad (3)$$

It is based on the 31 irregular wave tests that were not contaminated by seiche and is shown in Figure 6. The correlation coefficient, r^2 is 0.81 and the different symbols represent ranges of groupiness. A consistent trend with groupiness is not apparent. This is, most likely because the calculation of the Groupiness Factor was affected by the reflected long wave at the offshore probe.

Long Wave Reflection Model

The cross-shore profiles of long wave height, H_{mol} , with distance offshore showed partial nodes and antinodes (the solid triangles in Figure 7). This indicates the long waves may be simulated by superimposing a reflected and absorbed long wave component. Thus, the Longuet-Higgins and Stewart (1964) development, suitably modified using partial long wave reflection is needed to explain the experimental results.

The fully reflected component was simulated by the solution presented in Lamb's (1932) for the reflection of a long wave over a sloping bottom. The height

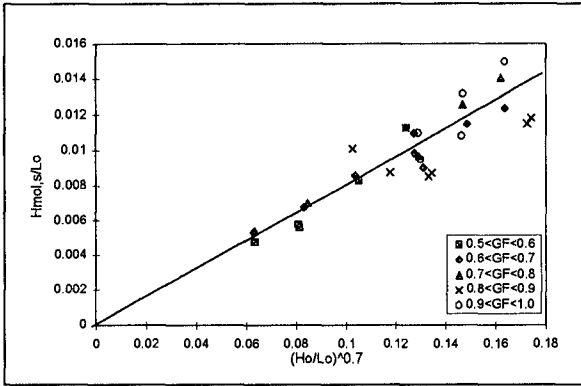


Figure 6 Regression Results for All Irregular Wave Tests

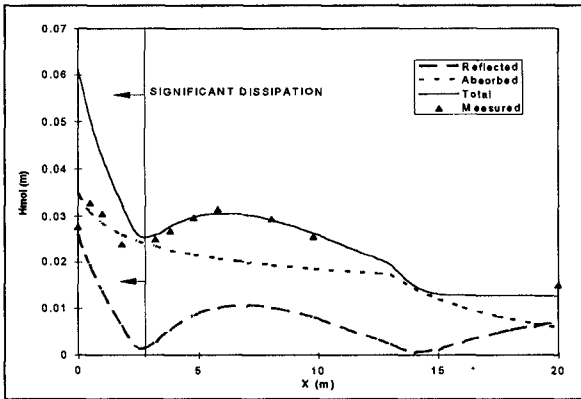


Figure 7 Example Model Results for Bichromatic Wave Test

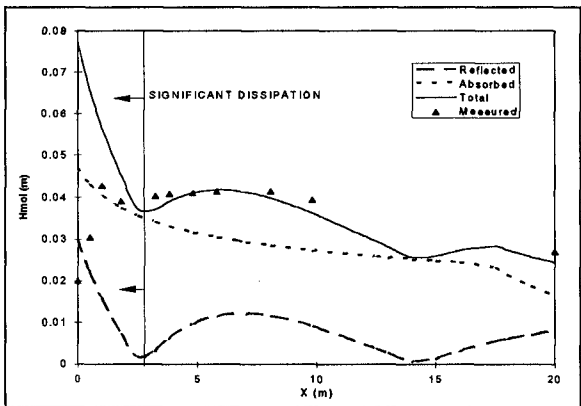


Figure 8 Example Model Results for Irregular Wave Test

of the standing wave envelope, ζ_r , is twice the absolute value of Lamb's Bessel function solution,

$$\zeta_r = 2\zeta_{r,s} \left| J_0 \left(\sqrt{\frac{4\sigma^2 x}{g\beta}} \right) \right| \quad (4)$$

where ζ_r is the local reflected long wave height, $\zeta_{r,s}$ is the reflected long wave height at the shoreline, J_0 is the zero order Bessel function, σ is the angular frequency of the long wave, g is the acceleration due to gravity, β is the beach slope and x is the distance offshore of the still water line. The reflected long wave is shown as the dashed line in Figure 7.

The absorbed portion of the long wave energy shoals as it travels inshore; the dotted line in Figure 7. Prior to breaking, the shoaling of the short waves will increase the height of the bound long wave. Theoretically this rate has been shown to vary with depth according to $h^{-3/2}$ by Longuet-Higgins and Stewart (1964). They assume, however, that the depth varies slowly enough that the shoaling long wave attains equilibrium. In practice the depth probably changes too rapidly for the long wave to reach equilibrium. Typically the distance from the wave generator to the breakpoint was less than one wavelength of the bound long wave and hence the actual shoaling rate was considerably smaller than $h^{-5/2}$. Since the focus of this research was on the swash zone, few probes were placed in the outer surf zone and for most tests the offshore probe was the only measured point on the bound long wave shoaling profile. Thus, a precise quantification of the bound long wave shoaling rate was not possible from these results.

If it is assumed that the bound long wave becomes a free long wave upon breaking, Green's Law, which states that the wave height of a free long wave varies with depth according to $h^{-1/4}$, can be used inside the breaker. The transition from bound to free long wave shoaling should begin where breaking is initiated. The present model assumes an abrupt transition between the two shoaling rates at the onset of breaking, as estimated using the criteria of Kamphuis (1991). This is an over-simplification; the transition is more gradual and will occur over the width of the breaking zone.

In very shallow water, wave set-up contributes to the effective depth and must be included. Theoretically, wave set-up increases linearly from the maximum set-down at the breakpoint to maximum set-up at the shoreline (Longuet-Higgins and Stewart, 1964). This relationship was a good approximation to the actually measured values of set-up. Thus, the local absorbed long wave height, ζ_a , inshore of the breaking point for a coordinate system with its origin at the still water line may be expressed, using a combination of wave set-up and wave shoaling according to Green's Law as:

$$\zeta_a = \zeta_{a,s} \left(\frac{h_o + \bar{\eta}_b + (\bar{\eta}_s - \bar{\eta}_b) \left(1 - \frac{h_o}{h_b}\right)}{\bar{\eta}_s} \right)^{-1/4} \quad (5)$$

where ζ_a is the local absorbed long wave height, $\zeta_{a,s}$ is the absorbed long wave height at the shoreline, h_o is the local still water depth, h_b is the breaking depth, $\bar{\eta}_s$ is the set-up at the shoreline and $\bar{\eta}_b$ is the set-down at the breakpoint. Offshore of the breaker

$$\zeta_a = \zeta_{a,s} \left(\frac{h_b + \bar{\eta}_b}{\bar{\eta}_s} \right)^{-1/4} \left(\frac{h_o}{h_b} \right)^{-k} \quad (6)$$

where k is the shoaling rate for the bound long wave (equal to $5/2$ if the depth is changing very slowly).

Superimposing the wave reflection analyzed from Equation (4) on Equations (5) and (6) produced Figure 7, a prediction of the local long wave height, representing the partially reflected standing wave system for a linear long wave over a sloping bottom, in the absence of losses:

$$\zeta_i = \zeta_a + \zeta_r \quad (7)$$

The model can calculate the long wave height profile if $\zeta_{a,s}$, $\zeta_{r,s}$, and σ are known. Figure 7 compares the results of the model (solid line) with measured data for a bichromatic wave test with $H_1 = 0.1$ m, $H_2 = 0.05$ m, $T_{av} = 1.9$ s, $T_g = 18$ s; the reflected and absorbed components are respectively the dashed and dotted lines. The predicted long wave profile, offshore of the first partial node, matches the observed standing wave pattern well. Inshore of this node, (at approximately $X = 2$ m), the model overpredicts the measured H_{mol} profile severely. This is because energy dissipation removes energy from the long wave system, since the extremely shallow depths make bottom friction significant. The measured profile peaks at about 1 m offshore and then abruptly decreases. Figure 8 shows similar results for an irregular wave test with $H_o = 0.175$ m, $T_p = 0.5$ Hz, $GF = 0.9$. More long wave energy is absorbed in the irregular wave test (Figure 8) than in the bichromatic wave test (Figure 7), which translates into less reflection. This may be due to the broad-bandedness of the irregular wave group frequency.

Comparable results to Figures 7 and 8 were obtained for all 15 of the 24 bichromatic tests and the 9 irregular tests at NRCC which were not contaminated by seiche.

Long wave height at the shoreline was represented by a simple empirical expression (Equation 3).

Long waves are partially reflected from within the swash zone. A model was developed that predicts the shape of the observed partial standing long wave envelope by adding the absorbed and reflected long waves (Equations 4-7). These equations take into account shoaling.

Seiche at the natural frequency of the basin was found to be a much more important laboratory effect in contaminating long wave experiments than the spurious long waves off the generator. Bichromatic tests were found to be contaminated by the seiche, when the group period approached the natural period of the flume or its superharmonics. Irregular wave tests were only contaminated when longer test durations were used.

Acknowledgments

This study was funded by the operating grants programme of the National Sciences and Engineering Research Council. The assistance of Etienne Mansard and the facilities provided by the National Research Council of Canada Hydraulics Laboratory are greatly appreciated. The funding for Adam Shah to attend ICCE '96 was provided by the Queen's University School of Graduate Studies.

References

- Flick, R.E. and Guza, R.T. (1980), "Paddle Generated Waves in Laboratory Channels," *Journal of the Waterway, Port, Coastal and Ocean Div.*, ASCE, Vol. 106, pp. 79-97.
- Funke, E.R. and Mansard, E.P.D. (1979), "On the Synthesis of Realistic Sea States," National Research Council of Canada, *Hydraulics Laboratory Technical Report*, LTR-HY-66.
- Kamphuis, J.W. (1991), "Incipient Wave Breaking" *Coastal Eng.*, Vol 15, pp. 185-203.
- Kraus, N.C., Farinto, R.S. and Horikawa, K. (1981), "Field Experiments on Longshore Sand Transport in the Surf Zone," *Coastal Engineering in Japan*, Vol. 24, pp. 171-194.
- Lamb, H. (1932), "*Hydrodynamics*," 6th Edition, Cambridge University Press, p. 738.
- Longuet-Higgins, M.S. and Stewart, R.W. (1964), "Radiation Stresses in Water Waves, a Physical Discussion, with Applications," *Deep Sea Res.*, Vol. 11, pp. 529-564.
- Ottensen - Hansen, N.E., Sand, S.E., Lundgren, H., Sorensen, T. and Gravesen, H. (1980), "Correct Reproduction of Group Induced Long Waves," *Proc. 17 Intl. Conf. Coastal Eng.*, Sydney, ASCE, pp. 784-800.
- Shah, A.M. (1996), "*The Swash Zone: A Focus on Low Frequency Motion*", M.Sc. Thesis, Queen's University, 138 pp.
- Symonds, G., Huntley, D.A. and Bowen, A.J. (1982), "Two Dimensional Surf Beat: Long Wave Generation by a Time Varying Breakpoint," *J. Geophys. Res.*, Vol. 87, pp. 492-498.
- Wilson, B.S. (1966), "Seiche", in *Encyclopedia of Oceanography*, R.W. Fairbridge ed., Academic Press, New York.

CHAPTER 112

THE DEVELOPMENT OF AN ON-LINE, INTERACTIVE, TSUNAMI-INFORMATION RESOURCE

Benjamin Cook¹, Catherine Petroff²

ABSTRACT

Tsunami! (<http://www.geophys.washington.edu/tsunami/welcome.html>) is a WWW site developed at the University of Washington with collaborative support from the global tsunami research community. The site originated as an on-line documentation of the 1994 East Java tsunami survey. The field survey documentation was developed to serve as a prototypical WWW resource whose form can be amended and improved upon for future on-line tsunami survey documentation. Educational and hazard mitigation resources were added to the site to provide the general public with an on-line source of tsunami information. The site's content and interface design were strongly influenced by the wide range of network connections and browser applications utilized by the target audience.

INTRODUCTION

The World-Wide Web (WWW) can be thought of as the virtual network of information accessible over the Internet using the HyperText Transmission Protocol (HTTP), the WWW communication standard. A collection of WWW documents with a common theme served by a computer(s) is often called a WWW or Web site. *Tsunami!* is a prototypical WWW site developed at the University of Washington with collaborative support from tsunami researchers around the world. Multimedia-supported resources currently available through the site include the following: Explanations of the physics of tsunamis; case studies of significant historical

1) Hydraulic Engineer, WEST Consultants, 2101 4th Avenue, Suite 1050, Seattle, WA 98121, USA.

2) Assistant Professor, Department of Civil Engineering, University of Washington, Seattle, WA 98195, USA.

tsunamis; hazard management and prevention information; recent event documentation; and an index of tsunami-related WWW sites.

The site originated as an on-line documentation of the 1994 East Java tsunami survey. On June 3, 1994, a large earthquake occurred off the southeastern coast of Java near the east end of the Java Trench in the Indian Ocean (Figure 1). The 7.2 M_s earthquake generated a devastating tsunami that took the lives of approximately 200 East Java residents (Synolakis et al., 1995). An international tsunami survey team, which included tsunami scientists and engineers from Indonesia, Italy, Japan, and the United States, visited the impacted areas of Bali and Java from June 20 to June 25, 1994. Survey team members measured runup heights along the southwestern coast of Bali and the southeastern coast of Java (Figure 2), and examined tsunami-induced sedimentation and structural damage. They also interviewed coastal residents to determine the distribution of seismic intensity and collect eyewitness accounts of the tsunami attack (Tsuji et al., 1995). In addition to the quantitative data collected during the survey, visual data such as slides, photographs, and video footage were also gathered. The visual data include photographs that depict sedimentation and structural damage observed by survey team members (Figure 3), as well as water and debris marks noted in the runup surveys.

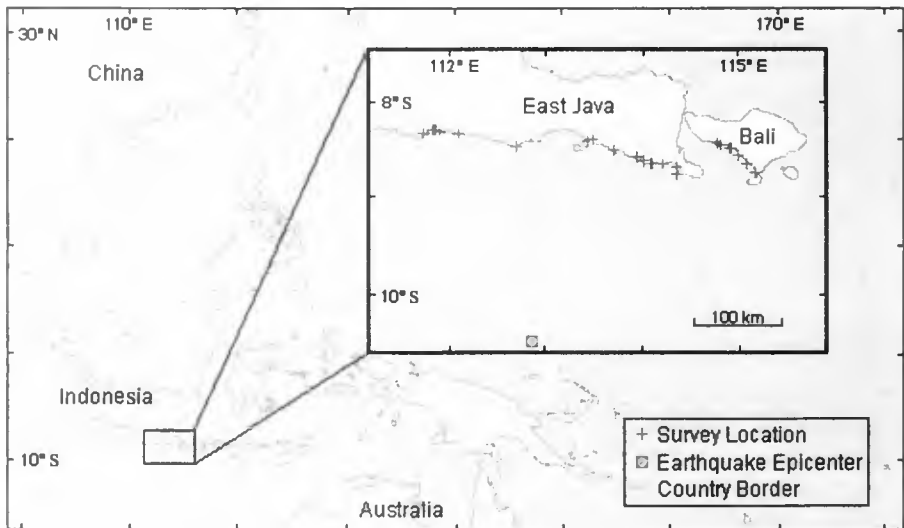


Figure 1. Locator map for the 1994 East Java survey.

Due to the limited number of tsunami scientists who were able to participate in the field survey, dissemination of the visual and quantitative data gathered during the survey was considered to be an important part of the documentation effort. Since the physical duplication and distribution of the visual data to tsunami scientists located throughout the world was logistically impractical, the feasibility of

distributing digitized visual data with an Internet information-exchange service was explored. It was found that the WWW allowed for an easily implemented and distributed multimedia presentation of the survey data. Non-platform specific, the WWW enables the electronic publishing of documents, which can include both text and graphics, to any computer connected to the Internet and equipped with browser software. Browser applications, through their graphical interface, allow users to access and view WWW documents, often referred to as WWW pages. A variety of media resources, including graphics such as survey maps, as well as audio and video clips, can be incorporated into a WWW page. Another WWW feature, interactive graphics called image maps, allows users to retrieve information associated with a particular region of an image.

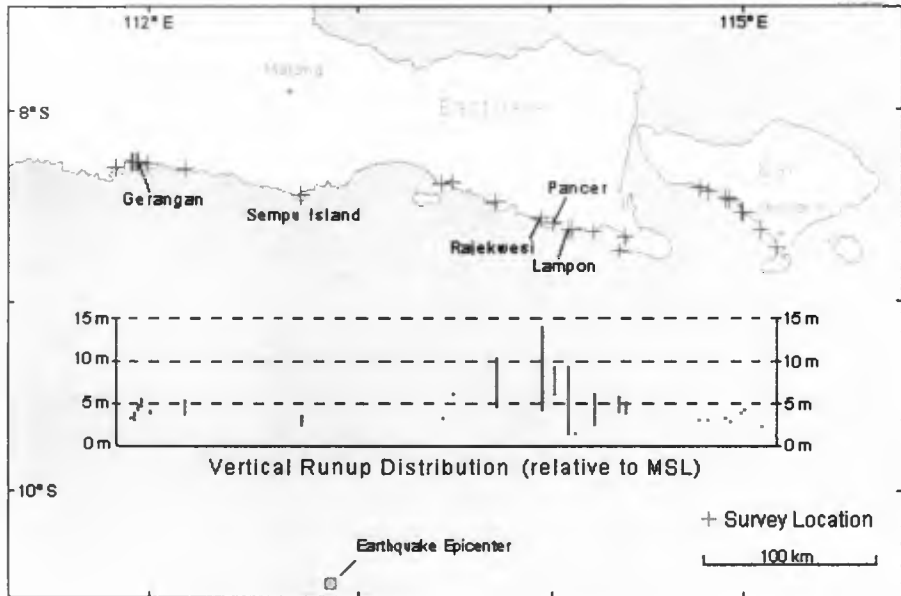


Figure 2. Interactive runup distribution map of 1994 East Java survey area.

FIELD SURVEY DOCUMENTATION

For the East Java survey, visual, damage, and runup data related to the event are accessed through an interactive runup distribution map of the survey area (Figure 2). Site-specific survey data are downloaded by selecting the survey location of interest from the image map. Runup data are presented in a tabular format including raw data (as recorded in the field) and corrected data that have been adjusted for the difference in the tidal level at the time of the tsunami attack and the time of the runup measurements (Tsuji et al., 1995). The visual data were prepared in two resolution formats. By default, the user is presented with small, low-resolution annotated



Figure 3. Sample digitized slide showing a scarp in Rajekwesi, East Java formed by tsunami-induced erosion.

digital images called in-line images. Relatively small in file size (less than 10 kilobytes), the in-line images are more quickly transferred over the Internet, facilitating the rapid navigation of the visual data. The in-line images function as links to higher-resolution images, which can be accessed by clicking on the in-line image of interest.

The East Java tsunami survey documentation was developed to serve as a prototypical document whose form can be amended and improved upon for future WWW tsunami-survey documentation. As shown schematically in Figure 4, a more comprehensive on-line documentation is proposed for future tsunami surveys that would serve as a data source for tsunami scientists and hazard management professionals. An event overview section could provide summary information about the event, the survey itinerary and team members, as well as links to other related WWW documents. Data sections accessible through the event overview could include earthquake source information provided by seismologists, historical data pertaining to local seismic and tsunami activity, and instrument records (when available) from tide gauges, deep-ocean pressure transducers, and remote sensing.

Data pertaining to specific survey sites could be accessed through an interactive survey area map, such as the one used in the East Java documentation (Figure 2). Survey site overviews could provide brief descriptive summaries of the observed local runup and flow characteristics, and tsunami-induced sedimentation and structural damage. A local map could be presented in conjunction with audio-visual data gathered at the survey location. Site-specific runup, sedimentation, damage, and emergency management data could be presented in subordinate sections. For example, a runup data section for a specific survey site might include an

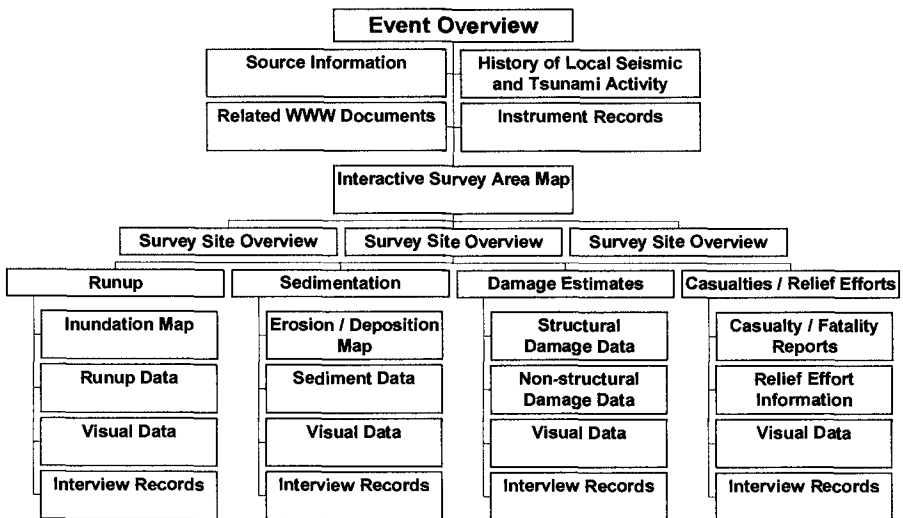


Figure 4. Resource hierarchy tree for tsunami survey documentation.

inundation map, surveyed runup measurements, annotated visual data showing water marks, trace evidence, and indicative debris, and interview records. Borrowing on the multimedia capabilities of the WWW, interview records could be presented in written form and as audio clips, both in the native language of the interviewee and in English.

At present, the preparation of an on-line multimedia survey documentation is technically challenging and labor intensive. Emerging software and hardware technologies should greatly facilitate future tsunami survey documentation efforts. For example, the use of digital cameras in field surveys would allow for the direct uploading and WWW publication of visual data. The level of detail of future documentation will vary as a function of the perceived scientific importance and human impact of a particular tsunami event. With limited public funding available for tsunami field surveys, the WWW enables the cost-effective documentation and world-wide dissemination of field survey data to tsunami scientists and emergency management professionals.

SITE RESOURCES

Additional resources were added to the site to meet the general public's broader needs for hazard mitigation and educational information. In addition to researchers and hazard management professionals interested in recent event data, the site's audience includes secondary and university students, and residents of tsunami-threatened coastal communities. In recognition of the diverse information needs of this group, *Tsunami!*'s on-line resources include educational information about the physics of tsunamis, significant historical tsunamis, the Tsunami Warning System and hazard mitigation. A top-level flow chart of the subject material presented on the site is shown in Figure 5. Referred to as a resource hierarchy tree, it represents, in a general sense, the logical order in which the site developers attempted to present the resources. The site's directory structure reflects the resource hierarchy tree, assuring continuity for inter-linked documents throughout the development process.

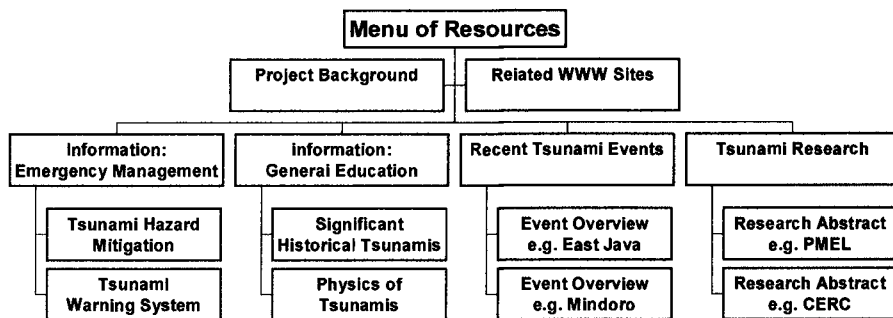


Figure 5. Top-level resource hierarchy tree for the WWW tsunami site.

With roughly 500 animation, audio, image, and text files accessible through the site, link management was an important issue that had to be addressed in site development. Similar subordinate flow charts were conceived for several of the more extensively-developed sections shown in Figure 5, including the "Physics of Tsunamis" and "Event Overview" sections (for example, see Figure 4).

CONTENT AND INTERFACE DESIGN

The site's content and interface design were strongly influenced by the technical constraints imposed by the wide range of network connections and browser applications utilized by the target audience. At present, there are some inherent technical limitations, such as network bandwidth, that strongly impact the design of a WWW site. Restricted local and global network bandwidth often prevents the rapid transfer of information necessary to allow the interactive navigation of the WWW. WWW-related computer hardware, software, protocols, and languages are also swiftly changing.

Several types of Internet connections exist. The fastest connections, commonly available on university campuses and at large corporate facilities, are Ethernet connections. Users accessing the Internet over Ethernet connections can consistently realize file transfer rates, or throughput, of over 100 kilobytes per second (KB/s). However, many of site's potential users are limited to dial-up Serial Line Internet Protocol (SLIP) or Point-to-Point Protocol (PPP) connections through modems, with typical baud rates (bits per second) of 9,600 - 28,800, limiting theoretical throughput over these dial-up connections to between one and three KB/s (Krol, 1994). Throughput can be further diminished by heavy local and regional network traffic.

This wide range in throughput poses a significant development problem as multimedia resources are information-rich and hence inherently large in file size. Image files, even when stored in the compressed formats cited later in this paper, can be well over 100 KB in size. Animations, even relatively short clips several seconds in length, can be one or more megabytes. Considerable effort was taken to present information on the site in the least data-intensive format for the primary links. Additional link-options, intended for users on high-bandwidth connections, are available to provide access to data-rich resources such as high-resolution images and animations. With the exception of the high-resolution images and animations, most of the site's pages have been kept to well under 50 KB, allowing even dial-up users to quickly download and browse through pages containing in-line images.

Compounding the at least two order of magnitude difference in throughput experienced by the site's target audience, the language used to format documents, HyperText Markup Language (HTML), continues to evolve. At the time of the site's initial development (summer 1995), most graphics-capable browsers supported HTML 2.0, but did not support the then newly-proposed standard, HTML 3.0. HTML 3.0 implemented several features, including table formatting and sophisticated image formatting, not available with HTML 2.0, and was used exclusively for the site's page development because of these advanced features. For site resources to be easily accessed and properly displayed, developers need to

accurately assess the hardware and software capabilities of their site's prospective audience. Following this assessment, document formatting standards and multimedia content can be appropriately selected.

RESOURCE DEVELOPMENT AND SITE IMPLEMENTATION

The site presents a variety of media resources, including graphics, sounds, and animations. These resources were originally delivered to users over the Internet by a dedicated server set up specifically to support the site. It is beyond the scope of this paper to discuss in detail the digitization techniques and editing employed in the development of the site's multimedia resources. Digitization considerations include data preparation (e.g., cleaning of slides), digitization device and resolution selection. Post-digitization filtering, such as image sharpening, can greatly improve digital image quality. Various compression algorithms are available that significantly reduce file size while preserving visual and audio quality. The interested reader is referred to numerous on-line resources or in-print publications (see, for example, Murray, 1994).

Digitization Techniques

A variety of digitization devices are currently available for converting hard-copy images and analog audio and video signals into digital data. For this project, flatbed scanners were used to digitize hard-copy images such as slides and photographs. A Macintosh Quadra with hardware-assisted compression provided by a Digital Film frame-grabber board was used to capture video footage. *Adobe Premier* was used as the software interface for the capture board and served as a powerful editing environment for the acquired digital clips. Sounds were digitized with an analog-to-digital converter supported by the Macintosh's built-in sound capabilities.

Two types of graphics file formats were used to store the images presented on the site; the Joint Photographic Experts Group (JPEG) format is used for in-line and high-resolution digital images produced from photographic images, while the Graphic Interchange Format (GIF) format is used for maps, image maps, and icons that were digitally generated. JPEG images, with their 24-bit pixel depth, can contain over 16 million colors, while GIF images are limited to 256 colors because of the format's 8-bit pixel depth. Digital movies were stored in the cross-platform flattened QuickTime format with Cinepak compression. Lastly, the AU file format was used for audio clips.

HTTP Server Setup

WWW documents are distributed over the Internet by HTTP servers. In many cases, organizations may have an existing HTTP server, and the publication of WWW documents simply requires that newly-developed HTML files be transferred to the HTTP server. Although a departmental HTTP server was available with limited storage space, for this project a Macintosh HTTP server was initially set up to facilitate site development. The creation of the dedicated server allowed for the autonomous administration of the WWW tsunami site during the development

period. The HTTP server consisted of a Macintosh SE-30 running *MacHTTP 2.2* that was connected to the University of Washington's Ethernet network. Remarkably, this somewhat outdated configuration performed almost flawlessly for one year, distributing data to the more than 10,000 users who accessed the site over this period. Increased server demand during the summer of 1996 necessitated the site's move to a UNIX-based workstation.

FUTURE WORK

As the tsunami research and hazard management community's information exchange and dissemination needs become better defined, *Tsunami!* can be easily expanded and revised. Future development efforts that have been considered include real-time tsunami warning dissemination, event management, and post-event survey administration. In cooperation with the Pacific Tsunami Warning System, tsunami warnings and preliminary event information could be globally disseminated over the WWW. Event information could be complemented by regional hazard management resources, including inundation maps and evacuation procedures. Post-event data collection could be facilitated with the on-line distribution of survey guidelines, survey itineraries, and preliminary visual and runup data. Finally, educational offerings could be expanded to include interactive demonstrations, which could be developed in the Java programming language, of tsunami generation, propagation, and inundation mechanisms.

ACKNOWLEDGMENTS

Funding for *Tsunami!*'s development was provided by the U.S. Department of Defense, through the National Defense Science and Engineering Graduate (NDSEG) Fellowship Program. Researchers who contributed to the development of the site are acknowledged individually at the following on-line location: (<http://www.geophys.washington.edu/tsunami/background/acknow.html>).

REFERENCES

- Krol, E. *The Whole Internet User's Guide & Catalog*. Sebastopol, CA: O'Reilly and Associates, Inc. 1994.
- Murray, and William vanRyper. *Encyclopedia of Graphics File Formats*. Sebastopol, CA: O'Reilly and Associates, Inc. 1994.
- Synolakis et al. "Damage, Conditions of East Java Tsunami of 1994 Analyzed." *Eos*. 76.26 (1995).
- Tsuji et al. "Field Survey of the East Java Earthquake and Tsunami of June 3, 1994." *Pure and Applied Geophysics*. 144.3/4 (1995).

CHAPTER 113

LONG WAVE RUNUP ON COASTAL STRUCTURES

Utku Kânoğlu¹ and Costas Emmanuel Synolakis²

Abstract

We present a general method for determining the runup and the amplification explicitly for nonbreaking long waves propagating over piecewise linear topography, using the linear shallow water wave equations. We associate each constant-depth segment and each linearly-varying depth segment with (2×2) matrices and we calculate the transmitted wave amplitude after propagating over any number of segments explicitly. We then extend our methodology to the three dimensional topography of a conical island. Our method is applicable in the design of dikes, sea-walls and other coastal structures.

INTRODUCTION

The September 2, 1992 Nicaragua tsunami, the December 12, 1992 Flores island tsunami, the July 12, 1993 Hokkaido tsunami, the June 2, 1994 East Java tsunami, on October 2, 1994 Kuril Islands, Shikotan tsunami, the November 11, 1994 Mindoro Island tsunami, the February 17, 1996 Biak, Irian Jaya tsunami, and the February 27, 1996 Peru tsunami were eight major devastating geophysical events that caused severe property damage and killed an estimated 2000 people. Field observations raised new questions about the suitability of the standard paradigm of a tsunami model, i.e. a solitary wave attacking a plane beach. For one, most of the eyewitness reported waves which caused the shorelines to recede first before advancing; these waves were studied by Tadepalli and Synolakis and they are now called leading-elevation N-waves (Tadepalli and Synolakis, 1994). Then, practically all field-measured

¹Research associate, School of Engineering, University of Southern California, Department of Civil Engineering, University Park, Los Angeles, California 90089-2531, USA.

²Professor, School of Engineering, University of Southern California, Department of Civil Engineering, University Park, Los Angeles, California 90089-2531, USA.

runup distribution showed three-dimensional effects which had been counter-intuitive. For example, during the 12/12/92 Flores Island tsunami, 263 people were killed and two fishing villages completely annihilated on Babi Island, a small volcanic islet off Flores; all damage concentrated on the tsunami wise and wind-wave wise lee side of the island. During the 9/2/92 Nicaraguan tsunami, the runup varied by a factor of 4 between locations distant less than a mile from each other, suggesting that even though the tsunamis are long waves, local bathymetric features of much smaller length scale did influence the wave runup. A recent increase in tsunami incidence and an abundance of new observations of coastal effects added urgency to the resolution of the question to determine a priori how a given topography will affect the wave evolution.

Besides tsunamis, the long wave theory presented here can be used for the calculation of the runup and evolution of certain wind generated waves particularly in the infragravity spectral band. The numerical solution of the nonlinear shallow-water wave equation were used to calculate the runup of wind swell (Raubenheimer *et al.*, 1995). Also, it has long been known that the runup predicted by the nonlinear shallow-water wave equation is mathematically the same of that predicted by the linear shallow-water wave equation for the one slope beach case (Carrier, 1966; Synolakis, 1987).

FORMULATION OF THE PROBLEM

We will describe a new general method that will provide a closed form analytical solution to determine the relationship between the amplification factor and the incident wave amplitude for the two-dimensional topographies. Given that any physically realistic topography is unlikely to consist entirely of a single-sloping beach or a single constant-depth segment, and to allow the use of analytical (non-numerical) solutions, it is incumbent to be able to break down the physical propagation problem into a series of linear problems which can then be solved with standard method analytically. The proposed method of solution consists of representing a given topography by a series of constant-depth and linearly-varying depth segments.

We will use the linear shallow-water wave equation to solve the propagation problem over linear topographies; this equation is

$$\eta_{tt} - (\eta_x h)_x = 0. \quad (1)$$

We introduce dimensionless variables using a reference undisturbed offshore water depth d as the characteristic length scale, and $\sqrt{d/g}$ as the characteristic time scale. With time harmonic dependence of the form $\eta(x, t) = \zeta(x) e^{-i\omega t}$, for the wave evolution over the dimensionless constant-depth $h(x) = h_c$, equation

(1) becomes,

$$h_c \frac{d^2 \zeta(x)}{dx^2} + \omega^2 \zeta(x) = 0. \quad (2)$$

The general solution is

$$\eta(x, t) = \{A_1 e^{-\frac{i\omega x}{\sqrt{h_c}}} + B_1 e^{\frac{i\omega x}{\sqrt{h_c}}}\} e^{-i\omega t}, \quad (3)$$

where A_1 and B_1 are arbitrary constants. If the depth is linearly-varying and defined by $h(x) = mx + n$ with $m \neq 0$ and n constant, the field equation is

$$(mx + n) \frac{d^2 \zeta(x)}{dx^2} + m \frac{d\zeta(x)}{dx} + \omega^2 \zeta(x) = 0. \quad (4)$$

The eigenfunctions of the field equation are two zeroth-order linearly independent solutions of Bessel's equation, e.g. J_0 and Y_0 . Then the solution for evolution over variable depth is

$$\eta(x, t) = \{A_2 J_0(2\omega\sqrt{\xi}) + B_2 Y_0(2\omega\sqrt{\xi})\} e^{-i\omega t}, \quad (5)$$

with $\xi = \sqrt{(x + n/m)/m}$, where A_2 and B_2 are arbitrary constants.

From the solutions (3) and (5), the appropriate form of η is chosen for each segment. Continuity of the surface elevation and of the mass flux provides two equations at each transition point between the adjacent segments and the unknowns such as A_1 , B_1 , A_2 , B_2 can be calculated from these interface matching conditions.

In general, an m -segment topography involves m -sets of (3) and (5) type eigenfunction expansions, each with 2 unknown coefficients. Given that the incoming wave height is known, $(2m - 1)$ coefficients have to be determined, requiring $(2m - 1)$ equations for closure. To this end, continuity of the surface elevation and of the mass flux boundary conditions must be considered at each transition point between the adjacent segments. These boundary conditions provide $(2m - 2)$ equations. The conditions of transmission at the segment, or the condition of bounded solution at the coastline or perfect reflection off a wall provide one additional equation. Adding a new segment introduces two more unknown coefficients, but at the same time also allows to write two new boundary conditions. This extends the order of the system of equations by two. Thus the wave evolution over any topography composed of any number of piecewise linear segments can be calculated.

Our method consists of establishing basic topography segments, i.e. a constant-depth segment, a linearly-varying depth segment. Each segment has a (2×2) matrix that incorporates its topographic feature. We associate each constant-depth segment of depth h_r with a segment matrix,

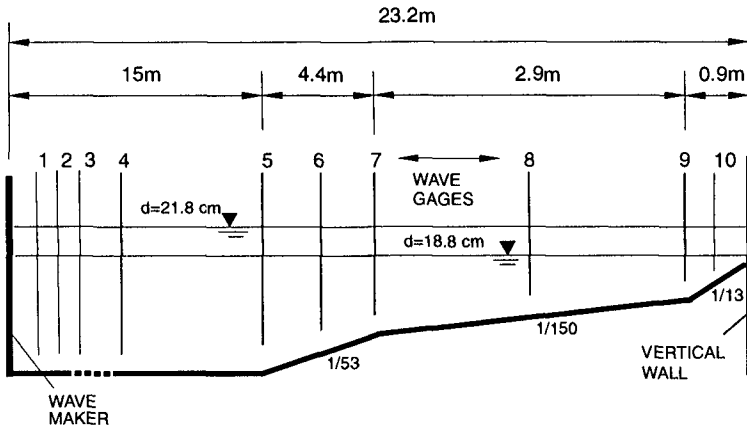


Figure 1. Definition sketch of the Revere Beach topography (not to scale).

$$K_{pr} = \begin{pmatrix} e^{-\frac{i\omega x_p}{\sqrt{h_r}}} & e^{\frac{i\omega x_p}{\sqrt{h_r}}} \\ i e^{-\frac{i\omega x_p}{\sqrt{h_r}}} & -i e^{\frac{i\omega x_p}{\sqrt{h_r}}} \end{pmatrix}. \quad (6)$$

We associate each linearly-varying depth segment with $h_r(x) = m_r x + n$ with $m_r \neq 0$ and n constant with the segment matrix,

$$S_{pr} = \begin{pmatrix} J_0(2\omega\sqrt{\xi_{pr}}) & Y_0(2\omega\sqrt{\xi_{pr}}) \\ J_1(2\omega\sqrt{\xi_{pr}}) & Y_1(2\omega\sqrt{\xi_{pr}}) \end{pmatrix}, \quad (7)$$

with $\xi_{pr} = \sqrt{(x_p + n/m_r)/m_r}$. The subscripts p and r identify the transition point and the segment number increasing from the seaward to the shoreward.

Using these topographic-feature matrices, it is possible to write a matrix equation between the unknowns of the eigenfunction expansion. We will provide a specific example for application of this general method.

REVERE BEACH

A physical model of the Revere Beach—located approximately 6 miles northeast of Boston City of Revere, Massachusetts—was constructed at Waterways Experiment Station (WES), US Army Corps of Engineers Coastal Engineering Research Center (CERC), by Ward who investigated the beach erosion and flooding problems (Ward, 1995). Moreover it presented a unique opportunity to evaluate the predictions of the general method presented here. The model of the Revere Beach consisted of three piecewise linear, 1 : 13,

1 : 150 and 1 : 53 slopes from seaward to shoreward respectively, with a vertical wall at the landward end of the compound slope and it is shown in figure 1.

Analytical Solution

Alternative to the conventional method of solution –try to solve $(2m - 1)$ equation numerically– using the general methodology presented here boundary conditions for each transition point can be written as a matrix equation;

$$S_w A_1 = V_1, \quad (8)$$

$$S_{11} V_1 = S_{12} V_2, \quad (9)$$

$$S_{22} V_2 = S_{23} V_3, \quad (10)$$

$$S_{33} V_3 = K_{34} V_4, \quad (11)$$

and finally

$$S_w A_1 = S_{11}^{-1} S_{12} S_{22}^{-1} S_{23} S_{33}^{-1} K_{34} V_4. \quad (12)$$

Here V_1, V_2, V_3 and V_4 are column unknown vectors for each segment. Using the naming style presented for the topographic–feature matrices,

$$\begin{pmatrix} 1 \\ -J_1\left(\frac{2\omega\sqrt{h_w}}{m_1}\right)/Y_1\left(\frac{2\omega\sqrt{h_w}}{m_1}\right) \end{pmatrix} A_1 = \begin{pmatrix} J_0\left(\frac{2\omega\sqrt{h_1}}{m_1}\right) & Y_0\left(\frac{2\omega\sqrt{h_1}}{m_1}\right) \\ J_1\left(\frac{2\omega\sqrt{h_1}}{m_1}\right) & Y_1\left(\frac{2\omega\sqrt{h_1}}{m_1}\right) \end{pmatrix}^{-1} \begin{pmatrix} J_0\left(\frac{2\omega\sqrt{h_1}}{m_2}\right) & Y_0\left(\frac{2\omega\sqrt{h_1}}{m_2}\right) \\ J_1\left(\frac{2\omega\sqrt{h_1}}{m_2}\right) & Y_1\left(\frac{2\omega\sqrt{h_1}}{m_2}\right) \end{pmatrix} \begin{pmatrix} J_0\left(\frac{2\omega\sqrt{h_2}}{m_2}\right) & Y_0\left(\frac{2\omega\sqrt{h_2}}{m_2}\right) \\ J_1\left(\frac{2\omega\sqrt{h_2}}{m_2}\right) & Y_1\left(\frac{2\omega\sqrt{h_2}}{m_2}\right) \end{pmatrix}^{-1} \begin{pmatrix} J_0\left(\frac{2\omega\sqrt{h_2}}{m_3}\right) & Y_0\left(\frac{2\omega\sqrt{h_2}}{m_3}\right) \\ J_1\left(\frac{2\omega\sqrt{h_2}}{m_3}\right) & Y_1\left(\frac{2\omega\sqrt{h_2}}{m_3}\right) \end{pmatrix} \begin{pmatrix} J_0\left(\frac{2\omega\sqrt{h_3}}{m_3}\right) & Y_0\left(\frac{2\omega\sqrt{h_3}}{m_3}\right) \\ J_1\left(\frac{2\omega\sqrt{h_3}}{m_3}\right) & Y_1\left(\frac{2\omega\sqrt{h_3}}{m_3}\right) \end{pmatrix}^{-1} \begin{pmatrix} e^{-\frac{i\omega x_3}{\sqrt{h_4}}} & e^{\frac{i\omega x_3}{\sqrt{h_4}}} \\ i e^{-\frac{i\omega x_3}{\sqrt{h_4}}} & -i e^{\frac{i\omega x_3}{\sqrt{h_4}}} \end{pmatrix} \begin{pmatrix} A_i \\ A_r \end{pmatrix}. \quad (13)$$

Notice that first the matrix equation (8) represents perfect reflection boundary condition, $\partial\eta/\partial x = 0$, since the topography has finite depth (h_w) at the shoreline ($x = 0$). We evaluate the following integral to find time histories of surface elevation at any given location;

$$\eta_j(x, t) = \int_{-\infty}^{+\infty} \Phi(\omega) \{A_j J_0\left(\frac{2\omega\sqrt{h_j(x)}}{m_j}\right) + B_j Y_0\left(\frac{2\omega\sqrt{h_j(x)}}{m_j}\right)\} e^{-i\omega t} d\omega, \quad (14)$$

where $j = 1, 3$ represents the segment number. The unknowns of the eigenfunction expansion can be determined equations (8) through (12). Here $\Phi(\omega)$

is the Fourier transform of the initial solitary wave profile located at $x = x_s$ and given by $(2/3)\omega \operatorname{cosech}(\alpha\omega) e^{i\omega x_s}$ with $\alpha = \pi/2\gamma$ and $\gamma = \sqrt{3H/4}$ (Synolakis, 1986). H is the dimensionless incoming waveheight.

We evaluated the integral (14) at the shoreline ($x = 0$) using the contour integration technique to find an analytical expression for the maximum runup (Kânoğlu, 1997). With asymptotic analysis, we found that the maximum runup for the Revere Beach can be given by

$$R = 2 h_w^{-1/4} H; \quad (15)$$

the maximum runup depends only on the incoming waveheight H and on the depth at the wall h_w .

Experimental Results

We performed the experiments 23.2m-long, 45cm-wide glass-walled flume. The wave maker was located 23.22m away from the wall. Ten wave gages were located to record time histories of free surface displacements as shown in figure 1. Gage 4 was moved to a half-wavelength away from the toe of the 1 : 53 slope. This gage was used to define the waveheight of the incoming wave and its location, ensured that all waves propagated the same relative distance of a half wavelength ($L/2 = (1/\gamma)\operatorname{arccosh}\sqrt{20}$) between the reference location and the toe of the beach. This localization is the standard method for referencing the heights of solitary waves climbing up a sloping beach (Synolakis, 1986 and 1987). Experiments were carried out at two different water depths, 18.8cm and 21.8cm. The experiments are described elsewhere in detail (Briggs *et al.*, 1997; Kânoğlu, 1997).

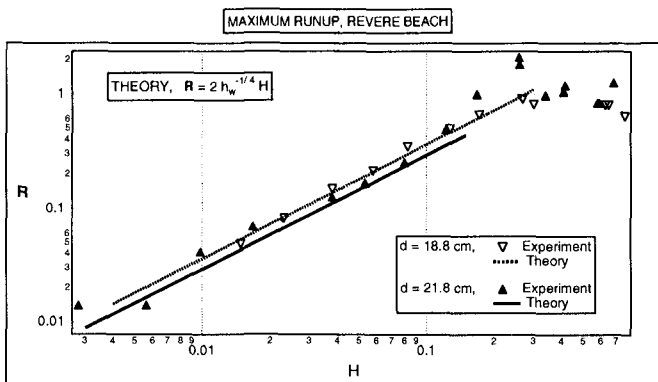


Figure 2. Comparison of the maximum runup between the analytical solution and the laboratory data for two different depth $d = 18.8\text{cm}$ and $d = 21.8\text{cm}$.

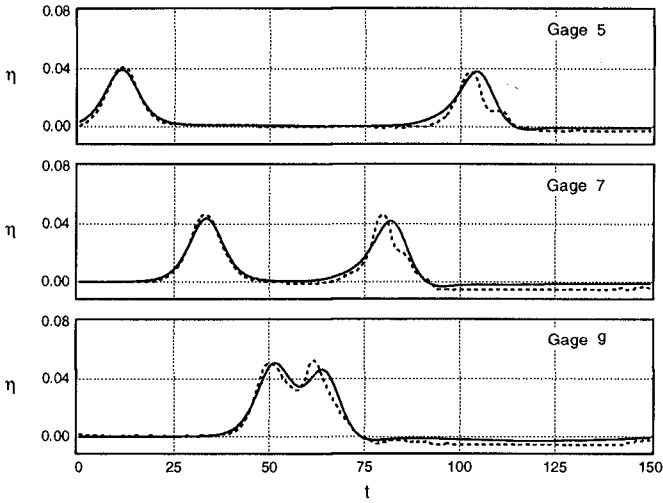


Figure 3. Comparison of the time histories of surface elevations between the analytical solution (evaluation of the integral 14) and the laboratory data for $d = 21.8\text{cm}$ and $H = 0.0378$ case at three gages. Dotted lines represent the laboratory results.

A comparison of theory predictions with laboratory data is presented here. We compared the maximum runup heights and the time series of surface elevations predicted by the general method with the laboratory data in figure 2 and figure 3 respectively.

THE CONTINENTAL SHELF AND SLOPE

Our objective is to obtain the amplification factor \mathcal{A} in the first segment and the reflection coefficient A_r in the third segment in terms of the incident wave amplitude A_i . We use general methodology to write a matrix equation to obtain analytical solution;

$$S_{11} \mathcal{A} = S_{12} V_2, \tag{16}$$

$$S_{22} V_2 = K_{23} V_3, \tag{17}$$

Combining the two matrix equations, it is possible to write the following matrix equation;

$$S_{11} \mathcal{A} = S_{12} S_{22}^{-1} K_{23} V_3. \tag{18}$$

Using the naming style for the topographic-feature matrices,

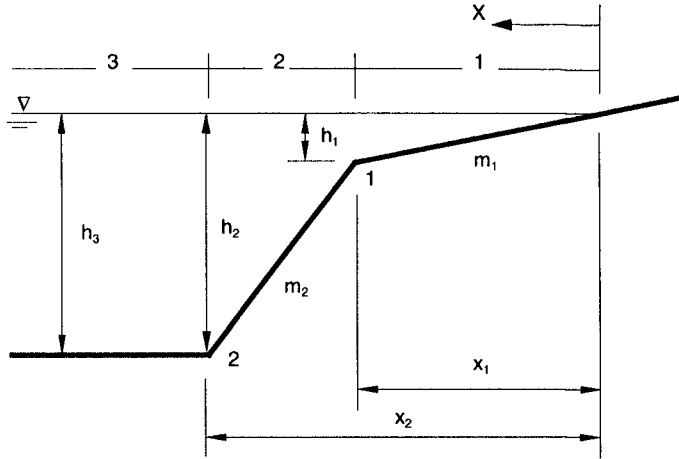


Figure 4. Definition sketch for the continental shelf and slope topography.

$$\begin{pmatrix} J_0\left(\frac{2\omega\sqrt{h_1}}{m_1}\right) \\ J_1\left(\frac{2\omega\sqrt{h_1}}{m_1}\right) \end{pmatrix} \mathcal{A} = \begin{pmatrix} J_0\left(\frac{2\omega\sqrt{h_1}}{m_2}\right) & Y_0\left(\frac{2\omega\sqrt{h_1}}{m_2}\right) \\ J_1\left(\frac{2\omega\sqrt{h_1}}{m_2}\right) & Y_1\left(\frac{2\omega\sqrt{h_1}}{m_2}\right) \end{pmatrix} \begin{pmatrix} J_0\left(\frac{2\omega\sqrt{h_2}}{m_2}\right) & Y_0\left(\frac{2\omega\sqrt{h_2}}{m_2}\right) \\ J_1\left(\frac{2\omega\sqrt{h_2}}{m_2}\right) & Y_1\left(\frac{2\omega\sqrt{h_2}}{m_2}\right) \end{pmatrix}^{-1} \begin{pmatrix} e^{-\frac{i\omega x_2}{\sqrt{h_3}}} & e^{\frac{i\omega x_2}{\sqrt{h_3}}} \\ i e^{-\frac{i\omega x_2}{\sqrt{h_3}}} & -i e^{\frac{i\omega x_2}{\sqrt{h_3}}} \end{pmatrix} \begin{pmatrix} A_i \\ A_r \end{pmatrix}. \tag{19}$$

Here \mathcal{A} is the unknown scalar – To ensure a bounded solution at the coastline, as in the single beach case, the unknown coefficient in the eigenfunction equation for Y_0 must be set equal to zero. This gives a scalar unknown for this segment.– for the first segment and V_2 and V_3 are the column unknown vectors for the second and third segments respectively.

The transmitted wave to the beach is given by

$$\eta_1(x, t) = \int_{-\infty}^{+\infty} \Phi(\omega) \mathcal{A} J_0\left(\frac{2\omega\sqrt{h_1(x)}}{m_1}\right) e^{-i\omega t} d\omega. \tag{20}$$

Again here $\Phi(\omega)$ associated with initial solitary wave profile. Amplification factor \mathcal{A} can be determined from equation (19). Using the asymptotic analysis, the maximum runup can be given by

$$R = 2.831 \sqrt{1/m_1} H^{5/4}. \tag{21}$$

This is the same analytical expression that Synolakis (1986) found for the single sloping beach case, implying that at least for long waves the runup only depends on the beach slope closest to the shoreline. To better understand these results, different hypothetical topographies of the continental shelf and slope will be investigated next, by changing the transition point and the wave height H the effects of the slopes on the maximum runup are analyzed. Maximum runup calculations are based on the evaluation of the maximum of the integral (20). Maximum runup calculations are shown in figure 5 for the different ranges of parameters; i.e. H , h_1 , m_1 and m_2 . It is clear from the figure that the most dominant parameter on the maximum runup is the slope of beach closest to the shoreline; i.e. m_1 . More parametric analysis can be found elsewhere (Kânoğlu, 1997).

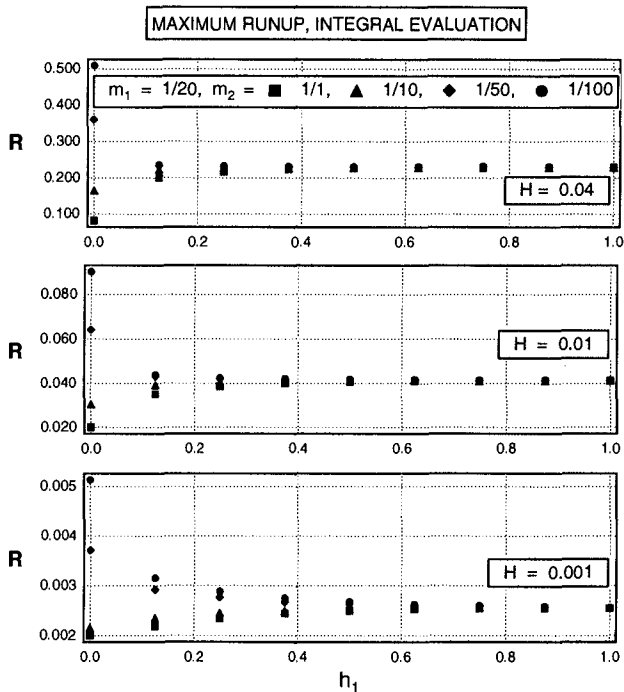


Figure 5. The effect of the parameters m_2 , h_1 and H on the maximum runup for the continental shelf and slope with $m_1 = 1/20$ - $h_1 = 0$ means topography only with m_2 slope and $h_1 = 1$ means topography only with m_1 slope-.

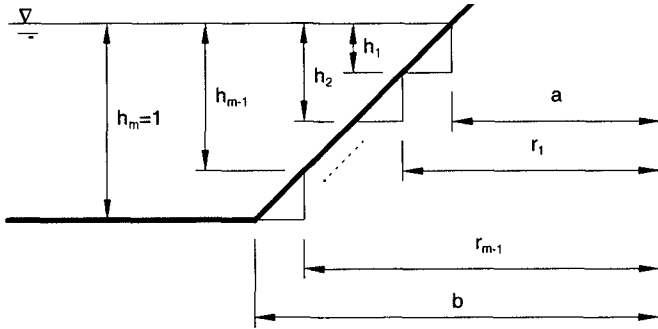


Figure 6. Island slope in a stepwise fashion.

CONICAL ISLAND

The overall good agreement between the analytic results and the laboratory data for the two-dimensional topography of the Revere Beach suggested the implementation of a similar methodology, i.e. usage of piecewise linear topographies for the three-dimensional topographies.

Analytical Solution

Here we will use linear shallow-water wave equation in polar coordinates. Given the singularity of the equation of motion in the case of the conical island $h(r) = m(r - a) - m$ and a are the slope and the waterline radius of the conical island, respectively— one method of removing it is to approximate the surface of cone with cylindrical boxes—Henceforth a cylindrical box will be referred to as a sill— in a stepwise fashion as in figure 6. For example in the segments, the basic solutions are

$$\eta_j = \sum_{n=-\infty}^{+\infty} e^{i(n\theta - \omega t)} \begin{cases} \{A_{n,i} e^{-\frac{i n \pi}{2}} J_n(kr) + A_{n,r} H_n^{(1)}(kr)\} & r \geq b, \\ \{A_n J_n(kr) + B_n Y_n(kr)\} & r_j \leq r \leq r_{j+1}, \end{cases} \quad (22)$$

where b is the radius of the conical island at the toe, $k = \omega/\sqrt{h_j}$ and j represents the segment number. Given that the solution is known for evolution over a sill, the dividing the solution over the conical surface involves matching solutions at the interface of steps on segments. At the edge of each sill, in other words at a discontinuity in h , it will be required that the surface elevation and the normal component of the mass flux are continuous. At the shoreline ($r = a$); the later matching condition requires that $\partial\eta/\partial r|_{r=a} = 0$. Again here instead of trying to solve the system of equations which can be set up from the matching conditions, we will use (2×2) matrices to get solutions as described two-dimensional case. Details of the analytical study are described by Kânoğlu (Kânoğlu, 1997).

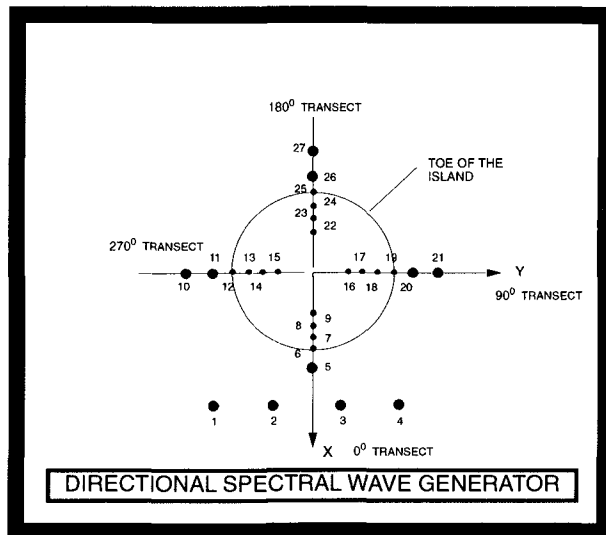


Figure 7. Definition sketch of the basin (not to scale).

Experimental Study

We performed a series of large scale laboratory experiment –in a 30m wide and 25m long basin– at CERC for a conical island. Conical island –60cm high, 7.2m toe diameter and 2.2m crest diameter and 1 : 4 slope– was located in the middle of the basin as shown in figure 7. We varied the water depth, the solitary wave height, the horizontal length of the source and the eccentricities. We recorded the time histories of surface elevation at 27 locations and we measured maximum runup heights at 24 locations around the island. The experiments are described elsewhere in detail (Liu *et al.*, 1995; Briggs *et al.*, 1994; Kânoğlu, 1997). In most cases, the maximum runup heights are the largest at the front of the island and it decreases gradually toward the lee side of the island. Because of the collision of the two trapped waves, there is a drastic increase in the maximum runup height at the lee side of the island. Furthermore, in some cases as in figure 8, the maximum runup heights at the lee side of the island are larger than that of the front side.

We compared the maximum runup heights and the time series of surface elevations predicted by the general method with the laboratory data. Comparisons for the maximum runup and time histories of surface elevation are shown in figure 8 and 9 respectively.

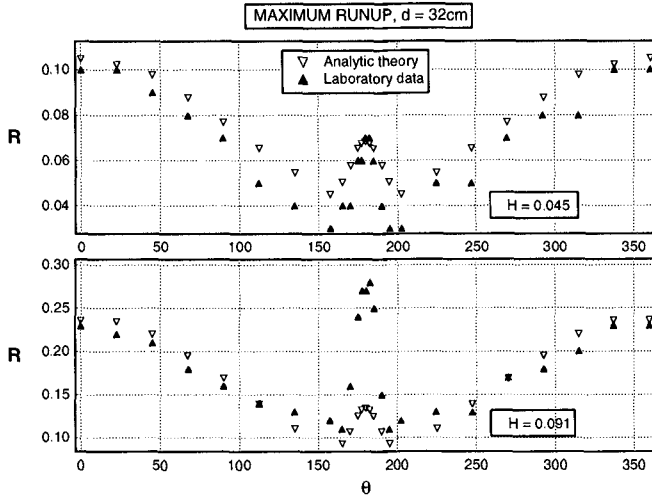


Figure 8. Comparison between analytical solution and experimental results for maximum runup for two different waveheights H .

CONCLUSIONS

Comparisons between the analytical and experimental results are in good agreement for the maximum runup and the time series of surface elevation in both cases, i.e. the Revere Beach and the conical island experiments. For the conical island, we observe that the maximum runup height is largest in the front of the island and it decreases gradually toward the lee side of the island. Because of the collision of the two trapped waves, there is a drastic increase in the maximum runup height at the lee side. As suggested by Yeh (Yeh *et al.*, 1994), our results also confirm the mechanism of catastrophe around Babi island.

ACKNOWLEDGEMENT

We are grateful to the National Science Foundation of the United States for its support through grant BCS-9201326 and a PYI grant.

REFERENCES

- Briggs, M. J., Synolakis, C. E., Harkins, G. S. and Green, D. 1994. Laboratory experiments of tsunami runup on a circular island. *PAGEOPH*, **144**, 569-593.
- Briggs, M. J., Synolakis, C. E., Kanoglu, U., Green, D. R. 1997. Benchmark problem 3, Runup of solitary waves on a vertical wall. *Proceedings of the Second Workshop on Long Wave Runup Models*. In press.

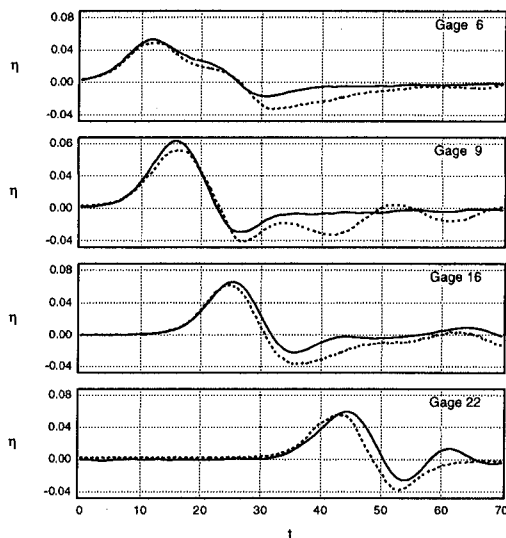


Figure 9. Comparison between the laboratory data and the analytical solution for the time histories of the surface elevation for a $H = 0.045$ solitary wave, at four different locations. Dotted lines represent the laboratory results.

Carrier, G. F. 1966. Gravity waves on water of variable depth. *J. Fluid Mech.*, **24**, 641-659.

Kânoğlu, U. 1997. *The runup of long waves around piecewise linear bathymetries*. Ph.D. Thesis. University of Southern California, Los Angeles, California, 90089.

Liu, P-L, Cho, Y-S, Briggs, M. J., Kanoglu, U., and Synolakis, C. E. 1995. Runup of solitary waves on circular islands. *J. Fluid Mech.*, **320**, 259-285.

Raubenheimer, B., Guza, R. T., Elgar, S. 1995. Wave transformation in the surf zone. *EOS*, AGU 1995 Fall Meeting, November 7, p. 282.

Synolakis, C. E. 1986. *The Runup of Long Waves*. Ph.D. Thesis. California Institute of Technology, Pasadena, California, 91125. 228 pp.

Synolakis, C. E. 1987. The runup of solitary waves. *J. Fluid Mech.*, **185**, 523-545.

Tadepalli, S. and Synolakis, C. E. 1994. The run-up of N-waves on sloping beaches. *Proc. of R. Soc. Lond. A*, **445**, 99-112.

Ward, D. 1995. Physical model study of Revere Beach, Massachusetts. US Army Corps of Engineers, Waterways Experiment Station Technical Report CERC-95-2, March 1995.

Yeh, H., Liu, P-L., Briggs, M., Synolakis C. E. 1994. Tsunami catastrophe in Babi island. *Nature*, **372**, 353-358.

CHAPTER 114

OFFSHORE TSUNAMI PROFILES OBSERVED AT THE COASTAL WAVE STATIONS

Toshihiko NAGAI¹, Noriaki HASHIMOTO²,
Kazuyoshi SHIMIZU³, and Fujio KITAMURA⁴

ABSTRACT

This paper presents offshore tsunami profiles observed by NOWPHAS (Nationwide Ocean Wave Information Network for Ports and Harbours) wave-measuring instruments installed at various coastal wave stations and tide stations in Japan. Included are wave profiles of damage-inflicting tsunamis generated by the 1993 Hokkaido-Southwest Earthquake, the 1994 Hokkaido-Eastoff Earthquake, the 1996 Iri-Anjaya Earthquake, and other smaller recently occurring tsunamis. Also presented are characteristics and phenomena of interest clarified through various analyses performed on observational data.

Introduction

Analysis of observed offshore tsunami profiles provides valuable information for clarifying their characteristics, which is essential for preventing disastrous consequences. Here, we present profiles of several damage-inflicting tsunamis which recently struck Japan, i.e., tsunamis generated by the 1993 Hokkaido-Southwest Earthquake on Jul. 12, 1993, the 1994 Hokkaido-Eastoff Earthquake on Oct. 4, 1994, the 1995 Hyogo-South Earthquake on Jan. 17, 1995, and the 1996 Irianjaya Earthquake on Feb. 17, 1996. Wave data was measured by NOWPHAS (Nationwide Ocean Wave Information Network for Ports and Harbours) wave-measuring instruments installed at various coastal wave stations and tide stations in Japan. Also presented are characteristics and phenomena of interest clarified through various analyses performed on observational data.

¹ Chief, Marine Observation Laboratory, Hydraulic Engineering Division, Port and Harbour Research Institute (PHRI), Ministry of Transport (MOT), 3-1-1 Nagase, Yokosuka, 239, Japan

² Chief, Hydraulic Laboratory, Marine Environmental Division, PHRI, MOT

³ Ex-Senior Research Engineer, Hydraulic Engineering Division, PHRI, MOT

⁴ Ex-Senior Research Engineer, Coastal Development Institute of Technology, 6F 3-16 Hayabusa-cho, Chiyoda, Tokyo, 102, Japan

Wave-Measuring Instrumentation

Figure 1 shows the NOWPHAS wave observation network in Japan (Nagai et al., 1996, 1994a) which is operated under the auspices of the Ports and Harbours Bureau of the Ministry of Transport (MOT) and its associated agencies including the Port and Harbour Research Institute (PHRI). This nationwide network of wave-measuring instrumentation is the product of long-term intensive efforts directed at obtaining more precise and reliable coastal wave information for disaster prevention purposes and the planning, design, and construction of ports and other coastal structures.

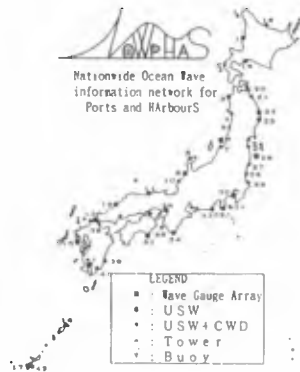


Figure. 1 NOWPHAS Wave Observation Network

Figure 2 shows three types of wave-measuring instruments employed in the NOWPHAS network: (1) The ultrasonic wave (USW) gauge, a widely employed instrument (jointly developed by the Kaijo Co. and PHRI in the 1960s) which precisely determines wave surface elevation by measuring the time for an ultrasonic wave to travel between the seabed and water surface, (2) The current wave directional (CWD) gauge, a widely employed instrument (developed in the 1970s) which determines wave direction by measuring wave-induced horizontal current fluctuations along the seabed, and (3) The Doppler wave directional meter (DWDM), a newly employed instrument (jointly developed by the Kaijo Co., Marine Surveyors Association, and PHRI in 1995) which uses a single sensor to determine with sufficient accuracy the height, period, and directional spectra of waves. DWDMs have been installed at four coastal stations (Fig.1) (Takayama et al., 1995), and in the future are expected to be the main wave-measuring instrument employed under NOWPHAS.



Figure. 2 USW, CWD, and DWDM Wave Gauges

Hokkaido-Southwest Earthquake OffshoreTsunami Profile

Figure 3 shows 20 min of offshore wave records observed at coastal station No.8 Wajima (Sta.8) before arrival of the 1993 Hokkaido-Southwest Earthquake tsunami. Shown are water surface elevation, horizontal current at the seabed in vector form, and the corresponding vector components of water velocity U (m/s) and water direction θ . A USW installed at 50 m measures η and a CWD installed at 27 m measures U and θ . Figure 4 shows corresponding records observed just after the arrival of the tsunami (Nagai et al., 1993, 1994b, 1995a), where it can be seen from the center line determined by low-pass filtering that distinct, long-period oscillations are generated in η . The wave current is also clearly affected as indicated by the long-period oscillations in the horizontal current vectors numerically determined using a triangular low-pass filter of 10s in length.

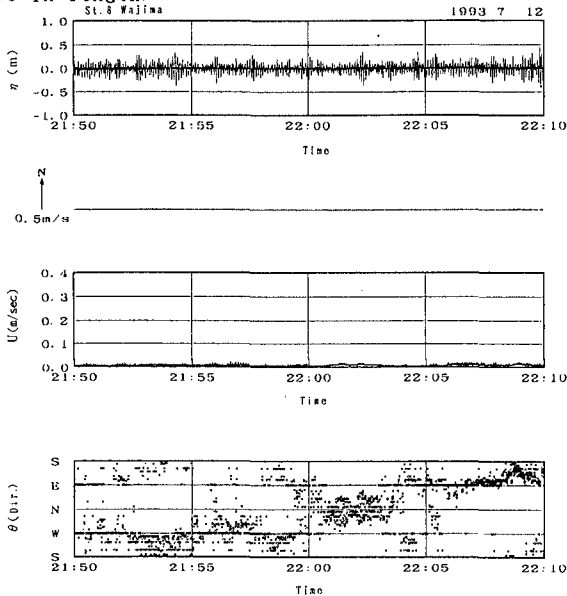


Figure. 3 Offshre Wave Gauge Data before the Tsunami Attack

Shown in Figure 5 are pair values of USW-measured filtered η and CWD-measured differential change in seabed pressure p observed at Sta.4 Akita before (left) and after (right) tsunami arrival; where for each case, 20 min of data are plotted at a sampling interval of 0.5s. Before arrival, most values are concentrated around the origin ($\eta = p = 0$) indicating no long-period oscillations in η or seabed current. In contrast, however, after the tsunami arrives they are concentrated along the line $\eta = p$; thereby indicating long-period oscillations occur as expected under linear long wave theory. Taken together, these results confirm the reliability of the observed.

Under linear progressive long wave theory, the following relationship should hold:

$$U_{max} = (\eta / 2)(g/h)^{-1/2} \tag{1}$$

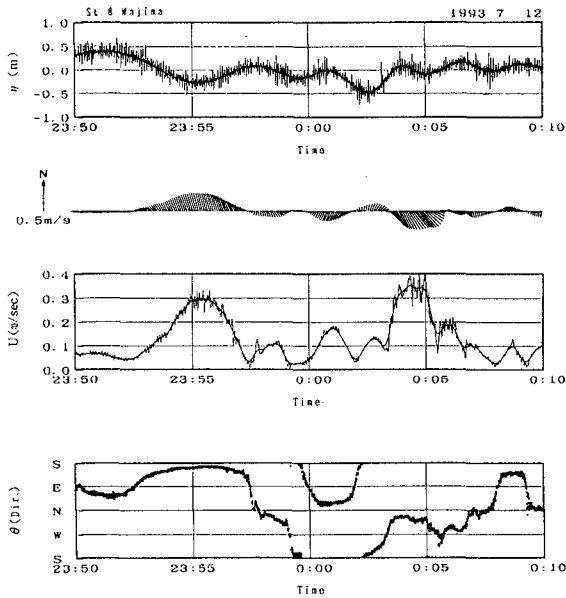


Figure. 4 Offshore Wave Gauge Data after the Tsunami Attack

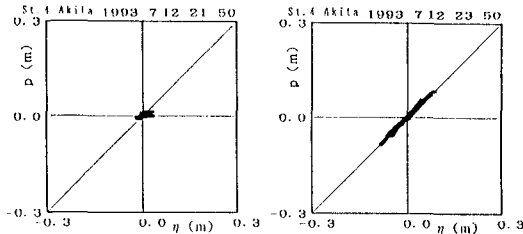


Figure. 5 Comparison of η and p

where U_{max} is the maximum horizontal water velocity at the seabed, $\eta/2$ the amplitude of water surface elevation $(\eta_{max} - \eta_{min})/2$, g the acceleration of gravity, and h the water depth. These parameters are respectively plotted as pair values in Figure 6 for various wave stations over a 20-min period following the arrival of the tsunami. If eq. (1) is satisfied, then the plotted values should fall on the indicated 45 degree line. For standing waves, $\eta=0$ at the nodes (y-axis) and $U=0$ at the antinodes (x-axis). Considering the results, it appears that the observed tsunami is not completely progressive, but rather exhibits characteristics of standing waves due to the effect of wave reflection.

Integration of current velocity over time gives the motion of water particles at the seabed, being shown in Figure 7 for 20 min before and after the tsunami's arrival at Sta. 8 with and without tide corrections. Motion is shown in the horizontal plane in which the x- and y-axis indicate directions East(+) and West(-) and North(+) and South(-). The effect of the tsunami is quite apparent, especially when considering tide effects. Note that the direction of the constant-velocity tidal current is shown before arrival, and that after correction it is

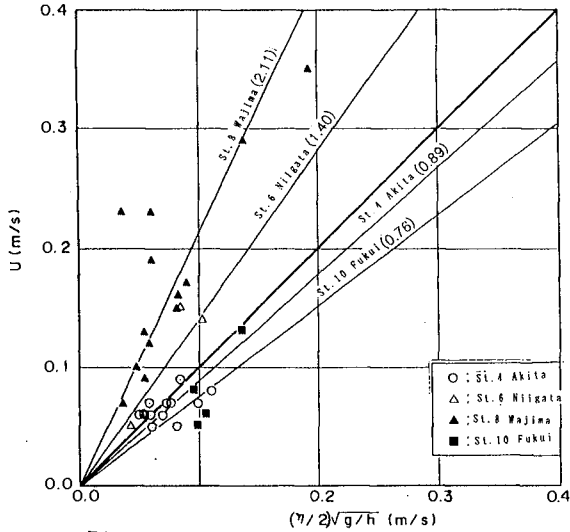


Figure. 6 Comparison of η and U

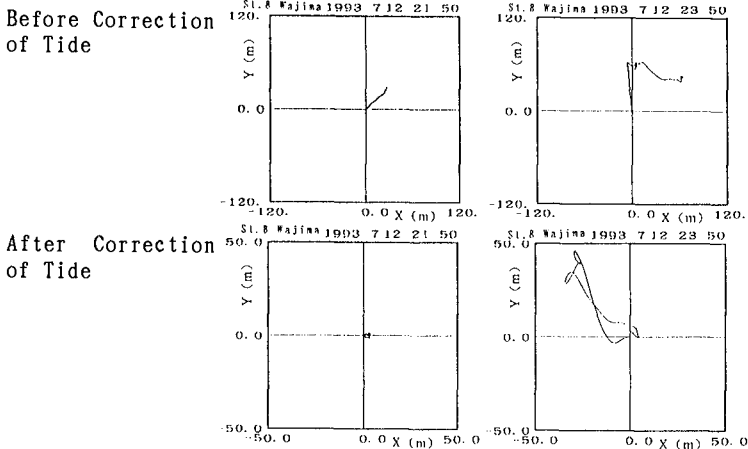


Figure. 7 Seabed Water Particle Movement

properly accounted for. The amplitude of seabed particle motion due to the tsunami is shown to be about 50m, i.e., a distance much greater than can be explained by even the strongest wind-wave conditions.

Figure 8 shows the low-pass filtered offshore wave profile η and tide record Z , before and until more than 6 hours after tsunami arrival as measured at Sta.8 (3km offshore), and the Wajima Port tide station, respectively. Upon tsunami arrival just after 0:00LT, both records show a large peak which cannot be accounted for by the effects of wind or tidal motions. In addition, short-period oscillations less than 10 min, i.e., such as those clearly shown in η , cannot be observed in tide records due to the occurrence of low-pass-filter effects in the measuring instrument's seawater drain tube; thereby demonstrating the

necessity for deploying offshore wave-measuring instrumentation.

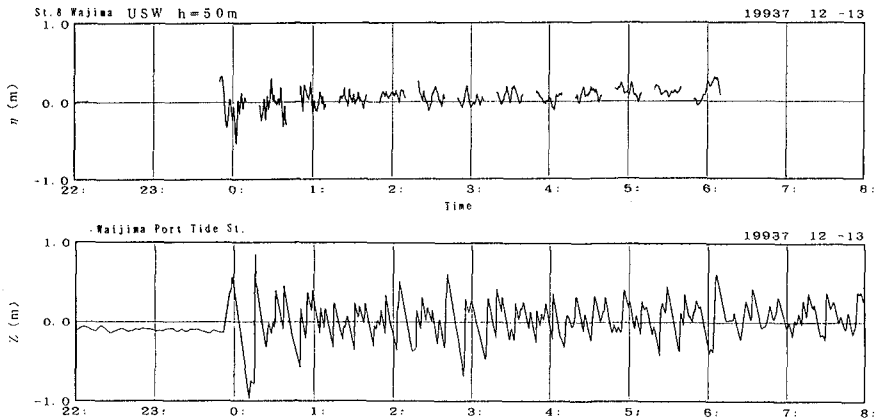


Figure. 8 Comparison of Offshore Wave Profile and Tide Record

Hokkaido-Eastoff Earthquake Offshore Tsunami Profile

Figure 9 summarizes the heights and periods of the tsunami generated by the 1994 Hokkaido-Eastoff Earthquake as observed along Japan's Pacific Ocean coast by NOWPHAS wave-measuring instrumentation (Nagai et al., 1995b, 1995c). Individual tsunami waves were defined by the zero-up-cross method. A "*" denotes wave station data while all other data is from tide stations. Note that individual tsunami waves show a long period of about 40 min.

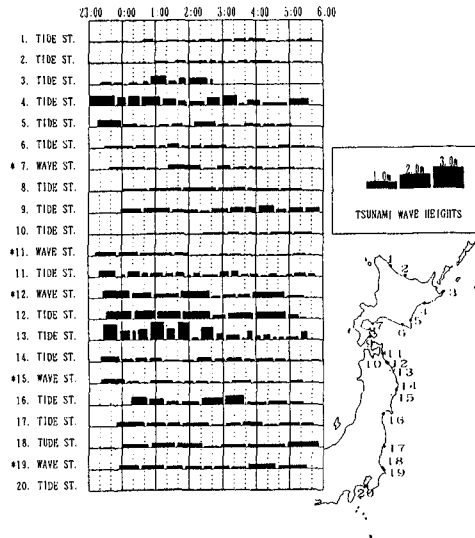


Figure. 9 Tsunami Heights and Periods of the 1994.10 Earthquake

Figure 10 shows a continuous offshore profile η of the tsunami as observed at Sta.19 off Tomakomai Port at a water depth of 18.5 m. This data was obtained as part of a continuous offshore long wave observation project conducted in Oct.1994 by the Tomakomai Port Construction Office of the Hokkaido Development Agency in order to investigate a port resonance problem caused by long waves. Although η is low-pass filtered, clearly distinguishing the tsunami from wind waves and tides is difficult due to the presence of waves with significant wave heights of more than 2 m and a large range of tidal motion. Nevertheless, when these observations are considered in conjunction with those in Figure 10, this confirms the presence of tsunami-generated waves with very long periods of 30 to 80 min.

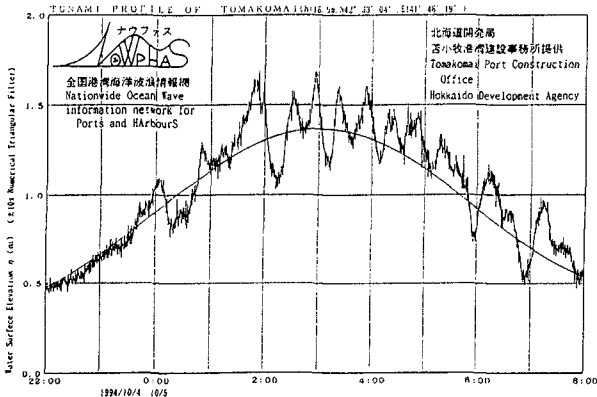


Figure. 10 Tsunami Profile of the No.7 Tomakomai Port

Figure 11 also shows continuous tsunami wave data observed by tide and offshore wave stations at Sta.20 Mutsu-Ogawara for the tsunamis generated by the Hokkaido-Eastoff and 1994 Sanriku-Faroff (Dec.28,1994) Earthquakes. Also shown are the predicted tides, as well as seabed horizontal current vectors for the Hokkaido-Eastoff tsunami.

The results of applying frequential spectral analysis to the data in Figure 11 are presented in Figure 12, which shows corresponding power spectra and the response functions of the wave and tide gauges for each tsunami. Note that both tsunami show the same correlation between their wave and tide spectra; thereby indicating accurate and reliable measurements even under transient, unstable conditions caused by a tsunami.

Figure 13 shows the results of a spectral correlation analysis between η and Z power spectra determined from observation data of the Hokkaido-Eastoff tsunami. Coherence and phase values indicate high stability for measurements at frequencies less than 10^{-8} Hz, which includes the frequency range where dominant tsunami energy exists.

Shown in Figure 14 are corresponding results for spectral correlation analysis between η and the two vector components of seabed horizontal current velocity u and v , where u is the east-west (on-off shore) direction and v the north-south (longshore) direction.

Evaluation of the respective coherence and phase values indicates consistent results with those shown in Figure 13.

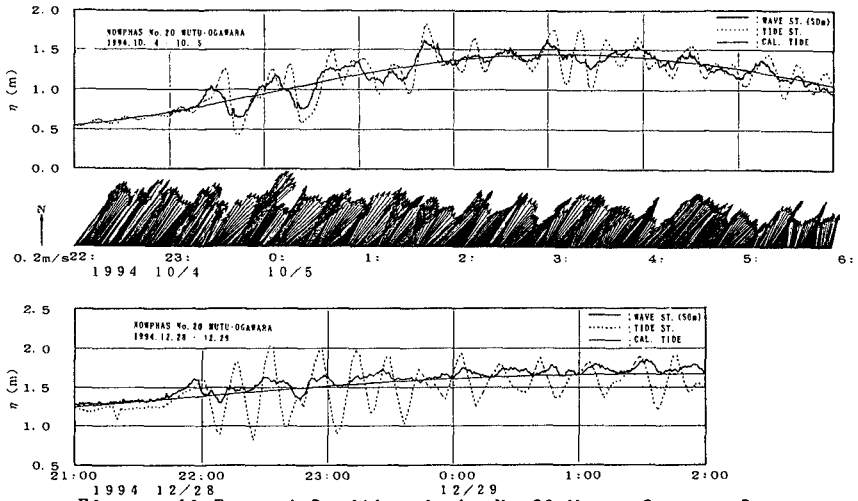


Figure. 11 Tsunami Profile of the No. 20 Mutsu-Ogawara Port

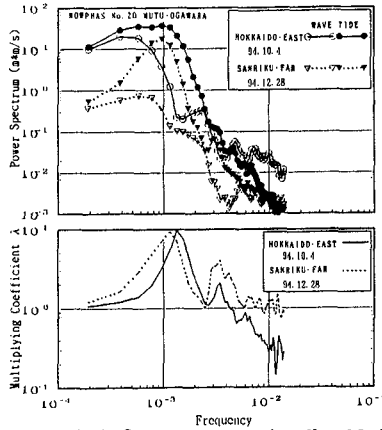


Figure. 12 Frequential Spectra of the No. 20 Mutsu-Ogawara Port

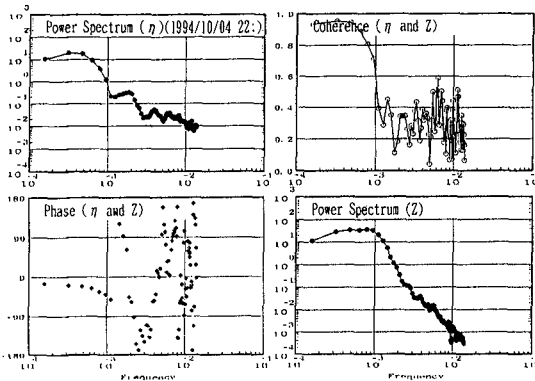


Figure. 13 Spectra Correlation between η and Z

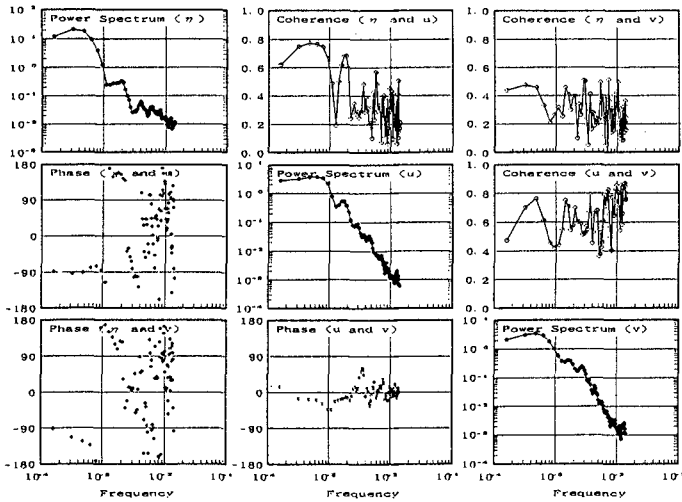


Figure. 14 Spectra Correlation among η , u and v

Figure 15 shows pair values of u and η (g/h)^{-1/2} plotted over three 15-min periods in which the first-arriving individual Hokkaido-Eastoff tsunami wave was observed by Sta.20, where the values should fall on the straight line passing through the origin under linear progressive wave theory. In this case, the difference between the observation depth of the USW (50m) and CWD (28m) gauges is accounted for. A comparison of observed values indicates the presence of standing wave characteristics at the early stage of observation due to wave reflections off the coast.

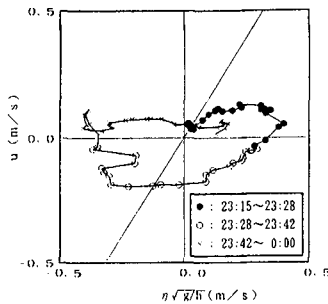


Figure. 15 Relation between η and U for the First Tsunami Wave

Continuous-observed offshore wave profiles provide a good benchmark from which to evaluate numerical models for simulating tsunami characteristics. Figure 16 compares observed wave/tide station η/Z and u of the Hokkaido-Eastoff tsunami obtained at Sta.20 with those calculated by a numerical simulation model of 3 km grid based on linear long wave propagation characteristics(Aida,1962), and the initial seabed movement determined by the DCRC-3b model (Table 1) developed at the University of Tohoku. Good agreement is present for all three measured parameters, possibly being due to employing a grid size that is relative

-ly small compared to tsunami wave length with a 40-min period.

Table. 1 The 1994 Tsunami Model (DCRC-3b Model by Univ. of Tohoku)

Origin of Fault	43.210°N, 146.120°E
Length	140km
Width	70km
Strike	52°
Dip Angle	77°
Slip Angle	128°
Depth	30km
Dislocation	7.62m

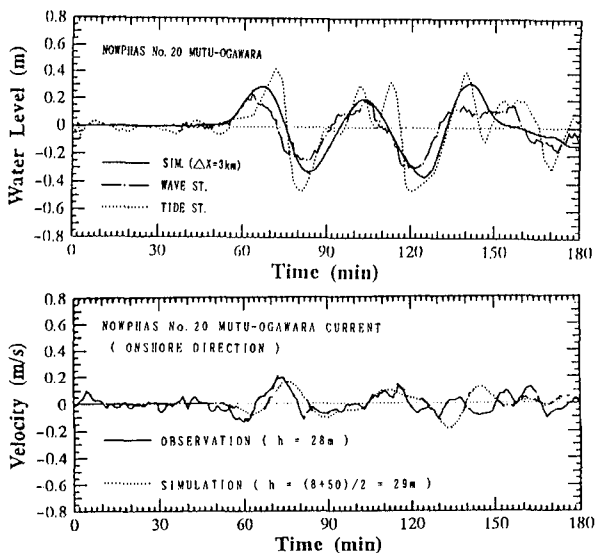


Figure. 16 Comparizon of the Observed and Calculated Tsunami Profile

Hyogo-South Earthquake Tsunami Profile

The city of Kobe and its surrounding region suffered tremendous damage and loss of life when the 1995 Hyogo-South Earthquake struck during the early morning hours (05:47). Figure 17 shows USW-measured off-shore wave profile before and immediately after striking as observed by Sta. 36 Kobe, where amplitudes of several centimeters and periods of 1 or 2 min are indicated by the low-pass-filtered line, i.e., most of the earthquake's energy was expended on land areas such that its effect generated only slight movement of the seabed.

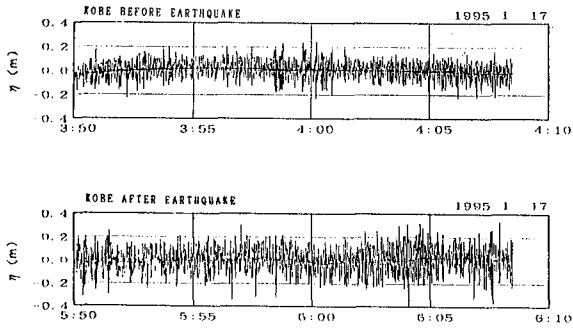


Figure. 17 The 1995 Hygo-South-Earthquake Tsunami Profile

Irianjaya Earthquake Tsunami Profile

Figure 18 shows the wave profile of the tsunami generated by the 1996 Irianjaya-Earthquake as observed by Sta. 31 Habu (USW, 50 m) and PHR1 (USW and tide station) at the entrance to Tokyo Bay 50 km distant. The tsunami arrived at the bay entrance 20 to 30 min after initial observation at Sta. 31, which indicates that continuous observation and monitoring of offshore waves at this offshore station would allow predicting the strike time and provide an early warning for the Tokyo area. Note that the maximum wave heights are about 10 and 70 cm, respectively, with this amplification in height being due to topographical resonance effects.

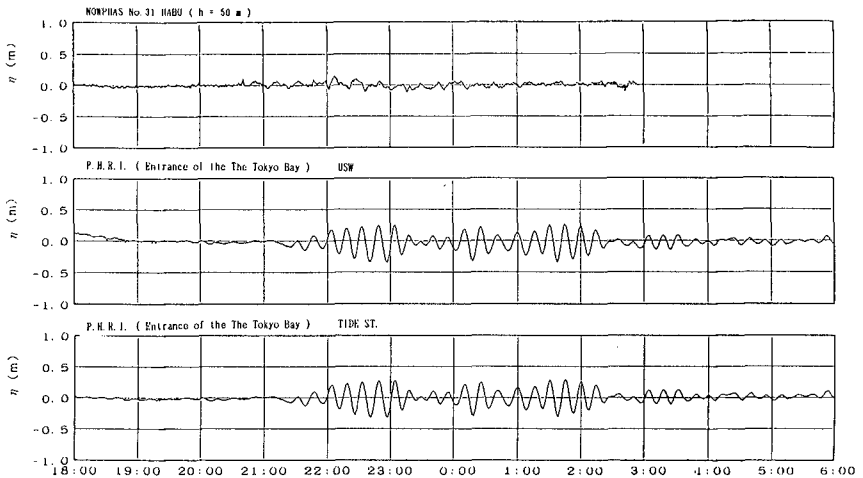


Figure. 18 The 1996 Irianjaya-Earthquake Tsunami Profile

The results of applying frequential spectral analysis to the data in Figure 18 are presented in Figure 19, where a distinct resonance peak is apparent and indicates that amplification occurs in the frequency band of $0.9 \cdot 10^{-3}$ and $1.5 \cdot 10^{-3}$ Hz ($T = 18.5$ and 11 min).

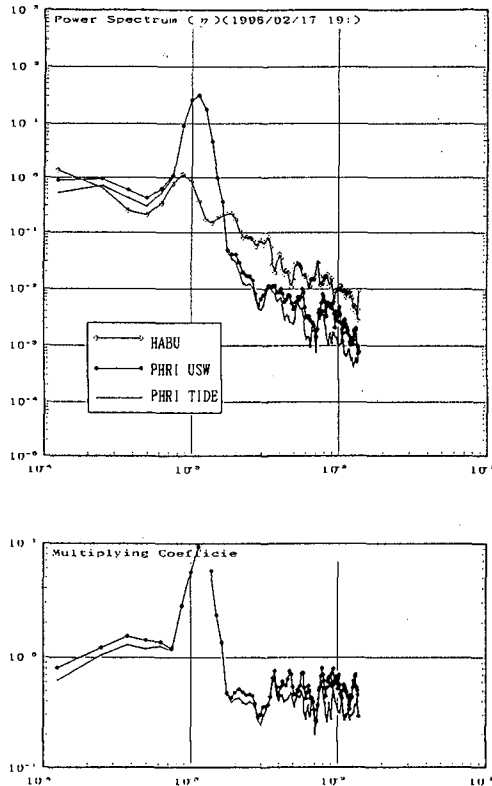


Figure. 19 Frequential Spectra of the 1996 Irianjaya-Earthquake Tsunami

Summary

We have analyzed selected wave profiles and associated data of large, recently striking tsunami as observed by NOWPHAS offshore wave-measuring instruments and harbor tide stations throughout Japan. As a result of our analysis, several tsunami characteristics and phenomena of interest have been clarified, and through our better understand we can expect to improve observation capability. To fully understand the characteristics of tsunamis and long waves, however, the data acquisition system of NOWPHAS must be reconfigured to a more continuous observation scheme as wave observations are at the present time only performed for 20min every 2h. Efforts to realize such an observation system are now in progress (Nagai et al., 1995d).

Acknowledgments

For their outstanding cooperation, sincere gratitude is extended to all personnel involved with NOWPHAS, with a special thank you to those from the Ports and Harbours Bureau, District Port Construction Bureaus of MOT, Hokkaido and Okinawa Development Agencies, and PHRI.

REFERECES

- Aida, I. (1962), "Numerical Experiments for Tsunami Caused by Moving Deformation of the Sea Bottom, Bull. Earthqu. Res. Inst., vol.47, pp. 849-862
- Nagai, T., Sugahara, K., Hashimoto, N., and Asai, T. (1996), "Annual Report on Nationwide Ocean Wave information network for Ports and HarbourS (NOWPHAS 1994)", Technical Note of the PHRI, No. 821, 313p.
from 1970 to 1993 year's versions of the same series of the Annual Reports, See the Technical Notes of the PHRI, No. 137, 158, 178, 209, 233, 258, 282, 311, 332, 373, 417, 445, 480, 517, 545, 574, 612, 642, 666, 712, 721, 745, 770, and 796 respectively
- NAGAI, T., HASHIMOTO, N., SHIMIZU, K., and TAKAYAMA, T. (1995a), "Tsunami Profiles Observed at the NOWPHAS Offshore Wave Stations", Second International Workshop on Wind and Earthquake for Offshore and Coastal Structure, UJNR at Berkeley, California
- Nagai, T., Hashimoto, N., Hiraishi, T., and Shimzu K. (1995b), "Characteristics of the 1994 Hokkaido-Eastoff-Earthquake Tsunami", Technical Note of the PHRI, No. 802, 97p.
- Nagai, T., Hashimoto, N., Hiraishi, T., Shimzu K., Ichikawa, T., Miyabe S., Kudaka, M., and Kawamata, S. (1995c), "Characteristics of the 1994 Hokkaido-Eastoff-Earthquake Tsunami based on the Field Observation Data", Proceedings of Coastal Engineering, Vol. 42, Japan Society of Civil Engineers, pp. 351-355
- Nagai, T., Hashimoto, N., Asai, T., Tobiki, I., Ito, K., Toue, T., Kobayashi, A. and Shibata, I. (1995d), "Relationship of a Moored Vessel in a Harbour and a Long Wave Caused by Wave Groups", Proceedings of the 24th International Conference on Coastal Engineering (ICCE' 94), vol.1, pp. 847-860
- Nagai, T., Sugahara, K., Hashimoto, N., Asai, T., Higashiyama, S., and Toda, K. (1994a), "Introduction of Japanese NOWPHAS System and its Recent Topics", Proceedings of HYDRO-PORT' 94, PHRI, pp. 67-82.
- Nagai, T., Sugahara, K., Hashimoto, N., and Asai, T., Higashiyama, S., Toda, K. (1994b), "Offshore Tsunami Profiles of the 1993 Hokkaido-Southwest-Earthquake Tsunami", Proceedings of Coastal Engineering, Vol. 41, Japan Society of Civil Engineers, pp. 221-225.
- Nagai, T., Hashimoto, N., and Asai, T. (1993), "The Hokkaido-Southwest-Earthquake Tsunami profiles observed at the NOWPHAS offshore stations", Rept. of PHRI, Vol. 32, No. 4, pp. 51-97
- TAKAYAMA, T., HASHIMOTO, N., NAGAI, T., TAKAHASHI, T., SASAKI, H., and ITO, Y., (1995), "Development of Submerged Doppler-type Directional Wave Meter", Proc. of the 24th International Conference on Coastal Engineering (ICCE' 94), vol.1, pp. 624-634

CHAPTER 115

A REALISTIC MODEL FOR THE 1992-96 TIDAL WAVES

Srinivas Tadepalli†

Costas Emmanuel Synolakis‡

ASCE, Associate Member

I. ABSTRACT

Tidal waves or tsunamis are long water waves of small steepness generated by impulsive geophysical events of the seafloor or by coastal landslides. Whereas their coastal evolution is now well-understood, their generation is not. Until recently (Tadepalli and Synolakis 1994a, 1996), numerous anecdotal records of historic tsunamis where shorelines significantly retreated before the tidal waves advanced up the coastline have been disregarded; the prevailing paradigm for tsunami studies is the modeling of the evolution and runup of a single-hump leading-elevation waves which offshore have solitary-wave profiles. We propose a model for the leading-wave of tsunamis to explain why the coastal manifestation of most tsunamis suggests a leading-depression N-wave, a waveform which causes the shoreline to recede before advancing up the beach. Farfield, we use the Korteweg-De-Vries equation, and we find that N-waves of geophysical scales do not fission over transoceanic propagation distances and no leading solitary waves emerge. Nearshore, we use shallow water theory to calculate the evolution and runup of emerging non-breaking waves, and we observe that they evolve according to Greens' law (Green, 1837, Lamb, 1945, Synolakis, 1991). We discuss the effects of certain ground deformation parameters and provide one application of our theory by modeling the Nicaraguan tsunami of September 1, 1992.

II. INTRODUCTION

The study of the generation, evolution and coastal effects of tidal waves is one of the classic problems in coastal engineering. Tsunamis are generated by impulsive geophysical events such as submarine earthquakes, volcanoes and landslides. The understanding of their coastal effects has progressed considerably in the last four years, both due to detailed field observations of tsunami inundation (Satake et al, 1993, Yeh et al, 1993, Synolakis et al, 1994, Imamura et al, 1995) and due to the availability of large scale laboratory data (Briggs et al, 1994 and 1995), all of which have helped validate inundation calculations in hydrodynamic models. Yet, the process of tsunami generation is less-understood,

† Environmental Fluid Mechanics Laboratory, Department of Civil Engg., Stanford Univ., Stanford, CA 94305-4020.

‡ Associate Professor, School of Engg., Univ. of Southern California, Los Angeles, CA 90089-2531.

and only very recently there has been an effort to understand the effects of seismic parameters on the leading-wave evolution at generation (Geist and Yoshioka, 1996). In fact as Tadepalli and Synolakis (1994) showed, the sign of the leading-wave which is a reflection of the direction of ground motion is of paramount importance in the determination of coastal effects.

Several recent earthquakes in Nicaragua [Sept. 1, 1993], Flores, Indonesia [Dec. 12, 1992], Okushiri, Japan [July. 7, 1993], East Java, Indonesia [Jun. 6, 1994], Kuril Islands, Russia [Oct. 4, 1994], and Mindoro, Philippines [Nov. 14, 1994] have produced tsunami waves which caused nearby shorelines to first recede before advancing. These observations have challenged further the prevailing paradigm for studying the coastal effects of tsunamis, i.e., the canonical model of a Boussinesq solitary wave profile propagating over constant depth and then climbing up a sloping beach (Liu et al, 1991). To quantify the persistent field observations and tsunami folklore, a class of water waves referred to as N-waves have been proposed (Tadepalli and Synolakis, 1994a) for nearshore-generated tsunamis, and it was observed that at least for three different types of N-waves, leading-depression N-waves climb up higher on sloping beaches than leading-elevation N-waves with the same leading-wave amplitude. They also derived asymptotic relationships referred to as runup laws, whose utility was recently demonstrated (Geist and Yoshioka, 1996) to supplement numerical computations for a Cascadia Subduction Zone giant earthquake. However, unresolved questions persist as to the long-distance hydrodynamic stability of these waves. Also, given the uncertainty associated with inferring the seafloor displacement from distant strong-motion records (Yamashita and Shato, 1974) there is little understanding as to the relative effects of the vertical deformation, of the deformed or of the relative magnitudes of subsidence and uplift, forcing laboratory modelers to work exclusively with solitary waves or periodic long waves, and numerical modelers to routinely introduce arbitrary large "amplification" factors to fit their results to runup field observations. We will attempt to address these questions here, by first deriving an initial sea-surface profile for the leading wave of a tsunami from a specification of the sea-bottom deformation and by demonstrating that this profile encompasses as special cases all N-wave like and solitary wave like profiles used in earlier studies (Synolakis, 1987, Tadepalli and Synolakis 1994a, Carrier, 1993). We then will discuss their stability with respect to fission in far field evolution, and we derive nearshore evolution relationships. We will then obtain asymptotic estimates of the relative effects of some generation parameters on the runup of non-breaking waves.

We therefore propose as a model for the leading wave of tidal waves the following normalized waveform,

$$\eta(x) = (\mathcal{E}_g \mathcal{H}) \cdot (x - X_2) \operatorname{sech}^2[\gamma(x - \theta)]|_{t=0} \quad (2.1)$$

where $\gamma = \sqrt{3\mathcal{H}p_0}/4$, $\theta = X_1 + ct$, $L = X_1 - X_2$, $c = 1$ and p_0 is a steepness parameter. We have nondimensionalized all variables with the offshore depth d , and in this normalization, $c = 1$. $\mathcal{E}_g < 1$ is a scaling parameter defining the crest amplitude introduced only for reference to ensure that the wave height (2.1) is \mathcal{H} ; \mathcal{E}_g can be chosen to fit desired field-inferred surface profiles. \mathcal{H} and the wavelength of the profile inferred from (2.1) are vertical and horizontal measures of the ground deformation respectively.

When the crest of the wave at generation is ahead of the trough, we will refer to this wave as a leading-elevation N-wave (LEN); when the trough starts propagating ahead of the crest, we will refer to these waves as leading-depression

N-waves. As suggested by Carrier (1993), multi-lobe waves similar to (2.1) can be described by combinations of Gaussian profiles; we prefer (2.1) because it allows direct derivation of asymptotic results. Here, for brevity, we will refer to all multilobe waveforms as N-waves. We will also use the qualifier non-breaking to refer to waves which do not break in the specific evolution problem, and we note that the same leading wave which evolves to its maximum penetration without breaking on a steep beach may break on a gentle beach; in the steepness range of geophysical interest the leading waves of most tsunamis do not break on most natural beaches[†], but they may break when advancing up rivers, during overland flow, or when focused on headlands.

III. TIDAL WAVE GENERATION

To motivate the generation of N-waves and our particular choice of the initial profile, consider the normalized linearized shallow-water equation (LSW) for propagation over constant depth, long believed as the physically realistic generation approximation (Tuck, 1972, Carrier, 1966) i.e.,

$$\eta_{tt} - \eta_{xx} = h_{0,tt} \quad (3.1)$$

and we consider the following seafloor motion,

$$h_0 = -\frac{2\mathcal{E}_g\mathcal{H}}{\gamma}\tanh[\gamma(x - \theta)] \quad (3.2)$$

where $h_0(x, t)$ is the ground motion, measured from a horizontal datum. Most submarine earthquakes are bipolar, and $h_0(x, t)$ is a motion with both a sudden uplift and subsidence such as would occur with a normal or oblique thrust fault. In nature, the ground deformation would stop quickly after the rupture and the deformation would not propagate indefinitely as the definition of h_0 suggests. Nonetheless, since our objective is only to determine an initial profile valid only for short times, the above ground deformation is adequate. It can be verified directly that (2.1) is an exact solution of the equation (3.1) with ground deformation given by (3.2). The ground deformation that generates a leading depression N-wave is shown in figure 1. Other ground motions (Tuck, 1972, Carrier, 1966) would also produce multi-lobe waves, but not of the same mathematical form; the advantage of the ground deformation h_0 in (3.2) is that it allows for the explicit evaluation of the nearfield and farfield effects in terms

[†] Since quite often tsunamis/tidal waves are reported in the press as giant walls of breaking water, we quote from the Proceedings of the 1979 NSF Workshop on Tsunamis, reported by E.O. Tuck and P. L.-F. Liu who wrote, "of course the physical mechanism has nothing to do with astronomical tides, but the common term "tidal waves" surely arose because most tsunamis are quite satisfactorily described as giving the appearance of a 'fast-rising' tides . . . we should be pleased that it (the term tidal wave) provides a correct picture of what actually happens . . . A near vertical moving wall of water as in movies like the Poseidon Adventure is unlikely to occur in the open ocean and it is the exception rather than the rule for coastal impact of tsunamis." Therefore we will resurrect the term tidal wave and use it interchangeably with the term tsunami.

of simple and intuitive asymptotic formulae.

To appreciate the range of surface profiles that (2.1) describes, figure 2(a) compares a classical Boussinesq solitary-wave profile with the surface profile obtained by (2.1), and for reference, with an isosceles[‡] leading-elevation (LEN) wave with the same leading wave steepness $p_0 = 1$ and a Gaussian profile suggested by Carrier (1993). Figure 2(b) shows leading-depression (LDN) profiles generated by equation (2.1) for a fixed \mathcal{H} and different values of L and, for reference, an isosceles LDN and a combination of Gaussian profiles (Carrier, 1993).

As an initial condition we will use the N-wave of (2.1), and then we will solve the Korteweg-De-Vries equation to calculate transoceanic propagation over constant depth. Once the wave arrives nearshore, we will use the LSW equation (Liu, 1991); it is well-established that for the non-breaking waves we are considering here, dispersive effects do not have sufficient time to manifest over the relatively short propagation distances on a sloping beach. We will show that both LDNs and LENs evolve according to a relationship equivalent to Greens' law (1837). Finally, we will provide results for the maximum runup and we will discuss the relative importance of certain generation parameters.

IV. PROPAGATION DISTANCE FOR SOLITARY WAVE EVOLUTION

Since, we are most interested in the effective propagation distance over which the leading solitary waves emerge, we propagated LDN waves by solving the KDV equation numerically (Synolakis, 1990). The prevailing paradigm would suggest that leading solitary waves should emerge rapidly, and therefore the leading tidal wave attacking nearby coastlines would be a solitary wave. LDN waves with geophysically-realistic initial height-to-depth ratio of 0.001 were practically unchanged after a transoceanic propagating distance of 2000 depths (see figure 3 (a)), indicating the hydrodynamic stability of N-waves and explaining anecdotal reports of LDN waves striking Hawaii after the Chilean 1960 event. No distinct solitary waves emerge even when LDN waves with initial height-to-depth ratio of 0.01 (much larger amplitude than a possible transoceanic tsunami) are propagated through twice the typical transoceanic distances, of about 4000 depths (see figure 3 (b)).

V. COASTAL EVOLUTION OF N-WAVES

We will now solve the propagation problem described by linearized shallow water equations (LSW) for variable depth $h_0(x)$, i.e.,

$$\eta_{tt} - (\eta_x h_0)_x = 0 \tag{5.1}$$

normalized with the offshore depth d as the characteristic length scale, and

[‡] Isosceles N-wave is a wave with equal peak and trough heights.

$\sqrt{g/d}$ as the time scale, $h_0(x) = x/\cot\beta$, when $x \leq \cot\beta$ and $h_0(x) = 1$ otherwise. It is widely believed that these equations describe the essential physics of the coastal tsunami evolution problem well (Liu et al, 1991). When the incident wave from infinity is of the form $\int_{-\infty}^{\infty} \Phi(\omega)e^{-i\omega t}d\omega$, then the transmitted wave to the beach is given by :

$$\eta(x, t) = 2 \int_{-\infty}^{\infty} \frac{\Phi(\omega)J_0(2\omega\sqrt{x\cot\beta})e^{-i\omega(\cot\beta+ct)}}{J_0(2\omega\cot\beta) - iJ_1(2\omega\cot\beta)}d\omega, \tag{5.2}$$

where $\Phi(\omega)$ is the transform function of the incoming wave. When $x = 0$, $R(t) = \eta(0, t)$ and its maximum value R is the maximum runup i.e., the elevation above the shoreline at the point of maximum penetration of the wave. Carrier (1966) and Synolakis (1987) have proved the runup invariance between linear and non-linear theory, and it has been repeatedly (Synolakis, 1991, 1993) shown that linear theory describes well the evolution of the maximum height of long waves which offshore had a Boussinesq solitary-wave profile. Therefore, without loss of generality, we will use linear theory for non-breaking waves we are considering here, to calculate the evolution of the wave height and the maximum runup.

The transform $\Phi(\omega)$ of (2.1) is obtained through contour integration (Tadepalli and Synolakis, 1994a) along a semi-circular contour in the upper half plane and is given by :

$$\Phi = \frac{2\mathcal{E}_g}{3p_0} \text{csh}\left(\frac{\pi\omega}{2\gamma}\right) \left[L\omega - i\left[1 - \frac{\pi\omega}{2\gamma} \text{coth}\left(\frac{\pi\omega}{2\gamma}\right)\right] \right] e^{i\omega X_1} \tag{5.3}$$

The evolution of this wave is obtained by substituting equation (5.3) into equation (5.2). We write $\eta(x, t) = F_1(x, t) + F_2(x, t) + F_3(x, t)$ and introduce $\theta = X_1 - X_0 - ct$. Then,

$$F_1(x, t) = \frac{4\mathcal{E}_g}{3p_0} L \int_{-\infty}^{\infty} \frac{\omega \text{csh}\left(\frac{\pi\omega}{2\gamma}\right) J_0(2\omega\sqrt{xX_0}) e^{i\omega\theta}}{J_0(2\omega X_0) - iJ_1(2\omega X_0)} d\omega. \tag{5.4}$$

Noting that $J_0(z) - iJ_1(z)$ is entire in the upper half-plane (Synolakis 1988, Tadepalli and Synolakis, 1994b), we use contour integration and compute the Laurent expansion to obtain :

$$F_1(x, t) = \frac{32}{3} \mathcal{E}_g \gamma_s^2 L \sum_{n=1}^{\infty} \frac{(-1)^{n+1} n I_0(4n\gamma\sqrt{xX_0}) e^{-2n\gamma\theta}}{I_0(4n\gamma X_0) + I_1(4n\gamma X_0)}, \tag{5.5}$$

where $\gamma_s = \sqrt{3\mathcal{H}/4}$. Using the asymptotic expansions for the modified Bessel functions (Abramowitz, 1970), we approximate F_1 by

$$F_1 = \frac{16}{3} \mathcal{E}_g L \frac{\gamma_s^2}{h^{1/4}} \sum_{n=1}^{\infty} (-1)^{n+1} n e^{-2n\gamma\phi'}, \tag{5.6}$$

where $\phi' = X_1 + X_0 - ct - 2\sqrt{xX_0}$. Similarly we find that,

$$F_2(x, t) = -\frac{8\mathcal{E}_g \gamma_s}{3\sqrt{p_0} h^{1/4}} \sum_{n=1}^{\infty} (-1)^{n+1} e^{-2n\gamma\phi'}, \tag{5.7}$$

and

$$F_3(x, t) = -\frac{4\pi^2 \mathcal{E}_g}{3\gamma_s p_0^{\frac{3}{2}}} \sum_{n=1}^{\infty} a_n \tag{5.8}$$

where,

$$a_n = \lim_{\omega \rightarrow 2n\gamma_i} (\omega - 2n\gamma_i)^2 f(\omega) e^{i\omega\theta} \times \frac{\cosh(\frac{\pi\omega}{2\gamma})}{\sinh^2(\frac{\pi\omega}{2\gamma})} \left\{ 1 + i\omega\theta + \frac{\omega f'(\omega)}{f(\omega)} \right\}, \tag{5.9}$$

with,

$$f(\omega) = \frac{J_0(2\omega\sqrt{xX_0})}{J_0(2\omega X_0) - iJ_1(2\omega X_0)}. \tag{5.10}$$

On further simplifying we find that

$$a_n = \frac{2(-1)^n \gamma_s^2 p_0}{\pi^2 h^{1/4}} \left\{ \frac{3}{2} - 2n\gamma\phi' \right\} e^{-2n\gamma\phi'}, \tag{5.11}$$

and therefore,

$$F_3(x, t) = \frac{8\mathcal{E}_g \gamma_s}{3\sqrt{p_0} h^{1/4}} \sum_{n=1}^{\infty} (-1)^{n+1} \left\{ \frac{3}{2} - 2n\gamma\phi' \right\} e^{-2n\gamma\phi'}. \tag{5.12}$$

where $\gamma_s = \sqrt{3\mathcal{H}/4}$. Using the asymptotic expansions for the modified Bessel functions (Abramowitz, 1970), we approximate F_1 by

$$F_1 = \frac{16}{3} \mathcal{E}_g L \frac{\gamma_s^2}{h^{1/4}} \sum_{n=1}^{\infty} (-1)^{n+1} n e^{-2n\gamma\phi'}, \tag{5.13}$$

where $\phi' = X_1 + X_0 - ct - 2\sqrt{xX_0}$. Similarly we find that,

$$F_2(x, t) = -\frac{8\mathcal{E}_g \gamma_s}{3\sqrt{p_0} h^{1/4}} \sum_{n=1}^{\infty} (-1)^{n+1} e^{-2n\gamma\phi'}, \tag{5.14}$$

and

$$F_3(x, t) = -\frac{4\pi^2 \mathcal{E}_g}{3\gamma_s p_0^{\frac{3}{2}}} \sum_{n=1}^{\infty} a_n \tag{5.15}$$

where,

$$a_n = \lim_{\omega \rightarrow 2n\gamma_i} (\omega - 2n\gamma_i)^2 f(\omega) e^{i\omega\theta} \times \frac{\cosh(\frac{\pi\omega}{2\gamma})}{\sinh^2(\frac{\pi\omega}{2\gamma})} \left\{ 1 + i\omega\theta + \frac{\omega f'(\omega)}{f(\omega)} \right\}, \tag{5.16}$$

with,

$$f(\omega) = \frac{J_0(2\omega\sqrt{xX_0})}{J_0(2\omega X_0) - iJ_1(2\omega X_0)}. \tag{5.17}$$

On further simplifying we find that

$$a_n = \frac{2(-1)^n \gamma_s^2 p_0}{\pi^2 h^{1/4}} \left\{ \frac{3}{2} - 2n\gamma\phi' \right\} e^{-2n\gamma\phi'}, \tag{5.18}$$

and therefore,

$$F_3(x, t) = \frac{8\mathcal{E}_g \gamma_s}{3\sqrt{p_0} h^{1/4}} \sum_{n=1}^{\infty} (-1)^{n+1} \left\{ \frac{3}{2} - 2n\gamma\phi' \right\} e^{-2n\gamma\phi'}. \tag{5.19}$$

Summing (5.13), (5.14) and (5.19) and evaluating the series expansions, we obtain

$$\eta(x, t) = \eta_0 \left[\gamma d_0 \operatorname{sech}^2(\gamma\phi') + \frac{1}{2} e^{-\gamma\phi'} \operatorname{sech}(\gamma\phi') \right] \tag{5.20}$$

where $\eta_0 = 4\mathcal{E}_g \gamma_s / (3\sqrt{p_0} h^{1/4})$, $\gamma_s = \sqrt{3\mathcal{H}/4}$, $\phi = X_1 + \cot\beta - ct$, $\phi' = \phi - 2\sqrt{x \cot\beta}$ and $d_0 = L - \phi'$. Note that only η_0 depends on the local depth h . Solving $\partial\eta/\partial\phi' = 0$, the extremum η_{ext} for any location x , we obtain

$$\left| \frac{\eta_{\text{ext}}(x)}{\mathcal{H}} \right| = \frac{F(\gamma, \phi'_m)}{h^{1/4}} \tag{5.21}$$

where ϕ'_m is the phase corresponding to η_{ext} . Therefore for any given initial LEN or LDN wave, η_{ext} is independent of L and depends only on the local depth h . N-waves are therefore seen to evolve far from the shoreline in a manner similar to what is referred to as Greens' law (Green, 1837, Lamb 1945, Synolakis, 1991) whether a leading-depression or leading-elevation wave.

VI. RUNUP OF N-WAVES

To calculate the maximum runup, the maximum of equation (5.2) at $x = 0$ has to be evaluated; proceeding as in the previous section, we find that

$$\eta(0, t) = R_0 \sum_{n=1}^{\infty} (-1)^{n+1} n^{\frac{1}{2}} \left\{ 2n\gamma(L - \phi) + \frac{1}{2} \right\} e^{-2n\gamma\phi}, \tag{6.1}$$

where $R_0 = \frac{16}{3} \mathcal{E}_g \gamma_s^3 / 2(2\pi \cot\beta)^{\frac{1}{2}} / p_0^{\frac{1}{4}}$. Here, we compute the maximum runup of a N-wave (2.1) explicitly; in Tadepalli and Synolakis (1994a), only an upper limit had been calculated. We first note that the phase ϕ_m at the extremum runup satisfies

$$-\frac{4\gamma}{3} (L - \phi_m) = \frac{\sum_{n=1}^{\infty} (-1)^{n+1} n^{\frac{3}{2}} e^{-2n\gamma\phi_m}}{\sum_{n=1}^{\infty} (-1)^{n+1} n^{\frac{5}{2}} e^{-2n\gamma\phi_m}}. \tag{6.2}$$

Denoting

$$S(\phi_m) = \sum_{n=1}^{\infty} (-1)^{n+1} n^{\frac{3}{2}} e^{-2n\gamma\phi_m}, \quad (6.3)$$

we rewrite the equation for ϕ_m as

$$\frac{dS(\phi_m)}{d\phi_m} = \frac{3S(\phi_m)}{2(L - \phi_m)} \quad (6.4)$$

Solving for $S(\phi_m)$ for LDN ($L - \phi_m > 0$), we find that $S(\phi_m) = S_o(L - \phi_m)^{-\frac{3}{2}}$. We then note that

$$-2\gamma \int S(\phi_m) d\phi_m = \sum_{n=1}^{\infty} (-1)^{n+1} n^{\frac{1}{2}} e^{-2n\gamma\phi_m} \quad (6.5)$$

and obtain the maximum runup of a non-breaking leading-depression N-wave,

$$\mathbf{R} = 3.3\mathcal{E}_g p_0^{\frac{1}{4}} Q(L, \gamma) \mathbf{R}_{\text{sol}}. \quad (6.6)$$

Here \mathbf{R}_{sol} is the runup of a Boussinesq solitary wave of the same \mathcal{H} , and (6.6) is asymptotically close to runup law for solitary waves given by Synolakis (1987). This is reassuring; as figure 2(a) shows in the asymptotic limit LEN profiles describe solitary waves, for example when $L = 30$, $\mathcal{E}_g = 0.032$, $Q \approx 10$ and $p_0 = 1$.

This relationship (6.6) referred to as the N-wave runup law is valid when $4\gamma\cot\beta \gg 1$ for non-breaking LDN waves. The limiting wave amplitude for the validity of the above runup law can be obtained from the non-linear shallow water theory using Carrier and Greenspan hodographic transformation (Carrier, 1958) and is the same amplitude as outlined in Tadepalli and Synolakis (1994a) for $p_0 = 1$. $Q(L, \gamma)$ has to be determined numerically, but to the same order of approximation as (6.6) and over a wide range, Q varies linearly with L .

As examples, figures 4(a) and 4(b) show the variation of maximum runup with L and \mathcal{H} respectively. Clearly in the region of physical interest the runup increases almost linearly with \mathcal{H} .

Figure 5 shows the maximum runup variation with the crest-to-trough heights ratio; this parameter is uniquely determined from (2.1) through \mathcal{H} , L and p_0 . Notice that the maximum runup decreases from the isosceles N-wave limit to the solitary wave limit as the crest-to-trough ratio increases, consistent with the earlier observation that LDNs and LENs climb further than the equivalent solitary waves of the same \mathcal{H} and steepness.

VII. DISCUSSION

We have presented a model for the leading wave of tsunamis, encompassing as special cases waves similar to the Boussinesq solitary wave profiles, N-waves, and the certain combinations of Gaussian profiles (Carrier, 1993). The function can be fully described by specifying the crest amplitude \mathcal{H} , the steepness

parameter p_0 and L , and it includes the individual classes of N-waves outlined earlier by Tadepalli and Synolakis (1994a).

Our conjecture is that tsunamigenic faulting generates multi-lobe waves, and that the leading wave of the tsunami is important for estimating coastal effects, at least along open coastlines. Most physically realistic tsunamis retain their overall N-wave character even after transoceanic propagation. Nearshore-generated tsunamis do not have sufficient propagation distance to fully evolve, and their nearshore manifestation is almost invariably N-wave like. We found that the maximum runup decreases as the ratio of trough height-to-crest height decreases, confirming that the dip angle is an important parameter for tsunami characterization, as suggested by Yamashita and Shato (1974) and Geist and Yashioka (1996).

The two-dimensional character of the generation region limits the application of our proposed model, even though the canonical model itself is two-dimensional. We do note, however, that two-dimensional SW propagation models are still used extensively by oceanographers for calculating wave evolution and runup of wind-generated swell (Raubenheimer et al 1995, Raubenheimer and Guza, 1996), a wave motion presumably much shorter than tsunamis.

Nonetheless, we are reluctant to draw excessive physical conclusions other than claim that our initial profile provides a conceptual framework for analysis and for explaining certain field observations qualitatively, or even certain local numerical calculations as demonstrated by Geist and Yashioka (1996). Yet, we did perform simple calculations using our model in one of the recent tsunami catastrophes, where the coastal topography allowed it. One segment of the pacific coastline of Nicaragua is a 73km long with almost uniform plane beach slope ($\cot\beta = 33.18$), fronted by a continental shelf. This simplicity has allowed the use of two-dimensional numerical shoreline models coupled with three-dimensional offshore propagation models to calculate the runup and inundation. Figure 6 shows a comparison between the numerically generated surface profile for the Nicaraguan tsunami with that of equation (2.1), at the time when the wave reaches the toe of the beach (Titov and Synolakis, 1993, Satake, 1995). The measured and numerically computed maximum runup values were $6\text{m} \pm 2\text{m}$, while the runup law (6.6) predicts 3.5m .

We envision our model being applied for first-order estimates of tsunami or tidal wave inundation, as the realistic alternative to the solitary wave model. Given an approximate seafloor deformation area and an average seafloor displacement and the known dip angle of a fault, the parameters $\mathcal{E}_g, \gamma, \mathcal{H}$ can be estimated, and our N-wave model can provide an initial condition for numerical computations. It can also provide an estimate of the runup through the runup law (6.6), when the coastline is fronted by a fairly uniform beach. The runup of a real tsunami may vary substantially in the longshore direction due to local topographic features, yet the model will provide representative values for preliminary design purposes.

ACKNOWLEDGMENTS

We are grateful for the generous support of the National Science Foundation (Program Director, Dr. Cliff Astill, CMS 9201326). We would like to thank Professor J.B. Keller, Dr. Eric L. Geist for several useful discussions and Vassili V. Titov for providing the Nicaraguan profile.

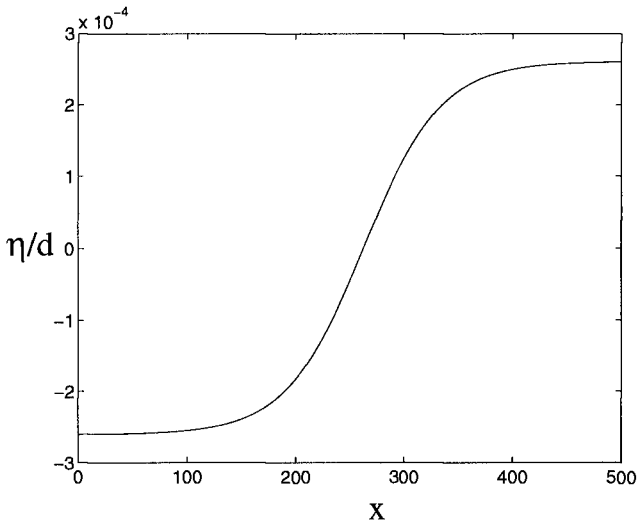


Figure 1 Bottom displacement (3.2) that describes leading depression N-wave (2.1) for $X_1 = 262.5$ and $\gamma = 0.014$.

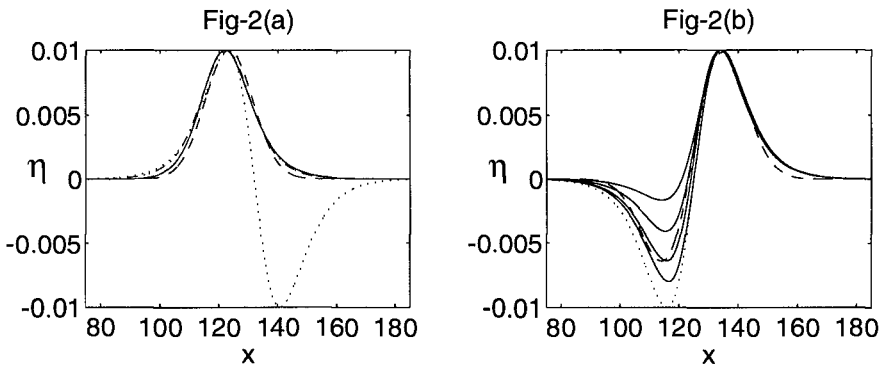


Figure 2(a) Comparison of Boussinesq solitary profile (---), N-wave solitary profile (—) ($L=30$, $\mathcal{E}_g=0.032$), Gaussian profile (- -) and leading elevation isosceles N-wave (· ·)

Figure 2(b) A family of leading-depression waves generated by N-wave (—) for $L = 8, 4, 2, 1$; $p_0 = 1$, combination of Gaussian profiles (- -) and leading-depression isosceles N-wave (· ·) generated with $L = 0$, $p_0 = 1$.

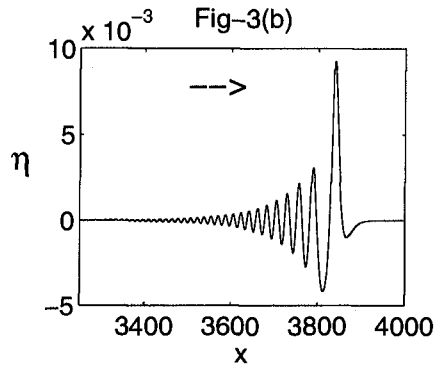
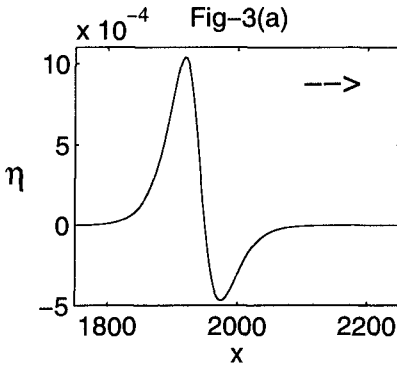


Figure 3(a) LDN N-wave generated by equation (2.1) for $(X_1 = 190, X_2 = 200, \mathcal{H} = 1.E - 03)$ propagated by KDV to 2000 depths.

Figure 3(b) LDN N-wave generated by equation (2.1) for $(X_1 = 98, X_2 = 100, \mathcal{H} = 1.E - 02)$ propagated by KDV to 4000 depths.

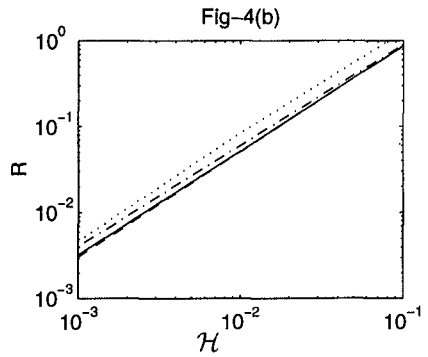
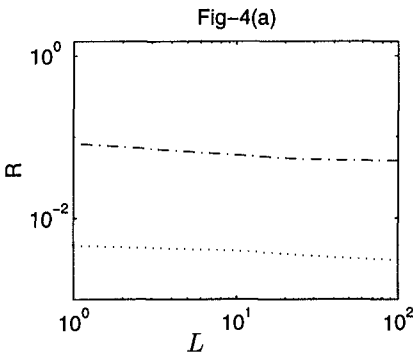


Figure 4(a) **R** vs. **L** for $\mathcal{H} = .001(\cdot\cdot)$ and $\mathcal{H} = .01(\cdot\cdot\cdot)$.

Figure 4(b) **R** vs. \mathcal{H} for $L = 1(\cdot\cdot)$, $L = 10(\cdot\cdot\cdot)$, $L = 50(\cdot\cdot\cdot\cdot)$ and $L = 100(\cdot\cdot\cdot\cdot)$.

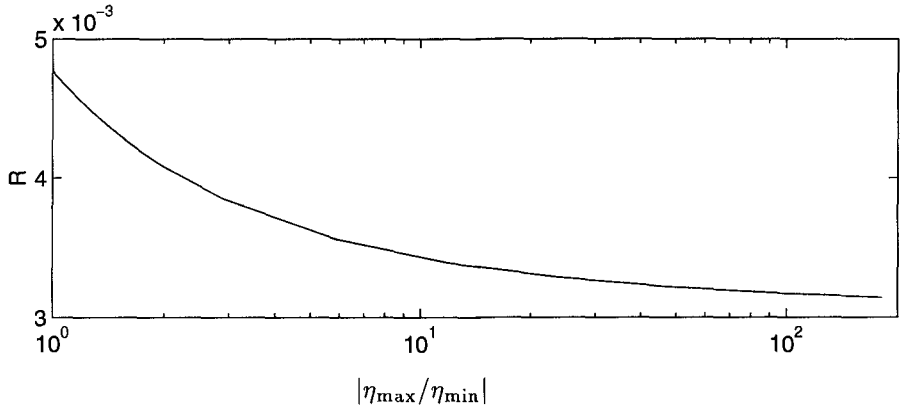


Figure 5 Variation of maximum-runup with peak-trough amplitude ratio for $\mathcal{H} = 0.001$, $L = 0 - 75$, $X_0 = 30$.

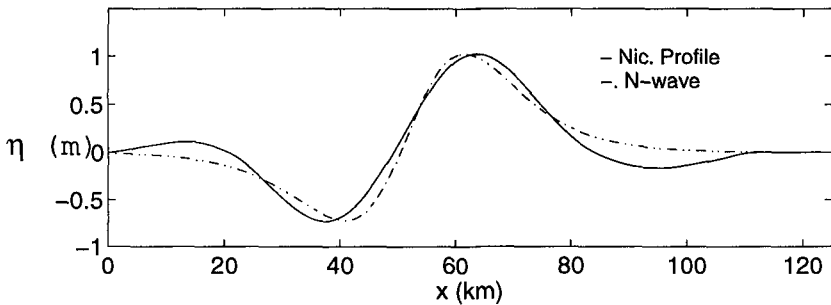


Figure 6 Comparison of Nicaraguan tsunami profile at the toe of the beach using N-wave [equation (2.1)] with $L = 9$, $\mathcal{E}_g = 0.4823$ and $\gamma_s = 0.015$.

VIII. REFERENCES

- [1] Abramowitz, M. and Stegun, I.A., Dover Publications Inc., New York (1970).
- [2] Carrier, G.F. and Greenspan, H.P., *J. Fluid Mech.*, **17**, pp. 97-109 (1958).
- [3] Carrier, G. F., *J. Fluid Mech.* **24**, 641-659 (1966).
- [4] Carrier, G. F., International Tsunami Symposium, Wakayama, Japan, Aug. 23-27 (1993).
- [5] Geist, E. and Yoshioka, S., *Natural Hazards*, **13**, (2), 151-177 (1996).
- [6] Green, G., *Trans. Camb. Phil. Soc.* 1838 (1837).
- [7] Imamura, F., Synolakis, C.E., Gica, E., Titov, V., Listanco, E., Lee, H.-J., *PAGEOPH*, **144** (3/4), 875-889 (1995).
- [8] Keller, J.B. and Keller, H.B., 1964, ONR contract NONR-3828(00), Washington, D.C., 1-40.
- [9] Lamb, H., Dover Publications Inc., New York (1945).
- [10] Liu, L.-F. P., Synolakis, C.E. and Yeh, H., *J. Fluid Mech.* **229**, 675-688 (1991).
- [11] Raubenheimer, B., Guza, R.T., Elgar, S., Kobayashi, N., *J. Geoph. Res.*, **100** (C5), 8751-8760 (1995).
- [12] Raubenheimer, B. and Guza, R.T. Observations and Predictions of Runup *J. Geoph. Res.*, *In Press* (1996).
- [13] Satake, K., *Pure Appl. Geoph.*, **144** (3/4), 455-470 (1995).
- [14] Satake, K., Bourgeois, J., Abe, K., Tsuji, Y., Imamura, F., Iio, Y., Katao, H., Nogeura, E., Estrada, F., *EOS, Trans. AGU*, **74**, 145 and 156-157 (1993).
- [15] Synolakis, C.E., *J. Fluid Mech.* **185**, 523-545 (1987).
- [16] Synolakis, C.E., *Qu. Appl. Math.* **46**, 105-107 (1988).
- [17] Synolakis, C.E., *J. of Waterway, Harbors Port, Coastal and Ocean Engineering*, **116**, (2), 252-266 (1990).
- [18] Synolakis, C.E., *Phys. Fluids A* **3**(3), 490-491 (1991).
- [19] Synolakis, C.E., Imamura, F., Tsuji, Y., Matsutomi, H., Tinti, S., Cook, B., Chandra, Y.P., Ushman, M., *EOS, Trans. AGU*, **76**, 257 and 261-262 (1995).
- [20] Synolakis, C.E. and Skjelbreia, J.E., *J. Waterway, Harbor, Port, Coastal and Ocean Engineering*, **119**, 323-342 (1993).
- [21] Tadepalli, S. and Synolakis, C.E., *Proc. of R. Soc. A Lond.* **445**, 99-112 (1994a).
- [22] Tadepalli, S. and Synolakis, C.E., *Qu. Appl. Math.* **51**, 103-112 (1994b).
- [23] Tadepalli, S. and Synolakis, C.E., *Phys. Rev. Lett.* **77**, 2141-2144 (1996).
- [24] Titov, V.V. and Synolakis, C.E., Tsunami 93 Proc. IUGG/IOC, Wakayama, 627-635 (1993).
- [25] Tuck, E.O. and Hwang, Li-San, *J. Fluid Mech.*, **51**, 440-461 (1972).
- [26] Yamashita, T. and Sato, R., *J. Phys. Earth*, **22**, 415-440 (1974).
- [27] Yeh, H., Imamura, F., Synolakis, C.E., Tsuji, Y., Liu, P. L.-F., Shi, S. *EOS, Trans. AGU*, **74**, 369 and 371-373 (1993).

CHAPTER 116

LONG-PERIOD OSCILLATIONS IN A HARBOUR CAUSED BY TYPHOON

Wataru Kioka¹

ABSTRACT

A nonlinear model for predicting the resonant oscillations in a harbour due to typhoon is developed and its validity is evaluated through the comparisons with filed measurements obtained in Yui Fishery Harbour facing Suruga Bay in Japan. The numerical model is based on a time domain solution of Boussinesq equations proposed by Nwogu(1993) with an additional Forchheimer resistance term in the momentum equation to take account of the reflection characteristics of permeable seawalls in the field. It is shown that the numerical model predicts well the low-frequency oscillations inside the harbour exited by incident wave groups.

1. INTRODUCTION

Excessive long-period oscillations are often observed in relatively small harbours along sea coasts when typhoons or atmospheric low pressures pass over sea area. Such oscillations often lead to the breaking of mooring lines and the flooding on the wharf. Recent filed observations reveal that locked or bound long waves accompanied by incident wave groups have relevance to large oscillations in a harbour (e.g., Okihiro *et al.*, 1993). The resonance phenomena due to such infragravity forcing are essentially nonlinear as the locked long waves exist under wave groups through nonlinearity. In this study, a nonlinear model for predicting the low-frequency oscillations inside a harbour due to the typhoon is developed using the Boussinesq equations. The validity of the model is evaluated through the comparisons with field measurements obtained during Typhoon in Yui Fishery Harbour facing Suruga Bay in Japan.

2. MATHEMATICAL MODEL

¹ Professor, Dept. of Civil Eng., Nagoya Institute of Technology, Nagoya, 466 Japan.

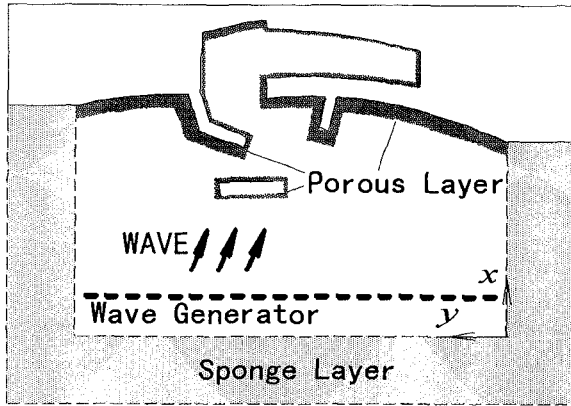


Fig. 1 Sketch of numerical model

2.1 Model Equations

The numerical model is based on a time domain solution of Boussinesq equations proposed by Nwogu (1993) with an additional absorbing term in the momentum equation and a source generation term in the continuity equation (Borsen and Larsen, 1987) :

$$\zeta_t + \nabla \cdot [(\zeta + h)\mathbf{u}] + \nabla \cdot \left[\left(\frac{1}{2} z_\alpha^2 - \frac{1}{6} h^2 \right) h \nabla (\nabla \cdot \mathbf{u}) + \left(z_\alpha + \frac{1}{2} h \right) h \nabla \{ \nabla \cdot (h\mathbf{u}) \} \right] - U^* = 0 \quad (1)$$

$$\mathbf{u}_t + (\mathbf{u} \cdot \nabla) \mathbf{u} + g \nabla \zeta + \left[\frac{1}{2} z_\alpha^2 \nabla (\nabla \cdot \mathbf{u}_t) + z_\alpha \nabla \{ \nabla \cdot (h\mathbf{u}_t) \} \right] + f_s \left[\mathbf{u} + \left[\frac{1}{2} z_\alpha^2 \nabla \cdot (\nabla \cdot \mathbf{u}) + z_\alpha \nabla \{ \nabla \cdot (h\mathbf{u}) \} \right] \right] = 0 \quad (2)$$

where $\zeta(x, y)$ is the water surface elevation, $\mathbf{u}(x, y, t)$ is the velocity at an arbitrary elevation $z = z_\alpha(x, y)$, U^* is the vertical source distribution extending from the bottom to free surface, and $f_s(x, y)$ is the distribution function for the sponge layer. The instantaneous horizontal volume flux of the source distribution is included only in the continuity equation, provided that the weak nonlinearity represented by the ratio of wave amplitude to water depth, $\varepsilon = a_0/h_0$, is in the same order of magnitude as the frequency dispersion represented by the square of the ratio of the water depth to wavelength, $\mu^2 = (h_0/l_0)^2$. The distance z_α is determined using an error-minimizing criterion for the dispersion relation. Following Nwogu (1993), the elevation z_α is set

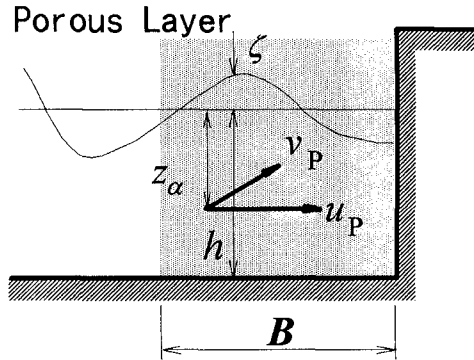


Fig. 2 Definition sketch of porous structure model

to be $-0.53h$. On the upwave control boundary and sides of the computational domain, all outgoing waves are absorbed by using sponge layers and applying the Sommerfeld radiation condition at the outer boundaries of the sponge region (see Fig. 1). The radiation condition is prescribed from the linear long wave theory. The function $f_s(x, y)$ varies linearly over the sponge region, i.e. increases linearly with the distance from fluid boundary lines, so that local disturbances due to the sponge layers are kept to a minimum. A harbour with fully reflective boundaries is treated as the solid walls.

2.2 Modeling Porous Structures

For the cases of partially reflective boundaries, the Boussinesq equations (1) and (2) are further modified to account for the reflection characteristics of permeable seawalls, assuming Forchheimer resistance law for the fluid motion in porous structures, as in the forms (Kioka et al., 1996)

$$\zeta_t + \nabla \cdot [(\zeta + h)\mathbf{u}_p] + \nabla \cdot \left[\left(\frac{1}{2} z_\alpha^2 - \frac{1}{6} h^2 \right) h \nabla (\nabla \cdot \mathbf{u}_p) + \left(z_\alpha + \frac{1}{2} h \right) h \nabla \{ \nabla \cdot (h \mathbf{u}_p) \} \right] = 0 \quad (3)$$

$$\frac{\tau}{\lambda} \mathbf{u}_{p,t} + \frac{1}{\lambda^2} \frac{1}{2} \nabla (\mathbf{u}_p^2) + g \nabla \zeta + \frac{\tau}{\lambda} \left[\frac{1}{2} z_\alpha^2 \nabla (\nabla \cdot \mathbf{u}_{p,t}) + z_\alpha \nabla \{ \nabla \cdot (h \mathbf{u}_{p,t}) \} \right] + \alpha \left[\mathbf{u}_p + \left[\frac{1}{2} z_\alpha^2 \nabla (\nabla \cdot \mathbf{u}_p) + z_\alpha \nabla \{ \nabla \cdot (h \mathbf{u}_p) \} \right] \right] + \beta |\mathbf{u}_p| \mathbf{u}_p = 0 \quad (4)$$

where \mathbf{u}_p is the discharge velocity vector at the distance z_α in porous structures, λ is the porosity, τ is the inertial coefficient given as $\tau = 1 + \kappa(1 - \lambda)$ with κ being the added mass coefficient, α and β are the linear and nonlinear damping coefficients in the unsteady Forchheimer equation, respectively. The flow in the porous domain is

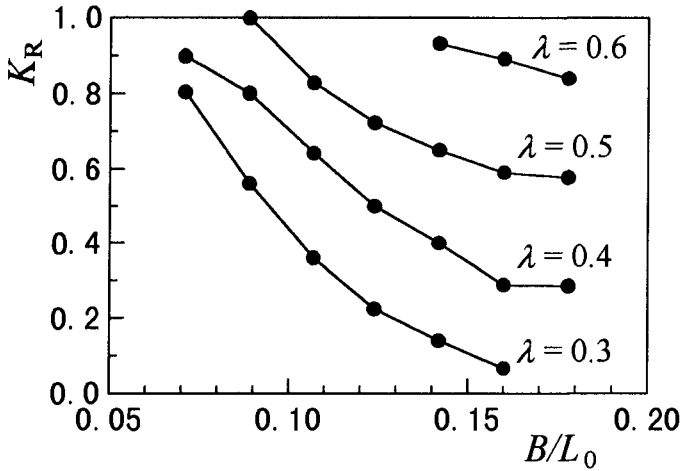


Fig. 3 Reflection coefficients ($h = 4.0$ m)

assumed irrotational. The damping coefficients α and β are respectively given after van Gent (1995) as

$$\alpha = 1000 \frac{(1-\lambda)^2}{\lambda^3} \frac{\nu}{D^2} \quad (5)$$

$$\beta = 1.1 \left(1 + \frac{7.5}{KC} \right) \frac{(1-\lambda)}{\lambda^3} \frac{1}{D} \quad (6)$$

where ν is the kinematic viscosity coefficient, D is the mean grain size of the material of the porous media, and KC is the Keulegan-Carpenter number. The contribution of the added mass to the total inertial resistance is assumed to be disregarded ($\tau = 1$).

The damping coefficients of porous structures cannot be exactly determined from the field measurements, as methods for evaluating these coefficients of large blocks are, at present, not fully established. In the numerical analysis, the porosity λ is adjusted to suit the observed reflection coefficients while the damping coefficients α , β are held fixed. Fig. 3 shows the computed reflection coefficients K_R as a function of the ratio of the thickness of porous body B to the deepwater wavelength L_0 , using sinusoidal waves in the constant water depth of $h = 4.0$ m. The coefficients K_R are simply given as the ratio of the maximum wave height measured in front of the porous structure to the incident wave height. For example, in the case of wave period $T = 9.5$ s and $B = 20$ m, the porosity $\lambda = 0.4$ approximately gives $K_R = 0.4$, according to Fig. 3. The energy dissipation of the incident waves due to the porous

the porous structure, however, decreases with the increase of the water depth. In the case of $h = 6.0$ m, K_R nearly equals 1.0 in the range of $\lambda > 0.4$ and $B/L_0 < 0.2$. For porous structures in relatively deep water depths, the reflection coefficients are underestimated even when using an unrealistic value of the porosity λ . In the deeper water depth, the thickness of the porous structure B is then taken longer than the actual width of the wave-dissipating blocks in the field. The wider porous body leads to better agreements with the observed reflection coefficients, but yields slightly different reflection characteristics of the short waves.

2.3 Numerical Scheme

The equations (1)-(4) are numerically solved using a finite difference scheme. The spatial derivatives in one direction are approximated using 5grid-point centered differences with fourth-order accuracy, leading to a truncation error that is small relative to all retained terms in the equations. Although the finite difference approximations of the xy -, xyx - and yyx -derivatives can be respectively approximated with fourth-order accuracy using 3grid-point centered differences per a direction, 5grid-point approximations are adopted here in order to avoid numerical instabilities. For the temporal integral, an iterative scheme based on the 3rd-order Adams-Bashforth-Moulton method is employed. The water surface elevation ζ can be obtained explicitly. As the velocity component in the x -direction u is solved by calculating matrices, the derivatives of the component in the y -direction v can be treated explicitly for the sake of efficient calculations.

The directional spreading of incident wave energy has a significant influence on the long-period oscillations, and thus must be taken into account for the quantitative prediction. The wave condition at the upwave boundary is then specified in terms of a directional wave spectrum. The single direction per frequency method is used to describe the first-order water surface elevations with the parametric cosine power function for the directional distribution. Since the contribution of second-order waves, especially sub-harmonic waves, is important for the quantitative prediction, i.e., for preventing the generation of spurious free waves at the incident boundary, all the sub-harmonics and super-harmonics in directional wave fields are included in the incident waves through the quadratic transfer function. The characteristics of the groupiness of individual waves and the associated long-period waves are influenced by the initial phase angles of the different frequency components. In the numerical analysis hereafter, the computations are carried out three times for each set of the initial phases. The effective duration of each run is about 1200s.

3. FIELD OBSERVATIONS

Yui Fishery Harbour is a relatively small harbour facing Suruga Bay in Japan (see Fig. 4). Two breakwaters are constructed at the eastern and western side of the harbour entrance, and the offshore breakwater (under construction) is located about 70 m away from the tip of the western breakwater. These breakwaters and the

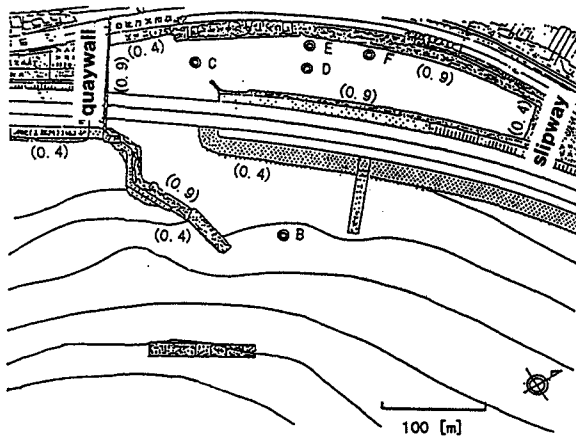


Fig. 4 Layout of Yui Fishery Harbour

revetments facing open sea are covered with wave dissipating blocks. The field measurements of the water surface elevations have been carried out for two months from August to October in 1994, at station about 300 m offshore from the southern offshore breakwater, station at the harbour entrance and 4 stations inside the harbour basin, as shown in Fig. 4. The time series of surface elevation with the significant wave height $H_{1/3} = 3.7$ m and period $T_{1/3} = 9.5$ s have been obtained at the offshore station due to Typhoon 26, September 29-30 in 1994. The wave heights of the short-wave components were significantly reduced inside the harbour. The low-frequency waves in the range from 0.0025 Hz to 0.013 Hz were, however, amplified to a certain degree due to resonant oscillations inside the harbour.

4. NUMERICAL CONDITIONS AND RESULTS

4.1 Numerical Conditions

The directional spectra have not been observed at the offshore station. The measured time series of the surface displacements cannot be directly used for the incident waves in the numerical calculations. The incident short-wave components are given from the Bretschneider-Mitsuyasu spectrum assuming the Mitsuyasu-type directional function for the directional distributions. The water depth at the offshore station is 25.0 m. The significant wave height $H_{1/3} = 3.7$ m and the period $T_{1/3} = 9.5$ s observed during Typhoon 26, 1994 are used for the numerical simulations. The parameter S_{\max} indicating the degree of directional spreading was not directly measured but estimated from the measured wave steepness using the procedure proposed by Goda and Suzuki (1975). Their estimation method gives $S_{\max} = 40$ at

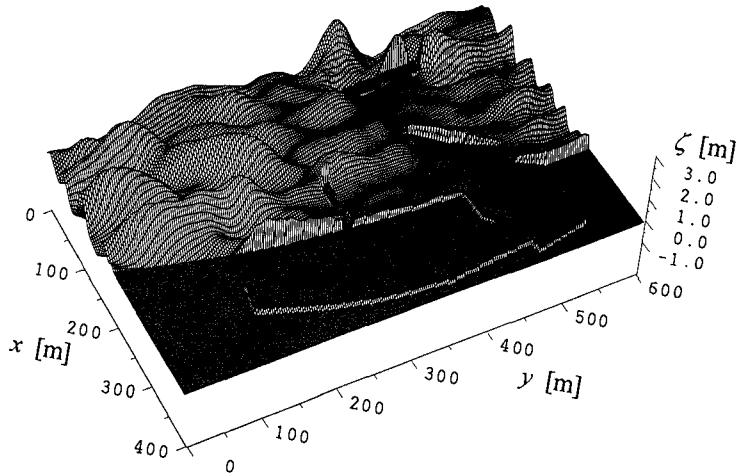


Fig. 5 Snapshot of free-surface displacements

the offshore station. The frequency bands of $0.4 \sim 2.0$ times the peak frequency are decomposed into 100 first-order wave components. The directional spread of $\pm 50^\circ$ from the principal wave direction is modeled using 20 components. The wave directions are selected in a random order within each frequency band. The set-down wave components defined as low-frequency waves below the bands of short-waves are calculated through the quadratic transfer function, and are added to the short-waves at the incident boundary. The super-harmonic wave components are also included, but with no effect on the long-period oscillations in the harbour. Since the inclusion of all second-order waves requires a large computational effort, only the contribution of the sub-harmonic components may be considered for the second-order waves. The numerical simulation is carried out using a time interval $\Delta t = 0.1$ s, and spatial grid sizes $\Delta x = 5$ m, $\Delta y = 5$ m.

The water depths at each grid-points are counted, referring to the mean water level observed at the offshore station. The 1:6 constant slope slipway is located at the end of harbour basin. The short-wave components are expected to break on the slope. The wave heights are, however, very small inside the basin, so that the influence of long-period free waves caused by the wave breaking on the slope of the slipway may be disregarded for predicting the harbour oscillations. The slipway inside the harbour is then assumed to be an upright porous structure similar to the other partially reflective boundaries.

4.2 Numerical results

Fig. 5 shows the snapshot of the free-surface displacements in the vicinity of Yui Fishery Harbour due to Typhoon 26, 1994. The offshore breakwater, being under

construction, is not effective in reducing the transmitted waves on the leeward side. The incoming short-waves considerably attenuate inside the harbour basin primarily by the breakwaters and the wave absorbing works.

The comparisons of the time series between the numerical results and the observations are shown in Fig. 6. In the case of offshore station, the temporal profiles of the long-period components are exaggerated by multiplying by 5. The set-down waves generated by the short-waves crossing at small angle tend to be underestimated in the region of relatively deep water depth. This may result in the slightly smaller long-period components as compared with the observations at the offshore station. At the station D inside the basin the low-frequency oscillations near 0.013 Hz are clearly reproduced, but their amplitudes are slightly smaller than the measured ones. The computed short-wave components inside the basin appear to be calmer than the measurements. The wave dissipation inside the harbour is possibly overestimated from the porous structure model.

The computed spectra at the stations C and D inside the harbour are compared with the measurements in Fig. 7. The numerical model predicts well the amplification in the low-frequency range. It should be noted the secondary peak near 0.013 Hz is slightly larger than the first peak near 0.0025 Hz. The linear model gives much smaller amplification for the secondary peak.

The spatial profiles of the long-period components are plotted in Fig. 8. The long-period components of near the peak frequencies $f = 0.0025$ Hz, 0.0090 Hz and 0.013 Hz are extracted from the computed spectra inside the harbour. The long-period oscillations are seen to be not multi-directional, but quite uni-directional in the y -direction (in the direction of the longer side of the basin). Near the first peak ($f = 0.0025$ Hz), the surface elevations within the harbour rise more or less in unison. At the second and third peaks (0.0090 Hz, 0.013 Hz), the long-period waves behave as a standing wave, respectively corresponding to two and three anti-nodes in the y -direction.

5. CONCLUDING REMARKS

A nonlinear model, which takes account of the multi-directional features of the incoming waves as well as the partially reflecting boundaries, is developed for predicting the resonant oscillations in a harbour due to typhoon. The spectra observed in Yui Fishery Harbour are well reproduced in the low-frequency range of interest by the present numerical model. Possible countermeasures against the resonant oscillations observed in a small harbour like Yui Fishery Harbour are currently under investigation using the present model.

ACKNOWLEDGEMENTS

The research has been funded by the Grand-in-Aid for Scientific Research from the Ministry of Education, Science and Culture of Japan. The author would like to thank Dr. M. Tanaka of Shimz Corp. and Yui Fisheries Co-operative Organization for

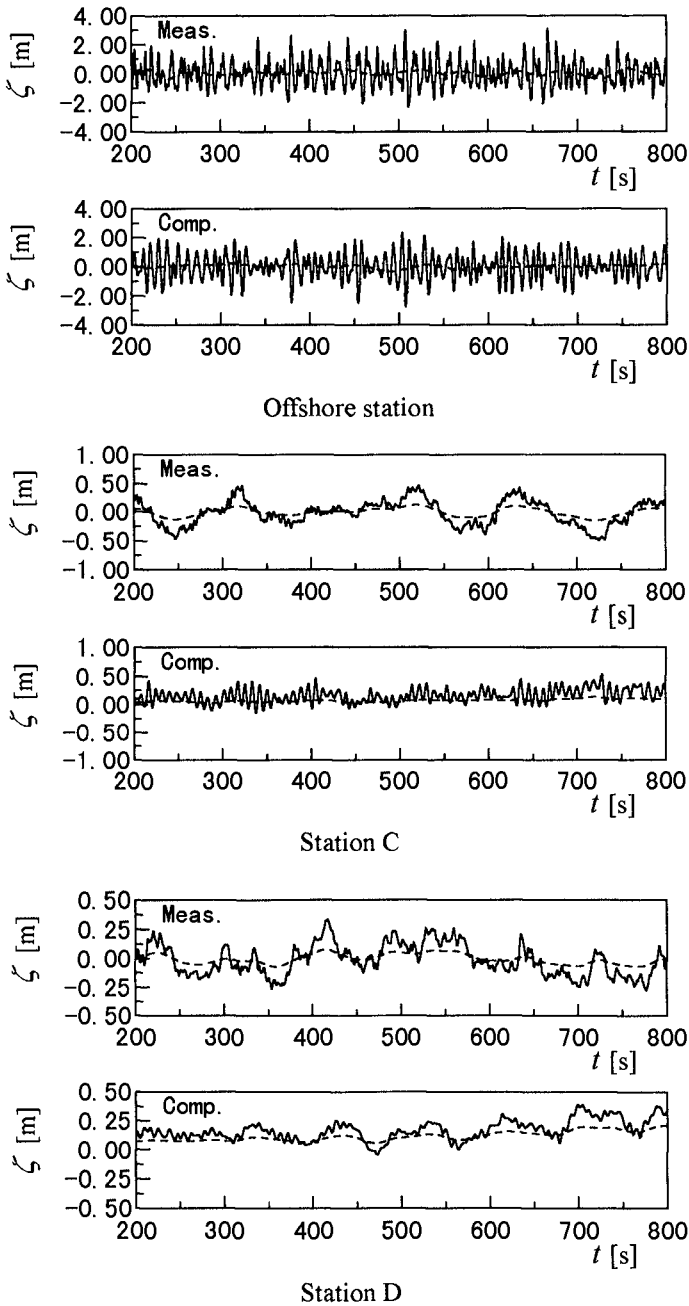


Fig. 6 Comparison of temporal profiles (- - - - : long-wave components)

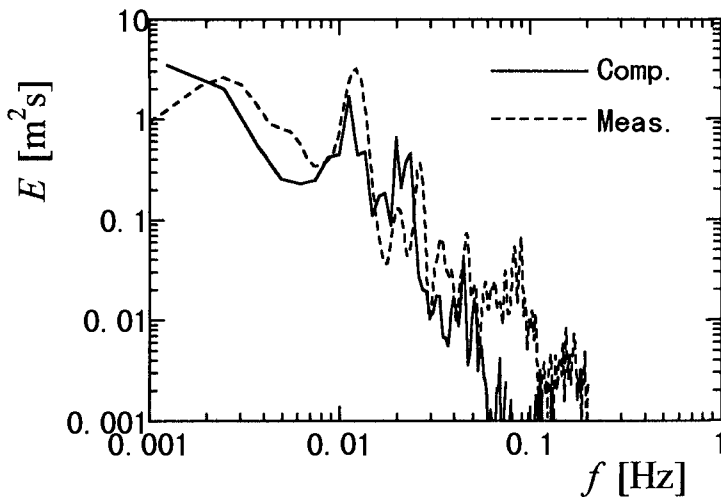
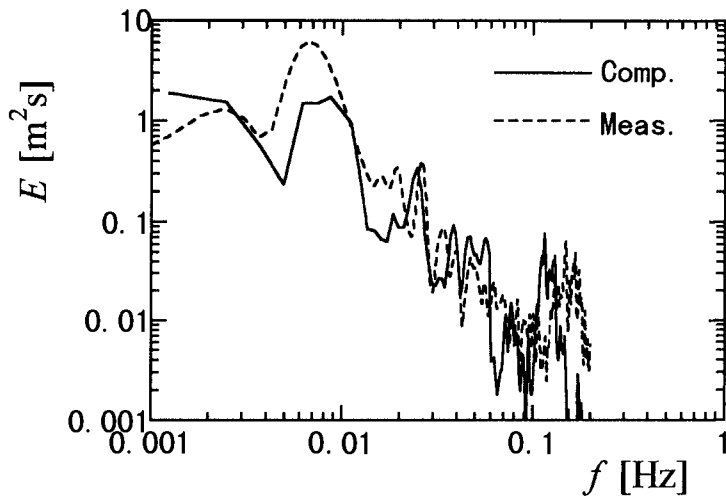


Fig. 7 Comparison of spectra inside the harbour

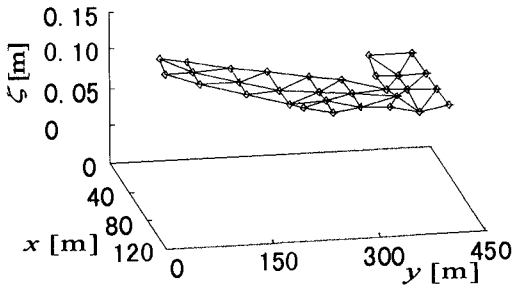
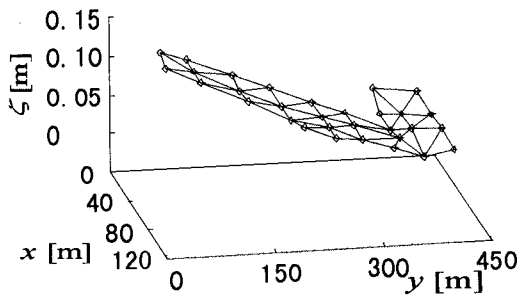
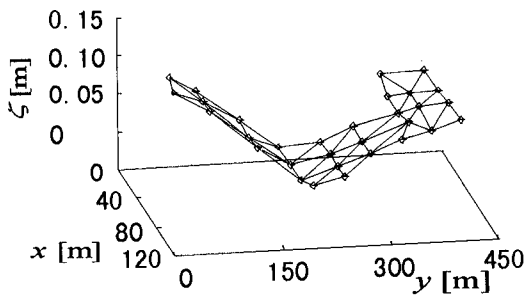
(a) $f = 0.0025$ Hz(b) $f = 0.0090$ Hz(c) $f = 0.0130$ Hz

Fig. 8 Spatial profiles of long-period wave components

their contribution and cooperation in obtaining the filed data. Thanks are also due to K. Kashihara and H. Aikawa for their assistance in carrying out the numerical simulations.

REFERENCES

- Brorsen, M. and Larsen, J. (1987) : Source generation of nonlinear gravity waves with the boundary integral equation method, *Coastal Eng.*, No. 11, pp. 93-113.
- Goda, Y. and Suzuki, Y. (1975) : Computation of refraction and diffraction of sea waves with Mitsuyasu's directional spectrum, *Technical Note of the Port and Harbour Research Institute Ministry of Transport*, No. 230, pp.4-18 (in Japanese).
- Kioka, W., Kai, H. and Yasue, T. (1996) : Numerical analysis of wave deformation over a porous bottom by Boussinesq equations, *Proc. Coastal Eng., JSCE*, Vol.43, pp.101-105 (in Japanese).
- Nwogu, O. (1993) : Alternative form of Boussinesq equations for nearshore wave propagation, *J. Waterway, Port, Coastal, and Ocean Eng.*, Vol. 119, No.6, pp. 618-638.
- Okiihiro, M., Guza, R. T. and Seymour, R. J. (1993) : Excitation of seiche observed in a small harbor, *J. Geophys. Res.*, Vol. 98, pp. 18201-18211.
- van Gent, M. R. A. (1995) : Porous flow through rubble-mound material, *J. Waterway, Port, Coastal and Ocean Eng.*, Vol. 121, No. 3, pp.176-181.

CHAPTER 117

ESTIMATION OF WAVE GROUPS PARAMETER FROM WAVE CLIMATE STATISTICS

Satoshi Nakamura¹

Abstract

Field measurement of sea surface elevation for analysis of wave groups have been carried out at the 4 wave observation points around Japan about for 6 months. As the result of analysis of coefficient variation of wave group parameter, that a record length of wave data needs more than 60 minutes for the reliable statistics of wave groups. Using the wave record of the enough length for wave groups analysis, the empirical relationship between wave group statistics and wave climate statistics is estimated.

Introduction

We have well known that wave groups cause hydraulic problems near the surf-zone, for example harbor tranquillity due to long period oscillations taken by wave groups, abrupt beach erosion due to the infragravity waves generated by breaking of wave groups, a sliding of breakwaters by continuous high waves, and fluctuations of over-topping volume on sea-walls. In spite that the grouping waves are the origin force of hydraulic problems, the research on the statistics of the wave groups which incident to beaches and harbor has not been carried out sufficiently yet. For indicating the degree of wave grouping, a lot of parameters have been proposed. For example, Goda(1970) proposed the peakedness parameter of spectral distribution, Q_p , Funke-Mansard(1979) proposed the groupiness factor, GF , Kimura(1980) shows theoretically relationship between

¹ Senior research engineer, Marine Environment Division
Port and Harbour Research Institute, MOT
3-1-1 Nagase, Yokosuka 239, JAPAN

the run length, j , and the correlation coefficient with succeeding waves, γ_{HH} , and Battjes(1984) proposed the correlation coefficient of wave envelop curve, κ . It is no problem to use whichever parameter for the statistics of wave groups, because they have an adequate correlation each other. The statistical variability of the parameters with record length of the data is rather more important for the analysis.

This study is to discuss on the statistical variability of a wave group parameter for reliable information of wave groups and to propose the empirical formula to estimate the wave groups parameter from wave climate statistics in case of no information on the wave groups.

Field Observation

There are many wave observation stations to observe waves and to get wave climate statistics around Japan. Figure 1 shows the location of wave gages connected to the nationwide ocean wave information network(Nowphas)

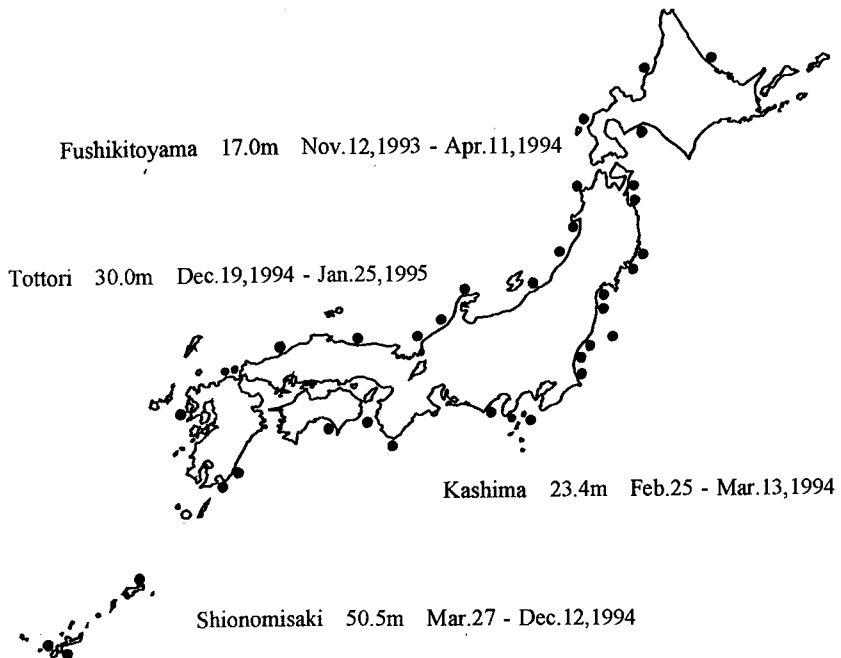


Figure 1 Location, water depth of wave gages, and observation terms

and some of the independent wave gages. This network consist of the wave gages near the big harbors. The data of this network is generally collected about 100 waves every 2 hours and sent to the Port and Harbour Research Institute. The representative value of the wave such as mean wave height and period and the significant wave height and period are computed. The data of un-networked wave gages is similarly processed at each station. This record length is enough for analysis of the representative value of the individual waves distribution, but for analysis of wave groups, it is too short to get the reliable results. Therefor, the special recordings of continuous 119 minutes every 2 hours for about 6 months of sea surface elevation are done at the 4 wave stations (Toyama, Kashima, Tottori and Shionomisaki) which are selected with a basis of the different sea condition. The locations, the establishment water depths and the observation periods of the stations are shown in the figure 1. The sea surface data divided every 2 hours is A/D transformed with a sampling interval 2 Hz and stored in MO disk. After whole data recorded, the data which has some noise was removed and the data was deducted in the tide level change. Table 1 shows the value of skewness and kurtosis of sea surface elevation each observation

Table 1 Skewness and kurtosis of surface elevation

	Skewness	Kurtosis
Fushikitoyama	0.068 ± 0.054	3.0 ± 0.079
Kashima	0.086 ± 0.041	3.0 ± 0.069
Shionomisaki	0.059 ± 0.036	3.0 ± 0.086
Tottori	0.086 ± 0.036	3.0 ± 0.081

points and their standard deviation. At the each points, the skewness almost equals to zero and the kurtosis equals to 3. These value indicate that the distribution of surface elevation is not affected of wave breaking and wave shoring.

Parameter to Identify Wave Groups

There are several parameter of wave groups. The groupiness factor GF is calculated in the value of coefficient variation of smoothed instantaneous wave energy history(SIWEH). The run length j is calculated in how many time the wave height which is higher than the standard height such as $H_{1/3}$ or H_{mean} happens continuously after defining the lines of individual wave heights. The γ_{HH} is by the correlation coefficient of consecutive wave heights. The spectral peakedness Q_p is the moment of spectral distribution. The envelope correlation κ is the correlation coefficient of wave

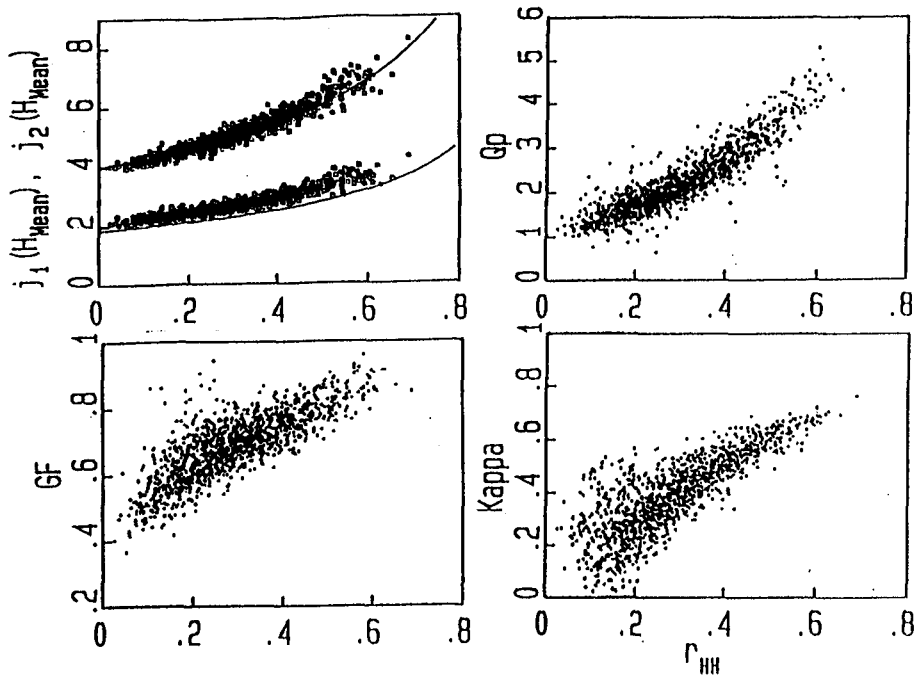


Figure 2 Relationship between γ_{HH} and others

envelop curve. The each correlation of these parameters are adequate. Among these parameters, the parameter γ_{HH} are used following analysis. Because it is easy to calculate in a series of analysing wave climate statistics based on the individual wave analysis and it is possible to change from the γ_{HH} into the others using the relationships which was gotten from field observation. Figure 2 show the relationship between γ_{HH} and other parameters. In the upper left graph, solid lines are theoretically given by Kimura. The relation in each graphs can be approximated with the simple functions. Suzuki and Kawai et al.(1994) also showed the relationships among them by numerical simulations.

Statistics Variability of Wave Groups Parameter γ_{HH}

In order to estimate statistical variability of the parameter γ_{HH} which is related to the record length, the value of coefficient variation, C.V., of the standardized parameter $\gamma_{HH}(t)/\gamma_{HH}(119)$ is used, where $\gamma_{HH}(t)$ is calculated with the record length of variable t minutes and $\gamma_{HH}(119)$ is the value with 119 minutes of data length. Figure 3 shows the change of statistical variability γ_{HH} with the record length t minutes. The solid line is the mean value of the 372 various conditions of wave groups. As the record length becomes

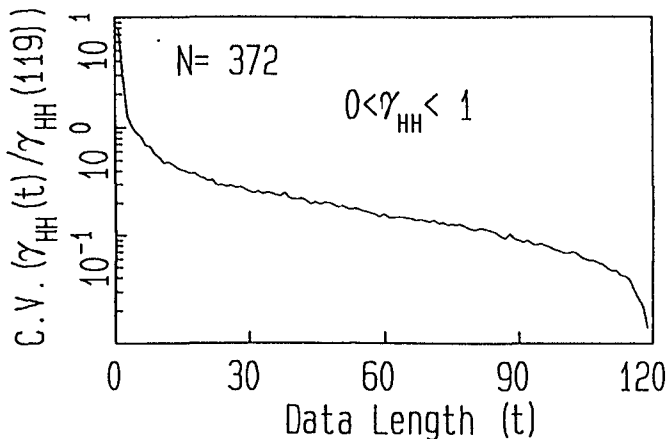


Figure 3 Change of statistical variability of γ_{HH} with the record length

long, the variability of γ_{HH} becomes small rapidly until 30 minutes and decrease of it tend to stable longer than 30 minutes. The value of γ_{HH} is reliable with a record length of 60 minutes although there is some variability in the value of γ_{HH} . As considering the sea condition change of itself, for example, the change due to the movement of the low atmosphere pressure, it is necessary for wave groups analysis to observe among from 60 minutes to 120 minutes. In this paper, the record length of 119 minutes is used for further analysis. Figure 4 show the relative frequency of the parameter γ_{HH} at the 4 observation points. In each figure, The symbol N shows total number of records. There is a difference in the occurring frequency of the large value of γ_{HH} , because the total number is not equal.

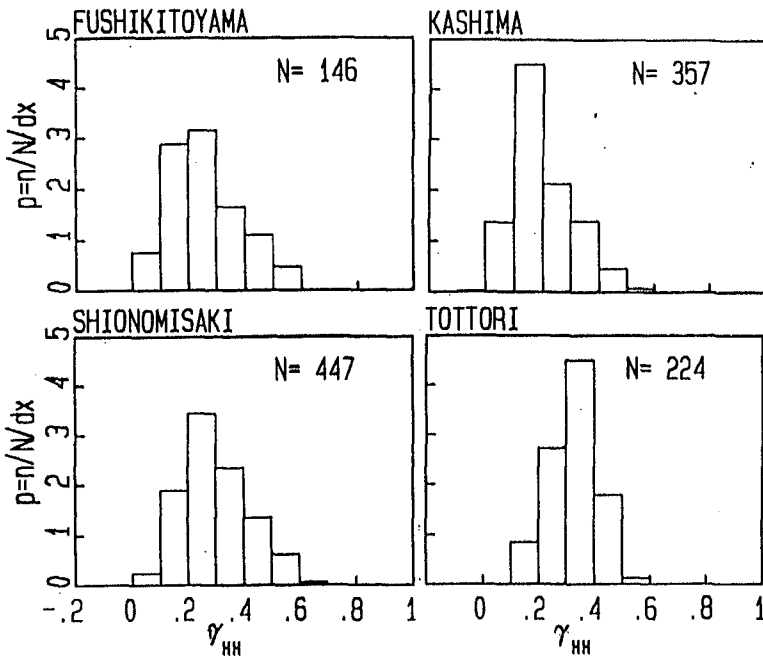


Figure 4 Relative frequency of γ_{HH}

Relationship between Wave Group Statistics and Wave Climate Statistics

It is necessary to record as a lot of waves as possible from now, to study on wave groups structure, and to process statistics of the wave group characteristics. As for getting a statistical value of it, however, the long terms are needed by getting a reliable value because strong wave groups happens rarely. Then, for information of wave groups, it is necessary to show the degrees of the wave group using the characteristics of wave climate such as $(H_{1/3}, T_{1/3})$ and (H_{mean}, T_{mean}) which is obtained enough at many ports. As for the study on the statistics of the wave characteristics, a principal objective is placed in the height of the waves. For example, above-mentioned $T_{1/3}$ is average period with higher 1/3 rank wave height and also the peak period T_p obtained by spectral analysis is the period with highest spectral density. In case of analysis of the wave group, the analysis to have paid attention to the period must be done. Figure 5a and 5b

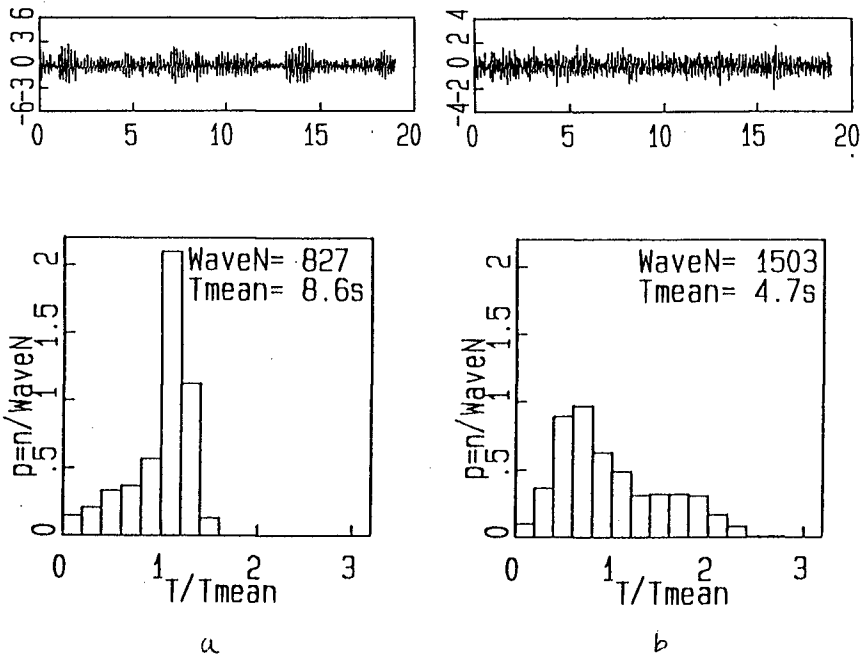


Figure 5 Time series of surface elevation and its period distributions

are the time series of surface elevation and the its non-dimensional periods distribution obtained different wave groups condition. When the wave grouping appears strongly in the time series(5a), the non-dimensional distribution of periods has a peak towards long period side. The other hand, when the wave grouping does not appear clearly(5b), the distribution has a peak towards short period side. This fact indicates that the skewness of periods distribution is related with the wave group parameter γ_{HH} . The skewness can be easily measured with the quartile skewness, QS , with the definition of the following:

$$QS = \frac{(T_{75} - T_{50}) - (T_{50} - T_{25})}{T_{75} - T_{25}} \quad \dots (1)$$

where the quartile value of periods, T_{xx} , is selected in ascending order of wave period until the subscript xx percentage of the total number of waves is reached. When the peak leans to the large percentage with the condition of the distribution has a one peak, the value of the index QS is negative. When the peak leans to small side, the QS is positive. Figure 6 shows the

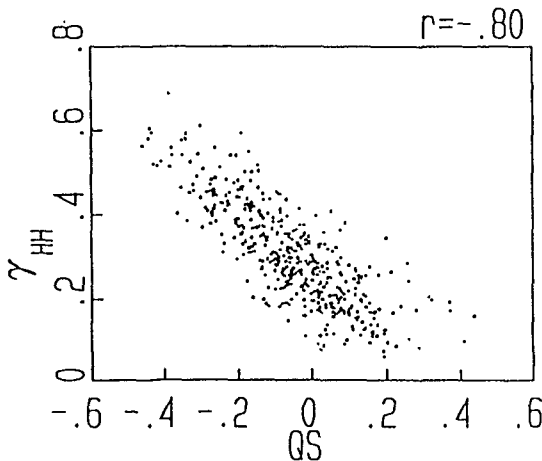


Figure 6 Relationship between γ_{HH} and QS

relationship between QS and γ_{HH} . Their coefficient of correlation is 80%. We find that the wave groups influence strongly in the distribution of periods. In our field wave climate observation, however, a standard procedure is not to define representative wave period such a T_{xx} , depend on the distribution of wave periods. Therefor, I use the combination parameter wave height ratio and the period ratio, which is calculate the characteristics of wave such a (H_{max}, T_{max}) , $(H_{1/3}, T_{1/3})$, and (H_{mean}, T_{mean}) depend on the wave height, instead of the distribution representative period T_{xx} . For estimating the value of γ_{HH} from the value of wave heights and periods, the combination parameter $\chi^n \tau^m$, which composed of wave periods ratio $\tau = T_{1/3} / T_{mean}$ and wave height ratio $\chi = H_{1/3} / H_{mean}$ is used as the parameter QS . The powers of this parameter are defined on condition that the parameter has high correlation with γ_{HH} . Figure 7 shows the correlation coefficient between γ_{HH} and $\chi^n \tau^m$ with value of n and m . The combination parameter $\chi^n \tau^m$ has

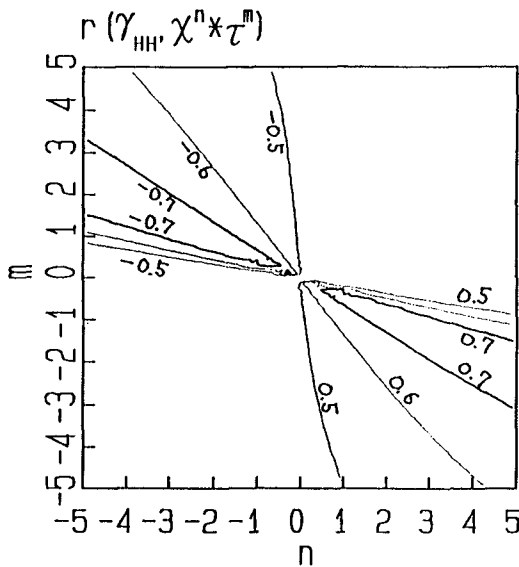


Figure 7 Correlation coefficient between γ_{HH} and $\chi^n \tau^m$

high correlation with the ratio of n and m on 5 to -2. This ratio of n and m is same at this 4 observation points. The value of $n=2.5$ and $m=-1$ are chose because the combination parameter has positive correlation coefficient and the relationship between γ_{HH} and this parameter is almost linear. The γ_{HH} is approximated with a first order function of $\chi^{2.5} \tau^{-1}$ as follows:

$$\gamma_{HH} = a \chi^{2.5} \tau^{-1} + b \quad \dots(2)$$

and determined the constant a and b using the least squares method. Table 2 shows the pair of coefficients a and b at each observation points. These pair of coefficients are approximately same value at the 4 observation points in spite of different sea condition

Table 2 Pair of coefficients a and b

	a	b
Fushikitoyama	0.74	-1.69
Kashima	0.69	-1.50
Shionomisaki	0.69	-1.52
Tottori	0.72	-1.57

of wave energy and direction. This result shows that the degree of wave groupiness is independent to the location of wave gages. On all seashore, the grouping waves come. Figure 8 shows a comparison of the observed γ_{HH} with the estimated one at the Shionomisaki observation point. There is a close agreement between them. The empirical formula to estimate the wave groups parameter from wave climate statistics is proposed.

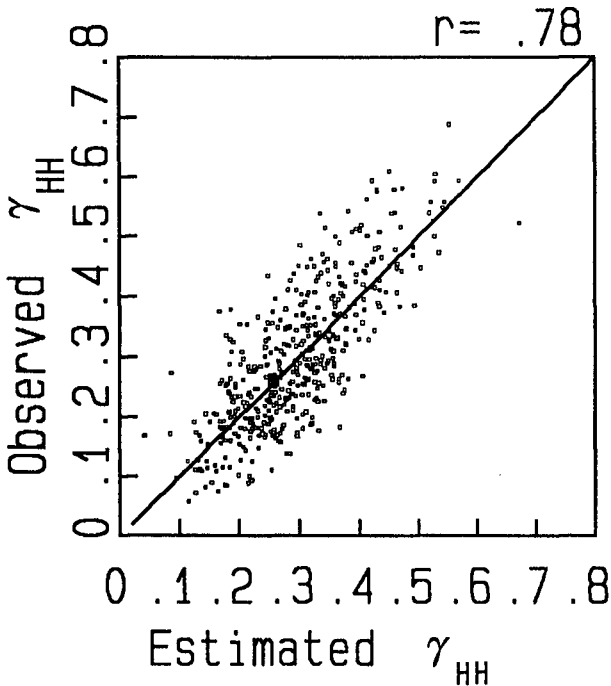


Figure 8 Comparison of observed γ_{HH} and estimated one

Conclusions

To identify wave groups, the correlation coefficient of consecutive wave heights, γ_{HH} , is easy to add in a series of analysing wave climate statistics based on the individual wave analysis. It is possible to change from the γ_{HH} into the other parameter proposed by many researchers using the relationships obtained from field observation.

The value of wave group parameter γ_{HH} is corresponded to the data record length. The reliability of γ_{HH} increases rapidly until 30 minutes of data length and increase of it tend to stable longer than 30 minutes. The value of γ_{HH} is reliable with a record length of 60 minutes although there is some variability in the value of γ_{HH} . Using the enough record length of sea surface elevation data, the relative frequency of the parameter

γ_{HH} based on the 6 months observation at 4 points are shown.

The degree of wave grouping appears on the skewness of distribution of periods strongly. The relationship between quartile skewness of distribution of periods, QS and γ_{HH} has 80% coefficient of correlation. In case that the distribution of wave periods is not calculated, standard wave climate procedure don't define representative wave period such a T_{xx} , the combination parameter, $\chi^{2.5}\tau^{-1}$, composed of wave climate statistics ($H_{1/3}, T_{1/3}$) and (H_{mean}, T_{mean}) have an adequate correlation with wave groupiness.

Empirical formula of the wave groupiness to estimate from wave climate (equation 2) is proposed. The coefficients are constant regardless of the observation points.

References

- 1) Battjes, J.A. and G.Ph. van Vledder (1984): Verification of Kimura's Theory for Wave Group Statistics, Proc. 19th Int. Conf. Coastal Engineering, pp.642-648.
- 2) Funke, E.R. and Mansard, E.P.D. (1979): On the Synthesis of Realistic Sea States in a Laboratory Flume, National Research Council Technical Report LTH-HY-66.
- 3) Goda, Y. (1970): Numerical Experiments on Wave Statistics with Spectral Simulation, Report of the Port and Harbour Research Institute, Vol.9, No.3, pp.3-57.
- 4) Kimura, A (1980): Statistical Properties of Random Wave Groups, Proc. 17th Int. Conf. on Coastal Engineering, pp.2955-2973.
- 5) Suzuki, Y and Kawai, H (1994): Effect of Spectral Peakedness on Wave Grouping Characteristics (in Japanese), The report of the port and harbour research institute, Vol.33, No.2, pp.3-58.



Professor Robert L. Wiegel and Rebecca D. Edge at San Francisco Seawall, California. Photo courtesy of Billy L. Edge.

PART III

Coastal Structures



Detached breakwaters at Caxambas Pass, Marco Island, Florida. Photo courtesy of Coastal Engineering Consultants, Inc.

CHAPTER 118

REFLECTION COEFFICIENTS OF THE STEP-SHAPED SLIT CAISSON ON THE RUBBLE MOUND

Sung Mo. Ahn,¹ Ryuichi Fujiwara², Hiroshi Matsunaga³,
Katsuhiko Kurata⁴, Shohachi Kakuno⁵

ABSTRACT

The characteristics of the reflection coefficients of a step-shaped slit caisson on the rubble mound are examined by experimental data. A numerical analysis which combines the method of matched asymptotic expansions with a boundary element method has been applied for the calculation of the reflection coefficients of the caisson on the rubble mound. Numerical results are compared with experimental data to show the validity. Dimensions of the preferable cross-section of the step-shaped slit caisson on the rubble mound are discussed and obtained through the numerical results.

1. INTRODUCTION

Many kinds of perforated breakwaters, seawalls, and quay-walls have been constructed in Japan. A large number of studies about the hydraulic characteristics of this type of breakwaters have been performed since Jarlan's original work (1961). Reflection coefficients of the structures of this type depend strongly on the relative wave chamber width, the ratio of the wave chamber width to the wave length, and low reflection coefficient can be expected only in a narrow band of wave frequency. From this reason, a new type of breakwater with a step-shaped slit wall, whose cross section is shown schematically in **Fig. 3**, has been developed recently and some very fascinating

1 Research Engineer, Hydraulic Engineering Laboratory, Technical Research Institute
, Toyo Const. Co. Ltd. 3-7-16, Naruo -hama , Nishinomiya, Hyogo, Japan

2 Senior Research Engineer, ditto

3 Senior Engineer, Osaka Branch, Toyo Const. Co. Ltd.

4 General Manager, Technical Research Institute Toyo Const. Co. Ltd.

5 Assoc. Prof., Dept. of Civil Engrg., Osaka City Univ. 3-3-138, Sugimoto, Sumiyoshiku,
Osaka, Japan

results have been found. It was found that this breakwater has low reflection in a wider range of wave frequency compared to conventional slit-type breakwaters. Although a numerical analysis which combines the method of matched asymptotic expansions with a boundary element method (BEM) has successfully been applied for calculation of the reflection coefficients of this structure (Kakuno et al., 1989), the previous analysis was on the condition of non rubble mound. It is essential to verify the effect of rubble mound and to discuss the preferable shape of the *step-shaped slit caisson* (SSC) on the rubble mound for the objective of the construction of this breakwater in the field.

The main objective of the present study is to present the preferable shape and dimensions of the SSC on the rubble mound from the viewpoint of the reflection coefficient. Wave flume experiments were carried out for this objective and the results were compared with those of a modified numerical model which was modified to take the effect of the rubble mound into consideration.

2 NUMERICAL ANALYSIS

2-1 Assumptions and the Boundary Conditions

We consider two-dimensional problem as shown in Fig.1. Assuming non-viscous and incompressible fluid except the region of the vicinity of the slits, we may have the velocity potential for the fluid motion in the whole fluid domain Ω . The velocity potential $\phi(x, z)$, which excludes the time term $\exp(-i\sigma t)$ satisfies the governing equation and the boundary conditions as follows :

$$\nabla^2 \phi = 0 \quad ; \text{in } \Omega \quad (1)$$

$$\partial \phi / \partial y - v \phi = 0 \quad ; \text{on } y = 0 \quad (2)$$

$$\partial \phi / \partial y = 0 \quad ; \text{on } y = -h \quad (3)$$

$$\partial \phi / \partial n = 0 \quad ; \text{on } S_U \quad (4)$$

$$\partial \phi / \partial x = 0 \quad ; \text{on } x = l \quad (5)$$

$$\lim_{|x| \rightarrow \infty} (\partial \phi_{sc} / \partial |x| - ik \phi_{sc}) = 0 \quad ; x \rightarrow -\infty \quad (6)$$

Radiation condition, Eq.(6), can be rewritten for this problem with a complex reflection coefficient ρ as follows:

$$\phi(x, y) \Big|_{x \rightarrow -\infty} \rightarrow (e^{ikx} + \rho e^{-ikx}) \cosh k(y+h) / \cosh kh \quad (7)$$

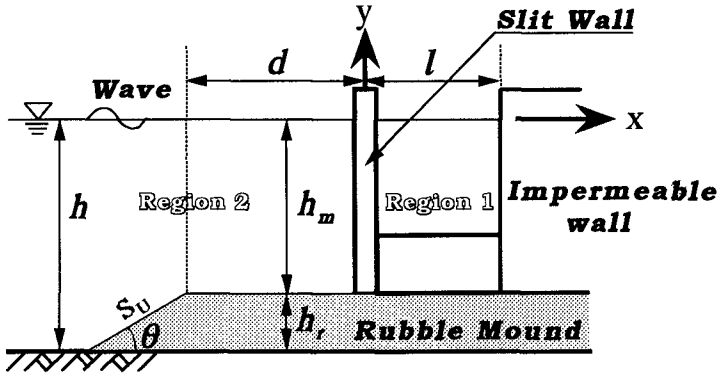


Figure 1. Definition sketch

2-2 A Method of Matched Asymptotic Expansions

(1) Far-field Solutions

The flow domain is divided into two fields; one is the region 1 and the other the region 2 as shown in Fig. 1. Applying Green's theorem to the governing equation in each region, far-field solutions having no local influence by slit walls are derived as follows:

$$\begin{aligned} \phi_1(\xi, \eta) = & \int_{-h_m}^0 \left[\frac{\partial \phi_1}{\partial x}(0_+, y) G_1(0_+, y; \xi, \eta) - \phi_1(0_+, y) \frac{\partial G_1}{\partial x}(0_+, y; \xi, \eta) \right] dy \\ & + \int_{-h_m}^0 \phi_1(l, y) \frac{\partial G_1}{\partial x}(l, y; \xi, \eta) dy \end{aligned} \tag{8}$$

$$\begin{aligned} \phi_2(\xi, \eta) = & \phi_0(\xi, \eta) \\ & + \int_{-h_m}^0 \left[\phi_2(0_-, y) \frac{\partial G_2}{\partial x}(0_-, y; \xi, \eta) - \frac{\partial \phi_2}{\partial x}(0_-, y) G_2(0_-, y; \xi, \eta) \right] dy \\ & + \int_{-d}^0 \phi_2(x, -h_m) \frac{\partial G_2}{\partial y}(x, -h_m; \xi, \eta) dx + \int_{\Gamma} \phi_2(x, y) \frac{\partial G_2}{\partial n}(x, y; \xi, \eta) ds \end{aligned} \tag{9}$$

where G_1 and G_2 are Green's functions, (ξ, η) is a coordinates in the fluid domain, (x, y) is a coordinates on the pass of integration, Γ is the pass of integration on the slope of the rubble mound, $\phi_2(x, y)$ is the velocity potential on the Γ , and $\phi_2(x, -h_m)$ is the velocity potential on the flat top of the rubble mound. $\phi_0(\xi, \eta)$ is the velocity potential of the incident waves which may be written as:

$$\phi_0(\xi, \eta) = \exp(ik\xi) \cosh k(\eta + h) / \cosh kh \quad (10)$$

(2) Near-field Solutions

The near-field solutions which must satisfy the boundary condition on the surfaces of cylinders may be taken as an oscillating flow through the slits between cylinders with a velocity amplitude $U(\eta)$

$$\phi(\xi, \eta) = (\xi \pm C(\eta))U(\eta) + C'_0(\eta) \quad (11)$$

where the positive and negative signs correspond to region 1 and region 2, respectively, $C'_0(\eta)$ is a complex constant, and $C(\eta)$ is a complex blockage coefficient (Kakuno et al., 1993) whose real part corresponds to the coefficient of the inertia resistance and imaginary part to the coefficient of energy dissipation due to the separation at slits.

(3) Matching and reflection coefficient of the SSC

In order to match the inner expansions of the far-field solutions and the outer expansions of the near-field solutions, we have to obtain the limit form for $\xi \rightarrow \pm 0$ in Eq.(8) and Eq.(9):

$$\begin{aligned} \phi_1(0_+, \eta) &= 2 \int_{-h_m}^0 \frac{\partial \phi_1}{\partial x}(0_+, y) G_1(0_+, y; 0_+, \eta) dy \\ &\quad + 2 \int_{-h_m}^0 \phi_1(l, y) \frac{\partial G_1}{\partial x}(l, y; 0_+, \eta) dy \end{aligned} \quad (12)$$

$$\begin{aligned} \phi_2(0_-, \eta) &= 2\phi_0(0_-, \eta) - 2 \int_{-h_m}^0 \frac{\partial \phi_2}{\partial x}(0_-, y) G_2(0_-, y; 0_-, \eta) dy \\ &\quad + 2 \int_{-d}^0 \phi_2(x_1, -h_m) \frac{\partial G_2}{\partial y}(x, -h_m; 0_-, \eta) dx \\ &\quad + 2 \int_{\Gamma} \phi_2(x, y) \frac{\partial G_2}{\partial n}(x, y; 0_-, \eta) ds \end{aligned} \quad (13)$$

Equation (12) and (13) may be matched with Eq.(11) to yield unknown parameters, $U(\eta)$, $\phi(x, y)$ and $\phi_2(x, y)$ and we may have:

$$\begin{aligned} C(\eta)U(\eta) + \phi_0(0_-, \eta) &= \int_{-h_m}^0 U(y) \cdot [G_1(0_+, y; 0_+, \eta) + G_2(0_-, y; 0_-, \eta)] dy \\ &\quad + \int_{-h_m}^0 \phi_1(l, y) \frac{\partial G_1}{\partial x}(l, y; 0_+, \eta) ds - \int_{-d}^0 \phi_2(x, -h_m) \frac{\partial G_2}{\partial y}(x, -h_m; 0_-, \eta) dx \\ &\quad - \int_{\Gamma} \phi_2(x, y) \frac{\partial G_2}{\partial n}(x, y; 0_-, \eta) ds \end{aligned} \quad (14)$$

Also we may derive three equations as the limit form of Eqs. (8) and (9) making (ξ, η) approach impermeable surfaces:

$$\phi_1(l, \eta) = 2 \int_{-h_m}^0 \left[\frac{\partial \phi}{\partial x}(0+, y) G_1(0+, y; l, \eta) - \phi_1(0+, y) \frac{\partial G_1}{\partial x}(0+, y; l, \eta) \right] dy \quad (15)$$

$$\begin{aligned} \phi_2(\xi, -h_m) - \int_{-d}^0 \phi_2(x, -h_m) \frac{\partial G_2}{\partial y}(x, -h_m; \xi, -h_m) dx &= \phi_0(\xi, -h_m) \\ + \int_{-h_m}^0 \left[\phi_2(0-, y) \frac{\partial G_2}{\partial x}(0-, y; \xi, -h_m) - \frac{\partial \phi_2}{\partial x}(0-, y) G_2(0-, y; \xi, -h_m) \right] dy \\ + \int_{\Gamma} \phi_2(x, y) \frac{\partial G_2}{\partial n}(x, y; \xi, -h_m) ds & \quad (16) \end{aligned}$$

$$\begin{aligned} \phi_2(\xi, \eta) - \int_{\Gamma} \phi_2(x, y) \frac{\partial G_2}{\partial n}(x, y; \xi, \eta) ds &= \phi_0(\xi, \eta) \\ + \int_{-h_m}^0 \left[\phi_2(0-, y) \frac{\partial G_2}{\partial x}(0-, y; \xi, \eta) - \frac{\partial \phi_2}{\partial x}(0-, y) G_2(0-, y; \xi, \eta) \right] dy \\ + \int_{-d}^0 \phi_2(x, -h_m) \frac{\partial G_2}{\partial y}(x, -h_m; \xi, \eta) dx + \int_{\Gamma} \phi_2(x, y) \frac{\partial G_2}{\partial n}(x, y; \xi, \eta) ds & \quad (17) \end{aligned}$$

Obtaining $U(\eta)$, $\phi_1(l, y)$, $\phi_2(x, -h_m)$, $\phi_2(x, y)$ from Eqs.(14) through (17), we may calculate limit values for Eq.(8) and (9). Comparing these limit values with Eq.(7), the reflection coefficient can be obtained. The numerical method for the type of those equations has been discussed in detail, for example, by Macaskill(1979).

3 EXPERIMENTS

A wave flume in which model tests were conducted is 40m long, 1.0m wide and 2.0m deep, and is shown in Fig. 2. The slope of the foreshore was uniform with 1:100. The cross section of the breakerwater model is shown in Fig.3, where the water depth on the horizontal bottom was kept constant: $h = 50\text{cm}$. To examine the characteristics of the reflection coefficient and to verify the validity of the calculation, we used 12 types of model caissons with 2 types of rubble mound. The test conditions are shown in Table 1. From measured wave profiles in front of the caisson, the reflected wave height and

the reflection coefficients were estimated by using Goda's method (Goda et al., 1976).

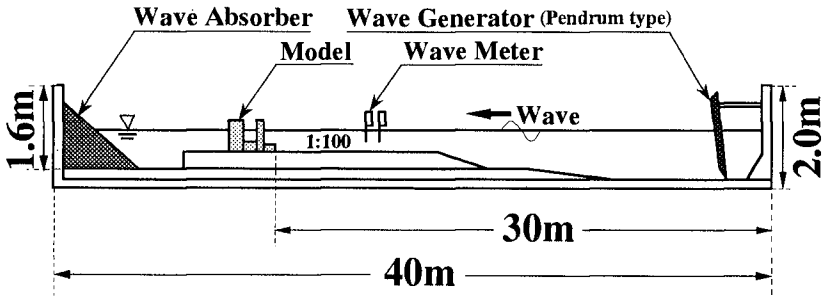


Figure 2. Wave Flume

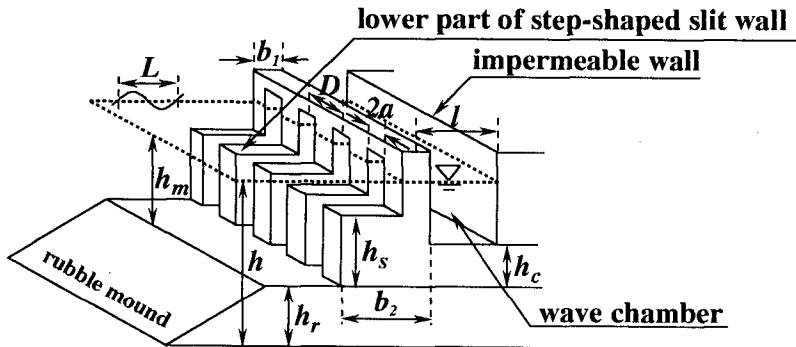


Figure 3. Cross Section of Breakwater

Table 1. Test Condition

Water Depth (h)	50 cm
Height of Rubble Mound (h_r)	$h_r / h = 0.14, 0.33$ (2 Types)
Wave Period (T)	0.73~2.19 sec (6 Types)
Wave Height (H)	$H / L = 0.01, 0.02$ (2 Types)
Model Breakwater	12 Types

4 DISCUSSION

4-1 Results of Experiments

In Fig. 4, the variation of the reflection coefficients as a function of the

relative wave chamber width, l/L , is presented with a parameter h_s/h_m , where h_s is the height of the lower part of the slit wall and h_m the depth of the top of the rubble mound. From Fig. 4, it is observed that the reflection coefficients K_R become slightly smaller at larger period as h_s/h_m becomes large, that is, the height of the lower part of the slit wall (h_s) increases. Fig. 5 shows the variation of the reflection coefficients as functions of the relative wave chamber width and a parameter h_c/h_m , where h_c is the height of the bottom of the wave chamber. From the figure, it is obvious that the reflection coefficients K_R become smaller at longer period as the height of the bottom of the wave chamber becomes large. However, in the shorter period the reflection coefficients become large with increasing h_c/h_m . Also, the value of l/L where the reflection coefficient attains minimum value becomes small. These results implies wave energy must be dissipated effectively by raising the bottom of the wave chamber; that is, the flow through the gaps of the lower part of slit wall is directed upward and is merged with the flow through the gap of the upper part of slit wall. Therefore, the flow through the gap of slit wall is accelerated and more energy loss due to eddy-formation and flow separation may be expected. From these results, lower part of the slit wall and raised bottom of the wave chamber may be effective for the reduction of the reflection coefficient. Fig. 6 and Fig. 7 show the reflection coefficients as functions of the relative wave chamber length and h_r/h (Fig.6), where h_r is the height of the rubble mound, or the wave steepness, H/L (Fig.7). From these figures, as h_r/h increases from 0.14 to 0.33, or as the wave steepness increases, the reflection coefficients K_R become small.

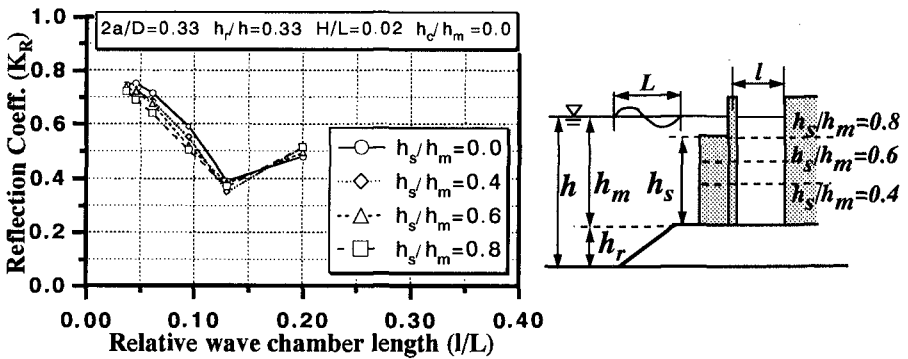


Figure 4. Effect of the height of the lower part of slit wall

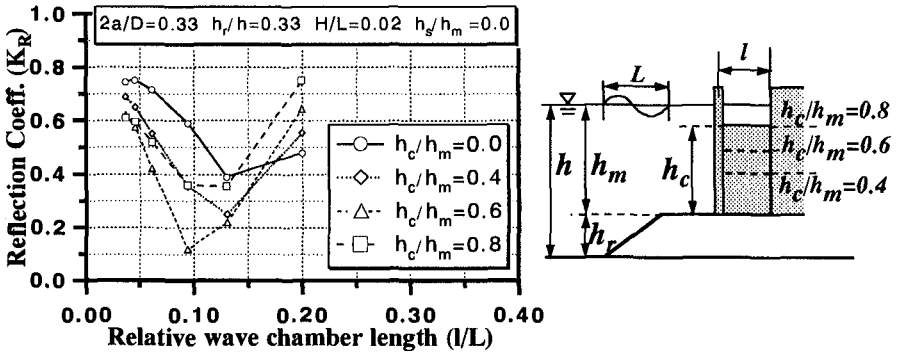


Figure 5. Effect of the depth of the wave chamber

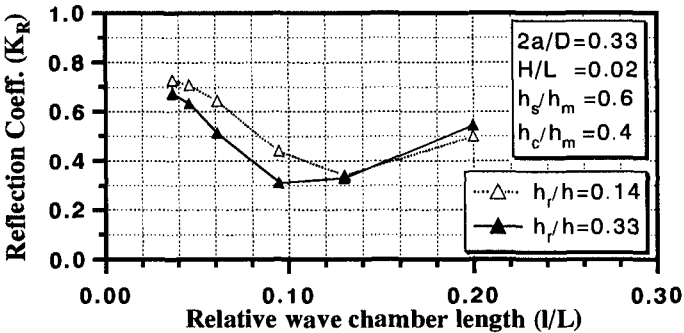


Figure 6. Effect of the height of rubble mound

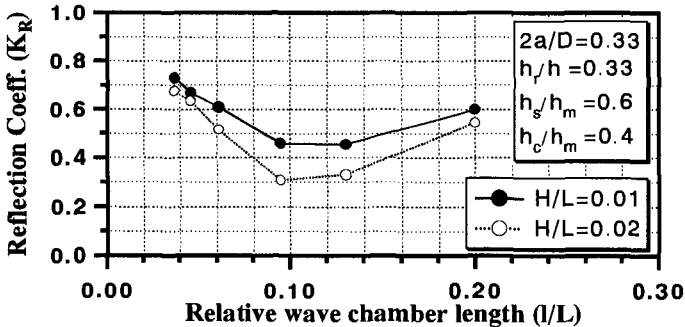


Figure 7. Effect of the wave steepness

4-2 Comparison of Numerical and Experimental Results

In Fig. 8, an example of the comparison of numerical results and experimental data for the reflection coefficients is shown. From Fig. 8, it is obvious that the numerical results of the reflection coefficients agree well with the experimental ones and the validity of the present numerical scheme is shown.

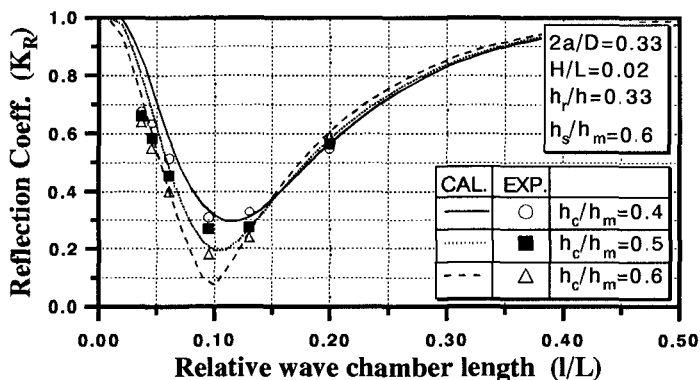


Figure 8. Comparison of numerical and experimental reflection coefficient

4-3 Preferable Shape and Dimension of the SSC on the Rubble Mound

The preferable shape and dimensions of the SSC are discussed on the basis of the criteria as follows:

- 1) *for short-period waves, the value of the reflection coefficient is almost the same as one of the conventional slit-type caisson.*
- 2) *for long-period waves, the value of the reflection coefficient is smaller than the conventional slit-caisson in a wider range of wave period.*

Fig.9 shows the relation between the reflection coefficients K_R and the relative wave chamber width, l/L , with a parameter h_s/h_m , of the SSC on the rubble mound and the conventional slit-type caisson. As the height of the lower part of the slit wall increases, the minimum value of K_R shifts to longer period slightly. In order to decide the preferable dimension of the SSC, the criteria as mentioned above was applied in the range of the relative wave chamber width where the reflection coefficients become smaller than 0.5. Table 2 shows the range of the relative wave chamber width for $K_R \leq 0.5$ read from Fig. 9. From Table 2, the preferable height of lower part of the slit wall, h_s , should be taken as 0.6 times the depth of the top of the rubble mound, h_m . The same routine may be performed for the preferable depth of the wave chamber, and the results of that are shown in Fig.10 and Table 3. From Table 3, the preferable height of the raised bottom of the wave chamber, h_c , may be judged to be 0.4 times the depth of the top of the rubble mound, h_m . Therefore, dimensions of the most preferable cross-section of the SSC is a combination of, $h_s = 0.6h_m$ and $h_c = 0.4h_m$. Now, as readily expected, the gap-ratio $2a/D$, where $2a$ is the gap, or slit, width and D is the distance between adjacent cylinders, is very effective parameter on the reflection coefficients of this type of structure. Fig. 11 shows the effect of the gap-ratio $2a/D$ for the cross

section of the SSC with $h_s = 0.6h_m$ and $h_c = 0.4h_m$. Table 4 shows that the most preferable gap-ratio $2a/D$ of the SSC is 0.25.

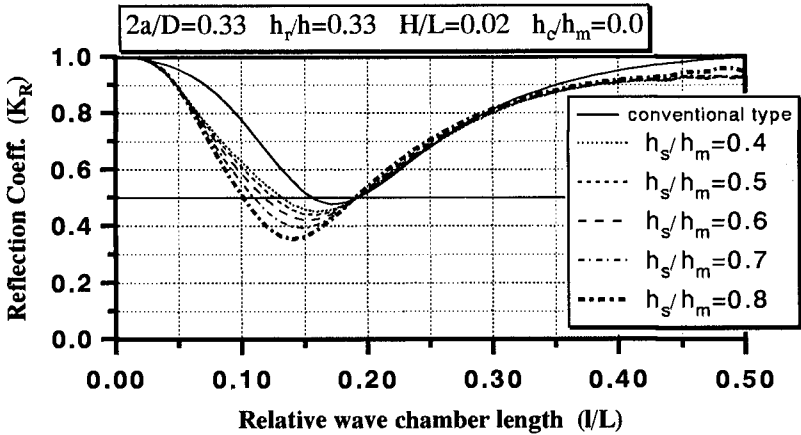


Figure 9. Preferable height of the lower part of the slit wall

Table 2. Range of relative wave chamber length l/L

h_s/h_m	the range of l/L with $K_R \leq 0.5$
Conventional type	0.15~0.19
0.2	0.14~0.19
0.3	0.13~0.19
0.4	0.12~0.19
0.5	0.11~0.18
0.6	0.10~0.18

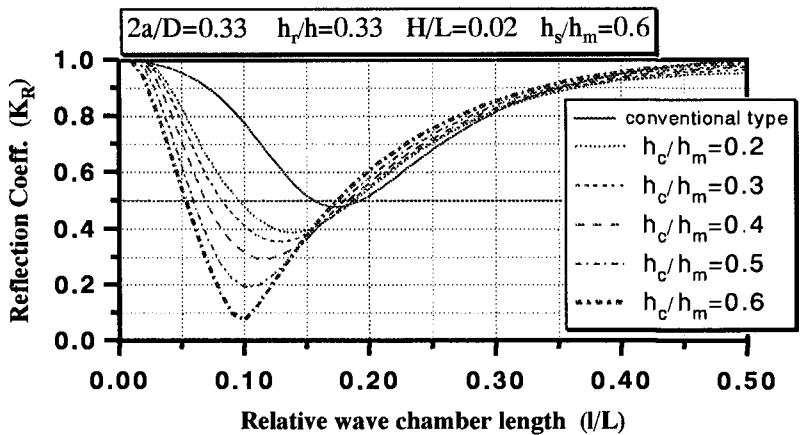


Figure 10. Preferable depth of the wave chamber

Table 3. Range of relative wave chamber length l/L

h_c/h_m	the range of l/L with $K_R \leq 0.5$
Conventional type	0.16~0.19
0.2	0.10~0.18
0.3	0.09~0.18
0.4	0.07~0.18
0.5	0.06~0.17
0.6	0.06~0.17

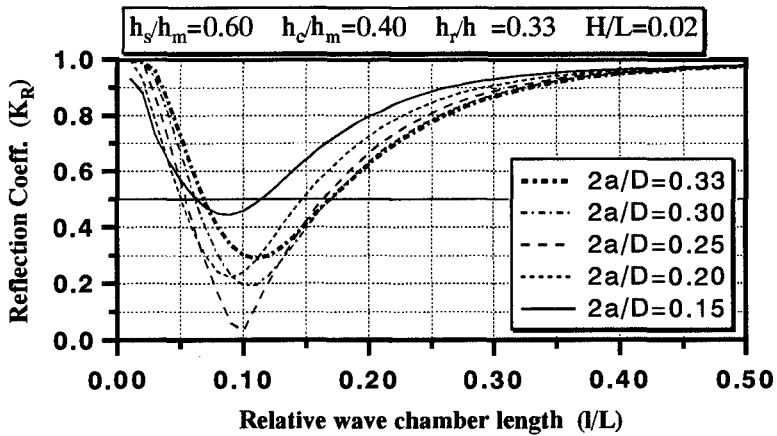


Figure 11. Preferable gap ratio of the slit wall

Table 4. Range of relative wave chamber length l/L

$R_g (= 2a/D)$	the range of l/L with $K_R \leq 0.5$	minimum value of K_R
0.33	0.10~0.18	0.28
0.30	0.09~0.18	0.19
0.25	0.07~0.18	0.03
0.20	0.06~0.17	0.22
0.15	0.06~0.17	0.44

CONCLUSION

The main conclusions obtained from this study can be summarized as follows:

- 1) Lower part of the slit wall and raised bottom of the wave chamber are effective for reduction of the reflection coefficient. The reflection coefficient of the *SSC* becomes low in a wider range of wave frequency than the conventional slit type caisson .
- 2) The numerical analysis which combines the method of the matched asymptotic expansion with BEM is supported and verified by the results of experiments on the reflection coefficients of the *SSC* on the rubble mound for regular waves.
- 3) Dimensions of the most preferable cross-section of the *SSC* is a combination of, the lower part of slit wall whose height is 60% of the water depth of the top of the rubble mound and, the raised bottom of the wave chamber whose height is 40% of the water depth of the top of the rubble mound, and the gap-ratio is 25%.

The next step we should take is to examine the stability of the *SSC*, for the purpose of the construction of the *SSC* in deeper seas.

References

- Fujiwara, R., T. Yosida, K. Kurata, S. Kakuno and K. Oda (1994) : A new type of breakwater with a Step-shaped slit wall, *Int. Conf. on Hydro-Technical Engrg. for Port and Harbor Const.*, pp. 543-562.
- Goda, Y., Y. Suzuki (1976) : Estimation of incident and reflected waves in random wave experiments, *Proc. ICCE*, pp. 828-845.
- Jarlan, G.E. (1961) : A perforated vertical wall breakwater, *The Doc & Harbour Authority, Vol. XLI*, No. 486, pp. 394-398.
- Kakuno, S., K. Oda, T. Muramoto and T. Yosida (1986) : A concept of a complex blockage coefficient for evaluating energy loss effects at slit of structures, *Proc. Japanese Conf. on Coastal Engrg.*, Vol. 33, pp. 407-411. (in Japanese)
- Kakuno, S., K. Oda, T. Fujita, S. Teraoka and T. Yosida (1989) : Wave behavior around slit-type structures with arbitrary vertical cross-sections, *Proc. Japanese Conf. on Coastal Engrg.*, Vol. 36, pp. 499-503. (in Japanese)
- Kakuno, S., K. Oda, and P.L.-F. Liu (1993) : Scattering of water waves by vertical cylinders with a backwall, *Proc. ASCE*, pp. 1258-1270.
- Macaskill, C. (1979) : Reflection of water waves by a permeable barrier, *J. Fluid Mech.*, Vol. 95, pp. 141-157.

CHAPTER 119

BERM BREAKWATER TRUNK EXPOSED TO OBLIQUE WAVES

A. Alikhani¹, G. R. Tomasicchio² and J. Juhl³

ABSTRACT

Comprehensive three-dimensional model tests with a berm breakwater round-head and the adjacent trunk section were carried out at the Danish Hydraulic Institute (DHI) and at the Hydraulic & Coastal Engineering Laboratory of Aalborg University (AAU). This paper describes the influence of wave obliquity on the profile shape, on the initiation of longshore transport and on the longshore transport rate at the trunk section both during and after the profile reshaping, whereas the roundhead stability is described in Juhl et al (1996). Furthermore, tests were made for studying the influence of storm duration and of short crested waves. Equations for calculation of profile development and longshore transport rate under oblique wave attack are introduced.

keywords: berm breakwaters, reshaping, threshold values, longshore transport.

1. INTRODUCTION

A berm breakwater exposed to head-on waves can hardly be destroyed unless it is overtopped, whereas for oblique waves the stones can move along the breakwater. Burcharth and Frigaard (1987) made the first systematic study of oblique wave attack on reshaping breakwaters by testing with angles of wave attack of 15° and 30°. As guideline they recommend $H_o < 4.5$ for a trunk exposed to steep oblique waves, $H_o < 3.5$ for a trunk exposed to long oblique waves and $H_o < 3$ for a roundhead, where

$$H_o = \frac{H_s}{\Delta D_{n50}} \quad (1)$$

is the stability number, Δ is the relative density, D_{n50} is the equivalent cube side length and H_s is the significant wave height. Dependency on wave obliqueness was not described. Burcharth and Frigaard (1988) mentioned that H_o is insufficient to describe the phenomena as it among other things does not contain the effect of wave length and the effect of the duration of the sea storm.

¹Ph.D. student., Aalborg University, Sohngaardsholmsvej 57, DK-9000 Aalborg, Denmark

²Ph.D. Assoc. Prof., Università degli Studi di Perugia, S. Lucia, I-06125 Perugia, Italy

³Senior Eng., Danish Hydraulic Institute, Agern Allé 5, DK-2970 Hørsholm, Denmark

They concluded that the erosion in oblique waves has a non-linear dependency of the sea state.

Van der Meer (1988) introduced the product of dimensionless wave height and wave period parameters for the design of a reshaping breakwater:

$$H_o T_{op} = \frac{H_s}{\Delta D_{n50}} T_p \sqrt{g/D_{n50}} \quad (2)$$

where T_p is the peak period and g is acceleration due to gravity.

Vrijling and Swart (1991) used data from tests of Burcharth and Frigaard (1988) and data from Delft Hydraulics to fit a formula for the transport of stones along the trunk of a breakwater under oblique wave attack. The formula gives the along-structure transport measured as the number of stones per wave, S :

$$S = 4.8 * 10^{-5} (H_o T_{op} - 100)^2 \quad (3)$$

The effect of obliquity of the incident waves is not included in Eq. (3). In average the onset of transport corresponds to $H_o T_{op} = 100$. van der Meer and Veldman (1992) presented Eq. (3) in a slightly different form. They concluded that the longshore transport for larger angles of wave attack such as 50° is much smaller than for 15° and 30° ; their formula is:

$$S = 5.0 * 10^{-5} (H_o T_{op} - 105)^2 \quad (4)$$

The influence of angle of wave attack for shingle beaches was studied by Van Hijum and Pilarczyk (1982) who proposed Eq. (5) for the along-structure volume transport rate under different angles of wave attack. The formula is only valid for shingle beaches, $H_o = 12 - 27$, and can thus not be applied for berm breakwaters.

$$\frac{S_V}{g D_{90}^2 T_s} = 7.12 * 10^{-4} \frac{H_{so} \sqrt{\cos \psi}}{D_{90}} \left(\frac{H_{so} \sqrt{\cos \psi}}{D_{90}} - 8.3 \right) \frac{\sin \psi}{\tanh kh} \quad (5)$$

where ψ is the incident wave angle, H_{so} is the deep water significant wave height, T_s is the 15% excess value of wave period, D_{90} is the sieve diameter for which 90% of the stones (by weight) are smaller, k is the wave number at the structure toe, h is the water depth at the structure toe, g is the acceleration of gravity and S_V is the bulk volume transport rate. With regard to the geometry of a reshaped breakwater Van Hijum and Pilarczyk (1982) concluded that profile parameters should be reduced by $\sqrt{\cos \psi}$. However, van der Meer (1988) re-analysed the data and came to a reduction factor of $\cos \psi$. The analysis was done only for 30° of wave attack and for finer material ($12 < H_o < 27$).

In the Shore Protection Manual (CERC, 1984) a longshore transport formula is given by the following relationship which is valid for H_o larger than 50 (i.e. for sand beaches):

$$S_V = 0.12 * 10^{-4} \pi H_s^2 c_{op} \sin 2\psi \quad (6)$$

where c_{op} is the wave celerity associated to the peak wave period. The formula includes the effect of the wave angle, but does not consider the grain size.

Tomasicchio et al. (1994) and Lamberti and Tomasicchio (1996) on the basis of flume tests, proposed a conceptual model relating longshore transport due to oblique wave attack to stone mobility. The transport model assumes that stones move during up-rush and down-rush in the direction of incident and reflected waves and that movement statistics is affected by obliquity through a modified stability number:

$$N_s^{**} = \frac{H_k}{C_k \Delta D_{n50}} \left(\frac{s_{mo}}{s_{mk}} \right)^{-1/5} (\cos \psi)^{2/5} \quad (7)$$

where H_k is a characteristic wave height for the phenomena under study. For stone movements at a berm breakwater $H_k = H_{1/50}$ is assumed; C_k is the ratio between the characteristic and significant wave height and has a value 1.55 if a Rayleighian wave height distribution is valid. The second factor in Eq. (7) is such that $N_s^{**} = H_o$ for $\psi = 0$ if $s_{mo} = s_{mk}$, where s_{mo} is the wave steepness in deep water based on the mean wave period and s_{mk} was assumed to be 0.03. Tomasicchio et al. (1994) defined the longshore transport, S , as the number of stones moved per wave to be related to the displacement length, l_d , a standard measure for damage, N_{od} , and to the incident wave angle, ψ . The damage index N_{od} was found to

$$N_{od} = 2.05 N_s^{**} (N_s^{**} - 2.0)^{2.2} \quad (8)$$

and for $N_s^{**} > 2.0$, S is given by:

$$\frac{S}{\sin \psi} = \frac{l_d}{D_{n50}} \frac{N_{od}}{1000} \quad (9)$$

In the following, the analysis of the effect of incident wave angle will be presented but also some other important parameters will be discussed.

2. EXPERIMENTS AND TEST PROGRAM AT DHI

2-1. Model set-up

An experimental investigation has been carried out at DHI in a 23 x 30 m wave basin in order to study the stability of a berm breakwater roundhead and the adjacent trunk section under the exposure of oblique waves. Fig. 1 shows a plan of the model basin including the various positions of the two 5.5 m wide wave generators capable of generating irregular long crested waves. Fig. 2 shows the initial profile at the trunk section, and the roundhead was made by rotating the profile around the centreline.

2-2. Stone characteristics

The berm breakwater was constructed of two stone classes, i.e. one for the core and the scour protection and one for the berm, the crest and the rear side protection. The core material had a nominal diameter of $D_{n50} = 0.010m$. A relative wide stone gradation was used for the berm, $\frac{D_{n85}}{D_{n15}} = 1.8$, with an equivalent cube length of $D_{n50} = 0.023m$. The density of the stone material was $\rho_s = 2.68t/m^3$.

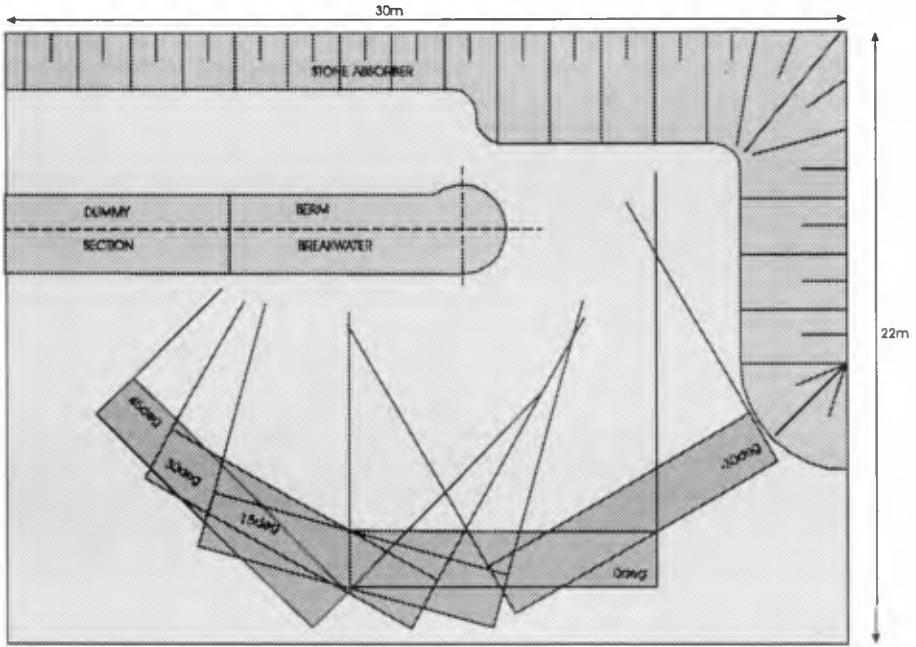


Figure 1: Plan view of the experimental set-up at DHI showing different positions of the wave paddle.

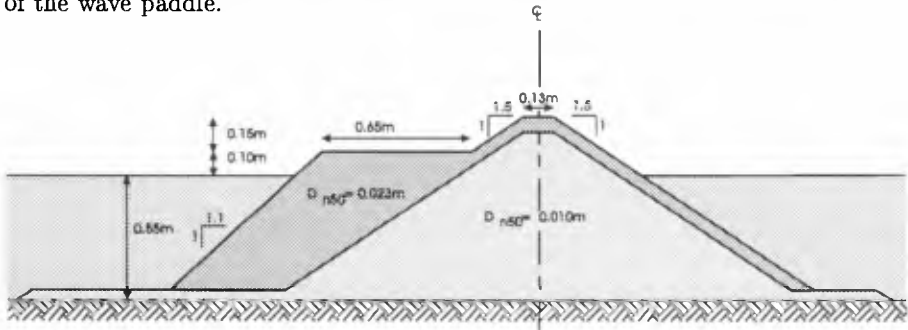


Figure 2: Initial profile for tests at DHI.

2-3. Test program

A total of six test series with irregular long crested waves were carried out in order to consider five angles of incident waves with a wave steepness of 0.05 (-30° , 0° , 15° , 30° , and 45° ; 0° is perpendicular to the trunk, see Fig. 1) and two wave steepnesses for the angle of incidence of -30° ($s_m = 0.03$ and 0.05). Each test series consisted of five tests ($H_0 = 2.0, 2.5, 3.0, 3.5,$ and 4.0) with a duration corresponding to 2,000 waves for initial reshaping of the berm breakwater followed by four tests with a duration of 1,000 waves for studying the stone movements on the reshaped profile ($H_0 = 2.5, 3.0, 3.5,$ and 4.0). All waves were generated on the basis of a Pierson Moskowitz spectrum.

2-4. Measurements

The waves were measured at 14 positions in the wave basin by the use of resistance type wave gauges. The wave conditions were checked by five reference wave gauges placed in a way to minimise the effect of reflection from the berm breakwater. Spectral analysis and zero-crossing analysis were carried out.

A total of 38 profiles along the 8.5 m long breakwater were measured after its construction (initial profile) and after each test run. The profiling was made with a laser running on a beam across the breakwater trunk. The horizontal position of the laser along the beam was measured by another laser, whereas the location along the breakwater axis was fixed manually. The profiles were measured for each 0.5 m along the trunk and for each 0.1 m at the roundhead. Assessment of the stone movements was made based on visual observations, photos taken after each test run and video recordings. Observations were made both during the reshaping process involving a large number of stone movements and after the reshaping. In order to facilitate observations of the threshold conditions for longshore transport and the longshore transport rate, all the armour stones in a one meter wide section of the trunk were painted (immersed in paint) before the reshaping phase and the surface was painted again before the stone movement tests.

3. EXPERIMENTS AND TEST PROGRAM AT AAU

3-1. Model set-up

A model test program for studying the effect of directionality of the waves and the effect of the number of waves on the behaviour of a berm breakwater trunk section exposed to oblique waves has been carried out in a 8.5 x 15.7 m directional wave basin at Aalborg Hydraulic & Coastal Engineering Laboratory. Fig. 3 shows the layout of the model basin and the cross section of the structure. The waves were generated by 9 paddles each 0.9 m wide.

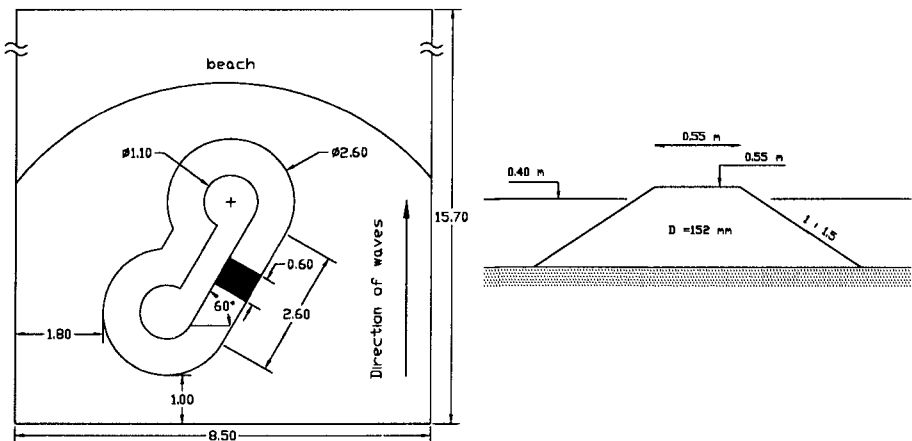


Figure 3: Lay-out of model basin and breakwater cross-section used for the directional wave tests at Aalborg University.

3-2. Stone characteristics

The berm breakwater was constructed with only one stone class having a nominal diameter of $D_{n50} = 0.0152m$ and $\frac{D_{n85}}{D_{n15}} = 1.44$. The density of the stone material was measured to $\rho_s = 2.70t/m^3$.

3-3. Test program

A total of 20 tests with irregular waves were carried out. The reshaping phase considered 5 wave attacks ($H_o = 2.2, 2.7, 3.3, 3.8,$ and 4.1) with long crested oblique waves. The tests were made with an angle of incidence of 60° with respect to the breakwater and a duration of 2,000 waves. The reshaping phase was followed by 4 tests with long crested oblique waves (60°) for studying the stone movements on the reshaped profile ($H_o = 2.9, 3.2, 3.5,$ and 4.0); each test with a duration corresponding to 1,000 waves.

After these stages, long duration tests with a total duration corresponding to 11,000 waves were carried out (11 tests with $H_o = 4.0$). Two of the tests were made with directional waves having an angle of incidence of 60° and a cosine spreading function of $s = 10$. All waves were generated on the basis of a JON-SWAP type spectrum with peakedness parameter $\gamma = 3.3$, width parameters $\sigma = 0.10$ for $f \leq f_p$ and $\sigma = 0.50$ for $f > f_p$.

3-4. Measurements

Prior to the initiation of the model tests, the directional waves were calibrated with a very gentle stone absorber in order to minimise wave reflection. The waves were measured at 6 positions in the wave basin by the use of resistance type wave gauges. The wave conditions have been checked by five reference wave gauges placed in positions with minimum effect of reflection from the berm breakwater. For the long crested waves the incident wave height was calculated using the method of Funke and Mansard (for separation of incident and reflected waves) and for the directional waves the calibrated target waves were used.

A total of 3 manual profile measurement were made: the initial profile, the profile after reshaping of the trunk and the profile after the long duration test with $H_o = 4.0$. Assessment of the stone movement was made based on visual observations and photos taken after each test. Observations were made both during the reshaping process involving a large number of stone movements and on the reshaped profile. In order to facilitate observations of the threshold conditions for the longshore transport and of the longshore transport rate, all the berm stones in a 0.6 m wide section of the trunk were painted (immersed in paint).

4. DISCUSSION

Three effects will be discussed in the following:

1. effect of wave obliquity on threshold of movement;
2. effect of wave obliquity on profile shape and sorting of the stones;
3. effect of wave obliquity on longshore transport.

4-1. Threshold of stone movement

For smaller angles of incidence the unstable stones will first start rocking and/or rolling and will not move in the longshore direction as long as the longshore

component of the energy flux is not big enough to move them. Table 1 shows the longshore transport (stones per wave) on the reshaped profile as a function of $H_o T_{op}$ for different angles of wave attack.

$H_o T_{op}$	15°	30°	45°
40	0.000	0.000	0.000
55	0.000	0.000	0.000
80	0.002	0.003	0.005
100	0.008	0.014	0.015
131	0.021	0.05	0.07
161	0.2	-	-

Table 1: Longshore transport after reshaping (tests made at DHI).

In general, the largest transport distance occur for $\psi = 45^\circ$ with a decreasing tendency for smaller and larger angles of wave attack. Now the threshold values are described as:

$$H_o T_{op} > \frac{50}{\sqrt{\sin 2\psi}} \quad (10)$$

during the reshaping phase, and

$$H_o T_{op} > \frac{75}{\sqrt{\sin 2\psi}} \quad (11)$$

after the reshaping phase

4-2. Sorting and profile shape

With regard to the tests made at DHI, Fig. 4 shows the as built structure stone distribution as well as the stone distribution around the water level and in the lower steep part of the reshaped breakwater after exposure to head-on waves with $H_o = 4.0$. w_{50} around the water level is found to be half the w_{50} in the lower

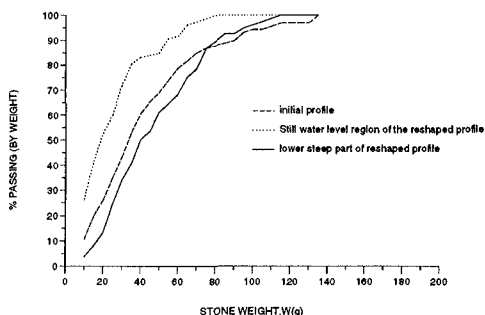


Figure 4: Stone distribution after exposure to 2,000 head-on waves with $H_o = 4.0$ (DHI tests).

steep part, where w_{50} is defined as the stone weight for which 50% of the stone are smaller. However, for more narrow stone gradations the differences will be less pronounced showing that the stone distribution might be an important parameter. The result of the tests at AAU with larger angle of wave attack and narrower stone gradation indicate less sorting of the stones. The major part of the resorting happens in the first 1000 waves. Due to the less sorting of stones for larger ψ and narrower stone gradation, a modification should be applied to the D_{n50} value. This modification might be dependent on the incident wave angle as well as on the value of $\frac{D_{85}}{D_{15}}$. From Fig. 5 it is seen that in long duration tests the lower part of the profile is not changing but the upper part is developing as a function of duration. The reason for this continued recession is lack of nourishment from the upstream of the breakwater. In the test of Van Hijum and

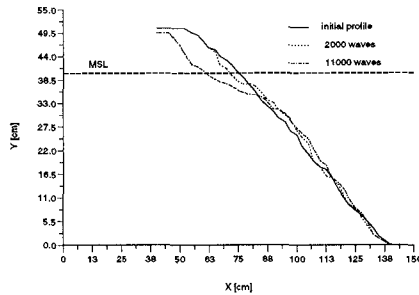


Figure 5: AAU tests, initial and reshaped profile at trunk section ($\psi = 60^\circ$).

Pilarczyk (1982) some of the structural parameters are neither fitting to $\sqrt{\cos \psi}$ nor to $\cos \psi$ as re-analysed by van der Meer (1988), e.g for the crest width the reduction factor is even bigger than unity. The fact is that the reduction factor for the upper part of the profile under oblique waves is more dependent on the storm duration, while for head-on waves this is not the case. Therefore, due to the longer duration sea state the recession of the berm under oblique waves can exceed the value for head-on waves for fixed equivalent wave parameters. Thus, a reduction factor for the upper part of the profile is meaningless under a long duration sea storm.

Equations were developed to calculate the reshaped profile under head-on and oblique wave attack. For reshaped profiles there is always a point, below SWL, which indicates the change of the curvature of the profile, see Fig. 6. This step point, h_s , can be described by

$$h_s = \frac{H_o T_{op} D_{n50} N^{0.07} \sqrt{\cos \psi}}{40} \quad (12)$$

where N , is the number of waves. From this point, depending on the water depth, wave parameters, stone weight, incident wave angle, initial shape of the profile, and repose angle of the stones, two power functions can represent the reshaped

profile namely upper part and lower part. The lower part can be described as:

$$Y = -hm_1\left(\frac{X}{h}\right)^{1.7} + h - h_s \quad (13)$$

where X and Y are the length and height of the reshaped profile counted from the center line of the breakwater, h is the water depth at the toe of the breakwater and coefficient m_1 is given by

$$m_1 = \frac{1.7e^{(-0.013H_oT_{op})}}{\cos \psi} \quad (14)$$

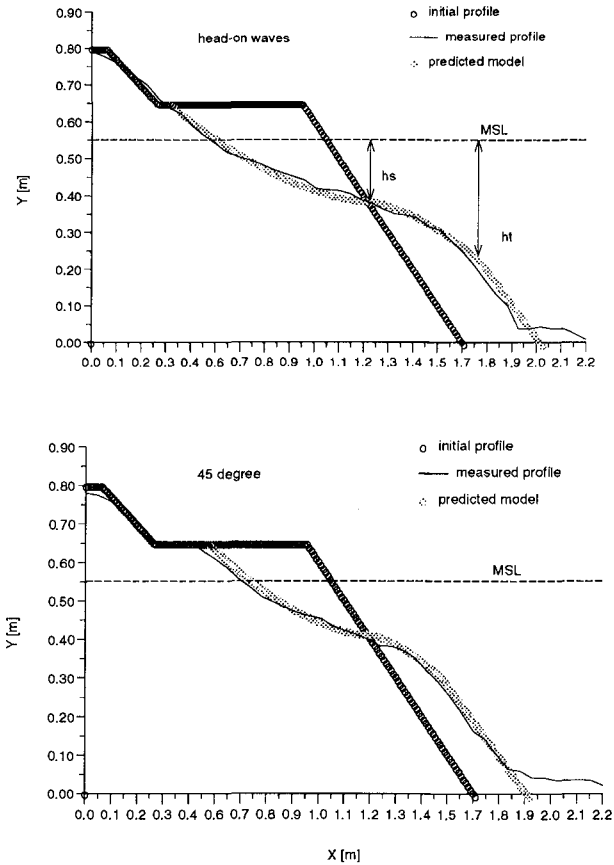


Figure 6: Initial, predicted and measured reshaped profiles for $H_oT_{op} = 161$.

Tests result at DHI show that the part of the profile below the transition point h_t follows the repose angle of the stones under water, where h_t is given by

$$h_t = H_s \cos \psi + h_s \quad (15)$$

The upper part can be described as:

$$Y = hm_2\left(\frac{X}{h}\right)^{1.7} + h - h_s \quad (16)$$

where

$$m_2 = \frac{1.7e^{(-0.01H_oT_{op})}}{\cos \psi} \quad (17)$$

The upper part above still water line is more depending on the initial shape of the profile. Tests result at DHI show that the part of the profile above the berm is following the initial profile shape.

A computer program "RESHAPED" is developed for calculating the profiles, see examples in Fig. 6. The profiles are drawn from an arbitrary point say from the center line of the breakwater and then by the use of an iterative procedure shifted along still-water line until the mass balance is fulfilled. In the case, where enough nourishment is not supplied from upstream, additional erosion due to longshore transport must be considered. For this purpose the longshore transport rate described in Eq. 18 can be used. RESHAPED is calibrated for a breakwater with core material and a relatively wide stone gradation. Comparison was made with some of the tests at AAU with a structure without core material and narrower gradation, showing more resistance of the breakwater compared to the tests at DHI. Calculations of the profile developments for the tests at DHI were also made using BREAKWAT, see van der Meer (1992), showing an overestimation of the structure response.

4-3. Longshore transport

Eq. 4 seems to be adaptable for berm breakwaters, but no influence of the wave angle is included, i.e the formula does not consider any difference between the effect of head-on waves and of oblique waves on the longshore transport.

One of the most important parameters influencing longshore transport is the longshore component of the incident wave energy. Therefore it is rational to relate the longshore transport to this parameter and consequently Eq. 4 is modified as:

$$S = 0.8 * 10^{-6} \sqrt{\cos \psi (H_o T_{op} \sqrt{\sin 2\psi} - 75)^2} \quad (18)$$

The formula is calibrated to give the maximum longshore transport for $\psi = 45^\circ$ and zero transport for head-on waves and waves propagating parallel to the breakwater axis. As the test conditions at laboratories were different (e.g water depth, nearshore slope, stones characteristics, initial profiles, wave generation and calibration procedures, and analysis of incident and reflected waves), each set of laboratory data will be discussed separately. Eq. 18 is shown in Fig. 7 together with data from DHI tests after reshaping. The test results and Eq. 18 show comparable relationships of the wave conditions and angle of wave attack. Fig. 8 shows Eq. 18 together with longshore transport data from the tests by Burcharth and Frigaard (1987). The tests for studying the influence of the wave angle were all made with a breakwater constructed with a profile as will develop after exposure to head-on waves, as they assumed the profile to be almost independent of the wave angle. Three points may concern here:

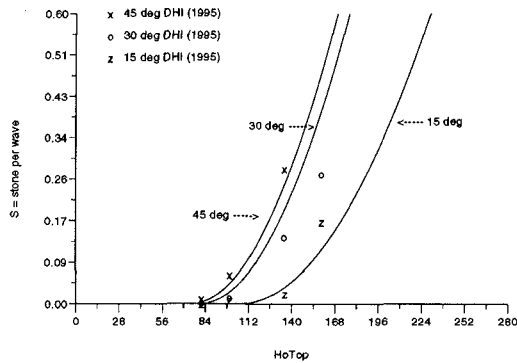


Figure 7: Longshore transport, in form of stone per wave, S , as function of $H_o T_{op}$.

- 1) The structure was not compacted during a reshaping process and redistribution of the stones did not take place. By constructing a breakwater in this manner, the additional stability due to the natural armouring that occurs as a result of stone motion induced by wave attack will not develop. This can have more influence on the tests with 15° than on the tests with 30° .
- 2) Results have shown that the profile reshaping is larger for head-on waves than for oblique waves. Running tests with oblique waves on a more reshaped profile will result in more energy dissipation and thus reduced longshore transport, which could be the reason for the small difference in longshore transport rate between 15° and 30° .
- 3) In some of the tests with increasing wave parameters the longshore transport was not increased; which can be due to the breakwater becoming more consolidated during exposure to more and more waves.

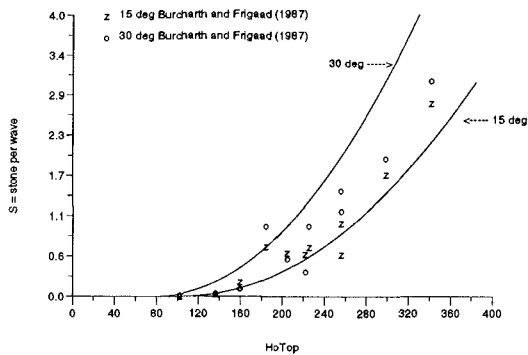


Figure 8: Longshore transport for data of Burcharth and Frigaard (1987).

Fig. 9 shows the longshore transport after reshaping based on data from van der Meer and Veldman (1992).

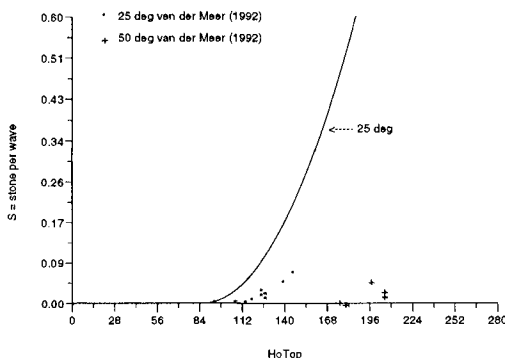


Figure 9: Longshore transport for data of van der Meer and Veldman (1992).

This figure confirms that other important parameters are the directionality of waves and the number of waves. Test results from AAU for directional waves have shown that the longshore transport is much lower than for long crested waves. For example for $s = 10$, where s is a parameter that controls the angular distribution in the cosine power spreading function, the longshore transport was 1/4 of the case for long crested waves for $H_o = 4.0$. More tests with different s values are necessary in order to formulate the directionality effects. Fig. 10 shows a plot of the data of the tests of van der Meer and Veldman (1992), where the directionality has been taken into account applying a reduction factor of 4.

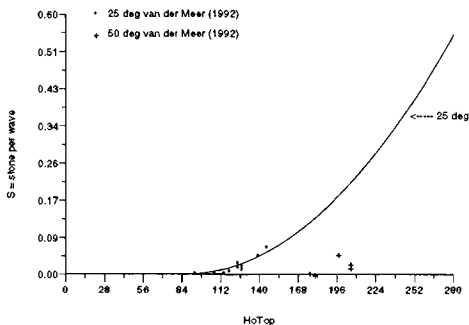


Figure 10: Longshore transport for data of van der Meer and Veldman (1992), with a reduction factor of 4 for directional waves.

For an angle of wave attack of 25° the data fit very well, but for 50° there must be some other reason which is not explainable.

In order to show the effect of the storm duration, long duration tests were carried out with a total of 11,000 waves. The number of moved stones was counted after each 1,000 waves. The longshore transport rate was decreasing with increasing number of waves, see results presented in Fig. 11. Experimental data fit in with an exponential function:

$$S = \frac{ae^{-bN}}{1000} \quad (19)$$

For tests at AAU with $\psi = 60^\circ$ and $H_o = 4.0$, a was found to be equal to 350.

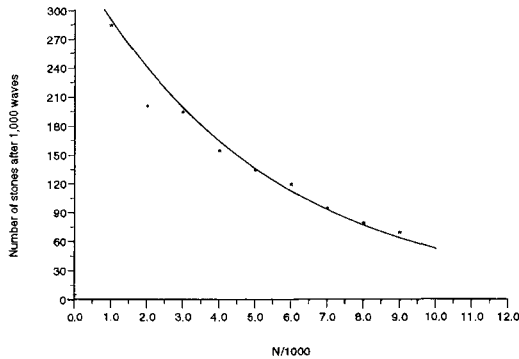


Figure 11: Long duration tests at Aalborg University $H_o = 4.0$, $\psi = 60^\circ$.

5. CONCLUSIONS

Three-dimensional experiments both at DHI and Aalborg University shown that the threshold value of the stone movement, the shape of the profile and the rate of longshore transport are dependent on both the angle of wave attack and the wave energy.

Laboratory investigations shown that due to the wave induced sorting of the stones, D_{n50} does not remain constant during the reshaping process at certain locations on the cross section. The sorting is a function of the hydrodynamic vector in front of the structure and will change as a function of the incident wave energy and the wave direction.

An equation for calculation of the longshore transport rate on a reshaped berm breakwater is established, see Eq. 18. Criteria for initiation of stone movements both during and after reshaping are given, see Eq 10. and 11. Moreover, laboratory investigations from Aalborg University shown that directional waves reduce the longshore transport rates (a specific test with a wave angle of 60° showed a reduction of 4) and that the longshore transport is reduced by an exponential function when increasing the number of waves.

The presented longshore transport formula can not necessarily fit all the data because it does not consider the effects of the stone gradation, the shape of the stones, the permeability, the armour layer thickness, the spreading function and the number of waves considered for each test at different laboratories. Further analysis are required to study the influence of especially stone gradation and directional waves.

The profile of a reshaped profile can be described by two equations, one for the part above a defined step point and one below this point, see Eq. 13 and 16. It was found that the angle of wave attack can be included by a reduction factor of $\cos \psi$.

ACKNOWLEDGEMENTS

The present study was carried out as part of the research project on Berm Breakwater Structures and was co-sponsored by the European Commission as part of the research and development program in the field of Marine Science and Technology (MAST) through contract MAS2-CT94-0087.

REFERENCES

- Alikhani, A., Frigaard, P., and Burcharth, H.F. (1996). "Design Construction and Maintenance of Reshaping Breakwaters. The Second International Conference on Coasts, Port, and Marine Structures." , "ICOPMAS", Tehran, Iran.
- Burcharth, H.F. and Frigaard, P. (1988). "On 3-Dimensional Stability of Reshaping Berm Breakwaters." ASCE, Proc. 21th ICCE, Malaga, Spain.
- Frigaard, P., Hald, T., Burcharth, H.F. and Sigurdur Sigurdarson (1996). "Stability of Reshaping Breakwaters with Special Reference to Stone Durability." ASCE, Proc. 25th ICCE, Orlando, USA.
- Juhl, J., Alikhani, A., Sloth, P., Archetti, R. (1996). "Roundhead Stability of Berm Breakwaters." ASCE, Proc. 25th ICCE, Orlando, USA.
- Lamberti, A., Tomasicchio, G.R. (1996). "Stone Mobility and Longshore Transport at Reshaping Breakwaters." Coastal Engineering (Pending Publication).
- Tomasicchio, G.R., Lamberti, A. and Guiducci, F. (1994). "Stone Movement on a Reshaped Profile." ASCE, Proc. 24th ICCE, Kobe, Japan.
- Van der Meer, J.W. (1988). "Rock Slopes and Gravel Beaches under Wave Attack." Ph.D.-Thesis, publication no. 396, Delft Hydraulics, The Netherlands.
- Van der Meer, J.W. and Veldman, J.J. (1992). "Singular Points at Berm Breakwaters: Scale Effects, Rear, Roundhead and Longshore Transport." Coastal Engineering, 17, pp 153-171.
- Van Hijum, E. and Pilarczyk, K.W. (1982). "Equilibrium profile and longshore transport of coarse material under regular and irregular wave attack." Publication No. 274, Delft Hydraulics, The Netherlands.
- Vrijling, J.K., Smit, E.S.P. and De Swart, P.F. (1991). "Berm Breakwater Design; The Longshore Transport Case: A Probabilistic Approach." ICE, Proc. Coastal Structures and Breakwaters, London, UK.

CHAPTER 120

INTERACTION BETWEEN MAIN ARMOUR AND TOE BERM DAMAGE

by P. Aminti¹ and A. Lamberti²

ABSTRACT

Wave flume tests were carried out aiming to describe and quantify the interaction between main armour and toe-berm damage up to failure. Experiments are described in brief, as well as the qualitative combined damaging process. An interaction scheme is formulated; data and formulae are provided for the quantification of the risk implied in the combined failure.

1. INTRODUCTION

The toe berm of a breakwater is primarily supposed to provide static support to main armour layer, avoiding that its lower units might roll down on the sloping lower surface.

Regarding the effects on the armour layer, if, on one hand, the whole toe-berm upper surface is eroded and erosion undermines the lowest units of the armour layer, the armour units may slide down producing relevant damage of the main armour layer. On the other hand, if the berm is wide enough and almost horizontal, units which are removed from the overlaying armour layer can be retained on the berm itself, reducing the effective slope of the layer and possibly increasing armour resistance to waves. Secondarily and proportionally to its width, the toe berm acts on the water flow, modifying for instance the wave breaking process and the boundary layer evolution at the breakwater surface.

In the case the armour layer is damaged when the berm still shows a significant retaining capacity, armour stones held on the berm can hinder its further erosion.

Some information regarding rubble mound toe protection stability in front of an impermeable vertical wall may be found in the Shore Protection Manual referring to Brebner & Donnelly (1962). Similar information drawn from Japanese experience can be found in Tanimoto & al. (1982) or Goda (1985).

Regarding toe berm stability at a rubble mound breakwater van der Meer (1992) presented a first design formula for depth limited wave conditions desumed from model tests of seven breakwaters with alternatives, whereas Gerding (1993) performed several tests for the specific purpose and derived a verification and design formula valid also for deep water conditions.

No precise information could be found in literature about damaging interaction,

¹ Professor, DIC, University of Florence, via Santa Marta 3, 50129 Firenze, Italy

² Professor, DISTART, University of Bologna, viale del Risorgimento 2, 40136 Bologna, Italy

and only an indirect and qualitative statement, van der Meer (1992), that berm damage greater than 3-10% may cause the berm to lose its functionality and should therefore be considered not acceptable.

In order to quantify the outlined interaction between toe-berm and armour layer a set of laboratory experiments was performed aiming:

- to identify the effect of a stable berm on main armour damage;
- to analyse the damaging process of the berm in a wide set of structure and wave conditions;
- to identify the berm damage level which forces the downsliding failure of the armour layer.

Analysing the wide set of experimental data obtained from our tests we have finally

- compared results from our tests and Gerding tests
- derived revised damage formulae for the berm including the effect of factors not variables in Gerding data set or not represented by Gerding formula;
- derived a relation between the berm width and the critical damage level causing main armour failure;
- analysed the statistical errors of Gerding and our revised formulae.

2. PERFORMED TESTS

Tests were performed in Florence. The wave channel used has a 0.8x0.8 m² section, is 40 m long and is equipped with a wave paddle of the absorbing type; water depth at the wave paddle is 0.5 m. A 1:100 bed slope reduces water depth to 0.34 or 0.20 m in front of the tested structure. The maximum significant wave height that could be produced in the test section is 0.15 m.

The test section was divided into three parts 0.265 m wide where structures were built with an identical profile, but with stone of different size in the berm. This enabled to test contemporary three berm conditions, but forced also to use a smaller scale than usual. The absence of scale effects was checked reproducing tests T23, T25 and T27 of Gerding (1993) in 1:2 scale. All the geometrical dimensions of the breakwater were accurately reproduced as well as the testing procedure used by Gerding at DH De Voorst: in these tests (only in these) no settling wave attack was run before the nominal ones and berm was rebuilt after each wave attack. Only the foreshore slope, which was yet prepared with a slope 1:100 in our channel, while it was 1:20 in DH experiments, is different. . The milder foreshore slope caused in our tests a reduced wave height at breaking and a slight distortion of the wave height distribution which was accounted for by assuming as characteristic wave height for stone mobility $H_{2\%}$; no significant scale effects could be observed with this assumption.

Several test structures were designed keeping fixed some parameters and others variable. Fixed were: armour stones (weight 32 g, density 2.6 g/cm³, equant shape) breakwater crest elevation (15 cm, irrelevant overtopping), berm base depth (25 cm in deep water, fig 1, and 15 cm in shallow water), shape and grading of berm stones (equant, very well sorted) and, approximately, the wave height likely to produce structure failure ($H_{s\sigma}=8$ cm). Variable were: water depth at structure toe, armour

slope, toe berm depth and width (the mentioned parameters define a structure shape) as well as wave steepness and toe berm stone size.

The criterion for the choice of variable parameters characterising each test series was to select combinations of reasonably extreme parameters. Each structure shape is identified by four parameters and denoted by four letters specifying in the order:

- water depth at structure toe h_m : D (deep) $\Leftrightarrow h_m=34$ cm, S (shallow) $\Leftrightarrow h_m=20$ cm; in the first case wave are not depth limited, whereas in the second case extreme waves are depth limited;
- berm depth h_f : H (high berm) $\Leftrightarrow h_f=H_{sd}$; L (low berm) $\Leftrightarrow h_f=1.6H_{sd}$; in the first case berm stones almost as great as armour stone are requested, in the second case almost as great as the underlayer ones;
- berm width b_f : F (no berm) $\Leftrightarrow b_f=0$, the berm depth marks a reduction in armour size; N (narrow) $\Leftrightarrow b_f=3D_{n50td}$; W (wide) $\Leftrightarrow b_f=10D_{n50td}$; D_{n50td} is our conventional design size of berm stones, i.e. the size satisfying Gerding berm stability formula () with damage $N_{odt}=b_f D_{n50t}$ (1 in the case of no berm)
- armour slope: S (steep) $\Leftrightarrow \cot\alpha=1.5$; M (mild) $\Leftrightarrow \cot\alpha=2.5$; it was supposed that milder slopes could hinder armour sliding even in the case of severe berm erosion.

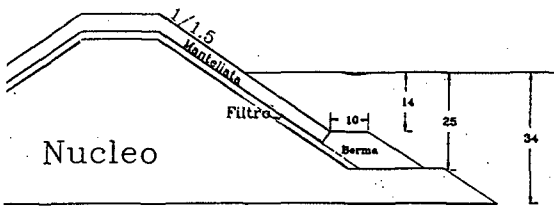


Fig. 1 Section of the tested structure DLWS

Figure 1 shows the DLWS structure.

Different berm stone size were tested corresponding to more and less stable berms than provided by the design criterion. The actual number of stones in the berm width can be significantly different from one of the nominal values (0,3,10), ranging actually from 0 to 25.

Each structure was attacked with waves of increasing intensity up to failure. Wave conditions were drawn from a fixed wave signal set providing a wave height increase around 10-12% per step. For each test series the wave spectrum shape was kept constant and in all cases each wave attack lasted 3000 waves. Two combinations of wave steepness and spectral shape were used: a PM spectrum giving $H_s/L_{om}=0.05$ (short waves, identified by a 5th letter S in test series code) and a JONSWAP spectrum with $\gamma=5$ and $H_s/L_{om}=0.02$ (long waves, L).

12 structure shapes (8 in deep water and only 4 in shallow water conditions, since low berm are unrealistic in this case) and 73 test series, i.e. combinations of structure shape, wave steepness and berm stability conditions, were tested systematically.

Waves were generated using the same signals and target wave conditions were preliminarily measured at structure toe in the absence of any structure. Measurements

were repeated during tests for control purposes but target values were used for analysis.

Damage to the armour layer and to the berm was measured:

- by profiling the structure with a rod array after each wave attack and deriving erosion area (A_e) from profiles (erosion damage $S \equiv A_e/D_{n50}^2$) and
- by counting over a certain observation area (the relevant part of the structure times an observation width B_o) the number of stones (N_d) displaced from the armour layer or removed from the berm ($N_{od} \equiv N_d/(D_{n50} \cdot B_o)$).

3. QUALITATIVE RESULTS AND CLASSIFICATION OF FAILURE PROCESS

Figure 2 shows some typical results of one test series.

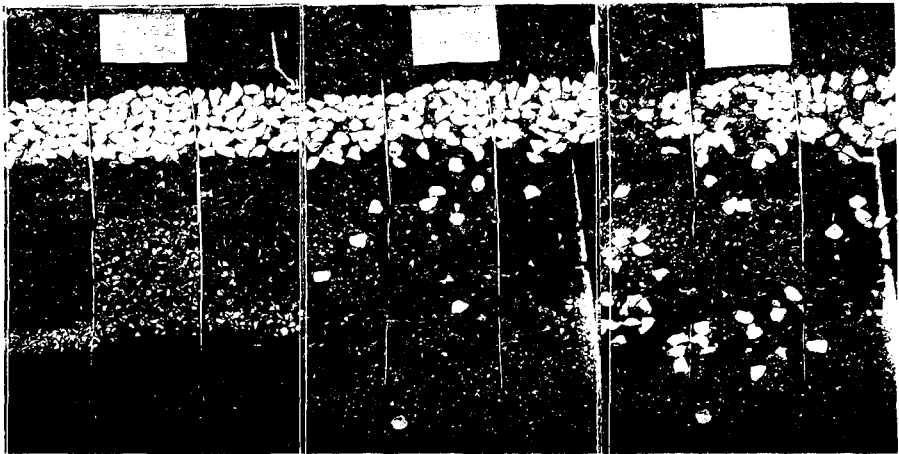


Fig. 2 Structure DHNS at start of test and after the 3rd and last wave attacks. Remark in the central photo how a moderate berm damage in the left structure (dark-coloured stones removed) does not induce any incremental damage on main armour compared to the central structure, whereas the right photo shows how a relevant berm damage forces the armour down sliding in the left structure and a significant incremental damage in the central structure, where the narrow flattened berm is unable to stop falling units, compared to the right structure.

Since every stone moved on the armour layer is displaced downwards and almost certainly removed from it, erosion and displacement damage of the armour are strictly linked and represent a single damaging process.

This is not the case for the berm when the armour layer is damaged, see fig. 3, since profiles do not distinguish armour from berm stones, whereas the distinction was natural while counting removed stones. Berm apparent erosion usually decreased when the armour layer was severely damaged, whereas the number of stones displaced from it is regularly increasing with wave height. As index of damage to the berm the displacement damage is therefore used in principle. A qualitative description of the damaging process must however accompany the damage quantification in order to

avoid ambiguities.

Referring to failure conditions the following classification was used:

1. stable and wide berm: the berm maintains its initial shape up to armour layer failure, most of falling armour stones are stopped by the berm causing a reduced damage increase with wave intensity;
2. stable but narrow berm: the berm maintains its initial shape but most of the armour stones fall below it;
3. wide berm less stable than the armour layer but effective in retaining falling units;
4. berm less stable than the armour layer and ineffective in retaining falling units;
5. severely unstable berm: the armour layer fails due to lack of support provided by the berm.

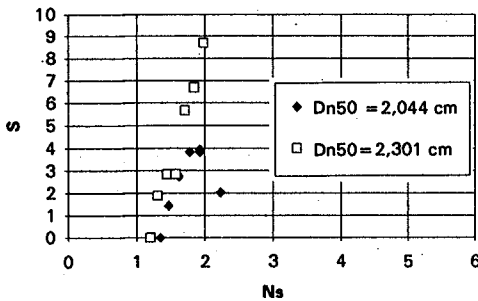


Fig. 3 Damage progress for a typical structure: DHNS, long waves, $D_{n50t} = 2.04 \text{ cm}$

By decreasing berm stability wide berm structures move from type 1 to 3 ending at 5; narrow berm structures normally follow the sequence 2, 4 and 5.

Figure 4 shows schematically the damage progress in berm and main armour for a non effective (left) or effective (right) berm. The three progress lines represent in left to right order a stable berm, a moderately unstable and a severely unstable one. The right figure shows also how a stable and wide berm retards the damaging of the main armour, the effect being cancelled in a weak berm, and how, hypothetically, main armour damage can retard the berm damage causing armour down sliding.

Since the damage causing main armour failure is well documented in literature

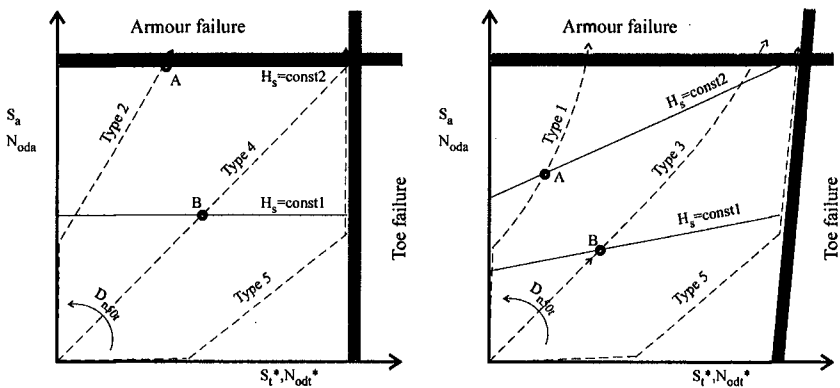


Fig. 4 Damage progress in a non effective berm case (left side) and in an effective berm case (right)

($S_a = 8 \div 12$ depending on slope, van der Meer 1988), the main aspects requiring quantification are:

- the benefit of a stable berm if any,
- the berm damage threshold causing armour down sliding
- a reliable relation providing berm damage (in the stable armour case at least).

Figure 5 shows the comparison of main armour damage over berm of different stability. In the presented cases the sudden damage increase due to berm flattening is evident. A curve is shown representing van der Meer formula, i.e. the usual increase of damage with increasing incident wave height. Erosion damage is converted to displacement damage dividing by 2.0.

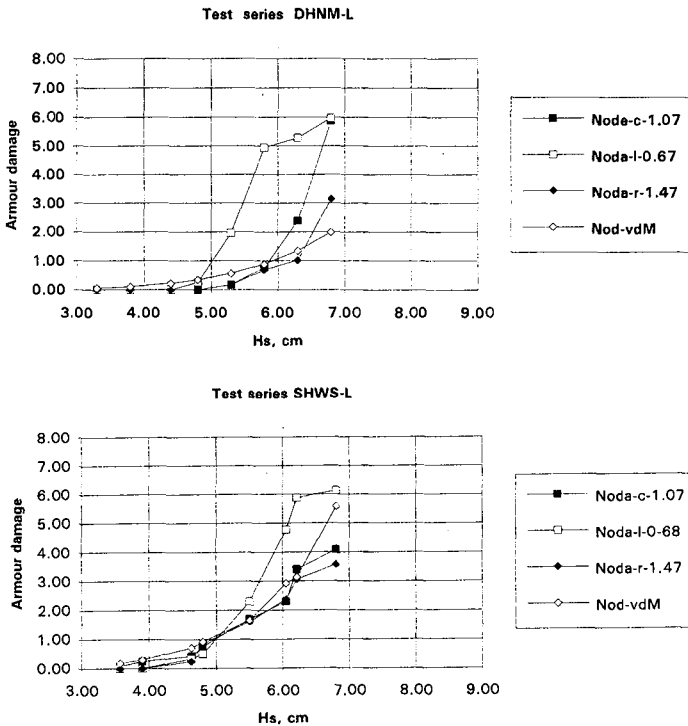


Fig. 5 The effect of berm stability on main armour damage in two tested structures

4. POSITIVE EFFECTS OF A STABLE BERM ON THE ARMOUR LAYER

The positive effect of a stable berm can be desumed from the comparison of observed armour damages over a certainly stable berm with damage estimates obtained from van der Meer (1988) formulae. This formula is actually deduced mostly from experiments on slopes, i.e. in the absence of any berm; the comparison with the formula is quantified by evaluating the average ratio of observed and

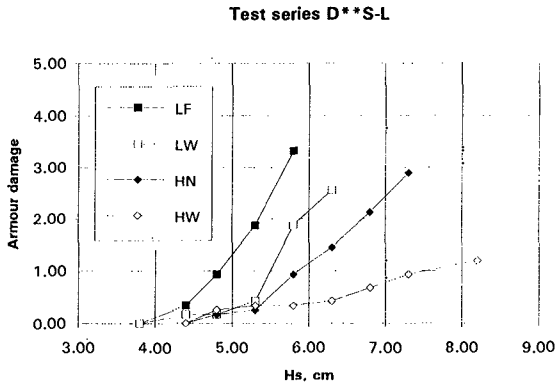


Fig. 6 Comparison among experimental displacement damages due to long waves in deep water acting on steep armour slopes over berms of varying width and depth

correlated: we have observed $S_a = 2.5 \cdot N_{oda} \pm 0.8$; but, while the first is subject to the evaluation error due to the limited number of profiles and includes structure settlement, the second is not subject of any measurement error, since counting is exact and displaced stones are clearly recognizable. Displacement damage was therefore preferred. Figure 6 shows the comparison of armour damages due to long waves on steep armour slopes in deep water. The compared results are derived from cases where the berm was very stable and show the effect of berm width and height. Every existing formula, as e.g. Van der Meer's formula, returns equal damages for the four structures. The effect is comparable to discrepancy observed between data in extreme conditions and van der Meer formula were observed also by Mase & al. (1995). The effect is in this case out of discussion: both the height and width of the berm have evident and positive effects. The effect is similar but smaller for mild armour slope and/or in shallow water, supporting the interpretation that the positive effect is due to

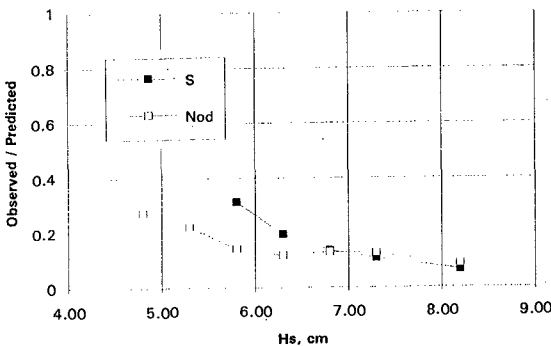


Fig. 7 Typical ratio of observed damage to the damage derived from van der Meer eq.. Structure DHWS with long waves (most effective berm among tested ones)

computed damages presented in table 1. Since formulae include the effects of wave and of armour layer parameters (wave height and period, armour slope, stone size and density) the ratio even if not constant is less variable than the damage itself and can characterize the damage relation below the threshold.

Armour damage was measured both as erosion and as displacement damage. The two damage estimates are well correlated: we have observed $S_a = 2.5 \cdot N_{oda} \pm 0.8$; but, while the first is subject to the evaluation error due to the limited number of profiles and includes structure settlement, the second is not subject of any measurement error, since counting is exact and displaced stones are clearly recognizable. Displacement damage was therefore preferred. Figure 6 shows the comparison of armour damages due to long waves on steep armour slopes in deep water. The compared results are derived from cases where the berm was very stable and show the effect of berm width and height. Every existing formula, as e.g. Van der Meer's formula, returns equal damages for the four structures. The effect is comparable to discrepancy observed between data in extreme conditions and van der Meer formula were observed also by Mase & al. (1995). The effect is in this case out of discussion: both the height and width of the berm have evident and positive effects. The effect is similar but smaller for mild armour slope and/or in shallow water, supporting the interpretation that the positive effect is due to reshaping of the armour layer sustained by the berm in the most severely attacked zone.

Figure 7 presents a typical behaviour of the ratio between observed damage and the damage estimated by van der Meer formulae.

Table 1 shows the average ratio between the observed damage and the damage foreseen by the formula. Due to the recognized inaccuracy of the

formula (6-7% on H_s) and due to the recognized lack of reproducibility of armour strength ($\approx 30\%$ on damage) only discrepancies greater than 40% are singularly evident.

Table 1. Average reduction factor to be applied to van der Meer equation below the negative effect threshold

	Long waves						Short waves					
	FS	NS	WS	FM	NM	WM	FS	NS	WS	FM	NM	WM
DH	---	0.4	0.2	---	0.8	0.4	---	0.5	0.4	---	0.9	0.6
DL	1.0	---	0.5	1.6	---	1.0	0.5	---	0.7	---	---	0.8
SH	1.2	0.9	0.8	---	---	0.8	0.8	1.1	0.6	---	---	0.6

Some conclusions may be drawn:

- positive effects are evident only in deep water;
- the effect normally increases with berm height and width;
- the effect is greater for steep armour slopes;
- strong positive effects are possible only when the berm can retain displaced stones from falling to a depth where they would be of no use for the portion of the profile that is attacked by waves.

5. NEGATIVE EFFECTS OF AN UNSTABLE BERM ON THE ARMOUR LAYER

In most cases armour damage increased quite abruptly as a consequence of berm flattening, see fig. 5. In a few others it raised more gradually. The damage increase shows always some irregularity due to the limited number of armour stones in the test area, and this makes the identification of small deviations questionable.

As long as the berm damage is significantly below the critical threshold no evident correlation between armour and berm damage could be observed.

Actually the erosion and flattening of the berm is supposed to cancel progressively the beneficial effect of the stable berm, but this is covered by the "noise" in most cases.

On the other side, when the armour is severely damaged and armour stones cover the berm, the conditions for experimental evaluation of the berm damage are the worst and only the order of magnitude of the damage can be assessed. Visual inspection showed also that armour stones were never covering with sufficient and uniform density the berm, so that a compensation between the shelter effect of a dense armour stone cover and the erosive effect of isolated stones is likely to occur.

When eventually erosion undermines the armour layer, a rather sudden incremental damage $\Delta N_{od} = 3 \div 4$ takes place.

Since the flattened berm has an almost constant shape (slope 1:4÷5), the corresponding berm damage level measured either as erosion or as displacement damage should depend only on the nodimensional berm width: berm damage, represented by either the erosion area A_e (volume of erosion per unit length) or by the number of displaced stones N_{dt} (proportional to the length where removed stone are

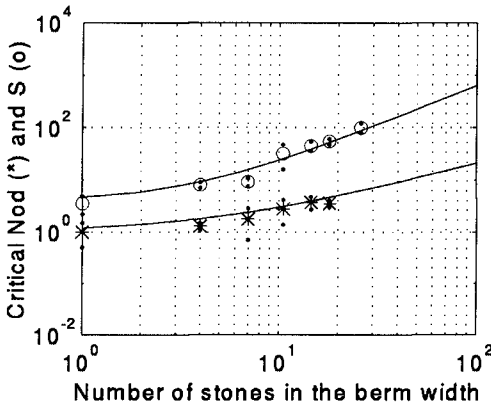


Fig. 8 Empirical relation between the critical berm erosion and the relative berm width

counted), should depend only on berm width B_t and stone size D_{n50t} , the nondimensional version of this relation is a relation between N_{odt} or S_t and B_t/D_{n50t} .

Figure 8 shows the two average empirical relations. For each substructure the critical damage was assessed (either as a value, when sliding was observed, or as a bound, when sliding was not observed) and statistics were evaluated for berm-width classes. Figure 8 shows the

average values and the 2 standard deviation range.

The two lines represent relations fitted to the average raw values; from these a unique corrected relation for the damage can be derived (following paragraph describes the correction):

$$S_t^c \cong 2.0 \cdot N_{odt}^c = 3 + 0.7 \cdot (B_t/D_{n50t})^{5/4} \quad (1)$$

The final interaction scheme is:

- if the berm damage is below critical threshold, the effect on the armour is normally weak; it can be:
 - disregarded (traditional approach, using e.g. van der Meer formulae) increasing parallelly the estimate error;
 - pointed out by some new method (e.g. Mase & al., 1995) or derived from tests; in this case the benefit should be reduced progressively to zero with increasing berm damage up to the critical value;
- if the berm damage reaches the critical value the upper layer of the armour will slide down causing a considerable increase of damage and reaching, for any reasonably safe design, armour failure ($N_{oda} \cong 4$).

6. RELIABILITY OF OUR DAMAGE ESTIMATES

For several reasons raw estimates of the berm damage S_t and N_{odt} are only moderately correlated and show an average ratio far greater than 2.0. If every removed stone causing erosion is counted in N_d and if no other mechanism but erosion causes profile modification, then the relation between the two variables would be

$$S \cdot (1 - n) = N_{od} \quad , \quad (2)$$

where n is the void fraction near the surface ($\cong 0.5$), expressing in non dimensional form the fact the eroded part of the initial profile was occupied by stones and by

interstitial void.

But actually settlement do occur, particularly for the berm since it was reconstructed after each test series, and some error in counting the removed stones could not be avoided. Berm stones were made recognisable by colouring the top layer, and removed stones were counted only when they were removed outside the berm including its face. Some berm stones were removed from the berm and not counted, because maybe they were hidden by fallen armour stones or among armour stones (particularly when in order to obtain a very unstable berm berm stones were smaller than those in the underlayer), some more eroded by the second layer were not counted because they were uncolored and confused with stones of the lower layers, some others were not counted because they moved within the berm.

The best experimental relation between the two variables in our experimental set-up and procedure was

$$S_t = 5.2 \cdot N_{odt} + \frac{0.5 \cdot B_t}{D_{n50t}^2} \quad \text{c.det.} = 0.76$$

It can be interpreted as:

- the average structure show a berm settlement of approximately 0.5 cm;
- on the average only 38% of berm stones contributing to erosion are positively counted as removed.

The first assumption corresponds to observations. The second was controlled in some final tests series where the upper first three layer of the berm where coloured differently from the front face, eliminating the second and partly the third cause of counting errors. It was observed that stones of the upper first layer transported out of the berm were on the average 45% of those that were counted as moved, i.e. that were moved outside they colour area. The difference (45-38%) can be easily explained by the remainin error causes.

The above empirical relation was used to correct raw berm damage estimates and combine them into "true" berm erosion and displacement damage indexes

$$S_t^* \equiv 2.0 \cdot N_{odt}^* \equiv \text{avg} \left(S_t - \frac{0.5 \cdot B_t}{D_{n50t}^2}, 5.2 \cdot N_{odt} \right)$$

The relation compensates for some systematic errors performed in the evaluation but shows also the errors present in the raw estimates.

Likely errors of compensated values are about 40% (less or more depending on the number of original raw estimates available: in some cases counting was impossible, in some others berm stones erosion area could not be assessed).

7. REVISION OF TOE BERM DAMAGE FORMULAE

Tests were programmed making use in a predictive sense of Gerding formula,

$$\frac{H_s}{\Delta_t D_{n50t}} = \left(1.6 + 0.24 \cdot \frac{h_t}{D_{n50t}} \right) \cdot N_{odt}^{0.15} \quad (3)$$

The results of the tests substantially confirm the formula.

Comparing the two sets of experimental results and or the derived formulae a few differences must be remarked. Formula (3) is based on a series of tests expressly designed for the evaluation of berm damage under a fixed armour layer, whereas our tests were primarily focused on the influence on armour damage and were therefore carried in a more complex and difficult experimental environment. The berm in Gerding's tests was reconstructed every time and damage are the damages of the wave attack, whereas in our tests the berm was reconstructed at the beginning of the test series and the observed damage is the cumulated effect of all the wave attacks in the current progression. Foreshore slope was different in the two experiments, as mentioned before. Armour slope in Gerding test was fixed: 1:1.5. Wave steepness in Gerding tests varied in {0.02, 0.03, 0.05} with preference with the central steepness, i.e. varied significantly less than in our experiments.

The main differences we observed are:

- the average exponent of displacement damage was higher: 0.2;
- the average sensitivity to berm depth was lower 0.15;
- a systematic effect of wave steepness (or wave period) was evident as in Benoit & Donnars (1996).

A formula similar to (3) that fits our results is:

$$\frac{H_s}{\Delta_t D_{n50t}} = \left(1.1 + 33 \cdot s_m + 0.15 \cdot \frac{h_t}{D_{n50t}} \right) \cdot N_{odt}^{0.20} \quad (4)$$

We have also reanalysed berm damage data with a more free approach since some aspects of formulae (3) and (4) did not convince us.

Let $u_c \equiv \sqrt{g \cdot H_s}$ be the conventional reference velocity (the velocity scale in the breaker area), let u_t be the maximum velocity at the toe-berm i.e. the real cause of damage, and let $v_t \equiv u_t/u_c$ be the non dimensional velocity at the berm. The erosion of toe berm stones depends on the ratio between the hydrodynamic force on the stones and their submerged weight

$$N_{odt}^* = \text{funct} \left(\frac{H_s}{\Delta_t D_{n50t}} \cdot v_t^2 \right) \quad (5)$$

where 1) *funct* should be a monotonic increasing function with no upper bound, and 2) v_t should depend only on what influences the flow field and not on Δ_t .

The non dimensional velocity at the berm should depend on:

- a location parameter specifying where the berm is located with special refence to breakers: h_t/H_s ;
- a roughness ratio, ratio between the flow field dimension and the surface roughness: h_t/D_{n50t} ;
- wave period and armour slope, determining wave penetration into depth, reflection, run down: s_m and $tg\alpha$
- berm width: B_t/D_{n50t} .

Formulae (3) and (4) conform to the above scheme but represent the influence of the roughness ratio which seems of secondary importance compared to the location parameter. Making use of the fact that Δ_t was practically constant in Gerding tests,

formula (3), for instance, can be easily transformed into an equivalent relation involving the location parameter:

$$\frac{H_s}{\Delta_t D_{n50t}} = \left(1.6 + 0.4 \cdot \frac{h_t}{H_s} \cdot \frac{H_s}{\Delta_t D_{n50t}} \right) \cdot N_{odt}^{0.15} \tag{6}$$

This relation however shows an upper limit in the damage $\left(\frac{H_s}{0.4 \cdot h_t} \right)^{1/0.15}$ which was almost reached in some of our experiments.

We have therefore interpreted also our data according to a power regression equation returning toe berm damage as function of the independent variables described above. The relation is fitted on our data and checked with Gerding's results.

The best representation is obtained with different equations fitting for h_t/H_s greater and smaller than 1.35; the separation value is empirical but not far from the condition that berm emerge at extreme run down; in the tested conditions the average run-down according to van der Meer (1992) is $R_{d2\%}/H_s = 0.75$.

All the independent variables were initially included in the regression; the less influent were progressively discarded until the loss of of determination (percentage of explained variance) became greater than 0.01. The final regression are:

- for $h_t/H_s < 1.35$

$$N_{odt}^* = 3 \cdot 10^{-6} \cdot \left(\frac{H_s}{\Delta_t D_{n50t}} \right)^{4.0} \cdot \left(\frac{H_s}{L_{om}} \right)^{-3.1} \cdot \left(\frac{B_t}{D_{n50t}} \right)^{-0.4} \tag{7}$$

on our data the coeff. of determination is 0.75 and r.m.s. log deviation is 0.48; on Gerding data r.m.s. log deviation is 0.85;

- for $1.35 < h_t/H_s$

$$N_{odt}^* = 9 \cdot 10^{-6} \cdot \left(\frac{H_s}{\Delta_t D_{n50t}} \right)^{3.5} \cdot \left(\frac{H_s}{h_t} \right)^{1.9} \cdot \left(\frac{H_s}{L_{om}} \right)^{-3.0} \cdot (tghkh_m)^{4.8} \cdot \left(\frac{B_t}{D_{n50t}} \right)^{-0.3} \tag{8}$$

on our data the coeff. of determination is 0.73 and r.m.s. log deviation 0.71; r.m.s. log deviation is 1.43 on Gerding data. As a comparison the r.m.s. log deviation of N_{odt} in Gerding's relation is 1.50 on our data, and 0.75 on Gerding's data.

Figure 9 gives an impression of data fitting to equation (7).

8. CONCLUSIONS

An effective berm (high, wide and stable) can reduce significantly the damage progress of a steep armour layer, particularly in deep water conditions;

The effect is significantly greater than the error range usually attributed to design formulae, particularly to van der Meer's one, which is quoted as providing estimates with a 6-7% error on H_s . The effect may be as great as 40 % on H_s at start of damage level ($N_{oda} = 1$) and is in several tested cases above 20%.

A berm damage above a critical threshold causes the rapid regressive erosion of a one stone layer (sliding) and the failure of the armour layer for every tested conditions ($tga \geq 1 / 2.5$). The threshold damage value increases with berm width; a graph representing the critical damage is provided.

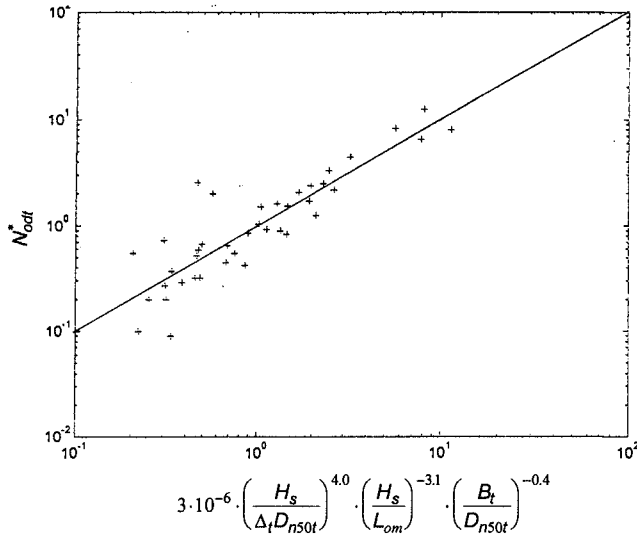


Fig. 9. Comparison of our experimental data with damage relation (7)

The armouring process of an unstable berm by displaced armour units, visually observed, does not produce evident effects in our tests, mainly because the surface armouring layer never was so dense everywhere to induce an effective protection of the underlying berm stones.

The test showed that wave steepness has an evident effect on berm damage. The berm depth influence is secondary if the berm is struck by breakers ($h_t/H_s < 1.35$ in our tests or berm above run-down level in a more general case), whereas it becomes predominant if the berm is deeper.

Secondary effects of berm width and of depth at structure toe are recognizable.

A formula for toe-berm damage is provided representing principal and secondary effects. In all tested conditions Gerding's formula gives however reasonable results. Correction terms in Gerding formula are provided in order to represent all the principal effects.

The design criterion "failure of the main armour (i.e. filter visible) and of the berm (i.e. erosion undermining armour units) for the same wave conditions" provides a balanced design. The criterion used for programming the tests, "failure of the main armour for wave conditions that, according to Gerding formula, cause as many displaced stones in the berm as they are in the top layer", lead to failure types 2 or 3 and can also be considered a balanced criterion, showing only minor unrepresented effects of wave steepness and berm width.

ACKNOWLEDGMENTS

The financial support by the Commission of the European Communities by way of contract MAS2-CT92-0042 "Rubble Mound Breakwater Failure Modes" is gratefully acknowledged.

REFERENCES

- Brebner A. & Donnelly P., 1962. Laboratory study of rubble foundations for vertical breakwater. Engineer Rep No. 23, Queen's University, Kingston, Ontario, Canada.
- British Standard, (1991). Maritime structures. Part 7. Guide to the design and construction of breakwaters. BS 6349: Part 7, 1991.
- Burcharth H. F., (1993). Structural integrity and Hydraulic Stability of Dolos Armour Layers. Dept. Civil Eng., Aalborg Univ., Series paper 9.
- CERC, (1984). Shore Protection Manual Department of the Army, US Army Corps of Engineers, Washington DC 20314.
- Gerding E. (1993). Toe structure stability of rubble mound breakwaters. Master's thesis at Delft University of Technology, August 1993, DH Report H 1874.
- Goda, Y, (1985). Random Seas and Design of Maritime Structures. University of Tokyo Press.
- Ierpi M., (1994). Stabilità di dighe a gettata: indagine sperimentale sulla interazione fra il danno sulla berma e sulla mantellata - criteri di progetto. Univ. di Firenze, Facoltà di Ingegneria, Tesi di laurea a.a. 1993-94.
- Jensen, O. J., (1984). A Monograph on Rubble Mound Breakwaters, DHI, Horsholm, Denmark, 1984.
- Lamberti A. (1994). Preliminary results on Main-Armour Toe-Berm Interaction. RMBFM 3rd Workshop - DH, De Voorst - 15-16 November 1994
- Lamberti A. & Aminti P. (1994). Program of Tests on Main-Armour Toe-Berm Interaction and Preliminary Check of Scale Effects. Proceedings of RMBFM 2nd Workshop, Brixen, Jan 1994.
- Lamberti A. (1996). Toe berm main armour interaction. In University of Bologna final report for Rubble Mound Breakwater Failure Modes CEC research project.
- PIANC - PTC II WG 12 (1992). Analysis of Rubble Mound Breakwaters, Supplement to PIANC Bulletin 78/79, 1992
- Tanimoto K., Yagyu T. & Goda Y, (1982). Irregular wave tests for composite breakwater foundations. Proc. 18th Int. Conf. Coastal Engg., Cape Town, pp. 2144-2163.
- Tomasicchio, G.R., O.H. Andersen & P. Norton (1992). Measurements of individual stone movements on reshaping breakwaters. MAST Coastal Structures Final Workshop, Lisbon, Nov. 1992.
- van der Meer J. W. (1988). Rock Slopes and Gravel Beaches under Wave attack. Doctoral thesis DUT. Also: DH communication no. 396.
- van der Meer J. W. (1992). Conceptual Design of Rubble mound Breakwaters. In Design and Reliability of Coastal Structures, Proceedings of the Short Course 23rd ICCE, Venice.

CHAPTER 121

Stability of artificial roughness elements and run-up reduction

M. Klein Breteler¹ and K. W. Pilarczyk²

Abstract

Smooth concrete slope protection structures are an interesting alternative to rip-rap slopes for areas with a mild wave climate (up to $H_s = 3$ m), especially where the accessibility and the aesthetic appearance of the slope is of great importance. The smooth surface makes the water line accessible to bathers and fishermen and it also enables an integrated design in the scenery.

Unfortunately the smooth surface gives a much higher wave run-up, leading to a higher structure. To tackle this problem one can use a smooth surface with artificial roughness elements.

The present research leads to the conclusion that relatively small roughness elements reduce wave run-up considerable, but don't effect the stability of the cover layer.

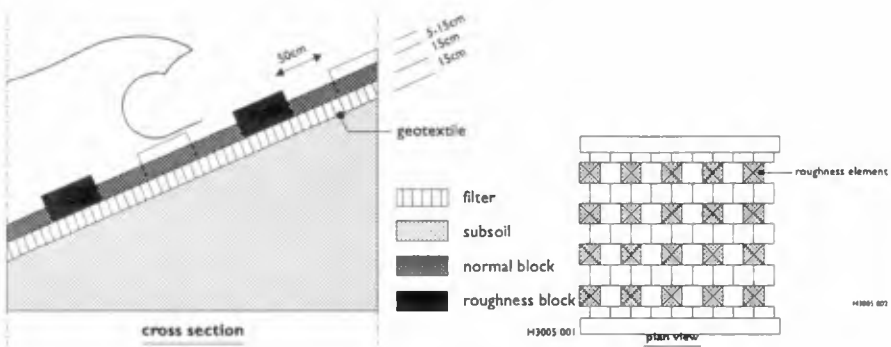


Figure 1, Cross section and plan view of smooth slope with artificial roughness

¹ Project manager at DELFT HYDRAULICS. P.O.Box 177, 2600 MH Delft, The Netherlands, telephone +31 15 2858585, fax +31 15 2858582

² Manager Research and Development department of Rijkswaterstaat. Road and Hydraulic Engineering division, P.O. Box 5044, 2600 GA Delft, The Netherlands

Introduction

Smooth concrete slope protection structures are used throughout the world, especially in areas where the accessibility and the aesthetic appearance of the slope is of great importance. The smooth surface allows recreation and makes the water line accessible to bathers and fishermen but it also enables an integrated design in the scenery.

On the other hand there are important disadvantages that cannot easily be overcome. For example, the smooth surface gives a much higher wave run-up. Consequently, the height of the structure must be much larger than that for an alternative structure with e.g. rip-rap. This leads not only to higher construction costs, but it is also undesirable in areas where the view over the sea should not be hindered by coastal structures.

To illustrate the problem an example has been presented in Figure 2. It shows the necessary height of the structure with slope of 1:3 for a wave attack of 2 m high waves with wave period of 5 s. The crest of the smooth slope with height of 2.85 m will have the same amount of wave overtopping as the rip-rap slope of 1.70 m height.

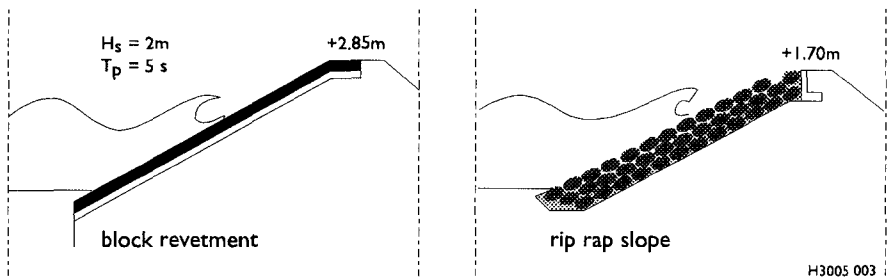


Figure 2, example of crest height for a smooth structure and a rip-rap structure

These problems can be tackled by using a smooth surface with artificial roughness elements. Walking across a slope, on which 5 to 15% of the surface is covered with block-shaped roughness elements with a height of less than 20 cm, is almost as easy as on a smooth slope. It is even easier when the slope is a bit slippery.

As a covered slope decreases the wave run-up, one can expect larger hydraulic forces on the structure. The influence of these extra hydraulic forces on the stability of the cover layer is investigated by way of large-scale model tests.

The tests have also resulted in new wave run-up data, which are compared to earlier small-scale test results.

The research was commissioned by the Rijkswaterstaat of the Dutch Ministry of Transport and Public Works (Road and Hydraulic Engineering division) and was performed by Delft Hydraulics in co-operation with Delft Geotechnics.

Reduction of wave run-up

The influence of artificial roughness elements has first been studied in a small-scale model with wave heights ranging from $H_s = 0.11$ up to 0.25 m. Various types of elements were used, resulting in reduction factors depending on the type of element and the relative spacing and dimensions of the roughness element. These results were described briefly by De Waal and Van Der Meer (1992).

The spacing and dimensions of the roughness elements in the small scale model is shown in Figure 3. All tests have been performed on a slope with steepness of 1:3, which is a common steepness for Dutch dikes.

The amount of roughness elements is expressed in a percentage: the total area of the roughness elements compared to the total area of the slope. In this way the first configuration in Figure 3 has 4% roughness.

schematised cross section

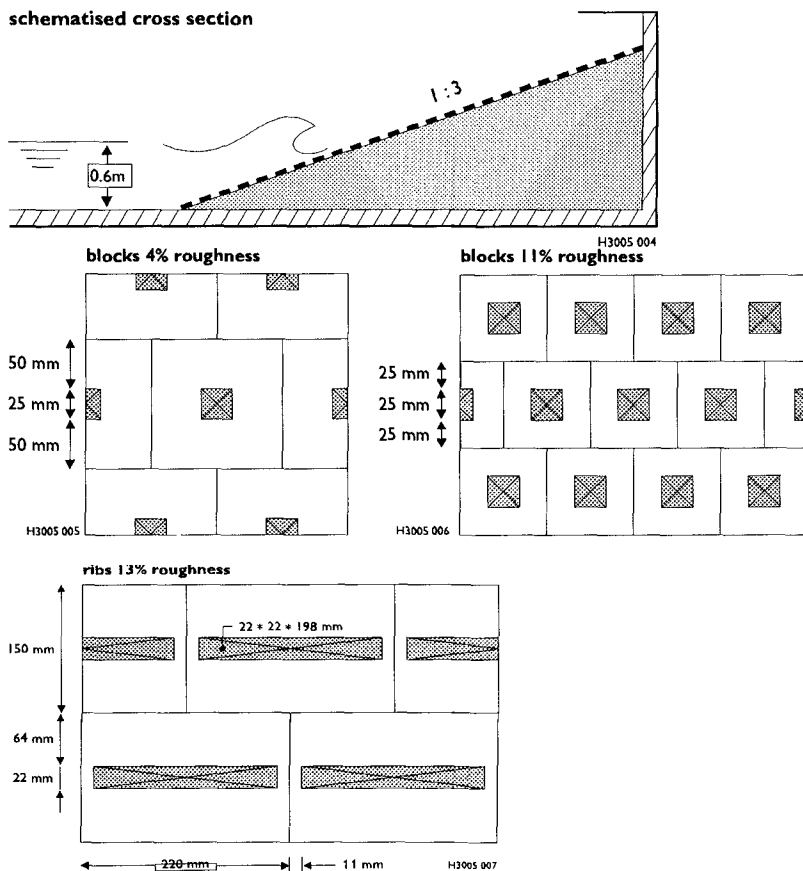


Figure 3, Small scale model of smooth slope with roughness elements.

An important parameter for designing the height of a structure is the wave run-up level which is seldom exceeded. For practical reasons $R_{u2\%}$ has been chosen, which is the run-up level relative to the still water level with exceedence frequency of 2%. The exceedence frequency is defined as the number of run-ups exceeding the $R_{u2\%}$ level divided by the number of incoming waves.

The test results are plotted in a dimensionless form in Figure 4. In the Figure one can see that the tests on a very smooth slope (plastic) and the tests on a smooth concrete slope give the same results. These test results can be summarised with the following formula (De Waal and Van der Meer, 1992):

- if $\xi_{op} \leq 2$:
$$\frac{R_{u2\%}}{H_s} = 1.5 \cdot \xi_{op} \quad (1)$$

- if $\xi_{op} \geq 2$:
$$\frac{R_{u2\%}}{H_s} = 3 \quad (2)$$

with: $R_{u2\%}$ = level of run-up which is exceeded by 2% of the incoming waves, relative to the still water level (m)

H_s = significant wave height of the incoming waves at the toe of the structure (m)

ξ_{op} = breaker parameter (-)
 $= \tan\alpha / \sqrt{(H_s/L_{op})}$

α = slope angle ($^\circ$)

L_{op} = wave length at deep water (m)
 $= gT_p^2 / (2\pi)$

T_p = wave period at the peak of the spectrum (s)

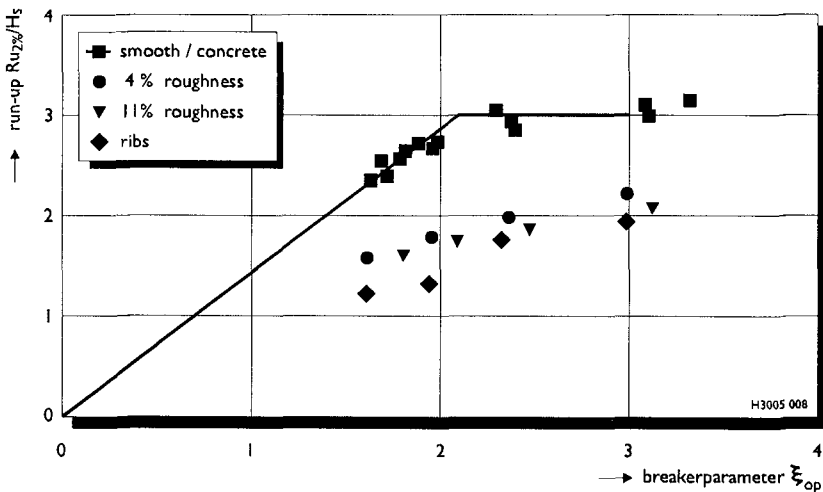


Figure 4, results of small scale run-up tests.

The tests with the roughness elements show a considerable lower wave run-up than the tests with a smooth slope. The following reduction factor is introduced:

$$f = \frac{[R_{u2\%}]_{rough}}{[R_{u2\%}]_{smooth}} \tag{3}$$

with: $[R_{u2\%}]_{rough}$ = wave run-up on a slope with roughness elements (m)
 $[R_{u2\%}]_{smooth}$ = wave run-up on a smooth slope without roughness elements (m)
 f = run-up reduction factor (-)

The smaller the reduction factor, the more the wave run-up is reduced. The range of the reduction factors is as follows:

- blocks with 4% roughness: $f = 0.61$ to 0.73 (average: 0.66)
- blocks with 11% roughness: $f = 0.58$ to 0.68 (average: 0.62)
- ribs with 13% roughness: $f = 0.46$ to 0.65 (average: 0.55)

The smallest reduction factors are measured with the ribs on the slope. The largest factors are found for the slope with 4% roughness, but the differences are only small. It means that with only a small amount of roughness elements, such as only 4% of the surface, one can obtain a considerable run-up reduction.

These results have been checked in the Deltaflume of Delft Hydraulics. In this large scale flume we can make waves up to 2 m high. For the present study a slope with steepness of 1:4 was installed with 4% roughness elements. A roughness element of $0.10 \times 0.10 \text{ m}^2$ and 0.088 m high was placed on each area of $0.5 \times 0.5 \text{ m}^2$, resulting in a 4 times larger model than during the small scale tests. The significant wave height was varied between 0.41 m and 0.82 m at a water depth of 5 m .

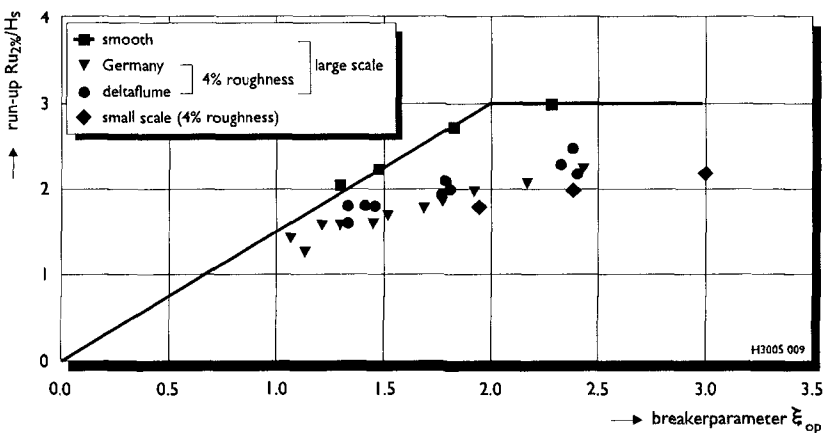


Figure 5, Results of large scale tests in comparison with small scale tests

In Figure 5 the results of the large scale model tests on a 1:4 slope in the Deltaflume are presented together with the small scale tests on the 1:3 slope and results of large scale tests performed in the Large Wave Channel in Germany

(Führböter et al '89). The German tests were performed on a slope with steepness of 1:6 and 4% roughness elements. The size of the roughness elements were $0.16 \times 0.16 \text{ m}^2$ and 0.14 m high. The wave height was varied between 0.75 m and 1.25 m with relatively large wave period (small wave steepness).

From the results with a smooth slope we can conclude that the large scale model also matches the formula (1) and (2) very well.

The results with roughness elements, however, show a difference. The large scale tests in the Deltaflume and from Germany both give an average reduction factor of 0.78, which is considerably higher than the small scale tests (0.66). This difference can not be explained with the difference in the slope angle, because the Deltaflume tests (slope of 1:4) and the German tests (slope 1:6) give the same result.

Probably there is a scale effect that can not be neglected. The influence of the Reynolds number may be of influence. Therefore we should be cautious when using the reduction factors from small scale tests. For now we estimate the run-up reduction for a slope with 4% roughness to be $f = 0.75$ to 0.80.

Stability of block revetments without roughness elements

The smooth surface of a block revetment and its nice interaction between the blocks leaves only one possible damage mechanism under wave attack: the uplift of blocks due to a pressure difference over the cover layer.

This damage mechanism is explained with Figure 6.

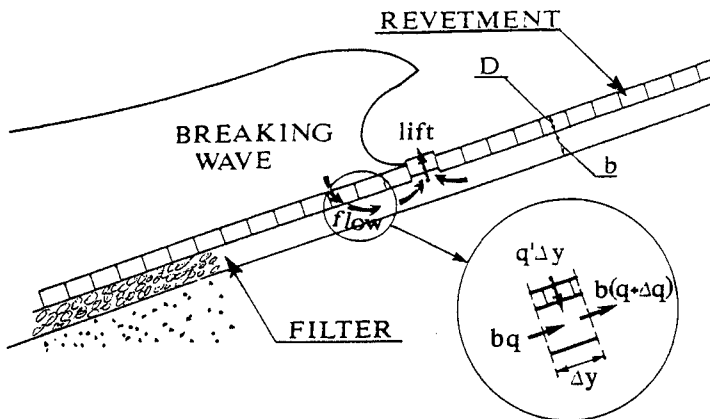


Figure 6, Damage mechanism of block revetment

Figure 6 shows the most important moment during wave attack. The previous wave has resulted in maximum wave run-down and the next wave is going to plunge on the slope. At this moment, which lasts for approximately $0.15T_p$ to $0.25T_p$, there is a region with a large pressure on the slope (under the oncoming wave) and a region with a low pressure on the slope (almost dry region above wave run-down level). The high pressure is transmitted through the filter, which is filled with water to at

least the still water level and probably even higher. The transmitted pressure leads to an upward pressure difference in the region with low pressure on the slope.

The wave impact itself lasts very short (less than a $0.1T_p$) and therefore can not be responsible for lifting a heavy block: The inertia dominates the motion.

The pressure transmission and resulting uplift pressure is influenced by the ratio of permeability's of cover layer and filter layer and the thickness of the cover layer and filter layer. Based on the assumption that each infinitesimal segment of filter cannot store water, a differential equation can be derived (Klein Breteler et al 1991), which can be used to quantify the uplift pressure. The uplift pressure turns out to be influenced only by the leakage length:

$$\frac{\Lambda}{D} = \sqrt{\frac{kb}{k'D}} \quad (4)$$

with: Λ = leakage length (m)
 D = thickness of cover layer (m)
 b = thickness of filter layer (m)
 k = permeability of filter layer (linearized) (m/s)
 k' = permeability of cover layer (linearized) (m/s)

A large leakage length will lead to a large pressure difference over the cover layer and a small stability. A small leakage length can be achieved by applying an open cover layer with large permeability of the cover layer (relative to the filter layer). An open cover layer will easily relief the high pressure in the filter, without resulting in an uplift force on the blocks.

The stability calculation of a block revetment follows several steps:

1. calculation of the decisive pressure on the slope for the given wave conditions.
 2. calculation of the permeability of filter and cover layer and calculation of leakage length.
 3. calculation of pressure difference over the cover layer (load on the blocks)
 4. calculation of weight of the blocks, friction between blocks and other aspects of the strength of the cover layer.
 5. comparing the load and strength leads to a conclusion about the stability.
- All of these aspects are dealt with by Klein Breteler (1995).

Stability of slope protection with artificial roughness elements

The stability of a smooth block revetment under wave attack is hardly affected by the water motion along the surface, because the hydraulic forces have no grip on the surface. This apparent advantage, compared to a rip-rap slope for example, does no longer hold when large artificial roughness elements are applied. If, however, the dimensions of the roughness elements are small compared to the thickness of the cover layer, it is possible to minimise the influence on the stability and still provide a large reduction in wave run-up.

This concept has been tested in the Delta flume of Delft Hydraulics with regular waves ranging from $H_i = 0.3$ m up to 1.0 m. The sand slope of the dike in the flume was protected against wave attack with a geotextile, a granular filter of 0.15 m thick and a cover layer of rectangular blocks of 0.5×0.5 m². The thickness of the cover layer was 0.15 m, but the roughness of the cover layer was created by replacing 25% of the blocks by thicker blocks. Most of these so called 'roughness blocks' were 0.238 m thick, giving a roughness height of 0.088 m.

To study the influence of the roughness height on the stability also blocks without extra thickness were used (no roughness), 0.200 m thick blocks (roughness height of 0.05 m) and 0.300 m thick blocks (roughness height of 0.15 m).

The test set up is given in Figure 7.

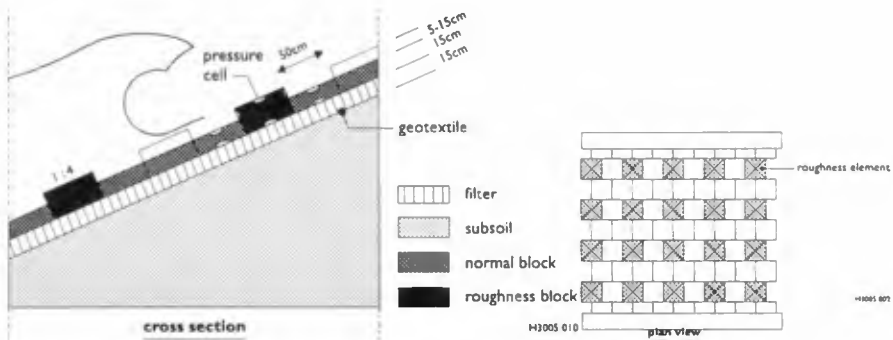


Figure 7, Model set up in Deltaflume for stability tests.

The objective of the study was to compare the uplift pressures on the cover layer with roughness elements and on a smooth cover layer. Regular waves were used as they were sufficient for the experiments.

The stability of a smooth cover layer can be jeopardised by the uplift pressure as is described in the previous chapter. For a rough surface one should anticipate on other forces as well. Führbötter (1986) described serious damage to the bottom protection of the Eider Barrage in Germany. This bottom protection was constructed with blocks with various thicknesses on a filter layer, comparable to the structure presently studied. The structure was seriously damaged after a period with large flow velocities. Supported by scale model tests he found that the stability was influenced by the flow that causes a high pressure against the roughness elements, see Figure 8.

The high flow pressure against the side of a roughness element is transmitted to the filter, contributing to an uplift pressure. At the Eider Barrage the blocks could also move aside by the flow pressure and rotate out of the bottom protection. The latter mechanism is not possible on our slope protection.

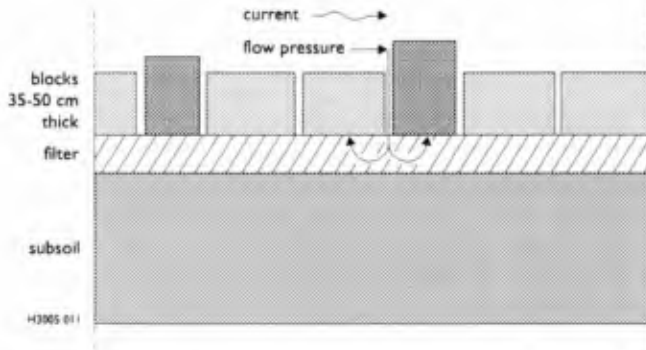


Figure 8, Flow pressure against roughness element is transmitted to filter

The two major causes of forces on the blocks on a slope protection:

1. The large pressure gradient on the slope during maximum wave run-down, just before the wave impact, leads to transmission of pressure through the filter to the blocks in the low pressure region. This results in an uplift force on the blocks near the wave run-down level.
2. The flow over the slope causes a flow pressure against the roughness elements, leading to a horizontal force on the blocks. But it is also transmitted to the filter contributing to an uplift force. The largest forces can be found at locations with largest velocities along the slope: near the level of wave impact.

Since it could not be foreseen which mechanism would give the largest uplift pressure on the slope with roughness elements, the model lay-out anticipated on four different levels of maximum wave forces, relative to the still water level.

At each level several blocks were equipped with pressure gauges and instruments to measure the displacement of blocks. The instrumentation was such that hydraulic loads on the roughness element itself and on adjacent blocks could be measured (see figure 7).

The levels of the roughness elements equipped with pressure gauges and displacement devices ranged from SWL-H_i up to SWL.

In addition, two water velocity meters were installed to measure the velocity parallel along the slope in front of roughness elements. These devices were installed to support the derivation of (theoretically based) formulas to quantify the influence of the roughness elements on the stability.

Typical test results are presented in Figure 9.

The measured uplift pressure in Figure 9 is drawn with the solid line. It should be compared to the weight of the blocks, which is drawn with the dotted line. With increasing height of the roughness elements we see an increasing uplift pressure, but since the weight of the roughness elements is larger as well, the stability does not decrease.

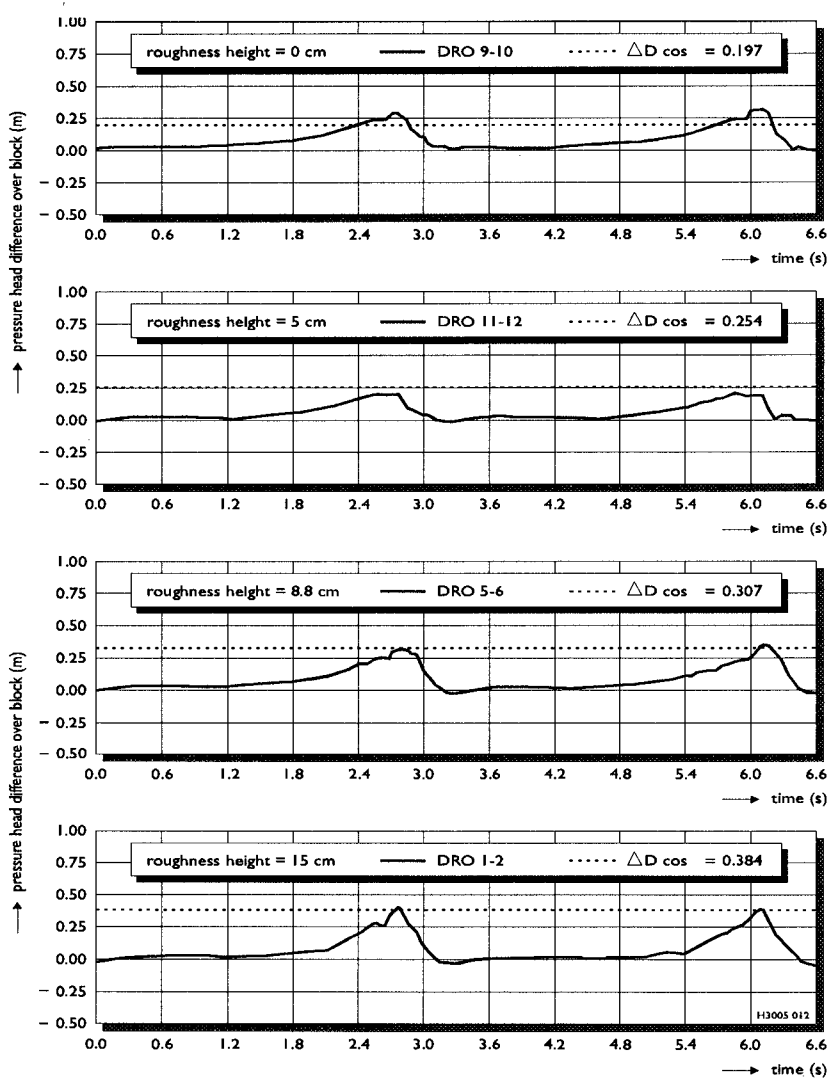


Figure 9, Pressure difference over the cover layer ($H_i = 0.80$ m and $T = 3.3$ s).

Also the uplift pressure over an adjacent block in the same row, in one row lower and in one row higher is measured. The influence of the roughness elements on the uplift of these adjacent blocks was negligible.

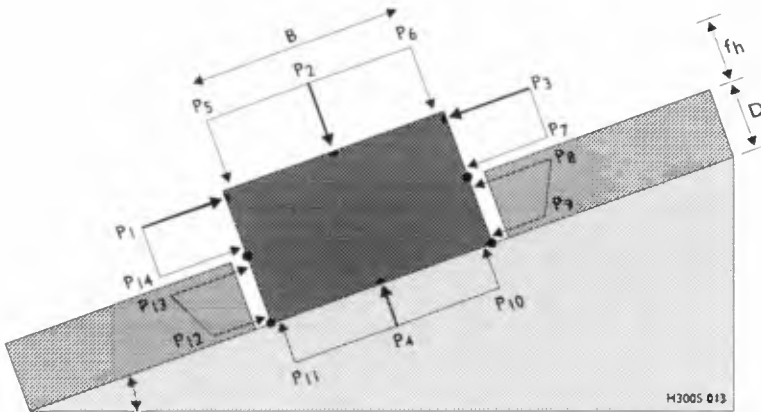


Figure 10, Forces acting on a roughness block.

A theoretical analysis of the relation between the water velocity on the slope, the pressure against the roughness elements and the uplift pressure on the cover layer was performed to see if the results of the measurements are applicable to all kinds of revetment and roughness geometry's. Figure 10 shows the pressures and forces acting on a roughness element. By considering the balance of forces and momentum it was possible to distinguish two damage mechanisms, each relevant for a certain type of roughness elements:

1. Wide blocks (width measured perpendicular to the water line) with relatively small roughness height: $f_h/B \ll 0.5$. The influence of the horizontal forces is small. The uplift pressure is the most important force and the block will slide out of the revetment during instability. Instability will not occur at a lower wave height than for a slope without roughness elements
2. Small blocks (width measured perpendicular to the water line) with relatively high roughness height: $f_h/B \gg 0.5$. The influence of the horizontal forces is large. The uplift pressure and forces along the slope result in a rotating motion if the blocks have open joints (such as at the bottom protection of the Eider Barrage, see Führbötter 1986). Instability may occur at a lower wave height than for a slope without roughness elements.

The exact criteria to distinguish these types have not yet been established. The preliminary advice is to make roughness elements smaller than 1/3 of the width of the blocks:

$$f_h/B < 0.33$$

with: f_h = height of the roughness element (m)
 B = width of the block, measured perpendicular to the water line (m)

In that case the roughness elements will not decrease the stability.

Conclusions

For areas with a mild wave climate (up to $H_s = 3$ m) a smooth concrete slope protection structure is an interesting alternative to rip-rap slopes. The smooth surface makes the water line accessible to bathers and fishermen and it also enables an integrated design in the scenery.

Unfortunately the smooth surface gives a much higher wave run-up, leading to a higher structure. This extra construction height can be kept within acceptable limits if artificial roughness elements on the smooth surface are used.

Small scale tests are performed to find the wave run-up reduction f , defined as a multiplication factor. The smaller the reduction factor, the more the wave run-up is reduced. The range of the reduction factors from small scale tests is as follows:

- blocks with 4% roughness: $f = 0.61$ to 0.73 (average: 0.66)
- blocks with 11% roughness: $f = 0.58$ to 0.68 (average: 0.62)
- ribs with 13% roughness: $f = 0.46$ to 0.65 (average: 0.55)

The first type of structure (4% roughness) is also tested on a large scale, with waves up to 1.2 m high. The large scale tests in the Deltaflume and from Germany both give an average reduction factor of 0.78, which is considerably higher than the small scale tests (0.66).

Probably there is a scale effect that can not be neglected. The influence of the Reynolds number may be of influence. Therefore we should be cautious when using the reduction factors from small scale tests. For now we estimate the run-up reduction for a slope with 4% roughness to be $f = 0.75$ to 0.80 .

The present conclusion for the reduction factor means the following for the example structure given in Figure 2:

- crest height for smooth surface: +2.85 m
- crest height for surface with 4% roughness elements: +2.20 m
- crest height for rip rap structure: +1.70 m

We see that with only 4% roughness the crest height can be reduced considerable and is now not that much higher than the rip rap structure.

From a theoretical analysis of the water motion and loads following two major causes of forces on the blocks on a slope protection has been identified:

1. The large pressure gradient on the slope during maximum wave run-down, just before the wave impact, leads to transmission to transmission of pressure through the filter to the blocks in the low pressure region. This results in an uplift force on the blocks near the wave run-down level.
2. The flow over the slope causes a flow pressure against the roughness elements, leading to a horizontal force on the blocks. But it is also transmitted to the filter contributing to a uplift force. The largest forces can be found at locations with largest velocities along the slope: near the level of wave impact.

The forces on the blocks were measured in the Delta flume of Delft Hydraulics with regular waves ranging from $H_i = 0.3$ m up to 1.0 m. Based on these measurements and on a theoretical analysis of the balance of forces on the blocks it was concluded that stability is not decreased by roughness elements when these are small compared to the width of the blocks (measured perpendicular to the water line): $f_i/B < 0.33$.

References

- J.P. De Waal and J.W. Van Der Meer, 1992.
Wave run-up and overtopping on coastal structures
Proceedings of the twenty-third international conference on Coastal Engineering, Venice, 1992
- Führböter, A., U. Sparboom und H.H. Witte
Großer Wellenkanal Hannover: Versuchsergebnisse über de Wellenauflauf auf glatt und rauhen Deichböschungen mit der Neigung 1:6.
Die Küüste, Heft 50, 1989
- Führböter, A.
Hydrodynamische Belastungen der Sohlsicherung des Eidersperrwerkes
Bauingenieur 61, pp 319-328
Springer Verlag, 1986
- Klein Breteler, M. and A. Bezuijen, 1991.
Simplified design method for block revetments
Coastal Structures and Breakwaters, Proceedings of the conference held in London 1991
- Klein Breteler, M., 1995
Design Manual for pitched slope protection
CUR report 155
Balkema, Rotterdam 1995, ISBN 90 54 10 6069

CHAPTER 122

WAVE INDUCED VELOCITIES AT A RUBBLE MOUND BREAKWATER

Bruno Brunone¹, member ASCE, and Giuseppe R. Tomasicchio¹

Abstract

An experimental study has been carried out concerning horizontal velocities induced by a regular wave acting on a rough permeable steep slope. Time-histories of vertical distributions of the horizontal component of local velocity observed for all the considered wave conditions have been compared with results from 1st and 2nd order wave theories. Further analysis has concerned water surface elevation, depth-averaged velocity and uniformity level of velocity profiles. For both local and global characteristics of velocity field, results from wave theories expected to apply are not in good agreement with experimental data. 1st order theory appears satisfactory for the shorter waves but departs significantly from data as the Ursell number increases.

INTRODUCTION

Despite their importance in design of rubble mound breakwaters, kinematics of waves propagating along a steep slope has received little experimental attention (Tørum and Gudmestad 1990). On the contrary, a large amount of experimental data is available for the case of a wave propagating over a horizontal impermeable smooth bottom (e.g. Ragone 1983) or over a gentle slope (e.g. Iwagaki et al. 1974; Stive 1980). Due to the lack of data, no comparison between theoretical and experimental vertical distributions of velocity on a steep slope is available. In the last decade, interest for systematic experimental investigations has grown up due to the

¹ University of Perugia, Institute of Hydraulics, Località S. Lucia, 06125, Perugia - Italy.
e-mail: brunone@unipg.it; tomas@unipg.it

development of 1-D numerical models simulating the wave induced kinematic field along and inside a rubble mound breakwater (Kobayashi and Wurjanto 1990; van Gent 1993). Comparisons between 1-D model provisions and experimental values have been carried out for the case of regular waves spilling on a rough, impermeable mild (1:35) slope (Cox et al. 1995) while with regard to steep slopes, only not consistent comparisons between computed depth-averaged velocity, U , and experimentally observed values of the mean local velocity, u , are available (e.g. Tørum and van Gent 1992). Moreover, 1-D numerical models have been extended to the formulation of a vertically 2-D shallow-water model (Bradley et al. 1996) and even to the reshaping simulation of a berm breakwater (Norton and Holmes 1992; van Gent 1995). The purpose of this paper is to present and discuss results from an experimental investigation concerning regular waves acting on a rough permeable steep slope. Data from this study are discussed from two complementary points of view. The first of them relates vertical distributions of the horizontal component of local velocity; the second one concentrates on the characteristics of some selected global quantities of the wave induced flow field which are provided by 1-D numerical models. In both cases comparisons are provided with wave theories which are expected to apply.

EXPERIMENTS

Laboratory tests were carried out in a wave flume 35 m long and 0.75 m wide equipped with a piston-type wave maker generating regular waves. The water depth, constant along the flume, was equal to 0.50 m. The breakwater, with a 1:2 uniform slope, was composed of an armour layer $2D'_{n50}$ thick, with nominal diameter $D'_{n50} = 0.027$ m, a filter layer $6D''_{n50}$ thick, with $D''_{n50} = 0.015$ m, and an impermeable core (Fig. 1).

Wave conditions were selected in order to produce no damage or overtopping of the structure and breaking waves of surging type. Table I shows the considered wave conditions at the structure toe with T and H' being the wave period and the wave height (incident + reflected), respectively.

Water surface elevation, η , was contemporary measured by standard conductivity-type gauges at the structure toe and at the section where velocity measurements were taken. Time-histories of the vertical distribution of the horizontal component of the mean local velocity, u , at four sections along the slope ($x = 0.0, 0.3, 0.4$ and 0.5 m) were obtained placing a single micro-propeller at different depths.

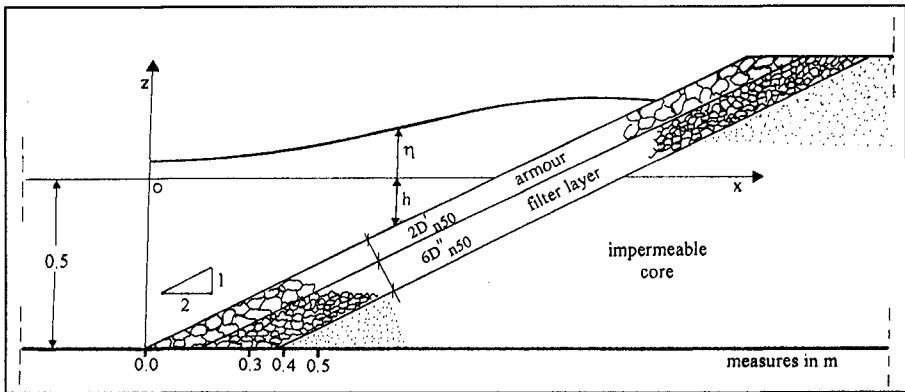


Figure 1 - Geometry of the tested structure and co-ordinate system.

The deepest point for velocity measurement was at 3.5 cm from the surface of the mound. Due to the use of a single micro-propeller, velocity measurements along the vertical were synchronised by superimposing measurements of free surface elevation at the considered section; synchronisation of velocity measurements at different sections was reached by superimposing measurements of η at the structure toe. Velocity signals presented noise which was removed by a Butterworth lowpass digital filter. Finally, according to observations by Tørum and van Gent (1992) and Cox et al. (1994), a phase averaging was made in order to reduce the remaining small irregularities in the velocity time series.

TABLE I. Wave characteristics

wave condition	symbol	T (s)	H' (cm)
1	o	0.80	3.51
2	•	1.50	4.91
3	□	1.50	5.48
4	×	1.70	7.59
5	▲	1.25	3.10

EXPERIMENTAL OBSERVATIONS AND THEORETICAL RESULTS

Local Characteristics of the Velocity Field

Time-histories of the vertical distributions of the horizontal component of local velocity were obtained for all the five wave conditions at the four considered sections. All velocity distributions present values of u with the same sign along the vertical. A time shift can be observed between the extreme values of the free surface elevation η and those of u . Absolute values of u at the passage of the wave through result systematically larger than the corresponding ones at the wave crest. Finally, the non-uniformity of the velocity profile depends on the wave characteristics; in particular, non uniformity increases for decreasing wave period.

Before introducing comparisons between experimental and theoretical velocity distributions, a selection of wave theories to consider was made, even if in a somewhat arbitrary and merely qualitative way, by evaluating the following dimensionless parameters (Le Méhauté 1976): relative water depth, h/gT^2 , and relative wave height, H/gT^2 , where H = wave height, h = water depth, and g = acceleration due to gravity. Ursell number, $U_R = HL^2/h^3$, with L = wave length, related to the ratio of the convective inertia term to the local inertia one, was also considered. Table II reports the values of the three above mentioned dimensionless parameters for the considered experimental conditions.

TABLE II. Wave dimensionless parameters

wave condition no.	1	2	3	4	5	
h/gT^2	$x = 0.0$ m	0.0796	0.0226	0.0226	0.0176	0.0326
	$x = 0.3$ m	0.0557	0.0158	0.0158	0.0123	0.0228
	$x = 0.4$ m	0.0478	0.0136	0.0136	0.0105	0.0195
	$x = 0.5$ m	0.0398	0.0113	0.0113	0.0088	0.0163
H/gT^2	$x = 0.0$ m	0.0056	0.0023	0.0025	0.0026	0.0020
	$x = 0.3$ m	0.0072	0.0023	0.0018	0.0020	0.0032
	$x = 0.4$ m	0.0059	0.0021	0.0015	0.0017	0.0033
	$x = 0.5$ m	0.0057	0.0016	0.0013	0.0013	0.0031
U_R	$x = 0.0$ m	0.2823	4.3470	4.8407	8.5617	1.4858
	$x = 0.3$ m	1.0551	9.4812	7.2463	13.6100	6.1511
	$x = 0.4$ m	1.3674	11.294	8.3772	15.3138	8.5275
	$x = 0.5$ m	2.2798	13.0164	10.3179	17.1729	11.5205

The range of experimental conditions include relative depths, h/gT^2 , from 0.0398 to 0.0796 for wave condition no. 1 and from 0.0088 to 0.0326 for wave

conditions no. 2 to 5; relative wave height, H/gT^2 , from 0.0056 to 0.0072 for wave condition no. 1 and from 0.0013 to 0.0033 for wave conditions no. 2 to 5; Ursell number, U_R , from 0.2823 to 2.2798 for wave condition no. 1 and from 1.4858 to 17.1729 for wave conditions no. 2 to 5. Thus, values of the three dimensionless parameters for wave condition no. 1 are significantly different from those attained in conditions no. 2 to 5. Specifically, wave motion no. 1 appears to be characterised by quasi-deep water conditions and by very small values of the Ursell number with respect to the other cases. On the basis of Fig. 2 (Le Méhauté 1976), for wave condition no.1, 2nd order and only marginally 3rd order theories apply; for the case of wave conditions no. 2 to 5, 2nd order theory should be taken into account. As a term of reference, also 1st order theory was considered in calculations.

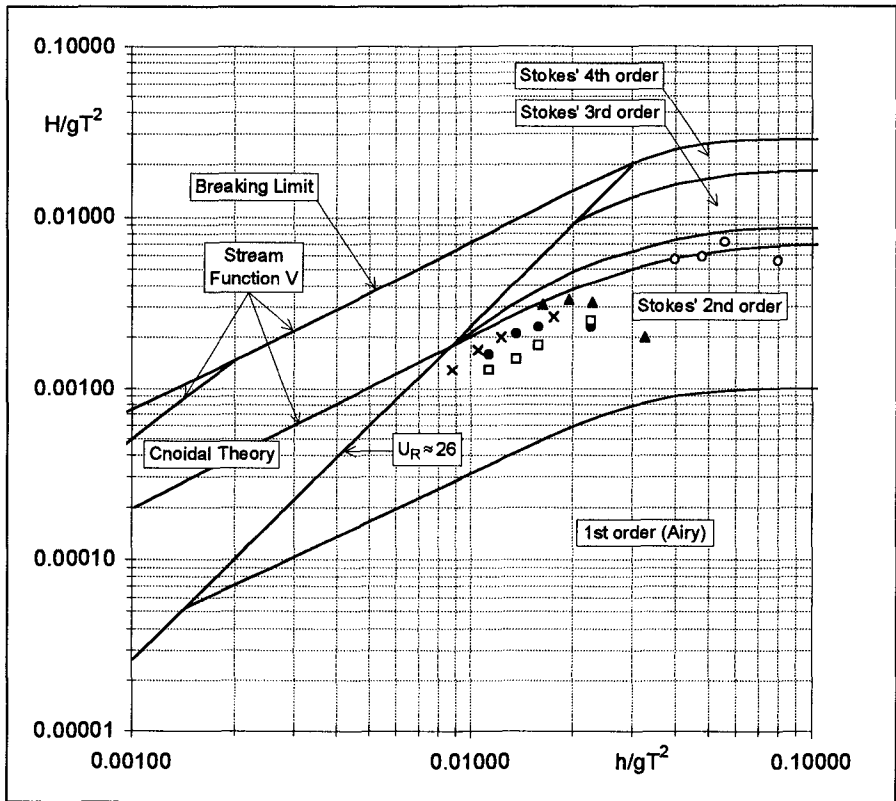


Figure 2 - Regions of validity for various wave theories and experimental conditions from the present study (modified from Le Méhauté 1976).

Comparisons have been carried out between observed and calculated velocity

distributions at some selected times counted in terms of $t^* = t/T$, with $t^* = 0$ corresponding to $\eta = \eta_{\max}$ at the considered section. Figs. 3a and 3b refer to section $x = 0.3$ m and to wave conditions no. 2 to 5; in plots, z is the vertical co-ordinate, positive upward with $z = 0$ at the armour surface. Fig. 3a shows the comparison between experimental and 2nd order theory velocity profiles, while in Fig. 3b 1st order theory results are considered. It is noted from these figures that nor the 2nd nor the 1st order theory is valid and that only small differences between them arise. Analogous results (not shown) are found at the other sections for wave conditions no. 2 to 5. On the contrary, with regard to wave condition no. 1, values from the 2nd and 1st order theories are practically indistinguishable and therefore in Fig. 4 only results from the 1st order theory are reported. A rather good agreement is found at section $x = 0.0$ m; further landward it gets slightly worse but it can be noticed that the 1st order theory well approximates the velocity profiles of wave condition no. 1.

As a preliminary result, it can be stated that the 1st order theory well simulates experimental velocity profiles characterised by a noticeable disuniformity and corresponding to a short period wave. Moreover, in accordance with the results of Le Méhauté et al. (1968) for a horizontal bottom, also for the case of a steep slope, the selection of the appropriate wave theory to describe the velocity field on the basis of relative water depth, h/gT^2 , and relative wave height, H/gT^2 , appears to be not completely reliable.

With regard to the wave kinematics field on a steep slope, more precise indications on the wave theory selection can be obtained by evaluating the influence of different terms like local inertia, convective inertia, wave reflection, energy dissipation due to surface roughness and flow in the mound. For wave condition no. 1, where U_R ranges from 0.2823 to 2.2798, accordance between the 1st order theory and the experimental velocity profiles suggests the predominance of the local inertia term with respect to the others. This is probably due to the small wave period which determines a so rapid change in the kinematic characteristics in one section that the effect of different conditions in the adjacent sections can be considered negligible. For the case of wave conditions no. 2 to 5, where U_R ranges from 1.4858 to 17.1729, other terms become more important than the local inertia one and there is no agreement with 1st and 2nd order theories. In other words, when in a given section the wave field characteristics vary very rapidly due to the small wave period, there is a minor influence of the contemporary changes in the adjacent sections.

The not large number of the examined experimental conditions and the lack of velocity measurements at the surface and close to the bottom give no possibility to

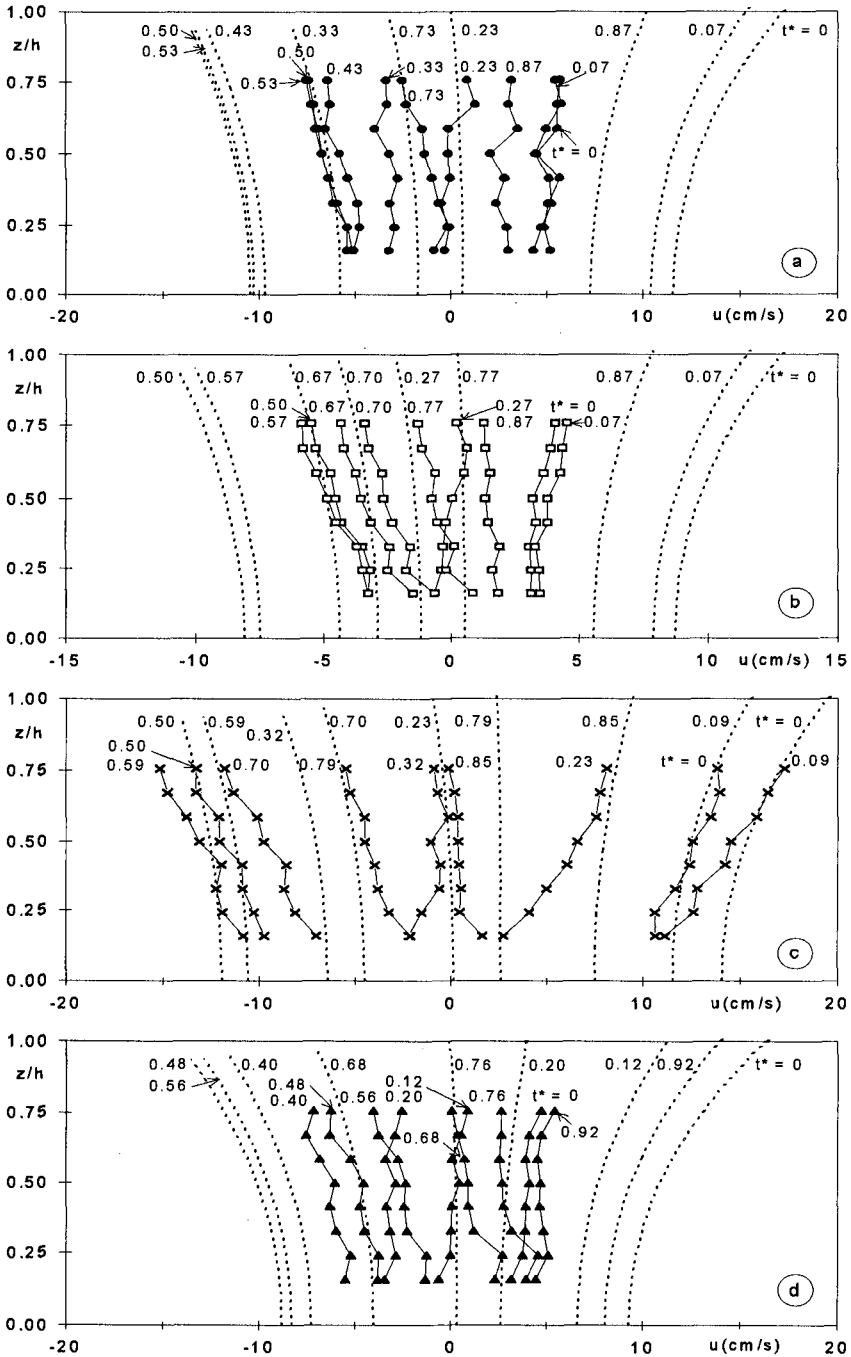


Figure 3a - Vertical distributions of the horizontal component of mean local velocity at section $x = 0.3$ m for wave condition: a) no. 2, b) no. 3, c) no. 4, d) no. 5 (dotted lines: 2nd order theory).

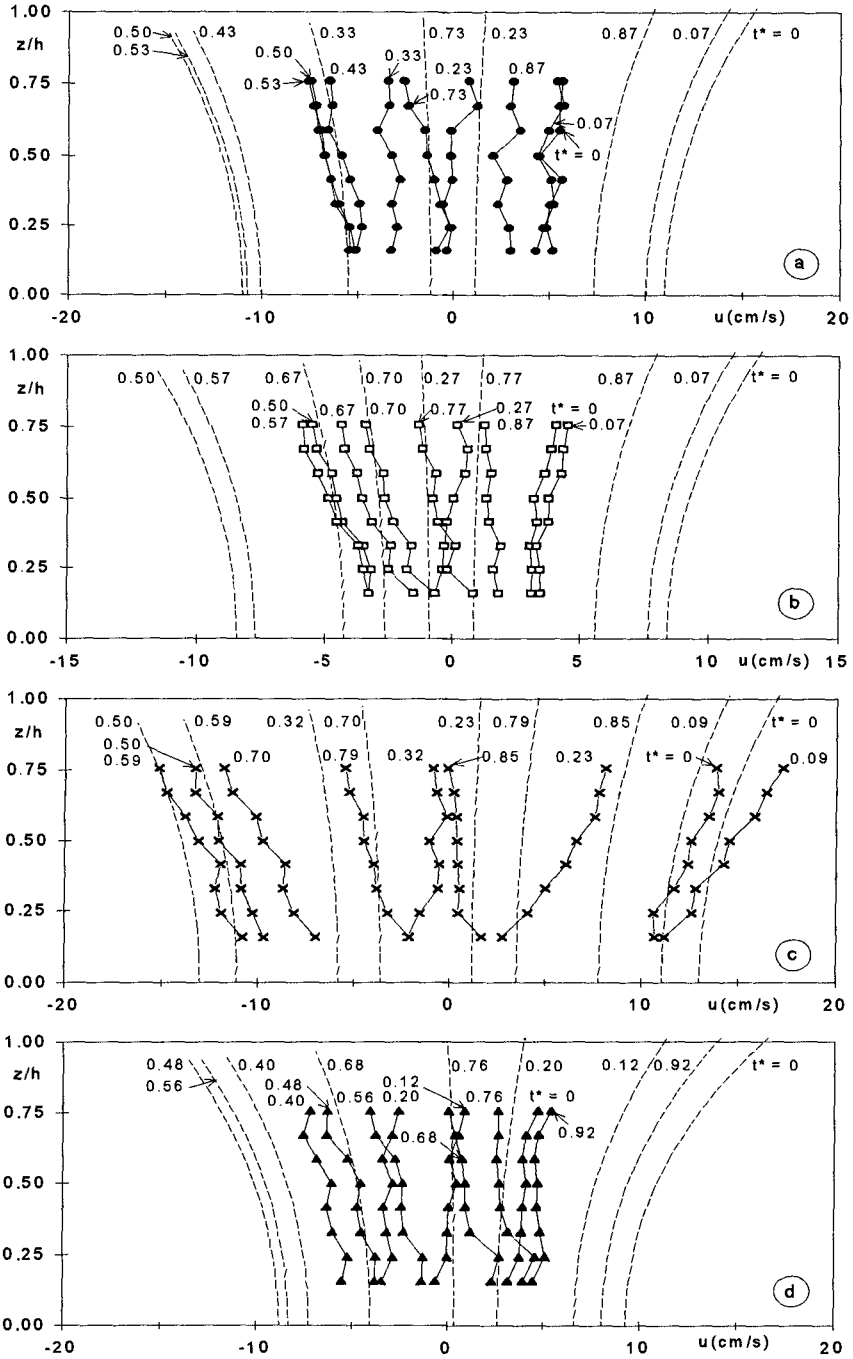


Figure 3b - Vertical distributions of the horizontal component of mean local velocity at section $x = 0.3$ m for wave condition: a) no. 2, b) no. 3, c) no. 4, d) no. 5 (broken lines: 1st order theory).

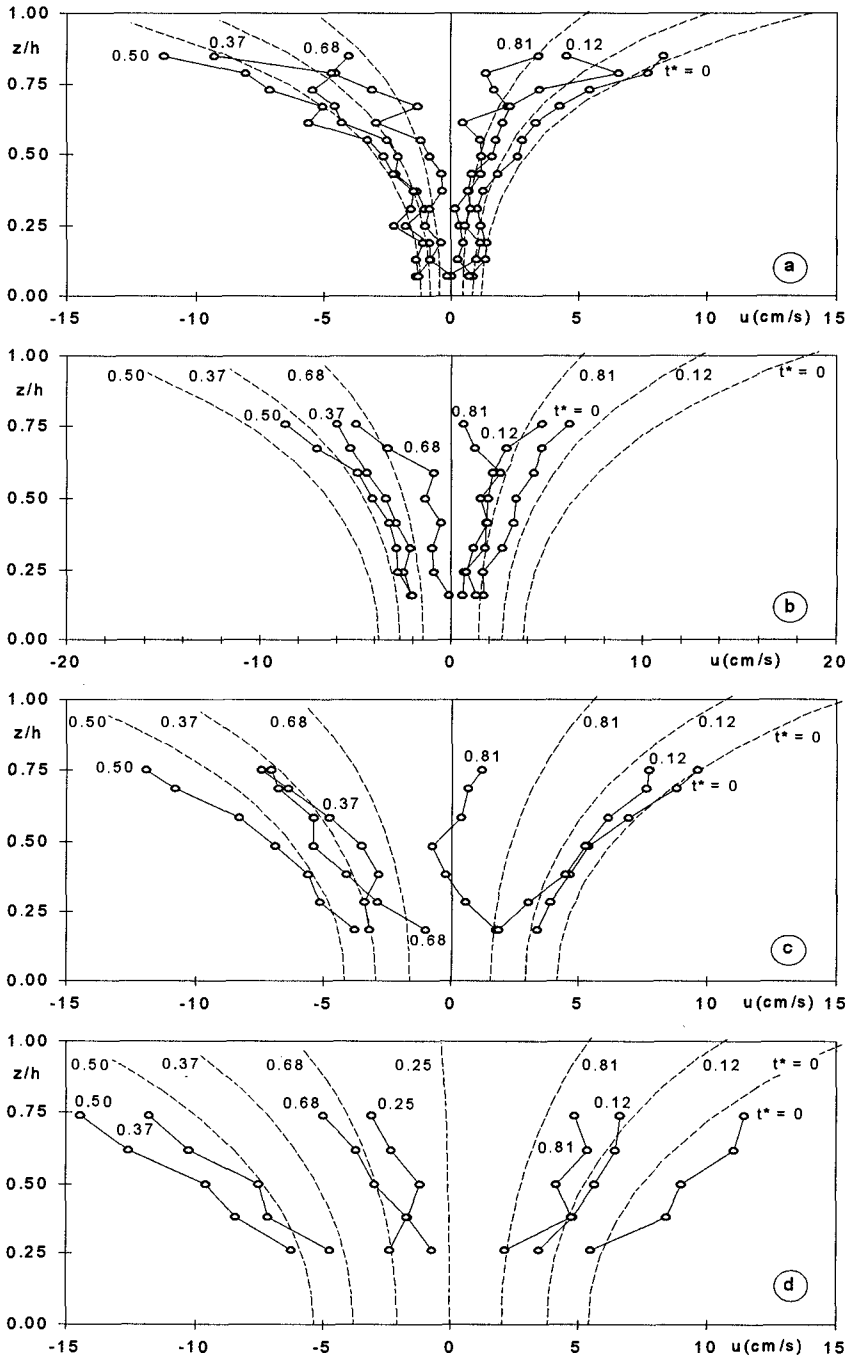


Figure 4 - Vertical distributions of the horizontal component of mean local velocity for wave condition no. 1 at section: a) $x = 0.0$ m, b) $x = 0.3$ m, c) $x = 0.4$ m, d) $x = 0.5$ m (broken lines: 1st order theory).

discuss further in terms of velocity profiles and makes not convenient to consider higher-order wave theories.

Global Characteristics of the Flow Field

In the present section the discussion refers to global quantities of the flow field, provided by 1-D numerical models, such as water surface elevation, η , and depth-averaged velocity, U , defined as:

$$U = \frac{\sum_{i=1}^{n'} u_i \Delta z_i}{h + \eta} \quad (1)$$

where $n' = n + 2$, with n being the number of the velocity measurement points along the vertical at the considered section. The extension of the experimental velocity profiles to the bottom and to the surface has been obtained by extrapolation. Because the momentum flux correction coefficient, β , is not defined when U is close to zero, the variance, σ^2 (Brunone and Tomasicchio 1996) defined as:

$$\sigma^2 = \frac{\sum_{i=1}^{n'} (u_i - U)^2}{n' - 1} \quad (2)$$

must be introduced. It allows to describe the uniformity level of velocity profiles and to evaluate 1-D approximations during the whole wave period.

With regard to η , for all the considered cases, in agreement with Le Méhauté et al. (1968), also when a steep slope is considered, differences between experiments and theory are not as great as that for local velocities since the most significant feature, the wave height, is imposed by experiments. For wave condition no. 1, Fig. 5 presents the experimental and calculated (1st order theory) time-histories of η , U and σ^2 through the wave period at the four different sections. Small differences and a moderate phase shift are observed between the experimental and calculated values of U . Maximum and minimum values of U happen at the same time of the corresponding extreme values of η . In agreement with the experimental observations (Brunone and Tomasicchio 1996), the calculated time-history of variance σ^2 presents a bimodality with two relative maximum (minimum) values. At section $x = 0.0$ m, calculated variance of velocity profiles simulates rather well the experimental data; further landward, differences increase and approximation is not satisfactory even if the

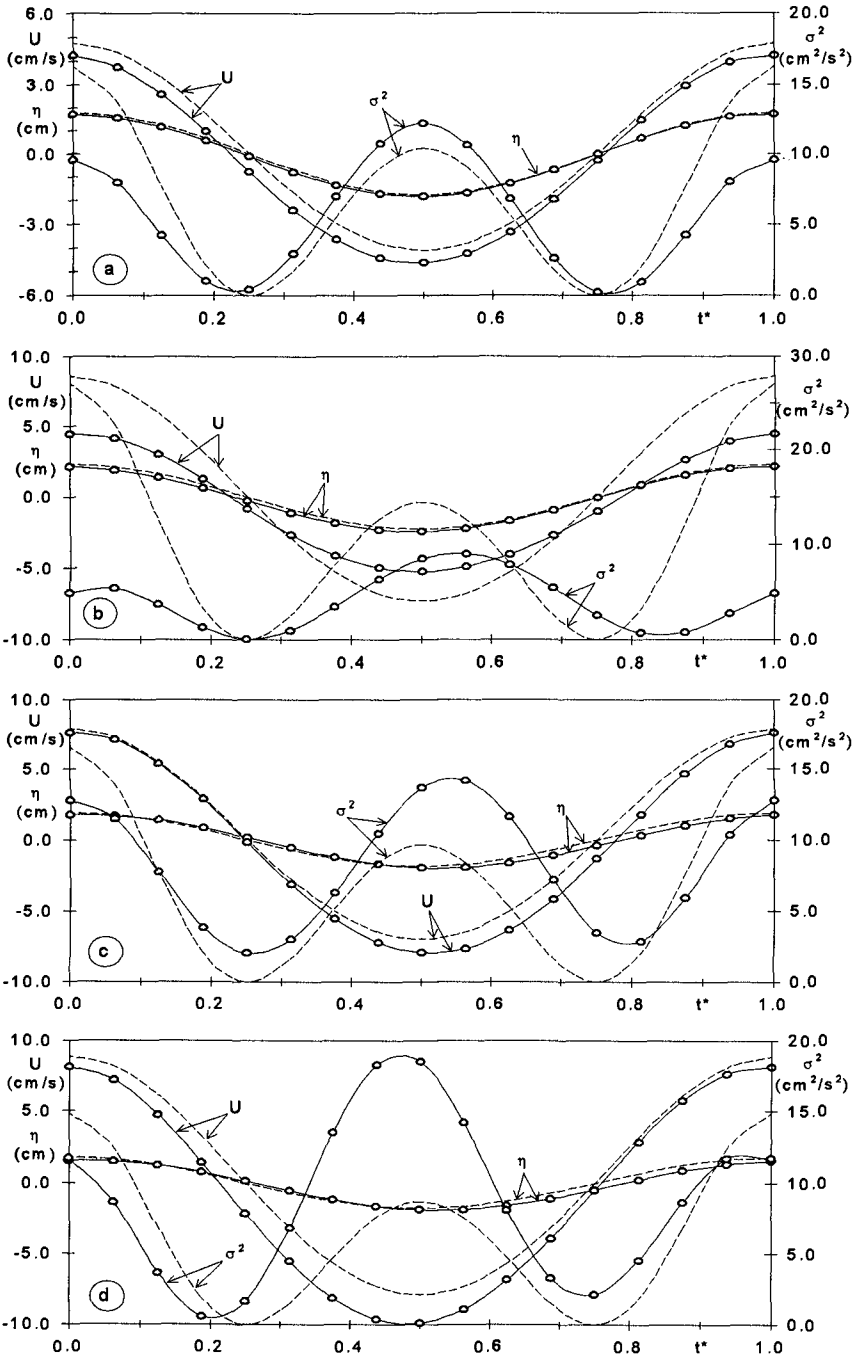


Figure 5 - Time-history of water surface elevation, depth-averaged velocity and variance of velocity profiles for wave condition no. 1 at section: a) $x = 0.0$ m, b) $x = 0.3$ m, c) $x = 0.4$ m, d) $x = 0.5$ m (broken lines: 1st order theory).

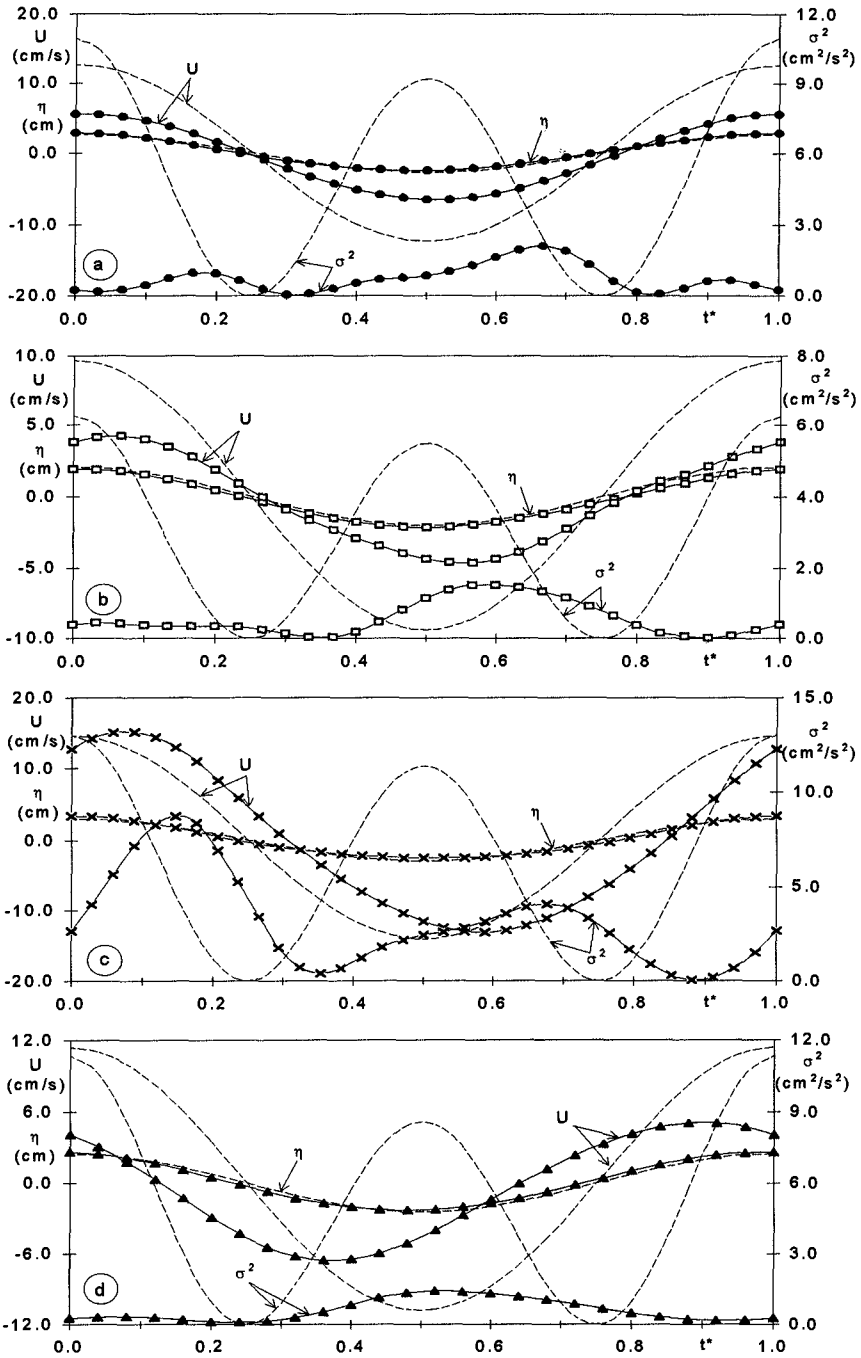


Figure 6 - Time-history of water surface elevation, depth-averaged velocity and variance of velocity profiles at section $x = 0.3$ m for wave condition: a) no. 2, b) no. 3, c) no. 4, d) no. 5 (broken lines: 1st order theory).

behaviour of the experimental values of the variance is certainly captured. Fig. 6 presents time behaviour of η , U and σ^2 at section $x = 0.3$ m for wave conditions no. 2 to 5. Still the experimental and calculated values of η are almost identical. This is not the case for the values of the depth-averaged velocity, for which differences are large and only a certain similarity in the shape can be found. Calculated time-histories of the variance present values much larger than the experimental ones and a very different shape.

CONCLUSIONS

Water surface elevation and horizontal velocity profiles at some sections along a rough permeable steep slope were observed for different wave conditions. Two different groups of wave conditions were identified by evaluating relative water depth, relative wave height and Ursell number. For wave condition no.1, 2nd order and only marginally 3rd order theories are expected to apply; for the case of wave conditions no. 2 to 5, 2nd order theory should be considered. As a term of reference, also 1st order theory was taken into account in calculations. Accordance between experimental and calculated values of water surface elevation was found for all the cases. Only for wave condition no. 1, where U_R ranges from 0.2823 to 2.2798, experimental and 2nd order theory velocity profiles show a satisfactory agreement and accordance is noticed also when 1st order theory is considered. Analogous considerations are valid for global characteristics of flow field such as depth-averaged velocity U and variance of velocity profiles σ^2 . For the case of a rough permeable steep slope, as a preliminary result of the study, it can be stated that wave kinematics is not correctly described by wave theories which are expected to apply considering only the values of relative water depth and relative wave height. Phenomena like wave reflection, energy dissipation due to slope roughness and flow in the permeable layer should be necessarily taken into account in description of wave induced kinematics on a steep slope.

Acknowledgement

The writers thank Mr. M. Barigelli for the very careful lay-out of the present paper.

References

- Bradley, D.J., Kobayashi, N., and Cox, D.T. (1996). "Formulation and validation of vertically 2-D shallow water wave model." *Proc. 25th Int. Conf. on Coast. Eng.*, Orlando, USA.

- Brunone, B., and Tomasicchio, G.R. (1995). Contribute to the Discussion on "Impact of coefficients in momentum equation on selection of inertial models" by Xia, R., *J. of Hydraulic Research*, IAHR, 720-722.
- Brunone, B., and Tomasicchio, G.R. (1996). "On wave kinematics at steep slopes: a second order model." Submitted to *J. Wtrwy., Port, Coast., and Oc. Engrg.*, ASCE.
- Cox, D.T., Kobayashi, N., and Okayasu, A. (1994). "Vertical variations of fluid velocities and shear stress in surf zones." *Proc. 24th Int. Conf. on Coast. Eng.*, Kobe, Japan, 98-112.
- Cox, D.T., Kobayashi, N., and Okayasu, A. (1995). "Experimental and numerical modeling of surf zone hydrodynamics." *Res. Rept. No. CACR-95-07*, Ctr. for Applied Coast. Res., University of Delaware, Newark, DE.
- Le Méhauté, B., Divoky, D., and Lin, A. (1968). "Shallow water waves: a comparison of theories and experiments." *Proc. 11th Int. Conf. on Coastal Eng.*, London, England, 86-107.
- Le Méhauté, B. (1976). "An introduction to hydrodynamics and water waves." Springer-Verlag.
- Kobayashi, N., and Wurjanto, A. (1990). "Numerical model for waves on rough permeable slopes." *J. Coast. Research*, SI(7), 149-166.
- Norton, P., and Holmes, P. (1992). "Reshaping simulation model for dynamically stable breakwaters." *Proc. 23rd Int. Conf. on Coast. Eng.*, Venice, Italy, 1448-1460.
- Ragone, A. (1983). "Experimental investigation on wave induced particle kinematics through laser Doppler anemometer." *Proc. of the Symposium on the use of laser Doppler anemometry in hydraulic experimentation*, Rome, Italy, 95-109 (in Italian).
- Stive, M.J.F. (1980). "Velocity field and pressure of spilling breakers." *Proc. 17th Int. Conf. on Coastal Eng.*, Sidney, Australia, 547-566.
- Tørum, A., and Gudmestad, O.T. (1990). "Report from the NATO ARW on water wave kinematics, May 1989." *Proc. 22nd Int. Conf. on Coast. Eng.*, Delft, The Netherlands, 1 (71), 934-958.
- Tørum, A., and van Gent, M.R.A. (1992). "Water particle velocities on a berm breakwater." *Proc. 23rd Int. Conf. on Coast. Eng.*, Venice, Italy, 1651-1665.
- van Gent, M.R.A. (1995). "Wave interaction with berm breakwaters." *J. Wtrwy., Port, Coast., and Oc. Engrg.*, ASCE, 121 (5), 229-238.

CHAPTER 123

Natural Periods of Armor Stones

Fred E. Camfield¹, Fellow, ASCE

Abstract

Results of a laboratory investigation were analyzed to determine the response of quarystone armor units to particular wave periods. Results indicate that individual stones appear to respond to particular wave periods depending on the stone's mass, shape, and placement in the structure's armor layer. Results also indicate that the wave period critical for design may not be the longest wave period in the incident waves, and investigations must be carefully conducted to determine the critical design conditions.

Introduction

Variables affecting stability of armor stones include wave height, wave period, water depth at the structure, foreslope of the shoreline, structure slope, structure porosity, and armor stone variables. Armor stone variables include stone density, mass, stone shape, orientation of the stone in the structure, contact with adjoining stones, and location of the stone in the armor layer with respect to the still water line (SWL).

Structures, in general, have natural frequencies and can be excited into motion by impulses applied at that frequency. Likewise, individual armor units on a coastal structure will have a natural frequency dependent on the mass, shape, and orientation of the armor unit in the structure. For concrete armor units, with a fixed mass and shape and uniform interlocking, this should be a

¹Research Hydraulic Engineer, Coastal and Hydraulics Laboratory, U.S. Army Engineer Waterways Experiment Station, Vicksburg, MS 39180-6199

single frequency. For armor stones, with variations in mass, shape, and orientation, there would be a range of natural frequencies due to the variations in the units.

Results of laboratory investigations were analyzed to compare motion of armor stones with various incident wave periods for different cases where the foreslope, water depth, structure slope, structure porosity, and stone density were held constant. Both monochromatic and spectral waves were used for the investigations. Separate investigations were carried out for three revetment slopes and one breakwater cross-section.

Laboratory Investigations

Investigations were carried out as part of a research effort to study the stability of selectively placed armor stones. Field practice is to place quarystone armor units to provide the best fit obtainable for particular site conditions. The selective placement of quarystones, i.e., the selection and placement of armor stones one at a time to achieve the best fit (often call Standard Placement), is known to provide better stability. The tighter fit of armor stones using this placement method may also allow the use of a single layer of armor stones which will result in significant construction cost savings when compared to the traditional use of two armor layers. Guidelines for selective placement specifications are given by the Coastal Engineering Research Center (1995).

Laboratory tests were conducted at the U.S. Army Engineer Waterways Experiment Station's Coastal and Hydraulics Laboratory in a two-foot wide wave flume. The flume is equipped with a programmable wave generator capable of producing both spectral and monochromatic waves. A long, two percent (1:50) foreslope was constructed in front of the model structures to produce breaking waves on the structure.

Tests were for model revetments having slopes of 1:1.5, 1:2, and 1:3, and for a breakwater cross-section with a 1:1.5 structure slope. The model revetments were constructed to be "impermeable" with a dense sand core overlaid with filter cloth. Layers of smaller bedding stone were used under the model armor stone. This bedding stone conformed to the present guidance in the Shore Protection Manual (1984), i.e., w50/10 for a first underlayer and w50/200 for a second underlayer. The tests on the breakwater cross section used the second underlayer stone as the structure core.

Tests were conducted for single layers of armor stones. Revetment tests were conducted using model armor

stones with a median weight of 0.47 lbs, and a range from 0.31 - 0.70 lbs (0.66 w50 - 1.49 w50). Breakwater tests were conducted using stones with a median weight of 0.43 lbs, with a range from 0.33 - 0.66 lbs (0.77 w50 - 1.53 w50).

Tests were conducted with waves breaking on the model structures. A total of 11 model revetments and five model breakwaters were tested. The water depth was varied to produce breaking waves of different heights. Tests were conducted using both monochromatic waves and spectral waves with periods (peak spectral periods) ranging from 1.3 to 3.0 seconds in the model. Waves were analyzed using a three-gage array (Hughes, 1993). Visual observations were made of armor stone movement for the various test conditions.

Repetitive tests were conducted to determine the stability of the armor stones. Initial tests were conducted using spectral waves with varying peak periods until rocking motion was detected in the armor stones. These tests were followed by tests using monochromatic waves with various periods that were embedded in the spectral waves. Tests continued until the structure failed, i.e., several stones rolled out of the armor layer, after which the revetment structure was reconstructed and retested.

Observations of Armor stone Movement

Observations indicated that different wave periods often affected different armor stones. Stone movement generally occurred at or somewhat above the still water line. With other variables, including water depth, held constant, breaking waves were generated with variations in wave period. If waves having a particular period caused motion, i.e., rocking of an armor stone, waves were then generated at periods slightly higher and/or lower than the initial period. It was found that moderate changes in wave period could cause changes in which stones exhibited motion, i.e., a stone which appeared stable at one wave period would be set in motion by a slightly different wave period, while a stone that initially had exhibited motion would become stable when the wave period changed. Examples of observations for three test set-ups are shown in Table 1. For each set-up shown, the only variables were the wave period and wave height, all other parameters being held constant.

Placement of the individual stones played a role in stone movement but did not appear to be the controlling factor. Stones that appeared to be less well placed (fewer points of contact) often remained stable while

stones with seemingly better placement moved when subjected to particular wave periods.

TABLE 1. Stone Movement vs. Wave Period			
Test	T (s)	H _{1/3} (cm)	Comments
13 Sep 95 Run No. 13	1.5	21.3	Breaking Waves, movement in stones above SWL
13 Sep 95 Run No. 14	1.7	21.3	Breaking waves, movement of different stone above SWL
13 Sep 95 Run No. 15	2.0	21.6	Breaking waves, movement of a stone in a different location
29 Jan 96 Run No. 5	2.0	19.5	Plunging breakers, Movement in stones above SWL
29 Jan 96 Run No. 10	2.5	22.3	Breaking waves, movement of different stone above SWL
14 Mar 96 Run No. 2	1.5	14.3	Surging breakers, movement in one stone near SWL
14 Mar 96 Run No. 3	1.7	18.3	Breaking waves, movement in same stone plus one additional stone
14 Mar 96 Run No. 12	2.0	19.0	Breaking waves, movement in second stone, other not moving
14 Mar 96 Run No. 18	2.5	19.2	Surging breakers, stone near SWL (not previously moving) came out

Consideration needs to be given to the different equations used for armor stone stability. The Hudson equation (Shore Protection Manual, 1984) does not include wave period, and bases stability on stone movement at whatever period may cause motion. This approach would appear to be correct if testing is conducted at a full range of wave periods. The stability equation proposed by van der Meer (1987, 1988) incorporates wave period which could be incorrect as it assumes a significant effect at all wave periods and lower stability at longer wave periods. The present tests showed that shorter wave periods often caused motion in stones and structural failure while longer wave periods, at similar wave heights, did not cause instability. Tests by others (Mansard, et al., 1996) also show that the longest wave period may not be the critical period for design. Previous tests by

McCartney and Ahrens (1975) for a concrete revetment unit also showed lower stability at a shorter wave period.

Investigations comparing wave spectra with monochromatic waves showed that wave spectra sometimes caused movement in armor stones while monochromatic waves having a period equal to the peak spectral period did not cause stone movement. This has also been observed by Kamphuis (1996). As noted above, minor variations in wave period can cause major changes in the response of the armor stones. As a wave spectrum contains waves at many periods, it is possible that an armor stone may respond to a period other than the peak spectral period. As an example, one test set-up for a breakwater cross-section (8 Jul 96) exhibited stronger motion of armor stones when subjected to a wave spectrum with a peak spectral period of 2.0 seconds than when the test section was subjected to 2.0 second monochromatic waves, even though the monochromatic waves had a higher wave height. Lowering the wave period of the monochromatic waves to 1.8 seconds produced stronger motion and one stone was displaced from the structure. It should be noted that comparisons between spectral and monochromatic waves were not consistent. In some cases wave spectra did not cause stone motion and monochromatic waves caused motion, and in other cases both the wave spectra and the monochromatic waves caused movement of the armor stones.

Conclusions

While this paper presents a concept for consideration, additional testing is needed to more completely investigate the natural periods of armor stone. The scalability of natural periods has not been established, and tests at different scales are needed. Finally, a practical method of applying the knowledge gained from this research to field use must be determined.

Acknowledgments

A field office working group was formed to provide input to the Waterways Experiment Station on field practice and experience in the placement of quarystone armor units on Corps structures. Members of this working group who participated in meetings at the Waterways Experiment Station were Messrs. Douglas Pirie, Bradd Schwichtenberg, Thomas J. Bender, Jeff Wiggan, George Young, and Jack McKellar. Messrs. Raymond Reed and John Williams, civil engineering technicians, Mr. David Daily, electronics technician, Mr. Bryan Johnston, contract student, and Ms. Dynisha Hayes, science and engineering apprentice, assisted in the testing. This paper was prepared under the Coastal Structures Evaluation and

Design Research Program of the U.S. Army Corps of Engineers Civil Works Research Program at the U.S. Army Engineer Waterways Experiment Station, Coastal and Hydraulics Laboratory. A draft of the material presented in this paper was technically reviewed by Messrs. C. Eugene Chatham, Jr., D. D. Davidson, and Donald L. Ward. Permission of the Chief of Engineers to publish this paper is appreciated.

References

Coastal Engineering Research Center. (1995). Specification Guidelines for the Placement of Quarystone Armor Units - Lessons Learned, *Coastal Engineering Technical Note (CETN) III-59*, U.S. Army Engineer Waterways Experiment Station, Vicksburg, MS.

Hughes, S. A., (1993). Laboratory Wave Reflection Analysis Using Co-Located Gages, *Coastal Engineering*, 20(3), 223-248.

Kamphuis, J. W., (1996). Depth-Limited Design Wave, *Proceedings, 22nd International Conference on Coastal Engineering*, ASCE.

Mansard, E. P. D., Davies, M. H., and Caron, O., (1996). Model Study of Reservoir Riprap Stability, *Proceedings, 22nd International Conference on Coastal Engineering*, ASCE.

McCartney, B. L., and Ahrens, J. P., (1975). Stability of Gobi Block Revetment to Wave Attack, *CERC TM-55*, U.S. Army Engineer Waterways Experiment Station, Vicksburg, MS.

Shore Protection Manual, (1984). 4th Ed., 2 vols., U.S. Army Engineer Waterways Experiment Station, Coastal Engineering Research Center, U.S. Government Printing Office, Washington, D.C.

Van der Meer, J. W., (1987). Stability of Breakwater Armour Layers-Design Formulae, *Coastal Engineering*, 11(3), 219-240.

Van der Meer, J. W., (1988). Deterministic and Probabilistic Design of Breakwater Armor Layers, *Journal of Waterways, Ports, Coastal, and Ocean Engineering*, 114(1), 66-80.

CHAPTER 124

Reliability based optimal design of vertical breakwaters modelled as a series system of failure

E. Christiani ¹ H.F. Burcharth ² J. Dalsgaard Sørensen ³

Abstract

Reliability based design of monolithic vertical breakwaters is considered. Probabilistic models of important failure modes such as sliding and rupture failure in the rubble mound and the subsoil are described. Characterisation of the relevant stochastic parameters are presented, and relevant design variables are identified and an optimal system reliability formulation is presented. An illustrative example is given.

Keywords: Vertical wall breakwaters, sliding failure, rupture failure, design optimisation, reliability

Introduction

A number of breakwater failures have been reported during the last 20 years for rubble mound breakwaters as well as for vertical breakwaters e.g. Sines (Portugal), Arzew (Alger), Mutsu-Ogawara Port (Japan), Gela (Italy) and Algeciras Port (Spain). This has resulted in new ways of approaching the design problems related to breakwaters. Probabilistic methods have been introduced to solve breakwater design problems in the early stage of planning. Reliability based design of breakwaters has been discussed by Nielsen et. al. (1983), Burcharth (1991), (1992a), (1992b), Burcharth et al. (1994) and (1995) and by Takayama (1994).

In the following a caisson vertical breakwater is analysed with respect to probability of failure for single failure modes. Emphasis is put on the foundation failure modes and their relative importance.

Identification of the failure modes

Sliding and rupture failure in the rubble mound foundation and in the subsoil are usually the most critical failure modes for vertical breakwaters. Other failure modes exist e.g. settlement of the caisson, seaward sliding, scour at the toe (subsoil and/or rubble mound), instability of the armour stones in the foundation, and structural failure of the caisson.

¹Ph.D.-student, Hydraulics and Coastal Eng. Lab., Dept. of Civil Eng., Aalborg University

²Prof. dr.techn., Hydraulics and Coastal Eng. Lab., Dept. of Civil Eng., Aalborg University

³Assoc. Prof. Ph.D., Dept. of Building Technology and Structural Engineering, Aalborg University

Nine foundation failure mechanisms including sliding are identified cf. Figure 1. Overturning is a relevant failure mode only in the cases of monolithic structures placed on very strong foundation soils or rock. The designs considered cover vertical breakwaters placed on low or high rubble mounds and sand or clay subsoils.

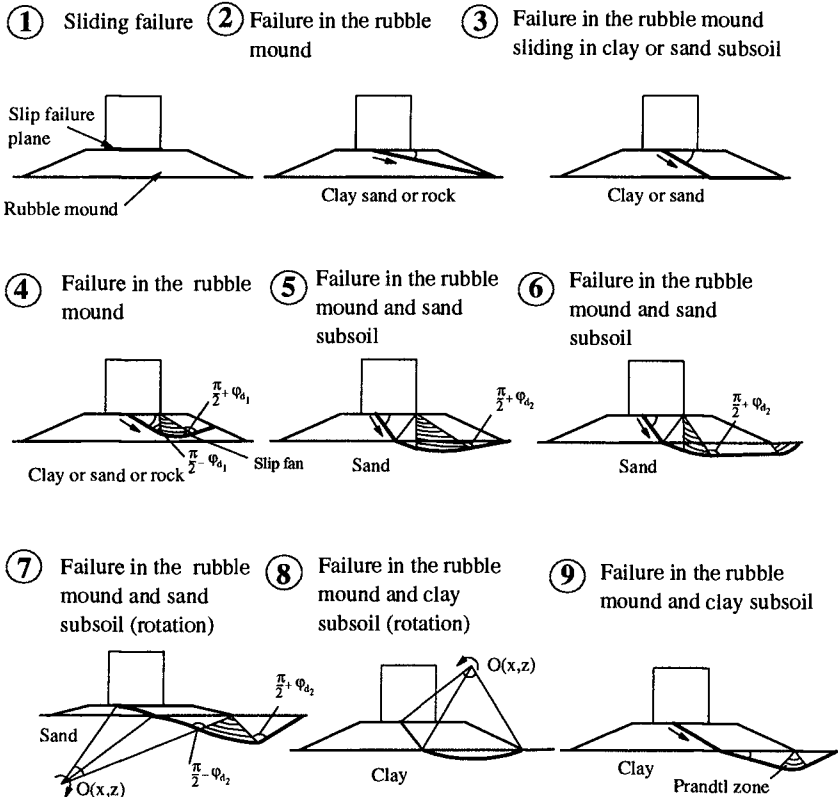


Figure 1: *Nine foundation rupture failure mechanisms*

Sliding

Sliding, i.e. horizontal displacement of the caisson, can occur as a slip either at the interface between the caisson concrete base plate and the rubble material, or entirely in the rubble material.

Corresponding to the first mentioned case stability against sliding exists when the ratio of the resultant horizontal force, F_H , to the resultant vertical force is equal to or less than $\tan \mu$, i.e.

$$F_H \leq (F_G - F_V) \tan \mu \tag{1}$$

where F_G is the weight of the caisson reduced for buoyancy, F_U is the wave induced uplift force on the base plate, and μ is the angle of friction between the concrete base plate and the rubble mound or the bedding layer. Reference is given to Takayama (1992) for values of $\tan \mu$.

If the sliding failure takes place entirely in the rubble material, e.g. in the bedding layer, then μ must be substituted by the effective angle of friction φ' of the material. The most critical of the two cases should be considered in the design.

F_H and F_U are in this paper calculated by using the wave load formulation by Goda et al. (1972) and (1974) extended to include impulsive pressure, Takahashi (1994). The design wave height is adjusted in the surf zone as described by Goda (1975).

The resultant of the forces F_H , F_G and F_U is indicated in Figure 2 as F_R .

Rupture failure in rubble, sand and clay subsoil - cases 1 - 9

To evaluate the stability of the foundation, consisting of the rubble mound, sand or clay subsoil, the upper bound theorem of general plasticity theory is used. This theorem can also be applied in a probabilistic approach of design.

Application of the upper bound theorem requires that the normality condition is fulfilled. Experience shows that good estimates of the bearing capacity can be obtained by introduction of a reduced effective angle of friction φ_d , Hansen (1979) defined by

$$\tan \varphi_d = \frac{\sin \varphi' \cos \psi}{1 - \sin \varphi' \sin \psi} \quad (2)$$

Both φ' and ψ are dependent on the stress level for which reason either reasonable mean values must be used, or calculations must be performed on increments.

Three dimensional effects are not included in the derivation of the zone rupture mechanism. The plane failure mode corresponding to case 8 is shown in Figure 2, where the line AB is approximately assumed to be a straight line. Note that it is assumed that tensile stresses cannot occur under the caisson base plate. Also note that because the caisson is a stiff body, the failure mechanism shown is not fully kinematic admissible. Actually, the intersection point A should be at the corner of the caisson, and the slip surface A-B is not necessarily a straight line. However, the rupture configuration is a close approximation as to the exact rupture mode can be demonstrated by comparison with results of finite element analyses.

Since the derivation of the mathematical formulation of the rupture failure modes 1 - 9 is rather lengthy, only rupture failure mode 8 will be discussed. Reference is given to Christiani (1996) for the rest of the failure modes.

Foundation in rubble and clay (rotation mechanism)

Case 8 in Figure 1 is considered.

The slip line AB is theoretically a logarithmic spiral. The areas, 1 and 2 move as stiff zones and interact with the clay subsoil, where a circular rupture zone evolves. The kinematic admissible rupture figure is described by a rotation mechanism about point D.

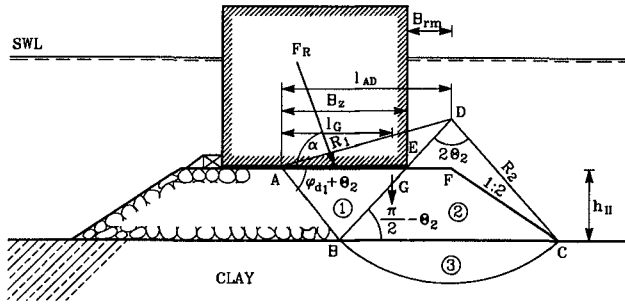


Figure 2: Rupture in the rubble mound and clay subsoil.

The geometrical lengths and the radius for the kinematically admissible rupture figure are cf. Figure 2.

$$l_{BC} = B_z + B_{rm} + 2h_{II} - \frac{h_{II}}{\tan(\varphi_{d1} + \theta_2)} \tag{3}$$

As noted above, the slip line AB is approximated by a straight line. The radius R_2 then becomes

$$R_2 = \frac{1}{2} l_{BC} / \sin \theta_2 \tag{4}$$

Further l_{AD} becomes

$$l_{AD} = \frac{h_{II}}{\tan(\varphi_{d1} + \theta_2)} + \frac{1}{2} l_{BC} \tag{5}$$

The centre of gravity for zone 1 and 2 is defined by the length l_G , cf. Figure 2

$$l_G = \frac{(l_{AD} - \frac{1}{2} l_{BC})(\frac{1}{3} l_{AD} + \frac{5}{6} l_{BC} - h_{II}) + \frac{1}{2} (l_{BC} - 2h_{II}) l_{BC} + \frac{2}{3} h_{II}^2}{\frac{1}{2} l_{AD} + \frac{3}{4} l_{BC} - h_{II}} \tag{6}$$

External work done

The external work W_E done by the wave loads, the pore pressure along the rupture boundary line and the weight of the vertical breakwater is for an infinitesimal rotation δ around point D

$$W_E = \delta M_o \tag{7}$$

where M_o is the moment around D of the wave loads, the pore pressure and the weight of the caisson.

The work done due to the weight of zones 1 and 2 is a rotation around D

$$W_{1,2} = \delta(\gamma_s - \gamma_w)(l_{AD} - l_G)(\Omega_1 + \Omega_2) \tag{8}$$

where Ω_1 and Ω_2 are the areas of zone 1 and 2, and $l_{AD} - l_G$ is the perpendicular length between the point of rotation and the center of gravity for zone 1 and 2.

The work done by the weight of zone 3 is zero as the resultant displacement of the centre of gravity is horizontal.

The internal work done in zone 3 along the rim of the rupture boundary BC is

$$W_3 = \delta R_2^2 \int_0^{2\theta_2} c_u(\theta) d\theta \tag{9}$$

where c_u is the undrained shear strength of the clay.

The limit state equation for the rupture mechanism in Figure 2 is then:

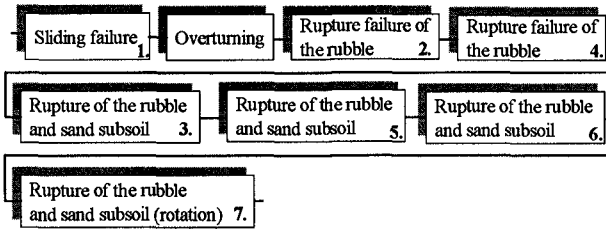
$$W_3 - W_{1,2} - W_E = 0 \tag{10}$$

θ_2 is the unknown angle to be determined by minimising the ratio between the stabilising work and driving work.

System model of failure modes for rupture failure and overturning

In design of vertical breakwaters, the main concern is sliding, overturning, and rupture failures in the rubble mound and in the subsoil. These failure modes can be modelled by a series systems cf. Figure 3.

a) Rubble mound and sand subsoil



b) Rubble mound and clay subsoil

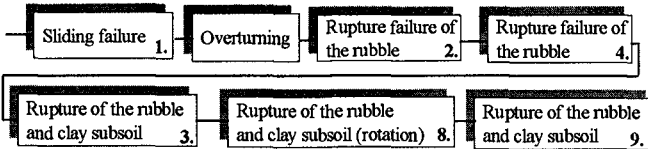


Figure 3: Series system of failure modes for rupture failure of the sand and clay subsoil.

Characterisation of the stochastic variables

All variables are in principle stochastic variables in a limit state formulation. Some parameters e.g. geometrical parameters have small coefficient of variation and might be regarded as deterministic variables. The parameters which have a significant degree of uncertainty in breakwater design will be discussed in the following. It is assumed that all stochastic variables are independent, unless otherwise stated in the text.

The wave induced horizontal force and the uplift force can be calculated from equations given by Goda et. al. (1974) and Takahashi (1994). The model uncertainty related to the *Goda wave load* is modelled by a normal distribution. This has been clarified by Bruining (1994) who compared a number of laboratory tests results with the Goda formula in order to evaluate the uncertainty related to the horizontal wave load, the wave induced uplift force, the horizontal moment and the wave induced uplift moment. The model uncertainties are represented by variables $U_{F_H}, U_{F_U}, U_{M_H}$ and U_{M_U} . Expected values (bias) and standard deviations are given in Table 2.

The *deep water wave climate* characterised by the significant wave height H_{so} is assumed to follow a Weibull distribution. The distribution function of the maximum significant wave height within T years is given by

$$F_{H_{so}^T}(H_{so}) = \left[1 - \exp \left(- \left(\frac{H_{so} - B_w}{A} \right)^k \right) \right]^{\lambda T} \tag{11}$$

where λ is the average number of H_{so} data values per year. $B_w = 2.69$ is usually regarded as a deterministic parameter.

Due to the limited number of data A and k are subject to statistical uncertainty. A and k values are modelled as normal distributed stochastic variables with a variance based on the maximum likelihood estimates. The expected value and the standard deviation of A and k are presented in Table 1.

	mean	standard deviation, σ
k	μ_k	$\simeq \sqrt{\frac{1}{N}}$ (approximation)
A	μ_A	$\left[\frac{\mu_A^2}{N} \left(\frac{\Gamma(1 + 2/\mu_k)}{\Gamma^2(1 + 1/\mu_k)} - 1 \right) \right]^{0.5} \simeq \mu_A \left(\frac{0.3}{N} \right)^{0.5}$

Table 1: Mean and standard deviation of A and k values in the Weibull distribution.

In Table 1 N is the number of available H_{so} -values and Γ is the gamma function. $\mu_A = 0.58$ and $\mu_k = 1.14$ and $N = 30$ will be used in the illustrative example, cf. Table 2.

As the water depth decreases from deep water to shallow water, wave transformation will result in refraction (when waves are not head on), shoaling and finally wave breaking. Therefore the uncertainty of the breaker heights should be considered in design in depth limited cases.

The *design wave height* $H_{design} = H_{1/250}$ to be applied in the Goda formula is in case of no surf zone in front of the structure taken as $1.8 \cdot H_{so}$.

i	X_i	Definition	Mean μ_{X_i}	Standard deviation σ_{X_i}	$\frac{\sigma_{X_i}}{\mu_{X_i}}$	Distribution	Reference
1	H_{so}	Deep water significant wave height (m)				weibull	Burcharth (1992)
2	k	Weibull parameter	1.14	0.15	0.13	normal	Burcharth (1994)
3	A	Weibull parameter	0.58	0.047	0.08	normal	Burcharth (1994)
4	ζ	Tidal elevation wave height (m)				cosine	Takayama (1992)
5	U_{FH}	Goda horizontal wave load	0.90	0.25	0.28	normal	Bruining (1994)
6	U_{Fv}	Goda wave induced uplift	0.77	0.25	0.32	normal	Bruining (1994)
7	U_{MH}	Horizontal moment about the heel	0.81	0.41	0.51	normal	Bruining (1994)
8	U_{Mv}	Uplift moment about the heel	0.72	0.37	0.51	normal	Bruining (1994)
9	ρ_c	Average density of the caisson (t/m^3)	2.15	0.11	0.05	normal	Burcharth (1994)
10	ψ_1	Angle of dilation rubble mound (rad.)	0.40	0.04	0.10	normal	
11	ψ_2	Angle of dilation sand subsoil (rad.)	0.30	0.03	0.10	normal	
12	φ'_1	Effective friction angle of rubble mound (rad.)	0.73	0.066	0.10	normal	
13	φ'_2	Effective friction angle of sand subsoil (rad.)	0.60	0.06	0.10	normal	
14	Z	Uncertainty of the rupture equation	1	0.10	0.10	normal	Sørensen C.S. (1993)
15	μ_f	Friction factor	0.636	0.0954	0.15	normal	Takayama (1992)

Table 2: Stochastic model of the stochastic variables

In case of a surf zone in front of the structure the breaker height is taken as (Goda, 1994)

$$H_b = L_0 0.17 \left(1 - \exp \left(-1.5 \frac{\pi h_b}{L_0} \left(1 + 15 \tan^{4/3} \theta \right) \right) \right) \quad (12)$$

where h_b is the water depth at a distance $5H_s$ seaward of the structure, and $L_0 = H_{so}/0.035$ is the deepwater wavelength. Consequently, $H_{design} = \min[H_{so}, H_b]$.

Tidal elevation ζ is assumed to follow a cosine distribution function, see Takayama (1992).

$$F_\zeta(\zeta) = -\frac{1}{\pi} \arccos \left(\frac{\zeta}{\zeta_a} - 1 \right) - 1 \quad (13)$$

where ζ varies between $\pm \zeta_a = 0.75 \text{ m}$.

Storm surge η_s should be considered when the structure is in shallow water, due to possible change in breaker wave heights and buoyancy of the structure. For simplicity the storm surge is not taken into account.

The total water depth in front the structure is $h_{tot} = h_s + \zeta$, where h_s is the mean sea water level at the foot of the structure, without influence from the storm surge or tidal level.

The average mass density of a conventional vertical breakwater including sand ballast, reinforced concrete walls and concrete cap can be assumed to be normal distributed with a mean value in the range $\rho_c = 2.15 - 2.3 \text{ t/m}^3$ and a coefficient of variation of 5%, Burcharth (1992).

It is generally accepted that the variability of the effective friction angle of a well known soil sample is small, but authors such as Nadim et al. (1994) and Cherubini (1992) have encountered variation coefficients in the range 3% to 15%. It is assumed in this paper that the angle of dilation and effective friction angle have a variation coefficient corresponding to 10 %.

The friction coefficient between the base plate and rubble is assumed normal distributed with a mean value $\tan \mu = 0.636$ and a coefficient of variation of 15 %, Takayama (1992).

Even homogeneous soil layers exhibit change in strength from point to point. The undrained shear strength of clay is an example where spatial variability exists. It is assumed to be modelled by a log-Gaussian stochastic field $\{c_u(x, z)\}$ where x is the horizontal coordinate and z the vertical coordinate, see e.g. Andersen et al. (1992). The mean value function and covariance function are in this paper assumed to be

$$E[c_u(x, z)] = \mu_{c_u} + az \quad (14)$$

$$Cov[c_u(x_1, z_1), c_u(x_2, z_2)] = \quad (15)$$

$$\sigma_{c_u}^2 \exp\left(-\left|\frac{z_1 - z_2}{3.0}\right|\right) \exp\left(-\left(\frac{x_1 - x_2}{30.0}\right)^2\right)$$

where c_u is in kPa and x, z are taken in metres with origo $(x, z) = (0, 0)$ equal to point B, see cf. Figure 2, μ_{c_u} is the expected value of the undrained shear strength, σ_{c_u} is the standard deviation of the undrained shear strength and $a = 3 \text{ kPa/m}$ is a constant signifying the linear increase of the undrained shear strength of the clay subsoil.

Method of reliability analysis

The uncertainties (physical, statistical and model) related to the above failure modes cf. Figure 1 are modelled as stochastic variables, and limit state functions for the failure modes are formulated as described above. The wave loads are estimated using the Goda formula, (including impulsive pressure modification) with model uncertainty included. For the foundation failure modes the strength of the clay subsoil is modelled as a stochastic field and a probabilistic limit state function is then formulated using kinematically admissible failure mechanisms, Christiani (1996).

The probability of failure of the failure modes are estimated using First Order Reliability Methods. System failure is modelled by a series system and the system probability of failure can be evaluated on the basis of the FORM analysis of the single failure modes, see Madsen et al. (1986) and Burcharth (1992).

Limit state functions

Sliding failure.

Failure corresponding to sliding can be modelled by the limit state function, cf eq. (1):

$$g_{sliding} = (F_G - F_U) \tan \varphi' - F_H \quad \begin{cases} < 0 & \text{failure} \\ = 0 & \text{limit state} \\ > 0 & \text{no failure} \end{cases} \quad (16)$$

Foundation failure in the rubble and clay subsoil

As mentioned above the undrained shear strength of the clay is modelled as a log-Gaussian stochastic field $\{c_u(x, z)\}$. The correlation lengths for $\{c_u(x, z)\}$ are small compared to the integration intervals and it follows from the central limit theorem that the total internal work in the clay subsoil can be approximated by a normal distributed stochastic variable W_3 with mean value μ_{W_3} and standard deviation σ_{W_3} . The limit state function is written, see eq. (10)

$$g_{clay} = E[W_3] + u_W \sigma_{W_3} - W_{1,2} - W_E \quad (17)$$

where u_W is a realization of a normal distributed stochastic variable U_W with mean 0 and unit standard deviation.

The expected value of W_3 is

$$E[W_3] = \delta R_2^2 \int_0^{2\theta_2} E[c_u(\theta)] d\theta \quad (18)$$

where $E[c_u(\theta)]$ is the expected value of c_u at the position described by the angle θ along the circular rupture line BC.

The variance of W_3 is

$$Var[W_3] = \sigma_{W_3}^2 = \delta^2 R_2^4 \int_0^{2\theta_2} \int_0^{2\theta_2} Cov[c_u(\theta), c_u(\theta_1)] d\theta_1 d\theta \quad (19)$$

where $Cov[c_u(\theta), c_u(\theta_1)]$ is the covariance function of c_u at the positions corresponding to θ and θ_1 .

Systems reliability of the series systems involving sand and clay subsoils

The single failure modes in Figure 1 are regarded as m failure components. It is clear from a deterministic design of a monolithic structure that if one of the failure components fail then the system fails, i.e. the breakwater has no load carrying capacity after the failure of one component. The system probability of failure P_f^s can be written as a probability of unions.

$$P_f^s = P \left(\bigcup_{i=1}^m g_i(\mathbf{x}) \leq 0 \right) = \int_{\bigcup_{i=1}^m g_i(\mathbf{x} \leq 0)} f_{\mathbf{x}}(\mathbf{x}) d\mathbf{x} \quad (20)$$

where $g_i(\mathbf{x})$ is the failure function corresponding to components $i = 1, 2, \dots, m$. The FORM approximation of the generalised systems reliability index β^s can be estimated as:

$$\beta^s = -\Phi^{-1}(1 - \Phi_m(\boldsymbol{\beta}^c, \boldsymbol{\rho})), \quad \text{or} \quad P_f^s = 1 - \Phi_m(\boldsymbol{\beta}^c, \boldsymbol{\rho}) \quad (21)$$

where Φ_m is the m -dimensional standardised normal distribution function, $\boldsymbol{\beta}^c$ is the vector of the reliability indices of the individual failure modes $\boldsymbol{\beta}^c = (\beta_1^c, \beta_2^c, \dots, \beta_m^c)$ and $\boldsymbol{\rho}$ is the correlation coefficient.

If the failure modes are fully correlated then $P_f^s = \max_{i=1}^m P_i$, where $P_i = \Phi(\beta_i^c)$ is the probability of failure for component i . If only failure modes involving foundation failure are considered the correlation coefficients are fairly close to 1. Taking $P_f^s = \max_{i=1}^m P_i$ is then a good approximation, although it is on the unsafe side.

Reliability based optimisation

In design of breakwaters the main objectives are usually to obtain an inexpensive structure and to have a satisfactory structural reliability.

Cost optimal design of a breakwater for construction or rehabilitation is always of interest to the design engineer. An example is presented in the following where the minimum reliability index is fixed and the decision variables are the geometrical values from a cross section of a vertical breakwater cf. Figure 4.

The design (decision) variables are denoted $\mathbf{b} = (b_1, \dots, b_N)$, i.e. the number of design variables is N .

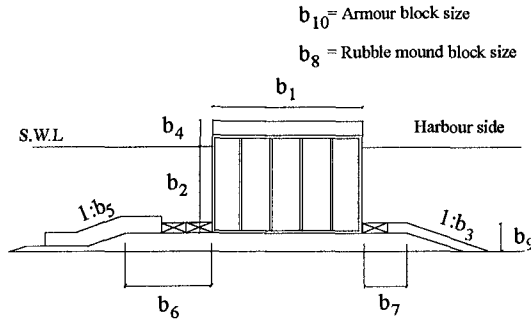


Figure 4: Definition of the design variables for optimal reliability design.

If the objective function is chosen as the total expected costs C_T of the structure during the lifetime, the optimal design can be found as the solution to the optimisation problem

$$\min_{\mathbf{b}} \quad C_T(\mathbf{b}) = C_I(\mathbf{b}) + C_F P_f(\mathbf{b}) \tag{22}$$

$$b_i^l \leq b_i \leq b_i^u \quad , \quad i = 1, \dots, N \tag{23}$$

where b_i^l and b_i^u are lower and upper bounds to b_i . C_I is the initial/construction costs, C_F is the costs of failure, and P_f is the probability of failure during the expected lifetime of the breakwater.

Alternatively an element reliability-index based optimisation problem can be formulated

$$\min_{\mathbf{b}} \quad C_I(\mathbf{b}) \tag{24}$$

$$s.t. \quad \beta_i(\mathbf{b}) \geq \beta_i^{min} \quad , \quad i = 1, \dots, m \tag{25}$$

$$b_i^l \leq b_i \leq b_i^u \quad , \quad i = 1, \dots, N \tag{26}$$

where β_i is the reliability index for failure mode i and β_i^{min} is the corresponding lower bound on the reliability index. Equivalent solutions from (22)-(23) and (24)-(25) can be obtained by suitable choices of β_i^{min} $i = 1, \dots, m$. The above optimisation problems are usually non-linear and non-convex. The optimisation problems can be solved effectively using non-linear optimisation algorithms and FORM.

The reliability indices in (25) are determined on the basis of limit state functions written as $g_i(\mathbf{x}(\mathbf{b}), \mathbf{b}) = 0$, $i = 1, \dots, m$. In a traditional deterministic design the design (optimisation) problem the constraint (25) is exchanged by the deterministic constraint

$$B_i(\mathbf{b}) = g_i(\mathbf{x}^D(\mathbf{b}, \boldsymbol{\gamma}), \mathbf{b}) \geq 0 \quad , \quad i = 1, \dots, m \tag{27}$$

where x^D are design values calculated using the statistical parameters for the stochastic variables X and γ are partial safety factors.

Evaluation of the failure modes

Reliability analysis of an engineering example is performed to show the significance of the failure modes in two series systems involving sand and clay subsoils.

The deterministic design of the vertical breakwater is designed according to Goda's pressure formulation (1974), considering recommended Japanese design guidelines for sliding (safety factor 1.2), overturning (safety factor 1.2) and max heel pressure ($400 - 600 \text{ kN/m}^2$), the tidal elevation $\zeta = 0$ and friction coefficient between base plate and rubble is taken as 0.6 cf. Figure 5.

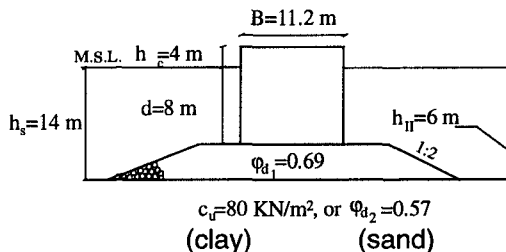


Figure 5: Illustration of a monolithic vertical breakwater.

The sensitivity of the caisson width on the probability of failure considering shoaling and breaker heights in the surf zone is shown in Figure 6

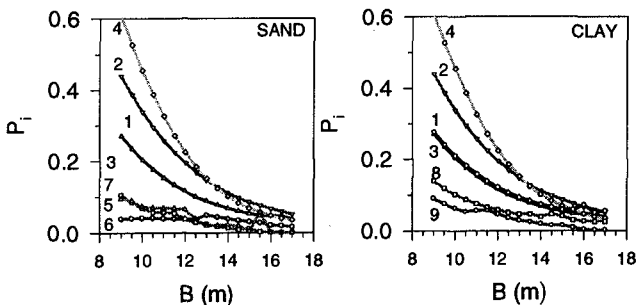


Figure 6: Effect of the width B of the caisson on the probability of failure P_i within 50 year structure lifetime, considering shoaling and breaker heights.

Numbers in the graphs refer to type of foundation failure mechanisms cf. Figure 1. From Figure 6 it is seen that the failure modes (4) and (2) are the most critical failure modes. It is also seen that the probability of failures for the deterministically determined caisson width of 11.2 m are very high.

Optimal design

Optimal design of the example cf. Figure 5 is determined on the basis of the formulation in equations (24) - (26) i.e. the cost of failure is neglected. The initial costs are divided into weight contributions from the rubble mound and the caisson. As design (decision) variables the width (B) and the height (h_{II}) of the rubble mound are chosen.

$$C_I(B, h_{II}) = C_{I_1} \cdot W_{caisson}(B) + C_{I_2} \cdot W_{rubble}(h_{II}) \quad (28)$$

where $W_{caisson}$ is the weight of the caisson and W_{rubble} is the corresponding weight of the rubble. The difference in price per unit weight between the weight of the rubble and caisson is chosen as $\frac{C_{I_1}}{C_{I_2}} = 2$. The cost of construction is minimised with upper bounds on the probability of failure of the significant failure modes.

Optimal designs for different levels of the acceptable probability of failure P_f without considering wave height reduction in the surf zone is presented in Table 3:

Applying Japanese design guidelines	P_f	B (sand & clay), h_{II}	B (sand & clay), h_{II}
$H_s^{50} = 5.56m, B = 17.8m, h_{II} = 6m$	0.1	24.7 (m), 5.0 (m)	26.5 (m), 6.0 (m)
waterdepth at the toe $h_s = 14m$	0.2	20.6 (m), 5.0 (m)	21.6 (m), 6.0 (m)
waterdepth, foot of the caisson $d = 8m$	0.3	18.2 (m), 5.0 (m)	19.0 (m), 6.0 (m)

Table 3: Optimal design for different levels of acceptable probability without considering shoaling and breaker heights in the surf zone.

Conclusions

Foundation failure modes for vertical breakwaters are formulated such that reliability analyses can be performed. The failure modes include sliding failure and failure modes involving sand and clay subsoils. Stochastic models for uncertain parameters are described using the information from experimental tests and from the literature. Further it is mentioned that foundation failure modes can be modelled as components in a series system.

Reliability based optimisation formulations for rational design of vertical wall breakwaters are given. Finally an illustrative example is presented, where the reliability of a breakwater on a high rubble mound is investigated and optimal designs are determined.

Acknowledgements

This work is supported by the Danish research program "Marin Teknik" sponsored by the Danish Technical Research Council.

References

- Andersen, E.Y. & B.S. Andreasen & P. Ostenfeld-Rosenthat (1992). *Foundation Reliability of Anchor Block for Suspension Bridge*. Proc. IFIP WG7.5, Lecture notes in Eng. Vol. 76, Springer Verlag, 1992 pp. 131-140.
- Bruining, J.W. (1994). *Wave forces on vertical breakwaters. Reliability of design formula*. Delft Hydraulics Report H1903, MAST II contract MAS2-CT92-0047.
- Burcharth, H.F. (1991). *Introduction of partial coefficients in the design of rubble mound breakwaters*. Conf.- on Coastal Structures and Breakwaters, Inst. of Civil Engineering, London.
- Burcharth, H.F. (1992a). *Development of a partial coefficient system for the design of rubble mound breakwaters*. PIANC PTC II Working Group 12, Subgroup F report.
- Burcharth, H.F. (1992b). *Reliability evaluation of a structure at sea*. Proceedings of the Short Course on Design and Reliability of Coastal Structures. Venice, Scuola di S. Giovanni Evangelista, 1992. 23rd International Conference on Coastal Engineering.

- Burcharth, H.F. & J.D. Sørensen & E. Christiani (1994). *On the Evaluation of Failure Probability of Monolithic Vertical Wall Breakwaters*. Proc. "Wave Barriers in Deepwater", Port and Harbour Research Institute, Yokosuka, Japan, 1994, pp. 458-46.
- Burcharth H.F., J.D. Sørensen & E. Christiani (1995): *Application of reliability analysis for optimal design of monolithic vertical wall breakwaters*, Proc. COPEDEC 1995, Rio de Janeiro, Brazil.
- Cherubini C. & Giasi C.I. (1993). *The coefficient of variations of some geotechnical parameters*. Probabilistic methods in geotechnical, A.A Balkema (1993).
- Christiani, E. (1996). *Statistically based design methods for breakwaters*. Ph.D., Aalborg University (in print).
- Goda, Y. and T. Fukumori (1972). *Laboratory investigation of wave pressures exerted upon vertical and composite walls*. Coastal Engineering in Japan, Vol. 15. pp 81-90, 1972.
- Goda, Y. (1974). *A new method of wave pressure calculation for the design of composite breakwater*. Proc. 14th Int. Conf. Coastal Eng., Copenhagen, Denmark.
- Goda, Y. (1975). *Irregular wave deformation in the surf zone* Coastal Engineering in Japan, JSCE, Vol.18 pp. 13-16.
- Hansen, B. (1979). *Definition and use of friction angles*. Proc. Int. Conf. VII ECSMFE, Brighton, UK, 1979.
- Nadim, F. & S. Lacasse, and T.R. Cuttormsen (1994). *Probabilistic foundation stability analysis: Mobilised friction angle vs available shear strength approach*. Structural Safety & Reliability, 1994, Balkema, Rotterdam.
- Nielsen S.R.K. and Burcharth H.F. (1983). *Stochastic design of rubble mound breakwaters*. Proc. 11 th IFIP Conference on system modelling and optimization, Copenhagen.
- Madsen, H.O., S. Krenk & N.C. Lind (1986). *Methods of Structural Safety*. Prentice-Hall, 1986.
- Sørensen, J.D., H.F. Burcharth and E. Christiani (1994). *Reliability analysis and optimal design of monolithic vertical wall breakwaters*. Proc. 6th IFIP WG7.5 Assisi, Italy. Chapman & Hall.
- Sørensen, C.S., Clausen, C.J.F., Andersen, H., (1993). *Bearing Capacity Analyses for the Great Belt East Bridge Anchor Blocks. Limit State Design in Geotechnical Engineering*. ISLAD 93, pp. 305-312
- Takahashi, S., Tanimoto, K., and K. Shimosako (1994). *Dynamic Response and Sliding of Breakwater Caisson against Impulsive Breaking Wave forces*. Proc. "Wave Barriers in Deepwater", Port and Harbour Research Institute, Yokosuka, Japan, 1994, pp. 362-399.
- Takayama, T. (1992). *Estimation of sliding Failure Probability of present Breakwaters for Probabilistic Design*. Report of Port and Harbour Research Inst., Vol. 31, No. 5, 1992.

CHAPTER 125

OVERALL SLOPE STABILITY ANALYSIS OF RUBBLE MOUND BREAKWATERS

Julien DE ROUCK¹, member ASCE
Luc VAN DAMME²

ABSTRACT

In this paper a “semi-dynamic approach for the slope stability analysis of rubble mound breakwaters” is presented. The principles of the method are described. Tide and wave action are taken into account in the slope stability analysis of deep slip-surfaces. For these slip-surfaces the moment of maximum wave run-up is most critical.

Pore water pressure variations at the seabottom are also measured below the seabottom but attenuated and approximately up to the so called influence depth h_{IP} . The fact that the pore pressure variation is attenuated leads to “overpressures” at the moment of low water and below the wave trough. The attenuation depends mainly on the wave period T and soil characteristics k (permeability) and E_{oed} (oedometric compression modulus).

INTRODUCTION

The design of a rubble mound breakwater normally starts with the determination of the overall geometry: crest level, crest width and slope angles of both seaward and rear slope. Once the overall geometry is fixed most attention is paid to the design of the armour layer: choice of the type of armour unit (rock or concrete block and in the latter the type of block: cube, tetrapod, dolos, ACCROPOD[®], HARO[®], ...) and the weight of the armour unit.

On behalf of the design of the armour layer, several design rules are available. These rules are based on extensive research: theoretical but mainly scale model tests in hydraulic laboratories. The main loading for the armour layer is the wave attack. Furthermore it is common use to carry out scale model tests on behalf of the design of (important) rubble mound breakwaters.

With regard to the overall slope stability of the slopes of a breakwater, distinction has to be made between the seaward slope and the rear slope. For the rear slope, which is normally not subjected to wave attack, one can apply calculation methods normally used for banks of a river, a canal, ... The seaward slope however is subjected to wave attack. Considering the seaward slope, designers and researchers were used to pay too little attention to the hydrodynamic effect of wave attack.

1) Civil Engineering Dept., University of Gent; HAECON N.V.; Technologiepark 9, B-9052 Gent, Belgium.

2) Ministry of Flemish Community, Coastal Division, Vrijhavenstraat 3, B-8400 Ostend, Belgium.

Frequently the experience gained on land is applied (Quinn, 1972 ; Fisher et al., 1975 ; Toppler, 1982 ; Chew, 1990 ; Murray et al, 1990 ; Koutitas, 1992). Only Barends takes into account the effect of waves. But he focuses on slip surfaces inside the breakwater core (Barends, 1983, 1985). Only in his paper of 1985 he presents some results with regard to the influence of (partial) liquefaction of the foundation layer due to wave attack.

During the design of the Zeebrugge breakwaters, extensive studies, research, testing and investigation into the geotechnical stability of rubble mound breakwaters have been carried out. One of the results is the proposed calculation method which takes into account the dynamic impact of waves and tides. The method is focusing on deep slip-circle stability analysis. As the dynamic effect of waves and tides is taken into account, we call it **“a semi-dynamic approach for the slope stability analysis of rubble mound breakwaters”**.

DESCRIPTION OF THE PROPOSED METHOD

Principles

The slope stability analysis can be carried out by using different methods: Fellenius, Bishop ... for circular slip surfaces and Nonveiller, Janbu, Morgenstern and Price, ... for non circular slip surfaces. In the analysis the friction angle ϕ' and the cohesion c' based on the effective stresses, are used. For the results shown in this paper, the Bishop formula has been applied. However the principles described further can be used for any other analysis method.

A sensitivity analysis has been carried out in order to learn which parameters are really influencing the overall stability of the seaward slope of a rubble mound breakwater. The following characteristics influencing the geotechnical safety factor F are considered: overall geometry, external forces, geotechnical characteristics (ρ , c' , ϕ') of both the material (mainly the breakwater core) and the subsoil, and pore water pressures. The sensitivity analysis showed the paramount importance of the pore water pressures along a potential slip surface: they are as important or even more important than the shear resistance characteristics.

Figure 1 shows a simplified cross-section of a rubble mound breakwater with a possible slip surface DEFA. All forces acting on the volume ABCDEFA are considered: weight of the volume, external forces acting on the faces AB, BC, DE, EFA. In that way the water pressures influence the overall geotechnical stability:

- water mass in front of the breakwater (AB);
- pressure on the breakwater slope (BC);
- pore pressure within the mound, influencing shear resistance along DE;
- pore pressure within the foundation layers, influencing the shear resistance along EFA.

To find the most critical load situation, two load conditions called A and B are considered: **tide action (A)** and **tide combined with wave action (B)**.

The first case, only tide action without considering any wave action, occurs at the rear slope of a breakwater. In that case low tide is the most critical situation.

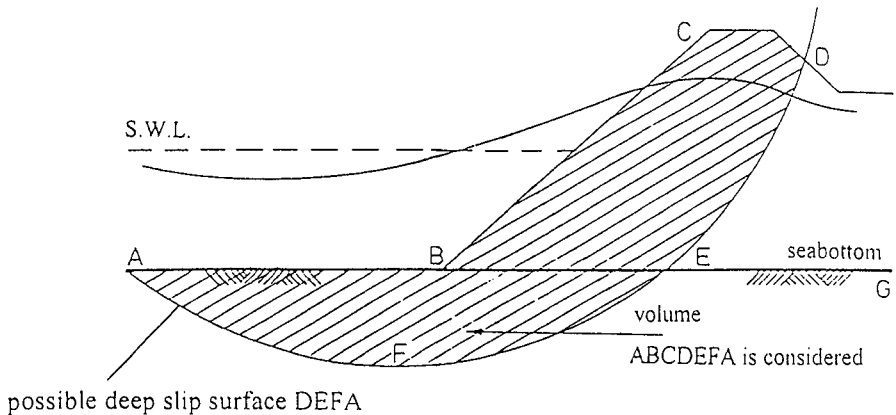


Figure 1. Simplified cross-section of a rubble mound breakwater (max. wave run up)

In the second case tide and wave action are acting together. The determining situation is the maximum wave run-up (wave crest) combined with the most critical moment in the tide cycle. A thorough investigation has shown that for a breakwater constructed in shallow water the most critical situation exists at high tide at the moment of maximum wave run-up, in fact immediately after maximum wave run-up. At that moment the wave action is changing from “pushing on the slope” into seepage forces, in fact “pulling on the mass CDEB”. For a breakwater in transitional water depths the most critical situation will occur at maximum wave run-up at either low water (L.W.), mean water or high water (H.W.). This is in clear contradiction with the widespread idea that the moment of maximum wave run-down, with the wave through in front of the breakwater is the most critical. The latter is only valid for slip surfaces which fully develop in the breakwater core.

Weight of the volume ABCDEFA

The weight of the considered volume (partially of the breakwater and partially of the foundation layer) can easily be calculated based on the geometry and the unit mass of the breakwater material and subsoil.

Watermass in front of the breakwater: forces acting on surface AB

We can easily take into account the water mass in front of the breakwater by suggesting that the slip surface reaches the water surface, calculating with following water characteristics: $\rho_w = 1 \text{ t/m}^3$; $c' = 0$; $\phi' = 0$ (De Beer, 1959). This is only valid for a horizontal water surface in rest, e.g. case A, because the water level is varying with a great period, so very slowly. Combining tide and wave action the sea level is going up and down and the surface isn't horizontal any more, the water pressure won't be hydrostatic: the so called Still Water Level (S.W.L.) is varying between low

and high tide and the waves are characterised by a wave height H , a wave period T and wave length L .

Several wave theories describe the water surface, determined by those parameters: Airy (linear wave theory), non linear wave theory, cnoidal waves ... As breakwaters are normally constructed in shallow water the cnoidal wave theory has to be applied, although the cnoidal theory is very complicated. Grace showed that for both cnoidal and Airy theory correction coefficients have to be used (Grace, 1978). So pressures on the surface AB can be calculated with sufficient accuracy using the Airy theory but taking into account the correction coefficients proposed by Grace.

Water pressure on the slope surface: forces acting on surface BC

In the case of not overtopped breakwaters the pressure on the slope surface of the breakwater is directly influenced by the shape of the incident wave. Based on results published by Brandtzaeg (Brandtzaeg, 1962 ; Brandtzaeg et al, 1966, 1969) and based on the measurements taken during the scale model tests for the Zeebrugge breakwaters, we recommend to registrate the wave form in front of the slope up to one wave length. Having determined the wave form at the time of maximum wave run-up allows to calculate forces on the slope. Essential in this method is the determination of maximum wave run-up. The run-up height R_u is defined as the vertical distance between S.W.L. and the highest point to which water from an incident wave will run up the slope of a structure. The value of R_u/H depends on the wave characteristics (H , T , L) and slope characteristics (slope angle, roughness, porosity, ...).

Pore pressure within the mound: forces acting on surface DE

On surface DE shear forces are acting. These shear forces depend on the shear strength characteristics of the material and on the effective stress. The latter depends on the pore pressures.

Involving water pressures in the mound, a distinction is made between tide action (case A) and tide and wave action (case B). In case A we can adopt a hydrostatic pressure for the water pressures along the slip surface.

Wave action (case B) on the seaward slope results in a water level set up inside the core. This is due to the fact that the inflow surface during wave run-up is greater than the outflow surface during run-down. In addition the mean flow path for inflow is shorter than that for outflow. This set up leads to higher mean pore pressures. Due to wave action pore pressures are varying within one wave period, depending on the location and on the attenuation through the armour layer, filter layer and core (Troch P. et al, 1996a and b).

Pore pressures within the foundation layers: forces acting on surface EFA

As for surface DE, on surface EFA shear forces are acting which depend on the pore pressures. The sensitivity analysis has shown the predominant importance of the pore pressures along EFA.

If these pressures are hydrostatic with regard to the seawaterlevel, they can be defined easily. But the question has to be put whether they are hydrostatic or not. The

sea waterlevel is continuously changing: slowly (tide with a period = 12h25min) or fast (waves: with periods between 6, ..., 20 s).

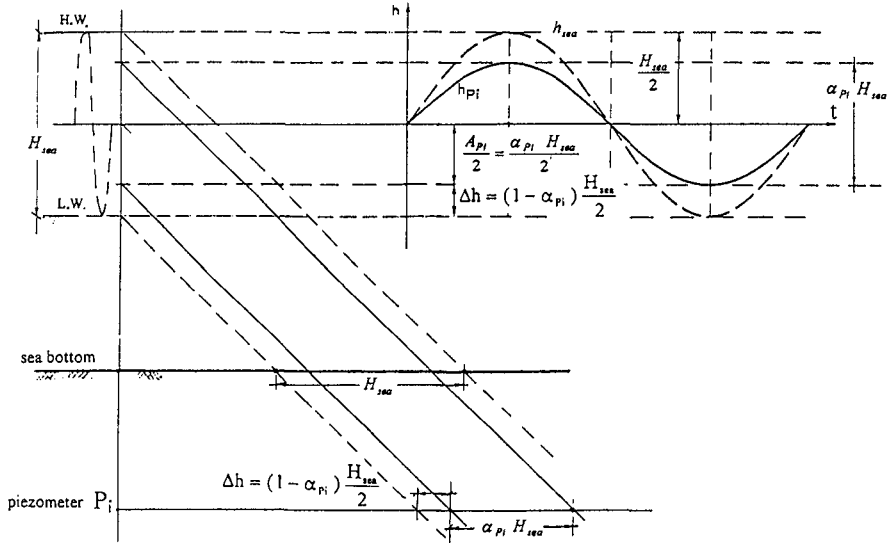


Figure 2. Definition sketch of attenuation of tide

Figure 2 shows the principle of wave attenuation in the subsoil. This attenuation results in an “overpressure” in the pores at the moment of L.W. or below the wave through. For tides the overpressure can be written as:

$$\begin{aligned} \Delta u &= \rho_w g \Delta h \\ &= \rho_w g (1 - \alpha_{Pi}) \frac{H_{sea}}{2} \end{aligned} \quad (1)$$

with	Δu	:	overpressure at low tide (in kPa)
	ρ_w	:	unit mass of seawater (t/m ³)
	Δh	:	overpressure at low tide (in m seawater)
	α_{Pi}	:	attenuation coefficient of piezometer Pi (-)
	H_{sea}	:	tidal range H.W. - L.W. (m)

This overpressure highly influences the overall slope stability.

ON SITE MEASUREMENT OF TIDE AND WAVE ATTENUATION IN THE SUBSOIL

Test set-up

In order to investigate the attenuation of varying water pressures (at the seabottom) in the subsoil four measurement campaigns have been carried out on behalf of the design of the Zeebrugge breakwaters. In this paper we will focus on the 4th campaign, taking into account both tides and waves.

In general this 4th campaign has the following characteristics:

- The seabottom is located at ca. Z-5,50.
- From the seabottom the following layers are found:
 - up to -14,00 : coarse sand with shells
 - up to -15,50 : a clayey sand layer
 - a stiff clay layer (Tertiary, Bartonian clay) up to much greater depths.
- In the harbour area M.L.W.S. is situated at the level Z+0,32 and M.H.W.S. at the level Z+4,62, i.e. waterdepths of about 5,80 m to about 10,10 m at the location of the multiple piezometer probe. The design wave height for the main breakwaters amounts 6,20 m, at design waterlevel Z+6,76.

A general view of the measuring system is given in fig. 3. The pore pressures in the seabottom are measured by electrical pressure transducers, mounted at seven levels in a multiple piezometer probe which was jacked into the seabottom. The pressure transducers are connected by a cable bundle to a measuring platform installed on top of a steel tube pile in the vicinity of the probe. The measuring platform contains the conditioning for the piezometer probe, a transmitter and all the related equipment. The measured values are sent by the transmitter to the coast by an UHF link. At the coast, the measured values are caught by a receiver and sent to a computer by telephone link where they are stored on disk and subsequently analysed.

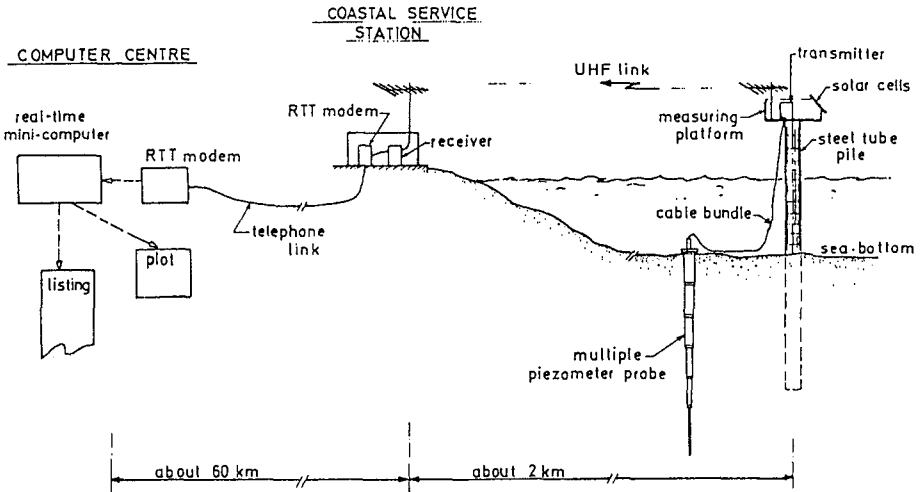


Figure 3. Lay-out of the measuring system for the 4th campaign

The multiple piezometer probe consists of six steel pipes linked together by stainless steel nipples containing the pressure transducers. Below each nipple a decrease in diameter was chosen to prevent direct contact between the different piezometer levels along the mantle of the probe. The diameters of the elements of the probe were kept as small as possible in order to keep the penetration forces within acceptable limits and to minimize soil disturbances. The pressure transducers are of the semi-conductor strain gauge type with very fast response and suitable electric output signal; they have a very small volume displacement, no moving parts and a low energy consumption.

More details about the lay-out of the system and the multiple piezometer probe, even about the measuring platform and equipment, data acquisition system and installation procedure are given in De Wolf et al. (1983) and De Rouck (1991).

Results

The tide is transmitted up to the tip of the probe at 13,00 m below the seabottom: within the sand layer only slightly attenuated but strongly attenuated in the clay layer.

Even wave action is registered up to the tip of the probe: the amplitude of the waves decreases very quickly from the seabottom to a depth of about 2,00 m underneath the seabottom, with further attenuation for greater depths.

THEORETICAL MODEL OF WATER PRESSURE PROPAGATION IN THE SUBSOIL

Out of the results of the measuring campaign it can be concluded that the water pressure in the subsoil is not hydrostatic due to the continuously changing seawaterlevel. The amplitude of the pressure variation is attenuated.

The differential equation governing the pore water pressure change during one tide (and one wave) has been written based on the Darcy equation and the continuity equation.

Consider an elementary volume $dx \cdot dy \cdot l$ and the effect of tides (fig. 4).

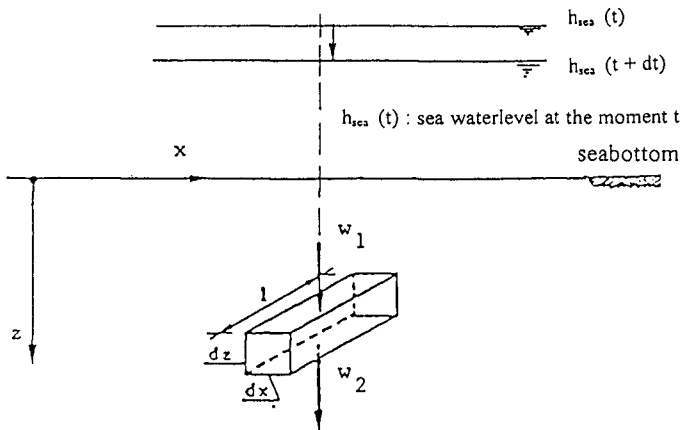


Figure 4. Tide: pore water flow in the subsoil due to seawater lowering

The equation of Darcy:

$$w = -\frac{k}{\rho_w g} \frac{\partial u}{\partial z} \quad (2)$$

with: w : flow velocity in z-direction
 u : pore water pressure
 k : permeability coefficient of the soil
 ρ_w : specific mass of seawater

The continuity equation takes into account following phenomena:

- if the seawater level drops from high tide to low tide, the pore water pressure decreases; the pore water expands, so some water is pressed out of the considered volume;
- at the same time the total effective stress decreases (both the vertical and horizontal stress decrease): the grain skeleton expands, so some water is sucked.

The continuity principle leads to:

$$\frac{\partial w}{\partial z} = -\left(\frac{1}{E_{oed}} + \frac{n}{K_w}\right) \frac{\partial u}{\partial t} \quad (3)$$

with E_{oed} : oedometric compression modulus of the soil
 n : porosity of the soil
 K_w : compression modulus of seawater

As all soil layers are situated below the seabottom it has been assumed that they are fully saturated.

Combining the equation of Darcy and the continuity equation leads to the differential equation for pressure response in the soil underneath the seabottom:

$$\frac{\partial^2 u}{\partial z^2} = \frac{\rho_w g}{k} \left(\frac{1}{E_{oed}} + \frac{n}{K_w}\right) \frac{\partial u}{\partial t} \quad (4)$$

- via $\frac{1}{E_{oed}}$ the compressibility of the grain skeleton is taken into account
- via $\frac{n}{K_w}$ the compressibility of seawater is taken into account

Comparing the order of magnitude of both terms for clay and sand learns that $\frac{n}{K_w}$ is

clearly smaller than $\frac{1}{E_{oed}}$, so $\frac{n}{K_w}$ can be neglected. Equation (4) can be simplified to

$$\frac{\partial^2 u}{\partial z^2} = \frac{\rho_w g}{k E_{oed}} \frac{\partial u}{\partial t} \quad (5)$$

In a similar way the general equation for water flow in the subsoil due to wave action can be written as:

$$\frac{\partial^2 u}{\partial x^2} + \frac{\partial^2 u}{\partial z^2} = \frac{\rho_w g}{k} \left(\frac{1}{E_{oed}} + \frac{n}{K_w} \right) \frac{\partial u}{\partial t} \quad (6)$$

As for tides the term $\frac{n}{K_w}$ can be neglected, leading to:

$$\frac{\partial^2 u}{\partial x^2} + \frac{\partial^2 u}{\partial z^2} = \frac{\rho_w g}{k E_{oed}} \frac{\partial u}{\partial t} \quad (7)$$

Comparison of the order of magnitude of $\frac{\partial^2 u}{\partial x^2}$ and $\frac{\rho_w g}{k E_{oed}} \frac{\partial u}{\partial t}$ for normal waves (e.g.

as measured during the 4th campaign) and for both clay and sand shows that $\frac{\partial^2 u}{\partial x^2}$ is

clearly smaller than $\frac{\rho_w g}{k E_{oed}} \frac{\partial u}{\partial t}$. So $\frac{\partial^2 u}{\partial x^2}$ can be neglected.

Equation (7) can be simplified to:

$$\frac{\partial^2 u}{\partial z^2} = \frac{\rho_w g}{k E_{oed}} \frac{\partial u}{\partial t} \quad (8)$$

Equation (5) and (8) are identical.

Solving this differential equation is done taking into account the following boundary conditions:

a) at the sea bottom (z = 0)

$$u(0,t) = u_o \cos \left(\frac{2\pi x}{L} - \frac{2\pi t}{T} \right) \quad (9)$$

Or, for a fixed spot, take x = 0

$$u(0,t) = u_o \cos \frac{2\pi t}{T} \quad (10)$$

with u_o - for tides $u_o = \rho_w g H_{sea}$

with H_{sea} : tidal range H.W. - L.W.

$$\text{- for waves } u_o = \frac{\rho_w g}{n} \frac{H}{2 \cosh \frac{2\pi d}{L}}$$

with H: wave height

L: wave length

d: water depth

n: correction coefficient of Grace

b) at great depth ($z = \infty$)

$$\lim_{z \rightarrow \infty} u(z,t) = 0 \tag{11}$$

This leads to the following solution:

$$u(z,t) = u_o e^{-Az} \cos\left(\frac{2\pi x}{L} + \frac{2\pi t}{T} - Az\right) \tag{12}$$

with:

$$A = \sqrt{\frac{\rho_w g \pi}{k E_{oed} T}} \left[\frac{1}{m} \right] \tag{13}$$

- with L : wave length
- T : wave period
- k : permeability coefficient of the soil
- E_{oed} : oedometric compression modulus of the soil

Figure 5 shows the pore water pressure variation in a soil layer due to tide or wave action. Curve 1 is valid for $x = 0$, $t = T/2$ and $A = 0,3$, while curve 2 is the envelope. Approximatively curve 1 can be replaced by the straight line AB. The distance OB is the so called "influence depth". This influence depth has proven to be a very handsome tool to introduce the variation of the pore water pressure in the subsoil into the slope stability analysis.

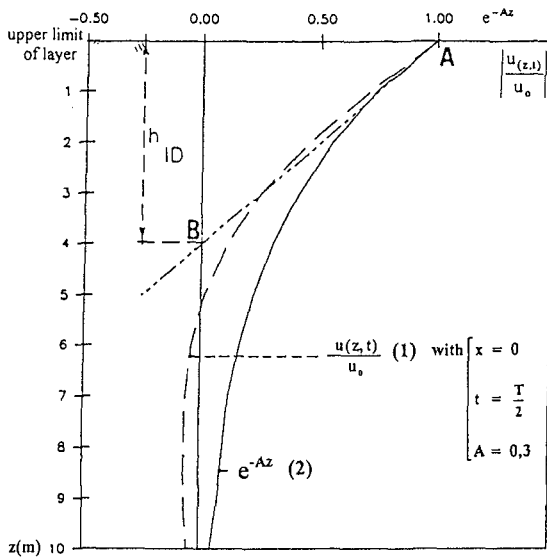


Figure 5. Pore water pressure variation in a soil layer due to tide or wave action

The attenuation decreases when the influence depth h_D increases, i.e. when A decreases. A decreases when the product $k \cdot E_{\text{sed}} \cdot T$ increases: a more permeable and less compressible soil combined with longer wave period (and subsequent longer wave length).

Comparison of on site measurement results with the theoretical model

It is investigated how the results of the on site measurements fit with the theoretical model. On the one hand the results for tides for respectively the stiff Bartonian clay and all sand layers (in which pore water pressure measurements have been carried out) and on the other hand the results of the 4th campaign for waves for the sand layer are considered.

For both tides and waves the attenuation coefficient is "measured on site" (i.e. determined based on the measurements on site). The attenuation coefficient is also "calculated" (i.e. by introducing soil characteristics in equation (13)). It is found that "measured" and "calculated" values coincide quite well (De Rouck, (1991)).

APPLICATION OF THE PROPOSED METHOD FOR SLOPE STABILITY ANALYSIS

The proposed method for analysing the overall slope stability has been applied at numerous occasions. Within this paper an example for Zeebrugge (Belgium) and Antifer (France) will be given.

Zeebrugge inner harbour breakwater

Figure 6 shows the most critical slip circle for a Zeebrugge inner harbour breakwater when considering the design water level $Z+6,76$. The crest of the breakwater is situated at $Z+10,30$. Maximum run-up will not fully occur as the considered extreme wave will pass over the crest (overtopping). The safety factor $F_{\text{min}} = 1,42$, which is rather high.

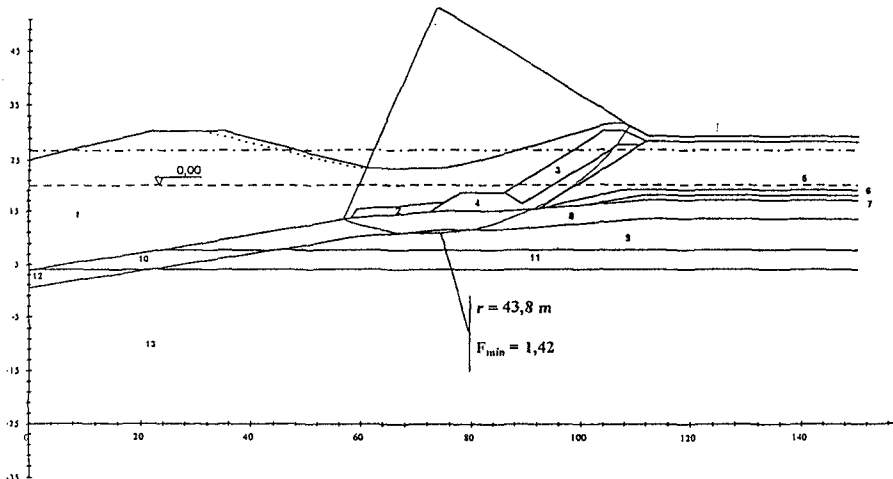


Figure 6. Zeebrugge breakwater slope stability analysis

Antifer main breakwater

Based on the geometry as given in Feuillet et al. (1987) the slope stability analysis is carried out. As no exact geometric data and hydraulic data (tide, waves) and no exact characteristics of the materials were available, approximative geometry and wave loading and approximative but realistic values for the characteristics of all layers (breakwater and subsoil) have been introduced in the slope stability analysis. Regarding these circumstances the result has to be considered as approximative as well. The analysis has been carried out for high tide and low tide. Low tide is clearly more critical. So fig. 7 shows the result for max. wave run-up at low tide: $F_{\min} = 1,13$. For the design of the Zeebrugge breakwaters for the case B (tide combined with wave attack) an $F_{\min} \geq 1,10$ has been required.

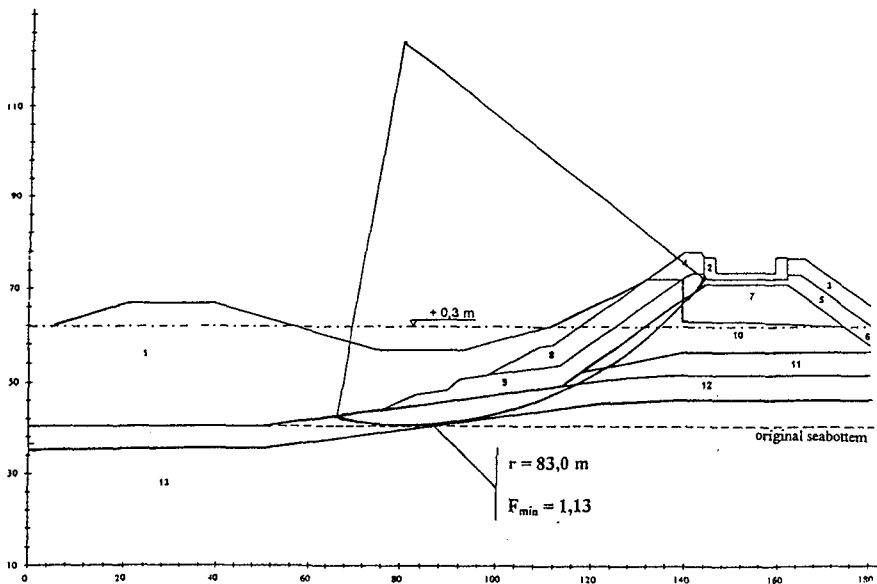


Figure 7. Antifer main breakwater slope stability analysis

FURTHER USE OF RESULTS

Knowledge of the water pressures in the soil layers below the seabottom, resp. below the bottom of a river subjected to tides, allows to explain unexpected behaviour of structures. Two examples are given.

An intake of water, constructed on a sand layer on top of a 12 m thick clay layer subsides at high tide and rises at low tide. This is completely unexpected regarding the higher submerged part at high tide. The phenomenon can be explained by taking into account the water pressures in the clay layer (De Rouck, 1991).

The crest of a quaywall subjected to tides, constructed on a claylayer or on a sandlayer on top of a claylayer may move towards the river at high tide and return at low tide. This will be the case if the effect of compression of the claylayer at high tide is dominant compared with the effect of the higher stabilising forces at high tide.

CONCLUSIONS

Within this paper a method for slope stability analysis of the seaward slope of a rubble mound breakwater has been described. The dynamic effect of both tides and waves has been taken into account.

The main conclusions are:

- Slope stability analysis of the slopes of the breakwater, especially the seaward slope, deserves as much attention as the design of the armour layer.
- The slope stability can be carried out by considering a volume ABCDEFA (fig. 1) which reaches into the soil layer underneath the seabottom.
- Pore water pressure variation (due to waves and tides) at the seabottom are also measured below the seabottom but attenuated and approximatively up to the so called influence depth h_{ID} . The fact that the pore pressure variation is attenuated leads to "overpressures" at the moment of low water and below the wave trough (for both L.W. and H.W.)
- The attenuation decreases with increasing influence depth h_{ID} , i.e. with decreasing factor A. The factor A on his turn decreases when the product $k.E_{oed}.T$ increases.

REFERENCES

- Barends F.B.J., Van Der Kogel H., Uijtewaal F.J. en Hagenaar J. (1983): West Breakwater Sines: Dynamic geotechnical stability of breakwaters. Proc. Conf. on Coastal Structures, Arlington, 1983, pp. 31-44.
- Barends F.B.J. (1985): Geotechnical aspects of rubble mound breakwaters. Proc. of the Conf. on Breakwaters, Institution of Civil Engineers, London, October 1985, pp. 155-174.
- Bishop A.W. (1955): The use of the slip circle in the stability analysis of slopes. Geotechnique 1955, Vol. 5, pp. 7-17.
- Brandtzaeg A. (1962): A simple mathematical model of wave motion on a rubble mound breakwater slope. Coastal Engineering, chapter 26, 1962, pp. 444-468.
- Brandtzaeg A. (1966): A simple mathematical model of wave motion on a rubble mound breakwater front. Coastal Engineering, chapter 57, 1966, pp. 977-989.
- Brandtzaeg A., Törum A. and Östby O.R. (1968): Velocities in downrush on rubble mound breakwaters. Proc. 11th I.C.C.E., 1968, pp. 815-832.
- Chew S.Y. en Wei J. (1980): Major reclamation scheme for Marina city, Singapore. Proc. 17th I.C.C.E., Sydney, 1980, pp. 2245-2260.
- De Beer E.E. (1959): Grondmechanica, Deel IV, Algemene Theorieën van het glijdingsevenwicht - Evenwichtsproblemen van taluds. N.V. Standaard Boekhandel, 1959.
- De Rouck J. (1991): De stabiliteit van stortsteengolfbrekers: Algemeen glijdingsevenwicht - Een nieuw deklaagelement, 1991, 525 pp.

- De Wolf P., Carpentier R., Verdonck W., Boullart L., De Rouck J., de Saint Aubin T. and De Voghel J. (1983): In situ pore water pressure measurements for the construction of the breakwaters of the new outer harbour at Zeebrugge. Havencongres, Antwerpen, 1983, 13pp.
- Feuillet J., Bernier J., Coeffé, and Chaloin B. (1987): Le dimensionnement des digues à talus. Collection de la Direction des Etudes et Recherches d'Electricité de France, 1987, 172 pp.
- Fisher J.A. and Lu B.T.D. (1975): Evaluation of offshore breakwater stability under wave action. Offshore Technology Conference, 1975, O.T.C. 2394, pp. 577-589.
- Grace R.A. (1976): Surface wave heights from pressure records. Coastal Engineering 2, 1978, pp. 55-67.
- Koutitas C. (1982): A numerical model for rubble mound breakwaters stability. Proc. Seminar on Maritime Engineering, Brugge, 1982.
- Meerschaut Y.(1995): Algemene stabiliteit van een golfbreker - Golf voor de dam. Universiteit Gent, 1995, 188 pp.
- Murray M. en Sayao O.J. (1990): Offshore breakwater for the Sergipe Marine Terminal, Brazil. Book of Abstracts of the 22nd I.C.C.E., Delft, 1990, pp. 163-164.
- Quinn A.D. (1972): Design and Construction of ports and marine structures. Mc Graw-Hill Book Compagny, 611 pp.
- Toppler J.F., Groeneveld R.L. en Van den Berg J. (1982): Design of breakwaters in deep water. Proc. Seminar on Maritime Engineering, Brugge, 1982, pp. 81-85.
- Troch P., De Rouck J., De Somer M., Saey D., Andersen H., and Schlütter F., 1996. MAST II-project MAS2-CT92-0023. Vol. 1, Report D: Internal hydraulic response, 87 pp.
- Troch P., De Somer M., De Rouck J., Van Damme L., Vermeir D., Martens J-P, Van Hove C. (1996): Full scale measurements on wave attenuation inside a rubble mound breakwater, ICCE, 1996, 14 pp.

CHAPTER 126

INTERACTIONS IN THE STABILITY OF TOE-BERM AND MAIN-ARMOUR FOR RUBBLE-MOUND BREAKWATERS : AN EXPERIMENTAL STUDY

Philippe DONNARS ¹ and Michel BENOIT ¹

Abstract

This experimental study is concerned with one particular aspect of possible failure modes for a rubble-mound breakwater : the interactions between the toe-berm and the main-armour of the breakwater. Through a series of laboratory tests in a wave basin under long-crested and short-crested waves, we investigate the mutual influence of both these component parts of the breakwater on its general stability. The effects of several wave parameters are examined for four sizes of toe-berm stones. For the trunk section, experimental results are found to compare quite satisfactorily with existing design formulas both for the main-armour and the toe-berm. As a general trend from the tests results, the interaction processes appear to have only moderate effect. Their major feature is an increase of damage to the armour when the toe-berm is unstable. On the opposite, minor effects of main-armour on toe-berm stability were observed. In particular, the "toe-berm armouring process" (by units falling from the armour) appears to occur only marginally and under precise conditions.

1. INTRODUCTION - SCOPE OF WORK

The common practice for designing a breakwater is usually to use existing design formulas and rules for each individual part of the breakwater (main armour, rear armour, crest,...). This design approach is quite well documented in the scientific literature, in particular for the main armour (e.g. Van der Meer, 1992). In a following step, the whole breakwater profile has to be further tested and optimized through model tests in wave flume or basin, to obtain a reliable and safe structure.

The overall stability of the breakwater is however not only a function of the stability of each individual component part of the breakwater, but also of the interaction mechanisms between these parts. Present knowledge on the latter point is quite limited and it is not straightforward to find in the literature precise and quantitative descriptions of these possible interaction effects. Improving this knowledge was the main objective of the European Research Project "Rubble-Mound Breakwater Failure Modes (RMBFM)" of MAST-2. The study presented in this paper is concerned with one particular aspect of these possible failure modes : the interactions between the toe-berm and the main-armour of a breakwater.

¹ Research Engineer — Maritime Group
EDF - Laboratoire National d'Hydraulique, 6, quai Watier 78400 CHATOU, FRANCE

This experimental study continues previous tests performed in a wave flume at the University of Bologna (UB) in Italy (Lamberti and Aminti, 1994) within the same RMBFM project. In particular, Lamberti (1994) emitted the idea that, for sufficiently wide toe-berms, the main feature of this interaction process could be a phenomenon of "toe-armouring" by stones falling down from the damaged armour. If these stones remain on the toe-berm, they may increase its stability (lower damage to the toe-berm). Still addressing these possible interactions, we focus here more closely on three-dimensional effects, by considering the following aspects :

- wave obliquity (effect of angle of wave incidence)
- wave directionality (effect of angular spreading of wave energy)
- behaviour on the trunk section and at round-heads. Within the frame of this paper, attention will be mainly paid to the trunk section. Additional results for the round-head section may be found in Benoit and Donnars (1996).

In the present study, these effects are investigated through a series of laboratory experiments in a multidirectional wave basin. The experimental conditions and procedure are described in Section 2. Results for the main-armour and the toe-berm are presented and compared with other experimental results and existing design formulas in Section 3 and 4 respectively. The effects of the interaction processes are discussed in Section 5. The conclusion of Section 6 summarizes the main findings of this study and gives some recommendations for practical design.

2. EXPERIMENTAL SET-UP AND TEST CONDITIONS

2.1 Brief description of the wave basin used for laboratory tests.

The tests have been conducted in the multidirectional wave basin of Laboratoire National d'Hydraulique (LNH) in Chatou (France) (Figure 1). This experimental facility is dedicated to physical modelling applied to maritime and coastal studies. The overall dimensions of the basin are 54 m x 31 m x 1.3 m (maximum water depth for operational use : 0.80 m). This basin is fitted out with a multidirectional piston-type wave-maker composed of 56 paddles (segment width : 0.40 m).

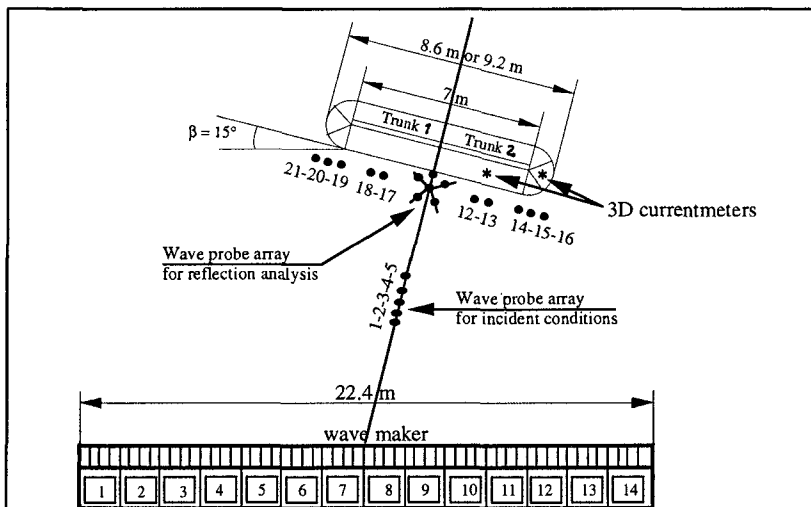


Figure 1 : General lay-out of experimental set-up in LNH wave basin.

The total length of the wave-maker thus reaches 22.4 m. It can operate in the frequency range [0.2 ; 2.0 Hz]. During the experiments, vertical side-walls (of 2 m in length) were set up at each side of the wave-maker in order to increase the work area by making use of "corner-reflection" method (Funke and Miles, 1987).

2.2 Breakwater lay-out and cross-sections.

The present tests were aimed to continue previous tests, performed within the same research project in a wave flume at the University of Bologna (UB) in Italy (Lamberti and Aminti, 1994). So, we started from the same breakwater characteristics, except that the geometric scale was multiplied by a factor of 1.32 with respect to UB tests in order to adapt to the characteristics of LNH wave basin.

The main features of breakwater cross-sections (Figure 2 for the slope of 1:1.5) are summarized below :

- tests are performed with a flat bottom at a water depth of $d=0.45$ m.
- the ratio of water depth above toe-berm h_t to design wave height H_{sd} is about 1 ($h_t/H_{sd} \approx 1$)
- the width of toe-berm B_t is constant over the whole test programme and is taken to be three times the diameter of design toe-berm stones $D_{n50t(\text{design})}$
- the thickness of the toe-berm is constant and is taken to be that of two layers of design toe-berm stones $D_{n50t(\text{design})}$.
- two armour slopes are considered : 1:1.5 ($\cotg \alpha = 3/2 = 1.5$) and 1:2.5.

The breakwater is not parallel to the wave-maker, but there is an angle of 15 degrees between them (Figure 1). This orientation has been chosen in order to ensure a sufficiently high frequency limit for generated waves even for oblique incidences. In the paper, we only make use the direction of incidence as referred to the breakwater (for instance, a 0° direction corresponds to normal wave attack).

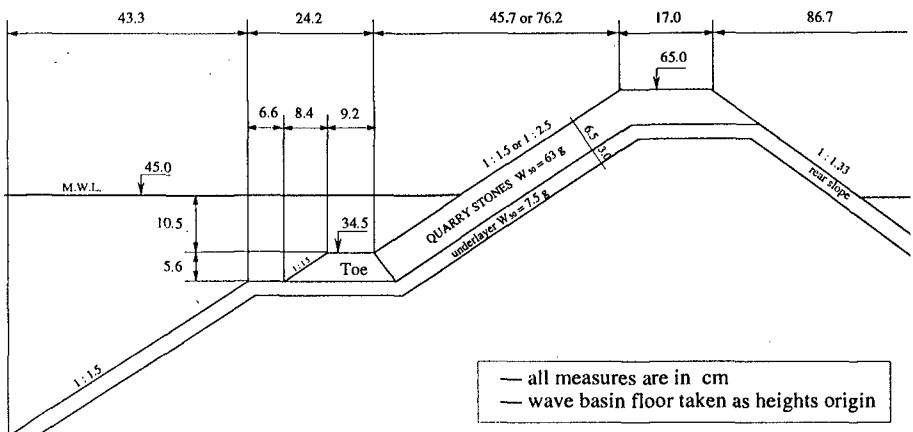


Figure 2 : Cross-section of breakwater (slope 1:1.5).

The breakwater used for the experiments consists in two half-breakwaters, each of them being composed of a trunk section and a round-head section (Figure 3). Each half-breakwater has the same armour units, but different toe-berm stones. A 1 m long test section is considered on each trunk section. The round-head sections are divided in 6 angular sectors of 36 degrees (Figure 3). By this way, it is possible to test simultaneously 4 sections (2 trunks and 2 round-heads) under normal waves and 3 sections under oblique waves (2 trunks, 1 round-head).

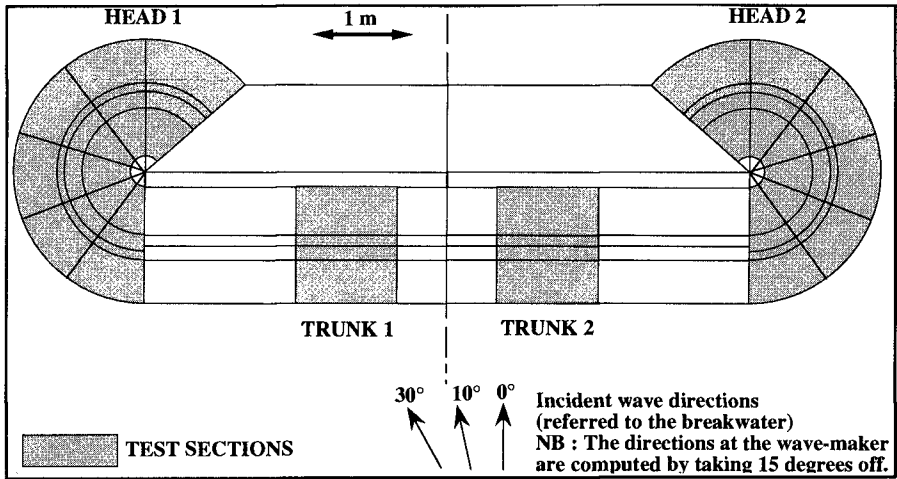


Figure 3 : Test sections on the breakwater and wave directions.

2.3 Choice of governing parameters and test programme.

The choice of varying governing parameters for the experimental tests is based on the analysis performed by Gerding (1993) and Lamberti (1994) :

- the **nominal diameter of the toe-berm stones** [4 values]. The first value corresponds to the "design" value as determined by a conventional design approach, whereas the other ones lead to "unstable" berms (see § 2.5).
- the **slope of the main-armour** [2 values : 1:1.5 and 1:2.5] (see § 2.2).
- the **wave steepness** [2 values : $s_{om} = 2\%$ and $s_{om} = 5\%$]
The wave steepness is defined as : $s_{om} = H_s/L_{0m} = H_s/1.56T_m^2$. As "longer" waves ($s_{om} = 2\%$) are thought to be more severe for the stability of the breakwater than "shorter" waves ($s_{om} = 5\%$), most of tests are performed with the 2 % steepness for incident waves.
- the **angle of wave incidence** [2 values : $\beta = 0^\circ$ and $\beta = 30^\circ$]. One test has also been conducted under a $\beta = 10^\circ$ angle of wave incidence to check whether such a value could lead to higher damage, as shown by Galland (1994) for toe-berm stability at concrete armoured structures or by Juhl and Sloth (1994) for wave overtopping.
- the **angular spreading of energy** [2 values : $s = \infty$ (unidirectional waves) and $s = 15$]. The spreading index s corresponds to the exponent in the model of directional spreading function used for generating drive signals for the wave-maker $D(\theta) = 1/\Delta \cos^{2 \cdot s}(\theta)$. The short-crested case ($s = 15$) produces a directional sea-state with moderate angular spreading (directional width of about 10 degrees).

The test programme is based on the above choice of governing parameters. Due to this rather large number of parameters, it was not possible to test all the combinations between all parameters, which would have resulted in $4 \times 2 \times 2 \times 2 \times 2 = 64$ tests. This number has been reduced to 30 by considering only some of the above combinations (Benoit and Donnars, 1996). Because two half-breakwaters are tested simultaneously, the overall number of tests is finally equal to 15. Due to the fact that only three sections are tested under oblique wave, the total number of sections (trunk + round-head) examined during the experiments is equal to 52.

2.4 Review of incident wave conditions.

A JONSWAP-type spectrum is used for the distribution of wave energy over frequencies with a value of the peak enhancement factor $\gamma = 5$ for the tests at steepness $s_{om} = 0.05$ and a value of $\gamma = 1$ for the tests at steepness $s_{om} = 0.02$.

For a given test, the wave steepness is constant and the target wave height is increased by successive steps : each step corresponds to a run. A test is thus composed of 7 runs. The target wave characteristics for the experiments (in terms of significant wave height H_s and mean period T_m) are summarized in Table 1.

Each run has a duration of about 2000 waves of target mean period T_m .

run n°	$s_{om} = 0.05$ ($\gamma = 5$)		$s_{om} = 0.02$ ($\gamma = 1$)	
	H_s (m)	T_m (s)	H_s (m)	T_m (s)
1	0.060	0.88	0.045	1.20
2	0.071	0.95	0.053	1.30
3	0.082	1.02	0.061	1.40
4	0.093	1.09	0.069	1.49
5	0.104	1.15	0.077	1.57
6	0.115	1.21	0.085	1.65
7	0.126	1.27	0.093	1.73

Table 1: Target wave characteristics for model experiments (H_s , T_m).

2.5 Review of incident wave conditions.

• **Armour stones** : The following characteristics were obtained for the stones of the main armour (two layers) : Density=2.55 ; Nominal diameter $D_{n50a} = 2.91$ cm ; Nominal weight $W_{n50a} = 63$ g ; $\Delta.D_{n50a} = 4.51$). Same stones are used for the armour-layer both at the trunk sections and at the round-heads.

• **Toe-berm stones** : The "design" value of toe-berm stones for trunk section (labelled T1) was determined according to the design formula of Gerding (1993), leading to the following characteristics : Density=2.72 ; Nominal diameter $D_{n50t} = 2.58$ cm ; Nominal weight $W_{n50t} = 47$ g ; $\Delta.D_{n50t} = 4.44$)

From the design value of toe-berm stones, the three other values (termed T2 to T4) are computed from the relationship proposed by Lamberti (1994) :

$$W_{n50t}(T_j) = \frac{W_{n50t}(T_1)}{2^{K_j}} \quad \alpha \quad K_j = \ln_2 \left(\frac{W_{n50t}(T_1)}{W_{n50t}(T_j)} \right)$$

The values of K_j are chosen to be :

- toe-berm stones T2 : $K_2 = 1.2$ $W_{n50t}(T2) = W_{n50t}(T1) / 2.3 \approx 20$ gr
- toe-berm stones T3 : $K_3 = 2.5$ $W_{n50t}(T3) = W_{n50t}(T1) / 5.66 \approx 7.5$ gr
- toe-berm stones T4 : $K_4 = 4.5$ $W_{n50t}(T4) = W_{n50t}(T1) / 22.6 \approx 2.2$ gr

The weight of toe-berm stones at the round-head are increased by about 25 % from the above values determined for the trunk section.

The sorting index D_{85} / D_{15} for the various toe-berm stones lies in the range [2 ; 2.5]. It must be emphasised that this sorting index is much larger (but also more representative of natural conditions) than the value of 1.1 used during the flume experiments at UB (Lamberti, 1994).

2.6 Measurement and analysis of damage.

There is no rebuilding of the breakwater between consecutive steps of a test : cumulative damage is observed and reported during the experiments.

Damage is first evaluated by counting the number of units displaced from the armour-layer and the toe-berm. This is the standard method for measuring damage during the tests. For the trunk section, the damage index is given by the number N_{od} of units displaced within a strip of width equal to one D_{n50} :

$$N_{od} = N_d \frac{D_{n50}}{l} \quad \text{where } l \text{ is the width of the trunk section.}$$

An optical sensor has also been used for several tests in order to get information on the changes in the profile of the breakwater and to estimate the eroded area A_e in the breakwater profile. The damage level is then defined as : $S = A_e / D_{n50}^2$.

By combining present experimental results and previous observations (Van der Meer, 1992 ; Burcharth, 1993), the relationship : $S \approx 2 \cdot N_{od}$ is obtained and will be used further in the analysis of test results.

3. STABILITY OF THE MAIN-ARMOUR FOR THE TRUNK SECTION

3.1 Descriptive analysis of the stability of the main-armour of the trunk

We only report here the main observations from the tests. A more complete description and analysis of results may be found in Benoit and Donnars (1996).

3.1.1 Influence of wave direction and directionality (angular spreading)

Examples of test results for the stability of the main-armour are plotted on Figure 4 for four wave conditions and the four toe-berm stone sizes (armour-slope 1:2.5 only). In the range of tested values, the wave direction does not appear to have a significant effect on the stability of the main-armour as long as the toe-berm is stable (toe-berms T1 and T2). When the toe-berm is unstable, damage levels are higher on the armour layer and the normal direction seems to be more severe than an oblique (30°) direction.

Damage on the main-armour is higher under short-crested waves (only one tested value of angular spreading) than under long-crested waves for the same incident wave height. This is a clear observation from present experiments, which appears to be in some contradiction with other experimental test results. For instance, Thunbo Christensen *et al.* (1984) found from model tests on a breakwater armoured with quarry stones that uni-directional waves result in 30-40 % more damage to the breakwater when compared to short-crested waves. Canel and De Graauw (1992) also concluded that short-crested waves result in an increase of the stability number (from 0 to 60 %) for rock for the 1 % damage level. Although no definite conclusion may be drawn from the rather low number of present experiments, this increase of damage under short-crested waves appears quite clearly. It is assumed to be due to a rather low angular spreading of wave energy.

This increase of damage under short-crested waves is clearly observed for the normal attack, but seems to be quite feeble for the 30° direction.

3.1.2 Influence of wave steepness (long-crested waves ; armour slope 1:2.5)

The effect was examined for toe-berms T1 and T2 only. For the same wave height, it is observed that the "longer" waves ($s_{om} = 2$ %) clearly result in more damage to the armour-layer than the "shorter" waves ($s_{om} = 5$ %).

3.1.3 Influence of toe-berm stones weight (long-crested waves only)

For the normal wave attack, a clear increase of damage to the main-armour with decreasing toe-berm stone weight is observable. For toe-berm stones T1 and T2, damage to the armour remains at an acceptable and comparable level. But for lighter stones (toe-berm stones T3 and T4), the main-armour is significantly more damaged. Severe damage occurs for the lightest toe-berm stones T4.

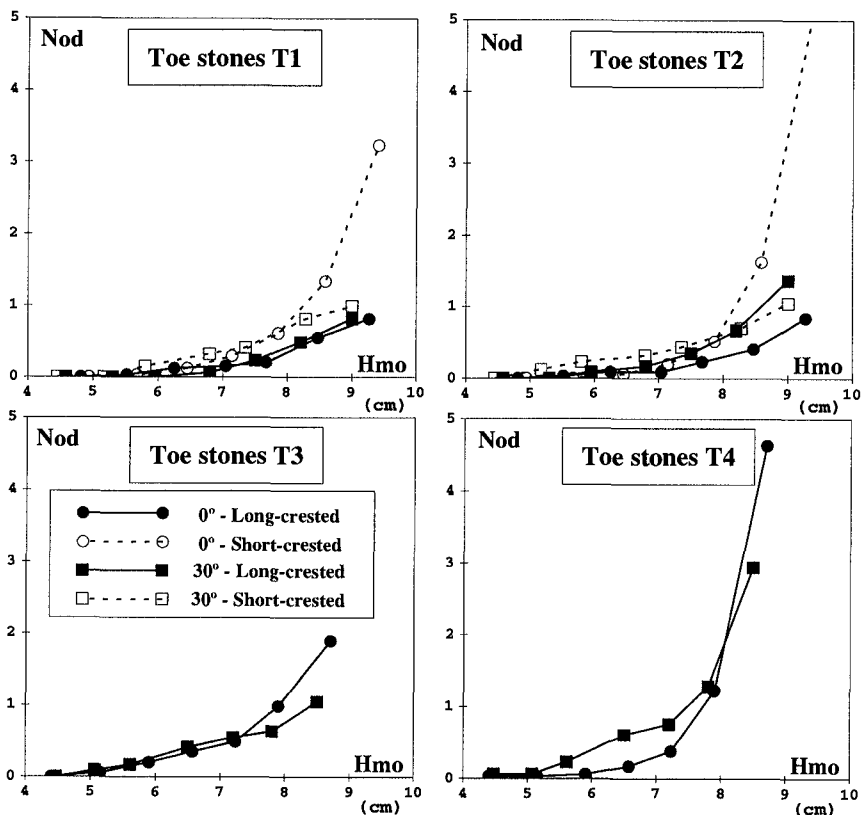


Figure 4 : Evolution of observed damage to the main-armour for four wave conditions (armour-slope 1:2.5 only).

3.2 Synthetic analysis of the stability of the main-armour of the trunk

In order to compare our test results to existing design formulas, we consider the Van der Meer design formulas (Van der Meer, 1988) for the armour layer :

$$\text{Plunging waves } (\xi_m < \xi_{mc}) : \frac{H_s}{\Delta \cdot D_{n50a}} = 6.2 \frac{P^{0.18}}{\sqrt{\xi_m}} \left(\frac{S}{\sqrt{N}} \right)^{0.2}$$

$$\text{Surging waves } (\xi_m > \xi_{mc}) : \frac{H_s}{\Delta \cdot D_{n50a}} = 1.0 P^{-0.13} \left(\frac{S}{\sqrt{N}} \right)^{0.2} \sqrt{\cotg \alpha} \xi_m^P$$

where N is the number of waves in a storm or in the test (N=2000), S is the damage index defined from the eroded area A_c (here, S is computed from N_{od} by : $S = 2 \cdot N_{od}$; see § 2.6), ξ_m is the surf-similarity parameter defined from the mean wave period T_m , P is the notional permeability factor (taken to be 0.4 as suggested by Van der Meer (1988) for a permeable core with a filter and an armour composed of two layers of natural rocks). ξ_{mc} is the critical value of surf-similarity parameter ξ_m , determining the transition from plunging waves to surging waves :

$$\xi_{mc} = \left[6.2 P^{0.31} \sqrt{\tan \alpha} \right]_{P+0.5}^{-1}$$

The values surf-similarity parameter ξ_m depend on both the steepness (two possible values) and the slope of the armour (two possible values). From these

values, it appears that tests performed for the 1:1.5 slope are of "surging" type whereas they are of "plunging type" for the 1:2.5 slope (and 2 values of steepness).

The tests results are plotted and compared to Van der Meer stability formulas on Figure 5.a (plunging waves) and 5.b (surging waves). Experimental points from Van der Meer (1988), Galland (1994) and Lamberti (1994) are also superimposed.

— Analysis of the "plunging waves" tests (figure 5.a) :

An acceptable agreement is found between experimental points and the formula. However, one can observe that the lower values of damage are overpredicted by the formula, whereas the higher values seem to be underpredicted. This is in particular quite clear for the tests with 5 % steepness, which may indicate that the effect of steepness is not perfectly resolved in the Van der Meer formula for plunging waves. If we consider the experimental points from Van der Meer (1988) for permeable core, we again note that most of points lie above the design curve.

— Analysis of the "surging waves" tests (figure 5.b) :

Based on present experiments, the general trend of the formula is to overpredict the observed damage levels. The use of Van der Meer formula on these experiments thus seems to lead to a conservative design of the armour. Test results from Lamberti (1994) also confirm this trend in spite of a rather high scatter. However, one should also note that Van der Meer formula appears to be a good fit to the Van der Meer (1988) test results obtained with a permeable core. Additional analysis and comparisons should be performed in order to check this point. In particular, it was observed that the permeability factor P may play a significant role in the formula and the precise determination of P for an existing breakwater is not straightforward.

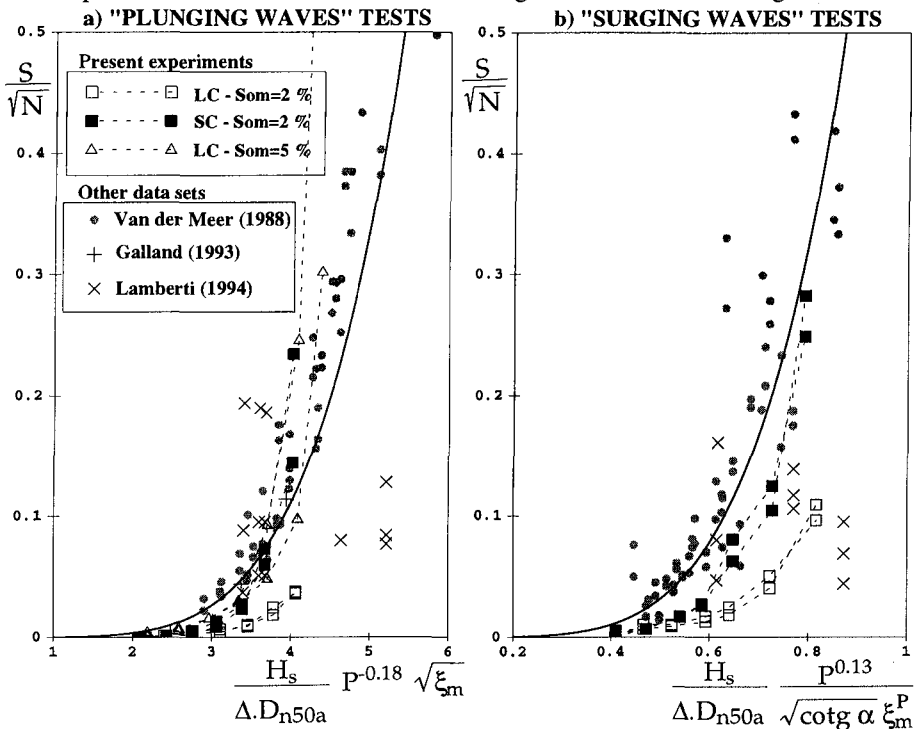


Figure 5 : Comparison of present test results with Van der Meer (1988) formula for the stability of the main armour (tests under normal wave attack).

4. STABILITY OF THE TOE-BERM FOR THE TRUNK SECTION

4.1 Descriptive analysis of the stability of the toe-berm of the trunk

4.1.1 Influence of wave direction and directionality (angular spreading)

Examples of test results are plotted on Figure 6 for four wave conditions and the four toe-berm stone sizes (armour-slope 1:2.5 only). From the tests, we observe that the normal direction seems to be usually more severe than the 30° direction.

Damage to the toe-berm is higher under short-crested waves than under long-crested waves only for the normal attack, whereas long-crested waves produce more damage for the 30° direction.

The toe-berms are less stable for the slope 1:2.5 slope of armour than the same ones associated with the 1:1.5 slope. This may be related to slight different hydrodynamical conditions of wave breaking and run-down, resulting in stronger action to the toe-berm.

4.1.2 Influence of wave steepness (long-crested waves ; armour slope 1:2.5)

The longer waves ($s_{om} = 2\%$) create more damage to the toe-berm than shorter waves ($s_{om} = 2\%$), but this trend is stronger than for the damage to the main-armour (see § 3.12). This indicates that the toe-berm is more sensitive to the steepness of incident waves than the main-armour.

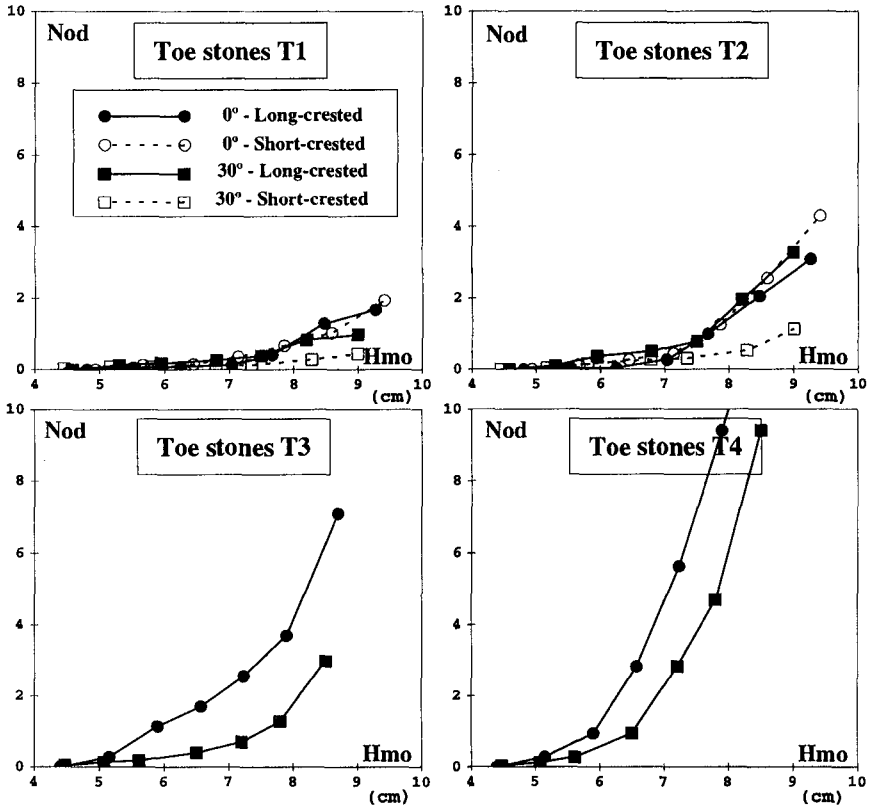


Figure 6 : Evolution of observed damage to the toe-berms for four wave conditions (armour-slope 1:2.5 only).

4.1.3 Influence of toe-berm stones weight (long-crested waves only)

For the normal wave attack, damage to the toe-berm increases with decreasing toe-berm stone weight. The effect of the toe-berm stone size is clearly more sensitive on the damage to the toe-berm itself than on the damage to the main-armour. However, one may distinguish two different behaviour : toe-berms T1 and T2 are quite stable with low damage levels, whereas toe-berms T3 and T4 are clearly unstable with higher damage levels.

4.2 Synthetic analysis of the stability of the toe-berm of the trunk

In this section, we consider the formula established by Gerding (1993) for the stability of the toe-berm of a rubble-mound breakwater :

$$\frac{H_s}{\Delta \cdot D_{n50t}} = \left(0.24 \frac{h_t}{D_{n50t}} + 1.6 \right) N_{od}^{0.15}$$

where Δ is the relative buoyant density of toe-berm stones ($\Delta = \rho_r / \rho_w - 1$), D_{n50t} is the nominal diameter of stones composing the toe-berm, h_t is the depth of toe-berm below the Mean Water Level and N_{od} is the damage index to the toe-berm.

The damage level is classified as : $N_{od} = 0.5$: hardly any damage ; $N_{od} = 2$: acceptable damage (design criteria) and $N_{od} = 4$: unacceptable damage.

On Figure 7, the experimental data points plotted on the graph are composed of all the present experiments conducted with normal wave attack and long-crested waves (including 2 slopes of main-armour, 4 toe-berm stone sizes and 2 values of wave steepness). On this figure, an acceptable agreement between present experiments and the formula from Gerding (1993) is obtained. However, one must note that the effects of mound-slope and wave-steepness are not included in Gerding's formula. Although these effects do not appear as dominant on experimental points, it is possible to distinguish on Figure 7 the data points for the 1:1.5 slope (triangles) and for the 1:2.5 slope (circles). The effect of steepness is more sensitive (compare crosses and circles for toe-berm stones T1 and T2), indicating that damage to the toe-berm appears to be lower for the "shorter" waves than for the "longer" waves. The inclusion of these effects in an extended formula appears as an interesting research item.

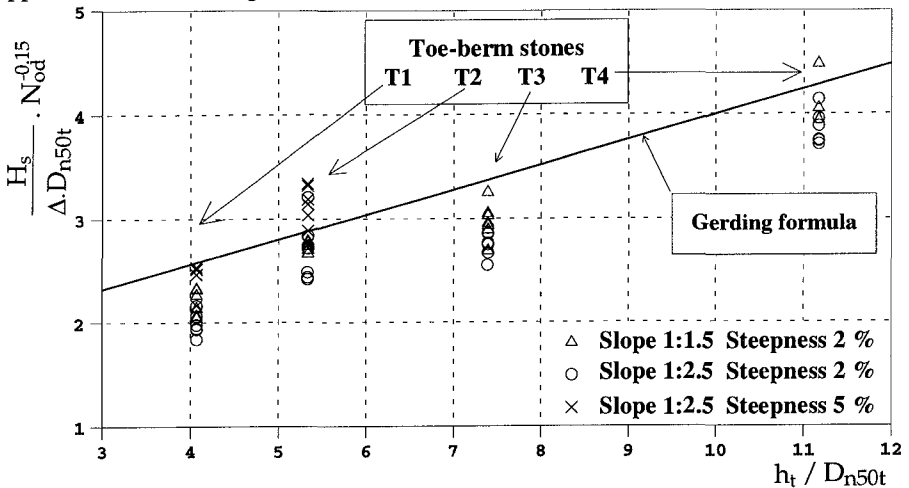


Figure 7 : Comparison of present test results with Gerding (1993) formula for the stability of the toe-berm (tests under normal wave attack only).

5. DISCUSSION OF THE INTERACTION PROCESSES

During the experiments, the following points have been observed :

- For most of tests, as the wave height increases between each run, damage first appears on the toe-berm and then on the main-armor. This is not really surprising, as the main-armor is made of stones whose weight is determined from "standard" design value whereas the toe-berm stones weight are equal (toe-berm stones T1) or lower than the design value (toe-berm stones T2 to T4). It is thus quite a "normal" behaviour that toe-berms are damaged first.
- The stability of the toe-berm continuously decreases as the weight of toe-berm stones decreases. The stability of the main-armor is also decreasing with the size of toe-berm stones (in particular for toe stones T3 and T4).
- Damage to the main-armor for the trunk section is mainly located between the toe (- 0.10 m referred to MWL) and about + 0.05 m referred to MWL.

In order to describe the interaction processes between the main-armor and the toe-berm, we start from the classification of evolution mechanisms proposed by Lamberti (1994). We further tentatively propose a correlation diagram between damage to toe-berm and damage to main-armor where the evolution processes (A, a, B, b, c) from Lamberti (1994) are schematically summarized (figure 8).

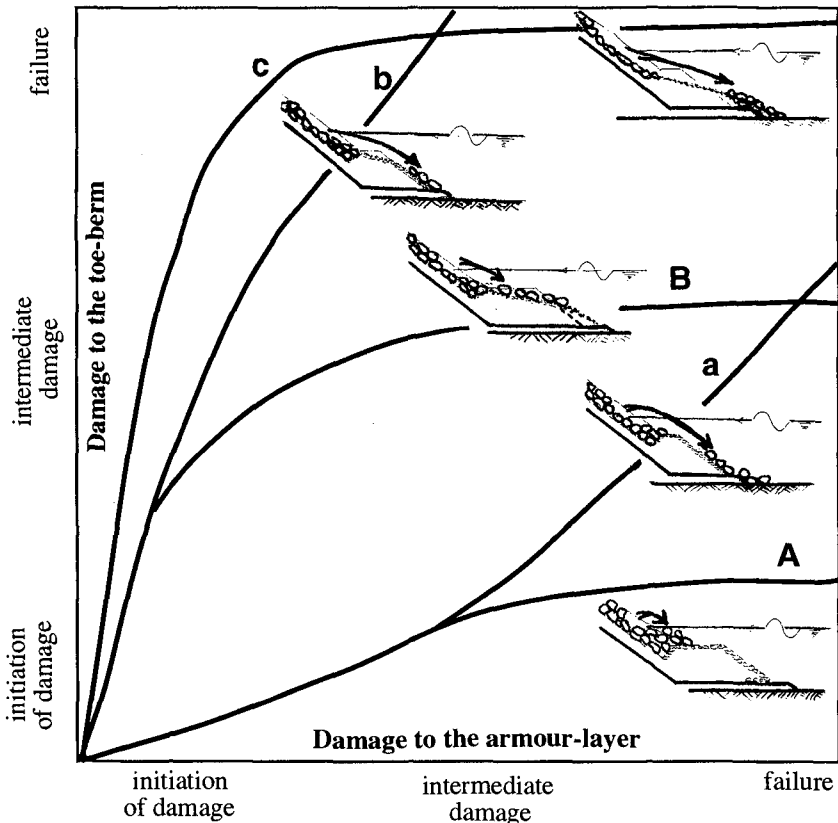


Figure 8 : Tentative analysis of correlation between damage to armour and damage to toe-berm after a classification of mechanisms from Lamberti (1994)

Based on the data from our experiments, it is possible to build such plots for the four toe stones used and for different wave conditions (Figure 9). On these plots, we can directly compare the synthetic evolution of the observed interaction process to the classification of evolution processes of figure 8. The main comments raising from this analysis are summarized below :

• **Toe-berm stones T1 and T2 : evolution process : a**

The toe-berm is rather narrow, but quite stable for the various wave conditions. Damage appears approximately at the same time on the main-armour and the toe-berm. There is no significant effect of toe-armouring process. As the toe-berm is quite narrow, the stones falling down from the armour do not stop on the toe-berm.

• **Toe-berm stones T3 : evolution process : b**

The toe-berm is less stable than the armour layer and is damaged first. It thus becomes narrower and is then not very effective in retaining armour units when damage further appears on the main armour.

• **Toe-berm stones T4 : evolution process : c**

The toe-berm is severely unstable and the static support of the armour layer fails when the toe-berm is fully damaged. The armour layer may then slide down abruptly, exposing the underlayer.

In particular, the evolution process B (stones falling down from the armour layer stop on the toe-berm and enhance its stability : toe-armouring process) only rarely occurred and then exhibited quite feeble effect on the stability of the toe-berm. Most

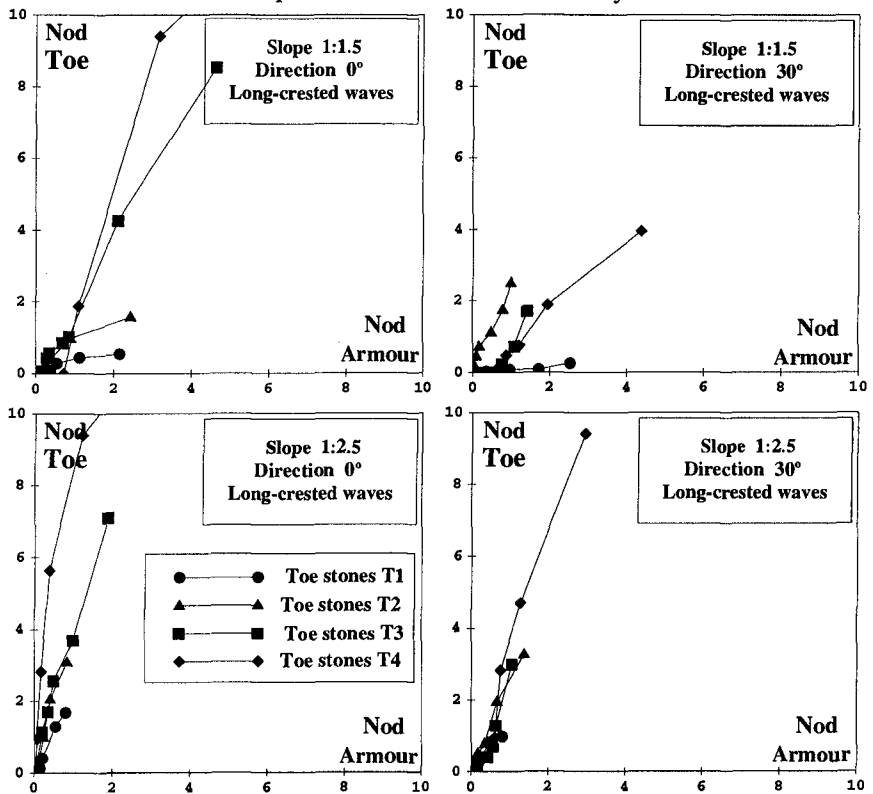


Figure 9 : Correlation diagrams based on present experiments for various conditions

of stones falling from the armour went directly to the floor of basin either because the berm was too narrow (toe-berm stones T1 and T2) or because it was already significantly damaged when damage started on the main-armour (toe-berm stones T3 and T4). For the breakwater profiles tested in the present study, there thus appears to be only a weak coupling in the stability of the main-armour and the toe-berm for the trunk section. It is suspected that the considered toe-berms were either too unstable or too narrow for the occurrence of the "toe-armouring" process. Such a process could maybe be observed with a wider and still quite stable toe-berm, but tests in this direction remain to be performed.

6. CONCLUSIONS

The major observations and conclusions raising from present experiments are **very briefly** summarized below for the trunk section of the breakwater :

- Effect of wave incoming direction : No definite effect emerges from the tests results for the main-armour. For the toe-berm however, the normal direction seems more severe than the 30° direction, at least for long-crested waves.
- Effect of wave directionality : More damage to the main-armour and to the toe-berm is observed under short-crested waves, in particular for normal wave attack. This point is rather in contradiction with previous experiments (Thunbo Christensen *et al.*, 1984 ; Canel and De Graauw, 1992), but is rather clear from present tests. It is supposed to be related to a quite low angular spreading of energy, which could be more severe for the stability. This point has however to be addressed by additional tests.
- Effect of wave steepness : Among the two tested values of steepness (2 % and 5%), the one corresponding to "longer" waves results in more damage both to the armour-layer and to the toe-berm. However, the toe-berm appears to be more sensitive to the steepness of incident waves than the main-armour.
- Effect of toe-berm stones size : when the toe-berm is "stable" (T1 or T2), the stability of the armour is not significantly affected by the stability of toe-berm. However, when the toe-berm is unstable (T3 or T4), higher damage is observed on the main-armour, leading sometimes to its failure. As expected, damage to the toe-berm increases as the toe-berm stone size decreases.

Comparing present results with existing design formulas, acceptable agreement was observed with the Van der Meer formulas for the stability of the main-armour. However some differences were also noted, in particular for the "plunging waves" formula : the lower values of damage to the armour-layer are overpredicted by the formula, whereas the higher values seem to be underpredicted. The Van der Meer formula for "surging waves" appears to lead to a somewhat conservative design. For the toe-berm, the formula from Gerding (1993) lies in acceptable agreement with present results, although the effects of wave steepness and mound-slope (not included in the formula) slightly increase the scatter of experimental points.

As a matter of conclusion, it appears from the present tests that the major feature of the interaction process between main-armour and toe-berm is an increase of damage to the armour when the toe-berm is unstable. This may lead to a total failure of the armour if the toe-berm is sufficiently eroded to fail in providing static support to the armour-layer. On the opposite, minor effect of main-armour on toe-berm stability was observed. In particular the "toe-armouring" process appeared to occur only marginally and under precise conditions. This process is thus regarded as a particular mechanism, which will occur only under specific conditions (precise relative stability of the toe-berm and the armour-layer, wide berm, ...).

As the effects of interaction processes between main-armour and toe-berm appear quite weak (unless toe-berm stones are significantly lighter than their design value), it appears both more natural and safe to use state-of-the-art stability formulas to establish a first design of both the toe-berm and the armour-layer independently. The full breakwater profile should then be tested in a wave flume, or preferably in a wave basin with a correct representation of the actual bathymetry in order to validate its design.

7. ACKNOWLEDGEMENTS

This work was funded partly by the European Union (Directorate General XII of the European Communities) under contract MAS2-CT92-0042 of MAST-2 programme and partly by the French Sea State Secretary (Service Technique Central des Ports Maritimes et Voies Navigables). The authors are grateful to the participants of the Rubble-Mound Breakwater Failure Modes (RMBFM) project for their fruitful discussions and suggestions.

8. REFERENCES

- Benoit M., Donnars P. (1996) : Interactions in the stability of main-armour and toe-berm for a rubble-mound breakwater : an experimental study under both long-crested and short-crested waves. *MAST II RMBFM Project, Final report, January 1996.*
- Burcharth H.F. (1993) : Structural integrity and hydraulic stability of dolos armour layers. *Series paper N°9. Aalborg University (Denmark).*
- Canel M., De Graauw A. (1992) : Rubble-mound breakwater stability with multidirectional waves. *MAST I G6-S Project. Final report. Sogreah Ing. (France).*
- Funke E.R., Miles M.D. (1987) : Multi-directional wave generation with corner reflectors. *National Research Council Canada. Technical report TR-HY-021.*
- Galland J.-C. (1994) : Rubble mound breakwater stability under oblique waves : an experimental study. *Proc. of the 24th Int. Conf. on Coastal Eng. (ASCE), pp 1061- 1074, Kobe (Japan).*
- Gerding E. (1993) : Toe structure stability of rubble mound breakwaters. *Master's Thesis, Report H1874 - Delft University of Technology (The Netherlands).*
- Juhl J., Sloth P. (1994) : Wave overtopping of breakwaters under oblique waves. *Proc. 24th Int. Conf. on Coastal Eng. (ASCE), pp 1182-1196, Kobe (Japan).*
- Lamberti A., Aminti P. (1994) : Program of tests on main armour - toe berm interaction and preliminary check of scale effects. *MAST II RMBFM Project, Proc. of the 2nd workshop, Bressanone (Italy), 20-21 January 1994.*
- Lamberti A. (1994) : Preliminary results on main-armour toe-berm interaction. *MAST II RMBFM Project, Proc. of the 3rd workshop, De Voorst (The Netherlands), 15-16 November 1994.*
- Thunbo Christensen F., Broberg P.C., Sand S.E., Tryde P. (1984) : Behaviour of rubble-mound breakwater in directional and uni-directional waves. *Coastal Engineering, Vol 8, pp 265-278.*
- Van der Meer J. W. (1988) : Rock slopes and gravel beaches under wave attack. *Doctoral thesis. Publication N°396, Delft Hydraulics (The Netherlands).*
- Van der Meer J. W. (1992) : Conceptual design of rubble-mound breakwaters. *Proc. of the Short Course on Design and reliability of coastal structures. 23rd Int. Conf. on Coastal Eng. (ASCE), Venice (Italy).*

CHAPTER 127

POTENTIAL USES FOR THE RAPIDLY INSTALLED BREAKWATER SYSTEM

Jimmy Fowler¹, Donald Resio², Michael Briggs¹, Cheryl Pollock¹
Members, ASCE

Abstract

Engineers and scientists at the U.S. Army Engineer Waterways Experiment Station (WES) are developing a Rapidly Installed Breakwater (RIB) System specifically designed to address problems associated with the military's efforts to off-load ships during Logistics Over The Shore (LOTS) operations. Problems arise with these operations when seas become energetic and limit capabilities of crane operators and stevedore crews. The RIB System is designed to solve this problem by creating a 'pool' of calmer water where these operations occur so that crews can continue to function. A series of small-scale laboratory experiments conducted in 1995 and 1996 at WES's facilities in Vicksburg, Miss., and at the O. H. Hinsdale Wave Research Laboratory at Oregon State University in Corvallis, laid the groundwork for the RIB System development and yielded an optimum RIB System configuration known as the "Double Delta". Laboratory results, obtained with the Double Delta configuration, showed that wave heights could be reduced by more than 80 percent. During the spring and summer of 1996, a mid-scale RIB System successfully demonstrated its capabilities during a field deployment, with wave height reduction on the order of 75 percent. Based on these results, it is believed that the RIB System will be integrated into the Army's LOTS asset inventory and become a key part of the solution to the military's LOTS problems.

¹ Research Hydraulic Engineer, USAE Waterways Experiment Station, Coastal and Hydraulics Laboratory, 3909 Halls Ferry Road, Vicksburg, MS, USA 39180-6199

² Senior Scientist, USAE Waterways Experiment Station, Coastal and Hydraulics Laboratory, 3909 Halls Ferry Road, Vicksburg, MS, USA 39180-6199

Introduction

For many years, the US Army Engineer Waterways Experiment Station (WES) has been involved with the design and deployment of floating breakwaters, primarily for application within bays or estuaries which are semi-protected from large waves. Such structures typically are intended to attenuate waves with heights not exceeding 4 ft and periods not exceeding 4 sec. Extrapolation to an open ocean environment is at least an order of magnitude greater in difficulty. In an oceanic environment, waves with heights and periods up to 10 ft and 10 seconds respectively, are common during storm conditions. Previous experiments have shown that to be effective, floating breakwaters must have widths on the order of 1/4 of the wavelength being attenuated, and hence, must be very massive to be effective. Such structures are simply not feasible for most temporary and rapidly installed floating breakwater applications, since it would be necessary to transport large volumes of construction materials to the site being sheltered. As described below, this problem was the driving force behind recent floating breakwater developments at the WES.

During energetic seas, the primary problem occurs in key offshore areas (anchorage) where containerships and roll-on/roll-off (RO/RO) vessels discharge cargo and unit equipment onto much smaller vessels, collectively termed lighterage. Hence, WES efforts were directed towards creating sheltered areas in which these anchorages could be located and operated more effectively. A Tactical Auxilliary Crane Ship (TACS) anchorage for offloading containerships offshore is shown in Figure 1 while a Roll On/Roll Off anchorage for offloading rolling stock, such as

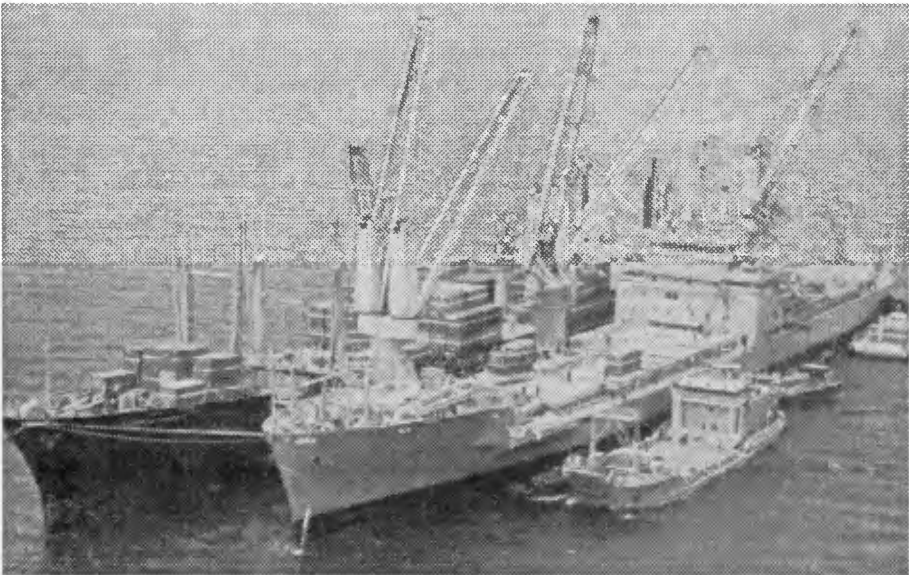


Figure 1. Example of Crane Ship (TACS) Anchorage.

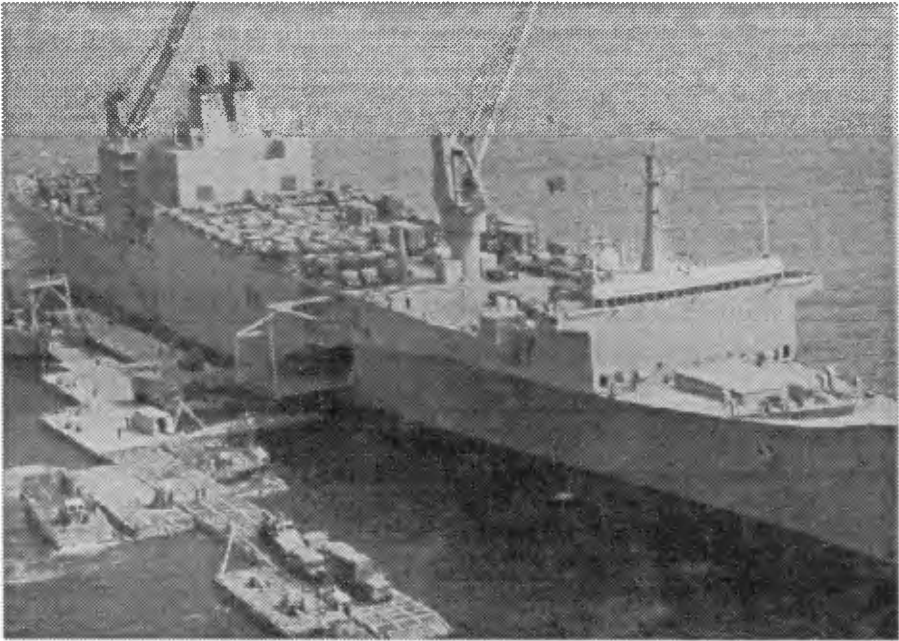


Figure 2. Example of Roll On/Roll Off Anchorage.

tracked and wheeled vehicles, is shown in Figure 2. The ability to move vehicles, equipment, and supplies from ship to shore in a rapid manner is considered vital to existing military force deployment operations such as humanitarian relief efforts or supporting a war-fighting effort. Therefore, a key feature of the RIB System is the ability to use existing assets to transport and deploy the system within acceptable time constraints. In light of this, the RIB System will very likely be stockpiled at various pre-positioned locations around the world in fairly large modular components. When exercises or real-world events require its use, the RIB System would then be loaded from the nearest pre-positioned site and transported via sealift to the LOTS site, where it would be assembled with the assistance of either Fast Sealift Ships or TACS in combination with Army and/or Navy tugs.

Operational Requirements of the RIB System.

The main problem to be overcome during these operations is the demonstrated inability to effectively conduct LOTS offloading operations when wave climate conditions exceed what is commonly termed "sea state 2", as given by the Pierson-Moskowitz scale for characterizing energetic seas. The Army uses the period of maximum energy associated with a given significant wave height as found in the Pierson-Moskowitz scale to characterize sea state, which has categories ranging between zero and nine. Figure 3 is provided to demonstrate the relationship between sea state, significant wave height, and period as found in the Pierson-Moskowitz scale. The problematic condition described above is commonly known as the "sea

state 3 problem" and exists when significant wave height is between 3 to 5 feet and periods range from about 3 to 7 seconds. The military considers the sea state 3 problem to be critical since these conditions exist a significant percent of the time worldwide, and in fact is considered to be a potential "war stopper" for present force projection plans and technology.

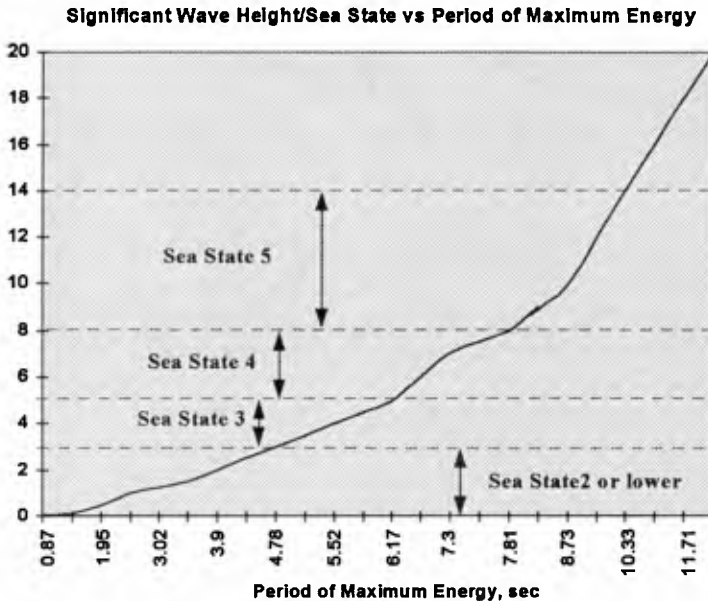


Figure 3. Relationship Between Sea State, Significant Wave Height and Period.

In light of the above, for the RIB System to be effective, it should be deployable during sea state 3 conditions and should reduce incident waves to create a "pool" of calmer water in the immediate vicinity of these anchorages which is below the sea state 3 threshold. With this scenario, crane operators and stevedore crews could continue to function during sea state 3 and even greater, since existing lighters can operate effectively in sea state 3, once safely loaded. An efficiently performing RIB System would cause the limiting sea state condition to be determined by capabilities of the various lighterage and equipment being used during the LOTS operation.

WES-Developed Rapidly Installed Breakwater System.

The RIB System is presently being developed and evaluated by research coastal engineers at WES. The RIB System consists of a V-shaped structure in plan view, with vertical barrier curtains extending from the surface of the water toward the bottom for a distance sufficient to preclude excessive wave energy from penetrating beneath the structure (see Figure 4). The RIB system concept was initially developed to address specific problems encountered by military personnel during LOTS operations, primarily those affected by sea state conditions characterized by relatively short period waves.

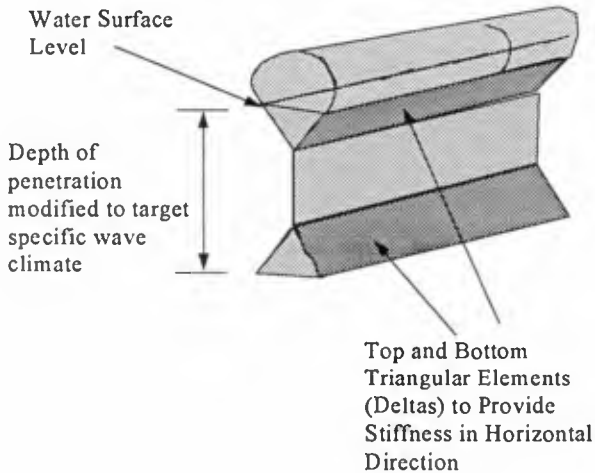


Figure 4. Double Delta Version of the RIB System

When deployed, the tip of the V-shape is oriented into approaching waves and spreads wave fronts apart based on geometric spreading and coupled deflections of wave motion. Ships and lighterage are moored in the lee of the V-shape for offloading. Depending on the specific location where the RIB System is to be employed, the legs of the "V" will vary, but for maximum effectiveness, each leg should be at least three wavelengths in length. The legs are joined at the front of the RIB System and supported with braces to insure structural stiffness. Wave-related mooring loads are relatively small due to two factors. First, the structure is designed to deflect waves rather than absorb them. Second, since the structure is oriented at an angle and is several wavelengths long, the oscillatory nature of the wave forces associated with the crest are simultaneously reduced by the force associated with the trough, which acts in the opposite direction.

Small Scale Laboratory Model Experiments.

During the early stages of the RIB System development, scale model studies were conducted at WES and Oregon State University (OSU) to test the concept, refine the initial design, and subsequently to test enhancements and various modifications. Results indicated that a significant "offshore" area could be effectively reduced from sea state 3 to sea state 1 by the RIB system. The objective of this effort was to obtain data relating to wave transmission in the lee of the RIB system, by evaluating multidirectional waves with both frequency and directional spreading. Wave heights were recorded at 15 locations throughout the sheltered region to ascertain diffraction effects around the ends of the RIB System. Laboratory experiments evaluating the Double Delta configuration which yielded the favorable results are depicted in Figure 5, with each plotted line representing a different wave period. Results are presented as the ratio of recorded wave height in the lee of the system divided by measured incident wave height approaching the RIB System versus distance from the leading edge of the RIB system. As shown below, it was possible to obtain up to 83 percent attenuation (19 percent transmitted height ratio) for some of the wave conditions, for the Double Delta configuration RIB system arrangement.

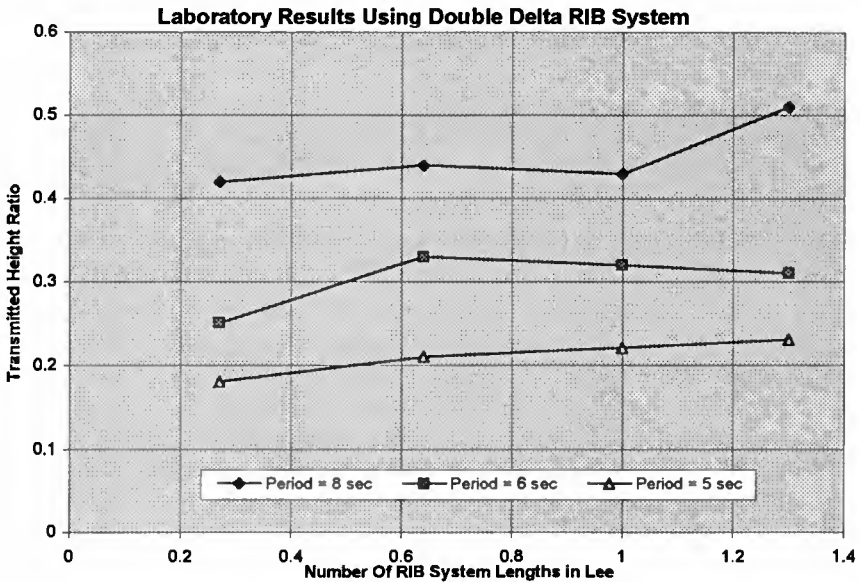


Figure 5. Laboratory Results Using Double Delta RIB System.

Figure 6 is a photograph which shows the wave basin setup and wave reduction achieved by the RIB System during one of the Double Delta experiments conducted at the OSU facilities. Based on the successes achieved in laboratory environments, a mid-scale field experiment was designed and subsequently conducted in the Currituck Sound during May 20 - 14 June 1996.



Figure 6. Laboratory Experiment Conducted at OSU Using the Double Delta Version of RIB System with Significant Height = 5 ft, Period = 6 sec..

RIB System Field Experiment

The field study was performed at WES's Field Research Facility, located on the Outer Banks in Duck, North Carolina. Since the model was constructed at a 1 to 4 scale, open ocean deployment was not suitable, and the somewhat milder wave climate of the Currituck Sound was selected. The RIB System deployed at Duck consisted of a combination of welded steel structure and closed cell foam floatation. The model was designed as a modular system capable of being assembled using simple hand tools on the beach at Currituck Sound. The deployment featured two 150-ft long RIB System legs, which were assembled from 30 RIB System modules and a nose buoy which was designed and constructed to expedite connecting the two legs. Each leg was assembled on the beach and subsequently towed into deeper water,

where they were joined to the previously positioned nose buoy as shown in the photo in Figure 7. Following attachment to the nose buoy, the trailing ends of each leg were attached to prepositioned anchors to achieve the desired "V" configuration. Instrumentation to measure wave height and weather conditions along with video recordings were used to document the effectiveness of the model used during the field investigation. During the two

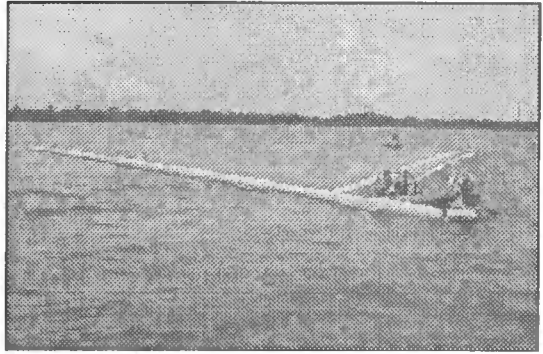


Figure 7. Joining of RIB System Legs.

week period, the RIB System was successfully deployed, and data were collected to document wave reduction capabilities and allow comparison to the laboratory data. The comparison indicated that the mid-scale field deployment performed quite similar to the laboratory version, again reducing incoming wave heights by about 75 percent. Figure 8 is a photograph of the RIB System as it was functioning during the field deployment. Incident waves in the photograph scaled to mid- to upper sea state 3, while the wave climate in the lee of the RIB System scaled to sea state 1.

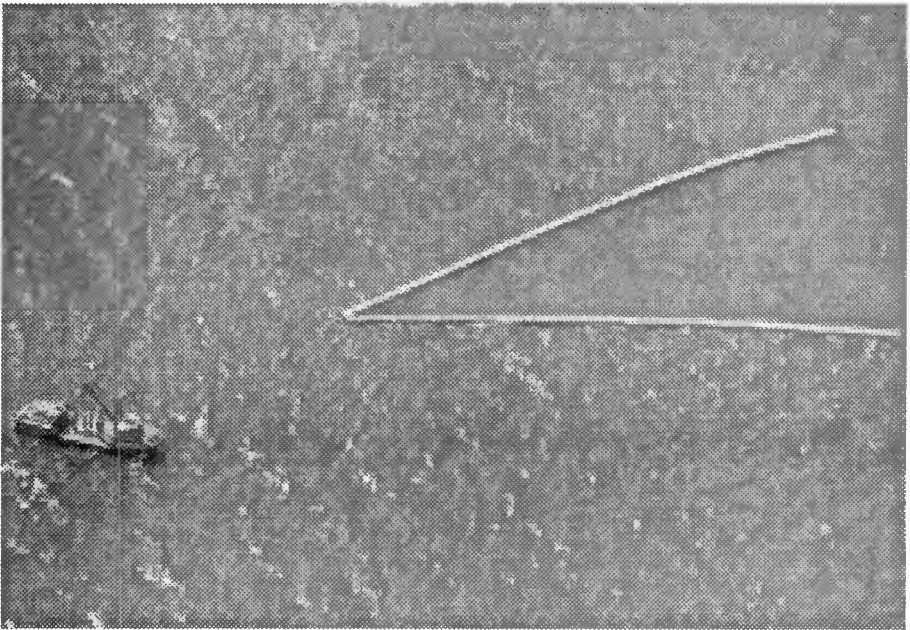


Figure 8. Aerial View of RIB System During 1996 Field Deployment.

Future Plans.

The next step in the development of the RIB System will be additional laboratory investigations to study deployment options, construction materials, and mooring requirements. These efforts will be followed by the construction, and field deployment of a larger, near full size version in 1997. This will in turn be followed by design, construction and deployment of a full-scale version during an actual LOTS operation exercise in the year 2000.

Conclusions

Based on results such as those obtained in the extensive laboratory studies and observations made during the field study in May-June 1996, the RIB System being developed at WES holds great promise for alleviating the military's ship offloading problems associated with higher sea states during LOTS operations. Additional laboratory investigations oriented towards mooring techniques and methods of deployment are scheduled for 1997. These studies will be designed to optimize present design and examine potential alternative uses for the RIB System. A second field deployment of the RIB System constructed at a 1 to 3 scale, will occur during the summer of 1997, primarily to evaluate mooring and deployment options developed during the laboratory studies. These efforts will be followed by a full-scale demonstration, and by research to evaluate other potential applications of the RIB system, including protection of shore-based offloading sites, protection of nearshore construction/repair sites such as for jettys or breakwaters, and temporary small boat harbors.

Acknowledgements

The authors acknowledge Headquarters, U.S. Army Corps of Engineers, for authorizing preparation and publication of this paper. It was prepared as part of the Military RDT&E Program of the U.S. Army Engineer Waterways Experiment Station's Coastal and Hydraulics Laboratory. The RIB System deployed during the field study was fabricated by Kepner Plastics Fabricators, Inc., Torrance, California. M. J. Plackett & Associates (MJP&A) provided technical assistance and support to WES related to the design, planning, structural analysis and fabrication of the RIB System models used in both the field and laboratory studies. The authors thank John Evans, Debra Green, Raymond Reed, O.H. Hinsdale Wave Research Laboratory, and M.J. Plackett & Associates, and the staff of the Field Research Facility for their help during this project.

CHAPTER 128

Stability of Reshaping Breakwaters with Special Reference to Stone Durability

P. Frigaard ¹, T. Hald ¹, H.F. Burcharth ¹, Sigurdur Sigurdarson ²,

1 Introduction

Traditionally, conventional rubble mound breakwaters are designed with stable armour units, and consequently, very large stones or even artificial armour units are required. Reshaping breakwater designs allow reshaping of the seaward slope thus involving stone movements. Ultimately, dependent on the degree of safety in the design, this reshaping process might end up in a stable profile where no changes in the cross sections occur even though stone movements are allowed.

Unfortunately, large movements of the protecting stones during the structural lifetime in combination with high stone velocities inherently cause some breakage and abrasion of the individual stones and thereby also reduced stability. In order to avoid excessive abrasion a high stone quality is demanded or larger stones must be applied when constructed. To allow the designer to account for abrasion and armour stone breakage due to the stone motion a description of the overall wave climate during the structural lifetime must be derived involving knowledge of transport rates, movement patterns, stone velocities and stone quality.

The main objective of the paper is to describe a tool enabling calculation of the anticipated armour stone movements. Also tensile stresses occur, as a result of stone against stone impact are discussed in order to make a more close connection between wave climate, stone movements and abrasion/breakage. Finally, a comparison to selected prototype structures is made to compare the armour stone movement model with visual profile observations of existing breakwaters.

¹Hydraulics & Coastal Engineering Laboratory, Aalborg University, Sohngaardsholmsvej 57,
DK-9000 Aalborg, Denmark, tel + 45 98158522, fax +45 98142555

²Icelandic Harbour Authority, Vesturvör, 2200 Kopavogur, Iceland

2 Longshore Transport Rate

Motion of stones along the active profile occurs when even slightly oblique waves attack the breakwater. This longshore motion has been evaluated in model tests performed by Burcharth and Frigaard (1988) and by van der Meer and Veldman (1992). Longshore transport was measured by observing the movements of stones layed out in coloured bands over the profile. To calculate the steady state transport the number of stones per wave passing a specific cross section at each sea state was divided by the number of waves. This ratio is termed the longshore transport rate S_x .

In Figure 1 the measured longshore transport rate is plotted against the mobility index $H_oT_{op} = \frac{H_a}{\Delta D_{n50}} T_p \sqrt{\frac{g}{D_{n50}}}$. The longshore transport rate seems to be described quite well by a power function as originally proposed by Vrijling (1991). The best fit of the power function to the data is:

$$S_x = 85 \cdot 10^{-6} (H_oT_{op} - 105)^2 \tag{1}$$

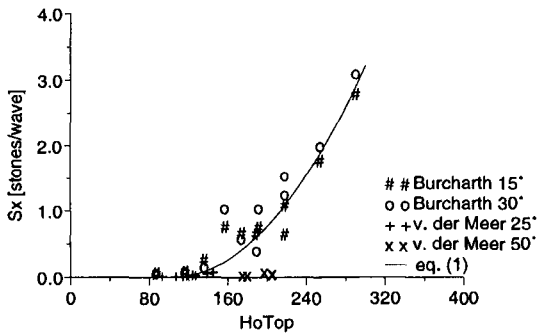


Figure 1: Longshore transport rate for reshaping breakwaters.

One might argue if the model in eq. (1) is too simple because of the absence of obliquity. The model can however, easily be adjusted to include the angle of incidence θ as discussed by Alikhani et al. (1996). Though the effect of obliquity is small.

Another aspect of the transport model is the obvious sensitivity to the onset of motion. From the model it is seen that sea states slightly above those corresponding to the onset of motion result in significant transport due the rapid increase of the power function. The latter comparison with prototype breakwaters outlines this sensitivity.

3 Longshore Distribution of Transported Material

To characterize the motion of the individual stones on the breakwater several video recordings from the model tests performed by Burcharth and Frigaard (1988) have

been reanalysed thoroughly.

The main conclusion based on the analysis of the video recordings was a typical zigzag motion pattern as shown in Figure 2. The typical upward motion of the stone follows

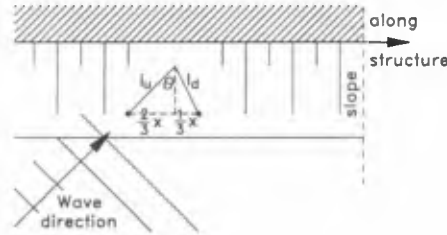


Figure 2: Typical pattern for single stone motion.

the wave direction θ whereas the downward motion is more controlled by gravity and an angle of half the angle of incidence seems more appropriate, see Figure 2. From Figure 2 the total travelled longshore distance can be calculated, assuming the upward and downward distances orthogonal to the structure in average are equal

$$l = l_u + l_d = \frac{2x}{3 \sin(\theta)} + \frac{x}{3 \sin(\frac{1}{2}\theta)} \tag{2}$$

To quantify the travelled longshore distance x the longshore distribution of the transported material has been derived from the same tests. The longshore distribution was derived from recordings of the number of stones positioned in 5 cm wide bands over the profile along the entire length of breakwater. From these recordings the number of stones per m, the position of the individual stones and the mean stone movements are calculated. Figure 3 shows an example from a single longshore transport test.



Figure 3: Example of the longshore distribution of transported material.

In Figure 4 the longshore distribution is shown for all 22 tested wave conditions. As abscissa the travelled longshore distance x is normalized by the mean travelled distance \bar{x} and as ordinate the stone distribution along the structure $s(x)$ (unit: stones/m per wave) is normalized by multiplying with $\frac{\bar{x}}{S_x}$.

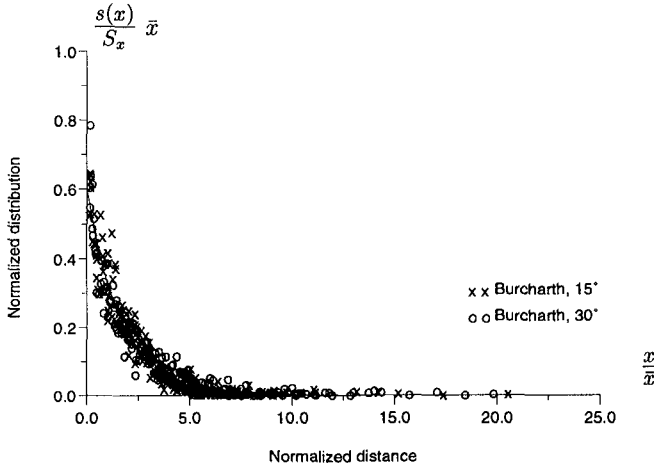


Figure 4: Longshore distribution of transported material.

From Figure 4 an excellent uniformity of the distribution curves for different wave climates and different angles of incidence is seen. Hence, a general exponential function can be fitted to the entire data set

$$s(x) = 0.6 \exp\left(-0.6 \frac{x}{\bar{x}}\right) \frac{S_x}{\bar{x}} \tag{3}$$

In Figure 5 the mean stone movement is plotted against the mobility index for all 22 tested wave climates.

The mean stone movement is described by

$$\bar{x} = 5.3 \cdot 10^{-3} D_{n50} (H_o T_{op} - 105) \sin^{0.8}(2\theta) \tag{4}$$

or by inserting the longshore transport model eq. (1).

$$\bar{x} = 0.6 D_{n50} \sqrt{S_x} \sin^{0.8}(2\theta) \tag{5}$$

Inserting the mean travelled distance in the expression for l , eq. (3) gives the average distance moved per wave. Knowing the wave height/period scatter diagram describing the storm history for a specific area, it is possible to calculate the accumulated average distance moved by each single storm during the structural lifetime simply based on the easy accessible parameters, H_s , T_p , θ , number of waves and D_{n50} .

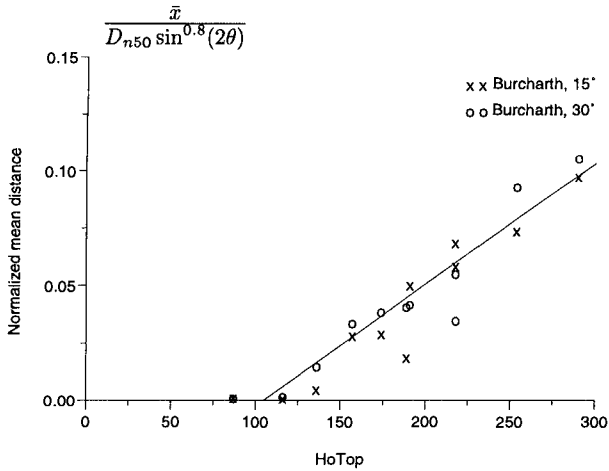


Figure 5: Mean stone movement versus the mobility index.

4 Impact Stresses in Armour Stones

A more close description than the stone motion connecting abrasion and breakage is to consider the tension stresses as a result of armour stones impacting armour stones during movements. This impact results in a shock wave propagating through the stone which is reflected at the edge structure resulting in a reverse propagating tensile stress wave. In case the tensile stress is too high the stone may crack depending on the stone quality.

In Figure 6 an idealized static model of a stone impact is sketched where the impacted stone remains at rest after impact. This is modelled by giving the stone infinity mass and zero velocity.

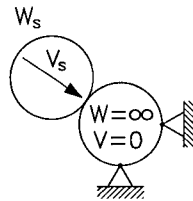


Figure 6: Static model

Applying Hertz' law to the system in Figure 6 results in the following equation

$$\sigma_{max} \propto \left(\frac{V_s^4}{D_{n50}} \right)^{0.2} E \tag{6}$$

where:

- W_s = Stone weight
- V_s = Stone velocity
- D_{n50} = Nominal stone diameter
- E = Young's Modulus

Generally, eq. (6) describes the stresses with reason: a high velocity yields high stresses, a small diameter signifies large curvature and thus larger impact stresses because of the smaller contact area, and finally the elasticity of the stone is described by Young's Modulus. Another aspect is that by simple Froude scaling larger stones gain larger stresses.

From the previously described tests typical stone velocities during both run-up and run-down were investigated by video. A typical stone velocity during run-down equals the wave run-down velocity whereas the typical stone velocity during run-up is approximately 50-70% of the wave run-up velocity.

Several attempts to assess the run-up and run-down velocities have been made showing that the maximum expected velocity can be well described by H_s and $\xi = g(\alpha, H_s, T_p)$. The overall maximum velocity is expected to be in the order of $1.5\sqrt{gH_s}$, e.g. Sawaragi, (1995).

From the above considerations it seems that the impact stresses can be described by the same easy accessible parameters as the movement model. The model still needs verification and calibration to physical model tests as well as prototype measurements. More work has to be done into these subjects.

5 Comparison with Prototype Breakwaters

For prototype comparison four sites are investigated with wave and structural characteristics given in the two tables 1 and 2. The accumulated travelled mean distance have been calculated followingly:

- Calculation of longshore transport rate from eq. (1) for each storm.
- Calculation of mean position moved from eq. (5) for each storm.
- Calculation of total travelled distance from eq. (3) for each storm.
- Summation of total travelled distance during lifetime.

Regarding

1. Caldera, Costa Rica: Estimated stone movements are rather small indicating little stone movements during lifetime. Observations show little profile changes but some broken stones. This might be due to the very poor quality of the stones.
2. St. Paul, Alaska: Vast stone movements are estimated. Total damage of the breakwater was observed.
3. Racine, Wisconsin: Long travelled distance is estimated. Severe breakage and large profile changes were observed.

4. Bolungarvik, Iceland: Little stone motions were estimated. Little profile changes observed.

It seems that the calculated distance corresponds very well to what might have happened. Though, it is clear that actual damage depends on both the travelled distance and the quality of the stones. In all, the comparison indicates that there is reason in relating breakwater damage to the armour stone motion.

6 Conclusions

A model enabling calculation of the accumulated travelled stone distance is given based on the easily accessible parameters such as H_s , T_p , θ , number of waves and D_{n50} . Furthermore, a short discussion focusing on the structural integrity is given. It is argued that the anticipated maximum tensile impact stresses can be evaluated by the same easily accessible parameters, though more work need to be done into this subject.

A comparison with selected prototype structures is presented showing that there is reason in relating breakwater damage to the armour stone motion. The comparison also signifies that only little transport should be allowed in order to avoid severe damage.

In areas where sufficiently large armour stones can be difficult to get, the stone quality is often poor. Even little stone transport or stone motion will in these cases result in breakage and abrasion of the armour stones. In practice it is difficult to avoid the abrasion and breakage of the armour stones and thus little transport should be allowed. The best possible design of the berm breakwater with maximum utilization of the quarry when possible is suggested by Sigurdarson et al. (1995). The aim is to minimize stone movements and make a more or less statically stable structure with little expected movements during the lifetime if suitable quarries are found in the vicinity. Still if stone movements occur on the berm breakwater no abrupt failure occur. By the berm concept up to 100% of the quarry yield can be used. This design approach have been used videly in Iceland with succes, see Sigurdarson and Viggosson (1994).

7 Acknowledgement

The work carried out is partly sponsored by the Danish Technical Research Council and partly by the Commission of the European Community under the MAST II Berm Breakwater Structure project, contract no. MAS2-CT94-0087.

8 References

- Alikhani, A., Tomasicchio, R. and Juhl, J., *Berm Breakwater Trunk Exposed to Oblique Waves*, to be published in Proc. 25th ICCE, Orlando, USA, 1996.
- Burcharth, H.F., Frigaard, P., *On 3-Dimensional Stability of Reshaping Breakwaters*, Proc. 21th ICCE, Malaga, Spain, 1988.
- CIRIA/CUR, *Manual on the Use of Rock in Coastal and Shoreline Engineering*, Published jointly by the Construction Industry Research and Information Association in the UK and the Centre for Civil Engineering Research, Codes and Specifications in the Netherlands, 1991.
- Lamberti, A., Tomasicchio, G.R., *Stone Mobility and Abrasion on Reshaping Breakwaters* to be published in Coastal Engineering, 1996.
- van der Meer, J.W., Veldman, J., *Singular Points at Berm Breakwaters: Scale Effects, Rear, Round Head and Longshore Transport*, Coastal Engineering, Vol. 17, Nos. 3,4, August 1992.
- Vrijling, J.K., Smit, E.S.P. and Swart, P.F., *Berm Breakwater Design; the Longshore Transport Case: a Probabilistic Approach*, ICE, Proc. Coastal Structures and Breakwaters, London, 1991.
- Sawaragi, T., *Coastal Engineering - Waves, Beaches, Wave-Structure Interactions*, Developments in Geotechnical Engineering, 78, Elsevier Science B.V., 1995.
- Sigurdarson, S., Viggosson, G., *Berm Breakwaters in Iceland, Practical Experiences*, Proc. Int. Conf. on Hydro-Technical Engineering for Port and Harbour Construction, Yokosuka, Japan, October 1994.
- Sigurdarson, S., Viggosson, G., Benediktsson, S., Samarason, O. B. *Berm Breakwaters and Quarry Investigations in Iceland*, Proc. 4th Int. Conf. on Coastal & Port Engineering in Developing Countries, Rio de Janeiro, Brazil, September 1995.

Location	W_{50} [t]	ρ [t/m ³]	storm	duration [waves]	H_s [m]	T_p [sec]	Θ [deg]	H_0	$H_0 T_{0p}$ [stones/wave]	S	l_i [m]
Caldera, Costa Rica	5.0	2.40	21.09.78	3000	3.65	18.7	50	2.1	109.5	$1.7 \cdot 10^{-3}$	155
	5.0	2.40	21.05.81	3000	3.55	17.9	50	2.1	101.2	0	0
	5.0	2.40	18.07.83	3000	3.47	17.1	50	2.0	95.2	0	0
	5.0	2.40	18.06.78	3000	3.30	17.5	50	1.9	92.6	0	0
St. Paul, Alaska	1.5	2.77	13.11.84	1900	5.34	31.0	15	3.8	417.1	8.3	7886
	1.5	2.77	07.12.84	4000	5.34	15.0	15	3.8	201.8	0.8	5155
Racine, Wisconsin	0.82	2.61	08.03.87	2500	4.4	11.2	15	4.15	176.6	0.4	1984
Bolungarvik, Iceland	6.0	2.85	27.10.95	3000	6.0	15	10	2.65	109.9	$2.0 \cdot 10^{-3}$	338

Table 1: Experienced wave conditions and structural parameters for selected prototype structures.

Location	St. type/ shape	W_{50} [t]	ρ [t/m ³]	$\frac{W_{65}}{W_{15}}$	$H_{0,max}$	$H_0 T_{0p,max}$	S_{max} [st./wave]	$\sum l_i$ [m]	Visual profile observations
Caldera, Costa Rica	Sand stone/ Rough angular	5.0	2.40	1.5	2.1	110	$1.7 \cdot 10^{-3}$	155	app. 5-10% broken stones, severe abrasion little profile changes and longshore transport. total damage, 150 m recession of breakwater head. severe breakage of armour stones, large profile changes and longshore transport.
St. Paul, Alaska	Crushed stone	1.5	2.77	3.0	3.8	417.1	8.3	13041	
Racine, Wisconsin	Crushed limestone	0.82	2.61	2.5	4.15	176.6	0.4	1984	
Bolungarvik, Iceland	Quarry stone/ Rough angular	6.0	2.85	2.5	2.65	109.9	$2.0 \cdot 10^{-3}$	338	no armour stone breakage, little profile changes, no longshore transport.

Table 2: Comparison of experienced wave conditions, structural parameters and profile observations for selected prototype structures.

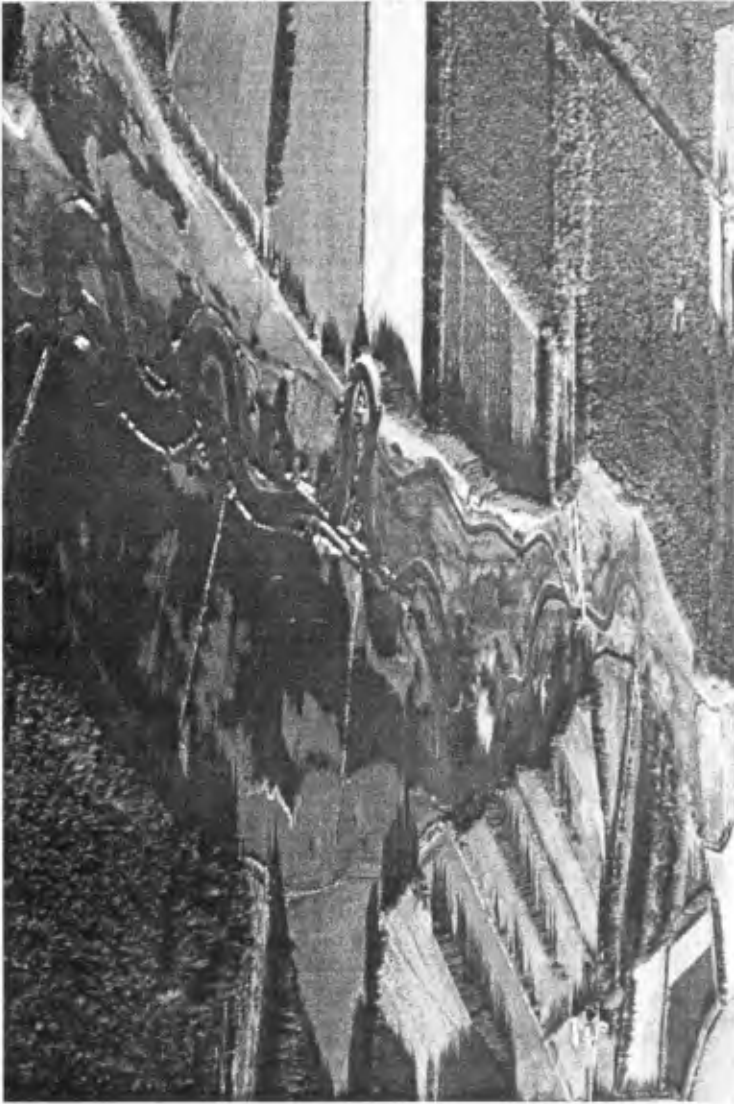




Photo from Icelandic berm breakwater



Photo from Norwegian berm breakwater

CHAPTER 129

FIELD INVESTIGATIONS ON WAVE-DISSIPATING CONCRETE BLOCKS COVERING VERTICAL WALL BREAKWATER

Michio Gomyoh¹, Kazuhiko Sakai², Tomotuka Takayama³,
Kojiro Suzuki⁴, Shigeo Takahashi⁵

Abstract

The failures experienced in Japan by wave-dissipating concrete blocks (WDCB) covering vertical wall breakwaters are investigated, and the deformation characteristics such as failure features and factors are examined.

Typical examples for failures are illustrated, and two main types for failures are suggested: (a) scattering of WDCB due to shortage of their weight, (b) settlement of WDCB following deformation of the toe area. These types are analyzed and then the latter is discussed with some preliminary experiments. The results suggested that both stability of WDCB and applicability of the Hudson formula depend on the location and their cross-sectional shape, and that a weakening of sand bed due to wave action, especially wave-induced liquefaction, is an important factor of settlement deformation as well as scouring.

From these results and additional field surveys, finally, two parameters are suggested which can explain the effect of stability of WDCB and toe area on both scattering and settlement behavior, and a classification of resultant failure characteristics and a conceptualized diagram of failure behavior of WDCB are presented.

1. Introduction

Throughout the world, and especially in Japan, the Hudson formula has

¹Senior Research Engineer, Technical Research Institute, Toa Corporation, 1-3, Anzen-cho, Tsurumi-ku, Yokohama, 230 Japan.

²Deputy General Manager, Technical Development Division, Toa Corporation, 5, Yonban-cho, Chiyoda-ku, Tokyo, 102 Japan.

³Professor, Disaster Prevention Research Institute, Kyoto University, Uji Gokasho, Kyoto, 611 Japan.

⁴Research Engineer, Maritime Structure Laboratory, Port & Harbor Research Institute, Ministry of Transport, 3-1-1, Nagase, Yokosuka, 239 Japan.

⁵Chief, Maritime Structure Laboratory, Port & Harbor Research Institute, Ministry of Transport, 3-1-1, Nagase, Yokosuka, 239 Japan.

been applied in the design process used to evaluate the stability of WDCB which cover the front of large-scale vertical wall breakwaters. However, based on the fact that this design tool was not for WDCB, but originally formulated for evaluating the armor layers of rubble mound breakwaters, WDCB may show different stability properties in the applied fields.

Therefore, firstly, we performed field stability investigations to determine the deformation characteristics and resultant suitability of the Hudson formula in designing Japan's recently built vertical breakwaters covered with such blocks. Secondly, we also carried out some preliminary experiments and field surveys to understand a unique failure characteristics of settlement deformation observed at Miyazaki Port. Finally, in discussion, we classified these complicated failure features and explained them quantitatively, so that the results will be helpful to develop an improved design method.

2. Investigation method

Field investigations were conducted in Japan on major breakwaters located at 16 ports among more than a hundred as shown in Figure 1. Failure

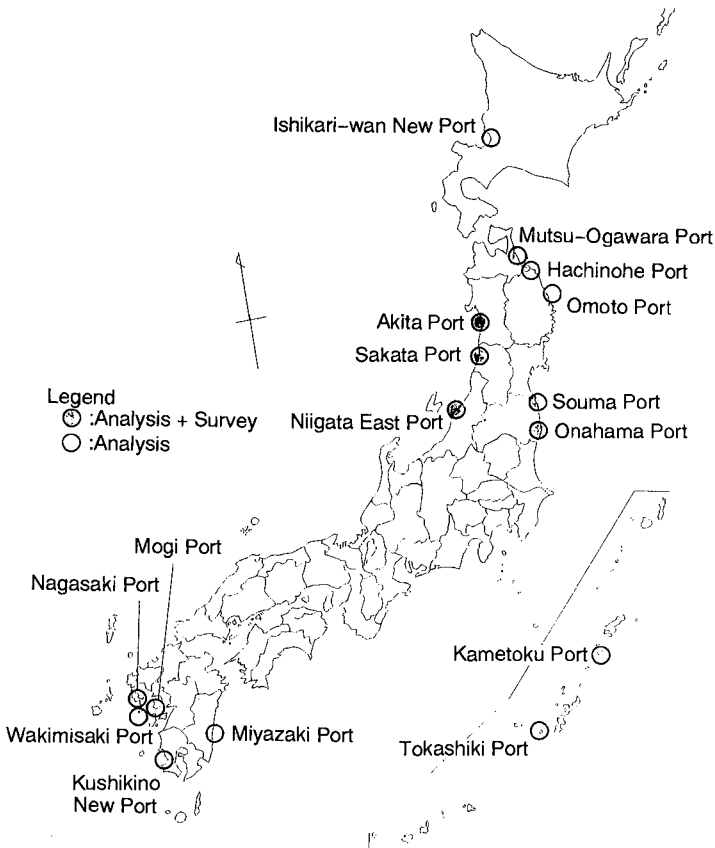


Figure 1. Map of ports investigated in this study

Table 1. Summary of failures of WDCB

No.	Disturbance	Port: Breakwater	Location	Sectional Shape	Design: $H_{1/3}, T, I$
1	'91, Feb.	Mutsu-Ogawara: East	trunk	sectional end	7.1m/ 13.0s/ 1:50
2				fully covered	
3				sectional end	
4		Hachinohe: No.1	head	sectional end	6.3m/ 13.0s/ 1:100
5				fully covered	
6		Hachinohe: No.2	head	sectional end	6.6m/ 13.0s/ 1:100
7				fully covered	
8		Omoto: Offshore	head	fully covered	7.9m/ 12.0s/ 1:30
9	'91, Sep.	Nagasaki(Oe): Offshore	head	sectional end(berm)	5.5m/ 10.7s00/ 1:30
10	Typhoon 19			sectional end	
11				fully covered	
12		Wakimisaki: South	trunk	sectional end	3.9m/ 10.0s
13				fully covered	
14		Kusikino New: West	trunk	fully covered	6.0m/ 13.0s
15				fully covered	7.7m/ 13.8s
16		Mogi: Offshore	head	fully covered	4.5m/ 12.5s
17			trunk	fully covered	
18	'87, Aug.	Kametoku: South	head, on a reef	fully covered	10.2m/ 16s/ 1:50
19		Tokashiki: South	head	fully covered	-
20	'88 - '90	Miyazaki: South	trunk	fully covered	8.9m/ 14.0s/ 1:200
21	'85, Nov.	Ishikari-wan New	trunk	fully covered	5.6m/ 11.0s
22	'93, Aug.	Onahama: No.1, West	trunk	fully covered	6.2m/ 14.0s/ 1:100
23	Typhoon 11	Onahama: No.2, West	trunk	fully covered	8.1m/ 14.0s/ 1:100
24		Souma: South2	trunk	fully covered	4.5m/ 15.0s
25	'80 - '90	Sakata: North	trunk	temporaly low crest	7.5m/ 11.0s
26	'93 - '94	Akita: South(E)	trunk	fully covered	7.5m/ 13.5s
27	'95, Nov.	Niigata East: West	trunk	sectional end, fully covered	8.3m/ 12.9s

cases investigated in this study are limited to those which recently occurred remarkably and whose data have been accumulated enough to analyze their features and factors. As the result, 27 cases including both damage and no damage were analyzed using pertinent data including wave conditions, damage features (area, type, and weight of blocks), and design conditions. After these analyses some preliminary experiments were done to study a unique failure at Miyazaki port. Furthermore, in order to see not only failure results but also its process going on in site, 6 cases (Case 22 to 27 in Table 1) were surveyed noting the physical conditions before and/or after deformation. All cases are summarized in Table 1.

3. Investigation results

From all the cases in Table. 1, the following specific features of WDCB failures are obtained:

1) Few failure cases of WDCB are reported in spite of the fact that they are used in many sites.

Table 1 (continued)

No.	Block*	Wave conditions**: $H_{1/3}$, T, θ	Failure features of WDCB	Other failure features
1	T:50t, S:50t (1:4/3)	9.6m/ 13.4s/ -7.1°	scattering, settlement	caisson sliding, breakage
2	T:50t (1:4/3)		a little settlement (0-1.5m)	
3	S:50t (1:4/3)		scattering, settlement	
4	T:50t (1:4/3)	7.5m/ 11.4s/ 8.9°	scattering, settlement	caisson sliding
5			a little settlement	
6	T:50t (1:4/3)	5.9m/ 11.4s/ 23.8°	scattering, settlement	caisson sliding
7			a little settlement	
8	T:64t (1:4/3)	9.3m/ 13.7s/ 31.8°	scattering, breakage	caisson sliding, breakage
9	T:20t (1:4/3)		scattering, breakage	caisson sliding
10	T:20, 40t (1:4/3)		scattering, settlement	
11	T:20, 40t (1:4/3)		no damage	
12	T:32t (1:4/3)	4.8m/ 15.1s	scattering, settlement	
13			no damage	
14	T:50t (1:4/3)	-	scattering, settlement,	
15	T:64t (1:4/3)		breakage	
16	T:16t (1:4/3)	-	scattering	caisson sliding
17			no damage	
18	D:50t (1:1.3)	5.9m/ 12.2s/ 39°	scattering	caisson sliding
19	T:5, 32t (1:4/3)	7.0m/ 14.4s/ 51°	settlement	caisson sliding, breakage
20	T:64t (1:4/3)	-	settlement	scouring at the toe area
21	T:4, 20t	-	settlement	scouring at the toe area
22	T:25t (1:4/3)	6.6m/ 12.0s	scattering, settlement	scouring at the toe area
23	T:50t (1:4/3)	9.1m/ 12.0s	scattering, settlement	scouring at the toe area
24	H:25t (1:1.5)	5.0m/ 10.8sec	scattering, settlement	scouring at the toe area
25	T:32, 50t (1:1.5)	-	settlement	
26	T:40t (1:1.5)	-	settlement	
27	T:50t (1:1.5)	-	settlement	

* T: Tetrapods, S: Sealock, D: Dolos, H: Hexa-leg-block

** Incident wave conditions calculated by wave hindcasting when the failures occurred

2) Though the predominant disturbances are typhoons in summer and depressions in winter, gradually advancing deformations during about one year are also observed.

3) Tetrapods and its normal slope gradient of 1:4/3 are used for more breakwaters, however, gentler slope of 1:1.5 is locally adopted at the ports facing to the Sea of Japan where scouring at the toe area of composite type breakwater is remarkable.

4) Occurrence of the breakage of blocks is less than that of scattering and settlement which seem to be typical failure features.

5) Other two failure features, caisson sliding and breakage, and scouring at the toe area, are observed at the breakwater head/sectional end and breakwater trunk, respectively.

In the following paragraphs, the investigation results on scattering and settlement of WDCB will be indicated.

3.1 Scattering failures of WDCB

Typical examples

Figure 2 shows the scattering of WDCB, 40 t Tetrapods, and the damage of caissons of No.2 breakwater at Hachinohe Port (Case 6,7). The important point to note in these cases is that the scattering of WDCB was found to be severe at the breakwater head/sectional end, A-A line, and that it was very mild at the trunk section, B-B line, in spite of neighboring the damaged area. The predominant reason responsible for the former is the action of severe wave force at the sectional end as pointed out by Takahashi et. al.(1993). A nesting process of the scattering of WDCB and the caisson sliding due to increase of wave force acting on the caisson wall lead to the larger scattering. Similar failure features like this are observed at east breakwater in Mutu-Ogawara Port (Case1,2,3), No.1 breakwater in Hachinohe Port (Case 4,5), Nagasaki Port (Case9,10,11), and Wakimisaki Port (Case12,13).

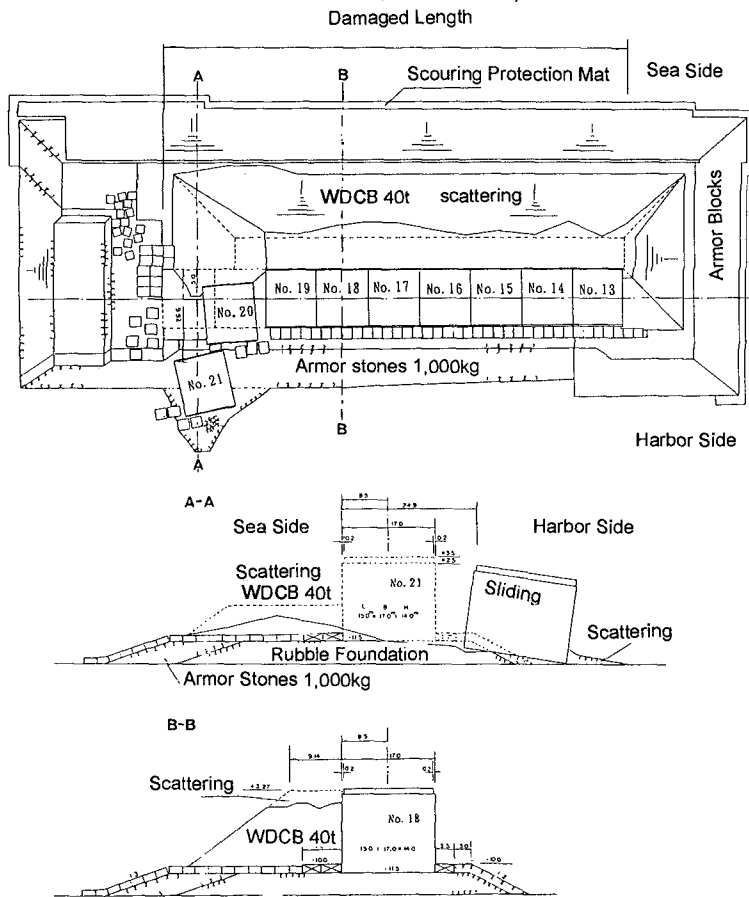


Figure 2. Scattering of WDCB at breakwater trunk section and head sectional end (Hachinohe Port)

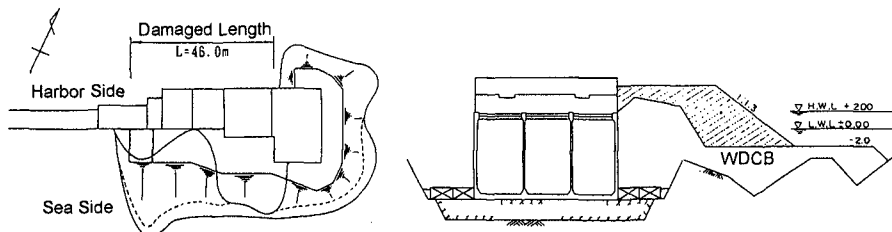


Figure 3. Scattering of WDCB covering a reef (Kametoku Port)

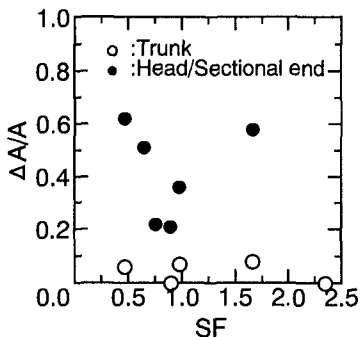


Figure 4. Relationship between degree of scattering and safety factor

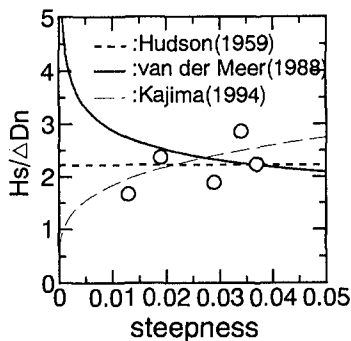


Figure 5. Effect of steepness on stability number as determined by three formulas and observed failure cases

Figure 3 shows the scattering of WDCB, 50t Dolos, covering the reef at Kametoku Port (Case18). Here, the south breakwater is located on the natural reef around the Tokunosima island, and its head on the edge of reef whose bottom slope is steep. This scattering occurred due to both waves breaking there suddenly and resultant severe currents.

Relationship between degree of scattering and safety factor

Judging from the above, the degree of scattering of WDCB seems to depend on its location and cross-sectional shape. Figure 4 shows the relationship between the degree of scattering of WDCB and the safety factor, where $\Delta A/A$ is the ratio of the cross-sectional damaged area to design area, and SF shows the ratio of the actual weight to the calculated weight when failure occurred. It is clear that WDCB at the trunk section remains stable at a safety factor as low as 0.5, and in contrast, the scattering of WDCB at the breakwater head/sectional end occurs severely even though the safety factor is as high as 1.7. Consequently, it is indicated that the applicability of the Hudson formula is adequate at the breakwater trunk section and marginal at the head/sectional end.

Applicability of stability formulas for WDCB

Corresponding analyses are also performed using the design formulas by van der Meer(1988) and Kajima(1994) as well as the Hudson formula. Figure 5 shows the effect of steepness on the stability number by comparing the no

damaged cases at trunk section to the results calculated by three formulas in such conditions that relative damage level in van der Meer(1988), $N_o=0.2$; deformation level in Kajima(1994); $S=1.2$, and wave number; $N=1000$. It is found that they show similar applicability when considering limited amount of field data though the effects of steepness varies among them. In other words, there is almost no difference among them in a practical wave steepness ranging from 0.01 to 0.05.

3.2 Settlement failure of WDCB

Typical examples

Of particular interest, the failure at Miyazaki Port is a typical one caused by long-term, gradual settlement of blocks, being a sometimes hard-to-recognize type of damage that frequently occurs in areas where sand transport is significant. Figure 6 shows that the cross-sectional change such as settlement of WDCB, 64t Tetrapods and armor blocks. Although the nesting process of blocks and/or scouring at the toe area have generally been considered to be the main cause, block settlement may instead be due to various wave actions weakening the sand bed to such an extent that the blocks literally sink into it. Figure 7 shows a photograph supporting this possibility, i.e., the entire body of blocks appears to have moved toward and down during settling. This characteristic feature is also observed at Kushikino Port.

Reproduction of settlement behavior at Miyazaki Port

In order to discuss this type of settlement behavior in detail, wave flume experiments designed to reproduce the breakwater deformation at Miyazaki Port were conducted with reduced scale of 1:55. It was found that block scattering did not occur, even when attacked by waves exceeding the design wave height, and scouring was produced at the toe area, though the use of gravel mats prevented subsequent deformation of the block section.

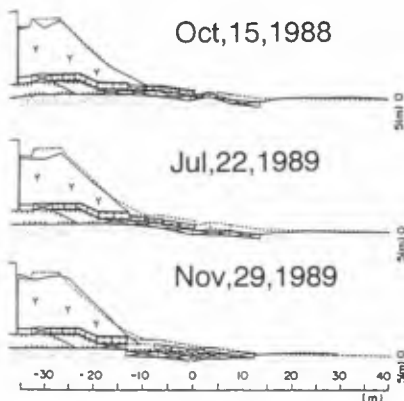


Figure 6. Cross-sectional change of south breakwater at Miyazaki port



Figure 7. Settlement deformation of WDCB at Miyazaki Port

Then, to clarify whether weakened strength of the sand bed is responsible for settlement of blocks, we liquefied it by supplying pore water from bottom of the bed. Figure 8 shows a photograph of the results. The important point to note is that the settlement of the block section is quite definitive, i.e., the blocks at the toe area have sunk into the sand bed and the entire body of blocks has moved forward and down (Figure 8(b), (c)), being a similar behavior to that actually observed (Figure 7) and quite different from the not-liquefied case (Figure 8(a)). These results indicate that weakening of the bed caused such settlement deformation, and that as wave loadings most likely lead to bed weakening, the phenomenon of wave-induced liquefaction may play a key role.

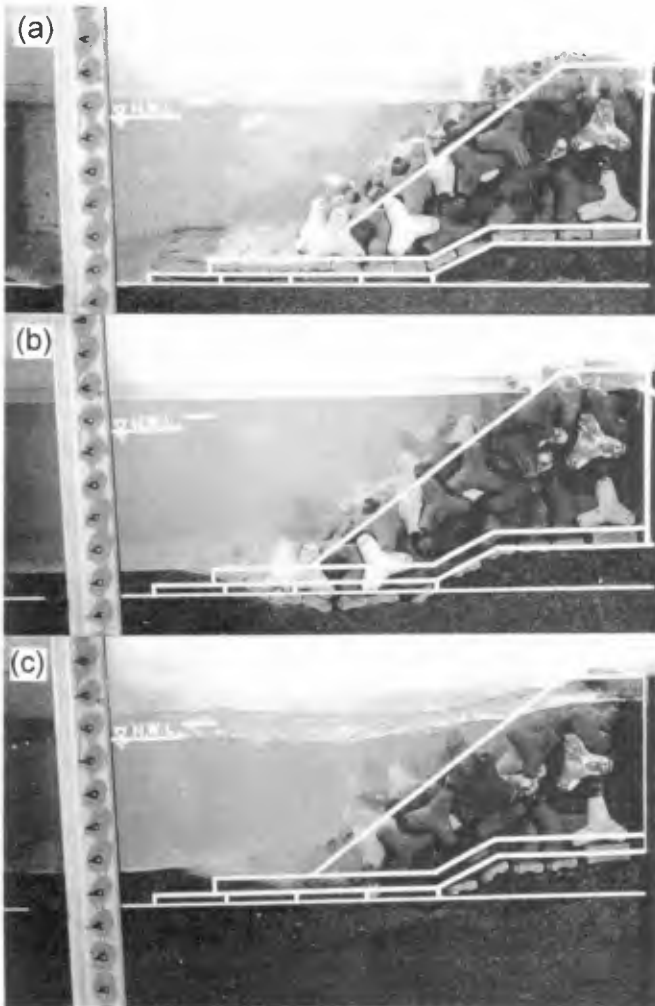


Figure 8. Block settlement deformation due to weakening the sand bed by liquefaction

3.3 Surveys of settlement deformation

During Dec. 1995 to Mar. 1996, field surveys were carried out at 5 ports as shown in Table 1, to examine whether a similar settlement deformation like Miyazaki Port is observed or not. The results indicate that there are two patterns of settlement, excluding the initial settlement due to compaction by wave attack after construction. These are 1) settlement of the top of WDCB due to scattering, a pattern which looks like true settlement, and 2) settlement of an entire body of WDCB following the deformation of a toe area. Furthermore, it is reasonable to think that these features are possible to occur either alone or together.

4. Discussions

The discussions were made below towards a better understanding of the scattering and settlement behavior of WDCB.

Classification of predominant failure characteristics of WDCB

The following classification and identification of failures can be obtained from the investigated failure cases:

- 1) Failure features
 - Direct and independent:
 - Scattering
 - Breakage
 - Others
 - Indirect and complex:
 - Scattering with caisson sliding
 - Settlement following deformation of toe area
 - Others
- 2) Failure factors except for waves exceeding the design condition
 - Major factors for scattering
 - Sea bottom topography: reef and steep slope
 - Location: breakwater head
 - Cross-sectional shape: sectional end
 - Major factors for settlement
 - Soil condition: sand
 - Toe structure

In the following discussions, the scattering and settlement at the breakwater trunk will be discussed in particular.

Structural Parameterization

Considering the settlement feature and its process, it seems reasonable to suppose that both material and dimension of the toe area are important factors to prevent settlement deformation of blocks. Therefore, the structures including WDCB in front of a vertical wall are represented with dimensionless parameters as shown in Figure 9. In this figure, x and z indicate the distance measured from the vertical wall and sea bottom, and h and L show the water depth and wave length in design, respectively. Furthermore, the following abbreviations are used: AB (armor block), AS (armor stone), FPB (foot protection block), FPS (foot protection stone), G (gabion), GM (gravel mat), M

(asphalt mat or scour protection mat), RF (rubble foundation).

As illustrated in this figure, the structures for toe area have a certain range from the thick and wide to the thin and narrow. Consequently, we parameterized the structure for toe area by its thickness; t and width; s as shown in the top right, where st shows an index of cross-sectional area of toe structure.

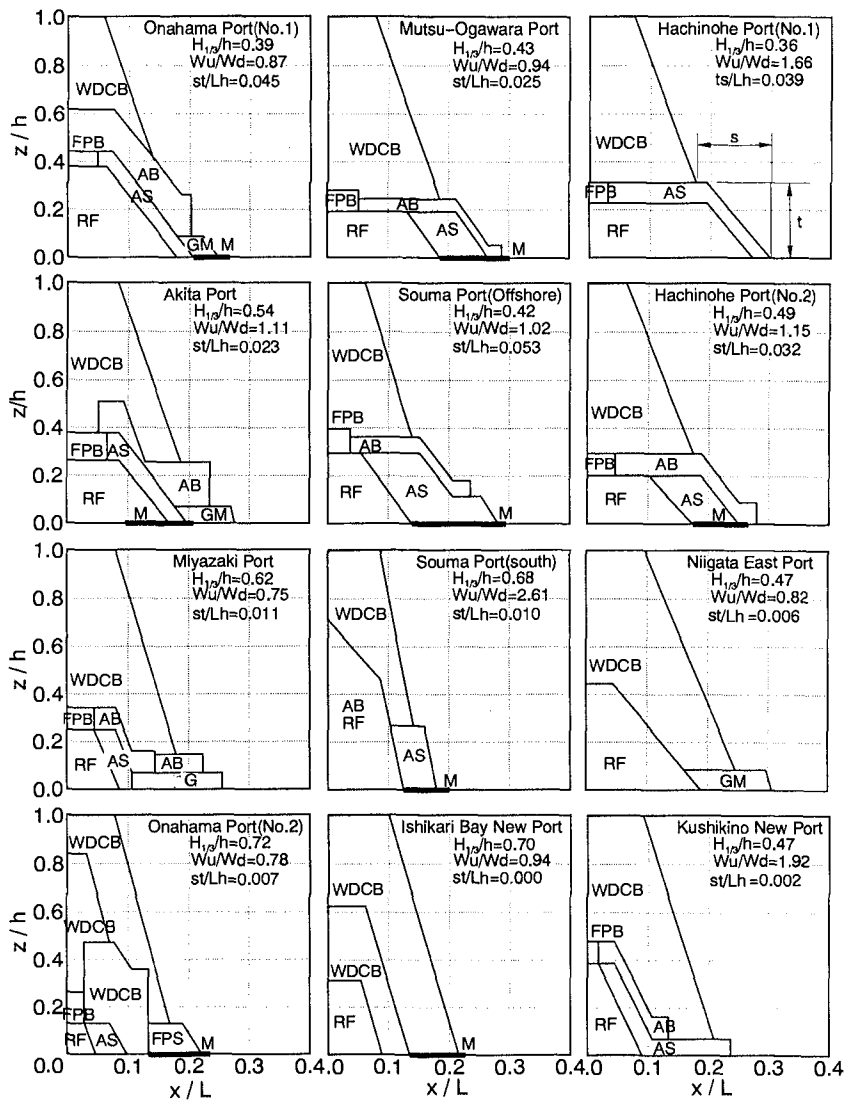


Figure 9. Structure parameterization

Effects of stability of WDCB and toe area on scattering and settlement behavior

To discuss both effect of stability of WDCB and toe area on scattering and settlement behavior, two parameters are suggested: $st/LH_{1/3}$ which indicates the stability of toe area being non-dimensional parameter with st , design significant wave height; $H_{1/3}$ and wave length; L , and W_u/W_d which indicates the stability of WDCB by using actual weight; W_u and design weight; W_d . Figure 10 shows the relationship between two parameters and the degree of deformation at trunk section. As shown in this figure, deformation becomes larger when $st/LH_{1/3}$ is smaller than 0.04 and the failures can be divided into four regions in this figure: no failure, settlement, settlement and scattering, and scattering.

Furthermore, each failure case can be explained reasonably and estimated. For example, the following consideration is possible:

1) Both Miyazaki Port and Kushikino Port are unstable for settlement and indicate similar failure feature, however, if severe waves exceeding the design wave condition attack, they will show different failure features, with scattering or no scattering, because of the difference in the stability of WDCB.

2) The failure case observed at Souma Port (south) shows the severe deformation against the wave attack slightly exceeding the design wave condition although the weight of WDCB is enough to keep itself stable under such a wave condition. This case can be explained as typical one caused by settlement deformation.

3) The case at Onahama Port (No.2), where the blocks less than design weight were used, the value of $st/LH_{1/3}$ is 0.01, and the exceedance of wave design condition was experienced, seems to indicate a complex failure feature which both settlement and scattering occurred at the same time.

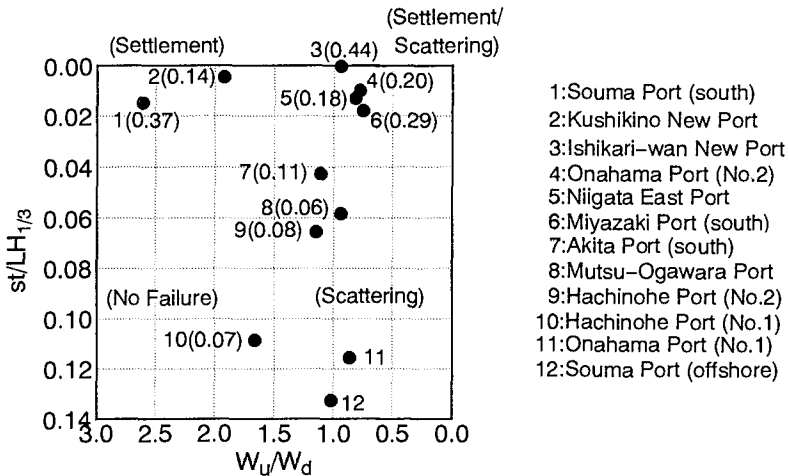


Figure 10. Influence of stability of toe area and WDCB on scattering and settlement behavior (values in parentheses indicate $\Delta A/A$)

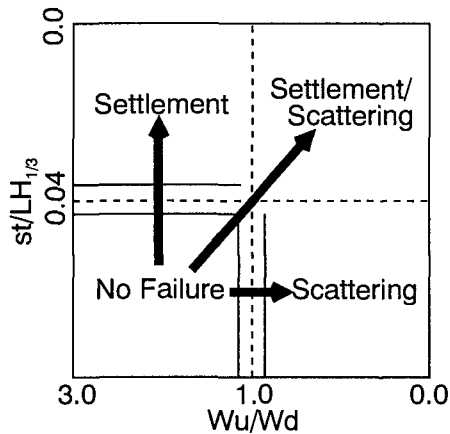


Figure 11. A diagrammatic representation of Figure 10

Conceptualization of failure behavior of WDCB

Based on the above discussion and Figure 10, the failure behavior can be conceptualized as shown in Figure 11. This diagram shows a summary representation of the effects of stability of toe area and WDCB on failure behavior of WDCB.

5. Conclusion

The following main conclusions can be drawn from these investigations:

- 1) Few failure cases of WDCB covering vertical breakwaters are reported in spite of the fact that they have been used in many sites.
- 2) WDCB designed by using the Hudson formula are very stable at the breakwater trunk. On the other hand, those at the breakwater head/sectional end are less stable and have experienced the typical scattering failures consequently.
- 3) Of the failures which have been considered as scattering failures, not a few failures due to settlement are observed like Miyazaki Port and Kushikino Port.
- 4) Not only scouring at the toe area but also liquefaction due to waves may play a key role on the settlement failure, and to clarify its cause, further research is necessary.
- 5) However, a suggestion is possible as a countermeasure for the settlement failure that one adopts a large value of the parameter st , that is, makes a toe structure wider and thicker.

Acknowledgements

Thanks are due to the members of District Port Construction and Bureaus of Ministry of Transport and Civil Engineering Research Institute Hokkaido Development Bureau for providing us with the materials and valuable comments.

References

- Kajima,R.(1994): A new method of structurally resistive design of very important seawalls against wave action, Proc. of International Workshop on Wave Barriers in Deepwater, PHRI, pp.518-536.
- Takahashi, S., Tanimoto,K. and Shimosako,K.(1993): Experimental study of impulsive pressures on composite breakwaters, Rest. of PHRI, Vol.31, No.5, pp.33-72.
- Takahashi, S.(1996): Design of vertical breakwaters, Reference Document No.34, PHRI, 85p.
- van der Meer, J. W.(1988): Stability of Cubes, Tetrapods and Acropode, Proc. of Conf. Breakwater '88, pp.59-68.

CHAPTER 130

NEW STABILITY FORMULA FOR WAVE-DISSIPATING CONCRETE BLOCKS COVERING HORIZONTALLY COMPOSITE BREAKWATERS

Minoru Hanzawa¹, Hirokazu Sato¹, Shigeo Takahashi², Kenichiro Shimosako²,
Tomotsuka Takayama³ and Katsutoshi Tanimoto⁴

ABSTRACT

A new stability formula for wave-dissipating concrete blocks covering horizontally composite breakwaters is proposed after reviewing the existing stability formulae and verified using experimental data. A method for estimating the expected value of the accumulated damage to wave-dissipating concrete blocks within their lifetime using the Monte Carlo simulation follows thereafter and the practicability of this method for reliability based design of wave-dissipating concrete blocks is shown.

1. INTRODUCTION

Horizontally composite breakwaters (Fig. 1), covered with wave-dissipating concrete blocks, are widely employed in Japan (Takahashi, 1996) due to their proven effectiveness in reducing (i) wave forces acting on caissons, (ii) reflected waves and (iii) overtopping.

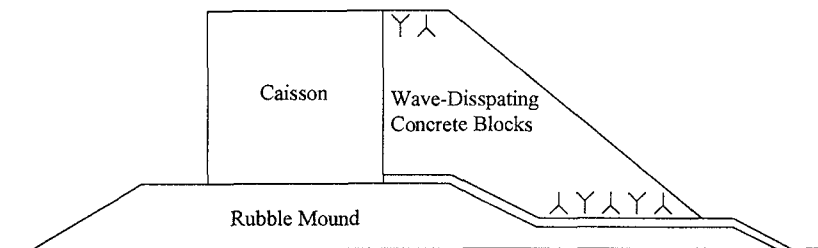


Figure 1 Typical cross section of horizontally composite breakwaters

¹ Tetra Co., Ltd., 2-7 Higashi Nakanuki, Tsuchiura, Ibaraki, 300, Japan

² Port and Harbor Research Institute, Ministry of Transport, 3-1-1 Nagase, Yokosuka, 239, Japan

³ Professor, Disaster Prevention Research Institute, Kyoto University, Gokasho, Uji, 611, Japan

⁴ Professor, Saitama University, 255 Shimo-okubo, Urawa, 338, Japan

The design process used in Japan for horizontally composite breakwaters has strongly relied on the Hudson formula (Hudson, 1959) to provide the design weight of these blocks. Van der Meer (1987, 1988) developed stability formulae for rock/stone and armor unit breakwaters, both of which include parameters not considered by Hudson, i.e., damage level, wave steepness, and wave number.

The formula for armor units, however, is based on a two-layer type rubble-mound breakwater with a high crest level. This results in characteristics such as permeability and run-up/run-down features which are quite different from the case in horizontally composite breakwaters. The stability of wave-dissipating concrete blocks has been investigated by many researchers. For example, Kajima (1994) proposed a stability formula applicable to Tetrapods, as used in the protective covering of vertical seawalls. This formula, however, can not determine a specific design value to correspond to the assurance of no damage.

The above considerations have led to the present study and a new design formula specifically formulated to analyze the stability of wave-dissipating concrete blocks covering horizontally composite breakwaters is proposed herein.

In recent years reliability based design has been introduced to port and coastal structures. Takayama et al. (1994) developed a probabilistic design for caissons in composite breakwaters in order to estimate the probability of slide and overturn of caissons. As for probabilistic design for wave-dissipating concrete blocks, the total damage level accumulated within the life time of these structures proves very important as well as the probability of occurrence of damage. The authors in this study demonstrate a method for probabilistic design for wave-dissipating concrete blocks by Monte Carlo simulation with a new stability formula.

2. NEW STABILITY FORMULA

2.1 Example of Experimental Data

Various kinds of experimental research for wave-dissipating concrete blocks has been carried out in Japan. The several available data sources shown in Table 1 were carefully examined in this study. The type of structure is a typical horizontally composite breakwater.

Table 1 Example of experimental data

(Figures in Model)

No.	Port Name	Water Depth (cm)	Sea Bed Slope	$T_{1/3}$ (sec)	$H_{1/3}$ (cm)	Wave Steepness	Mass of Tetrapod (gf)
1	General. Tanimoto (1979)	39.0~48.0	1/100	2.5	16.2~25.9	0.017~0.027	743.3
2	General. Tanimoto (1985)	39.7	1/50	2.46	12.0~23.0	0.013~0.024	296.0, 596.4
3	S	25.0~31.3	1/15	1.95	8.0~15.0	0.013~0.025	91.7, 128.6
4	Mu	29.3	1/50	1.95	11.4~17.1	0.019~0.029	171.7
5	K	24.3	1/50	1.91	12.9~18.6	0.023~0.033	235.0
6	A	37.5~42.0	1/100	1.74~2.37	13.0~20.0	0.015~0.040	449.2
7	Mi	27.2	1/50	1.94	16.8	0.029	297.4

The Tetrapod was applied as it is a typical example of a wave-dissipating concrete block. The scales of the experiments vary from 1/40 to 1/80. The water depth ranges from 25 to 50cm in the model (14 to 20m in the prototype), the seabed slope is from 1/15 to 1/100, and the mass of the blocks is from 90 to 700gf in the model (32 to 80 tf in the prototype). All experiments were carried out under irregular waves of wave height 6.5 to 12m and wave period 11 to 17s in the prototype, and wave steepness 0.013 to 0.04.

2.2 Review of Existing Formulae

(1) Hudson's formula

Hudson (1959) carried out an experimental study on 2-layer type armor units under regular waves and proposed his stability formula to calculate a mass of units as shown below.

$$W = \frac{\rho_r H^3}{Ns^3(Sr - 1)^3} \quad (1)$$

where W is the mass of the armor unit, Ns the stability number, $Sr = \rho_r / \rho$, ρ_r the mass density of the unit, ρ the mass density of water, H the wave height.

Then Hudson obtained expression of Ns as a function of the slope angle α and the stability coefficient K_D as shown below.

$$Ns^3 = K_D \cot \alpha \quad (2)$$

Figure 2 shows the relation between the damage D(%) and K_D for the data from Table 1. D(%) denotes the ratio of the number of displaced units to the total number of units. K_D was calculated by Eqs.(1) and (2) using $H_{1/3}$ as H corresponding to the damage D(%). The data is scattered in a wide range and it is difficult to find any certain trend. The reason behind the data scatter is that the damage D(%) is affected by the size of the structure and the duration of wave attack is not considered in the Hudson's formula.

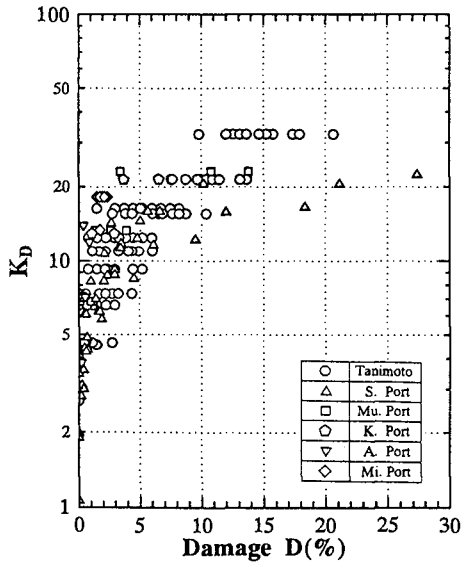


Figure 2 Relation between K_D and damage D(%)

(2) Van der Meer's Expression of Stability Number

Van der Meer (1988) proposed the following expression of stability number for 2-layer Tetrapod armoring on a rubble slope of 1 on 1.5.

$$Ns \approx H_{1/3}/(\Delta Dn) = \left(3.75N_0^{0.5}/N^{0.25} + 0.85\right) Sz^{-0.2} \tag{3}$$

where Δ is Sr-1, Dn the nominal diameter of the unit ($=V^{1/3}$), V the volume of the unit, N_0 the relative damage level defined by van der Meer (1988) as the actual number of displaced units related to the width (along the breakwater alignment) of one nominal diameter Dn , N the number of waves, Sz the wave steepness ($=2\pi H_{1/3}/gTs^2$) and, Ts the wave period.

Figure 3 shows the results from Eq. (3) with the model test data employed. The abscissa is calculated using the right side of Eq.(3) with N_0 , N and Sz , and the ordinate is calculated using the left side with $H_{1/3}$, Δ and Dn .

The difference between the model test data and those calculated is not acceptable, even when the slope difference between 1:4/3 of the model data in Table 1 and 1:1.5 of Eq. (3) by van der Meer is considered. This result shows that Eq. (3) derived for the 2-layer type can not be directly used on wave-dissipating concrete blocks covering horizontally composite breakwaters. The reason behind this is considered to be mainly from the difference of permeability as van der Meer (1987, 1988) incorporated permeability into his stability formula for the armor stones.

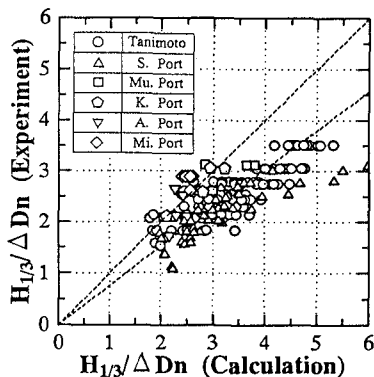


Figure 3 Comparison of van der Meer's formula with model test data

(3) Kajima's Expression of Stability Number

Kajima (1994) proposed the following expression of stability number applicable to Tetrapods for horizontally composite breakwaters.

$$Ns = H_{1/3}/(\Delta Dn) = 8.5(S/N^{0.5})^{0.16} \xi^{-0.5} \tag{4}$$

where S is the deformation level defined by van der Meer (1987) for rubble mound breakwaters as A/Dn^2 , A the sectional area of erosion, ξ the surf similarity parameter ($=\tan\alpha/(H_{1/3}/L_0)^{0.5}$, L_0 the offshore wave length).

Kajima et. al. (1993) showed that the deformation parameter S is related to the damage D' (%) corresponding to the 2-layers as follows.

$$S = 0.6 D' \tag{5}$$

Figure 4 shows the relation between $H_{1/3}/(\Delta Dn)\xi^{0.5}$ and $S/N^{0.5}$.

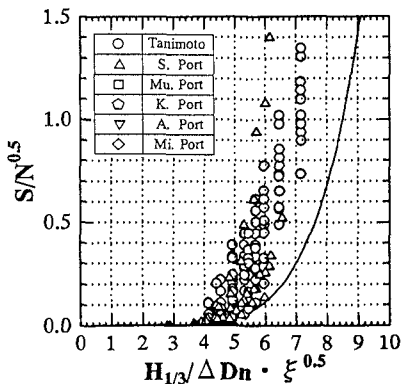


Figure 4 Relation between $H_{1/3}/(\Delta Dn)\xi^{0.5}$ and $S/N^{0.5}$

The solid line indicates the relation derived from Eq.(4). In the model test data, S was calculated from damage D' based on Eq.(5). Eq.(4) was verified by model test data from Kajima et. al. (1993). Eq.(4) however does not agree well with the model test data employed from Table 1.

One of the reasons for this disagreement is considered to be that Eq.(4) is formulated so as to cover a range of relatively high damage level which is usually not seen in the ordinary design of port structures. Also, the water depth of the structure Kajima investigated was greater than those in Table 1 resulting in a bigger cross section. This is considered to affect parameter S calculated through D' from our data.

2.3 Basis of Formulation

To establish a new stability formula, the above mentioned three formulae, i.e. Hudson, van der Meer, and Kajima were comparatively evaluated and various main parameters in the formulae were investigated. These subsequently led to the determination of the basis of a new formula as summarized below:

- 1) *Type of Formula*: The type of formula desired is for use to obtain the stability number $N_s = H_{1/3}/(\Delta D_n)$ by parameters of damage and number of waves.
- 2) *Damage*: Damage to wave-dissipating concrete blocks is expressed as N_0 following van der Meer. According to the preliminary investigation for a typical horizontally composite breakwater, the relation between N_0 and D(%) is considered as $N_0 = 0.2$ to $0.3 D$.
- 3) *Duration of Wave Attack*: Damage to blocks is considered to be proportional to the root of the duration of wave attack (van der Meer, 1988 and Kajima, 1994). So the number of waves N is incorporated into the formula as the form $N_0 N^{0.5}$.
- 4) *Wave Steepness*: This parameter is treated somewhat differently among the formulae, with Fig. 5 showing how it respectively varies with respect to wave steepness. Note that the relationship derived by van der Meer and Kajima show opposite behaviors, i.e., increasing wave steepness either decreases (van der Meer) or increases (Kajima) stability. The stability itself however is relatively similar at wave steepness values from 0.02 to 0.04, and this is the normal design condition. In accordance to this discussion, wave steepness is neglected as a parameter.

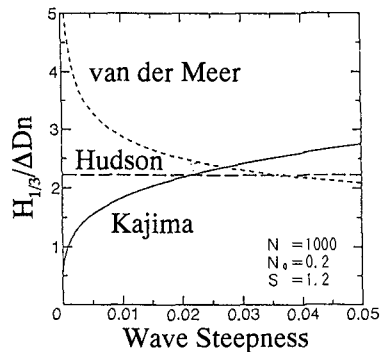


Figure 5 Comparative formula evaluation on the effect of wave steepness on stability

5) *Design for No Damage*: The formula was constructed so as to be able to determine the weight of blocks resulting in no damage.

6) *Type of Block*: Tetrapods with a 1 : 4/3 slope.

2.4 New Stability Formula

Detailed analysis of the experimental data in Table 1 was carried out on the above mentioned basis and the resultant stability formula was expressed as follows.

$$Ns = H_{1/3}/(\Delta Dn) = 2.32(N_0/N^{0.5})^{0.2} + 1.33 \tag{6}$$

Figure 6 compares the results from Eq. (6) with the model test data employed, and good agreement is clearly indicated. Figure 7 also shows another evaluation where the proposed stability formula shows markedly better agreement with experimental data when compared with Figure 3.

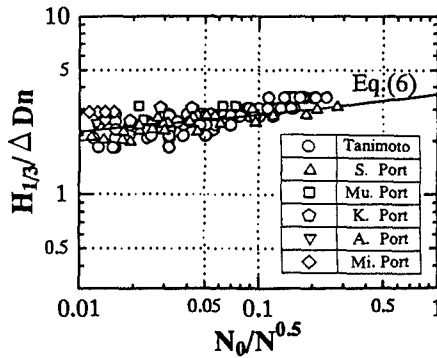


Figure 6 Comparison of proposed new formula with experimental data

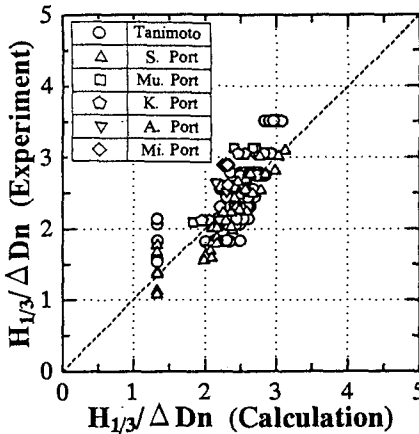


Figure 7 Comparison of proposed new formula with experimental data

Figure 8 compares the mass of the Tetrapod using the new formula having $N_0=0.1, 0.3, 0.6, 1.0$ and $N=1000$ with that using Hudson's formula using $K_D=8.3$ and $\cot\alpha=4/3$. As shown in the figure the new formula, using $N_0=0.3$ and $N=1000$, corresponds to conventional design using Hudson's formula. Figure 9 shows the mass variation against N_0 and N with the wave height of $H_{1/3}=8.0\text{m}$ fixed. As shown in the figure, the change in mass against N_0 up to 0.5 and N up to 1000 is significant.

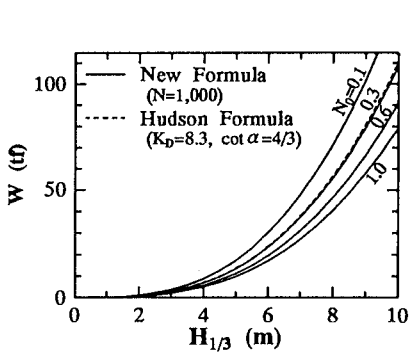


Figure 8 Relation between W and $H_{1/3}$

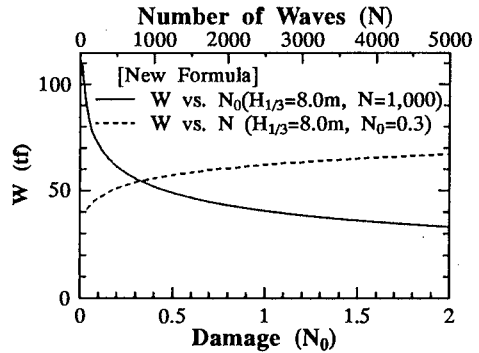


Figure 9 Mass change with N_0 and N

3. APPROACH TO PROBABILISTIC DESIGN

3.1 General Method

Reliability based design is a design methods which incorporate uncertainty and statistical deviation of design parameters. It is considered to be requisite for port and coast related structures from the view point of economic design especially for wave-dissipating concrete blocks. For the design of wave-dissipating concrete blocks, damage level accumulated within the lifetime of the structure is considered to be necessary. Therefore the process of damage accumulation in structures within their lifetime should be taken into consideration.

Design for port related structures includes many parameters to be treated probabilistically such as offshore wave height, wave period, tide, wave deformation by refraction, diffraction, shoaling and breaking for wave calculation. After calculation of the waves, the statistical uncertainty of damage to blocks should be taken into account specifically for wave-dissipating concrete blocks.

In this study, the authors demonstrate a procedure for the estimation of the expected value of damage accumulated within the lifetime of horizontally composite breakwaters incorporating statistical deviation of the offshore wave height, tide, shoaling, wave breaking, and damage to wave-dissipating concrete blocks.

The Monte Carlo simulation is used in probabilistic treatment, because of the advantage in handling physical phenomena using many sequential steps like the design process mentioned here. The simulation is considered to be a useful tool well supported by the advance of personal computers in recent years.

3.2 Detailed Calculation Method

(1) Offshore Wave Height

Damage to wave-dissipating concrete blocks is generally considered to be caused by large waves comparable to design waves. Therefore the yearly maximum offshore wave height is considered sufficient to be incorporated into the calculation. This offshore wave height H_{0e} is sampled from an extreme distribution of offshore waves. The estimated value of the offshore wave height is considered to include a statistical deviation. An average value H_0 is considered to follow a normal distribution with a bias (mean shift) α_{H0} , a standard deviation σ_{H0} and a deviation coefficient γ_{H0} as expressed as follows (Takayama et. al., 1994)

$$H_0 = (1 + \alpha_{H0})H_{0e}, \quad \sigma_{H0} = \gamma_{H0}H_{0e} \quad (7)$$

The sample offshore wave height datum H_{0c} to be used in the calculation is determined by a normalized random number based on Eq.(7).

(2) Tide

The tide is assumed to change sinusoidally between the High Water Level and the Low Water Level. A sample of tide value η is determined based on this assumption using a uniformly distributed random number as a phase of the sinusoidal curve.

(3) Wave Transformation (Shoaling, Breaking)

The height of wave incident to the structure $H_{1/3e}$ is calculated by the Goda method (1975) and the average value $H_{1/3}$ is expressed in a way similar to the offshore wave height, i.e.

$$H_{1/3} = (1 + \alpha_{H1/3})H_{1/3e}, \quad \sigma_{H1/3} = \gamma_{H1/3}H_{1/3e} \quad (8)$$

where $\alpha_{H1/3}$ is the bias, $\sigma_{H1/3}$ the standard deviation and $\gamma_{H1/3}$ the deviation coefficient. The sample wave height $H_{1/3c}$ at the structure is determined by a normalized random number based on Eq.(8) similar to that used for the offshore wave height.

(4) Stability Formula and Damage

As described before, in the reliability based design for wave-dissipating concrete blocks, the total damage level should be taken into account. Therefore the following formula derived from Eq.(6) is employed in order to estimate the damage level.

$$N_0 = \left(\frac{H_{1/3}/\Delta Dn - 1.33}{2.32} \right)^5 N^{0.5} \quad (9)$$

As for the uncertainty of damage to wave-dissipating concrete blocks, a statistical deviation of the increment of damage is taken into consideration. Tanimoto et. al. (1985) carried out a model test for wave-dissipating blocks and duplicated tests against the same wave condition with 6 to 7 wave height levels providing statistical data for damage increment. Figure 10 shows a sample of the distribution histogram of damage increment ΔN_0 , while the solid line indicates the

normal distribution function. The increment of damage is considered to be roughly distributed as the normal distribution function. Analysis of the data from Tanimoto et. al. shows that the larger the damage increase, the larger the standard deviation. Figure 11 shows the relation between damage increase ΔN_0 and standard deviation $\sigma_{\Delta N_0}$. The solid line indicates their relation as shown below.

$$\sigma_{\Delta N_0} = 0.36\Delta N_0^{0.5} \quad (10)$$

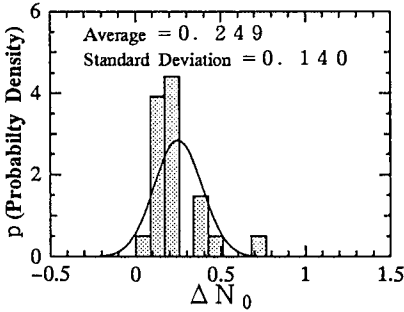


Figure 10 Example of histogram of ΔN_0

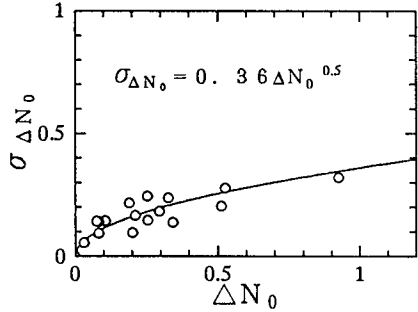


Figure 11 Relation between ΔN_0 and $\sigma_{\Delta N_0}$

(5) Damage Accumulation

Damage to wave-dissipating concrete blocks is considered to occur under rough sea conditions with a range of wave height of design level or larger in a cumulative way within the lifetime of the structures. This accumulation of damage is calculated in the following manner. Supposing the wave height at the structure for the i -th year is $H_{1/3c}(i)$ and the total damage up to the $(i-1)$ -th year is $N_0(i-1)$, the equivalent wave number $N=N'$ is determined by the following equation derived from Eq.(6) by substituting $H_{1/3c}(i)$ and $N_0(i-1)$ into $H_{1/3}$ and N_0 respectively.

$$N = \left(\frac{H_{1/3c}/\Delta Dn - 1.33}{2.32} \right)^{-10} N_0^2 \quad (11)$$

The total damage up to the i -th year $N_0(i)$ is calculated by Eq.(9) with $N=N'+N(i)$. The first estimation of ΔN_0 is calculated as $N_0(i)-N_0(i-1)$ and the sample data of ΔN_{0c} , taking into consideration the uncertainty of damage increment, is determined by the normalized random number with the standard deviation defined by Eq.(10). The estimated damage up to the i -th year is finally calculated as $N_0(i)=N_0(i-1)+\Delta N_{0c}$.

(6) General Flow of Calculation

The method described above is the procedure for calculating damage up to a certain year and the sample data of total damage accumulated within one lifetime is calculated by repeating this process for corresponding years of the total lifetime. Figure 12 shows the schematic flow of calculation. After obtaining several thousand

samples, statistical values such as the expected mean of total damage can be calculated.

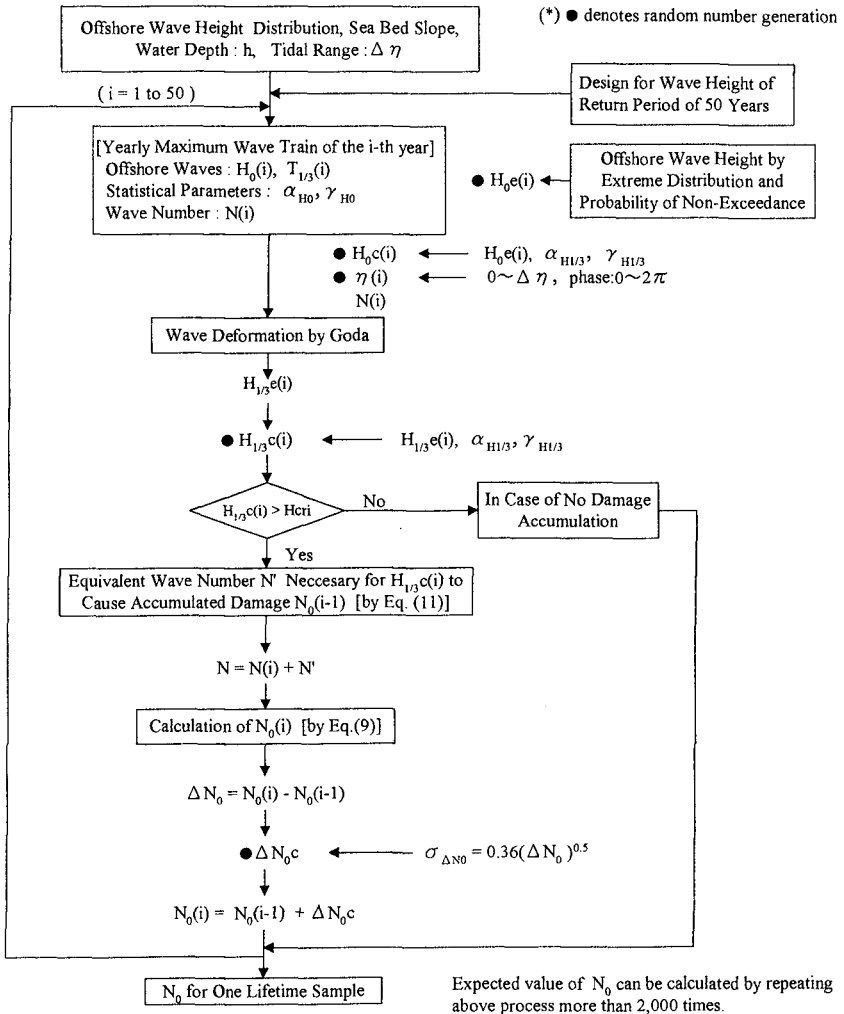


Figure 12 General calculation flow of one lifetime sample

(7) Calculation Sample of One Lifetime

Figure 13 shows an example of the offshore wave height, wave height at the structure and damage in chronological order. The design wave heights offshore and at the structure taken as a conventional manner with return period of 50 years for this example are $H_0=9.2\text{m}$ and $H_{1/3}=8.7\text{m}$ with a wave period $T_{1/3}=14.0\text{s}$. According to the figure, the offshore wave heights in the 33rd and 48th years exceeded the design

level. The wave height at the structure exceeds the design level in the 33rd year and the heaviest damage is accrued in the same year. Other smaller incidents of damages were recorded in the 2nd, 19th and 48th years resulting in a total damages of 0.45 accumulated within the lifetime of this one sample.

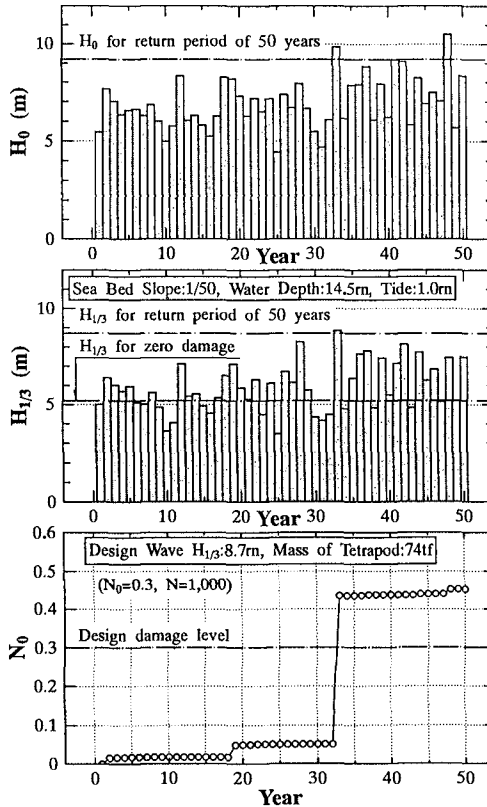


Figure 13 Example of lifetime sample

(8) Number of Lifetime Samples

In the example shown in the next sub-section, 5,000 samples of lifetime were computed for the statistical treatment for estimating total damage. Preliminary analysis, however, showed that 2,000 samples are considered to be enough to obtain a stable statistical result in this method from the practical view point.

3.3 Example of Estimation of Expected Value of Damage

In this sub-section, some examples of calculation based on the method mentioned previously are shown. The conditions of computation are as follows.

- a) *Wave Height* : A Weibull distribution with parameters $k=2.0$, $A=2.23$ and $B=4.78$ is assumed to be the extreme function for the offshore wave height ($H_0=9.2$ for return period of 50 years). The parameters expressing uncertainties for the offshore wave height and wave deformation mentioned in Eqs.(7), (8) were set as $\alpha_{H0} = 0$, $\gamma_{H0} = 0.1$, $\alpha_{H1/3} = -0.13$, $\gamma_{H1/3} = 0.09$ (Takayama et.al., 1994).
- b) *Wave Period and Number of Waves* : The wave periods for the examples here were determined so as to correspond to a wave steepness of 0.03 at the offshore. The wave period for the wave height $H_0=9.2$ m (50 year event) is $T_{1/3}=14.0$ s accordingly. The number of waves was set as 1,000 for all wave heights in these examples.
- c) *Tide* : The tide range of 1.0m (L.W.L. 0.0m, H.W.L. +1.0m) was assumed
- d) *Design of Wave-dissipating Concrete Blocks* : The mass of Tetrapods was calculated by Eq.(6) under the criteria of $N_0=0.3$ and $N=1,000$ against wave height for the 50 year event.
- e) *Sea Bed Slope* : Sea bed slopes of 1/50 and 1/10 were employed.
- f) *Water Depth* : Water depths of 7, 9, 11, 13 and 15m at low tide were examined.

Table 2 summarizes the parameters of the simulation such as the design wave heights and masses of the Tetrapods at each location based on the conditions above in a conventional design for a 50 year event.

Table 2 Design wave height and mass of Tetrapod

Case No.	1	2	3	4	5
Sea Bed Slopes	1/50	1/50	1/50	1/50	1/50
Water Depths (m)	7.0	9.0	11.0	13.0	15.0
Design Wave Heights (m)	5.57	6.64	7.59	8.34	8.81
Mass of Tetrapods (tf)	18.7	31.8	47.6	63.0	74.3
Case No.	6	7	8	9	10
Sea Bed Slopes	1/10	1/10	1/10	1/10	1/10
Water Depths (m)	7.0	9.0	11.0	13.0	15.0
Design Wave Heights (m)	8.16	9.41	10.18	10.31	10.13
Mass of Tetrapods(tf)	59.0	90.5	114.5	118.9	112.9

Figure 14 shows the variation of the expected value of $\max H/H_s$ with water depth, where $\max H$ is the maximum significant wave height at each location within the lifetime, H_s is the design wave height. As shown in Figure 13, the total damage to the wave-dissipating concrete blocks was significantly affected by the maximum wave height within the lifetime. The expected value of $\max H/H_s$ tended to decrease against the water depth in the case of the sea bed slope of 1/50. However, it had a minimum at around 11m for a 1/10 slope.

Figure 15 shows the calculated results of the expected accumulated damage at each location. The expected accumulated damages for these examples are estimated as larger than the design criteria of $N_0=0.3$. This is considered reasonable because of the possibility of occurrence of a wave height larger than the design level. The damage accumulation is accurately taken into account as shown in Figure 13.

From the conventional deterministic design view point, the masses shown in Table 2 are considered to equally assure the damage level of $N_0=0.3$ against each design wave height with a safety factor of 1.0. The present simulation shows that the expected total damage within the lifetime on the probabilistic basis depends on such parameters as the sea bed slope and water depth. It is also found that the expected value of total damage to wave-dissipating concrete blocks varies corresponding to the variation of $\max H/H_s$ shown in Figure 14.

Figure 15 also shows the effect of mass increase on the damage in the case of a 1/50 slope. It can be roughly said that a 10% to 20% mass increase caused a 30% to 50% decrease in total damage accumulated. This result means that the mass of the wave-dissipating concrete block might be adjusted to account for certain conditions by some percentage higher than that determined by the stability formula when based on the probabilistic design. This would assure the same level of total damage within the lifetime.

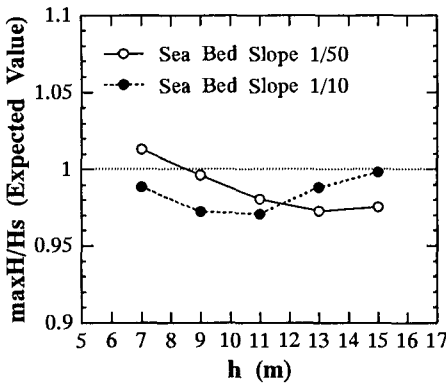


Figure 14 Expected values of $\max H/H_s$

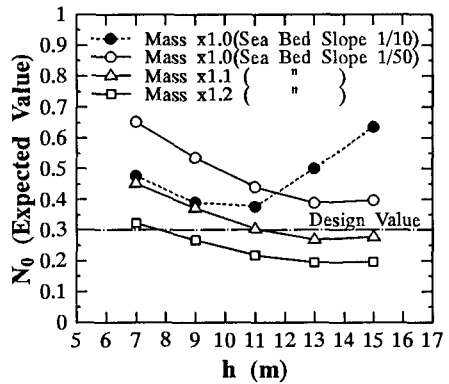


Figure 15 Expected values of N_0

4. CONCLUSIONS

- 1) A new stability formula for wave-dissipating concrete blocks covering horizontally composite breakwaters was proposed and the applicability of this formula was verified by experimental data.
- 2) A probabilistic approach to the estimation of total damage to wave dissipating concrete blocks accumulated within a life time by Monte Carlo simulation was proposed and the applicability of this method for reliability based design of wave-dissipating concrete blocks was proved.

Acknowledgements

The authors wish to thank Mr. R. Ojima, Head of the Hydraulic Engineering Division, Port and Harbor Research Institute, Ministry of Transport and Dr. K. Kobune, from the Overseas Coastal Area Development Institute of Japan for their valuable insight to this study. The authors wish to express gratitude to the Hokkaido and Okinawa Development Bureaus, and the 1st to 5th District Port Construction Bureaus, Ministry of Transport, for their kind cooperation in supplying the model test data.

References:

- Goda Y. (1975): Deformation of irregular waves due to depth-controlled wave breaking, Report of the Port and Harbour Research Institute, Vol.14, No.3, pp. 59-106 (in Japanese)
- Hudson, R.Y. (1959): Laboratory investigation of rubble-mound breakwater, Proc. A.S.C.E. Vol. 85, WW3, pp. 93-121.
- Van der Meer, J.W. (1987): Stability of breakwater armor layer design formulae, Coastal Engineering, Vol. 11, pp. 219-239.
- Van der Meer, J.W. (1988): Stability of Cubes, Tetrapods and Accropode, Proc. of Conf. Breakwaters '88, pp. 59-68.
- Kajima, R., Sakakiyama, T., Shimizu, T., Sekimoto, T., Kunisu, H., Kyoya, O. (1993): A formula for estimating deformation level of wave-dissipating concrete blocks under irregular waves, Proc. of Coastal Engineering, vol. 40, pp. 795-799 (in Japanese).
- Kajima, R. (1994): A new method of structurally resistive design of very important seawalls against wave action, Proc. of International Workshop on Wave Barriers in Deepwaters, pp. 518-536.
- Takahashi, S. (1996): Design of vertical breakwaters, Reference Documents, No.34, Port and Harbour Research Institute, 85p.
- Takayama, T., Ikeda, N. (1994): Estimation of encounter probability of sliding for probabilistic design of breakwater, Proc. of International Workshop on Wave Barriers in Deepwaters, pp. 438-457.
- Tanimoto, K., Kitatani, T., Osato, M. (1979): Example of model test for wave dissipating concrete blocks against irregular waves, Technical Note of the Port and Harbour Research Institute, No.321, 60p. (in Japanese)
- Tanimoto, K., Haranaka, S., Yamazaki, K. (1985): Experimental study of wave dissipating concrete blocks against irregular waves, Report of the Port and Harbour Research Institute, Vol.24, No.2, pp. 85-121 (in Japanese)

CHAPTER 131

Breakwater Stability under Regular and Irregular Wave Attack

Thomas Jensen^{*}, Henning Andersen^{*}, John Grønbech^{**}
Etienne P.D. Mansard^{***} and Michael H. Davies^{***}

Abstract

The main objective of the present study was to compare the damage to a rubble mound breakwater under regular and irregular wave attack, and thereby identify an irregular wave height parameter that corresponds to the wave height of a regular wave in terms of inducing a similar degree of damage to the structure. The 1984 edition of the Shore Protection Manual recommends this irregular wave height parameter to be $H_{1/10}$ (the average of the highest one-10th of the waves in a sea state), but other researchers recommend $H_{1/30}$ (e.g. Vidal et al., 1995). For the present study, $H_{1/20}$ is the irregular wave height parameter that yields the best correspondence between irregular and regular waves. However, this result is dependent on the length of the time series and on the number of times this time series is recycled to achieve a given damage level. The new wave height parameter H_n (the average of the n highest waves in a sea state) proposed by Vidal et al. (1995) takes into account the statistics of the large waves contained in the time series as well as the number of times this time series is recycled. The present study indicates that H_{250} (the average of the highest 250 waves in the sea state) is a suitable wave height parameter for characterizing breakwater stability under irregular waves.

1 Introduction

Over the years, several formulae have been proposed for predicting the hydraulic stability of armour layers; All of them are empirical and do not account for all of the parameters that affect the stability. One of these formulae is the well-known Hudson

* Danish Hydraulic Institute. Agern Allé 5, DK-2970 Hørsholm, Denmark.

** Department of Civil Engineering. Aalborg University, Sohngaardsholmsvej 57, DK-9000 Aalborg, Denmark

*** Canadian Hydraulics Centre, National Research Council of Canada, Ottawa, Ontario K1A 0R6, Canada.

formula, developed by R.Y. Hudson in 1958. Although this formula was developed on the basis of regular waves, it has been applied for irregular waves by replacing the regular wave height by the significant wave height H_s (i.e. $H_{1/3}$) of irregular waves.

The Shore Protection Manual (1984) recommends the use of $H_{1/10}$ instead of $H_{1/3}$. However, authors such as Vidal et al. (1995) claim that a wave height parameter such as $H_{1/10}$ or $H_{1/3}$ does not describe the large waves in a wave train sufficiently well. They argue that additional information is required on the length of the time series and the number of times it is recycled to achieve a given degree of damage. They also show that a new wave height concept H_n , based on the average of the n highest waves in a sea state, can account for the statistics of the large waves contained in the sea state as well as for the number of times it is recycled for achieving a certain degree of damage.

The main objective of the present study was to compare breakwater stability under regular and irregular waves in terms of measured damage. Whether or not H_n is a suitable wave height parameter for carrying out this comparison will also be established.

2 Experimental Set-up and Test Series

The experimental investigations were carried out in the Wave Research Flume at the Canadian Hydraulics Centre (CHC) of the National Research Council of Canada (NRC) at a Froude scale of 1:15 (Andersen et al., 1995). This flume is 97 m long, 2 m wide and 2.75 m deep. The wave generator in the flume uses active wave absorption, which allows the wave paddle to absorb reflected waves during wave generation thereby eliminating re-reflections (Davies et al., 1994a).

The tested structure was composed of a core, filter and an armour layer placed on a uniform slope of 1:1.8. The gradation of the armour stones was such that the ratio of $M_{max}/M_{min} \approx 2.5$. The median mass of the rocks, M_{50} was 2600 kg. A sketch of the tested structure is shown in Figure 1.

An array of five capacitance-type wave gauges was placed in front of the structure in order to separate the incident and reflected wave components. The applied reflection analysis was based on the least-squares technique described by Mansard et al. (1980). The incident sea state parameters obtained in the tests with regular and irregular waves are shown in Table 1 together with the number of repetitions of each sea state. For irregular waves the sea state was characterized by the incident significant wave height ($H_{s,i}$), derived from the incident wave spectrum and the spectral peak period, T_p . The incident sea state parameters for regular waves were also determined from reflection analysis.

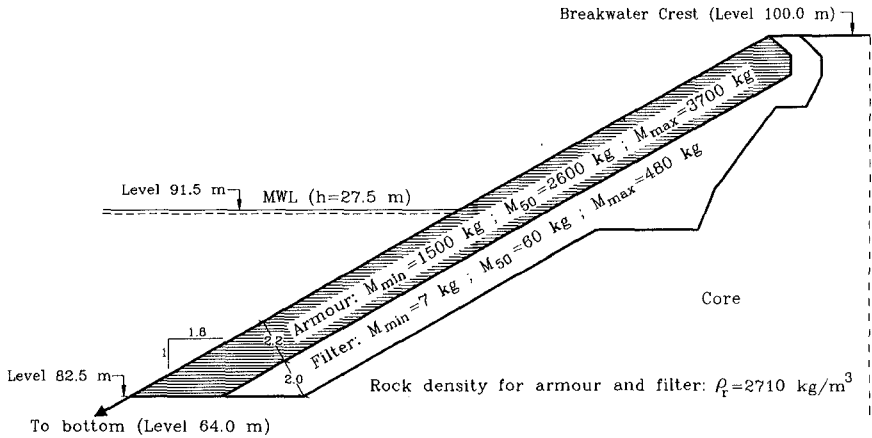


Figure 1 - Sketch of the tested breakwater cross-section (prototype units).

Irregular Waves			Regular waves		
$H_{s,i}$ (m)	T_p (s)	Repetitions	H_i (m)	T (s)	Repetitions
1.0	4.1	1	1.3	3.8	1
1.5	5.0	1	1.7	4.7	1
2.0	6.0	4	2.3	5.6	1
2.3	6.4	4	2.7	5.9	1
2.6	6.6	4	2.9	6.4	1
2.8	7.1	4	3.3	6.7	1
3.1	7.3	4	3.7	7.0	3
-	-	-	3.9	7.2	2
-	-	-	4.2	7.5	2
-	-	-	4.5	7.7	2

Table 1 - Incident sea state parameters for regular and irregular waves.

For each irregular wave condition a time series was synthesized using the random phase spectrum method, which combines the amplitude spectrum derived from the JONSWAP spectrum with a random phase spectrum (Mansard et al., 1994b). The prototype length of the time series for irregular waves was chosen to be relatively long (i.e. 2 hours) in order to minimize any of the potential variability in wave parameters often associated with shorter time series. Thus the time series contained 1200 to 2100 waves depending on the peak period of the sea state.

In order to ensure that the damage had stabilized under each wave condition, each time series was recycled four times resulting in approximately 5000 waves. Damage patterns generally stabilized after about 5000 waves. Since damage patterns develop much more quickly for regular waves, the length of the regular wave time series was

chosen to contain approximately 300 to 600 waves (depending on the period). For incident waves with $H_i > 3.3$ m it was necessary to repeat the time series 2 or 3 times in order for the damage to stabilize. This illustrates a fundamental difficulty with the concept of damage stabilization. The tendency for breakwater damage to stabilize and the time-frame within which this stabilization occurs are in fact directly related to the stability number, N_s .

Table 1 shows the wave parameters that were used in this study. These are the incident waves that were determined from reflection analysis. When generating the regular waves, an appropriate wave period had to be chosen for each wave height. Based on earlier works suggesting that either $H_{1/10}$ or $H_{1/20}$ are appropriate parameters when comparing regular and irregular waves, the wave periods for the regular waves in this study were chosen to be equal to the average of the wave periods corresponding to $H_{1/10}$ and $H_{1/20}$ of the corresponding irregular wave trains (i.e. the bivariate statistics were used).

3 Damage Measurements

After each test series the damage to the breakwater was estimated by computing the eroded area (A_e) using an electro-mechanical profiler. The performance of this profiler has been found to be very reliable and it has also been compared with the estimates of eroded area derived by counting the number of displaced armour stones (Davies et al., 1994b).

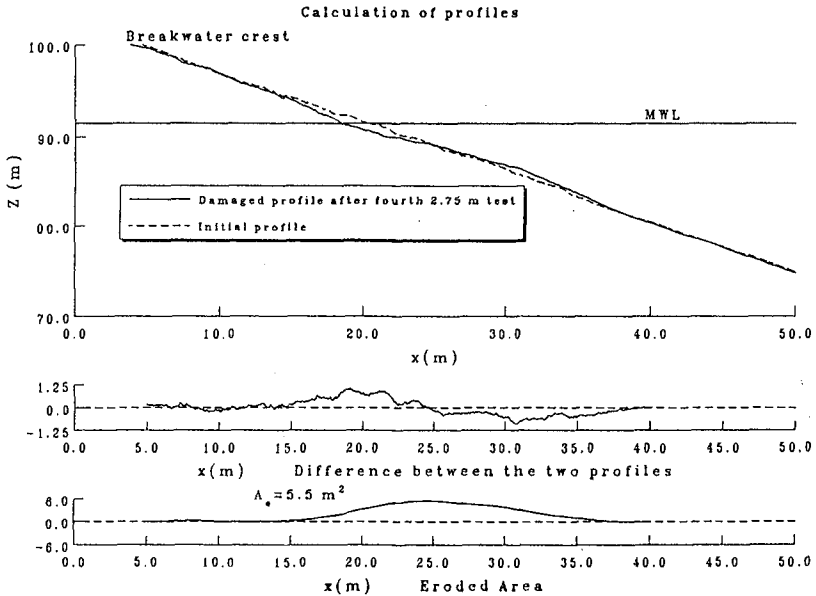


Figure 2 - Damaged breakwater profile after 4th irregular test with $H_{s,i} = 2.8$ m.

The damaged profile is determined as the average of nine evenly spaced profiles across the flume. The cross-sectional area of erosion is calculated by integrating the vertical difference between the damaged profile and the initial profile. Integrating from the crest of the breakwater, the eroded area is defined as the maximum value of this integral as a function of the distance x (see Figure 2). The eroded area is interpreted as the eroded volume/metre breakwater length.

When analyzing damage on rubble mound breakwaters, a dimensionless damage parameter S is often introduced:

$$S = \frac{A_e}{D_{n50}^2}$$

where A_e is the eroded area and $D_{n50} = (M_{50}/\rho_r)^{1/3}$ is the nominal diameter of the armour stones. The damage parameter can be visualized as the number of cubic stones of dimension D_{n50} eroded within a D_{n50} wide strip of the breakwater. $S = 2$ corresponds to the initiation of damage and is equivalent to the 0-5% damage defined in Shore Protection Manual (1984). Failure is defined as exposure of the filter layer and for a two diameter thick armour layer, this occurs for S -values of approximately 8 (van der Meer, 1988).

4 Evolution of Damage under Irregular Waves

In Figure 3 the damage parameter S is shown as a function of the number of waves for each of the four test sequences carried out.

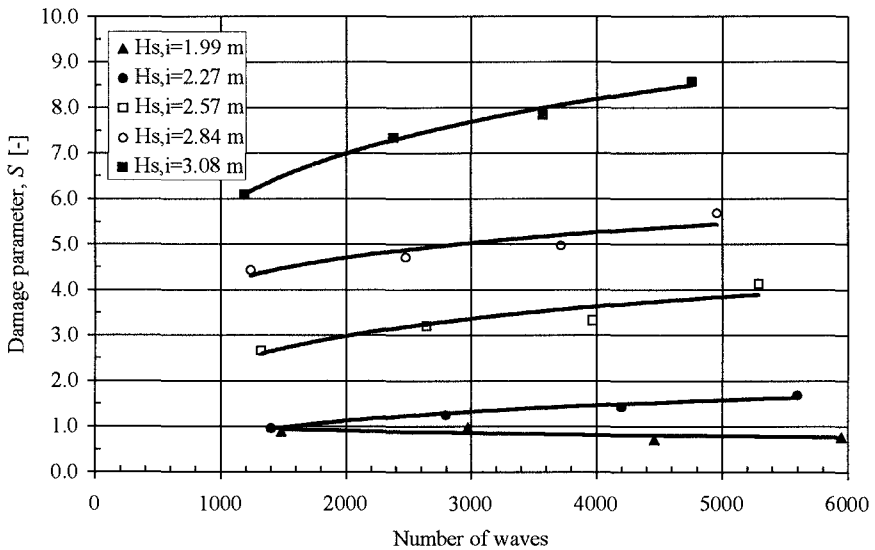


Figure 3 - Evolution of damage for irregular waves.

It can be seen from Figure 3 that the damage tends to stabilize in about 5000 waves. Based on approximately 50 tests with irregular waves, van der Meer (1988) proposed an equation for describing the damage evolution as a function of the number of waves. However, the results used to develop this equation were based on tests that started with zero-damage when the wave heights were changed. This means that the breakwater was rebuilt after each sea state. In this study the breakwater was not rebuilt after each severity of the sea state. Hence, the expression of van der Meer (1988) is not directly comparable to the evolution of damage shown in Figure 3. The evolution of damage is also seen in Figure 4 where the cumulative damage is plotted as a function of the cumulative number of waves.

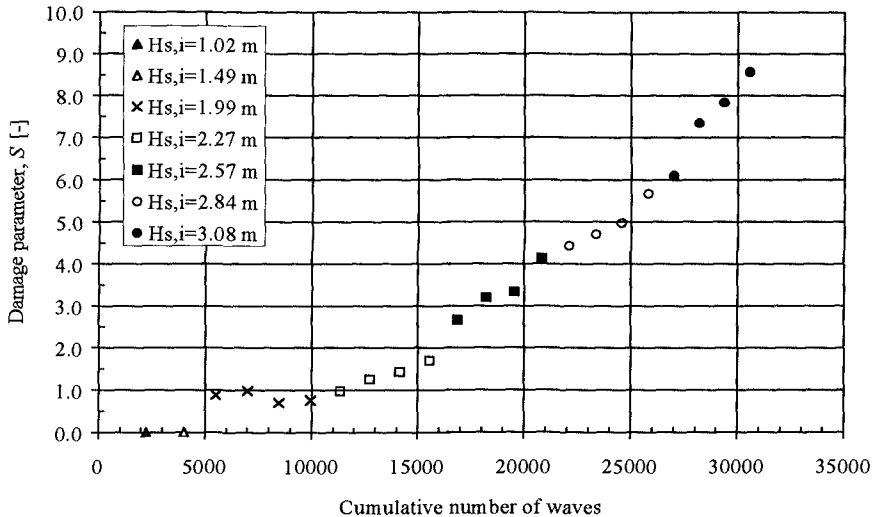


Figure 4 - Damage versus the cumulative number of waves (irregular waves).

5 Evolution of Damage under Regular Waves

According to Vidal et al. (1995) it takes about 100 to 400 waves for the damage to attain its equilibrium under regular waves. Hence, a 10 minutes long time series containing approximately 300 to 600 waves (depending on the period) was used in regular wave tests.

In Figure 5 the damage parameter S is shown as a function of the cumulative number of waves for the tests with regular waves. For $H_i = 3.7$ m the time series had to be repeated three times before the damage patterns stabilized. This indicates that the number of waves required to reach a state of equilibrium is larger than the value suggested in Vidal et al. (1995). Further tests should be carried out to verify this observation. It is possible that the number of waves required to stabilize the damage patterns can also vary with the degree of breakwater damage.

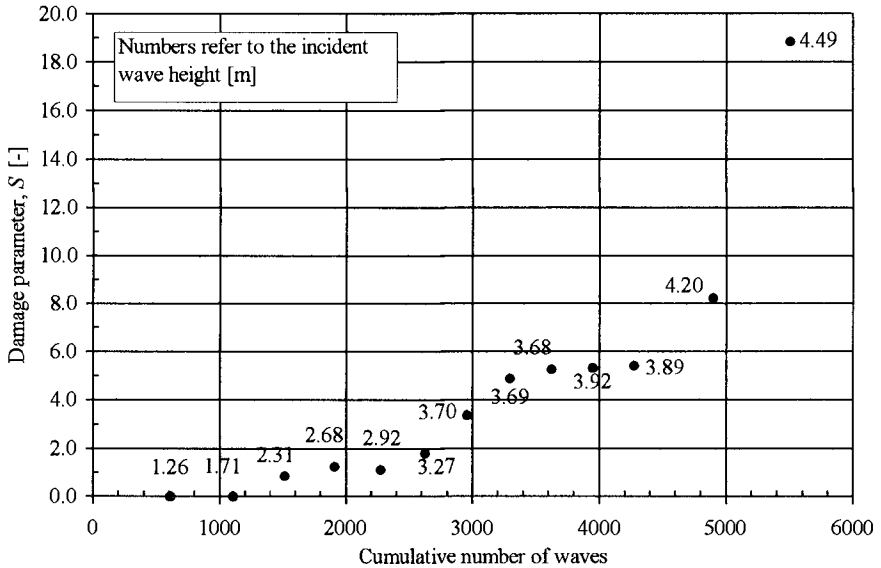


Figure 5 - Damage versus the cumulative number of waves (regular waves).

The regular wave tests showed that a damage level of $S = 2$ corresponds to a regular wave height of $H_i = 3.3$ m. In Hudson's formula, this would correspond to a value of $K_D = 4$, which agrees well with published values.

6 Comparison between Regular and Irregular Waves

In Figure 6 the damage is plotted against the stability number, N_s given by:

$$N_s = \frac{H}{\Delta D_{n50}} \quad ; \quad \Delta = \frac{\rho_r}{\rho_w} - 1$$

where H is the wave height and ρ_w is the mass density of water.

Figure 6 compares the damage caused by irregular waves characterized using four different wave height parameters in the calculation of the N_s parameter: $H_{1/3}$ ($\approx H_s$), $H_{1/10}$, $H_{1/20}$ and the average of $H_{1/10}$ and $H_{1/20}$.

A time-domain reflection analysis recently developed by Mansard (1994) showed that the average ratio between $H_{1/10}$ and $H_{1/3}$ and the ratio between $H_{1/20}$ and $H_{1/3}$ were 1.28 and 1.42, respectively, in the irregular wave tests. Since the corresponding values from the theoretical Rayleigh distribution are 1.27 and 1.40 respectively, this suggests that the incident wave heights were Rayleigh distributed.

From Figure 6 it appears that the best correspondence between the damage levels for regular and irregular waves is obtained when the irregular waves are

characterized by $H_{1/20}$. A comparison of the results of the present study with results of previous tests with the same breakwater is shown in Figure 7.

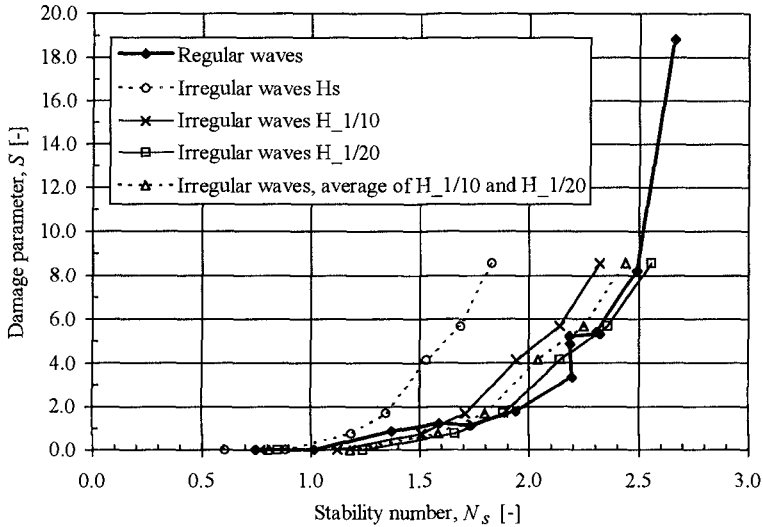


Figure 6 - Comparison between damage for regular and irregular waves.

In terms of Hudson's stability formula it is seen from Figure 7 that there is a good agreement between the results of the present study and the results obtained previously. The K_D -factor for this study using $H_{1/3}$ as the wave height parameter and $S = 2$ as damage level is approximately 1.4. In similar tests undertaken at CHC (e.g. Laurich et al., 1995) with the same breakwater the K_D -factor was found to range between 1.2 and 1.7.

Shore Protection Manual (1977) recommends the use of $H_{1/3}$ in Hudson's stability formula for design of breakwaters. The K_D -values suggested for breaking and non-breaking waves for rough angular quarry stone were 3.5 and 4.0, respectively (note that these K_D -values were established using only regular wave tests). Shore Protection Manual (1984) recommends the use of $H_{1/10}$ instead of $H_{1/3}$, and also recommends that the K_D -values for breaking and non-breaking waves should be changed to 2.0 and 4.0, respectively. The recommendation of $H_{1/10}$ in Hudson's formula rather than $H_{1/3}$ was supported by hydraulic tests by Feuillet et al. (1980); However, tests by Tanimoto et al. (1982) suggested a design wave height of $H_{1/5}$ when comparing regular and irregular wave tests. Furthermore, Allsop (1993) suggests that the application of $H_{1/10}$ in Hudson's formula is overly conservative.

For irregular waves, van der Meer (1988) proposed the following general damage equation:

$$N_s = a(K_D \cot \theta)^{1/3} \cdot S^b$$

where N_s is determined using $H_{1/3}$, θ is the slope of the armour, and a and b are empirical coefficients ($a = 0.7$, $b = 0.15$) determined by regression analysis. The K_D -value corresponds to Shore Protection Manual (1984), here the use of $H_{1/10}$ in the Shore Protection Manual is taken into account by the value of the a -coefficient. If this formula is applied to the results of the present study the damage to the breakwater is underestimated. This may be attributable to the fact that $H_{1/20}$ is a better parameter than $H_{1/10}$ for comparing regular and irregular waves for this structure (see Figure 6).

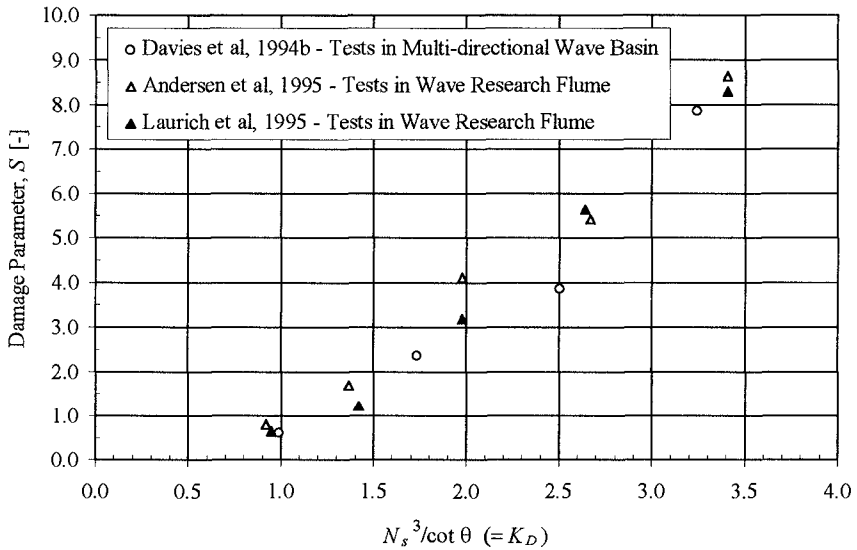


Figure 7 - Comparison with previous studies. N_s is computed from $H_{1/3}$.

Based on the results of a number of laboratory tests performed to study damage mechanisms of riprap, Ben Belfadhel (1993) found $H_{1/10}$ to be an acceptable wave parameter for use in stability formulae developed from regular wave tests. However, based on CHC data for steep slopes (1:1.5) Ben Belfadhel* has found that $H_{1/20}$ may be a more suitable parameter.

A comparison between the results of Vidal et al. (1992) obtained under irregular waves and the results established by Givler et al. (1986) using regular waves was carried out by Vidal et al. (1995). They found a good correspondence between the damage of regular and irregular waves with $H_{1/30}$ as the wave height parameter in the stability expression. However, from Figure 5 in Vidal et al. (1995) it seems that an

* Personal communication between Dr. E.P.D. Mansard and Dr. B. Belfadhel.

even better correspondence could have been obtained if a wave height parameter closer to $H_{1/20}$ was applied.

7 Potential Sources of Inaccuracy

When dealing with irregular waves, the choice of an appropriate wave height parameter for use in the Hudson's formula is a continuous source of debate. Independent experiments by different researchers have failed to achieve consensus. Discrepancies between the findings of the various researchers could be partly due to different test methods used in different laboratories. Two potential sources of inaccuracies in experimental methods are described in the following.

Active Absorption of Waves

A commonly used technique for determining incident waves in flume tests is to calibrate sea states in the test flume with an efficient absorber in place before the breakwater is constructed, - thereby eliminating the need for sophisticated reflection analysis. During the breakwater stability tests, the damage is expressed as a function of the incident wave height obtained during this wave calibration procedure. Without active absorption, re-reflections can modify this incident wave height. This is discussed below:

Waves reflected by the breakwater propagate towards the wave generator and generally get re-reflected if the installation is not equipped with the capability for active absorption. These re-reflected components then propagate toward the breakwater as part of the incident waves. Depending on the differences between the phase angles of the original incident component and the re-reflected component, the net incident wave height attacking the breakwater could either be lower or higher than intended. Studies recently performed at CHC by Laurich et al. (1995) showed that active absorption can eliminate the inaccuracies introduced by these re-reflections.

The importance of using active wave absorption is shown in Figure 8, which shows the results of separate breakwater stability tests conducted with regular waves with periods of 2.0 and 1.94 s, respectively. No active absorption (position control) was used in these tests. For the test with $T = 1.94$ s, the phases of the re-reflected waves and the incident waves were such that they caused a higher than intended incident wave height at the structure (and correspondingly, a high degree of damage). The reverse was true when $T = 2.0$ s - the phasing of the re-reflected waves was such that incident wave energy (and damage levels) were reduced. If these test results were interpreted neglecting the effects of re-reflections, the damage levels seen in the two tests would have suggested two quite different conclusions. Using the results of the present study, the $T = 1.94$ s test would suggest that $H_{1/10}$ is the appropriate

wave parameter for comparison of irregular and regular waves, while the $T = 2.0$ s test would suggest that $H_{1/50}$ is more suitable.

This example shows that if active absorption is not used (or if the actual incident waves attacking the breakwater are not determined accurately), the interpretation of results could be quite different depending on the experimental installation.

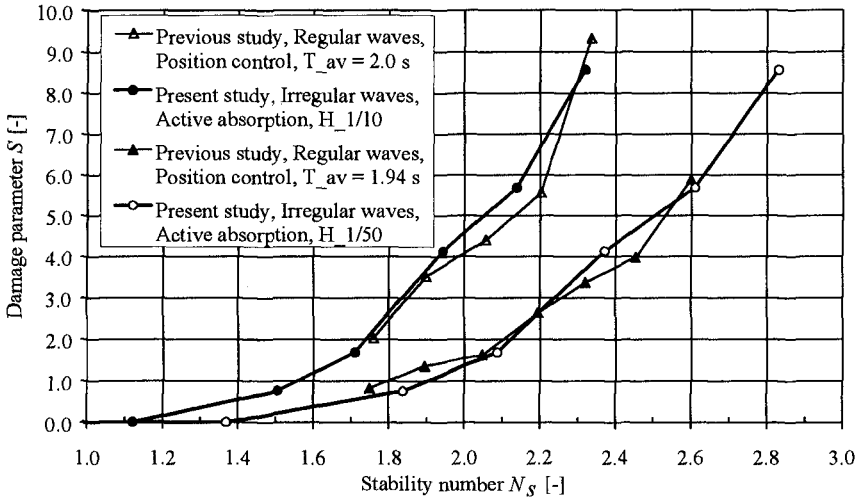


Figure 8 - Comparison of damage between two regular and two irregular wave tests.

Stabilization of Damage

In order to perform a reliable comparison between the damage obtained under regular and irregular waves, the rate of damage progression must be considered. Ideally one should compare regular and irregular wave tests at some equilibrium damage level. This can be difficult because true equilibrium is rarely attained in breakwater testing, however the rate of damage progression does slow with time. Choosing an equivalent number of cycles for regular and irregular wave tests is thus somewhat arbitrary. It takes fewer waves (i.e. 300 to 600) for the damage to stabilize if these waves are regular. In the case of irregular waves, 5000 waves or more are required to approach stabilization. It is important to make damage comparisons after ensuring that the level of damage “equilibrium” in the regular and irregular wave tests is equivalent. Otherwise misleading conclusions can be drawn.

9 Suitable Wave Height Parameter

Although $H_{1/20}$ has been identified as the most appropriate irregular wave parameter in this study, it does not consider the role of storm duration. Since each of the four

tests was carried out by recycling the same time series, the value of the $H_{1/20}$ parameter remains the same (i.e. $1.42 \cdot H_{m0}$), whether one or four cycles were used. Vidal et al. (1995) suggest a technique to incorporate both the effects of wave height and the number of waves to which a structure is exposed. They introduce H_n , which is defined as the average of the n highest waves used in achieving a certain damage. To apply this concept to the present study, H_n would be computed based on all four cycles of the time series used in the experiments. For instance, since a total of nearly 5000 waves were used in this particular study, the average of the highest one 20th corresponds to a wave height parameter H_{250} . Vidal et al. (1995) report that the parameter H_{250} describes not only the damage that has attained its equilibrium but also the intermediate ones.

To illustrate the suitability of the H_n parameter, Vidal et al. (1995) assumed that damage is proportional to the 5th power of the H_n wave height as follows:

$$S_{nz} = K_1 \left(\frac{H_n}{H_{1/3}} \right)^5$$

where S_{nz} is the damage after n_z waves, and K_1 is a constant. The damage can also be predicted by applying the following equation of van der Meer (1988):

$$S_{nz} = S_{5000} 1.3 \left[1 - \exp(-3 \cdot 10^{-4} n_z) \right] = K_2 f(n_z)$$

Equating these two damage levels gives:

$$\frac{K_2}{K_1} = \frac{(H_n / H_{1/3})^5}{f(n_z)}$$

i.e., the right hand side of this equation should be constant for different n_z . Vidal et al. (1995) show that for Rayleigh distributed wave heights an appropriate value for n is approximately 100. It is presumed that this proportionality is applicable to a breakwater section that was tested if it had undergone no damage by previous wave heights. Since in this study, lower wave heights have already caused some initial damage, a somewhat different form of the relationship was anticipated. Consequently, both linear and parabolic relationships were considered in determining a suitable relationship, i.e.

$$S \propto H_n \quad \text{and} \quad S \propto H_n^2$$

For each cycle, the wave height parameter ($H_{1/m}$) is determined corresponding to the actual damage level (Rayleigh distribution of wave heights is assumed. This assumption has been verified in the wave analysis). Since $H_{1/20}$ was shown to be the best parameter in Figure 6, it is also used in the following illustration:

For example: after the 1st cycle of $H_{s,i} = 3.1$ m the damage level is 72% of the corresponding equilibrium damage level. Hence the wave height parameter is $0.72 H_{1/20}$ for the linear assumption and $\sqrt{0.72} H_{1/20}$ for the parabolic assumption, corresponding to $H_{1/3.0}$ and $H_{1/6.8}$, respectively, using the Rayleigh distribution. Based on the cumulative number of waves (determined from the mean period) the corresponding n -value can be determined for H_n .

Using this approach for the present study, the n -value can be determined for all the test series (i.e. including the intermediate damage levels). The average value of n was found to be 250 with a coefficient of variation of approximately 10 %. This indicates that the H_n parameter is a more suitable parameter to characterize breakwater damage than the conventional $H_{1/n}$ (e.g. $H_{1/10}$ or $H_{1/20}$) which does not take into account the number of waves.

10 Conclusions

The best correspondence between regular and irregular waves in terms of the damage is obtained when the irregular waves are characterized by $H_{1/20}$. Other researchers have proposed e.g. $H_{1/10}$ and $H_{1/30}$ to characterize irregular waves. These different results may be associated, to a certain extent, with variations in test methods.

Vidal et al. (1995) proposed the H_n concept to characterize irregular waves. This concept, defined as the average of the n highest waves, has the advantage of including the length of the time series, the number of times it is recycled, and the statistics of the highest waves. In this particular study, an n -value of approximately 250 was found to be suitable. Further research is necessary to verify the suitability of H_n to characterize breakwater damage under irregular waves and to determine a suitable n -value.

Acknowledgements

The authors gratefully acknowledge the Canadian Hydraulics Centre of the National Research Council of Canada for generously providing the facilities for these investigations. Thanks are also due to the entire staff of CHC for their assistance.

References

- Allsop, N.W.H. (1993): *Formulae for Rubble Mound Breakwater Failure Modes*. PIANC Report, Analysis on Rubble Mound Breakwaters, Sub-Group A.
- Andersen, H., Grønbech, J. and Jensen, T. (1995): *Model Study of Rubble Mound Breakwater under Regular and Irregular Wave Attack*. NRC Controlled Technical Report, HYD-CTR-001.

- Ben Belfadhel, M., Lefebvre, G. and Rohan, K. (1993): *Clarification on the use of Hudson Formula for Riprap Design*. Proc. of 25th IAHR Congress, Tokyo, Japan, 1993.
- Davies, M.H., Laurich, P.H., Mansard, E.P.D. and Miles, M.D. (1994a): *A new Wave Research Flume at NRCC*. Proc. of the 24th International Symposium on Waves, Vancouver, 1994.
- Davies, M.H., Mansard, E.P.D, and Cornett, A.M. (1994b): *Damage analysis for rubble mound breakwaters*. Proc. 24th ICCE, Kobe, 1994.
- Feuillet, J., and Sabaton, M. (1980): *Stability of Rubble-Mound Breakwater*. Proc. 17th ICCE, Sydney, 1980.
- Givler, L.D. and Sørensen, R.M. (1986): *An investigation of the stability of submerged homogeneous rubble mound structures under wave attack*. H.R. IMBT Hydraulic Report IHL-110-86, Lehigh University, Bethlehem, Pa.
- Laurich, P.H., Mansard, E.P.D. and Davies, M.H. (1995): *Active Wave Absorption for Improved Modelling of Breakwater Stability*. Proc. XXVI IAHR Congress, London, 1995.
- Mansard, E.P.D. (1994): *On the Estimation of the Incident Wave Train from Reflection Analysis*. Proc. 9th Congress of Asia-Pacific Division of IAHR, Singapore, 1994.
- Mansard, E.P.D. and Funke, E.R. (1980): *The Measurement of Incident and Reflected Spectra using a Least Squares Method*. Proc. 17th ICCE, Sydney, 1980.
- Mansard, E.P.D., Davies, M.H., Caron, O. and Parkinson, F.E. (1994a): *Model Study of Riprap Stability Under Wave Action at the LG3 Reservoir, La Grande Hydroelectric Project*. Proc. of the Seminar on Case Histories for the Design, Construction and Maintenance of Rubble-Mound Structures, Eureka, 1994.
- Mansard, E.P.D., Miles, M.D., and Nwogu, O.G. (1994b): *Laboratory Simulations of Waves: An Outline of Wave Generation and Analysis Procedures*. Proc. of the 24th International Symposium on Waves, Vancouver, 1994.
- Shore Protection Manuals (version 1977 and 1984). Coastal Engineering Research Center, Waterway Experiment Station, U.S. Corps of Engineers, Department of the Army, Vicksburg, Mississippi, U.S.A.
- Tanimoto, K., Yagyo, T., and Goda, Y. (1982): *Irregular Wave Tests for Composite Breakwater Foundations*. Proc. 18th ICCE, Cape Town, 1982.
- Van der Meer, J.W. (1988): *Rock Slopes and Gravel Beaches Under Wave Attack*. PhD. Thesis, Delft University of Technology, Delft, The Netherlands.
- Vidal, C., Losada, M.A., Mansard, E.P.D., and Gomez-Pina, G. (1992): *A universal analysis for the stability of both low-crested and submerged breakwaters*. Proc. 23rd ICCE, New York, 1992.
- Vidal, C., Losada, M.A. and Mansard, E.P.D. (1995): *Suitable Wave Height Parameter for Characterizing Breakwater Stability*. Journal of Waterway, Port, Coastal and Ocean Engineering, Vol.121, No.2, 1995. ASCE.

CHAPTER 132

Roundhead Stability of Berm Breakwaters

Jørgen Juhl¹, Amir Alikhani², Peter Sloth¹, Renata Archetti³

Abstract

Three-dimensional (3D) model tests were carried out for studying the stability of a berm breakwater roundhead and the adjacent trunk section. The present paper describes the influence of the wave incidence angle and wave steepness on the roundhead stability. The test results are described in terms of profile development, recession of the berm, eroded and deposited volumes and the transport of stones during reshaping. Results from analysis of the influence of wave obliquity on profile shape, initiation of longshore transport and longshore transport rate at the trunk section are presented in Alikhani et al (1996).

Introduction

For berm breakwaters as compared with traditional rubble mound breakwaters, special measures have to be taken for the breakwater roundhead. If stone displacements occur on a roundhead, the stones will be moved in the wave direction and will loose most of their stabilising effect. A point of special concern is whether, and under which conditions, a berm breakwater roundhead after some initial reshaping may develop into a stable shape that is not subject to continued erosion, or at least such slow erosion that it may be acceptable for a permanent structure.

The major part of the research on berm breakwaters has concentrated on the reshaping of the seaward side of the trunk under perpendicular wave attack. In 1988, van der Meer pre-

¹ Danish Hydraulic Institute, Agern Allé 5, DK-2970 Hørsholm, Denmark

² Aalborg University, Sohngaardsholmsvej 57, DK-9000 Aalborg, Denmark

³ University of Bologna, 2 Viale de Risorgimento, I-40136 Bologna, Italy

sented results from a series of flume model tests with gravel beaches and rock slopes which led to a set of parameters equations for assessing the profile development of berm breakwaters. Also Kao and Hall (1990) presented results on various aspects influencing the stability of berm breakwaters. Analysis of flume tests concentrating on the rear side stability was presented by Andersen et al (1992).

Only a little research has been made to study the stability of berm breakwater roundheads. Burcharth and Frigaard (1987) described results from model tests with reshaping breakwaters exposed to head on waves and waves having a wave incidence angle of 15° and 30° . The analysis concentrated on the stability of roundheads and trunk erosion in oblique waves, and some preliminary recommendations for berm breakwater trunks and heads were given.

Jensen and Sørensen (1992) presented results from a 3D model study of a berm breakwater including trunk and roundhead. Comparison of the profile development on the trunk and head was made.

Van der Meer and Veldman (1992) made a discussion on roundhead stability based on analysis of results from a series of wave basin tests.

Description of Model Tests

Model Set-Up

The model tests were carried out in a 22 x 30 m wave basin at the Danish Hydraulic Institute, see Figure 1, which also shows the various positions of the two 5.5 m wide movable wave generators for generating long-crested irregular waves. A stone absorber was placed along the basin boundary in order to minimise wave reflections. The berm breakwater profile used for the trunk section is shown in Figure 2. The roundhead was constructed by rotating the profile around the centreline.

The berm breakwater was constructed from two stone classes, ie one for the core and the scour protection and one for the berm, the crest and the rear side protection. The core material had a nominal diameter of $D_{n,50}=0.010$ m. A relative wide stone gradation was used for the berm, ie $D_{n,85}/D_{n,15}=1.80$ with a nominal diameter of $D_{n,50}=0.023$ m. The density of the stone material was $\rho_s=2.68$ t/m³ and the density of the water was $\rho_w=1.00$ t/m³.

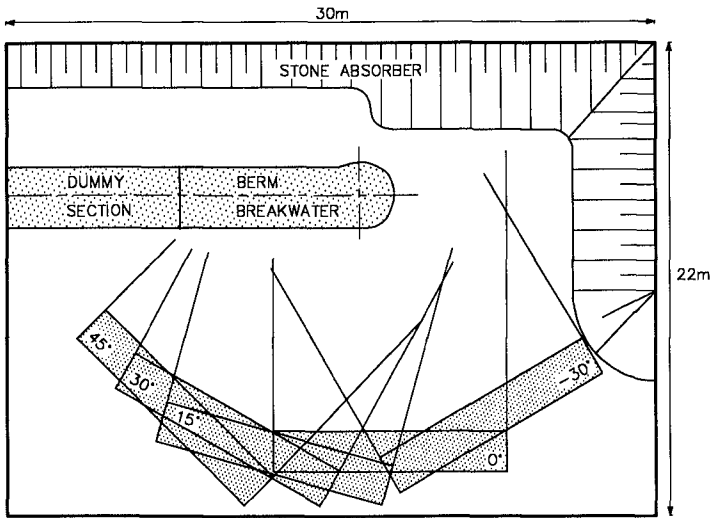


Figure 1. Model plan, including positions of the wave generators.

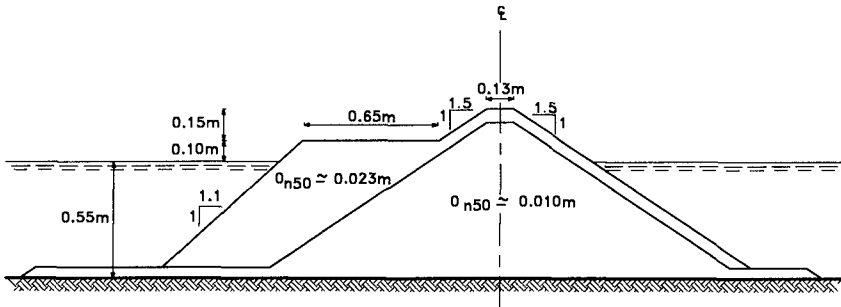


Figure 2. Cross-section of the initial profile for the trunk.
The roundhead was made by rotating the profile around the centreline

Test Programme

A total of six test series were carried out with irregular waves, covering five angles of incident waves with a wave steepness of $S_m=0.05$ (45° , 30° , 15° , 0° and -30° ; where 0° is perpendicular to the trunk) and two wave steepnesses for -30° ($S_m=0.03$ and 0.05). The wave steepness, S_m , is given by $H_{m0}/L_{m0}=H_{m0}/(g/2\pi \cdot T_m^2)$, where H_{m0} is the wave height, L_{m0} is the deep water wave length, and T_m is the mean wave period.

Each test series consisted of five tests with a duration corresponding to 2,000 waves for reshaping of the berm breakwater ($H_0=H_{m0}/\Delta \cdot D_{n,50}=2.0, 2.5, 3.0, 3.5,$ and 4.0 ; where Δ is the relative density, and $D_{n,50}$ is the nominal stone diameter) followed by four tests with a duration of 1,000 waves for studying the stone movements on the reshaped profile ($H_0=2.5, 3.0, 3.5,$ and 4.0).

All waves were generated on basis of a Pierson-Moskowitz spectrum.

Measurements

The waves were measured in 14 positions in the wave basin by use of resistance type wave gauges. The incoming wave conditions were checked by five reference wave gauges placed in a way to minimise the effect of reflections. Spectral analysis and zero-crossing analysis were carried out.

A total of 38 profiles along the 8.5 m long breakwater were measured after construction of the breakwater (initial profile) and after each test run. The profiling was made with a laser running on a beam across the breakwater trunk. The horizontal position of the laser running on the beam was measured by another laser, whereas the position along the breakwater was fixed manually. The profiles were measured for each 0.5 m along the trunk and for each 0.1 m at the roundhead.

The data from the 38 profile measurements were interpolated into a 3D representation of the breakwater from which it was possible to extract profiles in arbitrary cross-sections and to make contour plots of the breakwater as shown in Figure 3.

Definitions and Analysis

Sections and Wave Directions

The 3D representation of the test results was used to calculate the results for 10° sections on the breakwater head and 10 cm sections on the trunk with the convention as shown in Figure 4, which also shows the wave direction convention. This means that

section 0 is the section covering 10° in continuation of the breakwater centreline and -90° is the section perpendicular to the centreline, where the trunk meets the roundhead.

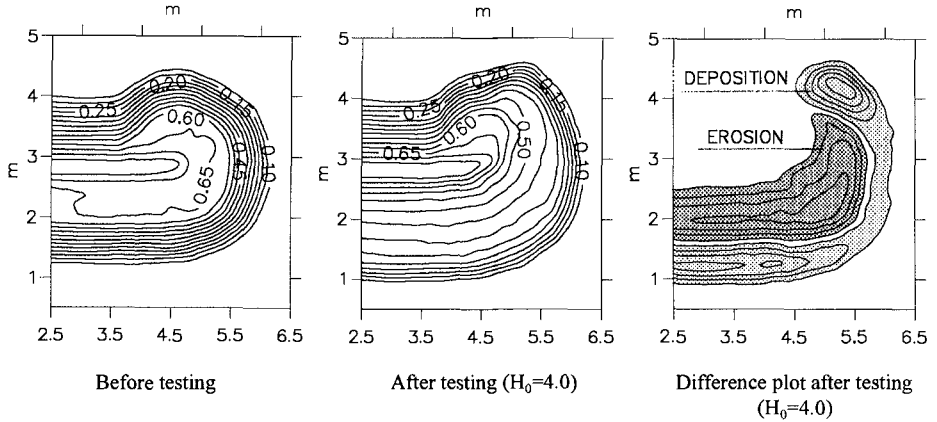


Figure 3. Contour (m) plots of breakwater. Wave direction 0°

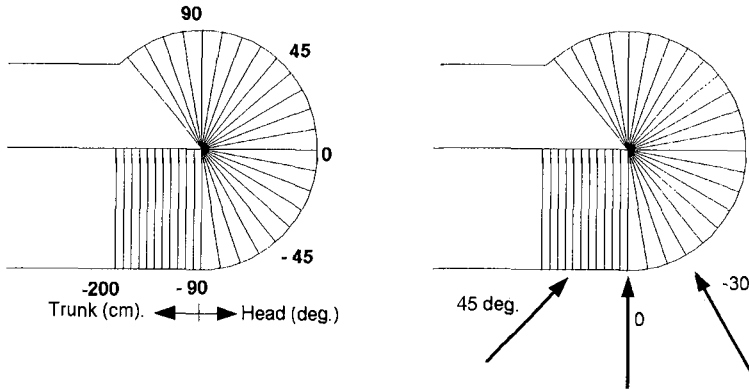


Figure 4. Profile definition.

Definition of wave direction

Relative Angle

When comparing results at the roundhead for different wave directions, a relative angle is introduced, defined as the angle between the incident waves and the considered section on the head, see Figure 5. For example, a relative angle of 0° corresponds to the section pointing directly towards the waves, whereas a relative angle of 90° corresponds to the section perpendicular to the wave direction.

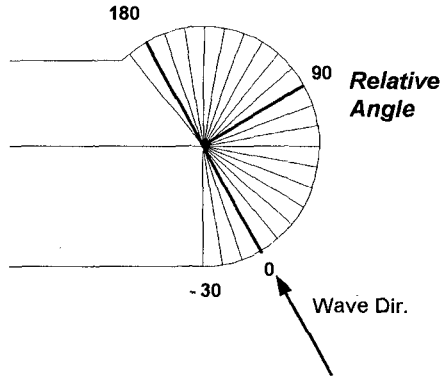


Figure 5. Definition of relative angle

Investigated Parameters

During the analysis, the following parameters have been investigated:

Recession

The recession is defined as the width of the berm eroded, see Figure 6. For the investigated breakwater profile with an initial berm width of 0.65 m, a recession of 0.65 m thus corresponds to a fully eroded berm with a directly exposed breakwater crest.

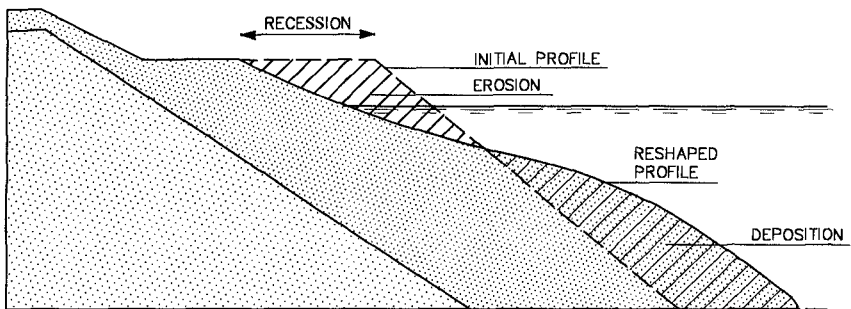


Figure 6. Definition of recession, erosion and deposition

Erosion

The erosion is defined as the volume eroded for the individual sections as shown in Figure 6. The erosion is presented as the eroded volume relative to the initial volume of berm material for the section. An erosion equal to 0.2 thus corresponds to the case where 20 per cent of the initial berm volume is eroded at the considered section. The erosion is presented as negative values.

Deposition

The deposition is defined as the deposited volume at the individual sections, as shown in Figure 6. As for the erosion, the deposition is presented as the deposited volume relative to the initial volume of berm material for each section. The deposition is presented as positive values.

Transported volume

This parameter is defined as the volume which has passed a given section since the start of the test series. The transport is defined positive in the anti-clockwise direction on the head (towards the rear of the head). On the trunk, the transport is positive towards the head. The volume is calculated directly from the measured profiles (ie including voids).

The transported volume is calculated by accumulating the volume changes from the rear of the roundhead - where no changes occur - clockwise around the head.

Stone transport

The stone transport is the estimated number of stones per wave passing a given section for a given H_0 . The number of stones is estimated by correcting the calculated transported volumes for porosity and dividing by the average stone weight.

Presentation of Results

This section presents the results of the analysis of the profile measurements and concentrates on recession, erosion and deposition, transported volume and finally stone transport during the reshaping process.

Recession

Figure 7 presents the recession at the head found for wave direction 45° , respectively 0° , for increasing H_0 .

It is seen that the recession for head on waves (wave direction 0°) is significantly higher than for 45° .

Plotting the recession measured after $H_0 = 4.0$ for all wave directions as function of the relative angle, see Figure 8, shows that the recession pattern follows the wave direction, and that maximum recession occurs at an area directly exposed to the waves. It is found that the maximum recession on the head occurs for wave direction 0° , where the recession reaches the initial berm width for H_0 between 3.5 and 4.

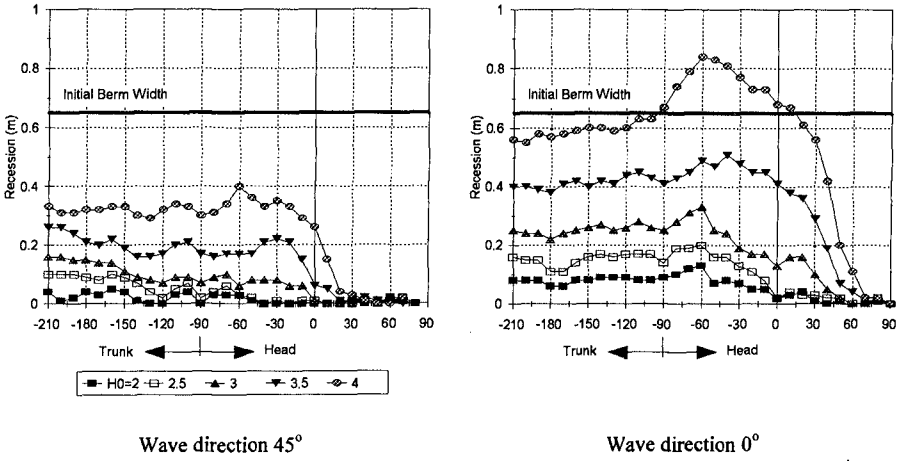


Figure 7. Recession of head and adjacent trunk

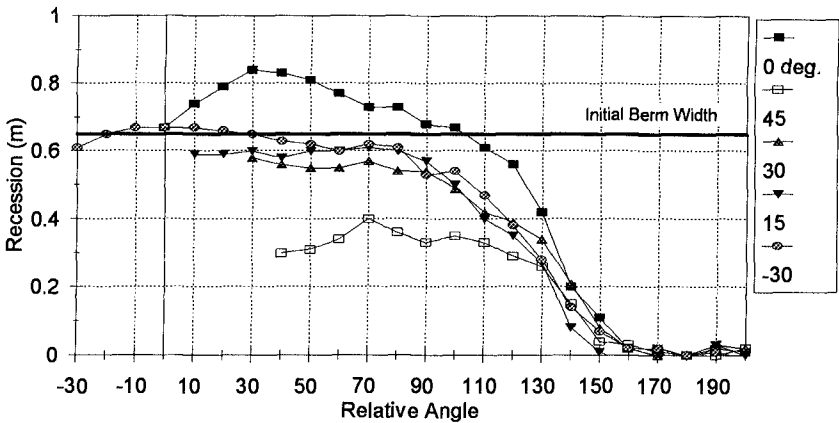


Figure 8. Recession. All wave directions. After $H_0 = 4.0$, $S_m = 0.05$

Comparing the maximum recession found at the head with the recession on the trunk, see Figure 9, it is found that only in the case with wave direction 45° the maximum recession on the head is equal to or less than the recession on the trunk section. In the case with wave direction -30° , the recession on the head is up to 75 per cent higher than for the trunk section. For head on waves, the maximum recession on the head is 50 per cent higher than the recession on the trunk.

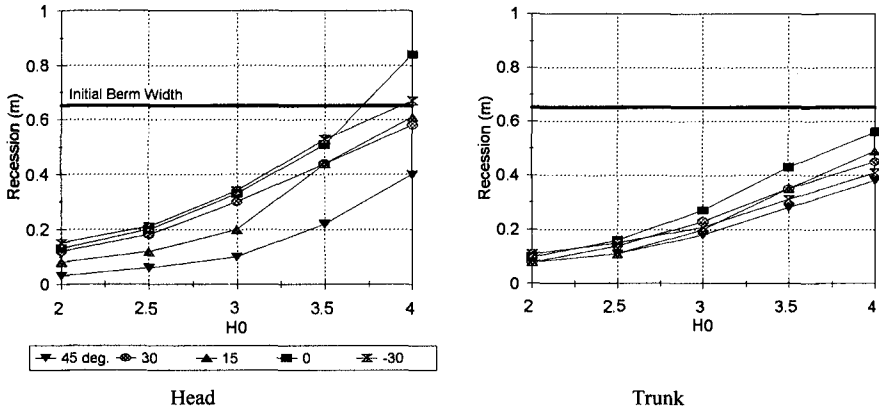


Figure 9. Maximum recession on head, respectively trunk

When analysing the maximum recession as function of the wave direction, it can be seen that the maximum recession on the head is increased by a factor of up to 2 comparing the results for wave directions 45° and 0° , whereas the recession on the trunk is increased by a factor of about 1.4. The recession on the head is thus more sensitive to changes in the wave direction than the recession on the trunk. For comparison, a cosine (cos) and a cosine² (cos²) distribution of the recession found for wave direction 0° for $H_0=4$ were compared to the results, showing that the variation of the maximum recession with the wave direction, on the head, can be approximated by a cos² distribution for the higher H_0 's. At the trunk, the results show a distribution closer to a cos distribution.

The influence of the wave steepness was investigated for wave direction -30° . The results showed a strong influence by the wave steepness, as the maximum recession on the head for $S_m=0.03$ was almost twice the recession found for $S_m=0.05$. On the trunk, the influence was less pronounced. Analysis showed that a good agreement between the two data sets ($S_m=0.03$ respectively 0.05) was obtained when plotting the recession as function of H_0T_0 , especially for the trunk section. T_0 is given by $T_0=T_m \sqrt{g / D_{n,50}}$.

Erosion and Deposition

Figure 10 presents the erosion and deposition pattern around the breakwater head, after $H_0=4.0$ for all wave directions as function of the relative angle, again showing that the reshaping pattern follows the wave direction closely. A pronounced deposition area at the rear of the roundhead and a relative wide area of erosion is found.

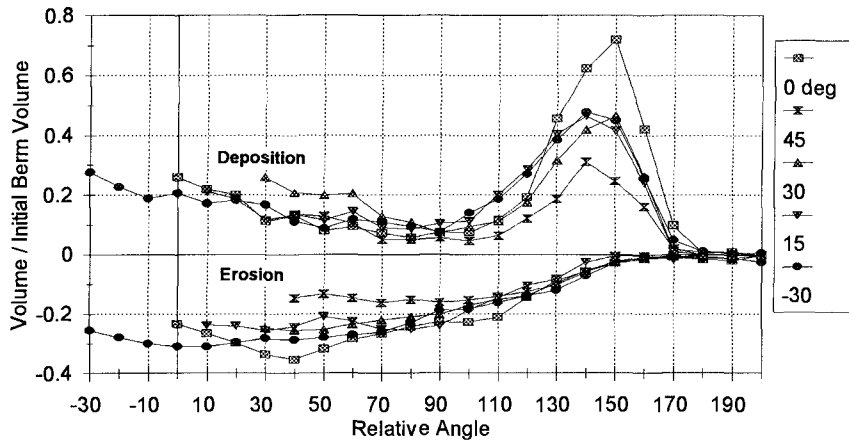


Figure 10. Erosion and deposition after $H_0=4.0$. All wave directions

For an infinitely long trunk, the erosion and deposition areas are equal (disregarding compaction), whereas for a roundhead stones will be transported towards the rear side of the roundhead. At the directly exposed part of the head, the erosion will be larger than the deposition, whereas the opposite will be the case at the rear of the head. This can also be seen from the contour plots presented in Figure 3 showing the height contours of the breakwater before and after the test series with wave direction 0° together with a difference plot.

As seen from Figure 11, the erosion at the head accelerates for $H_0 > 2.5$. The influence of the wave steepness can be seen from Figure 12 presenting the maximum erosion and deposition as function of both H_0 and $H_0 T_0$ for the two wave steepnesses, $S_m=0.03$ and 0.05 , respectively (wave direction -30°). Plotting the maximum erosion and deposition as function of $H_0 T_0$ shows a better agreement between the two data sets than when plotting against the wave height parameter, H_0 .

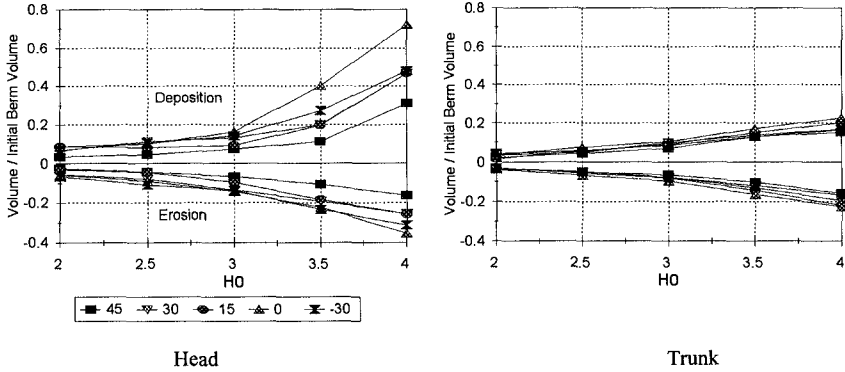


Figure 11. Maximum erosion and deposition

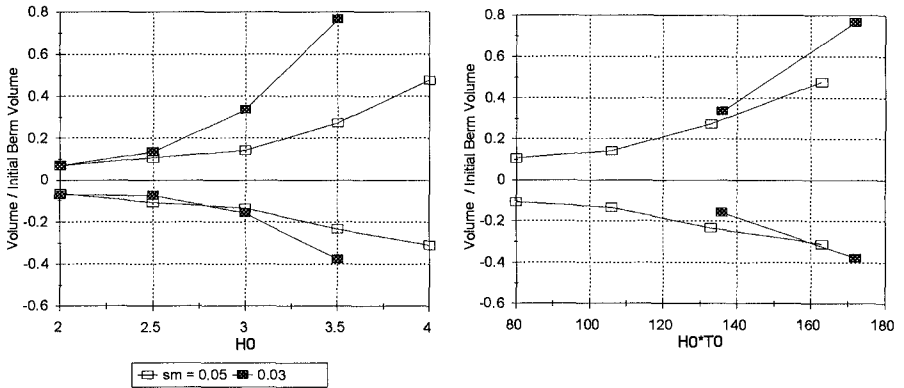


Figure 12. Influence of wave steepness on erosion/deposition.
Wave direction -30°

Transported Volume

Figure 13 presents the transported volume at the roundhead for all wave directions as function of the relative angle after $H_0=4.0$ ($S_m=0.05$), showing that the section which experiences the heaviest traffic during the test series is located $110^\circ-130^\circ$ anti-clockwise from the angle of wave attack.

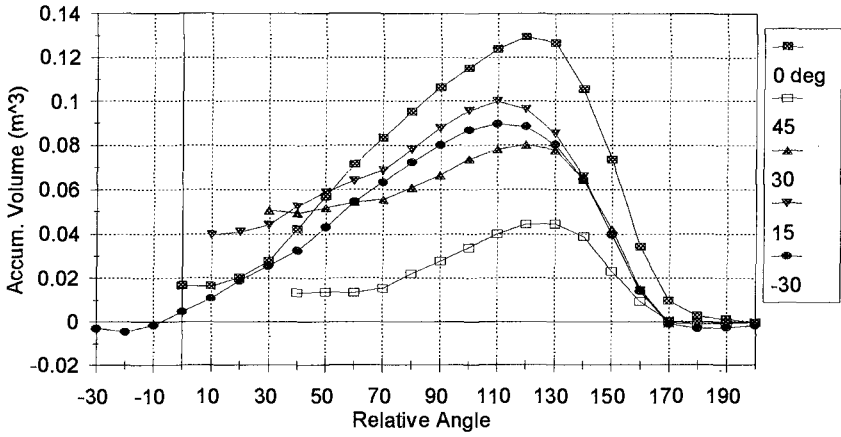


Figure 13. Transported volume on head after $H_0=4$. All wave directions

Figure 14 shows the maximum transported volume on the roundhead as function of H_0 revealing that the transport accelerates for $H_0 > 2.5$.

As for the recession on the head, the sensitivity to the wave direction can clearly be seen on the transport. The results indicate that the decrease in transported volume with the wave direction can be estimated by a \cos^3 distribution for the higher H_0 's comparing with the transport for wave direction 0° .

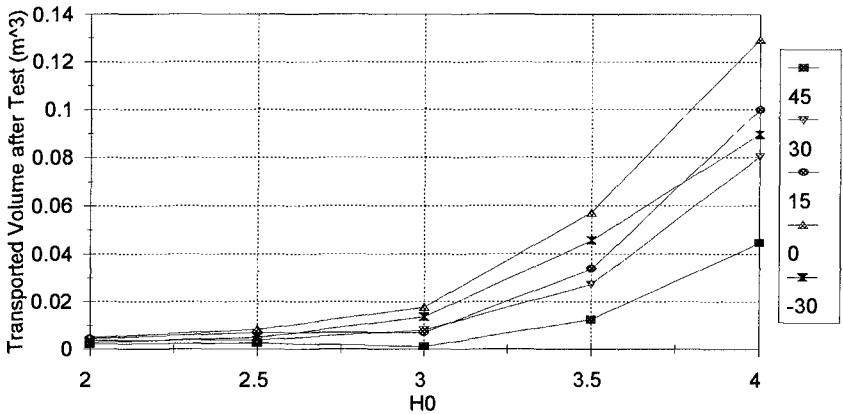


Figure 14. Maximum transported volume on head

Stone Transport

In Figure 15, the stone transport for $H_0=4.0$ is plotted for all wave directions as function of the relative angle, again showing that the maximum transport takes place at the sections 110° - 130° relative to the wave direction. The maximum stone transport on the head occurs with head on waves (0°), being up to three to four times higher than for wave direction 45° .

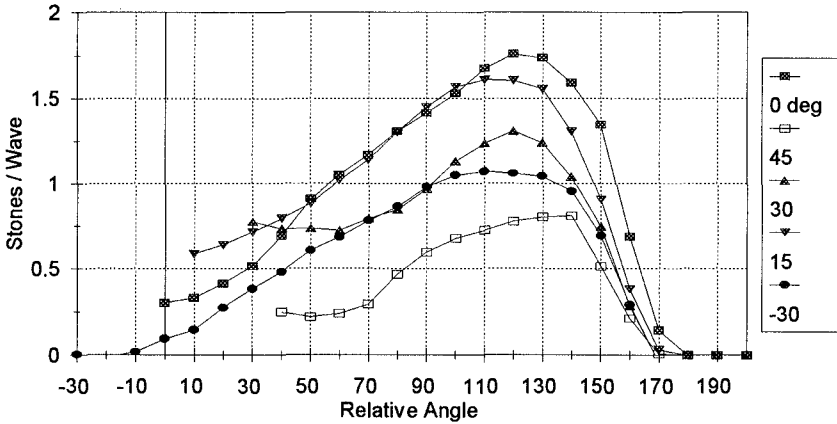


Figure 15. Stone transport for $H_0=4.0$. All wave directions

Conclusion

A total of six test series were carried out in a wave basin for studying the development of berm breakwater roundheads. Five wave incidence angles were tested together with two wave steepnesses. All tests were carried out with irregular long-crested waves, and each test series consisted of five tests for reshaping of the breakwater ($H_0=2.0, 2.5, 3.0, 3.5$ and 4.0).

The measurements included a total of 38 profiles along the breakwater which were interpolated into a 3D representation of the breakwater. This formed the basis for detailed calculations of the profile development, recession of the berm, eroded and deposited volumes and transport of stones in arbitrary sections of the breakwater.

The main findings of the work are summarised below :

- The maximum recession occurs at the area directly exposed to the waves.
- The recession/erosion pattern follows the wave direction.
- On the head, the maximum recession was observed for head-on waves (0°) being up to two times higher than for 45° . For the trunk section, the increase was less than 1.5. The recession on the head is thus more sensitive to changes in the wave direction than on the trunk.
- For 45° wave direction, the maximum recession on the trunk and on the head is of the same magnitude, whereas the maximum recession on the head is 75 per cent higher than on the trunk for wave direction -30° . For 0° , the maximum recession on the head is about 50 per cent higher than on the trunk.
- The results for the two wave steepnesses, $S_m = 0.03$ and 0.05 , showed that the wave steepness is of paramount importance, and that H_0T_0 is a good parameter when comparing the results - better than H_0 .
- The reshaping of the head accelerates for $H_0 > 80-100$.
- The maximum transport of stones takes place $100^\circ-130^\circ$ anti-clockwise from the angle of wave attack.
- The maximum stone transport rates were found for wave direction 0° , being up to three to four times higher than for wave direction 45° .

Acknowledgements

The research was carried out as part of the project on Berm Breakwater Structures co-sponsored by the European Commission under the second Research and Development Programme on Marine Science and Technology, MAST II (Contract MAS2-CT94-0087).

References

- Alikhani, A et al (1996): *Berm breakwater trunk exposed to oblique waves*. Proceedings of ICCE'96, Florida, USA.
- Andersen, OH; Juhl, J; and Sloth, P (1992): *Rear side stability of berm breakwaters*. Proceedings of ICCE'92, Venice, Italy.
- Burcharth, HF and Frigaard, P (1987): *On the stability of berm breakwater roundheads and trunk erosion in oblique waves*. Workshop on Berm Breakwaters: Unconventional Rubble-Mound Breakwaters, Ottawa, Canada.
- Jensen, OJ and Sørensen, T (1992): *Hydraulic performance of berm breakwater heads*. Journal of Hydraulic Research, Vol 29, No 6.
- Kao, JS and Hall, KR (1990): *Trends in stability of dynamically stable breakwaters*. Proceedings of ICCE'90, Delft, The Netherlands.
- Van der Meer, JW (1988): *Rock slopes and gravel beaches under wave attack*. PhD Thesis, publication No 396, Delft Hydraulics, The Netherlands.
- Van der Meer, JW and Veldman, JJ (1992): *Singular points at berm breakwaters: scale effects, rear, round-head and longshore transport*. Coastal Engineering, 17, pp 153-171.

CHAPTER 133

Improvement of Composite Breakwater on Solid Bottom Against Severe Tsunamis

Yoshiaki KIMURA¹, Hideo KONDO², Shinji KUWABARA³ and Akira KAWAMORI⁴

1. Introduction

Recent diversification in the use of coastal areas has increased the importance of tsunami prevention measures in the areas. To prevent disasters, it is important to set up various facilities, including tsunami breakwaters and tide embankments, and to improve systems to ensure the safety of people escaping from tsunamis with larger waves than predicted when designing the facilities. Previous studies showed that coastal and port structures are effective to decrease damage caused by tsunamis. These structures are, however, easy to overturn or slide, since they are designed without considering tsunamis as external forces on them. The North Breakwater in Okushiri Port damaged by the tsunamis of the Hokkaido Nanseioki Earthquake in 1993 is an example of a damaged composite breakwater (Photo 1).

Recently, a composite breakwater has become popular as a port structure to cope with enlargement of ports and weak ground of coastal areas. It has two tiers: a caisson functioning as an upright breakwater on top, and a mound (rubble-mound foundation) functioning as a sloping breakwater on the bottom. Though a composite breakwater is frequently used as a tsunami breakwater, damage to it by wave forces larger than the external forces predicted for its design has not been sufficiently taken into account. In most cases, an incident wave of a tsunami on the composite breakwater is broken up due to the influence of the water depth, to become a tsunami. Tsunamis have the largest destructive force on a breakwater.

1) Formerly Graduate Student (presently Nishimatsu Construction Co., Tokyo)

2) Professor, Dept. of Civil Engrg. & Architecture, Muroran Institute of Tech., 27-1 Mizumoto-Cho, Muroran, 050 JAPAN

3) Engineer, North Japan Port Consultants, Heiwa-Dori 2, Shiroishi-Ku, Sapporo, 003 JAPAN

4) President, Alpha Hydraulic Eng. Consultants, Hassamu 9-14, Nishi-Ku, Sapporo, 062 JAPAN

This study clarifies the features of damage by a surge tsunami to composite breakwaters designed without considering tsunamis as external forces by model experiments.



Photo 1 Damaged composite breakwater(1993 Okushiri Port)

2. Dimensional Analysis

A simple dimensional analysis was made to examine factors influencing the amount of damage to a breakwater Δ (horizontal displacement).

$$\Delta = F \left\{ \frac{W'}{\ell \rho g a (d + h_c)}, \frac{P_h}{\rho g a (d + h_c)}, \frac{P_u}{\rho g a b}, \frac{\ell_f}{a}, \frac{\ell_r}{a}, \frac{d}{a}, \frac{h}{a}, T \sqrt{\frac{a}{g}}, f, \dots \right\} \quad (1)$$

where W' = weight in water, P_h = horizontal wave force, P_u = uplift pressure, a = amplitude of a tsunami, T = period of a tsunami, f = friction coefficient. Fig. 1 shows other variables.

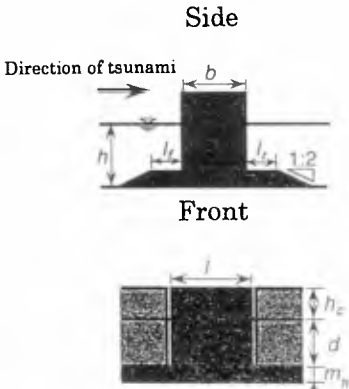


Fig-1 Variables

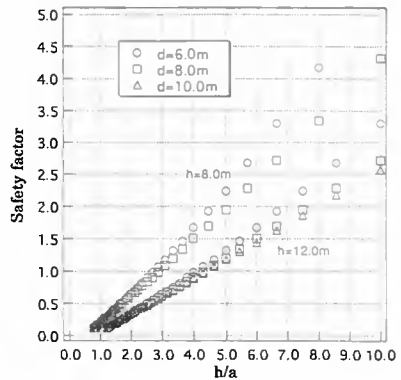


Fig-2 Relationship between Sf and h/a

Generally, Δ depends mainly upon a safety factor of the upright part against sliding. The first term of the right side F in equation (1) is almost equal to the safety factor. In Fig. 2 the axis of ordinates represents the safety factor against sliding and the axis of abscissas represents h/a . The parameters here are the water depth at the upright part (d) and the water depth (h). The wave force was calculated by the wave force formula of a surge tsunami by Tanimoto et al. This figure shows that the safety factor is proportional to h/a and is more influenced by the water depth (h) than the water depth at the upright part (d).

3. Experimental Equipments

3.1 Two-dimensional open channel

In this experiment, a steel two-dimensional open channel (Fig. 3) 15.0 m long, 0.6 m wide and 0.5 m deep was used. The gate was suddenly opened to produce a tsunami. Both sides of the channel were glass and the bottom was steel coated with paint. A gate to adjust the water depth was installed at one end. The breakwater model was placed with its front 3.5 m from the back of the channel. Pipes to adjust the water depth were installed along both side walls of the channel to level the water depths at the front and back of the breakwater. A tsunami was produced by a wave making gate, or a wave paddle, installed at 5.55 m from the breakwater.

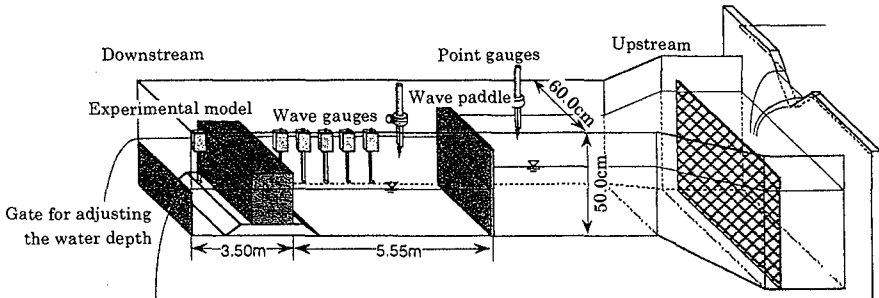


Fig-3 Experimental channel and position of the experimental model

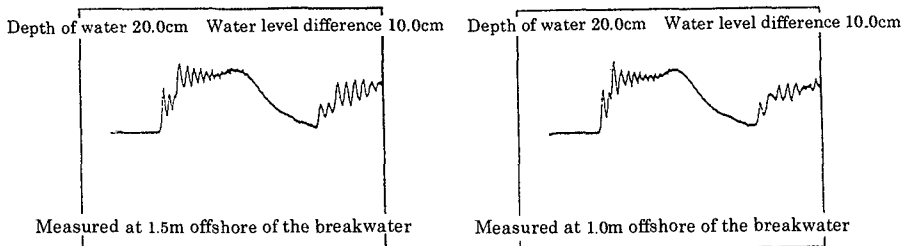


Fig-4 Wave form in the experiment

The difference in the water depths at the front and back of the gate was measured with a point gauge, and the gate was suddenly opened to produce a surge tsunami when the difference reached a specified amount. The installed gate was a wooden, hand-operated vertical lift gate. In this experiment, the difference in the water surfaces at two sides of gate almost corresponded to the amplitude of a surge tsunami. Six capacitance-type wave gauges were installed, and a video camera was installed at the side of the channel to confirm the wave form. Fig. 4 shows examples of wave form in the experiment.

3.2 Experimental model

The experimental model was made from the design of the North Breakwater in Okushiri Port (Photo 1). The North Breakwater in Okushiri Port was constructed recently to increase the calmness in the port located behind the island from the hypocenter. Tsunamis at the time of the earthquake caused foot-protection blocks at the back of the breakwater to drift away; the upright part, especially around the center, overturned and slid; and the mound deformed. The dimensions of a real-size breakwater were assumed from the central part of the North Breakwater which had slid so much. The assumed breakwater was scaled down to 1/40 for the experiments to make a model made of mortar. The dimensions of the assumed breakwater (1/40 figures for each is in brackets) were: height: 10.0 m (25.0 cm); width: 8.0 m (20.0 cm); length: 10.0 m (25.0 cm); height of the mound: 2.0 m (5.0 cm); water depth (h): 8.0 m (20.0 cm). We called the size of the 1/40 model the standard type in this study. The height, width and material of the mound and the water depth (h) were varied during the experiments. And also the weight of the model was varied as an experimental condition, a void of 10.0 cm × 10.0 cm × 15.0 cm (Fig. 5) was made inside the caisson model to make it lighter than reality.

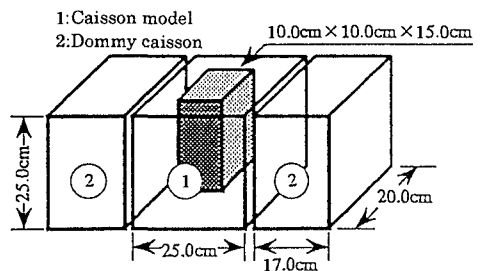


Fig-5 Upright part model

3.3 Mound

The length of the mound was set at the same width of the channel (0.6 m). The standard size of the mound was 5.0 cm in height, 40.0 cm in width, and with the gradient of its slope was 1:2 (standard type). Rubble was used as the mound material, with the equivalent weight of 400 kg (6.0 g for each piece of rubble). Foot-protection blocks placed on the surface of the mound were ignored. By assuming that the mound was a sloping breakwater, the stability number and the Reynolds number of the surface layer of the sloping breakwater were calculated to investigate the mounds stability and scale effect. As a result, we found that the

scale effect need not to be considered and that the stability number was larger than that of the sloping breakwater, in spite of the low critical wave height for stability. From these findings, the weight and the size of the rubble seemed to be sufficient. Also, the experimental result that the rubble of the mound at the front of the breakwater did not move corresponded to the theory that rubble does not move. The reason why the rubble of the mound at the back of the breakwater moved seemed to be due to sliding of the upright part.

4. Experimental Procedure

The experiments were designed to investigate the behavior of the breakwater sliding (the sliding distance which is defined as the distance of the horizontal movement of its upright part), when receiving a surge tsunami produced at a specified water level difference. Tsunami amplitude was increased by 1.0cm, until all number of times became fatal damage. However the results varied much depending on the conditions of the mound and the breakwater. To understand the trend of the results of the experiments, a wave was produced 10 times for each amplitude. If a sliding distance of the caisson model exceeded 20.0 cm, the effect on the breakwater was different from the expected one. We called this effect on the breakwater fatal damage, and only the number of times was counted.

4.1 Effect of the water depth

Influenced by astronomical tides, storm surges and wind waves, the actual water level varies from the standard water level when an incident wave acts on a breakwater. In this experiment, therefore, we investigated the behavior of the upright part and the damage to the mound part, when the breakwater model and the mound had the standard type, and only the water depth (h) was varied from 16.0 cm to 24.0 cm.

4.2 Effect of the configuration of the mound

Composite breakwaters have varied shapes according to the design conditions, including the water depth (h), the design wave, and the purpose of the installment. This experiment, therefore, was designed to see how the damage of the breakwater was affected by changes in the height and width of the mound.

(1) Height

This experiment determined the behavior of the breakwater, when the water depth at the upright part (d) was constant(15cm) and the height of the mound was 5.0 cm, 7.0 cm, and 9.0 cm.

(2) Width

This experiment determined the changes in the behavior of the breakwater, when

the width of the mound was increased by 10.0 cm from the standard type.

4.3 Effect of the weight of breakwater

A general and popular way to increase the stability of the breakwater against wave forces is to increase its weight. This method is effective for waves smaller than the design waves. However, its effectiveness for tsunamis larger than the design waves has not been clarified. This experiment investigated changes in the damage, when a weight was placed on the breakwater.

4.4 Effect of W'

In the experiment where the water depth was changed, the results were difficult to interpret due to the changes in buoyancy and wave forces caused by the changing water depth. In this experiment, the weight offsetting the increased buoyancy caused by the changing water depth was placed on the breakwater to keep constant the underwater weight. The experiment aimed to understand the changes in the behavior due to changes in wave forces.

4.5 Effect of the restraining the settlement of breakwater

Previous experiments showed that fatal damage of the breakwater and its settlement often happened at the same time. We considered that a reinforced mound could be effective to prevent damage by tsunamis. Damage was investigated after installing supporting rods in the mound under the back of the breakwater to restraining the breakwater settlement (Fig. 6).

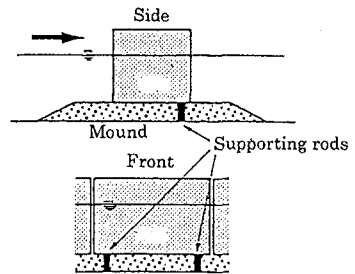


Fig-6 Effect of restraining the settlement of breakwater

5. Results and Discussion

5.1 Effect of the water depth (Fig. 7)

To understand the basic trend, the standard type for this experiment with the water depth at 20.0 cm (c) was investigated. As tsunami amplitude increased, the sliding distance and the number of cases of fatal damage increased, though the results were partly contradictory. When tsunami amplitude was 8.0 cm or less, the breakwater did not slide, and when it was 14.0 cm or more, the breakwater always underwent fatal damage. The sliding distances varied less when the amplitude was close to 7.0 cm or to 16.0 cm, and they varied more when the amplitude was halfway between these two distances. Such a wide variation in sliding distances halfway between 7.0 cm and 16.0 cm seemed to be caused by all

the manual operations, including molding the mound and installing the caisson model.

We found that, in general, the deeper was the water depth, the easier the breakwater slid. The number of cases of complete fatal damage increased almost in proportion to the increase in the water depth. It means that as the water depth increased, the influence from front wave pressure and buoyancy increase.

5.2 Effect of the configuration of the mound

(1) Height (Fig. 8)

Fig. 8 (a) shows the experimental results of the mound in the standard type with the water depth at 20.0 cm. As the mound height increased, the number of cases of fatal damage increased compared to the standard type. This trend was particularly obvious when the mound was 9.0 cm high, because the higher mounds seemed to have less stability and tended to fall down on a large scale when the breakwater began to slide. The critical point of sliding in terms of the tsunami amplitude was irrelevant to the height of the mound, because the constant water depth in front of the breakwater contributed to maintaining the same wave pressure on the breakwater front. The tendency for shorter sliding distances for the mound 7.0 cm high than those for the mound 5.0 cm high (standard type) was considered to be due to experimental errors from different experimental conditions.

(2) Width (Fig. 9)

Wider mounds brought better stability. No fatal damage was recorded especially when the mound was extended 10 cm toward the rear, though the sliding distance increased due to the shorter front side of the mound. This must be because more energy was required for the sliding while the mound at the rearside of the breakwater was settling.

5.3 Experiment of the weight of breakwater (Fig. 10)

Fig. 10 (a) is the standard type, with the weight of the breakwater of the standard weight +0.0 kg. When the tsunami amplitude was the same, as the weight increased the sliding distance decreased, because a larger horizontal wave force was required for sliding as the weight increased. However, when the weight was +3.0 kg, the breakwater had fatal damage at tsunami amplitude of 12.0 cm and the sliding distance was fairly large, because the bearing capacity of the mound did not sufficiently accommodate the increase in the vertical load. Therefore, once the mound starts to fall down, it falls down completely to the solid bottom of channel. The results of this experiment cannot be simply compared to the other results, since the installment conditions of the breakwater in this experiment were slightly different from those of the others.

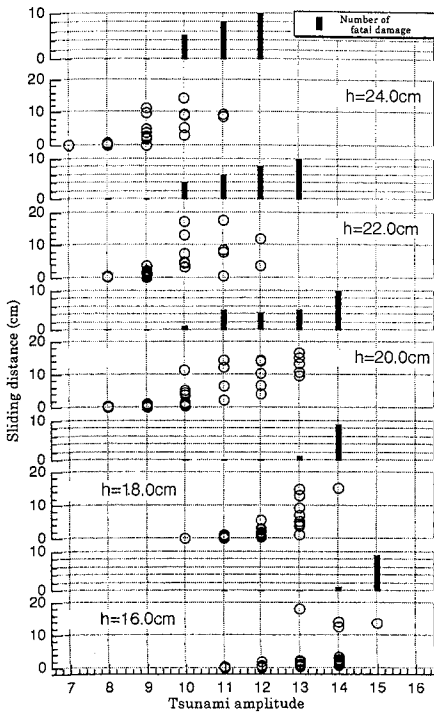


Fig-7 Effect of the water depth

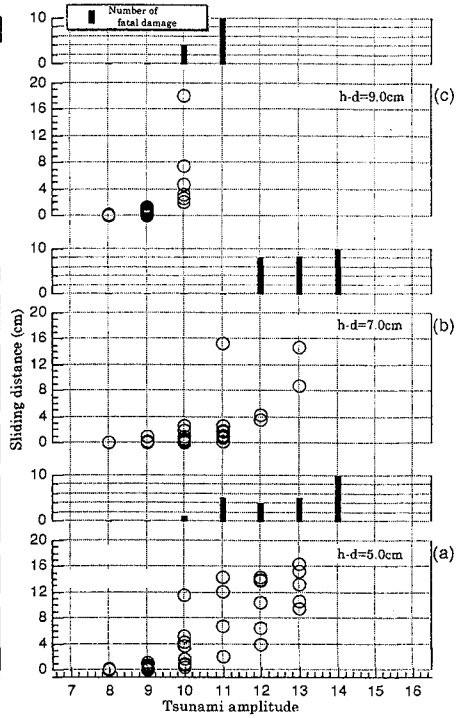


Fig-8 Effect of the mound height

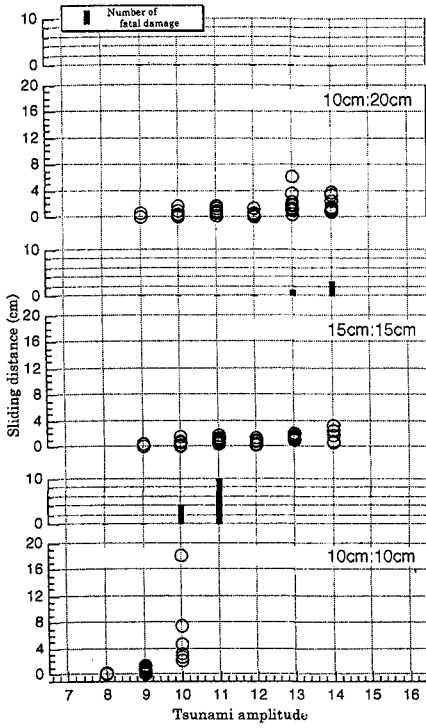


Fig-9 Effect of the mound width

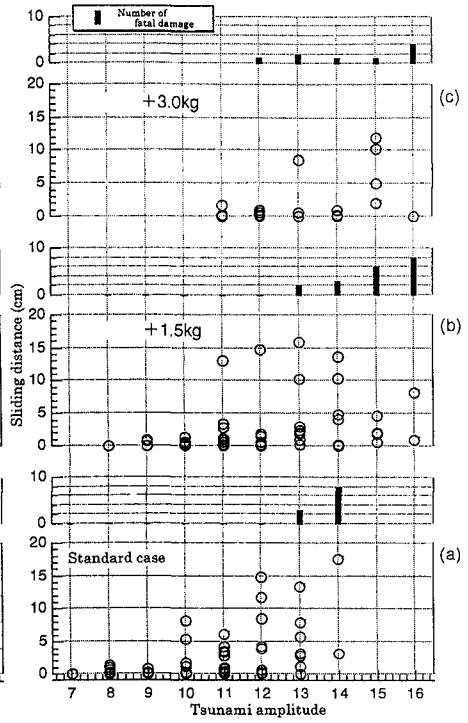


Fig-10 Effect of the weight of breakwater

5.4 Effect of W' (Fig. 11)

Fig. 11 (a) shows the standard type. Breakwater with a weight on top slid less, in the same way as in the experiment by changing the weight. The critical point of sliding for each case was mostly the same. Also, the trend towards fatal damage and the tsunami amplitude causing fatal damage were almost the same. As a result, we found that buoyancy change had a greater influence than the change in wave force caused by the water depth change.

5.5 Effect of restraining the settlement of breakwater (Fig. 12)

This experiment shows the least sliding distance and the least number of cases of fatal damage, compared to other experiments, because the falling down of the mound was restrained by supporting the breakwater. This means that the stability of the mound was dominant in influencing the sliding distance of the breakwater.

5.6 Features of Damage

Fig. 13 is from the data of the experiments on the water depth and the mound height. The axis of abscissas represents the water depth at the breakwater divided by the water depth, and the axis of ordinates represents the sliding distance divided by the water level difference producing a tsunami. Each figure is non-dimensional. Within the region of these experiments, the figures on the axis of ordinates did not exceed 2.0 unless the breakwater had fatal damage. This shows that the sliding distance was under twice the tsunami amplitude. The results corresponded to those of the experiment by changing the width of the mound, where the mound was moved toward the rearside. Moving toward both edges of the axis of d/h indicates the breakwater became less stable and easier to slide or have fatal damage, but near the axis center indicates the breakwater was most resistive to slide. As a result, the breakwater with d/h around 0.7 appears to be the most stable.

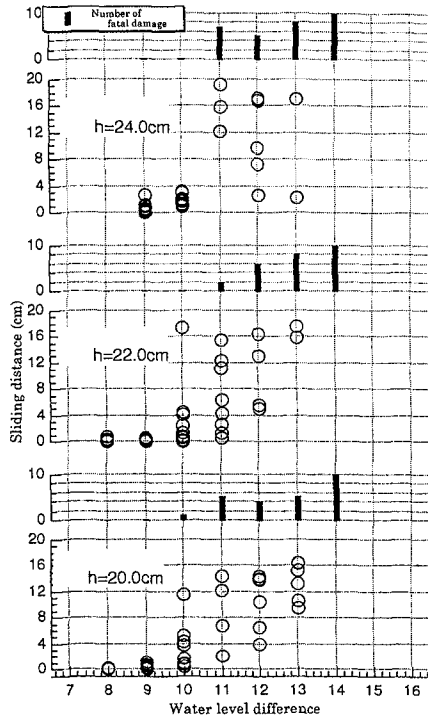


Fig-11 Effect of W'

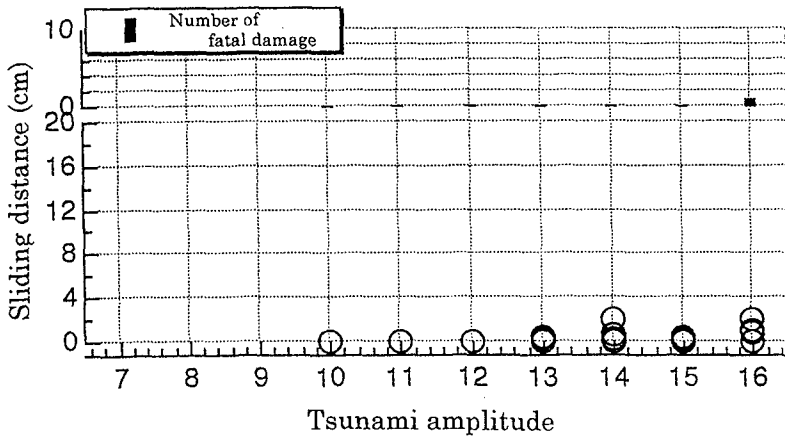


Fig-12 Effect of the restraining settlement of breakwater

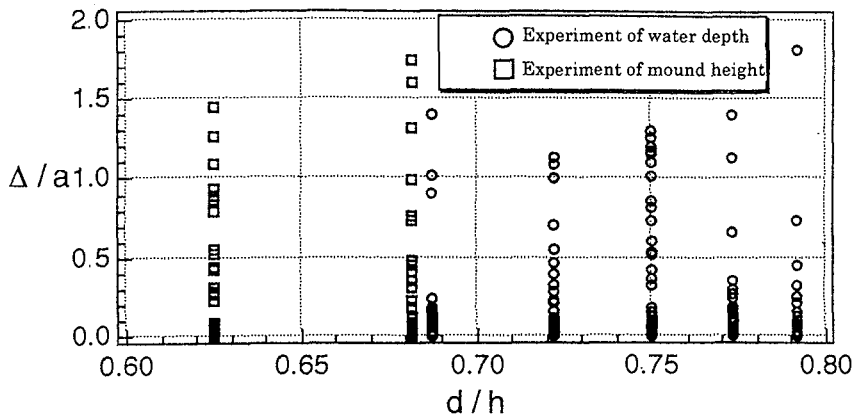


Fig-13 Features of damage

6. Conclusion

This study aimed to clarify the features of damage of a composite breakwater by tsunamis through experiments, and to find better damage prevention measures. As a result of this study, the following have been clarified.

6.1 Effect of breakwater configuration

- 1) An increase in buoyancy was more responsible for damage than an increase in wave pressure on the front of the breakwater due to the increase in the water depth.
- 2) Stability against sliding was remarkably influenced by the mound conditions. The stability increased, especially when the mound was prolonged toward the rear and when the mound was reinforced with body supporting rods.
- 3) A heavier weight of a breakwater for stabilizing the breakwater or an unnecessarily higher mound was not advisable, since it was easier to have fatal damage when exceeding the critical values.
- 4) For stability of a breakwater, the desirable ratio of the water depth (h) and the water depth at the upright part (d) was when the d/h ratio was around 0.7.

6.2 Proposed stability criteria

Stability criteria of composite breakwaters against tsunami wave action are deduced from the experimental result employing a dimensionless displacement, as,

$$\text{Heavy Damage } \Delta/a > 1.0 \text{ for } \mu W_u' / Ph \leq 1.0$$

$$\text{Slight Damage } \Delta/a < 0.1 \text{ for } \mu W_u' / Ph \geq 2.0$$

where a is tsunami amplitude, μ is the friction coefficient between the upright structure and the mound, W_u' ($=W' / \ell$) is weight of upper structure per unit length in water and Ph is the horizontal tsunami wave force per unit length. (Fig. 14)

6.3 Countermeasures

1) To increase simply the weight of upper structure is effective to the critical tsunami height, but Δ becomes abruptly greater for the tsunamis higher than it.

2) Prolongation of the rear shoulder ℓ_r is effective to lessen Δ to prevent the earlier falling down.

3) Most effective way to decrease Δ is to strengthen the mound surface around the heel of upright structure since Δ gradually becomes large as the stress concentration near the heel proceeds during the tsunami colliding on upright structure.

7. Acknowledgement

The authors thank to Hokkaido Development Bureau for kindly offering the valuable data. Special thank also goes to Mr. A. Hakozaiki, former student of the institute for his eager support during the course of experiment.

References

Hokkaido Development Bureau, Hakodate Development Construction Division(1995):The report of repair work to the calamity of Okusiri port (in Japanese).

Tanimoto, K. et al.(1984):Analysis of damaged reclamational shore protection, influenced by tsunami force occurred by Japan Sea earthquake in 1983, Proc. 33th Japanese Conf. on Coastal Eng., pp. 257-261 (in Japanese).

Kondo, H. and Tkakeda, H.(1983):Wave Dissipating Structures, Morikita Syuppan Co.Ltd.,(in Japanese).

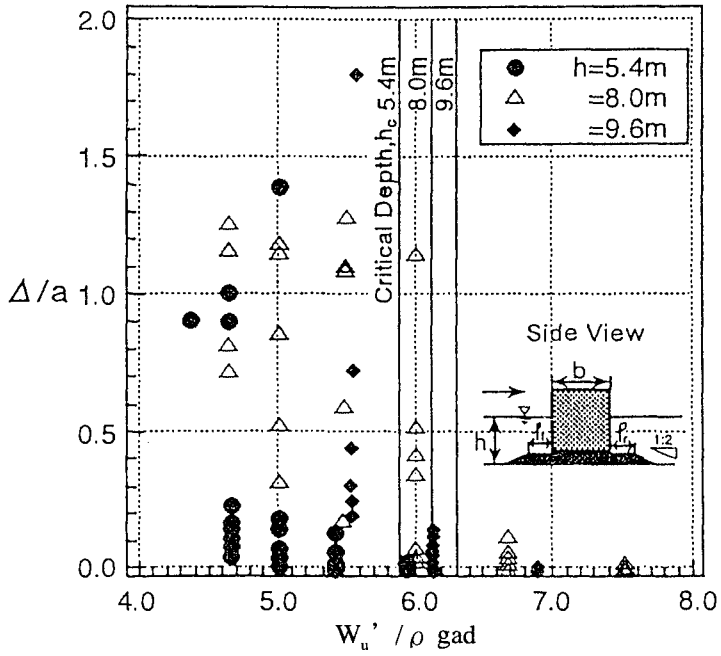


Fig-14 Dimensionless displacement of caisson by model tsunami

CHAPTER 134

Hydraulic Stability Analysis of Leaside Slopes of Overtopped Breakwaters

M. D. Kudale¹ and N. Kobayashi²

Abstract

The hydraulic stability of armor units on the leaside slope of an overtopped breakwater is analyzed using the velocity and depth of overtopping water on the crest computed by an existing numerical model. The stability analysis is carried out considering the hydrodynamic forces of the overtopping jet impinging on a leaside armor unit. A traditional force balance method is used to predict the stability number N_s for initiation of armor movement. The computed critical stability numbers N_{sc} for stones compare well with the observed stability numbers, provided that the hydrodynamic force coefficients are calibrated once for the stone stability on leaside slopes. The computed results indicate that the minimum stability of the leaside armor units occur at intermediate crest heights. The stability of leaside armor improves as the seaward slope is made flatter. The leaside slope of a breakwater in relatively deeper water is more stable. The leaside stability of a breakwater in shallower water with its crest height near still water level (SWL) can be improved by increasing the the back slope angle. A wider crest also improves the leaside stability.

Further studies are required to refine the developed stability model. The influence of tailwater in reducing the water velocity of overtopping jet needs to be included which has not been considered in the present analysis. The developed model would be very useful in designing the geometry of an overtopped breakwater and the size of leaside armor units because of a large number of design parameters.

Introduction

Low-crested breakwaters are usually constructed when only partial protection from waves is required landward of breakwaters. Low-crested breakwaters are more economical. Also, a significant amount of wave energy is transmitted due to overtopping, which results in the reduction of wave energy actually dissipated on the seaward slope of the breakwater. The weight of the armor units on the seaward slope can be reduced significantly by allowing overtopping. However, the armor units on the crest

¹Senior Research Officer, Central Water and Power Research Station, Pune-411 024, India

²Professor & Associate Director, Center for Applied Coastal Research, University of Delaware, Newark, Delaware 19711, USA

and leeside slope become vulnerable under overtopping waves. The weight of these armor units may need to be increased to withstand the forces of overtopping water.

The stability of a traditional non-overtopped rubble mound breakwater depends primarily upon the stability of individual armor units on its seaward slope. A major factor in the design of rubble mound breakwaters is hence the minimum weight of the armor units on the seaward slope, required to withstand the design waves. Many studies were carried out on the hydraulic stability of individual armor units on the seaward slope. Several empirical formulae such as Van der Meer formula (1988) are available for the estimation of the minimum weight. The present practices for the design of rubble mounds are based on hydraulic model tests and empirical formulae. A few numerical models have also been developed recently for the design of rubble mound structures. Kobayashi et al. (1989, 1994) developed a numerical model for the design of coastal rubble mound structures, which predicts wave reflection, runup and armor stability on the seaward slope.

For low-crested overtopped rubble mound breakwaters, the stability of leeside armor units also becomes an important design aspect. A few studies have been reported on this design aspect. Walker et al. (1975) indicated that the leeside slope was subjected to more damage than the seaward slope. Wave run-down on the seaward slope is reduced due to overtopping and the weight of the armor units may be significantly reduced as suggested empirically by Van der Meer (1988). However, armor units on the crest and leeside slope are more exposed to the wave forces and their weight may need to be increased. Ahrens and Cox (1990) suggested that the increased stability of the seaward slope and the decreased stability of the crest and leeside slope could lead to stability minimum of the entire structure at an intermediate crest elevation. Van der Meer and Veldman (1992) proposed simple empirical formulae for different damage levels for the design of leeside armor of berm breakwaters. Anderson et al. (1992) carried out a hydraulic stability analysis of leeside armor for berm breakwaters and suggested a semi-empirical formula for the size of leeside stone. In their analysis, the velocity of overtopping water on the crest was estimated using an empirical formula for wave runup and only the stability of armor units slightly above SWL was analyzed. Losada et al. (1992) used the velocity obtained from the numerical model of Kobayashi et al. (1987, 1989) and showed that the minimum armor stability on the crest occurred when the crest level of a submerged breakwater was at the mean water level. Vidal et al. (1992) carried out random wave tests in a three dimensional wave basin and presented the stability curves for different portions of a low-crested breakwater. The stability number plotted as a function of the normalized crest height showed that the minimum armor stability against the initiation of damage on the leeside slope occurred at an intermediate crest height.

In the present study, the stability of the leeside armor units is analyzed considering the drag, inertia and lift forces caused by the overtopping jet of water impinging on the leeside slope above or below the still water level. The structure with its crest at or above the SWL under the attack of normally incident wave trains has been considered. The numerical model RBREAK2 by Kobayashi and Poff (1994) is used to compute the temporal variations of the horizontal velocity and thickness of the overtopping jet on the crest. The jet of water issuing from the crest is treated as a free jet in a

quasi-steady manner. The stability of leeside armor units is expressed in terms of the stability number, N_s as a function of the impinging jet velocity and direction as well as the leeside slope. The computed stability number is shown to be in good agreement with the measured stability number for the initiation of damage presented by Vidal et al. (1992). The stability model is then used to perform sensitivity analyses to gain insight into the mechanisms of the leeside armor stability.

Armor Stability Model

Overtopping Flow on Crest

Kobayashi and Otta (1987) developed a numerical flow model to predict the flow characteristics on rough slopes for specified normally incident wave trains. The wave motion on the slope of a structure is described by the one-dimensional finite-amplitude, shallow water equations including the effect of bottom friction. An explicit dissipative Lax-Wendroff finite difference method is used to solve these equations. This numerical flow model was extended to predict the temporal variations of the velocity and depth of the overtopping flow on the crest of the structure by Kobayashi and Wurjanto (1989). The velocity and depth of the overtopping jet at the landward edge of the crest are the input to the stability analysis of leeside armor units presented in this paper. The numerical model called RBREAK2 (Kobayashi and Poff, 1994) for random waves is used for the computations made herein.

Free Jet Impinging on Leeside Slope

Walker et al. (1975) depicted three possible causes of the failure of the leeside of a low-crested breakwater: 1) pore pressure induced by waves striking the seaward slope; 2) overtopping jet of water impinging on the slope; and 3) toe scouring of the leeside slope by the impinging jet. Out of these causes the impinging jet on the leeside slope appears to be the most common. The wave-induced pore pressure would be significant only for a porous breakwater with a small width and porous material near the still water level. The toe scouring of the leeside slope may be important in very shallow water but is beyond the scope of this study. The breakwater is assumed to be essentially impermeable and only the stability of leeside armor units under the impinging jet is considered in the following.

The jet of overtopping water issuing from the landward edge of the crest impinges on the leeside slope. The jet may directly hit the leeside slope above SWL as shown in Figure 1 or it plunges into the tailwater and then attacks the leeside slope as shown in Figure 2. The properties of jet striking the leeside slope are analyzed using the following symbols shown in Figures 1 and 2:

- x_e = landward edge of the breakwater crest
- d_t = water depth below SWL at the seaward toe of the breakwater
which is assumed to be the same as the tailwater depth
- θ = seaward slope angle of the breakwater
- θ_l = leeside slope angle of the breakwater
- u = depth-averaged horizontal velocity of the overtopping water
at x_e computed by RBREAK2
- h = thickness of the overtopping jet at x_e computed by RBREAK2

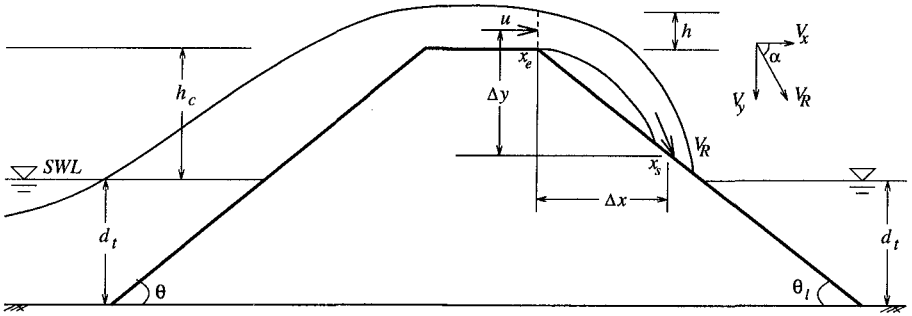


Figure 1: Jet of Water Impinging on Leaside Slope Above Tailwater Surface

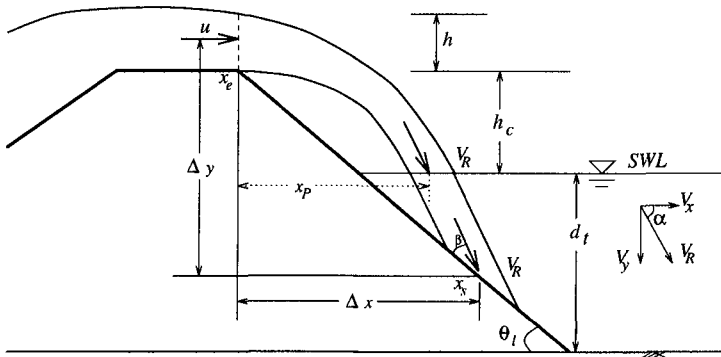


Figure 2: Jet of Water Impinging on Leaside Slope Below Tailwater Surface

- h_c = crest height of the breakwater above SWL
- x_s = impinging point of the jet on the leaside slope
- Δx = horizontal distance between the crest edge and the point x_s
- Δy = vertical distance between the center of the jet at x_e and the point x_s
- V_x = horizontal water velocity of the jet at x_s
- V_y = vertical water velocity of the jet at x_s
- V_R = resultant velocity of the jet striking the slope at x_s
- α = angle of V_R with the horizontal at x_s
- β = angle of V_R relative to the leaside slope given by $\beta = \alpha - \theta_l$

The jet of thickness h issuing from the crest with the computed horizontal velocity of u is assumed to fall freely due to gravity. The initial vertical velocity is zero. The horizontal velocity of the freely falling jet remains to be the initial value u if air friction is neglected. However, the vertical velocity accelerates under the influence of gravity and the vertical acceleration is assumed to be the same as the gravitational acceleration g until the jet impinges on the leaside slope above SWL or the tailwater surface. In the following the unknown values of V_R , α , Δx and Δy are expressed in terms of the known values of u , h , θ_l and h_c .

For the case of the jet impinging on the leaside slope above SWL, a simple analysis

of the quasi-steady jet falling freely due to the gravitational acceleration g yields the following expressions:

$$V_x = u \quad (1)$$

$$\Delta x = g^{-1} \left[u^2 \tan \theta_l + \left(u^4 \tan^2 \theta_l + gh u^2 \right)^{1/2} \right] \quad (2)$$

$$\Delta y = \Delta x \tan \theta_l + \frac{h}{2} \quad (3)$$

$$V_y = \frac{g \Delta x}{u} \quad (4)$$

$$V_R = \left(V_x^2 + V_y^2 \right)^{1/2} \quad (5)$$

$$\alpha = \tan^{-1} \left(\frac{V_y}{V_x} \right) \quad (6)$$

The impinging point x_s in Figure 1 can be found from the calculated values of Δx and Δy . If the point x_s is located below SWL, the jet plunges into the tailwater first and then strikes the leeside slope below SWL. For this case, the jet follows the path of a projectile up to the water surface only. After entering the tailwater, the jet is not falling freely due to gravity. It may be assumed as a first approximation that the jet penetrates straight with the same velocity as the jet velocity at the free surface. Blaisdell and Anderson (1988) made a similar assumption for their analysis of scour at cantilevered pipe outlets. The horizontal distance Δx from the crest edge to the impinging point on the leeside slope is the sum of the free-fall distance x_p to the entry point at the water surface and the horizontal distance of the straight jet penetration below the tailwater surface. The expression for Δx is obtained geometrically using Figure 2.

$$\Delta x = x_p + \frac{(x_p \tan \theta_l - h_c)}{\tan \alpha - \tan \theta_l} \quad (7)$$

where the horizontal distance x_p of the free fall is

$$x_p = u \sqrt{\frac{2(h_c + h/2)}{g}} \quad (8)$$

The vertical velocity V_y at the impinging point x_s in Figure 2 is assumed to be the same as the vertical velocity of the jet at the entry point at the free surface.

$$V_y = \frac{g x_p}{u} \quad (9)$$

The horizontal velocity V_x at the point x_s is assumed to be the same as u and given by (1). The values of Δy , V_R and α are given by (3), (5) and (6), respectively.

The assumption of the constant jet velocity below the tailwater surface may be reasonable for a short penetration distance and result in the overestimation of the jet velocity at the impinging point x_s for a long penetration distance. It is noted that if the horizontal distance Δx calculated by (7) exceeds the horizontal extent of the leeside slope, the jet will impinge on the seabed but the toe scour landward of the leeside slope is not analyzed herein.

Hydrodynamic Forces and Armor Stability

The hydrodynamic forces acting on an individual armor unit on the leeside slope are the drag, lift and inertia forces. These forces may be expressed by the following Morison-type equations:

$$\text{Drag Force; } F_D = \frac{1}{2} \rho C_D C_2 (d)^2 V_R^2 \tag{10}$$

$$\text{Lift Force; } F_L = \frac{1}{2} \rho C_L C_2 (d)^2 V_R^2 \tag{11}$$

$$\text{Inertia Force; } F_I = \rho C_M C_3 (d)^3 \left(\frac{dV_R}{dt} \right) \tag{12}$$

- where, ρ = fluid density which is assumed constant
- C_D, C_L and C_M = drag, lift and inertia coefficients
- C_2 and C_3 = area and volume coefficients of the armor unit
- d = characteristic length of the armor unit
- $\frac{dV_R}{dt}$ = acceleration of the impinging water

The drag force is assumed to act in the direction of the impinging jet as shown in Figure 3. The acceleration of the jet falling freely is vertically downward and its magnitude equals the gravitational acceleration g . The corresponding inertia force acting vertically downward is given by (12) with $dV_R/dt = g$. On the other hand, the inertia force is assumed to be zero where the impinging point x_s is located below SWL. This assumption is consistent with the assumption of the constant jet velocity below the tailwater surface. For simplicity, it may be assumed that the lift force acts upward normal to the slope.

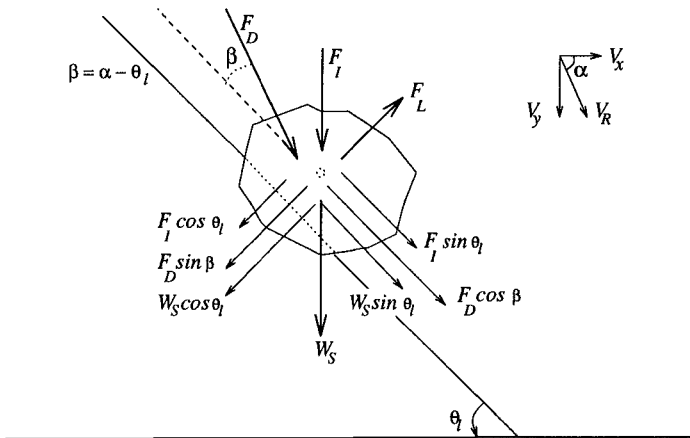


Figure 3: Forces Acting on Armor Unit

In addition to these hydrodynamic forces, the submerged weight of the armor unit acts vertically downward.

$$\text{Submerged Weight; } W_s = \rho g (s - 1) C_3 (d)^3 \tag{13}$$

where s = specific density of the armor unit, which is assumed to be fully submerged.

These forces acting on the armor unit may be resolved in the directions parallel and normal to the slope as shown in Figure 3. The static stability condition against sliding or rolling may be given by

$$F_D \cos \beta + F_I \sin \theta_l + W_s \sin \theta_l \leq (F_D \sin \beta + F_I \cos \theta_l + W_s \cos \theta_l - F_L) \tan \phi \quad (14)$$

in which ϕ = angle of repose of the armor units.

The stability of armor units is traditionally expressed in terms of the stability number, N_s , defined as

$$N_s = \frac{H_s}{(s-1)D_{n50}} \quad ; \quad D_{n50} = C_3^{1/3}d \quad (15)$$

where D_{n50} is the nominal diameter defined as $D_{n50} = (M_{50}/\rho s)^{1/3}$ with M_{50} being the median (50% exceedance) mass of the stones. Accordingly, the characteristic armor length d is taken as the length corresponding to $M_{50} = C_3 \rho s d^3$. The wave height in (15) is generally taken as the significant wave height H_s .

Substitution of (10), (11), (12) and (15) with $dV_R/dt = g$ or 0 into (14) yields

$$N_s \leq N_R = \frac{2C_3^{2/3} \sin(\phi - \theta_l)}{C_2 V_*^2 [C_L \sin \phi + C_D \cos(\phi + \alpha - \theta_l)]} \left[\frac{C_M}{(s-1)} + 1 \right] \quad (16)$$

where $V_* = V_R/\sqrt{gH_s}$ is the impinging jet velocity normalized by the significant wave height. Eq. (16) corresponds to the case of $dV_R/dt = g$. For the case of $dV_R/dt = 0$ below the tailwater surface, N_R is given by (16) without the term $C_M/(s-1)$.

The temporal variations of u and h on the crest for the specified incident wave duration are computed using the numerical model RBREAK2 for the specified geometry of the seaward slope and crest as well as the specified incident wave train. For the specified geometry of the leeside slope, (1)-(9) are used to calculate the location of the jet impinging point x_s and the impinging velocity V_R and its direction α at each instant when the computed u and h are stored. The value of N_R at that instant is computed using (16). The critical stability number, N_{sc} , for the initiation of armor movement is defined as the minimum value of N_R during the entire duration of the incident wave action.

Assuming that C_2, C_3, ϕ, C_L, C_D , and s are constant and C_M is constant but zero if point x_s is below SWL, (16) clearly shows the increase of N_R and hence N_s with the increase of C_3 and C_M and the decrease of C_2, C_L and C_D . Also the leeside slope angle θ_l can be adjusted to increase N_R and hence N_s .

There are only two hydrodynamic variables in (16): i) $V_* = V_R/\sqrt{gH_s}$ with the jet impinging speed V_R at point x_s ; and ii) α = jet angle at point x_s . Eq. (16) clearly indicates the increase of N_R and hence N_s as V_* decreases and α increases. However, if $\alpha \leq \theta_l$, the jet will not strike the leeside slope. For the jet to strike the leeside slope, α should be greater than θ_l as shown in Figures 1 and 2. This implies that the increase of the leeside slope angle θ_l increases α and increase N_s . The increase of θ_l , however, will also decrease $\sin(\phi - \theta_l)$ and increase $\cos(\phi + \alpha - \theta_l)$ where $\phi > \theta_l$ for the

stone stability. In addition, V_R^2 is proportional to u^2 and can be reduced by reducing u^2 using a wider crest or a gentler seaward (front) slope.

The sensitivity of the stability criterion (16) to the force coefficients and the leeside slope is evaluated using the following basic values:

$$C_2 = 0.9, C_3 = 0.66, \phi = 50^\circ, s = 2.65, \cot \theta_l = 1.5, V_*^2 = 2.0, \alpha = 40^\circ \\ C_D = 0.1, C_L = 0.025, C_M = 0.1 \text{ (or zero if } x_s \text{ is below SWL)}$$

Figure 4(a) shows the variations of the stability function N_R with C_D , C_L and C_M where these coefficients are varied one by one from the above basic values. N_R increases with C_M and decreases with C_D and C_L as can also be seen in (16). C_M has a minor effect on the value of N_s . The value of N_s significantly depends upon C_D and C_L in the range of C_D and C_L less than about 0.1. Figure 4(b) shows the sensitivity of N_R to the leeside slope $\cot \theta_l$. For this example, N_R increases fairly rapidly as the leeside slope becomes gentler.

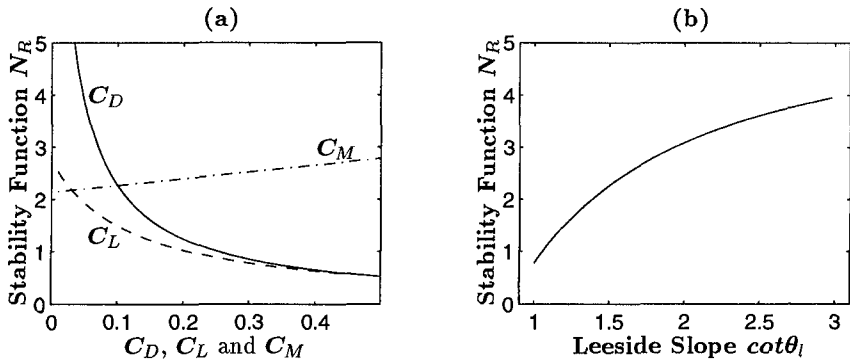


Figure 4: Sensitivity of Stability Function N_R to (a) Drag, Lift and Inertia Coefficients and (b) Leeside Slope $\cot \theta_l$

Comparison With Available Data

Vidal et al. (1992) carried out a series of tests in a three-dimensional wave basin for the stability of stones on the seaward slope, crest and leeside slope of a low-crested rubble mound breakwater. The present numerical model is compared with their test data for the initiation of damage on the leeside slope. The characteristics of the tested breakwater were as follows:

$$\begin{array}{ll} \text{seaward slope } \cot \theta & = 1.5 & ; & \text{leeside slope } \cot \theta_l & = 1.5 \\ \text{crest width} & = 15 \text{ cm} & ; & \text{water depth at toe } d_t & = 38 - 60 \text{ cm} \\ \text{stone diameter } D_{n50} & = 2.49 \text{ cm} & ; & \text{specific density } s & = 2.65 \end{array}$$

Some of the input parameters for the numerical model are based on those used for the armor stability on the seaward slope computed by Kobayashi and Otta (1987). The friction factor, f' , used in RBREAK2 is taken as 0.3 for the seaward slope and crest. The effect of permeability is neglected. The area coefficient, C_2 , and the volume coefficient, C_3 , of the stone are assumed as 0.9 and 0.66, respectively, and the angle of repose, ϕ , for the stone is assumed to be equal to 50° .

In the numerical model RBREAK2 the input time series of the incident wave train needs to be specified at the seaward toe of the structure. The one hour time series based on JONSWAP spectra with its peak period, $T_p = 1.4$ or 1.8 sec, and its peak enhancement factor, $\gamma = 3.3$, are used as the input to comply with the wave conditions used in their experiment. The zero-moment wave height H_{m0} was varied in their experiment to produce the different damage levels. Four tests in their experiment corresponded to the initiation of damage (ID) on the leeside slope of the low-crested breakwater. The corresponding significant wave height H_s for these four tests is calculated from the observed N_s using (15). Based on these values of H_s the time series of incident wave trains are then simulated numerically using the random phase method for the input to RBREAK2. The conditions of the four ID tests are listed in the rows of test 1-4 in Table 1.

Table 1: Test Conditions and Stability Numbers

Test No.	h_c (cm)	d_t (cm)	T_p (sec)	H_{m0} (cm)	H_s (cm)	h_c/H_s	N_s (data)	N_{sc} (computed)
1	0	40	1.4	11.5	11.1	0.00	2.70	2.56
		60	1.4	11.5	11.1	0.00		2.46
2	2	58	1.8	9.1	8.8	0.23	2.15	1.97
		58	1.4	9.1	8.8	0.23		2.20
		38	1.4	9.1	8.8	0.23		1.98
3	4	56	1.4	8.3	8.0	0.50	1.95	2.11
4	6	54	1.4	8.5	8.2	0.73	2.00	2.02
		54	1.8	8.5	8.2	0.73		1.91
5	8	54	1.4	8.5	8.2	0.98	-	2.00
6	10	54	1.4	8.5	8.2	1.22	-	2.02
7	12	54	1.4	8.5	8.2	1.46	-	2.25
8	14	54	1.4	8.5	8.2	1.71	-	2.53
9	16	54	1.4	8.5	8.2	1.95	-	2.80
10	18	54	1.4	8.5	8.2	2.20	-	3.47

Vidal et al. (1992) did not indicate the specific values of d_t and T_p for these four tests. As a result, all the values of d_t and T_p listed in their Table 2 are considered as indicated in the rows of test 1-4. It is noted that test 5-10 listed in Table 1 is hypothetical and used to examine the effect of the crest height h_c greater than the upper limit of $h_c = 6$ cm tested by Vidal et al. (1992). The computed time series of u and h at the landward edge of crest are stored at the rate of 40 points for each T_p .

The stability model was then calibrated to fit the computed values of N_{sc} with the observed values of N_s for initiation of damage for the leeside slope stones. A good agreement was obtained with the values of force coefficients as $C_D = 0.1$, $C_L = 0.025$, and $C_M = 0.1$. Figure 4(a) based on (16) suggests that a similar agreement might be obtained using different values of these coefficients. These values of the force

coefficients appear to be small as compared to the force coefficients for the stones on the seaward slope of the breakwater calibrated by Kobayashi and Otta (1987). Data on the values of C_D , C_L and C_M for the leeside slope stones will be required to resolve the different values of these coefficients for the seaward and leeside slope stones.

Figure 5 shows the comparison of the computed and observed stability numbers plotted against the normalized crest height, h_c/H_s , for test 1-4 listed in Table 1. It can be seen that by adopting the values of the force coefficients as mentioned above, the computed values of N_{sc} for all the four tests are in good agreement with the observed values of N_s .

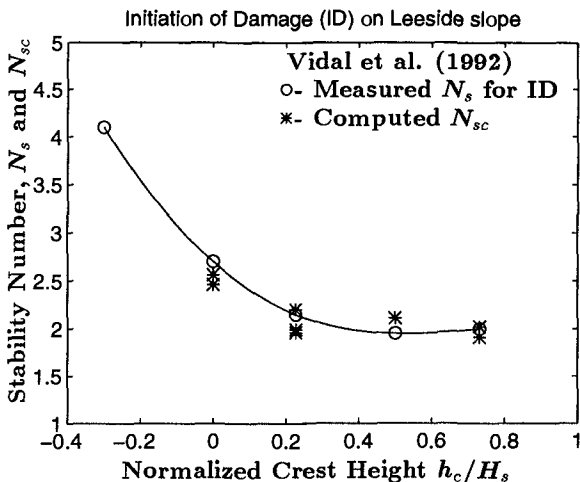


Figure 5: Comparison of Computed N_{sc} with Measured N_s

Influence of Various Parameters

In order to study the effect of the increased crest height on the leeside stability above the range tested by Vidal et al. (1992), computations are carried out using the test conditions for test 4 with the crest height being increased in an increment of 2 cm as listed as test 5-10 in Table 1. The critical stability numbers for the leeside slopes $\cot \theta_l = 1.25$ and 2 are also calculated for all the tests listed in Table 1 where $\cot \theta_l = 1.5$ in Table 1. Figure 6 shows the variation of N_{sc} with the crest height normalized by H_s for $\cot \theta_l = 1.25$, 1.5 and 2 where the fitted curved line for each slope is added for clarity. For the leeside slope of 1:1.5 the minimum stability occurs at intermediate crest heights and the range of h_c/H_s for the minimum stability is wider. However, for the leeside slope of 1:2, the stability minimum moves towards zero crest height and N_{sc} increases monotonically with the increase of h_c/H_s . Figure 6 also shows that the stability increases rapidly as the crest height is increased beyond the minimum stability range. The stability at zero crest height shows the trend of increasing stability for the negative crest heights, consistent with the computed results by Losada et al. (1992). For this particular case with the normalized depth $d_t/H_s = 6.6$, the armor stability improves significantly as the leeside slope is made flatter.

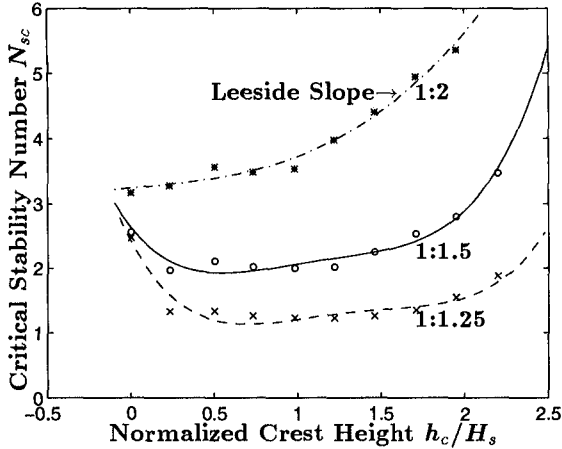


Figure 6: Computed Variation of N_{sc} with Normalized Crest Height h_c/H_s for Leeside Slopes of 1:1.25, 1:1.5 and 1:2

Computations are also carried out to study the influence of the seaward slope, water depth, crest width and spectral peak period on the leeside armor stability. The basic characteristics of the breakwater and wave conditions chosen for the computations are as follows:

seaward slope $\cot \theta$	= 2.0	;	leeside slope $\cot \theta_l$	= 1.5
crest width	= 15 cm	;	crest height above SWL h_c	= 0 - 20 cm
water depth at toe d_t	= 60 cm	;	peak period T_p	= 1.4 sec
significant wave ht. H_s	= 10.0 cm	;	zero-moment wave ht. H_{m0}	= 10.1 cm

The seaward slope $\cot \theta$, the water depth d_t , the crest width and the peak period T_p are varied one by one from these basic values in the following sensitivity analyses. The values of the critical stability number are computed for different crest heights. However, the computations for the influence of the crest width and peak period are made only for the single crest height of 4 cm above SWL, that is, $h_c/H_s = 0.4$.

Figure 7 shows the influence of the seaward slope on the leeside armor stability where the seaward slope affects the depth-averaged velocity u and the water depth h at the landward edge of the crest computed by RBREAK2. The leeside stability improves as the seaward slope is made flatter. The range of h_c/H_s for the minimum stability becomes smaller and tends to move towards zero crest height for the flatter seaward slope. As the seaward slope becomes flatter, the velocity u of overtopping water is reduced and the stability of leeside armor is increased.

Figure 8 shows the variation of the computed stability number N_{sc} with the water depth at the toe, d_t , normalized by H_s . The stability of the leeside slope is generally larger for the deeper water. However, for the small crest heights at about zero, the leeside armor stability is greater for the shallower water. This is because the overtopping water with the higher velocity for the shallower water impinges beyond the toe of the leeside slope. The intense jet strikes the seabed instead of the leeside armor slope. For the shallower depth the leeside slope stability of a breakwater with a crest

near SWL could be increased by increasing the leeside slope angle. However, scour of the seabed landward of the leeside slope may become serious.

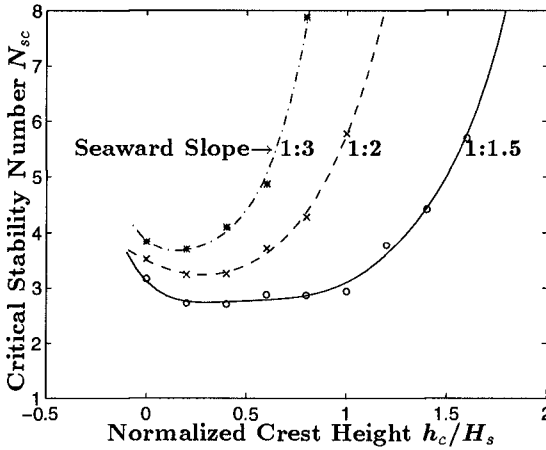


Figure 7: Variation of N_{sc} with Seaward (Front) Slope

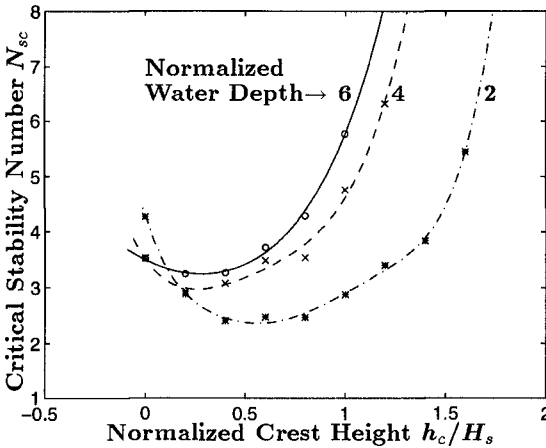


Figure 8: Variation of N_{sc} with Normalized Water Depth d_t/H_s

Figure 9(a) shows the variation of the computed stability number N_{sc} with the crest width normalized by H_s . The increase of the crest width of the breakwater improves the stability of the leeside. This is obvious because the increased crest width provides additional friction to the overtopping water on the crest and reduces the velocity u at its landward edge. However, the stability number increases only slowly with the crest width increase and this option may not be very economical.

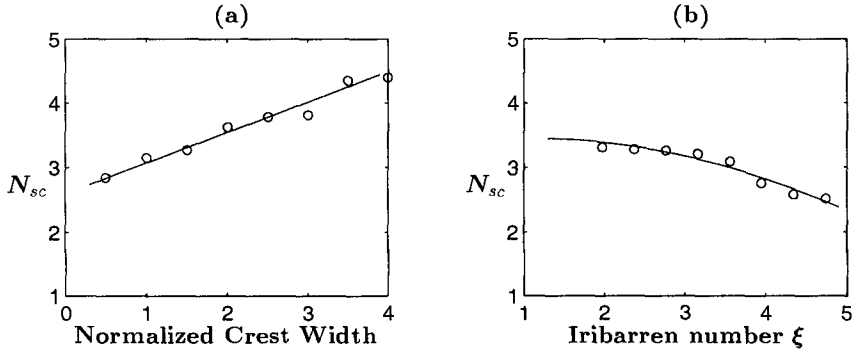


Figure 9: Computed Variation of N_{sc} with (a) Crest Width Normalized by H_s and (b) Iribarren Number by Varying T_p for $h_c/H_s = 0.4$

The peak period T_p of the incident wave spectrum has also a noticeable effect on the leeside armor stability. Figure 9(b) shows the variation of the computed stability number N_{sc} with the Iribarren number ξ defined as $\xi = \tan \theta / \sqrt{(2\pi H_s)/(gT_p^2)}$.

Figure 9(b) indicates that the stability of the leeside slope decreases with the increasing wave period for this case. The longer period waves increase the overtopping water velocity u for this geometry of the breakwater. A similar result was also observed experimentally by Van der Meer and Veldman (1992).

Conclusions and Recommendations

A hydraulic stability model for armor units on the leeside slopes of overtopped rubble mound breakwaters has been developed using the water velocity and depth of the overtopping flow computed by the existing time dependent numerical model RBREAK2. A good agreement has been obtained with available limited data. Some of the empirical coefficients used in the model have been calibrated using the same data. Consequently, more extensive data will be required to verify the developed model in a more rigorous manner. The limited computed results presented herein indicate the following qualitative conclusions:

- The flatter leeside slope increases the armor stability.
- The flatter seaward slope of a breakwater improves the leeside armor stability and the crest height for the minimum stability tends to approach zero at SWL for the flatter seaward slopes.
- The leeside slope of a breakwater is more stable in deeper water. Also, the crest height for the minimum stability approaches zero at SWL.
- For relatively shallow water depths the minimum armor stability on the leeside slope occurs for wide intermediate crest heights.
- For the shallower water depths the leeside slope stability of a breakwater with a crest near SWL could be increased by increasing the leeside slope angle.
- The stability of the leeside slope can be improved somewhat by increasing the crest width of a breakwater.

These conclusions are based on the specific computations made in this paper. It is difficult to obtain simple general conclusions because the number of parameters involved in this problem is large. The developed hydraulic model will allow one to examine the hydraulic stability of leeside armor units under various wave conditions and breakwater configurations. Consequently, the model is very useful in designing the geometry of an overtopped breakwater and the size of leeside armor units.

Acknowledgment

The study was carried out during the fellowship training of the first author at the University of Delaware. The fellowship was sponsored by the United Nations Development Programme (UNDP) under the Project IND/90/038 at the Central Water and Power Research Station, Pune, India.

References

- Ahrens, J.P. and Cox., J., 1990, 'Design and Performance of Reef Breakwaters', *J. Coastal Research*, SI(7), 61-75.
- Blaisdell, F.W. and Anderson, C.L., 1988, 'A Comprehensive Generalized Study of Scour at Cantilevered Pipe Outlets', *J. Hydraulic Research*, 26(4), 357-376.
- Anderson, O.H., Juhl, J. and Sloth, P., 1992, 'Rear Side Stability of Berm Breakwaters', *Proc. 23rd Coast. Engrg. Conf.*, ASCE, 1020-1029.
- Kobayashi, N., and Otta, A.K., 1987, 'Hydraulic Stability Analysis of Armor Units', *J. Waterway, Port, Coast. and Ocean Engrg.*, ASCE, 113(2), 282-298.
- Kobayashi, N., and Wurjanto, A., 1989, 'Numerical Model for Design of Impermeable Coastal Structures', *Res. Rep. No. CE-89-75*, Ctr. for Applied Coast. Res., Univ. of Delaware, Newark, Del., USA.
- Kobayashi, N., and Poff, M.T., 1994, 'Numerical Model RBREAK2 for Random Waves on Impermeable Coastal Structures and Beaches', *Res. Rep. No. CACR-94-12*, Ctr. for Applied Coast. Res., Univ. of Delaware, Newark, Del., USA.
- Losada, M.A., Kobayashi, N. and Martin, F.L., 1992, 'Armor Stability on Submerged Breakwaters', *J. Waterway, Port, Coast. and Ocean Engrg.*, ASCE, 118(2), 207-212.
- Van der Meer, J.W., 1988, 'Rock Slopes and Gravel Beaches Under Wave Attack', *Delft Hydraulics Communication No. 396*, Delft, The Netherlands.
- Van der Meer, J.W., and Veldman, J.J., 1992, 'Singular Points at Berm Breakwaters: Scale Effects, Rear, Roundhead, and Longshore Transport', *Coastal Engrg.*, 17, 153-171.
- Vidal, C., Losada, M. A., Medina, R., Mansard, E. P. D. and Gomez-Pina, G., 1992, 'A Universal Analysis for the Stability of Both Low-Crested and Submerged Breakwaters', *Proc. 23rd Coast. Engrg. Conf.*, ASCE, 1679-1692.
- Walker, J. R., Palmer, R. Q. and Dunham, J. W., 1975, 'Breakwater Backslope Stability', *Proc. Civil Engrg. in Oceans*, ASCE, 879-898.

CHAPTER 135

Influence of the core configuration on the stability of berm breakwaters

Nikolay Lissev¹
Alf Tørum²

Abstract

An experimental study has been carried out to investigate the concept of extending the core into the berm of a berm breakwater. Five different core configurations were tested. The reshaped profiles were not significantly influenced by the core configuration. The core configuration should be such that the core material is not directly exposed to the waves during the reshaping.

The concept of extending the core into the berm will lead to cheaper berm breakwater structures since the core material is cheaper than the armour stones.

Introduction

Berm breakwaters was introduced as a economical breakwater concept in the beginning of the 1980'ties. Baird and Hall (1987) discussed the main advantage of the concept. The main advantage of the berm breakwater concept is that smaller stone weights can be used in a berm breakwater than in a conventional rubble mound breakwater. Hence general contracting equipment can be used instead of more costly speciality equipment.

Several investigations have been carried out on the stability of berm breakwaters. van der Meer (1988) have carried out the most comprehensive study

¹ University of Architecture, Civil Engineering and Geodesy, 1421Sofia, Bulgaria

² Prof, SINTEF Civil and Environmental Engineering/Norwegian University of Science and Technology, 7034 Trondheim, Norway

on the stability of static and dynamic stable breakwaters, including the berm breakwater. Burchart et al (1988) carried out tests on berm breakwaters in which they concentrated mainly on 3-dimensional effects, i e transport of stones along the structure exposed to oblique waves and deformation of roundheads.

Much research on berm breakwaters was carried out during the EU MAST I (1992-1994) and MAST II (1994-1996) program. The present study was initiated by the second author when he participated in MAST I. Up to that time most of the systematic laboratory work had been carried on berm breakwaters as shown in Figure 1A. A cross section as shown in Figure 1B could be more economical since more of the (cheaper) core material can be used. The experimental study on the influence of the core configuration on the berm breakwater stability was reported in detail by Lissev (1993). This paper is a summary of the report.

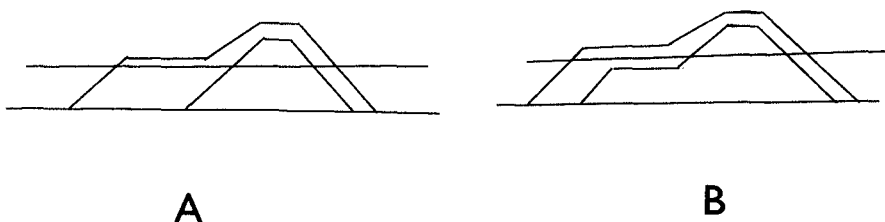


Figure 1 Berm breakwater cross-sections

Test set-up

The model testing was carried out in a wave flume as shown in Figure 2. The width of the flume is 1.0 m.

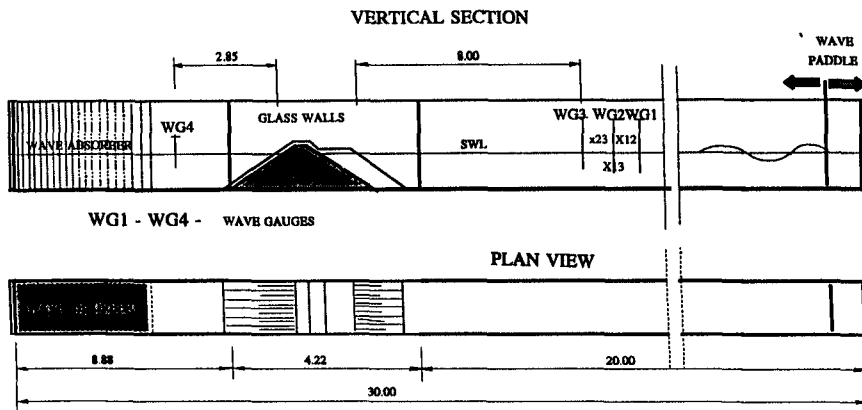


Figure 2 Wave flume with berm breakwater model

Five different cross sections as shown in Figure 3 were tested.

The gradation curves for the berm stone material and the core material are shown in Figure 4. The nominal diameter is defined as $D = \sqrt[3]{W / \rho_s}$, where W = mass of the stone, ρ_s = specific mass of the stone.

Wave measurement

The surface elevations were measured with conductive type wave gauges. In order to be able to sort out the incoming and reflected waves the three gauges were placed with individual distances as recommended by Mansard and Funke (1980).

The group of three gauges were placed 8 m in front of the breakwater. This is more than one wave length, as recommended by Goda (1985).

To decompose the wave field into incoming and reflected waves a method based on linear wave theory and developed by Zelt and Skjelbreia (1992) was used.

Figure 5 shows reflection coefficients as obtained for profiles 1, 2 and 3 compared with coefficients obtained by Andersen et al (1992).

Test program

As mentioned five initial profiles with the same outer profile configuration were used, but with different configuration of the core, Figure 3. Two types of model tests were conducted for profiles 1, 2 and 3: Stability tests and tests for measuring some of the hydraulic responses of the developed profile of the breakwater after finishing the stability tests. For the initial profiles 4 and 5 only stability tests were conducted.

The tests were carried out with irregular waves with increasing peak period T_p with increasing significant wave height such that the wave steepness $s_{02} = 2\pi H_s / gT_{02}^2$ was kept approximately constant, $s_{02} = 0.045$. The lowest peak period was $T_p = 1.32$ s and the highest peak period $T_p = 2.8$ s. H_s = significant wave height, $T_{02} = 2\pi\sqrt{m_0 / m_2}$, m_0 = area under the wave spectrum, m_2 = second area moment of the wave spectrum.

The time duration of the different significant wave height steps are shown in Figure 6. Table 1 shows significant parameters for the tests.

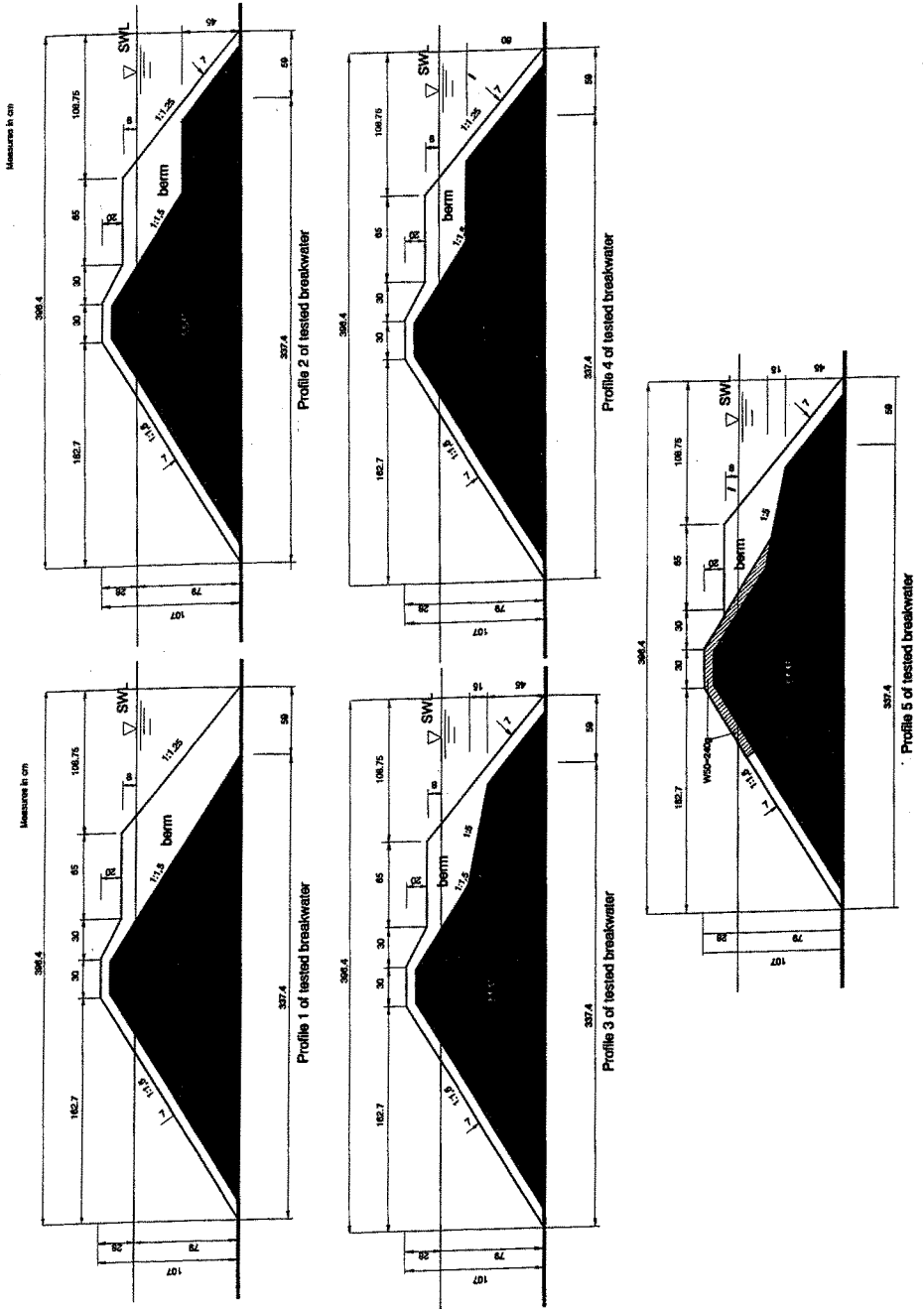
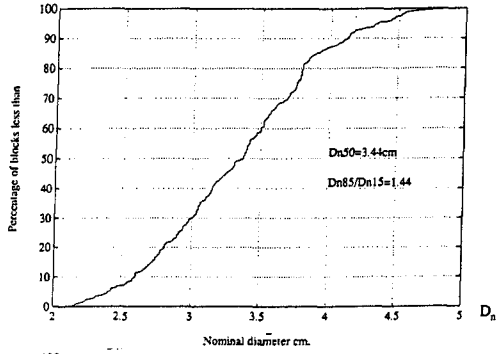


Figure 3 The five tested cross sections

A



B

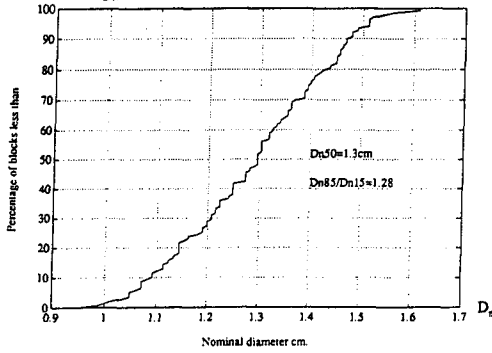


Figure 4 Gradation curves A) Berm stones B) Core stones

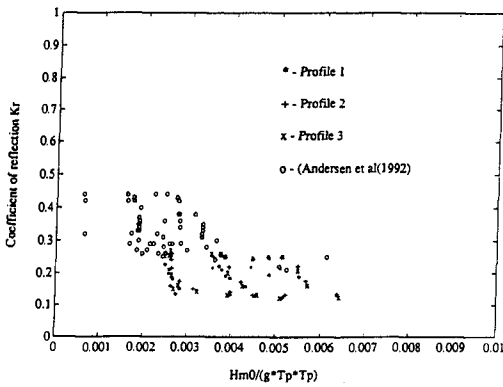


Fig 5 Reflection coefficients

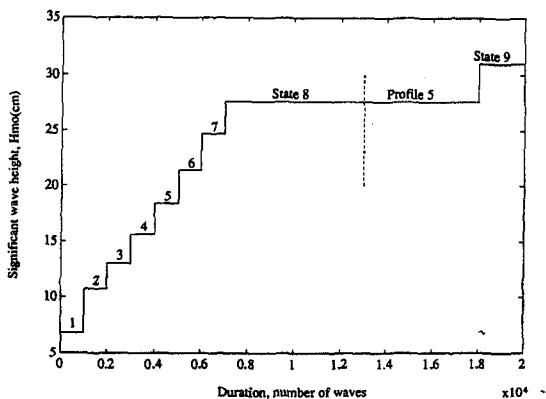


Figure 6 Time duration of the significant wave height

Table 1 Tested sea states

State no.	T_p (sec)	T_{02} (sec)	H_{m0} (cm)	S_{02}	$H_{m0}/D_{n50} \Delta$
1	1.32	1.05	6.8	0.040	1.18
2	1.55	1.24	10.7	0.044	1.86
3	1.75	1.36	13.0	0.046	2.26
4	2.00	1.51	15.6	0.044	2.72
5	2.20	1.65	18.4	0.044	3.20
6	2.40	1.74	21.4	0.046	3.72
7	2.60	1.87	24.7	0.046	4.30
8	2.80	2.00	27.6	0.046	4.80

Test results

Reshaped profiles after attacks of 1000 waves for each wave state between state 4 and state 8 and for every one of the five tested initial profiles are shown in Figure 7. The most significant changes for every wave state took place after the attack of the first two-three hundred waves for every wave state. For wave states 4, 5 and 6 only very small changes of the profile were observed after this time.

In Figure 8 are shown the reshaped breakwater profiles for all five initial profiles measured after finishing the tests with 1000 waves for every wave state 1-8. In Figure 9 are shown the final profiles after completing the tests with additional 5000 waves for wave state 8 for every of the five initial profiles.

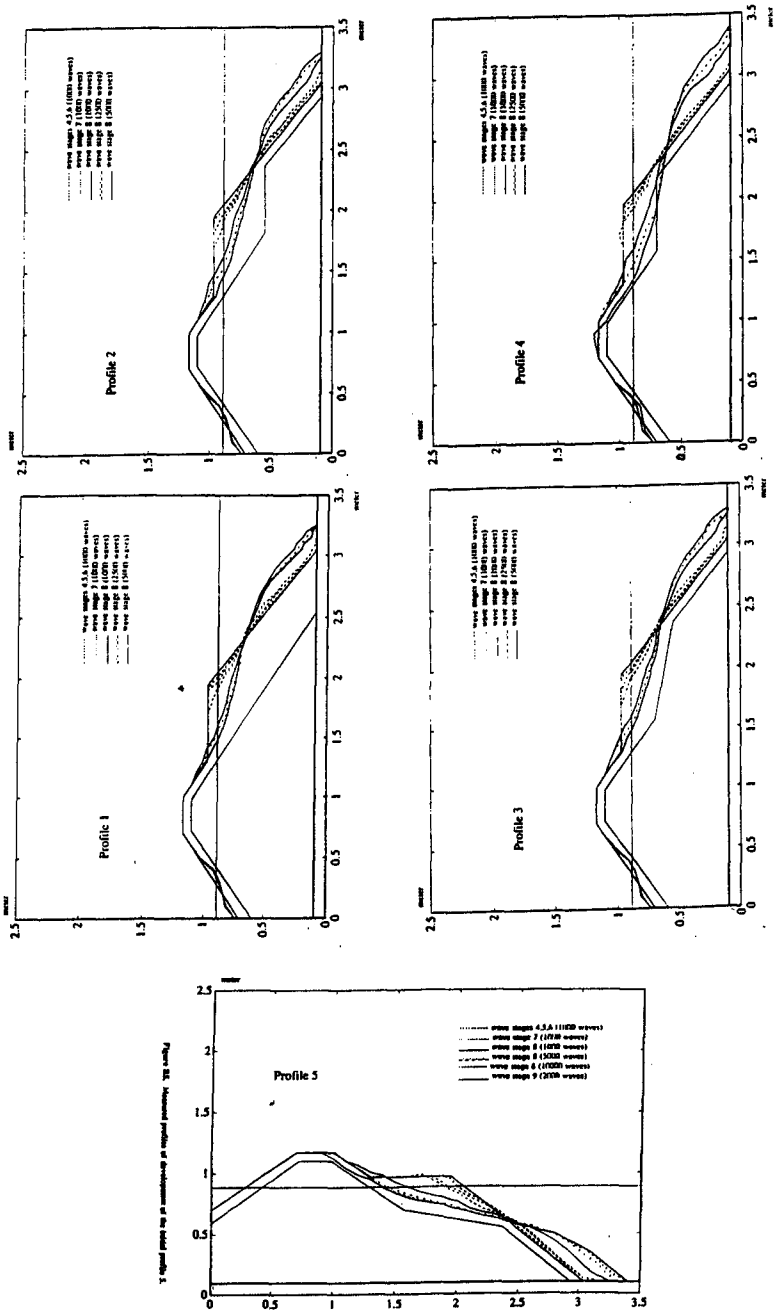


Figure 7 Reshaped profiles for the different initial profiles

Figure 8 shows that there are no significant differences for all five tested initial profiles after completing the sea wave states 1-8 with 1000 waves in each state. The profiles are almost identical with small deviations at the upper and lower berm slope. In this case the width of the berm was reduced from 0.65 m to 0.10 - 0.13 m. This means that for no one of the tested profiles seaward damage conditions are reached. The damage to the seaward side of the berm breakwater is defined to occur when the entire width of the top berm is eroded.

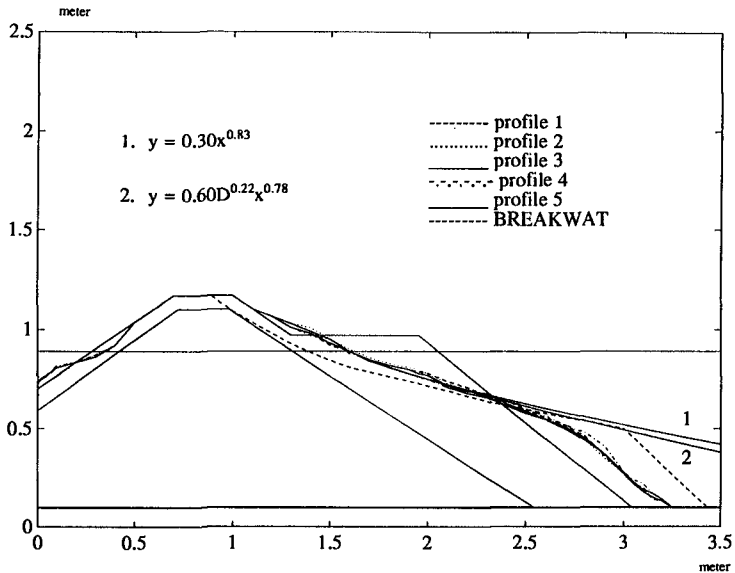


Figure 8 Reshaped profiles for every initial profiles 1-5 after completing every wave state 1-8 with 1000 waves for each state.

For profile 4 there was another critical point close to the dynamic stable profile. The berm stones were removed at this point and the core became directly exposed to the waves after completing the test with sea states 1-8 with 1000 waves in each sea state. Even though a critical condition was reached for profile 4 then it was decided to continue the experiments with the 5000 waves for wave state 8 for this profile to see if a complete failure would develop.

The experiments with additional 5000 waves for wave state 8 show almost the same reshaping for the initial profiles 1, 2 and 3. At the end of the tests for all these three profiles the width of the horizontal berm was reduced to zero. The results from the tests with the initial profiles 1, 2 and 3 gave the idea to use somewhat larger stones over the breakwater crest, Profile 5, Figure 3. Profile 5 is a modified

version of profile 3. The medium weight of the stones over the crest is $W_{50} = 0.24$ kgs, which is approximately twice the weight of the stones in the berm.

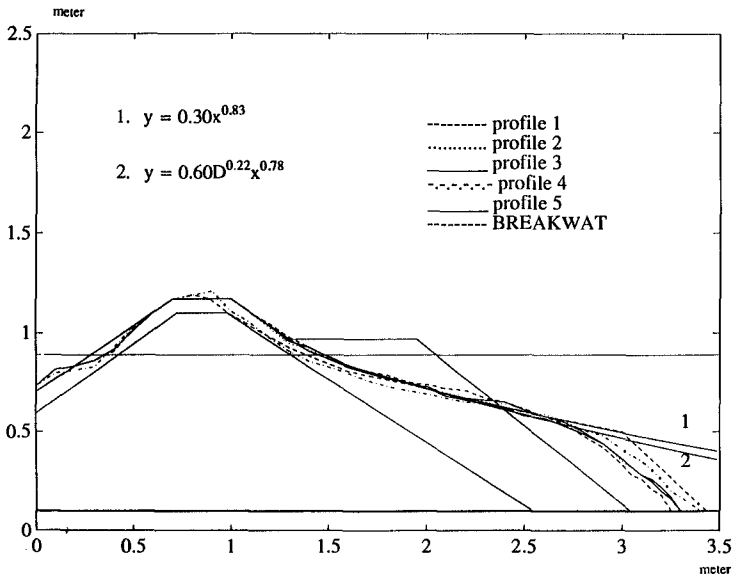


Figure 9 Reshaped profiles for every initial profiles 1-5 after completing every wave state 1-8 with 1000 waves for each state plus additional 5000 wave for wave state 8.

The development of Profile 5 up to 5000 waves is similar to the profiles 1, 2 and 3. For Profile 5 an additional 5000 waves of wave state 8 were run. During these 5000 waves there were only small changes in the upper and lower part of the profile. This means that the profile is dynamically stable for this wave state. Only some few stones were moved from the additional armour layer to the toe of the breakwater.

After completing the tests with wave state 8 for Profile 5, the wave height was increased to wave state 9, $H_s = 0.31$ m and $T_p = 2.8$ s. After 2000 waves with this wave state the armour layer was almost completely destroyed and the test was stopped. In this wave state the dynamic stable profile in the middle part was the same. The main development was in the upper and lower part of the berm slope. Bigger stones from the upper part of the profile were moved to the toe of the breakwater.

For Profile 4 the "failure" which started during the first 1000 waves with wave state 8 increased with the number of waves. Part of the core which was directly exposed to the wave action migrated gradually towards the crest of the breakwater. It is important to point out that this process developed gradually with time. Even without armour stones on the flat part, the profile was relatively stable because stone prism formed in the front part of the profile supporting finer core material. This is a good example that processes of destruction of the berm breakwaters are relatively slow in comparison with conventional mound breakwaters where failure is very fast after some critical stage has been reached.

The curves marked BREAKWAT in Figure 8 are results obtained with the computer program BREAKWAT developed by Delft Hydraulics (1990) based on the extensive tests by van der Meer (1988).

The curves in Figure 8 represented by the equations

$$y = a_4 x^{0.83}$$

$$y = p \cdot D^{0.22} x^{0.78}$$

comes from van der Meer (1988) and a modified version of Vellinga's (1986) equations for dune erosion during storm surges.

There is fair agreement between the results obtained in this study and previous studies.

Overtopping

Tests to determine irregular wave overtopping were carried out on the reshaped breakwater after the stability tests had been completed for Profiles 1 and 3. Figure 10 shows the test set-up to measure overtopping.

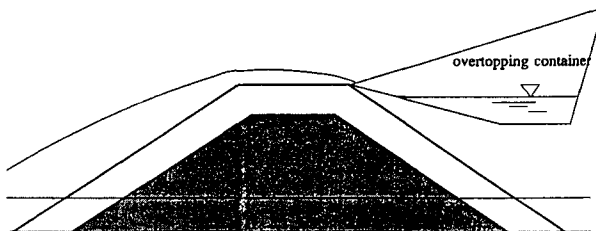


Figure 10 Scheme of measuring overtopping

We used the dimensionless freeboard parameter F' , Ahrens (1986):

$$F' = \frac{F}{(H_s^2 L_p)^{1/3}}$$

where F = freeboard, i.e. the vertical difference between the crest height of the berm breakwater and the still water line, SWL. L_p is the Airy wave length based on the peak period T_p and the water depth in front of the breakwater.

The overtopping rate Q is defined as the volume of water overtopping the breakwater per unit length of breakwater per unit time.

In Figure 11, Q is plotted versus F' . The curve shown in Figure 11 represents an equation of the general form due to Owen (1982):

$$Q = Q_o \exp(C_1 F')$$

The curve shown in Figure 11 is an eyefitted curve. The coefficients Q_o and C_1 leave in this case the values $Q_o = 4600 \text{ cm}^3/\text{cm s}$ and $C_1 = -21$.

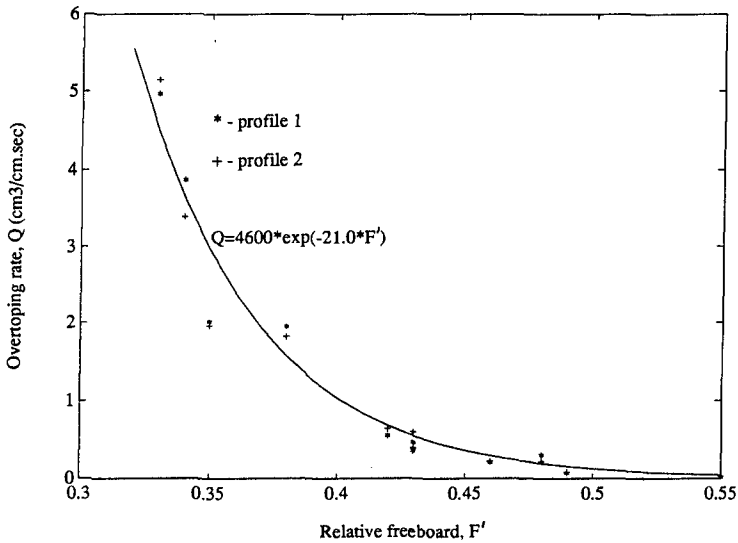


Figure 11 Overtopping rate versus relative freeboard

Rear side damage

No special tests for rear side stability were included in this study. We only registered the beginning of the damage processes on the rear side. Some comparisons were made with Andersen et al (1992) on rear side damage. There was a fair agreement between the two test series.

Conclusion

Based on the results obtained in this study it can be concluded that the core can be extended into the berm of a berm breakwater. Since the core material is generally cheaper than the armour stones, the concept of extending the core material into the berm will give a cheaper berm breakwater structure.

Acknowledgement

This study was conducted by the first author under the supervision of the second author when the first author stayed for 9 months 1992/93 at the Norwegian University of Science and Technology on a scholarship from the Norwegian Research Council for Science and Humanities (NAVF). We appreciate this financial support from NAVF.

References

- Ahrens, J.P., Heimbaugh, M.S. and Davidson, D.D. (1986). Irregular wave overtopping of seawall/revetment configurations, Roughans point, Massachusetts. Experimental model investigation, Technical Report CERC-86-7, US Army Engineer Waterways Experiment Station, Vicksburg, MS.
- Andersen, O.A., Juhl, J. and Sloth, P. (1992). Rear side stability of berm breakwaters. Proc. 23rd International Conference on Coastal Engineering, ASCE, Venice, Italy.
- Baird, W.F., Hall, K.R. (1984). The design of breakwaters using quarried stones. Proceedings of the 19th International Conference on Coastal Engineering, Houston, USA.
- Burchart, H.F. and Frigaard, P. (1988). On 3-dimensional stability of reshaping breakwaters. Proceedings of the 21th International Conference on Coastal Engineering, Malaga, Spain, Ch 169.

Delft Hydraulics (1990). BREAKWAT, Design tool for rubble mound breakwaters. Manual.

Goda, Y., Suzuki, Y. (1976). Estimation of incident and reflected waves in random wave experiments. Proceedings of the 15th International Conference on Coastal Engineering, Ch 48.

Goda, Y. (1985). Random sea and design of maritime structures. University of Tokio Press.

Lissev, N. (1993). Influence of the core configuration on the stability of berm breakwaters. Report R-6-93, Department of Structural Engineering, University of Trondheim, The Norwegian Institute of Technology, June 1993.

Mansard, E.P.D., Funke, E.R. (1980). Proceedings of the 17th International Conference on Coastal Engineering, Ch 8.

van der Meer, J.W. (1988). Rock slopes and gravel beaches under wave attack. Doctoral thesis. Delft University of Technology. Also: Delft Hydraulics Communication No. 396.

Vellinga, P. (1986). Beach and dune erosion during storm surges. Delft Hydraulic, Communication No 372.

Zelt, J.A., Skjelbreia, J.E. (1992). Estimating incident and reflected wave fields using an arbitrary number of wave gauges. Proceedings of the 23rd International Conference on Coastal Engineering, 4-9 October 1992, Venice, Italy.

CHAPTER 136

Model Study of Reservoir Riprap Stability

Etienne P.D. Mansard¹, Michael H. Davies¹ and Octave Caron²

Abstract

A series of large scale (1:15) experiments have been undertaken to assist the Société d'Énergie de la Baie James (SEBJ) in the development of new design guidelines for riprap. The stability of revetments resting on 1:1.8 and 1:2.25 (V:H) slopes is considered. In an attempt to quantify the relative roles of stone size, gradation and armour layer thickness, these tests were undertaken with stone gradations varying from (M_{\max}/M_{\min} ranging from 1 to 10) and with armour layers both $2.2D_{n50}$ and $2.7D_{n50}$ thick.

Introduction

The La Grande Hydroelectric complex includes over 100 km of earth dykes. Over the past 15 years a small percentage of these dykes have suffered wave damage and have needed repair. (Caron et al, 1993, Levay et al, 1993 and 1994). The Société d'Énergie de la Baie James (SEBJ) was mandated to review the designs of these dykes and contracted the Canadian Hydraulics Centre (CHC) to undertake a physical model testing program. In the first phase of this study, repair schemes were developed for several dykes which have experienced damage (Mansard et al, 1994) The second phase of this study focused on improving riprap design techniques. This paper reviews some of the findings of this second phase.

In undertaking the original construction and the repair works, SEBJ has garnered extensive experience with riprap design and construction. Their experience suggests that riprap specifications based on a minimum acceptable stone size (M_{\min}), along with controls on stone gradation can provide an efficient and practical method for design, construction and quality control (Tournier et al., 1996).

1 Canadian Hydraulics Centre, Bldg. M-32, National Research Council Canada, Montreal Road, Ottawa, K1A 0R6.

2 Hydro-Québec, 75 Boul. René Lévesque Ouest, Montréal, Québec, H2Z 1A4.

Experimental configuration

The cross-sections studied in these experiments were typical designs for earth dykes in reservoirs exposed to wave action (see Figure 1). These are adaptations of the earth dyke designs used in the La Grande Hydroelectric Complex. A Froude-scaled model of these cross-sections (scale 1:15) was built in a 2m wide flume built within the Multidirectional Wave Basin (MWB) at the Canadian Hydraulics Centre. The basin configuration is shown in Figure 2. This layout allowed waves reflected by the structure to diffract and dissipate as they propagate towards the wave generator. This minimises the presence of re-reflected waves at the test section.

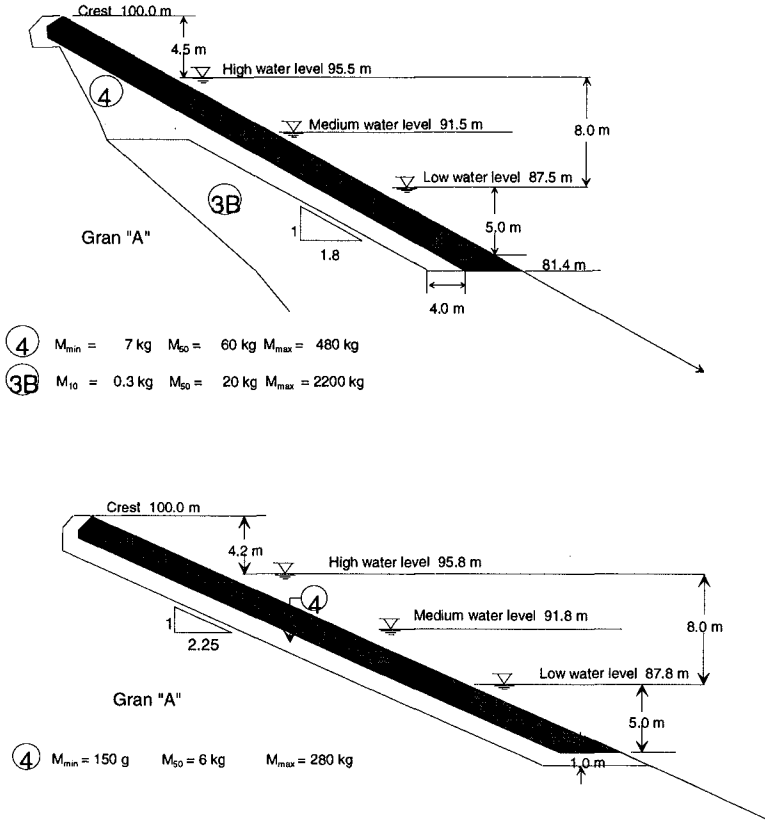


Figure 1 Cross-sections used in test program

Armour layer gradations for the model were obtained from crushed limestone from a local quarry. This rock was first mechanically sorted using the CHC's high capacity rock sizing facility. The tightly controlled gradations required for the armour layer were then obtained by individually weighing the stones from the mechanical sorting. Approximately 1 tonne of armour stone was required for each test configuration.

Test Conditions

Table 1 summarises the tests undertaken. The two slopes were both nominally designed to withstand a design storm of $H_s=2.5\text{m}$. This resulted in median stone masses (M_{50}) for the two slopes of 2600 and 2100kg for the 1:1.8 and 1:2.25 slopes, respectively. This typical design is listed at Tests 1 and 4 in Table 1. Tests were conducted with extremely uniform stone distributions where the median stone mass was set equal to the value of the minimum stone mass of the initial tests (see Tests 2, 3, 5 and 6 in Table 1). These uniform gradations of minimal stone size were tested with layers both $2.2D_{n50}$ and $2.7D_{n50}$ thick. Additional tests were also undertaken with two broader gradations $M_{\max}/M_{\min}=5$ (Test 7), and $M_{\max}/M_{\min}=10$ (Test 8) along with a final test (Test 9) with a uniform gradation ($M_{\max}/M_{\min}\approx 1$) in which the median stone mass was the same as in the original design. Tests on the typical designs were conducted at three water levels; high, medium and low, in order to establish any potential influence of overtopping and toe instability on the overall stability of the dyke.

Table 1 Test Program

<i>Test</i>	<i>Slope</i>	<i>M</i> ₅₀ [kg]	<i>D</i> _{n50} [m]	<i>Armour layer</i> <i>thickness, t_a</i> [m]	<i>Filter layer</i> <i>thickness [m]</i>	<i>Gradation</i> <i>M_{max}/M_{min}</i>	<i>Elevation of</i> <i>SWL [m]</i>
1	1:1.8	2600	0.99	2.2 (2.2) <i>D</i> _{n50}	1.9 (1.92 <i>D</i> _{n50})	2.5	95.5, 91.5 and 86.5m
2	1:1.8	1500	0.82	2.2 (2.7) <i>D</i> _{n50}	1.9 (2.32 <i>D</i> _{n50})	1	91.5
3	1:1.8	1500	0.82	1.8 (2.2) <i>D</i> _{n50}	1.9 (2.32 <i>D</i> _{n50})	1	91.5
4	1:2.25	2100	0.92	2.0 (2.2) <i>D</i> _{n50}	1.5 (1.63 <i>D</i> _{n50})	2.5	95.8, 91.8 and 87.8 m
5	1:2.25	1200	0.76	2.0 (2.7) <i>D</i> _{n50}	1.5 (1.97 <i>D</i> _{n50})	1	91.8
6	1:2.25	1200	0.76	1.6 (2.2) <i>D</i> _{n50}	1.5 (1.97 <i>D</i> _{n50})	1	91.8
7	1:1.8	2600	0.99	2.2 (2.2) <i>D</i> _{n50}	1.9 (1.92 <i>D</i> _{n50})	5	91.5
8	1:1.8	2600	0.99	2.2 (2.2) <i>D</i> _{n50}	1.9 (1.92 <i>D</i> _{n50})	10	91.5
9	1:1.8	2600	0.99	2.2 (2.2) <i>D</i> _{n50}	1.9 (1.92 <i>D</i> _{n50})	1	91.5

Note: Tests were performed at a scale of 1:15, the structures had a crest elevation of 100.0m, and the basin floor was at elevation 59m. This table reflects target values for gradations and armour layer thickness.

Figure 1 shows the three water levels tested. Water depths and freeboard (the vertical distance between the still water level and the crest of the structure) were varied in the tests to cover the full range of likely operating conditions for the reservoirs. Table 1 lists the water depth for each test. The majority of the tests reported here were conducted at the medium water level, that is with a water depth of 32.5m and a freeboard of 8.5m. This represents a non-overtopping condition for the design wave height of $H_s=2.5\text{m}$, and the structure's behaviour approaches that

of a uniform, infinite slope. The milder 1:2.25 sloped structure required a slightly lower stone mass for stability and required less freeboard to minimise overtopping (i.e. 4.2m instead of 4.5m).

Wave conditions used in test program

All sea states used in this study were irregular waves based on the JONSWAP spectrum ($\gamma=3.3$). Waves were synthesised using the method of random phases as described in Funke et al (1988). The time series of each sea state was chosen to be rather long in order to minimise any statistical variability of wave parameters associated with short records. The length of time series corresponded therefore to two hours of storm duration at prototype scale, containing approximately 1100 to 2600 waves depending on wave period (see values of N in Table 2). This choice of long records also ensured that the wave heights fit a Rayleigh distribution. The ratio of H_{\max}/H_s was between 1.8 and 2.0 for all sea states. Table 2 summarises the wave conditions used in this study.

Wave Calibration

Generally, waves are calibrated in the basin (with an efficient absorber in place) prior to building the breakwater. During the testing program (with the breakwater in place) reflection analysis is performed on the measured wave records to separate the incident and reflected significant wave heights. Since the design of the 2 m section within the 30 m wide basin ensured a good diffraction zone for minimising the re-reflected components (see Figure 2), good agreement was obtained between the incident wave heights measured during calibration and those measured during the testing program. (This comparison can be found in Mansard et al, 1994). This good agreement, in conjunction with the CHC technique for dynamic wave machine calibration, allowed the use of the reflection analysis results (with the structure in place) for establishing incident wave conditions during the tests. Furthermore, during this testing program, CHC had developed and validated a new algorithm that can provide not only the significant wave heights but also the statistics of the incident wave train (Mansard, 1994).

Experimental Procedure

Testing involved the exposure of the structure to a sequence of wave conditions of increasing severity. Testing started at a 'no-damage' wave height and built in 0.5 m wave height increments to a wave height sufficient to cause major damage to the revetment (see Table 2). Each sea state that induced damage to the breakwater was run for approximately 5000 waves (corresponding to 8 hours of storm duration). For this test program, sea states with $H_s < 2.0$ m did not cause any significant damage to the structure.

The 5000 wave duration was chosen to represent relatively long-term exposure at each storm level. This is supported by the work of Thompson and Shuttler

(1975) and by van der Meer (1988) who both show damage evolution varying logarithmically with time and reaching roughly 80% of the maximum possible damage levels within 5000 waves.

Table 2 Wave conditions used in testing.

H_{m0} [m]	T_p [s]	Number of waves per cycle, N	Number of cycles tested	Total number of waves, N_{tot}
1.0	4.0	2600	1	2600
1.5	5.0	1750	1	1750
1.75	5.4	1613	1	1613
2.0	6.0	1487	4	5948
2.25	6.4	1377	4	5508
2.5	6.75	1328	4	5312
2.75	7.25	1239	4	4956
3.0	7.5	1162	4	4648

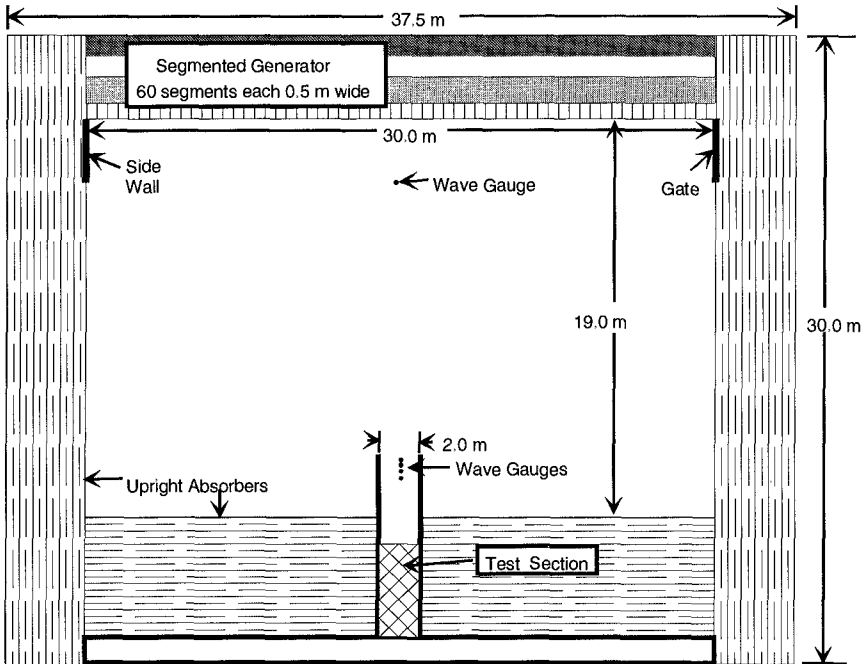


Figure 2 Test layout in Multidirectional Wave Basin

Measurement of damage

During construction of the underlayer and the armour layer the NRC electro-mechanical profiler was used to ensure model tolerances were met. This profiling system is described in Davies et al, 1994. This instrument uses a contact wheel on a pivot arm which is mounted to a traversing carriage. High-precision potentiometers

are used to measure the horizontal and vertical location of the contact wheel on the revetment slope. The slope is located using a counter-balanced mechanical contact wheel. This technique provides profiles of the structure accurate to within ± 2 mm and can be used either above or below the water line. This avoids the need for either draining or flooding the basin as is common with other techniques such as acoustic or electrical resistivity methods.

Profiles are analysed to determine the eroded cross-sectional area, A , by comparing the damaged profile at the end of each storm sequence to the original profile. The damage index, S , is then calculated as:

$$S = A/D_{n50}^2 \quad \text{where } D_{n50} = \sqrt[3]{M_{50}/\rho_s} \quad \text{Equation 1}$$

where ρ_s is the density of the armourstone [kg/m^3]. Damage was also measured by counting the number of stones displaced. For low damage levels these two methods provide comparable results (see Davies et al, 1994), while for high damage levels, the counting of stones become impractical.

Another damage index used in this study is the concept of depth of cover, d_c , presented in Davies et al (1994). This index provides a measure of the thickness of protection that remains on the breakwater section after every storm sequence rather than the area eroded from it. It is calculated as the minimum slope-normal armour layer thickness within the zone of wave action. This is based on the measured armour layer profile and the profile of the filter layer obtained during construction. Viewing damage in terms of the depth of cover remaining on the structure can facilitate the interpretation of the results, particularly if the breakwater sections is not a classical 2-layered section.

Test results for typical design revetment

Figure 3 shows typical damage progression for the 'typical revetment', with $M_{\max}/M_{\min}=2.5$ results are presented in terms of the damage level, S as a function of the cumulative number of waves to which the structure was exposed. Note that only the data at high and medium water levels are shown here since a different test protocol was followed for the low water level test. The low water level test was carried out only at the design wave height mainly to verify that there was no toe instability when the level of protection extends to 2 times the design significant wave height below the low water level.

Figure 3 shows that the damage progression curves for the 1:1.8 sloped structure are similar at the high and medium water levels. During the $H_s=3.0\text{m}$ test at the high water level, reduced damage levels were observed. This is possibly attributable to the high degree of overtopping observed during this test.

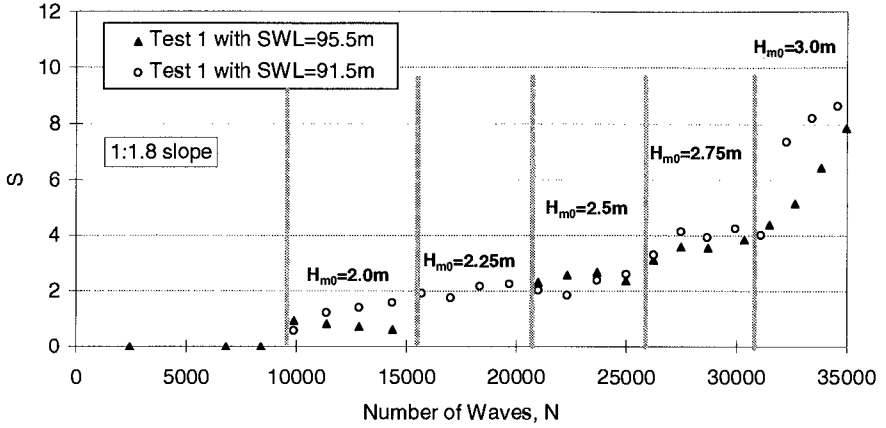


Figure 3 Damage progression for 1:1.8 slope - typical revetment (Test 1).

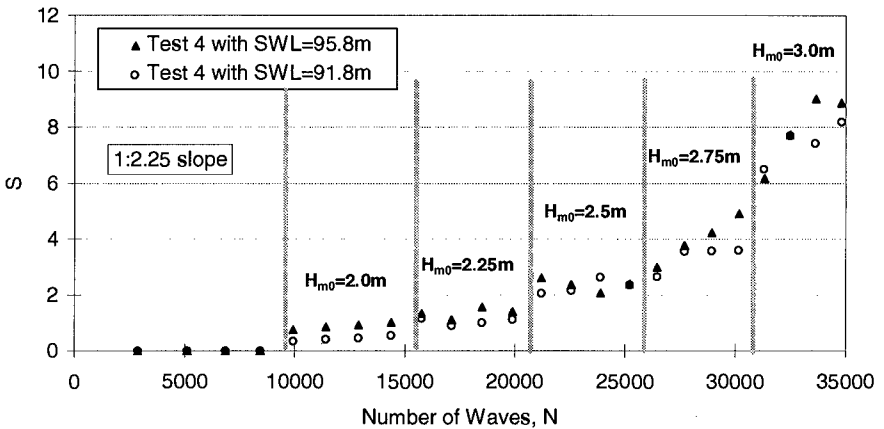


Figure 4 Damage progression for 1:2.25 slope - typical revetment (Test 4).

Similar damage evolution curves were observed for the mild sloped structure. Figure 4 shows the good agreement between the high and medium water level results for a 1:2.25 slope.

The Shore Protection Manual (SPM 1977, 1984) uses Hudson’s formula to evaluate riprap stability as a function of stone size, incident wave height, and structure slope. Using the stability number, $H_o = H_s / (\Delta D_{n50})$, Hudson’s relationship can be expressed as:

$$S = \varphi \left(\frac{H_o^3}{\cot \theta} \right)$$

The coefficient, K_d is the threshold for the onset of damage, commonly taken to be at $S=2$. K_d is the value of $H_o^3/\cot \theta$ at $S=2$. Figure 5 presents the S values, obtained after 5000 waves at each sea state, plotted as a function of $H_o^3/\cot \theta$. Through inclusion of the structure slope, θ , in the abscissa, both the steep and mild sloped structures can be viewed on the same plot. Results from the low water level test are also included in this figure. It can be seen from this figure that for a damage equivalent to $S = 2$, the K_d value ranges between 1.2 to 1.7. Note that this value of K_d is based on the significant wave height (H_s) of the sea states and not on the value of $H_{1/10}$ proposed in the Shore Protection Manual of 1984. Davies et al (1996) compared these experimental results with predictions using the formulae of van der Meer (1988). A good match between measured and predicted values exists for values of van der Meer's permeability factor P around 0.14. Here, the van der Meer formula was applied with $N=5000$ waves. For a more exact comparison, the cumulative effects of antecedent storm conditions should be included.

Overall results

The results discussed so far correspond only to the first test series where graded revetment with $M_{max}/M_{min} = 2.5$ was used. A similar comparison of the entire dataset in one figure is difficult because of differences in the stone masses, stone gradation and layer thicknesses listed in Table 1. Furthermore, the damage index S discussed above is the eroded area normalised by the square of the nominal diameter of the stone which is also different in the subsequent tests. It is possible, however, to review the ensemble of the results using simpler parameters such as eroded area, A , and significant wave height, H_s .

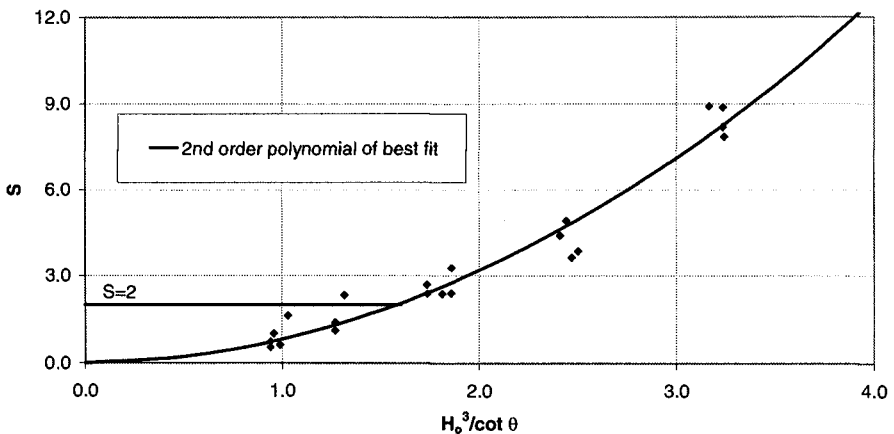


Figure 5 Damage S vs $H_o^3/\cot \theta$ - results for both Test 1 (1:1.8 slope) and for Test 4 (1:2.25 slope).

Figure 6 shows the values of A vs H_s for all the structures listed in Table 1. Note that for the graded revetment the averages of the values obtained during high and low water levels are presented here. This figure shows that the eroded area remains nearly the same for all configurations -- there is little difference in the values of the eroded area of the structures $2.2D_{n50}$ thick, whether they are made up of uniform or graded revetment. There is however a trend for the eroded area to be smaller when the layer thickness increases from 2.2 to $2.7D_{n50}$. The following sections provide different interpretations of the dataset which more clearly illustrate the effects of these various parameters.

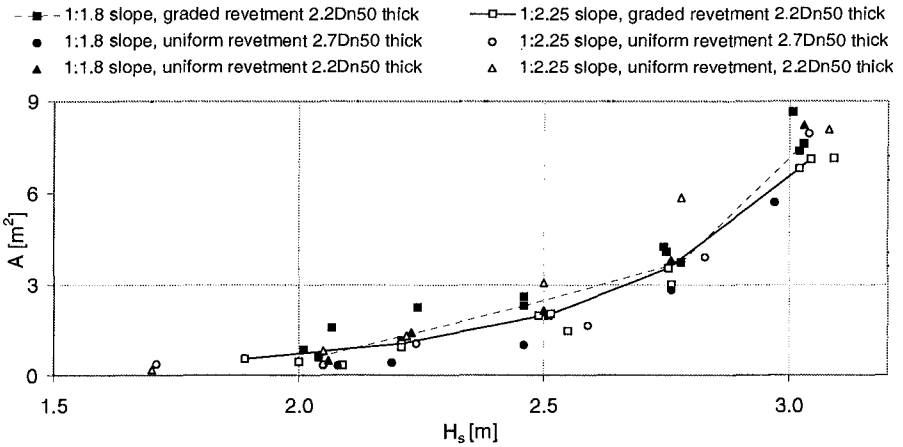


Figure 6 Eroded area, A vs significant wave height, H_s .

Effect of uniform gradation

Figure 7 presents the results of the graded and uniform revetments $2.2D_{n50}$ thick in terms of S versus $H_o^3/cot \theta$ for the 1:1.8 slope. Here, we have not included test results performed with the reduced median mass (i.e. Tests 2 and 3). Tests 2 and 3 were performed using the same filter layer geometry as the rest of the tests, consequently, the relative permeability of these tests is higher (i.e. the ratio of filter layer thickness to D_{n50} is larger for these tests). This figure shows a trend for uniform revetments to provide higher stability. The influence of gradation is small, particularly at low damage levels. Values of M_{max}/M_{min} between 10 and 2.5 all show quite similar stability. For extremely narrow gradations (M_{max}/M_{min} approaching 1), stability is seen to increase.

Figure 8 shows the influence of gradation in terms of the value of $H_o^3/cot \theta$ required to cause a given damage level ($S=2$ and $S=8$). This figure shows that the extremely uniform gradation is more stable than the broader gradations. Similar analysis was undertaken by van der Meer (1988) – in considering two gradations

(equivalent to M_{max}/M_{min} of 11 and 2) he concluded that gradation had “no or minor influence on the stability and that, within this range, the armour layer can be described simply by the nominal diameter, D_{n50} ”. The present work is in general agreement with these findings, however, these results show that for extremely narrow gradations ($M_{max}/M_{min} < 2.5$) the gradation can significantly improve stability.

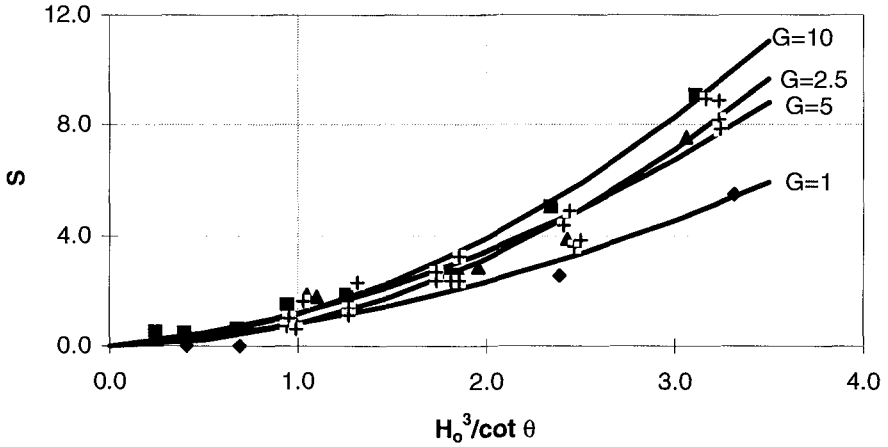


Figure 7 Influence of gradation, 1:1.8 slope (Tests 1, 7, 8 and 9)

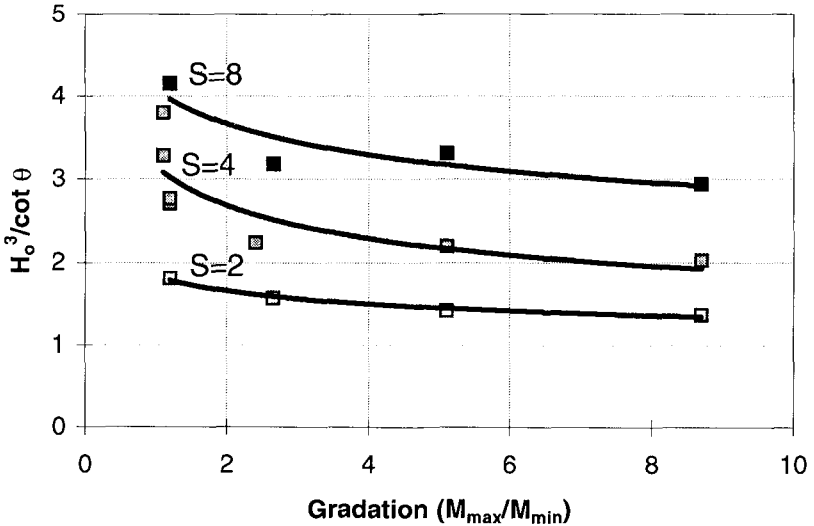


Figure 8 $H_o^3/cot \theta$ to cause a given damage level as a function of gradation (Tests 1, 7, 8 and 9).

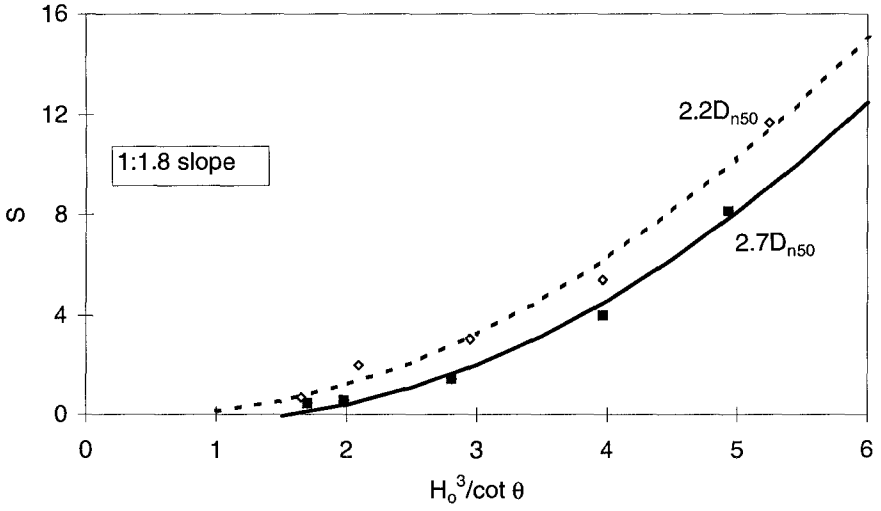


Figure 9 Effect of layer thickness for 1:1.8 slope (Tests 2 and 3).

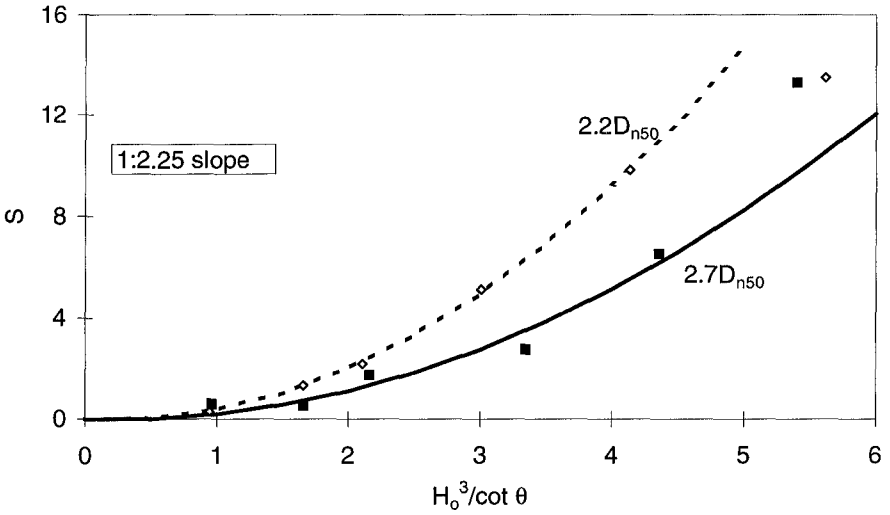


Figure 10 Effect of layer thickness for 1:2.25 slope (Tests 5 and 6).

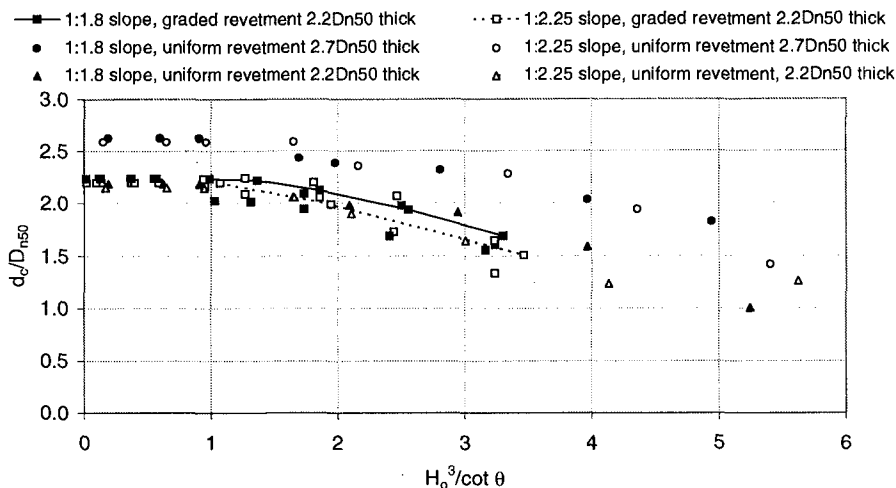


Figure 11 Response in terms of depth of cover, d_c

Effect of layer thickness

Figures 9 and 10 show the effects of layer thickness for the steep and mild slopes, respectively. All other test conditions were held constant for these tests so that layer thickness is the only variable. It can be seen that the thicker armour layer ($2.7D_{n50}$) provides better stability. This is as would be expected through the influence of permeability – as layer thickness increases, the ability of the slope to ‘absorb’ wave-induced flows increases.

The influence of layer thickness can also be viewed in terms of the depth of protection, d_c . Figure 11 presents the depth of protection normalised with respect to the nominal median diameter, d_c/D_{n50} as a function of $H_o^3/cot \theta$. As one would expect, the tests with greater layer thickness show a smaller loss in the depth of protection compared to its counterparts with two layers. Furthermore, the remaining protection on the structure is also higher – that is, not only are the damage levels lower (i.e. the amount of material removed is reduced) but, by virtue of the three-layer thickness, the structure can tolerate a higher damage level before the underlayers are endangered.

Conclusions

This study has led to the creation of a large-scale dataset on revetment stability. The parameters S and $H_o^3/cot \theta$ have been seen to accurately describe the revetment stability. The results for the typical revetment design lead to values of K_d ranging between 1.2 and 1.7 (for a damage level of $S=2$). In establishing these K_d values the median mass of the revetment and the significant wave heights of the sea states were used.

Uniform stone distributions have been shown to provide better stability than graded revetment. However, the influence of gradation is small for ratios of M_{\max}/M_{\min} between 2.5 and 10. For uniform stone distributions, increased layer thickness reduces actual damage levels and increases tolerable damage levels. This response is described well by the remaining depth of cover, d_c .

Application of these test results into practical design techniques for dam revetment have been undertaken by the Société d'énergie de la Baie James and are presented by Tournier et al (1996).

Acknowledgements

This study is the result of close cooperation between Hydro-Québec, the Société d'Énergie de la Baie James, and the Canadian Hydraulics Centre. In particular, the authors would like to thank J. Levay, J-P. Tournier and P. Dupuis of SEBJ for their support throughout this study and for their comments in reviewing this paper. The technical support of Dave Watson (CHC) was key to the successful completion of this study.

References

- Caron, O., Dupuis, P., and Tran Van, T. (1993). *The hydraulics of riprap design applied to the repairs of dams and dykes of the La Grande Hydroelectric Complex, Phase I*. Proceedings of the 5th Canadian Dam Safety Conference, CDSA-CANCOLD, St. John's, Nfld, Canada, Sept. 1993, pp. 121-135.
- Davies, M.H., Mansard, E.P.D., and Cornett, A.M. (1994). *Damage Analysis for Rubble-mound Breakwaters*. Proc.24th ICCE Conf., Kobe, Japan, pp. 1001-1015
- Davies, M.H., Mansard, E.P.D., and Parkinson, F.E. (1996). *Études sur modèles de la stabilité des concepts types*. Controlled Technical Report, Canadian Hydraulics Centre, National Research Council of Canada, HYD-CTR-007
- Funke, E.R., Mansard, E.P.D., and Dai, G. (1988): Realizable wave parameters in a laboratory flume. Proc. 21st ICCE, Spain, June.
- Levay, J., Tournier, J-P., Arès, R., and LeBoeuf, D. (1993). *Riprap stability studies on dams and dykes of the la Grande Complex (Phase I)*. Proceedings of the 5th Canadian Dam Safety Conference, CDSA-CANCOLD, St. John's, Newfoundland, Canada, September, 1993, pp. 137-150.
- Levay, J., Caron, O., Tournier, J.P. and Arés, R. (1994). *Assessment of riprap design and performance on the La Grande Complex - James Bay, Québec*. Transactions of the 18th Congress on Large Dams, ICOLD, Durban, South Africa, Vol. 1 (Q.68,R.25), pp. 369-389.
- Mansard, E.P.D.(1994). *On the estimation of the incident wave train from reflection analysis*. Proc. 9th Congress, Asian Pacific Division, IAHR, 24-26 Aug., Singapore.

- Mansard, E.P.D., Davies M.H, Caron, O. and Parkinson F.E. (1994). *Model study of riprap stability under wave action at the LG3 Reservoir, La Grande Hydroelectric Project*. Proc. of Seminar on Case Histories for the Design, Construction and Maintenance of Rubble-mound Structures, Eureka, Calif., USA.
- SPM, 1977 and 1984 *Shore Protection Manual*, Coastal Engineering Research Centre, U.S. Army Corps of Engineers, 3 volumes.
- Thompson, D.M., and Shuttler, R.M. (1975). *Riprap design for wind wave attack – A laboratory study in random waves*. HRS, Wallingford, Report EX707.
- Tournier, J-P, Dupuis P, and Arès R. (1996). *An improved design method for the riprap of earthfill dams of large reservoirs*. Proc.25th ICCE Conf., Orlando USA
- van der Meer, J.W. (1988). *Rock slopes and gravel beaches under wave attack*. Delft Hydraulics Publication No. 396.

CHAPTER 137

PROTOTYPE MEASUREMENTS OF WAVE PRESSURES ON A WAVE SCREEN: COMPARISON TO PHYSICAL AND ANALYTICAL MODELS

Martin¹, F. L., Losada², M. A., Vidal³, C., Diaz Rato⁴, J.L.

ABSTRACT

The results of a field campaign of measurements of pressures on a prototype wave screen are analyzed and compared to the results of laboratory tests and to the calculation methods proposed by Jensen, 1984, Günbak et al., 1984, and Martin et al. 1995. Both the field campaign data and the lab tests results seem to fit quantitatively better to the method of Martin et al. than to other proposed formulae. Moreover, the proposed modelization and description of the process employed to develop the method of Martin et al., 1995, are consistent to the measured pressure profiles and time-pressure series.

INTRODUCTION

Most of the rubble-mound breakwaters have a crown wall on their top. These superstructures may help to control wave overtopping and to limit the height of the main layer. Moreover, they may provide access to the breakwater and give support and protection to wiring and pipelines along the breakwater crest. There are few methods to evaluate wave forces on wave screens: Iribarren et al., 1964, Günbak et al., 1984, Jensen, 1984, revisited by Bradbury et al., 1988, and Pedersen et al., 1992, Martin et al. 1995. However, others consider physical modelling as the unique reliable method. The Spanish experience is that the wave screens may withstand without failure higher waves than expected by using Engineering methods.

¹ *Asistant Professor, ² Professor, ³ Associate Professor.
Ocean and Coastal Research Group. University of Cantabria. 39005 Santander (Spain).*

⁴ *Engineer in chief. Port Authority of Gijón. Claudio Alvargonzalez s/n. Gijón (Spain)*

The main objectives of the present paper are (1) to describe the instrumentation of the Gijón breakwater wave screen and (2) to compare the prototype measurements to model test and to several formulae being used in the engineering practice.

In this paper the reader will find a brief description of the field campaign, the lab tests and the engineering methods employed in the comparison, then a qualitative check of the hypothesis employed in the calculation methods by analyzing the measurements and finally a quantitative comparison of results.

PROTOTYPE INSTRUMENTATION AND MEASUREMENTS

Gijón is located at the Cantabrian Sea, in the north of Spain (fig. 1). It is exposed to sea states from N-NW, which are the most severe sea states in that zone. The 100-year return period significant wave is 10.5 m which can lead to wave heights greater than 18 m.

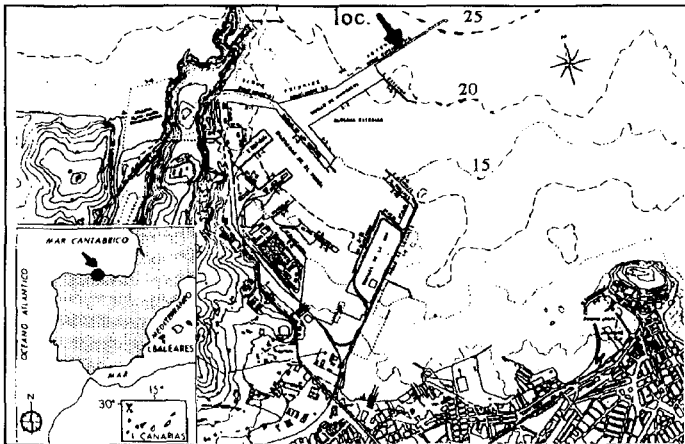


Fig. 1. Prototype location.

Three wave recorders (W1-W3) were installed in front of the breakwater to be able to separate the incident and the reflected wave trains. One directional wave recorder (W4) is placed at the leeside of the instrumented section to identify the transmitted energy across the breakwater and the diffracted energy around the breakwater head. Five specially designed pressure gages were placed in the wall front (P1-P5), while three pressure cells were drilled across the wall basement to record the uplift pressures (S1- S3) (fig. 2). Moreover, there are two wave riders installed close to the breakwater by Puertos del Estado (Ministry of Public Works) continuously recording wave heights and periods.

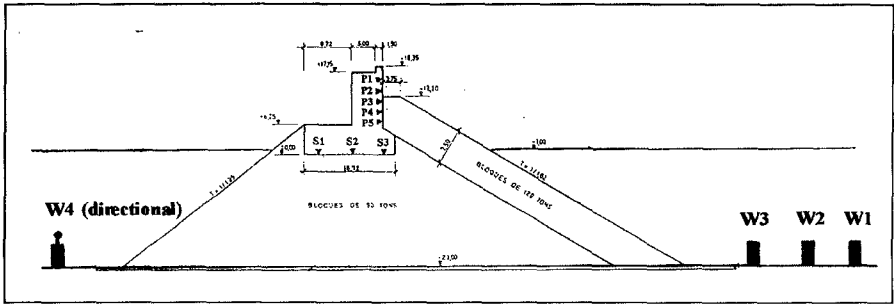


Fig. 2. Instrumentation setup.

The sampling rate of pressures in the wave screen is 20 Hz, which is enough to record the main characteristics of interest of the time-pressure series being researched. The system is continuously logging data in 45-min. bursts. After the burst is finished, the system checks if a given minimum level of pressures is exceeded. If so, the data is stored and if not, it is deleted.

The sampling rate for the wave recorders is 0.5 Hz. Notice that, for a 16-second wave period this data rate gives 8 data/wave period which is enough to define the wave shape. Waves shorter than 8 seconds will be underdefined, but their forces on the wave screen are not expected to be noticeable. Moreover, the wave recorders are fixed in 25 m water depth, and the information of short period waves in this depth will be strongly affected by the difficult-to-define pressure/free surface oscillation transfer function.

The system was set up in February 95 and is still working. During the February-April 1995 period, two storms of $H_s = 5.9$ m and 4.5 m respectively were recorded. In the second period (December-April, 1996) two more storms were measured corresponding to 6.0 m and 5.2 m significant wave height. Due to the tidal level at the instant of maximum wave height only three of these four storms produced significant pressures on the wave screen. The selected storms are described in Table 1. The tidal level is defined above the zero datum (minimum low tide level)

Date	Signif. wave height	Peak period	Tidal level
16/2/95	5.9 m	20 s	4.1 m
10/2/96	6.0 m	19 s	3.9 m
19/2/96	5.5 m	16 s	4.3 m

As the system is to exposed to the natural and port labour actions, some measuring problems appeared in different instants of the field campaign: some electrical noise in the signal and power outages in the initial months, lightning which hit the amplifiers and affected almost all of the system, etc. In figure 3, an abstract of the field work development and incidences is represented.

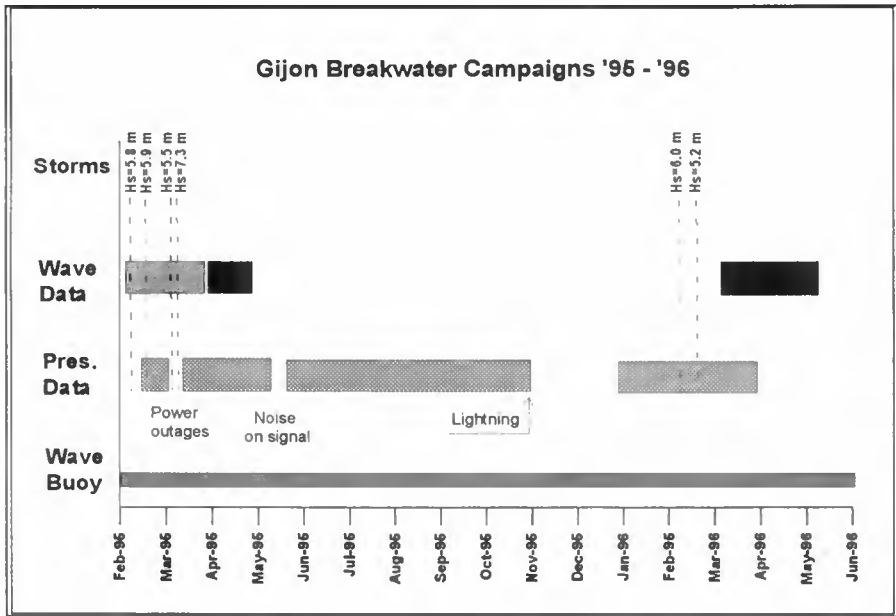


Figure 3. Field campaign schedule and incidences

LABORATORY EXPERIMENTAL SETUP

Model scale lab tests tests were conducted in the 70 m long, 2 m wide, 2 m high wave flume at the Oceanographical and Coastal Engineering Lab at the University of Cantabria. The test model consists of a 1/90 scale section of the Príncipe de Asturias breakwater at Port of Gijón (Spain) shown in figure 2. This breakwater has a wave screen based at low tide level (0.0) and crowned 18.3 m above. The main layer is built of 120-Ton parallelepipedical blocks, and the core is built of 90-Ton blocks. The water depth was set to correspond to high tide level in the prototype. Regular cnoidal waves were generated by a piston-type wavemaker. Wave heights ranging from 9 to 13.5 m and periods from 11 to 17 s were tested. Moreover, irregular wave series were generated. The irregular wave characteristics are represented in Table II.

Table II. Model scale 1/90. Irregular wave series.

Significant wave height	4 m	6 m	8 m	10 m	12 m
Peak period	12 s	14 s	16 s	18 s	20 s

Free surface in front of the structure was measured by three resistance gages and a reflection analysis of the free surface time series was done. By using this technique it is possible to obtain the incident and the reflected wave height. The transmitted wave height was measured by one free surface gage located 1 m from the lee side toe of the breakwater. Four strain-gage type pressure gages were installed in the wave screen basement while eight gages were fixed to the structure front.

One of the main targets of the tests was to identify and quantify the effect of the berm length on the resulting pressures. Three berm lengths were tested, corresponding to the length of 1 mound unit, 2 units and 3 units. Two types of parallelepipedic blocks were used corresponding to 90 and 120 tons.

ENGINEERING ANALYTICAL METHODS

There are few methods available for the calculation of forces on wave screens, some are mainly analytical: Iribarren et al., 1964, which largely overpredicts the resulting pressures, and Günbak et al., 1984; some are mainly experimental: Jensen, 1984, revisited by Bradbury et al., 1988, and Pedersen et al., 1992, which makes a probabilistic approach to the horizontal forces (not pressure distributions or uplift forces). The parametrization selected in Jensen, 1984, generates a relatively large dispersion in the results, and Bradbury et al., 1988, found that the influence of wave period on the resulting forces is not represented adequately.

Generally speaking, the response of the built wave screens reveals that the calculating methods available overpredict the wave induced forces, with the related influence on the construction costs. Therefore, it is clear that a deeper study of these forces was needed. The Ocean and Coastal Research Group of University of Cantabria has been working for several years in the conceptualization of the process and the study of the procedures of momentum transfer between a bore and a vertical surface. Finally, Martin et al. (1995) developed a new method for the calculation of the pressure profiles acting in the wave screen front and base due to bores hitting the superstructure in the run-up process.

From the results of the experimental study conducted at the Oceanographical Eng. lab at University of Cantabria (Losada et al. 1995, Martin, 1995) it can be concluded that two maxima of force occur due to each single wave; the former peak is generated during the abrupt change of direction of the bore front due to the wave screen (horizontal decelerations), while the latter maximum occurs after the instant of maximum run-up and is related to the vertical acceleration of the water mass piling in front of the wave screen (early Run-down movement).

The distinct nature of these force peaks is well revealed in the vertical distribution of pressures. In figure 4 an interval of the time-force curve obtained from lab tests is shown, and the two force maxima (A and B) are pointed out. The vertical distribution of pressures at the wall in the instants A and B are shown in the same figure. The pressures due to the first peak (A), hereafter denoted as Shock pressures (P_s), present an almost vertically uniform profile, where two zones are well distinguished: the upper zone, not protected by the rubble-mound layer, and the lower zone, protected by the rubble-mound layer. The pressure profile due to the second peak (B), hereafter denoted as Reflecting pressure (P_r), grows vertically with an almost constant increasing factor, always equal to or smaller than ρg . Martin et al., 1995, proposed a method to calculate the pressure profiles in the two instants of maximum force (P_s, P_r).

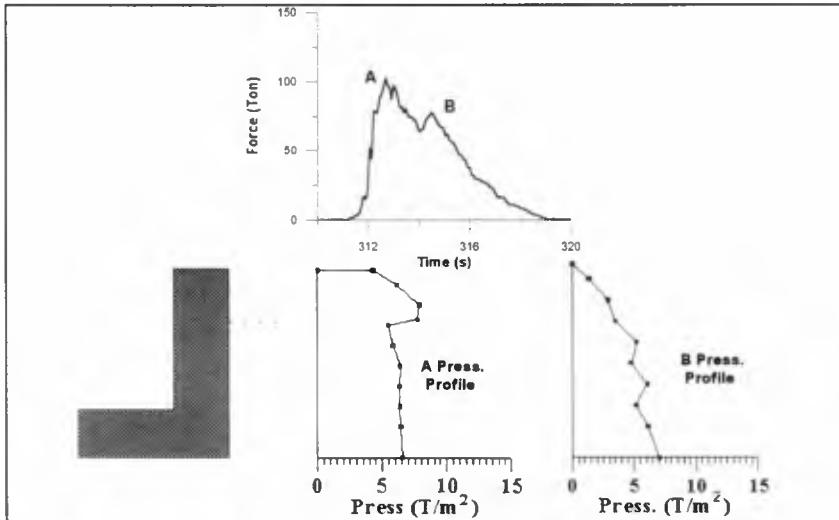


Figure 4. Force-time series and pressure profiles in instants A and B.

In this paper, the results from the lab and field campaigns are compared to the methods proposed by Jensen, 1984, Günbak et al., 1984 and Martin et al., 1995. The methods of Martin et al., 1995, and Günbak et al., 1984, are defined wave to wave and provide the pressure profiles in the maximum force instant, while the method of

Jensen provides the force of 0.1% of probability of occurrence under a given sea state defined by the significant wave height (H_s). As was said before, the method proposed by Jensen neither predicts the pressure profiles nor the uplift pressures and therefore, can not be used to predict the overturning momentum on the wave screen.

QUALITATIVE COMPARISON OF RESULTS

This comparison is done in order to achieve two main targets: 1) To make a qualitative check of some of the hypothesis in which the methods of Günbak et al., 1984 and Martín et al., 1995 are based and; 2) To identify any possible qualitative scale effects between lab and prototype results. To do that, comparison of force-time series and pressure profiles measured in the field campaign, in the lab and proposed by the methods, are done.

In figure 5, a brief interval of force-time series measured in the lab is presented. The wave train characteristics are $H_s = 9.0$ m and $T_p = 18$ s and the tests were done with a tidal elevation of 4.0 m above the zero datum. In this figure, two impinging wave forces are pointed up. The former (time 310-320 s) shows a double peak pattern while the latter (447-457 s) shows a single peak pattern. The only difference between the two impinging waves was the Run-up height. The former wave, slightly larger wave height and period, produced a Run-up tongue which overcame the main layer berm level (Ac) while the latter almost reached the level Ac.

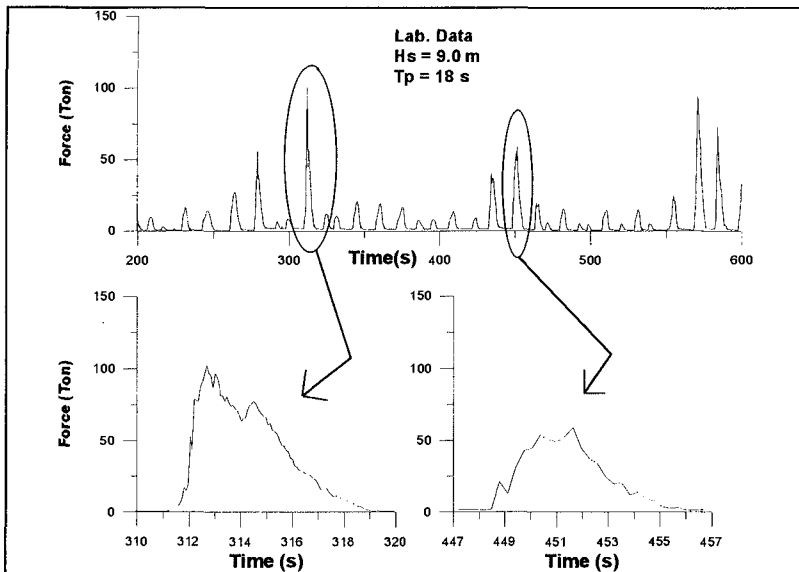


Figure 5. Experimental time-force series.

If the main layer units can stand the rush-up wave action, most of the bore front horizontal momentum is transmitted to these units, in the region below A_c . If the bore does not overcome A_c level, the former peak of force (shock pressures) is smoothed, with only more or less noticeable pressure oscillations appearing, depending on the berm length and main layer porosity. The second peak (reflecting pressure) always occurs because it is generated by the water mass piled by the wall developing a pseudohydrostatic pressures profile.

In Günbak et al., 1984, only one maximum force situation obtained as the sum of the shock and reflecting pressures is defined. These two pressure maxima occur at different instants in the evolution of the bore and are due to different processes that must be analyzed separately.

From lab tests over regular shaped breakwaters (uniform slopes 1:1.5- 1:2, main layer porosity ranging 0.3-0.4) it can be estimated that shock pressure maximum of force is expected to appear in the cases when $H_s/A_c \geq 0.7$. Of course, this value heavily depends on the Run-up and thus, on the breakwater characteristics.

In the case of Gijón Breakwater, A_c level is 12 meters above the zero datum. In high tide situations (+4.0 m), the berm freeboard is 8.0 m. Thus, shock pressures are expected to occur for significant wave heights above $0.7 \times 8.0 = 5.60$ m. In figure 6, a pressure-time series corresponding to gages P3, P4 and P5 in the prototype front are represented. These series were measured during the storm on February 10, 1996. Recalling Table I, the characteristics of this storm were $H_s = 6.0$ m and $T_p = 19$ s. In the instant of the measurements shown in fig. 6, the tide level was 3.9 m.

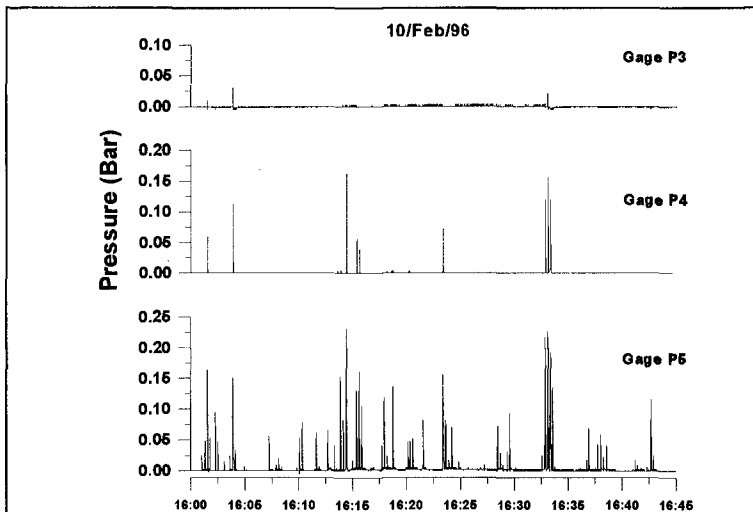


Figure 6. Pressure-time series measured in the prototype front face.

Figure 6 shows that only three waves reached gage P3 (0.4 m below Ac level) in 45 minutes. This is consistent with the test results in 1/90 scale model under $H_s = 6.0$ m, where bores do not overcome Ac level.

One of the main hypotheses introduced in Martín et al., is the assumption that the basic run-up tongue characteristics (thickness, bore front velocity, etc...) on breakwaters with wave screens are similar than those in bores running-up on infinite slopes and, thus, the effect induced by the presence of the wave screen can be neglected. Under this assumption, the classical Run-up formulae can be employed. As an example, estimating $Ru \approx H$, the maximum run-up in a given sea state can be calculated. A sea state of $H_s = 6.0$ m and 150 waves (45 minutes of storm on 10/2/96) will lead in maximum waves about 8-9 meters. These waves would run-up 8-9 meters above the SWL (4.0 m tidal level) and merely reach the Ac level. This is consistent with the prototype measurements. Although this comparison is rough, it can be used as a engineering check of the hypothesis. The Run-up on rough permeable slopes is a process with high experimental variability, and all engineering formulae for Run-up are "best fit" methods. The hypothesis included in Martín et al., can not be experimentally distinguished from the experimental "noise".

In figure 7, a stretching of the previous fig. 6 is done in order to show three wave actions. It can be noticed that the shock pressure peak is not clear and only some pressure oscillations appear. These measurements are as expected because the ratio H_s/Ac in this storm is around the 0.7 limit. Once again, this is consistent with the lab results and the modeling of the double peak effect done in Martín et al., 1995.

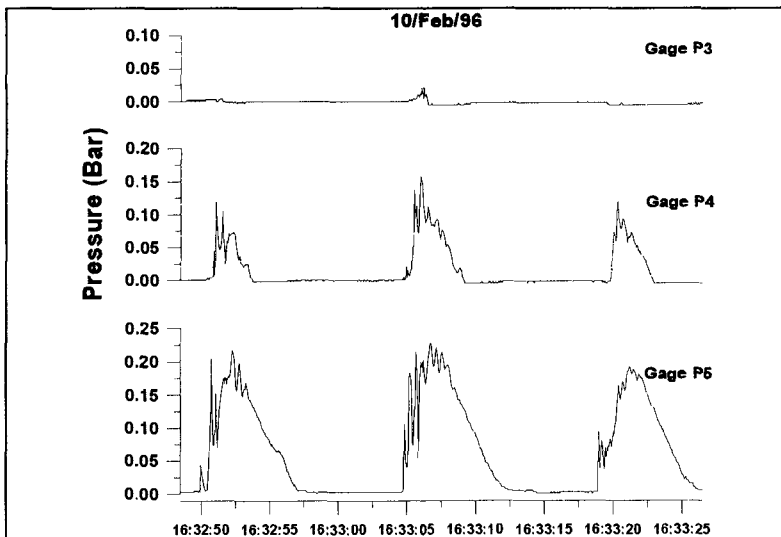


Figure 7. Pressure-time series in prototype.

Finally, the vertical profiles of pressure due to a selected single wave of 8.3 m height and 16.2 s period measured in the prototype, measured in the lab and proposed by Martin et al., 1995 were compared. The results are shown in figure 8. It can be noted that the shock pressures profile is quite similar in the prototype and in the lab, and fits the homogeneous vertical distribution proposed for shock pressures in Martin et al., 1995, quite well. Generally speaking, the total force produced by the shock oscillations in the cases when $Ru < Ac$ are low and smaller than the reflecting force. In Martin et al., when $Ru < Ac$, it is assumed that the shock forces are always smaller than the reflecting forces and can be neglected.

In the reflecting pressures there are some differences between the quantitative values of the measuring points in the lab and in the prototype, but the overall trend of the pressure profile is quite similar. Notice that this comparison is done in qualitative terms. It is easy to understand the difficulty of make a deterministic comparison between the results in the prototype and the lab, trying to simulate exactly the same wave height, period, tidal condition, etc...

The dashed lines in Figure 8 show the proposed reflecting pressure by Günbak et al., 1984 and Martín et al., 1995. The overall trend is well simulated by both methods, but the profile proposed by Martín et al., 1995, fits better the actual quantitative values measured.

As a result of the quantitative comparison, it can be concluded that there are not large and noticeable qualitative scale effects between lab and prototype results, and that Martin et al., 1995, method adequately represents the main characteristics of the process.

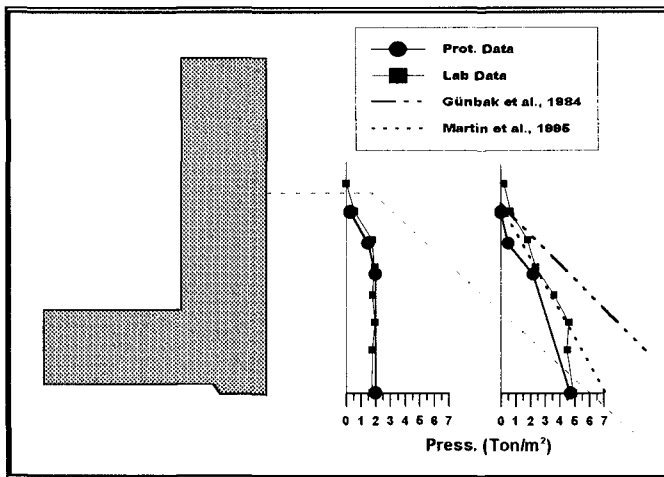


Figure 8. Pressure profiles in prototype, lab tests and analytical methods

QUANTITATIVE COMPARISON OF RESULTS

As the method proposed by Jensen, 1984, provides the 0.1% probability force, this force has been selected as a comparison parameter. In figure 9 the net 0.1% horizontal force given by the lab tests, the methods from Jensen, Günbak et al. and Martin et al., and the three storms measured up to now in the prototype are given.

The method from Jensen is basically empirical and must be applied using some experimental parameters. In this case, it is applied using the experimental data collected by Pedersen and Burcharth, 1992. This data shows a wide spreading that makes it difficult for the engineer to define design values of the parameters. In this case, an upper and lower value of the parameters are selected and, thus, an upper and lower 0.1 % force is given for each wave height. These two lines define a region assigned as Jensen's results region in figure 9.

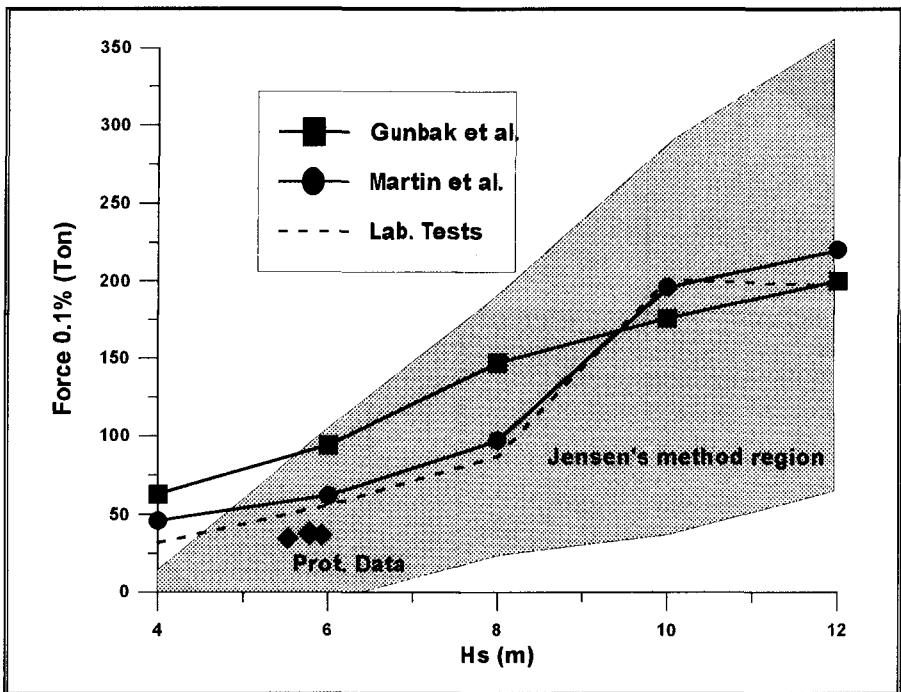


Figure 9. Quantitative comparison of results.

The 0.1 % force produced by the three storms are obtained by extrapolating the probability curve of forces in 45-min. burst, because in the next 45-min. burst the tidal range is different and the "test conditions" are not homogeneous. The maximum forces

are measured in the high tide situation (about 4.0 m in the three storms) and is equal to the tide level employed in the lab tests. Notice that in 45-min. burst, an average of 150 waves are measured and the 0.1% force requires 1,000 waves (about 6 hours).

The prototype results are 15% smaller than those of the lab results. Regarding the qualitative comparison done, it is clear that all the forces measured in the prototype under such storms are due to reflecting pressures. In the comparison of vertical pressure profiles, it was noticeable that the pressures measured in the lab were slightly larger than those measured in the prototype. This can be explained regarding the breakwater core. In the lab the core was built by small scale 90-T blocks, which can simulate the same porosity but not the same permeability. As the reflecting pressures are due to the water mass piled by the wall, larger wave transmission across the breakwater will produce less water accumulation by the wave screen.

Martin et al., 1995 and Günbak et al., 1984 methods are developed to be applied wave to wave. In this case the hypothesis of equivalence (Saville, 1962) is assumed and the methods are applied to a series of 3,000 synthetic simulated individual waves that represent a TMA spectrum. The fitting of Martín et al., 1995 to the lab results is not surprising as the parameters of the method were adjusted to this breakwater from the experimental results. The difference in the 12 m wave height is due to the breaking of waves in the wave flume, which occurs for breaking parameters (H_b/d , breaking wave height over depth) smaller than in the nature.

The results of Günbak et al., 1984, overpredicts the results (100% respect prototype, 60 %, respect experimental results) for smaller wave heights while for larger wave heights the results are smaller than the experimental. Perhaps the most important characteristic to point out is the different trend shown by Günbak et al. results (quasi linear) and Martín et al. results (quasi parabolic). It is clear that the shock forces on the wave screen front face depend on the pressure on the wall (horizontal momentum related to the water mass and the bore celerity) and on the area of wall exposed to the pressure (Run-up). Both of them are related to the wave height and, thus, the wave height must have an effect on the resulting forces at least in a quadratic form. It is clear that once the wall is overtopped ($H_s > 10$ m in fig. 9) the quadratic trend disappears.

Figure 10 represents the probability distribution of forces measured in the prototype on 19/2/96 ($H_s = 5.5$ m, $T_p = 16$ s) and the lab tests results for $H_s = 6$ m and $T_p = 14$ s which are the most similar cases available nowadays. The differences for smaller waves and the better fit for larger waves can be noticed.

Small scale effects are apparent by comparing the two probability curves. As no shock pressures occur for these wave heights these effects are not expected to be related to the water compressibility or aeration and perhaps more related to the core permeability

in the scale model or the differences in the wave trains between the lab and the prototype.

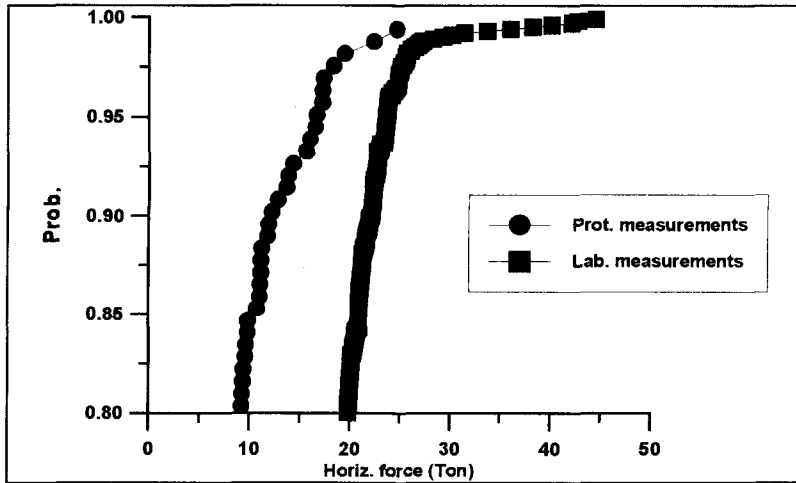


Figure 10. Force probability distributions.

CONCLUSIONS

- A field campaign is being developed as well as intensive lab tests over the 1/90 scale model of Príncipe de Asturias breakwater. The results of the field campaign and the lab tests are used to check the validity of some analytical methods employed in engineering practice to design wave screens. Moreover, the comparison of the results between the prototype and the 1/90 model allows to analyze the scale effects.
- The lab test results and the analytical methods seem to slightly overpredict the forces measured in the prototype.
- Maximum forces measured in the prototype up to now are due to reflecting pressures, where Froude scaling works properly, and the discrepancies must be explained by other modelling effects (core permeability, wave modeling, etc).
- No severe scale effects between lab results and prototype results are identified in a qualitative analysis.
- The method proposed by Martín et al., 1995 produces results which fit the lab test results well and 60% more accurately than Günbak et al., method. Jensen's method is difficult to apply by the designing engineers.

- The field campaign will provide more fruitful results when $H_s > 7$ m occur and shock pressures are measured.

ACKNOWLEDGEMENTS

This project is partially funded by the European Communities Research Programme, MAST III (Marine Science and Technology), Project PROVERBS (Probabilistic design tools for vertical breakwaters) under EU contract MAS3-CT95-0041. We appreciate this financial support very much.

The authors are grateful to the participants of PROVERBS for fruitful discussions and comments during workshops.

The authors wish to thank the Port Authority of Gijón for the unconditional technical and financial support to this project.

REFERENCES

- Bradbury, A.P., Alsop, N.W.H., Stephens, R.V., (1988). Hydraulic performance of breakwater crown walls. Report SR 146. H.R. Wallingford.
- Günbak, A. R., Gökce, T., (1984). Wave screen stability of rubble-mound breakwaters. International symposium of maritime structures in the Mediterranean Sea. Athens, Greece. pp 99-112.
- Iribarren, R., Nogales, C., (1964). Obras marítimas. Ed. Dossat. Madrid.
- Jensen, O.J., (1984). A monograph on rubble mound breakwaters. Ed. Danish Hydraulic Institute.
- Losada, M.A., Martín, F.L., Medina, R., (1995). Wave kinematics and dynamics in front of reflective structures. Wave forces on inclined and vertical wall structures. Task committee on forces on inclined and vertical wall structures. ASCE. pp 282- 310
- Martín, F.L., Losada, M.A., Medina, R., Vidal, C., (1995). Un método para el cálculo de las acciones del oleaje sobre los espaldones de los diques rompeolas. Revista de Ingeniería del Agua, Ed. Unidad docente de mecánica de fluidos. Univ. politécnica de Valencia Vol. 2, n° 3. pp 37-52. (In spanish, available in english).
- Pedersen, J., Burcharth, H. F., (1992). Wave force on crown walls. Proc. 23rd Int. Conference on Coastal Engineering, ASCE. Venice, Italy, pp 1489-1502.
- Saville, T., (1962). An approximation of the wave run-up frequency distribution. Proc. 8th International Conference on Coastal Engineering, ICCE. Mexico.

CHAPTER 138

Velocity Field Measurements over Breakwater Heads under 3D Waves

Yoshiharu Matsumi ¹, Akira Kimura ² and Kenichi Ohno ³

Abstract

The measurements of wave kinematics over the breakwater heads under uni and multidirectional waves attack were undertaken to achieve an improved understanding of the influence of wave directionality on the stability of heads. The characteristics of the magnitudes and directions of velocity vectors under 3D waves were assessed by comparing with those measured under 2D waves. The sensitive zones of the initial damage in the head sections were evaluated by linking the measurements of velocity components with a stability formula for armour stones on the heads, which was derived in this study.

Introduction

Breakwater designs have been generally evaluated using unidirectional waves, because they are widely considered to be conservative. This may be true for the trunk section of the breakwater where the directional spread associated with the multidirectional seas tends to reduce the wave loads imparted on the structure. However, for the breakwater heads, multidirectional waves could be expected to induce more loads on the structure due to their geometry.

The previous study which was carried out by Matsumi and Mansard et al. (1994), was the first step towards an experimental program achieving the realistic stability criteria for breakwater heads under multidirectional seas. It presented a comparison for the performance of breakwater heads under 2D and 3D waves attack. However, those experimental results could not draw general conclusion that the head sections were prone to more or less damage under 3D waves.

-
- 1 Associate Professor, D. Eng., Dept. of Social Systems Eng., Tottori University, Tottori 680, Japan.
 - 2 M. ASCE, Professor, D. Eng., Dept. of Social Systems Eng., Tottori University
 - 3 Graduate Student, M. Eng., Dept. of Social Systems Eng., Tottori University

The objective of this study is, as a continuation of that program, to explore a better insight into the reasons for the damage results of the heads in previous study through the measurements of wave kinematics over the heads under uni and multidirectional waves. Furthermore, directly unexpected waves attack under 3D waves may lead to higher loads to armour stones at some local position in the heads. Namely, the locality in location of the sensitive zones of the initial damage in the heads for 3D waves is deemed to be stronger than the case of 2D waves. This initiation of damage is relevant to trigger of breakwater failure. Therefore, the second purpose is to investigate the locality in spatial occurrence of the initial damage over the heads for 2D and 3D waves, which is evaluated by linking the measurements of velocity components with a stability formula for the armour stone.

Experimental Setup

Layout of the basin

The physical model tests were carried out, at the Tottori university, in the multidirectional wave basin with a length of 14m and a wide of 8.4m. Figure 1 shows a plan view of the experimental set-up. A fourteen-segment generator of the snake type is located along one of the 8.4m sides of the basin. Expanded polystyrene absorbers with permeability, capable of limiting wave reflections to 20% for most frequencies of interest, are installed along the two sides of the basin. On the side opposite the wave generator, the slope with 1:10 is placed in order to ensure an efficient dissipation of wave energy.

Layout of current meters and wave gauges

The velocity field over the head was measured using 6 bi-axial electromagnetic current meters at 6 different locations indicated by dots in Figure 1. The positions of these probes were fixed before placing the structure. The initial deflection of the U and V components of each current meter, by placing against the coordinate system located in the basin, was established by means of the preliminary regular wave tests without the breakwater. In Figure 1, θ shows the directions of velocity vector, minus θ and V(-) velocity component indicate flow towards armour layer of the head. The water surface elevations of the sea states in the proximity of the model were measured using 8 wave gauges at 8 different locations.

Layout of breakwater model

The layout of the breakwater model had to be designed carefully to ensure homogeneous sea states on the breakwater. For this purpose, the numerical model which was based on the diffraction theory and boundary integral equation was used. This model, developed by Isaacson (1992), can predict the water surface elevation and kinematics of the sea states prevailing at different locations in the basin. A

sample output resulting from this numerical model is presented in Figure 2. It illustrates the spatial distribution of wave heights in the basin without the breakwater model in place, under a multidirectional sea state. The expected wave heights presented in this figure were normalized with respect to target wave height. Note that their maximum value is only 0.9. This is due to the diffraction processes and can be increased by applying an amplification factor. It can be seen from this figure that the useful test area, over which the sea state is homogeneous, is limited by a triangular boundary. According to this figure, the best location for the model would be close to the paddle. However, since this wave basin is not yet equipped with active absorption, in order to minimize re-reflections from the paddles, the model is placed with its longitudinal axis rotated 20° with respect to the paddles, as shown in Figure 1.

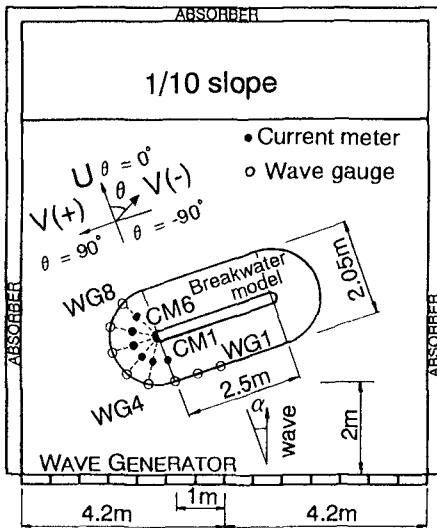


Figure 1 Plan view of the experimental set-up.

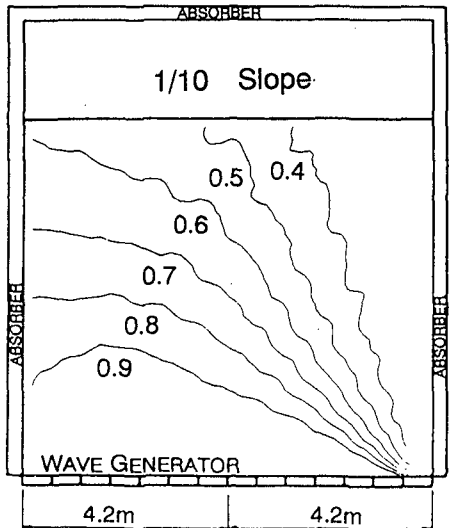


Figure 2 Spatial distribution of wave heights in the basin without the model.

Characteristics of the breakwater model

Figure 3 shows both plan and profile views of the breakwater model. The three dimensional rubble-mound breakwater with 2 layers of armour stones and a relatively porous core was built with a slope of 1:2. Its height was 50cm and it performed as a non-overtopping structure in a water depth of 30cm. Since this study was to focus on the wave velocity field over the heads without any damage, the whole surface of breakwater was covered with a hard nylon mesh to restrain armor stones. The reflection characteristics of the breakwater were estimated under unidirectional waves of normal incidence. The reflection coefficient was about 25%.

The characteristics of the armour and core stones used in the experiments are presented in Table 1. The weight of armour stones, W_{50} , was 42 grams, this value was 1.5 times the weight estimated by van der Meer's formula (1987) with damage parameter $S=2$ against the targeted significant wave height, $H_{m0}=6\text{cm}$, and peak wave period, $T_p=1.4\text{s}$. The gradations of armour stones were meticulously checked and the resulting D_{n85}/D_{n15} ratio for the armour was 1.1.

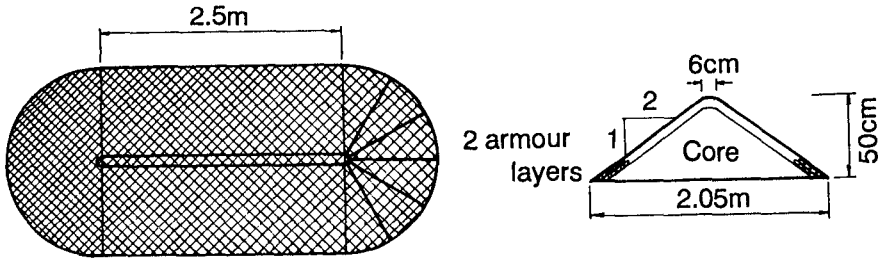


Figure 3 Plan and profile view of the breakwater model.

Table 1 Summary of the breakwater characteristics.

W_{50} weight of armour (g)	42
W_{a50} weight of core (g)	3.75
D_{n50} weight of armour (cm)	2.51
Porosity	0.45
D_L Length of head (cm)	205
T_L Length of trunk (cm)	250
Crest breadth (cm)	6
Height of breakwater (cm)	50

$$D_{n50} = (W_{50} / \rho_s)^{1/3} , \rho_s : \text{unit weight of armour stone}$$

Table 2 Characteristics of waves in experiments.

Spectrum	T_p (s)	γ	H_{m0} (cm)	α (deg.)	S_{max}	T_R (min.)	N	D_L/L	T_L/L
JONSWAP	1.0	3.3	6, 8.5	0, -15	10, 20, ∞	20	1440	1.49	1.82
JONSWAP	1.4	3.3	6, 8.5	0, -15	10, 20, ∞	20	1028	0.95	1.16

Test series

Table 2 indicates the characteristics of the waves adopted in the experiments. The spectra were the JONSWAP type with two different peak periods ($T_p=1.0s$ and $T_p=1.4s$). The peak enhancement factor γ was chosen to be equal to 3.3. The multidirectional waves were simulated by using the well known Single Summation Method in order to eliminate spatial variability of sea states. For the directional spreading function, the Mitsuyasu-type (1975) was chosen, the spreading parameter s was given by the following form (Goda 1985):

$$s = \begin{cases} S_{max} \cdot (f/f_p)^5 & : f \leq f_p \\ S_{max} \cdot (f/f_p)^{-2.5} & : f \geq f_p \end{cases}$$

Here f_p denotes the frequency at the spectral peak. Values of $S_{max}=10, 20$ and $S_{max}=\infty$ were applied to simulate multi and unidirectional waves respectively. In order to assess the influence of obliqueness, two different mean angles of incidence $\alpha = 0^\circ$ and $\alpha = -15^\circ$ were used, ensuring at the same time homogeneity of the sea state at the head sections.

In order to minimize statistical variability associated with short lengths of wave records, a recycling period of 20 minutes in model scale was used in the synthesis. This storm duration corresponded to about 1400 waves when $T_p=1.0s$ and 1000 for $T_p=1.4s$. The ratios of diameter of the head over wave length and length of trunk over wave length are indicated in Table 2.

Table 3 Significant wave heights in the experiments.

Wave Condition	H_{m0}	H_{s_no} ($T_p=1.0s$)	H_{s_no} ($T_p=1.4s$)	H_{m0}	H_{s_no} ($T_p=1.0s$)	H_{s_no} ($T_p=1.4s$)
Uni Normal ($S_{max}=\infty$)	6.0	6.01	6.17	8.5	8.68	8.42
Uni Oblique ($S_{max}=\infty$)	6.0	6.12	6.15	8.5	8.65	8.66
Multi Normal ($S_{max}=20$)	6.0	5.99	5.99	8.5	8.75	8.70
Multi Oblique ($S_{max}=20$)	6.0	6.16	6.16	8.5	8.77	8.49
Multi Normal ($S_{max}=10$)	6.0	6.01	6.05	8.5	8.63	8.40
Multi Oblique ($S_{max}=10$)	6.0	6.13	5.94	8.5	8.70	8.52

(Units : cm)

Twenty-four test series were carried out using different combinations of spreading index and mean angle of incidence. In each series, the spectrum-based

significant wave heights, H_{m0} , were 6cm and 8.5cm. These sea states were pre-calibrated in the basin without the structure in position, while keeping all wave gauges and current meters in place. The water depth was 30cm.

Table 3 provides a summary of wave heights measured under different experimental combinations without the breakwater model. The values of H_{s_no} are given by averaging the significant wave heights at every wave gauges. It can be found that there is not so much difference between values of H_{m0} and H_{s_no} of incident waves under uni and multidirectional waves.

Characteristics of Velocity Field over Breakwater Head

Armour stones of the breakwaters may be strongly prone to move under a condition of faster flow velocities. Therefore in this study, larger magnitudes of velocities in the time series data of the measurements were discussed. Figure 4 shows the comparison of the U and V component velocities at 4 different locations (CM-2, CM-3, CM-4, CM-5 shown in Figure 1) on the head under 3D waves and those under 2D waves, when H_{m0} is 6cm and Tp is 1.4s. The velocities employed in this figure are the average of the highest 1/3 of the time series data from each current meter. The ordinate in this figure indicates the ratio of the values of U, V for 3D waves to those under 2D waves. Therefore, when these values exceed one, velocities under 3D waves become larger than those under 2D waves. It can be seen that for 3D waves, the V(-) component which is towards the armour layer causing severe damage is larger than those for 2D waves. In even back head section, this value under 3D waves is nearly 1.2 to 1.3 times larger than the values measured under 2D waves.

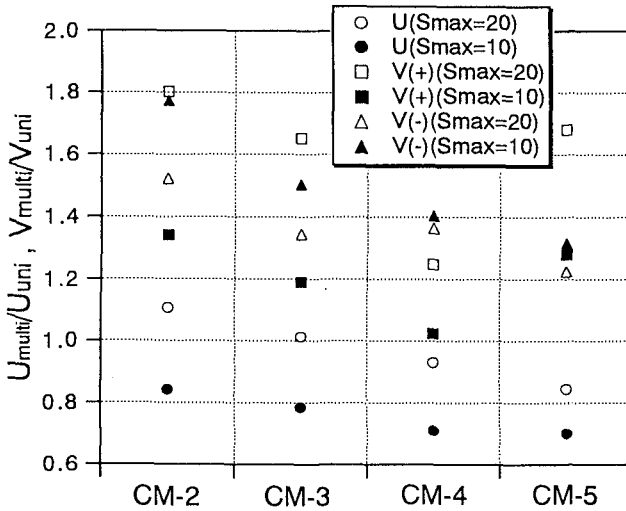


Figure 4 Comparison between U, V component velocities under 3D and 2D waves.

Figure 5 shows the spatial characteristics in correlation of the magnitude of velocity vectors at every current meter. In these figures, the value of R indicates the coefficient of the correlation between measurements at every current meter and that at CM-1 current meter placed on the top of the front head section. It can be seen that in the case of multidirectional waves, the correlation in the middle and back head section is very poor regardless of the mean direction of waves and peak periods. From these results, the possibility of waves attacking directly the heads due to the directional spread associated with 3D waves may be supported.

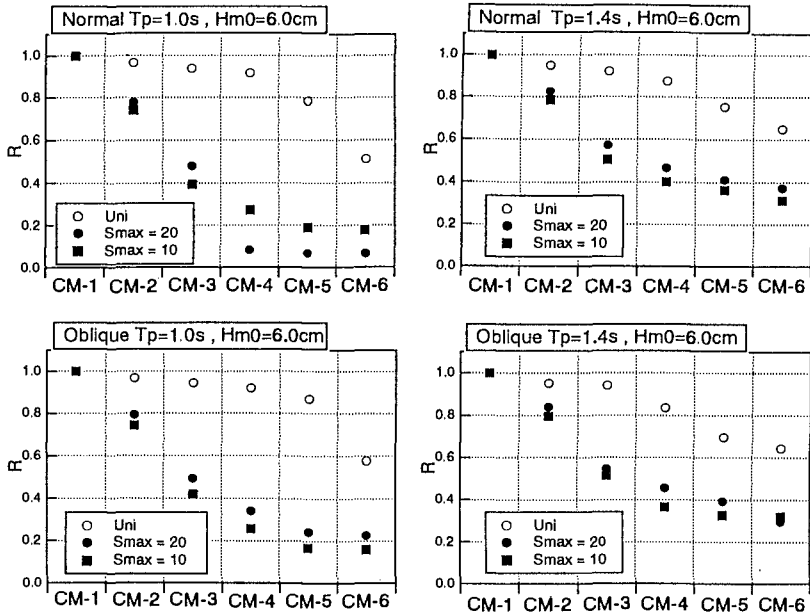


Figure 5 Spatial characteristics in correlation of velocities over the head.

In order to achieve a better understanding of these results, the directionality of velocity vectors on the heads was investigated. Figure 6 (a) and (b) show examples of the directionality of the highest 1/100 of the velocity vectors evaluated from the time series data of U and V at CM-3 (Middle section) and CM-5 (Back section) under 2D and 3D waves, respectively. Especially in the back head section, velocity vectors ($\theta < 0$) under 2D waves wrap around there. Conversely, in the case of 3D waves, the velocity vectors ($\theta > 0$) towards the down-slop of the head appear to be remarkable. The reason may be explained by the influence of the reflection of oblique waves directly attacking the front and middle head sections due to the directional spread in multidirectional waves. From these measurements, it is pointed out that in stability design for the heads, waves attacking directly the front and middle heads in 3D seas cannot be negligible.

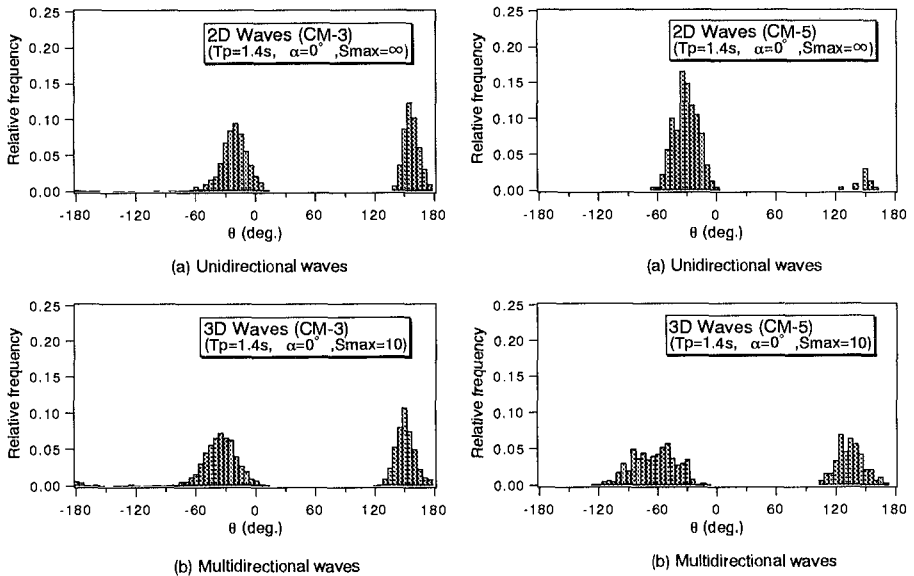


Figure 6 Directionality of velocities over the head.

Consideration on Stability of Armour Stones

The stability of armour stones on the heads is deeply concerned with the magnitudes and directions of the attacking velocity vectors, besides the slope of armour layer with respect to the velocity vectors (Jensen 1984). In this section, an equation about critical current velocity, when the armour stone movement in the heads is brought, is derived by taking account of tangential slope of the heads with respect to the direction of velocity vectors. The sensitive zones of initial damage in the heads will be evaluated by linking this stability formula for armour stones with the measurements of velocity components.

Critical velocity for stability of armour stones

The armour sphere (A) is placed on the head with the horizontal angle β for the velocity vector v_r with horizontal angle θ , as shown in Figure 7. By assuming the shape of the head as a circular cone, the curve of intersection between the vertical plane and the cone becomes a hyperbola. In this study, the only drag force was considered as hydrodynamic force. Then, the equilibrium equation between the armour weight and the drag force can be derived by balancing the moment about point O in this figure:

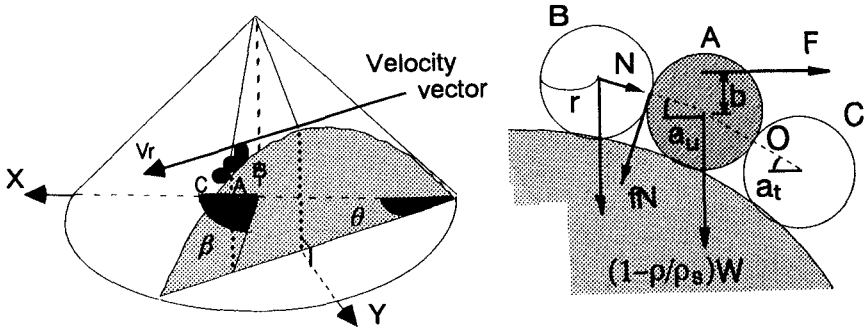


Figure 7 Attacking velocity and hydrodynamics force on armour stone.

$$\left(1 - \frac{\rho}{\rho_s}\right) W \left[\cos a_t + f \sin a_u \left\{ 1 + \cos(a_t - a_u) \right\} \right] = F \left(\sin a_t + \frac{b}{r} \right) \quad (1)$$

where W and r are weight and diameter of armour stone, ρ_s and ρ are unit weight of stone and water, F is drag force, f is friction coefficient between stones. The parameters a_u and a_t in Eq.(1) are respectively the angle of elevation of armour sphere (A) from (C), and (B) from (A) as shown in Figure 7. The drag force is described by the following formula:

$$F = m' \rho \pi r^2 v_r^2 \quad (2)$$

where m' is drag coefficient of armour stone, v_r is magnitude of attacking velocity vector. The velocity can be expressed by substituting Eq.(2) into Eq.(1) as:

$$\frac{v_r^2}{gr} = \frac{\left(1 - \frac{\rho}{\rho_s}\right) \left[\cos a_t + f \sin a_u \left\{ 1 + \cos(a_t - a_u) \right\} \right]}{\frac{3}{4} m' \frac{\rho}{\rho_s} \left(\sin a_t + \frac{b}{r} \right)} \quad (3)$$

where g is gravitational acceleration. In Eq.(3), f , m' , r and b are unknown parameters, a_u and a_t can be derived from tangential slope of the head with respect to the velocity vector as the following.

The cone is mathematically expressed by following formula in X-Y coordinate system shown in Figure 7:

$$Z = a - \frac{1}{2} \sqrt{X^2 + Y^2} \quad (4)$$

where a is the height of the cone, Z is distance from bottom. The coordinate (X, Y) of center of armour sphere (A) becomes $(R \cos(\beta - \theta), R \sin(\beta - \theta))$ in X-Y coordinate system. The tangential slope of the heads with respect to the velocity vector can be derived by partially differentiating Eq.(4) with respect to X , and inserting the (X, Y) of the point A:

$$\text{Tangential slope} = -\frac{1}{2} \cos(\beta - \theta) \tag{5}$$

Assuming that a_t is equal to a_u for simplicity in this study, they are given as:

$$a_t = a_u = \tan^{-1} \left\{ \frac{1}{2} \cos(\beta - \theta) \right\} \tag{6}$$

Finally, the critical velocity, v_{rc} , for armour stone movement in the heads is expressed by substituting Eq.(6) for a_t and a_u into Eq.(3):

$$\frac{v_{rc}^2}{gr} = \frac{\left(1 - \frac{\rho}{\rho_s}\right) \{1 + f \cos(\beta - \theta)\}}{\frac{3}{4} m' \left(\frac{\rho}{\rho_s}\right) \left[\frac{\cos(\beta - \theta)}{2} + \frac{b}{r} \sqrt{1 + \left\{ \frac{\cos(\beta - \theta)}{2} \right\}^2} \right]} \tag{7}$$

When the tangential slope with respect to attacking velocity vector becomes positive, in Eq.(7), the plus sign before the friction coefficient, f , is replaced by the minus sign. The unknown parameters m' , b and f in Eq.(7) were considered as $m'=1$, $b=0.5r$ and $f=0.4$, for simplicity in this paper.

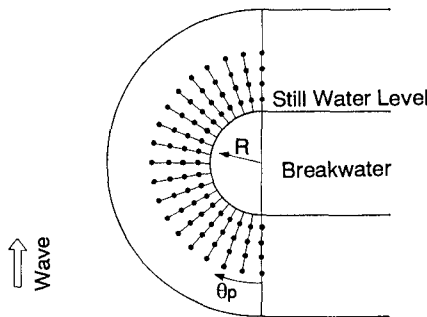
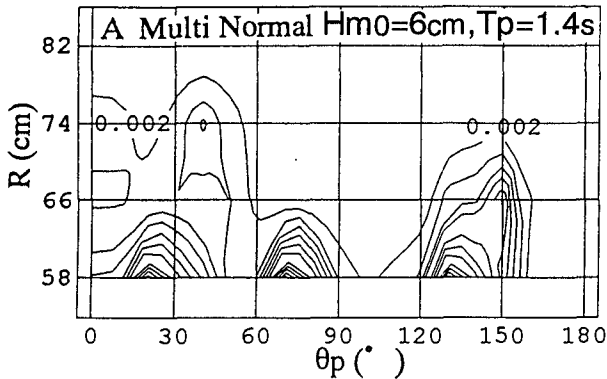


Figure 8 Measuring points of velocity components over the head.

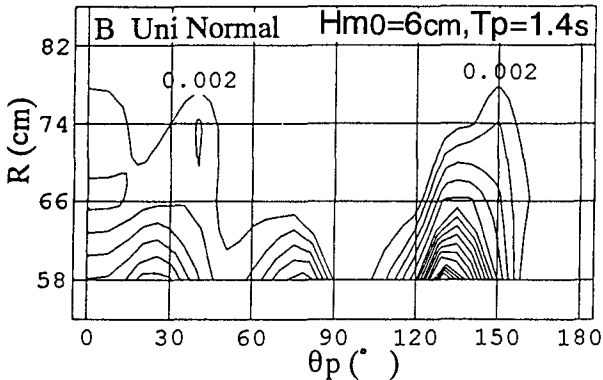
Influence of wave directionality on sensitive zone for initial damage

In this section, in order to investigate the influence of wave directionality on the stability of breakwater heads, the spatial occurrence frequencies for armour stone movement in the head sections were estimated by linking Eq.(7) and the velocity vectors which were newly measured at 76 points over the head shown in Figure 8.

Figure 9(a) and 9(b) show the spatial distribution of calculated occurrence frequencies for armour stone movement in the head under conditions of the normal 3D waves and 2D waves with $T_p=1.4s$ and $H_{m0}=6cm$ respectively, in which θ_p is the angle from the front head and R is the distance in the radial direction from the center of head as shown in Figure 8. In these figures, contour lines of relative occurrence frequencies which are normalized with respect to the total number of velocities measured for 20 minutes are indicated with interval every 0.002.



(a) Multidirectional waves ($S_{max} = 10$)



(b) Unidirectional waves ($S_{max} = \infty$)

Figure 9 Spatial distribution of occurrence frequencies for armour stone movement.

In order to investigate the reliability of those calculated results, the initial damage tests of armour stones in the head sections were carried out under the same incident wave conditions as those in the velocity measuring tests. The resulting initial damage zones in the head under 3D and 2D waves attack are shown in Figure 10(a) and 10(b), respectively. In these figures, the hatched parts mean that the second armour layer is clearly exposed due to the displacement of the first armour layer. By comparing these initial damage patterns with the spatial distributions of occurrence frequencies for armour stone movement shown in Figure 9, it can be seen that the results of the calculations evaluating the locations of the initial damage are fairly close to the experimental locations.

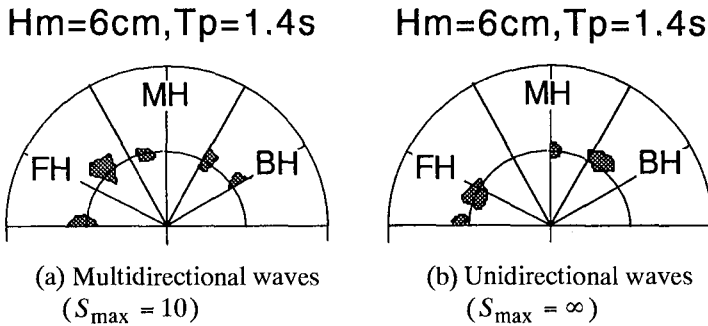


Figure 10 Initial damage zones in the head.

It can be found from Figure 9 that the sensitive zones for armour stone movement in the head sections are appeared at three locations; the front, middle and back head section respectively. Although there is not so much difference in these locations under 3D and 2D waves, there is obvious difference between the values of both occurrence frequencies, that is, in the case of the unidirectional waves, the back head section is more sensitive part for armour stone movement. Under unidirectional waves attack, it could be observed in the damage tests that the damage in the back head section was caused to plunge of the strong current with the high velocities generated by refraction, shoaling and diffraction processes. On the other hand, under multidirectional waves attack, the front and middle section are more sensitive part for the initial damage, because of the oblique waves attacking directly these sections due to the directional spread associated with the multidirectional seas. This consideration may be supported, since in the case of the multidirectional waves of Figure 6(b), the direction ($\theta > 0$) of velocity vectors outwards from the armour layer in the back head section is remarkably recognized in comparison with those under unidirectional waves.

Under oblique incidence, the multidirectional waves resulted in larger occurrence frequencies in the three sensitive zones (FH, MH and BH) for armour

stone movement than those under unidirectional waves. This is caused by the waves attacking directly the back head section due to the oblique incidence. When T_p was equal to 1.0s, the difference in calculated occurrence frequencies for armour movement in the head sections between uni and multidirectional waves was relatively small.

Conclusion

In this study, the characteristics of velocity field over the head under 2D and 3D waves were investigated. The V velocity component under multidirectional waves was larger than those under unidirectional waves. A noteworthy finding was that those on the back head section under 3D waves were larger by nearly 1.2 to 1.3 times the values measured under 2D waves, and that the direction of velocity vectors downing slope in the back section under 3D waves were remarkably recognized.

The presented equation of the critical velocity for armour stone movement in the heads could satisfactorily explain the initial damage zones in the damage tests. The front and middle head section were more sensitive zone for the initial damage under multidirectional waves attack. This result provided a better insight into previous study.

Further the unknown parameter in the presented equation will be investigated by physical experiments or theoretical techniques, the stability of breakwater heads will be evaluated by linking the equation of the critical velocity for armour stone movement with a numerical analysis of wave kinematics over the heads.

References

- Jensen, O.J. (1984). "A monograph on rubble mound breakwaters", Danish Hydraulics Institute, Denmark.
- Matsumi, Y., Mansard, E.P.D. and Rutledge, J. (1994). "Influence of wave directionality on stability of breakwater heads", Proc. 26th Int. Conf. on Coast. Engrg., ASCE, 1397-1411.
- Mitsuyasu, H. et al (1975). "Observation of the directional spectrum of ocean waves using a cloverleaf buoy", Jour. Physical Oceanography, Vol.5, 750-760.
- Van der Meer, J.W. (1987). "Stability of breakwater armour layers - design formulae", Coastal Engrg., 219-239.
- Y. Goda (1985). Random seas and design of maritime structures, University of Tokyo Press, Japan.

CHAPTER 139

WAVE CLIMATE SIMULATION AND BREAKWATER STABILITY

Josep R. Medina¹

Abstract

The nonstationarity of the sea waves is usually significant for periods longer than 3 hours (1,000 waves) with a correlation coefficient $r_{HH}(3)$ below 95% on most coasts of the world. Therefore, the actual engineering problem is to define an appropriate armor damage model applicable for nonstationary processes and not only for stationary sea states with a given storm duration. In deep water, five conditions are identified for any rational armor damage model to properly take into consideration the storm duration. A new exponential model applied on individual waves is shown to accomplish the five necessary conditions identified, and is compared with the Teisson's and Vidal's models based on totally different assumptions, but accomplishing most of the conditions. The three models provide similar results for a wide range of values if the parameters are $n_{63\%}=30$ and $N_w=50$ for the exponential and Vidal's models respectively. An example of the application of the exponential model to nonstationary processes is given, applying the new method to the case of the partial failure of the Zierbana breakwater (Port of Bilbao, Spain) under construction in February 1996.

Introduction

The duration of the storm and the wave groupiness are design factors not explicitly addressed by the Hudson formula. The storm duration obviously increases the expected damage on the armor layer because it increases both the number and the size of the individual waves above the corresponding damage threshold level. On the other hand, some characteristics of wave groups are related to the variability of variance and storm duration. A number of models and stability formulae considering storm duration have been

1) Professor, Departamento de Transportes, Univ. Politécnic de Valencia, Camino de Vera s/n, 46022 Valencia, SPAIN. // E-mail: jrmedina@tra.upv.es

developed during the last decade, introducing a variety of empirical relations based on different interpretations of test results up to 16,000 waves. The relationships between wave groupiness and extreme waves was considered by Vidal et al.(1995) to introduce a new discrete wave parameter to characterize design storms, instead of wave spectrum and storm duration. However, the problem of defining an appropriate and simple method to take into account storm duration and stochastic variability, is not solved.

The stationarity of the process is a basic assumption of most methods for analyzing breakwater stability; however, although the random sea waves were stationary, the significant wave height shows a natural variability that increases when spectral peakedness increases and record length decreases. Therefore, a larger storm duration increases the expected armor damage. Moreover, it is obvious that sea waves are never stationary and stationarity only should be considered a reasonable approximation for short periods of time. When long storm durations are considered for designing ($N > 1,000$ waves), the influence of nonstationarity on sea waves should be taken into consideration.

This paper compares first some of the most common methods and formulas proposed to analyze the influence of storm duration on the estimation of the armor damage. Secondly, the influence of the intrinsic variability of variance of the stationary processes related to wave groups on the expected armor damage is evaluated. Thirdly, the wave climate simulators and the need of multivariable stochastic models to describe the wave climate are justified. Fourthly, the necessary conditions are given to build up rational armor damage models for nonstationary processes. Fifthly, a new exponential model on individual waves are described and compared to the Teisson's and Vidal's models. Finally, an example of application is given to the case of the partial damages occurred at the Zierbana breakwater (Port of Bilbao, Spain) under construction during February 1996.

Armor Damage as Function of Storm Duration

Using SPM(1984) as the basic methodology for designing rubblemound breakwaters, the expected armor damage would not be dependent of the storm duration. However, it is obvious that given a design storm, the armor damage increases if the storm duration increases. There are significant discrepancies among different authors to quantify the relationship D versus N . Taking into consideration a reference storm duration of 1,000 waves, Fig. 1 shows the relative damage estimated by the models proposed by SPM(1984), Van der Meer(1988), Medina and McDougal(1990), Teisson(1990), Smith et al.(1992), and Vidal et al.(1995). Vidal's model has been applied considering a Rayleigh wave height distribution; therefore, the model may be considered an upper limit of the armor damage as function of the number of waves of a given sea state. The models compared in Fig. 1 have different variables and assumptions; the relative armor damages, $D(N)/D(1000)$, have been calculated referring the damage estimated by each model to the damage estimation for 1,000 waves in deep water conditions.

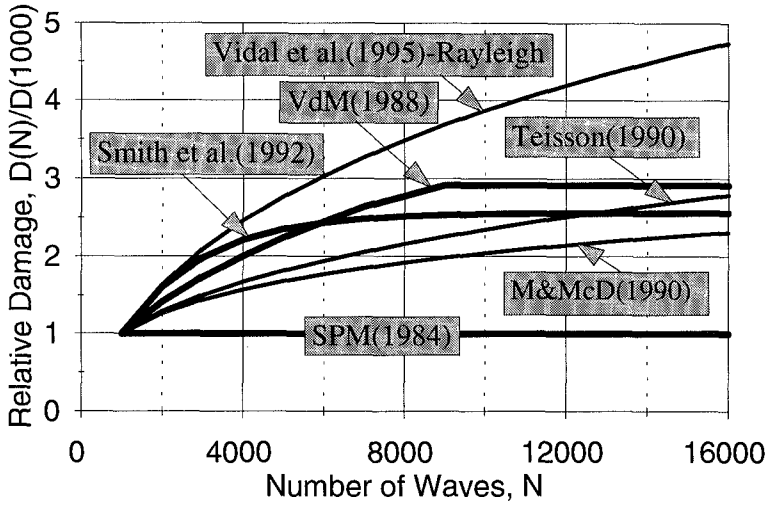


Figure 1.- Armor Damage as Function of Storm Duration.

Variability of Variance

The stationarity of the process is a basic assumption of most methods for analyzing breakwater stability; however, although the random sea waves were stationary, the significant wave height shows a natural variability that increases when spectral peakedness increases and record length decreases. Therefore, the storm duration affects not only the expected armor damage but also the variability. According to Medina and Hudspeth(1987), the coefficient of variation of H_{m0} is given by

$$CV(H_{m0}) \approx \sqrt{\frac{Q_e}{8 N}} \tag{1}$$

in which Q_e is the spectral peakedness parameter given by

$$Q_e = \frac{2m_1}{m_0^3} \int_{f_{min}}^{f_{max}} S_n^2(f) df \tag{2}$$

in which $S_n(f)$ is the variance spectrum, and m_0 and m_1 are the zeroeth and first spectral moments respectively. Assuming a perfect stationarity of the process, the variable H_{10} of finite records of 1,000 waves, $\{H_{10}\}_{1000}$, is a Gaussian random variable; therefore, the maximum $\{H_{10}\}_{1000}$ increases when the storm duration increases so do the corresponding armor damage (see Medina et al.,

1994) according to

$$\frac{H_{10}}{H_d} = \left[\frac{D}{1.6} \right]^{\frac{1}{5}} \quad (3)$$

in which $H_{10} = 1.27 H_{m0} > H_d$, H_d is the design wave height, and D is the armor damage. Eq. 3 fits the failure data given by the SPM(1984) and may be considered a reasonable good approximation for estimating damages of tests with wave runs around 1,000 waves. For very long wave runs, it may be reasonable to select the highest $\{H_{10}\}_{1000}$ to estimate the damage according to Eq. 3.

Fig. 2 shows the relative damage corresponding to the highest $\{H_{10}\}_{1000}$ when the storm duration increases up to $N=16,000$ waves; the values of the spectral peakedness parameter $Q_e = 2.3, 4.4,$ and 6.2 correspond to the JONSWAP spectral shapes $\gamma = 1, 5,$ and 10 and are related to different wave grouping characteristics (see Medina and Hudspeth, 1990). The variability of variance increases significantly the expected damage, but far below that observed in Fig. 1.

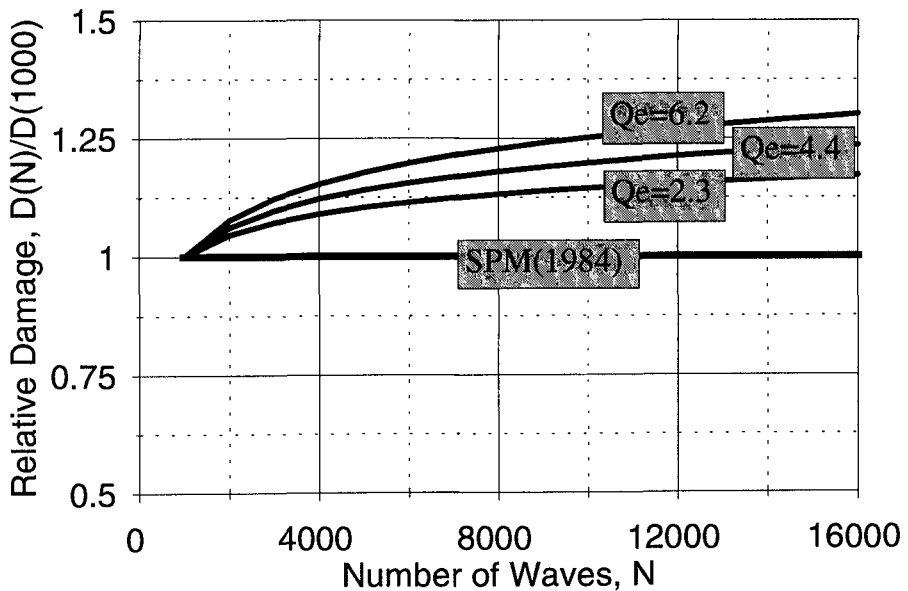


Figure 2.- Effect of Variability of Variance on Expected Armor Damage.

WAVE CLIMATE SIMULATION

The quantitative estimation of storm-induced beach change, as function of the time-dependent forcing conditions, has proved to be a powerful technique that may be applied in project designing of coastal structures. The basic input of the numerical models for simulating beach profile changes are the evolution in time of the wave climate variables. By analogy, it is reasonable to consider that reliable models for quantitative estimation of armor damage as function of the time-dependent forcing conditions will be developed in the near future. In this scenario, new wave climate models will be necessary to provide the appropriate input variables as do the wave climate simulators.

Fig. 3 shows a typical wave climate simulation corresponding to the first hours of the year on the coast of Oregon, according to Medina et al.(1991). The nonstationarity is significant for periods as short as 3 hours ($N < 1,000$ waves). The correlation coefficient of Oregon, $r_{HH}(3) = [r_{HH}(6)]^{1/2} = +0.92$, is similar to the $[r_{HH}(6)]^{1/2}$ given by Rossouw(1988) for the South African coast, slightly lower than the $r_{HH}(3) = +0.94$ given by Bettencourt et al.(1995) for the coast of Portugal, but higher than the $r_{HH}(3) = +0.89$ calculated for the coast of Valencia with shorter fetchs in the Western Mediterranean. Therefore, the actual problem is not to estimate the armor damage corresponding to a given design storm, $D[H_{m0}, T_{01}, N]$, but to estimate the evolution in time of damage for nonstationary processes, $D[\{H_{m0}, T_{01}\}(t)]$.

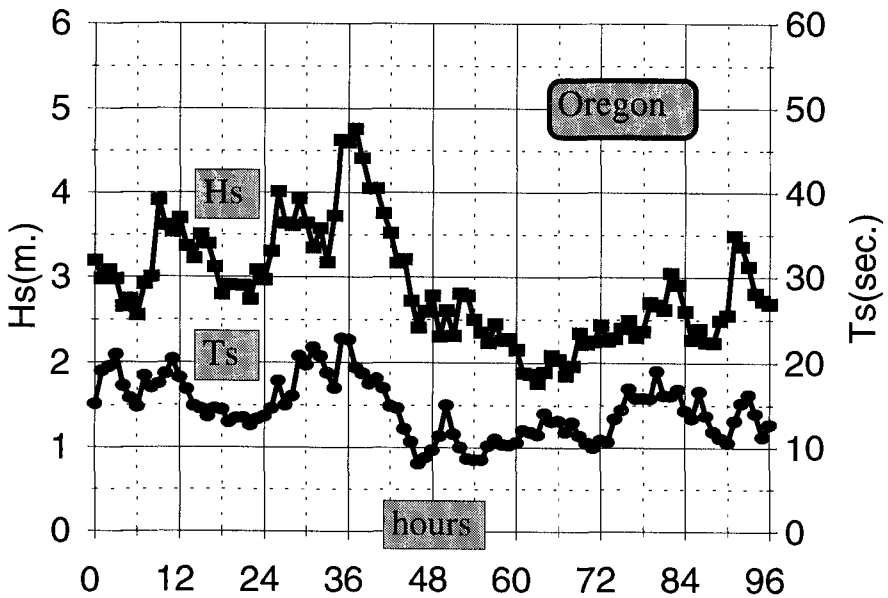


Figure 3.- Hourly Simulation of {Hs,Ts} Corresponding to January (Oregon)

Armor Damage Models for Nonstationary Processes

The armor damage models compared in Fig. 1 are based on different assumptions, some of them inappropriate for nonstationary processes. The design method proposed by SPM(1984) is based on a wide range of laboratory tests only with regular waves; the extrapolation to random waves has been changing in time with $H_{D=0}=H_s$, proposed by SPM(1975), and $H_{D=0}=H_{10}$ proposed ten years later by SPM(1984). In deep water conditions, the storm duration obviously affects the armor damage, because changes both the expected largest wave and the number of waves above any threshold level; therefore, armor damage must increase when storm duration increases, and no fixed equivalence independent of duration exists between regular waves and random waves.

The models proposed by Van der Meer(1988) and Smith et al.(1992) are based on laboratory tests only with random waves; both have an equilibrium limit for the armor damage under random wave attack in stationary conditions. However, armor damage must increase when storm duration increases for the reasons given above; therefore, no equilibrium limit is acceptable for random waves in deep water conditions. The empirical model of Medina and McDougal(1990) based on the Van der Meer's results avoid this problem but is difficult to be applied to nonstationary processes.

The method proposed by Teisson(1990), based on the test results with random waves given by Lepetit and Feuillet(1979) is directly applicable to nonstationary processes. The design wave height, H_D , producing similar damages with regular waves is

$$H_D = 1.18 H_{1/3} t^{0.085} \quad (4)$$

in which H_D and $H_{1/3}$ are given in meters and t in hours. For rubblemound breakwaters and nonstationary process the damage is calculated according to:

$$D(t) = 0.706 \left(\sum [H_{1/3}(\Delta t)]^{10.64} \Delta t \right)^{0.37} ; t = \sum \Delta t \quad (5)$$

in which Δt is small enough to admit the nonstationary process correctly composed by a succession of short stationary sea states characterized by $H_{1/3}$.

Vidal et al.(1995) proposed the use of the average height of the $N_w=100$ largest waves in a sea state, as the characteristic wave height which take into consideration both the intensity and duration of the sea state. Although these authors indicated that the most suitable value of N_w is still a subject of continuing research, their method may easily be applied to nonstationary processes. The armor damage would then be related to the average of the highest N_w waves in the storm, whatever was the evolution of the significant wave height in time during the storm.

Any rational model to estimate the evolution in time of the armor damage of rubblemound breakwaters in deep water conditions should fit reasonably well the existing test results with regular and random waves. Therefore, the following necessary conditions for acceptability of an armor damage model applicable to nonstationary processes are:

- (1) Under regular wave attack, the maximum damage must be limited by the existence of an equilibrium profile, $D(H,T,N) < D_0(H,T)$.
- (2) The maximum damage under regular waves may be approximated (if wave periods are not considered) by Eq. 3.
- (3) There is no equilibrium profile under random wave attack in deep waters; the damage must grow with the storm duration without any limit.
- (4) The armor damage should be insensitive to the waves below some threshold level related to the design wave height, $H_i < H_d$; only the large waves are relevant to the armor damage.
- (5) The characteristics of a few highest waves should have a significant effect on the armor damage.
- (6) The method must be applicable to nonstationary processes where the characteristics of the sea states are continuously changing in time.

Only Teisson's model, based on hypothesis of equivalence for damages, and Vidal's model, based on a parameter $N_w=100$ not well justified, may be applied to nonstationary processes and accomplish most of the necessary conditions given above. Laboratory test are rarely conducted considering nonstationarity; furthermore, long runs in wave flumes have a low reliability because of the difficulty in controlling the stochastic structure of random waves for a long time. As a result, the overall quality of data supporting the models compared in Fig. 1 has to be considered low, because observations are partially contaminated by assumptions not compatible with the necessary conditions given above.

Exponential Model on Individual Waves

A simple method that accomplish the six conditions given above is the exponential model applied on individual waves. The exponential model is normally used for describing events occurring at random time with a constant future lifetime, and in life-testing applications. The evolution of damage of the armor layer of a rubblemound breakwater in deep waters shows some of the characteristics suitable for the exponential model.

The exponential model for regular waves may be described by

$$D(H,T,N) = D_0(H,T) [1 - \exp(-kN)] \quad ; \quad k = \frac{1}{n_{63\%}} \quad (6)$$

in which $n_{63\%}$ is the number of waves that causes 63% of damage in a regular wave attack. Fig. 4 shows the evolution of damage in time, under regular waves, corresponding to the exponential model.

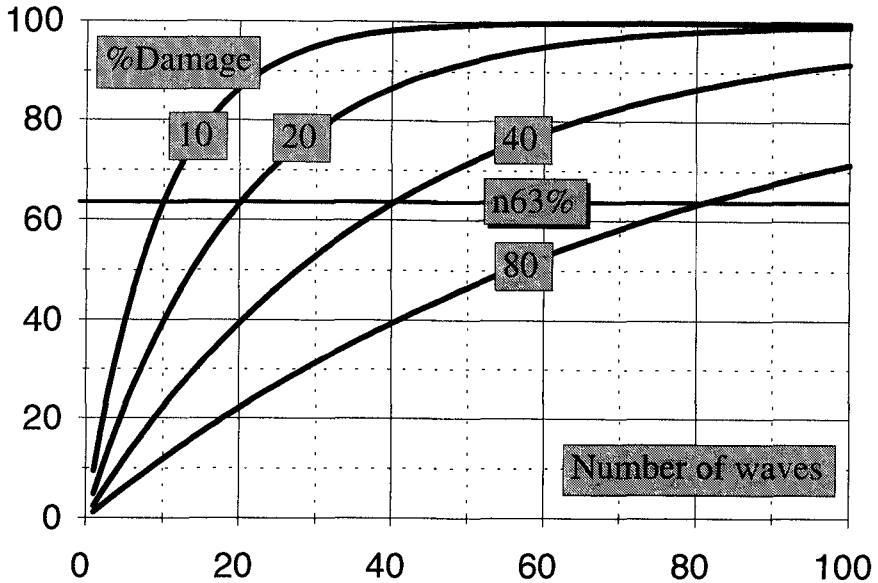


Figure 4.- Parameter n63% Controlling the Evolution of Damage in Time.

The exponential model for random waves requires first the identification of the individual waves, $\{H_i, T_i\}$, in a continuous record. In this paper, the orbital criterion proposed by Giménez et al.(1994) has been selected. The model could be extended to both wave heights and periods; a simplified version considering only wave heights may be described by

$$D_i = D_{i-1} + \left(\frac{1}{n63\%} \right) [D_0(H_i) - D_{i-1}] \quad \text{if } D_0(H_i) > D_{i-1} \quad (7a)$$

$$D_i = D_{i-1} \quad \text{if } D_0(H_i) < D_{i-1} \quad \text{or} \quad H_i < H_{min} \quad (7b)$$

in which $D_0(H_i) = 1.6 (H_i/H_d)^5$. Eqs.7 are the discrete derivative version of Eq. 6, if wave periods are not included in the armor damage model. The different armor damage models were compared on the basis of numerical simulations and the orbital criterion shown by Giménez et al.(1994). Fig. 5 shows the evolution of damage corresponding to the exponential model with n63% ranging from 10 to 40, compared to the estimations given by the models of Teisson(1990) and Smith et al.(1992). Teisson's model gives similar results to the exponential model with n63%=30; on the contrary, Smith's model shows radically different results. On the other hand, Fig. 6 compares the exponential model and the model of Vidal et al.(1995).

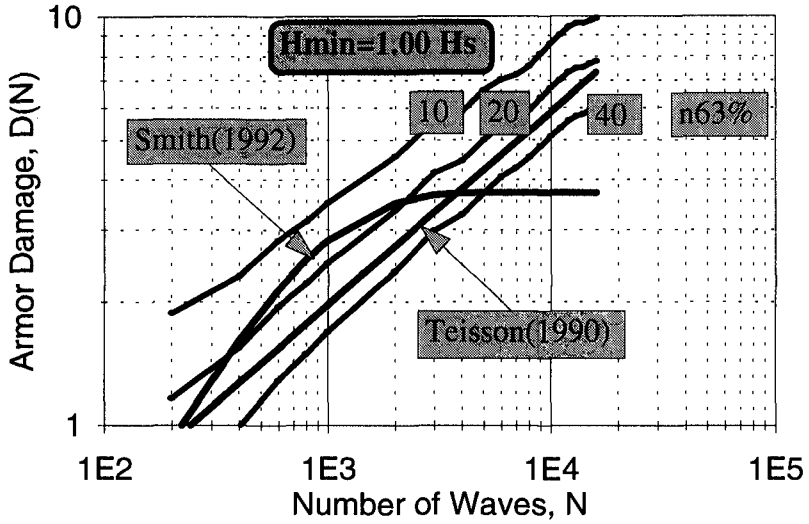


Figure 5.- Damage Estimations Compared to Teisson's and Smith's Models.

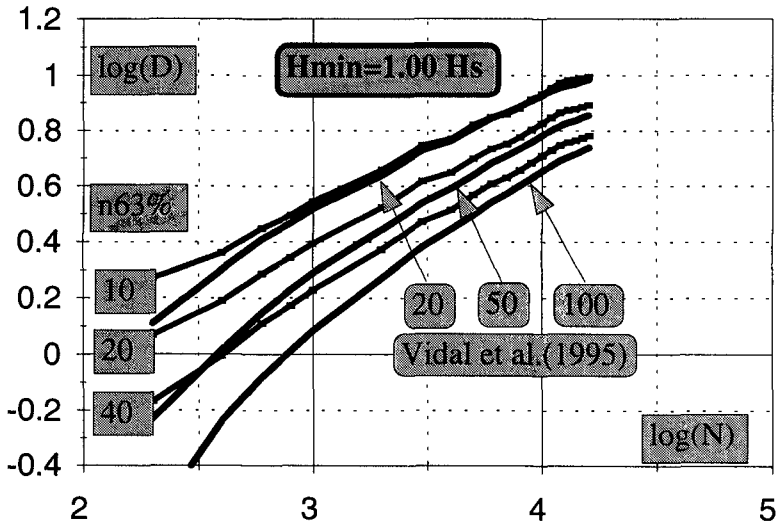


Figure 6.- Damage Estimations Compared to Vidal's Model.

The results provided by the exponential and Vidal's model for $N > 5,000$ waves suggest that only the largest waves in a record are relevant to estimate armor damages. Fig.7 shows the sensitivity of the armor damage estimated by the exponential model to the threshold level H_{min} of Eq. 7b. The significance of

damages caused by the lowest waves ($H_i < H_{min}$) in a storm decreases when the storm duration increases. Considering the exponential model with $n_{63\%}=30$, 95% of damage are produced by less than 1% of the highest waves in a random wave train of 10,000 waves.

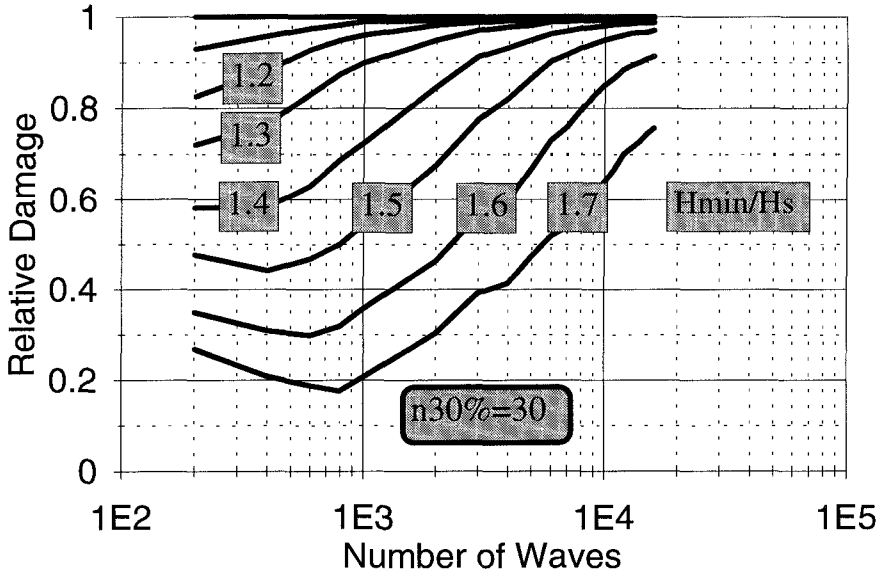


Figure 7.- Sensitivity of the Exponential Model to H_{min}/H_s .

Example: Partial Damages on the Zierbana Breakwater in the Port of Bilbao (Spain) under Construction During February 1996.

The development of the Port of Bilbao in the outer Abra is described by Losada et al.(1996). The Zierbana Breakwater under construction in 1996 was partially damaged in February 1996. The part of the breakwater with the armor completed with the 100 tn concrete blocks was not damaged; on the contrary, the advanced part of the breakwater protected only with the secondary layer of 8 tn concrete blocks collapsed. Additionally, the crane used for installing the armor units was lost in the storm.

Uzcanga and González(1992) describe the technical and economic design criteria and laboratory tests conducted to justify the breakwater design under construction. Taking into consideration the technical information given by the above mentioned authors, the data provided by the waverider buoy operating during the peak of the storm (7-8 February 1996), and the observation of armor damages in different parts of the breakwater, the Zierbana case has been selected to show the possible applications of the exponential model to the analysis of the evolution of the armor damage.

Fig. 8 shows the evolution in time of the H_{m0} and T_{01} measured by the waverider buoy off Bilbao during the damaging storm in February 1996. The wave measurements were taken at one hour interval (about 300 waves/hour), the peak of the storm had about 1,000 waves with $H_{m0} \approx 8$ meters and $T_{01} \approx 12$ sec.; according to Fig. 7, more than 95% of damage is caused by $H_i > 1.2 H_{m0} \approx 9.6$ meters. The maximum individual wave height is expected to be $(H_{max}) \approx 1.7 H_{m0}$; therefore, the minimum H_{m0} significant for estimating the armor damage is $(H_{m0})_{min} \approx 9.6/1.7 = 5.6$ meters. Therefore, the damages are expected to be suffered between the 15:00 p.m. (7 Feb 96) and 7:00 a.m. (8 Feb 96) with a probable maximum wave height of 15 meters.

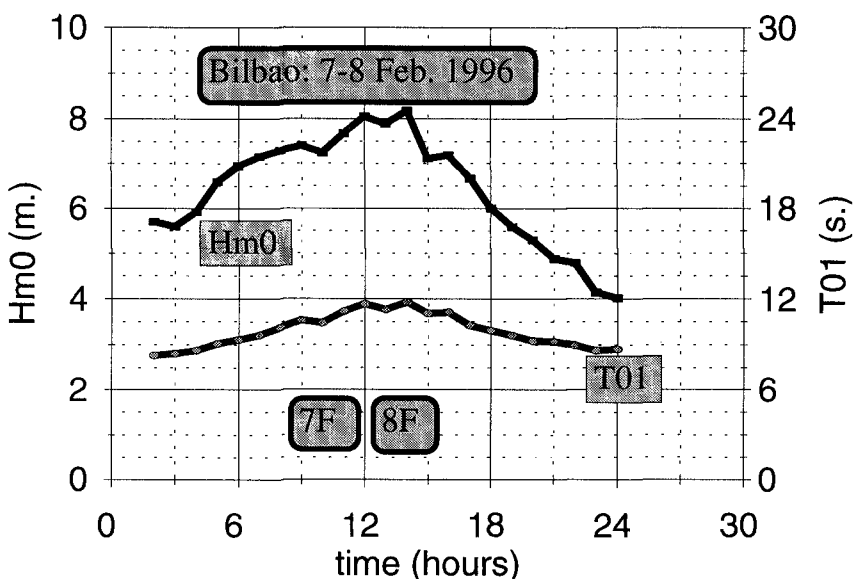


Figure 8.- Evolution of H_{m0} and T_{01} (7-8 February 1996).

Considering the evolution in time of H_{m0} and T_{01} given in Fig. 8, and the numerical simulations described by Giménez et al.(1994) used in Figs. 5 and 6, it is possible to estimate the evolution in time of the damage on the armor layer applying the exponential model described previously. The technical information provided by Uzcanga en González(1992) are used to link the waverider measurements and structural response to the wave characteristics. Fig. 9 shows the estimations of the armor damage evolution in time considering the exponential model on individual waves with $n_{63\%}=30$, and three different armor blocks ($W= 8$ tn, 16 tn and 100 tn). The model predicts only minor damages on the armor of 100 tn blocks, and total destruction of the armor of 8 tn, in agreement to what was observed in the Zierbana Breakwater. According to the exponential model, a secondary layer of more than 16 tn was

necessary to resist the wave storm measured during February 1996.

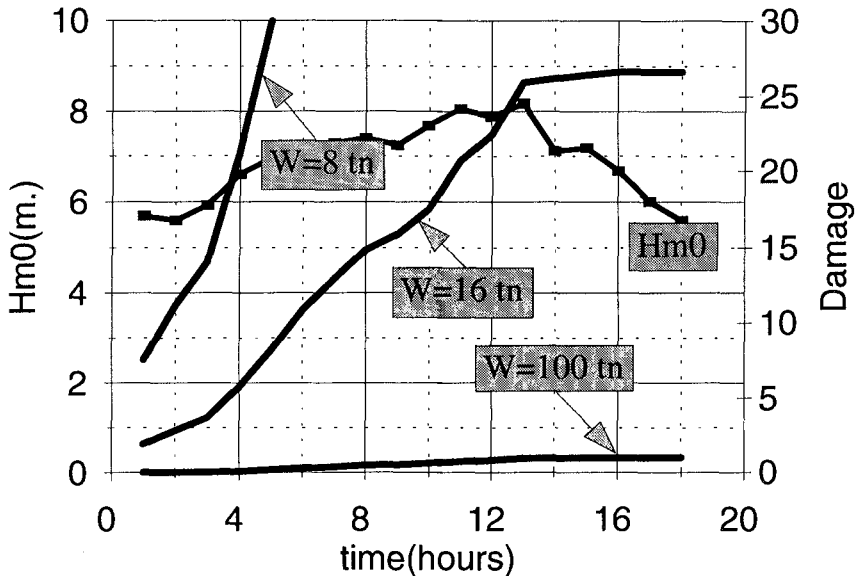


Figure 9.- Estimation of the Evolution in Time of the Armor Damage.

The damages caused in the Zierbana Breakwater suggest the need of re-analyzing the risk associated with the construction during winter months. Considering the measurements given by the Bilbao waverider buoy before 1991, ROM 0.3-91(1992) provides an estimation of $R=7$ years ($R=3$ years is the 90% confidence band limit) for a wave storm of $H_s=8$ meters. However, it is possible to apply the method given by Rossouw and Medina(1996) to estimate the risk associated with each month independently. Taking into consideration the wave measurements before 1994, and based only on the monthly average and standard deviations, it is possible to estimate the intensity of the storm having a 10% and 2% annual risk of being overpassed during a specific month. Fig. 10 describes the monthly average, $E[H_{m0}]$, the monthly standard deviation, $std[H_{m0}]$, and the H_{m0} (storm duration: $Dt = 3$ hours) having 10% and 2% annual risk ($R=10$ and $R=50$) of being overpassed during each month.

According to Fig. 10, during the months of December and February it is probable to suffer a wave storm of $H_{m0} \approx 8$ meters ($1/R \approx 10\%$ each month) while there is a low additional risk during January, March, April, October, and November ($1/R \approx 2\%$ each month). The total annual risk of the event ($H_{m0}=8$ meters, $Dt = 3$ hours) is approximately 30%; therefore, the damaging storm measured by the waverider buoy off Bilbao shown in Fig. 8 ($H_{m0} \approx 8$ meters, $Dt \approx 3$ hours) was likely to happen during the four year construction period of the Zierbana Breakwater. Furthermore, February is the most risky month to work

with partially protected breakwater during construction. The failure of the forecasting system used in Bilbao during construction may be responsible for losing the main crane, able to place the 100 tn blocks at 50 meters; however, from the climatic point of view, it is difficult to justify the work in February.

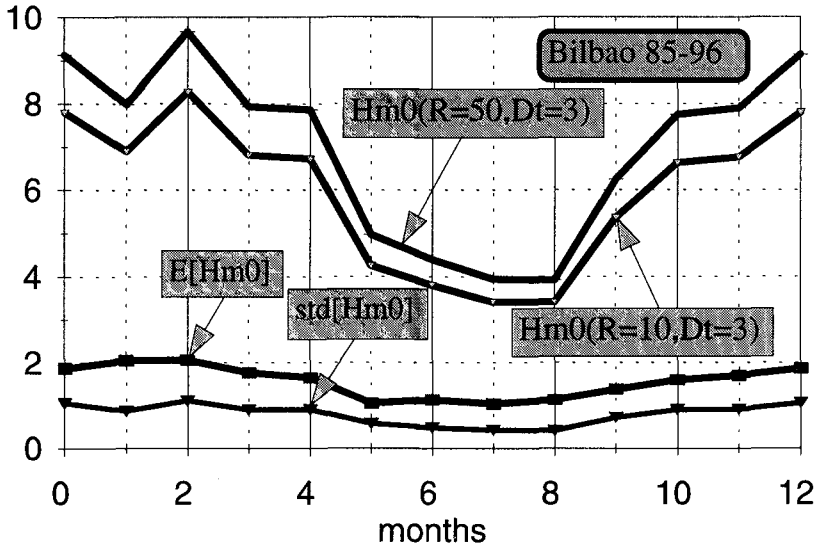


Figure 10.- Characteristics of the Wave Climate in the Coast of Bilbao.

CONCLUSIONS

New models for describing the armor damage evolution in time have to be developed. Existing $D(N)$ models are not appropriate to be applied for nonstationary stochastic models which are the most adequate for modelling real waves. The models must accomplish four basic conditions: (1)unlimited damage if unlimited duration, (2)unsensitive to characteristics of waves below a threshold level, (3)higher relative effect associated with the largest waves, and (4)simple to be applied to nonstationary stochastic models.

ACKNOWLEDGEMENTS

The author acknowledge the financial support provided by the Dirección General de Investigación Científica y Técnica, under Grant PB94-0534, and the wave data provided by the Programa de Clima Marítimo (CEDEX) of Puertos del Estado.

REFERENCES

Bettencourt, J., Aguiar, R., and Pontes, T.(1995). Long Time Series of 3-Hourly Spectral Shape Parameters, *Proc. OMAE-95-339:1-10*.

- Giménez, M.H., Sánchez-Carratalá, C. , and Medina, J.R.(1994).** False Waves in Wave Records and Numerical Simulations. *Proc. , 24th Int. Conf. on Coastal Engr.*, ASCE, 192-206.
- Losada, M.A., Medina, R., Vidal, C., and Losada, I.J.(1996).** History of Coastal Engineering in Spain, *History and Heritage of Coastal Engineering (Ed. N. Kraus)*, ASCE, 465-499.
- Lepetit, J.P., and Feuillet, J.(1979).** Study of the Stability of a Rubble Mound Breakwater under Random Waves. Quantification of the Effect of Duration, *EDF-LNH Report 42/79.15* (in French).
- Medina, J.R. and Hudspeth, R.T. (1987).** Sea States Defined by Wave Height and Period Functions. *Proc., IAHR Seminar on Wave Analysis and Generation in Laboratory Basins, 22nd IAHR Congress, Lausanne, Switzerland*, 249-259.
- Medina, J.R. and Hudspeth, R.T. (1990).** A Review of the Analyses of Wave Groups. *Coastal Engineering*, 14, 515-542.
- Medina, J.R. and McDougal, W.G. (1990).** Deterministic and Probabilistic Design of Breakwater Armor Layer (Discussion). *Journal of Waterway, Port, Coastal and Ocean Engineering*, 116(4), 508-510.
- Medina, J.R., Giménez, M.H., and Hudspeth, R.T.(1991).** A Wave Climate Simulator. *Proc. XXIV IAHR Congress, Madrid*, 9-13 Sep. 1991, (B)521-528.
- Medina, J.R., Hudspeth, R.T., and Fassardi, C.(1994).** Breakwater Armor Damage due to Wave Groups. *Journal of Waterway, Port, Coastal and Ocean Engineering*, 120(2), 179-198.
- ROM 0.3-91(1992).** *Waves. Anexo I: Wave Climate on the Spanish Coast.* Puertos del Estado, Publicaciones Técnicas. 76p.
- Rossouw, J.(1988).** Design Waves and their Probability Distributions. *Proc. , 21st Int. Conf. on Coastal Engr.*, ASCE, 822-834.
- Rossouw, J., and Medina, J.R.(1996).** The Stability of Design Wave Estimates. *Book of Abstracts, 25th Int. Conf. on Coastal Engr.*, ASCE, 50-51.
- Shore Protection Manual(1975).** Coastal Eng. Res. Center, Dep. of the Army, Waterways Exp. Stat., Vicksburg, Miss.
- Shore Protection Manual(1984).** Coastal Eng. Res. Center, Dep. of the Army, Waterways Exp. Stat., Vicksburg, Miss.
- Smith, W.G., Kobayashi, N., Kaku, S.(1992).** Profile Changes of Rock Slopes by Irregular Waves. *Proc., 23rd Int. Conf. on Coastal Engr.*, 1559-1572.
- Teisson, C.(1990).** Statistical Approach of Duration of Extreme Storms: Consequences on Breakwater Damages. *Proc., 22nd Int. Conf. on Coastal Engr.*, ASCE, 1851-1860.
- Uzcanga, J., and González, B.(1992).** Algunas Consideraciones sobre el Diseño de Diques (in Spanish). *Proc. I Jornadas Españolas de Ingeniería de Costas y Puertos, Santander 7-8 May 1992*, UPV, 84-130.
- Van der Meer, J.W. (1988).** Deterministic and Probabilistic Design of Breakwater Armor Layer. *Journal of Waterway, Port, Coastal and Ocean Engineering*, 114(1), 66-80.
- Vidal, C., Losada, M.A., and Mansard, E.P.D.(1995).** Suitable Wave-Height Parameter for Characterizing Breakwater Stability. *J. Waterway, Port, Coastal and Ocean Engineering*, 121(2):88-97.

CHAPTER 140

INCIPIENT MOTION OF BREAKWATER ARMOR UNITS

J. A. Melby¹, M. ASCE, and N. Kobayashi², M. ASCE

ABSTRACT

This paper describes observations made of incipient motion on both stone and sphere armor layers. Velocity measurements were made during these experiments both inside and just outside the armor layer. It is shown that the vertical convective acceleration across the armor layer is proportional to the square of the vertical velocity. An incipient lifting motion criterion is derived based on Morison forcing for the dominant mode of motion: vertical lift under the steep breaking-wave face. The experimental observations and measurements are used to validate the incipient motion criterion for breakwater armor.

1 INTRODUCTION

Extensive research on breakwater armor stability has produced many empirical stability models. These models predict minor damage reasonably well. Many investigations have also quantified the wave forces on undamaged armor; and these force measurements have been used to compute more explicit stability criteria. But few studies have been done to observe and quantify the wave and structure conditions under which armor just begins to move, i.e. incipient armor motion.

The Iribarren (1938), Hudson (1958), and other empirical armor stability models are based on a free body analysis of an armor unit undergoing forcing due to breaking waves. Early stability models assumed the principle wave force was 1) due to down-or up-rush on an unsheltered and unrestrained unit, 2) drag dominance, and 3) that the drag force would be critical if the maximum horizontal fluid velocity was used, which was considered to be proportional to the incident wave celerity. But for an intact structure and prior to initiation of incipient motion, the armor units are typically partially hidden and restrained from up or down slope movement; so lift, inertia, and convection across the armor layer must be considered. Moreover, Sawaragi et. al. (1982) showed that the maximum fluid velocity on a rubble mound was not necessarily proportional to the wave celerity. Sigurdsson (1962) made force measurements on sphere armor at extremely steep slopes with an impermeable underlayer and with no underlayer and derived incipient equations of motion; but concluded by stating that the

¹ Res. Engineer, USAE Waterways Experiment Station, CERC, 3909 Halls Ferry Rd., Vicksburg, MS, 39180

² Professor, Center for Applied Coastal Research, University of Delaware, Newark, Delaware, 19716

dominant mechanism of initiation of armor motion was still unknown and required further investigation. Although many authors have discussed wave kinematics and dynamics on armor layers and the resulting forces, including Mizutani et. al (1992), Torum and van Gent (1992), Torum (1994), and Cornett and Mansard (1994), there have been few observations of incipient movement of armor units discussed in the literature. As such, the relationships between incipient motion, wave kinematics, and forces on armor units is still unknown.

Kobayashi et al. (1990) presented a numerical model for predicting the displacement of armor on a traditional rubble mound. The shallow water wave model interacted with a permeable flow model and hydrodynamic drag, inertia, and lift forces were computed using a Morison type of formulation (Morison et al. 1950). The model was limited to forces parallel to the structure because the hydrodynamics were one-dimensional vertically averaged. Torum and van Gent (1992) discussed a similar model and compared it to velocity measurements above a berm breakwater. Torum (1994) discussed the measurements further. Although two dimensional velocities were measured, vertical flow in the breaking wave was not modeled numerically. In addition, Torum noted that the inertial force was not well defined by the traditional inertia term of the Morison equation. Cornett and Mansard (1994) described an experiment where forces were measured on a panel of stones. This approach was unique and yielded insight into the average frictional force on sections of the armor layer. The results were used to develop a stability model for armor sliding.

The present article discusses a series of physical model experiments to identify and develop predictive models for breakwater armor incipient motion and to relate this motion to existing empirical stability relationships. The experiments were done in wave flumes at the Waterways Experiment Station in Vicksburg, Mississippi. The first experiment consisted of measuring wave-induced fluid velocities on and within the armor layer and runup/down. In addition, free surface oscillations were measured while observing armor motion on stone and Core-Loc armor. The observations from this early study led to an incipient motion experiment using a fixed-sphere armor layer with several loose spheres placed at various depths within the armor layer. A dominant incipient armor motion mode and predictive stability equation were verified.

EXPERIMENTAL SETUP

The initial experiments were conducted to determine the nature of armor incipient motion and surrounding flow. The instrumentation included a laser Doppler velocimeter (LDV), high resolution video, and runup and vertical free-surface-piercing gages near and within the armor layer. The experiments discussed herein were all carried out using regular monochromatic waves. The analysis techniques were done using short segments of between five and ten uniform waves to develop clear relationships between wave parameters and armor motion.

The primary study was done in a 46m long by 0.46m wide by 1m deep flume, with an offshore slope of 1V:30H. A conventional rubble mound cross section was constructed with various seaward slopes and armor types (Figure 1). Table 1 lists the different test plans. In this paper, only the sphere and stone armor plans will be discussed (Test Plans 3 and 4). Velocity measurements, sampled at 100 Hz, were made

throughout the water column from the toe to two armor dimensions above the still water level. The ranges of physical quantities and common dimensionless parameters for plans 3 and 4 are listed in Table 2.

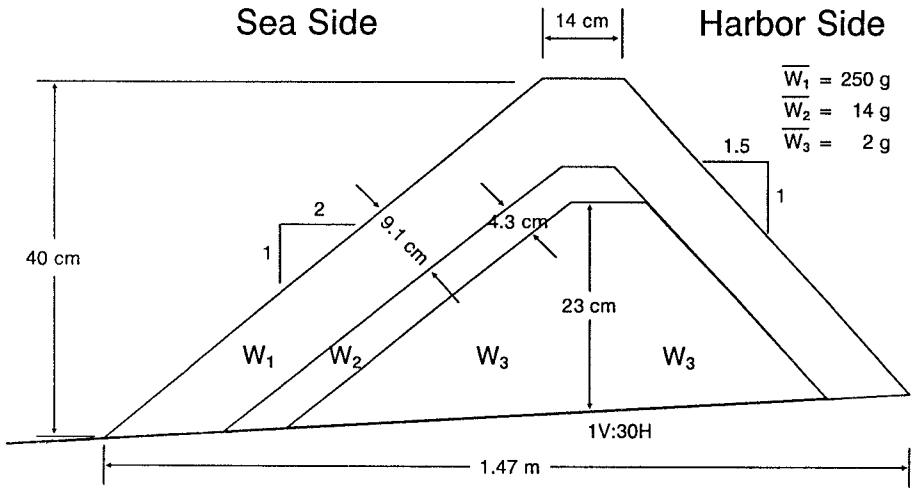


Figure 1. Definition sketch for typical structure profile.

Table 1. Experimental Plans							
Plan	Armor Type	Armor Weight W, g	Nominal Armor Dia. $D_n = (V)^{1/3}$ cm	Structure Slope, cot θ	Off-shore Slope cot α	Runup down Meas.	Force Meas.
1	Core-Loc	220	4.6	1.33	100	no	no
2	Core-Loc	105	3.6	1.5	20	no	no
3	Stone	200	4.6	2.0	30	yes	no
4	Sphere	58	3.8	2.0	30	yes	no
5	Sphere	212	5.6	2.0	30	yes	yes

Table 2. Ranges of Measured Physical Quantities and Common Dimensionless Parameters for Plans 3 and 4	
Parameter	Range
Wave height at toe, H_t	2.4 to 18 cm
Wave period, T	0.75 to 4.0 sec
Water depth at toe, d_t	15 to 24 cm
Wave steepness, $S_z = H_t / L_o$ L_o = deepwater wave length	0.007 to 0.1
Surf similarity parameter, $\xi = \tan \alpha / (H_t / L_o)^{1/2}$ $\tan \alpha = 1/30$ = beach slope	0.1 to 1.4
Surf similarity parameter, $\xi = \tan \theta / (H_t / L_o)^{1/2}$ $\tan \theta = 1/2$ = structure slope	1.5 to 21
Relative depth, d_t / L_o	0.009 to 0.28
Relative wave height, H_t / d_t	0.06 to 0.88

The LDV was a two-watt argon-ion two-component device assembled by the Dantec Corporation. The version used works in the back scatter mode using a non-intrusive probe which contains both the emission and receiving optics. The benefits of this device included nonintrusive measurements, small measurement volume, clean drop outs, high sampling rate, and no required calibration. The LDV is unique in that the probe can be pointed through the glass flume wall into the voids within the armor layer and allow measurements of the internal flow within the porous media. Many of the voids are more than a nominal armor diameter deep so the measurements can be made outside the flume wall boundary layer. One drawback to the LDV is it requires a full time operator with continuous attention to detail. Also, because of the small measurement volume, small changes in measurement location often yield large variations in measured velocities, especially near or within the breakwater armor layer. Therefore, the instrument requires many measurements to map the flow field. So data analysis requirements were substantial for this experiment.

The wave heights were determined using free surface measurements from a capacitance-type gage positioned at the location of the structure toe with no structure in place. Synthetic rubberized horse-hair mats were placed landward of the structure location to absorb the waves. The sampling rate for free surface measurements was 20 hz. The zero-downcrossing wave height was computed as the average height from a burst of approximately ten regular waves.

INCIPIENT MOTION OBSERVATIONS

Several dominant incipient motion modes were identified during the stone stability experiment in Plan 3, Table 1. The following descriptions pertain to initial armor

motion on an intact, as-built structure. Rolling was the only mode of motion for stones on the toe. Although both onshore and offshore motion was observed, the toe units always moved out of the layer in the onshore direction. For upslope armor, armor near the still water level was more likely to displace than armor in other areas. This appeared to be due to the fact that the armor was loosened in this area due to high velocities in the breaking wave jet. Once loosened, the motion would depend on the armor shape and its position. If the armor shape was flat, then the armor unit would flop back and forth until it rolled out of the armor layer, generally rolling upslope during uprush. If the armor shape was rounded, which was normally the case, the armor units would jump vertically under the steep wave face if the wave was severely plunging or collapsing. If the wave was surging, then loose units would only be displaced if they were exposed. There did not appear to be sufficient lift in downrush or uprush flows along the armor layer to displace the stones unless they were odd shaped (flat). The only displacement mechanism observed for rounded stones sufficiently hidden in the armor layer was uplift under the steep wave face.

These observations indicated that a fluid velocity or acceleration component in the vertical direction is normally required to initiate armor motion for hidden armor units. Additionally, this early qualitative study indicated that, for a wave of given energy, incipient motion was primarily influenced by wave shape, stone position, stone exposure, and stone looseness.

EXPERIMENTAL MEASUREMENTS

Throughout the experiments, vertical and horizontal wave velocities were measured in the vicinity of the armor layer. Figure 2 shows typical time series of the horizontal and vertical velocities on the structure. The sign convention was such that the horizontal velocity was positive seaward while the vertical velocity is positive upward. Note that the horizontal velocity amplitudes are very regular while the vertical velocity typically varies considerably. Figure 3 shows a velocity vector time series over one wave period, measured just above the armor layer one-third of the depth down from the still water level, and the wave profile at the point of maximum vertical velocity. The plot shows a large vertical velocity vector just below the steep wave front. Observed maximum stone movement for this wave profile position is also shown. Figure 4 shows an example of vertical velocities outside and inside the armor layer. The measurement locations for these time series are shown in Figure 5, where the structure slope is 1V:2H. Here it is clear that the velocities within the armor layer are highly irregular due to turbulence.

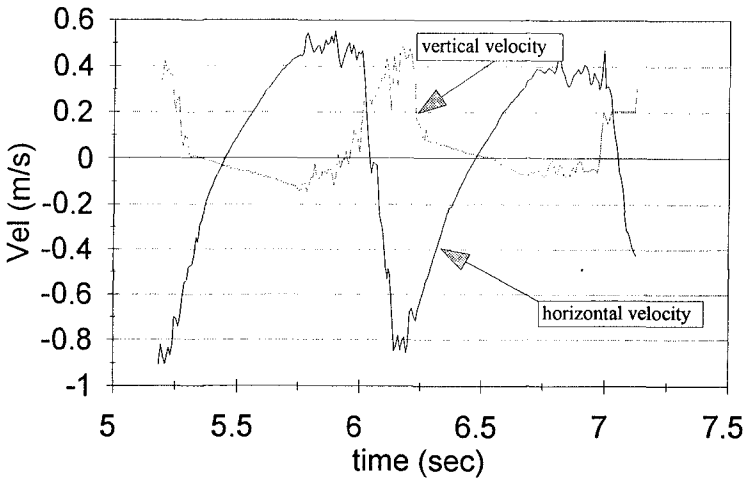


Figure 2. Velocity time series for one wave period, $H_t = 12\text{cm}$, $T = 1\text{ sec}$, $d_t = 24\text{ cm}$.

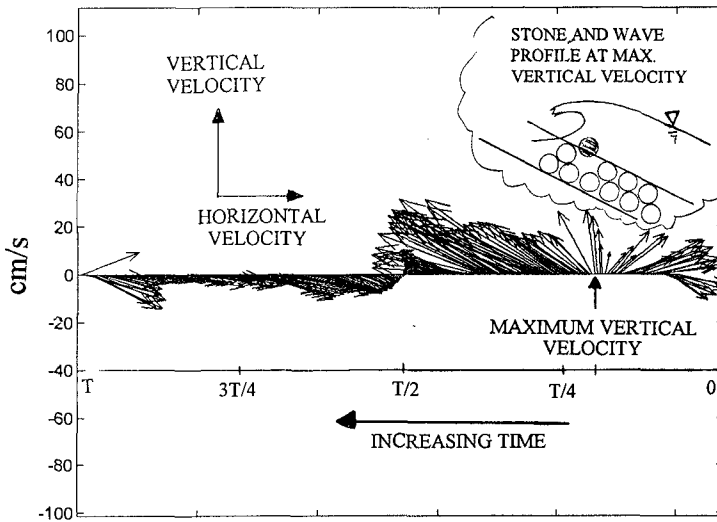


Figure 3. Velocity vector for one wave period for armor lifting.

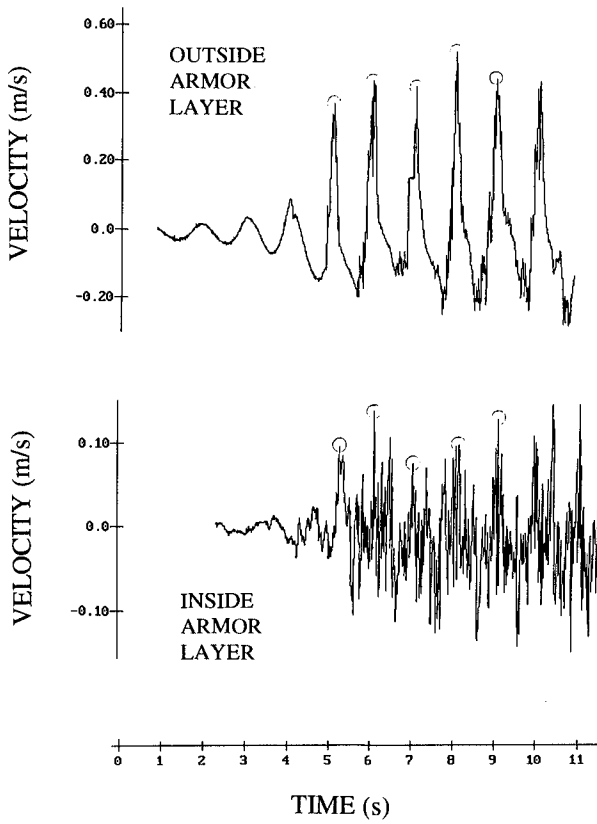


Figure 4. Vertical velocity time series outside and inside the armor layer

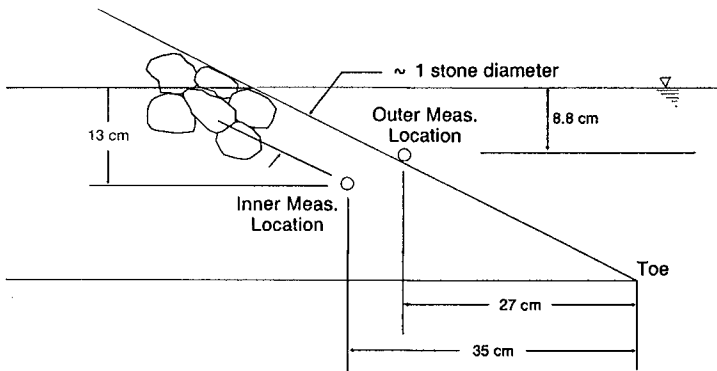


Figure 5. Measurement locations for vertical velocities shown in Figure 4.

Figure 6 shows a typical plot of vertical velocity $v_{1/3}/(gH_t)^{1/2}$, measured just above the armor layer at various depths, versus the square root of wave steepness, where $v_{1/3}$ is the average of the highest one-third peak velocities, g the gravitational acceleration, H_t the toe wave height, structure slope = 1V:2H, and L_o the deep water wave length. For simplicity, v is used instead of $v_{1/3}$ in Figure 6 and hereafter. Relative laser depth, rd , is the ratio of the depth of the laser to the depth at the toe, measured from the still water level. As noted by Sawaragi et al. (1982), maximum non-dimensional velocities commonly occurred for collapsing to plunging breaking waves. The peak vertical velocities for given wave period decreased downward with increase of rd in this figure.

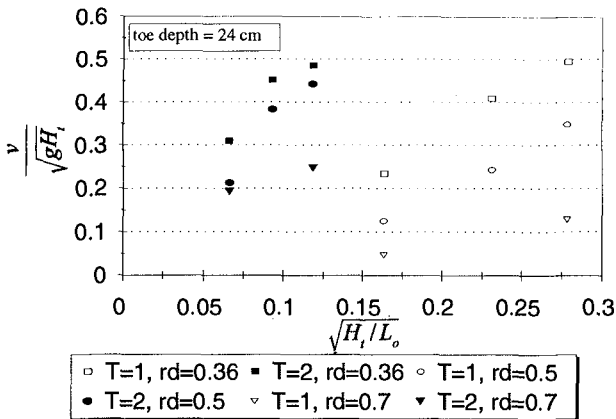


Figure 6. Maximum vertical velocity versus the square root of wave steepness for wave periods $T = 1$ and 2 s and relative depths $rd = 0.36, 0.5,$ and 0.7 .

INCIPIENT MOTION PREDICTION

The previous experimental results indicated that one of the dominant incipient motion modes was due to the vertical force occurring under the steep wave front. The balance of forces for vertical incipient armor motion with no external restraints yields the equality between the submerged armor weight and the vertical fluid force; $W' = F_v$. The vertical force at the steep wave front can be described by the Morison equation (Morison et al. 1950).

$$F_v = \frac{\rho}{2} A C_D v^2 + \rho V C_m \frac{dv}{dt} \quad (1)$$

where ρ = fluid density, A = cross sectional area of armor unit in direction of flow, C_D = drag coefficient, v = peak vertical velocity just above the armor layer as plotted in Figure 6, V = armor unit volume, C_m = inertia coefficient, and dv/dt = total fluid acceleration. The drag force can be expressed as a function of the armor nominal

diameter, D_n , by introducing an armor shape factor, K_A , as follows

$$A = K_A D_n^2 \tag{2}$$

The drag force in (1) is then given by

$$F_D = \rho D_n^2 C'_D v^2 ; \quad C'_D = \frac{K_A C_D}{2} \tag{3}$$

where the nominal diameter is defined as

$$D_n = V^{1/3} = \left(\frac{W}{\gamma_r} \right)^{1/3} \tag{4}$$

where W = armor weight, V = armor volume, and γ_r = armor specific weight.

At the point of maximum vertical fluid velocity, the local vertical fluid acceleration, $\partial v/\partial t$, and horizontal velocity, u , are negligible. As such, the total acceleration reduces to a convective term.

$$\left(\frac{dv}{dt} \right)_{\max} = \left(\frac{\partial v}{\partial t} + u \frac{\partial v}{\partial x} + v \frac{\partial v}{\partial y} \right)_{\max} \approx v \frac{\partial v}{\partial y} \tag{5}$$

where x = horizontal coordinate and y = vertical coordinate. If we assume the convective acceleration across the armor layer to vary linearly vertically, then the acceleration can be expressed as

$$\left(\frac{dv}{dt} \right)_{\max} \approx v \frac{\partial v}{\partial y} = K_c \frac{v^2}{D_n} \tag{6}$$

where K_c is an empirical coefficient on the order of unity. The maximum inertial fluid force in (1) can thus be reduced to

$$F_i = \rho D_n^2 C'_m v^2 \tag{7}$$

with

$$C'_m = K_c C_m \quad (8)$$

Substituting (3) and (7) into the stability criterion $W' = F_v$ with $W' = \rho g(S_r - 1)D_n^3$ yields a stability relation in form similar to Shields criterion for the initiation of motion of sediment particles

$$\frac{v_c^2}{D_n g(S_r - 1)} = (C'_D + C'_m)^{-1} \quad (9)$$

where S_r = armor specific gravity, g = acceleration of gravity, and v_c = critical vertical velocity at which armor just begins to lift. In terms of N_s = armor stability number, (9) becomes

$$N_s = \frac{H_c}{D_n(S_r - 1)} = \frac{gH_c}{v_c^2} (C'_D + C'_m)^{-1} \quad (10)$$

where H_c = critical wave height at toe. It is interesting to note that the stability number is primarily a function of the Froude number, $v_c / (gH_c)^{1/2}$. This formula ties the traditional stability relations to local vertical velocity measurements.

Based on results of detailed velocity measurements in the interior and just outside the armor layer, the vertical velocity gradient was found to be proportional to the ratio of the vertical velocity and the armor diameter, as assumed in (6). This is shown in Figure 7 for a typical case. The empirical convection coefficient is $K_c = 0.67$ for these tests.

The drag and inertia coefficients can be more accurately defined if we assume spherical armor. Based on previous studies of forces on armor by Mizutani et al. (1992) and Torum (1994), reasonable estimates for drag and inertia coefficients are $C_D = 0.8$ and $C_m = 0.4$ yielding

$$C'_D = \frac{K_A C_D}{2} \approx 0.5 \quad (K_A = 1.21) \quad (11)$$

$$C'_m = K_c C_m \approx 0.3 \quad (K_c = 0.67) \quad (12)$$

where $K_A = 1.21$ corresponds to a sphere. The critical vertical velocity, v_c , for the

incipient vertical armor movement reduces to

$$\frac{v_c^2}{D_n g(S_r - 1)} = 1.3 \tag{13}$$

where the critical vertical velocity, v_c , depends on the nominal diameter, D_n , and the specific gravity, S_r , only, for a loose armor unit.

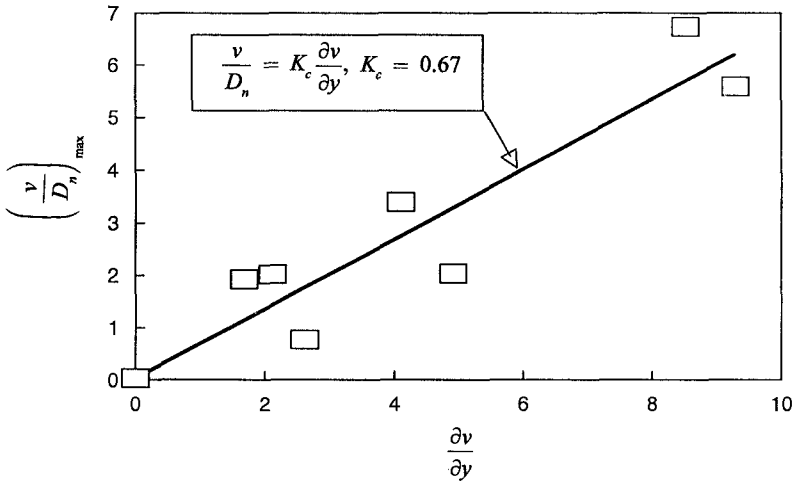


Figure 7. Vertical variation of vertical velocity under steep wave front.

Plan 4 in Table 1 was designed to test the above criterion. For Plan 4, the armor layer was constructed using silicon rubber spheres which were glued together and attached to an inflexible yet porous metal mat. The metal mat was placed directly on the underlayer and fixed to the flume walls. Several loose concrete spheres were placed in the armor layer along a line from above the still water level down to the toe. Each two loose spheres were separated by two glued spheres so that there was no interaction between loose spheres. The sphere layer of Plan 4 was constructed to have the minimum porosity of 0.33.

For Plan 4, the loose spheres would not move under any conditions unless they were slightly raised in the armor layer. This was accomplished by placing a 0.5-cm-thick washer under each sphere. The primary effect of this was to raise the porosity surrounding the loose sphere slightly, providing a path for water motion under the sphere. The only motion observed for the raised loose spheres was vertical motion under the steep wave front, following a slightly elliptical path, and landing back in their hole after the wave front passed. For tests with vertical velocities corresponding to the critical value, the spheres were just lifting off. For the larger vertical velocities, the

spheres were lifting entirely out of their initial holes, but settling back into their holes. Spheres at a depth of one-third the toe depth were the most mobile while spheres at the still water level were somewhat less mobile. This movement corresponded to the variation of the vertical velocities in the water column as shown in Figure 6. Figure 8 shows the incipient motion criterion versus wave steepness for Plan 4 using a few representative points from each motion category. The dark horizontal line represents the theoretical incipient motion criteria while the velocity measurements are represented by the dark dots. Observed movement is noted for each data point. For the drag and inertia coefficients selected, the incipient motion criteria agrees quite well with the observed movement.

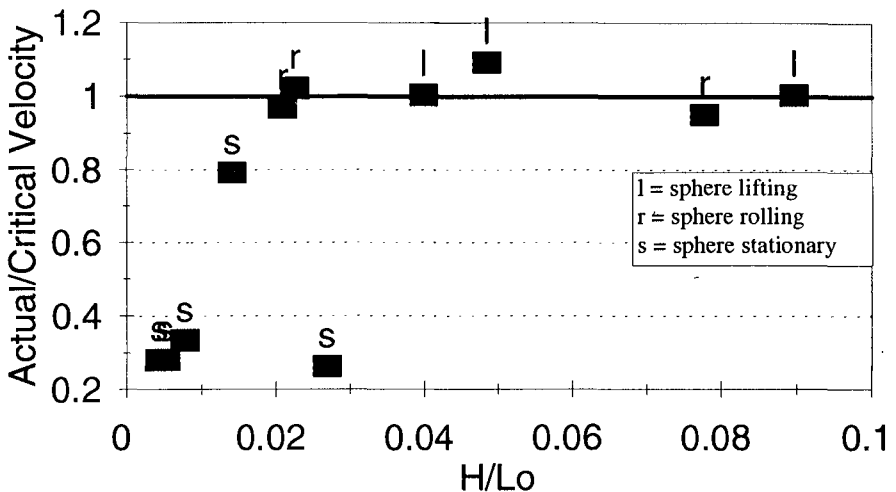


Figure 8. Incipient motion criterion versus wave steepness

CONCLUSIONS

Experiments on incipient motion of breakwater armor showed several modes of displacement. One dominant mode was due to vertical wave forces which are shown to occur at the point of maximum vertical velocity under the steep wave front. A simple relation was derived assuming a Morison-like wave force balanced by the armor unit submerged weight. The wave force model was composed of drag, due to the maximum vertical velocities, and inertia, due to the vertical convective accelerations. The maximum vertical convective acceleration is shown to be roughly linearly related to the square of the velocity, which puts the inertial force term into the same form as the drag term. The resulting incipient motion stability relation is similar in form to the Shields sediment motion criteria. Further, when expressed as a traditional stability number, incipient motion is shown to be a function of the Froude number, $v/(gH)^{1/2}$. The incipient motion criterion is shown to predict the incipient motion of spheres well for the conditions tested.

ACKNOWLEDGEMENT

This study was conducted and this article prepared with funding from the U.S. Army Engineer Coastal R&D Program. Permission to publish this article was granted by the Office, Chief of Engineers. Dr. Steven Hughes, U.S. Army Engineer Waterways Experiment Station, is acknowledged for his helpful suggestions regarding interpretation of data throughout the study.

REFERENCES

- Hudson, R.Y., 1958. "Design of quarry-stone a cover layers for rubble-mound breakaters," *RR 2-2*, USAE WES, Vicksburg, MS.
- Iribarren, R., 1938. "Una formula para el calculo de los diques en escoller (A formula for the calculation of rock-fill dikes)," *Revista de Obras Publicas*, Madrid, Spain. Translated by D. Heinrich, Tech. Rep. HE-116-295, Fluid Mech. Lab., Univ. of Calif., Berkeley, CA, 1948.
- Kobayashi, N, Wurjanto, A., and Cox, D. 1990. "Rock slopes under irregular wave attack," *Proc. 22nd ICCE*. ASCE, NY, NY, 1306-1319.
- Mizutani, N., Iwata, K., Rufin, T.M., and Kurata, K. 1992. "Laboratory investigation of the stability of a spherical armor unit of a submerged breakwater," *Proc. 23rd ICCE*. ASCE, NY, NY, 1400-1413.
- Morison, J., O'Brien, M., Johnson, J., Scaaf, S. 1950. "The force exerted by surface waves on piles," *Petroleum Trans.* 189, TP 149-154.
- Sawaragi, T., Iwata, K., and Kobayashi, N., 1982. "Conditions and probability of occurrence of resonance on steep slopes of coastal structures," *Coastal Engineering in Japan*, 25, 75-90.
- Sigurdsson, G. 1962. "Wave forces on breakwater capstones," *J. Wirwy. and Harb. Div.*, ASCE, WW3, 27-60.
- Torum, A., van Gent, M. 1992. "Water particle velocities on a berm breakwater," *Proc. 23rd ICCE*, ASCE, NY, NY, 1651-1665.
- Torum, A. 1994. "Wave-induced forces on armor units on berm breakwaters," *J. Wirway, Port, Coast., and Oc. Engrg.*, ASCE, 120(3), 251-268.

CHAPTER 141

OVERTOPPING REDUCTION IN CROWNWALL DESIGN

José Luis Monsó ¹

Alfonso Vidoar ²

Cristina Cadevall, Cristina García ³

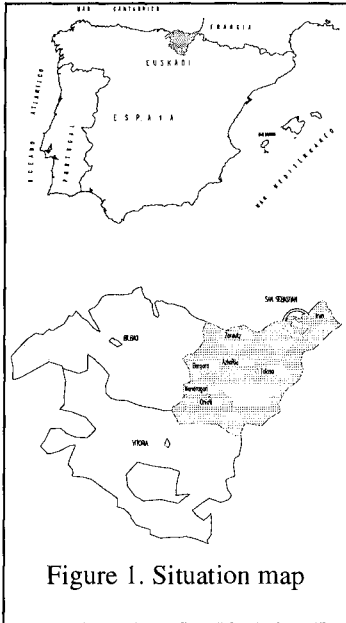


Figure 1. Situation map

1. ABSTRACT

This study for overtopping reduction in crownwall design presents several results of 2D (wave flume) and 3D (wave basin) tests on irregular wave overtopping of different configurations for breakwater sections were obtained by the Applied Hydrodynamics Institute (INHA) in order to improve the design of the small-craft harbour at San Sebastian in the North of Spain (fig.1).

San Sebastian is one of the most well-known and beautiful tourist cities in Europe and for that reason aesthetic as well as environmental aspects of construction had to be taken into account.

¹ Director, Instituto de Hidrodinámica Aplicada (INHA), Parc Tecnològic del Vallès, 08290 Cerdanyola, Spain. Prof. Dr. in Civil Engineering, Dept. Maritime Eng. UPC, 08034 Barcelona, Spain.

² Director, Civil Engineer, Europrincipia S.L., Parc Tecnològic del Vallès, 08290 Cerdanyola, Spain.

³ Research Engineers, Instituto de Hidrodinámica Aplicada (INHA), Parc Tecnològic del Vallès, 08290 Cerdanyola, Spain

2. INTRODUCTION

The San Sebastian harbour (fig.2) was designed by Europrincipia in 1995. The harbour would like to become a centre of attraction to citizens and tourists, not merely a berthing area for vessels. For this reason the creation of a new shopping and recreational area and urban integration with the city, which is extended to the end of the harbour by a promenade, are some of the issues that have to be dealt with.

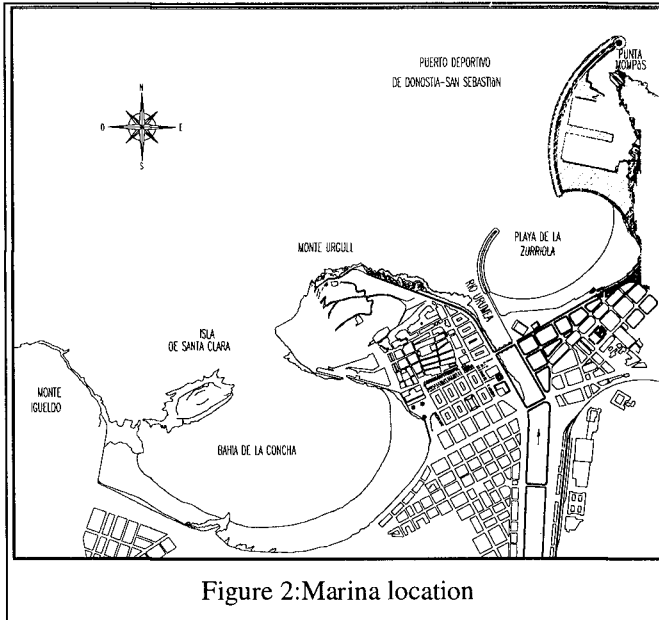


Figure 2:Marina location

From an engineering stand point the most important issue is, however, the wave climate, which is very severe in that area. The design incident wave height is $H_s=10.5\text{m}$ at a depth of $h=-20\text{m}$ and the average wave period is $T_z=15\text{s}$. The tidal regime in this area is $\text{hw}l=+4.8\text{m}$ and $\text{lw}l=0\text{m}$. The water depth at the toe of the berm can reach -15m and therefore important non breaking waves can reach the structure. For this reason, and also because the visual impact of a very high crownwall to prevent overtopping would be of significant importance for the city, it was necessary to determine a freeboard height of the crownwall that agreed with both requirements.

Some strategies for improving the performance of the main breakwater of San Sebastian harbour were therefore tested.

The design of a recurved breakwater in plan view (Figure 3) resulted in a reduction of overtopping rates due to oblique wave attack as well as a reduction of wave induced forces in the crownwall. These results can be shown by comparing 2D tests (straight breakwater) and 3D tests (curved breakwater).

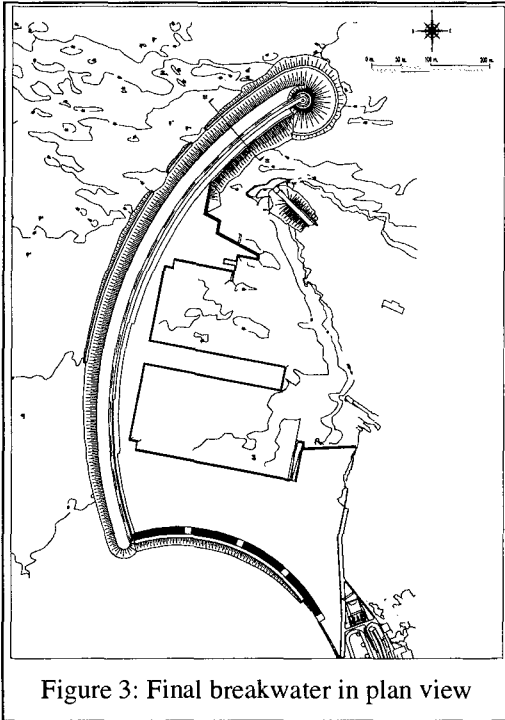


Figure 3: Final breakwater in plan view

3. PHYSICAL MODEL TESTS

The 3D model tests were conducted in a wave basin 28m long, 23m wide and 1.2 m high at scale 1/50 and the 2D model tests were performed at a scale of 1/30 in a wave flume with dimensions of 52m long, 1.8m wide and 2 m high.

In both facilities, tests of irregular waves with a Jonswap type spectrum were considered.

$$S_f = \alpha H_{1/3}^2 T_p^{-4} f^{-5} \exp[-1.25(T_p f)^{-4}] \gamma^{\exp[-(T_p f^{-1})^2 / 2\sigma^2]} \quad \text{with}$$

$$\alpha = \frac{0.0624}{0.230 + 0.0336\gamma - 0.185(1.9 + \gamma)^{-1}}$$

$$\sigma = \begin{cases} \sigma_a; f \leq f_p \\ \sigma_b; f \geq f_p \end{cases} \quad \sigma_a = 0.07 \quad \text{and} \quad \sigma_b = 0.09$$

$$\gamma = 1.9$$

The quantity f_p is the frequency at the spectral peak and T_p is the inverse of f_p

$$\text{with } T_z = 1.3T_p$$

The experiments were performed for 4 different water levels, and for 7 significant wave steps.

The section that was compared in 2D and 3D experiments is the one shown in fig.8. (fourth alternative) with a toe depth of 13m.

4. STRATEGIES TO REDUCE OVERTOPPING

The initial design (fig.4), almost a straight breakwater in plan view, was a stepped crownwall with height as reduced as possible in order to minimise visual impact. Rubble mound units were used instead of artificial blocks taking advantage of a nearby stone quarry which is able to provide parallelepipedic blocks of up to 70 Tn perfectly cut with explosives. The main features of this initial configuration are:

- Crownwall height : +14 m
- Weight of slope rubble mound units : 27 Tn
- Length of the berm: 45 m
- Depth of the berm : -5.5 m
- Weight of berm rubble mound units :17 Tn.

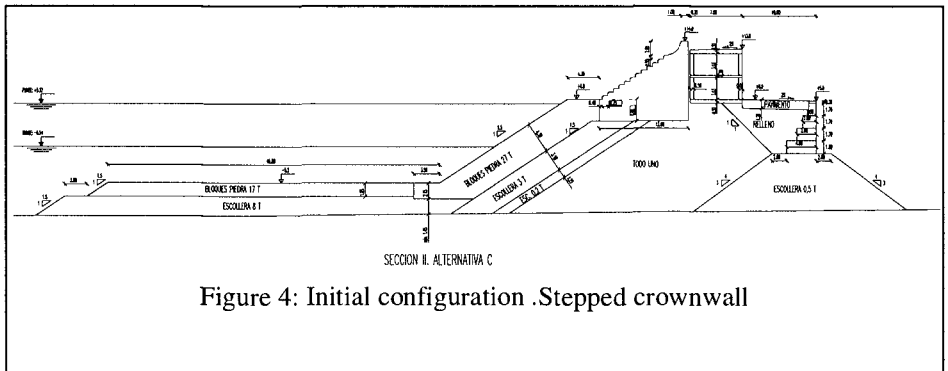


Figure 4: Initial configuration .Stepped crownwall

In order to analytically estimate the wave run-up and the overtopping rate several formulations were used. The initial configuration used the J.P. de Waal and J.W. van der Meer formula proposed in Coastal Engineering 1992. In this formula the expression that describes the average overtopping is an exponential function :

$$\frac{Q}{\sqrt{gH_s^3}} = 8 \cdot 10^{-5} \exp \left[3.1 \frac{Ru2\% - Rc}{H_s} \right]$$

where

$$\frac{Ru2\%}{H_s} = 1.5 \gamma_f \gamma_h \gamma_\beta \zeta_{p,eq} \quad \text{with a maximum of } 3.0 \gamma_f, \gamma_h, \gamma_\beta$$

The theoretical values obtained differed from the experimental ones. Some reasons for this can be : the stepped crownwall does not act like a rough slope and, moreover, the stepped crownwall design has a ramp effect, as was shown in the overtopping tests performed.

As soon as the experimental values did not reach the requirements, 4 strategies to reduce overtopping rates were evaluated:

- To raise the height of the berm
- Design a crownwall topped with a recurved wall
- Raise the freeboard of the crownwall
- Design a curved breakwater in plan view.

These strategies were implemented in 4 new design alternatives.

a) First alternative:

In this case, the strategy of raising the height of the berm up to the MWL has the effect of a reduction of the initial overtopping rate as can be seen in several experiments carried out recently by Van der Meer (1990).

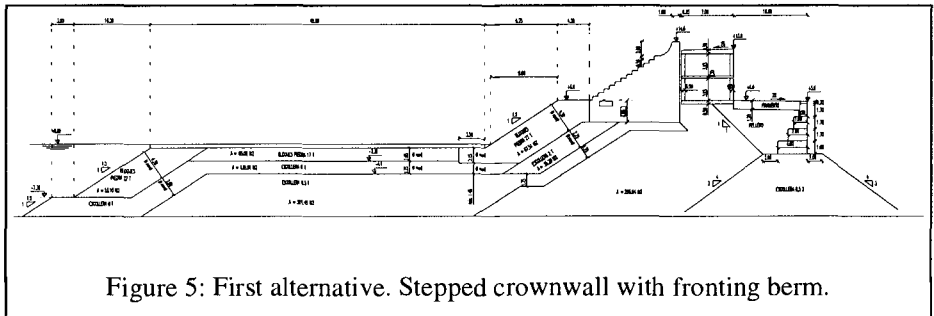


Figure 5: First alternative. Stepped crownwall with fronting berm.

The average overtopping rates for the section described above were still unacceptable. The reasons for these high values of Q_r were the relatively low freeboard and the ramp effect induced by the stepped crownwall.

b) Second alternative:

The second design alternative (fig.6) combines three more strategies in order to improve the overtopping rates: raise the freeboard, construct a recurved crownwall and ,finally, design a curved breakwater in plan view.

Raising the freeboard of the crownwall has an immediate reductive effect as expected by theory. Considering the simplified theoretical model of Jensen and Juhl (1987) or Ahrens (1988), the overtopping rate Q is an exponential function of the dimensionless freeboard, $F' = F/H_s$, with F the freeboard of the structure and H_s the incident significant wave height. The limitation of this strategy is the visual impact of construction, which should be kept to a minimum.

The construction of a crownwall topped with a recurved wall has also a beneficial effect. Experimental tests showed that overtopping rates are considerably reduced due to the effectiveness of the recurved wall.

c) Third alternative:

The third design alternative (fig.7) consisted of reducing the long berm at MWL and constructing a short berm high up the crownwall instead. For this configuration, as can be seen in figure 9, the overtopping rates increased again

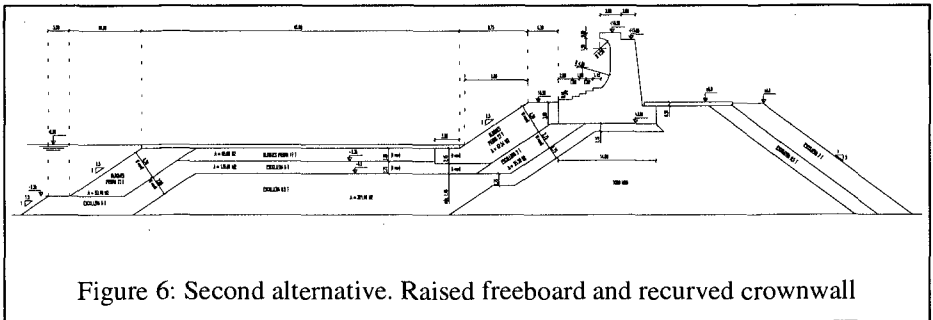


Figure 6: Second alternative. Raised freeboard and recurved crownwall

probably due to the fact that the recurved wall partially blocked by the berm is not effective enough from a hydraulic point of view. Therefore, the rubble mound berm in front of the recurved wall should not reach high up the wall, as in this case the small curve above would be ineffective. This means that the corresponding rubble mound slope produces a ramp effect on the waves, resulting in disappointing performance.

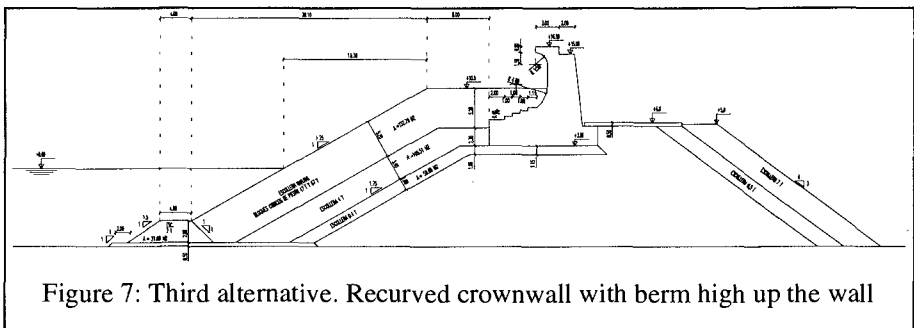


Figure 7: Third alternative. Recurved crownwall with berm high up the wall

d) Fourth alternative:

The final section proposed, corresponding to the fourth alternative (fig.8), has the following characteristics:

- Crownwall height : +16.5m
- Weight of slope rubble mound units : 27 and 47 Tn

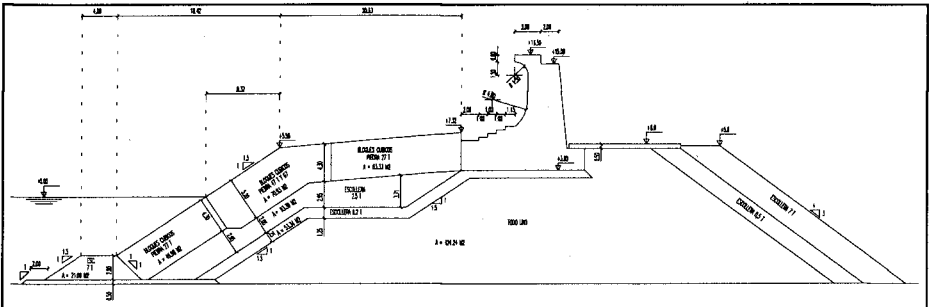


Figure 8: Fourth alternative. Final proposed section

- Length of the berm: 45 m
- Height of the berm : +7.5 m

Figure 9 shows the results of Q_r for the four alternatives.

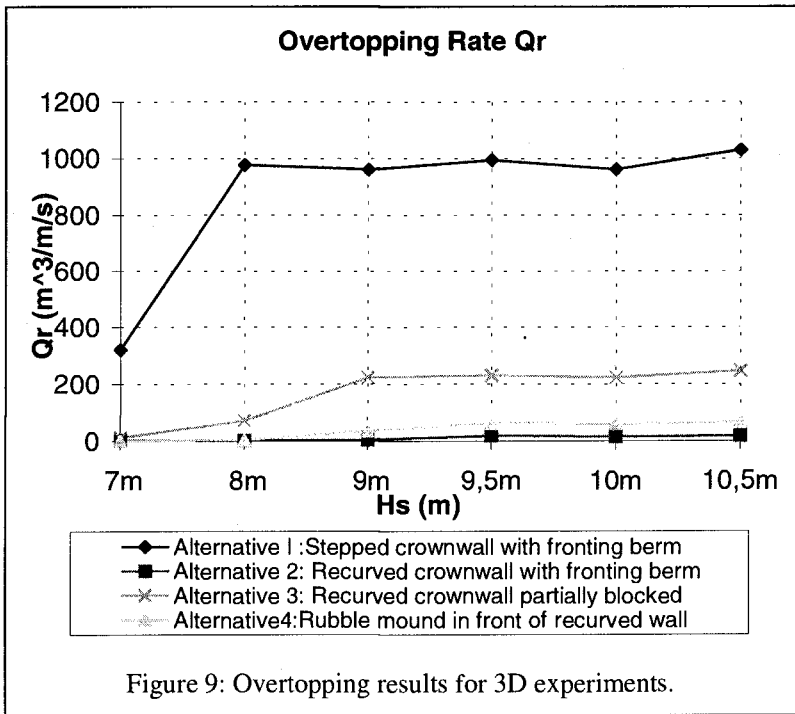


Figure 9: Overtopping results for 3D experiments.

5. COMPARISON BETWEEN 2D AND 3D RESULTS

Up to now, nothing has been said about the effect of a curved breakwater in plan view on the reduction of overtopping.



Figure 10: 3D model tests

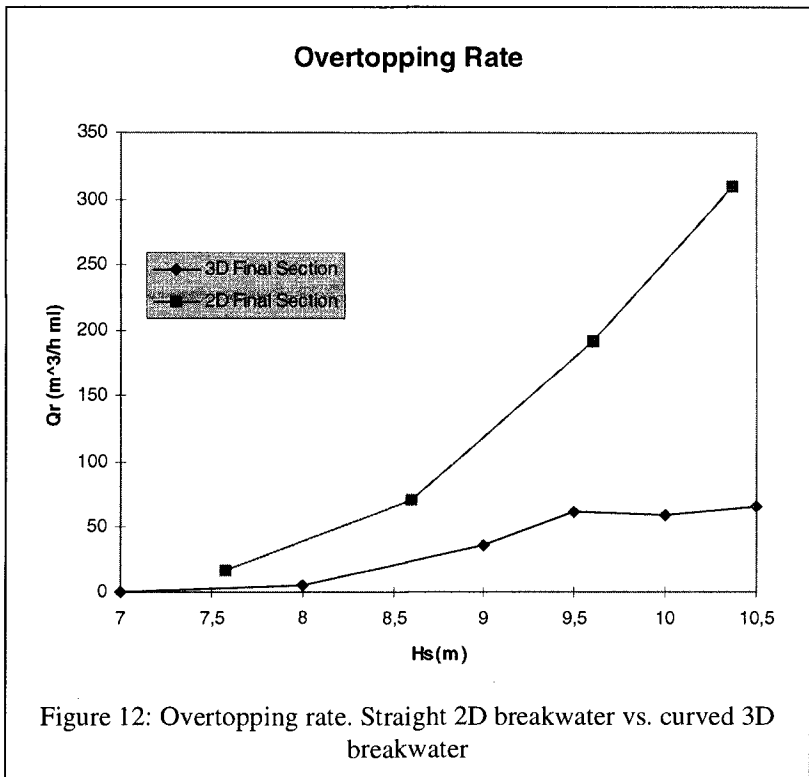


Figure 11: 2D model tests

In order to assess such an effect, 2D tests of alternative 4 were performed in a wave flume. Incidentally, stability tests of the crownwall were also performed in order to approve a final design of the breakwater.

Figure 11 shows the good performance of the curved breakwater making the wave return seaward.

Figure 12 shows the differences in overtopping reduction between a straight and a curved breakwater in plan view.



Apart from possible scale or laboratory effects that may somewhat reduce the difference in the overtopping rate, the tests performed confirm that the curved breakwater considerably improves the hydrodynamic performance of the water flowing along the crownwall, reducing wave overtopping.

All these results could be compared with some state of the art formulas for overtopping rates like for instance Van der Meer's. Unfortunately, the geometry did not meet the hypothesis or requirements to fit these formulas.

6. CONCLUSIONS

The laboratory tests conducted at INHA in Barcelona (Spain) with different configurations of the breakwater of San Sebastian have shown various alternatives as ways to reduce the overtopping rates. First of all, there is a more or less exponential relationship between dimensionless freeboard and overtopping. Moreover, the use of a rubble berm in front of the structure is also an improvement, as is the construction of a recurved crownwall of an appropriate shape. Finally, as determined by comparing wave flume tests with basin tests, the design of a curved breakwater in plan view instead of a straight one considerably

improves the hydrodynamic performance of the water flowing along the recurved wall and reduces wave overtopping. This series of strategies makes it possible to design an optimised breakwater compatible with the visual impact limitations of the site.

7. REFERENCES

- Ahrens, J.P., and Heimbaugh, M.S., "Seawall Overtopping Model", Proceedings of the 21st Coastal Engineering Conference, Malaga, Spain, June 1988.
- Jensen, O.J. and Juhl, J., "Wave Overtopping on Breakwaters and Sea Dikes", International Conference on Coastal and Port Engineering in Developing Countries, Benjing, China, Sept. 1987.
- Van der Meer, J.W. and Pilarczyk, K.W., "Stability of lowcrested and reef breakwaters", Proceedings of the 22nd Int. Conf. on Coastal Engineering, Delft, 1990.
- Battjes, J.A., "Wave Runup and Overtopping", Report to the Technical Advisory Committee on Protection Against Inundation, Rijkswaterstaat, the Hague, the Netherlands, 1974.
- Owen, M.W., "The Hydraulic Design of Sea-Wall Profiles", Proceedings of the International Coastal Engineering Conference, University of Southampton, England, Sept. 1982a
- Goda, Y., "Random Seas and the Design of Maritime Structures", University of Tokyo Press, Tokyo, Japan, 1985.

CHAPTER 142

Stable Profiles of Reshaping Breakwaters with a Berm Below the Water Level

C.I.Moutzouris¹

Abstract

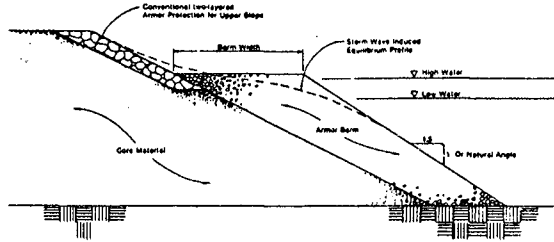
An experimental study of breakwaters with an initially horizontal berm below the SWL was conducted in a wave flume. The study aimed at defining the shape and geometrical features of the adjusted stable profiles and at confirming the existence of a zone of non-significant profile adjustment below the initially flat and horizontal slope.

Indroduction

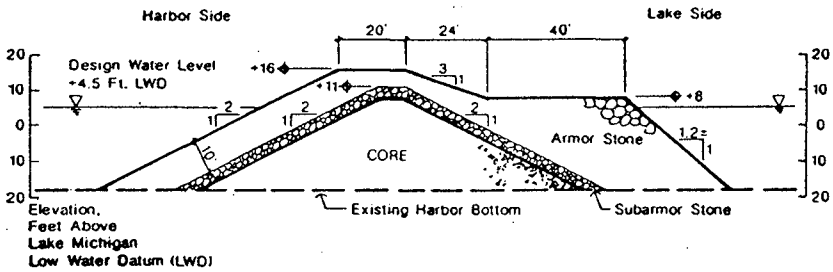
Berm breakwaters are increasingly recieving attention from researchers and practicing engineers (see f.i.van der Meer, 1988, Hall & Kao 1991, Tomasicchio et al., 1994, etc.), because they are considered to be economically attractive, to minimise rock movement and to reduce the time required for natural stability to be obtained. The concept of the berm is to pre-break incident waves further out and the stability is greatly enchanced due to waves breaking on a level surface instead of on a slope. As an almost general rule, the berm is placed slightly above the still water level(SWL), as it can be seen in Fig. 1.

Although the existence of a berm above the SWL facilitates the position of construction equipment

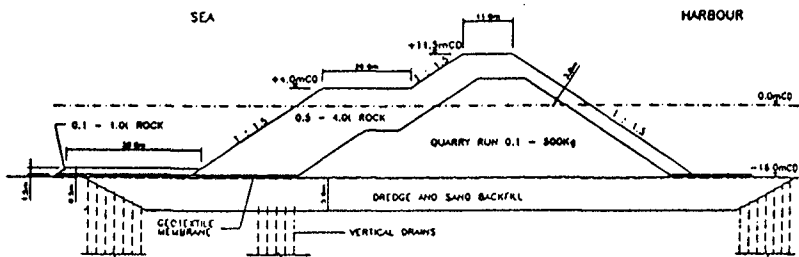
¹Professor, Laboratory of Harbour Works, Civil Engineering Department, National Technical University of Athens (NTUA), 5 Iroon Polytechniou Str., Zografou, 15773 Athens, Greece



from Rauw, 1988



from Montgomery et al., 1988



NOTE : DIMENSIONS AND ELEVATIONS SHOWN ARE FOR BREAKWATER LAYOUT NO. 1.

from Lingteringen et al., 1992

Figure 1. Typical breakwaters with a berm above the SWL

physical evidence seems to indicate that in reshaping (or dynamically stable) breakwaters flat slopes form below the SWL. The model tests reported by Foster and Hall show that flatter slopes tend to develop in the area below the SWL, but above the level of the lowest wave rundown, which is an area of maximum hydrodynamic forces. It is, therefore, surprising that very little

data exist on the response of profiles with a berm built below the SWL.

An experimental study of breakwaters with an initially horizontal berm below the SWL was conducted in a wave flume of the Laboratory of Harbour Works, NTUA. The study aimed at defining the shape and geometrical features of the adjusted stable profiles and at confirming the existence of a zone of non-significant profile adjustment below the initially flat and horizontal slope.

Experimental Conditions and Procedure

The wave flume was 25m long and 0.6m wide. The wave generator was placed at one end of the flume and generated regular waves. Crushed stones with a density of $\rho_s = 2.6\text{t/m}^3$ were used for the armour layer of the breakwaters. Nominal armour diameter D_{n50} defined as $(W_{50}/\rho_s)^{1/3}$, where W_{50} is the 50% value of armour mass distribution, was equal to 3.5cm.

A total of 258 experiments were carried out. The seaward slope underwent reshaping under the wave action until a stable (or final) profile developed. The influence of numerous initial conditions were examined, namely (see Fig.2 and Table 1): initial berm height d_a and width b , water depth d , wave height and length H and L , respectively, initial slope of the armour layers in the upper and lower parts 1:n and 1:m, respectively. For comparison reasons numerous experiments with $b = 0$ (conventional breakwater or no berm conditions) were carried out. Some experiments with a berm built above the SWL ($d_a > d$) were also performed. Finally, a number of experiments with an initially sloping berm (1:k) were executed.

The stability (or mobility) number N_g defined as $H/\Delta D_{n50}$ ranged in all cases examined from 2 to 3.5, which indicates a conservative design of the initial profile. Δ is the boyant mass density. The ratio h/d ranged from 0.2 to 0.35 indicating rather shallow water conditions.

The following geometrical features of the final profiles were measured (see Fig.3): slopes of the fronts and the berm, the final berm height d_b , the height h_c of the adjusted profile above the SWL, the length l_c of the adjusted profile above the SWL and the height of the zone of non-significant profile

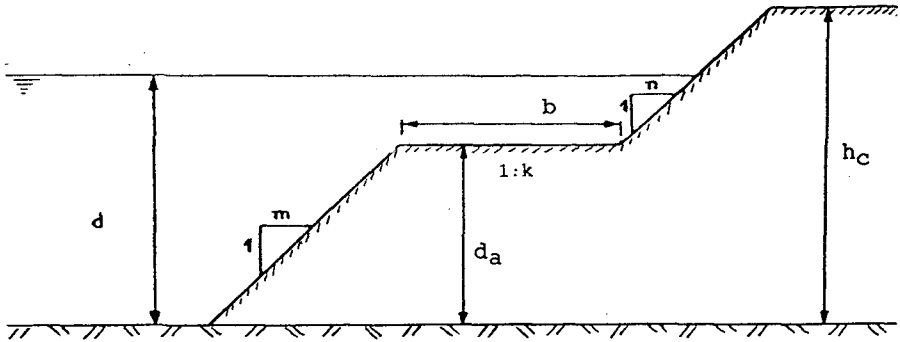
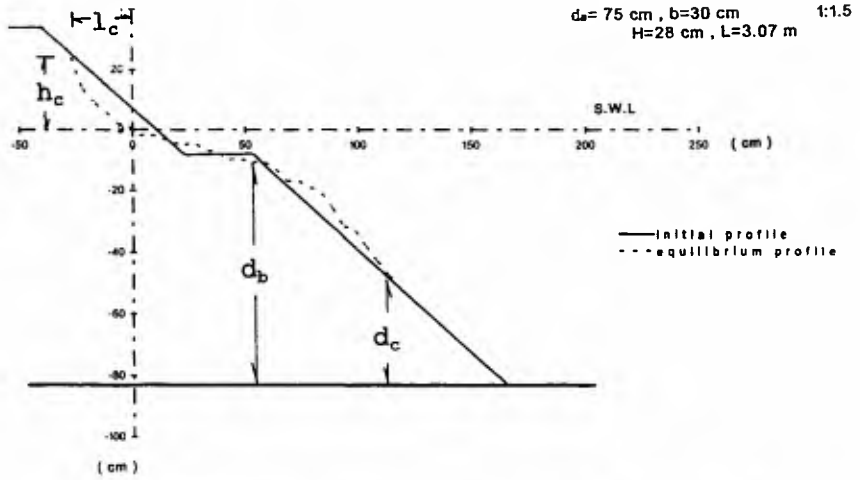


Figure 2. Definitions

water depth at the structure toe d	83 cm
water depth at the horizontal berm (or berm height) d_a	73, 83 and 91 cm
berm width b	0, 15, 30, 50 and 70cm
initial slope of the armour layer UPPER PART $1:n$	1 : 1.5 and 1 : 2
initial slope of the armour layer LOWER PART $1:m$	1 : 5 and 1 : 8
offshore wave length L	231 and 307 cm
H/L	0.05 to 0.12
b/L	0 to 0.30
wave height to water depth H/d	0.20 to 0.35 (Greek conditions)
H/D_{n50}	3.0 to 5.6
stability number $N_s = H/\Delta * D_{n50}$	2 to 3.5 (conservative design)

Table 1. Initial conditions in the experiments

adjustment d_c . Finally, the shape of the adjusted seaward profile above and below the SWL were studied.



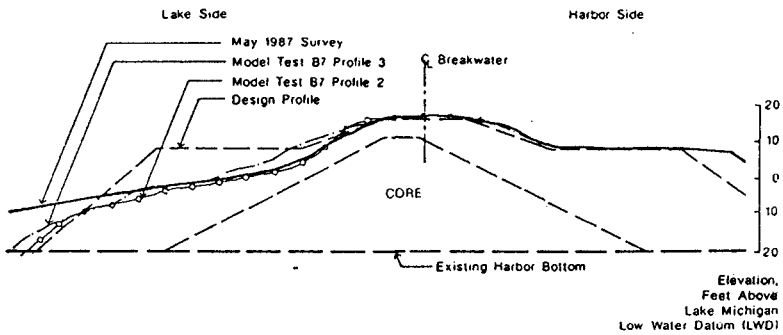
$b=15\text{cm}$ $d_a=83\text{cm}$ $L=3.07\text{m}$ $H=28\text{cm}$

Figure 3. Initial and final profiles

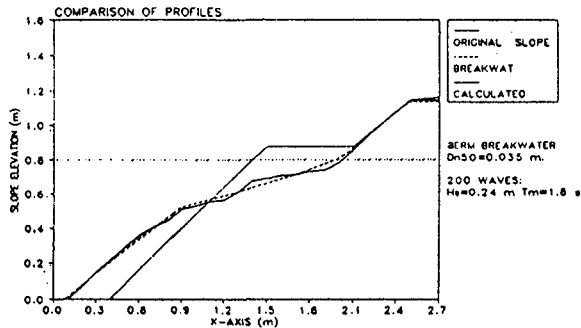
Results

In the paper results from the experiments are presented on the following features of the reshaped and finally stable profile of the breakwaters: final slope of the initially horizontal berm, non-dimensional height of the zone of non-significant profile adjustment, non-dimensional height and length of the adjusted profile above and below the SWL, final berm height and finally shape of the profile above and below the SWL.

Berms initially built horizontal tend to become sloping as a result of wave action, as it can be seen in Fig.4. In the present experiments it was found that



from Montgomery et al., 1988



from van Gent, 1995

Figure 4. Sloping final berm

always the final (or stable) berm was curvilinear with a central part nearly rectilinear. This central part was found to be almost always sloping with slopes ranging from 1:8 to 1:1 (vertical : horizontal). Most frequent final slopes were from 1:6 to 1:3. Slopes as steep as 1:2 or 1:1 were rare. No influence of the initial berm slope was detected (see Fig. 5).

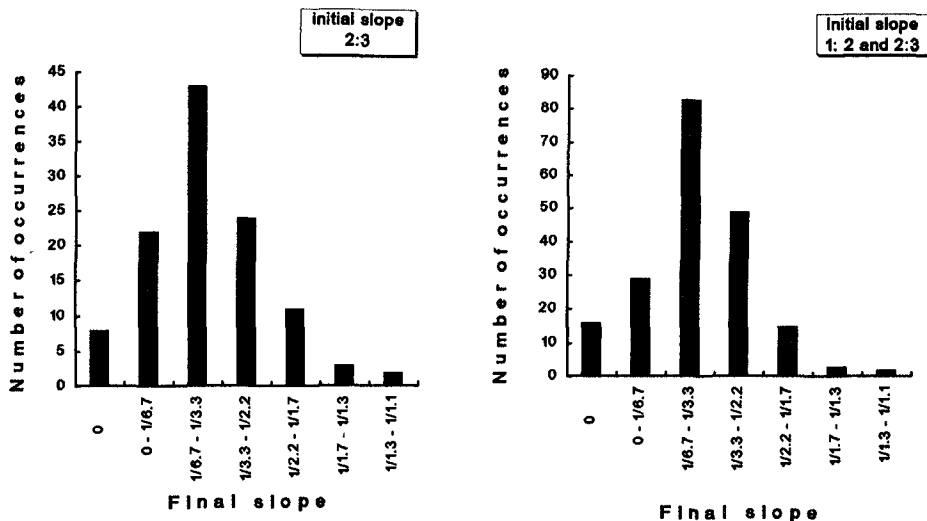


Figure 5. Slopes of the final berm

A considerable part of the profile remained always as it was built and did not deform under the wave action. The so-called "zone of non-significant profile adjustment" is the lower part of the seaward profile with a height above the flume bed equal to d_c . The values of d_c/d were found to range between 0.4 and 0.6 (see Fig.6). d_c/d was increasing when the initial slope was decreasing and this could be explained as follows: Changes in the breakwater profile are mainly due to wave breaking. As it is known, steeper breakwater slopes lead to a higher degree of wave reflection and to less pronounced wave breaking, which explains the experimental result. The initial height of the berm d_a was not found to influence the ratio d_c/d .

The conclusion that at least 40% of the height of the initial profile remains always stable and does not change is rather interesting.

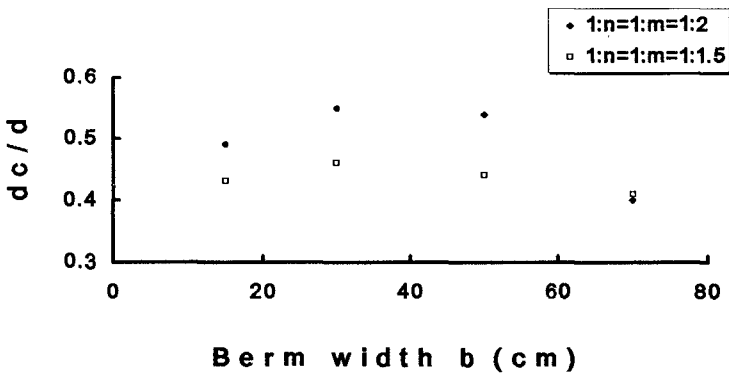
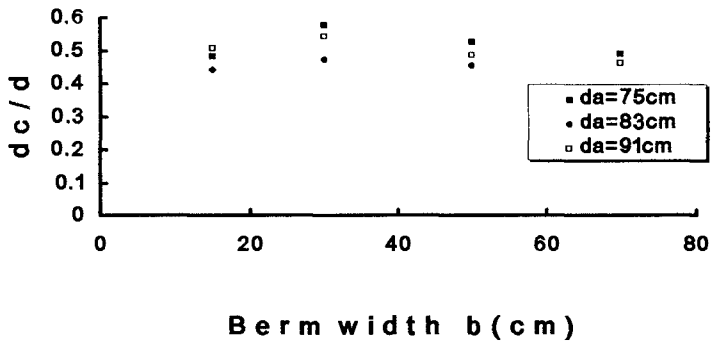
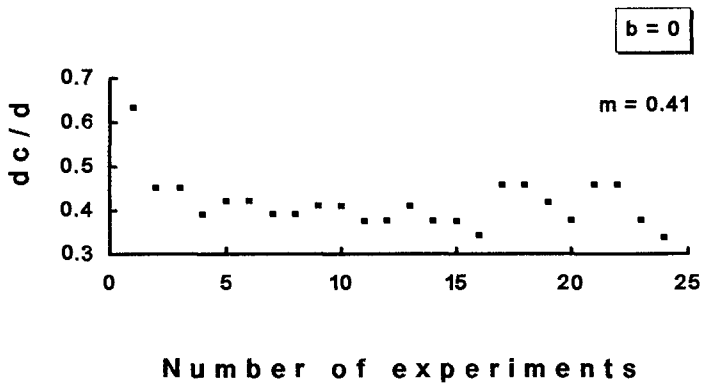


Figure 6. Height of the zone of non-significant profile adjustment

The height of the adjusted profile above the SWL was found to be strongly influenced by the width of the berm (see Fig. 7). In the case of a conventional breakwater (no berm) h_c was of the order of the deforming wave height (0.7 to 1.2 H). When a berm 70cm wide was present, h_c decreased to less than half the wave height. This could be explained as follows: Waves break directly on the slope of a conventional breakwater and cause extensive deformation of the profile. A wide berm forces the waves to break further offshore and, therefore, the zone of deformation becomes smaller.

Similar conclusions were drawn from the experimental results on the length l_c of the adjusted profile above the SWL. l_c was decreasing as the berm width was increasing. The wave length was in most cases in the order of 10 to 20 times the length of the adjusted profile (see Fig.8). Van der Meer (1988) proposed an empirical expression for l_c . The present results concerning l_c were not always in good agreement with van der Meer's $l_{c,VM}$.

The seaward profile of a berm breakwater is often predicted by simple models (f.i. van der Meer, 1988) based on physical model tests of the following type:

$$y = ax^b \quad (1)$$

where a and b are empirical coefficients. The present experiments showed that both the sections below and above the SWL of the deformed profile could be represented by an equation of the same type as equ.(1), namely:

$$y = a_1 x^{b_1} \quad \text{for the section below the SWL}$$

and

$$y = a_2 (-x)^{b_2} \quad \text{for the section above the SWL}$$

The range of values of b_1 and b_2 were as follows:

$$b_1 = 0.70 \text{ to } 1.15$$

$$b_2 = 0.98 \text{ to } 1.12$$

Table 2 contains the values of b_1 and b_2 as found in the present experiments and as proposed by various authors. According to a PIANC report, for values of N_s lower than about 10 to 15 the prediction model of van der Meer seems to be less reliable than for larger values of N_s .

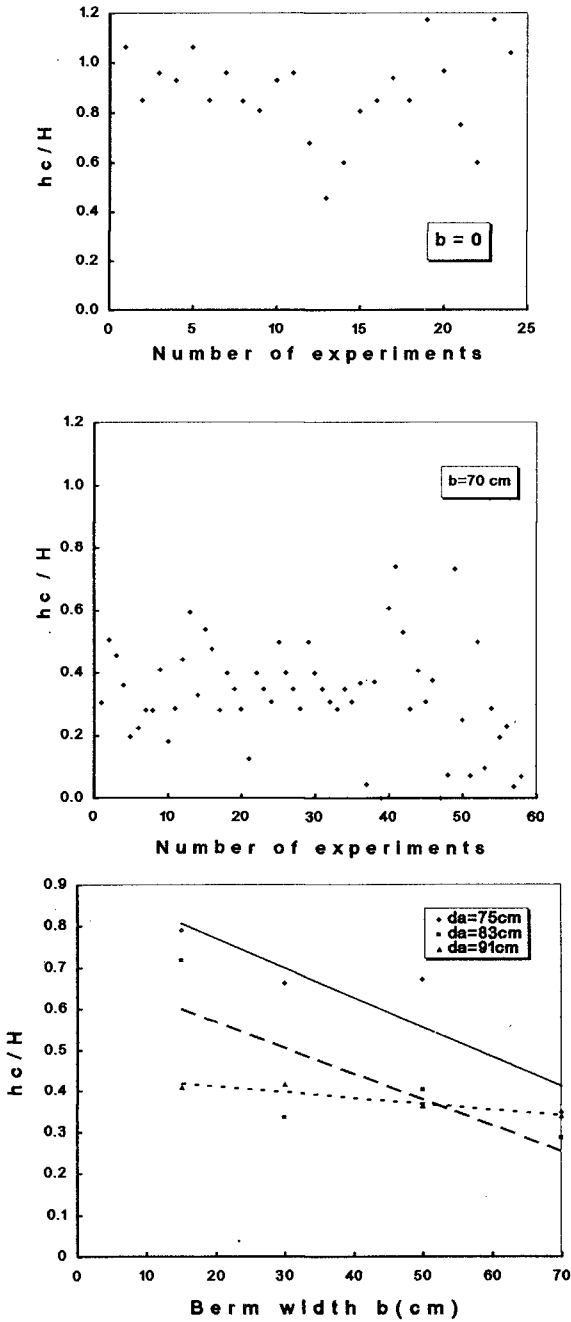


Figure 7. Height of the adjusted profile above the SWL

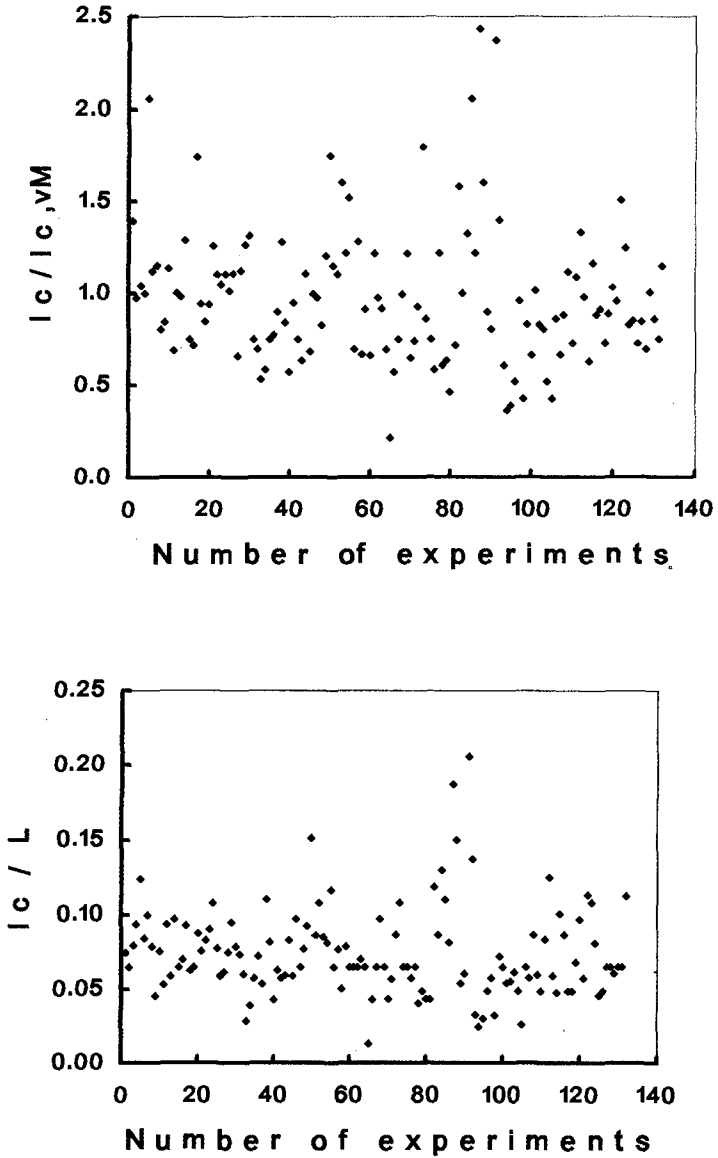


Figure 8. Length of the adjusted profile above the SWL

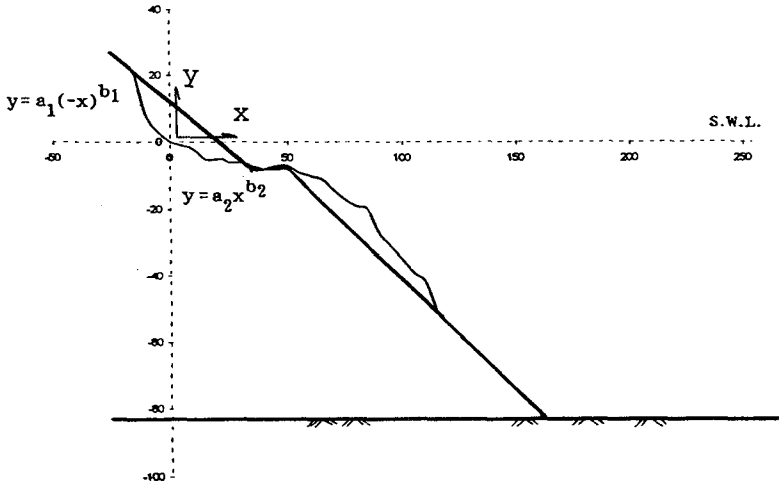


Figure 9. Final profile above and below the SWL

Researcher	b ₁	b ₂
Dean (1977)	-	0.67
Vellinga (1986)	-	0.78
Van der Meer (1988)	1.15	0.83
Present experiments		
(a) 1:n=1:m=1.5 and 1:2, 1:k=0 (250 exper.)	1.09	0.98
(b) 1:n=1:2, 1:m=1:1.5, 1:k=0 (8 exper.)	1.00	1.12
(c) 1:n=1.5, 1:m=1:2, 1:k=0 (21 exper.)	1.13	1.03
(d) 1:n=1:m=1:2, 1:k=0 (84 exper.)	0.99	1.05
(e) 1:n=1:m=1:1.5, 1:k=0 (112 exper.)	1.02	1.10
(f) 1:n=1:1.5, 1:m=1:2, 1:k=1:5 and 1:8 (8 exper.)	0.74	-

Table 2. Values of b₁ and b₂

The range of values of a_1 and a_2 was rather broad. No conclusion could be drawn.

The final height of the berm d_b is defined as the height above the flume bed of the center of the rectilinear part of the final sloping berm. d_b was always found to be in the order of 80% to 100% of the initial berm height d_a (see Fig.10). In many cases d_b was almost equal to d_a , which means that the final position of the berm did not change considerably in its central part.

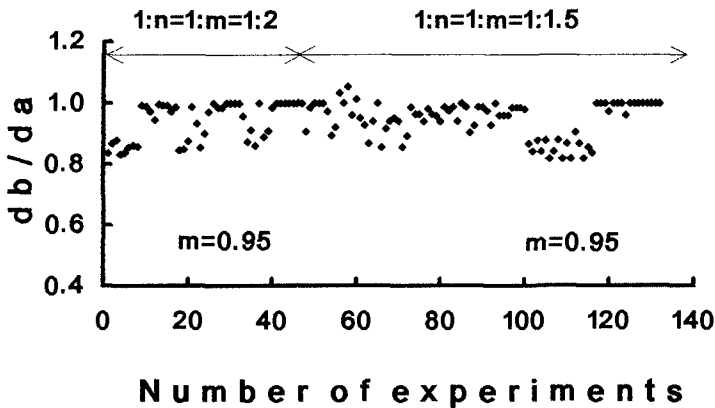


Figure 10. Final berm height

Conclusions

Some rather interesting conclusions are drawn from the results. The adjusted berm height was found to be in the order of 80% to 100% of the initial height. The height of the zone of non-significant profile adjustment was in all cases in the order of 40% to 50% of the water height.

Appendix: References

Hall K.R. & Kao J.S., (1991). *The influence of armour stone gradation on dynamically stable breakwaters*. Coastal Engineering, 15, pp. 333 -346

Laboratory of Harbour Works, N.T.U.A., (1996). *Breakwaters with a berm above the SWL - Experimental data*. Final Report from 6 Diploma Thesis, Athens (in Greek)

Ligteringen H., Rowe H.J.D., Hight D., Swetsloot P.A.J & Chan K.K., (1992). *The preferred concept for the Lamma breakwater, Western Harbour, Hong Kong*, Proc. PORTS 2000, Hong Kong, pp.401 -408

Montgomery R.J., Hofmeister G.J. & Baird W.F., (1988). *Implementation and performance of berm breakwater design at Racine, W.I.*, in BERM BREAKWATERS, ASCE, pp.229 - 249

Rauw C.I., (1988). *Berm type armor protection for a runway extension at Unalaska, Alaska*, in BERM BREAKWATERS, ASCE, pp. 251 - 269

Sigurdarson S.& Viggooson G., (1994). *Berm breakwaters in Iceland, Practical experiences*, Proc. HYDRO - PORT '94, Yokosuka, pp. 651 - 671

Tomasicchio G.R., Lamberti A. & Guiducci F., (1994). *Stone movement on a reshaped profile*, Proc. 24th Int. Conf. on Coastal Eng., Kobe, pp 1625 - 1639

van Gent M.R.A., (1995). *Wave interaction with berm breakwaters*, Jour. Wat. Ports Coast. Ocean Engineering, ASCE, Vol 121, No5, pp. 229 - 238

van der Meer J.W., (1988). *Rock slopes and gravel beaches under wave attack*. Delft Hydraulics Publ. No 396

Vellinga P., (1986). *Beach and dune erosion during storm surges*. Ph.D. thesis, Delft University of Technology

Widagdo A.B. & Istiyanto D.C., (1994). *Hydraulic model test on stability of a low crest breakwater with tetrapod armour layer*, Proc. HYDRO - PORT '94, Yokosuka, pp. 641 - 649

Yang D.W., Lindo M.H., Schemltz E.J. & Gomez D., (1994). *Design and construction of an extended berm breakwater at port of Haina, D.R.*, Proc. 24th Int. Conf. Coastal Eng., paper. No. 177

CHAPTER 143

Experiments on a non-wave overtopping type seawall

Keisuke Murakami,* I.Irie[†] and Y.Kamikubo[‡]

Abstract

A new type of seawall is proposed in this study. The seawall has a deep circular arc cross section and allows no wave overtopping any more. The critical crest elevation of the seawall, which defined as the minimum crest elevation on which the wave overtopping dose not occur at all, is investigated through the wave tank experiments. The wave pressures and wave forces acting on the seawall are also measured, and the characteristics of the wave pressure distribution and wave forces are examined.

1. Introduction

The landward area of a seawall provides an excellent space for various use so long as it is protected from the wave overtopping. Recently, the coastal areas are planned for land use which is very sensitive to the spray falls such as the electronic power plant and the airport, and the very small quantity of the wave overtopping rate is allowed. Furthermore the reduction of the seawall height is also required to afford unobstructed view as well as to save the cost. Though some types of seawall were proposed for the purposes of the reduction of the rate of wave overtopping and the height of seawall (Inoue, 1974; Takata, 1979; Kono, 1993), those could not release the land from hazard by the wave overtopping thoroughly.

In this study, a new type of seawall is proposed(referred as *Flaring Shaped Seawall (FSS)* ; see **Fig.-1**). The seawall has a deep circular arc cross section and no wave overtopping is allowed any more. The critical crest elevation of the *FSS*,

*Research Associate, Dept. of Civil Eng., Kyushu Univ., Fukuoka, 812-81, JAPAN

[†]Professor, Ditto

[‡]Graduate Student, Ditto

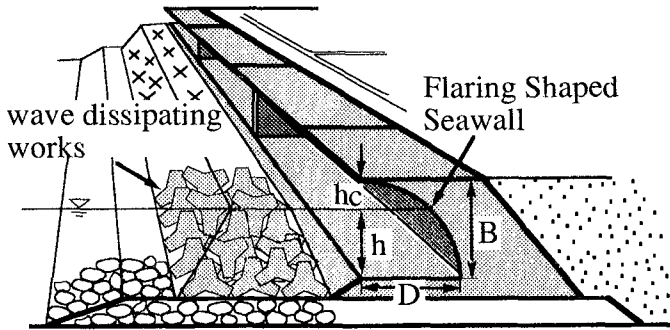


Fig.-1: Conceptual sketch of the *FSS*

which defined as the minimum crest elevation on which the wave overtopping dose not occur at all, was investigated through wave tank experiments, and the required crest elevation which satisfies the non-wave overtopping condition was examined. The wave pressures and uplift wave forces acting on the *FSS* were also measured through wave tank experiments and characteristics of the wave pressure were discussed by classifying the wave colliding patterns in front of the *FSS*.

2. Experimental conditions

2.1 Measurement of the critical crest elevation

As shown in **Fig.-2**, the experiments were conducted with two-dimensional wave tank of $28m$ in length, $0.5m$ in height and $0.3m$ in width. The water depth was maintained at $h_0 = 35cm$ and the impermeable slope with $1/20$ was installed at the end of the wave tank. Four types of seawall with the same seawall

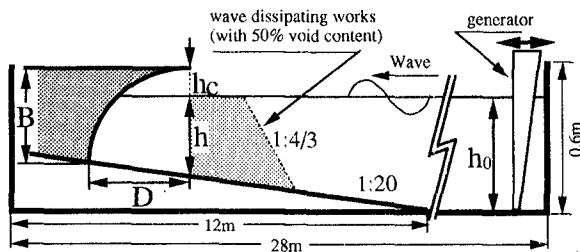


Fig.-2: Schematic of wave tank facility

Table-1: Wave conditions for the measurement of the critical crest elevation

$B(cm)$	D/B	H_0/L_0	$H_0(cm)$
15	0	0.012	4,6,7,8,9
		0.036	
	0.5	0.012	
		0.036	
	1.0	0.012	
		0.036	
	2.0	0.012	
		0.036	

height, $B = 15cm$, and the different arc depth, $D/B = 0, 0.5, 1.0$ and 2.0 , were tested. The tip of these seawall was made with a thin plate and its thickness did not affect to the wave overtopping. The critical crest elevation depends on the configurations of the wave dissipating works such as crest elevation, crown width, location and void content (e.g., Yamamoto, 1984, Takayama, 1988, Sasajima, 1993). In this study, the wave dissipating works with 50% void content was installed in front of the seawall and its crest elevation was coincide with the still water level. The wave dissipating works was made by using 1/25 scale model of 2t type blocks, and these blocks were piled one upon another in the layers.

Table-1 shows the incident wave conditions, where H_0 and L_0 indicate the incident wave height and wave length respectively. Two kinds of incident wave steepness of $H_0/L_0 = 0.012$ and 0.036 were used in this experiment, and the incident wave height, H_0 was changed in the range from $4cm$ to $9cm$. With changing the location of the seawall and incident wave height, the critical crest elevation, h_c for these incident wave condition was measured. The critical crest elevation was obtained by observing whether the wave overtopping occur or not.

2.2 Measurement of the wave pressure

The experiments were conducted with two-dimensional wave tank of $20m$ in length, $1.2m$ in height and $0.6m$ in width. The water depth was maintained at $h_0 = 85cm$. Four types of seawall with the combinations of the different seawall height, $B = 22.5cm$ and $36.4cm$, and the different relative arc depth, $D/B = 1.0$ and 0.5 were tested. The wave dissipating works with 50% void content and crest elevation in the still water level was installed in front of the seawall.

Table-2 shows the incident wave conditions. The incident wave steepness of $H_0/L_0 = 0.036$ was used in this experiment, and the incident wave height, H_0 was changed in the range from $4cm$ to $13cm$. With changing the location of the seawall and incident wave height, the wave pressure distributions on the seawall were measured by the pressure gauges of $8mm$ diameter attached on the face of

Table-2: Wave conditions for the measurement of the wave pressure

B (cm)	D/B	h (cm)	H_0 (cm)	B (cm)	D/B	h (cm)	H_0 (cm)
22.5	0.5	11	6,8,10,11,12,13	36.4	0.5	27	7,9,11,13
		13	6,8,10,11,12,13			30	3,5,7,9
		15	6,8,10,12,13			32	4,5,6,7
		18	4,6,8,9,10				
	1.0	11	6,8,10,11,12,13		1.0	24	7,9,11,13
		13	6,8,10,11,12,13			27	7,9,11,13
		15	6,8,10,12,13			30	7,9,11,13
		18	4,6,8,9,10			34	3,4,5,6

the seawalls. The output signals were recorded in the digital data recorder with 1000Hz sampling frequency.

3. Characteristics of the critical crest elevation

Fig.-3 shows the characteristics of the critical crest elevation, h_c/H_0 for the incident wave steepness of $H_0/L_0 = 0.012$ on which the wave dissipating works are installed in front of the seawall. **Fig.-4** also shows the characteristics of h_c/H_0 for $H_0/L_0 = 0.036$. In these figures, the symbols \circ , \diamond , and \triangle show the results of the *FSS* with $D/B = 0.5$, 1.0 and 2.0 respectively. The symbol \bullet also shows the results of the conventional upright seawall which has the same seawall height as other *FSS*. The thick line in **Fig.-4** shows the relative crest elevation of the upright seawall with wave absorber proposed by Goda(1985) for $H_0 = 2\text{m}$ as a model scale of 1/20. The wave overtopping rate, $q = 2 \times 10^{-4}(\text{m}^3/\text{m} \cdot \text{sec.})$ was employed as a level where the wave overtopping rate can be considered negligible.

The critical crest elevation, h_c/H_0 of the conventional upright seawall increase linearly with increase of the relative water depth, h/H_0 . On the other hand, the critical crest elevation of the *FSS* decrease with increase of h/H_0 , and the differences of the critical crest elevation between *FSS* and conventional upright seawall become larger. The *FSS* checks the wave overtopping more effectively than the upright seawall, and the crest elevation, h_c of the *FSS* can be reduced to about a half of the offshore wave height even under the non-wave overtopping condition.

Fig.-5 and **Fig.-6** show the critical crest elevation for $H_0/L_0 = 0.012$ and 0.036 on which the wave dissipating works is not installed in front of the seawall. Though the characteristics of the critical crest elevation are similar to the results shown in **Fig.-3** and **Fig.-4**, the differences of the critical crest elevation between

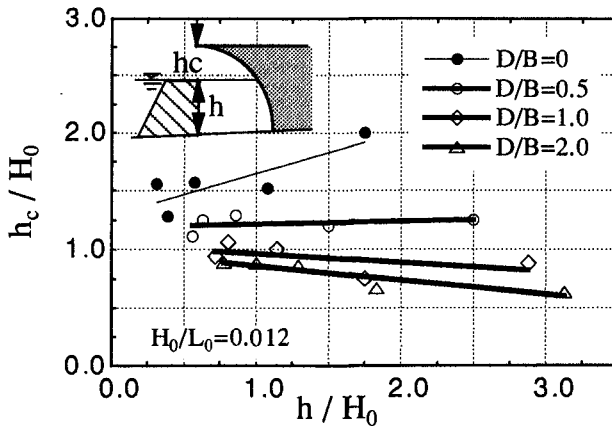


Fig-3: Critical crest elevation for $H_0/L_0 = 0.012$ (with wave dissipating works)

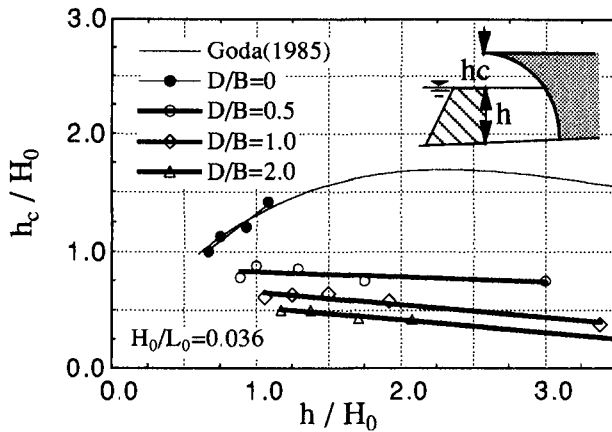


Fig-4: Critical crest elevation for $H_0/L_0 = 0.036$ (with wave dissipating works)

the *FSS* and upright seawall become significant because h_c/H_0 of the upright seawall increase rapidly with increase of h/H_0 .

Comparing with the results of $D/B = 0.5, 1.0$ and 2.0 in **Fig.-3** and **Fig.-4**, the checking capability of the wave overtopping becomes higher along with the increase of the relative circular arc depth, D/B . **Fig.-7** shows the relationship between the critical crest elevation and relative arc depth, D/L_0 . h_c/H_0 decreases monotonously with increase of D/L_0 . So that, the *FSS* with deep arc depth relative to the incident wave length is effective for the prevention of the

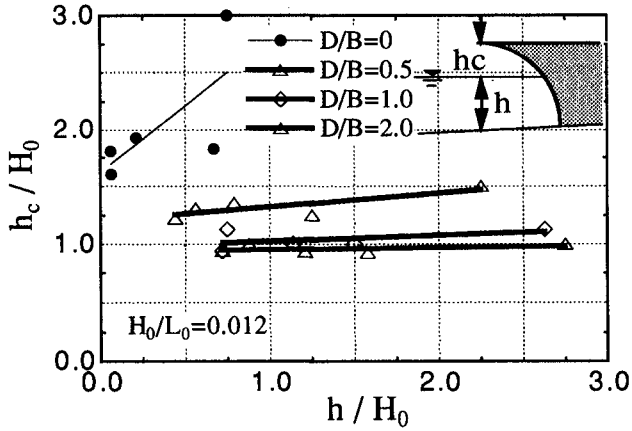


Fig-5: Critical crest elevation for $H_0/L_0 = 0.012$ (without wave dissipating works)

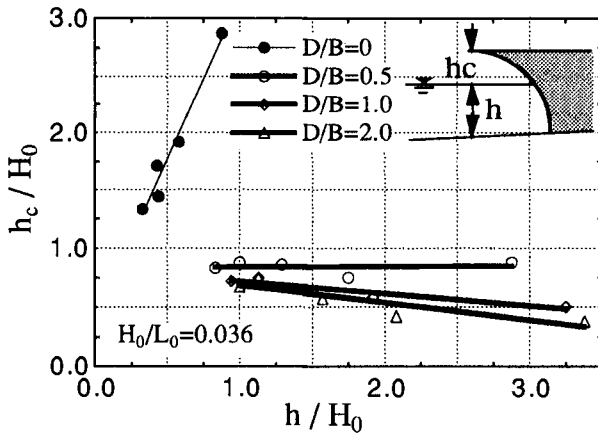


Fig-6: Critical crest elevation for $H_0/L_0 = 0.036$ (without wave dissipating works)

wave overtopping.

The critical crest elevation, h_c/H_0 is deeply related to h/H_0 , D/B , H_0/L_0 , H_0/h_0 , $\tan \beta$ and f_D , where f_D means a wave damping rate by the wave dissipating works. The linear multiple regression analysis was carried out with using above factors to obtain the approximate equation for h_c/H_0 , and the equation was obtained as follows:

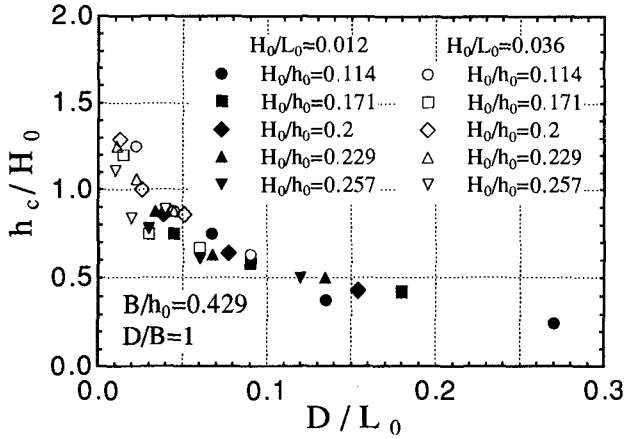


Fig.-7: Relationship between h_c/H_0 and D/L_0

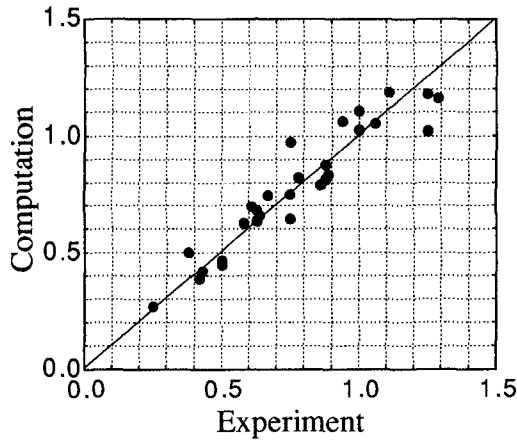


Fig.-8: Results of the regression analysis

$$\frac{h_c}{H_0} = -0.24 \frac{h}{H_0} - 0.18 \frac{D}{B} - 11.59 \frac{H_0}{L_0} - 2.63 \frac{H_0}{h_0} + 2.17 \quad (1)$$

where $\tan \beta$ and f_D are constant in this study.

Fig.-8 shows a result of the regression analysis. The computed results show fairly good agreements with experimental ones, and h_c/H_0 is estimated with high correlation coefficient of $\gamma = 0.95$ by Eq.(1).

4. Wave pressure acting on FSS

Fig-9 and Fig-10 show the wave pressure distributions on the *FSS* of $D/B = 1.0$ and 0.5 at different water depth, h/h_0 , where the seawall height is $B = 22.5\text{cm}$. The lateral axis shows the location of the wave pressure gauges and coordinate z is taken upward from the still water surface. Each symbol in

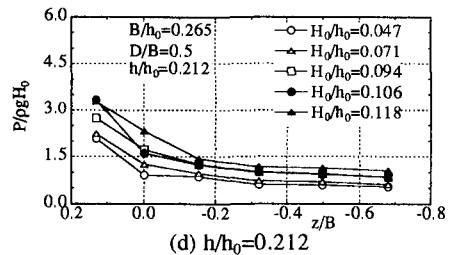
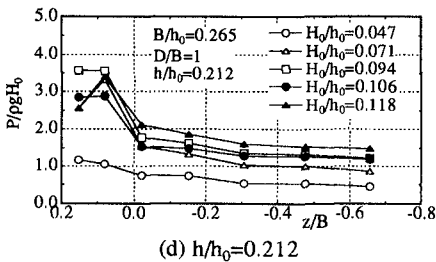
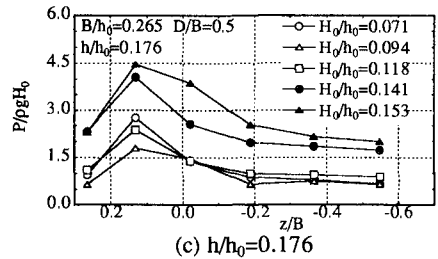
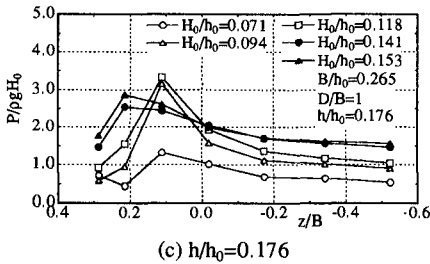
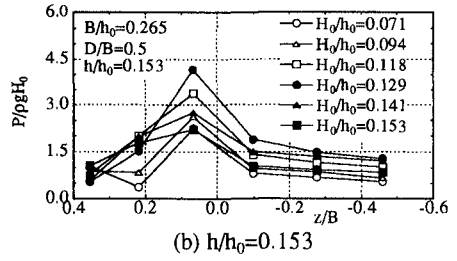
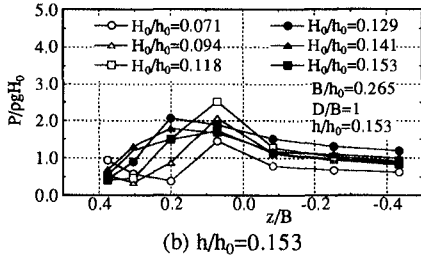
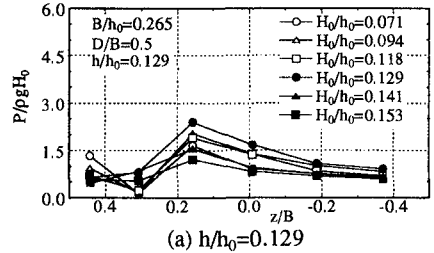
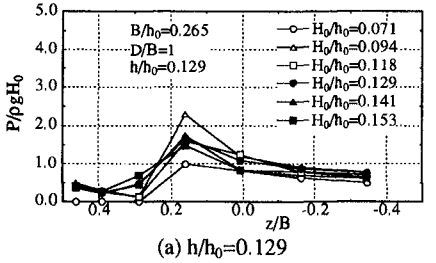


Fig-9: Wave pressure distributions on *FSS* of $D/B = 1.0$

Fig-10: Wave pressure distributions on *FSS* of $D/B = 0.5$

the figures mean the difference of the incident wave height, H_0/h_0 .

The patterns of the wave pressure distribution are varied with the incident wave height, H_0/h_0 and the water depth, h/h_0 . The maximum wave pressure appears between $z/B = 0$ and 0.2 , and the pressure in the range from $P_{max}/\rho g H_0 = 1.2$ to 4.5 were observed. The values of the maximum wave pressure closely relate to the wave colliding patterns in front of the *FSS*.

Fig.-11 and Fig.-12 show the variation of the maximum wave pressure,

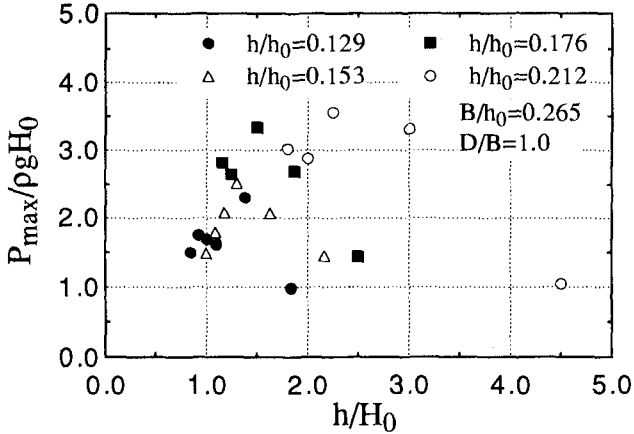


Fig.-11: Variation of the maximum wave pressure to the relative water depth, h/H_0 ($D/B = 1.0$)

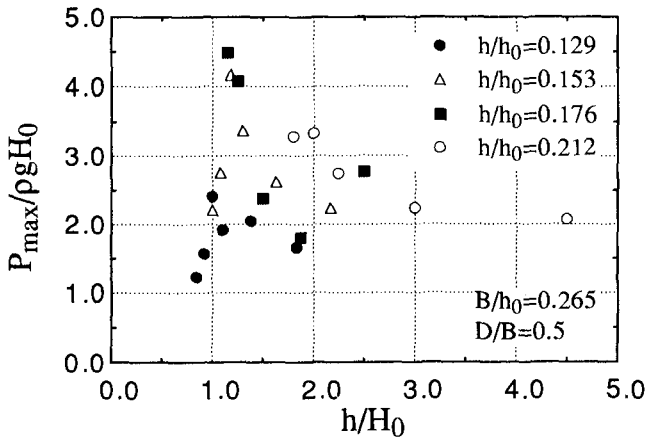


Fig.-12: Variation of the maximum wave pressure to the relative water depth, h/H_0 ($D/B = 0.5$)

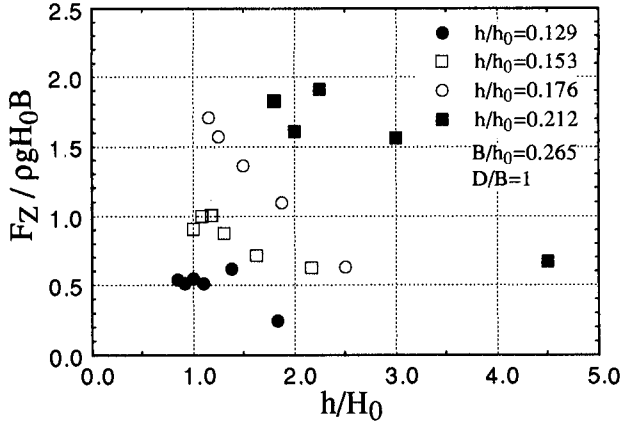


Fig-13: Variation of the vertical wave force to the relative water depth, h/H_0 ($D/B = 1.0$)

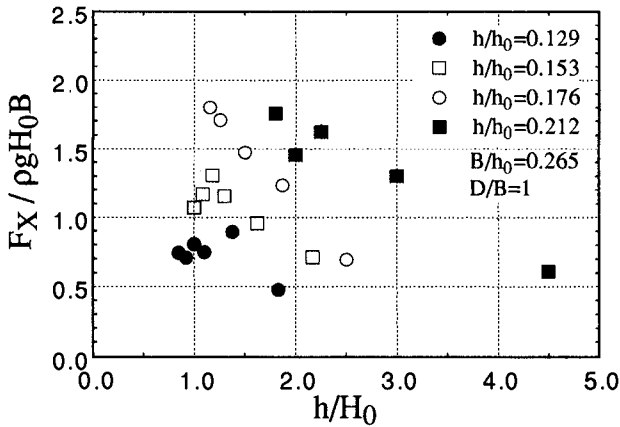


Fig-14: Variation of the horizontal wave force to the relative water depth, h/H_0 ($D/B = 1.0$)

$P_{max}/\rho g H_0$ to the relative water depth, h/H_0 for $D/B = 1.0$ and 0.5 . In the range of the small relative water depth, h/H_0 , the maximum wave pressure is relatively small, because the incident waves break on the offshore side of the wave dissipating works and fully dissipated waves attack the seawall. With increase of h/H_0 , the maximum wave pressure increases because the wave breaking point approaches to the seawall. The maximum value of $P_{max}/\rho g H_0$ appears when the waves break just in front of the seawall. After taking the maximum value, the maximum wave pressure decreases with increase of h/H_0 . In the range of the

large relative water depth, h/H_0 , the maximum wave pressure becomes small because the waves attack the seawall without wave breaking.

Fig.-13 and **Fig.-14** show the vertical and horizontal wave forces acting on the *FSS* of $D/B = 1.0$. The profiles of the wave pressure at each measuring point were assumed to be synchronized, and the wave forces were obtained by integrating the maximum wave pressures along the seawall face.

The variations of the vertical wave force are similar to that of the horizontal wave forces. The magnitude of the vertical wave force takes nearly the same value of the horizontal wave force, and the vertical force acting on the *FSS* is relatively larger than that on the upright seawall. The same tendencies were observed in the *FSS* of $D/B = 0.5$. In that case, the values of the vertical wave force took about 50%~60% of the horizontal wave force.

5. Conclusions

A new type of seawall (*FSS*) with deep circular arc cross section was proposed. The relative critical crest elevation of the *FSS* was extremely smaller than that of the conventional upright seawall, and the crest elevation could be reduced to about a half of the offshore wave height even under the non-wave overtopping condition. Further, the critical crest elevation of the *FSS* was estimated with fairly good correlation coefficient by using the approximate equation obtained from the experimental results.

The characteristics of the wave pressure were investigated. The values of the maximum wave pressure deeply related to the wave colliding patterns in front of the seawall, and those values change with the relative water depth, h/H_0 .

The maximum wave pressure appears near the still water surface and this pressure causes the large vertical wave force. The increase of the vertical wave force reduces the stability of the seawall, and a new type of wave dissipating works which could reduce the maximum wave pressure effectively must be investigated in further studies.

References

- Inoue, M.: Hydraulic characteristics of seawall with inverted slope, Proc. 21th Conf. on Coastal Eng. in Japan, pp.417-421, 1974. (in Japanese)
- Takata, A., Y. Yoshida, H. Fujikawa: Relationships of sectional forms of seawall and wave overtopping, Proc. 26th Conf. on Coastal Eng. in Japan, pp.285-289, 1979. (in Japanese)
- Kono, T., S. Takano, H. Tsuda: Comparison of wave overtopping rate between seawalls with various kind of cross section, Proc. 40th Conf. on Coastal Eng. in Japan, pp.681-685, 1993. (in Japanese)

- Yamamoto, M., Y. Nishi: Developments of the seawall having remote absorber to reduce overtopping, Proc. 31th Conf. on Coastal Eng. in Japan, pp.537-541, 1984. (in Japanese)
- Takayama, T., N. Ikeda, T. Nagai, M. Takayama: Model tests on the reduction of wave overtopping rate by a broad submerged breakwater, Proc. 35th Conf. on Coastal Eng. in Japan, pp.587-591, 1988. (in Japanese)
- Sasajima, T., K. Yamanaka, K. Kimura, Y. Mizuno, S. Kikuchi: Study on hydraulic characteristics of double alignment breakwater, Proc. 40th Conf. on Coastal Eng. in Japan, pp.645-649, 1993. (in Japanese)
- Goda, Y.: Random seas and design of maritime structures, University of Tokyo Press, 1985.

CHAPTER 144

A Condition and Performance Rating System For Breakwaters and Jetties

John Oliver¹, Don Plotkin²,
John Lesnik³, Douglas Pirie⁴

Abstract

This paper describes one aspect of a series of projects which the U. S. Army Corps of Engineers has undertaken to improve maintenance management of coastal and navigational structures. At the core of these projects is the development of procedures for more uniformly evaluating and describing the physical condition and functional performance of structures, and further, the development of methods where the condition and performance of structures, and their parts, can be expressed numerically to take best advantage of the benefits available from the use of microcomputers in maintenance management. These procedures are designed to allow the condition and performance of different structures to be more easily compared and more uniformly tracked over long time periods and to aid the repair budgeting prioritization process. This paper briefly

¹ Consulting Engineer, 20525 SW Mountain Home Road, Sherwood, OR 97140 (formerly, U. S. Army Corps of Engineers).

² Civil Engineer, U. S. Army Construction Engineering Research Laboratory, P. O. Box 9005, Champaign, IL 61826.

³ Vice President, Moffatt & Nichol Engineers, 3717 National Drive, Raleigh, NC 27612.

⁴ Consulting Engineer, 2960 Ascot Circle, West Linn, OR 97068 (formerly, U. S. Army Corps of Engineers).

describes the performance-based assessment method for breakwaters and jetties, primarily of rubble construction.

System Philosophy

The most important analysis within this system is on structure performance, with physical condition taking a secondary role. In this performance-based system, the difference between current structure condition and as-built (or "like new") condition is not, in itself, a deciding factor on the need for repair. Rather, it is a structure's documented loss of function as a result of structural deterioration which is most important. When performance is judged unsatisfactory, then repairs are considered which would raise performance back to satisfactory levels. Evidence of near-term structural instability is also an important consideration, as it could adversely affect performance.

The Eight System Steps

Table 1 lists the eight steps in the implementation and use of the system. A brief description of these steps is given below. A more complete system description is contained in Oliver, Plotkin, Lesnik, and Pirie 1996. This document will be referred to as the "system manual" in the rest of the paper.

Assigning Functions and Defining Reaches

The first step is to determine which functions the structure is intended to perform, according to the four main functional areas and nine functional rating categories, as listed in Table 2. These are described in the system manual which also contains a spreadsheet to assist in performing the complete functional assessment.

Generally, Harbor Area and Navigation Channel cover how well the structure controls waves and currents with respect to the categories listed for those areas. To avoid confusion and duplication of defect reporting, all sediment control aspects are grouped together under Sediment Management. Structure Protection refers mainly to how well a structure protects adjacent structures against attack by waves and currents. This function may apply to an outer breakwater protecting an inner breakwater, or to one jetty protecting the one on the opposite side of the channel.

Table 1. Eight Steps in the Rating System

Step Number (1)	Description (2)
	Steps 1-5 are Initial (One Time Only):
1	Determine What Functions Structure Serves.
2	Divide Structure into Major Reaches - by Function.
3	Establish Functional Performance Criteria.
4	Establish Structural Requirements.
5	Further Divide Reaches into Subreaches - by Structural and Length Criteria
	Steps 6 - 8 are Repeated as Required:
6	Inspect Structure - Produce Structural Rating.
7	Assess Functional Performance - Produce Functional Rating.
8	Review Structural Requirements.

The Toe Erosion and Trunk Protection categories serve as a useful reference but are not included in the Condition Index calculations, as their effect is covered by the structural rating categories.

Next is the initial step in dividing the structure along its length into reaches. The functions provided by different portions of the structure are determined, using the categories listed within the four main functional areas. Initial reach limits are set where functional changes occur. The head of a structure is always considered to be a separate reach.

Performance Criteria and Structural Requirements

Step 3 is to determine, for each reach and for each functional category which applies to it, what level of performance is expected. This performance expectation is

Table 2. Functional and Structural Rating Categories.

Functional Area (1)	Functional Rating Categories (2)	Structural Rating Categories (3)
Harbor Area	Harbor Navigation Harbor Use	Breach
Navigation Channel	Entrance Use Channel	Core Exposure/Loss
Sediment Management	Ebb Shoal Flood Shoal Harbor Shoal Shoreline Impacts	Armor Loss
Structure Protection	Nearby Structures Toe Erosion * Trunk Protection	Loss of Armor Contact/Interlock
		Armor Quality Defects
		Slope Defects

Not included in Condition Index calculation.

indicated by the acceptable number of annual disruptions, or periods of disruption for each of the required navigation and related activities. The allowable disruption will vary not only with navigation activity, but also by size and type of vessel.

Performance is referenced to three levels of storm events:

1. Design Storm: This is the largest storm (or most adverse combination of storm conditions) which the structure (or project) is intended to withstand, without allowing disruption of navigation or harbor activities, or damage to the structure or shore facilities. The design storm is usually designated by frequency of occurrence or probability of occurrence.
2. Intermediate Storms (2X Design Storm Frequency): This level refers to storms (or combinations of adverse conditions) of intermediate intensity, which occur on the order of twice as often as the design storm. This level is intended to represent a midway point between the maximum storm levels (design storm) and small or minor intensity storms which may occur more frequently, especially during certain periods of the year.

3. Low Intensity Storm Conditions: This level refers to storms (or combinations of adverse conditions) of low intensity, which may occur frequently throughout the year, such as common rain storms or periods of above normal winds. This level is the next stage above normal non-storm conditions.

The design storm is the main reference point for establishing expected structure performance. Authorizing documents, design notes, project history, and current requirements are used to confirm the appropriate design storms for a project. For systems designed for seasonal use or for interrupted use, the expected non-use periods must be allowed for in arriving at a design storm. Design storm conditions include: wave height, direction, and period; water level; storm duration; and combinations of these factors.

The design storm typically varies from one project to another, and for different activities or areas within a single project. For example, disruption of cargo handling or limitations on channel entrance use might be tolerated more frequently than disruption in the harbor area. Thus the design storms for the navigation channel, damage to harbor facilities, vessel damage, and disruption of cargo handling are, or should be, at different return intervals.

For many harbor entrances, design depths and channel orientation are indications of design intent. For example, a 10 foot channel will have breaking waves at a wave height of 8 feet. At this wave height, about 4 feet of channel depth is lost at the wave trough and waves are steep enough to cause broaching of a craft with less than 5 feet of draft. Thus, with an 8-foot wave, the channel is impassable for all vessels due to either limited depth (for larger vessels) or excessive wave steepness (for smaller vessels). At this location, an 8-foot wave height can then be tied to a storm of a certain frequency or probability, and a tolerable frequency for closing the channel can then be determined. In a similar fashion, safety in the harbor berthing area and disruption to cargo handling could be analyzed.

When structure performance is rated later in the process, the ratings are based on storms of the greatest intensity which have occurred during the last rating period. Having three levels allows ratings to be produced during intervals when only storms of less than design intensity have occurred.

Once performance expectations are established for each function, it is then necessary to determine what structural requirements the structure must fulfill to allow performance requirements to be met. Seldom does a rubble coastal structure require full structural integrity to have continuity in function. In fact, most rubble structures are built with some allowance for damage before function is compromised, and many are overbuilt for constructability. Thus, structural damage does not automatically equate to loss of function.

Determining structural requirements involves estimating the minimum cross section dimensions, crest elevation, and level of structural integrity needed to meet functional performance requirements. Initial efforts in visualizing these dimensions can be aided by estimating the impact on functions if the reach under study were to be completely destroyed. Project history, authorizing documents, public input, and analysis may also be required to adequately determine these dimensions. As this is not an exact science, application of significant engineering judgment will be necessary to produce a reasonable estimate. Once this is done, these structural requirements are used to help identify sources of functional deficiencies in the existing structure.

Final Reach Division

At this point, the reaches which were initially divided according to function are now further divided according to the following two criteria:

1. By Construction: Further division is made based on changes in structural characteristics.
2. By Length: Where function and construction are uniform over a long length, divisions are made to keep reaches in the range of 60 to 150 meters (200 to 500 feet).

Divided in this fashion, the reaches now represent convenient-sized management units with similar properties. Reach definition is permanent, unless major changes are made to the structure.

At this point, all the initial steps in implementing the system are complete and need not be repeated. The following steps are then performed on a recurring basis, as needed.

Structural Inspection and Rating

Structural ratings are produced by comparing the current physical condition, alignment, and cross sectional dimensions of a structure to that of a "like new" structure which was built as intended and according to good practice, and with good quality materials.

For structural rating, each reach is divided into three cross sectional areas: the crest (or cap), the seaside, and channel or harborside. Each cross sectional area is given 0 to 100 ratings in five of six rating categories, as listed in the right-hand column on Table 2. (Slope Defects is not rated for the crest, and Breach is not rated for the two side slopes). These ratings are determined primarily from visual inspections of the structure, although additional information, such as hydrographic surveys, may also be used.

The system manual contains a rating table for each structural rating category. While these tables are specific to each category, they follow the basic format of the General Condition Index Scale shown in Table 3. Values are usually selected as multiples of 5 (60,65,70, etc). The system includes a field form for recording the ratings, inspector comments, and other information useful in producing a thorough inspection.

The ratings are then entered into the BREAKWATER computer program which calculates a composite structural index (SI) for each of the three cross sectional areas, a single SI for the whole reach, and finally an SI for the whole structure (Aguirre and Plotkin 1996). The SI value for a structure or structural component indicates its level of physical condition and structural integrity.

Functional Assessment and Rating

Functional assessment begins with a review of the functional performance criteria for the structure. Then, the environmental setting (wave and current energy, water level variability, sediment transport, etc.) is examined, followed by a review of the structural ratings, SI values, and comments made during the structural inspection. The intent is to determine the extent to which structural deterioration has adversely affected function.

As for structural rating, the system also contains rating tables for each functional rating category which likewise follow the general format of Table 3. After the

Table 3. General Condition Index Scale.

Observed Damage Level (1)	Zone (2)	Index Range (3)	Condition Level (4)	Description (5)
Minor	1	85 to 100	EXCELLENT	No noticeable defects. Some aging or wear may be visible.
		70 to 84	GOOD	Only minor deterioration or defects are evident.
Moderate	2	55 to 69	FAIR	Some deterioration or defects are evident, but function is not significantly affected.
		40 to 54	MARGINAL	Moderate deterioration. Function is still adequate.
Major	3	25 to 39	POOR	Serious deterioration in at least some portions of the structure. Function is inadequate.
		10 to 24	VERY POOR	Extensive deterioration. Barely Functional.
		0 to 9	FAILED	No longer functions. General Failure or complete failure of a major structural component.

ratings are chosen, a check is made to ensure that each rating is made based on how the structure itself (its presence or condition) has affected the rated functional categories.

The ratings are then entered into the BREAKWATER computer program which calculates a composite functional

index (FI) for the whole reach and then for the whole structure. The FI values for a structure or reach indicate how well it performs its intended functions. The FI values then lead to a condition index for the reach or whole structure.

Review of Structural Requirements

Finally, structural ratings and functional ratings are compared to the initial structural requirements. The intent is to perfect the relationship of performance to structural deterioration, which will occur over the long term through repeated analysis.

Budgeting for Repairs

Through use of the method outlined above, sufficient data and experience will be accumulated to track structure condition over time and properly relate physical condition with functional performance. At this point, general deterioration rates can be determined, along with minimum condition levels which will provide the required performance. From this information, the required repairs can be budgeted to the extent needed and at the appropriate timing.

While it is recognized that catastrophic effects of major storms can result in a clear need for immediate repair, these major events will not necessarily dictate the decision process or dominate a structure's overall long-term structural deterioration and accompanying loss of function. Even the repair of major storm damage is still appropriately assessed through the above method.

Conclusions

This system establishes a rational and systematic method for assessing the physical condition and performance of breakwaters and jetties. It emphasizes the need to establish performance expectations for coastal structures, and further, to relate the need for structural repairs to documented loss of function. The system for rubble breakwaters and jetties is currently being implemented throughout the U. S. Army Corps of Engineers. Similar procedures will also be developed for breakwaters and jetties of non rubble construction, and later, for seawalls, bulkheads, revetments, and groins.

Acknowledgements

Development of the system described here depended on the assistance of many within the Corps of Engineers' coastal community. Their efforts and ideas contributed greatly to the final product.

Appendix. References

Aguirre, R., and Plotkin, D. (1996). "BREAKWATER Computer Program User Manual," U. S. Army Construction Engineering Research Laboratory, Champaign, IL, (Draft Technical Report).

Oliver, J., Plotkin, D., Lesnik, J., and Pirie, D. (1996). "REMR Management Systems - Condition and Performance Rating Procedures for Rubble Breakwaters and Jetties," U. S. Army Construction Engineering Research Laboratory, Champaign, IL, (Draft Technical Report).

CHAPTER 145

Wave overtopping and stability of armor units under multidirectional waves

T.Sakakiyama¹ and R.Kajima²

Abstract

This paper describes the wave overtopping along a seawall of a man-made island where nuclear power plants are projected to construct and the stability of armor units at the concave section of seawall. Effects of the wave directionality on them were investigated by using multidirectional wave basin not only for a design wave but also larger waves than the design one to ascertain the durability and margin of the safety of seawall.

1 Introduction

To extend siting area for power plants, a synthetic project for new siting technologies has been undertaken by Central Research Institute of Electric Power Industries(CRIEPI). One of the most promising technologies is to site them in a man-made island instead of on coastal land. A new design method for very important coastal structure of the man-made island has been proposed by Kajima(1994).

Concerning the power plants on the man-made-land, the wave overtopping and the stability of armor units for the new design concept has been investigated mostly with two-dimensional physical model tests (Kajima *et al.*,1993; Kaijma, 1994; Sakakiyama *et al.*, 1994a; Sakakiyama *et al.*,1994b). Because the man-made island will be constructed offshore, effects of the wave directionality on the wave

¹ Central Research Institute of Electric Power Industry, 1646, Abiko, Abiko-city, Chiba, 270-11, Japan. e-mail:sakaki@criepi.denken.or.jp

² Ditto, e-mail:kajima@criepi.denken.or.jp

overtopping and the stability of armor units are of great importance for rational design of the seawall.

Works on the wave overtopping recently performed were aiming at design formula (de Waal and van der Meer, 1992; Herbert *et al.*, 1994). Although multidirectional wave basins are available nowadays, research on the overtopping rate was carried out for oblique waves (Juhl and Sloth, 1994) and for two-dimensional coastal structure due to multidirectional waves (Hiraishi *et al.*, 1995).

Effects of the wave directionality on the overtopping rate and the stability of armor units were investigated in the wave field where the diffracted waves were caused by three dimensional coastal structure. To ascertain the durability and margin of the safety of seawall of the man-made island, not only a design wave but also larger waves than the design one were applied for the structure.

2 Design concept

To guarantee the safety of man-made island where a nuclear power plant is supposed to be constructed, a new design method was proposed by Kajima (1994). That design concept is based on the following two-step design: At first step, according to the current design method, coastal structure should be stable for a "fundamental design wave". That wave condition is determined with 100-year return period.

In addition to the present design concept, functions of the seawall are confirmed for a severer wave than the fundamental design wave height, where it is named the "functional check wave".

In this research, to demonstrate this two-step design method, design wave conditions are supposed as shown in Table 1. The deep-water significant wave height $H_0=10\text{m}$ and wave period $T=16\text{s}$ are taken as the fundamental design wave with 100-year return period.

For second step, a wave condition to check up functions of the coastal structure is determined: The wave height is one and a half times larger than that of the fundamental design wave, $H_{F0}=1.5\times H_{0D}=15\text{m}$. Water depth of the man-made

Table 1 Design wave conditions

fundamental design wave		functional check wave
return period	100 years	roughly 1000 years
conditions in deep-water conditions		
wave height $H_0(\text{m})$	10m	15m(= $1.5\times H_0$)
wave period $T_0(\text{s})$	16s	16s
conditions at man-made island		
wave height $H_D(\text{m})$	10.3m	12.8m(= $1.24\times H_D$)
wave period $T_D(\text{s})$	16s	16s
armor units	stable	slight deformation
allowable overtopping rate	$0.05\text{m}^3/\text{s}/\text{m}$	$0.2\text{m}^3/\text{s}/\text{m}$

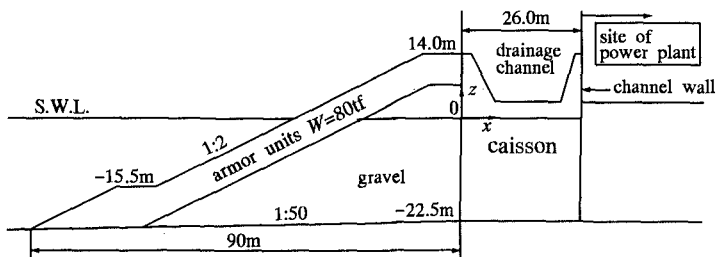


Fig.1 seawall covered with armor units

island is assumed as $h=22.5\text{m}$ including the high tidal range. An incident significant wave height at the water depth $h=22.5\text{m}$ applied in the tests ranges from the design wave height $H_D=10.3\text{m}$ to $H=1.24\times H_D=12.8\text{m}$.

Coastal structure should be stable for the fundamental design wave according to the current design method. However, it is allowed to get slight damage of the armor layer within keeping its functions.

Coastal structure to protect the man-made island consists of wave dissipating work and caisson on which drainage channel for overtopping water is constructed. Fig. 1 shows a cross section of the seawall and it is designed to be stable for the fundamental design wave condition with 100-year return period. The incident significant wave height for the fundamental design is $H_D=10.3\text{m}$ at the water depth $h=22.5\text{m}$ where the seawall is constructed. Armor units used in the present experiments is Tetrapod and its weight $W=80\text{tf}$ which is determined by Hudson formula ($K_D=8.2$). A crest elevation of the seawall was estimated as $h_c=14\text{m}$ above S.W.L. for an allowable overtopping rate, $q_{da}=0.05\text{m}^3/\text{s}/\text{m}$. For the functional check wave, the allowable overtopping rate was also given. But the crest elevation of the seawall is lower than that of the fundamental wave condition. For those given wave conditions, the relationship between the crest elevation and the overtopping rate was obtained by using the diagrams for wave overtopping proposed by Goda's (1985). Area inside the channel wall is site of the power plant. So extremely large amount of water due to the wave overtopping is not allowed in this area.

Coastal structure should keep its functions to protect the power plant inside of man-made island. Therefore, investigation was also performed in this research from this point of view. Dimensions of drainage channel was determined with two-dimensional wave flume tests including large- and small-scale test (Sakakiyama *et al.*, 1994b).

3 Experimental method

The experiments were carried out by using a multidirectional wave basin (35.0m long, 45.0m wide and 1.1m deep) equipped with a 48-segmented wave maker (19.2m

wide) as shown in Fig. 2. A scale factor of physical model test is $\lambda=1/88.1$. A model of man-made island is 5.7m long in the direction on-offshore and 11.4m wide in the direction alongshore(500m by 1000m in full-size). It is protected with seawalls consisting of caissons covered with armor units as shown in Fig. 1. The model of man-made island was located as shown in Fig. 2 to make center lines of the wave generator and of a half section of offshore-side seawall on the same line. Measurement of wave overtopping was done in a half section of seawall. Guide walls were settled during the tests for both normal and obliquely incident waves. Uniformity of wave heights at the water depth of offshore-side seawall was checked parallel to the shoreline

Table 2 shows the experimental conditions. Three kinds of wave directional conditions were selected, CASE A: multidirectional wave with normal incident($\theta=0$ deg.), CASE B: uni-directional irregular wave($\theta=0$ deg.) and CASE C: obliquely uni-directional irregular wave($\theta=30$ deg.). The wave directionality is expressed with the spreading parameter for wave energy S_{max} defined by Goda(1985). When S_{max} is small, e.g., waves with $S_{max}=10$ corresponds to wind waves. The wave of which S_{max} tends to the infinity is a uni-directional wave. Multidirectional wave used in the test has $S_{max}=25$ which corresponds to swell at short decay distance with relatively large wave steepness(Goda, 1985). The wave height ranges from the design wave height($H_D=11.7$ cm in model and $=10.3$ m in full-size) to the functional check wave height($1.24H_D=14.5$ cm in model and $=12.8$ m in full-size). The wave period is constant sa $T=1.71$ s(16s in full-size).

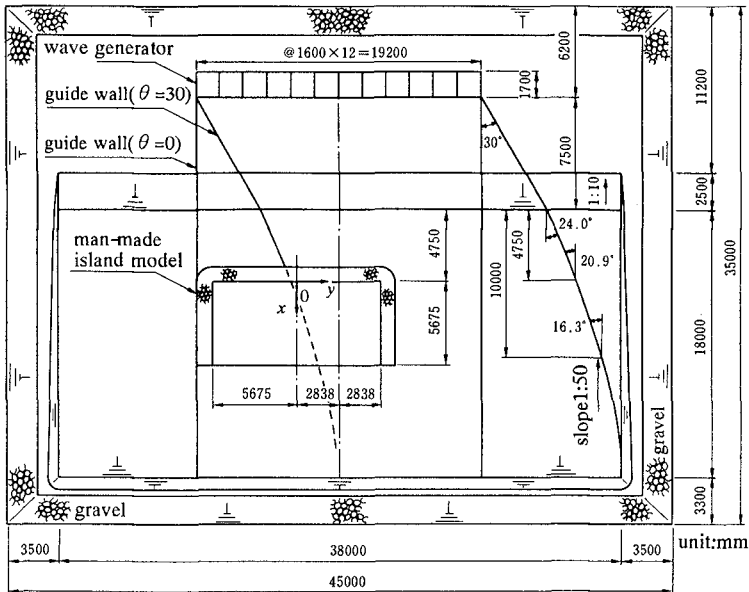


Fig.2 Multidirectional wave basin and man-made island model

Table 2 Experimental conditions(scale factor $\lambda=1/88.1$)

CASE	wave directionality	S_{max}	θ (deg.)	wave height	wave period(s)
A	multi-directional	25	0	H_D	1.71
B	uni-directional	∞	0	to	
C	obliquely uni-directional	∞	30	$1.24H_D$	

H_D is design wave height =11.7cm
water depth at seawall is 25.5cm.

Fig. 3 shows an experimental set-up for measurement of the overtopping volume. Local change of the wave overtopping was measured at a half of the offshore-side seawall alongshore for both in the drainage channel and onto the site of power plant. A half length of the test section is divided into ten parts to make tanks for water storage. Channel wall as shown in Fig. 3

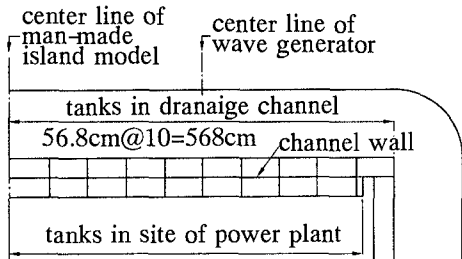


Fig.3 tanks to measured overtopping volume

was scaled down to be 15.9cm high. To store the overtopping water beyond the channel wall and onto the site of the power plant, 50-cm high wall was set to the tanks in site of power plant. It was caused mainly by spray.

A number of wave trains was 250 in one test run. Because amount of water beyond the channel wall was very small, tests were repeated three or more times under the same wave condition to get sufficient volume of water. Mean overtopping rate was obtained from the measured volume and the wave duration time. Physical values are converted to full-sized ones in the following.

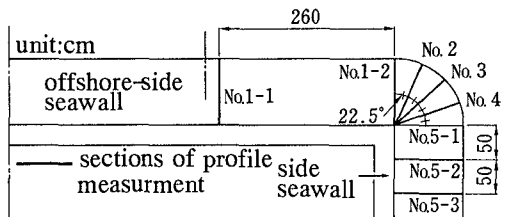


Fig.4 measuring sections of profiles

Fig. 4 shows the lines(No.1-1 to No.5-3) along which profiles of the armor layer were measured with depth-meters. Basically the armor units in two-dimensional section(Line No.1-1 in Fig. 4) are stable for the normal incident design waves. Interest in the stability of armor units is concentrated on critical part, that is, concave section. Profiles were measured at initial and several stages in the wave duration up to 3000 times the significant wave period($t/T=0, 250, 500, 1000$ and 3000). "Damage level S " defined by van der Meer(1987) is used to quantify the deformation of the armor layer. Fig. 5 shows its definition. The damage level physically means a number which is proportional to armor units number in an eroded area per width of the nominal diameter of the armor units D_n .

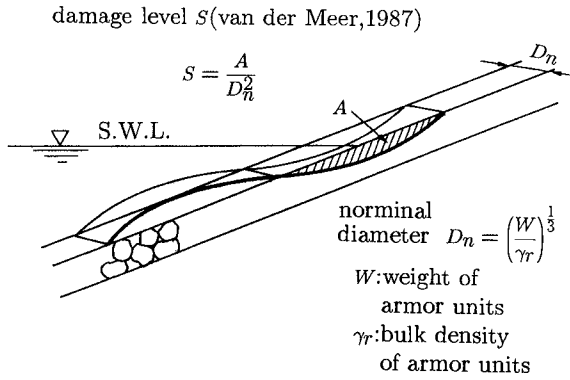


Fig.5 Definition of damage level

4 Overtopping rate

Fig. 6 shows distribution of the local overtopping rate along the seawall due to the multidirectional wave, where the local overtopping rate is defined as the discharge per unit length normal to the seawall. It was measured for several wave heights ranging from the design wave height (denoted by $H/H_D=1.0$) to the functional check wave height ($H/H_D=1.24$). Because the man-made island has finite length, diffracted waves were generated from ends of the structure. They cause the wave height change along the seawall. Consequently they results in change of the overtopping rate as shown in Fig. 6. The diffracted waves consist

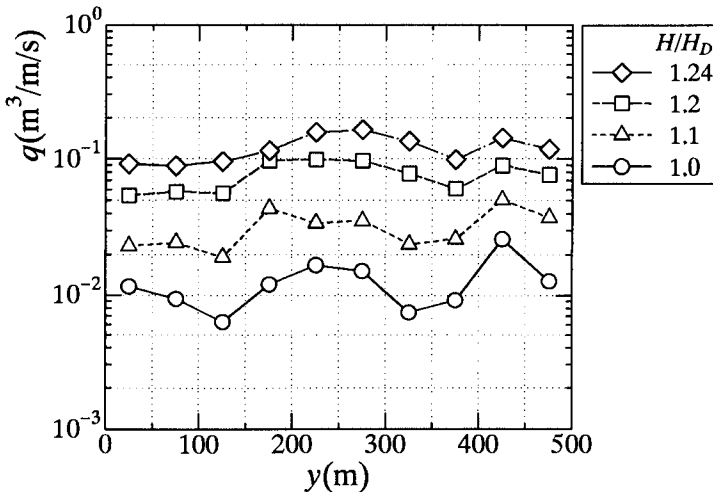


Fig.6 Local overtopping rate along seawall due to multidirectional wave

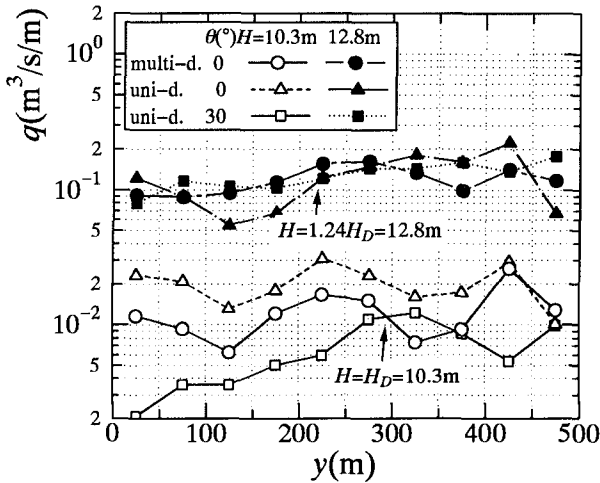


Fig.7 Overtopping rate change along seawall on wave directionality

of plain waves and cylindrical scattered waves. The scattered wave propagates along the seawall not normal to that. Effect of the cylindrical scattered wave on the overtopping rate is smaller than that of the normal incident wave but not null. The diffracted wave causes an increase in the mean water level along the seawall as a function of wave height. A ratio of the maximum to minimum local overtopping rate is about four at the design wave height denoted with a hollow circle, $H/H_D=1.0$. The ratio decreases as the wave height increases. The ratio due to the functional check wave (with a diamond, $H/H_D=1.24$) is about two.

Dependency of the local overtopping rate on the wave directionality is shown in Fig. 7. The results of large waves show the overtopping rate of uni-directional wave denoted with solid triangle fluctuates most, the second is uni-directional wave and the smallest due to the obliquely uni-directional wave. This tendency agrees with the diffracted wave height distribution. Trend due to the design wave height slightly differs from the previous one. It is because that the overtopping rate is nonlinear to the wave height. The diffracted wave height due to the multidirectional waves is smoother than the uni-directional irregular wave ones.

Roughly speaking, the local overtopping rate fluctuates from a half to twice the mean value in space except the result of the obliquely incident wave with the design wave height. The diffracted wave from another corner of the model was not included from the experimental restriction. A ratio of the length of man-made island to the significant wave length is 4.5. It means that the man-made island is relatively long. Therefore, it is considered that the scattered wave from one corner dissipated at another. Experiments were also performed by capping the tanks in the drainage channel to investigate that the water can be drained through the channel. Outlets of the drainage channel were located at the landward ends of the side seawall. It was confirmed that most of water over the

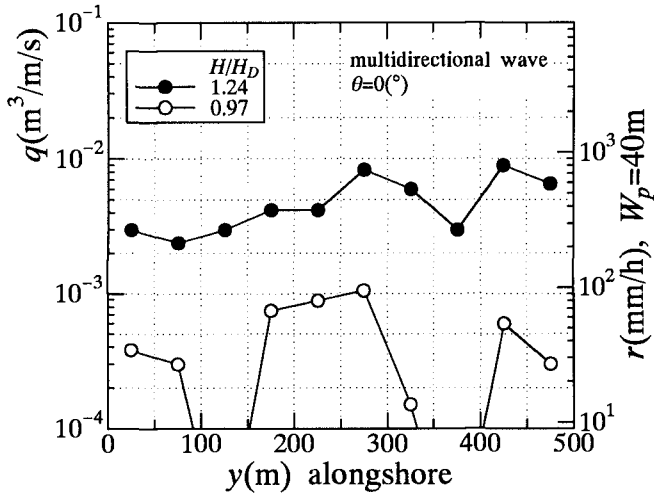


Fig.8 Overtopping rate in drainage channel

parapet was drained through the channel on the caisson. Maximum water depth in the drainage channel was about 4m. Comparing with the height of channel wall 10.5m, the channel has sufficient capacity for draining. Dimensions of the drainage channel was determined mainly to reduce the overtopping water onto the site of power plant.

Overtopping water onto the site of power plant is caused by splash. Spray is not avoidable by the channel wall with reasonable height. Critical situation due to the wave overtopping is flood into the power plant. Therefore, it is required to estimate discharge in the site to design a drainage pumping system.

Fig. 8 shows the local overtopping rate onto the site. The right axis of ordinate shows the equivalent precipitation. A distance of drainage W_p is assumed as 40m from the channel wall which was estimated by observation in the experiments. Although the scale factor of this experiment is small and an accuracy for such small amount of water should be taken into account, the equivalent precipitation due to the design wave fluctuates from less than 10mm/h to 100mm/h. A mean equivalent precipitation over the seawall is O(10)mm/h. It is acceptable. Owing to the functional check wave, it will be about 500mm/h. It is equivalent to rainfall by a very strong typhoon. Drainage pumping system should be reinforced by double within this range of $W_p=40m$ for both the wave overtopping as well as the rainfall.

Fig. 9 shows an effect of the wave directionality on the overtopping rate which is averaged rate over the offshore-side seawall. The axis of abscissas indicates the incident significant wave height. The uni-directional wave with the principal wave direction $\theta=0deg$. causes the largest overtopping rate, the multi-directional wave with $\theta=0 deg$. medium and the oblique uni-directional wave with $\theta=30 deg$. the smallest. This results of the comparison between the multidirectional

and uni-directional waves agrees with that obtained by Hiraishi *et al.*(1995). The overtopping rate due to the multidirectional waves is smaller than that due to the uni-directional waves by about 30%. Results obtained with two-dimensional tests overestimates the overtopping rate when it will be applied for offshore structure in the multidirectional waves. The obliquely incident uni-directional waves produces the smallest overtopping rate among three wave directionality. Under such conditions, wave dissipating work becomes relatively long on wave run-up, although its slope becomes milder. This effect is valid for the multidirectional waves which come from the various directions.

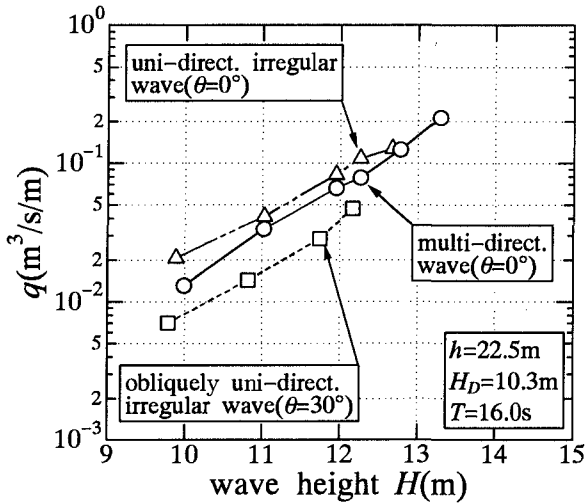


Fig.9 Overtopping rate q dependent on wave directionality

5 Stability of armor units

Fig. 10 shows the profiles of deformed armor layers due to the multidirectional wave with the design wave height at $\alpha=67.5$ deg. of the concave section. Under the design wave conditions for three wave directionality, the multidirectional wave gives the largest damage to the profile change although the differences are small. It is seen from the difference between the initial($t/T=0$) and final($t/T=3000$) profiles that small area just below the still water level was eroded and accumulated close to by down the slope. This eroded area is quantified with the damage level $S \approx 4$. Although the area eroded is small, it is not allowed under the current design concept. The armor units used in the experiments correspond to the maximum one available in practice. So it is necessary to do further work to make alternative ways to satisfy the present design method, i.g., to use high density armor units or to use more stable armor units.

Fig. 11 shows the profiles due to the functional check wave at the same section. The armor units initially placed near the still water level were removed by much severer waves than the design wave. In this figure, an eroded area is seen but accumulated one is not. Change of area does not balance between the initial and final profiles. It is because the armor units were removed in the wave propagation direction, not down the slope. The damage level S at the final profile at $t/T=3000$ is about 11. For the functional check wave as well as the design wave, the damage does not reach the crest level of armor layer.

Figures 12 and 13 show the damage level change dependent on the time of wave duration. Deformation occurs at an early stage of the wave duration. This tendency is same as the previous results obtained using two dimensional tests(Kajima *et al.*, 1994). The damage level due to the design wave height reaches at most five at $\alpha=45(\text{deg.})$ denoted with the solid square as shown in Fig. 12. The damage level of $\alpha=67.5(\text{deg.})$ at $t/T=3000$ is four of which the profiles were shown in Fig. 10. It is considered that the damage level around five indicates small damage

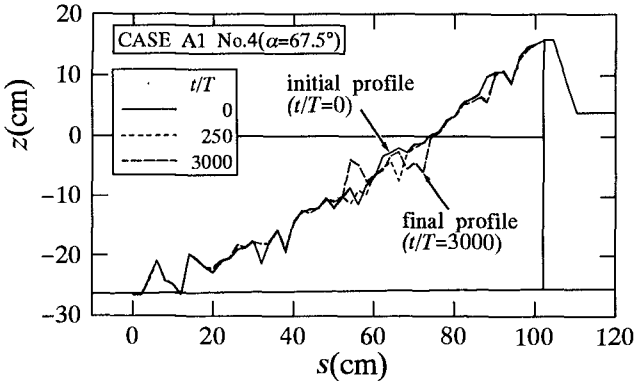


Fig.10 Profiles deformed with design wave($H/H_D=1.0$)

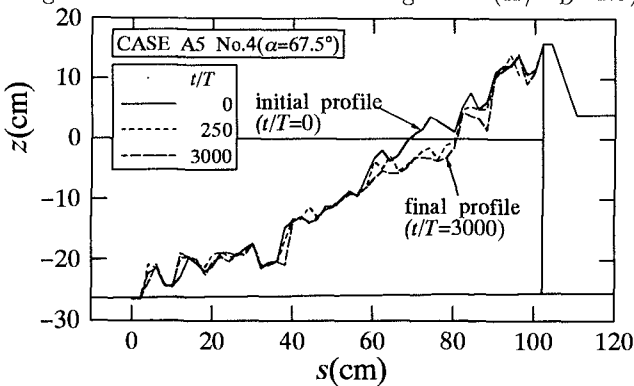


Fig.11 Profiles deformed with functional check wave($H/H_D=1.24$)

from the geometrical point of view.

Fig. 13 shows the damage level change due to the functional wave. The most serious damage occurred at $\alpha=67.5(\text{deg.})$ of which profiles were given in Fig. 11. The damage due to the larger wave also occurred at the early stage of wave duration. The damage level does not increase significantly compared with the results of the design wave height. However, it was observed that more armor units were removed by the functional check wave than the design wave. They were carried away in the direction of wave propagation not down the slope. Some of the removed armor units might fill up the eroded part at the different sections. Consequently, the obtained damage levels are rather small compared with the results of the design wave height.

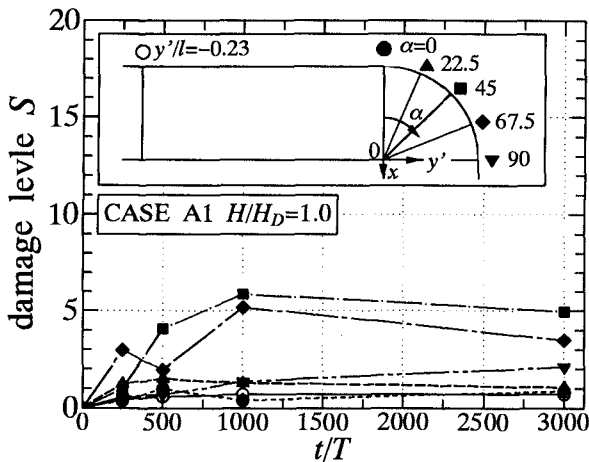


Fig.12 Time history of damage level (multidirectional wave, Case A1)

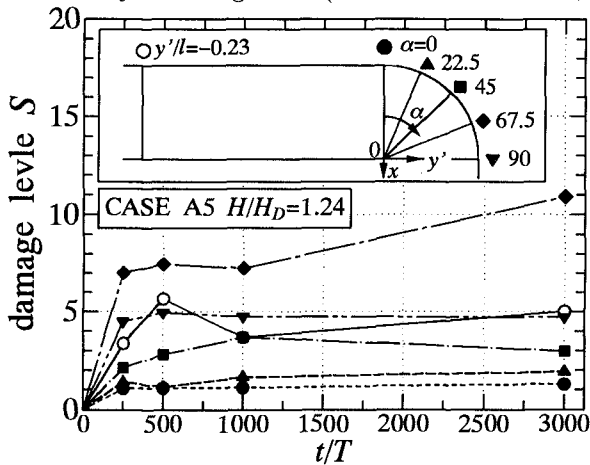


Fig.13 Time history of damage level (multidirectional wave, Case A5)

The hollow circle in Figures 12 and 13 shows the damage level at the offshore-side seawall where the wave motion is expected as two-dimensional. Its damage level is very small for the design wave height but somewhat large due to the functional check wave.

In this experiment, the wave was applied for 3000 times the significant wave period which is equivalent to more than 13-hour duration. It is expected that the extremely large wave does not last such long time. Therefore, the damage level will be reduced by taking account of the wave duration. It is required for estimation of the damage level in practical use that the duration time should be considered as a function of the wave height and period.

Fig. 14 shows the damage level at the final stage ($t/T=3000$) around the concave section, where the effect of the wave directionality is compared for the design wave height. The damage level around the center of the concave section has peaks for three different kinds of wave directionality. Although it is seen that the damage level due to the design wave height of multidirectional wave is the largest, which is up to five, it is not concluded that the effect of the wave directionality is significant by considering the magnitude of damage which are small. The damage level at the side seawall is invisible.

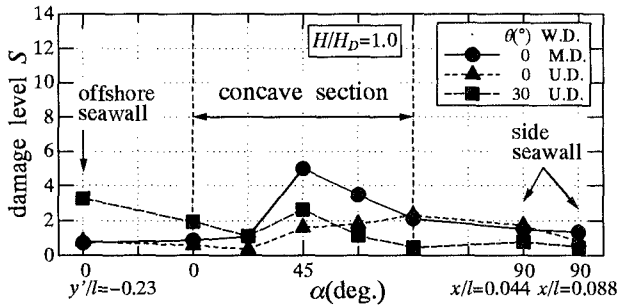


Fig.14 Damage level at concave section due to design wave

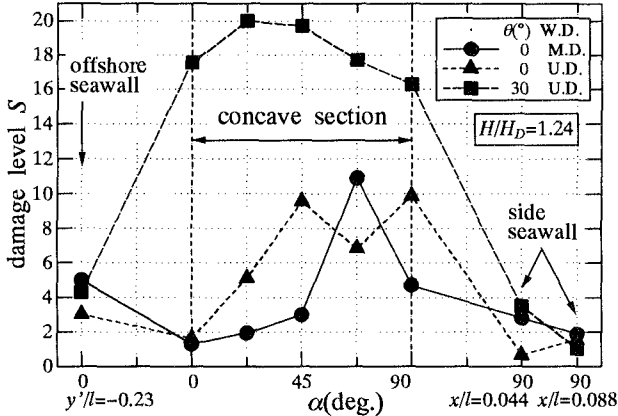


Fig.15 Damage level at concave section due to functional check wave

Fig. 15 shows the result by the functional check wave height. Larger waves than the design wave cause more serious damage as expected. The obliquely uni-directional irregular wave caused the most serious damage around the whole concave section and the damage level becomes 20. However, it is considered that such condition resulted in an overestimated one. The normal incident waves caused the maximum damage level about ten for both the multidirectional and uni-directional waves. As the results of two normal incident waves, the wave directionality does not influence the damage at the concave section.

Considering reparability of the damaged section, it have to be estimate an allowable damage level for the severer wave than the design wave. Under both the design and functional check conditions, the deformation of the armor layer does not reach the crest elevation. It is important that damage does not reach the crest elevation in order to keep functions of seawall. Otherwise seawall collapses in a short time like the result of the obliquely incident wave.

6 Conclusions

The effect of the wave directionality on the overtopping rate was confirmed by tests using the multidirectional wave basin. It is caused by the diffracted waves generating at the concave section of the man-made island. The durability of the armor layer is confirmed for both the design wave and the larger wave than it. The margin of the safety can be expected to a certain degree against the larger wave than the design wave. The following s are main conclusions obtained by the present work.

Conclusions:

- 1 The multidirectional waves give smaller overtopping rate than uni-directional waves for normal incident condition. Oblique wave gives the smallest.
- 2 The overtopping rate was estimated for both in the drainage channel and onto the site of power plan. The later case is important for the safety of power plant. The equivalent precipitation can us information to design the drainage pumping system in the site power plant.
- 3 No serious damage at the concave section of seawall was confirmed for keeping seawall's functions.

Future works:

- 1 To make a model to estimate the overtopping rate with a numerical model to simulate wave height around an man-made island.
- 2 To make no damage at concave section for the design wave. Alternative ways are to use high density armor units and to use more stable armor units.

Acknowledgements

This research has been supported by nine Japanese electric power companies

and the Japan Atomic Power Co. through "Studies on advanced siting civil engineering technology for nuclear power plant". The support is greatly appreciated.

References

- De Wall, J.P. and J.W. van der Meer(1992): Wave runup and overtopping rate on coastal structures, *Proc. 23rd Coastal Engineering Conf.*, ASCE, Vol.2, pp.1758-1771.
- Goda, Y.(1985): Random seas and design of maritime structures, University of Tokyo Press, 323p.
- Herbert,D.M., N.W.H. Allsop and M.W. Owen(1994): Overtopping of sea walls under random waves, *Proc. 24th Coastal Engineering Conf.*, ASCE, Vol.2, pp.1130-1142.
- Hiraishi, T. and N. Mochizuki(1995): Wave overtopping rate of seawall in directional sea, *Proc. 26th Congress of IAHR*, HYDRA 2000, pp.251-256.
- Juhl, J. and P. Sloth(1994): Wave overtopping of breakwaters under oblique waves, *Proc. 24th Coastal Engineering Conf.*, ASCE, Vol.2, pp.1182-1196.
- Kajima, R., T.Sakakiyama, M.Matsuyama, T.Sekimoto and O.Kyoya(1993): Stability of armor layer of man-made island sea-wall and overtopping due to extremely large irregular waves, *Proc. 40th Japanese Conf. on Coastal Engineering*, JSCE, vol.2, pp.686-690(in Japanese).
- Kajima,R.(1994): A new method of structurally resistive design of very important seawall against wave action, *Proc. Wave barriers in deepwaters*, pp.518-536.
- Sakakiyama,T.,R.Kajima and O.Kyoya(1994a): Wave force on caisson due to large waves causing deformation of armor layer, *Proc. Waves- physical and numerical modelling*, pp.1384-1393.
- Sakakiyama,T.,R.Kajima and Y.Kubo(1994b): Evaluation of overtopping rate onto site of power plant on man-made island, *Proc. 41st Japanese Conf. on Coastal Engineering*, JSCE, vol.2, pp.661-665(in Japanese).
- Van der Meer, J. W.(1987): Stability of breakwater armour layers design formulae, *Coastal Engineering*, 11, pp.219-239.

CHAPTER 146

NUMERICAL MODELING OF BREACH GROWTH IN A SANDDIKE

by

Guus S.Stelling, Willem T.Bakker, Christine van Kuik and Christel Somers¹²

ABSTRACT.

On October 7, 1994 a full scale breach growth experiment has been carried out at the Dutch- Belgium border, in the Zwin at the west-end of the Dutch-Belgian border. A small breach was initiated in a sanddike with a height of 3.25 m and the breaching process was monitored. The present paper focusses on the numerical modeling (hindcasting) of the breach growth process.

1 INTRODUCTION; GOAL OF THE INVESTIGATIONS.

De Looff et al.(1996) give a summary of the current breach research in the Netherlands. The present paper reports on a part of these investigations, i.e.:

- . the full scale field experiments of 1994 (Zwin);
- . the present research, which should lead to a comprehensive numerical model for breaching processes.

On October 7, 1994 a full scale breach growth experiment has been carried out at the Dutch- Belgium border, in the Zwin [1], [2]. Fig. 1 shows the site of the experiment at the west-end of the Dutch-Belgian border.

A small breach was initiated in a sanddike with a height of 3.25 m and the breaching process was monitored. The experiment was carried out by Rijkswaterstaat and Delft University of Technology, with aid of Delft Hydraulics Laboratory.

Ultimate goal of the investigations, which are reported on is extrapolation of the behaviour of the Zwin breach to other circumstances:

- . Construction of the dike: use of other materials (clay instead of sand);
- . Larger areas of the submerged basin;
- . Other bottom level of the submerged basin.

The present paper focusses on the numerical modeling (hindcasting) of the breach growth process.

2 MEASUREMENTS.

The Zwin experiment has been reported before (Visser et al.,1995a,b): an experimental closure of a tidal basin near the Dutch-Belgian border, which is a historic residual of the former tidal entrance to the Belgian city of Brugge, called "the Zwin" (fig.1). Twice in 1994, on October 6 and 7, the inlet was closed off by a sanddam; breaching was simulated by digging a small trench in it at High Tide.

¹All:Civ. Engng.Depth.:Delft University of Technology,P.O. 5048:2600GA Delft

²Respectively :Professor; Principal Scientific Officer; Graduate engineer (2x)

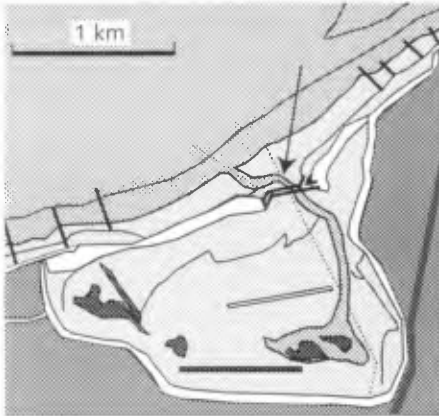


Fig. 1. Situation

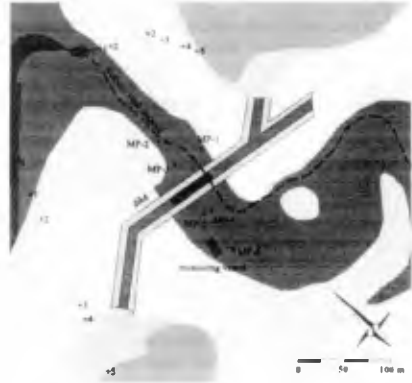


Fig. 2. Site of measuring poles

Fig.2 shows the measuring site with the artificial dam. MP 2..6 are measuring poles in which the water level and the current velocities were measured. Maximum velocities were of the order of 4.2 to 4.4 m/s.

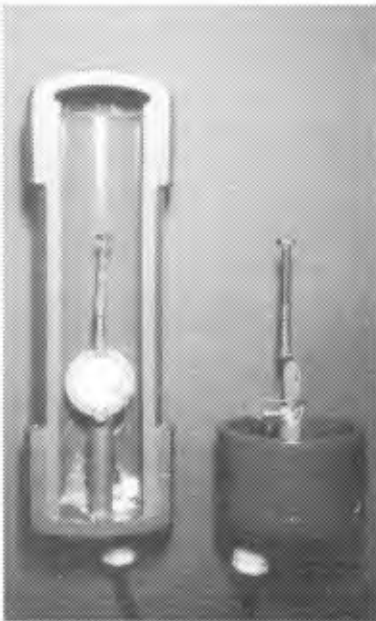


Fig. 3. Trillo's

An array of burglar alarms was placed in and underneath the dike in order to monitor the breaching process.

These alarms, specially developed for these tests were called: "Trillo". Fig.3 shows the instrument, with a PVC bar fixed to a watertight PVC cylinder (length 20 cm). The alarm consists of a piezo-electric element, reacting on the motion of a bolt, which is attached to it with a spring. When the PVC cylinder, buried in the sand, turns loose the bolt will tremble, which is monitored by an electrical signal in the piezo-electric element.

Fig.4 shows the sites, where the burglar alarms were placed in and underneath the dike and furthermore the dimensions of the dike.

¹Dutch: translated in English: "Tremblo".

It reaches up to a level of 3.30 m above NAP (which is about OD). The high water level at which the breach was initiated was NAP 2.75 m. An initial trench in the dike was dug to a level of NAP +2.50 m. Poles had been placed in a 5m-pattern underneath the dike. The Trillo's were attached on these poles at a mutual distance of 75 cm (4 Trillo's per pole). This paper reports on the second day of experiments. At that time the Trillo's in the body of the dike were not present any more because of the experiments of the first day. Also the Trillo's in the front of the dike disfunctioned the second day. Before looking to some results of the measurements it is useful to

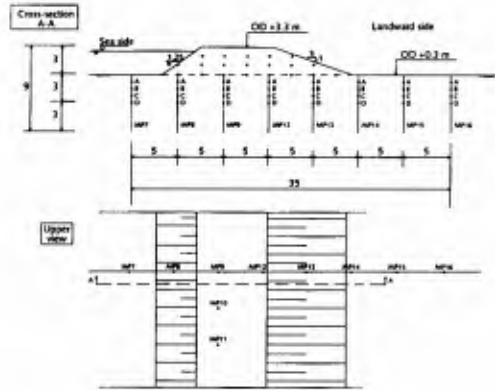


Fig. 4. Site of the trillo's

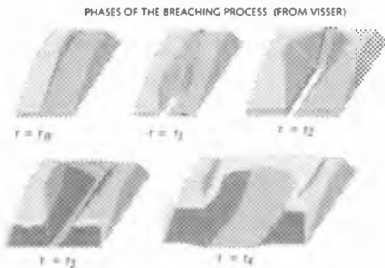


Fig. 5. Phases

the experiment. The dip "a" in the water level on the seaside of the dike is caused by the Bernoulli term. Measuring gauges in deeper water show a convex curve in this hour. The thin lines (with the scales on the right) show the measured velocities in course of time on the seaward and landward side (maximum velocities 4.3 m/s).

remind to the various phases of breaching, as indicated by Visser (1995). Successively, one observes the steepening of the inner slope, backscour of the inner slope and removal of the sill at the seaside of the dike. After this happens, the breaching process reinforces itself and a quick growth of width takes place. Refer to fig.5 and the photo's 1 to 8. The thick lines in fig.6 show the water level at the seaside and the inner side of the dike as function of time. Indicated is the moment of initiation of the breach and the moment of the turning of the tide; furthermore the end of

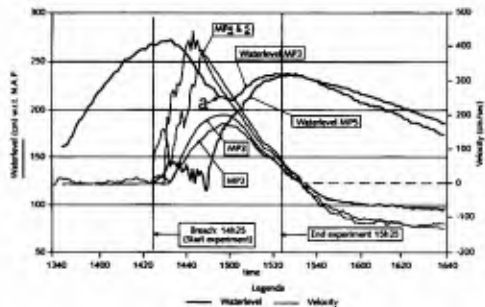


Fig. 6. Measured waterlevels and velocities

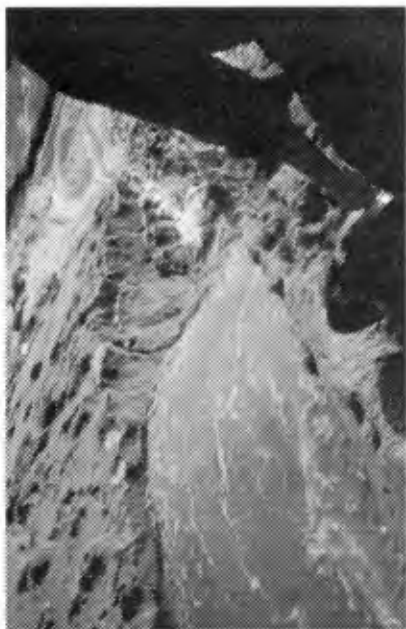


Photo.2 Current velocities after 1 min.



Photo.4 Current velocities after 7 min.



Photo.1 Initial trench

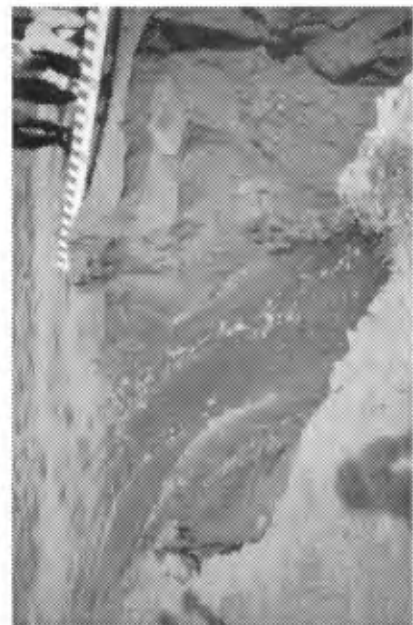


Photo.3 Current velocities after 6 min.



Photo.5 Current velocities after 12.5 min.

Photo.7 Current velocities after 12.5 min.



Photo.6 Current velocities after 12.5 min.

Photo.8 Current velocities after 60 min.



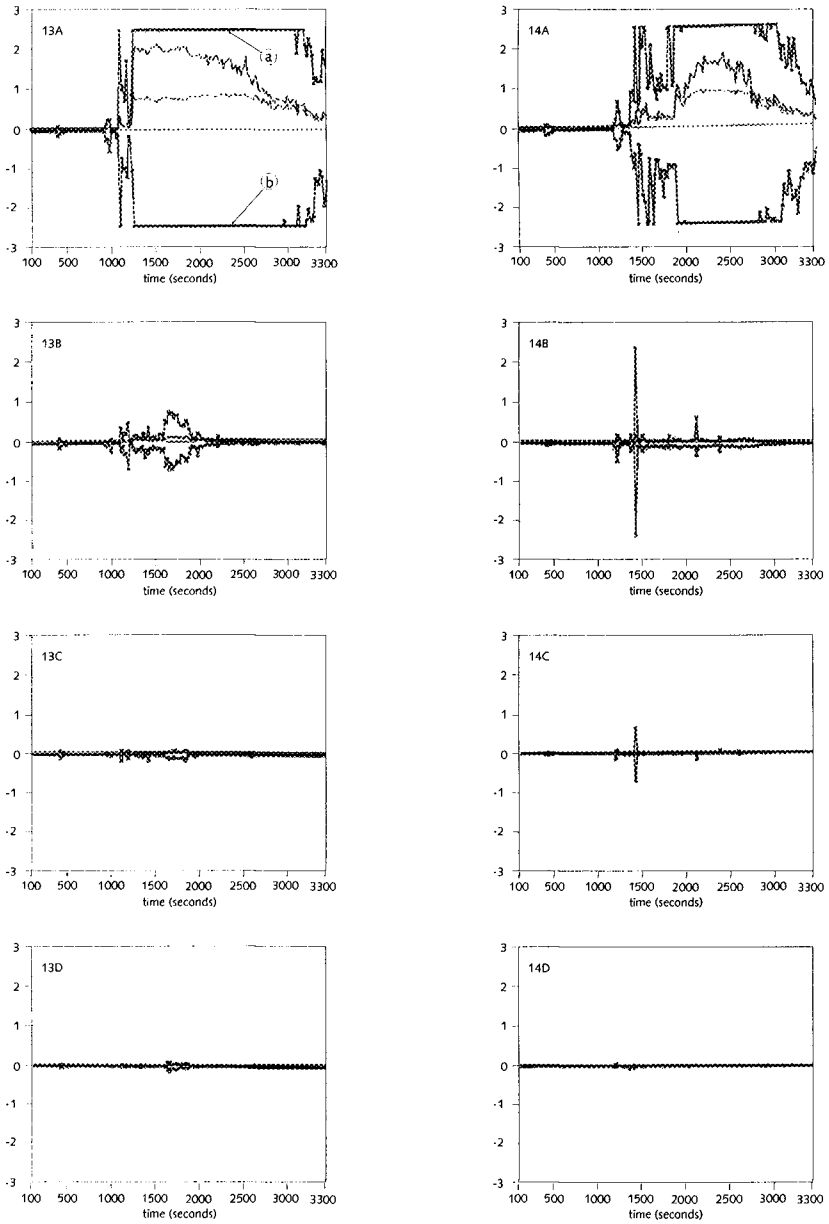


Fig.7 . Trillo registrations

Fig.7 shows the 8 registrations of two vertical rows of each 4 Trillo's, somewhat landward of the center of the dike. The larger the deviations between the lines "a" and "b", the larger the motion of the Trillo's.

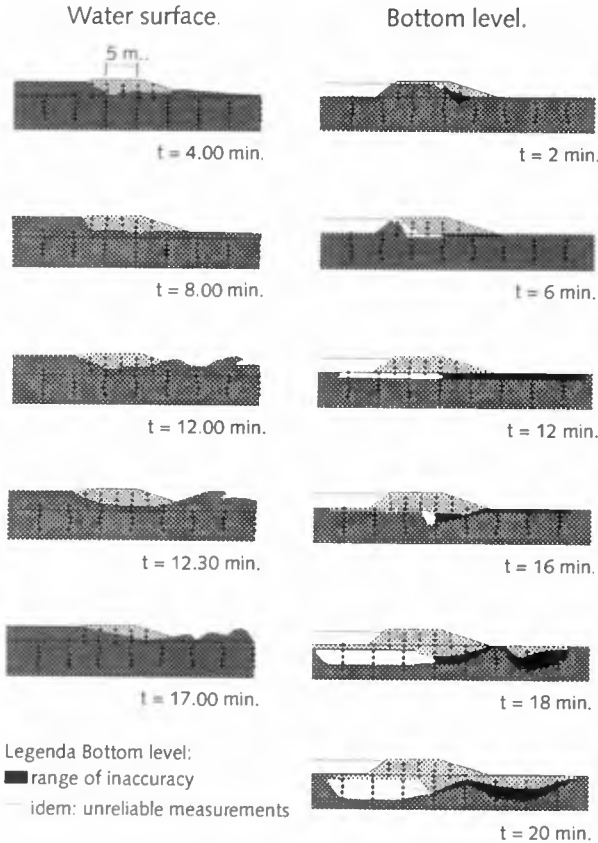


Fig. 8. Waterlevel and bottom depth

From visual analysis of the video's and slides and from the Trillo's figure 8 resulted concerning the relation between the water motion and the scour.

In the lefthand figures the dike and the watersurface at various times are indicated. No attention to the bottom is given. In the right-hand picture the bottom development is shown.

The black and white band show the rate of inaccuracy. The white band was caused by malfunctioning of the Trillo's; the black band by inaccuracy of interpretation. In both cases the upper side of the band is more likely than the lower extreme (in the white area this lower extreme is even very unlikely).

It doesnot seem likely, that much deeper scour holes occurred than 2m below the original bottom level. These scour holes were formed not before the phase of the breach, in which the sill at the seaside was removed.

COMPUTATIONS.

Numerical computations were made with the 3-D Trisula model of Rijks waterstaat and Delft Hydraulics. Fig.9 shows a 2DH-current pattern.

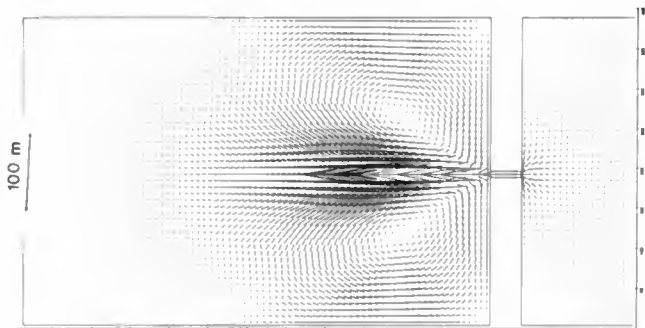


Fig.9 . Trisula model

With a flat sloping bottom (dotted line in fig.10), the water surface (in the center line of the breach) according to the line, indicated with diamonds was computed. The stars show the measured values after 12.5 minutes. If scour holes were introduced (lines with triangles; fig.10), the water surface as indicated by blocs was the result.

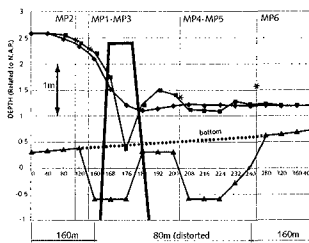


Fig.10. Water surface

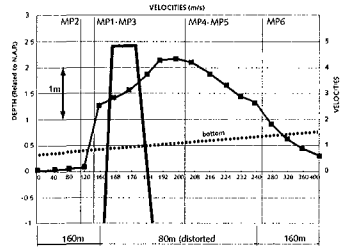


Fig.11. Velocities

Current velocities (for the case with flat bottom) are as given in fig. 11. Maximum velocity found was 4.3 m/s.

IMPRESSIONS.

From the investigations, the following impressions resulted concerning the hydraulic aspects:

- . The maximum velocities occurred shortly after washout of the dike in the breach;
- . At that time the water level in the breach is mainly determined by the Bernoulli term;
- . The Froude number of the maximum velocity occurring in the breach was of the order of 1.5;
- . The current has a jet-like character; a Bernoulli-trough with a depth of ca. 1 m could be observed, ending in an undular jump.

Concerning morphology the following observations c.q. impressions seem relevant:

- . The dike washed away with a velocity of 2 m/minute; the sand consisted at some places of coarse sand, originating from a former artificial sand supply with a grain diameter of .315 mm and at other places of local sands with a diameter of .185 mm.
- . Scour started to develop at the landward side of the dike; this might have triggered an undular jump.
- . The bottom changes show some similarity with the dynamics of antidunes.

SEDIMENT TRANSPORT MODEL (under development).

A pick-up transport model (appendix B) is developed with the following characteristics. The acting forces are: self-weight; shear stress on the surface and the horizontal pressure gradient.

Hindered entrainment is implemented, caused by:

percolation resistance.

This is the resistance which occurs if a mass of grains is moved in vertical sense through a mass of ambient fluid.

Percolation resistance does not imply changes in the grain structure.

Suction forces in the contact points between the grains.

Additionally to the percolation resistance, there should be accounted for viscous suction forces, caused by opening of the grain structure, at the sites, where originally touching grains are quickly separated.

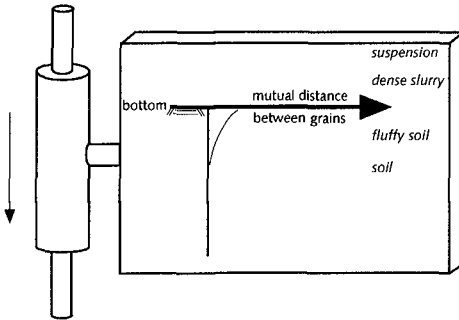


Fig.12. Zip-erosion.

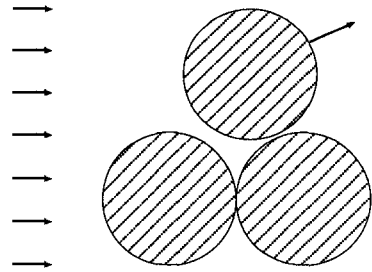


Fig.13. Virtual reduction self-weight by horizontal pressure gradient.

The feature to be simulated is called: "zip-erosion" (fig.12).

In the course of the breaching process, the career of a grain is as follows. First it makes part of the soil, then of fluffy soil, then of dense slurry and it ends as suspension transport.

When the thick horizontal line in fig.12 is the bottom, the curved line shows the mutual distance between the grains, i.e.: an average gap width. The mutual distance between the grains is negative-exponential in downward direction.

During "Zip-erosion" the process of detaching propagates (as a zipper) with constant velocity in downward direction.

In the area just below the bottom line dilatation takes place. In the model, this process is simulated because the grains play leap-frog, triggered by gravity and pressure. Instability occurs, when the layers play leap-frog; this doesnot lead to infinite transports.

The model starts from the presumption of perfect spheres, which gives instability under an angle of repose of 30^0 in the case of a horizontal water surface, but 15^0 in case of a water level, parallel to the slope. This because of the effect of the horizontal water pressure.

Based upon hydrology and soil mechanics considerations, essentially the same mechanism was indicated by Edelman (1960).

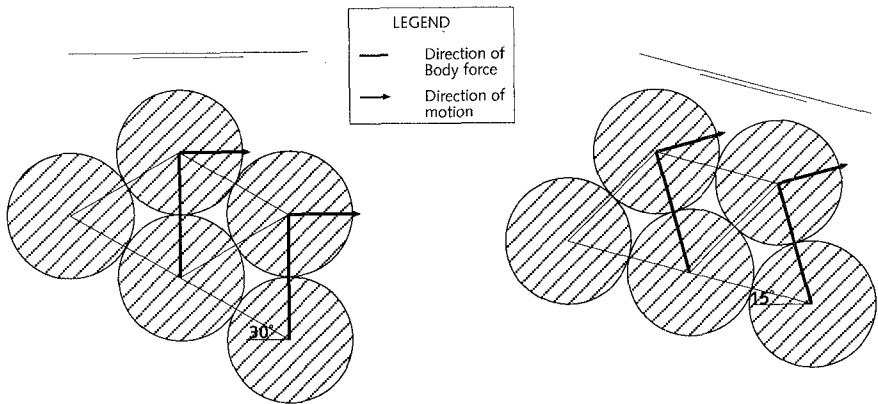


Fig.14. Direction motion grains for horizontal water level and for water level parallel to slope.

6 ACKNOWLEDGEMENT.

The Zwin experiment and its elaborations were made possible by funding of the Technical Advisory Committee and the Road and Hydraulic Engineering Division of the Rijkswaterstaat. The Marine Survey Department of the Directorate of Zeeland of the Rijkswaterstaat carried out the current measurements and surveys; the Section Zeeuws Vlaanderen helped with the organization. Furthermore, collaboration is gratefully acknowledged of the Foundation "The Zeeland Landscape", the Belgian Service for Coastal Harbours, the Royal Dutch Army (the Corps of Military Engineers and the Military Command of Zeeland), the contractors Aertssen NV and Janson Bridging. Supervised by W.T.Bakker, P.J.Visser, A.W. Kraak, H.J.Steetzel and J.v.d.Graaff preparation of the experiment was carried out by M.J.Smit and D.W.Snip as part of their M.Sc.thesis work at Delft University of Technology. Many students of the Coastal Engineering Department assisted with the measurements. The authors acknowledge the contribution of P.J.Visser concerning fig.5 and photo 1,7 and 8 and of Mr.C.A.Pugh of the Bureau of Reclamation, who is the photographer of the other photos. Graphical assistance concerning the other figures by the Dept. for Visual Display of Rijkswaterstaat and by mr.M.Voorendt of Delft University should be gratefully acknowledged.

7 APPENDIX A. Hydraulic Model

MODEL EQUATIONS

The numerical model is based upon approximations for continuity, momentum, and transport equations for salinity, heat, turbulent kinetic energy k and its dissipation rate ϵ . The equations are based upon the hydrostatic pressure assumption. In cartesian coordinates they are given by:

continuity equation:

$$\frac{\partial u_i}{\partial x_i} = 0 \quad (1.a)$$

momentum equations in the horizontal:

$$\frac{\partial u_i}{\partial t} + \frac{\partial u_i u_j}{\partial x_j} + \frac{1}{\rho_0} \frac{\partial p}{\partial x_i} + \frac{\partial R_{ij}}{\partial x_j} = f_i, \quad i=1, 2 \quad (1.b)$$

hydrostatic pressure assumption:

$$\frac{\partial p}{\partial x_3} = -\rho g \quad (1.c)$$

transport equations:

$$\frac{\partial c}{\partial t} + \frac{\partial F_i}{\partial x_i} = P \quad (1.d)$$

where u_i is the velocity in x_i direction, p is the pressure, ρ is the density, ρ_0 is a reference density, g is the acceleration due to gravity, c is the concentration, f is the external forcing, e.g. wind, F is the concentration flux due to convection and diffusion, R is the Reynolds stress tensor, and P is the dissipation and/or production function. The Reynolds stresses are modeled via the well-known eddy viscosity concept. The density ρ is supposed to be constant i.e. $\rho = \rho_0$.

The equations are transformed via a transformation given by:

$$\xi = \xi(x_1, x_2), \quad \eta = \eta(x_1, x_2), \quad \sigma = \frac{x_3 - \zeta}{h} \quad (2)$$

in which ζ is the free surface elevation, and h is the water depth. In the horizontal the transformations are orthogonal, in the vertical it is the well-known sigma transformation.

For the numerical approximation a "C grid", i.e. a fully staggered grid has been chosen. As far as the spatial derivatives are concerned the approximation method is based upon second order central differences for the continuity equation and for the pressure terms in the momentum equation. For the advection terms some weighted average is being used of second order upwind differencing and second order central differences. The integration in time is based upon a second order ADI and AOI (alternating operator implicit) type of factorization technique. Details are given by Leendertse (1989), Stelling and Leendertse (1992).

8 APPENDIX B. Sediment transport model

The principles of the sediment transport model, which will be used, are described in Bakker & van Kesteren (1986), Bakker, van Kesteren & Klomp (1990), Bakker & van Kesteren (1994) and Bakker & van Kesteren (1996). A comprehensive report concerning the theory will be published in 1997.

9 REFERENCES

- Bakker, W.T. & W.G.M. van Kesteren, (1986)
The dynamics of oscillating sheetflow
Proc. 20th Int.Conf. on Coastal Engng., Taipei; RO China
- Bakker, W.T., W.G.M. van Kesteren & W.H.G.Klomp, (1990)
Grain-fluid interaction in Couette flow
Proc. 22nd Int.Conf. on Coastal Engng., Delft; the Netherlands
- Bakker, W.T. & W.G.M. van Kesteren, (1994)
Flirting with Anna Lyse
Proc. Int. Conf. on Hydrodynamics, ICHD'94; Wuxi, PR China
- Bakker, W.T. & W.G.M. van Kesteren (1996)
Zipper Consolidation and Zip-Erosion
Proc. Second Int. Conf. on Hydrodynamics, ICHD'96 Hong Kong
- Edelman, T. (1960),
The failure of dikes in 1953 (in dutch)
De Ingenieur 72, no.11; March 11, 1960
- Leendertse, J.J.(1989)
A New Approach to Three-Dimensional Free-Surface Flow Modelling
The RAND Corporation, R-3712-NETH/RC, 1989.
- de Loeff, H., H.J.Steetzel & A.W.Kraak (1996)
Breach Growth: Experiments and Modeling
Proc. 25th Int.Conf. on Coastal Engng., Orlando; USA
- Stelling, G.S., and Leendertse, J.J. (1992)
Approximation of convective processes by cyclic AOI methods.
Proc. 2nd Int. Conf. Estuarine and Coastal Modelling, Tampa, FL, 771-782.
- Visser, P.J. (1995)
Application of sand transport formulae to sand-dike breach erosion.
Comm. on Hydr. and Geotechn.Engng.(78pp.)
- Visser, P.J., A.W.Kraak, W.T.Bakker, H.J.Steetzel, M.J.Smit & D.W.Snip (1995a)
A large scale experiment on breaching in sand dikes
Proc. Coastal Dynamics Conf., Gdansk; Poland
- Visser, P.J., W.T.Bakker, J.v.d.Graaff, A.W.Kraak, M.J.Smit, D.W.Snip & H.J.Steetzel (1995b)
Breaching experiment in Zwin succeeded (in dutch)
Otar, 7/8; September; p.227-231

CHAPTER 147

AGING AND STABILITY OF PLACED BLOCK REVETMENTS

Theo Stoutjesdijk¹⁾, Hans Johanson²⁾ and Mark Klein Breteler³⁾

Abstract

Since the early 1980's fundamental research on the behaviour of placed block revetments has been carried out in the Netherlands. This research has focussed on understanding the physics of this particular revetment type, which has resulted in empirical (Pilarczyk, 1985), analytical (Burger et al, 1990) and numerical (Bezuijen et al, 1987) design methods. These methods have been tested extensively in large and small scale model tests (for instance Klein Breteler, 1988, den Boer et al, 1983).

During the last years extensive field research has been carried out (Stoutjesdijk, 1992). This research has shown that a large difference in physical behaviour can exist between newly placed revetments or large scale models, and older ('aged') revetments in the field. To investigate this phenomenon further, field work, laboratory tests and modelling efforts have been carried out. This paper describes the current state of affairs. Purpose of this research is to quantify the net effect of aging on the stability of placed block revetments. If the net effect proves to be positive, it may prove possible to upgrade the stability of revetments by artificial simulation of aging effects.

Historical development of placed block revetments

In the Netherlands dikes of clay have been built since approximately 1200 AC. Especially in the coastal and estuarian zone some type of revetment protecting the dike from erosion by waves has been necessary. Originally wooden pile

¹⁾ Delft Geotechnics, P.O. Box 69, 2600 AB Delft, the Netherlands

²⁾ Dutch Ministry of Transport and Public Works, Department of Road and Hydraulic Engineering, P.O. Box 5044, 2600 GA Delft, the Netherlands

³⁾ Delft Hydraulics, P.O. Box 177, 2600 MH Delft, the Netherlands

constructions were used for this purpose. Later, the soil was protected by stone. In the absence of rock quarries to provide sufficient amounts of stone, revetments were constructed by placing the stones manually in a closed pattern. Originally natural stone such as basalt was used, but in more recent years also concrete blocks are used at a large scale.

Beneath the blocks it was common practice to use reed mats to protect the soil. On top of this mat layers of bricks were placed to provide a smooth surface. To deal with the unequal sizes of the stones in the top layer rubble stone of smaller size was used. This rubble stone acts as a filter layer, but is relatively coarse for this purpose, and originally was not used knowingly for this purpose. Newer dikes were no longer exclusively built by using clay. With increased dredging capability sand became a cheap material. A large number of dikes have been constructed by placing quays of mine stone and placing sand in between them. These mine stone quays can also be identified as permeable sublayers of the placed blocks. Between the mine stone and the top layer a thin layer of filter material is present.

With the availability of concrete blocks, all of the same size, this rubble stone layer or filter layer is no longer absolutely necessary. It was thought advantageous to place the blocks directly on the clay layer. Because clay is a relatively impermeable material no uplift pressures beneath the blocks would be expected. In practice however, some problems with this type of revetment occur. In time, clay can be eroded from beneath the blocks, forming gaps between the blocks and the surface, thus causing a stability problem. Secondly, the clay dries out, cracks, becomes more permeable and if the top layer fails, the clay layer is more erodable by wave activity than thought earlier.

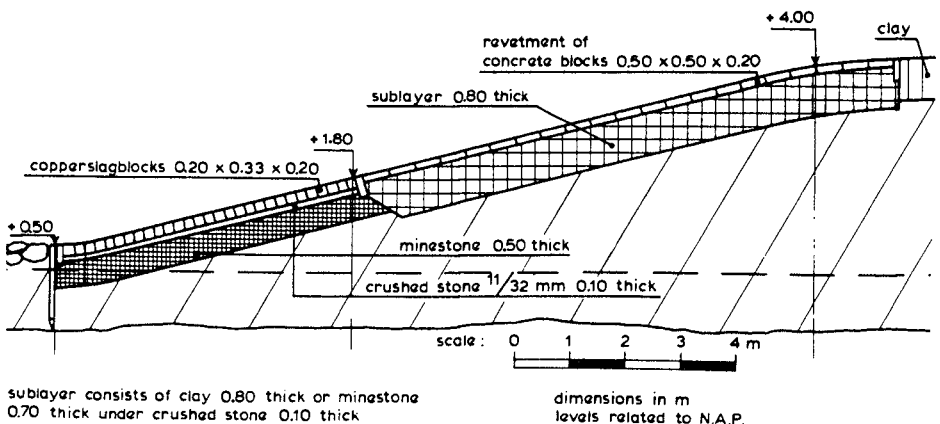


Figure 1 Example of a placed block revetment

Until the 1980's no design criteria on the stability of placed block revetments were available. Revetment design was based on experience. This experience was strongly damage-related, meaning that if blocks of a certain size at a certain location experienced too much damage during storms subsequently heavier blocks would be used. In the frequently loaded zones lower on the revetment this can work satisfactorily; waves can be depth-limited so that a revetment experiences waves that are almost design waves during its lifetime. In seldomly loaded areas of the revetment the design wave attack is more severe and there is no experience showing that heavier blocks are needed. Therefore, a lot of these revetments will not meet today's design standards and will have to be reinforced.

Figure 1 shows an example of a placed block revetment. As the term 'placed blocks' already indicates the top layer consists of blocks that are placed together in a closed pattern. The sublayer consists either of a filter layer of granular material or a clay layer, or in some cases both.

In time, and especially in the tidal zone, sand and other material from the foreshore is washed into the revetment. This causes the physical properties of the revetment to change quite dramatically (Stoutjesdijk et al., 1992).

The definition of aging, as used in this paper, is: "Aging is migration of sand from the foreshore into the top layer and/or filter layer."

The physical behaviour of a placed block revetment on a filter layer can be described by use of the so-called "leakage length":

$$\Lambda = \sqrt{\frac{b \cdot D \cdot k}{k'}}$$

with:

Λ	leakage length [m]
b	thickness of filter layer [m]
D	thickness of top layer [m]
k	permeability of filter layer [m/s]
k'	permeability of top layer [m/s]

By means of the leakage factor the hydraulic head (difference) over the top layer can be described analytically.

Background of research

In the 1980's a fundamental research program on the stability of placed block revetments was started. Design formulae based on model tests and descriptions of the physical behaviour of placed block revetments were developed.

In the 1990's attention has been paid to measuring field performance of existing revetments (Stoutjesdijk et al (1992)) and it was found that existing

revetments can show a different behaviour from that found in model tests. This was subscribed to the fact that, especially in the tidal zone, sand and other material from the foreshore had migrated into the filter layer and the top layer. Because the behaviour of the revetments was different from that of newly constructed revetments this was referred to as 'aging effects'.

The reason to research the effect of aging on stability is twofold. On the one hand, it is necessary to determine the actual strength of existing revetments, especially in the tidal zone. On the other hand, if aging proves to have a positive effect on revetment stability, it may be possible to upgrade the stability of existing revetments (above the tidal zone) by artificially filling them with sand.

Aging

Aging is defined as the migration of sand from the foreshore into the revetment. Both filter layer, which consists of coarse grains, and the cracks between the blocks can in time become completely filled with sand.

The most obvious way to see whether or not aging has taken place is to lift some blocks out of the revetment and inspect the filter layer and the cracks between the blocks. This has been done at several locations. Sieve analysis of samples of the filter layer has shown that weight percentages up to 30 % of sand can be present between the coarse filter material. The cracks between the blocks can be almost completely filled with sand, silt, shells and small stones. In one instance, when a bore hole was drilled through the top layer to place a pressure transducer in the filter layer, it was found that about 20 cm sand had sedimented into the bore hole during one single storm.

These extreme conditions are found in the tidal zone. More extensive investigations indicate that higher on the revetment less and less sand is found in the revetment.

In the tidal zone marine growth is common. Higher on the revetment, above the splash zone, grasses, wild plants and flowers are found.

Field measurements

To gain more insight into the actual behaviour of existing placed block revetments a field measurement campaign was initiated. A fairly simple method to measure the permeability of the top layer is to place a square box with no bottom on top of the revetment, fill this with water and monitor the speed with which the water level decreases. This can be supplemented by placing pressure transducers in the filter layer to check the pressure difference (hydraulic head) over the top layer. Usually no pressure built-up takes place in the filter layer, due to the limited permeability of the top layer.

Results of these tests indicate that permeability varies with the height at which the measurement takes place. One event showed a permeability 10.000 times less in the tidal zone compared to that high on the revetment.

Another type of test is the infiltration test. One or two blocks are lifted out of the top layer, and an infiltration box is placed directly on the filter layer. Water is pumped into this box until a more or less stationary situation is obtained. At several points around the infiltration point pressure transducers are placed in the filter layer. The pressure differences between the infiltration point and the pressure transducers can be used to estimate the leakage length.

This method has first been tried out in a large scale model. These results were encouraging. In the field problems were encountered with filters that consisted of more than one layer, and 'leakage' of pressure towards the sand core, whereas the model assumes a impermeable lower boundary. Also, it can occur that higher on the revetment, permeabilities are very high and that pumping capacity is inadequate to obtain sufficient pressure in the filter layer.

Measurements have also been performed during storm conditions. On the top layer a beam with several pressure transducers is fixed. Next to this beam bore holes are made in the top layer to place pressure transducers in the filter layer. In this way the reaction in the filter layer to wave pressures on the top layer are determined. These measurement can be numerically simulated to obtain the leakage length of the revetment. Because of practical reasons this type of measurement can only be performed in or just above the tidal zone, where moderate storms (several times per year) occur. In one instance, a leakage length of more than 10 m was found in the tidal zone. On another occasion the leakage length varied over a short distance: a leakage length of 6 m in the tidal zone was determined, while just above high water level the leakage length appeared to be 0.5 m.

During a third measurement a surprising new phenomenom was found. In expectation of a rather high water level the measurement beam was fixed higher on the revetment than usual. It appeared that, although the water level was high enough to record significant waves with the measurement beam, in the filter layer no pressures were recorded at all. As it appears, due to the limited permeability of the top layer and the filter layer, the rise in sea water level does not coincide with an equal rise in water level in the filter layer. There is both a phase lag and an amplitude damping. The water level in the filter layer never reached the level of the pore pressure transducers.

To see if this phenomenom could be measured and hindcasted several measurements of tides and corresponding water levels in the filter layer were carried out, all of which confirmed this theory. Due to the slow variation of water levels, it appears that if the subsoil consists of sand, this has a large influence on the flow of water to and from the filter layer. Also the permeability of the toe construction can have a large influence on the inflow of water into the filter layer. In some cases this has made interpretation difficult.

Pulling tests

As discussed in the previous paragraph, on several occasions decreased permeabilities led to larger values of the leakage length. This leads to an increase in load on the top layer during storms. If only the weight of the blocks is taken into account, severe damage in the tidal zone would be expected even during moderate storms. This is not the case. Even though in practice some damage occurs during 'once a year' storms, no major damage is found.

The presence of material in the cracks between the blocks appears to have a stabilizing effect. The interaction between blocks is improved, but also very important is the fact that the probability of very loose blocks is reduced.

At a number of locations pulling tests have been performed. To perform this test a specially designed pulling unit is manoeuvred into a position above a block, the pulling unit is attached to the block and then the block is pulled out perpendicular to the revetment. The pulling force and the corresponding movement of the block are registered.

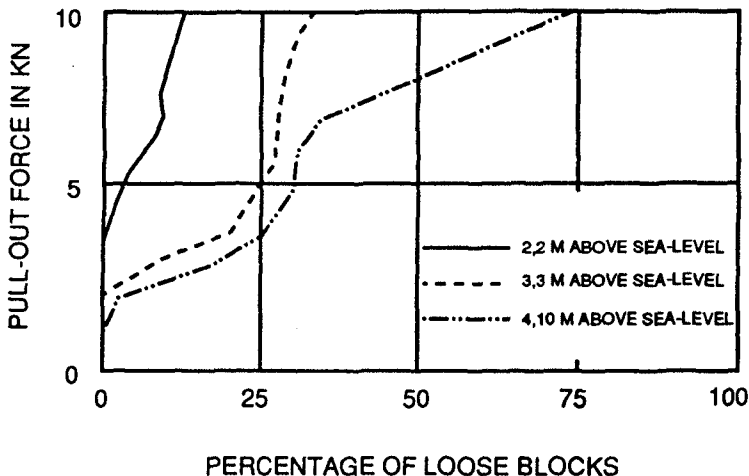


Figure 2 Example of the results of pull out tests on square concrete blocks

One example of these pulling tests is shown in Figure 2. Shown are the results of tests on square, concrete blocks (size 0.5 x 0.5 m and 0.25 m thick) on different levels of the revetment. On the vertical axis the pull-out force is given in kN. The weight of one single block is about 1.35 kN. Only at the levels which are high above mean sea level a few 'very loose' blocks are found.

Not shown in Figure 2 is the fact that in the tidal zone no blocks could be pulled out at all, not even with a pulling force of six times the weight of one block.

Since then, a number of sites were visited with this equipment, and more insight into the strength of the top layer has been gained. To properly evaluate the strength it is necessary to statistically analyze these pulling tests. The approach aims at a lower boundary criterium of the strength that can be taken into account that is exceeded with a known, high reliability.

Application of these statistical methods to the results of pulling tests shows that, even though high pulling forces can be found for the majority of blocks, the net effect of this extra strength still is limited to factors 1.1 to 1.2 for large square concrete blocks. In the tidal zone higher factors can be found, and also polygon shaped blocks which have been washed in with gravel can have significant additional strength due to clamping forces.

Test location

The fact that in the tidal zone high pulling forces are found was subscribed to the fact that the revetment was entirely filled with sand at these lower levels. At a test location artificial filling of the top layer with sand was applied.

The test location consisted of six sections. The top layer in five of these sections was recently placed. The sixth section had been constructed in 1984, and had quite a lot of vegetation growing in the cracks between the blocks. The newer sections consisted of a reference section, where no special measures were taken, and four sections where coarse sand and fine sand, and different ways of filling the top layer (brushing in, washing in, densification) were tried. All of these attempts were succesfull.

In Figure 3 the results of pulling tests on this test location are shown. On the vertical axis the pulling force is expressed as 'Times blockweight'. On the horizontal axis the frequency or percentage of blocks that can be pulled at a certain pulling force is given. As an example, from the graph can be read that at a pulling force of 5 times the block weight only 1 % of the blocks in the old section can be pulled out. For the reference section this amounts to about 1.5 times the block weight and for the artificially filled sections a value of about 2 times the block weight is found.

In Figure 3 the symbols indicate the following sections:

- ∇ the old vegetated section
- the new reference section
- + new section, brushed in with coarse sand
- ⊗ new section, brushed in with fine sand
- △ new section, brushed in with fine sand and densified
- x new section, fine sand is washed in with water

As it appears two conclusions can be drawn from these results. Clearly the

strength of the older, vegetated top layer is much larger than the newer sections. This can be due to the influence of vegetation. Perhaps there is also some effect of cementing between the sand particles.

Secondly, the artificially filled sections perform slightly better than the reference section. The expected benefit lies in a range of 20 to 50 % increase in strength of the top layer.

In 1997 this location will be revisited to see if the sand is still present or that the sand has to be supplemented periodically. It would also be interesting to see whether the artificially filled sections can in time reach the same level of stability as is the case the old section.

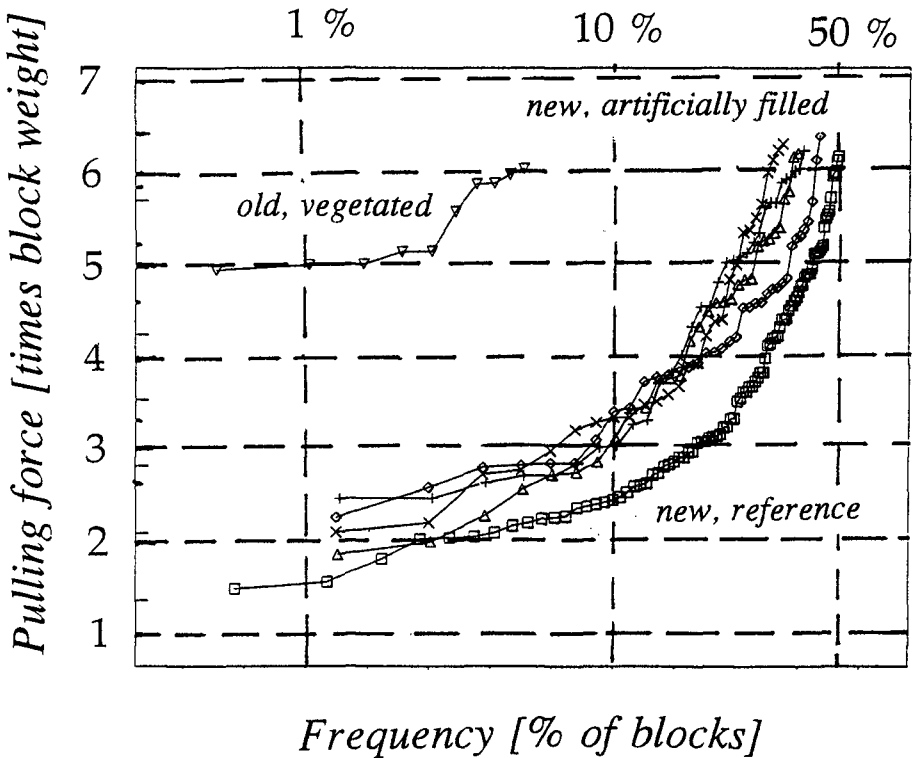


Figure 3 Results of pull out tests on test section

Stability of sand in small cracks

One of the questions regarding the presence of sand in a revetment is whether the sand remains in the revetment during storm conditions or is washed out during wave attack. This was investigated in model tests using a set up as shown in Figure 4. The general idea is very simple: between two plates a small crack with a width of 1.5 to 6 mm is created. In this crack sand is placed. Then an upward hydraulic head is applied to the sand. The critical hydraulic head at which the sand is washed out is recorded.

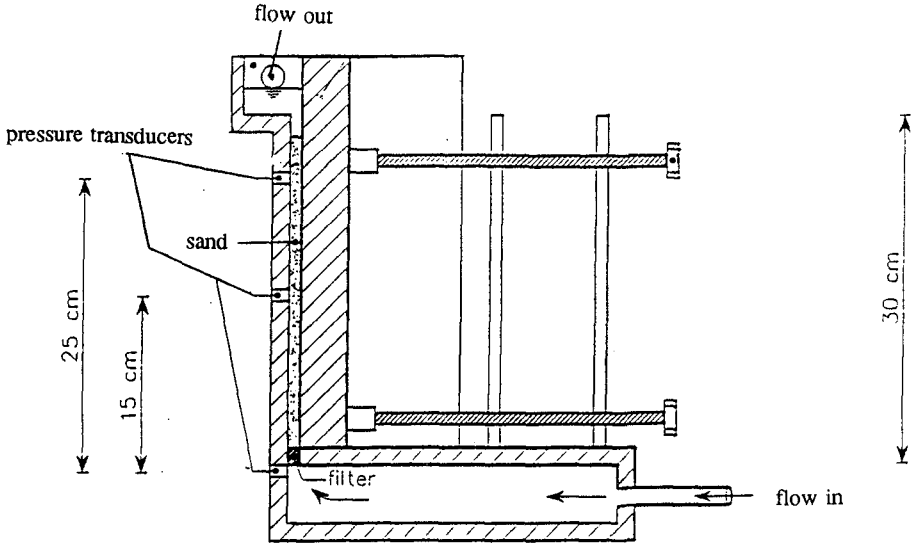


Figure 4 Set up of model to test the stability of sand in small cracks

In Figure 5 some of the results from these tests are presented. A line has been fitted through the results of the tests with a static hydraulic head, using the equation:

$$i_{crit} = 6.2 \cdot D_r^{0.25} \cdot N^{-0.3} \cdot U^{0.4}$$

- with: i_{crit} the critical hydraulic head
 D_r the relative density of the sand $(n_{max} - n)/(n_{max} - n_{min})$
 n porosity (n_{max} , n_{min} are the maximum and minimum porosity)
 N the ratio between crack width and grain diameter
 U the uniformity of the sand (D_{60}/D_{10}) .

From Figure 5 it appears that some of the tests show high values for the critical head. It is assumed that the sand forms arches between the two walls of the

crack, and is thus able to withstand a considerable upward hydraulic head. As the ratio between crack width and grain diameter becomes larger this effect decreases, and eventually the critical hydraulic head will become close to 1.

There is some effect of density of the material. It is not entirely clear whether this has to do with material behaviour (dilatancy) of sand or with a more efficient way of forming arches in dense sand.

The uniformity of the material is demonstrated most clearly if a small layer of coarse material is placed upon a larger layer of fine material. Due to the higher permeability of the coarse material there is no built up of uplift pressure on this layer, and therefor the layer acts as a plug.

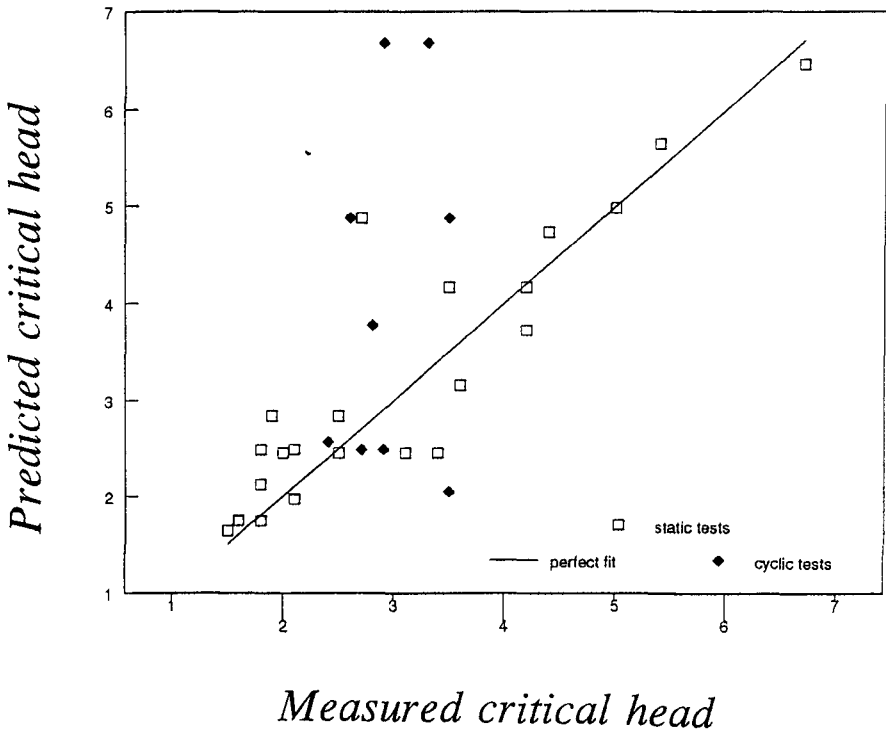


Figure 5 Results of static and cyclic head tests

The tests where a cyclic hydraulic head instead of a constant hydraulic head was used indicate that in general lower critical heads are found in the cyclic tests. The sand is washed out more easily. This can be subscribed to the fact that if arches are being formed by flow of water into one direction, these arches are continuously being formed and destroyed by a cyclic flow of water. Thus the sand is homogenized and washes out more easily than during tests with a constant hydraulic head.

In the cyclic tests there is a difference between 'start of movement' and 'wash out'. Once the sand is observed to start moving in one direction there is some time required to actually form a sand-water mixture that is washed out. During this time the flow can change direction.

In all cases however the critical head lies above the value of 1, which is the threshold value where the sand is supposed to liquefy and wash out.

Stability of sand in a filter layer

The stability of sand in a layer of granular material (gravel) has also been tested. Figure 6 shows the test set up. In a test cel with a diameter of 30 cm a gravel layer is placed. Then the sand is washed in and an upward hydraulic head is applied. Again the critical head at which the sand is washed out is recorded. Typical values for this critical head are 0.6 for loose sand and larger than 1 if the sand has been densified before the test is begun.

The mode of failure as observed during these tests is that at lower hydraulic heads small wells at the surface and pipes in the sand between the grains occur. At the critical value of the hydraulic head the entire sand mass is 'boiling' and can easily be transported away.

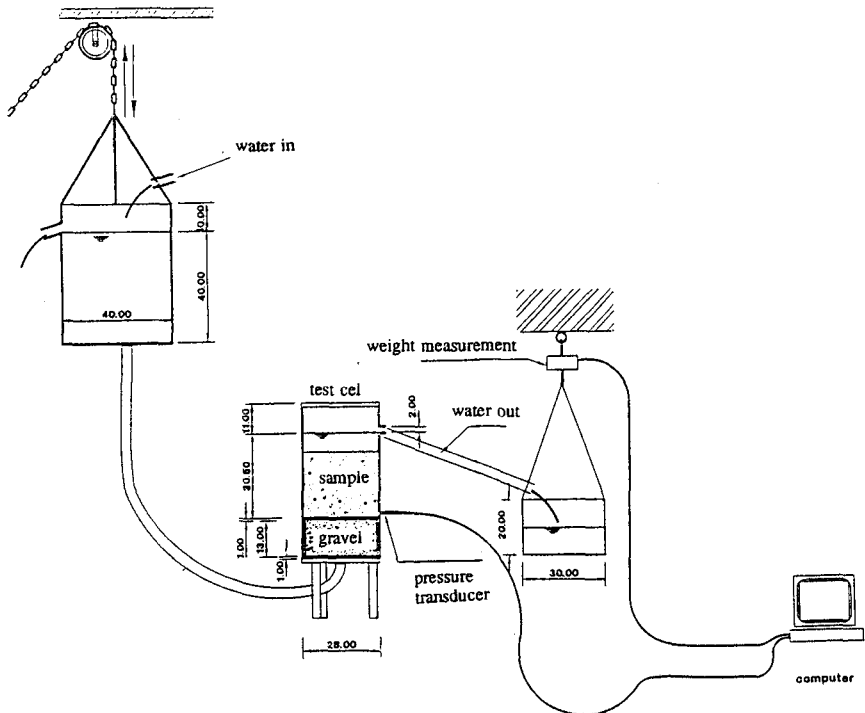


Figure 6 Set up for tests on sand-grain mixtures

The tests also permitted for the permeability of the sand-grain mixture to be measured. It was found that the permeability of these gap-graded mixtures was about equal to 0.3 times the permeability of the sand used in the tests. This seems a logical result, considering the fact that flow takes place through the sand and that the sand is present in the 30 % pore space between the gravel.

Modelling

Obviously, aging, in other words the presence of sand in the construction, causes permeabilities to decrease. This can lead to an increase in hydraulic load over the top layer.

On the other hand, due to the presence of sand, interaction between the blocks is improved, and if the cracks are completely filled with sand, the probability of loose blocks (blocks that do not interact with other blocks when loaded) is strongly reduced.

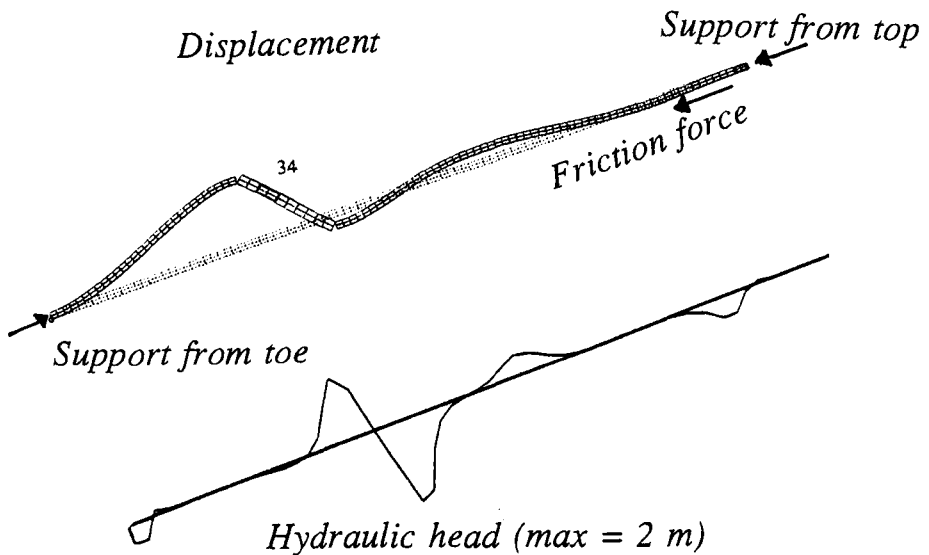


Figure 7 Hydraulic head difference (lower part) and corresponding displacement (upper part)

Modelling of different aspects has consisted of simple models, such as spreadsheet models or analytical, conceptual models, and more sophisticated modelling. Bezuijen (1994) is an example of an approach to describe hydraulic loads,

block movement and subsequent clamping forces in a revetment during oblique wave attack using the numerical STEENZET code.

In order to be able to simulate the complex event of block movement during wave-attack calculations have been made with the STEENZET-model to establish the hydraulic load on the top layer. The corresponding movement of the blocks in the top layer has been calculated with the Finite Element code DIANA. If the blocks are all touching each other the vertical movement causes large horizontal forces in the plane of the slope. These horizontal forces have to be counteracted by support (or stiffness) of the toe and top structure, and by friction between the blocks and the sublayer. An example of this procedure is shown in Figure 7. In the lower part of the figure the hydraulic head difference of a revetment at the moment of the impact of a breaking wave is shown. Above and below this point an upward hydraulic head is generated. The upper part of the figure represents the calculated response of the block revetment in terms of displacement. The movement is scaled up for presentation. Just to give an idea of the real dimensions it can be mentioned that this calculation gives an upward hydraulic head of about 1.75 m, which results in a movement of block 34 in the figure of about 7 cm. The upward water pressure is compensated by the weight of the blocks as due to clamping forces a lot more blocks are lifted than just block 34.

It is now thought that in the case of square concrete blocks the stability of a row of blocks parallel to the waterline is more critical for the stability of the top layer than the situation for blocks in a column parallel to the slope shown in Figure 7. This is because in the case of perpendicular wave attack an entire row of blocks is loaded with almost the same upward load. Theoretically all the blocks in this row would show the same upward movement and clamping can not take place. From calculations for this type of problem it appears that the presence and the stiffness of the material in the cracks is very important. Additional top layer strength is calculated to be 10 to 40 %, which is in reasonable agreement with the results of pull out tests on this type of revetment.

From the pull out tests a larger degree of additional strength is expected from polygon shaped blocks which are washed in with gravel. This is because the blocks do not spread the load into one direction (row or column) but in different directions. In the future 3D simulations will be performed to investigate this.

Conclusion

Finally, the balance between positive effects of aging, such as an increase in top layer stability by an improved interaction between blocks, and negative

effects, such as a possible increase of load on the top layer, has to be made up. Question marks in this process are the stability of sand in the revetment during storm conditions and the possibility to artificially fill filter layers with sand. The overall net effect of aging is, qualitatively, expected to be positive. There is a strong need for quantitative measures. This will take a lot more study of detail processes using for instance sophisticated models, large scale model tests but on the other hand also simple pragmatic tests, field research and test locations.

References

Bezuijen, A., M. Klein Breteler and K. J. Bakker (1987), Design criteria for placed block revetments and granular filters, Int. Conf. on Coastal Eng. in Developing Countries, Beijing, China

Bezuijen, A., M. Klein Breteler and A. Burger (1990), Placed block revetments, in: Coastal Protection, Pilarczyk (ed.), Balkema, Rotterdam, ISBN 90 6191 1273

Bezuijen, A. (1994), Friction and clamping forces in wave loaded placed block revetments, 24th Int. Conf. on Coastal Eng., Kobe, Japan

Burger, A. M., M. Klein Breteler, L. Banach and A. Bezuijen (1990), Analytical design method for relatively closed block revetments, ASCE Journal of Hydr. Eng.

Den Boer, K., C. J. Kenter and K. W. Pilarczyk (1983), Large scale model tests on placed block revetments, Coastal Structures, Washington D.C.

Klein Breteler, M. (1988), Stability of block revetments. Evaluation of the wave pressures on a slope. Delft Hydraulics H195.

Pilarczyk, K. W. (1985), Stability of revetments under wave and current attack, 21st Int. Ass. for Hydr. Research Congress (IAHR), Melbourne

Stoutjesdijk, T. P., A. Bezuijen and B. P. Rieger (1992), Field measurements on placed block revetments, 23rd Int. Conf. on Coastal Eng., Venice, Italy

CHAPTER 148

Experimental Analysis of the Settlement Failure Mechanism Shown by Caisson-Type Seawalls

Shigeo TAKAHASHI¹,
Kojiro SUZUKI¹,
Katsumasa TOKUBUCHI²
Ken-ichiro SHIMOSAKO¹

ABSTRACT

We conducted a series of model in a wave flume measuring pore pressures in the reclaimed soil (sand) to investigate the settlement failure mechanisms of caisson type seawalls. Settlement of reclaimed soil was reproduced by considering that the geotextile sheet, which separates the backfill and reclaimed soil regions, had an opening ripped in it such that soil rapidly leaks out. Also reproduced were the phenomenon of sand boiling (liquefaction), the presence of saturated reclaimed soil above the backfill stones, seawall construction with no backfill stones, and impulsive pressures acting on the joint plate connecting two caissons. Experiment results further clarified the fundamental mechanisms of the settlement failures.

INTRODUCTION

The recent utilization of reclaimed land to provide large-area, man-made islands, e.g., those used for airports, has necessitated their construction in relatively deep seas, which naturally requires them to be surrounded by seawalls that are directly exposed to strong waves since no protective breakwaters are present. Consequently, failures frequently occur during and after construction. The settlement of reclaimed soil behind the seawalls is considered to be responsible for most, and while this type of failure *does not* result in complete failure of the seawall, it *does* lead to land-usage problems and expensive long-term maintenance requirements.

*1 Maritime Structures Lab., Port and Harbour Res. Inst.,
MOT, Japan, 3-1-1 Nagase, Yokosuka 239,
Fax:+81-468-42-7846 Tel:+81-468-44-5011

*2 R&D Div., Shibata Industry Co., Ltd., Japan

Photo 1(a) shows a typical seawall failure by settlement, occurring at S Port located along the Pacific Coast in Japan, where a large hole is formed behind the seawall. This type settlement failure occurred during construction, being the end result of wave actions from a strong storm. Figure 1 shows the cross section of the seawall, a relatively deepwater seawall protecting a large, man-made island; being particularly chosen due to a water depth of more than 10 m and a design significant wave height of about 8 m. The caisson is 12 m wide and covered by wave-dissipating concrete blocks. Backfill stones placed behind the caisson reduce the soil pressure acting on it. The large holes were formed in the reclaimed soil located above the backfill stones. A permeable geotextile sheet laid on the top of the backfill stones should prevent such soil leakage; thus, we surmise that it was damaged by waves either during and/or after placement of reclaimed soil.

The seawall failure in S Port is unique in that it also provided evidence of air blow, which can be seen in Photo 1(b), i.e., air is being blown out a gap between the caisson and reclaimed soil. Air blow occurs when wave motion inside the



Photo 1(a) A large hole formed behind a seawall.

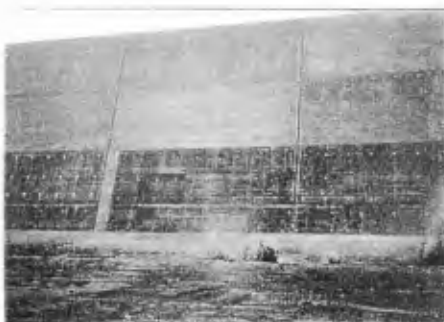


Photo 1(b) Air blow occurring from a gap between the caisson and backfill stones.

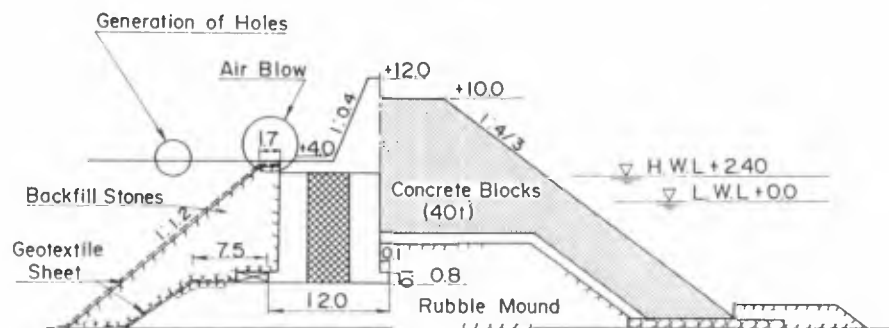


Fig. 1 Cross section of a caisson type deepwater seawall.

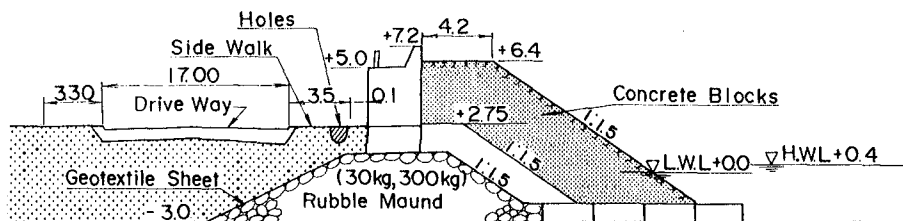


Fig. 2 Cross section of a rubble mound type shallow water seawall.

backfill stones compresses the air within the stones such that it blows out through the gap; a phenomenon that occurs even at not-so-large wave heights.

Figure 2 shows another settlement failure, in this case for a rubble mound type seawall located in relatively shallow water. The apparent damage was caused by a winter storm, leaving numerous holes in the sidewalk. Note that the interlocking blocks in the sidewalk have been upturned/knocked out of place; a phenomenon thought to occur when the pore pressure in the backfill stones exceeds the overburden soil pressure in the overlying reclaimed soil.

Three years ago, a comprehensive study on the mechanisms of settlement failures was initiated at the Port and Harbour Research Institute (PHRI), Japan. The study is considered comprehensive due to the inclusion of hydraulic, geotechnical, and material aspects in conjunction with determining practical construction methods. Here, we report the results of hydraulic model experiments which further elucidate the mechanisms leading to settlement failures of seawalls.

EXPERIMENTAL PROCEDURES

Experiment series

Four series of model experiments were conducted. In series 1, the settlement failures of reclaimed soil were reproduced, and in series 2, pore pressures in the backfill stones and reclaimed soil were measured. Standard and special cross sections were tested along with a cross section in which the boiling type of failure can easily occur.

In the series 3 experiments, we measured the impulsive pressure acting on the joint plate connecting two caissons, as destruction of the plate is known to result in damage to the geotextile sheet and subsequent settlement of the reclaimed soil; while in series 4, a cross section with no backfill stones was tested to show the effect of the stones in preventing settlement failure. In this case, no reduction occurs in the ground pressure acting on the caisson, nor in the direct wave actions affecting the reclaimed soil. Pore pressures were also measured for this cross section.

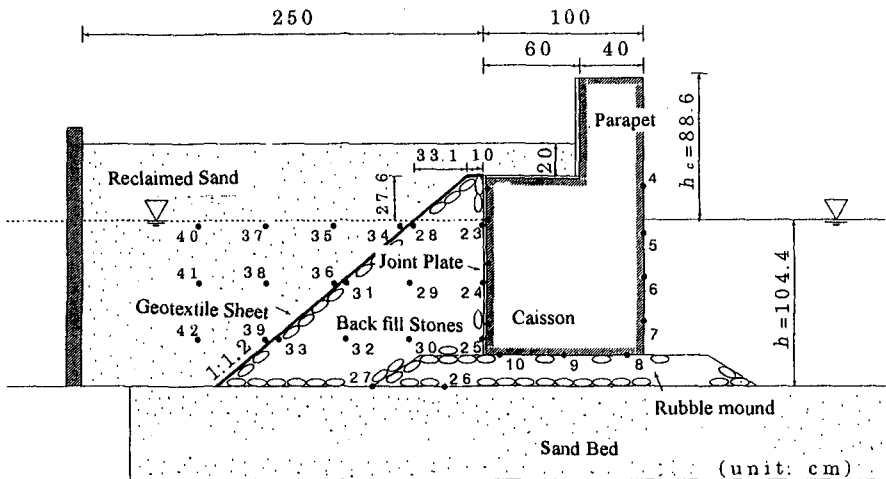


Fig. 3 Cross section of the standard seawall model.

Seawall Model

Figure 3 shows a cross section of the standard seawall model in which the geotextile sheet is placed between the backfill stones and reclaimed sand (soil) in order to stop sand from leaking through the backfill. Although the surface of the reclaimed soil is usually paved, this was not simulated in the model.

Models at 1/16-scale were installed in a wave flume on top of a sand bed. The water depth and caisson width were both about 1 m, and crest elevation of the seawall was 88.9 cm, which is relatively high compared to the water depth. Equivalent water depth is about 16 m and crest elevation about 14 m. The locations of more than 40 wave pressure and pore pressure transducers are indicated.

We also tested a model cross section similar to one occurring during the construction period, where the reclaimed sand is filled just up to the top of the backfill stones. In this case, which was mainly considered in series 1 experiments, the crest height of the caisson is relatively low at 58.1 cm.

Waves

Regular and irregular waves were generated in the experiments, with wave height being varied from 25 to 61 cm and wave period from 2.1 to 3.5 s. The standard case uses a wave height of 52.4 cm and wave period of 3.04 s, i.e., equivalent to 8.4 m and 12.2 s for actual waves.

EXPERIMENTS REPRODUCING SETTLEMENT FAILURE

Soil leakage due to geotextile sheet damage

In series 1 experiments, under the assumption that the settlement of reclaimed soil was caused by an opening being

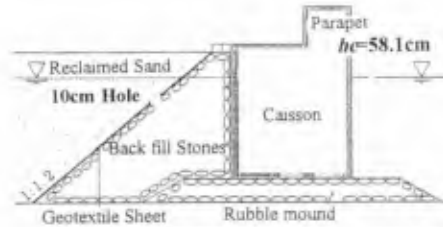
ripped in the geotextile sheet either during or after construction, we cut a relatively large, 10-cm diameter hole in the sheet, laying it between the backfill stones and reclaimed sand such that the hole was situated below the still water level.

Photo 2 shows the effect of sand leakage before applying wave action. After adding the overlying reclaimed sand, while slowly filling the wave flume with water, sand started leaking through the hole right after the water reached its level, with the end result being the formation of the large tunnel (cave) shown in the photo.

Upon commencing wave action after crushing the tunnel and refilling in the sand lost by leakage, the water surface in the backfill stones began moving up and down and gradually sand began leaking through the hole, in turn forming another tunnel. Some sand is trapped in the backfill stones, but most passes through them and piles up on the seabed.

Although larger waves led to a larger tunnel, when wave overtopping occurred, the water motion in the backfill region increased, leading to a higher leakage rate and rapid growth of the tunnel until the weight of the overlying sand suddenly collapsed it. Photo 2 also shows the resultant settlement of the reclaimed sand which is greatest just above the location of the hole.

Experiments to Reproduce the Settlement Failures



Generation of Cave before Wave Action



Generation of Cave by Wave Action



Collapsing of Soil by Overtopping Waves

Photo 2 Soil leakage through a 10-cm hole in the geotextile sheet at a location below the still water level.

Effect of hole size and location

To further investigate this behavior, we varied the size and location of the hole. Although the rate of sand leakage naturally increased with the size of the hole, for very small holes with a diameter of 1 cm, the leakage stopped due to the hole being blocked by sand that is trapped nearby between backfill stones. In addition, the rate of leakage is highest for holes located just below the still water level, being substantially increased by overtopping waves, or by rainfall which was also simulated.

Behavior of reclaimed sand without a geotextile sheet

Because some seawalls have been constructed in Japan without a geotextile sheet, under the premise that adding reclaimed soil to the backfill section during construction will prevent subsequent leakage upon completion, this case was also examined in the experiments.

As expected under this situation, the sand literally flowed into the backfill stone section during the filling process. Also, small wave actions promoted infiltration into the backfill section. In fact, even if reclaimed sand is added to fill all the void spaces in the backfill stones, the sand in the backfill stones located just behind the caisson is still carried away through the rubble mound. Such behavior indicates a good possibility that leakage will continue after construction, especially if large waves attack the seawall.

MEASUREMENT OF PORE PRESSURES

Pore pressure distribution

Figure 4 shows typical analogue data for the standard cross section measured at four channels, i.e., the front and bottom of the caisson (7, 10), in the backfill stones (23), and in the reclaimed sand (38). Channels 7 and 10 indicate ordinary standing wave pressure that is simultaneously transmitted to the backfill stones, where slight damping is apparent and negative pressures indicate higher damping than positive ones. Also, pore pressure in the reclaimed sand is highly damped and shows a very smooth pressure curve. Pore pressures in the backfill stones and reclaimed sand provide important data as settlement failure is more likely to occur at high positive and/or negative values.

Peak pore pressure for standard cross section

Figure 5 shows the corresponding pressure distribution for the standard cross section, where the size of the arrows indicates the relative magnitude of nondimensionalized positive peak pressure, while its inclination indicates the phase difference at peak pressure. Note that the pore pressure in the backfill stones is almost constant, being quite high at about 80% of the wave pressure at the front of the caisson. Pressure is not substantially reduced because the water and air in the backfill stones are enclosed relatively tightly by the reclaimed sand, i.e.,

the movement of pore water in the rubble mound and backfill stones is very limited by the reclaimed sand and the dissipation of pore pressure is low. This pore pressure, however, rapidly damps out as shown by the pore pressure in the reclaimed sand.

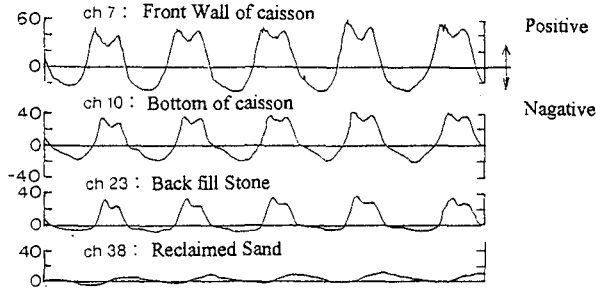


Fig. 4 Analogue data for the standard cross section indicating pore pressures measured at indicated channels.

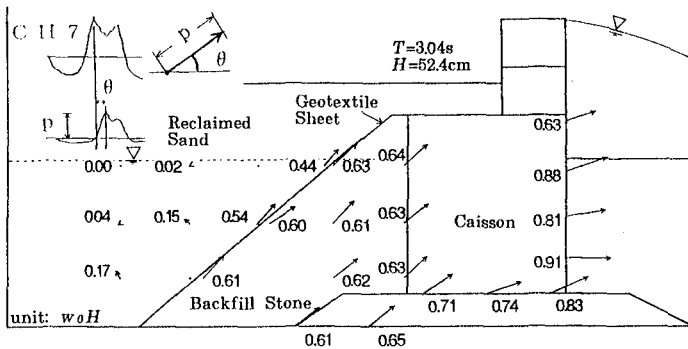


Fig. 5 Distribution of positive peak pressures in the standard cross section in which reclaimed sand above the backfill region is not in a saturated condition.

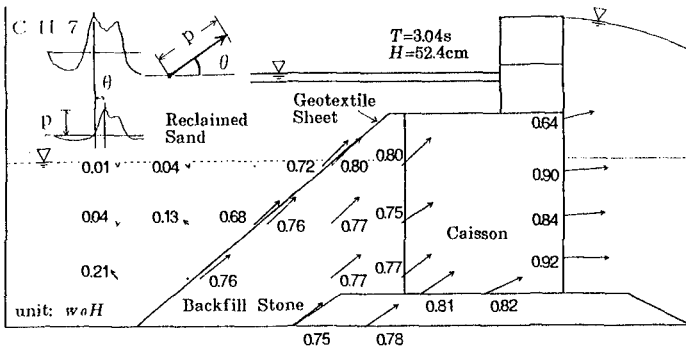


Fig. 6 Distribution of positive peak pressures for a cross section in which the reclaimed sand above the backfill region is maintained in a saturated condition.

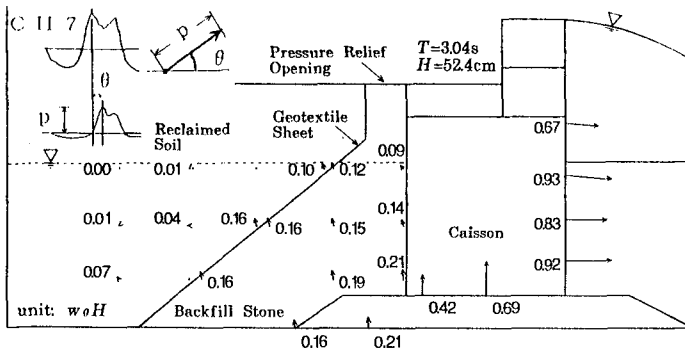


Fig. 7 Distribution of positive peak pressure using pressure relief opening.

Pressure increase due to saturation of reclaimed soil

Due to wave overtopping and rain, the reclaimed soil will normally be water saturated; thus, to simulate the strong effect of this condition on pore pressure in the backfill region, we added water as necessary to ensure the reclaimed sand stayed saturated during the experiments.

By comparing Figs. 5 and 6, which show the resultant pressure distribution of peak pressures with and without saturation, it is clear that much higher pore pressures are present when the reclaimed sand is saturated, being nearly equal to the wave pressure in front of the caisson. This phenomenon is a result of the backfill region being tightly enclosed by the saturated reclaimed sand above the still water level, i.e., pore pressure is transmitted without damping in the backfill stones.

Pressure relief measures

The transmission of pore pressure in the backfill region without damping can be prevented, however, by providing a vent path or opening in the backfill stones, which can be established if a portion of the upper surface of the stones is situated at or above the level of reclaimed soil. Figure 7 shows the resultant pressure distribution if such an opening is established, where the peak values are significantly reduced to about 10% of the wave pressure acting on the front of the caisson; and accordingly, the pressure in the reclaimed sand is reduced as well.

As another method for reducing pore pressure in the backfill stones, a pressure relief opening was made in the rear chamber of the caisson, with results indicating a substantial reduction in pressure, (although the data are not shown here).

Water level oscillation in backfill stones

Movement of pore water, especially that of the water level in the backfill stones, is another important factor affecting sand leakage. For the standard cross section, the level of water fluctuated between 10 and 20% of incident wave height as shown

in Fig. 8. Note that the magnitude of fluctuations decreases as wave height increases. Naturally the fluctuations in water level are smaller when the reclaimed sand is in a saturated condition, being less than 10% of the incident wave height. If, however, a pressure relief opening is established in the backfill region, the size of the fluctuations increases, ranging from 23 to 32% of the incident wave height.

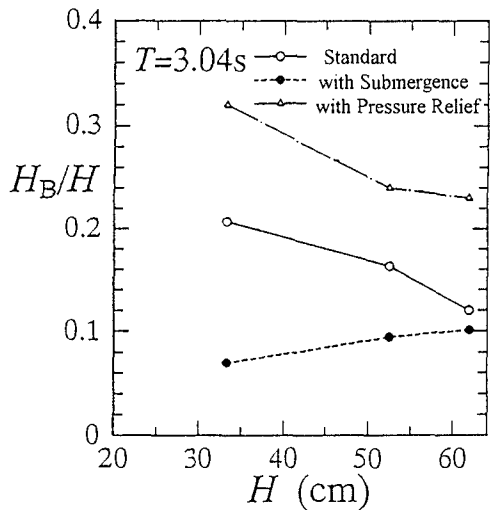


Fig. 8 Water level oscillations in backfill region.

BOILING OF RECLAIMED SOIL

As boiling or liquefaction of sand is considered a major factor causing settlement failures of seawalls, we modified the cross section of the standard seawall to experimentally reproduce this behavior. That is, a 20-cm-thick layer of reclaimed sand was used to cover the backfill stones, and the level of water was maintained at the surface of the reclaimed sand in order to limit the overburden soil pressure acting on the stones.

Although no unusual behavior was observed at small wave heights, at a wave height of 42.8 cm, the entire layer of sand appears to lift up as shown in Fig. 9. This is the first indication of sand boiling (liquefaction), with increases in the wave height forcing the sand further upward until boiling occurs. The effect of boiling is disastrous as can destroy both the layer of reclaimed soil and any type of pavement covering this region. As another consequence, the geotextile sheet can be ripped such that an opening occurs.

Figure 10 shows the pore pressure distribution when boiling occurs, where the pore pressure in the backfill stones reaches about 17.8 gf/cm^2 (14.5 kN/m^2), approaching close to the overburden soil pressure. Note that the pore pressure stays at this level even though wave height is increased.

These experiments confirm that boiling of reclaimed soil occurs when the pore pressure in the backfill region increases close to the overburden soil pressure acting on the backfill region. Consequently, to withstand large wave heights, the layer of the reclaimed soil should be sufficiently thick such that the force produced by the weight of the soil counteracts that produced by the increase in pore pressure in the backfill region;

or alternatively, the backfill pore pressure should be reduced by establishing a pressure relief path.

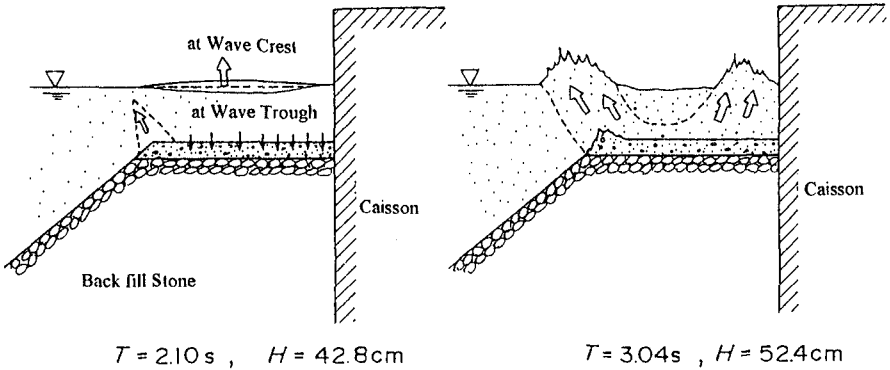


Fig. 9 Boiling of reclaimed sand.

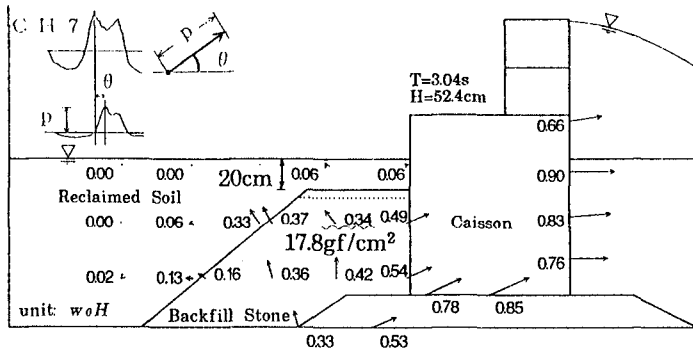


Fig. 10 Distribution of peak pore pressure in the case of sand boiling.

IMPULSIVE PRESSURE ON A JOINT PLATE

Caisson joint model

In series 3 experiments, the impulsive pressures acting on the joint plate connecting two caissons were measured, being done in response to learning that destruction of the joint plate leads to the damaging the geotextile sheet and settlement failure due to soil leakage.

Figure 11 shows the cross section and front view of the seawall model, where a 1.5-cm joint plate has been installed between the caisson and a glass observation window. Several pressure transducers were placed to measure impulsive pressures on the joint plate.

Wave action and impulsive pressure on the joint plate

Figure 12 shows typical analogue measurements indicating wave pressure on the caisson's front wall and joint plate

respectively. Channel 11 provides pressure on the joint plate at the still water level, while channel 4 provides the pressure on the caisson at the same level, and channel 14 on the plate near the caisson bottom. As shown, an impulsive pressure appeared near the water surface, having an intensity of more than $3 w_0H$. Also shown is the movement of the wave front which contains a layer of air such that it generates an impulsive pressure upon impact against the plate.

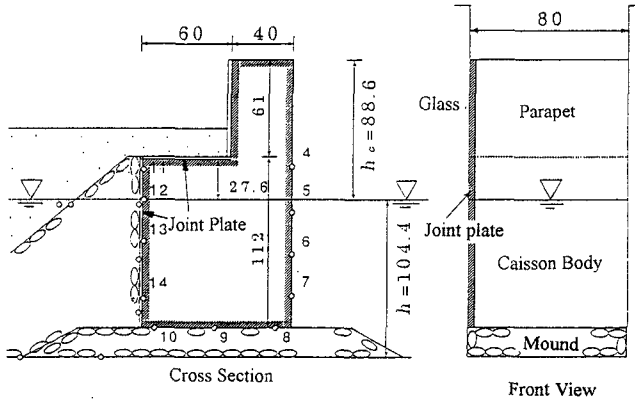


Fig. 11 Seawall model with a caisson joint plate.

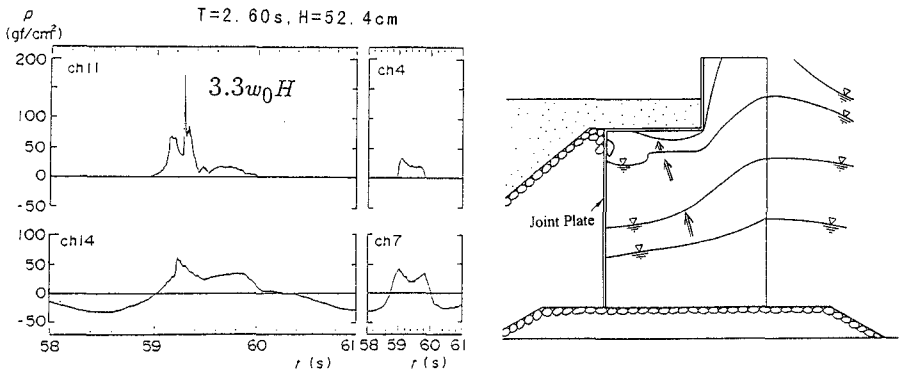


Fig. 12 Generation of impulsive pressure on joint plates.

Peak impulsive pressure on the joint plate

Figure 13 shows nondimensionalized peak pressure acting on the joint plate near the still water level, where experimental values are plotted for four different wave periods as a function of wave height. Due to data scatter, the ranges and mean values are indicated, with pressure ranging from 1 to 4 w_0H and having an average value of about 2 w_0H .

The impulsive pressure acting on the joint plate above the still water level is very similar to the uplift pressure on the horizontal plate, e.g., the superstructure of a pillar quay or that

acting on the ceiling slab of a wave chamber in a perforated wall caisson. Based on this similarity, the methods used to determine these pressures can be applied here for determining the impulsive pressure.

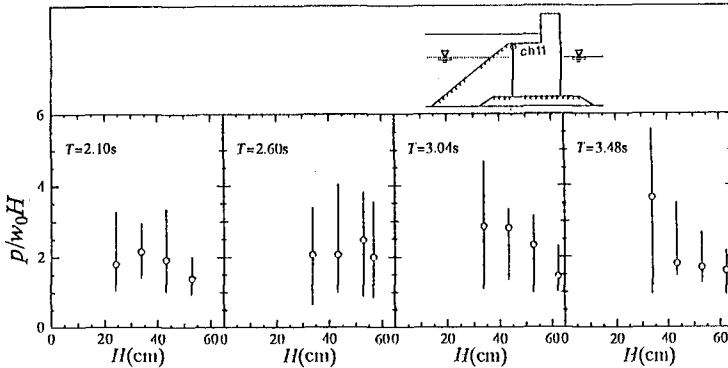


Fig. 13 Impulsive pressure intensity on a joint plate.

Reduction of impulsive pressure by spacer plates

The impulsive pressure on the joint plate can be reduced by narrowing the gap (space) between two caissons using spacer plates. Figure 14 shows that two spacer plates installed in the gap between the caisson and observation window can substantially reduce impulsive pressure, although one spacer plate works almost as well.

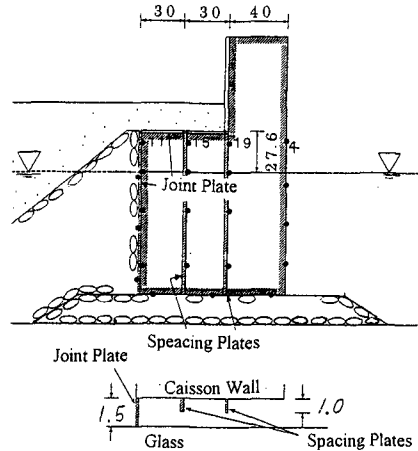


Fig. 14 Spacer plates to reduce the impulsive pressure.

SEAWALLS WITHOUT BACKFILL STONES

Loss of reclaimed soil due to joint plate damage

The main purpose of using backfill stones is to reduce ground pressure acting on the caisson. If, however, the wave pressure is large compared to ground pressure, then backfill stones need not be used. This is commonly the case in Japan where the design wave height is large and the design acceleration produced by an earthquake is small. In addition, if backfill stones are not used construction costs will be lower.

Using backfill stones along with a geotextile sheet reduces the risk of the leakage of reclaimed soil through the joint plate should it be damaged. In fact, the stones function as a filter medium which reduces direct wave pressure acting on the

reclaimed soil. When a small hole was made in the joint plate, wave actions led to a continuous leakage of sand from the back region of seawall.

Pore pressure in the reclaimed sand

Figure 15 shows the pressure distribution for a cross section without backfill stones, where the high pressure in the reclaimed sand near the rubble mound should be noted, being almost 90% of the frontal wave pressure. Consequently, the pressure gradient in the sand near the rubble foundation will be large, which might easily lead to the adverse consequence of damaging the geotextile sheet placed between the sand and rubble mound.

The pore pressure in the reclaimed sand can be reduced using an opening in the caisson. Figure 16 shows the pressure distribution with an opening in the rear chamber of the caisson, which reduces the pressure near the sand and rubble mound to 10% of the frontal wave pressure. If the backfill stones are not used, then obviously measures such as this one must be taken in order reduce pore pressure in reclaimed soil.

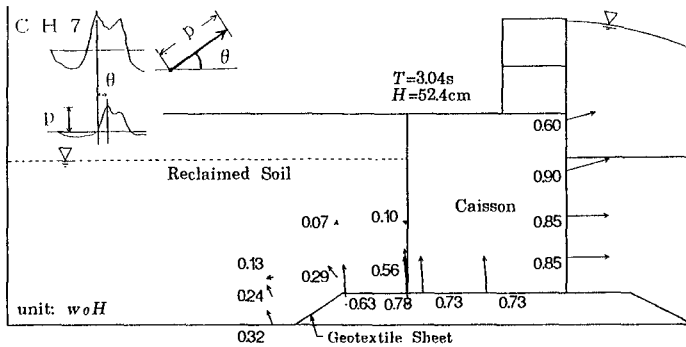


Fig. 15 Distribution of peak pore pressure without backfill stones.

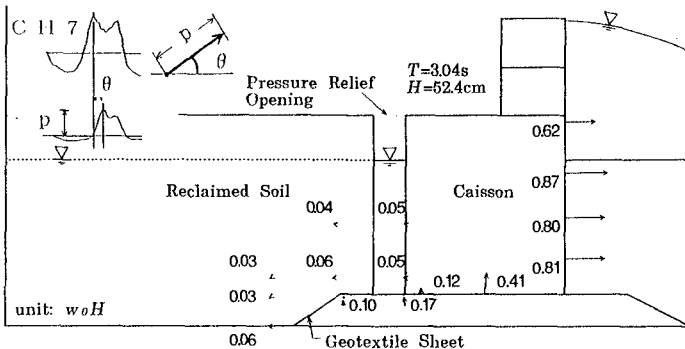


Fig. 16 Distribution of peak pore pressure with a pressure relief opening.

CONCLUDING REMARKS

By combining the present experimental results with those from field surveys various mechanisms were found to cause leakage of reclaimed soil, with the loss of this soil subsequently leading to seawall failure by settlement. Figure 17 shows the resultant settlement failure mechanisms using a failure path diagram. For example, failure occurs if the wave actions during and/or after construction breach the integrity of the geotextile sheet, where the soil can then leak into the backfill stone region due to wave actions. The occurrence of sand boiling and damage to the joint plate were also implicated as being important settlement failure mechanisms.

Although we have obtained a relatively sound qualitative understanding of settlement failure mechanisms, being an essential aspect towards realizing practical seawall designs, only with a sound quantitative understanding of the mechanisms can a full understanding be obtained.

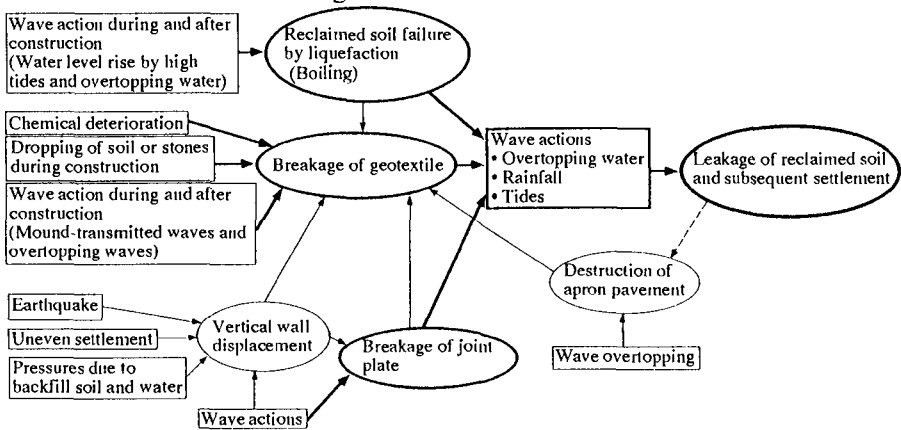


Figure 17 Diagram of mechanisms leading to seawall failure by settlement.

ACKNOWLEDGEMENTS

The authors wish to express their thanks to Drs. K. Kobune, R. Ojima, K. Zen and H. Yamazaki of PHRI for their precious comments on the present study. The author is also grateful to Messrs. S. Yamamoto, H. Miura, T. Okamura, and Y. Saito of PHRI for their collaboration in the experimental works.

REFERENCES

- Takahashi, S., Tanimoto, K., and Miyanaga, S. (1985)
 "Uplift force due to compression of enclosed air layer and their similitude law," Coastal Eng. in Japan, JSCE, Vol. 28, pp.191-206.
- Williams, A.F., Burcharth, H.F., den Adel, H. (1992)
 "The permeability of rubble mound breakwaters, New measurements and new ideas, Proc. of 23rd International Conference on Coastal Engineering, ASCE, pp. 1720-1733.

CHAPTER 149

FULL SCALE MEASUREMENTS OF WAVE ATTENUATION INSIDE A RUBBLE MOUND BREAKWATER

Peter TROCH¹, Marc DE SOMER¹, Julien DE ROUCK¹, Luc VAN DAMME²,
Dierik VERMEIR³, Jean-Pierre MARTENS⁴, Conan VAN HOVE⁴

ABSTRACT

At the Zeebrugge harbour (Belgium) a cross-section of the N.W.-breakwater has been instrumented for the study of physical processes related to the behaviour of a prototype rubble mound breakwater in random wave conditions. Within the EC MAST programme (project MAS02-CT92-0023) this monitoring system has been re-engineered and extended to a high-quality full scale data acquisition centre (Troch et al., 1995).

The development of the prototype monitoring system to a world-wide unique system with respect to the infrastructure available at Zeebrugge, the instrumentation installed on site, and the data management developed, is briefly summarised.

Filed measurements of wave attack in front of the breakwater, and pore pressure response inside the breakwater core, have been analysed in order to determine the hydraulic response of the full scale breakwater. Analysis results on wave run-up/run-down measurements, phreatic set-up calculations, and pore pressure wave attenuation are presented here in more detail.

INFRASTRUCTURE

The port of Zeebrugge is situated on the eastern part of the Belgian coastline, and is protected by two main breakwaters (Fig. 1). The Zeebrugge breakwater constitutes of a conventional rubble-mound breakwater with a low superstructure and an armour layer consisting of grooved cubes (25 ton). The breakwater core consists of quarry run 2-300 kg, the filter layer is made of rock 1-3 ton. On the breakwater crest, a service road enables easy access of the breakwater. The tidal range at spring tide is 4.3 m.

A measurement jetty of 60 m length supported by a steel tube pile at the breakwater toe and by concrete columns on top of the breakwater is situated on the NW-breakwater, Fig. 2. Six boreholes have been drilled in the core: four vertical boreholes and two oblique boreholes. Galvanised steel casings are placed in these boreholes. These casings are perforated in order not to disturb the overall permeability. Pressure sensors are mounted in these casings. Each pressure sensor cable is protected by a high density polyethylene tube provided with a perforated nylon head at the sensor end.

1) Civil Engineering Dept., University of Gent, Technologiepark 9, B-9052 Gent, Belgium.

2) Ministry of Flemish Community, Coastal Division, Vrijhavenstraat 3, B-8400 Ostend, Belgium.

3) Dept. Information Technology, HAECON, Deinssesteenweg 110, B-9031 Gent, Belgium.

4) ELIS, University of Gent, St-Pietersnieuwstraat 41, B-9000 Gent, Belgium.

In an air-conditioned container, placed on the landside of the breakwater, signal conditioning apparatuses and a data acquisition system (DAS) are installed. All electric cables from the measuring sensors are lead towards the container.

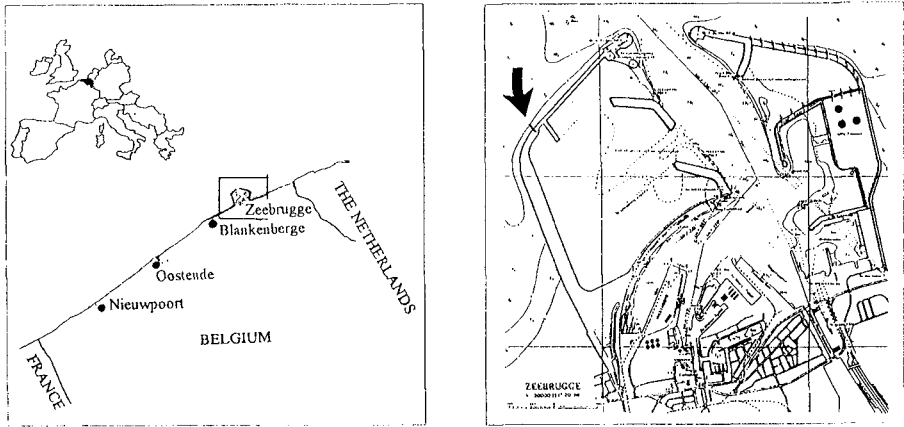


Fig. 1. Location of the prototype monitoring system on the NW breakwater at Zeebrugge harbour (Belgium).

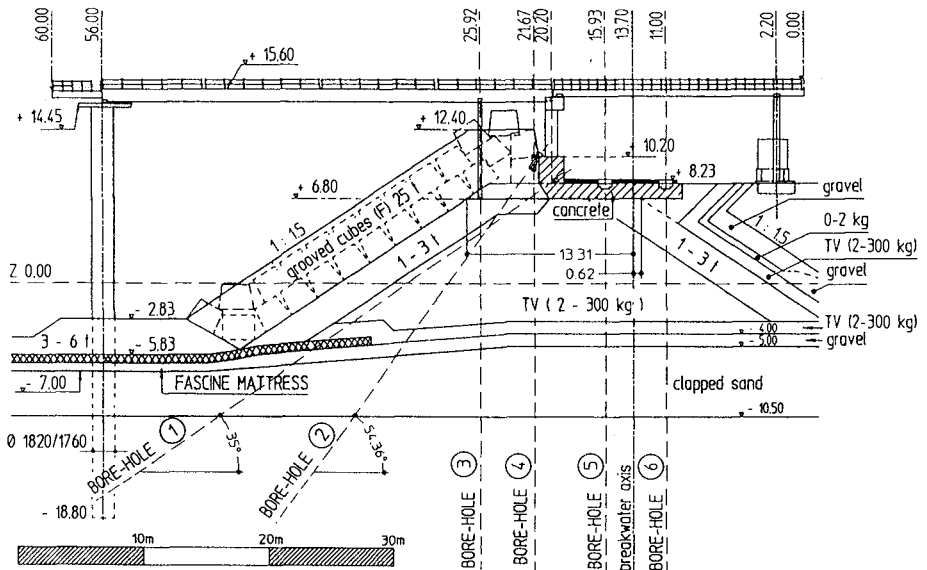


Fig. 2. Cross-section of the Zeebrugge rubble mound breakwater.

INSTRUMENTATION

An overview of instrumentation installed on the measurement jetty is given in Fig. 3, and summarised in Table 1.

Full Scale Measurement Jetty at Zeebrugge Breakwater

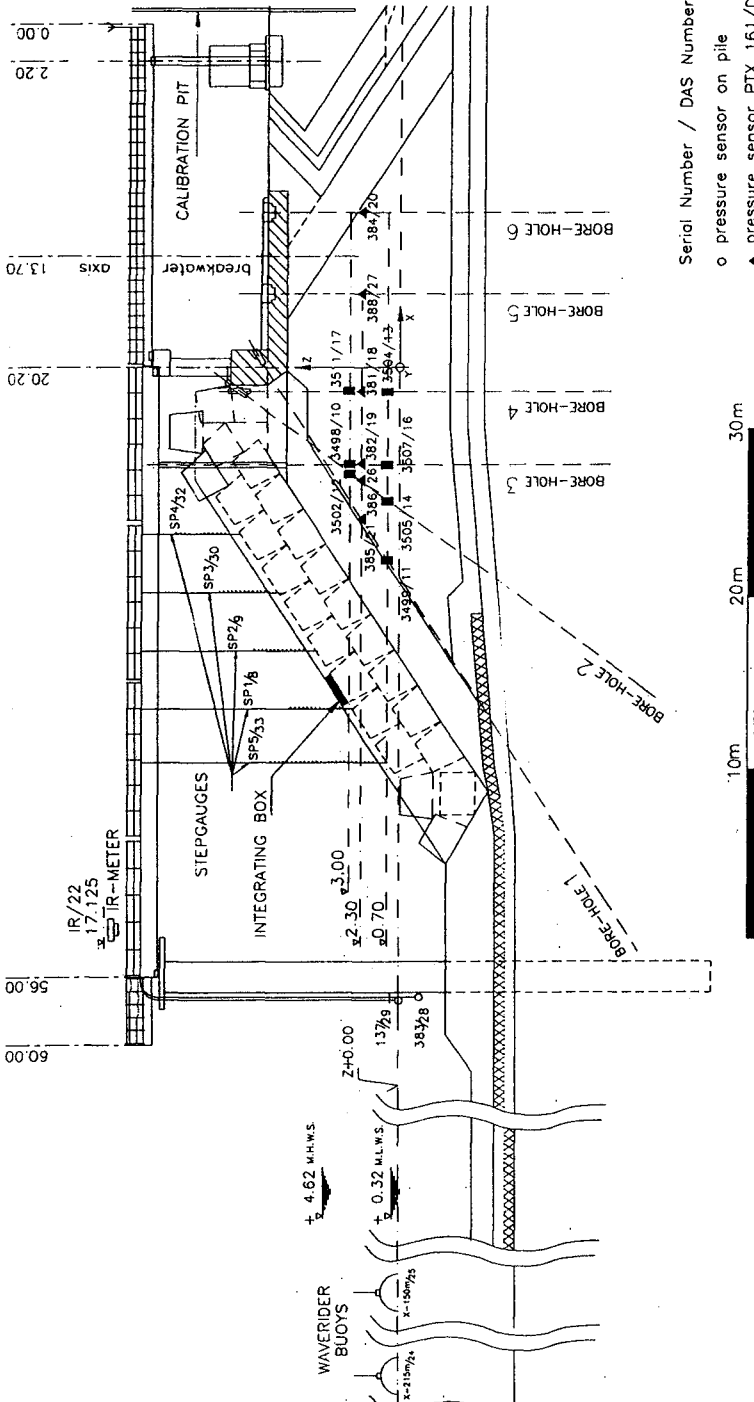


Fig. 3. Zeebrugge breakwater: Location of instrumentation since 1994.

Wave rider buoys are located in front of the breakwater and measure the incident waves. The water level at the toe of the breakwater is measured by an infra-red wave height meter and by two submerged pressure sensors located in front of the steel tube pile.

A set of vertically placed stepgauges between the measurement jetty and the armour layer is able to registrate the wave run-up and run-down on the armour layer.

Inside the core 13 pressure sensors are installed in the six boreholes for the measurement of the internal pore pressures induced by the waves. Assembly of the sensors is conceived to allow flexible placement in the boreholes, ease of maintenance and ease of calibration.

A device called "integrating box" is designed for the measurement of wave forces, i.e. the integrated pressures on (a part of) an armour unit face. The solid steel box is filled with water under pressure. A pressure sensor mounted in the box measures the pressure variation in the enclosed box volume. The device has been calibrated extensively in the laboratory. The pressure inside the box is related to the wave force applied on the box membrane.

INSTRUMENTATION	LOCATION	AIM OF MEASUREMENT
2 waverider buoys	150 m and 215 m from breakwater	wave records
infra-red wave height meter	near steel tube pile	wave records, tide level
2 submerged pressure sensors	near steel tube pile	wave records, tide level
5 vertically placed stepgauges	between armour layer and jetty beam	run-up/run-down wave profiles
'integrating box'	on one face of armour unit	wave forces on an armour unit
13 pressure sensors	inside rubble core	pressure records

Table 1. Instrumentation of Zeebrugge breakwater.

DATA MANAGEMENT

A strategic data management plan is developed for acquisition, processing and distribution of all full scale data.

Each sensor has its dedicated signal conditioner providing individual isolated power supply and converting the current of the pressure sensor circuit to a voltage output -proportional to the physical input- which is galvanically isolated from the sensor circuit. The voltage outputs of all sensors are separately connected to an isolation amplifier followed by a lowpass-filter before being connected to the data acquisition system. Special care with regard to groundings and shielding of the electronic devices has been taken in order to prevent ground loops.

A scanner samples all analog data at 10 Hz. After analog-to-digital conversion raw data are stored as binary files on a hard disk of the computer. The data acquisition computer manages the hard disk as a ringbuffer.

An software package, written in ANSI C and portable on several systems, is included for presentation, evaluation and signal analysis. Software tools were written to read data from file, display data on screen, select pieces of data and analyse the selected

data. Routines for input and output have been implemented allowing the user to output measurements values and computational results and to input signals having a format different from the one of Zeebrugge data. Procedures have been developed for the quality control of raw data. This way an interface today is available for the input of external data from scale models and numerical models for comparison and research activities.

The acquired time series are edited for the elimination of errors in the signals. A very valuable technique, developed in speech analysis, and applied here to the signals, is the calculation of a spectrogram of a signal. The spectrogram (Fig. 4) consists of consecutive spectra, calculated for consecutive windows on the time series and placed vertically. The spectral energy information per frequency interval is converted towards a proportional line length. This way, errors in the signal, such as high frequency noise or sample gaps, are easily detected and edited.

Up to date about 16 storms with significant wave heights ranging between 1.00 m and 3.50 m, and wind directions from N.W. -allowing almost perpendicular wave attack- have been registrated. Continuously improvements and new instruments are prepared and installed, keeping the prototype monitoring system highly operational. For more detailed information and technical details of instrumentation and data acquisition, the reader is referred to (Troch et al., 1996-a; Troch et al., 1996-b).

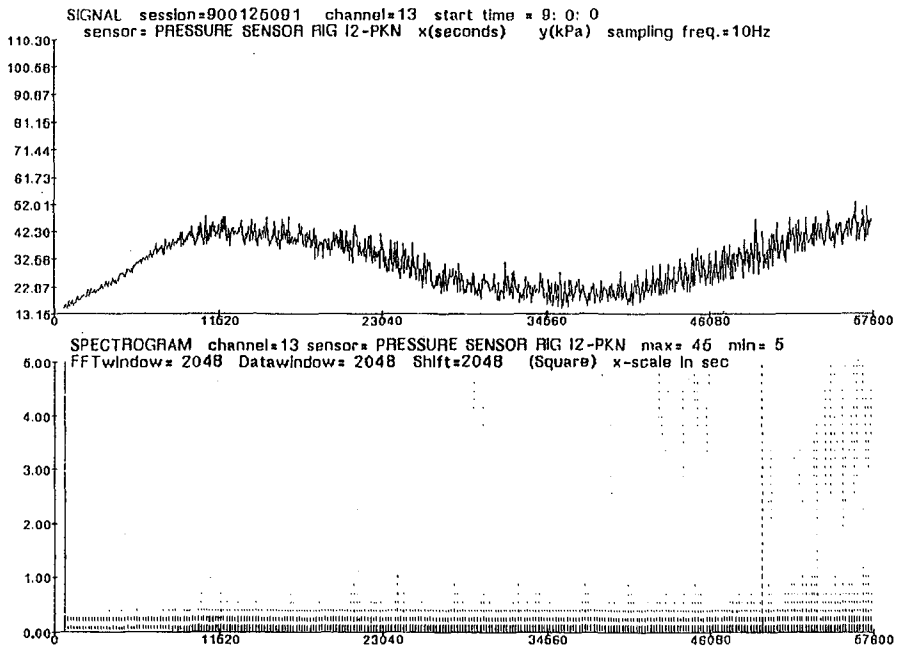


Fig. 4. Typical acquired time series and spectrogram of pressure sensor signal.

FULL SCALE DATA ANALYSIS RESULTS

Wave run-up measurements

The wave run-up (run-down) derived from full scale measurements is defined as the vertical distance between Mean Water Level (MWL) and the highest (lowest) point attained by the wave up-rush (down-rush) on the slope. The run-up height R_u is one of the most important parameters associated with wave loading on rubble mound structures and their stability. It, along with the highest still water level, determines the necessary crest level of the breakwater.

At each stepgauge mounted along the breakwater slope, the instantaneous water surface level is measured. From these time series, the instantaneous wave profile on the slope is derived. At one instant, the wave profile is taken as the polygon connecting the water surface levels measured at all stepgauges. The instantaneous wave run-up height is defined here as the vertical distance between MWL, and the intersection of the breakwater slope with an extrapolated line, constructed through the two highest water surface levels measured at that instant. MWL is calculated as the mean of a water surface measurement using a submerged pressure sensor mounted in front of the steel tube pile. When the intersection is positioned below MWL, instantaneous wave run-down is identified.

The relevant run-up level of an irregular wave signal is taken as $R_{u,2\%}$. This is the level exceeded by only 2% of the waves running up the armour slope. The run-down level considered is the $R_{d,98\%}$ which is the level exceeded by 98% of the waves. The reference number of waves used for the computation of the exceedence level, is taken here as the total number of run-up waves on the slope. The non-dimensional run-up ratio $R_{u,2\%}/H_{mo}$, where H_{mo} is the significant incident wave height, and run-down ratio $R_{d,98\%}/H_{mo}$, are plotted versus the deep water Iribarren number of the wave form:

$$\xi = \frac{\tan \alpha}{\sqrt{\frac{H_{mo} 2\pi}{gT_{(0,2)}^2}}} \quad (1)$$

where α = slope angle ($^\circ$); significant wave height $H_{mo} = 4(m_0)^{1/2}$ (m); wave period $T_{(0,2)} = (m_0 / m_2)^{1/2}$ (s), where m_n is the n^{th} moment of spectral density.

Allsop et al. (1985) presented model test run-up results on a 1:1.5 Antifer cube slope with irregular waves, using Losada et al.'s (1982) relationship:

$$\frac{R}{H} = A[1 - \exp(B\xi)] \quad (2)$$

where R = run-up/run-down level, defined as: $R_{u,2\%}$ or $R_{d,98\%}$; $H = H_{mo}$; A , B = experimental coefficients; ξ = Iribarren number. Allsop reported:

$$\text{run-up: } A=1.52 \quad B=-0.34$$

From physical model tests on the identical Zeebrugge breakwater cross-section, carried out in the MAST II project (Kingston et al., 1996), it is found that for irregular waves the coefficients are:

$$\begin{array}{ll} \text{run-up:} & A=1.76 \quad B=-0.28 \\ \text{run-down:} & A=-1.05 \quad B=-0.43 \end{array}$$

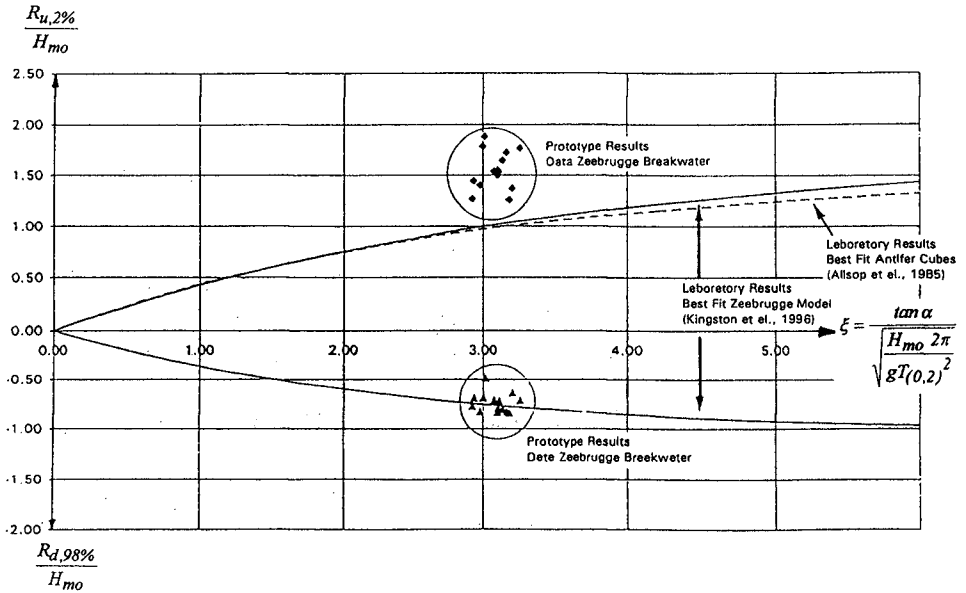


Fig. 5. Comparison between prototype and scale model wave run-up results.

In Fig. 5 non-dimensional wave run-up heights and wave run-down heights obtained from Zeebrugge prototype measurements using the vertically placed stepgauges are plotted as a function of the Iribarren number ξ . Note that the range for ξ is small due to the occurred wave and breakwater characteristics. As a result, for $\xi \approx 3$ the wave run-up $R_{u,2\%}/H_{m0}$ has order of magnitude 1.50, and the wave run-down $R_{d,98\%}/H_{m0}$ has order of magnitude -0.75.

Comparing with the laboratory wave run-up measurements (Allsop et al., 1985; Kingston et al., 1996), it appears that from this analysis of prototype data the wave run-up is about 50% higher than the well-accepted wave run-up, based on laboratory results. Wave run-down agrees well with laboratory data. Due to the measurement technique, mainly the remaining distance between the gauge and the slope, the run-up measured in laboratory tests might be underestimated by up to 20 %.

This high run-up $R_{u,2\%}$ confirms the practical experience in Sines (Portugal) and Zeebrugge harbours that wave overtopping is higher than expected during design. As prototype results are only available for one storm within a narrow range of Iribarren numbers, they have to be confirmed by future measurements. It is clear that a better measurement accuracy is needed before final conclusions are drawn. However, this remarkable result, if confirmed, would have large impact on social, economic and environmental aspects of coastal protection works. As a conclusion, more detailed research and measurements on wave run-up are necessary in order to acquire a better understanding of prototype wave run-up.

Internal phreatic set-up

Due to the geometric non-linear effect on the slope subjected to waves, swell or tides, an internal phreatic set-up in a breakwater may occur. As the inflow section along the slope at the moment of a high water level is larger than the outflow section at the moment of a low water level, and as the average inflow path is shorter than the outflow path, more water will enter the breakwater than can leave during cyclic water level changes. Consequently, an average internal set-up of the water level inside will occur.

This internal maximum average set-up occurring after several cycles may be described by a simple theoretical formula (Barends, 1988):

$$\frac{s}{D} = \sqrt{I + \xi \cdot F} - 1 \quad (3)$$

with:

$$\xi = \frac{0.1cH^2}{n\lambda D \tan\alpha}, \quad \lambda = 0.5 \sqrt{\frac{DKt}{n}} \quad (4)$$

where s = maximum average set-up (m); D = depth at toe of slope (m); c = constant depending on effects of air entrainment and run-up ($c > 1$); H = wave height at slope (m); n = porosity (-); λ = penetration length of the cyclic water level into the porous structure (m); α = slope angle ($^\circ$); K = permeability coefficient (m/s); t = period of cyclic loading (s); F = function related to two cases (open or closed lee-side). For a closed lee-side the maximum set-up s is found at the lee-side.

As a practical example of the theoretical formula the Zeebrugge case is worked out. Barends (1983) assumed that the permeability $K \approx 0.50$ m/s and the porosity $n = 0.40$. The incident wave is characterised by $H = 6.50$ m and $T = 9$ s. The waterdepth D is 11 m. The penetration length is approximated by $\lambda = 5.56$ m. The situation corresponds to a closed lee-side and s occurs at lee-side. With $L \approx 85$ m and $L/\lambda = 85/5.56 = 15.3$ m, $F(\text{closed}) = 1$. With $\tan\alpha = 0.67$, $c = 1.25$ (according to Barends, 1988) and $H = 6.50$ m, ξ becomes 0.32. The maximum average set-up s derived from the theoretical formula (3) finally is 1.65 m. This theoretical result is in between the rule of thumb values proposed by Barends. With $D = 11$ m, $s = 0.15D$: the magnitude of the internal set-up is within 10-20 % of the waterdepth at the toe of the breakwater.

A permeability coefficient K with the same order of magnitude is found by (Gudehus, 1974) from tests on rock samples characterised by $d_{10} = 60$ mm, $d_{50} = 140$ mm, $d_{90} = 190$ mm. Dimensions of the test specimen are: height = 1.20 m, diameter = 1.22 m. The rock dimensions are clearly lower than the 2-300 kg rock used in the core. From this consideration, it may be assumed that the permeability of the core is higher than 0.50 m/s, however no measured values are available. Assuming that the permeability is 10 times higher, $K = 10 \times 0.50 = 5$ m/s, the set-up reduces to 0.50 m.

Thus, set-up is very sensitive to some of the parameters included, such as the permeability and the air entrainment factor. These are difficult to estimate. The results need to be treated with much care.

In order to study the stability of the filter layers of the Zeebrugge breakwater, a calculation with the mathematical model HADEER (Barends, 1983) was part of the study. Results from these calculations show similar set-up values as calculated from (3).

From full scale measurements, maximum average set-up values s , calculated at the position of the pressure sensor located closest to the leeside, are reported in Table 2. The Mean Water Level (MWL) is derived by calculating the mean of a wave record registrated by the infra-red meter. Inside the breakwater core pressure data (Pa) are converted into water level data (datum Z) by assuming a hydrostatic section where the density is constant. Those assumptions do not apply in the hydrodynamic area near the armour layer, but become more reasonable moving in the leeward direction. Internal phreatic set-up is calculated as the difference between mean values over a time interval of 180 s of the infra-red wave meter outside and the pressure sensors inside the core.

H_i [m]	s [m]	s/D [%]	s/H_i [%]
3.50	0.29	2.6	8.3
3.05	0.33	3.0	10.8
2.25	0.37	3.4	16.4
2.00	0.36	3.3	18.0

Table 2. Maximum average set-up s and rule of thumb ratios.

Comparison is made of calculated prototype set-up values with orders of magnitude proposed in literature: the results from prototype data are not within the range proposed by (Barends, 1988): $0.10D \leq s \leq 0.20D$, but the results have the same order of magnitude, as found by (Bürger et al., 1988) on large scale models: $0.10H_i \leq s \leq 0.20H_i$, where H_i = incident wave height $H_{1/3}$ (m). Ratios s/D and s/H_i used in the rules of thumb are summarised in Table 2.

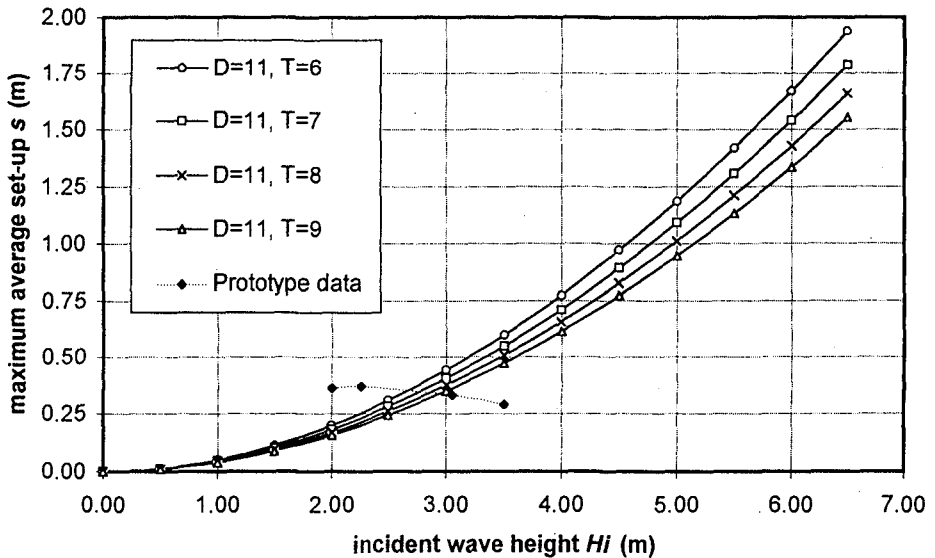


Fig. 6. Comparison between theoretical and prototype set-up calculations.

Barends' theoretical formula (3), where depth at toe $D=11\text{m}$, wave height $H=3\text{m}$, wave period $T=7.2\text{ s}$ gives a setup value of $s=0.41\text{ m}$ at the landward side. This result is of the same order of magnitude of the full scale data, as extrapolating the pressure gradient towards the landward side yields $s=0.39$. Using $K=5\text{ m/s}$, set-up reduces to 0.12 m .

Fig. 6 shows the set-up for the Zeebrugge case as a function of wave height and period for $D=11\text{ m}$. Further to Barends' theoretical formula the setup increases with increasing wave height. Plotting prototype setup as a function of H_i on Fig. 6 shows no agreement with this suggested non-linear relationship between setup and H_i .

The set-up is evaluated as a function of the horizontal distance from the interface between the filter and the core. It is concluded from prototype measurements that the set-up increases with the distance to the outer face of the breakwater. This is in agreement with the Barends' formula, because the breakwater is backfilled.

Pore pressure wave attenuation

The main objective of a breakwater is to dissipate incident wave energy when waves propagate through the porous breakwater core. This points out the relevance of investigating the breakwater's capability in this respect. In this section, results of full scale wave attenuation are presented. It is not the wave heights which are measured in the core, but the pore pressures.

Theoretical work dealing with oscillatory flow in porous media was carried out by Biesel (1950) who identified the form of the spatial and temporal relationships which describe a linearly damped oscillatory flow. Le Méhauté (1957) applied this relationship to rubble mound breakwaters by introducing parameters accounting for porosity and inertia effects of the porous material. Oumeraci (1990) summarises Le Méhauté's theory on this topic and concludes that the height of the pore pressure oscillation $p(x)$ of a propagating pressure wave decreases exponentially with the distance to the breakwater interface according to the linear damping model:

$$p(x) = p(0) \exp(-\beta \frac{2\pi}{L'} x) \quad (5)$$

where x = co-ordinate across core (m); $p(x)$ = pore pressure at x (N/m^2); $p(0)$ = pore pressure at $x = 0$ (N/m^2), i.e. the first pressure sensor location, L' = wave length within breakwater (m), β = damping factor (-).

The wave length within breakwater L' is calculated by $L' = L/\sqrt{1.4}$, (Oumeraci, 1990). The wavelength L is calculated by the dispersion relationship using wave period $T_{(0,2)}$, and waterdepth in front of the breakwater toe D . The pore pressure height $p(x) = 4(m_0)^{1/2}$, is calculated from the energy content of the signal.

The magnitude of the damping factor β depends on the distance y_s of the horizontal level of the sensors to the MWL: the lower the location under MWL, the smaller the friction losses will become as the degree of turbulence decreases, and the smaller the damping factor β becomes.

In Fig. 7, a number of wave records of 15 minutes are considered for the horizontal level of sensors at $Z+2.30$. The ratio $p(x)/p(0)$ is plotted versus the relative distance x/L' . An exponential curve is fitted through the data, the resulting damping factor $\beta=0.68$. In Fig. 8 curves with damping factors 0.81 ($Z+3.00$), 0.53 ($Z+0.70$) are plotted as well. As seen from this Fig. 8 the damping factor β decreases with increasing distance

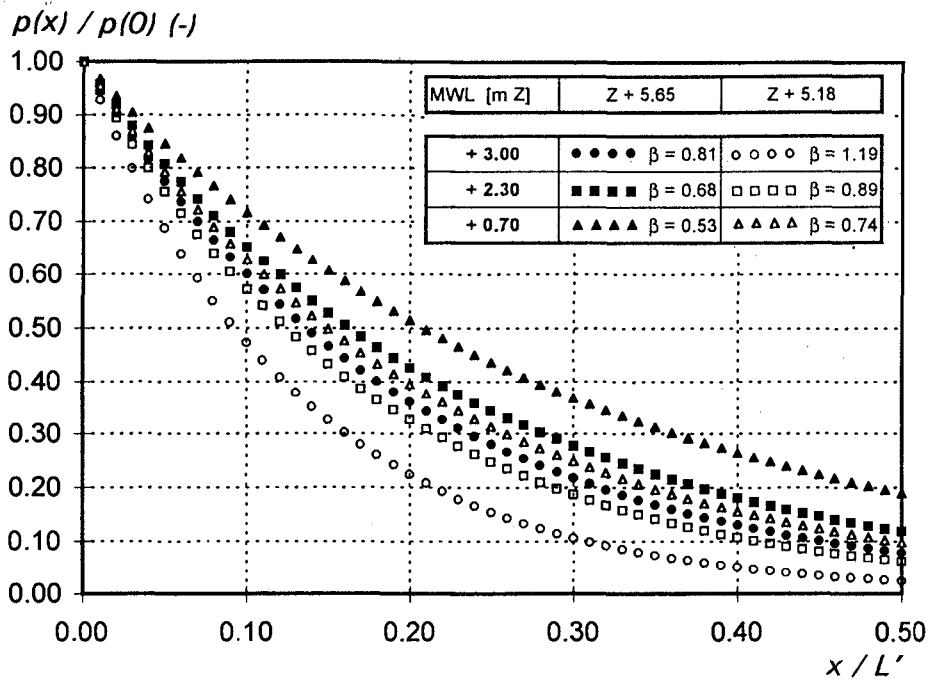


Fig. 7. Damping factor β from the three sensor levels for two MWL's.

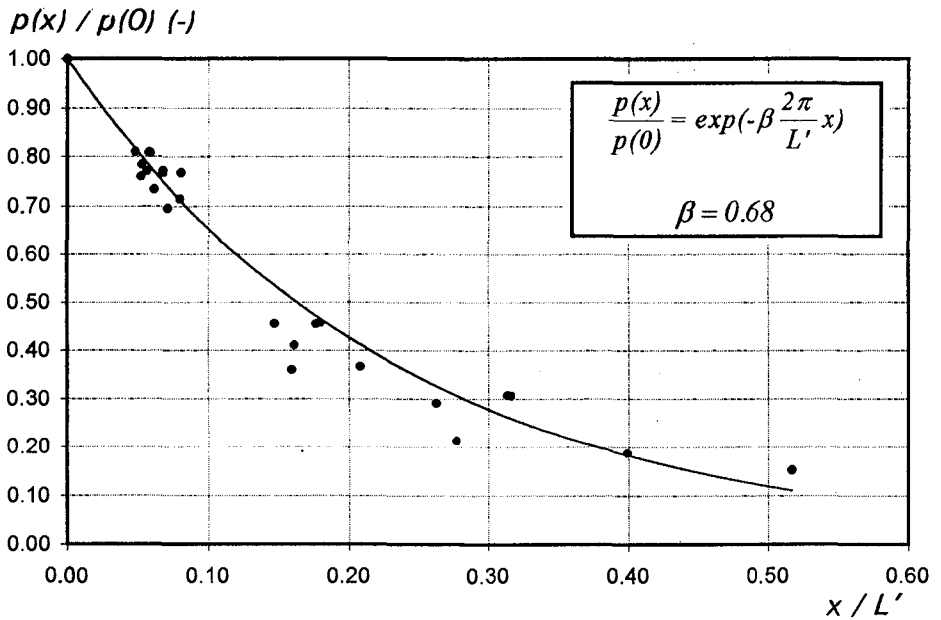


Fig. 8. Prototype pore pressure wave attenuation inside breakwater core: prototype data and fitted linear damping model.

from the MWL (MWL at $Z+5.65$). In the same Fig. 8 the blank dotted lines have resulting damping factors β for a situation with lower MWL (at $Z+5.18$). Compared to the former β values at each level, the latter values are higher (e.g. 0.89 versus 0.68 at sensor level $Z+2.30$). Indeed there is more turbulence due to the lower MWL, and the damping factor β depends on the distance y_s .

Analysis of a comprehensive set of data (Troch et al., 1996-c) shows that the energy content of steeper waves decays much nearer to the front of the core, where $x=0$. In other words, the rate of attenuation within the core for a given wave period increases with increasing wave height. In contrast the opposite trend is evident for a constant incident wave height. Increasing the wave period resulted in a decrease in the rate of attenuation in the mound. Summarised, the damping factor β also depends on the incoming wave height and period.

It is assumed (Burcharth et al., 1995) that the extended Forchheimer equation models the flow resistance in porous media:

$$i = au + bu^2 + c \frac{\partial u}{\partial t} \quad (6)$$

where i = hydraulic gradient (-); u = bulk (or filter) velocity (m/s); a , b , and c = constants. However, the turbulent term (u^2) in equation (6) is normally predominant when considering internal flow in breakwaters, and this turbulent term does not occur in (5). Hence there is no evident purpose in relating the β -value in equation (5) to the coefficients in the Forchheimer equation. From the above it is suggested that the model derived by (Oumeraci et al., 1990) is too simple being a linear model compared with the non-linear Forchheimer model. Moreover a straight comparison between calculated β values, based on prototype results, and the value reported by (Oumeraci et al. 1990), $\beta=2$ is not possible because of the different geometrical shape factors, the different breakwater cross section and scaled core materials affecting the core permeability, and different position of the first pressure sensor (the first reference pressure sensor in Oumeraci's analysis is positioned in the filter layer between armour and core).

CONCLUSIONS

This paper briefly outlines the prototype monitoring system installed at the Zeebrugge rubble mound breakwater. To date a comprehensive set of full scale data have been acquired at this unique monitoring system during storm conditions with significant wave heights ranging between 1.00 m and 3.50 m, and are available for validation of physical and numerical models. Prototype measurements consisting of incident wave data, wave run-up data, and pore pressure data have been analysed in order to determine the hydraulic response of the full scale Zeebrugge breakwater. As hydraulic responses the following phenomena are included: wave run-up/run-down, internal phreatic set-up and pressure wave attenuation.

Comparing prototype wave run-up measurements with well-accepted laboratory results, it appears that the prototype wave run-up is about 50% higher than the wave run-up on armoured slopes of scale models. Wave run-down agrees well with laboratory data. This remarkable result, if confirmed, would have large impact on social, economic and environmental aspects of coastal protection works. As a

conclusion, more detailed research and measurements on wave run-up are necessary in order to acquire a better understanding of prototype wave run-up.

Prototype set-up measurements are compared with a simple theoretical formulation. For the range of wave heights available, there is good agreement between prototype and theoretical set-up. However no clear dependence of set-up on wave height, as suggested by the theoretical formulation (3), is found. The order of magnitude of calculated set-up from prototype measurements is between 10 and 20 % of the incident wave height.

Results show that the pore pressure height $p(x)$ of a wave travelling through a rubble mound breakwater in the horizontal direction decreases exponentially, and the magnitude of β depends on the distance from the horizontal plane to the mean water level. Finally some remarks on the applicability of the linear damping model, based on the Oumeraci formulation are made. There is a clear dependence of the damping factor on the incident wave height and period, which is neglected by the linear damping model. There is no non-linear Forchheimer term present in the linear damping model, although this term is predominant for internal porous flow.

Acknowledgements

The research presented was carried out as a part of the research and technological development programme in the field of Marine Science and Technology (MAST) financed by the Commission of the European Communities, Directorate-General for Science, Research and Development, MAST II, contract MAS02-CT92-0023. The funding by EC is very much appreciated.

References

- Allsop N.W.H., Hawkes P.J., Jackson F.A. and Franco L. (1985).* Wave Run-up on Steep Slopes - Model Tests under Random Waves. Report No. SR2, Hydraulics Research Wallingford, 54 pp.
- Barends F.B.J. (1983).* Venting study of Zeebrugge breakwater. Report of Delft Soil Mechanics Laboratory.
- Barends F.B.J. (1986).* Geotechnical aspects of rubble mound breakwaters. Developments in breakwaters, Thomas Telford Ltd, London.
- Barends F.B.J. (1988).* Discussion on paper by Simm and Hedges: 'Pore pressure response and stability of rubble mound breakwaters', Breakwaters 1988.
- Biesel F. (1950).* Equations de l'écoulement non lent en milieu perméable. La Houille Blanche, No 2.
- Burcharth H.F., Andersen O.H. (1995).* On the one-dimensional steady and unsteady porous flow equations. Coastal Engineering 24, pp.233-257.
- Bürger W., Oumeraci H., Partenscky H.W. (1988).* Geohydraulic investigations of rubble mound breakwaters. Proc. 21st ICCE Malaga.
- Gudehus G. (1974).* Annexe au rapport 6632/b-73/17 de IGE Proces verbal relatif aux résultats des essais géotechniques effectués sur des enrochements dont l'utilisation est prévue pour la construction du barrage de l'Eau d'Heure.
- Kingston K., Murphy J. (1996).* Wave run-up/run-down. Thematic report B of the Detailed scientific report MAS02/1-893/PTH, project MAS02/CT92/23, Editors Troch P., De Rouck J.

- Le Méhauté B. (1957).* Perméabilité des digues en enrochements aux ondes de gravité périodiques. La Houille Blanche No 6, (1957); No 2,3 (1958).
- Losada M.A., Giménez-Curto L.A. (1982).* Mound breakwaters under oblique wave attack, a working hypothesis. Coastal Engineering 6, pp. 83-92.
- Oumeraci H., Partenscky H.W. (1990).* Wave induced pore pressure in rubble mound breakwaters". Proc. 22th ICCE.
- Troch P., De Somer M., De Rouck J. (1995).* Full scale dynamic load monitoring of rubble-mound breakwaters. Proc. 2nd MASTDAYS and EUROMAR-market, Sorrento, Italy.
- Troch P., De Somer M., De Rouck J., Van Damme L., Vermeir D. (1996-a).* In situ load monitoring of rubble mound breakwaters. Proc. 11th Int. Harbour Congress, Antwerpen, Belgium.
- Troch P., De Rouck J., Van Damme L. (1996-b).* Instrumentation and prototype measurements at the Zeebrugge rubble mound breakwater. To be published in Special Issue Coastal Engineering Journal, Elsevier, Amsterdam, Netherlands.
- Troch P., De Rouck J. (1996-c).* Detailed scientific report MAS02/1-893/PTH, project MAS02/CT92/23.

CHAPTER 150

NUMERICAL MODELLING OF WAVE INTERACTION WITH DYNAMICALLY STABLE STRUCTURES

Marcel R.A. van Gent¹

ABSTRACT: Wave interaction with dynamically stable structures is simulated by means of a numerical model based on finite-amplitude shallow-water wave equations. The model can simulate wave motion on and inside permeable structures. For dynamically stable structures, including berm breakwaters, reef-type structures and gravel beaches, a procedure is developed to simulate the natural response to wave attack. This procedure is extended, for instance by implementing effects of grading and effects of seawalls, to increase the applicability for practical applications.

1. INTRODUCTION

Coastal structures that consist of rubble mound material and are designed to undergo reshaping under severe storm conditions, while their seaward slope is stable under normal wave conditions, are called here dynamically stable structures. These structures such as berm breakwaters and reef-type structures can be economically attractive since their natural response to hydrodynamic loads causes that smaller rock material can be used than with conventional statically stable coastal structures. On the other hand, the dynamic behaviour needs to be predicted to assess the performance of such structures. For berm breakwaters this dynamic behaviour of the seaward slope is very much depending on the hydrodynamic loads and vice versa. This interactive character of the hydrodynamics and the reshaping process are studied here by means of a numerical wave load-response model.

A verified wave model has been combined with a procedure to simulate the response of dynamic structures (Van Gent, 1995-c). Procedures for initiation of movement of individual stones and for the reshaping of the structure as a result of moving stones determine the response of the structure. Both the wave motion and the response of the structure are simulated in the time-domain which means that the response of a structure immediately effects the computed wave motion.

1) Delft Hydraulics, P.O.Box 177, 2600 MH Delft, The Netherlands.

2. MODELLING OF WAVE ATTACK

A numerical model for simulating wave motion on and inside permeable structures is described in Van Gent (1994, 1995-b,c). The wave dynamics of normally incident wave attack on various types of structures are approximated by the non-linear shallow-water wave equations with steep wave fronts represented by bores. The model is based on concepts by Hibberd and Peregrine (1979) who developed a numerical model with an explicit dissipative finite-difference scheme (Lax-Wendroff) for impermeable slopes without friction. Using this concept, many practical applications have been obtained, see for instance Kobayashi *et al.* (1987) for wave reflection and run-up on impermeable rough slopes. For the permeable part of a structure the same types of equations can be applied although the friction coefficients for porous media needed to be assessed, see Van Gent (1995-a,c). The coupling of the external flow to the internal flow is determinative for the accuracy of such a wave model, see Van Gent (1994, 1995-c).

The model is able to deal with waves either regular or irregular which attack various types of structures with arbitrary seaward slopes, smooth or rough, permeable or impermeable, overtopped or not. Although the model uses a one-dimensional description of the flow it can, however, give a useful impression of the flow field in two dimensions, see Figure 1 and Figure 2.

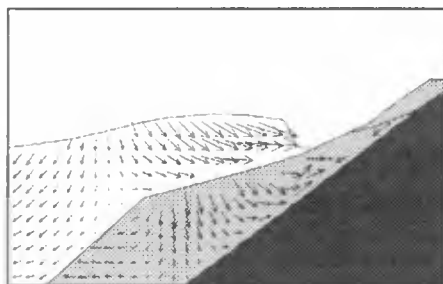


Fig.1 Computed flow-field for a berm breakwater with an impermeable core.

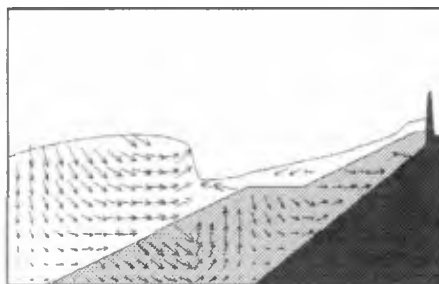


Fig.2 Computed flow-field for a permeable breakwater with crown-wall.

3. MODELLING OF RESHAPING OF STRUCTURES

3.1 APPROACH FOR SIMULATING PROFILE DEVELOPMENT

The stability of the stones is strongly dependent on the hydrodynamic properties. Several expressions for this stability have been developed. Although these design recommendations are rather accurate for many applications, more generally applicable results can be obtained by simulating the wave motion first and then using flow properties like the velocities and accelerations to predict forces on stones. This can be done numerically.

In the approach towards a numerical wave load-response model several model formulations are required. Firstly, the hydrodynamic flow, both outside and inside the structure, need to be known and modelled numerically. The mentioned one-dimensional model can be used as a first approximation. Secondly, information concerning the magnitude of forces on stones is necessary. Thirdly, relations between the forces on stones and the hydrodynamic behaviour are necessary. As mentioned before, the hydrodynamics can be represented by local velocities and local accelerations. As a first approximation, a Morison-type of expression (Morison *et al.*, 1950) can be used, see for instance Kobayashi and Otta (1987) or Tørum (1992). Fourthly, information concerning failure mechanisms and forces causing damage is needed. Often failure mechanisms referred to as *rolling*, *sliding* or *lifting* are distinguished. These mechanisms or other failure mechanisms need to be modelled. Finally, the new positions of unstable stones need to be known if the complete reshaping process is to be simulated. For most breakwaters no severe damage is allowed, so for those cases it is not of primary interest to study the new positions of the stones. However, for berm breakwaters and gravel beaches these new positions are of primary concern. Only the main aspects of the wave load-response model are mentioned in the following sections. A more detailed description, including the calibration and validation of the model, can be found in Van Gent (1995-c).

3.2 MODELLING OF FORCES ON STONES

The hydrodynamic loadings on a single stone can be modelled using a number of forces. For the relation between the hydrodynamics and the forces, local velocities and local accelerations are required. The numerical model provides these local properties although averaged over the depth. Differences between these properties at the position of the particles and the depth-averaged velocities naturally cause inaccuracies.

Three forces as a result of the hydrodynamic loadings have been distinguished; the drag force acting parallel to the slope in the direction of the velocity, the inertia force acting parallel to the slope and the lift force acting perpendicular to the slope:

$$F_D = \frac{1}{2} \rho c_D k_2 D^2 u |u| \quad (1)$$

$$F_I = \rho c_M k_1 D^3 \frac{Du}{Dt} \quad (2)$$

$$F_L = \frac{1}{2} \rho c_L k_2 D^2 u^2 \quad (3)$$

where the acceleration Du/Dt is approximated with $\partial u/\partial t$; c_D , c_M , c_L are the drag coefficient, the inertia coefficient and the lift coefficient respectively; k_1 and k_2 are the volume shape factor and the area shape factor respectively. With the area shape

factor k_2 the actual projected area in the flow direction can be incorporated. Since a cover particle is partially sheltered by other particles, the actual projected area is smaller than for a single particle in a flow. The sheltering effect has not been incorporated separately and therefore affects the values of the coefficients which are derived through calibration. In all computations $k_1=0.66$ and $k_2=0.9$ were used. For the stone diameter the equivalent sphere diameter D_{EQ} is taken as the characteristic stone size ($D_{EQ} \approx 1.24 \cdot D_{n50}$).

The submerged weight is taken as the counter-acting force. The submerged weight acts vertically and can be written as (ρ_s is the density of the stone material):

$$W_s = (\rho_s - \rho) g k_1 D^3 \quad (4)$$

Several concepts can be used for initiation of movement. Stability criteria for the phenomena referred to as *lifting* and *sliding* can respectively be expressed by:

$$F_L \leq W_s \cos \phi \quad (5)$$

$$|F_D + F_I - W_s \sin \phi| \leq \tan \mu (W_s \cos \phi - F_L) \quad (6)$$

where μ denotes the angle of internal friction and ϕ the local slope angle. The phenomenon *rolling* is assumed to occur if both stability conditions are not satisfied.

3.3 MODELLING OF STONE DISPLACEMENTS

If at a certain position a stone in the slope is unstable, the direction in which the stone will move has to be determined. It is assumed that the drag and inertia forces and the weight of the stone determine in which direction an unstable particle will move after one of the stability criteria is (Eq.5 and/or Eq.6) not satisfied:

$$(F_D + F_I - W_s \sin \phi) > 0 \Rightarrow \text{UPWARD} \quad (7)$$

$$(F_D + F_I - W_s \sin \phi) < 0 \Rightarrow \text{DOWNWARD} \quad (8)$$

In Van Gent (1995-c) erroneously an additional force (F_p) was taken into account in equations 7 and 8. Although this force did not have any effect on the computations, this force has been omitted in the new computations.

After determining the direction in which an unstable particle may move, the local hydrodynamic properties at a position one space-increment (Δx) away from the original position, are regarded. It is verified whether the particle would be stable or unstable in that neighbouring position. If the particle is stable at that position, the particle will stay at its original position. If the particle is also unstable at the

neighbouring position the particle is moved to this position. This is done without any time-delay which means that the particle is moved over a space-increment Δx within a period of Δt . The choice of Δt depends on the space-increment Δx and the wave celerity which means that the velocity of the stones is in fact related to the (average) wave celerity.

This response model for cross-structure transport is interactive with the hydraulic model. At each time-step (Δt) the hydraulic properties are determined at all positions. At each position and each time-step it is verified whether the particles are stable at their present position or not and whether they need to be displaced. The profile changes due to the movement of the particles while the new profile is immediately incorporated in the hydraulic model.

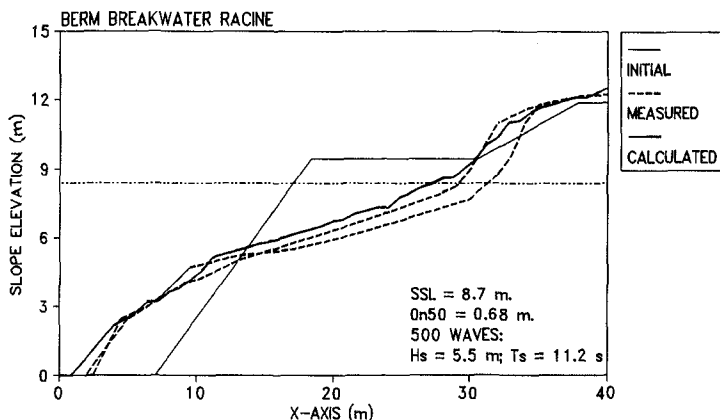


Fig.3 Comparison between measured and computed reshaped profiles of a prototype berm breakwater.

A few examples of performed computations are shown here. Figure 3 shows a comparison between measured (Montgomery *et al*, 1988) and computed reshaped slopes of a (prototype) berm breakwater. Computations for reef-type structures were performed after verification of wave transmission coefficients. Tests by Ahrens (1987) were used for comparisons of the dynamical response of reef-type structures, see Figure 4.

4. MODELLING OF EFFECTS OF GRADING

Besides a quantitative validation of the model also trends that have been observed in physical model tests have been studied. This concerns the effects of wave height, wave period, stone size and initial slopes. The wave load-response model has been extended to also include the effects of variations in stone size along the slope and stone size segregation.

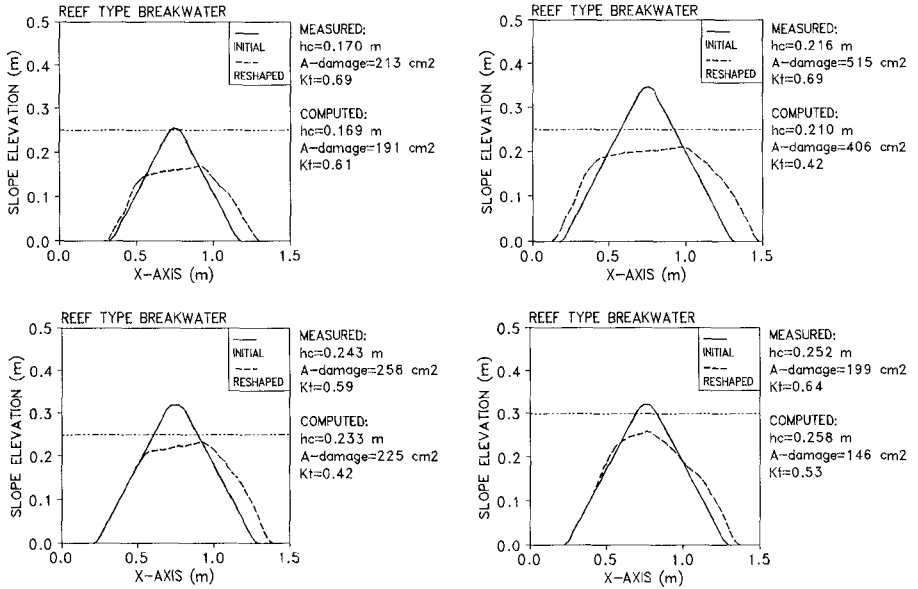


Fig.4 Computations with reef-type structures, initial profiles and reshaped profiles (stable).

To include these effects of the stone size distribution, the initial slope is made out of stones with at each position (each Δx) a stone with a different size. This is done randomly but such that the slope has a prescribed grading curve. At each position the forces are determined on the stone with its particular size. If a stone is unstable and moved in the upward or downward direction, the stone (size) in the second layer is treated as the exposed stone. At the position where the stone is moved to, this stone becomes the exposed stone while the originally exposed stone becomes the stone in the second layer. In this treatment the thickness of the layers is not equal to one stone diameter. Despite this simplification the effects of material with a range of sizes can be studied numerically.

The effect of grading on the reshaping process is not only determined by the size distribution of the stones. A wider stone size grading also has a lower permeability than a narrow grading. Grading might also affect the friction but since this phenomenon is not sufficiently quantified, the friction has not been varied in these computations ($f=0.10$).

The reshaping of gravel beaches with three different gradings are computed; $D_{n85}/D_{n15}=1.0, 1.33$ and 2.0 . For the grading curve a linear distribution is taken. Because the original wave load-response model was calibrated on a physical model test with material with a grading of $D_{n85}/D_{n15}=1.5$, while in the numerical model a grading of $D_{n85}/D_{n15}=1.0$ was used, the coefficients c_L , c_M and c_D should in fact

have been determined again after implementing the effect of grading. Since no recalibration was done, the analysis performed here is concentrated on the effects of grading itself and not into detail on the magnitude of the erosion and accretion on the reshaped profiles.

In Figure 5 reshaped profiles of three gravel beaches are shown. First only the effect of permeability is studied. For gradings of $D_{n85}/D_{n15}=1.0, 1.33$ and 2.0 the effect of decreasing permeability has been taken into account by simply reducing the porosity from $n=0.45$ for $D_{n85}/D_{n15}=1.0$ to $n=0.40$ for $D_{n85}/D_{n15}=1.33$ and $n=0.35$ for $D_{n85}/D_{n15}=2.0$. The results of this variation in permeability is shown in the upper graph of Figure 5. The second graph shows the effect of the variation in stone sizes along the slope while in the lower graph both effects are simultaneously taken into account. It is clear from the figures that reducing the permeability leads to more erosion of the slope. This seems reasonable since a increased permeability reduces the velocities along the slope. The variation in the size distribution shows a counteracting effect; a wider distribution shows a less affected profile. Apparently, after some reshaping the larger material of the distribution forms the toplayer and reduces further reshaping of the slope.

Combining the two effects shows (lower graph of Figure 5) that for the narrow grading the effect of lower permeability is slightly larger than the effect of the wider size distribution (slight increase in erosion from $D_{n85}/D_{n15}=1.0$ to 1.33). For wider gradings the effect of the wider size distribution becomes slightly more important (slight decrease in erosion from $D_{n85}/D_{n15}=1.33$ to 2.0). Similar conclusions were obtained by Kao and Hall (1990) who studied the effects of grading on a reshaping berm breakwater through physical modelling.

Figure 6 shows the computed effects of three different gradings for reshaped profiles with different material size (D_{n50}). As can be expected, larger material leads to less erosion of the initial slope; this also leads to a smaller effect of a wider gradation for larger material. Figure 7 shows the effects on reshaped profiles for different initial slopes; steeper initial slopes are much more affected than milder slopes. For slopes where considerable erosion of the initial slope occurs again the effects of a wider gradation is obvious. Apparently, the larger material of the distribution forms the exposed layer after some reshaping and reduces further reshaping of the slope. The computations also show that for wider gradings more material is moved upward; the forming of a beach crest is more substantial for wider gradings while the forming of a submerged bar is more apparent for narrow gradings.

Since the motion of material with different sizes within one slope is modelled, also the effect of stone segregation is simulated. Figure 8 shows the stone size distribution of material along the slope after reshaping. The stone size distribution is given for the exposed stones and also for the average of the ten upmost stones. In Figure 8 the stone size material is averaged over some sections of the slope in

which the variation in size is relatively small. Two examples for different initial slopes are shown in Figure 8. The general conclusion is that in the region around and just below the still-waterline the material in the toplayer is relatively large. More downward and more upward from this region around the still-waterline, the material is somewhat smaller. The main conclusion is that after reshaping relatively large material is located in the region where the largest velocities occur, i.e. just below the still-waterline.

5. MODELLING OF EFFECT OF TOP-LAYER WITH HIGHER WEIGHT

In practice sometimes the largest stones from a quarry are positioned on top of the primary armour layer of a berm breakwater. This causes that initial reshaping occurs for somewhat more severe wave conditions than without this measure. By using the numerical model it is studied whether positioning the largest stones on top has effect on the final reshaped profile. The computations shown in Figure 9 indicate that these largest stones are moved either upward or downward and do not remain in the section around the waterline where the largest velocities occur. This also causes that the final reshaped profile is almost not affected.

6. MODELLING OF EFFECTS OF A SEAWALL

Some computations are performed with a fully reflecting impermeable boundary landward from the gravel beach. If such a seawall is positioned in the region that is affected by reshaping under conditions without a seawall it is obvious that the seawall can change the reshaping process. Since a one-dimensional model is applied here for conditions where vertical accelerations cannot always be neglected, the results are affected by extra inaccuracies and must not be taken too seriously.

Figure 10 shows results for three different initial slopes. For each initial slope the first reshaped profile shows the situation without a seawall, the second profile the effect of a seawall located on the beach and the third profile the effect of a seawall at the initial waterline. In general the trend is that the seawall causes the submerged bar to develop more seaward, as can be expected since the reflected waves cause increased velocities in the seaward direction. The computations do not show a clear local effect on the reshaped profile near the seawall; in some computations the local erosion increases slightly but in some other computations some piling-up of stones against the seawall occurs.

CONCLUDING REMARKS

The reshaping of dynamic structures such as berm breakwaters, reef-type structures and gravel beaches has been simulated numerically. This approach

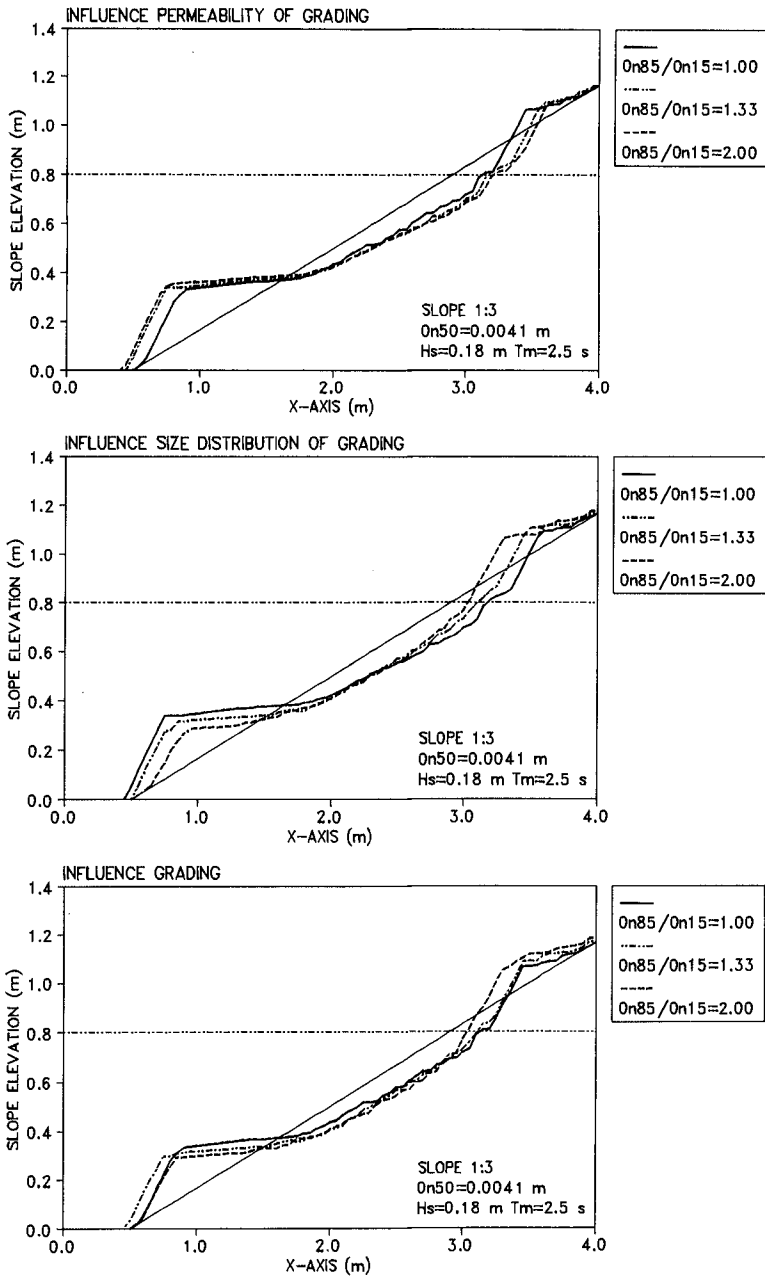


Fig.5 Influence of permeability, size distribution and combined effects of grading on reshaped profiles.

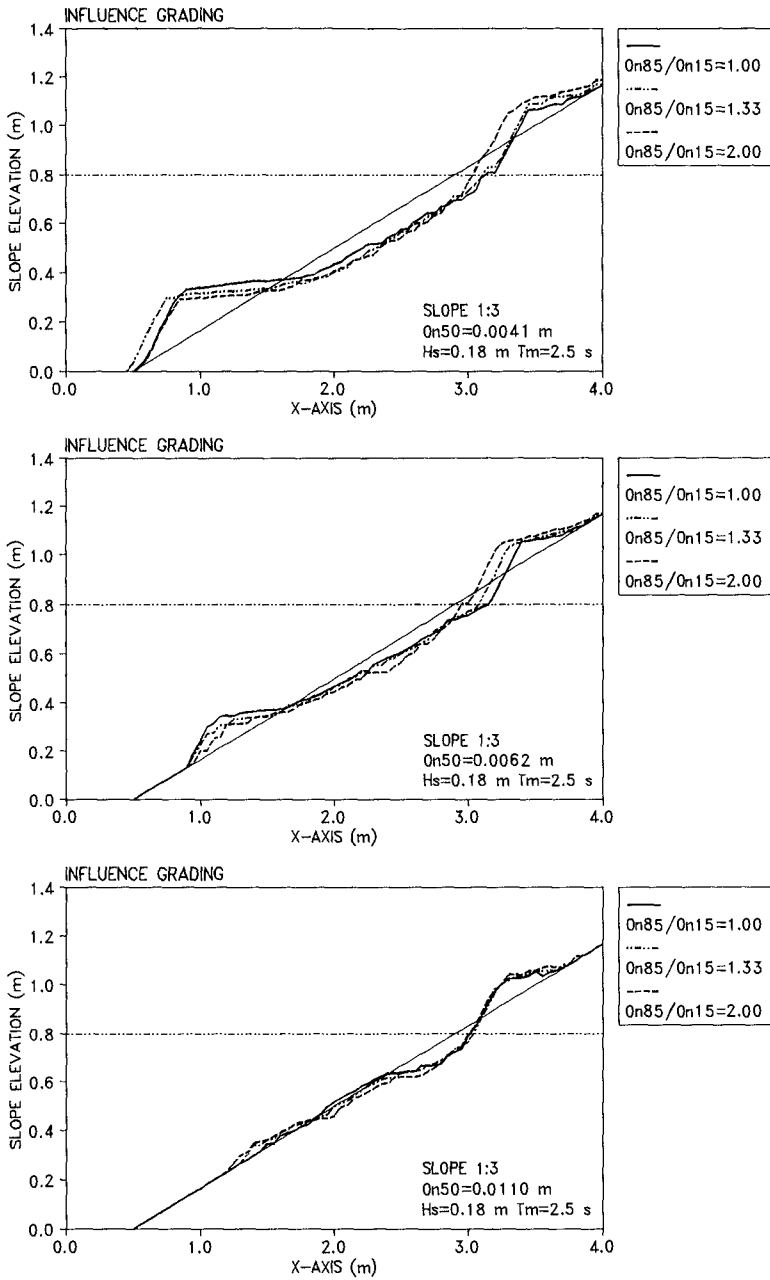


Fig.6 Influence of grading on reshaped profiles for different stone sizes.

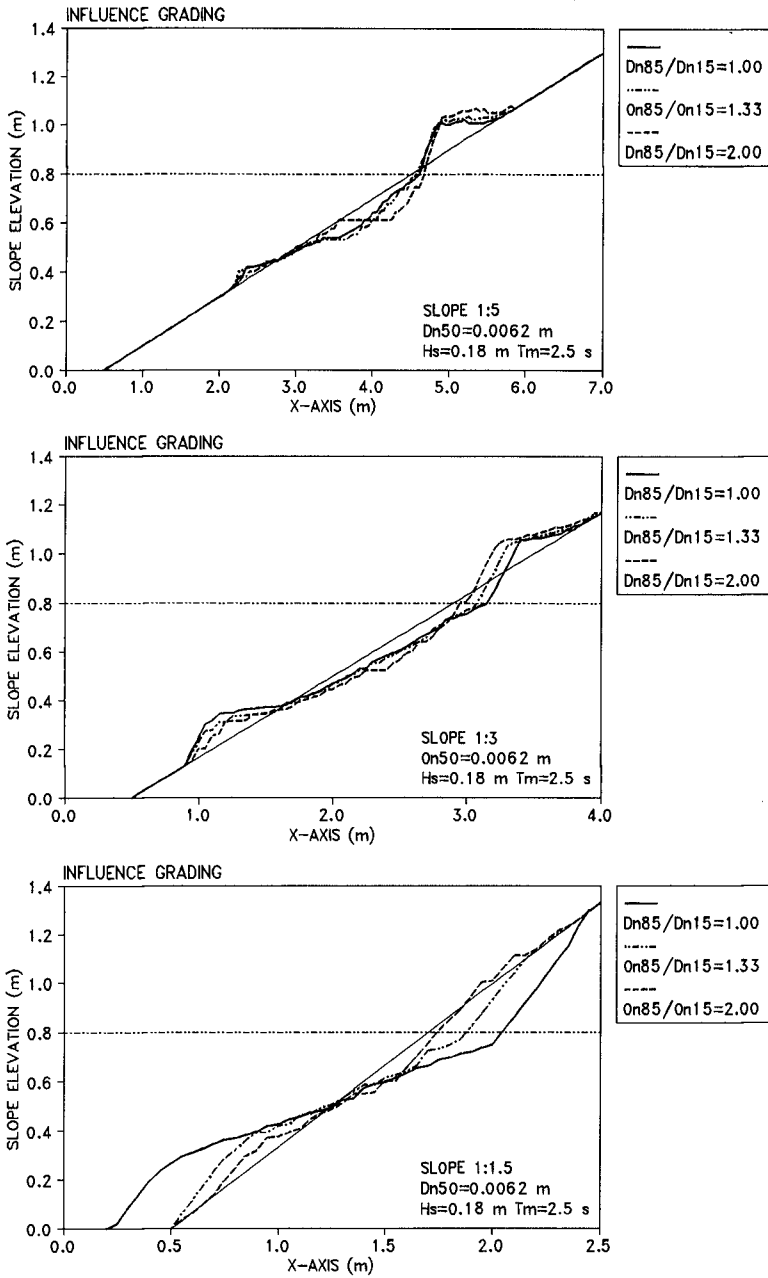


Fig. 7 Influence of grading on reshaped profiles for different slope angles.

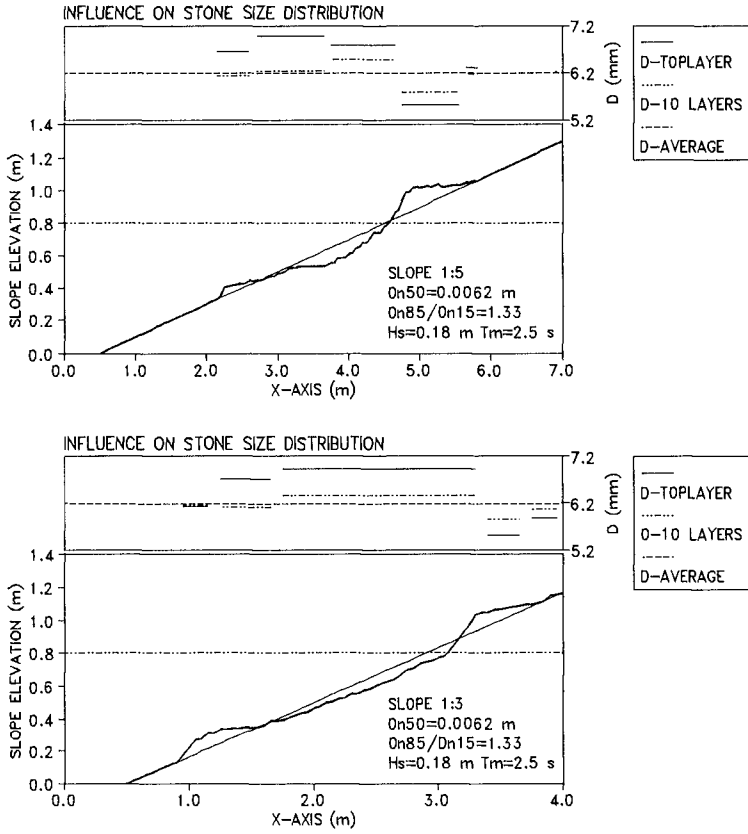


Fig.8 Stone size distribution along reshaped slopes.

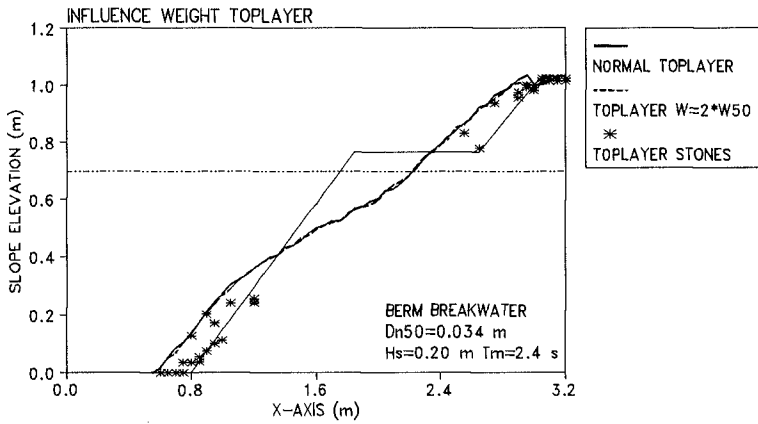


Fig.9 Influence of an increased weight of toplayer stones.

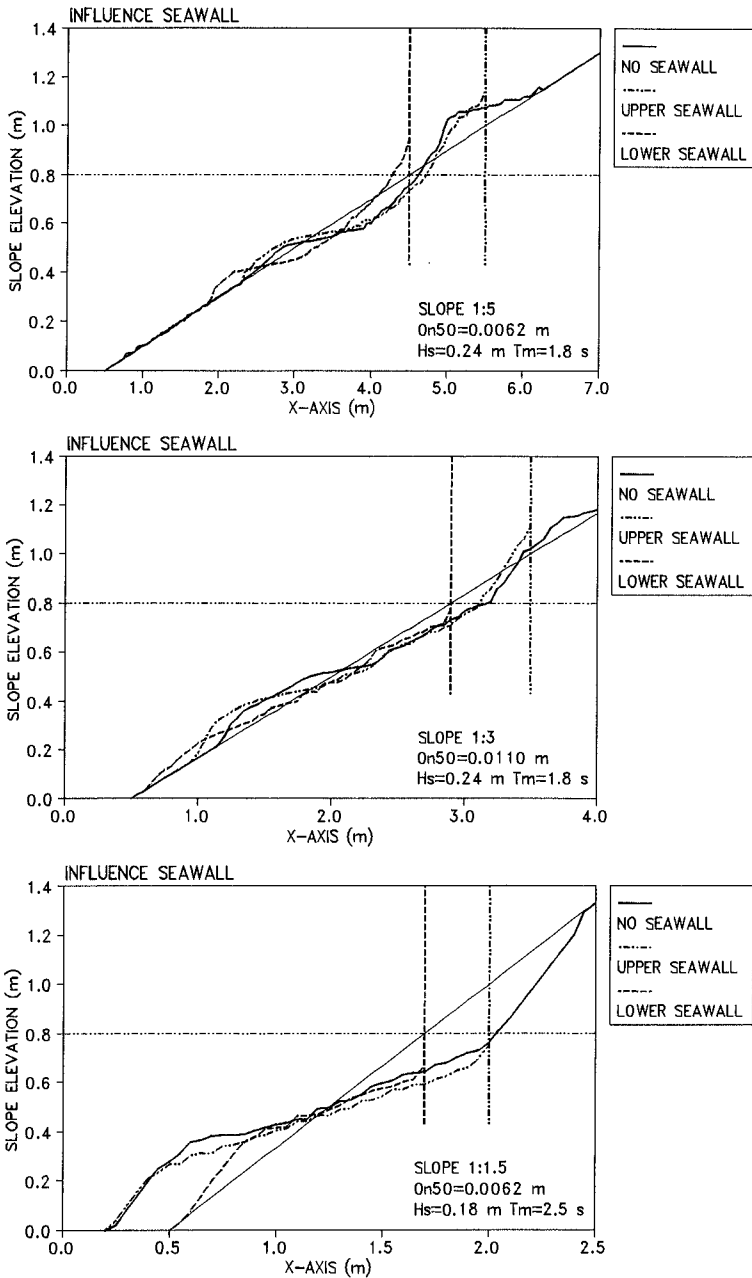


Fig. 10 Influence of a reflecting seawall in front of a reshaping profile.

appeared to be successful for predicting trends in the effects of variations of the wave height, wave period, stone material and initial slope. Although not validated, also effects of grading of stone material and effects of a seawall on a beach were incorporated. Further improvements to this wave load-response model might be obtained by applying a model which provides more detailed and more accurate information on the wave motion; the two-dimensional model (2DV) described in Van Gent *et al.* (1994, 1995-c), which includes detailed modelling of breaking waves, can be applied but this requires considerable computational efforts.

ACKNOWLEDGEMENTS

The financial support by the Commission of the European Communities by way of the MAST-Berm Breakwater project (contract MAS2-CT94-0087) is gratefully acknowledged. Thanks are also due to Prof. K. d'Angremond from the Delft University of Technology since a large part of the research concerning this paper is performed at this University.

REFERENCES

- Ahrens, J.P. (1987), *Characteristics of reef breakwaters*, Report CERC-87-17, Vicksburg.
- Hibberd, S. and D.H. Peregrine (1979), *Surf and run-up on a beach: a uniform bore*, J. of Fluid Mechanics, Vol.95, part 2, pp.323-345.
- Gent, M.R.A. van (1994), *The modelling of wave action on and in coastal structures*, Coastal Engineering, Vol.22 (3-4), pp.311-339, Elsevier, Amsterdam.
- Gent, M.R.A. van, P. Tönjes, H.A.H. Petit and P. van den Bosch (1994), *Wave action on and in permeable structures*, Proc.ICCE'94, Vol.2, pp.1739-1753, Kobe.
- Gent, M.R.A. van (1995-a), *Porous flow through rubble mound material*, J. of Waterway, Port, Coastal and Ocean Engineering, ASCE, Vol.121, no.3, pp.176-181.
- Gent, M.R.A. van (1995-b), *Wave interaction with berm breakwaters*, J. of Waterway, Port, Coastal and Ocean Engineering, ASCE, Vol.121, no.5, pp.229-238.
- Gent, M.R.A. van (1995-c), *Wave interaction with permeable coastal structures*, Ph.D.-thesis, Delft University of Technology, ISBN 90-407-1182-8, Delft University Press.
- Kao, J.S. and K.R. Hall (1990), *Trends in stability of dynamically stable breakwaters*, Proc. ICCE'90, Vol.2, pp.1730-1741, Delft.
- Kobayashi, N., A.K. Otta and I. Roy (1987), *Wave reflection and run-up on rough slopes*, J. of Waterway, Port, Coastal and Ocean Engrg, ASCE, Vol.113, no.3, pp.282-298.
- Kobayashi, N. and A.K. Otta (1987), *Hydraulic stability analysis of armour units*, J. of Waterway, Port, Coastal and Ocean Engineering, ASCE, Vol.113, No.2, pp.171-185.
- Morison, J.R., M.P. O'Brien, J.W. Johnsen and S.A. Schaff (1950), *The forces exerted by surface waves on piles*, Petrol. Trans. AIME, Vol.189, pp.149-154.
- Montgomery, R.J., G.J. Hofmeister and W.F. Baird (1988), *Implementation and performance of berm breakwater design at Racine, WI*, Berm breakwaters; (ed. D.H. Willis *et al.*), derived from Workshop Ottawa, September 1987, pp.230-249.
- Tørum, A (1992), *Wave induced water particle velocities and forces on an armour unit on a berm breakwater*, MAST-G6s report STF60-A92104, NHL-Trondheim, Norway.

CHAPTER 151

MONITORING OF ZEEBRUGGE BREAKWATERS

Luc VAN DAMME¹, Julien DE ROUCK²,

ABSTRACT

From the moment they are constructed, rubble-mound breakwaters are due to be damaged someday. Accepting damage is one of the basic principles of mound breakwaters design. Damage can take place either gradually in time or catastrophically after a major storm. Gradual deterioration of the armour layers or foundation may be unnoticed without the aid of a monitoring program and may ultimately result in the failure of the armour layer, in slope instability or in unacceptable large settlements. By comparison of measurements of the state of the structure at a number of points in time, a monitoring program allows these changes to be identified at an early stage, thus enabling the appropriate maintenance action to be carried out.

Several structural and environmental monitoring techniques are used in Zeebrugge. Three structural monitoring techniques are presented in more detail.

The emerged armour units of the Zeebrugge breakwaters are monitored using aerial remote sensing. An observation flight is made once a year. Each time, the position of over 15,000 armour units is very accurately retrieved by stereometric digitization. The coordinates are stored in a computer database. Several types of data visualization have been developed for a fast and efficient evaluation of the survey results.

For the underwater inspections of the breakwater two acoustic techniques are used. On the one hand, digital side-scan sonar recordings are used to produce high-resolution and contrasting images of the breakwaters' underwater armour layer. Such images allowed the detection of structure modifications in the breakwaters' toe protection.

On the other hand, high-frequent multibeam echosoundings, allow to exactly quantify the actual underwater armour unit movements in time.

-
- 1) Ministry of Flemish Community, Coastal Division, Vrijhavenstraat 3, B-8400 Ostend, Belgium.
 - 2) Civil Engineering Dept., University of Ghent, HAECON NV, Technologiepark 9, B-9052 Ghent, Belgium.

THE MONITORING PROGRAMME OF ZEEBRUGGE

The monitoring programme of Zeebrugge breakwaters is composed of the following parts : visual control of the armour layer, the crest of the breakwater and the filter construction next to the road; topographic survey, bathymetric soundings of the different zones around and in the harbour; aerial remote sensing of the armour units ; side scan sonar recordings of the underwater part of the armour layer and the wave breaking carpet and berms coupled to multibeam recordings; evaluation of the hydraulic design conditions on the basis of data collected by five measurement stations and seven waverider buoys in the neighbourhood of the harbour. The monitoring programme is now running for more than 10 years.

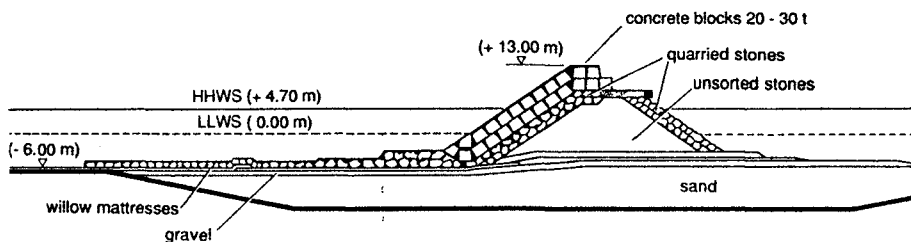


Figure 1 - Cross-section NW breakwater

Two parts of the monitoring programme will be treated in detail : aerial remote sensing of the armour units and the underwater inspections. Figure 1 is a typical cross-section of the Zeebrugge breakwaters. The toe of the breakwater is protected by a berm in 3-6 ton stones. The armour layer of the breakwater consists of antifer cubes 20 to 30 ton.

AERIAL REMOTE SENSING OF THE ZEEBRUGGE BREAKWATER ARMOUR LAYER

Several techniques are used for the survey of armour units. Soon after the construction of the Zeebrugge outer harbour breakwaters, an attempt was made to determine the position of the individual armour units, using land-based photographic recordings. This method was labourintensive and time-consuming, and posed serious problems in the areas that cannot be accessed on foot. Indeed, the vast majority of the armour units are inaccessible, or even out of sight for a land-based surveyor. Therefore, the use of aerial photography was proposed.

A survey based on this method offers the advantages proper to aerial photography: high accuracy, rapid (instantaneous) coverage of the complete breakwater length, recorded documents (photographs) allowing objective interpretation and verification, highly automated data handling and preparation for interpretation.

Execution of the photoflight

The aerial photographic recordings are carried out at low water during spring tide, to ensure maximum coverage of the breakwaters, i.e. a maximal number of armour units is visible.

The flight axis is located above the seaward side of the breakwaters so that the breakwaters take a central position in the aerial photographs.

The flight altitude is a major key to the success and accuracy of the survey. First, the mean square error on height data, obtained by photogrammetric digitization, is directly proportional to flight altitude. As a rule of thumb, the error on altimetry is approximately 1/10,000 of the flight altitude. This clearly illustrates the advantage of low altitude recording.

Another advantage of very low flight altitudes is that recordings can be made under a cloud cover. The diffuse light favours the image quality of the objects surveyed (i.e. the individual armour units), as there are no deep shadows. This, however, is only possible using technical features to enhance the quality and contrast of pictures realized under such reduced light conditions. As a wide lens aperture ($f/4$) and a relatively long exposure time are needed, the use of forward-motion compensated (FMC) cameras is indispensable. The cameras are mounted in twin-prop aircraft of the STOL (short take off and landing) type, so as to realize the best stability at low flight altitude and low speeds.

At low-altitudes, the speed of the aircraft in relation to the reloading of the cameras determines the stereoscopic coverage of the area. As a minimum photographic overlap of 60 % in the flight direction is needed for adequate stereoscopic vision, a coupled system of two alternating photogrammetric cameras is used.

A first survey flight took place on 2 July 1988 ; a second flight was carried out on 18 October 1989. Each time, the flight altitude was situated between 150 and 200 m. About 7 km of the seaward sides of the breakwaters were covered. The recordings allowed the survey of over 15,000 concrete blocks from the upper layer of the breakwater armour layer.

Photogrammetric digitization of the armour units

The orientation of the photogrammetric couples in the stereoplotter poses a special problem. For the relative and absolute orientation of each stereocouple, use is normally made of six control points. The control points should be distributed equally over the area which is covered by the stereocouple. If the condition of aerial distribution is not met, inadmissible errors in the accuracy will occur as a result of the orientation procedure.

Aerial photographs of breakwaters, however, show large surfaces of water that do not allow the determination of fixed calibration points.

The breakwaters take up only the central portion of the aerial photographs, and so, no calibration points along the sides are available. The orientation problem was overcome by the use of a specially developed software orientation programme. After mounting the two aerial photographs that constitute a stereocouple into an analogous stereoplotter, the position is measured in stereoplotter coordinates of six arbitrarily chosen field points that can be recognized on both photographs and are sufficiently well distributed over the area. Also, the centre point of each photograph is determined. The computer program then calculates the parameters needed for the relative orientation of the stereocouple. The operator manually sets the stereoplotter using these parameters. Afterwards, use is made of field control points (situated on the breakwater), to perform the absolute orientation (i.e. relative to the known standard grid "Lambert"). This operation has to be performed on an analogous stereoplotter, because analytical stereoplotters have a built-in orientation program that continuously recalculates the orientation and repositions the photographs.

The digitization of the armour units is also performed using a non-standard procedure. Of every armour unit, a minimum of four well-defined points are digitized.

These points determine the exact position of each armour unit with sufficient redundancy. A computer program controls and corrects the digitization of the armour units, given that the exact dimensions of each type of armour unit are known. This operation minimizes operator-induced uncertainties. The high quality of the aerial photography recordings, the efficiency of the dedicated software and the skill and experience of the stereogrammetric digitization operators combined reduce the error on the altimetry of the armour units to below 5 cm. The accuracy was confirmed on a special occasion. In October 1989, some 20 armour units had to be displaced in order to improve the cover. Before the operation, their position was measured using classical, land-based methods. The position of those blocks that could be accessed was measured with high precision. Table 1 compares the centre point coordinates with those retrieved from the 1988 observation flight. It is clear that the differences in position are completely within the accuracy range stated above. Thus, the position of each armour unit is known with the utmost precision, as required to detect slight variations in position between consecutive flights.

Furthermore, if armour units are damaged, the entire cleavage area is digitized. The volume percent of the armour unit lost by breakage is calculated accordingly. If an armour block is broken up into several, almost equally large pieces, then these pieces are digitized separately.

The armour unit database

Each flight results in the creation of three data files, containing all the information for further data handling and visualization, which are incorporated in the overall breakwater database.

The main data file, the so-called master file, contains an identification number, the absolute position of the centre point of the upper plane and the relative coordinates of the corner points of all the armour units measured. The absolute position is specified by the planimetric coordinates (with respect to the national grid Lambert '72) and by the altimetric coordinate (with respect to the level datum "Z" of the Ministry of Public Works). A second data file, called pointer file, contains the armour unit type and links the block identification number of the current survey to the reference breakwater survey (i.e. the first survey, performed on 18 October 1989). In the third output file, called cleavage file the information regarding the damaged armour units is stored, i.e. the armour unit identification number, and the absolute coordinates of the cleavage line.

The displacement of the centre point of the armour units is calculated for each inspection flight. This data, together with the information on breakage, is represented in an updated report table.

In the table 1 the measurement some results of the 1989 and 1991 surveys of a selected area of the Westdam (between the P2810 and P2910 marks) are listed.

Block Number	Block Type	Top Plane Centre at Reference			Displacement (cm)			Breakage (%)
		X(Lambert)	Y	Z	dX	dY	dZ	
3925	25TP	66594,840	227772,352	10,181	0	-11	-21	1,1
3926	25TP	66590,628	227772,288	7,957	5	-1	-15	
3927	25TP	66592,556	227773,504	8,381	15	0	-2	
3928	25TP	66590,904	227774,560	6,774	2	1	-14	

Table 1 - Armour Unit Data table

This table consist of five primary columns, containing the following information:

1. The armour unit ID number : a unique number allotted to each armour unit at the photogrammetrical digitization of the 18 October 1989 reference survey. The position of the armour units can be found in the armour unit location plan.
2. The armour unit type : 20TP, 25TP, 25T or 30T.
3. The coordinates (respectively Lambert-72 X and Y (in metres), and Z (in metres as well) with respect to the Z datum of the Ministry of Public Work) of the centre of the armour unit's upper face, as measured at the 18 October 1989 survey.
4. The displacement of the armour unit's centre, in centimetres, i.e. the difference in position between the reference survey and the present survey.

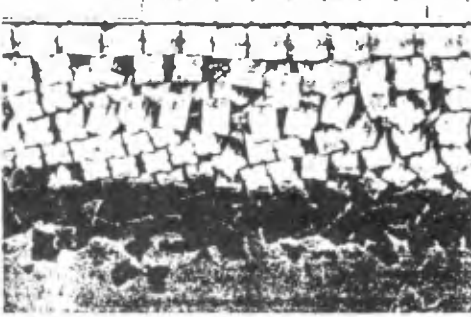
The displacement is calculated by defining the difference between the reference survey coordinates and the present coordinates along each coordinate axis (X, Y, Z).

5. The breakage volume rate. The rate of volume loss due to breakage is calculated for each armour unit that has suffered breakage.

From the table (with armour unit identification numbers identical to those of the armour unit location plan) it can be quickly determined which armour units have undergone a displacement with respect to the reference survey, how large the displacement is, and in which direction it has occurred. This gives a quantitative overview of the displacements between the different surveys.

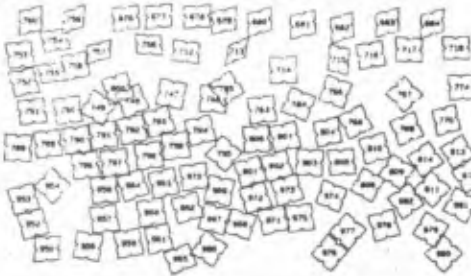
It can also be seen which armour units have suffered breakage, and how important the damage is. The armour unit displacement plans visualize the block's displacements.

VISUAL REPRESENTATION OF THE BREAKWATER SURVEYS



In order to allow a quick and accurate interpretation of the vast amount of data involved in the breakwater armour survey and several cartographic representations were developed. The definition and the main characteristics of the different ways of representation are briefly outlined below.

Armour unit location plan



The armour unit location plans show the position of each armour unit in the upper layer. The slope plane, as defined above, is taken as the projection plane. All upper surfaces are shown in projection.

It follows that the upper surfaces of all regularly-positioned blocks of the slope plane are shown as squares in an optimal projection.

Irregularly positioned or tilted units are represented by flat parallelograms.



Figure 2 - Unit location plan

The central part of Fig. 2 is an extract of the 1989 armour unit location plan corresponding to the part of the breakwater shown in the upper aerial photograph.

On the armour unit location plan, three digits identifying each block are indicated. Areas of tilted blocks or regularly-positioned blocks can immediately be recognized. Also, a qualitative picture is provided of the density of the breakwater cover. Furthermore, the blocks affected by breakage are hatched.

Armour unit occupation plans

Different ways of visualizing the positioning density of the armour units on the breakwater slopes have been established. Each method emphasizes one particular aspect with respect to the protective function of the armour layer:

- the mean occupation plan highlights the positioning density of the armour units as a function of their spacing and orientation. The plan shows the values of the "mean occupation density", calculated for each point of the slope plane. The mean occupation density assumes high values when armour unit spacing is smaller than originally designed (i.e. the units clump together), while low values indicate a poor block density.

Low values are also achieved when the armour units are irregularly oriented (i.e. the basal surface of the block is at angles to the slope plane). Therefore, a low mean occupation density always indicates a poorer protection of the breakwater at the location considered ; either the blocks make irregular angles with respect to the slope plane, or their spacing is too high ;

- the differential mean occupation plan compares the mean occupation density as calculated for a specific observation flight with the design mean occupation density. As different types of armour units and patterns of positioning were applied, part of the variation of the mean occupation density is due to the design. The differential mean occupation plan singles out this part of the variation and only shows discrepancies in occupation between the current survey and the design situation. Of course, this technique can be applied to any two surveys;
- the porosity plan regards the occupation density as an inverse function of the occurrence of hollows and spaces between the armour units of the upper layer. The plan represents the real porosity of the outer armour layer, such as calculated for a given observation flight. It does not conform with the design porosity, as the latter is calculated over the two armour layers, in which all armour units have the same orientation.

The values, represented in each type of plan are, respectively, the mean occupation density, the relative mean occupation density and the porosity.

These values are calculated for each point of the slope plane. For computational reasons, these points are positioned on a rectangular grid.

The unit spacing of the calculation grid can be chosen according to local conditions. For the Zeebrugge breakwaters, a 1-m spacing was adopted. All values determined are averages calculated over a unit surface, of which the centre is located successively in each grid point. In Zeebrugge, a unit surface of $6 \times 12 \text{ m}^2$ was found to provide the most relevant areal detail after some preliminary tests. The long axis of the unit surface is oriented parallel to the long axis of the breakwater. The rectangular shape of the unit surface provides a better sensitivity to density variations in the slope direction.

The dimensions of the unit surface were chosen so that it contains 15 to 20 armour units at a time. The values calculated in each grid point therefore represent the point itself and its immediate environment.

The armour unit occupation plans are produced in colour. In each of the three approaches, red corresponds to a poor condition, yellow represents the ideal or mean situation and green is used for a too close armour. The use of this colour representation of the occupation values described, enables a very precise and fast overview of the condition of the breakwater armour layer. The lower part of Fig. 3 is an extract of the porosity plan of the section shown above.

Though the figure is in black and white, the relation to the aerial photograph and the location plan above is still clear. Parts of the breakwater having a dense occupation of armour units are characterized by a low porosity, and vice versa.

Armour unit displacement plans

An essential indication of breakwater instability is the movement of the individual armour units. In order to detect such movements and their rate, inspection flights are carried out every year. As the aerial photography, the photogrammetric digitization and the subsequent computer processing are carried out with utmost care, absolute shifts in position of armour units can be traced once they exceed about 5 cm.

Therefore, a link is provided between the block coordinate lists of the reference flight and the last flight performed. Using a dedicated software program, the armour units of the last flight are automatically linked with the corresponding armour unit of the reference flight. The link method is based on the position of the centre of gravity of each block. Once this identification procedure has been carried out, the displacement of the individual armour units is readily established. The armour unit displacement plan represents, by the same projection method as the one used for the location plans, the displacement of all individual armour units between two surveys by means of colour coding.

DIGITAL SIDE-SCAN SONAR RECORDINGS

Side-scan sonar is basically an imaging technique whereby sound pulses are transmitted at both sides of a towed 'fish'. The pulses are sent perpendicular to the track of the vessel under approx. 90° , allowing a full coverage of the sea bottom on both sides of the vessel from the water surface to below the survey vessel. As the ship advances, a complete image of the seabottom along-track the survey vessel is created.

The strength and delay of the returned signals are measured and presented to the user on an analog thermal paper output. The returned signals are indicated by black dots on white thermal paper. As the initial sound pulse covers an angle of 90° , return signals from within this entire lookangle are received. The darkness of the dot corresponds to the strength of the returned signal. Usually, 16 or 64 discrete levels of black can be shown. The dot is positioned away from the centre of the paper roll proportional to the time delay of the returned signal. With each new emitted sound pulse, the time delays of the returned signals are measured with respect to the new trigger point (i.e. the new pulse). This provides information about the distance from the source the reflecting substance can be found, not however on the direction in which to search for this distance.

The maximum time allowed to wait for a returned pulse is a measure for and proportional with the distance the sidescan sonar is allowed to 'look' under the water. The thermal paper of the analog output is advanced at regular speed, which can be set manually or automatically to reflect, as much as possible, the speed of the survey vessel. By doing so, as one line of information is written with each emitted and returned pulse and consecutive pulses create consecutive lines in the output, an image of the seabottom is created.

However, because exact directional information (from where the return signal is coming) is missing, side-scan sonar measurements do not provide absolute positioning of the recorded features. This is the main difference with the other measuring technique used, multibeam (see below).

All objects under water, when hit by the sound pulse, will reflect part or whole of the incident energy back to the source. Some objects, such as stone, are much better reflectors than others, e.g. silt. The strength of the return signal, duly amplified because of the attenuation of the signal with distance from the source creates an image, that gives an impression of the kind of materials detected under water. Also, objects by returning the sound pulse create a shadow zone behind them, effectively hiding part of the seabottom or underwater part of the breakwaters from detection by the side-scan sonar.

Such shadow areas are normally indicated as white - blank areas on the visualisation output.

The description above applies to standard side-scan sonar. However in Zeebrugge the analog output of the side-scan sonar is systematically digitized, in real-time and this information is stored in digital form. That technique is therefore dubbed digital side-scan sonar.

The side scan sonar used is a dual-frequency instrument, with analog output and recording. The analog output is digitized in real-time and connected to a VME-computer for data logging. The VME-computer also records the GPS information as well as the information of the vessel's roll, pitch and heading, destined for geometric corrections later on.

The digital storage of the side-scan sonar output is in 12 bit, allowing 4096 distinct data values (or 'grey values' in terms of analog output), while normal analog output on thermal paper only allows 16 or 64 grey values. All subsequent data treatment is also performed digitally.

Processing of the digital side-scan recordings

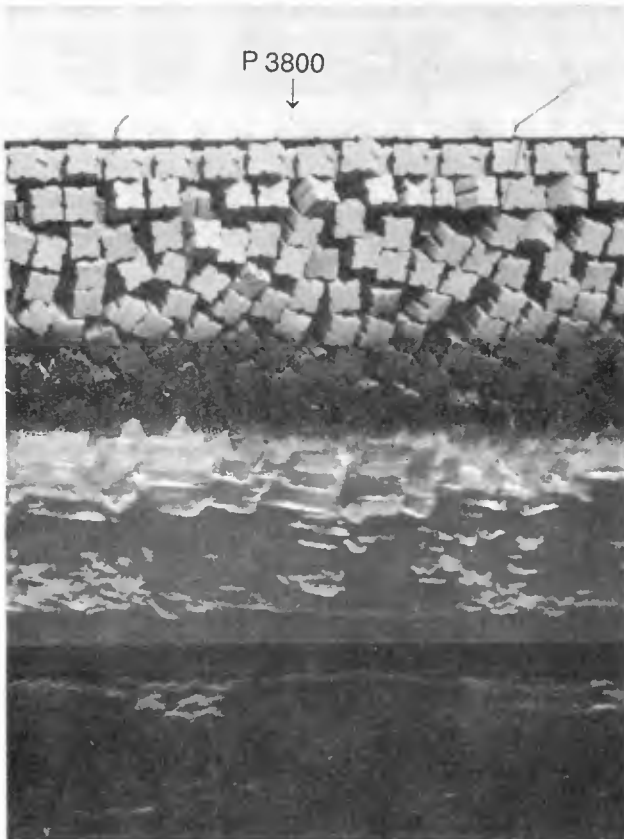


Figure 3 - SSS-recordings

First, geometric corrections are applied, together with a straightening of the sounded track. Geometric corrections are needed because the sounding vessel's speed nor behaviour (roll, pitch) are constant during the recording.

Also, the followed path is not a perfect straight line parallel to the breakwater. Corrections are based on the continuously stored positioning, heading, roll and pitch data.

A further data treatment arranges the sonar recordings into a straight strip parallel to the breakwater.

Adequate along-track way-points ensure a uniform scale in this direction, to which the transversal scale is adapted. After the geometric corrections, a number of digital imaging techniques is applied to render the side-scan sonar image easy to read and interpret. This step is largely made possible by the great number of recorded grey levels. Figure 3 contains an example of enhanced side-scan sonar recordings, fit to aerial photographs showing the subaerial part of the breakwater. The armour units below and above water level are clearly detectable.

The aerial photographs are rectified grey-scale images of the breakwater, above the low-water line. Both types of recording are fitted together without transition break, so that a continuous image of the breakwaters is created, showing them from the breakwater crest till its toe. On the image, distance indications and other marks are added, so as to facilitate the interpretation.

MULTIBEAM RECORDINGS

With multibeam, as the name implies, a number of discrete sound pulses (or 'beams') are emitted and the returned signal is recorded within well specified angles. Basically the same information is thus collected as with side-scan sonar, only now because of the known direction of the returned signal, the exact distance and hence location of the underwater object can be determined. In multibeam, the output of the device is always in digital form, needing often not more than serial RS-232 connection to have access to the measured data. While, side-scan sonar can be considered an 'imaging' technique, multibeam is a real 'measuring' technique.

Multibeam principle and deployment geometry

Multibeam systems emit a number of discrete sound pulses and record the returned signal within well-specified angles. The system used in the Zeebrugge breakwater monitoring programme, emits 60 beams at a time in a profile, perpendicular to the track. The beams have an aperture angle of 1.5° so that a complete profile covers an angle of 90° . The basic geometry of the system deployment much resembles the one used in side-scan sonar surveying, only now, because both the delay time and the direction of the returned signal are known, the exact location of the reflecting underwater object with respect to the sensor head can be determined.

For the breakwater surveys, the sensor head is rigidly fixed to the vessel's starboard side in an angle of 45° from the vertical, so that the beams look sideward from the sea bottom over the toe protection and armour layer to the watersurface.

Contrary to the side-scan sonar measurements however, with the used multibeam, only on one side of the track are measurements possible at any one time. As the survey operation takes place in very shallow water, a high beam update frequency can be obtained.

A high frequency is advantageous to increase the number of measured profiles, so that a high data density is achieved. In the Zeebrugge breakwater surveys, update frequencies in the order of 13.5 Hz yielded the best results. This rate corresponds to 810 measured points per second, or, at a survey speed of 1 to 1.5 m/s at least 100 measured points per armour unit.

Processing and interpretation of the survey results

The output of multibeam echosoundings is typically a map showing all measured points (on their true location x,y), together with an indication of the measured depth (z , with reference to the chart datum).

Such a basic visualization poses some difficulties, especially when one is interested in comparing the results of successive surveys. Two different approaches to this problem can be used, depending on the type of breakwater material.

For quarry stone layers, such as the toe protection of the Zeebrugge breakwaters, a digital terrain model (DTM) can be fitted through the measured points that are located on the top of the rubble mound surface.

When a second survey has been completed, e.g. one year later, a new DTM of the rubble mound slope can be established. The difference of both DTMs can then be represented in a map, displaying areas where changes in the rubble mound topography have occurred.

If the breakwater is protected by armour units, such as in Zeebrugge (grooved cubes), this method no longer applies. Here, the exact location of the armour units is needed to assess the breakwater's safety, so that displacements per unit can be calculated. The determination of the exact location of the underwater units is possible, as sufficient points are measured per armour unit, with an absolute accuracy of approx. 20 cm in all three axes. This is less than 1/10 the dimensions of the armour unit. Comparison of the same unit, measured at a later stage, e.g. a year later, at the same accuracy, allows the production of differential maps of the submerged armour units with an approximate precision better than 40 cm, 1/5 the dimensions of armour units. Considering that only displacements equal to the unit length are significant in breakwater stability rules and equations, it is evident that the measuring technique effectively and quantitatively allows the assessment of breakwaters' stability.

CONCLUSION

The measurement of the position and displacement of individual armour units of a rubble mound breakwater is the most straightforward method for early detection of breakwater changes.

Due to the difficult and dangerous access, aerial remote sensing is one of the most appropriate ways to obtain the position of those blocks of the outer armour layer that are emerged at low tide.

Aerial photography moreover adds the advantages of high accuracy, fast speed of observation and automated data acquisition and processing.

Appropriate tools have been developed to obtain and evaluate the volume of information. The unit data tables, armour unit location plans, occupation plans and displacement plans provide an effective and accurate picture of the actual condition of the armour layer and the movement of the armour units since a reference situation.

The use of digital side-scan sonar recordings allow qualitative assessment of the stability of the underwater part of breakwaters. Multibeam recordings are very useful when quantitative data are needed.

Since 1993, the determination of the exact position of the Zeebrugge breakwaters underwater armour units, as well as of the exact underwater topography of the breakwaters' toe protection, is based on high-accuracy multibeam echosounding. Successive surveys allow the movements of the armour units and changes in the toe protection topography to be mapped and analyzed.

These three structural monitoring techniques are excellent tools to organize adequate maintenance and to keep the breakwaters in optimum condition.

Acknowledgement

Part of the work leading to this paper is carried out within the MAST II-project: MAS2/CT92-0023, funded by the European Commission.

References

- Van Damme L., De Wolf P., Fransaer D., Braet K., Van Rensbergen J. (1990).* Breakwater armour units monitored using aerial remote sensing. PIANC-Bulletin n° 70, pp 22-28.
- Van Damme L., Vandenbossche D. (1992).* Port of Zeebrugge breakwater monitoring. Coastal structures and breakwaters. Thomas Telford, London, pp. 165-170.
- De Putter B., Van Damme L., Fransaer D., Claeys F. (1996).* High-quality quantitative and qualitative underwater inspections of breakwaters. Proc of the 11th International Harbour Congress, Antwerp, Belgium.
- Eurosense NV (1995).* Zeebrugge breakwaters Survey. Overview report. Western Breakwater. P2810-P2910.

CHAPTER 152

Influence of rock shape and grading on stability of low-crested structures

Jentsje W. van der Meer¹
W.H. Tutuarima²
G. Burger³

Abstract

The stability of low-crested rubble mound structures has been treated before by various researchers. In the first phase of this study two data sets from different laboratories were combined to one homogeneous data set. Re-analysis of these data resulted in a design diagramme for the stability of the seaward side, the crest, the rear and the total armour layer of the structure. Secondly, model tests were performed on carefully selected rock with different rock shapes (angular, flat and rounded) and different gradings, all for a low-crested structure. Results show that the differences between the various rock types were small, especially for the start of damage. The influence of the length/thickness ratio showed even no influence at all which means that the sometimes strict requirements in construction may be released.

Combination of existing results

Low-crested rubble mound structures were treated by Van der Meer and Pilarczyk (1990) and were divided into three types: reef type structures and conventional structures with, respectively, the crest above or below the still water level. For all three types design formulas were given, based on a limited number of tests. In fact the division between structures with the crest above or below still water is not really practical as both situations can happen for the same structure.

Vidal et al. (1992) treated low-crested structures in three parts: the front

¹ Delft Hydraulics, P.O. Box 177, 2600 MH Delft, The Netherlands

² Delft University of Technology and Royal Boskalis Westminster nv, Papendrecht, The Netherlands

³ Delft University of Technology and Grabowsky & Poort Consulting Engineers, The Hague, The Netherlands

slope, the crest and the rear slope. Their tests were complementary to the available data of Van der Meer and Pilarczyk (1990). The first part of the present study was to analyse both data sets in the same way and bring them together. All data were submitted by Vidal.

Vidal et al. (1992) accounted for the development of damage onto the entire structure, where Van der Meer and Pilarczyk (1990) only looked at the stability of the front side including a small part of the crest. In addition, Vidal et al. divided the damage in three segments: the front, the crest and the rear. The division in these three segment, used for the present re-analysis, is given in Fig. 1.

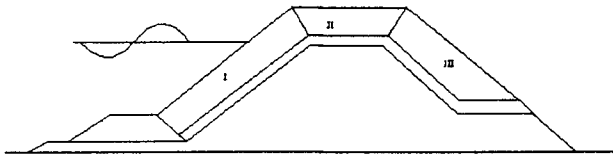


Figure 1. Division of armour layer in three segments

The damages to the structures of Van der Meer and Pilarczyk (1990) and of Vidal et al, were re-established according to Fig. 1. All data and the analysis have been described in Burger (1995). The damage is defined according to Van der Meer (1988):

$$S = A_e / D_{n50}^2 \quad (1)$$

Where: S = damage; A_e = surface of eroded area; D_{n50} = nominal diameter (cubical size) of the rock. S -values between 1-3 mean start of damage and values higher than 8-12 give "failure", this means holes in the armour layer and visible underlayer or core. With steep slopes and small areas subjected to wave attack, the smaller S -values should be used.

Parameter	Van der Meer	Vidal
D_{n50} (m)	0.0344	0.0249
Δ (-)	1.61	1.65
H_s (m)	0.073-0.229	0.047-0.152
T_p (s)	1.96 and 2.56	1.4 and 1.8
s_p (-)	0.010-0.036	0.010-0.049
B/D_{n50} (-)	8	6
R_c/D_{n50} (-)	-2.9 to 3.0	-2.0 to 2.4

Table 1. Test conditions for Van der Meer and for Vidal

The stability number is given by $N_s = H_s / \Delta D_{n50}$, where H_s = the significant wave height and Δ = the relative buoyant density. The stability of low-crested structures will be dependent on the relative crest freeboard. This is defined by R_c / D_{n50} , the number of rock sizes that the crest is above (positive) or below (negative) the still water level. Other used parameters are the peak wave period T_p , the wave steepness s_p , and the crest width B . Table 1 gives the test conditions for both Van der Meer (1990) and Vidal et al. (1992).

Re-analysis of existing results

The parameters used by Vidal et al. are not fully the same as those by Van der Meer and Pilarczyk. Vidal et al. used a front slope with an angle of 1:1.5, whereas Van der Meer and Pilarczyk used 1:2. The comparison between the two test series was carried out as follows: from the damage curves various fixed damage levels S were chosen and the corresponding stability numbers were determined. Then figures were drawn of stability number against crest freeboard for the various damage levels. Fig. 2 gives an example of the front slope.

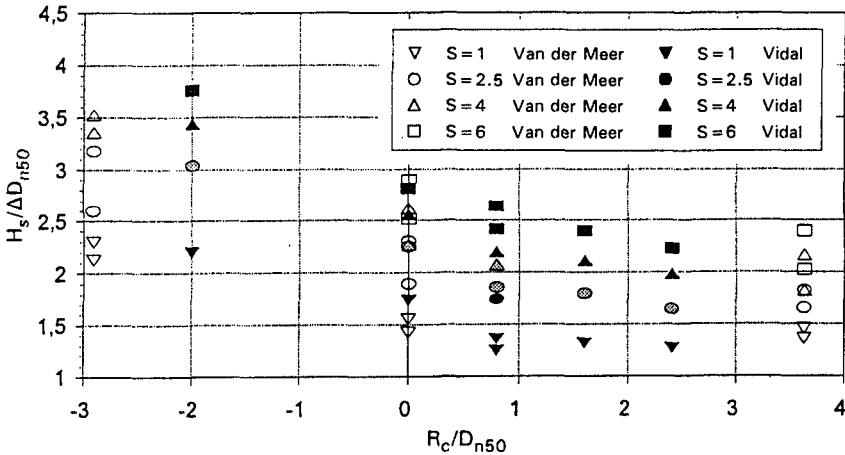


Figure 2. Stability at the front for fixed damage levels S

This figure shows that the two different data sets give a fairly good agreement, although some scatter is present. In order to make the analysis easier, in the following only start of damage will be considered. For the whole structure start of damage is given as $S = 2$. In order to remain consistent start of damage to the different segments separately should be lower, but in total again $S = 2$. The following distribution was chosen for start of damage: front 50% ($S = 1$), crest 25% ($S = 0.5$) and rear 25% ($S = 0.5$). The real distribution of the damage will vary with the freeboard. Fig. 3 gives the same data as Fig. 2 for the front, but now only for start of damage $S = 1$.

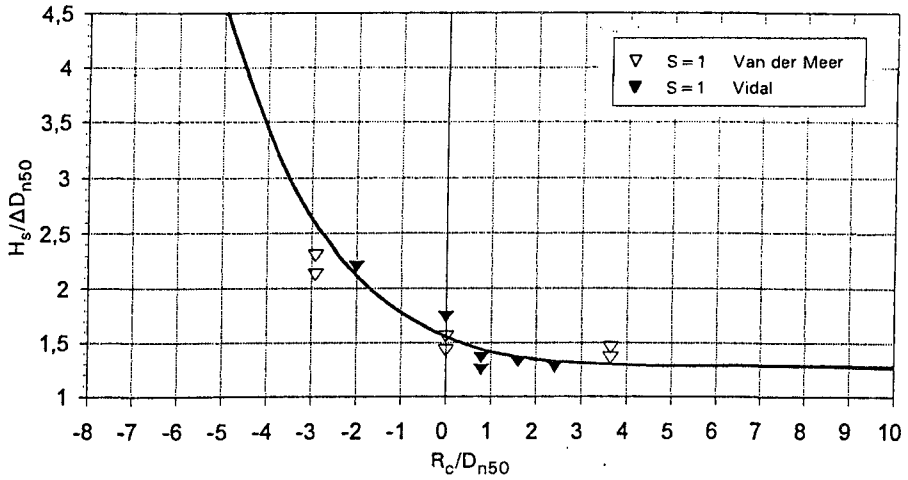


Figure 3. Stability front for start of damage

A curve is drawn through the data points and this curve is also extended beyond the range of test data. For positively increasing freeboard the value of the stability number can be determined easily. Because as the freeboard increases there will not be any more overtopping and the structure will behave according to the formulas by van der Meer (1988). The accompanying stability with the damage $S = 1$ is then $H_s/\Delta D_{n50} = 1.3$. For negatively decreasing freeboard the development is less easy to predict. However, it is evident that the stability will increase with a freeboard decreasing.

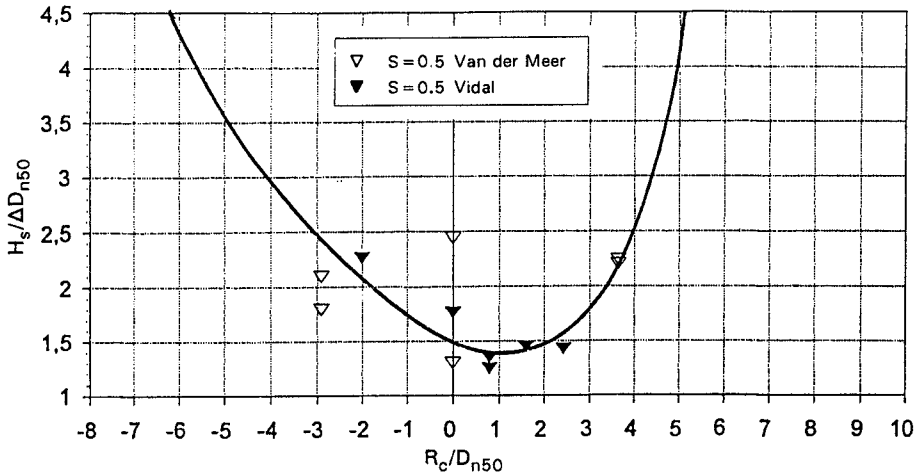


Figure 4. Stability of the crest for start of damage

Fig. 4 gives the data points for start of damage of the crest. Although some scatter is present, especially for the crest at the still water level, the trend is clear. The crest is most vulnerable for freeboards around the still water level. For high crest heights there will be hardly any or no overtopping and the curve will raise sharply. For negative freeboards the stability will increase with decreasing freeboards, more or less according to the front. Although the crest for large negative freeboards will show more damage than the front due to the wave attack directly on the crest for (very) low structures.

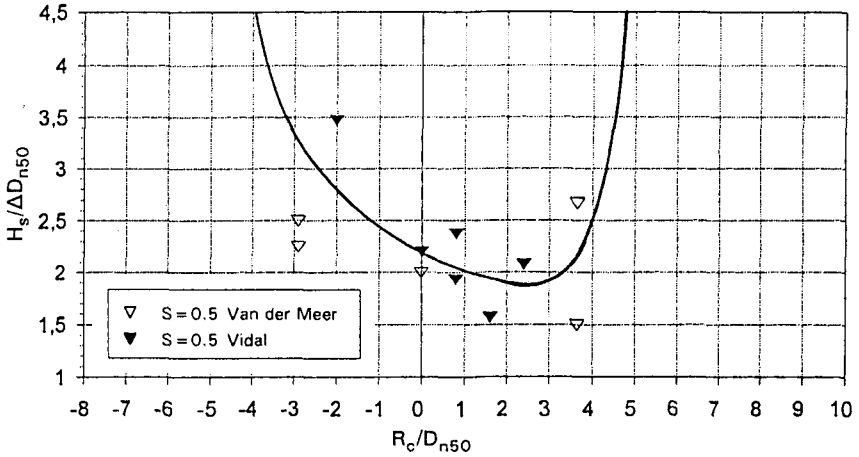


Figure 5. Stability rear for start of damage

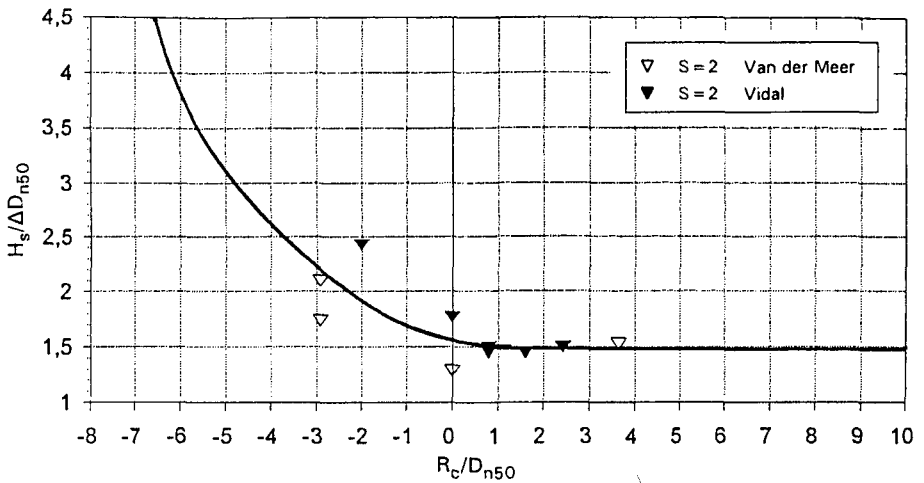


Figure 6. Stability of entire structure

Fig. 5 gives the data points for start of damage ($S=0.5$) for the rear. Considerable scatter is present. For increasing positive freeboards stability should increase as soon as overtopping waves can hardly reach the rear. Therefore, the curve should go up quite steep. Again the stability of the rear should increase for very low structures, according to front and crest.

The total stability is shown in Fig. 6 where the curve is similar to the one for the front side. All four graphs together give a design graph for stability of low-crested rubble mound structures at start of damage. This design graph is given in Fig. 7. The crest and front slope are always normative in this figure. The crest is normative for a crest under water up to a crest height of 1 to 2 D_{n50} . Above that level the front is the least stable segment.

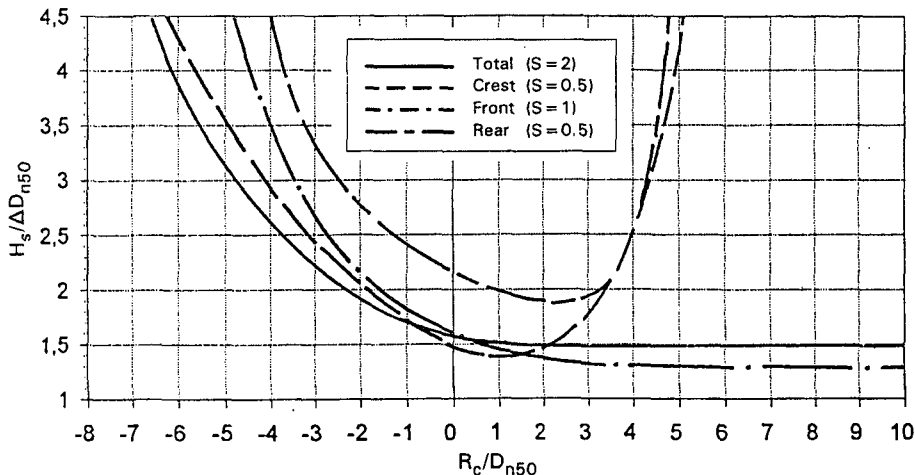


Figure 7. Design graph for low-crested rubble mound structures, for start of damage of various segments, front, crest, rear and entire structure

The design graph in Fig. 7 can be used in various ways. If the structure will be always under water it could be possible to use the armour layer only on the crest and to reduce the size at front side and rear. It is also possible to place the heaviest rock from the quarry at the least stable segment, which is determined from Fig. 7. Or one can design front, crest and rear with different rock gradings according to their required stability number. This may benefit the output yield curve of a quarry.

Tests on rock shape and grading

Requirements on rock shape and grading for construction of rubble mound structures are often fairly strict, see the CUR/CIRIA-manual (1991). The rock shape can roughly be determined by the L/D -ratio and by a description of the

shape (angular, round, etc.), see Figs. 8 and 9. Here L is the largest dimension and D the smallest. $L/D=1$ is a sphere or cube, $L/D=3$ is a fairly long and/or flat rock. In many cases values larger than 2 are not permitted, which in reality is difficult to obtain. Furthermore, such requirements are hardly based on testing. Also one is often strict as regards the demands for grading. The value of D_{85}/D_{15} may not exceed 2.0, implying that the quarry must produce uniform material.

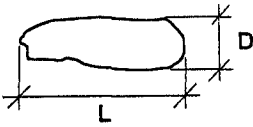


Figure 8. Rock shape L/D

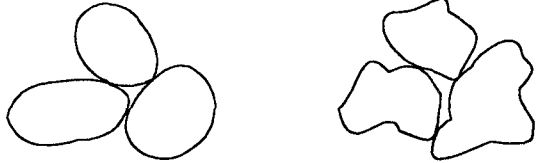


Figure 9. Round and angular rock

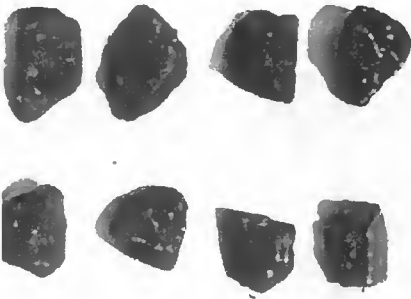
The above requirements give both delay as well as an increase of the costs of building the structure. It is remarkable, though, that none of these requirements have been tested sufficiently so as to substantiate them. However, a number of researchers have already determined (Van der Meer, 1988; Bradbury et al. 1990) for the grading that, within reasonable limits ($D_{85}/D_{15} < 2.5$), the grading has a negligible impact on the stability, but for low breakwaters this has not yet been investigated.

Tests were performed at Delft Hydraulics with six categories of rock which were very carefully prepared. Each individual rock was weighed and all three length dimensions were measured. These rocks were placed in fractions of 5 mm size difference (25-30 mm, 30-35 mm, etc.) and then further in three fractions with different shape: $L/D < 2$; $2 < L/D < 3$; and $L/D > 3$. These fractions were put together to form a predescribed grading and shape.

Table 2 shows the six different types of rock gradings and shapes. Three categories were used with angular rock, the same L/D -distribution, but with different gradings: $D_{85}/D_{15} = 1.25$ (uniform rock); 1.75 (normal grading); 2.5 (very wide grading). Two other categories were also made of angular rock, but had different L/D -ratio's. One of these categories had 40% rock with $L/D > 3$ (type 5). The sixth category was made of shingle which is very rounded rock. Fig. 10 shows a picture of each of the six different types of rock gradings.

Rock type	Shape	D_{85}/D_{15} (-)	$L/D > 2$ (%)	$L/D > 3$ (%)
1	angular	1.25	20	0
2	angular	1.75	20	0
3	angular	2.50	20	0
4	angular	1.75	50	15
5	angular/flat	1.75	80	40
6	rounded	1.75	50	15

Table 2. Rock types tested on a low-crested breakwater



Type 1. Angular; $D_{85} / D_{15} = 1.25$
 $L/D > 2$: 20% $L/D > 3$: 0%



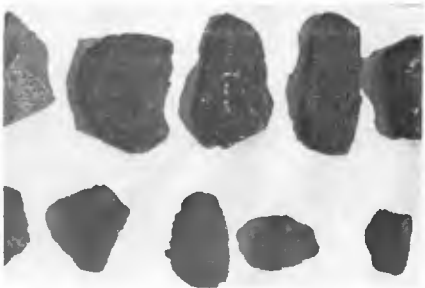
Type 2. Angular; $D_{85} / D_{15} = 1.75$
 $L/D > 2$: 20% $L/D > 3$: 0%



Type 3. Angular; $D_{85} / D_{15} = 2.50$
 $L/D > 2$: 20% $L/D > 3$: 0%



Type 4. Angular; $D_{85} / D_{15} = 1.75$
 $L/D > 2$: 50% $L/D > 3$: 15%



Type 5. Angular/flat; $D_{85} / D_{15} = 1.75$
 $L/D > 2$: 80% $L/D > 3$: 40%



Type 6. Rounded; $D_{85} / D_{15} = 1.75$
 $L/D > 2$: 50% $L/D > 3$: 15%

Figure 10. Pictures of the six tested gradings

Tests were performed on a cross-section as given in Fig. 11. The prepared rock was placed on the upper sections only, as for the lower sections (shaded) no damage was expected. The seaward slope was 1:2, the rear 1:1.5. The water depth for all tests was 0.6 m, the structure height 0.67 m (crest freeboard of 0.07 m). The nominal diameter of the rock was around 0.035 m. Tests were performed with a Jonswap spectrum. The significant wave heights varied from 0.07 to 0.18 m. For each rock type two test series were done, one with a wave steepness of $s_p = 0.02$ (fairly long waves) and one with $s_p = 0.04$ (storm waves). A test series consisted of 6 to 7 test runs with different wave height in order to establish the damage curve (damage versus wave height). The structure was reconstructed after each test run (6 or 7 times during each test series). This procedure gives damage data that are independent and have no cumulative effect.

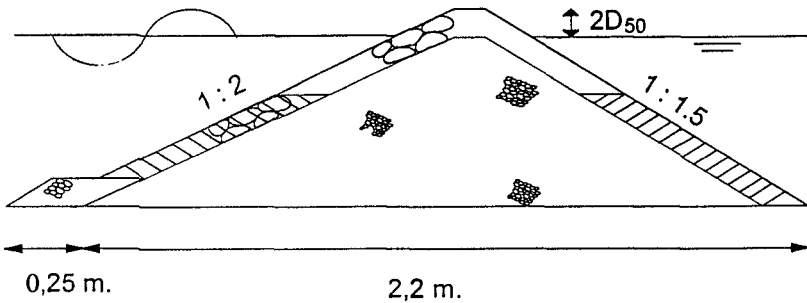


Figure 11. Tested cross-section

After each test run (of 1000 waves) the profile was sounded. Each time four cross-sections were measured with a sounding rod and a recording was taken every 0.039 m. Then the average profile was calculated and compared with the original profile. The final result was the damage area A_c and the damage S . The underside of the sounding rod had a circle shaped bulge with a radius of $0.5 D_{n50}$. The test data are given in Burger (1995).

For each test series a damage curve can be drawn. This gives two damage curves for each rock type, one for low and one for high wave steepness. With certain combinations of rock types in one graph the influence of rock shape and grading can be established. Figures 12 - 14 give all these combinations for the influence of:

- rock shape L/D
- rock shape angular/rounded
- rock grading D_{85}/D_{15}

Influence of rock shape L/D

Fig. 12 gives the results of rock types 2, 4 and 5, which have similar gradings, but have different shapes of L/D . Rock type 2 is almost cubical, where

rock type 5 has many long and flat stones (see also Fig. 10). The upper graph of Fig. 12 gives the results for a steepness of 0.02 and the lower graph for 0.04.

The influence of the rock shape L/D can hardly be traced in Fig. 12. In particular at the wave steepness of 0.04 the three rock types virtually overlap;

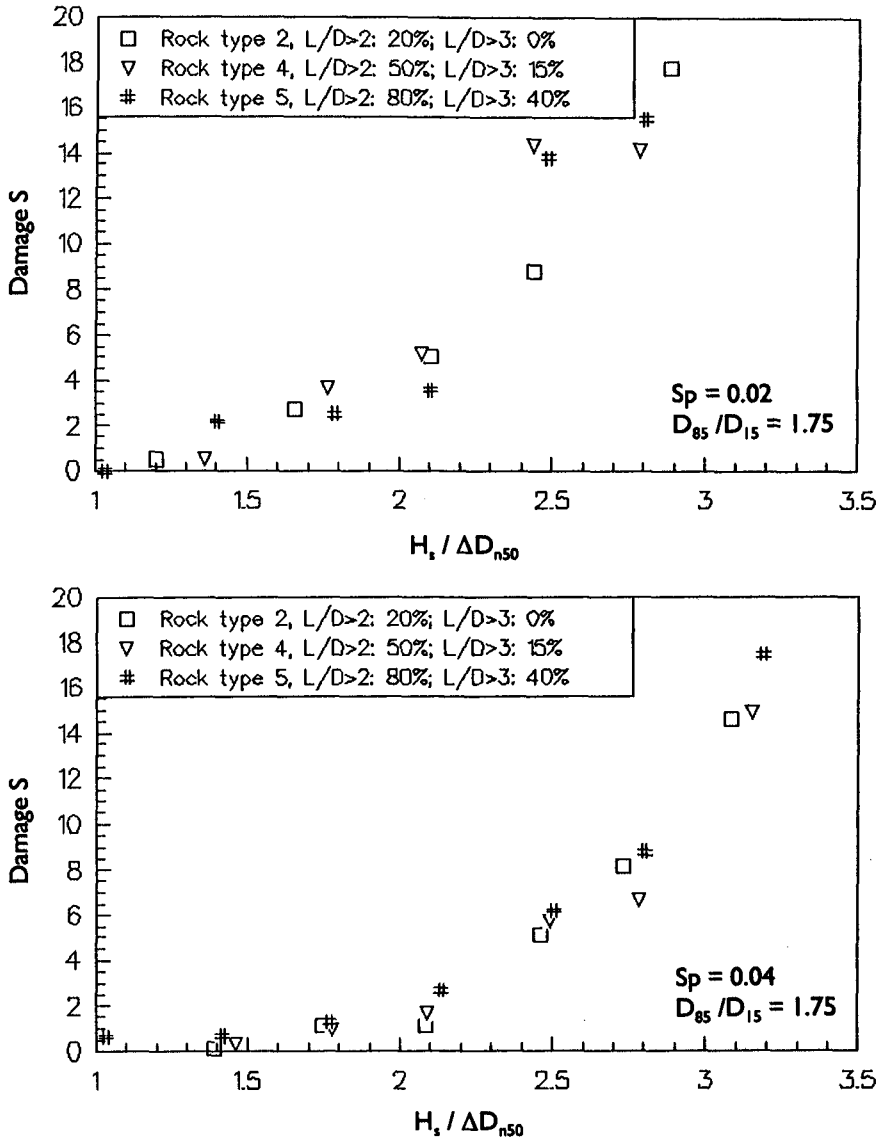


Figure 12. Influence of rock shape L/D on stability

results are virtually all on one line. With $s_p = 0.02$ there is no difference until a damage of $S = 4$; a little beyond that the more uniform material is more stable. At a yet higher stability number this is, remarkably enough, the least stable material.

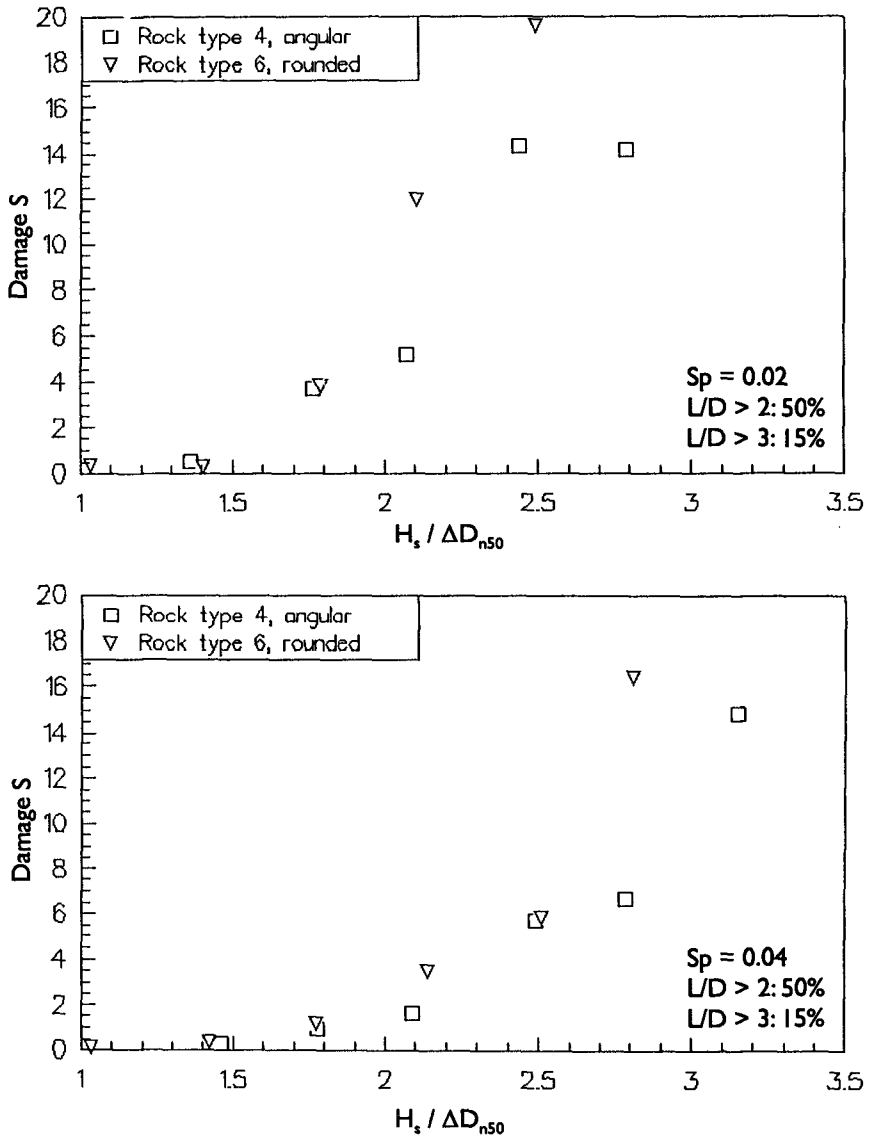


Figure 13. Influence of angularity on stability

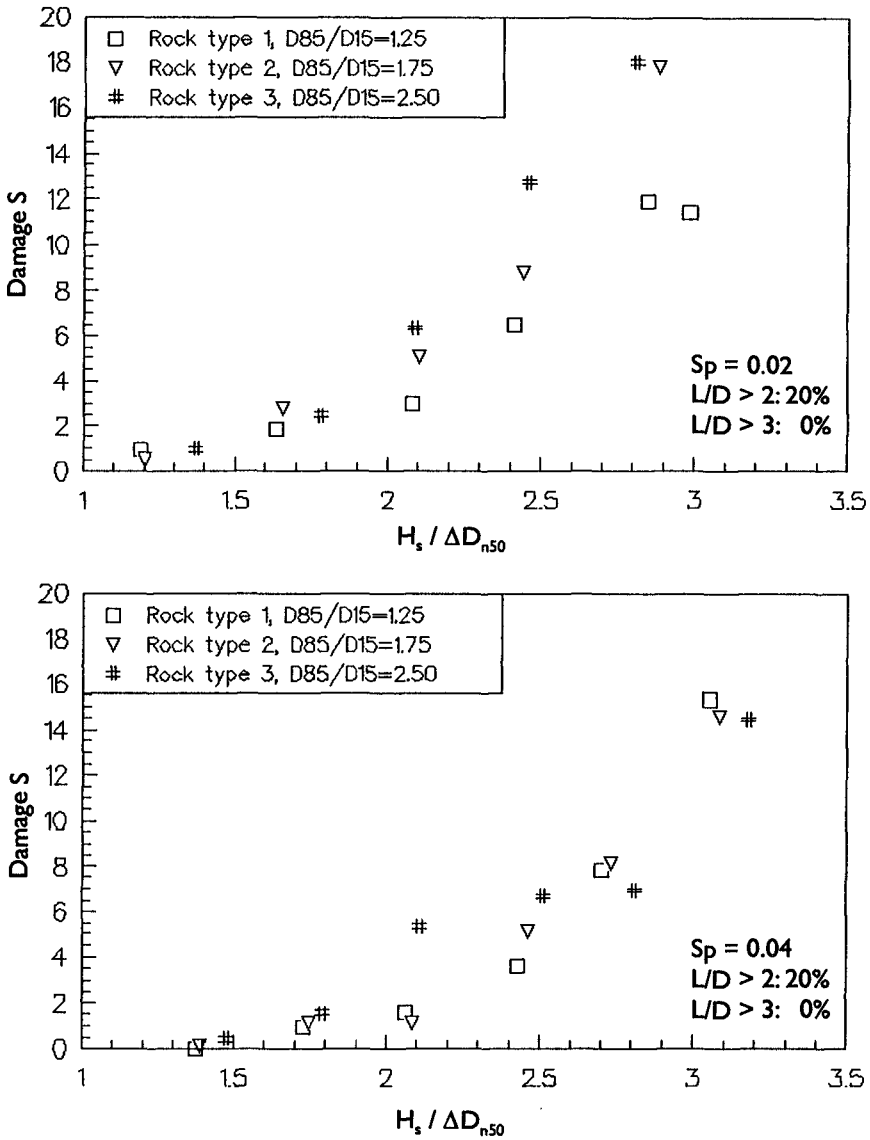


Figure 14. Influence of grading on stability

Influence of rock shape: angular/rounded

In Fig. 13 the results of the angular and rounded rock are given. Rock type 6 is composed of round shingle. For a wave steepness of $s_p = 0.02$ the data points up to a damage of $S = 4$ overlap one another exactly. The damage curves

for $s_p = 0.04$ are similar up to $S = 6$. Apparently the rounded material does not roll that easily as one would expect. However, when it does start rolling, the development of damage will occur progressively in comparison to the angular material.

Influence of grading D_{85}/D_{15}

Fig. 14 gives the damage curves for the first three rock types which all have the same shape, but different gradings. Up to start of damage, $S = 2$, there is hardly any difference between damage development. Beyond that and with a wave steepness of 0.02 one can recognise a difference in damage development. There is hardly difference for the wave steepness of 0.04. The scatter in results is largest for the widest grading with $D_{85}/D_{15} = 2.5$. This is similar to tests performed at HR Wallingford, for a very wide grading with $D_{85}/D_{15} = 4.0$ (CUR/C-IRIA-manual, 1991, page 271). There it is recommended not to use gradings with $D_{85}/D_{15} > 2.5$. The results in Fig. 14 show that upto this value the differences are small.

Conclusions

The existing test results of Vidal et al. (1992) and Van der Meer and Pilarczyk (1991) are reasonably in agreement, certainly if the differences in slope angle and crest width are considered. A design graph for start of damage was composed for stability of low-crested rubble mound structures (stability number versus relative crest freeboard). This design graph contains four curves: for the entire structure, the front slope, the crest and the rear.

Material factors of rock such as shape and grading appear to be of little influence on the stability of the armour layer of low-crested rubble mound structures. The length-width ratio L/D of the rock showed no influence at all on stability. A rock type with relatively many elongated/flat rocks is just as stable as a more uniformly shape rock type. There was hardly difference between the angular and rounded (shingle) shaped rock up to a damage of $S = 4-6$. After that the rounded rock showed a more progressive development of damage. Still the conclusion can be that also more rounded rock can be used for design of low-crested structures.

The grading has only little influence. It has no influence if the grading D_{85}/D_{15} is smaller than about 2. With $D_{85}/D_{15} = 2.5$ the stability can be the same, but the reliability of the results is smaller (the scatter is larger), probably due to unsorting of the grading, etc. It is recommended not to use gradings with $D_{85}/D_{15} > 2.5$.

The material factors as described above give hardly cause for the rejection of amounts of rock during construction. Hence, in future it is recommendable to be less strict as to the requirements for constructing (low) breakwaters than was

customary up to now. In particular, for the differences in length/width ratios of the rock this will yield gains in time and material to be used. This will benefit both principal and contractor.

Acknowledgements

Prof. Vidal of the University of Stantander, Spain, is acknowledged for the release of all his test data.

References

Bradbury, A.P., Latham, J.P. and Allsop, N.W.H. (1990). Rock armour stability formulae influence of stone shape and layer thickness. ASCE, 22nd ICCE, Delft, The Netherlands

Burger, G. (1995). Stability of low-crested breakwaters. Stability of front, crest and rear. Influence of rock shape and gradation. MSc. thesis Delft University of Technology and Delft Hydraulics Report H1878/H2415.

CUR/CIRIA-manual (1991). Manual on the use of rock in coastal and shoreline engineering. CUR-report 154, Gouda, The Netherlands. CIRIA special publication 83, London, United Kingdom.

Van der Meer, J.W. (1988). Rock slopes and gravel beaches under wave attack. PhD-thesis Delft University of Technology. Also Delft Hydraulics Publication No. 396

Van der Meer, J.W. and K.W. Pilarczyk (1990). Stability of low-crested and reef breakwaters. ASCE, 22th ICCE, Delft, The Netherlands.

Vidal, C., M.A. Losada, R. Medina, E.P.D. Mansard and C. Gomez-Pina (1992). A universal analysis for the stability of both low-crested and submerged breakwaters. ASCE, 23rd ICCE, Venice, Italy.

CHAPTER 153

TOE STABILITY OF RUBBLE MOUND BREAKWATERS

Ton van der Meulen, Gerrit J. Schiereck, Kees d'Angremond¹

ABSTRACT

At the Congress on Coastal Structures and Breakwaters, a stability relation for toe structures of rubble mound breakwaters was presented, see Van der Meer et al., 1995. In that relation the relative stone density, Δ , was used in the stability parameter $H_s/\Delta D_{n50}$. In the tests on which the relation was based, however, Δ was not varied, so some uncertainty remained on the influence of this parameter. Additional tests were therefore carried out with different stone densities, leading to the conclusion that there is no influence of the stone density, other than represented in the stability parameter $H_s/\Delta D_{n50}$. Computations were done, coupling the orbital velocities in the waves in front of the breakwater to the stability of the stones of the toe structure leading to encouraging results. Both computations and tests show an influence of the waterdepth in front of the breakwater which is not yet included in the stability relation.

1. INTRODUCTION

Figure 1 shows a typical cross-section of a rubble mound breakwater, consisting of several layers, covered with an armour layer bordered by a toe structure. The function of the toe is mainly to support the armour layer, and to provide a transition to low(er) weight units in the base of the structure. Data about the stability of the toe are less in number than about the stability of armour layers. That is the reason to attach special attention to this part of the structure.

¹Delft University of Technology, Faculty of Civil Engineering,
P.O. Box 5046, 2600 GA Delft, The Netherlands

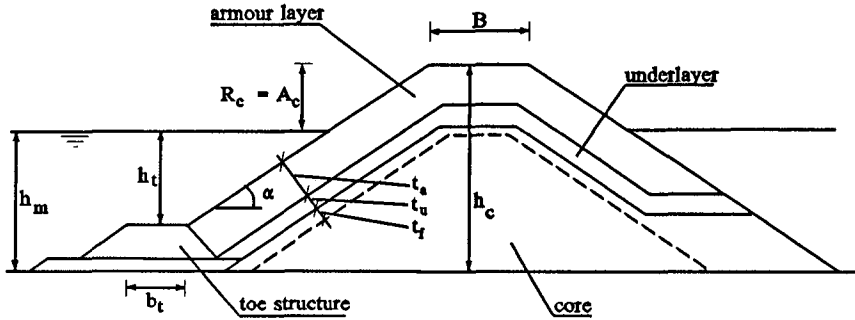


Figure 1 Cross-section rubble mound breakwater

Stability of the toe was traditionally related to the stability of the armour layer. For values of $h_t/H_s = 1.5$, a minimum weight of the units in the toe was given as $W/2$. For a greater submergence, with values of $h_t/H_s > 2$, toe unit weight could be reduced to $W/10$ to $W/15$ (Shore Protection Manual, 1984). These design rules were attractive because of their simplicity. They were, however, not based on extensive research or comprehensive theoretical considerations.

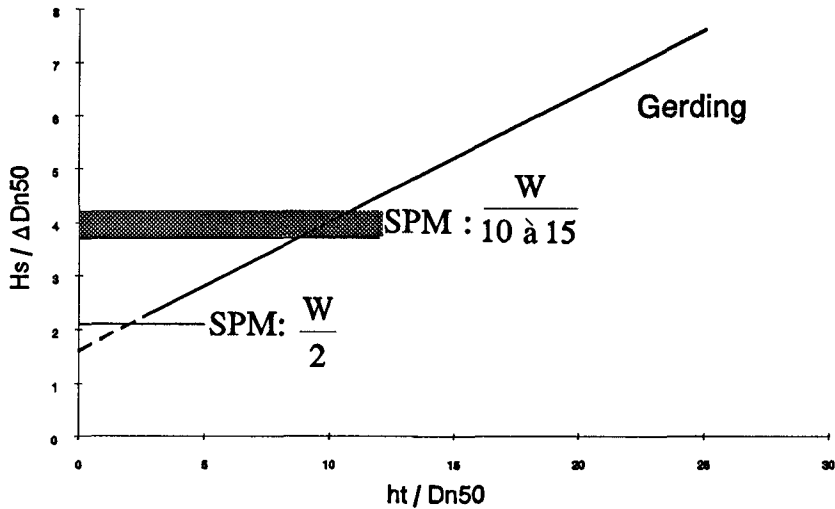


Figure 2 Existing relations for toe stability

Several other investigations on the stability of breakwater toes have been done. Van der Meer et al., 1995 presented the following expression, based on the MSc work of Gerding at Delft University of Technology (DUT):

$$\frac{H_s}{\Delta D_{n50}} = \left(0.24 \frac{h_t}{D_{n50}} + 1.6 \right) N_{od}^{0.15} \quad (1)$$

in which N_{od} is defined as the number of stones removed from the toe structure divided by the number of stones in a strip with a width of one D_{n50} and a length equal to the width of the test section (Van der Meer, 1993)

In this equation, the submergence of the toe is expressed as h_t/D_{n50} instead of h/H_s , since that gave a better fit with the experimental data. Figure 2 shows equation (1) for $N_{od} = 0.5$ (threshold of motion), together with the values from the Shore Protection Manual.

The stability parameter, $H_s/\Delta D_{n50}$, in equation (1) contains the relative density of the stones of which the toe structure consists. In the tests on which the equation is based, however, Δ was constant. The question therefore remains whether the influence of Δ is represented correctly in the equation. For another MSc-thesis, see Docters van Leeuwen, 1996, tests were done with a range of stone densities in order to check this.

The second item in this paper is an attempt to link the experimental results to the wave motion in front of the breakwater. Hydraulic engineering knows (too) many empirical relations. This makes application without sufficient knowledge of the backgrounds dangerous. The hydraulic engineering department at DUT has a policy, for reasons of didactics, to try to relate as much as possible stability of stones to the water motion.

2. EXPERIMENTS

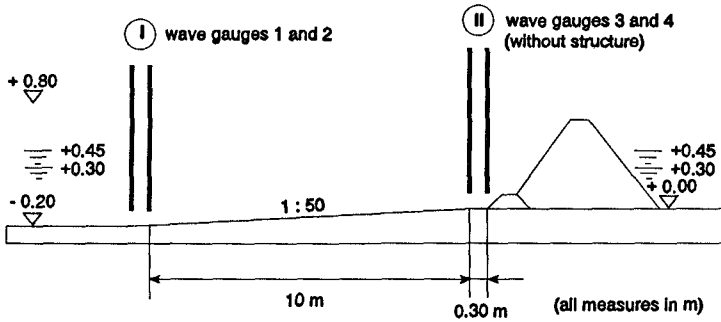


Figure 3 Test set-up in wave flume

The tests were performed in a wave flume (length 40 m, width 0.8 m and depth 0.9 m) at the Laboratory of Fluid Mechanics at Delft University of Technology (DUT). An overview of the test set-up is given in Figure 3. In the flume a fixed bed foreshore with a slope of 1:50 was constructed. The length of the foreshore was 10 m. The rubble mound breakwater and toe structure were placed on a horizontal bed at a distance of 0.3 m from the end of the foreshore.

Irregular waves were generated according to a JONSWAP-spectrum. During a test the significant wave height was increased in 4 steps from about 0.1 m up till about 0.2 m. The peak period to match followed from the selected steepness s_{op} . In the research of Gerding the influence of the wave steepness on the stability of the stones in the toe appeared to be small (due to the selected steep front slope giving little variation in reflection with the wave steepness, hence in load on the toe). Therefore the steepness was kept constant at a value $s_{op} = 0.04$.

The wave heights used in the analysis are the measured wave heights at the beginning of the foreshore, reduced with the reflection and adapted for shoaling due to the sloped foreshore. The in this manner processed wave heights are indicated as incoming wave heights. The wave generator was provided with a reflection compensation. During the tests an average value of the reflection coefficient $C_r = 0.25$ was found with a minimum of 0.185 and a maximum of 0.315.

The breakwater was constructed with rubble according to Figure 4 to create a porous structure with a reflection coefficient similar to the one in prototype. The front slope was kept constant (2:3).

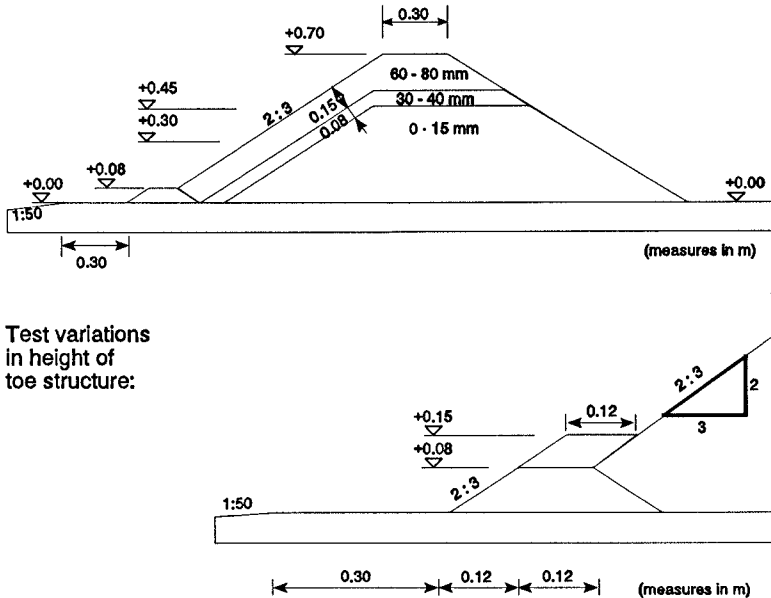


Figure 4 Cross-sections tested breakwater with toe

The tests by Gerding showed little to no influence of the width of the toe, therefore the toe structure width, b , (perpendicular to the length axis of the breakwater) was kept constant (0.12 m). Two toe heights were used in the tests, namely $z_t = 0.08$ m and 0.15 m. Each toe height was tested for two water depths $h_m = 0.30$ m and 0.45 m in front of the toe structure (0.50 m and 0.65 m at the beginning of the foreshore respectively). For the rubble of the toe structure three different materials with varying size were used:

Material	ρ (kg/m ³)	D_{n50} (mm)	D_{n85}/D_{n15}
basalt	2850	10.2	1.4
basalt	2850	15.1	1.2
porphyry	2550	9.8	1.34
porphyry	2550	14.4	1.31
porphyry	2550	21.0	1.26
brick	1900	23.1	1.45

The use of 6 stone types (ρ, D_{n50}), 2 waterdepth, 2 toe heights and 4 different wave heights led to a total number of 96 tests.

After each test the damage was determined by counting and weighing the total number of stones removed from the toe structure in the seaward direction. The damage is expressed with the damage number N_{od} .

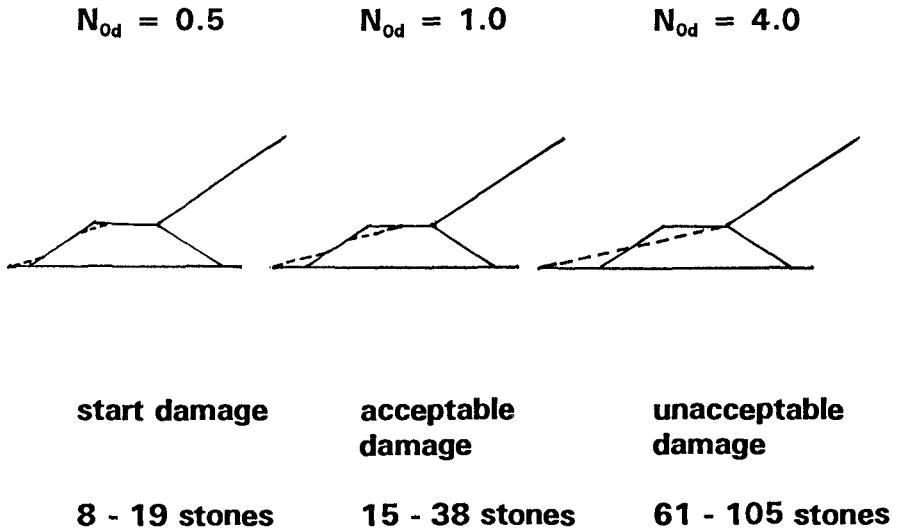


Figure 5 Sketch of damage for various values of N_{od}

Figure 5 shows various damage stages. $N_{od} = 0.5$ was chosen as the threshold of motion in this study.

N.B. Gerding found in his tests no influence of the berm width on the damage level. Of course, the acceptability of damage does depend on the berm width.

3. RESULTS

For the 96 tests, mentioned in the previous section, the damage results were plotted against the (incoming) wave height. Figure 6 shows an example of these results.

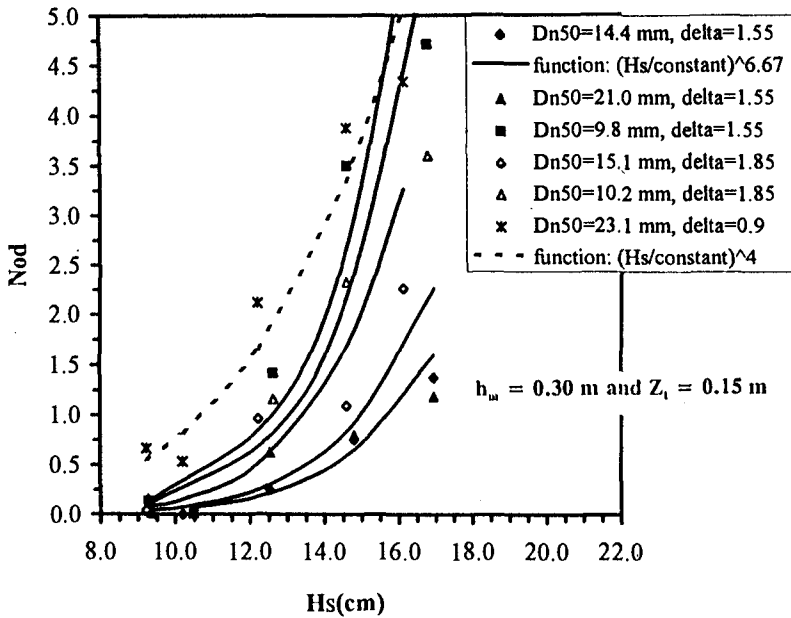


Figure 6 Example of damage as function of wave height

First, to check the influence of the density in the Gerding formula, $(H_s/\Delta D_{n50})/N_{0d}^{0.15}$ was plotted against h_t/D_{n50} . The results showed considerable scatter, making it difficult to draw a firm conclusion on the influence of Δ in the equation. Figure 7 shows the results limited to the threshold of motion, $N_{0d} = 0.5$. There is no clear distinction in this graph between the result points for the various densities. This justifies, for practical purposes, the use of $H_s/\Delta D_{n50}$ as a single stability parameter, indicating that there is no secondary effect of Δ on the stability (of course, there is a primary effect of Δ via the stability parameter).

In a more detailed investigation into the scatter of the results as presented in Figure 7, the data was also sorted out for toe height and waterdepth with the same horizontal and vertical axis. The toe height appeared to give no difference, but the waterdepth h_m shows definitely two different lines, see Figure 8. This makes that h_m should be involved, actually, in the stability relation, equation (1), although the differences are small.

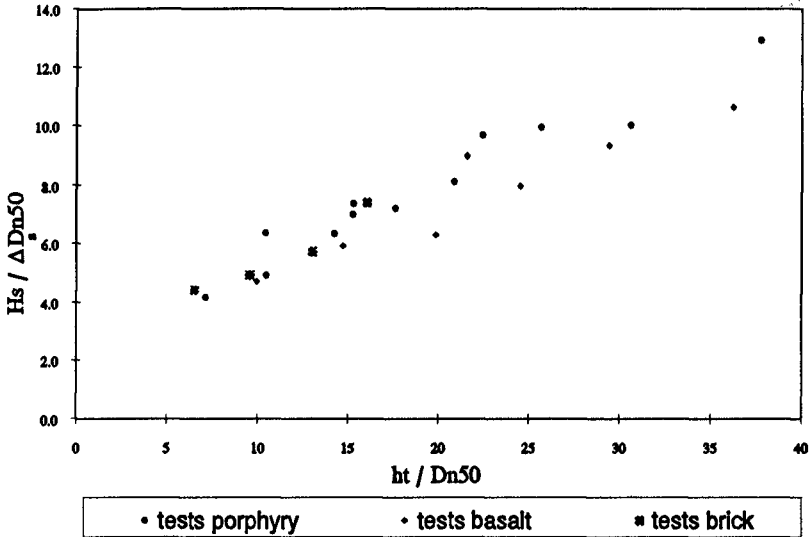


Figure 7 Stability sorted out to stone density

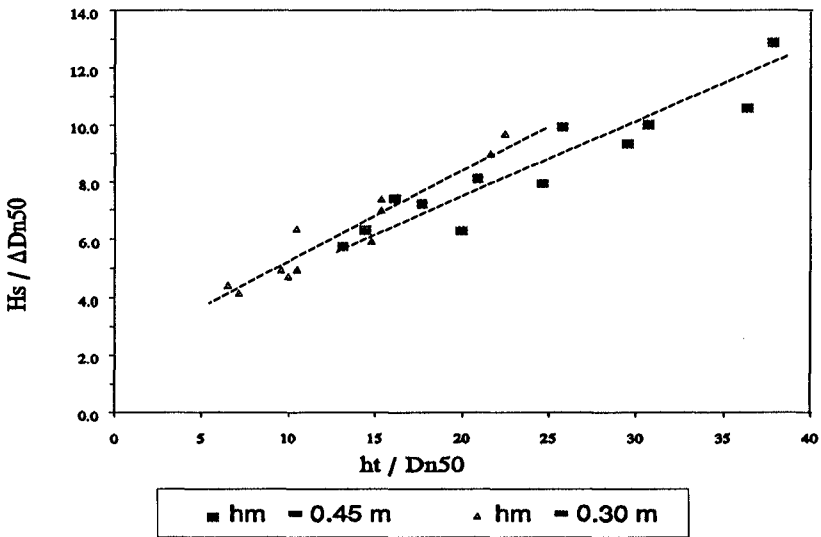


Figure 8 Stability sorted out to water depth h_m

4. COMPUTATIONS

Empirical relations like equation (1) are only valid for the range of parameters that has been investigated. Application outside that range can be dangerous. Closely related to this drawback is the fact that empirical relations contribute very little to the understanding of the phenomena involved. In an attempt to understand more of the mechanisms behind the stability of toe structures and to extend the range of applicability of existing relations, computations were done, in which the orbital wave motion was linked to the stability of stones in the toe of a breakwater.

The orbital motion at the toe surface (at $h_m - h_t$) is derived from the linear wave theory:

$$\hat{u}_h = \frac{\omega H}{2} \frac{\cosh k(h_m - h_t)}{\sinh kh_m} \quad (2)$$

where the hat denotes the amplitude of the orbital velocity. The stone stability in orbital motion is approximated with the experimental results of Rance & Warren, 1968, see also Schiereck et al., 1994:

$$\frac{a_h}{T^2 \Delta g} = 0.025 \left[\frac{a_h}{D_{50}} \right]^{-\frac{2}{3}} \quad (3)$$

in which a_h is the orbital stroke at the breakwater toe, which is equivalent to \hat{u}_h/ω .

Both equations need some adjustment. The orbital motion at the toe is not only due to incoming waves, but is also influenced by reflection from the breakwater. Furthermore, incipient motion will not be caused by H_s , but by a larger wave in an irregular wave field, e.g. $H_{1\%}$. Equation (2) is therefore rewritten into:

$$\hat{u}_h = \frac{\omega (1 + C_r) F * H_s}{2} \frac{\cosh k(h_m - h_t)}{\sinh kh_m} \quad (4)$$

in which F is a "tuning" factor.

In the tests by Rance & Warren, the sieve diameter D is used, while in the investigations by the authors, the nominal diameter D_n is used, which is somewhat smaller. With $D_{n50} \approx 0.84 * D_{50}$ and $a_h = \hat{u}_h/\omega$, equation (3) becomes:

$$D_{n50} = \frac{2.15 * \hat{u}_h^{2.5}}{\sqrt{T_P} * (\Delta g)^{1.5}} \quad (5)$$

With these two equations the necessary stone size was computed for incipient motion in the experiments ($N_{od} = 0.5$). The accompanying, measured, incoming wave height H_s was used, together with the measured reflection, C_r . The resulting, computed, diameters, together with the other relevant parameters from the tests, were adapted to the same dimensionless parameters as used with the test results, $H_s/\Delta D_{n50}$ and h_t/D_{n50} . Figure 9 shows the results.

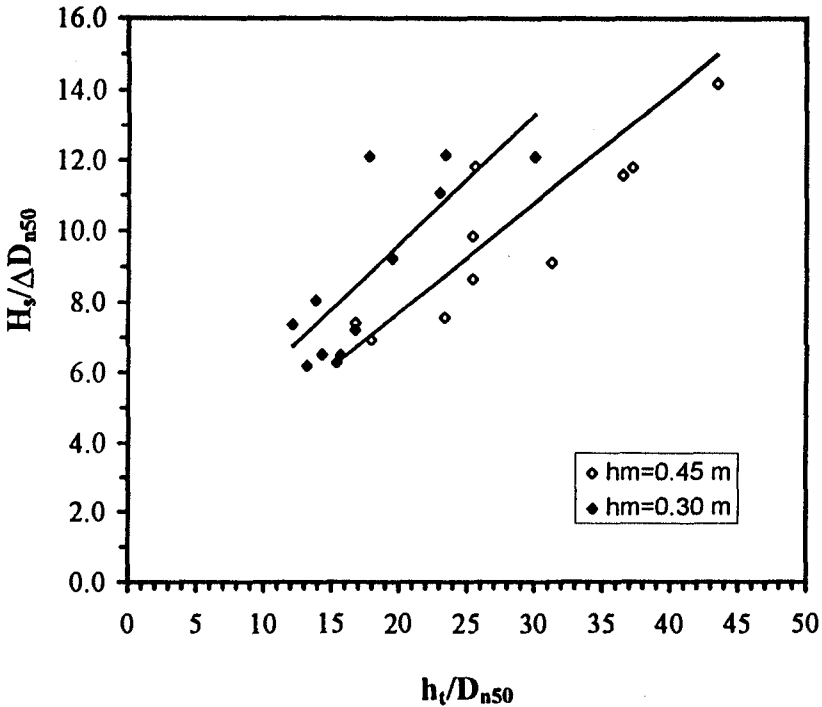


Figure 9 Results of computations

The tuning factor, necessary to give more or less equal results as the tests, appeared to be 1.7. This means that, assuming a Rayleigh distribution, $H_{0.5\%}$ is responsible for incipient motion, which seems reasonable. This, together with the trend of the computational results and the fact that the same influence of h_m is found in computations and experiments, is encouraging.

5. DISCUSSION

Stability of any structure is the relation between load and strength, in this case expressed as $H_s/\Delta D_{n50}$. The strength of a stone on the toe of a breakwater is expressed as ΔD_{n50} . This is, of course, a simplification of the strength mechanism in which e.g. also friction between the stones plays a role. The idea, however, exists that this is reasonably satisfying. The load is expressed as H_s which is a much more far-reaching simplification.

Stones in the toe of a breakwater move because of lift, drag and shear forces which again come from the velocity field in waves in front of the breakwater. This is a highly complex motion, even in a regular wave system, while, moreover, waves in nature are irregular. To this background it seems almost naive to try to catch the stability of stones in waves in simple formulas like equation (1).

Waves approaching a breakwater deform, mainly due to shoaling, bottom friction, reflection and breaking on the slope of the breakwater or the foreshore. All these processes can not be expressed by just including H_s as the single load parameter. The reflection, for example, plays definitely a role in the load on the toe, but is not used in equation (1), since the incoming wave is regarded as the load. This seems logically, since the incoming wave is the boundary condition as offered by nature. The reflection is a response of the structure, but any difference in this response is not expressed in the equation, so it will appear as scatter in the experimental results.

The only way to include these aspects, is a model in which the complete water motion is represented correctly. This is, however, not very practical. The procedure followed in this paper can be seen as a compromise between simplicity and correctly representing the physical processes involved. The path is promising enough to walk on. Results will not only be easier to understand and to explain, but there will also be a wider application. An example may be the design of a foundation sill under a vertical, caisson-type, breakwater, which is loaded in a very similar way.

6. CONCLUSIONS AND RECOMMENDATION

CONCLUSIONS

1. Tests in which the stone density is varied between $\rho = 1900$ and 2850 kg/m^3 show that there is no effect of the density on the stone stability in the relationship as proposed by Gerding:

$$\frac{H_s}{\Delta D_{n50}} = \left(0.24 \frac{h_t}{D_{n50}} + 1.6 \right) N_{od}^{0.15} \quad (6)$$

other than expressed in the stability parameter $H_s/\Delta D_{n50}$.

2. Simple computations, relating the orbital wave motion to the stone stability on the toe structure, give promising results.
3. Both computations and experiments show an influence of the waterdepth in front of the breakwater on the stability, which is not expressed in the Gerding's relationship.

RECOMMENDATION

It is worthwhile to put more effort into computations. Equations like Gerding's stability relationship have both the advantage and disadvantage of simplicity. The advantage is obvious, the disadvantage is that it is impossible to capture all aspects of the physical reality in one equation. Possibly a combination of hydrodynamic equations, describing the velocity field in the waves and experimental results, describing the relationship between the velocity field and the stone stability, leads to a relatively simple, but more comprehensive, model. Such a model, including the wave reflection caused by any structure, could be applied not only for toes of rubble mound breakwaters, but also for foundations of caisson type, vertical breakwaters.

SYMBOLS

b_t	width of the toe structure		m
D_{n50}	median nominal diameter of material	$(d_{n50} = (M_{50}/\rho_s)^{0.33})$	m
D_{50}	median sieve diameter of material		m
g	acceleration due to gravity		m/s ²
h_m	water depth near structure		m
h_t	water depth above the toe structure		m
H	wave height		m
H_s	significant wave height		m
k	wave number	$(k = 2\pi/L)$	1/m
L	wave length		m
L_0	deep-water wave length	$(L_0 = gT_p^2/2\pi)$	m
M	mass		kg
s	wave steepness	$(s = H/L_0)$	-
T_p	peak wave period of spectrum		s
\hat{u}	amplitude of orbital velocity		m/s
z_t	height of toe		m
Δ	relative mass density of material	$(\Delta = (\rho_s - \rho_w)/\rho_w)$	-
ρ_s	mass density of material		kg/m ³
ρ_w	mass density of water		kg/m ³
ω	angular frequency	$(\omega = 2\pi/T)$	1/s

REFERENCES

Docters van Leeuwen, L., *Toe stability of rubble-mound breakwaters*, MSc-thesis, Delft University of Technology, October 1996

Rance, P.J., and Warren, N.F., *The threshold of movement of coarse material in oscillatory flow* Proc. 11th Conf. on Coastal Engineering, London, pp. 487-491, 1968

Schiereck, G.J., Fontijn, H.A., Grote, W. and Sistermans, P.G.J., *Stability of rock on beaches*, Proceedings 21th Int. Conf. on Coastal Eng. ASCE, Kobe, 1994

Shore Protection Manual, Coastal Engineering Research Center, Waterways Experiment Station, Vicksburg Miss., U.S.A., 1984

Van der Meer, J.W., d'Angremond, K., and Gerding, E., *Toe structure stability of rubble mound breakwaters*, Proceedings Coastal Structures and Breakwaters, ICE, London, U.K., 1995

Van der Meer, J.W., *Conceptual design of rubble mound breakwaters*, Delft Hydraulics, Publication no 483, Delft, 1993

CHAPTER 154

SEAWALL EFFECTS ON HISTORICALLY RECEDING SHORELINES

Bryan N. Jones¹ and David R. Basco²

ABSTRACT

This paper presents the results of a study using 15 years of beach profile data to determine how the presence of seawalls influences the existing erosional trends of the beach at Sandbridge, Virginia (USA). Three analysis methods using historic and seasonal time scales were used to answer three questions about the possible effects seawalls may have on adjacent nonwalled beaches. The results show that, statistically, there is no difference in the erosion rates of walled and nonwalled beaches. Seasonal variability of volume is greater for walled profiles. Seasonal recovery rates for both profile types are similar. Finally, the claim that the erosion of landward volumes at nonwalled beaches is increasing due to the presence of nearby seawalls is not supported by the evidence at Sandbridge beach.

INTRODUCTION

Great debate has arisen over the long term impacts seawalls may or may not have on the erosion rate of an historically receding shoreline. An obstacle to the formation of definite conclusions about seawall and beach interaction is the lack of long term physical data, which must be collected prior to and following seawall construction. Kraus (1988), and Kraus and McDougal (1996), summarize the state of knowledge on seawall and beach interaction.

Sandbridge is a coastal residential and commercial community within the City of Virginia Beach, Virginia. Sandbridge is located 25 km south of Cape Henry at the entrance to the Chesapeake Bay and 25 km north of the Virginia-North Carolina border. The historical shoreline recession rate over the past 140 years varies linearly from -1.1 m/yr on the north end to -2.9 m/yr at the south end of the study area (Everts, et al., 1983; Dolan, 1985). The first seawalls were built at Sandbridge around 1978, with a peak construction period between 1987 and 1989. At present, about 62 percent of the study

¹Project Engineer, Collins Engineers Inc., 745 Bluecrab Road, Newport News, VA 23606.

²Professor, Coastal Engineering Program, Old Dominion University, Norfolk, VA 23529.

area is walled and 38 percent is nonwalled. The length of the study area is 7.7 km.

This paper presents a statistical analysis of subaerial beach profile data collected over the past 15 years in an effort to determine how the seawalls influence the existing erosional trends of the beach at Sandbridge, Virginia (USA). To achieve this goal, this study addresses the following three questions:

Question 1: Is the sand volume seaward of walled profiles disappearing at a faster rate than a similar volume defined at adjacent nonwalled profiles?

This question can be answered by analyzing the long term and seasonal trends for the volume of sand located seaward of the walls at walled and nonwalled profiles. A statistical analysis of profile data was performed to show any differences between the rate of change of these volumes. If the seawalls are responsible for increasing beach erosion, the trends should show that the volume seaward rate of change for the walls is greater than that for the nonwalled profiles.

Question 2: Are the seawalls responsible for delaying beach recovery during the seasonal transitions?

Another way in which seawalls may detrimentally affect beaches is by interfering with the processes responsible for the natural recovery of sand volumes with the change in seasons. This question can be answered by looking at when the walled and nonwalled profiles make their seasonal transitions.

Question 3: Following seawall construction, does the volume landward of an adjacent nonwalled profile erode at a faster rate than was previously recorded before the construction?

Because upland sand trapped by the seawalls is essentially removed from the littoral system, less sand is available to replace that removed by natural long-term erosion processes. If seawalls are increasing the erosion rate of the beach, then there should be evidence of an increase in the erosion rate of sand for the nonwalled profiles after the seawalls were built. This question is addressed by using 15 years of profile data divided into time intervals before and after construction of nearby walls.

DATA COLLECTION AND ARCHIVES

In August 1990, Old Dominion University began collecting subaerial beach profile data at 28 locations along a 7.7 km study area at Sandbridge. Surveys were made at these locations monthly and following significant coastal storms. Other agencies, including the City of Virginia Beach, have contributed profile data collected over the past 15 years at Sandbridge. At present, 13 of the ODU profiles are located at walled sections and 15 are located at nonwalled (dune) sections. The current data set contains more than 2700 profiles taken at 53 different locations over 15 years (October 1980 to September 1995). The 15 year data set includes several years before and after a boom in seawall

construction during the late 1980's.

Volumetric beach parameters were defined to quantify changes in space and time, as shown in Figure 1. For profiles at walled locations, the volume of sand located seaward of the wall and above MLW is called the volume seaward (V_S). Volume landward (V_L), therefore, is the volume of sand located behind the wall, down to the MLW elevation. For profiles at nonwalled locations, an imaginary partition is extended from adjacent walls parallel to the shoreline. This imaginary partition becomes the boundary separating V_S and V_L for the nonwalled profiles. The volumetric parameters (V_S and V_L) are the best indicators of long-term beach erosion trends for this study, using volume loss with time as the key variable of interest (Basco, et al., 1996).

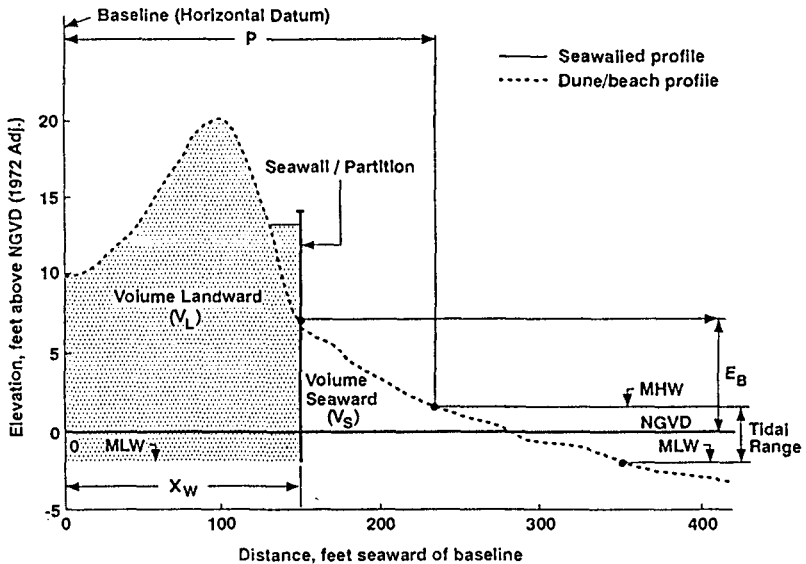


Figure 1. Beach Parameter Definitions.

The measured volumetric beach parameters are known to vary with the seasons. In general, subaerial beach sand is dragged offshore onto bars during frequent storms in the winter months (October to March), and is pushed back onto the beach by the long swells of the summer (April to September). The seasonal variability was modeled as a sinusoidal wave with a period of one year. The seasonal amplitude of the sinusoidal wave was found using the value that produced the least variance between the measured parameter and the calculated seasonal signal. A linear regression analysis using the method of least squares was performed to estimate the annual rate of change for each profile parameter and each profile type. The null hypothesis test was performed to determine if one parameter's slope was statistically greater than the other.

ANALYSIS METHODS

Over the five-year ODU monitoring study, three methods were developed to analyze the observed changes in V_s and V_L . These methods included the Weighted Average Method (WAM), the Sectional Weighted Average Method (WAMSECT), and the Individual Profile Method (IPM).

The WAM method used only the 28 ODU profile locations surveyed since October 1990, and was useful to characterize generalized beach change for the entire study area. The 28 profiles were grouped into two sets by type, walled or nonwalled (dune). Each profile was assigned a representative length of beach which was assumed to represent the walled or nonwalled conditions along that particular length of shore. For each profile, the volumetric parameters were multiplied by that profile's representative length. All of the wall profile products were then summed for each parameter, then divided by the total wall length. The result was a set of weighted averaged parameters (V_s and V_L) for each survey that singularly represented the walled profiles at Sandbridge. A set of weighted average nonwalled profile parameters were found in the same manner, using different representative lengths of nonwalled beach.

The Sectional Weighted Average Method (WAMSECT) divided the Sandbridge study area into three distinct reaches (North End, Middle Section, South End) to recognize differences in barrier island elevation and historic shoreline erosion rates. As with the WAM, weighted averages were employed for each type (walled or nonwalled) based on the lengths of walled and nonwalled beach in each section.

Differences in the parameter change rates before and after seawall construction were studied using the individual profile method (IPM). Beach profiles taken prior to October 1990 varied in location, and were not sufficient in number to permit accurate use of the WAM or WAMSECT averaging methods. The volumetric beach parameters were calculated for all surveys dating back to October 1980 for each profile, thus permitting the profile history to be analyzed beyond the five years of ODU monitoring. Parameter rates of change could then be compared for the periods of time before and after wall construction, but only for each individual profile location. The results of this analysis could then be used to form conclusions regarding Question No. 3.

RESULTS

Seasonal trends are best identified by plotting the WAM and WAMSECT results for the volume seaward difference (ΔV_s) for the five full wave years of ODU profile data. The initial value of each parameter is taken as the regression line intercept for October 1, 1990. The differences, therefore, represent the change in time over five years. Comparisons of the trends between walled and nonwalled profiles were made in an attempt to find supporting evidence for Questions No. 1 and No. 2. Transition from winter to summer was defined by when the ΔV_s parameter passed from below to above the regression line for each profile type. Likewise, the summer to winter transition was said to occur once the ΔV_s parameter moved below the regression line.

WAM Results

Using the WAM, Figures 2 and 3 show the long term change in ΔV_s for the walled and nonwalled profiles, respectively. The negative regression slopes in these figures demonstrate the imbalance of the seasonal cycle, which is caused by the chronic long term erosion rates at Sandbridge. Volume seaward from the walled and nonwalled profiles is disappearing at yearly rates of $1.58 \text{ m}^3/\text{m}$ and $1.80 \text{ m}^3/\text{m}$, respectively. This difference in the change rates of the two profile types is not statistically significant, as determined from the null-hypothesis test.

It is apparent from Figures 2 and 3 that the winters of 1992-1993 and 1994-1995 were the most severe. Volumes seaward in each of these years were below the mean decreasing value for each profile type. By comparison, the winters of 1990, 1991 and 1993-1994 were very mild. The summer beach rebuilding periods also demonstrate variability from year to year. With the exception of the 1994-1995 wave year, the walled profiles recovered to about $\Delta V_s = +7 \text{ m}^3/\text{m}$ during each summer, which was the summer value prior to October 1990. In contrast, the nonwalled sections continued to fall below the seaward volume present during the summer of 1990.

A comparison of seasonal transition times showed that the walled profiles recovered in the summer of 1991 first. The dunes made the summer transition first in 1992. Both profile types recovered simultaneously in 1993 and 1994. In 1995, the severely eroded beach never quite recovered in front of the walls while the dunes eventually did recover near the end of the summer season. The summer to winter transitions occurred at the same time for both types in 1990, 1992, 1993, and 1994. In 1991 and 1995, the winter transition was observed earlier for the dune sections.

WAMSECT Results

Figures 4 and 5 show the trends in the North End seaward volumes for walls and dunes, respectively. Similar plots were generated for walled and nonwalled profiles in the Middle Section and South End. Differences in the rates of change and seasonal variation amplitudes between each WAMSECT subsection are apparent. The results of the WAMSECT linear regression analysis of volumetric change rates are summarized in Table 1.

At the North End, the linear regression analysis showed that the ΔV_s rates of change for dunes and walls are negative and statistically equivalent. In addition, the amplitudes of the calculated seasonal variation are also equivalent. Beach recovery following the winter season occurred simultaneously for both profile types from 1990 to 1993. The walled profiles recovered first in the 1993-1994 wave year. Wave year 1994-1995 was characterized by two hurricanes along the mid-atlantic coast (Gordon, Nov. 1994 and Felix, Aug. 1995) in addition to a stronger wave climate generated by hurricane activity in the Caribbean. While the nonwalled profiles eventually recovered, the data shows ΔV_s for the walled profiles never recovered above the regression line for this section. Both profile types made the transition from "summer" to "winter" characteristics (seasonal erosion) around the same time for the first four years of the

WAM Wall - Volume Seaward

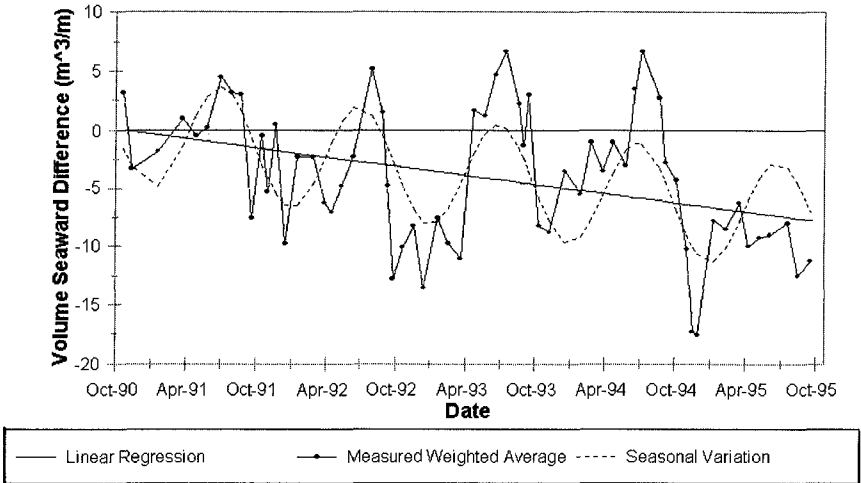


Figure 2 WAM seasonal variations in volume seaward for walled profiles.

WAM Dune - Volume Seaward

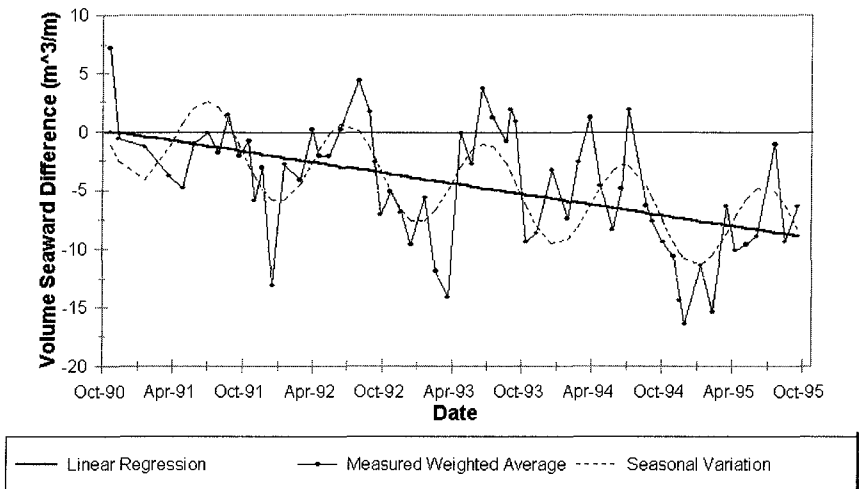
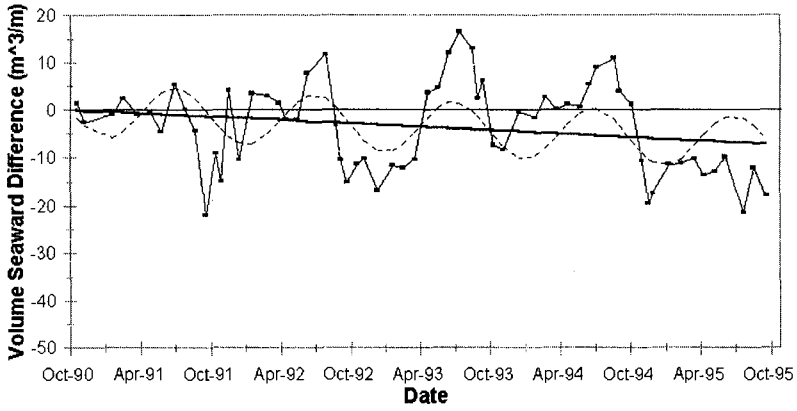


Figure 3 WAM seasonal variations in volume seaward for nonwalled profiles.

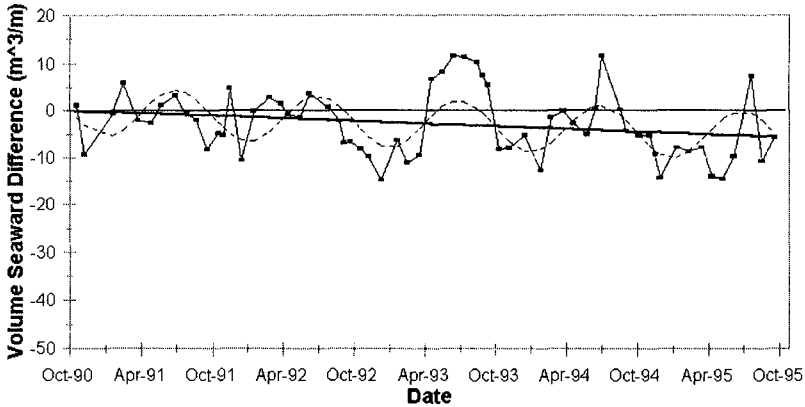
WAMSECT Wall - Volume Seaward North End



— Linear Regression — Measured Weighted Average - - - Seasonal Variation

Figure 4 North End WAMSECT Seasonal Variations in Vs for walled profiles.

WAMSECT Dune - Volume Seaward North End



— Linear Regression — Measured Weighted Average - - - Seasonal Variation

Figure 5 North End WAMSECT seasonal variations in Vs for nonwalled profiles.

Table 1. WAMSECT volumetric rates of change.

	Profile Type	WAMSECT Subsection					
		North End Oct 90 - Sept 95		Middle Section Oct 90 - Sept 95		South End Oct 90 - Sept 95	
		Rate of Change	Seasonal Amplitude	Rate of Change	Seasonal Amplitude	Rate of Change	Seasonal Amplitude
ΔV_s (m^3/myr)	Wall	-1.44	-5.6	-0.61	-6.8	-3.2	-2.5
	Dune	-1.14	-5.2	-1.50	-3.6	-4.0	-3.9
Sectional make-up (by length)		75% walled		44% walled		73% walled	
		25% nonwalled		56% nonwalled		27% nonwalled	

ODU study. During the stormy 1994-1995 season, the dunes made the transition first.

The results for the Middle Section showed the rates of change for ΔV_s were statistically equivalent for both walled and nonwalled profiles. Seasonal amplitudes in ΔV_s were greater for the walled profiles in this region. Beach recovery occurred simultaneously for both profile types in the first three years (1990-1993). The walled profiles recovered before the nonwalled profiles in the 1993-1994 summer season. Like the North End, the walled profiles never recovered above the regression line following the stormy 1994-1995 season. Transition from summer to winter levels occurred first for the walled profiles in 1990-1991. Both profile types changed at the same time in the three years between 1991-1994. The nonwalled profiles eroded to winter levels before the walls in the turbulent 1994-1995 wave year.

As in the North End and Middle Section, the rates of change for ΔV_s in the South End are statistically equivalent for both walled and nonwalled profile types. The greater historic erosion rates for the South End are clearly demonstrated by the greater change rates in Table 1. The walled profiles recovered first during the summer beach rebuilding season for the first two years of the study (1990-1992). In the 1990-1991 season, however, the nonwalled profiles did not recover above the ΔV_s regression line. In the remaining three years of the study, both profile types recovered simultaneously. Seasonal transition from summer to winter occurred at the same time for walled and nonwalled profiles for 1990-1994. The 1994-1995 season showed that the walls eroded to winter levels before the dunes, conflicting the trends observed for this wave year in the North and Middle regions.

IPM Long-Term Rates of Change

Comparisons of the volume rates of change for each of the profiles used in the IPM were made in three groups (North End, Middle Section, and South End) to recognize the regional differences in physical characteristics. The key variable is V_L of

the seawall or partition. A large decrease in the V_L after adjacent wall construction meant that Question No. 3 was supported, i.e., at one profile location, the volume of sand retained behind nearby walls is unavailable, causing adjacent, nonwalled locations to erode at a faster rate. Profile 1 is a good example as shown in Figure 6. For eight years (October 1980 - July 1988) and for 24 surveys, V_L "before" nearby wall construction was $+0.8 \text{ m}^3/\text{m}/\text{yr}$. Seawalls were built during the spring of 1989 about 30m south of Profile No. 1 so that for five years (July 1989 - June 1994) with 54 surveys the rate became $-9.0 \text{ m}^3/\text{m}/\text{yr}$. Unfortunately, the lot owner at Profile No. 1 leveled the dune in June 1994, so that some question remains as to how much affect the adjacent wall really has at this location.

By this same method of comparison for other profiles in the North End, supporting evidence does exist for Question No. 3. However, this is not true for the Middle Section or South End. A conflicting example in the Middle section lies at Profile 161. Figure 7 shows a similar eight year period (October 1980 - October 1988) for this profile. After 50 surveys, V_L "before" nearby construction was $-2.2 \text{ m}^3/\text{m}/\text{yr}$. Seawalls were built during 1989 starting 30m south so that after 5 years and 70 surveys, the "after" rate became $-0.8 \text{ m}^3/\text{m}/\text{yr}$. This evidence, and many other examples in the Middle section does not support Question No. 3. The South End includes both supporting, nonsupporting and inconclusive results so that it must be concluded that the evidence is inconclusive for this region.

Non-Wall Profile No. 1 Sand Volume

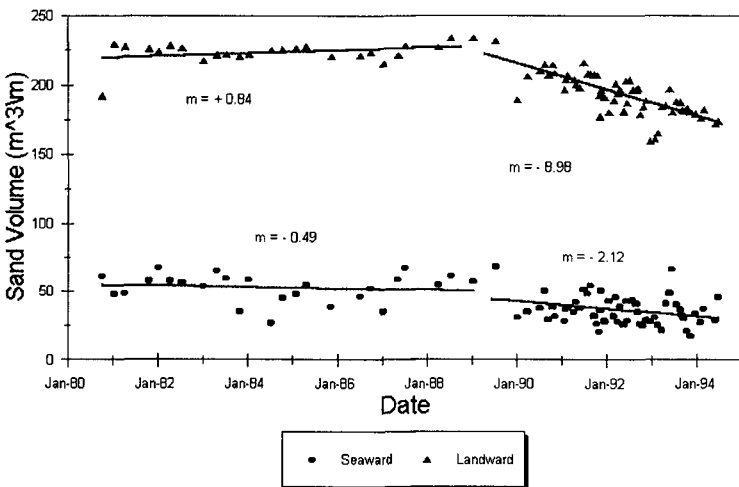


Figure 6 IPM analysis of Profile 1. Supporting evidence for Question No. 3.

Non-Wall Profile No. 161 Sand Volume

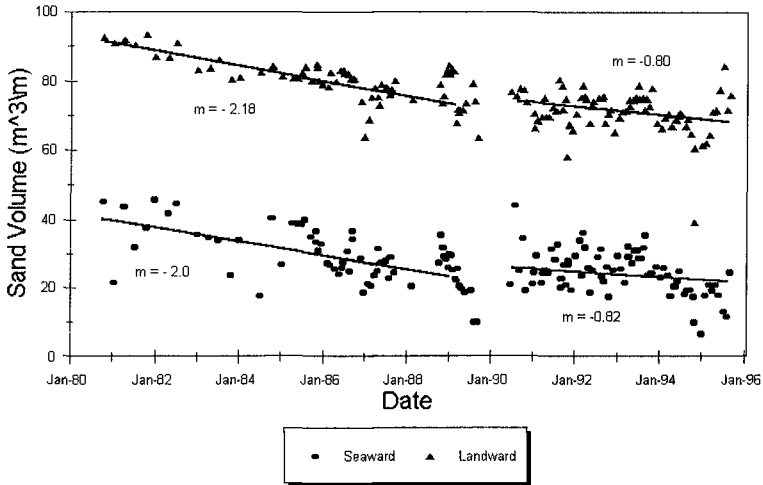


Figure 7 IPM analysis of Profile 161. Nonsupporting evidence for Question 3.

SUMMARY

The three basic methods (WAM, WAMSECT, and IPM) used in this study consider seawall and beach interaction on an increasingly more focused spatial scale. The WAM model provides trends for the Sandbridge area as a whole. The WAMSECT model concentrates on the effects of seawalls on a more localized level, and the IPM method considers each profile separately. Long-term effects are obtained from the results of all three methods using the five year ODU data set (15 years for profiles in the IPM). Seasonal variations are seen using both the WAM and WAMSECT methods.

Question No. 1: Does the sand volume seaward of the walls erode faster than a similar volume defined at adjacent nonwalled profiles?

Statistical comparison of parameter change rates (ΔV_s) using the null-hypothesis test revealed that the erosional trends are *statistically equal* for walled and nonwalled profiles. The results are the same for the WAM analysis and for each section in the WAMSECT analysis. Using five years of statistical data, there is no evidence to support the conclusion that the seaward volumes in front of seawalls is disappearing any faster than the seaward volumes in front of nonwalled profiles.

Seasonal variations in seaward volume were modeled using the five-year WAM and WAMSECT data. The WAM results show the amplitude of the seasonal variation

in V_s is greater for walled profiles. Because seawalls provide an impermeable barrier for cross-shore transport, sand is piled up against the walls by long period swells during seasonal recovery, resulting in larger relative seaward volumes for walled profiles during the summer. Likewise, winter erosion removes more sand from in front of the walls, since sand located landward of the partition is readily available to replenish sand removed seaward at the nonwalled profiles.

In the North End, the seasonal amplitudes for V_s were found to be the same for both profile types. Seasonal amplitudes in V_s were highest for walls in the Middle Section. The results indicate that the five-year seasonal variations in V_s are greater for the nonwalled profiles in the South End. Because not as much sand is available to replace that removed from in front of the walls during seasonal transitions, we might expect the walled profile variations to be less for the South End than in the North End and Middle Section.

Question No. 2: Do seawalls delay beach recovery during seasonal transitions?

Seasonal beach recovery was studied using the WAM and WAMSECT results over the five-year ODU monitoring period. Using the WAM, seasonal transitions generally occurred about the same time for both walled and nonwalled profiles. During the abnormally high erosion experienced by storm activity in the 1994-1995 wave year, the nonwalled sections eventually recovered while the walled sections did not. Continued monitoring for 1995-1996, however, shows that the walled profiles have recovered.

The North End WAMSECT trends indicate that seasonal beach recovery occurred simultaneously for both profile types in three of the five years studied. In 1995, the walled profiles never recovered above the regression line. In the Middle Section, seasonal recovery also occurred simultaneously for both profile types in three of five years. As in the North End, the walled profiles did not recover above the regression line in 1995. As for the South End, seasonal beach recovery for walls and dunes occurred at the same time for the last three years of this study.

Question No. 3: Does seawall construction increase the natural erosion rate of the sand volume landward of the walls at adjacent nonwalled locations?

After a seawall has been built, the sand trapped behind the wall is no longer available for transport to adjacent beaches during storms. This reduction in sediment supply is thought to place additional erosional pressure on beaches adjacent to walls. The IPM was the only method which provided enough long term data to form conclusions regarding Question No. 3. Linear regression was used to determine trends in the nonwalled V_L parameter before and after seawall construction. The individual profile results were compared according to region (North End, Middle Section, South End).

In the North End, evidence exists to support Question No. 3. None of the Middle Section profiles demonstrated an increase erosion rates, in fact, each of the profiles compared showed evidence to argue that erosion rates *decreased* following the

nearly addition of seawalls. The IPM results for the South End are inconclusive and include two instances where no significant change was noted, one instance where the change rate decreased, and one where the rate increased.

CONCLUSIONS

Seawalls are not responsible for the erosion problem at Sandbridge, they are a result of it. Three different spatial and time scales have been used to analyze fifteen years of subaerial beach profile data. While the results clearly show differences in short term coastal processes between walled and nonwalled beaches, the long-term and seasonal effects are very nearly the same.

With regard to Question No. 1, the results from the five-year WAM and WAMSECT trends clearly indicate that volumes seaward of walls *are not* eroding faster than volumes in front of nonwalled profiles. These results are consistent with the conclusions made by other researchers reviewed in Kraus (1988), and Kraus and McDougal (1996). The results do show that seasonal variation in volume is greater for walled profiles, however, these variations are temporary.

The results for Question No. 2 show that seawalls *do not* inhibit seasonal recovery for either profile type. The five-year seasonal recovery trends using both the WAM and WAMSECT methods yielded the same results.

Despite the use of over 15 years of profile data, no clear conclusions can yet be made regarding Question No. 3. Comparison of change rates before and after seawall construction yielded supporting evidence in the North End, nonsupporting evidence in the Middle Section, and inconclusive results for the South End. The results for the study area as a whole, therefore, must be considered inconclusive for Question No. 3.

The study at Sandbridge is continuing. As the ratio of volume trapped behind the seawalls to that remaining on the subaerial beach increases, some evidence to support Question No. 3 may be found in the future.

ACKNOWLEDGMENTS

Special thanks are due to the following graduate students who participated in the ODU beach monitoring program at Sandbridge over the course of this five year study: Tim Blankenship, Maolong Cai, Quin Chen, Gary Hobson, Bruce Husselbee, C.S. Shin, Murat Utku, Greg Ward and Rob Webb. The initial project engineer was Doug Bellomo, who was followed by John Hazelton.

This study was supported by the "Impacts of Coastal Armoring on Beaches" Work Unit (32747) of the USAE, Waterways Experiment Station (CERC), Vicksburg, MS. The conclusions are not necessarily those supported by the Army Corps of Engineers.

REFERENCES

Basco, D.R., Bellomo, D.A., Hazelton, J. M., and Jones, B. N. (1996) *The Influence of Seawalls on Subaerial Beach Volumes With Receding Shorelines*, Coastal Engineering Research Center, WES, U.S. Army Corps of Engineers, Vicksburg, MS. (In preparation)

Dolan, R. (1985) *Sandbridge Beach and Back Bay*, Tech. Rpt., Sandbridge Beach Restoration Association.

Everts, C.H., et al. (1983) *Shoreline Movements: Cape Henry, Virginia to Cape Hatteras, North Carolina, 1849-1980*, Rpt. No. 1, Tech. Rpt. CERC-83-1, U.S. Army Coastal Engrg. Res. Ctr., Vicksburg, MS.

Kraus, N.C. (1988) "The Effects of Seawalls on the Beach: An Extended Literature Review." *Journal of Coastal Research*, Spec. Iss., No. 4, Autumn.

Kraus, N.C. and McDougal, W.G. (1996) "The Effects of Seawalls on the Beach: Part I, An Updated Literature Review." *Journal of Coastal Research*, Summer.

CHAPTER 155

CONTROL OF WAVE PROPAGATION ANGLE BY TAPERED-SUBMERGED BREAKWATER

Satoshi TAKEWAKA¹ and Isao IRIE²

ABSTRACT

A new type of submerged breakwater with a triangular plane form which modifies the wave propagation angle is proposed. Its performance is demonstrated and assessed analytically. Preliminary movable bed experiments were conducted. The breakwater was installed in front of the beach to modify the wave propagation angle in the offshore zone. Longshore current and littoral drift were driven through the effect of wave angle modification.

INTRODUCTION

A beach remains stable in the long term when supply and loss of sediment are equally balanced. Offshore structures often break this equilibrium state and the beach profile as well as the shoreline configuration change to a new state, which resulting in erosion problems in most cases. The deformation of the shore may be suppressed when sediment movement of the original state is preserved by regulating the wave height and propagation angle by some offshore structures.

In this context, a new type of submerged breakwater with triangular plane-form, Tapered-Submerged Breakwater (hereafter referred as TSB), is proposed. Its functions are reduction of wave height by reflection and wave breaking, and modification of wave propagation angle on downwave side as shown in Fig. 1.

This study describes and evaluates the performance of TSB in controlling wave propagation angle. Then results of preliminary movable bed experiments are demonstrated, which were conducted to test out the applicability of TSB in regulating wave field, current system and sediment transport of a beach.

¹Research Associate, Dept. of Civil Eng., Kyushu University, Fukuoka, Japan 812-81.

Email : takewaka@civil.kyushu-u.ac.jp

²Professor, ditto, Email : irie@civil.kyushu-u.ac.jp

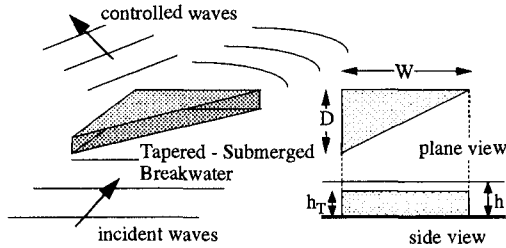


Figure 1 The concept of Tapered-Submerged Breakwater

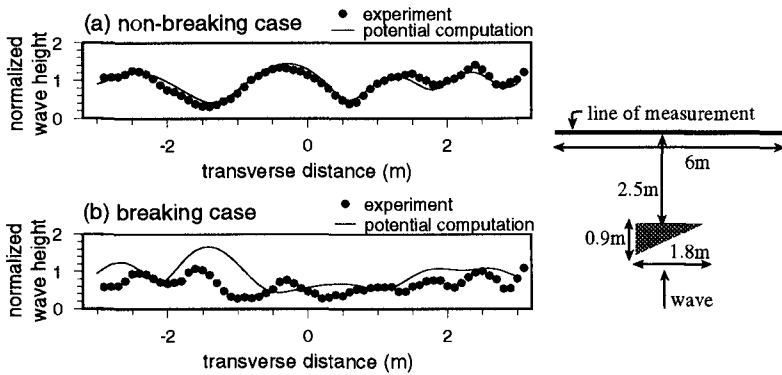


Figure 2 Normalized wave height distribution on downwave side of the breakwater. Wave height is normalized with the incident wave height. Experimental conditions : $T = 0.76s$, $h = 0.14m$, incident wave height = $0.015m$, $W = 1.8m$, $D = 0.9m$, (a) $h_T = 0.07m$, $h_T/h = 0.5$, (b) $h_T = 0.11m$, $h_T/h = 0.8$.

MODIFICATION OF WAVE PROPAGATION ANGLE

The shape of a TSB is characterized with three parameters, height of breakwater h_T , plane depth D and plane width W , as shown in Fig. 1. All these parameters were varied in a wide range in this study to find out an optimum configuration of TSB in wave angle modification.

Wave field around TSB subjected to regular incident waves was computed with *Collocation Method of Matched Eigenfunction Expansions* which was developed by Yoshida et al.(1992). This method provides linear potential solution of wave field over a submerged structure with an arbitrary plane form. Prior to the analytical work, experiments in a wave tank were made to examine the validity of the potential solutions. Figure 2(a) and (b) show the comparison of measured and computed wave height distribution normalized with the incident wave height on the downwave side of the TSB.

A fairly good agreement is observed in Fig. 2(a), while discrepancy becomes

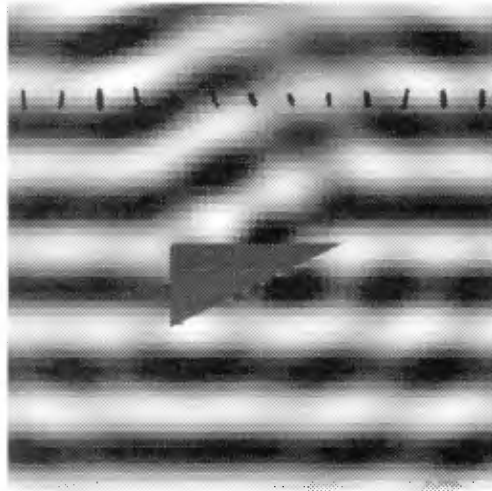


Figure 3 Wave pattern and trajectories of water particles. $T = 0.76s$, $h = 0.14m$, $W = 1.8m$, $D = 0.9m$, $h_T = 0.11m$, incident wave height = $0.01m$. Incident wave travels from bottom to top in the figure.

apparent in Fig. 2(b) where wave breaking above the TSB was observed in the experiment. Since the potential solution fails to describe the wave field when wave breaking occurs, this study concentrates on non-breaking cases.

The wave height distribution shown in Fig. 2(a) oscillates remarkably which is a typical feature of wave diffraction from submerged a structure. Since the plane form of the submerged body is asymmetric in this study, the most energetic part appears aside from the center of the wave height distribution. This is an indication that the TSB modifies the direction of wave energy propagation.

The distribution of instantaneous water surface elevation and the horizontal trajectories of the water particle motion around the TSB is shown in Fig. 3. The incident wave travels from bottom to top of the figure. The water surface are shaded in this figure with the highest levels being white and trajectories of water particles are depicted with solid lines. Declined crest lines are apparent on the downwave side of the TSB. The main semiaxes of the water particle trajectory are almost perpendicular to the crest line which assures that the waves travel obliquely to the incident.

EVALUATION OF THE WAVE ANGLE CONTROL PERFORMANCE

The performance of the wave propagation angle modification is assessed by analyzing the character of the potential solution provided from the Collocation Method. The Collocation Method gives the complex amplitude potential Φ for the wave field by superposing two solutions : (i) known incident wave solution

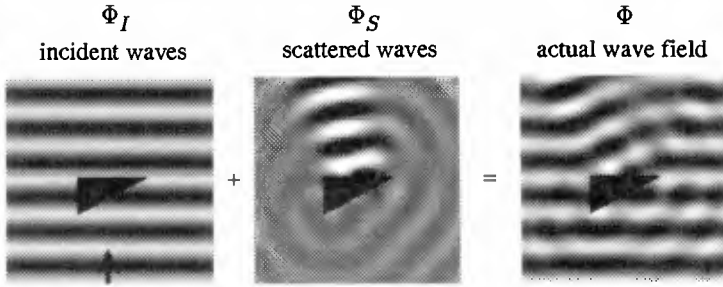


Figure 4 Collocation Method of Matched Eigenfunction Expansions

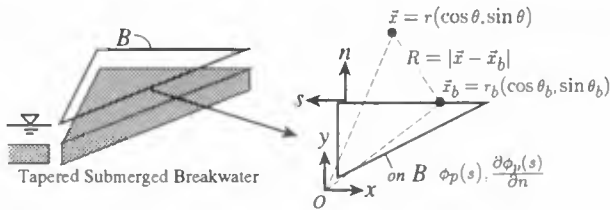


Figure 5 Definition of the symbols and integral path

Φ_I and (ii) unknown scattered wave solution Φ_S which is determined so that the whole solution ($\Phi = \Phi_I + \Phi_S$) satisfies the boundary conditions on the submerged body and Sommerfeld's radiation condition at far field (see Fig. 4).

The scattered wave solution Φ_S is expressed in terms of Green's law :

$$\Phi_S(r, \theta) = \oint_B \left\{ \phi_B(s) \frac{\partial}{\partial n} - \frac{\partial \phi_B(s)}{\partial n} \right\} G(R, \theta) ds. \tag{1}$$

Here, ϕ_B and $\frac{\partial \phi_B(s)}{\partial n}$ are the potential of the scattered waves and its derivatives on the path B above the breakwater as indicated in Fig. 5, and G is the Green function. Further definitions of the symbols are depicted in the same figure.

The scattered wave solution ϕ_B consists of evanescent wave mode ϕ_E and progressive wave mode ϕ_P . The former (ϕ_E) is apparent only in the close vicinity of the structure and the latter (ϕ_P) is the wave which travels to the infinity by decaying its amplitude. Neglecting the evanescent wave, following equation for the scattered wave solution is obtained which is valid except in the vicinity of the structure :

$$\Phi_S(r, \theta) = \frac{i}{4} \oint_B \left\{ \phi_P(s) \frac{\partial}{\partial n} - \frac{\partial \phi_P(s)}{\partial n} \right\} H_0^{(1)}(kR) ds \tag{2}$$

where $H_0^{(1)}$ is the Hankel function of the first kind of the 0th order and k is the wave number of the incident wave.

A further approximation is adapted to Eq.(2) to split it into radial part r and directional part θ . Following relationships of R for $r \gg r_b$ and Hankel function

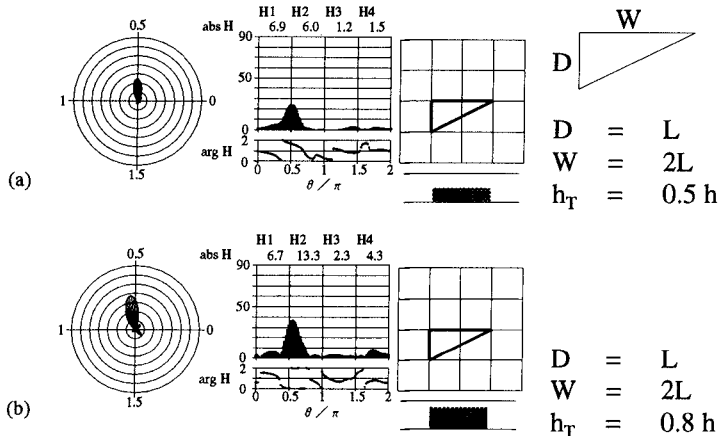


Figure 6 Distribution of Kochin function $H(\theta)$. L = incident wave length ($kh = 1.18$).

with large argument are substituted :

$$R = |\vec{x} - \vec{x}_b| \approx r - r_b \cos(\theta - \theta_b) \tag{3}$$

$$H_0^{(1)}(z) \approx \sqrt{\frac{2}{\pi z}} e^{i(z - \pi/4)} \tag{4}$$

$$\frac{dH_0^{(1)}(z)}{dz} = -H_1^{(1)}(z) \approx -\sqrt{\frac{2}{\pi z}} e^{i(z - 3\pi/4)}. \tag{5}$$

The result of the substitution is

$$\Phi_S(r, \theta) \approx -\frac{i}{4} \sqrt{\frac{2}{\pi kr}} e^{i(kr - \pi/4)} \times \oint_B \left\{ ik \cos(\theta - \theta_n(s)) \phi_P(s) + \frac{\partial \phi_P(s)}{\partial n} \right\} ds \tag{6}$$

where θ_n the angle of the integral path s to the y axis.

The scattered wave solution $\Phi_S(r, \theta)$ is now separated into radial part which expresses the decay of the scattered waves travelling to the infinity, and directional part which stands for the complex amplitude of the scattered waves. The directional part is termed as *Kochin function* $H(\theta)$ (Mei, 1983).

The wave angle modification performance is estimated by comparing the characteristics of the Kochin function distribution of different TSBs. The idea is to evaluate the directional amplitude of scattered waves from Kochin function and use it as a measure of the performance. Figure 6 shows the distributions of Kochin function for TSBs with the same plane form, but of different heights. The directional distribution of $H(\theta)$ is displayed in different expressions in the figure : left diagram displays magnitude of $H(\theta)$ as a radar chart and center diagram displays magnitude and phase of $H(\theta)$. Since the incident wave travels into $\theta = 0.5\pi$, scattered waves must have wave components which travel into

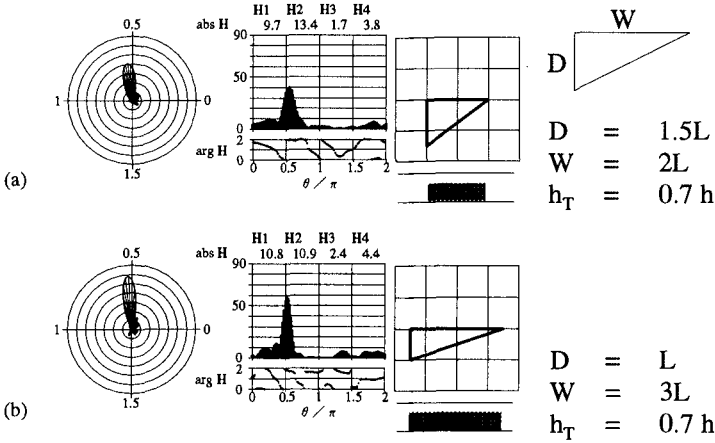


Figure 7 Distribution of Kochin function $H(\theta)$. L = incident wave length ($kh = 1.18$).

$0.5\pi < \theta < \pi$ if the wave angle modification is achieved properly. The comparison of the Kochin function distributions suggests that the TSB with larger height h_T is effective in wave angle modification.

Figure 7 shows the distributions of Kochin function for TSBs with the same height, but of different plane forms. It is hard to rate the efficiency of the two breakwaters from simple comparison of the Kochin function distributions. In this case, the integral of $H(\theta)$ in $0.5\pi < \theta < \pi$ (H_2) was estimated and used as a measure of the wave angle modification effect. The value of the integrals of different ranges is depicted in the top of the center diagram (H_1, H_2, H_3, H_4). The TSB with larger plane depth D is judged superior in wave angle modification, since it possesses a larger value.

A large number of tests for TSBs with different shapes were conducted to seek optimum configuration. It was found that heightening the height h_T and broadening the plane depth D of the breakwater enhance the effect of wave angle modification in general. It was also found that the plane depth D and the plane width W must be at least as large as incident wave length L , which means that the breakwater needs to a large structure to work well.

APPLICATION TO BED PROFILE MODIFICATION

Preliminary experiments on movable bed were conducted to test out the applicability of the TSB in topography modification. The experimental setup is shown in Fig. 8. The experiment is designed to observe the effect of wave angle modification in the offshore region on bottom topography variation and does not imply any realistic situation. The experiment started from a 1:10 slope beach made from fine glass beads with $0.08 \mu m$ mean diameter and 2.6 specific gravity.

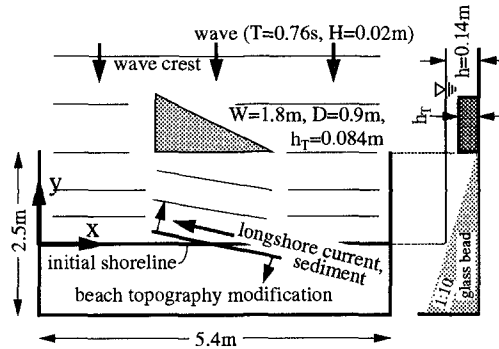


Figure 8 Experimental setup of the movable bed experiment

Regular waves with 0.76s period and 0.02m wave height were acted for 2 hours without installing the TSB to excite the initial off-onshore sediment movement. Then the TSB was installed in front of the slope and the experiment was proceeded further for 8 hours. Bed elevations were measured for several times during the experiment.

Figure 9(a) and (b) show the depth contour lines of the bed form at $t = 2hrs.$ and $t = 10hrs.$ for the run with single TSB. No wave breaking above the breakwater was observed. In the region of $1.7 < x < 2.8m$, the shoreline and the depth contour lines in front of it inclined remarkably at $t = 10hrs.$ which were almost straight and parallel at $t = 2hrs.$ This region was affected by the waves whose propagation angle was modified by the TSB. The distribution of total longshore sediment rate (Fig. 9(c)) estimated from the results of bed profile measurements shows that the sediment was transported unidirectional as a whole.

The wave angle modification accompanies wave concentration on the down-wave side of the breakwater which results in the alongshore variation of the wave breaking point. Accordant with this breaking point variation, several circulations cells along the shore were observed which transported sediments alongshore.

Numerical computations of the wave and current field were conducted to give insight of the sediment transport. The wave field was computed with parabolic mild slope equation starting from the initial value given by the potential solution described in the previous chapter. Flow field was computed with the conventional ADI method inputting the radiation stress derived from the wave field computation. Bed profile data measured in the experiment was entered for wave and current computations.

Figure 10(a) and (b) show the computed wave height distribution and flow field at $t = 2hrs.$ The effect of wave angle modification concentrates the waves. This is shown in the figure of wave height distribution as strips of contour lines of high and low wave region. Since the high waves break at an earlier stage, the distribution of the breaking points varies alongshore. Accordant with this variation, the distribution of radiation stresses becomes complicated, and several

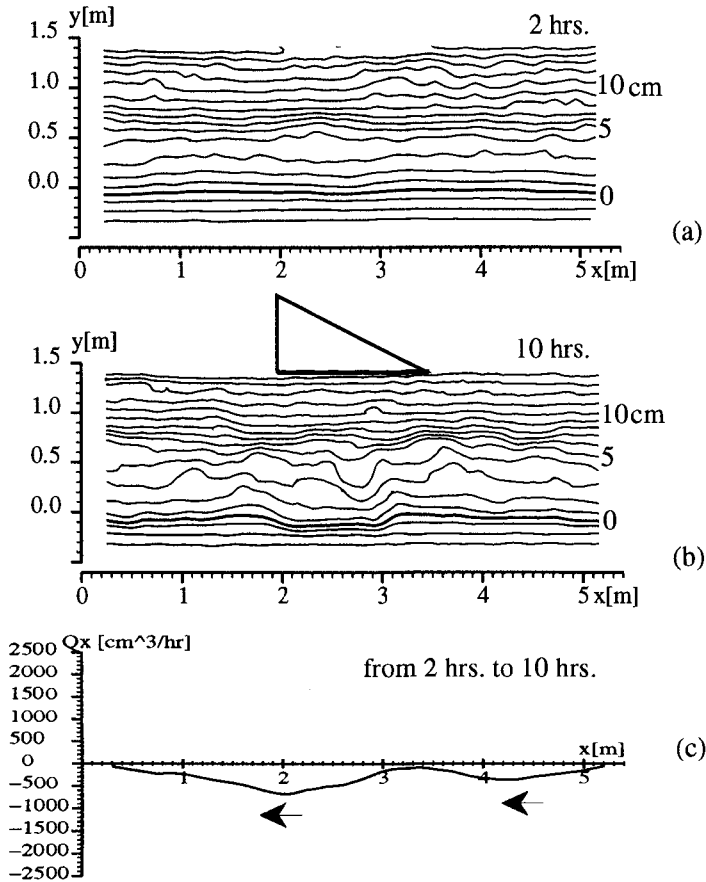


Figure 9 Resultant bed form and total longshore sediment rate, (a) $t = 2$ hrs., (b) $t = 10$ hrs., (c) Total longshore sediment rate (from $t = 2$ hrs. to $t = 10$ hrs.). $W = 1.5$ m, $D = 0.75$ m, $h_T = 0.084$ m.

circulation cells including two major counter-rotating cells are reproduced in the flow computation. Their number, position and scale agreed fairly with the experiment. It is supposed that the sediment is mainly transported by the current system. Bottom material is eroded where high waves attack. The current system then transports it as suspended sediment and deposits it finally where wave motion becomes calm.

Figure 11 shows the resultant bed form in case of two TSBs were installed in sequence. With this arrangement, it is expected that the effect of the wave angle modification extends to a wider range. The bed form at $t = 10$ hrs. shows that

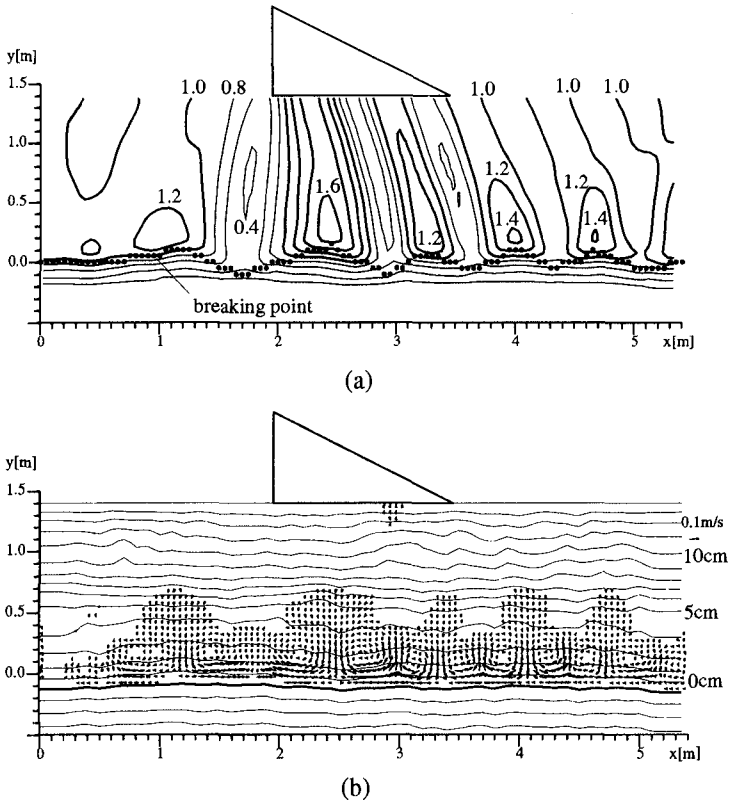


Figure 10 Computational result of wave and current system at $t = 2$ hrs., (a) Normalized wave height distribution and breaking points, (b) Current field and bed form. $W = 1.5m$, $D = 0.75m$, $h_T = 0.084m$.

each breakwater affected the sediment process individually. The distribution of total longshore sediment rate (not listed) indicates that the sediment is transported generally in the aimed direction in a wide range. It is, however, hard to conclude that the attempt is a full success. The shoreline, or depth contour lines become highly irregular and the beauty of the coast with gentle-curved or straight shoreline is lost. Further studies on this point, how to obtain a smoother shore line, are required.

CONCLUSIONS

A new type of submerged breakwater (Tapered submerged breakwater) which modifies the wave propagation angle is proposed. Its ability and performance were demonstrated and assessed analytically. TSBs with different shapes were

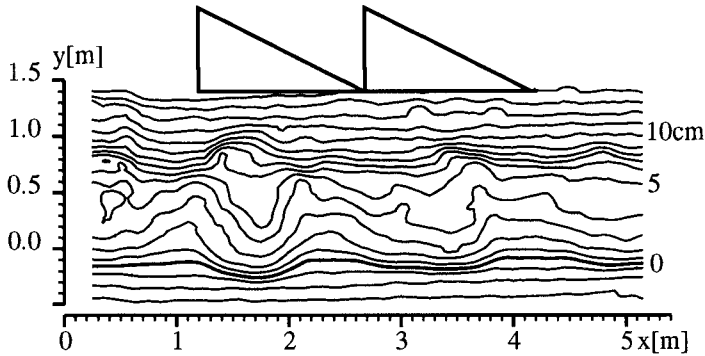


Figure 11 Resultant bed form at $t = 10\text{hrs.}$ for two TSBs run. $W = 1.5\text{m}$, $D = 0.75\text{m}$, $h_T = 0.084\text{m}$.

tested and it was found that broadening of the plane depth D and heightening the breakwater height h_T enhances the wave angle modification performance. It was also found that D and the plane width W of the TSB must be at least as large as incident wave length L to be effective. This means that the TSB needs to be a large structure to work well.

Preliminary movable bed experiments were conducted. The TSB was installed in front of the beach to modify the wave propagation angle in the offshore zone. The alongshore wave height distribution varied in the nearshore zone due to the effect of wave angle modification. Several flow circulations appeared subsequently which transported longshore sediment. The total longshore sediment rate indicates that the sediment moved unidirectional as a whole. The resultant bottom configuration, however, was highly irregular, even when two TSBs were installed in sequence. Further studies are required on this point to refine the conception acceptable.

ACKNOWLEDGMENT

Authors are indebted to Hiroshi Yamaguchi, graduate student of Kyushu University, for his collaboration in movable bed experiment.

REFERENCES

- Mei, C.C (1983) : The applied dynamics of ocean surface waves, World Scientific.
- Yoshida, A., Murakami K. and Ono M. (1992) : Collocation Method of Matched Eigenfunction Expansions, Proc. Japanese Conf. on Coastal Eng., JSCE, Vol.39, pp. 756 - 760 (in Japanese).

CHAPTER 156

MULTIDIRECTIONAL WAVE LOADS ON VERTICAL BREAKWATERS

Claudio Franco¹, Jentsie W. Van der Meer², Leopoldo Franco³

Abstract

An extensive 3-D model test program has been performed to study the effects of wave obliquity and multidirectionality on the hydraulic response of vertical (caisson) breakwaters. In this paper the results of the wave forces and pressures are shown. The measurements are compared with the Goda's formula with some divergences. The tests show that multidirectional wave loads do not reduce with increasing obliquity of the mean direction, whereas a reduction occurs for oblique long-crested waves. Three-dimensional effects on the uplift forces are better described by Goda formulations and smaller scatter is observed when comparing with measurements. The analysis of the longitudinal distribution of the horizontal pressures confirmed that the global wave load decays with increasing multidirectionality and obliquity, with clear advantages for the design of long monolithic breakwaters.

Introduction

The design of coastal structures has been typically based on formulae developed for head-on long crested waves. After the development of 3D basins in hydraulics laboratories, the effect of wave three-dimensionality on structure loading has been considered mainly for the design of offshore platforms. More recently 3-D waves were found to have influence also on the long period wave components associated to the short period waves which induce harbour oscillations (Bowers, 1987) or on the stability of rubble mound breakwaters (Galland, 1994). Very little attention has been addressed so far to the influence of wave multidirectionality on the response of vertical face structures in intermediate or shallow water .

¹ Ph.D. Student, DIAR, Politecnico di Milano, P.Leonardo da Vinci 32, 20133 Milano, Italy
² Dr., Delft Hydraulics, p.o.box 177, 2600 MH Delft (NL) e-mail: jentsie.vdmeer @wl.delft.nl
³ Prof. Eng., Dept.Civil Eng., 3rd University of Rome, via C.Segre 60, 00146 Rome, Italy, e-mail: leofranc@fenice.dsic.uniroma3.it

A 3-D model investigation has been carried out at Delft Hydraulics, within a joint European research project, in order to assess the effects of the obliquity and “multidirectionality” of wave attack on the hydraulic performance of caisson breakwaters. Tests have been performed with attack angles up to 60° to the normal and directional spreadings up to 30° on different structure geometries such as caissons with vertical plain wall, with perforated front wall, with an additional curved parapet and with a high impermeable slope and berm, measuring wave forces, horizontal and uplift pressures, reflection coefficients and overtopping.

Only the results of the analysis on horizontal and uplift forces on the plain wall vertical caisson are here presented in order to provide useful guidance for the design of caisson breakwaters. Comparisons are made with the more abundant results obtained by Goda (1985) on the simple vertical face structure under long-crested wave attacks.

Model setup and test conditions

The hydraulic model tests were carried out in the 26.4 m wide and 23 m long multidirectional-wave “Vinjè basin” at DH - De Voorst during summer 1994. The structure (Fig.1 and 2), consisting of 13 caissons, each 0.9 m wide, with curved roundheads at the two ends, was placed on a flat concrete bottom, and linked to the floor through a permeable two layer rock basement.

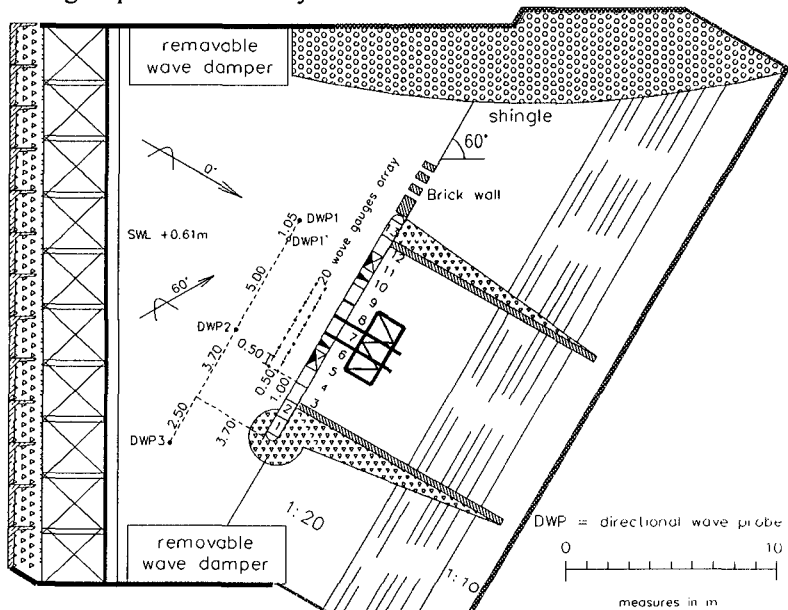


Figure 1.: Plan view of the basin and model layout

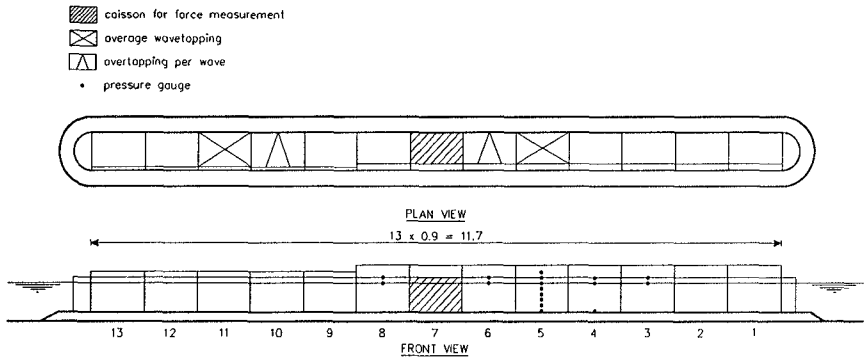


Figure 2 Plan and front view of the model caisson breakwater with location of measuring devices

Being a research model, there is no actual reference to particular prototype conditions, but a Froude scaling of 1:30 could be considered as an approximate scaling ratio for typical real structures. Crest elements were made removable in order to adjust the relative crest height (freeboard $R_c/H_s = 1.18, 1.50$ and 1.63).

The target significant wave height was kept fixed to 0.14 m throughout all tests, but the actual H_s was a little bit lower due to technical wave generation limits for the most angled wave conditions. The constant water depth in front of the caissons was 0.61 m in all tests, giving a relative water depth $h/H_s=4.3$. Peak periods (T_p) of standard ($\gamma=3.3$) JONSWAP spectra were 1.5 s and 2.12 s to give theoretical peak wave steepnesses $s_{op}=2\pi H_{os}/gT_p^2$ of 0.04 and 0.02 respectively. The minimum number of waves per test was 1000. Mean wave attack angles β varied with 10° steps from 0° (orthogonal to the structure axis) to the most oblique 60° . Energy dispersion around the mean direction was Gaussian with target standard deviations σ set equal to $0^\circ, 15^\circ$ and 30° (the latter two were actually 22° and 28°).

Wave conditions in front of the model have been analysed through a set of 20 gauges placed in two rows at 1.0 m distance offshore of the structure. The methods of analysis used to separate incident and reflected wave energy are the Maximum Likelihood and the Bayesian approach as explained by Frigaard et al. (1994).

A total of 84 tests with non-breaking wave conditions were performed. Of course wave breaking actually occurred before the wall when testing the caisson configuration with the frontal slope and berm. An extensive set of tests was performed for the simplest case of a straight vertical plain wall, whereas a more limited number of tests were conducted for the alternative structure geometries.

The selection of the structural configurations was based on the similarity with typical prototype conditions and with previous 2-D model studies. The basic caisson geometry (Fig. 3) was in fact designed in close agreement with a model structure

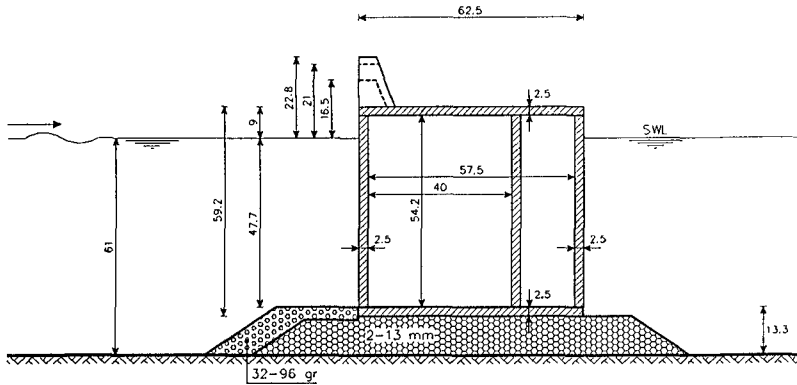


Figure 3 : Cross-section of the caisson with the simple plain vertical wall

tested in Milan for overtopping (Franco et al., 1994), while perforated walls were also designed in order to be comparable with a similar 2-D model investigation simultaneously going on at HR Wallingford, within the same MAST project. In one alternative configuration a small additional “nose” (with the same geometry tested in Milan) was placed at the top of the parapet wall, which is useful for reducing overtopping rates.

Two different types of devices have been used in the model to measure the wave-induced loads on the model structure. One central caisson (N.7 in Fig.2) was suspended above the floor of the basin by rigid metal plates attached to the inner section of the laboratory force metering frame. The inner section of the metering frame was supported by a rigidly mounted external frame section through six suspensions with strain gauges, three in the horizontal and three in the vertical planes to derive the total horizontal force F_h , the total uplift force F_u and the total overturning moment M . A clearance of approximately 2.5 mm was left around the front and sides of the measuring caisson to ensure complete freedom of movement during the force measuring tests. Two brick walls placed behind the caisson row (Fig. 1) avoided wave disturbances behind the force measuring caisson.

Wave loads were also obtained by integrating data from a set of 21 pressure transducers, which were positioned on the outer vertical face (8 cells on caisson n.5), on the bottom slab (5 on caisson n.4) and along the longitudinal direction of the caisson structure (Fig.2). All pressure signals have been combined into a total horizontal force and a total uplift force by multiplying each cell output with different factors, representing the respective influence area. The uplift force was therefore achieved only from the pressure cells measurements. The output signals from both the strain gauges of the measuring frame and from the set of pressure cells were sampled at 25 Hz and filtered analogically in real-time at 12.5 Hz. This means that only the “pulsating forces” and no wave impacts would have been recorded.

Horizontal forces

The comparison between the measurements obtained with the two systems (applied on different caissons) could be performed only in the four tests with long-crested (or unidirectional) waves approaching the structure perpendicularly ($\beta=0^\circ$). The total force over the two different longitudinal influence areas (a vertical line for the pressure transducers and a band-width of 0.9 m for the force-metering caisson) is in fact influenced by wave obliquity and multi-directionality.

With the longer period waves ($s_{op}=0.02$) the horizontal force obtained with the pressure cells showed values 8-9% higher than those derived with the force metering frame, thus revealing a standing wave pattern along the structure length with consequent non-homogeneity of the incident wave field (Fig.4a). Other reasons that can partially explain this divergences may be the dynamic response of the free caisson (n^o7) with consequent inclusion of additional inertia forces, or the different force application area which can have a small effect even under head-on wave conditions which are never perfectly two-dimensional. With the shorter waves ($s_{op}=0.04$) the comparison between the two measurements revealed an exact coincidence of the total force series, exception made for the highest two or three higher values (Fig.4b). In such case the pressure transducers were able to record also the faster transients that, acting only on a local scale, are not represented by the whole caisson metering system.

The general good matching of the force series confirmed the overall homogeneity of the incident wave field and thus the data reliability.

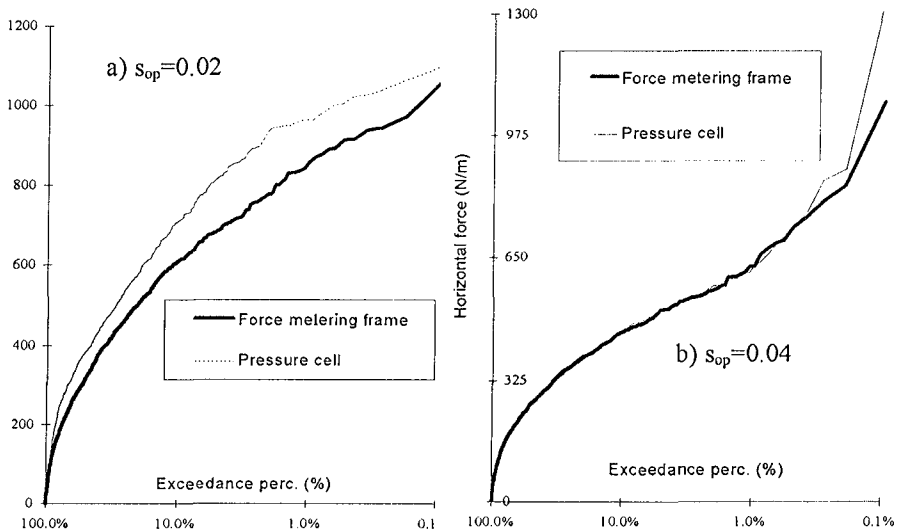


Figure 4 : Comparison between the force measurements of the pressure cells and the caisson frame outputs

The analysis has been mainly addressed to the pressure cell records, also to be consistent with the uplift force measurements which have been recorded only through the set of pressure cells. The analysis, however, demonstrated that the effects of the different wave conditions are similarly represented by both types of recordings.

The most commonly adopted prediction formula for determining the pulsating loads on vertical face structures, under long-crested attacks, is the Goda formula (1985). Design wave parameters are the maximum wave height in front of the structure H_{max} and the significant wave period T_s , which is close to the peak period T_p . Goda suggests to use as H_{max} the mean of the highest 1/250 part of the total number of waves. If Rayleigh is assumed as the probability distribution of wave heights in deep water, then $H_{max} = H_{1/250} = 1.8 H_{si}$. Thus, the analysis has been concentrated on the $F_{h,1/250}$ statistical value, which is the average of the four highest recorded forces in each of the 1000 waves-long tests. Other statistical values such as $F_{h,95\%}$, $F_{h,99\%}$, $F_{h,99.6\%}$, $F_{h,99.8\%}$, $F_{h,99.9\%}$ (the latter being the actual maximum measured force) have been used for further verification.

The little variations of the incident wave heights are taken into account when comparing forces of different tests by using the dimensionless force $F_{h,1/250}/\rho g h H_{si}$ as proposed by Goda (1985). h is the water depth in front of the structure, $\rho g = w_0$ is the specific weight of the water and H_{si} is the significant wave height measured at the structure. The graph of figure 5 clearly shows the change of this dimensionless parameter with the angle of wave attack β only for the tests with high crest. At perpendicular wave attacks, short-crestedness produces horizontal loads that are about 30% less than those acting under long-crested seas.

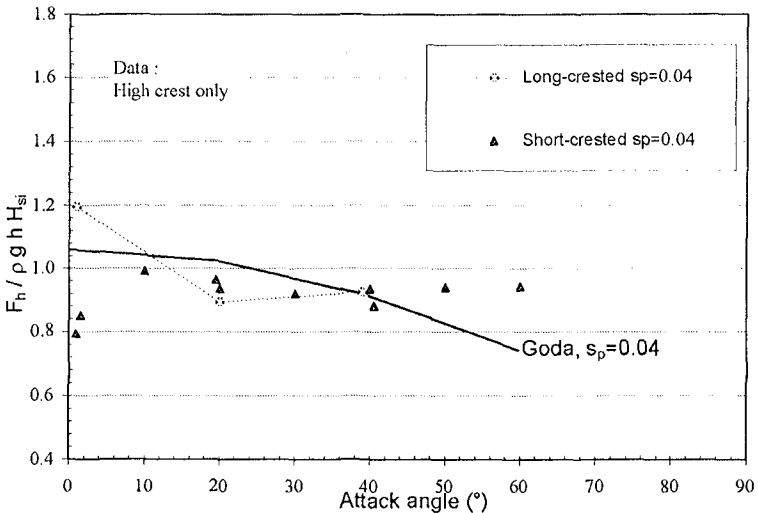


Figure 5: Horizontal forces: comparison of measurements with Goda's prediction. "h" on the y-axis is the water depth in front of the structure

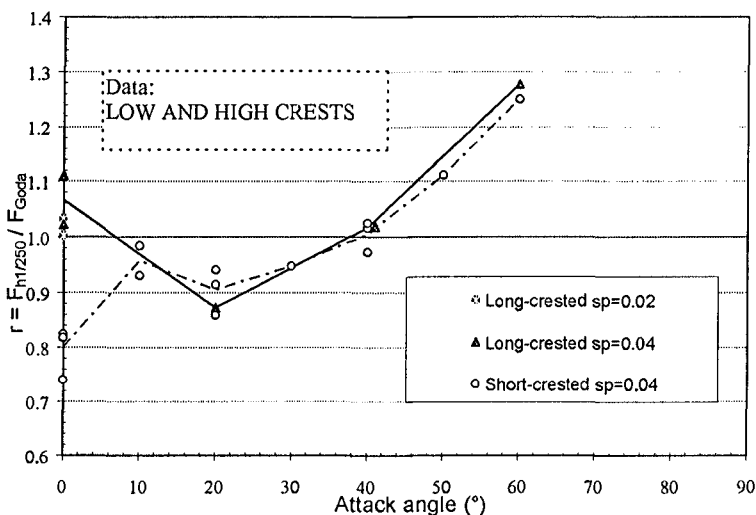


Figure 6 : Horizontal forces: reliability of the Goda formula.

This applies also for the $s_p=0.02$ data set, for which such comparison can be performed at $\beta=0^\circ$ only.

The most direct way to present the measured forces compared with the Goda prediction is to plot $r=F_{h,1/250} / F_{h,Goda}$ versus the angle of attack as shown in Figure 6 in which the 3-D effects are described. A general increase of r with increasing wave obliquity is clearly noted, which is due to the fact that Goda assumes a load decay with obliquity proportional to a cosine function which is not confirmed by these tests.

The average ratios between the measured $F_{h,1/250}$ and the calculated horizontal forces $F_{h,Goda}$, together with the relative standard deviations, are given in Table 1.

Table 1: r factor and shape parameter b for different wave conditions

	s_{op}	$r = F_{h,1/250} / F_{h,Goda}$		Shape parameter b	
		Mean	St.dev.	Mean	St.dev.
Long-crested waves	both	1.11	0.12	2.15	1.08
Short-crested waves (3-D)	0.04	0.96	0.14	2.00	0.47
Short-crested waves (3-D)	0.02	0.96	0.20	1.86	0.28
ALL WAVE CONDITIONS		0.99	0.14	1.95	0.67

Variation coefficients, σ/μ , amount to 10-15% . Other conclusions can be drawn from the analysis of Figures 5 and 6:

- Generally for the long-crested case, a load reduction due to the obliquity of wave attack is observed. Goda predicts this reduction fairly well ($\pm 10-12\%$) up to attack

angles $\beta=40^\circ$. At $\beta=60^\circ$ however, the measured force is more than 25% higher than predicted by Goda.

- With long-crested head-on waves, Goda formula slightly (7%) underestimates the force for both wave conditions with $s_{op}=0.04$ and $s_{op}=0.02$.
- With short-crested seas, the force shows no reduction with increasing angle of attack. Then it appears that Goda formula underestimates loads with large wave obliquities ($\beta>40^\circ$), so it may not be suitable for representing the effect of wave obliquity in short-crested seas.
- With head-on short-crested seas, Goda prediction tends to overestimate the total horizontal force by 20% on average.

When short-crested wave conditions dominate, Goda’s formulation may be modified to take into account wave multi-directionality, by including a reduction factor $r_{3D} \approx 0.8 \sim 0.85$ on the total load and disregarding all the effects related due to wave obliquity β .

As far as the response of the alternative geometry with recurved parapet top (“nose”), little differences of the total F_h have been observed when comparing with the case of a simple plain wall, despite the effectiveness in reducing overtopping.

The loads acting on the tested structures have been analysed statistically. A two-parameter Weibull distribution, which is often used in extreme value problems, has been fitted to the measured horizontal forces with exceedance probability of 5%, 2%, 1%, 0.4%, 0.2% and 0.1% (the latter is the actual maximum measured force) as:

$$P(F_h) = \exp -(F_h/a)^b \tag{1}$$

where a is the scale parameter, b is the shape parameter and $P(F_h)$ the exceedance probability. Fig.7 shows an example of force data fitting with a two-parameter Weibull. The calculated shape parameters b are presented in Table 1 for different incident wave conditions.

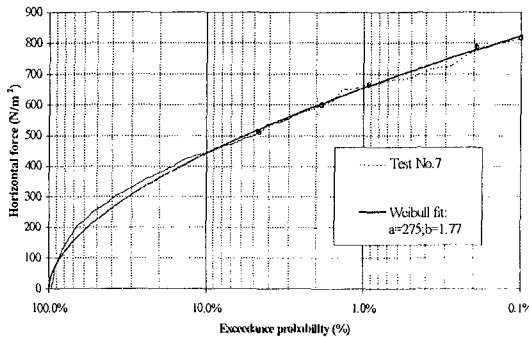


Figure 7 : Example of data fitting with the Weibull distribution.
 ($\beta=20^\circ, \sigma=22^\circ, s_{op}=0.04$)

Even though variation coefficients, σ/μ , are quite large (25-50%), the mean values of “b” are found to be close to 2.0, which correspond to a Rayleigh distribution.

A design formula (Van der Meer et al., 1995) may thus be derived from equation (1) for the exceedance probability of the highest forces, based on Goda’s method:

$$P(F_h) = \exp -(2.547 F_h / (r F_{h,Goda}))^b \tag{2}$$

where some “indicative” values of the shape parameters b and of the factors r are given in Table 1 for various 2-D and 3-D seastates. The coefficient 2.547 (=1/a) is obtained by substituting $P(F_{h,1/250})=0.00152$ into equation (1).

Uplift forces

The uplift force measurements are shown in Figure 8 by using the dimensionless uplift force $F_{u1/250} / \rho g B H_{si}$, as proposed by Goda (1985), where B is the bottom width of the caisson. A consistent decay of the uplift force with increasing wave obliquity for the steeper sea-state is shown, as also described by the Goda formula. A little difference (7-8%) is found at perpendicular wave attacks between the long and short-crested wave loads, but not as large as found for the horizontal force measurements. When waves are oblique the two seastates give similar results up to $\beta=60^\circ$, where a reduction of 30-35% on the total load is observed if compared to the head-on case. The crest “nose”, as expected, was found to have a marginal influence on the uplift forces. The force decay with wave obliquity matches that of the simple wall without nose for both long and short-crested wave attack.

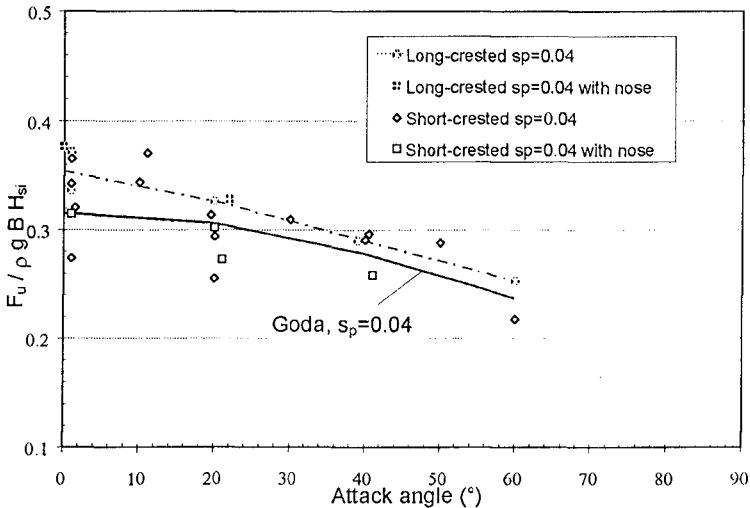


Figure 8 : Uplift forces: comparison of measurements with Goda’s prediction. “B” on the y-axis is the caisson width.

The Table 2 shows the mean values and the standard deviations of $r = F_{u,1/250} / F_{u,Goda}$ obtained for different wave steepnesses and multidirectionality indices. Standard deviations are generally lower than those of the horizontal forces and the mean values show a little reduction with short-crested waves. It is observed however, that wave obliquity effects on the uplift load are substantially well described by Goda's prediction. Some inaccuracy is noticed for angles up to $\beta = 20^\circ$ for which the measured $F_{u,1/250}$ can be on average $\pm 15\%$ of $F_{u,Goda}$. In the range $\beta = 30^\circ$ up to $\beta = 60^\circ$ the discrepancy reduces down to $\pm 10\%$.

Table 2: Uplift forces: r factor and shape parameter b for different wave conditions

	s_{op}	$r = F_{u,1/250} / F_{u,Goda}$		Shape parameter b	
		Mean	St.dev.	Mean	St.dev.
Long-crested waves	both	1.04	0.08	2.47	0.95
Short-crested waves (3-D)	0.04	1.03	0.10	2.29	0.74
Short-crested waves (3-D)	0.02	0.93	0.10	2.15	0.22
ALL WAVE CONDITIONS		0.99	0.10	2.30	0.70

Measured uplift force series have been fitted by a Weibull distribution, enabling the derivation of the scale and shape parameters for each test. Generally, the mean values of the shape parameter "b" were found to be higher than those relative to the horizontal forces, thus confirming a similar result obtained by Bruining (1994). For wave attack angles greater than 20° the shape parameter was found to be consistently higher than 2.0 (Rayleigh). For design applications the factors in Table 2 may be used as input for relation (1) with reference to F_u .

Wave pressure diagram shape

The analysis of the pressure distributions underneath and in front of the caisson revealed that few significant changes in the diagram shape occur with increasing obliquity of wave attack. When the 0.1%, 0.4%, 1%, 2%, 10% exceedance values of the total horizontal load were reached, the concurrent pressure values at the various locations have been recorded. The resulting instantaneous pressure distributions have been plotted in Fig.9 and 10 together with the calculated distribution of Goda. In the figures, attention is only focused on the diagram "shape" since comparisons in absolute terms cannot be performed, given the difference of the incident wave height in each data set and being the pressures not dimensionless.

The horizontal pressure distribution along the vertical wall, is fairly well predicted by the Goda's formula for both two and three-dimensional sea states, although the concave shape between the S.W.L and the sea bed differs from the simply linearized one by Goda. In Figure 9 the influence of wave obliquity is shown for long-crested seastate with $s_p = 0.04$: it can be observed that the vertical distribution of the horizontal pressures is not affected by the variability of the incidence angle.

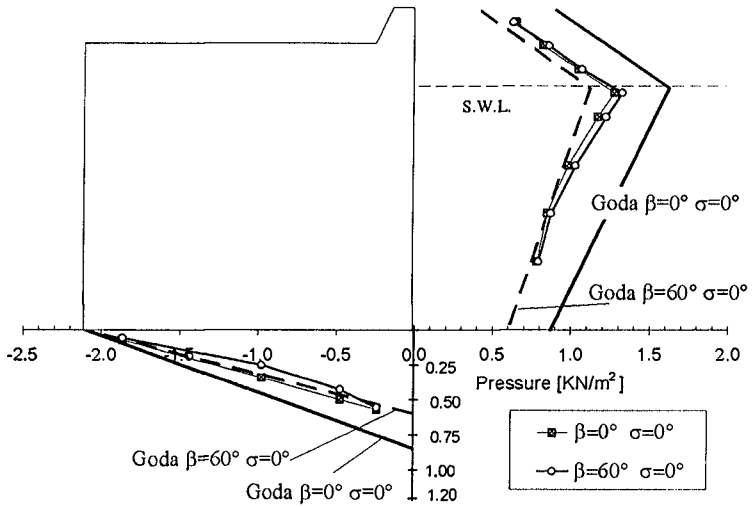


Figure 9 : Wave pressure diagram: effect of wave obliquity

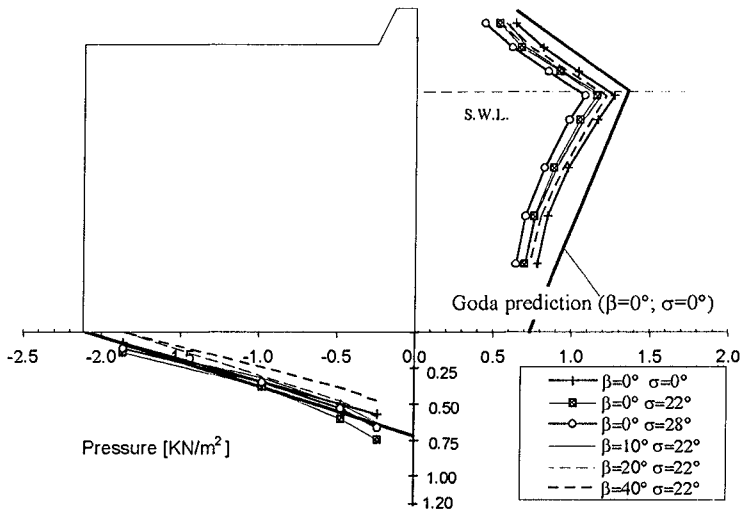


Figure 10: Wave pressure diagram: effect of wave spreading

For the uplift pressures, on the contrary, considerable changes in the diagram shape occur with increasing angle of wave attack. For large obliquity the uplift pressure distribution is not triangular (as predicted by Goda and as found in the head-on wave cases), but shows a slight concavity that shifts the centre of gravity to the seaward toe of the caisson, thus increasing the overturning moment M_u . However, the absolute value of the uplift force reduces with obliquity (not properly shown in the figure given the non-dimensionless force), so that the overall moment reduces,

even with larger arm. For most tests, the uplift distribution is fairly well in agreement with the Goda's prediction.

The effect of wave directional spreading on the uplift pressure diagram is similar to that induced by wave obliquity (Fig.10), whereas the influence of the pressure exceedance level on both the horizontal and uplift pressure distributions was found to be negligible.

Longitudinal distribution of the horizontal loads

Additional analysis has been addressed to the longitudinal distribution of the horizontal loads by coupling pressure signal time histories from adjacent caissons in various multiple combinations. Under oblique wave attack, in fact, long structures are not simultaneously subjected to the peak loads. Moreover, in short-crested seas, in which wave crests are characterised by a finite length, the correlation between the wave motion at distinct locations is lower than that achieved with long-crested waves. A global load reduction on long monolithic structures can thus be expected.

In this study, the total load decay with increasing longitudinal caisson lengths (L), as a function of peak wave length (L_p), attack angle and spreading, has been compared with the theoretically derived Battjes (1982) formula: as shown in the example of Figure 11, the agreement is reasonable for both long-crested and short-crested sea-states. Even under unidirectional head-on attack the 3-D tests showed a small load reduction, due to the finite wave width. With oblique and short-crested wave attacks the actual global load is underestimated by the theory for about $L/L_p > 0.5$.

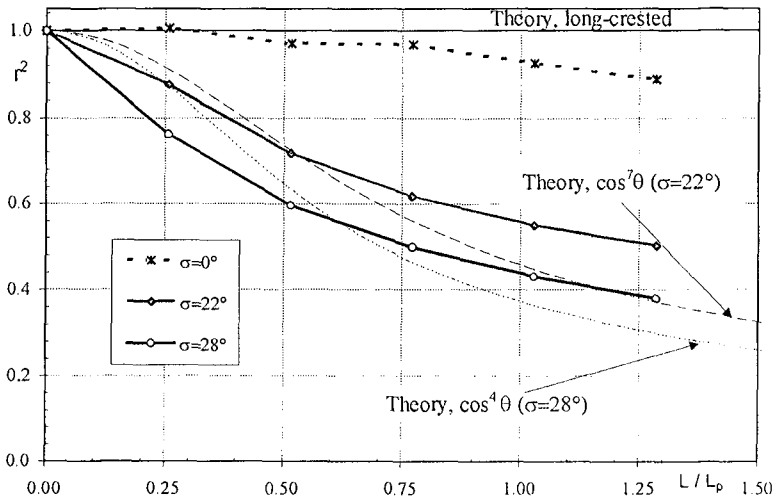


Figure 11 : Longitudinal load decay for head-on long and short-crested waves

Real 3-D waves can produce substantially reduced total loads on a vertical structure even with length as short as $0.25 L_p$. Therefore the construction of new longer caissons may allow valuable savings. Various graphs from this new data set provide useful guidance for caisson breakwaters design (Franco C., 1996).

Conclusions

The results of an extensive model study on the three-dimensional wave loads on simple vertical face caissons (with and without an additional nose) has lead to the following conclusions:

- The current practice for the evaluation of design wave loads on monolithic vertical breakwaters subjected to pulsating wave loads may not be adequate in three-dimensional sea-states. The total horizontal force acting on a whole caisson should be calculated first by considering the pressure integral along a vertical section of infinitesimal width and afterwards by applying a reduction factor proportional to the caisson relative length. This reduction can be significant even for the structures commonly constructed in the practice ($l=20-40$ m) and it is even larger in case of impact loads, which are typically applied only on limited areas. In fact the analysis of 3-D model tests showed the coincidence of the total horizontal force measurement on a whole free caisson and the reduced averaged pressure integral of two adjacent caissons.
- The Goda formula gives a good prediction of the horizontal forces for long-crested waves approaching the breakwater at angles less than $\beta=40^\circ$ with respect to the normal. However, in short-crested sea-states it should include a correction factor of 0.8-0.85 and disregard all effects of wave obliquity.
- Three-dimensional effects on the uplift forces are better described by Goda formulations and smaller scatter is observed when comparing with measurements. However, minor changes in the shape of the pressure diagram are observed for the most oblique wave attacks.
- Even though the Weibull shape parameter b of the fitted probability distribution presents a large scatter, the highest horizontal forces can be described with Rayleigh ($b=2.0$), whereas slightly higher b values are found for the uplift force series.
- The global wave load on monolithic caissons with lengths as short as $0.25L_p$ are substantially reduced, as predicted fairly well by Battjes theory.

Additional analysis on the longitudinal decay of 3-D wave loads and on the distribution of the mean and individual wave overtopping for the various tested geometries are extensively presented in other papers (Franco et al., 1995) and in the final internal report of the research project team.

Acknowledgements

This 3-D model investigation has been financed by the UE under the Large Installation Programme (LIP) and the MAST II-MCS project and partly by Dutch Rijkswaterstaat (TAW committee). The research program was proposed and coordinated by L.Franco and J.Van der Meer; model testing was directed by J. Wouters; data analysis and interpretation was mainly conducted by C.Franco. The authors wish to thank J.P.de Waal and P.Pasterkamp (Delft Hydraulics) and C.Restano (Politecnico Milano) for their productive cooperation and advice. The good collaboration of the LIP-MAST partners, H.Burcharth, P.Frigaard and J.H.Petersen (Aalborg University, DK), of the other European MAST partners H. Oumeraci (LWI,D), W.Allsop (HR, UK), J.Juhl (DHI, DK), M.Canel (SOG, F) and P.Tonjes (RWS, NL) is also acknowledged .

References

- BATTJES J (1982) Effects of short-crestedness on wave loads on long structures, *J Applied Ocean Research*, Vol.4 No.3 pp 165-172
- BOWERS E (1987) Short-crested seas in harbour modelling, *Rep Sr141* HR Wallingford.
- BRUINING J W (1994). Wave forces on vertical breakwaters. Reliability of design formula. *Msc. Thesis*, Delft Univ. of Technology. Also *D.H. report H1903*.
- FRANCO C (1995) "3-D wave overtopping on caisson breakwaters", Student competition, *XXVI IAHR congress*, , London
- FRANCO C., (1996), "Wave three-dimensional effects on long maritime structures" (in Italian), *IV° AIOM Congress*, Padua (I)
- FRANCO C., FRANCO L., RESTANO C., PASSONI G., V.D.MEER J, (1995), "The effect of wave obliquity and short-crestedness on the overtopping rate and volume distribution on caisson breakwaters", *MAST II-MCS Final Project Proceedings*
- FRANCO L., DE GERLONI M., VAN DER MEER J.W. (1994), "Wave overtopping on vertical and composite breakwaters", *Proc.of the 24th ICCE*, Kobe, ASCE, NY
- FRIGAARD P PETERSEN J H (1994) Estimation of incident wave height. *MAST II-MCS LIP, 3rd Workshop*, Nov 94, De Voorst, The Netherlands.
- GODA Y.(1985), Random seas and design of maritime structures .University of Tokyo Press.
- VAN DER MEER, J.W. D'ANGREMOND K, JUHL J (1995) Probabilistic calculations of wave forces on vertical structures.. *DELFT HYDRAULICS publication n.487*

CHAPTER 157

MODELLING THE IMPACT OF DETACHED BREAKWATERS ON THE COAST

K.J. Bos¹, J.A. Roelvink¹ and M.W. Dingenans¹

1. Introduction

Detached breakwaters alter the nearshore wave climate and hence the wave-driven current and sediment transport patterns. They obstruct a part or all of the longshore sediment transport and because of this they play a role in the large-scale sediment budget of the coasts where they are applied. Their local effect on the coast is to form single or double salients or tombolos. Which of these beach shapes will develop may be important for the attractiveness of the beach, in terms of visual aspects and water quality.

Besides having a function as part of a coastal management scheme, detached breakwaters with a jetty to the shore may be designed as a low-maintenance port. Obviously, one hopes that in such cases a salient rather than a tombolo will develop.

Clearly, engineers need to have means to assess the bypass-characteristics and the local impact of detached breakwaters if they want to apply them in a responsible manner. Several methods are at their disposal.

First, there are rules-of-thumb, based on field and lab experience. These are quite useful to get a first rough idea of the possible impacts, but generally do not give answers that are conclusive enough: a typical result is of the form that two design rules say you'll get a salient and three say you'll get a tombolo.

The most common tools applied at present are coastline models. They assume that the coastal profile is more or less constant in shape, and that the longshore sediment transport is related to the local angle of incidence of the waves. Several commercially available packages have special options to assess the local wave climate behind detached breakwaters. Effects that are not included in the current and transport models, such as circulations induced by set-up gradients, can be simulated by adjusting transport parameters locally. Generally, a lot of calibration is required, and the predictive capability is often uncertain. The calibrated models often show nice comparisons with data, especially for the initial stages. The development towards equilibrium is generally not represented at all.

Recently, more sophisticated "area models" have matured to the point that fully dynamic wave, current, transport and bed evolution simulations can be carried out over a period which is long enough to approach equilibrium conditions (see for instance Johnson et al., 1994). The advantages are obvious: these models explicitly take into account the most important processes, and therefore the amount of heuristic modelling is reduced substantially.

In the light of the ongoing efforts of devising coastal area morphological models, the performance of DELFT HYDRAULICS morphological model is tested on the simple situation of a detached breakwater in a coastal area with parallel iso-baths. This also furnishes a test for the DELFT3D system and has proven an opportunity of improving the model.

Netherlands Centre for Coastal Research (NCK), Delft University of Technology, c/o DELFT HYDRAULICS, PO Box 177, 2600 MH Delft, the Netherlands.

2. The model

The model system which is tested is DELFT HYDRAULICS morphological model DELFT3D. This model allows a flexible integration of the models for currents, waves, sediment transport, bottom changes, water quality and ecology (Roelvink and Van Banning, 1994; Roelvink et al., 1995). The morphological system contains the first four models and a control model. This control model allows the user to prescribe any combination of processes and arranges the time-progress of each model and possible iterations between models. The models relevant to morphological simulations are outlined below:

waves

Stationary multi-directional (short-crested) wave model HISWA (Holthuijsen et al., 1989). The model solves the spectral wave action balance equation assuming a frequency spectrum of fixed shape. The model includes directional spreading, wave shoaling, refraction, dissipation by bottom friction and wave breaking, current refraction and wave blocking.

Hydrodynamics

2D or 3D flow model DELFT3D-FLOW (formulae TRISULA) based on the shallow water equations, including effects of tides, wind, density currents, waves, spiral motion and turbulence models up to k- ϵ ; for morphodynamic computations, a quasi-3D option to account for wave-driven cross-shore currents is available.

Sediment transport

The sediment transport can be calculated according to several formulae, including bed-load and suspended load transport. Typical cross-shore effects such as return flow and wave asymmetry can be accounted for. The model includes a quasi-three-dimensional advection diffusion solver for suspended sediment, including temporal and spatial lag effects.

Bottom change

The bottom changes are computed from the sediment mass continuity equation. This equation is solved with a forward-time, central space (FTCS) explicit numerical scheme. The model contains a built-in time step optimization procedure.

The flow diagram for the combination of models applied in this study is given in Figure 1. Starting from an initial bathymetry, a wave computation is carried out followed by a run of the flow model. The wave and current computation can be iterated to account for full wave-current interaction. Sediment transport computations are carried out for a number of steps. After each step the bathymetry is updated based on the residual transport pattern. A very important branch in this scheme is denoted by B. Here, the discharge pattern is kept constant and (small) bottom changes are assumed to affect the current only locally: at a constant discharge rate, the current velocity increases if depth decreases. This is a reasonable assumption as long as the bottom changes are small and lead to an enormous reduction in computational cost. Typically, 20-40 so-called continuity correction steps can be taken in between full hydrodynamic runs (branch A).

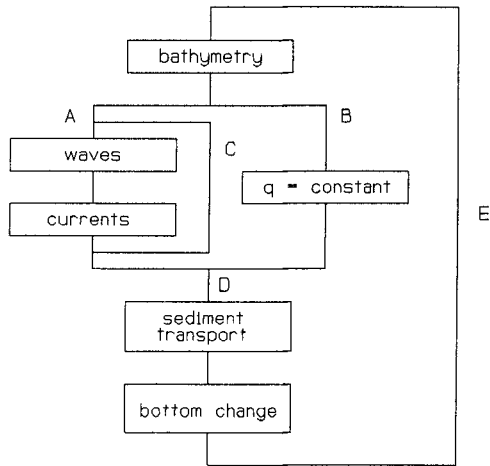


Figure 1 Flow diagram of morphological model system.

3. Test case

The breakwater lay-out to be simulated exists of a single offshore breakwater placed on a plane sloping 1:50 beach profile. The breakwater has a length of 300 m and is subjected to the action of normal or oblique incident storm waves, $H_{rms} = 2.00$ m. The relevant parameters are summarized below:

breakwater lay-out

beach slope	= 1:50	
L_b	= 300 m	breakwater length
X_b	= 220 m	breakwater axis-to-shore distance
h_b	= 4.6 m	depth at the seaward side of the breakwater

wave data

H_{rms}	= 2.0 m	root mean square wave height
T_p	= 8.0 s	peak wave period
θ	= 0° or 30°	mean wave direction

hydrodynamic data

tide = absent

sediment data

ρ	= 2650 kg/m ³	mass density of sediment
d_{50}	= 250 μ m	median diameter
ϵ	= 0.4	porosity of sediment

4. 2DH results

Within the 2DH computations the transport formula of Bijker is used.

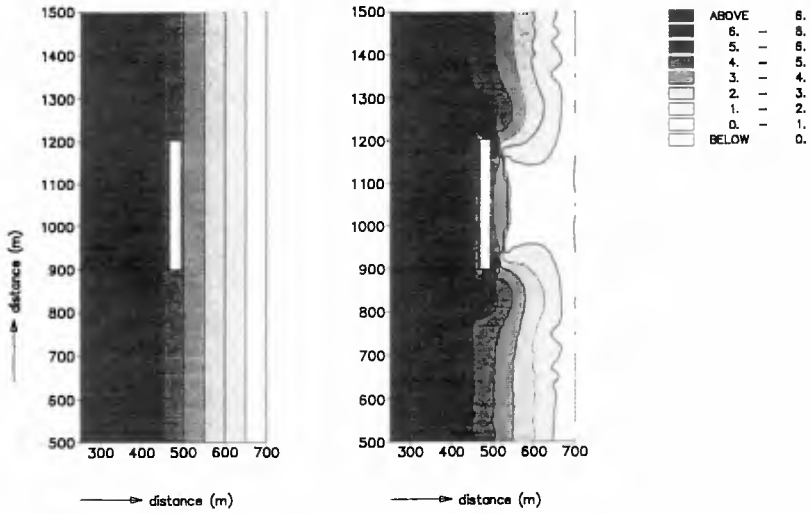


Figure 2 Left: Initial bathymetry; right: Bathymetry after 200 hours.

Normal incident waves

In the left part of Figure 2 the initial bathymetry is shown. In Figure 3 the initial wave pattern, water level and flow field are presented for normal incident waves.

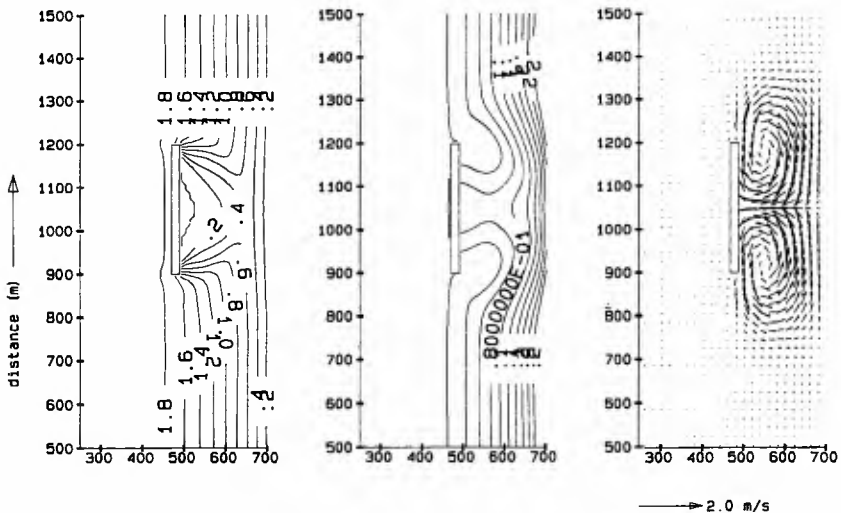


Figure 3 Left: Initial wave pattern; middle: Initial water level; right: Initial flow pattern.

The waves penetrate into the sheltered area as a result of diffraction. Although wave diffraction is not accounted for in HISWA its effect is limited in view of the wide directional

spreading used. Comparison of HISWA and a parabolic model by DHI (Johnson et al., 1994) showed that HISWA yields less wave activity and induced current behind the breakwater. However, these differences are partly due to the directional spreading accounted for in HISWA (and not in the parabolic model) since directional spreading has a smoothing effect on the wave and current field.

The isolines plot of the wave height shows that the breakwater is placed in the breaker zone which extends over about 300 m. As a result of the difference in wave height in longshore direction a water level gradient is present which generates two circulatory cells in the lee of the breakwater. These gyres have high current velocities up to 0.88 m/s at the breakwater tips which are able to transport sediment towards the lee of the breakwater (Figure 4).

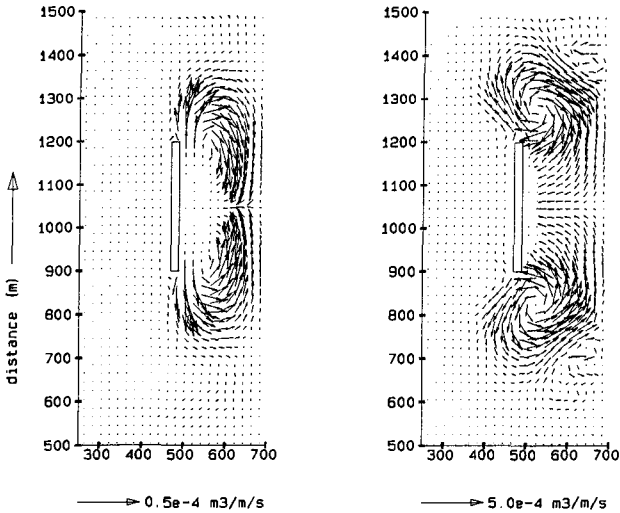


Figure 4 Left: Initial sediment transport pattern; right: Sediment transport pattern after 200 hours.

The situation after 200 hours of wave action is shown in the right part of Figure 2. From this Figure it can be expected that a tombolo will be formed in the lee of the breakwater. At each breakwater tip a large scour hole develops. The sediment transport pattern after 200 hours is shown in the right part of Figure 4. Due to the formed tombolo in the lee of the breakwater the gyres are migrated towards the exposed area. The same happens to the sediment transport field which in the Bijker formula depends strongly on the flow pattern.

Oblique incident waves

If the waves are arriving at an angle to the shore a wave driven longshore current is present. In the left part of Figure 5 the initial flow field is shown. The longshore current reaches values up to 0.5 m/s. In the lee of the breakwater two gyres are generated but at the up-stream side this gyres is very much smaller and weaker compared to the down-stream gyre. The sediment transport related to this flow field is shown in the middle part of Figure 5. Sediment is trapped into the lee of the breakwater at the up-stream side by the longshore current while erosion occurs at the down-stream breakwater tip due to the strong current velocity of combined gyre and longshore current.

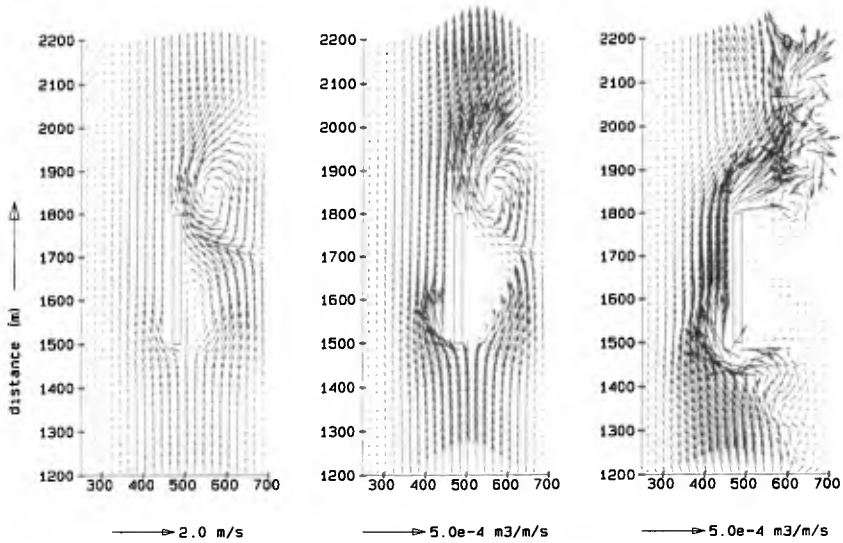


Figure 5 Left: Initial flow pattern; middle: Initial sediment transport pattern; right: Sediment transport pattern after 40 days.

Figure 6 shows the bathymetry after 200 hours and after 40 days respectively. Sediment is trapped into the lee of the breakwater forming a tombolo while a scour hole is generated at the down-stream breakwater tip. However, after some time the up-stream bathymetry is reshaped by the blocking of the sediment transport resulting in natural by-passing. This is shown in the right part of Figure 5. Almost all sediment passes the breakwater at the seaward side of the breakwater filling the scourhole at the down-stream side which result in a migrating scour hole in down-stream direction.

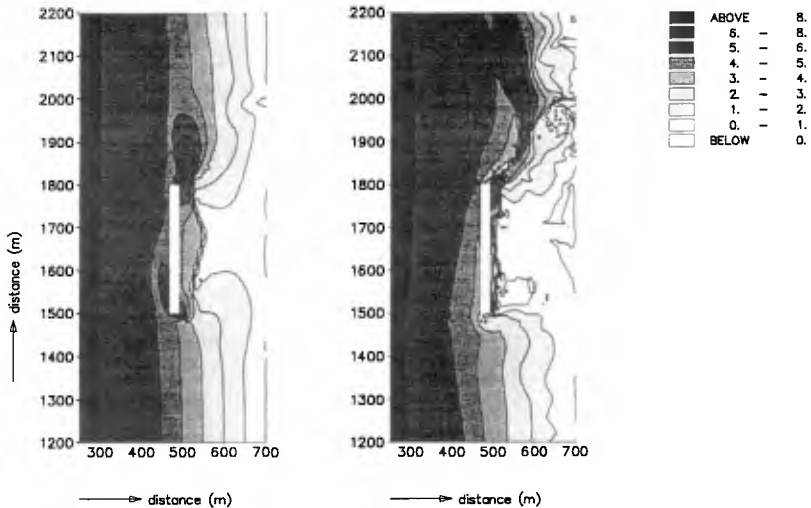


Figure 6 Left: Bathymetry after 200 hours; right: Bathymetry after 40 days.

Finally, the deposition in the lee of the breakwater is shown in Figure 7 for both normal and oblique incident waves.

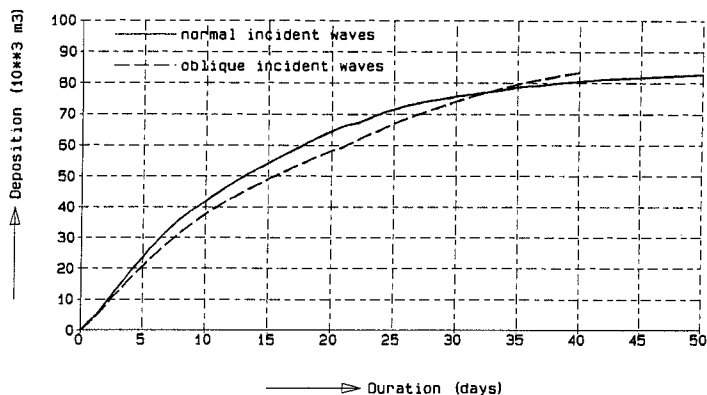


Figure 7 Deposition behind the breakwater.

5. Q3D model

Within the DELFT3D model the transport formula of Van Rijn/Ribberink is used. The transport formula of van Rijn/Ribberink contains a Q3D approach of the nearshore flow pattern. The depth-averaged flow being the result of the TRISULA computation serves as input for a Vertical Structure Model (VSM). This VSM computes the vertical distribution of the horizontal flow velocity components including wind and wave effects and the orbital velocity. The local flow and orbital velocity as computed by the VSM are subsequently used for the prediction of the sediment transport.

Mean current profile

The VSM computes the vertical velocity profile based on the assumption of quasi-steady flow and the assumption that the flow is locally uniform in the horizontal plane. These assumptions follow from the different time and length scales in the nearshore zone. The time and length scales in the vertical plane are much smaller than the time and length scales for the horizontal pattern. Hence, the vertical profile will adjust much faster to changes in external conditions than the horizontal flow pattern.

Primary and secondary current

The description of the primary and secondary current is based on the concept of de Vriend and Stive (1987). Their approach will be outlined in short below.

The current can be split into a primary and a secondary current, according to the definition:

$$u = u_p + u_s \quad \text{with} \quad u_p = \bar{u}(x, y, t) f_p \left(\frac{z - z_b}{h} \right), \quad \bar{u}_s = 0 \quad (1)$$

with a similar expression for the velocity in y-direction. The suffix p denotes the primary

current, the suffix *s* the secondary current. From this definition it follows that the depth-averaged flow is determined entirely by the primary current.

After substitution of the definitions for the primary and secondary current into the Reynolds equations for turbulence-averaged flow and integration from the bottom to a point above the highest water surface elevation the primary current can be defined such that:

$$\frac{\partial}{\partial z} \left(\nu_t \frac{\partial u_p}{\partial z} \right) + \frac{\tau_{bpx}}{\rho_w h} = 0 \quad (2)$$

Here ν_t is the turbulence viscosity, τ_{bpx} is the bottom shear stress related to the primary flow, ρ_w is the mass density of water and *h* is the water depth.

For the secondary current a more complicated expression was found with contributions of different sources. For practical reasons only the secondary flow resulting from the vertical non-uniformity of the wave-induced forces is taken into account. To describe this wave-induced secondary current the water column is divided into three layers:

1. Surface layer, above the wave trough level
2. Middle layer
3. Bottom boundary layer

Next step in their approach was to reduce the description of the surface layer to its effects on the middle and bottom layer. The effects which should be accounted for are wave breaking and mass flux.

The effect of the wave breaking is taken into account by imposing an effective shear stress at the wave trough level. This representing the transfer of momentum across the wave trough level into the flow. This stress is given by:

$$\tau_{wave} = \frac{D_b}{c} \quad (3)$$

in which:

τ_{wave}	=	shear stress at wave trough level representing wave breaking
D_b	=	dissipation due to wave breaking
<i>c</i>	=	wave propagation speed

Non-breaking progressing waves cause an onshore mass flux above the wave trough level in the direction of wave propagation. Since there is no net flux this has to be compensated by an averaged velocity at lower levels that is opposite to the wave direction (undertow). The mass flux follows from:

$$m = \frac{E}{c} \quad (4)$$

in which:

<i>m</i>	=	mass flux
<i>E</i>	=	wave energy
<i>c</i>	=	wave propagation velocity

The equation for the wave-induced secondary flow could now be derived from the momentum equation for the middle layer and the expression of the primary flow. After some reduction the equation for the secondary flow in the relatively shallow breaker zone yields:

$$\frac{\partial}{\partial z} \left(v_t \frac{\partial u_s}{\partial z} \right) = \frac{\tau_{sxx} - \tau_{bxx}}{\rho_w (z_t - z_b)} \quad (5)$$

In which τ_{sxx} is the effective shear stress at the wave trough level, τ_{bxx} is the bottom shear stress related to the secondary flow, z_t the wave trough level and z_b the bottom level. Equation 5 can be solved with the integral condition of continuity which yields that the mass flux in the surface layer must be compensated by a return flow in the lower layers:

$$\int_{z_b}^{z_t} u dz = -\frac{m}{\rho_w} \quad (6)$$

Eddy viscosity model

Within DELFT3D the mean current profile in the remaining two layers is computed using an eddy viscosity model according to van Rijn et al. (1995). The viscosity is written as the product of a scale factor and a shape function. The distribution of the eddy viscosity is assumed to be parabolic in both layers and zero at $z = 0$.

Since there are different sources which contribute to the turbulence viscosity the VSM distinguished three limit cases for which the combined viscosity must reduce. These cases are:

1. Turbulence viscosity for purely slope-driven currents. In this case the distribution of the eddy viscosity is parabolic and zero at the bottom level and the water surface.
2. Turbulence viscosity for purely wind-driven currents. In this case a maximum is expected near the surface, so the eddy viscosity distribution is taken half-parabolic.
3. Turbulence viscosity generated by wave breaking. The distribution of in this case is assumed to be similar to that induced by wind stress.

Near-bed orbital velocity

The model of the time-variation of the near-bed velocity (orbital motion) is based on the concept described in Roelvink and Stive (1989). They suggested to split this oscillatory part of the near bottom flow, \bar{u} into a component varying on the time scale of the wave groups, u_1 and a component varying on the time scale of the individual waves, u_2 .

Assuming that $u_1 \ll u_2$, two contributions can be distinguished which contribute to the time-varying flow; non-linear short waves and long waves/short wave interaction. The contribution due to non-linear short waves is computed using Rienacker and Fenton's method (1981) for monochromatic waves while the contribution due to bound long waves is based on Sand (1982), and an empirical relationship for the phase of the bound wave relative to the short wave envelope.

In the transport model of van Rijn/Ribberink a complete representative time-series of the near-bed velocity is made. This time-series has the same characteristics of asymmetry, long waves and amplitude modulation. The method followed is outlined in DELFT HYDRAULICS (1995).

Continuity correction

Based on the concept outlined above the test case was applied to the Q3D model. From the first runs it appeared that a lot of sediment was transported by the secondary current in

offshore direction, creating a huge bar (see also left part of Figure 8). This was caused by the return flow which remains constant and at the same location in between full hydrodynamic runs (branch A in the model scheme). Since this enormous bar seems quite unrealistic the number of sediment transport steps was decreased which lead to better results. However, this results in higher computational costs since more hydrodynamic runs has to be carried out. Therefore it was suggested to update the undertow by the continuity corrections.

The secondary current is determined by eq. 5. From this equation it can be seen that the wave breaking-induced shear stress τ_{tsx} at the wave trough level is a very important parameter in the driving of the undertow. This parameter is defined by:

$$\tau_{tsx} = \tau_{wind} + \frac{D_b}{c} \tag{7}$$

with τ_{wind} is the shear stress at the wave trough level due to wind.

The effect of the decreasing water depth on the undertow can be taken into account by updating the wave energy dissipation D_b after each transport and bottom step. The wave energy dissipation is determined from the dissipation model of Battjes and Janssen (1978):

$$D_b = \frac{1}{4} \rho_w g Q_b \frac{H_{max}}{T_m} \tag{8}$$

with:

- H_{max} = maximum wave height according to Miche criterion
- T_m = mean wave period
- Q_b = fraction of breaking waves

Updating the wave energy dissipation improves the simulation of the waves breaking on the generated bar and result in a stronger undertow at these particular locations. When the wave action and the undertow are strong enough this will cause the bar to travel further downward the cross-shore profile and reduces the amount of sediment deposited at the same location. The resulting profile development with the improved model is shown in the right part of Figure 8.

It should be noticed that the wave height during the transport and bottom steps still remains constant. Since the wave height is needed to determine the fraction of breaking waves Q_b , the dissipation is still not updated completely.

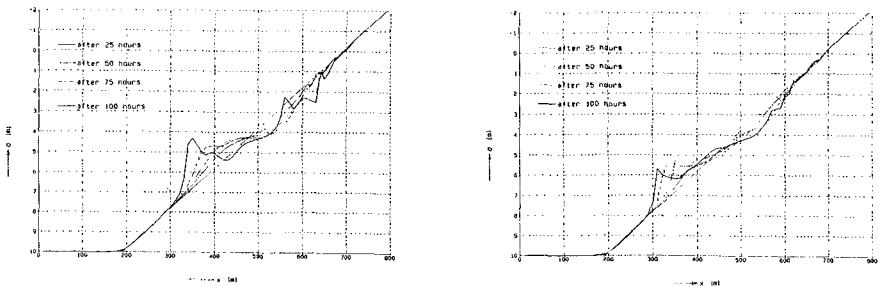


Figure 8 Left: Profile development without updating return flow; right: Profile development with updating return flow.

6. Q3D results

Normal incident waves

Since the hydrodynamic results are the same for both the 2DH and Q3D model here the attention is focused on the sediment transport and bottom changes.

The initial sediment transport pattern is presented in the left part of Figure 9. Sediment is transported by the return flow in offshore direction, while the gyres in the lee of the breakwater transport sediment towards the centre line of the sheltered area. The resulting bathymetry after 100 hours of wave action is shown in the right part of Figure 9. A double salient is generated at the moment while the bottom profile in the exposed area is changed in a similar way as shown in Figure 8. The resulting bathymetry contains very irregular contour lines which affect the progress of the computation (disturbing effect on the flow pattern).

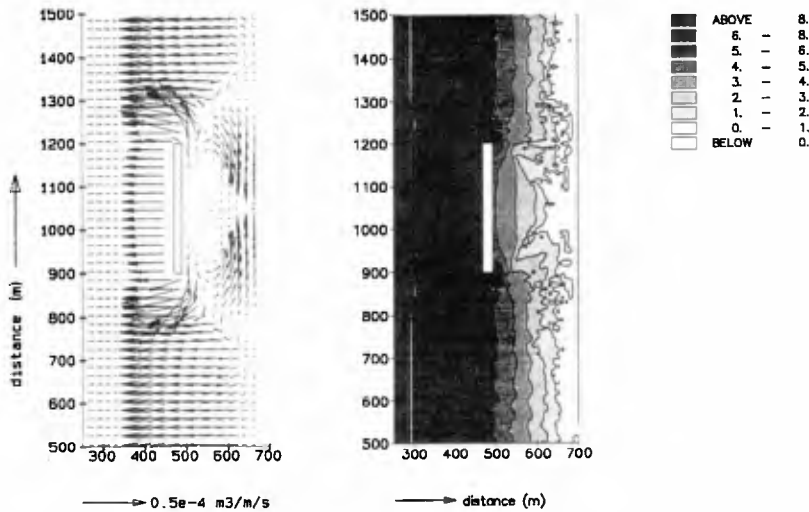


Figure 9 Left: Initial sediment transport pattern; right: Bathymetry after 100 hours.

Oblique incident waves

The initial sediment transport and resulting bathymetry after 100 hours is shown in Figure 9. The sediment transport pattern shows that the cross-shore sediment transport is still dominating over the longshore sediment transport. This seems to be one of the causes of the same irregularities occurring in the bottom contour lines.

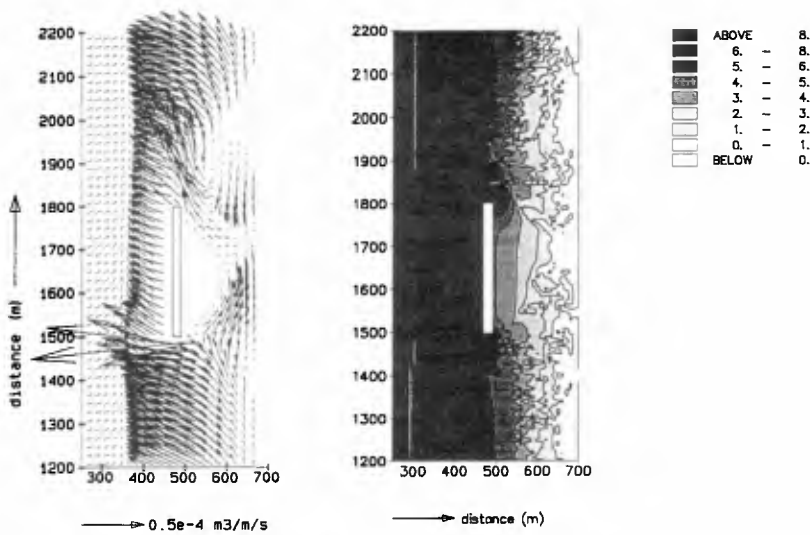


Figure 10 Left: Initial sediment transport pattern; right: Bathymetry after 100 hours.

5. Discussion

In Table 1 criteria for the formation of salients and tombolos, derived from laboratory and field data are given. From this table it can be concluded that most criteria pointed to the formation of a tombolo for the simulated test case. Based on these criteria it can be concluded that the 2DH model results show good qualitative agreement. With this model the equilibrium situation can approximately be simulated.

Reference	Criterion	Present case
Gourlay (1981)	$L_b/X_b \geq 0.67$ Tombolo	$L_b/X_b = 1.36$ Tombolo
Dally and Pope (1986)	$L_b/X_b \leq 0.5$ Salient $L_b/X_b \geq 1.5$ Tombolo	$L_b/X_b = 1.36$ Salient/Tombolo
Harris and Herbich (1986)	$L_b/X_b < 1$ Salient $L_b/X_b > 1$ Tombolo	$L_b/X_b = 1.36$ Tombolo
Suh and Dalrymple (1987)	$L_b/X_b > 1$ Tombolo	$L_b/X_b = 1.36$ Tombolo
Hanson and Kraus (1990)	$L_b/\lambda_b \leq 48(1-K_t)H_0/h_b$ Salient $L_b/\lambda_b \leq 11(1-K_t)H_0/h_b$ Tombolo	$\frac{L_b/\lambda_b}{(1-K_t)H_0/h_b} = 1$ Salient
Hsu and Silvester (1990)	$L_b/X_b > 1.33$ Tombolo	$L_b/X_b = 1.36$ Tombolo

Table 1 Criteria for the formation of salients and tombolos (L_b =breakwater length, X_b =breakwater axis-to-shore distance, K_t =transmission of the breakwater, H_0 =deep water wave height and λ_b =wave length at the breakwater)

The 2DH results with normal incident waves were also compared with other model results by Nicholson et al. (1996). From this comparison it was concluded that the area models are able to reproduce the major morphological features associated with offshore breakwaters. However, it also became clear that the choice of the sediment transport formula had a pronounced influence on the resulting morphology. This is also shown within this study by comparison between the sediment transport rates computed with the formula of Bijker and the formula of van Rijn/Ribberink.

Within this study the Q3D model has been improved so that the breakwater test case can be reproduced. From the results it is shown that the sediment transport by the undertow is a dominating feature in the initial state. However, since the prediction of the bathymetry contains very irregular contour lines, the equilibrium state can not be simulated until now.

References

- Dally, W.R. and Pope, J., 1986. Detached breakwaters for shore protection. Tech. Report CERC-86-1, U.S. Army Engineer Waterways Experiment Station, Vicksburg, U.S.A.
- Delft Hydraulics, 1995. Yearly averaged sediment transport along the Dutch shore. Report H2129.
- Gourlay, M.R., 1981. Beach processes in the vicinity of offshore breakwaters. In: Proc. 5th Australian Conference on Coastal and Ocean Engineering, Perth, Australian.
- Hanson, H. and Kraus, N.C., 1990. Shoreline response to a single transmissive detached breakwater. In: Proc. 22th International Conference on Coastal Engineering, Delft.
- Harris, M.M. and Herbich, J.B., 1986. Effects of breakwaters spacing on sand entrapment. In: Proc. IAHR-Symposium-86 on scale effects in modelling sediment transport phenomena, Toronto, Canada
- Holthuijsen L.H., Booij N. and Herbers T.H.C., 1989. A prediction model for stationary, short-crested waves in shallow water with ambient currents. Coastal Engineering, Vol. 13, pp. 23-54, Elsevier.
- Hsu J.R.C. and Silvester R., 1990. Accretion behind single offshore breakwater. J. Waterway, Port, Coastal and Ocean Engineering, ASCE, 116(3): 362-380.
- Johnson, H., Brøker I. and J.A. Zyserman, 1994. Identification of some relevant processes in coastal morphological modelling. Proc. 24th Int. Conf. on Coastal Engineering, pp. 2871-2885.
- Nicholson J., Brøker I., Roelvink J.A., Price D., Tanguy J.M. and Moreno L., 1996. Intercomparison of coastal area morphodynamic models.
- Reinecker, M.M. and Fenton, J.D., 1981. A Fourier approximation method for steady water waves. Journal Fluid Mech., Vol. 104, pp. 119-137.
- Roelvink, J.A. and G.K.F.M. van Banning, 1994. Design and development of DELFT3D and application to coastal morphodynamics. Proc. Hydroinformatics '94, Balkema, Rotterdam, pp. 451-456.
- Roelvink, J.A., D.J.R. Walstra and Z. Chen, 1994. Morphological modelling of Keta Lagoon case. Proc. 24th Int. Conf. on Coastal Engineering, pp. 3223-3236.
- Roelvink, J.A. and Stive, M.J.F., 1989. Bar-generating cross-shore flow mechanisms on a beach. Journal of geophysical research, Vol. 94, no. C4, pp.4785-4800.
- Reinecker, M.M. and Fenton, J.D., 1981. A Fourier approximation method for steady water waves. Journal Fluid Mech., Vol. 104, pp. 119-137.
- Sand, S.E., 1982. Long wave problems in laboratory models. Journal, Waterway, Port, Coastal, and Ocean Engineering, Div. Am. Soc. Civ. Eng., Vol. 108, pp. 492-503.
- Suh, K. and Dalrymple, R.A., 1987. Offshore breakwaters in Laboratory and field. Journal, Waterway, Port, Coastal, and Ocean Engineering, Div. Am. Soc. Civ. Eng., Vol. 113,

pp 105-121.

Van Rijn, L.C., Reniers, A., Zitman, T. and Ribberink, J.S., 1995. Yearly-averaged sand transport at the 20 m and 8 m NAP depth contours of the JARKUS-profiles 14, 40, 76 and 103, Report H1887, Delft Hydraulics.

Vriend, H.J. de and Stive, M.J.F., 1987. Quasi-3D modelling of nearshore currents. In: P.P.G. Dyke (ed), JONSMOD'86, Coastal Eng. 11, pp. 565-601.

CHAPTER 158

Evaluation of beach modelling techniques behind detached breakwaters

Philip Axe¹, Suzana Ilic¹ and Andrew Chadwick²

1 Abstract

This paper presents an evaluation of current design formulae for beach response to multiple breakwaters, comparing the predictions of the design guidelines with observations of beach response made during the large scale field experiment carried out at Elmer, on the UK south coast. The introduction describes typical shoreline response to breakwaters, the forcing mechanisms responsible and the characteristics of macro-tidal beaches. The remainder of the paper presents the empirical design tools, and the results of the evaluation.

2 Introduction

Detached breakwaters have been used for coastal protection throughout this century. Experience of the effects of such structures on macro-tidal beaches is limited however, and little information is available to design engineers on the response of coarse grained beaches to detached breakwaters. Salient and tombolo formation has been observed behind both natural and man-made coastal structures. Circulatory gyres in the lee of these structures, responsible for this planshape development, have long been observed (e.g. Sauvage *et al*, 1954). The forcing mechanisms responsible for these gyres have been identified as due to longshore currents set up by oblique breaking of diffracted waves, and also due to differences in set-up at the shoreline, due to longshore differences in wave height, again due to diffraction.

2.1 Shoreline response to single units

Shoreline response to single offshore breakwaters is dominated by the ratio of breakwater length to offshore distance. The influence of this ratio can be seen in the data collated in Hsu and Silvester's (1990) paper. This data is plotted in figure 1 as

¹ Researchers, ² Reader, School of Civil and Structural Engineering, University of Plymouth, PL4 8AA, United Kingdom

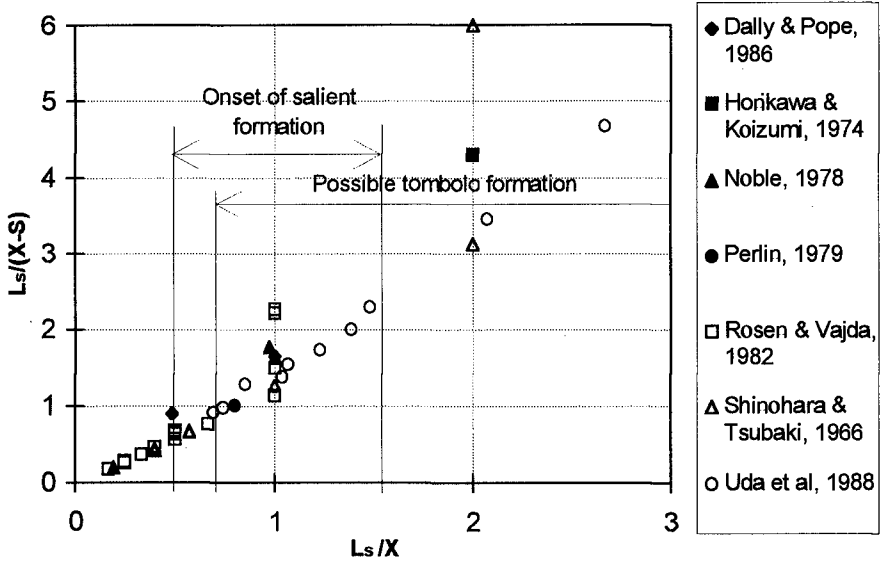


Figure 1. Ratio of breakwater length to breakwater-salient tip distance, plotted against breakwater length to offshore distance, collated by Hsu and Silvester, 1990

the ratio of breakwater length (L_s) to breakwater-salient tip distance ($X-S$), against the ratio of breakwater length to offshore distance (X). (A schematic diagram showing the meaning of the various dimensions is shown in the appendix. The data has been replotted in this way to illustrate clearly both the clarity of the relation, and also the spread of data, especially at higher values of L_s/X . This variability is not apparent in the original graph, where the data is fitted to a $1/x$ type curve.). This data is obtained from a variety of prototype schemes, physical models and a set of numerical tests (Perlin, 1979).

The importance of the ratio of L_s/X has been observed by many researchers, and forms the basis of several empirical prediction schemes. The exact shoreline response to a particular value of L_s/X is not definable, but in the literature, the onset of tombolo formation has been observed for values of L_s/X between 0.67 and 2.5, while salients begin to form for values between 0.5 and 1.5. No shoreline response is observed for values of L_s/X less than 0.5. Chasten *et al* (1993) presents a good review of the literature.

The uncertainty in predictions of shoreline response to single units is due to the combined influence of other factors, such as the size and availability of sediment, structural properties (such as the porosity- determined by armour and core sizes, and packing and freeboard, which control wave transmission) of the breakwater, and wave conditions (such as the directional spread of the incident wave energy).

2.2 Multiple breakwaters

For multiple detached breakwaters, the task of predicting shoreline response is more complex. In addition to the parameters controlling beach response described previously, the breakwater gap width has a major effect on the final beach plan shape. The gap width controls the amount of energy reaching the shoreline and thus available to drive longshore currents. The relative gap width (that is, the ratio of the gap width to the incident wavelength) also controls the way in which incident waves are diffracted, which in turn affects the currents responsible for the beach planform development. Where the gap is large compared to the incident wavelength, wave diffraction is considered to occur at the breakwater tip, and the breakwater may be considered to behave as an individual structure. Where the gap width is small, the diffraction appears to be from the centre of the gap, and the shoreline response to the two breakwaters can be considered to be governed by both breakwaters.

Previously, experience of detached breakwater design has been concentrated in micro- and meso-tidal regimes, such as Japan (see, for e.g., Seiji *et al*, 1987) the Italian Adriatic (Liberatore, 1992), the Spanish Mediterranean (Berenguer and Enriquez, 1988), or the Great Lakes (e.g. Pope and Rowen, 1983). The UK south coast is a strongly macro-tidal environment, and this has implications for detached breakwater design.

Current design guidance gives predictions of the still water shoreline position. In a macro-tidal regime, in order to maintain a suitable berm width under storm conditions, the design engineer is interested in knowing the high water shoreline position. Figure 2 highlights the problem, showing a 3D surface of a section of the Elmer frontage, with the shoreline positions at low water, mid tide and mean high water marked. It can be seen from this figure that at low tide, the breakwaters are above the water line, and only operate as the tide rises. The tidal rise increases the offshore distance of the breakwaters.

In addition to the varying geometry of the system, the changing water levels also affect the incoming waves. At lower tidal levels, waves are more likely to be depth limited, and the breakwaters lie within the surf zone. This condition is favourable to tombolo formation (Gourlay, 1987). At high water, the breakwaters are well offshore, and waves break straight onto the beach. The wavelength of an incoming wave is reduced at low water, which changes the relative gap width, which in turn is responsible for controlling whether the breakwater acts as a single unit, or as part of an array. The question that we want to answer is this:

'Is an equilibrium beach planform reached for every tidal level (in which case it would be simple to map the 3D morphology of the beach), or does the beach only come into equilibrium at the high and low water stands (where the rate of change in water depth is a minimum)?'

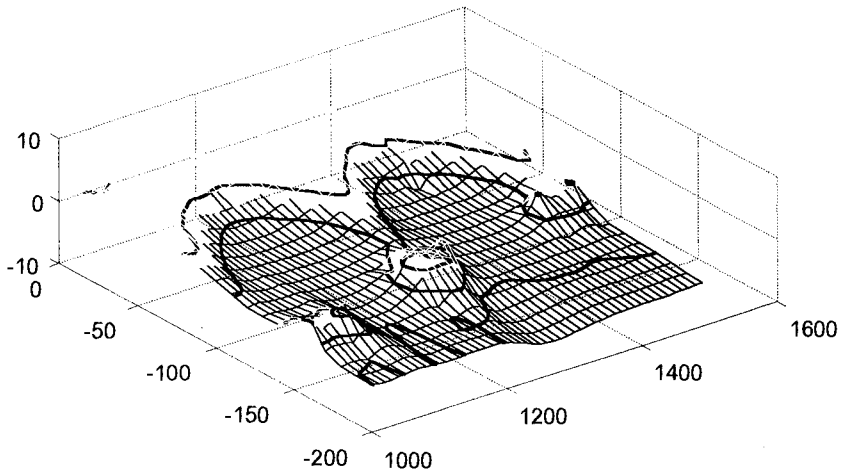


Figure 2 Positions of low water, mid tide and high water shorelines (solid black lines) at Elmer. All dimensions are in metres

2.3 Field Study

A field experiment, to study the shoreline response to a new set of breakwaters was devised and carried out at Elmer, between 1993 and 1995. Elmer lies on the UK south coast, 15 km from the western boundary of the Selsey Bill - Thames estuary coastal cell. The predominant drift direction along this coast is from west to east. The study site is the most seaward protrusion along an otherwise straight stretch of coastline, and has thus behaved as a headland area. In the winter of 1989, severe storms led to flooding of the residential hinterland. Works were planned, and constructed between 1992 and '93. These consisted of a 239,000 m³ beach fill along 2 km of frontage, stabilised by eight shore-parallel offshore breakwaters and a terminal rock groyne (described in Holland and Coughlan, 1993). A plan of the scheme is shown in figure 3.

The field work program provided wave data recorded simultaneously at the shoreline and offshore. Data was processed using common spectral and directional analysis routines. Beach surveys were taken concurrently with the wave data collection. Data was collected for at least one year, to avoid seasonal bias.

One wave recorder (a pressure transducer array described in Bird, 1993) was deployed 650 metres offshore, towards the western end of the scheme. This provided the incident wave conditions. At the shoreline, the Inshore Wave Climate Monitor (IWCM- described in Chadwick, Borges, Pope and Ilic, 1995) was deployed to provide directional wave conditions after the waves had been diffracted through the gap between breakwaters three and four.

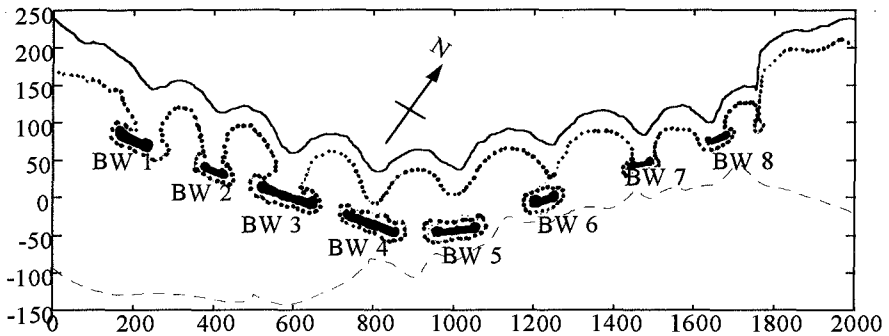


Figure 3. Elmer frontage, showing numbering scheme for breakwaters, and levels of highest (solid line) spring, mid (dotted line) and lowest spring (dashed line) tides

Photogrammetric surveys of the beach were commissioned in collaboration with the local coastal protection authority. Aerial surveys provided overlapping colour prints, at a contact scale of 1:3000, of the coastline up to 2 kilometres east of the scheme, and 1 kilometre west. Profile data was provided along profile lines set in discussion with the local coastal protection authority. This gave 65 cross shore profile lines, and 4 longshore lines. Within the scheme, profile line spacing was 30 metres, with the exception of the instrumented area, where a line spacing of 10 metres was provided. Beyond the limits of the scheme, line spacing was 50 metres. The first survey was produced on completion of the scheme (September '93), and then on the following dates: 2 February '94; 29 May '94; 16 September '94; 29 January '95 and 16 May '95. Below the low tide limit, bathymetric data was obtained by an echo sounder survey. A summary of data collected is presented in table 1, and monthly averages of wave conditions are shown in figure 4.

Parameter measured	Method	Start date	End date	Data availability
Directional wave conditions (offshore)	Sub-surface pressure transducers	23 September 1993	14 January 1995	2776
Directional wave conditions (inshore)	Direct measurement by resistance staffs	5 October 1993	13 December 1994	1550
Wave induced currents	Electromagnetic current meters, float tracking	18 April 1994	24 April 1994	24
Beach profiles	Aerial survey	September 1993	May 1995	6 surveys
Beach samples	Direct sampling	April 1994	June 1995	22 samples

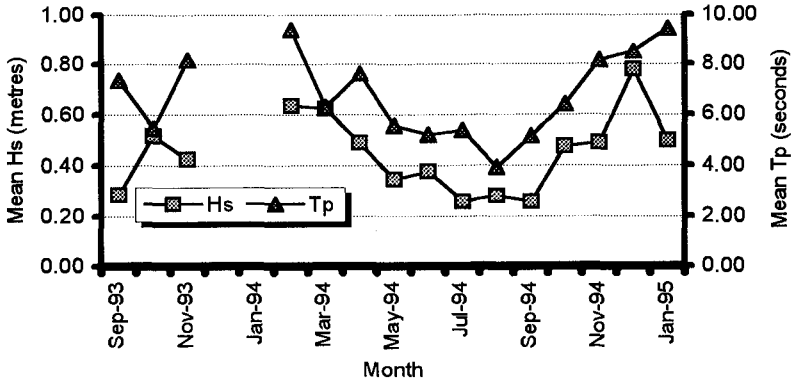


Figure 4. Monthly averaged wave conditions (offshore)

1 Evaluation of empirical models

Four models were selected for evaluation. These were : Pope and Dean (1986); Suh and Dalrymple (1987); Ahrens and Cox (1990); and McCormick (1993). Of these, Suh and Dalrymple and McCormick’s models provide values of salient length (Suh and Dalrymple) or of shoreline position (McCormick), whereas the Pope and Dean, and Ahrens and Cox models both describe the beach response in general terms.

The Suh and Dalrymple model is based on a set of physical model tests carried out in a spiral wave basin, and on prototype and model tests described in the literature. The equation presented to fit this data is:

$$S^* = 14.8 \left(\frac{G_B^*}{L_B^*} \right) \exp \left[-2.83 \left(\frac{G_B^*}{L_B^*} \right)^{\frac{1}{2}} \right] \tag{Equation 1}$$

where X_s is the salient length, G_B is the gap width, and L_B is the breakwater length. Characters marked with an asterisk represent values non-dimensionalized with respect to the offshore distance of the structure.

The McCormick (1993) model is based on the observation that bays formed behind detached breakwaters tend to be ellipsoid. This observation was based on aerial photographs, and on selected physical model data of Shinohara and Tsubaki (1966) and of Rosen and Vajda (1982). Validation for the model was carried out on four breakwaters within the ‘Bay Ridge’ prototype scheme in Chesapeake Bay. This model is more complex than the others studied. It is still based primarily on the ratio of offshore distance to breakwater length, but also includes the effects of wave steepness, direction and beach slope. These values are used to predict the size and locations of the ellipses that define the shoreline position. For the purposes of this

evaluation, the predictions of salient length were extracted from this information. The reader is recommended to read McCormick's original paper for details of the application of this model.

Pope and Dean (1986) proposed a system of classifying the effect of breakwater schemes in terms of their shoreline response. Beach response was divided into five bands, ranging from 'no sinuosity' through 'subdued salients', 'well developed salients', and 'periodic tombolos' to 'permanent tombolos'. The classification is based on the degree of protection afforded to a coastline (in terms of the ratio of breakwater length to gap length) plotted against the ratio of offshore distance to water depth at the structure. Preliminary results of a validation of this method were presented for low to moderate wave climates.

Ahrens and Cox (1990) followed the classification scheme proposed by Pope and Dean, defining a beach response index I_s . The index is defined below, in equation 2.

$$I_s = e^{\left(1.72 - 0.41 \frac{L_s}{X}\right)} \quad \text{Equation 2}$$

Values of I_s less than 1 predict permanent tombolo formation, while values greater than 5 predict no sinuosity. The method is based purely on the breakwater length and offshore distance, and therefore ignores any effects of variable gap width.

To apply these models to the Elmer site, the profile data and construction plans were analysed to provide information on the scheme geometry. Because of the interest in the ability of these schemes to predict beach response at varying tidal levels, measured salient lengths, offshore distances, beach slopes and water depths were extracted at 0.3 metre intervals, from the mid tide level up to mean high water springs (2.4 metres higher). This information was then used to drive the models, and the predictions were compared with the observed findings. Offshore distances of the breakwaters are presented in Table 2, while measured salient lengths are presented in Table 3.

Water level (over mean water level)	Break water 1	Break water 2	Break water 3	Break water 4	Break water 5	Break water 6	Break water 7	Break water 8
0	50.6	48.7	0	40.9	54.5	44.3	25.5	10.4
0.3	68.2	65.3	3.9	42.9	57.1	47.3	29.1	13.5
0.6	72.1	68.2	51.3	45.8	59.7	50.4	32.2	16.7
0.9	73.1	72.1	54.5	48.7	62.3	53.4	34.3	19.8
1.2	76	74	57.1	52.6	64.9	56.5	36.4	21.9
1.5	77.9	77.9	59.7	55.5	67.5	59.5	38.4	24
1.8	80.8	80.8	62.3	58.4	70.1	62.6	41	27.1
2.1	83.8	82.8	66.2	60.4	72.7	65.6	43.6	29.2
2.4	85.7	85.7	68.2	66.2	75.3	68.7	46.2	32.3

Table 2. Breakwater-shoreline distances at various tidal levels

Water level (over mean water level)	Break water 1	Break water 2	Break water 3	Break water 4	Break water 5	Break water 6	Break water 7	Break water 8
0	51	49	0	41	30	44	26	10
0.3	68	65	4	43	21	15	29	14
0.6	72	64	51	46	18	9	32	17
0.9	54	35	55	16	16	5	34	20
1.2	35	27	38	14	14	1	34	19
1.5	27	23	28	5	12	-1	34	19
1.8	22	19	23	2	8	-2	35	20
2.1	22	11	21	0	8	-5	32	18
2.4	20	10	18	0	6	-7	31	17

Table 3. Observed salient lengths at various tidal levels

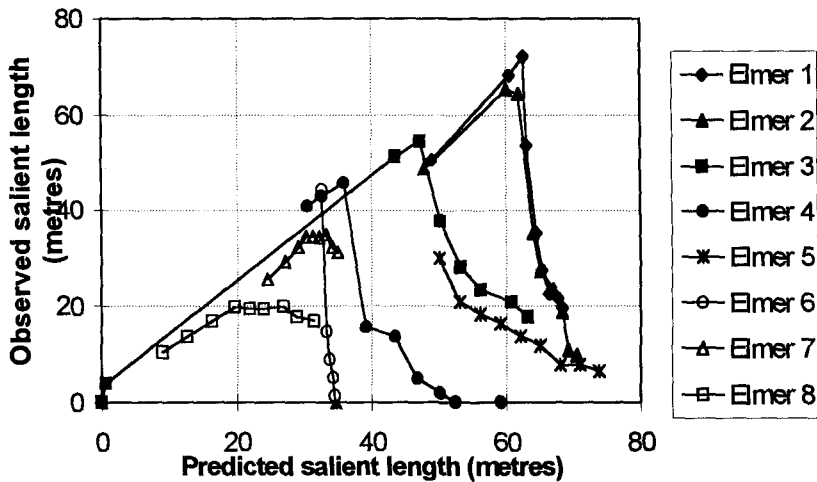


Figure 5. Comparison of observed and predicted salient lengths, based on Suh and Dalrymple, 1987

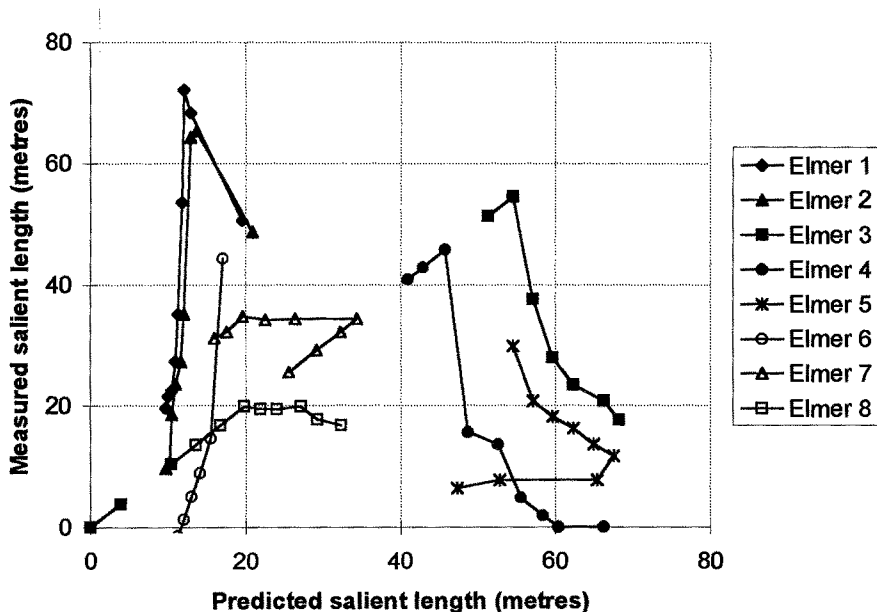


Figure 6. Comparison of observed and predicted salient lengths, using McCormick, 1993

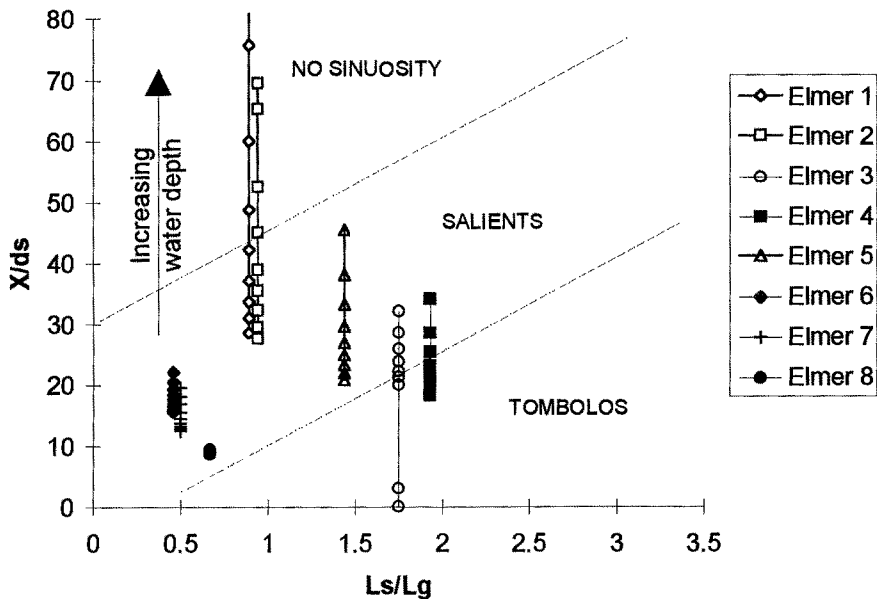


Figure 7. Elmer breakwaters plotted according to the classification scheme of Pope and Dean (1986)

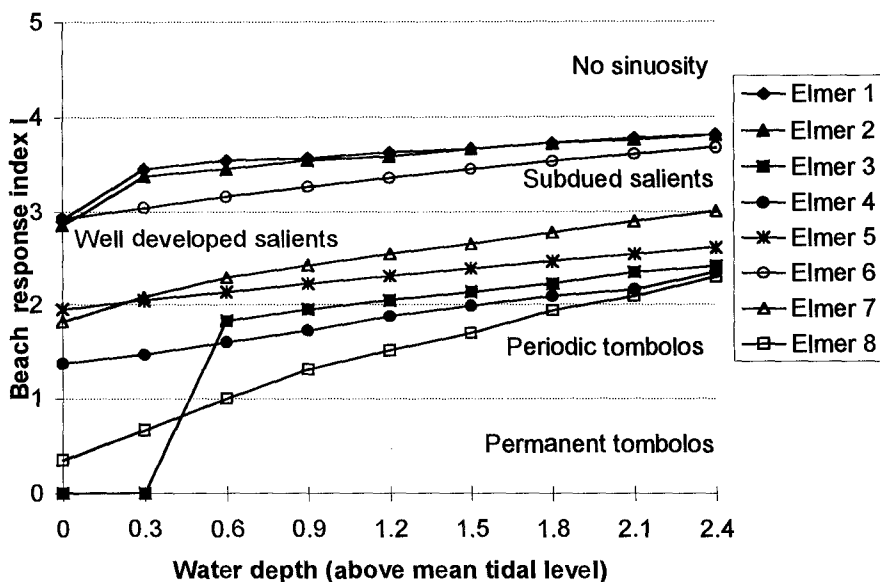


Figure 8. Variation in breakwater index with tidal level, according to the classification scheme of Ahrens and Cox (1990)

4 Results

The model predictions from Suh and Dalrymple (1987) shown in figure 5, show excellent agreement between observed and predicted salient lengths at the lower levels- when tombolos occur. As the tide rises, this model predicts steadily increasing salient lengths. This is counter to the observed salient behaviour, but in line with the observations reported in Chasten *et al* (1993). The response predicted by McCormick's model (shown in figure 6) differs from this. Similar tombolo formation was predicted at the lower tidal levels. Salient length was predicted to decrease behind breakwaters 1,2,6 and 7, and predicted to increase behind breakwaters 3,4 and 8. In the case of breakwaters 1 and 2, this decrease in salient length improved the quality of the predictions, but for the other breakwaters, the predictions worsened at the higher tidal levels.

Figure 7 shows the predictions according to Pope and Dean's classification. Tombolo formation is only predicted to occur behind breakwaters 3 and 4, although the prediction of the limit between salient and tombolo for breakwater 3 is perfect. The limited shoreline response behind breakwaters 1 and 2 at high tide is also represented well, but tombolo formation at low water is not predicted. Figure 8 shows the effect of varying water depth on Ahrens and Cox's beach response index. Tombolo formation is predicted at mid tide behind breakwater 3,4,5,7 and 8. A tombolo does

not form behind breakwater 5 however, and the tombolos behind breakwaters 1 and 2 were not predicted to occur. As the water depth is increased, the transition from tombolo to salient is reasonably well described.

5 Discussion

From these results, it appears that the methods of Suh & Dalrymple, and of McCormick, work very well for describing tombolo formation, but do not appear to be as reliable when modelling salient formation. This may be due to a tendency to over predict salient lengths, which is a characteristic that would be masked when comparing these models with field tombolos. This tendency has been observed previously and reported in Chasten *et al* (1993). As a counter to this however, both models described the lower salient and tombolo formation behind breakwater 4.

The Suh and Dalrymple model was developed from physical model tests and prototype data where the gap widths between breakwaters was constant, and the beach response averaged across a scheme was evaluated. Where the gap widths are variable, as at Elmer, and individual salient lengths are required, the limits of applicability of this model may have been exceeded. Additionally, the study site is characterised by the bimodal nature of the beach. In the updrift west of the scheme, the tombolos are formed of sand, while the upper beach is gravel. In the (downdrift) east of the scheme, where the gap widths are wider, the tombolos are predominantly gravel. The formation of tombolos from finer material to the remainder of the beach leads to a difference in beach slope in the bays and on the tombolos. This in turn affects the rate at which parameters (non-dimensionalized against offshore distance) vary with depth. In the east of the scheme, this problem is less pronounced, due to the more uniform nature of the beach.

The more general predictors, of Pope and Dean, and Ahrens and Cox, were more successful in predicting beach response- due in part to the fact that as they only give general descriptions of a likely response. To illustrate this, it is clear that in figure 7, tombolos were not predicted to occur behind breakwaters 7 or 8. The observed response, shown in figure 3, is that tombolos formed. The response predicted by this method does however lie close to the limit of salient tombolo formation presented by Pope and Dean. Thus the predictions are reasonable. The prediction of the response to 3 and 4 was excellent. The method failed in the predictions of 1 and 2. As mentioned previously, the net drift direction at Elmer was from west to east, and this has led to an increased accumulation of material behind the first two breakwaters, that has not (yet?) been passed through the system. It may be supposed therefore that the Pope and Dean predictions are best used where longshore transport into a system is not significant, such as in a pocket bay, or indeed in the middle of a scheme of breakwaters. This failure to predict the beach response to breakwaters 1 and 2 also occurs with Ahrens and Cox's technique, although this method does succeed in predicting the tombolos behind breakwater 8 (and less well) breakwater 7.

6 Conclusions

From the comparison of the predicted and observed salient lengths during this exercise, three of the predictive schemes (Ahrens and Cox, McCormick, and Pope and Dean) were unable to predict the behaviour of the updrift breakwaters. This suggests that these techniques are not suitable for use where there is significant longshore transport into a scheme, which restrict their use to the design of pocket beaches, or to the central portions of multiple breakwater schemes, where net longshore transport is expected to be low. The robustness of the simplest technique (Ahrens and Cox) is surprising, suggesting that even in multiple breakwater schemes, the ratio of breakwater length to offshore distance is still paramount in determining shoreline response. This would seem to be contrary to other research (such as, for example, Hanson, Kraus and Nakashima, 1989), which suggested that wave transmission, for example, was an important parameter in determining shoreline response. The findings in this work are most likely to be a result of this evaluation being well within the range of applicability of the Ahrens and Cox method.

The inability of these methods to predict shoreline positions behind detached breakwaters does make them of less use to design engineers. To improve our design capability, physically based numerical process models, validated against field measurements, are needed before we can confidently develop 'rules of thumb' to simplify design.

7 Acknowledgements

The authors would like to express their thanks to Arun District Council and to the Hydraulics Engineering Research Unit of the University of Brighton for their help in this project. They would also like to thank Dr. P.A.D. Bird for his assistance in preparing equipment for the fieldwork stages of the project. The fieldwork was supported by the UK Engineering and Physical Sciences Research Council Grants GR/H 82969 and GR/H 74360. Data processing and analysis was financially supported by Arun District Council and SCOPAC, the Standing Conference on Problems Associated with the Coastline.

8 References

- Bird P.A.D.**, 1993, Measurement and analysis of sea waves near a reflective structure. *Unpublished PhD thesis, University of Plymouth, 282 p*
- Chadwick A.J., Pope D.J., Borges J. and Ilic S.**, 1995, Shoreline directional wave spectra. Part 2. Instrumentation and field measurements, in: *Proceedings of the Institution of Civil Engineers (Water, Maritime and Energy)*, September 1995, pp 209-226
- Chasten M.A., Rosati J.D., McCormick J.W. and Randall R.E.**, 1993, Engineering design guidance for detached breakwaters as shoreline stabilisation structures. *Tech. Rep CERC-93-19. US Army Corps of Engineers Waterways Experiment Station, Vicksburg, Mississippi.*

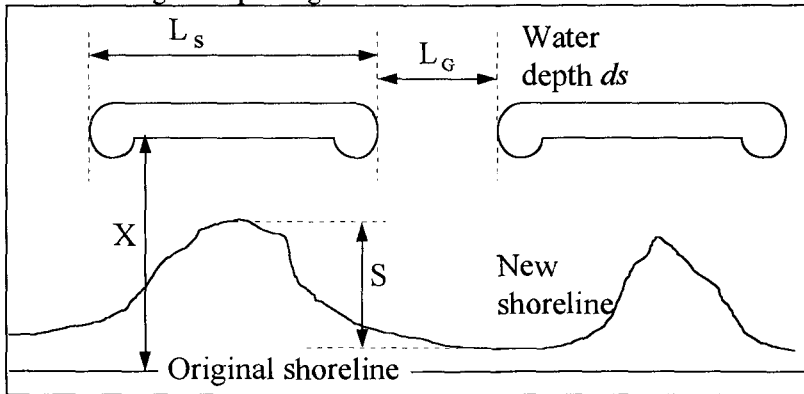
- Dally W.R., and Pope J., 1986, Detached breakwaters for shore protection, Tech. Report CERC-86-1, US Army Engineers Waterways Experiment Station, Vicksburg, Mississippi.**
- Berenguer J.M., and Enriquez J., 1988, Design of pocket beaches: the Spanish case, in: *Proc. Conference on Coastal Engineering, ASCE, 1411-1425***
- Gourlay M., 1987, discussion of: Offshore breakwaters in laboratory and field, in: *Journal of Waterways, Port, Coastal and Ocean Engineering, vol 113 (4)***
- Hanson H., Kraus N.C., and Nakashima L., 1989, Shoreline change behind transmissive detached breakwaters, *Proceedings of coastal zone '89, ASCE, 568-582***
- Holland B. and Coughlan P., 1993, The Elmer Coastal Defence Scheme, *Proceedings of MAFF Conference on River and Coastal Engineering, Keele, UK***
- Horikawa K., and Koizumi, 1974, An experimental study on the function of an offshore breakwater, *29th Annual Conference, Japanese Society of Civil Engineers, pp 85-87***
- Hsu J.R.C., and Silvester R., 1990, Accretion behind single offshore breakwater, in: *Journal of Waterways, Port, Coastal and Ocean Engineering, vol 116 (3), 362-379***
- McCormick M.E., 1993, Equilibrium shoreline response to breakwaters, in: *Journal of Waterways, Port, Coastal and Ocean Engineering, vol 119 (6), 657-670***
- Noble, R.M., 1978, Coastal structures' effects on shorelines, *Proceedings of 16th International Conference on Coastal Engineering, ASCE, vol 3, 2069-2085***
- Perlin, M. 1979, Predicting beach planforms in the lee of a breakwater, *Proceedings of Coastal Structures '79, ASCE, vol 2, pp 792-808***
- Rosen D.S., and Vajda M., 1982 Sedimentological influence of detached breakwaters, *Proceedings 18th International Conference on Coastal Engineering, ASCE, 1930-1949***
- Sauvage de St. Marc M.G., and Vincent M.G., 1954, Transport littoral, formation de fleches et de tombolo, in: *Proceedings of 5th Conference on Coastal Engineering, Council on wave research, 296-327***
- Suh K. and Dalrymple R.A., 1987, Offshore breakwaters in laboratory and field, in: *Journal of Waterways, Coastal and Ocean Engineering, v 113 (2), 105-121.***
- Shinohara and Tsubaki, 1966, Model study on the change of shoreline of sandy beach by offshore breakwater, *Proceedings 10th Coastal Engineering Conference, ASCE, vol 1, pp 550-563***
- Toyoshima O., 1982, Variation in foreshore due to detached breakwaters, in: *Proc. 18th International Conference on Coastal Engineering, ASCE, 1873-1892***
- Uda T., Omata, A., and Yokoyama, Y., 1988, On the formation of artificial headland beach using detached breakwater, *Proceedings of 35th Japanese conference on coastal engineering, JSCE, p 26-30***
- Walker J.R., Clark D., and Pope J., 1980, A detached breakwater system for shore protection, *Proc. 17th International Conference on Coastal Engineering, ASCE, Sydney, 1968-1987***

9 Notation

L_s	Breakwater length (metres)
X	Offshore distance of breakwater (metres)
S	Salient length (metres)
L_G	Gap width
d_s	Water depth at seaward side of breakwater
λ	Water wavelength
*	Non-dimensionalised with respect to X

10 Appendix

Schematic diagram explaining notation



CHAPTER 159

Numerical Modelling of Bed Evolution Behind a Detached Breakwater

Philippe P  chon¹ and Charles Teisson¹

Abstract

The sedimentological impact of waves on a sandy beach with a detached breakwater is simulated using a compound system of models. The results are satisfying since a salient could be generated behind the structure. They are in agreement with bed evolutions surveyed in experimental facilities and in nature. A quantitative analysis of the results performed in the framework of the working group 'Coastal Area Modelling' of the project MAST G8M shows that the volume of accretion computed here is in good agreement with the volumes obtained by other models and empirical formula.

Introduction

A numerical system has been developed for simulating bed evolution due to breaking waves. Wave, current, sediment, transport and bed evolution are computed successively. Since the wave field is affected by sea bed changes, hydrodynamic phenomena are up-dated when bed evolution is significant. The system of models is illustrated on figure 1.

The three numerical models belong to the library TELEMAC based on finite element technic. They are coupled within an automatic procedure.

Comparisons of the numerical results with measurements in flume cases were carried out in the past. They gave satisfying results (Broker Hedegaard et al 1992, P  chon 1994), undertow as well as bed evolution were well predicted. Standard parameters were used for these simulations except for the sediment transport formula where the suspended load was increased in the surf zone to account for breaking effect.

¹ Laboratoire National d'Hydraulique, EDF.
6, quai Watier, 78400 Chatou. France

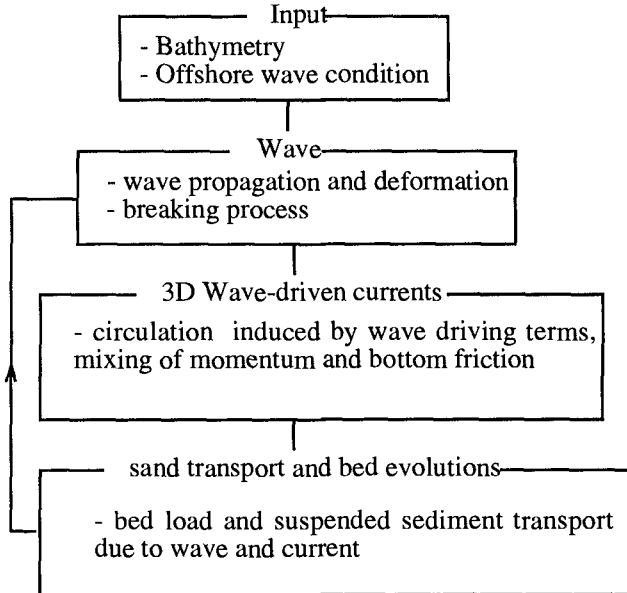


Fig.1 Structure of models

The present article deals with the application of the models on a three-dimensional case ; the impact of a detached breakwater built along a rectilinear beach is investigated. In a previous study (Péchon et al., 1995) the good agreement of computed currents with measurements collected in a basin (Mory and Hamm, 1995) was exhibited on the same but reduced scaled structure. Accurate data of seabed movement and wave climate are not available for the present full scaled test. However the effect of breakwaters is qualitatively known according to surveys in coastal zones, and the ability of models to reproduce realistic morphological changes can be checked. Moreover an intercomparison exercise with other modellers was performed (Nicholson et al 1995) in the framework of the European program MAST2 G8M.

The numerical models

The wave model

The model ARTEMIS V1.0 solves the complete mild-slope equations :

$$\text{div} (C C_G \vec{\text{grad}}\varphi) + \omega \frac{C_G}{C} \varphi = 0$$

with $C = w / k$ C : phase celerity

$C_G = \frac{1}{2} (1 + \frac{2kh}{sh 2kh}) C$ C_G : wave group celerity

φ : complex horizontal part of the potential

$$\varnothing (x, y, z, t) = Z(z) \varphi(x, y) e^{-i\omega t}$$

where $Z(z) = \frac{ch(k(h+z))}{ch(kh)}$

According to the rather schematised bathymetry tested here, the wave height decay in the surf-zone is given by the formula $H_b = 0.8 h$ where H_b is the breaking wave height and h the still water depth.

The radiation stress can be calculated knowing the wave potential. However this leads to a very irregular radiation stress field which has to be smoothen. So it is preferred here to express the driving terms in function of the dissipation of breaking waves.

The computed instantaneous wave velocity follows an ellipse, therefore there is not a simple incidence. In the following current and transport models, the required incidence is supposed to be given by the large axis of the ellipse.

The time-averaged current model

The model TELEMAC-3D V3.0 solves the time-averaged three-dimensional equations accounting for the vertical variability of the forces due to breaking waves and especially roller effect (Péchon 1994). They read, in the case of a flume for clarity :

$$\frac{\partial U^2}{\partial x} + \frac{\partial UW}{\partial z} + \frac{\partial(\overline{u_w^2} - \overline{w_w^2})}{\partial x} + \frac{\partial \overline{u_w w_w}}{\partial z} = -g \frac{\partial \xi}{\partial x} - \frac{\partial \overline{u'w'}}{\partial z} + t$$

$$\frac{\partial U}{\partial x} + \frac{\partial W}{\partial z} = 0$$

with U, W : time-averaged current due to breaking waves
 u_w, w_w : instantaneous wave velocity
 u', w' : turbulent fluctuations of velocity
 x : free surface level
 t : contribution of the roller of breaking waves

The overbar indicates time-averaged quantities.

The following closures are taken :

$$\frac{\partial(\overline{u_w^2} - \overline{w_w^2})}{\partial x} = \frac{1}{\rho h} \frac{D}{C} \quad \text{with}$$

$$\frac{\partial \overline{u_w w_w}}{\partial z} = \frac{1}{2\rho h} \frac{D}{C} \quad \begin{array}{l} D : \text{energy dissipation} \\ C : \text{wave celerity} \\ h : \text{mean water depth} \end{array}$$

$$\overline{u'w'} = -v_t \frac{\partial U}{\partial z} \quad v_t = Mh \left(\frac{D}{\rho}\right)^{1/3}, \text{ constant } M = 0.4$$

$$t = \frac{14}{\rho} \frac{D}{g HT} \quad \begin{array}{l} T : \text{wave period} \\ H : \text{wave height} \end{array}$$

The sediment transport model

The sediment transport is calculated by a satellite version of the numerical model TSEF V3.0 using Bailard formula (1981) in terms of the near-bed velocity field resulting from the previous model. The bed load and suspended load transport rates are expressed as :

$$\vec{q}_b = \frac{f_{cw} \epsilon_b}{\Delta g \operatorname{tg} \phi} \left[\langle |\vec{u}|^2 \vec{u} \rangle - \frac{\operatorname{tg} \theta}{\operatorname{tg} \phi} \langle |\vec{u}|^3 \vec{i} \rangle \right]$$

$$\vec{q}_s = \frac{f_{cw} \epsilon_s}{\Delta g W_s} \left[\langle |\vec{u}|^3 \vec{u} \rangle - \frac{\epsilon_s}{W_s} \operatorname{tg} \theta \langle |\vec{u}|^5 \vec{i} \rangle \right]$$

in which

\vec{q}_b bed-load transport rate m²/s

\vec{q}_s suspended load transport rate

f_{cw} friction factor wave+current

ϵ_b efficiency factor for bed-load transport $\epsilon_b = 0.13$

ϵ_s efficiency factor for suspended load transport $\epsilon_s = 0.024$

\vec{i} unit vector directed downslope

ϕ internal angle of friction of the sediment

W_s fall velocity

Δ apparent density

\vec{u} instantaneous nearbed velocity vector

$\operatorname{tg} \theta$ bed slope

$\langle \cdot \rangle$ time-averaged quantity

This formula is expected to give the transport rate inside and outside the surf-zone. The friction factor is adopted for the wave alone :

$$f_w = \exp \left(-6. + 5.2 \left(\frac{A_w}{k_s} \right)^{-0.19} \right)$$

with $A_w = \frac{H}{2 \sin kh}$ orbital excursion

$k_w = \frac{3}{D_s}$ roughness coefficient

D_s grain size diameter

In the present model the velocity \vec{u} is the summation of the time-averaged velocity and the instantaneous orbital wave velocity near the bed.

At the present state of knowledge, sediment transport formulae have broad correlation between predicted and observed values. Soulsby et al (1995) compared Bailard formula with data and they showed that only 57% of the predicted transport rate lay within a factor of 5 of the data. In the following application, it has been observed that the original formula overestimates the transport rate. So it is divided by 10 here, which is equivalent to increase the time scale.

Bed evolution model

The mass conservation of sand is also computed by the previous model which solves the equation for mass conservation of sediment.

Wave and current fields are updated when the bed evolution is greater than 0.5 time the water depth at 3 nodes of the mesh or 0.3 time at 10 nodes. In the following application this criteria occurs about every 30 hours.

Application

Description of the case

The domain of computation is presented on figure 2. At the initial time the bottom slope is 1:50 nearshore and the bed is horizontal offshore where the bottom level is -7.4 m.

The four lateral boundaries are closed for current and sediment transport. Only the offshore boundary is open for waves.

The generated wave at the offshore boundary is perpendicular to the shoreline. In the present model the wave is supposed to be regular, with a period of 8.0 s. The wave height is 1.2 m. The median grain size is 250 μ .

The mesh grid for wave computation contains 10500 nodes. It is refined in order to have at least 10 nodes per wave length. The horizontal mesh grid for current and sediment transport (fig 3) has 1450 nodes and each vertical profile has 9 nodes in the three-dimensional computation of currents.

Results

For the initial bottom, along a current cross-shore profile the wave height increases and reaches 1.6 m at the distance of the structure $y = -110$ m where the still water depth is -2.0 m (fig. 4), then it breaks. Wave pattern diffracts behind the structure.

In spite of the account for three-dimensional effects, the velocity field is nearly homogeneous over the water depth. In fact in this case the currents are mainly generated by alongshore gradient of surface elevation because the wave direction is nearly normal to the shoreline, and this gradient is constant over the vertical. The 3D effect would be stronger with oblique wave direction because the current would be also generated directly by driving terms with non-uniform vertical profile.

The near-bed velocity field displays a large eddy behind the breakwater (fig. 5). In the shallower part the intensity reaches 1.0 m/s whereas it is less along the structure in deeper part. In the open area the velocity field is very irregular because of variations of wave height. A cell takes place in the right hand side of the beach because of the closed boundaries at this corner. 2DV undertows are not

generated. The irregularities of the velocity field near the breaking line are due to the variation of the wave height in the longshore direction (fig. 4).

The resulting sand transport pattern displays very strong rate of $0.013 \text{ m}^2/\text{s}$ behind the breakwater in shallower water (fig. 6). Out of this area, the transport rate is very small except locally such as on the right hand side of the beach.

After 10 days of cumulative wave action, the accretion behind the breakwater is very strong, often greater than 2.0 m, creating a salient (fig. 7). The thickness of erosion in the bordering area is generally smaller, less than 1.5 m .

The wave, current and sediment transport patterns calculated with this new bathymetry are modified (fig. 8, 9 and 10). The wave field is more irregular. The velocities and transport rates behind the breakwater are more intense because of the reduction of the water depth. The cell seen initially on the right hand side of the beach creates disturbances which extends along the beach. The choice of constant wave conditions is probably responsible for this situation ; in prototype situation the variation of wave incidence for instance contributes to smooth bathymetry and avoid extension of such phenomenum.

Comparison with other models and available data

In a literature review reported by Moreno (1995), a similar case was mentioned. The shoreline evolution behind a detached breakwater with a normal wave was investigated in a wave tank (Rosen and Vajda 1982). The beach was built of coarse bakelite. In the computation, the offshore steepness H_0/L_0 is equal to 0.012 which is close to the experimental condition 0.015. The ratio of structure length on the distance from shoreline is 1.4 in the computation, 1.0 and 2.0 in tests 6 and 7 of the experiments.

In the experiments a salient is created behind the breakwater with one prominence in test 6 and two symmetrical prominences in test 7. Regarding the computed bed evolution after 10 days (fig. 7), the numerical modelling leads to formation of two salients (or one in the half-domain) as in test 7. However the immersed area was not measured in the basin, so it is not possible to go further in the comparison. Moreover the numerical modelling does not reproduce the stirring up of sand in the emerged part.

Watanabe et al (1986) also tested a detached breakwater in a experimental basin with movable bed. The beach was made of sand of 0.2 mm. In this test the wave breaks in deeper water than in the numerical simulation, roughly at the same distance offshore than the breakwater. According to the different conditions the numerical and experimental results cannot be superimposed. However it is seen that in intermediate water, the contourlines -3.0 m in the field case (fig. 7) and -6 cm in the basin for instance have the same curvature. In shallow water a prominence is created in both tests but the shoreline moves offshore just out of the lee of the structure in the basin whereas it is eroded in the same area in the field test.

After 15 days the volume of accretion behind the structure is equal to $23\ 000 \text{ m}^3$ according to the readjusted transport formula. This value is in good

agreement with other models of DHI, Uni. Liverpool, HR and STCPMVN developed in the project MAST2 G8M where it ranges from 21 000 to 29 000 m³ (Nicholson et al 1995).

It is noted that these two tests in experimental basins were not chosen for the present simulation because on one hand the transport formula of Bailard was elaborated for real life conditions and would not be appropriate for a reduced scale simulation. On the other hand the hydrodynamic results of the present simulation was already validated in a wave tank with fixed bed (Péchon et al 1995).

Conclusion

A compound system of models of the library TELEMAC have been developed in order to reproduce the refined evolution of the sea-bed in the surf-zone. In order to facilitate its use in practical applications, the codes have been coupled in an automatic procedure.

The sedimentological impact of waves on a sandy beach with a detached breakwater have been reproduced. The results are qualitatively satisfying since a salient have been generated behind the structure. They are in agreement with bed evolutions surveyed in experimental facilities and in nature. A quantitative analysis of the results performed in the framework of the working group 'Coastal Area Modelling' of the project MAST G8M shows that the volume of accretion computed here was in good agreement with the values obtained by other models.

Improvement of the models can be expected in the future by calculating instantaneous wave velocity field solving Boussinesq equations which include non-linear effects. Moreover Soulsby et al (1995) showed deficiencies of the transport formula compared with measurements. So further work is required for having a more reliable one.

Additional applications have to be done with this system of models in order to get experience and to appraise its limitations. More complex situations have to be investigated, for instance by accounting for tidal range.

Acknowledgement

This work was carried out as part of the G8 Coastal Morphodynamics research programme. It was funded partly by the Service Central Technique du Secrétariat d'Etat à la Mer and the Commission of the European Communities, Directorate General for Science, Research and Development, under contract n°MAST2-CT92-0027.

References

- Bailard, J.A., 1991, An energetics total load sediment transport model for plane sloping beach. *J. Geophys. Res.*, Vol. 86, No. C11.
- Broker Hedegaard, I., Rolvink, J.A., Southgate, H., Péchon, P., Nicholson, J. and Hamm, L., 1992, Intercomparison of coastal profile models. *23rd International Conference on Coastal Engineering*, Venice.
- Nicholson, J., Tanguy, J-M., Roelvink, J. A., Price, D., Péchon, P., Broker, I. and Moreno, L., 1996, Intercomparison of coastal area morphodynamic models. *Coastal Engineering* (submitted paper).
- Moreno, L., 1994, Minutes of MAST2 G8M Workshop, Gregynog.
- Mory, L. and Hamm, L., 1995, Experimental study of wave propagation, set-up and current around a detached breakwater. *Coastal Dynamics'95*, Gdansk.
- Péchon, P., 1994, Advances in 3D modelling of wave-driven currents. *Coastal Dynamics' 94*, Barcelone.
- Péchon, P., 1994, Numerical modelling of wave-driven currents in the surf-zone. *International Conference on Coastal Engineering*, Kobe.
- Péchon, P., Rivero, F., Johnson, H., Chesher, T., O'Connor, B., Tanguy, J-M., Karambas, T., Mory, M. and Hamm, L., 1996, Intercomparison of Wave-Driven Current Models, *Coastal Engineering* (submitted paper).
- Rosen, D. S. and Vajda, M., 1982, Sedimentological influences of detached breakwaters. *International Conference on Coastal Engineering*.
- Soulsby, R. L., 1995, The Bailard sediment transport formula : comparison with data and models. G8M final overall meeting, abstracts-in-depth.
- Watanabe, A., Maruyama, K., Shimizu, T., Sakakiyama, T. , 1986, Numerical prediction model of three-dimensional beach deformation around a structure. *Coastal Engineering in Japan*, Vol. 29.

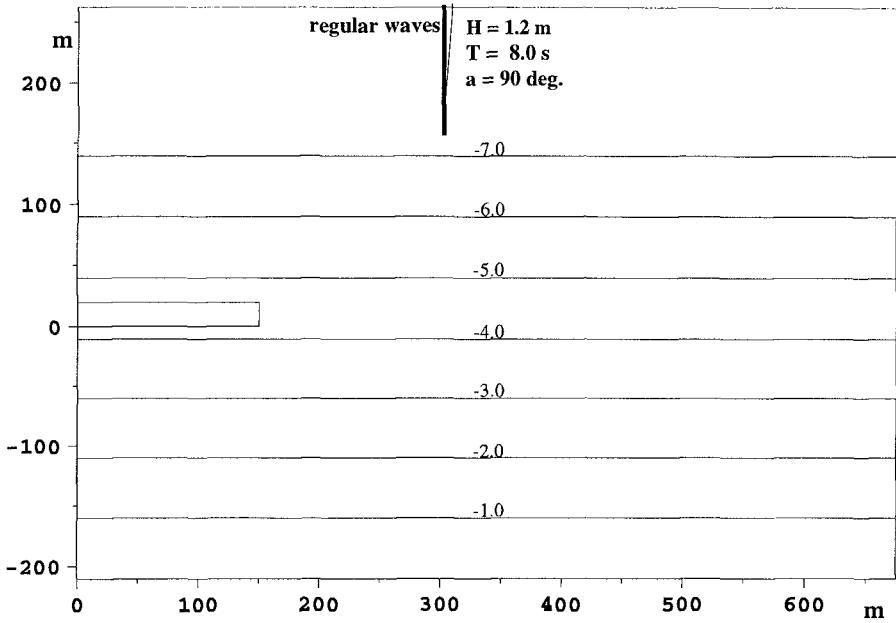


Figure 2 Bathymetry, initial time

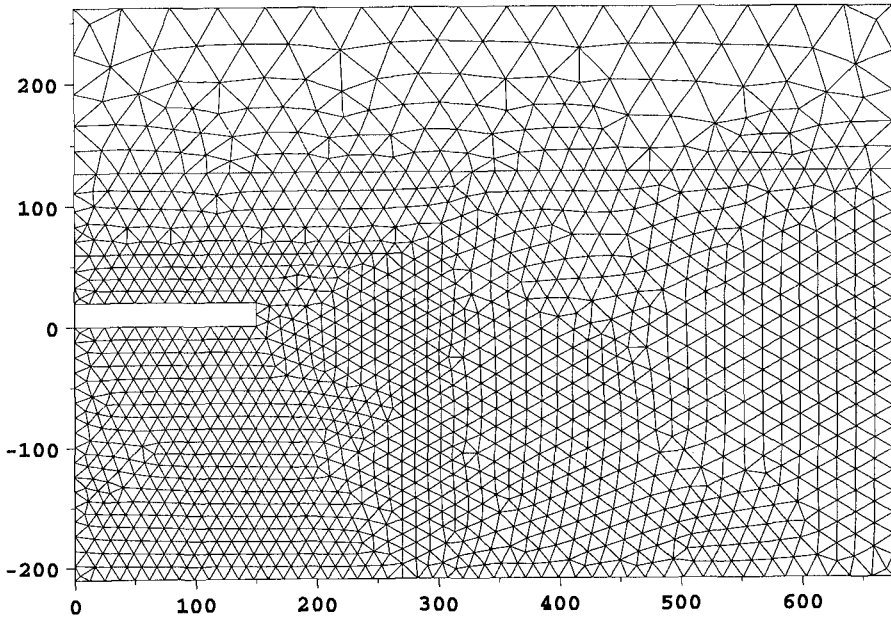


Figure 3 The mesh grid for computation of current and sediment transport

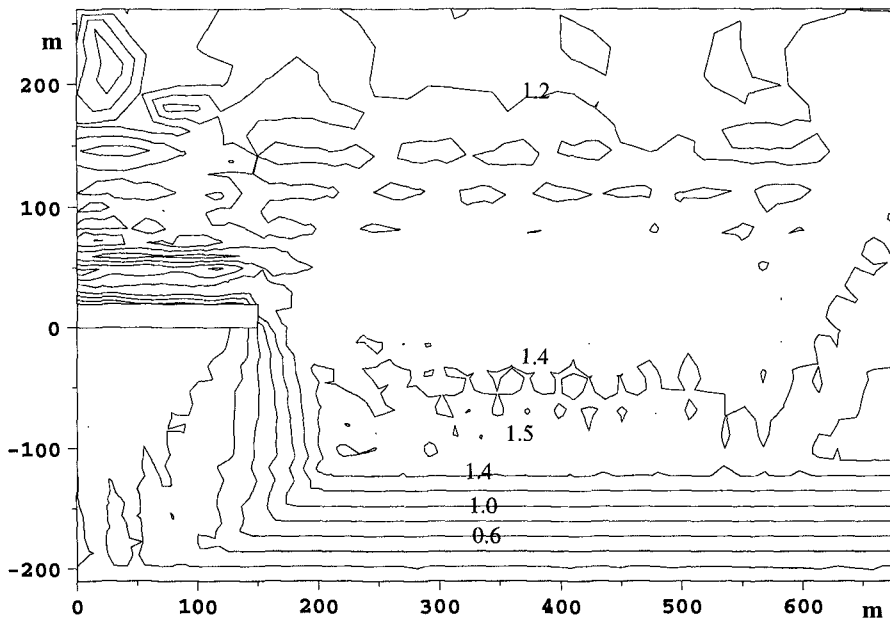


Figure 4 Wave field, initial time

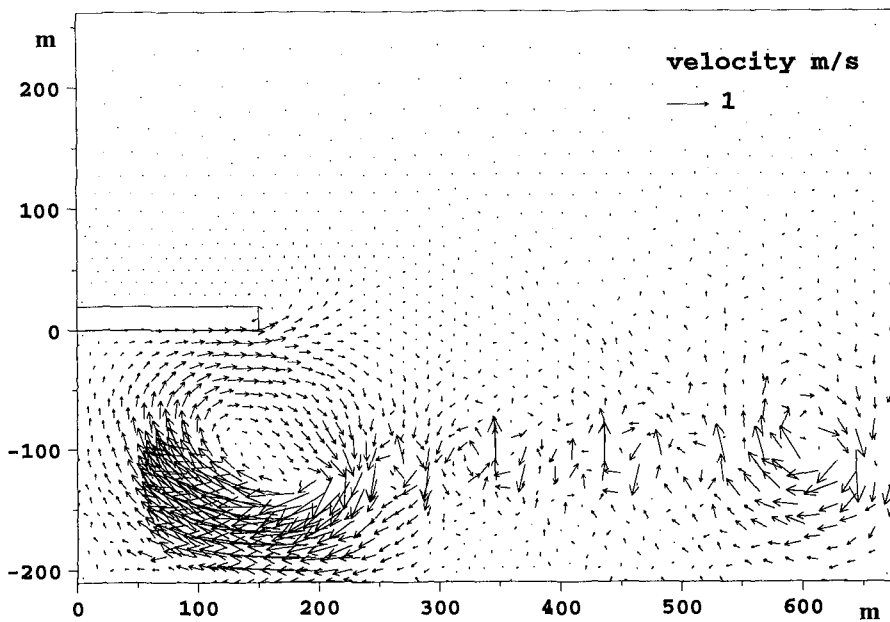
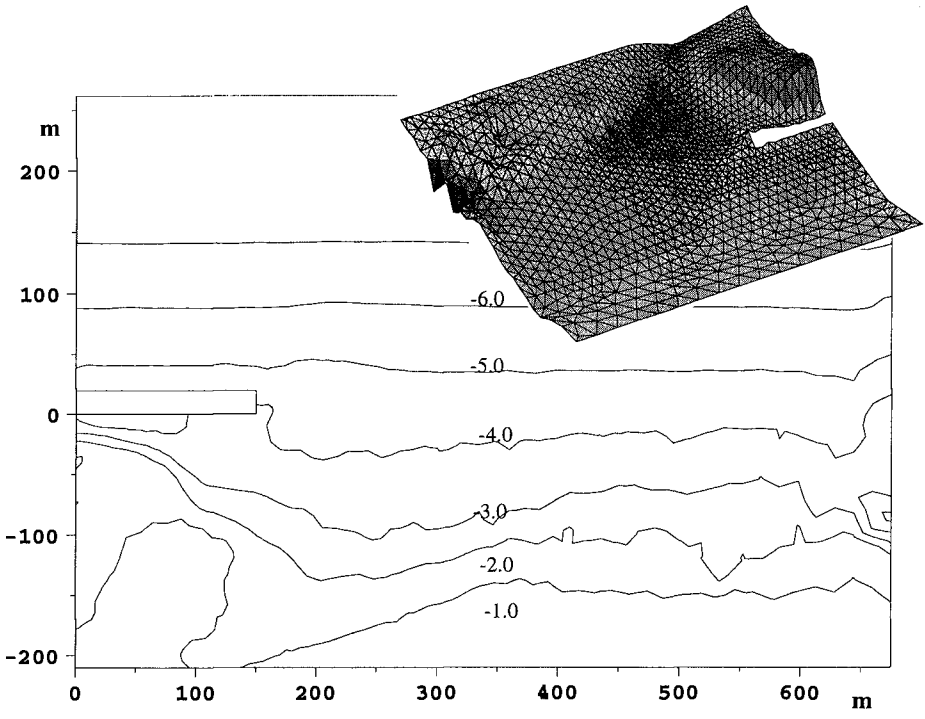
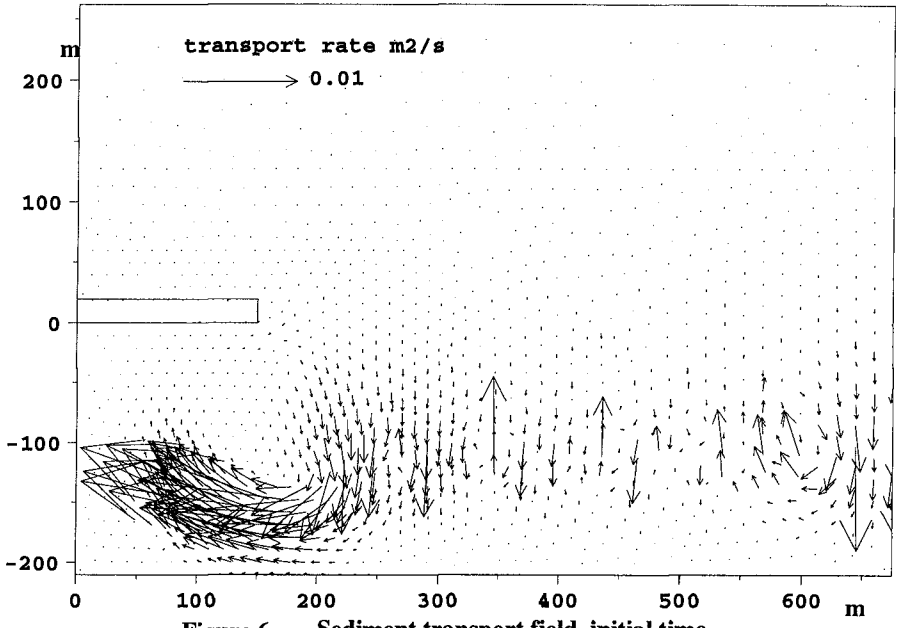


Figure 5 Velocity field near the bed, initial time



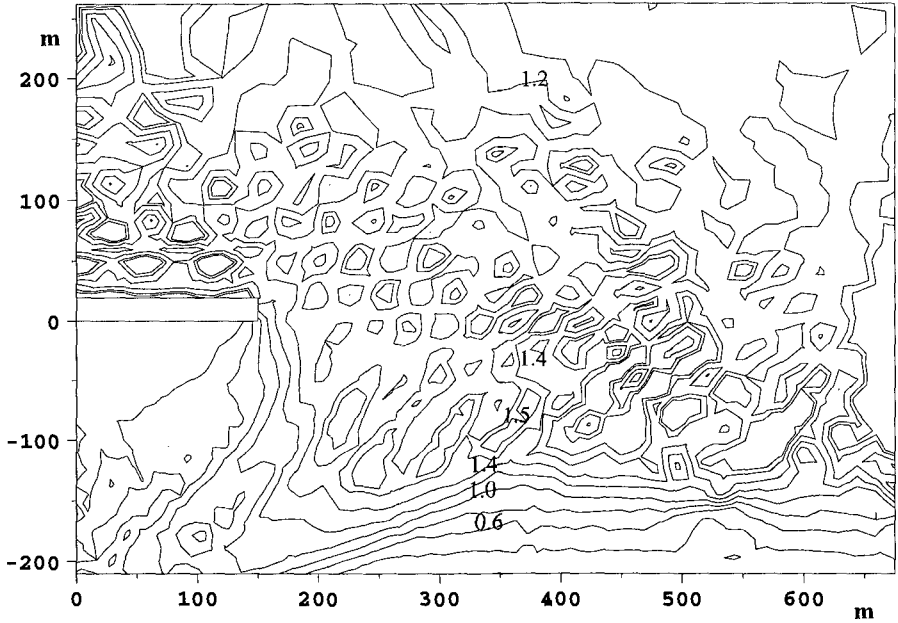


Figure 8 Wave field, time = 10 days

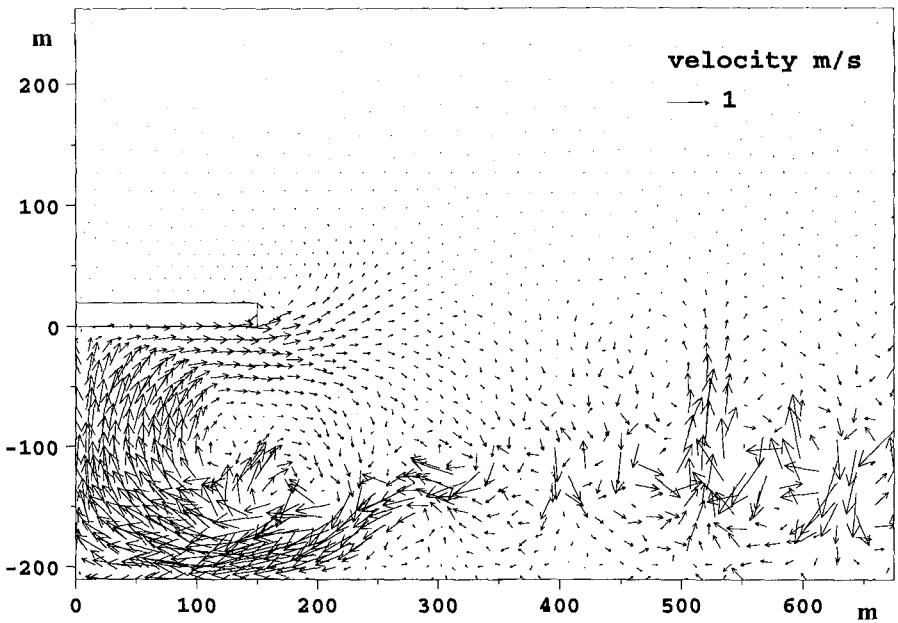


Figure 9 Velocity field near the bed, time = 10 days

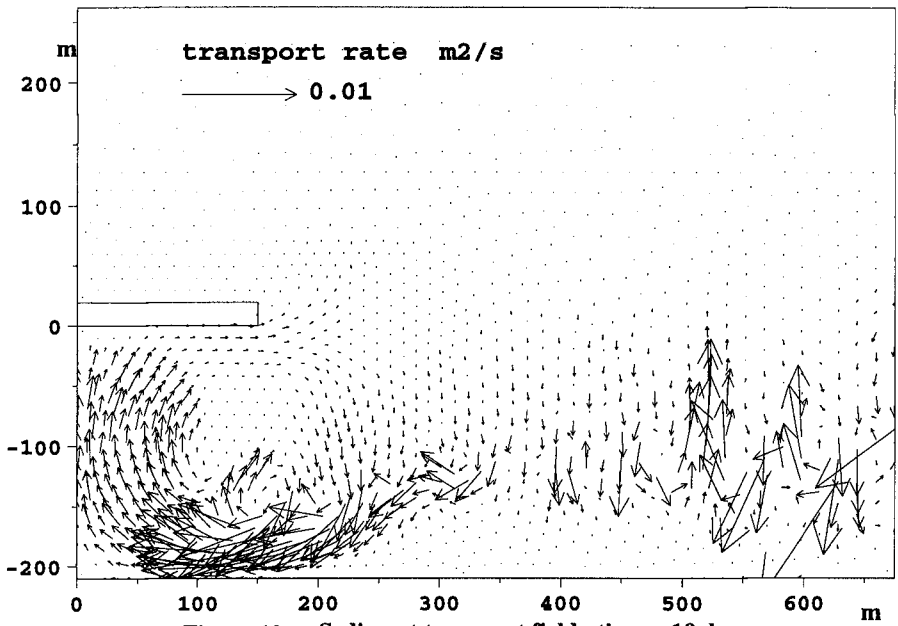


Figure 10 Sediment transport field, time = 10 days

CHAPTER 160

COMBINED DIFFRACTION AND TRANSMISSION OF WATER WAVES AROUND A POROUS BREAKWATER GAP

Xiping Yu¹ *and* Hiroyoshi Togashi²

ABSTRACT

An analytic method for the combined diffraction and transmission around a porous breakwater gap is presented. The method can be summarized as follows. First of all, it is necessary to decompose the incident wave into two components, according to the incidence angle and the permeability of the two breakwaters that form the gap. Then, let the breakwaters be completely transparent to the relevant component of the incident wave and ascertain the transmission field. Next, treat the breakwaters as solid to the other component of the incident wave and solve the diffraction field. Finally, superpose the transmission and the diffraction to give the objective wave motion. The available analytic methods for the diffraction by an aperture on solid wall are comparatively studied since they play the central role in working out the final solution of a real problem with combined diffraction and transmission. Sample computations are carried out for typical cases with both regular and irregular incidence. The computational results show that the phase effects of the porosity of the breakwaters on a combined wave field can be significant.

INTRODUCTION

Being constructed with rocks or concrete blocks in most of the engineering practices, segmented offshore breakwaters for the purpose of shore protection are usually of greater or lesser permeability. For this reason, it has long been a keen

¹Assoc. Prof., Dept. of Civ. Eng., Nagasaki Univ., 1-14, Bunkyo-Machi, Nagasaki City, Nagasaki 852, Japan.

²Prof., ditto.

interest of not only the scientific researchers but also the practicing engineers to have a good understanding on the effects of the permeability of a porous breakwater on the pertinent wave motion.

There exist possibly a few very different approaches to water wave problems with porous breakwaters involved. The one appeared to be relatively dogmatic is to isolate the region occupied by the porous skeleton and consider the details of the flow within the porous medium, which is in general of a complex picture and needs to be treated as viscous and turbulent. A solution of such configured problem also requires the relevant exterior flow to be matched with the flow inside the pores. Since both a straightforward look at the pore water flow and the matching procedure are extremely sophisticated, studies in the past decades, instead of dealing with Navier-Stokes flows, have been directed to modeling the effects of the porous skeleton on the fluid motion. There have been a few effective models based on such consideration established. The one by Sollitt and Cross (1972) and Madsen (1974), which includes both the resistance and the inertia forces exerted on the fluid by the porous skeleton, has indeed been applied to many practical problems.

Even with modeling, treatment of the flow inside a porous medium is still not easy at all. Practical solutions can only be obtained under very simplified conditions. This situation has motivated a more pragmatic approach that is to treat the surface of the porous structure as an absorptive or partial reflective boundary of the problem concerned. With this consideration, however, prescription of the amplitude and phase of the reflected wave relative to the approaching wave is necessary (Chen, 1986; Isaacson and Qu, 1989). Extension of the applicability of this approach thus requires continued efforts to establish highly accurate empirical formulas for the reflection coefficient and the phase trapping property of a structure with given porosity and known hydraulic conditions behind the structure.

The approach adopted in the present study is yet another one. It was originally proposed by Yu and Chwang (1994) and Yu (1995). As a porous breakwater is thin when compared to the local wavelength, the normal component of the seepage velocity through the porous body was noted to be proportional to the difference of the wave function at both sides of the breakwater. The proportionality coefficient is a function of the physical thickness, the porosity as well as the other properties of the porous medium and the wave.

The primary objective of the present study is to provide an analytic method for the combined diffraction and transmission around a porous breakwater gap. We shall try to find a method that takes advantage of the well established techniques for diffraction by a solid aperture. Emphasis will also be paid on the phase effects of the porosity of breakwaters.

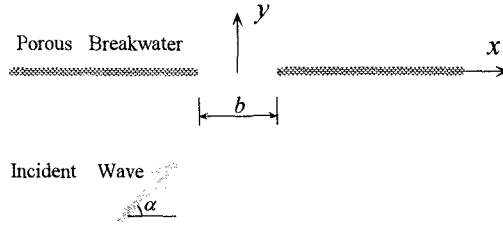


Fig. 1. Definition sketch of a porous breakwater gap.

THORRY

Formulation

The physical problem is sketched in Fig. 1. Outside the porous breakwaters we adopt the conventional assumptions that the fluid is inviscid and incompressible, and moreover, the fluid motion is irrotational. The three dimensional wave field can then be represented by a scalar velocity potential ϕ that satisfies the Laplace equation. Let the waves of interest be sinusoidal with respect to time and be of small amplitude. Hence, we can express the velocity potential in the following form with the time and the vertical coordinate separated:

$$\phi(x, y, z, t) = F(x, y) \cosh k(h + z)e^{i\sigma t} \tag{1}$$

where σ is the angular frequency of the wave motion, k is the wave number, h is the water depth, x and y are the horizontal coordinates, z is the vertical coordinate, and t is the time. F , usually called the wave function, is complex-valued with its modulus proportional to the amplitude and its argument equal to the relative phase of the surface oscillation. It can be readily confirmed that Eq. (1) satisfies the impermeable bottom condition and also the free surface condition as far as σ , k and h are related to each other through the dispersion equation:

$$\sigma^2 = gk \tanh kh \tag{2}$$

where g is the gravitational acceleration. By substituting Eq. (1) into the Laplace equation for ϕ we can show that $F(x, y)$ is governed by the following Helmholtz equation:

$$\nabla^2 F + k^2 F = 0 \tag{3}$$

where ∇ is the horizontal gradient operator.

For the problem concerned in the present study the boundary conditions include the incidence condition, the radiation condition at infinity and a partial

transmission condition along the permeable breakwaters. The incident wave, long-crested and propagating in the direction that forms an angle α with the positive x -axis, can be described by

$$F_0 = A_0 e^{ik(x \cos \alpha + y \sin \alpha)} \quad (4)$$

where $A_0 = gH/2\sigma \cosh kh$ and H is the incident wave height. The partial transmission condition at the porous breakwaters can be written as:

$$\left. \frac{\partial F}{\partial y} \right|_{y=0+} = \left. \frac{\partial F}{\partial y} \right|_{y=0-} = -ikG(F|_{y=0+} - F|_{y=0-}) \quad (5)$$

where $G = \gamma/k\delta\{f - i[1 + C_m(1 - \gamma)/\gamma]\}$ represents the permeability of the breakwaters while, δ is the physical thickness of the breakwaters (geometrically, the thickness of the breakwaters is considered to be zero) and, γ , f and C_m are the porosity, the linearized resistance coefficient and the added-mass coefficient of the porous medium, respectively. $y = 0+$ and $y = 0-$ indicate respectively the downwave and the upwave side of the breakwaters. As the ratio of the physical thickness of the breakwaters to the local wavelength is less than about 0.2, which is right in most of the practical situations, Eq. (5) has been shown to be in good agreement with experimental data (Yu, 1995). Since the wave function and its gradient are proportional to the dynamic pressure and the velocity of the fluid, respectively, in a linear wave theory, Eq. (5) is apparently identical to the Darcy's law which states that the velocity of the fluid flow in a porous medium is directly proportional to the pressure gradient. The actual difference between Eq. (5) and the Darcy's law is that we allowed a phase lag between the velocity and the pressure gradient to represent the inertia effects of the porous flow. This is trivial if the porous medium is closely-packed and the resistance dominates the flow. But it might be important if the porosity of the breakwaters is relatively large.

Reflection and Transmission

Consider the special case where the opening of the porous breakwater gap described in Fig. 1 approaches zero, or the two semi-infinite breakwaters are connected to become a continuous one extending to infinity at both ends. On this particular occasion, we are able to derive an explicit solution for both the reflected and transmitted waves under arbitrary incidence conditions.

Let the reflection and transmission coefficients of an infinite breakwater be defined as the ratios of the amplitudes of the reflected and the transmitted wave to the incident wave. Denoting the reflection and the transmission coefficient by K_r and K_t , respectively, we can formally express the wave field in the reflection region and that in the transmission region by

$$F_r = F_0 + K_r A_0 e^{ik(x \cos \alpha - y \sin \alpha)} \tag{6}$$

$$F_t = K_t A_0 e^{ik(x \cos \alpha + y \sin \alpha)} \tag{7}$$

Both K_r and K_t are assumed to be complex-valued so that information on not only the magnitude but also the phase of the reflected and transmitted waves is included. To satisfy the partial transmission condition (5) at the porous breakwater, we attain the following relations:

$$K_t \sin \alpha = (1 - K_r) \sin \alpha = G(1 + K_r - K_t) \tag{8}$$

which yields

$$K_r = \frac{\sin \alpha}{2G + \sin \alpha} \tag{9}$$

$$K_t = \frac{2G}{2G + \sin \alpha} \tag{10}$$

Back substitution of Eqs. (9) and (10) into Eqs. (6) and (7) gives rise to the final solution of the simple reflection-transmission problem. It must be pointed out that verification of Eqs. (9) and (10) by measured data under general conditions has not been carried out. It is because they were demonstrated to be in satisfactory agreement with laboratory experiments at $\alpha = \pi/2$ or under the normal incidence conditions we give credence to these equations in the present study.

Diffraction

In both the reflection and transmission regions we decompose the wave function F into two parts: the transmitted wave F_t and the diffracted wave F_d . That is, we let

$$F = F_t + F_d \tag{11}$$

where F_t is given by Eq. (7) with K_t defined by Eq. (10). For F_t is known we need only to fix F_d to finally determine F .

Since both F and F_t satisfy the Helmholtz equation, which is linear and homogeneous, F_d should do likewise to ensure Eq. (11). That is,

$$\nabla^2 F_d + k^2 F_d = 0 \tag{12}$$

At $x \rightarrow \pm\infty$, the effects of the breakwater gap on the wave field die off and, therefore, F approaches the relevant solution for a continuous breakwater. This can be written as

$$F_d \rightarrow 2K_r A_0 e^{ikx \cos \alpha} \cos(ky \sin \alpha) \quad \text{at } y \leq 0 \text{ and } x \rightarrow \pm\infty \tag{13}$$

$$F_d \rightarrow 0 \quad \text{at } y \geq 0 \text{ and } x \rightarrow \pm\infty \quad (14)$$

Along the porous breakwater, Eq. (5) leads to

$$\frac{\partial F_d}{\partial y} = 0 \quad \text{at } y = 0 \text{ and } |x| > \frac{b}{2} \quad (15)$$

Eqs. (12), (13), (14) and (15) are in fact the formulation for diffraction by an impermeable breakwater gap provided the incident wave is given by

$$F_2 = K_r A_0 e^{ik(x \cos \alpha + y \sin \alpha)} \quad (16)$$

which is the original incident wave expressed by Eq. (4) with a phase shift (since K_r is complex-valued) and an amplitude reduction (since $|K_r| < 1$).

It becomes now very obvious that the wave field around a porous breakwater gap can be treated as the superposition of a transmission and a diffraction by impermeable structures. Namely, we can split the incident wave (F_0) into two component waves ($F_1 = K_t A_0 e^{ik(x \cos \alpha + y \sin \alpha)}$ and $F_2 = K_r A_0 e^{ik(x \cos \alpha + y \sin \alpha)}$). To one of these components (F_1) the breakwater is completely transparent and transmission of wave into the region behind the breakwater is totally free. To the other component wave (F_2), on the other hand, the breakwater works like a solid wall. A complete reflection in front of it will occur and transmission of the wave energy into the region behind the breakwater is only by the diffraction process. Since both K_r and K_t are complex-valued in general, it should be emphasized that split of the incident wave is not simply a proportional division of the incident wave energy or amplitude. The phase effects of the porosity of the breakwater must be correctly considered.

A different way to view the combined diffraction and transmission around a porous breakwater gap can be explained as follows. Instead of Eq. (11) we let

$$F = K_r F_0 + K_t F_{0d} \quad (17)$$

where F_0 is interpreted as the wave field due to transparent breakwaters and F_{0d} as the wave field due to solid breakwaters (the relevant incidence is F_0 in either case). Considering the fact

$$K_r + K_t = 1 \quad (18)$$

we can treat a porous breakwater as the proportional combination of a transparent one and a solid one. The resulted wave field associated with the porous breakwater can also be interpreted as the similarly proportioned combination of the relevant wave field as the breakwater is transparent and solid. Again, it is important to notice that the proportional factors are complex-valued, so disintegration of breakwaters depends on not only the porosity of the breakwaters but also the properties of the wave.

ANALYTIC METHODS FOR DIFFRACTION

By the concept described in the previous section, the solution of wave motion around a porous breakwater gap can be obtained as long as the principle for decomposition of the incident wave or disintegration of the breakwaters in addition to an effective solution method for the diffraction by solid breakwater gaps are available. The theoretical elements which underlie the decomposition and disintegration course for given incidence condition and the porous properties of breakwaters has been discussed in details. In the following we shall give a brief summary of the useful methods for the diffraction by solid breakwater gaps with emphasis on their limitations when recently available numerical recipes are employed.

Water wave diffraction by solid breakwater gaps is one of the most classical subjects of coastal and harbor hydrodynamics. The problem has its analogy in both acoustics and electromagnetics. A large number of studies, analytical and numerical, have been carried out in the past half century. Exact solutions of the problem can be obtained by separation of variables in the elliptic coordinates. This elegant method is usually attributed to Morse and Rubenstein (1938) who gave the first outline of application for the diffraction of sound and electromagnetic waves by a slit in the infinite plane. Its effectiveness in solving the relevant water wave problems was widely recognized after Carr and Stelzriede's work (1952). The method is essentially straightforward but it does involve substantial efforts if numerical results are necessitated. The difficulty is owing to the appearance of the unusual Mathieu functions, for which advanced computational programs do not seem to have been readily available until this manuscript is to be finalized (although no sign showed they are more accurate than the present development, the routines in the recent book by Zhang and Jin (1996) are valuable). Even the excellent work by Sobey and Jonsson (1986) still had to partially rely on tables for some characteristic values. In principle, Morse and Rubenstein's method is valid with no restriction. However, accurate evaluation of the modified Mathieu functions of the third kind, which are involved in the solution, is rather difficult if the breakwater gap is wide. Owing to this fact, the exact solution method has not been recommended if the ratio of the opening of the breakwater gap to the local wavelength is larger than 3 (Carr and Stelzriede, 1952). Whether this suggested limit is still reasonable at present and how accurate is Morse and Rubenstein's solution near this limit are, however, not known.

The standard method for the diffraction by a solid breakwater gap with relatively large opening is attributed to Penney and Price (1952). The method is based on the Sommerfeld solution for the diffraction around the tip of a semi-infinite wall. It was widely promoted in the coastal engineering society (CERE, 1984), because of its relative simplicity from the numerical point of view when

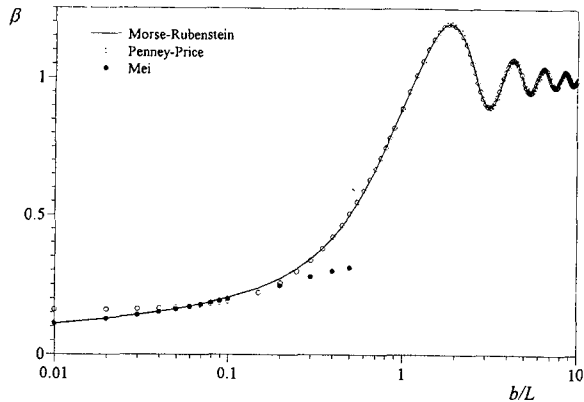


Fig. 2. Computed wave height at $x = 0$ and $y = L$ for varying opening of breakwater gap. Morse and Rubenstein's solution, Penney and Price's solution and Mei's solution are compared.

compared to Morse and Rubenstein's method. One needs only to evaluate the Fresnel integrals for determining the wave motion. Penney and Price's solution is not exact because it assumed that the scattered waves due to one breakwater arm produce no transverse flow at the position of the other arm and this assumption is approximately valid only when the opening of the breakwater gap is larger than a few wave length depending on the accuracy requirement.

Approximate solution for the diffraction by a breakwater gap with small opening is also available (Mei, 1989). This is called Mei's method and is based on matched asymptotic expressions. It assumed that the gap is equivalent to a singularity to a far-field observer. In the near-field, on the other hand, general representation of the wave field can be derived by conformal mapping. Mei's solution is concise but it can not be applied to cases with large ratio of the opening of the breakwater gap to the local wavelength. The limit for given accuracy is yet open to question.

Owing to the fact that practical problems in coastal and harbor engineering may not always fall inside the limits of the approximate solutions for large and small gaps, we developed a highly accurate numerical method for evaluating Morse and Rubenstein's solution in the present study. The characteristic values of the Mathieu functions in the method are determined through finding the eigenvalues of real-symmetric tridiagonal metrics with elements differing widely in order of magnitude. The relevant eigenvalue problems are solved by the QL method with implicit shifts (Press et al., 1989) in double precision. The computer codes were strictly checked by the tables given in Abramowitz and Stegun (1972). The Bessel functions of the various kinds involved in the expansions of the Mathieu functions are also evaluated in double precision, following the

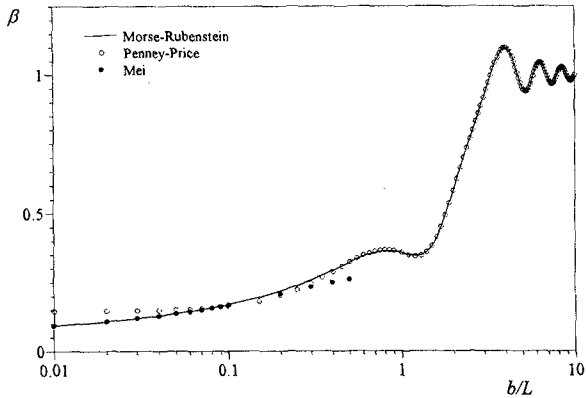


Fig. 3. Computed wave height at $x = L$ and $y = L$ for varying opening of breakwater gap. Morse and Rubenstein's solution, Penney and Price's solution and Mei's solution are compared.

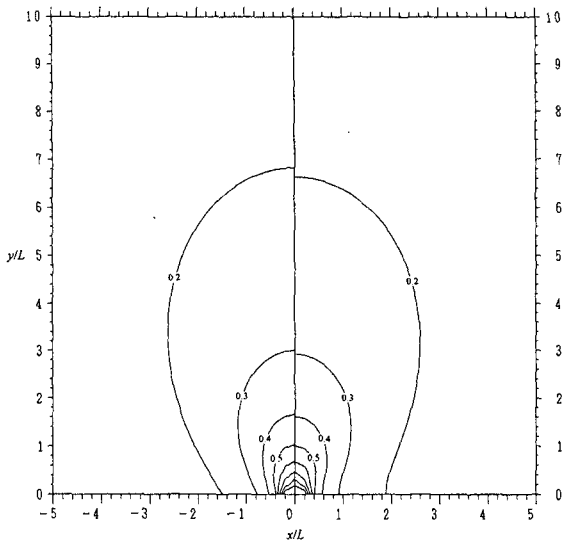


Fig. 4. Comparison of the wave height distribution around the breakwater gap. The left half is Penney and Price's solution. The right half is Morse and Rubenstein's solution. $b/L = 0.5$.

schemes given by Watanabe et al. (1989).

Figs. 2 and 3 are the plots of the relative wave height β (= the ratio of the local wave height to the incident wave height) against the relative opening of the breakwater gap (= the ratio of the opening b to the wavelength L) at two different positions. It can be noticed that the agreement between Morse and Rubenstein's solution and Penney and Price's solution is fairly good if b/L is larger than about

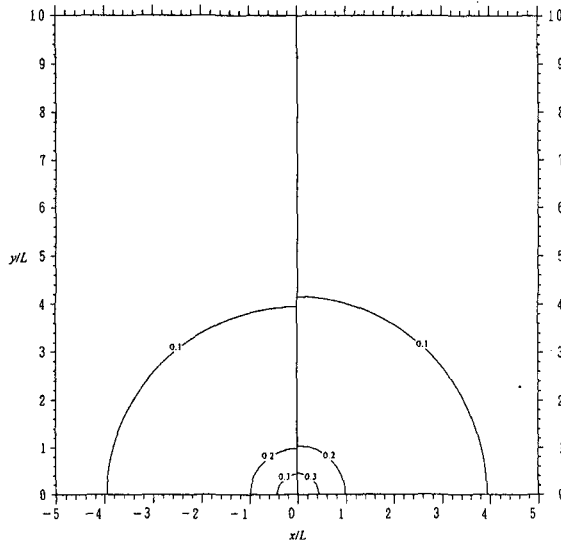


Fig. 5. Comparison of the wave height distribution around the breakwater gap. The left half is Mei's solution. The right half Morse and Rubenstein's solution. $b/L = 0.1$.

0.5. At the other end, Morse and Rubenstein's solution almost coincides with Mei's solution if b/L is less than about 0.1. Accurate evaluation of Morse and Rubenstein's solution has been successfully done for b/L up to more than 10, which is much larger than the number reported previously.

Figs. 4 and 5 also compare Morse and Rubenstein's solution with Penney and Price's solution and Mei's solution. The comparisons are made for the wave height distribution around the breakwater gap at $b/L = 0.5$ and $b/L = 0.1$, respectively. The selected ratios of the opening of the breakwater gap to the wavelength can actually be viewed as the limits of the approximate solutions. The agreement, as can be seen, is fairly good from the engineering point of view.

COMBINED DIFFRACTION AND TRANSMISSION

Hereinbelow we examine the combined diffraction and transmission around a porous breakwater gap with numerical examples. The first case under consideration is of an oblique incidence with $\alpha = \pi/4$. The relative opening of the gap is 1.0. For reference, the diffracted wave height distribution as the breakwaters are solid, which can also be treated as a limiting case of the combined diffraction and transmission at $G = 0$, is shown in Fig. 6. The wave pattern we can have is evidently a typical one for pure diffraction which represents the dynamic

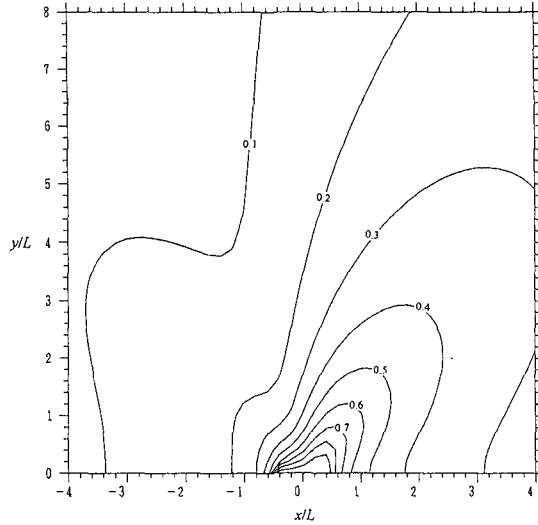


Fig. 6. Wave height distribution around a solid breakwater gap. $b/L = 1.0$ and $\alpha = \pi/4$.

processes of essentially radial waves.

The combined diffraction and transmission around the gap formed by breakwaters with any permeability can be readily assembled from a unidirectional wave and the diffracted wave as depicted in Fig. 6. Fig. 7 presents an example for $G = 0.25 + 0.25i$, that is, $K_r = 0.500 - 0.207i$ and $K_t = 0.500 + 0.207i$. What we can recognize from this figure is that the wave pattern for combined diffraction and transmission is very different from the one for a pure diffraction. This may have to be explained by the phase interactions between the diffraction (an essentially radial wave) and the transmission (a unidirectional wave).

To understand the combined diffraction and transmission of random waves, we turn to a case with normal incidence of the Bretschneider-type spectrum:

$$S(f) = 0.430\bar{H}^2\bar{T}(\bar{T}f)^{-5} \exp[-0.675(\bar{T}f)^{-4}] \tag{19}$$

where \bar{H} is the mean wave height, \bar{T} is the mean wave period and $f = \sigma/2\pi$ is the frequency. Fig. 8 is a comparison of the energy-spectrum of the wave at $x = \bar{L}$ and $y = \bar{L}$ (\bar{L} is the mean wavelength) under various conditions of the porosity of the breakwaters. In the computations, the mean wave period is 10 s and the still water depth is considered to be 5 m. The opening of the breakwater gap equals to the mean wavelength. The permeability of the breakwaters in terms of the mean wavelength is assumed to take different values representing structures with different porosity ($G = 0$ is for solid breakwaters; $G = 0.1$ for densely-packed and resistance dominated breakwaters; and $G = 0.25(1 + i)$ for loosely-packed and

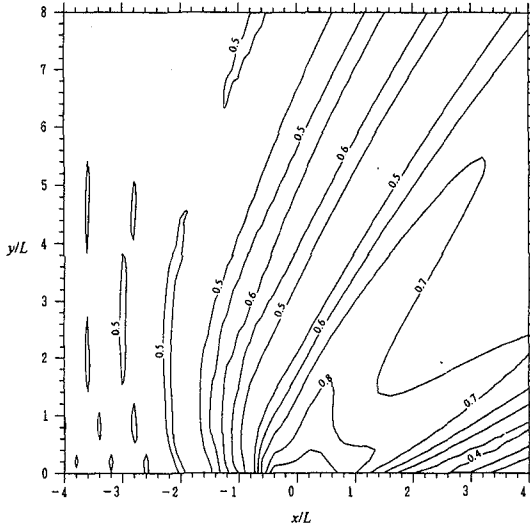


Fig. 7. Wave height distribution around a porous breakwater gap with combined diffraction and transmission. $b/L = 1.0$, $\alpha = \pi/4$ and $G = 0.25(1 + i)$.

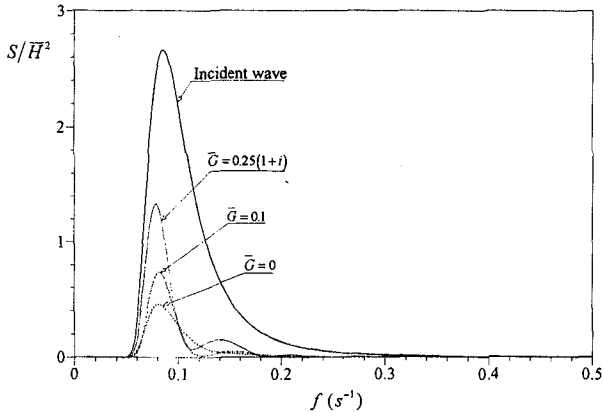


Fig. 8. Spectrum of the combined diffraction and transmission at $x = \bar{L}$ and $y = \bar{L}$ with various permeability of the breakwaters. Incidence is of the Bretschneider-type. $b/\bar{L} = 1.0$.

moderately dissipative breakwaters). The important information included in the figure is that the wave spectrum behind the breakwater undergoes significantly different transformation for different properties of the breakwaters. When the breakwaters are impermeable, the spectrum is of only one peak, like the incident wave. When they are porous, however, the spectrum shows at least two peaks. This implies that the performance of the breakwaters depends closely on the

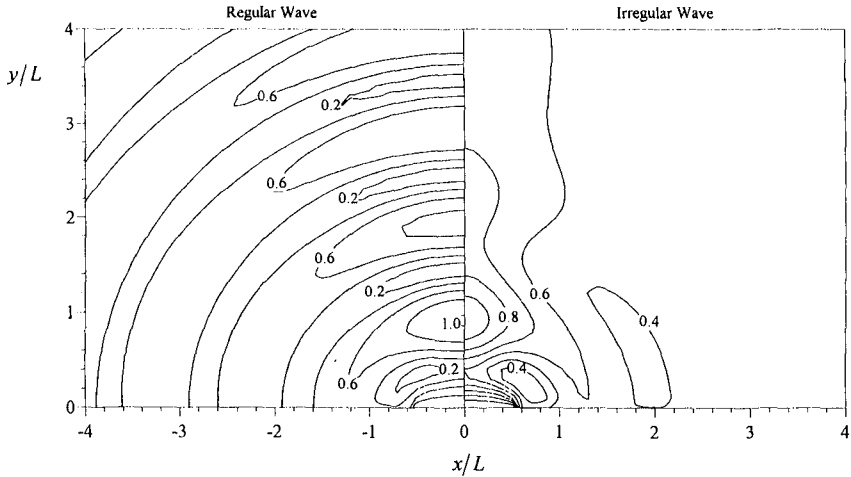


Fig. 9. Comparison of the wave height distribution for regular and irregular waves. Normal incidence is considered. $b/L = 1.0$ and $G = 0.25(1 + i)$.

wavelength. It should also be noted that as the permeability increases, wave energy behind the breakwater increases, as it should be. But, the increase of the energy related to long waves is particularly remarkable. This indicates that a porous breakwater is less effective to long waves.

Fig. 9 compares the wave height distribution around the porous breakwater gap with $G = 0.25(1 + i)$ when the incident wave is regular and irregular. We are able to observe totally different wave patterns for monochromatic and spectral waves. This is again explained by the effects of phase interactions between diffracted and transmitted waves.

SUMMARY AND CONCLUSIONS

We presented an useful method for the combined diffraction and transmission around porous breakwater gaps. The method can be summarized as follows: (1) we need to decompose the incident wave into two components, according to the incidence angle and the permeability of the breakwaters which form the gap; (2) we assume the breakwaters to be completely transparent to the relevant component of the incident wave and ascertain the transmission field; (3) we treat the breakwaters as solid to the other component of the incident wave and solve the diffraction field; (4) we superpose the transmission and the diffraction to obtain the objective wave. Since they play the central role in working out the final solution of a real problem with combined diffraction and transmission, methods for the diffraction by solid breakwater gaps were comparatively stud-

ied. Limitations of the approximate solutions for large and small breakwater gaps were demonstrated. Sample computations were done for typical cases with combined diffraction and transmission. The computational results showed that the effects of phase interactions between diffracted and transmitted waves, which result from the porosity of the breakwaters, are not insignificant.

REFERENCES

- Abramowitz, M. and Stegun, I. A. (1972). *Handbook of mathematical functions*, Dover Publications, New York, USA.
- Carr, J. H. and Stelzriede, M. E. (1952). "Diffraction of water waves by breakwaters." *Proc., Symp. on Gravity Waves*, NBS Circ. 521, 109-125.
- CERC (1984). *Shore Protection Manual*, US Army Corps of Engineers, Washington, DC, USA.
- Chen, H. S. (1986). "Effects of bottom friction and boundary absorption on water wave scattering." *Appl. Ocean Res.*, 8(2), 99-104.
- Isaacson, M. and Qu, S. (1989). "Waves in a harbour with partially reflecting boundaries." *Coast. Engrg.*, 14, 193-214.
- Madsen, O. S. (1974). "Wave transmission through porous structures." *J., Wtrwy., Harb. and Coast. Engrg. Div.*, ASCE, 102(1), 169-188.
- Mei, C. C. (1989). *The Applied Dynamics of Ocean Surface Waves*, World Scientific, Singapore.
- Morse, P. M. and Rubenstein, P. J. (1938). "The diffraction of waves by ribbons and by slits." *Physical Review*, 54, 895-898.
- Penney, W. G., and Price, A. T. (1952). "The diffraction theory of sea waves and the shelter afforded by breakwaters." *Phil. Tran., Royal Soc. London*, 244(A), 236-253.
- Press W. H., Flannery, B. P., Teukolsky, S. A. and Vetterling, W. T. (1989). *Numerical Recipes*, Cambridge University Press, New York, USA.
- Sobey, R. J., and Johnson, T. L. (1986). "Diffraction patterns near narrow breakwater gaps." *J., Wtrwy., Port, Coast. and Oc. Engrg.*, ASCE, 112(4), 512-528.
- Sollitt, C. K., and Cross, R. H. (1972). "Wave transmission through porous breakwaters." *Proc., 13th Conf. on Coastal Engrg.*, ASCE, 1827-1846.
- Watanabe T., Natori, M. and Oguni, T. (1989). *Numerical Methods and Software*, Maruzen, Tokyo, Japan.
- Yu, X. (1995). "Diffraction of wave waves by porous breakwaters." *J., Wtrwy., Port, Coast. and Oc. Engrg.*, ASCE, 121(6), 275-282.
- Yu, X. and Chwang, A. T. (1994). "Wave induced oscillation in harbors with porous breakwaters." *J., Wtrwy., Port, Coast. and Oc. Engrg.*, ASCE, 120(2), 125-144.
- Zhang, S. and Jin, J. (1996). *Computation of Special Functions*, Wiley Interscience, New York, USA.

CHAPTER 161

PREDICTION OF WAVE REFLECTION FROM ROCK STRUCTURES: AN INTEGRATION OF FIELD & LABORATORY DATA.

Mark A. Davidson¹, Paul A.D. Bird², David A. Huntley¹, and Geoff N. Bullock².

ABSTRACT: An empirical predictive scheme for wave reflection from rock island breakwaters is derived from a multiple regression analysis of a large data set (780 data points) which includes both laboratory and full-scale measurements. The large parameter space embraced due to the inclusion of both laboratory and field data leads to a robust solution for the prediction of wave reflection. The resulting equation expresses the reflection coefficient as a function of a number of dimensionless parameters which can be identified with specific physical processes. These include wave breaking, dissipation due to friction and turbulence induced by structural roughness, and transmission into and through the breakwater.

SYMBOLS

d_t	Depth at the toe of the structure relative to the still water level.
D	Significant armour diameter $= (W_{50}/\rho)^{1/3}$
H_i	Significant wave height
K_r	Frequency averaged reflection coefficient $= \sqrt{\int S_r df / \int S_i df}$
f	Frequency
L_o	Deep water wavelength
P	Notional permeability (Van der Meer, 1988)
r	Multiple regression correlation coefficient
R	Reflection number $= \frac{L_o^2 d_t \tan \beta}{H_i D^2}$, (Davidson <i>et al.</i> , 1996)
S_i, S_r	Incident and reflected spectral estimates
W_{50}	Median mass of rock armour
β	Average structure slope
ρ	Density of rock armour
σ	Standard error in multiple regression analysis
ξ	Iribarren number $= \tan \beta / \sqrt{H_i / L_o}$

¹Institute of Marine Studies, University of Plymouth, Drake Circus, Plymouth, Devon, PL4 8AA, UK.

²School of Civil & Structural Eng., University of Plymouth, Palace Court, Palace St., Plymouth, Devon, PL1 2DE, UK.

INTRODUCTION

Much attention has been focused on the prediction of wave reflection from rubble mound structures (e.g. Seelig and Ahrens 1981, Postma 1989, Van der Meer 1992, Allsop and Channell 1989, Hughes 1995, Davidson *et al.* 1994.). A recent review can be found in Davidson *et al.*, 1996. Most predictive schemes for wave reflection have been based on empirical relationships involving the Iribarren number derived from laboratory experiments. Whilst the Iribarren number describes well the form of breaking waves (Battjes, 1974) and hence dissipation due to breaking, the processes of turbulent dissipation due to the roughness of the structure and transmission into and through the structure are not obviously related to the Iribarren number and have normally been accounted for through additional empirical coefficients. The combined effects of the empirical nature of these equations and the inevitable limited parameter space have meant that these solutions are rarely universal particularly at full-scale. This problem is compounded by potential scale effects and inconsistencies in the method of analysing wave reflection.

Davidson *et al.*, 1996, collected full-scale data seawards of a rock island breakwater both before and after the addition of more armour to the seawards face of the structure. This modification was designed to reduce the slope of the structure hence enhancing structural stability and ameliorating wave reflection. Conventional plots of reflection coefficient versus Iribarren number showed the pre- and post- modification data sets as two distinct populations. The failure of the Iribarren number to condense both data sets on to a single curve severely limits the accuracy of predictive schemes which express wave reflection as some function of ξ .

For these full-scale data an improved parameterization of wave reflection was derived in terms of a dimensionless reflection number R where:

$$R = \frac{L_o^2 d_t \tan \beta}{H_t D^2} = \xi \left(\frac{L^{3/2} d_t}{H^{1/2} D^2} \right) \quad (1)$$

and;

$$K_r = \frac{0.635 \sqrt{R}}{41.2 + \sqrt{R}} \quad \text{or} \quad K_r = 0.151 R^{0.11} \quad (2)$$

It can be seen from Equation 1 that R revises the relative weighting of wave height and wavelength in the Iribarren number and includes other physically significant parameters such as the depth at the toe and the characteristic armour diameter.

Whilst equations based on R provide an excellent prediction of wave reflection ($r=0.87$, $\sigma=0.055$) for these full-scale data (within the parameter space of the measurements) poor predictions were found for laboratory data. These inconsistencies can be explained in part due to the potential scale effects which may significantly contribute to differences between the field and laboratory data (up to 10%, Shimada *et al.*, 1986), but more significantly to the empirical nature of Equations 1 and 2 and the limited parameter space of the data from which they were derived.

This contribution aims to minimise problems associated with limited parameter space by integrating both laboratory and field investigations. The advantage of this approach is that although it is empirical the resulting predictive scheme is remarkably robust over a broad range of scale and incident wave conditions.

The problem of predicting wave reflection is essentially the solution to the energy balance equation including the processes of wave reflection, dissipation (due to breaking, turbulence and friction) and transmission (both through and over the structure). Therefore an accurate solution for the reflection coefficient intuitively should include parameters which relate (even if only empirically) to each of the most significant processes involved (Figure 1). Thus, solutions based on a single parameter like the Iribarren number which only obviously relate to the process of dissipation due to breaking are only likely to provide a ubiquitous solution for wave reflection where breaking is the dominant process.

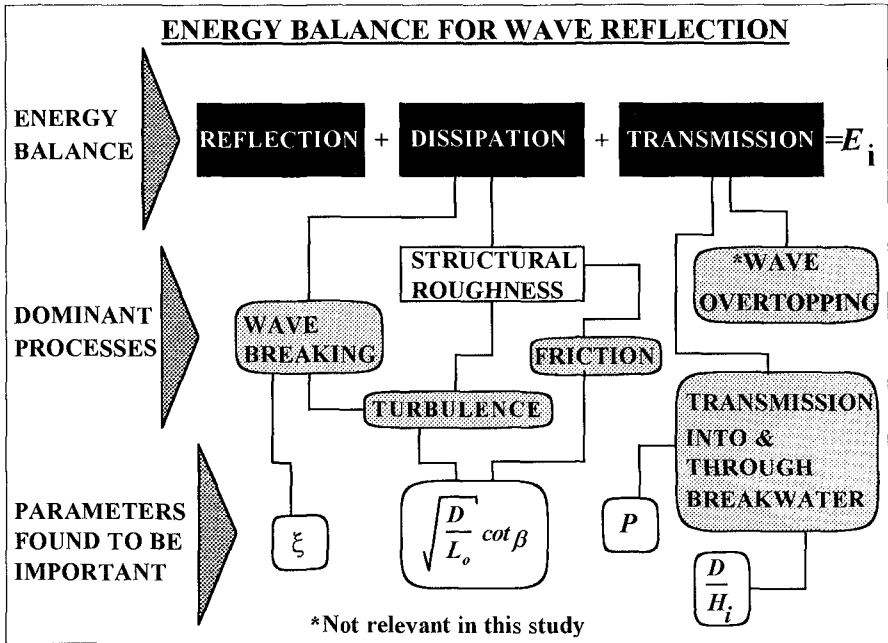


Figure 1: Schematic diagram illustrating the dominant processes affecting wave reflection and some of the parameters associated with them. Here E_i is the incident wave energy.

DATA BASE

Data analysed here includes laboratory tests from Seelig and Ahrens (1981), Allsop and Channell (1989), Postma (1989), and field data from a natural rock island breakwater, both before and after a modification of the seawards slope of the structure (Davidson *et al.*, 1996). The reader is referred to the original references for details of these experiments. A summary of each of these experiments including the ranges of specific dimensionless variables have been summarised in Table 1. All available information from each experiment was entered into a data base. For each experiment information was available on; wave height, deep/shallow water

wavelength, structure slope, armour diameter, permeability, the number of armour layers and depth at the toe of the structure. In all cases wave overtopping was not significant.

Author (s)	Field or Lab. F / L	$\frac{H_i}{L_o}$	$\cot \beta$	$\frac{D}{H_i}$	$\sqrt{\frac{D}{L_o}} \cot \beta$	P	$\frac{d_r}{L_o}$	$\frac{H_i}{H_b}$	ξ	K_r	Analysis Method / No. of Gauges
Seelig & Ahrens, 1981	L	0.005-0.050	2.5	0.52-1.67	0.12-0.57	0.04	0.015-0.369	0.49-0.11	1.8-7.5	0.115-0.561	Goda & Suzuki, 1976 / (3)
Allsop & Channell, 1989	L	0.003-0.040	1.50-2.50	0.31-0.94	0.08-0.29	0.04-0.1	0.075-0.342	0.06-0.29	2.0-11.7	0.170-0.700	Goda & Suzuki, 1976 / (3)
Postma, 1989	L	0.002-0.057	1.50-3.00	0.16-0.87	0.07-0.65	0.1-0.6	0.02-0.289	0.09-0.95	0.7-8.9	0.122-0.738	Kajima, 1969 / (2)
Davidson <i>et al.</i> , 1996	F	3×10^{-4} -0.036	0.82	1.19-23.39	0.02-0.30	0.6	0.003-0.360	0.03-0.46	10.0-113.	0.263-0.734	Gaillard <i>et al.</i> , 1982 / (3)
Davidson <i>et al.</i> , 1996	F	8×10^{-4} -0.021	1.55	0.98-9.60	0.09-0.51	0.6	0.007-0.074	0.08-0.68	3.0-26.5	0.274-0.600	Gaillard <i>et al.</i> , 1982 / (3)

Table 1: A summary of the data sets, parameter space and analysis techniques used in this study.

RESULTS

A multiple regression analysis technique was used in order to determine the relationship between the frequency averaged reflection coefficient and various non-dimensional variables which are identifiable with of specific physical processes affecting wave reflection. The results of this analysis are summarised in Table 2. A number of parameters were tested, and the impact of each parameter on the wave reflection was assessed through the correlation coefficient (r) and standard error (σ). If the addition of a parameter led to a reduction in the standard error and an increase in the correlation coefficient then the parameter was assessed as being significant and left in the equation for further analysis. If however, the addition of a parameter lead to an increase or no significant change in the standard error (or rise in correlation coefficient) it was neglected in subsequent tests.

Parameters which were found to significantly improve predictions of wave reflection are shown in Figure 1 and listed below:

- 1) The Iribarren number which characterises the form of the breaking waves and hence relates to the dissipation of wave energy due to breaking.
- 2) A relative diameter term (D/H_b , referred to here as the transmission parameter) which Van der Meer, 1992 has shown empirically to be related to wave transmission.
- 3) A roughness parameter ($\sqrt{\frac{D}{L}} \cot \beta$, Seelig & Ahrens, 1981). The effective roughness of the structure increases both as the armour diameter increases relative to the wavelength of the waves, and as the slope of the structure is reduced. Gentler slopes give rise to increased energy dissipation due to the effect of turbulence and viscosity of water close to the sea bed.

4) Van der Meer's Permeability parameter (Van der Meer, 1988).

5) The relative toe depth $\left(\frac{d}{L_o}\right)$. The exact physical significance of this parameter in the process of wave reflection is not clear. The effect of decreasing the depth at the toe will ultimately lead to breaking offshore of the structure, thus reducing reflection. Conversely, in the case of a fully permeable breakwater transmission of wave energy through the structure may increase (reducing wave reflection) with increasing d_t as the width of the breakwater (at mean water level) is reduced.

The relationship between K_r and some of the variables tested was non-linear and an improved correlation could be obtained if the logarithm of the variable was taken prior to carrying out the regression analysis. This is true if the effect of a given variable on wave reflection diminishes as the value of that variable increases. The Iribarren number provides a good example of this. When waves are steep enough to break (low Iribarren numbers, $\xi < 4$) wave reflection increases proportionately with the Iribarren number through the continuum of breakers from the extremes of spilling to surging. However, when waves cease to break further increase in wave reflection produces no change in the reflection coefficient.

No. of Variables	$\xi = \frac{\tan \beta}{\sqrt{H_i/L_o}}$	$\frac{D}{H_i}$	$\sqrt{\frac{D}{L_o}} \cot \beta$	P	$\frac{d_t}{L_o}$	c	r	σ
	Iribarren Number	Transmission	Roughness	Permeability	Rel. toe depth	y-axis Intercept	Correlation coeff.	Standard error
1	0.02					0.203	0.622	0.1218
1	0.442*					0.065	0.828	0.0873
2	0.585*	-0.027				0.024	0.884	0.0727
3	0.354*	0.014	-0.596			0.288	0.904	0.0667
3	0.282*	-0.013	-0.383*			-0.071	0.910	0.0645
4	0.327*	-0.012	-0.388*	-0.192		-0.058	0.931	0.0568
5	0.298*	-0.011	-0.321*	-0.191	-0.358	0.049	0.943	0.0521

Table 2: Multiple regression analysis statistics showing parameter coefficients, correlation coefficients and standard errors. Note that * sign indicates that the logarithm of the variable has been taken prior to the regression analysis.

Table 2 gives a number of predictive equations for wave reflection based on these data. The number of parameters and the accuracy of the equations increasing towards the bottom of the table. Also given are the linear, multiple regression coefficients. The best predictor of wave reflection is given at the bottom of this table (in bold type) and yields the following equation:

$$K_r = 0.298 \log(\xi) - 0.011 \left(\frac{D}{H_i}\right) - 0.321 \log\left(\sqrt{\frac{D}{L_o}} \cot \beta\right) - 0.191P - 0.358 \left(\frac{d_t}{L_o}\right) - 0.049 \quad (3)$$

Predicted and observed reflection coefficients from Equation 3 are shown in Figure 2.

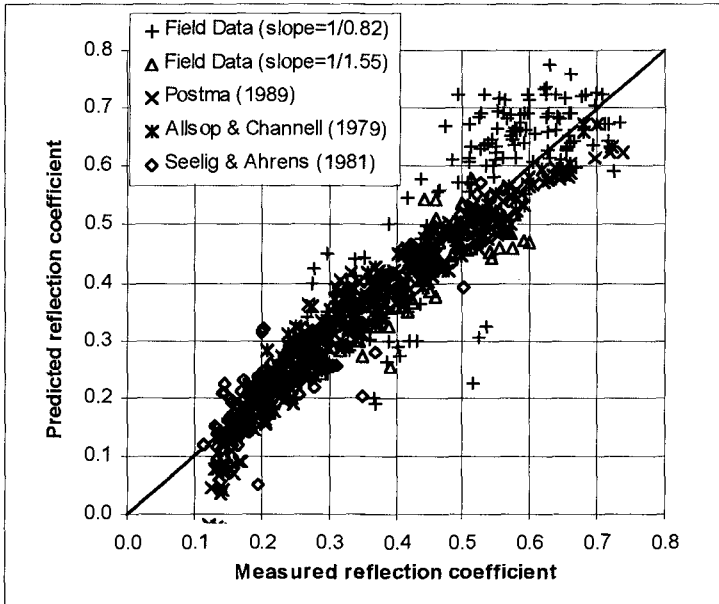


Figure 2: Predicted and measured reflection coefficients for both field and laboratory data.

DISCUSSION

Inspection of Table 2 shows that the accuracy of the predictive scheme for wave reflection is significantly improved (as indicated by the correlation coefficient and standard error statistics) through the addition of each of the 5 variables. It should be noted that several other combinations of variables (not shown here) were tested and shown not to significantly improve (or even worsen) predictions of K_r . Equation 3 provides a remarkably robust solution for wave reflection given the exceedingly broad parameter space covered by the 780 data points. The equation includes parameters which have physical significance in the processes of wave dissipation due to breaking (ξ), turbulence /friction induced by structural roughness ($\sqrt{\frac{D}{L_o} \cot \beta}$), and transmission through and into the breakwater ($\frac{D}{H_i}$ & P) (see Figure 1). The relative toe depth (d/L_o) is also seen to significantly improve reflection estimates although the physical significance of this parameter is less clear.

The excellent correlation between observed and predicted reflection coefficient for these data is shown in Figure 2. The correlation coefficient and standard error for the data shown in Figure 2 are 0.943 and 0.0521 respectively. A conservative estimate of K_r for which 98% of the data does not exceed is given by adding two times the standard error ($=0.1042$) to Equation 3.

Inspection of Figure 2 shows that there is evidence of some systematic deviation of the reflection estimates for low measured values of K_r (<0.18). These discrepancies probably arise due to errors in analysis techniques which are sensitive to bias due to signal noise for low

reflection conditions. However, these deviations are of little significance since reflected wave energy is less than 4% of the incident value in this area of the graph.

Correlation coefficients and standard errors associated with field data alone ($r=0.815$) are poorer than those associated with the laboratory data ($r=0.962$). This is perhaps to be expected to some extent since there are a greater number of variables associated with the field situation. For example, non-uniformities in the wave field, oblique wave approach and irregularities in the structure may all contribute to uncertainties in K_r . However, Davidson *et al.*, (1996) conducted numerical tests indicated that errors in estimates of K_r due to oblique wave approach and low signal coherence between sensor pairs are generally low (error in $K_r < \pm 0.09$) for these data. It is valid therefore to consider other potential reasons for the increased scatter in the predictions associated with the field data.

Table 1 shows that the field data embraces a considerably broader range of Iribarren numbers. In particular the field data extends to much higher Iribarren numbers where waves of low steepness surge (un-broken) against the structure. In this regime dissipation due to wave breaking is of little importance and the processes of transmission and dissipation due to turbulence and friction promoted by the roughness of the structure most significantly affect the energy balance (Figure 1). It is under these highly reflective conditions that there is considerably more scatter in the estimates of reflection coefficient (Figure 2). This may indicate that the processes of transmission, and dissipation due to structural roughness are less well represented by Equation 3 than those associated with wave breaking. This hypothesis is supported by the fact that the data from the second deployment which has the reduced slope ($\tan \beta = 1/1.55$) and lower Iribarren numbers shows less scatter than the data collected in more reflective conditions in the first deployment ($\tan \beta = 1/0.82$).

It should also be noted that Equation 3 is some what biased towards the model scale tests since the ratio of laboratory to field data analysis here is of the order 3:1. Hence if the solution given by Equation 3 is more suited to the laboratory data, scale effects may significantly contribute to the scatter in the field data. More field data is required to clarify this issue.

Although Equation 3 provides a good and versatile estimate of wave reflection within a very broad parameter space, an improved prediction of wave reflection ($r=0.87$, $\sigma=0.055$) at full-scale is given by Equations 1 and 2 within the range of field measurements summarised in Table 1.

Figure 3 shows a series of plots illustrating the relative impact of each of the terms in Equation 3 on the overall estimate of reflection across the measured parameter space. In these figures the range of the value of each term in the field and laboratory is represented by lines joined by open circles and crosses respectively. Also shown are the 95% confidence intervals for each parameter. Inspection of Figure 3 shows that the dissipation, transmission and roughness parameters have a first order effect on wave reflection with relatively small contributions ($\Delta K_r < 0.15$) from the permeability and relative depth terms.

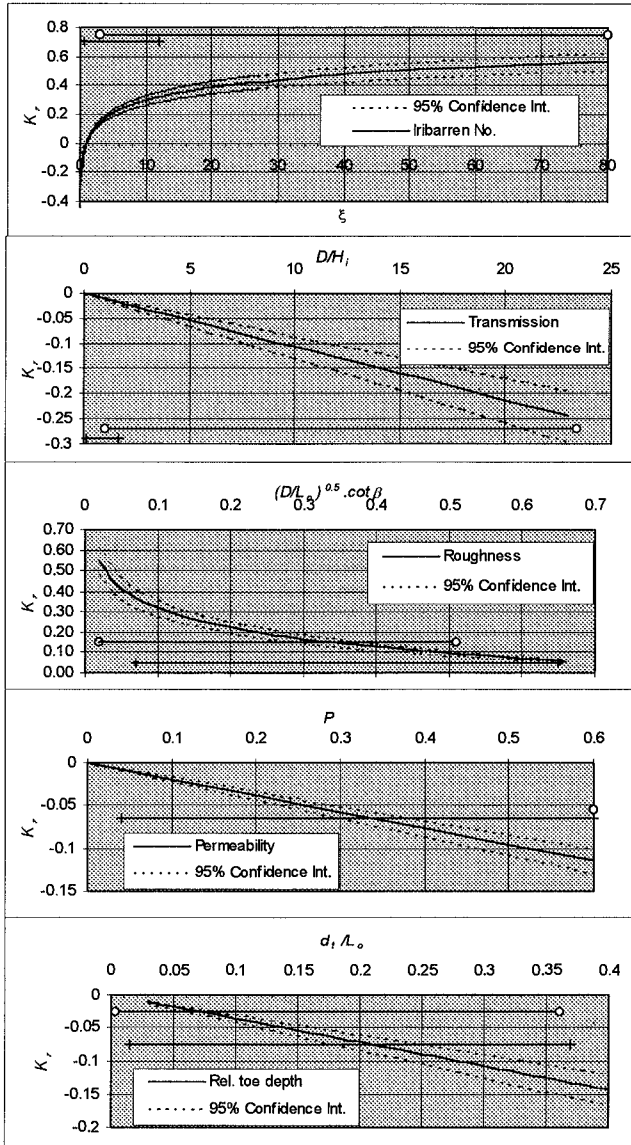


Figure 3: Figure showing the relative influence of each of the five terms in Equation 3 on the reflection coefficient estimate over the field and laboratory parameter space. Note that the field and laboratory range for each variable are indicated by lines joining open circles and crosses respectively.

The relative impact of each term in Equation 3 on the reflection estimate is in some cases very different for the field and laboratory data. For example the Iribarren number is very significant across the full range of the laboratory data but has little impact on K_r for much of the field data which corresponds to high Iribarren numbers and non-breaking waves. Conversely, the transmission parameter has a much more significant effect on K_r for the field data. Table 2 (line 3) shows that the addition of the transmission parameter to the equation significantly increases the correlation coefficient ($r=0.622 \rightarrow 0.828$). Plots of predictions based on the Iribarren number alone (not included here) show the field and laboratory data as two distinct series. Inclusion of the transmission term effectively brings together the field and laboratory data. This emphasises the importance of the effects of wave transmission which perhaps have not been fully appreciated previously from laboratory experiments which have a much more limited range in Iribarren number.

It should also be mentioned that there may be several other parameters which are significant in the process of wave reflection which have not been considered in Equation 3. In particular, Van der Meer (1992) sites the relative crest freeboard height R_c/H_i as being an important factor influencing wave transmission. Unfortunately statistics for R_c (height of the structure crest above mean sea level) were not available for all data and therefore the effect of R_c/H_i could not be tested here. Other significant factors might include the effective breakwater width corresponding to the still water level and wave frequency. Thornton and Calhoun (1972) found also that wave transmission was a frequency dependent process with lower frequency wave propagating more readily through the structure. The effect of wave overtopping and strongly oblique wave approach are also not accounted by Equation 3.

CONCLUSIONS

Multiple regression analysis of this large data base (780 data points) including both field and laboratory data provides a robust predictive scheme for wave reflection and an insight into the relative importance of parameters affecting this process. The results of this study can be summarised as follows:

- 1) An accurate prediction of wave reflection ($r=0.943$, $\sigma=0.0521$) over the sampled parameter space (Table 1) is given by:

$$K_r = 0.298 \log(\xi) - 0.011 \left(\frac{D}{H_i} \right) - 0.321 \log \left(\sqrt{\frac{D}{L_o}} \cot \beta \right) - 0.191P - 0.358 \left(\frac{d_i}{L_o} \right) - 0.049 \quad (3)$$

A conservative estimates which of wave reflection not exceeded by 98% of data is given by addition of two times the standard error (0.1042) to this equation. Equation 3 is valid for normally incident waves and no overtopping.

- 2) Equation 3 includes parameters which are physically significant in the processes of wave dissipation through breaking (ξ), turbulence and friction induced by structural roughness $\left(\sqrt{\frac{D}{L_o}} \cot \beta \right)$ and transmission into and through the breakwater (P , D/H_i).
- 3) In Equation 3 the Iribarren number (relating to dissipation through breaking), transmission and roughness parameters exert a first order effect on wave reflection estimates with smaller contributions ($\Delta K_r < 0.15$) from the permeability and relative depth terms.

- 4) More field data is required in order to test the validity of Equation 3 at full-scale and the potential importance of scale effects.
- 5) For conditions corresponding to the parameter space covered in the field experiment (Davidson *et al.*, 1996, see Table 1) Equations 1 and 2 are recommended for the prediction of wave reflection.

ACKNOWLEDGEMENTS

The authors would like to extend their thanks to the Engineering and Physical Sciences Research Council (EPSRC, Grant no. GR/H17183) and MAST (Grant no. MAS2-CT92-0030) for funding this research. We would also like to acknowledge the technician support in the School of Civil & Structural Engineering and Arun District Council for their co-operation in the field.

REFERENCES

- Allsop and Channell, 1989, Wave reflection in harbours. Reflection performance of rock armoured slopes in random waves. Hydraulics Research Report OD 102.
- Battjes, J.A., 1974, Surf similarity. Proc. 14th Coastal Eng. Conf., vol. 1, pp 466-480.
- Davidson, M.A., Bird, P.A.D., Bullock, G.N. and Huntley, D.A., 1994, Wave reflection: Field measurements, analysis and theoretical developments, Proc. Coastal Dynamic, '94 Barcelona, pp 642-654.
- Davidson, M.A., Bird, P.A.D., Bullock, G.N. and Huntley, D.A., 1996, A new non-dimensional number for the analysis of wave reflection from rubble mound breakwaters., Coastal Engineering, 28 pp93-120.
- Hughes, S.A. and Fowler, J.E., 1995, Estimating wave induced kinematics at sloping structures, J. of Waterway, Port, Coastal and Ocean Engineering, pp 209-215.
- Postma, G.M., 1989, Wave reflection from rock slopes under random wave attack, Unpub. M.Sc. thesis, Delft Univ. of technology, 106pp.
- Seelig, W.N and Ahrens, J.P., 1981, Estimation of wave reflection and energy dissipation coefficients for beaches revetments and breakwaters., Technical paper, Tp 81-1, Dept. of the Army Coastal Eng. Research Centre, Kingman Building, Fort Belvoir, Virginia 22060.
- Shimada, A., Fujimoto, T., Saito, S., Sakikiyama, T. and Hirakuchi, H., 1986, Scalc effects on stability and wave reflection regarding armour units. Proc. 20th Coastal Eng. Conf., Vol. 3, pp2238-2252.
- Thornton, E.B. and Calhoun, R.J., 1972, Spectral resolution of breakwater reflected waves. Proc. ASCE J. of waterways, Harbours and Coastal Eng., Vol. 98, WW4.
- Van der Meer, J.W., 1988, Rock slopes and gravel beaches under wave attack. Ph.D. thesis, Delft Univ. of Technology. Also: Delft Hydraulics Communication No. 396.
- Van der Meer, J.W., 1992, Conceptual design of rubble mound breakwaters. Proc. of a short course on the design and reliability of coastal structures, 23rd Conf. Coastal Eng., Venice. pp447-510.

CHAPTER 162

PERFORMANCE EVALUATION OF BUOY-MEMBRANE WAVE BARRIERS

M.H. Kim¹, B.L. Edge², S.T. Kee³, and L. Zhang⁴
Department of Civil Engineering
Texas A&M University
College Station, TX 77843, USA

ABSTRACT

The interaction of water waves with a tensioned, inextensible, vertical flexible membrane hinged at the sea floor and attached to a solid cylindrical buoy at its top, was investigated in the context of two-dimensional linear wave-body interaction theory. A two-domain boundary element program was developed based on a discrete-membrane dynamic model and simple-source distribution over the entire fluid boundaries. To verify the numerical results, a series of experiments were conducted with two different models in the two-dimensional wave tank. For each model, both surface-piercing and submerged cases were tested. The numerical prediction was generally in good agreement with experimental results except resonance regions. The comparison was improved after including viscous or material damping effects. It is shown that the buoy/membrane system can be a very effective wave barrier if it is properly designed.

INTRODUCTION

A flexible membrane can be used as a portable and sacrificial breakwater, containment boom, underwater screen (Huygens et al., 1994), and silt curtain (Sawaragi et al., 1989). It has the advantage of being lightweight, inexpensive, reusable, and rapidly deployable. Since it can be easily removed, we expect minimum environmental impacts on various coastal processes. Using inflatable buoy, it can be air-dropped and self-erected. Its shape and mass can be easily controlled by filling with air or water optimized for various sea conditions (e.g. Ohyama et al., 1989; Broderick & Jenkins, 1993; Zhao, 1994). In this paper, we will particularly focus on the use of floating or submerged buoy/membrane as a breakwater (Thompson et al., 1992).

Most floating breakwaters proposed so far (e.g. Seymour & Hanes, 1979; Sollitt et al., 1986; Isaacson et al., 1994) have been relatively transparent to the incident wave field especially in the long wave regime. In order to improve the performance in long waves, it is necessary for the structure to occupy a major fraction of the water column. In view of this, numerous flap-type or elastic-beam breakwaters have been investigated but they were not greatly successful primarily due to the motion-induced waves in the lee side. The effectiveness of this kind of vertical breakwaters was improved by tuning structural responses (Sollitt et al, 1986; Evans & Linton, 1991; Abul Azm, 1994) or by adjusting structural flexibility (Lee & Chen, 1990; Williams et al., 1991,1992) and porosity (Wang & Ren, 1993).

¹ Associate Prof., Dept. of Civil Engrg, Texas A&M Univ., College Station, Texas, 77843

² Prof., Dept. of Civil Engrg., Texas A&M Univ., College Station, Texas, 77843

³ Res. Asst. Dept. of Civil Engrg., Texas A&M Univ., College Station, Texas, 77843.

⁴ Res. Asst., Dept. of Civil Engrg., Texas A&M Univ., College Station, Texas, 77843.

In Kim & Kee (1996), the wave interaction with a tensioned vertical flexible membrane hinged or elastically supported at the seabed and the mean free surface was considered. Both analytic and numerical solutions were developed and used to assess the performance with varying various parameters such as membrane tension, length, mass, and mooring stiffness. It was found that almost complete reflection was possible despite large vertically-sinusoidal membrane motions which tended to generate only exponentially decaying local (evanescent) waves in the lee side. Consequently, the efficiency was in general higher than conventional floating breakwaters. The overall performance, however, depended on the magnitude of membrane tension and types of boundary conditions.

In Kee & Kim (1997), more practical buoy-membrane systems were considered. A special two-domain boundary element method was developed to solve the interaction of a rigid buoy and flexible membrane with regular waves. It was observed that diffracted and radiated waves by a buoy tended to diminish the efficiency of the membrane-alone case. However, it was shown that the practical system with a floating buoy can still be highly efficient if it is properly designed.

To validate the numerical results of Kee & Kim (1997), a series of experiments were conducted in a 35-m long, glass-walled two-dimensional wave tank at Texas A&M University. Two different models were tested both in regular and irregular waves. Reasonable agreement was observed between theory and experiment. The representative results of this experimental study are reported in this paper.

Key Words: flexible membrane, floating breakwater, submerged breakwater, potential theory, hydroelasticity, two-domain BEM, performance evaluation, model experiment

THEORY AND NUMERICAL METHOD

The interaction of a buoy/membrane wave barrier with long-crested monochromatic waves is solved in the context of potential theory. Buoy and membrane motions are assumed to be uniform in the longitudinal direction thus allowing two-dimensional analysis. It is also assumed that wave and membrane motions are small so that linear theory may be applicable. For analysis, the Cartesian coordinate system with the origin on the mean free surface and the y axis positive upward is used. Assuming ideal fluid and harmonic motion of frequency ω , the velocity potential can be written as $\Phi(x, y, t) = \text{Re}[\phi(x, y)e^{-i\omega t}]$. The velocity potential of a monochromatic incident wave of amplitude A and wavenumber k , propagating in the positive x direction is given by

$$\phi_0 = \frac{-igA \cosh k(y+h)}{\omega \cosh kh} e^{ikx} \quad (1)$$

where $\omega^2 = kg \tanh kh$ with g and h being the gravitational acceleration and water depth, respectively. The complex disturbance velocity potentials, ϕ_1 and ϕ_2 , in two fluid domains I and II (see Figure 1) satisfy Laplace equation $\nabla^2 \phi_l = 0, (l = 1, 2)$ and the following linearized free-surface (Γ_f), bottom (Γ_b), and radiation conditions:

$$-\omega^2 \phi_l + g \frac{\partial \phi_l}{\partial y} = 0 \quad (\text{on } \Gamma_f) \quad (2)$$

$$\frac{\partial \phi}{\partial n} = 0 \quad (\text{on } \Gamma_b) \tag{3}$$

$$\lim_{|x| \rightarrow \infty} \left(\frac{\partial}{\partial x} \pm ik \right) \begin{pmatrix} \phi_1 \\ \phi_2 \end{pmatrix} = 0 \quad (\text{on } \Gamma_c) \tag{4}$$

where $\mathbf{n} = (n_x, n_y)$ is the unit outward normal vector.

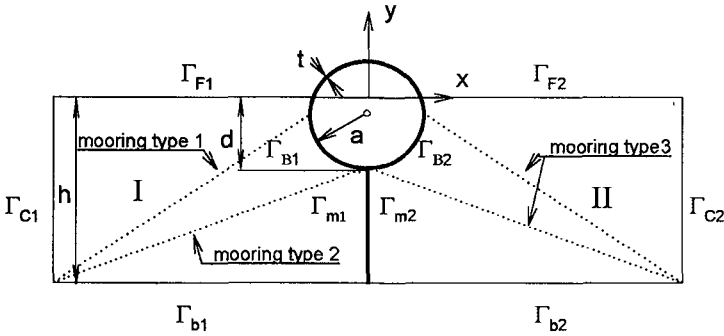


Figure 1. Computational domain.

Under large initial tension, we assume, for simplicity, that the membrane is inextensible and the heave motion of the buoy is negligible. Then the boundary condition on the buoy is

$$\frac{\partial \phi}{\partial n} + i\omega \{ \eta_h n_x + \eta_b n_y \} + \delta_{11} \frac{\partial \phi_b}{\partial n} = 0 \quad (\text{on } \Gamma_b) \tag{5}$$

where δ is the Kronecker delta function, and $n_\theta = xn_y - yn_x$. The symbols η_h and η_b represent complex sway and roll responses respectively. In addition, the disturbance potentials must satisfy the following linearized kinematic and dynamic boundary conditions on the membrane surface:

$$\frac{\partial(\phi_1 + \phi_b)}{\partial x} = \frac{\partial \phi_2}{\partial x} = -i\omega \xi \tag{6}$$

$$\frac{d^2 \xi}{dy^2} + \lambda^2 \xi = \frac{\rho i \omega}{T} (\phi_2 - \phi_1 - \phi_b) \quad (\text{on } \Gamma_m) \tag{7}$$

in which $\lambda = \omega \sqrt{m/T}$ with T and m being the membrane tension and mass per unit length, respectively. In (6) and (7), ρ is the fluid density, and the harmonic membrane motion $\Xi(y, t) = \text{Re}[\xi(y)e^{-i\omega t}]$. The dynamics of the tensioned membrane is modeled as that of the tensioned string which satisfies one-dimensional wave equation. Unlike rigid body hydrodynamics, the body boundary condition on the flexible membrane is not known in advance. Therefore, the

membrane motions and velocity potentials need to be solved simultaneously. If buoy is submerged, the continuity of pressure and normal velocity must be satisfied along the fictitious vertical centerline above buoy:

$$\phi_1 = \phi_2, \quad \frac{\partial \phi_1}{\partial n} = -\frac{\partial \phi_2}{\partial n} \quad \text{at } \Gamma_f \quad (8)$$

To solve the above boundary value problem, a two-domain boundary element method using simple sources along the entire boundary is developed. The details are given in Kee & Kim (1997). Two auxiliary vertical boundaries (Γ_{e1}) and (Γ_{e2}) are located sufficiently far from the membrane such that the radiation condition (4) is valid. The discrete membrane equation is given in the following form:

$$\rho i \omega (\phi_{0j} + \phi_{1j} - \phi_{2j}) l_j - T_j \left(\frac{\partial \xi}{\partial \zeta} \right)_j + T_{j+1} \left(\frac{\partial \xi}{\partial \zeta} \right)_{j+1} = -m l_j \omega^2 \xi_j \quad (9)$$

where

$$\left(\frac{\partial \xi}{\partial \zeta} \right)_j = (\xi_j - \xi_{j-1}) / \Delta \zeta_j$$

The symbol l_j is the length of the j -th segment, and $\Delta \zeta_j = \frac{l_j + l_{j+1}}{2}$. The geometric boundary conditions at the seabed and the top connection point $(0, -R)$ are

$$\xi = 0 \quad \text{at } z = -h, \quad \xi = \eta_h + R\eta_b \quad \text{at } z = -R \quad (10)$$

The equation (9) can in principle be solved for variable tensions. In the present study, however, we assume that the initial tension T is much greater than membrane weight or dynamic tension thus can be regarded as constant. The sway-roll coupled equation of buoy motion is given by

$$M(-\omega^2)X = F_p - (K_{HS} + K_m)X - F_T + F_D \quad (11)$$

where $X = [\eta_h \ \eta_b]^T$, M =buoy mass matrix, K_{HS} =hydrostatic restoring coefficients, K_m =mooring stiffness, F_p =potential force, F_D =linearized drag force, and F_T =force at the connection point. The force F_T caused by membrane tension can be either restoring force or excitation. The detailed expression of these variables is given in Kee & Kim (1997).

EXPERIMENT

In order to validate the theory and numerical procedure developed in the preceding section, we conducted a series of experiments using a two dimensional wave tank (37-m long, 0.91-m wide, and 1.22m deep) equipped with a dry-back, hinged flap wave maker capable of producing regular and irregular waves (see Figure 2). The wave elevation was measured with a resistance wave gauge having an accuracy of ± 0.1 cm. A probe measuring incident and reflected wave heights and another probe measuring the transmitted wave heights are placed at 9.14m and 24.38m from the wavemaker, respectively. The wave barrier model was placed at 18.29m from the wavemaker between the two probes. Regular waves were generated by a user-defined time-voltage input to the wave maker. The wave period range used in our experiments was from 0.7 to 2.5. The wave heights used in the experiments range from 3cm to 6cm.

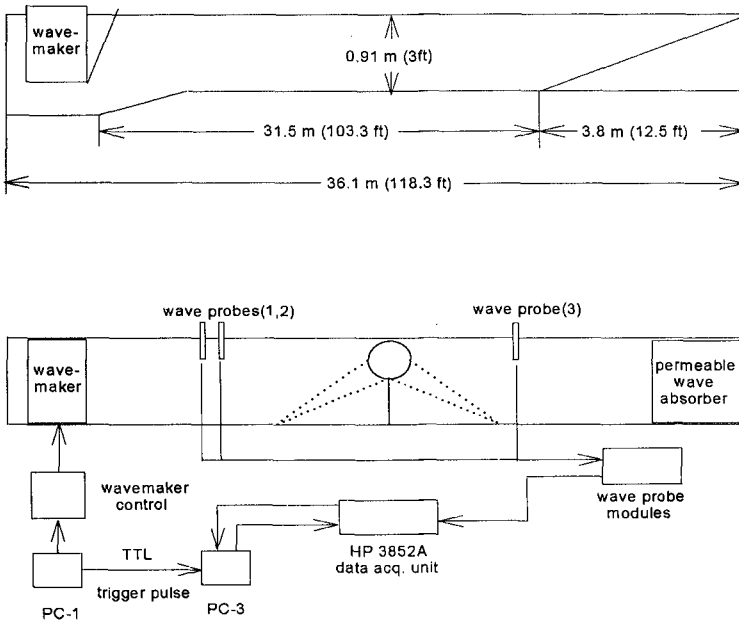


Figure 2. Wave tank and experimental set-up.

A sinusoidal regular wave was generated with the beginning and end of the series attenuated in amplitude. Two models were constructed for the present study. The buoy of model I is relatively small and heavy and made of PVC pipe. The buoy of model II is relatively large and light and made of foam wrapped by plastic sheet. The models consisted of a flexible membrane suspended from a cylindrical buoy and hinged at the sea floor. The flexible membrane was made of a thin stretching-resistant plastic material resembling a plastic tarpaulin. The total length of the buoy with side caps was 86cm. The membrane was attached to the bottom by clamping it between two angle irons which were fastened to the bottom. Four (type 1) or eight (type 3) taut mooring (two at each end) lines are used and they consist of unstretchable steelon-nylon wire that can resist up to 534N and a spring near the bottom connection. When mooring type 3 is used, two taut cables having the same anchoring point are connected to the side and bottom of a buoy, respectively. The stiffness of each spring was measured by applying static loads. The stiffness per length was found to be piece-wise linear as displacement increases. To avoid being slack, each mooring line is slightly pre-tensioned. Table 1 and 2 summarize the principal characteristics of the model I and II used in the experiment. The signal of the incident wave train was obtained (see Figure 3a,b) as it passed the probe toward the membrane breakwater. Then, the reflected wave train was recorded as the reflected waves pass the probe again in the opposite direction. After averaging the wave heights for the incident and reflected, and transmitted wave trains, the reflection coefficient R_f and transmission coefficient T_f can be calculated from the ratio of the averaged reflected and transmitted wave height to the averaged incident wave height.

TABLE 1. Particulars and Experimental conditions for Model I

	Surface Piercing System	Submerged System
Density of PVC buoy	1690 kg / m ²	1690 kg / m ²
Radius of Cylindrical Buoy	10.65(cm)	10.65(cm)
Thickness of Cylindrical Buoy	0.6(cm)	0.6(cm)
Buoy weight per unit length	6.6 kg/m	6.6 kg/m
Water depth	54.94 cm	66.45 cm
Buoy Draft	11.50 cm	
Location of mass center from S.W.L.	-0.85(cm)	-12.25(cm)
Wave amplitude range without mooring	3-2 (cm)	2(cm)
with mooring	2.5-1.5(cm)	2(cm)
Wave Period	0.74-2.1(sec)	0.82-2.5(sec)
Mooring line stiffness (average)	1.65 kg/cm	1.65 kg/cm
Initial tension of mooring line	1.81 kg/cm	1.81 kg/cm
Mooring angle (degrees) type 1.	33°	33°
Clearance		1.6 (cm)
Mooring attachment point from S.W.L.	-0.85 (cm)	-12.25(cm)

TABLE 2. Particulars and Experimental conditions for Model II

	Surface Piercing System	Submerged System
Density of Cylindrical Buoy	42 kg / m ²	42 kg / m ²
Radius of Cylindrical Buoy	17.5(cm)	17.5(cm)
Thickness of Cylindrical Buoy	14.5(cm)	14.5(cm)
Buoy weight per unit length	3.9 kg/m	3.9 kg/m
Water depth	70.0 cm	90.0 cm
Buoy Draft	25.75 cm	
Location of mass center from S.W.L.	-8.25(cm)	-28.25(cm)
Wave amplitude range without mooring	3-2 (cm)	2(cm)
with mooring	2.5-1.5(cm)	2(cm)
Wave Period	0.69-2.0(sec)	0.78-2.0(sec)
Random Wave Spectrum(Jownswap $\gamma = 1$)	1/50 scale $H_{1/3} = 1.5m$, $T_p = 6.5$ see	
Mooring line stiffness (average)	1.28 kg/cm	1.28 kg/cm
Initial tension of mooring line type1	2.00 kg/cm	2.00 kg/cm
Initial tension of mooring line type2	2.50 kg/cm	2.50 kg/cm
Mooring angle (degrees) type 1.	40.2°	40.2°
Mooring angle (degrees) type 2.	23.4°	23.4°
Clearance		10.75 (cm)
Mooring attachment point from S.W.L. (type1)	-8.25 (cm)	-28.25(cm)
Mooring attachment point from S.W.L. (type2)	-25.75 (cm)	-45.75(cm)

Reflected and transmitted waves were repeatedly reflected from the wave maker and beach as time goes on. In order to minimize the effects of multiple reflection, the fixed single probe method was adopted in favor of moving single probe method and three-probe method (Isaacson, 1991). It is shown in Hagen (1994) that the present method is more reliable than the moving or three-probe methods when nonlinear phenomena or multiple reflections exist. In most of our surface-piercing-buoy experiments, the errors estimated from the energy relation were kept within 10%. The difference can be attributed to viscous, gap, and nonlinear effects, and mooring/material damping etc.

RESULTS AND DISCUSSION

The boundary element program developed as described in the preceding section was used to predict the performance of surface-piercing or submerged buoy-membrane wave barriers. The computational domain is defined as in Figure 1. The error was calculated from the energy conservation relation $R_f^2 + T_f^2 = 1$. It is seen that the errors uniformly decrease as the number of segments is increased.

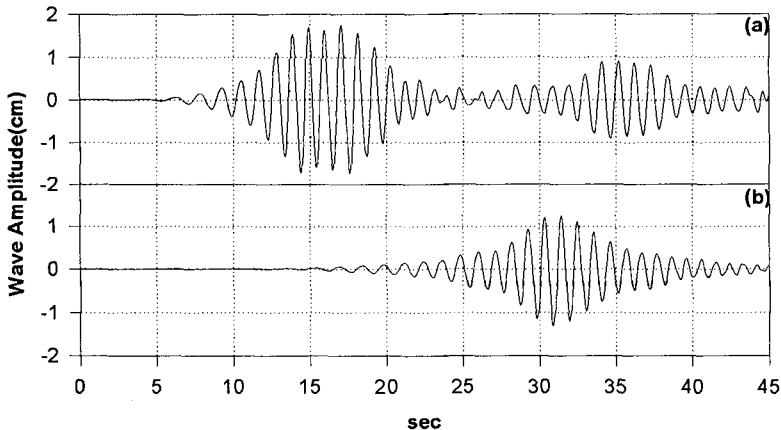


Figure 3. (a) Incident and reflected, and (b) transmitted wave packet for wave period 1.08 sec.

Figure 4 shows comparison between the numerical results and measurements for a surface-piercing buoy/membrane breakwater (model I) without mooring lines. In this experiment, both small and large amplitude waves were used to see the sensitivity to wave heights. As can be seen in the figure, experimental data agree well with the present numerical results. As expected, smaller-amplitude waves correlate better with the linear wave-body-interaction theory. The discrepancy for large-amplitude waves can mainly be attributed to nonlinear effects since it is more pronounced in the high-frequency region. The experimental results satisfied the energy conservation with less than 8% error in the whole frequency range. To account for viscous and material damping effects, 2.5% of the sway and roll critical damping of the cylinder as well as 0%, 2.5%, and 5% of membrane critical damping was included in the cylinder and membrane equations of motions. The results are also plotted in Figure 4. As can be seen in this figure, its effect is not significant in the wave frequency range considered, which is not surprising because the relevant Keulegan-Carpenter (KC) number is smaller than 1.

Figure 5 shows the result of the same case (model I, surface piercing) except that the buoy is moored by a pair of weakly pre-tensioned springs (type 1) located at both ends of the cylinder. As mentioned earlier, the spring exhibited piece-wise nonlinear behavior, and thus the averaged stiffness was used in this computation. The computed results correlate well with the measured data except for the resonance region characterized by the sharp increase of the reflection coefficient. The discrepancy near resonance can mainly be attributed to the increased viscous and nonlinear effects. Actually in this case, we observed large buoy and membrane motions in the experiment. To assess the effects of increased damping due to viscosity and mooring lines, the same damping parameters as in Figure 4 were used in the motion calculation and the results are also shown in Figure 5. It is seen that viscous effects are increased near the resonance region.

In Figure 6, the experimental results for a moored (type 1), submerged wave barrier (model I) are compared with numerical prediction. The overall correlation of the potential theory with experiment is somewhat worse than the surface-piercing cases, indicating that viscous or material damping effects play a more important role for submerged breakwaters. The experimental results do not accurately satisfy the energy relation because of the increased viscous and nonlinear effects. In addition, we observed, especially for short waves (or large kh), mild wave breaking above the buoy surface, which can also contribute to energy loss. To see the viscous effects more clearly, we first included the sway drag force on the cylinder through Morison's formula as explained in the preceding section with 5% roll damping ratio. We can see in the figure that its effect is small. To have further insight, we also presented the cases in which the sway and roll damping ratios of the cylinder are 5%, and membrane damping ratio is increased from 0% to 5%. It tends to lower both reflection and transmission coefficients except near $kh \approx 2.8$, where reflection increases. The new results with viscosity tend to correlate better with measured data.

Since the buoy of model I is relatively small and heavy, its wave-blocking performance is not very impressive. For comparison, the performance of a similar system with larger and lighter buoy (model II) was also tested and compared with numerical prediction. Figure 7 shows the performance of the model II without mooring for various kh values. Figure 8 shows the performance of the same system with type 3 mooring lines. In both cases, the predicted results agree well with measured data except the resonance region, where nonlinear effects can be significant. It is also seen that the efficiency in long waves can be significantly enhanced by adding mooring lines. The efficiency for $kh > 3$ is very high regardless of the presence of mooring lines.

Figure 9 shows the performance of the submerged system (model II) with type-3 mooring in regular waves. Compared to the surface-piercing case, the efficiency in long waves is greatly enhanced, while that in short waves becomes poor. The predicted results again correlate reasonably with measured data. The results of Figure 8 and 9 indicate that high performance can be achieved for a variety of wave conditions if the submerged and surface-piercing systems are combined. Finally, In Figure 10a, the performance of the surface-piercing model II in irregular waves is shown. As a typical operational condition in a partly protected sea, a two-parameter Pierson-Moskowitz spectrum with significant wave height=1.5m and peak period=6.5s was selected. We can see that the transmitted wave spectrum is greatly less than the incident wave spectrum. In this experiment, due to the accumulated multiple reflection from both wave maker and beach, the duration of the time series cannot be long. Therefore, five different time series of 180-s duration were generated and the averaged spectra were presented in Figure 10a. Figures 11a,b show the typical time series of wave elevation recorded by wave probes 1 and 3. Figure 10b shows the performance of the submerged system in irregular waves. For this plot, four different time series are averaged. One of such time series is shown in Figure 11c,d.

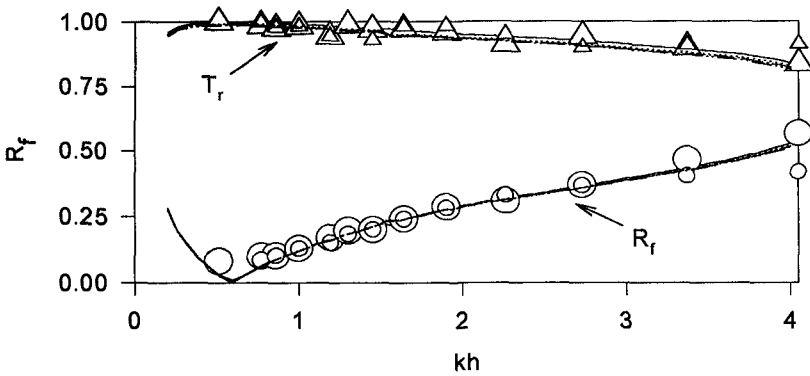


Figure 4. Comparison of the present numerical results with measured data for a surface-piercing membrane breakwater (model I) without mooring lines. Num. R_f and T_r (—), Exp. with small wave amplitudes{ R_f (O), T_r (Δ) }, Exp. with large wave amplitudes{ R_f (o), T_r (Δ)}. Additional lines are for 2.5 % sway and roll damping ratio of the cylinder and membrane damping ratio of 0% (.....), 2.5% (- - - - -), and 5.0% (- · - · - ·).

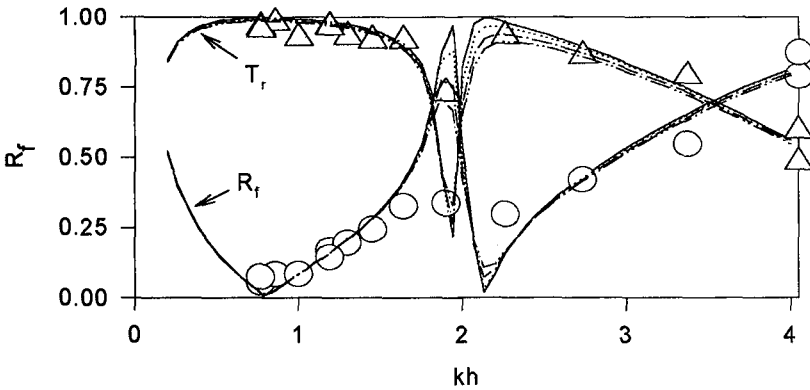


Figure 5. Comparison of the present numerical results with measured data for a surface-piercing membrane breakwater (model I) with type 1 mooring. Num. R_f and T_r (—), Exp. { R_f (O), T_r (Δ)}. Additional lines are for 2.5 % sway and roll damping ratio of the cylinder and membrane damping ratio 0% (.....), 2.5% (- - - - -), and 5.0% (- · - · - ·).

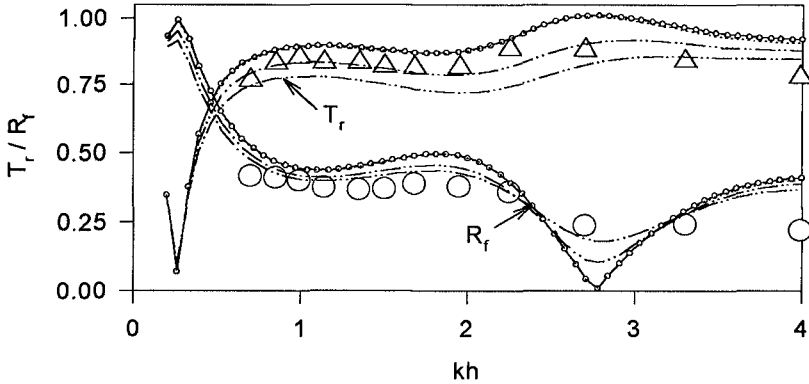


Figure 6. Comparison of the present numerical results with measured data for a fully submerged membrane breakwater (model I) with type 1 mooring. Num. R_f and T_r (—), Exp. { R_f (O) , T_r (Δ) }. Circles (\circ) represent the results for which Morison equation for sway and 5 % roll damping ratio of the cylinder are used. Additional lines are for 5 % sway and roll damping ratio of the cylinder and membrane damping ratio of, 0 % (.....), 2.5 % (-.-.-.-), 5.0 %(-.-.-.-)

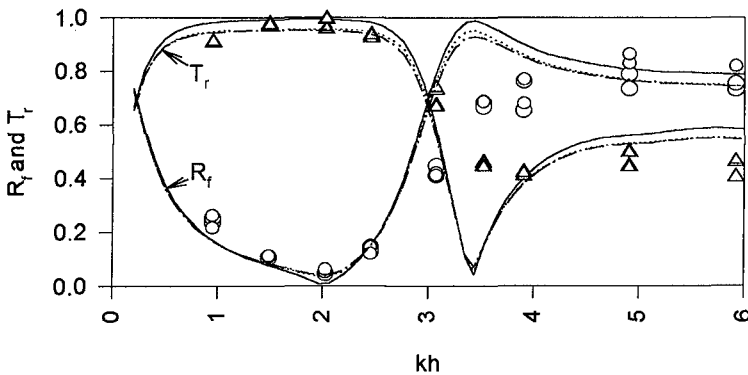


Figure 7. Comparison of the present numerical results with measured data for a surface-piercing membrane breakwater (model II) without mooring lines. Num. R_f and T_r (—), Exp. { R_f (O), T_r (Δ) }. Additional lines are for 5.0 % sway and roll damping ratio of the cylinder and membrane damping ratio of 5.0% (.....), and 10.0% (-.-.-.-)

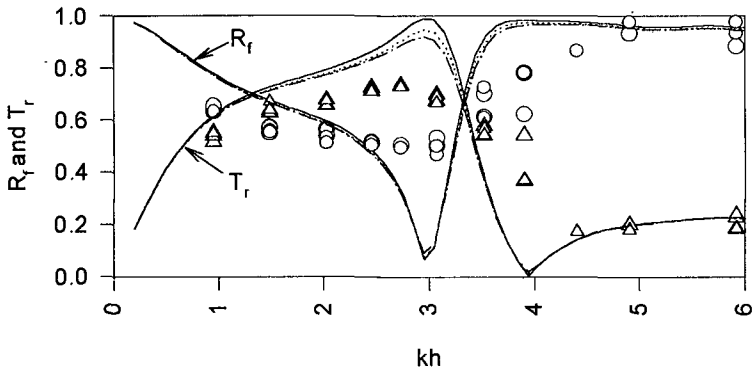


Figure 8. Comparison of the present numerical results with measured data for a surface-piercing membrane breakwater(model II) with type 3 mooring. Num. R_r and T_r (—), Exp. $\{R_r(O), T_r(\Delta)\}$. Additional lines are for 5.0 % sway and roll damping ratio of the cylinder and membrane damping ratio 5.0 % (.....), 10. % (- - - - -).

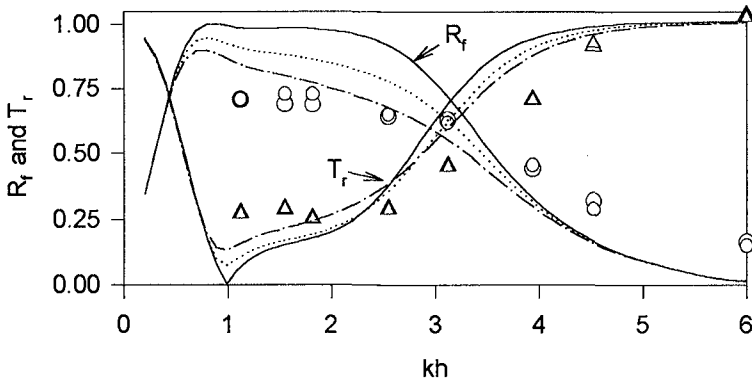


Figure 9. Comparison of the present numerical results with measured data for a fully submerged membrane breakwater (model II) with type 3 mooring. Exp. $\{R_r(O), T_r(\Delta)\}$, Num. R_r and T_r for sway and roll damping ratio of the cylinder and membrane damping ratio of 0 % (—), 5.0 % (.....), 10.0 % (- - - - -).

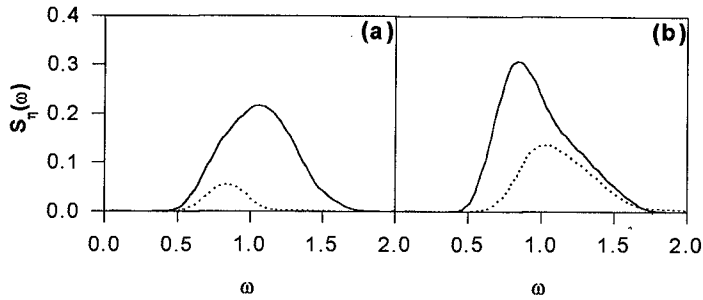


FIG. 10. The spectra of incident (—) and transmitted (---) irregular waves for a surface-piercing model II (a) and a fully submerged model II (b).

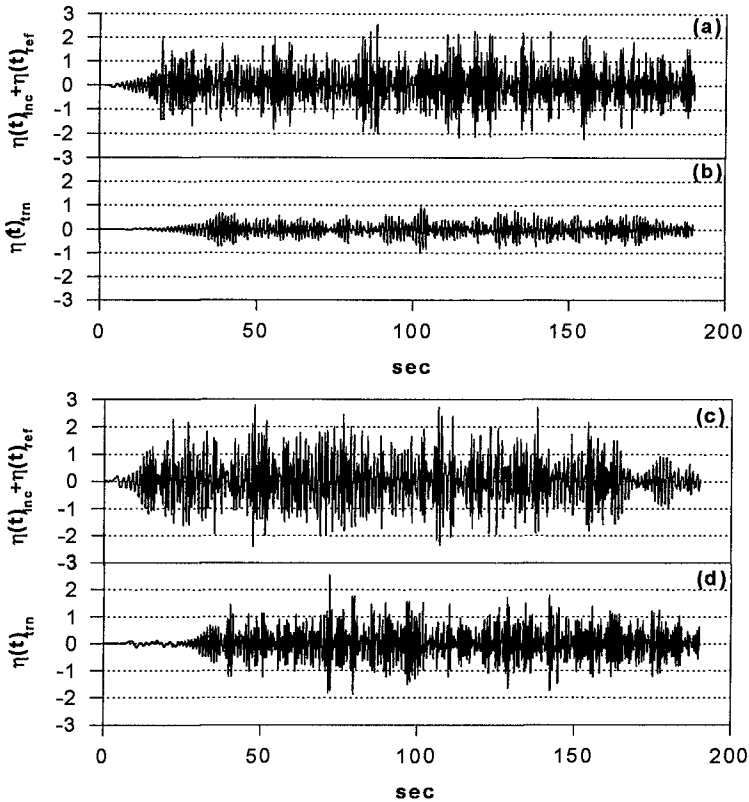


FIG. 11. Time series of incident (a) and transmitted (b) waves for a surface-piercing model II, and incident (c) and transmitted (d) waves for a fully submerged model II

CONCLUDING REMARKS

The interaction of waves with a tensioned, inextensible, vertical flexible membrane hinged at the sea floor and attached to a rigid cylindrical buoy at its top, was solved in the context of two-dimensional linear wave-body interaction theory. Both submerged and surface-piercing buoy/membrane system were considered. A boundary element program was developed based on a discrete-membrane dynamic model and simple-source distribution over the entire fluid boundaries. A two-domain BEM was employed since the membrane is infinitely thin. Membrane motions and velocity potentials were solved simultaneously because the body-boundary condition on the membrane is not known in advance. The accuracy and convergence of the developed program were verified through comparison with analytic solutions.

To verify the numerical results, a series of experiments were conducted with two different models, in the two-dimensional wave tank. For each model, both surface-piercing and submerged cases were tested. The model I with a small buoy was efficient only for limited wave frequency bands, while the model II with larger and lighter buoy performed well for a wider range of wave conditions. The model II successfully reduced the sea state 3-4 to sea state 2. It was also found that submerged systems can be effective in blocking long waves, while surface-piercing systems are more effective for larger kh values. The numerical prediction was generally in good agreement with experimental results except resonance regions. The comparison was improved after including viscous or material damping effects.

ACKNOWLEDGMENT

This research was sponsored by the Korea Research Institute of Ships & Ocean Engineering (KRISO) through a KRISO/TAMU cooperative research program. This work was also partly supported by the Offshore Technology Research Center through the National Science Foundation Engineering Research Centers Program, Grant Number CDR-8721512.

REFERENCES

- Abul-Azm, A.G. (1994), "Wave diffraction by double flexible breakwaters" *Journal of Applied Ocean Research*, Vol.16, 87-99.
- Broderick, L.L. & Jenkins, C.H. (1993) "Experimental investigation of fluid-filled membrane breakwaters" *ASCE J. of Waterway, Port, Coastal & Ocean Engineering*, Vol 119, #6, 639-656.
- Evans, D.V. & Linton, C.M. (1991) "Submerged Floating Breakwaters" *J. of Offshore Mechanics & Arctic Engr.*, Vol 113, 205-210.
- Hagan, C.L. & Kim, M.H. (1994), "A theoretical/experimental study of a perforated wall wave absorber" *M.S. Thesis*, Texas A&M University.
- Huygens, M., Verhoeven, R., Wachter, D.D., Himpe, J., Buyck, S., & Wens, F. (1994), "Underwater screens for shore protection" *Intl. Symp. Waves-Physical & Numerical Modeling*, Vancouver, Canada, 1503-1512.
- Isaacson, M. (1991), "Measurement of regular wave reflection" *ASCE J. of Waterway, Port, Coastal & Ocean Engineering*, Vol 117, 553-569.
- Isaacson, M., Whiteside, N., Gardiner, R., & Hay, D. (1994), "Modelling of a circular section floating breakwater" *Intl. Symp. Waves - Physical & Numerical Modeling*, Vancouver.

Kee, S. T. & Kim, M. H. (1997 March issue). "Flexible membrane wave barrier. Part 2. Floating/submerged buoy-membrane system." *ASCE J. of Waterway, Port, Coastal & Ocean Engineering*, (In Press).

Kim, M.H. & Kee, S.T. (1996) "Flexible membrane wave barrier. Part 1. Analytic and numerical solutions" *ASCE J. of Waterway, Port, Coastal & Ocean Engineering*, Vol.122, No.1, 46-53.

Lee, J.F. & Chen, C.J. (1990) "Wave interaction with hinged flexible breakwater" *J. of Hydraulic Research*, Vol 28, 283-295.

Ohyama, T., Tanaka, M., Kiyokawa, T., Uda, T., & Murai, Y. (1989) "Transmission and reflection characteristics of waves over a submerged flexible mound" *Coastal Engineering in Japan*, Vol.32, No.1, 53-68

Sawaragi, T., Aoki, S., & Yasui, A. (1989), "Tensions on silt curtains in currents and waves" *Proc. Offshore Mechanics & Arctic Engr. Conf.*, Hague, 13-21.

Seymour, R.J. & Hanes, D.M. (1979) "Performance analysis of tethered float breakwater" *ASCE J. of Waterway, Port, Coastal & Ocean Engineering*, Vol 105, #3, 265-281.

Sollitt, C.K., Lee, C.P., McDougal, W.G., & Perry, T.J. (1986) "Mechanically coupled buoyant flaps: theory and experiment" *Proc. 20th Coastal Engineering Conf.*, Vol.3, 2445-2459.

Thompson, G.O., Sollitt, C.K., McDougal, W.G. & Bender W.R. (1992) "Flexible membrane wave barrier" *ASCE Conf. Ocean V*, College Station, 129-148.

Wang, K.H. & Ren, X. (1993), "Water waves on a flexible and porous breakwater" *Journal of Engineering Mechanics*, Vol.119, 1025-1048.

Williams, A.N., Geiger, P.T., & McDougal, W.G. (1991), "Flexible floating breakwater" *ASCE J. of Waterway, Port, Coastal & Ocean Engineering*, Vol 117, #5, 429-450.

Williams, A.N., Geiger, P.T., & McDougal, W.G. (1992), "A submerged compliant breakwater" *J. of Offshore Mechanics & Arctic Engr.*, Vol 114, 83-90.

Zhao, R. (1994), "Hydroelastic analyses of a floating flexible body in waves" *9th Int. Workshop Water Waves & Floating Bodies*, Japan, 241-244.

CHAPTER 163

An Improved Design Method for the Riprap of Earthfill Dams of Large Reservoirs

Jean-Pierre Tournier¹, Pierre Dupuis¹, Raymond Arès²

Abstract

Since impounding of the various reservoirs of the La Grande Complex in northern Québec, the riprap of several dams and dykes suffered some damage during the fifteen-year period which followed. A mandate was given to the Société d'énergie de la Baie James (SEBJ) in January 1992 to review the riprap design and evaluate the necessary repairs. The paper focuses on this work. An improved design method, for the riprap of earthfill dams of large reservoirs, is proposed based on four years of intensive studies and fifteen years of field data. Large scale model tests with irregular waves completed the studies.

Introduction

The construction of the various structures on the La Grande Complex (Phase 1), in northern Québec (figure 1), was done over a period of twelve (12) years between May 1973 and December 1985.

The project required the building of 215 embankment dams and dykes along with three powerhouses producing 10 000 megawatts and had a total cost of 13,7 billion dollars (Canadian). Since the filling of the reservoirs, which took place between 1978 and 1983, the upstream protection of some structures underwent damage and had to be repaired. Until 1992, a total of 19 structures required work varying from minor repairs to repeated dumping of rockfill on the upstream slopes.

In January 1992, La Société d'énergie de la Baie James (SEBJ) was mandated by Hydro-Québec to review the overall design of riprap, taking into account the actual condition of the dams and dykes on the Complex and to estimate the work to be done using existing techniques. To fulfill its mandate, SEBJ conducted extensive field measurements, including wind and wave measurements on four reservoirs and large scale model tests of various repair schemes using irregular waves. This paper focuses on riprap design and repair. Reevaluation of the design wave with a revised wave hindcast formula is presented by Dupuis et al. (1996), while large scale model testing of the repairs is described by Mansard et al. (1996).

¹La Société d'Énergie de la Baie James, 500 Boul. René-Lévesque Ouest, Montréal, Québec, Canada, H2Z 1Z9

²Rousseau, Sauvé, Warren, inc., 500 Boul. René-Lévesque Ouest, Montréal, Québec, Canada, H2Z 1Z9



Figure 1. La Grande Hydroelectric Complex

Original riprap performance

The results of extensive studies indicate that the riprap of most of the embankments has performed satisfactory since reservoir filling. In general, the most important damage was caused by the presence of fine material in the riprap. In a few cases, when systematic repairs were required, the riprap was undersized because the wave height was underestimated in the original design or the riprap specifications were sometimes relaxed during construction. Experience has shown that the use of graded riprap evaluated with the median mass M_{50} increases the risk of having local areas of undersized riprap. Of the 215 earth structures, seventeen needed general repairs.

According to the findings, coarser riprap with a narrow gradation was specified for repairs with a strict control on the minimum size to eliminate any contamination by fine material.

Repair work

The decision to do repair work on a given structure is based on the present condition of the structure, the historical performance of the riprap and on the requirement that the in-place riprap meets the dimensions required. Dams and dykes with steep slopes, in general, were treated with special attention due to their importance and the fact that the mode of failure of the riprap was more severe and rapid and could cause sliding or sloughing of the crest. Damage observed on structures with flatter slopes and adequate protection was generally limited and

evolved slowly.

Structures which had adequate protection but had minor local damage associate with weak zones needed maintenance or local repairs. The local repairs consisted essentially of repairing the damaged or weak zones by rearranging the existing stones and adding stones of appropriate size. In cases where the structures had generalized damage and the riprap was, in whole or in part, undersized, systematic repairs were done. The design and repair techniques were verified and optimized with large scale model tests at the National Research Council of Canada (NRC) that reproduced the natural conditions found on the reservoirs.



Figure 2. Typical systematic repairs (1)



Figure 3. Typical systematic repairs (2)

The method retained for systematic repairs consisted of dumping the riprap from the crest (figure 2) or on the slope, one meter above the maximum water level (figure 3), depending on the required quantity and the width of the berm.

This berm was then cut back with a backhoe and the rockfill rearranged down to 1 meter below the maximum water level. When required, the freeboard was heightened by adding a layer of rock to form a cap-like protection (figure 4).



Figure 4. Systematic repairs at the Dam KA-03 with heightened freeboard.

At the end of 1997, more than two million tons of riprap will be placed on some fifty embankment dams and dykes, ranging from minor to systematic repairs. The know-how acquired during the execution of this mandate enabled new concepts to be elaborated regarding riprap design. This new approach was also verified in the field and lab, with tests on large scale models.

Design considerations

The following well-known Hudson formula is used to evaluate the mass that should resist a certain wave height for specific conditions such as embankment slope and rockfill characteristics:

$$M = \frac{\rho_r H_s^3}{K(S_r - 1)^3 \cot \alpha} \quad [1]$$

with M the rockfill mass in kg, ρ_r the rockfill mass density in kg/m^3 , S_r the rockfill specific density, $\cot \alpha$ the slope, H_s the significant wave height and K the stability coefficient.

Recently, Van der Meer (1988) proposed elaborate equations for irregular wave

climates with various types of wave attack (spilling, plunging or surging). However, for the worst wave conditions these equations can be reduced to the same form as the Hudson formula. Along with the required parameters (slope of fill, mass and density of the rockfill), the formula which gives the mass as a function of the wave height contains a stability coefficient K which takes into account all other factors and corresponds to a safety factor. In the literature, this coefficient is known as K_d or K_r according to different conditions. If all the physical and geometrical parameters are fixed, the calculated resisting mass corresponds to a value for the stability coefficient.

For a given test, if the mass is "unique", that is, if all the blocks are identical (as was the case for Hudson's tests) the definition of this coefficient is straightforward and unique (K_d). On the other hand, when mass variation is allowed within the riprap, it is common practice to define this coefficient (K_r) for the average mass M_{50} . However, if all other parameters are constant, each mass can be considered to be associated to a given value of the stability coefficient. Therefore a variation in mass, in effect, translates into a variation in the stability coefficient which is inversely proportional to the mass (figure 5).

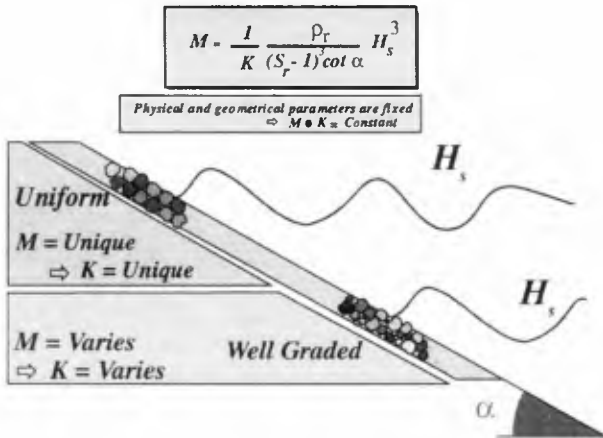


Figure 5. Schematic representation of the relation between M and K

By using this approach, the variations in the mass according to the different methods can be represented in terms of the variations in the stability coefficient equivalent (figure 6). It can be noted that a wide range in the variation of the mass, as in the case for well graded riprap, implies that a large portion of the rockfill has a stability coefficient above 5,0, and can reach 9, 10 or even 17,6 depending on the case and corresponds to the fine part of the riprap. This confirms the results of our

studies that the damage was due mainly to the presence of fines and to our approach of using graded or uniform riprap.

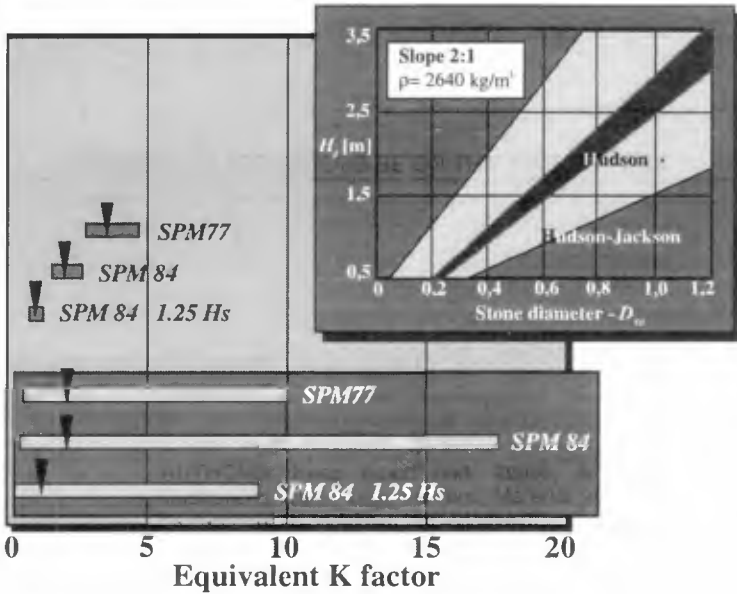


Figure 6. Effect of gradation on the equivalent *K* coefficient

Therefore, for the design, we should determine an acceptable lower limit of the mass, that is an upper limit to the stability coefficient which will resist a given wave height with an acceptable damage index value. In common practice, the damage index *S* is defined as follows:

$$S = \frac{A}{D_{n,50}^2} \quad M_{50} = \rho_r D_{n,50}^3 \quad [2]$$

where *A* is the eroded cross-section area and *D_n* the nominal stone diameter.

For the evaluation of this upper value of the stability coefficient, a new damage index is proposed, based on the minimum mass:

$$\hat{S} = \frac{A}{D_{n,\min}^2} \quad M_{\min} = \rho_r D_{n,\min}^3 \quad [3]$$

The ratio of damage between the two indexes, for a given area of damage, is:

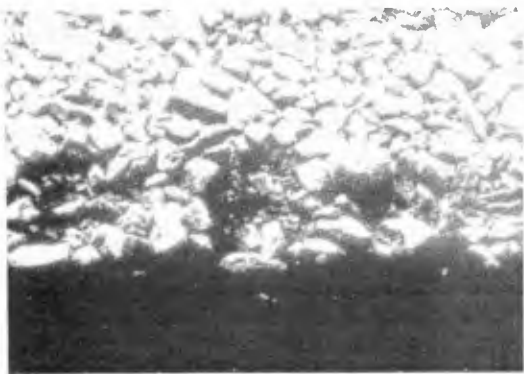
$$\frac{\hat{S}}{S} = \sqrt[3]{\left(\frac{M_{50}}{M_{\min}}\right)^2} \quad [4]$$

Practically, a value of \hat{S} equal to 2,5 is considered as the beginning of damage while a value of 5 is defined as tolerable damage. The results indicate that beyond values of 7 or 8, the damage rate tends to accelerate and can lead to major damage. It should be noted that the condition $\hat{S} = 2,5$ or $5,0$ is more severe than the condition $S=2,0$ or $4,0$ generally used.

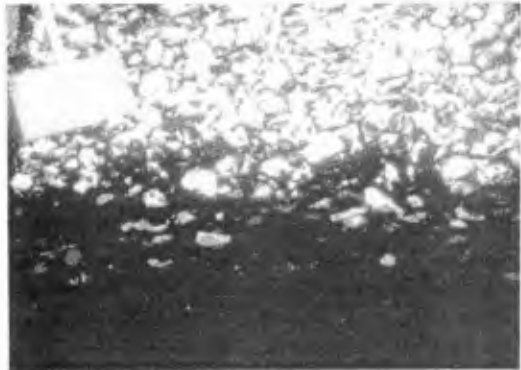
Tests conditions

SEBJ designed test cases for riprap that could withstand events with a significant wave height of 2,5 m with an accepted degree of damage ($\hat{S} = 5$). Large scale tests (15:1) were performed by the NRC for two different slopes with irregular waves. In the first phase, irregular wave trains were generated with spectral characteristics similar to those measured in the reservoirs and tests were conducted to check if observed damage could be reproduced. As can be seen on figure 7, similar damage zones indicate that the tests were conclusive.

Preliminary large scale model tests allowed a stability coefficient value of 3,5 to be used by SEBJ. Typical wave trains were generated following analysis of wave records gathered at the site. For both steep (1,8:1) and flat (2,25:1) slopes the minimum rock mass was calculated using formula [1]. The rock mass gradation was specified with a ratio, between maximum and minimum mass equal to 2,5.



Dyke TA-13



Scale Model

Figure 7. Comparison of damage

The riprap layer thickness is given by:

$$d_c = 2D_{50} \quad D_{50} = \sqrt[3]{\frac{M_{50}}{C_f \rho_r}} \quad [5]$$

with d_c the depth of cover and C_f a form factor taken to be 0,6. Gradations of 2,4 and 2,9 were realized respectively for steep (CTR) and flat (CTD) slope tests. There were three different levels of attack. The riprap thickness (d_c) was taken as the average thickness of the riprap within the zone of influence, that is 5 meters above and below the level of attack which was 2 times the target design wave height. Other tests (CTRU, CTDU) were performed with uniform blocks ($M_{max}/M_{min} < 1,2$) to confirm that the minimum mass was a key parameter for graded riprap design. Finally, some tests were conducted to verify the influence of a greater ratio between M_{max} and M_{min} (up to about 9 which could occasionally occur in the field) on the performance of riprap designed according to this new approach.

Results

As a first step, SEBJ designed tests with a stability coefficient $K=3,5$ applied to the minimum mass for an accepted degree of damage ($\hat{S} = 5$). A graded material (M_{max}/M_{min} around 2,5 to 3,0) was specified for the riprap and two different slopes were tested. The data, obtained from the tests, was as follows:

Test	Slope [H:V]	M_{min} [kg]	M_{50} [kg]	M_{max} [kg]	M_{max}/M_{min}	$d_c/D_{n,min}^{(*)}$	$d_c/D_{n,50}^{(*)}$
CTR	1,80	1515	2585	3686	2,43	2,6	2,2
CTD	2,25	1023	2052	3007	2,94	3,1	2,5

(*) Mean value at intermediate level.

The rockfill mass density is 2710 kg/m^3 and the theoretical values of H_s , according to equation [1] are respectively 2,60 and 2,46 for steep and flat slopes. The results, as shown on figure 8, represent the variations in the equivalent coefficient K obtained as a function of the damage index after 4 cycles of waves for a given H_s applied to the intermediate level for steep and flat slopes. After 4 cycles, or about 5000 waves, the level of equilibrium was obtained, at least, up to a damage index $S=4$ or $\hat{S} = 6$. For these conditions, a linear variation in the equivalent coefficient K can be noted for the same reference mass (minimum, median or maximum) as a function of the damage index. Similar results are obtained for different attack levels.

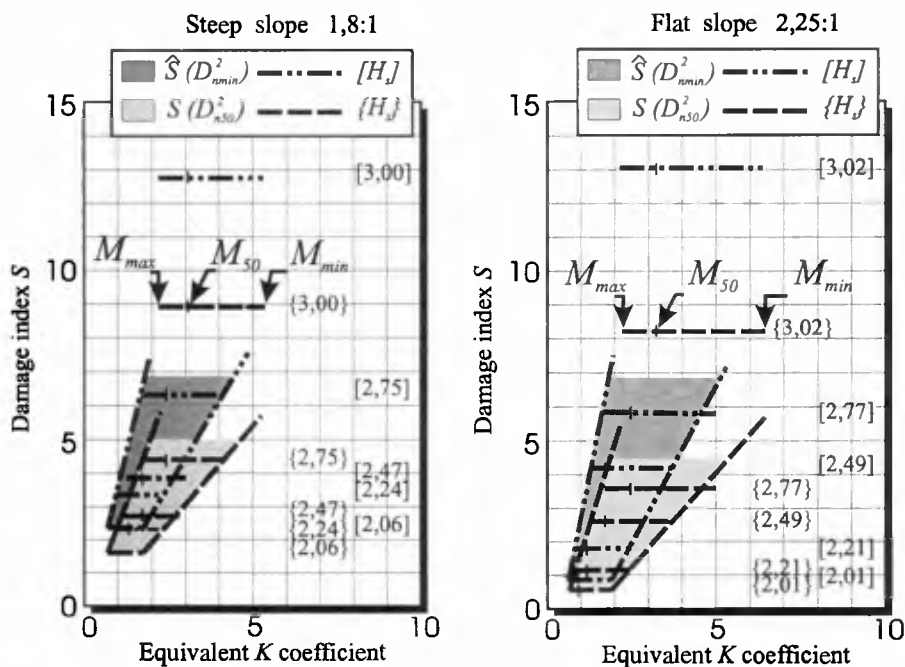


Figure 8. Relation between K and S

These results were obtained using a graded riprap with a tolerance for the rockfill of $M_{max}/M_{min} = 2,4$ and $2,9$. In order to verify if this tolerance had an influence on the upper limit obtained for the coefficient K, similar tests with uniform rock equal to the minimum mass were performed. The data, obtained for the tests, was as follows:

Test	Slope [H:V]	M_{min} [kg]	M_{50} [kg]	M_{max} [kg]	M_{max}/M_{min}	$d_c/D_{n,min}^{(*)}$	$d_c/D_{n,50}^{(*)}$
CTRU	1,80	1499	1596	1681	1,12	2,6	2,6
CTRUM	1,80	1499	1596	1681	1,12	2,1	2,0
CTRU5	1,80	2342	2552	2913	1,24	2,2	2,1
CTDU	2,25	1154	1252	1340	1,16	3,0	2,9
CTDUM	2,25	1154	1252	1340	1,16	2,1	2,0

(*) Mean value at intermediate level.

Figure 9 shows the variation in the equivalent coefficient K obtained as a function of the damage index after 4 wave cycles for tests with uniform material and the equivalent test with graded material.

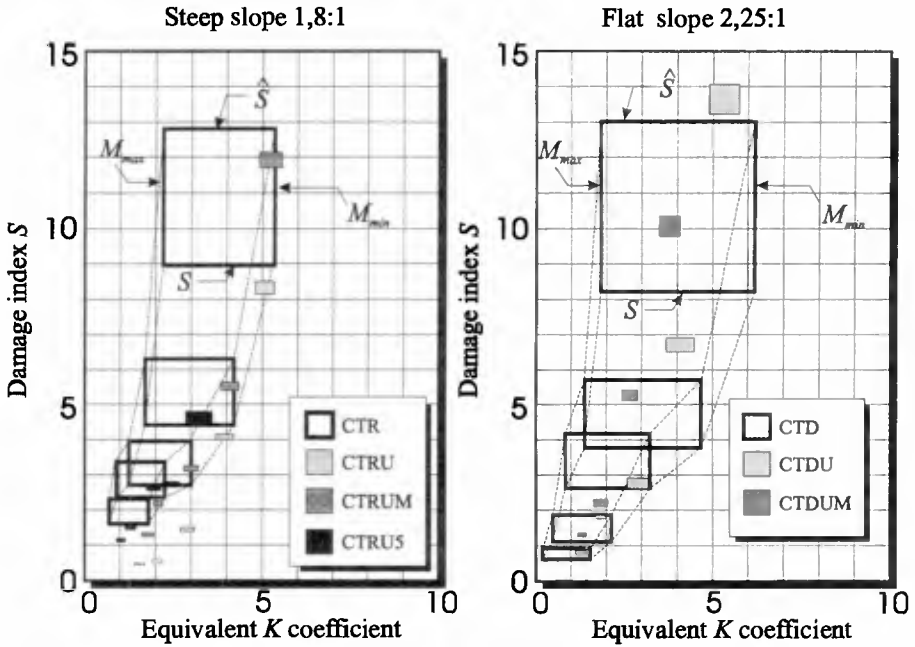


Figure 9. Comparison between graded and uniform material

The values obtained for K with tests on material with a uniform mass are comparable to the corresponding values for the minimum mass for tests with graded material or slightly superior for low values of the damage index and a steep slope. These results indicate that the minimum mass controls the resistance of the riprap for these gradations. It can be noted that a uniform material test (CTR5), on a steep slope, with a larger minimum mass (2342 kg in comparison to 1499 or 1515 kg) shows the same trend. In the same way, the apparent discrepancy of test CTDUM on a flat slope is explained by the influence of the riprap thickness ($d_c/D_{n,min} = 2,1$ in comparison to 3,0 or 3,1). The results confirm that a thicker riprap is more resistant.

Finally, in the field, it is difficult to keep a ratio M_{max}/M_{min} lower or equal to 3,0 as specified. Experience has shown that a ratio between 4 to 6 can be readily obtained. So tests on steep slopes were conducted to verify the influence of such a ratio on the performance of riprap.

The data, as obtained for these tests, was as follow:

Test	Slope [H:V]	M_{min} [kg]	M_{50} [kg]	M_{max} [kg]	M_{max}/M_{min}	$d_c/D_{n,min}^{(*)}$	$d_c/D_{n,50}^{(*)}$
CTR3	1,80	854	2498	4323	5,06	3,1	2,2
CTR4	1,80	543	2606	4725	8,70	3,6	2,1

(*) Mean value at intermediate level.

The results of these tests (CTR3 and CTR4) are shown on figure 10, along with the results of the other tests on steep slopes, as a function of equivalent coefficient K obtained with minimum mass to damage index \hat{S} also according to a minimum nominal diameter. The K values obtained from tests with a ratio M_{max}/M_{min} up to 5,1 are almost identical, and superior for CTR4 test with a ratio equal to 8,7. The higher value is due partly to a relative larger thickness ($d_c/D_{n,min} = 3,6$ in comparison with a mean value of 2,6) and also due to the more severe conditions imposed on a well graded material using minimum mass. In fact, back calculations indicate that the performance of CTR4 corresponds approximately to the resistance of M_{10} . So the use of a minimum mass approach is a conservative approach and finer material of at least 10% can be tolerated without much effect on the required resistance.

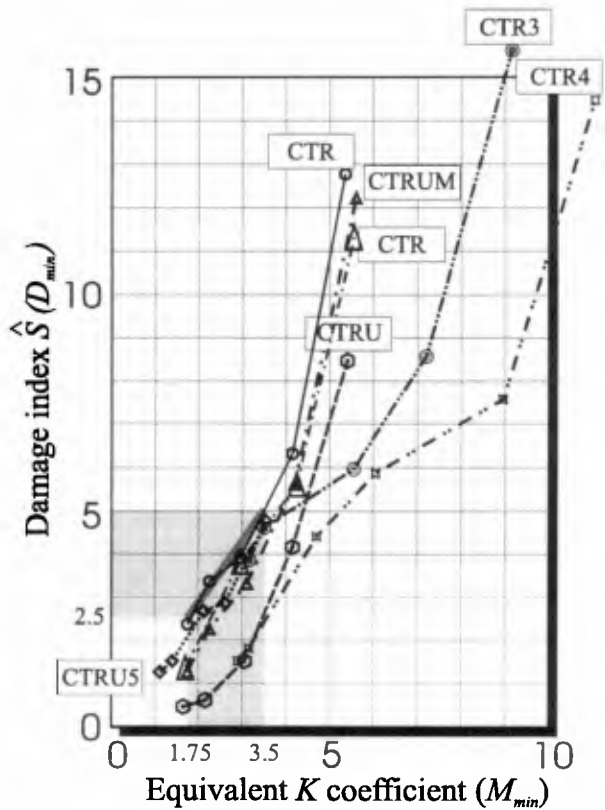


Figure 10. Relation of K versus \hat{S} for all tests (steep slope)

performance of CTR4 corresponds approximately to the resistance of M_{10} . So the use of a minimum mass approach is a conservative approach and finer material of at least 10% can be tolerated without much effect on the required resistance.

It is generally accepted that a damage index, based on the median mass, of 2 or 3 is considered as no damage and that a value of 4 or 5 is a level of acceptable damage. Using the minimum mass approach, a damage index value of 2,5 and 5 respectively is recommended to define the limits of no damage and acceptable damage, which, in terms of median mass, translates into values less than to 2 and 4.

Figure 10 represents the variation of the stability coefficient as a function of the damage index using the minimum mass approach for all the tests done on a steep slope with a minimum acceptable riprap thickness of two layers. The upper limit obtained for the coefficient K , which allows for the calculation of the minimum mass, is 3,50 (as predicted) for tolerable damage and 1,75 for no damage. The test results on flat slopes are quite similar and confirm the values for the coefficient K .

To sum up, the riprap design for the tests was based on the coefficient $K = 3,5$ for the minimum mass with a tolerance in the variation of mass $M_{max}/M_{min} = 2,4$ to 2,9 and an acceptable damage ($\hat{S} = 5$). The results are:

Tests	H_s	
	Design	Observed
Steep slope (1,80:1)	2,60	2,61
Flat slope (2,25:1)	2,46	2,59

and confirm that these parameters are justified.

In terms of design, the choice of the damage index should be related to the selected period of occurrence of the maximum wave attack. We recommend the tolerable damage for a return period of 1000 years and no damage for a period of 100 years.

Conclusion

Tests results show good behaviour of the riprap layer designed according to the approach based on the minimum mass and even some reserve for flat slopes. Tests have indicated that protection should extend to 2 times the design wave height below the attack level.

Uniform riprap is at least as resistant as graded riprap and for these gradations, stability is controlled by the minimum mass.

Results of tests and performance of riprap are more easily explained in terms of the minimum mass concept. Using this concept, values of 2,5 and 5 are proposed for the damage index respectively for the start of damage and acceptable damage. Within these boundaries, evolution of the damage index is linear with respect to the stability coefficient.

In accordance with Hudson's original work, the studies showed that a relatively uniform riprap performs best, so a ratio of 3,0 between the maximum and minimum mass is used for design purposes. In the field, however, it is difficult to preserve such a ratio. Experience has shown that a ratio between 4 and 6 can be readily obtained and is acceptable. The Hudson formula is used to obtain the minimum

mass of the rock. For the design, the significant wave height is used with a return period of 1:1000 years and a stability coefficient equal to 3,5. These values correspond approximately to the no damage condition with a 100 year return period and a stability coefficient of 1,75.

Resistance to wave action is a combination of both rock mass and permeability of the riprap. Sufficient void volume within the riprap allows for efficient wave energy dissipation. Rocks uniformly sized and uniformly graded with sufficient thickness achieve this objective.

Acknowledgements

The authors wish to thank La Société d'Énergie de la Baie James for permitting this paper to be published and Hydro-Québec for use of the information acquired during the mandate.

References

- CERC, 1977 *Shore Protection Manual*. U.S. Army Corps of Engineers, Coastal Engineering Research Center, Fort Belvoir, Virginia, 3 volumes, 1977 edition.
- CERC, 1984 *Shore Protection Manual*. U.S. Army Corps of Engineers, Coastal Engineering Research Center, Fort Belvoir, Virginia, 3 volumes, 1984 edition.
- Dupuis P., J.P. Tournier, O. Caron, 1996, *Wave Climate of Large Reservoirs and Revised Wave Hindcast formula*. 25th International Conference on Coastal Engineering, CERC ASCE, Orlando, Florida, U.S.A, Book of abstracts, Paper no 24, September 1996.
- Hudson R. Y., 1959 *Laboratory investigation of rubble-mound breakwaters*. Journal of the Waterways and Harbour Division, ASCE, 85 (3), pp. 93-121.
- Levay J., O. Caron, J.P. Tournier, R. Arès, 1994. *Assessment of Riprap Design and Performance on the La Grande Complex - James Bay, Québec*. Transactions of the 18th Congress on Large Dams, ICOLD, Durban, South Africa, vol. 1 (Q.68, R.25), pp. 369-389.
- Levay J., J.P. Tournier, R. Arès, D. LeBoeuf, 1993. *Étude de stabilité du riprap des digues et barrages du Complexe La Grande (Phase I)*. Compte-rendu du 1^{er} congrès national des grands barrages, Alger, Algérie, Mai 1993.
- Levay J., J.P. Tournier, R. Arès, D. LeBoeuf, 1993. *Riprap Stability Studies on Dams and Dykes of the La Grande Complex (Phase I)*. Proceedings of the 5th Canadian Dam Safety Conference, CDSA-CANCOLD, St. John's, Newfoundland, September 1993 pp. 137-150.
- Mansard E., M.H. Davies, O. Caron, 1996. *Model Study of Reservoir Riprap Stability*. 25th International Conference on Coastal Engineering, CERC-ASCE, Orlando, Florida, U.S.A, Book of abstracts, Paper no 94, September 1996.
- Van der Meer J.W., 1988. *Rock Slopes and Gravel Beaches under Wave Attack*. Ph.D. Thesis, Delft University of Technology, Delft Hydraulics Publication no 396.

CHAPTER 164

GEOTEXTILE SYSTEMS IN COASTAL ENGINEERING- an overview -

Krystian W. Pilarczyk, M.Sc.¹

Abstract

Geosystems has gained popularity in recent years because of their simplicity in placement and constructability, cost effectiveness and their minimum impact on the environment. An overview is given on application of the existing geosynthetic systems in hydraulic and coastal engineering.

Introduction

Various structures/systems can be of use in coastal engineering, from traditional rubble or concrete systems to more novel methods as geosystems and others. There is a growing interest both in developed and in developing countries in low cost or novel methods of shoreline protection particularly as the capital cost of defence works and their maintenance continues to rise. The shortage of natural rock in certain geographical regions can also be a reason for looking to other materials.

The geotextile systems as bags, mattresses, tubes and containers filled with sand or mortar, and artificial seaweed and geotextile curtains, can be a good and mostly cheaper alternative for more traditional materials/systems as rock, concrete units or asphalt. These new systems were applied successfully in number of countries and they deserve to be applied on a larger scale. Because of the lower price and easier execution these systems can be a good alternative for coastal protection and coastal structures in developing countries. The main obstacle in their application is however the lack of proper design criteria. An overview is given on application of the

Manager R&D, Rijkswaterstaat, Hydraulic Engineering Division, P.O. Box 5044, 2600 GA, Delft, The Netherlands, Fax +31-15-2611361

existing geosystems and reference is made to the design criteria.

Systems and applications

Geotextile systems utilize a high strengt synthetic fabric as a form for casting large units by filling by sand or mortar, or as curtains collecting sand. At this moment there is a relative large number of products of this type on the markt provided by some specialistic companies all over the world.

The following types and applications of geosynthetic systems can be distinguished:

1. Closed forms/units filled with sand, gravel or mortar: bags, mattresses, tubes, containers
2. Open-matting bags filled with stone or asphalt
3. Geotextile forms/moulds sand-filled structures
4. Geosynthetic sheets for dune reinforcement
5. Geotextile curtains for shore erosion control
6. Artificial seaweed mainly for scour prevention
7. Silt fences with various applications (pollution)
8. Geocells for surface (slope) erosion control
9. Geocomposite mats for drainage/erosion control
10. Traditional applications as geotextile filters
11. Water- or air-filled dams
12. Other (unclassified) systems (bearer for blockmats, temporary slope protection, landfill covers, cabling, pins, pipes, connections).

More informations on these systems can be found in (Pilarczyk, 1995, Pilarczyk & Zeidler, 1996) and in references.

Geosynthetic forms

Mattresses are mainly applied as slope and bed protection. Bags are also suitable for slope protection and retaining walls or toe protection but the main application is construction of groynes, perched beaches and offshore breakwaters. The tubes and containers are mainly applicable for construction of groynes, perched beaches and offshore breakwaters.

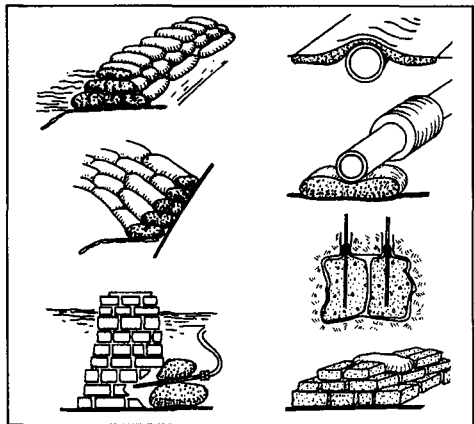


Figure 1. Application of bags

They can form an individual structure conform some functional requirements for the project but also they can be

used complementary with the artificial beach nourishment to increase its lifetime. Especially for creating the perched beaches the sand bags and /or sand tubes can be an ideal (often low-cost) solution for constructing the submerged sill (with a low wave loading).

Some coastal engineering concepts are shown in Figure 2. Underwater breakwaters and sills (perched beaches) are not easy to construct with traditional materials. In this respect (sand)tubes, although based on the same principle, are more advanced even by comparison with sandbags, which are only 1.0 to 5.0 m³ in capacity and are time-consuming as concerns both manufacturing and installation while hydraulic filling of tubes provides a few hundreds m³ of sand in few hours.

The sand-filled bags and /or tubes can be of use for constructing of groynes. Up till now there is no reliable design methods concerning the functioning of groynes. When the groyne will work satisfactorily such groyne can be strengthened additionally (if necessary) to get a permanent function. If not, the groyne can be easily demolished. In general, the sand-filled structure can be used as a temporary structures to learn the natural interactions/ responses, or as the permanent structures

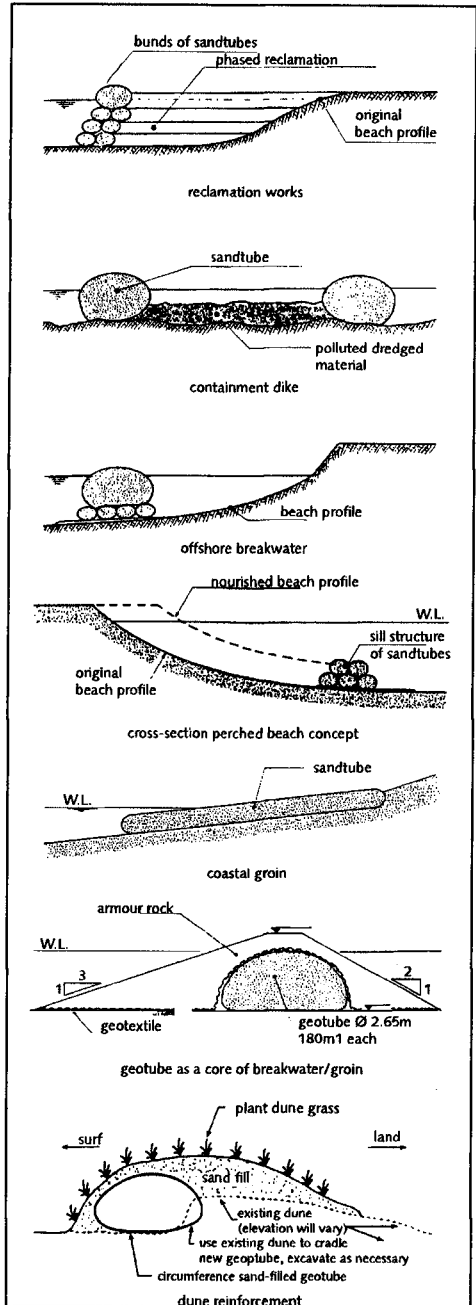


Figure 2. Coastal applications of geotubes/containers

at locations with relatively low wave attack ($H < 1.5\text{m}$), or as submerged structures where direct wave forces are reduced by submergence. The units (if necessary) can be interconnected by bars or by creating a special interlocking shape.

These systems can also be applied in hydraulic/river engineering for constructing of spur dikes, guide dams, revetments, bottom groins, bottom protection, etc.. As other possible applications can be mentioned: containment dikes for storage of (contaminated) dredged material, dike or dune reinforcement, moulds for artificial sand structures, etc.

The main advantages of these systems in comparison with more traditional methods (rock, prefabricated concrete units, blockmats, asphalt, etc.) are: a reduction in work volume, a reduction in execution time, a reduction in cost, a use of local materials, a low-skilled labour and (mostly) locally available equipment.

That means that in most, not too extreme cases/conditions the work can be done by a local contractor under supervision of the specialistic experts/company.

Geocurtains

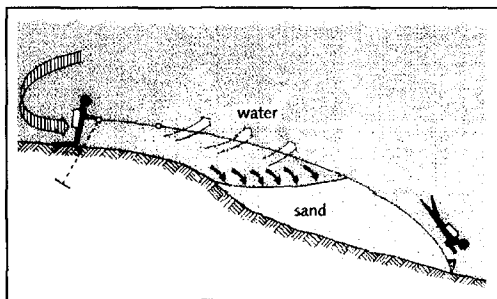
There are a number of various applications of geocurtains, i.e. silt- and/or pollution curtains, guiding screens for sediment control in rivers and harbours, fences for surface erosion control, etc.

Information on these systems can be found in references.

An interesting application for shore erosion control is the geocurtain known under the name **BEROSIN** (Fig. 3).

Figure 3. Application of geocurtains (**BEROSIN**)

The **BEROSIN** curtain is a flexible structure made of various woven geotextiles which after placing by divers near the shore and anchoring to the bed catches the sand transported by currents and waves providing accretion on a shore and preventing the erosion. The horizontal curtain (sheet) can be easily spread (at proper sea conditions) by a small workboat and two divers. The upper (shore-side) edge, equipped with some depth-compensated floaters, should be properly anchored at the projected line. The sea-side edge is kept in position by the workboat. By ballasting some of the outside pockets at the lower edge with sand or other



materials and with help of divers, the lower edge is sinking to the required position. The proper choice of permeability of geotextile creates the proper conditions for sedimentation of suspended sediment in front/or under the curtain and at the same time allowing the water to flow out without creating too high forces on the curtain and thus, on the anchors. In case of coast of Vlieland (NL), some of the horizontal curtains placed in the intertidal zone have provided a growth of a beach/foreshore of 0.5 to 1.0 m within a week while others within a few weeks. It was also recognized that the sheets (curtains) can be easily damaged in vicinity of rock due to abrasion (one curtain was connected to the existing rock groyne). On the other hand, the heads of the existing groynes were badly damaged and the beach between the groynes was eroded during the storms while the area protected by the curtains remained in proper condition.

It seems that this system can provide a low-cost measure for steering of the morfological processes. However, more prototype experiments in various wave climate are needed before the final conclusions on the effectiveness and durability of this system in various design conditions can be drawn.

The most recent development concerns the application of a number of (anchored) floating screens (grids), placed in a certain pattern along the sea bed (Huygens et al, 1995). However, the first in site experiment has failed because of high wave induced forces and resulting anchorage problems.

Artificial seaweed

The field observations provided that in some coastal areas the natural seaweed plays an important role in retaining sand along the coastlines due to the reduction of the shear stresses exerted by currents and waves on the seabed. This fact was the base of the idea to produce and apply the artificial seaweed for erosion control. The first users of artificial fibres for erosion control and/or to prevent marine scouring date back to the 60-ies (England, Denmark, Netherlands). The artificial seaweed was composed on polypropylene tape (having a specific gravity of less than one), 3 to 10 mm wide, connected edge to edge to form a continuous serrated sheet. In some cases dozens of tapes were bundled together to form individual tufts of seaweed. Fronds varied from 1 to 2 m in length. In the Netherlands, research on artificial seaweed has been conducted in cooperation with the Shell Plastics Laboratory, Nicolon Geotextiles Company and the Rijkswaterstaat (Dutch Public Works), (Bakker et al, 1972) The improper anchorage was the main reason of the failures with this system .

The experience from US and European projects indicate

that the artificial seaweed can be successfully applied for scour prevention around the legs of offshore platforms and around offshore pipelines when the anchorage is designed properly. Applications of artificial seaweed to beach erosion control were till now less successful. There were often no discernable differences between the shoreline protected with artificial seaweed and adjacent unprotected shorelines. The materials appear to be inadequate to survive moderate to high wave activity. One of the main reason for that was again the problem with anchoring (Rogers, 1987). Due to the high forces of breaking waves in a surf zone the necessary anchorage needs special expensive measures which makes this system less competitive with more conventional solutions.

The past experience with the artificial seaweed indicates that the most promising application for this product is prevention of localized scour at offshore structures (platforms, pipelines, etc.). The wave induced currents are there of a limited strength (less problems with proper anchorage), because of larger depths no problem with UV-resistance, and less problems with effect of fouling and debris. That also explains why the recent developments and applications are related (limited) to that area.

The product which actually successfully operates on the markt for offshore applications has a form of a underwater artificial sea grass field/mats (developed in 80-ies), and is known as Seabed Scour Control System (SSCS, 1995). Based on the artificial seaweed concept of "arrested sedimentation" SSCS system (mat) suffers none of the drawbacks of similar previous systems. It has superb positional stability, it is not prone to phylloplankton colonisation, it requires no special tools or skills for installation and it actually serves to enhance its own effectiveness and that of other conventional sea defence forms.

The functioning principles are straight-forward; buoyant fronds floating upright from the seabed act to reduce seabed and near-seabed current velocities, encouraging the deposition of transported (eroded) seabed material. In conjunction with this action, at relatively shallow water the fronds also interfere with wave-induced orbital forces, effectively causing waves to break early and thus reducing the impact on threatend shorelines, breakwaters, etc.

This technique employs chemically inert materials to create a flexible barrier to retard the flow of water. The SSCS scour control mats are retained on the seabed by anchors hydraulically driven to a depth of 1 m. The system has been designed and tested for stability in current velocities in excess of 10 knots (> 0.5 m/s). The flexible fronds-mat can also be incorporated into flexible concrete block mats to provide added effectiveness in

stability and in wave dissipation. The main applications are in protecting fixed offshore platforms, mobile rigs and pipelines from the effects of scour.

Stability of geosystems

The main obstacle in application of geosystems is the lack of proper design criteria. However, from the literature review it is possible to formulate some stability criteria based on small scale experiments. It can be concluded that the stability of the coastal structures composed of geosystems (bags, mattresses, geotubes) can mostly be expressed in the similar way as for rock, namely in term of $H_s/\Delta D$ parameter.

* Sand and mortar filled bags

For the time being it can be concluded that the stability of sandbags with the width-length ratio not larger than 1 to 3 and properly filled (> 70%), can be computed in the similar way as riprap. It is recommended to calculate the stability acc. to Pilarczyk's formula (Pilarczyk, 1990) with stability coefficient $c = 2.5$, nl.:

$$H_s/\Delta D = c \cos\alpha \xi^{-1/2} \quad \text{for } \xi \leq 3 ,$$

(for $\xi > 3$, the values calculated for $\xi = 3$ can be used),

where: H_s = significant wave height, Δ = relative density of the bags, $(\rho_s - \rho_w)/\rho_w$, D = average thickness of bags, c = stability coefficient defined at $\xi = 1$, $\cos\alpha$ = slope angle (it can be neglected for slopes milder than 1 on 3), ξ = surf-similarity parameter equal to $\tan\alpha/(H_s/L_o)^{1/2}$, and L_o = wave length. The density of bags (ρ_s) can be assumed 2000 and 2300 kg/m³ resp. for sand and concrete (Δ resp. 1 and 1.3).

Note: Sand-filled units exposed to direct wave attack are applicable till $H_s = 1.5$ m (max. 2 m).

* Stability of foreshore protection mattresses incl. sand-sausage mattresses (ProFix-mats)

For the first approximation of stability of sand- or mortar-filled mattresses (i.e. ProFix or Fabriform mats) of more or less uniform thickness the formula proposed by Pilarczyk (1990) can be used:

$$H_s/\Delta D_{eq.} = c \cos\alpha \xi^{-2/3} \quad \text{for } \xi \leq 3$$

(for $\xi > 3$, the values calculated for $\xi = 3$ can be used) where: Δ = relative density of the mattress, $D_{eq.}$ = equivalent (average) thickness of mattress, c = stability coefficient defined at $\xi = 1$ (definition of other parameters is the same as above).

The value of coefficient 'c' depends on the failure

mechanism and the ratio between the permeability of the mattress and the permeability of the subsoil, k_m/k_s :

$c = 3$ to 4 when $k_m/k_s < 1$ with the uplift of mattress and deformation of subsoil as main failure mechanism, and

$c = 4$ to 6 when $k_m/k_s \geq 1$ with the deformation of subsoil as the main failure mechanism.

The range of c -values follows from the research projects of Delft Hydraulics with placed block revetments/block-mats and different type of mattresses. It should be noted that the uplift can already start at $c = 2$, but it is so small and of such short duration that it will no result in a serious damage to the mattress protection. Therefore $c = 3$ to 4 can be treated as a design value.

In special cases as large mattresses of temporary use and/or when some deformation of the subsoil can be accepted or the subsoil is more resistant to deformation (i.e. clay) the higher values of ' c ' can be chosen (max. 6). The research described in (Delft Hydraulics, 1975; large mattresses on circular island) can be illustration of such case. Using these high c -values the structure should be controlled on sliding, and in most cases it will require a special anchoring of mattresses.

Sand-filled units applicable till $H_s \leq 1.5$ m.

* General stability criteria for geotubes filled with sand or mortar (Wouters, 1995)

Based on small scale investigations by Delft Hydraulics (Breakwater of concrete filled hoses, M 1085, 1973) and other literature informations, the following stability criteria for geotubes can be formulated:

- tubes on the crest (at S.W.L. or submerged) lying parallelly to the axis of breakwater

$$H_s/\Delta B = 1$$

where B is the width (horizontal ovality measure) of a tube; one may roughly assume $B = 1.1 D$ (original diameter of a tube).

Note: when the crest layer is composed of two tubes connected artificially to each other (i.e. re-bars) the equivalent width is equal to $2B$.

- when the tube is placed perpendicularly to the axis of a breakwater the stability can be approximated by

$$H_s/\Delta L = 1$$

where L is the length of a tube.

Sand-filled units are applicable till $H_s = 1.5$ m (max. 2m).

Due to the absence of reinforcement in the mortar filled units it is very likely that for long tubes (say longer than 3D) also cracks will occur; some reinforcement should be recommended or an equivalent length should be taken equal to $L < (3 \text{ to } 4) D$.

Conclusions

The geotextile systems can be a good and mostly cheaper alternative for more traditional materials/systems. These new systems were applied successfully in number of countries and they deserve to be applied on a larger scale.

In the past the design of these systems was mostly based on rather vague experience than on the general valid calculation methods. Actually, more proper design rules have been established based on some scale investigations and experience from realized projects. However, more research, especially concerning the large scale tests and evaluation of performance of already realized projects, is still needed.

The technologies related to geotextile systems have been utilized extensively in Europe, Northern America, Mexico, Japan and Australia, producing often successful installations but only few technical details. Some manufacturers and contractors are inclined to protect know-how to preserve market advantages. Therefore, to effectively commercialize these technologies it is necessary to uncover the technical details. Technically the methodologies have shown to be feasible but there are design and constructibility uncertainties that still must be addressed.

A number of weak points of above reviewed systems can be omitted when the actual knowledge/experience will be applied in the design and technological improving of these systems including such aspects as fabric choice, fabric coating, filling method, installation techniques, stability criteria, and life-time.

The intention of this literature search is to uncover, as far as possible, the technical informations on these systems and make them available for the potential users. It will help to make a proper choice for specific problems/projects and it will stimulate the further developments in this field.

There are more applications of geosynthetic (geotextile) systems in coastal engineering than those mentioned above. It is going too far in the scope of this paper to review all of them. However, the main other applications can be found in the references.

There is a rapid development in the field of geotextiles and geotextile systems and there is always a certain time gap between new developments and publishing that in specialistic books. Therefore, it is recommended to follow the professional literature on this subject (Jour-

nal of Geotextiles and Geomembranes, Geotextiles Congresses, Coastal Engineering Congresses, etc.) and manufacturer's brochures for updating the present knowledge.

References and Bibliography

- Ahrends, J., 1976, Wave Attenuation by Artificial Seaweed, Miscellaneous Papers, No. 76-9, CERC, US Army Corps of Engineers, Fort Belvoir.
- AKZO, 1991, Armater, Enkamat, Company Publications, Arnhem, the Netherlands.
- Armstrong, J.M. and C.L. Kureth, 1979, Some observations on the Longard tube as a coastal erosion protection structure, ASCE, Coastal Structures '79.
- Anwar, H.O., 1967, Inflatable Dams, Journal of Hydraulics Division, ASCE, HY 3, May.
- Bakker, W.T. et al, 1972, Artificial Seaweed: coastal and submarine pipeline protection studies with stretched polypropylene foam strands, Shell Plastic Laboratory, Delft, the Netherlands.
- BEROSIN/Bureau van der Hidde, 1995, Product information, P.O. Box. 299, 8860 AG Harlingen, Netherlands.
- Bogossian, F., R.T. Smith, J.C. Vertimatti and O. Yazbek, 1982, Continuous retaining dikes by means of geotextiles, Proc. 2d Intern. Conf. on Geotextiles, Las Vegas.
- Brian, E.W. and Dowse, P., 1979, Hydrostatically supported sand coastal structures, Coastal Structures '79.
- Davis, G.A., D.J. Hanslow, K. Hibbert and P. Nielsen, 1992, Gravity drainage: a new method of beach stabilisation through drainage of the watertable, Proc. 23rd ICCE, Venice.
- Delft Hydraulics Laboratory, 1973, Artificial weed as bed protection, Report M 1162.
- Delft Hydraulics Laboratory, 1973, Breakwater of concrete filled hoses, Report M 1085.
- Delft Hydraulics Laboratory, 1975, Artificial Islands in the Beaufort-sea: M 1271 part III, comparison of stability of shore protection with gabions and sand sausages (2-dim.); M 1271 part V, stability of shore protection with sand sausages on circular island.
- Delft Hydraulics Laboratory/Delft Soil Mechanics Laboratory, 1983, Stability of ProFix sand filled mattresses under wave action, Report of model investigation, R1903.
- Delft Hydraulics/Nicolon, 1994, Stability of breakwaters constructed with Geotubes or Geocontainers, Two-dimensional model tests, Report on the model investigation, H2029.
- den Hoedt, G., Metz, H.E., Voskamp, W., 1987, Cost-effective building of breakwaters using geotextiles, 2nd Int. Conf. on Coastal and Port Engineering in Developing Countries, Beijing.
- den Hoedt, G., Metz, H.E., Veltman, M. and Voskamp, W.,

- 1987, Cost-effective reduction of sedimentation and maintenance dredging using geotextile flow diversion screens, 2nd Int. Conf. on Coastal and Port Engineering in Developing countries, Beijing, China, Vol. II.
- Dette, H.H. and Raudkivi, A.J., 1994, Dune Protection, Inter. Symposium "WAVES '94", Vancouver, Canada (see also, 24th ICCE, Kobe).
- Deron Austin of Jessup, 1992, Steep slope protection using geocells, Geosynthetics World, 4/5.
- Foreman J.F., 1986, Generalized monitoring of SEASCAPE installation at Cape Hatteras Light-house, North Carolina, Miscell. Paper CERC-86-2, US Army Corps of Eng., Vicksburg.
- Gadd, P.E., 1988, Sand bag slope protection: design, construction and performance, Arctic Coastal Processes and Slope Protection Design, ASCE.
- Gutman, L., 1979, Low-cost shoreline protection in Massachusetts, Coastal Structures '79.
- Hall, C.D., 1992, The contemporary approach to the role of vegetation in erosion control, Geosynthetics World, April/May.
- Hendrikse, C., 1995, Geocontainers; report test programma (prototype), Van Oord ACZ - Nicolon, the Netherlands.
- Huygens, M., de Wachter, D., Verhoeven, R., Himpe, J., Buyck, S. and Wens, F., 1994, Underwater screens for shore protection, Symposium WAVES, Vancouver, Canada.
- Huygens, M., de Wachter, D., Verhoeven, R., Himpe, J., Buyck, S., Wens, F., de Putter, B. and de Wolf, P., 1995, Model simulation of the impact of underwater screens on shore protection, PIANC Bulletin No. 86.
- Hydraulics Research, 1984, A Review of Novel Shore Protection Methods, Volume 2 - Sand or mortar-filled fabric bags, by J.M. Motyka and J. Welsby, Wallingford, England.
- Italian Public Works, 1992, Coasts, Harbours and Lagoons Protection Works.
- Jackson, L.A., 1987, Evaluation of sand filled geotextile groyne constructed on the Gold Coast, Australia, Proc. 8th Australian Conf. on Coastal & Ocean Engng., Launceston.
- Jacobs B.K. and Nobuhisa Kobayashi, 1983, Sandbag stability and wave runup on bench slopes, University of Delaware, Dpt. of Civil Engineering, Research Report No. CE-83-36, July.
- Kato, M. and Hamanaka, K., 1993, Analytical and Experimental Study of Characteristics of Textile Sheets Structure, 11th Australasian Conference on Coastal and Ocean Engineering.
- Kazimierowicz, K., 1994, Simple Analysis of Deformation of Sand-Sausages, 5th Inter. Conf. on Geotextiles, Geomembranes and Related Products, Singapore.
- Kobayashi N. and B.K. Jacobs, 1985a, Stability of armor units on composite slopes, ASCE, Journal of Waterway,

- Port, Coastal and Ocean Engineering, Vol. 111, No. 5, September.
- Kobayashi N. and B.K. Jacobs, 1985b, Experimental study on sandbag stability and runup, ASCE, Proc. Coastal Zone '85, Vol.2, pp.1612.
- Lamberton, B.A., 1983, Fabric-formed revetment technology opens new engineering opportunities, Geotechnical Fabrics Report.
- Lamberton, B.A., 1983, Fabric forming for underwater concrete, Coastal Structures'83.
- Lamberton, B.A., 1989, Fabric forms for concrete, Concrete International, December.
- Linear Composites, 1986, Erosion Control Systems, ICI Fibres, Product info., North Yorkshire, UK.
- Longard, 1985, Flexible sand-filled tubes used for constructing underwater breakwaters in coast protection plans, Company publication.
- Nicolon Corporation, 1985, Artificial Seaweed Protects the Seabed, Estuaries and Submerged Pipelines, Product literature, the Netherlands.
- Perrier, H., 1986, Use of soil-filled synthetic pillows for erosion protection, Proc. 3rd Intern. Conf. on Geotextiles, Vienna.
- PIANC, 1992, Guidelines for the design and construction of flexible revetments incorporating geotextiles in marine environment, Brussels, Belgium.
- Pilarczyk, K.W., 1990, Coastal Protection, A.A. Balkema Publisher, Rotterdam.
- Pilarczyk, K.W., 1994, 1995, Novel systems in coastal engineering; geotextile systems and other methods, Rijkswaterstaat, Delft, the Netherlands
- Pilarczyk, K.W. and M. K. Breteler, 1994, Designing of revetments incorporating geotextiles, 5th Int. Conf. on geotextiles, Geomembranes and Related Products, Singapore.
- Pilarczyk, K.W. and Zeidler, R.B., 1996, Offshore breakwaters and shore evolution control, A.A. Balkema Publ., Rotterdam.
- Pildysh M. and K. Wilson, 1983, Cooling ponds lined with fabric-formed concrete, Concrete International, September.
- Porraz, M., 1976, "Textile Forms Slash Costs of Coastal Zone Structures", Ocean Industry Magazine, October 1976. pp. 61 - 64.
- Porraz, M., José A. Maza and Ricardo Medina, 1979, Mortar-filled containers, Lab and Ocean Experience, Coastal Structures'79.
- Rankilor, P.R., 1989, The reduction of soil erosion by pre-formed systems, The International Erosion Control Association, Symposium on Soil Erosion and Its Control.
- Ray, R., 1977, A laboratory study of the stability of sand-filled nylon bag breakwater structures, Miscella-

- neous report no. 77-4, US Army Corps of Engineers.
- Rijkswaterstaat - Nicolon, 1988, Bed protection, Old Meuse, by means of geocontainers, report VXT/HJ88.168, Publication of Nicolon B.V.
- River and Harbour Laboratory, 1976, Scour prevention system, Hydraulic flume study, SINTEF, Trondheim, Norway.
- Rogers, Spencer M. Jr. 1987, Artificial Seaweed for Erosion Control, Shore and Beach, Vol. 55, No. 1.
- Saathoff, F. and Witte J., 1994, Use of geotextile containers for stabilizing the scour embankments at the Eidersperrwerk (in German), Deutsche Textvorlage für Geosynthetics World.
- Sarti, G. and J. Larsen, 1983, Underwater filling of Longard tubes, Coastal Structure '79.
- Silvester, R., 1986, Use of grout-filled sausages in coastal structures, ASCE, J. Waterway, Port Coastal and Ocean Engineering, Vol. 112, No. 1, January.
- Silvester, R., 1990, Flexible Membrane Units for Breakwaters, in 'Handbook of Coastal and Ocean Engineering, John B. Herbich, ed., Vol. 1, pp. 921-938.
- Sprague, C.J. and M.M. Koutsourais, 1992, Fabric formed concrete revetment systems, published in 'Geosynthetics in Filtration, Drainage and Erosion Control, R.M. Koerner, ed., Elsevier Applied Science (reprinted from Geotextiles and Geomembranes, V. 11, No. 4-6).
- Sprague, C.J., 1994, Dredged material filled geotextile containers, prepared for the US Army Corps of Engineers, Vicksburg, MS.
- SSCS, 1995, Eliminate the High Cost of Scour: an engineering solution to seabed erosion, Product information of Seabed Scour Control Systems Limited, Great Yarmouth, England.
- Stark K.P. and Johnston, A.J., 1985, A marine building material of the future, 7th Australasian Conference.
- Stephenson, R.W., 1982, A study of soil-filled synthetic fabric "Pillows" for erosion protection, 2nd Inter. Conf. on Geotextiles, Las Vegas, U.S.A.
- SUT Seminar, 1980, Scour prevention techniques around offshore structures, One-day Seminar on 16 December 1980, Society for Underwater Technology, London.
- Taiyo Kogyo Corporation, 1994, Design of Silt Protector, Company Publication, Tokyo, Japan.
- ten Hoopen, H. 1976, Recent Applications of Artificial Seaweed in the Netherlands, Coastal Engineering Conference, ASCE, New York.
- Tutuarima, W.H. and W. van Wijk, 1984, ProFix mattresses - an alternative erosion control system, in Flexible Armoured Revetments incorporating geotextiles, Thomas Telford, UK.
- Tetra Tech, 1982, Longard Tube Applications Manual (Aldek A-S Longard), Tetra tech, U.S.A.
- US Army, 1981, Low Cost Shore Protection, Final report on the Shoreline Erosion Control Demonstration Program

- (Section 54), Published by the US Army Corps of Engineers.
- van Santvoort, G./Veldhuijzen van Zanten, R./, 1994, Geotextiles and Geomembranes in Civil Engineering: a handbook, A.A. Balkema Publ., Rotterdam.
- Voskamp, W., 1983, Construction of steep slopes of sand under water using synthetic fiber screens, 2nd Int. Offshore Mechanics and Arctic Engineering Symposium, Houston, Texas.
- Watson, R., 1985, A note on shape of flexible dams, J. Hydraulic Research, Vol. 23, No. 2.
- Wouters, J., 1995, Stability of geosystems, Open Taludbekledingen, Delft Hydraulics, H 1930, March (concept, in Dutch).

CHAPTER 165

Groynes on the East Frisian islands: History and experiences

Hans Kunz ¹

Abstract

Groynes can be a valuable shore-protection structure. An example for this fact are the 'Strombuhnen' ('stream groynes') which have been constructed on most of the East Frisian islands throughout the last hundred years. These groynes are integrated in an engineering coastal protection system, which includes seawalls, dune revetments, 'Strandbuhnen' ('beach groynes') and artificial beach-restoration. The modern approach of society in Germany (and many other countries) towards nature preservation and integrated management of the coastal zone discourages use of 'hard' constructions. However, there are several demands of society, for which we have to concede, that properly designed 'stream groynes' can function effectively and economically; under certain conditions; this can also be the case for 'beach groynes'. According to the stated demands, these constructions have, more or less, the target to govern natural processes; hence they are principally objectable from an environmental point of view.

Introduction

The seven East Frisian islands extend along the North Sea in the western part of Germany (Fig. 1). The chain of barrier-islands is broken by inlets and separated from the mainland by a tidal flat system (Fig. 2). The semi-diurnal tides and wave action generate a net littoral drift from West to East. With respect to hydrodynamical boundary conditions and sediment transport, the islands experience both, erosion and accretion. The processes at the spits of the islands are governed by the tidal inlet, associated with the sediment transport processes in the ebb delta-shoals and the tidal

Director, Dr., Coastal Research Station (CRS) of the Lower Saxonian Central State Board for Ecology, An der Mühle 5, D-26548 Norderney/Germany

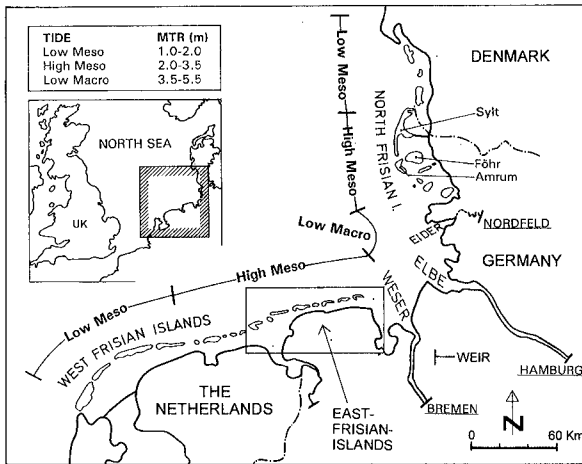


Fig. 1: The German, Dutch and Danish Waddensea - North Sea coast.

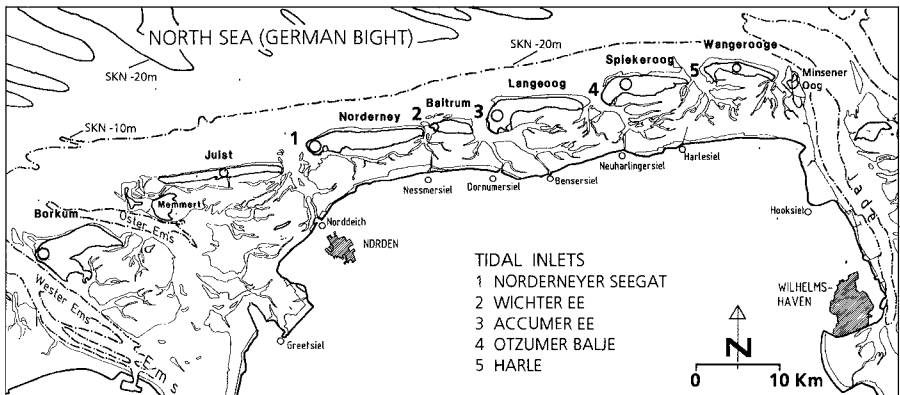


Fig. 2: The East Frisian islands and tidal inlets.

basin. The inlets are the most active part of the system; in the past they permanently changed their location as a reaction on structural changes within the sea/inlet/basin-system (naturally or man made). A migrating inlet can lead to erosion of an island, by the strong currents in the tidal channel and by effects on the ebb-delta shoals ('reef bow') which decrease the sand supply from the littoral system (negativ sand budget). The morphological development of the East Frisian islands is well recorded since 1650 (e.g. Homeier, 1962).

Groynes on the East-Frisian islands

Groynes are shore-perpendicular (normal) constructions. Professional terms in German literature distinguish 'Strandbuhnen' ('beach groynes') and 'Strombuhnen'

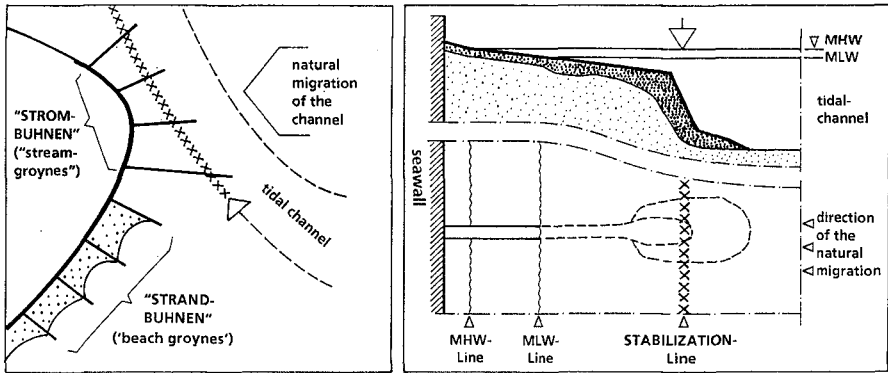


Fig. 3: Groyne-types (left). Stream-groyne (right).

('stream groynes') - see Fig. 3. The definition of 'beach groynes' has stated the purpose, quite similar to SPM (1984), as trapping littoral drift, building a beach, defending the removal of sand from the beach. 'Stream groynes' are structures to withstand and to govern the eroding forces (currents) of migrating tidal channels - e.g. KFKI (1993), TAW (1995).

The first solid construction (groynes, revetments) on the East Frisian islands were directed against dune and beach erosion. They failed in the beginning, because they could not stop migration of the inlets and they did not trap sand. The effects of scouring in front of the revetment and lee-erosion, prompted the extension of the protection means (expansion, displacement of the problems). Later on, the functional purposes of the groynes had been focused on the stabilization of the tidal inlet, leading to controversial discussions on the extension of groynes into deep water. The extreme high expenses for these 'Strombuhnen' finally had been justified by different targets (e.g. Witte, 1970):

- protection of the settlements (residential, recreational, commercial purposes).
- Preservation of the existing coastal protection constructions.
- Stabilization of the Ems- and Jade-waterway (Borkum- and Wangerooge-island).
- Stabilization of the tidal inlets and by this maintenance of the wadden-waterways to small harbors and of drainage channels.
- Protection of the mainland (dikes, foreland) against the impact of stormfloods.

The construction of 'stream groynes' started around 1900 and had been carried out on the western spits of four East Frisian islands. In every case these groynes had been constructed by extending existing 'beach groynes' into the deep water of the channel (response to the fact that the implemented groynes failed to stop erosion). Hence, these groynes are a combination of both types, depending on the crest-height; the lower part is addressed as 'underwater-groynes'. Since 1951/52 the technique of beach restoration has frequently applied to compensate sand losses by maintaining beaches within the groyne fields, which are high enough to protect the structures against failure caused by stormfloods.

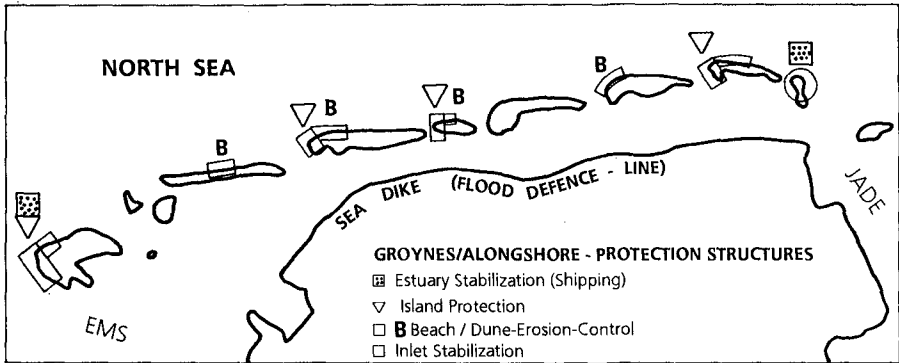


Fig. 4: Groynes on the East Frisian islands and their different targets.

The development of the groynes as part of the engineering coastal protection systems on the East Frisian islands is well known and described (e.g. Fülischer (1905), Gaye & Walther (1929), Kurzack et al. (1950), Witte (1970)).

Fig. 4 displays the groynes of the East Frisian islands (124); all are incorporated in protection structures (about 20 km length in total) which include shoreparallel constructions (seawalls, revetments). The different main targets with respect to the island/inlet are marked by signatures. The islands, tidal flats, forelands (saltmarshes), sea dikes (flood defence line) form one unit; hence the areas behind the islands benefit from the island protection means. The construction of groynes has rather based on a 'guidance on functional design', (e.g. Kraus et al., 1994) than on 'roles of thumb'; adaptations derived from 'lessons learnt from experience' and from changing hydrographic and morphological boundary conditions. The effects of groynes had been studied in physical models, especially for Norderney-island (hydrodynamical preinvestigations go back to the end of the last century; in the forties of this century they had been combined with morphodynamics (movable bed using amber grains) - Pr. Versuchsanstalt, 1940.

Examples

Fig. 5 shows, as an example, the actual situation of Baltrum-island: the western spit is totally armored, the inlet (Wichter Ee) has been fixed by 'stream groynes', the shoals (littoral drift) feed only areas eastward of the exposed spit. This situation is comparable with Norderney-island (e.g. Fig. 2 in Kunz, 1993a) and the problems are principally the same (e.g. Luck 1976, Kunz 1987).

The migration-history of the Wichter Ee inlet is shown on Fig. 6 by the development of: the Wichter Ee itself (ΔW), the watersheds of the Wichter Ee tidal basin (to the West (ΔN) and to the East (ΔB)), the shore-line of Baltrum West. The definition of the terms is illustrated on Fig. 7. The construction of 'beach-groynes' started earlier on Norderney than on Baltrum (see (N) and (B) on Fig. 6); the exten-



Fig. 5: Aerial view of Norderney (left), Accumer Ee-inlet, Baltrum (right). Situation 1966, low water.

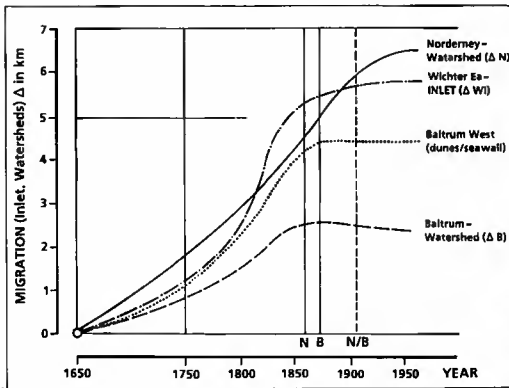


Figure 6

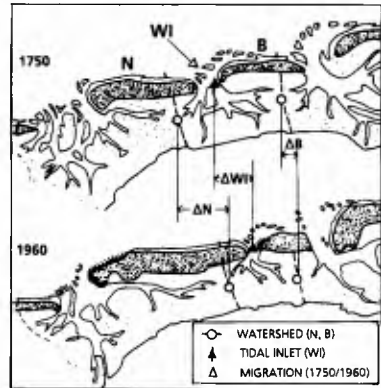


Figure 7

Fig. 6: Migration of the Wichter Ee-inlet (ΔWI), of the watersheds (ΔN , ΔB), of the Baltrum-spit. Data from Homeier (1962), Luck (1975).

Fig. 7: Situation of Norderney (N), Baltrum (B), Wichter Ee-tidal inlet (WI) around 1750 and in 1960. Illustration of the terms ΔWI , ΔN , ΔB (see fig.6).

sion of the existing beach groynes into the tidal inlet (conversion into 'stream groynes') is marked by (N/B). The stabilization-effects are obvious: the system lost it's dynamic behavior and became static. This happened to the East Frisian islands as a whole, as three more inlets (see Fig. 4) had been stabilized (e.g. Luck 1976). Society

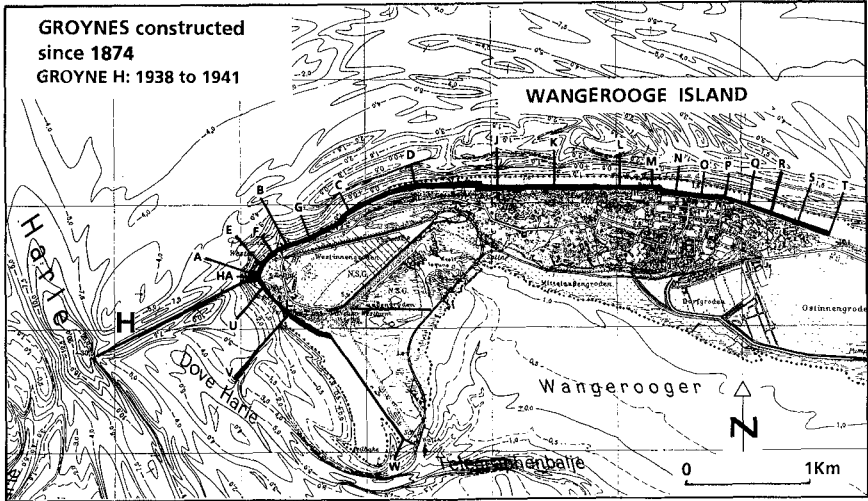


Fig. 8: Groynes on Wangerooge-island. Forschungsstelle (1980).

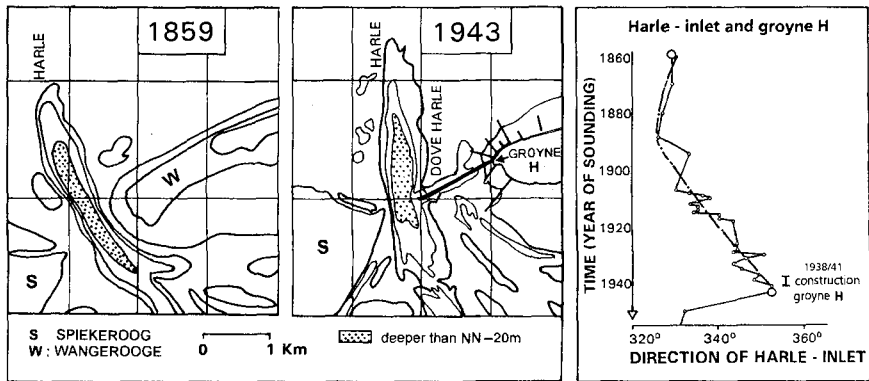


Fig. 9 : Harle inlet and Wangerooge island in 1859 and 1943. Turning of the Harle-inlet-direction before and after the construction of groyne H - Lüders (1952).

valued this result as a success; nowadays there are complains arising from the new targets of nature conservation, which society has more and more agreed on throughout the last decades (e.g. Kunz, 1993b).

The western spit of Wangerooge-island and additionally about four more kilometers of the shoreline to the East are protected by groynes (Fig. 8). The history of the island-protection is closely associated with the Jade-waterway and the harbor of Wilhelmshaven (e.g. Krüger 1911, Witte 1970). The Harle-inlet migrated to the East and turned clockwise (Fig. 9), a trend which can be explained by natural and by man made reductions of the attached catchment area 'Harle tidal basin' - Homeier (1973).

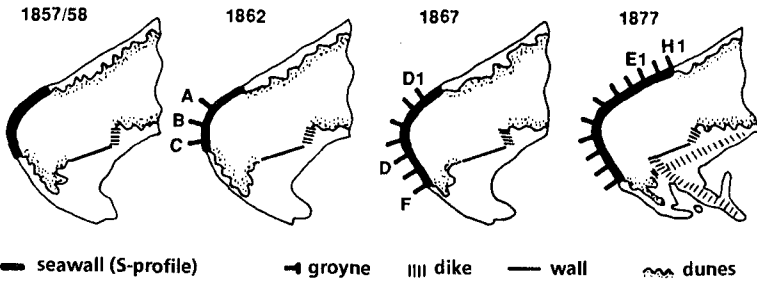


Fig. 10: Development of the protection on Norderney west (1857 to 1877).

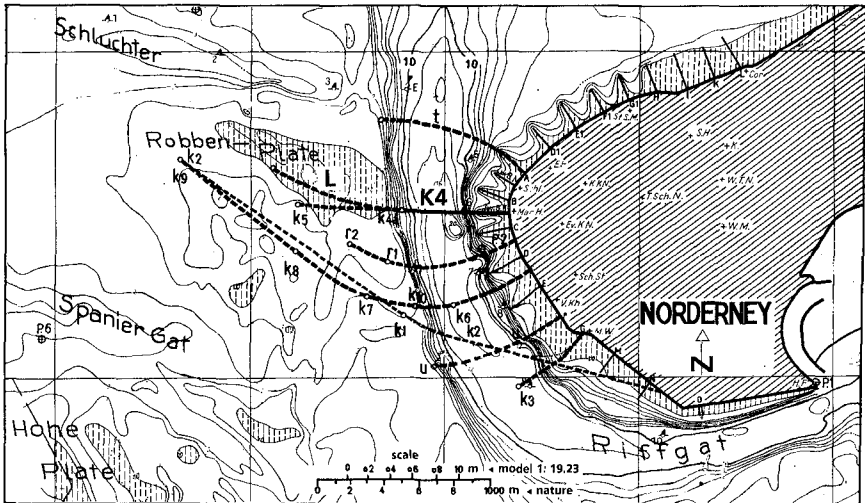


Fig. 11: Proposed groyne-extensions and training dams into the Norderney-inlet: physical model with movable bed (Pr. Versuchsanstalt, 1940).

The western spit of Wangerooge-island and additionally about four more kilometers of the shoreline to the East are protected by groynes (Fig. 8). The history of the island-protection is closely associated with the Jade-waterway and the harbor of Wilhelmshaven (e.g. Krüger 1911, Witte 1970). The Harle-inlet migrated to the East and turned clockwise (Fig. 9), a trend which can be explained by natural and by man made reductions of the attached catchment area 'Harle tidal basin' - Homeier (1973). By the extension of groyne H from 290 m to 1460 m with a crest height of about MLW it was possible to close the secondary channel 'Dove Harle' and to restore a morphodynamic situation almost similar to the middle of the last century by returning the direction of the Harle-inlet (Fig. 9, right), which has been more favorable for the island with respect to the island stabilization-targets (Lüders 1952).

The groynes and shore-parallel structures on the East Frisian islands have been implemented 'step by step' since the middle of the last century. In each case the first

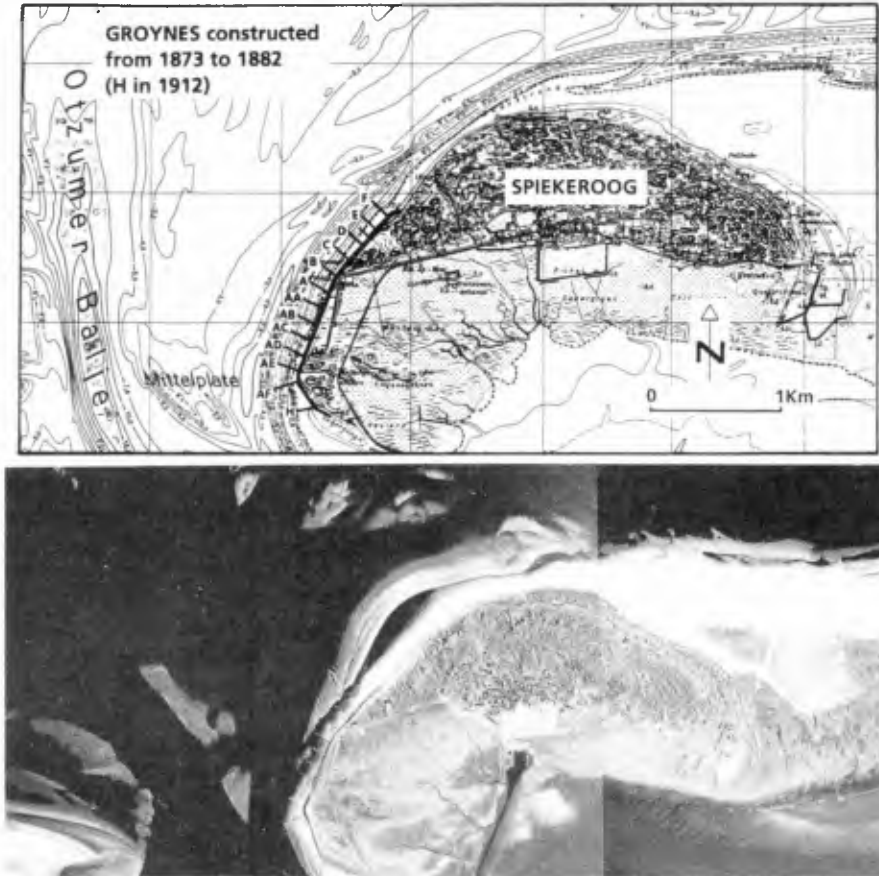


Fig. 12: Spielerog West. Above: groynes and dune revetment. Below: Aerial view, May 1989, shortly before landing of an accumulated shoals.

step had been a technical response to the respective problem: short stretch of dune revetment against dune-losses; a few short 'beach groynes' against beach-scouring; extensions against effects of lee-erosion etc.. Thus, the first 'voluntary step' had been followed by further steps which had been determined by the natural processes in interaction with the coastal defence-constructions (man made boundary conditions). This history is especially well documented for Norderney (e.g. Fülischer (1905), Gaye & Walther (1929), Kurzack et al. (1950), Peper (1956), Witte (1970)). Fig. 10 describes this history for the first two decades after a short solid seawall had been constructed in 1957/58 (still in place!). Under the existing conditions (tidal channel is migrating towards the island, lack of sand supply by cross-shore transport, unfavorable balance between net and gross longshore transport, bypassing) the construction had to be adapted or given up. The adaptation by 'stream groynes' stopped the inlet movement, but it didn't solve the erosion-problems. Therefore the question had been investigated, how the morphological and hydrographical boundary condi-

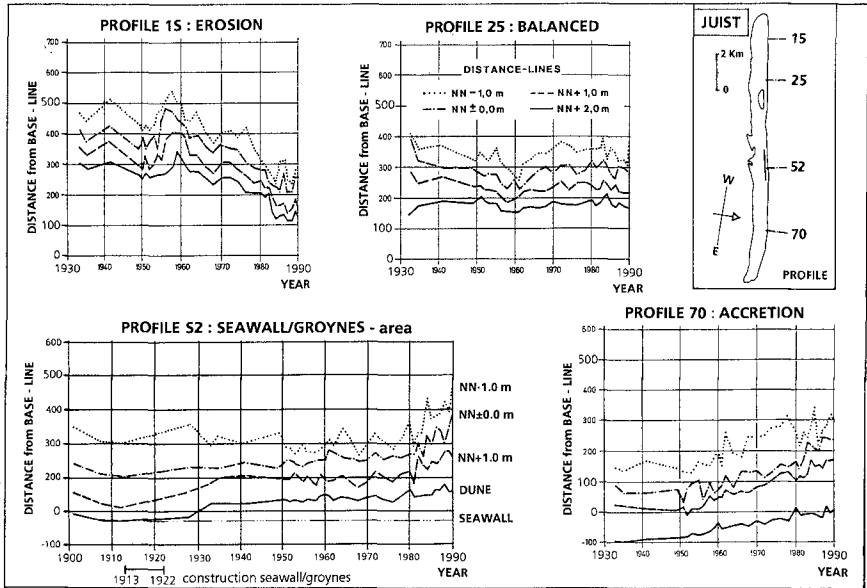


Fig. 13: Time-Distance-Lines for profiles on Juist island. Profile 52: construction of groynes with seawall from 1913 to 1922. Data: Archive CRS, Norderney.

had been investigated, how the morphological and hydrographical boundary conditions could be changed by groynes and training dams in such a way, that a new tidal inlet (displacement to the West, anticlockwise turning of the direction up to 45°) could be established and maintained - Pr. Versuchsanstalt (1940), Kurzack et al. (1950). Fig. 11 gives an idea about the enormous dimensions of the discussed plans. Fortunately an especially established expert-group worked out an alternative (Küstenausschuß, 1952) and the decisionmakers followed their recommendations. Subsequently the first large scale beach nourishment in Europe (1.25 Mio m^3) had been carried out on Norderney-island in 1951/52 (see Fig. 14).

The morphological development of Spiekeroog-island since the Middle Ages had been substantially affected by natural sedimentation in the related tidal basin (Harle-bay) and by land reclamation means (poldering): persevering recession of the coastline in the West, accretion in the East - Homeier (1961). This led to a break through of the foredunes in 1832. The following construction of dikes (embankments) failed; consequently a solid construction work (groynes and dune revetment) had been implemented between 1873 and 1884, with supplements in 1912 and 1936/37 (Fig. 12, above). The construction works were successful; the large scale morphological features fluctuated around a generally stable stage and, in average, the natural sand supply from the 'reef bow' (merging shoals) has been sufficient. Critical situations occur when approaching shoals accumulate in front of the shore line, creating a shore-parallel channel (last phase before merging). In this phase the groynes combine more or less stabilization functions of beach- and stream-groynes (Fig. 12, below).

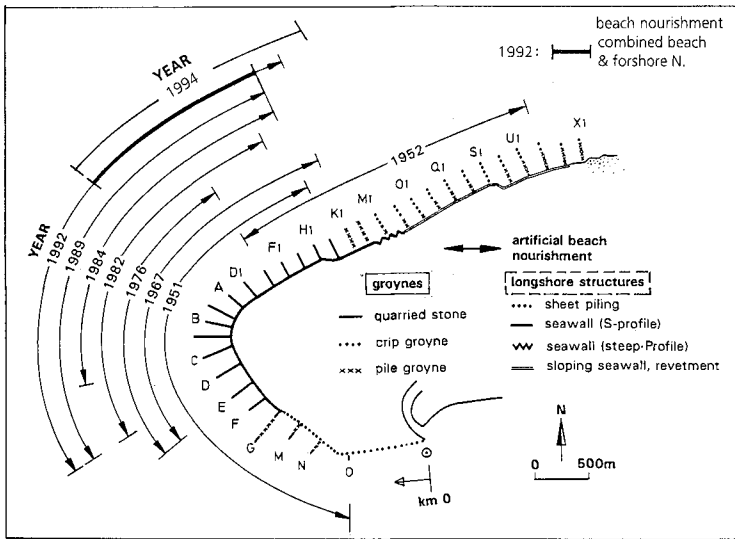


Fig. 14: Combined coastal protection system on Norderney-island.

The last groyne-seawall system on the East Frisian islands had been constructed on Juist between 1913 and 1922. Fig. 13 demonstrates long term trends of shore line developments: erosion in the West (prof. 15), accretion in the East (prof. 70), intermediate stages inbetween (prof. 25 & 52). The general trends are overlapped by short term variations. The displayed trends can not be extrapolated without taking into account the possibility, that there may be a kind of cycle with a very long time-period (see prof. 52). Unfortunately we have only a few records on profile mapping available, which reach far enough back into the past, to work on this question. On Juist the settlement seemed to be endangered by dune-erosion in the first decade of this century. The construction of the protection-system coincided with the transition from an erosive to an accretional trend (see prof. 52). Subsequently the groyne and the seawall had been buried under sand (up to 10 meters).

Groyne as part of a coastal defence strategy

The groyne on the East Frisian islands are incorporated into an engineering coastal defence system. This system has been successful in stopping the migration of tidal inlets and it preserved endangered parts of the island. The groyne were not effective in reducing beach erosion; but they can stabilize artificially restored beaches, if appropriately designed. Beach restoration is carried out as part of the maintenance. Fig. 14 demonstrates the strategy by the Norderney-example:

- Stream Groyne to stop the eastward directed migration tendency of the tidal inlet.
- Beach Groyne to stabilize the beaches in front of the shore-parallel structures.
- Shore-parallel Structures to protect the foredunes against erosive forces.
- Artificial beach nourishment of groyne fields to protect the existing structures against damage during storm floods.

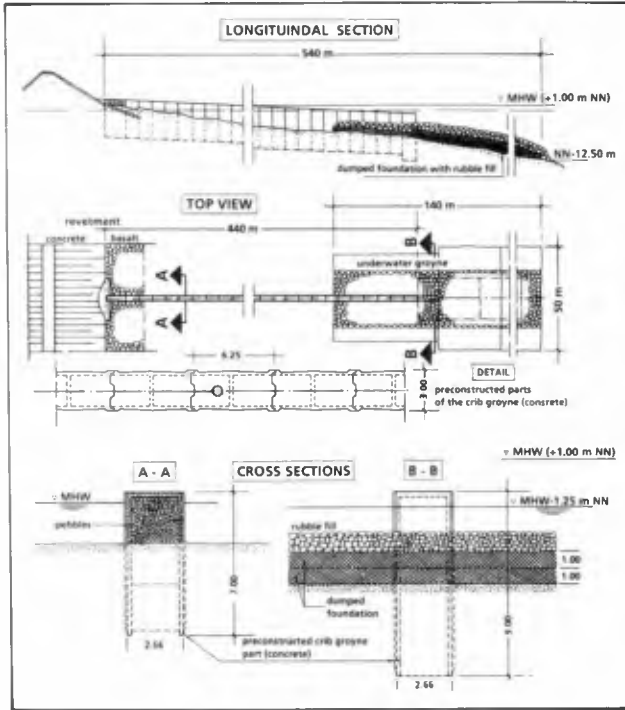


Fig. 15: Crib groyne No. 33 on Borkum island. Aster et. al. (1989), KFKI (1993).

The groynes need to be maintained and restored. A restoration-example is shown on Fig. 15 to give an idea about the dimensions - e.g. Aster et al. (1989), KFKI (1993).

The existing coastal defence systems on the East Frisian islands demonstrate, that they are sound tools to fix the shoreline. On the other hand they show, how expensive these systems are and how strongly they interfere with nature. There is an increasing demand by the island population to defend shoreline retreat with the 'hard' technique which has been proven as successful in the past. Fig. 16 deals with actual problems on Borkum-island. The western spit has been protected since the middle of the last century - e.g. Witte (1970), Aster et al. (1989). The north-eastern part of the island reacts (erosion, accretion) on structural developments of tidal channels and the foreshore (e.g. Kunz et al. 1996). The existing erosional trend and the expected development in future (szenario 2045) makes it understandable, that protection demands arise. However, if we take into account the aspects of an integrated coastal zone management, we should learn from history, that society has to take into account the problem as a whole, including the large scale processes (time & space). She also has to remember the fact, that an armoring of the existing intermediate stage is not favorable. The displayed hydro-morphological situation explains, together with the other examples, why proposed 'head-land' solutions (e.g. Silvester, 1978) provide no realistic alternatives for the East Frisian islands.

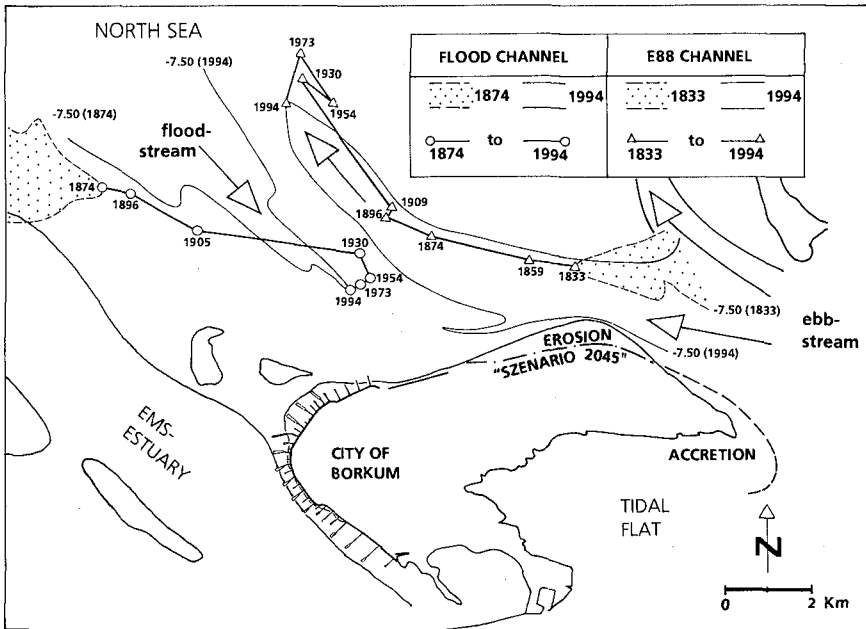


Fig. 16: Development (1874 to 1994) of the flood- and ebb-stream channels which impact the northern part of Borkum-island. "Szenario 2045" for erosion. Existing groyne-sea-wall system around the western spit.

Conclusions

Man started to protect the islands against erosion by solid structures since the middle of the last century. Groynes had been proven as an essential part of the coastal protection systems. The groynes are incorporated into a system which consists of different types of groynes, seawalls & dune-revetments and of artificial beach/foreshore-nourishment. The system had been successful in stopping the migration of tidal inlets and it preserved endangered western parts of the islands. The groynes were not effective in reducing beach erosion - but the existing groynes can stabilize artificially restored beaches, if the restoration is appropriately designed.

The existing groynes have to be maintained and enhanced, as far as they are essential to protect the historically developed situation. Beach groynes may be given up, instead of being reconstructed. This has to be investigated sitespecifically.

If we combine the lessons learned from the groyne-history with the recently developed demands of society (environmental issues & cost-benefit-ratio) we can not recommend to continue with the strategy of the past. Future strategies for the coastal-protection of the East Frisian barrier-islands should not include the construction of groynes, except in special cases, where no shore-line-retreat is acceptable and no solutions are possible, which are less static.

References

- Aster, D., H.-H. Jürgens & H. Weitzel (1989): Bühnenbauten auf Borkum (Groyne constructions on Borkum). HANSA, No. 21, 1474-1481.
- Forschungsstelle (1980): Reisefibel (coastal guide-book). Report Coastal Research Station (CRS), 240 pages.
- Fülscher, J. (1905): Über Schutzbauten zur Erhaltung der ost- und nordfriesischen Inseln (On protection structures for the preservation of the East and North Frisian islands). Zeitschr. f. Bauwesen, Publ.: Ernst & Sohn, Berlin, 305-342, 527-562, 681-722.
- Gaye, J. & F. Walther (1929): Bericht über die Schutzbauten zur Erhaltung der Ostfriesischen Inseln Juist, Norderney, Langeoog und Spiekeroog in der Zeit von 1900 bis 1928 (Report on the constructions for the coastal protection of the East-Frisian islands Juist, Norderney, Langeoog and Spiekeroog between 1900 and 1928). Report Wasserbauamt Norden, 62 pages (unpublished).
- Homeier, H. (1961): Die morphologische Entwicklung der Insel Spiekeroog und die Auswirkungen der Strandschutzwerke (The morphological development of Spiekeroog-island and the impact of the dune protection works). Jahresber. 1960 d. Forschungsstelle, Norderney (annual report 1960, CRS), Vol. 12, 49-79.
- Homeier, H. (1962): Historisches Kartenwerk 1:50 000 der niedersächsischen Küste (Historical charts 1:50 000 for the coast of Lower Saxony). Jahresber. 1961 d. Forschungsstelle, Norderney (annual report 1961, CRS), Vol. 13, 11-29.
- Homeier, H. (1973): Die morphologische Entwicklung im Bereich der Harle und ihre Auswirkungen auf das Westende von Wangerooge (The morphological development in the Harle-area and its impacts on the western spit of Wangerooge-island). Jahresber. 1972 d. Forschungsstelle, Norderney (annual report 1972, CRS), Vol. 24, 15-44.
- KFKI (1993): Empfehlungen für die Ausführung von Küstenschutzwerken (Recommendations for Coastal Protection Constructions) - EAK 1993, Die Küste, Vol. 55, 541 pages.
- Kraus, N.C., H. Hanson & S.H. Blomgren (1994): Modern functional design of groin systems. Proc. 24th Coastal Eng. Conf., ASCE, 1327-1342.
- Krüger, W. (1911): Meer und Küste bei Wangerooge und die Kräfte die auf ihre Gestaltung einwirken (Sea and coast in the Wangerooge-area and the forces which have an impact on the morphological development). Publ.: Wilhelm Ernst & Sohn, Berlin, 22 pages.
- Küstenausschuß (1952): Gutachtliche Stellungnahme des Küstenausschuß Nord- und Ostsee, Arbeitsgruppe Norderney zu den "Untersuchungen über die Ursachen der Abbrucherscheinungen am West- und Nordweststrand der Insel Norderney sowie zu den zum Schutze der Insel vorgeschlagenen seebautechnischen Maßnahmen" (Expertise of the Expert Board for the North- and Baltic-Sea, Working Group Norderney on the Report "Forschungsstelle, 1950"), Die Küste, Vol. 1, 27-42.
- Kunz, H. (1987): History of seawalls and revetments on the island of Norderney. Proc. Coastal Sediments '87, ASCE, 974-989.
- Kunz, H. (1993a): Sand losses from an artificially nourished beach stabilized by groynes. Coastal Zone '93 - Special Volume: Beach Nourishment Engineering and Management Considerations (ed.: Stauble & Kraus), ASCE, 191-205.

- Kunz, H. (1993b): Coastal Protection in the past, Coastal Zone Management in Future? Case Study for the Ems-Weser Area, Germany. CZ '93, Special Volume 'Coastlines of the Southern North Sea' (ed. Hillen & Verhagen), ASCE, 314-335.
- Kunz, H., G. Ragutzki, H.-J. Stephan & U. Abels (1996): Schutz des Nordteiles der Insel Borkum - Generelle Untersuchung (Protection of the northern part of Borkum-island). Report NLO-Coastal Research Station (CRS), No. 7/1996, 53 pages (unpublished).
- Kurzack, G., O. Linke, W. Dechend, H. Krause & R. Thilo (1950): Die Ursachen der Abbrucherscheinungen am West- und Nordweststrand der Insel Norderney und die Beurteilung der zum Schutz der Insel vorgeschlagenen seebautechnischen Maßnahmen (Causes for erosion of the western and northwestern shores of the island of Norderney and evaluation of the recommended engineering protection means). Jahresber. 1949 d. Forschungsstelle, Norderney (annual report 1949, CRS), 181 pages (unpublished).
- Luck, G. (1976): Inlet Changes of the Eastfrisian Islands. Proc. 15th ICCE, ASCE, 1938-1957.
- Lüders, K. (1952): Die Wirkung der Buhne H in Wangerooge West auf das Seegat "Harle" (The impact of groyne H, Wangerooge West, on the Harle-tidal inlet). Die Küste, Vol. 1, 21-26.
- Peper, G. (1956): Die Entstehung und Entwicklung der Inselschutzwerke auf Norderney mit besonderer Berücksichtigung der Bauten der letzten Jahre (Origin and development of the island protection on Norderney with special reference to the constructions of the recent years). Neues Archiv für Niedersachsen, Vol. 8(13), No. 3, 175-196.
- Pr. Versuchsanstalt (1940): Modellversuche für das Norderneyer Seegat und Ergänzungsversuch mit Damm k4 und Leitwerk (Investigations with a physical model for the Norderney-tidal inlet, groyne k4 and trainig wall). Report Preussische Versuchsanstalt für Wasser-, Erd- u. Schiffbau, Berlin, Vol. 3 and 5 (Kopp & Berg), 17 and 14 pages (unpublished).
- Silvester, R. (1978): Some facts and fancies about beach erosion. Proc. 16th ICCE, ASCE, 1888-1902.
- SPM (1984): Shore Protection Manual-Groins. Coastal Eng. Res. Center, US Army Corps of Engineers, U.S. Govt. Printing Office, Washington, D.C., 5.35-5.56.
- TAW (1995): Basisrapport Zandige Kust (Basis Report on Sandy Coasts). Technische Adviescommissie voor de Waterkeringen, Drukkerij & DTP-Service Nivo, Delft, 507 pages.
- Witte, H.-H. (1970): Die Schutzarbeiten auf den Ostfriesischen Inseln (The protection works on the Eastfrisian Islands). Die Küste, Vol. 19, 68-124.

CHAPTER 166

PERMEABLE PILE GROINS

Thomas Trampenau¹, Frank Göricke², Arved J. Raudkivi³

ABSTRACT: Permeable pile groins have been built on the southern shores of the Baltic Sea in large numbers for the past century and a half, yet no detailed literature has been written on how these structures function. The study of the groin system at Warnemünde, has shown that this type of groin causes a reduction of the littoral current and elimination of the local rip currents. This, in turn, causes underwater profiles to raise, a widening of the beach and a seaward movement of the shoreline.

INTRODUCTION

Groins are one of the oldest forms of coastal protection structures used in a multitude of forms and types of material the world over. Their expected effects, however, are still only loosely predictable. Groins are generally solid structures extending from the shoreline into the surf zone. These may be short or long, high or low groins, where the latter are frequently overtopped by waves. There are also groins that slope from the beach or revetment down to the sea bed at the seaward end. Groins may also be classified by the type of construction and materials used. Rubble-mound, concrete, steel or wood are examples of materials used in construction. Many groins are permeable, but mainly as a result of leakage rather than intention. For example, rubble-mound groins may become less pervious as sand and slit block the voids.

The following discussion is restricted permeable pile groins. These are pervious by nature and built using piles rammed with predetermined spacing that may vary along the groin. Such a groin is illustrated in Fig. 1.

-
- 1) Dipl.-Ing., Leichtweiß-Institut, Techn. Univ. Braunschweig, Beethovenstr. 51a, 38106 Braunschweig, Germany.
 - 2) Dipl.-Ing., Staatl. Amt für Umwelt und Natur Rostock, Parkstr. 46, 18119 Warnemünde, Germany.
 - 3) Em. Prof., Dr.-Ing. Univ. Auckland, New Zealand, 7 Coates Road Howick, Auckland 1705, New Zealand.



Figure 1. A permeable pile groin field in the test area Warnemünde during low water (caused by wind set-down)

The use of pile groins has been primarily confined to the southern coast of the almost tideless Baltic Sea, where over 900 pile groins have been built along the German coastline since 1843 (Weiss 1991) and about 950 along the Polish shores (Basinski 1963; Onoszko 1984). The permeabilities (the ratio of the pile diameter to the pile spacing) vary up to about 50%.

Frequently, the food of the groin has been rammed tight (permeability = 0%). The groins typically protrude 0.5 m above the sea level. Unlike non-permeable groin fields which cause a saw-tooth shoreline to form, permeable pile groins fields retain a continuous, straight shoreline (Fig. 2).

Consequently, the explanations of performance of groin, as expounded in literature, are not directly applicable to permeable pile groins. A discussion of the functioning of the permeable pile groins was published by Raudkivi (1996). The primary effect of permeable pile groins is the slowing down of wave induced longshore current in the groin fields and an elimination of rip currents along the groins (Fig. 3). This results in the raising of the profile within the reach of groin field and the development of a terrace. The following is a representation of field data from the groin system Warnemünde near Rostock, Germany.



Figure 2. Typical shoreline alignment of a permeable groin field at low water

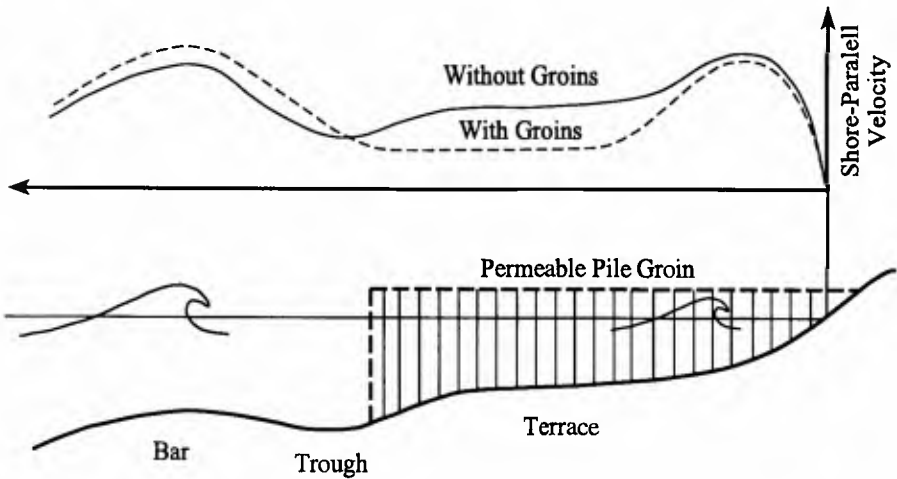


Figure 3. Schematic beach profile and wave-induced longshore current distribution with and without permeable pile groins

THE TEST AREA

The coastline of the test area faces northward. The predominant wind direction is from west to northwest that leads to a net eastward component of annual energy flux. An aerial view of the groin system is shown in Fig. 4.

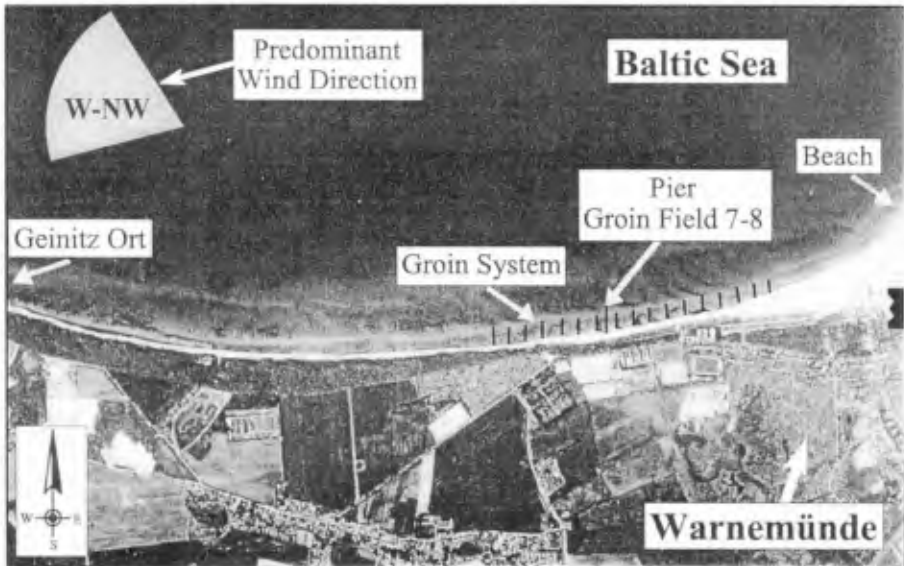


Figure 4. Aerial view of the groin system at Warnemünde

Although typical fluctuation of the water level due to wind setup/setdown is less than ± 0.5 m, storm tides up to 2.8 m above MSL have been recorded. Severe storm tides are associated with weather systems of lows in the North Atlantic or Mediterranean that move to the Baltic area and meet with Northern European high pressure systems. This leads to severe winds from the northeast. These have a mean return period of about 6 years. The frequency of significant wave heights H_S higher than 1.0 m is approximately 5%. The predominantly fine-grained sediment of the coastline has a narrow swash zone, followed by an upward concave slope (terrace) that ends with a steeper slope down to the trough landward of the first shore-parallel bar. The term "first bar" is used because in the tideless Baltic Sea frequently more than one shore-parallel bar is present (Fig. 5).

Temporary bar-trough features (inner bar) occur on the nearshore slope due to local breaking of waves. In the swash zone the middle and coarse fractions of the local sand dominate. On the terrace about 90% are finer than 0.2 mm. The sand grain diameters increase down to the trough (0.35-0.63 mm). On the bar, though, about 90% of the sand is finer than 0.2 mm.

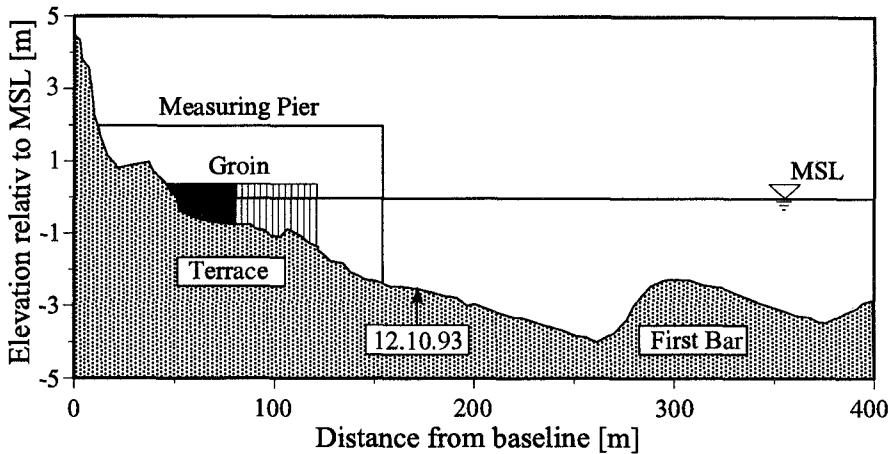


Figure 5. Typical shoreline profile in the test area

Field data has been collected from the Warnemünde test area since 1989. 17 pile groins were installed during 1991-92 and extend 120 m seaward from a baseline that is about 20 m landward from the water's edge. They are spaced 80 m apart. The top of the piles are 0.5 m above mean sea level. The groin system Warnemünde is shown in Fig 6.

The permeability (P) of the groins varies. The groins in the centre of the groin system are rammed tight for the first 80 m of their seaward reach. The permeability of the remaining 40 m displays an increase of spacing between the piles. The permeability of the groins also decreases between groins in the field. The groins furthest east and west exhibit the lowest mean permeabilities. Groin 8 and 9 have the highest permeabilities. The dotted area on Fig. 6 delineates the area where the groins are rammed tight. Groins 2 and 3 have pile spacings up to 0.25 m compared with pile diameter of 0.22 m. Permeability increases from 30% up to 55% with a mean over the groin length of 40%. The groins 5 and 6 have permeabilities from nominal zero up to 40% with an average of 20%, and groins 7 and 8 have permeabilities up to 40% with a mean of 13%. To verify the efficacy of the permeable groin field after construction, a profile 140 m westward of the first groin was used for reference. Regular surveying along this profile as well as within the groin fields between groins 2-3, 5-6 and 7-8 have been carried out since 1991.

RESULTS

The bands of annual wave-induced profile variations at the groinless reference station are shown in Fig. 7 for the year 1990/91 superimposed onto the bands of the years 1992 up to 1995. Other years depict an essentially identical picture of small profile changes dependent on sea conditions. Changes between the underwater profile in the groin field 2-3, (of relatively high permeability) from that before the installation of groins, is illustrated in Fig. 8.

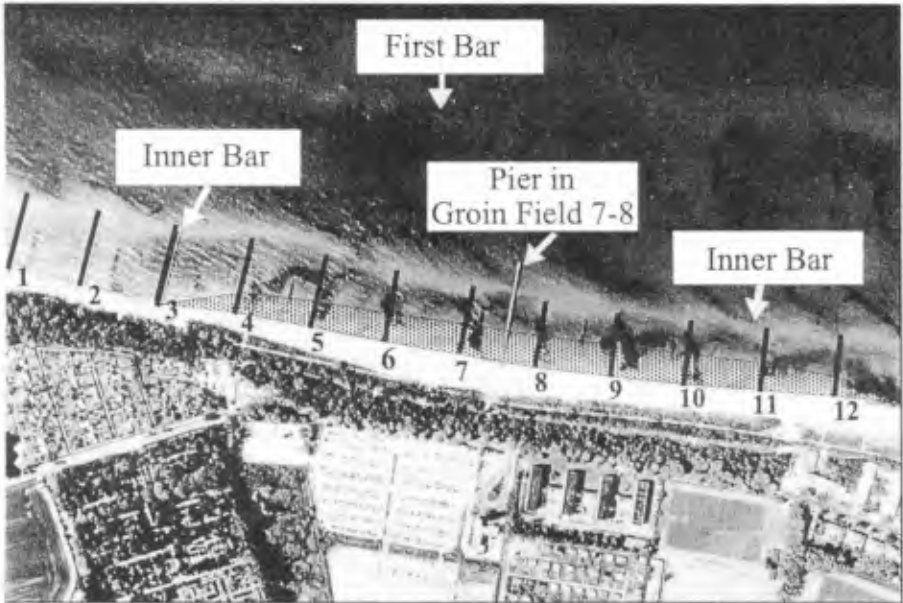


Figure 6. Aerial photo of the test area Warnemünde (enlargement)

A time span of almost two years past before a change of the profile become noticeable. In 1995 a significant widening of the beach and development of an underwater terrace is apparent. It is also noticeable that the terrace now extends beyond the end of the groins. The underwater profile development in the groin field 5-6 is shown in Fig. 9. Also to be noted is the seaward shortening of the terrace, a rise of the underwater profile near the shoreline and a widening of the beach about 20 m in seaward direction.

The changes of underwater profile in the permeable groin field 7-8, with the lowest permeability ($P=13\%$) over their entire length, is shown in Fig. 10. The comparison of the annual profile bands, before and after groin installation, were is informativ. The differences in band variation (1990 and 1991) before groin installation are relatively small and comparable with those at the reference station that shows no trends. After installation of the groins in autumn 1991, 1) the shoreline has moved steadily in seaward direction, 2) the terrace has narrowed considerably, 3) the beach level has been raised, 4) the underwater profile in the groin field has lifted 0.5 m and 5) its slope at the groin toe has become steeper.

At the reference profile (groinless coast) only small profile changes have been recorded. The results show that permeable groins with relatively high permeability over their entire length lead to a shift of the shoreline seaward (note groin field 2-3). A further reduction in permeability and a tighter inshore segment lead to a raising and seaward shift of the underwater profile, as seen in groin fields 5-6 and 7-8.

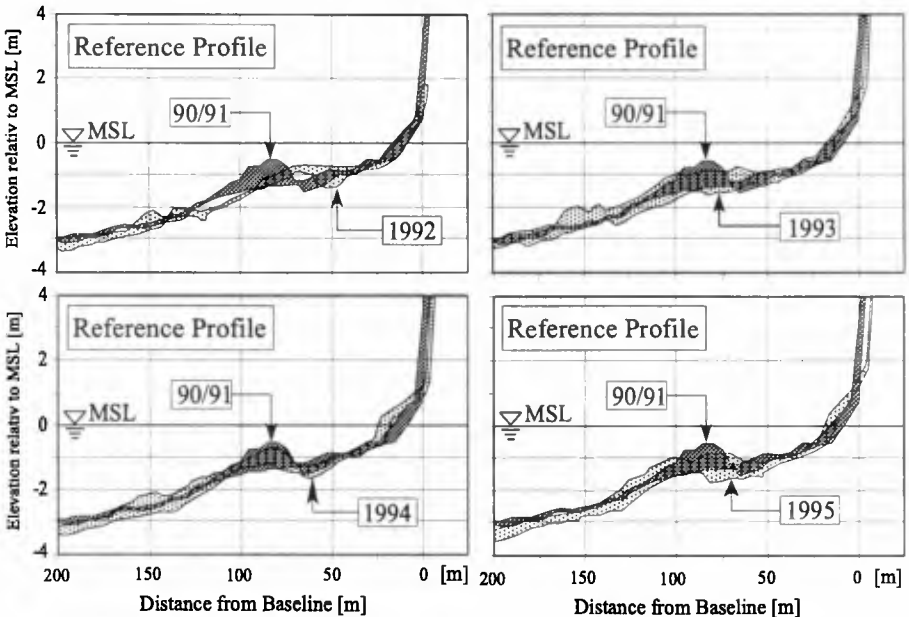


Figure 7. Bands of profile movements at reference station from 1992 up to 1995 compared with the band from 1990/91

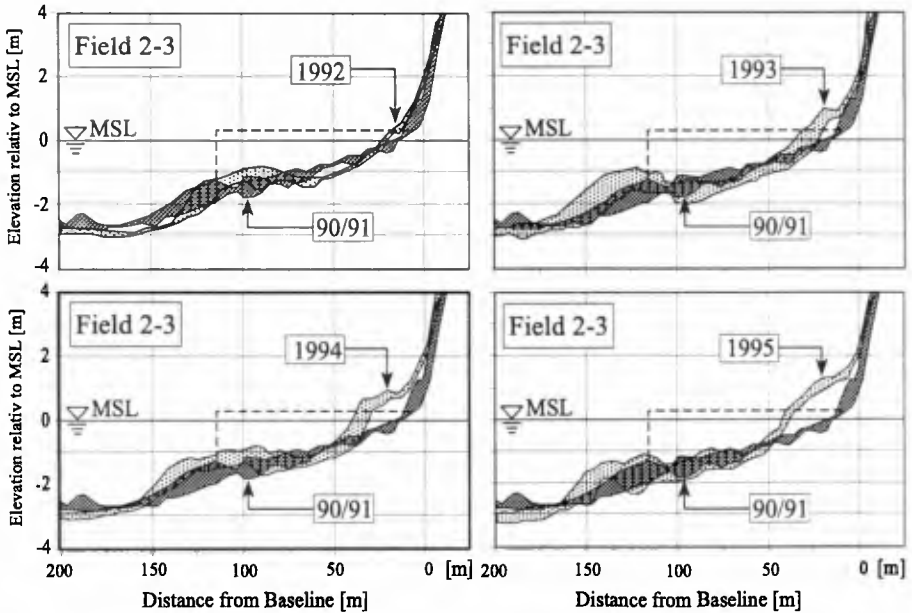


Figure 8. Bands of profile movements in groin field 2-3 from 1992 up to 1995 compared with the band from 1990/91 before groin installation

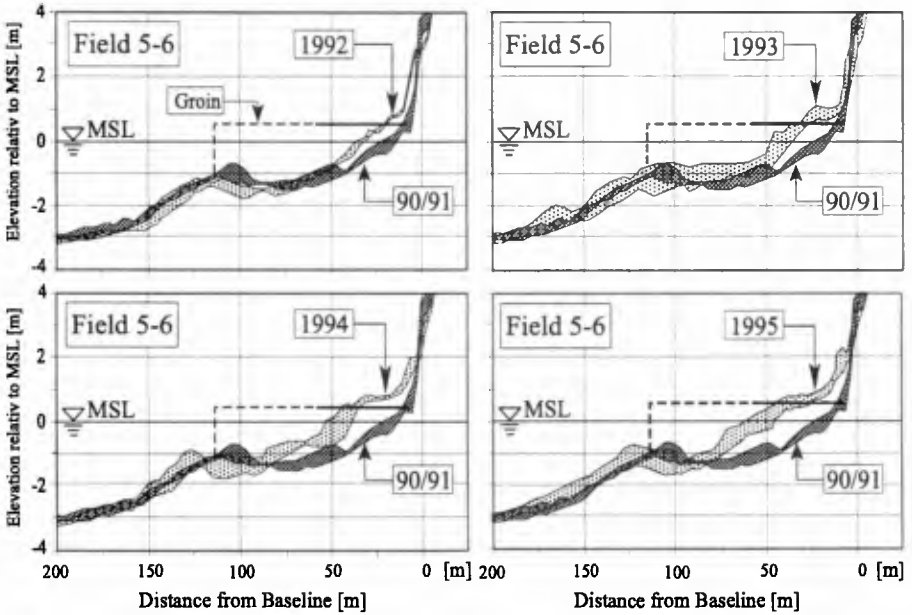


Figure 9. Bands of profile movements in groin field 5-6 from 1992 up to 1995 compared with the band from 1990/91 before groin installation

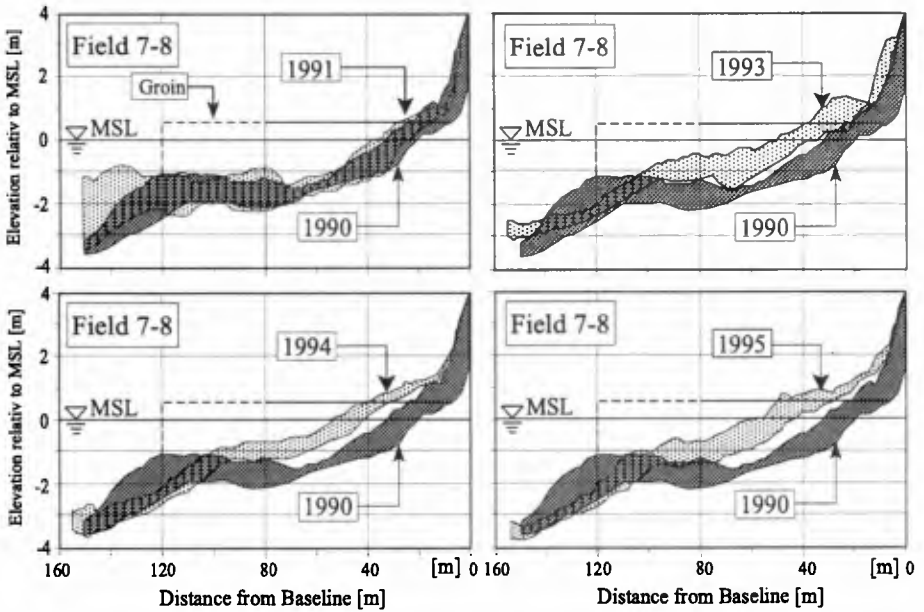


Figure 10. Bands of profile movements in groin field 7-8 from 1991 up to 1995 compared with the band from 1990 before groin installation

Significantly low permeability at the seaward end appears to concentrate the longshore current and erode the slope as seen from comparison of profiles of groin field 7-8.

The development of the shoreline over the time is illustrated in Fig. 11. No changes in the location of the depth contours are indicated at the reference location (Fig. 11 A) since 1990. No trends are recognizable in the groin fields before construction of the groin field.

Response to groin construction was slow in groin field of relatively high permeability (e.g. 2-3). However, a slow movement of the shoreline and the -2 m contour line is apparent after installation of the groins (Fig. 11 B). In groin fields 5-6 (Fig. 11 C) and 7-8 (Fig. 11 D) the shoreline and the -1 m contour line started moving steadily seaward soon after installation of the groins, whereas at 7-8 the -2 m contour line moved landward.

Tests with tracer sands showed that sand placed at the edge of the seaward limit of the terrace moved predominantly along the slope to the trough. A small amount of the sand was carried in the direction of wind into the groin field. Tracer sand placed in the swash zone was transported partly into the corner of the groin field. However, the sand suspended in the swash zone was transported in a narrow band seaward normal to the beach. The width and alignment of this transport path indicate that the sand was transported in suspension by the return current.

DISCUSSION

It is apparent from the field data that pile groins have reduced the wave-induced longshore current without creating rip currents. This has led to two beneficial effects:

- widening of the beach, and
- raising the level of the terrace.

The more gradual slope of the underwater profile and the shallower water over the terrace distributes the conversion of wave energy over a broader area and reduces the energy loading per unit area. This leads to a reduction of the erosion potential of the shoreline breakers and hence increases the stability of the beach. Groins with insufficient permeability, cause increased velocities past the ends of the groins and erosion of the seaward slope from the terrace to the trough. The groins should, therefore, be accordingly permeable (even in the swash zone) to eliminate local rip currents.

ACKNOWLEDGMENTS

This study was supported by the Federal German Ministry for Education, Science, Research and Technology and by the Committee for Coastal Engineering.

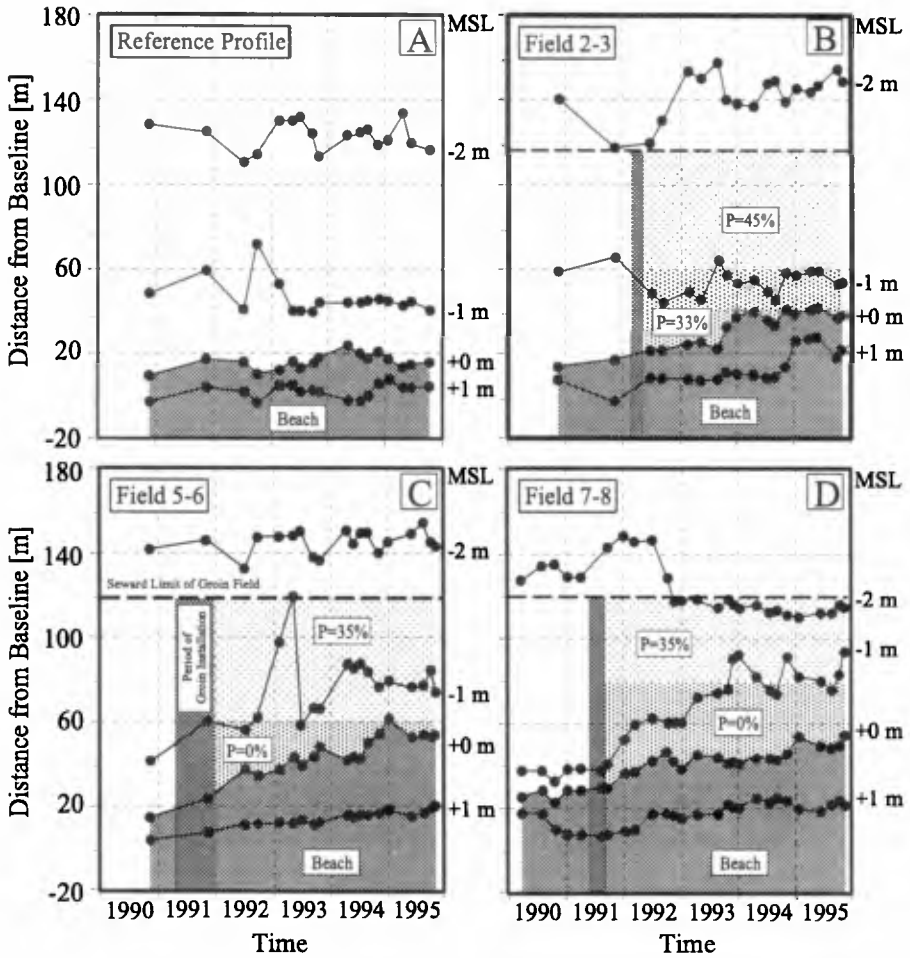


Figure 11. Changes in the location of contour lines during the period of observations

REFERENCES

- BASINSKI, T. (1963) Budowe ochronne na poskin wybrzezu Baltyku, [w:] Materiały do monografii polskiego brzegu morskiego, PWN, Gdansk-Poznan, Poland (in Polish).
- RAUDKIVI, A. J. (1996) Permeable pile groins. *Journal of Waterway, Port, Coastal and Ocean Engineering*, Vol. 122, No. 6.
- ONOSZKO, J. (1984) Ochrona brzegu morkiego w minionym 40-leciu, *Inzynieria Morska* No. 5, Poland (in Polish).

CHAPTER 167

THE EFFECT OF GROUNDWATER ON SCOUR NEAR STRUCTURES

John H Loveless¹, Geoffrey T Grant² and Robert I Karlsson²

ABSTRACT

A previously unreported mechanism which is believed to be a key process in the formation of shingle beaches is identified. It is proposed that this mechanism be called "winnowing".

Several new considerations relating to the selection of appropriate model sediments for shingle beach models are discussed. It is shown that lightweight sediments are subject to a significant scale effect and a compromise solution is suggested.

The results of some experiments, never previously performed, of beach scour in front of sea walls resulting from various combinations of wave attack and groundwater flow in the beach are presented. These show that the presence of groundwater flow in the beach has a significant impact on the amount of toe scour to be expected.

INTRODUCTION

A thorough understanding of all the major mechanisms involved in the formation of beaches is necessary if effective remedies to coastal erosion problems are to be established. This paper suggests that the study of the movement of sediment on beaches has until recently tended to ignore or misjudge the effects of flow into and out of the beach. It has only recently been discovered that under-drainage can be used as an effective method of beach accretion and it would be highly surprising if we have nothing more to learn about how beaches behave.

Beach or seabed scour in front of and around coastal structures is possibly their most frequently occurring failure mechanism. However, the reliability of the advice that coastal engineering researchers can provide is dependent on how well these processes can be modelled.

-
- 1) Senior Lecturer, Dept of Civ. Eng. Univ. of Bristol, Bristol BS8 1TR
 - 2) Research Asst., Dept. of Civ. Eng. Univ. of Bristol, Bristol BS8 1TR

The spectacular failure of several large breakwaters around the world and the discovery that scour is occurring near to many of them has led to increased interest in this area of research. Scour predictions are still usually derived from physical model studies with length scales of 1:20 or less. It is impossible to satisfy all the criteria for similarity in these models which are therefore subject to scale effect errors.

HOW SHINGLE BEACHES FORM

Coarse Material Transport

Broadly speaking the creation of a shingle beach is usually explained by reference to two mechanisms. First the movement of coarse material to the upper beach is explained on the assumption that coarse material moves as bed load and the peak bed velocity over each wave cycle is greater inshore than offshore. Also, since there is significant percolation into a shingle beach, the energy of the backwash is less than the energy of the swash. For example (Muir Wood, 1970) described this process admirably as:

“Whereas sand is moved by the sea predominantly in saltation and, near and inshore of the breaker line, in suspension, shingle is shifted by sliding and rolling along the bottom. The significance of this difference is that, whereas sand will tend to be moved in the direction of the vector representing residual wave velocity plus tidal velocity, shingle is only moved during that part of the wave cycle in which a certain threshold value is exceeded”.

Beach Slope

He also showed that the local slope of a beach is given by;

$$\tan \alpha = \frac{(1 - c)}{(1 + c)} \tan \phi$$

where α is the local beach angle, ϕ the angle of repose of the local beach material and c the ratio of the energy flux E_2 of the backwash to the energy flux E_1 of the upwash. This equation results in the limiting conditions of $c = 0$ at the top of the beach giving $\alpha = \phi$ and far offshore where $c = 1$ giving $\alpha = 0$ between these limits the equation results in the prediction of a parabolic beach form.

Fine Material Transport

The second mechanism which has been adduced to explain the formation of shingle beaches is the well known theory of Dean (Dean 1973). The theory has been shown to give extremely good correspondence with field results and it is highly probable therefore that it is essentially correct. However, the theory starts with an assumption for which no explanation has yet been given, viz. “It is assumed that the action of breaking waves is sufficient to place sand into suspension over at least a portion of the water column”.

Dean then goes on to explain how the relative fall times of the sediment lifted into suspension when compared to the wave period determines whether the sediment will move onshore or offshore.

Thus the analyses of both Dean and Muir Wood while both being clear and highly plausible do not provide a complete explanation. There is one piece missing from the jig-saw. How is the fine sediment carried into suspension not only from the surface, but also from within the beach? The jet caused by plunging waves creates a scour trench an associated bar and turbulence which could be deemed sufficient, but is there something else at work?

Winnowing

It is now suggested that there is a third mechanism at work which operates rather like the process of winnowing. As a wave approaches the breaking point the hydraulic gradient in the surface layers of the beach just in front of the wave reach a maximum. A number of experiments were carried out to investigate the nature and magnitude of these hydraulic gradients and to predict their possible consequences on sediment transport in the beach.

In one experiment dye was injected into a model shingle beach ($D_{50} = 5.6$ mm) near the breaker line. The movement of the dye indicated the direction of the instantaneous seepage velocity within the beach. The motion was seen to be rotary and in phase with the wave with the maximum velocity in the horizontal (onshore) direction just beneath the breaking wave. Just in front of the breaking wave the percolation velocity is vertically upwards and this was clearly visible as shown in Figures 1 & 2 as a jet of dye ejected into the flow. When the wave passes the dye cloud is swept forward up the beach.

Further experiments were carried out using a small probe inserted into the bed on which a cruciform of wire was fixed. Using electrolysis the wires were made to emit hydrogen bubbles as the waves passed and their movement was recorded on video. These experiments showed similar results and, because the probe could be moved about easily it was possible for a complete flow net to be constructed showing the hydraulic gradients in the beach beneath the breaking wave. Although these experiments proved that just in front of a breaking wave the upward direction of the seepage velocity in the bed is capable of squirting dye into the flow above the bed, it did not explain why this should preferentially eject the fine sediments.

In a third set of experiments some small pressure transducers were immersed in the bed. These showed that the hydraulic gradient in the bed frequently exceeded 1.0 in front of the breaking wave. This is the hydraulic gradient usually thought of as necessary to fluidise a soil sample.

Permeameter Tests

To investigate the hydraulic gradients needed to start soil migration a series of experiments was carried out using combinations of gravel and sand in a permeameter. These were reported briefly (Loveless & Grant, 1995) and showed conclusively that for gap-graded sediments the fine particles will start to migrate at very low hydraulic



Dye plume emerging from a shingle beach ($D_{10} = 4.0$ mm) under a breaking wave ($f = 0.5$ Hz).

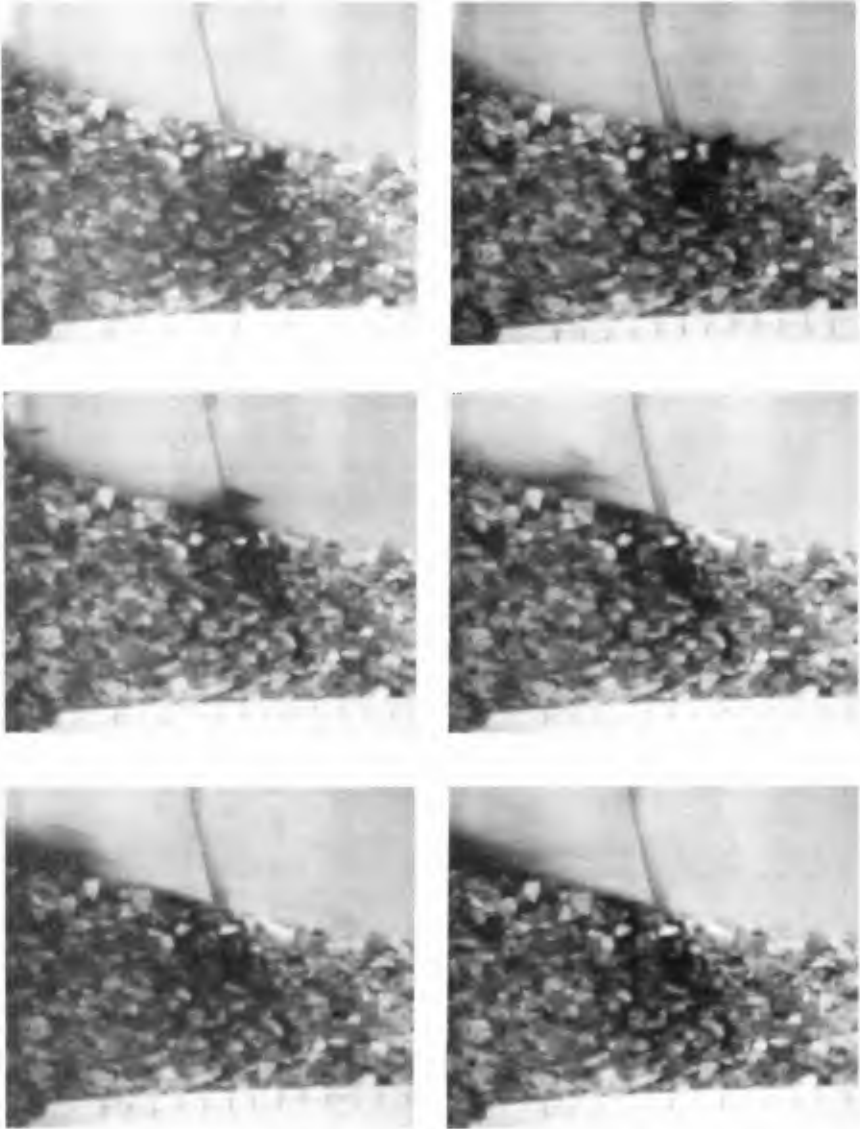


Figure 2: Detail of dye plume emerging from shingle beach under a breaking wave ($f = 0.5$ Hz).

gradients, as low as 0.2 or 0.25. The results of these (and other) experiments are shown on Figure 3. The Stability Index is a measure of how gap-graded the soil is. It is defined as the percentage of a soil sample passing at a diameter $4D$ minus the percentage passing at a diameter D all divided by the percentage passing at a diameter D . A Stability Index less than 1.0 is a potentially unstable soil. Where the soil is gap-graded, as in a shingle beach, the hydraulic gradient required to initiate fine soil migration is only around 0.2 not 1.0 as for a normal soil as shown in Figure 3.

The Dynamics of the Swash Zone

Finally, it is readily observed in the field and laboratory that the swash zone is a very dynamic environment for the sediment. During storm events the face of the beach, to a considerable depth, is being reworked and this reworking it is suggested provides the final element in the process which leads to marked size segregation which is the hallmark of a shingle beach.

Thus to summarise it is suggested that fine sediments are ejected from the bed just in front of breaking waves by a winnowing like process as vertical hydraulic gradients in excess of 0.5 act on a bed which is effectively being fully fluidised at the same time by peak horizontal hydraulic gradients in excess of 1.0. The finer particles are more mobile and are moved both upwards and downwards. The process naturally strengthens as segregation causes the beach to become more and more permeable.

The fine material carried to the surface can be carried both inshore and offshore. This leaves the part of the beach subjected to the highest hydraulic gradients to protect itself with a shingle beach and what nature chooses to defend itself may not be able to be bettered by man.

SEDIMENT SELECTION AND SCALING FOR MODELS OF SHINGLE BEACHES

Since laboratory models of shingle beaches are still the ultimate source of design guidance for both physical and mathematical models it is very important that the best possible physical models should be constructed and the greatest care be taken to identify the various mechanisms at work.

It has recently been shown (Loveless 1994), that for normal wave approach, there are nine separate mechanisms which can produce scour near to the toe of a coastal structure. It has also been shown (Loveless & Grant 1995) that certain aspects of model sediment selection are commonly misunderstood or ignored.

Lightweight sediments

In the UK lightweight sediments have been used for over 30 years to construct models of shingle beaches. It has been shown however (Loveless 1994) that this means that one of the important forces is in error by a factor of six for an upward hydraulic gradient in the beach. Figure 4 is a diagram (not drawn to scale) of the main forces acting on a particle on a beach under the trough of a wave. The upward percolation force is significant when the upward hydraulic gradient is large as it is just

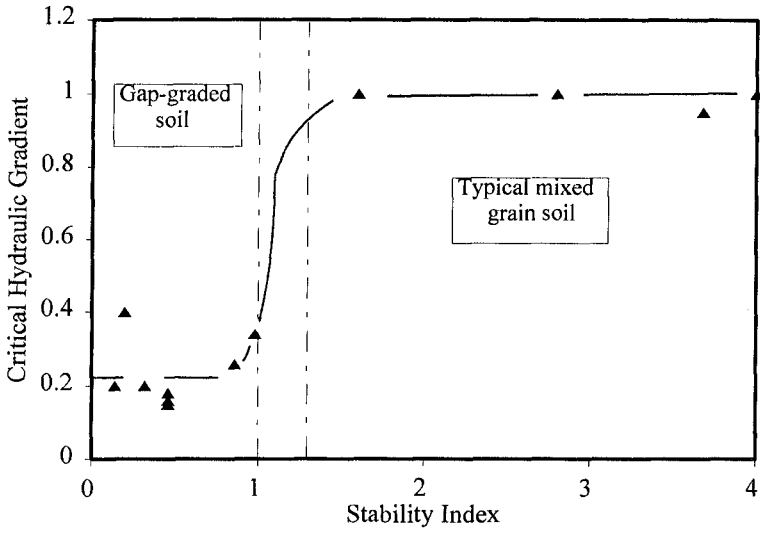


Figure 3: Critical hydraulic gradient against Stability Index.

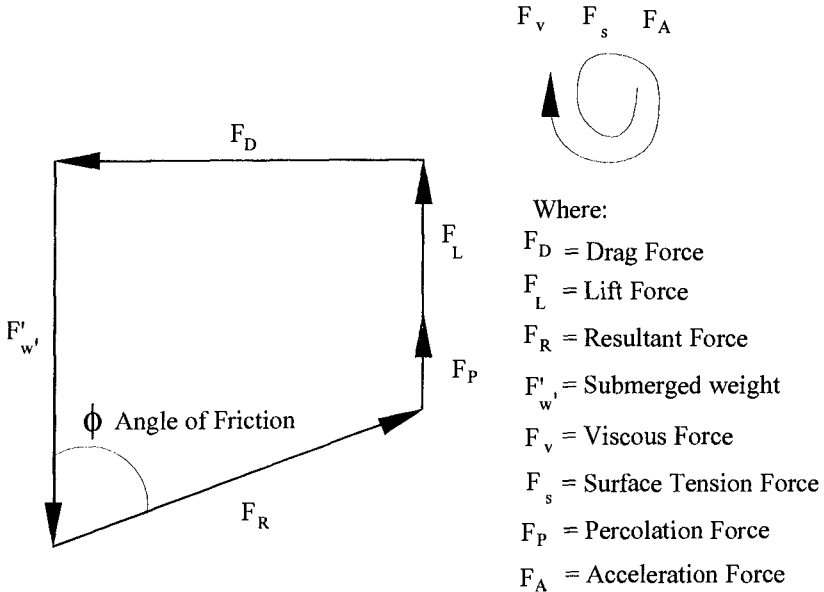


Figure 4: Forces on a sediment particle beneath a wave trough.

in front of a breaking wave. For similarity the ratio of the submerged weight and the upward percolation force should be the same in model and prototype. The ratio is given by,

$$\frac{F_{w^t}}{F_p} = \frac{i}{(1-n)(s-1)}$$

where i is the hydraulic gradient, n is the porosity of the soil and s is the specific gravity. If i and n remain the same, but s (model) equals say, 1.27 then a scale effect error of 6.1 would result if the prototype sediment had a specific gravity $s = 2.65$. Hence lightweight sediments will grossly overpredict scour at the toe of coastal structures.

If however a lightweight sediment is not used it is not possible to model the rate of percolation into the beach correctly for a sediment which satisfies similarity of the threshold of motion condition. In recent research we have found that a sediment having a specific gravity of about 2.0 would give scale effect errors not exceeding 3.0 for both percolation rate and percolation force. This may be the ideal compromise if such a material can be obtained at a reasonable price.

Angle of Repose

Another factor which appears to be ignored by researchers, but which is nevertheless important is the angle of repose of the sediment in model and prototype. To obtain similarity of the threshold of motion between model and prototype it can be shown that the following condition must be satisfied.

$$\frac{\lambda U_b}{\lambda_{W_s} \lambda_{\tan \phi}} = 1$$

where λ is the scale factor, U_b the near bed velocity, W_s the fall velocity of the sediment and ϕ the angle of repose. Hence ϕ directly affects one of the key similarity parameters and therefore must not be ignored.

A further important aspect of the variable ϕ is that it is reduced when a finer material is added to a gravel even when only 50% of the sample is sand. This effect was measured in the laboratory and a typical result is shown in Figure 5.

SCOUR EXPERIMENTS WITH GROUNDWATER FLOWS SUPERIMPOSED

A sea wall that is subjected to waves breaking near the toe of the structure, may at the same time experience a seaward groundwater flow under it. The experiments reported here show that the severity of scour is dramatically increased when these two scour mechanisms are combined. Similarly, if on the other hand the groundwater flow is reversed, accretion can be made to occur even under storm wave conditions and where, with no groundwater flow, a considerable scour hole would be formed. Although an experiment of this kind, with ground water flow being taken into account, is obviously a more realistic one than one which only considers waves we have not been able to trace a report of any such experiment having been performed

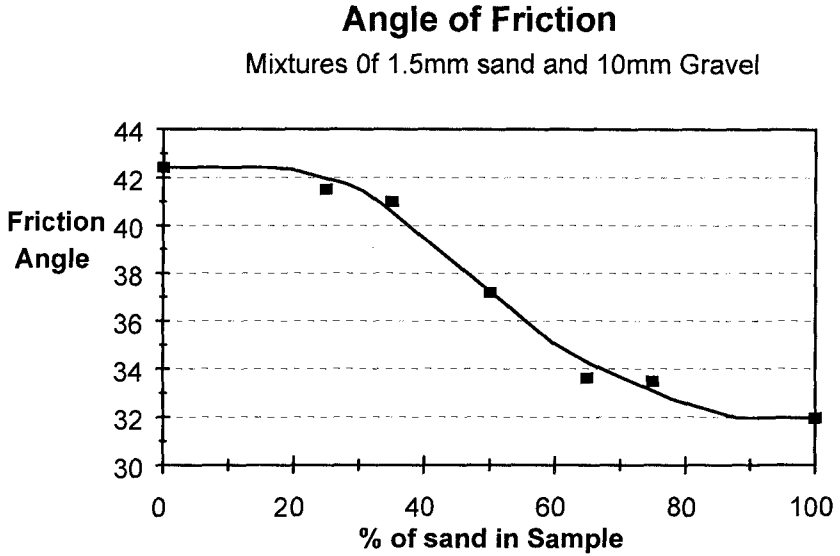


Figure 5: Value of ϕ for various combinations of sand and gravel.

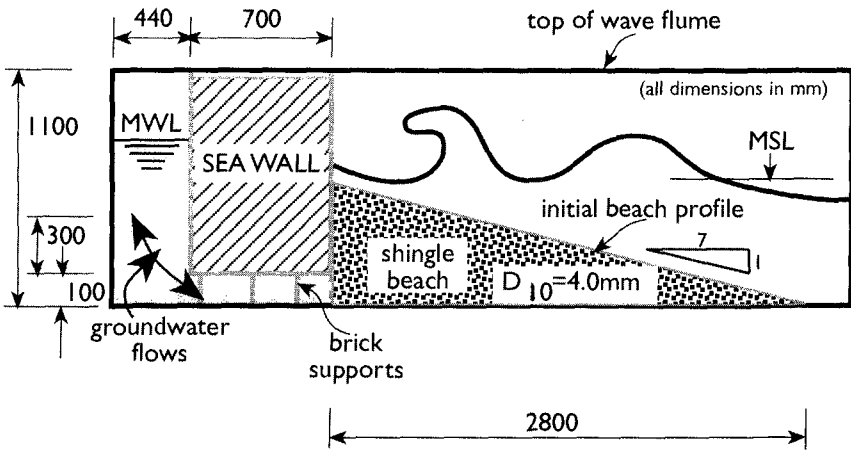


Figure 6: Cross-section of the arrangement of the model beach and sea wall.

before. Figure 6 shows the arrangement that was used to test these conditions for both shingle and sand beaches. The experiments were conducted in a large 1.5m wide wave flume at the end of which there was a test section of 0.5m width. The dimensions of the shingle beach were as shown in Figure 6, giving an initial beach slope of 1:7. The sand beach however was arranged with a gap beneath the sea wall of 70 mm and a depth above this of 230 mm giving a total depth of sand of 300 mm at the sea wall. The beach extended for 800mm giving a beach slope of 1:26.7. The gravel used in the model had a $D_{10} = 4.0$ mm and a $\phi = 36^\circ$. It was selected to model, at a scale of 1:20, a shingle beach having a $D_{10} = 14$ mm. The reasons for this selection have been reported earlier (Loveless & Grant, 1995). The sand used in the model had a $D_{50} = 0.33$ mm and $\phi = 30^\circ$. It was used to model a beach sand having $D_{50} = 1.5$ mm and $\phi = 32^\circ$.

The beaches were subjected to regular waves except that, for the sand beach only, the beach was exposed to a JONSWAP Spectrum with the following characteristics for two hours: $f_p = 0.7$ Hz, $H_s = 7.4$ cm, σ_1 , left = 0.7, σ_1 , right = 0.09; water level, $h_o = 0$ or 170 mm above datum at the flume floor level.

The groundwater flows in the beach were created by means of a small submersible pump. To create an offshore flow the pump was placed in the main flume and water was pumped to the back of the sea wall. To create an onshore flow the pump was instead placed behind the sea wall. The maximum capacity of the pump was $2.0 \ell / s$ and with the gravel beach this flow created a difference in mean water levels of 80 mm in both directions. The sand beach was exposed to an increasing hydraulic gradient until at a difference of 280 mm it failed by boiling. During the tests it was subjected to water level differences of +20, +10 and -20 cms. These corresponded to pumping rates of +0.30, +0.15 and -0.30 ℓ / s .

The range of tests completed is shown in Tables 1 & 2. In these tables, h_o represents the mean sea level at the sea wall above the level of the beach. The scour depth, Y is measured at the structure and H_i is the offshore wave height incident on the beach and structure.

Figure 7 is a summary of the gravel beach results and shows clearly that the presence of a groundwater flow in the beach has a significant impact on scour at the structure. The most dramatic difference was obtained with Test 15 and the resulting profiles for this test are shown in Figure 8.

The toe scour occurring with offshore flow was much greater than the no flow case and the onshore flow actually caused accretion. Figure 9 again shows the significant difference in the resulting beach profile. The results for sand beaches, while not showing such dramatic changes in scour near to the toe of the structure nevertheless resulted in very different beach profiles as shown in Figure 10.

CONCLUSIONS

The paper has identified a new mechanism which it is believed is a fundamental mechanism in the formation of shingle beaches. It is proposed to call this mechanism "winnowing".

Test	Freq.	Hydraulic difference	Toe water depth	Incom. wave height	Steepness	Rel. depth	Rel. scour	No. of waves
	f (Hz)	Δh (cm)	h_0 (cm)	H_i (cm)	H_i/L	h_0/H_i	Y/H_i	
4	0.7	+8	0	5.5	0.017	0	0.41	-
4	0.7	0	0	5.5	0.017	0	0.69	1260
11	0.7	+8	+5	9.0	0.028	0.56	-0.25	-
11	0.7	0	+5	9.0	0.028	0.56	-0.21	1092
12	1.0	+8	-3	12.5	0.080	-0.24	-0.32	-
12	1.0	0	-3	12.5	0.080	-0.24	0.15	-
15	0.7	+8	+5	18.4	0.058	0.27	-0.43	-
15	0.7	0	+5	18.4	0.058	0.27	-0.24	-
15	0.7	-8	+5	18.4	0.058	0.27	0.14	-
18	1.0	+8	+10	11.5	0.074	0.87	-0.36	-
18	1.0	0	+10	11.5	0.074	0.87	-0.26	-
21	0.7	+8	+10	18.7	0.059	0.53	-0.21	-
21	0.7	0	+10	18.7	0.059	0.53	-0.11	812
21	0.7	-8	+10	18.7	0.059	0.53	-0.03	-

Table 1 Comparator scour test results for a gravel beach ($\phi = 36^\circ$).

Test	Freq.	Hydraulic difference	Toe water depth	Incom. wave height	Steepness	Rel. depth	Rel. scour	No. of waves
	f (Hz)	Δh (cm)	h_0 (cm)	H_i (cm)	H_i/L_0	h_0/H_i	Y/H_i	
5	1.0	+10	+5	7.0	0.045	0.71	0	1500
5	1.0	+20	+5	7.0	0.045	0.71	-0.43	3300
5	1.0	0	+5	7.0	0.045	0.71	-0.61	2820
8	0.5	+10	+8	10.5	0.017	0.76	-0.95	1500
8	0.5	+20	+8	10.5	0.017	0.76	-1.29	1500
8	0.5	0	+8	10.5	0.017	0.76	-1.27	1500
8	0.5	-20	+8	10.5	0.017	0.76	-0.95	1500
14	1.0	+10	+10	11.0	0.070	0.91	-0.50	2100
14	1.0	+20	+10	11.0	0.070	0.91	-0.73	1800
14	1.0	0	+10	11.0	0.070	0.91	-0.70	1800
14	1.0	-20	+10	11.0	0.070	0.91	-0.45	1800

Table 2: Comparator scour test results for a sand beach ($\phi = 30^\circ$).

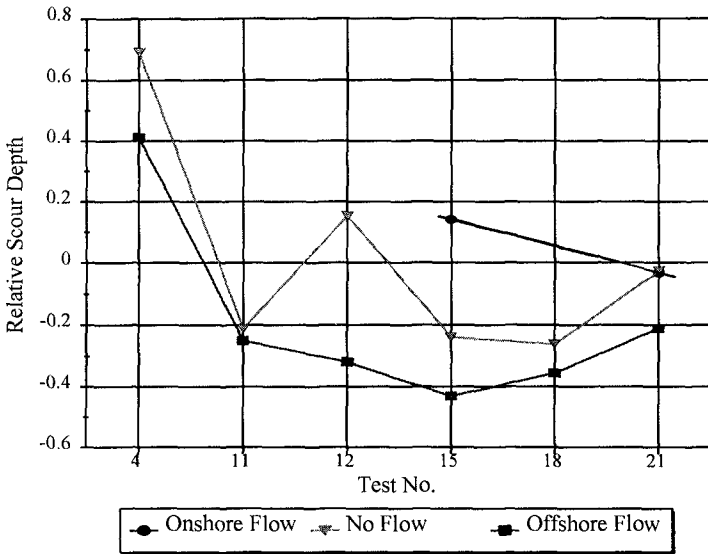


Figure 7: Relative scour depth (scour at toe/wave height) for various tests on a gravel beach.

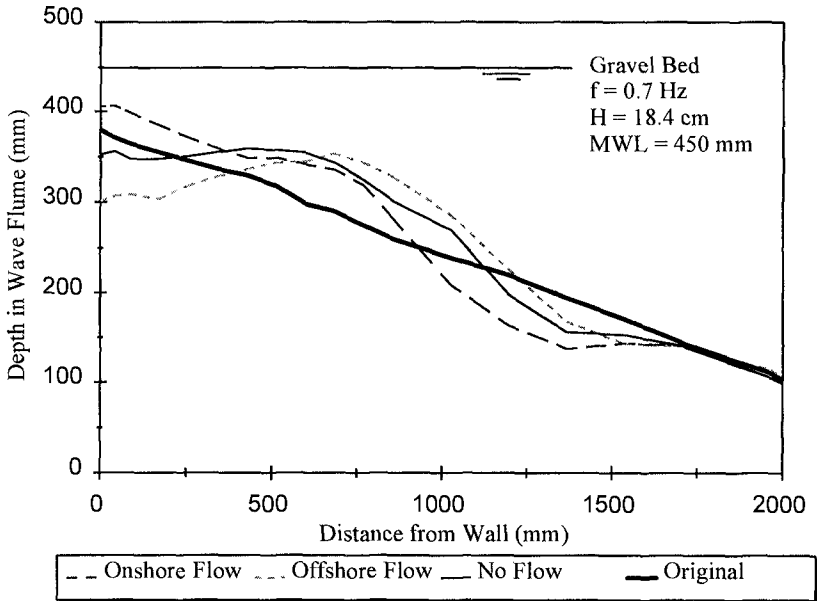


Figure 8: Resulting beach profiles after Test 15 (gravel beach).

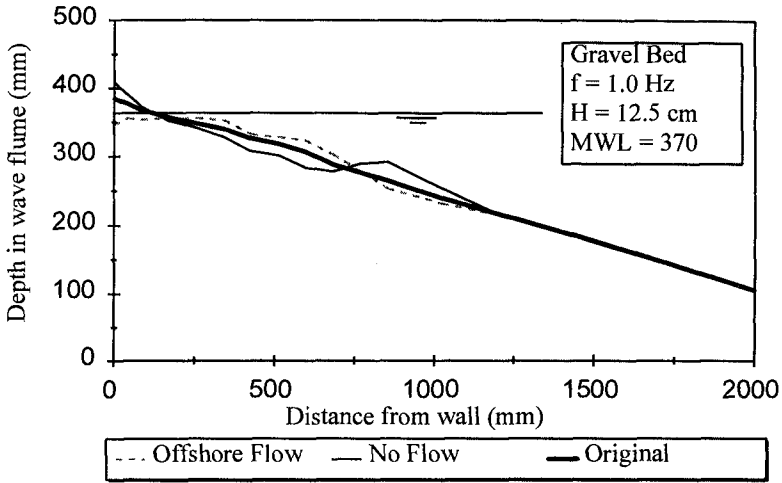


Figure 9: Resulting beach profiles after Test 12 (gravel beach).

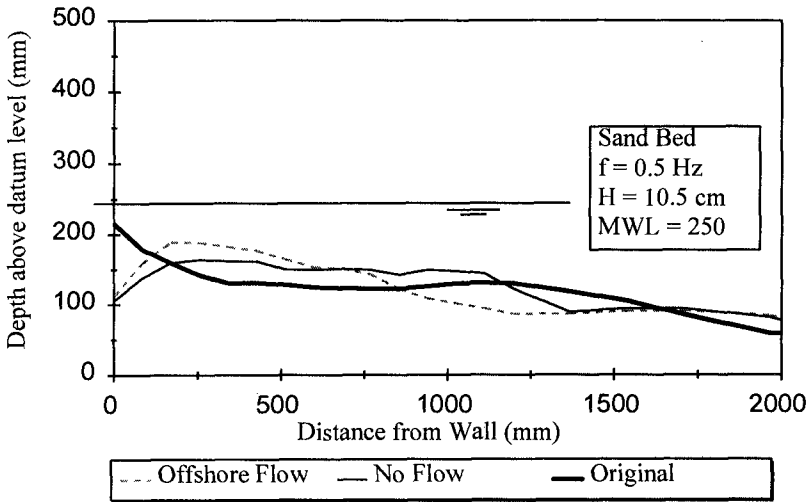


Figure 10: Resulting beach profiles after Test 8 (sand beach).

The paper has also suggested that aspects of the selection of model beach sediments which have tended to be ignored, such as the percolation force and the angle of repose of the sediment, should be taken into account when designing models.

The paper has reported on experiments which have shown how toe scour and beach profiles in the vicinity of coastal structures are affected by groundwater flows in the beach.

ACKNOWLEDGEMENT

Much of this research was conducted with the assistance of a grant from the UK Engineering and Physical Sciences Research Council for which the authors are grateful.

REFERENCES

- 1 Dean R G. "Heuristic models of sand transport in the surf zone." Conf. on Engg. Dynamics in the Coastal Zone. 1973. Inst. of Engineers of Australia.
- 2 Loveless J H. "Modelling toe scour at coastal structures." 2nd International Conference on Hydraulic Modelling, June 1994. BHR Group. England.
- 3 Loveless J H and Grant G T. "Physical Modelling of Scour at Coastal Structures." 26th Congress, Int. Ass. for Hydraulic Res. , London, UK. Sept. 1995.
- 4 Loveless J H and Grant G T. "Discussion of Skempton A W and Brogan J M. Experiments on piping in Sandy soils." Geotechnique 45, No 3. Sept 1995 p565-567.
- 5 Muir Wood A M. "Characteristics of shingle beaches: The solution to some Practical Problems." Proc. 12th Conf. on Coastal Engineering 1970 Chapter 68, p1059-1075.

CHAPTER 168

Abrasion of Steel Pipe Piles by Sediment Motion in Coastal Zones

Gaku Matsuoka¹, Shinichi Ito², Toshihiko Yamashita³
Hiroshi Saeki⁴, Yoshihisa Kariyazono⁵, and Koichi Sato⁶

ABSTRACT

In the outer coastal zones, where wave conditions are severe, steel-pipe piles often undergo abrasion due to the collision of sand particles. The abrasion characteristics of steel-pipe piles were clarified from the results of full-scale experiments. The abrasion rate of steel-pipe piles was found to be approximately proportional to the second power of the amplitude of flow velocity. The larger the ratio of sand particle diameter to pile diameter was, the higher was the abrasion rate. As the collision energy of sand particles obtained by numerical analysis was nearly proportional to the measured abrasion rate, it was considered that the abrasion rate can be estimated from the collision energy.

INTRODUCTION

Large amounts of sand particles sometimes drift around pipe piles due to the action of waves, especially in outer coastal zones. Steel-pipe piles exposed to these drifting sand particles undergo abrasion due to the collision of sand particles with the piles. Durability is an important consideration in the construction of steel structures in coastal zones. Culbertson W. Ross (1949) reported severe abrasion and corrosion of

-
- 1) Graduate Student, Dept. of Civil Engineering, Hokkaido University, Kita-13 Nishi-8 Sapporo 060 JAPAN
 - 2) Civil Engineer, Niigata Prefectural Government, 4-1 Sinkoucho Niigata 950-70 JAPAN
 - 3) Associate Professor, Dept. of Civil Engineering, Hokkaido University, Ditto
 - 4) Professor, Dept. of Civil Engineering, Hokkaido University, Ditto
 - 5) Senior Researcher, Kimitsu R & D Laboratories, Nippon Steel Corporation, Kimitsu-1 Kimitsu-city Chiba 299-11 JAPAN
 - 6) Senior Manager, Sapporo Sales Office, Nippon Steel Corporation, Kita-2 Nishi-4 Sapporo 060 JAPAN

steel-pile groins at Palm Beach, Florida. There have also been reports of large decreases in the wall thickness of steel-pipe piles (more than 1mm/year) due to abrasion and corrosion in other outer coastal zones. The reported rates of decrease in the wall thickness are more than 10 times greater than the allowable corrosion rate of steel in sea water (0.1mm/year). However, except for our previous studies (Yamashita et al., 1989, 1990, 1991, 1992; Kariyazono, 1992), there have been very few experimental or theoretical studies on the abrasion of steel piles due to sediment motion. The behavior of sand particles during collision with the surface of piles and the resulting abrasion of the surface have not yet been clarified.

In the present study, full-scale experiments were carried out to investigate the abrasion characteristics of steel-pipe piles from the viewpoint of the effects of flow velocity, diameter of sand particles and diameter of piles. Also, from numerical analysis of the motion of suspended sand particles, the characteristics of the collision energy of sand particles against steel piles were investigated, and the relationship between collision energy and abrasion rate was clarified.

EXPERIMENTS

A series of abrasion tests on steel-pipe piles were carried out in the laboratory using a large-scale U-shaped tube that could generate a strong oscillatory flow with sand drift (Fig. 1). The tube is 10m in horizontal length, 5m in height and 1m in width. The horizontal part of the apparatus, which is 500mm in height, was filled with sand to a height of 400mm. Thus, the flow took place in the upper 100mm of the horizontal part. The experimental flow conditions were as follows: the period of oscillatory flow was 7.1 or 7.4 sec and the amplitude of velocity (u_0) was 2.0m/s ~ 4.0m/s. Three sizes of pipe piles (267, 140 and 76mm in diameter(ϕ)), and four grades of sand (0.75, 1.5, 4.0 and 7.0mm in diameter(d)) were used. The specific gravity was 2.65 in all sand particles. The steel piles, which were made of 392N/mm² carbon steel, were fixed securely to the bottom of the horizontal part of the apparatus

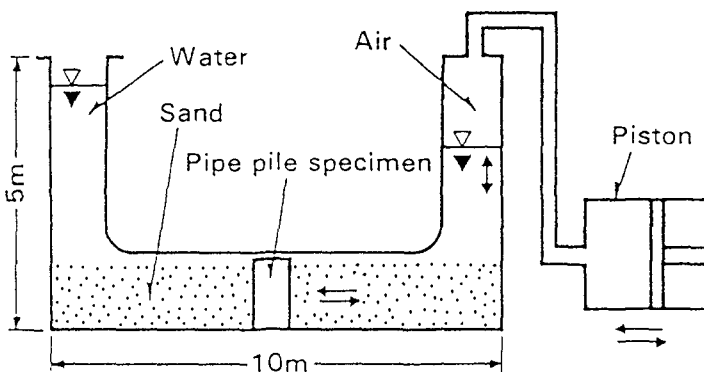


Fig. 1 Large-scale U-shaped tube that can generate a strong oscillatory flow with sand drift.

by steel caps and bolts. Rubber bands were wrapped around both ends of each steel-pipe specimen to prevent abrasion of the surface during the test. Most of the tests were carried out under conditions in which the period was 7.4 sec and the amplitudes of flow velocity were 2.0 or 3.0m/s. Flow velocity of 2.0 and 3.0m/s are equivalent to strong waves of 5.4 and 8.1m in height, respectively, which occur in coastal zones with a water depth of 10m.

Fig. 2 shows a schematic diagram of the apparatus used to measure the surface profile of each specimen. The surface profiles were measured in the longitudinal direction by a dial gage before and after each abrasion test. Surface profile measurements were carried out at intervals of 15 degrees to the main flow direction.

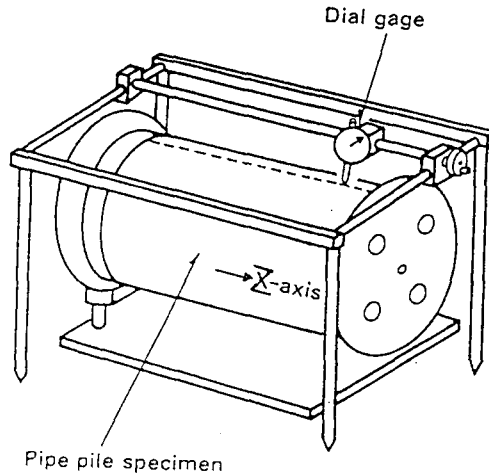


Fig. 2 Measurement of the surface profile of a pipe pile specimen.

RESULTS and DISCUSSION

Fig. 3 shows an example of the surface profiles of a steel pipe pile before and after the abrasion test. The Z-axis is the distance from the upper standard line of the pipe (see Fig. 4). The upper and lower parts of the pile were covered with rubber bands to prevent abrasion during the test. The amount of abrasion was obtained from the difference between surface profiles before and after the test.

Fig. 4 shows an example of the profile of the sand bed around a steel pipe pile after the test at a flow velocity of 3.0m/s. The diameter of the steel pipe pile was 267 mm. The depth of the sand far from the pile was about 440mm, while but sand around the pile was scoured to a depth of about 120mm. The degree of scouring was greater at a flow velocity of 3.0m/s than at 2.0m/s.

Fig. 5 shows an example of the distributions of the amount of abrasion. The dotted lines indicate the surface of the sand bed at the pile surface. The solid lines indicate the surface of the sand bed far from the pile. At the upper part of sand bed

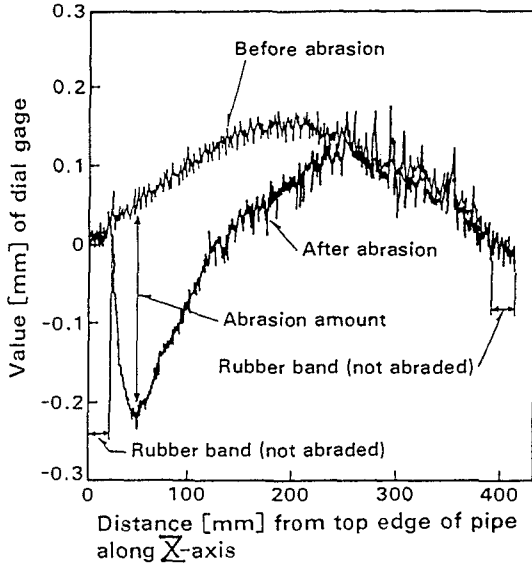


Fig. 3 Surface profiles of a specimen before and after abrasion.

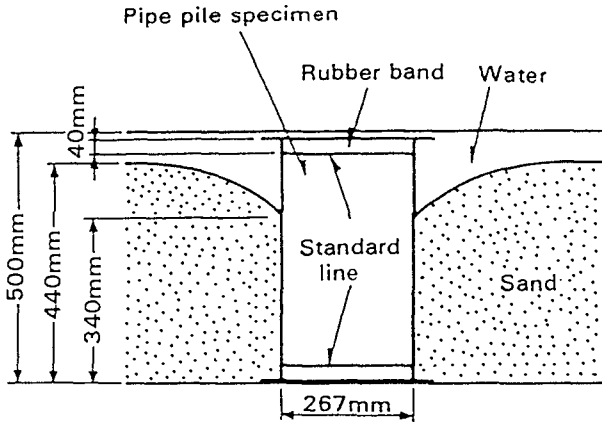


Fig. 4 Profile of the sand bed around the pipe pile specimen.

surface from the dotted line, the amount of abrasion was largest at 15 or 30 degrees and smallest at 90 degrees. The maximum amount of abrasion was observed at about 50mm above the sand bed and at 15 or 30 degrees to the main flow direction. In the

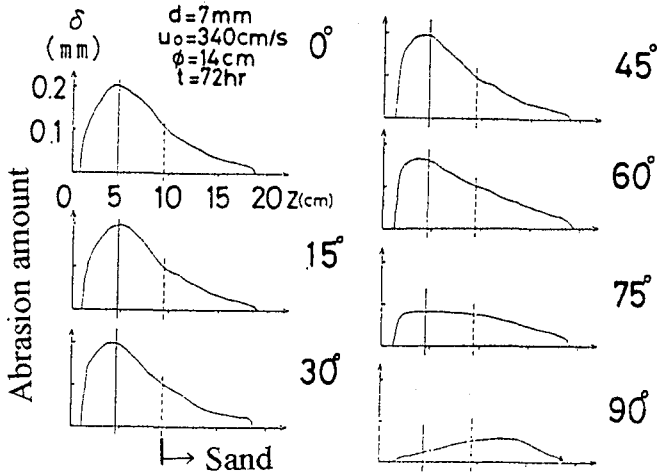


Fig. 5 Distributions of the amount of abrasion of the pile along the distance from the top standard line.

case where the sand particle diameter was 7mm and the flow velocity was 3.4m/sec, the maximum amount of abrasion was 0.2mm/3days. This value corresponds to 2mm/month. Thus, it was confirmed that a serious loss of 1mm/year in wall thickness was expected in coastal zones with severe sand motion. At the lower part of the sand bed surface, the amount of abrasion was rather small and was independent of the angle. At the upper part of the sand bed surface, abrasion occurred due mainly to the collision of suspended sand particles against the pile surface. At the lower part of the sand bed surface, however, the pile underwent sliding abrasion caused by sand particles in a state of liquefaction.

The results of the experiments indicate that the collision energy of suspended sand particles affects the maximum amount of abrasion on the surface of a steel pile. To determine the collision energy of sand particles against the surface of the pile, numerical analysis of the motion of suspended sand particles was performed.

Fig. 6 shows a sketch of sand particle motion. It was assumed that the fluid flow in the front of a pile was a two-dimensional, steady, potential motion. The sand particle motion was determined by Eq. 1.

$$M \frac{d\bar{U}}{dt} + C_M m \frac{d(\bar{U} - \bar{u})}{dt} = m \frac{d\bar{u}}{dt} + \frac{1}{2} C_D \rho_w A |\bar{u} - \bar{U}| (\bar{u} - \bar{U}), \quad (1)$$

where M and m are the mass of the sand particle and the mass of water displaced by the sand particle, respectively; \bar{U} and \bar{u} are the velocity vectors of the sand particle and fluid particle, respectively; A is the cross-sectional area of the sand particle; ρ_w

is the density of the fluid; and C_M and C_D are the virtual mass coefficient and the drag coefficient, respectively. From the study of Sawamoto (1979), we assumed C_M to be 0.5, and C_D was determined by Eq. 2.

$$C_D = 0.4 + \frac{24}{Re}, \tag{2}$$

where Re is Reynolds number. As we assume that abrasion of a pile occurs due to the collision energy of sand particles against the pile, dimensionless collision energy is defined as follows:

$$\text{Dimensionless collision energy} = \frac{CVn|\vec{U}|}{u_0^2}, \tag{3}$$

where \vec{U} is the collision velocity vector of sand a particle; Vn is the normal component of \vec{U} to the pile surface; u_0 is the amplitude of main flow velocity; and C is the dimensionless number of collision particles, defined as the ratio of the volume flux of sand particles at a point far from the pile to the volume flux when sand particles collided with the surface of the pile.

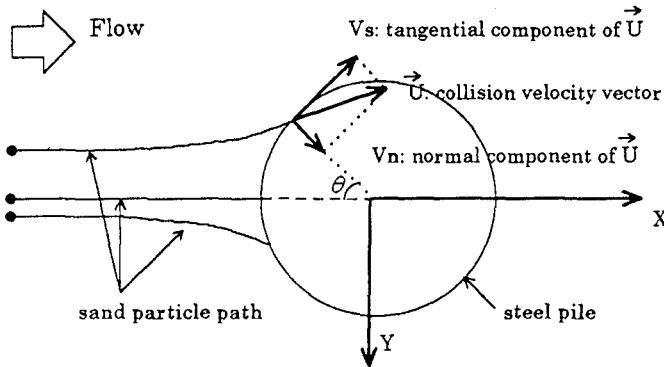


Fig. 6 Sketch of sand particle motion.

Fig. 7 shows the relationship between sand particle diameter, the calculated dimensionless collision energy, and the measured abrasion rate around a pile. Numerical analysis was carried out under the following conditions: flow velocity u_0 and diameter of pile ϕ were 3.0m/s and 30cm, respectively, and the diameters of sand d were 1, 4 and 10mm. Fig. 7 also shows the measured abrasion rates of steel piles of 267mm in diameter in a large U-shaped tube with sand of 7, 4, 1.5 and 0.75mm in diameter at a maximum flow velocity of 3.0m/s for 3 days. The horizontal axis θ is the angle of the pile surface. The collision energy increased as the sand particle diameter increased. The collision energy of large sand particles was distributed over

a wider range of angles θ compared with that of small sand particles. The rate of abrasion also increased as the diameter of the sand particles increased. The abrasion rate of large sand particles was distributed over a wider range of angles θ than that of small sand particles. The collision energy distributions obtained by numerical analysis almost coincide with the distributions of measured abrasion rates.

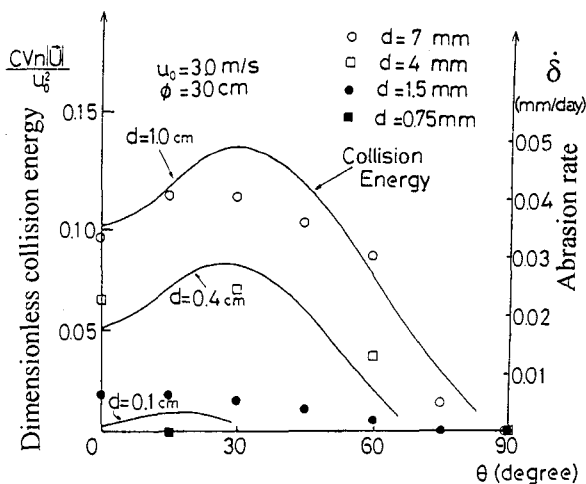


Fig. 7 Relationship between sand particle diameter, collision energy, and rate of abrasion around a pile.

Fig. 8 shows the relationship between sand particle diameter, maximum dimensionless collision energy, and maximum abrasion rate obtained from Fig. 7. The maximum collision energy of sand particles increased with increases in the sand particle diameter. The maximum collision energy was nearly proportional to the measured maximum abrasion rate.

Fig. 9 shows the relationship between pile diameter, dimensionless collision energy, and the rate of abrasion of the pile. The conditions for calculation were as follows: flow velocity is 3.0 m/s, sand particle diameter is 8 mm and pile diameters are 7.5, 10, 15, 30 and 100 cm. Fig. 9 also shows measured rates of abrasion of the steel piles of diameters of with 7.6, 14.0 and 26.7 cm under conditions in which the sand particle diameter is 7 mm and the amplitude of flow velocity is 3.0 m/s. The collision energy of the sand particles increased with decreases in the pile diameter. The collision energy of a small pile was distributed over a wider range of angles θ compared with that of a big pile.

Thus, the larger the sand particle diameter and the smaller the pile diameter are, the higher the abrasion rate and the wider the abrasion area become. The reason for this is as follows. Fig. 10 shows an illustration of the collision behavior of sand particles and the streamlines of fluid near a pile without sand particles. When the diameter of

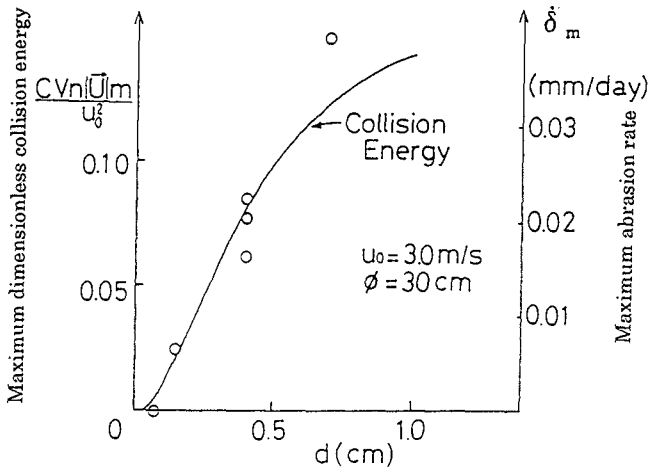


Fig. 8 Relationship between sand particle diameter, maximum collision energy and maximum abrasion rate.

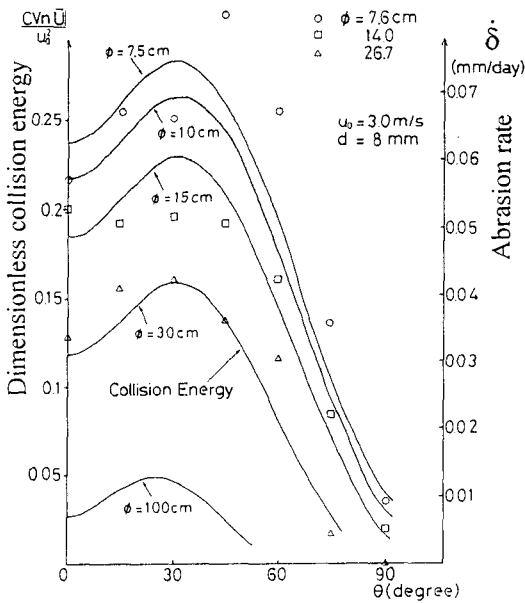


Fig. 9 Relationship between pile diameter, collision energy, and rate of abrasion around pile.

the sand particles is small, most of the sand particles tend to follow the fluid particles and do not contact with the surface of the pile because they have low inertia. Thus, the collision energy at the surface of the pile is very small. When the diameter of sand particles is large, however most of the particles collide with the surface of pile regardless of the flow of fluid around the pile, and thus the collision energy is very large. On the other hand, when the diameter of the pile is large, streamlines begin to curve at a point far away from the pile because of the pile's wall effect. When the diameter of pile is large, most of the sand particles closely follow the streamlines and do not contact with the surface of the pile due to the large wall effect.

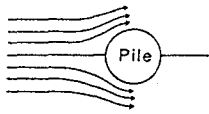
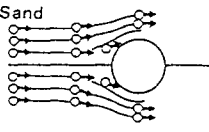
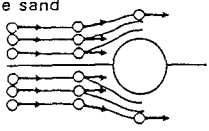
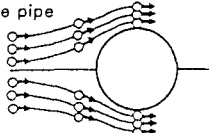
	Streamline without sand.
	Most fine sand follows the streamline without collision because it has low inertia. The energy transferred to the pile is low.
	Most large sand particles collide with the pile due to inertia. The energy transferred to the pile is high.
	Most sand particles follow the streamline without collision because of the large wall effect. The energy transferred to the pile is low.

Fig. 10 Illustration of the collision behavior of sand.

Fig. 11 shows the relationship between the ratio d/ϕ of sand particle diameter to diameter of the pile and dimensionless maximum collision energy. The maximum collision energy is a function of only the ratio d/ϕ approximately. The larger d/ϕ is, the larger the maximum collision energy becomes.

Fig. 12 shows the relationship between d/ϕ , maximum dimensionless collision energy, and maximum abrasion rate. The maximum abrasion rate is also a function of only the ratio d/ϕ approximately. The collision energy obtained by numerical analysis is nearly proportional to the measured abrasion rate. This relationship is as follows. Dimensionless collision energy of 1.0 corresponds to an abrasion rate of 0.21mm/day at a flow velocity of 3.0m/s.

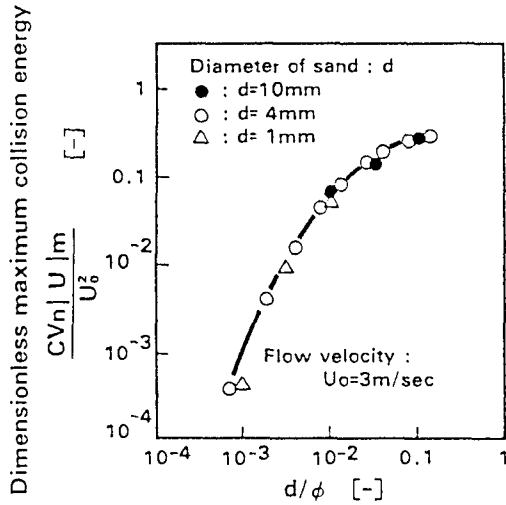


Fig. 11 Relationship between ratio of diameter (d) of sand to diameter (ϕ) of pipe and dimensionless maximum collision energy.

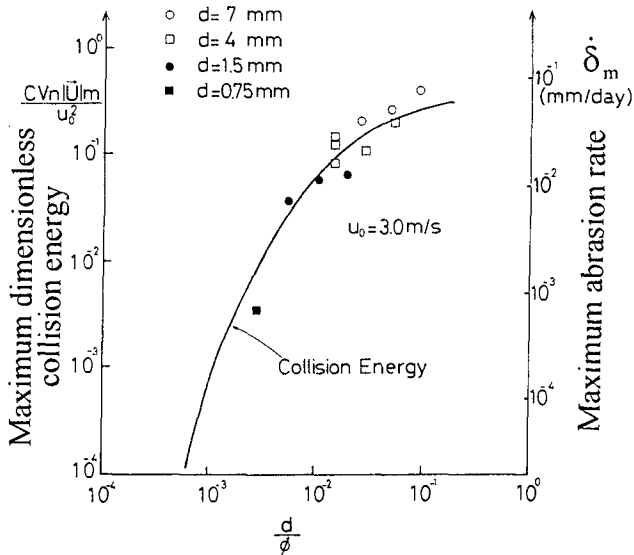


Fig. 12 Relationship between d/ϕ , maximum collision energy, and maximum abrasion rate.

Fig. 13 shows the relationship between flow velocity, dimensionless maximum collision energy, and maximum abrasion rate. If flow velocity is larger than 1.0m/s,

the dimensionless maximum collision energy is nearly constant. The maximum abrasion rate is roughly proportional to the maximum collision energy. The rate of abrasion of a steel pile is roughly proportional to the second power of flow velocity.

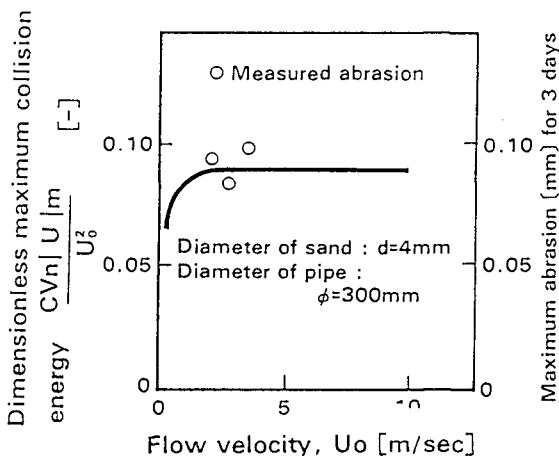


Fig. 13 Relationship between flow velocity and dimensionless maximum collision energy.

CONCLUSIONS

The distributions of abrasion rate around and along steel pipe piles were clarified. The maximum abrasion rate was observed about 50mm above the sand bed and 15~30 degrees in the main flow direction. It is confirmed that an abrasion rate of 1mm/year can be expected in coastal zones with severe sand motion.

The abrasion rate of a steel pipe pile is roughly proportional to the second power of the amplitude of flow velocity.

The larger the sand particle diameter is and the smaller the pile diameter, the higher the abrasion rate becomes and the wider the abrasion area. This reason for this is as follows. When the diameter of sand particles is small and the diameter of the pile is large, more of the sand particles tend to follow the fluid particles and do not contact with the surface of the pile due to their low inertia and the large wall effect, respectively. The collision energy of sand particles obtained by this numerical analysis is nearly proportional to the measured abrasion rate.

The maximum collision energy is approximately a function of only the ratio d/ϕ (sand particle diameter to pile diameter). The larger d/ϕ is, the larger the maximum of abrasion rate and the maximum collision energy become.

As the relationship between collision energy and measured abrasion rate has been clarified, the abrasion rate can be estimated from the collision energy.

REFERECES

- Culbertson W.Ross(1949): Deterioration of Steel Sheet Pile Groins at Palm Beach, Florida, Corrosion, Vol.5, pp.339-342.
- Yamashita,T., H.Saeki, N,Asakawa, K.Sato and Y.Kariyazono(1989): Experimental Study on Abrasion of Steel Pile by Sediment Transport, Proceedings of Civil Engineering in the Ocean, JSCE, Vol.5, pp.109-112.(in Japanese)
- Yamashita,T., H.Saeki, Y.Senda, K.Sato and Y.Kariyazono(1990): Abrasion of Heavy Duty Anti-Corrosion Steel Pile due to Sand Transport under Oscillatory Flow, Proceedings of Coastal Engineering, JSCE,Vol.37, pp.394-398.(in Japanese)
- Yamashita,T., H.Saeki, Y.Senda, K.Sato and Y.Kariyazono(1991): Relation between Abrasion of Heavy-Duty Coated Steel Pipe and Collision Energy of Sand Particle due to Sediment Transport in Coastal Zone, Proceedings of Civil Engineering in the Ocean, JSCE,Vol.7, pp.231-236.(in Japanese)
- Yamashita,T., H.Saeki, Y.Senda, T.Someya, K.Sato and Y.Kariyazono(1992): The Effects of Sand Particle Diameter and Pile Diameter on the Abrasion Rate of Steel Pile by Littoral Drift, Proceedings of Coastal Engineering, JSCE, Vol.39, pp.481-485.(in Japanese)
- Kariyazono,Y., K.Sato, T.Yamashita and H.Saeki(1992): Abrasion of Heavy-Duty Coated Steel Piles by Sediment Transport in Coastal Zone, Proceedings of 1st International Conference of CORROSION ASIA' 92, pp.341-351.

CHAPTER 169

A Viscous Rotational Model for Wave Overtopping over Marine Structure

Fei Zhuang,¹ Jiin-Jen Lee²

Abstract

Wave overtopping problems continue to require more attention due to the complexity of the physical process and the lack of available predictive models. In a recent experimental study on the kinematics of wave overtopping on marine structure by Lee, Zhuang and Chang (1993), it was found that the overtopping wave constitutes a jet-like water mass impacting the shoreward region of the breakwater. This jet-like water mass induces strong vortices and large water particle velocities in both the horizontal and vertical direction in the shoreward region behind the marine structure. The large rotational velocity field is capable of removing the armor units of the breakwater and scouring the bed in the shoreward region of the breakwater. In the study of Zhuang, Chang and Lee (1994), a numerical model capable of generating the rotational velocity field in the vicinity of the shoreward face of the breakwater was proposed. This paper presents the computation results from a refined viscous rotational model and their comparisons with newly acquired experimental data.

1. Introduction

¹Postdoctoral Research Associate, Department of Civil Engineering, University of Southern California, Los Angeles, CA 90089-2531

²Professor of Civil Engineering, University of Southern California, Los Angeles, CA 90089-2531, Member of ASCE.

Overtopping of ocean waves over marine structures has been an important problem for ocean and coastal engineers due to the fact that it may severely damage the marine structure. The overtopping process may transmit significant wave energy toward the coastal zone which the marine structure (such as breakwater) is supposed to protect.

In a recent experimental study on the kinematics of wave overtopping on marine structure by Lee, Zhuang and Chang (1993), it was found that the overtopping wave constitutes a jet-like water mass impacting the shoreward region of the breakwater. This jet-like water mass induces strong vortices and large water particle velocities in both the horizontal and vertical direction. Moreover, the overtopping wave also generates waves in the shoreward region possessing significant wave energy with oscillatory wave trains. These two major conclusions have significant practical implications: The large rotational velocity field can remove the armor units of the breakwater and scour the bed. The generated waves could induce significant basin oscillations in the shoreward basin with resonant frequencies which are different from the incident wave frequencies. Such experimental results deviated significantly from the potential flow theory in certain regions. Thus, computational results based on the potential flow theory can not fully explain the experimental data without incorporating additional features. In the study of Zhuang, Chang and Lee (1994), a numerical model capable of generating the rotational velocity field in the vicinity of the shoreward face of the breakwater was proposed. This paper presents the computation results from a refined viscous rotational model and their comparisons with newly acquired experimental data.

2. Experiments

Experiments involving propagation of solitary waves over various submerged breakwater configurations are conducted in a wave tank 37.73 meter long, 39.4 centimeter wide, and 61 centimeter deep. A programmable piston type wave generator is installed at one end of the tank and a sloping beach is installed at the other end of the tank to aid the wave dissipation for the purpose of reducing the waiting time between experimental runs. Three different breakwater configurations are used in the experiment. Three resistance type wave gauges are installed at desired locations to make simultaneous wave profile measurements.

The water particle velocities are measured using a portable four-beam, two-component, fiber optic Laser Doppler Velocimeter (LDV) manufactured by TSI Inc.. Titanium Dioxide powder (TiO_2) is used in the experiments as

a seeding agent.

3. Numerical Models

The refined viscous rotational flow model consists of two basic elements: The velocity field generated by using the potential flow theory and the rotational velocity field generated by the separated flow (vortices) of the overtopping waves as they leave the breakwater site. For the potential flow theory, the Boundary Element Method has been used. The nonlinear boundary condition at the free surface is satisfied in the numerical model to allow simulation of large amplitude waves. The transient non-rotational flow field obtained by the potential flow theory is combined with the time dependent rotational flow field due to vortices generated in the separation zone.

The potential flow theory formulation using boundary element method has been presented in Lee, Chang and Zhuang (1992). The problem of wave overtopping on marine structure is formulated as a two-dimensional boundary value problem. The fluid in the solution domain is assumed to be incompressible and the flow is assumed to be irrotational. Viscous force is also neglected. Application of potential theory leads to the governing Laplace's equation for the velocity potential function ϕ :

$$\nabla^2 \phi(\mathbf{x}, t) = 0 \quad \mathbf{x} \in \Omega(t) \quad (1)$$

with the kinematic and the nonlinear dynamic free surface conditions as the boundary conditions on the free surface Γ_s :

$$\frac{D\mathbf{r}}{Dt} = \left(\frac{\partial}{\partial t} + \mathbf{u} \cdot \nabla \right) \mathbf{r} = \mathbf{u} = \nabla \phi \quad (2)$$

$$\frac{D\phi}{Dt} = -gy + \frac{1}{2} |\nabla \phi|^2 - \frac{p_a - p_o}{\rho} \quad (3)$$

where \mathbf{r} is the position vector of a free surface fluid particle, g the acceleration due to gravity, y the vertical coordinate, p_a the pressure at the surface, p_o a reference pressure and ρ the fluid density.

The solution to the boundary value problem is expressed as a boundary integral using the free space Green's function $G(\mathbf{x}_i, \mathbf{x}_j) = -\frac{1}{2\pi} \log |\mathbf{x}_i - \mathbf{x}_j|$ and Green's theorem:

$$\alpha(\mathbf{x}_i) \phi(\mathbf{x}_i) = \int_{\Gamma(\mathbf{x})} \left[\frac{\partial \phi}{\partial n} G(\mathbf{x}, \mathbf{x}_i) - \phi(\mathbf{x}) \frac{\partial G(\mathbf{x}, \mathbf{x}_i)}{\partial n} \right] d\Gamma(\mathbf{x}) \quad (4)$$

where \mathbf{x}_i and \mathbf{x} are position vectors for points on the boundary (\mathbf{x}_i can also be any where within the domain), $\Gamma(\mathbf{x})$ is the boundary of the fluid domain Ω , \mathbf{n} the unit outward normal vector and $\alpha(\mathbf{x}_i)$ a geometric coefficient. The boundary integral equation is then solved using the Boundary Element Method.

A time marching procedure which was first suggested by Dold and Peregrine (1986) has been used in the present analysis to update both the new position of the free surface and the potential value ϕ on the free surface at the next time step:

$$\mathbf{r}(t + \Delta t) = \mathbf{r}(t) + \sum_{k=1}^n \frac{(\Delta t)^k}{k!} \frac{D^k \mathbf{r}(t)}{Dt^k} + O[(\Delta t)^{n+1}] \quad (5)$$

$$\phi(\mathbf{r}(t + \Delta t), t + \Delta t) = \phi(\mathbf{r}(t), t) + \sum_{k=1}^n \frac{(\Delta t)^k}{k!} \frac{D^k \phi(\mathbf{r}(t), t)}{Dt^k} + O[(\Delta t)^{n+1}]. \quad (6)$$

The Boundary Element Method together with the time marching procedure form a unique solution technique for solving transient nonlinear wave problems.

The rotational flow field in the vicinity of the shoreward breakwater is simulated with the governing equations for the vorticity stream function formulation of incompressible laminar flow. Figure 1 shows the computational domain for this rotational flow field (ABCDE). The governing equations are:

$$\frac{\partial \omega}{\partial t} + u \frac{\partial \omega}{\partial x} + v \frac{\partial \omega}{\partial y} = \nu \left(\frac{\partial^2 \omega}{\partial x^2} + \frac{\partial^2 \omega}{\partial y^2} \right) \quad (7)$$

$$\frac{\partial^2 \psi}{\partial x^2} + \frac{\partial^2 \psi}{\partial y^2} = \omega \quad (8)$$

where ω is the vorticity vector; u, v are the horizontal and vertical components of the velocity vector, and ν is the kinematic viscosity of the fluid. The boundary conditions in conjunction with the governing equations (7) and (8) are listed as follows:

A-B and A-E:

$$u = 0, \quad v = 0, \quad \psi = 0$$

B-C:

$$\frac{\partial \psi}{\partial y} = u, \quad \omega = \frac{\partial u}{\partial y} - \frac{\partial v}{\partial x}$$

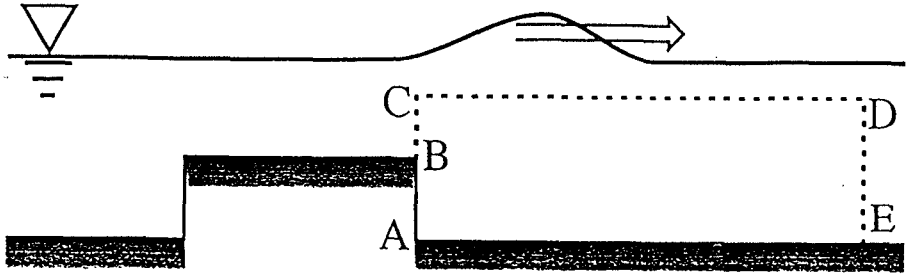


Figure 1: Sketch of the computational domain.

C-D:

$$\frac{\partial \psi}{\partial x} = -v, \quad \omega = \frac{\partial u}{\partial y} - \frac{\partial v}{\partial x}$$

D-E:

$$\frac{\partial \omega}{\partial x} = 0, \quad \frac{\partial^2 \psi}{\partial x^2} = 0$$

For each time step, the particle velocity solution is collected along B-C and C-D from the computational results based on the boundary element method (potential flow theory). These are used as the boundary conditions for the vorticity stream function formulation, hereafter we refer it as combined rotational model. Equation (8) is solved using Successive Over Relaxation method. Equation (7) is then solved using Alternating Direction Implicit method. The same computational procedure is repeated over the successive time steps. For detailed description of the numerical model, the reader is referred to Zhuang (1996).

For the two dimensional wave overtopping problem, potential theory with boundary element method has shown to have the following advantages: (1) the boundary element method can reduce the dimension of the original problem by one, thus reduce the computer storage requirements and speed up the computation. (2) the boundary element method is especially suitable for problems where the variables of primary interest are mainly located on the boundary, such as wave-related problems. (3) it has been proved by previous study (Lee, Chang and Zhuang (1992)) that potential theory results agree

well with the experimental data for the region near the free surface and the region far away from the separation zone near the breakwater. But, it is also shown through the present experimental data that in the separation zone (where vortex generation and large induced flow velocities are prevailing) potential theory can not be valid.

As for the vorticity stream function formulation with finite difference method, it includes elements of rotationality and viscous effect, and it can be used to describe flow separation and vortex generation. However, this formulation is difficult in dealing with free surface calculation and is not economical in terms of computational cost compared with the boundary element method.

In order to make the numerical model capable of simulating the whole wave overtopping process, and to take advantages of both the potential flow theory and the vorticity stream function formulation, the present study proposes a combined numerical model. In this model, potential flow theory with boundary element method is used to obtain the wave profile and flow field information in the region where the flow can be assumed inviscid and irrotational, i.e. the region near the free surface and the region far away from the separation zone. In the region near the shoreward breakwater, where flow separation and vortex generation are dominant, vorticity and stream function formulation is employed to capture the rotational flow motion in this region.

It is reasonable to expect that the computational results from the boundary element method based on the potential flow theory would fail at the separation zone due to its imposed assumption of inviscid fluid and irrotational condition. However, the computational results should be reasonably valid in the region far away from the separation zone. Therefore, our modeling strategy for the region near the separation zone is adopted as follows: As the incident wave propagates over the breakwater, the computed velocity field from the boundary element method in the regions BC and CD are used as input boundary condition for the rotational flow simulations based on equations (7) and (8). In this approach, the domain of computation is fixed thus the computational effort is greatly simplified.

4. Results and Discussion

During the experiment we have observed flow separation and vortex generation near shoreward face of the breakwater. These observed phenomena

and the inability of the potential flow theory to describe the flow phenomena motivated the development of the present combined rotational flow model. In this section, the focus will be in the separation zone. Flow patterns, detailed particle velocity time history obtained from both the experiments and the present combined rotational flow model will be presented.

Figure 2 and 3 present a series of four photographs taken during one experimental run of $H/d=0.3$ solitary wave overtopping on submerged Breakwater C (height=4.5in and width=15in) with water depth $d=9$ in. The blue dye is injected in the shoreward region of the breakwater before the wave is generated. The solitary wave propagates from left to right direction in the pictures. The breakwater can be seen at the lower left corner of the pictures. From Figure 2(A), we can see a vortex is starting to form at the shoreward edge of the breakwater while the wave crest is approximately on the top of the edge. The following three pictures show a complete process for the generation of a vortex. It is observed that a strong rotational flow field has been generated in the vicinity of the shoreward breakwater. Since this is a transient process, the vortex will grow bigger and bigger after the wave has passed and eventually move downstream and become disintegrated. A practical point to remember is that the rotational field so generated will induce more scouring capability in the shoreward region of the breakwater.

The velocity time history comparisons between the model results and the experimental data are presented in Figures 4 and 5. Figure 4 shows the velocity time history at a location P-825. The location P-825 is at the vertical position $-0.825d$ from the still water surface and $0.15d$ from the breakwater shoreward surface. Included in the figure are the results of the potential flow theory (solution from boundary element method) shown in solid line. The results from the combined rotational flow model are shown in dotted line. The velocity time history obtained by using the Laser Doppler Velocimeter measurement are plotted using the star symbols. The ordinates in both figures are the velocity components normalized with respect to \sqrt{gd} (the wave celerity in water depth d). The abscissa is the real time normalized as $t\sqrt{g/d}$. Examining both the horizontal and vertical velocities, it is seen that, at location P-825, both the combined rotational flow model and experimental data reveal that the horizontal velocity changes direction from positive to negative and the vertical velocity changes the direction from negative to positive. That means the flow direction at that point changes from forward and downward to backward (seaward) and upward. It clearly shows that a vortical motion has been generated during the wave overtopping process.



Figure 2: Pictures (A) and (B) of an experimental observation of vortex generation for solitary wave overtopping submerged breakwater. $H/d=0.3$, $d=9\text{in}$, Breakwater C.

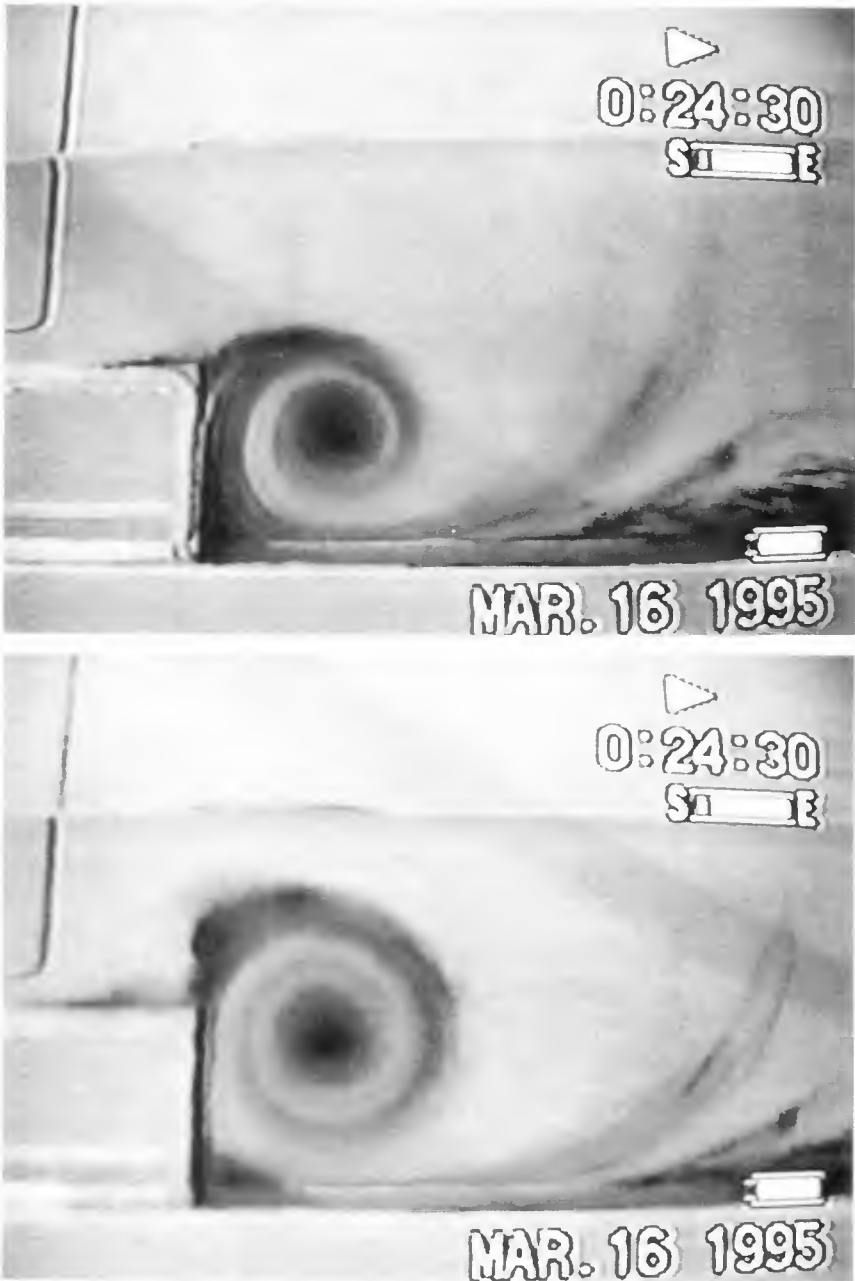


Figure 3: Pictures (C) and (D) of an experimental observation of vortex generation for solitary wave overtopping submerged breakwater. $H/d=0.3$, $d=9\text{in}$, Breakwater C.

The present combined rotational flow model predicts this feature of particle movement and agree well with the experimental data. As expected, the potential theory predicts only positive horizontal velocity and negative vertical velocity. The results from the potential flow model deviate significantly from the experimental data beyond a very short time after the arrival of the waves. Thus, according to the potential flow theory, the particles are always going forward and downward directions during the overtopping process, representing no rotational motion. It is reasonable to expect that the computational results from the boundary element method based on the potential flow theory would fail in the separation zone due to its imposed assumption of inviscid fluid and irrotational condition.

Another noticeable feature to be observed from this time history graph is the magnitude of the positive vertical velocity and negative horizontal velocity, both are much greater than the particle velocities associated with an unmodified solitary wave. This feature of increased particle motion could contribute to the destabilization of the breakwater armor units in the shoreward face.

Figure 5 shows horizontal and vertical velocity time history comparisons between the present model and the experimental results at location P-75 for 0.3 solitary overtopping on Breakwater C. Location P-75 is $-0.75d$ from the still water surface and $0.15d$ from the breakwater shoreward surface. It is $0.075d$ above location P-825. As observed from Figure 4, velocity at location P-75 also shows the reversal of horizontal velocity from shoreward to seaward direction and the reversal of vertical velocity from downward to upward. Although location P-75 is very close to location P-825, we can see the velocity time histories from the two locations have significant differences. It indicates that there is a rapidly changing velocity field in this region. Notice that the vertical velocity reached the maximum when the horizontal velocity becomes small, indicating location P-75 is in the middle left portion of the clockwise rotating vortex, where the flow is basically going up. Again Figure 5 shows the results from the present rotational flow model agree quite well with experiments.

5. Conclusions

The major conclusions drawn from this study can be summarized as follows:

1. A numerical model has been developed to simulate wave induced vis-

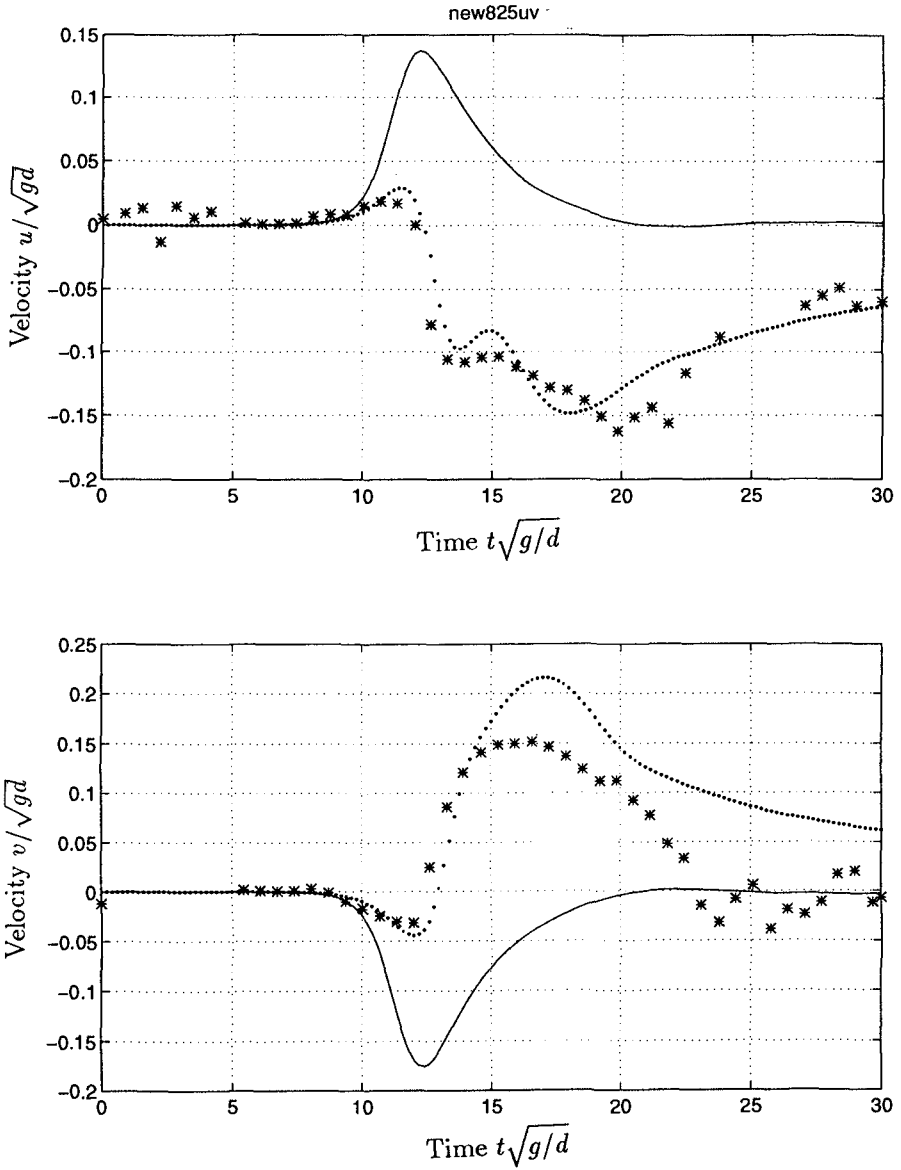


Figure 4: Comparison of particle velocity results from the present model, potential flow theory and experiment at $x^* = 0.15$ and $y^* = -0.825$ for solitary wave overtopping on breakwater C, $H/d = 0.3$, $d = 9in$; \cdots present model; $—$ potential flow model; $***$ experiment.

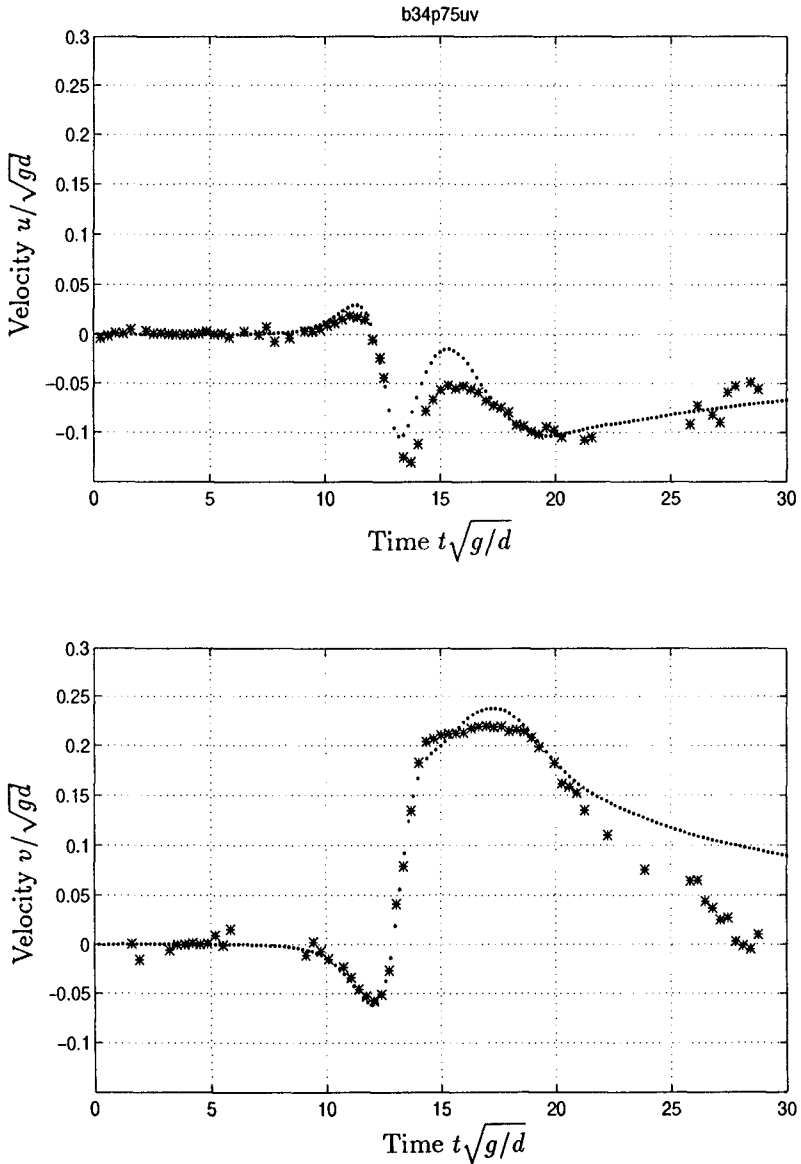


Figure 5: Comparison of particle velocity results from the present model and experiment at $x^* = 0.15$ and $y^* = -0.75$ for solitary wave overtopping on breakwater C. $H/d=0.3$, $d=9\text{in}$; \cdots present model; $***$ experiment.

cous rotational flow in the separation zone near shoreward breakwater surface. This model is referred as the combined rotational flow model because it combines two distinct theories and corresponding solution methods and it is capable of evaluating rotational separating flow field. It is seen that the combined rotational flow model describes the flow field quite well when compared with the experimental data. It offers a tool for modeling the flow field in the vicinity of the shoreward region of the breakwater. It is also seen that the potential flow results deviate from the experiments significantly. This demonstrates the importance of incorporating the rotational feature for modeling the flow field in the vicinity of the shoreward region of the breakwater.

2. Based on both the numerical and experimental results it is found that there is a vortex generated by the overtopping of solitary wave in the vicinity of the shoreward breakwater. The vortical motion remains there even when the wave has traveled to the region far away from the breakwater. This vortical motion produces a velocity field which could cause significant scouring in the region close to the breakwater.
3. Because of the vortex motion, there is a relatively large velocity component in the upward and seaward direction. This velocity component could produce a lifting force which could destabilize the armor units in the shoreward face of the breakwater.
4. The present combined rotational flow model can be easily implemented because of its time-saving feature. It only computes rotational flow field in a relatively small local domain, while the efficient potential theory using boundary element method offers the information away from the separation zone, where the irrotationality assumption is valid. Furthermore, this model can be extended to solve other wave-structure interaction problems.

Acknowledgment

This study is supported by USC Foundation for Cross-Connection Control and Hydraulic Research. The LDV System is supported by NSF under Grant No. 8906898. The authors are grateful for the generosity of Dr. Fredric Raichlen for permitting them to conduct the experiments at Caltech's W.M. Keck Laboratory of Hydraulics and Water Resources.

References

1. Dold, J.W. & Peregrine, D.H., "An Efficient Boundary Integral Method for Steep Unsteady Water Waves", Numerical Methods for Fluid Dynamics II (ed. K.W. Morton & M.J. Baines), pp.671-679, Clarendon Press, Oxford, 1986.
2. Fletcher, C.A.J., "Computational Techniques for Fluid Dynamics", Second Edition, Springer-Verlag, 1991.
3. Lee, J.J., Zhuang, F. and Chang, C., "Kinematics of Wave Overtopping on Marine Structure", Proceedings of the Second International Symposium on Ocean Wave Measurement and Analysis (Wave 93), July 25-28, 1993, New Orleans, Louisiana, pp. 821-834.
4. Lee, J.J., Chang, C. and Zhuang, F., "Interaction of Nonlinear Waves with Coastal Structures", Proceedings of the Twenty-Third International Conference on Coastal Engineering, ASCE, Venice, Italy, Oct.4-9,1992, pp.1327-1340.
5. Raichlen, F., Cox, J.C. and Ramsden, J.D., "Inner Harbor Wave Conditions due to Breakwater Overtopping", Proceedings of Coastal Engineering Practice '92, ASCE, March 1992.
6. Zhuang, F., Chang, C. and Lee, J.J., "Modeling of Wave Overtopping over Breakwater", Proceedings of the Twenty-Fourth International Conference on Coastal Engineering, pp.1700-1712, ASCE, Kobe, Japan, Oct. 23-28, 1994.
7. Zhuang, F., "Experimental and Numerical Investigation of Wave Overtopping over Coastal Structures", Ph.D. Thesis, University of Southern California, Los Angeles, CA, August 1996.

CHAPTER 170

Overtopping of waves at a wall: a theoretical approach

M. Jervis ¹ and D.H. Peregrine ².

Abstract

The flow of water due to the overtopping of a vertical wall by waves is modelled. The waves are computed with an accurate irrotational flow solver. The case where a jet of water is projected up the face of the wall is considered. A simple estimation is made from the computation of the amount of water that can pass over the crest of a wall of finite height. The results for overtopping volume per wave show a roughly exponential decaying dependence on the height of the wall above the still water level. Results are given for waves of differing height and also for various sizes of berm in front of the wall. The effects of surface tension are included to investigate the possibility of errors in scaling experimental results to prototype scale. These are larger than expected.

Introduction

In many locations sea walls and breakwaters are built to prevent water from the open sea spreading inland, or disturbing harbours and their installations. There are many reasons for estimating how much water may overtop a wall of given height in given wave conditions. With sea walls, erosion of the back side may be the greatest danger, whereas damage to people and port installations may be of concern behind a breakwater.

Previous study of overtopping at vertical walls has been almost entirely based on small scale experiments (e.g. Franco 1994, Juhl & Sloth 1994). This is a theoretical study of wave overtopping. We focus on the case where waves slosh against a vertical wall sending a jet of water up to a height which may be as much as three times the height of the incident wave. Numerically accurate irrotational flow computations model the upward jet, then a simple model described in the next section is used to estimate how much of the water in the jet would overtop a wall of given height.

The results we present here are all for steep solitary waves meeting a wall. The solitary wave is the largest wave that can propagate on water of a given depth. As well as considering a vertical wall, bounding water of constant depth,

¹Research student, School of Mathematics, University of Bristol.

²Professor of Applied Mathematics, School of Mathematics, University of Bristol, University Walk, Bristol BS8 1TW, UK. (*D.H.Peregrine@bristol.ac.uk*)

cases of walls with berms are also presented. There is interest in several aspects of the hydrodynamics of such flows, but we concentrate on the overtopping. The effect of a berm depends on both its horizontal extent and height. Small low berms have little effect. Larger berms change the wave behaviour.

There are two types of behaviour characteristic of extreme standing waves, or waves reflecting (Thais & Peregrine, in preparation). One is the thin sheet like jet that we see in figure 1, but a berm can also give the other almost "table-like" elevation as in figure 6, or wave breaking at or before the wall. The computations show strong variation of overtopping depending on the berm size, but are not capable of dealing with the cases of wave breaking.

A further variation is introduced to give an indication of scale effects. Often, experiments are performed on rather shallow water, e.g. 0.1m or less especially when a three-dimensional wave field is being modelled. In such cases surface tension is likely to have a significant influence on the tip of wave jets. By including surface tension in the program to calculate the incident wave and jet this scale effect is quantified and found to be more important than originally expected.

Overtopping model

The program used is that of Cooker, Peregrine, Vidal & Dold(1990) which is based on the accurate irrotational flow solver of Dold & Peregrine(1986). The computation assumes inviscid, irrotational and incompressible flow, solving Laplace's equation with a boundary-integral method, and using the fully non-linear boundary conditions to time step the computation. High-order numerical approximations are used.

The reflection of waves by a vertical structure such as a breakwater means that the waves in front of the structure are well modelled by standing or near-standing waves if no breaking occurs. Breakwaters are sometimes designed so as to guarantee the formation of standing waves in front of the structure. In this way the chances of the occasional very high impact pressures which might lead to structural failure are reduced. The appearance of the standing waves becomes more like a reflecting solitary wave as water depth is decreased. The largest waves that can approach any structure are shallow water waves whose crests are very similar to solitary waves. Thus we use solitary waves as incident waves for the examples here.

Impact on a vertical wall is modelled by considering the symmetrical collision of two steep solitary waves. That is, the initial condition in the computation corresponds to two accurate solitary waves heading towards each other, but sufficiently far apart that there is no initial interaction between them. An initial solitary wave of any height can be accurately modelled using Tanaka's (1986) method. The program can include simple deformations to a flat bed, such as beaches and half ellipses. A berm of quarter-elliptical shape in front of the wall is modelled by placing a semi-ellipse on the bottom directly below the line of symmetry of the surface, where the two solitary waves collide. Results for such cases are also reported. For sufficiently steep waves a vertical jet forms at the wall (see figure 1).

We are not able to explicitly model a wall of finite height using the present code. Substantial changes would be needed to do this. However, we make use of a feature of common to all jets arising from unsteady waves. That is once the jet forms the pressure field within the jet is very weak. This means that almost all the motion of water in the jet is close to purely inertial. Thus we assume that

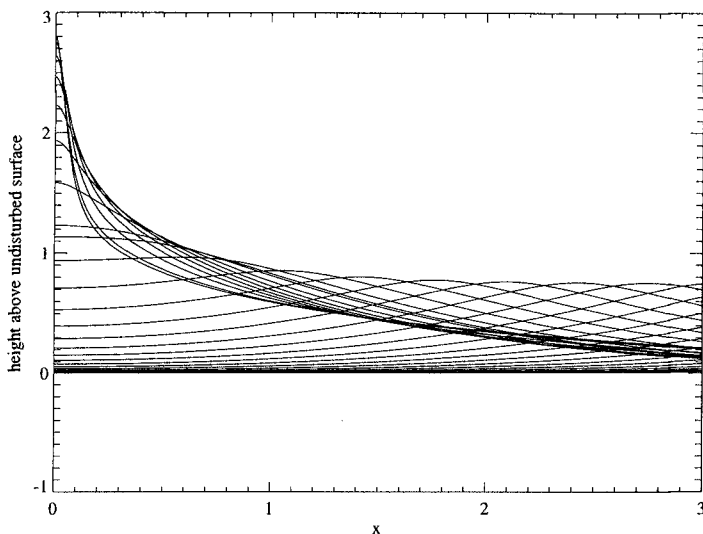


Figure 1: Solitary wave collision with vertical wall. Wave height, $H = 0.75d$

once the jet has formed, the motion of any fluid particle in the jet is governed by its initial momentum and gravity. Portions of fluid are modelled by considering their motion once above the crest of the wall as if they are free particles moving under gravity, that is

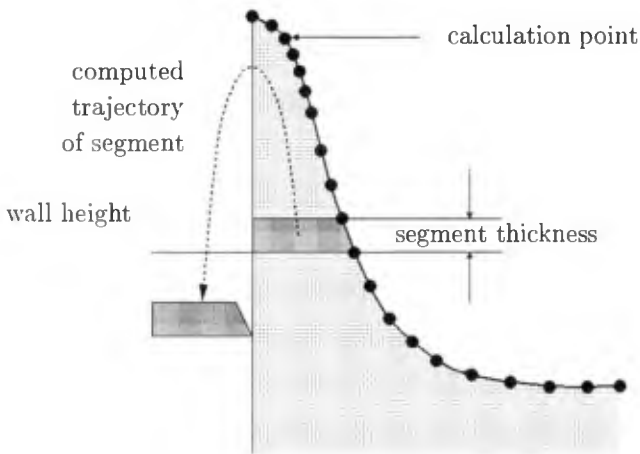
$$y(t) = y_0 + v_0(t - T_0) - gt^2/2 \quad (1)$$

$$x(t) = x_0 + u_0(t - T_0) \quad (2)$$

where the fluid particle has position (x_0, y_0) and velocity (u_0, v_0) at a time T_0 when it passes the crest of the wall.

As a jet ascends a wall there is some slight pressure against it. This is due to motion towards the wall as each portion of the jet stretches and thins. As the water passes the top of the wall this slight pressure drops to atmospheric, but the motion towards the line of wall continues. This means any portion of fluid passing the top of the wall has some momentum in a direction towards the wall which can carry it over the wall face and cause overtopping. Thus our model is as follows:

- Take horizontal slices of water as they pass the level chosen to represent the top of the wall.
- Work out their horizontal momentum.
- Treat each slice as a particle moving under gravity as in equations (1) and (2).
- Consider each slice as it returns to the level of the top of the wall. Use the position of its centre of mass to decide how much, if any, of the water has moved horizontally past the face of the wall and hence counts as overtopping.
- Add the contribution from all the slices that flow past the top of the wall to give an estimate of the total volume of water overtopping due to that wave.



This calculation could be further refined by allowing for the contraction of each slice under its initial velocity field. However, such contraction is influenced by the slight pressures exerted by adjacent slices, so that to try and include it would mean going beyond the simple modelling we wish to present here.

Slices were identified by stepping in time. The length of each time step and the vertical velocity together determining the thickness of each slice. Too short a time-step means good resolution but long computation times, too long a time step gives poor resolution. A time step size was chosen such that the thickness was always less than $10^{-4}d$, where d is the undisturbed water depth.

Limitations of simple model

In these calculations it is assumed that solitary waves are an accurate representation of the likely steepest incoming waves (see previous section). For the collision of solitary waves only the case of no surface tension and constant depth has been previously studied. When the waves are steepened by interaction with the berm a range of motions can develop, including flip-through motions as described by Cooker & Peregrine (1990). Flip-through motion is very sensitive to wave shape and can produce very violent jets. The present model is only applied to situations in which the free surface calculated by the potential flow solver has reached or passed the time of maximum run-up before breaking down. Thus we cannot model overtopping from breaking waves such as in figure 2, or the strong 'flip-through' impacts described by Cooker & Peregrine since in such cases we cannot compute up to the time of maximum elevation. On the other hand these give very thin jets. If the wave has already broken any resulting jet is small and mostly fails to overtop the structure. Thus the cases to which our model is restricted are those which happen to be responsible for a significant amount of overtopping.

Our model is inaccurate for wall heights below the height of jet formation, or for waves where no significant jet is formed, i.e. where the force due to internal pressure on a fluid particle is not negligible compared to gravity. Thus for example it does not apply to surging over low walls. In practice this means that

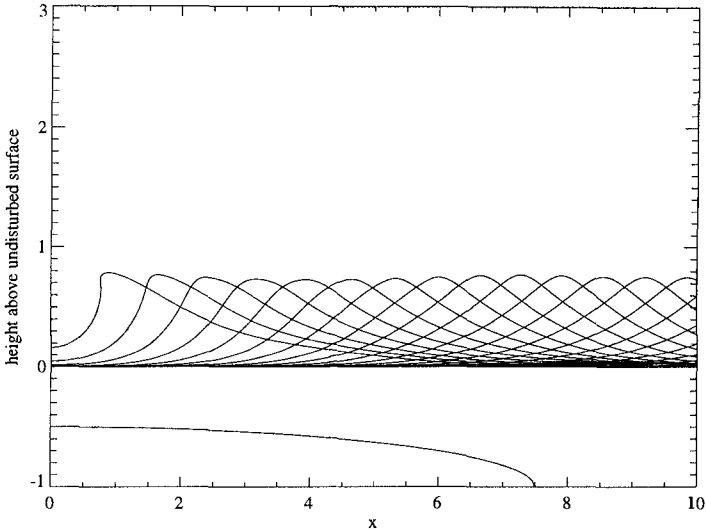


Figure 2: Solitary wave steepening over wide berm.

only solitary waves of steepness greater than $0.5d$ were used, and the results are restricted to the higher end of the dimensionless freeboard range (approximately to above $R/H=1.8$ in the calculations presented here).

Results with gravity waves.

Since these calculations assume two-dimensional waves the overtopping volumes calculated are volume per unit length of the wall, Q . The undisturbed water depth, d , is used as the unit of length in computations, so for example the wave height, H , is a dimensionless ratio of wave height to that water depth. Following the presentation of results in previous papers on overtopping rates, the quantities presented in the following section are in terms of the overtopping volume Q/H^2 , and dimensionless wall crest free board R/H , where R is the height of the top of the wall above the undisturbed water level. Note, for these solitary wave computations the undisturbed level corresponds to trough level in a periodic or irregular wave train.

Figure 3 shows the results of dimensionless overtopping against dimensionless crest free board for the case of a horizontal bed. The dimensionless overtopping volume is plotted on a logarithmic scale. For solitary waves of amplitude 0.5 or less, no significant jet is formed at the wall. Thus our model is less accurate for the wave of lower amplitude for which it is only likely to give a rough indication of overtopping volumes. The variation with wave height reflects the greater height of run-up at wall for the highest waves. This is described in Cooker *et al.* (1997). Dimensionless overtopping volume increases with wave height.

For the case of a berm in front of the wall figures 4 and 5 show the results of dimensionless overtopping volume against dimensionless crest free board for a solitary wave with amplitude $0.7d$ for berm widths d and $2d$. These include a range of results for berms of different heights. Rather surprisingly, for berms of

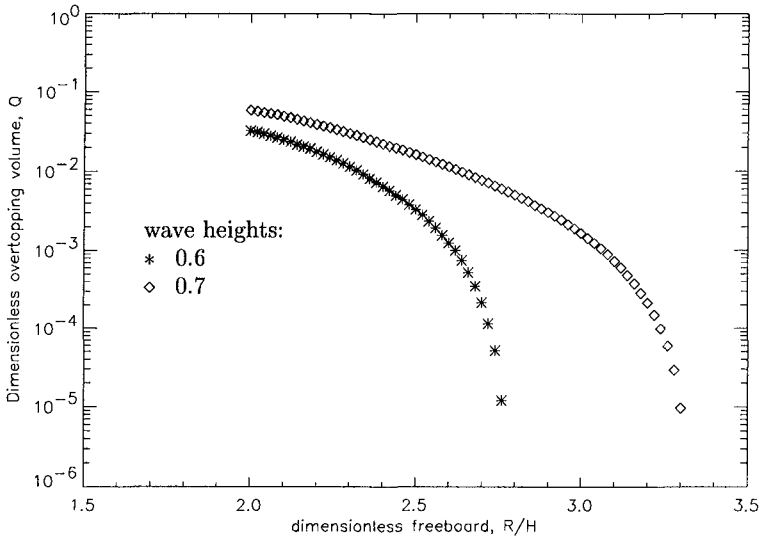


Figure 3: Solitary wave overtopping on water of constant depth; different wave heights, H

width d , $2d$, the overtopping decreases with increasing berm height. For these short berm widths, the higher berm interferes with the water motion near the wall. The influence on the shape of the resultant jet shape is small in the case of length d , but strong for the berm of length $2d$ (see figure 6 for example), making it increasingly wide and short.

It can be seen in figure 6 that the berm forces the water level at the wall up earlier than in the case with no berm. The result is that the strong accelerations normally seen at this time are reduced and the water just sloshes smoothly against the wall. In this case the reduction in the violence of the collision also corresponds to a reduced impact pressure at the wall. However, since the motion of the water is directed up by the berm at the wall this may give larger overtopping volumes at low crest free-boards. This is beyond the scope of our current model. For berms of width $3d$, the effect seen with the $2d$ berm and that of wave steepening appear to cancel each other. The overtopping predicted is very close to that with no berm. For wider berms still, wave steepening is the dominant effect, which increases the violence of the motion and the corresponding overtopping volume.

Figure 7 shows the dimensionless overtopping volume against dimensionless crest free board for berms of fixed height but different width. For dimensionless free-boards up to 2.5 there is little difference; it is only in the free-boards near the maximum run-up height that the influence of the berms can be clearly seen. Results show that a berm of width less than $3d$ decreases Q , compared to the no berm case. Over wider berms, the wave steepens giving a stronger jet on impact. A roughly exponential relation between individual dimensionless overtopping volume and dimensionless free-board (i.e. a straight line on the graph) can be seen over much of the valid range.

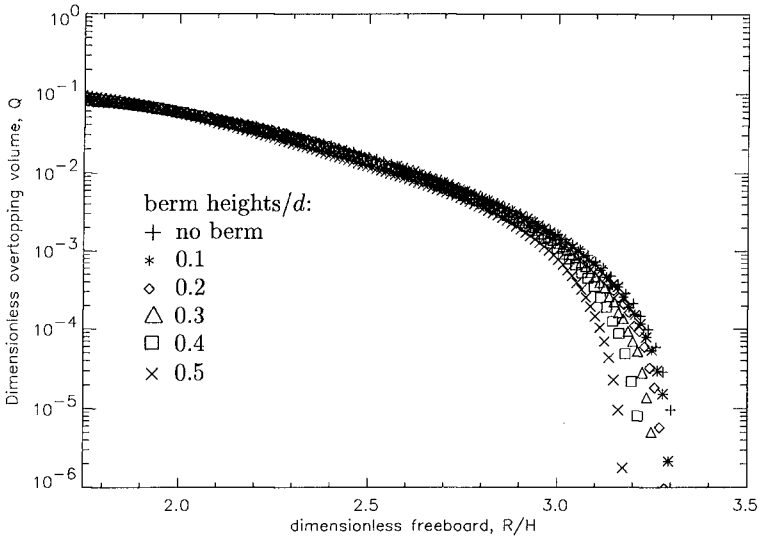


Figure 4: Solitary wave overtopping; berm width = d , different berm heights.
 $H = 0.7d$

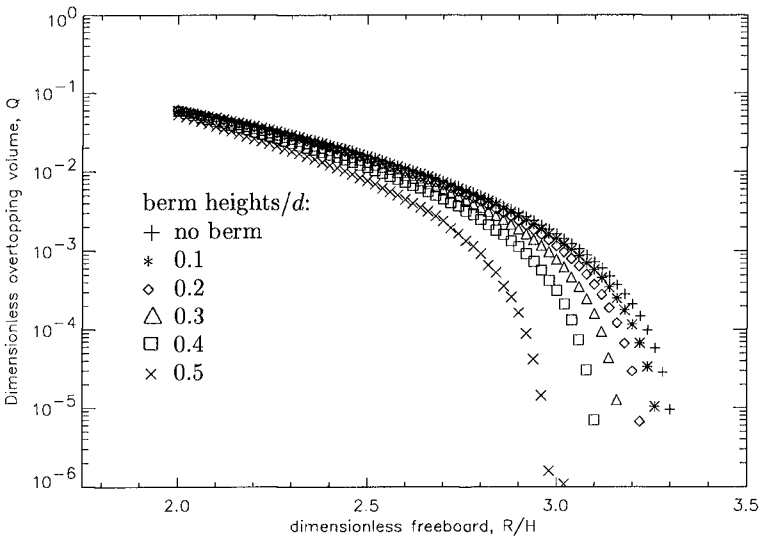


Figure 5: Solitary wave overtopping; berm width = $2d$, different berm heights.
 $H = 0.7d$

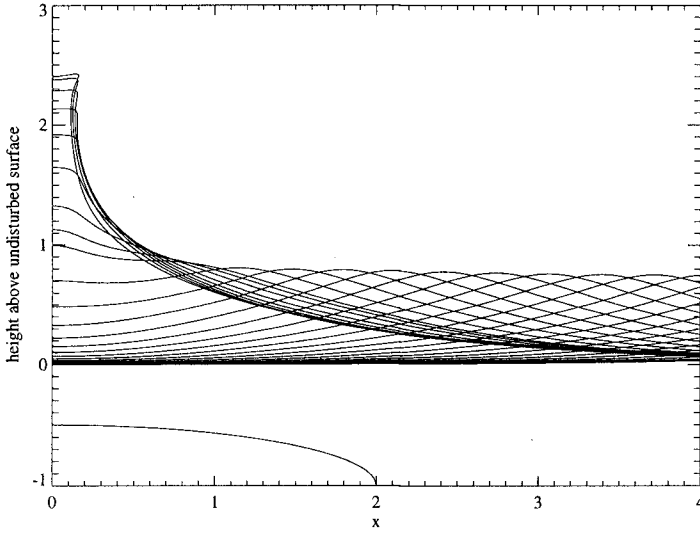


Figure 6: Vertical wall with berm width $2d$, height $0.5d$. $H = 0.75d$

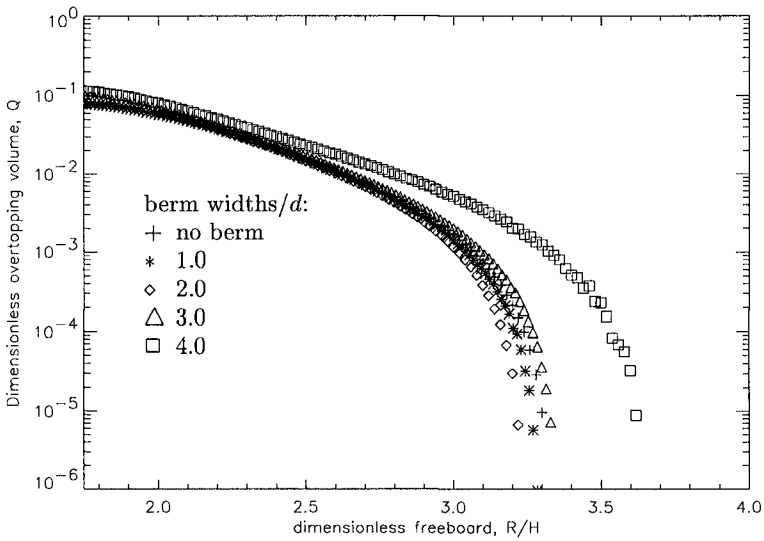


Figure 7: Solitary wave overtopping; berm height = $0.2d$, $H = 0.7d$.

Comparison to existing experimental data

To the authors' knowledge there are no experimental results for individual overtopping volumes for a vertical breakwater in which the required geometric and hydraulic characteristics are all given. Indeed, the purpose of this study is partly to fill that gap. We can however draw some parallels between the calculations presented here and experimental results. From the knowledge of wave steepnesses (defined in related experimental work as wave height/distance between crests) and the nondimensional wave speed in our model, we can work out a rough overtopping rate. Values for wave heights are given in terms of a significant wave height, defined as the mean height of the 1/3 highest waves. In conversion to approximate rates we use this as equivalent to the height of our test wave. Where a range of significant wave heights is given our test wave is chosen equal to the mean of the range.

The overtopping rate is defined as the overtopping volume divided by the time between overtopping events. The time between overtopping events usually differs from the wave period as only a limited percentage of the incident waves produce overtopping.

A series of model test are carried out by Juhl (1995). Results for dimensionless overtopping rates are presented for differing angles of wave attack and wind velocities. Our model is only applicable to the results with zero wind velocity and normal wave attack. Again, we have to be careful when comparing our model to results with overtopping rates. Suppose we assume that only 10% of waves produce overtopping, a likely figure from various experimental results. Our model thus only gives a rough approximation to the experimental data.

Figure 8 compares the rate of overtopping found with zero wind velocity and 0° angle of wave attack to that predicted by our simple model over its range of validity. The period between overtopping events used to find the rate is derived by assuming the a periodic train of solitary waves which give a steepness equal to the average used in the tests, multiplied by the probability. We see that our model produces results that are of the same order of magnitude over most of the range. However there is a tendency for under-prediction at higher dimensionless free boards. This is explained earlier. The non-dimensional overtopping rate compares well to that of Juhl for dimensionless free boards in the range 2 to 3.

Overtopping with gravity-capillary waves

Surface tension plays an important local role where-ever the surface curvature is sufficiently high. In the calculations above, extremely thin jets are often produced which have a region of very high curvature at the tip. Surface tension can have a significant effect on the shape of the jet at this tip. This in turn might effect the predicted overtopping volumes. There are two ways in which surface tension is likely to effect overtopping - by affecting the profile of the incident wave, and by affecting the resulting jet shape. We ask, at what scale would surface tension become significant in overtopping experiments? The lack of data on scale correction factors to date has been reported as substantially hindering the application of research results to practical engineering analysis or design. Our model permits the inclusion of surface tension in the evolution of the surface. There are, of course, other scale effects not included in our model. These include the break up of jets into water drops and the effects of any wind. There may also be problems including any air entrainment effects.

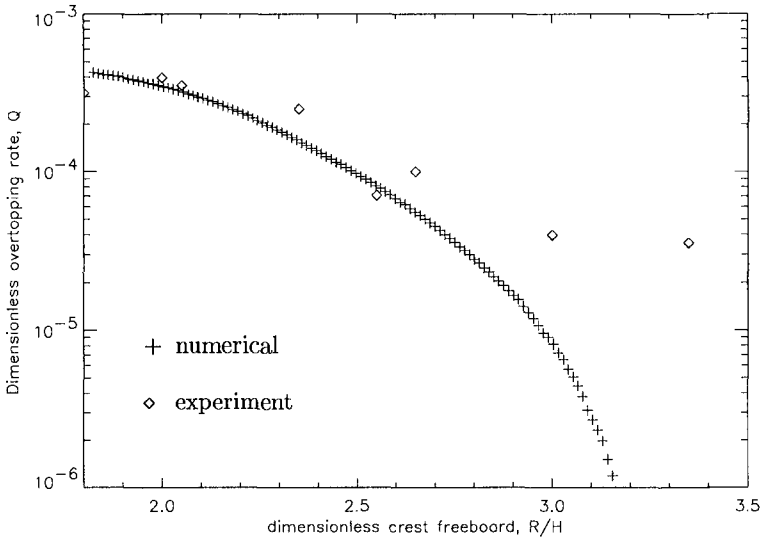


Figure 8: Comparison of estimated overtopping rates with Juhl (1995) (wind speed=0, angle of attack= 0°)

The results are described in terms of the properties of clean water. Hence the description of water depth is used to specify scale of motion and thus the relative strength of surface tension. In our symmetric approximation we implicitly assume a contact angle $\theta = 90^\circ$. In practice the contact angle may differ from this, and the water is not usually clean.

Run-up of solitary type waves with surface tension

Figure 9 shows the jet at the time of maximum run-up for a solitary waves of $a = 0.7d$ with $d = 5\text{cm}$. In Jervis (1996), it was found that for the particular case of a solitary wave with $a = 0.7d$, propagating on depths 5cm and larger no noticeable capillary waves formed. Experimenters might then expect surface tension to play no measurable role in experiments. The main effect of the inclusion of surface tension is to modify the shape of the jet produced in the solitary wave collision. The jet is generally broader and shorter due to surface tension. A decreasing non-dimensional run-up height with increasing surface tension (i.e. decreasing scale) is found. For the $d = 5\text{cm}$ case for example, the decrease in non-dimensional run-up height is approximately 10%.

Overtopping volumes with surface tension

Figure 11 shows the dimensionless overtopping predicted by our model for a solitary wave of amplitude $a = 0.7d$. Results for depths of 5cm, 10cm, 20cm and 50cm are shown alongside the result for no surface tension. Results for depth 2cm are not shown: at this scale surface tension restricted the formation of a jet too much for our overtopping model to be valid. For small dimensionless free-boards we see that the results coincide. At higher dimensionless free-boards the

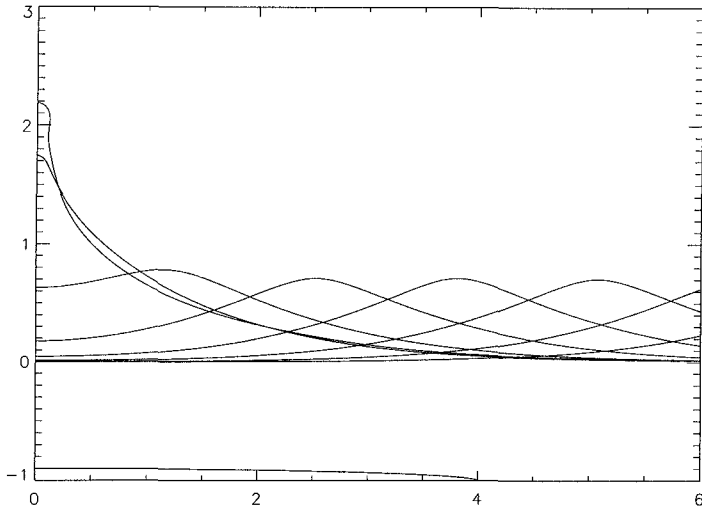


Figure 9: y/d against x/d at time up to maximum run-up for a solitary wave $a=0.7d$, $d=5\text{cm}$, berm width= $4d$, berm height= $0.1d$.

difference in jet shape shown in figure 10 is affecting overtopping volumes. At smaller scale (higher nondimensional surface tension values) the run-up height is less, and the average velocity towards the wall is reduced. Even for the calculation for $d=50\text{cm}$ there is a noticeable underprediction.

We can then see that even experiments carried out on depths of the order 20 to 50cm there is an underprediction at the upper limits of dimensionless free-board. For experiments where the incident wave is only 5-10cm relatively large underpredictions of overtopping volume and wave run-up can occur when scaling results back to full scale for use in breakwater design for $R/H > 2.6$. Of course here we are modelling only the non-breaking waves. More violent impacts produce jets beyond the scope of this simple model.

Figure 12 shows dimensionless overtopping for a wave on 5cm depth where the wave is steepened by a berm of width $4d$. As with no surface tension, wave steepening increases the strength of the jet produced. This can be seen in the trend towards a straight line for much of the range on figure 12 for higher berms. Without surface tension, overtopping is recorded for dimensionless crest free-boards of over 3.6, compared to only 2.85 with the corresponding 5cm calculation. It is clear then that extrapolating experimental results from such a small scale can give misleading values at high relative crest free-boards.

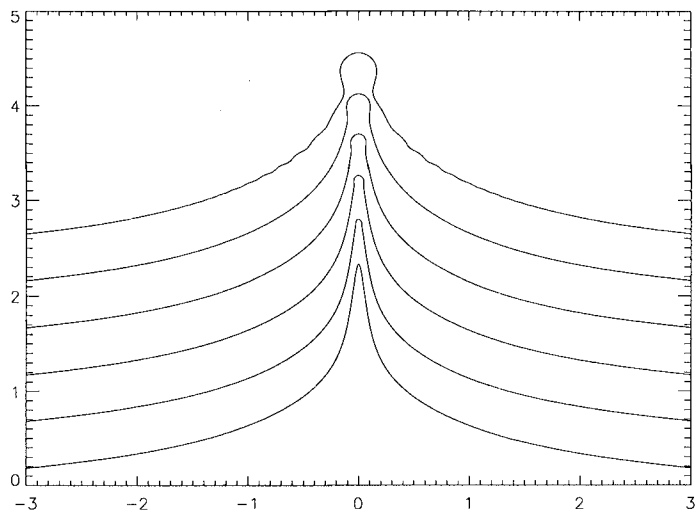


Figure 10: y/d against x/d at time of maximum run-up for a solitary wave $a = 0.7d$, for $d=2\text{cm}$, 5cm , 10cm , 20cm , 50cm and with no surface tension. (Surfaces have been shifted vertically for clarity).

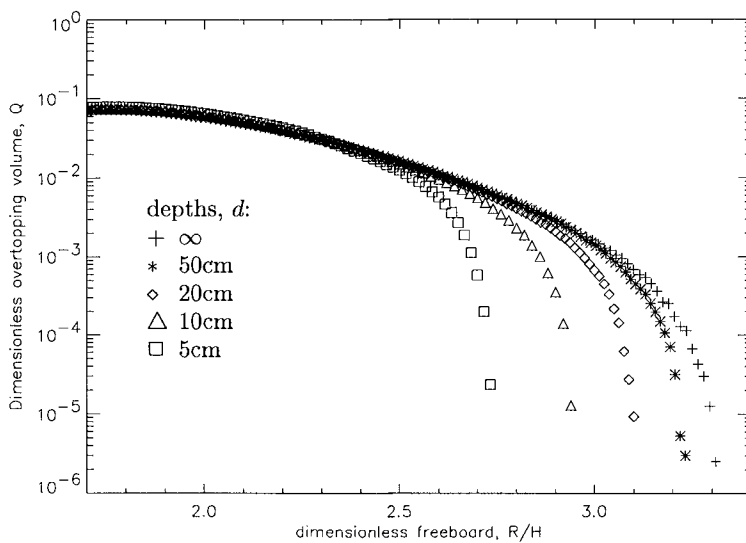


Figure 11: Dimensionless overtopping volume against dimensionless free-board for a solitary wave $a = 0.7d$, $d= 5\text{cm}$, 10cm , 20cm , 50cm and ∞ i.e. no surface tension.

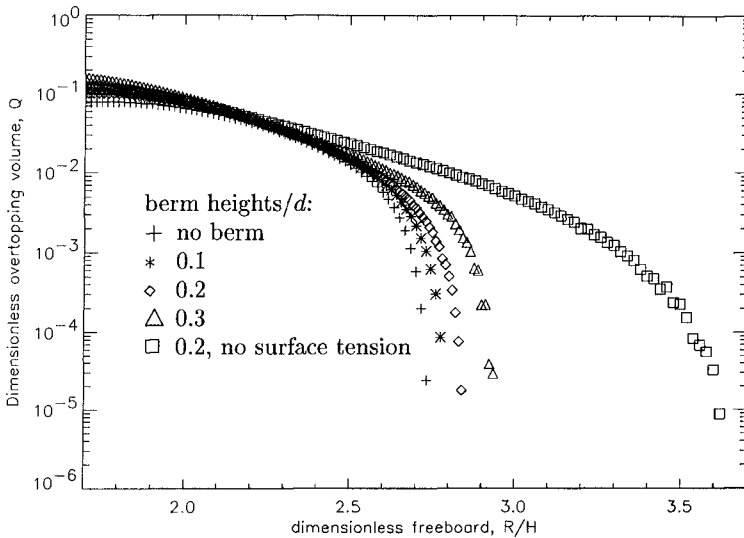


Figure 12: Dimensionless overtopping volume against dimensionless free-board on a berm of width $4d$ for a solitary wave $a = 0.7d$, for $d=5\text{cm}$ with surface tension.

Further work and conclusion

It appears that this simple theoretical approach gives plausible results for overtopping volumes per wave for non-breaking solitary waves. When strong jets are formed, particularly in calculations where the wave is steepened by interaction with a long berm, it is found that the overtopping volumes have a roughly exponential dependence on run-up for waves of a given height. Such an exponential relationship is similar to experimental results on overtopping rates (Franco, 1994, Juhl and Sloth, 1994, for example). The method predicts the same trends as previously reported in measurement of overtopping rates. A comparison of the results to measured overtopping volumes per wave is needed to validate the method however. Quantitatively, overtopping rates compare well with experimental results of Juhl (1995), allowing for the expected underprediction at high relative crest free boards.

From the results it appears that for the parameter range studied the short high berms decrease overtopping perhaps by interfering with the water motion near the wall, whereas wider berms steepen the incoming wave and make its encounter with the wall more violent and increase overtopping. Wide berms act to steepen the incident wave. In case where the flow was calculated up to the maximum run-up, wide berms tended to increase overtopping volume. Cases where the flow could not be computed up to the time of maximum run-up involved wave steepening often to the point of breaking before impact with the wall. In this case the likely impact pressures can be considerably higher (see Cooker 1990 for example). For the higher berms the shape of the jet can vary significantly, as can be seen in figure 6.

Wind can also play a role in overtopping. A wind force can break jets into spray above wall height. It can thus act to significantly increase or decrease overtopping, according to direction. Such a wind force could easily be incorporated into the simple mathematics of this overtopping model.

Most experiments are carried out at scales where surface tension plays a role in the jet dynamics. The effect of surface tension is generally not taken into account when extrapolating experimental results to full scale. Results here show that for overtopping rates that the effect of surface tension cannot be ignored for high crest free-boards. The action of surface tension on the tip of the jet leads to a considerable reduction in overtopping volume at relative crest free-boards greater than 2.6 for wave on depths up to the order of 20cm, and a corresponding reduction in non-dimensional run-up height. Since our model fits the most common mode of overtopping, we expect experimental results to be affected also, even though they generally include other modes of overtopping not covered here.

Acknowledgements

We acknowledge support from the U.K. Engineering and Physical Sciences Research Council and from the Commission of the European Communities, Directorate General for Science, Research and Development under MAST Contract MAS3-CT95-0041.

References

- COOKER, M. & PEREGRINE, D.H. (1990) A model for breaking wave impact pressures. *Proc. 22nd Int. Conf. Coastal Eng.* ASCE, Delft. 1473-1486.
- COOKER, M., PEREGRINE, D.H., VIDAL, C. & DOLD, J.W. (1990) The interaction between a solitary wave and a submerged semi-circular cylinder. *J.Fluid Mech.* **215**, 1-22.
- COOKER, M., WEIDMAN, P.D. & BALE, D.S. (1997) Reflection of a high amplitude solitary wave at a wall. *J.Fluid Mech.* to appear.
- DOLD, J.W. & PEREGRINE, D.H. (1986) An efficient boundary integral method for steep unsteady surface waves. *Numerical methods for fluid dynamics II*, (ed. Morton, K.W., Baines, M.J.) Oxford.U.P. 671-679.
- FRANCO, L. (1994) Further results of hydraulic model tests on wave overtopping: probability distribution of overtopping volumes per wave. *Proc. 2nd Workshop, Monolithic Coastal Structures Project, E.C. MAST 2, Milan.*
- JERVIS, M. (1996) Some effects of surface tension on water waves and water waves at a wall. *PhD. thesis.* University of Bristol.
- JUHL, J. & SLOTH, P. (1994) Wave overtopping of breakwater under oblique waves. *24th Int. Conf. on Coastal Eng.*, ASCE, Kobe.
- JUHL, J. (1995) Wave overtopping of vertical walls and the influence of wind. *Proc. Monolithic Coastal Structures Project, Final Workshop. E.C. MAST 2 Programme.*
- TANAKA, M. (1986) The stability of solitary waves. *Phys. Fluids.* **29** 650-655.

CHAPTER 171

Wind Effects on Runup and Overtopping of Coastal Structures

by Donald L. Ward¹, Assoc. Member, ASCE; Jun Zhang², Assoc. Member, ASCE;
Christopher G. Wibner³; and Charles M. Cinotto⁴

ABSTRACT

Effects of strong onshore winds on runup and overtopping of coastal revetments were studied in a wave flume with wind-generating capabilities. Runup and overtopping were measured during tests with onshore wind blowing over mechanically-generated waves. The addition of a constant wind over monochromatic waves added substantial energy to the wave field but the energy spectrum remained single peaked if the generated wave period was short (one second). These single-peaked incident spectra of the combined wind/wave tests were then reproduced mechanically using just the mechanical wave generator, with runup or overtopping again being measured. Runup and overtopping were both found to be considerably higher with similar incident spectra under the influence of onshore winds. Results are presented for a range of structure slopes, wind speeds, wave periods, and wave heights. Both smooth and rough revetments were tested.

¹Research Hydraulic Engineer. US Army Engineer Waterways Experiment Station CW-R, 3909 Halls Ferry Rd, Vicksburg, Mississippi 39180-6199, USA.

²Assoc. Professor. Texas A&M University, Mail Stop 3136, Ocean Engr. Program, Dept. of Civil Engr., College Station, Texas 77843-3136, USA.

³Engineer. Aker Omega, Inc., 11757 Katy Freeway, Suite 1300, Houston, TX 77079, USA.

⁴Graduate Student. Texas A&M University, Mail Stop 3136, Ocean Engr. Program, Dept. of Civil Engr., College Station, Texas 77843-3136, USA.

I. INTRODUCTION

Design storm conditions for coastal structures typically include strong onshore winds that play an obvious role in transport of splash and spray, and may have a significant effect on wave runup elevations and overtopping rates. Design for runup and overtopping on coastal structures, however, typically ignores wind effects. Traditionally, runup distances and overtopping rates have been calculated from empirical equations determined from series of small-scale physical model tests (e.g., Weggel 1976, Ahrens and Martin 1985, Ahrens and Heimbaugh 1988, de Waal and van der Meer 1992, Ward 1992, Yamamoto and Horikawa 1992, van der Meer and Janssen 1994) that were conducted in the absence of wind. Numerical models currently available for runup and overtopping also neglect effects of onshore winds (e.g., Kobayashi and Wurjanto 1989, Wurjanto and Kobayashi 1991, van der Meer et al. 1992, Kobayashi and Poff 1994).

Because of the importance of accurate estimates of runup heights and overtopping rates, the Coastal Engineering Research Center (CERC) of the US Army Engineer Waterways Experiment Station has initiated a joint research project with Texas A&M University (TAMU) to investigate effects of onshore winds on runup and overtopping of coastal structures. Using a wave flume with wind-generating capabilities at TAMU, a series of tests were conducted on model revetments using a range of structure slopes, incident wave conditions, and wind speeds. Runup elevations or overtopping rates were measured, along with changes in the incident wave spectra due to influence of the wind.

II. TEST FACILITY

The two-dimensional wind/wave flume at TAMU is a glass-walled flume 36.0-m-long by 0.6-m-wide and 0.9-m-deep (Figure 1). Wave generation was by a pair of Seasim Ltd. (presently Commercial Hydraulics) dry-back hinged-flap wavemakers. Wave generation was controlled by an IBM personal computer interfaced to the wavemaker through an analog output card using software developed at TAMU.

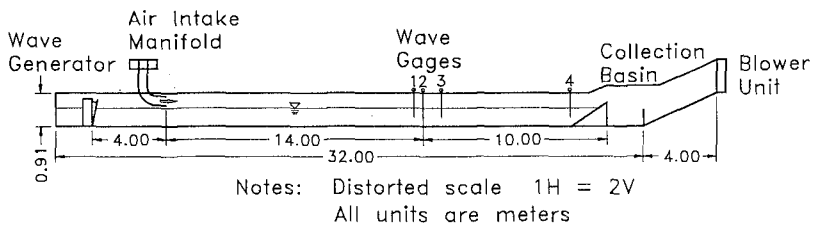


Figure 1. Wind/wave test facility at Texas A&M University

Wind generation was provided by an exhaust blower connected to the end of the flume away from the wavemakers. Air was pulled into the flume through a vertically-adjustable intake manifold equipped with horizontal vanes to help introduce a uniform flow field into the flume.

Runup tests were conducted on plywood test structures with slopes of 1:1.5 (V:H), 1:3, and 1:5. Each slope was tested both as a smooth slope and as a rough slope. Rough slopes replicated riprap revetments and were covered with a filter layer and two-layer-thick riprap armor layer designed in accordance with Engineering Manual EM 1110-2-1614, Design of Coastal Revetments, Seawalls, and Bulkheads (1995).

Data inputs included twin-rod resistance-type wave gauges, resistance-type and capacitance-type runup gauges on the test structures, and a three-cup anemometer for measuring wind speeds. In addition, visual observations of runup elevations were recorded, wind speeds were measured by a pitot-static tube connected to an oil-filled manometer with wind speeds being visually observed, and overtopping rates were determined by measuring water surface elevations in an overtopping basin located behind the test structures at the beginning and end of each test run.

III. TEST PROCEDURE AND RESULTS

A. Determination of Incident Wave Conditions

All tests were conducted with monochromatic waves produced in short bursts such that wave generation would cease before waves reflecting off the test structures could reach the wave board and contaminate the incident wave train. Selection of wave heights was limited by the capabilities of the wavemaker. Wind speeds selected were 50%, 75%, and 100% of blower capacity (providing wind speeds of 6.5 m/s, 12 m/s, and 16 m/s, respectively), as well as the no-wind condition. Tests were conducted at a constant depth of 0.5 m; all wave tests conducted were classified as intermediate waves.

To determine incident wave spectra under the influence of wind, a 1:5 plywood slope was placed in the flume and covered with a wave absorber comprised of several layers of rubber matting ("horse hair") to a thickness of approximately 30 cm near the toe and 23 cm near the crest. A wave gauge placed near the toe of the structure (26 m from the wavemaker) recorded the incident wave train. The method of Goda and Suzuki (1976) was used to examine the recorded signals from a set of wave gauges centered 23 m in front of the wavemaker to separate incident and reflected wave trains and confirm that reflection was minimal. Each of the test conditions was run with the wave-absorbing slope to establish incident wave

conditions. Energy spectra showing the effects of wind are given in Figure 2 for generated waves with a 1-sec period and wave heights of 5, 7, and 10 cm.

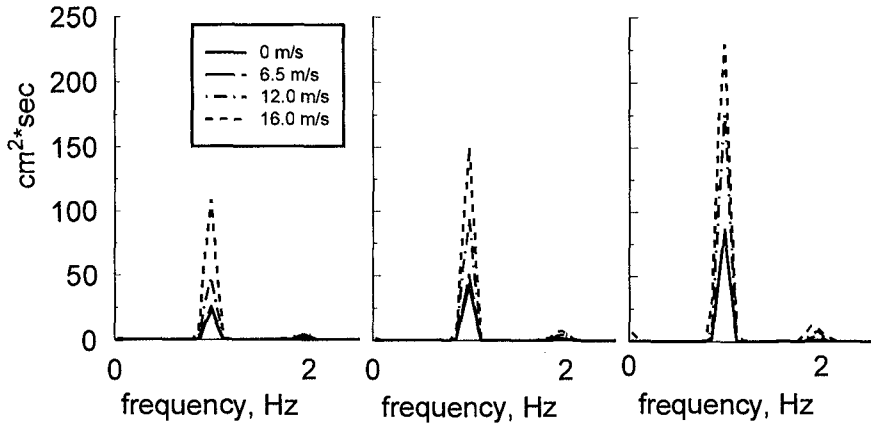


Figure 2. Wave energy growth for 1-sec mechanically-generated monochromatic waves of wave heights (left to right) 5 cm, 7 cm, and 10 cm.

During tests of wind-wave energy growth and tests to establish incident wave conditions for the combined wavemaker/wind generator tests, the amount of wind-induced setup at the revetment was measured. It was found that the wind-induced setup remained constant for each wind velocity, virtually independent of incident wave conditions or structure slope. Observed wind-induced setup elevations were 1 cm, 3 cm, and 5 cm for wind speeds of 6.5 m/s, 12 m/s, and 16 m/s, respectively.

The addition of wind energy to the generated wave train clearly adds energy to the wave spectrum. Earlier tests with mechanically-generated wave periods of 1.75 and 2.5 sec had demonstrated that the majority of the energy increase due to wind produced a second peak in the spectrum at a frequency of about 2 Hz. This second peak is missing in Figure 2 for wave spectra with mechanically-generated wave periods of 1.0 sec, where the additional energy is shown as an increase in the single peak of the mechanically-generated wave. There are two reasons the spectra of the one-second waves remain as a single peak. First, as the wind-wave field developed during the first several meters of fetch, the wind-wave field was characterized by a high-frequency, short wave length wave field. As the steep one-second mechanically-generated waves propagated down the wind-wave flume, high frequency wind waves were blocked at the forward face of the steep mechanical waves and the wind waves were not allowed to form. This phenomenon of capillary/gravity wave blockage was described by Phillips (1984), Shyu and Phillips (1990) and Zhang (1995). Phillips (1984) noted that while this phenomenon is not

of great significance in the field, it can significantly affect the wave spectrum in laboratory wind-wave flumes with short fetches.

The second factor restricting development of the second peak in the wave spectra was the significant growth of the mechanically-generated waves due to modulation of the air pressure field. Because the crests of the large mechanically-generated waves were closer to the top of the flume than were the troughs, airflow was constricted by the reduction in cross-sectional area above the crests, resulting in higher local wind velocities at the crests. The opposite, of course, was true at the troughs. This modulation of wind velocities resulted in modulation of the air pressure field according to the Bernoulli equation. The modulated air pressures were in phase with the mechanically-generated waves and led to the growth of the mechanically-generated waves. The modulation of air pressure was not as significant for the longer wave lengths due to the smaller heights used due to limitations of the wave generator.

B. Runup Tests

For the runup tests, the wave-absorbing slope was removed and test slopes of 1:1.5, 1:3, and 1:5 were installed. Each slope was tested both as a smooth slope and built as a typical riprap revetment.

As was seen in Figure 2, the addition of wind to a mechanically-generated wave period of 1 sec remained as a single-peaked spectrum. For these single-peaked cases, it is possible to determine wind effects on runup by mechanically reproducing the combined wind/wave spectra. That is, the stroke of the wave generator can be increased to produce a similar spectrum to that obtained by a lesser stroke under the influence of wind.

Figure 3 plots runup on smooth slopes of 1:1.5, 1:3, and 1:5; Figures 4 plots runup on rough slopes. In both Figures 3 and 4, the abscissa is significant wave height (average of one-third highest waves) recorded near the structure toe, regardless of the height of the mechanically-generated wave. The ordinate is "equivalent" runup, that is, maximum runup adjusted for the increase in still water level due to wind setup. Symbols used in the figures indicate wind velocity used during each test. Figures 3 and 4 clearly illustrate the wind effects: for waves of similar wave height, the runup is considerably greater when the wave height is obtained by a small mechanically-generated wave plus influence of a strong wind, than when the wave height is purely mechanically driven (in the absence of wind).

Overtopping occurred in all tests conducted on the smooth 1:1.5 slope with wind speeds of 12 m/s and 16 m/s, and on the smooth 1:3 slope with wind speeds of 16 m/s and all but one test at 12 m/s. If overtopping occurred, maximum runup is not defined and no data are presented in the figures. On tests with smooth slopes

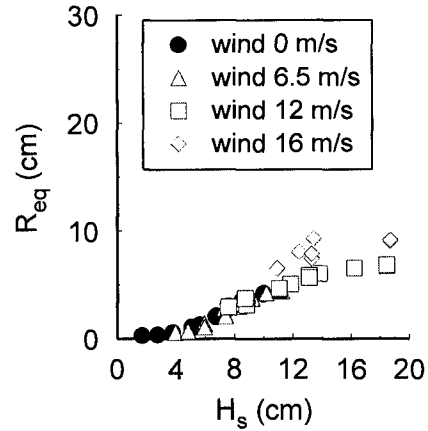
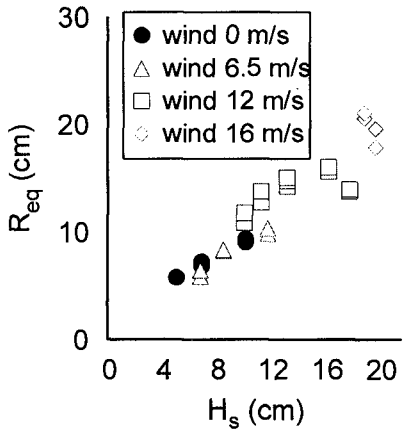
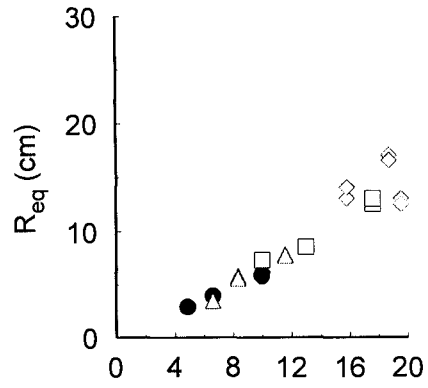
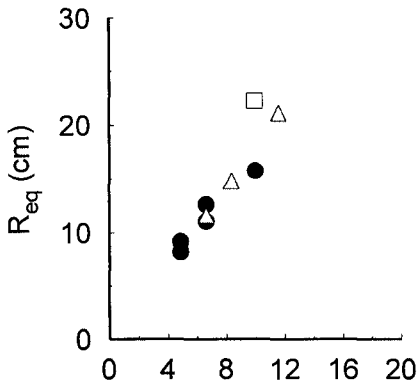
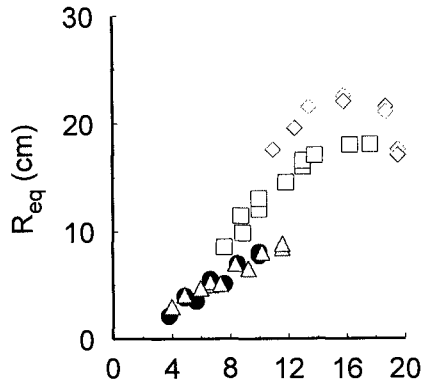
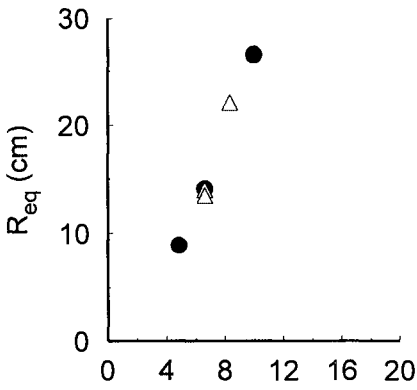


Figure 3. Runup elevations for (top to bottom) 1:1.5, 1:3, and 1:5 smooth slopes.

Figure 4. Runup elevations for (top to bottom) 1:1.5, 1:3, and 1:5 rough slopes.

(Figure 3) and rough slopes (Figure 4), the 6.5 m/s wind is seen to have negligible effect on runup elevations. Wind speeds of 12 m/s and 16 m/s cause significant increases in runup elevations on the smooth slopes, and on the rough 1:1.5 slope. For flatter rough slopes, the 12 m/s wind has little effect and only the 16 m/s wind significantly increases runup elevations.

Runup under the influence of the 12 m/sec wind and 16 m/sec wind is seen to increase linearly with incident wave height, then the runup tapers off or even decreases with increasing incident wave height. This is due to wave breaking under the influence of the wind prior to the wave reaching the test structure.

C. Overtopping Tests

In cases where the crest elevation was lower than the wave runup, overtopping was collected and measured in a basin behind the revetment. Different crest elevations on the revetment were tested, therefore a given incident wave condition may appear both in the runup figures (high crest elevation) and in the overtopping data (lower crest elevation).

Figure 5 plots overtopping on smooth slopes of 1:1.5, 1:3, and 1:5. The abscissa is "equivalent" crest elevation (crest elevation adjusted for wind-induced setup) divided by significant wave height measured near the structure toe. Ordinate of the

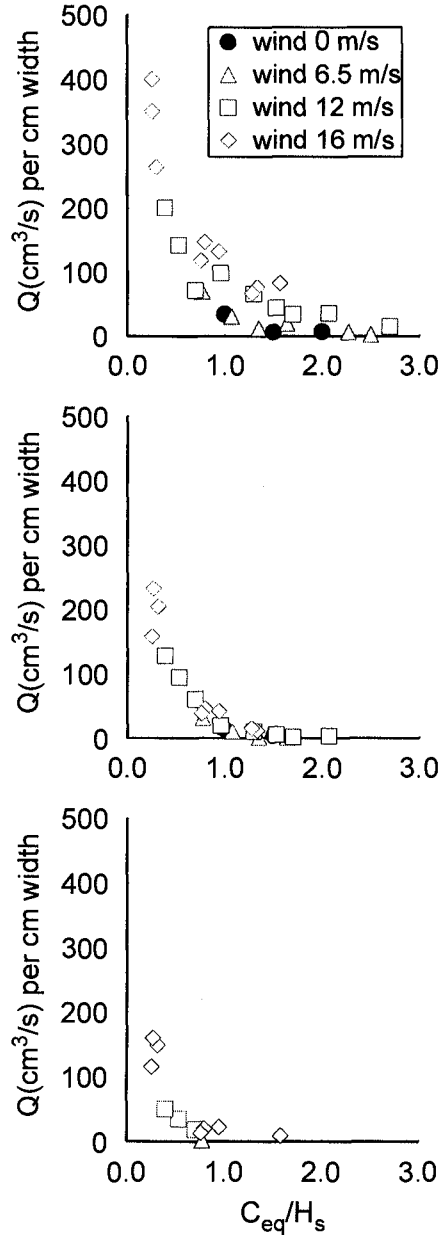


Figure 5. Overtopping tests for (top to bottom) 1:1.5, 1:3, and 1:5 smooth slopes.

figure is overtopping rate per cm of revetment width.

Overtopping results were similar to the runup results: higher wind speeds produced higher overtopping for similar wave heights, and wind effects were more pronounced on steeper slopes.

For no-wind conditions, measurable overtopping was only obtained on the smooth 1:1.5 slope and 1:3 slope. On the smooth 1:1.5 slope, winds of 6.5 m/s are seen to have negligible effect over the no-wind tests, but winds of 12 m/s and 16 m/s produced significant increases in overtopping rates. On the smooth 1:3 slope, winds of 6.5 m/s and 12 m/s appear to have little effect on overtopping rates, and only the 16 m/s winds show an appreciable effect.

IV. DISCUSSION

Physical model studies of prototype locations will typically reproduce certain parameters of a design storm wave environment, but do not reproduce storm winds associated with the design storm. Selected design storm wave heights are reproduced in a wave flume by a mechanical wave generator in the absence of wind. The study reported herein examines the effects on wave runup elevation and overtopping rates of reproducing a given wave height by purely mechanical means and failing to include the associated onshore winds.

Strong onshore winds have been shown to produce appreciably higher wave runup elevations and overtopping rates for waves of similar heights at the structure toes. Wind speeds of 6.5 m/s (23 km/hr) showed little effect on runup or overtopping, but wind speeds of 12 m/s (43 km/hr) and higher greatly increased both runup and overtopping. The significance of the wind effects, however, requires a consideration of the scaling effects involved.

Wind effects on runup and overtopping include wind energy input into the wave energy spectrum and wind induced setup. Both of these factors have been fully accounted for in the study reported herein. However, mechanically reproducing a wind/wave spectrum does not necessarily reproduce the *shape* of the individual waves. Different wave shapes due to wind forces acting on the waves, and changes in wave breaking due to wind effects, may change the wave kinematics at the structure causing the observed increases in runup and overtopping. Additionally, wind effects on the wave upwash on the structure slope may affect runup not only by helping “push” the upwash up the slope but possibly by reducing the effects of downwash on the subsequent wave. Wind advection of splash and spray has an obvious affect on overtopping rates. Each of these factors is currently being further studied.

V. ACKNOWLEDGEMENT

The testing program reported herein is funded by the U.S. Army Corps of Engineers, and the authors gratefully acknowledge this support. Permission to publish this paper was granted by the Office, Chief of Engineers.

APPENDIX: References

- Ahrens, J.P., and Heimbaugh, M.S. 1988. "Approximate upper limit of irregular wave runup on riprap," Technical Report CERC-88-5, U.S. Army Engineer Waterways Experiment Station, Vicksburg, Mississippi.
- Ahrens, J.P., and Martin, F.T. 1985. "Wave run-up formulas for smooth slopes," *J. Waterway, Port, Coast. and Oc. Engrg.*, ASCE, 111(1), 128-133.
- de Waal, J.P., and van der Meer, J.W. 1992. "Wave runup and overtopping on coastal structures," *Proc. 23rd Coastal Engr. Conf.*, Venice, Italy, ASCE.
- Goda, Y., and Suzuki, T. 1976. "Estimation of incident and reflected waves in random wave experiments," *Proc. 15th Coast. Engr. Conf.*, Honolulu, Hawaii, ASCE.
- Kobayashi, N., and Poff, M.T. 1994. "Numerical model RBREAK2 for random waves on impermeable coastal structures and beaches," Research Report No. CACR-94-12, Center for Applied Coastal Research, Univ. of Delaware, Newark, Delaware.
- Kobayashi, N., and Wurjanto, A. 1989. "Numerical model for design of impermeable coastal structures," Research Report No. CE-89-75, Center for Applied Coastal Research, Univ. of Delaware, Newark, Delaware.
- Phillips, O.M. 1984. "The dispersion of short wavelets in the presence of a dominant long wave," *J. Fluid Mech.*, 107, 465-485.
- Shyu, J.H., and Phillips, O.M. 1990. "The blockage of gravity and capillary waves by longer waves and currents," *J. Fluid Mech.*, 217, 115-141.
- U.S. Army Engineer Coastal Engineering Research Center. 1985. *Design of Coastal Revetments, Seawalls, and Bulkheads*. Engineering Manual 1110-2-1614, U.S. Government Printing Office, Washington, D.C.

- van der Meer, J.W., and Janssen, J.P.F.M. 1994. "Wave run-up and wave overtopping at dikes and revetments," Publication No. 454, Delft Hydraulics, Delft, The Netherlands.
- van der Meer, J.W., Petit, H.A.H., van den Bosch, P., Klopman, G., and Broekens, R.D. 1992. "Numerical simulation of wave motion on and in coastal structures," *Proc. 23rd Coast. Engrg. Conf.*, Venice, Italy, ASCE.
- Ward, D.L. 1992. "Prediction of overtopping rates for irregular waves on riprap revetments," Miscellaneous Paper CERC-92-4, U.S. Army Engineer Waterways Experiment Station, Vicksburg, Mississippi.
- Ward, D.L., Wibner, C.G., Zhang, J., and Edge, B. 1994. "Wind effects on runup and overtopping," *Proc. 24th Coast. Engrg. Conf.*, Kobe, Japan, ASCE, 1687-1699.
- Weggel, J.R. 1976. "Wave overtopping equation," *Proc. 15th Coast. Engrg. Conf.*, Honolulu, Hawaii, ASCE, 3, 2737-2755.
- Wurjanto, A., and Kobayashi, N. 1991. "Numerical model for random waves on impermeable coastal structures and beaches," Research Report No. CACR-91-05, Center for Applied Coastal Research, Univ. of Delaware, Newark, Delaware.
- Yamamoto, Y., and Horikawa, K. 1992. "New methods to evaluate run-up height and wave overtopping rate," *Proc. 23rd Coastal Engr. Conf.*, Venice, Italy, ASCE.
- Zhang, X. 1995. "Capillary-gravity and capillary waves generated in a wind wave tank: observations and theories," *J. Fluid. Mech.*, 289, 51-82.

CHAPTER 172

Wave Overtopping of Vertical Structures including Wind Effect

Johannes P. de Waal¹, Patrick Tönjes², Jentsje W. van der Meer³

ABSTRACT

The influence of both wave breaking and wind on the wave overtopping discharge of vertical sea-walls were assessed. In a qualitative way the influences of wave breaking agreed with the trends as pointed out by Goda (1985). The influence of wind on overtopping appears to be only relevant in specific conditions related to wave breaking. Even in these conditions the influence appeared to be smaller than expected.

1 INTRODUCTION

Intuitively, the influence of wind on wave overtopping is regarded to be relevant, but it is not clear to what extent. There are several types of possible wind influences. In this study the possible influence of wind on wave overtopping was subdivided as follows:

- Wind may cause overtopping of the part of the breaker spray which would have fallen back into the sea in a situation without wind;
- Wind may cause the breaker type to change by deforming the incident waves;
- Wind may cause overtopping by so-called "basic" spray, that is, spray which is generated by the wind at open sea.

Wind influence on the water level at the structure is assumed to be accounted for in the assessment of the design water level. A problem which is closely linked to the different (though coupled) wind influences is the measurability, especially the appropriate interpretation of measurements in a small scale model.

¹Project engineer, Rijkswaterstaat, Institute for Inland Water Management and Waste Water Treatment RIZA, PO Box 17, 8200 AA Lelystad, The Netherlands (formerly project engineer at Delft Hydraulics)

²Project manager, Rijkswaterstaat, Road and Hydraulic Engineering Division, PO Box 5044, 2600 GA Delft, The Netherlands

³Manager and senior engineer, Delft Hydraulics, PO Box 177, 2600 MH Delft, The Netherlands

2 SET-UP OF THE INVESTIGATION

Due to the large number of relevant parameters and the very complex water motion at the structure, a theoretical approach to the wave overtopping problem is hardly feasible. Therefore, it was decided to perform physical model tests in a wave flume in order to develop a set of empirical formulae for overtopping. However, in a physical scale model one should be aware of the following scale effects:

- Water drops in the air are not to scale: they are far too big in the model.
- The drop transport capacity of wind is not known.
- The influence of wind on the wave-form depends on the shear stress on the water surface, therefore the shear velocity of the wind should be to scale.
- The "flip-through" breaker type (see Section 4.4) probably occurs more often than in prototype, because the air entrainment is not to scale. At this point also the salinity of water is of significance, which makes the problem very complicated.

Due to these scale effects the three possible wind influences could not be modelled at one time in a physical scale model. For this reason, it was decided to focus the physical model investigation on an accurate modelling of the influence of wind on the breaker-spray transport only. The other two wind effects were studied theoretically.

The following basic dimensionless parameters are identified:

$$\text{Mean overtopping discharge} \quad Q = q/\sqrt{gH_{os}^3} \quad (2.1)$$

$$\text{Relative crest height} \quad R = R_c/H_{os} \quad (2.2)$$

$$\text{Wave steepness} \quad S = H_{os}/L_{op} \quad (2.3)$$

$$\text{Relative local water depth} \quad D = d_t/H_{os} \quad (2.4)$$

With:

g	= acceleration due to gravity (= 9.81)	(m/s ²)
d_t	= water depth at the structure	(m)
H_{os}	= significant wave height at deep water	(m)
L_{op}	= wave length in deep water, based on T_p	(m)
q	= average overtopping discharge per metre structure width	(m ² /s)
R_c	= crest level with respect to SWL	(m)
T_p	= wave period at the peak of the spectrum	(s)

These dimensionless parameters will provide a basis both for the set-up of test programmes and for the development of (empirical) overtopping formulae. A generally applicable form of the wave overtopping formula is the basic relationship between the dimensionless overtopping discharge Q and the relative

crest height R:

$$Q = c_1 \exp(c_2 R) \quad (2.5)$$

The coefficients c_1 and c_2 are also dimensionless and may be dependent upon all parameters except Q and R. A common way to present a measured or computed relationship between Q and R is a plot of $\log(Q)$ (or Q on a logarithmic scale) against R. Formula (2.5) implies that this type of presentation yields a straight line. In some other approaches the lines are curved very slightly downward, as indicated by Battjes (1974, for slopes) and Goda (1985, for vertical walls). However, the proposed straight line has proven to be a very good approximation and is fairly comfortable in computations.

The wave height H_{os} is very important in the basic overtopping formula and should be accurately assessed. If overtopping data are available in which the value of the wave height is uncertain within a band between plus and minus 10%, then the overtopping data lie within a band of which the maximum values are 3 to 6 times the minimum values, even when all other measured parameters are exact!

3 ANALYSIS OF GODA'S GRAPHS

Goda (1985) presents six separate graphs for wave overtopping of a vertical wall at specific combinations of the foreshore slope and the wave steepness. Compared with other information on wave overtopping in literature these graphs have proven to be very well applicable. The dimensionless overtopping discharge is plotted on a logarithmic scale against the relative local water depth, identifying lines for constant values of the relative crest height. Note the small difference between the definition of the dimensionless overtopping discharge used by Goda and the one used in this paper:

$$\text{Goda: } Q^* = q/\sqrt{2gH_{os}^3}; \quad \text{this paper: } Q = q/\sqrt{gH_{os}^3}$$

The information in the graphs was tabulated for $D \geq 1.0$. This table provided the opportunity to analyze the influences of the relative crest height R, the local water depth D, the wave steepness S and the foreshore slope $\cot\alpha_f$ on the dimensionless overtopping discharge Q. These aspects are discussed below in a qualitative way.

For constant values of $\cot\alpha_f$, S and D the relation between Q and R is well approximated by an exponential relation. A linear regression analysis has yielded the coefficients c_1 and c_2 . The value of c_1 appeared to be almost independent of $\cot\alpha_f$, S and D: $c_1 \approx 0.045$. This result proves to be very convenient, because the analysis of Goda's graphs may now be restricted to c_2 as a function of $\cot\alpha_f$, S and D. The optimum values of c_2 have been calculated again, but now with the assumption that $c_1 = 0.045$. The resulting c_2 -values have been plotted against D, identifying the different combinations of S and $\cot\alpha_f$, see

Figure 1.

In this Figure the following trends may be identified:

- The influence of S and D are approximately independent of $\cot\alpha_f$ if $D > 3.0$. In other words: the influence of the foreshore slope on wave overtopping is negligible for relatively deep water. This seems quite reasonable.
- If $1.0 \leq D < 3.0$, the c_2 -values (read: overtopping discharges) for $\cot\alpha_f = 10$ are greater than those for $\cot\alpha_f = 30$. This also seems reasonable because at a steeper foreshore the waves have less time and space for breaking. For milder foreshore slopes more wave energy is lost on the foreshore before the waves reach the wall.
- With increasing D the c_2 -values decrease. This is probably caused by the decreasing peakedness of the wave crests, but this effect is intuitively expected to be smaller than Goda's graphs suggest.
- The influence of S decreases with an increasing D . However, even at very deep water this influence seems fairly significant in Goda's graphs, whereas the influence of the wave steepness is expected to vanish at already intermediate relative water depths.

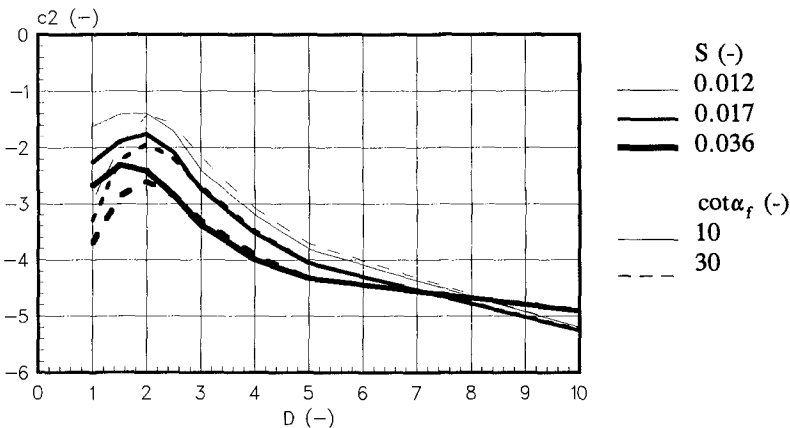


Figure 1. Influence of wave steepness, relative water depth and foreshore slope

4 TESTS ON THE INFLUENCE OF BREAKER SPRAY TRANSPORT

4.1 Model set-up

The objective of this model investigation was to assess the maximum possible influence wind can have on the mean wave overtopping discharge. The experiments were carried out in the Scheldt Flume of DELFT HYDRAULICS, De Voorst location in October 1993.

The foreshore was 8 m long and had a slope of 1:20. The vertical structure was 0.40 or 0.60 m high and had a sharp crest. Five vertical plates were installed perpendicularly to the structure in order to prevent or reduce transverse

oscillations in the flume. In order to prevent the loss of spray out of the flume the side walls of the flume were heightened after which a sort of a tunnel was created by covering this part of the flume with a horizontal board.

Scale effects in the total volume of water rising above the crest are intuitively considered to be small and the essential assumption in this investigation is that these scale effects may be neglected. In the second half of the test programme all spray rising above the crest was mechanically transported over the crest by means of a rotating paddle wheel, whose dimensions are presented in Figure 2. The optimum rotation speed is the maximum speed at which there is still enough time for all the water collected by a paddle to drain from the paddle and be collected behind the crest. This rotation speed appeared to be 21.4 revolutions per minute, which implied that the average number of strokes (paddles passing the crest) was 4.3 per second.

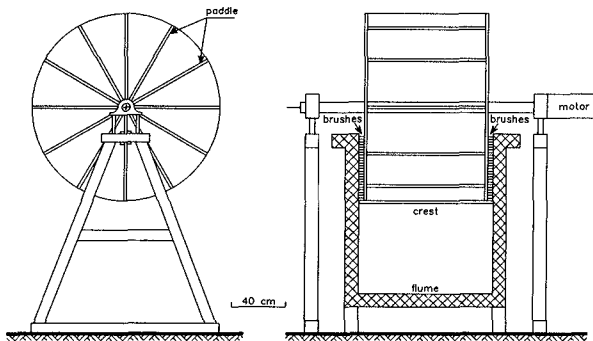


Figure 2. Paddle wheel for mechanical breaker spray transport

Irregular waves were generated according to a JONSWAP spectrum. Two wave gauges at deep water were used for the wave analysis. The signals of the wave gauges were sampled at 25 Hz. The test duration was 30 minutes.

The wave overtopping was characterized by the average overtopping discharge only. The storage capacity of the reservoir was about 300 litres. In addition, pumps with a constant discharge were used at intervals when this was necessary in order to prevent the reservoir from overflowing. The total pumping time was measured with a stopwatch. A water level gauge was installed at the reservoir for the measurement of water levels before and after each test.

The test programme consisted of two series. In the first series the overtopping was measured without the paddle wheel. Table 1 presents the target values of the dimensionless parameters. However, not all the possible combinations were tested. The first test series consisted of 18 tests. After installation of the paddle wheel this series was repeated, yielding the second test series. During the four tests with $D = 1.5$, video recordings of the water motion at the structure and of the performance of the paddle wheel were made.

Parameter	Notation	Values in test programme
Relative local water depth	D	1.0 1.5 2.0 3.0
Relative crest height	R	1.4 1.7 2.0 2.3
Wave steepness	S	0.02 0.04

Table 1. Target values of dimensionless parameters in overtopping tests

4.2 Analysis method

In order to describe the influence of a specific dimensionless parameter, such a parameter should have been varied while keeping all other relevant dimensionless parameters unchanged. Although the test programme was set up to account for such series, the actually measured wave conditions were not exactly equal to the desired values. Interpolation techniques were applied in order to obtain representative test results at the target values of the dimensionless test conditions.

For the quantitative analysis of the influence of spray transport we introduced a so-called "spray transport factor" W_s , defined as:

$$W_s = \frac{Q_{\text{with spray transport}}}{Q_{\text{without spray transport}}} \quad (4.1)$$

W_s is calculated on the basis of the test results at the target values of the dimensionless parameters.

In the analysis the definition of the significant incident wave height was based on spectral analysis. The incident and reflected wave energy (m_{oi} and m_{or}) were calculated from a cross-spectrum analysis of the recordings of the two wave gauges. The significant incident wave height was defined as:

$$H_{os} = 4\sqrt{m_{oi}} \quad (4.2)$$

4.3 Observations during tests

The water motion at the structure and the process of wave overtopping vary strongly, even during a single test:

- Ordinary overtopping occurs when the crest of a standing wave reaches higher than the crest of the structure: so-called "green water" flows over the crest.
- Collision of a steep wave crest with the wall results in an upward accelerating compact body of water, which spurts up moderately high and almost completely overtops the crest.
- When air entrainment at the wall is about to occur, the collision of the wave crest with the wall will result in a so-called "flip-through". The sound of the collision is still more like "zip" instead of a bang. A thin water sheet spurts up extremely high, almost vertically. The water sheet rapidly disperses into drops. About half of the upspurting water volume falls back into the flume.

- Wave slamming together with a loud bang will occur when a wave crest hits the wall about horizontally and some air is entrained. The water spurts up high, in big drops, in a great variety of directions.
- When the wave crest tip is already moving downward as it collides with the wall and much air is entrained, there is no clear "bang" heard any more. There is a lot of turbulence and the water spurts up chaotically and moderately high.
- When the wave is already broken as it reaches the wall almost no "bang" will be heard any more, partially due to the fact that the breaking wave itself already produces noise. The water does not spurt up very high and most of the big drops fall back into the flume.

The sequence of the phenomena described above corresponds with the transition from relatively deep local water to relatively shallow local water at the structure. In a single test with irregular waves this development corresponds with the transition from relatively small waves to relatively large waves. In tests with an intermediate relative local water depth ($D = 1.5$ to 2.0) this whole variation of phenomena could be observed.

The effectiveness of the mechanical spray transport was assessed by means of extensive visual inspections during the tests. These inspections led to the estimation that at least 90% of the volume of water which should have been transported by the paddles actually was transported. (Of course one can see some water falling back into the flume but it is very hard to conclude whether or not this water actually had risen higher than the crest). This estimated effectiveness is considered to be amply sufficient for this investigation.

4.4 Tests results

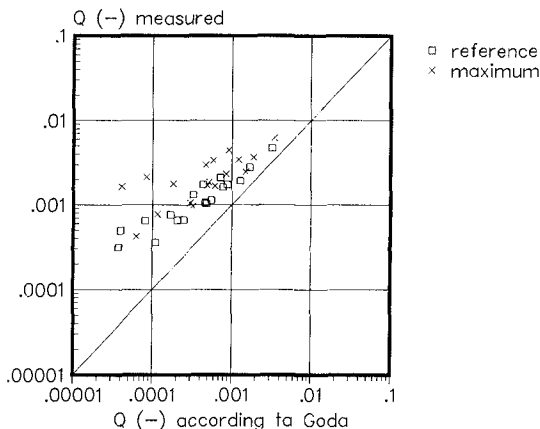


Figure 3. Comparison of test results with values based on Goda's graphs

Figure 3 shows the comparison between the measured overtopping and the calculated overtopping on the basis of Goda's graphs. The calculated values were

based on the measured hydraulic conditions. Most of the measured overtopping discharges appear to be considerably greater than the values according to Goda's lines.

The results for tests without spray transport are presented in Figure 4 and 5.

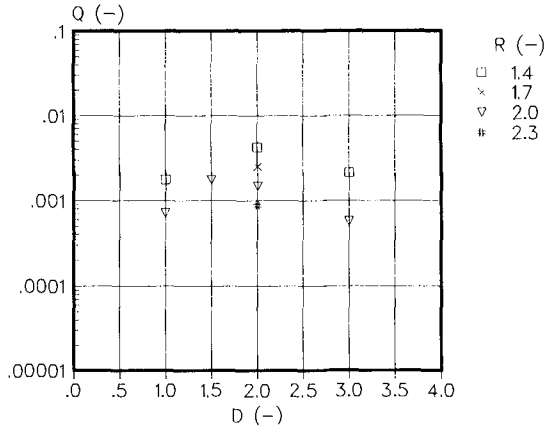


Figure 4. Influence of relative local water depth and relative crest height without mechanical breaker spray transport for $S = 0.02$

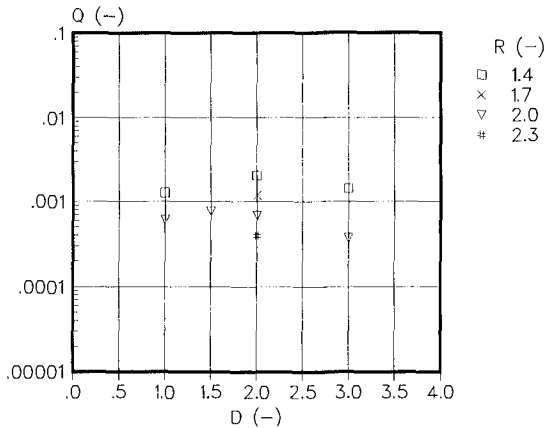


Figure 5. Influence of relative local water depth and relative crest height without mechanical breaker spray transport for $S = 0.04$

From these Figures the following conclusions may be drawn:

- The overtopping discharge clearly decreases with an increasing relative crest height. The four measurement points from the test series with $D = 2.0$ are at equidistant positions. This confirms the assumed linear relationship between $\log(Q)$ and R for tests without spray transport. (From a closer analysis it is concluded that the c_1 and c_2 values are not constant for the different values of

- D. The c_1 values may be approximated by a single constant of about 0.050 for $D = 2$, which agrees with the value based on Goda's graphs, but for $D = 1$ the measurements show a different tendency.)
- The overtopping decreases with increasing wave steepness, which agrees with Goda's graphs. This influence is the most obvious for tests with $D = 2.0$.
 - The overtopping discharge seems to reach a maximum at $D = 1.5$ to 2.0 , which agrees with Goda's graphs. For $S = 0.02$ this maximum is clearer than for $S = 0.04$.

Figure 6 and 7 show the results for the spray transport factor.

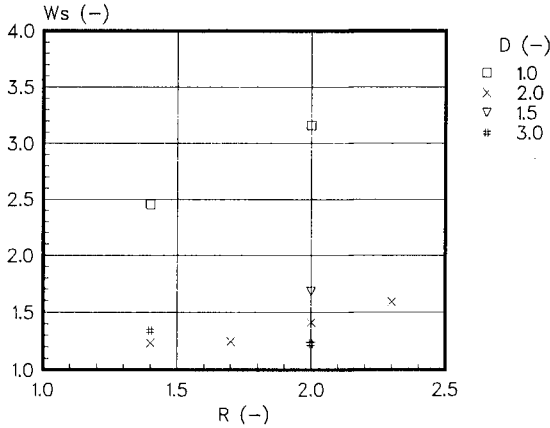


Figure 6. Measured spray transport factor for $S = 0.02$

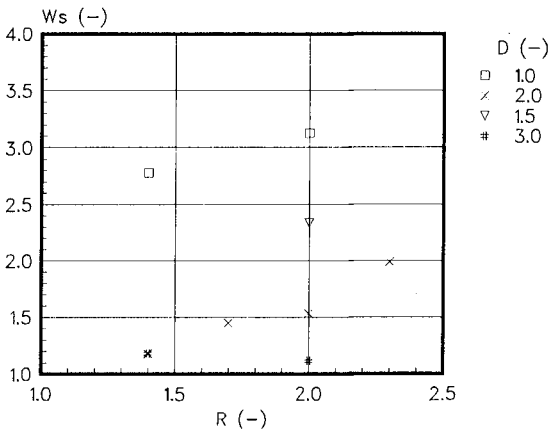


Figure 7. Measured spray transport factor for $S = 0.04$

All tests with spray transport resulted in more overtopping than the corresponding tests without spray transport ($W_s > 1$). This seems a trivial conclusion, but a greater scatter in the measurement results could have caused less

consistency. The maximum value of the spray transport factor was about 3.2. The overtopping discharge in tests with spray transport still decreased with an increasing relative crest height, but the linear relationship between $\log(Q)$ and R appeared to be no longer valid.

From Figure 6 and 7 it may be concluded that the influence of spray transport increases with increasing relative crest height. This may be explained by the fact that the horizontal velocity of the water rising above the crest is smaller for a higher crest. This implies that for a higher crest a larger portion of the water falls back into the flume and the effect of spray transport may therefore be larger.

The spray transport factor sharply decreases with increasing relative local water depth. The explanation of this trend is similar to the explanation of the relative crest height influence. In shallower water, more waves have already broken when they reach the structure. The spray, resulting from collision of broken (or breaking) waves and the wall, has a great variety of directions. A relatively large portion of the water volume (spray) rising above the crest of the structure falls back into the flume. The influence of spray transport is considerable.

A comparison between Figure 6 and 7 leads to the conclusion that the influence of spray transport hardly depends on the wave steepness. In only a few tests the spray transport factor appears to be greater for the steeper waves.

5 INFLUENCE OF WIND ON WAVE OVERTOPPING

5.1 Additional breaker-spray transport due to wind

The physical model investigation has yielded fairly accurate quantitative information about the maximum additional breaker-spray transport due to wind. The upper limit of this wind occurs for breaking or broken waves and appears to be about 3 times the overtopping discharge for a vertical wall without wind. This factor may be regarded to be relatively small; it is of the same order as the scatter in overtopping data from other investigations. Therefore, the assessment of the relation between the actual wind speed and the additional portion of transported breaker spray is not considered to be very useful. The relatively small factor also implies that the error in past investigations due to the absence of additional spray transport was small.

5.2 Influence of wind on the wave breaker type

The effect of wind on the wave height at the structure should be accounted for in the substitution of the significant wave height term in the overtopping formula. However, wind may also change both the wave shape and the wave breaker type at the structure. As yet, there are no computation methods to assess this effect. Qualitatively, the influence of onshore wind on wave breaking can be summarized as follows (Douglass, 1989):

- Waves tend to break earlier (in deeper water).
- The type of wave breaking tends towards a spilling breaker type.

Douglass (1989) discusses only waves breaking on a mild slope, such as a beach. By a first approximation, the above tendencies may also be assumed to be valid for a mild slope ending in a vertical wall. However, the wave reflection with a vertical wall differs completely from that without a wall. The influence of wave reflection on the wave deformation by wind may be significant but is as yet unknown.

The wind effects on wave breaking are similar to the influences of a decrease in local water depth together with a decrease in foreshore slope. A decrease in local water depth causes the wave-breaking location to change: a decrease in foreshore slope the wave breaker type to change. This implies that an approximation of the influence of wind on wave breaking may consist of a reduction in both the local water depth and the foreshore slope in the overtopping formulae. This approximation is first roughly quantified and substituted afterwards into the overtopping formula.

On the basis of information from literature, Douglass suggests that the water particle velocity in the wave crest be increased by 3% of the wind speed to account for the onshore wind. The wave is assumed to break as soon as this water particle velocity exceeds the wave phase velocity. The reduction of the water depth at which wave breaking occurs may be approximated by:

$$\frac{d_b \text{ (with wind)}}{d_b \text{ (without wind)}} = \left(1 + 0.03 \frac{u_{a,10}}{\sqrt{g d_b}}\right)^2 \quad (5.1)$$

with:

$$\begin{aligned} d_b &= \text{water depth at which wave breaking occurs} \quad (\text{m}) \\ u_{a,10} &= \text{wind speed at 10 m height} \quad (\text{m/s}) \end{aligned}$$

For a numerical example of this wind effect a situation is considered in which waves break at a water depth of 5.0 to 10.0 m if there is no wind. Now a heavy onshore storm is considered in which the wind speed reaches 30 m/s. From Equation (5.1) it is concluded that the wind effect causes the same waves to break in 1.27 to 1.19 times deeper water than without wind. This change in location of wave breaking would also be caused by a reduction in water depth by about 20%.

The wave breaker type is characterized by the breaker parameter ξ_{op} , which is in this case determined by the slope of the foreshore instead of the slope of the structure:

$$\xi_{op} = \tan \alpha_f / \sqrt{S} \quad (5.2)$$

However, the type of wave breaking is very difficult to quantify and the

influence of wind on the breaker type is only qualitatively described. For a first indication, the influence of wind on the breaker type is approximated arbitrarily by a reduction in foreshore slope by 20%. This effectively decreases the value of the breaker parameter, thereby representing a transition towards a more spilling breaker type. In view of this arbitrary decision, the small influence of the reduction of the foreshore slope on the wave-breaking location has been neglected.

In order to estimate the order of magnitude of this wind effect on overtopping the influence of the representative changes in the foreshore on overtopping is assessed using Goda's lines. Figure 8 presents the wave-deformation factor due to wind, defined as:

$$W_d = \frac{Q_{\text{with wave deformation due to wind}}}{Q_{\text{without wind}}} \quad (5.3)$$

From this Figure it can be concluded that due to this wind effect, the overtopping discharge increases by a factor of about 3.0 for a relatively high crest and an intermediate relative local water depth ($D \approx 3$). On the other hand, the overtopping discharge decreases for a smaller relative local water depth ($1 \leq D \leq 2$).

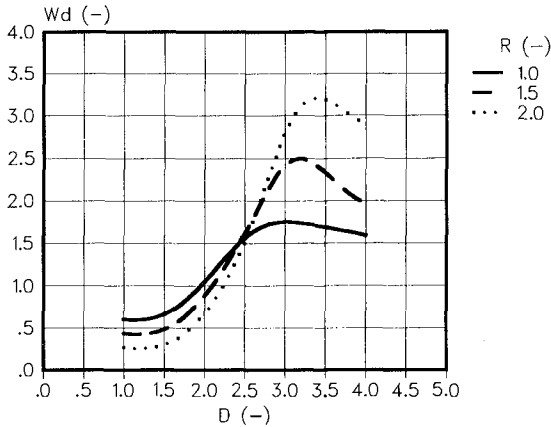


Figure 8. Wave deformation factor due to wind for $\cot \alpha_f = 20$ and $S = 0.03$

The wind effect in question seems to have the same order of magnitude as the influence of wind on the breaker-spray transport, although it reaches a maximum under different circumstances. However, the verification tests showed that the influence of the relative water depth on overtopping is less pronounced than Goda's graphs suggest. This implies that the maximum factor of increase in overtopping due to wave deformation is probably less than 3. Still, one should be aware of the rough approximations which form the basis of this conclusion. This wind effect requires further investigation before it can be quantified accurately.

5.3 Contribution of basic spray to overtopping

In storm conditions the air above the sea surface is filled with spray. This spray is called "basic spray" in this paper. There is a dynamic equilibrium of the spray distribution over the height above the sea surface. This equilibrium is maintained by spray generation and turbulence in the air on the one hand and gravity on the other hand. The equilibrium is disturbed at the transition from sea to land, where the spray starts to be deposited. The amount of this type of overtopping was compared with the overtopping by waves (including breaker spray) and rainfall.

The following simple exponential equation for the spray concentration is applied:

$$c = c_0 \exp\left\{-\frac{w}{D_t}(z - z_0)\right\} \quad (5.4)$$

With:

- c = volumic spray concentration (-)
- c_0 = average spray concentration at $z = z_0$ (-)
- t = time (s)
- z = vertical coordinate, positive upward and $z=0$ at mean sea level (m)
- z_0 = reference level for spray concentration distribution (m)
- w = average fall velocity of spray (drops) in air (m/s)
- D_t = turbulent diffusion coefficient (m^2/s)

We introduce a horizontal coordinate x , being zero at the structure crest and negative at the open sea. We assumed a stationary situation. We assumed that the vertical distribution of spray concentration is transported with the horizontal wind velocity u_a , which was assumed to be uniform (independent of z). The total spray discharge (per m crest width) over the crest level R_c is given by:

$$q_b = \int_{R_c}^{\infty} c u_a dz \quad (5.5)$$

As soon as this spray distribution passes the structure crest (at $x = 0$), the production of basic spray at $z = 0$ stops. For $x > 0$ we neglect the influence of diffusion and simply assume that all spray falls down, having a velocity w . The total discharge of basic spray falling on the first L metre behind the crest (per metre crest width) is now given by:

$$q_b = \frac{D_t}{w} u_a c_0 \exp\left\{-\frac{w}{D_t}(R_c - z_0)\right\} \left(1 - \exp\left\{-\frac{w}{D_t} L\right\}\right) \quad (5.6)$$

The governing parameters in this formula were chosen as follows. The amount of spray strongly depends on the wind velocity. In the calculations a wind velocity u_a of 30 m/s is applied, representing wind force 11 on the Beaufort scale. The spray fall velocity w strongly depends on the drop size. Since the variety of drop sizes in the spray is very great, the representative fall velocity is difficult to assess. Therefore, two values have been applied, namely 0.5 and 2.5 m/s, representing a low and a high estimate respectively. The turbulent diffusion

coefficient D_t is unknown but is at first approximation regarded to be related to the average wind velocity. Two values have been applied, namely 5.0 and 50 m/s. The average spray concentration c_0 at the reference level $z = z_0$ is based on a rough estimation. The concentration of water in air during intensive rainfall is estimated at 10 ml/m^3 . This yields $c_0 = 10^{-5}$. The level of z_0 is assumed to be equal to the level of R_c . For the length L behind the structure crest in which basic spray is deposited two values were applied: 50 m and 100 m.

An estimation of the contribution of rainfall to the average overtopping was based on an intensity of 10 mm/hr. A representative value for the wave overtopping discharge was based on $H_{os} = 5 \text{ m}$, $S = 0.04$, $D = 2.0$ and $R = 1.7$. This yields $Q \approx 0.001$, which results in $q = 0.035 \text{ m}^2/\text{s}$. The results of the computations are presented in Table 2.

	w (m/s)	D_t (m^2/s)	q (l/m/s)	
			L = 50 m	L = 100 m
Basic	0.5	5	0.2	0.5
	0.5	50	0.2	0.5
Spray	2.5	5	0.5	0.6
	2.5	50	1.1	2.0
Rainfall			0.1	0.3
Wave overtopping			35	

Table 2. The contribution of basic spray to overtopping

From these results we concluded that the contribution of basic spray to the overtopping discharge is only slightly greater than the contribution of rainfall and is still negligibly small in comparison with representative wave overtopping discharges.

ACKNOWLEDGEMENTS

The Dutch Rijkswaterstaat and the Technical Advisory Committee for Water Defences are gratefully acknowledged for their substantial financial contribution and scientific support to this project.

REFERENCES

- J.A. Battjes, 1974. Wave run-up and overtopping. Technical Advisory committee on protection against inundation, The Hague.
- S.L. Douglass, 1989. The influence of wind on nearshore breaking waves. Drexel University.
- Y. Goda, 1985. Random seas and design of maritime structures. University of Tokyo Press.

CHAPTER 173

Bridge Pier Scour Assessment for the Northumberland Strait Crossing

C.D. Anglin¹, Associate Member, R.B. Nairn¹,
A.M. Cornett², L. Dunaszegi³, J. Turnham⁴, G.W. Annandale⁵

Abstract

In 1997, the Northumberland Strait Crossing will form a 13 km fixed link (bridge) between New Brunswick and Prince Edward Island in the Canadian Maritimes. This \$800 million project has presented many engineering challenges, one of which has been the assessment of scour protection requirements for the 65 bridge piers. A multi-faceted coastal engineering investigation was undertaken by Baird & Associates to assess the potential for scour, and, where required, to design scour protection. Key activities included geotechnical investigations to define the seabed characteristics, numerical modelling to define the wave, current and water level conditions at the crossing site, physical modelling of wave-current interaction with the bridge piers, and the development of a new methodology to estimate the erosion potential of the seabed under extreme wave and current conditions.

The direct application of standard scour prediction techniques was not possible for this project due to the combination of complex flow conditions (waves and currents), complex pier geometry (conical base, with some piers located in dredged pits), and complex seabed conditions (highly weathered and fractured bedrock). A new methodology to estimate the potential for scour, considering these complex conditions, was developed using the empirical erodibility approach of Annandale (1995). Measurements of actual scour around one of the first four bridge piers installed early in the project were used to calibrate/verify the methodology. Using this new methodology, scour protection was recommended at approximately one-quarter of the bridge piers. The protection system consists of a 10 m wide band of either armour stone or tremie concrete placed around the base of the piers.

1 - Baird & Associates, 1145 Hunt Club Rd., Suite 1, Ottawa, ON, Canada K1V 0Y3

2 - Canadian Hydraulics Centre, National Research Council, Ottawa, ON, Canada K1A 0R6

3 - SLG Stanley Consultants Inc., Suite 400, 1122 - 4th St. SW, Calgary, AL, Canada T2R 1M1

4 - Strait Crossing JV, Trans Canada Hwy at Dickie Rd., Borden-Carleton, PEI, Canada C0B 1X0

5 - Golder Associates, 200 Union Blvd., Suite 500, Lakewood, CO, USA 80228

Overview of Project

The Northumberland Strait separates Prince Edward Island (PEI) from the mainland provinces of New Brunswick (NB) and Nova Scotia (NS), as shown in Figure 1.

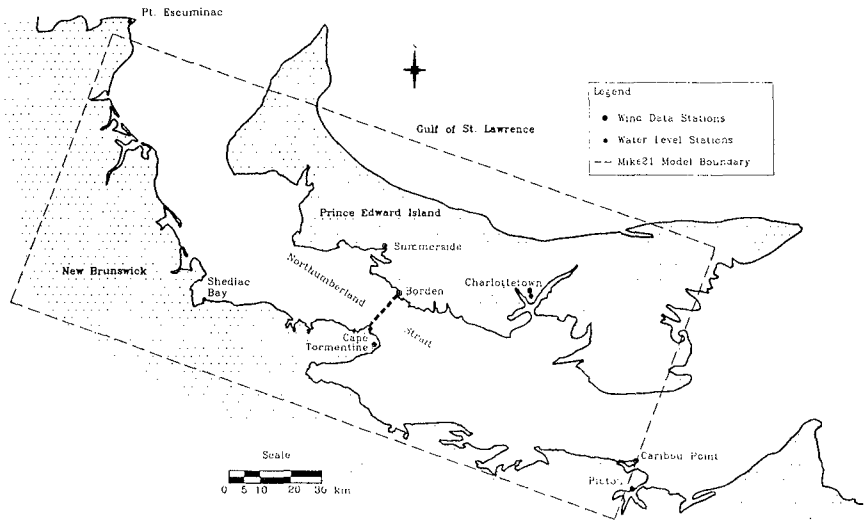


Figure 1 - The Northumberland Strait

At the crossing location, the Strait is approximately 13 km wide, with water depths ranging from 0 to 30 m (typically in the order of 15 m). Under extreme design conditions, this site (and the bridge) may be exposed to 120 kph winds, 4.5 m/9 s waves (H_s/T_p) and 2.5 m/s currents (the latter generated by the combined effects of tides, surges and wave-driven longshore currents). In addition, the Strait has a very dynamic ice environment, with ice present two to three months per year, level ice thicknesses of up to 1.2 m, and first year pressure ridges with keel depths of up to 15 m.

Ice forces on the bridge, and the effect of the bridge on ice breakup in the Strait, were the dominant design considerations for the bridge. The bridge structure consists of the east (PEI) and west (NB) approach bridges (93 m spans) and the main bridge (250 m spans). There are 7 approach piers on the PEI side and 14 on the NB side, and 44 main piers in between. Figure 2 provides a schematic illustration of one of the main piers, and shows the conical pier base, the conical ice shield and the pier shaft. For the approach piers, which are located in shallow water (depth < 8 m), the conical pier base is also the ice shield.

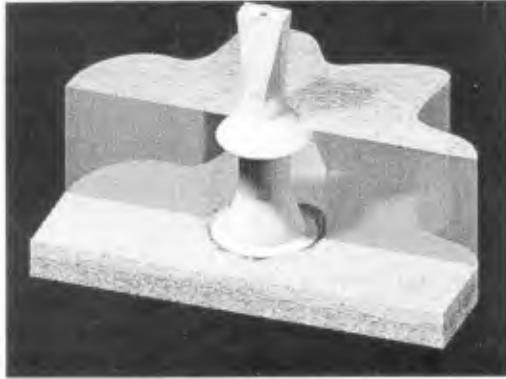


Figure 2 - Typical Main Bridge Pier

In order to meet the very tight project schedule, the primary bridge components (pier bases, ice shield/pier shaft, approach spans, main spans and drop-in spans) were all pre-cast in two production yards. Simultaneously, the pier foundations were prepared, including dredging/excavation to the founding elevation, and the placement of "hardpoints" to provide a level surface on which to place the pier bases. The main bridge components were then transported and placed using the heavy lift vessel (HLV) "Svanen" (see Figure 3), followed by connection of individual components. Construction began in the middle of 1994, and the final main bridge component was placed by the "Svanen" in November 1996. The bridge is scheduled to open in May 1997.



Figure 3 - Bridge Under Construction and HLV "Svanen" (view from PEI)

Overview of Development of Scour Assessment Methodology

Initially, an extensive literature survey was undertaken in an attempt to identify scour assessment techniques that could be applied to the Northumberland Strait Crossing Project (NSCP) (Baird, 1996). After reviewing all of the available information, including the HEC-18 manual of the U.S. Department of Transportation (1993), it was concluded that there was no acceptable technique to define scour potential for the NSCP bridge piers due to the following unique features/conditions associated with the project:

- combined waves and currents;
- conical shape of the pier bases;
- location of some pier bases in dredged pits (up to 7 m deep); and
- highly weathered/fractured and variable bedrock seabed.

An initial laboratory study was undertaken (Cornett et al, 1994) in an attempt to characterize and quantify the erosion potential of the various seabed materials at the crossing location. This investigation was completed in a tilting flume, and consisted of exposing intact samples (both slabs and cores) of various materials (glacial till, mudstone, siltstone and sandstone) to both open channel flows and submerged jet flows. The erosion process was found to be quite complex, and it was not possible to reliably quantify erosion of these materials as a function of either near bed velocity or shear stress.

Following these tests, the literature review was updated (Baird, 1996), leading to the identification of a promising new approach (Annandale, 1995) to estimate the erosion potential of “complex materials” (such as weathered and fractured bedrock). In general terms, Annandale’s (1995) approach relates the driving force for scour, as defined by the “stream power” parameter, P (which provides a measure of the rate of energy dissipation in the near bed flow), to the resistance to scour, as defined by the “erodibility index” parameter, EI (which provides a measure of the in-situ strength of the material based on data derived from borehole logs). Annandale’s (1995) database, and his relationship between stream power and erodibility index (which defines the threshold for scour) is based on observations of scour (or no scour) in spillways downstream of dams. In order to develop and apply this methodology to the NSCP, it was necessary to not only define the stream power (driving force for scour) and erodibility index (resistance to scour) for the unique conditions associated with the NSCP, but also to calibrate and verify the methodology for the assessment of scour potential around conical bridge piers exposed to combined waves and currents.

Driving Force for Scour

Two general issues must be addressed with respect to quantifying the driving force for scour for the NSCP bridge piers. First, the ambient flow conditions (waves and currents) at the crossing location must be defined, and second, the local influence of the bridge piers on these flow conditions must be defined.

Ambient Flow Conditions

Numerical modelling techniques were utilized to define the ambient flow conditions at the crossing location. A parametric wind-wave hindcast model was used to estimate the wave height, period and direction at four points along the crossing alignment on an hourly basis between 1960 and 1995. This 36 year period corresponded to the duration of available wind data in the vicinity of the Northumberland Strait. The hindcast model was calibrated (through modification of the overland wind data to represent overwater winds) against recorded wave data (five months) available in the immediate vicinity of the crossing, and excellent agreement was obtained for both wave height and period. Weekly composite ice charts were also reviewed, and wave conditions were set to zero during periods of significant ice cover on the Strait (typically two to three months per year).

The MIKE21 hydrodynamic model, developed by the Danish Hydraulic Institute, was used to estimate water levels and currents throughout the Strait on an hourly basis for the 23 year period between 1973 and 1995. The model utilized a 2.5 km grid spacing, and covered a total area of 95 by 208 km. The model boundary conditions were defined by recorded water level data at the model boundaries (Pictou, NS, and Pt. Escuminac, NB), thereby incorporating the effects of both tides and surges. The model was calibrated using recorded current data in the vicinity of the crossing location, and was verified against recorded water level data at locations on either side of the crossing (Charlottetown, PEI and Shediac Bay, NB). The model provided excellent agreement with the recorded current data, and also provided a good simulation of the very different tidal conditions at the two intermediate water level stations. The model results (hourly estimate of water level and current speed and direction) were extracted for the same four points as used in the wind-wave hindcast analyses. A sample output (vector plot of currents) for the hydrodynamic model is provided in Figure 4.

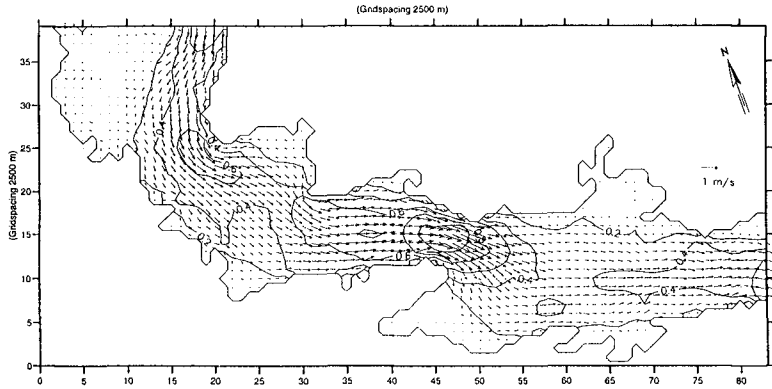


Figure 4 - Sample of Hydrodynamic Model Results (vector plot of currents)

A combined database (23 year hourly time series) was then developed for the four points along the crossing alignment, including wave height, period and direction, current speed and direction and water level. Shallow water processes, including refraction, shoaling, breaking and wave-driven longshore currents, were then estimated using the COSMOS model of coastal processes (Southgate and Nairn, 1993) in order to estimate the wave conditions at the shallow water approach piers (depth < 8 m). The stream power parameter, P , which defines the rate of energy dissipation in the flow, was then calculated as the product of the near bed shear stress and the near bed velocity, considering the combined effect of both waves and currents. The combined near bed shear stress was calculated using the method of Myrhaug and Slaatelid (1990), as presented in Soulsby et al (1993). The combined near bed velocity was calculated as the vector sum of the maximum wave orbital velocity and the depth-averaged tidal/surge current. Stokes second order wave theory was used in “deep” water (Ursell number < 26.3), while Cnoidal wave theory was used in “shallow” water (Ursell number > 26.3). Given the importance of water depth on wave orbital motions, these calculations were completed for a range in water depths representative of the 65 bridge pier locations.

Based on these calculations, a 23 year hourly time series of stream power was developed for a range in representative water depths. Severe stream power events were identified and extracted for each water depth, and extreme value analyses were completed to define the stream power parameter as a function of return period. The 100 year stream power event (considering the combined effect of waves and tidal/surge currents) was selected as the ambient design event for this project.

Local Influence of Bridge Piers

The presence of the piers in the Strait will result in accelerated flows and vortices in the immediate vicinity of the piers, leading to an increase in the driving force for

scour around the base of the piers. The influence of the various pier shapes and dredged pit depths (0 to 7 m) on the local flow conditions around the base of the piers was investigated for a representative range of water depths using a 1:70 scale model in a test flume at the Canadian Hydraulics Centre (Cornett, 1996). Figure 5 shows a photograph of typical model approach and main piers.

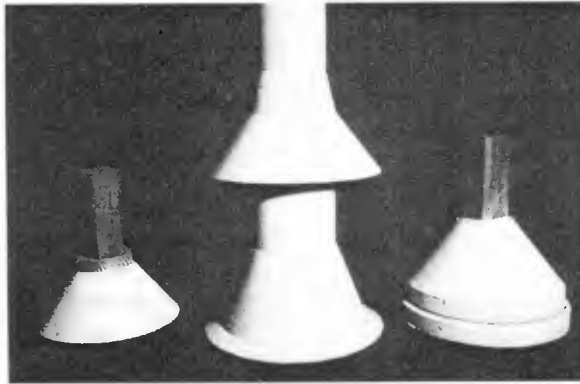


Figure 5 - 1:70 Scale Models of Bridge Piers
(L - West Approach Pier, C - Main Pier, R - East Approach Pier)

The test flume was connected to a 0.2 m³/s pump and flow circulation system to generate unidirectional currents, and a wave generator at both ends of the flume capable of generating both regular and irregular wave conditions. As such, it was possible to test waves with both following and opposing currents. The test section was located on a raised floor in the center of the flume. The flow patterns around the base of the pier were defined with the aid of a laser doppler velocimeter, acoustic velocity meters, flow visualization and tracer materials. Figure 6 presents a schematic diagram of the test flume.

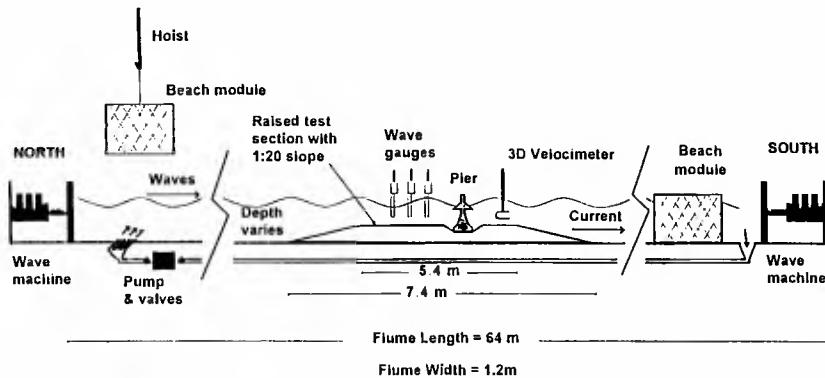


Figure 6 - Schematic Diagram of Test Flume

Stream power magnification factors were developed for the various water depths and pier geometries encountered at the 65 bridge piers through a comparison of the stream power required to initiate the scour of a tracer material (coarse sand or fine gravel) with and without the pier in place. The stream power magnification factors varied from 1.5, for a deepwater main pier founded in a 7 m dredged trench (Figure 7), to approximately 6, for a shallow water approach pier founded directly on the seabed (Figure 8). The product of the local 100 year ambient stream power and the local pier influence factor (stream power magnification factor) defined the design driving force for scour at each of the 65 bridge piers.



Figure 7 - Scour in Tracer Material for Main Pier Founded in a Dredged Pit



Figure 8 - Scour in Tracer Material for Approach Pier Founded on Seabed

Seabed Resistance to Scour

Estimating the erodibility of the various highly weathered bedrock materials was one of the most challenging aspects of this project. As noted earlier, the laboratory tests in the initial phase of the investigation revealed that the erosion process was very complex, and was not a direct function of either near bed shear stress or near bed velocity. Ultimately, the empirical erodibility approach developed by Annandale (1995) was adopted. In this approach, the erosion resistance of the material is quantified by the “erodibility index”, EI, which characterizes in-situ strength of the material, considering the mass strength of the material, the typical “particle” size, and the interparticle “friction”. This parameter is calculated as the product of four dimensionless variables, all defined from information derived from standard geotechnical borehole logs, as summarized below:

$$EI = K_m * K_b * K_d * J_s$$

where EI = Erodibility Index
K_m = Mass Strength Number
K_b = Block Size Number
K_d = Joint Roughness Number
J_s = Joint Structure Number

As part of the geotechnical investigation undertaken to support the design of the NSCP bridge piers and foundations, between two and ten boreholes were drilled at each of the 65 bridge piers locations. For the scour assessment study, erodibility indices were calculated by the geotechnical engineer (Golder Associates) for each core run (approximately 0.3 m lengths) for each of these boreholes (approximately 300 in total). In general, the erodibility indices showed considerable variation (orders of magnitude) in both the horizontal and vertical dimensions. This variation reflected the highly variable nature of the materials on which the bridge piers are founded. In addition, it is noted that all of the boreholes were located under the pier bases, and not in the zone surrounding the pier bases where scour would initiate. This variability and uncertainty in the strength (erosion resistance) of the seabed materials was a primary consideration in the incorporation of a factor of safety in the assessment of scour potential for the bridge piers.

Calibration of Methodology

The NSCP represents the first application of Annandale’s (1995) approach to bridge piers, waves and currents, or design of any kind. As such, calibration and verification of the methodology was a key component of the investigation.

Fortuitously, observations of actual scour experienced around one of the first four approach piers installed early in the project provided valuable information for calibration of the new methodology. More specifically, scour around one of these approach piers (Pier E7) was noted following a storm event (in November 1994) during construction of the piers. Figure 9 provides a schematic illustration of the observed scour, which extended up to 5 m out from the base of the pier, with undermining up to 1 m in and 1.5 m below the base. Scour was not observed around the other piers in place at the time of this event.

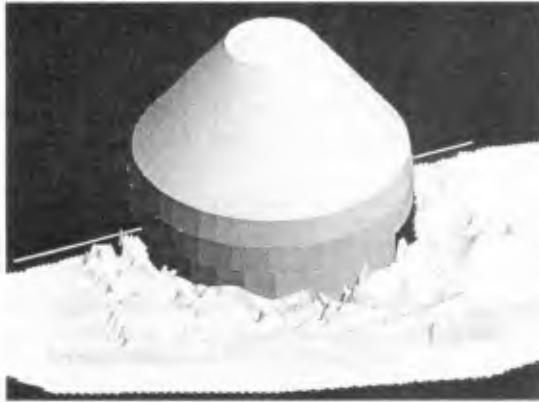


Figure 9 - Scour in Bedrock Observed Around and Under Pier E7

The wave and current conditions which caused the scour during this event were hindcast using the numerical models described earlier, and indicated that the event had a return period (based on the stream power parameter) of approximately five years. The flow patterns around the pier were modeled for this event in the 1:70 physical model investigation. Based on this information, along with the geotechnical data describing the seabed conditions in the vicinity of the four approach piers, an attempt was made to calibrate Annandale's (1995) methodology for this project. The key calibration parameters were the wave height (ie. H_{avg} , H_s , $H_{1/10}$, H_{max}), the wave period (ie. T_{avg} , T_p , T_{max}), the shear stress (ie. T_{mean} , T_{max}) and the bottom roughness (k_s). Ultimately, the best comparison between estimated and observed scour at Pier E7 was obtained using H_{max} , T_{max} , T_{max} and a bottom roughness of 0.3 m. The use of the maximum wave height, period and shear stress values can be qualitatively justified by the hypothesis that the erosion of the highly weathered and fractured bedrock materials present at this site is a threshold process, and that once a rock fragment has been dislodged and removed from the matrix, the remaining material can be readily eroded. The lack of scour at the other three piers in place at the time of the November 1994 storm event can be explained by the presence of stronger materials (ie. higher EI values) on the seabed at these pier locations.

A qualitative confirmation of the scour assessment methodology was also made through consideration of the morphological development of the sea bed across the Strait. Through the application of the erodibility index approach, it was possible to explain the existence of a glacial till (soft clay/silt/sand) over the underlying bedrock for areas with depths greater than about 13 m. More specifically, in these areas, the 100 year stream power was less than the stream power required to erode the till material according to Annandale's (1995) approach. Together, the quantitative and qualitative observations of scour substantiated the methodology for the assessment of scour potential for the Northumberland Strait conditions.

A detailed review of Annandale's (1995) database, in particular the critical data points which describe the threshold condition for scour for erodibility indices similar to those encountered at the pier bases for the NSCP, was also undertaken in order to assess the compatibility of Annandale's database to the hydrodynamic and geotechnical conditions associated with the NSCP. In general, it was found that the critical data points which define the threshold condition for rock and complex earth materials represent similar rock conditions to those encountered in this project. Further, the hydrodynamic conditions for these data points, although not generated by wind-waves and tidal/surge currents, were associated with high velocities and turbulent flow conditions. As such, it was concluded that Annandale's (1995) scour threshold relationship could be applied to the NSCP.

Requirement for Scour Protection

A pier by pier assessment was undertaken in order to assess the requirement for scour protection at each of the 65 bridge piers. In general, this assessment consisted of the following steps:

- define the "critical depth zone" beneath the foundation of each pier (considering the allowable scour, which varies from 0 to 0.5 m the various approach and main pier foundation designs);
- define erodibility indices (based on available borehole data) within the critical depth zone, and estimate the corresponding threshold stream power for scour;
- compare local design stream power (100 year ambient value times pier magnification factor) to local threshold stream power;
- recommend protection if factor of safety is less than two to four.

The factor of safety was incorporated to address uncertainties associated with the driving forces, resisting forces and scour threshold relationship. The key uncertainty was the highly variable seabed conditions. A higher factor of safety was applied at piers with greater variation in seabed conditions, and/or where the tolerance for scour was lower. Ultimately, scour protection was recommended for approximately one quarter of the 65 bridge piers.

Design of Scour Protection

The design of the scour protection system around the base of the piers was developed and optimized using a physical model investigation. The test facilities and setup were very similar to that described earlier for the tracer tests undertaken to quantify the pier magnification factors. In general, these tests indicated that the influence of the piers on flow conditions extended approximately 7 to 9 m out from the toe of the conical pier bases. As such, a 10 m wide band of scour protection was adopted. Scour protection designs were initially developed using either one or two layers of armour stone. For the shallow water approach piers, these armour stones were in the order of 2 to 7 tonnes. Smaller armour materials were adequate for deep water piers. Figure 10 shows a picture of a scour protection test in progress.



Figure 10 - Scour Protection Test at Shallow Water Approach Pier

Subsequently, construction considerations led to the development of a scour protection system using tremie concrete. Again, this system extended out 10 m from the base of the pier. The key design details associated with the tremie concrete solution were careful cleaning of the seabed prior to concrete placement, and construction and monitoring operations adequate to provide a minimum 0.5 m thick mat of concrete over the seabed.

Monitoring Program

An extensive monitoring program has been recommended in order to quantify potential scour events over the design life of the Northumberland Strait Crossing Project, and to document scour which may occur around the base of the bridge piers. This monitoring program has been recommended for several reasons, as noted below:

- the scour assessment methodology utilized for this project is new, and has never been applied to bridge piers, waves and currents, or design of any kind;
- there are uncertainties associated with the estimation of both the driving forces for scour and the seabed resistance to scour;
- there is a desire to minimize seabed survey requirements around the base of the bridge piers associated with the monitoring program.

The monitoring program will consist of a near real-time wave and tide prediction system installed at the site. The prediction system will utilize numerical models similar to those used to develop the design database for this project. This system will run continuously, and will quantify the magnitude of potential scour (ie. stream power) events to which the bridge is exposed. Over time, a data base will be developed for each pier documenting the conditions to which the pier has been previously exposed (based on the prediction system) and the response of the seabed to these conditions (ie. scour or no scour, based on detailed surveys of the seabed). The database will be updated on a regular basis, and the system will identify any requirement for action by the bridge operation and maintenance staff. For example, additional surveys of the seabed around any particular pier will be required if the pier has been exposed to an event greater than any prior event, or if a certain period of time has elapsed since the last survey.

Conclusions

A multi-faceted coastal engineering investigation has been completed to support the assessment of scour around bridge piers for the Northumberland Strait Crossing Project. The application of conventional scour design techniques to this project was precluded by the unique conditions associated with this project, including complex flow conditions (combined waves and currents), complex pier base geometry (conical pier bases, with some located in dredged pits), and complex foundation materials (highly weathered and fractured bedrock).

The investigation has led to the development of a new methodology to assess scour potential around bridge piers which can address the unique conditions noted above, but can also be applied to more conventional/less complicated scour design problems. The new methodology is based on the empirical erodibility approach of Annandale (1995), and has been developed, calibrated and verified, to the extent possible, for this project. A detailed, long-term monitoring program will be implemented upon completion of the project in 1997, and will be used to verify this new scour design methodology.



Photograph of Bridge Nearing Completion

References

- Annandale, G.W. (1995), "Erodibility", Journal of Hydraulic Research, IAHR. Vol. 33, No. 4, pp. 471-494.
- Baird & Associates (1996), "Northumberland Strait Crossing - Assessment and Development of Scour Protection Requirements", final report prepared for JMI Stanley Joint Venture.
- Cornett, A.M., Sigouin, N. and Davies, M.H. (1994), "Erosive Response of Northumberland Strait Till and Sedimentary Rock to Fluid Flow", National Research Council of Canada, Institute of Marine Dynamics, Report TR-1994-22.
- Cornett, A.M. (1996), "Model Tests in Support of Scour Protection Design for the Northumberland Strait Crossing", National Research Council of Canada, Canadian Hydraulics Centre, Report HYD-CTR-008.
- U.S. Department of Transportation (1993), "Evaluating Scour at Bridges", Hydraulic Engineering Circular (HEC) No. 18, Report No. FHWA-IP-90-017, Federal Highway Administration, Washington, D.C.
- Myrhaug, D. and Slatelid, O.H. (1990), "A Rational Approach to Wave-Current Friction Coefficients for Rough, Smooth and Transitional Turbulent Flow", Coastal Engineering, Vol. 14, pp. 265-294.
- Soulsby, R.L., Hamm, L., Klopman, G., Myrhaug, D., Simons, R.R. and Thomas, G.D. (1993), "Wave-Current Interaction Within and Outside the Bottom Boundary Layer", Coastal Engineering, Vol. 21, pp. 41-69.
- Southgate, H.N. and Nairn, R.B. (1993), "Deterministic Profile Modelling of Nearshore Processes - Part 1 - Waves and Currents", Coastal Engineering, Vol. 19, pp. 27-56.

CHAPTER 174

WAVE SETUP AT RIVER ENTRANCES

David J Hanslow¹, Peter Nielsen² and Kevin Hibbert¹

Abstract

Detailed mean water level measurements from the Brunswick River on the NSW North Coast have, to date, suggested that the contribution of wave setup to the super-elevation of river entrance water levels is quite small. Data indicate that the over heights inside the area of wave breaking in rivers are typically smaller than at the same depth in a beach surf zone with the same waves. It is thought that difference between beach surf zones and river mouths is due to the momentum flux of the river current and the current's influence on the wave breaking process. Nevertheless, tidal anomalies of the order 0.5m are measured once or twice a year by tide gauges just inside river entrances along the east coast of New South Wales. These anomalies are thought to be mainly due to freshwater outflow and/or oceanic phenomena.

Introduction

The largest part of disaster relief in Australia is related to flooding by river systems. In New South Wales alone the cost of flooding from coastal rivers is of the order M\$50 per annum. Hence, realistic modelling of flood flows and water levels in the rivers is a national concern. The State of the art of flood modelling is however unsatisfactory because the interaction between the ocean and the river systems is poorly understood.

A flood model of a river system will have two main inputs namely rainfall over the catchment and tail water level, i.e., the water level where the river meets the sea. The present paper addresses the estimation of these tail water levels.

The tail water level at a river mouth is influenced by several processes not all of which are well understood. The most predictable component is the astronomical tide. Its origin relating to the gravitational influence of the sun and the moon. In most places this component is quite predictable based on long tidal records.

Differences between the astronomical tide and the actual tide level are often referred to as tidal anomalies. In the deep ocean anomalies occur due to barometric pressure variations

¹ Coastal Management Program, NSW Department of Land and Water Conservation, Sydney, NSW, Australia

² Department of Civil Engineering, University of Queensland, St Lucia, Queensland, Australia

and to temperature variations in the water. In coastal areas additional anomalies can be caused by winds and waves, and in estuaries the water levels may be increased due to fresh water outflow.

The following contains a review of available theory and recent observations of tidal anomalies in the lower parts of a few rivers on the east coast of Australia, and the contribution of wave setup to these anomalies.

The main emphasis is on the Brunswick River in Northern New South Wales which is trained by almost parallel breakwaters that are approximately 40m apart at the seaward end. It has a catchment of 200 km² and a (spring) tidal prism of 4.8×10^6 m³ (Figure 1). The Brunswick River has a fairly shallow bar where even the smallest waves tend to break, and was therefore considered ideal for studying the contribution of wave setup to river tail water levels. The "ocean tide gauge" on the Brunswick River is situated at the confluence of Simpson's Creek with the River approximately 640m upstream from the ends of the breakwaters (Manly Hydraulics Laboratory, 1993).

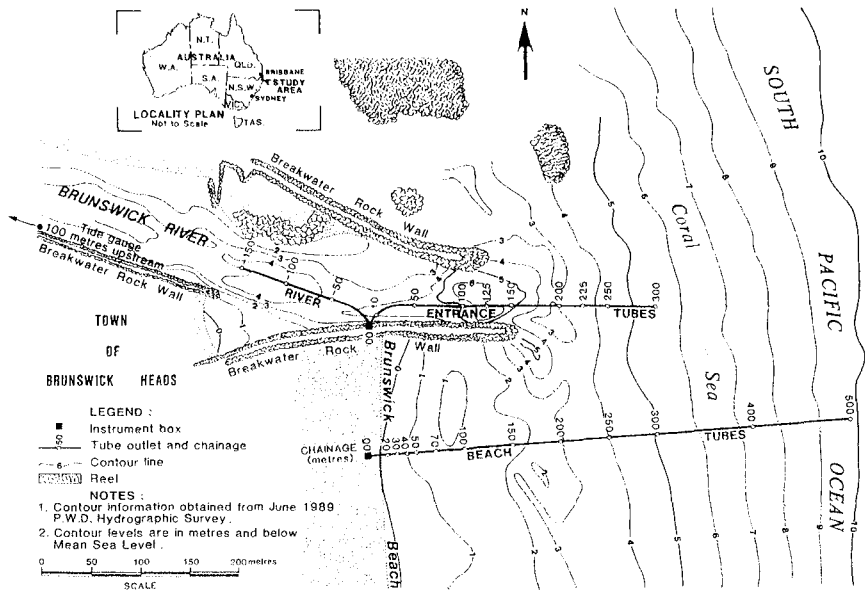


Figure 1. The Manometer tube system at the Brunswick River.

Anomaly Statistics for the Brunswick River

In the period 1986 to 1995 there were eight events during which the Brunswick Ocean tide gauge recorded water levels greater than 0.5m above the predicted astronomical tide level. The largest of these tidal anomalies was 0.87m occurring on April 11 1988. Of these major anomalies, all except for 17/3/1993 (Cyclone Roger), were associated with very large daily rainfalls on the catchment (more than 65 mm at Mullumbimby).

An example of two different anomaly events is shown in figures 2 and 3. In these figures anomalies recorded at the Brunswick tide gauge and at an offshore pressure gauge located in 26m of water offshore of Tweed Heads (30 km north of Brunswick Heads) are presented for the periods 24-29 April 1989 and 7-11 March 1990. Also presented are the offshore root mean square wave height (H_{orms}) recorded at the Byron Bay wave rider (located approximately 10km south of Brunswick Heads in 80m water depth) and the hourly rainfall recorded at Huonbrook in the Brunswick hinterland. As seen in these figures both events saw similar wave conditions with maximum RMS wave heights of around 4m in each event (5.8m significant wave height). Rainfall patterns were however very different for each event with a total of 369mm of rain being recorded over the period 24-29 April 1989, but only 35 mm recorded over the period 7-11 March 1990.

During the March 1990 event maximum anomalies recorded at both the offshore gauge and the Brunswick River entrance were of similar order (0.38m and 0.42m at the offshore gauge and the Brunswick river entrance respectively). The similarity of anomalies recorded between the two locations during this event suggests the absence of any effects of wave setup within the Brunswick River Entrance. During the April 1989 event however, maximum tidal anomalies measured at the two sites are significantly different with the Brunswick River site being elevated approximately 0.44m above the offshore water level. (0.33 and 0.77m were measured at the offshore site and the Brunswick River gauge respectively). Given the similar wave conditions during each of these events the difference between the offshore anomalies and that recorded in the river entrance between these two events appears to be related to the effects of rainfall and the resulting flood gradient.

The correlation of tidal anomalies with daily rainfall is indicated in figure 4A. For a few major events 24 hourly anomaly values have been plotted against the same daily rainfall total. This leads to the "vertical clusters" where the lower anomalies would have occurred before the bulk of the rainfall is felt at the tide gauge.

The incorporation of more detailed (spatially and temporally) rainfall information combined with the cumulative effect of rain on previous days would enable closer correlation to be obtained.

In contrast to this obvious correlation between tidal anomalies and rainfall, there is virtually no correlation between tidal anomalies and offshore wave height. This is shown by figure 4B where the tidal anomalies at the Brunswick "ocean tide gauge" are plotted against the root mean square wave height H_{orms} off Cape Byron. Both gauges are operated by the Manly Hydraulics Laboratory. The plot shows no significant correlation between tidal anomaly and wave height. An explanation for this lack of correlation may be found in the following discussion of wave set up in surf zones.

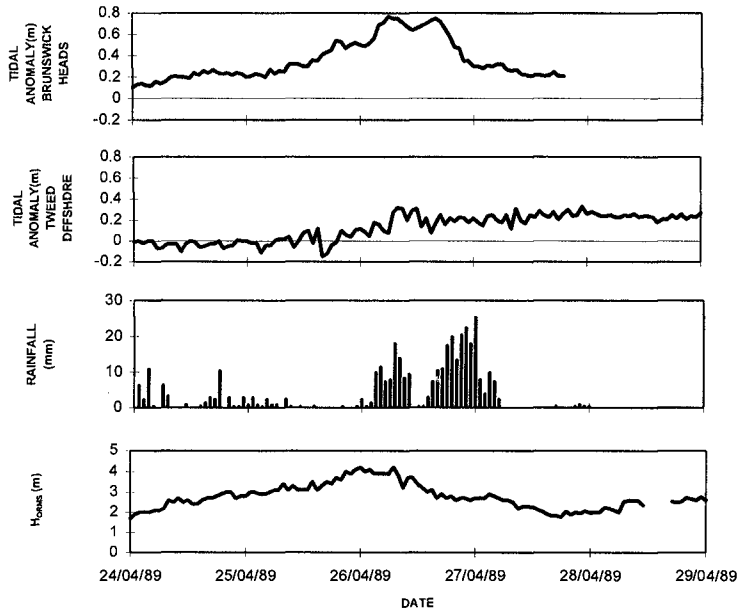


Figure 2. The tidal anomalies measured at the Brunswick River gauge and the Tweed offshore aandraa, hourly rainfall at Huonbrook, and RMS wave height at the Byron Wave rider for the period 24-29 April 1989. Data courtesy of Manly Hydraulics Laboratory.

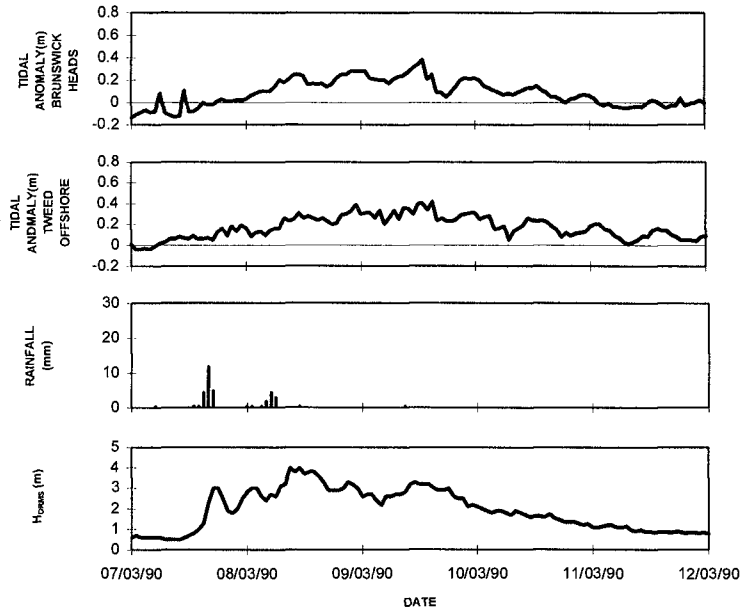


Figure 3. The tidal anomalies measured at the Brunswick River gauge and the Tweed offshore aandraa, hourly rainfall at Huonbrook, and RMS wave height at the Byron Wave rider for the period 7-11 March 1990. Data courtesy of Manly Hydraulics Laboratory.

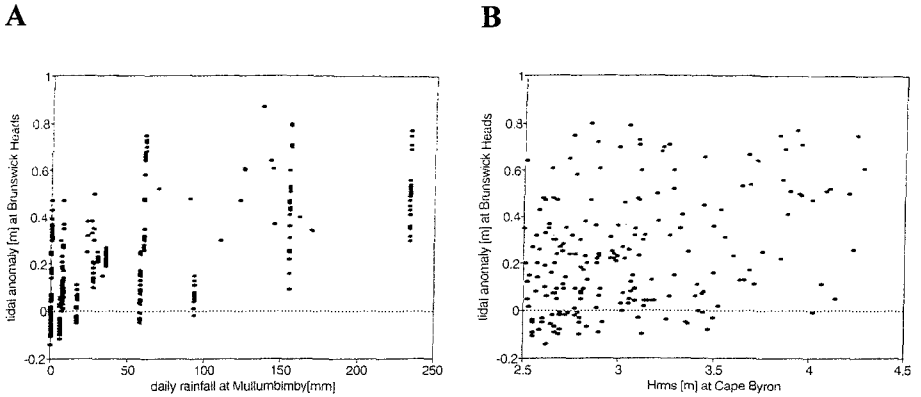


Figure 4. The tidal anomalies observed at the “ocean tide gauge” in the Brunswick River plotted versus (A) Daily Rainfalls at Mullumbimby; and (B) offshore wave height H_{oms} off Cape Byron for wave heights $H_{oms} > 2.5\text{m}$. Vertical clusters in the rainfall data occur where several anomalies are plotted against the same daily rainfall value. Data courtesy of Manly Hydraulics Laboratory.

Wave Setup

Surf Zone Wave Setup

The phenomenon of wave setup in surf zones has been known from observations (eg. Savage 1957) since the nineteen fifties and quantitatively understood since the development of the concept of wave radiation stress by Longuet-Higgins and Stewart (1964).

It occurs because the radiation stress or thrust S_{xx} of the waves is gradually translated into a mean water surface overheight, the setup B , as the waves decay towards the shore. Based on the force balance on a surf zone control volume, the governing equation is found to be

$$\rho gh \frac{dB}{dx} = -\frac{dS_{xx}}{dx} + \tau_w + \tau_b \quad (1)$$

where the wind τ_w and the bed shear stress τ_b are often neglected.

The earliest setup models by Longuet-Higgins and Stewart (1964) and Bowen et al (1968) which assume a constant ratio between wave height and depth ($H - \gamma h$) through the surf zone and use linear wave theory to express the radiation stress.

$$S_{xx} = \frac{3}{16} \rho g H^2 \quad (2)$$

lead to a linearly increasing setup towards the shore. However, experiments, eg. van Dorn (1976), have shown that such a distribution is only realistic for short waves on flat slopes or more precisely for small values of the surf similarity parameter $\xi = \tan\beta L_o/H \leq 0.2$, where L_o is the deep water wave length and $\tan\beta$ is the beach slope.

For larger values of the surf similarity parameter, the H/h ratio is not constant through the surf zone and Equation (2) is not a good approximation. The result is an upward concave mean water surface (MWS), see eg. Nielsen (1989) and Gourlay (1992).

The variability of the height of natural (irregular) waves also tends to make the MWS upward concave even at small values of ξ see eg. the field data of Nielsen (1988). The reason is that the onset of breaking occurs at different depths for waves of different heights.

While setup profiles due to regular laboratory waves show great shape variability depending on the surf similarity parameter, it turns out that the shape of setup profiles on natural beaches varies very little. An empirical description of these profiles will be given in the following.

An Empirical Model for Setup on Natural Beaches

The shoreline setup level (that is the setup at zero water depth) varies very little between natural beaches and between naturally occurring wave conditions as documented by Hanslow & Nielsen (1994). They found that data from the full spectrum of New South Wales beaches showed no systematic deviations from either of the shoreline setup (B_s) formulae

$$B_s = 0.38 H_{orms} \quad (\text{correlation coefficient } 0.65) \quad (3)$$

or

$$B_s = 0.048 H_{orms} L_o \quad (\text{correlation coefficient } 0.77) \quad (4)$$

where H_{orms} is the deep water root mean square wave height and L_o is the deep water wave length. Correspondingly, the whole setup distributions measured on different beaches under not too unusual wave conditions are very similar. (Note that laboratory conditions with very flat waves on steep slopes corresponding to $\xi = \tan\beta_F L_o/H_o > 3.0$ may lead to very large relative shoreline setup, eg., $B_s/H > 2.0$ and that very long swell waves might generate similar results in the field. Such conditions would however be very rare).

A typical set of setup profile data from a single storm event (Brunswick Heads 22/8 1989) is shown in Figure 5.

The curve fitted to this setup profile is given by

$$B(h) = \frac{B_s}{1 + \alpha h / H_{orms}} \quad \text{with } \alpha = 10 \quad (5)$$

For other beach topographies the shape is similar, but the value of α may vary by a factor 2 either way, i.e. $5 < \alpha < 20$.

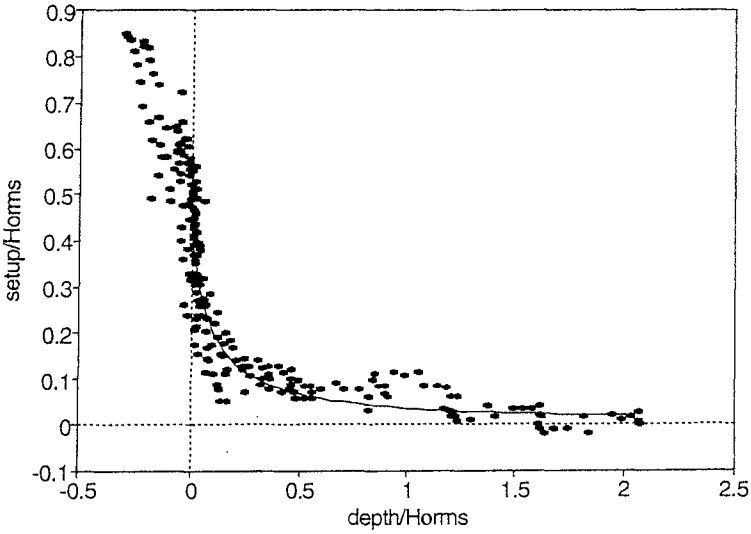


Figure 5. Measured setup profile data from Brunswick Beach August 22 1989.

S_{xx} according to measured setup profiles

The simplified setup equation $\rho gh \frac{dB}{dx} = -\frac{dS_{xx}}{dx}$ which for a monotonically sloping bottom can be rewritten $\frac{dS_{xx}}{dh} = -\rho gh \frac{dB}{dh}$ gives through integration by parts

$$S_{xx} = -\rho g \left[Bh - \int B dh \right] \tag{5}$$

which with (5) inserted gives

$$S_{xx}(h) = \rho g H_{orms}^2 \frac{B_y}{H_{orms}} \left[\frac{1}{\alpha} \ln \left(1 + \alpha \frac{h}{H_{orms}} \right) - \frac{h / H_{orms}}{1 + \alpha h / H_{orms}} \right] + \text{constant} \tag{6}$$

The constant of integration is found by matching with S_{xx} for non breaking waves at a suitable depth outside the surf zone. The alternative: $S_{xx}(0) = 0$ does not apply for natural beaches where runup occurs beyond $h = 0$.

Estimation of River Mouth Setup from Surf Zone Profiles

If one boldly assumes that a similar relation exists between depth and setup in a river entrance as in a surf zone (Equations 2 and 9) one might use the following estimate for the wave setup contribution to the river tailwater level

$$B_{\max} = \frac{B_y}{1 + \frac{\alpha h_{\min}}{H_{orms}}} \tag{7}$$

where h_{min} is the minimum depth in the river mouth. The shoreline setup B_s , determined from either (3) or (4).

As an example with reference to the Brunswick River one might choose $H_{min} = 2.0, \alpha = 10$ and $H_{orms} = 2.5m$, which gives $B_{max} \approx 0.2m$. We shall see in the following that this estimate is quite excessive which indicates that the assumptions required (see Section 8 for details) for this approach are not satisfied.

Detailed Mean Water Surface Measurements from the Brunswick River

In order to obtain detailed experimental data on river mouth water levels a manometer tube system, similar to the surf zone system described by Nielsen (1988), was installed in the Brunswick river in 1988 and extended in 1990, see Figure 1

From this system a large data base has been accumulated including river water levels during the flood event of April 26-27 1989 shown in Figure 6.

These measurements show that during this event the water level at the tide gauge was considerably above the ocean level due to the hydraulic gradient in the entrance.

In contrast, events with moderately large waves but little rainfall show very little water level difference between the inner and outer tubes, see Figure 7.

The fact that a water level difference of about 1m exists between the swash zone on the beach and the river on the other side of the breakwater some times results in large scour holes.

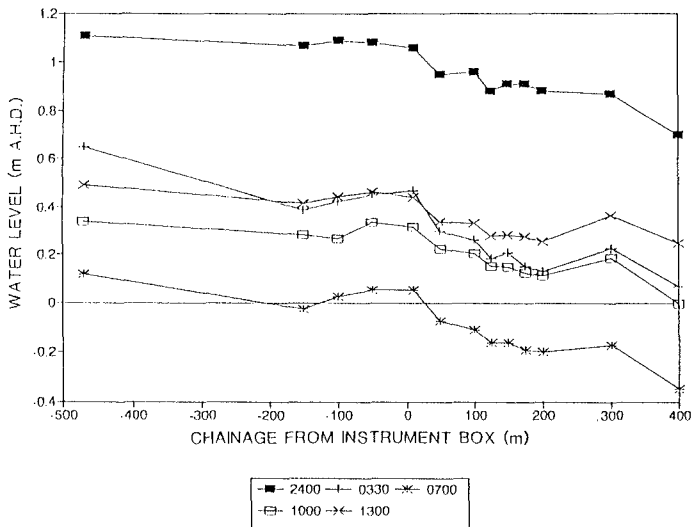


Figure 6. River water levels during a flood event (26/4/89), even at high tide the hydraulic gradient in the river generates water level differences of over 30 cm between the tide gauge (chainage -460m) and the ocean (chainage +150m).

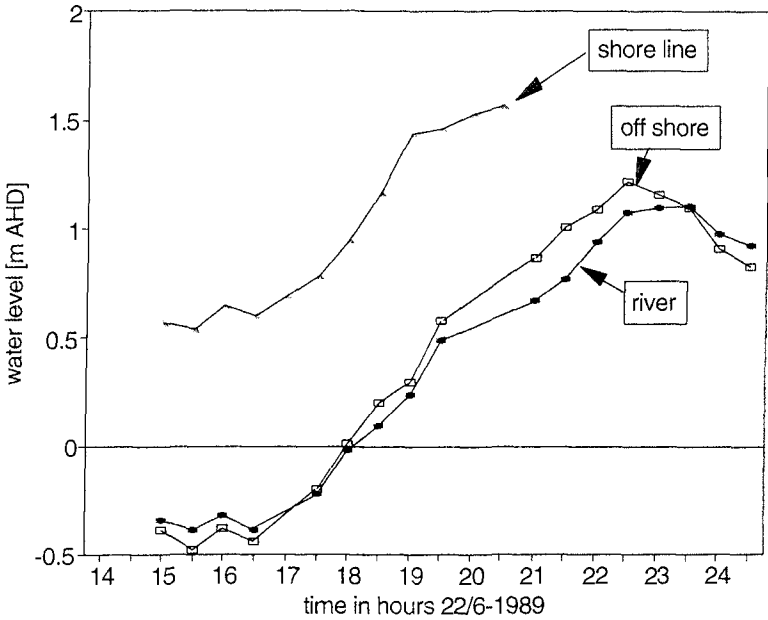


Figure 7. Time series of water levels offshore, inside of the wave breaking in the river and at the shoreline of the southern adjacent beach 22/6/89. A shoreline setup of the order of 1.0m is observed while the river levels only reflect the small tidal gradient ie. no setup was observed during Cyclone Nancy (2-4 March 1990).

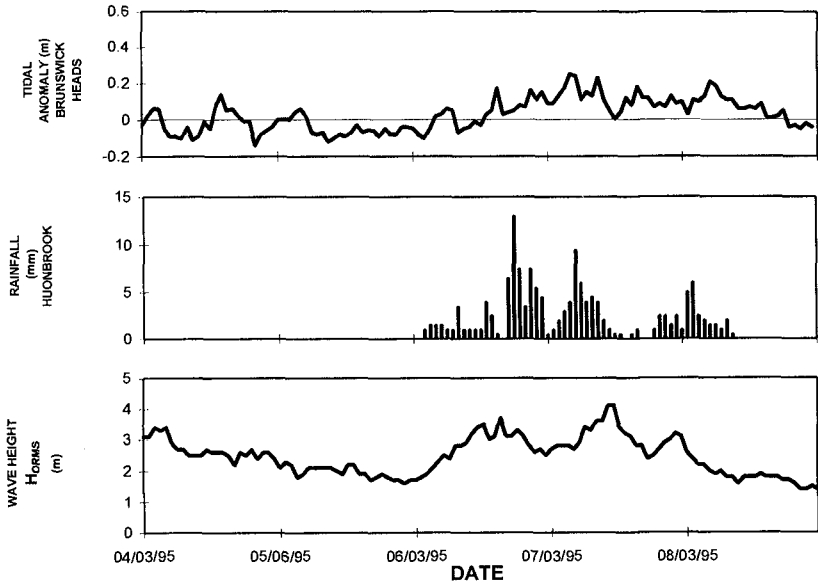
The occurrence of the scour holes is of course conditional upon the water finding a path through the breakwater, which is not supposed to occur as most breakwaters are designed to be impermeable. Nevertheless, they are not uncommon. Professor M. Losada of the University of Cantabria has observed them at river entrances on the North Coast of Spain (personal communication 1992) and Mr J Bodycott (personal communication 1990) has reported on “mystery sand banks” occurring inside some of the New South Wales rivers with no other plausible explanation that the sand being washed through the breakwater by the mechanism shown above.

Anomalies due to Long Period Waves in the Ocean

Storm events which seem quite similar in intensity and shape may cause very different amounts of tidal anomaly. For example, Cyclone Roger (March 1993) produced an anomaly of about 0.5 m while Cyclone Violet (March 1995) produced an anomaly of only half this amount. This is despite the fact that several of the contributing mechanisms would have been stronger at Brunswick Heads during Cyclone Violet. See the time series of rainfall, wave height and measured anomaly in Figures 8a,b.

These figures show that the tidal anomaly caused by Cyclone Roger was two times greater than that caused by Cyclone Violet even though the wave height at the nearby Cape Byron wave rider was greater during Violet and the rainfall was greater as well. Furthermore, the atmospheric pressure in the Brunswick area would have been considerably lower during Cyclone Violet, which came very close to Brunswick Heads, than during Roger which came no further south than Maryborough.

A



B

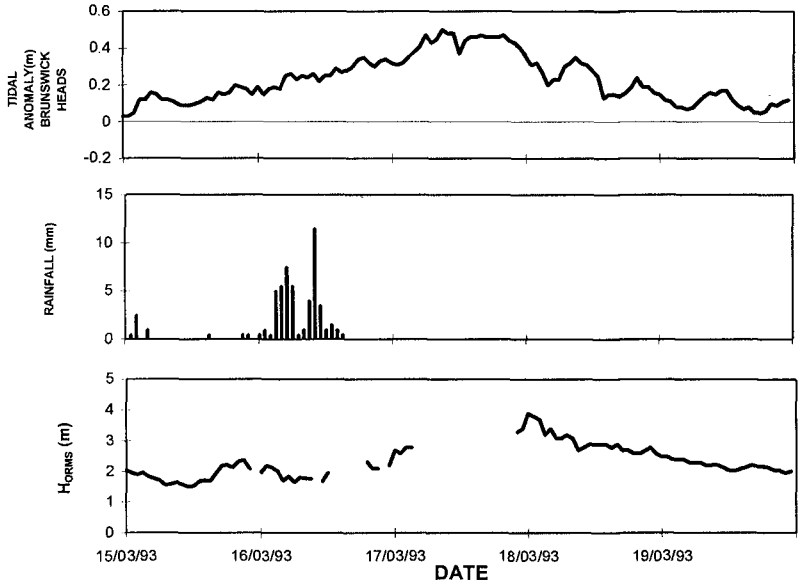


Figure 8. Time series of rainfall, wave height and measured tidal anomaly in the Brunswick River during (A) Cyclone Roger and (B) Cyclone Violet.

These observations point towards long periodic ocean waves as the main contributors to tidal anomalies in the absence of rainfall effects. These long waves would also contribute to tidal anomalies measured at Coffs Harbour and in Sydney Harbour where the effect of waves and fresh water flow would be negligible. For a discussion of tidal anomalies in Sydney Harbour, see Wyllie et al (1993).

The fact that anomalies of the ‘‘Cyclone Roger type’’ do not occur in connection with all cyclones underlines the complication nature of the long periodic ocean waves that might cause them (eg Tang & Grimshaw, 1995).

Modelling River Entrance Water Levels

The approximate role of waves, winds and currents in generating river entrance water levels can be understood using a fairly simple numerical model as indicated in the following.

Governing equations

The model is based on the momentum principle applied to the control volume in Figure 9.

The x- momentum equation for this volume can be written:

$$\rho h \delta x W \frac{\partial U}{\partial t} = -\delta(\rho[D + \eta]WU^2) - \delta(\rho g \eta[D + \eta]W) - \delta(S_{xx}W) + \tau_w \delta_x W - \tau_b \delta_x W \tag{8}$$

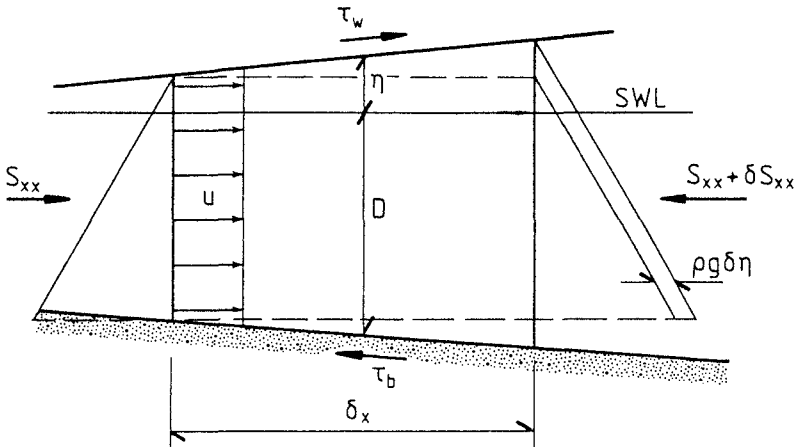


Figure 9. Control volume at a river mouth. The width of the channel is $W=W(x)$, h is the total depth $h=D+\eta$, and x is positive landwards.

Where U is the velocity averaged over a wave period so that the left hand side represents acceleration of the mean flow for example due to tidal changes. On the right hand side, the first term represents the change in current momentum flux over the length δ_x . The second term is the change in the hydrostatic pressure force, the third is the wave radiation stress force, the fourth is the wind stress force and the fifth is the bed shear stress force. Friction

along the sides of the channel is also included in the last term. As usual, ρ is the density of water and g is the acceleration of gravity.

If the length of the model area is short compared to $T_{tidal} \sqrt{gD}$ quasi steadiness can be assumed and the left hand side becomes zero. Then division by $\rho g W [D + \eta]$ leads to

$$\delta\eta = -\delta\left(\frac{U^2}{2g}\right) - \frac{1}{\rho g [D + \eta]} \delta S_{xx} + \frac{\tau_w \delta x}{\rho g [D + \eta]} - \frac{\tau_b \delta x}{\rho g [D + \eta]} \tag{9}$$

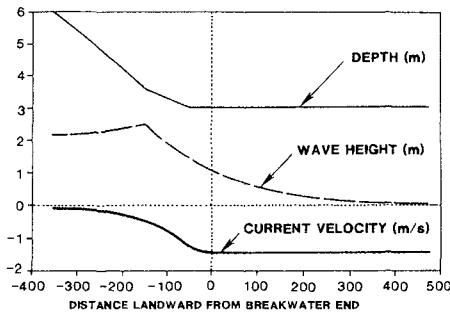
This equation can, with a given discharge $Q = UW (D + \eta)$ be used alternatively to find the setup $\eta (x)$ starting from the seaward boundary (x_s, D_s, η_s) with $D + \eta \approx D$ in the first iteration.

Preliminary Results

To gain a general impression of the behaviour of the system an example is shown in Figure 10 a, b.

These results show that the spreading current generates a set down effect of the order U^2_{max}/gh at the end of the breakwaters ($x=0$) which works opposite to the setup caused by wave breaking in the same area. This is probably why the detailed water level measurements from the Brunswick River show no measurable setup even in conditions with a metre or more of shoreline setup at the neighbouring beach. For the case above, the shoreline setup would be of the order $0.4 H_o = 0.8m$.

A



B

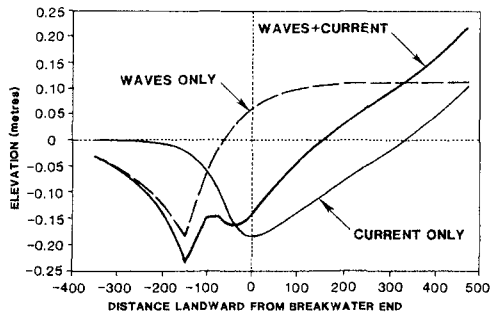


Figure 10(A) Assumed distributions of wave height, depth and current velocity. (B) Resulting surface elevations with current alone, waves alone and with both waves and current. The bed (+side) friction was calculated as: $\tau_b = 0.5\rho f_c |U| U$ with $f_c = 0.001$, and the wind stress as: $\tau_w = C_{10} \rho_{air} U_{10}^2 \cos\alpha_w$ with $U_{10} = 10m/s$, $C_{10} = 0.003$ and $\alpha_w = 20^\circ$.

Conclusions

Detailed mean water level measurements from the Brunswick River suggest that waves generate very little setup at river entrances of this type. Measurements indicate that over heights inside the area of wave breaking in the Brunswick River are typically smaller than at the same depth in the neighbouring surf zone with the same waves. This difference between surf zones and river mouths is thought to be due to the momentum flux of the river current and the current's influence on the wave breaking process. Nevertheless, tidal anomalies of the order 0.5m are measured once or twice a year by tide gauges just inside river entrances along the east coast of New South Wales. These anomalies are thought to be mainly due to freshwater outflow and/or oceanic phenomena which have yet to be fully explained.

Acknowledgments

This study was funded through the Floodplain, Estuary and Coastal Management Programs of the NSW Department of Land and Water Conservation.

Tidal anomaly, wave and rainfall data used in the paper were supplied Manly Hydraulics Laboratory. The assistance of Steve Wyllie and Peter Davidson is gratefully acknowledged.

References

- Goring, D G & R G Bell (1993): Effect of barometric pressure on sea level in the Bay of Plenty, New Zealand, *Proc. 11th. Australasian Conference on coastal Engineering, Townsville*, pp 415-419.
- Gourlay, M R (1992): Wave set-up, wave run-up and beach water table: Interaction between surf zone hydraulics and ground water hydraulics. *Coastal Engineering*, Vol.17, pp 93-144.
- Hamon, B V (1966): Continental shelf waves and the effect of the atmospheric pressure and wind stress on sea level. *J. Geophysical Research*, Vol. 71, No. 12, pp 2883-2893.
- Hanslow, DJ & P Nielsen (1992): Wave setup on beaches and in river entrances. *Proc. 23rd Int. Conference Coastal Engineering, Venice*, pp 240-252.
- Longuet-Higgins, MS & RW Stewart (1964): Radiation stress in water waves, a physical discussion with applications. *Deep Sea research*, Vol. 11, pp 529-562.
- Manly Hydraulics Laboratory (1993): NSW ocean tide levels annual summary 1992/93. Report MHL658.
- Nielsen, P (1988): Wave setup: A field study. *J. Geophysical Research*, Vol. 93, No C3, pp 15643-15652.
- Nielsen, P (1989): Wave setup and runup: An integrated approach. *Coastal Engineering*, Vol. 13, pp 1-9.

Nielsen, P, G A Davis, JM Winterbourne & G Elias (1988): Wave setup and the watertable in sandy beaches. New South Wales Public Works Department, TM 88/1, 132pp.

Savage, R P (1957): Model tests for hurricane protection project. Technical Bulletin, US. Army Corps of Engineers, Washington DC.

Tang, YM & R Grimshaw (1995) A model analysis of coastally trapped waves generated by tropical cyclones. *J. Physical Oceanography*, Vol. 25 pp 1577-1598.

Toba, Y, I Noriko, H. Kawamura, E. Naoto and ISF Jones (1990): Wave dependence of sea surface wind stress. *J. Physical Oceanography*, Vol. 20, No. 5, pp 705-721.

Van Dorn, W G (1976): Setup and runup in shoaling breakers. *Proc. 15th. International Conference on Coastal Engineering*, ASCE, pp 738-751.

Wyllie, SJ, DJ Gorham & PJ Davidson (1993): Understanding tidal anomalies along the NSW Coast. *Proc. 11th. Australasian Conference on Coastal Engineering*, Townsville, pp 421-425.

CHAPTER 175

Scour at Coastal Inlet Structures

Steven A. Hughes¹ and J. William Kamphuis²

Abstract: Scour at inlet navigation structures was investigated using a series of movable-bed physical models. Experiments included ebb and flood flows, sometimes combined with wave action. A new and potentially important scour mechanism was identified for situations where the ebb-flow discharge is redirected by a navigation structure. As ebb flow is deflected, flow velocities increase and a scour trench forms adjacent to the jetty.

In this paper formulations from inviscid jet theory are used to develop an easily-applied, but crude, prediction capability for maximum flow velocity in terms of entrance channel velocity and inlet geometry. A simplified scour prediction method is also provided, but much needs to be done to make it more realistic. Preliminary conclusions are given about scour produced by flood flow combined with waves.

1 Introduction

Scour hole formation adjacent to the channel-side toe and near the head of protective inlet jetty structures is a troublesome problem at many navigation inlets. Without remedial action, continued scour hole growth may result in jetty instability and partial collapse of the structure. In addition, deep scouring adjacent to the channel side of a protective jetty may be accompanied by shoaling of the maintained navigation channel, shifting the navigation channel dangerously close to the jetty.

These inlet scour problems were investigated through a comprehensive set of movable-bed model experiments conducted jointly by Queens University in Canada and the Coastal Engineering Research Center (CERC) in the United States. The experiments examined flood-flow and ebb-flow scour that develops at inlets under various combinations of tidal flow discharge, flow direction, and incoming wave action. The goal of the experiments was to develop simple empirical relationships for

¹Research Hydraulic Engineer, US Army Engineer Waterways Experiment Station, Coastal and Hydraulics Laboratory, 3909 Halls Ferry Road, Vicksburg, Mississippi 39180-6199 USA.

²Professor, Department of Civil Engineering, Ellis Hall, Queens University, Kingston, Ontario, K7L 3N6 CANADA.

estimating maximum scour depth in terms of easily determined parameters related to tidal discharge, channel geometry, and incident wave parameters.

From a survey of scour problems experienced at inlets (Lillycrop and Hughes 1993), it appears that one of the more important physical mechanisms causing scour at inlets during ebb flow is strong ebb currents that exit the inner bay and impinge on the structure at an angle as shown schematically by Figure 1. Laboratory observations indicated that as the ebb flow is deflected, the width of the flow parallel to the navigation structure is reduced, much like the deflection of a water jet. This results in increased flow velocity adjacent to the structure in order to maintain the same flow discharge over the reduced cross-section. Over many ebb-tidal cycles the increased velocities scour the bottom and enlarge the flow cross-sectional area until eventually flow velocities are reduced to non-scouring levels. The scour process is further complicated by the influence of short-period waves in the channel, entrainment at the flow shear interface, changes in flow velocity over the ebb cycle, and the influence of a porous jetty structure.

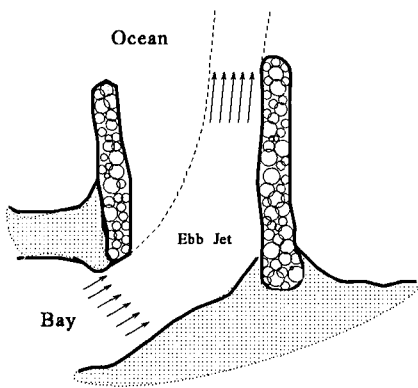


Figure 1: Ebb Flow Deflection.

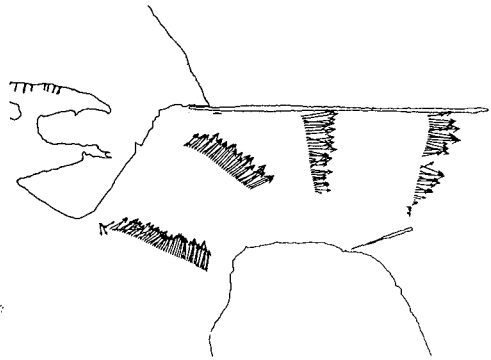


Figure 2: Depth-Averaged Ebb-Flow Velocities at Ponce de Leon Inlet.

Field evidence of velocity increases due to ebb-flow deflection is shown in Figure 2, which plots depth-averaged ebb-flow velocity measurements obtained at Ponce de Leon Inlet, Florida. At the time of these measurements a scour trench had already formed adjacent to the jetty. Otherwise, the velocities would likely be even greater next to the jetty.

2 Laboratory Experiments

A series of deflected ebb-flow laboratory movable-bed model tests were conducted in a 15-m-wide wave flume at CERC with an undistorted nominal length scale of 1:20 and a water depth of 30 cm. These tests expanded on earlier studies conducted at Queens University at 1:30 scale. The experiment layout is sketched in Figure 3.

A conventional model jetty was constructed on a 45-cm-deep flat bed of fine quartz sand having mean diameter of 0.13 mm. The jetty toe was protected with a small stone scour blanket. The current manifold position and angle were adjustable to allow

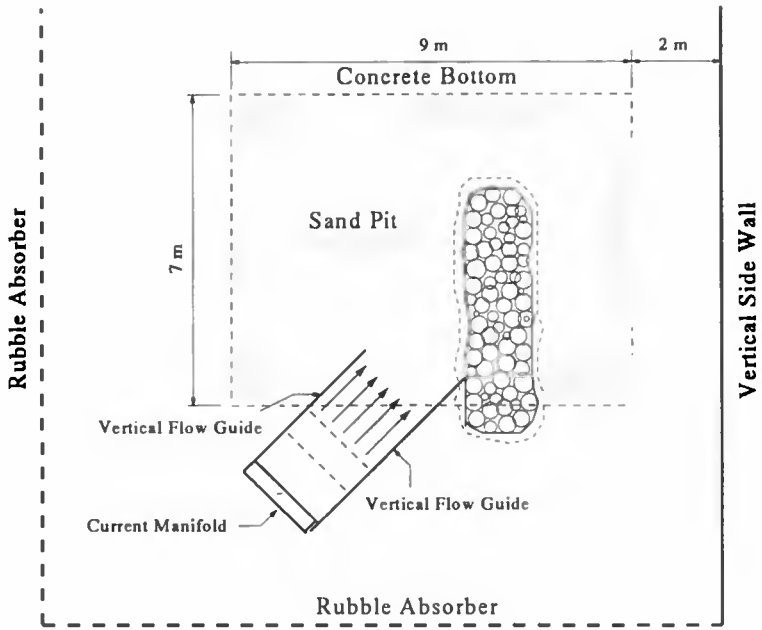


Figure 3: Ebb Flow Experiment Layout.



Figure 4: Scour After 10 Hours with 60° Deflection (View from Seaward of Jetty).

different deflection angles (30° , 45° , 60°) relative to the jetty centerline. Adjustable vertical flow guides were used to direct the ebb flow, and flow straighteners helped to make the flow more uniform before passing over the movable bed. Total flow discharge was monitored and controlled at an upstream valve.

Laboratory measurements of flow velocity throughout the study region were accomplished using an array of three SonTek acoustic Doppler current meters (ADV's) mounted on an instrument catwalk spanning the flume. At each location the ADV's recorded a 3-minute velocity time series (25-Hz sample rate) at a depth 15 cm below the water surface. (All measurement values throughout this paper are in model units.)

Mean velocity at the input entrance channel was adjusted to be slightly above the 28–30 cm/s estimated to be required for incipient motion of the sediment. Dye injection indicated the deflected flow width adjacent to the jetty narrowed considerably similar to Figure 1. This gave rise to increased velocities adjacent to the jetty and significant scour along the jetty structure. Depending on the flow deflection angle, mid-depth mean velocities adjacent to the structure varied between 40–50 cm/s at the start of the experiments while the sand bed was still horizontal and scour was in initial stages.

Experiments continued for a total of 10 hours by which time it appeared that scour had reached an equilibrium for that flow condition. A portion of the scoured sediment was transported seaward by the ebb flow and deposited in a “fan” in a deeper part of the flume, whereas some sediment was deposited in a “berm” running parallel to the scour trench. Typical scour results are illustrated by the photograph in Figure 4, which was taken from a seaward position after an experiment with a 60° deflection angle. The photograph shows that the scour apron may have helped protect the armor slope.

Post-experiment surveys of the bed were completed using a Delft bed profiler mounted on the traversing catwalk. Bed elevation data were obtained at 4-cm spacings on survey lines running perpendicular to the jetty centerline. There was 20-cm spacing between survey lines.

3 Deflected Ebb Jet Theory

3.1 Analogy to Jet Flow

The deflected ebb-flow observed in the laboratory experiments is quite similar to a two-dimensional jet impinging on a solid boundary, and an analytical approach to deflected ebb-flow hydrodynamics was developed based on this analogy. Using the notation and coordinate system detailed in Figure 5, an inviscid, potential flow solution can be specified that links the flow field to the geometry of the solid boundaries.

The assumptions associated with this flow solution are given as:

- Incompressible, nonviscous, ideal fluid (no boundary layers, boundary layer separation, or flow entrainment at the jet “free boundary”)¹
- Steady flow in two dimensions (horizontal bottom)

¹The term “free boundary” refers to the interface between the jet and the adjacent still water as represented by the dashed line in Figure 1.

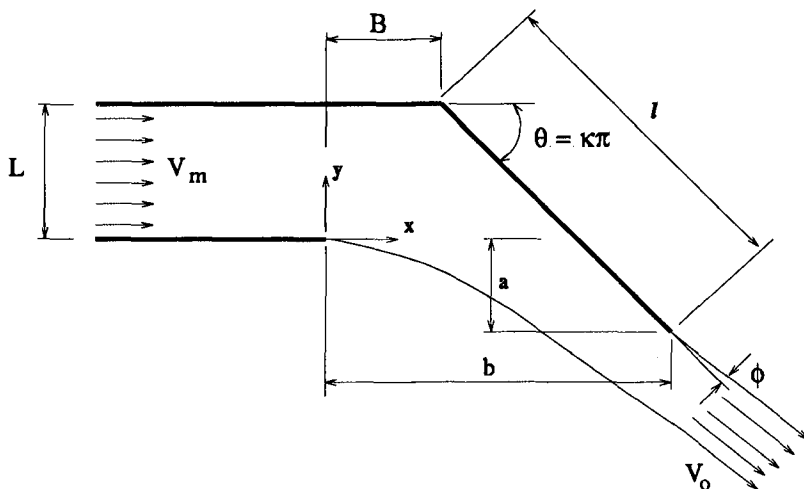


Figure 5: Ebb Jet Coordinate System.

- Nonrotational flow (velocity potential exists)
- Gravity has no effect on flow (implies relatively high velocities, and no cross-channel water surface setup due to centrifugal forces)

On solid boundaries and on flow streamlines there is the “no-flow” condition, i.e.,

$$\frac{\partial \phi}{\partial n} = 0 \tag{1}$$

and on the “free boundaries” pressure is assumed constant. This means that on the free boundary streamline, Bernoulli’s Equation is given as

$$\frac{V_o^2}{2} + gz = constant \tag{2}$$

Neglecting gravitational effects reduces the free-boundary condition of Eqn. (2) to

$$V_o = Constant \tag{3}$$

3.2 Potential Flow Solution

The solution to this particular jet-flow problem was given in Gurevich (1965). Without presenting details, the solution was found by conformally mapping the jet and its boundaries into a unit circle in the complex plane. Conformal mapping is a typical approach for this family of jet-flow problems. Other techniques are unsuccessful because the location of the jet free boundaries is not known *a priori*.

The resulting solution² is expressed as the following three equations (Eqns. 4-6)

²Note that in Gurevich (1965), page 63, the denominator of the second term under the integral of Eqn. (6) was incorrectly given as “ $t + (1/h)$ ” rather than the correct value of “ $t - (1/h)$ ”.

$$\frac{\ell}{L} = \frac{h^\kappa}{\pi} \int_0^1 \frac{d\xi}{\xi^\kappa} \left[\frac{1}{\xi+h} + \frac{1}{\xi+(1/h)} - \frac{2[\xi+\cos(\beta)]}{\xi^2+2\xi\cos(\beta)+1} \right] \quad (4)$$

$$\frac{a}{L} = 1 - \frac{\ell}{L} \sin(\pi\kappa) \quad (5)$$

$$\frac{b}{L} = \frac{\ell}{L} \cos(\pi\kappa) - \frac{h^\kappa}{\pi} \text{V.P.} \int_0^1 \frac{dt}{t^\kappa} \left[\frac{1}{t-h} + \frac{1}{t-(1/h)} - \frac{2[t-\cos(\beta)]}{t^2-2t\cos(\beta)+1} \right] \quad (6)$$

where "V.P." in Eqn. (6) means take the Cauchy principal value of the integral. In these equations, the parameter h is defined by the expression

$$h^\kappa = \frac{V_m}{V_o} \quad (7)$$

and the angle β is related to the jet exit angle, ϕ , by the geometric relationship

$$\beta = \frac{\phi}{\kappa} + \pi \quad (8)$$

with both angles given in radians.

The main difficulty with this solution is that the equations explicitly solve for the deflected jet geometry (ℓ/L , a/L , b/L) given the entrance and exit velocities (V_m , V_o), jet deflection angle ($\theta = \kappa\pi$), and jet exit angle (ϕ). In application to inlets, the geometry is usually known, and the flow solution is sought. Because the equations cannot be inverted, the only recourse is an iterative or nomogram solution.

Figure 6 presents an example of a nomogram that was generated for an ebb-flow deflection angle of 45° ($\kappa\pi = \pi/4$). This nomogram was constructed by solving Eqns. (4) and (6) at over 850 evenly distributed grid points bounded by the axes shown in Figure 6, and then contouring the results. The solid lines are contours of equal values for ℓ/L and the dashed lines represent constant values of b/L . For a given inlet geometry the unique solution is found at the intersection of the appropriate values of ℓ/L and b/L . The jet exit angle, ϕ , in degrees is read from the abscissa, and the velocity function, h , is read from the ordinate. The unknown velocity, V_o , corresponding to a value of V_m can now be determined from Eqn. (7). Figure 7 illustrates the variation in velocity ratio, V_o/V_m as a function of ebb-jet deflection angle, θ , and geometry parameter, B/L (see Figure 5 for definition of B).

Once values of h and ϕ are known, it is also possible to specify the location of the inviscid "free boundary" using the following equations that were derived based on Gurevich's (1965) formulation of the complex velocity potential.

$$dx = \frac{Lh^\kappa}{\pi} \left[\frac{\sin\sigma\kappa + h\sin\sigma(1-\kappa)}{(\cos\sigma-h)^2 + \sin^2\sigma} + \frac{\sin\sigma\kappa + \frac{1}{h}\sin\sigma(1-\kappa)}{(\cos\sigma-\frac{1}{h})^2 + \sin^2\sigma} - \frac{\sin\sigma\kappa + \sin[\sigma(1-\kappa)-\beta]}{2-2\cos(\sigma-\beta)} - \frac{\sin\sigma\kappa + \sin[\sigma(1-\kappa)+\beta]}{2-2\cos(\sigma+\beta)} \right] d\sigma \quad (9)$$

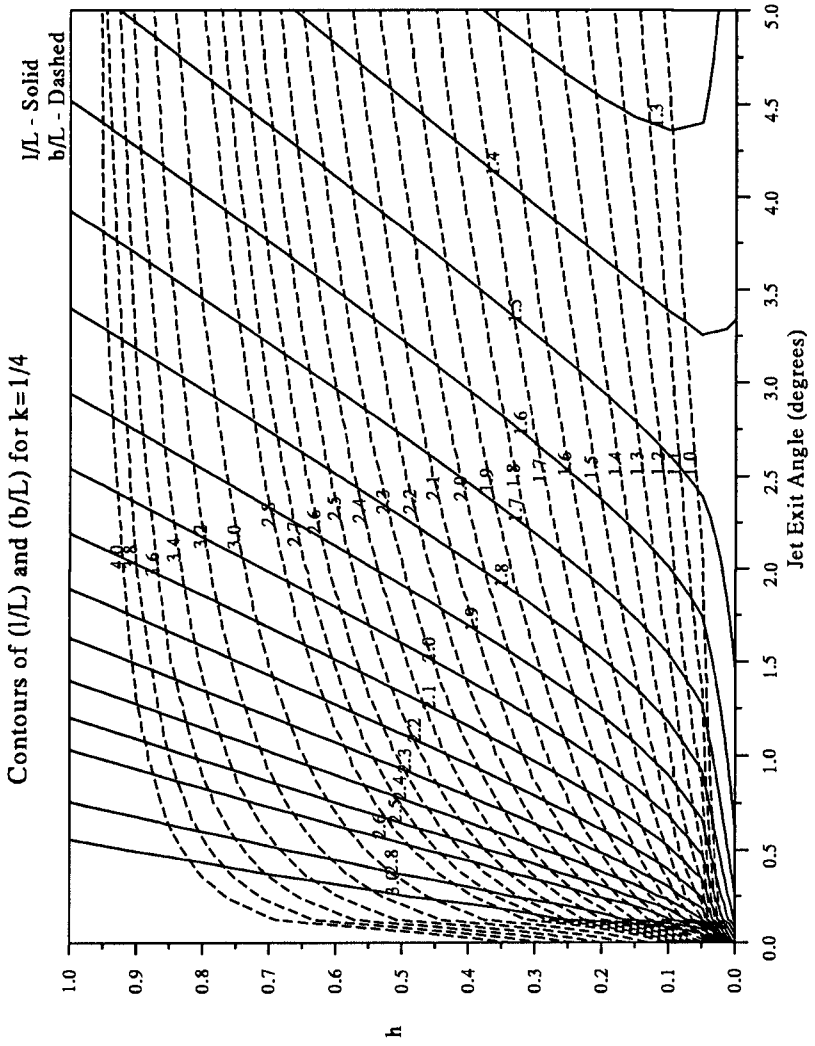


Figure 6: Nomogram for Ebb-Flow Deflection Angle of 45°.

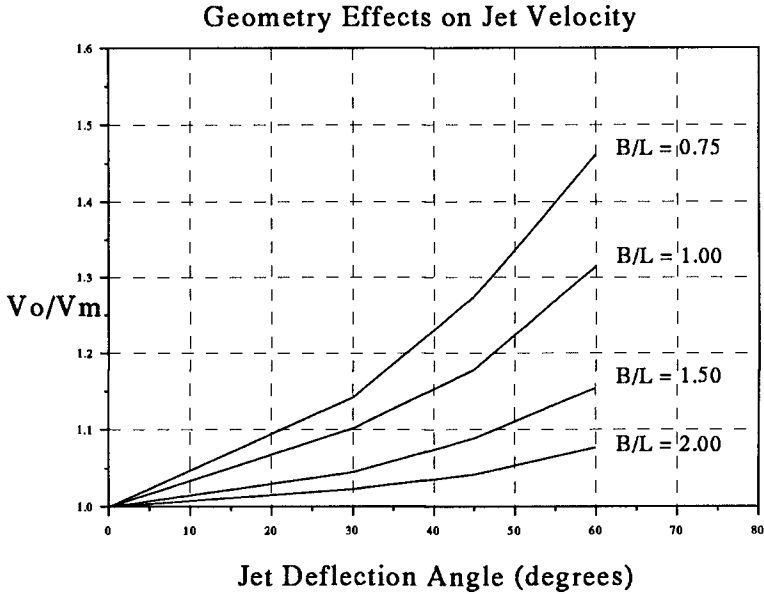


Figure 7: Effect of Geometry on Ebb Jet Velocity Ratio.

$$\begin{aligned}
 dy = \frac{Lh^\kappa}{\pi} & \left[\frac{\cos \sigma \kappa - h \cos \sigma (1 - \kappa)}{(\cos \sigma - h)^2 + \sin^2 \sigma} + \frac{\cos \sigma \kappa - \frac{1}{h} \cos \sigma (1 - \kappa)}{(\cos \sigma - \frac{1}{h})^2 + \sin^2 \sigma} - \right. \\
 & \left. - \frac{\cos \sigma \kappa - \cos [\sigma (1 - \kappa) - \beta]}{2 - 2 \cos(\sigma - \beta)} - \frac{\cos \sigma \kappa - \cos [\sigma (1 - \kappa) + \beta]}{2 - 2 \cos(\sigma + \beta)} \right] d\sigma
 \end{aligned} \quad (10)$$

Values of x , y on the free boundary relative to the origin shown in Figure 5 are found by numerically integrating Eqns. (9-10) between zero and different values of σ lying between $0 \rightarrow \beta$, where β (in radians) is given by Eqn. (8).

3.3 Caveats!

It is important to note that the inviscid jet theory does **NOT** include any allowance for the following important “*real world*” effects related to deflected ebb flow at inlets:

- Turbulent flow entrainment between the ebb jet and adjacent still water
- Boundary layer losses due to the jetty structure and the bottom
- Effects of gravity on the ebb flow (possible secondary flows)
- Sloping, porous rubble-mound structures rather than vertical side walls

- Nonuniform entrance flow distribution
- Nonuniform depth in approach channel
- Wave effects on the ebb jet

Nevertheless, this initial flow approximation technique provides a conservative estimate of maximum flow velocity that would occur in the absence of the "real world" effects, and it can be used as a foundation on which to incorporate empirical approximations for these effects.

4 Comparison to Measurements

Figure 8 plots time-averaged velocity vectors measured at mid-depth for an experiment where the entrance channel was oriented 60° to the jetty. The average entrance velocity was $V_m = 32$ cm/s, and the dashed line in the figure is the inviscid "free boundary" calculated using Eqns. (9) and (10) with appropriate values of h and ϕ from the nomograms. Velocity increase along the jetty is clearly evident, as is flow entrainment along the ebb jet free boundary.

Ebb-jet theory estimates of maximum velocity, V_o , are compared to measured values near the seaward end of the jetty in Figure 9. Flow deflection angles of 60° (upper) and 45° (lower) are shown, and the plots are oriented with the structure to the left side (view from offshore). The theory predicts a constant velocity from the jetty out to the jet free boundary, at which point the velocity becomes zero at the interface.

Close to the jetty, the inviscid jet theory provides good estimates based only on geometry and entrance velocity, V_m (32 cm/s). Further away from the structure, flow entrainment between the ebb jet and adjacent still water had a significant impact.

Neglected altogether is the possibility that some of the flow acceleration might be due to secondary flows generated by a slope in the water elevation caused by centrifugal forces as the flow is deflected. This mechanism is thought to be important in river bends. Field measurements at an inlet where ebb flows are deflected by a structure would provide insight into whether secondary flows may also be an important factor in flow acceleration and subsequent scour.

5 Conservative Scour Prediction

Inviscid jet theory, coupled with flow continuity, can provide very crude (and overly conservative) scour estimates for deflected ebb-jet flows. Flow continuity requires the discharge at the entrance section (Q_m) be equal to the discharge at the narrowest part of the jet (Q_o), i.e.,

$$V_m d_m L = V_o d_o W_o \quad \text{or} \quad \frac{V_m}{V_o} = \frac{d_o}{d_m} \frac{W_o}{L} \quad (11)$$

where d_m and d_o are the total depths at the entrance and narrow section, respectively, and W_o is the width of the jet at its narrowest. Assuming an initially flat bottom where $d_m = d_o$, the width ratio W_o/L in Eqn. (11) can be expressed as

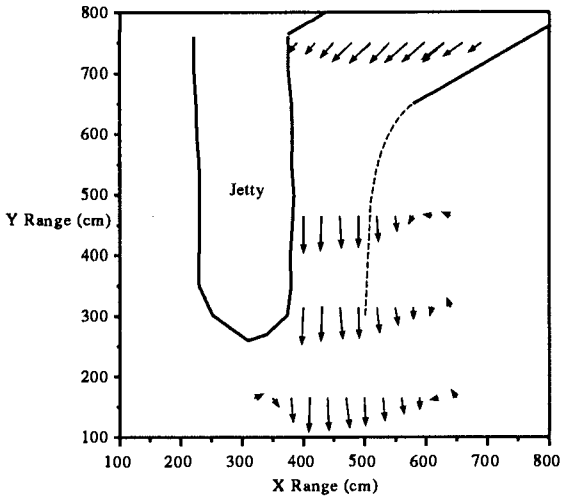


Figure 8: Measured Mid-Depth Velocities for 60° Deflection Angle.

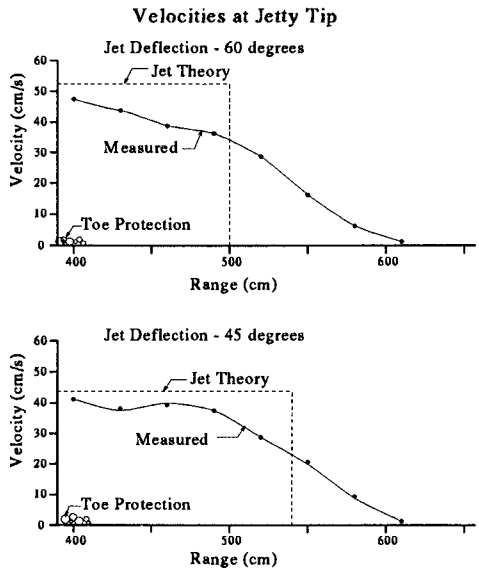


Figure 9: Ebb-Jet Theory Compared to Mid-Depth Velocity Measurements.

$$\frac{W_o}{L} = h^\kappa \quad (12)$$

where the velocity ratio was replaced by Eqn. (7). If we assume the velocity, V_m , in the entrance channel is just at the sediment incipient motion criteria, we expect the bottom to erode at the narrowest part of the ebb jet until the velocity at that location reduces from V_o to V_m . Provided the width of the jet does not change, the depth increase necessary to maintain flow discharge is found from Eqn. (11) with $V_o = V_m$ and W_o/L given by Eqn. (12), i.e.,

$$\frac{d_o}{d_m} = h^{-\kappa} \quad (13)$$

Figure 10 shows two applications of this simplified scour prediction method compared to movable-bed model scour results. The dashed line indicates scour prediction using inviscid jet theory. Obviously, neglecting the effects of shear flow entrainment and bottom boundary layer flow reduction (and possibly secondary flows) has resulted in substantial over-prediction of scour. The assumption of constant W_o is also suspect.

6 Flood Scour Observations

Kidney-shaped scour holes situated at the tips of coastal inlet structures are a commonly observed type of scour. In some instances these scour holes are permanent features, but don't appear to threaten the structure toe. In other cases, structure toe instability has resulted with subsequent unraveling of the head armor layer and structure damage.

Preliminary tests conducted at Queens University examined development of scour holes at jetty heads under various combinations of flood-flow magnitude and direction, wave severity, and incident wave directions of -20° , 0° , and $+30^\circ$ relative to the jetty axis. In these tests the most severe jetty-tip scouring under flood flow currents occurred when both waves and currents approached from a -20° direction as illustrated in Figure 11.

Apparently, flood flow is accelerated as it is bent around the jetty tip similar to the classical case of potential flow around a sharp corner. The addition of waves from the same direction as the current resulted in wave diffraction around the jetty tip, which when combined with the current, increased the depth and areal extent of the scour.

7 Conclusions

Based on movable-bed laboratory experiments, a new and potentially important scour mechanism has been identified for situations where the ebb-flow discharge is redirected by an inlet navigation structure. As the ebb flow is deflected, flow velocities increase resulting in the formation of a scour trench adjacent to the jetty structure toe. This flow situation was recognized to be somewhat analogous to a free jet impinging on a wall, and inviscid jet theory was used to develop an easily-applied, but crude, prediction capability for maximum velocity in terms of entrance channel velocity and

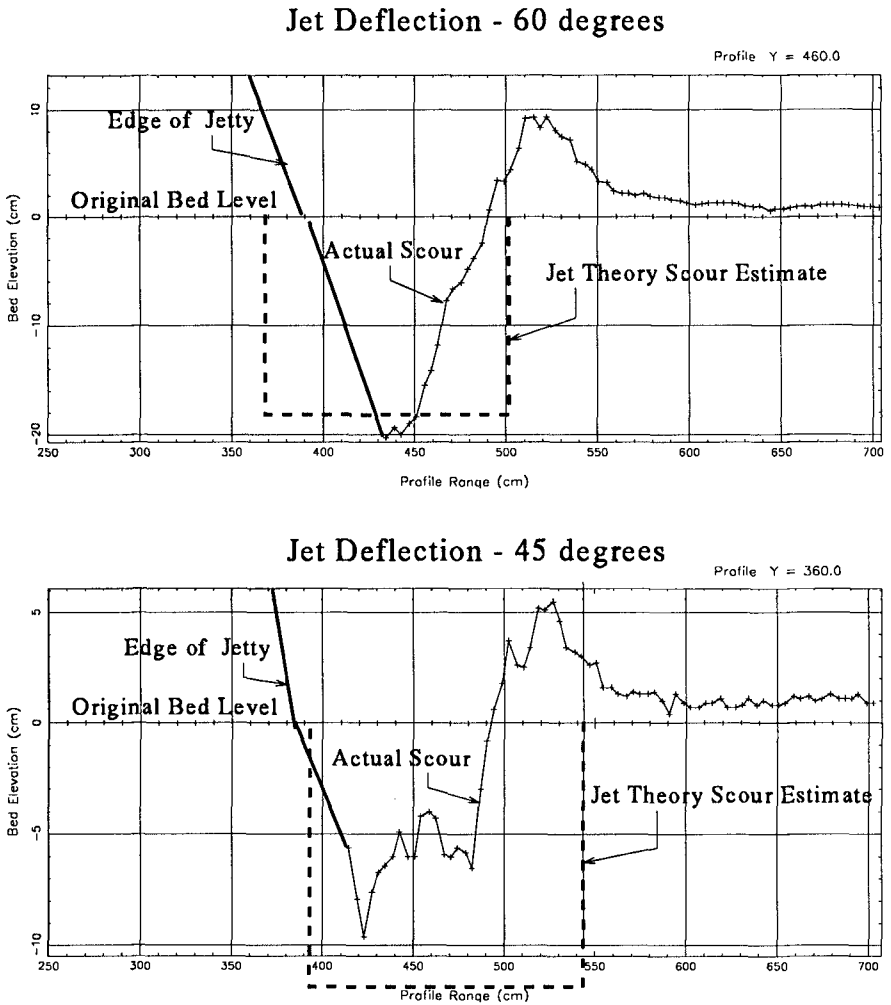


Figure 10: Conservative Scour Estimates for Two Experiments.

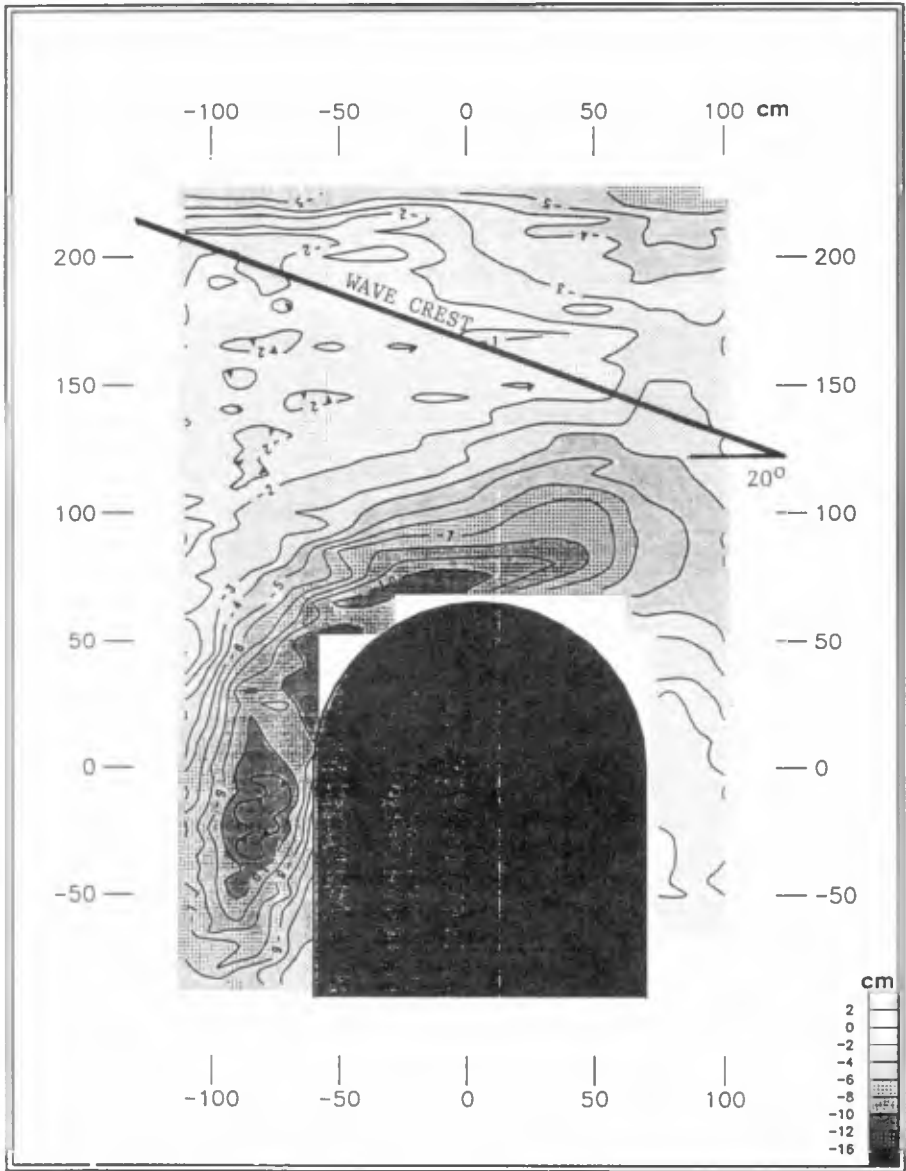


Figure 11: Example of Flood-Flow Scour Model Results.

boundary geometry. Comparison of inviscid theory to laboratory measurements indicated reasonable agreement near the jetty structure, but over-prediction away from the structure due to flow entrainment at the shear interface between the ebb-jet and adjacent still water.

A simple, overly conservative, scour prediction method was offered based on inviscid jet theory, but the method suffers from not including empirical adjustments for the "real world" effects of shear flow entrainment and bottom boundary layers. However, this inviscid theory could be used as a starting point for incorporating these necessary features. Future efforts will extend and refine these preliminary design tools.

An initial examination of movable-bed model experiments simulating scour holes produced near the tips of jetties by flood currents indicated that the most severe erosion occurs on the lee side of the jetty tip when currents and waves approach at an angle to the jetty centerline. Although currents alone are sufficient to create scour holes, the addition of waves promotes more rapid scour to greater depths over a wider area.

8 Acknowledgements

The research described and the results presented herein, unless otherwise noted, were obtained from research conducted under the *Scour Holes at Inlet Structures* work unit in the *Coastal Inlets Research Program* at the US Army Engineer Waterways Experiment Station (WES). Permission to publish this information was granted by the Chief of Engineers. Mr. Raymond Reed (WES) and Ms. Catherine Bishop and Mr. Jack Kooistra (Queens University) are acknowledged for their valuable contributions to the laboratory experiments.

9 References

- Gurevich, M. I. (1965). *Theory of Jets in Ideal Fluids*, Translated from the Russian by R. L. Street and K. Zagustin, Academic Press, New York.
- Lillycrop, W. J., and Hughes, S. A. (1993). "Scour Hole Problems Experienced by the Corps of Engineers; Data Presentation and Summary," Miscellaneous Paper CERC-93-2, US Army Engineer Waterways Experiment Station, Coastal Engineering Research Center, Vicksburg, Mississippi.

CHAPTER 176

Probability distribution of the maximum wave height along a sea wall with finite width

Akira Kimura ¹ and Takao Ohta ²

Abstract

A probability distribution of the simultaneous maximum wave amplitude within a finite width along a virtual vertical plane placed in a 3-dim. irregular sea state is studied theoretically. The probability distribution differs considerably from the Rayleigh distribution even when the width of the structure is an order of 1/10 significant wave length. The difference increases with the interval width. Especially, apparent probability of large amplitude is considerably larger than that expected from the Rayleigh distribution. Coastal structures which were designed with sufficient safety margin have sometimes failed. There are possibilities that the structures were not attacked by "unexpectedly large waves" but large waves which could have been possibly expected if we had taken the width effect into account.

1. Introduction

Probability distribution of zero-crossing irregular wave heights measured by a "fixed wave gauge" agrees well with the Rayleigh probability distribution regardless of a wave spectrum. A zero-crossing wave height is defined as a difference between the maximum and minimum water levels within a zero-crossing wave period in the ordinary definition. When a short crested irregular wave acts on the structure such as a breakwater, wave height along it changes spatially. Although visual observation can roughly recognize a maximum wave height and its location, but single wave gauge can not always catch 3-dim. wave peaks and troughs of the short crested waves but only record a water surface displacement at its fixed position (Fig.1). However, if a big wave hits any part of the structure, it is recognized that the structure is attacked by a big wave. Suppose many wave gauges

¹Prof. of Tottori Univ., Faculty of Eng., Koyama Minami 4-101, Tottori, Japan

²Research Associate of Tottori Univ., Faculty of Eng., Koyama Minami 4-101, Tottori, Japan

are set up with negligibly small intervals on the structure, even though it seems unpractical. And if the largest one is adopted selectively among measured wave heights with these wave gauges as a simultaneous wave height during an action of a single (short crested) wave, a probability distribution of the wave height defined in this way may change according to the width of the structure. Statistical properties of the selectively defined wave height seems necessary to consider in a design of structure, if the structure is such a type that a local damage may induce a failure of the whole structure. This study deals with a theoretical probability distribution of the spatially maximum wave amplitudes along a structure with a finite width placed in a 3-dim. irregular sea state. A quite different probability distribution of wave amplitudes from the Rayleigh distribution is obtained if the width is not small.

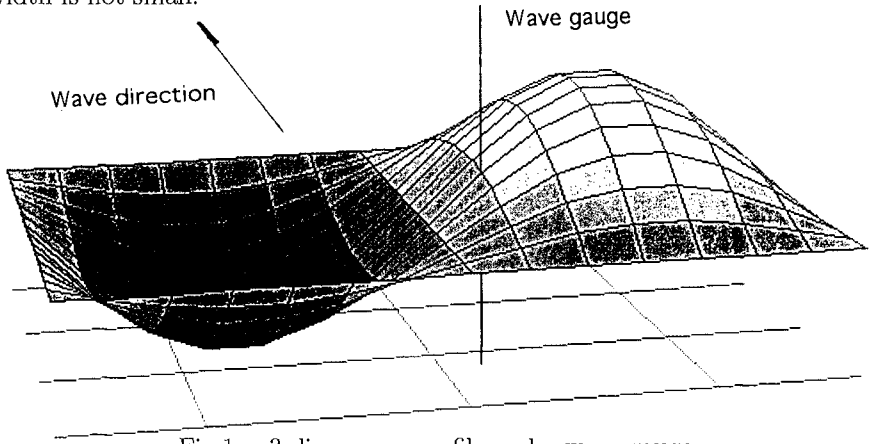


Fig.1 3-dim. wave profile and a wave gauge

2. Wave number spectrum

x and y axes are taken on a still water level so that x axis takes a dominant wave direction and z axis is taken positive upward. Water surface elevation ξ of a 3-dim. short crested irregular wave is expressed as,

$$\xi = \sum_{i=1}^{\infty} c_i \cos(\mathbf{k}_i \mathbf{x} + 2\pi f_i t + \varphi_i) \tag{1}$$

in which c_i , \mathbf{k}_i , f_i and φ_i are amplitude, wave number, frequency and phase angle of the i -th component wave respectively, $\mathbf{x}=(x, y)$ and t is time. c_i is determined from

$$\sum_{f_i, \theta_i}^{f_i+df, \theta_i+d\theta} c_i^2/2 = E(f_i, \theta_i) df d\theta = S(f_i)G(\theta_i; f_i) df d\theta \tag{2}$$

where θ and $E(f, \theta)$ are the direction of wave and the directional wave spectrum, $S(f)$ is a power spectrum, $G(\theta; f)$ is a directional function. A wave number

spectrum $E(k_x, k_y)$ is derived from $E(f, \theta)$ as,

$$E(k_x, k_y) = C_g/2\pi \mathbf{k} \cdot E(f, \theta) \quad (3)$$

where k_x , k_y and C_g are x, y components of a wave number \mathbf{k} and group velocity corresponding to the frequency f respectively. New x , y axes which are anti-clockwise rotation of x and y axes around z axis are taken. The angle between x and x axes is θ . The wave number components on the new axes are expressed as,

$$\begin{aligned} k_x &= k_x \cos \theta + k_y \sin \theta \\ k_y &= -k_x \sin \theta + k_y \cos \theta \end{aligned} \quad (4)$$

For simplicity, k_x , k_x , k_y and k_y are replaced by u , u , v and v respectively. Wave profile in the new coordinate is expressed as,

$$\xi = \sum_{n=1}^{\infty} C_n \cos(u_n x + v_n y + 2\pi f_n t + \varepsilon_n) \quad (5)$$

and if a vertical virtual plane H is placed on the new x axis, cross section of ξ on H at $t = 0$ is given as,

$$\zeta = \sum_{n=1}^{\infty} C_n \cos(u_n x + \varepsilon_n) \quad (6)$$

where C_n and ε_n are amplitude and phase angle of the n -th component wave. C_n is determined from,

$$\sum_{u_n, v_n}^{u_n+du, v_n+dv} C_n^2/2 = E(u_n, v_n) du dv \quad (7)$$

The wave number spectrum $E(u, v)$ in eq.(3) is transformed into $E(u, v)$ using the relations,

$$\begin{aligned} u &= u \cos \theta - v \sin \theta \\ v &= u \sin \theta + v \cos \theta \end{aligned} \quad (8)$$

and

$$E(u, v) = \frac{\partial(u, v)}{\partial(u, v)} E(u, v) \quad (9)$$

where $\partial(u, v)/\partial(u, v) = 1$. One dimensional wave number spectrum $E_\theta(u)$ for ζ is given by an integration of $E(u, v)$ in terms of v ,

$$E_\theta(u) du = \sum_{du, v} C^2/2 = du \int_{-\infty}^{\infty} E(u, v) dv \quad (10)$$

When $\theta = \pi/2$, $E_\theta(u)$ is symmetry about $u = 0$. Small angle shift from $\theta = \pi/2$ brings, however, less unsymmetry on $E_\theta(u)$.

3. Maximum amplitude within a finite interval

Amplitude of zero-crossing wave is approximated with a wave envelope. Solid line in Fig.2 shows schematically a wave envelope $R(x)$ on H for $\zeta|_{t=0}$. $R(x)$ is determined by the Rice(1945) method (eq.20). Taylor series expansion of $R(x)|_{t=0}$ around $x = 0$ is given as,

$$R(x) = R(0) + R'(0) x + R''(0) x^2/2 + \dots \dots \dots \tag{11}$$

$R(0)$, $R'(0)$ and $R''(0)$ are amplitude of $R(x)$, its first and second derivative in terms of x at $x = 0$ respectively. First three terms in eq.(11) are used to approximate $R(x)$ in this study assuming the width of concern in Fig.2 ($-\Delta L \leq x \leq \Delta L$: width of the structure) is not large. A difference between the maximum amplitude R_m within the interval and $R(0)$ is given as

$$\begin{aligned} |R'(0)/R''(0)| &\leq \Delta L ; \\ R_m - R(0) &= -\{R'(0)\}^2/2R''(0) \end{aligned} \tag{12}$$

$$\begin{aligned} |R'(0)/R''(0)| &> \Delta L ; \\ R'(0) &\geq 0 \\ R_m - R(0) &= R'(0) \Delta L + R''(0) (\Delta L)^2/2 \\ R'(0) &< 0 \\ R_m - R(0) &= -R'(0) \Delta L + R''(0) (\Delta L)^2/2 \end{aligned} \tag{13}$$

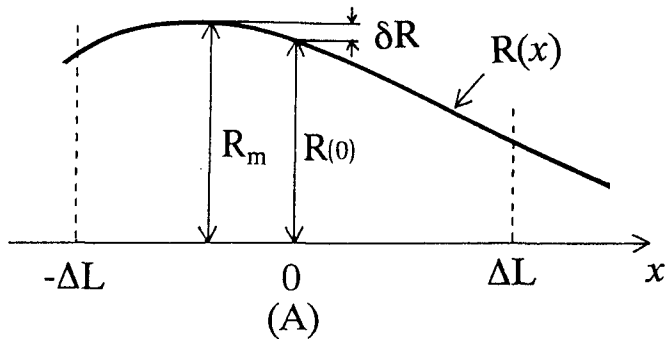


Fig.2 $R(x)$, $R(0)$ and R_m ; wave envelope its amplitude at $x = 0$ and its maximum amplitude within the interval $-\Delta L \leq x \leq \Delta L$

Putting $\delta R = R_m - R(0)$, probability distribution of δR is defined as

$$P(\delta R)_R = \int_S P [R'(0), R''(0); R(0)] dS \tag{14}$$

in which $P[R'(0), R''(0); R(0)]$ is a conditional joint probability distribution for $R'(0)$ and $R''(0)$ and S is a region in which $\Delta R < \delta R < \Delta R + dR$ on condition $R(0)$. Figure 3 schematically shows the region S . Since S is symmetry about R'' axis, a half region ($R' > 0$) is shown. A probability distribution for the maximum amplitude R_m within the interval $-\Delta L \leq x \leq \Delta L$ is defined by

$$P_m(R) = \int_S P(\delta R)_R P [R(0)] dR(0) \tag{15}$$

where $P [R(0)]$ is a probability distribution of $R(0)$ (Rayleigh distribution). Connecting eqs.(14) and (15), $P_m(R)$ is calculated from

$$P_m(R) = \int_R^\infty \int_S P [R(0), R'(0), R''(0)] dS dR(0) \tag{16}$$

in which $P[R(0), R'(0), R''(0)]$ is a joint probability distribution of $R(0), R'(0)$ and $R''(0)$. For simplicity, $R(0), R'(0)$ and $R''(0)$ are expressed as R, R' and R'' respectively.

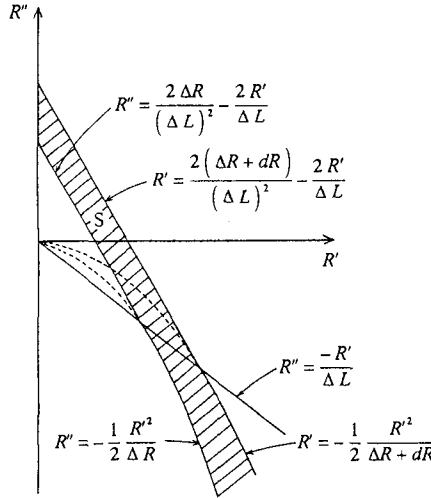


Fig.3 Region of integration S

4. Joint probability distribution for R, R' and R''

Following Rice (1945), joint probability distribution for R, R' and R'' is given as,

$$p(R, R', R'') = \frac{R^3}{8\pi^3 B} \int_0^{2\pi} d\phi \int_{-\infty}^{\infty} d\phi' \int_{-\infty}^{\infty} d\phi''$$

$$\begin{aligned} & \times \exp \left\{ -\frac{1}{2B^2} \left[B_0 R^2 + 2B_1 R^2 \phi' - 2B_2 (RR'' - R^2 \phi'^2) \right. \right. \\ & + B_{22} (R'^2 + R^2 \phi'^2) \\ & - 2B_3 (RR'' \phi' - 2R'^2 \phi' - R' R \phi'' - R^2 \phi'^3) \\ & \left. \left. + B_4 (R''^2 - 2RR'' \phi'^2 + 4R'^2 \phi'^2 + 4RR' \phi' \phi'' + R^2 \phi'^4 + R^2 \phi''^2) \right] \right\} \end{aligned} \tag{17}$$

in which

$$\begin{aligned} B_0 &= (b_2 b_4 - b_3^2) B, & B_{22} &= (b_0 b_4 - b_2^2) B, \\ B_1 &= -(b_1 b_4 - b_2 b_3) B, & B_2 &= (b_1 b_3 - b_2^2) B, \\ B_3 &= -(b_0 b_3 - b_1 b_2) B, & B_4 &= (b_0 b_2 - b_1^2) B, \\ B &= b_0 b_2 b_4 + 2b_1 b_2 b_3 - b_2^3 - b_0 b_3^3 - b_4 b_1^2 \end{aligned} \tag{18}$$

b_n , ($n = 0, 1, 2, 3, 4$) is determined as,

$$\begin{aligned} b_0 &= \langle I_{c1}^2 \rangle = \langle I_{s1}^2 \rangle \\ b_2 &= \langle I_{c2}^2 \rangle = \langle I_{s2}^2 \rangle \\ b_4 &= \langle I_{c3}^2 \rangle = \langle I_{s3}^2 \rangle \\ b_1 &= \langle I_{c1} I_{s2} \rangle = \langle I_{c2} I_{s1} \rangle \\ b_3 &= \langle I_{s2} I_{c3} \rangle = \langle I_{c2} I_{s3} \rangle \end{aligned} \tag{19}$$

in which $\langle \rangle$ means an ensemble mean, I_{ci} , I_{si} , ($i = 1, 2, 3$), R and ϕ are given as,

$$\begin{aligned} I_{c1} &= \sum_{n=1}^{\infty} C_n \cos(u_n x - u_m x + \varepsilon_n) \\ I_{s1} &= \sum_{n=1}^{\infty} C_n \sin(u_n x - u_m x + \varepsilon_n) \\ R &= \sqrt{I_{c1}^2 + I_{s1}^2} \\ \phi &= \tan^{-1}(I_{s1}/I_{c1}) \end{aligned} \tag{20}$$

and

$$I_{c2} = (I_{c1})', \quad I_{s2} = (I_{s1})', \quad I_{c3} = (I_{c1})'', \quad I_{s2} = (I_{s1})'' \tag{21}$$

u_m is a mean wave number of $E_\theta(u)$ (eq.10). In these equations ' and '' mean the first and second derivative in terms of x respectively. For simplicity $E_\theta(u)$ is assumed to be symmetry about $u = 0$. This assumption approximately holds if $|\theta - \pi/2|$ is not large. Integrating eq.(17) in terms of ϕ and ϕ'' ,

$$p(R, R', R'') = 2\alpha \int_0^\infty \exp\{-\beta\phi'^4 - \gamma\phi'^2\} d\phi' \quad (22)$$

$$\alpha = \frac{R^2}{(2\pi)^{3/2} \sqrt{B_4}} \exp\left\{-\frac{1}{2B^2} (B_0 R^2 - 2B_2 R R'' + B_{22} R'^2 + B_4 R''^2)\right\} \quad (23)$$

$$\beta = B_4 R^2 / 2B^2 \quad (24)$$

$$\gamma = (B_{22} R^2 - 2B_4 R R'' + 2B_2 R'^2) / (2B^2) \quad (25)$$

Although Rice(1945) gave an analytical solution for eq.(22), calculation is made numerically in this study.

5. Probability distribution of the maximum amplitude

Bretschneider-Mitsuyasu type wave spectrum is applied for $S(f)$ in eq.(2).

$$S(f) = 0.257 H_{1/3}^2 T_{1/3} (T_{1/3} f)^{-5} \exp[-1.03(T_{1/3} f)^{-4}] \quad (26)$$

where $H_{1/3}$ and $T_{1/3}$ are significant wave height and period. Mitsuyasu type directional spreading function $G(\theta; f)$ modified by Goda et al. (1975) is used.

$$G(\theta; f) = G_0 \cos^{2S}(\theta/2) \quad (27)$$

in which

$$G_0 = 2^{2S-1} \Gamma^2(S+1) / [\pi \Gamma(2S+1)] \quad (28)$$

and

$$S = \begin{cases} S_{\max} \cdot (f/f_p)^5 & : f \leq f_p \\ S_{\max} \cdot (f/f_p)^{-2.5} & : f > f_p \end{cases} \quad (29)$$

f_p is a peak frequency of $S(f)$. Goda et al.(1975) showed that $S_{\max} = 10, 25$ and 75 are suitable for fully saturated sea state, swell sea states with short and long decay distances respectively. Significant wave height and period of $H_{1/3} = 5.5m, T_{1/3} = 10s$ are used to realize a fully saturated sea state in the present calculation. $L_{1/3}, R(0)_{rms}$ and $H_{1/3}/L_{1/3}$ are $156m, 1.35m$ and 0.035 respectively in deep sea condition.

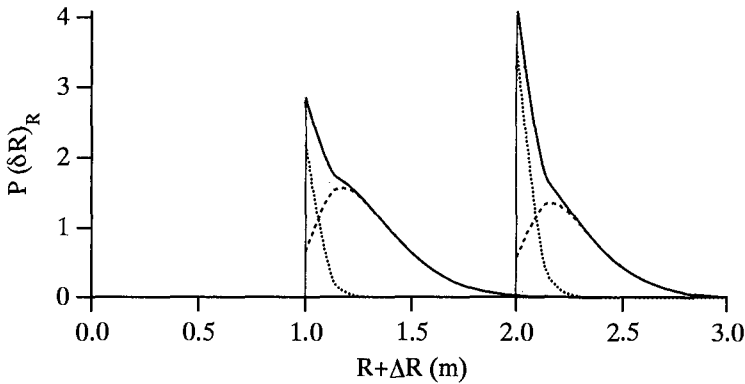
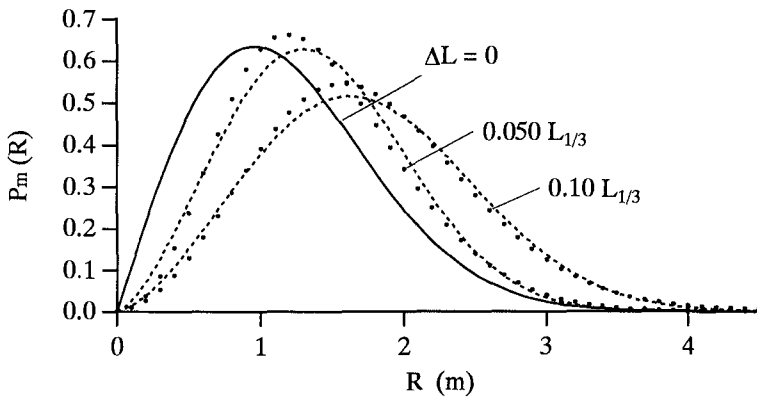
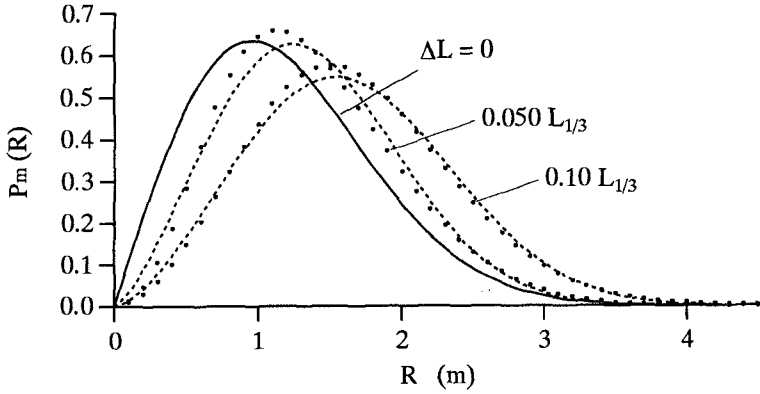


Fig.4 Distributions of δR on conditions $R = 1.0m$ and $R = 2.0m$
 ($S_{max} = 10, \Delta L = 0.05L_{1/3}$)

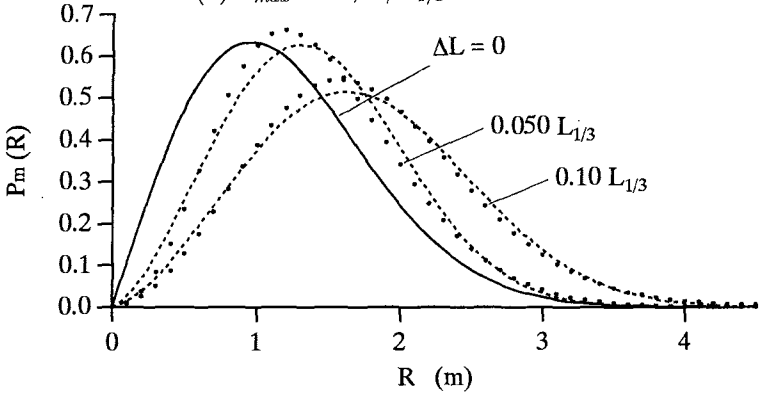
Figure 4 shows $P(\delta R)_R$ when $R = 1.0m$ and $2.0m$ for $\Delta L = 0.05L_{1/3}$, $h/L_{1/3} = 1.0$, and $S_{max} = 10$. Dotted line shows a part of the distribution when local maxima (eq.12) appear within $-\Delta L \leq x \leq \Delta L$ and chain line shows a part of the distribution when local maxima appear outside of the interval. Maximum amplitude within the interval is $R(-\Delta L)$ or $R(\Delta L)$ in the latter distribution (eq.13). Total of the dotted and chain lines gives $P(\delta R)_R$. When $R = 2.0m$, total distribution is narrower than that of $R = 1.0m$. This may correspond that when $R(0)$ is large, R_m presumably exist within a vicinity of $x = 0$. When $R(0)$ is small, on the contrary, the probability that the local maximum exist outside of the interval becomes large.



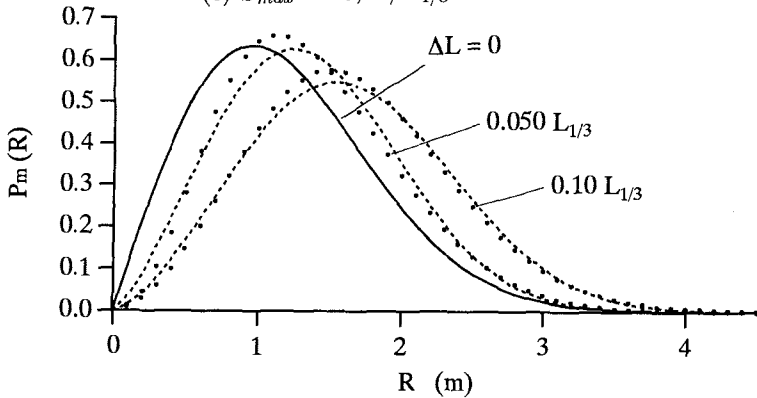
(a) $S_{max} = 10, h/L_{1/3} = 1.0$



(b) $S_{max} = 10, h/L_{1/3} = 0.25$



(c) $S_{max} = 20, h/L_{1/3} = 1.0$



(d) $S_{max} = 20, h/L_{1/3} = 0.25$

Fig.5 $P_m(R)$ (●), Rayleigh (solid line) and Weibull (broken line) distributions.

Figure 5 shows a calculated example of $P_m(R)$ (•) when (a) $h/L_{1/3} = 1.0$, $S_{max} = 10$, (b) $h/L_{1/3} = 0.25$, $S_{max} = 10$, (c) $h/L_{1/3} = 1.0$, $S_{max} = 20$, and (d) $h/L_{1/3} = 0.25$, $S_{max} = 20$. Two values for ΔL ($0.05L_{1/3}$, $0.1L_{1/3}$) are used in the calculations. Solid line shows the Rayleigh distribution ($\Delta L = 0$). Increasing interval brings a larger departure from the Rayleigh distribution. Broken lines are the Weibull distribution shown for comparisons. Shape parameters for the Weibull distribution are calculated using a Weibull probability paper (Yamauchi, 1972). Agreements of the calculated results and the Weibull distributions are fairly well in all cases.

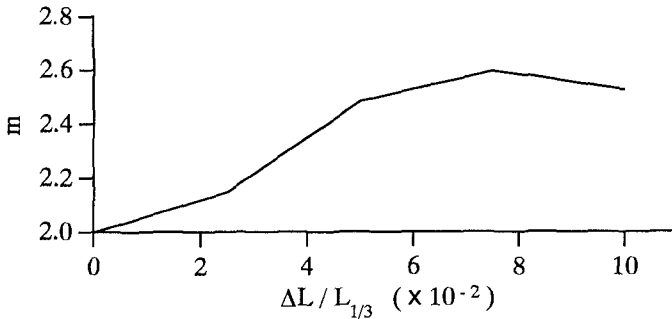


Fig.6 Change of the shape factor with $\Delta L/L_{1/3}$
($h/L_{1/3} = 1.0$, $S_{max} = 10$)

Figure 6 shows a change of the shape factor with $\Delta L/L_{1/3}$ when $h/L_{1/3} = 1.0$, $S_{max} = 10$ (Fig.5(a)). It increases with ΔL while it is small but takes almost constant value $2.5 \sim 2.6$ where $\Delta L/L_{1/3} > 0.06$. Figure 7 shows a change of rms value for R_m calculated from $P_m(R)$ in Fig.5(a). Similar results as shown in Figs.6 and 7 are obtained in other cases. $P_m(R)$ (•), Rayleigh (solid line) and Weibull (broken line) distributions are compared for large value of R ($> 3.8m$) in Fig.8 ($h/L_{1/3} = 0.1$, $S_{max} = 25$ and $\Delta L/L_{1/3} = 0.1$). $P_m(R)$ is considerably larger than the Rayleigh and Weibull distribution in this area.

6. Modification of the spectrum

High frequency component of a wave spectrum brings small fluctuations on R (Tayfun et al., 1989). Sometimes a few local maxima appear on R within a given width. Eqs.(12), (13) may give δR between the nearest local maximum and $R(0)$, instead of between the maximum R_m within the interval and $R(0)$ in this case. To eliminate insignificant fluctuations on R , high frequency (large wave number; $k > 0.2$, $L \leq 0.2L_{1/3}$) part of the spectrum is neglected so that no wave component has shorter wave length than the mentioned widest width ($-\Delta = 0.1L_{1/3}$) in this study.

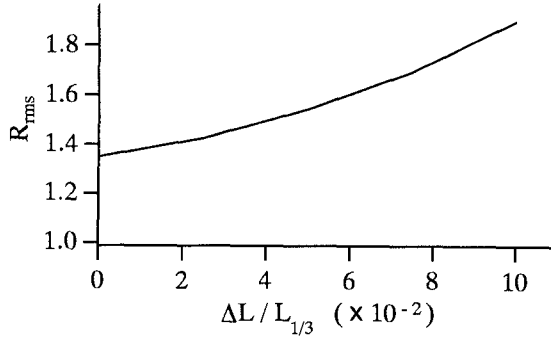


Fig.7 Change of the rms value for R_m with $\Delta L/L_{1/3}$ ($h/L_{1/3} = 1.0, S_{max} = 10$)

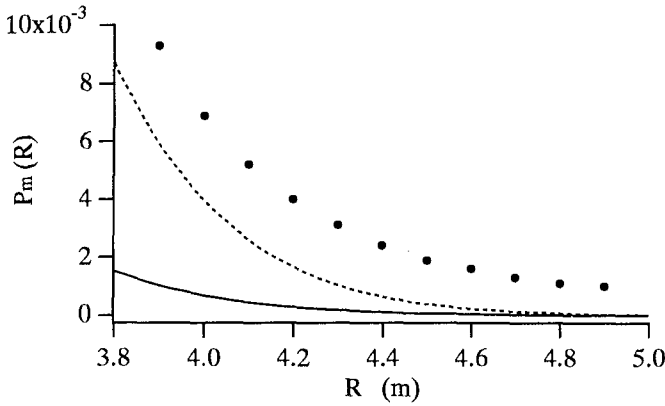


Fig.8 $P_m(R)$ (●), Rayleigh (solid line) and Weibull (broken line) distributions in a large R region. ($h/L_{1/3} = 1.0, S_{max} = 10$)

7. Concluding remarks

This study deals with a probability distribution of the maximum wave amplitude within a finite width along a virtual vertical plane placed in a 3-dim. irregular sea state. The probability distribution departs considerably from the Rayleigh distribution. This difference increases with the interval width. Especially, probability of the large amplitude is considerably larger than that of the Rayleigh distribution. It could be considered that unexpectedly large wave, appearance probability of which is very small, attacked when failure of coastal structures took place. However, the width effect for the apparent probability of large waves we has not been taken into account. Some of the failure may take place since this width effect on the probability distribution of wave heights is neglected. When structures are planed, three-dimensional properties of waves seems necessary to consider.

References

- [1] Goda, Y. and Y. Suzuki: Computation of refraction and diffraction of sea waves with Mitsuyasu's directional spectrum, tech. note of the PHRI, No.230, 45p., 1975.
- [2] Longuet-Higgins, M. S.: Statistical properties of wave groups in a random sea state, *Phil. Trans. Roy. Soc. London, Ser. A*, vol. 312, pp.219-250, 1984.
- [3] Rice S. O.: *Mathematical analysis of random noise, Selected papers on noise and stochastic processes* (ed. Nelson Wax), Dover, pp.133-294, 1954.
- [4] Tayfun, M. A. and Jen-Men, Lo.: Envelope, phase, and narrow-band models of sea waves, *Jour. of Waterway, port, coastal, and ocean eng.*, vol. 115, No.5, pp.594-613, 1989.
- [5] Yamauchi, Z. (ed.): *Statistical tables, Japanese standards association*, 451p., 1972. (in Japanese)

CHAPTER 177

Beach Response in Front of Wave-Reflecting Structures

Roy C. Seaman¹ and Tom O' Donoghue²

Abstract

The results of an experimental study of beach response in front of wave-reflecting structures are presented. The particular beach response problem is the so-called "N-type" response where sand is eroded in the area between the node and antinode and is transported towards the node. The characteristics of the equilibrium beach profile are presented and an equation describing the profile is proposed. The beach response is fundamentally dependent on the interaction between the flow and the ripples superimposed on the larger bedforms. Particle image velocimetry (PIV) has been used to look closely at the ripples and the flow. It is found that the sand transport towards the node results from larger vortex growth on the antinodal side of ripples than on the nodal side caused by the asymmetry in the main flow velocity time history which itself is a result of the superposition of the non-linear incident and reflected waves.

Introduction

Under a standing wave two main types of sediment transport can occur: transport of sand in suspension from under nodes towards antinodes or transport of sand as bed-load from between node and antinode towards the node. The former is often referred to as "L-type" movement and the latter as "N-type" movement. Previous notable research in this area (de Best *et al* (1971), Irie and Nadaoka (1984) and Xie (1985)) has shown that a "movability parameter", defined as the ratio of shear velocity to sediment fall velocity, can be used to determine which of the two types of transport is likely to occur for a given set of conditions. For relatively low values of the movability parameter, beach material transport is N-

¹) Research Student, University of Aberdeen, Department of Engineering, King's College, Aberdeen AB24 3UE, Scotland, U.K.

²) Lecturer, University of Aberdeen, Department of Engineering, King's College, Aberdeen AB24 3UE, Scotland, U.K.

type and for relatively high values of the movability parameter, the transport is L-type.

N-type movement is demonstrated very easily in the laboratory by sprinkling some sand onto a fixed flat bed: under a standing wave the sand, provided the movability parameter is sufficiently low, oscillates on the bed and gradually advances towards the node. The reason why this occurs is because the direction of mass transport at the bottom of the wave boundary layer under a standing wave is towards the node as described originally by Longuet-Higgins (1953) and, in the context of the development of offshore sand bedforms, by Carter, Liu and Mei (1973). However, for a fully-mobile bed under a standing wave, ripples form very quickly and subsequently play a crucial role in the sand transport process.

The present paper presents the results of an experimental investigation of N-type beach response. Two main aspects of the problem are addressed: first, the characteristics of the "equilibrium" beach profile and, second, the fundamental dependence of the sand transport on the interaction between the flow and the ripples superimposed on the larger bedforms.

Experimental Set-up

All experiments were conducted in a 20m long, 0.45m wide random wave flume with a water depth at the paddle of 0.7m (Figure 1(a)). A horizontal tray, approximately 3m long and supported in the wave tank by a frame fixed to the tank, held a 200mm deep sand bed, the top 100mm or so consisting of a well-sorted sand with $D_{50}=0.32\text{mm}$. A vertical, impermeable wall was located at the shoreward end of the sand bed. The water depth in front of the wall was 150mm. Waves approached the sand bed from the deeper 0.7m depth at the paddle via a sloping false floor with a 1:20 slope over most of its length and constructed from perspex panels supported on an aluminium frame.

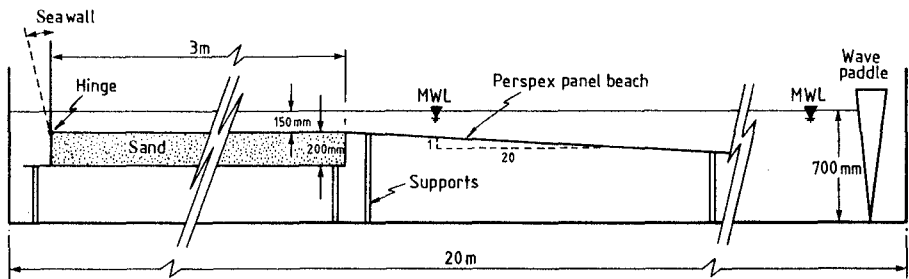


Figure 1(a): Experimental Set-up

Seventeen experiments corresponding to a wave frequency range of 0.7-1.1Hz and incident wave height range of 30-60mm were conducted in which the bed development from flat bed to equilibrium profile was observed. Once the equilibrium condition was reached for a given wave condition, the water level in the tank was lowered and the beach measured using a laser displacement sensor. The sensor has a spot diameter of 1mm and a resolution of 50 μ m and was mounted on a computer-controlled x-y table. For each experiment a total of 31 profiles were measured at 10mm intervals across the wave tank over a 300mm wide central section and at a resolution of 2mm in the longitudinal direction stretching from the wall to the first offshore antinode.

In order to study the underlying processes of the beach response, the detailed flow behaviour for a single wave condition ($f = 0.9$ Hz and $H = 50$ mm) was examined using particle image velocimetry (PIV). At selected stages in the development of the beach profile the bed was made rigid by sprinkling a thin layer of cement over the bed and allowing it to harden. PIV was then used to measure the instantaneous 2-d velocity field over and around individual ripples at selected phases of the wave cycle.

The PIV system used is based on a cross-correlation camera with two 756x458 CCD arrays. The camera is part of a completely integrated imaging system which includes the camera, PCI frame-grabber and camera-control card and Windows-based image acquisition and processing software. The camera views a part of the seeded, illuminated flow-field. Illumination was achieved using an 18W argon-ion laser beam carried by fibre-optic cable to a rotating mirror positioned above the wave tank which directed the beam via a lens to a thin sheet of glass held semi-immersed in the water (Figure 1(b)). The plane of the glass sheet was perpendicular to the mean water level and parallel to the sides of the wave tank. The purpose of the glass sheet was to avoid problems associated with bringing the laser beam through a fluctuating air-water interface. The light sheet was approximately 300mm long but only a fraction of this was viewed by the camera when measuring flow over the ripples.

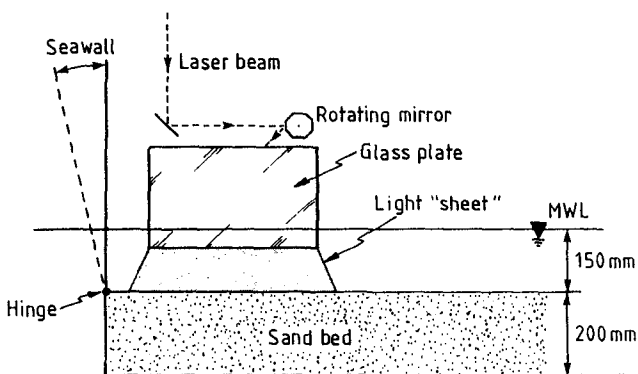


Figure 1(b): Illumination for PIV

Overview of Beach Response

Figure 2 illustrates the typical development of the beach with time from the initial flat bed condition to the final, equilibrium profile. At the beginning of an experiment sand on the flat, horizontal bed began to oscillate back and forth. Oscillations were most vigorous underneath the node where velocity amplitudes were highest resulting in the rapid development of ripples here. Ripple formation then propagated towards the antinodes on either side until a point was reached beyond which the near-bed velocities were too low to initiate movement of the sand. These points are referred to as the limits of movement in the present paper. The ripple wavelength and height decreased with distance from the node, a result which is consistent with the reduction in the radius of water particle orbits with distance from the node. The characteristics of the ripples remained largely unchanged throughout the experiment as the underlying larger bedform developed. Beach development progressed as sand continued to move towards the node from the areas close to the limits of movement resulting in areas of scour adjacent to the limits of movement and a zone of accretion around the node. The scour holes deepened with time and velocities within the scoured areas decreased until no further sand transport could occur. At this stage sand movement towards the node ceased. Sand close to the node continued to oscillate back and forth under the high velocity amplitudes present there, but no further net transport was produced and the bed was said to have reached "equilibrium".

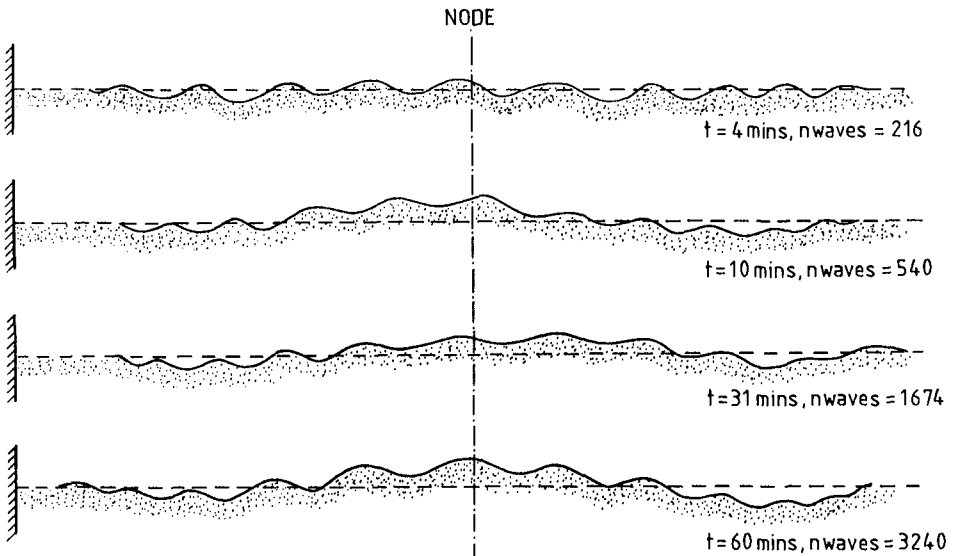


Figure 2 Sample beach profiles through time for $f=0.9\text{Hz}$ and $H=0.05\text{m}$

The Equilibrium Profile

The underlying larger bedform of the equilibrium profile is of significant engineering interest. The following equation is proposed to describe its major features:

$$\text{for } x_l \leq x \leq \left(\frac{\lambda}{2} - x_l\right) \quad \eta_b = \frac{a}{3} \sin\left\{\frac{2\pi}{3\lambda_b}(x - x_l)\right\} - a \sin\left\{\frac{2\pi}{\lambda_b}(x - x_l)\right\} \quad \dots[1]$$

where x is distance from the wall, x_l is the distance from the wall to the first limit of movement (equal to the distance from the second limit of movement to the offshore antinode), λ is the wave wavelength, η_b is the bed elevation above the initial flat bed level, a is a measure of the amplitude of the profile and λ_b is the bed profile wavelength where

$$\lambda_b = \frac{4}{3} \left(\frac{\lambda}{4} - x_l \right) \quad \dots[2]$$

For a given incident wave wavelength the function is fully defined if the positions of the limit of movement x_l and the amplitude factor a are known. The integral of the function over a half wavelength (antinode to antinode) is zero. The highest point on the profile is

$$\eta_{b_{\max}} = \frac{4}{3}a \quad \dots[3]$$

$$\text{The maximum scour depth is } \eta_{b_{\min}} = -\frac{5}{6}a \quad \dots[4]$$

For a given measured profile the limits of sand movement can be determined by calculating the local bed gradient as one advances from the antinode (where the bed gradient is zero) to a point where the gradient suddenly changes. The a value is then determined from a least squares regression of equation [1] onto the measured data. Two examples of measured profiles and their corresponding fitted functions are presented in Figure 3. Generally the function provides a good fit to the overall bed profile shape: it picks out the positions of maximum accretion and maximum scour satisfactorily and the method used to establish the limits of movement is seen to be successful. However, the function does tend to slightly under-predict the maximum scour and the gradient of the slopes leading up to the peak.

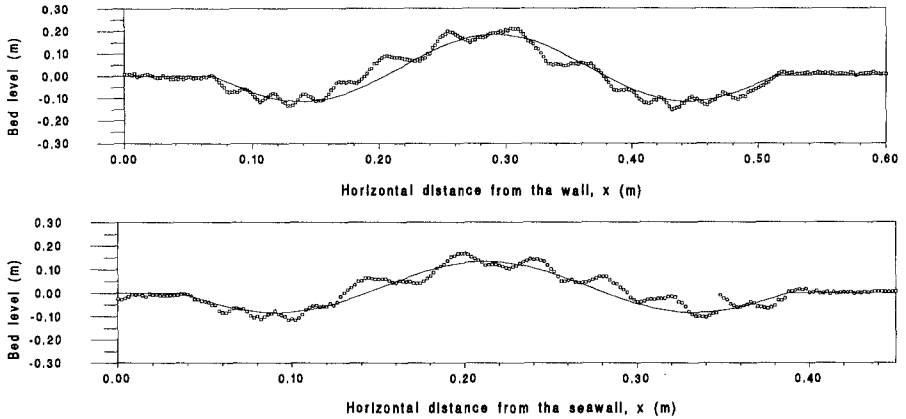


Figure 3: Measured profiles and corresponding best-fit of equation [1]. Top: $f=0.9\text{Hz}$, $H=30\text{mm}$; Bottom: $f=1.1\text{Hz}$, $H=40\text{mm}$

The values of x_l were determined for each of the 31 longitudinal profiles of each experiment. Of course two limits are obtained for each profile: the first limit is the shoreward limit denoted x_{l1} (i.e. the limit closest to the wall); the second is the seaward limit and is denoted x_{l2} . Figure 4 shows the results obtained for the limits of movement for three different wave period conditions. The results show the expected shift seaward of the limits of movement as the wave period increases, reflecting the seaward shift of the node of the standing wave. The results also show that the limits of movement are generally reasonably consistent across the width of the wave tank, significant scatter being observed only in the seaward limit of the longest period waves.

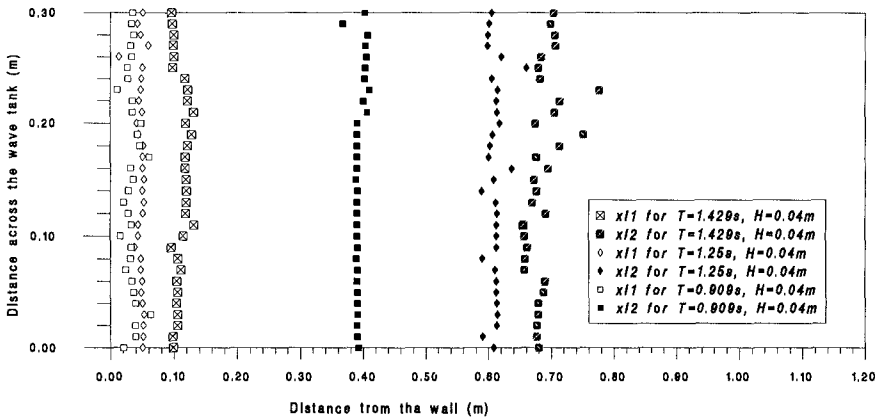


Figure 4. Measured limits of movement for 3 experiments.

A comparison of the measured limits of movement with the limits predicted using an incipient motion criterion is presented in Figure 5. The incipient motion criterion used is that proposed by Losada and Desire (1985) given by

$$\frac{A}{D_{50}} = \alpha' \left(\frac{Re^{\frac{2}{3}}}{D_*} \right)^{\frac{9}{5}} \quad \text{with} \quad D_* = D_{50} \left(\frac{\gamma g}{\nu^2} \right)^{\frac{1}{3}} \quad \text{and} \quad Re = \frac{u_{max} A}{\nu} \quad \dots[5]$$

where A is the amplitude of water particle excursion at the bed, D_{50} is the sediment size, γ is sediment specific gravity, ν is kinematic viscosity and u_{max} is the amplitude of horizontal water particle velocity at the bed. A limited study on the point of incipient motion of the sand used in this study was undertaken prior to the main body of experiments. For a number of wave periods, the wave height was increased in increments of 10mm until a value was reached at which movement of the sand could be clearly seen. The positions of the two points, one either side of the node, marking the separation of the area of bed where sand moves and the area where no sand movement occurs were measured and from this a threshold velocity calculated. The results obtained agreed very well with Losada and Desire's presentation of Goddet's data with α' equal to 1.34.

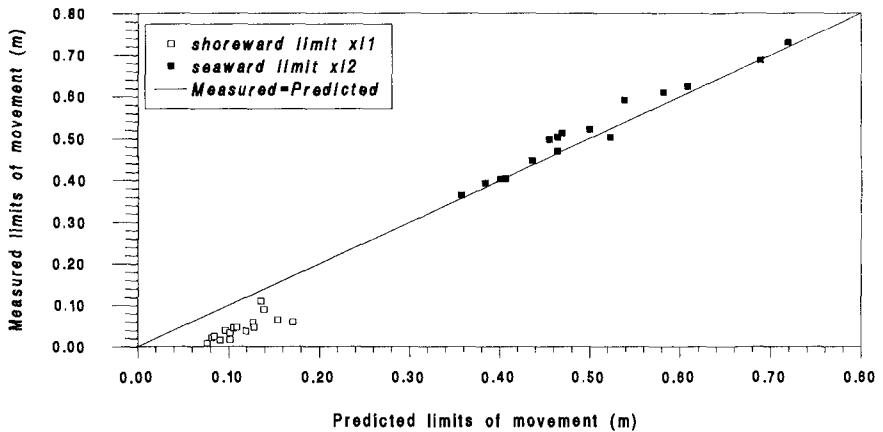


Figure 5 Comparison of predicted and measured limits of movement.

In Figure 5 the measured limits of movement are the average values of the 31 profiles. Figure 5 shows that the seaward limits of movement of the equilibrium profiles are well predicted using the incipient motion criterion. However, there is poor agreement between the measured and predicted shoreward limits. It is not known at this stage why this should be the case: the measured results suggest that the threshold velocity for sand movement near the wall is less than the threshold velocity away from the wall; of course the predicted threshold velocity is the same at the seaward and shoreward predicted limits of movement.

Although care was taken during the experiments to ensure that the wall was perfectly perpendicular to the incident waves, the response of the beach was never perfectly 2-dimensional, i.e. the beach profile varied across the width of the tank. Some evidence of this was seen in Figure 4 in respect of the limits of movement. Figure 6 shows the variation in a across the width of the tank for three different wave periods; a has been non-dimensionalised with respect to the mean value of the 31 a values of each test. The results show that a can deviate from the mean a value by as much as 20% of the mean value. This is an important result in that it illustrates the extent to which the developed beach is not perfectly 2-dimensional and reveals the dangers of obtaining results from a single longitudinal profile.

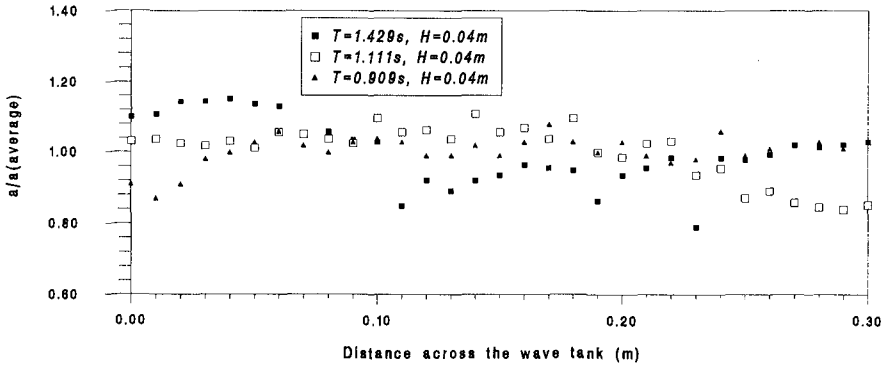


Figure 6 Variation in a across the wave tank for three example conditions.

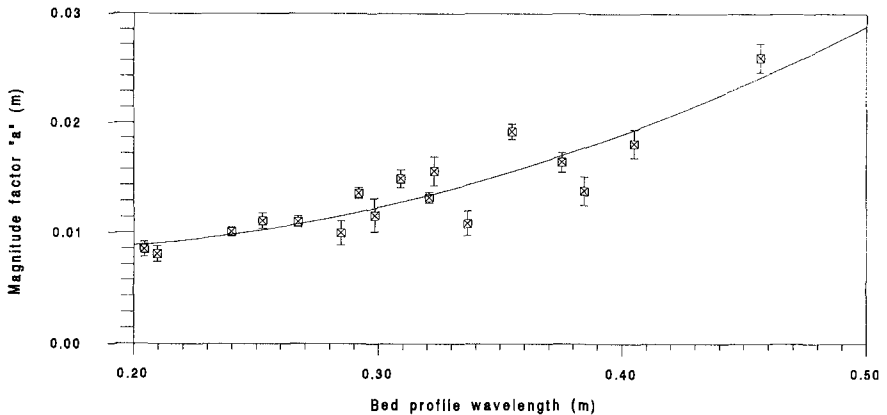


Figure 7: Relationship between the amplitude and wavelength of the equilibrium bed profile.

The average a and its standard deviation was calculated from the 31 profiles of each experiment. The average bed profile wavelength λ_b was calculated from the measured limits of movement of the 31 profiles. Figure 7 shows the plot of average a against average λ_b , the error bars on a corresponding to \pm the standard deviation of a . Although there is some scatter, there is a reasonably good correlation between a and λ_b , particularly at lower values of λ_b . The results show that, for the conditions of the present study, the value of a is between 1/20th and 1/30th of the bed profile wavelength λ_b .

Mechanism of Sand Transport Towards the Node

During the very early stages of the beach development the primary mechanism causing sand transport towards the node is mass transport at the bottom of the wave boundary layer as described by Carter, Liu and Mei (1973). However, as the ripples grow, first at the node and later further out, they become large enough to shed vortices. Observations indicated that these vortices then become the dominant mechanism in further sand transport. In order to study the behaviour of the vortices, a single experimental condition was selected ($f = 0.9\text{Hz}$, incident $H = 50\text{mm}$) and flow around the ripples was studied using PIV.

Before looking at some of the PIV results it is first necessary to look at the characteristics of the main flow, i.e. the flow at a position away from the bed. LDA measurements of velocity were made at a height of 25mm above the initial flat bed at 8 positions in front of the reflecting wall. Figure 8 presents the results for the horizontal component of velocity along with a prediction of the horizontal velocity based on the superposition of two Stokes second order waves. There is good agreement between the measured and predicted velocity time series. The maximum velocity towards the wall (positive velocity) and away from the wall (negative velocity) are approximately equal to each other at each of the 8 positions. However, the velocity function is generally asymmetrical, meaning that accelerations are not of the same magnitude in the two directions. For example, at position 1 maximum acceleration away from the wall is much greater than the maximum acceleration towards the wall, or, in other words, acceleration is greater towards the node; at the corresponding position on the other side of the node, position 7, maximum acceleration towards the wall is much greater than that away from the wall, or, again, maximum acceleration is greater towards the node. So, maximum acceleration is always greater towards the node than away from the node and, because the degree of asymmetry decreases as the node is approached, the difference between maximum acceleration towards and away from the node decreases as the node is approached.

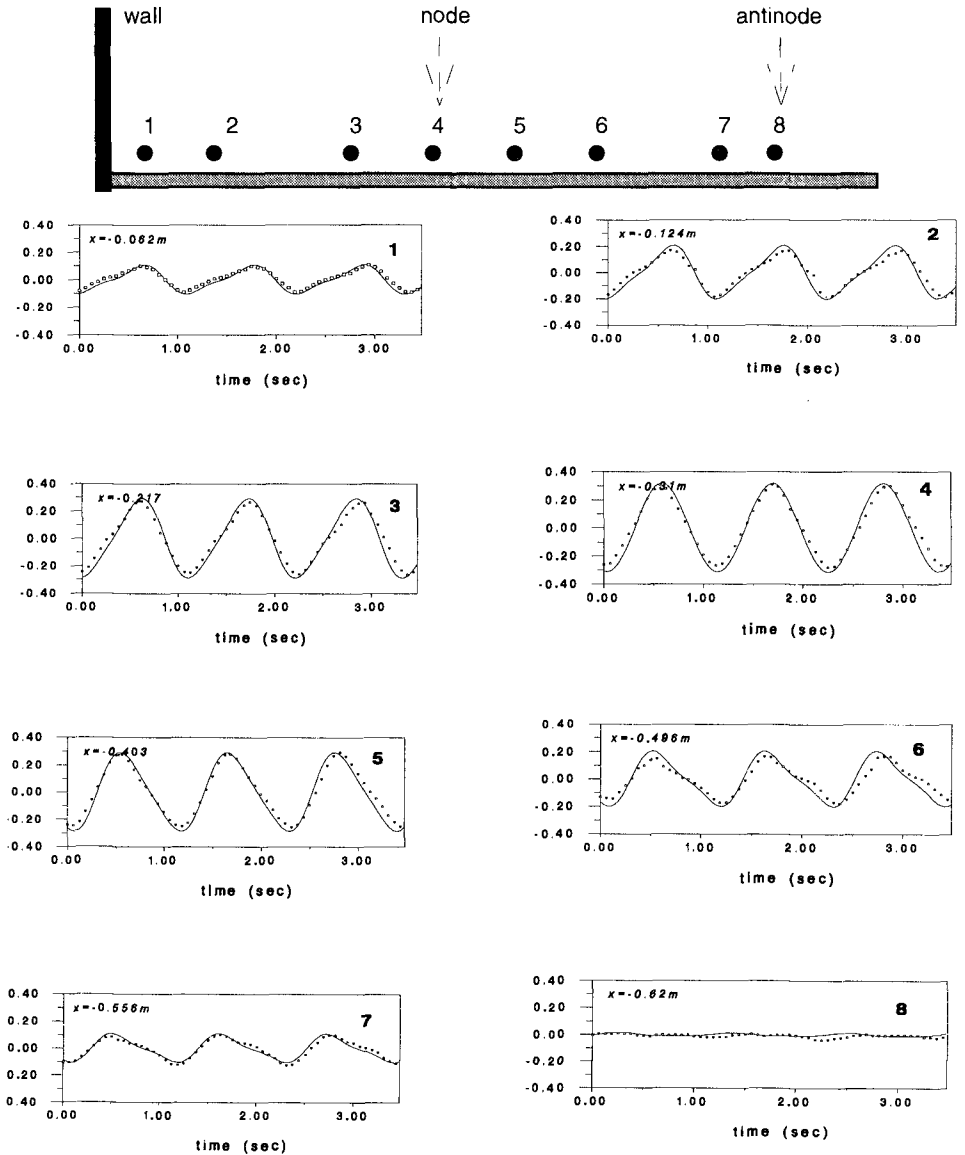


Figure 8: Time-history of horizontal velocity at 8 positions in front of the wall, 25mm above flat bed, $f=0.9\text{Hz}$, $H=50\text{mm}$. The node is at $x=-0.31\text{m}$ (posn.4) approximately; $x=-0.062\text{m}$ (posn.1) and $x=-0.558\text{m}$ (posn.7) correspond approximately to the shoreward and seaward limits of movement; $x=-0.62\text{m}$ (posn.8) corresponds to the offshore antinode. The solid line is the velocity predicted using Stokes 2nd order theory; the discrete symbols are the LDA measurements of the velocity.

A vortex grows in the lee of a ripple as the main flow velocity decreases from maximum velocity to zero velocity at flow reversal. Vortex growth on the antinodal side of a ripple occurs as the main flow acceleration is increasing from zero to maximum acceleration towards the node and vortex growth on the nodal side of a ripple occurs as the main flow acceleration is increasing from zero to maximum acceleration towards the antinode. Because the maximum acceleration towards the node is greater than the maximum acceleration towards the antinode, a larger vortex forms on the antinodal side of the ripple than on the nodal side. The larger vortex entrains more sand as it grows making it available for transport towards the node as the flow reverses.

Figure 9 presents PIV-measured vector plots of the flow over and around a ripple located at a position between 2 and 3 in Figure 8. Flow to the left is towards the wall/antinode; flow to the right is towards the node. Six vector plots are shown corresponding to 6 different phases of the wave. In Figure 9(a) the main flow has just started to decrease from maximum velocity towards the wall. The beginning of the vortex growth on the antinodal side of the ripple can be seen. Figure 9(b) shows the vortex well established as the flow reversal stage is approached while Figure 9(c) shows flow reversal with the vortex lifting off the bed. Figure 9(d) shows the situation before maximum velocity towards the node is reached while 9(e) and 9(f) show the vortex growth on the nodal side of the ripple with 9(f) corresponding to flow reversal.

Figure 9 clearly illustrates the asymmetry in vortex generation: a much larger vortex is formed on the antinodal side of the ripple than on the nodal side. As a result, when the bed is mobile, a larger volume of sand is entrained by the larger vortex on the antinodal side of the ripple than is entrained by the smaller vortex on the nodal side half a wave cycle later. The larger volume of sand is available for transport towards the node at flow reversal, while the smaller volume is available for transport towards the antinode. Therefore, the effect over a complete wave cycle is net transport of material towards the node.

The present description of the role played by the vortices in determining the net sand transport under standing waves echoes what has been observed by others for the case of nonlinear progressive waves (e.g. Sato and Horikawa (1986). Like the standing wave case, vortex growth is not the same on the two sides of a ripple in the case of non-linear progressive waves. However the reason for the asymmetry in vortex growth is not the same for progressive and standing waves: in the case of non-linear progressive waves the velocity function is skewed with the maximum shoreward velocity greater than the maximum seaward velocity. The result is larger vortex growth on the shoreward side of the ripple as the flow velocity decreases from maximum velocity shoreward to zero velocity at flow reversal. The net effect is greater sand transport seaward than shoreward.

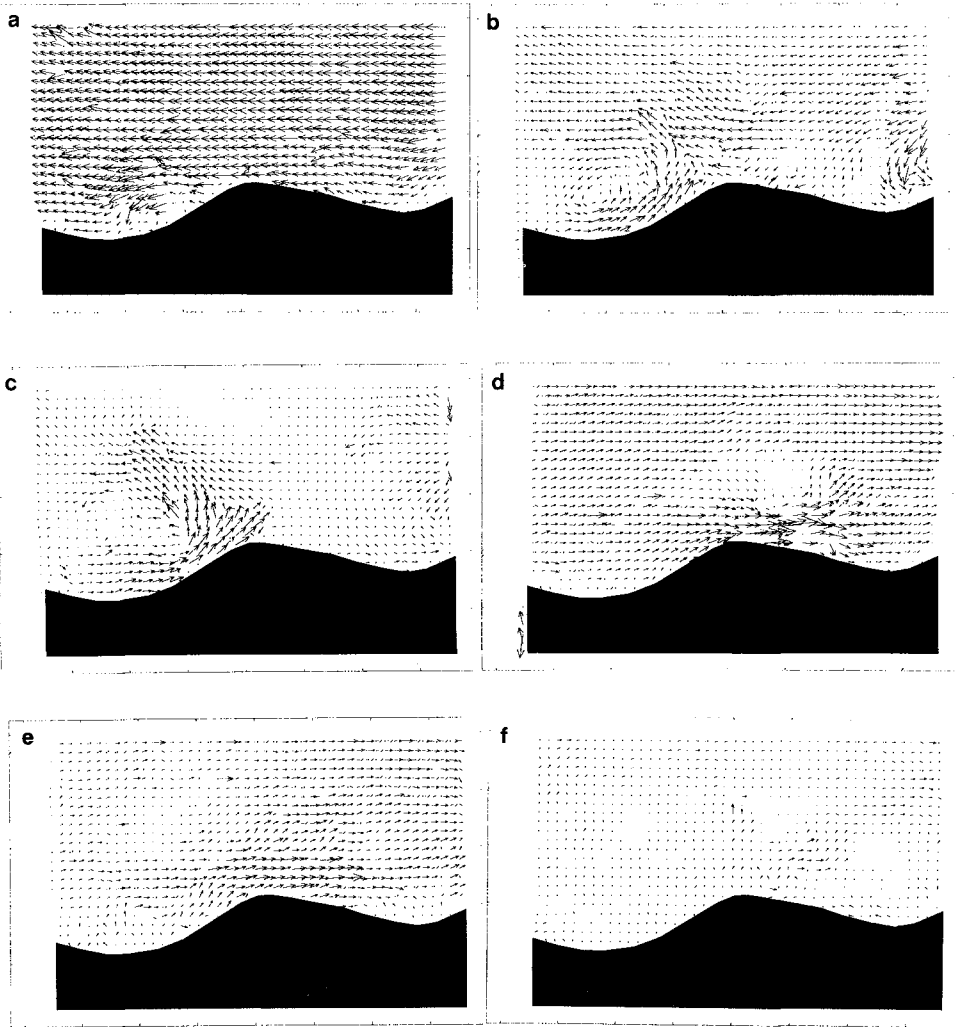


Figure 9: PIV-measured velocity fields corresponding to 6 phases of the wave, $f=0.9\text{Hz}$, $H=50\text{mm}$; the ripple shown is located between positions 2 and 3 in Figure 8.

Conclusions

Two main aspects of N-type beach response in front of wave-reflecting structures have been studied: (i) the characteristics of the equilibrium beach profile and (ii) the underlying mechanism causing sand transport towards the node.

The major features of the underlying larger bedforms of the equilibrium beach profile are well characterised by an equation which is fully defined for a given wave condition if the positions of the limits of movement and the amplitude factor a are known. The limits of movement can be estimated using an incipient motion condition although good agreement was not achieved in the present study between the predicted and measured shoreward limits. For the sand used in the study the amplitude factor a is approximately 1/25th of the equilibrium bed profile wavelength λ_b ; maximum scour depth is therefore approximately 1/30th of λ_b . Further work is needed at larger scale with different sand sizes to see if these results have general application.

The ripples superimposed on the larger bedforms play a crucial role in the sand transport process. Asymmetry in the main flow velocity time-history, resulting from the superposition of non-linear incident and reflected waves, causes larger vortex growth on the antinodal side of the ripple than on the nodal side. Because vortex growth occurs as the flow is slowing down and the vortex is at its largest and lifting off the bed at flow reversal, more sand is transported towards the node than towards the antinode with each wave cycle. PIV is a very effective way of studying the flow over and around the ripples.

Acknowledgements

Mr. Seaman acknowledges the support of Aberdeen University through the receipt of an Aberdeen University Research Studentship. The assistance of Bill Lowson with the laboratory work is gratefully acknowledged.

References

- de Best, A., Bijker, E.W., and Wichers, J.E.W., (1971), *Scouring of a Bed in Front of a Vertical Breakwater*, Proc. 1st P.O.A.C. Conf., Vol. II, p1077-1086.
- Carter, T.G., Liu, P.L-F., and Mei, C.C. (1973), *Mass transport by waves and Offshore sand bedforms*, ASCE, Journ. Waterways, Harbours and Coastal Engineering, Vol 99, no. ww2, p165-184.
- Irie, I., and Nadaoka, K., (1984), *Laboratory Reproduction of Seabed Scouring Front of Breakwaters*, Proc. 19th Conf. on Coastal Engineering, p1715-1731.

- Longuet-Higgins, M.S. (1953), *Mass Transport in Water Waves*, Phil. Trans. Royal Society of London, Vol 245, p535-581
- Losada, M.A., and Desire, J.M., (1985), *Incipient Motion on a Horizontal Granular Bed in Non-breaking Water Waves*, Coastal Engineering, 9, p357-369.
- Sato, S. and Horikawa, K. (1986), *Laboratory Study on Sand Transport over Ripples due to Asymmetric Oscillatory Flows*, Proc. 20th Coastal Engng. Conf., Chap. 109, p1481-1489
- Xie, S., (1985), *Scouring Patterns in Front of Vertical Breakwaters*, Acta Oceanologica Sinica, Vol. 4, No. 1, p153-164.

CHAPTER 178

Fundamental Characteristics of Wave Transformation Around Artificial Reefs

Toshio Aono¹

Eric C. Cruz²

Abstract

The fundamental characteristics of the wave field around an existing artificial reef in Japan are studied based on field measurements and wave simulations using a nonlinear wave model that takes reef porosity into account. Results of two-dimensional simulations and comparison with field data of significant wave heights and reef velocities indicate characteristic wave evolution of nonbreaking and breaking waves and confirm the damping effect of the reef.

1. INTRODUCTION

Artificial reefs are a type of submerged breakwater. Unlike ordinary submerged breakwaters, however, they are usually designed with a permeable interior, a broad crown and steep face slopes. A permeable interior allows better water exchange with the sea when incident waves are small and yet induces wave energy dissipation through porous damping when the incident waves are high. A broad crown improves the damping effect of the reef over a wider frequency range while the steep face slopes are structural merits exploited when certain types of armor units are used to protect the reef when used as a breakwater. Hence, there are at least three important properties which must be considered when analyzing an actual artificial reef: (1) porosity (2) a wide depth regime, that is, shallow on the reef crown and deep on either side; and (3) steep face slopes.

A considerable number of artificial reefs have been constructed near the coasts in Japan, but there are no published reports on detailed field measurements around such structures. Part of this paper reports on a series of field measurements around Yugawara artificial reef which is one of such existing reefs in a Japanese coast. These measurements include the water surface profiles as well as reef velocities on

¹ Senior Research Engineer, Numerical Analysis Laboratory, Technical Research Institute, Toa Corporation, 1-3 Anzen-cho Tsurumi-ku Yokohama 230, Japan.

² Research Engineer, ditto

the reef crown.

Results obtained from a synthesis from these field measurements were used to verify the applicability of a mathematical model originally developed for wave transformation on porous beds. Mathematical models have been proposed in recent years to model the wave field around submerged structures. Inclusion of wave non-linearity in these models is important due to the small depth on the crowns of submerged structures. A second requisite is good dispersivity in order to reproduce frequency-dependent phenomena such as propagation in deep water, transformation and wave grouping of irregular waves and wave decomposition at the lee. For an artificial reef used as a submerged breakwater, the porous interior dissipates wave energy and hence porosity is an important property that affects the evolution of the wave.

This paper is part of a study which aims to analyze the effects of the existing Yugawara reef with a broadened crown on the surrounding coastal environment, particularly on the revetment which protects the adjacent coast. As an initial step, a simplified treatment of the wave field is chosen to serve as basis for launching a more detailed set of computations. The objective of the present paper is therefore to identify basic characteristics of the wave field based on field measurements and wave simulations with practical assumptions on reef composition and wave dimensionality.

2. FIELD MEASUREMENTS

General Description of Yugawara Artificial Reef

The layout of the existing reef is shown in **Fig. 1(a)** and the section through the center is shown in **Fig. 1(b)**. The reef was constructed to reduce the damage during high wave conditions to the vertical wave-absorbing revetment onshore which, in turn, protects the structures on the coast used for commercial fishing. The reef crown is 170m long and 70m wide. The crown width was increased from the previous 32m (shown dashed in **Fig. 1**) to make it more effective in dissipating the wave energy over a wider range of relative

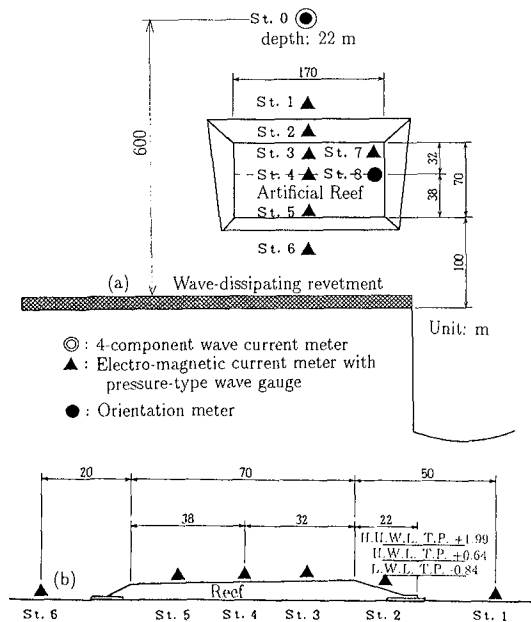


Fig.1 Layout of Yugawara artificial reef and measuring devices. (a)plan view (b)cross section

water depths. The seaward slope is 1:3 while the shoreward slope is 1:2. The seaward slope and the seaward 32m of the crown are protected with 10-ton X-block armor units while the shoreward slope and the remaining portion of the crown are covered with 2-ton armor stones. The reef interior consists of 30 to 200kg medium-sized stones. The crown is submerged about 1.5m from mean water level and the depth to the seabed is around 8.5m at the crown center.

Field Measurements

Field measurements were conducted continuously for 2 months from February 1 to March 31, 1994. The measuring devices and their location are shown in Fig. 1. The water depths and surface elevations were measured by pressure-type gauges and velocity components at a fixed distance from the reef bed were measured directly using electro-magnetic current meters. Incident wave conditions were based on measurements at station 0 located 600 m from the revetment at a depth of 22 m. Six stations were disposed along the reef centerline with Stations 3, 4 and 5 on the shallow crown while Stations 7 and 8 were installed as shown to evaluate the effect of reef edge. The bed configuration and reef shape were determined from design drawings. However, field measurements of depths indicate that the bed slope has changed from its design value of 1:30 to 1:39 and the seaward slope from its design value of 1:3 to 1:3.16 due probably to slump of the reef and scouring at the toe. These measured slopes were applied to the bathymetry used in the computations .

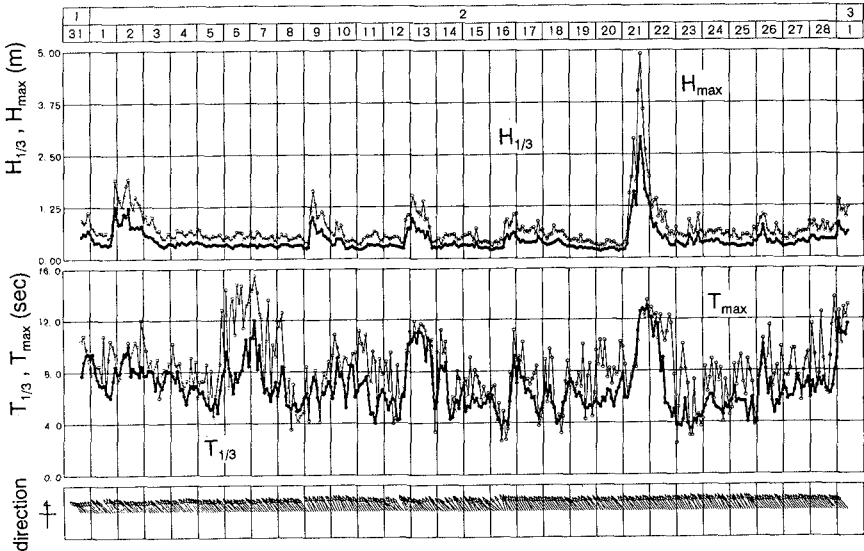


Fig. 2 Time series of $H_{1/3}$, $T_{1/3}$, H_{max} , T_{max} and incident wave direction

Fig. 2 shows the observed time series of the significant wave height and period, maximum wave height and period and incident wave direction. The critical wave occurred on February 21 with a significant wave height of 2.90m and maximum

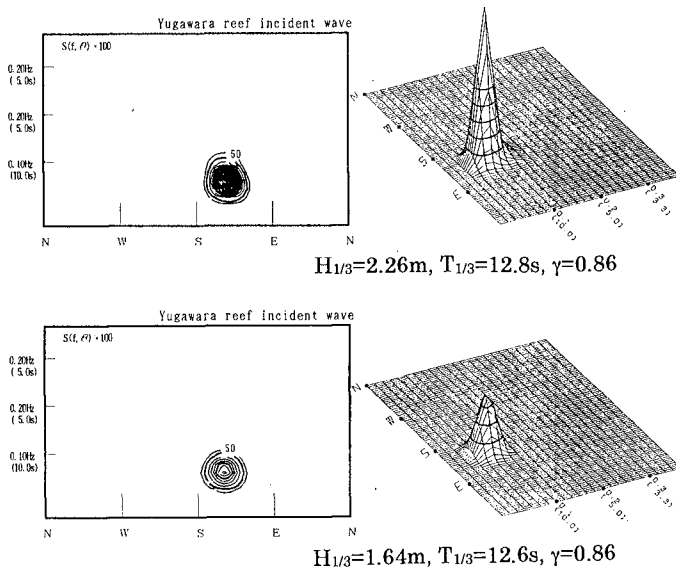


Fig.3 Directional spectrum (incident wave)

wave height of 5m. This wave was due to a low-pressure atmosphere. The significant wave period fluctuates but the highest value coincided with the significant wave height. This critical wave condition was used in the simulation. Incident wave direction was almost constant during the entire observation period. The wave direction was oriented almost normally to the reef. **Fig.3** shows the directional spectrum of incident wave. The method of calculation is EMEP by Hashimoto(1992). The shape of this directional spectrum is a single peak type and the long crestedness parameter is 0.86 so the directional spreading is relatively small. Observed directional spectrum data show an almost similar tendency.

Fig.4 shows the significant wave heights $H_{1/3}$ at stations along the center of the reef. We observed that it first increases on approaching the reef's seaward slope. Then it decreases abruptly due to breaking. Along the reef crown, the significant height continues to decrease due to the damping action of the porous interior. However, the rate of decrease is smaller than that due to

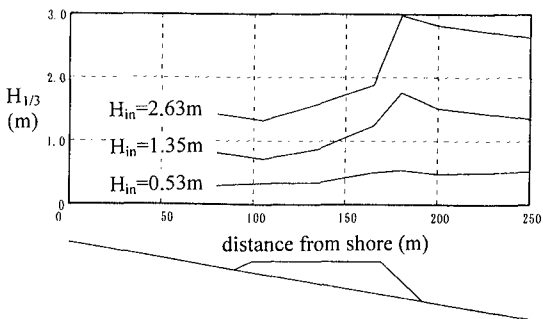


Fig.4 Distribution of $H_{1/3}$ along the center of reef

breaking. At the back of the reef, the wave height can still increase depending on the incident wave conditions.

3. MODEL EQUATIONS FORMULATION AND ANALYSIS

Model Equations

The basic depth-averaged nonlinear equations for horizontal one-dimensional wave transformation over porous beds have been derived using the perturbation method (Isobe et al., 1991; Cruz, et al., 1992). The leading order of nonlinearity has been included but nondispersive waves were vicariously assumed. The model can reproduce the generation of higher harmonics on the shallow crown but cannot predict the decomposition of waves beyond the structure. By reformulating the basic governing equations in the water and porous layers as a potential flow problem in terms of nondimensionalized variables, Cruz et al. (1996) obtained a set of Boussinesq equations for porous beds. These equations possess a second-order accurate linear dispersion relation and are applicable to weakly dispersive waves. By extending the linear dispersion relation to fourth-order accuracy through the addition of higher-order momentum terms, the Extended Boussinesq Equations for Porous Beds were obtained. For two-dimensional wave transformation, they are written as:

$$\eta_x + [(h + \eta)u]_x + (\varepsilon h_s u_s)_x = 0 \quad (1)$$

$$u_t + \frac{1}{2}(u_s^2)_x + g\eta_x - \varphi + F_\varepsilon + F_B = O(\delta\mu^2, \mu^4) \quad (2)$$

$$C_r \left[u_{st} + \frac{1}{2}(u_s^2)_x \right] + g\eta_x + \alpha u_s - \varphi_s = O(\delta\mu^2, \mu^4) \quad (3)$$

where η is the water surface displacement, u and u_s the depth-averaged velocities in the water and porous layers, ε the porosity, g the gravity acceleration, h and h_s the thickness of the water and porous layers, respectively, F_ε the boundary absorption term, F_B the wave breaking dissipation term, C_r the inertial coefficient, t the time and x the horizontal coordinate. Subscripts denote partial differentiation. α denotes the resistance coefficient of the porous medium:

$$\alpha \equiv \alpha_1 + \alpha_2 |u_s| = \frac{\nu\varepsilon}{K} + \frac{C_f \varepsilon^2}{\sqrt{K}} |u_s| \quad (4)$$

where ν is the kinematic viscosity, K the intrinsic permeability and C_f is the turbulent friction coefficient. φ and φ_s are the extended dispersion terms defined as

$$\varphi \equiv \left(\frac{1}{3} + \gamma \right) h^2 u_{xxt} + \left(\frac{1}{2} + \gamma \right) h h_x u_{xt} + \left(\frac{1}{2} + \gamma \right) h (h_x u_t)_x + \gamma g h (h \eta_x)_{xx} + \frac{1}{2} h (h_p u_{st})_{xx} \quad (5)$$

$$\begin{aligned} \varphi_s \equiv & \frac{1}{2} C_r \left[\frac{2}{3} h_s^2 u_{sxx} + h_s (h_{bx} u_{st})_x - h_s (h_x - h_{sx}) u_{sxt} - 2 h_x h_{bx} u_{st} \right] \\ & + \frac{1}{2} \alpha \left[\frac{2}{3} h_s^2 u_{sxx} + h_s (h_{bx} u_s)_x - h_s (h_x - h_{sx}) u_{sx} - 2 h_x h_{bx} u_s \right] + \frac{1}{2} (h^2 u_t)_{xx} \\ & + (1 + \beta) \left[h (h_p u_{st})_x \right]_x + \frac{\beta g}{C_r} \left[h (h_p \eta_x) \right]_x + \frac{\beta g}{C_r} \left[h (h_p u_s)_x \right]_x \end{aligned} \quad (6)$$

where $h_p \equiv \epsilon h_s$ is the effective porous thickness, $h_b \equiv h + h_s$ the bottom depth, and γ and β the celerity and damping extension factors. The right sides of **Eqs. (1) to (3)** indicate the truncation error in the dispersivity parameter $\mu \equiv h_o/l$ and nonlinearity parameter $\delta \equiv a/l$ where h_o , l and a are the characteristic depth, wavelength and amplitude, respectively.

Linear Analysis of Model Equations

A linear analysis of the model equations has been carried out by neglecting the dynamic volume flux term in Eq. (1), the convective terms in Eqs. (2) and (3) and the nonlinear resistance term α_2 in α . This leads to the following dispersion relation for porous beds:

$$\frac{\omega^2}{k^2 gh} \left[1 + \left(\frac{1}{3} + \gamma \right) k^2 h^2 \right] \left\{ \left(C_r + i \frac{\alpha}{\omega} \right) \left(1 + \frac{1}{3} k^2 h_s^2 \right) + k^2 h h_p \left(1 + \beta + i \frac{\beta \alpha}{\omega C_r} \right) \right\} = \left(1 + \gamma k^2 h^2 \right) + \frac{h_p}{M h} \left[1 + \left(\frac{1}{3} + \gamma \right) k^2 h^2 \right] \left[1 + \frac{\beta}{C_r} k^2 h h_p \right] \tag{7}$$

$$- \frac{k^2 h h_p}{2 M} \left[\left(1 + \frac{\beta}{C_r} k^2 h h_p \right) - \frac{\omega^2 h}{g} + \left(1 + \gamma k^2 h^2 \right) \right]$$

$$M = \left(C_r + i \frac{\alpha}{\omega} \right) \left(1 + \frac{1}{3} k^2 h_s^2 \right) + \lambda k^2 h h_s \left(1 + \beta + i \frac{\beta \alpha}{\omega C_r} \right) \tag{8}$$

For progressive waves of angular frequency ω , the complex wave number k consists of a real part k_r that governs the phase celerity and an imaginary part k_i which gives the spatial porous damping rate. The values of γ and β have been determined by comparing these wave properties with those of the theoretical dispersion relation for porous beds up to deep water. Eq. (7) reduces to the dispersion relation of Madsen et al. (1991) when $h_p=0$. **Fig. 5(a)** plots the normalized celerity r_1 as a function of frequency in terms of h/L_0 , where $L_0=2\pi g/\omega^2$, for various relative porous thickness h_s/h . **Fig.5(b)** shows the dependence of the normalized damping rate r_2 on frequency. Plots similar to **Fig. 1** were obtained for values up to $\epsilon=0.7$

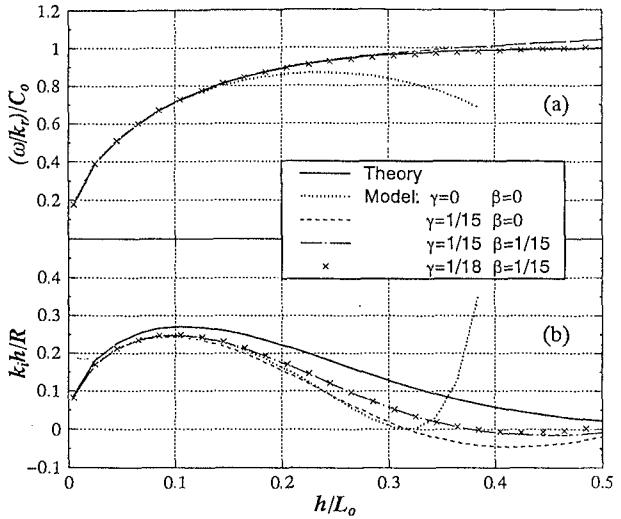


Fig.5 Summarized curve of r_1 (a) and r_2 (b) of the extended model equations

which leads to the optimum values $\gamma=1/21$ and $\beta=1/15$ up to $h/L_0=0.50$, $h_s/h=10$, $\varepsilon=0.7$ and $R=1.0$. These upper limits of the wave and porous layer parameters already encompass their practical limits.

Wave Breaking Dissipation

Due to the steep seaward slope, wave breaking occur mostly as plunging breakers. At present however, there is no adequate model for plunging random breakers even for solid beds. In this simplified treatment, a surface roller approach (Deigaard, 1989; Schaffer et. al., 1992) ignoring the effects of the porous bottom is employed.

$$F_B = \frac{\partial \psi}{\partial x} = \frac{\partial}{\partial x} \left[\frac{\delta(h + \eta - \delta)}{(h + \eta)^2} (C - u)^2 \right] \tag{9}$$

Where, ψ is momentum flux correction, δ the roller thickness, C the wave celerity. In this model, breaking is determined based on the crest toe angle. The roller approach is adopted due to its ability to deal with temporally and spatially migrating breakers as obtained in an irregular wave field on a non-monotonic bathymetry.

Velocity Field

The fluid particle horizontal velocities can be obtained from the depth-averaged velocities by invoking their definitions in terms of the velocity potentials. The horizontal velocity U in the water layer is given by

$$U(z) = u - \frac{1}{2} \left[(z + h)^2 - \frac{h^2}{3} \right] u_{xx} - \frac{1}{2} (h + 2z) [(h_x u)_x + h_x u_x] - \frac{\varepsilon}{2} (h + 2z) (h_s u_s)_{xx} \tag{10}$$

and the velocity U_s in the porous layer by

$$U_s(z) = u_s + \frac{1}{2} \left\{ \left(\frac{h_s^2}{3} + h h_b - z^2 \right) u_{sxx} + [h_s - 2(z + h_b)] (h_b u_s)_{xx} \right\} \tag{11}$$

where z is taken positive upward from the still-water level. Eqs. (10) and (11) satisfy the following boundary condition at the interface $z = -h(x)$,

$$U_n = \varepsilon U_{s,n} \tag{12}$$

where n denotes the direction normal to the interface. The velocity potential, when truncated at the order consistent with Eqs. (2) and (3), therefore, prescribes a parabolic vertical distribution of horizontal velocities in both layers.

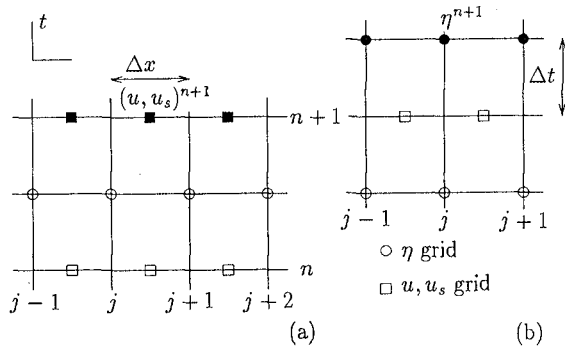


Fig.6 Finite difference module for solution of model equations.

4. NUMERICAL COMPUTATIONS

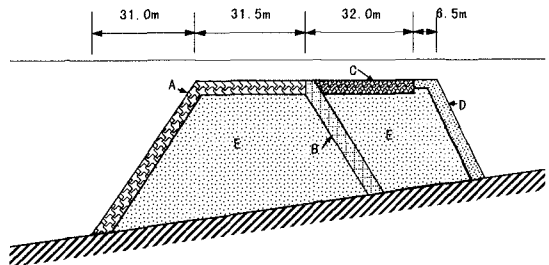
Eqs. (1) to (3) were discretized using the finite difference method on a staggered grid (Fig. 6). η is defined on the main grid, u and u_s on the secondary grid and the depths h, h_s on both grids. Eqs. (2) and (3) are first solved for u and u_s , and then Eq. (1) is used to solve for η in alternating time steps spaced at $\Delta t/2$.

Waves are introduced at the left end of the computation domain and the transmitted waves exit the open boundary at the right end. Because waves are reflected from the steep seaward slope of the reef, numerical wave absorbers were placed on both ends to absorb the outgoing wave components. The properties of the absorber, namely, its damping distribution, maximum damping coefficient and absorber width were determined from simulation aid graphs theoretically developed for regular and irregular wave fields (Cruz and Isobe, 1994). Computations were continued until the wave profile has become stable from one period to the next. Considering the presence of absorbers at both ends, this condition is achieved after the first crest has traveled a distance of about $5X_D$, where X_D is the total width of the computation domain.

Reef Material Distribution

The vertical section at the centerline of the reef, Fig. 1(b), was taken as the representative section for the preliminary one-dimensional calculation reported here. Due to the variability of materials in the reef armor and interior, reef porosity is not uniform. Fig. 7 shows the cross-section make-up of the present Yugawara Reef along its centerline. The previous 32-meter reef was formed with medium-sized rocks and covered with 10ton X-blocks. The added portion has an interior similar to the older one but was protected with different armors. To carry out wave simulations, however, it was necessary to use a uniform porosity in the model equations. Noting that the flow field near the seaward corner of the crown is critical, we used values of the material properties based on the X blocks and assumed that the entire reef is a homogeneous structure. For purposes of analysis, it was assumed to be uniform. In the simulation, The following parameters were used:

$$\begin{aligned} \epsilon &= 0.20, \quad \nu = 1.3 \times 10^{-6} \text{ m}^2/\text{s} (10^\circ \text{C}), \\ K &= 8 \times 10^{-7} \text{ m}^2, \quad C_f = 0.20 \end{aligned}$$



Zone	Material	Weight
A	X-Blocks	10tons
B	armor rocks	250kg
C	armor rocks	2tons
D	armor rocks	500~800kg
E	medium-size rocks	30~200kg

Fig.7 Reef material distribution of Yugawara artificial reef.

K and C_f were obtained by linearly extrapolating the data of Sollit and Cross (1972) for a mean block size of 1.0m.

Simulation of the Regular Wave Field (Non-breaking)

To examine the characteristic of the model, simulation is performed using regular waves. In order to utilize the field data, the incident wave has the properties of the significant wave, namely, $T_{in} = (T_{1/3})_{Sta.0}$ and $H_{in} = (H_{1/3})_{Sta.0}$. The spatial profiles of η at $T_{in}/8$ intervals beginning at $t=t_{rec}$ are shown in Fig. 8(a). The incident wave is linear at station 0 (Ursell No. $Ur=0.17$) and becomes

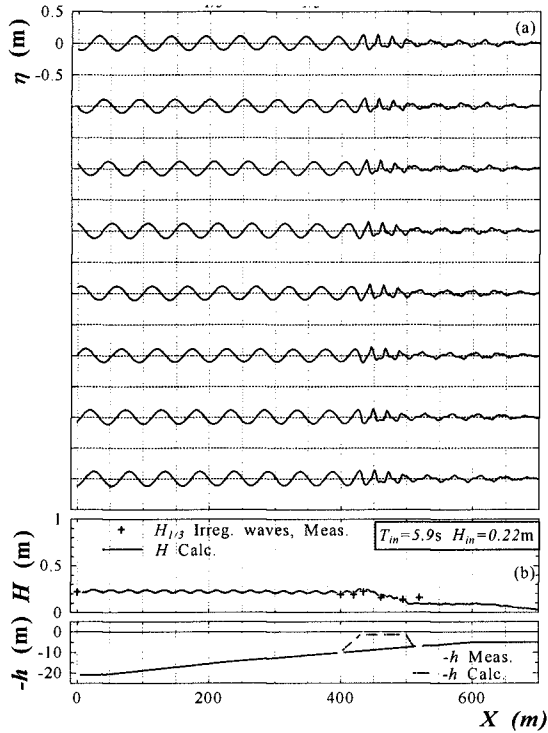


Fig. 8 Wave field (a) Simulated evolution of η (b) Comparison of calculated and measured

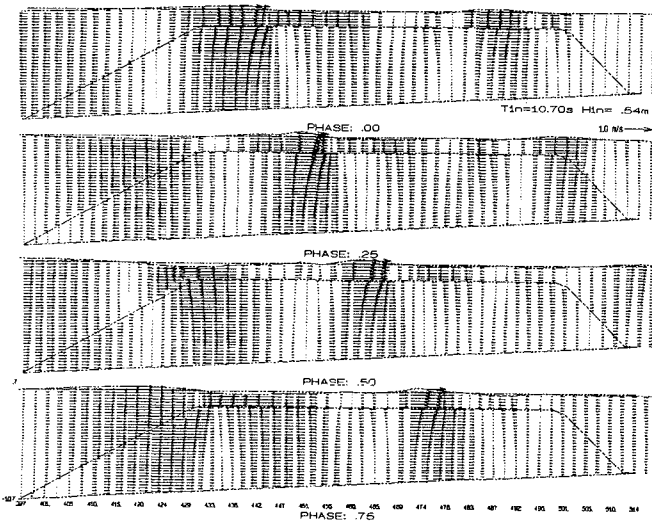


Fig. 9 Vertical field of U and U_s at $T_{in}/4$ intervals

nonlinear at the reef crown because of its shallowness. Higher harmonics are generated on the crown and the resultant wave propagates largely undeformed on the crown (ignoring the damping effect of the reef) because the higher harmonics and the primary wave travel at essentially at the shallow-water celerity. These bound harmonics are released behind the reef as free-waves that travel at their frequency-dependent celerities. Further leeward, the free waves interact with each other and the primary wave resulting in the nonpermanent profiles as seen in the figures.

Fig. 8(b) show the comparison of the simulated wave heights H and the significant wave heights $H_{1/3}$ of the field data. Prior to the crown, these wave heights agree very well. The underestimation of H at station 6 is partly due to the neglect of reflection from the revetment which has been confirmed in the field measurements (Ohnaka and Yoshizawa, 1994).

The spatial distribution of the velocities can be used to obtain the vertical field of fluid particle velocities U and U_s through Eqs. (10) and (11). **Fig. 9** show the velocity profile at the reef toe is that of linear wave. As the wave moves into the crown, the upper portion of the reef is engaged in redistributing the wave energy through the interface boundary conditions, for example, Eq. (11). The wave crest does not have to travel far into the crown because a relatively thick porous medium is available to dissipate a relatively small interface velocity.

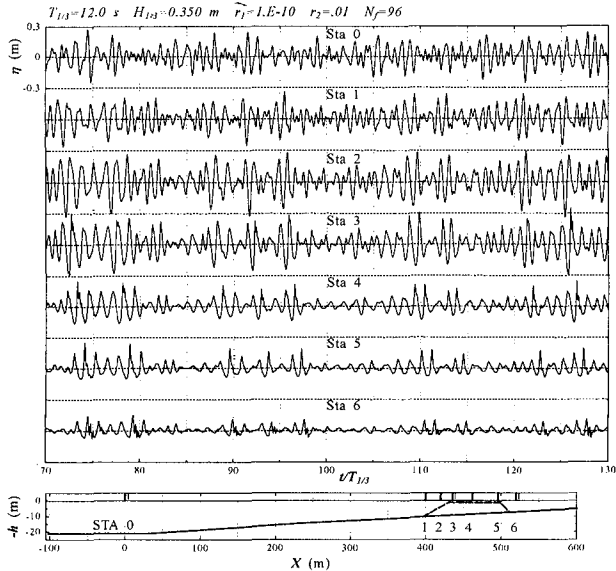


Fig. 10 Simulated evolution of η

Simulation of Irregular Wave Field Non-Breaking Wave

Fig. 10 shows the results of the simulation of an irregular non-breaking

wave. The input frequency spectrum is Bretschneider-Mitsuyasu type with a period of 12.0 s and height of 0.35m. The time profile at Station 0 is generated using linear random wave theory consisting of 256 waves with random phases. Simulations are done for 138 significant periods and the last 128 periods

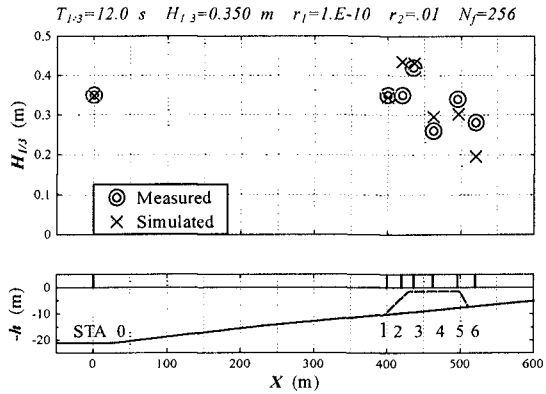


Fig. 11 Comparison of calculated and measured wave heights are used for synthesis.

In Fig. 10, the time profiles at Stations 0 to 6 for the last 60 periods is shown. In particular, the frequency components are reduced drastically by passage on the reef. At the back, the high-frequency portion is somewhat recovered. Fig. 11 shows the measured and simulated significant wave heights. Dominant shoaling effect at Station 1 is simulated well and the high wave on Station 3 is satisfactorily predicted. However, deviations are noticeable for the shoreward Stations.

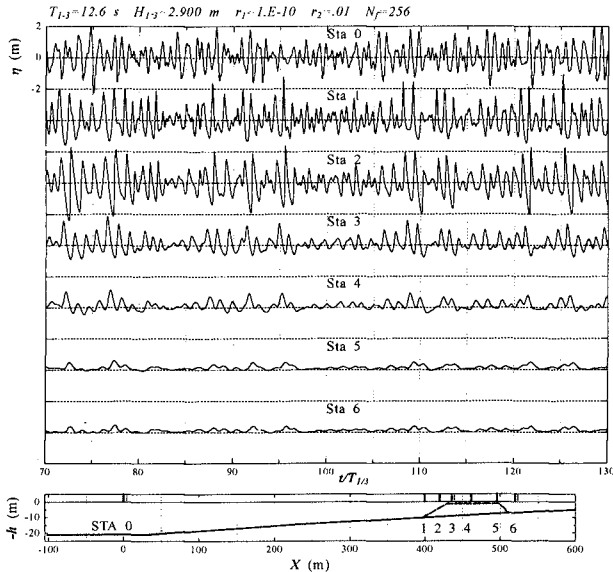


Fig. 12 Simulated evolution of η (breaking wave)

Breaking Wave

Fig. 12 shows the time profiles for the simulation of the highest recorded significant wave at Station 0 with incident wave height of 2.90 m and period of 12.6 s. Compared to the nonbreaking case, high-frequency reduction of the incident profile

occurs earlier. This is attributed to the active damping by the porous layer when the velocity penetrates the reef interior. However, breaking between Stations 2 and 3 still causes the major reduction in wave energy. **Fig. 13** shows the significant wave heights. The high wave on the slope is still predicted well but there is considerable underestimation of wave energy beginning at Station 3. The trend of wave height is still predicted correctly.

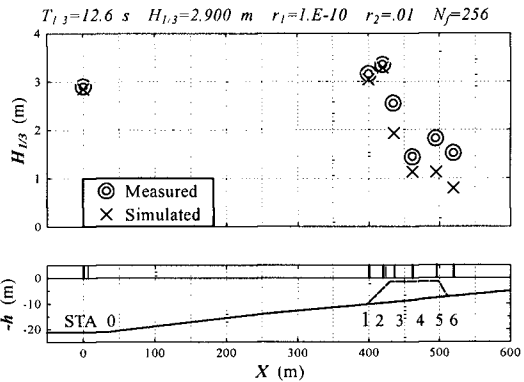


Fig. 13 Comparison of calculated and measured wave height (breaking wave)

Simulation of the Velocity Field

The velocity field is obtained simultaneously in the solution of Eqs. (1) to (3). **Fig. 14** shows the time series of depth-averaged horizontal velocity in water layer at Stations 3 and 4 on the reef crown for the breaking wave case. Since the crown is shallow at these stations, the measured point velocity essentially represents the depth-averaged value. Segments of the velocity measured at the current meters located 70 cm above the crown are shown for comparison. Although a direct comparison of the ob-

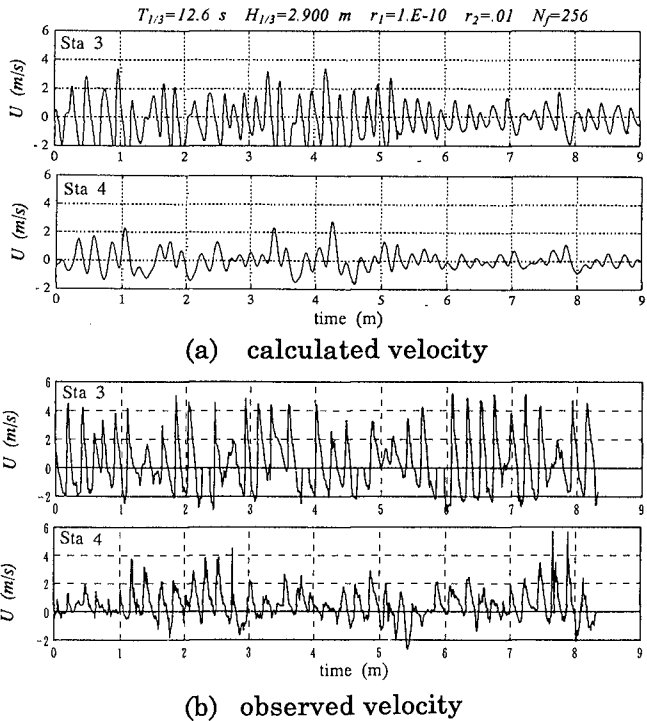


Fig. 14 Time series of the calculated and measured velocity *u*.

served and simulated velocities is strictly not meaningful due to the different phase relationships in the incident wave, the profiles indicate the velocity magnitudes after breaking. The simulation based on a depth-averaged treatment of the momentum exchange in a breaker tends to overestimate the amount of energy dissipated on the crown primarily because the breaking point predicted by the model occurs seaward of the reef crown, resulting in a wider region within which energy is apparently decimated. A surface roller approach tends to be sensitive to reflection which leads to a preemptive prediction of breaking.

Fig.15 shows the root-mean-square depth-averaged velocities u_{rms} obtained by a second run in which the roller parameters were determined such that the breaking point occurs just before the reef crown. In this case, u_{rms} are closer to the measured values especially before the breaking point and the general trend is predicted well. However, the values are significantly underestimated beyond Station 3 due to various factors, the most important of which is the variable material makeup of the actual reef.

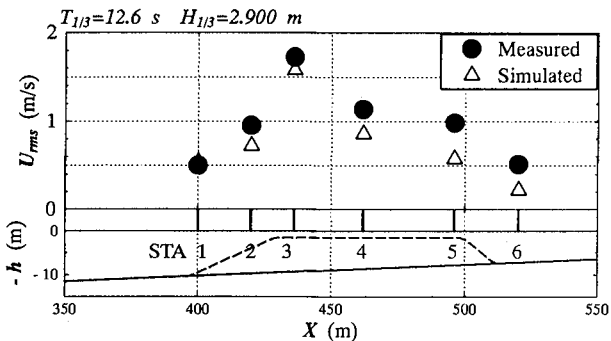


Fig. 15 Comparison of calculated and measured rms value of velocities.

5. CONCLUSIONS

The following summarizes the leading conclusions of this study:

- a. Measurements of the wave and current fields around the existing Yugawara Reef in Japan are reported. A synthesis of the significant wave parameters is discussed.
- b. A set of nonlinear wave equations with an extended range of dispersivity and porous damping rate is used to simulate the nonbreaking wave field along the reef centerline. Breaking waves are modelled using surface rollers.
- e. The wave field is generally characterized by a strong seaward reflection, decaying

wave heights on the crown and decomposing waves beyond the reef.

- d. There is a general agreement of wave energy distribution around the reef. However, deviations from measured values are observed. These are attributed to the simplifications in modelling the material composition of the reef, directional nature of the incident wave spectrum, the assumed two-dimensionality of the wave field and boundary influences such as external reflections.

Reference

- Cruz, E.C., M. Isobe and A. Watanabe (1992): Nonlinear wave transformation over a submerged permeable breakwater. Proc., Int. Conf. Coastal Eng., pp.1101..1114.
- Cruz, E.C., M. Isobe and A. Watanabe (1996): Boussinesq equations for wave transformation on porous beds, Coastal Eng., CENG 00727.
- Cruz, E.C. and M. Isobe (1994): Numerical wave absorbers for short and long wave modelling. Proc., Int. Symp. on Waves -- Phys. and Num. Modelling. Univ. of British Columbia, pp.992..1001.
- Deigaard, R.(1989): Mathematical modelling of waves in the surf zone, Progress Rep. 69, ISVA, Tech. Univ., Lyngby, Denmark, pp.47-59.
- Hasimoto, N., T. Nagai and T. Asai (1994):Extension of the maximum entropy principle method for directional wave spectrum estimation, Proc., Int. Conf. Coastal Eng., pp.232..246.
- Isobe, M., K. Shiba, E.C. Cruz and A. Watanabe (1991): On the nonlinear deformation of waves over submerged permeable breakwaters. Proc., Coastal Eng. Conference in Japan (in Japanese). pp.551..555.
- Ohnaka, S. and T. Yoshizawa (1994): Field observation on wave dissipation and reflection by an artificial reef with varying crown width. Proc., Int. Conf. Hydro-Technical Eng. for Port and Harbor Construction, pp.365..376.
- Madsen, P.A., R. Murray and O.R. Sorensen (1991): A new form of the Boussinesq equations with improved linear dispersion characteristics. Coastal Eng., 15, pp. 371..388.
- Schaffer, H.A., R. Deigaard and P.A. Madsen(1984): A two dimensional surf zone model based on the Boussinesq equations, Proc., Int. Conf. Coastal Eng., pp.576-589.

CHAPTER 179

Performance of a Submerged Breakwater for Shore Protection

Albert E. Browder¹, A. Member, ASCE; Robert G. Dean², Member, ASCE;
and Renjie Chen³

Abstract

A summary is presented of the results from a 3-year monitoring study of a submerged breakwater placed alongshore for shore protection. The experimental breakwater project, located in Palm Beach, Florida, USA, was concluded in August, 1995. The monitoring program was instituted to determine changes in wave climate and bathymetry, and to assess the shoreline response relative to pre-project conditions. The Palm Beach breakwater consisted of 330 interlocking concrete units, each 1.8 meters in height, 3.7 m long, and 4.6 m wide, which formed a 1,260 m-long shore parallel barrier. The breakwater, termed the Prefabricated Erosion Prevention (P.E.P.) Reef was placed in approximately 3 m of water roughly 73 m from the shoreline. The project was intended to increase shore protection against storm waves and to create a wider beach in the lee of the Reef. Wave transmission measurements indicated a 5 to 15% reduction in incident wave heights due to the Reef. The results of the monitoring program at the end of two years indicated erosion throughout the project area, primarily in the lee of the Reef, where the annual volumetric erosion rate was measured to be 2.3 times higher than the pre-project rate. The submerged breakwater is interpreted to have increased the longshore currents via ponding of water trapped behind the breakwater, which was then diverted alongshore. Laboratory experiments were conducted to investigate this ponding phenomenon and to test the performance of various segmented and repositioned breakwater arrangements. Shoreline erosion in the lee of the Reef was sufficiently severe to warrant removal of the structure in August, 1995.

¹Coastal Engineer, Olsen Associates, Inc., 4438 Herschel St., Jacksonville, FL, 32210 USA, 904-387-6114.

²Chairman & Graduate Research Professor, Coastal & Oceanographic Engineering Dept., University of Florida, Gainesville, FL 32611, USA.

³Graduate Research Assistant, Coastal & Oceanographic Engr. Dept., U. of Florida.

Introduction

The Town of Palm Beach lies on the southeast coast of Florida, U.S.A. The project site is 7.2 km south of the Port of Palm Beach Entrance (see Figure 1). This tidal entrance was created artificially in 1918, followed by the construction of jetties on either side of the inlet in 1925. The excavation of the inlet resulted in the rapid recession of the shoreline to the south along Palm Beach Island. The erosion problems experienced alongshore prompted the Town of Palm Beach to take action in three ways:

- ◆ The construction of seawalls alongshore,
- ◆ The use of beach nourishment, beginning in 1944,
- ◆ The construction and operation of a sand bypassing plant at the Port entrance, which was built in 1958. The plant operated until 1990, when it was damaged by storms. The plant re-opened in 1996.

The latter two actions resulted in the placement of over 5.86 million m³ of sand along the shoreline south of the Port entrance between 1944 and 1990. As a result, the average shoreline position in 1990, from the Port entrance southward 11 km, lies some 18 m seaward of its 1944 location, despite a persistent background erosion rate attributed mainly to the Port Entrance. This background erosion rate was estimated to be about 9.3 m³/m/yr by the U.S. Army Corps of Engineers (1987).

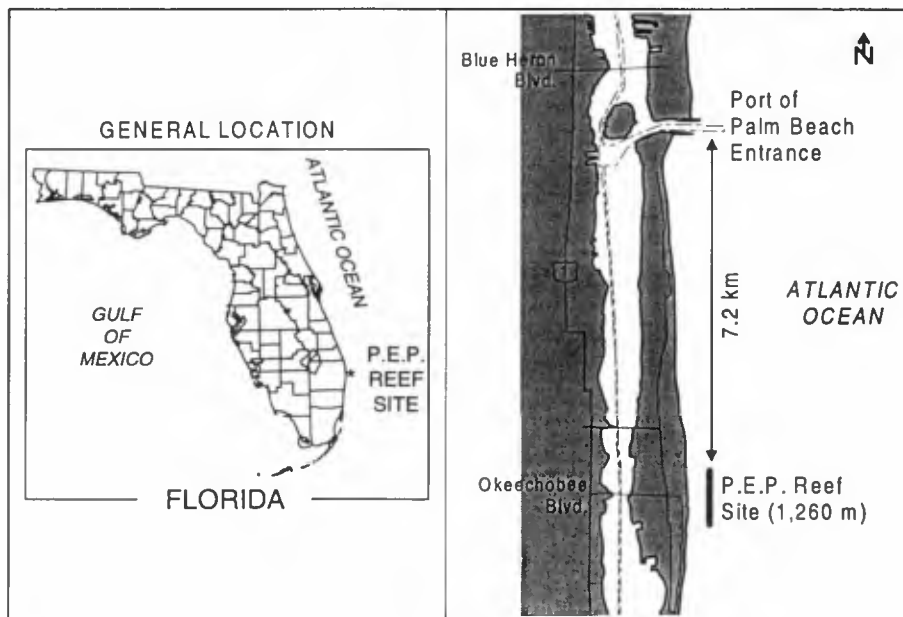


Figure 1 Location of P.E.P. Reef Site in the Town of Palm Beach, FL. The site lies approximately 7.2 km south of the Port of Palm Beach Entrance.

In an effort to provide a long-term "hard" solution to the erosion problem, the Town of Palm Beach investigated the use of a narrow-crested submerged nearshore breakwater, which was intended to increase shore protection against storm waves and to create a wider beach in the lee of the Reef.

The project involved the installation of 330 pre-cast concrete P.E.P. Reef units, each of which weighed 23 metric tons. The units were 1.8 m in height, 4.6 m in cross-shore width, and 3.7 m in length alongshore. When assembled the units extended 1,260 m alongshore. The units were placed in approximately 3 m water depth, about 73 m from the existing seawall along the heavily armored shoreline (see Figure 2).

Construction of the project began in July, 1992, with the placement of 57 units. Hurricane Andrew passed through southeast Florida in August, 1992, after which significant settling of the placed units was observed. The settlement of the units suspended construction of the project until the following summer. The remaining 273 units were placed between May and August, 1993. All 330 units were placed directly on the sandy bottom with no underlayment or foundation bedding.

To gauge the performance of the installation against its pre-project expectations, a monitoring program was conducted by the University of Florida Coastal and Oceanographic Engineering Department beginning in August, 1993. The program included quarterly topographic and hydrographic surveys of the site, wave transmission and unit settlement measurements, and an analysis of the background erosion processes and rates.

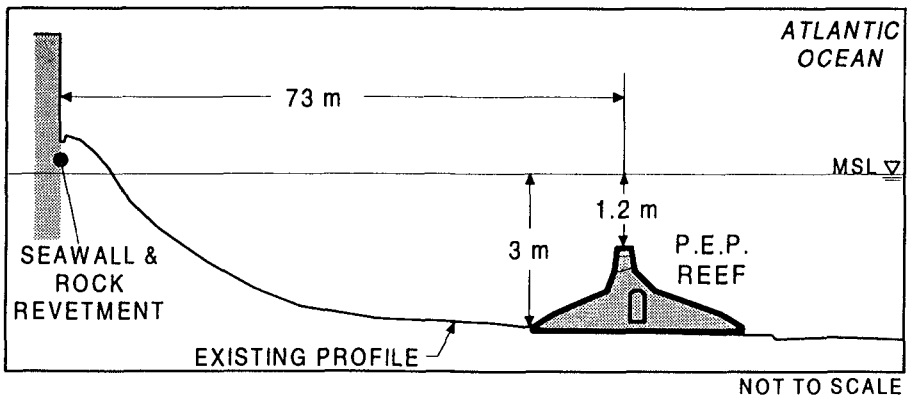


Figure 2 Schematic profile illustrating the relative location of the P.E.P. Reef structure to the shoreline.

Wave Transmission

To measure the effects of the Reef on the incident wave climate, two bottom mounted pressure-velocity gages were installed approximately 25 m on either side of the Reef just south of the centerline of the structure. The offshore and inshore gages were deployed in 4 and 2 m water depths, respectively. These gages collected data on an hourly basis, taking average pressure and bi-directional current measurements. Wave measurements were collected beginning in October, 1993, and continuing to the end of the monitoring period in June, 1995. Transmission coefficients were computed from each hourly measurement by calculating the ratio of the measured nearshore wave height to the wave height measured offshore, after shoaling the offshore wave height to the depth of the nearshore gage via linear wave theory. Figure 3 illustrates a schematic of the wave measurement arrangement and the summarized results.

Results from the initial wave measurements indicated a wave height reduction of as much as 15 to 25% (Dean and Chen, 1995). The range in wave height attenuation reflects the variable water levels and wave heights in the project area. The structure would have a greater effect (i.e., more wave height reduction) on larger waves and/or at lower water levels. The wave measurements indicated wave height reductions somewhat greater than anticipated by published literature (e.g., 0 to 10%, Ahrens, 1987). Additional wave measurements were taken at similar cross-shore locations south of the Reef structure. Analysis of the resulting data indicated a partial reduction in wave height due to natural effects such as wave breaking and bottom friction of approximately 10% (Browder, 1994). Thus, for an overall wave height reduction of 15 to 25%, the reduction due to the Reef was estimated to be 5 to 15%.

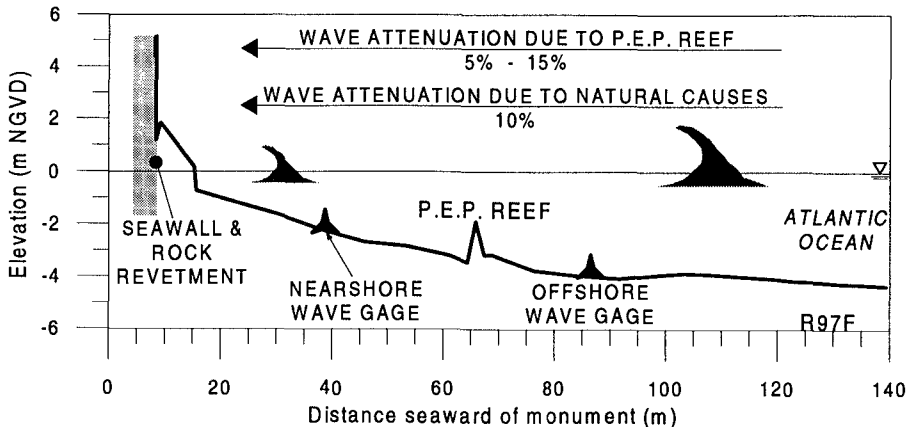


Figure 3 Schematic illustrating the cross-shore location of the wave gages and the P.E.P. Reef. The Reef was found to reduce incident wave heights by 5 to 15%, with another 10% reduction attributed to natural causes.

Littoral Performance

The littoral performance of the P.E.P. Reef project was measured via extensive hydrographic surveys, conducted on a quarterly basis during the project. The performance of the project was gaged against the historical shoreline behavior in the area. Ten surveys were conducted during the monitoring program, beginning in July, 1992, with the pre-construction survey. Each survey included 75 profile lines based from the Florida Department of Environmental Protection (FDEP) "R" monuments, which are spaced approximately 300 m apart alongshore. Additional profiles were surveyed between R-monuments at spacings of between 23 and 122 m.

The beach profiles were surveyed using standard land surveying techniques (swimming surveys with a rod and level) and boat/fathometer surveys. The swimming portion of the surveys extended at least 15 m seaward of the Reef to provide adequate overlap with the boat surveys. Each profile extended at least 365 m offshore. On annual surveys, the profiles were surveyed out to 1,070 m offshore. Profiles surveyed from R-monuments extended offshore 1,980 m. The hydrographic surveys were conducted on the following dates: July, 1992; April, August, and December, 1993; March, July, November, and December, 1994; and March and June, 1995. The November and December, 1994, surveys represent pre- and post-storm surveys of the area due to the passage of Tropical Storm Gordon.

Figure 4 shows the change in location of the Mean High Water Line (MHWL, approximately +0.6 m above the National Geodetic Vertical Datum, NGVD, which is approximately Mean Sea Level of 1929) measured alongshore over the course of the monitoring period. In the figure, the MHW shorelines are plotted relative to the July, 1992, *pre-project* shoreline location. It is important to note that in many places alongshore, the pre-project MHWL as well as the various surveyed project MHW shorelines fall on the seawall, thus limiting the landward recession of the shoreline in these areas.

Figure 4 indicates that during the first 13-month monitoring period, the shoreline south of R-98, in the vicinity of the original 57 units, advanced seaward an average of over 11 m. Along the remaining project shoreline north of R-98, recession of 2.8 m on average was measured, with some areas experiencing over 10 m of recession at the MHWL. Once again the presence of the seawall limited recession at many locations.

Following complete installation of all 330 units in August, 1993, the shoreline in the lee of the reef began to recede landward toward the seawall, as indicated by the July, 1994, surveyed MHWL. This recession continued through the end of the monitoring program, at which time (June, 1995) the shoreline along the majority of the 1,260-m project length had retreated to the seawall (with the exception of the shoreline at R-96 (Clarke Avenue), where there is no seawall; whereat the shoreline receded almost 23 m over 35 months).

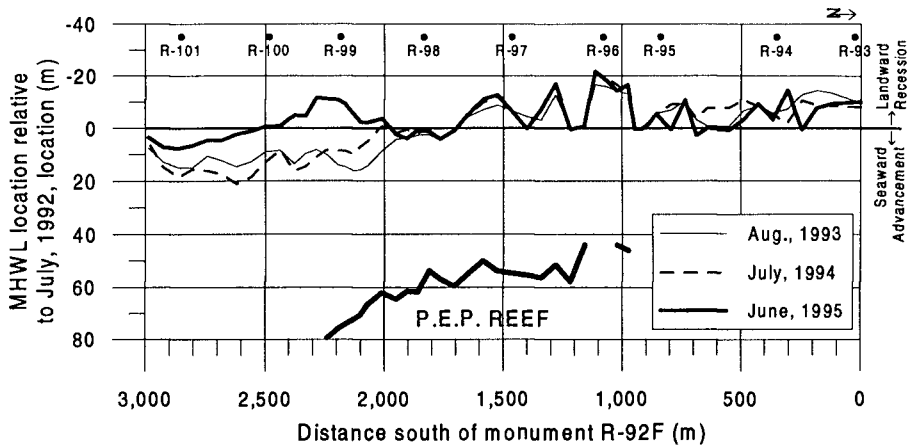


Figure 4 Location of the Mean High Water Line (MHWL) relative to the July, 1992, *pre-project* shoreline. The figure indicates the recession of the shoreline along the southern portion of the project, while the central and northern portions remain mostly unchanged. This is due to the presence of the seawall alongshore. Most of the central and northern MHWL was located at the seawall prior to the project, and no seaward advancement of the MHWL occurred at these locations.

Figure 5 illustrates the changes in one beach profile measured over the 35-month period between July, 1992, and June, 1995, at monument R-98J, approximately 23 m north of monument R-99, at the southern end of the Reef. Inspection of the three profiles plotted in the figure indicates that between July, 1992, and August, 1993, the shoreline had advanced seaward roughly 15 m (measured at Mean High Water). This time period spans the time in which the first 57 Reef units were already in place and the remaining 273 units were installed.

Between August, 1993, and June, 1995, however, the profile at R-98J retreated landward of the pre-project, July, 1992, position, to the seawall. The profile lowered over 2 m in front of the seawall in the 22-month period following completion of the entire Reef structure. Over the entire area in the lee of the 1,260-m long structure, i.e., between the Reef and the seawall, the seabed lowered an average of 0.7 m between August, 1993, and June, 1995.

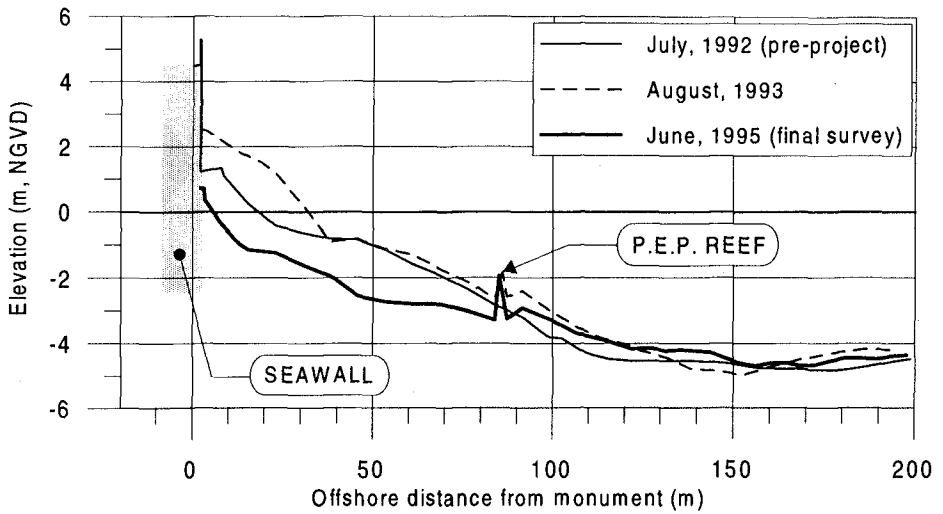


Figure 5 Profile changes measured at monument R-98J, near the southern terminus of the Reef. The plot indicates an initial seaward advance of the upper beach, followed by extreme erosion over the last 22 months of the monitoring program.

On a volumetric basis, analysis of the survey data indicates a net erosional signal in the area surrounding the installation. Figure 6 presents the measured volumetric changes in six zones surrounding the P.E.P. Reef installation. During the first year following complete installation (August, 1993, to August, 1994), the area in the lee of the Reef lost $28,600 \text{ m}^3$ of material while the area immediately to the south gained $13,500 \text{ m}^3$ (Dean & Chen, 1995). It is noted that of the $28,600 \text{ m}^3$ of erosion measured in the lee of the Reef, the majority (over 80%) of the erosion occurred in the first four months following complete installation of the Reef. Figure 6 indicates that in the remaining 4 zones, very little volumetric change occurred during this 12-month period.

Over the last year of monitoring, from July, 1994 to June, 1995, the area in the lee of the Reef continued to erode at roughly the same rate, losing $36,500 \text{ m}^3$ while the area immediately to the south lost $40,500 \text{ m}^3$ of material. Volumetric changes to the north of the project and offshore of the Reef again were relatively small (Figure 7).

Overall, during the full 35-month monitoring period, the area between the Reef and the seawall lost some $81,700 \text{ m}^3$ of sand (Figure 8). This loss translates to an average lowering of the seabed of 0.9 meters. Cumulative measurements of scour in the vicinity of the Reef's northern end indicate that the seabed immediately adjacent to the Reef had lowered between 0.5 and 1.05 m during the monitoring study.

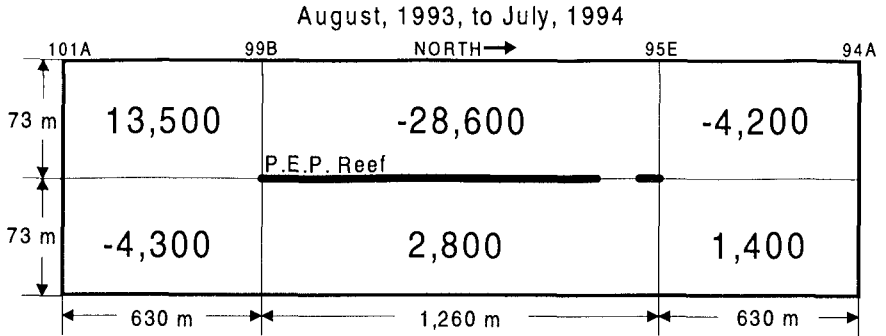


Figure 6 Volumetric changes (m^3) measured in six zones surrounding the P.E.P. Reef Installation between August, 1993, and August, 1994.

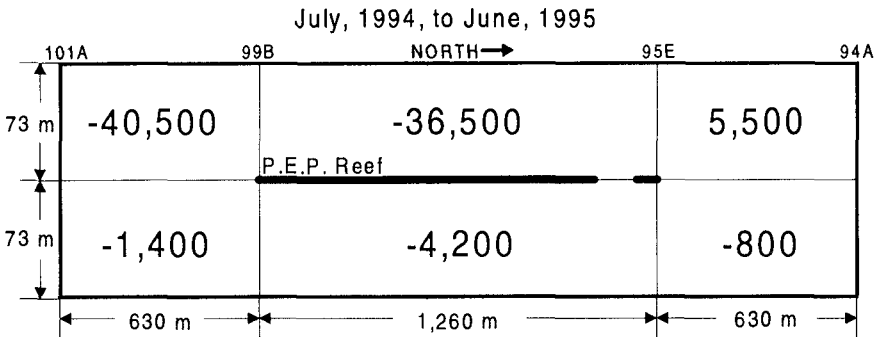


Figure 7 Volumetric changes (m^3) measured in six zones surrounding the P.E.P. Reef Installation between July, 1994, and June, 1995.

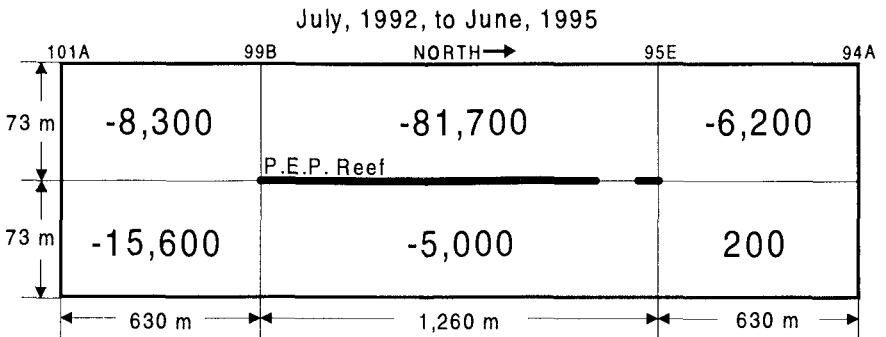


Figure 8 Volumetric changes (m^3) measured in six zones surrounding the P.E.P. Reef Installation between July, 1992, and June, 1995.

While the area to the south of the Reef had indicated accretion during the first two years of the study, erosion in the last year (40,500 m³, Figure 7) resulted in a net erosional signal south of the Reef over the 35-month monitoring period. Referring back to Figure 4, by June, 1995, only the southernmost 500 meters of the shoreline (some 300 meters south of the southern terminus of the Reef) were significantly seaward of the July, 1992, pre-project shoreline at the end of the study. Over the entire monitored area, 116,600 m³ of sand eroded during the 35-month period.

Pre-project data indicate that the project area is sediment-starved, due at least in part to the presence of the Port of Palm Beach Entrance. To compare the erosion rates measured during the monitoring program to the background erosion rates, two separate comparisons are investigated. Inspection of Figure 8 reveals that over 35 months, the erosion rate immediately in the lee of the Reef was 5.6 times higher than the rate along a combined equivalent shoreline distance north and south of the Reef. During the 23 months that the entire 330 Reef units were in place, the erosion rate was 2.5 times higher in the lee of the Reef than the adjacent shorelines (Figures 6 & 7). By reference to approximately 50 years of historical shoreline data, the overall erosion rate during the project was found to be 2.3 times higher than the pre-project rate estimated by the U.S. Army Corps of Engineers (1987)⁴.

The degree of erosion immediately landward of the Reef as compared to the areas to the north and south suggests the following mechanism for the overall erosion patterns. The monitoring data suggest that waves 'pump' water over the Reef, creating a ponding situation in which the ponded water is prevented from returning offshore in the normal return flow fashion and is instead redirected alongshore. This augments the natural longshore current and increases sediment transport in the lee of the Reef (Figure 9). With very little sediment supplying the area in pre-project conditions, the addition of the Reef (which did not introduce additional sand) caused a 'pumping out' of sediment from behind the Reef. This sediment was transported predominantly south to the adjacent shoreline, where it was temporarily deposited until the natural littoral transport carried it farther southward, resulting in an overall erosive condition.

Unit Settlement

In addition to the beach profiles, measurements of the top elevations of each unit were conducted during each quarterly survey to document the vertical settlement of the 330 units. The units were placed directly on the sandy bottom, with no foundation bedding or underlayment. The analysis of the settlement is divided into the average settlement of the original 57 units, which were in place a total of 35 months, and the remaining 273 units, which were in place 23 months.

4

USACE (1987) estimates the erosion rate to be 9.3 m³/yr/m alongshore. Along the 1,260 m shoreline in the lee of the Reef, this translates to 11,720 m³/yr of erosion.

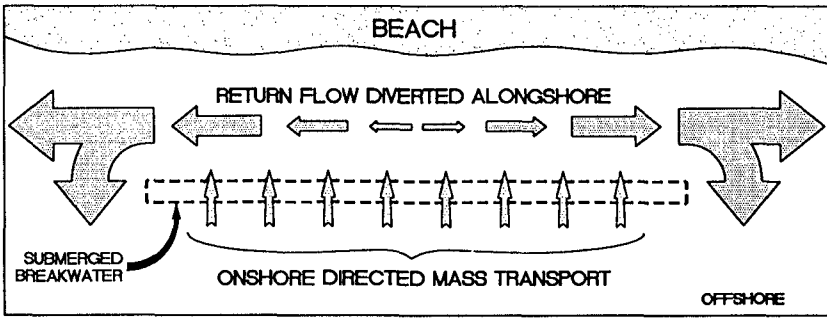


Figure 9 Schematic of Currents Generated Leeward of a Submerged Breakwater

Figure 10 illustrates the settlement of the units over time, relative to their estimated design depth. The original 57 units settled an average of 0.84 m, over 46% of the height of the Reef units (1.8 m). The remaining units settled an average of 0.60 m, 33% of the structure’s height. While it is unclear exactly how much the passage of Hurricane Andrew in August, 1992, affected the first 57 units, Figure 10 suggests that the hurricane may have contributed significantly to the settlement of these units.

The settlement of the units reduced the degree to which the units block the water column, which directly relates to the level of protection from wave attack afforded by the structure. At the same time, however, the lower structures may have prevented additional erosion caused by diverting more return flow water alongshore. Inspection of the bathymetric surveys and scour rod measurements conducted adjacent to the Reef suggests that the settlement was due primarily to the overall lowering of the sea floor in the vicinity of the Reef, rather than locally, structure-induced scour.

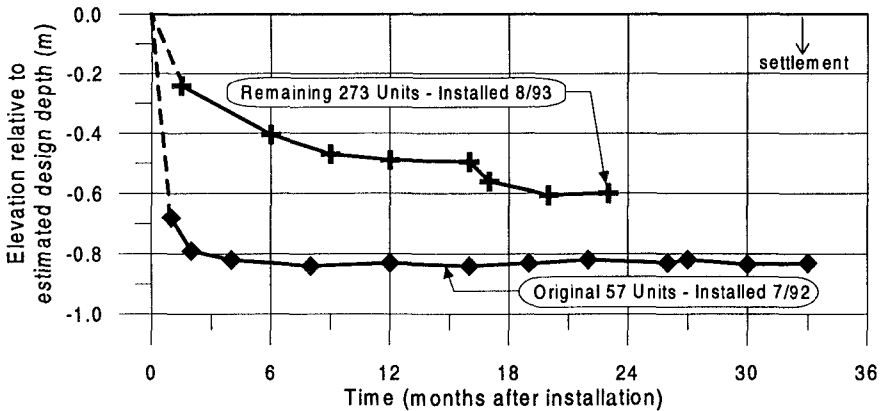


Figure 10 Average settlement of the first 57 units and the later 273 units.

Laboratory Findings

Laboratory experiments were conducted in conjunction with the monitoring program to investigate the ponding and associated phenomenon and to test the performance of various segmented and repositioned breakwater arrangements. Previous laboratory tests with two-dimensional tanks could not reveal the longshore current generation. Using the 3-d wave basin at the University of Florida Coastal and Oceanographic Engineering Laboratory, 1:16 scale models of the P.E.P. Reef units were tested on a fixed bed.

Laboratory measurements in this study included wave transmission and current velocities. Wave height measurements yielded transmission coefficients of approximately 95% for conditions simulating the Palm Beach P.E.P. Reef (i.e., continuous Reef structure with less than 50% of the vertical water column blocked by the Reef).

The lab tests, for all arrangements of the units, were able to reproduce the “pumping current” hypothesized from the littoral performance of the structure in the field (see Figure 9). Figure 11 illustrates the trajectories of bottom drogues documented in the laboratory report (Dean et al., 1994). Figure 11 indicates that for normally incident waves, in which there is no predominant wave or tidal generated longshore current, the presence of the submerged breakwater generates a longshore current that originates from the centerline of the structure in the lee of the Reef and flows toward the open ends, where the current is reduced through expansion.

While this longshore current was never directly measured in the field, the patterns of erosion measured in the lee of the Reef, relative to the volumetric changes along the adjacent shorelines, suggests that this “ponding and pumping” mechanism does in fact exist. It is believed that the pumping current existed as a secondary current to the longshore current, and was sufficient to increase the sediment transport rates along the seabed in the lee of the Reef, resulting in the substantial erosion measured between the Reef and the shoreline.

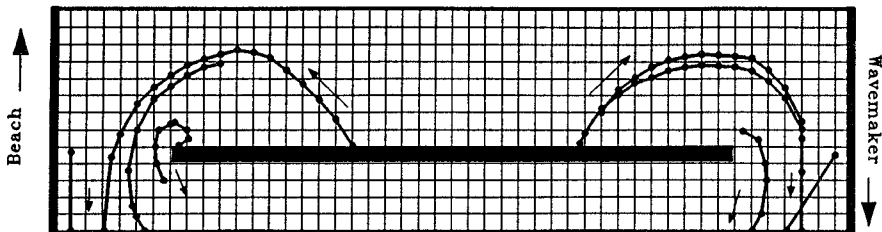


Figure 11 Typical circulation patterns witnessed in laboratory study using neutrally buoyant drogues. The patterns indicate that the Reef generates longshore currents in its lee that flow toward the ends of the Reef.

Summary

The results from a 3-year monitoring study of the Palm Beach, FL, Prefabricated Erosion Prevention Reef (P.E.P Reef), indicate that the reef modified both the incident wave climate and the nearshore current patterns. As defined by the State of Florida Department of Environmental Protection (FDEP), the project was intended to increase shore protection against storm waves and to create a wider beach in the lee of the Reef. Wave transmission measurements indicated a 5 to 15% reduction in incident wave heights due to the Reef. The results of the monitoring program at the end of two years indicated erosion throughout the project area, primarily in the lee of the Reef, where the annual volumetric erosion rate was measured to be 2.3 times higher than the pre-project rate. The submerged breakwater was found to have increased the longshore currents via ponding of water trapped behind the breakwater, which was then diverted alongshore. Laboratory experiments were conducted to investigate this ponding phenomenon and to test the performance of various segmented and repositioned breakwater arrangements.

Shoreline erosion in the lee of the Reef was sufficiently severe to warrant removal of the structure in August, 1995. Immediately following the dismantling of the submerged breakwater, a large-scale beach nourishment project was constructed on the site. This project utilized some of the P.E.P. Reef units as the core material for shore-perpendicular groins within the beach-fill. The remaining units were moved into deeper water offshore to create artificial reef habitat

Acknowledgements

The authors would like to express their appreciation to FDEP and the Town of Palm Beach for supporting the project. Sea Systems, Inc., of Pompano Beach, FL, conducted the surveys in a professional and timely manner.

References

Ahrens, J.P., 1987, "Characteristics of Reef Breakwaters," Coastal Engineering Research Center, Technical Report CERC-87-17.

Browder, A.E., 1994, "Wave Transmission and Current Patterns Associated with Narrow-Crested Submerged Breakwaters," M.Eng. Thesis, Coastal and Oceanographic Engineering Department Rpt. No. UFL/COEL-94/022, University of Florida.

Dean, R.G., Browder, A.E., Goodrich, M.S., and Donaldson, D.G., "Model Tests of the Proposed P.E.P. Reef Installation at Vero Beach, FL," Coastal and Oceanographic Engineering Department Rpt. No. UFL/COEL-94/012, University of Florida.

Dean, R.G., and Chen, R., 1995, "Performance of the P.E.P. Reef Installation, Town of Palm Beach, Seventeen Months Results," Coastal and Oceanographic Engineering Department Rpt. No. UFL/COEL-95/004, University of Florida.

U.S. Army Corps of Engineers, 1987, "Beach Erosion Control Project, Palm Beach County, FL," Jacksonville District, FL.

CHAPTER 180

Nonlinear Wave Transformation over a Submerged Triangular Breakwater

Lifen Dong¹ Akira Watanabe and Masahiko Isobe²

Abstract

This study deals with wave transformation over a submerged triangular breakwater that is composed of a series of elements with a triangular horizontal cross-section. The idea of such a triangular breakwater is founded on the use of the wave refraction due to peculiar spatial change in water depth around it.

A numerical model is developed to predict nonlinear wave transformation over and around the breakwater on the basis of fully nonlinear wave equations proposed by Isobe (1994). Laboratory experiment has also been conducted in a wave basin. The validity of the numerical model is examined by comparing the computations with the measurements.

1. Introduction

When waves propagate over a submerged triangular breakwater, wave refraction will happen. The superiority of a submerged triangular breakwater lies in its capability of controlling the wave direction as well as the height as compared to conventional submerged breakwaters with rectangular cross-section. For example, a breakwater as shown in Fig. 1 (a) can control even the longshore current through the change in the wave direction, whereas the one as illustrated in Fig. 1 (b) may be employed to increase the wave height in the locations where the waves converge for purposes such as effective wave energy use and surfing.

This paper presents the results of numerical computation based on fully nonlinear mild-slope equations proposed by Isobe and compares them with those of a laboratory experiment for breakwaters of the type (b).

¹Research Engineer, River Engineering Consultants Co., Ltd., Ohyama Higashichou 40-5, Itabashi-ku, Tokyo, 113, Japan.

²Professor, Dept. of Civil Eng., Univ. of Tokyo, Tokyo, 113, Japan.

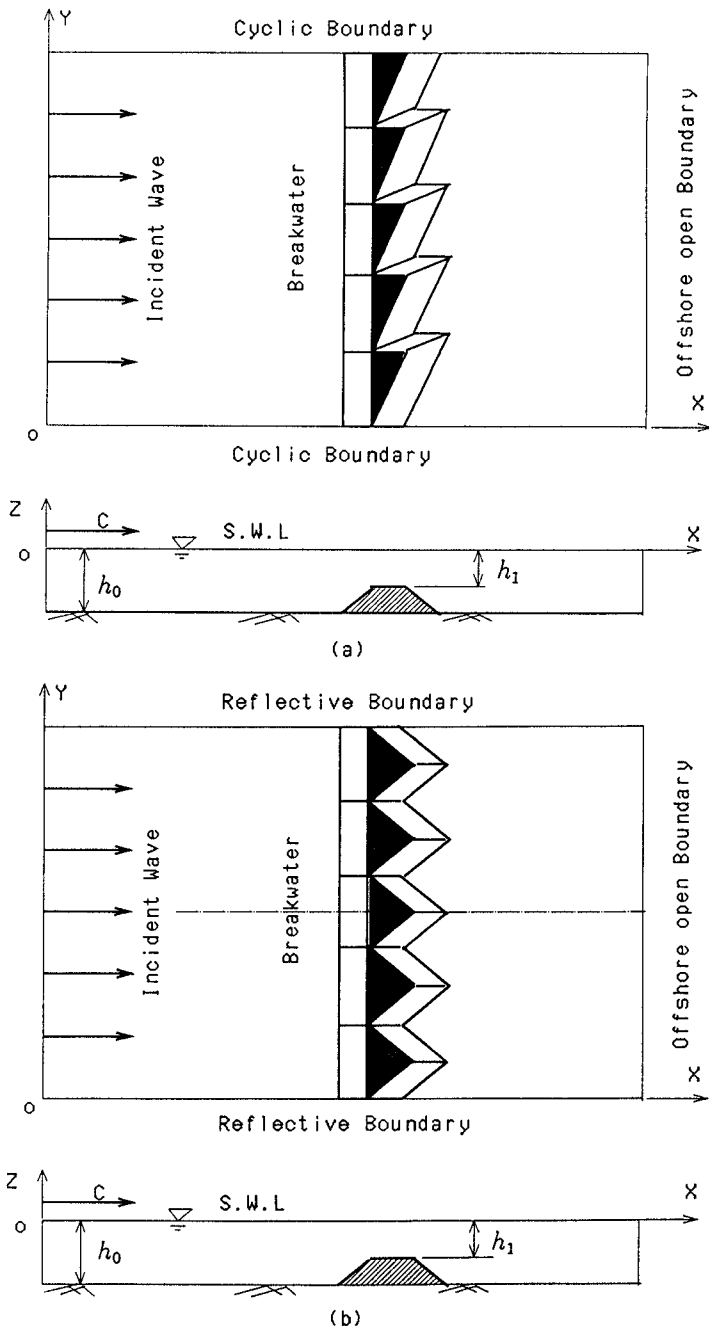


Fig. 1 Two types of submerged triangular breakwaters.

2. Numerical Model

2.1 Governing equations

The mild-slope nonlinear equations proposed by Isobe (1994) are as follows:

$$Z_\alpha^\eta \frac{\partial \eta}{\partial t} + \nabla(A_{\alpha\beta} \nabla f_\beta) - B_{\alpha\beta} f_\beta + (C_{\beta\alpha} - C_{\alpha\beta}) \nabla f_\beta \nabla h + \frac{\partial Z_\beta^\eta}{\partial h} Z_\alpha^\eta f_\beta \nabla \eta \nabla h = 0 \quad (1)$$

$$g\eta + Z_\beta^\eta \frac{\partial f_\beta}{\partial t} + \frac{1}{2} Z_\gamma^\eta Z_\beta^\eta \nabla f_\gamma \nabla f_\beta + \frac{1}{2} \frac{\partial Z_\gamma^\eta}{\partial z} \frac{\partial Z_\beta^\eta}{\partial z} f_\gamma f_\beta + \frac{\partial Z_\gamma^\eta}{\partial h} Z_\beta^\eta f_\gamma \nabla f_\beta \nabla h = 0 \quad (2)$$

where $Z_\alpha^\eta = Z_\alpha|_{z=\eta}$, h is the water depth, and the water surface elevation η and the function f_α are unknown variables. The vertical distribution function Z_α is related to the velocity potential ϕ and defined as

$$\phi(x, y, z, t) = \sum_{\alpha=0}^N Z_\alpha(z, h(x, y)) f_\alpha(x, y, t) \quad (3)$$

$$Z_\alpha(z, h(x, y)) = \left(1 + \frac{z}{h}\right)^{2\alpha} \quad (4)$$

The coefficients $A_{\alpha\beta}$, $B_{\alpha\beta}$ and $C_{\alpha\beta}$ can be obtained from Z_α by

$$A_{\alpha\beta} = \int_{-h}^{\eta} Z_\alpha Z_\beta dz \quad (5)$$

$$B_{\alpha\beta} = \int_{-h}^{\eta} \frac{\partial Z_\alpha}{\partial z} \frac{\partial Z_\beta}{\partial z} dz \quad (6)$$

$$C_{\alpha\beta} = \int_{-h}^{\eta} \frac{\partial Z_\alpha}{\partial h} Z_\beta dz \quad (7)$$

2.2 Boundary conditions

For the present case, the following perfectly reflective boundary condition is imposed on the side boundaries by virtue of the symmetry of the structure and the resulting wave field.

$$\frac{\partial \phi}{\partial y} = 0 \quad (8)$$

By substituting the expression of ϕ into Eq. (8), the following two expressions are obtained as side boundary conditions.

$$\frac{\partial \eta}{\partial y} = 0, \quad \frac{\partial f_\alpha}{\partial y} = 0 \quad (9)$$

The Sommerfeld radiation condition is used on the onshore open boundary.

$$\frac{\partial \phi}{\partial t} + C \frac{\partial \phi}{\partial \bar{n}} = 0 \quad (10)$$

The substitution of ϕ yields the onshore boundary conditions as follows:

$$\frac{\partial \eta}{\partial t} + C \frac{\partial \eta}{\partial \bar{n}} = 0, \quad \frac{\partial f_\alpha}{\partial t} + C \frac{\partial f_\alpha}{\partial \bar{n}} = 0, \tag{11}$$

in which \bar{n} is the length of the mean direction vector of transmitted waves and C denotes the wave celerity.

The offshore boundary condition is given by

$$\cos \bar{\alpha}_r \frac{\partial \phi}{\partial t} - C \frac{\partial \phi}{\partial x} = (1 + \cos \bar{\alpha}_r) \frac{\partial \phi_0}{\partial t} \tag{12}$$

where ϕ_0 , the potential of the incident waves, is expressed as

$$\phi_0 = \sum_{\alpha=0}^N Z_\alpha f_{\alpha 0} = Z_\alpha f_{\alpha 0} \tag{13}$$

Substituting of the expressions of ϕ and ϕ_0 into Eq. (12), we obtain

$$\cos \bar{\alpha}_r \frac{\partial \eta}{\partial t} - C \frac{\partial \eta}{\partial x} = (1 + \cos \bar{\alpha}_r) \frac{\partial \eta_0}{\partial t} \tag{14}$$

$$\cos \bar{\alpha}_r \frac{\partial f_\alpha}{\partial t} - C \frac{\partial f_\alpha}{\partial x} = (1 + \cos \bar{\alpha}_r) \frac{\partial f_{\alpha 0}}{\partial t} \tag{15}$$

where η_0 is the water surface elevation of the incident waves and $\bar{\alpha}_r$ is the mean direction of reflected waves.

2.3 Expression of incident waves

Even in the computation of nonlinear wave transformation, the incident waves will be reasonably expressed by a small amplitude wave theory if the Ursell number is not so large at the offshore boundary. Assuming that the incident waves are monochromatic sinusoidal waves propagating along the x -direction, their potential ϕ_0 can be expressed as

$$\phi_0 = \frac{a_0 g}{\sigma} \frac{\cosh k_0(z + h_0)}{\cosh k_0 h_0} \sin(k_0 x - \sigma t) \tag{16}$$

$$= \sum_{\alpha=0}^N Z_\alpha f_{\alpha 0} \tag{17}$$

which corresponds to the water surface displacement η_0 given by

$$\eta_0 = a_0 \cos(k_0 x - \sigma t) \tag{18}$$

where a_0 and k_0 are the amplitude and the wave number of the incident waves, h_0 is the offshore water depth, and σ is the angular frequency.

By expanding $\cosh k_0(z + h_0)$, ϕ_0 can be expressed as

$$\phi_0 = \sum_{\alpha=0}^N \frac{a_0 g}{\sigma} \frac{(k_0 h_0)^{2\alpha}}{(2\alpha)! \cosh k_0 h_0} \sin(k_0 x - \sigma t) \left(1 + \frac{z}{h_0}\right)^{2\alpha} \quad (19)$$

From this equation we obtain

$$f_{\alpha 0} = \frac{a_0 g}{\sigma} \frac{(k_0 h_0)^{2\alpha}}{(2\alpha)! \cosh k_0 h_0} \sin(k_0 x - \sigma t) \quad (20)$$

2.4 Finite difference equations

Numerical solutions of the governing equations are obtained using a finite difference technique. Central difference and forward difference are adopted in space and in time, respectively. To the nonlinear equations into a finite difference form for the present two-dimensional problem, ADI (Alternating Direction Implicit) scheme (Fletcher, 1987) is employed, namely, Eqs. (4.1) and (4.2) are splitted into x -sweep and y -sweep finite difference equations.

x -sweep

During the first half-step the following discretization is made.

$$\begin{aligned} & Z_\alpha^\eta \frac{\eta_{i,j}^{m+\frac{1}{2}} - \eta_{i,j}^m}{\Delta t/2} + A_{\alpha\beta i,j} \frac{f_{\beta(i+1),j}^{m+\frac{1}{2}} + f_{\beta(i-1),j}^{m+\frac{1}{2}} - 2f_{\beta i,j}^{m+\frac{1}{2}}}{\Delta x^2} \\ & + A_{\alpha\beta i,j} \frac{f_{\beta i,j+1}^m + f_{\beta i,j-1}^m - 2f_{\beta i,j}^m}{\Delta y^2} - B_{\alpha\beta} f_{\beta i,j}^{m+\frac{1}{2}} \\ & + \frac{A_{\alpha\beta(i+1),j} - A_{\alpha\beta(i-1),j}}{2\Delta x} \frac{f_{\beta(i+1),j}^{m+\frac{1}{2}} - f_{\beta(i-1),j}^{m+\frac{1}{2}}}{2\Delta x} \\ & + \frac{A_{\alpha\beta i,j+1} - A_{\alpha\beta i,j-1}}{2\Delta y} \frac{f_{\beta i,j+1}^m - f_{\beta i,j-1}^m}{2\Delta y} \\ & + (C_{\beta\alpha} - C_{\alpha\beta}) \frac{f_{\beta(i+1),j}^{m+\frac{1}{2}} - f_{\beta(i-1),j}^{m+\frac{1}{2}}}{2\Delta x} \frac{h_{i+1,j} - h_{i-1,j}}{2\Delta x} \\ & + (C_{\beta\alpha} - C_{\alpha\beta}) \frac{f_{\beta i,j+1}^m - f_{\beta i,j-1}^m}{2\Delta y} \frac{h_{i,j+1} - h_{i,j-1}}{2\Delta y} \\ & + \frac{\partial Z_\beta^\eta}{\partial h} Z_\alpha^\eta f_{\beta i,j}^{m+\frac{1}{2}} \left(\frac{\eta_{i+1,j}^m - \eta_{i-1,j}^m}{2\Delta x} \frac{h_{i+1,j} - h_{i-1,j}}{2\Delta x} + \frac{\eta_{i,j+1}^m - \eta_{i,j-1}^m}{2\Delta y} \frac{h_{i,j+1} - h_{i,j-1}}{2\Delta y} \right) \\ & = 0 \end{aligned} \quad (21)$$

$$\begin{aligned} & g\eta_{i,j}^{m+\frac{1}{2}} + Z_\beta^\eta \frac{f_{\beta i,j}^{m+\frac{1}{2}} - f_{\beta i,j}^m}{\Delta t/2} + \frac{1}{2} Z_\gamma^\eta Z_\beta^\eta \left(\frac{f_{\gamma(i+1),j}^m - f_{\gamma(i-1),j}^m}{2\Delta x} \frac{f_{\beta(i+1),j}^{m+\frac{1}{2}} - f_{\beta(i-1),j}^{m+\frac{1}{2}}}{2\Delta x} \right) \\ & + \frac{1}{2} Z_\gamma^\eta Z_\beta^\eta \left(\frac{f_{\gamma i,j+1}^m - f_{\gamma i,j-1}^m}{2\Delta y} \frac{f_{\beta i,j+1}^{m+\frac{1}{2}} - f_{\beta i,j-1}^{m+\frac{1}{2}}}{2\Delta y} \right) + \frac{1}{2} \frac{\partial Z_\gamma^\eta}{\partial z} \frac{\partial Z_\beta^\eta}{\partial z} f_{\gamma i,j}^m f_{\beta i,j}^{m+\frac{1}{2}} \end{aligned}$$

$$\begin{aligned}
 & + \left(\frac{f_{\beta(i+1),j}^{m+\frac{1}{2}} - f_{\beta(i-1),j}^{m+\frac{1}{2}}}{2\Delta x} \frac{h_{i+1,j} - h_{i-1,j}}{2\Delta x} + \frac{f_{\beta i,j+1}^m - f_{\beta i,j-1}^m}{2\Delta y} \frac{h_{i,j+1} - h_{i,j-1}}{2\Delta y} \right) \\
 & \frac{\partial Z_\gamma^\eta}{\partial h} f_{\gamma i,j}^m Z_\beta^\eta \\
 & = 0
 \end{aligned} \tag{22}$$

in which, Δx and Δy are the space intervals and Δt is the time interval. The quantities $\eta_{i,j}^{m+\frac{1}{2}}$ and $f_{\beta i,j}^{m+\frac{1}{2}}$ are the unknowns, whereas $\eta_{i,j}^m$, $f_{\beta i,j}^m$ and other parameters are given in the previous time step m .

y-sweep

During the second half-step the following discretization is made.

$$\begin{aligned}
 & Z_\alpha^\eta \frac{\eta_{i,j}^{m+1} - \eta_{i,j}^{m+\frac{1}{2}}}{\Delta t/2} + A_{\alpha\beta i,j} \frac{f_{\beta(i+1),j}^{m+\frac{1}{2}} + f_{\beta(i-1),j}^{m+\frac{1}{2}} - 2f_{\beta i,j}^{m+\frac{1}{2}}}{\Delta x^2} \\
 & + A_{\alpha\beta i,j} \frac{f_{\beta i,j+1}^{m+1} + f_{\beta i,j-1}^{m+1} - 2f_{\beta i,j}^{m+1}}{\Delta y^2} - B_{\alpha\beta} f_{\beta i,j}^{m+1} \\
 & + \frac{A_{\alpha\beta(i+1),j} - A_{\alpha\beta(i-1),j}}{2\Delta x} \frac{f_{\beta(i+1),j}^{m+\frac{1}{2}} - f_{\beta(i-1),j}^{m+\frac{1}{2}}}{2\Delta x} \\
 & + \frac{A_{\alpha\beta i,j+1} - A_{\alpha\beta i,j-1}}{2\Delta y} \frac{f_{\beta i,j+1}^{m+1} - f_{\beta i,j-1}^{m+1}}{2\Delta y} \\
 & + (C_{\beta\alpha} - C_{\alpha\beta}) \frac{f_{\beta(i+1),j}^{m+\frac{1}{2}} - f_{\beta(i-1),j}^{m+\frac{1}{2}}}{2\Delta x} \frac{h_{i+1,j} - h_{i-1,j}}{2\Delta x} \\
 & + (C_{\beta\alpha} - C_{\alpha\beta}) \frac{f_{\beta i,j+1}^{m+1} - f_{\beta i,j-1}^{m+1}}{2\Delta y} \frac{h_{i,j+1} - h_{i,j-1}}{2\Delta y} \\
 & + \frac{\partial Z_\beta^\eta}{\partial h} Z_\alpha^\eta f_{\beta i,j}^{m+1} \left(\frac{\eta_{i+1,j}^{m+\frac{1}{2}} - \eta_{i-1,j}^{m+\frac{1}{2}}}{2\Delta x} \frac{h_{i+1,j} - h_{i-1,j}}{2\Delta x} + \frac{\eta_{i,j+1}^{m+\frac{1}{2}} - \eta_{i,j-1}^{m+\frac{1}{2}}}{2\Delta y} \frac{h_{i,j+1} - h_{i,j-1}}{2\Delta y} \right) \\
 & = 0
 \end{aligned} \tag{23}$$

$$\begin{aligned}
 & g\eta_{i,j}^{m+1} + Z_\beta^\eta \frac{f_{\beta i,j}^{m+1} - f_{\beta i,j}^{m+\frac{1}{2}}}{\Delta t} + \frac{1}{2} Z_\gamma^\eta Z_\beta^\eta \left(\frac{f_{\gamma(i+1),j}^{m+\frac{1}{2}} - f_{\gamma(i-1),j}^{m+\frac{1}{2}}}{2\Delta x} \frac{f_{\beta(i+1),j}^{m+\frac{1}{2}} - f_{\beta(i-1),j}^{m+\frac{1}{2}}}{2\Delta x} \right) \\
 & + \frac{1}{2} Z_\gamma^\eta Z_\beta^\eta \left(\frac{f_{\gamma i,j+1}^{m+\frac{1}{2}} - f_{\gamma i,j-1}^{m+\frac{1}{2}}}{2\Delta y} \frac{f_{\beta i,j+1}^{m+1} - f_{\beta i,j-1}^{m+1}}{2\Delta y} \right) + \frac{1}{2} \frac{\partial Z_\gamma^\eta}{\partial z} \frac{\partial Z_\beta^\eta}{\partial z} f_{\gamma i,j}^m f_{\beta i,j}^{m+1} \\
 & + \left(\frac{f_{\beta(i+1),j}^{m+\frac{1}{2}} - f_{\beta(i-1),j}^{m+\frac{1}{2}}}{2\Delta x} \frac{h_{i+1,j} - h_{i-1,j}}{2\Delta x} + \frac{f_{\beta i,j+1}^{m+1} - f_{\beta i,j-1}^{m+1}}{2\Delta y} \frac{h_{i,j+1} - h_{i,j-1}}{2\Delta y} \right)
 \end{aligned}$$

$$\frac{\partial Z_\gamma^n}{\partial h} f_{\gamma_{i,j}}^m; Z_\beta^n = 0 \quad (24)$$

in which $\eta_{i,j}^{m+1}$, $f_{\beta_{i,j}}^{m+1}$ are the unknowns, and $\eta_{i,j}^{m+\frac{1}{2}}$, $f_{\beta_{i,j}}^{m+\frac{1}{2}}$ and other parameters are given at the previous time step ($m + \frac{1}{2}$).

2.5 Numerical solutions

Solutions of the finite difference equations are obtained by using the boundary conditions given above. In the numerical computation, the intervals of space and time are taken as follows: $\Delta x < L_0/20$, $\Delta y < L_0/20$, $\Delta t = T/250$, where, T is the wave period and L_0 is the wavelength.

At any time step m , the water surface elevation $\eta_m(x_i, y_j)$ can be obtained by solving the above equations. Then the root mean square value of the water surface displacement $\eta_{\text{rms}}(x_i, y_j)$ can be given by

$$\eta_{\text{rms}}(x_i, y_j) = \sqrt{\sum_{m=1}^n \eta_m^2(x_i, y_j)/n} \quad (25)$$

where n is the total sampling number of water surface elevation within several wave periods.

3. Laboratory Experiment

3.1 Experimental setup

In order to observe the wave deformation process and to examine the numerical computation model, a two-dimensional laboratory experiment on wave transformation over submerged triangular breakwaters has been made in a wave basin, of which the flow domain is 3.55×0.75 m. A flap-type wave maker is equipped to generate regular waves, and a wave absorber is placed on the onshore boundary in order to avoid the wave reflectoin.

Only a half element of the breakwater has been taken in the experiment (as well as in the computation) because of the symmetry of the breakwater as shown in Fig. 1 (b). Two types of model breakwaters have been modeled. The first one has a purely triangular horizontal cross-section with seaward and shoreward side slope of $1/3$, whereas the second one has a cross-section composed of triangular and rectangular parts as shown in Fig. 2. In all the cases, the direction of incident waves is in parallel to the x -axis and no wave breaking over the breakwater has occurred.

3.2 Data acquisition and processing

The water surface displacement was measured at many points with small spacing in the x -direction along the nine sections shown in Fig. 2 with the capacitance-

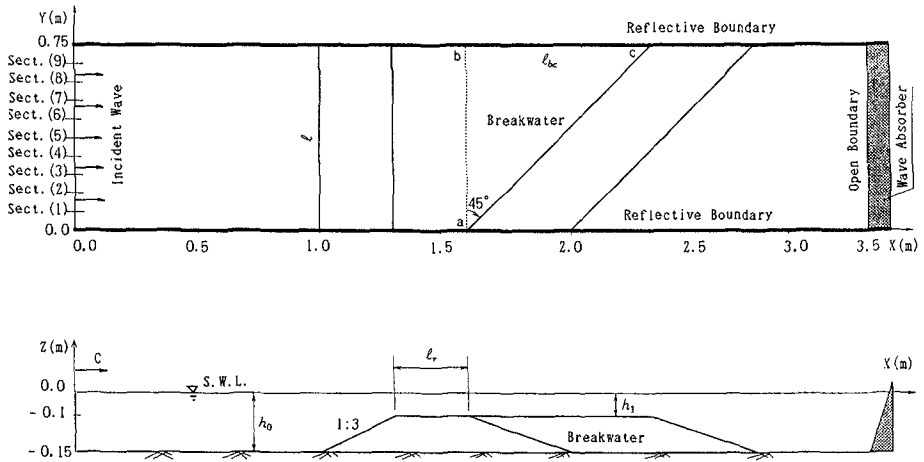


Fig. 2 Experimental setup.

type wave gages. After preliminary processing, the root mean square value of the water surface elevation η_{rms} was obtained for every point.

$$\eta_{rms} = \sqrt{\sum_{i=1}^n \eta^2(t_i) / n} \tag{26}$$

By utilizing the separation technique for incident and reflected wave components (Goda and Suzuki, 1976) from two adjacent wave records measured along the x -direction at the same time, the amplitude of incident waves a_{0j} was evaluated. Then the root mean square of water surface displacement of the incident waves was obtained by using the following expression.

$$\eta_{0rms} = \sqrt{\sum_{j=1}^m \frac{a_{0j}^2}{2}} \tag{27}$$

where m is the number of incident wave components.

Finally relative values of the water surface elevation η_{rms} / η_{0rms} were calculated.

4. Results and Conclusions

4.1 Results

For the two types of breakwaters, the experiment and computation were carried out under various incident wave conditions. In the numerical computation, the mean direction angle of reflected waves $\bar{\alpha}_r$ was taken as 0.0 degree for all the cases, and the mean direction of transmitted waves was assumed to be parallel to the x -direction at any grid point on the onshore boundary. The range of α in the vertical distribution function $Z_\alpha(z)$ is taken from 0 to 3, i.e., four terms are taken in the expression of velocity potential ϕ .

Fig. 3 shows examples of the comparisons between the measurements and the computations of the relative root mean square of the water surface displacement along the sections (1), (3), (5), (7) and (9) for the first type of the breakwater. The total water depth is 15 cm, the breakwater height is 10 cm, and the incident wave height and period are 0.85 cm and 1.0 s. Fig. 4 shows the comparisons between the measurements and the computations of time histories of the water surface displacements at several points along the x -direction for the same condition. Both the figures demonstrate a rather good agreement between the measurements and the computations.

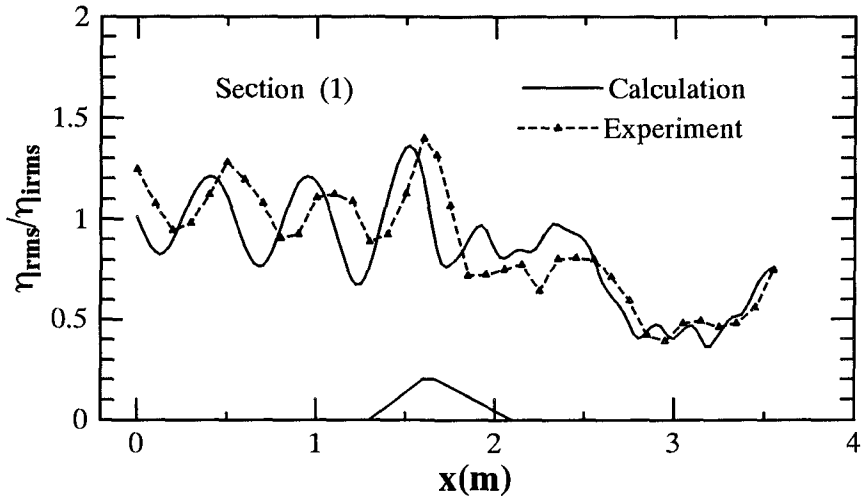


Fig. 3.1 Distributions of RMS of surface displacements.

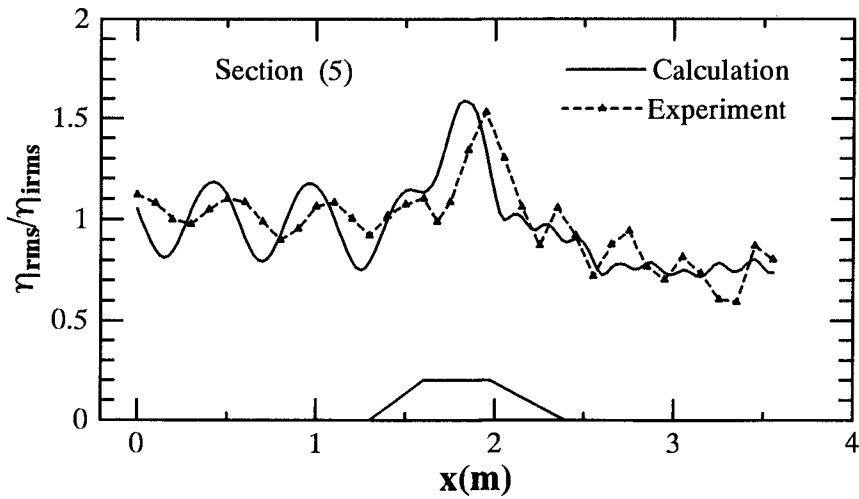
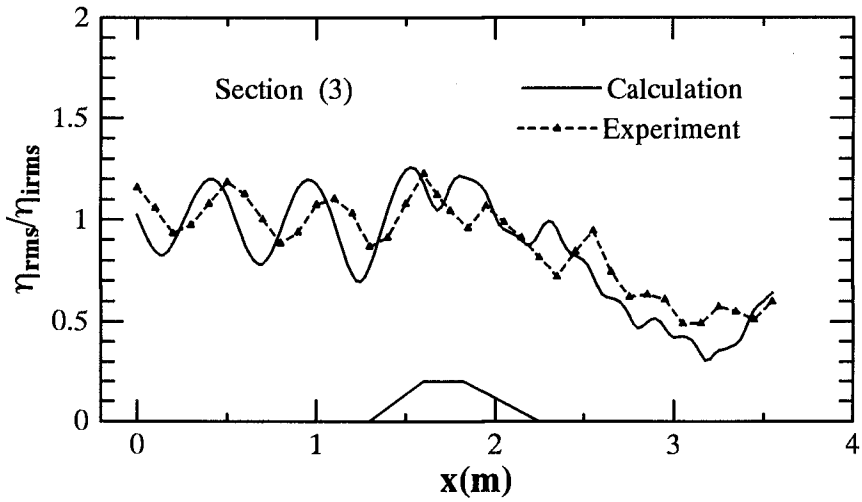


Fig. 3.2 Distributions of RMS of surface displacements.

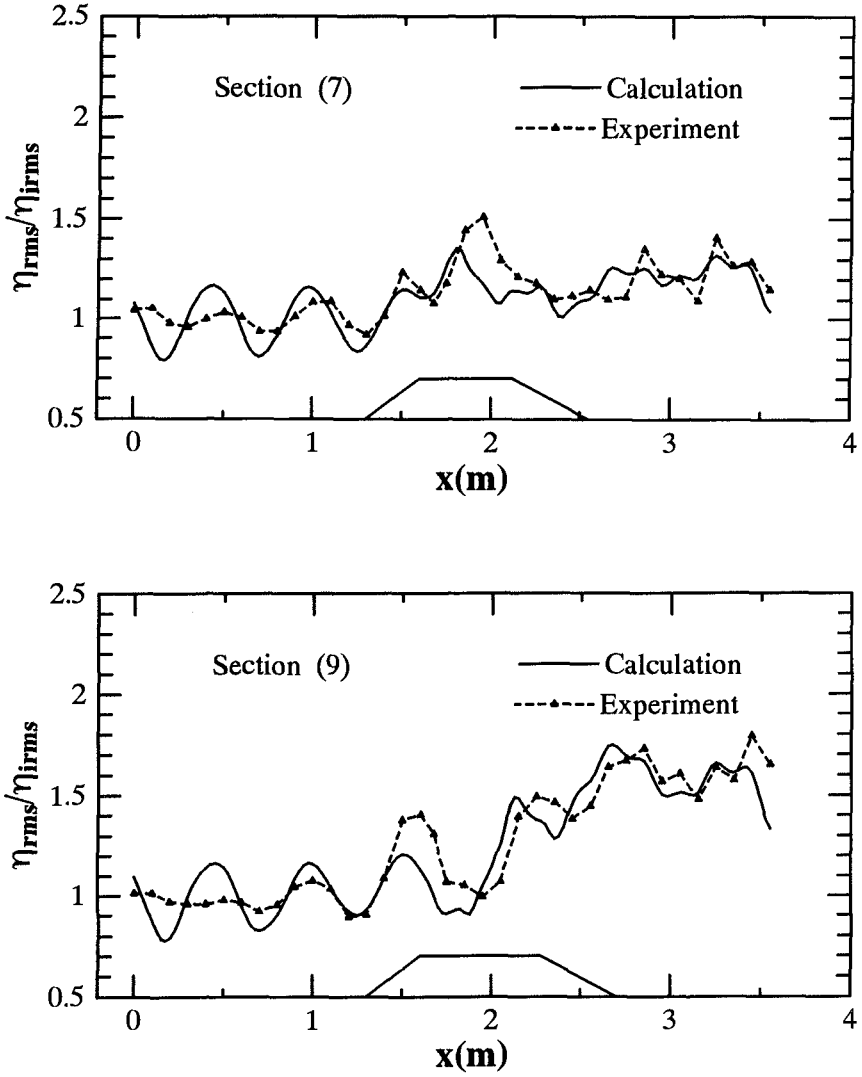


Fig. 3.3 Distributions of RMS of surface displacements.

In Fig. 3, we can see significant variations in the cross-shore distributions of water surface displacements for different sections. Usually the water surface displacement in the region behind the breakwater increases from section (1) to section (9); the mean relative water surface elevations are less than unity from sections (1) to (7), while they are larger than unity for the section (9). The mean value of the transmission coefficients reaches a value of 0.85.

In Fig. 4, a remarkable change in the time histories of the water surface displacements along the x -direction can be seen. In the region before the breakwater, the water surface elevation at position 1 ($x = 0.5$ m) behaves without peculiarities, whereas the time history at position 4 ($x = 2.0$ m) on the top of the breakwater shows strongly nonlinearity with steep peaks. In the region behind the breakwater, two peaks appear in the wave profiles at position 5 ($x = 2.5$ m), i.e., higher harmonics exist.

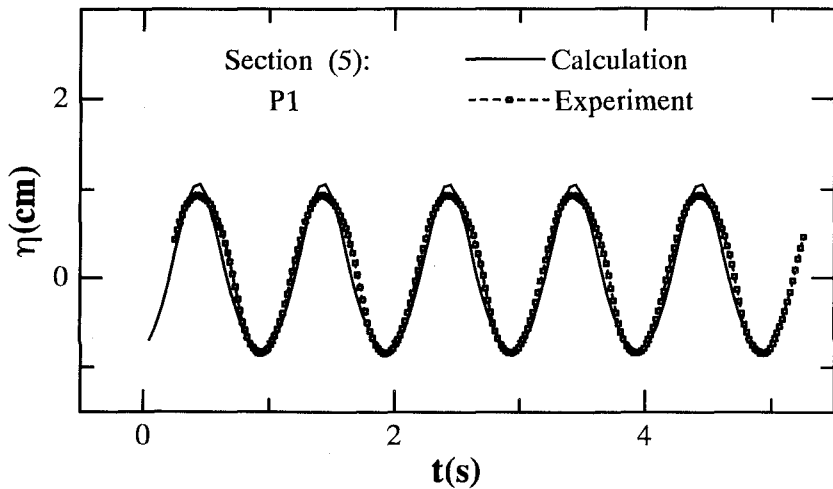


Fig. 4.1 Time history of the surface displacements.

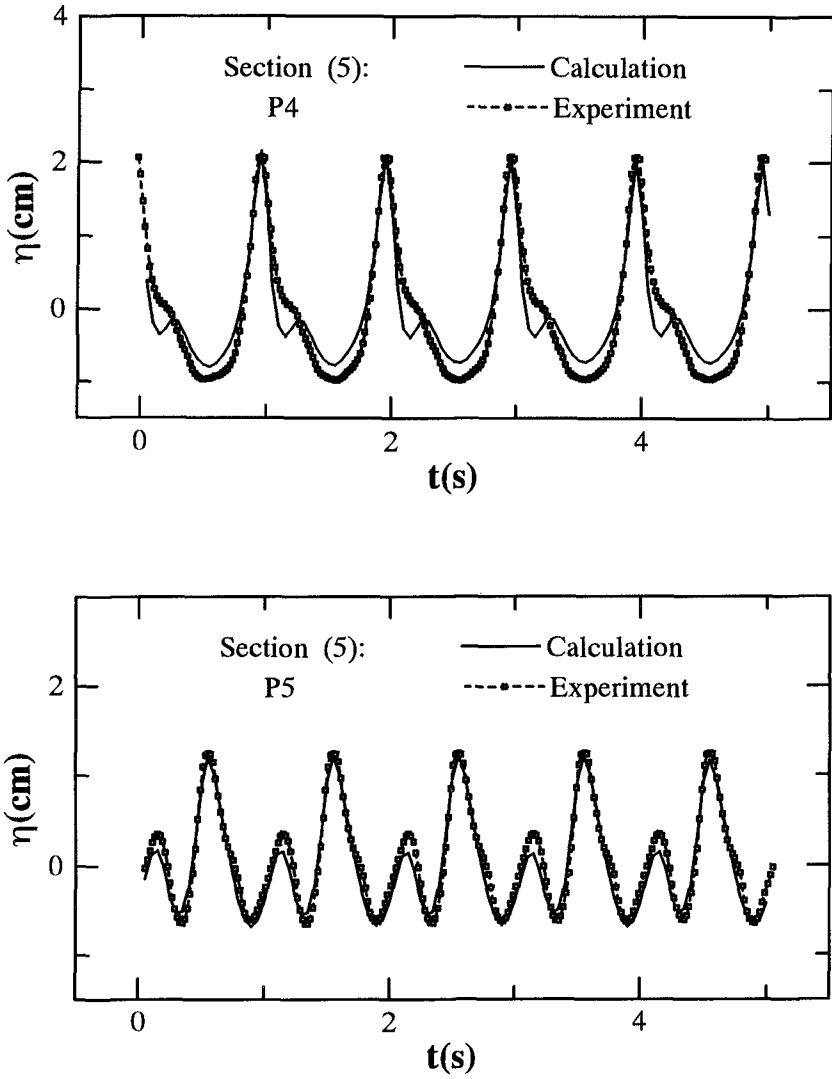


Fig. 4.2 Time history of the surface displacements.

4.2 Conclusions

It has been shown that the agreement between the measurements and the computations is good enough for practical use. For all the other cases, the agreement has been as good as for this case. It will be concluded that the present model reproduces well not only the root mean square wave height distribution but also the temporal variations of surface displacement at every point even when higher harmonic components strongly appear above and behind the breakwater owing to the high nonlinearity of waves.

These results indicate the validity of the present model as well as the interesting effects of the wave direction change due to the presence of a submerged triangular breakwater on the wave deformation.

References

- [1] Fletcher, C.A.J. (1987): Computational Techniques for Fluid Dynamics, Vol. I, Springer-Verlag, 252p.
- [2] Goda, Y., and Y. Suzuki (1976): Estimation of incident and reflected waves in random wave experiments, Proc. 15th Coastal Eng. Conf., ASCE, pp. 828–845.
- [3] Isobe, M. (1994): Time-dependent mild-slope equations for random waves, Proc. 24th Int'l Conf. on Coastal Eng., ASCE, pp. 285–299.

CHAPTER 181

BREAKING LIMIT, BREAKING AND POST-BREAKING WAVE DEFORMATION DUE TO SUBMERGED STRUCTURES

Koichiro IWATA¹, Koji KAWASAKI², and Do-Sam KIM³

ABSTRACT

The aim of this paper is to investigate experimentally and numerically the breaking limit, breaking and post-breaking wave deformation due to three different types of submerged structures such as bottom-seated, non-bottom-seated fixed and tautly-moored structures. Based on laboratory experiments, the breaking limits have been formulated for three different types of the submerged structures. Moreover, a modified SOLA-VOF method with the non-reflective wave generation method has been proposed and found to be very effective in evaluating the wave breaking process and post-breaking wave characteristics.

INTRODUCTION

An accurate prediction of the wave deformation due to a submerged structure is very important for the nearshore sea environment. Most of the foregoing researches have discussed wave breaking and breaking wave deformation only due to bottom-seated submerged structures. On the other hand, the breaking limit and breaking wave deformation for other types of submerged structures have been little investigated. Recently, a research and development of numerical computation techniques has been highlighted to evaluate the wave breaking process with a strong energy dissipation (for example; Miyata et al., 1988, Takigawa et al., 1991, Park and Miyata, 1994, and van Gent et al., 1994). A reliable numerical analysis model, however, has not been established yet to compute the wave deformation after breaking.

This paper is aimed to discuss experimentally and numerically the breaking limit, length of breaker zone, and post-breaking wave deformation due to three different submerged structures such as bottom-seated, non-bottom-seated, and tautly-moored structures. First of all, breaking limits, breaker

1) Professor, Dept. of Civil Eng., Nagoya Univ., Nagoya 464-01, JAPAN

2) Doctoral Course Student, Dept. of Civil Eng., Nagoya Univ., Nagoya, JAPAN

3) Assoc. Professor, Dept. of Ocean Eng., Korea Maritime Univ., Pusan 606-791, KOREA

types and length of breaker zone are experimentally investigated for three different submerged structures in a two-dimensional regular wave field. Next, a numerical analysis model which combines the SOLA-VOF method (Hirt and Nichols, 1981) with the non-reflective numerical wave source (Brorsen and Larsen, 1987) has been developed to evaluate the wave breaking and its post deformation in the regular wave field. The validity of the present numerical calculation method is proved by comparing the computed results with the experimental ones.

LABORATORY EXPERIMENTS

Two-dimensional laboratory experiments were carried out using a wave tank at Nagoya university. The still water depth h was 40, 50 and 60cm. The structural types employed in this experiment are bottom-seated (Type I), non-bottom seated (Type II) and tautly-moored structures (Type III), as shown in Fig. 1. The non-dimensional structural width B/L (B : width of the structure, L : incident wavelength) for Type I ranged from 0.025 to 1.2, and the non-dimensional structural height D/h (D : height of the structure) was 0.4, 0.6 and 0.8. The length and height of the structures (Type II and III) were 68cm and 23 or 34cm, respectively. The initial angle θ_0 of the mooring line to the bottom was 45 degrees in case of Type III. The submerged water depth h_d was 6, 9 and 12cm. The regular waves with periods $T=0.6 \sim 1.68$ s and steepness $H/L=0.02 \sim 0.13$ (H : incident wave height) were generated. The total number of experimental runs was about 540. For each experimental run, the water surface profile η and the water particle velocities u and w were measured with capacitance-type wave gages and electromagnetic type velocimeters, respectively. Also, the wave breaking process was recorded using a video camera.

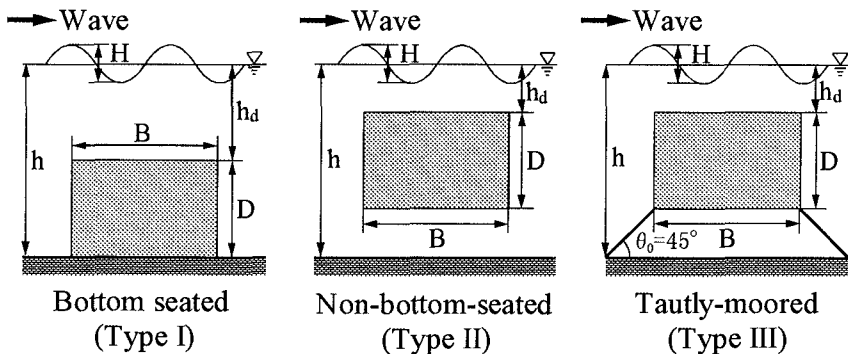


Fig. 1 Structural Types

NUMERICAL ANALYSIS

The numerical analysis model which combines the SOLA-VOF method with the non-reflective numerical generator has been proposed. The governing equation consists of the continuity equation Eq.(1), Navier-Stokes equations Eqs.(3) and (4) for incompressible fluid, and the advection equation Eq.(5)

which represents the behavior of the free-surface. These equations involve the source term because the wave generation source is placed within the computational domain.

$$\frac{\partial u}{\partial x} + \frac{\partial w}{\partial z} = q(x, z, t) = \begin{cases} q^*(z, t) & : x = x_s \\ 0 & : x \neq x_s \end{cases} \quad (1)$$

$$q^*(z, t) = \begin{cases} \{1 - \exp(-0.5t/T)\} \cdot 2U & : t/T \leq 3 \\ 2U & : t/T > 3 \end{cases} \quad (2)$$

$$\frac{\partial u}{\partial t} + \frac{\partial u^2}{\partial x} + \frac{\partial(wu)}{\partial z} = -\frac{1}{\rho} \frac{\partial p}{\partial x} + \nu \left(\frac{\partial^2 u}{\partial x^2} + \frac{\partial^2 u}{\partial z^2} \right) + uq \quad (3)$$

$$\frac{\partial w}{\partial t} + \frac{\partial(uw)}{\partial x} + \frac{\partial w^2}{\partial z} = -g - \frac{1}{\rho} \frac{\partial p}{\partial z} + \nu \left(\frac{\partial^2 w}{\partial x^2} + \frac{\partial^2 w}{\partial z^2} \right) + wq + \frac{1}{3} \nu \frac{\partial q}{\partial z} \quad (4)$$

$$\frac{\partial F}{\partial t} + \frac{\partial(Fu)}{\partial x} + \frac{\partial(Fw)}{\partial z} = Fq \quad (5)$$

where the Cartesian coordinate system (x, z) is employed, and u and w are the velocity components in the respective directions of x and z , t the time, p the pressure, ρ the fluid density, ν the kinematic viscosity, g the gravitational acceleration, and q the wave generation source with q^* as the source strength which is only located at $x = x_s$. The wave generation source q^* with the horizontal velocity U corresponding to the third-order Stokes wave is gradually intensified, as given in Eq.(2), in order to produce a regular Stokes wave train and T is the incident wave period. The VOF function F represents the volume fraction of the cell occupied by the fluid; the cell with $F=0$ is the air cell (the empty cell), the cell with $0 < F < 1$ is the air and water mixture cell (the surface cell) and $F=1$ is the water cell (the full cell).

Employing the modified SOLA-VOF method with the wave generation source, the velocity components (u and w) and the pressure p at the next time step are determined by using the continuity and momentum equations (Eqs.(1), (3) and (4)). The staggered mesh was adopted for discretization of the calculational domain. The flow chart of this numerical scheme is shown in Fig. 2, where $D = \partial u / \partial x + \partial w / \partial z - q$. Regarding the boundary conditions, Sommerfeld radiation condition Eq.(6), where Q is a quantity representing the velocities u , w and C is the wave celerity, is applied for the open boundaries. The non-slip condition is used on both the structure surface and the sea bed.

$$\frac{\partial Q}{\partial t} \pm C \frac{\partial Q}{\partial x} = 0 \quad (6)$$

The computational domain is taken as 500cm times 70cm in the respective directions of x and z . As shown in Fig. 3, the wave generation source is located at an appropriate location determined according to the wavelength, and the origin of x coincides with the wave generation source. While, the positive direction x -axis is taken toward the structure and the vertical axis z is taken positive upward with its origin being on the still water level. The cell

length Δx and Δz are $1/50L$ and $1/40h$ in respective directions of x and z , and the successive time interval Δt , initially $\Delta t_i=0.01s$, is determined at every time step so that the Courant condition Eq.(7) is satisfied. Here, $\gamma=0.5$ in this study, and $|u|_{\max}$ and $|w|_{\max}$ are, respectively, maximum velocity of u and w .

$$\Delta t < \gamma \cdot \min \left\{ \frac{\Delta x}{|u|_{\max}}, \frac{\Delta z}{|w|_{\max}} \right\} \tag{7}$$

Figure 4 shows one example of the time history of the calculated water surface profile $\eta(t)$ (solid line) in which the theoretical value of third-order Stokes wave (open circle) is simultaneously shown for comparison. It is obvious that the calculated water surface profile becomes stable and regular after the fifth generated wave. Moreover, both the calculated and theoretical results

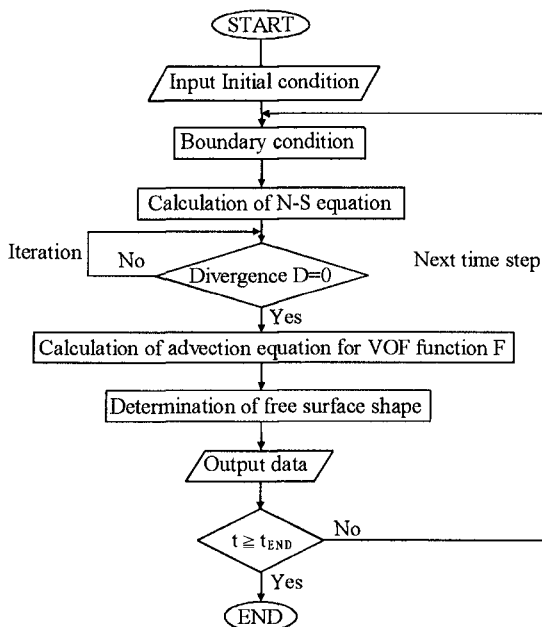


Fig. 2 Flow chart of Numerical Calculation

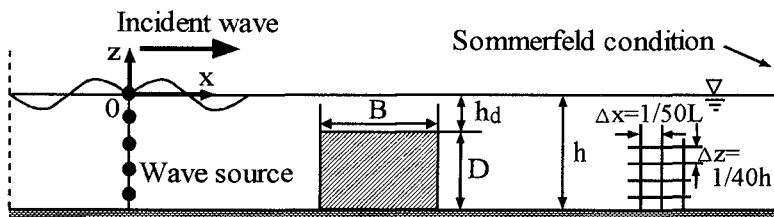


Fig. 3 Definition Sketch

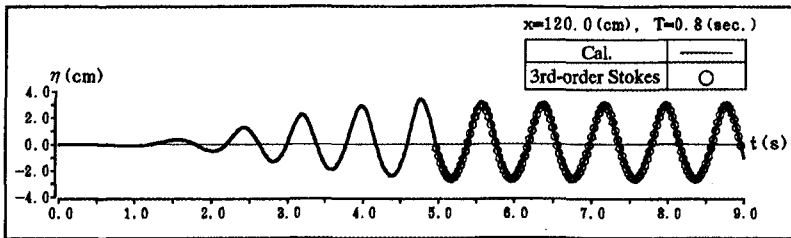


Fig. 4 Time History of Water Surface Profile ($h/L=0.5$ and $H_i/L=0.057$)

agree well and, hence, the validity of the wave generation by the wave source method is proved.

RESULTS AND DISCUSSIONS

I. Laboratory Experiment

a) Breaking Limit : Analyzing the laboratory experiments, the breaking limit for three different structures is, first of all, discussed. Figures 5(a) and (b) show the relationship between the wave steepness H/L and the non-dimensional submergence depth h_d/L in cases of Type II and III structures, respectively. The critical wave steepness $(H/L)_b$ in case of Type II structure can be represented only by one curve, regardless of the values of h_d/h , while the critical value $(H/L)_b$ in case of Type III structure takes a peak value at certain value of h_d/L according to h_d/h , as shown in Fig. 5(b). This took place under the resonance condition that the natural period of the motion of the tautly-moored structure is close to the wave period. Employing the concept of breaking limit of partial standing wave (Iwata and Kiyono, 1985), the breaking limit for Type II and III structures can be formulated as

$$\left(\frac{H}{L}\right)_b = \xi \left[0.0845 \left\{ 1 - \exp\left(-1.675\pi \frac{h_d}{L_0}\right) \right\} \left(\frac{1 - K_R}{1 + K_R}\right) + 0.218 \tanh\left(\frac{2\pi h_d}{L_b}\right) \left(\frac{2K_R}{1 + K_R}\right) \right] ; \xi = \beta / [\{\alpha(T_n - T)\}^2 + 1] + 1 \quad (8)$$

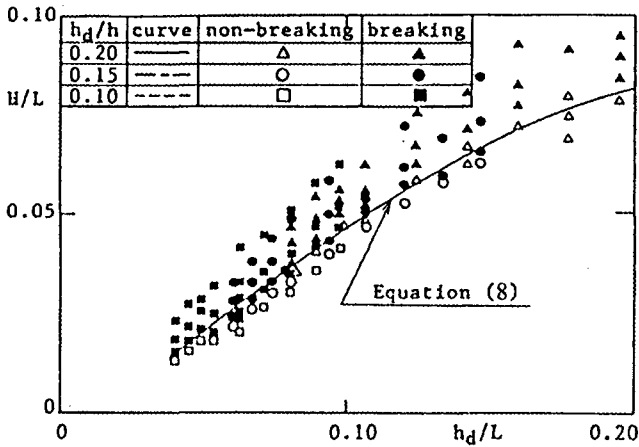
where, $(H/L)_b$ is the critical wave steepness, K_R the reflection coefficient, L_0 the wavelength at deep water, T_n the natural period of the tautly-moored structure, and α and β are numerical constants (see Fig. 5(b)) which are zero for fixed structures.

Equation (8) agrees well with the experimental values, as shown in Fig. 5. The comparison between Figs. 5(a) and (b) shows that the breaking limit $(H/L)_b$ in case of Type III structure is slightly larger than that in case of Type II structure. In other words, the non-bottom-seated structure is more effective to break waves than the tautly-moored structure.

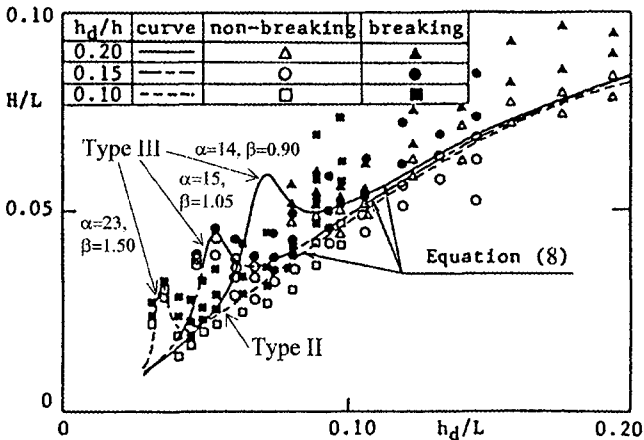
Equation (8) can be also applied to define the breaking limit for Type I structure. In addition, the breaking limits $(H/h_d)_b$ for Type I structure can be

formulated, as shown in Fig. 6, in terms of B/L for $h/L=0.13$ and 0.4 without using the reflection coefficient K_R . The breaking limits for Type I structure are formulated as follows:

$$\left. \begin{aligned} (H/h_d)_b &= 0.3656 + 0.3668 \exp(-10B/L) \\ &\quad ; 0.1 \leq B/L \leq 0.6 \text{ for } h/L = 0.13 \\ (H/h_d)_b &= 0.3641 + 0.2313 \exp(-10B/L) \\ &\quad ; 0.1 \leq B/L \leq 0.6 \text{ for } h/L = 0.2 \\ (H/h_d)_b &= 0.4417 + 0.2252 \exp(-10B/L) \\ &\quad ; 0.1 \leq B/L \leq 1.0 \text{ for } h/L = 0.4 \end{aligned} \right\} \quad (9)$$



(a) Non-Bottom-Seated Structure (Type II)



(b) Tautly-Moored Structure (Type III)

Fig. 5 Breaking limit

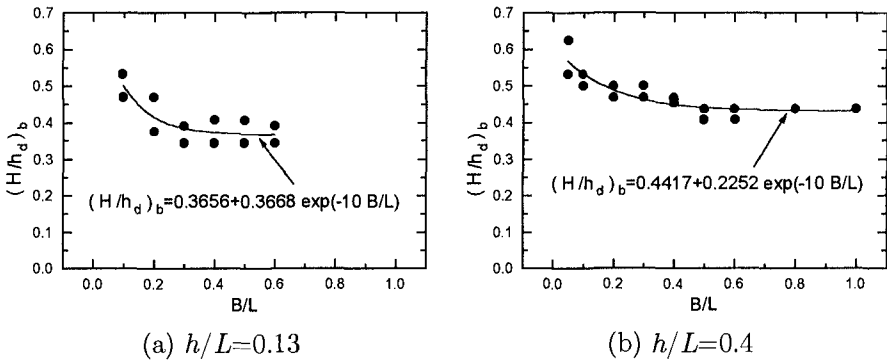


Fig. 6 Breaking Limit for Bottom-Seated Structure (Type I)

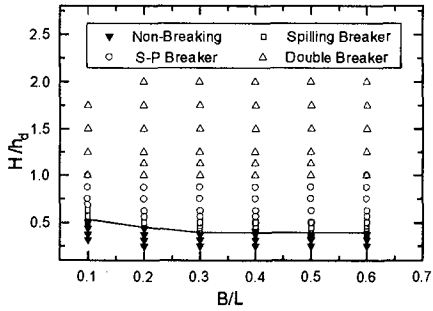
b) Breaker Type : As shown in Figs. 6 and 7, the change in the breaking limit and the breaker type become very small for $B/L > 0.5$ in case of $h/L=0.2$ and 0.4 , and for $B/L > 0.3$ in case of $h/L=0.13$. The breaker type changes from Spilling breaker to S-P breaker (an intermediate type between Spilling and Plunging breaker) and finally to Double breaker (Katano et. al., 1992) as H/h_d increases. It is also revealed from Fig. 7 that the critical values of H/h_d for the wave breaking and the breaker type classifications in case of $h/L=0.4$ is larger than other cases. Also, the non-bottom-seated structure, among three different types of the submerged structures, is found to be the most effective one to break waves because a strong circulating flow is usually formed around the structure.

c) Breaking Position : As shown in Fig. 8, the non-dimensional breaking position x_b/L (x_b : distance from the front of the structure to the breaking position) shifts to the offshore side of the structure by an increment of H/h_d and is almost constant at $x_b/L \approx -0.05$ near the antinode position of the partial standing wave in front of the submerged structure for $H/h_d \geq$ about 1.0. Inspection of Figs. 7 and 8 reveals that x_b/L shifts to the offshore side of the structure according to the change of the breaker types from Spilling to S-P, and to Double breakers.

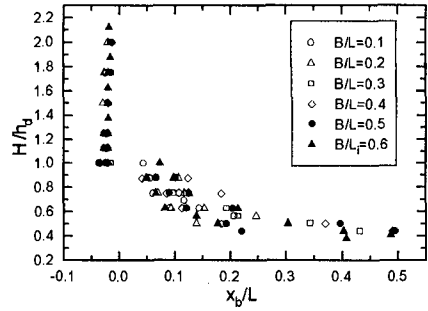
d) Breaker Zone Length : Non-dimensional breaker zone length L_b/L is plotted versus H/h_d in Fig. 9 with parameters of h_d/h and B/L , where L_b is the distance from the breaking point to the location where the breaking wave-caused turbulence with air entrainment disappears. As H/h_d increases, L_b/L becomes larger regardless of h_d/h . Further, L_b/L for $h_d/h=0.2$ is larger than that for $h_d/h=0.4$ because of the stronger non-linear interaction between the wave and the structure.

e) High Harmonic Components : Figure 10 shows the spatial distribution of the non-dimensional wave height spectrum $2A(f)/H$ around the submerged structure, where $A(f)$ is the amplitude spectrum for frequency f and B.P. is the breaking point. It is found from Figs. 10(a) and (b) that the fundamental harmonic component increases in front of the structure and decays toward the

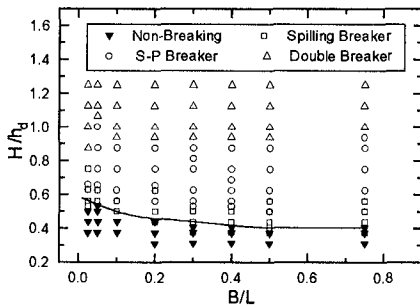
onshore side of the structure because of the wave energy dissipation due to the wave breaking. On the other hand, higher frequency components grow up above the structure, especially the second harmonic component becomes larger around the submerged structure. This is accounted by the wave energy transfer from the fundamental harmonic component to the second harmonic component due to the non-linear interaction between the wave and the structure. Figures



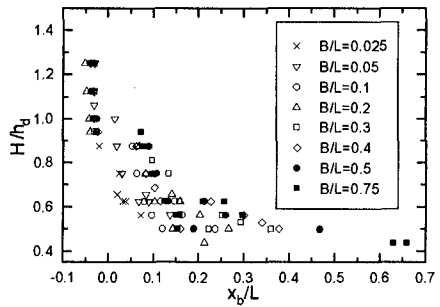
(a) $h/L=0.13$



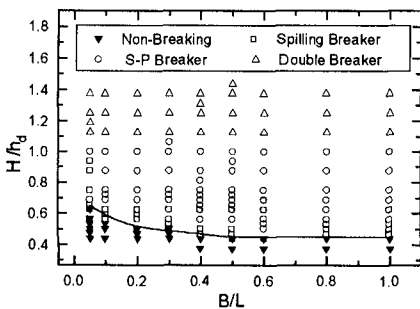
(a) $h/L=0.13$



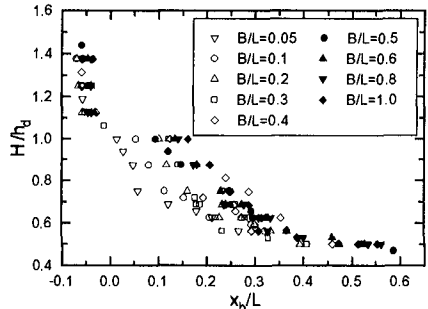
(b) $h/L=0.2$



(b) $h/L=0.2$



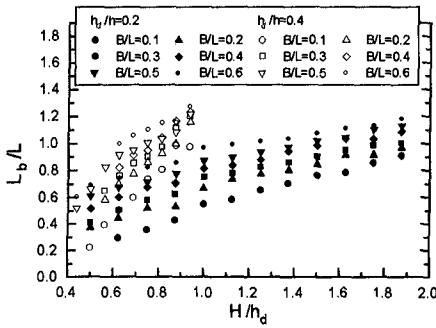
(c) $h/L=0.4$



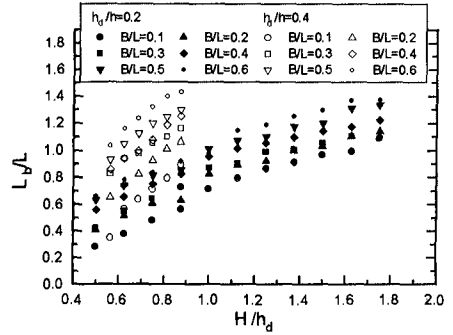
(c) $h/L=0.4$

Fig. 7 Breaking limit and breaker type (Type I)

Fig. 8 Breaking Position (Type I)

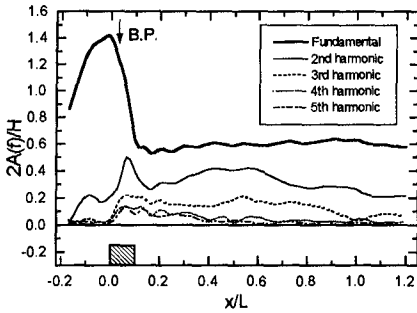


(a) $h/L=0.13$

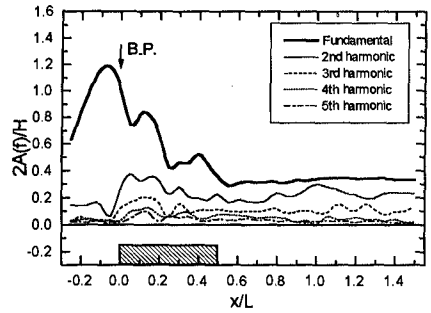


(b) $h/L=0.2$

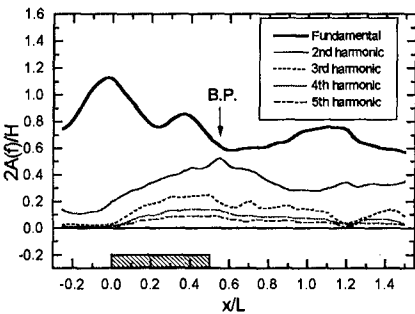
Fig. 9 Breaker Zone Length (Type I)



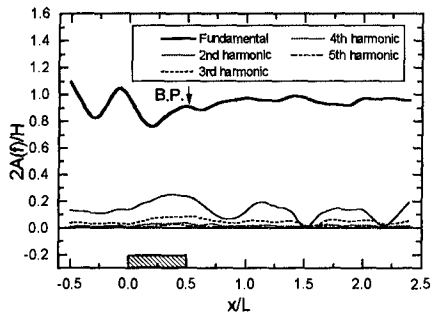
(a) $h/L=0.13, B/L=0.1, h_d/h=0.2, H/L=0.022$



(b) $h/L=0.2, B/L=0.5, h_d/h=0.2, H/L=0.044$



(c) $h/L=0.2, B/L=0.5, h_d/h=0.4, H/L=0.044$



(d) $h/L=0.4, B/L=0.5, h_d/h=0.4, H/L=0.067$

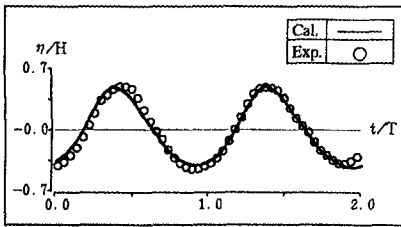
Fig. 10 Spatial Distribution of Non-dimensional Wave Height Spectrum (Type I)

10(b) and (c) reveal that the spatial distribution of $2A(f)/H$ depends on h_d/h and that larger wave energy dissipation takes place with decreasing h_d/h . It is obvious from Fig. 10(d) (case of a weak Spilling breaker) that the second harmonic component is seen to change periodically after breaking. According to Massel(1983) who calculated the wave transformation due to submerged structures for non-breaking waves, the beat length λ_2 has been formulated in Eq.(10), where k_1 and k_2 are the wave numbers for the fundamental and second harmonic components, and σ is the angular frequency of the fundamental component. Applying Eq.(10) to the case presented in Fig. 10(d), $\lambda_2/L \cong 0.6$ is obtained and found to coincide with the corresponding experimental one. Therefore, it can be thought that the free second harmonic component wave is generated even under the breaking wave condition.

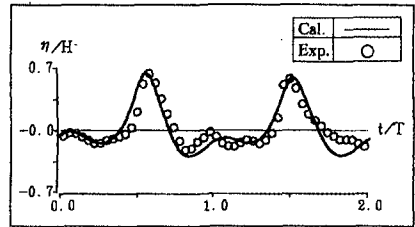
$$\lambda_2 = 2\pi / (k_2 - 2k_1) \quad ; \quad \sigma^2 = gk_1 \tanh k_1 h_d, \quad 4\sigma^2 = gk_2 \tanh k_2 h_d \quad (10)$$

II Numerical Calculation

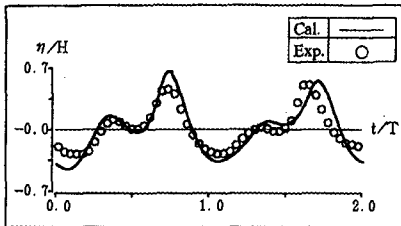
The post-breaking wave deformation due to a submerged structure is computed using the modified SOLA-VOF method. The non-dimensional water surface profiles η/H_i measured at $x=174\text{cm}$ offshore side and $x=290, 314$ and 338cm onshore side of the Type II structure are plotted versus t/T in Figs. 11(a)~(d) in case of a spilling breaker. In Fig. 11, laboratory experimental values are also shown for comparison. It is found that higher frequency component waves are generated as mentioned above and, hence, the time history



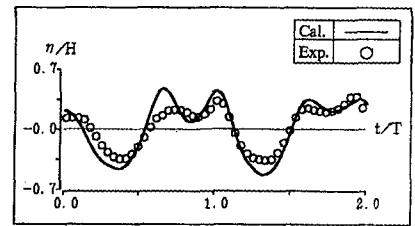
(a) 36cm offshoreward from structure
($x/L=1.15$)



(b) 12cm onshoreward from structure
($x/L=1.92$)



(c) 36cm onshoreward from structure
($x/L=2.08$)



(d) 60cm onshoreward from structure
($x/L=2.24$)

Fig. 11 Comparison of Calculated and Experimental Water Surface Profile (Type II ; $H/L=0.04, h/L=0.33$)

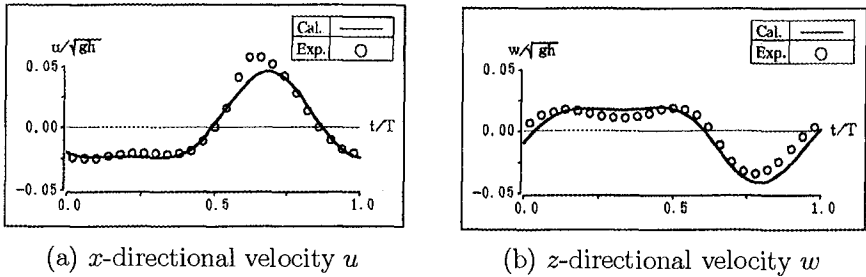
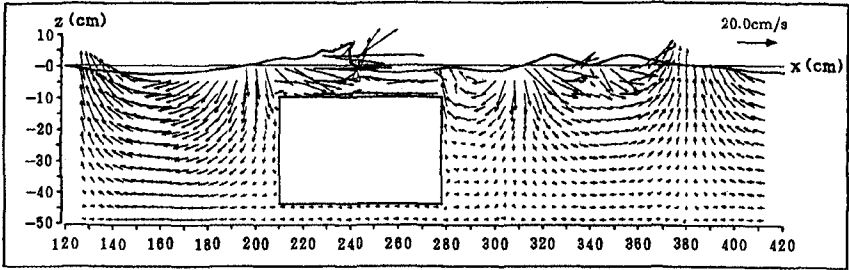


Fig. 12 Comparison of Calculated and Experimental Velocity Profile
(Type II ; $H/L=0.04$, $h/L=0.33$, $x/L=1.92$, $z/h=-0.2$)

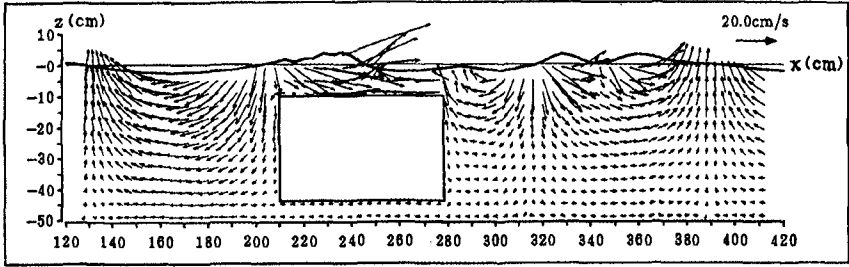
of the water surface profile has a complex form in the onshore region of the structure after breaking. From Fig. 11, the calculated values are found to be in good agreement with experimental ones. Good agreement between the calculated values and laboratory experiments is also confirmed for the water particle velocity, as shown in Fig. 12. Therefore, it is demonstrated that the present numerical calculation method can reproduce well the water surface profile and the water particle velocity before and after breaking due to a impermeable submerged structure.

Figures 13(a)~(d) show the spatial variations of the water surface profiles and the particle velocities around the structure at $t=7.55$, 7.60, 7.72 and 7.83s, respectively, under the same condition stated in Fig. 11. Figures 13(a) and (b) show that the wave passing over the submerged structure breaks with an overturning wave front, and Figs. 13(c) and (d) show that the broken wave is deformed into several wave components with two or three peaks in one wavelength. According to Fig. 14, in case of Type I structure, large vortex is found to be formed on the onshore side of the submerged structure after the wave passes over it. In addition, analysis of video tape recorder confirms that the breaker type and wave deformations evaluated with the numerical calculations are very similar to those measured at the laboratory. However, the air-bubbles entrainment due to wave breaking, which was observed by the video tape recorder and the visual observations, cannot be simulated in the numerical calculations.

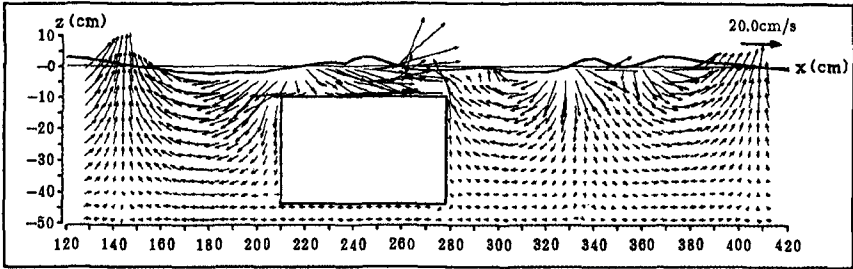
As shown in Fig. 15, both the numerical and experimental results show that the high mean onshore velocity is generated near the free-surface onshore side of the structure and the high mean downward velocity is observed to occur near $x=340\text{cm}$. The mean offshore velocity, i.e. the return flow, is also generated to compensate the onshore mass transport caused by wave breaking around the still water level. The return flow is, in particular, strong below the structure because the flow cross sectional area below the structure abruptly diminishes from the onshore side of the structure, which could accelerate the flow velocity. According to Fig. 15(a), the upward velocity takes place in front of the structure where the antinode of the partial standing wave seems to appear, and the offshore steady flow takes place just above the crown of the structure. However, it is expected that there is a strong onshore steady flow above the wave trough (i.e. around the still water level) over the structure. Judging from



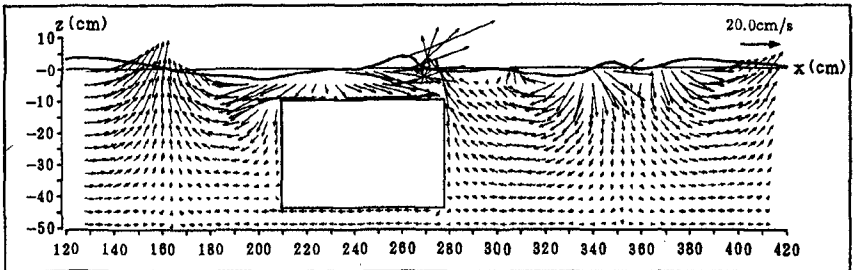
(a) $t=7.55s$



(b) $t=7.60s$



(c) $t=7.72s$



(d) $t=7.83s$

Fig. 13 Results of Numerical Calculation (Type II)
 $(H/L=0.04, h/L=0.33)$

the above-stated, it can be said that a circulating flow is formed around the submerged structure. Judging from Figs. 15(a) and (b), the proposed numerical calculation scheme is shown to agree well with the measured mean wave velocity field in laboratory experiments.

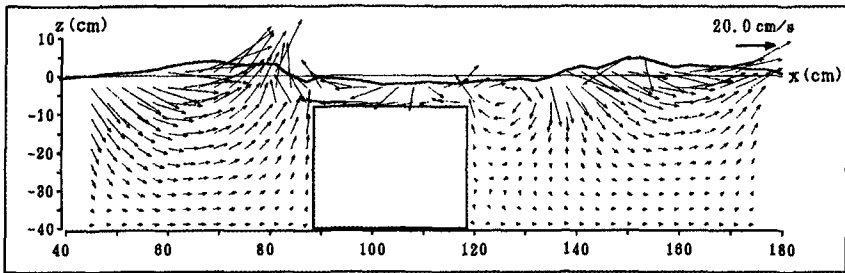
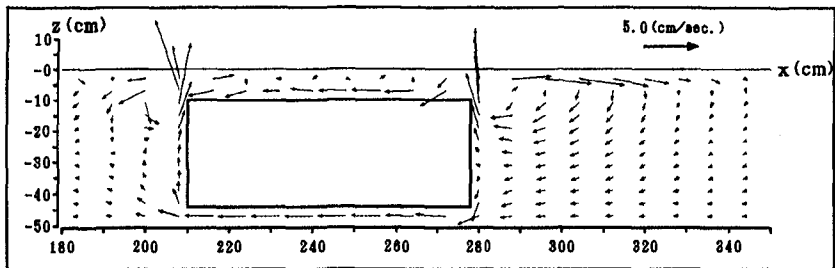
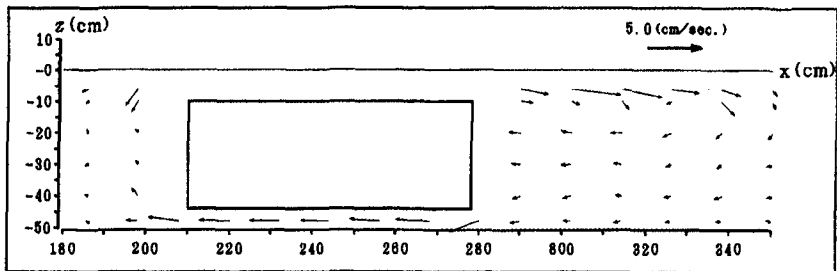


Fig. 14 Results of Numerical Calculation (Type I)
($H/L=0.077$, $h/L=0.4$)



(a) Calculation



(b) Experiment

Fig. 15 Spatial Distribution of Mean Velocity around Structure (Type II)
($H/L=0.04$, $h/L=0.33$)

CONCLUSIONS

The breaking limit, breaking and post-breaking wave deformation due to three different types of submerged structures have been discussed experimentally and numerically. Main conclusions in this study are summarized as follows:

- 1) Breaking limits have been formulated experimentally for three different types of submerged structures.
- 2) Breaker types have been also formulated experimentally for two types of submerged fixed structures.
- 3) Among the three types of structures, the non-bottom-seated structure has been found to be the most effective one to break the waves.
- 4) A numerical model using the modified SOLA-VOF method has been found to evaluate well the wave deformation before and after breaking in case of a spilling breaker.

REFERENCES

- Brorsen, M. and Larsen, J. (1987). "Source Generation of Nonlinear Gravity Waves with Boundary Integral Equation Method", *Coastal Eng.*, Vol. 11, pp. 93-113.
- Hirt, C.W. and Nichols, B.D. (1981). "Volume of Fluid (VOF) method for the Dynamics of Free Boundaries", *J. Comp. Phys.*, Vol. 39, pp. 201-225.
- Iwata, K. and Kiyono, H. (1985). "Breaking of Standing Two-Component Composite and Irregular Waves", *Coastal Eng. in Japan*, Vol. 28, pp. 71-87.
- Katano, A., Murakami, S., and Hattori, M. (1992). "Relevant Parameters Representing Energy Dissipation due to Submerged Breakwaters", *Proc. Coastal Eng., JSCE*, Vol. 39, pp. 646-650 (in Japanese).
- Massel, S.R. (1983). "Harmonic Generation by Waves Propagating over a Submerged Step", *Coastal Eng.*, Vol. 7, pp. 357-380.
- Miyata, H., Katsumata, M., Lee, Y.-G., and Kajitani, H. (1988). "A Finite-Difference Simulation Method for Strongly Interacting Two-Layer Flow", *J. Soc. Naval Arch. Japan*, Vol. 163, pp. 1-16.
- Park, J.C., and Miyata, H. (1994). "Numerical Simulation of the 2D and 3D Breaking Waves by Finite-Difference Method", *J. Soc. Naval Arch. Japan*, Vol. 175, pp. 11-24 (in Japanese).
- Takigawa, K., Yamada, Y., Arimoto, M., and Tabuchi, Y. (1991). "Development of Numerical Analysis System on Deformation and Breaking of Waves on Sloping Bottom", *Proc. Coastal Eng., JSCE*, Vol. 38, pp. 61-65 (in Japanese).
- van Gent, M.R.A., Tönjes, H.A.H. and van den Bosch, P. (1994). "Wave Action on and in Permeable Structure", *Proc. 24th ICCE, ASCE*, Vol. 2, pp. 1739-1753.

CHAPTER 182

ITALIAN EXPERIENCE ON SUBMERGED BARRIERS AS BEACH DEFENCE STRUCTURES

by Alberto Lamberti* & Alessandro Mancinelli**

Abstract

The use of submerged barriers in Italy is rather new starting in the first 80's. Since that time more than 50 submerged barrier defence system were constructed and this type of structure is progressively complementing and substituting the traditional use of parallel emerging breakwaters.

The paper presents documentation about the experience gained on the topic and describes and compares to prototype experience the design criterion suggested by the authors, based essentially on the selection of a proper wave attenuation necessary to obtain to desire profile modifications.

1 Introduction

Since the XV century, beach erosion has been taking place in many parts of the Italian coastline. The numerous historical maps document, for instance, erosion due to the construction of channel-harbour in the Adriatic Sea such as Cesenatico, Rimini, Pesaro, Fano, Senigallia, Pescara, etc. The extension of jetties in these ports carried out at different times in order to avoid silting up of the entrance, gave rise to down drift erosion (in the Adriatic sea north of these structures).

The first coastal defence structures built in Italy date back to the beginning of this century. An exception though, is to be found in the Venetian Republic which had already started to construct seawalls in the XVII century, to protect the sandy strip which separated the lagoon from the sea, the so-called "murazzi".

The erosion phenomenon remarkably increased between the 50's-60's largely due to the extension of existing ports or to the construction of new harbour and to the first structures of river engineering works.

* Professor, DISTART, University of Bologna, viale del Risorgimento 2, 40136 Bologna, Italy

** Professor, Hydraulics Institute, University of Ancona, via Breccie Bianche, 60131 Ancona, Italy

In addition to the causes mentioned above, the indiscriminate extraction of sand and gravel from the low-water bed of rivers was also responsible for the rapid beach erosion.

The first defence interventions carried out on the Adriatic coast consisted of natural rubble-mound seawalls or breakwaters of the emerging type. Instead, in Liguria, beach nourishment using a narrow strip of sand has been adopted since the 1950's (Savona, Lavagna).

The construction of longitudinal detached emerging breakwaters which determine down drift erosion, forced the Administrations of Emilia Romagna and Marche to build breakwaters of the emerging type for almost 80 km. Beaches are essential in supporting the tourist economy which has been rapidly growing since the 1960's.

At the end of the 1970's, the erosive phenomenon aggravated and this was particularly severe in Emilia Romagna because of subsidence. Therefore, the Administrations of the two Regions predisposed for legislative interventions which prohibited extraction of sand and gravel from the low-water bed and limited the gas and water extraction from the subsoil. Regional Plans were also set up to protect the coast. Their aim was to study and gain knowledge on this phenomenon in addition to finding alternative interventions to breakwaters of the emerging type.

Thus, at the beginning of the 80's, submerged barriers were tested. When the first author was performing his first analysis and tests on this type of structure, Lamberti & Tomasicchio (1981), only very few real life applications were observable in Italy and all of them were using a very special technology (Longard tubes). Since then, more than 50 submerged barrier defence systems have been constructed and this type of structure is progressively complementing and substituting the traditional use of parallel emerging breakwaters.

Two main types of structures have been constructed:

- sand-bag barriers, mainly used in combination with beach nourishment, and characterised by a high submergence and small section; they do not provide a significant reduction of wave height nor an effective retaining capacity on sand, but they are supposed to provide stabilization of natural sand bars and are appreciated because of their very low impact;
- rubble-mound submerged breakwaters, used alone or in combination with nourishment, with or without gaps, with or without a bed protection at the gaps, used to reduce wave transmission through the gaps of emerging parallel breakwater systems or to protect the bed from erosion in correspondence of the gaps.

In the meantime, many model tests have been carried out, Aminti & al. (1983), Lamberti & al., (1985), DH (1983, 1989, 1990) and others. Detailed monitoring of their behaviour in nature was also performed in some cases, Ferrante & al. (1992).

The evolution of defence systems with the introduction of submerged barriers will be examined for typical cases in three Italian regions: Veneto, Emilia Romagna and Marche situated on the Adriatic sea.

The Adriatic Italian coast is low and very flat in the Northern reach pertaining to Veneto and Emilia Romagna, and is an alternation of alluvial plains and moderately high erosion coasts in Marche region. Tidal excursion at spring ranges from 1.0 m in

Venice to 0.6 m in southern Emilia Romagna. Tide is substantially lower and mainly diurnal in the Marche region. Extreme storm surge ranges from 1.1m in Venice to 0.8 m in Ancona.

Typical 1 year return period waves are about 3.5 m and extreme about 6.0 m

2 Case histories

2.1 Emilia Romagna

The protective systems built after 1983 are nourishments protected by submerged barriers formed with sand-bags. Transversal groins made with sand-bags or rock in the emerging part and connected to the submerged barriers, are almost always present.

The new intervention extend for about 13.8 km in length with the use of 2.130.000 m³ of sand nourishment coming from borrowed land quarries.

In these first interventions, sand-bag barriers had a small section, a volume of 1 m³ and were generally arranged in two rows of 3 and 2 bags at a depth of -2.50, -3 metres.

The high submergence of these barriers does not produce any appreciable reduction of wave action. The barriers, however, stabilize the natural sand bars giving rise to a localized inshore erosion and to raising of the bed offshore (see Fig. 1).

Frequently sand-bag barriers can undergo static failures. To avoid erosion produced by breakers falling on the sand, the dimensions of the sand-bags and the width of the barriers were enlarged during subsequent interventions (see Fig. 2).

The only work carried out in Emilia Romagna with submerged barriers of natural rock is that of Lido di Dante (Ravenna) (see Fig. 3) where a series of emerged groins had been incapable of preventing erosion. The submerged barriers have a crown width of 12 m and are 0.5 m deep in water, as shown in Fig. 3. The last groin is connected to the barrier in order to prevent leakage of the sediments northwards. The volume of nourishment is such that the equilibrium profile has a closure depth between the coastline and the submerged barrier, producing a maximum shoreline advancement of about 30 metres from the.

Figure 4 shows the beach of Lido di Dante after the above intervention was carried out. Before the intervention the shoreline was just at the toe of the house.

2.2 Marche

Since 1982-83, in alternative to breakwaters of the emerging type or rubble-mound seawalls, a series of defence interventions were performed in the Marche region. Submerged barriers with nourishment were used for low coasts while those without nourishment were used for rocky coasts [Fiorenzuola (PS), Sirolo and Numana (AN)]. In some cases (Pesaro, Fano, Montemarçiano) the typology was the same as in Emilia Romagna with sand-bag barriers or Longard tube barriers. In other cases, south of Ancona, the first submerged barriers in natural rock were used, both as breakwaters and as a defence at the foot of the nourishment. Figure 5 shows an intervention at Grottammare; the characteristics of a submerged barrier can be seen

with a crown width of 3.00 m and a submergence of 0.90 m. The barriers have gaps of 30 m and link two stretches of emerged breakwater barriers.

The drawbacks of these first submerged barriers are the following:

- heavy erosion in the gaps and in the terminal head arising from strong return currents;
- scouring effects at shore-side foot of the barriers;

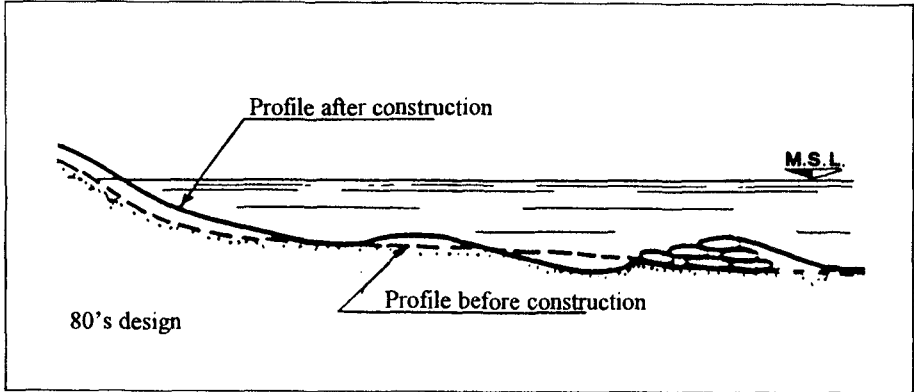


Fig. 1 – Sand bags submerged barriers and their effects - First intervention.

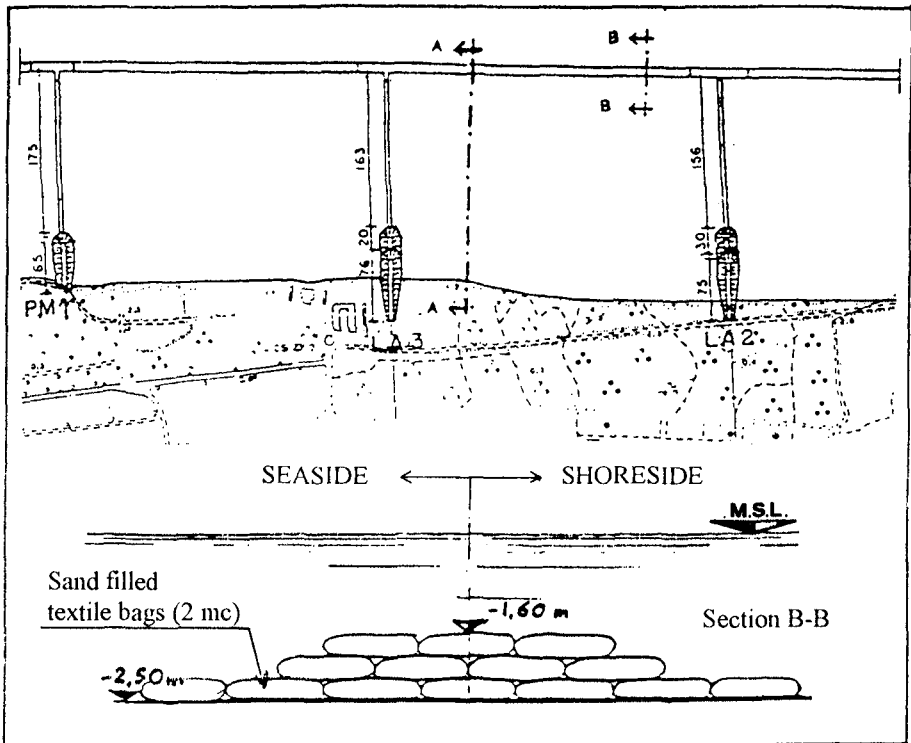


Fig. 2 – Protective system whit sandbags - New intervention.

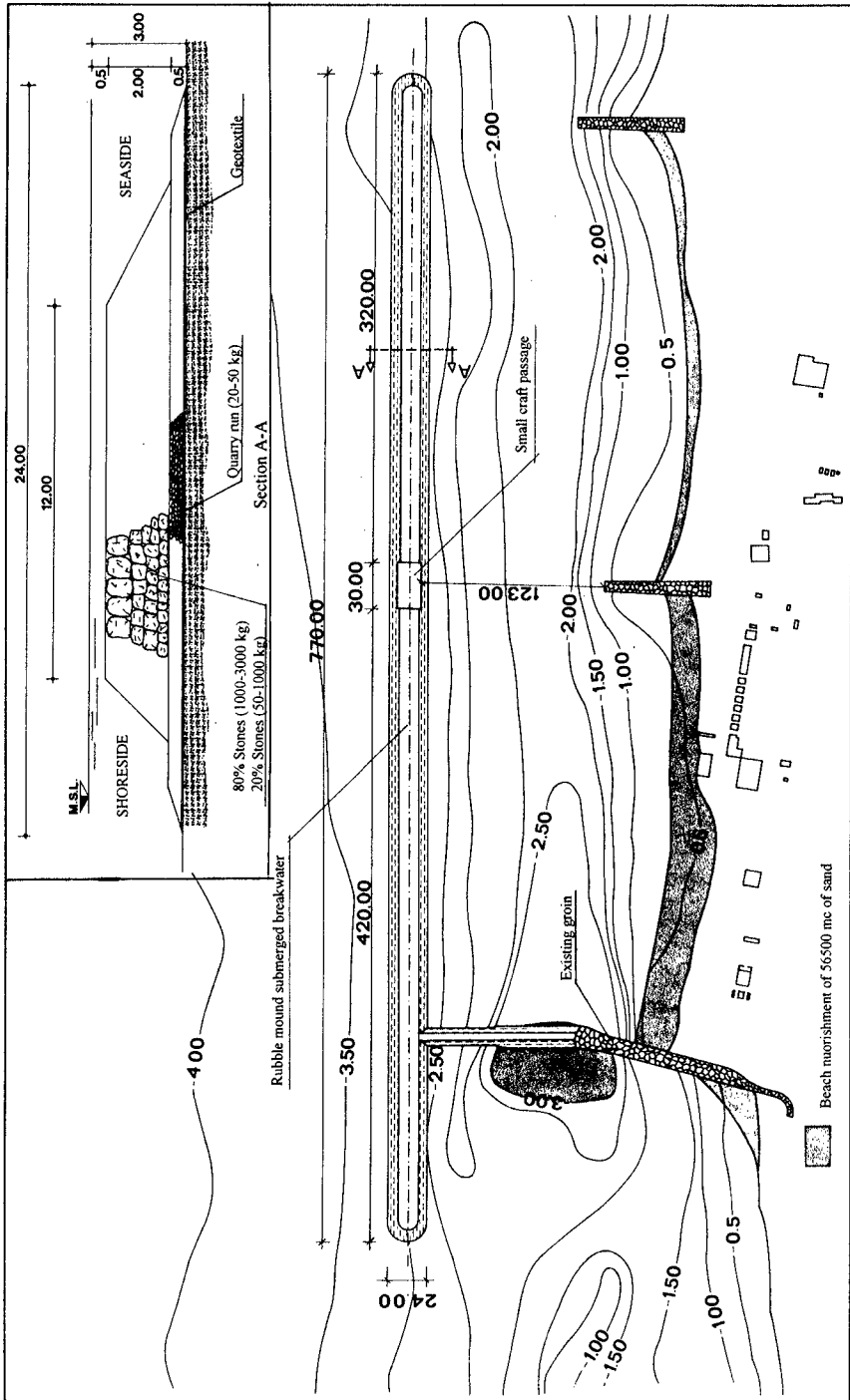


Fig. 3 - Protected nourishment at Lido di Dante (RA, Emilia Romagna): plan of the area and section of the submerged breakwater.



Fig. 4 – Lido di Dante after intervention.

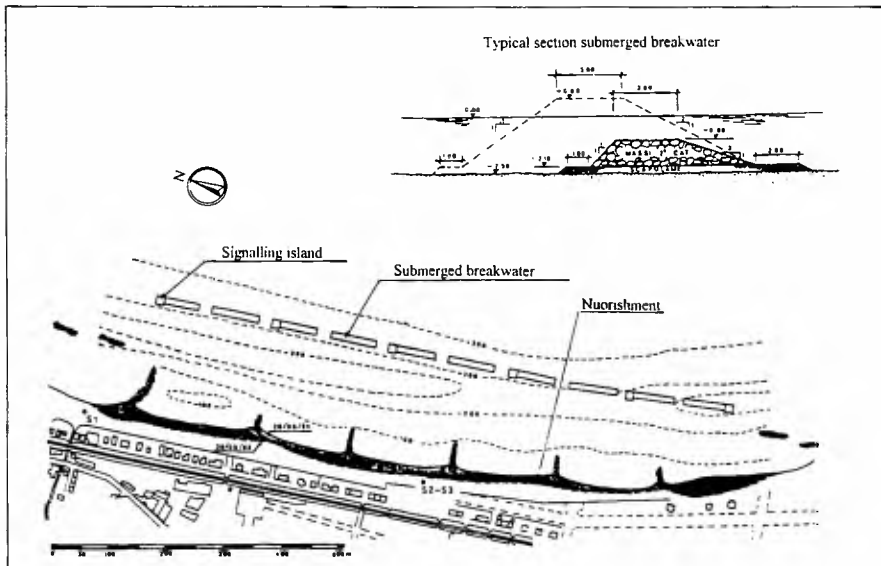


Fig. 5 – Protective system at Grottammare (AP, Marche)

- rock displacement due also to an imperfect execution when building the barriers, since it is difficult to place rocks in cloudy water;
- high submergence particularly stressed during Southeast sea-storms characterized by a remarkable rising of the average sea level. This produces an insufficient dissipation of wave energy.

The second generation of submerged barriers carried out in the Marche region have a considerably wider transversal section. This was done by increasing the crown width to 10-12 m, by lowering the submergence to -0.5 m and by increasing the slope of both barriers sides (see Fig. 6).

The gaps between the barriers are covered with a quarry run mattress in order to extend the base of the foundation between one gap and the next.

Second generation submerged barriers were used in place of emerging breakwaters or along stretches of the coast subjected to new erosion, without nourishment (see Fig. 7 on the intervention in Montemarignano (AN)). These replacements were carried out with the aim of improving the quality of the water and the sediments.

When emerging barriers are placed close to the shoreline, an insufficient water circulation is created which leads to the formation of slimy and annoying deposits of material for bathers.

In Montemarignano, the submerged barriers defend the facing coast. These barriers have been subjected to displacement of the stones along the slopes facing the shore and sea. The erosive process moves down drift (see Fig. 8), similarly to what happens with the emerging barriers.

Bathymetric measurements carried out at different intervals, show the formation of scouring effects both offshore and inshore of the structures and in proximity of the head of the extreme segments.

In Senigallia, the substitution of emerging barriers with submerged ones has led to the disappearance of sand "tombolo" and subsequent withdrawal of the shoreline by 20-30 metres (see Fig. 9).

Longard tubes and sand-bag barriers have not been used anymore in the Marche. The negative results of these typologies were seen in those beaches with a steep bed slope.

2.3 Veneto

In interventions regarding the defence of venetian beaches which began in the 60's, the structures used were mainly groins with rigid seawall. Breakwaters of the emerging type were used only in a small stretch off the coast of Jesolo.

On the coast of Caorle (1985), submerged barriers in Longard tubes or sand-bags were experimented to create a protective nourishment.

At present, a project predisposed by the Consorzio Venezia Nuova is underway for interventions regarding the defence of the Cavallino and Pellestrina shores situated in the stretch of coast which separates the lagoon of Venice from the sea. The work which has been underway since 1995, foresees the construction of an artificial beach contained inside areas delimited by lateral groins, in part submerged and in part emerging, and by a submerged structure which connects these groins.

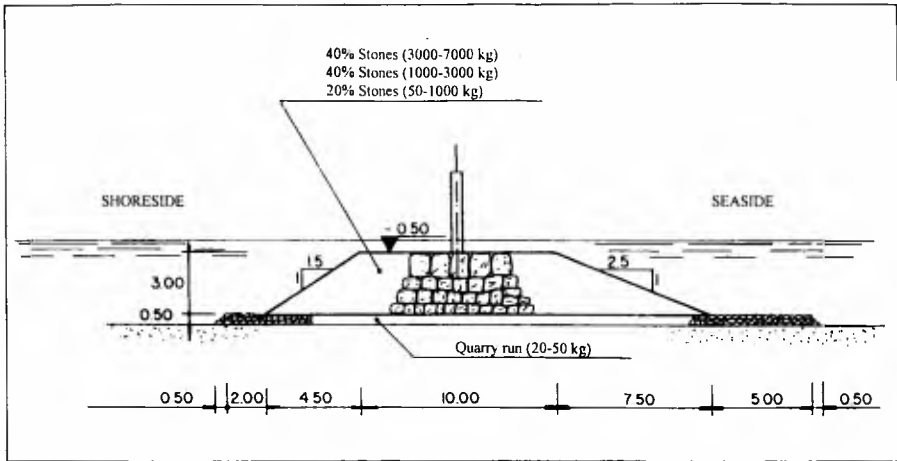


Fig. 6 – Submerged breakwater at Marina di Montemarcano (AN, Marche).



Fig. 7 – Protective system at Marina di Montemarcano (AN, Marche).



Fig. 8 – Down drift erosion of the submerged breakwater Marina di Montemarciano.



Fig. 9 – Protective system at Senigallia (AN, Marche).

Once finished, the artificial beach will stretch for 9 km with an average width of 100 metres at the time of sand-filling which should stabilize around 70 metres.

The main source supplying nourishment sand (12.000.000 m³) has been individuated off Malamocco, 20 km from the coast at an average depth of -20 metres.

The characteristics of the intervention are visible in figures 10, 11 and 12.

3 The suggested design criterion

3.1 Relevant components of the dynamics of submerged barriers

The most important effect of submerged barriers is the depth induced wave breaking; even in the absence of breaking relevant effects on wave agitation take place. The limited submergence cause the generation of higher harmonics, see Fig. 7, and the relevant friction exerted by armour stones in the shallow stream flowing over the crests cause significant energy dissipation and modification of wave spectrum.

The breaking of wave over the crest is the cause of a potentially high wave set-up inshore the barrier. Set-up is significantly reduced by gaps in the barrier or at the ends of the barrier, but contemporary strong currents are induced through the gaps, where the bed must be adequately protected.

The mutual effects of energy dissipation by breaking and by friction must be adequately balanced because while they cooperate in reducing wave energy, they act in an opposite direction on wave set-up and currents, which are recognized as negative effects of the barriers.

3.2 Criterion For Global Retaining Efficiency

As a consequence of turbulence induced by breakers, the resuspension capacity of waves just inshore of the barriers is greater than for normal waves of the same height. Therefore, if sand is transported from the shore to the barrier, it will probably be resuspended and transported out of the barrier.

In order to be retained, sand should not reach the barrier, i.e. the reduction of wave height on the barrier should be strong enough to ensure the formation inshore of the barrier itself of a beach profile down to its closure depth.

Wave transmission is evaluated by formulae or experiments. Approximately $H_{st} \cong s_c$ (H_{st} = transmitted wave; s_c = barrier submergence).

Transmission coefficient depends on scaled values of:

- barrier submergence
- crest-berm width
- stone size
- wave steepness

Closure depth (h_c) for sandy beaches is evaluated by formulae or, approximately, as $h_c = 2H_{st}$. On gravel beaches a no movement condition at the foot of the inshore barrier can be imposed. The equilibrium beach profile is evaluated according to Dean 2/3 power relation. The turbulence decay area of the breaker can be approximately evaluated as $10h$.

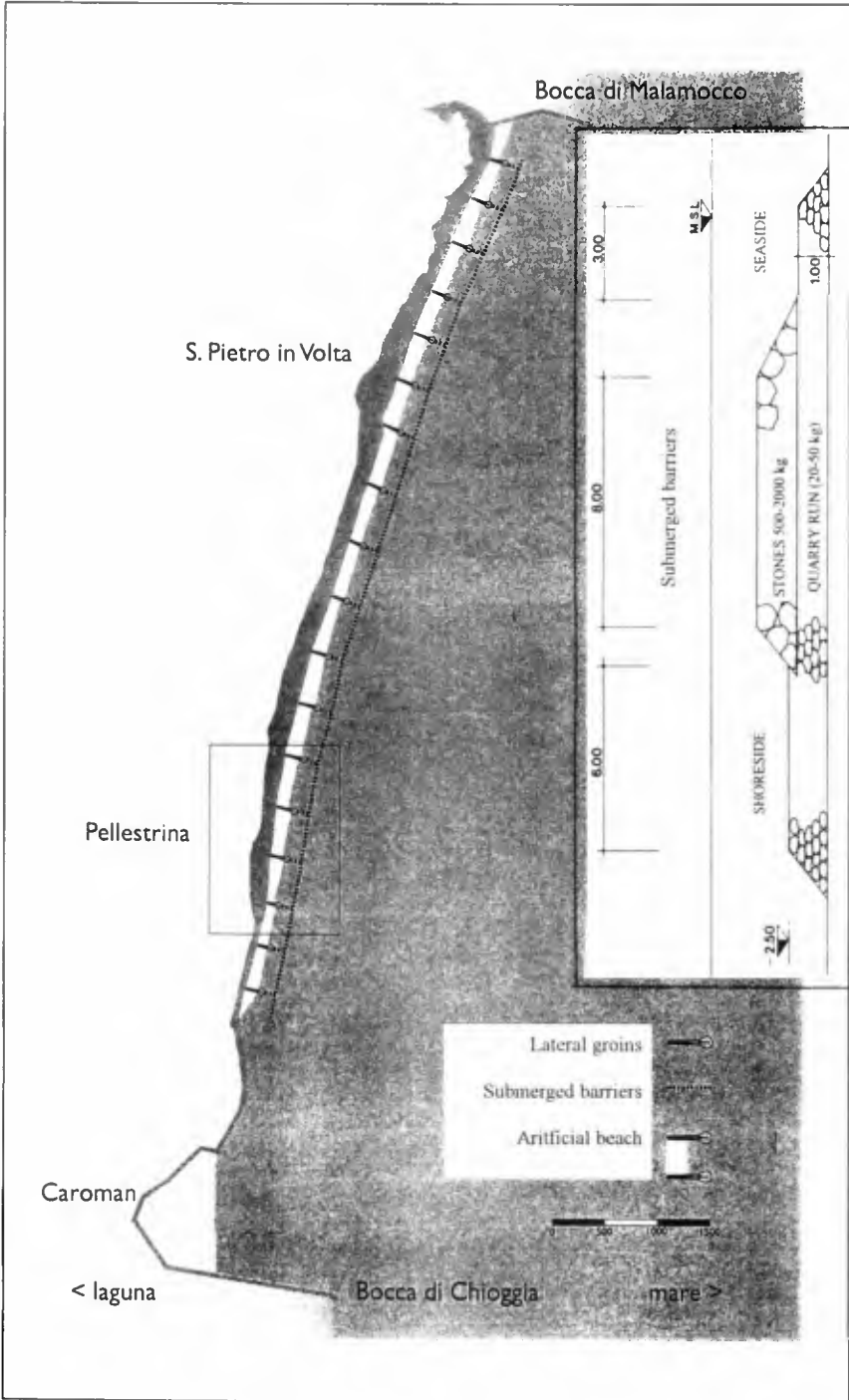


Fig. 10 – Protected nourishment at Pellestrina (VE, Veneto): plan of the area and section of the submerged barrier.



Fig. 11 – Pellestrina litoral before the works.



Fig. 12 – Pellestrina litoral after the interventions.

High water conditions are obviously the most severe for the beach stability; since $h_c \approx 2s_c$, a sea level rise cause an almost double increase of closure depth and an almost equal lowering of the closure point.

3.3 Most frequently used formulae

The Goda-Seelig (SPM), (Goda, 1985) and Van der Meer & Daemen (1994) formulae are most frequently used to calculate the wave transmission from the barrier.

For the closure depth of the equilibrium beach profile, Hallermeir's (1980, 1981) formula is used for sandy sediments.

For gravel beaches a modified Shield criterion is used in combination with a friction formula returning shear velocity from the orbital wave velocity at the bed.

For the armour stones stability Van der Meer (1993), Vidal (1995) and other formulae are normally used.

4 Open problems

The development of currents induced by the barrier is a 3-D complicated phenomenon, since the limited size of the barrier make the use of a mild slope approximation questionable. As a consequence the capacity of providing quantitative and reliable predictions of sediment transport by rip and longshore currents is limited and consequently of erosion in the vicinity of the structure and of effects on the beach.

Even if barriers made of rocks are stable according to the calculation formulae used, their transversal section show changes probably due to sinking of the rocks in the sediments of the bottom. This could be due to a probable underestimation of the structure-foundation interactions caused by the dynamic actions induced by the waves.

The structural resistance of sand bags showed to be insufficient. Most works constructed with this technique were destroyed after few years and in some case the remnants could not be found after 8-10 years.

Some damages to bags are probably caused during construction. During lifetime bag are covered with vegetation and mussels, the effects of which is poorly known, or abided by sand.

Finally quite often the sandy bed on which they are posed is ploughed by mussels fishers damaging the barrier.

5 Conclusions

In order to be efficient sand retaining structures, submerged barriers should be:

- sufficiently high and wide, so that they cause a significant reduction of the transmitted wave height and avoid erosion of the bed at their inshore foot:
 - $s_c < h/2$ ($s_c = h/3$ at high water level)
 - $b_c < 3h$ ($b_c = 3h$ at high water level)
- sufficiently distant from the shoreline, so that turbulence produced by induced

breakers decays before reaching the inner beach.

Wave transmission and hydraulic stability of their stones are rather well known, particularly in the absence of cross-currents.

The knowledge of barrier behaviour is nevertheless still insufficient regarding several aspects:

- induced set-up and currents influencing sediment transport and water quality;
- related sediment transport causing littoral sand trapping efficiency or sand losses;
- local bed erosion at inshore and offshore toe of the barrier and in the gaps;
- barrier sinking mechanism, which must be controlled in order to preserve barrier submergence and efficiency.

References

- Aminti, P. & al. (1983). *Experimental studies on submerged barriers as shore protection structures*. Int. Conf. COPEDEC, Colombo, March 20-26 1983.
- Beji, S. & Battjes, J.A. (1992). *Experimental investigation of wave propagation over a bar*. Coastal Eng., 151-162.
- Delft Hydraulics, (1983). *Lido di Dante - Morfologic behaviour of beach fill with underwater dam*. Rep. On model investig. M 1891.
- (1989). *Coastal protection Plan Lido di Ostia*. H 891, Rep. on math. Computation and scale model tests.
- (1990). *Beach nourishment schemes for the coast of Riccione and Cesenatico*. H 725, Rep. On model investig.
- Ferrante, A., Franco, L., Boer, S. (1992). *Modelling and monitoring of a perched beach at Lido di Ostia (Rome)*. Proc. 23rd ICCE Venice, pp. 3305-3318.
- Hallermeir, R.J. (1980). *Sand motion initiation by water waves: two asymptotes*. J.Wtrwy Port Coast. and Oc. Div., ASCE, 106(3), 299-318.
- Hallermeir, R.J. (1981). *A profile zonation for seasonal sand beaches from wave climate*. Coastal Eng., 4, 253-277.
- Lamberti, A. & Tomasicchio, U. (1981). *Le barriere sommerse possibili strutture a difesa della costa*. Porti Mare Territorio, Anno III n° 1, pp. 29-37.
- Lamberti, A. & al. (1985). *A comparative analysis of some types of submerged barriers as beach defence structures*. Proc. 21st IAHR Congress, Melbourne, pp.27-34.
- Seelig, W.N. (1979). *Effect of breakwaters on waves: laboratory tests of waves transmission by overtopping*. Coastal Eng., 2, 941-961.
- Van Der Meer, J.W. (1993). *Conceptual design of rubble mound breakwaters*. Delft Hydraulics Publications, n° 483.
- Van Der Meer, J.W., Daemen, I.F.R. (1994). *Stability and wave transmission at low crested rubble-mound structures*. J.Wtrwy Port Coast. and Oc. Engrg., ASCE, 120(1), 1-19.
- Vidal, C. & al. (1995). *Suitable wave-height parameter for characterizing breakwater stability*. J.Wtrwy Port Coast. and Oc. Engrg., ASCE, 121(2), 88-97.
- Vidal, C. & al. (1995). *Stability of low-crested rubble-mound breakwaters heads*. J.Wtrwy Port Coast. and Oc. Engrg., ASCE, 121(2), 114-122.

CHAPTER 183

Resonant Reflection and Refraction-Diffraction of Surface Waves due to Porous Submerged Breakwaters

Hajime Mase¹⁾, Akira Kimura²⁾ and Hiroshi Sakakibara³⁾

ABSTRACT: A wave equation, taking account of the effects of porous medium, is transformed into coupled parabolic equations. It is assumed in the theory that the mean water depth and the thickness of porous layer are slowly varying and the bottom undulation is rapidly varying compared to the wavelength of surface waves. Though we can utilize the Bragg reflection to reduce transmitted waves behind breakwaters in one-dimensional case, wave heights behind breakwaters do not always decrease due to wave refraction-diffraction in horizontal two-dimensional case. By adding a dissipation term to the coupled parabolic equations, we can calculate the wave breaking deformation.

INTRODUCTION

Porous submerged coastal structures are superior from the view points of seascape, water quality conservation, and fishery resources. If artificial reefs for fish habitat, consisted of blocks, are arranged to form a suitable bar field, we can expect a function of wave control as well as the function of creating fishery resources. Such porous bar fields make wave reflection and transmission smaller than those by impermeable bar fields.

Davies and Heathershaw (1984) studied the reflection from sinusoidal undulation over a horizontal bottom and derived a solution of reflection coefficient. Mei (1985) and Naciri and Mei (1988) developed theories of wave evolution at and close to the resonant condition by shore-parallel sinusoidal bars and two-dimensional doubly sinusoidal undulations over a slowly varying topography. Kirby (1986) derived a general wave equation which extends the mild slope equation of Berkhoff (1972). These existing theories don't take account of the effects of seabed permeability. Izumiya (1990) obtained an extended mild slope equation for waves propagating over a permeable submerged breakwater. However, since the assumption that the slope of the structure is very gentle is employed, the theory cannot be applied to the case of seabed with rapidly varying undulations.

In this study, a wave equation over porous rippled beds (Mase and Takeba, 1994), taking into account the effects of porous medium, is transformed into coupled para-

1) Assoc. Prof., Disaster Prevention Research Institute, Kyoto Univ., Gokasho, Uji, 611, Japan

2) Prof., Dept. of Social Systems Eng., Tottori Univ., Koyama Minami, Tottori, 680, Japan

3) Engineer, NEWJEC, 1-20-19 Shimanouchi, Chuo-ku, Osaka, 542, Japan

bolic equations of forward- and backward-scattering waves. Numerical calculations are carried out to examine wave transformations or the Bragg scattering by a group of porous submerged breakwaters over constant and sloping beaches in horizontal two-dimension.

WAVE EQUATION OF ELLIPTIC TYPE

Mase and Takeba (1994) and Mase et al. (1995) derived a wave equation over porous rippled beds:

$$\nabla_h \cdot (\alpha \nabla_h \hat{\phi}) + \alpha k^2 \hat{\phi} - \frac{\cosh^2 kh_s}{D^2} (1 - \gamma) \nabla_h \cdot (\delta \nabla_h \hat{\phi}) = 0 \tag{1}$$

where

$$\alpha = \frac{1}{4kD^2} \left\{ \cosh^2 kh_s \sinh 2kh \left(1 + \frac{2kh}{\sinh 2kh} \right) + \gamma \sinh 2kh_s (\cosh 2kh - 1) + \gamma^2 \sinh^2 kh_s \sinh 2kh \left(1 - \frac{2kh}{\sinh 2kh} \right) + \gamma \sinh 2kh_s \sinh 2kh \left(1 + \frac{2kh_s}{\sinh 2kh_s} \right) \right\} \tag{2}$$

$$D = \cosh kh_s \cosh kh (1 + \gamma \tanh kh_s \tanh kh) \tag{3}$$

$$\gamma = n / (\tau + i f) \tag{4}$$

$$\omega^2 = gk \frac{\tanh kh + \gamma \tanh kh_s}{1 + \gamma \tanh kh \tanh kh_s} \tag{5}$$

where $\hat{\phi}$ is the complex amplitude of velocity potential, δ is the rapidly varying undulation, h and h_s are slowly varying water depth and thickness of porous layer, ∇_h is the horizontal gradient operator, f is the linearized friction factor, n is the porosity, τ is the inertia coefficient, and ω is the angular frequency. The effects of the porous medium are taken into account through the complex wavenumber k given by Eq.(5) and the complex coefficients α and γ .

Eq.(1) contains the existing models such as the mild slope equation by Berkhoff (1972) and the general wave equation by Kirby (1986), see Mase and Takeba (1994).

COUPLED PARABOLIC EQUATIONS

We need the boundary condition along a closed curve surrounded an analytical domain to solve Eq.(1) of elliptic type. In problems of predicting wave transformations over sloping topography, we cannot set the shoreward boundary condition a priori. A parabolic approximation method developed by Radder (1979) is useful for such problems. Here, following Kirby (1986), we transform Eq.(1) into coupled parabolic equations.

Multiplying Eq.(1) by the gravity acceleration g makes the dimension of αg same as that of CC_g (phase velocity \times group velocity). Hereafter, αg and $g \cosh^2 kh_s / D^2$ are described as α and β , respectively. Manipulating Eq.(1) yields

$$\{\alpha - \beta(1-\gamma)\delta\}\phi_{xx} + \{\alpha_x - \beta(1-\gamma)\delta_x\}\phi_x + \alpha k^2\phi + (\alpha\phi_y)_y - \beta(1-\gamma)(\delta\phi_y)_y = 0 \quad (6)$$

and Eq.(6) is rewritten as

$$\phi_{xx} + v^{-1}v_x\phi_x + v^{-1}\alpha k^2\phi + v^{-1}(\alpha\phi_y)_y - v^{-1}\beta(1-\gamma)(\delta\phi_y)_y = 0 \quad (7)$$

where

$$v = \alpha - \beta(1-\gamma)\delta \quad (8)$$

$$v_x = \alpha_x - \beta(1-\gamma)\delta_x + O(k\delta)^2 \quad (9)$$

$$v^{-1} = \alpha^{-1} \left\{ 1 + \frac{\beta}{\alpha}(1-\gamma)\delta + O(k\delta)^2 \right\} \quad (10)$$

Let's introduce the following pseudo-operator:

$$\mu^2\phi = k^2 \left[\left\{ 1 + \frac{\beta}{\alpha}(1-\gamma)\delta \right\} \phi + \frac{1}{k^2\alpha}(\alpha\phi_y)_y - \frac{\beta(1-\gamma)}{k^2\alpha}(\delta\phi_y)_y \right] + O(k\delta)^2 \quad (11)$$

Treating μ^2 to be a numerical value and taking the square root of it gives

$$\mu\phi = k \left[\left\{ 1 + \frac{\beta}{2\alpha}(1-\gamma)\delta \right\} \phi + \frac{1}{2k^2\alpha}(\alpha\phi_y)_y - \frac{\beta(1-\gamma)}{2k^2\alpha}(\delta\phi_y)_y \right] + O(k\delta)^2 \quad (12)$$

Now we express the potential ϕ as a sum of the forward-scattered potential, ϕ^+ , and the backward-scattered potential, ϕ^- , as

$$\phi = \phi^+ + \phi^- \quad (13)$$

and express their derivatives as

$$\phi_x^+ = i\mu\phi^+ + F(\phi^+, \phi^-) \quad (14)$$

$$\phi_x^- = -i\mu\phi^- - F(\phi^+, \phi^-) \quad (15)$$

where $F(\phi^+, \phi^-)$ is a coupling term, and μ is a kind of wavenumber. Using Eq.(11), Eq.(7) is expressed as follows:

$$\phi_{xx} + \frac{v_x}{v}\phi_x + \mu^2\phi = 0 \quad (16)$$

$F(\phi^+, \phi^-)$ is found to be

$$F(\phi^+, \phi^-) = -\frac{(\mu\nu)_x}{2\mu\nu}(\phi^+ - \phi^-) \tag{17}$$

by substituting Eqs.(13)~(14) into Eq.(16). The pseudo-operator $\mu\nu$ can be given by

$$\mu\nu = k\left\{\alpha - \frac{\beta}{2}(1-\gamma)\delta\right\} + O(k\delta)^2 \tag{18}$$

Differentiating Eq.(18) with respect to x yields

$$(\mu\nu)_x = (k\alpha)_x - \frac{1}{2}\{k\beta(1-\gamma)\delta\}_x \tag{19}$$

Using Eq.(12) and Eqs.(17) ~ (19), Eqs.(14) and (15) can be expressed as follows:

$$\begin{aligned} \phi_x^+ = ik \left[\left\{ 1 + \frac{\beta}{2\alpha}(1-\gamma)\delta \right\} \phi^+ + \frac{1}{2k^2\alpha}(\alpha\phi_y^+)_y \right. \\ \left. - \frac{\beta}{2k^2\alpha}(1-\gamma)(\delta\phi_y^+)_y \right] - \left\{ \frac{(k\alpha)_x}{2k\alpha} - \frac{\beta}{4\alpha}(1-\gamma)\delta_x \right\} (\phi^+ - \phi^-) \end{aligned} \tag{20}$$

$$\begin{aligned} \phi_x^- = -ik \left[\left\{ 1 + \frac{\beta}{2\alpha}(1-\gamma)\delta \right\} \phi^- + \frac{1}{2k^2\alpha}(\alpha\phi_y^-)_y \right. \\ \left. - \frac{\beta}{2k^2\alpha}(1-\gamma)(\delta\phi_y^-)_y \right] + \left\{ \frac{(k\alpha)_x}{2k\alpha} - \frac{\beta}{4\alpha}(1-\gamma)\delta_x \right\} (\phi^+ - \phi^-) \end{aligned} \tag{21}$$

The relation between the potential amplitude and the wave amplitude is

$$\phi^+ = -\frac{ig}{\omega} A e^{ik_0x} \tag{22}$$

$$\phi^- = -\frac{ig}{\omega} B e^{-ik_0x} \tag{23}$$

where k_0 is a reference wavenumber. Substituting Eqs.(22) and (23) into Eqs.(20) and (21) yields

$$\begin{aligned} A_x + \left[ik_0 - ik \left\{ 1 + \frac{\beta(1-\gamma)\delta}{2\alpha} \right\} + \frac{(k\alpha)_x}{2k\alpha} - \frac{\beta(1-\gamma)\delta_x}{4\alpha} \right] A \\ - \frac{i}{2k\alpha}(\alpha A_y)_y + \frac{i\beta(1-\gamma)}{2k\alpha}(\delta A_y)_y = \left\{ \frac{(k\alpha)_x}{2k\alpha} - \frac{\beta(1-\gamma)\delta_x}{4\alpha} \right\} B e^{-2ik_0x} \end{aligned} \tag{24}$$

$$\begin{aligned}
 B_x + \left[-ik_0 + ik \left\{ 1 + \frac{\beta(1-\gamma)\delta}{2\alpha} \right\} + \frac{(k\alpha)_x}{2k\alpha} - \frac{\beta(1-\gamma)\delta_x}{4\alpha} \right] B \\
 + \frac{i}{2k\alpha} (\alpha B_y)_y - \frac{i\beta(1-\gamma)}{2k\alpha} (\delta B_y)_y = \left\{ \frac{(k\alpha)_x}{2k\alpha} - \frac{\beta(1-\gamma)\delta_x}{4\alpha} \right\} A e^{2ik_0x} \quad (25)
 \end{aligned}$$

Eqs.(24) and (25) are the coupled parabolic equations for forward- and backward-scattered waves. Detail deviation is seen in Mase et al. (1995).

BRAGG SCATTERING DUE TO POROUS SUBMERGED BREAKWATERS

Procedure of numerical calculations

Eqs.(24) and (25) were finite-differentiated by the Crank-Nicolson method. The procedure of numerical calculations is as follows:

- 1) Setting $B = 0$ in the right hand side of Eq.(24), we calculate Eq.(24) for A in the forward direction;
- 2) Using the calculated A for the right hand side of Eq.(25), we calculate Eq.(25) for B in the backward direction;
- 3) Using the calculated B in the previous step, we solve Eq.(24) for A ;
- 4) Using the calculated A in the previous step, we solve Eq.(25) for B .

The procedure of 3) and 4) is repeated until getting convergence of the calculated results of A and B . A preliminary calculation revealed that four repetition was enough to reach the convergence.

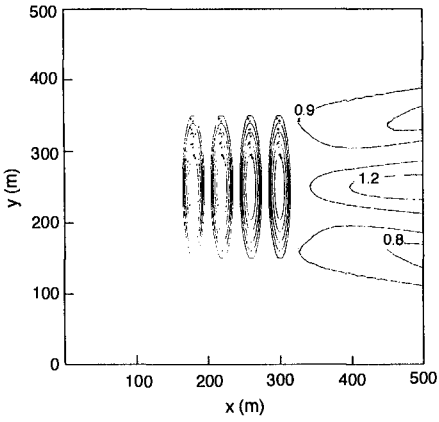
Numerical conditions

The following conditions were adopted in the numerical calculations:

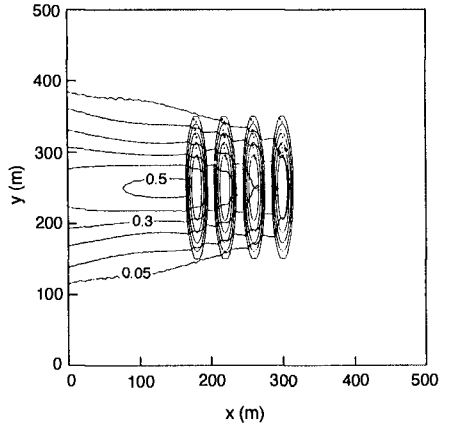
- 1) The analytical domain is 500 m \times 500 m;
- 2) The model beaches are constant water depth of 8 m, and 1/25 uniform slope;
- 3) Impermeable and permeable submerged breakwaters of elliptic shape (see, Mase et al., 1995), are installed at the interval of 40 m over constant and sloping beaches;
- 4) The height of the breakwaters is changed by 1.5 m and 2.5 m;
- 5) Characteristics of porous medium are selected as $n = 0.4$, $\tau = 1.0$, and $f = 1.0$;
- 6) Waves propagate in the direction of x axis. The incident wave amplitude is 1 m, and the wave period is changed by 8 s, 10 s, and 12 s.

Calculated results and discussions

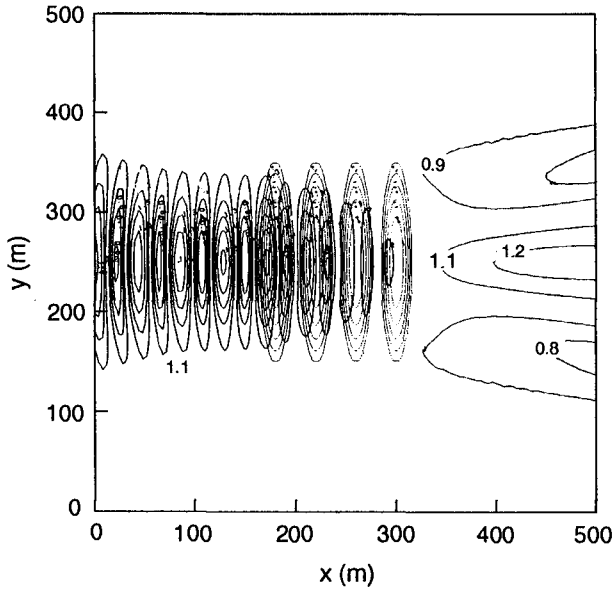
When the wave period is 10 s, the resonant Bragg reflection condition is satisfied in the constant water depth. The calculated results to be shown hereafter are those in the case of wave period of 10 s. Figure 1(a) shows the contour of the forward-scattered wave amplitude, Fig.1(b) the backward-scattered wave amplitude, and Fig.1(c) the total wave amplitude for the case of impermeable submerged breakwaters of which height is 2.5 m. It is seen from Fig.1(a) that the amplitude becomes large behind the elliptic breakwaters similar to the case of a large shoal. Fig.1(b) indicates that the breakwaters generate the reflected waves. In Fig.1(c), the two-dimensional standing wave pattern can be seen.



(a) Incident Wave Amplitude



(b) Reflected Wave Amplitude



(c) Total Wave Amplitude

Fig.1 Wave Transformation due to Impermeable Submerged Breakwaters over Constant Water Depth

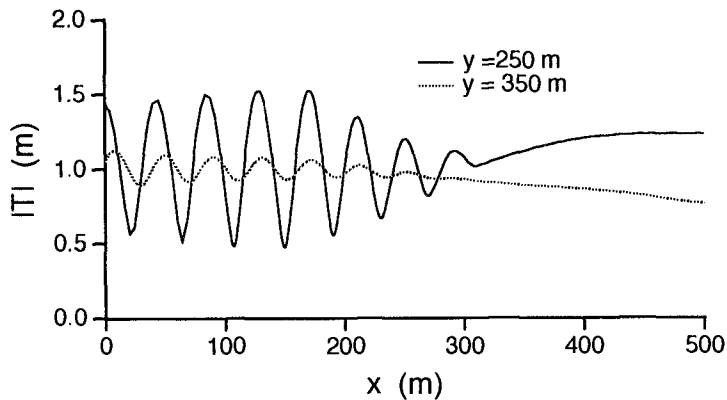


Fig.2 Spatial Change of Total Wave Amplitude along Two Lines

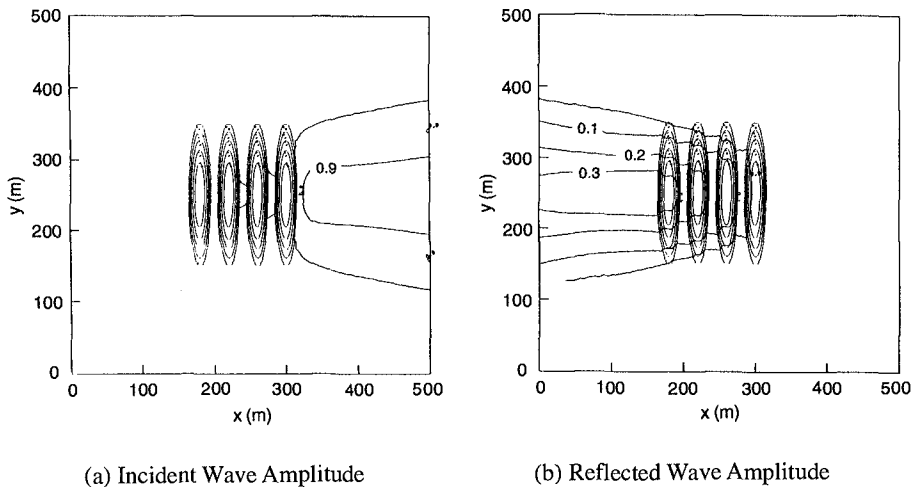
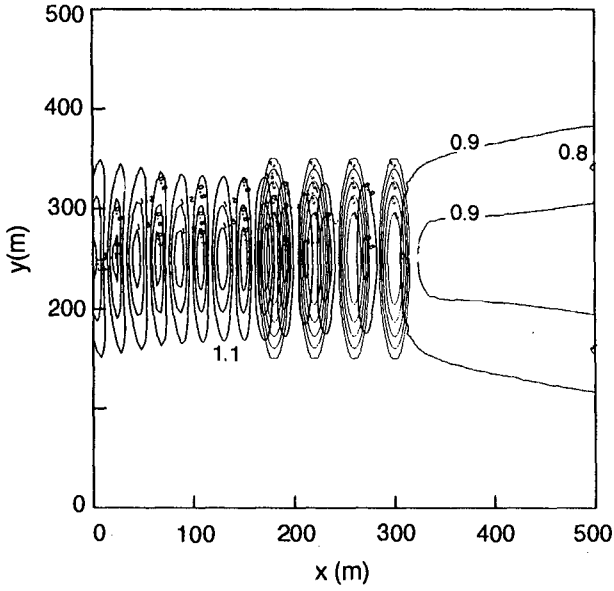


Fig.3 Wave Transformation due to Permeable Submerged Breakwaters over Constant Water Depth
(Continued)

The spatial distribution of the wave amplitude along $y = 250$ m and $y = 350$ m is shown in Fig.2. In an one-dimensional case, we can see that the transmitted waves downstream the ripples are reduced by utilizing the Bragg resonant scattering (Mase and Takeba, 1994); however, in a two-dimensional case, the wave height behind submerged breakwaters does not become small.



(c) Total Wave Amplitude

Fig.3 Wave Transformation due to Permeable Submerged Breakwaters over Constant Water Depth

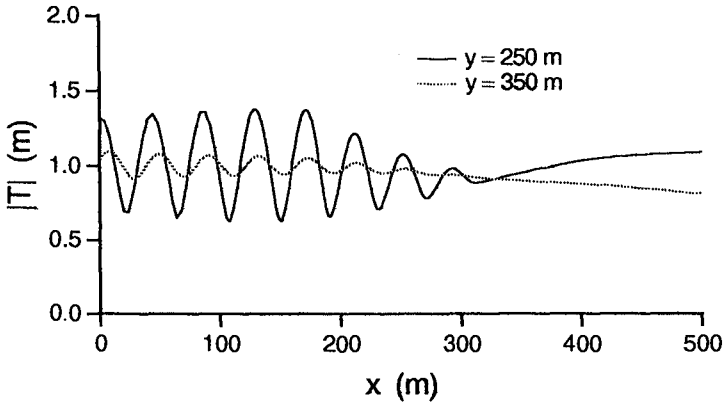


Fig.4 Spatial Change of Total Amplitude along Two Lines

Figure 3 shows the result of the case of permeable breakwaters of 2.5 m in height, where the figure (a) is the contour of the forward-scattered wave amplitude, the figure (b) the back-scattered wave amplitude, and the figure (c) the total wave amplitude. Figure 4 is the spatial change of total wave amplitude along $y = 250$ m (solid line) and $y = 350$ m (dotted line). Comparing these figures with those of Figs.1 and 2, we can see that the standing wave pattern and the increase in wave height behind the breakwaters are weakened due to energy dissipation in the porous medium.

Within the surf zone, wave energy is dissipated. To include the energy dissipation due to wave breaking in the coupled parabolic equations, an energy dissipation term is required. Dally et al. (1985) proposed an energy dissipation model which assumed that there is a stable wave height after breaking equal to some fraction of the water depth and that the rate of energy dissipation in the surf zone is proportional to the difference between the actual wave energy flux and the stable wave energy flux, $(EC_g)_s$. The model is as follows:

$$\frac{d(EC_g)}{dx} = -W = -\frac{K}{h} \{ EC_g - (EC_g)_s \} \quad (26)$$

where E is the wave energy. The stable wave height is given by $H_s = \gamma h$. In this study,

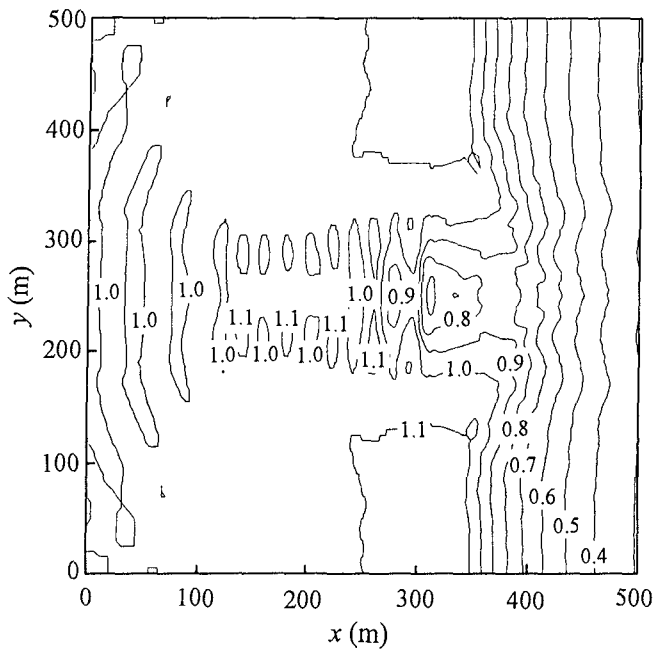


Fig.5 Wave Transformation due to Permeable Submerged Breakwaters over Sloping Beach

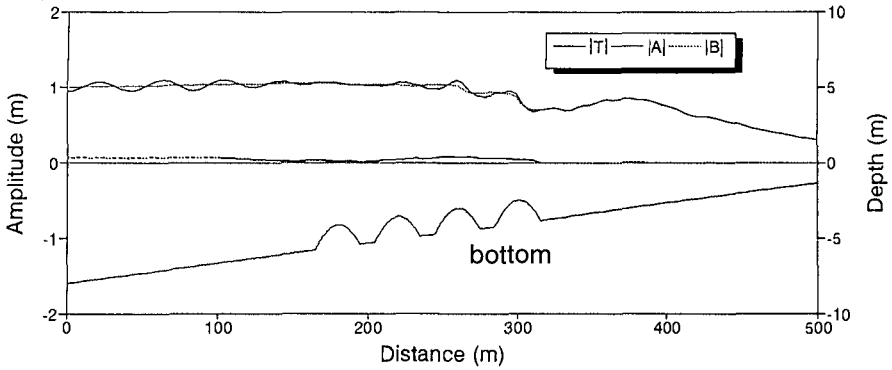


Fig.6 Spatial Change of Total Amplitude along Line of $y = 250$ m

$K = 0.15$ and $\gamma = 0.4$ were adopted. And the wave breaking condition of $H_b = 0.78h$ was employed, where wave height H is defined as $2|A|$.

A coefficient of energy dissipation is defined as

$$W_r = W / E \tag{27}$$

In order to include energy dissipation in the coupled parabolic equations, the term of $W_r A / (2C_g)$ was added in the left hand side of Eq.(24).

Figure 5 shows the wave transformation over a uniform sloping beach existing a group of permeable submerged breakwaters. Figure 6 shows the spatial distribution of wave amplitude along the line of $y = 250$ m. Wave breaking occurs around $x = 300$ m, and wave begins to decrease and again increases toward the shore. Second wave breaking occurs around $x = 380$ m, and wave amplitude continues to decrease.

CONCLUSIONS

In order to deal with wave transformations due to permeable submerged breakwaters, we developed a wave equation of elliptic type taking account of the effects of porous medium, and the wave equation was transformed into coupled parabolic equations. It was assumed, in the theory, that the mean water depth and the thickness of porous layer were slowly varying and the bottom undulation was rapidly varying compared to the wavelength of surface waves.

Numerical examples of the Bragg scattering were shown in horizontal two-dimensional case. Wave amplitudes became large behind a group of submerged breakwaters due to the wave refraction-diffraction, even when the resonant Bragg reflection condition was satisfied. When the breakwaters were permeable, the standing wave pattern and the increase in wave height behind the breakwaters were weakened due to energy dissipation in the porous medium.

REFERENCES

- Berkhoff J.C.W. (1972), Computation of Combined Refraction- Diffraction, Proc. 13rd Int. Conf. Coastal Eng., ASCE, pp.471-490.
- Dally, W.R., Dean, R.G. and Dalrymple, R.A. (1985), Wave height variation across beaches of arbitrary profile, Jour. Geophys. Res., Vol.90, No.C6, pp.11917-11927.
- Davies, A.G. and Heathershaw, A.D. (1984), Surface-Wave Propagation over Sinusoidally Varying Topography, Jour. Fluid Mech., Vol. 144, pp.419-443.
- Izumiya, T. (1990), Extension of Mild Slope Equation for Waves Propagating over a Permeable Submerged Breakwater, Proc. 22nd Int. Conf. Coastal Eng., ASCE, pp.306-315.
- Kirby, J.T. (1986), A General Wave Equation for Waves over Rippled Beds, Jour. Fluid Mech., Vol. 162, pp. 171-186.
- Mase, H. and Takeba, K. (1994), Bragg scattering of waves over porous rippled bed, Proc. 24th Int. Conf. on Coastal Eng., ASCE, pp.635-649.
- Mase, H., Takeba, K. and Oki, S. (1995), Wave equation over permeable rippled bed and analysis of Bragg scattering of surface gravity waves, Jour. Hydraulic Res., Vol.33, No.6, pp.789-812.
- Mei, C.C. (1985), Resonant Reflection of Surface Waves by Periodic Sand-Bars, Jour. Fluid Mech., Vol. 152, pp.315-335.
- Naciri, M. and Mei, C.C. (1988), Bragg Scattering of Water Waves by a Doubly Periodic Seabed, Jour. Fluid Mech., Vol. 192, pp.51-74.
- Radder, A.C. (1979), On the Parabolic Equation Method for Water-Wave Propagation, Jour. Fluid Mech., Vol.95, pp. 159- 176.

CHAPTER 184

BEM-FEM COMBINED ANALYSIS OF NONLINEAR INTERACTION BETWEEN WAVE AND SUBMERGED BREAKWATER

N.Mizutani¹, W.G. McDougal², A.M. Mostafa³

ABSTRACT:

A combined BEM-FEM model has been developed to study the nonlinear dynamic interaction between a submerged breakwater and waves. The resistance coefficients in the equations of motion inside the porous media have been experimentally determined based on measured values of the wave forces on spherical armor units in a submerged breakwater. Comparisons of the numerical model results with the experimental measurements indicate that this modification has improved the model accuracy in simulating the wave deformation and the energy dissipation due to a submerged breakwater. Results also show that the model gives good estimates for the wave kinematics inside and around the breakwater which are necessary to compute the stable armor stone weight.

INTRODUCTION:

Submerged breakwaters have several advantages over the conventional surface piercing structures including aesthetics, less impact on the near shore water quality and ability to trigger early wave breaking. Their use is also recommended on recreational beaches to ensure safe conditions. They are usually constructed from rubble and may be protected by an armor layer of large stones or concrete blocks.

Earlier researchers focused on wave deformation and energy dissipation due to submerged breakwaters, but less interest was given to their internal properties and shape. Driscoll et al. (1992) studied the harmonic generation and transmission past

¹ Assoc. Prof., D.Eng., Dept. of Civil Eng., Nagoya University, Nagoya 464-01, Japan

² Prof., Dept. of Civil Eng., Oregon State Univ., Corvallis, OR 97331, USA

³ Graduate student, M.Eng., Dept. of Civil Eng., Nagoya University, Nagoya 464-01, Japan

a submerged impermeable rectangular obstacle. They conducted laboratory experiments and compared the results with a linear scattering model and a fully nonlinear model. Cruz et al (1992) derived a set of nonlinear vertically integrated equations similar to that of Boussinesq to estimate the wave transformations past a submerged permeable breakwater. They found that their equations work well in the region of cnoidal waves, but the transmitted and the broken wave characteristics could not be well predicted. Gu and Wang (1992) linearized the porous flow equations inside the submerged breakwater using the equivalent energy principle and developed a model based on the Boundary Equation Method (BEM). They found that maximum wave energy dissipation can be achieved at practical permeability levels.

Based on modified Navier-Stokes equations, McCorquodale and Hannoura (1978) developed the flow equations inside the porous media and applied them to the case of rubble mound breakwaters. A mixed numerical model was also developed to simulate the wave motion inside rubble mound breakwaters and, hence, check the stability of the seaward slope (Hannoura and McCorquodale, 1985). Ohyama and Nadaoka (1991) developed an idealized numerical wave tank consisting of sponge layer(s) and the non-reflective wave source developed by Brorsen and Larsen (1987). They used the BEM and proved that their proposed wave tank is applicable for use with irregular and nonlinear wave fields.

Sakakiyama et al. (1991) developed a porous body model analysis of nonlinear wave transformations to study the velocity, pressure fields and free surface displacement in and near rubble mound and composite breakwaters. They considered the flow to be rotational inside and outside the porous media, but their numerical model required a very long CPU run-time. Moreover, in a comparison between permeable and impermeable submerged breakwaters, it has been found that the wave reduction is slightly affected by the porosity of the breakwater (Sakakiyama, 1992).

For wide crown submerged breakwaters, the flow velocities and the wave field behind the breakwater are small and assuming irrotationality of the flow in the wave field may be reasonable. This will reduce the computation time and cost. Therefore, a hybrid-type numerical model has been developed and used to simulate the non-linear dynamic interaction between waves and rectangular permeable submerged breakwater considering irrotational flow in the wave field, but rotational flow inside the porous media (Mizutani et al., 1995).

This study has been conducted to develop an accurate numerical model for the simulation of the nonlinear dynamic interaction between waves and submerged breakwater with irregular cross section. An idealized wave tank, similar to that of Ohyama and Nadaoka (1991), has been used to simulate the nonlinear wave field. Modified Navier-Stokes equations have been employed to simulate the flow inside the porous media (McCorquodale and Hannoura, 1978). The Boundary Element Method (BEM) has been used to develop a numerical model for the wave field.

The Finite Element Method (FEM), based on the weighted residual technique, has been used to solve the flow problem inside the submerged breakwater. The link between the two models has been maintained through boundary conditions on the interface between the wave and porous media fields. The BEM-FEM model computes the wave deformations and the flow inside the submerged breakwater simultaneously at each time step in a time marching scheme.

The resistance coefficients in Navier-Stokes equations have been modified through comparison with a Morison type equation for evaluating the wave forces on a spherical armor unit. The measured values of the wave forces and velocities in the experiments (Mizutani et al., 1994) have been used to estimate the drag and inertia coefficients.

GOVERNING EQUATIONS AND MODEL DEVELOPMENT

Wave Field

The flow in the wave field has been assumed to be irrotational and the water is considered inviscid and incompressible. The idealised wave tank used in this study is shown in Fig.1 and it is governed by the following Poisson equation (Brorsen and Larsen, 1987).

$$\frac{\partial^2 \phi}{\partial X^2} + \frac{\partial^2 \phi}{\partial Z^2} = q^* \tag{1}$$

$$q^* = U^*(Z, t)\delta(X - X_s) \tag{2}$$

where ϕ is the velocity potential; X and Z are the horizontal and vertical coordinates, respectively; q^* corresponds to the flux density at the wave-making source and is zero elsewhere; U^* is the flux density at the wave-making source; δ is Dirac's delta function and X_s is the X -position of the wave-making source. Eq.1 is subjected to the following boundary conditions (see Fig.1):

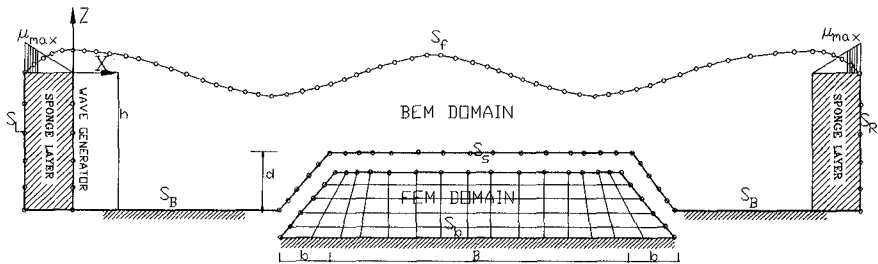


Fig.1 Wave tank for wave-submerged breakwater dynamic interaction

$$\frac{\partial \phi}{\partial n} = n_z \frac{\partial \eta}{\partial t} \quad (\text{on } S_f) \quad (3)$$

$$\frac{\partial \phi}{\partial n} = 0 \quad (\text{on } S_b) \quad (4)$$

$$\frac{\partial \phi}{\partial n} = V_n \quad (\text{on } S_s) \quad (5)$$

$$\frac{\partial \phi}{\partial t} + \frac{1}{2}(\nabla \phi)^2 + g\eta + \mu\phi - \int_{X_1}^X \frac{\partial \mu}{\partial X} \phi dX = 0 \quad (\text{on } S_e) \quad (6)$$

$$\frac{\partial \phi}{\partial X} = \frac{1}{\sqrt{gh}} \left(\frac{\partial \phi}{\partial t} + \mu\phi + \int_{X_2}^X \frac{\partial \mu}{\partial X} \phi dX \right) \quad (\text{on } S_L) \quad (7)$$

$$\frac{\partial \phi}{\partial X} = -\frac{1}{\sqrt{gh}} \left(\frac{\partial \phi}{\partial t} + \mu\phi - \int_{X_3}^X \frac{\partial \mu}{\partial X} \phi dX \right) \quad (\text{on } S_R) \quad (8)$$

$$\mu_{\max} = (0.25 \sim 0.50) \sqrt{\frac{g}{h}} \quad (9)$$

where n_z is the directional cosine of the normal outward from the boundary with the Z axis; t is time; V_n/m is the porewater velocity normal to the boundary; m is the porosity; h is the water depth; and η is the water surface elevation above SWL. μ is a damping factor which varies linearly inside the sponge layer from zero at the beginning of the layer to μ_{\max} at the open boundary (see Fig. 1).

Ohyama and Nadaoka (1991) have found that if the value of the coefficient in Eq. 9 ranges from 0.25 to 0.50 and the sponge layer width is more than one wave length, the coefficient of reflection from the sponge layer will be less than 2%. Eq. 6 can represent the free surface inside and outside the sponge layer since $\mu = \partial \mu / \partial X = 0$ outside the layer and, hence, the equation is reduced to the original dynamic boundary condition.

Applying Green's theorem, the integral form of Eq. 1 can be written as follows (Brebbia and Walker, 1980):

$$\alpha(q)\phi(q) + \int_s \left(\phi \frac{\partial G}{\partial n} - \frac{\partial \phi}{\partial n} G \right) ds + \iint_{\Omega} q * G d\Omega = 0 \quad (10)$$

where $\alpha(q)$ and $\phi(q)$ are the internal boundary angle and velocity potential at point (q) , respectively; s represents the outer boundary; and G is the Green's function defined as:

$$G = \ln(1/r) + \ln(1/R) \quad (11)$$

where r is the distance between the point of interest (q) and other domain points and R is the distance between the point (q) and the image of other domain points considering the seabed as a mirror line.

The weighted residual method has been applied to integrate the dynamic boundary condition on the free surface using linear elements and weighting factor ϖ resulting in the following integral equation.

$$\int \varpi \left\{ \frac{\partial \phi}{\partial t} + 0.5 \left(n_z^2 \left[\frac{\partial \eta}{\partial t} \right]^2 + \left[\frac{\partial \phi}{\partial s} \right]^2 \right) + g\eta + \mu\phi - \int \frac{\partial \mu}{\partial X} \phi dX \right\} ds = 0 \quad (12)$$

Further details about this method are given in Ohyama and Nadaoka (1991).

Initial condition:

The water surface elevation above the SWL, the velocity potential and their time derivatives are set to zero at the initial time step of the program (cold start). The model ramps up from this condition. Iterations for the location of the nonlinear water surface are made at each time step in a time marching scheme.

Porous Media

The flow in the porous media is considered to be rotational and the porewater is assumed to be incompressible but viscous. The continuity equation and the equations of motion (McCorquodale and Hannoura, 1978) for the flow inside the porous media are as follows:

$$\frac{\partial U}{\partial X} + \frac{\partial W}{\partial Z} = 0 \quad (13)$$

$$A \frac{\partial U}{\partial t} + BU \frac{\partial U}{\partial X} + CW \frac{\partial U}{\partial Z} + D \frac{\partial P}{\partial X} + EU + FU \sqrt{U^2 + W^2} = 0 \quad (14)$$

$$A \frac{\partial W}{\partial t} + BU \frac{\partial W}{\partial X} + CW \frac{\partial W}{\partial Z} + D \frac{\partial P}{\partial Z} + EW + FW \sqrt{U^2 + W^2} = 0 \quad (15)$$

where

$$A = \frac{\left(1 + \frac{1-m}{m} C_{AX}\right)}{mg}, \quad B = C = \frac{1}{m^2 g}, \quad D = \frac{1}{\gamma}, \quad E = \frac{4.6\nu}{gmD^2}$$

$$F = \frac{0.79}{gm^{1/2}D}, \quad P = p + \gamma Z$$

and U, W, P are the horizontal and vertical water particle velocities and the porewater pressure, respectively; p is the dynamic porewater pressure; C_{AX} is the added mass coefficient; g is the acceleration of gravity; ν is the kinematic viscosity of water; γ is the unit weight of water; and D is the mean particle diameter.

The porous media equations are subjected to the following boundary conditions:

$$P = -\frac{\partial \phi}{\partial t} - \frac{1}{2} \left\{ \left(\frac{V_n}{m} \right)^2 + V_s^2 \right\} - \gamma Z \quad (\text{on } S_s) \quad (16)$$

$$V_n = (W \cos \theta \pm U \sin \theta) \quad (\text{on } S_s) \quad (17)$$

$$V_s = \frac{\partial \phi}{\partial S} \quad (\text{on } S_s) \quad (18)$$

$$V_n = 0 \quad (\text{on } S_b) \quad (19)$$

where V_s is the water particle velocity in the tangential direction to the boundary and θ is the inclination of the permeable boundary on the X axis.

The continuity of the normal velocity component (V_n) and the porewater pressure have been considered along the surface boundary of the submerged breakwater. The tangential component of the water velocity along the breakwater surface has been solved using the Finite Difference Method (FDM).

The FEM in the porous media is based on the weighted residual method. A special isoparametric trapezoidal element has been considered for discretization of the FEM domain. A four node element for the velocity (u and w) and eight node element for the pressure (p) have been employed to solve the problem. Linear interpolation and weight functions have been used for the continuity equation but a special technique has been applied to the equations of motion (Mizutani et al., 1995).

Initial conditions:

The velocity, pressure and their derivatives have been set to zero at the initial time step of the program (cold start) and a time marching scheme has been used to compute the flow inside the porous media at subsequent steps.

BEM-FEM Model Development

The BEM model for the simulation of the wave motion and the FEM model for porous flow have been linked together into one model that computes simultaneously the wave deformations outside the breakwater and the porous media flow inside the breakwater. The time derivative of any variable ψ at any time step (n) in the porous media or the wave field equations is solved using Taylor series expansion as follows:

$$\left(\frac{\partial \psi}{\partial t}\right)^n = 2 \frac{\Delta \psi}{\Delta t} - \left(\frac{\partial \psi}{\partial t}\right)^{n-1} \quad (20)$$

The nodes along the surface boundary of the breakwater and the water surface are located at spacing less than $L/20$ (where L is the wave length). The location of the FEM nodes are selected to be the same as that of the BEM along the interface between the breakwater and the wave domain. The time step of the model is initially selected to be $T/24$ and then the results are compared to the experimental results. If the difference between the numerical and experimental results is more than an accepted tolerance, smaller time steps are selected. It has been found that time increments less than $T/24$ may be needed for steep waves.

PHYSICAL MODEL

Submerged breakwater experiments were conducted in the coastal engineering laboratory at Nagoya University. These experiments measured the wave forces on spherical armor units (F_x and F_z), wave deformations and the water velocity around the surface of the breakwater. The submerged breakwater was constructed of spherical glass balls 3.0 cm in diameter and placed in a wave tank of 25.0 m long and 0.70 m wide. The breakwater had a crown width of 220 cm, height of 21 cm, and the seaward face had a slope of 3.2 (horizontal) : 1 (vertical). The balls were arranged to produce the maximum densely packed arrangement and their computed corresponding porosity was 26%. Two possible positions were considered for the spheres, namely, embedded and non-embedded positions (Mizutani et al., 1992). The experiments were conducted in a water depth of 28.0 cm so that the still water depth over the crown was 7.0 cm. Wave heights (H) of 3.0, 5.0, 7.0 and 10.0 cm and wave periods (T) of 1.0, 1.40 and 1.80 sec were examined. Records were sampled for one minute at a rate of 50 Hz.

It was observed that the waves pass over the breakwater without breaking for wave heights 3.0 and 5.0 cm, but break for larger heights. Studies were formerly conducted to estimate the wave forces on armor units over a submerged breakwater and proved that the dimensionless non-breaking wave force, normalised by the wave height, on the armor is higher than the breaking one (Mizutani et al., 1992). Therefore, the non-breaking wave conditions will only be used for comparison and discussions in this study.

ESTIMATION OF WAVE FORCES

Standard Morison type equations have been found to be generally applicable to estimate the horizontal wave forces on the spherical armor units of submerged breakwaters (Rufin et al., 1996). However, in this study, the wave force has been considered to be composed of three components as follows:

$$F_x = \frac{1}{6}C_{MX}\rho\pi D^3 \frac{\partial u_r}{\partial t} + \frac{1}{8}C_{DX1}\rho\pi D^2 u_r \sqrt{u_r^2 + w_r^2} + 3C_{DX2}\rho v\pi D u_r \quad (21)$$

By applying Eq.21, the horizontal wave force acting on a small element of a homogeneous porous submerged breakwater can be written as follows:

$$F_x = \rho V C_{MX} \frac{\partial u_r}{\partial t} + \frac{1}{2} C_{DX1} \rho A_x u_r \sqrt{u_r^2 + w_r^2} + C_{DX2} \frac{3\rho v S}{D} u_r \quad (22)$$

where u_r and w_r are the porewater velocity components in the horizontal and vertical directions, respectively; S is the surface area of the armor unit affected by friction with the flow; ρ is the porewater density; C_{MX} is the coefficient of mass; and C_{DX1} and C_{DX2} are the drag coefficients in the X direction. A_x is the projected area of the armor unit in the X direction and V is its volume. This form of the Morison equation includes the common inertia and quadratic drag terms but also has a linear drag term. This linear term is analogous to Darcy flow in groundwater.

To solve the modified Morison equation, the porewater velocities (u_r , w_r), V , S and A_x have been expressed as follows and inserted into Eq.22.

$$A_x = (1 - m)\Delta Z \quad (23)$$

$$V = (1 - m)\Delta X\Delta Z \quad (24)$$

$$S = 2(1 - m)\Delta X \quad (25)$$

$$u_r = \frac{U}{m}, \quad w_r = \frac{W}{m} \quad (26)$$

where ΔX , ΔZ are the horizontal and vertical dimensions of the computational unit, respectively. Therefore, Eq.22 can be now expressed in terms of the flow parameters inside the porous media and the computational unit size as follows:

$$F_x = \rho \frac{(1-m)}{m} C_{MX} \frac{\partial U}{\partial t} \Delta X \Delta Z + \frac{1}{2} C_{DX1} \rho \frac{(1-m)}{m^2} U \sqrt{U^2 + W^2} Z + C_{DX2} \frac{3\rho v S}{D} U \quad (27)$$

Furthermore, the force per unit weight of the porewater (f_x) can be expressed as follows:

$$f_x = \frac{(1 - m)}{gm^2} C_{MX} \frac{\partial U}{\partial t} + \frac{C_{DX1}(1 - m)}{2m^3 g \Delta X} U \sqrt{U^2 + W^2} \Delta Z + \frac{3C_{DX2} v}{gmd} U \quad (28a)$$

$$d = \frac{m\Delta X\Delta Z}{S} \quad (28b)$$

By comparing Eq.28 with the horizontal equation of motion in the porous media (Eq.14), the coefficients E and F are now modified and can be expressed as follows:

$$E = \frac{3C_{DX2} v}{gmd} \quad (29a)$$

$$F = \frac{C_{DX1}(1 - m)}{2m^3 g \Delta X} \quad (29b)$$

The size of the computation unit should be selected such that the side length is not less than D and, therefore, the value of $\Delta X = \Delta Z = D$ has been used in Eq.29 to compute the resistance coefficients as shown in Eq.30. Consequently, the coefficients C_{MX} , C_{DX1} and C_{DX2} should be first estimated in order to be able to use the modified equations of motion.

$$E = \frac{6(1 - m)C_{DX2} v}{gm^2 D^2} \quad (30a)$$

$$F = \frac{C_{DX1}(1 - m)}{2m^3 g D} \quad (30b)$$

ESTIMATION OF THE RESISTANCE COEFFICIENTS

Using the experimentally measured values of the wave forces and water velocities, the values of the coefficients (C_{MX} , C_{DX1} and C_{DX2}) have been estimated for the previously described wave conditions by means of the least square technique applied to Eq.21. The corresponding values of these coefficients for the case of non-embedded spheres have been plotted against, the Keulegan-Carpenter number, KC_x in Figs. 2-4. The KC_x number is $U_m T/D$ where U_m is the maximum horizontal porewater velocity. Also shown are the data for the case of isolated spheres by Iwata and Mizutani (1989).

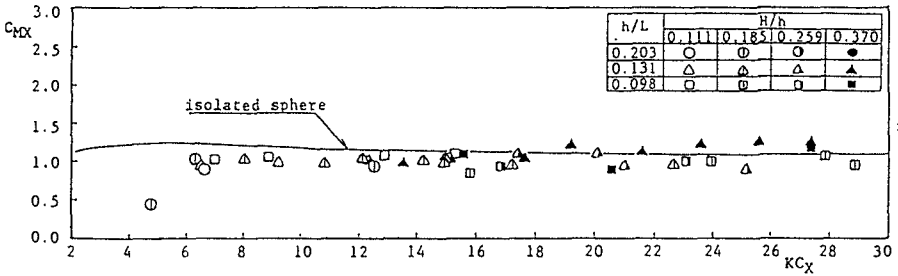


Fig.2 Coefficient of mass (C_{MX}) versus KC_x

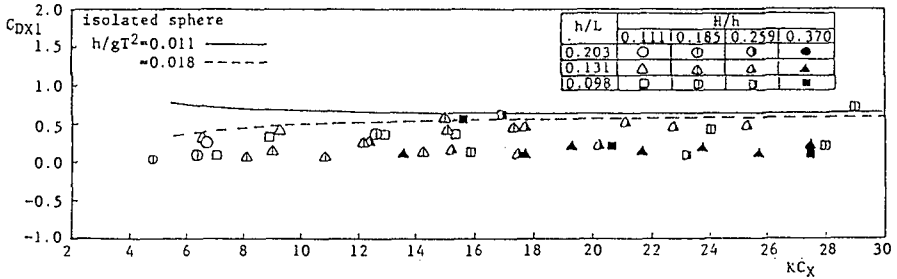


Fig.3 Coefficient of drag (C_{DX1}) versus KC_x

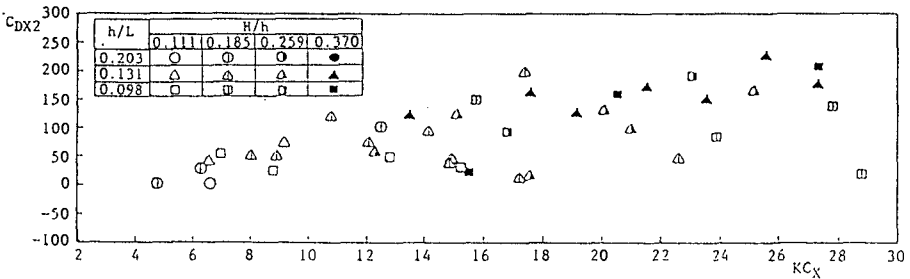


Fig.4 Coefficient of drag (C_{DX2}) versus KC_x

It is clear in Fig.2 that the value of C_{MX} is almost constant and independent of KC_x . Also, the values for isolated spheres and armor spheres are very similar. The value of C_{MX} has been estimated to be 0.96 ($C_{AX} = -0.04$) by taking the average over all computed values. This value has been used in the numerical model for comparison with the experiment.

The value of C_{DX1} ranges from 0.20 to 0.60 and is only weakly dependent upon KC_x as shown in Fig.3. The values of C_{DX1} for isolated spheres are generally higher than that for the armor units of a submerged breakwater. It is worth mentioning that the coefficient of drag C_{DX1} , formerly estimated by a standard Morison type equation and neglecting the linear friction term, experienced large scatter at small values of KC_x (Rufin et al., 1996). It has been estimated that $C_{DX1} = 0.45$ for use in the numerical model computations by taking the average over all the computed values.

The experimental results for C_{DX2} show large scatter, especially at large KC_x . The range is from a minimum of near zero for low KC_x to a maximum near to 200 for high KC_x . However, it has been found that the relative importance of the linear friction term including the drag coefficient C_{DX2} is very small at values of $KC_x > 10$, where flow separation occurs. Its effect is only considerable at low values of KC_x . Therefore, a value of $C_{DX2} = 25.0$ has been estimated for use in the numerical model by considering the average of its computed values for the range of $KC_x < 10.0$.

RESULTS AND DISCUSSIONS

The BEM-FEM model, employing modified resistance coefficients and their experimentally estimated values, has been used to model waves over a submerged breakwater. The comparisons with experimental results confirm the importance of the modified coefficients.

A velocity vector diagram and the wave profile along the wave tank at $t/T=5.0$ are shown in Fig.5. It is obvious that the water flows into the breakwater at the locations of the wave crests and flows out of it at locations of the wave trough. The areas over the leading edge of the crown and on the offshore slope have higher velocities than the other locations inside the breakwater. There is a rapid change in the free surface as the waves encounter the structure.

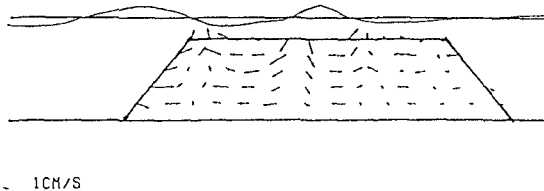


Fig.5 Wave deformation around and water velocity inside the breakwater at $t/T=5.0$ ($h/gT^2 = 0.029$, $H/h = 0.11$)

The computed and measured water surface levels over the crown of the breakwater at $X/L=0.30$ and $X/L=0.50$ for a wave height (H) 3.0 cm and period (T) 1.40 sec are plotted in Fig.6. The BEM-FEM model agrees well with the measured water levels along the crown of the submerged breakwater. The waves are very nonlinear and asymmetric. Computations have also been conducted to evaluate the average wave setup ($\bar{\eta}$) at $X/L=0.30$ and 0.50 over the crown. It is obvious that the differences between the BEM-FEM model results and the experiment are small (Fig.6).

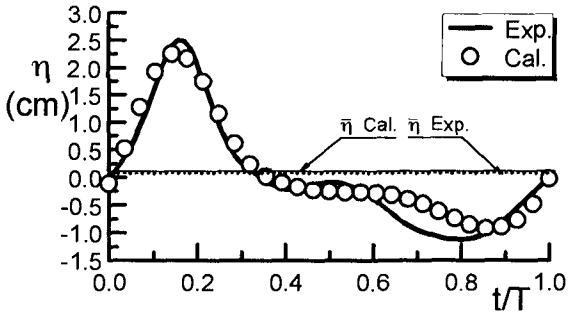


Fig.6a Free surface elevation at $X/L=0.30$ over the crown
($h/gT^2 = 0.015$, $H/h = 0.11$)

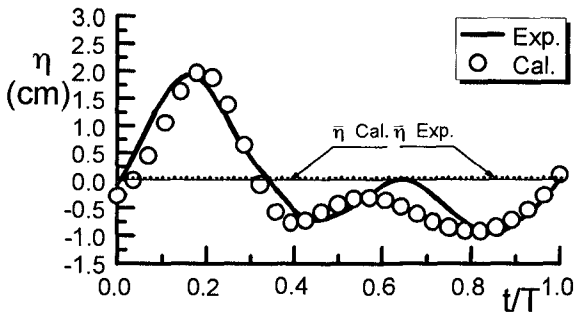


Fig.6b Free surface elevation at $X/L=0.50$ over the crown
($h/gT^2 = 0.015$, $H/h = 0.11$)

The value of η_{rms} along the wave tank has been used to represent the wave energy and comparison has been made between its measured and computed values along the wave tank (Fig.7). The measured and computed values are in good agreement. A partial standing wave is formed offshore of the breakwater and nonlinear wave damping occurs across the crown leading to a small transmitted wave to the lee side.

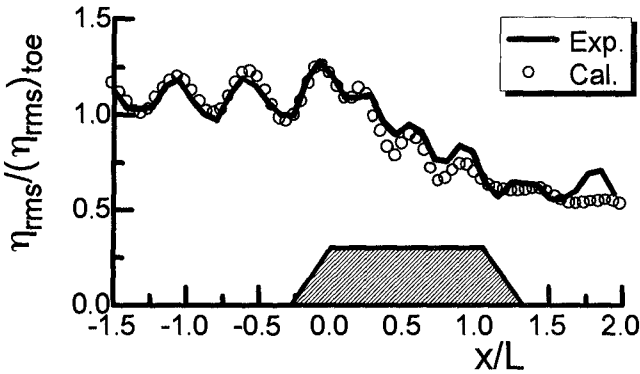


Fig.7 water level variation along the wave tank ($h/gT^2 = 0.015, H/h = 0.11$)

The computed and measured values for the maximum water particle velocity components (U_m and W_m) along the crown of the breakwater are shown in Fig.8. While U_m has been used to denote the maximum horizontal porewater velocity over the crown, W_m has been used to express the maximum vertical seepage velocity along it. The results are compared for a wave height (H) of 3.0 cm and period (T) of 1.0 sec. It can be observed that the numerical model results agree qualitatively well with the experimental ones. However, the values computed by the numerical model seem to be higher than that in the experiment. The velocities have been measured in the experiment at a small distance over the crown but, in the BEM-FEM model, the velocities have been computed exactly on the crown surface. It has been found that the locations of the maximum horizontal and vertical velocities are located at the offshore crown corner of the breakwater. This is in agreement with earlier investigations that have also proved experimentally that the point of maximum wave force is at the same location (Mizutani et al., 1992).

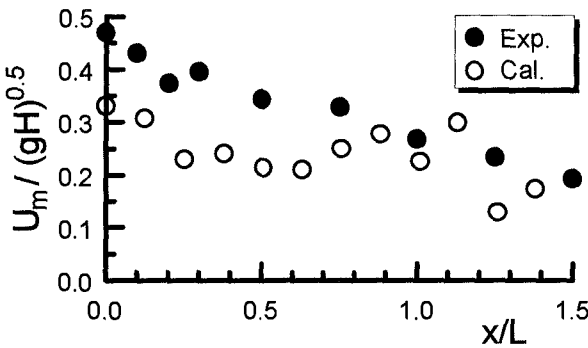


Fig.8a Maximum horizontal porewater velocity along the crown ($h/gT^2 = 0.029, H/h = 0.11$)

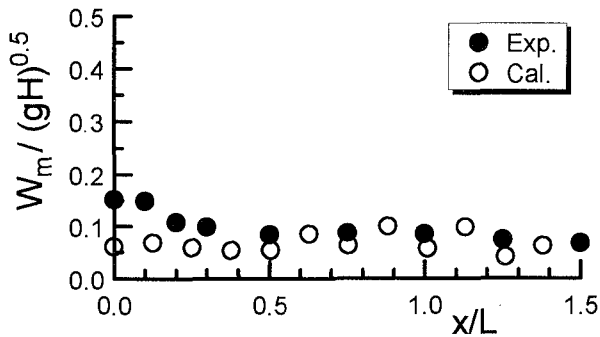


Fig.8b Maximum vertical seepage velocity along the crown
($h/gT^2 = 0.029$, $H/h = 0.11$)

CONCLUSIONS AND PERSPECTIVES

- 1) A numerical model is presented which simulates the nonlinear interaction between free surface waves and a submerged permeable breakwater. Modified resistance coefficients have been developed from experimental measurements and improved the results of the BEM-FEM model.
- 2) The model accurately predicts the partial standing wave that is formed offshore of the breakwater and the damping which occurs along it causing a small wave to be transmitted to the lee of the breakwater. The model can accurately estimate the transmitted wave height resulting from the combined effects of reflection, shoaling and dissipation.
- 3) The numerical model has been shown to compute with good accuracy the wave kinematics inside and around the submerged breakwater. Therefore, this model can be used further for studying the stability of the armor of the breakwater.
- 4) The point of maximum velocity along the submerged breakwater is at the offshore corner of the crown for all wave conditions tested in this study. As a result, the location of the maximum wave forces on the armor units is also at the offshore crown corner.
- 5) The model may be used to optimize the submerged breakwater shape, size and properties for site specific design requirements.

ACKNOWLEDGEMENT

The first author is grateful to and acknowledges the financial support of Kajima Foundation during his stay in Oregon State University at the initial stage of this research. The second author was supported by the Oregon State University Sea Grant Program. The authors are grateful to Prof. K. Iwata of Nagoya University for his valuable advice and guidance in this research.

REFERENCES

- Brebbia, C. A. and Walker, S. (1980). *Boundary element techniques in engineering*, Butterworths, London.
- Brorsen, M. and Larsen, J. (1987). *Source generation of nonlinear gravity waves with the boundary integral equation method*, Coastal Eng. 11, pp. 93-113.
- Cruz, E.C., Isobe, M. and Watanabe, A. (1992). *Nonlinear wave transformation over a submerged permeable breakwater*, Coastal Eng. 23, ASCE, pp. 1101-1114.
- Gu, G. Z. and Wang, H. (1992). *Numerical modelling for wave energy dissipation within porous submerged breakwaters of irregular cross section*, Coastal Eng. 23, ASCE, pp. 1189-1202.
- Hannoura, A.A. and McCorquodale, J.A. (1985). *Rubble mounds: numerical modelling of wave motion*, J. WatWay, Port, Coastal Ocean Eng., ASCE 111, pp. 800-816.
- Iwata, K. and Mizutani, N. (1989). *Experimental study on wave force acting on a submerged sphere*, Proc. of 8th Conf. on Offshore Mechanics and Arctic Eng., OMAE, pp.145-152.
- McCorquodale, J.A. and Hannoura, A.A. (1978). *Hydraulic conductivity of rockfill*, J. Hydraulic Research, No. 2, pp. 123-137.
- Mizutani, N., Iwata, K., Rufin, T.M., Jr. and Kurata, K. (1992). *Laboratory investigation on the stability of a spherical armor unit of submerged breakwater*. Coastal Eng. 23 , ASCE, pp.1400-1413.
- Mizutani, N., Rufin, T.M.Jr. and Iwata, K. (1994). *Stability of armor stones of a submerged wide-crown breakwater*, Coastal Eng. 24 , ASCE, pp.1439-1453.
- Mizutani, N., Goto, T. and McDougal, W. (1995). *Hybrid-type numerical analysis of wave transformation due to a submerged permeable structure and internal flow*. Proc. of Coastal Eng., JSCE, Vol. 42(1), pp.776-780. (in Japanese)
- Ohyama, T. and Nadaoka, K. (1991). *Development of a numerical wave tank for analysis of nonlinear and irregular wave field*, Fluid Dynamics Research 8, pp. 231-251.
- Rufin, T.M. Jr., Mizutani, N. and Iwata, K. (1996). *Estimation method of stable weight of spherical armor unit of a submerged wide-crown breakwater*, Coastal Eng., Elsevier, Vol.28, pp. 183-228
- Sakakiyama, T., Kajima, R., and Abe, N. (1991). *Numerical simulation of wave motion in and near breakwaters*, Proc. of Coastal Eng., JSCE, Vol.38(2), pp. 545-550. (in Japanese)
- Sakakiyama, T. (1992). *Numerical analysis of wave disintegration due to submerged breakwaters*, Proc. of Coastal Eng., JSCE, Vol. 39(2), pp. 626-630. (in Japanese)

CHAPTER 185

Regulation of Nearshore Circulation by Submerged Breakwater for Shore Protection

Hisamichi Nobuoka¹, Isao Irie², Hajime Kato¹ and Nobuo Mimura¹

Abstract

A submerged breakwater induces a circulation with onshore currents over the structure and offshore currents through gaps, resulting in sediment loss to the offshore region. A new submerged breakwater with inclined multiple blades is tested by laboratory experiments and numerical simulations. This breakwater can generate offshore currents over the structure and onshore currents through gaps suggesting onshore sediment supply.

1. Introduction

Submerged breakwaters and artificial reefs have been widely constructed to prevent coastal erosion without spoiling landscapes of coast. However, wave set-up induced in the onshore area of the structure by wave breaking often generates strong nearshore circulation. The directions of cross-shore currents of the circulation are onshore above the structures and offshore in their gaps (**Figure 1(a)**) (Browder, 1996; Uda, 1987).

These currents reduce the efficiency of shore protection, since the current crossing over the structure does not bring sediment onshore, while the offshore current takes sediment away to the offshore. If an opposite pattern of circulation, in which the direction of flow is onshore in the gaps of the structures (**Figure 1(b)**), can be formed, sediment will be supplied from offshore to onshore. In order to generate such current, it is need to develop a structure which dose not induce wave set-up in the onshore area. Authors have proposed such structures (e.g. Irie 1991).

This study aims at finding a technical solution which can meet the above requirement to control current's direction. To this end, a new

1 Dept. of Urban and Civil Eng., Faculty of Eng., Ibaraki University Nakanarusawa, Hitachi, Ibaraki, 316, Japan

2 Dept. of Civil Eng. Faculty of Eng., Kyushu University, Hakozaki, Fukuoka, 812, Japan

submerged breakwater with multiple inclined blades shown in **Figure 2** is proposed.

In the study, experiments were performed to measure the wave set-up and patterns of the induced circulation around a structure in a wave flume and a wave basin. Numerical calculations using a two-dimensional model were also performed to simulate the nearshore currents around a structure. Finally, the functional capacity of these structures for shore protection was evaluated on the basis of the numerical simulation.

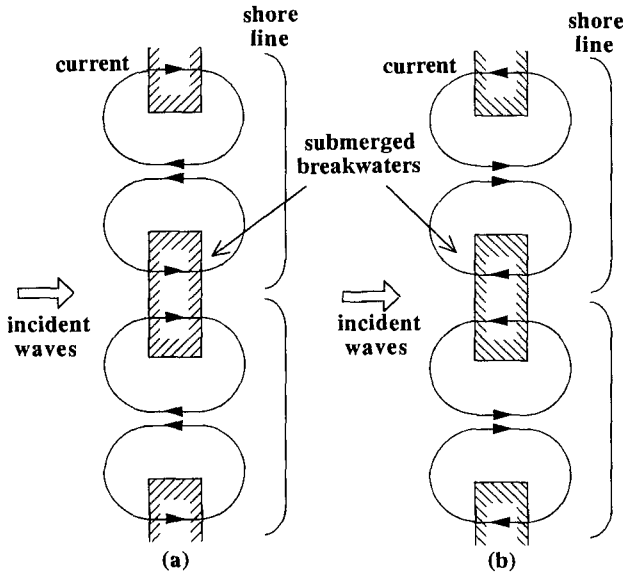


Figure 1 Patterns of nearshore circulation

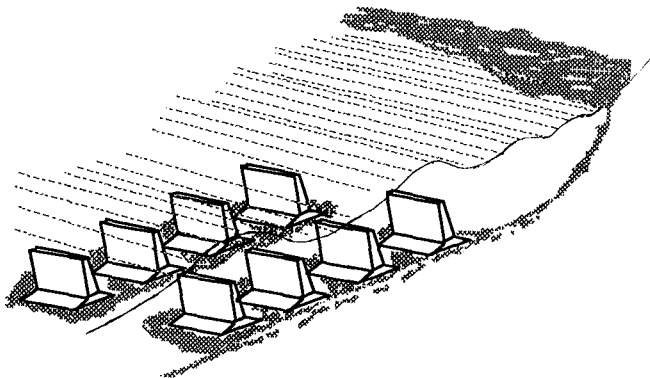


Figure 2 Sketch of a new submerged breakwater with multiple inclined blades

2. Methods of Experiments for Wave Set-up and Currents

Experiments were performed to examine the distributions of wave height and wave set-up and set-down around breakwaters under the condition of the uniform water depth ($h=0.35\text{m}$) in a wave flume whose length, width and height were 35m, 0.3m and 0.5m respectively. The structures examined were an artificial reef and four types of new submerged breakwaters with multiple blades; a type of blades was upright, and the others were inclined offshore as shown in **Figure 3**. The angle of blades was 15° , 30° and 45° . The height (D), spacing of the blades (B) and total length of the body (WT) was $0.5h$, $2.0h$ and $6.0h$ respectively. Each structure was set in the flume at the point of 12m onshore from the wave maker. In each case, the condition of incident waves was 6.0cm in height, and 1.02, 1.27 and 1.83s in period. Fluctuations of water surface were measured around the structure at intervals of 7cm, i.e. $0.2h$.

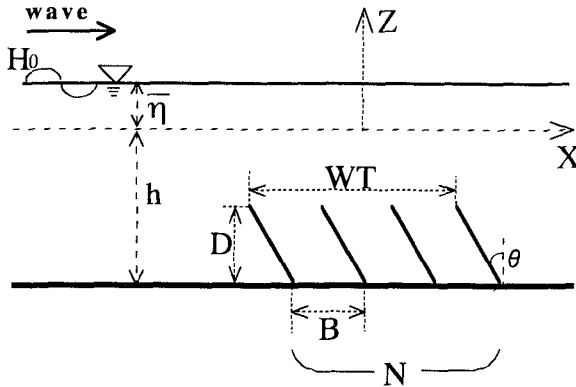


Figure 3 Scale of multiple blades

Another experiments were performed to measure currents around the breakwaters in a wave basin with a uniform water depth ($h=0.1\text{m}$). The basin was 246cm long, 170cm wide and 30cm high, and was equipped with a wave maker, wave absorber and filter as shown in **Figure 4**. In the experiments, models of detached breakwater ($20\text{cm}\times 60\text{cm}$), artificial reef ($60\text{cm}\times 60\text{cm}$, 6.5cm high) and multiple blades ($60\text{cm}\times 60\text{cm}$, 6.5cm high, $\theta=30^\circ$, $B=2.0h$) were set in the center of the wave basin. The conditions of incident wave were 1.7cm in height and 1.1 and 0.76s in period.

To measure the patterns of currents, floats having a diameter of 1cm were used. The weight of the floats was adjusted so that they stayed in the surface layer and bottom layer respectively. The movement of the floats was recorded by a video camera, and traced at an interval of 5 or 20s.

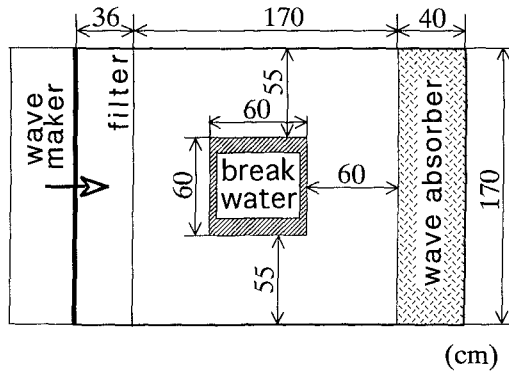


Figure 4 Experimental wave basin

3. Wave Set-up and Set-down Around the Multiple Inclined Blades

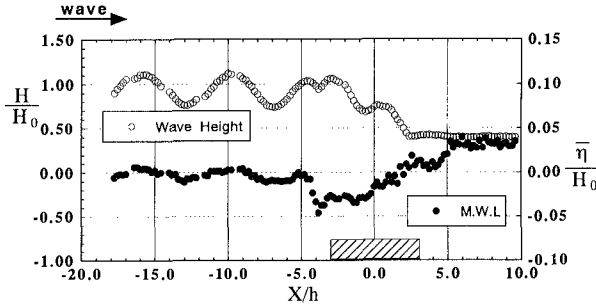
Figure 5 shows the distributions of wave heights and mean water level around the artificial reef (a) and multiple blades inclined by 30° (b).

In the case of artificial reef, wave transmission coefficient is approximately 40% and standing waves is observed in the offshore side. On the other hand, for the multiple blades, the transmission coefficient is approximately 70% and no standing waves form. The coefficient changed from 60 to 70% with blade slant angle and wave period.

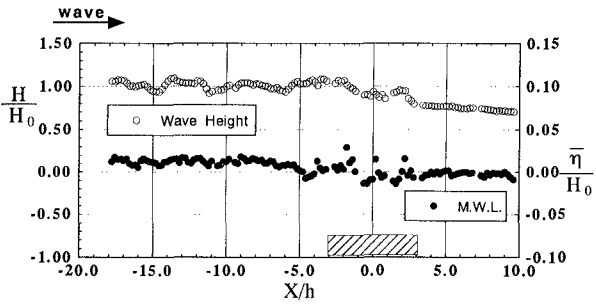
It was found by observation of the water motion that strong wave breaking occurred on the reef. On the other hand, at the top of the multiple blades, large eddies occurred. It can be concluded that the decreases in wave height were caused by wave breaking and reflection for artificial reef and eddy formation for multiple blades.

Regarding the mean water level distributions, wave set-up occurred in the onshore area in the case of reef. While, for the case of multiple blades, the mean water level decreased gradually in the onshore direction. Wave set-down occurred in the onshore area.

For all cases of blade's slope type and wave conditions, the mean water level is rather constant except just above the breakwater. Figure 6(a) shows the difference between the mean water levels of offshore and onshore sides around the five structures, respectively. Since the water depth is constant, it was taken as the reference level. The distribution of mean water level around the structure varies systematically depending on structure's type and the slope of the inclined blades. In the case of the reef, wave set-up occur in the onshore area. For the breakwaters with blades, the larger is the blade slope, the lower is the wave set-up in the onshore area. Even wave set-down takes place for the blade slopes of 30° and 45° .



(a) artificial reef



(b) multiple blades ($\theta = 30^\circ$, $T = 1.1s$)

Figure 5 Distribution of wave height and mean water level

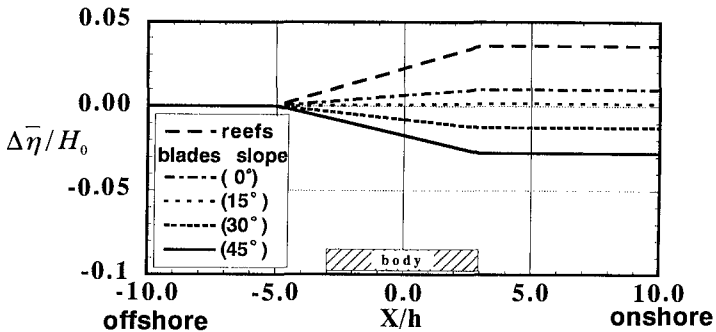


Figure 6(a) Difference in mean water level around the structure

The results of the cases with different wave periods are shown in Figure 6(b). The horizontal axis is a wave period and the vertical the difference in mean water level. The same tendency as mentioned above was obtained; when the slant of blades is large, the wave set-down is also large. This tendency becomes more profound as the wave period becomes large.

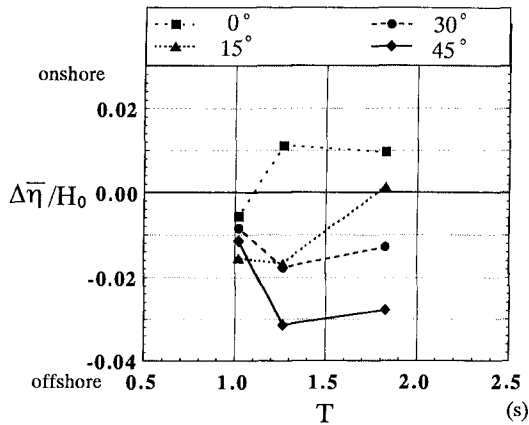


Figure 6 (b) Difference of mean water level in all the case of multiple blades

4. Experimental Results on Nearshore Currents

Figure 7 (a),(b),(c) show the currents at surface layer around the detached breakwater, the reef and multiple blades inclined by 30°. The wave conditions are $H=1.7\text{cm}$ and $T=1.1\text{s}$. Filled dots in the figure indicate the location of floats at an interval of 5 or 20 seconds and the square in the center of figure shows the corresponding structure.

Around the detached breakwater (**Figure 7(a)**), the flow is so weak that a circulation is not very clear. At the side of the structure, onshore and offshore currents occur near the structure and far away from the structure.

For the case of the artificial reef (**Figure 7(b)**), a clear circulation is formed around the reef, in which currents flow in the onshore and offshore directions above the structure and on its both sides, respectively. The directions of the circulation at the bottom layer were same as that of the surface layer.

A completely opposite pattern of circulation is generated for the case of breakwater with inclined blades by 30° as shown in **Figure 7(c)**; the current flows to the shore through the gaps, and juts out over the blades. In the bottom layer except above the structure, the flow is very weak and goes toward onshore. The case with different wave condition, which is 0.76s in wave period, is shown in **Figure 7(d)**. Though a pattern of circulation around the multiple blades was not so clear, the pattern of currents was same as that in the case of wave period which was 1.1s.

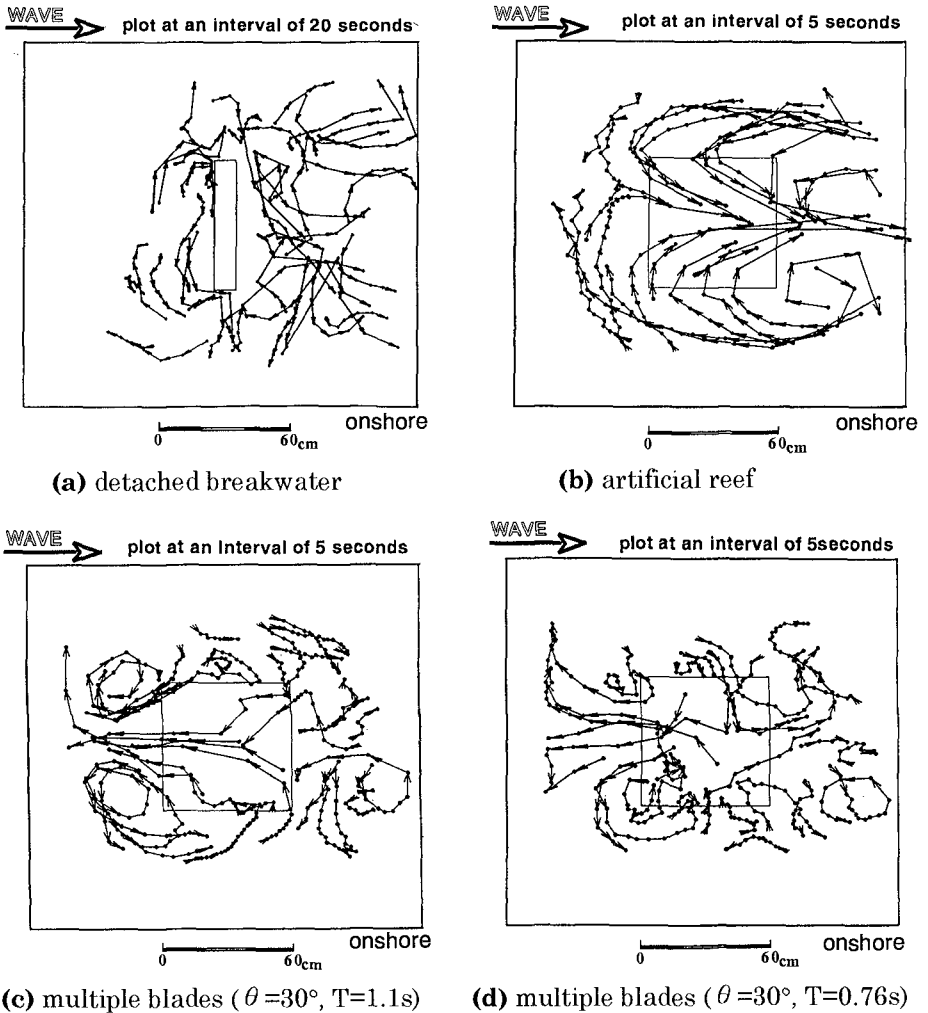


Figure 7 Nearshore currents around the structure (experiment)

5. Evaluation of Functional Capacity of Currents for Shore Protection

In order to study the currents around the submerged breakwaters in detail, a numerical model was developed.

5-1. Government Equation

Equations of conservation of mass and momentum (1), (2) and (3) for nearshore currents were used, with two additional terms to express special conditions imposed by the existence of the breakwater.

$$\frac{\partial \bar{\eta}}{\partial t} + \frac{\partial u (\bar{\eta} + h)}{\partial x} + \frac{\partial v (\bar{\eta} + h)}{\partial y} = 0 \quad (1)$$

$$\frac{\partial u}{\partial t} + u \frac{\partial u}{\partial x} + v \frac{\partial u}{\partial y} + F_x - M_x + S_x + g \frac{\partial \bar{\eta}}{\partial x} = 0 \quad (2)$$

$$\frac{\partial v}{\partial t} + u \frac{\partial v}{\partial x} + v \frac{\partial v}{\partial y} + F_y - M_y + S_y + g \frac{\partial \bar{\eta}}{\partial y} = 0 \quad (3)$$

where, u , v are x and y components of the velocity, $\bar{\eta}$ mean water level, F_x , F_y bottom friction, M_x , M_y horizontal mixing terms, and S_x , S_y radiation stress term. The bottom friction was formulated according to Longuet-Higgins(1970) with the Manning roughness coefficient being $0.013[\text{m}^{-1/3}\text{s}]$. These equations were calculated by ADI method.

5-2. Special Term

The one of special terms is needed to express the onshore momentum transport due to strong wave breaking above the reef. If this effect is not introduced, the reproduction of the flow is insufficient (Sasaki, 1990). In this study, this phenomenon was expressed by increasing the gradient of radiation stress at onshore side from wave breaking point.

The other special term is to express the mean resistance force of the inclined blades which appears as a residual stress over a period. This mean force was caused by the difference in the resistance force between the onshore and offshore directions. When the direction of water particle's motion is the same as the blade's inclination, the resistance force acting on the water mass is weak(**Figure 8(a)**). On the other hand, when the direction of flow is opposite to the blade inclination, the resistance force becomes strong(**Figure 8(b)**). Such a mechanism, therefore, can induce the difference of onshore and offshore resistance forces in a wave period. Since the offshore resistance force is stronger than onshore one, the blades exert offshore force on the water body and cause wave set-up on the offshore side.

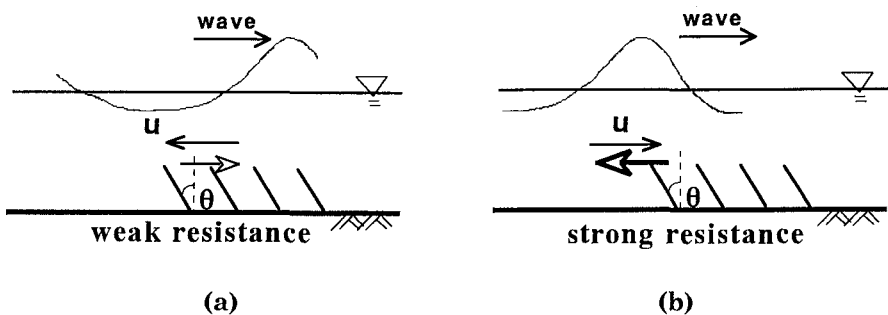


Figure 8 Generation of the offshore residual resistance force

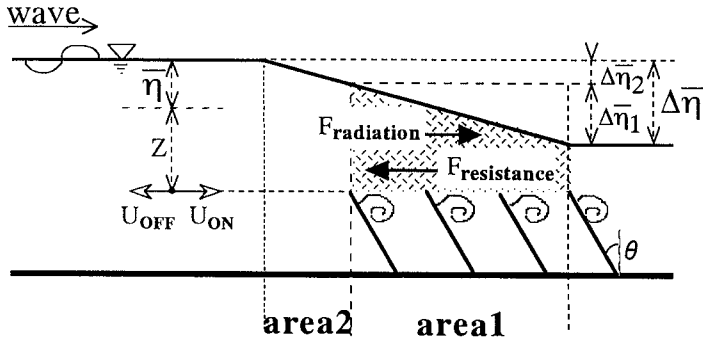


Figure 9 Balance of power around the multiple blades

It is assumed that the onshore and offshore resistance forces caused by blades are proportional to the square of the horizontal velocity of wave motion, and act in the direction opposite to the flow above the blades. It is also assumed that the resistance force integrated over the period of onshore or offshore flow is also proportional to the square of the maximum velocity in the corresponding period. The residual resistance force can be, therefore, evaluated by the difference in the square of maximum velocity. In this study, the horizontal maximum velocity was calculated by second-order stokes wave theory.

The three forces, which are the gradient of hydrostatic pressure, the gradient of radiation stress and the resistance force, balance near the multiple blades. This relation in area 1 shown **Figure 9** can be formulated as **Equation 4**.

$$g (\bar{\eta} + h) \frac{\Delta \bar{\eta}_1}{\Delta x} = - \frac{1}{\rho} \frac{\Delta S_{xx}}{\Delta x} + C_\alpha D \sum_1^N (u_{on(max)}^2 - u_{off(max)}^2) \quad (4)$$

The left hand side is the gradient of hydrostatic pressure. The first and the second terms in the right hand side are the gradient of the radiation stress in the water column on the blades and the mean resistance force in a wave period, respectively. C_α is a kind of resistance coefficient and was obtained by a least squares method for the cases of different blades angle.

Mean water level varied even in the offshore area of the structure, which is indicated as area 2 in **Figure 9**. It is assumed that the resistance force also acts this area. The balance of forces in area 2 is, therefore, formulated in the same way as Equation (4) using a coefficient of C_β instead of C_α , although the water depth is different from the area 1.

$$C_\alpha = -0.010 \times \theta - 0.016 \quad (5)$$

$$C_\beta = -0.013 \times \theta - 0.022 \quad (6)$$

here, the unit of θ is degree.

When the simulation of nearshore currents around the multiple blades was performed using the government equations with this resistance term, the velocities of flow became too strong. This is because the present model includes only the resistance force caused by wave motion, and does not take into account that by the currents. The coefficient of C_γ which modify the coefficient of C_α , C_β was evaluated so as to reproduce the currents well.

$$C_\gamma = 1.2 - 0.88 \times T \quad (7)$$

where, a range of a wave period, T , is from 0.76s to 1.1s for the water depth of 0.1m.

5-3. Results of Simulations for Nearshore Circulation

Figure 10(a) illustrates the currents around the detached breakwater. Very weak circulation flow occurred around the body.

For the case of artificial reef, a clear circulation was formed as shown in **Figure 10(b)**. The direction of circulation is onshore above the structure and offshore both sides of structure.

On the other hand, for the case of multiple blades, a completely opposite pattern of circulation was generated as shown in **Figure 10(c)**; the current flow to the shore through the gaps, and juts out over the blades. For the case with different wave period, the circulation was not much clear, but the same pattern appeared (**Figure 10(d)**).

These results of simulations show fairly good agreement with those obtained by experiments.

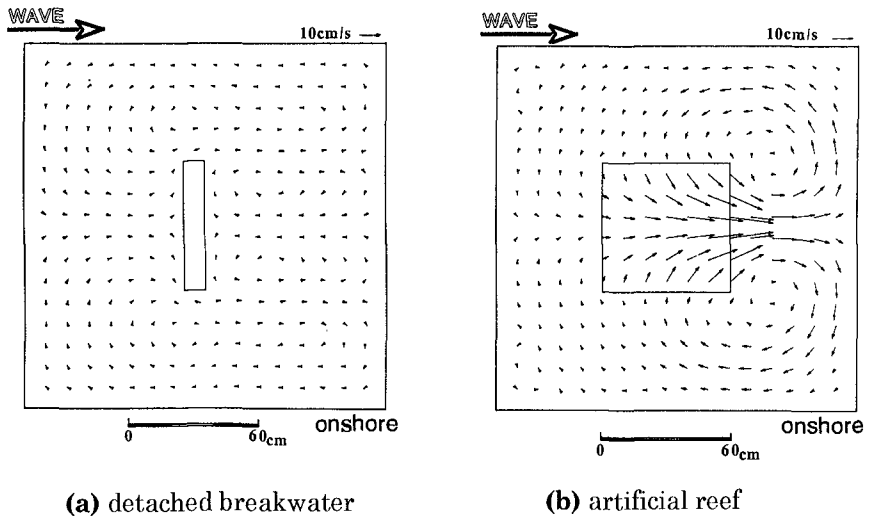
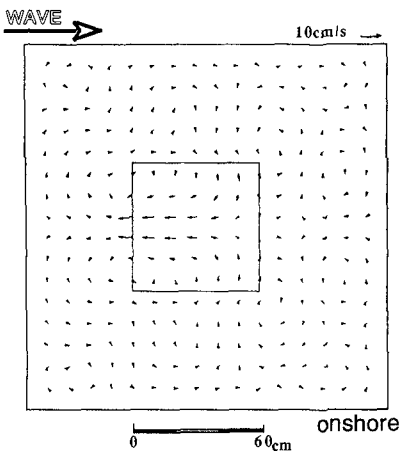
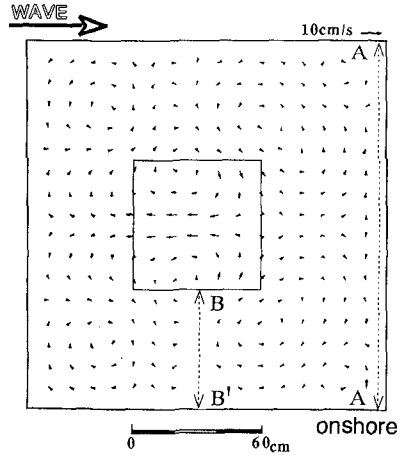


Figure 10 Nearshore currents around the structure (simulation)

(c) multiple blades ($\theta = 30^\circ$, $T = 1.1$ s)(d) multiple blades ($\theta = 30^\circ$, $T = 0.76$ s)

Continue Figure 10

5-4. Functional Capacity of Currents for Shore Protection

The effect of the induced currents for shore protection is evaluated on the basis of the result of the calculation. There are two disputed points; the one is wave set-up near shoreline, and the other is currents on the sides of breakwater. The examined structures were the detached breakwater, the artificial reef and the new submerged breakwater with multiple blades.

Wave set-up near the shoreline causes shoreline retreat, and the difference in wave set-up along the shoreline induces strong longshore currents which transport the sediments.

The wave set-up at line A-A' in **Figure 10(d)** are showed in **Figure 11**. The horizontal axis is long shore distance and the square of the center indicates the position of the structure. For the case of reef, highest wave set-up appears. On the other hand, for the case of multiple blades and detached breakwater, wave set-up was low, and the difference of mean water level in longshore direction was small, that indicates the beach would be protected.

The offshore currents on the side of the structure bring sediment offshore, resulting in shore erosion. The flow rates across the line B-B' in **Figure 10(d)** are indicated in **Figure 12**. The vertical axis shows the cross-shore flow rates; a positive value indicated the onshore flow rates.

In the cases with detached breakwaters and multiple blades inclined by 15° , no or little currents occurred, so there are no bars on the graph. The case of artificial reefs shows strong offshore currents. For the case of multiple blades, with the blade angle, the onshore currents become stronger. For the

case of multiple blades inclined by 45°, most strong onshore currents occur. It may be expected that the onshore currents supply sediment onshore.

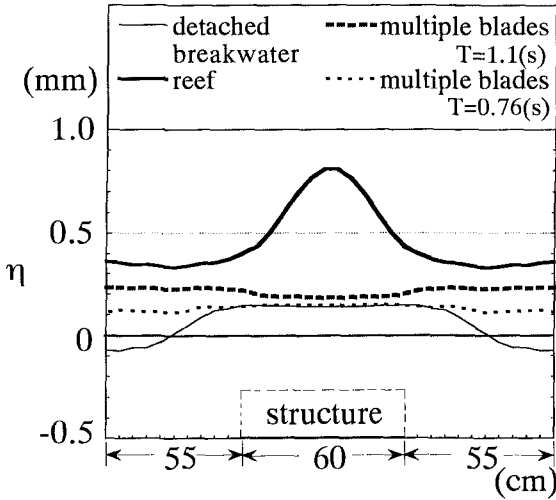


Figure 11 Wave set-up near the shoreline

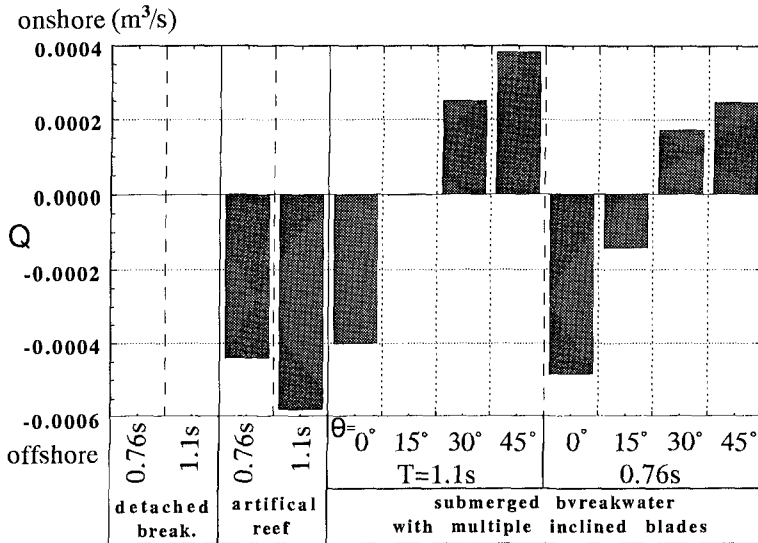


Figure 12 Cross-shore flow rates on the side of structure

6. Conclusions

This study confirmed the principle and effectiveness of a new type of breakwater with multiple blades to generate a preferable circulation pattern for preventing beach erosion. Three points should be emphasized as the conclusions of this study.

1. Wave set-down occurred in the onshore area of the new submerged breakwater with multiple inclined blades in laboratory experiments with a two-dimensional wave flume.
2. The direction of nearshore circulation around the multiple inclined blades is offshore above the structure and onshore on the sides of the structure. This pattern of the flows is opposite to that of nearshore circulation induced by artificial reefs.
3. The structure with multiple blades inclined by 45° caused the most strong onshore currents on the side of structure, which suggested that onshore transport of sediments was expected.

Reference

- Browder A. E., R. G. Dean and R. Chen(1996):Performance of submerged breakwater for shore protection, Book of abstracts 25th ICCE, ASCE, pp.244-245
- Irie I., H. Nobuoka, H. Kojima and Y. Mihara(1991):Wave attenuation by deeply submerged plates, Proc. of 38th Japanese Conf. on Coastal Eng., JSCE, pp.561-565(in Japanese)
- Longuet-Higgins M. S.(1970):Longshore currents generated by obliquely incident sea waves, 1, Journal of Geophysical Research Vol.75, pp.6778-6789
- Sasaki M., A. Sato and A. Takeshita(1991):Numerical simulation of nearshore dynamics around a submerged breakwater, Proc. of 37th Japanese Conf. on Coastal Eng., JSCE, pp.404-408(in Japanese)
- Uda T., A. Omata and Y. Yokoyama(1987):Nearshore current and topographic change around artificial reefs, Proc. of 34th Japanese Conf. on Coastal Eng., JSCE,pp.337-341(in Japanese)

CHAPTER 186

Submerged breakwaters for the defence of the shoreline at Ostia Field experiences, comparison

by

Ugo Tomasicchio, Member ASCE ¹

Summary

An important study case with different defence structures and the results of the monitoring data of are reported. Field experiences are specially usefull to compare two soft structures used to defend the Lido of Ostia, i.e. the coastline of Rome at the mouth of river Tevere (Tiber)²

Introduction

Erosion phenomena along the almost 7500 km of the Italian coast are widespread and certainly have been increasing more and more during the last decades. The main causes of this aggravation are the large number of protection works against the landslides, the use of material from the river basins for building purposes and the construction of reservoirs for water supply.

Disappearance or reduction of the sandy beaches often determines a too heavy damage for the economy related to the tourism. This encourages the State or the local administrations to try to contrast the phenomena. A large number of defence interventions has been realized starting since the sixties and their importance and cost have been raising through the years. Adopted techniques have been paying an increasing attention to the results effectiveness and to the costs benefits optimization. For this last evaluation, the environmental parameters have assumed a big importance. In fact, it is clear that every defence intervention in areas which have particular tourist attractions can only be directed towards protection and, possibly, improvement of these amenities. During the recent years, the deeper attention for the environment has induced preference for soft structures like the beach nourishment and the submerged breakwaters. Even if the experience from the wide use throughout the sixties to the

¹ Politecnico di Bari, via Re David 200, 70125-Bari, Italy.

² Rome was for many centuries the *Caput Mundi* = Capital of the World (Tiber is the name in latin language; in the Roman time usual its pronunciation was Tiver, from wich many scholars consider to deduce the common name river).

eighties of the detached emerged breakwaters is only sufficient, this structure resulted to be effective for the defence of eroded beaches with a reasonable cost. A detached emerged breakwater interrupts the natural sediment longshore transport therefore the sand material which is entrapped in the sheltered area is subtracted to the downdrift coastline.

This phenomena, like the domino game, is visible at most of the Italian coasts and has given extension of this type of structure to very long coastlines (e.g. the Adriatic coastline).

Of course, their environmental result is not highly appreciated. In fact in addition to an inconvenience in the sometime wonderful seaweaves, the emerged breakwaters have often induced a worsening of the water quality in the protected area together with a strong and fast erosion phenomena at the openings between the barriers.

If the second effect, as well known, gives troubles to the swimmers, the first can induce the Health Authority to forbid the recreational use of the beach. If we realize that, generally, the defence work aim is to preserve the beach for a recreational use, the previous discussion shows, *ad abundantiam*, the unacceptableness of the emerged structures. In fact, during the Summer season, the water circulation, which is ensured only by the openings, is often insufficient for a tendentially eutrophic water. These are some of the reasons which have driven to the use of soft defence interventions, like the combination of a beach nourishment with the submerged breakwaters.

Sand material which is compatible for a beach nourishment can not easily be found in the Italian seas. Therefore, the required large volumes of necessary material for a beach nourishment are usually taken from quarries whose travel distance from the intervention area is giving sometime a too high cost. Use of the quarry must consider that the Italian territory is highly used for different purposes and, environmentally speaking, the areas still free of buildings are not less important and sometime they are in a preserved zone. On the other hand, the submerged detached breakwaters offer big benefits. They can be considered as soft structures; in fact, their environmental impact is soft (nature uses the coral reef) and they offer a low cost and effective defence of the beaches. The submerged breakwaters have been recreating sandy beaches which were completely lost with only a small negative impact on the adjacent coastline and, more important, without any reduction of the water circulation in the sheltered area during the summer. These benefits are attainable under the condition of a careful structure design. The design should consider the stability of the rubble mound, the transmission coefficient (which is related to the crest width, its submergence and wave climate) and the verification that the residual wave energy is not able to erode further the beach.

Many laboratory tests and field study have been carried out in Italy. The results from these studies allowed a verification of the indications published on this subject since the seventies and a better calibration of the relationships used for the design. Obviously, the field gives the best results for the interpretation of the phenomena and the calibration of the interventions.

The present paper aims to refer about and to discuss one of the most noising Italian defence work intervention. In particular, the purpose is to carry out a technical economical comparison between two different defence structures (beach nourishment

with reef and submerged breakwater) which have been built along two adjacent coastlines at Ostia (Roma). Their behaviour we compare. The first is an expensive - composite structure (beach nourishment and submerged barrier or reef defending a 3 km stretch). The second is a submerged rubble mound breakwater defending a 1 km long stretch. Results obtained suggest a preference for the second cheaper structure.

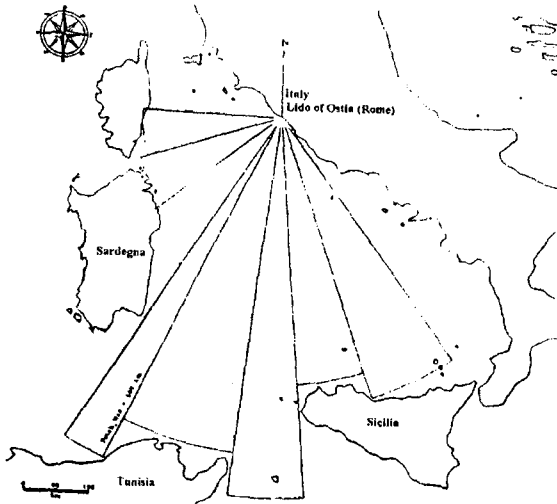


Fig. 1 The site of Lido of Ostia in front of Tirrenian sea

The littoral of Ostia

The littoral of Ostia extends itself to South-west and to South-east of the two mouths in which the sacred river Tevere forks itself, before flowing into the sea.

History says that the area around the river mouth has always been extending seaward.

The increment of the distance between the shoreline and the antique port of Ostia, the port of Rome at Empire time, was very rapid, causing not few problems to the transport from the Africa and Sicily regions of the provisions for the two millions of citizens.

Fig.2 (an old map of year 1680 by Mayer) shows the distance between the ports of Traiano and Claudio (Roman Emperors of the first century a.C.) and the sea. It's interesting to remember that the Port of Traiano and the next of Claudio were interested by silting up, soon after the end of their construction.

In fig. 3 (Caputo and al., 1992) the shoreline changes among 1873 and 1987 are represented. So, until year 1950, a shoreline advancement of about 2-3 m/y it has verified. No more accretion of the land area after 1950, due to the drastic reduction of the sediment transport from the river Tevere (use of material from the river basin for building purpose and the construction of about 20 reservoirs for water supply).

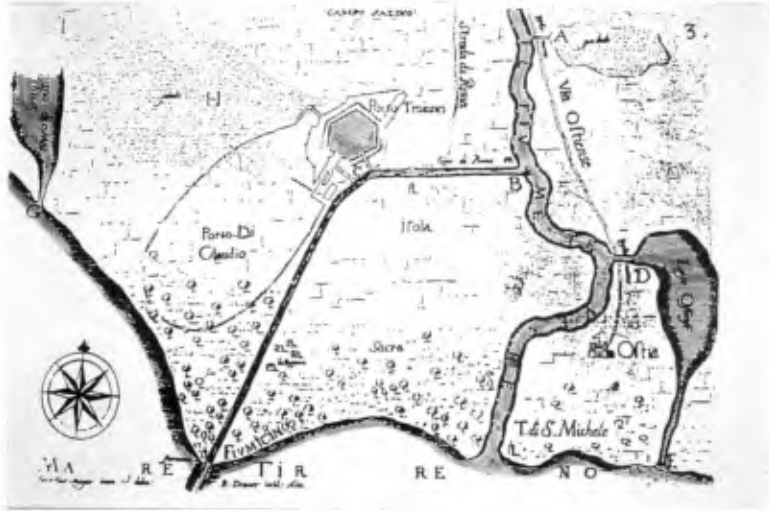


Fig. 2 Coastline as in old Map of Mayer (1680)

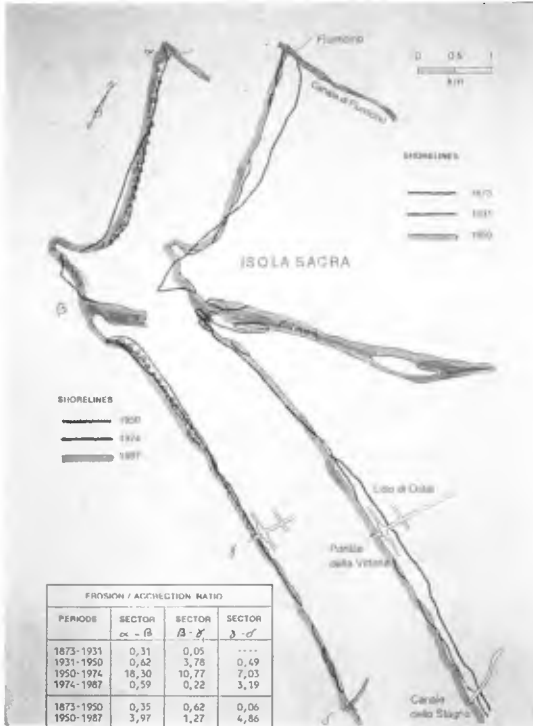


Fig. 3 Shoreline changes in the last century and in the last decades

Actually the river bed of the terminal zone has retreated, on the average, of 2 meters and the sediment transported by river has a very little size, not sufficient to stay in the inshore zone.

The result of this new situation was the erosion of the beach, in the left of the fig.3.

In the fig.4 the Lido of Ostia from the Nautical Map of 1983 is reported; in the same map four zones are distinguished (A, B, C, D) according to the years of the construction of the defence structures (the letters from A to C indicate the real time sequence of the building).



Fig. 4 Shoreline in a map of 1983. The four zones A,B,C,D.



Fig. 5 In the map of Consiglio Nazionale delle Ricerche, many results of study.

In the map (fig.5) many results of investigations and studies by National Research Council are presented: arrow shows the direction of the net longshore transport, as monitored by the sedimentologist research group.

Defence works in two last decades

To stop the shore erosion and its unacceptable effects, some defence structures were built, beginning from the years seventies; in the eighties was an hard structure consisted in a few segments of detached emerged rubble mound breakwaters (about one meter over the m.s.l.) founded in 2-3 meters depth with the crest 3-5 meters width.

Each one of the four zones (fig. 4) corresponds to a different defence structure used. The emerged detached breakwaters are in the **zone A**.

That hard structure, being the first structure downdrift to the mouth, was able to capture large volume of sediment transported by longshore and to enlarge the beach. Such design solution corresponds to the people request of that time.

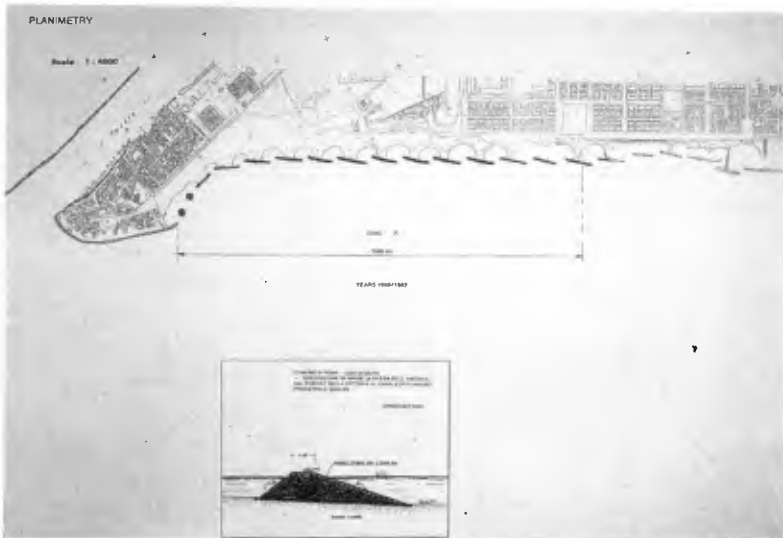


Fig. 6 Aerial photo of zone A and cross section of the emerged segmented breakwater

Aerial photo (fig.6) shows the increase of land **area A** with the formation of the tombolos.

This result is good for the defence of the beach from the erosion but is not well accepted for the bathing use of the sea water in the tombolo areas. In fact, these areas are too receptive to the bacterial colonies, and so they are interdicted to the bathers like dangerous for their healthiness. (Italian law permits the water bathing use only if the number of the bacteria coli, per liter, is less than 100; for many other national laws - as in USA - is 500/liter). Also the emerged rubble mound breakwaters are very good sites for the development of the bacterial colonies (especially in the sea level exchange band by tide).

It's clear that each one structure, going from North to South, has conditioned the downside structure behaviour.

New design demands. Soft structures for the defence of the zones B and C.

In the second part of the years '80, the demand of more space for the recreational use of the beach increased very fast; moreover, the environmental culture was more developed in the people. Consequently, in order to prevent the erosive action of the sea in the littoral of Ostia, where the sediment balance is poor, to reduce the impact of the works on the environment, to limit the effects on the adjacent beaches, to ensure the exchange of protected areas, many technical solutions were investigated.

Mathematical and physical models were used to study the beach stability and to reduce the cost (first and of the maintenance) of the intervention.

The preference went, not without oppositions, to the soft structures, and mainly to the beach nourishment.

But, where to find the borrow areas for so large volume of suitable sand for an artificial beach, both from a quantitative as a qualitative by?

Many environmental investigations, supported by scientific criteria, were done; the search of the suitable sand was very difficult and the results suggest to take all the necessary materials from the land quarries (that means a greater cost of the intervention), relying the artificial beach nourishment and submerged rubble mound (a reef), as in fig. 7 for the **zone B**, 3000 m. long.

The width of the artificial beach in the design was of 40+90 m. (gravel and gross sand nourishment), while the crest of the reef was 15 m wide and 1,5 m deep under m.s.l. with the slopes $1/3$ seaside and $1/2$ landside on the bottom of about 4 m under m.s.l. (quarry stones among 5 and 1000 kg). The reef section hydraulic stability was tested in wave flume.

This solution was the more pleasant to the people of the bathers, but the question was: how will the reef be able to reduce significantly the wave energy and to maintain sufficiently stable that artificial beach through the years?

Due to the very high cost of the intervention, the Public Administration financed it as experimental project. Obviously a monitoring plan was also financed.

The construction was carried out 1989-1991 (not in the Summer season). But, already when the works were in progress and soon after, a not negligible erosion phenomenon started updrift (see aerial photos Fig. 9). The dimension of erosion pointed out the necessity of a periodic maintenance having a too high cost for the public administration.

So, in the 1992 decided to use a different cheaper soft structure to defend the neighbour new part of the coast, 700 m. long (zone C in fig. 8.). Fig. 8 shows also the cross section of the submerged breakwater used for the **zone C** and the aerial photos fig. 9 the shoreline exchanges between 1991 and 1995 years.

The depth of the crest of submerged barrier in this case was lowered only to 0,5 m under m.s.l., while the bottom is on 3 m about. In the zone C no artificial nourishment was done. Main reason of this decision was the reduced money availability. The first idea was to provide the artificial nourishment of the zone C, if necessary, in the future.

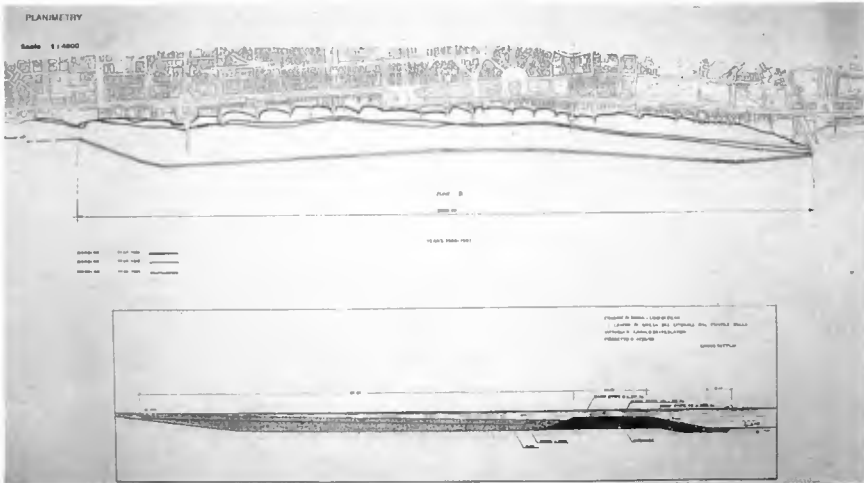


Fig. 7 Aerial photo of the zone B and cross section of the defence composite structure

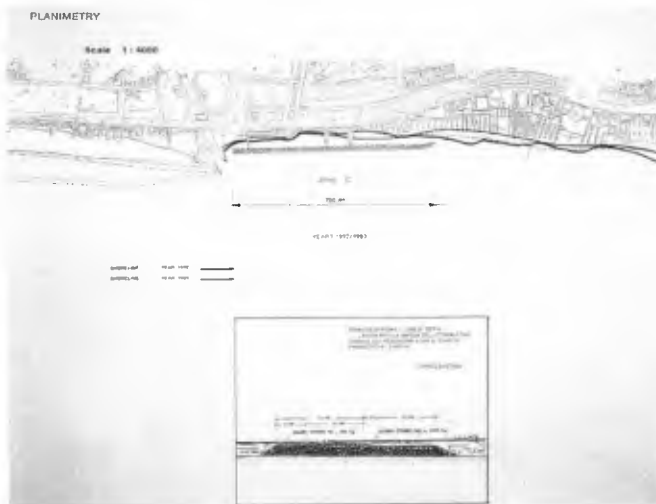


Fig. 8 Aerial photo of the zone C and cross section of the defence structure

It can be also observed that between the zones B and C there is a big groyne (the inlet of the Canale dei Pescatori) that reduces significantly the sediment transport capacity of the natural drift. In spite of this, not few inspectors hoped too much in submerged breakwaters defence action.

Pay attention that we distinguish between submerged barrier, like breakwater, and reef; the first is able to reduce significantly the wave energy, the second can not (in the submerged breakwaters depth of the crest has to be not large than 50 cm.).

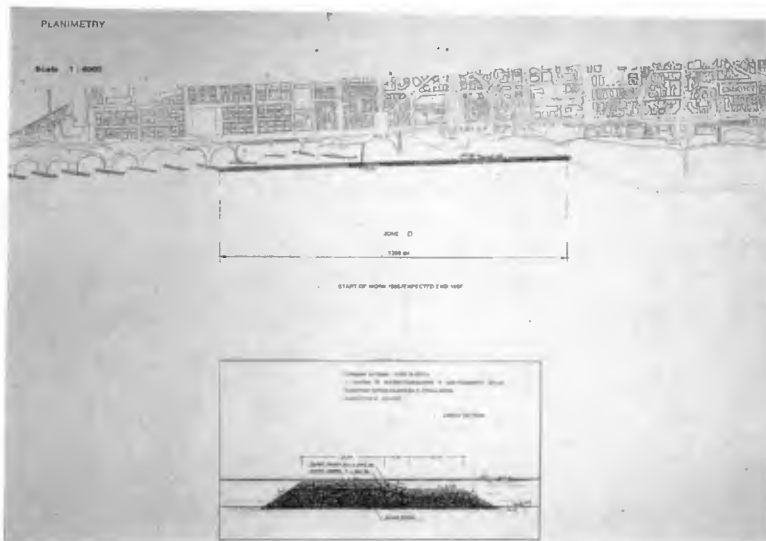


Fig. 9 *The Zone D - Works in progress*

Both the defence soft structures used for the zones B and C are able to assure the healthiness of waters in the protected areas.

In fact, thinking that the water transport by sea waves travels in maximum part on the surface, it means that a well designed submerged barrier can defend the shoreline stability by reducing the highest waves energy and can permit the transmission in protected area to the low waves mass transport (low waves and high temperatures are characteristic of Summer time in Italy) to assure a well exchange of water between offshore and inshore areas (id est the healthiness of recreational bathing water).

But, already at the end of the construction of the submerged rubble mound breakwater for the zone C, it was possible to see there a not little shifting of the shoreline seaward due to the natural sand capture.

Monitoring results

The aerial photos in fig. 10 show the shoreline exchanges of the artificial beach in the **zone B** between the years 1991-1995.

Cross sections (Fig. 11 and 12) northside and in the middle of the zone B taken in the year 1989 (before the works), in the 1992 (one year after the end of the works) and in the year 1995. Erosion action by waves is evident; southside is smaller due to long groin (at the inlet of the Canal).



Fig. 10 *In the aerial photographs the shoreline exchanges among 1985 - 1995 years*

The width of the emerged beach northside is reducing almost at the same size of the 1989; in all cases the erosion action by waves on the artificial beach is very clear both landside and seaside the reef.

As in Dean tests (1995), these results make evident that a similar reef can't defend the beach by waves and, also, breaking, does not reduce significantly the energy of waves passing in the area, increases the erosion in both sides; so, its presence can be, at the limit, dangerous rather than useful.

Viceversa, for the **zone C**, the defence utility of the submerged breakwater of the fig. 8 is demonstrated from the aerial photos in Fig. 10 and from the profiles of the cross section of Fig. 13.

No sand artificial nourishment was done in the zone C, so it's easily understandable that the submerged breakwaters can not only defend the coastline but it is able to capture the fine sediments by longshore drift and to assure them a dynamic sufficient stability.

These results have been observed also in not few field experiments (as at the mouth of Volturno river Napoli, like other example) and in laboratory tests (Chiaia and al., 1992). These results suggested to the public administration to continue in the defending of the **zone D** with the same structure as in zone C (works in progress).

Costs and benefits, comparison

First cost of the defence structure of the zone A (segmented detached emerged breakwaters) is the same of those of the zones C and D, fig. 9 (continuous submerged breakwaters), i.e. about 2 million US dollars/km.

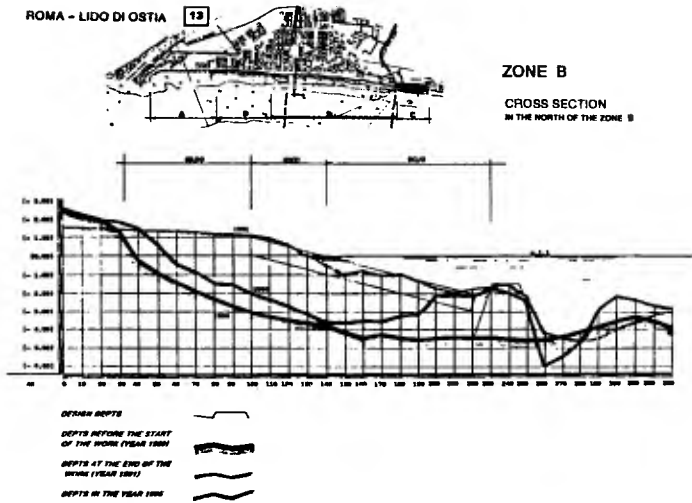


Fig. 11 Zone B - Cross section in the north of zone B.

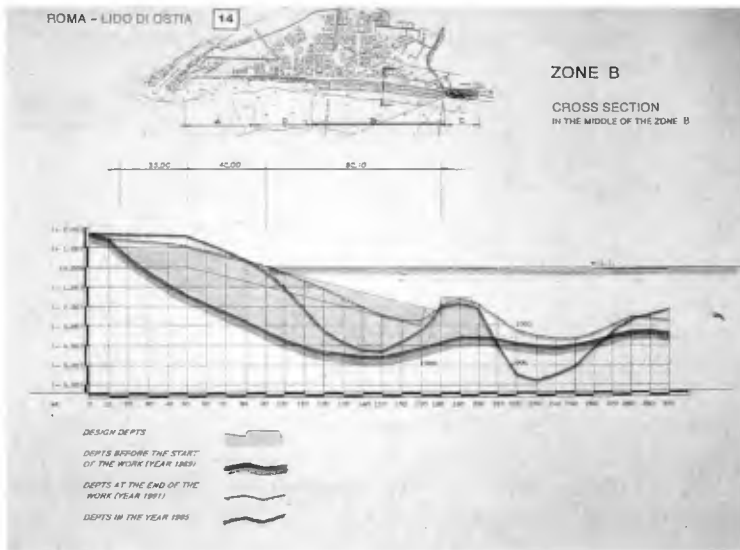


Fig. 12 Zone B - Cross section in the middle of zone B.

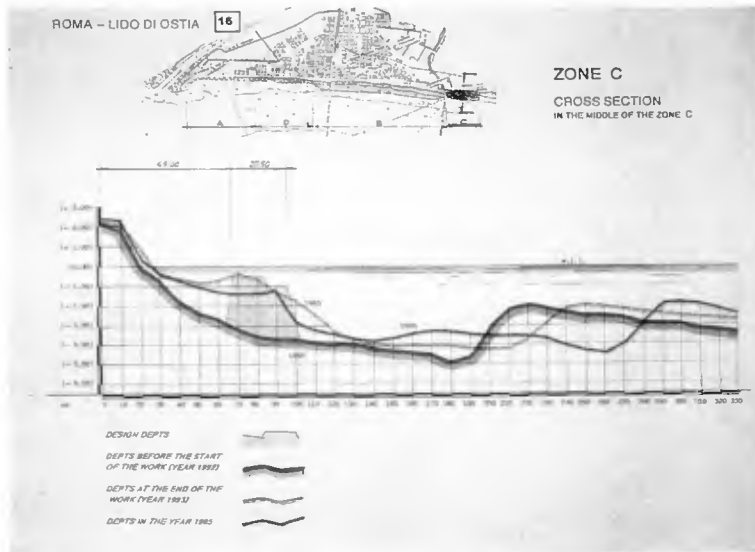


Fig. 13 Zone C - Cross section in the middle of zone C.

The barrier of the zone C is long 700 m, that of the zone D 1,300 m. For the nourishment of the zone B (3 km long), cubic meters 502,000 of fine sand and 880,000 of gravel mixed with coarse sand were used; the cross section volume of the stone reef in the zone B is very similar to that of the submerged breakwater in the zone C. So the first cost of the artificial beach in the **zone B** (artificial sand nourishment and stone reef) is very bigger (about 6.2 million US dollars/km) that the cost of the defence structure (only a submerged breakwater) in the **zone C** (about 2 million US dollars/km).

The monitoring control of the works suggests, also, a necessity of about 15,000 cubic meters/km of sand supply for the maintenance of the artificial beach in the zone B; none cost of the maintenance for the beach in the zone C, because there the nourishment is natural, i.e. it is due to the capture action of the downdrift sediment by the submerged breakwater. Comparison of the above results shows that in both cases of the two soft structures used for the zones B and C the principal scope of the defence from waves erosion has been obtained, also the healthiness of the bathing water was assured; moreover in the zone B a large artificial beach results (in the year 1995 the width was between 30 and 100 m. in going from north to south), while in the zone C the width of the natural beach was smaller (between 15 and 30 m.). It is interesting, also, to look at the favorable action of the special shape of the cross section of the submerged barrier used (two different steps to reduce the reflection of incident waves and, consequently, the energy of the breaking waves at the foot seaside of the barrier). Above the costs of both the soft structures are reported with the benefits for all the beach of very high tourist interest: the comparison is easy.



Fig. 14 Zone B - Before and after the works



Fig. 15 Zone C - Before and after the works

Considerations

The above experiences suggest the following considerations:

- a) both the soft structures have a very low environmental impact;
- b) well designed submerged breakwater is able to defend the coastline from erosion by seawaves, permits a sufficient water exchange between offshore and inshore areas during the summertime, can capture the sediment transport (when it there is) for a natural, low price and enough stable sand beach (pay attention that, for the Italian seas, the maximum spring-tide is generally about 30 cm);
- c) a reef does not assure the stability of the shoreline and increases the erosion landside due to the waves breaking on it (it's too much the energy of the highest waves that comes in the landside area);
- d) the costs of construction and maintenance of the defence soft structure, as in the example of the zone B, is very high and hardly supportable from the community. As benefits, it is a very acceptable soft structure, the area of emerged sand beach is large and better responds to the requests of the people for the recreational and bathing use. But, really, the defence structure is the coarse sand and gravel nourishment, while the effect of the reef is more negative than doubtfull. The laboratory tests demonstrate that an increase of the sand and gravel dimensions are more usefull to stabilize the beach (Aminti,1987).
- e) use of a submerged breakwater as in zone C and D has to be favourite when you want to defend from erosion the shoreline and also to build an artificial beach to reduce the sand supply necessity.
- f) In fact, it does not disturb the landscape scenery, permits to preserve the healthiness and the bathing use of the water in the protected area, assures a good

shoreline stability because it can reduce notably the energy of the highest erosive waves.

References

- Aminti, (1987) *Prove su modello bidimensionale di protezioni di spiagge con ripascimenti artificiali*. Atti IV Colloquio Nazionale AIOM
- Aminti, P. & al. (1983) *Experimental studies on submerged barriers as shore protection structures*. Int. Conf. COPEDEC, Colombo, March 20-26, 1983.
- Benassai E., Gentilomo M., Ragone A., Setaro F., Tomasicchio U. (1992). *Littoral Restoration by means of protected beach nourishment. Recent Italian Works*. PIANC Bulletin, May 1997.
- Caputo C. & al. (1993) *La ricostruzione dei litorali in erosione mediante ripascimento artificiale e il problema del reperimento degli inerti*. Università La Sapienza, Roma.
- CERC, US Army Corps of Engineers. (1977), *Shore Protection Manual*
- Chiaia G. & al., (1992) *Evolution of a beach with and without a submerged breakwater*. 23rd ICCE, Venezia ottobre 1992.
- Autori vari (Tomasicchio etc.) *Raccomandazioni tecniche per la difesa delle coste in erosione*. Progetto finalizzato Conservazione del Suolo, sott. Dinamica dei Litorali. Pubbl. n.156.
- Consiglio Superiore dei Lavori Pubblici (1991) *Istruzioni tecniche per la progettazione e l'esecuzione di opere di protezione delle coste in erosione*. Giornale del Genio Civile, Fasc.10,11,12,1991.
- Dean R.G. & Browder A.E. (1995) *Full scale monitoring study of a submerged breakwater*. Testo del Seminario tenuto all'Università di Perugia nell'ottobre 1995.
- Dean R.G. (1992) *Defence of Shorelines by Structural Approaches*. Proceedings of the Short Course on Design and Reliability of Coastal Structures. ICCE 1992, Venezia
- Dean R.G. *Beach nourishment, Design Principles*. Proc. ICCE '92, Venezia
- Dean R.G. and Tomasicchio G.R (1995) *Effetti della costruzione di un porto turistico sulla linea di riva adiacente*. Giornate italiane di ingegneria costiera. Ravenna.
- Delft Hydraulics (1989) *Coastal Protection Plan Lido di Ostia*. H 891, Rep. On math. Computation scale model tests.
- De Santis, M. & Ruol, P. (1987) *Studio sperimentale su un particolare intervento per la salvaguardia delle spiagge in erosione*. Atti IV Colloquio Nazionale AIOM
- Ferrante, A., Franco, L., Boer, S. (1992). *Modelling and monitoring of a perched beach at Lido di Ostia (Rome)*. Proc. 23rd ICCE, Venice.
- Lamberti, A. & Tomasicchio, U. (1981) *Le barriere sommerse, possibili strutture a difesa della costa*. Porti Mare Territorio, anno III, n.1.
- Silvester, R. *Coastal Engineering* (1974) Elsevier, Amsterdam
- Tomasicchio, U. (1993) *Difese costiere e loro inserimento nel paesaggio litoraneo*. 10° Corso di aggiornamento sulle tecniche per la difesa dall'inquinamento. Università degli Studi della Calabria. Editoriale BIOS. L
- Tomasicchio, U. (1991) *Presentazione delle situazioni tecniche per la progettazione e l'esecuzione di opere di protezione delle coste in erosione*. Giornale del Genio Civile, Fasc. 10, 11, 12 - 1991.
- Tomasicchio, U. (1983) *La conservazione dei lidi a protezione della laguna di Venezia*. Convegno di Studi "Laguna, fiumi, lidi: cinque secoli di gestione delle acque nella laguna di Venezia". Giugno 1983, Venezia.

CHAPTER 187

WAVE TRANSMISSION AT LOW-CRESTED STRUCTURES

Kees d'Angremond¹, Jentsje W. Van Der Meer², Rutger J. De Jong³

Abstract

Existing data on wave transmission have been critically examined to obtain a homogenous data base. These data have been re-analyzed, and an expression has been derived relating the transmission coefficient to structural parameters and wave parameters.

Introduction

One of the main aims of breakwaters is improving the tranquility in designated areas to facilitate cargo handling or to protect natural shorelines. Economic considerations often indicate that the structural integrity of the breakwater shall be such that the structure is able to survive severe weather conditions without major damage. The functional requirements, however, do not always require that absolute tranquility is maintained under such extreme conditions. Since the volume of material involved in the structure (and thereby its cost) is proportional to the square of its height, it is worthwhile to consider the minimum crest level as carefully as the structural strength of the armor layer. Therefore it is necessary to give a good prediction of wave transmission of low-crested structures. This is the main reason for the continued attention for wave transmission at Delft University and Delft Hydraulics.

¹ Delft University of Technology, P.O. Box 5048, 2600 GA Delft, the Netherlands

² Delft Hydraulics, P.O.Box 152, 8300 AD Emmeloord, the Netherlands

³ MSc-Student, Faculty of Civil Engineering, Delft University of Technology, at present: Grabowsky and Poort, Consulting Engineers, The Hague, The Netherlands.

Run-up, Overtopping and Transmission

Before analyzing the phenomenon of wave transmission it may be wise to define the three related subjects, run-up, overtopping and transmission, since there seems to be a lot of misunderstanding about the meaning of these words.

Wave run-up is the phenomenon that when a wave approaches a sloping face, a wave tongue runs up the slope. The tongue reaches a maximum elevation above still water level, which is the run-up level. This is thus a vertical distance above the momentary sea level. When the crest of the slope is lower than the run-up level, the wave tongue will pass over the crest.

The average quantity of water passing over the crest is called wave transmission. It is expressed in m^3 per running meter crest per second, and it can therefore be compared with the specific discharge per unit width (q) in open channel flow. In case the area behind the sloping structure is dry land, the quantity of overtopping may be used to design the capacity of the drainage system.

In case the area behind the structure is a plane of water, the masses of water spilling over the crest from time to time will generate waves in the basin. These waves will generally be smaller than the waves at the outside of the structure. The ratio between the wave height behind the structure (H_t) and the wave height in front of the structure (H_i) is the transmission coefficient K_t .

The governing parameters related to transmission are: structural geometry, permeability, crest freeboard, crest width, surface roughness, water depth and the hydraulic parameters wave height and wave period. A definition sketch is given in Figure 1.

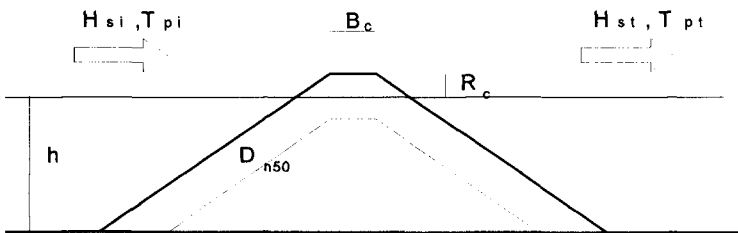


Figure 1. Definition Sketch

Existing Transmission Formulae

Two formulae describing wave transmission at low-crested structures have already been published by the authors in previous papers. In the first formula, derived

by Van der Meer (1990, a and b), the transmission coefficient was related to the crest freeboard R_c , divided by the incident significant wave height H_{si} .

$$K_t = 0.46 - 0.3 \frac{R_c}{H_{si}}$$

K_t is limited between 0.8 and 0.1.

Figure 2 shows an indication of the scatter obtained in this way. In particular, it is remarkable that the transmission coefficient does not reach the value 1 for relatively low structures, and that it remains quite above 0 for structures with a considerable relative freeboard.

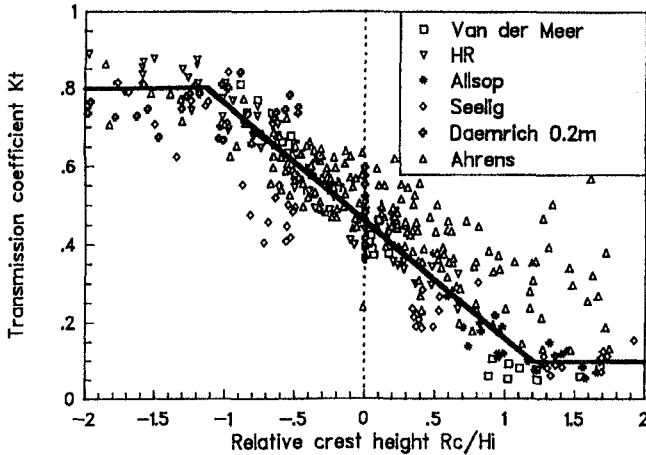


Figure 2. Wave transmission versus relative crest height R_c/H_i

The second formula was derived by Daemen in his Master's thesis (Daemen 1991) and published by Van der Meer et al (1991). Daemen attributed part of the scatter to permeability of the armor layer, specifically for those structures that had a crest slightly above MSL. It was concluded that the scatter could be reduced by introducing a different dimensionless expression for the freeboard i.e. R_c/D_{n50} , in which D_{n50} is the nominal stone diameter of the armor layer.

Eventually, an expression was developed of the shape:

$$K_t = a \frac{R_c}{D_{n50}} + b$$

in which

$$a = 0.031 \frac{H_{si}}{D_{n50}} - 0.24$$

and

$$b = -5.42 s_{op} + 0.0323 \frac{H_{sj}}{D_{n50}} - 0.0017 \left(\frac{B}{D_{n50}} \right)^{1.84} + 0.51$$

Boundaries were set at $K_t \text{ max.} = 0.75$ and $K_t \text{ min.} = 0.075$, while the validity of the formulae was limited for $1 < H_s/D_{n50} < 6$ and $0.01 < s_{op} < 0.05$.

Daemen further noted that the data by Ahrens, based on the behavior of reef-type breakwaters were so much different that other formulae were required to describe transmission over such structures. A comprehensive analysis of the background of the tests by Ahrens justifies the separation of reef type structures from regular breakwaters. At the same time, Daemen suggested a modified expression valid for reef type breakwaters. The results obtained by Daemen for regular breakwaters are presented in Figure 3.

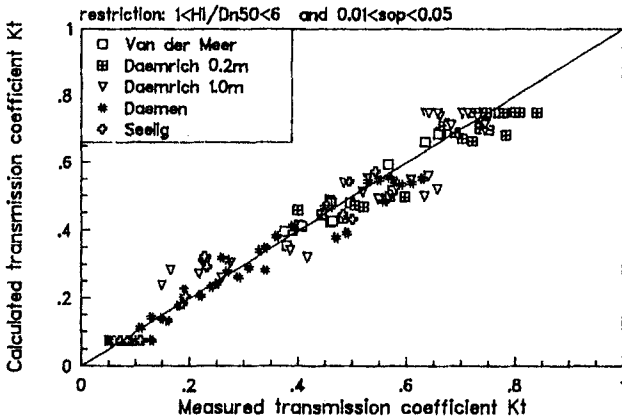


Figure 3. Calculated and measured transmission for conventional breakwaters (Daemen)

Although the result of Daemen looks quite promising considering the scatter, there is one obvious disadvantage: the formula is not valid for structures that have no characteristic diameter, or that have a low or zero permeability in the region around MSL. Examples of such structures are asphalt grouted breakwaters and groynes, caisson type breakwaters, and breakwaters with large solid superstructures. It was therefore decided to continue the work by Daemen and to try and find an expression for the transmission that is primarily based on the outer dimensions of the structure, with correction factors for roughness and permeability. Before starting the new analysis, it was decided to examine existing data sets critically to obtain a homogenous data base.

Existing Data Sets

Van der Meer and Daemen both used various sets of data that were gathered and published by various researchers. It was mentioned already that the test results by Ahrens were omitted by Daemen because of the completely different character of the reef type breakwater. The test series by Seelig (1980), Allsop (1983), Daemrich and Kahle (1985), Powell and Allsop (1985), Van der Meer (1988) and Daemen (1991) that had been used by both, van der Meer and Damen, were studied again for the present work, and new data from site specific model investigations by Delft Hydraulics (mainly carried out in 1993 and 1994) could be added. In these series also impermeable submerged breakwaters were included.

All data, however, have there specific character. Seelig used waves with an extremely large wave steepness of 0.10, which could not be reproduced in other laboratories due to wave breaking. Allsop restricted his studies to structures with a relatively high crest level. Daemrich and Kale used tetrapods as armor units, instead of quarry stone used by many other authors. Probably, the permeability is thus slightly larger, which results in a larger transmission. Powell and Allsop carried out their tests at extremely shallow water depths. Some of the recent investigations by Delft Hydraulics were also on armor layers with Tetrapods and Accropods, with consequences for the permeability. All authors are a little ambiguous about the definition of the crest level. This may explain systematic deviations between various data sets.

In spite of the inconsistency of the various data sets, all data, except those of Ahrens for reef type breakwaters were used. From the data sets, some tests were discarded, however, i.e. those sets with extremely steep or breaking waves ($s_{op} > 0.6$ and $H_{si}/h > 0.54$). Tests with $R_c/H_{si} > 2.5$ and with $R_c/H_{si} < -2.5$ were considered less relevant and therefore not taken into account either.

The complete set of data used during the present study is compiled in Figure 4, which gives the raw relation between R_c/H_{si} and K_t .

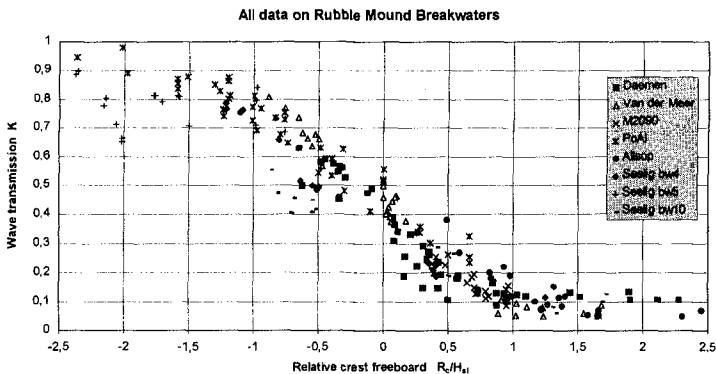


Figure 4. Homogenous Data on Transmission

Analysis

The analysis of data was taken up in a similar way as was done originally by van der Meer. This resulted in a relation of the form:

$$K_t = a \frac{R_c}{H_{si}} + b$$

in which

- a* determines the slope of the curve, and appears to be independent of any of the parameters considered, and
- b* determines the value of the transmission coefficient K_t when the relative crest height equals zero. This coefficient appears to be a function of crest width and breaker parameter.

Because of the trend in all data, the coefficient *a* could be set at -0.4. The coefficient *b* was expected to depend on crest width and breaker parameter ξ . It was attempted to find a dimensionless expression for the crest width by combining it with wave height and wave length respectively. Eventually, the best result was obtained by the expression

$$0.54 \left(\frac{B}{H_{si}} \right)^{-0.31}$$

The coefficient 0.54 in this expression could, however, not be considered a real constant yet. Because of the similarity between wave transmission and wave run-up, it was expected that the Iribarren parameter, $\xi = \tan \alpha / \sqrt{H/L}$ would play a role. It was found that the expression $(1 - e^{-0.5\xi}) * C$, (with $C = 0.64$) yielded optimum results.

The remaining scatter is due to the influence of the stone size D_{n50} . This influence becomes noticeable for values of $H_{si}/D_{n50} < 2$. The influence, however, is two-fold and works in different ways, depending on the crest level: small values of H/D indicate the presence of relatively large armor stones, which increase the permeability and thus increase the transmission by water flowing through the breakwater, but which increase the surface roughness at the same time and thus reduce transmission by water flowing over the breakwater. There were insufficient data to establish a final relation. Therefore, it is suggested to maintain the coefficient 0.64 for the time being. The deviation by this choice mainly influences the results for extreme values of K_t and thus of R_c/H_{si} (see figure 5).

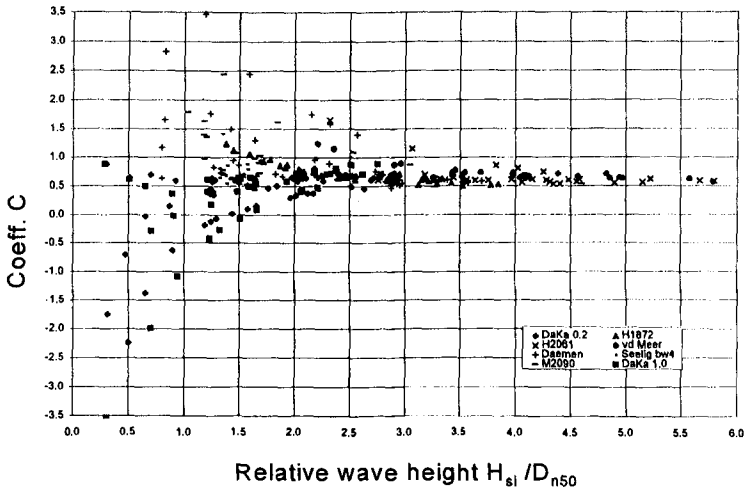


Figure 5. Remaining scatter due to armor size

Conclusions

In conclusion, the expression proposed for permeable breakwaters is:

$$K_t = -0.4 \frac{R_c}{H_{si}} + \left(\frac{B}{H_{si}}\right)^{-0.31} * (1 - e^{-0.5\xi}) * 0.64$$

with limits for the value of K_t :
 $0.075 < K_t < 0.80$.

In a similar way, an expression for impermeable structures was derived:

$$K_t = -0.4 \frac{R_c}{H_{si}} + \left(\frac{B}{H_{si}}\right)^{-0.31} * (1 - e^{-0.5\xi}) * 0.80$$

with the same limits.

Measured and calculated results for compared for permeable and impermeable structures respectively. The results are presented in Figures 6 and 7. For permeable structures, the standard deviation σ was 0.060, resulting in a 90% confidence band of $K_t \pm 0.10$. For impermeable structures, the standard deviation was found to be 0.053, with 90% confidence level for $K_t \pm 0.087$.

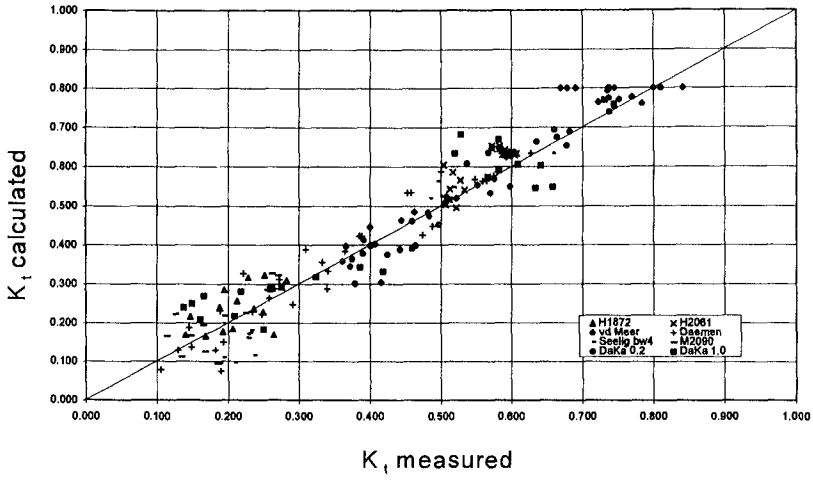


Figure 6. Measured and calculated transmission permeable structures

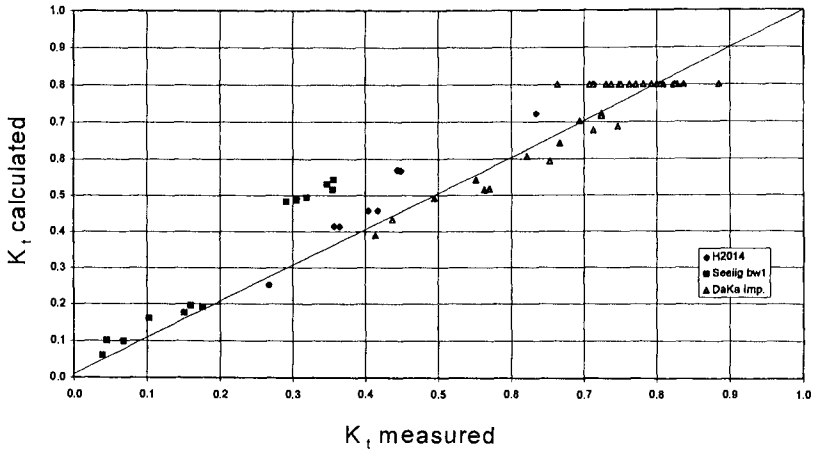


Figure 7. Measured and calculated transmission impermeable structures

Recommendations

The main problem in finding a reliable expression for wave transmission is the fact that available data do not form a homogenous data base. Model tests have been carried out by several different laboratories, where it is not certain that always the same definitions have been used. This mainly applies to the crest level. Further, many model tests were carried out with emphasis on other aspects of structural behavior. It is therefore recommended that special tests be carried out with the main aim to establish a homogenous data base for transmission of permeable and non-permeable breakwaters.

References

- Ahrens, J.P. (1987) Characteristics of reef breakwaters, CERC, Vicksburg, *Technical Report CERC-87-17*.
- Allsop, N.W.H. (1983) Low-crest breakwaters, studies in random waves. *Proc. Coastal Structures '83, Arlington, Virginia, pp. 94-107*.
- Daemen, I.F.R. (1991) Wave transmission at low crested structures. *MSc Thesis Delft University of Technology, Faculty of Civil Engineering, Delft Hydraulics Report H 462*.
- Daemrich, K. and Kahle, W. (1985) Schutzwirkung von Unterwasser Wellen brechern unter dem Einfluss unregelmässiger Seegangswellen. *Eigenverslag des Franziskus-Instituts für Wasserbau und Küsteningenieurwesen, Heft 61 (in German)*.
- Powell, K.A. and Allsop, J.P. (1985) Low-crest breakwaters, hydraulic performance and stability. *Hydraulics research, Wallingford, Report SR 57*.
- Seelig, W.N. (1980) Two-dimensional tests of wave transmission and reflection characteristics of laboratory breakwaters. *WES, CERC, Fort Belvoir, Technical Report No. 80-1*.
- Van der Meer, J.W. (1990a) Data on Wave Transmission due to overtopping. *Delft Hydraulics report no. H 986, prepared for CUR C67*.
- Van der Meer, J.W. (1990b) Low-crested and reef breakwaters. *Delft Hydraulics report no. H 986 II, prepared for CUR C67*.
- Van der Meer, J.W. and d'Angremond, K. (1991). Wave transmission at low-crested structures. *Coastal Structures and Breakwaters, ICE, London, pp. 25-42*.
- Van der Meer, J.W. and Daemen, I.F.R. (1994). Stability and wave transmission at low-crested rubble mound structures. *ASCE, J. of Waterways, Ports, Coastal and Ocean Engineering, Vol. 120, Jan/Feb, pp. 1-19*.

CHAPTER 188

EFFECT OF SUBMERGED BREAKWATER ON PROFILE DEVELOPMENT

Martin D. Groenewoud¹, Jan van de Graaff², Edward W.M. Claessen³
and Stephan C. van der Biezen¹

ABSTRACT

The project “Dynamics of Beaches” is carried out by a network of six European Universities within the framework of the Human Capital and Mobility Program of the European Union. The aim of the project is to improve the existing knowledge on physical processes governing the nearshore zone due to effects of submerged breakwaters. Within the project hydrodynamic and morphological experiments have been carried out.

This paper discusses the results of the experiments that took place in a wave flume and the large wave basin at Delft University of Technology. The experiments were carried out with movable beds and varying wave conditions.

INTRODUCTION

Structural erosion and dune erosion during severe storm surges threaten large parts of coasts. Proper protection of threatened coasts is often an important aim in coastal engineering practice. Apart from this type of protection, sometimes new reclaimed areas have to be protected from attacks from the sea.

Coastal engineers must always select the proper protection method out of the many available methods; e.g., beach nourishments, series of groins, series of offshore breakwaters, submerged breakwaters, seawalls and revetments. In order to apply a specific method its physical effects on the surrounding area should be well known.

¹ Researcher; Delft University of Technology; Stevinweg 1; 2628 CN Delft; the Netherlands

² Senior scientific officer; Delft University of Technology; Stevinweg 1; 2628 CN Delft; the Netherlands

³ formerly Msc. student DUT

One of the promising methods of coastal protection is the use of submerged breakwaters. Within the framework of the Human Capital and Mobility program of the European Union six universities [Barcelona (Spain), Thessaloniki (Greece), Ghent (Belgium), Liverpool (U.K.), Cork (Ireland) and Delft (the Netherlands)] work together in solving some of the unknown aspects related to the use of submerged breakwaters along sandy coasts.

The primary aim of this project called "Dynamics of Beaches" is to obtain a valuable database which is available for further modelling studies.

In the research program many experiments in wave flumes and wave basins have been carried out by the partners with the main emphasis on the effects of a submerged breakwater on hydrodynamics. Table 1 gives an overview.

Laboratory	Facility	Bottom	Waves
Barcelona	Flume	Rigid	Irregular
Liverpool	Flume	Rigid	Regular/Irregular
Cork	Basin	Rigid	Irregular
Delft	Flume	Movable	Regular/Irregular
Delft	Basin	Movable	Regular

Table 1 Overview experiments "Dynamics of Beaches" project.

This paper discusses the results of the experiments in Delft with main emphasis on the wave flume experiments. First a general evaluation of the applicability of submerged breakwaters is given.

OBJECTIVES OF APPLICATION

The erosion of coasts can often be divided in two types of problems, viz.:

1 - Structural erosion

Structural erosion of a stretch of coast means that the stretch loses sediments at a regular basis. Typical for structural erosion is the fact that it is an irreversible process. In a certain cross-shore profile the amount of sediment diminishes as a function of time. Eventually all parts of the profile will suffer from this type of erosion.

Often a gradient in the longshore transport is the cause for this erosion. Fig.1 shows a simple schematization of the coast. If $S_b > S_a$ then the shoreline will retreat.

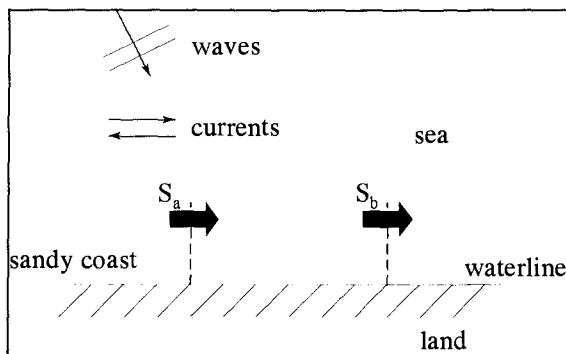


Fig.1 Longshore sediment transport

2 - Retreat of coastline during severe storm surges

A retreat of the (sandy) coast can take place during severe storm surges. Typical for this type of erosion is that it is a reversible process. Sediment is lost from the upper part of the profile to the shoreface, but will be transported in opposite direction again during calm weather conditions.

The second type of erosion should in principle not be battled by submerged breakwaters. During storm surges the combination of wave set-up, wind set-up and high (spring) tide leads to a high water level. The height of the submerged breakwater relative to water depth will become smaller. The influence of the breakwater will decrease at the time its presence is needed mostly. Therefore submerged breakwaters are not a proper solution to that kind of problem. It is stressed that of course the level of the crest is very important in this case.

Undesired structural erosion can be battled either by 'hard' or by 'soft' measures. 'Hard' measures are supposed to interfere with the sediment transports in such a way that the erosion is reduced or stopped at all. Well-known examples of such methods are: groins, offshore breakwaters, dikes etc. The erosion problem often is shifted to the adjacent leeside of the structure, which is a serious disadvantage of these types of countermeasures.

'Soft' measures (e.g. artificial nourishments) can avoid the disadvantage of leeside erosion. Nourishments, however, only treat the symptoms of the erosion; no permanent solution can be offered by these methods.

The general desire to solve erosion problems has stimulated the research of more structural solutions to the problem.

One of the promising methods is the use of submerged breakwaters. Basically the submerged breakwaters are supposed to reduce the wave heights landward of the structure. Because of this the wave-driven longshore current will be reduced. The decrease of the wave-driven longshore current will in principle lead to a reduction

of the longshore transport capacity. By fine-tuning the dimensions of the breakwaters (e.g. crest-height, gap size, orientation etc.) the desired reduction in transport capacity can be achieved. In other words, structural erosion can be avoided. More detailed descriptions of the effect of offshore breakwaters in general can be found elsewhere, e.g.: CUR, 1997; Pilarczyk and Zeidler, 1996.

The experiments as carried out in the framework of the 'Dynamics of Beaches' project are meant to increase the knowledge about the effects of submerged breakwaters on hydro- and morphodynamics.

THE DELFT EXPERIMENTS IN A WAVE FLUME

Experimental set-up

Several agreements concerning the experiments were made between the different partners of the Dynamics of Beaches project. Wave conditions and breakwater layout were in principle defined for a (fictitious) submerged breakwater at scale 1:1.

The experiments were carried out in one of the wave flumes of the Laboratory of Fluid Mechanics at Delft University of Technology (DUT). The dimensions of the wave flume are: length: 32.0 m; width: 0.8 m; height: 1.0 m.

The wave board is able to generate irregular waves. Because of the dimensions of the wave flume it was decided to perform the experiments at scale 1:15. Prototype wave conditions and breakwater layout were scaled down. Only the scaled parameters of the experiment will be mentioned in this paper.

The layout of the flume is shown in Fig.2. The layout of the cross-section of the submerged breakwater is presented in detail in Fig.3. According to the test programme the experiments were done with and without breakwater with a 1 in 15 slope and a movable bed. The bed consisted of sand with $D_{50} = 95 \mu\text{m}$ ($D_{10} = 76 \mu\text{m}$, $D_{90} = 131 \mu\text{m}$) which is relatively fine for sand along a beach. The purpose of using this type of sand is that the ratio between bed transport and suspension transport will be closer to the ratio that would occur if the experiments were performed at scale 1:1.

Because the erosion near the seaward toe of the breakwater was not a research topic, the first part of the slope is made out of concrete (see Fig.2). An advantage of a concrete slope seaward of the breakwater is that possible amounts of sediment transport over the breakwater can be measured very accurately.

Five different wave conditions with varying wave heights and wave periods (A through E, see Table 2) were defined in the Test Definition Report. By means of varying wave height and wave period the influence of these parameters on hydro- and morphodynamics can be investigated. One wave condition with regular waves was added (test F) to the program. In this way a coupling between the results of these 2DV tests and the 3D tests with regular waves can be made.

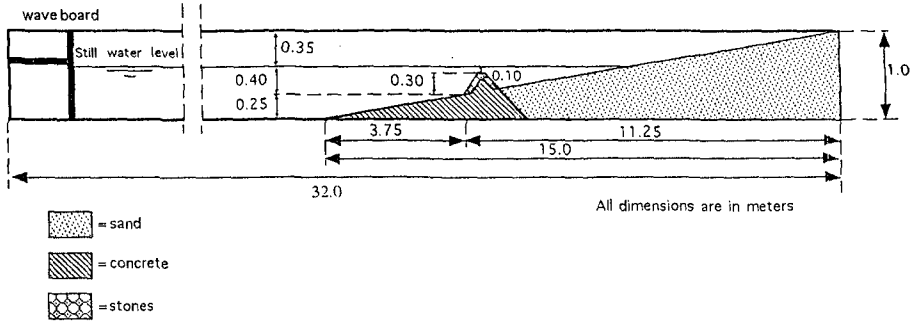
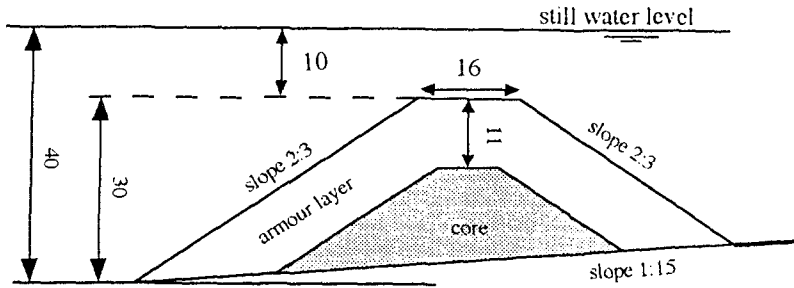


Fig. 2 Layout experiment (wave flume DUT).



All dimensions are in centimeters

Fig. 3 Layout of the breakwater in detail.

Six experiments were carried out without breakwater, each of them with one of the predefined wave conditions (A through F). The same strategy was repeated with the breakwater present. By using similar conditions for the tests with and without breakwater it is possible to make a true comparison between both situations.

Wave condition (irr. waves)	F/H _s (-)	H _s /L _{0p} (%)	T _p (s)	H _s (m)	h (m)	F (m)	H _s /L _p (%)
A	1.00	1.50	2.07	0.10	0.4	0.1	2.61
B	1.00	2.67	1.55	0.10	0.4	0.1	3.67
C	1.00	3.84	1.29	0.10	0.4	0.1	4.66
D	0.75	2.61	1.81	0.133	0.4	0.1	4.06
E	1.50	2.56	1.29	0.067	0.4	0.1	3.01
Wave condition (reg. waves)	F/H (-)	H/L ₀ (%)	T (s)	H (m)	h (m)	F (m)	H/L _p (%)
F	1.00	2.67	1.55	0.10	0.4	0.1	3.67

Table 2 Wave conditions

Each experiment lasted for 7.5 hours. The period of 7.5 hours was divided in four intervals with durations of respectively 0.5, 1.0, 2.0 and 4.0 hours.

The following types of measurements were carried out:

- wave height measurements (electrical resistance method)
- flow velocity measurements (electromagnetic fluid-velocity meters, (EMS))
- sediment concentrations measurements (transverse suction method with intake tubes)
- profile measurements (electronic profile follower)

The wave height, flow velocity and sediment concentration measurements were carried out during the different intervals at specific places (see Fig.4). Profile measurements were carried out between these intervals. Some of the results will be presented. (For a detailed description of measurements and results reference is made to Claessen and Groenewoud, 1995).

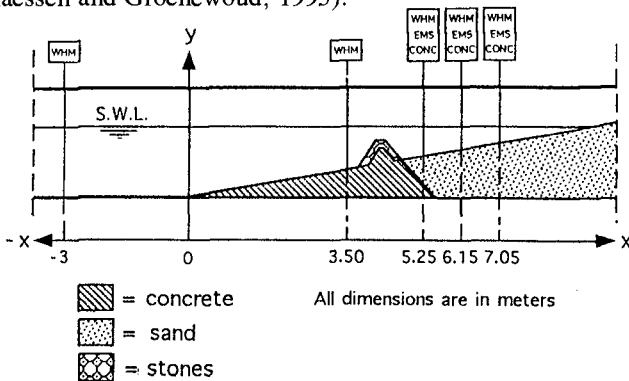


Fig.4 Cross-section of the flume and measuring positions

Analysis of results

As an example some of the results of the experiments with condition D ($H_s = 0.137$ m and $T_p = 1.81$ s) will be presented.

Profile measurements

The initial profile has a 1 in 15 slope. This relatively steep profile is far from equilibrium. Fast adaptations were therefore expected. After a test duration of 7.5 hours equilibrium is not yet reached. Aim of the tests was to see at what rate the adaptations would take place and what the influence of a submerged breakwater under varying wave conditions would be.

Fig.5 shows as an example the profile development of experiment D without breakwater. The other experiments without breakwater showed similar trends in profile development; erosion takes place around the shoreline and the sand is transported in offshore direction where a bar is formed. The size of the bar increases in time; the center of the bar moves seaward.

Fig.6 shows the profile development of experiment D with breakwater. Again, erosion around the waterline takes place. Part of the sediment settles against the breakwater. A bar in between the waterline and the breakwater is also formed.

Fig.7 compares the profiles after 7.5 hours of both experiments. The scourhole is less pronounced in case of the experiment with breakwater. The submerged breakwater clearly forms an obstacle for the sediment moving in seaward direction. Without the breakwater more sediment has moved in offshore direction.

Fig.8 shows the sediment transport through the vertical indicated in Fig.7. The transport in offshore direction was smallest for the experiment with breakwater. Other experiments gave similar results.

The experiments in the wave flume are strictly 2 dimensional. Therefore the mass flux due to (partly) breaking over the submerged breakwater has to return through the same cross-sections.

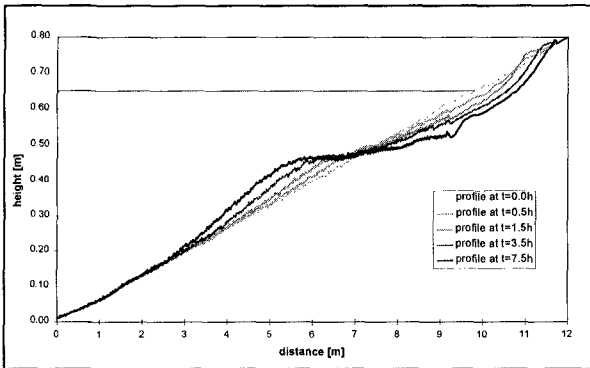


Fig.5 Profile development experiment D without breakwater ($H_s = 0.137$ m, $T_p = 1.81$ s)

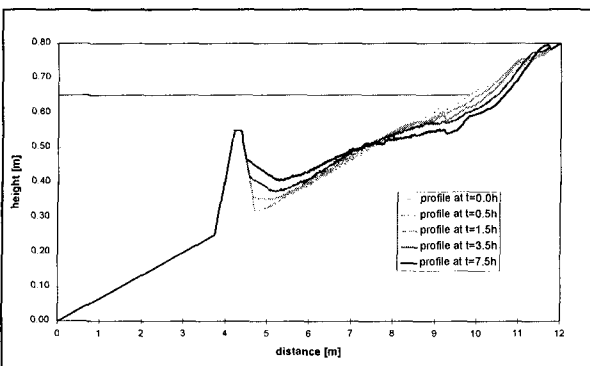


Fig.6 Profile development experiment D with breakwater ($H_s = 0.137$ m, $T_p = 1.81$ s)

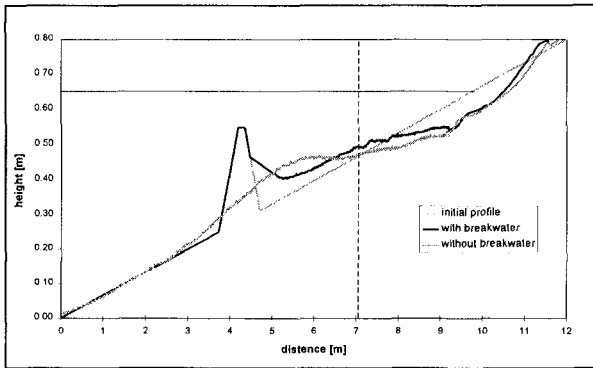


Fig.7 Comparison profiles experiment D with and without breakwater ($H_s = 0.137\text{ m}$, $T_p = 1.81\text{ s}$)

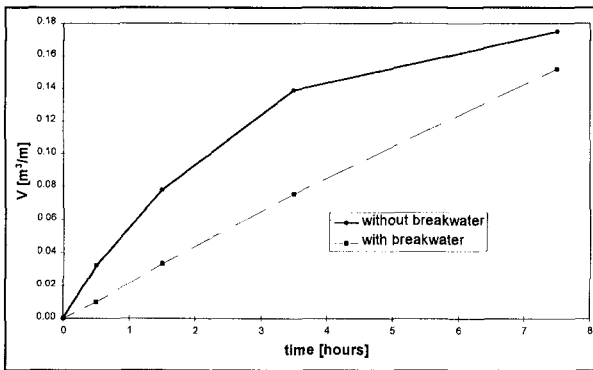


Fig.8 Comparison transport volumes through vertical ($x = 7.05\text{ m}$)

Simulation experiments with 2DV model

The experiments have been simulated with the computer programme Unibest- TC (Unibest is a program package of Delft Hydraulics). Measured wave heights and measured profile development have been compared with calculations.

Wave heights: measured and calculated

The results of the wave height measurements have been compared with calculations executed with Unibest-TC. The results of this comparison for experiment D are shown in Fig.9 and Fig.10. (In the figures the H_{rms} have been plotted).

For the situation with breakwater the Unibest-TC model calculates a sudden increase in wave height at the position of the breakwater. In reality the wave height and wave form will change less instantaneously as the effect of abrupt changes in the bottom profile.

Profile development: measured and calculated

Unibest-TC predicts the profile development for the situation without breakwater rather well (see Fig.11). Only the retreat of the waterline is not modelled satisfactory. This is due to the fact that the used equations are not valid near the waterline. The differences between measured and calculated development become larger with the breakwater present (see Fig.12). The calculated size of the scourhole lags behind in comparison to the measured development. Again, the retreat of the waterline is not modelled correctly.

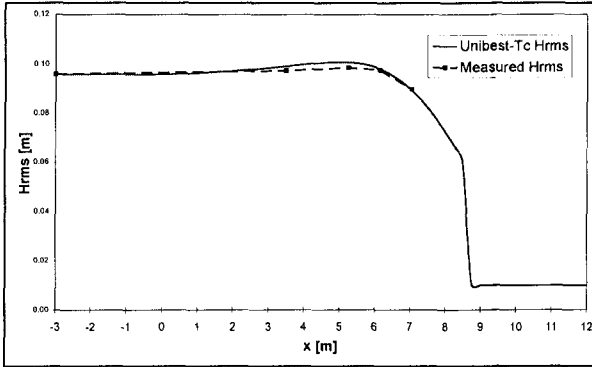


Fig.9 Comparison measured and calculated wave heights experiment D with breakwater ($H_s = 0.137$ m, $T_p = 1.81$ s)

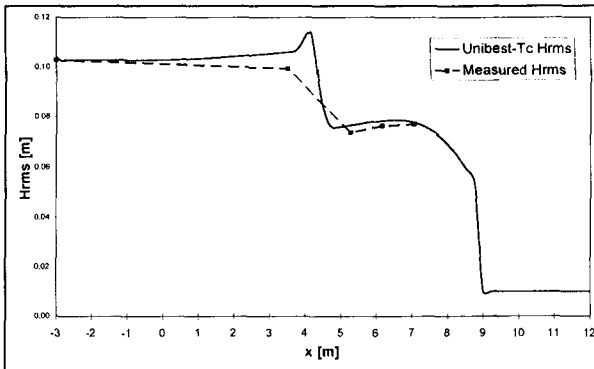


Fig.10 Comparison measured and calculated wave heights experiment D with breakwater ($H_s = 0.137$ m, $T_p = 1.81$ s)

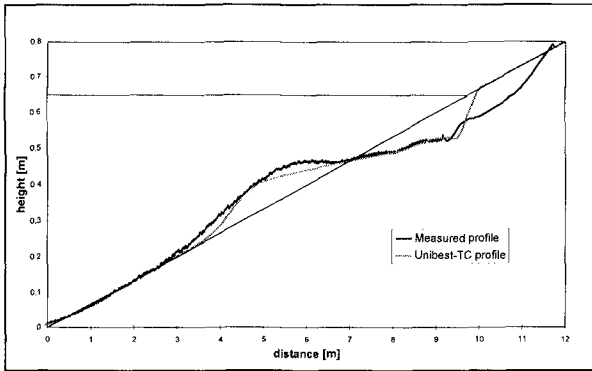


Fig.11 Comparison measured and calculated profiles experiment D without breakwater ($H_s = 0.137$ m, $T_p = 1.81$ s) after 7.5 hours wave action

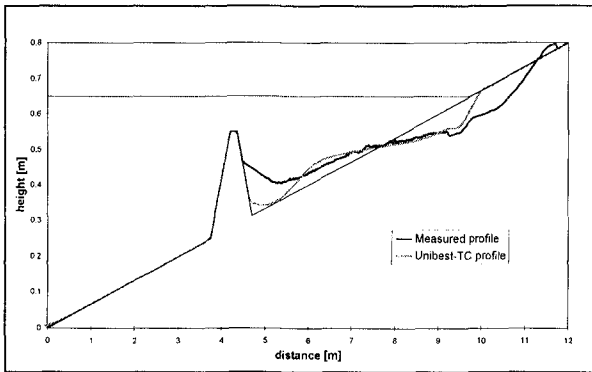


Fig.12 Comparison measured and calculated profiles experiment D with breakwater ($H_s = 0.137$ m, $T_p = 1.81$ s) after 7.5 hours wave action

RESULTS OF THE 2DV MOVABLE BED TESTS IN BRIEF

In most cases the presence of the breakwater has reduced the sediment transports in offshore direction. In some cases there was a small amount of sediment transport over the breakwater in offshore direction. This sediment can be considered as lost.

The breakwater causes much dissipation of wave energy. The wave heights offshore have increased due to reflection against the breakwater.

High sediment concentrations were measured behind the breakwater caused by the increased turbulence as effect of wave breaking.

The experiments showed that with the used variety in wave conditions a change in wave height had much stronger effects on morpho- and hydrodynamics than a change in wave period.

The simulations with Unibest-TC showed that the wave height development along the profile is predicted quite well. The calculated profile development differed considerably from the measurements.

It has to be stressed that the experiments in the flume are strictly 2 dimensional. Therefore the mass flux in the top of the breaking waves has to return in the same cross-section. This also applies for waves breaking over the submerged breakwater.

3D MOVABLE BED TESTS

In order to investigate 3D effects near the gaps between submerged breakwaters, or at an end of a long submerged barrier, in the wave basin of the Laboratory of Fluid Mechanics at the Delft University of Technology a segmented type of submerged breakwater was focused upon. Small scale experiments were carried out with regular waves. The experiments were carried out in resemblance with experiments in the Hydraulics and Maritime Research Center in Cork, Ireland. Both universities used the same set-up, except that in Delft a movable bed was applied instead of a concrete slope.

Each experiment starts with the same initial profile, which is steeper than the theoretical equilibrium profile, and covers 7.5 hours of wave action. Three different mean wave heights H were applied: 0.08 m, 0.10 m and 0.12 m, defined at the seaward toe of the breakwater which had a crest submergence of 0.10 m. The mean wave period T was kept constant at 1.55 s. The sediment used in the basin was the same as used in the wave flume ($D_{50} = 95 \mu\text{m}$).

Experiments were carried out with and without breakwaters. The experiments without breakwaters show a slope adjusting offshore sediment transport, transforming the initial 1:15 slope into an ogee profile which tends to stability after 7.5 hours of wave exposure; a real equilibrium is, however, certainly not reached in 7.5 hours. The experiments were interrupted five times for profile monitoring, to visualize the profile development in time in five steps. For a wave height of 0.10 m, Fig.13 shows the final situation of the bed without breakwaters. The still water level is set at $z = 1.00$ m.

Repeating the tests with submerged breakwaters installed, the most noticeable observation is a strong offshore flow through the gaps between the breakwaters, apparently compensating for the mass flux over the breakwater crests. Fig. 14 shows the final situation of the bed with breakwaters.

The relatively high offshore velocities in the gaps lead to a profound sediment loss and a much larger retreat of the shoreline than observed without breakwaters. The same effect was found at Palm Beach, Florida, USA (Browder *et al.*, 1996). In an attempt to reduce beach erosion and wave impact on a protective seawall, an experimental submerged breakwater of 1,260 m length was installed in a water depth of approximately 3 m off the Town of Palm Beach, Florida. The profile data documented erosion in the entire monitored area with the greatest erosion landward of the submerged breakwater.

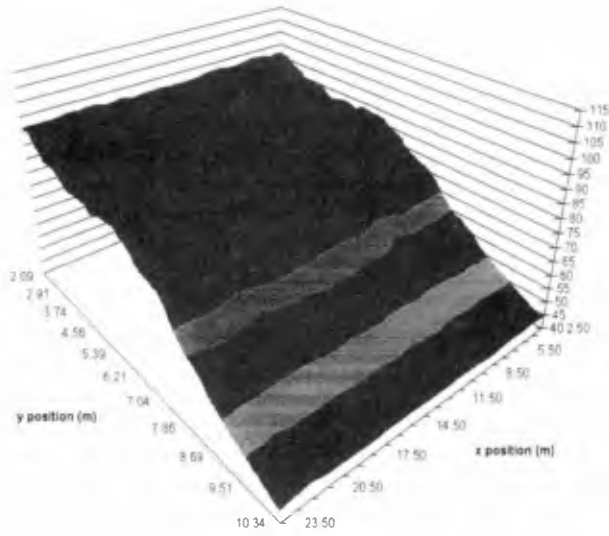


Fig.13 Final situation experiment without breakwaters

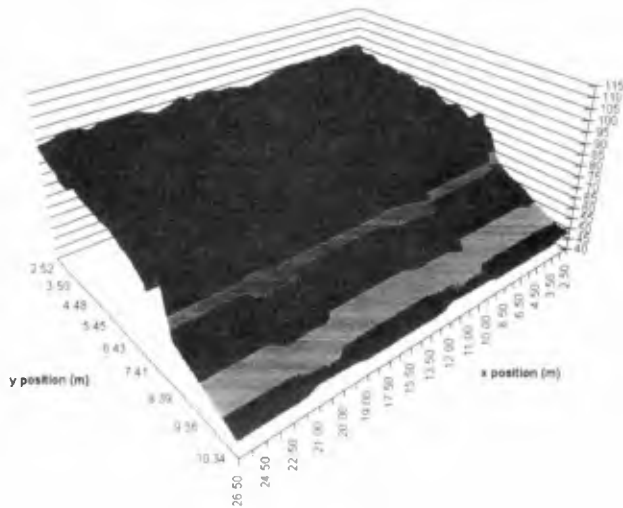


Fig.14 Final situation experiment with breakwaters

The current velocities measured relatively close to the bottom support the hypothesis that a surplus of water is built up landward of the breakwater. This can be seen from Figures 15 and 16.

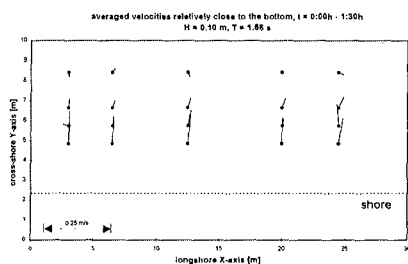


Fig.15 Velocities and directions without breakwaters

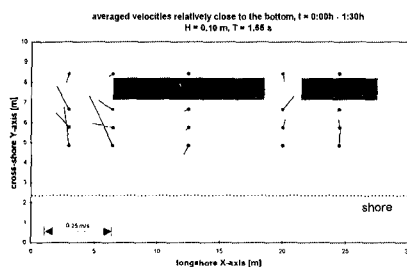


Fig.16 Velocities and directions with breakwaters

In Figs.15 and 16 averaged current patterns relatively close to the bottom are given for the first 1.5 hours, with and without breakwaters. Although the vectors can only provide a rough indication of what the current pattern in the basin will be like, intercomparison of these figures clearly shows the influence of the breakwater segments. The offshore undertow, uniformly distributed over the width of the basin in Fig.15, is channelled towards the gaps between the breakwaters as shown in Fig.16.

It has to be stressed that a main objective of tests with a movable bed is to achieve a reliable data set for verification purposes of mathematical morphological models. This comparison has not yet been carried out.

CONCLUSIONS ON THE 3D MOVABLE BED TESTS

Submerged breakwaters seem to offer a number of advantages over conventional coastal protection structures. However, 3D experiments indicate that one should be careful when applying submerged breakwaters with gaps. 2DV experiments often stress the reduction of the offshore sediment transport by the breakwater. This seems to justify the conclusion that the submerged breakwater creates a perched beach. The present 3D results, however, prove that it is important to count for the consequences of gaps between the submerged breakwaters. These can lead to unexpected scouring.

Furthermore, from the 2DV tests it is found that the submerged breakwaters reduce the wave heights in the lee. This is in accordance with the 3D results. In the gaps, however, the waves can pass and diffract around the ends of the breakwater into the lee side of the breakwater. For this reason, the amount of wave energy at the lee side of the breakwater becomes larger than indicated by 2DV testing.

To summarize, introduction of 3D properties such as gaps between breakwaters and breakwater endings affect the performance of submerged breakwaters as follows:

- the wave energy transmitted to the lee side of the breakwaters is much greater than predicted by 2DV testing (Murphy *et al.*,1996),
- submerged breakwaters allow a mass transport over the crest. The return flow is concentrated in the gaps resulting in local high velocities,
- although submerged breakwaters create a perched beach in a 2DV situation (an infinitely long breakwater), a significant amount of sand is removed from behind the structures and transported through the gaps when applying segmented breakwaters,
- the *exposure ratio*, defined as the ratio of gap width to the sum of the breakwater length and gap width, has a significant influence on the morphodynamic processes occurring in the nearshore region.

The equilibrium state was not reached during the present experiments, so the resulting profile shape after 7.5 hours of wave exposure is still partly determined by the initial steep slope. Therefore, a long term prognosis about the efficiency of segmented submerged breakwaters can not be made on basis of the present results.

OVERALL CONCLUSIONS

Especially the 3D experiments have shown that one should be careful with applying submerged breakwaters. Submerged breakwaters do not seem to be good solutions for an arbitrary structural erosion problem.

The gaps in between of the breakwaters effect the hydro- and morphodynamics very strongly.

Further research is necessary to increase the knowledge about the influence of parameters like gap size (exposure ratio).

ACKNOWLEDGEMENT

The “Dynamics of Beaches” project is sponsored by the Human Capital and Mobility programme (Scientific and Technical Cooperation Networks) of the Commission of the European Union, Directorate General for Science, Research and Development, under contract CHRX-CT93-0392.

REFERENCES

- Browder, A.E., R.G. Dean and R. Chen (1996)** Performance of a submerged breakwater for shore protection, Book of Abstracts 25th Int. Conf. on Coastal Eng., Orlando, USA.
- Claessen, E.W.M. and M.D. Groenewoud (1995)** Effect of submerged breakwater on profile development. Delft University of Technology, Fac. of Civil Eng., August 1995.
- CUR (Center for Civil Engineering Research, codes and specifications) (1997)** Soft sand & hard structures. Gouda, the Netherlands. (in preparation)
- Murphy, J.M., A.W. Lewis, C. Wall, J. van de Graaff and S. van der Biezen (1996)** Submerged breakwater research as part of the EU Human Capital and Mobility Programme. MAFF Conf. Of River and Coastal Engineers, Univ. of Keele, England.
- Pilarczyk, K.W. and R.B. Zeidler (1996)** Offshore breakwaters and shore evolution control, A.A.Balkema/Rotterdam/Brookfield.

CHAPTER 189

CAUSE AND CHARACTERISTICS OF IMPACT PRESSURE EXERTED BY SPILLING AND PLUNGING BREAKERS ON A VERTICAL WALL

Seyed Ali Azarmsa ¹, Takashi Yasuda ², Hidemi Mutsuda ³

Abstract

Detailed measurements of spilling and plunging wave pressures on a vertical wall are carried out to identify and compare their characteristics. Kinematical differences between the spilling and plunging breakers enable us to investigate better the generation mechanism and characteristics of the impact pressure. Further, the reliability of numerically computed breaking wave pressure is investigated through the comparisons with the experimental results. It is made clear that the impact pressure can be well expressed in terms of internal kinematics of breaking waves.

Introduction

Impact pressure of breaking waves has been studied by many investigators, but for only plunging breakers (e.g. Bagnold, 1939; Kirkgoz, 1982; Chan and Melville, 1988; Cooker and Peregrine, 1990; Oumeraci et al., 1992; Hattori et al., 1994). Since the impact pressure exerted by a plunging breaker on a vertical wall usually takes place near the elevations where air is entrapped, some of the investigators related the cause of occurrence of the impact pressure to entrapped air dynamics, to reduced velocity of sound in a water-air mixture etc. and thus much less attention is paid on the role and contribution of the kinematics of water particles to the impact pressure.

Discussing different ideas about the generation mechanism of the impact pressure, Azarmsa et al., (1996a) made clear that generation of the impact pressure is independent of breaker type and showed that even spilling breakers exert the impact pressure on a vertical wall. Besides, they made clear that entrapped air

¹Doctoral Student, Dept. of Civil Engineering, Gifu University, Yanagido 1-1, Gifu, 501-11, Japan.

²Professor, ditto.

³Research Associate, ditto.

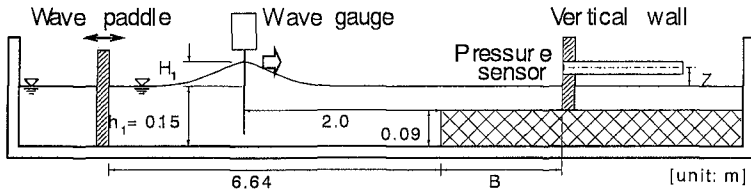


Figure 1: Experimental set-up.

does not play any role in generation of the impact pressure, although pressure oscillations are linked to entrapped air dynamics. Such conclusions turned our attention round from the entrapped air dynamics to the kinematics of the breaking waves as the key factor in generation of the impact pressure and related problems. To understand how the kinematics of breaking waves and the impact pressure are related, the internal kinematics of incipient breaking waves were computed numerically and applied to the calculation of the impact pressure in two different ways (Azarmsa et al., 1996a). The results indicated that both the horizontal and vertical components of velocity and acceleration of water particles should be considered in computations of the impact pressure.

In this study, spilling and plunging wave pressures exerted on a vertical wall are investigated to make clear the common and individual characteristics of the impact pressure exerted by these breakers. Moreover, the experimental and numerical results are compared to investigate the reliability of the vertical distribution of the maximum pressure computed on the base of the internal kinematics of breaking waves, as suggested by Azarmsa et al., (1996a). Further, since the internal kinematics of overturned waves is more critical than that of waves just at breaking, our attention is also focused on the pressure exerted by overturned waves. The results will be compared with the pressure exerted by waves which just break on the wall and the role of entrapped air will be discussed.

Experiments

Experiments were conducted in a 54m long, 1m wide, and 1m deep wave channel. A computer-controlled piston-type wave maker was used to generate the desired solitary waves.

Figure 1 shows a view of the wave channel and apparatus used for the experiments. A reef with the crown height of 9.0 cm was made of stainless steel plates and installed in the wave channel to make the generated solitary waves break. The dimensionless incident wave heights of generated spilling and plunging breakers are respectively ($H_1/h_1 = 0.24$) and ($H_1/h_1 = 0.55$), where $h_1 = 15\text{cm}$ is water depth in the wave channel. A vertical wall with 60.0 cm height and 2.0 cm thickness made of acrylic material was installed on the reef. In order to prevent probable vibrations of the vertical wall from transferring to the pressure trans-

ducers, the transducers were set not to the acrylic wall but to a rigid steel frame which was directly fixed to side walls of the wave channel. An acrylic frame was used to hold the transducers in a vertical slit which was already prepared in the wall so that the transducers were not in contact with the vertical wall. The small space less than 0.1 cm between the acrylic frame and the vertical wall was coated by gum tape.

Pin point pressure transducers with operational capacity of 500 gf/cm^2 and overload capacity of 120 % were used for pressure measurements. Natural frequency of the pressure transducers are 10 KHz. Adaptors filled with silicon grease were used with the pressure transducers. Each adaptor had a pin hole of only 0.5 mm in diameter which enabled us to measure pressure very locally. Pressure data were recorded and digitized with 20 KHz sampling frequency which was adequate for being able to record the peak pressure during the impact and to collect sufficient numbers of data around the peak, as the shortest pressure rise time was 0.4 ms.

The spilling and plunging wave pressures were measured in detail at various elevations (spaced 5 mm apart, above the wave through level, here S.W.L.) and for different wall locations in their breaking zones. Since the breaking point varies with the breaker type, we were obliged to locate the wall in two different areas on the reef to measure pressure in the breaking zones of the spilling and plunging breakers. Hence, for the purpose of comparison, dimensionless relative distance of the wall from the breaking point, $\delta x/h_1$, is adopted to show the wall location in the breaking zone.

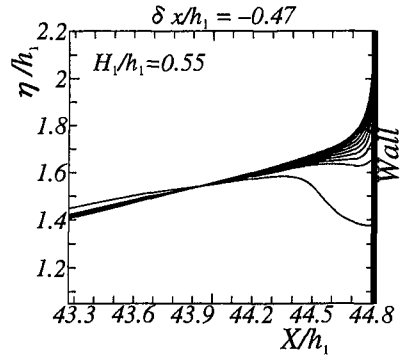
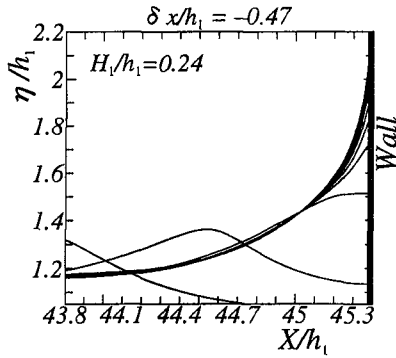
Numerical Simulations

Fully nonlinear BIM is used to compute the spilling and plunging wave profiles, the associated water particle velocities and accelerations, and the exerted pressure on a vertical wall installed in their breaking zones. Computations are made for the same incident waves and bottom topography used in the experiments. Details of the computational approaches, the concepts used for pressure computations and the computed free surface profiles of the spilling and plunging breakers (in the absence of the wall) at different stages of overturning process are presented in previous work of Azarmsa et al. (1996a).

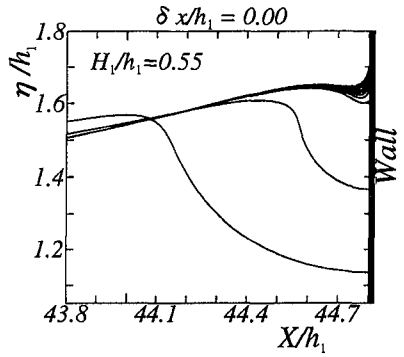
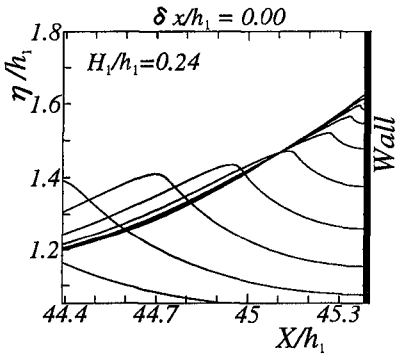
Figure 2 indicates how the spilling and plunging wave profiles vary during the collision with a vertical wall modeled at different locations on the reef. When these breakers collide with a vertical wall at a location before the breaking point (**Fig. 2 (a)**), their horizontal momentum smoothly converts into the vertical momentum and as a result, water rises up the wall. For the wall at the breaking point (**Fig. 2 (b)**), the front face of both the breakers converges toward a point on the wall. The elevation of the focus of the front face of the plunging breaker on the wall is only a little higher than the elevation of the incident wave crest. But since the slope of the front face of the spilling breaker is milder than that of the plunging breaker, the water line at the wall can considerably rises up the wall

Spilling

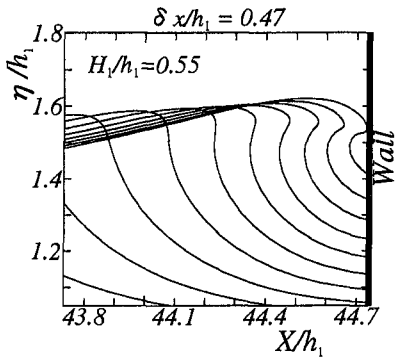
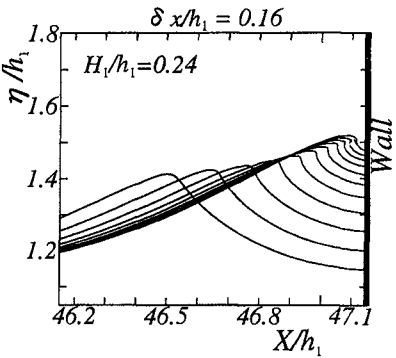
Plunging



(a) Before breaking



(b) Breaking point



(c) After breaking

Figure 2: Computed profiles for the spilling and plunging breakers during the collision with a vertical wall.

before that the wave crest could make a contact with the wall. As a result, the elevation of the focus of the front face of the spilling breaker on the wall is much higher than the elevation of the incident wave crest. **Figure 2** (c) indicates that collision of the plunging breaker with the wall at a location after the breaking point results in entrapping air. However, air is not entrapped between the front face of the spilling breaker and the wall, as expected.

Pressure Time Histories

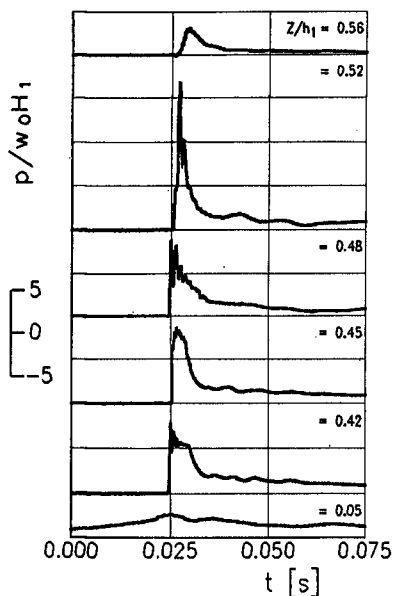
In order to investigate the characteristics of the plunging and spilling wave pressures, detailed measurements of pressure in both horizontal and vertical directions were carried out and variation of pressure time history with wall locations in the breaking zone and elevations along the wall are investigated.

a) Plunging Breaker

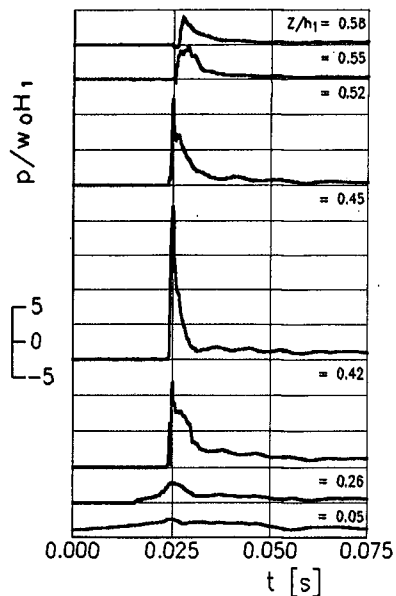
Pressure records on the wall installed in a location very near to the breaking point ($\delta x/h_1 = -0.13$) are shown in **Fig. 3** (a). The pressure measured near the still water level is very similar to the standing wave pressure and characterized by long pressure rise time and low maximum pressure value. However, as the elevation increases, the dimensionless value of maximum pressure exerted on the wall becomes larger so that $p_{max}/\omega_0 H_1 > 15$ is observed at the elevation of $z/h_1 = 0.52$ just below the wave crest. Comparisons among the pressure time histories measured between the elevations $z/h_1 = 0.42$ and 0.52 reveal that although the pressure rise times in these records are very short and more or less the same, the maximum pressure values and the pressure fall times differ from case to case.

Figure 3 (b) illustrates the pressure time histories recorded on the wall installed at the breaking point ($\delta x/h_1 = 0.00$). Comparisons between **Fig. 3** (a) and (b) reveal that for only a small (2.0cm) change in the wall location, the pressure time histories measured at the elevations of $z/h_1 = 0.42, 0.45$ and 0.52 have considerably changed. The maximum pressure value has increased more than twice at the elevations of $z/h_1 = 0.42$ and 0.45 , but it has decreased at the elevation of $z/h_1 = 0.52$.

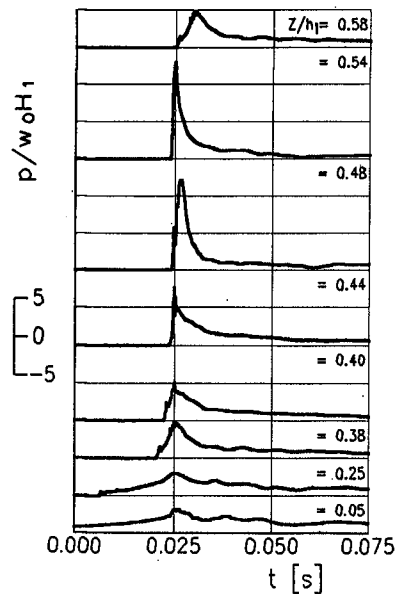
In fact, when the wall is located at the location of $\delta x/h_1 = -0.13$ violent vertical motion of the water on the wall prevents the wave crest from making a direct impact on the wall and causes the water particles near the wave crest to move upward. However, change of the wall location from $\delta x/h_1 = -0.13$ to the breaking point ($\delta x/h_1 = 0.00$) allows the wave to deform more before colliding with the wall. As a result, the wave front face becomes nearly vertical and the wave crest makes a direct impact on the wall just before that the water rising on the wall reaches the wave crest elevation. Therefore, change in the wall location allows a change in direction of movement of the water particles near the wave crest from an upward direction to a nearly horizontal one. Moreover, the water jet observed by video camera just starts forming at the breaking point. In other



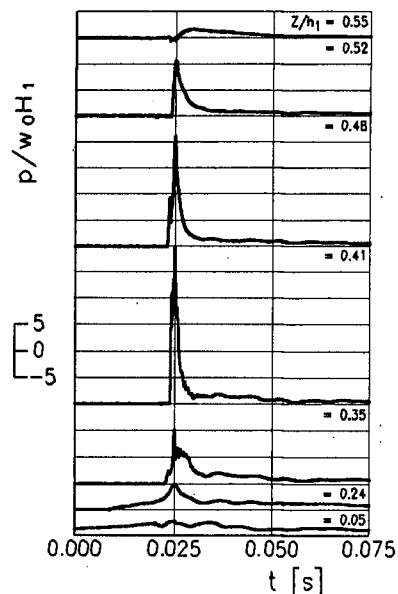
a) Near breaking ($\delta x/h_1 = -0.13$)



b) Breaking point ($\delta x/h_1 = 0.00$)



c) After breaking ($\delta x/h_1 = 0.07$)



d) After breaking ($\delta x/h_1 = 0.47$)

Figure 3: Time histories of the plunging wave pressure recorded on the wall at different locations.

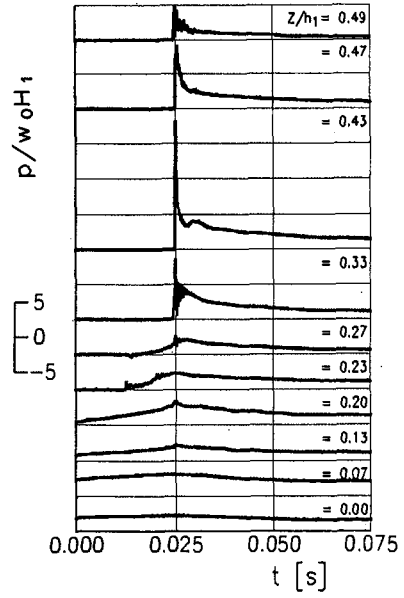
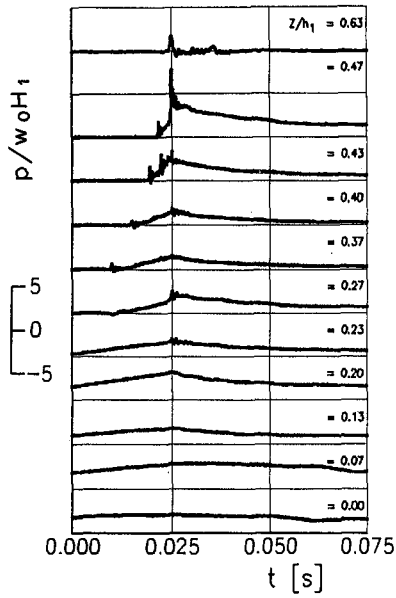
words, the velocity and acceleration of water particles which are near the wave crest and form the jet have also increased. Therefore, it can be concluded that the reason why both of the pressure intensity and the elevations at which high pressures take place change sensitively with the wall locations should be closely related to the rapid change in the wave kinematics.

Time histories of the pressure exerted on the wall installed at two different locations after the breaking point are shown in **Fig. 3** (c) and (d). Pressure time histories measured on the wall at different elevations, especially those near the still water level are characterized by low frequency oscillations which are supposed to be excited due to the dynamics of air entrapped between the curved front face of a plunging breaker and a vertical wall. Entrapped air also makes the pressure rise time become longer. Comparisons between **Fig. 3** (b) and (d) reveal that although the pressure rise time becomes longer due to the entrapped air influence, the maximum pressure value remains in the same order or becomes even larger (e.g. at the elevation of $z/h_1 = 0.41$, **Fig. 3** (d)) than those measured at the breaking point ($\delta x/h_1 = 0.00$). This confirms that the maximum pressure value does not necessarily change inversely with the pressure rise time, as mentioned before. Moreover, the impact pressure occurs in a wider area on the wall at the location of $\delta x/h_1 = 0.47$. Comparisons between the pressure time history recorded at the elevation of $z/h_1 = 0.41$ (**Fig. 3** (d)) and the pressure records on the wall at the breaking point (**Fig. 3** (b)) reveal that the overturned waves may exert even stronger impacts on the wall than the waves which just break on the wall with an almost vertically fronted face (see also **Fig. 6** (c) and (e)). As long pressure rise time, multiple peaks and low frequency oscillations following the peaks reveal and also as seen in **Fig. 2**, a big amount of air is entrapped between the front face of the overturned wave which collides with the wall at the location of $\delta x/h_1 = 0.47$. Therefore, occurrence of such a high impact pressure may be related to the velocity and acceleration of water particles which their values have also become larger, in comparison with their values at the breaking point. As a result, it can be concluded that although the entrapped air is generally supposed to reduce the intensity of the impact pressure, it does not necessarily control the occurrence of high impact pressures.

b) Spilling Breaker

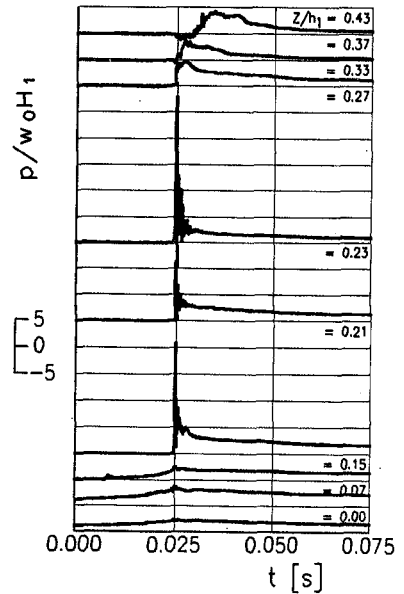
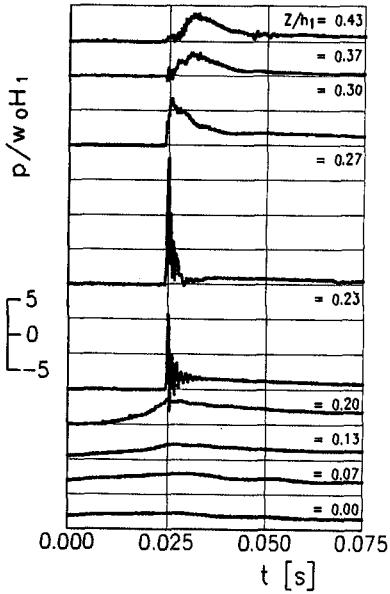
Figure 4 (a) indicates that for a wall location close to the breaking point ($\delta x/h_1 = -0.27$), the pressure recorded at and near the still water level is similar to the standing wave pressure. However, as the elevation increases, the pressure rise time becomes shorter and the maximum value of pressure increases so that it exceeds the value of $7\omega_0 H_1$ at the elevation of $z/h_1 = 0.47$.

The pressure time histories recorded at the breaking point (**Figure 4** (b), $0.33 < z/h_1 < 0.47$) are characterized by short rise time and high peak value. The pressure time history recorded at the elevation of $z/h_1 = 0.43$ reveals that even the spilling breaker exerts the impact pressure on the wall. This indicates



a) Near breaking ($\delta x/h_1 = -0.27$)

b) Breaking point ($\delta x/h_1 = 0.00$)



c) After breaking ($\delta x/h_1 = 0.67$)

d) After breaking ($\delta x/h_1 = 1.47$)

Figure 4: Time histories of the spilling wave pressure recorded on the wall at different locations.

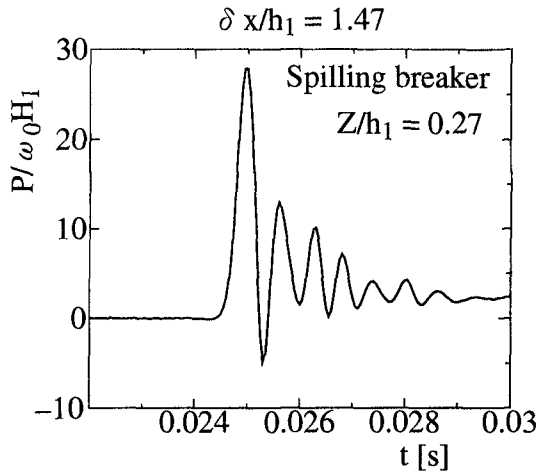


Figure 5: Oscillations in the time history of the spilling wave pressure.

that occurrence of the impact pressure is independent of breaker type, as concluded by Azarmsa et al., (1996a). Since a spilling breaker does not entrap an air pocket (as previously seen in **Fig. 2**), this result also indicates that the impact pressure may be generated even in the absence of entrapped air. As the elevation increases (above the elevation of $z/h_1 = 0.43$), the maximum value of pressure decreases, although the pressure rise time remains short.

The results shown in **Fig. 4** (c) and (d) make clear that as well as a plunging breaker, a spilling breaker also exerts the impact pressure on a vertical wall at a location after the breaking point. As seen previously (**Fig. 3**(c)), low frequency oscillations which demonstrates presence of an entrapped air pocket are observed in the time histories of the plunging wave pressure. In contrast, very high frequency oscillations are detected in the time histories of the spilling wave pressure. To see better these oscillations, one of these records is shown in **Fig. 5** in a smaller time scale. Frequency of these oscillations is more than 1.6 KHz which is much higher than the frequency of oscillations observed in the time histories of the plunging wave pressure (reported here or those reported in the literature). Besides, these oscillations are damped in less than 4ms. Therefore, it seems that these oscillations are excited by some small air bubbles temporarily entrapped between the unstable wave front and the vertical wall or resulted from partial compression and expansion of the air between the wall and upper side of the wave front when it is forced to go out rapidly (see wave profiles of the spilling breaker while colliding with a wall at a location after the breaking point, **Fig. 2** (c)).

Comparisons between the spilling (**Fig. 4**) and plunging (**Fig. 3**) wave pressures exerted on the wall in the after breaking area ($\delta x/h_1 > 0.00$) reveal that

air pocket entrapped by the plunging breaker causes the pressure rise time to increase. From the comparisons, it is also understood that for the records with almost the same maximum pressure values, the pressure rise times are different and vice versa, as also mentioned before. Therefore, it can be concluded that the maximum pressure value does not necessarily obey an inverse relation with the pressure rise time, although some empirical formulas for the peak value of pressure have been based on such an assumption (e.g. Weggel and Maxwell; 1970, Kirkgoz; 1990, Hattori et al.; 1994).

Vertical Distribution of the Maximum Pressure

The study of vertical distribution of the maximum pressure is important not only for evaluating the critical force and momentum working on the structure during the wave impact but also for investigating the localized characteristics of the impact pressure which may be the cause of the local damages in a vertical structure.

To derive the vertical distribution of the maximum pressure, the maximum pressure values of repeated tests carried out under the identical initial experimental conditions are averaged and normalized by $\omega_0 H_1$ at each measuring point. **Figures 6 and 7** respectively show the obtained results for the plunging and spilling breakers at different wall locations in their breaking zones. At each measuring point, the range of pressure variation and the mean value for repeated experiments are illustrated by the interval between two bars and open circle, respectively. From the comparisons, it is found that for both the breakers the peak value of pressure exerted on the wall increases as the wall is shifted more from the before breaking area ($\delta x/h_1 < 0.00$) toward the breaking point ($\delta x/h_1 = 0.00$).

At the breaking point ($\delta x/h_1 = 0.00$), both the experimental and numerical results are illustrated. The solid circle indicates the calculated peak value of the pressure resulted from the direct impact of the free jet on the wall. This value is calculated on the base of horizontal momentum and inertia of the jet (Azarmsa et al., 1996 (a)). The solid line represents vertical distribution of maximum pressure computed directly from the BIM by considering both of the horizontal and vertical components of water particle kinematics. Agreement between the experimental result and the numerical one using the BIM (the open circles and the solid line) reveals that vertical distribution of both the plunging and spilling wave pressures can be computed under the assumption of irrotational flow in the incompressible and inviscid fluid. Moreover, the difference between the peak values of the pressure resulted from each of the computational concepts (the solid circle and line) indicates the significant contribution of vertical velocity and acceleration of water particles in generation of the impact pressure.

As seen, both the breakers exert the impact pressure on the wall not only at the breaking point but also in the after breaking area ($\delta x/h_1 > 0.00$). From the comparisons, it is also found that as the wall is moved from the breaking point toward the after breaking area, size of the area on the wall subjected to

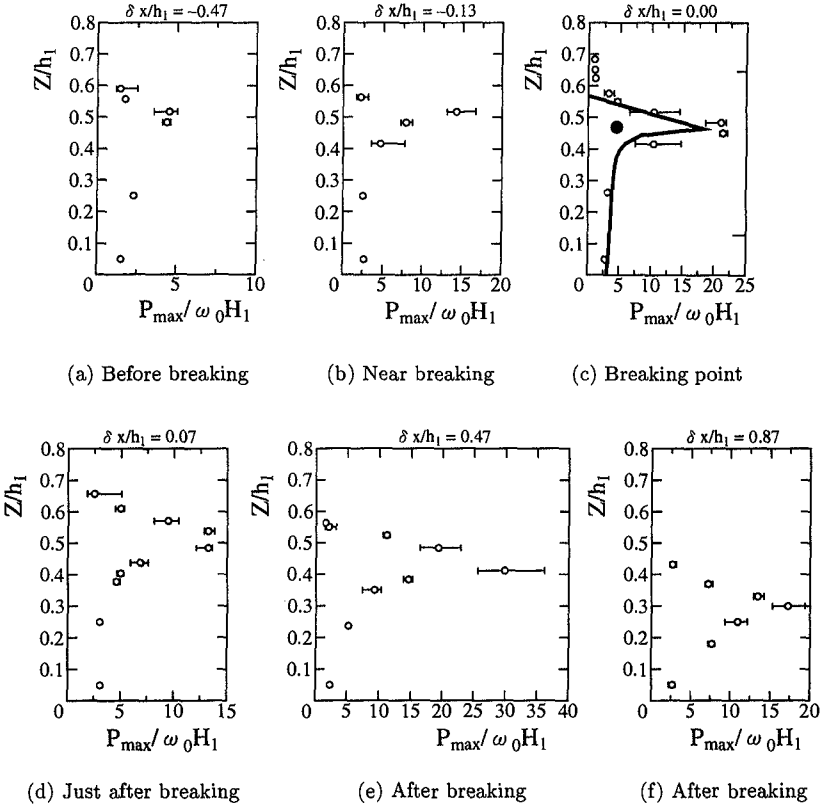


Figure 6: Vertical distribution of the maximum pressure exerted by the plunging breaker on the wall at different locations.

high pressures becomes larger and reach to its largest value at the location of $\delta x/h_1 = 0.47$ for the plunging breaker and $\delta x/h_1 = 1.47$ for the spilling breaker. Therefore, it can be concluded that the total force exerted on the wall in the after breaking area should be the largest. On the other hand, comparisons between Fig. 6 and Fig. 7 reveal that size of the impact zone for the spilling breaker is smaller than that for the plunging breaker. This is because size of the jet (which contains water particles of the most critical kinematics) excited by a spilling breaker is much smaller than that by a plunging breaker. From the comparisons, it is also found that the ranges of pressure variation for the repeated experiments are larger for the spilling breaker. The reason why in the impact zone the spilling wave pressure varies more sensitively with the repeats of the experiments is also related to the fact that size of the jet excited by a spilling breaker is small. In fact because of the smallness of the jet size, the elevation at which the impact pressure is exerted on the wall may change owing to a small

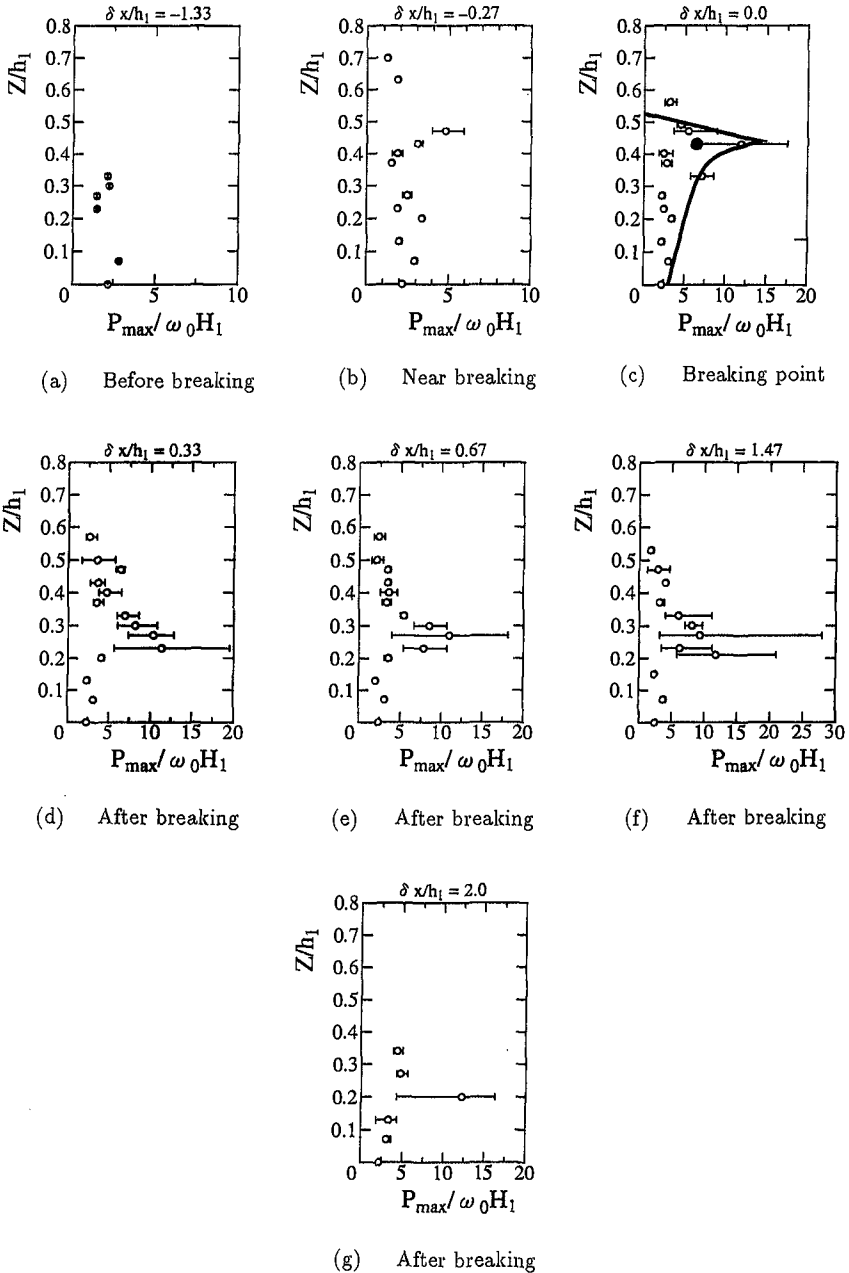


Figure 7: Vertical distribution of the maximum pressure exerted by the spilling breaker on the wall at different locations.

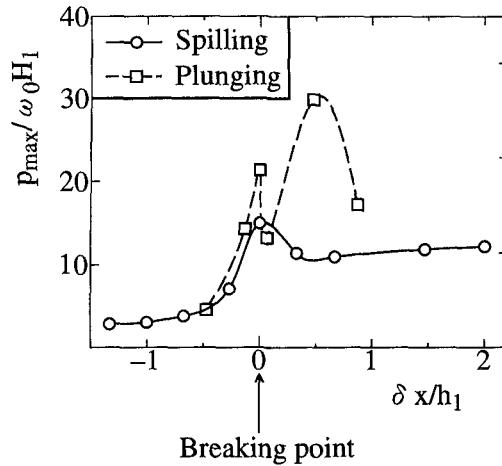


Figure 8: Variation of the peak value in the vertical distribution of maximum pressure with wall locations.

change in the collision condition of a spilling breaker with a vertical wall and as a result, a fixed pressure transducer may or may not be affected by strong impact pressure, from one to another repeat of the experiments. Therefore, it can be concluded that the variability of the maximum pressure in repeated tests is not only due to the randomness and dynamics of entrapped air, but also may be because of the size and elevation of the jet at the instant of collision.

For both of the breakers, variation of the peak value in the vertical distribution of the maximum pressure with wall locations is shown in **Fig. 8**. The results for the plunging breaker reveal that pressure exerted by an overturned wave may be even higher than that by a wave just breaking on the wall with an almost vertically fronted face. The reason may be related to the fact that kinematics of an overturned wave is more critical than the kinematics of the same wave just at the breaking point. In contrast, the pressure peaks recorded for the spilling breaker at different wall locations near the breaking point and in the after breaking area are almost the same. This is not unexpected because the kinematics of the spilling breaker does not change so much during the overturning process. **Figure 8** also reveals that the obtained values for the spilling breaker are smaller than those for the plunging breaker. Since there is a big difference between the spilling and plunging breakers with regard to the volume of entrapped air, if the impact pressure is related to the reduced velocity of sound in a water-air mixture (Schmidt et al., 1992; Hattori, 1994; Peregrine and Topliss, 1994), the pressure exerted by the spilling breaker is expected to be higher (see discussion made by Azarmsa et al., 1996a). However, the results of this study make clear that occurrence of the impact pressure can not be related to the water hammer effect even if the reduced velocity of sound in a water-air mixture is used.

Conclusions

The results of this study clearly show that different types of breaking waves at different steps of their overturning process exert the impact pressure on a vertical structure. It is made clear that occurrence of the impact pressure can not be related to the water hammer effect, even if the reduced velocity of sound in a water-air mixture is used. Besides, it is shown that although the entrapped air reduces the intensity of the impact pressure, it does not necessarily control the occurrence of high impact pressures. Further, it is made clear that occurrence of the impact pressure is closely related to the internal kinematics of breaking waves. Therefore, the condition under which the impact pressure may occur is not critically dependent on wave geometry, entrapped air dynamics and so on. In other words, the structures subjected to the breaking waves quite frequently experience the impact pressure. As a result, even if the impact pressure is supposed to cause local damage in the structure, after sufficient number of repeats of the event at different elevations the stability of the structure may be threaten in whole.

References

- Azarmsa, S. A., T. Yasuda, and H. Mutsuda (1996a):** Breaker-type effect on impact pressure exerted on a vertical wall, *J. Coastal Eng. in Japan*. Vol. 39, No. 1, JSCE, pp. 39-57.
- Bagnold, M. R. A.(1939):** Interim report on wave-pressure research, London, Engineering Research, pp. 202-226.
- Chan, E. S. and W. K. Melville (1988):** Deep-water plunging wave pressures on a vertical plane wall, *Proc. R. Soc. Lond., Vol.A* 417, pp. 95-131.
- Cooker, M.J. and D.H. Peregrine (1990):** Violent water motion at breaking-wave impact, *Proc. Coastal Eng. Conf.*, pp.164-176.
- Hattori M., A. Arami and T. Yui (1994):** Wave impact pressure on vertical walls under breaking waves of various types, *Coastal Engineering*, 22, pp. 79-114.
- Kirkgoz, M. S. (1982):** Shock pressure of breaking waves on vertical walls, *J. of the waterway, port, coastal and ocean division, ASCE*, Vol. 108, No WW1, pp. 81-95.
- Kirkgoz, M. S. (1990):** An experimental investigation of a vertical wall response to breaking wave impact, *Ocean Eng.*, 17(4), pp. 379-391.
- Oumeraci, H., H. W. Partensky, E. Tautenhain and H. Nickels (1992):** Large-scale model investigations: a contribution to the revival of vertical breakwaters, *ICE, Proc. of Coastal Structures and Breakwaters Conf. London*, pp. 207-220.
- Peregrine, D.H. and M.E. Topliss (1994):** The pressure field due to steep water waves incident on a vertical wall, *Proc. of Coastal Eng. Conf.*, pp. 1496-1510.
- Schmidt, R., H. Oumeraci and H. W. Partensky (1992):** Impact loads induced by plunging breakers on vertical structures, *Proc. 23rd Coastal Eng. Conf., Venice, ASCE*, pp. 1545-1558.
- Weggel, J.R. and W.H.C. Maxwell (1970):** Experimental study of breaking wave pressures, *Proc. Offshore Tech. Conf., Texas, OCT 1244*, pp. 175-188.

CHAPTER 190

DYNAMIC RESPONSE OF VERTICAL ELASTIC WALLS TO BREAKING WAVE IMPACT

Masatato Hattori¹ and Nobuaki Tsujioka²

Abstract

Experiments were focused on deflection responses of the wall member of upright structures to impulsive wave forces. The experiments revealed that the wall deflection response depends on wave loading modes as well as on natural frequency of the wall member system, f_{NW} . Single degree-of-freedom model of transient impact shows that the peak wall deflection is given as a function of the ratio between rise time of wave force τ_F and f_{NW} , representing characteristics of the wave load and the wall member. The measured peak deflection agrees well with the predicted by the model. In addition, the model indicates that with decreasing natural frequencies of the wall system, the wave load mode brought about greater peak deflections changes from the mode of short duration force to that of long-lasting force.

Introduction

Steep breaking waves impinging onto upright structures bring about high impact forces of short duration. It has been considered that such impact forces are not the cause of sliding and/or overturning of massive structures. On the other hand, some studies (e.g., Weggel and Maxwell, 1970; Mogridge and Jamieson, 1980) pointed out a possibility that the impact force will cause a cumulative and local damage due to shear and fatigue failures to the structure. As a result of successive attacks of the breaking wave, such damage grows likely into a sudden breakdown of the structure.

1 Professor, Department of Civil Engineering, Chuo University, Bunkyo-ku, Tokyo 112, Japan.

2 Graduate-Student, ditto.

The failure processes, therefore, seem to be relevant to deflection responses of the wall member to the impact.

Many studies have been conducted to provide functional information on the stability of upright structures. In contrast with this, as far as we know, only three previous studies (Witte, 1988; Kirkgöz, 1990; Hattori, 1994) have discussed dynamic responses of the vertical wall to impact wave pressures. Therefore, more precise studies are requested to deepen our understanding of the deflection response of elastic walls, as the first step toward the explication of failure processes of the wall member.

Accordingly, we conducted a series of comprehensive experiments with the following objectives;

- (1) to build up the reliable data base of deflection responses of the vertical wall due to impulsive wave forces for designing the structures,
- (2) to examine influences of the wave loading mode and the physical property of elastic walls on the wall deflection response, and
- (3) to discuss a critical condition, producing the greatest wall deflection, based on a single degree-of-freedom model of transient impact.

Experimental setup and Measurements

Figure 1 shows the general arrangement of experimental setup. Experiments were conducted in a glass-walled wave flume, 0.30 m wide, 0.55 m high, and 20 m long, in which a steel plane beach of 1/20 slope was installed. Regular waves were produced by a reflection-absorbing wave maker of flap-type, controlled by a programmed analogue signal yielding a regular wave train. Vertical wall complex was mounted rigidly on a plastic mound with a foreshore slope of 1/10. Except for the wall complex, the experimental setup and measuring techniques used in this study are basically the same as those used in the previous study (Hattori et al. 1994).

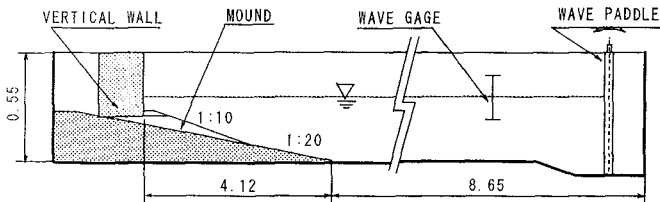


Fig. 1 General arrangement of the experimental setup. (units: m)

Vertical wall is composed of two parts, the rigid wall of 10 mm-thick steel plate (0.30 m wide and 0.50 m high) and the square elastic wall as shown in Fig. 2. The elastic wall is a thin plate fully fixed each side with rigid steel frames, and it is

inlaid into the lower section of the rigid wall. Taking into account influences of the wall physical property on the deflection response, we used three elastic plates with different properties (Table 1).

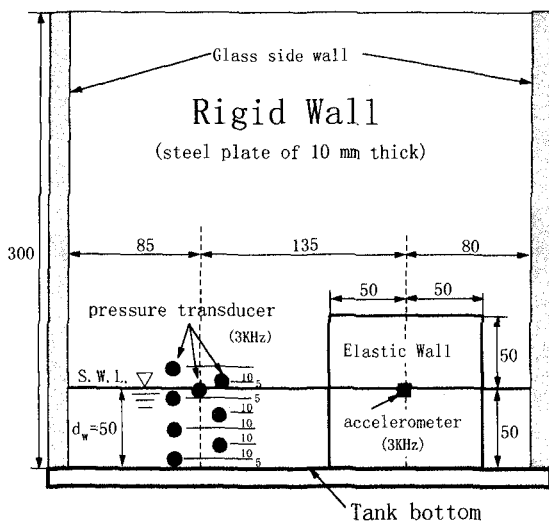


Fig. 2 Wave tank cross-section showing the location of rigid and elastic walls. (units: mm)

Table 1 Physical properties of the elastic plates.

Plate	Thickness (mm)	Density (g/cm ³)	E (KN/m ²)	f _{NW} (Hz)	
				in air	in water
Spring metal	1.0	9.0	1.0 × 10 ⁸	557	271
	0.5	9.0	1.0 × 10 ⁸	290	100
Polyvinyl chloride	0.5	1.14	1.6 × 10 ⁷	300	59

E: Modulus of elasticity.

In this study, the wall deflection response will be examined in terms of the natural frequency of the elastic wall system, f_{NW} , as a relevant parameter representing dynamic characteristics of the elastic wall. Taking account of added mass effect of ambient water in front of the wall, the natural frequency (first mode) of wall deflection system (abbreviated to W-D system) were calibrated by a pendulum test with changing the water depth in front of the wall. As an example, the natural

frequency of 1 mm-thick spring metal plate wall is given by Fig. 3, as a function of the relative water depth d_w/h_a (d_w : water depth at the wall, and h_a : elastic wall height).

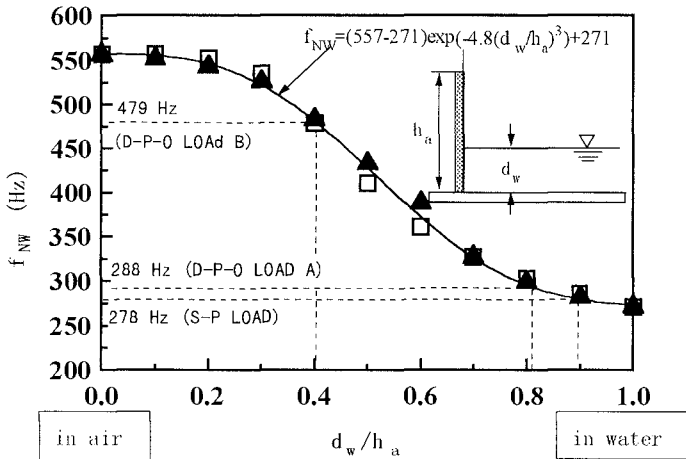


Fig. 3 Natural frequency of the spring metal wall. (1.0 mm-thick)

When pressure transducers are installed on the elastic wall, the output signals are usually contaminated by wall oscillations (Hattori, 1994). To avoid such undesirable effect, eight semi-conductor type transducers (10 mm ϕ , and natural frequency: 3 KHz) were deployed on the rigid wall (Fig. 2). Impact pressures were recorded on digital recorders over six wave periods at a sampling frequency of 5 KHz. The time history of the wave force per unit wall width, $F^*(t) [=F(t)/\gamma H_B^2]$, was computed by depth integration of the pressure time histories. γ is the specific weight of water, and H_B is the breaking wave height.

Wall oscillations excited by wave impact were detected by an accelerometer (natural frequency: 3 KHz) setting up at the elastic wall center (Fig. 2). Using time series data of the wall oscillations, the wall deflection at the wall center $\delta(t)$ was computed by means of a step by step integration of a linear acceleration method.

Experimental Results and Discussions

The wall deflection response depends closely on the magnitude and the rise time of impact forces (Hattori, 1994). Accordingly, we classify the wave loading into the three following modes (Hattori et al., 1994), according to the relationship between the wave force oscillation frequency f_{FO} and the natural frequency of W-D system f_{NW} . That is,

- (1) Single peaked load (S-P LOAD) with very short duration: $f_{FO} \gg f_{NW}$,

- (2) Damped pressure oscillation load A (D-P-O LOAD A): $f_{FO} > f_{NW}$, and
 (3) Damped pressure oscillation load B (D-P-O LOAD B): $f_{FO} < f_{NW}$.

Time history records of the wave force and the wall oscillations were examined by the aid of a frequency spectral analysis. The time history records taken from a breaking wave collision are transient data that result from short duration nonstationary phenomena with a clearly defined beginning and end. Hence, frequency spectra of these data will be analyzed by means of techniques commonly used for stationary data.

Figure 4 shows a typical experimental result obtained from the S-P LOAD, an extremely high peak pressure of $p_p=1030 \text{ N/m}^2$ [$p_p^* (=p_p/\gamma H_B)=80.1$] occurs at just above the still water level (pressure records not shown). Fig. 4 (A) is time history records of the wave force and the wall oscillations of spring metal of 1-mm thick. $t^* [= t/(H_B/C_S)]=0$ on the time axis refers to the time of the peak wave force. $C_S (=1500 \text{ m/s})$ is the sound velocity in water. Three video still pictures on the top of Fig. 4 provide a sequential change of impinging wave shape, at three different instants marked by thick arrows on the top of the time history records.

Fig. 4 (B) shows a comparison between the computed frequency spectra of the wave force and the wall oscillation data. From a comparison between time histories of the wave pressures (not shown) and the wave force (Fig. 4 (A)), we find that despite the peak wave pressures produced by S-P LOAD are extremely high magnitude, the maximum wave force does not attain a high magnitude ($F_M=1030 \text{ N/m}$), because of narrow region of the high peak pressures and of subtle time gaps between the peak pressures.

Just after impact, the wall starts to oscillate and keeps on oscillating with a natural frequency of the W-D system even after damping down the wave impact. In Fig. 4 (B), no any spectral peak appears on the frequency spectrum of wave force. In contrast with the wave force, on the frequency spectrum of wall oscillations, a distinct spectral peak is found at a frequency of 278 Hz correspond to the natural frequency of W-D system, in which the wall is almost in water (see Fig. 3, $d_w/h_a=0.9$).

Under D-P-O LOAD A, a thin air pocket is trapped between the wall and breaking wave front at impact, results in the wave force oscillations with higher frequencies than the natural frequency of the W-D system. Owing to short duration time of the wave force, the maximum wave force ($F_M=1720 \text{ N/m}$) is larger than that of S-P load (Fig. 4 (A)). Consequently, as seen in Fig. 5 (A), the spring metal wall of 1.0 mm-thick can not response to very rapid changes of the impact force and keeps to oscillate with its own natural frequency, even after the wave force oscillations damp down. The computed frequency spectrum of wave force record indicates a distinct spectral peak at a frequency of 479 Hz, while that of wall oscillation record shows the only peak at a frequency of 288 Hz, corresponds to the natural frequency of W-D system (see Fig. 3, $d_w/h_a=0.81$).

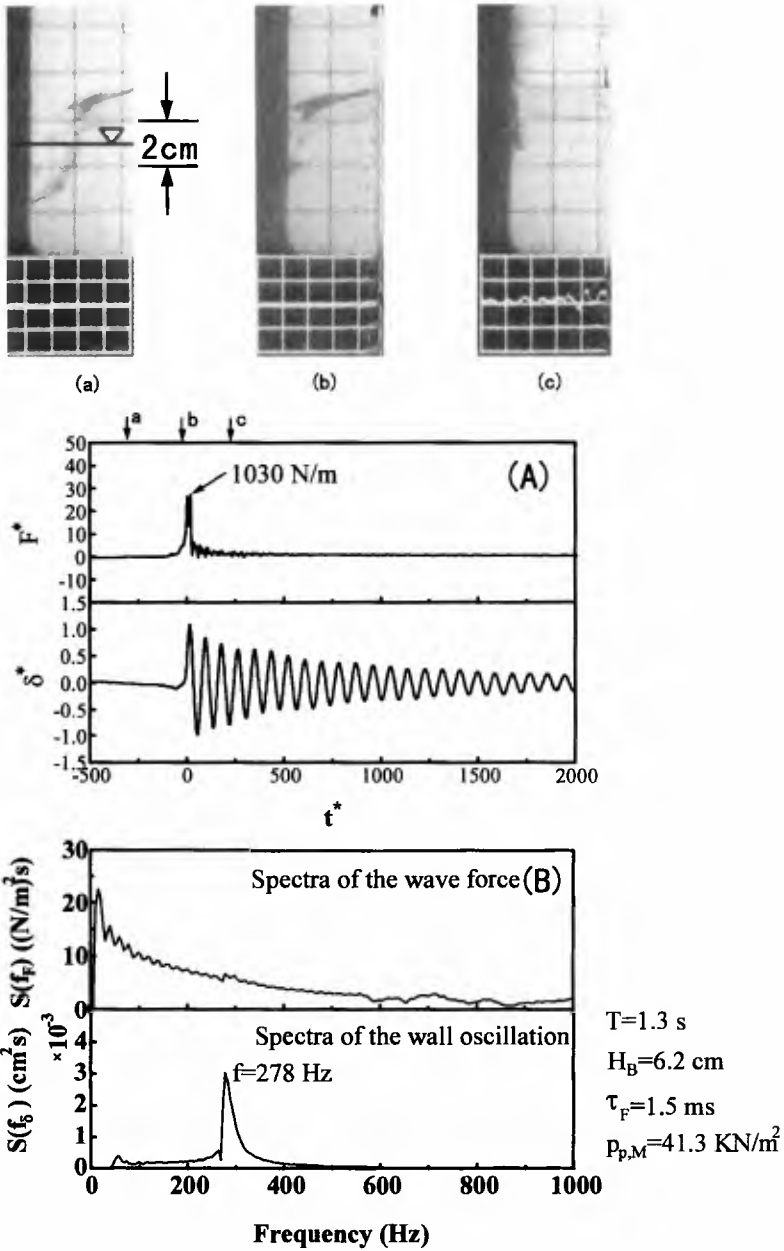


Fig. 4 Time history records of frequency spectra of the wave force and the wall deflection. (S-P LOAD)

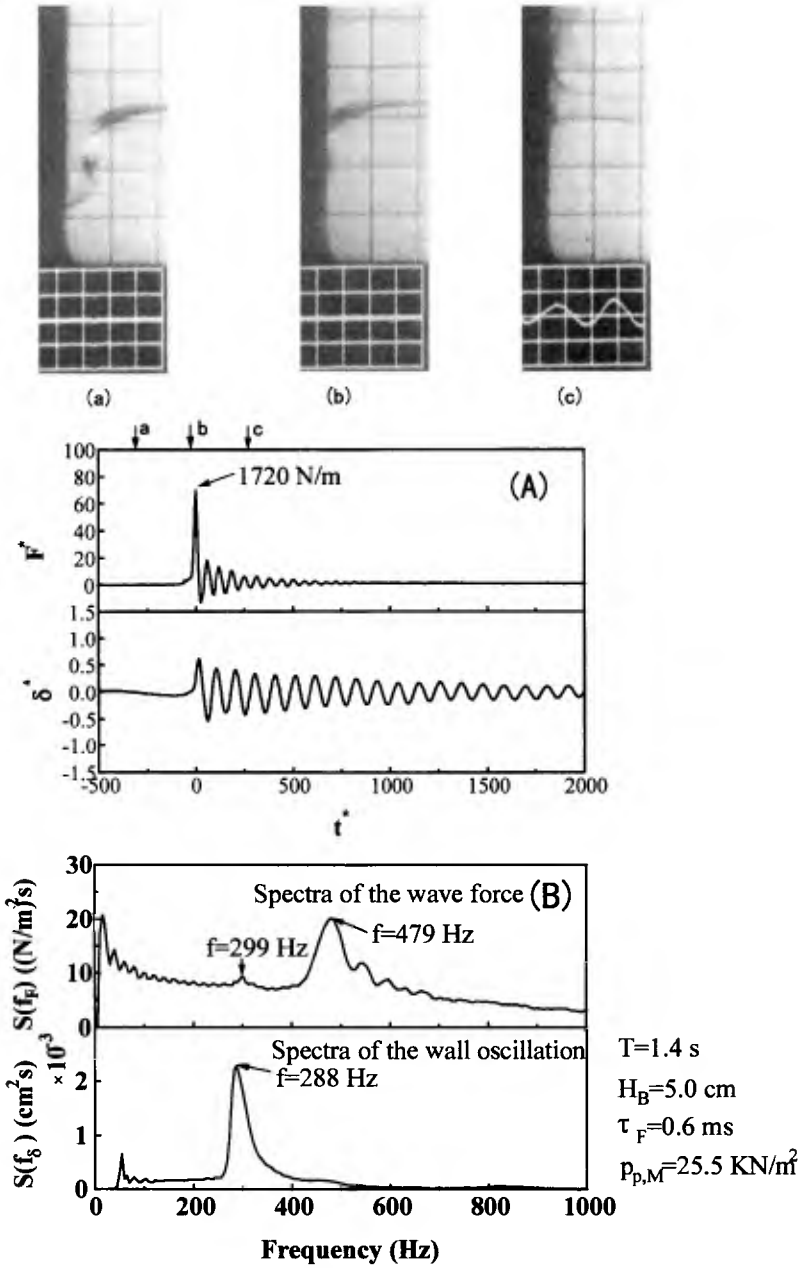


Fig. 5 Time history records and frequency spectra of the wave force and the wall deflection. (D-P-O LOAD A)

Figure 6 shows the time history records taken from D-P-O load B and these computed frequency spectra. The D-P-O LOAD B occurs when a larger air pocket is trapped at impact. Therefore, the peak pressure magnitudes decrease and the pressure rise times increase. These wave loading characteristics are clearly reflected in the wave force record (Fig. 6 (A)). The wave force record also displays a regularly damped oscillations, while the wall oscillation record indicates a rather complicated behavior owing to collisions of irregular wave front of impinging breakers on the wall, as seen in the still pictures on the top of Fig. 6 (A). Frequency spectrum of the wave force record indicates that the wave force oscillates with a frequency of 186 Hz. On the other hand, the wall oscillations are composed of two dominant components in frequency, the natural frequency f_{NW} of 479 Hz (see Fig. 3) and the frequency of 186 Hz, identical with the wave force oscillations. The wall oscillations with 186 Hz frequency attenuate rapidly with the wave force oscillations. It seems that the small spectral peak at 250 Hz indicates the occurrence of the free oscillation of second mode of W-D system.

From the experimental results, we notice the following facts;

- (1) When frequencies of the wave force oscillations are higher than the natural frequency of the W-D system (S-P LOAD and D-P-O LOAD A), the only wall oscillation with the natural frequency of W-D system is excited just after the wave impact. On the other hand, D-P-O LOAD B excites wall oscillations with two dominant components in frequency, the wave force oscillation and the natural oscillation of W-D system. In either case, the wall keeps on oscillating with the natural frequency even after the impact force damp down.
- (2) The natural frequency of W-D system changes with the contact length of entrapped air pocket with the wall, depends on the wave loading mode (see Fig. 3). Then, the contact length is measured from still video pictures taken at the instant of a wave impact, and the natural frequency of W-D system is estimated by using the pendulum test result. It is found that the natural frequency is almost the same as the measured one.
- (3) Wave pressure records taken from the D-P-O LOAD display regular pressure oscillations with almost the same changes in magnitude and in phase (not shown). A thinner air pocket entrapped at impact brings about a higher peak pressure of short duration and results in pressure oscillations with a higher frequency (Hattori et al., 1994). As the result, maxima of the wave force due to D-P-O LOAD tend to be larger than that due to S-P LOAD, which produces very high peak pressures over narrow zone near the still water level. On the basis of the measured pressure record, Figures 7 (a) and (b) show relations of $\dot{p}_{P,M} \sim \dot{\tau}_P$ and $\dot{F}_M \sim \dot{\tau}_F$. $\dot{p}_{P,M}$ ($= \dot{p}_{P,M}/\gamma H_B$) is the maximum peak pressure, and $\dot{\tau}_P$ ($= \dot{\tau}_P/(H_B C_S)$) and $\dot{\tau}_F$ ($= \dot{\tau}_F/(H_B C_S)$) are the rise time of wave pressure and wave force. The variation trend of \dot{F}_M with $\dot{\tau}_F$ is similar to that of $\dot{p}_{P,M}$ with $\dot{\tau}_P$. However, we notice that maxima of the wave force due to D-P-O LOAD (open triangles) tends to be greater than that due to S-P LOAD. This is a very important evidence for designing the structure.

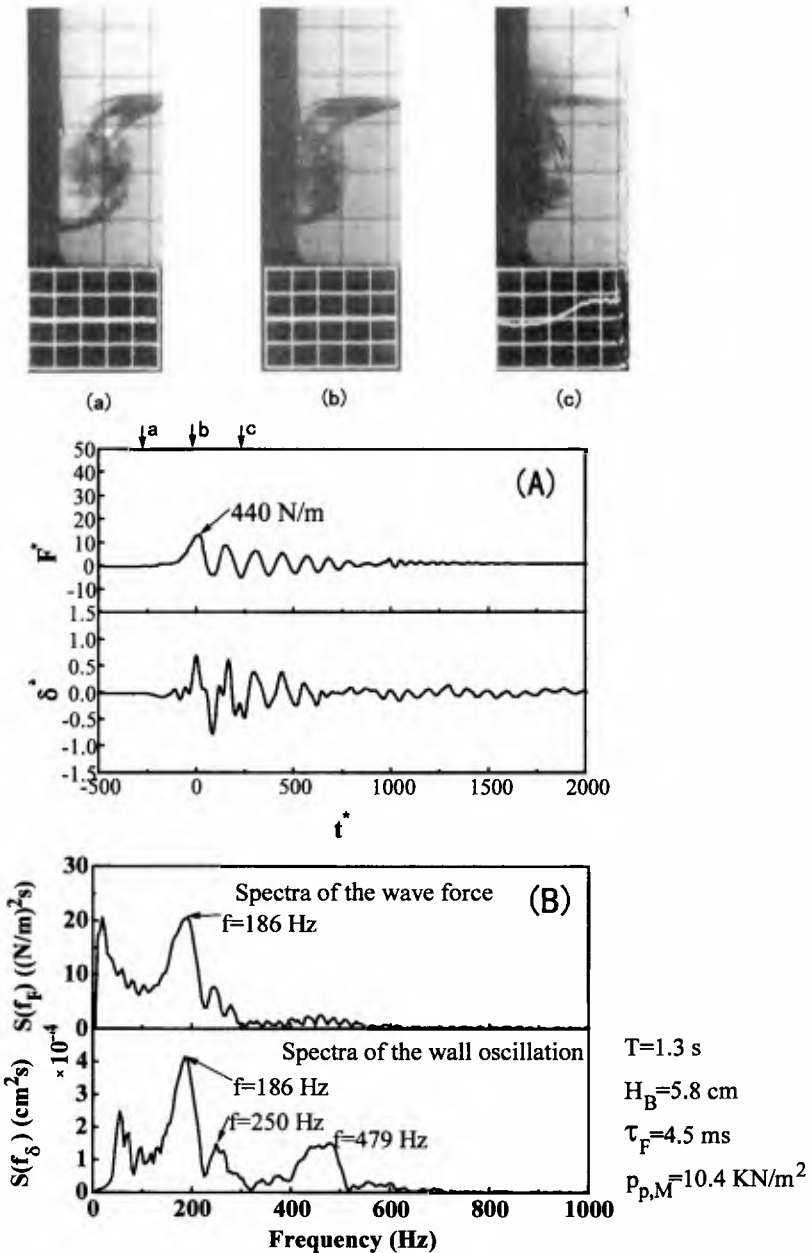


Fig. 6 Time history records and frequency spectra of the wave force and the wall deflection. (D-P-O LOAD B)

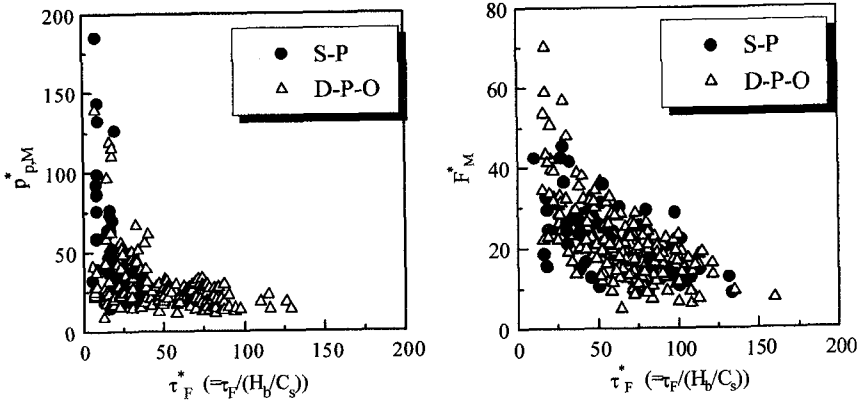


Fig. 7 Relation of $p^*_{P,M} \sim \tau^*_P$ and $F^*_M \sim \tau^*_F$.

(4) As seen in Fig. 4 (A) of the S-P LOAD, the wall oscillations lasting for a long time are gradually damped and maintains a almost constant frequency. This implies that both the fluid damping and the added mass due to the impinging water mass do not practically affect the wall deflection response to a transient impact.

Single Degree-of-Freedom Model for Transient Impact

In the following, we will discuss the wall deflection as a transient phenomenon caused by a wave impact of short duration. Based on the experimental results, assume that any damping and added mass effects caused by the water mass colliding on the wall can be neglected.

We use a single degree-of-freedom model of transient impact, in which the wall at rest is subjected a force input $F(t)$ and produces a wall deflection response $\delta(t)$. The equation governing the deflection response of the elastic wall system without damping (Fig. 8) is given by Eq. (1).

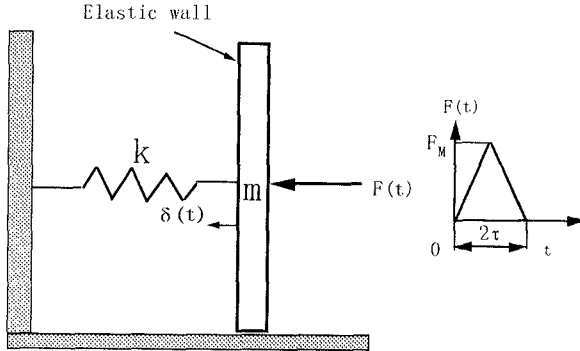


Fig. 8 Wall deflection system for transient impact.

$$m \frac{d^2\delta(t)}{dt^2} + k\delta(t) = F(t) , \tag{1}$$

where m is the wall mass including the virtual mass of impinging water, k is the spring constant, and t is the time. The input force $F(t)$ is assumed by a form of isosceles triangle with the height of F_M and the base of 2τ (Fig. 8). With the initial conditions of

$$\delta = d\delta(t)/dt = 0 : \text{at } t = 0, \tag{2}$$

the relative wall deflection δ/δ_s is obtained as Eqs. (3) to (5). δ_s is the wall deflection due to the maximum wave force F_M as a static load, distributed uniformly on the wall center elevation.

$$\delta/\delta_s = (t/\tau) - (\sin f_{NW}t / \sin f_{NW}\tau) ; (0 \leq t \leq \tau) \tag{3}$$

$$= (2\tau-t)/\tau + [2\sin f_{NW}(t-\tau) - \sin f_{NW}t] / \sin f_{NW}\tau ; (\tau \leq t \leq 2\tau) \tag{4}$$

$$= [2\sin f_{NW}(t-\tau) - \sin f_{NW}t - \sin f_{NW}(t - 2\tau)] / \sin f_{NW}\tau ; (2\tau \leq t) \tag{5}$$

, in which $f_{NW} = (1/2)(k/m)^{1/2}$: the natural frequency of the wall system. From Eqs. (3) to (5), we calculate the gain factor of wall deflection, $\delta_M^* (= \delta_M/\delta_s)$ and the relative lag time $\Delta t_\delta^* (= \Delta t \cdot f_{NW})$ between the maximum force F_M^* and peak deflection δ_M^* (Fig. 9), as a function of the relative rise time $\tau_F^* (= \tau_F \cdot f_{NW})$.

Variations of the gain factor δ_M^* and the lag time Δt_δ^* in terms of τ_F^* are shown in Fig. 9. The single degree-of-freedom model indicates that the largest peak wall deflection due to a given wave force attains 1.5 times as much as the static wall deflection, when the relative rise time $\tau_F^* = 0.45$, and that the peak wall deflection always appears after occurrence of the maximum wave force.

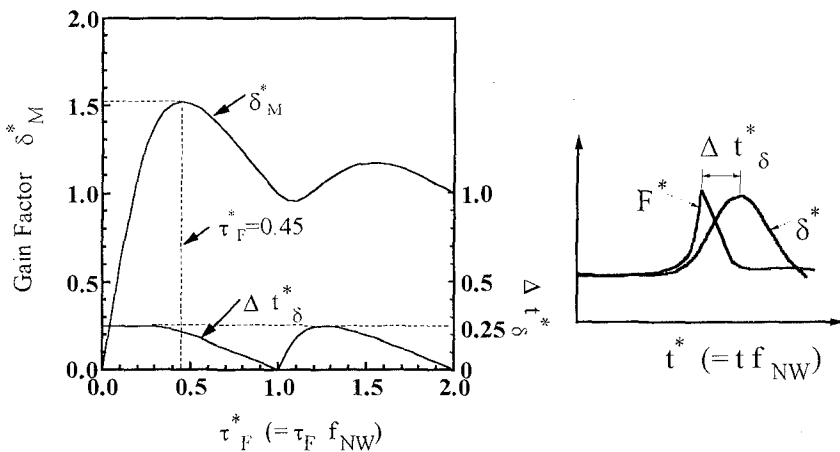


Fig. 9 Variations of δ_M^* and Δt_δ^* .

Figures 10 and 11 show respectively a comparison between the measured and predicted gain factor for 1 mm-thick spring plate and 0.5 mm-thick PVC plate walls.

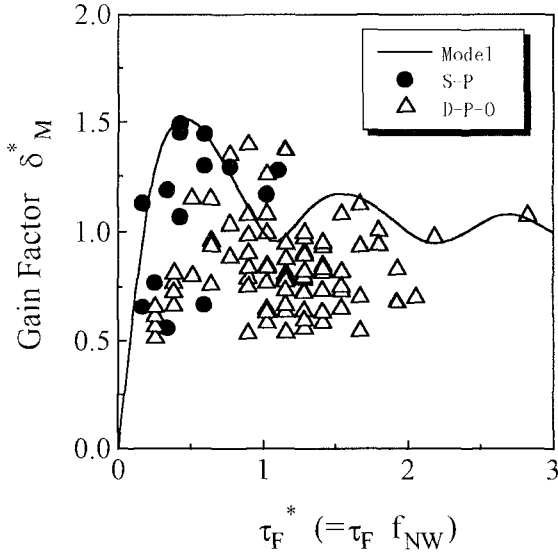


Fig. 10 Gain factor of the wall deflection.
(1.0 mm-thick spring plate wall)

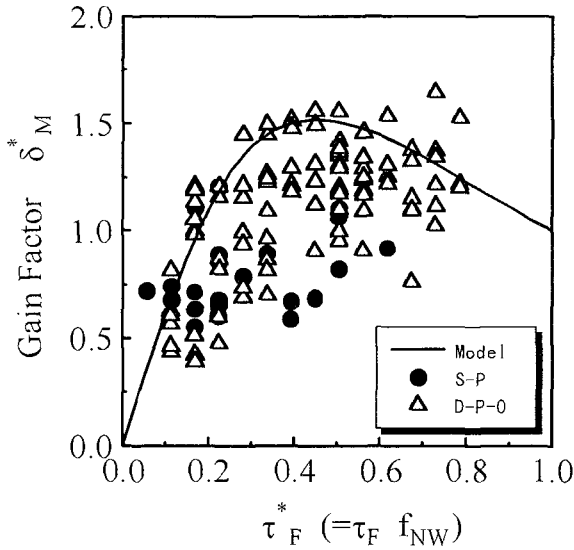


Fig. 11 Gain factor of the wall deflection.
(0.5 mm-thick PVC plate wall)

The solid line represents the model prediction. Although the experimental points are widely scattered owing to variability of the impact processes, the model agrees reasonably well with upper bounds of the experimental points. In case of the spring metal wall ($f_{NW}=557$ Hz in air), the large gain factor within range of $0 \leq \tau \leq 1$ is produced by the S-P LOAD (solid circles). On the other hand, in case of PVC plate ($f_{NW}=300$ Hz in air), the large gain factor within the same range appears under the D-P-O LOAD condition (open triangles).

Due to the three-dimensionality of the wave impact process, the convergent crest of breaking waves does not always hit simultaneously the rigid and elastic walls. As the result, we could not obtain reasonably good results on the variation of the delay time Δt^*_δ with the relative rise time τ^*_F .

Conclusions

We conducted laboratory experiments focused on wall deflection responses of the wall member of upright structures to impulsive wave forces. The wall deflection response relates closely not only to the wave load mode, the magnitude and the rise time of impact forces, but also to the natural frequency of the wall deflection system. The single degree-of-freedom model of transient impact describe well the wall deflection process. In addition, the experiments point out an very important fact that the wave force produced by single-peaked load is lower than that by the damped-pressure-oscillation load, such as D-P-O LOAD A. The main findings are as follows;

- (1) Both S-P LOAD and D-P-O LOAD A, $f_{FO} \gg f_{NW}$ and $f_{FO} > f_{NW}$, excite the wall oscillations only with the natural frequency of the W-D system. Such wall oscillations continue for a long time even after the wave impact damp down.
- (2) The wall oscillations due to the D-P-O LOAD B, $f_{FO} < f_{NW}$, consist of the two components in frequency, correspond to the wave force oscillations and the natural oscillations of W-D system.
- (3) The single degree-of-freedom model of transient impact describes well the wall deflection response and is verified by comparisons of the experiments. The gain factor of the wall oscillation δ^*_M is a function of the relative rise time τ^*_F , and the peak value of δ^*_M attains 1.5, when $\tau^*_F = 0.45$.

References

- Hattori, M.(1994): Wave impact pressures on vertical walls and the resulting wall deflections, Proc. of International Workshop on Wave Barriers in Deepwaters, Port and Harbour Research Institute, pp. 332-346.
- Hattori, M., A. Arami, and T. Yui(1994): Wave impact pressures on vertical walls

- under breaking waves of various types, Coastal Engineering, Elsevier, pp. 79-114.
- Kirkgöz, M.S.(1990): An experimental investigation of a vertical wall response to breaking wave impact, Ocean Engineering, Vol. 17, No. 4, pp. 379-391.
- Mogridge, G.R. and W.W. Jamieson(1980): Wave impact pressures, ASCE, Proc. 10th Int. Conf. on Coastal Engineering, pp. 1829-1848.
- Weggel, J.R. and W.H. Maxwell(1970): Numerical model for wave pressure distributions, Proc., ASCE. Jour. Waterways, Harbors and Coastal Engineering Div., No. WW3, pp. 623-641.
- Witte, H.H.(1988): Wave-induced impact loading in deterministic and stochastic reflection, Mitteilungen, Leichtweiss Institut für Wasserbau, Tech. University Braunschweig, 102, pp. 1-227.

CHAPTER 191

WAVE TRANSMISSION PAST VERTICAL WAVE BARRIERS

David L. Kriebel¹ and Chad A. Bollmann²

Abstract

Three theories for predicting regular wave transmission past vertical wave barriers are evaluated using three sets of experimental data. The three theories are: (1) the power transmission theory of Wiegel (1960), (2) and modified power transmission theory that includes effects of wave reflection, and (3) the eigenfunction expansion theory of Losada et al. (1992). Under deep and near-deep water conditions - which are typical of most design conditions - the theory of Wiegel is found to over predict wave transmission under most circumstances. The modified power transmission theory provides better agreement with the data. The eigenfunction method provides good agreement for deep wave barrier drafts but overestimates transmission for shallow drafts.

Introduction

For more than 30 years, estimates of wave transmission past vertical wave barriers (vertical wall breakwaters, sometimes called wave screens, wave fences, skirt breakwaters, or curtain walls) have been based primarily on the theory and experimental data published by Wiegel (1960). The "Wiegel Theory" has been adopted as the recommended practice by both the Army Corps of Engineers (1984) in the *Shore Protection Manual* and by the Naval Facilities Engineering Command (1982) in the *Coastal Protection Design Manual 26.2*. While other theories have been published since then, none has been as widely adopted for design purposes and none has been accompanied by new experimental data.

¹ Associate Professor, Ocean Engineering Program, United States Naval Academy, Annapolis, MD 21402 kriebel@nadn.navy.mil

² Ensign, United States Navy

Despite the widespread use of the Wiegel theory, questions have arisen recently³ concerning its accuracy. Wiegel himself recognized that the theory was not physically rigorous and he considered it a first approximation based on some limiting assumptions (Wiegel, 1995, personal communication). In general, a comparison of Wiegel's theory to his own data shows that his theory tends to overpredict wave transmission under deep water conditions and underpredict transmission as the relative water depth became more shallow. Since most wave barriers are built in deep or near-deep water conditions, use of this theory in design may produce deeper wave barrier drafts, at greater cost, than would actually be required to achieve some desired level of wave transmission.

Recently, several more sophisticated theories for wave transmission have been proposed based on numerical solutions of the boundary value problem for waves interacting with a vertical barrier. Liu and Abbaspour (1982) developed a numerical solution based on the boundary integral equation method, while both Losada, Losada, and Roldan (1992) and Abul-Azm (1993) developed numerical solutions based on the method of eigenfunction expansion. Compared to Wiegel's simple theory, these theories are more difficult to apply because they require complex matrix solutions. In addition, the numerical solutions have not been widely or rigorously verified through comparison to measurements.

In this paper, we evaluate three different theories for predicting the transmission of regular waves past wave barriers and we then compare these theories to some new experimental data for wave transmission past vertical wave barriers. The three theories that are evaluated include: (1) the original power transmission theory of Wiegel, (2) the eigenfunction expansion theory of Losada et al. and Abul-Azm, and (3) a modified power transmission theory which was developed in the course of this study. This modified theory is, like the original Wiegel theory, based on the wave power transmission past the wave barrier and, like the Wiegel theory, predicts the wave transmission is a simple closed-form equation. Unlike the original derivation, however, the modified theory accounts for the effects of partial wave reflection from the barrier and this results in different (lower) transmission than is predicted by the Wiegel theory

These theories are then evaluated using laboratory data from three different sources. This includes the original Wiegel data as well as additional laboratory tests data published by Peratrovich, Nottingham & Drage, Inc. (1992) based upon tests conducted by the British Columbia Research Corporation (BCRC). The third set of data was then collected as part of this study and is based on experiments conducted at the U.S. Naval Academy Hydromechanics Laboratory (NAHL).

³ Based on discussions at a Wave Barrier Design workshop, held by Peratrovich, Nottingham & Drage, Inc. in Seattle, Washington, on April 24-25, 1995

Definition of a Vertical Wave Barrier

A definition sketch of a vertical wave barrier is shown in Figure 1. The wave barrier consists of an impermeable vertical wall with a draft or penetration, w , in water of depth d . The wave field consists of incident regular waves with height H_i and frequency σ , along with transmitted waves of height $H_t = K_t H_i$, and reflected waves of height $H_r = K_r H_i$, where K_t and K_r are the transmission and reflection coefficients. The water depth is assumed uniform on both sides of the wall so that the wave length, L , and the wave group velocity, C_g , are equal on both sides. If we define the wavenumber as $k = 2\pi/L$, then the wave transmission is fundamentally dependent on two dimensionless variables: the relative water depth kd and the relative barrier penetration kw .

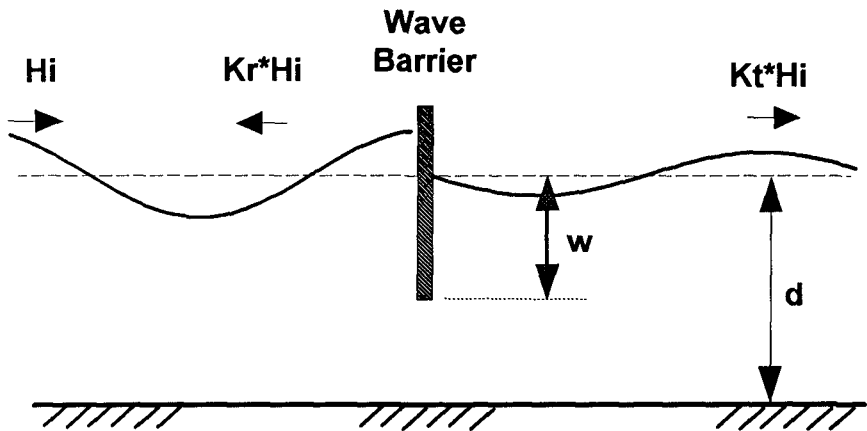


Figure 1. Definition sketch of wave interaction with a vertical wave barrier.

Wiegel Power Transmission Theory

The Wiegel theory is based on the concept that wave motions behind the wall (downstream) are related to the wave power transmission below the wall. Wave power is computed as the depth-integrated product of wave induced dynamic pressures, p , and wave-induced horizontal fluid velocities, u , time-averaged over one wave cycle. Wiegel then assumed that the net wave power transmitted behind the wall (over the full depth) was equal to the fraction of the incident wave power below the bottom of the wall as

$$\frac{1}{T} \int_0^T \int_{-d}^0 p_i u_i dz dt = \frac{1}{T} \int_0^T \int_{-d}^{-w} p_i u_i dz dt \tag{1}$$

Substituting the expressions for dynamic pressure and horizontal fluid velocity from linear wave theory and carrying out the integration then leads to the solution for the transmission coefficient given by Wiegel (1960) as

$$K_t = T_F^{1/2} \tag{2}$$

where we introduce the *transmission function*, T_F , which is given by

$$T_F = \frac{2k(d-w) + \sinh 2k(d-w)}{2kd + \sinh 2kd} \tag{3}$$

Modified Power Transmission Theory

In the modified power transmission theory, the same basic approach is used but the effects of wave reflection are also considered. This time, the dynamic pressures below the barrier are assumed to be given to first order by the sum of incident and reflected pressures, $p_i + p_r$. Because pressures are additive, the net pressure acting on a vertical plane below the wave barrier is greater than that assumed by Wiegel. In a similar way, the horizontal fluid velocities below the wave barrier are modified by reflection. However, the effective velocity is $u_i - u_r$, and is reduced from that assumed by Wiegel.

Based on the above arguments, the transmitted wave power downstream can be equated to the net wave power transmitted under the barrier as

$$\frac{1}{T} \int_0^T \int_{-d}^0 p_i u_i dz dt = \frac{1}{T} \int_0^T \int_{-d}^{-w} (p_i + p_r) (u_i - u_r) dz dt \tag{4}$$

Substituting the expressions for dynamic pressures and horizontal fluid velocities from linear wave theory and canceling common terms then gives:

$$K_t^2 = (1 - K_r^2) T_F \tag{5}$$

By including the effect of the reflected wave, the solution given above contains two unknowns and cannot be solved without introduction of another relationship between K_t and K_r . Since equation (5) implicitly assumes that there are energy losses in the system, the necessary relationship is one that guarantees conservation of fluid mass, or continuity of the fluid velocities, below the wave barrier as $u_t = u_i - u_r$. Ignoring any phase shifts that may occur across the wall, and assuming that velocities are described by linear wave theory, the matching condition requires that

$$K_t = 1 - K_r \quad (6)$$

Substitution of equation (6) into equation (5) then gives the following solution for transmission coefficient from the modified power transmission theory:

$$K_t = \frac{2 T_F}{1 + T_F} \quad (7)$$

where the transmission function T_F is defined in equation (3). Because of the inclusion of the effects of wave reflection, equation (7) predicts wave transmission coefficients that are smaller than those predicted by the Wiegel theory in equation (2). This may be seen most readily in equation (5) where it is clear that the effect of wave reflection (with reflection coefficient K_r greater than zero but less than one) is to decrease the wave transmission compared with that predicted by Wiegel.

The modified power transmission theory is, like the Wiegel theory, an approximation of the actual wave transmission process. From a theoretical standpoint, the method appears inconsistent because the usual balance of incident, reflected, and transmitted wave energy is not preserved. In addition, the modified theory, like the Wiegel theory, produces inconsistent results when taken in shallow water limit. However, the method is intended as a simple engineering solution and, as will be shown, it provides significantly better results when compared to measured wave transmission than the Wiegel theory for most conditions of interest.

Eigenfunction Solution

Because of the theoretical limitations of the power transmission theories, it is next of interest to consider mathematically exact solutions for linear water wave interaction with a thin vertical barrier. Such a solution has been given by both Losada et al. (1992) and Abul Azm (1993) based on eigenfunction expansion methods and their solution will be further considered here. In this paper, the method will only be presented in a summary form and the reader is referred to the original papers for a more thorough description of the method.

The eigenfunction expansion method involves solution for the velocity potentials on the upwave side (wavemaker or incident wave side) and on the downwave side (transmitted wave side) of the wave barrier. These upwave and downwave potentials must then be appropriately matched at the location of the wave barrier ($x=0$). Following Dalrymple and Martin (1990), these potentials must be harmonic in time with frequency σ and must have a spatial dependence (in x and z) given by

$$\Phi_{up} = Z_1 e^{-ik_1 x} + \sum_{n=1}^N R_n Z_n e^{ik_n x} \quad \Phi_{dn} = Z_1 e^{-ik_1 x} - \sum_{n=1}^N R_n Z_n e^{-ik_n x} \quad (8)$$

Equation (8) automatically satisfies the requirement that the velocities must be matched at all elevations on and below the barrier. In this form, the first term in each velocity potential is the incident progressive wave mode while the terms in the summation includes both the scattered progressive wave ($n=1$) and the evanescent wave modes ($n > 1$), all with unknown complex amplitudes R_n .

The functions Z_n in equation (8) describe the depth-dependence of the wave modes and are given by

$$Z_n = \frac{i g H_i}{2 \sigma} \frac{\cosh k_n (d+z)}{\cosh k_n d} \quad (9)$$

The wavenumbers k_n are given by the solution of the dispersion equation

$$\sigma^2 = g k_n \tanh k_n d \quad (10)$$

where the first (real) root is the linear progressive wavenumber, $k_1 = k$, and where there are then an infinite set of imaginary roots for $n > 1$.

The solution for the complex amplitudes R_n must satisfy two additional physical requirements: (a) the velocities must be zero on both sides of the barrier in the upper region where $-w < z < 0$, and (b) the velocity potentials (or equivalently the dynamic pressures) must match in the gap below the barrier where $-d < z < -w$. As a result, two distinct equations (from upper and lower regions) are obtained - the so-called dual-series relationships noted by Dalrymple and Martin (1990) - and both must be satisfied simultaneously to find the unknowns R_n .

It may then be shown that two equivalent methods may be used to satisfy the matching conditions: one through a least squares procedure and the other through a more direct procedure. In the first approach, used by Losada et al. (1992) and Abul-

Azm (1993), the matching conditions are first applied locally, retaining the vertical (z) dependence. The resulting dual series relationships are then combined and re-written as one mixed boundary condition which must equal zero over the full depth. This combined function is then solved in a least-squares sense in which the square of the function is minimized. In a second approach, used in this paper, the matching conditions are applied and are again combined into one mixed boundary condition. This combined function is then, however, multiplied by the orthogonal functions Z_n and depth-integrated over the full depth. This results in a single matrix equation that can be solved directly without the need a least-squares solution.

Following the second method, the mixed boundary condition to be satisfied, denoted $G(z)$ as in Losada et al. (1992), is defined for the upper and lower regions as follows. In the upper region, the horizontal velocities ($u = \partial\Phi/\partial x$) are set equal to zero at the wave barrier ($x=0$) resulting in

$$G(z) = -k_1 Z_1 + \sum_{n=1}^N R_n k_n Z_n = 0 \quad -w < z < 0 \quad (11)$$

In the lower region, the velocity potentials from equation (8) are matched directly under the wall ($x=0$) as

$$Z_1 + \sum_{n=1}^N R_n Z_n = Z_1 - \sum_{n=1}^N R_n Z_n \quad (12)$$

Following cancellation of the leading terms, and after multiplying by k_1 to make equation (12) dimensionally consistent with equation (11), the remaining portion of the mixed boundary condition is obtained as

$$G(z) = 2 k_1 \sum_{n=1}^N R_n Z_n = 0 \quad -d < z < -w \quad (13)$$

The mixed boundary condition $G(z)$ can then be satisfied in the usual way by employing the orthogonality properties of the depth-dependent eigenfunctions Z_n from equation (9) as

$$\int_{-d}^0 G(z) Z_m dz = 0 \quad (14)$$

This yields the following set of matrix equations which must be solved for the unknown amplitudes R_n

$$\sum_{n=1}^N R_n (2 k_1 X_{nm} + k_n Y_{nm}) = k_1 Y_{1m} \quad (15)$$

where the functions X_{nm} and Y_{nm} are defined by Losada et al. (1992) and are given by

$$X_{nm} = \int_{-d}^{-w} Z_n Z_m dz \quad (16)$$

$$Y_{nm} = \int_{-w}^0 Z_n Z_m dz \quad (17)$$

Once the matrix in equation (15) is solved for the unknowns R_n , the transmission coefficient is obtained from the first term, R_1 . The reflection and transmission coefficients for the progressive wave modes are given by

$$K_r = |R_1| \quad K_t = |1 - R_1| \quad (18)$$

Numerical computations have shown that the solution obtained by employing the orthogonality properties of the eigenfunctions is numerically equivalent to that obtained by Losada et al. (1992) using the least-squares solution procedure. It is noted, however, that the matrix in equation (15) is somewhat easier to solve than that given by Losada et al. in that it has stronger diagonal dominance.

Comparison to Data

The three theories for wave transmission past vertical wave barriers are now compared to available laboratory data for regular waves. Two sources of published data were considered: (1) the data given by Wiegel (1960) and (2) the data given by Peratovich, Nottingham, and Drage (1992) from tests conducted at the British Columbia Research Corporation (BCRC). These data were then supplemented by additional data collected in the Naval Academy Hydromechanics Laboratory (NAHL).

The NAHL tests were conducted in a wave tank 120 feet (36.6 m) long, 8 feet (2.43 m) wide, and 5 feet (1.52 m) deep. A thin rigid wall (2 inches or 5 cm thick) was placed about 60 feet (18.3 m) from the wavemaker. The wall was supported at the sides of the tank and was also backed by an aluminum frame to prevent deflection of the wall. With the fixed water depth, four wall penetrations were tested producing four values of the relative wall penetration, w/d , was 0.4, 0.5, 0.6, and 0.7.

In these experiments, 80 tests were performed with regular waves. The wave periods varied from 0.9 sec to 2.5 sec and wave heights ranged from 1 in (2.5 cm) to almost 9 inches (23 cm). Combinations of these parameters were used to obtain values of wave steepness, H_s/L , between 0.01 and 0.06 with most tests being in the range of 0.02 to 0.04. Incident waves were measured with a fixed wave gage near the wavemaker while transmitted waves were measured with the fixed gage located about 15 feet (4.6 m) behind the wall. In all tests, a series of 5 to 10 waves of uniform height was generated and measurements were limited to exclude any effects of wave reflection from the beach landward of the wall or from the wavemaker.

Figures 2a through 2h present comparisons of measured and predicted transmission coefficients for regular waves. Each figure represents a specific relative water depth, d/L . Transmission coefficients are then plotted as a function of the relative wall penetration, w/d . Note that in some cases where more than one source of data is used, the relative water depths were approximated in order to compare the various theories and data sets on the same graph. As an example, in Figure 2b, tests conducted by Wiegel used a relative depth of 0.68, while tests conducted by BCRC used a relative depth of 0.73. Theoretical results were based on an approximate average value of $d/L=0.70$.

Figures 2a, 2b, and 2c show measured and predicted wave transmission for deep water conditions where the relative depth is about 0.5 or higher. In these figures, it is evident that the Wiegel theory overestimates the wave transmission while the modified theory provides much better predictions at all values of relative depth and wave barrier penetration. For those cases where the penetration reached one-third to one-half of the water depth, wave reflection from the wave barrier is expected to have been most pronounced. It is for these conditions that the differences between the two theories are particularly large and the modified theory, which includes the effects of wave reflection, provides a significant improvement. The eigenfunction solution overestimates the transmission for small wall penetrations but then agrees with the modified theory and predicts the transmission quite well for deeper wall penetrations.

All other cases shown in Figure 2 represent intermediate or transitional water depths. In Figures 2d, 2e, and 2f it is evident that the modified theory yields improved prediction of wave transmission for most wave barrier penetrations when compared to the Wiegel theory. For barrier penetrations of 0.2 or less (wave barrier penetrations just below the wave trough level), both theories underpredict the measured wave transmission. For cases of deeper penetration, the Wiegel theory again tends to overestimate transmission while the modified theory is more accurate. In these cases, the eigenfunction solution again overestimates transmission for small wall penetrations and agrees with the modified power transmission theory - and with the data - at larger wall penetrations.

In Figures 2g and 2h, the relative depth is fairly shallow (though still greater than the normal limit between intermediate and shallow water wave conditions) and results of the three theories are mixed. Of the two power transmission theories, the Wiegel theory generally provides better predictions than the modified theory. Unlike the deep water conditions, the Wiegel theory no longer overestimates transmission and, in fact, has a tendency to underestimate transmission. The modified theory consistently underestimates the transmission more severely. In these "shallow water" conditions, the eigenfunction theory tends to overestimate the transmission at all values of wall penetration until the wall penetration is over 90 percent of the water depth.

Conclusion and Discussion

Results presented in this paper indicate that for most conditions of interest in engineering design - for deep water conditions with large wave barrier penetration (typically to mid-depth or deeper) - the Wiegel theory generally overestimates wave transmission while both the modified power transmission theory and the eigenfunction expansion theory produce more accurate predictions with little bias toward over or under-prediction of wave transmission. Neither the modified power transmission theory nor the eigenfunction expansion method produce improved estimates of wave transmission under all conditions, however. In near-shallow water, the modified theory tends to underestimate wave transmission while, for these same relative depth conditions, the eigenfunction method tends to overestimate wave transmission.

One puzzling feature of the results in Figure 2 is the degree to which the modified power transmission theory agrees with the complete eigenfunction solution for certain conditions, namely for deep water and large wall penetrations. This can be explained by considering the first term in the eigenfunction expansion. From equation (15), if $n=m=1$, the leading-order behavior of the eigenfunction solution is

$$R_1 = \frac{Y_{11}}{2X_{11} + Y_{11}} \quad (19)$$

The integrals Y_{11} and X_{11} may be expressed in terms of the transmission function, T_F , in equation (3) and it can be shown that $X_{11} \approx T_F$ and $Y_{11} \approx 1 - T_F$. As a result, the leading-order wave transmission from the eigenfunction solution can then be obtained from equation (11) in the following form

$$K_t = 1 - R_1 = \frac{2T_F}{1 + T_F} \quad (20)$$

This result is identical to that obtained from the modified power transmission theory in equation (7). The modified power transmission theory is therefore consistent with

the leading-order behavior of the progressive wave modes in the eigenfunction solution and is valid for conditions where the evanescent wave modes are not expected to be significant.

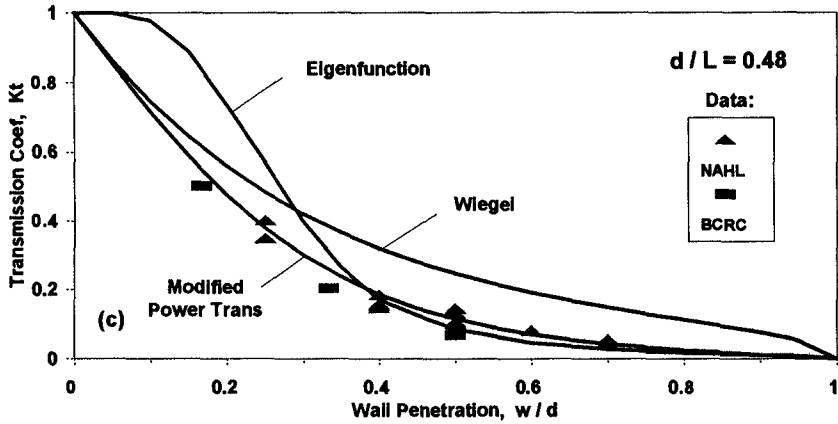
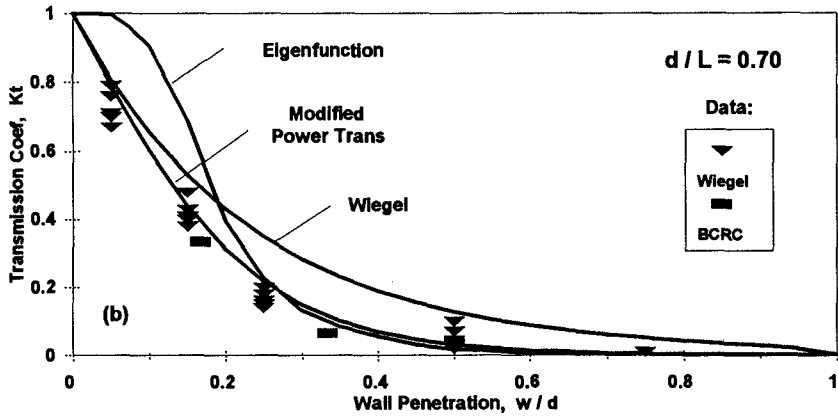
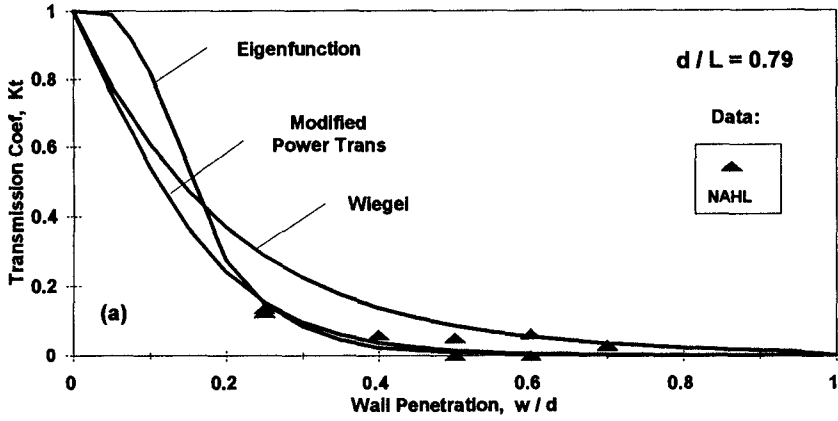
For conditions where the evanescent modes are important (small wave barrier penetrations), the eigenfunction solution tends to overestimate wave transmission and is less accurate than would be expected. The reason for this appears to be that frictional losses become important due to flow separation at the bottom of the wave barrier. In the NAHL tests, both dye studies and velocity measurements using an acoustic doppler velocimeter confirmed the presence of a large vortex at the bottom of the wall. The inclusion of friction in the eigenfunction solution dramatically improves its predictive ability and this will be the subject of future work.

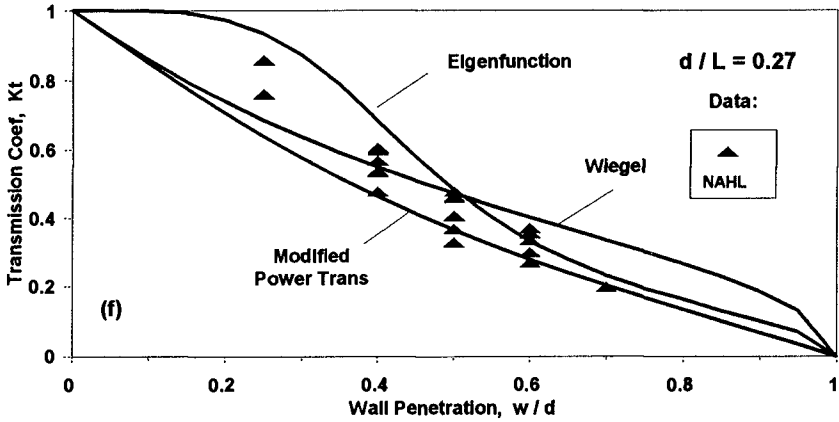
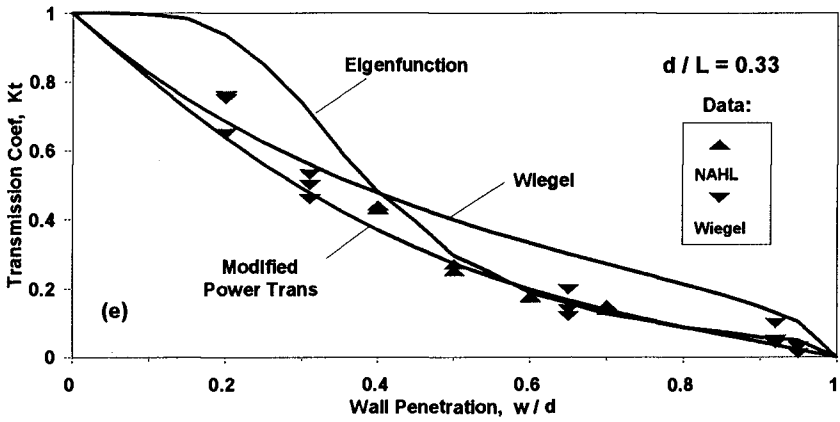
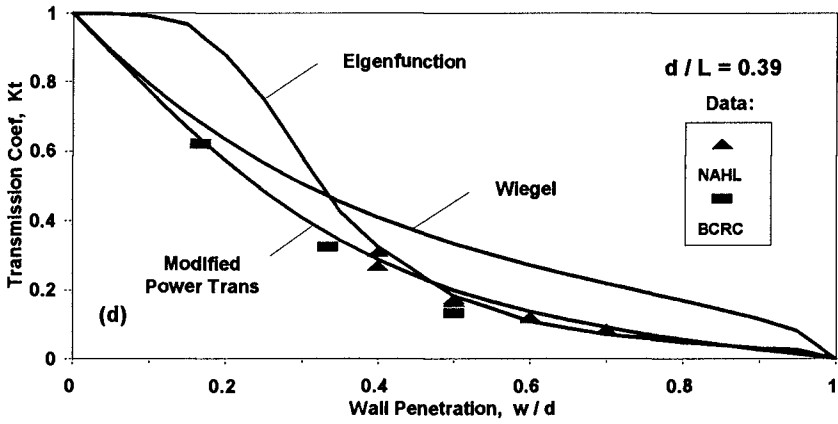
Acknowledgments

This work has been supported by the National Science Foundation and by the Alaska Science and Technology Foundation.

References

- Abul-Azm, A.G., 1993, "Wave Diffraction Through Submerged Breakwaters," *J. Waterway, Port, Coastal, and Ocean Engineering*, Vol. 119, No. 6, pp. 587-605.
- Dalrymple, R.A. and Martin, P., 1990, "Wave Diffraction Through Offshore Breakwaters," *J. Waterway, Port, Coastal, and Ocean Engineering*, Vol. 116, No. 6, pp. 727-741.
- Liu, P.L-F., and Abbaspour, M., 1982, "Wave Scattering by a Rigid Tin Barrier," *J. Waterway, Port, Coastal, and Ocean Engineering*, Vol. 108, WW4, pp. 479-491.
- Losada, I., Losada, M., and Roldan, A., 1992, "Propagation of Oblique Incident Waves Past Rigid Vertical Thin Barriers," *Applied Ocean Res.*, Vol. 14, pp. 191-199.
- Naval Facilities Engineering Command, 1984, *Coastal Protection Design Manual 26.2*, U.S. Government Printing Office, Washington, D.C.
- Peratrovich, Nottingham, and Drage, Inc., 1992, "Wave Barrier Development," Final report to the Alaska Science and Technology Foundation, Feb. 1992.
- U.S. Army Corps of Engineers, 1984, "Shore Protection Manual," 4th edition, U.S. Government Printing Office, Washington, D.C.
- Wiegel, Robert L., 1960, "Transmission of waves Past a Rigid Vertical Thin Barrier," *J. of the Waterways and Harbors Division, ASCE*, Vol. 86, No. WW1, pp. 1-12.





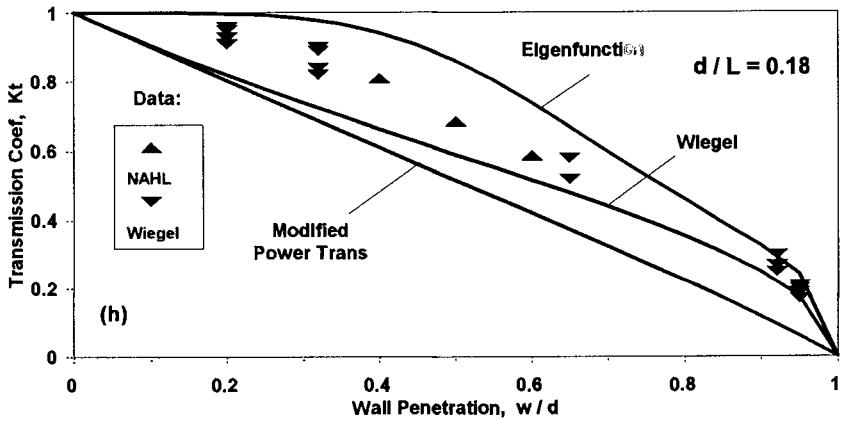
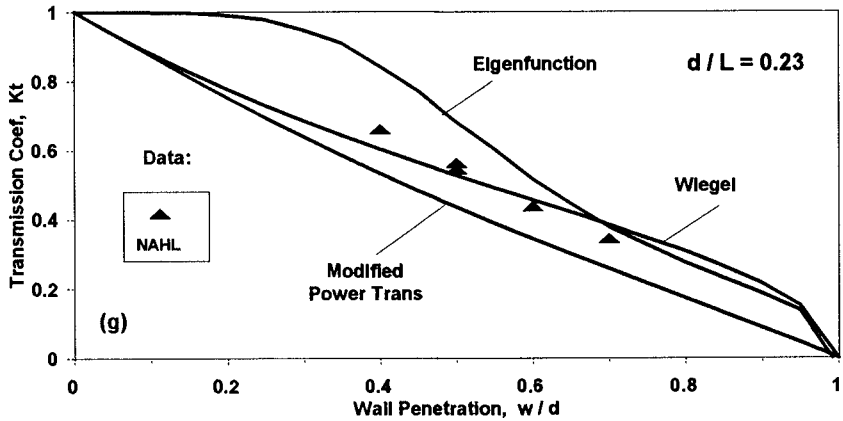


Figure 2a-2h. Comparisons of three theories to measured data for regular wave transmission past vertical wave barriers: (a) $d/L=0.79$, (b) $d/L=0.70$, (c) $d/L=0.48$, (d) $d/L=0.39$, (e) $d/L=0.33$, (f) $d/L=0.27$, (g) $d/L=0.23$, and (h) $d/L=0.18$.

CHAPTER 192

PHYSICAL STUDY OF THE NATURE OF HIGH PEAK WAVE PRESSURES

Jordan Marinski¹

ABSTRACT

In order to investigate the generation mechanism of high peak wave pressures on vertical/steep walls two physical experiments are carried out on a specially constructed research apparatus. It is found from present experiments that the enclosed air volume as a physical medium under compression could not be a cause for the high peak short-period wave pressures. The wave breaking on a vertical wall is accompanied by cumulating of the wave energy and its redistribution on the smaller area of the wall and conditions for shock wave are created after the collision of the streams.

INTRODUCTION

During the breaking of a wave on vertical/steep walls or elements very short-period peak pressures have been recorded. There are experimental data which prove their importance about coastal and harbours works stability,(OUMERACI et al., 1992). But in the literature there are different and inconsistent physical hypotheses which should explain one and the same phenomenon - high peak pressure generating mechanism. These hypotheses have become a physical basis of different formulas for calculation of the wave loading on vertical walls or elements used in the designing and building of vertical structures. In this way insufficient study of the nature of high peak pressures has contributed to many failures of the vertical structures.

1) Assoc. Professor, Bulgarian Academy of Sciences, Institute of Water Problems, Acad. G.Bonchev street, Block 1, 1113 Sofia, Bulgaria.

The aims of this experimental study are: 1) to model breaking wave impact out of wave flume if we accept in advance that those basic assumptions of BAGNOLD, (1939) for the appearance of this type of high pressures are truth, namely a) the wave motion turns into translational motion; b) shortly before the impact the wave front is vertical and smooth; 2) to learn the quantitative effects of a entrapped air volume on the impact parameters.

PROCEDURE

The reasons to be investigated high peak pressures out of wave flume are: 1) the experiments carried out in a wave flume show that such kind of breaking wave impact, when the high peak short-period pressure appears, repeats very rarely even if there are the same wave parameters and the same geometry of the bottom at the approach of waves; 2) it is not possible to give in advance one exactly fixed air volume on the wall and to study its quantitative effect during breaking wave impact in a wave flume.

The experimental study is carried out on a specially constructed research apparatus, Fig. 1.

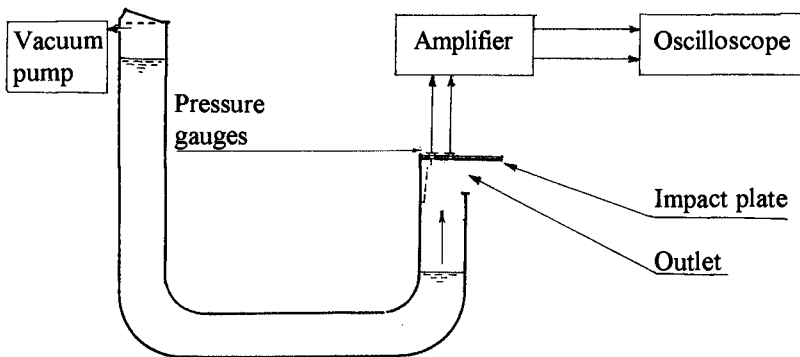


Fig. 1 Experimental set-up

One of the arms of "U"-shaped pipe is made of Plexiglas and has rectangular cross-section, which allows visual observation of the impact of the water column on a flat solid plate. Under the plate a water-air-outflow opening is left. Its dimensions are chosen in such a way that two requirements are met : 1) water column cross section remains the same until reaching the impact plate with velocity values from 0,8 to 1,5 m/s; 2) the spreading of a water hammer pressure is avoided.

The water column motion is a uniformly accelerated motion due to the head which is created beforehand by changing the pressure in one of the arms and instantly following equalising of that pressure. With this preliminary created head the water column velocity is regulated and it could reach the value of 1,5 m/s. At such velocity values in a wave flume, the high peak pressures at wave height of 6-10 cm has been registered, by SMIRNOFF, (1955) and RUNDGREN, (1958). The liquid

mass taking part in the impact is 7,65 kg. The experiment is filmed by a high speed camera (4000 frames per second).

The research working program includes the following two physical experiments:

EXPERIMENT A: *Quantitative study of the entrapped air volume effect on the impact parameters: p , dp/dt and t , where p - hydrodynamic pressure; dp/dt - rate of pressure change; t - rise time.*

The air quantity is given preliminary. Under the impact plate in the side outlet plane a replaceable water-and airtight "threshold" is fixed. Its height D is given beforehand and varies from $0,06 H$ to $0,22 H$, where H is the width of the water column, Fig.2.

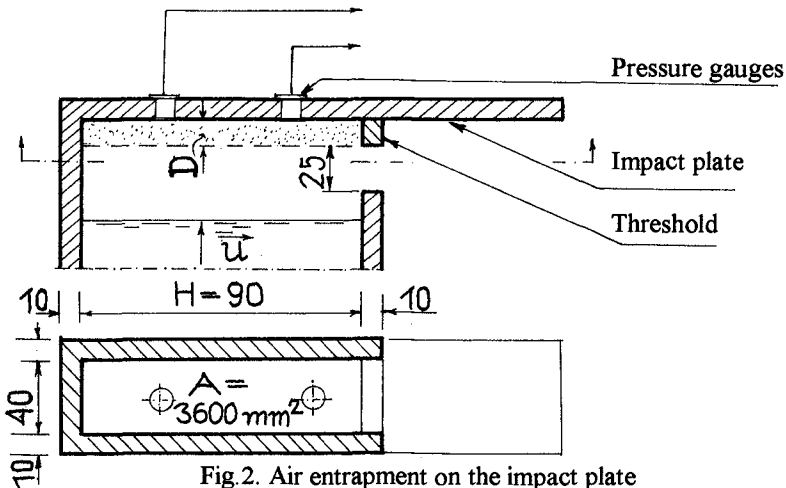


Fig.2. Air entrapment on the impact plate

In this way an air cushion with thickness equal to the threshold height and with a rectangular cross-section equal to that of the water column is created. The thickness of air cushion is as follows: $D = 0,06 H$; $D = 0,11 H$; $D = 0,16 H$; $D = 0,22 H$. The pressures are measured in two locations by membrane resistor transducers (gauges) whose natural frequency is 2000 Hz and operating pressure range of up to 100 kN/m^2 . The area of the membrane is 1 cm^2 .

EXPERIMENT B: *Modelling of the wave front surface F motion during the breaking wave impact on a wall.*

The shape and velocity of the oncoming wave are known from the experiments in wave flume, (DENNY, 1951). By changing the geometry of the profile of the approach before the impact plate an analogous kinematic profile can be achieved. The pressures are measured in two locations before the entrapment of air cushion (G_1) and in the location of the air entrapment (G_2).

RESULTS**EXPERIMENT A**

The recorded impact characteristics are shown in Fig.3.

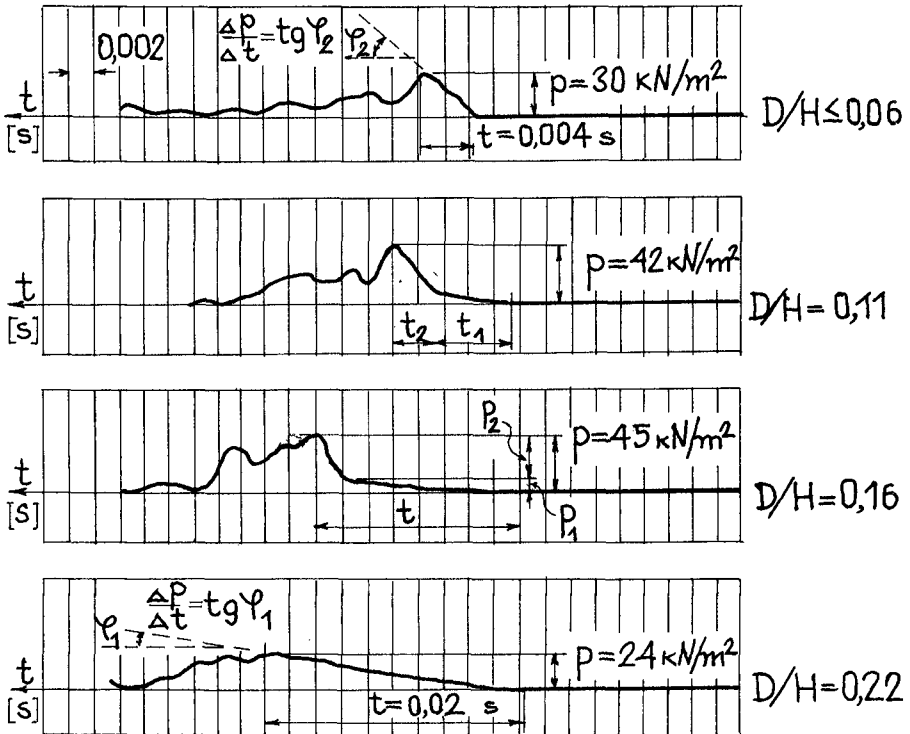


Fig.3. Effect of thickness of the entrapped air volume on impact parameters

The results could be divided in three different groups:

1. The effect of an air volume at $D/H \leq 0,06$
2. The effect of an air volume at $0,06 < D/H < 0,22$
3. The effect of an air volume at $D/H \geq 0,22$

1. $D/H \leq 0,06$. Compression of very thin air cushion.

During the impact the very thin air cushion is broken by the liquid to many small bubbles, which in practice do not reduce the kinetic energy of the water column. The pressure gauges do not catch the air compression of the small bubbles and register the impact pressure of the jets when the water gets in touch with the gauge membrane. Such insignificant small air quantities practically does not affect the character and the magnitude of the pressures.

2. $0.06 < D/H < 0.22$. *Compression of thin air cushion.*

The rate of pressure change clearly shows two physical processes from which the maximum pressure value has been formed. The first part of the pressure is generated as a results from the air compression, but the second is indicated at the time of contact between the liquid and the impact plate. The rate of pressure change at the time of the contact of the liquid with plate is four times bigger than the one with the air compression. However, unlike the first case, during the compression of the continuous thin air cushion a loss of kinetic energy is almost not observed, Fig. 3. The resulting magnitude of the peak pressure in spite of the compression is increasing, Fig. 4

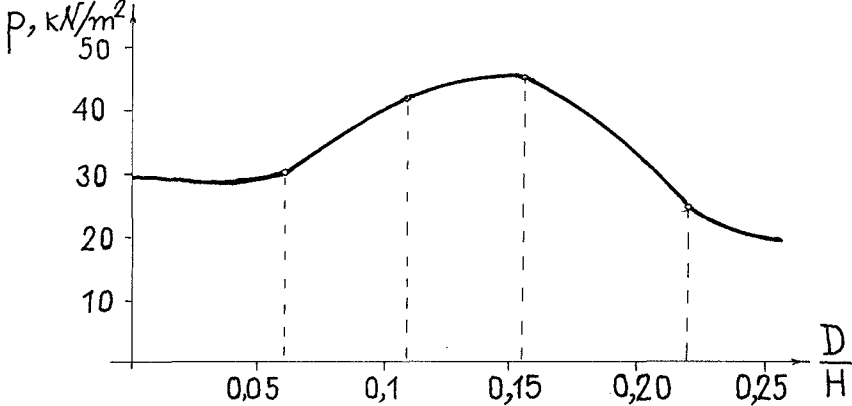


Fig. 4. Effect of dimensionless thickness (D/H) on magnitude of impact pressure

3. $D/H \geq 0.22$. *Compression of air cushion*

At this thickness of the air cushion the pressure is due only to the air compression. Here the kinetic energy of running water is being reduced by the compression of the air cushion. The pressure magnitude is decreasing, Fig. 4. The rate of pressure change with air compression is nearly 4 times less of the same with a direct impact of the liquid.

From the experimental study described above the following conclusion about the quantity influence of the air volume could be made:

- 1). The pressure from the air compression is negligibly small with insignificant air volumes due to breaking of the air cushion into bubbles.
- 2). When the air cushion keeps continuous before it is broken, the pressure from the air compression is added to the pressure from direct liquid impact.
- 3). At bigger air volumes the water column does not reach the plate during the impact and the air cushion acts as a damper.

EXPERIMENT B

The research apparatus allows the motion of the wave front, which surface is designated here as F , to be simulated before and during the impact. By changing the geometry of the profile of approach before the impact plate and using a high speed camera a kinematical profile analogous to that of the wave front surface F motion in a flume (DENNY, 1951) is achieved, Fig. 5.

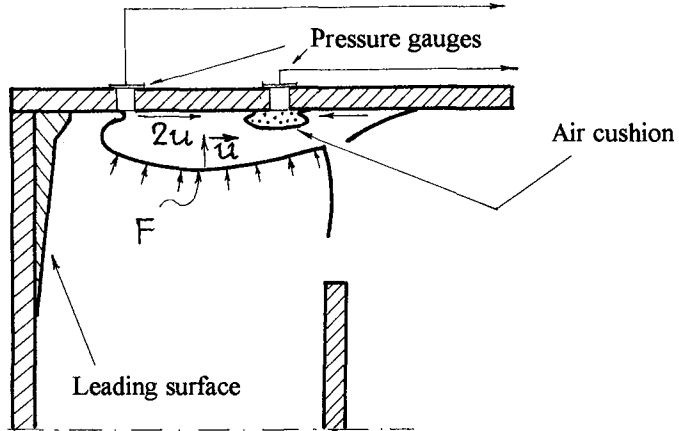


Fig. 5. Modelling of the wave front surface F motion

The Gauge 1 registers the pressure at the location where the water flow is deviated and accelerated upwards without air entrapment.

The Gauge 2 records the pressure where the air is entrapped, Fig. 6.

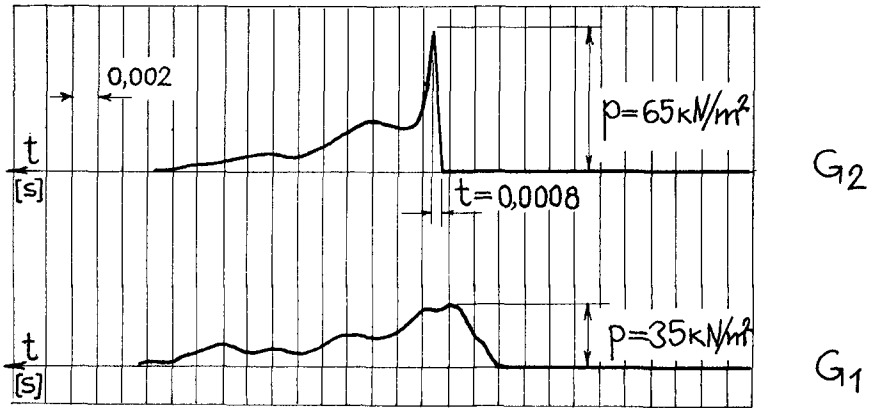


Fig. 6. Pressure-time records during the impact; G1: striking water column; G2: shock wave

The shape of the pressure curve obtained from Gauge 2 exactly repeats the records of high pressures in a wave flume made by numerous researchers (BAGNOLD, 1939; RUNDGREN, 1958; GODA & HARANAKA, 1967; PARTENSCKY, 1987; KIRGOZ, 1982; TAKAHASHI et al. 1994).

At the location of the entrapment of the air a counter stream appears and a free fluid issuing is strongly hampered. These conditions are of crucial importance for a shock wave to be created. It is confirmed from the record of Gauge 2 shown in Fig. 6 and after a comparison between the impact parameters from experiment A and experiment B, shown in Table 1.

Table 1. Comparison of impact parameters obtained from experiments A & B

Type of impact	u m/s	p kN/m ²	t s	dp/dt (tgφ) -
with air compression	1	24	0,02	0,14
water jet (column)	1	30	0,004	1
collision of streams and jets (shock wave)	1	65	0,0008	15

EXPLANATION OF THE GENERATION MECHANISM OF HIGH PEAK WAVE IMPACT PRESSURES

The physical experiments help to be established the following:

1. The enclosed air volume as a geometric space and a physical medium with density considerably smaller than that of water allows the focusing of the kinematical parameters vectors of the flowing liquid around the gas-liquid interface F.

2. The velocity values calculated using the data obtained with high speed camera are an experimental proof about the cumulative character of the wave flow rate during the breaking against the wall. The velocity of stream at the time of spilling on the plate is twice as much as the surface F velocity before its reaching the barrier. In physics the cumulative principle with water current motion is known, (LAVRENTIEV and SHABAT, 1977), (SLOBODETSKI and ASLAMAZOV, 1980). Its theoretical basis with waves breaking against a wall could be illustrated. If a water jet strikes a flat plate with velocity c, Fig. 7, the velocity values of both spilling jets on the plate are the same equal to c:

$$c_1 = c_2 = c \quad (1)$$

and it is not dependent on the angle of attack θ .

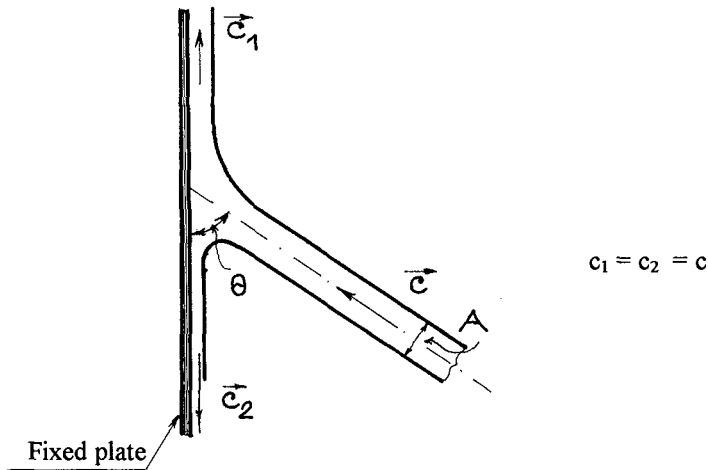


Fig. 7. Impact of a jet on a fixed flat plate

Now let examine this water mass of the wave which strikes the wall as it is shown in Fig. 8.

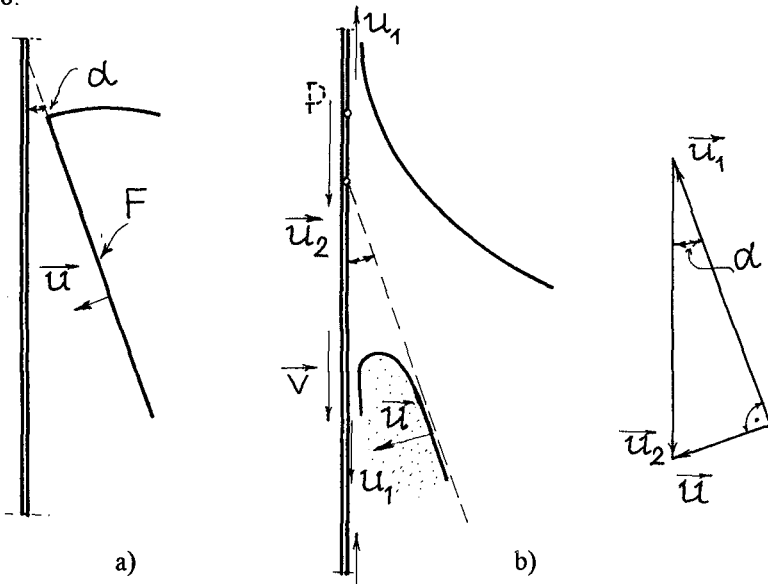


Fig. 8. Impact of a wave on a vertical wall

The velocity value of the front of wave respectively the water surface F before the impact u and the angle of attack between the wave front and the wall plane are known. Let find the stream velocity v with which it is spilling on the wall.

The velocity u could be shown by the vector equation

$$\vec{u} = \vec{u}_1 + \vec{u}_2 \tag{2}$$

where \vec{u}_1 is the velocity component that is paralleled to the wave front and \vec{u}_2 is the velocity of the cross point P of the wave front line and the wall line.

During the impact on the wall the velocity of the spilling stream is equal to the sum of both velocities

$$v = u_1 + u_2 \quad (3)$$

knowing that $c_1 = c_2 = c$.

The component velocities u_1 and u_2 could easily be found, ($u \perp u_1$).

Therefore $u_1 = u \cdot \cot\alpha$ and $u_2 = u/\sin\alpha$. Substituting these values in Eq. 3 gives

$$v = u \frac{1 + \cos\alpha}{\sin\alpha} \quad (4)$$

With small values of α , (such are made in practice) theoretically the velocity could reach values many times bigger than the velocity of the wave front before its contact with the wall. The same is the case considering the kinetic energy. The ratio of the energy per unit volume of such spilling stream on the wall $\rho v^2/2$ to the energy of moving water in the wave $\rho u^2/2$ is more than 1. When $\alpha = 10^\circ$, $v = 11u$, $\rho v^2/2 / \rho u^2/2 = 120$; at $\alpha = 2^\circ$, $v = 57u$, $\rho v^2/2 / \rho u^2/2 = 3200$.

3. Due to the entrapped air space and the field of the velocities (as well as field of the accelerations) the wave energy is being distributed on a smaller area on the wall which is proved from both gauges indications. The cumulative character of the water stream motion on the wall contributes to the wave energy convergence. The stream which is moving vertically upward has started from the lower part of the wave. The counter stream is created by the impact of the wave crest. No matter the mass in the central part of wave (say in the form of striking jets) reaches the wall before or after the collision of these two streams. The possibility for spilling of water streams and jets disappears and after their collision a zone of high shock hydrodynamic pressure is created at the location of the entrapped air cushion.

CONCLUSIONS

1. The wave breaking on a vertical wall is accompanied by cumulation of the wave energy and its redistribution on the smaller area of the wall, and conditions for a shock wave are created at the collision of the streams and jets.
2. The closed air volume as a physical medium under compression could not be a cause for the high peak short-period wave pressures.

ACKNOWLEDGEMENT

The experiments were carried out in Moscow Civil Engineering Institution, Department "Water resources and harbours" founded by Professor N. N. Dzhunkovski. The author wish to express his sincere gratitude to the Institution and

to the Department for their financial support and personally to Professor Gleb Smirnoff who was the initiator of this study.

REFERENCES

- BAGNOLD, R.A.(1939). "Interim Report on Wave Pressure Research." Jour. of the Inst. of Civil Eng., Vol. 12. No. 7, pp. 202-226.
- DENNY, D.K.(1951). "Further experiments on wave pressures." Jour. of the Inst. of Civil Eng., Vol.35, pp. 330-345.
- GODA, Y. & HARANAKA, S.(1967). "An experiment on the shock pressure of breaking waves." Technical note of Port and Harbour Research Institute Ministry of Transport, Japan, No.32, pp. 3-18, (in Japanese). KIRKGOZ, M.S.(1982). "Shock pressure of breaking waves on vertical walls." J. WatWay, Port Coastal Ocean Div., ASCE 108, 81-95.
- LAVRENTIEV, M.A. & SHABAT, B.V.(1977). Hydrodynamics problems and their mathematical models. Nauka Publishers, Moscow, 407 p.(in Russian).
- OUMERACI, H., PARTENSKY, H.W. & TAUTENHBAIN, E.(1992): "Breaking wave on vertical gravity structures." Pros. of the Second Int. Offshore and Polar Eng. Conf., San Francisco, USA, pp. 532-539.
- PARTENSKY, H.W.(1987). "Neue Bemessungskriterien für senkrechte und geschüttete Weienbrecher". Jahrbuch der Hafenbautechnischen Gesellschaft, Hamburg 42, 233-254.
- RUNDGREN, L.(1958). "Water wave forces." Bull. No 54. Inst. of Hydraulics Institute of Technology, Stockholm, Tekniska Hogskolan. 1-122.
- SLOBODETSKI, I.S. & ASLAMAZOV, L.G.(1980). Problems on physics. Nauka Publishers, Moscow, 173p. (in Russian).
- SMIRNOFF, G.N.(1955). "Pressure of breaking waves." Ph.D.- Thesis, Moscow Civil Engineering Institute, CIS, 138p, (in Russian).
- TAKAHASHI, S., TANIMOTO, K., SHIMOSATO, K.(1994). "Dynamic response and sliding of breakwater caissons against impulsive breaking wave forces." Proc. of Int. Workshop on Wave Barriers in Deepwaters, Jan. 10-14, Port and Harbour Research Institute, Yokosuka, Japan, 362-399.

CHAPTER 193

A Design Short-Crested Wave Force Model for Vertical Deep-Water Breakwaters

S.-Y. Tzang¹ and S.-R. Liaw²

Abstract

Fenton's short-crested wave force approximations were modified for designing a vertical breakwater in deep water regions. The theoretical water surface profiles and depth-distributions of hydrodynamic pressure in front of a vertical breakwater were first evaluated with field wave conditions of height $H_b=10\text{m}$ and period $T=9.6\text{s}$ at depths d from 20m to 40m. The calculations immediately illustrated characteristics of residual pressures at wave crest and exponentially decreasing profiles under design water level. As d increased, wave crest height decreased as well and the crest pressure deviations became negligible while overestimated pressure force by assuming linear under-water pressure distributions became more significant. Through appropriate modifications, a design wave force model were proposed and compared with Goda's design formulae for standing waves. Results clearly displayed that 45° incident short-crested waves could induce greater total wave forces on a vertical breakwater than those by Goda's formulae at the same depth. Differences became greater at $d=40\text{m}$ by about 12% ~ 17% for $T=10\text{s}$ and 17% ~ 29% for $T=18\text{s}$ based on Fenton's 2nd and 3rd-order approximations.

Introduction

Currently in many countries, up-surgng economic developments have made breakwaters, which were used to be constructed at water depths around 20m, now tend to be installed at water depths of more than 40m. For example in Japan, several port engineering require rather deep water breakwaters such as those in port Kamaish (deepest depth of 63m) etc.(Tanimoto & Takahashi, 1994). Similar challenges are also about to be encountered in Taiwan for its deep-water port projects in the near future. Thus, studies on the complex wave characteristics before a breakwater and

¹ Associate Professor, Dept. of Harbor and River Eng. National Taiwan Ocean University, Keelung, Taiwan 202, R.O.C.

² Chief Engineer, Harbor & Coastal Eng. Dept., China Eng. Consultants, Inc. 20th Fl., 185 Hsin-Hai Rd. Sec. 2, Taipei, Taiwan, R.O.C

related engineering techniques have become an urgent task.

In marine environments, waves generally attack breakwaters obliquely rather than normally resulting in a short-crested wave system (Jeffrey, 1924; Chappellear, 1961). It has been a common engineering assumption adopted for design purposes that normal incident wave forces are greatest than short-crested wave forces, e.g. Goda's formulae (1972, 1985). In fact, this is not always true as pointed out previously that short-crested waves could induce greater wave forces on vertical walls than standing waves (Silvester, 1974; Roberts and Schwartz, 1983). These findings simply suggested that in certain conditions Goda's formulae for standing waves might under-estimate the resulting total wave forces and the designed breakwaters are more susceptible to catastrophic damages during storm attacks.

Goda's Design Wave Force Formulae

As schematically represented by Figure 1 for a composite breakwater, Goda defined wave crest height η_c and wave pressures P_i at specified positions as follows :

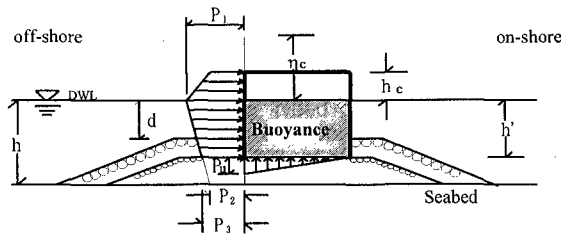


Figure 1. Definition Sketch of Goda's Design Standing Wave Pressures

Wave crest elevations

$$\eta_c = 0.75(1 + \cos \beta) \lambda H_{\max} \quad (1)$$

η_c : upper limit of wave pressure above design water level (DWL)

β : angle between incident wave and the normal of breakwaters

λ : pressure dissipation ratio (=1.0 for current paper)

Wave-induced pressures

$$P_1 = \frac{1}{2}(1 + \cos \beta)(\alpha_1 + \alpha_2 \cos^2 \beta) \lambda W_0 H_{\max} \quad ; \quad P_2 = \frac{P_1}{\cosh(2\pi h / L)}$$

$$P_3 = \alpha_3 P_1 \quad ; \quad P_u = \frac{1}{2}(1 + \cos \beta) \lambda \alpha_1 \alpha_3 w_0 H_{\max}$$

$$\alpha_1 = 0.6 + \frac{1}{2} \left[\frac{4\pi h / L}{\sinh(4\pi h / L)} \right]^2 \quad ; \quad \alpha_2 = \min \left\{ \frac{h_b - d}{3h_b} \left(\frac{H_{\max}}{d} \right)^2, \frac{2d}{H_{\max}} \right\} \quad (2)$$

$$\alpha_3 = 1 - \frac{h'}{h} \left[1 - \frac{1}{\cosh(2\pi h / L)} \right]$$

P_1, P_2, P_3, P_u : max. pressures at DWL, sea bed, caisson bottom and up lift pressure;

h, h', d : water depths from DWL to sea bed, caisson bottom, and rubble mound;

η_c, h_c : elevation of wave crest and caisson top above DWL;

$\alpha_1, \alpha_2, \alpha_3$: coefficients for pressure calculation.

For a vertical breakwater, it is shown that $h=d$ and $P_2=P_3$ while Eq.(1) and Eq.(2) confirm that Goda assumed maximum wave force by standing waves and those by obliquely incident waves decreased by a factor of $\cos\beta$.

Fenton's short-crested wave force theory

Based on Hsu et al's (1979) approximations of short-crested waves, Fenton (1985) further studied the surface wave profile, wave pressure and resulting total forces on a vertical wall. The short-crested wave system can be defined in Figure 2.

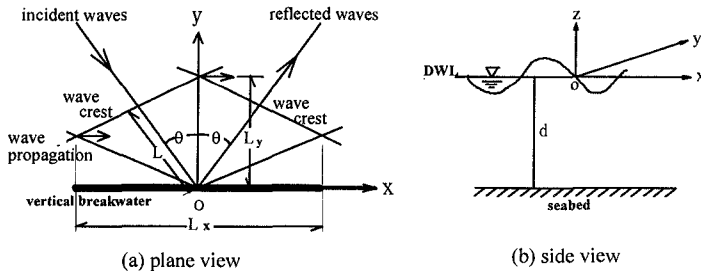


Figure 2. Definitions of A Short-Crested Wave System

As expressed in Figure 2, an obliquely incident wave and its reflected wave from a vertical wall can generate a short-crested wave system. Thus, short-crested waves are essentially three dimensional rather than the two dimensional standing waves, which approach a breakwater normally. According to Fenton in the case of total reflection, short-crested wave height H_{sc} is exactly equal to twice of the incident wave height H_D . Represented by Cartesian coordinates, the governing equation for the velocity potential ϕ simply satisfies the Laplace equation :

$$\nabla^2 \phi = \phi_{xx} + \phi_{yy} + \phi_{zz} = 0 \quad (3)$$

Solving with dynamic and kinematic boundary conditions on surface, at sea bed and on breakwater, Fenton derived a 3rd-order approximations with a variable $\delta = \frac{1}{2} k H_{sc}$ (H_{sc} : short-crested wave height) as expressed, respectively below :

Surface water profile :

$$k \eta(x, y, z, t) = \sum_{i=1}^3 \frac{\delta^i}{(i-1)!} \sum_{j=0}^i \cos j(mkx - \omega t) \sum_{l=0}^i B_{jil} \cos lnky + O(\delta^4) \quad (4)$$

Hydrodynamic pressure :

$$\frac{kp(x, y, z, t)}{\rho g} = -kz + \sum_{i=1}^3 \frac{\delta^i}{(i-1)!} \sum_{j=0}^i \cos j(mkx - \omega t) \sum_{l=0}^i C_{jil}(z) \cos lnky + O(\delta^4) \quad (5)$$

Total wave pressure force :

$$\begin{aligned} \frac{P^*}{\rho g d^2} &= \delta F_{11} \cos(mkx - \omega t) + \delta^2 [F_{20} + F_{22} \cos 2(mkx - \omega t)] \\ &+ \frac{1}{2} \delta^3 [F_{31} \cos(mkx - \omega t) + F_{33} \cos 3(mkx - \omega t)] + O(\delta^4) \end{aligned} \quad (6)$$

The dimensionless coefficients B_{ij} , C_{ij} , F_{ij} and the listed variables are all defined in Fenton (1985). To examine the short-crested wave characteristics before a vertical breakwater, both Fenton's 2nd and 3rd-order approximations shall be evaluated with field wave conditions and then modified for design applications. The results will also be compared with Goda's formulae to manifest the under-estimation of wave forces by standing wave theory in deeper water regions.

Wave Characteristics before A Deep-Water Vertical Breakwater

Both wave crest elevations and wave pressure at specified depths were first studied with a set of in-situ design wave conditions at installation depths of 20, 25, 30, 35, and 40m, respectively. The incident design wave height H_b is 10 meters, wave period T is 9.6 seconds and steady current along the breakwater is neglected in this paper. The seabed slope is assumed to be 1/50 for applying Goda's formulae and only incident angles $\theta=0.01^\circ$ and 45° were considered. Results calculated with water density $\rho=1.03 \text{ g/cm}^3$ and gravity acceleration $g=9.806 \text{ cm/s}^2$ are summarized in Table 1, where the shadowed areas denote results for $\theta=45^\circ$ by both approximations.

Water surface profiles

For water surface profiles, it is seen in Table 1 that short-crested wave crest heights η_c are decreasing with water depth and higher for normal incidence at each depth. The values at wave crest are exactly the same for both approximations but the phase variations of surface profiles are slightly different as illustrated in Figure 3. From both Table 1 and Figure 3, it is noted that short-crested η_c of both normal and oblique incidence are always smaller than those by Goda's formulae except for the case at $d=20\text{m}$. In fact, Goda's formulae gave a constant value of 15m regardless of the water depth and are even higher than short-crested waves by 1m to 2.9m at $d=40\text{m}$ for $\theta=0.01^\circ$ and 45° , respectively by different approximations.

Wave pressure depth distributions

Contrary to η_c , Table 1 shows that at each depth waves with the same height and period imposed greater maximum pressures for $\theta=45^\circ$ than those for normal incidence. This is clearly demonstrated by the phase variations of the wave pressure at half depth and seabed by both approximations as shown in Figure 4 and Figure 5, respectively. It is seen in both figures that maximum wave pressures of $\theta=45^\circ$ are greater than those of $\theta=0.01^\circ$ and maximum standing wave pressures occurred at phases deviated from phase of zero (wave crests) due to double hump structure. For waves of $\theta=45^\circ$, pressures at DWL and at seabed derived by 2nd-order approximation are all greater than those by 3rd-order approximation but the differences became quite small as water depth increased. By 2nd-order approximations, the residual errors of water pressure at wave crest tend to diminish with increasing depths except for the cases of $\theta=0.01^\circ$. This suggests that in deeper waters Fenton's approximations are more applicable due to negligibly small residual crest pressures and thus, resulting total wave pressure force on a vertical breakwater can be reasonably derived.

Table 1 Wave Characteristics by Fenton's and Goda's Approximations at Various Water Depths

$H_T=10\text{m}$, $T=9.6\text{sec}$, Slope= $1/50$ (for Goda's)

d=20m	θ	k	η_c	P_{crest}	P_1	$P_{1\text{max}}$	P_2	$P_{2\text{max}}$	d/L	H_{sc}/L	δ
3rd	0.01	0.058	15.61	52.75	40.40	52.28	8.44	46.69	0.185	0.184	0.578
	45	0.05	14.51	-75.35	68.48	*	50.04	*	0.159	0.160	0.503
2nd	0.01	0.058	15.61	192.30	109.20	*	48.30	*	0.185	0.184	0.578
	45	0.05	14.51	85.39	108.00	*	65.69	*	0.159	0.160	0.503
Goda's	0	0.055	15.0		72.93		43.71		$\alpha_1=0.72, \alpha_2=0.002$		
d=25m											
3rd	0.01	0.056	14.80	3.74	47.12	56.11	10.96	37.53	0.223	0.178	0.559
	45	0.048	13.35	-46.84	72.28	*	46.41	*	0.191	0.153	0.481
2nd	0.01	0.056	14.79	118.45	99.77	*	35.61	35.95	0.223	0.178	0.559
	45	0.048	13.35	34.13	94.50	*	52.85	*	0.191	0.153	0.481
Goda's	0	0.051	15		68.80		35.67		$\alpha_1=0.68, \alpha_2=0.0012$		
d=30m											
3rd	0.01	0.054	14.36	-7.56	51.18	57.86	9.64	30.64	0.258	0.172	0.540
	45	0.046	12.74	-29.71	74.41	*	41.08	*	0.220	0.146	0.459
2nd	0.01	0.054	14.36	86.54	95.10	*	26.45	28.58	0.258	0.172	0.540
	45	0.046	12.74	13.64	87.49	*	44.05	*	0.220	0.146	0.459
Goda's	0	0.049	15		65.72		28.7		$\alpha_1=0.65, \alpha_2=0.0007$		
d=35m											
3rd	0.01	0.052	14.12	-11.00	53.55	58.74	6.89	25.25	0.290	0.166	0.522
	45	0.045	12.37	-20.03	75.61	*	35.60	*	0.251	0.144	0.452
2nd	0.01	0.052	14.12	70.48	92.47	*	19.00	23.35	0.290	0.166	0.522
	45	0.045	12.37	3.56	83.34	*	37.06	*	0.251	0.144	0.452
Goda's	0	0.047	15		63.67		23.70		$\alpha_1=0.63, \alpha_2=0.0004$		
d=40m											
3rd	0.01	0.051	13.96	-12.15	55.07	59.26	3.88	21.41	0.325	0.160	0.503
	45	0.044	12.13	-14.28	76.30	*	30.44	*	0.280	0.140	0.440
2nd	0.01	0.051	13.96	61.48	90.93	*	12.91	19.63	0.325	0.160	0.503
	45	0.044	12.13	-2.07	80.70	*	31.20	*	0.280	0.140	0.440
Goda's	0	0.046	15		62.45		17.74		$\alpha_1=0.618, \alpha_2=0.0003$		

where

θ : incidence angle; k : wave number; η_c : wave crest elevation (unit: m); *: same as left

P_{crest} : wave pressure at η_c ; P_1, P_2 : wave pressure (phase $t/T=0$) at DWL & seabed

$P_{1\text{max}}, P_{2\text{max}}$: maximum wave pressure at DWL & seabed (unit: kN/m^2)

d/L : relative water depth; H_{sc}/L : short-crested wave steepness; δ : expansion parameter

Figure 6 and Figure 7 display both onshore and offshore pressures at different depths by both approximations, respectively. From the figures and Table 1, it is found that the residual errors at wave crest P_{crest} for 45° incident short-crested waves altogether decreased towards a theoretical zero to satisfy the Bernoulli assumptions at free surface boundary. The values decrease from 85 to -2 kN/m^2 by 2nd-order approximations and from -75 to -14 kN/m^2 by 3rd-order approximations at depths of 20m to 40m. For results by 2nd-order approximations, the deviations at wave crest seem more significant for normal incident waves than obliquely incident waves and pressure changes at DWL with depths were more notified than those by 3rd-order approximations. Being supported by negligible discrepancies between the two approximations at deep depths, it seems reasonable to apply either of the two approximations to estimate wave forces on a deep-water vertical breakwater.

Resultant wave forces estimations

Compared with the results by Goda's formulae, Table 1 shows that short-crested wave pressures of 45° incidence at DWL and seabed by both approximations were similarly greater than those by Goda's except at depth of 20m. The differences were gradually enlarged with increasing water depth at both locations, implying that Goda's formulae tend to under-estimate the resulting total pressure forces for obliquely incident waves on a deep water vertical breakwater. This is demonstrated with the calculated wave forces summarized in Table 2, in which numerical values were derived by summations of the approximated pressures directly from Eq.(6) at discretized depths. The reasons for utilizing discrete summations were mainly due to the avoidance of the residual effects of the surface errors on the resulting integration of Eq.(6) and the merits of estimations of wave forces between any two depths. Taking Figures 6 and 7 for illustrations, the pressure distributions above DWL were seen to be similarly linear for most depths but the surface residual errors would certainly cause calculated wave forces to be less reliable. If we correct this error by constraining the values of P_{crest} to be theoretically zero thus, wave forces can simply be calculated with known values of η_c and maximum pressure at DWL P_{1max} . However, this correction had resulted in an error equal to the triangle area with coordinates of $(P_{1max}, 0, P_{crest})$ and its magnitude is simply equal to $1/2 \times P_{crest} \times \eta_c$. Shown in Table 2, we notify the decreasing trends of the errors with increasing water depths since P_{crest} became much smaller as displayed in Figure 6 and 7. As a result, we found from Table 2 that errors are decreasing in deeper water by both approximations for 45° incident waves. However, the results for normal incidence have not shown similar tendency, rather are still significant at $d=30\text{m}$ and 40m , implying more attentions should be taken when applications.

On the other hand, the pressure force below DWL is simply the summation of the pressure force per unit depth. Usually for engineering applications as schematically shown in Figure 1 by Goda, the total on and off-shore pressure forces are derived by the magnitude of the area with linear distribution between P_1 and P_2 . The calculations are simple but may result in a significant error in resulting wave forces, especially for a deep water breakwater. As summarized in Table 2, the differences

between linear assumptions and the derived theoretical curves were exactly the shadowed areas shown in Figure 6 and 7. In this paper, the theoretical under-water total forces were approximated by summations of 20 trapezoidal pressure forces and more divisions can only slightly change the results. Obviously, linear assumptions of the pressure depth distributions result in an overestimation of the total force (the shadowed area), which became greater with increasing water depth. For 45° incident waves, Table 2 shows that for on-shore pressure force the over-estimations due to linear assumptions were about 10% at $d=20\text{m}$ to 19% at $d=40\text{m}$ greater than those due to theoretical profiles. They became even greater for the cases with normal incident waves, e.g. 46% and 26% for both 2nd and 3rd approximations. Overall, the over-estimations calculated by both approximations became closer in deep waters. This trend was also true for off-shore pressure force calculations. Therefore, linear assumptions always resulted in over-estimations and were more significant with increasing water depths. Besides, both approximations gave closer values at $d=40\text{m}$ than at $d=20\text{m}$, confirming the application of either of the two perturbed approximations in deeper water will not make much differences to each other.

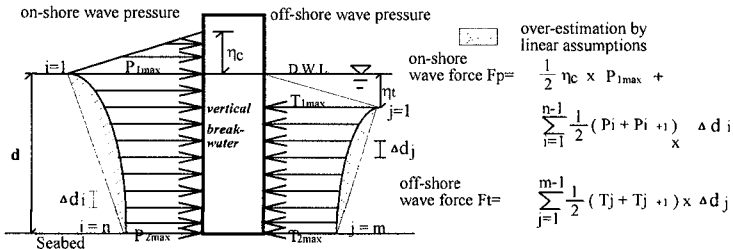


Figure 8. Definition Sketch for Design Short-Crested Wave Force Model

A Design Short-Crested Wave Force Model

According to above discussions, for a deep-water vertical breakwater we propose a design force model based on Fenton’s short-crested wave theory as schematically displayed in Figure 8. This model assumes that the residual surface pressure (on-shore) are negligible and set to be zero at the elevation of η_c . The pressures increase linearly to the maximum pressure at DWL (P_{1max}) such that the total wave pressure force above DWL is equal to the summation of each component pressure forces in the enclosed triangle area. The under water pressure force for both on and off-shore directions is the summation of the discrete unit pressure force derived directly from the theory for avoiding the over-estimations due to linear approximations. As a result, the total on and off-shore wave pressure forces at each depth calculated by this design model were summarized in Table 2. Table 2 illustrated that by this design wave force model the results were slightly different from those by Eq. 6 at water depths.

Comparisons of total pressure forces with depth

The comparisons with Goda’s formulae will mainly focus on the on-shore total

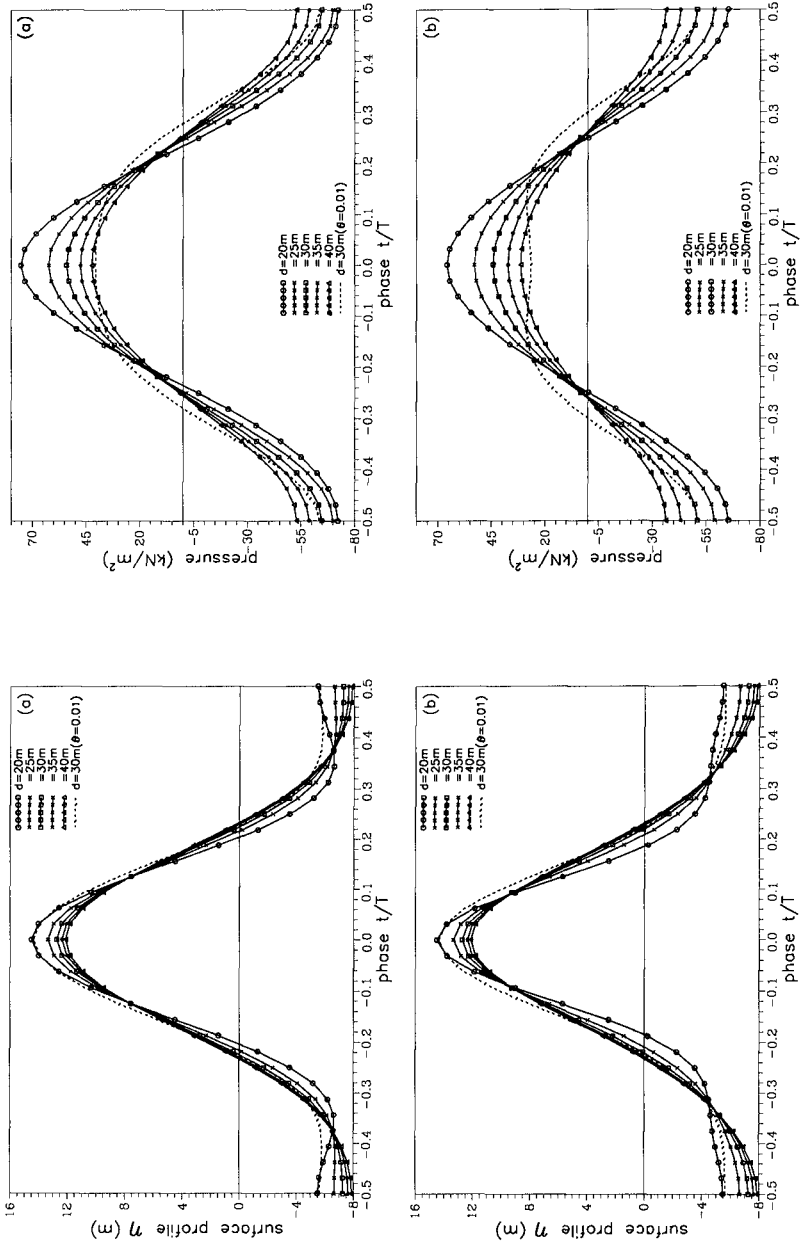


Figure 3. Surface Displacement with Phase by (a) 2nd-, (b) 3rd-Order S-C Wave Approx. ($\theta=45^\circ$)

Figure 4. Pressure Variations with Phase at (a) Mid-Depth, (b) Seabed by 2nd-Order Approx. ($\theta=45^\circ$)

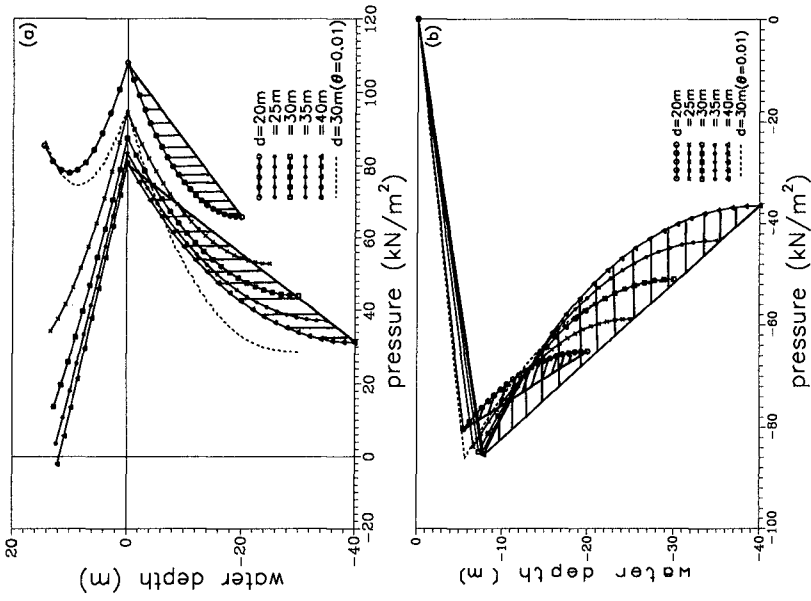


Figure 6. Vertical Distributions of S-C (a) On-, (b) Off-Shore Wave Pressures by 2nd-Order Approx. ($\theta=45^\circ$)

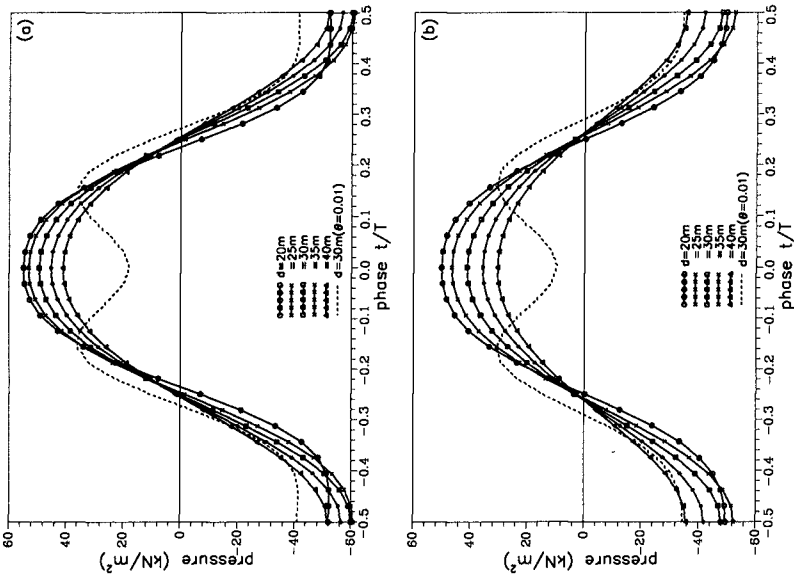


Figure 5. Pressure Variations with Phase at (a) Mid-Depth, (b) Seabed by 3rd-Order Approx. ($\theta=45^\circ$)

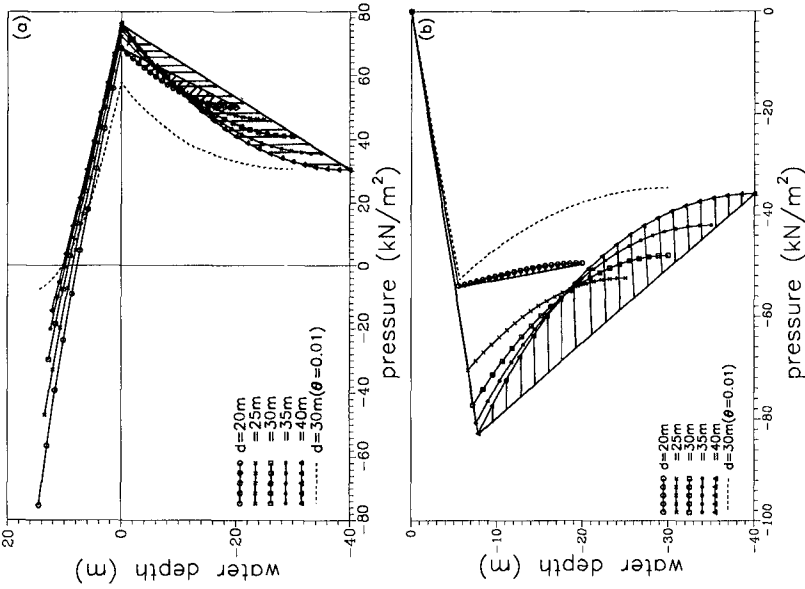


Figure 7. Vertical Distributions of S-C (a) On-, (b) Off-Shore Wave Pressures by 3rd-Order Approx. ($\theta=45^\circ$)

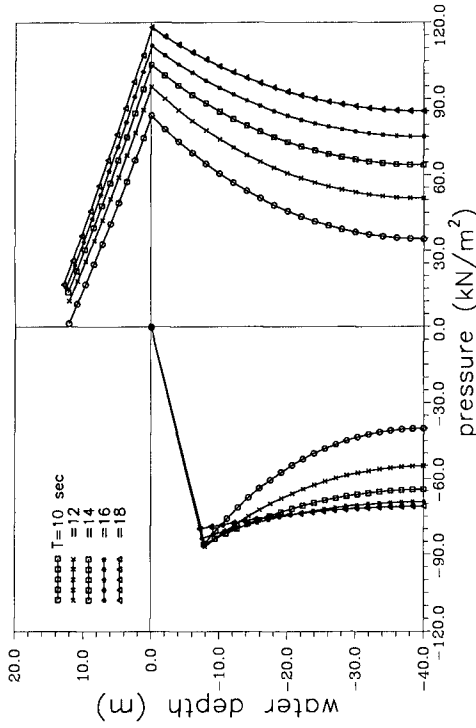


Figure 9. Vertical Distributions of S-C Wave Pressures with Period at $d=40\text{m}$ by 2nd-Order Approx. ($\theta=45^\circ$)

Table 2 Comparisons of Wave Forces on A Vertical Breakwater(unit : kN/m; $H_{\max}=10\text{m}$, $T=9.6\text{sec}$)

water depth (m)		20	25	30	35	40	30	40	
F above DWL		On-shore wave force ($\theta=45^\circ$)					($\theta=0^\circ$)		
(1) corrected	(3rd)	496.7	482.5	474.0	467.7	462.7	415.5	413.7	
	(2nd)	783.5	630.8	557.3	515.5	489.2	683.0	643.9	
(2) error ΔF	(3rd)	546.5	312.6	189.3	123.9	86.6	200.7	180.0	
	(2nd)	-466.7	-167.8	-56.2	-3.59	24.8	-472.2	-330	
Goda's		547.0	516.0	492.9	477.5	468.4			
F below DWL									
(3) curved	(3rd)	1129.5	1382.4	1567.9	1706.4	1808.9	1161.3	1274.2	
	(2nd)	1581.9	1652.3	1737.1	1813.2	1874.4	1429.8	1510.1	
(4) linear	(3rd)	1185.0	1483.6	1732.2	1946.1	2134.8	1327.5	1613.4	
	(2nd)	1737.1	1841.9	1973.1	2107.0	2236.8	1855.1	2211.2	
$\Delta F=(3)-(4)$		55.5	101.2	164.3	239.7	325.9	166.2	339.2	
$\Delta F / (3)$	(3rd)	(4.9%)	(7.3%)	(10.5%)	(14.0%)	(18.0%)	(14.3%)	(26.6%)	
	(2nd)	155.2	189.6	236	293.8	362.4	425.3	701.1	
		(9.8%)	(11.5%)	(13.4%)	(16.2%)	(19.3%)	(29.7%)	(46.4%)	
Goda's		1166.4	1305.9	1416.3	1528.9	1603.8			
Total wave force									
(5) (1) + (3)	(3rd)	1626.2	1864.9	2041.9	2174.0	2271.6	1576.8	1687.9	
	(2nd)	2365.4	2283.1	2294.4	2328.7	2363.6	2112.8	2145.0	
(6) Fenton's	(3rd)	1897.2	2023.9	2143.4	2242.3	2319.0	1427.7	1495.7	
	(2nd)	2086.5	2156.9	2241.6	2317.5	2378.6	1919.6	1927.3	
(7) Goda's		1713.4	1821.9	1909.3	2006.5	2072.2			
$\Delta F=(5)-(6)$		-271.0	-159.0	-101.5	-68.2	-47.3	-149.1	-192.2	
$\Delta F / (6)$	(3rd)	(-14.3%)	(-7.9%)	(-4.7%)	(-3.0%)	(-2.0%)	(-10.4%)	(-11.4%)	
	(2nd)	228.9	126.2	52.8	11.2	-15	193.2	217.7	
		(11.0%)	(5.9%)	(2.4%)	(0.5%)	(-0.6%)	(10.1%)	(11.3%)	
$\Delta F=(5)-(7)$		-87.3	43	132	167	199.5	-332.2	-416.4	
$\Delta F / (7)$	(3rd)	(-5.1%)	(2.4%)	(6.9%)	(8.3%)	(9.6%)	(-17.4%)	(-20.1%)	
	(2nd)	652	461.2	385.1	322.2	291.4	203.5	40.7	
		(38%)	(25.3%)	(20.2%)	(16.1%)	(14.1%)	(10.7%)	(2.0%)	
		Off-shore Wave Force($\theta=45^\circ$)					($\theta=0^\circ$)		
(8) curved	(3rd)	-743.2	-1073.3	-1308.0	-1483.4	-1614.7	-984.8	-1309.8	
	(2nd)	-1018.2	-1228.8	-1405.1	-1545.0	-1654.0	-1521.8	-1797.6	
(9) linear	(3rd)	-750.7	-1128.3	-1425.0	-1678.8	-1903.9	-1063.0	-1511.4	
	(2nd)	-1054.9	-1308.4	-1543.1	-1758.1	-1955.7	-1674.6	-2116.9	
$\Delta F=(8)-(9)$	(3rd)	46.8	55	117	195.4	289.2	78.2	201.6	
	(2nd)	36.7	79.6	138	213.1	301.7	152.8	319.3	

(2nd) and (3rd) denote results by Fenton's 2nd and 3rd-order approximations, respectively

Table 3 Summations of Short-Crested Swell Characteristics

$H_p=10m, d=40m, \theta=45^\circ$					
wave period T (sec)	10	12	14	16	18
wave crest elevation η_c (m)	12.095	12.071	12.22	12.50	12.87
wave trough elevation η_t (m)	-7.91	-7.93	-7.78	-7.51	-7.14
pressure at crest $P_{crest}(kN/m^2)$	-12.76	-7.28	-3.721	-0.86	1.80
	1.30	10.06	13.43	15.23	16.47
max. on-shore pressure at DWL	78.14	86.50	93.68	100.32	106.87
$P1_{max}$ (kN/m ²)	83.42	94.74	103.42	110.90	117.96
max. on-shore pressure at seabed	33.70	48.47	60.20	69.73	77.90
$P2_{max}$ (kN/m ²)	34.64	50.7	63.89	75.10	85.10
max. off-shore pressure at trough	-81.81	-81.66	-79.01	-75.16	-70.28
$T1_{max}$ (kN/m ²)	-85.86	-87.05	-86.14	-83.69	-80.00
max. off-shore pressure at seabed	-39.15	-52.91	-60.69	-63.94	-63.87
$T2_{max}$ (kN/m ²)	-40.08	-55.10	-64.38	-69.31	-71.08
$\Delta F_p = F_p(\text{linear}) - F_p(3rd)$	313.9	265.7	234.6	215.5	205
$\Delta F_p / F_p(3rd)$	(16.3%)	(10.9%)	(8.3%)	(6.8%)	(5.9%)
$\Delta F_p = F_p(\text{linear}) - F_p(2nd)$	345.4	321.9	285.6	256.7	233.7
$\Delta F_p / F_p(2nd)$	(17.3%)	(12.4%)	(9.3%)	(7.4%)	(6.1%)
Total on-shore wave force F_p	2395.5	2955.8	3415.4	3812.5	4178.1
	2500.3	3158.7	3692.5	4156.4	4586.6
$\Delta F_p = F_p(2nd) - F_p(3rd)$	104.8	202.9	277.1	343.9	408.5
$\Delta F_p / F_p(3rd)$	(4.4%)	(6.9%)	(8.1%)	(9.0%)	(9.8%)
Goda's design pressure force	2134.9	2524.8	2903.5	3250.3	3565.3
$\Delta F_p = F_p(3rd) - F_p(\text{Goda})$	260.6	431	511.9	562.2	612.8
$\Delta F_p / F_p(\text{Goda})$	(12.2%)	(17.1%)	(17.6%)	(17.3%)	(17.2%)
$\Delta F_p = F_p(2nd) - F_p(\text{Goda})$	365.4	633.9	789.0	906.1	1021.3
$\Delta F_p / F_p(\text{Goda})$	(17.1%)	(25.1%)	(27.2%)	(27.9%)	(28.6%)
Total off-shore wave force	-1694.6	-1997.1	-2152.2	-2201.1	-2171.5
(hydrodynamic components)	-1743.6	-2097.2	-2304.7	-2407.9	-2435.0
$\Delta F_T = F_T(\text{linear}) - F_T(3rd)$	-246.2	-160.7	-98.4	-58.6	-32.6
$\Delta F_T / F_T(3rd)$	(14.5%)	(8.0%)	(4.6%)	(2.7%)	(1.5%)
$\Delta F_T = F_T(\text{linear}) - F_T(2nd)$	-277.1	-182.2	-120.2	-77.6	-47.2
$\Delta F_T / F_T(2nd)$	(15.9%)	(8.7%)	(5.2%)	(3.2%)	(1.9%)

Note : the shadowed areas denote the calculations by the 3rd-order approximations

wave pressure forces in the following sections. The short-crested wave pressure forces were derived according to Figure 8 and standing wave pressure forces were based on Figure 1. From Table 2, the calculated total pressure forces by short-crested wave model were always greater than Goda's results, even though the over-estimation due to linear short-crested wave pressure distribution under DWL had been excluded. As water depths increased, the trends of depth distribution of wave pressure were opposite for both approximations and resulting total wave forces by 2nd-order were also greater than those by 3rd-order but the differences became smaller in deeper waters. At water depth of 40m, for example, the 45° incident short-crested waves could impose 10% to 14% greater pressure forces than standing waves on a vertical breakwater. Based on the findings and Table 2, it is expected that short-crested wave forces could still be significantly greater than standing waves forces at water depths over 40m. It is clearer that Goda's formulae tend to under-estimate total pressure forces especially for a deep-water vertical breakwater. Therefore, the traditional acknowledgment of standing waves to be the maximum imposing loading on a vertical breakwater should be corrected for future engineering practices.

Applications to short-crested swells

To further demonstrate the differences between current model and Goda's formulae, we shall briefly examine the variations of total wave pressure forces with longer waves at depth of 40m. The wave height is the same as discussed above but wave periods will be 10, 12, 14, 16, and 18 seconds, respectively. Results calculated by both short-crested wave approximations were summarized in Table 3. Figure 9 displays the phase variation of maximum on and off-shore pressure depth distributions by the 2nd-order approximations. It is observed from Table 3 that wave crest elevations η_c were only slightly increasing with wave periods and standing η_c are all higher than short-crested η_c but the differences decreased with longer wave periods. Figure 9 shows that the surface residual pressures were relatively small and Table 3 confirms the same trend for 3rd-order approximations. Besides, at this depth the curvature of the under-DWL on and off-shore pressure depth distributions were more significant for shorter-period waves by both approximations. Thus, the over-estimation by linear assumptions of the on-shore pressure depth distributions became less important such as were about 17.3% for T=10s to 6.1% for T=18s, respectively for 2nd-order approximations. But the variances in total wave forces derived according to Figure 8 between the two approximations became more significant with longer wave period. From Table 3, the total wave forces by 2nd-order were greater than those by 3rd-order approximations by about 4.4% for T=10s to 9.8% for T=18s. As a result for 45° incident short-crested waves acting on a vertical breakwater in such conditions, the total wave forces calculated by current model became greater with period than those by Goda's. For 3rd-order approximations, the trend could grow up about from 12% for T=10s to 17% for T=18s and became even more significant for those by 2nd-order approximations. The comparisons clearly suggest that the design forces could be under-estimated by Goda's formulae, especially in deep waters.

Conclusions and Suggestions

The evaluations with $\theta=45^\circ$ incident waves of $H_D=10\text{m}$ and $T=9.6\text{s}$ show that both Fenton's 2nd and 3rd-order approximations can be reasonably applicable at deep depths due to more negligible residual pressures at wave crest. Modified from the theory, present short-crested wave force model for deep-water vertical breakwaters defines maximum wave pressure P at DWL and linear distribution of P to zero pressure at wave crest. The resulting wave pressure forces are simply the summations of pressure distributions derived according to theoretical approximations at discrete depths. Linear assumptions for pressure depth distribution under DWL result in greater over-estimated total wave forces with increasing water depth or shorter waves. Differences between 2nd and 3rd-order approximations always become negligible as water depth increased but more significant for longer waves or for $\theta=0^\circ$. For $\theta=45^\circ$ and $T=9.6\text{s}$, the over-estimations by 3rd-order approximations could amount about from 5% to 18% at $d=20\text{m}$ to 40m but then decrease to 6% for $T=18\text{s}$ at $d=40\text{m}$. For current wave conditions, Goda's formulae for standing waves under-estimate the total pressure forces than short-crested waves of $\theta=45^\circ$ by at least 10% at depth of 40m and up to 17% or 28% for waves of $T=18\text{s}$ derived by 3rd-order and 2nd-order approximations, respectively.

It is recommended that more studies on the applications of the current model to field conditions to be carried out for further design needs of deep-water breakwaters. Three-dimensional hydraulic model tests are considered necessary for decisive selection between the two approximations. Further extension to establish a similar model for composite breakwaters will be very valuable for engineering practices.

References

- Chappellear, J. E. (1961), "On the description of short-crested waves," *Beach Erosion Bd, U.S. Army Corps Engrs. Tech. Memo*, No. 125.
- Fenton, J. D.(1985), "Wave forces on vertical walls," *J. of Waterway, Port, Coastal and Ocean Engineering*, Vol. 111, No. 4, pp. 193-717.
- Goda, Y. (1972), "New wave pressure formulae for composite breakwater," *Proc. of 14th Int. Conf. Coastal Engineering*, Copenhagen, pp. 1702-1720.
- Goda, Y. (1985), *Random Sea Waves and Engineering Applications*, University of Tokyo Press, Ch4.
- Hsu, J. R. C., Y. Tsuchiya, and R. Silvester (1979) "Third-order approximation to short-crested waves," *J. Fluid Mech.*, Vol. 90, No. 1, pp. 179-196.
- Jeffreys, H. (1924), "On water waves near the coast," *Phil. Mag. Ser.*, Vol. 6, No. 48, pp. 44-48.
- Roberts, A. J. and L. W. Schwartz, (1983) "The calculation of non-linear short-crested gravity waves," *Phys. Fluids*, Vol. 26, No. 9, pp. 2388-2392.
- Silvester, R.(1974), *Coastal Engineering*, Vol. 1, Elsevier, Amsterdam, Netherlands.
- Tanimoto, K. and S. Takahashi, (1994), "Design and construction of caisson breakwaters - the Japanese experience," *Coastal Engineering*, Vol. 22, pp. 55-77.

CHAPTER 194

New design methods for wave impact loadings on vertical breakwaters and seawalls

Allsop N.W.H.,¹ McKenna J.E.,² Vicinanza D.³ & Whittaker T.T.J⁴

ABSTRACT

This paper discusses wave impacts on vertical and composite breakwaters and related coastal structures. It describes types of vertical walls in use, with particular reference to older walls that may be much more influenced by wave impacts. Methods to estimate wave forces are identified. Analysis of performance suggests that these under-predict wave impact loads, and cannot identify combinations of geometry and wave conditions which lead to impacts.

Comprehensive 2-dimensional hydraulic model tests have been conducted using random waves to measure wave pressures (and other responses) on a wide range of simple and composite vertical walls. The test results have been used here to:

- Identify the ranges of geometry and wave conditions which lead to wave impacts;
- Develop a simple method to estimate wave forces under impact conditions.

Analysis of % of impacts has defined a new design diagram to identify wave conditions and wall / mound geometries which cause impacts. These results are intended for engineers analysing vertical or composite walls in deep water, in harbours, or along the shoreline.

1. VERTICAL WALLS

Seawalls or breakwaters around the world have often been built with vertical or steep faces formed by small blocks joined together. The structure relies on its weight to resist sliding or overturning forces, and on the bonding or jointing of the blocks to maintain its monolithicity. The integrity of blockwork walls depends on their resistance to local pressures or pressure gradients. Modern structures may be formed from larger elements, perhaps full-depth cellular caissons filled with sand or rubble, and founded on rubble. A few modern structures use concrete blocks bonded or keyed together, or thin concrete elements.

Much of the historical and experimental information discussed in this paper has been presented in the comprehensive research report by Allsop et al (1996a).

¹ Professor (associate), Department of Civil Engineering, University of Sheffield; Manager Coastal Structures, HR Wallingford, Howbery Park, Wallingford, UK; e-mail: w.allsop@sheffield.ac.uk

² Ph.D student, Department of Civil Engineering, Queen's University of Belfast.

³ Ph.D researcher, Department of Hydraulic Construction, University of Naples, Italy

⁴ Professor, Department of Civil Engineering, Queen's University of Belfast

Construction of breakwaters, piers, and seawalls

Unless founded directly onto rock, vertical breakwaters or piers built before about 1900 used rubble slightly below low water, and surmounted by blockwork walls. Hewn stones were laid in bond, generally slightly off vertical. Blocks were originally laid dry, or in lime / pozzolanic mortar. Cement mortars were used after about 1900, and concrete blocks after about 1880. Tensile, bending, or shear loads were transferred between adjoining blocks, or courses of blocks, by iron cramps, keys or joggle joints between blocks.

Concrete blocks were used at North Tyne in 1855 (Fig 1), for Dover breakwater, 1866, and at Cork in 1877. Concrete bags formed a foundation at Fraserburgh in 1877, and for Ardrossan Pier in 1892. Concrete filling was used for the later stages of Alderney breakwater 1849-1866, Aberdeen south breakwater, 1873; North Pier at Aberdeen, and the Fraserburgh breakwater, both in 1877. The Italian engineer Coen Cagli re-introduced vertical wall breakwaters to Italy after a visit to Britain in 1896 where he saw blockwork breakwaters at Dover, Sunderland, North Tyne, Peterhead, and Wick.

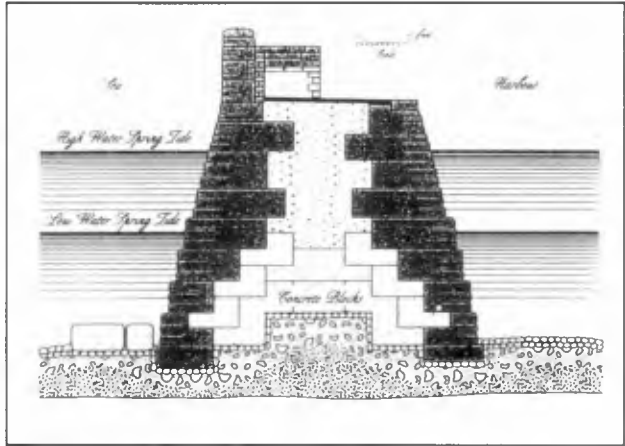


Figure 1 North Tyne Breakwater

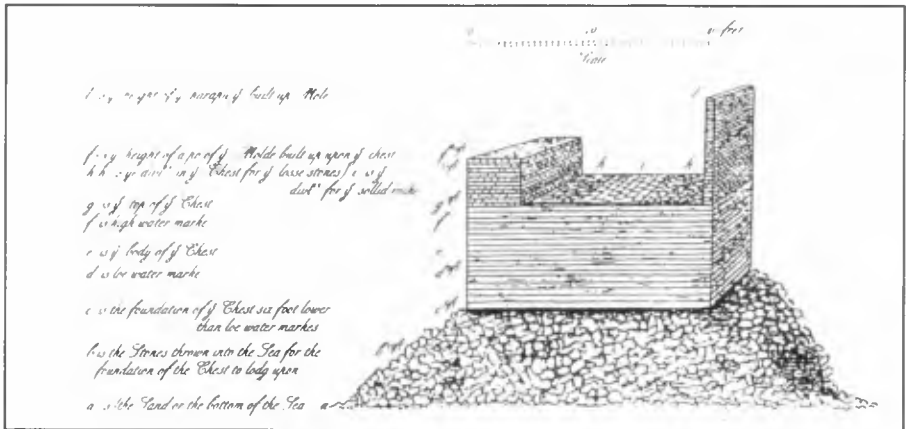


Figure 2 Timber caisson used for the Greate Mole at Tangier, 1677

Caissons were rarely used in the UK before 1900, but construction of the Greate Mole at Tangier by British engineers using caissons in 1660s is described by Routh cited by Allsop et al (1996a). The Mole was started with rubble foundations placed ahead of blockwork in August 1663, but only reached 350m by August 1668 due to adverse wave conditions; loss of

fill into the sand; diversion of the workforce to other (military) duties; difficulties in obtaining materials; and significant delays in payment for work completed. Construction re-started in April 1670 with the blockwork walls damaged and breached by storms. A new construction was copied from Genoa using "great wooden chests" bound in iron, and filled with stones and mortar. After much debate, some reported in Samuel Pepys' diaries, wooden caissons of 500 to 2000 tons were towed out from England, and sunk onto the foundation filled with stone bound in mortar (Fig 2). Progress was quicker with the new construction and suffered less delay than the blockwork sections. In 1680 however, peace was concluded, and the breakwater was then destroyed lest it provide shelter to a later enemy.

The development of many harbours around the UK between 1850 and 1900, and their survival, have reduced the need for new harbours around the UK, so relatively few have been constructed since 1900. Vertical breakwater exceptions to this are at the new marina harbour at Brighton protected by circular caissons based on those used at Hanstholm in Denmark; and the vertical wave screen breakwaters at Sutton Harbour, Plymouth, and Cardiff Barrage.

Performance in service

The life of a breakwater may be considered in three periods: construction; initial service; and extended service (often well beyond that used in design life calculations). Most damage occurs early in its life, even during construction, so most breakwaters which survive the first 5 years without damage are likely to survive the next 40-50 years. This simplification however ignores steady or accelerated deterioration which may lead to sudden failures in later life.

Stevenson describes construction at Wick started in 1863 using dry-placed blocks of 5 to 10 tons. During storms in 1870, about 115m was destroyed, presumably by breaching the wall. This section was then rebuilt using cement to bond the block facing, and iron dowels between courses. A storm in February 1872 gave impact pressures so severe that facing stones were shattered, although Stevenson does not identify whether this was by direct wave impact, or by stones from the mound being hurled against the face. In December 1872 a section of blockwork bonded together and estimated as weighing 1350 tons slid into the harbour. This was followed in 1873 by movement of another section of 2600 tons.

During construction of Catania breakwater in Sicily in 1930, large blocks slid backwards into the harbour under wave attack. The damage was repeated in 1933 when much of the upper part of the breakwater slid backwards, due to a lack of horizontal connectivity between layers. Later structures in Italy included connections to resist horizontal forces, but few if any existing structures were re-appraised or strengthened, and collapses continued at Genoa in 1955, at Ventotene in 1966, Palermo in 1973, Bari in 1974, and Naples in 1987.

Mutsu-Ogawara port on the Pacific coast of Japan was under construction in 1991, when it was hit by waves of $H_s=9.9\text{m}$, substantially above the 1:50 year design condition of $H_{so}=7.6\text{m}$. Damage was particularly severe where mounds of armour intended to cover the front face were incomplete and/or had already been damaged. Waves tripped over the part-height mounds causing impact forces so severe that two 24m long caissons suffered significant structural damage, one of them losing most of its upper part.

Sakata port is on the Japan Sea, less exposed than the Pacific coast. Even so, waves during winter 1973 / 74 reached $H_{so}=7.2\text{m}$ and exceeded $H_{so}=4.5\text{m}$ on 4 other occasions. In depths no more than 9-10m, these conditions would have reached or exceeded the breaking limit. Nearly all 39 caissons, each 20m long and 17m deep, slid during these storms, some by 4m.

In December 1990, a small breakwater was damaged at Amlwch, North Wales. It is about 60m long, slightly curved in plan, and is constructed using concrete blocks in slices on mass concrete on the rockhead. The outer end of the breakwater was slid backwards by about 0.3, cracking the crown wall in three places. Wave conditions are estimated as $H_{so} \geq 4\text{m}$, with

$T_m=9s$. The foreshore is very steep, approximately 1:13, falling outside of any established design method. The depth at the toe probably reached at least 11-14m. Allsop & Vicinanza (1996) estimated inshore wave conditions limited by depth to $H_{s0}=4m$ at MHWS, but reducing to $H_{s0}=3.6m$ at MLWS. Using the method of Vicinanza et al (1995), F_h was calculated as 1040kN/m at MHWS. With no up-lift force for blocks direct on concrete, and $\mu=0.5$, these give a factor of safety of $F_s = 0.9$ at high water, contrasted by predictions using Goda which give $F_s = 1.2$ at high water, and $F_s = 2.3$ at low water.

In late October 1966, the blockwork breakwater of Porthcawl in South Wales lost its capping wall over a length of about 55m, again probably due to a single direct wave impact.

These examples demonstrate that wave impact forces are very high, and the more recent damage suggest that predictions of wave loadings / responses remain very uncertain. As many blockwork walls approach 150 years old, and the potential for local or catastrophic collapse increases, it becomes more important to re-examine wave load prediction methods.

2. WAVE LOADINGS ON VERTICAL AND COMPOSITE WALLS

The main loadings acting on these types of walls arise from: direct wave pressures; up-lift forces; quasi-hydrostatic forces from internal water pressures; and geotechnical forces / reactions from backing or supporting materials. These structures resist wave and geotechnical forces essentially by their own weight, and by friction with the underlying materials. Interlock or bonding forces between component elements maintain continuity and avoid movement or loss of elements and/or fill.

The simplest failure mode for monolithic vertical structures is sliding under direct wave forces, primarily under horizontal loads, but also influenced by up-lift forces. Failure by overturning may be examined by assuming rotation about the rear heel of the caisson / wall, but the point of rotation depends upon bearing capacity and geotechnical characteristics of the mound / foundation. Analysis of foundation failures has been discussed by de Groot et al (1995), and constitutes a major part of the MAST III research project PROVERBS. Blockwork breakwaters may also fail by loss of integrity where a block is removed (seaward) by net suction forces, followed perhaps by progressive damage and then catastrophic collapse.

It is often convenient to treat wave pressures / forces on these structures as quasi-static / pulsating; of dynamic / impulsive or impact, see also Figure 4 in Section 3.

Quasi-static or pulsating wave pressures change relatively slowly. A wave impinges directly against the structure applying a (quasi-) static pressure difference. The obstruction of wave momentum causes the water surface to rise up, increasing the force on the wall. The net force is related closely to the peak water level, and can be estimated using simple methods. Most design methods assume static loadings, and simple equilibrium conditions.

Dynamic or impact pressures arise where the wave breaks directly onto the structure. Impact pressures are substantially greater than pulsating pressures, and of much shorter duration. The processes of wave breaking are not well understood and the occurrence of breaking cannot be predicted with reliability, so these pressures are extremely difficult to calculate, and have historically not been used in design calculations. Schmidt et al (1992) remind us that there are still two attitudes to impact loadings. The first simply assumes that impact pressures are not important and need not be adopted in design. The second is to skip the problem of evaluating impact loads by assuming that the structure can be designed so that impacts will not occur. A third (newer) approach is to conduct dynamic analysis of the structure, its foundation, and the loads. This requires high levels of data on wave loadings, and on the geotechnical response characteristics of structure / mound / foundation, but is likely to become more frequently used.

These problems are compounded by uncertainties in defining conditions that lead to impacts. Schmidt et al (1992) and Oumeraci (1994) define 7 breaker classifications in terms of H_b/d , but the breaker height H_b is extremely difficult to predict, so these classifications are of limited use. Klammer et al (1996) define 2 types of plunging and a "flip-through" breaker, but then derive a suggested force formula for all three types lumped together.

Goda (1985) described rules to identify whether particular structures or sea states will cause impulsive wave conditions, and that method is re-interpreted as Figure 3.

Wave force prediction methods

Hiroi's simple formula gives a uniform wave pressure p on the front face up to $1.25H$ above still water level where H the wave height, and $p = 1.5\rho_w gH$. Sainflou's method calculates a maximum pressure, p_1 , at static water level, tapering to zero at $H + \delta_0$ above SWL, and reducing linearly with depth from p_1 to p_2 at the rubble base. The Shore Protection Manual (1984) however suggests that Sainflou's method may over-estimate wave forces for short non-breaking waves, and uses Miche-Rundgren formulae to derive the clapotis height from which an (assumed) linear hydrostatic pressure is calculated. For long waves of low steepness, the SPM recommends Sainflou's method.

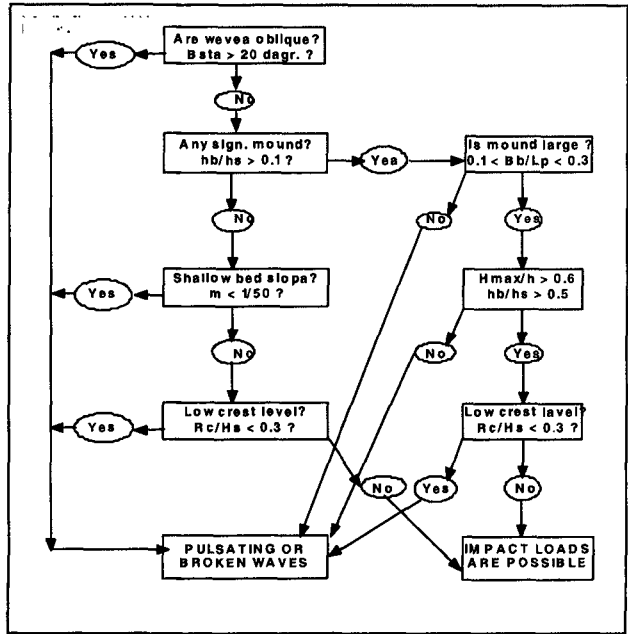


Figure 3 Impact breaking conditions, derived from Goda (1985)

Goda's method

The most widely used prediction method for wave forces on vertical walls was developed by Goda (1985), primarily to calculate horizontal forces for concrete caissons on rubble mound foundations, and calibrated against laboratory tests and back-analysis of historic failures. This method assumes wave pressures on the front face are distributed trapezoidally, reducing from p_1 at s.w.l. to p_2 at the caisson base. Above s.w.l. pressure reduces to zero at the (notional) run-up height $\eta^* = 1.5H_{max}$, where H_{max} is taken as $1.8H_b$. The method describes impulsive and deflected wave components by coefficients α_1 , α_2 , and α_3 . The effect of relative depth to wave length on the pulsating component is represented by α_1 ; the effect of impulsive breaking due to the mound is represented by α_2 ; and α_3 accounts for the relative crest level and relative depth over the toe. The depth h is taken at the mound toe, and d over the mound at the front face of the caisson, but h_b is taken $5H_b$ seaward.

The caissons on rubble foundations considered by Goda had natural periods around 0.1 to 0.3s. When subjected to loads of much shorter durations, the effective load is smaller than the applied load. Thus for the short peak pressures caused by wave impacts, Goda's formula

does not give actual pressures, but equivalent static loads for the dynamic system of caisson, mound and foundation. Goda noted that impulsive pressures caused by waves which break onto the wall may rise to $p=10\rho_w gH$, but judged that vertical breakwaters would not be designed to be exposed to direct impulsive pressures.

Wave impact force predictions

In Europe, engineers observed the effects of very large forces on some walls, and noted very short impacts coupled with very large pressures. Bagnold postulated a model of air compressed by the exchange of wave momentum, see Klammer et al (1996) for a simple description. At maximum pressure, all the wave momentum has been converted to pressure over the impact rise time. This approach however required identification of the thickness of the air pocket, and of the virtual length of the water piston, neither of which could be measured. Minikin's (1963) used Bagnold's model to develop to estimate impact pressures caused by waves breaking directly onto a wall, and therefore addressed the problems of impact pressures. The resulting expression for p_{max} may be written:

$$p_{max} = \frac{1}{2} C_{mk} \pi \rho_w g H_{max} (1+d/h) (d/L) \quad (1a)$$

where C_{mk} is defined to fit Rouville's data, accounting for typical sizes of air pocket. Minikin suggests $C_{mk}=2$, which is then cancelled within eqn. 1a to give the simpler version used in the British Standard, BS6349 Pt1, BSI (1984):

$$p_{max} = \pi \rho_w g H_{max} (1+d/h) (d/L) \quad (1b)$$

Unfortunately, this expression was re-written by Minikin with $\pi\rho_w g$ replaced by $2.9!$ This (mis)-use of dimensioned coefficients was later compounded by the Shore Protection Manual, and others. The total horizontal force may be written in dimensionally correct terms:

$$F_{hmax} = \frac{1}{2} C_{mk} \pi \rho_w g H_{max} d \left\{ (1+d/h) H/(3L) + 1/(2\pi) + H/(8\pi d) \right\} \quad (1c)$$

Many versions of Minikin's formula for total force, except that used by BSI (1984), included a factor of 101 replacing πg , but without qualification on the units. In imperial units this becomes more serious when later authors imply that $\pi g = 101$ can be used in other units than f.p.s, and have thus propagated the erroneous version of Minikin's formulae ever since! In practice the SPM version of Minikin's method gave so much greater pressures than other formulae that its use for calculations in practical design has been limited. Goda writing on wave force formulae in 1990 summarises the prevalent view on Minikin's method as "can be considered to belong to a group of pressure formulae of historical interest".

Takahashi extended Goda's method to include effects of breaking wave impacts. This was obtained by re-analysing tests of caissons sliding under wave impacts (regular waves), together with data on caisson movements at Sakata Port. The modification is applied by changing the α_2 coefficient to be the maximum of α_2 or a new impulsive coefficient α_1 , itself given by coefficients representing the effect of wave height on the mound, and mound shape.

Other methods for impact pressures

Partenscky quoting Oumeraci has used results from the large wave channel at Hannover / Braunschweig (GWK) to suggest that impact pressures of very short durations (0.01 to 0.03s) may be calculated the breaking wave height, and a coefficient K_1 given in terms of the air content a_o of the breaking wave.

Blackmore & Hewson conducted field measurements at four sea walls in the UK, from which they developed a model based on momentum exchange. Impact pressures p_i depend on the shallow water wave velocity, v_o ; the wave period, T ; and an aeration factor, λ , which depends on the roughness of the foreshore. A value of $\lambda = 0.3$ is recommended for a rough and rocky seabed, and $\lambda = 0.5$ for a regular seabed. Breaking wave heights are indirectly considered by using shallow water wave velocities calculated from the breaking water depth, h_b , and breaking wave height, H_b .

More recently, Klammer et al (1996) have developed a method to predict wave impact forces based primarily on solitary waves, but with some (rather tenuous) comparisons with data from random wave tests in the Large Wave Flume at Hannover / Braunschweig.

3. DESIGN OF MODEL STUDIES

3.1 Test structures and facility

Hydraulic model tests were conducted to measure wave pressures / forces on a range of simple vertical and composite wall configurations, using the Deep Random Wave Flume at Wallingford, which is 52m long and operates with water depths between 0.8m and 1.75m. The flume is configured to reduce reflection of waves from the test section in absorbing side channels. The bathymetry approaching the test section was formed to 1:50. The main caisson was formed as a hollow box with pressure transducers mounted flush with the front face and the underside. The design / construction of the model caissons, the measurement systems, and the test programme, have been described fully by Allsop et al (1996a).

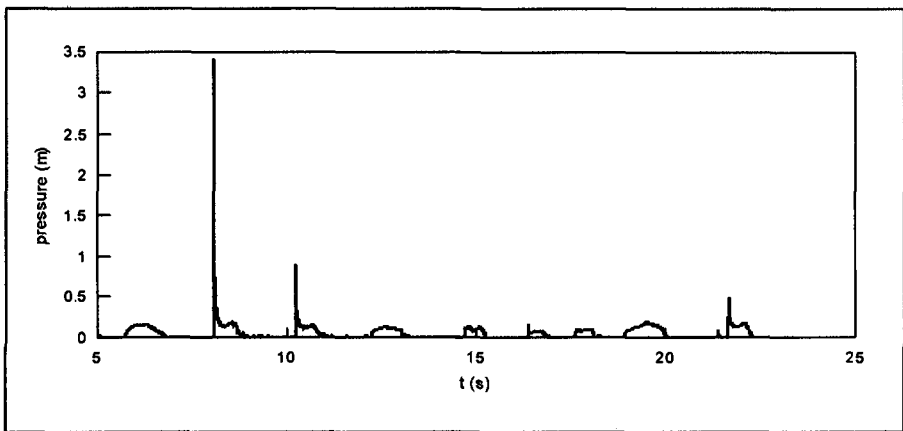


Figure 4 Wave pressure events from Test 10003 on Structure 1

The geometric and wave parameters that influence wave forces include: wave heights, H_{so} and H_b ; water depth in front of the structure, h_b ; crest freeboard, R_c ; wave steepness, s_{mo} ; wave length at structure toe, L_s ; water depth over mound at wall, d ; berm height, h_b ; berm width, B_b , and front slope of mound, α ; and the depth of embedment of caisson into mound, h_b-h_c . Systematic variations would have required more than 1 year testing, so drastic reductions were made by concentrating on the most important dimensionless parameters, particularly the relative wave height, H_b/d , berm length, B_b/L , and berm height, h_b/h_s .

For the simple wall, the parameters varied were the waves and water depth. The crest level was not changed. For composite walls, the main change was the relative height / depth of the mound in front of the wall, by varying the height of the mound, and the water level. The other changes were to the width of the berm (3 widths) and the front slope angle of the mound (1:1.5, 1:3 with most tests using 1:2). Eleven structures were tested in this study. Structure 0 was a simple vertical wall. The main composite walls were Structure 1 with a small mound; Structures 2 or 3 with intermediate mounds; and Structures 9 and 10 with large mounds.

Wave steepnesses of $s_{mo} = 0.02, 0.04$ and 0.06 were used for relative wave heights of $H_b/h_s = 0.1 - 0.6$, but restricted to $0.15 - 0.4$ for some structures. Up to 5 water levels were used.

Pressures / forces were measured by pressure transducers in the front and lower faces of the caisson. These gave high resolution measurements to about 8m (fresh) water head, and a maximum pressure before damage equivalent to 15m.

The sampling rate was 400Hz, and data were collected from 16 pressure transducers for 500 waves for each test. Oumeraci et al (1994) suggest reduction factors for impact pressures sampled at 400Hz may give under-estimates of maximum pressures by up to 50%, but the reduction for horizontal force is limited to 20%. At these rates, the total impulses are not significantly affected.

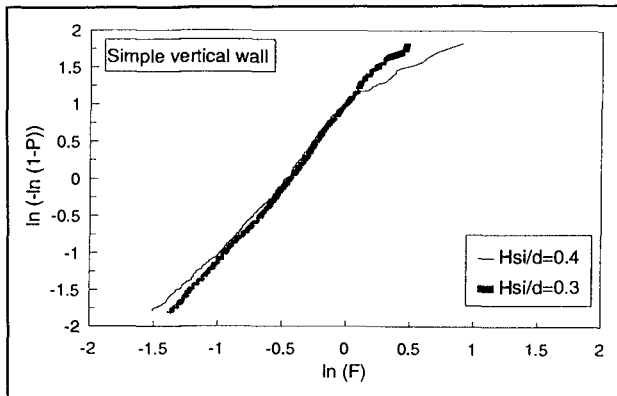


Figure 5 Weibull probabilities of horizontal forces, pulsating, and (few) impacts

4. RESULTS

In excess of 1 million waves were sampled in 217 tests. Pressures measured by a transducer at static water level are shown in Figure 4 for about 9 waves on Structure 1 with a low rubble mound. This shows some impact events; and others with substantially smaller pressures with much longer rise times, pulsating events. During other tests, severe impacts up to $p=40\rho_w g H_s$ were noted. Previous studies had suggested that severe impacts might be very variable, but repeated tests confirmed that these impacts were repeatable.

Simple vertical walls

In the first analysis, horizontal forces (and uplift where applicable) were calculated for each force event. The statistical distribution of horizontal forces were then plotted on Weibull axes for each test. Examples for simple vertical walls subject to waves of $H_s/h_s=0.3$ and 0.4 in Figure 5 show the start of impacts (about 2%) where the highest forces for $H_s/h_s=0.4$ start to deviate (upwards) from the linear Weibull line for the pulsating condition for $H_s/h_s=0.3$. Overall forces are not greatly increased by these impacts, but $F_{h99.6\%}$ and $F_{h1/250}$ are increased significantly. These increases further as waves approaches the breaking limit for shallow bed slopes around $H_s/h_s = 0.55$ to 0.6.

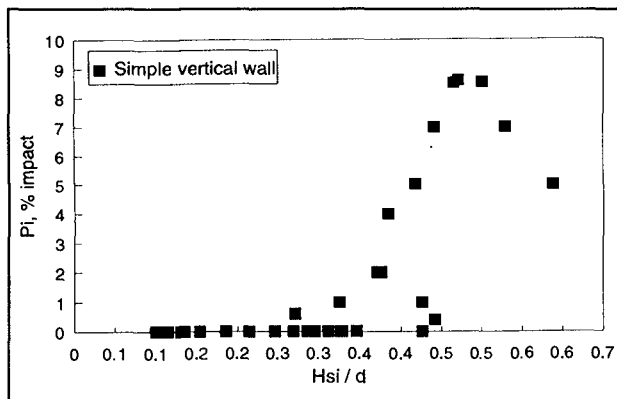


Figure 6 Influence of H_{st}/d on $P_{i\%}$ for simple walls

For the simple wall tests, impacts ($P_{i\%}$) are plotted against H_{si}/d (equal to H_s/h_s for simple walls) in Figure 6. Impacts start at $H_{si}/d > 0.35$, suggesting this simple limit for onset of impacts. $H_s/h_s=0.35$ is lower than the simple rule for wave breaking over shallow bed, but it is reasonable to expect some larger waves to break at conditions below $H_{si}/d=0.55$.

These limits identify different types of wave / structure interaction, but do not predict forces. Horizontal forces non-dimensionalised as $F_{h1/250}/\rho_w g d^2$ have been plotted against H_{si}/d in Figure 7. Force predicted by Goda's method are also shown, illustrating relatively good agreement for relatively small waves in the region $H_{si}/d \leq 0.35$, but significant errors for those waves which cause impacts, $H_{si}/d > 0.35$.

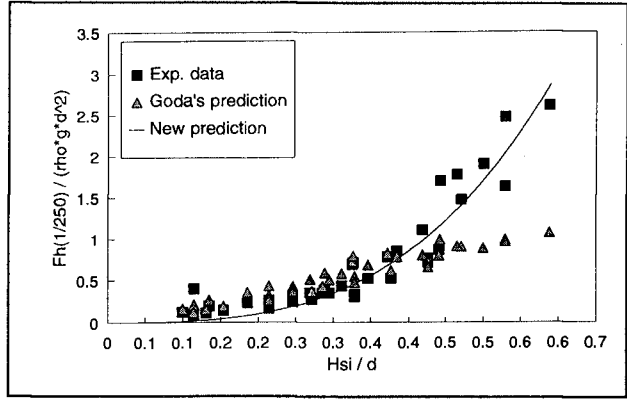


Figure 7 Dimensionless force against H_{si}/d for simple walls

Composite structures

Responses of composite structures are more complex, being influenced by the height, width and slope of the rubble berm, as well as by relative water depth and wave conditions. The first task was to separate data by the relative berm height, h_b/h_s into "low" and "high" mounds. Low mounds are described by $0.3 < h_b/h_s < 0.6$, and high mounds by $0.6 \leq h_b/h_s < 0.9$. These limits are not themselves of much significance, but give convenient divisions between regions of different response characteristics.

Low mounds.

$0.3 < h_b/h_s < 0.6$

For low mounds, the onset of breaking and hence of impact conditions is shifted by the presence of the mound to $H_{si}/d=0.65$, see Figure 8. For higher waves, $0.65 < H_{si}/d \leq 1.3$, the nearness of breaking and effect of the mound combine to increase $P_{i\%}$. The dimensionless forces in Figure 9 fit surprisingly well the simple prediction method in eqn. (2) derived initially for simple walls only.

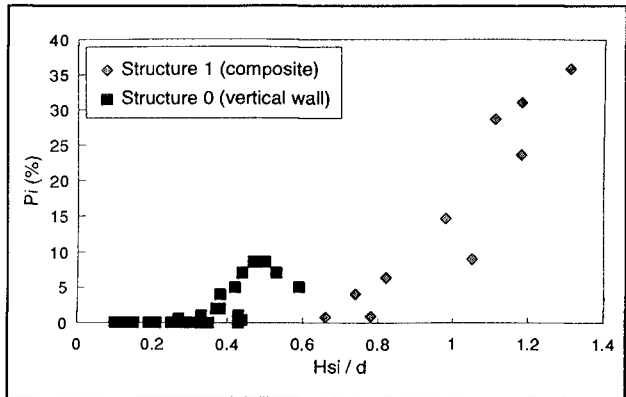


Figure 8 Influence of H_{si}/d on $P_{i\%}$ for low mounds

$$F_{h1/250}/(\rho_w g d^2) = 15 (H_{si}/d)^{3.134} \quad \text{for } 0.35 < H_{si}/d < 0.6 \quad (2)$$

High mounds. $0.6 \leq h_p/h_s < 0.9$.

Wave loads are again pulsating for high mounds with smaller waves ($0.3 < H_{sr}/d < 0.6$). Here Goda's equations give conservative predictions for horizontal wave forces. Then as wave heights increase, more waves break on the structure, and the situation becomes more complex. For small waves, $0.3 < H_{sr}/d < 0.55$, the loading conditions are primarily pulsating, and for larger waves, $0.65 < H_{sr}/d < 1.3$, primarily impacts.

Within the last zone examined here, covered by the largest waves tested $0.65 < H_{sr}/d < 1.3$, the influence of berm width expressed as B_{eq}/L_p is substantially more important. For short berms, given by $0.08 < B_{eq}/L_p < 0.14$, the waves are still pulsating with few if any impacts, and again Goda's method can be used to estimate wave forces. At the opposite end with long berms given by $B_{eq}/L_p > 0.4$, wave breaking occurs over the berm before the wall, and wave loads on the wall are due to broken waves. Again the use of Goda's method gives a safe estimation of forces, even though the process under broken waves will be rather different.

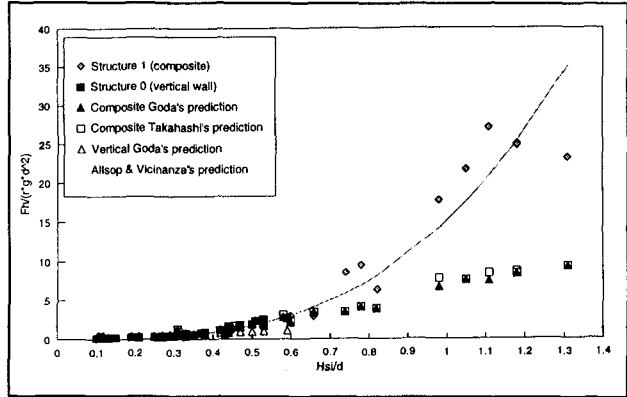


Figure 9 Dimensionless force against H_{sr}/d for low mounds

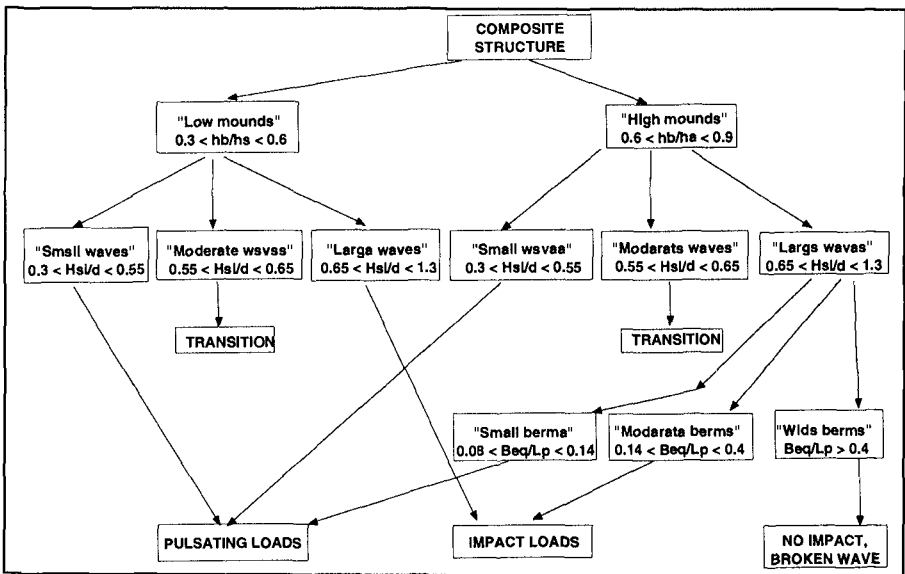


Figure 10 Decision chart for impacts on simple or composite walls

The overall picture of the different loading conditions over these regions is summarised in a type of flow chart in Figure 10. This was developed first by Allsop et al (1996c) and refined by Allsop et al (1996a). The parameter regions are divided by the relative berm height h_b/h_s , the relative wave height H_w/d , and the relative berm length B_{eq}/L_p . This chart represents a considerable simplification of the overall processes, but renders decisions on the type of wave loading substantially more tractable.

5. POSITION AND VARIATIONS OF IMPACTS

The major emphasis so far has been the extreme pressures / forces which determine overall stability of the structure. Data on local pressures and pressure gradients are also needed in any analysis of potential local damage or instability of blockwork.

Distribution of pressures

Goda's method assumes that wave pressures are distributed trapezoidally over the front face. For pulsating conditions this assumption is reasonably well-supported, but for impact conditions, agreement is much less good. For $H_w/d=0.4$ on the same simple wall, the peak pressures in Figure 11 are much more severe. The peak is greater than predicted, and here is slightly above the water level.

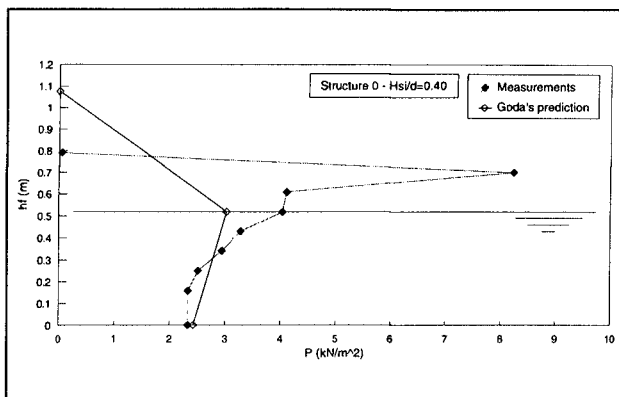


Figure 11 Vertical distribution of pressures, $H_w/d=0.4$, simple wall

Increasing impacts increase overall forces, but also substantially increases local pressure gradients, illustrated dramatically in Figure 12 where the difference between these tests is in the effective berm width, B_{eq} . The most uniformly distributed pressures occur for the simple wall, and for the composite structure with moderate berm, 3. Structures 4 and 7 have only slightly larger berms, yet the local pressures and pressure gradients increase significantly. Here increasing the berm width has initiated the breaking process, giving greater impact forces for greater relative berm width, and dramatically greater peak pressures.

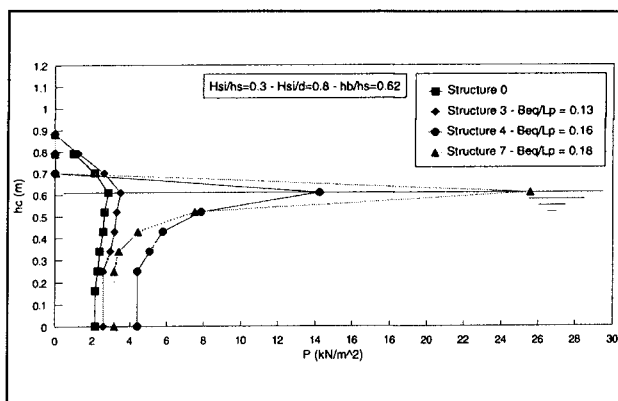


Figure 12 Effect of berm width on distribution of pressures, high mounds

Pressure gradients

Pulsating wave conditions give relatively low absolute values of wave pressure, so pressure gradients seldom exceed values of $dp/dz > 1$. The situation is however dramatically different for impact conditions, even on simple walls where peak local pressure gradients in these tests varied over $dp/dz=2$ to 70. These increased slightly for low mounds to $dp/dz=5$ to 90, and for high mounds to $dp/dz=2$ to 80. The mean value of these results, the standard deviations (s.d.) and coefficients of variation are summarised below:

Structure	range	mean (dp/dz)	s.d. (dp/dz)	coef. varn.
Vertical	2 - 70	13.2	15.9	1.19
Low mound	5 - 90	29.5	25.9	0.879
High mound	2 - 80	21.6	17.5	0.814

For impact waves, the greatest relative local pressure measured in these tests was given by:

$$p_{max} / (\rho_w g H_w) \leq 50 \tag{3a}$$

and the steepest pressure gradient was given by:

$$\max (dp / dz) \leq 90 \tag{3b}$$

6. DISCUSSION ON SCALE EFFECTS

Use of model tests should always include analysis of scale effects, particularly where key responses are influenced by the scale of the tests. Analysis of pressure measurements at laboratory scale here has not explicitly assumed any scale conversion, but use of parameters scaled by Froude implies that pressures measured here can be scaled by Froude unless corrected. Wave impacts in small scale hydraulic model tests are however greater in magnitude, but shorter in duration than their equivalents at full scale in sea water, so simple Froude scaling will over-estimate prototype loads, but under-estimate their durations.

New work discussed by Allsop et al (1996a, b) and Howarth et al (1996) has been used to develop a simple correction method for impact pressures. Measurements of wave impact pressures on concrete armour units on a prototype breakwater have been compared with measurements of equivalent pressures in laboratory tests at 1:32 scale in fresh water. These were used to calculate pressure impulse estimated by peak pressure multiplied by the rise time Δt . Values of this pressure impulse were compared at the same exceedance levels and show extremely close agreement over the regions of probability of interest, 90-99.9% non-exceedance.

Extreme impact pressures from field and model have then been compared by Allsop et al (1996a, b), see Figure 12, and these show that model results need to be corrected by factors between 0.45 to 0.40 for non-exceedances levels of 90 - 99.9%. It should however be borne in mind that the relatively slow rate of sampling

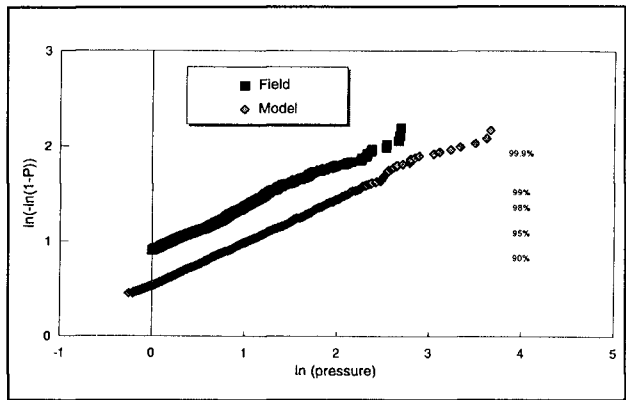


Figure 13 Weibull probabilities of impact pressures, field and model

used in the Wallingford / Belfast / Sheffield tests may imply that some peak pressures could have been under-estimated by up to 50%, so any scale correction to reduce predicted pressures should be used with care.

ACKNOWLEDGEMENTS

This work is based on studies completed at HR Wallingford for the Construction Sponsorship Directorate of the UK Department of Environment, under research contracts PECD 7/6/263, PECD 7/6/312, and CI 39/5/96; with support from the MCS project of the European Union's MAST II programme under contract MAS2-CT92-0047, and the PROVERBS project in MAST III under contract MAS3-CT95-0041.

Substantial additional support to the testing and/or data analysis has been given by the Queen's University of Belfast; the Department of Hydraulics of the University of Naples; and the University of Sheffield. Funding support for visiting researchers at Wallingford from TECHWARE, the international exchange programme of the University of Naples, and the Department of Education NI is also gratefully acknowledged.

The senior author acknowledges considerable assistance from his colleagues at Wallingford; advice by Mike Chrimes, librarian of the Institution of Civil Engineers; Gerald Müller of Queen's University of Belfast for discussions on wave impacts and advice on measurement devices; Mario Calabrese of University of Naples for assistance in the development of the initial flow diagram dividing parameter regions and pulsating / impact responses; and Andreas Kortenhaus of University of Braunschweig for advice on analysis and event definitions. The senior author is also grateful to the Port and Harbour Research Institute in Japan and JISTEC for supporting participation in the 1994 Wave Barriers workshop.

REFERENCES

- Allsop N.W.H. & Bray R.N. (1994) "Vertical breakwaters in the United Kingdom: historical and recent experience" Proceedings of Workshop on Wave Barriers in Deep Waters, pp76-100, Port and Harbour Research Institute, Yokosuka, Japan.
- Allsop N.W.H., Calabrese M., Vicinanza D. & Jones R.J. (1996b) "Wave impact loads on vertical and composite breakwaters" Proceedings 10th Congress of the Asia and Pacific Division of IAHR, 26-29 August 1996, Langkawi Island, Malaysia
- Allsop, N.W.H., Vicinanza, D & McKenna, J.E. (1996a) "Forces on vertical breakwaters and related structures" Strategic Research Report SR 443, HR Wallingford, Wallingford.
- Allsop N.W.H. & Vicinanza D. (1996) "Wave impact loadings on vertical breakwaters: development of new prediction formulae " 11th International Harbour Congress, Antwerp.
- Allsop N.W.H., Vicinanza D., Calabrese M. & Centurioni L. (1996c) "Breaking wave impact loads on vertical faces" 6th ISOPE Conference, Los Angeles, California, USA.
- British Standards Institution (1984) "British Standard Code of practice for Maritime structures, Part 1. General Criteria" BS 6349: Part 1: 1984, and Amendments 5488 and 5942, London.
- CERC (1984) "Shore Protection Manual" 4th ed. U.S. Govt. Printing Office, Washington D.C.
- Goda Y. (1985) "Random seas and maritime structures" University of Tokyo Press.
- Howarth M. (1997) "Wave impacts on hollow cube breakwater armour units" Ph.D thesis, University of Bristol.

Howarth M.W., Allsop N.W.H., Vann A.M., Jones R.J., & Davis J.P. (1996) "Scale effects of wave impact pressures on cob armour units" 25th International Conference on Coastal Engineering, Orlando, ASCE, New York.

Klammer P., Kortenhaus A & Oumeraci H. (1996) "Wave impact loading on vertical face structures for dynamic analysis- prediction formulae" 25th International Conference on Coastal Engineering, Orlando, ASCE, New York.

Kirkgoz M.S. (1995) "Breaking wave impact on vertical and sloping coastal structures" Ocean Engineering, Vol 22, No 1, pp 35-48

McKenna (1997) "Wave forces on caissons and breakwater crown walls" Ph.D thesis, Queen's University of Belfast, Belfast.

Minikin R.R. (1963) "Winds, Waves and Maritime Structures" 2nd ed., Griffin, London.

Oumeraci H. (1994) "Review and analysis of vertical breakwater failures - lessons learned" Coastal Engineering, Issue on Vertical Breakwaters, Vol 22, pp3-30, Elsevier, Amsterdam.

Schmidt R., Oumeraci H. & Partenscky H-W (1992) "Impact loads induced by plunging breakers on vertical structures" Proceedings of 23rd ICCE, Venice, publ. ASCE, New York.

Vicinanza D. (1997) "Pressioni e forze di impatto di onde frangenti su dighe a paramento verticale e composte" Ph.D thesis, University of Naples, Naples.

CHAPTER 195

Scale effects of wave impact pressures on cob armour units

M.W.Howarth†, N.W.H.Allsop‡, A.M.Vann†, R.J.Jones‡ and J.P.Davis†
† University of Bristol, UK ‡HR Wallingford, UK

Abstract

Froudian scaling laws are often used to convert model wave impact pressures to prototype scale. However, although many model studies have been performed in the past, the effects of scale on the magnitude and duration of wave impact pressures have yet to be determined.

Wave impact pressures were monitored on a Cob armoured breakwater at LaCollette Harbour, Jersey, UK, throughout the Winter of 1993/94. In addition, a 1:32 scale model of the prototype breakwater was constructed at the University of Bristol and subjected to a similar wave climate as was measured at prototype scale. A comparison of the pressures measured at the 2 scales has allowed the scale effects present in the wave impact process to be determined.

Introduction

Wave impact loading has long been of interest to designers and researchers, as it can be the most severe form of loading on coastal structures (e.g. Rouville 1938). Despite this, there is still considerable uncertainty about the magnitude of these loads and the physical processes which govern them. Although many model studies have been carried out, the scale effects present in the impact process remain uncertain.

Traditionally, Froudian scaling is used to convert model wave loads to prototype scale, as it is generally accepted that wave loads are gravity dominated. However, during the wave impact process the compressibility of the wave front may be the

dominating factor in determining the magnitude of the pressure generated (Führböter 1988, Kamel 1970). Many researchers have recognised that small scale experiments may overestimate the pressures measured at prototype scale when Froudian similarity is used. Very little research, if any, has adequately shown this to be the case by carrying out experiments at model and prototype scales and comparing the results.

In this study, impact pressures were measured on a typical hollow cube armour unit (a Cob unit) at LaCollette Harbour, Jersey. In addition, a 2-dimensional model of the breakwater at LaCollette Harbour was constructed at 1:32 scale in the small wave flume at the University of Bristol. The wave and tidal conditions measured at LaCollette Harbour were recreated as closely as possible in the laboratory. Any differences in the pressures measured at model and prototype scales are likely to be due to the scale effects present in the impact process.

Prototype pressure measurement

LaCollette breakwater was constructed in the early 1970s, and forms part of the outer coastal defence of St. Helier Harbour, Jersey. The breakwater is protected by Cob armour units, placed in a single layer, protecting a rubble core. The main axis of the breakwater runs WNW to ESE, and is subjected to wave loading from the South-west. A typical cross-section of the breakwater is shown in Figure 1.

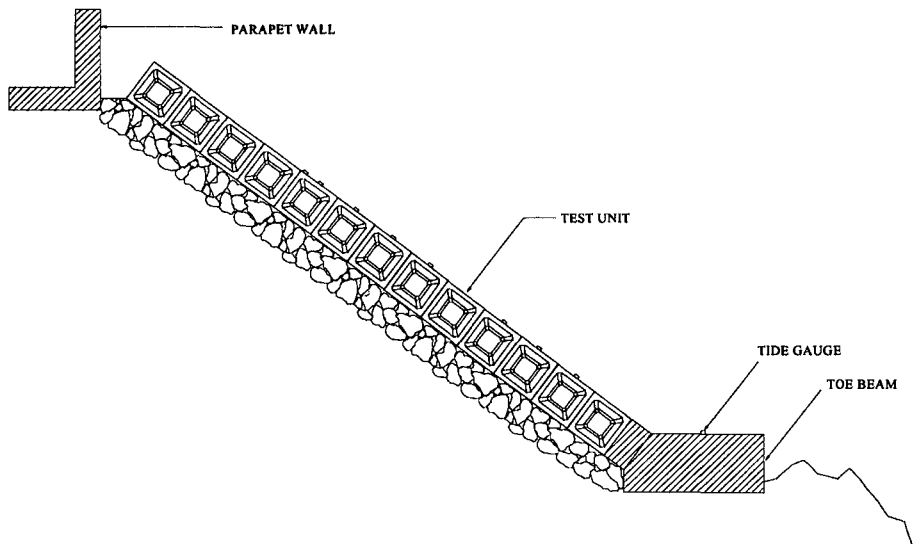


Figure 1: Typical cross-section of LaCollette Breakwater, Jersey, UK

Wave impact pressures were measured at 8 points on the surface of a single unit on row 5 of the breakwater. The unit was chosen as it received wave impact loading on every tide whilst being far enough up the breakwater slope to be relatively unaffected by the toe beam. Data Instruments AB pressure transducers were used to measure impact pressures. The transducers were placed flush with the surface of the Cob unit to ensure that the pressures measured were the same as those experienced by the unit. The pressures were sampled at 500Hz, which was adequate to ensure the vast majority of impact pressures were accurately captured. Wave height and tidal level were measured at the breakwater toe.

The long logging periods and the high sampling rates involved in measuring wave loads on a prototype breakwater can mean a huge volume of data can be collected, with relatively few impact 'events' occurring during that time. Intelligent monitoring techniques were used in an attempt to limit the volume of data stored whilst retaining all significant impact data. This was achieved by sampling pressure data for 1 hour as the tidal level increased towards the instrumented unit, and for 1 hour as the tidal level fell back below the unit. The logging period was sufficiently long to ensure that all impacts which occurred on the instrumented unit were measured. An analysis program was then implemented to detect the wave impacts measured during the logging period and to determine the magnitudes and rise times of the pressures. The details of each impact were then stored in a text file with the time and the tidal level at the time of impact. This process greatly reduced the amount of data stored whilst retaining all useful impact pressure information.

Pressure and wave data was monitored almost continuously between November 1993 and February 1994.

Model Pressure Tests

A 2-dimensional model of the LaCollette breakwater was constructed at 1:32 scale. A 1:50 slope was constructed in front of the breakwater, representing the average slope of the bathymetry at Jersey. Impact pressures were measured on the top limb of the Cob unit, as this was the position at which the largest pressures at prototype scale were measured. The pressure on the top limb was sampled at 10kHz. This is a faster sampling rate (to scale) than that used at prototype scale, as it has previously been found that wave impact pressures measured in the laboratory, using fresh water, can have an extremely short duration (e.g. Oumeraci 1993, Kirkgöz 1995). The pressure transducer used was the EP-101W-50 transducer supplied by Entran Ltd., chosen for its excellent frequency response and small size. The diameter of the sensing face roughly represented the diameter of the prototype scale transducer used in Jersey. The size of the sensing face of a pressure transducer is likely to affect the magnitude and rise time of the impact pressure measured, resulting in smaller magnitude, longer duration pressures being recorded. If accurate scaling between model and prototype scales is to be achieved it is likely that the linear dimensions of the transducer face should be subject to the same scale factor as the rest of the

model. If inappropriate transducers are used then the effects of scale in the impact process may not be detected (e.g. Führböter 1986).

The model breakwater was subjected to similar random wave conditions as those measured at LaCollette Harbour. The waves were always applied normal to the breakwater, which was not necessarily the case for the prototype structure. Despite this, it is thought that the waves applied to the model were a good representation of the prototype wave climate.

Prototype results

The site deployment at LaCollette Harbour was extremely successful. More than 4000 impact pressures above 1m head of water were recorded, with more than 3000 impacts measured on the vertical face of the top limb. Figure 2 shows pressures measured on instrumented unit caused by a typical wave - transducer 6 was situated on the vertical face of the top limb. In this case transducer 6 has measured an impact pressure equivalent to 3.5m head of water, whilst the other transducers have measured 'quasi-hydrostatic' pressures. The impact pressures measured exhibited typical wave impact features: a rapid rise in pressure (with a rise time generally below 30ms) as the wavefront impinged on the unit, followed by a longer duration pressure formed as the unit is submerged.

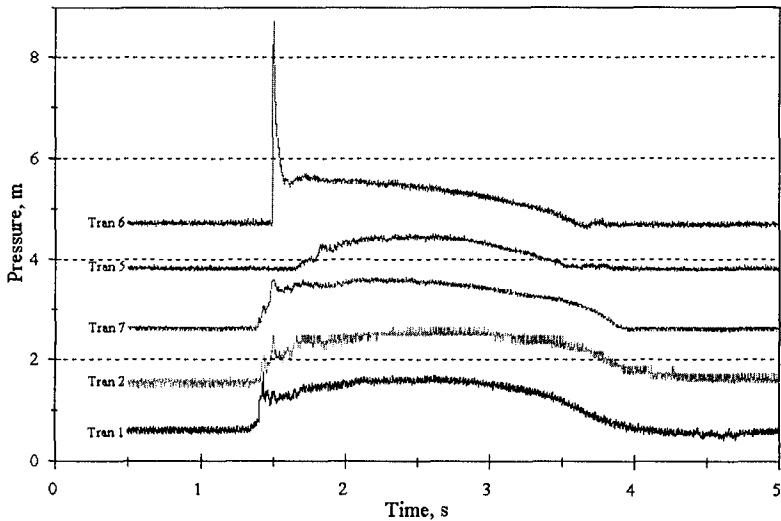


Figure 2: Typical pressure traces measured at prototype scale

All the impact pressures measured throughout the winter on the vertical face of top limb are plotted against probability of non-exceedence in Figure 3. The pressures followed a log-normal distribution very closely. The largest pressure measured was 14.6m head of water. The excellent correlation with a log-normal distribution suggests that more extreme impact pressures may be accurately predicted by extrapolating the graph.

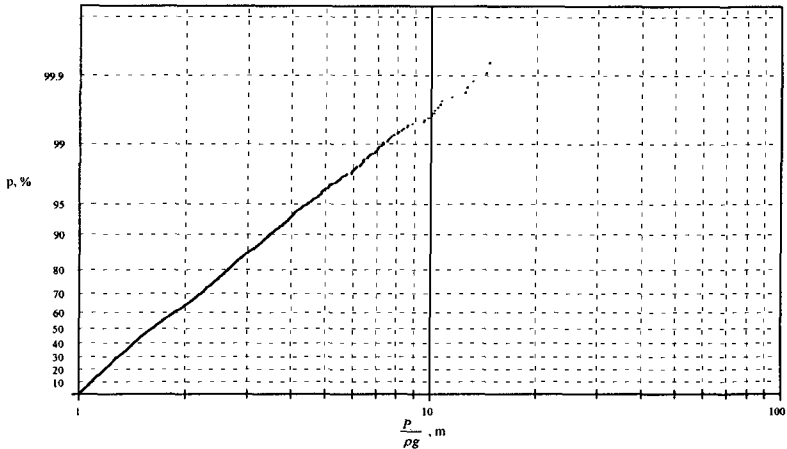


Figure 3: Log-normal distribution of impact pressure, prototype

The distribution of the rise times measured for each impact, plotted on log-normal axes, is shown in Figure 4. It can be seen that impact rise time follows a log-normal distribution well. Approximately 30% of the impact pressures measured had a rise time less than 10ms.

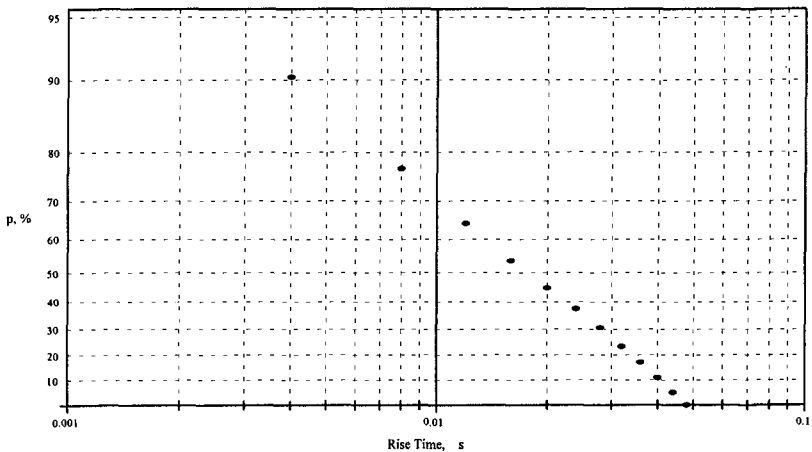


Figure 4: Log-normal distribution of impact pressure rise times, prototype

Model Test Results

The pressure transducer used in the model test programme performed excellently, and was found to be capable measuring the very rapid impact pressures found at small scales. The impact pressures measured exhibited similar features as those found at prototype scale. A typical impact pressure is shown in Figure 5. The pressure rise times were often very short, with many impacts being lower than 0.5ms.

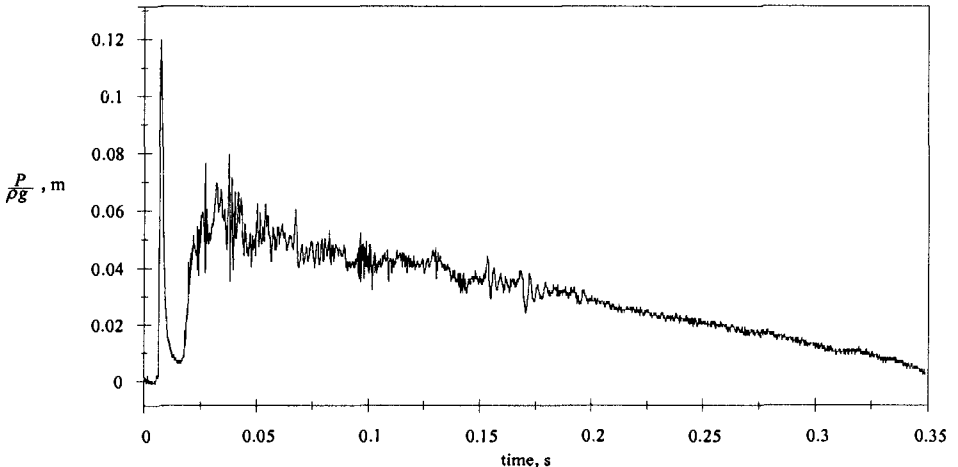


Figure 5: Typical impact pressure trace at model scale

The pressures measured during each test were plotted on statistical axes. It was found that a log-normal distribution accurately described the impact pressures measured in each test. The rise times of all the impact pressures measured during the test programme are shown in Figure 6. Log-normal axes have been used. It can be seen that the impact pressure rise times are accurately described by a log-normal distribution. It can also be seen that approximately 50% of the pressures measured exhibited a rise time of less than 1ms. A small number of impacts, approximately 1%, had a rise time of less than 0.1ms, equal to the sampling interval used throughout the test programme. Ideally, a higher sampling frequency would have been used so that even the most rapid impact pressures that occurred could have been accurately captured. However, an increase in the sampling rate would have led to increases in the already large volume of data recorded, and in any case the percentage of impact pressures which were affected by the sampling rate was small.

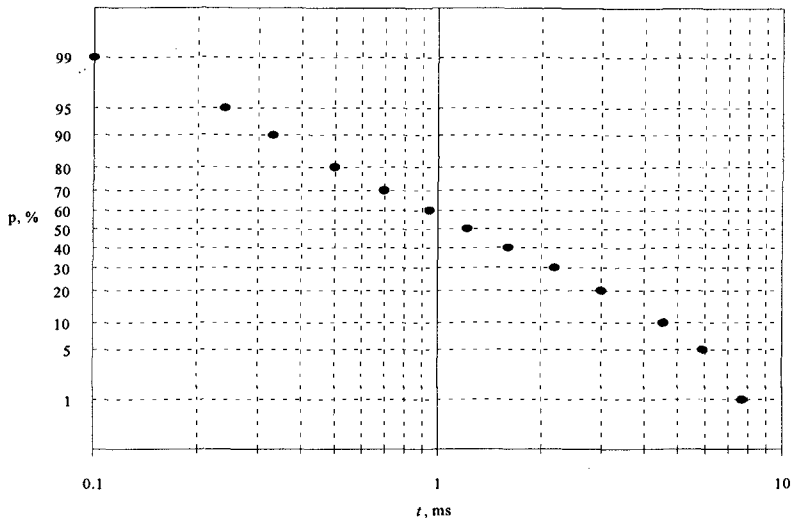


Figure 6: Log-normal distribution of impact pressure rise times, model

Scale Effects

The breakwater at LaCollette Harbour was modelled as closely as possible at 1:32 scale. The wave conditions measured at Jersey were reproduced accurately in the laboratory. The size of the pressure transducer was scaled as accurately as possible from prototype to 1:32 scale. Hence it can be assumed, with reasonable confidence, that any differences in the impact pressures measured at model and prototype scales are due to the scale effects present in the impact process.

It has generally been predicted by previous researchers (e.g. Führböter 1984) that Froudian scaling *overestimates* the magnitude of prototype impact pressures and *underestimates* their rise times. These results have been found in this research. It may be expected, therefore, that the magnitude of wave impact impulses will scale relatively accurately using Froudian scaling, since impulse is assumed to be the product of pressure magnitude and rise time.

Impulse data collected at model and prototype scale, scaled to prototype using Froudian scaling, is shown in Figure 7. The impulses are plotted on log-normal axes. It can be seen that for low probabilities of non-exceedence the values of model and prototype impulses differ significantly, with the model results underestimating the impulses measured at prototype scale. For more extreme impulses, however, the model and prototype data correlate well, suggesting that for the most severe impact events Froudian scaling can reasonably be used to predict prototype impulses from small scale data. Impulse is related to the wave momentum destroyed in the impact process. Wave momentum can be accurately scaled using Froudian similarity, and hence the value of impulse in the impact process can be modelled using Froudian

scaling. The difference in data at small values of impulse may be caused by the higher sampling rate (to scale) used in the laboratory, which allowed impact pressures with an extremely short rise time to be measured.

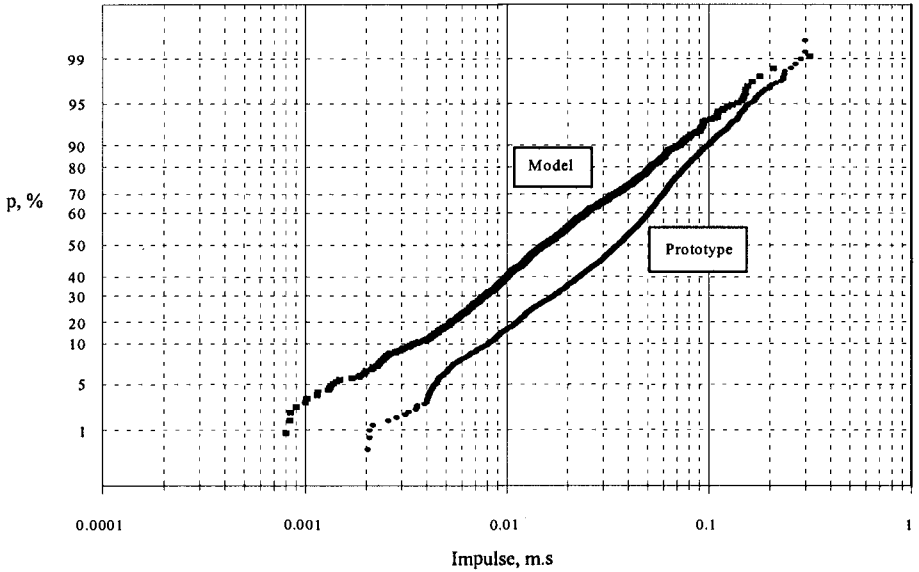


Figure 7: Comparison of impact impulses using Froudian scaling

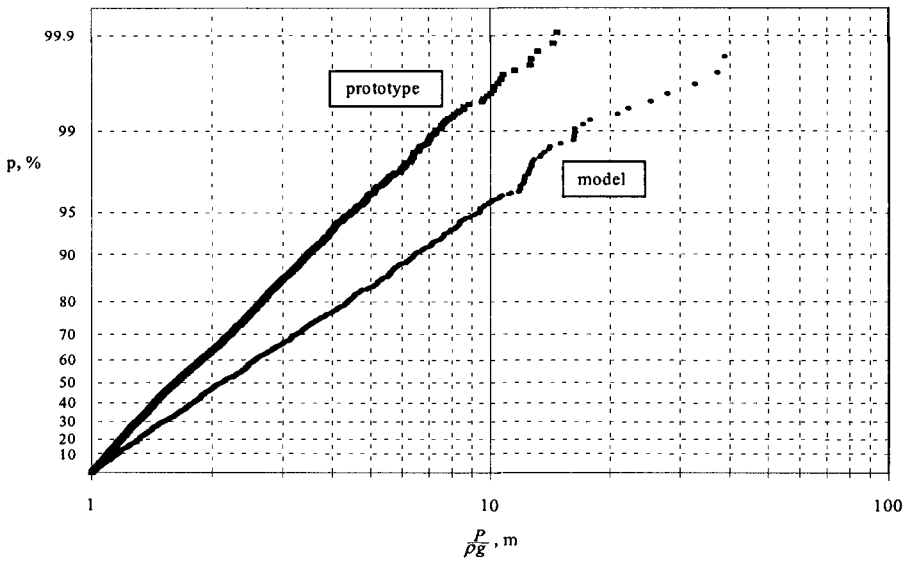


Figure 8: Comparison of pressure magnitudes using Froudian scaling

The distribution of all the impact pressures measured at prototype and model scale is shown in Figure 8. The model pressures have been scaled to prototype using Froudian similarity. It can be seen that the pressures at both scales follow a log-normal distribution extremely well. The distribution of pressures both start at 1m head of water as this was used as the threshold pressure magnitude for both scales. The pressures measured in the laboratory were generally larger than those measured at prototype scale. Although the magnitude of the pressures are different, the excellent correlation in the type of distribution data from both scales follow suggests that very similar processes are present at both scales.

The difference in the maximum pressures likely to occur at model and prototype scales increases as the likelihood of occurrence decreases. This is illustrated below:

Probability of non-exceedence, %	Model pressure, m	Prototype pressure, m	P_{model}/P_{proto}
50	2.13	1.68	1.27
90	6.35	3.26	1.80
99	18.1	7.20	2.51
99.9	40.4	12.50	3.24

As the impacts become more severe then the model pressures increasingly overestimate the magnitude of the pressure which will occur at prototype scale. The prototype and model pressures may be related, once Froudian scaling has been used, by the empirical equation:

$$\frac{P_{prototype}}{\rho g} = \left(\frac{P_{model}}{\rho g} \right)^{0.684}$$

It may be suggested that as the impact loading becomes more severe the effect of wave compressibility dominates over Froudian (gravity) forces. Hence, the increasing differences between model and prototype pressures is due to the increasing effect of wavefront compressibility on the impact process.

The largest non-dimensionalised pressure *likely* to occur in 100 waves, denoted by $P_{100}/\rho g H_s$, has been used to compare results from different model tests as well as being used in the prototype analysis. The value of $P_{100}/\rho g H_s$ is a good measure of the severity of wave impact loading, as it is a function of both the frequency of occurrence and the statistical distribution of the pressures measured. The effect of the still water level on the value of $P_{100}/\rho g H_s$ is shown in Figure 9. It can be seen that, for both scales, the most severe wave impacts occur when the still water level is below the level of the transducer. The pressures measured in the laboratory are much greater than those measured at prototype scale at this still water level, suggesting that compressibility effects are most important for the most severe

loading. As the water level rises towards the transducer then the pressures become less severe, with the pressures measured at both scales converging. This suggests that compressibility effects are less than Froudian effects for less severe impact pressures.

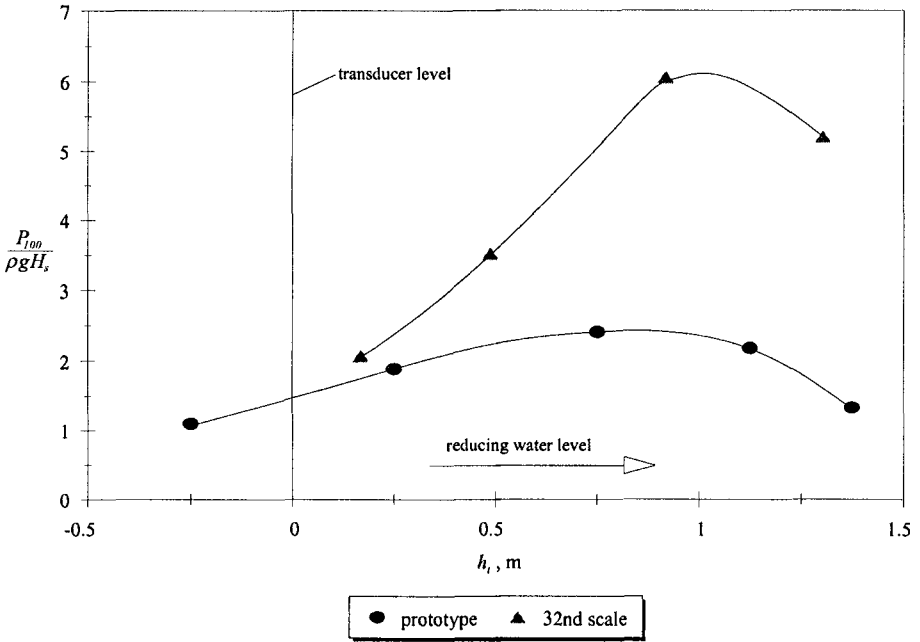


Figure 9: $P_{100} / \rho g H_s$ vs. relative water depth, h_t

It has been suggested previously (e.g. Oumeraci 1991) that impact pressures measured at small scales tend to have shorter rise times than would have been predicted using Froudian scaling. Figure 10 shows the percentage of impacts which occurred for given rise times. The data has been scaled to prototype scale using Froudian similarity. The results from both scales can be directly compared as the same definition of an ‘impact event’ was used at both scales. It can be seen from Figure 10 that a much higher proportion of impact pressures measured at 1:32 scale have short rise times compared to those measured at prototype scale.

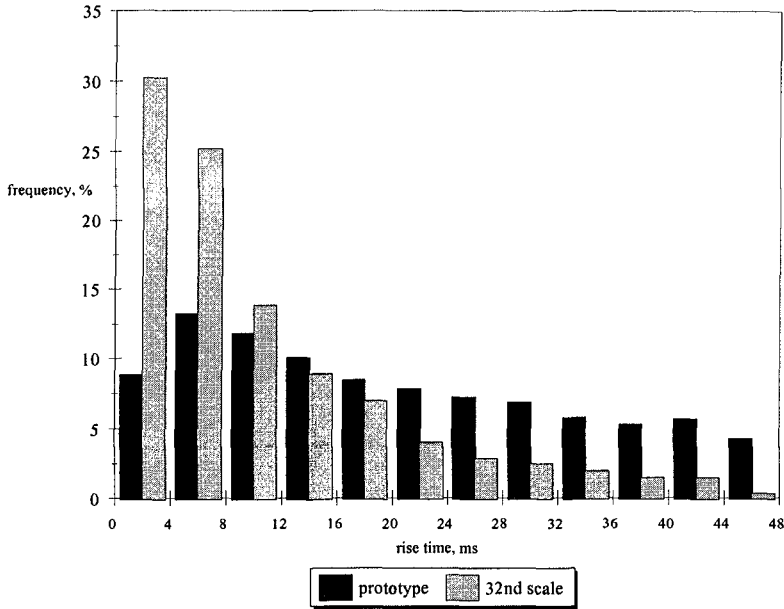


Figure 10: Comparison of impact pressure rise times using Froudian scaling

Figure 10 shows that great care must be taken when performing model wave impact tests. For example, it may be decided in the design of a coastal structure that impact pressures with a rise time below 5ms (for example) need not be considered, as it might be assumed that pressures of a shorter duration will have little effect on the prototype structure. However, Figure 10 shows that if model tests were carried out to determine the pressures likely to occur at prototype scale, rise times of less than this value (scaled down using Froudian scaling laws) should be considered. The short rise times which occur at small scales represent longer duration pressures at prototype scale which may be structurally important.

Conclusions

It has been shown that the physical effects present in model wave impact tests are similar to those found at prototype scale. For example, typical impact pressure traces are similar, the relationship between impact severity and still water level is similar, and pressures from both scales accurately follow a log-normal distribution. However, significant scale effects present in the wave impact process have been found:

The use of Froudian scaling to convert model impacts to prototype scale is likely to overestimate the pressures which will occur on the structure by up to 500%. The

error in the predicted pressures increases as the severity of the impact loading increases.

The rise times of impact pressures are underestimated at model scales if Froudian similarity is used. The reduced compressibility of the wavefront at model scale leads to sharper impact pressures with short rise times and large magnitudes. The reduction in compressibility is caused by less air entrainment present in the model waves, which in turn is caused by the use of fresh water in the laboratory as well as differences in the Weber number at the two scales.

Impact impulses scale reasonably well when Froudian scaling is used. The impulse generated in the impact process is principally related to the momentum of the wave, which may be accurately scaled using Froudian similarity.

A relationship between model and prototype pressures has been deduced. This allows Froudian scaling to be used to convert model data to prototype scale, as long as the appropriate adjustment is made to take scale effects into account.

References

1. Führböter A & Sparboom U. Full-scale wave attack of uniformly sloping sea dykes. *Proc.21st International Conference on Coastal Engineering*. 1988, pp.2174-2188.
2. Führböter A. Model and prototype tests for wave impact and run-up on a uniform 1:4 slope. *Coastal Engng*. Vol. 10, 1986, pp.49-84.
3. Kamel AM. Shock pressure on coastal structures. *J. Waterways, Harbors & Coastal Eng. Div. ASCE* , Vol. Xx, No. WW3 August 1970 pp.689-699.
4. Kirkgöz MS. Breaking wave impact on vertical and sloping coastal structures. *Ocean Engng*, Vol.22 No.1 1995 pp.35-48.
5. Oumeraci H, Klammer P & Partensky H-W. Classification of breaking wave loads on vertical structures. *J. Waterways, Harbors & Coastal Eng. Div. ASCE*, Vol. 119, No 4. July/August 1993 pp.381-397.
6. Rouville M, Besson P & Petry R. Etat actuel des études internationales sur les efforts dus aux lames. *Ann. Ponts Chaussées*, 1938 108 (2) pp.5-113.

CHAPTER 196

WAVE IMPACT LOADING OF VERTICAL FACE STRUCTURES FOR DYNAMIC STABILITY ANALYSIS - PREDICTION FORMULAE -

P. Klammer¹, A. Kortenhaus², H. Oumeraci³

ABSTRACT

Based on impulse theory and experimental investigations on breaking wave kinematics and impact loads, prediction formulae for impact forces have been derived for vertical face breakwaters and further monolithic structures where wave effects dominate design considerations. Hydraulic model tests have been performed to obtain the water mass involved in the impact process and to verify the theoretical results obtained from theory.

INTRODUCTION

The results of the re-analysis of vertical breakwater failures (*Oumeraci, 1994*) have highlighted the importance of breaking waves and the subsequent destructive potential of impact loads. One of the principal lessons drawn from these failures consists in the urgent need to supplement the present static design approach by dynamic stability analysis. For this purpose, the impact loads induced by breaking waves on vertical breakwaters must be specified. It is the main purpose of this paper to develop an approach for the prediction of the impact load as needed for dynamic analysis of caisson breakwaters and further monolithic structures where wave effects dominate design considerations.

For this purpose, a formula for the impact force will be derived using impulse theory and solitary wave theory. Missing parameters were obtained from PIV measurements (particle image velocity) conducted at the University of Edinburgh. The obtained formulae will be compared to hydraulic model tests performed in the Large Wave Flume of Hannover (GWK).

¹Dipl.-Ing., Leichtweiß-Institut, TU Braunschweig, Beethovenstr. 51a, 38106 Braunschweig, Germany, e-mail: p.klammer@tu-bs.de

²Dipl.-Ing., Leichtweiß-Institut, TU Braunschweig, Beethovenstr. 51a, 38106 Braunschweig, Germany, e-mail: a.kortenhaus@tu-bs.de

³Prof. Dr.-Ing., Leichtweiß-Institut, TU Braunschweig, Beethovenstr. 51a, 38106 Braunschweig, Germany, e-mail: h.oumeraci@tu-bs.de

THEORETICAL BACKGROUND

A breaking wave impinging on a vertical wall generally induces impulsive pressures on the wall which are difficult to predict in terms of their magnitude as well as in terms of their spatial and temporal distribution (Fig. 1).

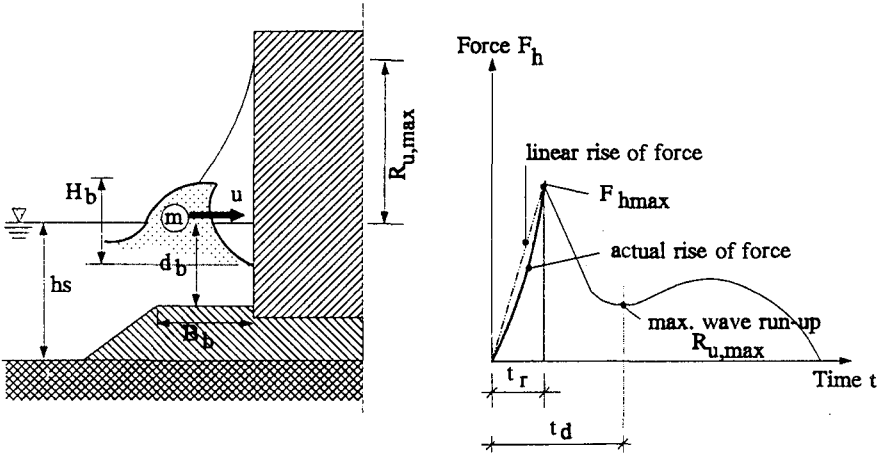


Fig. 1: Impact loading of vertical structure - definition sketch

The forward momentum of a fluid mass m hitting a wall with a horizontal velocity u will induce a force impulse (Fig. 1):

$$\int_0^{t_r} F_h(t) \cdot dt = m \cdot u \tag{1}$$

where t_r is the rise time up to the peak force $F_{h,max}$ and $F_h(t)$ is the horizontal force-time function. Assuming a linear temporal increase of the force $F(t)$, Eq. (1) yields:

$$\frac{1}{2} F_{h,max} \cdot t_r = m \cdot u \tag{2}$$

thus leading to the peak force:

$$F_{h,max} = 2 \cdot \frac{m \cdot u}{t_r} \tag{3}$$

Most of the difficulties encountered in applying Eq. (3) for the prediction of impact forces originate from the lack of information on the magnitude of the fluid mass m which is involved in the impact process and which accounts only for a small portion of the total mass M of the breaking wave impinging on the wall

$$m = k \cdot M \tag{4}$$

Assuming that the actual wave at breaking may be approximated by a solitary wave, its total mass M is given by the following relationship (Munk, 1949):

$$M = \rho \cdot \sqrt{\frac{16}{3} \cdot H_b \cdot d_b^3} \quad (5)$$

where ρ is the density of the fluid; H_b is the wave height at breaking and d_b is the water depth at the breaking point.

The maximum horizontal velocity approximates to (Munk, 1949):

$$u = \sqrt{g \cdot (d_b + H_b)} \quad (6)$$

and with the corresponding breaking criterion:

$$\frac{H_b}{d_b} = 0.78 \quad (7)$$

Eq. (6) yields:

$$u = \sqrt{g \cdot d_b \cdot (1 + 0.78)} \approx 1.33 \cdot \sqrt{g \cdot d_b} \quad (8)$$

and Eq. (5) yields:

$$M = \rho \cdot \sqrt{\frac{16}{3} \cdot H_b \cdot \left(\frac{H_b}{0.78}\right)^3} \approx 3.35 \cdot \rho \cdot H_b^2 \quad (9)$$

The forward momentum of the fluid mass m involved in the impact process is obtained from Eqs. (4), (8) and (9) to:

$$m \cdot u = (k \cdot M) \cdot u \approx 4.47 \cdot k \cdot \rho \cdot H_b^2 \cdot \sqrt{g \cdot d_b} \quad (10)$$

Considering Eq. (3) the dimensionless peak force is obtained as a function of the dimensionless rise time:

$$\frac{F_{h, \max}}{\rho \cdot g \cdot H_b^2} = k \cdot 8.94 \cdot \left(\frac{\sqrt{d_b/g}}{t_r} \right) = k \cdot 8.94 \cdot \left(\frac{t_r}{\sqrt{d_b/g}} \right)^{-1} \quad (11)$$

The nondimensional parameter k which represents the portion of the total mass of the breaking wave involved in the impact process has to be determined experimentally for each breaker type. According to *Bagnold (1938)* k is approximately 0.2. It can be concluded from Eq. (11) that the following issues will have to be further investigated:

- *Breaker types*: Breaker types have to be classified with respect to the loading induced in order to check the applicability of the proposed formula (impact loading and non impact loading)
- *Wave height H_b* : If H_b is not measured a method must be developed to determine the wave height at the breaker point taking into account the presence of the structure.
- *Mass parameter k* : for each loading case k has to be calculated from hydraulic model tests (see Eq. (4)).
- *Rise time t_r* : the determination of rise time t_r is dependent on the breaker type.

- *Occurrence frequency of relative horizontal force*: one of the two related parameters (relative horizontal force or relative rise time) in Eq. (11) must be taken from statistical analyses of hydraulic model tests.

(a) Typical Breaker Types

Model tests in the wave flume at the University of Edinburgh were conducted to experimentally define the water mass m involved in the impact process under different loading case conditions (Oumeraci *et al.*, 1995). In these tests velocity profiles for the following breaker types could be determined:

- well developed plunging breaker with large entrapped air-pocket
- plunging breaker with small entrapped air-pocket
- "flip-through" breaker

A rough classification of wave loading is given in Fig. 2 which distinguishes between 'pulsating' loads and impact loads. For the latter which is induced by waves plunging on the structure the Goda method (Goda, 1985) is not applicable (Takahashi *et al.*, 1993). The proposed method was therefore developed for this type of loading (Fig. 2c).

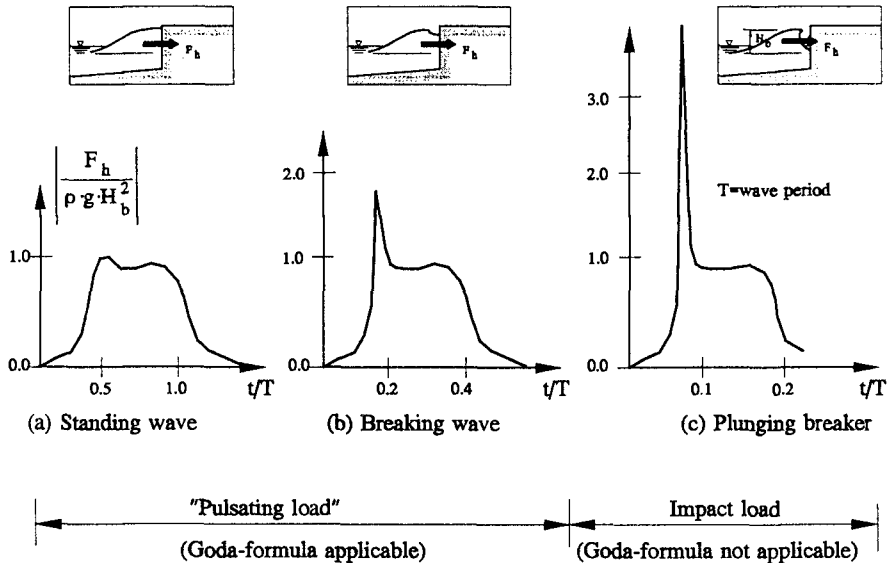


Fig. 2: Classification of wave loading

(b) Estimation of Incident Wave Heights

Wave breaking can be taken into account by a formula given in Oumeraci *et al.*, 1993 in which the total reflection of the structure and its influence on wave breaking is considered:

$$H_b = L_b \cdot \left[0.1025 + 0.0217 \left(\frac{1 - C_r}{1 + C_r} \right) \right] \cdot \tanh \left(2 \pi \frac{d_b}{L_b} \right) \quad (12)$$

In Eq. (12) d_b is the water depth at the breaking point of the wave, L_b is the wave length of the breaking wave and C_r is the reflection coefficient of the structure. The significant wave height can be calculated by a comparison between H_d (calculated from shoaling) and H_b in which H_d may not exceed H_b .

The water depth in front of the structure can be regarded as the governing parameter for the magnitude of the resulting wave height H_b . It can be assumed that a relatively short berm in front of the structure ($B_b/L \leq 0.15$) will have only a small influence on wave breaking. Therefore, it would not be correct to use the water depth d in front of the structure as an input ($d = d_b$) for Eq. (12). On the other hand using the water depth hs (Fig. 1) at the toe of the berm would certainly overestimate the breaker height as the influence of the berm on the breaking would be neglected. It is assumed that the berm width B_b , the wave length L and the slope of the berm 1:m ($m = \cot \alpha$) will influence the breaking of waves. Therefore an effective water depth d_m can be derived which takes into account the aforementioned parameters (Fig. 1):

$$d_m = d + B_{rel} \cdot m_{rel} \cdot (hs - d) \quad (13)$$

In Eq. (13) B_{rel} is the part of the berm width which influences the effective water depth:

$$B_{rel} = \begin{cases} 1 & \text{for } B_b/L > 1 \\ 1 - 0.5 \cdot B_b/L & \text{for } B_b/L \leq 1 \end{cases} \quad (14)$$

The parameter m_{rel} in Eq. (13) is a part of the slope of the berm which influences the effective water depth and is assumed to be:

$$m_{rel} = \begin{cases} 1 & \text{for } m < 1 \\ m^{-0.5} & \text{for } m \geq 1 \end{cases} \quad (15)$$

For solitary waves the effective water depth d_m is very close to the depth hs ($d_m = hs$), so that $B_{rel} = 1$ and $m_{rel} = 1$. This is confirmed by comparing the calculated wave height using Eq. (12) and this assumption with measurements in the Large Wave Flume of Hannover (GWK) (Fig. 3).

A relatively good agreement between measured and calculated values is also obtained for regular and random wave tests.

(c) Experimental Determination of Mass Parameter k

The basic concept for the evaluation of water mass m involved in the impact process is illustrated in Fig. 4. The impulse of a water mass m with a horizontal velocity $v(z)$ at a height z above the berm can be calculated as follows (Fig. 4a):

$$v(z) \cdot dm(z) = v(z) \cdot [\rho \cdot l(z) \cdot dz] \quad (16)$$

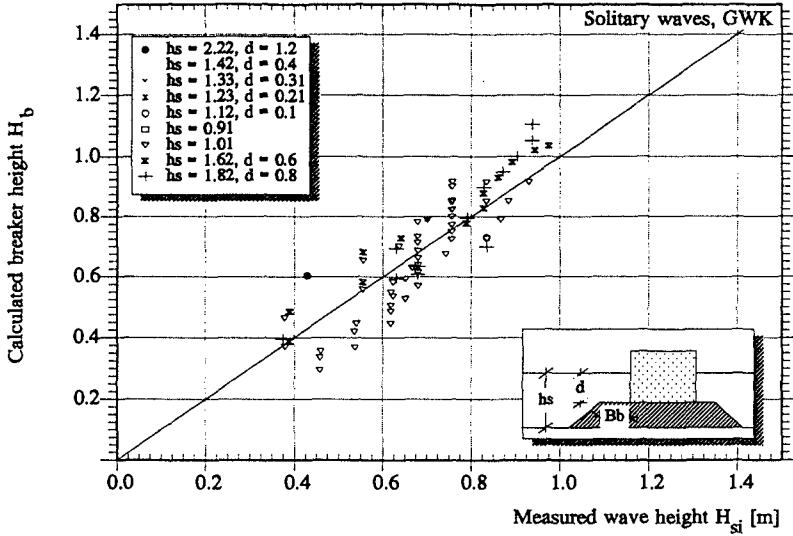


Fig. 3: Calculated vs measured wave height H_b for solitary waves

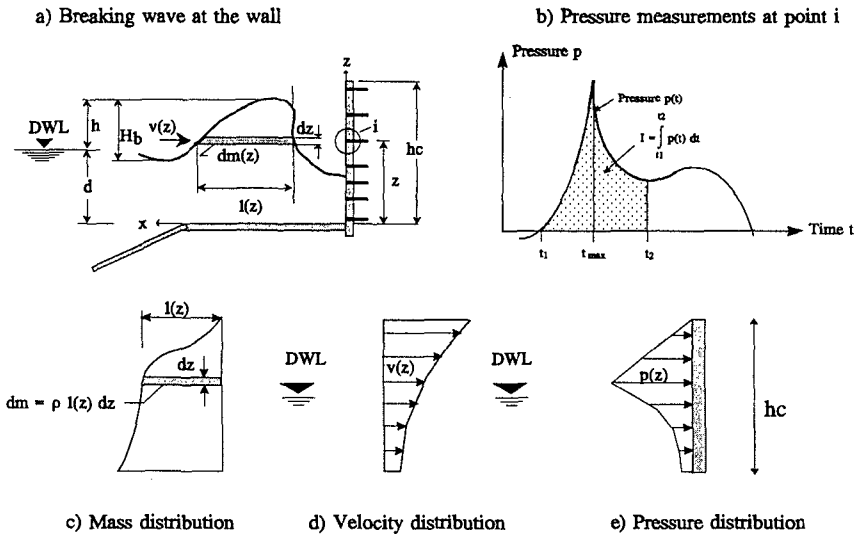


Fig. 4: Principal determination of wave induced loading

The vertical component of the velocity can be neglected. This impulse (Eq. (16)) is equal to the pressure impulse $dI = p(t) \cdot dt$ at the wall measured at a height z above the berm during the period t_1 to t_2 (Fig. 4b):

$$p(t) \cdot dt = [\rho \cdot l(z) \cdot dz] \cdot v(z) \tag{17}$$

Both the velocity (Fig. 4d) and the pressure distribution (Fig. 4e) were measured over the full height of the wall. From those, it is possible to determine the mass distribution for the respective breaker type (Fig. 4c).

The calculation of water masses involved in the impact process was performed according to the height of the pressure cells 6-12 at seven locations (Fig. 4a). The measured pressure distributions were integrated from time t_1 to the time of the maximum t_{max} (Fig. 4b) and from time t_1 to the time of maximum wave run-up at the wall t_2 (Fig. 4b). These values were multiplied by the horizontal velocities obtained from the PIV measurements.

Finally, the mass parameter k could be estimated for different breaker types (Tab. 1) (see also Fig. 4):

Tab. 1: Mass parameter and impulse ratio for different breaker types

Loading case	Breaker type	Mass parameter k [%]	Impulse ratio ^{*)} I_{rFh}/I_{dFh} [%]
2	Well developed plunging breaker with much air enclosed	11	9
3	Plunging breaker with little air enclosed	16	15
4	flip-through breaker	28	21

*) I_{rFh}, I_{dFh} : definition see Fig. 4

In Tab. 1 the experimentally determined mass parameter k (11-28%) are in the same order of magnitude as the average value $k \approx 0.2$ proposed by *Bagnold (1938)*.

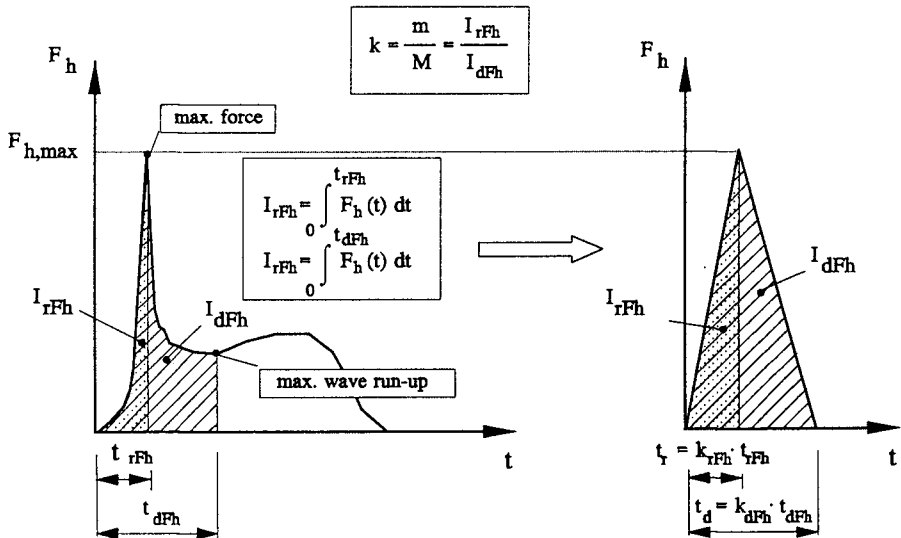


Fig. 5: Substitution of the real force history by an equivalent triangular force

Fig. 5 (left side) illustrates a typical horizontal force history induced by a wave impinging on the wall. The maximum load is reached after a time t_{rFh} and the maximum wave run-up after a time t_{dFh} . At that time it is assumed that the total mass M of the breaking wave has transferred its impulse I_{dFh} to the wall whereas the mass m inducing the impact transfers its impulse I_{rFh} to the wall over a duration t_{rFh} . Subsequently, the mass parameter k can be verified by the ratio of I_{rFh} and I_{dFh} as given in Fig. 5.

This force impulse ratio calculated for the same PIV tests as those used for the determination of k leads to results also given in Tab. 1. A comparison between the values of the PIV tests and the impulse ratio clearly shows that the latter are slightly smaller.

(d) Temporal Development of Horizontal Force

The theoretical approach is based on the assumption of a linear rise of the horizontal force to the maximum load (Fig. 5). Actually the shape of this force increase is strongly dependent on the breaker types.

Therefore two factors k_{rFh} and k_{dFh} are introduced which account for the different geometries of load histories in the case of breaking waves. The factor k_{rFh} is the value that has to be multiplied with the rise time t_{rFh} in order to obtain a triangle with the same area (force impulse). For the horizontal force this can be calculated as follows (Fig. 4):

$$k_{rFh} = \frac{2 \cdot I_{rFh}}{F_{h, \max} \cdot t_{rFh}} \quad \text{with } k_{rFh} < 1 \quad (18)$$

For k_{dFh} a similar approach yields:

$$k_{dFh} = \frac{2 \cdot \Delta I_{dFh}}{F_{h, \max} \cdot \Delta t_{dFh}} \quad \text{with } k_{dFh} < 1 \quad (19)$$

where the portion of impulse ΔI_{dFh} is defined as:

$$\Delta I_{dFh} = \int_{t_{rFh}}^{t_{dFh}} F_h(t) dt \quad (20)$$

(e) Prediction Formula for Impact Loading of Vertical Structures

Using the results derived in the previous sections Eq. (11) may be rewritten as:

$$\frac{F_{h, \max}}{\rho \cdot g \cdot H_b^2} = 8.94 \cdot \frac{k}{k_{r, Fh}} \cdot \left(\frac{t_r}{\sqrt{d_b/g}} \right)^{-1} \quad (21)$$

where k and $k_{r, Fh}$ are obtained from PIV tests:

- well developed plunging breaker: $k = 0.10$; $k_{r, Fh} = 0.80$
- plunging breaker: $k = 0.15$; $k_{r, Fh} = 0.80$
- 'flip-through': $k = 0.20$; $k_{r, Fh} = 1.00$

Since a distinction between these three loading cases based on simple parameter analysis is not yet available it is proposed to select a conservative value for $k = 0.20$ and $k_{r, Fh} = 0.80$, thus resulting in the following prediction formula:

$$\frac{F_{h,\max}}{\rho \cdot g \cdot H_b^2} = 2.24 \cdot \left(\frac{t_r}{\sqrt{d_b/g}} \right)^{-1} \quad (22)$$

This prediction formula can be compared with measurements obtained from GWK tests (Fig. 6) which are described in more detail in *Kortenhaus et al. (1994)*.

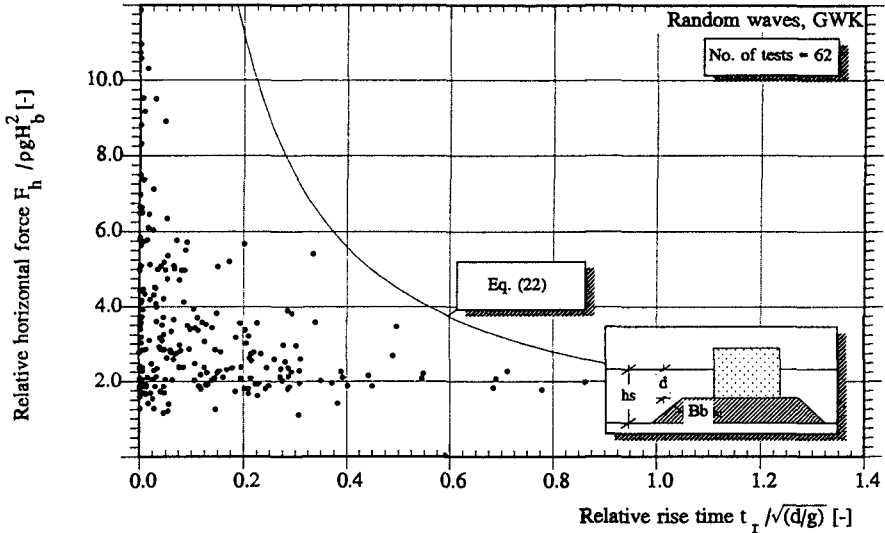


Fig. 6: Comparison of prediction formula to large-scale measurements (random waves)

It can be seen from Fig. 6 that the prediction formula in Eq. (22) represents approximately the upper envelope to the random wave test results. This was to be expected as a conservative approach was used where solitary wave theory was used. Therefore, for solitary waves the prediction formula better fits the data obtained from the model tests (Fig. 7). However, the large scatter in the data can be explained as follows:

- breaking processes at a vertical wall are extremely stochastic which can only be approximated by the aforementioned approach;
- the sampling frequency of the pressure transducers used in the tests was not high enough leading to errors in both defining the rise time and the maximum load;
- sampling noise during the measurements cause some problems in defining the zero crossings which are essential in defining the accurate rise times.

The relation between rise time t_r and total duration t_d of the load (both for triangular load geometries) can also be taken from large-scale measurements:

$$t_d = t_r + 0,35 \cdot \left(1 - \exp(-20 \cdot t_r) \right) \quad (23)$$

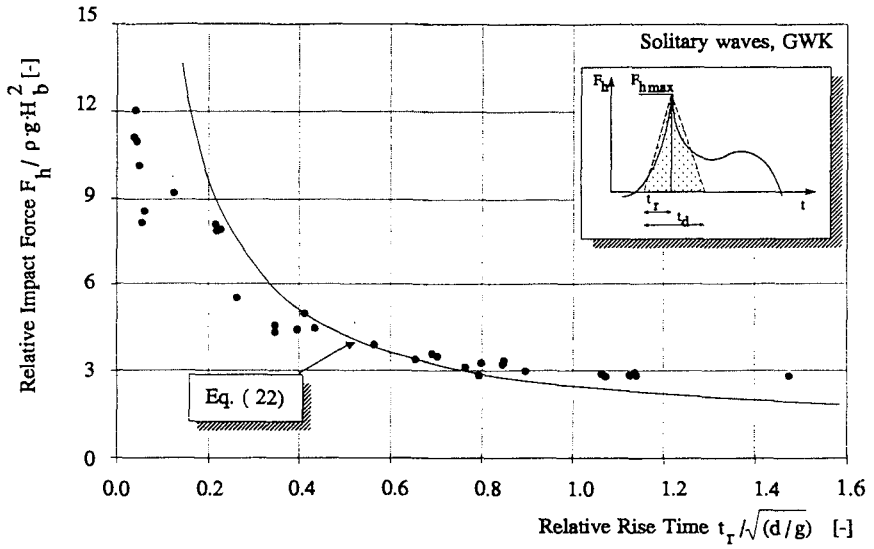


Fig. 7: Comparison of prediction formula to large-scale measurements (solitary waves)

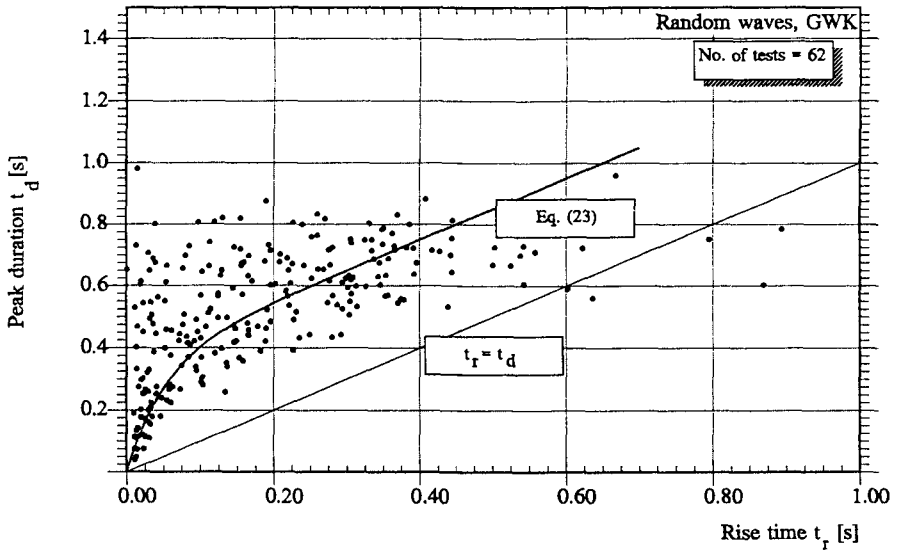


Fig. 8: Total duration t_d vs rise time t_r for random waves in large-scale model tests

(f) Statistical Distribution for Relative Horizontal Forces

In order to apply the prediction formula (Eq. (22)) a statistical distribution function for relative horizontal forces $F_h / \rho \cdot g \cdot H_b^2$ is needed. Such a distribution function has been developed by modifying the standard Weibull distribution (Weibull, 1951) as follows:

$$F(x) = 1 - \exp\left[-\gamma \cdot (\ln x - \beta)\right]^\alpha \quad x > 0 \tag{24}$$

In Eq. (24) α , β and γ are the parameters of the modified Weibull functions where $F(x)$ is the distribution function. Fig. 9 shows the non exceedance probabilities of relative horizontal forces taken from large-scale measurements with random waves.

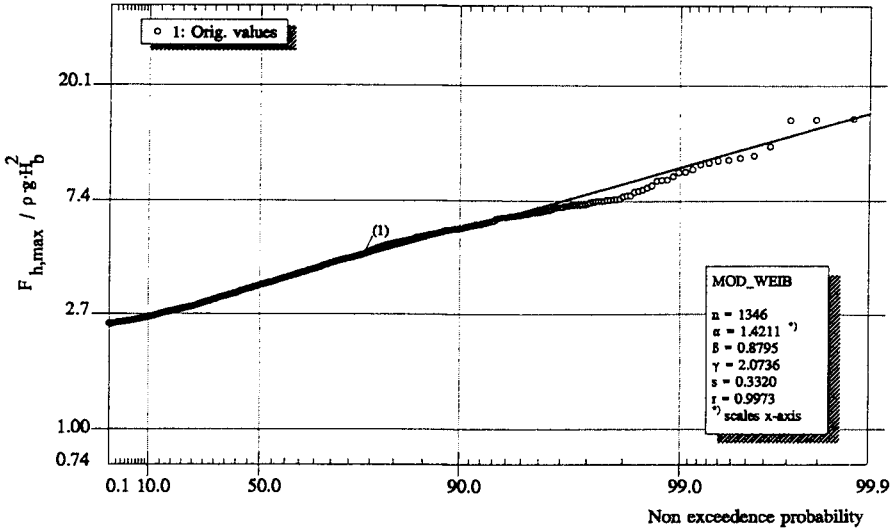


Fig. 9: Statistical distribution function of relative horizontal forces

Assuming a non exceedance value a relative horizontal force can be read from Fig. 9 or calculated by Eq. (24). In this approach no scale effects are considered but will have to be investigated further.

(g) Temporal Development of Pressure Distribution

For dynamic analyses it is very often necessary to apply pressure distributions at the front face of the structure instead of horizontal forces. Therefore, a pressure distribution has to be suggested. In Fig. 10 the temporal development of a typical pressure distribution for a well developed plunging breaker is shown over 30 time steps with the maximum impact force indicated in the centre of the figure.

It can be seen from Fig. 10 that the pressure distribution changes its shape significantly with time. Furthermore, the peak pressure close to the design water level (DWL) is very high at the time of the maximum force. As a result of the analysis of several distributions similar to that shown in Fig. 10 a very simplified pressure distribution at the time of peak force occurrence is proposed for design purposes in Fig. 11.

In Fig. 11 the height of the pressure distribution η^* above DWL is dependent on the wave height H_b and can be derived as follows:

$$\eta^* = 0.8 \cdot H_b \tag{25}$$

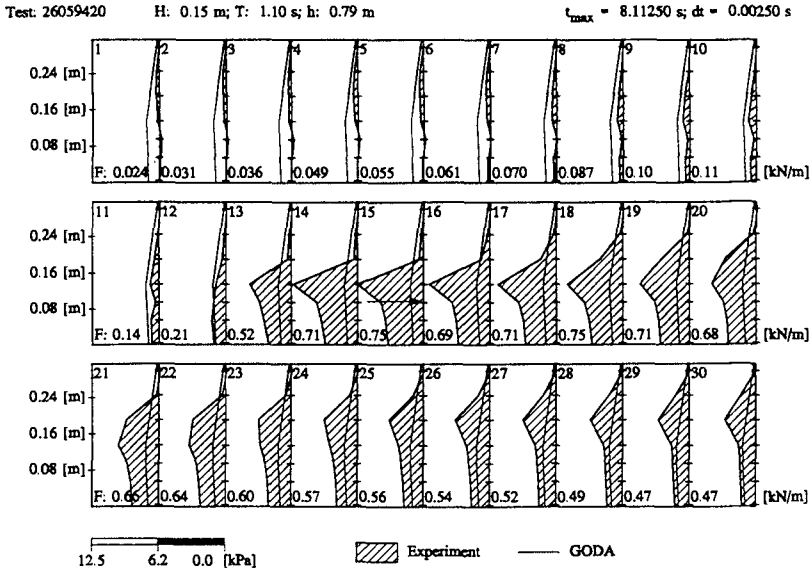


Fig. 10: Pressure distribution for a 'well developed plunging breaker'

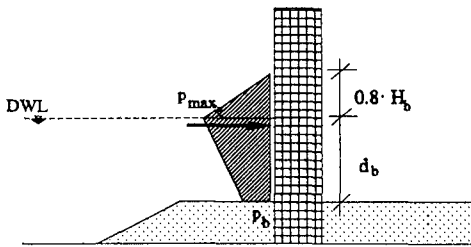


Fig. 11: Pressure distribution for breaking waves

In Eq. (25) H_b is the wave height of the breaking wave which can be taken from Eq. (12). The pressure head at the berm p_b can be approximated by:

$$p_b = 0.45 \cdot p_{max} \tag{26}$$

where p_{max} is the pressure at DWL. Therefore, p_{max} can be calculated from the horizontal force history by:

$$p_{max}(t) = \frac{F_h(t)}{0.4 d_b + 0.3 d_b + 0.4 H_b} = \frac{F_h(t)}{0.7 d_b + 0.4 H_b} \tag{27}$$

(h) Dynamic Load Factor

For practical design it might be desirable to use a static approach. This can be obtained by assuming an equivalent static load inducing the same response of the structure. The ratio between equivalent static and dynamic load, called dynamic load factor D, must be determined (*Oumeraci and Kortenhaus, 1994*).

DESIGN CONCEPT

For breaking waves at a structure prediction formulae have been developed in the previous sections. Therefore, an overall deterministic design concept can be derived which is principally summarized in Fig. 12.

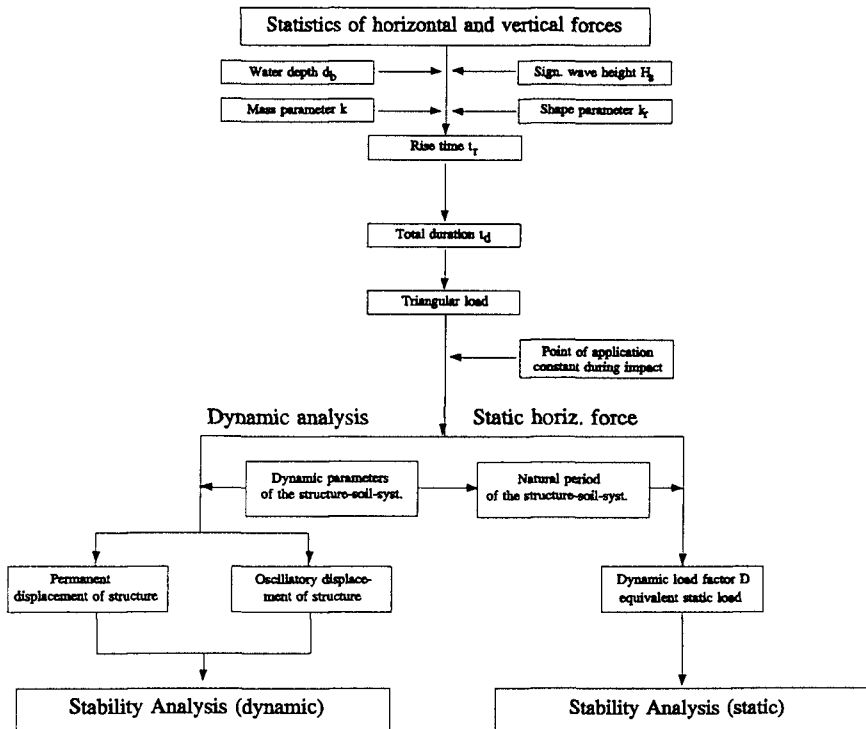


Fig. 12: Design concept for breaking wave loads

CONCLUDING REMARKS AND FUTURE WORK

Based on impulse theory and experimental investigations on breaking wave kinematics and impact loads, prediction formulae for impact forces have been derived for vertical face breakwaters.

Hydraulic model tests have been performed to assess the water mass involved in the impact process and to verify the results obtained from theory. It was found that the proposed formula represents the upper envelope of the measured values.

The ongoing and future research work is directed towards further improvement of the proposed prediction formulae. This will be particularly achieved by a better definition of the mass parameter k and of the pressure distribution for each breaker type. Moreover, a similar approach will also be developed for the uplift pressures and forces induced by breaking waves.

ACKNOWLEDGEMENTS

This study was supported by the German Research Council (DFG), Bonn. Additional support is provided by the European Union within the Research Programme MAST III (PROVERBS, contract no. MAS3-CT95-0041).

REFERENCES

- BAGNOLD, R.A. (1938): Interim Report on Wave-Pressure Research. *Journal of the Institution of Civil Engineers (ICE)*, vol. 12, pp. 202-226.
- GODA, Y. (1985): Random seas and design of maritime structures. Tokyo: University of Tokyo Press, 323 pp.
- KORTENHAUS, A.; OUMERACI, H.; KOHLHASE, S.; KLAMMER, P. (1994): Wave-induced uplift loading of caisson breakwaters. *Proceedings International Conference Coastal Engineering (ICCE)*, ASCE, Kobe, Japan, vol. 24, Part 2, pp. 1298-1311.
- MUNK, W.H. (1949): The solitary wave theory and its application to surf problems. *Annals of the New York Academy of Sciences*, pp. 378-424.
- OUMERACI, H.; KLAMMER, P.; PARTENSCKY, H.-W. (1993): Classification of breaking wave loads on vertical structures. *Journal of Waterway, Port, Coastal and Ocean Engineering*, ASCE, vol. 119, no. WW4, pp. 381-397.
- OUMERACI, H. (1994): Review and analysis of vertical breakwater failures - lessons learned. *Coastal Engineering, Special Issue on 'Vertical Breakwaters'*, Amsterdam, The Netherlands: Elsevier Science Publishers B.V., vol. 22, nos. 1/2, pp. 3-29.
- OUMERACI, H.; KORTENHAUS, A. (1994): Analysis of dynamic response of caisson breakwaters. *Coastal Engineering, Special Issue on 'Vertical Breakwaters'*, Oumeraci, H. et al., Amsterdam, The Netherlands: Elsevier Science Publishers B.V., vol. 22, nos. 1/2, pp. 159-183.
- OUMERACI, H.; BRUCE, T.; KLAMMER, P.; EASSON, W.J. (1995): Breaking wave kinematics and impact loading of caisson breakwaters. *Proceedings International Conference on Coastal and Port Engineering in Developing Countries (COPEDEC)*, Rio de Janeiro, Brazil, vol. 4, Part 3, pp. 2394-2410.
- OUMERACI, H.; KORTENHAUS, A.; KLAMMER, P. (1995): Displacement of caisson breakwaters induced by breaking wave impacts. *Proceedings of the Conference on Coastal Structures and Breakwaters*, ICE, London, U.K.: Thomas Telford Ltd.
- TAKAHASHI, S.; TANIMOTO, K.; SHIMOSAKO, K.-I. (1993): Experimental study of impulsive pressures on composite breakwaters. *Report. Port and Harbour Research Institute (PHRI)*, vol. 31, no. 5, Tokyo, Japan, pp. 33-72.
- WEIBULL, W. (1951): A statistical distribution function of wide applicability. *Journal of Applied Mechanics*, vol. 18, pp. 293-297.

CHAPTER 197

Analysis on the Interaction of Waves with Flexible Floating Structure by BE-FE Combined Method

Xiaodong Liu ¹ and Shigeki Sakai ²

Abstract

A numerical method is developed to analyze the dynamic responses of large-scale floating structures to waves. A boundary element method is applied to evaluate the fluid motion and a finite element method to analyze the response of structure. The BEM and FEM are combined to solve the wave-structure interaction problem by satisfying the continuity of the pressure and displacement on the fluid-structure interface. The unknown time-dependent boundary conditions on the free surface and the interface are evaluated by a time-stepping procedure, which gives a time domain solution. An implicit scheme ensures the calculation precision.

1. Introduction

In the analysis of floating structure, the dynamic responses of structure to waves are the most important factor. A small-scale floating structure can be analyzed as a rigid body. However, for a large-scale floating structure like floating pier, floating bridge or floating airport, the elastic deformation can not be ignored, and then the effect of flexibility should be considered in the wave-structure interaction.

In the previous studies, the wave-induced deformation of floating structure is calculated by the radiation-diffraction theory, in which the velocity potentials are expressed as a linear summation of incident, radiation and diffraction waves. This theory is available for the

1 Graduated Student, Dept. of Civil and Environmental Eng., Iwate University, 4-3-5 Ueda, Morioka, 020 Japan
2 Associate Professor, Dept. of Civil and Environmental Eng., Iwate University, 4-3-5 Ueda, Morioka, 020 Japan

analysis of periodic waves, however it is difficult to solve the problem with non-periodic waves, such as the random waves in actual seas. In the present study, a numerical approach is developed to simulate the interaction of floating structure with arbitrary waves.

In order to examine the validity and applicability of the proposed numerical implementation, the calculated results are compared with experimental data.

2. Numerical analysis

2.1 Governing equation and boundary conditions

The coordinate system of two-dimensional numerical flume is defined in Figure 1. The water depth is uniform. The waves generated on the wave maker boundary propagate in x direction, and pass through under the elastic structure, which is floating on water surface and can move freely in the vertical direction. A numerical wave filter is set up on the other end of water flume to absorb the waves. The property of fluid and the condition on fluid-structure interface are assumed as follows: (1)the fluid is incompressive and inviscid; (2)the flow is irrotational; (3)structure moves with fluid inseparably and satisfies both of the Bernoulli's equation and the bending equation of structure.

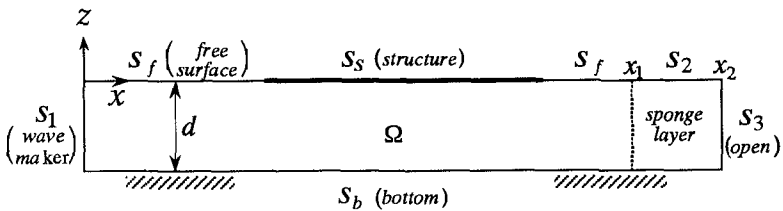


Figure 1. Definitions

According to assumption (2), a velocity potential ϕ will satisfy the following governing equation in the domain Ω :

$$\frac{\partial^2 \phi}{\partial x^2} + \frac{\partial^2 \phi}{\partial z^2} = 0 \quad \text{in } \Omega \quad (1)$$

Assuming that the waves excited on free surface is of small amplitude, the boundary conditions can be described as

$$\frac{\partial \phi}{\partial x} = V_n \quad \text{on } S_1 \quad (2)$$

$$\frac{\partial \phi}{\partial n} = 0 \quad \text{on } S_b \quad (3)$$

$$\frac{\partial \phi}{\partial n} = \frac{\partial z}{\partial t} \quad \text{on } S_f, S_s, S_2 \quad (4)$$

$$\frac{\partial \phi}{\partial t} + gz + \frac{p}{\rho} = 0 \quad \text{on } S_f, S_s \quad (5)$$

$$\frac{\partial \phi}{\partial t} + gz + \mu \phi - \int_{x_1}^x \phi \frac{\partial \mu}{\partial x} dx = 0 \quad \text{on } S_2 \quad (6)$$

$$\frac{\partial \phi}{\partial x} = -\frac{1}{\sqrt{gd}} \frac{\partial \phi}{\partial t} \quad \text{on } S_3 \quad (7)$$

where, t is time and n means the outward normal direction on boundary. (2) gives the water particle velocity of waves generated on wave maker boundary, and (3) is the impermeability condition on bottom boundary. (4) and (5) are the kinematic and dynamic conditions on the free surfaces and the interface. (6) is the dynamic condition on the free surface of the wave filter and (7) is the Sommerfeld equation on the outside boundary of the wave filter.

2.2 Boundary integral equations

As the velocity potential ϕ is a harmonic function, the Laplace equation in domain Ω can be derived as the boundary integral equation by using Green's equation.

$$c^*(\chi_l)\phi(\chi_l) = \int_{s(\chi)} \left[\frac{\partial \phi(\chi)}{\partial n} G(\chi, \chi_l) - \phi(\chi) \frac{\partial G(\chi, \chi_l)}{\partial n} \right] ds \quad (8)$$

$$G(\chi, \chi_l) = -\frac{1}{2\pi} \log|\chi - \chi_l|$$

where, $\chi = (x, z)$ and $\chi_l = (x_l, z_l)$ are the position vector on boundaries at the points of consideration and application respectively, and $c(\chi_l)$ is the parameter corresponding to the configuration of boundaries.

By substituting (2), (3), (4) and (7) into (8), the

relation between the unknowns of the velocity potential ϕ on all boundaries and the variable z on the free surface and the interface can be expressed by the following integral formulation.

$$c^*(\chi_l)\phi(\chi_l) = -\int_S \phi \frac{\partial G}{\partial n} ds + \int_{S_f, S_s, S_2} \frac{\partial z}{\partial t} G ds + \int_{S_1} V_n G ds + \int_{S_3} \left(\frac{\partial \phi}{\partial x} \right) G ds \quad (9)$$

On the right side of the above equation, the third term is known by giving the normal water particle velocity of waves on wave maker boundary. The fourth term is treated by the transformed Sommerfeld condition on the outside boundary of wave filter, which will be explained in part 2.4. The second term is the unknown time-dependent part including free surfaces and structure surface. To obtain the solution that satisfies equation (9), it is necessary to utilize the dynamic boundary conditions.

The dynamic boundary condition on free surface S_f is described by imposing $p=0$ into equation (5)

$$\frac{\partial \phi}{\partial t} + gz = 0 \quad \text{on } S_f \quad (10)$$

where z is the displacement measured from the equilibrium water surface.

The dynamic boundary condition on the free surface of wave filter is shown in equation (6). If $\mu = \partial \mu / \partial x = 0$, it will be identical with the general form, like equation (10).

The dynamic condition on structure surface is introduced in part 2.3 in detail.

2.3 Finite element analysis of structure

The flexible floating structure is considered as a plate with unit width, in which the effect of axis force is neglected. By discretizing the continuous body into elements, and converting the distribution force acting on each element into the concentrated force acting on the nodal points, the finite element analysis can give the solution of structure deformation from the dynamic condition on fluid-structure interface by satisfying the continuity of the nodal displacement.

The dynamic equilibrium equations for a finite element

system in motion can be written in matrix form

$$[M]\ddot{\{V\}} + ([K] + [K_d])\{V\} = \{F\} \quad (11)$$

where, $[M]$: the assembled mass matrix of structure
 $[K]$: the assembled stiffness matrix
 $[K_d]$: the converted coefficient matrix of the hydrostatic restoring force
 $\{V\}$: the displacement vector
 $\{F\}$: the external force vector

The mass matrix and stiffness matrix are calculated by the general approach of finite element method. The hydrostatic restoring force ($\rho g v(x)$), which is proportional to the displacement $v(x)$ of structure, is a distribution force along elements. By changing the distribution force into the equivalent concentrated forces at nodal points, the coefficient terms corresponding to the displacement can be described in the form of the element coefficient matrix $[K_d]^e$, which is

$$[K_d]^e = \frac{\rho g l}{420} \begin{bmatrix} 156 & 22l & 54 & -13l \\ 22l & 4l^2 & 13l & -3l^2 \\ 54 & 13l & 156 & -22l \\ -13l & -3l^2 & -22l & 4l^2 \end{bmatrix} \quad (12)$$

where, ρ is water density, g is the acceleration due to gravity, and l is the length of element. The coefficient matrix of the complete element assemblage is obtained by the direct addition of the element coefficient matrices similar to the assemblage of stiffness matrix.

Moreover, the fluid pressure ($p = -\partial\phi/\partial t$) that acts on floating body is a distribution force varying with the velocity potentials. It is also needed to convert the distribution force into the equivalent concentrated forces at nodal points. And then, the external force vector $\{F\}$ can be obtained by adding the nodal forces to the corresponding points.

In dynamic analysis, the equilibrium equations (11) are solved by using the Newmark integration scheme.

2.4 Wave filter boundary condition

In order to decrease the reflection waves from the far end of flume, a numerical wave filter proposed by Ohyama et al(1985) is employed to absorb the waves. The numerical wave filter consists of a sponge layer for absorbing the energy of incident waves and a Sommerfeld boundary for radiating the incoming waves. The sponge layer can be effectively used to absorb the component waves within a wide period range. But if the wave length is larger than the width of sponge layer, the efficiency of the sponge layer decreases. Therefore, the Sommerfeld condition applied on the outside boundary of the sponge layer can absorb the wave energy of long period waves.

Assuming that the attenuation coefficient μ in the sponge layer distributes linearly in horizontal direction and imposing eq.(6) to eq.(7), the boundary condition on S_3 that satisfies the continuity of velocity and pressure can be derived as follow

$$\frac{\partial \phi}{\partial x} = -\frac{1}{\sqrt{gd}} \left(\frac{\partial \phi}{\partial t} + \mu \phi - \int_{x_1}^{x_2} \phi \Big|_{on S_2} \frac{\partial \mu}{\partial x} dx \right) \quad \text{on } S_3 \quad (13)$$

2.5 Time-stepping procedure

The velocity potential ϕ on the discrete nodal points along all the boundaries and the nodal displacements on free surface and fluid-structure interface are time-defendant variables. The time under consideration is subdivided into the constant time intervals Δt , the motions of fluid and floating body can be described by a time-stepping scheme, in which a solution is established at each time step. Assuming that the velocity potential and its time derivatives at time t , denoted by $\phi^k, \dot{\phi}^k$ and $\ddot{\phi}^k$, respectively, are known, and that $\phi^{k+1}, \dot{\phi}^{k+1}$ and $\ddot{\phi}^{k+1}$ at time $t + \Delta t$ are unknown, the relation of the unknowns at time step $k+1$ and the knowns at time step k on nodal point i can be expressed by the constant-average-acceleration scheme, as follow.

$$\phi_i^{k+1} = \phi_i^k + \Delta t \dot{\phi}_i^{k+1} = \phi_i^k + \Delta t \dot{\phi}_i^k + \frac{\Delta t^2}{4} (\ddot{\phi}_i^k + \ddot{\phi}_i^{k+1}) \quad (14)$$

$$\dot{\phi}_i^{k+1} = \frac{2}{\Delta t} (\phi_i^{k+1} - \phi_i^k) - \dot{\phi}_i^k \quad (15)$$

$$\ddot{\phi}_i^{k+1} = \frac{4}{\Delta t^2} (\phi_i^{k+1} - \phi_i^k) - \frac{4}{\Delta t} \dot{\phi}_i^k - \ddot{\phi}_i^k \quad (16)$$

At the nodal point i on free and interface boundaries, the displacement, velocity and acceleration at step $k+1$ can be also expressed in the similar relation equation in terms of the previous solutions.

In the time-stepping calculation employed in this paper, at first, ϕ_i^{k+1} is predicted in relation (14), in which $\Delta\phi_i^{k+1}$ is approximately evaluated by the solution of the previous time step in relation (17).

$$\Delta\phi_i^{k+1} \approx \Delta t \dot{\phi}_i^k + \frac{\Delta t^2}{2} \ddot{\phi}_i^k \quad (17)$$

And then, the vertical velocity and displacement on free surface and interface are calculated from the boundary integration equation (9). The velocity potential ϕ_i^{k+1} required can be evaluated by the dynamic conditions of eq.(6),(10) and (11). For one step's calculation, it repeats until the relative error between ϕ_i^{k+1} evaluated and that predicted is smaller than a given value. The solution is given by an implicit method.

3. Calculated and experimental results

3.1 Experimental equipment

The wave flume used for the present experiments is 26m long, 0.8m wide and 1m deep, as illustrated in figure 2. The water depth is 60cm. A wave generator is placed at one end of the flume. The wave generator has an absorbing system so that any reflected waves from the floating structure will not be reflected by the paddle of the wave maker. At the other end a wave absorber is installed to decrease wave reflection. Three kinds of

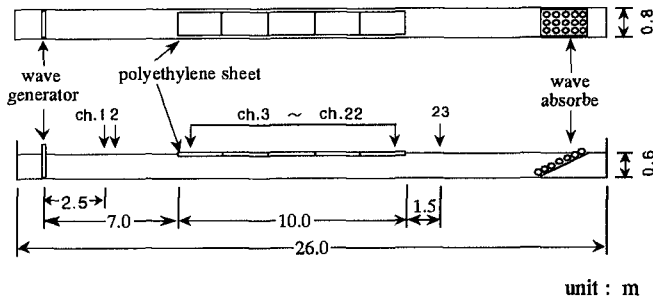


Figure 2. Experimental equipment

polyethylene plates with thickness 5mm, 10mm and 20mm are used as the model floating structure. The density of polyethylene plate is 0.941 and its elastic modulus is about 450 MPa. The wave profiles in the front open water are measured by two wave gauges. The vertical displacements of the floating body are measured at 20 points along the center of the flume by using an array of ultra-sonic sensors.

3.2 The numerical wave flume

The definition of the numerical two-dimensional wave flume is shown in figure 3. In the discretization of all boundaries, the element length on floating structure is 0.1m, 0.2m on free surface and 0.5m on the bottom. The calculation starts with a still water as the initial condition, and waves are produced by giving the water particle velocity and elevation on wave maker boundary. The step-by-step calculation proceeds with the time intervals of 1/100 wave period and the relative error 0.01 for each calculation step.

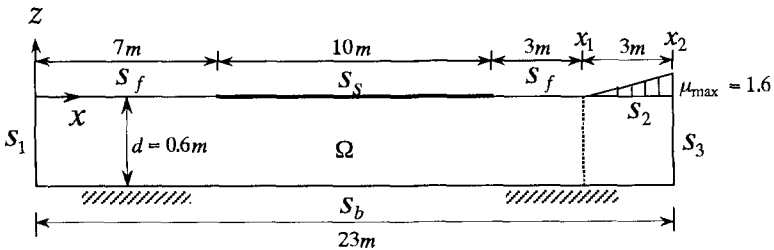


Figure 3. Definition of the numerical wave flume

3.3 Deformation of water surface and structure

Fig.4 shows an example of the calculated wave profile and the structure deformation at $t=24s$ after the waves are generated from a still water condition. In this case, the structure is 20mm thick and the wave period is 1.2 second. It can be seen clearly that the wavelength under the structure increases and the wave height (structure deformation amplitude) decreases significantly.

In figure 5, the time histories of deformation at several nodal points are plotted. The top one and the bottom one are in front and rear open waters respectively, and that in the middle part are on floating structure. In this figure, the vertical axis gives the value of vertical deformation and the horizontal axis is time.

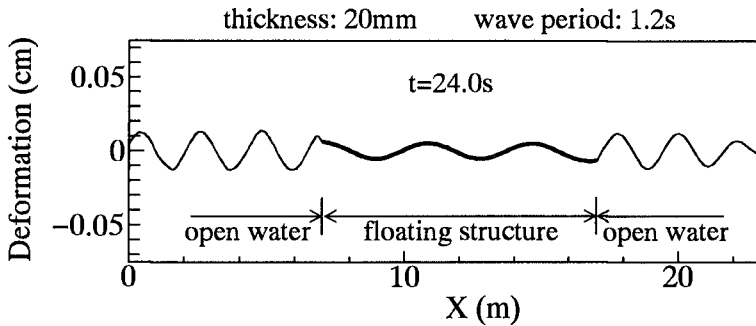


Figure 4. Deformation in open water and structure

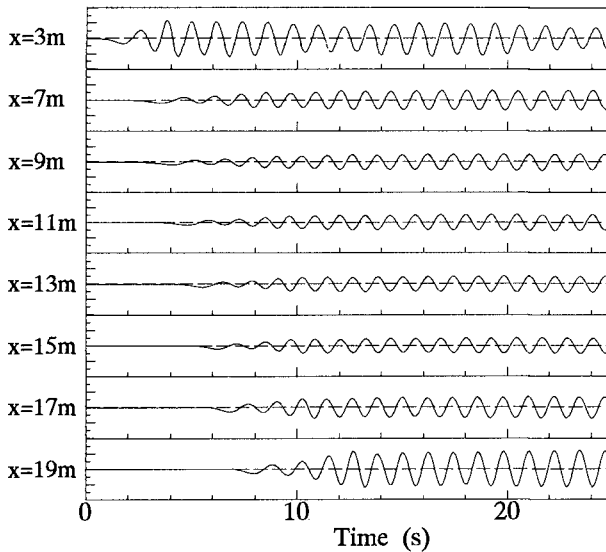


Figure 5. Time history deformation

The waves in front open water become stable, and then are influenced by the reflection waves due to the motion of floating body. For the deformation of structure, the amplitudes are large at both ends and small in structure. The motion of structure become stable after five waves pass through the structure. The variation of water surface elevation in front of wave filter is in steady state, therefore the waves are absorbed in the wave filter and the motion of floating structure is not influenced by the reflection waves.

3.4 Structure displacement response

Figure 6 shows the vertical deformation amplitude of structure with the thickness of 20mm and the wave periods of 0.8s and 1.4s. In this figure, the experimental data are the average values of wave heights measured by the time history deformation at the five waves that are in steady state. The amplitudes decrease significantly near the edge of the structure. This phenomenon is attributed to the energy conversion when the fluid motion changes into the structure-fluid combined motion. Both of the measured and the calculated results show that the deformation amplitudes exit the modes which depend on the length of structure and the period of incident waves, and they agree with each other very well.

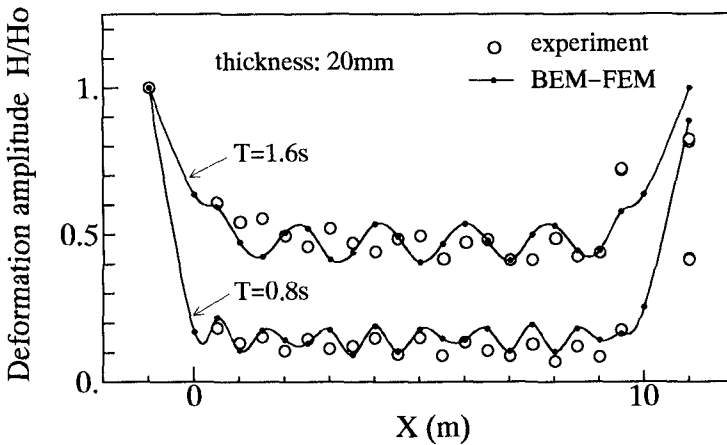


Figure 6. Deformation amplitude of structure

Figure 7 shows the changing rates of deformation amplitudes when waves propagate into structure by energy conservation method, potential matching method, the present method and experiments, respectively. The amplitude changing rates by the present method are calculated by evaluating the average amplitudes excluding the values near the edges of structure. The amplitude variations at structure edge based on the present method coincide with the measured data well.

3.5 Moment response

Figure 8 shows the response of bending moment for 20mm-thick floating structure. The peaks exist at several places and the mode observed depends on the incident wave periods. The longer the wave period becomes, the

lower the order of mode is and the greater the bending moment becomes.

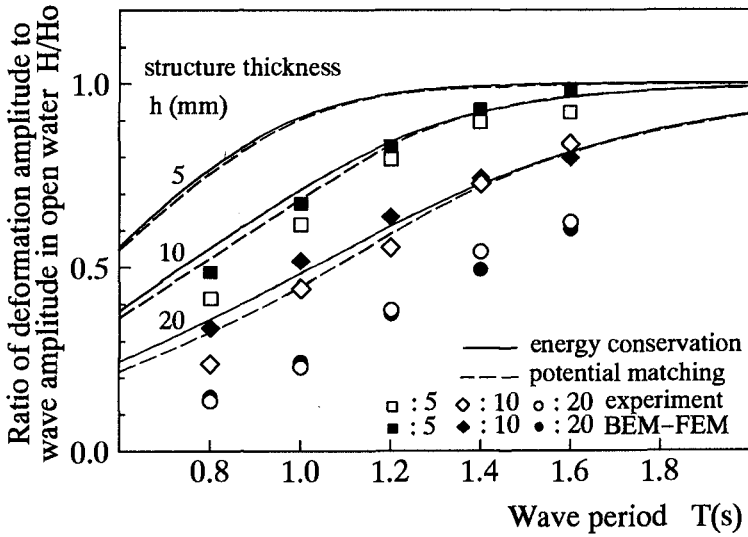


Figure 7. Comparisons of the amplitude changing rates at the edge of floating structure

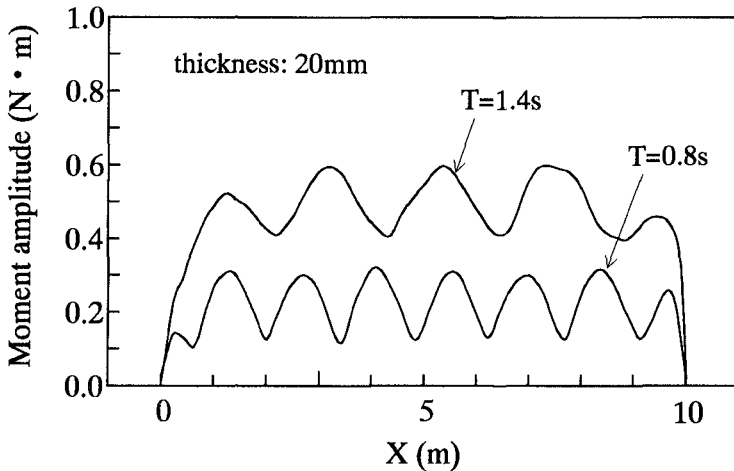


Figure 8. Moment response

4. Conclusions

The numerical approach proposed in the present study simulates the interaction of waves and flexible floating structure by employing BEM for evaluating the fluid motion and FEM for calculating the deformation of floating structure. By satisfying the continuity of the pressure and displacement on the fluid-structure interface, the BEM and FEM are combined to solve the interaction problem. The proposed method is of the following advantages: (1) The dynamic responses of structure to waves are calculated in a time-stepping procedure, which gives a time-domain solution; (2) The velocity potential is not expressed by any assumed function and is evaluated numerically. Therefore, the present method can be easily applied to any wave condition including random waves just by giving the values of incident waves on the wave maker boundary of the numerical wave flume; (3) The unknown time-dependent boundary conditions on the free surface and fluid-structure interface are evaluated by an implicit predictor-corrector scheme, which ensures a calculation precision.

The comparisons between the calculated and experimental results show that the present method is effective to the dynamic response analysis of flexible floating structures to waves.

Reference

1. Brebbia, C.A., "The Boundary Element Method For Engineers", Pentech Press, 1980
2. Sakai, S., "Interaction of Waves and Ice", Lecture Notes of the 31st Summer Seminar on Hydraulic Engineering, 95-B-2, JSCE, 1995 (in Japanese)
3. Ohyama, T. and Nadaoka, K., "Wave-Absorbing Filter for Open Boundary in Numerical Wave Tank", Proc. of Coastal Engineering, JSCE, Vol.37(1), pp.16-20, 1990 (in Japanese)
4. Suzuki Y., Tomita, Y. and Matumori, T., "Numerical Analysis of the Movement and Transmission Coefficient of Flexible Floating Structure in Waves", Proc. of Coastal Engineering, JSCE, Vol.40(2), pp.896-900, 1993 (in Japanese)

CHAPTER 198

Design wave height related to structure lifetime

Zhou Liu¹ Hans F. Burcharth²

Abstract

The determination of the design wave height (often given as the significant wave height) is usually based on statistical analysis of long-term extreme wave height measurement or hindcast. The result of such extreme wave height analysis is often given as the design wave height corresponding to a chosen return period. Sometimes confidence band of the design wave height is also given in order to include various sources of uncertainties.

In this paper the First Order Reliability Method (FORM) is used to determine the design wave height corresponding to a certain exceedence probability within the structure lifetime. This includes the statistical vagrancy of nature, sample variability and the uncertainty due to measurement or hindcast error. Moreover, based on the discussion on the statistical vagrancy of nature, a formula for the calculation of encounter probability is presented.

1 Introduction

The determination of the design wave height (often given as the significant wave height) is usually based on statistical analysis of long-term extreme wave height measurement or hindcast. The sources of uncertainty contributing to the uncertainty of the design wave height are (Burcharth 1992):

- 1) Statistical vagrancy of nature, i.e. the extreme wave height X is a random variable.
- 2) Sample variability due to limited sample size.
- 3) Error related to measurement, visual observation or hindcast.
- 4) Choice of distribution as a representative of the unknown true long-term distribution
- 5) Variability of algorithms (choice of threshold, fitting method etc.)
- 6) Climatological changes

The sources 1, 2 and 3 and their influence on the design wave height will be discussed in this paper.

¹Ph.D., Department of Civil Engineering, Aalborg University, Denmark

²Professor, dr.techn., Department of Civil Engineering, Aalborg University, Denmark

We use an example to demonstrate how the design wave height is determined. The data consist of 17 most severe storms in a period of 20 years for a deep water location. The Gumbel distribution curve in Fig.1 is obtained by fitting these 17 wave data to a Gumbel distribution.

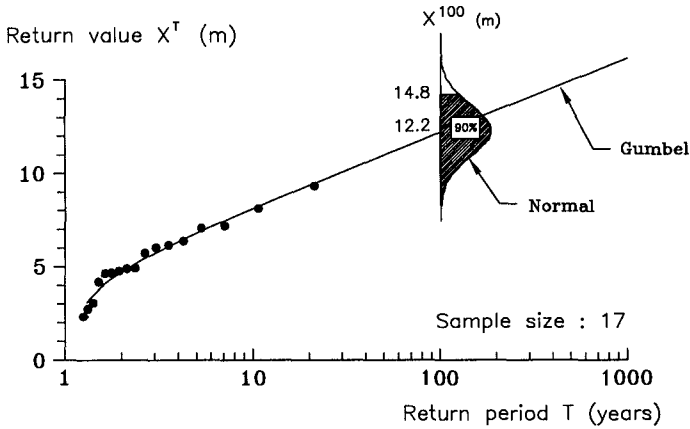


Fig.1. Design wave height.

If the design level for the design wave height is a return period of 100 years, i.e. $T = 100$, the design wave height is $x^{100} = 12.2 \text{ m}$, which means that on average this 12.2 m design wave height will be exceeded once in every 100 years.

The design wave height can be better described by the use of encounter probability, i.e. the probability that the design wave height will be exceeded within the structure lifetime. For example if the structure lifetime L is 25 years, the encounter probability of the design wave height x^{100} is

$$p = 1 - \exp\left(-\frac{L}{T}\right) = 22\% \tag{1}$$

Eq (1) is derived as eq (11) in section 2.

This means that the 12.2 m design wave height will be exceeded with 22% probability within a structure lifetime of 25 years.

If the sample variability is included, the design wave height x^{100} becomes a random variable. The distribution of the design wave height x^{100} , which is usually assumed to follow the normal distribution, can be obtained by numerical simulation, cf. Fig.1. If the upper bound with 90% confidence is taken as the design level, the design wave height is 14.8 m. What is the exceedence probability of the 14.8 m design wave height within the structure lifetime ? It cannot be calculated straight away but it might be guessed that it is

$$p = 1 - 0.9 (1 - 0.22) = 30\%$$

In this paper the First Order Reliability Method (FORM) is used to determine a design wave height corresponding to a certain exceedence probability within a specified structure lifetime. This includes the statistical vagrancy of nature, sample variability and the uncertainty due to measurement/hindcast error. Moreover, based on the discussion on the statistical vagrancy of nature, a formula for the calculation of encounter probability is presented.

2 Design wave height related to the statistical vagrancy of nature: Encounter probability

Even if we had an infinite quantity of historic true wave data and knew the related distribution precisely, there would still be uncertainty as to the largest wave which will occur during any period of time - simply due to the statistical vagrancy of nature. In this case the design wave height related to structure lifetime is characterized by the encounter probability, i.e. the probability that the design wave height will be exceeded within the structure lifetime.

Assume that the number of the extreme events is N within the structure lifetime L . X^1 denotes the maximum value in these N independent trials. Then the distribution function of X^1 is

$$F_{X^1}(x) = P(X^1 < x) = (F_X(x))^N \quad (2)$$

Note that F_{X^1} can be interpreted as the non-occurrence of the event ($X > x$) in any of N independent trials.

Assuming that the number of the extreme events $N = \lambda L$, where the sample intensity λ is

$$\lambda = \frac{\text{number of extreme events}}{\text{number of years of observation}} \quad (3)$$

From the definition of the return period T

$$T = \frac{1}{\lambda (1 - F_X(x))} \quad (4)$$

we get from eq (2)

$$F_{X^1}(x) = (F_X(x))^{\lambda L} = \left(1 - \frac{1}{\lambda T} \right)^{\lambda L} \quad (5)$$

The encounter probability of x , i.e. the probability that x will be exceeded within the structure lifetime L , is

$$p = 1 - F_{X^1}(x) = 1 - \left(1 - \frac{1}{\lambda T} \right)^{\lambda L} \quad (6)$$

For the case where $\lambda = 1$, eq (6) becomes

$$p = 1 - \left(1 - \frac{1}{T}\right)^L \quad (7)$$

However, the number of the extreme events within the structure lifetime N is also a random variable. N is usually assumed to follow the Poisson distribution

$$P(N = n) = \frac{(\lambda L)^n}{n!} \exp(-\lambda L) \quad n = 0, 1, 2, \dots \quad (8)$$

The probability of the event ($X^1 < x$ or $\bar{X} < x$) within the structure lifetime is

$$\begin{aligned} F_{X^1}(x) &= P(X^1 < x) = \sum_{n=0}^{\infty} [P(N = n) F_{X^1}(x, n)] \\ &= \sum_{n=0}^{\infty} \left[\frac{(\lambda L)^n}{n!} \exp(-\lambda L) (F_X(x))^n \right] \\ &= \sum_{n=0}^{\infty} \left[\frac{(\lambda L F_X(x))^n}{n!} \exp(-\lambda L) \right] \\ &= \exp(-\lambda L) \sum_{n=0}^{\infty} \left[\frac{(\lambda L F_X(x))^n}{n!} \right] \\ &= \exp(-\lambda L) \exp(\lambda L F_X(x)) \\ &= \exp[\lambda L (F_X(x) - 1)] \end{aligned} \quad (9)$$

Inserting eq (4) into eq (9) is obtained

$$F_{X^1}(x) = \exp\left(-\frac{L}{T}\right) \quad (10)$$

The encounter probability of x within the structure lifetime is

$$p = 1 - F_{X^1}(x) = 1 - \exp\left(-\frac{L}{T}\right) \quad (11)$$

Eq (11) is not only simpler than eq (6), but has stronger theoretical background as well because it treats N as a random variable.

3 Design wave height related to the statistical vagrancy of nature, sample variability and measurement/hindcast error

To exemplify the discussion, it is assumed that the extreme wave height follows the Gumbel distribution

$$F = F_X(x) = P(X < x) = \exp\left(-\exp\left(-\frac{x-B}{A}\right)\right) \quad (12)$$

where X is the extreme wave height which is a random variable, x a realization of X , A and B the distribution parameters.

Due to the sample variability and measurement/hindcast error, the distribution parameter A and B become random variables, and the maximum wave height within the structure lifetime, X^1 , becomes a conditional random variable $X^1|_{A,B}$. The probability of $X^1 > x_0$ within the structure lifetime is

$$P(X^1|_{A,B} \geq x_0) = P(x_0 - X^1|_{A,B} \leq 0) \quad (13)$$

Now consider the failure function

$$g(x^1, a, b) = x_0 - X^1|_{A,B} \quad \begin{cases} < 0 & \text{failure} \\ = 0 & \text{limit state} \\ > 0 & \text{no failure} \end{cases} \quad (14)$$

It can be seen that the failure probability of the failure function is actually the exceedence probability of the design wave height x_0 within the structure lifetime.

By the use of the Rosenblatt transformation, the Hasofer and Lind reliability index β for the failure function can be estimated by the First Order Reliability Theory (FORM). The failure probability, i.e. the probability of $X^1 > x_0$ within the structure lifetime, is calculated by

$$P(X^1|_{A,B} \geq x_0) \approx \Phi(-\beta) \quad (15)$$

where Φ is the standard normal distribution. The procedure for the calculation of β is detailed in the Appendix.

4 Numerical simulation of σ_A and σ_B

The only unknown in the calculation of β is the distribution of A and B .

Due to the sample variability, i.e. the influence of limited number of data, the distribution parameters A and B , estimated from a sample, are subject to an uncertainty.

Wave data set contains measurement/hindcast error. Measurement error is from malfunction and non-linearity of instruments, such as accelerometer and pressure cell, while hindcast error occurs when the sea-level atmospheric pressure fields are converted to wind data and further to wave data. The accuracy of such conversion depends on the quality of the pressure data and on the technique which is used to synthesize the data into the continues wave field. Burcharth (1986) gives an overview on the variational coefficient C (standard deviation over mean value) of measurement/hindcast error.

In order to account for the sample variability and measurement/hindcast error, A and B are assumed to follow the normal distribution. The mean values μ_A

and μ_B are obtained by fitting the data to the distribution by one of the fitting methods, such as maximum likelihood method or the least square method. The standard deviations σ_A and σ_B are obtained by numerical simulations, taking into account the sample variability and the hindcast error, as explained as follows:

A sample with size N is fitted to the Gumbel distribution

$$F_X(x) = P(X < x) = \exp\left(-\exp\left(-\left(\frac{x-B}{A}\right)\right)\right) \quad (16)$$

The obtained distribution parameters A_{true} and B_{true} are assumed to be the true values. Numerical simulation is applied to get the standard deviations of the estimators A and B , taking into account the sample variability corresponding to the sample size N . The procedure is as follows:

- 1) Generate randomly a number between 0 and 1. Let the non-exceedence probability F equal the number. the single extreme data x is obtained by

$$x = F_X^{-1}(F) = A_{\text{true}} [-\ln(-\ln F)] + B_{\text{true}} \quad (17)$$

- 2) Repeat step 1) N times. Thus we obtain a sample belonging to the distribution of eq (16) and the sample size is N .
- 3) Fit the sample to the Gumbel distribution and get the new estimated distribution parameters A and B .
- 4) Repeat steps 2) and 3), say, 10,000 times. Thus we get 10,000 values of A and B .
- 5) Calculate the standard deviations σ_A and σ_B .

In order to include the measurement/hindcast error it is assumed that the hindcast error follows a normal distribution. The following step can be added after step 1).

- 1*) Generate randomly a number between 0 and 1. Let the non-exceedence probability F be equal to the number. The modified extreme data x_{modified} is obtained by

$$x_{\text{modified}} = x + C x \Phi^{-1}(F) \quad (18)$$

where Φ is the standard normal distribution and C is the coefficient of variation of the measurement/hindcast error. C ranges usually from 0.05 to 0.2 as suggested by Burcharth (1986).

5 Examples

The deep water wave data presented in Fig.1 is used as an example to demonstrate the determination of the design wave height and the influence of sample variability and measurement/hindcast error.

The data set consists of 17 significant wave heights corresponding to the 17 most severe storms in a period of 20 years, i.e. $\lambda = 17/20$. By fitting a Gumbel distribution to the extreme data we obtain the distribution parameters $A = 1.73$ and $B = 4.53$, cf. Fig.1.

If only the statistical vagrancy of the nature is considered, i.e. A and B are exact values, the wave height corresponding to any return period can be found from the graph. The 100 year return period significant wave height is 12.2 m, which by use of eq (11) is found to correspond to 22% exceedence probability within 25 year structure lifetime.

Sample variability

Taking into account the sample variability, the distribution parameters A and B become random variables. Their distributions shown in Fig.2 are obtained by the Monto-Carlo simulation as explained in section 4.

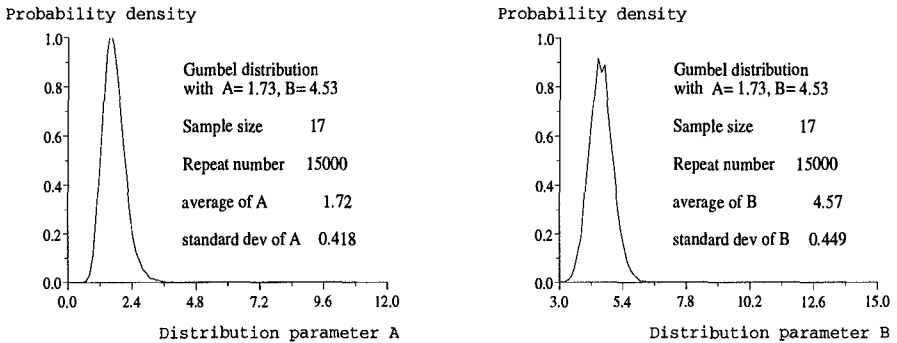


Fig.2. Distribution of the Gumbel parameters A and B by sample variability (N=17).

The probability density and the non-exceedence probability of the maximum significant wave height within any structure lifetime can be estimated by FORM. Fig.3 shows the results for a structure lifetime of 25 years. The figure includes for comparison also graphs where the sample variability is omitted. These graphs are obtained by eq (11).

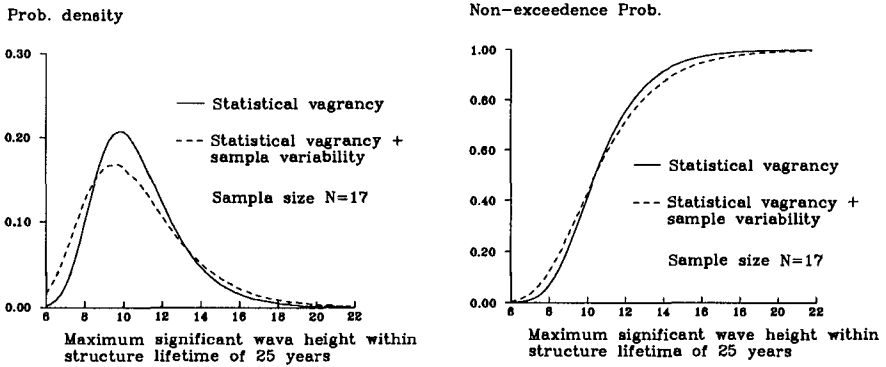


Fig.3. Distribution of maximum significant wave height (sample size $N=17$).

If the design level is the significant wave height corresponding to 22% exceedence probability within 25 years ($T = 100$ years), it can be seen from Fig.3 that the design wave height with consideration of the sample variability is 12.7 m, which is a little larger than the value without the consideration of the sample variability (12.2 m). It can also be seen that the design wave height of 14.8 m (upper bound with 90% confidence, cf. Fig.1) corresponds to 9% exceedence probability within 25 years, not 30% as guessed in Section 1.

In the case of a bigger sample size, e.g. $N = 100$, there is almost no difference between the design wave height with and without sample variability, cf. Fig.4. For comparison the same λ value is applied.

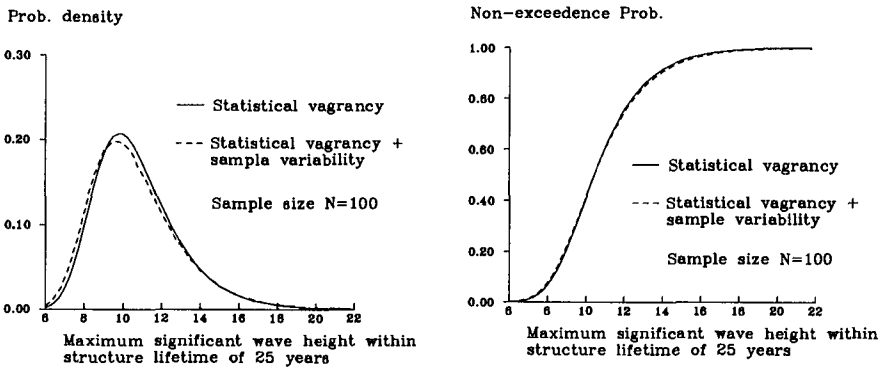


Fig.4. Distribution of maximum significant wave height (sample size $N=100$).

Table 1 shows the design wave height corresponding to different sample size. Sample size ∞ means that there is no sample variability. Keep in mind that a

typical sample size is about 20, it can be said that sample variability has some limited influence on the design wave height.

Table 1. Significant wave height corresponding to $p = 22\%$ within $L = 25$ years

sample size	10	17	50	100	∞
H_s (m)	13.0	12.7	12.4	12.3	12.2
relative difference	6.5%	4%	1.6%	0.8%	0

Measurement/hindcast error

The same procedure can be applied to further include the measurement/hindcast error.

The variational coefficient of the extreme data listed in Table 2 is taken from Burcharth (1986). Data based on visual observation from ships should in general not be used for determination of design wave height because ships avoid poor weather on purpose. With the advances in measuring techniques and numerical models, generally the C value has been reduced to app. 0.1 or less.

Table 2. Coefficient of variation for significant wave height (Burcharth 1986).

Methods of determination	Coefficient of variational
Accelerometer buoy	
Pressure cell	0.05 - 0.1
Vertical radar	
Horizontal radar	0.15
Hindcast, SPM method	0.15 - 0.2
Hindcast, numerical	0.1 - 0.2
Visual observation	0.2

In Fig.5 the coefficient of variation C of the extreme data due to measure-

ment/hindcast error is assumed a typical value of 0.1.

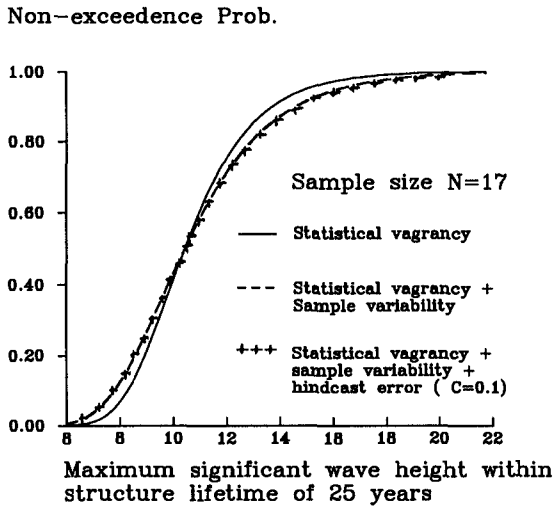


Fig.5. Distribution of maximum significant wave height ($N = 17, C = 0.1$).

In Table 3 is given values extracted from Fig.5 corresponding to an exceedence probability of $p = 22\%$.

Table 3. Significant wave height corresponding to $p = 22\%$ within $L = 25$ years

Case	H_s (m)	Remarks
Statistical vagrancy	12.2 m	
Statistical vagrancy + sample variability	12.71 m	sample size $N = 17$
Statistical vagrancy + sample variability + hindcast error	12.75 m	sample size $N = 17$ variational Coeff. $C = 0.1$

It can be seen from Fig.5 and Table 3 that the influence of measurement/hindcast error on the design wave height is very small.

6 Conclusions

The paper concentrates on the exceedence probability of the design wave height within the structure lifetime (encounter probability).

If only the statistical vagrancy of the nature is included, a new and simple encounter probability formula is derived which takes into account the randomness of the extreme events within the structure lifetime.

If other uncertainties should be considered, the paper shows that the reliability theory can be applied to determine the encounter probability of the design wave height. A practical example shows that normally sample variability has little influence on the design wave height, while the influence of measurement/hindcast errors is almost negligible.

7 References

- Burcharth, H.F. , 1986. *On the uncertainties related to the estimation of extreme environmental conditions*. Proceeding of Seminar on Uncertainties Related to the Design and Construction of Offshore Jacket Structures, Copenhagen, 1986, Published by Danish Society of Hydraulic Engineering
- Burcharth, H.F. and Zhou Liu , 1994. *On the extreme wave height analysis*. Proceedings of HYDRO-PORT'94, Yokosuka, Japan, 19-21 October, 1994
- Goda, Y. , 1988. *On the methodology of selecting design wave height*. Proc. 21st Int. Conf. on Coastal Engr., Spain.
- Thoft-Christensen, P. and Michael J. Baker , 1982. *Structural reliability theory and its application*. ISBN 3-540-11731-8, Springer-Verlag, 1982.

Appendix: Estimation of reliability index β

The followings explain the procedure for the calculation of β .

From eq (9) is obtained

$$\begin{aligned}
 F_{X^1}(x^1) &= \exp[\lambda L (F_X(x^1) - 1)] \\
 &= \exp\left[\lambda L \left(\exp\left(-\exp\left(-\left(\frac{x^1 - B}{A}\right)\right)\right) - 1\right)\right] \tag{19}
 \end{aligned}$$

which can be rewritten as

$$x^1 = A \left[-\ln \left(-\ln \left(1 + \frac{\ln F_{X^1}(x^1)}{\lambda L} \right) \right) \right] + B \tag{20}$$

X^1 can be converted to the standard normal distributed random variable U^1 by

$$\Phi(u_1) = F_{X^1}(x^1) \tag{21}$$

Inserting eq (21) into eq (20) is obtained

$$x^1 = A \left[-\ln \left(-\ln \left(1 + \frac{\ln \Phi(u_1)}{\lambda L} \right) \right) \right] + B \tag{22}$$

The failure function becomes

$$g(u_1, a, b) = x_0 - A \left[-\ln \left(-\ln \left(1 + \frac{\ln \Phi(u_1)}{\lambda L} \right) \right) \right] - B \tag{23}$$

The normal random variables A and B are converted into the standard normal distributed random variables U_2 and U_3 respectively

$$\frac{A - \mu_A}{\sigma_A} = u_2 \quad \frac{B - \mu_B}{\sigma_B} = u_3 \tag{24}$$

Insert eq (24) into eq (23) is obtained

$$\begin{aligned}
 g(u_1, u_2, u_3) &= x_0 - (\mu_A + \sigma_A u_2) \left[-\ln \left(-\ln \left(1 + \frac{\ln \Phi(u_1)}{\lambda L} \right) \right) \right] \\
 &\quad - (\mu_B + \sigma_B u_3) \tag{25}
 \end{aligned}$$

The differentiations of the failure function are

$$\begin{aligned}
 a_1 &= \frac{\partial g}{\partial u_1} = \frac{(\mu_A + \sigma_A u_2) \phi(u_1)}{\ln \left(1 + \frac{\ln \Phi(u_1)}{\lambda L} \right) \left(1 + \frac{\ln \Phi(u_1)}{\lambda L} \right) \lambda L \Phi(u_1)} \\
 a_2 &= \frac{\partial g}{\partial u_2} = -\sigma_A \left[-\ln \left(-\ln \left(1 + \frac{\ln \Phi(u_1)}{\lambda L} \right) \right) \right] \\
 a_3 &= \frac{\partial g}{\partial u_3} = -\sigma_B \tag{26}
 \end{aligned}$$

where ϕ is the density function of the standard normal distribution.

The iterative procedure for calculation of β is

- 1) Select trial values : $u^* = (u_1^*, u_2^*, u_3^*)$.
- 2) Insert u^* into eq (26) and get (a_1, a_2, a_3) .
- 3) Determine a better estimate of u^* by

$$u_i^* = a_i \frac{\sum_{i=1}^3 (a_i u_i^*) - g|_{u^*}}{\sum_{i=1}^3 a_i^2}$$

- 4) Repeat steps 2) and 3) to achieve convergence.
- 5) Calculate β by

$$\beta = \left(\sum_{i=1}^3 (u_i^*)^2 \right)^{\frac{1}{2}}$$

SUBJECT INDEX

Page number refers to the first page of paper

- Abrasives, 2166
Absorption, 55
Accretion, 2955, 4038
Accuracy, 2, 4770
Acoustic measurement, 275
Advection, 4024
Aeolian sands, 4214
Aerial surveys, 1944
Aging, 1888
Alaska, 1293
Algorithms, 914
Analytical techniques, 575, 1762,
1985
Anechorage, 1631
Anemometers, 602
Aquatic habitats, 4300
Armor units, 1542, 1583, 1617,
1640, 1665, 1679, 1721, 1735,
1748, 1789, 1803, 1862, 1944,
2377, 2418, 2522, 3006, 3791,
4228
Artificial islands, 754, 1862, 2298
Asymmetry, 3183, 3467
Australia, 4200, 4390
- Backfills, 3231, 4261
Baltic Sea, 2142
Barrier beaches, 247, 2732, 3391,
3546
Barrier islands, 2128, 2732, 2756,
2897, 4621
Barriers, 2087, 2352, 2470, 4505,
4601
Bars, 3680, 4289
Bars, riverine, 2884, 2897, 3546,
3588, 3600, 3666, 4491
Bathymetry, 731, 3521, 4376
- Bays, 4242, 4531
Beach erosion, 1349, 1985, 2352,
2666, 2691, 2705, 2718, 2732,
2756, 2770, 2820, 2857, 2871,
2884, 2911, 2918, 2955, 2982,
3115, 3295, 3378, 3442, 3521,
3874, 3976, 3986, 4038, 4583,
4613, 4650, 4717, 4744, 4756
Beach nourishment, 2746, 2770,
2857, 2897, 2911, 2918, 2927,
2941, 2955, 2982, 3115, 3642,
3708, 3722, 4014, 4390, 4440,
4613, 4621, 4650, 4730, 4756
Beaches, 151, 233, 261, 275, 602,
616, 717, 889, 955, 981, 1130,
2036, 2050, 2128, 2142, 2152,
2284, 2612, 2640, 2654, 2677,
2779, 2829, 2843, 2969, 2994,
3006, 3020, 3062, 3090, 3104,
3169, 3349, 3405, 3442, 3560,
3666, 3680, 3736, 3750, 3770,
3888, 3921, 3948, 3962, 3986,
4000, 4079, 4088, 4120, 4161,
4188, 4228, 4353, 4376, 4477
Bed load, 3467, 3913
Bed load movement, 3614
Bed movements, 3495
Bed ripples, 3129, 3183, 4079
Bed roughness, 3143
Bedforms, 3129, 3169, 3391, 3784
Belgium, 836
Benefit cost ratios, 2927, 4717
Berms, 1528, 1542, 1617, 1693,
1735, 1826, 1930, 2192, 2897,
2982, 3708, 3722, 4636
Blocks, 1888

Volume 1 1-1254, Volume 2 1255-2572, Volume 3 2573-3804, Volume 4 3805-4832

- Boundary conditions, 3770, 4120, 4134
- Boundary element method, 165, 1516, 2377, 2548
- Boundary layer, 3194, 3207, 3818
- Boundary layer flow, 3183, 3219, 4779
- Boussinesq equations, 95, 109, 123, 493, 589, 955, 1060, 1116, 1144, 1178, 1192, 1491, 3048, 3349, 4807
- Breaking, 1876
- Breaking waves, 2, 109, 151, 186, 200, 214, 233, 247, 261, 275, 286, 403, 527, 551, 602, 657, 754, 1144, 1156, 1178, 1192, 1219, 1321, 1403, 1803, 1826, 2216, 2244, 2298, 2338, 2366, 2442, 2456, 2484, 2598, 3104, 3194, 3588, 3805, 4228, 4793, 4807
- Breakwaters, 137, 186, 300, 767, 1280, 1528, 1542, 1589, 1640, 1652, 1665, 1693, 1707, 1721, 1735, 1789, 1803, 1816, 1826, 1852, 1930, 1998, 2008, 2022, 2036, 2050, 2063, 2178, 2192, 2216, 2312, 2324, 2352, 2366, 2377, 2391, 2404, 2428, 2470, 2494, 2508, 2522, 2534, 2584, 2770, 2871, 3830, 3976, 3986, 4664, 4676, 4689, 4744
- Bridges, piers, 2230
- Buoyant jets, 4325, 4569
- Buoys, 616, 743, 2087
- Caissons, 1516, 1902, 2008, 2584, 4583
- Calibration, 247, 1102, 3614
- California, 4214, 4636
- Canada, 2230
- Case reports, 1293, 2404, 2732, 3986, 4717
- Channel flow, 4491
- Channel improvements, 3323
- Channels, waterways, 1074, 4531, 4703
- Chaos, 864
- China, People's Republic of, 354
- Climatic changes, 314, 1349, 4364
- Climatic data, 81
- Closed form solutions, 3244
- Cnoidal waves, 2598
- Coastal engineering, 2, 67, 109, 286, 314, 328, 340, 354, 457, 465, 616, 1034, 1465, 1707, 2114, 3652, 3680, 4431
- Coastal environment, 314, 689, 794, 836, 1022, 1478, 2244, 3270, 3363, 3962, 4300, 4807
- Coastal management, 864, 1008, 1375, 2666, 2677, 2793, 2820, 2884, 2911, 2927, 3020, 3431, 4000, 4014, 4253, 4339, 4418, 4440, 4636, 4703, 4744
- Coastal morphology, 1349, 1417, 2770, 2806, 2829, 2897, 2955, 3048, 3090, 3391, 3521, 3534, 3560, 3574, 3600, 3750, 3762, 3830, 3913, 4024, 4038, 4079, 4477, 4517
- Coastal processes, 214, 2022, 2036, 2691, 2779, 2871, 3295, 3378, 3481, 3495, 3600, 3614, 3642, 3666, 3708, 3750, 3805, 3874, 3888, 4052, 4200, 4364, 4464, 4477, 4545, 4583, 4703, 4821
- Coastal structures, 43, 55, 214, 221, 314, 380, 389, 403, 616, 743, 981, 1452, 1569, 1735, 1852, 1862, 1876, 1957, 1971, 2008, 2114, 2128, 2142, 2152, 2166, 2178,

- 2206, 2216, 2258, 2272, 2284,
2338, 2352, 2391, 2404, 2418,
2456, 2560, 2573, 2718, 2918,
2969, 3507, 4397, 4440, 4531
- Coefficients, 1516
- Cohesive sediment, 3337
- Cold weather construction, 4397
- Colorado River, 3309
- Composite structures, 1707
- Computation, 537, 1102, 1130
- Computer aided design, 4650
- Computer aided drafting (CAD),
4650
- Computer networks, 1443
- Concrete blocks, 1652, 1665
- Concrete structures, 1556
- Configuration, 1735, 1816, 3155,
4636
- Construction, 4689
- Control, 493, 1998
- Control systems, 55
- Convection, 3784, 4098
- Coral reefs, 3143, 4261
- Core, 1735
- Corrosion, 2166
- Cost effectiveness, 2114, 4583
- Costs, 1735
- Cracks, 4411
- Crossflow, 175, 3378, 3405, 3666
- Currents, 30, 67, 95, 354, 629, 1060,
1219, 1247, 2391, 3363, 3431,
4066, 4079, 4569, 4730, 4807,
4821
- Curtain walls, 2470, 2484
- Cylinders, 380, 415
- Damage, 1233, 1789, 2969, 4261,
4676
- Damping, 2298, 2626, 3143, 4174
- Dams, 1233
- Dams, earth, 2101
- Data banks, 3652
- Data collection, 81, 137, 368, 629,
643, 677, 1916, 3722, 4200
- Data processing, 4770
- Databases, 81, 2418
- Decay, 300
- Decks, 2573
- Deep water, 2494
- Deflection, 2456
- Deformation, 261, 2338, 3062, 4411
- Deltas, 2806, 2820, 3270, 3284,
3976, 4505, 4545
- Denmark, 2927, 4703
- Density stratification, 4557
- Design, 314, 616, 1280, 1403, 1617,
1631, 1640, 1665, 1748, 1776,
1826, 1971, 2036, 2114, 2128,
2508, 2584, 2897, 2927, 3034,
3628, 4261, 4440, 4451, 4689,
4717
- Design criteria, 221, 354, 2352,
2534, 4397, 4431, 4591
- Design improvements, 2101
- Design waves, 328, 1233, 2494,
2560
- Dewatering, 2677
- Diffusers, 4325
- Diffusion, 3784, 4098
- Digital techniques, 657
- Dikes, 994, 1008, 1233, 1876, 1888,
2746, 2820
- Discharge, 3309
- Docks, 1293
- Documentation, 1443
- Dolos, 4664
- Doppler systems, 527, 629, 1060
- Drag, 3846
- Drag coefficient, 3363
- Drainage, 3507
- Drainage systems, 2640, 2654
- Drains, 2666, 2677
- Dredge spoil, 3708

- Dredging, 3284, 3708, 4274, 4289, 4390
- Ducts, 3913
- Dunes, 2793, 2884, 2955, 2969, 3034, 3115, 4148
- Dynamic response, 2456, 2584
- Dynamic stability, 1930, 2534
- Dynamics, 1178, 2955, 3560, 3805, 3846, 3921, 4052, 4364, 4601
- Earthfill, 2101
- Earthquakes, 1478
- Ecology, 4274
- Eddy viscosity, 200, 3194, 3419
- Education, 1443, 4431
- Effluents, 4325
- Egypt, 3976
- Eigenvalues, 1074, 2470
- Eigenvectors, 2829, 4730
- Embankments, 1707, 4188
- Energy conversion, 4591
- Energy dissipation, 261, 836, 1088, 1192, 1247, 2626, 3062
- Engineers, 4431
- Entropy, 643
- Environmental impact statements, 4274
- Equations of motion, 3846
- Equipment, 4591
- Erosion, 214, 1693, 2230, 2404, 3034, 4052, 4148, 4353, 4397, 4451, 4557, 4621, 4703
- Erosion control, 2666, 2677, 2820, 4038
- Estimates, 328, 3453
- Estimating, 16, 43, 2508
- Estimation, 30, 689, 794, 900, 981, 1389, 1503
- Estuaries, 2691, 4289, 4491, 4557
- Europe, 1375
- Evaluation, 340, 2036, 2677, 2857, 3652
- Experimentation, 443, 479, 516, 1617, 1840, 2640, 2746
- Extraction procedures, 4583
- Failure modes, 1902
- Failures, 1542, 1589
- Fatigue, 4664
- Feasibility studies, 4591
- Field investigations, 137, 994, 1652, 1876, 3600, 3901, 4000, 4491
- Field tests, 516, 689, 2077, 2612, 2654, 3257, 3323, 3962, 4052, 4111, 4591
- Finite element method, 2548
- Finite elements, 465
- Fisheries, 4253
- Floating breakwaters, 1631
- Floating structures, 2548
- Flood control, 2820, 4253, 4339, 4505
- Flood plain insurance, 4339
- Flooding, 1349, 2244, 2746, 4314, 4339, 4418
- Floods, 2258, 2705, 3284, 4491
- Florida, 2312, 3323, 3642, 4242, 4613
- Flow characteristics, 67
- Flow patterns, 4134
- Fluid flow, 3546
- Fluidizing, 4161
- Flumes, 300, 493, 575, 968, 1542, 1816, 1826, 1902, 2428, 3076, 3442
- Forecasting, 340, 743, 864
- Foundation performance, 3507
- Fourier analysis, 968, 1034
- Fourier transform, 3762
- Fractures, 4411
- Free surfaces, 389
- Frequency analysis, 123, 1144
- Frequency distribution, 16

- Friction, 836
Friction factor, 3143, 3495
- Gaging stations, 1465
Geographic information systems, 4650
Geometry, 1280
Georgia, 4314
Geotextiles, 1902, 2114
Germany, 2128, 3534, 4621
Gradient, 4161
Grain size, 4756, 4779
Gravel, 981
Gravity, 2640, 2654
Gravity waves, 1335
Great Lakes, 2705, 4289
Groins, structures, 2128, 2142, 2770, 3976, 4024, 4517, 4744
Ground water, 2152, 2654, 4120, 4601
Ground-water flow, 2640
Guidelines, 1748, 4188, 4253
Gulf of Mexico, 4770
- Harbors, 864, 889, 1256, 1268, 1280, 1491, 1816, 3284, 3986, 4014, 4451, 4744
Head loss, 1776
History, 457
Human factors, 275
Hurricanes, 781, 2756, 2982
Hydraulic design, 4314
Hydraulic models, 221, 443, 3169
Hydraulic performance, 1721
Hydraulic roughness, 3143
Hydraulics, 1679, 4531, 4545
Hydrodynamics, 109, 415, 668, 3419, 3546, 3680, 3948, 4289, 4491
Hydrology, 4274
- Ice forces, 4397
Ice loads, 4397
Ice sheets, 4411
Impact, 1640, 2022, 2442, 2573, 2779
Impact forces, 2456
Impact loads, 2508, 2522, 2534, 2584
Incipient motion, 1803
Indonesia, 1443
Infiltration, 2654
Inlets, waterways, 1219, 2258, 2779, 3270, 3284, 3295, 3323, 3642, 4464, 4477, 4517, 4531
Installation, 1631
Interactions, 1060, 1219, 2377, 2548, 3694, 4120, 4821
Ireland, 4557
Islands, 1452
Italy, 2404
- Japan, 137, 794, 1349, 1389, 1465, 1491, 4000, 4038, 4545, 4676
Jets, 4451
Jetties, 1852, 2573, 3295, 3309, 4531
- Kinematics, 502, 537, 565, 1034, 1247, 1776, 2442, 3481
- Laboratory tests, 43, 493, 927, 1022, 1307, 1321, 1583, 1631, 2077, 2626, 2746, 3295, 3628
Lagrangian functions, 4569
Landslides, 1293, 1478
Large structures, 380
Lasers, 527, 602
Leakage, 1556
Limit analysis, 3874
Liquefaction, 1902, 3860
Littoral currents, 175, 233, 602, 1361, 3391, 3419, 3481, 3560, 3628, 3666, 3860

- Littoral deposits, 2779
 Littoral drift, 1998, 2871, 2897,
 3270, 3309, 3628, 3652, 3830,
 4390, 4464, 4545
 Loading, 3507
 Long waves, 151, 493, 1307, 1321,
 1431, 1452, 1478, 3076, 3090
 Louisiana, 2756

 Maintenance, 1852, 2770
 Maintenance costs, 2969
 Mass transport, 4174
 Mathematical models, 589, 2941,
 3104
 Measurement, 286, 1762, 1916,
 3129, 3169, 3391, 3431, 3588,
 4079, 4098, 4161, 4569
 Measuring instruments, 643
 Mechanics, 4300
 Membranes, 2087
 Meteorology, 703, 822, 4200
 Mixing, 175, 3419, 4098, 4325, 4569
 Model studies, 1748, 4242
 Model tests, 1431, 1528, 1693, 1971,
 2428, 2484, 2534, 4689
 Model verification, 2806, 4730
 Modeling, 109, 186, 286, 565, 889,
 1205, 1247, 1375, 2036, 2230,
 2857, 2982, 2994, 3805, 3913,
 4120, 4464, 4477, 4621, 4821
 Models, 2, 81, 123, 165, 247, 403,
 429, 502, 703, 767, 781, 794,
 1048, 1060, 1116, 1144, 1168,
 1192, 1307, 1335, 1417, 1589,
 2008, 2022, 2178, 2298, 2456,
 2494, 3062, 3115, 3207, 3257,
 3405, 3419, 3467, 3574, 3784,
 3935, 4066, 4214, 4569, 4756,
 4770, 4779
 Momentum transfer, 175
 Monitoring, 889, 1944, 2312, 2871,
 4014, 4664, 4689, 4730

 Monte Carlo method, 822, 900, 1665
 Morphology, 3231
 Movable bed models, 1998, 2258,
 2428, 3169, 3295, 3495, 3628
 Mud, 3337, 4174

 Navier-Stokes equations, 200
 Navigation, 1074, 3231, 3284, 3323,
 4390, 4531
 Nearshore circulation, 808, 822, 878,
 1205, 1335, 1361, 1417, 2391,
 2843, 3020, 3694, 3722, 3830,
 4000, 4052, 4242
 Netherlands, 1876, 3600
 Networks, 616
 New Zealand, 3284
 Noise measurement, 275
 Nomographs, 781
 Nonlinear analysis, 165, 589
 Nonlinear response, 95, 717, 731,
 767, 850, 927, 955, 1034, 1048,
 1088, 1130, 1156, 1178
 Nonlinear systems, 657, 1491
 North Carolina, 3521, 3588, 3666,
 4517
 Numerical analysis, 575, 754, 927,
 1130, 1361, 1516, 2548
 Numerical models, 30, 95, 137, 200,
 233, 300, 340, 389, 465, 551, 668,
 941, 1074, 1219, 1256, 1268,
 1876, 1930, 2050, 2324, 2338,
 2666, 2746, 2770, 2969, 3614,
 3722, 3736, 3818, 3830, 3888,
 3962, 4174, 4289, 4601, 4807

 Ocean engineering, 457, 565
 Ocean waves, 16, 1465, 1789
 Oceanography, 3090
 Offshore structures, 1603
 Optimal design, 1589
 Optimization, 479
 Oregon, 2718

- Oscillations, 1268, 1491, 2884
Oscillatory flow, 3183, 3244, 3495,
4353, 4779
Outfall sewers, 4228
Outflows, 4120
Outwash, 4148
Overtopping, 1721, 1816, 1840,
1862, 2178, 2192, 2206, 2216,
2598
Oxygen transfer, 403

Parks, 4274
Particle motion, 3846
Peak values, 900, 2484
Performance, 1852, 4636
Performance evaluation, 2087
Permeability, 2142
Photogrammetry, 3750, 4664
Piers, 2573
Piles, 2142
Pipelines, 3231, 4228
Planning, 3986
Plunging flow, 2442
Polynomials, 1130
Ponding, 2312
Pore pressure, 1916, 3219, 3860
Porosity, 2366
Porous materials, 2063
Porous media, 2377
Ports, 1707, 4376, 4676
Predictions, 123, 314, 429, 502, 703,
743, 864, 878, 941, 1321, 1417,
2077, 2230, 2338, 2806, 2941,
3231, 3378, 3405, 3574, 3652,
4650, 4807, 4821
Pressure measurement, 429, 1034
Pressures, 4161
Probabilistic methods, 2793, 4717
Probabilistic models, 808
Probability, 2560, 4418, 4440
Probability density functions, 368,
850, 4793
Probability distribution, 328, 2272
Professional development, 4431
Profiles, 2829, 2982, 2994, 3006,
3020, 3048, 3104, 3169, 3194,
3349, 3405, 3442, 3736, 3750,
3784, 3901, 3921, 4052, 4650,
4756
Programs, 4613
Progressive waves, 3183
Projects, 1375, 2941
Propellers, 4451
Protective structures, 1403
Prototypes, 1762
Public land, 4418
Public opinion, 4253
Pumps, 4591

Quality control, 643
Quays, 4451

Radioactive tracers, 3901
Random waves, 2, 16, 30, 43, 261,
415, 537, 657, 754, 850, 914, 927,
1144, 1247, 2272, 3006, 3034,
3076, 3442
Ratings, 1852
Rayleigh waves, 914, 2272
Reaeration, 403
Recirculation, 3628
Recreational facilities, 2770
Reefs, 2298
Regulation, 2391
Reliability, 1589
Remote sensing, 1944
Repairing, 4689
Research, 286, 994, 1375, 1876,
1888, 3481
Reservoirs, 1233, 1748, 2101, 2918
Resonance, 1583
Resonators, 1280
Restoration, 4261

- Revetments, 1008, 1556, 1583, 1888,
 2206, 2718
 Reynolds stress, 200, 4079
 Rheological properties, 4174
 Rip currents, 1361, 2142, 3391,
 3680, 3694, 4000
 Riprap, 1233, 1748, 2101
 Risk analysis, 4339, 4440, 4717
 River flow, 4505
 River systems, 2244
 Rivers, 1349, 4545, 4557
 Rock structures, 2077
 Rocks, 1957
 Rotational flow, 2178
 Roughness, 3129, 3495
 Rubble-mound breakwaters, 1516,
 1569, 1589, 1603, 1617, 1679,
 1776, 1916, 1944, 1957, 1971,
 2418
 Russia, 2918

 Salt water, 1022
 Salt water intrusion, 4601
 Sand, 981, 1876, 2050, 2166, 2927,
 3034, 3219, 3600, 3642, 3770,
 3874, 3888, 3962, 4353, 4390,
 4505, 4613
 Sand transport, 137, 2284, 2829,
 2871, 2911, 2994, 3708, 3736,
 3784, 3791, 3846, 3948, 4111,
 4148, 4188, 4214, 4464, 4779
 Sand waves, 3183, 3521, 3574, 4024
 Satellite mapping, 81
 Satellite photography, 3762
 Scale effect, 403, 1762, 2152, 2192,
 2522
 Scale models, 1762, 1888, 2101,
 2152, 2941
 Scattering, 941
 Scour, 2152, 2230, 2258, 4397, 4517
 Scouring, 1652, 4451, 4676
 Screens, 1762

 Sea cliffs, 2793
 Sea floor, 941, 955, 2230, 3129,
 3155, 3207, 3378, 3507, 3860,
 4376
 Sea level, 1349, 1503, 3860, 4364,
 4418, 4583
 Sea state, 703
 Sea walls, 1022, 1403, 1840, 1862,
 1902, 1985, 2192, 2216, 2442,
 2456, 2508, 2612, 2718, 4621
 Sea water, 354
 Sediment, 2152, 2732, 4161
 Sediment concentration, 3901, 3935,
 4088
 Sediment deposits, 4200, 4214
 Sediment transport, 214, 1321, 2022,
 2612, 2691, 2756, 2843, 2941,
 2994, 3006, 3048, 3062, 3076,
 3104, 3115, 3155, 3194, 3231,
 3309, 3337, 3349, 3363, 3378,
 3405, 3467, 3534, 3546, 3560,
 3614, 3628, 3642, 3652, 3736,
 3770, 3791, 3805, 3818, 3860,
 3888, 3901, 3913, 3921, 4014,
 4289, 4300, 4376, 4545, 4744,
 4793
 Sediment yield, 2391
 Sedimentation, 3231
 Sedimentology, 2050
 Sensitivity analysis, 2746
 Sensors, 3453
 Settlement analysis, 1902
 Sewage disposal, 4325
 Shallow water, 95, 109, 123, 221,
 465, 502, 551, 589, 602, 668, 878,
 889, 955, 1088, 1452, 1930, 2192
 Shape, 1957
 Shear, 175, 3207
 Shear stress, 1168, 3155, 3194, 3337,
 3467, 3481, 3913, 4325
 Shellfish, 4300, 4353
 Ship motion, 1268

- Ships, 4261
- Shoaling, 2, 95, 151, 247, 537, 717, 754, 955, 1130, 3295, 4517
- Shore protection, 2063, 2114, 2128, 2206, 2312, 2352, 2391, 2404, 2418, 2428, 2470, 2640, 2654, 2705, 2718, 2911, 2918, 3034, 3976, 4440
- Shoreline changes, 1985, 2404, 2732, 2756, 2779, 2820, 2829, 2843, 2857, 2884, 2927, 3405, 3521, 3588, 3750, 3770, 3874, 3921, 4000, 4024, 4038, 4364, 4376, 4464, 4613, 4744
- Simulation, 16, 389, 657, 900, 914, 1431, 1789, 3442, 3560, 3818, 3976, 4024, 4242
- Simulation models, 67, 731, 2806
- Slope stability, 1556, 1603
- Slopes, 941, 3913
- Small structures, 380
- Soil mechanics, 1603
- Soil-structure interaction, 3507
- Solitary wave, 1156
- Sonar, 1944
- South Africa, 340
- Spain, 1816, 2806, 2871, 4014, 4418, 4730, 4744
- Spectral analysis, 43, 175
- Spraying, 994, 1022, 1840
- Sri Lanka, 4200
- Stability, 1583, 1617, 1640, 1652, 1665, 1679, 1721, 1748, 1776, 1789, 1803, 1826, 1862, 1888, 1957, 1971, 3534, 4161, 4228, 4664, 4756
- Stabilization, 2640, 2654, 2718, 2829, 3986
- Standing waves, 151, 3090
- Statistical analysis, 900, 914, 1985, 2560
- Statistical models, 1088
- Statistics, 123, 794, 808, 822, 1375, 1503
- Steel pipe piles, 2166
- Stochastic models, 1389, 4300
- Stochastic processes, 878
- Stones, 1583, 1640, 1693
- Storm surges, 822, 994, 1268, 1389, 1403, 1417, 4397
- Storms, 703, 743, 781, 1789, 2982, 3034, 3115, 3257, 3874, 3921, 4300, 4339, 4703
- Stratified flow, 4557
- Streams, 3183
- Stress, 3453
- Stress analysis, 4274
- Structural elements, 4261
- Structural response, 1617
- Submerged flow, 927
- Surf zone, 109, 151, 200, 214, 233, 286, 537, 551, 602, 1178, 1321, 1361, 1431, 3048, 3076, 3104, 3431, 3453, 3694, 3805, 3901, 4066, 4088, 4098, 4111, 4228, 4793
- Surface dynamics, 389
- Surface waves, 565, 1048, 3244, 3935
- Surveys, 2114, 3020
- Suspended sediments, 2612, 3076, 3207, 3257, 3736, 3784, 3791, 3888, 3935, 3948, 3962, 4088, 4098, 4111, 4793
- Tests, 30, 221, 286, 968, 1542, 1816, 3442, 3680
- Texas, 3736
- Theories, 443, 864, 3962
- Three-dimensional analysis, 1102
- Three-dimensional models, 233, 2843
- Tidal currents, 2691, 3722, 4491
- Tidal effects, 2994, 3090, 3574

- Tidal energy, 1478
Tidal flats, 994
Tidal waters, 3270, 3284, 3295,
3323, 3534, 3948, 4242, 4314,
4477, 4491
Tides, 629, 1603, 1707, 3431, 3442
Time studies, 1307
Toe aprons, 1971
Topography, 1349, 1417, 1452, 1998,
3534, 3560, 3762, 4545
Transducers, 3129
Trenches, 3231, 4188
Tributaries, 4289
Tsunamis, 1443, 1465, 1478, 1707,
4676
Turbidity, 4088
Turbulence, 186, 200, 214, 3207,
3818, 3935, 4111, 4228, 4325
Turbulent boundary layers, 3244
Turbulent diffusion, 4066
Turbulent flow, 200, 3453
Two-dimensional models, 3846
Typhoons, 1389, 1417, 1491
- Uncertainty analysis, 1256, 2560
Undertow, 3006, 3048, 3062, 3194,
3419, 3830
Underwater structures, 380, 927,
1998, 2312, 2324
Uniformity, 479
United Kingdom, 286, 3614, 4253,
4339
United States, 3020, 3708
Uplift pressure, 2008
- Validation, 551, 794, 1256, 3574
Vegetation, 2626, 3935, 4188
Velocity, 629, 677, 1116, 1168, 1803,
2666, 3244, 3431, 3453, 3818,
4066, 4353, 4793
Velocity distribution, 565, 1569
Velocity profile, 109, 527, 551
- Vietnam, 2820
Virginia, 1985
Viscosity, 2178
Vortices, 186, 1168, 3183, 3888,
3935, 4111, 4821
- Waste disposal, 4274
Water depth, 516, 677, 878, 1116,
2324, 3257
Water levels, 1205, 1826, 2244,
2793, 4148
Water pressure, 1603, 3155
Water quality, 403, 2677, 4557
Water surface, 850
Water surface profiles, 629
Water table, 3860, 4120, 4601
Water waves, 55, 81, 186, 275, 340,
457, 465, 502, 516, 527, 589, 657,
677, 717, 731, 878, 889, 1022,
1034, 1074, 1088, 1156, 1168,
1205, 1219, 1256, 1268, 1280,
1375, 1417, 1478, 1528, 1542,
1776, 1862, 2063, 2087, 2166,
2178, 2192, 2377, 2470, 2573,
3020, 3155, 3363, 4174, 4353,
4411
Wave action, 137, 175, 221, 380,
389, 415, 1603, 1679, 1693, 1930,
3048, 3337, 3507, 3784, 3791,
3948, 4038, 4088
Wave attenuation, 1022, 1916, 3349
Wave climatology, 314, 328, 575,
689, 808, 864, 1008, 1233, 1503,
1789, 2022, 2312, 4464, 4517,
4621
Wave diffraction, 2, 731, 754, 1048,
1862, 2063, 2366
Wave dispersion, 95, 300, 668, 767,
836, 941, 1048, 1060, 1116, 1144,
1631, 1652, 1665, 1840, 2077,
2298

- Wave energy, 261, 731, 767, 836,
1156, 1205, 2484, 2598, 2626,
3270, 4583, 4591
- Wave equations, 1452, 2324, 2366
- Wave forces, 415, 1168, 1528, 2008,
2050, 2377, 2494, 2508, 2522,
2534, 2548, 2573, 2584, 3129,
3155, 3467, 3481, 3495, 3507,
3694, 4676
- Wave generation, 55, 165, 443, 479,
493, 668, 677, 1293, 1307, 1321,
1335, 2338
- Wave groups, 151, 165, 493, 677,
1178, 1307, 1335, 1491, 1503,
3006, 3143, 3257, 3546
- Wave height, 67, 221, 247, 261, 300,
328, 368, 537, 689, 717, 743, 767,
794, 808, 850, 900, 1192, 1205,
1389, 1431, 1583, 1679, 2272,
2298, 2560, 2640, 2705, 3270,
4770
- Wave measurement, 354, 368, 429,
527, 537, 565, 616, 629, 643, 689,
703, 781, 1034, 1465, 4636, 4770
- Wave pressure, 575, 1403, 1556,
1762, 2442, 2484, 2522
- Wave propagation, 123, 165, 457,
589, 668, 878, 889, 1074, 1102,
1130, 1156, 1335, 1569, 1998,
2626, 3244, 4134, 4411, 4807
- Wave reflection, 43, 55, 443, 955,
968, 1516, 2077, 2284, 2338,
2366, 2418, 2470, 2598, 2612
- Wave refraction, 2, 754, 1048, 2324,
2366, 2691, 3762, 4505
- Wave runup, 233, 551, 981, 994,
1008, 1431, 1452, 1556, 1916,
2206, 2244, 2793, 3104, 3349,
3770, 4120, 4134, 4601
- Wave spectra, 16, 30, 43, 175, 368,
516, 629, 643, 689, 781, 822, 914,
927, 968, 1247, 2272, 3762
- Wave tanks, 479, 717, 1840, 2428,
3034, 3219, 3680, 3830
- Wave velocity, 502, 1569, 1776
- Waves, 3207, 3219, 3378, 3560,
3722, 4066, 4079, 4148, 4569,
4821
- Weibull density functions, 2272
- Weirs, 3309
- Wetlands, 4314
- Wildlife habitats, 4314
- Wind, 354, 1233
- Wind forces, 781, 2206, 2216, 3363,
4188, 4200, 4214, 4364
- Wind speed, 429, 4770
- Wind velocity, 2705
- Wind waves, 30, 429, 1088, 3363
- Yield strength, 3337

AUTHOR INDEX

Page number refers to the first page of paper

- Ahn, Kyungmo, 657
Ahn, Sung Mo., 1516
Ahrens, John P., 981, 3378
Akeda, Sadamitsu, 4353
Akiyama, Yoshinobu, 3860
Alikhani, A., 1528
Alikhani, Amir, 1693
Allsop, N. W. H., 2508, 2522
Allsop, N. William H., 389
Aminti, P., 1542
Andersen, Henning, 968, 1679
Anglin, C. D., 2230
Annandale, G. W., 2230
Aono, Toshio, 2298
Appleton, William S., 4664
Araki, Hideo, 275
Archetti, Renata, 1693
Arès, Raymond, 2101
Arntsen, Øivind A., 565
Asano, Toshiyuki, 3770
Axe, Philip, 2036
Azarmsa, Seyed Ali, 2442
- Baird, Andrew J., 4120
Bakker, Willem T., 1876, 2857
Baldock, Thomas E., 3006, 4161
Bando, Kozo, 3860
Banijamali, B., 95
Barker, Christopher H., 1034
Barnes, T. C. D., 186, 214
Bartels, A., 4689
Basco, David R., 1060, 1985, 2969
Bascom, Willard N., 3020
Battalio, Robert T., P.E., 2691
Battjes, J. A., 109, 1088, 3337
Battjes, Jurjen A., 175
Bauer, Bernard O., 4214
- Bazhenov, Yuri, 2918
Beach, R. A., 2793, 3207
Beachler, Kim E., P.E., 4613
Beale, Robert G., 389
Becq, Françoise, 465
Bedford, Keith W., 4289
Beji, Serdar, 1048
Benoit, Michel, 465, 1617
Berlamont, Jean, 836
Bian, J., 354
Bird, Paul A. D., 2077
Birkemeier, William A., 3874, 4052
Black, Kerry, 3284
Boczar-Karakiewicz, B., 3546
Bodge, Kevin R., P.E., 4261
Bollmann, Chad A., 2470
Bona, J. L., 3546
Booij, N., 668, 743
Bos, K. J., 2022
Bosboom, J., 109
Bosma, Kirk F., 2829
Bowen, A. J., 3207
Breeding, J. Ernest, Jr., 677
Breteler, M. Klein, 1556
Breteler, Mark Klein, 1888
Briggs, Michael, 1631
Briggs, Michael J., 1219
Brocchini, M., 186, 4134
Brodie, R. P. (Jock), 4390
Brøker, I., 3048, 4703
Brøker, Ida, 2927, 3805
Browder, Albert E., 2312
Brunone, Bruno, 1569
Bullock, Geoff N., 2077
Bullock, Geoffrey N., 2584
Burcharth, H. F., 1589, 1640

- Burcharth, Hans F., 2560
Burger, G., 1957
- Cadevall, Cristina, 1816
Caires, S., 743
Camfield, Fred E., 1583
Capobianco, Michele, 2884
Caron, Octave, 1233, 1748
Castañeda, A. M., 4014
Chadwick, Andrew, 2036
Chae, J. W., 1268
Chakrabarti, Subrata K., 380
Chakrabarti, Sumita, 380
Chan, Ray T. C., 3006
Chang, Kuang-An, 527
Chawla, Arun, 2
Chen, Qin, 1060
Chen, Renjie, 2312
Cho, Yong-Sik, 955
Christiani, E., 1589
Christopoulos, Spiros, 689
Cialone, Mary A., 3921, 4531
Cieslikiewicz, Witold, 703, 1375
Cinotto, Charles M., 2206
Claessen, Edward W. M., 2428
Clark, Stephen, 3784
Coates, L. E., 3257
Collins, Michael B., 3948
Cook, Benjamin, 1443
Cornett, A. M., 2230
Cox, Daniel T., 551, 3194
Craig, Kenneth R., II, 602
Creed, Christopher G., 4464
Cruz, Eric C., 2298
Curtis, William R., 2677
- Dally, W. R., 808
Dally, William R., 3419
Dalrymple, Robert A., 731, 1074,
2829
Dangaard, Jesper S., 3614, 3913
d'Angremond, Kees, 1971, 2418
- Davidson, Mark A., 2077
Davies, Michael H., 1679, 1748,
3507
Davies, P., 214
Davis, J. P., 2522
Davis, Jack E., 2677
Davis, Justin, 4242
Davis, Richard A., Jr., 2982
de Haas, Paul, 165
de Jong, Rutger J., 2418
de la Peña, Jose M., 889
de Lange, Willem, 3284
de Looff, A. P., 2770
de Looff, Harry, 2746
de Rouck, Julien, 1603, 1916, 1944
de Somer, Marc, 1916
de Vries, J. M., 4274
de Waal, Johannes P., 2216
Dean, Robert G., 2312, 3115, 3680
Deguchi, Ichiro, 3349, 3888
Deigaard, R., 3048
Deigaard, Rolf, 3805
Demirbilek, Zeki, 1219, 1256
Dennis, John M., 389
Dennis, William A., 4517
Dette, Hans-H., 3442
Diaz Rato, J. L., 1762
Dibajnia, Mohammad, 3104, 3791
DiCastro, Dan, 4376
Dingemans, M. W., 1156, 2022, 4821
Dingemans, Maarten, 165
Dombrowski, Michael R., 3270
Dong, Lifan, 2324
Dong, Ping, 4717
Donnars, Philippe, 1617
Douglass, Scott L., 3708
Dubai, Alfonse, 2626
Dunaszegi, L., 2230
Dupuis, Pierre, 1233, 2101
Duy, Nguyen The, 200

- Ebersole, Bruce A., 2779
Edge, B. L., 2087
Edge, Billy L., 941, 3309
Elbahrawy, Ali, 3976
Eldeberky, Y., 1088
Elfiky, Abd-Elfattah, 3976
Elfrink, Berry, 3805
Elgar, Steve, 3666
Elmongy, Abd-Elmohsen, 3976
Elsaeed, Gamal, 3976
Elwany, M. Hany S., 314
Escartín, F. Javier, 4014, 4744
- Falqués, Albert, 3560
Faria, A. F. Garcez, 3391
Feddersen, Falk, 3666
Fenton, J. D., 1130
Fenton, John D., 575, 1102
Fernández, A. J., 4418
Fisher, John S., 3750
Fisher, Paul R., 2994
Fleming, Chris, 4339
Fontijn, Henri L., 4228
Foster, D. L., 3207
Fowler, Jimmy, 1631
Fowler, Jimmy E., 3628
Franco, Claudio, 2008
Franco, Leopoldo, 2008
Fredsoe, Jørgen, 3231
Frigaard, P., 1640
Fujiwara, Ryuichi, 16, 1516
Fukumoto, Tadashi, 300
Fukunaga, Masahiko, 2666
Fukushima, Tadahiho, 2666
- Gadd, Peter E., 4397
Galofré, J., 4730
Galofré, Jordi, 4744
García, Cristina, 1816
Gares, Paul A., 4214
Gelfenbaum, Guy, 3453
Glodenis, Marina, 2918
- Gobbi, Maurício F., 1116
Goda, Yoshimi, 261, 629
Golan, Arik, 4376
Goldenbogen, Roland, 3534
Golik, Abraham, 4376
Gomyoh, Michio, 1652
Göricke, Frank, 2142
Gotoh, Hitoshi, 3155, 4300
Gouloumis, Spiros M., 429
Gracia, Vicente, 4098
Graff, Jerzy, 703, 1375
Grant, Geoffrey T., 2152
Gravens, Mark B., 4477
Greated, C. A., 214
Green, Debra R., 1219
Greenwood, B., 3546
Grilli, Stéphan T., 717
Groenewoud, Martin D., 2428, 2857
Grønbech, John, 968, 1679
Grüne, Joachim, 994, 1008
Guillen, Jorge, 2884
Guo, Lulin, 731
Guza, R. T., 3666
- Haines, John W., 3453
Hald, T., 1640
Hallermeier, Robert J., 2705, 3874
Hamill, G. A., 4451, 4557
Hamilton, David G., 3628
Hamm, Luc, 537
Hands, Edward B., 3378
Hanes, Daniel M., 3129, 3846
Hann, D. B., 214
Hansen, Erik Asp, 3805
Hansen, Mark E., 2756
Hanslow, David J., 2244
Hanson, Hans, 4024
Hanzawa, Minoru, 479, 1665
Harari, Pinkhas, 4376
Harcastle, P. J., 3257
Hasegawa, Iwao, 2640
Hashida, Misao, 1022, 3363

- Hashimoto, Noriaki, 30, 629, 1465
Hatada, Yoshio, 1389
Hathaway, Kent K., 4052
Hattori, Masatato, 2456
Haydon, T. R., 214
Healy, Terry, 3284
Hearon, G. E., 2718
Heilman, Daniel J., 3309
Hemsley, J. Michael, P.E., 616
Herbers, T. H. C., 3666
Herbich, John B., 3976
Hewson, Peter J., 2584
Hibbert, Kevin, 2244
Hinata, Hirofumi, 3431
Hoekstra, P., 2897
Holman, R. A., 3207
Holman, Rob, 3521
Holman, Rob A., 3588
Holmes, Patrick, 3006, 4161
Holthuijsen, L. H., 668, 743, 1247
Horikawa, Kiyoshi, 3405, 4188
Horn, Diane P., 4120
Horrillo, Juan, 717
Hosoi, Yoshihiko, 275
Hotta, Shintaro, 4188
Housley, John G., P.E., 2911
Houwman, K. T., 2897
Houwman, Klaas T., 4793
Howarth, M. W., 2522
Howell, Gary L., 3323
Hsu, John R. C., 3986
Huan, Nguyen Ngoc, 2820
Hubertz, Jon M., 4770
Hughes, Steven A., 2258
Hulscher, S. J. M. H., 3574
Humphery, J. D., 3257
Huntley, David A., 2077, 2612, 3090
Hwang, Ching-Her, 4088
Hwang, K. S., 3219
Hwung, H. H., 3219
Ikeno, Masaaki, 3076
Ilic, Suzana, 2036
Inman, Douglas L., 314
Iranzo, Vicente, 3560
Irie, I., 1840
Irie, Isao, 1022, 1998, 2391
Irish, Jennifer L., 3736
Ishii, Toshimasa, 754
Ishikawa, Motoyasu, 3860
Isobe, Masahiko, 16, 43, 443, 754, 767, 2324
Itabashi, Naoki, 137
Ito, Kazunori, 443
Ito, Shinichi, 2166
Itoh, Sadahiko, 275
Ivanova, Nadya, 2918
Iwata, Koichiro, 2338
Izumiyama, Koh, 4411
Jackson, Derek W. T., 4214
Jaffe, Bruce E., 2756
Jakobsen, Per Roed, 4703
Janssen, C. Marjolein, 4779
Jenkins, Scott A., 314
Jensen, Jacob Hjelmgager, 3231
Jensen, Robert E., 781
Jensen, Thomas, 968, 1679
Jeong, W. M., 1268
Jervis, M., 2192
Jetté, Christopher D., 3129
Jeuken, Claire, 4491
Jiang, Qin, 4174
Jiménez, José A., 2806, 4098
Johanson, Hans, 1888
Johnson, Bradley D., 551
Johnston, H. T., 4557
Jones, Bryan N., 1985
Jones, R. J., 2522
Juang, Jea Tzyy, 3762
Juhl, J., 1528
Juhl, Jørgen, 1693

- Jung, K. T., 1268
Justesen, Peter, 3805
- Kaczmarek, Jarka, 4364
Kaczmarek, Leszek M., 3467
Kaihatu, James M., 123, 1144
Kaiser, Ralf, 4621
Kajima, R., 1862
Kakuno, Shohachi, 1516
Kamikubo, Y., 1840
Kamphuis, J. William, 221, 1431, 2258
Kana, Timothy W., 2732, 4314, 4756
Kanada, Shigeo, 4411
Kanazawa, Hiroshi, 2640
Kang, Hong-Yoon, 4601
Kânog'lu, Utku, 1452
Kant, G., 2770, 2820
Kariyazono, Yoshihisa, 2166
Karjadi, Entin A., 233
Karlsson, Robert I., 2152
Kaskevitch, Liya, 2918
Katmarian, R. Eric, 4314
Kato, Hajime, 794, 2391
Kato, Kazumasa, 2640, 2654
Katori, Sadakazu, 3818
Katsui, Hidehiro, 443, 3183
Kawaguchi, Eiichi, 1349
Kawakami, Hiroshi, 3363
Kawamori, Akira, 1707
Kawanakajima, Y., 4000
Kawasaki, Koji, 2338
Kee, S. T., 2087
Kendall, Thomas, 4664
Kennedy, A. B., 1130
Kennedy, Andrew B., 1102
Khabidov, Alexander, 2918
Kim, Do-Sam, 2338
Kim, M. H., 2087
Kim, Taerim, 3830
Kimura, Akira, 864, 1776, 2272, 2366
- Kimura, Katsutoshi, 4676
Kimura, Yoshiaki, 1707
Kioka, Wataru, 1491
Kirby, James T., 2, 123, 1116, 1144, 1361
Kitamura, Fujio, 1465
Klammer, P., 2534
Klopman, G., 109
Klopman, Gert, 165
Knaack, Heiko, 4621
Kobayashi, N., 1721, 1803
Kobayashi, Nobuhisa, 233, 551, 3194, 4148
Kojima, Haruyuki, 927
Komar, P. D., 2718, 2793
Kondo, Hideo, 1707, 4583, 4591
Konicki, Kathryn M., 3588
Kortenhaus, A., 1403, 2534
Kos'yan, R. D., 4111
Koyabu, Tsuyoshi, 275
Kraak, Arie W., 2746
Kranenburg, C., 3337
Kraus, Nicholas C., 3020, 3034, 4024
Krecic, Michael R., 3846
Kriebel, David L., 2470
Kroon, A., 2897
Krylenko, M. V., 4111
Kudale, M. D., 1721
Kumagai, Takahiro, 2843
Kunz, H., 4111
Kunz, Hans, 2128, 3534
Kurata, Katsuhiko, 1516
Kuriyama, Yoshiaki, 247
Kuwabara, Shinji, 1707
Kuznetsov, S. Yu., 4111
Kwan, K. H., 4569
Kweon, Hyuck-Min, 261
- Lai, M.-Y., 914
Lamberti, A., 1542
Lamberti, Alberto, 2352

- Larson, Magnus, 3244
Laustrup, Christian, 2857, 2927
Lee, B. H., 3219
Lee, Jiin Jen, 1293
Lee, Jiin-Jen, 2178, 4325
Lee, Jong-In, 955
Lee, Jong-Kyu, 955
Leidersdorf, Craig B., 4397
Lesnik, John, 1852
Leyden, V. M., 808
Li, Li, 1074
Liaw, S.-R., 2494
Lillicrop, W. Jeff, 3736
Lin, Lihwa, 643, 3295
Lin, Paul C.-P., P.E., 3642
Lin, Po-Ching, 4088
Lissev, Nikolay, 1735
List, Jeffrey H., 2756
Liu, Paul C., 457
Liu, Philip L.-F., 527, 589
Liu, Xiaodong, 2548, 4411
Liu, Zhou, 2560
Long, Charles E., 4052
Losada, I. J., 4418
Losada, M. A., 1762
Loveless, John H., 2152
Lozano, José, 889
Lu, Chia-Chi, 822
Luo, Weimin, 836
Lupón, Nuria, 4014, 4744
- MacIver, Ruairi D., 3481
Maddrell, Roger, 4339
Madsen, Holger Toxvig, 2927
Madsen, P. A., 95, 1178, 3048
Madsen, Per A., 1060
Maeno, Yoshihiko, 3860
Mancinelli, Alessandro, 2352
Mann, Douglas W., P.E., 4613
Mano, Akira, 4505
Mansard, Etienne P. D., 1679, 1748
Manzenrieder, H. A., 4274
- Marcos, Frédéric, 465
Marinski, Jordan, 2484
Martens, Jean-Pierre, 1916
Martin, F. L., 1762
Mase, Hajime, 2366
Mason, Travis, 3948
Mason, Travis E., 4120
Masselink, Gerhard, 4200
Mathew, Joseph, 3284
Matsukawa, Fumihiko, 2640
Matsumi, Yoshiharu, 1776
Matsumoto, Akira, 479
Matsumoto, Teruki, 1321
Matsunaga, Hiroshi, 1516
Matsunaga, Nobuhiro, 1022, 3363
Matsuoka, Gaku, 2166, 4353
McClarty, A., 4689
McDougal, W. G., 2377, 2718, 2793
McGarvey, J. A., 4451
McKee, Philip A., 4314
McKenna, J. E., 2508
Medina, Josep R., 328, 1789, 2871
Medina, R., 4418, 4730
Mehta, Ashish J., 3270
Melby, J. A., 1803
Melby, Jeffrey A., 4664
Méndez, F., 4418
Mesa, Chuck, 4636
Miles, Jonathon R., 2612
Miller, C., 1403
Miller, Herman C., 4517
Mimura, Nobuo, 1349, 2391
Mitsui, Masao, 629
Mizuguchi, M., 493
Mizuguchi, Masaru, 1307, 2598, 3818
Mizuno, Yuzo, 4591, 4676
Mizutani, N., 2377
Mlynarski, Jeffrey M., 1074
Mochizuki, Hitoshi, 1280
Mochizuki, Masashi, 443
Mocke, G. P., 1205

- Moe, Geir, 565
Mohan, Ram K., P.E., 4756
Mohan, Ram Krishna, P.E., 2732
Monbaliu, Jaak, 836
Monsó, José Luis, 1816
Montoto, Amadeu, 3560
Montoya, F. J., 4730
Moore, S. P., 3257
Mori, Nobuhito, 850
Morita, Satoshi, 1280
Moriya, Yoichi, 2598
Mostafa, A. M., 2377
Mounsey, Chris, 4339
Moutzouris, C. I., 403, 1826
Murakami, Hitoshi, 275
Murakami, Keisuke, 927, 1840
Murray, Russell J., 4390
Mutsuda, Hidemi, 300, 2442
- Nadaoka, Kazuo, 1048, 3183, 3431
Nagai, Toshihiko, 629, 1465
Nagase, Satoru, 1307
Nairn, R. B., 2230
Nakagawa, Yasuyuki, 30, 4676
Nakamura, Satoshi, 1503
Nakamura, Takayuki, 1280
Nelson, Raymond C., 3143
Neshaei, M. Ahmad L., 3006
Newe, Jürgen, 3442
Nicholls, Robert J., 3874
Nielsen, Peter, 2244, 3495, 3784, 4066, 4601
Niemeyer, Hanz D., 4621
Nishi, Ryuichiro, 2666, 3034
Nobuoka, Hisamichi, 794, 2391
Nolten, R., 2770
Nwogu, Okey George, 4807
- Ochi, Michel K., 878
O'Donoghue, Tom, 2284
Oh, Tae-Myoung, 3680
Ohara, S., 4000
- O'Hare, Tim J., 2994, 3090
Ohno, Kenichi, 1776
Ohta, Takao, 864, 2272
Okayasu, Akio, 200, 1321
Oliver, John, 1852
O'Neil, Sean, 4289
Ono, Masanobu, 3349, 3888
Osanai, Senji, 4591
Osiecki, Daniel A., 3419
Ostrowski, Rafaxl, 3467
Otay, Emre N., 3722
Otta, A. K., 1156
Oumeraci, H., 1403, 2534
Overton, Margery F., 3750
Owczarczyk, Andrzej, 3901
Oya, Atsushi, 300
Özkan-Haller, H. Tuba, 2, 1361
- Palao, Ian M., 368
Panchang, Vijay, 1256
Panchang, Vijay G., 81
Park, W. S., 1268
Parson, Larry E., 3736
Pattiaratchi, Charitha, 4200
Péchon, Philippe, 2050
Peregrine, D. H., 186, 2192, 2573, 4134
Peters, Karsten, 3442
Petroff, Catherine, 1293, 1443
Phelp, D., 340, 4689
Pilarczyk, K. W., 1556
Pilarczyk, Krystian W., 2114
Pirie, Douglas, 1852
Plant, Nathaniel, 3521
Plotkin, Don, 1852
Pluijm, M., 2770
Podber, David P., 4289
Pollock, Cheryl, 1631
Polnikov, V., 1088
Porter, Mark, 4390
Pruszek, Z., 2820
Pruszek, Zbigniew, 3901

- Purnell, Reg, 4253
Pykhov, N. V., 4111
- Radder, A. C., 1156, 4821
Raichlen, Fredric, 1293
Rakha, K. A., 3048
Raudkivi, Arved J., 2142
Reniers, Ad, 175
Resio, Donald, 1631
Resio, Donald T., 3378
Ribberink, Jan S., 4779
Riddell, Keith J., 4717
Ris, R. C., 668, 1247
Rivero, Francisco J., 1168, 4098
Robillard, David J., 878
Robinson, David A., 4390
Rodríguez, Andrés, 4098
Roelvink, J. A., 109, 2022, 2897
Rogers, W. Erick, 2941
Romańczyk, W., 3546
Rønberg, J. K., 3048
Rosati, Julie D., 3628
Rosati, Julie Dean, 2779
Rose, C. P., 3257
Rosen, Dov S., 4376
Rossouw, Jan, 328
Rossouw, M., 340
Róz'yiński, Grzegorz, 4364
Ruessink, B. G., 2897
Ruessink, Gerben, 4793
Ruggiero, P., 2793
Russell, Paul E., 2612
Ryan, Joseph A., P.E., 4650
Rybak, Oleg, 2918
- Sabeur, Zoheir A., 389
Saeki, Hiroshi, 2166
Saito, K., 4000
Sakai, Kazuhiko, 1652
Sakai, Shigeki, 2548, 4411
Sakai, Tetsuo, 3155, 4300
Sakakibara, Hiroshi, 2366
- Sakakiyama, T., 1862
Saleh, Wameidh M., 3481
Sallenger, Asbury H., Jr., 2756
Sánchez-Arcilla, Agustín, 2806, 4098
Sancho, F. E., 1335
Santás, José C., 889
S.-Arcilla, Agustín, 1168
Sasamoto, Makoto, 4411
Sasso, R. Harvey, P.E., 3642
Sato, Hirokazu, 1665
Sato, Koichi, 2166
Sato, Michio, 2666
Savkin, Valery, 2918
Sawamoto, Masaki, 4505
Sawaragi, Toru, 3349, 3888
Schäffer, H. A., 95, 1178
Schäffer, Hemming A., 55
Scheffner, Norman W., 4440
Schiereck, Gerrit J., 1971, 4228
Schofield, Sidney, 643
Schoonees, J. S., 3652
Schroeder, Ernst, 3534
Seabergh, William C., 4531
Seaman, Roy C., 2284
Seelig, William N., 981
Serra, José, 2871
Shah, Adam M., 1431
Shak, Arthur T., P.E., 4650
Sharma, Jagat N., 354
Sheng, Y. Peter, 4242
Shepherd, Ian E., 3169
Sherman, Douglas J., 4214
Shibayama, Tomoya, 200, 3062
Shimizu, Kazuyoshi, 1465
Shimizu, Takao, 3076
Shimizu, Takuzo, 2843
Shimosako, Kenichiro, 1665
Shimosako, Ken-ichiro, 1902
Shin, Cheol S., 2969
Shoshany, Maxim, 4376
Siddabathula, M., 81
Sigurdarson, Sigurdur, 1640

- Silvester, Richard, 3986
Simmonds, David J., 3090
Simons, Richard R., 3481
Skaja, Marek, 4364
Skourup, Jesper, 55
Sloth, Peter, 1693
Smit, F., 1205
Smith, Jane M., 3628
Smith, Susan, 502
Soares, C. Guedes, 743
Sobey, Rodney J., 67, 1034
Solomonidis, Christos, 689
Somers, Christel, 1876
Sørensen, J. Dalsgaard, 1589
Sørensen, O. R., 95, 1178
Sørensen, Ole R., 1060
Sørensen, Per, 2927
Soulsby, Richard L., 3614, 3913
Southgate, Howard N., 286
Spanhoff, R., 2897
Spanhoff, Ruud, 2857
Stansby, P. K., 186
Stanton, T. P., 3391
Stanton, Timothy P., 4079
Stauble, Donald K., 3921, 4531
Steetzel, Henk J., 2746
Stelling, Guus S., 1876
Stive, Marcel J. F., 2884
Stoutjesdijk, Theo, 1888
Strange, R. Rea, III, 822
Stripling, Stuart, 286
Suriamihardja, D. A., 3694
Suzuki, Kojiro, 1652, 1902
Suzuki, Yasuyuki, 1321
Svendsen, I. A., 151, 1192, 1335
Swan, C., 4569
Swan, Christopher, 502
Synolakis, Costas Emmanuel, 1452,
1478

Tada, Akihide, 300
Tadepalli, Srinivas, 1478

Takahashi, Atsushi, 4545
Takahashi, Fumihiko, 4545
Takahashi, Shigeo, 1652, 1665, 1902
Takahashi, Tomoharu, 629
Takayama, Tomotsuka, 1665
Takayama, Tomotuka, 1652
Takewaka, Satoshi, 1998
Tanaka, Hitoshi, 4545
Tanimoto, Katsutoshi, 1665, 3405
Tega, Yukiko, 4148
Teisson, Charles, 2050
Teng, Chung-Chu, 368
Theron, A. K., 3652
Thevenot, Michelle M., 4024
Thieke, Robert J., 602
Thompson, Edward F., 4440
Thorne, P. D., 3257
Thornton, E. B., 3391
Thornton, Edward B., 4079
Togashi, Hiroyoshi, 2063
Toita, H., 493
Tokubuchi, Katsumasa, 1902
Tomasicchio, G. R., 1528
Tomasicchio, Giuseppe R., 1569
Tomasicchio, Ugo, 2404
Tönjes, Patrick, 2216
Tørum, Alf, 1735, 2626
Toue, Takao, 3183
Tournier, Jean-Pierre, 1233, 2101
Townsend, Murray, 575
Trampenau, Thomas, 2142
Trivedi, Dilip, P.E., 2691
Trizno, Anatoly, 2918
Troch, Peter, 1916
Tryggestad, S., 354
Tsai, Chin-Chi, 4088
Tsai, Li-Hung, 4088
Tsay, Ting-Kuei, 589
Tsoukala, V. K., 403
Tsuchiya, Yoshito, 3694, 4038
Tsujiimoto, Gozo, 3935
Tsujioka, Nobuaki, 2456

- Tsuruya, Hiroichi, 30, 4676
Turner, Ian L., 2677
Turnham, J., 2230
Tutuarima, W. H., 1957
Tzang, S.-Y., 2494
- Uchida, K., 4000
Uda, T., 4000
Uda, Takaaki, 137
Uittenbogaard, R. E., 4821
- van Damme, Luc, 1603, 1916, 1944
van de Graaff, Jan, 2428, 2857
van der Biezen, Stephan C., 2428
van der Meer, Jentsje W., 1957,
2008, 2216, 2418
van der Meulen, Ton, 1971
Van Dongeren, A. R., 1335
van Endt, M., 743
van Gent, Marcel R. A., 1930
van Hove, Conan, 1916
van Kessel, Thijs, 3337
van Kester, J. A. Th. M., 4821
van Kuik, Christine, 1876
Vann, A. M., 2522
Vaudrey, Kennon D., 4397
Veeramony, J., 151, 1192
Verhagen, Henk Jan, 4431
Verhagen, L. A., 516
Vermeir, Dierik, 1916
Vicinanza, D., 2508
Vidal, C., 1762
Vidaor, Alfonso, 1816, 4014, 4744
Vincent, Charles L., 781
Vinh, Ton That, 2820
Voulgaris, George, 3948
- Wada, Akira, 4353
Walkden, Michael J. A., 2584
Walker, S. A., 4557
Walstra, D. J. R., 1205
Wang, Hsiang, 643, 3295, 3830
Wang, Ping, 2982
Wang, Xu, 3295
Wang, Zeya, 1008
Ward, Donald L., 2206
Watabe, Tomiji, 4591
Watanabe, Akira, 754, 767, 2324,
2843, 3104, 3791, 3818, 4174
Watson, Gary, 1417
Watts, Philip, 1293
West, J. R., 3257
White, Thomas E., 3962
Whitehouse, Richard J. S., 3913
Whittaker, T. T. J., 2508
Wibner, Christopher G., 2206
Wiegel, Robert L., 3020
Wierzchnicki, Ryszard, 3901
Wijnberg, Kathelijne M., 3600
Williams, J. J., 3257
Wilson, D. J., 3257
Winyu, Rattanapitikon, 3062
Wood, D. J., 2573
Work, Paul A., 2941, 3722
Wu, Ji, 3762
Wu, Lilun, 4325
Wu, Nan-Jing, 589
Wutkowski, Michael, 4440
Wutkowski, Michael J., 4517
- Xu, Bingyi, 1256
Xu, Jianlu, 67
- Yabe, Kouichi, 3860
Yagi, Hiroshi, 3431
Yamaguchi, Masataka, 900, 1389
Yamaji, Kosuke, 137
Yamamoto, Shogo, 767
Yamamoto, Yoshimichi, 137, 3405
Yamashiro, Masaru, 927
Yamashita, Takao, 1417
Yamashita, Toshihiko, 2166, 4353
Yanagishima, Shin-ichi, 2654
Yano, Kenji, 4353

- | | |
|---------------------------------|---------------------------------|
| Yasuda, Takashi, 300, 850, 2442 | Zawadzka, Elz'bieta, 2955 |
| Yedapin, Veniamin, 2918 | Zeidler, Ryszard B., 3901, 4364 |
| Yim, John Z., 914 | Zelensky, Grigory, 2918 |
| Yokoki, Hiromune, 43 | Zhang, Jun, 2206 |
| Yokota, K., 4000 | Zhang, L., 2087 |
| Yoshida, Akinori, 927 | Zhang, Libang, 941 |
| You, Zai-Jin, 3495, 4066 | Zhang, Ning-chuan, 415 |
| Young, I. R., 516 | Zhao, Qun, 415 |
| Yu, Ke, 1192 | Zheng, Jie, 3115 |
| Yu, Xiping, 2063 | Zhuang, Fei, 2178 |
| Yu, Yu-xiu, 415 | Zyserman, J. A., 4703 |

Volume 3

Coastal Engineering 1996

Proceedings of the
twenty-fifth international conference

September 2-6, 1996
The Peabody Hotel
Orlando, Florida

Held under the auspices of the
Coastal Engineering Research Council of the
American Society of Civil Engineers

Edited by Billy L. Edge

Published by the

ASCE *American Society
of Civil Engineers*

345 East 47th Street
New York, New York 10017-2398

Abstract:

This proceedings contains over 370 papers presented at the 25th International Conference on Coastal Engineering which was held in Orlando, Florida, 2-6 September, 1996. The book is divided into six parts: 1) Characteristics of coastal waves and currents; 2) long waves and storm surges; 3) coastal structures; 4) coastal processes and sediment transport; 5) coastal, estuarine and environmental problems; and 6) case studies. The individual papers include such topics as the effects of wind, waves, storms and currents as well as the study of sedimentation, erosion and beach nourishment. Special emphasis is given to case studies of completed engineering projects. With the inclusion of both theoretical and practical information, these papers provide the civil engineer and professionals in related fields with a broad range of information on coastal engineering.

Library of Congress Cataloging-in-Publication Data

Coastal engineering 1996 : proceedings of the twenty-fifth international conference, September 2-6, 1996, The Peabody Hotel, Orlando, Florida / edited by Billy L. Edge.

p. cm.

"Held under the auspices of the Coastal Engineering Research Council of the American Society of Civil Engineers."

ISBN 0-7844-0242-6

1. Coastal engineering--Congresses. 2. Ocean waves--Congresses. I. Edge, Billy L. II. Coastal Engineering Research Council (U.S.) III. International Conference on Coastal Engineering (25th : 1996 : Orlando, Fla.)

TC203.5.C6184 1997

97-10664

627'.58--dc21

CIP

The Society is not responsible for any statements made or opinions expressed in its publications.

Photocopies. Authorization to photocopy material for internal or personal use under circumstances not falling within the fair use provisions of the Copyright Act is granted by ASCE to libraries and other users registered with the Copyright Clearance Center (CCC) Transactional Reporting Service, provided that the base fee of \$4.00 per article plus \$.25 per page is paid directly to CCC, 222 Rosewood, Drive, Danvers, MA 01923. The identification for ASCE Books is 0-7844-0242-6/97/\$4.00 + \$.25 per copy. Requests for special permission or bulk copying should be addressed to Permissions & Copyright Dept., ASCE.

Copyright © 1997 by the American Society of Civil Engineers,
All Rights Reserved.

Library of Congress Catalog Card No: 97-10664

ISBN 0-7844-0242-6

Manufactured in the United States of America.

Cover: One year after nourishment at Palm Beach, Florida. Photo courtesy of Applied Technology & Management, Inc. and Aerial Photography, Inc.

CONTENTS

Part I Characteristics of Coastal Waves and Currents

CHAPTER 1	
Experimental Study of Breaking Waves over a Shoal	2
<i>Arun Chawla, H. Tuba Ozkan-Haller, James T. Kirby</i>	
CHAPTER 2	
A Method for Estimating Standardized Bimodal Directional Spectra	16
<i>Ryuichi Fujiwara, Masahiko Isobe</i>	
CHAPTER 3	
The Effects of Currents on Estimations of Directional Wave Spectra	30
<i>Yasuyuki Nakagawa, Hiroichi Tsuruya, Noriaki Hashimoto</i>	
CHAPTER 4	
A Method for Estimating Directional Spectra in a Field of Incident and Reflected Waves	43
<i>Hiromune Yokoki, Masahiko Isobe</i>	
CHAPTER 5	
Active Absorption of Multidirectional Waves	55
<i>Hemming A. Schaffer, Jesper Skourup</i>	
CHAPTER 6	
Time-Averaged Wave Field Evolution in Coastal Zone	67
<i>Jianlu Xu, Rodney J. Sobey</i>	
CHAPTER 7	
Quality Control of GEOSAT Wave Data for Engineering Applications	81
<i>M. Siddabathula, Vijay G. Panchang</i>	
CHAPTER 8	
Boussinesq Type Equations with High Accuracy in Dispersion and Nonlinearity	95
<i>P.A. Madsen, B. Banijamali, H.A. Schaffer, O.R. Sorensen</i>	
CHAPTER 9	
Wave Kinematics Computations Using Boussinesq Models	109
<i>J. Bosboom, G. Klopman, J.A. Roelvink, J.A. Battjes</i>	
CHAPTER 10	
Effects of Mode Truncation and Dissipation on Predictions of Higher Order Statistics ...	123
<i>James M. Kaihatu, James T. Kirby</i>	
CHAPTER 11	
Field Observation of Movement of Sand Body Due to Waves and Verification of Its Mechanism by Numerical Model	137
<i>Takaaki Uda, Yoshimichi Yamamoto, Naoki Itabashi, Kosuke Yamaji</i>	

CHAPTER 12	
Wave Groups in the Surf-Zone: Model & Experiments	151
<i>J. Veeramony, I. A. Svendsen</i>	
CHAPTER 13	
Simulation of Propagating Nonlinear Wave Groups	165
<i>Paul de Haas, Maarten Dingemans, Gert Klopman</i>	
CHAPTER 14	
Cross-Shore Momentum Flux Due to Shear Instabilities	175
<i>Ad Reniers, Jurjen A. Battjes</i>	
CHAPTER 15	
Modelling Post-Wave Breaking Turbulence and Vorticity	186
<i>T.C.D. Barnes, M. Brocchini, D.H. Peregrine, P.K. Stansby</i>	
CHAPTER 16	
A Turbulent Flow Model for Breaking Waves	200
<i>Nguyen The Duy, Tomoya Shibayama, Akio Okayasu</i>	
CHAPTER 17	
Turbulence Structures in the Surf Zone	214
<i>T.R. Haydon, D.B. Hann, P. Davies, C.A. Greated, T.C.D. Barnes</i>	
CHAPTER 18	
Experiments on Design Wave Height in Shallow Water	221
<i>J. William Kamphuis</i>	
CHAPTER 19	
Time-Dependent Quasi-3D Modeling of Breaking Waves on Beaches	233
<i>Entin A. Karjadi, Nobuhisa Kobayashi</i>	
CHAPTER 20	
Models of Wave Height and Fraction of Breaking Waves on a Barred Beach	247
<i>Yoshiaki Kuriyama</i>	
CHAPTER 21	
A Parametric Model for Random Wave Deformation by Breaking on Arbitrary Beach Profiles	261
<i>Hyuck-Min Kweon, Yoshimi Goda</i>	
CHAPTER 22	
Generation Characteristics of Wave Sounds as a Factor of Beach Amenity	275
<i>Hitoshi Murakami, Sadahiko Itoh, Yoshihiko Hosoi, Hideo Araki and Tsuyoshi Koyabu</i>	
CHAPTER 23	
Measurements of Wave Breaking in the UK Coastal Research Facility	286
<i>Howard N. Southgate, Stuart Stripling</i>	
CHAPTER 24	
A New Type Breaker Forming a Giant Jet and Its Decaying Properties	300

CHAPTER 25	
Wave Climate Cycles and Coastal Engineering Practice	314
<i>Douglas L. Inman, Scott A. Jenkins, M. Hany S. Elwany</i>	
CHAPTER 26	
Stability of Design Wave Estimates	328
<i>Jan Rossouw, Josep R. Medina</i>	
CHAPTER 27	
An Evaluation of Two Wave Forecast Models for the South African Region	340
<i>M. Rossouw, D. Phelp</i>	
CHAPTER 28	
A Comprehensive Wind, Wave, and Current Measurement Program in the South China Sea	354
<i>Jagat N. Sharma, S. Tryggestad, J. Bian</i>	
CHAPTER 29	
Wave Height and Period Distributions from Long-Term Wave Measurement	368
<i>Chung-Chu Teng, Ian M. Palao</i>	
CHAPTER 30	
Interference of Small Structures in the Vicinity of Large Structures	380
<i>Subrata K. Chakrabarti, Sumita Chakrabarti</i>	
CHAPTER 31	
Wave Dynamics at Coastal Structures: Development of a Numerical Model for Free Surface Flow	389
<i>Zoheir A. Sabeur, N. William H. Allsop, Robert G. Beale, John M. Dennis</i>	
CHAPTER 32	
Scale Effects in Oxygenation in the Breaker Zone of Coastal Structures	403
<i>V.K. Tsoukala, C.I. Moutzouris</i>	
CHAPTER 33	
Wave Actions on a Vertical Cylinder in Multi-Directional Random Waves	415
<i>Yu-xiu Yu, Ning-chuan Zhang, Qun Zhao</i>	
CHAPTER 34	
Wind/Wave Relation and the Pressure Gradient Effect	429
<i>Spiros M. Gouloumis</i>	
CHAPTER 35	
Non-Reflected Multi Directional Wave Maker Theory and Experiments of Verification ..	443
<i>Kazunori Ito, Hidehiro Katsui, Masashi Mochizuki, Masahiko Isobe</i>	
CHAPTER 36	
Fifty Years of Wave Growth Curves	457
<i>Paul C. Liu</i>	

CHAPTER 37	
Development of a Third Generation Shallow-Water Wave Model with Unstructured Spatial Meshing465
<i>Michel Benoit, Frederic Marcos, Francoise Becq</i>	
CHAPTER 38	
New Optimization Method for Paddle Motion of Multi-Directional Wavemaker479
<i>Akira Matsumoto, Minoru Hanzawa</i>	
CHAPTER 39	
Generation of Second-Order Long Waves by a Wave Group in a Laboratory Flume and Its Control493
<i>M. Mizuguchi, H. Toita</i>	
CHAPTER 40	
Kinematic Predictions in Large Shallow Water Waves502
<i>Susan Smith, Christopher Swan</i>	
CHAPTER 41	
Fetch Limited Spectral Evolution in Finite Depth Water516
<i>I.R. Young, L.A. Verhagen</i>	
CHAPTER 42	
Measurement of Breaking Waves Using Particle Image Velocimetry527
<i>Kuang-An Chang, Philip L.-F. Liu</i>	
CHAPTER 43	
Computation of the Near-Bottom Kinematics of Shoaling Waves537
<i>Luc Hamm</i>	
CHAPTER 44	
Formulation and Validation of Vertically 2-D Shallow-Water Wave Model551
<i>Bradley D. Johnson, Nobuhisa Kobayashi, Daniel T. Cox</i>	
CHAPTER 45	
Particle Velocity Distribution in Surface Waves565
<i>Geir Moe, Oivind A. Arntsen</i>	
CHAPTER 46	
A Comparison of Analysis Methods for Wave Pressure Data575
<i>Murray Townsend, John D. Fenton</i>	
CHAPTER 47	
A Nonlinear Model for Wave Propagation589
<i>Ting-Kuei Tsay, Philip L.-F. Liu, Nan-Jing Wu</i>	
CHAPTER 48	
Application of a Digital Particle Image Velocimetry (DPIV) System to Breaking Waves in the Surf Zone602
<i>Kenneth R. Craig, Robert J. Thieke</i>	

CHAPTER 49	
Wave Gauging Networks Worldwide - An Overview616
<i>J. Michael Hemsley</i>	
CHAPTER 50	
Improvement of Submerged Doppler-Type Directional Wave Meter and its Application to Field Observations629
<i>Noriaki Hashimoto, Masao Mitsui, Yoshimi Goda, Toshihiko Nagai, Tomoharu Takahashi</i>	
CHAPTER 51	
Comparison of Directional Wave Data Quality from Two Different Monitoring Systems .	.643
<i>Lihwa Lin, Sidney Schofield, Hsiang Wang</i>	
CHAPTER 52	
The Digital Simulation of Non-Linear Random Waves657
<i>Kyungmo Ahn</i>	
CHAPTER 53	
The “SWAN” Wave Model for Shallow Water668
<i>N. Booij, L.H. Holthuijsen, R.C. Ris</i>	
CHAPTER 54	
Generation Depths from Water Wave Data677
<i>J. Ernest Breeding, Jr.</i>	
CHAPTER 55	
Wave Climate Assessment in the South Aegean Shelf689
<i>Spiros Christopoulos, Christos Solomonidis</i>	
CHAPTER 56	
Sea State Parameterisation Using Empirical Orthogonal Functions703
<i>Witold Cieslikiewicz, Jerzy Graff</i>	
CHAPTER 57	
Fully Nonlinear Properties of Periodic Waves Shoaling over Slopes717
<i>Stephan T. Grilli, Juan Horrillo</i>	
CHAPTER 58	
Water Wave Fluctuations Induced by Irregular Bathymetry731
<i>Lulin Guo, Robert A. Dalrymple</i>	
CHAPTER 59	
Integral Control Data Assimilation in Wave Predictions743
<i>L.H. Holthuijsen, N. Booij, M. van Endt, S. Caires, C. Guedes Soares</i>	
CHAPTER 60	
Two-Dimensional Analysis of Wave Transformation by Rational-Approximation-Based, Time-Dependent Mild-Slope Equation for Random Waves754
<i>Toshimasa Ishii, Masahiko Isobe, Akira Watanabe</i>	

CHAPTER 61	
Nonlinear Wave Transformation Due to a Submerged Breakwater	767
<i>Masahiko Isobe, Akira Watanabe, Shogo Yamamoto</i>	
CHAPTER 62	
Observed and Modeled Wave Results from Near-Stationary Hurricanes	781
<i>Charles L. Vincent, Robert E. Jensen</i>	
CHAPTER 63	
Estimation of Persistence Statistics of the Waves Observed on Japanese Coast in the Light of Recent Studies	794
<i>Hajime Kato, Hisamichi Nobuoka</i>	
CHAPTER 64	
Probabilistic Modeling of Long-Term Wave Climate	808
<i>V.M. Leyden, W.R. Dally</i>	
CHAPTER 65	
Monte Carlo Simulation for Nearshore Wave Statistics in Southern California	822
<i>Chia-Chi Lu, R. Rea Strange III</i>	
CHAPTER 66	
Bottom Friction Dissipation in the Belgian Coastal Regions	836
<i>Weimin Luo, Jaak Monbaliu, Jean Berlamont</i>	
CHAPTER 67	
Weakly non-Gaussian Model of Wave Height Distribution for Nonlinear Random Waves ..	850
<i>Nobuhito Mori, Takashi Yasuda</i>	
CHAPTER 68	
An Attempt at Applying the Chaos Theory to Wave Forecasting	864
<i>Takao Ohta, Akira Kimura</i>	
CHAPTER 69	
Transition of Stochastic Characteristics of Waves in the Nearshore Zone	878
<i>David J. Robillard, Michel K. Ochi</i>	
CHAPTER 70	
Monitoring and Modelling on Shallow Water Wave Propagations in “El Saler” Beach ..	889
<i>Jose C. Santos, Jose M. de la Pena, Jose Lozano</i>	
CHAPTER 71	
Intercomparison of Parameter Estimation Methods in Extremal Wave Analysis	900
<i>Masataka Yamaguchi</i>	
CHAPTER 72	
Influences of Spectral Shapes on the Statistical Properties of Simulated Random Waves ..	914
<i>John Z. Yim, M.-Y. Lai</i>	
CHAPTER 73	
Second-Order Interaction between Random Wave and Submerged Obstacle	927

CHAPTER 74	
A Uniform Mild-Slope Model for Waves over Varying Bottom941
<i>Libang Zhang, Billy L. Edge</i>	
CHAPTER 75	
Bragg Reflection of Shallow-Water Waves on a Sloping Beach955
<i>Yong-Sik Cho, Jong-In Lee, Jong-Kyu Lee</i>	
CHAPTER 76	
Reflection Analysis with Separation of Cross Modes968
<i>John Gronbech, Thomas Jensen, Henning Andersen</i>	
CHAPTER 77	
Wave Runup on Beaches981
<i>John P. Ahrens, William N. Seelig</i>	
CHAPTER 78	
Field Study on Wave Run-Up on Seadykes994
<i>Joachim Grune</i>	
CHAPTER 79	
Wave Run-Up on Revetments with Composite Slopes1008
<i>Zeya Wang, Joachim Grune</i>	
CHAPTER 80	
Landward Transport of Spray Generated from a Wave Absorbing Sea Wall1022
<i>Misao Hashida, Nobuhiro Matsunaga, Isao Irie</i>	
CHAPTER 81	
Irregular Wave Kinematics from a Pressure Record1034
<i>Christopher H. Barker, Rodney J. Sobey</i>	
CHAPTER 82	
Nonlinear Refraction-Diffraction of Surface Waves over Arbitrary Depths1048
<i>Serdar Beji, Kazuo Nadaoka</i>	
CHAPTER 83	
Boussinesq Equations with Improved Doppler Shift and Dispersion for Wave/Current Interaction1060
<i>Qin Chen, Per A. Madsen, Ole R. Sorensen, David R. Basco</i>	
CHAPTER 84	
The Propagation of Water Waves in Prismatic Channels1074
<i>Li Li, Robert A. Dalrymple, Jeffrey M. Mlynarski</i>	
CHAPTER 85	
A Statistical Approach for Modeling Triad Interactions in Dispersive Waves1088
<i>Y. Eldeberky, V. Polnikov, J. A. Battjes</i>	

CHAPTER 86	
A Fully Nonlinear 3D Method for the Computation of Wave Propagation	1102
<i>Andrew B. Kennedy, John D. Fenton</i>	
CHAPTER 87	
A Fourth Order Boussinesq-Type Wave Model	1116
<i>Mauricio F. Gobbi, James T. Kirby</i>	
CHAPTER 88	
Fast Methods for Computing the Shoaling of Nonlinear Waves	1130
<i>J.D. Fenton, A.B. Kennedy</i>	
CHAPTER 89	
Structure of Frequency Domain Models for Random Wave Breaking	1144
<i>James T. Kirby, James M. Kaihatu</i>	
CHAPTER 90	
A Hamiltonian Model for Nonlinear Water Waves and Its Applications	1156
<i>A.K. Otta, M.W. Dingemans, A.C. Radder</i>	
CHAPTER 91	
The Role of Wave-Induced Shear Stresses in the Momentum Balance Equations	1168
<i>Francisco J. Rivero, Agustin S.-Arcilla</i>	
CHAPTER 92	
Nonlinear Wave Dynamics in the Surf Zone	1178
<i>O.R. Sorensen, P.A. Madsen, H.A. Schaffer</i>	
CHAPTER 93	
A Boussinesq Breaking Wave Model with Vorticity	1192
<i>I.A. Svendsen, Ke Yu, J. Veeramony</i>	
CHAPTER 94	
Roller Contributions as Inferred from Inverse Modelling Techniques	1205
<i>D.J.R. Walstra, G.P. Mocke, F. Smit</i>	
CHAPTER 95	
Wave-Current Interaction in Inlets	1219
<i>Michael J. Briggs, Zeki Demirebilek, Debra R. Green</i>	
CHAPTER 96	
Wave Climate of Large Reservoirs and a Revised Wave Hindcast Formula	1233
<i>Pierre Dupuis, Jean-Pierre Tournier, Octave Caron</i>	
CHAPTER 97	
Spectral Modelling of Current Induced Wave-Blocking	1247
<i>R.C. Ris, L.H. Holthuijsen</i>	

Part II Long Period Waves, Storm Surges and Wave Groups

CHAPTER 98	
Uncertainties in the Validation of Harbor Wave Models	1256
<i>Zeki Demirbilek, Bingyi Xu, Vijay Panchang</i>	
CHAPTER 99	
Field Measurements and Numerical Modeling of Harbor Oscillations During Storm Waves	1268
<i>W.M. Jeong, J.W. Chae, W.S. Park, K.T. Jung</i>	
CHAPTER 100	
Performance of a Resonator Designed by the Wave Filter Theory - Applicability to a Harbor	1280
<i>Takayuki Nakamura, Hitoshi Mochizuki, Satoshi Morita</i>	
CHAPTER 101	
The Generation of Waves by a Landslide: Skagway, Alaska - A Case Study	1293
<i>Fredric Raichlen, Jiin Jen Lee, Catherine Petroff, Philip Watts</i>	
CHAPTER 102	
Laboratory Experiment on Long Wave Generation by Time-Varying Breakpoint	1307
<i>Satoru Nagase, Masaru Mizuguchi</i>	
CHAPTER 103	
Laboratory Experiments on Generation of Long Waves in the Surf Zone	1321
<i>Akio Okayasu, Teruki Matsumoto, Yasuyuki Suzuki</i>	
CHAPTER 104	
Generation of Infragravity Waves	1335
<i>A. R. van Dongeren, I.A. Svendsen, F.E. Sancho</i>	
CHAPTER 105	
Responses of Coastal Topography to Sea-Level Rise	1349
<i>Nobuo Mimura, Eiichi Kawaguchi</i>	
CHAPTER 106	
Numerical Study of Low Frequency Surf Zone Motions	1361
<i>H. Tuba Ozkan-Haller, James T. Kirby</i>	
CHAPTER 107	
Neptune - An Integrated Approach to Determining NW European Coastal Extremes ...	1375
<i>Jerzy Graff, Witold Cieslikiewicz</i>	
CHAPTER 108	
A Stochastic Typhoon Model and Its Application to the Estimation of Extremes of Storm Surge and Wave Height	1389
<i>Yoshio Hatada, Masataka Yamaguchi</i>	

CHAPTER 109	
Design of Vertical Walls Against Storm Surge	1403
<i>A. Kortenhaus, C. Miller, H. Oumeraci</i>	
CHAPTER 110	
Nearshore, Wave and Topographic Effects in Storm Surges	1417
<i>Gary Watson, Takao Yamashita</i>	
CHAPTER 111	
The Swash Zone: A Focus on Low Frequency Motion	1431
<i>Adam M. Shah, J. William Kamphuis</i>	
CHAPTER 112	
The Development of an On-Line, Interactive, Tsunami-Information Resource	1443
<i>Benjamin Cook, Catherine Petroff</i>	
CHAPTER 113	
Long Wave Runup on Coastal Structures	1452
<i>Utku Kanoglu, Costas Emmanuel Synolakis</i>	
CHAPTER 114	
Offshore Tsunami Profiles Observed at the Coastal Wave Stations	1465
<i>Toshihiko Nagai, Noriaki Hashimoto, Kazuyoshi Shimizu, Fujio Kitamura</i>	
CHAPTER 115	
A Realistic Model for the 1992-96 Tidal Waves	1478
<i>Srinivas Tadepalli, Costas Emmanuel Synolakis</i>	
CHAPTER 116	
Long-Period Oscillations in a Harbour Caused by Typhoon	1491
<i>Wataru Kioka</i>	
CHAPTER 117	
Estimation of Wave Groups Parameter from Wave Climate Statistics	1503
<i>Satoshi Nakamura</i>	

Part III Coastal Structures

CHAPTER 118	
Reflection Coefficients of the Step-Shaped Slit Caisson on the Rubble Mound	1516
<i>Sung Mo Ahn, Ryuichi Fujiwara, Hiroshi Matsunaga, Katsuhiko Kurata, Shohachi Kakuno</i>	
CHAPTER 119	
Berm Breakwater Trunk Exposed to Oblique Waves	1528
<i>A. Alikhani, G.R. Tomasicchio, J. Juhl</i>	
CHAPTER 120	
Interaction Between Main Armour and Toe Berm Damage	1542
<i>P. Aminti, A. Lamberti</i>	

CHAPTER 121	
Stability of Artificial Roughness Elements and Run-Up Reduction	1556
<i>M. Klein Breieler, K.W. Pilarczyk</i>	
CHAPTER 122	
Wave Induced Velocities at a Rubble Mound Breakwater	1569
<i>Bruno Brunone, Giuseppe R. Tomasicchio</i>	
CHAPTER 123	
Natural Periods of Armor Stones	1583
<i>Fred E. Camfield</i>	
CHAPTER 124	
Reliability Based Optimal Design of Vertical Breakwaters Modelled as a Series System of Failure	1589
<i>E. Christiani, H.F. Burcharth, J. Dalsgaard Sorensen</i>	
CHAPTER 125	
Overall Slope Stability Analysis of Rubble Mound Breakwaters	1603
<i>Julien De Rouck, Luc Van Damme</i>	
CHAPTER 126	
Interactions in the Stability of Toe-Berm and Main-Armour for Rubble-Mound Breakwaters: An Experimental Study	1617
<i>Philippe Donnars, Michel Benoit</i>	
CHAPTER 127	
Potential Uses for the Rapidly Installed Breakwater System	1631
<i>Jimmy Fowler, Donald Resio, Michael Briggs, Cheryl Pollock</i>	
CHAPTER 128	
Stability of Reshaping Breakwaters with Special Reference to Stone Durability	1640
<i>P. Frigaard, T. Hald, H.F. Burcharth, Sigurdur Sigurdarson</i>	
CHAPTER 129	
Field Investigations on Wave-Dissipating Concrete Blocks Covering Vertical Wall Breakwater	1652
<i>Michio Gomyoh, Kazuhiko Sakai, Tomotuka Takayama, Kojiro Suzuki, Shigeo Takahashi</i>	
CHAPTER 130	
New Stability Formula for Wave-Dissipating Concrete Blocks Covering Horizontally Composite Breakwaters	1665
<i>Minoru Hanzawa, Hirokazu Sato, Shigeo Takahashi, Kenichiro Shimosako, Tomotsuka Takayama, Katsutoshi Tanimoto</i>	
CHAPTER 131	
Breakwater Stability under Regular and Irregular Wave Attack	1679
<i>Thomas Jensen, Henning Andersen, John Gronbech, Etienne P.D. Mansard, Michael H. Davies</i>	
CHAPTER 132	
Roundhead Stability of Berm Breakwaters	1693

CHAPTER 133	
Improvement of Composite Breakwater on Solid Bottom Against Severe Tsunamis	1707
<i>Yoshiaki Kimura, Hideo Kondo, Shinji Kuwabara, Akira Kawamori</i>	
CHAPTER 134	
Hydraulic Stability Analysis of Leese Slopes of Overtopped Breakwaters	1721
<i>M.D. Kudale, N. Kobayashi</i>	
CHAPTER 135	
Influence of the Core Configuration on the Stability of Berm Breakwaters	1735
<i>Nikolay Lissev, Alf Torum</i>	
CHAPTER 136	
Model Study of Reservoir Riprap Stability	1748
<i>Etienne P. D. Mansard, Michael H. Davies, Octave Caron</i>	
CHAPTER 137	
Prototype Measurements of Wave Pressures on a Wave Screen: Comparison to Physical and Analytical Models	1762
<i>F.L. Martin, M. A. Losada, C. Vidal, J.L. Diaz Rato</i>	
CHAPTER 138	
Velocity Field Measurements over Breakwater Heads under 3D Waves	1776
<i>Yoshiharu Matsumi, Akira Kimura, Kenichi Ohno</i>	
CHAPTER 139	
Wave Climate Simulation and Breakwater Stability	1789
<i>Josep R. Medina</i>	
CHAPTER 140	
Incipient Motion of Breakwater Armor Units	1803
<i>J. A. Melby, N. Kobayashi</i>	
CHAPTER 141	
Overtopping Reduction in Crownwall Design	1816
<i>Jose Luis Monso, Alfonso Vdaor, Cristina Cadevall, Cristina Garcia</i>	
CHAPTER 142	
Stable Profiles of Reshaping Breakwaters with a Berm Below the Water Level	1826
<i>C.I. Moutzouris</i>	
CHAPTER 143	
Experiments on a Non-Wave Overtopping Type Seawall	1840
<i>Keisuke Murakami, I. Irie, Y. Kamikubo</i>	
CHAPTER 144	
A Condition and Performance Rating System for Breakwaters and Jetties	1852
<i>John Oliver, Don Plotkin, John Lesnik, Douglas Pirie</i>	

CHAPTER 145	
Wave Overtopping and Stability of Armor Units under Multidirectional Waves	1862
<i>T. Sakakiyama, R. Kajima</i>	
CHAPTER 146	
Numerical Modeling of Breach Growth in a Sanddike	1876
<i>Guis S. Stelling, Willem T. Bakker, Christine van Kuik, Christel Somers</i>	
CHAPTER 147	
Aging and Stability of Placed Block Revetments	1888
<i>Theo Stoutjesdijk, Hans Johanson, Mark Klein Breteler</i>	
CHAPTER 148	
Experimental Analysis of the Settlement Failure Mechanism Shown by Caisson-Type Seawalls	1902
<i>Shigeo Takahashi, Kojiro Suzuki, Katsumasa Tokubuchi, Ken-ichiro Shimosako</i>	
CHAPTER 149	
Full Scale Measurements of Wave Attenuation Inside a Rubble Mound Breakwater . . .	1916
<i>Peter Troch, Marc De Somer, Julien De Rouck, Luc van Damme, Dierik Vermeir, Jean-Pierre Martens, Conan van Hove</i>	
CHAPTER 150	
Numerical Modelling of Wave Interaction with Dynamically Stable Structures	1930
<i>Marcel R.A. van Gent</i>	
CHAPTER 151	
Monitoring of Zeebrugge Breakwaters	1944
<i>Luc van Damme, Julien de Rouck</i>	
CHAPTER 152	
Influence of Rock Shape and Grading on Stability of Low-Crested Structures	1957
<i>Jentsje W. van der Meer, W.H. Tutuarima, G. Burger</i>	
CHAPTER 153	
Toe Stability of Rubble Mound Breakwaters	1971
<i>Ton van der Meulen, Gerrit J. Schiereck, Kees d'Angremond</i>	
CHAPTER 154	
Seawall Effects on Historically Receding Shorelines	1985
<i>Bryan N. Jones, David R. Basco</i>	
CHAPTER 155	
Control of Wave Propagation Angle by Tapered-Submerged Breakwater	1998
<i>Satoshi Takewaka, Isao Irie</i>	
CHAPTER 156	
Multidirectional Wave Loads on Vertical Breakwaters	2008
<i>Claudio Franco, Jentsie W. Van der Meer, Leopoldo Franco</i>	

CHAPTER 157	
Modelling the Impact of Detached Breakwaters on the Coast	2022
<i>K.J. Bos, J.A. Roelvink, M.W. Dingsmans</i>	
CHAPTER 158	
Evaluation of Beach Modelling Techniques Behind Detached Breakwaters	2036
<i>Philip Axe, Suzana Ilic, Andrew Chadwick</i>	
CHAPTER 159	
Numerical Modelling of Bed Evolution Behind a Detached Breakwater	2050
<i>Philippe Pechon, Charles Teisson</i>	
CHAPTER 160	
Combined Diffraction and Transmission of Water Waves around a Porous Breakwater	
Gap	2063
<i>Xiping Yu, Hiroyoshi Togashi</i>	
CHAPTER 161	
Prediction of Wave Reflection from Rock Structures: An Integration of	
Field & Laboratory Data	2077
<i>Mark A. Davidson, Paul A.D. Bird, David A. Huntley, Geoff N. Bullock</i>	
CHAPTER 162	
Performance Evaluation of Buoy-Membrane Wave Barriers	2087
<i>M.H. Kim, B. L. Edge, S.T. Kee, L. Zhang</i>	
CHAPTER 163	
An Improved Design Method for the Riprap of Earthfill Dams of Large Reservoirs ...	2101
<i>Jean-Pierre Tournier, Pierre Dupuis, Raymond Ares</i>	
CHAPTER 164	
Geotextile Systems in Coastal Engineering - An Overview -	2114
<i>Krystian W. Pilarczyk</i>	
CHAPTER 165	
Groynes on the East Frisian Islands: History and Experiences	2128
<i>Hans Kunz</i>	
CHAPTER 166	
Permeable Pile Groins	2142
<i>Thomas Trampenau, Frank Goricke, Arved J. Raudkivi</i>	
CHAPTER 167	
The Effect of Groundwater on Scour Near Structures	2152
<i>John H. Loveless, Geoffrey T. Grant, Robert I. Karlsson</i>	
CHAPTER 168	
Abrasion of Steel Pipe Piles by Sediment Motion in Coastal Zones	2166
<i>Gaku Matsuoka, Shinichi Ito, Toshihiko Yamashita, Hiroshi Saeki, Yoshihisa Kariyazono, Koichi Sato</i>	

CHAPTER 169	
A Viscous Rotational Model for Wave Overtopping over Marine Structure	2178
<i>Fei Zhuang, Jiin-Jen Lee</i>	
CHAPTER 170	
Overtopping of Waves at a Wall: A Theoretical Approach	2192
<i>M. Jervis, D.H. Peregrine</i>	
CHAPTER 171	
Wind Effects on Runup and Overtopping of Coastal Structures	2206
<i>Donald L. Ward, Jun Zhang, Christopher G. Wibner, Charles M. Cinotto</i>	
CHAPTER 172	
Wave Overtopping of Vertical Structures Including Wind Effect	2216
<i>Johannes P. de Waal, Patrick Tonjes, Jentsje W. van der Meer</i>	
CHAPTER 173	
Bridge Pier Scour Assessment for the Northumberland Strait Crossing	2230
<i>C.D. Anglin, R.B. Nairn, A.M. Cornett, L. Dunaszegi, J. Turnham, G.W. Annandale</i>	
CHAPTER 174	
Wave Setup at River Entrances	2244
<i>David J. Hanslow, Peter Nielsen, Kevin Hibbert</i>	
CHAPTER 175	
Scour at Coastal Inlet Structures	2258
<i>Steven A. Hughes, J. William Kamphuis</i>	
CHAPTER 176	
Probability Distribution of the Maximum Wave Height along a Sea Wall with Finite Width	2272
<i>Akira Kimura, Takao Ohta</i>	
CHAPTER 177	
Beach Response in Front of Wave-Reflecting Structures	2284
<i>Roy C. Seaman, Tom O'Donoghue</i>	
CHAPTER 178	
Fundamental Characteristics of Wave Transformation around Artificial Reefs	2298
<i>Toshio Aono, Eric C. Cruz</i>	
CHAPTER 179	
Performance of a Submerged Breakwater for Shore Protection	2312
<i>Albert E. Browder, Robert G. Dean, Renjie Chen</i>	
CHAPTER 180	
Nonlinear Wave Transformation over a Submerged Triangular Breakwater	2324
<i>Lifen Dong, Akira Watanabe, Masahiko Isobe</i>	
CHAPTER 181	
Breaking Limit, Breaking and Post-Breaking Wave Deformation Due to Submerged	

Structures2338
<i>Koichiro Iwata, Koji Kawasaki, Do-Sam Kim</i>	
CHAPTER 182	
Italian Experience on Submerged Barriers as Beach Defence Structures2352
<i>Alberto Lamberti, Alessandro Mancinelli</i>	
CHAPTER 183	
Resonant Reflection and Refraction-Diffraction of Surface Waves Due to Porous Submerged Breakwaters2366
<i>Hajime Mase, Akira Kimura, Hiroshi Sakakibara</i>	
CHAPTER 184	
BEM-FEM Combined Analysis of Nonlinear Interaction between Wave and Submerged Breakwater2377
<i>N. Mizutani, W.G. McDougal, A.M. Mostafa</i>	
CHAPTER 185	
Regulation of Nearshore Circulation by Submerged Breakwater for Shore Protection ..	.2391
<i>Hisamichi Nobuoka, Isao Irie, Hajime Kato, Nobuo Mimura</i>	
CHAPTER 186	
Submerged Breakwaters for the Defence of the Shoreline at Ostia - Field Experiences, Comparison2404
<i>Ugo Tomasicchio</i>	
CHAPTER 187	
Wave Transmission of Low-Crested Structures2418
<i>Kees d'Angremond, Jentsje W. van der Meer, Rutger J. De Jong</i>	
CHAPTER 188	
Effect of Submerged Breakwater on Profile Development2428
<i>Martin D. Groenewoud, Jan van de Graaff, Edward W.M. Claessen, Stephan C. van der Biezen</i>	
CHAPTER 189	
Cause and Characteristics of Impact Pressure Exerted by Spilling and Plunging Breakers on a Vertical Wall2442
<i>Seyed Ali Azarmsa, Takashi Yasuda, Hidemi Mutsuda</i>	
CHAPTER 190	
Dynamic Response of Vertical Elastic Walls to Breaking Wave Impact2456
<i>Masatao Hattori, Nobuaki Tsujioka</i>	
CHAPTER 191	
Wave Transmission Past Vertical Wave Barriers2470
<i>David L. Kriebel, Chad A. Bollmann</i>	
CHAPTER 192	
Physical Study of the Nature of High Peak Wave Pressures2484
<i>Jordan Marinski</i>	

CHAPTER 193	
A Design Short-Crested Wave Force Model for Vertical Deep-Water Breakwaters	2494
	<i>S.-Y. Tzang, S.-R. Liaw</i>
CHAPTER 194	
New Design Methods for Wave Impact Loadings on Vertical Breakwaters and Seawalls . .	2508
	<i>N.W.H. Allsop, J.E. McKenna, D. Vicinanza, T.T.J. Whitaker</i>
CHAPTER 195	
Scale Effects of Wave Impact Pressures on Cob Armour Units	2522
	<i>M.W. Howarth, N.W.H. Allsop, A.M. Vann, R.J. Jones, J.P. Davis</i>
CHAPTER 196	
Wave Impact Loading of Vertical Face Structures for Dynamic Stability	
Analysis - Prediction Formulae -	2534
	<i>P. Klammer, A. Kortenhaus, H. Oumeraci</i>
CHAPTER 197	
Analysis on the Interaction of Waves with Flexible Floating Structure	
by BE-FE Combined Method	2548
	<i>Xiaodong Liu, Shigeki Sakai</i>
CHAPTER 198	
Design Wave Height Related to Structure Lifetime	2560
	<i>Zhou Liu, Hans F. Burcharth</i>
CHAPTER 199	
Wave Impact Beneath a Horizontal Surface	2573
	<i>D.J. Wood, D.H. Peregrine</i>
CHAPTER 200	
Wave Impulse Prediction for Caisson Design	2584
	<i>Michael J.A. Walkden, Peter J. Hewson, Geoffrey N. Bullock</i>
CHAPTER 201	
Wave Overtopping Rate and Reflection Coefficient for Obliquely Incident Waves	2598
	<i>Yoichi Moriya, Masaru Mizuguchi</i>
CHAPTER 202	
Sediment Transport and Wave Reflection near a Seawall	2612
	<i>Jonathon R. Miles, Paul E. Russell, David A. Huntley</i>

Part IV Coastal Processes and Sediment Transport

CHAPTER 203	
Wave Energy Dissipation in Kelp Vegetation	2626
	<i>Alfonse Dubi, Alf Torum</i>
CHAPTER 204	
Experimental Study on the Effect of Gravity Drainage System on Beach Stabilization . .	2640
	<i>Hiroi Kanazawa, Fumihiko Matsukawa, Kazumasa Katoh, Iwao Hasegawa</i>

CHAPTER 205	
Field Experiment on the Effect of Gravity Drainage System on Beach Stabilization . . .	2654
	<i>Kazumasa Katoh, Shin-ichi Yanagishima</i>
CHAPTER 206	
On the Change of Velocity Field in Nearshore Zone Due to Coastal Drain and the Consequent Beach Transformation	2666
	<i>Michio Sato, Tadahiro Fukushima, Ryuichiro Nishi, Masahiko Fukunaga</i>
CHAPTER 207	
Evaluation of a Beach Dewatering System: Nantucket, USA	2677
	<i>William R. Curtis, Jack E. Davis, Ian L. Turner</i>
CHAPTER 208	
Sediment Transport Processes at Ocean Beach, San Francisco, California	2691
	<i>Robert T. Battalio, Dilip Trivedi</i>
CHAPTER 209	
Two Treatments of Shore Erosion in Extreme Floods on U.S. Great Lakes	2705
	<i>Robert J. Hallermeier</i>
CHAPTER 210	
Long-Term Beach Response to Shore Stabilization Structures on the Oregon Coast . . .	2718
	<i>G.E. Hearon, W.G. McDougal, P.D. Komar</i>
CHAPTER 211	
Profile Volumes as a Measure of Erosion Vulnerability	2732
	<i>Timothy W. Kana, Ram Krishna Mohan</i>
CHAPTER 212	
Breach Growth: Experiments and Modelling	2746
	<i>Harry de Looff, Henk J. Steetzel, Arie W. Kraak</i>
CHAPTER 213	
The Impact of an Extreme Event on the Sediment Budget: Hurricane Andrew in the Louisiana Barrier Islands	2756
	<i>Jeffrey H. List, Mark E. Hansen, Asbury H. Sallenger, Jr., Bruce E. Jaffe</i>
CHAPTER 214	
Beach Maintenance Strategies, a Comparison for a Recreational Beach	2770
	<i>M. Pluijm, G. Kant, R. Noltén, A.P. de Looff</i>
CHAPTER 215	
Littoral Impact of Ocean City Inlet, Maryland, USA	2779
	<i>Julie Dean Rosati, Bruce A. Ebersole</i>
CHAPTER 216	
Extreme Water Levels, Wave Runup and Coastal Erosion	2793
	<i>P. Ruggiero, P.D. Komar, W.G. McDougal, R.A. Beach</i>

CHAPTER 217
A Morphological “Mixed-Type” Model for the Ebro Delta Coast2806
Agustin Sanchez-Arcilla, Jose A. Jimenez

CHAPTER 218
Sea Dike Erosion and Coastal Retreat at Nam Ha Province, Vietnam2820
Ton That Vinh, G. Kant, Nguyen Ngoc Huan, Z. Pruszek

CHAPTER 219
Beach Profile Analysis around Indian River Inlet, Delaware, U.S.A2829
Kirk F. Bosma, Robert A. Dalrymple

CHAPTER 220
Improved 3-D Beach Evolution Model Coupled with the Shoreline Model (3D-SHORE) .2843
Takuzo Shimizu, Takahiro Kumagai, Akira Watanabe

CHAPTER 221
Evaluation of Shoreface Nourishments by Line Modelling2857
*Martin D. Groenewoud, Willem T. Bakker, Jan van de Graaff, Ruud Spanhoff,
Christian Laustrup*

CHAPTER 222
Beach Monitoring Program of Valencia (Spain)2871
Jose Serra, Josep R. Medina

CHAPTER 223
Bar Migration and Duneface Oscillation on Decadal Scales2884
Marcel J.F. Stive, Jorge Guillen, Michele Capobianco

CHAPTER 224
Morphological Development of the Terschelling Shoreface Nourishment in Response to Hydrodynamic and Sediment Transport Processes2897
P. Hoekstra, K.T. Houwman, A. Kroon, B.G. Ruessink, J.A. Roelvink, R. Spanhoff

CHAPTER 225
Justification for Beach Nourishment2911
John G. Housley

CHAPTER 226
Beach Nourishment Versus Shore Protection Structures2918
*Alexander Khabidov, Yuri Bazhenov, Marina Glodenis, Nadya Ivanova, Liya Kaskevitch,
Oleg Rybak, Valery Savkin, Anatoly Trizno, Grigory Zelensky, Veniamin Yedapin*

CHAPTER 227
Comparison of Beach and Shoreface Nourishment Torsminde Tange, Denmark2927
Christian Laustrup, Holger Toxvig Madsen, Per Sorensen, Ida Broker

CHAPTER 228
Mathematical and Physical Modeling of Beach Nourishment Projects2941
W. Eric Rogers, Paul A. Work

CHAPTER 229	
Coastal Zone Dynamics during Artificial Nourishment	2955
<i>Elzbieta Zawadzka</i>	
CHAPTER 230	
Dune Damage Curves and Their Use to Estimate Dune Maintenance Costs	2969
<i>David R. Basco, Cheol S. Shin</i>	
CHAPTER 231	
Hurricane Opal Induced Changes on Natural and Nourished Beaches, West-Central Florida	2982
<i>Richard A. Davis, Jr., Ping Wang</i>	
CHAPTER 232	
Modelling Sand Transport and Profile Evolution on Macrotidal Beaches	2994
<i>Paul R. Fisher, Tim J. O'Hare</i>	
CHAPTER 233	
Beach Evolution Under Random Waves	3006
<i>Patrick Holmes, Thomas E. Baldock, Ray T.C. Chan, M. Ahmad L. Neshaei</i>	
CHAPTER 234	
Beach Profile Surveys Along the U.S. Pacific Coast 1945-1947	3020
<i>Nicholas C. Kraus, Robert L. Wiegel, Willard N. Bascom</i>	
CHAPTER 235	
Mechanism and Calculation of Sand Dune Erosion by Storms	3034
<i>Ryuichiro Nishi, Nicholas C. Kraus</i>	
CHAPTER 236	
Simulation of Coastal Profile Development Using a Boussinesq Wave Model	3048
<i>K.A. Rakha, R. Deigaard, P.A. Madsen, I. Broker, J.K. Ronberg</i>	
CHAPTER 237	
Cross-shore Sediment Transport and Beach Deformation Model	3062
<i>RattanapitikonWinyu , Tomoya Shibayama</i>	
CHAPTER 238	
Experimental Study on Sediment Transport in Surf and Swash Zones Using Large Wave Flume	3076
<i>Takao Shimizu, Masaaki Ikeno</i>	
CHAPTER 239	
The Influence of Long Waves on Macrotidal Beach Morphology	3090
<i>David J. Simmonds, Tim J. O'Hare, David A. Huntley</i>	
CHAPTER 240	
Mathematical Models for Waves and Beach Profiles in Surf and Swash Zones	3104
<i>Akira Watanabe, Mohammad Dibajnia</i>	

CHAPTER 241	
Comparisons of Erosion Models for Storms at Ocean City, Maryland	3115
<i>Jie Zheng, Robert G. Dean</i>	
CHAPTER 242	
Measurements of Wave Generated Bedforms	3129
<i>Christopher D. Jette, Daniel M. Hanes</i>	
CHAPTER 243	
Field Measurement of Bed Roughness for Waves on an Offshore Reef	3143
<i>Raymond C. Nelson</i>	
CHAPTER 244	
Effect of Wave-Induced-Pressure on Seabed Configuration	3155
<i>Tetsuo Sakai, Hitoshi Gotoh</i>	
CHAPTER 245	
The Measurement of Bed Form Shapes in Hydraulic Models	3169
<i>Ian E. Shepherd</i>	
CHAPTER 246	
Asymmetric Boundary Layer Flow above Sand Ripples under Progressive Waves	3183
<i>Takao Toue, Kazuo Nadaoka, Hidehiro Katsui</i>	
CHAPTER 247	
Undertow Profiles in the Bottom Boundary Layer under Breaking Waves	3194
<i>Daniel T. Cox, Nobuhisa Kobayashi</i>	
CHAPTER 248	
A Comparison of Field Observations and Quasi-Steady Linear Shear Instabilities of the Wave Bottom Boundary Layer	3207
<i>D.L. Foster, A.J. Bowen, R.A. Beach, R.A. Holman</i>	
CHAPTER 249	
Wave Boundary Layer Flows and Pore Pressures in Permeable Beds	3219
<i>H.H. Hwung, K.S. Hwang, B.H. Lee</i>	
CHAPTER 250	
Backfilling of Trenches Exposed to Waves	3231
<i>Jacob Hjelmager Jensen, Jorgen Fredsoe</i>	
CHAPTER 251	
A Closed-Form Solution for Turbulent Wave Boundary Layers	3244
<i>Magnus Larson</i>	
CHAPTER 252	
Observed Suspended Sediments in Storm Conditions	3257
<i>J.J. Williams, C.P. Rose, P.D. Thorne, L.E. Coates, J.R. West, P.J. Harcastle, J.D. Humphery, S.P. Moores, D.J. Wilson</i>	

CHAPTER 253	
Ebb Tidal Delta Evolution of Coastal Inlets	3270
<i>Michael R. Dombrowski, Ashish J. Mehta</i>	
CHAPTER 254	
Adjustments toward Equilibrium of a Large Flood -Tidal Delta after a Major Dredging Program, Tauranga Harbour, New Zealand	3284
<i>Terry Healy, Joseph Mathew, Willem de Lange, Kerry Black</i>	
CHAPTER 255	
Laboratory Mobile Bed Model Studies on Ebb Tidal Shoal Evolution	3295
<i>Xu Wang, Lihwa Lin, Hsiang Wang</i>	
CHAPTER 256	
Interaction of the Colorado River Project, Texas, with Longshore Sediment Transport ..	3309
<i>Daniel J. Heilman, Billy L. Edge</i>	
CHAPTER 257	
A Comprehensive Field Study of Tidal Inlet Processes at Ponce de Leon Inlet, Florida ..	3323
<i>Gary L. Howell</i>	
CHAPTER 258	
Transport of Fluid Mud Generated by Waves on Inclined Beds	3337
<i>Thijs van Kessel, C. Kranenburg, J.A. Battjes</i>	
CHAPTER 259	
Wave on Pebble Beach and Deformation of Pebble Beach	3349
<i>Ichiro Deguchi, Masanobu Ono, Toru Sawaragi</i>	
CHAPTER 260	
Wind-Induced Waves and Currents in a Nearshore Zone	3363
<i>Nobuhiro Matsunaga, Misao Hashida, Hiroshi Kawakami</i>	
CHAPTER 261	
Predicting Large-Scale, Cross-Shore Sediment Movement from Orbital Speeds	3378
<i>Edward B. Hands, John P. Ahrens, Donald T. Resio</i>	
CHAPTER 262	
Small-scale Morphology Related to Wave and Current Parameters Over a Barred Beach	3391
<i>A.F. Garcez Faria, E.B. Thornton, T.P. Stanton</i>	
CHAPTER 263	
Prediction of Shoreline Change Considering Cross-Shore Sediment Transport	3405
<i>Yoshimichi Yamamoto, Kiyoshi Horikawa, Katsutoshi Tanimoto</i>	
CHAPTER 264	
The Influence of Rollers on Longshore Currents	3419
<i>Daniel A. Osiecki, William R. Dally</i>	

CHAPTER 265	
Velocity Field Measurements in a “Coastal Buffer Zone”	3431
<i>Hiroshi Yagi, Hirofumi Hinata, Kazuo Nadaoka</i>	
CHAPTER 266	
Development of Underwater Beach Profile by Monochromatic and Random Waves ...	3442
<i>Karsten Peters, Jurgen Newe, Hans-H. Dette</i>	
CHAPTER 267	
Turbulent Stresses in the Surf-Zone: Which Way Is Up?	3453
<i>John W. Haines, Guy Gelfenbaum</i>	
CHAPTER 268	
Asymmetric and Irregular Wave Effects on Bedload: Theory Versus Laboratory and Field Experiments	3467
<i>Leszek M. Kaczmarek, Rafal Ostrowski</i>	
CHAPTER 269	
Kinematics and Shear Stresses from Combined Waves and Longshore Currents in the UK Coastal Research Facility	3481
<i>Richard R. Simons, Ruairi D. MacIver, Wameidh M. Saleh</i>	
CHAPTER 270	
Movable Bed Roughness in the Flow of Irregular Waves and Currents Over Movable Beds	3495
<i>Zai-Jin You, Peter Nielsen</i>	
CHAPTER 271	
Seabed and Foundation Response to Wave Loading	3507
<i>Michael H. Davies</i>	
CHAPTER 272	
Interannual Shoreline Variations at Duck, NC, USA	3521
<i>Nathaniel Plant, Rob Holman</i>	
CHAPTER 273	
Long Term Behaviour of the Sediment Volume inside a Tidal Basin after Poldering ...	3534
<i>Ernst Schroeder, Roland Goldenbogen, Hans Kunz</i>	
CHAPTER 274	
Wave Groups in a Barred Nearshore	3546
<i>B. Boczar-Karakiewicz, W. Romanczyk, J.L. Bona, B. Greenwood</i>	
CHAPTER 275	
Coastal Morphodynamic Instabilities	3560
<i>Albert Falques, Amadeu Montoto, Vicente Iranzo</i>	
CHAPTER 276	
On Validation of a Sand Waves and Sand Banks Model	3574
<i>Suzanne J.M.H. Hulscher</i>	

CHAPTER 277	
Transverse Bars in Duck, North Carolina	3588
<i>Kathryn M. Konicki, Rob A. Holman</i>	
CHAPTER 278	
On the Systematic Offshore Decay of Breaker Bars	3600
<i>Kathelijne M. Wijnberg</i>	
CHAPTER 279	
Longshore Bed-Load Transport	3614
<i>Jesper S. Damgaard, Richard L. Soulsby</i>	
CHAPTER 280	
Design Capacity of a Longshore Current Recirculation System for a Longshore 	
Sediment Transport Laboratory Facility	3628
<i>David G. Hamilton, Julie D. Rosati, Jimmy E. Fowler, Jane M. Smith</i>	
CHAPTER 281	
Influence of Nearshore Hardbottom on Regional Sediment Transport	3642
<i>Paul C.-P. Lin, R. Harvey Sasso</i>	
CHAPTER 282	
Improvement of the Most Accurate Longshore Transport Formula	3652
<i>J.S. Schoonees, A.K. Theron</i>	
CHAPTER 283	
Cross-shore Structure of Longshore Currents during Duck94	3666
<i>Falk Feddersen, R.T. Guza, Steve Elgar, T.H.C. Herbers</i>	
CHAPTER 284	
Three-Dimensional Hydrodynamics on a Barred Beach	3680
<i>Tae-Myoung Oh, Robert G. Dean</i>	
CHAPTER 285	
Rip Current Generation on a Plane Beach	3694
<i>D.A. Suriamihardja, Yoshito Tsuchiya</i>	
CHAPTER 286	
Nearshore Placement of Sand	3708
<i>Scott L. Douglass</i>	
CHAPTER 287	
Influence of Nearshore Berm on Beach Nourishment	3722
<i>Paul A. Work, Emre N. Otay</i>	
CHAPTER 288	
Accuracy of Sand Volumes as a Function of Survey Density	3736
<i>Jennifer L. Irish, W. Jeff Lillycrop, Larry E. Parson</i>	
CHAPTER 289	
Shoreline Analysis Using Digital Photogrammetry	3750

CHAPTER 290	
Application of Satellite Images to the Detection of Coastal Topography	3762
<i>Ji Wu, Jea Tzyy Juang</i>	
CHAPTER 291	
Sediment Transport in Swash Zone under Obliquely Incident Waves	3770
<i>Toshiyuki Asano</i>	
CHAPTER 292	
Sheet Flow Modelled As Pure Convection	3784
<i>Stephen Clark, Peter Nielsen</i>	
CHAPTER 293	
A Transport Rate Formula for Mixed-Size Sands	3791
<i>Mohammad Dibajnia, Akira Watanabe</i>	
CHAPTER 294	
Modelling of 3D Sediment Transport in the Surf Zone	3805
<i>Berry Elfrink, Ida Broker, Rolf Deigaard, Erik Asp Hansen, Peter Justesen</i>	
CHAPTER 295	
A Numerical Model of Sheet Flow Sediment Transport	3818
<i>Sadakazu Katori, Masaru Mizuguchi, Akira Watanabe</i>	
CHAPTER 296	
Numerical Modeling of Nearshore Morphological Changes under a Current-Wave Field	3830
<i>Taerim Kim, Hsiang Wang</i>	
CHAPTER 297	
An Analysis of Particle Saltation Dynamics	3846
<i>Michael R. Krecic, Daniel M. Hanes</i>	
CHAPTER 298	
Sediment Movement and Stress Condition in Sea Bed	3860
<i>Yoshihiko Maeno, Motoyasu Ishikawa, Kozo Bando, Yoshinobu Akiyama, Kouichi Yabe</i>	
CHAPTER 299	
Application of the Depth of Closure Concept	3874
<i>Robert J. Nicholls, William A. Birkemeier, Robert J. Hallermeier</i>	
CHAPTER 300	
Numerical Modeling of Sediment Transport for Various Mode	3888
<i>Masanobu Ono, Ichiro Deguchi, Toru Sawaragi</i>	
CHAPTER 301	
Nearbed Sediment Concentration from Tracer Studies	3901
<i>Zbigniew Pruszek, Ryszard Wierzchnicki, Andrzej Owczarczyk, Ryszard B. Zeidler</i>	

CHAPTER 302	
A Sloping Duct for the Study of Sediment Transport3913
<i>Jesper S. Damgaard, Richard J.S. Whitehouse, Richard L. Soulsby</i>	
CHAPTER 303	
Sediment Dynamics and Profile Interactions: DUCK943921
<i>Donald K. Stauble, Mary A. Cialone</i>	
CHAPTER 304	
A Study on Flow Structure and Suspended Sediment Concentration over Seaweed Bed ..	.3935
<i>Gozo Tsujimoto</i>	
CHAPTER 305	
An Energetics Approach for Suspended Sand Transport on Macrotidal Ridge and Runnel Beaches3948
<i>George Voulgaris, Travis Mason, Michael B. Collins</i>	
CHAPTER 306	
Field Tests of Suspended-Load Transport Theories Used in Numerical Models3962
<i>Thomas E. White</i>	
CHAPTER 307	
Shore Protection Studies for Ras-Elbar Area, Egypt3976
<i>John B. Herbich, Abd-Elfattah Elfiky, Abd-Elmohsen Elmongy; Ali Elbahrawy, Gamal Elsaeed</i>	
CHAPTER 308	
Stabilizing Beaches Downcoast of Harbor Extensions3986
<i>John R.C. Hsu, Richard Silvester</i>	
CHAPTER 309	
Observation of Nearshore Currents and Beach Changes around Headlands Built on the Kashimanada Coast, Japan4000
<i>K. Saito, T. Uda, K. Yokota, S. Ohara, Y. Kawanakajima, K. Uchida</i>	
CHAPTER 310	
Nourished Beach Control Between Balis and Arenys Harbours (Spain)4014
<i>F. Javier Escartin, Alfonso Vidaor, A.M. Castaneda, Nuria Lupon</i>	
CHAPTER 311	
Numerical Simulation of Shoreline Change with Longshore Sand Waves at Groins4024
<i>Hans Hanson, Michelle M. Thevenot, Nicholas C. Kraus</i>	
CHAPTER 312	
Erosive Waves in Shoreline Change Due to the Reduction of a River Delta4038
<i>Yoshito Tsuchiya</i>	
CHAPTER 313	
DELILAH, DUCK94 & SandyDuck: Three Nearshore Field Experiments4052
<i>William A. Birkemeier, Charles E. Long, Kent K. Hathaway</i>	

CHAPTER 314	
Eulerian Mean Velocities under Non-Breaking Waves on Horizontal Bottoms	4066
	<i>Peter Nielsen, Zai-Jin You</i>
CHAPTER 315	
Reynolds Stress and Small-Scale Morphology Measurements during DUCK94	4079
	<i>Timothy P. Stanton, Edward B. Thornton</i>
CHAPTER 316	
Studies on the Suspended Concentration in the Surf Zone	4088
	<i>Ching-Her Hwang, Li-Hung Tsai, Po-Ching Lin, Chin-Chi Tsai</i>
CHAPTER 317	
Suspended Sediment Mixing in the Surf Zone	4098
	<i>Jose A. Jimenez, Francisco J. Rivero, Agustin Sanchez-Arcilla, Vicente Gracia, Andres Rodriguez</i>
CHAPTER 318	
Sand Suspension Events and Intermittence of Turbulence in the Surf Zone	4111
	<i>R.D. Kos'yan, H. Kunz, S.Yu. Kuznetsov, N.V. Pykhov, M.V. Krylenko</i>
CHAPTER 319	
Mechanisms of Beach Ground Water and Swash Interaction	4120
	<i>Andrew J. Baird, Travis E. Mason, Diane P. Horn</i>
CHAPTER 320	
The Equations for Integral and Mean Flow Properties in the Swash Zone	4134
	<i>M. Brocchini, D.H. Peregrine</i>
CHAPTER 321	
Wave Overwash of Subaerial Dunes	4148
	<i>Yukiko Tega, Nobuhisa Kobayashi</i>
CHAPTER 322	
Pressure Gradients Within Sediment Beds	4161
	<i>Thomas E. Baldock, Patrick Holmes</i>
CHAPTER 323	
Analysis of Mud Mass Transport under Waves Using an Empirical Rheological Model . .	4174
	<i>Qin Jiang, Akira Watanabe</i>
CHAPTER 324	
Countermeasures Against Wind-Blown Sand on Beaches	4188
	<i>Shintaro Hotta, Kiyoshi Horikawa</i>
CHAPTER 325	
Sea Breeze Effects on Nearshore Coastal Processes	4200
	<i>Charitha Pattiaratchi, Gerhard Masselink</i>
CHAPTER 326	
Wind Blown Sand at Castroville, California	4214
	<i>Douglas J. Sherman, Bernard O. Bauer, Paul A. Gares, Derek W.T. Jackson</i>

Part V Coastal, Estuarine and Environmental Problems

CHAPTER 327	
Pipeline Protection in the Surf Zone	4228
<i>Gerrit J. Schiereck, Henri L. Fontijn</i>	
CHAPTER 328	
Modeling Tidal Circulation in Florida Bay	4242
<i>Y. Peter Sheng, Justin Davis</i>	
CHAPTER 329	
Recent Developments in Coastal Defence Policy and Guidance in England	4253
<i>Reg Purnell</i>	
CHAPTER 330	
Structural Restoration of Coral Reefs Damaged by Vessel Groundings	4261
<i>Kevin R. Bodge</i>	
CHAPTER 331	
Dredging and Disposal within the Limits of a National Park	4274
<i>H. A. Manzenrieder, J.M. de Vries</i>	
CHAPTER 332	
Storm-Derived Bar/Sill Dynamics in a Dredged Channel	4289
<i>Sean O'Neil, Keith W. Bedford, David P. Podber</i>	
CHAPTER 333	
Bivalve Habitat Based on Sediment-Transport Mechanics	4300
<i>Hitoshi Gotoh, Tetsuo Sakai</i>	
CHAPTER 334	
Hydraulic Controls on Tidal Wetlands	4314
<i>R. Eric Katmarian, Philip A. McKee, Timothy W. Kana</i>	
CHAPTER 335	
Enhanced Mixing Through Perforated Discs on Round Buoyant Jet	4325
<i>Lilun Wu, Jiin-Jen Lee</i>	
CHAPTER 336	
Assessing Coastal Flood Risks	4339
<i>Roger Maddrell, Chris Fleming, Chris Mounsey</i>	
CHAPTER 337	
Experimental Study on the Behavior of Bivalves by Oscillatory Flow	4353
<i>Toshihiko Yamashita, Akira Wada, Gaku Matsuoka, Kenji Yano, Sadamitsu Akeda</i>	
CHAPTER 338	
Wind- and Sea Level-Induced Shore Evolution in Poland	4364
<i>Ryszard B. Zeidler, Marek Skaja, Grzegorz Rozynski, Jarka Kaczmarek</i>	

CHAPTER 339
Ashdod Port's Effect on the Shoreline, Seabed and Sediment4376
Abraham Golik, Dov S. Rosen, Arik Golan, Maxim Shoshany Dan DiCastro, Pinkhas Harari

CHAPTER 340
Tweed River Sand Bypass: Concepts and Progress4390
Russell J. Murray, R.P. (Jock) Brodie, Mark Porter, David A. Robinson

CHAPTER 341
Design Considerations for Coastal Projects in Cold Regions4397
Craig B. Leidersdorf, Peter E. Gadd, Kennon D. Vaudrey

CHAPTER 342
Experimental Study on Deformation and Fracture of Ice Sheet by Propagating Water Wave4411
Shigeki Sakai, Xiaodong Liu, Makoto Sasamoto, Shigeo Kanada and Koh Izumiyama

CHAPTER 343
An Attempt to Determine the Spanish Public Domain Border4418
R. Medina, I.J. Losada, F. Mendez, A.J. Fernandez

CHAPTER 344
Education of Coastal Engineers for the 50th ICCE4431
Henk Jan Verhagen

CHAPTER 345
Risk-Based Analysis of Coastal Projects4440
Edward F. Thompson, Michael Wutkowski, Norman W. Scheffner

CHAPTER 346
Designing for Propeller Action in Harbours4451
G.A. Hamill, J.A. McGarvey

CHAPTER 347
Modeling Inlet Sand Bypassing4464
Christopher G. Creed

CHAPTER 348
An Approach to Modeling Inlet and Beach Evolution4477
Mark B. Gravens

CHAPTER 349
Hydrodynamics of a Bar in a Flood Channel - the Westerschelde Estuary4491
Claire Jeuken

CHAPTER 350
Interactions between a Sand Barrier and Flood Terrace at the Abukuma River Mouth .4505
Akira Mano, Masaki Sawamoto

CHAPTER 351
A Unique Look at Oregon Inlet, NC USA4517

CHAPTER 352	
Impacts of Inlet Structures on Channel Location	4531
<i>William C. Seabergh, Mary A. Cialone, Donald K. Stauble</i>	
CHAPTER 353	
Complete Closure of the Nanakita River Mouth in 1994	4545
<i>Hitoshi Tanaka, Fumihiko Takahashi, Atsushi Takahashi</i>	
CHAPTER 354	
The Erosion of a Salt Wedge Trapped Behind a Barrage Across An Estuary	4557
<i>S.A. Walker, G.A. Hamill, H.T. Johnston</i>	
CHAPTER 355	
Near-Field Measurements of a Buoyant Jet in Waves and Currents	4569
<i>K.H. Kwan, C. Swan</i>	
CHAPTER 356	
Cost Effectiveness of Wave Power Extraction at Erosive Coasts	4583
<i>Hideo Kondo</i>	
CHAPTER 357	
Feasibility Tests of New Pendular-Type Wave Energy Conversion Apparatus	4591
<i>Senji Osanai, Hideo Kondo, Yuzo Mizuno and Tomiji Watabe</i>	
CHAPTER 358	
Watertable Dynamics in Coastal Areas	4601
<i>Hong-Yoon Kang, Peter Nielsen</i>	
CHAPTER 359	
Long Range Positive Effects of the Delray Beach Nourishment Program	4613
<i>Kim E. Beachler, Douglas W. Mann</i>	
CHAPTER 360	
Effectiveness of a Combined Beach and Shoreface Nourishment on the Island of Norderney/East Frisia, Germany	4621
<i>Hanz D. Niemeyer, Ralf Kaiser, Heiko Knaack</i>	

Part VI Case Studies

CHAPTER 361	
Nearshore Berm Performance at Newport Beach, California, USA	4636
<i>Chuck Mesa</i>	
CHAPTER 362	
San Gabriel River to Newport Bay Erosion Control Project, Orange County, California—30 Years of Periodic Beach Replenishment	4650
<i>Arthur T. Shak, Joseph A. Ryan</i>	

CHAPTER 363	
A Ten-Year History of Dolos Monitoring at Crescent City	4664
<i>William S. Appleton, Thomas Kendall, Jeffrey A. Melby</i>	
CHAPTER 364	
Breakwater Damage in Okushiri Port Due to the Hokkaido Nansei-oki Earthquake Tsunami	4676
<i>Katsutoshi Kimura, Yuzo Mizuno, Hiroichi Tsuruya, Yasuyuki Nakagawa</i>	
CHAPTER 365	
Richards Bay North Breakwater - Repair of a Roundhead: Monitoring, Model Testing, Design and Construction	4689
<i>D. Phelp, A. McClarty, A. Bartels</i>	
CHAPTER 366	
Thyboron Coastal Investigations 1995: New Lessons from an Old Coastal Problem ...	4703
<i>I. Broker, J.A. Zyserman, Per Roed Jakobsen</i>	
CHAPTER 367	
Probabilistic Risk Assessment of Beach Erosion at Pevensey Bay in England	4717
<i>Ping Dong, Keith J. Riddell</i>	
CHAPTER 368	
Beach Nourishment in Altafulla, Spain: Verification of Theoretical Models	4730
<i>J. Galofre, F.J. Montoya, R. Medina</i>	
CHAPTER 369	
Alternatives to Beach Stabilization: Cambrils Coast Case Study (Spain)	4744
<i>Nuria Lupon, Alfonso Vidoar, Jordi Galofre, F. Javier Escartin</i>	
CHAPTER 370	
The Effect of Grain Sorting on Profile Stability of Nourished Beaches	4756
<i>Ram K. Mohan, Timothy W. Kana</i>	
CHAPTER 371	
The Use of Data Assimilation to Improve Wave Hindcast Results	4770
<i>Jon M. Hubertz</i>	
CHAPTER 372	
Grain-Size Influence on Sand Transport in Oscillatory Sheet Flow	4779
<i>C. Marjolein Janssen and Jan S. Ribberink</i>	
CHAPTER 373	
Cross-Shore Sediment Transport Mechanisms in the Surfzone on a Timescale of Month to Years	4793
<i>Klaas T. Houwman and Gerben Ruessink</i>	
CHAPTER 374	
Numerical Prediction of Breaking Waves and Currents with a Boussinesq Model	4807
<i>Okey George Nwogu</i>	

CHAPTER 375

The Effect of the CL-Vortex Force in 3D Wave-Current Interaction4821

M. W. Dingemans, J. A. Th. M. van Kester, A. C. Radder and R. E. Uittenbogaard

Subject Index4833

Author Index4847

CHAPTER 199

Wave impact beneath a horizontal surface.

D.J.Wood [†] and D.H.Peregrine [‡]

Abstract

Many coastal structures and natural coasts have openings, overhangs and projections which are open to impact by incident water waves. The sudden impact of a wave on a rigid surface leads to a rapid rise of pressure and consequent violent water motions. We consider the wave impact on the underside of a projecting surface. The example discussed is that of a flat deck close to the mean water level. A pressure-impulse approach is used, which has the advantage that given a solution for one problem it is possible to select pressure-impulse contours which give the solution to related problems. The pressure gradient on the underside of the deck is especially strong near the seaward edge of the impact region, so this is a region where any projections on the structure's surface may be subject to strong shearing forces. On the other hand the maximum pressure-impulse is at the landward end of the impact zone, it is here that the deck is most likely to be 'blown' upward.

Introduction

There are a number of circumstances in which the effect of the upward impact of a wave beneath a rigid horizontal surface needs to be estimated. For offshore oilrigs the lack of good estimates of such upward impacts leads to designs where the main platform of rigs is built to be out of reach of 'green water'. This may not be an option for some coastal structures, including piers and jetties, and temporary works in inter-tidal zones. Here we present pressure-impulse calculations for an impact on a horizontal surface near the surface of water of finite depth. For convenience we refer to the rigid surface as a deck.

In studies of wave impact on a wall Bagnold (1939) was the first to note that although pressure measurements show great variability between nominally identical wave impacts the integral of pressure over the duration of the impact,

[†]Ph.D. student, School of Mathematics, University of Bristol, University Walk, Bristol, BS8 1TW, UK, (*Deb.Wood@bristol.ac.uk*)

[‡]Professor of Applied Mathematics, School of Mathematics, University of Bristol, (*D.H.Peregrine@bristol.ac.uk*)

the pressure-impulse, is a more consistent measure of wave impact. This has been exploited theoretically by Cooker and Peregrine (1990 a,b, 1992, 1995) who show that the pressure-impulse and its distribution is not sensitive to the shape of the impacting water except in a region very close to the structure. Chan (1994) and Losada, Martin, and Medina (1995) show good agreement with experiment for wave impact on a wall.

Mathematical model

The geometrical simplifications we make may be seen in figure 1. The water is taken to be of finite depth $CD = a$, and to impact the horizontal deck BC of length L with an upward velocity V . The free surface outside the deck is taken to be flat, as BA , and to stretch to infinity. However, as indicated below alternative surface shapes are easily found by choosing different contours of pressure-impulse. The boundary conditions on CD given in figure 1 indicate that the problem can be reflected in the vertical plane of CD , corresponding to impact on a horizontal surface of length $2L$ with a central plane of symmetry.

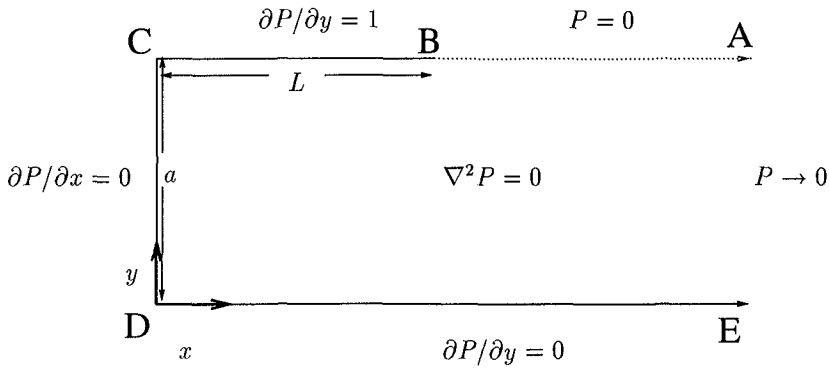


Figure 1: The problem to be solved.

Let the pressure be $p(x, y, t)$, then the pressure-impulse is

$$P(x, y) = \int_{t_b}^{t_a} p(x, y, t) dt \tag{1}$$

where t_a and t_b are the times after and before impact respectively, such that the time interval (t_b, t_a) is short compared with all other time scales in the problem. The main approximation is that during this short time the fluid motion changes so rapidly that the equation of motion may be approximated by

$$\frac{\partial \mathbf{u}}{\partial t} = -\frac{1}{\rho} \nabla p \tag{2}$$

where $\mathbf{u}(x, y, t)$ is the velocity field, and ρ the density which is assumed to be constant and uniform. The neglect of the convective terms $(\mathbf{u} \cdot \nabla) \mathbf{u}$ is consistent except in any small region near the impact where jets may form.

Integration of (2), with respect to time, yields

$$\mathbf{u}_a - \mathbf{u}_b = -\frac{1}{\rho} \nabla P \quad (3)$$

Incompressibility gives $\nabla \cdot \mathbf{u}_a = \nabla \cdot \mathbf{u}_b = 0$. Therefore we find

$$\nabla^2 P = 0 \quad (4)$$

in the region of the water.

The boundary condition at the free surface is that the pressure must be constant and continuous therefore $P = 0$. At the walls and on the bed, the normal velocity must be zero before and after impact, therefore using equation (3), $\partial P / \partial n = 0$, where n is the normal direction. As the water meets the deck BC, the water has vertical velocity V , which could be any function of x , and after impact the water has zero vertical velocity. Therefore, again using equation (3), we have $\partial P / \partial n = V$. For simplicity, we choose V to be constant. We make the problem dimensionless by choosing units for which $V = 1$ and $L = 1$.

Infinite depth solution

The problem of a wave hitting upwards under a deck jutting out from a wall, is mathematically equivalent to a plate dropping onto a body of water and setting the water in motion. Also when considering solving Laplace's equation we can use the direct analogy with the velocity potential of irrotational flow. If we consider the complex potential for a flow past a plate then we just need a change of reference frame to find the complex potential of a moving plate in a stationary fluid. With a complex potential $w = \phi + i\psi$, then $\partial \phi / \partial x = 0$ on $x = 0$, and $\partial \phi / \partial y = 1$ along the plate. These are the conditions that are required by P , and so the lines of constant pressure-impulse are given by lines of constant ϕ . The solution may be found in Lamb (1932, section 71), and in Milne-Thompson (1962, section 6.3), for a fluid flowing past an ellipse. If we allow one of the semi-axes to shrink to zero then we have a plate instead of an ellipse in the flow. Finally choosing the plate to be perpendicular to the flow, the length of the plate to be 2, and the velocity 1, we get an expression for the complex potential of a stream flowing past a plate:

$$w = -\sqrt{1 - z^2} \quad (5)$$

where the origin is taken to be the centre of the plate.

If we subtract the complex potential for a stream from this expression we have the potential for a moving plate. As the velocity of the stream is $(0, -1, 0)$, we must therefore subtract iz to get:

$$w = -iz - \sqrt{1 - z^2} \quad (6)$$

This solution is symmetric about the centre of the plate. This means that we can consider a line drawn perpendicular to the plate from the centre of the plate, to be a wall, bringing us back to the original problem of the water hitting a deck jutting out from a wall. Hence we have an expression for the pressure-impulse:

$$P = \text{Re}(-iz - \sqrt{1 - z^2}) \quad (7)$$

This is the infinite depth solution. Figure 2 shows contours of pressure-impulse. The total impulse on the deck is $\pi/4$, in dimensional terms $\pi \rho V L / 4$.

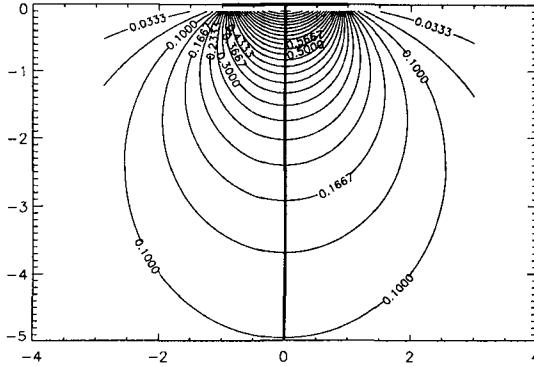


Figure 2: Infinite depth solution. Total impulse on deck (0,1) is $\pi/4$.

Infinitely long deck.

As a becomes small the effect of the free surface on the solution under the plate becomes small. This means it is possible to solve in that region by neglecting the condition at the free surface. Hence we solve Laplace's equation on a strip where $\partial P/\partial y = 1$ along the top, $\partial P/\partial n = 0$, where n is the normal direction, along the left-hand edge and bottom.

The solution is given by:

$$P = \frac{1}{2a} [y^2 - x^2] + K \tag{8}$$

where K is a constant which depends on the behaviour of P near $x = 0$, where this approximation fails. Figure 3 shows the case when $a = 0.1$, and K is set to zero.

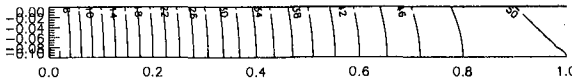


Figure 3: Analytic solution when a is small. ($a = 0.1, K = 0$)

In practice the 'filling flow' solution of Peregrine and Kalliadasis (1995) may be more relevant to this case.

More general solution

Consideration of the boundary conditions in Figure 1, or the solution (7) shows that at B there is a square root singularity. This singularity causes problems for many numerical solution methods. However, one way to eliminate the problem of the singularity is to map the original problem using conformal maps as follows. First map to a half-space, then use another conformal map to perform a shift and stretch so that by using a final conformal map we can bend the problem back to a semi-infinite strip but with the boundary conditions shifted round to a convenient position, i.e. shift the boundary conditions on the deck round to the vertical wall.

Let the original plane in which the problem is posed be the z plane. The first map we need is $w = u + iv = \cosh(\pi z/a)$. This gives the problem shown in figure 4. As we only use conformal maps P continues to satisfy Laplace's equation throughout.

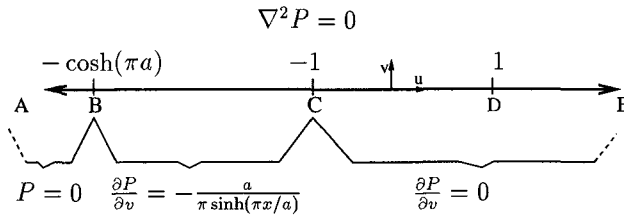


Figure 4: The problem in the w -plane after the first complex map.

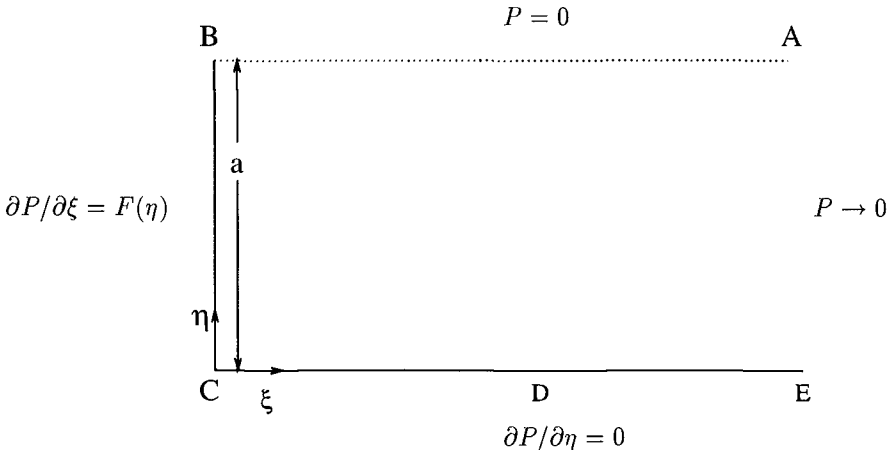


Figure 5. The final problem to be solved in the ζ -plane, where $F(\eta) = -\sin(\pi\eta/a)/(M\sqrt{b^2-1})$ with $b = [\cos(\pi\eta) - N]/M$.

We then use a translation and magnification to shift B to -1 , and C to 1 . The map required is $h = f + ig = Mw + N$ where $M = 2/(\cosh(\pi/a) - 1)$ and $N = M + 1$. The last step is to map this problem back to the strip. The final map required is $\zeta = \xi + i\eta = a \cosh^{-1}(h)/\pi$. This gives the problem as shown in figure 5, in a form with the singularity eliminated by being placed at a corner.

We solve Laplace's equation in this region by separation of variables. Let $P = f(\eta)g(\xi)$, giving $f'' = -\alpha^2 f$ and $g'' = \alpha^2 g$, where α is a constant. Solving for f , using the boundary condition that $f = 0$ at $\eta = a$, and $\partial f/\partial \eta = 0$ at $\eta = 0$, gives $f = A \cos(\alpha_n \eta)$ where $\alpha_n = (n + 1/2)\pi/a$. We now solve for g , using the condition that $P \rightarrow 0$ as $\xi \rightarrow \infty$. This gives $g = Re^{-\alpha_n \xi}$. Hence we have an expression for the pressure-impulse:

$$P = \sum_n A_n e^{-\alpha_n \xi} \cos(\alpha_n \eta) \quad (9)$$

Finally we use the condition that $\partial P/\partial \xi = -\sin(\pi \eta/a)/(M\sqrt{b^2-1})$, where $b = [\cos(\pi \eta) - N]/M$ along $\xi = 0$ to get expressions for the A_n . Using this condition we get:

$$-\sum_n A_n \alpha_n \cos(\alpha_n \eta) = -\frac{\sin(\pi \eta/a)}{M\sqrt{b^2-1}} \quad (10)$$

The final step is to multiply both sides by $\cos(\alpha_m \eta)$, and integrate along the line $\xi = 0$ to get:

$$A_m = \frac{2}{\alpha_m a} \int_0^a \frac{1}{M} \frac{\sin(\pi \eta/a) \cos(\alpha_m \eta)}{\sqrt{b^2-1}} d\eta \quad (11)$$

Similar results can be found for any velocity distribution $V = V(x)$.

Results and discussion

The integral in (11) is evaluated by using a numerical routine. For the cases of $a = 0.5$ and $a = 2.0$ taking thirty terms in the sum, gives an accuracy of 4 and 12 decimal places respectively. The distribution of pressure-impulse in the water beneath the deck is shown for deck width to depth ratios of 0.5, 1.0 and 2.0 in figures 6, 7 and 8 respectively. The values of the total impulse on the deck and on the wall beneath each deck are given in each caption.

In figures 6, 7 and 8 note the differing contour intervals, and the increasing impulse on the deck as the water depth a is decreased. The value of total impulse on the deck is given as a function of a in figure 9. This trend is for the impulse from impact of a given velocity and area to increase as the body of impacting water becomes more confined. The same trend is described by Cooker and Peregrine (1995) for impact on an interior wall of a rectangular box and by Topliss (1994) for impact within a circular cylinder. Consideration of flow in the most confined circumstances, as a becomes small, has given the concept of 'filling flows' (Peregrine and Kalliadasis, 1995). Further, an estimate of how the compressibility of dispersed air bubbles, such as those entrained in waves during breaking, may soften wave impact is given in Peregrine and Thais (1996).

The results are in dimensionless units, for practical use the dimensional pressure-impulse is needed; that is

$$P^*(x^*, y^*) = \rho VLP(Lx, Ly), \quad (12)$$

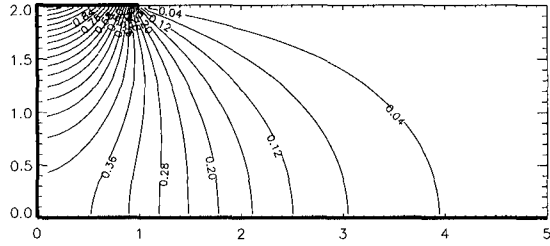


Figure 6: Pressure-impulse contours with $a = 2.0$. Total pressure-impulse on the deck and wall respectively are 0.81 and 1.02

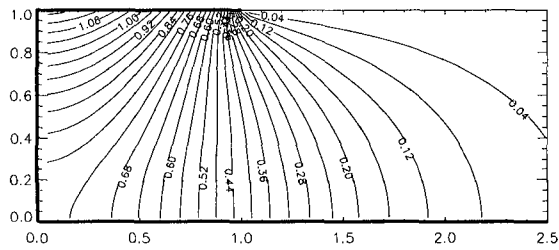


Figure 7: Pressure-impulse contours with $a = 1.0$. Total pressure-impulse on the deck and wall respectively are 0.92 and 0.74.

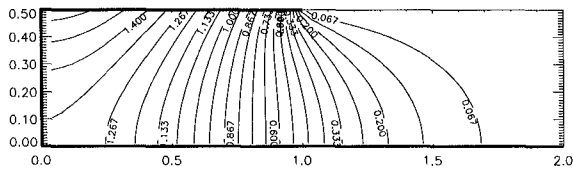


Figure 8: Pressure-impulse contours with $a = 0.5$. Total pressure-impulse on the deck and wall respectively are 1.193 and 0.44.

where * denotes the dimensional quantities. Whilst ρ and L will generally be known, V the vertical velocity of impact will need to be estimated. A simple method of estimating V is to first estimate how high a wave would be in the absence of the deck. Suppose it would have a height ΔH above the deck level. In simple projection of a particle this would require a velocity of $\sqrt{2g\Delta H}$. This is a reasonable, somewhat conservative, estimate for V .

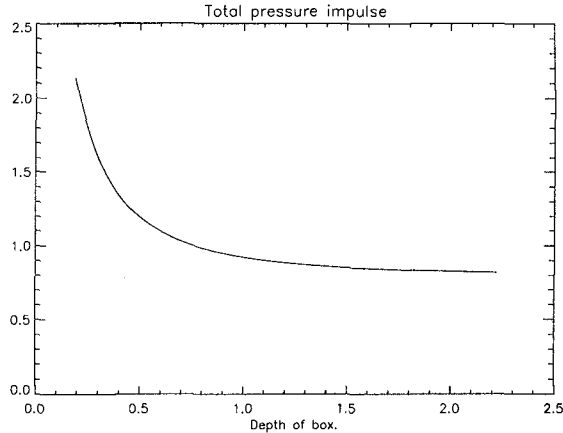


Figure 9: Total impulse on deck against depth a .

Note, the above solutions are not appropriate for impact from jets, e.g. see Cooker and Peregrine (1995), where the semi-infinite rectangular impact on a wall is equivalent to half of a plane jet and section 3.5 gives the solution for a circular jet. However, the solutions can be used for waves which are not nearly level with the deck as the figures indicate. By subtracting the appropriate constant from P , any of the contours of P can be chosen as an alternative free surface. Although such a surface tends downward rather than towards a horizontal level, this is not of great significance as long as the shape within roughly unit distance is appropriate. See Cooker and Peregrine (1995) for some examples.

Clearly the results presented here can be used to estimate the impulse and the spatial distribution of a wave impact. In addition, as illustrated by Cooker and Peregrine (1992) it is possible to estimate the impulse on smaller bodies on and near the wave impact area. The impulse may be derived from the local pressure-impulse gradient. Figure 10 shows the local gradient along the surface of the deck, and figures 11 and 12 show the gradient down the wall and along the bed respectively for a selection of values of a . On the wall and the bed the pressure gradient is tangential since $\partial P/\partial n = 0$. However, on the deck where the impact occurs $\partial P/\partial n \neq 0$ so that there is also a component of impulse perpendicular to the deck and downward.

Consideration of the gradient of pressure-impulse gradient near the edge of the deck shows alarmingly high values because the mathematical solution has a singularity at the edge of the deck. Clearly a better approximation is needed

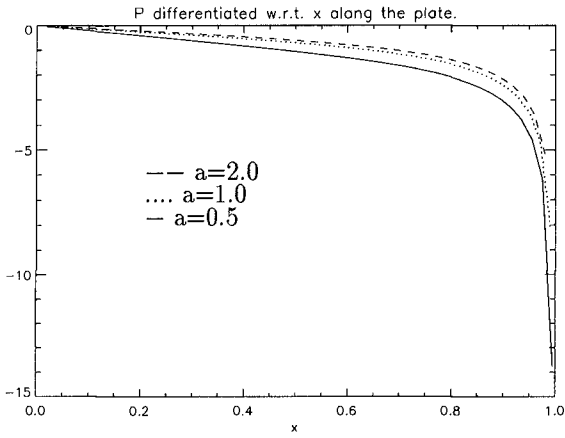


Figure 10: $\frac{\partial P}{\partial x}$ along the deck.

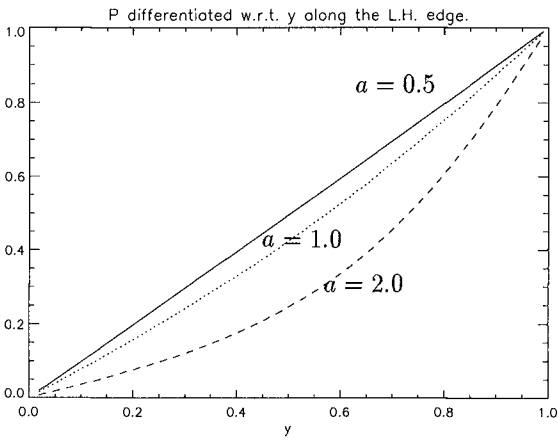


Figure 11: $\frac{\partial P}{\partial y}$ along the left hand wall.

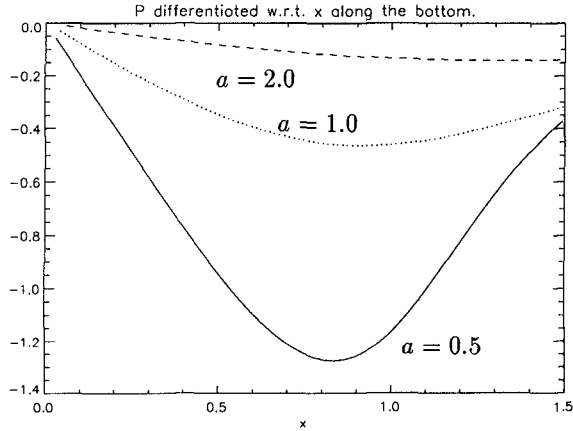


Figure 12: $\frac{\partial P}{\partial x}$ along the bottom.

there. One simple way of obtaining more realistic values is to consider how the solution is obtained for the infinite-depth case, $a = \infty$. There, the solution for the flow past a plate is used. This solution is a limit of flow past an ellipse. Thus a somewhat better solution could be obtained from the flow past a slender ellipse. In any case, it seems reasonable to conclude that attachments beneath a deck are vulnerable to especially large impact forces if they are near the edge of the deck, or the edge of the impact zone.

Three-dimensional effects

All the above work assumes uniformity perpendicular to the (x, y) plane, or some rigid boundaries parallel to that plane. In practice this is unlikely, and three-dimensional effects may be important. That is the impact area on the deck, rather than being a long strip of finite width L , should be taken as a finite area of an appropriate shape. This aspect of the problem is under study. For the present, we just note that for infinite depth solutions, a solution for impact on an elliptic area can readily be found from the potential flow round an ellipsoid.

Conclusions

A readily evaluated solution is presented for the pressure-impulse from waves hitting a deck from below. It is found that the impulse is greater if the water is shallow.

The same results may be useful for estimating the effects of upward impact by liquid confined within a container.

Acknowledgements

Support of the U.K. EPSRC and the European Commission, Directorate XII, Science, Research and Development, contract number MAS3-CT95-0041, is gratefully acknowledged.

References

- BAGNOLD, R.A. (1939). Interim report on wave pressure research. *J. Inst. Civil Engrs* **12**, 201-226.
- CHAN, E.S. (1994). Mechanics of deep water plunging-wave impacts on vertical structures. *Coastal Engng* **22**, 115-133.
- COOKER, M.J. & PEREGRINE, D.H. (1990a). Violent water motion at breaking wave impact. *Proc. 22nd Internat. Conf. Coast. Engng., ASCE* 164-176.
- COOKER, M.J. & PEREGRINE, D.H. (1990b). A model for breaking wave impact pressures. *Proc. 22nd Internat. Conf. Coast. Engng., ASCE* 1473-1486.
- COOKER, M.J. & PEREGRINE, D.H. (1992). Wave impact pressure and its effect upon bodies lying on the sea bed. *Coastal Engng.* **18** 205-229.
- COOKER, M.J. & PEREGRINE, D.H. (1995). Pressure-impulse theory for liquid impact problems. *J. Fluid Mech.* **297** 193-214.
- LAMB, H. (1932). *Hydrodynamics*. 6th Edn. Cambridge University Press.
- LOSADA, M.A., MARTIN, F.L. & MEDINA, R. (1995). Wave kinematics and dynamics in front of reflective structures. *Wave forces on inclined and vertical wall structures*. ASCE editors N. Kobayashi & Z. Demirbilek 282-310
- MILNE-THOMPSON, L.M. (1962). *Theoretical Hydrodynamics*. Macmillan.
- PEREGRINE, D.H. & KALLIADASIS, S. (1996). Filling flows, coastal erosion and cleaning flows. *J. Fluid Mech.* **310** 365-374.
- PEREGRINE, D.H. & THAIS, L. (1996). The effect of entrained air in violent water wave impacts. *J. Fluid Mech.* **325** 377-397.
- TOPLISS, M.E. (1994). Water wave impact on structures. Ph.D. dissertation, University of Bristol.

CHAPTER 200

WAVE IMPULSE PREDICTION FOR CAISSON DESIGN

Michael J.A. Walkden¹, Peter J. Hewson² and Geoffrey N. Bullock³

Abstract

Problems associated with the measurement of wave impact pressures are described and the poor comparison between the results of previous studies is outlined. It is argued that the force impulse form and magnitude are more relevant parameters for caisson design than maximum impact pressures. Data from small and large scale laboratory measurements are used to develop a simplified design approach for caisson breakwaters based on the limited magnitude of the force impulse. Comparison between large scale data and predictions based on small scale results show reasonable agreement.

Introduction

The form of breakwater selected for a particular site depends upon many physical, economic and political factors. Rubble mound constructions are popular in shallow water because they have proved reliable and easy to repair but they are expensive in deep water. Due to the growth of ocean going vessels and the associated need to provide mooring facilities in deeper water there is increasing interest in vertically sided breakwaters. Historically these have had a masonry construction, although in recent decades cellular caissons have provided a preferred alternative. The most common failure mode of caisson breakwaters has been sliding due to the impact of breaking waves (Oumeraci, 1994, Franco, 1994). Such impacts are highly complex events which can not yet be described theoretically. Small scale laboratory wave impacts are therefore a valuable source of information for both designers and those seeking to improve design methods. Due to the sensitivity of breaker shape to wave and physical boundary conditions and the transient and localised nature of impact pressures, results are frequently test specific. If this problem was successfully addressed then confidence in predictions of prototype loading conditions based on such small scale laboratory tests would be greatly enhanced.

¹ Research assistant,

² Principal lecturer,

³ Professor and Head of School, University of Plymouth School of Civil and Structural Engineering, Palace Court, Palace Street, Plymouth, PL1 2DE UK

Scatter of impulse pressures

Even the pressures generated by nominally identical consecutive breakers of a monochromatic wave train are only predictable in a statistical sense. Hayashi and Hattori, (1958) stated that "The initial shock pressure varies so enormously from test to test that it almost seems to have nothing to do with our theoretical considerations". There are many possible reasons for this, some due to random fluctuations in wave form, others due to test conditions and procedures.

Denny (1951) investigated high frequency random fluctuations in the wave form and took measurements of peak pressure from waves of various heights with two different levels of disturbance. This showed that the distribution of peak pressures normalised to wave height was identical for waves of different heights and similar disturbance, but for waves with less disruption, the distribution included much higher relative pressures. This effect may be due to differences in entrapped aeration, variations in the velocity field or some other process. The degree of disturbance and therefore the degree of pressure attenuation will depend on test facilities such as the wave generator and absorption system, and test procedures such as whether a solitary or regular wave train is tested, and how long the water is left to calm between tests.

Variation in pressure records between experiments will be compounded by effects specific to the wave channel and others resulting from the choice of equipment and procedure. The breaker shape depends, for the two dimensional case, mainly on the incident wave conditions, period, height and depth, and the physical boundary conditions mainly foreshore topography and permeability. Any difference in these between tests could be expected to alter impact pressures. The characteristics of the pressure transducers and their position are also significant because peak pressures are generally highly transient and localised. The number of transducers, their size and positions are significant to the spatial resolution, whilst frequency response and sample rate influence temporal resolution.

Impulse repeatability

The wide variation in peak pressure was first addressed by Bagnold who noted that the pressure rise impulse (see Figure 1) was far more repeatable. This observation was used to develop a concept of an 'effective length' of a piston like body of fluid extending horizontally into the wave from the front face. Because it was believed that the generation of the impulse was caused by momentum focusing through the pocket, it was the pocket dynamics and essentially its thickness which determined the impulse duration. Bagnold was unable to prove his model by measuring the air pocket. Also it is now known that an air pocket is not a necessary condition for the occurrence of an impulse load. The work has since been developed by other researchers, including Kirkgoz who measured a similar effective length for flat fronted waves as Bagnold found for air pocket waves, although with wide variation, and Weggel, *et al* (1970) who tried to show, but were unable to establish, that effective length varied with wave steepness.

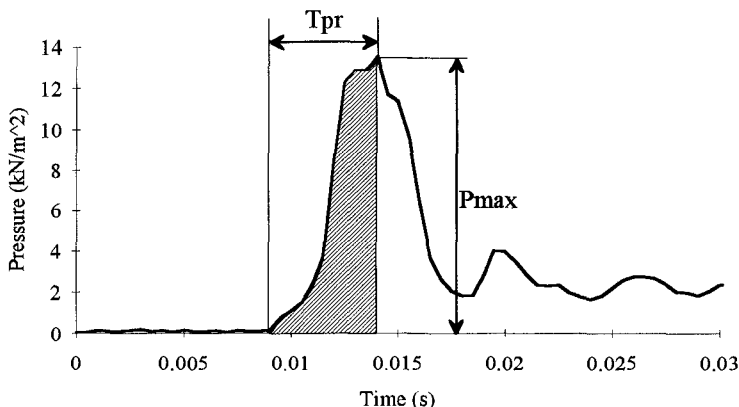


Figure 1. Definition of pressure rise impulse (shaded area)

P_{max} and T_{pr}

The consistency of wave pressure impulse has often been expressed as a relationship between the maximum impact pressure P_{max} , and the time for the pressure to rise to it, T_r of the form;

$$P_{max} = K \cdot T_{pr}^H$$

where K is a constant. Published examples include;

$P_{max} = 232T_{pr}^{-1}$, Weggel *et al*, (1970).

The upper envelope of 12 laboratory 2D measurements with a beach slope 1/20 and a discontinuous wave wall. Regular waves were used to form one breaker type, the heights and periods are not specified although the steepness is given as 70 mm/sec. Six pressure transducers were used which were located 19 mm apart. No information is provided on their characteristics or sample rate or the measures taken to ensure a calm water surface.

$P_{max} = 250T_{pr}^{-0.9}$, Kirkgoz (1990).

The best fit line to 70 laboratory 2D measurements with a beach slope of 1/10 and a continuous wave wall. Regular waves were used in still water depth of 0.61 m with an average height of 0.259 m and a 2 second period, these conditions produced plunging breakers. 10 pressure transducers with a 19 mm active surface diameter at 30 mm centres were sampled at 40 kHz. 1 hour was left between each test to allow the water surface to calm.

$P_{max} = 261T_{pr}^{-0.65}$, Witte.

The upper limit function to approximately 100 laboratory 2D events with a beach slope of 1/6. Regular waves of height 0.25 m and period 2 seconds were generated in a still water depth of 0.61 m (depth at wall 0.16 m). 25 waves were generated per train to prevent re-reflection. Steep, vertical and air pocket breaker types were examined. 14 pressure transducers with a minimum gap of 0.015 m and surface diameter of 3.7 mm were sampled at 62.5 kHz.

$P_{max} = 400T_{pr}^{-0.75}$, Hattori *et al*, (1994).

The upper limit function to a large number of laboratory events including a range of breaker shapes. The beach slope was 1:20 and the water depth at the wall was 50 mm. Regular wave trains were generated with an energy absorbing paddle with heights which varied from 40 to 120 mm and periods of 1.5, 1.7 and 2.0 seconds. Six pressure transducers were sampled at 5 kHz and located at 10 mm centres around still water level.

$P_{max} = 485T_{pr}^{-1}$, Weggel *et al*, (1970).

The test conditions were as described above, except the wave steepness was 17.9 mm/sec.

$P_{max} = 3100T_{pr}^{-1}$, Blackmore and Hewson (1984).

The upper limit function to approximately 80 full scale marine wave impacts on a sea wall. The wave heights ranged from 0.8 to 1.3 m with periods of from 2.67 to 8.5 seconds. The waves had mostly broken at impact. Seven 25 mm diameter pressure transducers were positioned at around 1 m intervals.

These functions appear because, as Bagnold noted, the pressure impulse is limited, if P_{max} is large, then T_{pr} tends to be small and *vice versa*. There are too many variables between each test to determine the effect of each on K and H although there seems to be some relationship between K and the size of the wave. For example the constant of 3100 calculated from the prototype sea wave impacts of Blackmore and Hewson is significantly higher than those derived from the laboratory data. The fact that this relationship between P_{max} and T_{pr} has been different in each case is probably due, at least in part, to the difficulties of recording consistent impact pressures between tests.

This pressure impulse appears to be a more consistent feature of impact loading than the pressure maxima, it may therefore be a more reliable basis for design if the structure response to the impulse is properly understood.

Structural Dynamics.

Structural response to loading is fundamentally important to design. Goda used a dynamic model to develop his method for breakwater design (Goda, 1974 and 1994) which has since become the standard in many countries. Oumeraci and Kortenhaus (1994) created a similar model which was calibrated with near prototype measurements recorded in the Grosser Wellen Kanal (GWK), see below. This was used to show how the structure responded to different force time histories. It was demonstrated that, for impacts without significant air pocket generated force oscillations, the dynamic response could be accurately predicted by simplifying the force time history to a triangular impulse described by the maximum force, F_{max} , the impulse duration, T_d and the rise time T_r . The results were presented in the form of dynamic amplification factors, ratios of force maxima to the equivalent static load which would have caused the same displacement (F_{stat}). The dynamic amplification factors depend upon the ratios of T_d and T_r to the natural period (T_n) of the structure

in question. In this way structural dynamic response can be accounted for and the problem for the designer is reduced to ensuring integrity under a known static load.

There are a series of problems to be overcome before adopting this approach. The form and magnitude of the force impulse has to be determined from the incident wave conditions and the physical boundary conditions. At present this can only be achieved through physical model tests. The natural variation in the magnitude and form of the impulses measured during such tests must therefore be accounted for and a reliable and appropriate method of scaling must be determined.

Scale effects

A comparison of similar wave impacts at significantly different scales have been conducted by Sakakiyama (1994) for the case of a submerged breakwater in front of a vertical wall, and by Fuhrboter (1986) for sloping revetments. To the authors knowledge no such data has been published for the case of a vertical wall experiencing direct wave breaking. The case for the existence of scale effects appears to be that field measurements provide relatively smaller peak impact pressures than have been measured in the laboratory and scaled with the Froude law. Aeration is often suggested as a probable cause although it seems probable that the above mentioned difficulties associated with measuring consistent impact pressures are at least partly responsible.

Aeration

Entrained aeration has a strong effect on the compressibility characteristics of water. It affects the rate of momentum exchange between the wave and wall (Blackmore and Hewson, 1984) and reduces the speed of sound in the fluid, altering the propagation of pressure waves (Topliss, 1994, Griffiths, 1994). It depends strongly on the chemistry and biology of the water. Bubbles of air in fresh water tend to be formed larger than in sea water due to increased surface tension, they also coalesce more readily and burst more easily at the surface. No direct measurements have yet been made of breaker aeration so its effects can only be assumed, however it has been shown that artificial aeration can reduce impact pressures (Crawford *et al*, 1994, Walkden *et al*, 1995).

If entrained aeration does affect impact pressures this does not necessarily mean that the impulse magnitude is affected. The force impulse represents the momentum of a proportion of the wave. Although aeration reduces water density, the wave mass remains essentially the same due to bulking. Also the wave kinematic pattern is probably not strongly effected, there is therefore reason to believe that the wave impulse might be reasonably independent of entrained aeration and so possibly free of associated scale effects.

Physical experiments

Measurements of wave impact forces were conducted at both small and near prototype scale in order to develop a way of accounting for wave impulse loading, for

impacts without significant air pocket oscillations. The following subjects were investigated;

The magnitude and form of the force impulse,

Linearisation of the impulse,

The significance of K and H,

Scale effects,

Transformation from dynamic loads to equivalent static loads.

University of Plymouth (UoP) small scale wave impact tests

Experiments were conducted in a 20 m long, 1.2 m deep and 0.9 m wide flume fitted with an energy absorbing wedge type wave paddle (Bullock and Murton, 1989).

Waves shoaled over a 1:4.5 sloping impermeable foreshore and broke onto a vertical wall made of 25 mm acrylic sheet. Five sealed gauge Kulite type 219 pressure transducers with an active surface diameter of 18 mm were used to record the pressures at the wall at 2 kHz. Three of these had a pressure range of from 0 to 100 kN/m², the others were designed for pressures of up to 400 kN/m². The transducer centres were 40, 55, 70, 90 and 110 mm above the toe of the wall, although during experiments the transducer at 90 mm was damaged. Data was recorded on a P.C. by means of a Microlink logger. Video records were made of each test.

GWK large scale wave impact tests

Experiments were conducted in Europe's largest wave flume, the GWK. The physical boundary conditions were not geometrically similar to those of the UoP flume but it was felt that adequately similar breaker geometry would be attainable. The GWK is a large concrete 'U' channel, with its base at ground level, internally it is 324 m long, 5 m wide and 7 m deep. Waves broke onto a sand filled concrete caisson mounted on a rubble foundation over a shallow sloping sand bed. Instrumentation was mounted on and built into a spar which was then attached to the caisson face. Four Kulite type 219 pressure transducers were installed which had a pressure range of 0 to 400 kN/m² (see above). They were positioned at 200 mm increments, 0.72 to 1.32 m from the top of the rubble mound. An additional pressure record was made with one of the transducers belonging to the Franzius Institut which was already built into the caisson and located 0.54 m above the rubble mound. Cabling was contained within the spar to protect it from the impacting waves. Pressures were recorded at 2 kHz. Video records of each test from two static and one mobile camera provided information on the breaker forms. Thirty eight tests were conducted in total in water depths ranging from 3.1 m to 3.3 m, including regular and pseudo random wave trains and solitary waves. Wave heights ranged from 0.5 to 1.1 m with periods from 3.5 to 5.5 seconds.

Results

Due to space limitations only the results from two tests will be shown, one conducted in the UoP flume, and one carried out in the GWK. In the former case 350 waves of height (H) 0.11 m, period 1.25 s and 79 mm water depth at the wall, broke with a near vertical, slightly overhanging wave front.

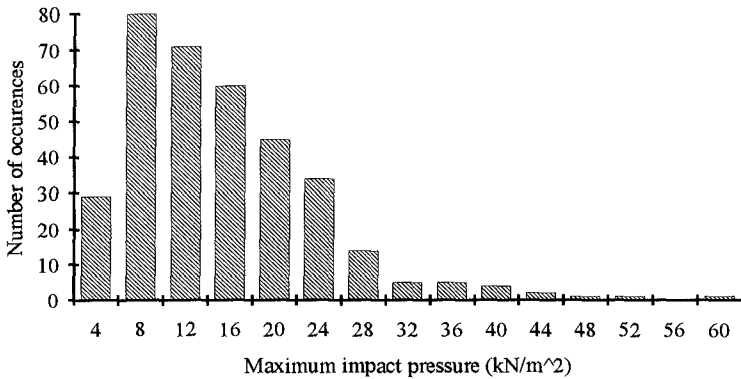


Figure 2. Maximum impact pressures from one transducer (UoP Data)

The data shown in Figure 2 illustrates the typically large spread in P_{max} . The mean value is 13.4 kN/m^2 , with a range from 2.3 kN/m^2 to 58.6 kN/m^2 . If this test had been conducted in order to model a design wave impact it might be concluded that the design event may produce a pressure maxima of anything from $2.13 \rho g H$ to $54.3 \rho g H$. It is not clear how such results should be interpreted.

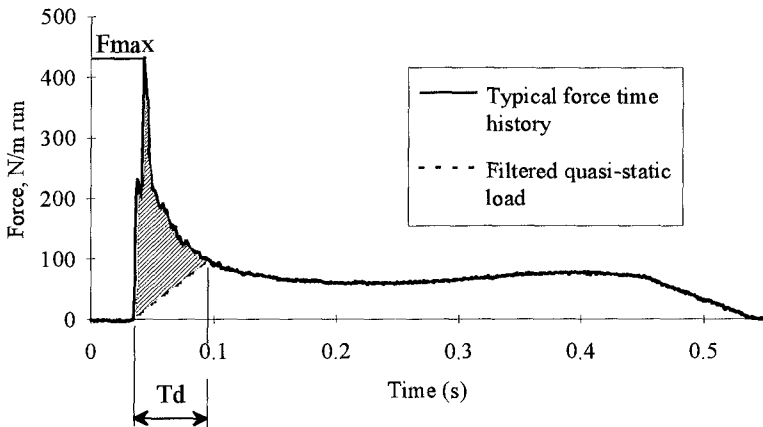


Figure 3. Typical force time history, the shaded area represents the impulse (UoP data)

In order to obtain the impulses, the force time histories were first calculated by spacewise integration of the pressures. The impulse is a dynamic load involving rapid variations in force, therefore a simple low pass filter was used to remove the quasi

static force component, see Figure 3. The distribution of the impulse was found to be compact, Figure 4 shows the results from the UoP test, normalised to the total momentum exchange caused by the wave at the wall. This implies that accounting for the impulse magnitude, with for instance a statistical confidence limit, may be fairly straightforward.

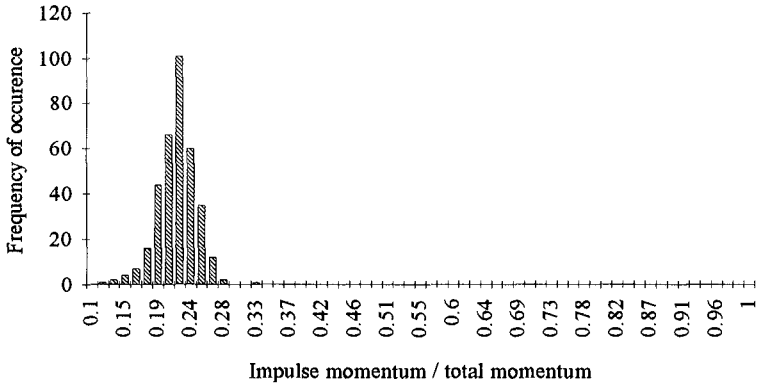


Figure 4. Frequency distribution of force impulse normalised to total momentum (Impulse momentum fraction, UoP data)

Partly because of this consistency, if the data is represented in the $F_{max} T_d$ domain it clusters around a similar function to those found in the $P_{max} T_{pr}$ domain, as shown in Figure 5.

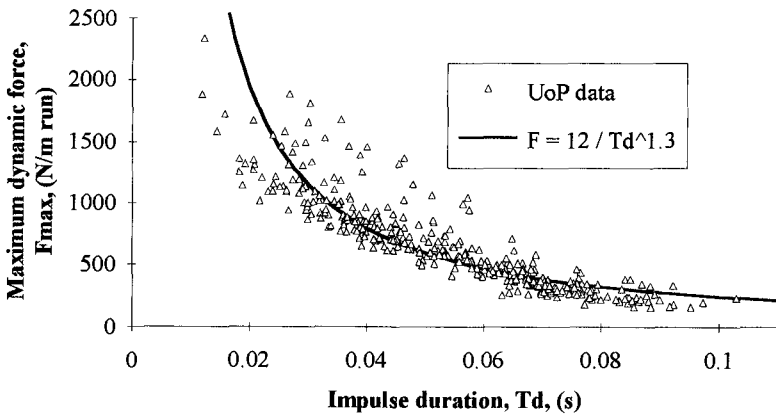


Figure 5. Relationship between maximum dynamic force and impulse duration

The values of F_{max} and T_d in Figure 5 are not suitable to be used to predict the structure response following the method described by Oumeraci and Kortenhuis. This is because the impulse is linearised to a triangle with base T_d and height F_{max} . Some of the data shows both a high peak force and a long duration which if used as a basis for linearisation results in an unrealistically high impulse magnitude and an over-prediction of structure response. This is because the form of the impulse tends to be concave as the force drops, as can be seen in Figure 3. In order to realistically predict structure response the magnitude of the impulse must be correct.

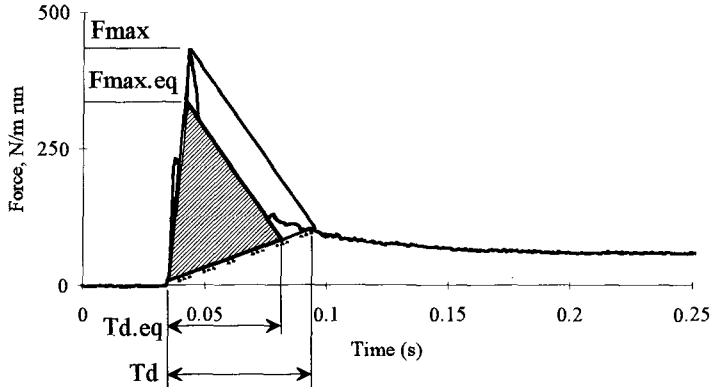


Figure 6. Method of processing the linearised force impulse

It was therefore decided to process the values of F_{max} and T_d to parameterise both the magnitude and the form of the impulse. Figure 6 demonstrates the method which was used. $T_{d.eq}$ and $F_{max.eq}$ are equivalent values which were calculated so that the area of the triangle they described is equal to the impulse magnitude, and the triangle they form is similar to the original linearised impulse. An alternative more ideal approach might account for the relationship between removed impulse frequencies and the natural frequency of the structure. The data in Figure 7 has been processed in this way.

The power of $T_{d.eq}$ in the best line fit in Figure 7 (shown with the dashed line) found through least squares regression, is 0.92. It can be seen that $T_{d.eq}^{-1}$ also provides a good fit. If the latter value is used then the constant assumes the value 16.3 and has units of Ns/m run or impulse per metre and is twice the average impulse magnitude. This data can now be used to account for dynamic response in the way Oumeraci and Kortenhuis suggest because both the impulse magnitude and its form are parameterised by $F_{max.eq}$ and $T_{d.eq}$.

Comparison with large scale test results

Similarity of physical boundary conditions between the large and small scale experiments was not possible. The small scale foreshore was impermeable and had a

regular slope, whereas the large scale foreshore was permeable and included a berm. If the incident wave conditions were geometrically similar then the breaker shapes would not be and no comparison between the results would be meaningful. It was therefore decided to base a scale comparison on the breaker shape and the wave momentum. The video records were used to match similar breaker shapes at small and large scale, then the wave momenta were used to obtain the scale ratio. The average momentum measured for the UoP waves was 39.2 Ns/m run and for the GWK data, 4545 Ns/m run, which provides a length scale of 6.7.

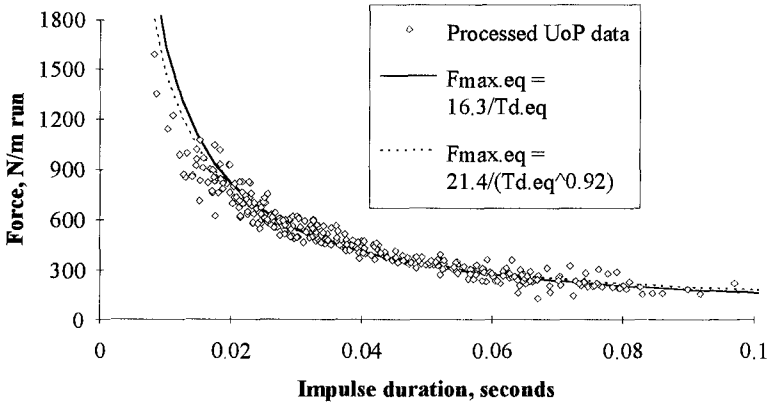


Figure 7. Impulse momentum and shape parameterised by F_{eq} and T_{eq}

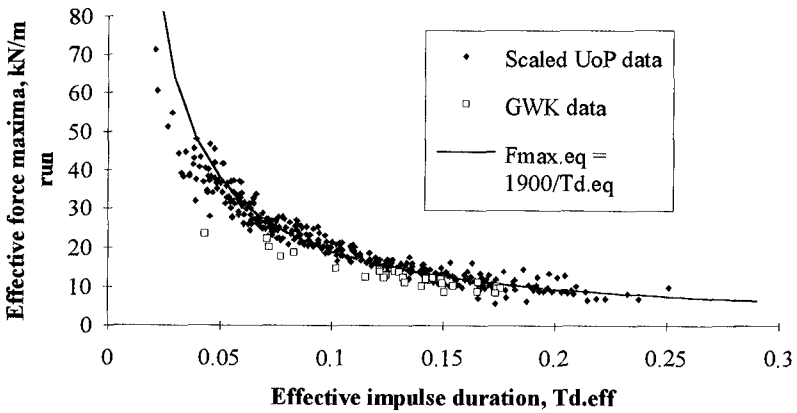


Figure 8. Comparison between scaled UoP data and GWK data

The values of $F_{max.eq}$ and $T_{d.eq}$ measured in the UoP flume were scaled according to Froude and compared to values obtained from the GWK test in Figure 8. The match is not perfect but when the lack of boundary condition similarity is considered the results might be considered close.

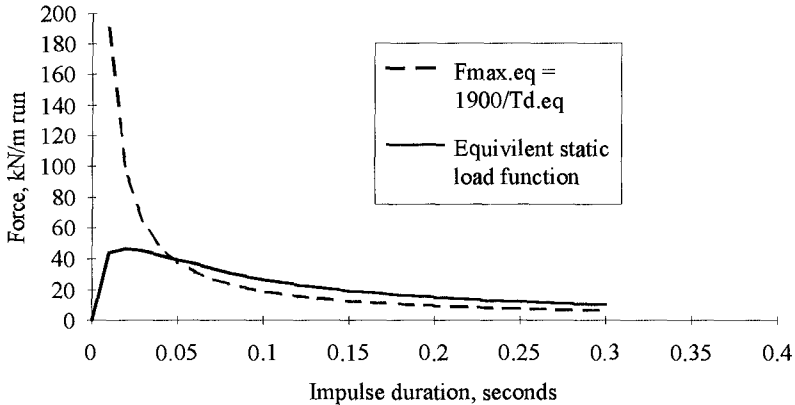


Figure 9. Equivalent static load function calculated from the dynamic amplification factors of Oumeraci and Kortenhaus, 1994. It is assumed that $T_n = 0.1$ and $T_r = 0$

In Figure 9 the dynamic force function $F_{max.eq} = 1900/T_{d.eq}$ has been multiplied by a dynamic amplification function to obtain the equivalent static load function. The maxima of this (in this case 45 kN/m run) might be considered the largest equivalent static force the impulse can generate and therefore the design load for this breaker.

Conclusions and discussion

- (I) Maximum impact pressures are highly variable and difficult to compare between tests. This is due to differences in test procedure and conditions as well as natural random scatter.
- (II) The magnitude of the force impulse is more consistent and more relevant to structural stability than a transient and localised pressure maxima.
- (III) The form of the force impulse is highly variable, this may be due to aeration effects, variations in breaker kinematics or some other unknown effect.
- (IV) Clustering occurs in the $F_{max} T_d$ domain due to points (II) and (III). This can be described with the dynamic force function $F_{max} = K \cdot T_d^H$, where K is a constant.
- (V) If the impulse is linearised to parameterise its magnitude and form by $F_{max.eq}$ and $T_{d.eq}$ then K is twice the mean impulse area, and H assumes the value -1.
- (VI) Scale effects can be reduced if experiments are conducted in large flumes however unless sea water is employed, similarity in aeration characteristics and therefore compressibility can not be assumed.

(VII) It was not possible to properly assess scale effects on the impulse because of a lack of geometric similarity, however a reasonably close comparison between large scale results and predictions based on small scale tests was obtained suggesting that scale effects on the impulse may be minimal.

(VIII) If T_r is assumed to be zero, and the structure natural frequency is known, then the maxima of the product of the dynamic force function and a dynamic amplification function might be considered the maximum static load for design purposes.

The analysis and interpretation presented is highly simplified and is intended to illustrate the basis of an approach. Areas of necessary further development include;

(I) Allowing non zero rise times.

The rise time can be measured fairly simply and used to select a more appropriate, dynamic amplification function. The ratio T_r/T_d may be affected by scale.

(II) Accounting for significant air induced force oscillations.

The entrapment of a long and large oscillating air pocket is recognised as resulting in a significant and dangerous loading condition. It is probably a relatively rare event because it requires a normal direction of approach and a relatively clean wave form. A similar danger may arise due to group dynamics of bubble clouds.

(II) The mean dynamic force function was used to predict equivalent static loads. For design purposes the loading should be calculated on the basis of the worst case with a chosen probability of occurrence within the design life. If the model test conditions have been chosen to represent events with a known return period then the smooth distribution of measured impulses should allow a confident estimate of a realistic design impulse magnitude.

(III) The method of impulse definition.

The use of a low pass filter to define the impulse seems to work well. The cut off frequency should be decided upon with a consideration of the way the structure will respond to that frequency. Similarly the process of obtaining $T_d.eq$ and $F_{max.eq}$ could be developed with more consideration of the structure dynamics.

(IV) Directionality.

The waves angle of approach has not been dealt with although its inclusion may be relatively straightforward. This method is based on momentum transfer at the plane of the caisson face which might be expected to vary relatively simply with angle of approach.

(V) Accounting for the structure response.

The conversion of dynamic loads to equivalent static loads has been based on the dynamic amplification factors published by Oumeraci and Kortenhaus (1994). These were derived by reducing the description of the caisson motion to a simplified single degree of freedom model. This was intended to "constitute a useful guide for judgement in developing design load specifications". There are many limitations which have been discussed in their paper regarding their model and modelling of structural dynamics in general. In the light of their comments it would be preferable, though more complex, to use a numerical model rather than a dynamic amplification function to account for structure response.

(VI) Assessment of the effect of breaker shape on the impulse momentum fraction. This varies with breaker type so it will reach a measurable maxima at some breaking condition. This might be multiplied by the design wave momentum in order to calculate a worst case impulse momentum. From this the constant K is obtained, and so the dynamic load function is known. The effect of variations in the incident wave and physical boundary conditions on the impulse momentum fraction should be easier to assess than for impact pressure maxima because of its more compact distribution. It is also far less sensitive to the characteristics of measurement equipment and test procedures. For these reasons scale effects may be also be easier to assess.

The main advantage of this approach is that it provides a means of interpreting the results of physical model tests in a way which is meaningful for structural design. This means that nature can be left to resolve the complexities of the breaker shape, a problem which can not yet be fully solved through numerical modelling.

Future work

Measurements of entrained and entrapped air are in progress at the University of Plymouth in order to examine their effect on the impulse form and magnitude and wave impact pressures. This work is being conducted both in the laboratory and in the field (Crawford, *et al* 1994, Walkden, *et al*, 1995 and Bird *et al*, 1997). It is hoped that the results will help explain the distribution of data along the dynamic load function, provide insights into the relationship between entrapped air and the force impulse and provide data with which to test possible scale effects.

Acknowledgements

The work described in this paper was in part carried out under contract MAS2-CT92-0047 of the European Union's Marine Science and Technology Programme. This, together with co-operation and facilities made available by the Franzius Institut, Universitat Hannover and the Technischen Universitat Braunschweig are gratefully acknowledged.

References

- Bagnold, R.A., (1939), "Interim report on wave pressure research". J. Instn. Civ. Engrs, Vol. 12, p. 201.
- Bird, P.A.D., Crawford, A.R., Hewson, P.J., and Bullock, G.N. (1997), "Measurement of wave impact pressures and sea water aeration". Paper in print for Coastal Engineering.
- Blackmore, P.A. and Hewson, P.J., (1984), "Experiments on full-scale wave impact pressures". Coastal Engineering, 8, pp 331-346.
- Bullock, G.N. and Murton, G.J., (1989), "Performance of a wedge type absorbing wave maker". Journal of Waterway, Port, Coastal and Ocean Engineering, Vol.115, No.1, pp.1-20.
- Crawford, A.R., Walkden, M.J., Bird, P.A.D., Bullock, G.N., Hewson, P.J. and Griffiths, J., (1994), "Wave impacts on sea walls and breakwaters". Proc.

- Coastal Dynamics, pp 656-670.
- Denny, D.F., (1951), "Further experiments on wave pressure". J. of the Institution of Civil Engineers, Vol. 35.
- Fuhrboter, A., (1986), "Model and prototype tests for wave impact and run-up on a uniform 1:4 slope". Coastal Engineering, 10, pp 49-84.
- Franco, L., (1994), "Vertical breakwaters: the Italian experience". Coastal Engineering 22, pp 31 - 55.
- Goda, Y. (1974), "New wave pressure formulae for composite breakwaters". Proc. 14th int. conf. Coastal Engineering, pp 1702 - 1720.
- Goda, Y., (1994), "Dynamic response of upright breakwaters to impulsive breaking wave forces", Coastal Engineering 22, pp 135-158.
- Griffiths, J., (1994), "The effects of aeration on wave impacts". Ph.D. Thesis, University of Plymouth. U.K.
- Hattori, M., Arami, A., and Yui, T., (1994), "Wave impact pressure on vertical walls under breaking waves of various types". Coastal Engineering, 22, pp 79-114.
- Hayashi, T., and Hattori, M., (1958), "Pressure of the breaker against a vertical wall". Coastal Engineering in Japan, pp 25 - 37.
- Kirkgoz, M.S., (1990), "An experimental investigation of a vertical wall response to a breaking wave impact". Ocean Engineering, 17(4): 379-391
- Oumeraci, H., (1994), "Review and analysis of vertical breakwater failures - lessons learned". Coastal Engineering 22, pp 3 - 29.
- Oumeraci, H. and Kortenhaus, A., 1994, "Analysis of the dynamic response of caisson breakwaters" Coastal Engineering 22, pp 159-183.
- Sakakiyama, T. and Ogasawara, M., (1994), "Scale effect on impulsive wave forces and reduction by submerged breakwater". Coastal Dynamics, pp 628 - 642
- Topliss, M.E., (1994), "Water wave impact on structures". Ph.D. thesis, University of Bristol, U.K.
- Walkden, M.J.A., Crawford, A.R., Hewson, P.J., Bullock, G.N., and Bird, P.A.D., (1995), "Wave Impact Loading on Vertical Structures", Proc. Coastal Structures and Breakwaters '95, London.
- Weggel, J.R., Hall, W. and Maxwell, C. (1970), "Numerical model for wave pressure distributions". ASCE. J. of waterways, harbours, and coastal engineering division, Vol. 96, No. WW3, pp 623 - 642.
- Witte, H.H., "Wave impact loading on a vertical wall with respect to structure response". Report for the Federal Waterways and Research Institute - Coastal Department - Coastal Department. 30 p.

CHAPTER 201

WAVE OVERTOPPING RATE AND REFLECTION COEFFICIENT FOR OBLIQUELY INCIDENT WAVES

Yoichi MORIYA¹ and Masaru MIZUGUCHI²

Abstract

Recently, wave overtopping over a vertical wall for normal incidence were treated analytically on the basis of the wave energy flux concept (Mizuguchi, 1993). In this study, the Mizuguchi's model for normal incidence is extended to oblique incidence. Incident wave angle effect on the wave overtopping rate is investigated. Validity of the extended model is checked experimentally. Satisfactory agreement between the extended model and the experimental results was found for the wave overtopping rate.

1. Introduction

Wave overtopping for oblique incidence has been studied experimentally in several papers. The influence of the incident wave angle on wave overtopping tests over a vertical wall was studied by using regular waves by Inoue and Tuchiya (1971) or using irregular waves by Takayama et al. (1984). Recently, several model tests have been performed, for example, de Waal and van der Meer (1992) ; Juhl and Sloth (1994), and so on. However, the quantitative estimation of wave overtopping rate does not agree among the previous studies. The disagreement partly comes from the varying wave height in front of the wall.

Recently, for normal incidence, a set of simple equation to estimate the wave overtopping rate over a vertical wall and the reflection coefficient were derived

¹Research Engineer; Penta-Ocean Construction Co., Ltd., Institute of Technology, Yonkucyo 1534-1, Nishinasuno-machi, Nasugun, Tochigi-Prefe., 329-27, JAPAN

²Professor; Dept. Civil Eng., Chuo Univ., Kasuga 1-13-27, Bunkyo-ku, Tokyo, 112, JAPAN

(Mizuguchi, 1993). The model, which does not include any experimental constants, is based on the energy flux concept with an assumption of partially standing waves. The validity of the model was confirmed by experiment (Yokoyama and Mizuguchi, 1993).

The purpose of this study is to investigate the influence of the incident wave angle on wave overtopping rate and reflection coefficient, by extending the model for normal incidence to oblique incidence. Validity of the extended model is checked experimentally.

2. Theoretical Approach

Wave field in front of vertical wall for oblique incidence

Figure 1 shows the coordinate system. When oblique waves incident a vertical wall, wave field in front of the vertical wall fully apart from the wall end is free from scattering waves forms bi-directional wave field. We supposed that wave field is uniform along the wall.

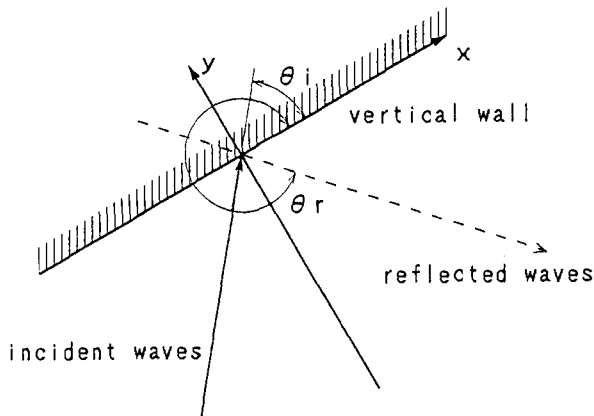


Figure 1 Coordinate system.

A finite amplitude wave theory is needed in evaluating the overtopping rate for waves with large height, especially in estimating the threshold wave height for overtopping. Since coastal structure are normally built in shallow water areas, the wave theory to be employed is the linear superposition of the first order cnoidal waves. The interaction between the incident waves and the reflected waves may be negligible as the interaction time is short. Surface elevation η in front of the vertical wall may be given by following formula:

$$\eta = \eta_i + \eta_r \quad (1)$$

$$= \frac{H_i}{2} [cn^2(\varphi_i; \kappa) - \overline{cn}] + \frac{H_r}{2} [cn^2(\varphi_r; \kappa) - \overline{cn}] \quad (2)$$

in which φ is the phase:

$$\varphi_j = \frac{K(\kappa)}{\pi} \{kx \cos \theta_j + ky \sin \theta_j - \sigma t\} \quad j=i, r \quad (3)$$

where, H is the wave height, k is the wave number, σ is the angular frequency, θ is the wave angle, $K(\kappa)$ is the complete elliptic integral of the first kind of modulus κ . The symbols cn denotes Jacobian elliptic function with modulus κ , and an overbar represents the average value over one period. The subscript i and r denote the quantity of the incident waves and the reflected waves, respectively.

Horizontal velocities of x and y direction, u and v , in front of the wall may be given by following formula:

$$u = \sqrt{\frac{g}{h}} (\eta_i \cos \theta_i + \eta_r \cos \theta_r) \quad (4)$$

$$v = \sqrt{\frac{g}{h}} (\eta_i \sin \theta_i + \eta_r \sin \theta_r) \quad (5)$$

where, g is the gravitational acceleration and h is the water depth.

Wave overtopping

Figure 2 shows schematic illustration of the wave overtopping over a vertical wall. For normal incidence, wave overtopping discharge is evaluated using an ideal fluid flow model over a sharp-edge weir by Kikkawa et al. (1967). When oblique waves are incident on a vertical wall, surface rise of the wave crest progresses along the wall. Wave overtopping for oblique incidence is supposed to be a kind of overflow of the surface rises over the wall. Then wave overtopping discharge, q_e , for oblique incidence averaged over one wave period may be given by following formula:

$$q_e = \frac{2\sqrt{2g}}{3T} \int_{\eta_t > H_c} \left\{ \left(\frac{v_w^2}{2g} + \eta_e - H_c \right)^{\frac{3}{2}} - \left(\frac{v_w^2}{2g} \right)^{\frac{3}{2}} \right\} dt \quad (6)$$

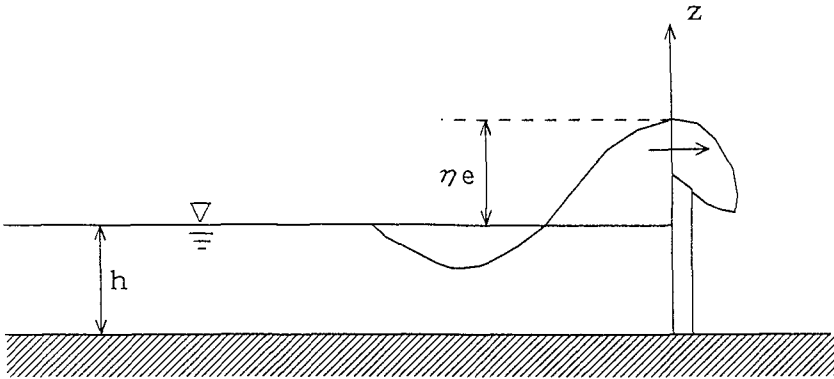


Figure 2 Schematic illustration of wave overtopping over a vertical wall.

where, T is the wave period, H_c is the crown height of the vertical wall above the still water level, η_e is the overtopping waves at the wall (η at $y = 0$) and v_w is the approaching velocity perpendicular to the wall.

Energy flux conservation

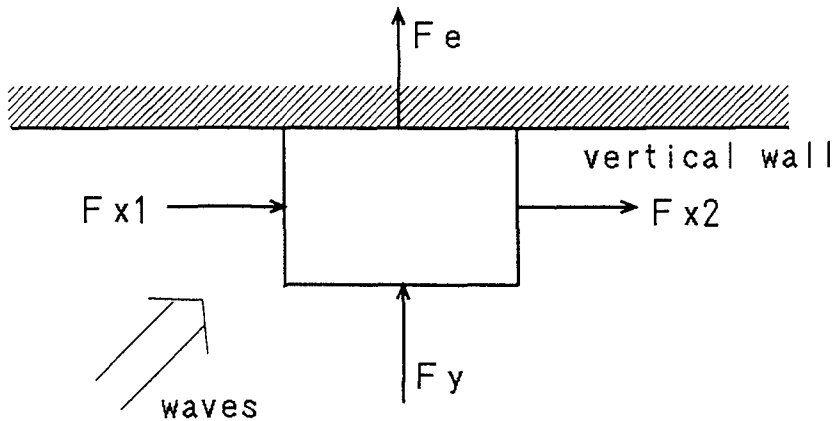


Figure 3 Schematic illustration of the energy flux conservation.

We consider the balance of the energy flux among the incident waves, the reflected waves and the wave overtopping flow. Figure 3 shows schematic illustration of wave energy

flux conservation. Here, F_x and F_y are the energy flux of x and y direction and F_e is the energy loss due to overtopping. We assume that the phenomenon of x direction (along the wall) is uniform, so the balance of energy flux yields following formula:

$$E_i c_g \sin \theta_i + E_r c_g \sin \theta_r = F_e \quad (7)$$

or

$$f_{2i} H_i^2 \sin \theta_i - f_{2r} H_i^2 K_r^2 \sin \theta_i = \frac{2\sqrt{2g}}{3T\sqrt{h}} \int_{\eta_e > H_c} \left\{ \left(\frac{v_w^2}{2g} + \eta_e - H_c \right)^{\frac{3}{2}} - \left(\frac{v_w^2}{2g} \right)^{\frac{3}{2}} \right\} \left(\eta_e + \frac{1}{2g} |u_w^2 + w_w^2|_{z=0} \right) dt \quad (8)$$

where, K_r is the reflection coefficient defined as the wave height ratio and u_w is the velocity along the wall. f_2 is the ratio between the energy and the wave height square on the first order cnoidal wave theory (Isobe, 1985), and is 1/8 for the small amplitude wave theory.

Equation (8) gives the reflection coefficient, when incident wave height, period and angle are prescribed together with geometry or the freeboard of the vertical wall. The wave overtopping discharge can be estimated from eq. (6) by using the reflection coefficient.

Numerical calculation

We performed numerical calculation of this model. We examine the influence of the incident wave angle and the incident wave height while water depth 20.0 cm and wave period 1.2 s are kept constant.

Figure 4 shows examples of the calculated non-dimensional overtopping rate q_e/q_0 and reflection coefficient K_r with respect to incident wave angle. Wave overtopping discharge, q_e , is non-dimensionalized with q_0 defined as

$$q_0 = \frac{H_i \sqrt{gh}}{2} \quad (9)$$

We performed the calculation using not only the first order cnoidal wave theory but also the small amplitude wave theory. It is clear that the wave overtopping rate and the reflection coefficient slightly decrease with the decrease of the incident wave angle. Significant decreases of more than 10%

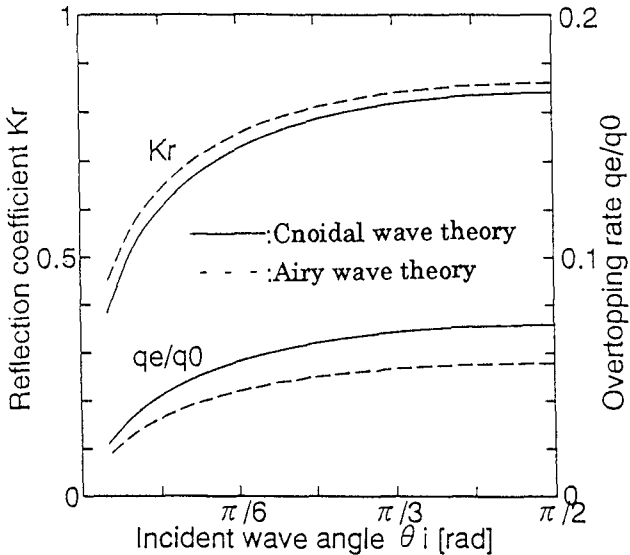


Figure 4 Examples of the calculated non-dimensional overtopping rate q_e/q_0 and reflection coefficient K_r with respect to incident wave angle. (calculation condition $h=20\text{cm}$, $T=1.2\text{s}$, $H_i=6\text{cm}$, $H_c=3\text{cm}$)

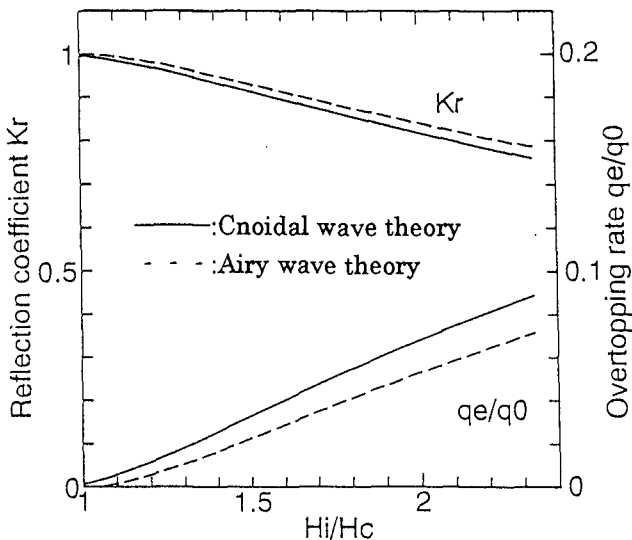


Figure 5 Examples of the calculated non-dimensional overtopping rate q_e/q_0 and reflection coefficient K_r with respect to incident wave height. (calculation condition $h=20\text{cm}$, $T=1.2\text{s}$, $\theta_i = \pi/3$, $H_c=3\text{cm}$)

are expected only for the incident wave angle less than $\pi/4$. Nonlinear effect yields the increase of the overtopping rate and the decrease of the reflection coefficient.

Figure 5 shows examples of the calculated non-dimensional overtopping rate q_e/q_0 and reflection coefficient K_r with respect to incident wave height. The difference between for the small amplitude waves and for the cnoidal waves in the overtopping rate and the reflection coefficient becomes larger as the incident wave height gets larger.

3. Experimental Confirmation

Experimental facilities

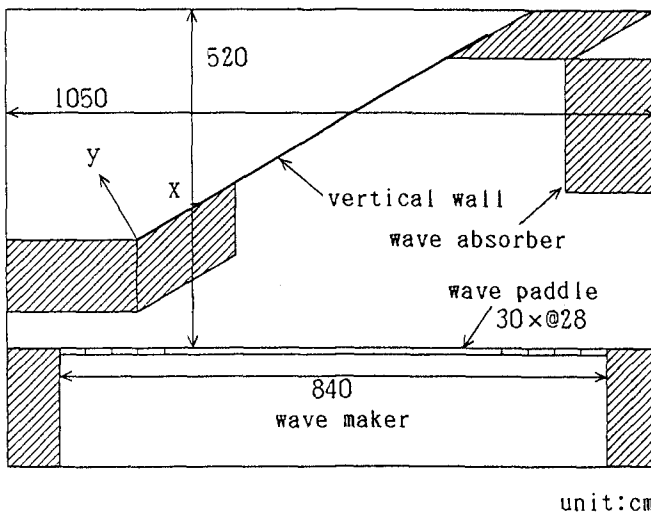


Figure 6 Experimental facilities and the coordinate system.

Experimental confirmation of this model is undertaken by using a multi-directional wave basin. Figure 6 shows the experimental facilities and the coordinate system. The basin is 10.5 m wide, 6.8 m long and 0.6 m depth. The distance from wave paddles to opposite end-wall is 5.2 m. The concrete floor of the basin is almost flat. The multi-directional wave maker consists of 28 piston-type wave paddles continuously linked or 29 sets of actuator rod. Each paddle is 30 cm wide and 50 cm high.

A vertical wall with 12.0 cm high and 540 cm long is installed in the basin. The influence of the scattering waves from the wall ends may be suppressed by placing wave absorbers around the wall ends.

In a multi-directional wave basin, generating a uniform wave field with the target value of wave height and angle is important. However, it is well known that both wave height and angle of generated regular waves show considerable spatial variation. The main cause is the finite length of the wave maker. The effect of the discontinuity at both ends of the wave maker may be suppressed by employing linear decrease of wave paddle amplitude (Mizuguchi, 1994). We applied this ends control method.

Water depth $h = 10.0$ cm, the crown height of the wall $H_c = 2.0$ cm, and a wave period of $T = 1.0$ s are kept constant. Incident wave height and incident wave angle are varied.

Wave field in front of the wall

Non-overtopping experiments (incident wave height $H_i = 1.0$ cm) were carried out in order to check the uniformity of the wave field in front of the vertical wall. Wave gauges are installed 1.0 cm distant perpendicularly to the wall. An array of wave gauge and electro-magnetic current meter measures the surface elevation and the horizontal velocity at the same point $1/12$ of wave length perpendicularly apart from the wall.

Figure 7 shows the wave height and the total amplitude of the horizontal velocity distribution in front of the vertical wall for non-overtopping cases. Wave field in front of the wall can be assumed to be uniform at the center of the wall. Where we measure wave overtopping discharge for all the cases.

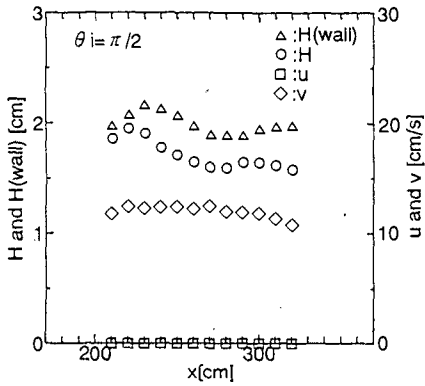
Separation method between incident and reflected waves

A separation method is developed to evaluate the reflection coefficient and the reflected wave angle from the measured data. The method assumes the linear superposition of the incident waves and the reflected waves, both of them being long waves.

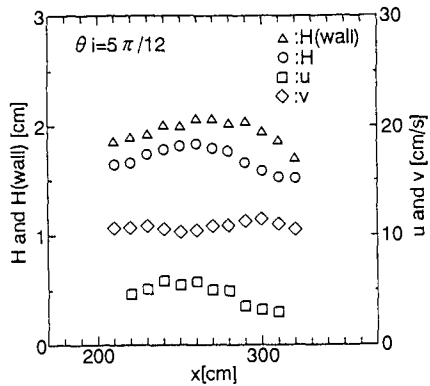
Mathematically, we have eq. (10), eliminating η_i and η_r from eqs. (1), (4) and (5),

$$\frac{\sqrt{h/gu} - \eta \cos \theta_i}{\sqrt{h/gv} - \eta \sin \theta_i} = \frac{\cos \theta_r - \cos \theta_i}{\sin \theta_r - \sin \theta_i} = \alpha \quad (10)$$

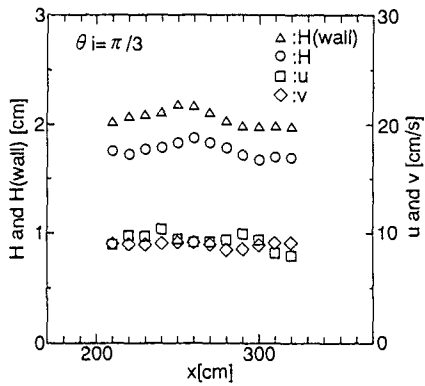
where, α is theoretically a constant, although α vary for a measured data. Symmetrical reflection ($\theta_r = 2\pi - \theta_i$) gives $\alpha = 0$. Incident waves and reflected waves are calculated by following formula,



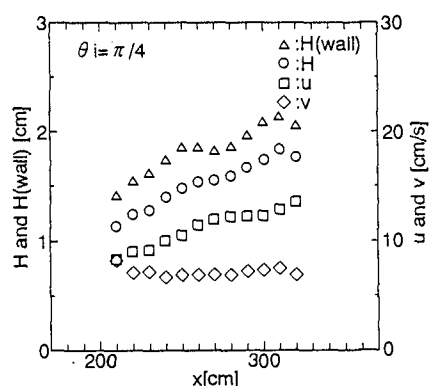
(a) $\theta_i = \pi/2$



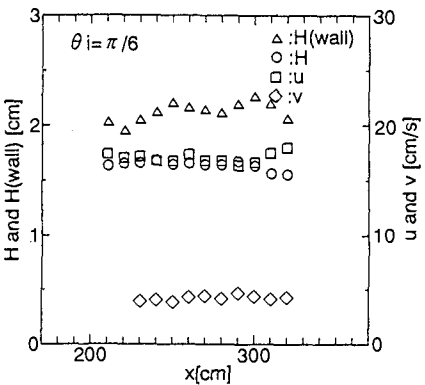
(b) $\theta_i = 5\pi/12$



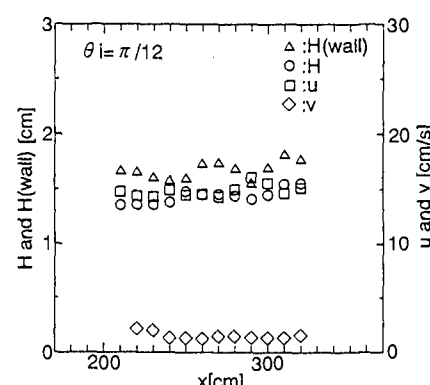
(c) $\theta_i = \pi/3$



(d) $\theta_i = \pi/4$



(e) $\theta_i = \pi/6$



(f) $\theta_i = \pi/12$

Figure 7 Wave height and total amplitude of horizontal velocity distribution in front of the wall.

$$\eta_i = \frac{\sqrt{h/gv} - \eta \sin \theta_r}{\sin \theta_i - \sin \theta_r} \left(= \frac{\sqrt{h/gu} - \eta \cos \theta_r}{\cos \theta_i - \cos \theta_r} \right) \quad (11)$$

and

$$\eta_r = \eta - \eta_i. \quad (12)$$

Reflection coefficient is the ratio between the incident wave height and the reflected wave height.

Wave overtopping rate and reflection coefficient

Incident wave heights are $H_i = 2.0, 2.5, 3.0$ and 3.5 cm in wave overtopping experiments. The wave overtopping discharge are measured by using a wave gauge in the box installed just behind the wall.

Figure 8 shows examples of measured data of surface elevation η and horizontal velocities u and v . Figure 9 shows separated incident waves and reflected waves calculated from equation (10) and (11) together with the time series of α , as using data shown in Fig. 8. Reflected wave angle is calculated by using mean value of α passed from -1 to 1.

Figure 10 shows reflected wave angle obtained from experimental data. When incident wave angle is large, the reflected wave angle shows almost symmetry. However, when incident wave angle is small, the reflected wave angle shows large discrepancy from symmetrical reflected angle. We may consider the reason why the separation method for incident and reflected waves suffers strongly influence from experimental noise. Figure 11 shows incident wave height obtained from experimental data. Incident wave height is almost the same as the target value. When incident wave angle is large, the validity of the separation method was confirmed.

Figure 12 shows measured and calculated wave overtopping rates and reflection coefficients with respect to the incident wave angle. Wave overtopping was not observed, for incident wave height $H_i = 2$ cm of all incident wave angles and $H_i = 2.5$ cm of incident wave angle $\theta_i = \pi/4, \pi/6$ and $\pi/12$. When wave overtopping occurs, good agreement between the model and the experiment results is found for the wave overtopping rate. The reflection coefficients for large incidence ($\theta_i = \pi/2, 5\pi/12$ and $\pi/3$) show reasonable values. For small incident wave angle, the reflection coefficient obtained from experimental data did not plot.

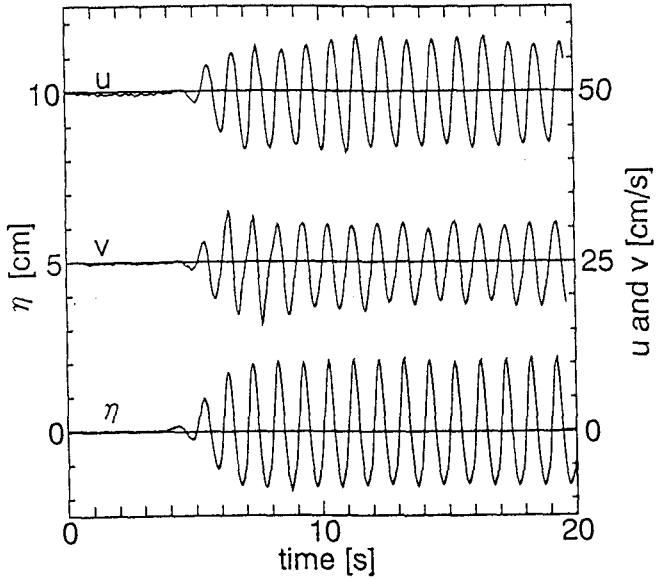


Figure 8 Examples of measured data of surface elevation η and horizontal velocities u and v . ($h=10\text{cm}$, $T=1.0\text{s}$, $H_i=3.0\text{cm}$, $\theta_i=\pi/3$)

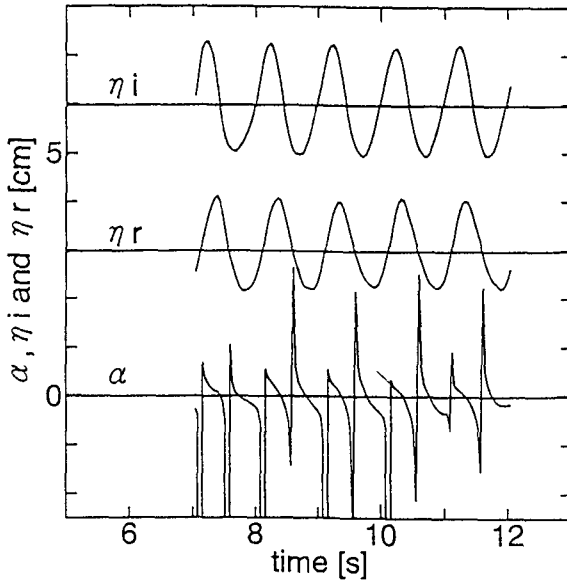


Figure 9 Time series of α , separated incident waves and reflected waves calculated as using data shown in Fig. 6.

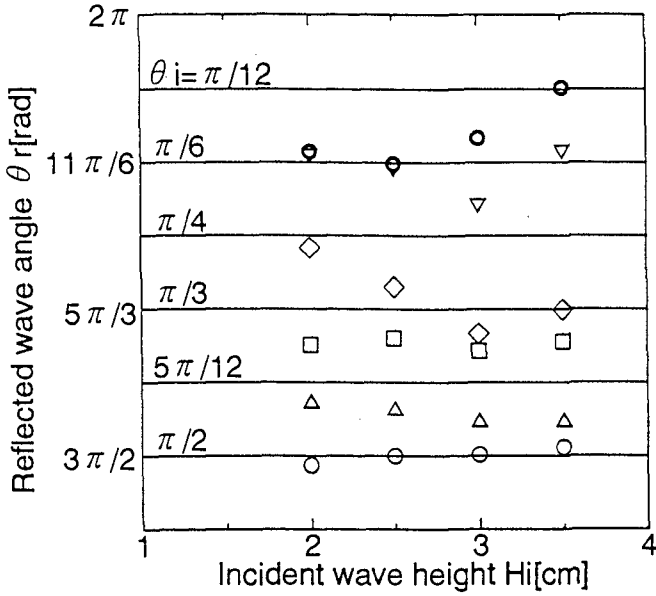


Figure 10 Reflected wave angle obtained from experimental data. (\circ : $\theta_i = \pi/2$, \triangle : $5\pi/12$, \square : $\pi/3$, \diamond : $\pi/4$, ∇ : $\pi/6$, \odot : $\pi/12$)

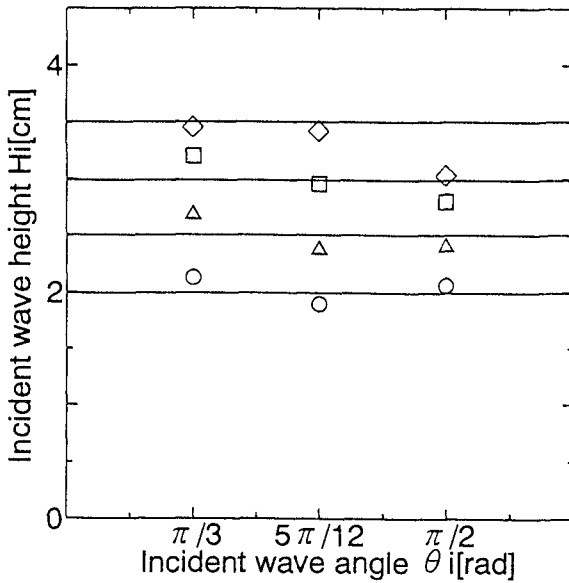


Figure 11 Incident wave height obtained from experimental data. (\circ : $H_i = 2.0$ cm, \triangle : 2.5 cm, \square : 3.0 cm, \diamond : 3.5 cm)

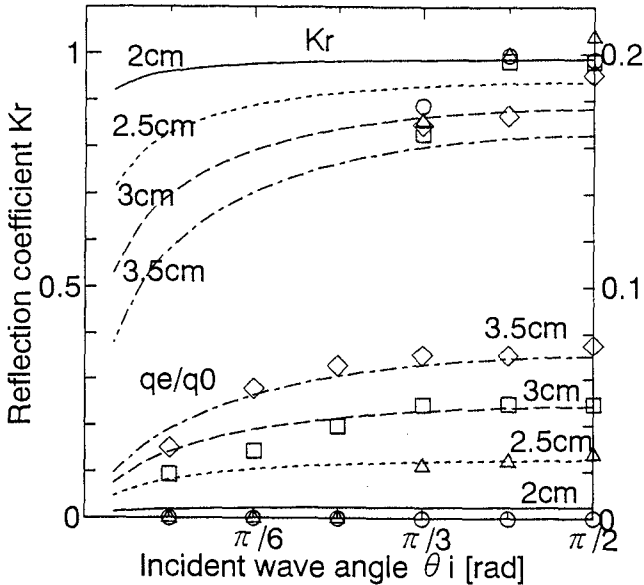


Figure 12 Measured and calculated wave overtopping rates and reflection coefficients with respect to the incident wave angle. (\circ : $H_1=2.0\text{cm}$, \triangle : 2.5cm , \square : 3.0cm , \diamond : 3.5cm)

4. Conclusion

Wave overtopping over a vertical wall for the oblique incidence were treated analytically by extending normal incidence (Mizuguchi's) model. Wave overtopping rate and reflection coefficient can be estimated from the extended model which does not include any experimental constants. The results of numerical calculation show the slightly decrease of the wave overtopping rate with the decrease of the incident wave angle.

Experimental confirmation of this model was undertaken by using a multi-directional wave basin. Satisfactory agreement between the model and the experimental results is found for the wave overtopping rate. The reflection coefficient for large incidence ($\theta_i = \pi/2, 5\pi/12$ and $\pi/3$) shows reasonable agreements. The validity of the model was confirmed at least for large incident wave angle.

Reference

de Waal, J. P. and J. W. van der Meer (1992): Wave runup and overtopping on coastal structures, Proc. 23rd, Conf.

- Coastal Eng., ASCE, pp.1758-1771.
- Inoue, M. and Y. Tuchiya(1971): Experimental study on wave overtopping over a vertical wall for oblique incidence, Proc, 18th, Japanese Conf. on Coastal Eng., JSCE, pp.259-264. (in Japanese)
- Isobe, M.(1985): Calculation and application of first order cnoidal wave theory, Coastal Eng., Elsevier, Vol.9, pp.309-325.
- Juhl, J. and P. Sloth(1994): Wave overtopping of breakwaters under oblique waves, Proc. 24th, Conf. Coastal Eng., ASCE, pp.1182-1196.
- Kikkawa, H., H. Shiigai and T. Kohno(1967): Basic study on wave overtopping for coastal embankment (1), Proc. 14th, Japanese Conf. on Coastal Eng., JSCE, pp.335-338. (in Japanese)
- Mizuguchi, M.(1993): Wave overtopping rate over a vertical wall and reflection coefficient, Coastal Eng. in Japan, Vol.36, No.1, pp.37-47.
- Mizuguchi, M.(1994): Uniformity of wave field produced by multi-directional wave maker, Abst. 24th, Conf. Coastal Eng., ASCE.
- Takayama, T., T. Nagai, K. Nishida and T. Sekiguchi(1984): Experiments on oblique random wave overtopping rates over seawalls, Proc. 31st, Japanese Conf. on Coastal Eng., JSCE, pp.542-546. (in Japanese)
- Yokoyama, K. and M. Mizuguchi(1993): Experimental study on wave overtopping over a vertical wall and reflection coefficient, Proc. Coastal Eng., JSCE, Vol.40, pp.676-680. (in Japanese)

CHAPTER 202

Sediment transport and wave reflection near a seawall.

Jonathon R. Miles¹, Paul E. Russell¹, David A. Huntley¹.

Abstract

This paper describes results of a field experiment to examine the effect of wave reflection on suspended sediment transport in front of a seawall. High frequency measurements of wave elevation, velocity and suspended sediment concentrations were made simultaneously on a natural beach and in front of a seawall at Teignmouth in South Devon (U.K.) in June 1995. Wave reflection at the natural beach was found to be dependent on frequency; low frequency waves being preferentially reflected while incident waves were dissipated. At the seawall the incident wave reflection coefficient was 0.9 indicating only a small amount of dissipation. The doubling of energy over the sea bed was found to greatly increase the suspended sediment concentrations in the water column, although the amount of this increase depended on the water depth. A data analysis technique was developed which allowed the incoming and outgoing wave contributions to the sediment transport to be analysed. In these accretionary conditions incoming waves transported sediment onshore in both wall and beach cases, while in the wall case sediment transported offshore by the outgoing waves balanced the onshore transport. Sediment build up which was observed at the top of the natural beach was not observed in front of the wall. Sediment maintained in suspension in front of the wall was available for longshore transport, and this was enhanced by the presence of the wall.

Introduction

Seawalls have been used for many years as a method of coastal protection on eroding shorelines. It has been suggested that the reflection of wave energy over the beach fronting the wall actually helps to erode the beach (Silvester 1977), but the processes controlling this erosion remain poorly understood. There has been considerable debate over the effect of the seawall on the beach in recent years

¹ Institute of Marine Studies, University of Plymouth, Drake Circus, Plymouth, U.K., PL4 8AA.

(Kraus, 1988; Kraus and McDougal, 1996), with experimenters carrying out laboratory experiments with moveable beds (e.g. McDougal et al., 1996) or carrying out surveys of defended and undefended coastlines (e.g. Griggs and Tait, 1988). Researchers into beach processes have identified driving forces behind beach morphology change using high frequency point measurements of suspended sediment concentrations and water velocities (e.g. Jaffe et al., 1984). This approach has been applied to the reflective seawall environment for the first time and the method and initial results are presented in this paper.

Method

To compare similar wave conditions in a surf zone with a reflective wall environment a location was required with a wall adjacent to a natural beach. The site chosen was Sprey point at Teignmouth in South Devon, UK which has a 7m high seawall fronted by a beach of slope 1/15. The sand in front of the wall is medium quartz sand with $D_{50}=0.24\text{mm}$. The beach is macro-tidal and morphodynamically intermediate. A rig designed to minimise interference with the hydro and sediment dynamic conditions whilst providing a stable base for instrumentation was built and bolted to the wall. An extendable rod was positioned on the front of the rig, extending close to the bed, to which the instruments were attached. Two EMCMs, (Electro Magnetic Current Meters) two OBSs (Optical Backscatter Sensors) and a PT (Pressure Transducer) were attached to this rod, 1.5m from the wall in a vertical array. A rig of instruments was also dug in to the adjacent beach on a similar depth contour so that comparisons could be made. This beach site had one EMCM, one OBS and one PT.

All of the *in-situ* monitoring devices were logged at a frequency of 8Hz and were pre-filtered between 3-4Hz. EMCM and PT offsets were determined in the field at the beginning and end of each tide. Surveys were carried out daily to establish beach morphology. Sediment samples were taken for size distribution analysis. During the period of observation and recording, in June 1995, the wind was generally light and the waves were, on average, 30cm in height at the breakpoint with an average period of 4 seconds. The robust design of the rig should enable measurements to be made in waves of up to 2m. The layout of the site is shown in figure 1:

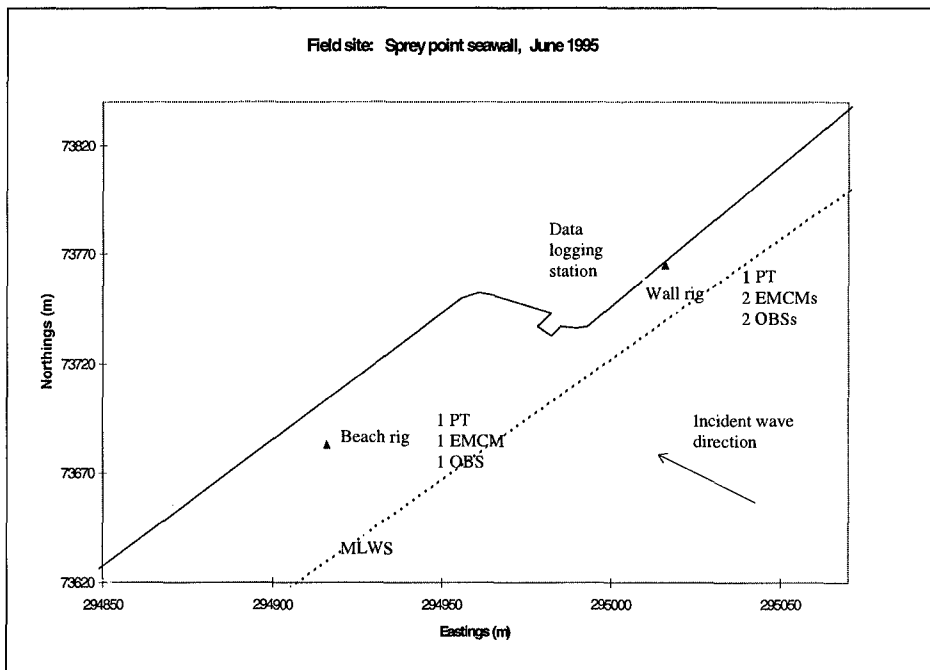


figure 1. Experiment site at Teignmouth.

Instruments were calibrated both before and after the experiment, and the calibrations were applied to the raw data. EMCs were calibrated in a tow tank at the Royal Naval Engineering College (RNEC) at Manadon, Plymouth (U.K.). Pressure transducers were calibrated for water depth in a 3m deep tank at the RNEC. OBSs were calibrated in the laboratory using sediment samples taken from the experiment site. To calibrate the OBSs a paint stirrer was used to suspend sediment in a tank while samples of the beach sediment were filtered from next to the OBS head. This calibration of the OBSs provided an excellent linear correlation between suspended sediment concentrations and voltage output.

Time series

Time series of surface elevation and suspended sediment concentration are shown in figure 2. Time series have been selected so that water depths are similar in the wall and beach examples, in this case the water depth is approximately 0.8m. Instruments suspended from the wall are 1.2m away from it. This puts them closer to the antinode at the wall than the node 2.7m away from the wall (for a wave period of 4 seconds). The maximum surface elevation deviation from the mean is therefore clearly larger than that observed at the beach rig. Suspended sediment data which is

compared in these examples is taken from OBSs at similar heights, both being approximately 18cm from the bed. The scale of the axis of the wall OBS is reduced so that the data fits the plot. In similar incident wave conditions levels of suspended sediment are clearly much larger at the wall, reaching 4 kg/m^3 at this height above the bed, while at the beach OBS sediment concentrations only reach 0.6 kg/m^3 .

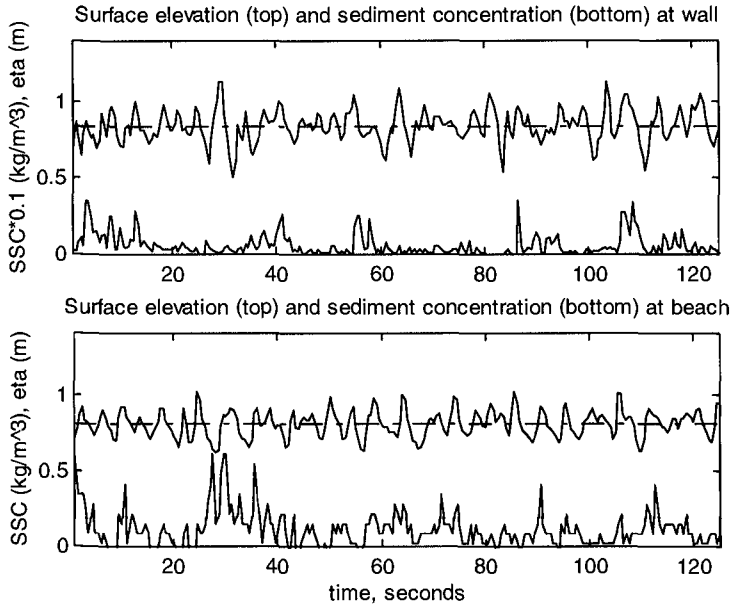


figure 2. Time series of surface elevation and suspended sediment concentrations at the wall and beach rigs. N.B. The sediment concentrations in the wall time series have been scaled down by a factor of 10.

Theory

Incoming and outgoing elevation time series were obtained from elevation and velocity time series using the method of Guza, Thornton and Holman (1984). The separation of incoming and outgoing waves forms the basis for most reflection analysis techniques which involve co-located elevation and velocity sensors. The analysis can also be extended to obtain the incoming and outgoing velocity time series. This allows the frequency dependent oscillatory sediment transport associated with the incident reflected waves to be found.

The derivation of Guza et al.'s (1984) time domain technique arises from linear shallow water theory:

The velocity potential for progressive water waves is as follows:

$$\phi = \frac{-a \cdot g}{\sigma} \cdot \frac{\cosh k(z+h)}{\cosh kh} \sin(kx - \sigma t)$$

The surface elevation can be obtained from this by differentiating with respect to time, and the attenuation term tends to 1 in shallow water.

$$\eta = \frac{1}{g} \left[\frac{\partial \phi}{\partial t} \right]_z = 0 \quad \text{giving} \quad \eta = a \cos(kx - \sigma t)$$

A similar equation for velocity is obtained by differentiating with respect to x

$$u = - \frac{\partial \phi}{\partial x} \quad \text{gives} \quad u = \frac{g a k}{\sigma} \cos(kx - \sigma t)$$

By dividing the elevation and velocity equations the following time domain transformation can be obtained relating velocity and surface elevation (provided the water is shallow).

$$\eta(t) = \frac{c}{g} u(t)$$

It is necessary to transform to the frequency domain and use full linear theory if this relationship is to be applied in intermediate or deep water.

Progressive wave surface elevation traces for waves incoming to a beach and outgoing from it can be obtained from the time series of elevation and velocity as follows:

$$\eta_{in}(t) = \left(\eta(t) + \frac{c}{g} u(t) \right) / 2$$

$$\eta_{out}(t) = \left(\eta(t) - \frac{c}{g} u(t) \right) / 2$$

In this case, a positive velocity implies an onshore flow, while a negative velocity an offshore flow. In order to obtain a frequency dependent reflection function (FDRF) it is necessary to carry out a spectral analysis of the incoming and outgoing elevation traces separately. After obtaining the power spectra of the incoming and outgoing elevation time series, $S_{ii}(f)$ and $S_{oo}(f)$ respectively, the frequency dependent reflection coefficient is simply:

$$R(f) = \sqrt{\frac{S_{ii}(f)}{S_{oo}(f)}}$$

This technique was examined for signal noise related bias by Huntley et al. (1995) who found that when the coherence between elevation and velocity was high, the bias in the FDRF was low. Two other techniques were discussed by Huntley et al. (1995). These were a frequency domain method by Tatavarti (1989) and a Principal Component Analysis method (Tatavarti et al., 1988). All three techniques were applied to the data in order that the frequency dependent reflection coefficient for the beach and wall cases could be identified. The three different methods were

found to offer similar results. This gives confidence in the time domain method which is the most simple to program and extend for incoming and outgoing sediment analysis.

In order to understand the effect of the reflected wave field on the suspended sediment transport, it is possible to carry out a cross-spectral analysis of the incoming and outgoing waves with the sediment.

It is first necessary to apply the transformation from elevation to velocity to obtain incoming and outgoing velocity time series. The appropriate transformations are:

$$u_{in} = \frac{g}{c} \eta_{in}$$

$$u_{out} = -\frac{g}{c} \eta_{out}$$

A wave crest (elevation maximum) correlated with onshore flow therefore represents a wave crest travelling onshore, while a wave peak correlated with an offshore velocity represents a wave crest travelling offshore. The equations for incoming and outgoing velocity are therefore:

$$u_{in} = \frac{1}{2} \left(u + \frac{g}{c} \eta \right)$$

$$u_{out} = \frac{1}{2} \left(u - \frac{g}{c} \eta \right)$$

It is next necessary to assume that the oscillatory sediment flux can be split into incoming and outgoing components. Jaffe et al. (1984) assumes a similar principle when considering the breakdown of the mean and oscillatory fluxes. They assume that the total velocity can be split into a mean and oscillatory component:

$$U = \bar{u} + u'$$

and that the sediment concentration is also separable into mean and oscillatory parts:

$$C_s = \bar{c}_s + c'_s$$

The time average of the flux therefore reduces to the mean flux and the flux coupling:

$$\overline{UC_s} = \bar{u} \bar{c}_s + \overline{u' c'_s}$$

Signals are routinely de-meant, and the remaining step is to split the oscillatory velocity into incoming and outgoing components before crossing with the suspended sediment to obtain the flux:

$$u' = u'_{in} + u'_{out}$$

The time average of the incoming and outgoing oscillatory flux is therefore:

$$\overline{u' c'_s} = \overline{u'_{in} c'_s} + \overline{u'_{out} c'_s}$$

Huntley and Hanes (1987) identified that the frequency dependent sediment transport could be found by taking the co-spectrum of the oscillatory cross shore velocity with the sediment concentration time series. The frequency dependent

sediment transport associated with the incoming and outgoing waves is therefore obtained from the co-spectrum of the incoming or outgoing velocity time series with the sediment time series. The contributions of the incoming and outgoing waves to the sediment transport can therefore be identified.

Frequency dependent wave reflection

Three methods were used to determine levels of energy incoming and outgoing from the natural beach and the wall. Incoming and outgoing wave spectra were obtained from the incident and reflected time series obtained using Guza et al.'s (1984) method. The frequency dependent reflection coefficient was then determined using this method and two frequency domain methods. All three methods require that the current meter and pressure transducers are co-located and log data simultaneously. The analysis was first applied to data from the beach rig (figure 3).

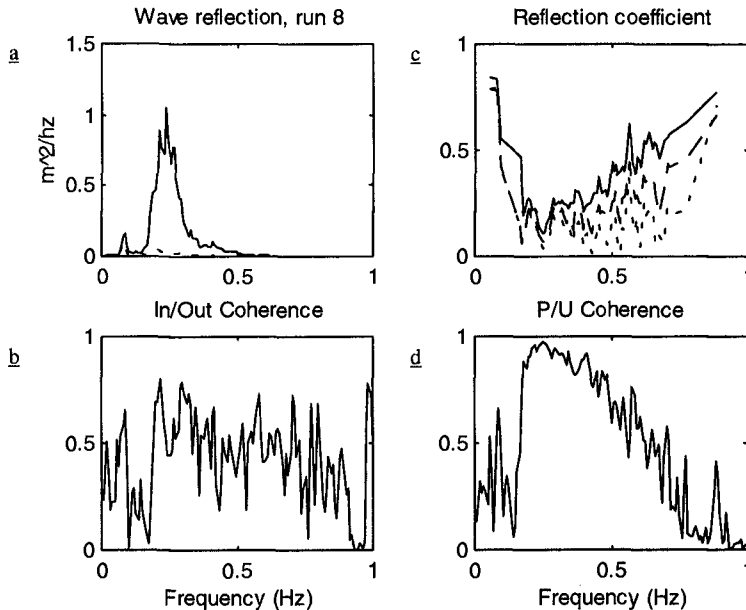


figure 3. Frequency dependent wave reflection at the beach. a: Incoming and outgoing wave spectra calculated using the time domain method. b: Coherence between calculated incoming and outgoing time series. c: Frequency dependent reflection coefficient calculated using time domain (solid), frequency domain (dashed) and principle component analysis (dotted) methods. d: Coherence between elevation and velocity. Water depth is 1.28m.

The energy spectra show clearly that the incident waves (frequency 0.25 Hz) are dissipated by the natural beach, while at a lower frequency (0.1Hz) wave reflection is taking place. By dividing the square root of the spectral estimates, the FDRF for this time domain method was obtained, and this shows a reflection coefficient of 0.1 for the incident waves on the natural beach while for the low frequency waves the reflection coefficient is 0.8. Of the three lines on the reflection coefficient figure above (top right), the lines show the methods of the time domain method (top), the frequency domain method (middle) and the Principal Component Analysis (bottom). The three methods give good agreement where there is good coherence between elevation and velocity.

A similar analysis was carried out to data from the wall rig. The results are shown in figure 4.

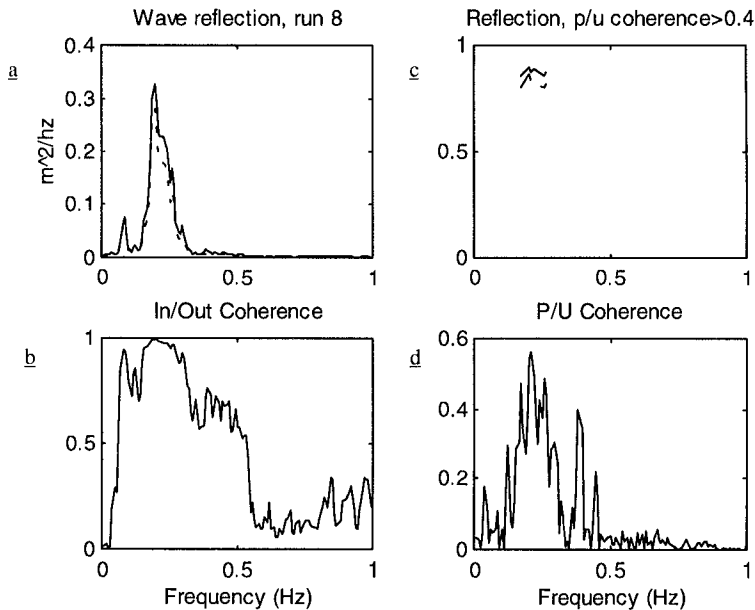


figure 4. Frequency dependent wave reflection at the wall. a: Incoming and outgoing wave spectra calculated using the time domain method. b: Coherence between calculated incoming and outgoing time series. c: Frequency dependent reflection coefficient calculated using time domain (solid), frequency domain (dashed) and principle component analysis (dotted) methods. Reflection estimates are plotted for values of P/U coherence > 0.4 so that there is 95% confidence in the coherence between P and U. This is necessary as cross spectral analysis is carried out in the determination of the FDRF using the frequency domain methods. d: Coherence between elevation and velocity. Water depth is 1.30m.

Similar amounts of energy were found in the spectra of both incoming and outgoing wave time series, indicating that reflection of the incident waves was occurring at the wall. At incident wave frequency all three methods of determining the frequency dependent reflection coefficient gave a value of 0.9 at the wall. The wall is in fact slightly sloping at the position of the rig and this may account for the reflection coefficient being less than unity.

Mean suspended sediment concentrations

The next part of the investigation was to examine the effect of the increase in reflection coefficient at the shoreline on concentrations of suspended sediment. To do this, data from OBSs on the beach and wall rig were compared. During the experiment OBSs were carefully positioned on each rig so that they were at the same height above the bed and are therefore comparable. Mean concentrations were calculated for each run. Mean water depths were also calculated and sediment concentrations in each case were then plotted against depth. The results are shown in figure 5.

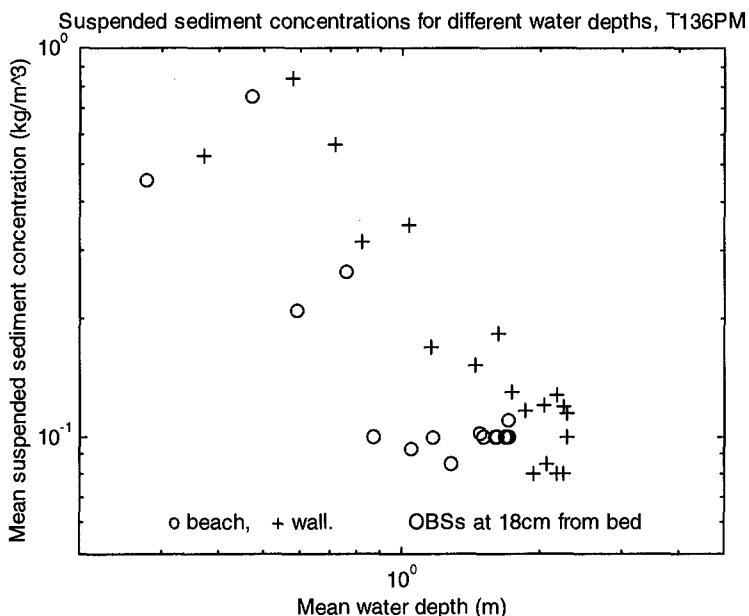


figure 5. Mean suspended sediment concentrations - comparison of data from wall and beach OBSs. Both instruments were mounted approximately 18cm from the bed. Incident waves were approximately 30cm high at the breakpoint.

The results show a greater concentration of sediment was in suspension in front of the wall than was in suspension on the natural beach when water depths were the same. Incoming wave conditions did not vary significantly during this tide, and the results therefore imply that it is the increase in wave reflection at the shoreline which must be responsible for increasing the concentrations of suspended sediment in front of the wall. The distinct linear trend in the data, especially in the wall rig data suggests that it may be possible to parameterise the mean suspended sediment concentrations in this region in terms of the reflection coefficient, water depth, height above bed and incident wave height. Further experimentation with a larger array of instruments would be necessary for this however.

Frequency dependent sediment transport

The incoming and outgoing frequency dependent sediment transport was obtained for both wall and beach rigs for each run of data logged. A clear picture emerged in all runs as to the nature of this transport and this is shown in figure 6.

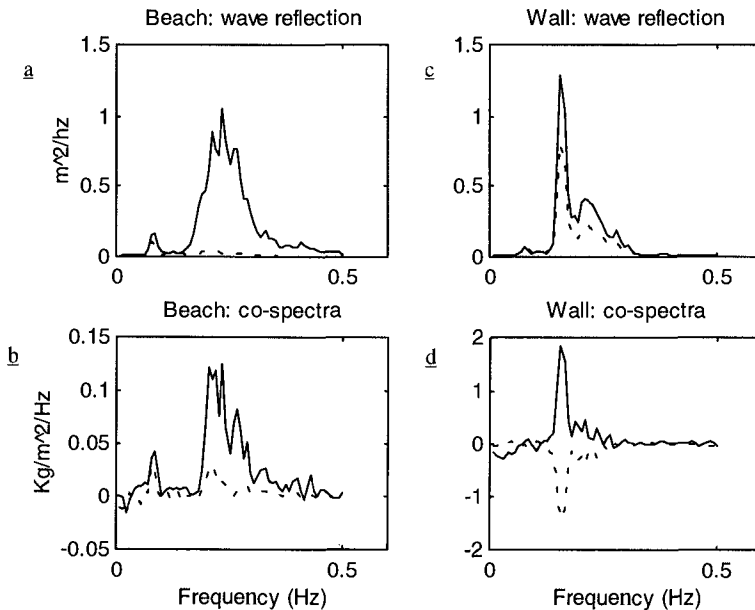


figure 6. Incoming and outgoing spectra and co-spectra in beach (a,b) and wall (c,d) cases. In the energy spectra plotted above, the solid lines represent incoming energy, the dashed lines represent outgoing energy. In the co-spectra, positive is onshore, solid lines are the cospectra between incoming waves and the sediment, dashed lines are cospectra between outgoing waves and sediment. Water depth is 1.3m

In the beach case (figure 6b), incoming waves are found to transport sediment onshore. This result is similar to that observed by Huntley and Hanes (1987). Suspension events occur at the same time as onshore directed flows, and the resultant transport is onshore. There is little energy outgoing from the beach however, and there is therefore little transport associated with the offshore directed waves.

At the wall, the situation is rather different (figure 6d). The incident waves are still responsible for onshore sediment transport, while the outgoing waves give rise to offshore transport. The onshore transport by the incoming waves is effectively halted by the outgoing waves. The net cross-shore oscillatory transport is therefore reduced. The fact that there is more sediment in suspension in front of the wall is also evident in this analysis as the magnitudes of the co-spectra are considerably larger in the wall case than in the beach case.

Longshore transport comparison

Mean longshore transport rates were calculated for both wall and beach rigs. The results are shown in figure 7.

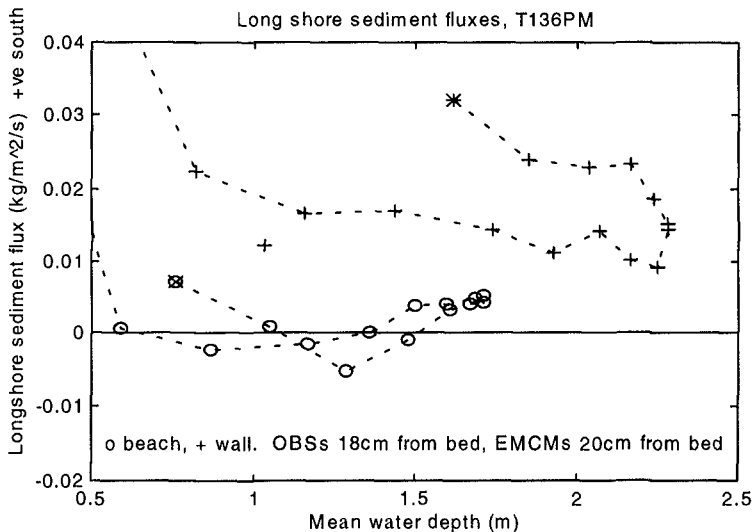


figure 7. Longshore transport rates measured at the beach and wall.

Longshore transport rates in front of the wall were found to be greater than at the beach rig at all times, and this was attributed to both the increase in suspended sediment concentrations and also an increase in the longshore current which passed

in front of the wall. The south-westward direction of longshore transport in the wall case is a result of the oblique wave approach from the east (see figure 1).

During the period of observation, morphology changes were monitored using surveying techniques. Increased levels of longshore transport along the Sprey point wall resulted in the development of a small bar to the south west of the wall. (extending SW from point 294990,73740; see figure 1). Shoreward of the beach rig, a net accretion was observed. This is likely to have resulted from the onshore transport by the incident waves. At the wall rig however there was no net accretion or erosion. The balance in transport between the incoming and outgoing waves prevented accretion taking place in this region, while increased levels of sediment in suspension led to an enhanced longshore transport of sediment in front of the wall.

Conclusions

This paper has described initial results of a field experiment to examine the effect of wave reflection on suspended sediment transport in front of a seawall. High frequency measurements of wave elevation, velocity and suspended sediment concentrations were made simultaneously on a natural beach and in front of a seawall. The doubling of energy over the sea bed was found to greatly increase the suspended sediment concentrations in the water column, although the amount of this increase depended on the water depth. A data analysis technique was developed which allowed the incoming and outgoing wave contributions to the sediment transport to be analysed. Incoming waves transported sediment onshore in both wall and beach cases, while in the wall case outgoing waves balanced the onshore transport. Sediment which was maintained in suspension in front of the wall was available for longshore transport, and this was enhanced by the presence of the wall.

Symbols

a	wave amplitude
c	wave celerity
c_s	sediment concentration
f	wave frequency
g	gravitational acceleration
h	water depth
k	wave number ($2\pi/\lambda$)
t	time
u	horizontal cross shore velocity
x	horizontal co-ordinate
z	vertical position. $z = 0$ at the surface, $z = -h$ at the bed
R(f)	frequency dependent reflection coefficient
S_{ii}	power spectrum of incoming wave time series
S_{oo}	power spectrum of outgoing wave time series
T	wave period

σ	angular frequency ($2\pi/T$)
η	surface elevation
λ	wavelength
ϕ	velocity potential
in	denotes incoming wave
out	denotes outgoing wave

References

- Griggs, G.B. and Tait, J.F., 1988. The effects of coastal protection structures on beaches along northern Monterey Bay, California. *Journal of Coastal Research, Special Issue No. 4*, 93-111.
- Guza, R.T., Thornton, E.B. and Holman, R.A., 1984. Swash on steep and shallow beaches, *Coastal Engineering*, 708-723.
- Huntley, D.A. and Hanes, D.M., 1987. Direct measurement of suspended sediment transport. *Proceedings, Coastal Sediments '87, ASCE*, 723-737.
- Huntley, D.A., Simmonds, D. and Tatavarti, R.S.V.N., 1995. On the measurement of coastal wave reflection using co-located elevation and current sensors. *Proceedings, Coastal Dynamics*, 57-68.
- Jaffe, B.E., Sternberg, R.W. and Sallenger, A.H., 1984. The role of suspended sediment in shore normal beach profile changes. *Proceedings, Coastal Engineering, 1983-1996*.
- Kraus, N.C., 1988. The effects of seawalls on the beach: extended literature review. *Journal of Coastal Research, Special Issue No. 4*, 1-28.
- Kraus, N.C. and McDougal, W.G., 1996. The effects of seawalls on the beach: part 1, an updated literature review. *Journal of Coastal Research*, 12 (3), 691-701.
- McDougal, W.G., Kraus, N.C. and Ajiwibowo, H., 1996. The effects of seawalls on the beach part II, numerical modelling of SUPERTANK seawall test. *Journal of Coastal Research*, 12 (3), 702-713.
- Silvester, R., 1977. The role of wave reflection in coastal processes. *Proceedings of Coastal Sediments '77, American Society of Civil Engineers*, 639-652.
- Tatavarti, R.S.V.N., 1989. The reflection of waves on natural beaches. Unpub. PhD thesis. Dalhousie University, Halifax, Nova Scotia, Canada. 175pp.
- Tatavarti, R.S.V.N. and Huntley, D.A., 1987. Wave reflections at beaches, *Proceedings, Canadian Coastal Conference*, Quebec City, Canada, 241-256.

Acknowledgements

The authors would like to thank Dr Mark Davidson at the University of Plymouth for helpful suggestions throughout the study, and Mr Peter Ganderton for his assistance with the field-work phase of the project.



Initial nourishment at Palm Beach, Florida. Photo courtesy of Applied Technology & Management, Inc. and Aerial Photography, Inc.

PART IV

Coastal Processes and Sediment Transport



One year after nourishment at Palm Beach, Florida. Photo courtesy of Applied Technology & Management, Inc. and Aerial Photography, Inc.

CHAPTER 203

WAVE ENERGY DISSIPATION IN KELP VEGETATION

Alfonse Dubi¹ and Alf Tørum²

ABSTRACT

A laboratory experiment was carried out to investigate wave energy dissipation in a coastal kelp field of *Laminaria hyperborea* with a purpose of finding the damping rate. Parameters measured were wave heights at 8 locations along the direction of wave propagation, forces on artificial kelp plants, and velocities in between the plants in 4 different water depths. It was found that in 4, 6, 8 and 10 meter water depths, the damping coefficient was 0.0094, 0.0032, 0.0014 and 0.0005m⁻¹ respectively. Results show that the damping rate varies with population density, size of plant, water depth and wave period.

1. INTRODUCTION

Through a variety of processes, waves lose energy. Among the commonly known processes are wave breaking, bottom friction, reflection and interaction with porous beds and soft muds. Waves propagating through vegetation also lose energy due the work done on the vegetation.

Following Ippen (1966), the wave amplitude attenuation can be evaluated through the steady-state conservation of wave energy flux equation:

$$\nabla \cdot (E \vec{C}_g) = -E_D \dots\dots\dots(1.1)$$

where $E = \frac{1}{2} \rho g a^2$ is the wave energy density, ρ is the density of water, C_g is the group velocity and E_D is the energy dissipation rate. The local wave amplitude a is found to decay exponentially (see for example, Asano et al., 1992) as

$$a(x) = a_o e^{-k_i x} \dots\dots\dots(1.2)$$

where k_i is the damping rate (also known as the damping coefficient) of the wave height with distance and $a = a_o$ at $x = 0$.

In a study on the interaction between ocean waves and a kelp farm, Dalrymple et al. (1982) arrived at a wave height attenuation formula of the form:

¹ Research Fellow, Institute of Marine Sciences, University of Dar Es Salaam, P.O. Box 668 Zanzibar, Tanzania.

² Professor/Head of Research, Dept. of Structural Eng., NTNU/SINTEF-NHL, N-7034 Trondheim, Norway.

$$\frac{a(x)}{a_0} = \left(\frac{1}{1 + \alpha_d x} \right) \dots\dots\dots(1.3)$$

where

$$\alpha_d = \frac{2C_D}{3\pi} \left(\frac{d_k}{b} \right) \left(\frac{a_0}{b} \right) \left[\sinh^3 kd + 3 \sinh kd \right] \left[\frac{4k}{3 \sinh kD (\sinh 2kD + 2kD)} \right] \dots\dots\dots(1.4)$$

in which only the real part of the wave number k is used. C_D is the drag coefficient assumed constant over depth, d is the height of plant above the bottom, d_k is the plant diameter, and b is the spacing between plants. This approximation, however, takes plants as rigid cylinders; an assumption which results in assigning different values to the drag coefficient to cover the ignorance of the plant motion. Dalrymple et al. (1982) applied Eq.(1.4) for waves propagating through *Macrocystis pyrifera* kelp forest using known values of $C_D = 1.0$, $d_k = 0.3$ meters, $b = 1.5$ meters and $D = 15$ meters. They found that incident wave heights of 6.1 meters with 10-20 seconds periods could be reduced by 50% over a distance of 800 meters. This is equivalent to $\alpha_d = 0.0013m^{-1}$ and applying the exponential law of attenuation, $k_i = 0.0009 m^{-1}$.

Recently, Kobayashi et al. (1991) developed an analytical model, hereafter known as the Kobayashi model, to describe a 2D problem of small amplitude waves propagating over submerged or subaerial vegetation. They assumed the effect of the vegetation to be expressible in terms of the drag resistance against the fluid motion. The vertical component of the drag resistance and the proximity effects of the surrounding strips on C_D were neglected. Although an analytical solution was obtained, the calibrated drag coefficient C_D varied widely due to the fact that the swaying motion of an individual vegetation stand had been neglected.

Later, Asano et al. (1992) improved the Kobayashi model by including the interaction between the wave and the vegetation motion. Whereas the Kobayashi gave the calibrated values of C_D to the order of 0.1, the model of Asano et al. produced C_D of the order unity and the vertical force was neglected while the horizontal drag force was assumed to be dominant and linearized as

$$F_x = \rho D_k u_2 \dots\dots\dots(1.5)$$

where D_k is a linear force coefficient determined by the least squares method, u_2 is the horizontal particle velocity in the vegetation zone. Solution of the linear model gives the dispersion equation as

$$\omega^2 = gk \frac{k \tanh kh + \alpha_k \tanh \alpha_k d}{k + \alpha_k \tanh \alpha_k d \tanh kh} \dots\dots\dots(1.6)$$

in which ω is the angular frequency, d is the vegetation height, h is the water depth above vegetation and

$$\alpha_k^2 = \frac{\omega k^2}{\omega + iD_k} \dots\dots\dots(1.7)$$

In the case of weak damping, $\omega \gg D_k$, separation of the real and imaginary parts of the dispersion equation yields the following

$$\omega^2 = gk_r \tanh k_r (h + d) \dots\dots\dots(1.8)$$

which implies that the presence of vegetation does not change the real wave number k_r as long as $\varepsilon_k \ll 1$. The damping rate is then approximated by

$$k_i = \varepsilon_k k_r \frac{2k_r d + \sinh 2k_r d}{2k_r (h + d) + \sinh 2k_r (h + d)} \dots\dots\dots(1.9)$$

where $\varepsilon_k = \frac{D_k}{2\omega} \dots\dots\dots(1.10)$

On the other hand, applying the energy conservation equation, Eq.(1.1), and invoking Eq.(1.2), the Kobayashi model gives the damping rate as

$$k_i = \frac{D_k}{C_g} \left(\frac{2k_r d + \sinh 2k_r d}{2 \sinh 2k_r (h + d)} \right) \dots\dots\dots(1.11)$$

A more recent theoretical model based on limited experimental data is that of Wang and Tørum (1994) in which the dispersion equation is given by

$$\omega^2 = \frac{\tanh kh - \frac{i}{\alpha f_x} \tanh k_s h_s}{1 - \frac{i}{\alpha f_x} \tanh k_s h_s \tan kh} \dots\dots\dots(1.12)$$

where $\alpha = \sqrt{\left| \frac{f_z}{f_x} \right|}$ is the force ratio $\dots\dots\dots(1.13)$

and $k_s = \alpha k$, f_x and f_z are linearized horizontal and vertical force coefficients respectively, h_s = height of plant. The complex wave number is solved by iteration for known parameters and an assumed value of $\alpha = 0.8$.

Results from this model show that the damping coefficient increases with increasing wave period until it reaches an asymptotic values of just below $0.0015m^{-1}$, $0.0020m^{-1}$ and $0.0025 m^{-1}$, for densities of 8, 12 and 16 plants/ m^2 .

In this paper three different ways of finding the damping rate are used and compared. The first way is to get an analytical expression of the energy dissipation rate E_D using the linearized dissipative force and then apply Eq. (1.1). The second way, is to get a numerical value of the dissipation rate from time series of the horizontal velocities measured in between the plants and the corresponding horizontal force on the plants and apply Eq.(1.1) again. The third way, is to solve the complex dispersion equation for the complex wave number k by iteration as proposed by Wang and Tørum, (1994).

2. THE DAMPING RATE

2.1 Energy dissipation and the damping rate

Energy dissipation considered to be real and positive takes place mainly in the vegetation zone and partly in the boundary layer at the interface and near the solid

bottom. For a given volume of the vegetation zone, energy dissipation during a time period T is given by (e.g Madsen, 1974)

$$E_D = \frac{1}{T} \int_t^{t+T} \int_V \vec{F} \cdot \vec{U} dV \dots\dots\dots(2.1)$$

where $\vec{F} = \vec{F}(x,y,z,t) = (F_x, 0, F_z)$ is the dissipative force vector in the vegetation zone and $\vec{U} = (u_2, 0, w_2)$ is the complex velocity vector for the 2D case. Defining the force and velocity vectors as $(\mathbf{i}, \mathbf{j}, \mathbf{k})$ in the (x, y, z) directions as

$$\left. \begin{aligned} \mathbf{F} &= F_x \mathbf{i} + F_z \mathbf{k} \\ \mathbf{U} &= u \mathbf{i} + w \mathbf{k} \end{aligned} \right\} \dots\dots\dots(2.2)$$

and substituting into Eq.(2.1) we get

$$\left. \begin{aligned} E_D &= \frac{1}{T} \int_t^{t+T} dt \int_{-(h+d)}^{-(h+l_k)} (F_x \cdot u_2 + F_z \cdot w_2) dz \\ &= \frac{1}{T} \int_t^{t+T} dt \int_{-(h+d)}^{-(h+l_k)} F_x \cdot u_2 \left(1 + \alpha^2 \left(\frac{w_2}{u_2}\right)\right) dz \end{aligned} \right\} \dots\dots\dots(2.3)$$

The second term under the integral in Eq.(2.3) is found to be at least of the order α^2 and if we assume that $w_2/u_2 = O(\alpha^2) \ll 1$, which is generally true in coastal waters (Mei, 1982), the time averaged energy dissipation then becomes

$$E_D = \frac{1}{T} \int_t^{t+T} dt \int_{-(h+d)}^{-(h+l_k)} F_x \cdot u_2 dz + O(\alpha^4) \dots\dots\dots(2.4)$$

The dissipative force is linearized and expressed as

$$F_x = \rho f_{dx} u_2 \dots\dots\dots(2.5)$$

where f_{dx} is a linear drag force coefficient (Dubi, 1995) given as

$$f_{dx} = \frac{4n_k \alpha_r F_\lambda k_s |1 - A_m| \cosh^2 k_s h_f}{\rho(2k_s d + \sinh(2k_s d))} \dots\dots\dots(2.6)$$

where n_k is the number of plants per unit horizontal area, α_r is a force reduction factor accounting for group shielding and is found experimentally as a fitting coefficient equal to 0.08. F_λ is an empirical force coefficient evaluated at the canopy level, i.e. at

$z = -(h + l_k)$ and $h_f = (d - l_k)$ where l_k is half length of the kelp frond. A_m is the velocity amplification factor obtained from the solution for the vegetation motion. The complex horizontal velocity in the vegetation zone is given in Dubi and Tørum (1994) as

$$u_2 = \frac{iCk}{\omega f_x} \cosh(k_s(h + d + z)) \exp[i(kx - \omega t)] \dots\dots\dots(2.7)$$

where

$$C = \frac{ga}{\cosh(k_s d) \cosh(kh) \left[1 - \frac{i}{\alpha f_x} \tanh(k_s d) \tanh(kh) \right]} \dots\dots\dots(2.8)$$

Substituting Eq.(2.7) into Eq.(2.4) we get the linearized form of energy dissipation, after time averaging, as

$$E_D = \frac{\rho f_{\dot{a}x}}{2} \int_{-(h+d)}^{-(h+l_k)} |u_2|^2 dz = \frac{\rho f_{\dot{a}x} |C|^2 |k|^2 \sinh(2k_s h_f) + 2k_s h_f}{2\omega^2 |f_x|^2 4k_s} \dots\dots\dots(2.9)$$

in which only the real part is considered. Substituting Eq.(2.9) into Eq.(1.1) for the 2D case we have

$$\frac{\partial}{\partial x} (EC_g) = \frac{1}{2} \rho g C_g \frac{\partial a^2}{\partial x} = -Ba^2 \dots\dots\dots(2.10)$$

in which C_g is assumed to be constant due to constant water depth and

$$B = \frac{\rho g^2 |\alpha k|^2 f_{\dot{a}x}}{2\omega^2 F^2 |\alpha f_x - iG|^2} \left(\frac{\sinh(2k_s h_f + 2k_s h_f)}{4k_s} \right) \dots\dots\dots(2.11)$$

where $F = \cosh k_s d \cosh kh$ and $G = \tanh k_s d \tanh kh$. The solution of Eq.(2.10) is

$$\frac{a}{a_0} = e^{-\frac{B'}{2}x} \dots\dots\dots(2.12)$$

where $B' = B/1/2\rho g C_g$. Equating Eq.(2.12) and Eq.(1.2) we find the damping rate to be

$$k_i = \frac{g|\alpha k|^2 f_{\dot{a}x}}{2\omega^2 F^2 |\alpha f_x - iG|^2 C_g} \left(\frac{\sinh(2k_s h_f + 2k_s h_f)}{4k_s} \right) \dots\dots\dots(2.13)$$

in which we shall adopt $|k| \cong k_r$ derived from the solution of the dispersion equation.

2.2 Solution of the complex dispersion equation and the damping rate.

The dispersion equation contains complex unknown variables k and f_x . The angular frequency ω is real and assumed to be known. The solution for the complex dispersion equation is found by iteration when Eq.(1.12) is rewritten as:

$$F(k, f_x) = \omega^2 \left(1 - \frac{i}{\alpha f_x} \tanh(k_s d) \tanh(kh)\right) - gk(\tanh(kh) - \frac{i}{\alpha f_x} \tanh(k_s d)) = 0 \dots (2.14)$$

The iteration scheme is carried out as follows:

(i) As a starting approximation we apply Eq.(2.14) for very small damping force coefficient, that is, for $f_x \rightarrow -i$, leading to an approximate solution for the wave number k_o for given α, ω, h and d . Then $k_1^{(o)} = \text{real}(k_o)$

(ii) With an initial guess $k_2^{(o)}$ for the imaginary part of k , we solve Eq.(2.14) with $k^{(o)} = k_1^{(o)} + ik_2^{(o)}$ as initial value input. The solution gives $k_r = \text{Re}(k)$ and $k_i = \text{Im}(k)$. The convergence criterion for the case is

$$\left| \frac{k^{(n)} - k^{(n-1)}}{k^{(n)}} \right| \leq e(k) \dots (2.15)$$

with $e(k)$ being an arbitrary small number which in our case is set equal to 10^{-5} . Results of the damping coefficient computed from the dispersion equation shall be compared with those obtained from the energy dissipation equation.

2.3 The damping rate from measured force and horizontal particle velocity

The damping rate can also be evaluated by making use of the measured force and horizontal velocity time series. Integrating the product of these two quantities and time averaging gives the energy dissipated per unit time as

$$E_D = \frac{1}{AT} \int_0^T F_m U_m \cos^2 \omega t \, dt = \frac{1}{2} \frac{F_m U_m}{A} \dots (2.16)$$

where F_m is the total measured force amplitude and U_m is the measured horizontal velocity amplitude. To get energy dissipation per unit horizontal surface area we have divided by $A = 8 \text{ m}^2$, which is the horizontal surface area of the shear plate used in the experiment. Inserting Eq.(2.16) into Eq. (1.1) we find that

$$k_i = \frac{1}{A} \frac{F_m U_m}{\rho g C_g \alpha_o^2} \dots (2.17)$$

in which ρ, g, C_g and maintain the same definition as in previous formulae, converted to full scale. For irregular waves we shall take significant force and significant velocity.

3. LABORATORY EXPERIMENT

The experiment was carried out in a 33 m long, 1 m wide and 1.6 m high wave tank as shown in Figure 1. The width of the channel was partitioned to give a width of 0.5 m. Five thousand models (scale 1:10) of *Laminaria hyperborea* plants were fixed on the bottom over a span of 9.3 meters. This represented a density of about 0.12 plants per horizontal square centimeter in the laboratory or 12 plants/square meter in the field. The setup consisted of eight capacitance wave gauges to measure surface elevations, one shear plate which was fixed flush with the bottom, to measure the horizontal force and a mini-current meter which was inserted in between the plants 4 centimeters above the shear plate to measure horizontal particle velocities. One of the wave gauges was placed above the shear plate. The first wave gauge, taken to be located at $x = 0$ and the last taken to be located at $x = 7$ m, were fixed about 1.2 meters inward from the inner and outer boundaries respectively.

We started with 6 m water depth and tested with regular waves with periods ranging from 4-14 seconds, full scale. With the same water depth, irregular waves with peak periods ranging from 4-14 seconds were tested. For each wave period, several wave heights were tested.

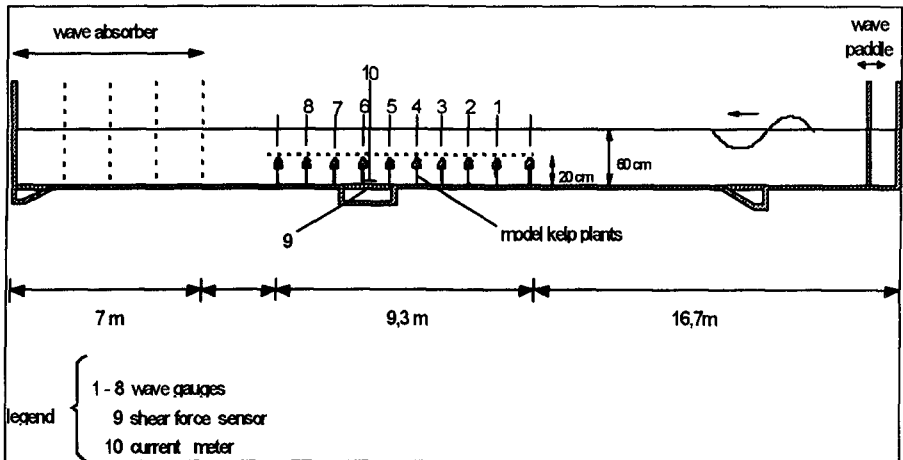


Figure 1 Laboratory experiment layout

4. RESULTS

(1) The exponential decay model given by Eq.(1.2) was fitted to measured data by regression analysis based on the least squares method. Figure 1 shows an overview of the exponential decay of the wave heights with respect to distance from the origin. Figure 3 shows theoretical variation of the damping rate with wave period T obtained from Eq.(2.14) and Eq.(2.13) for total water depth $D = 6$ m using the following kelp

plant properties: total kelp height $d = 2\text{m}$, frond half length $l_k = 0.5\text{m}$, density of kelp $\rho = 1120\text{ kg/m}^3$, mass of frond and stipe = 0.75 kg/m , linearized spring constant $k_o = 20\text{N/m}$, linearized (empirical) force coefficient $F_\lambda = 30\text{N}/(\text{m/s})$, added mass for both frond and stipe $C_a = 1$, number of plants per horizontal square meter $n_k = 12\text{plants/m}^2$. For the given parameters the damping rate using Eq.(2.13) increases with the wave period for small values of T to a maximum and then decreases gently for larger values of T to an almost asymptotic value. On the other hand, the damping rate from the dispersion equation decreases rapidly for larger values of T . In the same figure, we also compare the damping rates derived from Eq.(1.11) given by Asano et al. (1992) and the solution of the dispersion equation given by Wang and Tørum (1994).

(2) Figure 4 shows a comparison of theoretical values obtained from Eq.(2.13) with those obtained experimentally for irregular waves in a water depth of 4m. Theoretical models by Asano et al. (1992) and Wang and Tørum (1994) are also compared to the measured data points.

(3) Figures 5 through 8 show a comparison of theoretical values of the energy dissipation equation with measured values from regular and irregular waves in water depths of 6, 8 and 10 meters. From these figures we observe several things:

First, the experimental damping coefficient varies more widely for shorter peak periods and almost converges (narrower scatter) for longer peak periods.

Second, for longer peak periods the theoretical damping coefficient is almost independent of the peak period despite a gradual decrease.

Third, when we compare the damping rates in 4 and 6 meters water depths, we find larger values for the shallower water. We may conclude that the shallower the water, the higher the damping coefficient. This observation is also in agreement with field results by Mork (1995).

Fourth, The theoretical model by Asano et al. (1992) is good only for the prediction of the damping rate for small damping. For large damping, the model grossly overestimates the damping rate. The model by Wang and Tørum (1994) underestimates the damping rate for small waves and overestimates it for large damping. For the whole range and especially for practical wave periods (6-14 seconds), the present model is very good.

Fifth, the damping rate obtained from the experiment for regular waves shows a very wide scatter. However, the theoretically predicted values appear to fit within the range of scatter as shown in Figure 6.

Sixth, as the water depth increases, the energy dissipation equation (Eq.(2.13.)) tends to over-estimate the damping coefficient, while the dispersion equation (Eq.(2.14)) comes closer and closer to the measured values. The reason for this discrepancy is not clear. However, since the empirical force coefficient F_λ was evaluated at 6m water depth, in the absence of force data for other water depths, it may be that this coefficient is variable with water depth.

(4) Figures 9 and 10 show the general functional relationship between the damping coefficient and total water depth and the number of plants per square meter respectively. For all wave periods $k_t = 0.0658\exp(-0.5*D)$.

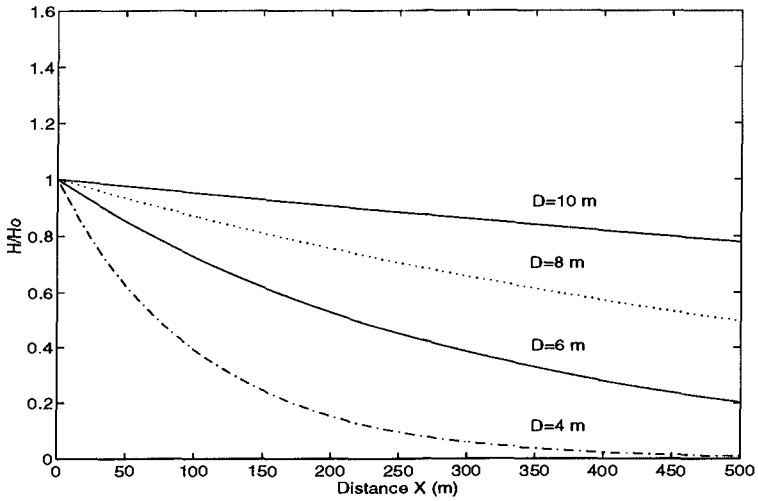


Figure 2 Comparison of exponential decay for different total water depths.

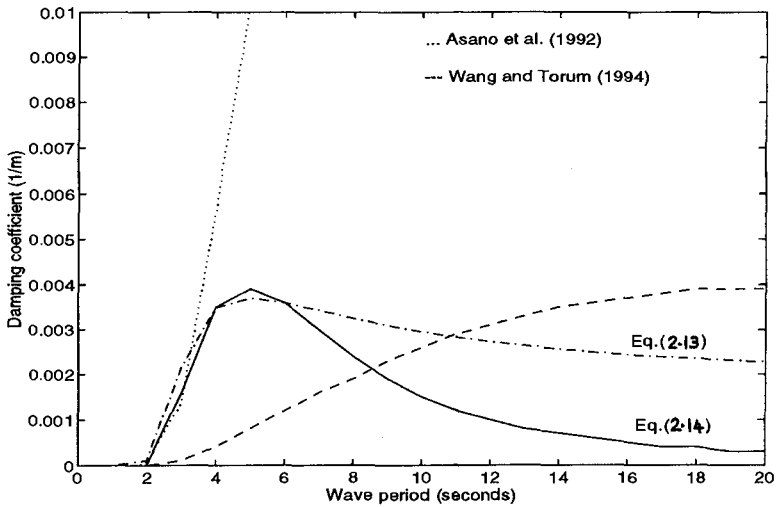


Figure 3 Comparison of theoretical models of Asano et al. (1992), Wang and Torum (1994) and the present model (Eq.(2.13) and Eq.(2.14)). Total water depth = 6 m.

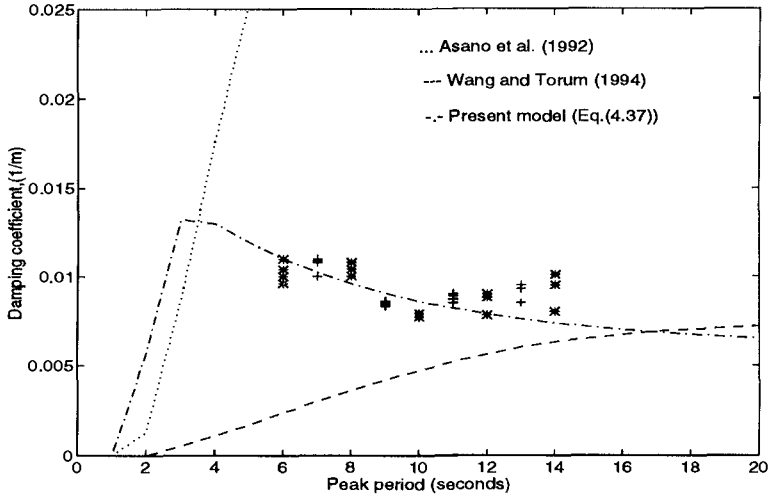


Figure 4 Comparison of theoretical values of previous models and the present model (Eq. (2.13) with measured values (*+). Total water depth = 4 m

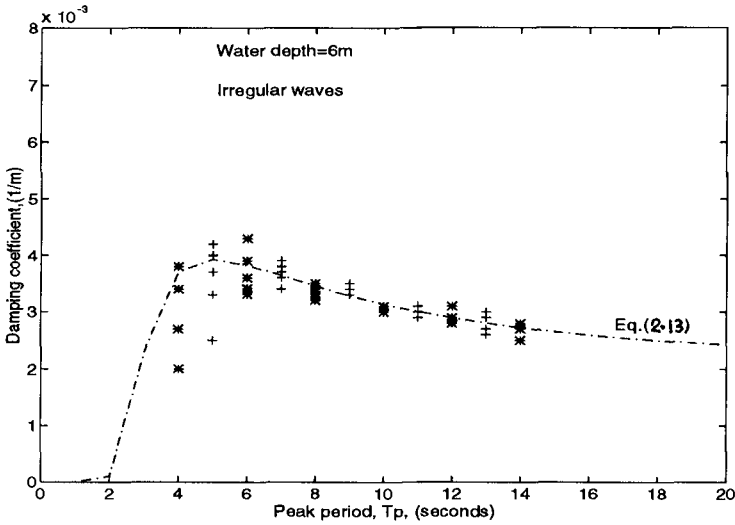


Figure 5 Comparison of theoretical values of Eq. (2.13) with measured values (*+). with irregular waves. Total water depth = 6 m

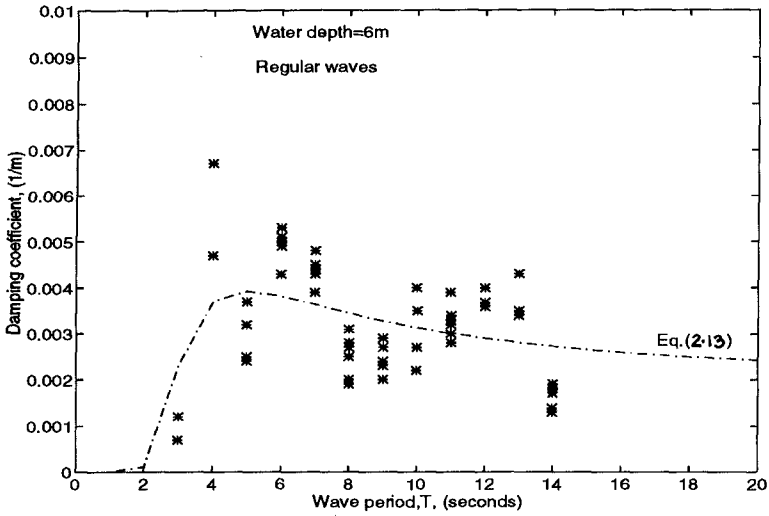


Figure 6 Comparison of theoretical values of Eq. (2.13) with measured values with regular waves (*+). Total water depth = 6 m

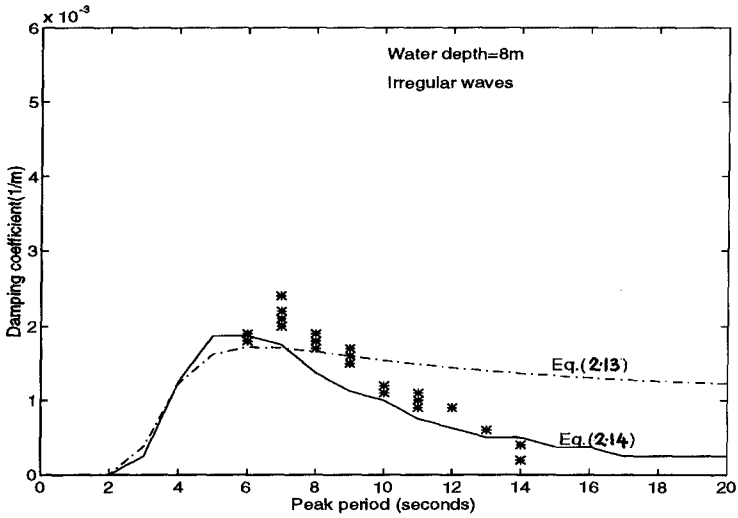


Figure 7 Comparison of theoretical values of Eq.(2.13) and Eq. (2.14) with measured values (*) with irregular waves. Total water depth = 8 m

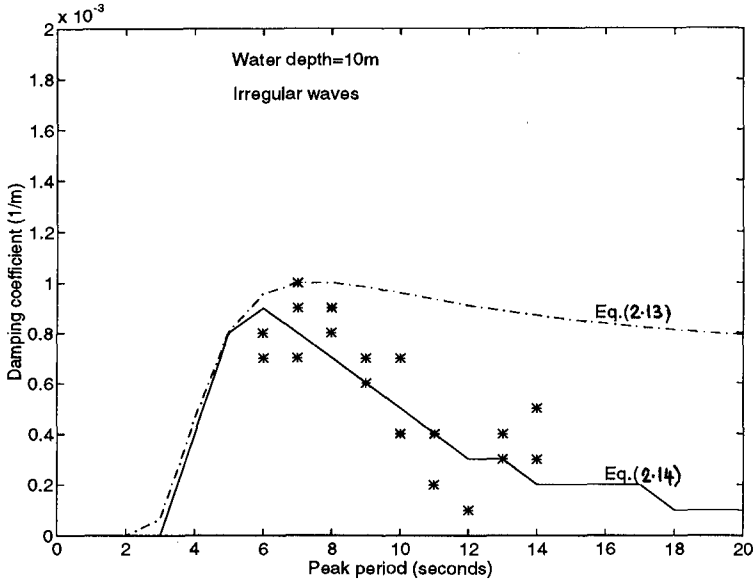


Figure 8 Comparison of theoretical values of Eq.(2.13) and Eq. (2.14) with measured values (*) with irregular waves. Total water depth = 10 m

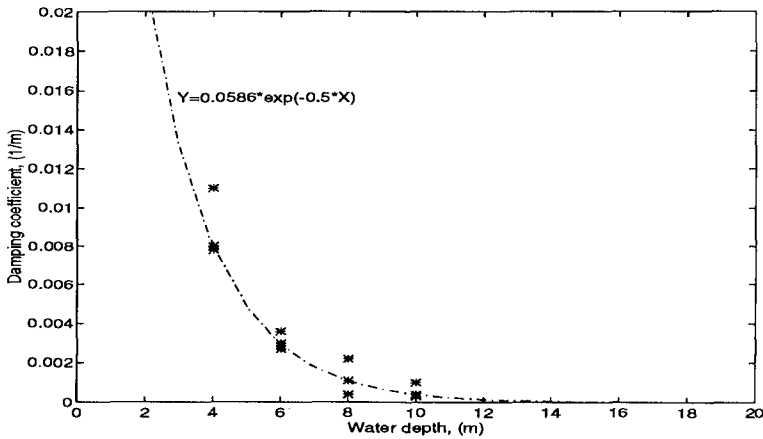


Figure 9 General functional relationship between damping coefficient and total water depth $D \geq d$, $T=7, 10$ and $14s$. For all wave periods $k_i = 0.0658 \exp(-0.5 \cdot D)$

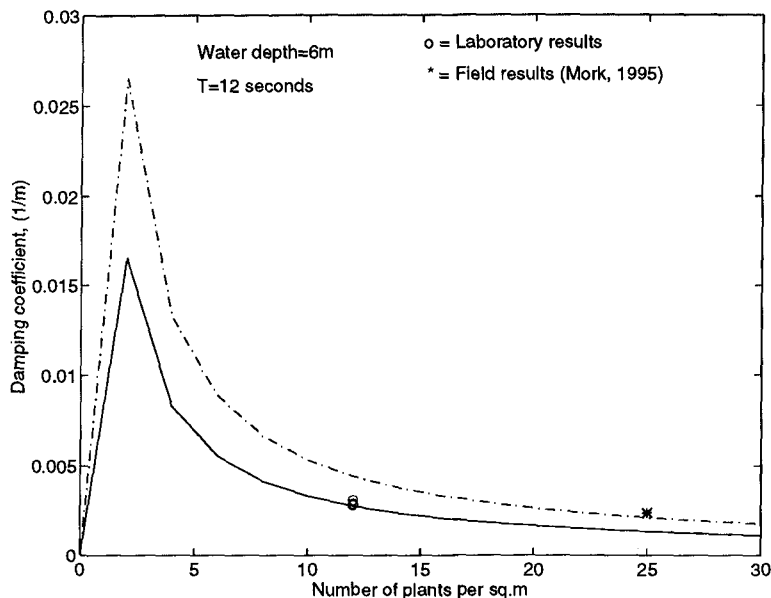


Figure 10 Variation of damping coefficient with number of plants per square meter. Total water depth = 6 m, ——— $d=2m$, - - - - - $d=3.2m$

CONCLUSION

(1) As waves propagate in kelp fields, their wave heights are reduced significantly and wave lengths are shortened. Both theoretical and experimental studies indicate that the damping coefficient is governed by the wave period. It increases with wave period for shorter periods, reaches a maximum and then decreases gradually with the wave period for longer periods (Figures 5 through 8)

(2) The damping coefficient is also governed by the water depth and population density of plants. Figure 9 shows that the damping coefficient decreases with increasing water depth. Figure 10 shows that it increases with increasing population density until it reaches a maximum, after which it decreases sharply with increasing density.

(3) Basing on the theoretical and experimental results, wave height attenuation is more substantial in shallow water than in deep water. In fact it is almost negligible in water depths greater than 10 meters. For a population density of 12 plants/m^2 , significant heights of irregular waves will be reduced by say 50% over a distance of 74, 216, 495 and 1390 meters in 4, 6, 8 and 10 meters mean water depth respectively.

(4) The linear assumption of the wave force in relation to the particle velocities leads to an exponential decay (damping) coefficient of the wave height with respect to distance.

ACKNOWLEDGEMENT

We wish to acknowledge with thanks the financial support we received from the Norwegian Directorate for Nature Management and the Norwegian Universities' Committee for Development Research and Education (NUFU). The first author is also grateful to the IOC of UNESCO for the travel grant to the Conference in Orlando, Florida.

REFERENCES

1. Asano, T., Deguchi, H., and Kobayashi, N. (1992). "Interaction between water waves and vegetation". *Proc. 23rd International Conference on Coastal Engineering*, Venice, Italy, pp. 2710-2723.
2. Dalrymple, R.A., Hwang, P.A. and Perlin, M. (1982): "Ocean Engineering aspects of coastal kelp farming". Report no. J-III, Coastal and Offshore Engineering and Research, Inc., Newark, Delaware.
3. Dean, R.G. and Dalrymple, R.A. (1984): *Water wave mechanics for engineers and scientists*. Prentice-Hall Inc., New Jersey.
4. Dubi, A.M. (1995): "Damping of water waves by submerged vegetation. A case study on *Laminaria hyperborea*". Dr. Ing. Thesis. University of Trondheim, The Norwegian Institute of Technology. Trondheim, Norway. ISBN 82-7119-859-9
5. Dubi, A.M. and Tørum, A., (1994): "Wave damping by kelp vegetation". *Proc. 24th International Conference on Coastal Engineering*, Kobe, Japan, pp. 142-156
6. Ippen, A.T. (1966): "*Estuary and Coastline hydrodynamics*". McGraw-Hill Book Co. Inc., New York.
7. Kobayashi, N., Raichle, A.W., and Asano, T. (1991). "Prediction of wave attenuation by vegetation and seaweed". Research report no. CACR-91-07, Center for Applied Coastal Research, Dept. of Civil Engineering, University of Delaware, Newark, Delaware 19716
8. Madsen, O.S. (1974). "Wave transmission through porous structures". *Journal of Water Ways Harbors and Coastal Engineering Division, Proc. of the ASCE*, Vol. 100, No. WW3, May, 1974 pp. 169-188
9. Mei, C.C. (1989): "*Applied Dynamics of Ocean Surface Waves*". World Scientific Publishing Co., Singapore, pp. 740.
10. Wang, H. and Tørum, A. (1994). 'A numerical model on beach response behind coastal kelp fields". SINTEF-NHL report no. STF60 A94092

CHAPTER 204

EXPERIMENTAL STUDY ON THE EFFECT OF GRAVITY DRAINAGE SYSTEM ON BEACH STABILIZATION

Hiroshi KANAZAWA ¹⁾, Fumihiko MATSUKAWA ¹⁾
Kazumasa KATO ²⁾ and Iwao HASEGAWA ³⁾

Abstract

In order to develop a new beach preservation technique which has two functions of protecting the beach in a storm and enabling utilization of beach during calm sea, we consider the system of controlling a groundwater level by burying a permeable layer under the foreshore. Since most of the components are buried underground, people on the beach do not notice the presence of the system, enabling preservation of the beach in its most natural state. The greatest challenge of the system is, however, whether installation of the permeable layer alone will fully prevent erosion. Authors therefore conducted an experiment to evaluate beach stabilization effect of the present system. The result indicates that the permeable layer buried in the sand can prevent rise in the groundwater level and the wave set-up. The critical wave height for the foreshore erosion is 1.66 times higher than that on the beach without the permeable layer.

1. Introduction

Against severe natural conditions in Japan, we have constructed seawalls with wave breaking blocks, jetties, detached breakwaters, and so on. These protection measures have stopped further erosion, and also protected the hinterland and people from large waves in a storm. However, in a calm sea condition, the structures keep the people away from the waterfront. Therefore, we are developing a new beach stabilization technique, which has functions of disaster prevention in a storm and beach utilization in a calm. In order to develop such a new beach stabilization technique, first of all a beach erosion mechanism

1)Yokohama Investigation and Design Office, the Second District Port Construction Bureau, Ministry of Transport, Kitanaka-dohri 5-57, Naka-ku, Yokohama, 231, JAPAN

2)Port and Harbor Research Institute, Nagase 3-1-1, Yokosuka, 239, JAPAN

3)ECOH co., Tsuruya-cho 2-19-4, Kanagawa-ku, Yokohama, 221, JAPAN

during stormy weather was investigated in the field (Katoh and Yanagishima: 1992, 1993). These investigations elucidated the relation between rise in the watertable due to wave run-up and the beach erosion. That is, when waves run-up beyond the berm crest in a storm, the sea water stays for a good while on the horizontal area of berm, which accelerates the infiltration of water into the beach. As a result, the watertable becomes higher, and the water exfiltrates through the surface of foreshore. The seepage level of water corresponds to the critical level of berm erosion. Taking this result into consideration, there are two countermeasures for reducing the beach erosion in a storm. One is a construction of a structure offshore to decrease the wave energy and to suppress the wave run-up on the beach. Another is to lower the watertable by some method.

As a latter measure, we consider a permeable layer setting up under the beach. In a storm, waves run-up to the high level and the water infiltrate into the beach. However, the groundwater may be gravitationally drained to the offshore through the layer. Concerning to the effect of permeable layers, two- and three-dimensional experiments were conducted with regular waves to compare the groundwater levels and the profiles on the beach with and without the permeable layer.

2. Details of Experiments

2.1 Aims of Experiments

Aims of two- and three-dimensional experiments are as follows:

- (1) Two-dimensional experiments : A purpose is to know the possibility of controlling watertable and reducing the beach erosion for three different kinds of permeable layers.
- (2) Three-dimensional experiments : There are two purposes in the three-dimensional experiments. One is to confirm the effect of the convergence type drainage system, in which the water gathered by the permeable layer is drained offshore through one pipe. Another is to evaluate the effect of permeable layer on beach stabilization quantitatively.

2.2 Conditions and Methods in Two-dimensional Experiments

The experiments were carried out in a experimental flume of 38.0 m long, 0.5 m wide and 1.5 m high. The movable profiles were made with sand of 0.135 mm in a median grain size. The permeability coefficient of sand is 6.28×10^{-3} cm/s, which is the result of permeability test.

As the permeable layer, three types shown in Figure 1 were tested. Features of these types are as follows, respectively.

- (1) Gravel Permeable Layer (GPL) : Gravels of 13 - 20 mm in size were laid with the thickness of 10 cm from the backshore to the breaker zone (Figure 1, top). Plankton nets were interposed between the sand layers and the gravel layer to prevent sand from intruding into the gravel layer. The sand layer above the permeable layer was 10 cm thick. A still water level was situated inside the permeable layer of horizontal part.

(2) Gravel Permeable Layer with Drainage Pipe (GPL-DP) : The thickness of the permeable layer and the sand layer were decreased to half that of GPL, respectively (Figure 1, middle). The permeable layer in the backshore was therefore situated above the still water level. A drainage pipe (44 mm in inner diameter) extended from the permeable layer near the shoreline toward offshore. The pipe was buried along the wall of experimental flume, with its outlet vent located at the wave breaking point.

(3) Permeable Pipe with Drainage Pipe (PP-DP) : Three permeable pipes were used in place of the permeable layer (Figure 1, bottom, Figure 2). The permeable pipe was a spring coil of 15 mm diameter wrapped up with a plankton net as shown in Figure 3. Groundwater percolates into the pipe through the plankton net. Three permeable pipes were buried under the beach with a 15 cm interval in the traverse direction. To protect the permeable pipes, a gravel layer was placed above the pipes. This gravel layer did not act as a permeable layer because sand was filled in the voids of gravel layer. The drainage pipe extending toward the offshore direction from near the shoreline was the same as that used in the GPL-DP.

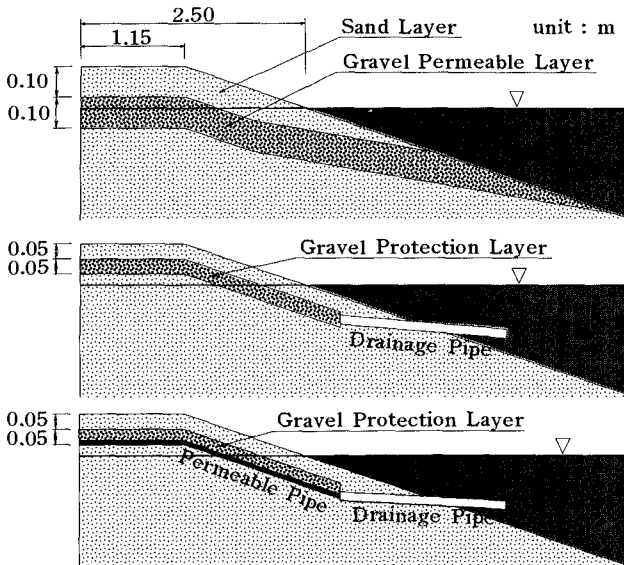


Figure 1: Types of Permeable Layer in Two Dimensional Experiment.

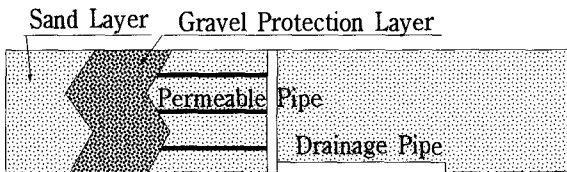


Figure 2 : Plane view of PP-DP.

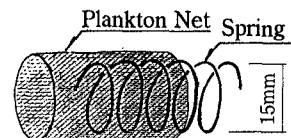


Figure 3 : Structure of Permeable Pipe.

Table 1 : Waves in Two Dimensional Experiments.

H_o (cm)	T (s)	H_o/L_o	GPL	GPL-DP	PP-DP	Without a Permeable Layer
8.4	1.34	0.03	○	○	○	○
10.0	1.79	0.03	○	○	○	○
15.0	1.79	0.03	○			○

The wave conditions in the two dimensional experiments are listed in Table 1, in which the cases with a circle were conducted. In the experiment, the level of groundwater in the section from the backshore to the shoreline, wave set-up in the surf zone, and the profile changes were measured. To measure the groundwater level and the wave set-up, a manometer using a vinyl tube 6 mm in inner diameter was used. Measurements were carried out with an interval of 25 cm along the wall of the flume in the cross-shore direction. Using a sand level meter, the profile changes were measured along three measurement lines in the traverse direction with an interval of 10 cm. The mean value of the profiles along the three measurement lines is calculated and used for further analysis of the profile changes. These result are compared with those obtained in the profile without permeable layer. In the profile without a permeable layer and the profile with GPL, a dye (methylene blue) was injected close to the glass wall of the flume. The seepage velocity inside the permeable layer and the sand layer above the permeable layer respectively were estimated from the travelling distance of the gravitational center of the dye patch and its elapsed time.

2.3 Conditions and Method in Three-Dimensional Experiments

Test conditions were primarily the same as those in the two dimensional experiments except the following.

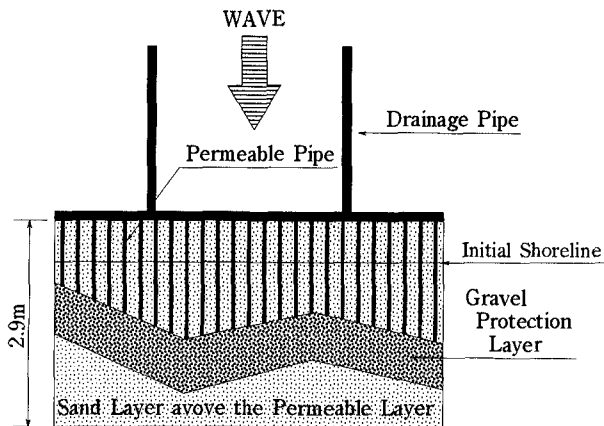


Figure 4 : Layout of Permeable Layer in Three-Dimensional Experiments.

A wave basin (35.0 m L × 1.1 m H × 15.0 m W) was divided into two sections (7.5 m W) to enable simultaneous experiments on the two beaches with PP-DP and without the permeable layer. Figure 4 shows the layout of PP-DP: 100 permeable pipes measuring 2.9 m in length and 15 mm in inner diameter were buried with a 7.5 cm longshore interval and eight drainage pipes measuring 44 mm in inner diameter with a 94 cm longshore interval. The outlet vent of the drainage pipe was positioned at the wave breaking line. The median grain size of the sand used in the experiments was $d_{50} = 0.16$ mm and the permeability coefficient was $k = 1.14 \times 10^{-2}$ cm/s.

Table 2 : Waves and Profile Changes in Three-dimensional Experiments.

T (s)	H _o (cm)	Value of C	Classification of Profile Changes	
			Without a Permeable Layer	PP-DP
1.34	1.5	2.0	II, III	III
	3.0	4.0	I, II	II, III
	4.5	6.0	I	II
	6.0	8.0	I	I
	7.5	10.0	I	I
	☆ 8.4	11.2	I	I
2.01	1.8	1.8	III	III
	3.7	3.7	I, II	II, III
	5.4	5.5	I	II
	7.2	7.4	I	I
	9.0	9.2	I	I
	☆ 12.5	12.8	I	I

The wave conditions used in the experiments are listed in the first two columns of Table 2. The waves were acted for one hour in each case. The three columns on the right in the table give information on the shoreline changes; the details are given later.

The groundwater level was measured with a 1.25 m interval in the longshore direction along the two measurement lines, the initial shoreline (shoreline at the time of still water) and the line near the tip of the wave run-up. Profiles were measured with a 0.125 m interval in the cross-shore direction along the three measurement lines set with a 2.25 m interval in the longshore direction. For the cases with the wave height values marked with asterisks in Table 1, additional measurements of profile were done along the measurement lines set with 0.25 m interval in the longshore direction.

3. Results of Experiments

3.1 Comparison of Groundwater Levels

Figure 5 shows the groundwater level in the two-dimensional experiment in which waves of 8.4 cm in height and 1.34 s in period were acted on the beach without the permeable layer. The reference level for elevation on the ordinate is the initial still water

level. The groundwater level begins to rise immediately after waves are acted, and substantially levels off after 11 minutes. The peak of the watertable near the location of 2.0 m substantially coincides with the tip end of the run-up, and the water level exceeds the still water level by 2 cm. The wave set-up at the shoreline located at 2.5 m is 1 cm above the still water level.

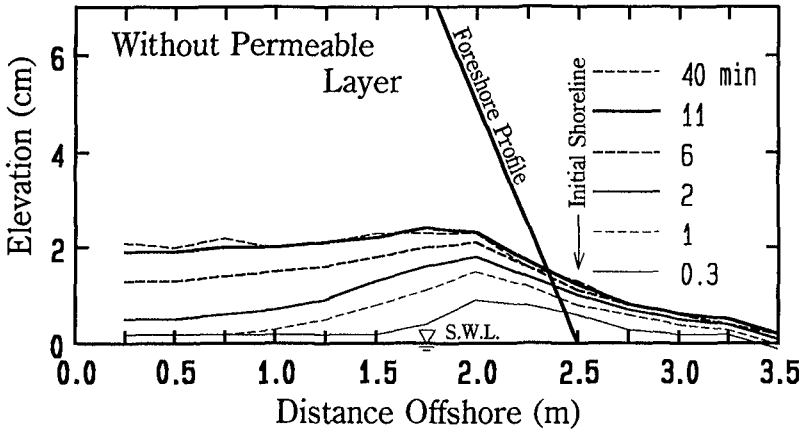


Figure 5 : Changes of Groundwater Level with Time in the Beach without the Permeable Layer (two-dimensional experiment).

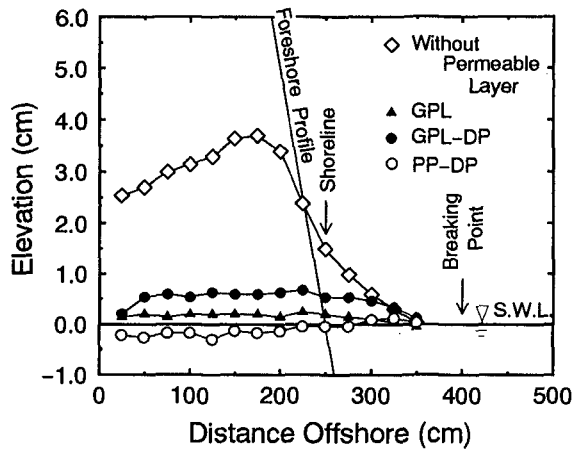


Figure 6 : Comparison of Groundwater Levels between Beaches with and without the Permeable Layer (two-dimensional experiment).

Figure 6 shows the distributions of groundwater level and the wave set-up measured ten minutes after the waves of 10.0 cm in height and 1.79 s in period were acted on the beaches without the permeable layer and with three types of permeable layer. Because of

the severe wave conditions, rise in the groundwater level and the wave set-up on the beach without a permeable layer are greater than those shown in Figure 5. In the beaches with the permeable layers, both the rise in the groundwater level and the wave set-up are quite insignificant. In particular, the groundwater level in the beach with PP-DP is lower than the initial still water level. This is considered to be the effect of wave set-down because the terminal end of the drainage pipe on the offshore side is located at the wave breaking point.

3.2 Wave set-up

It is confirmed that the permeable layer has a function to suppress rise in the groundwater level. The experiment results, however, suggest that it can also prevent the wave set-up. Figure 7 shows the relation between the wave set-up at the initial shoreline and the wave steepness in the two-dimensional experiment. For all cases, the values of wave set-up measured 10 minutes after the start of wave action are plotted. The broken line in the figure is a theoretical value of wave set-up according to Goda's theory (1975) when the bottom gradient is 1/10. The wave set-up on the beach without a permeable layer substantially agrees with Goda's theoretical value. On the beach with the permeable layer, particularly with PP-DP, no wave set-up is observed.

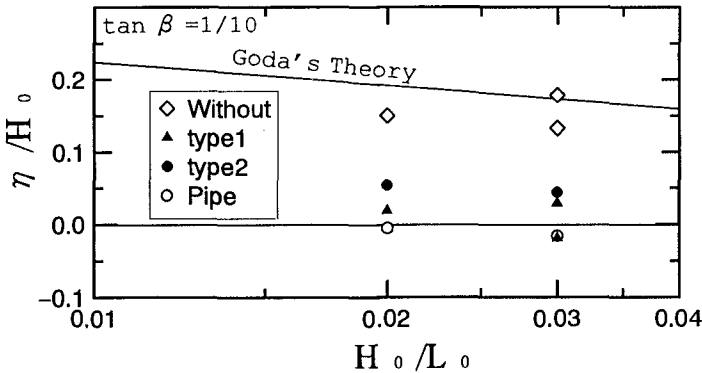


Figure 7 : Relation between Wave set-up and Wave Steepness
(two-dimensional experiment).

Figure 8 shows the longshore distributions of wave set-up at the shoreline on the beaches with and without the permeable layer in the three-dimensional experiments. The wave height was 12.5 cm and the period was 2.01 s, and the measurements were taken 30 minutes after the waves were acted. On the beach without the permeable layer, the wave set-up agrees with the theoretical value of Goda (1975) which is shown by a horizontal line in the figure. On the beach with the permeable layer, on the other hand, the average wave set-up is about 0.5 cm. The relative position between the measurement point of groundwater level and the position of the drainage pipe, which is shown by \uparrow in the Figure 8, changes from a location to a location. The wave set, however, is considered to

be constant in the longshore direction, although a slight fluctuation is observed. This result indicates that groundwater within the range of 0.94 m along the longshore direction could be discharged by one drainage pipe, suggesting that convergence type drainage system is feasible.

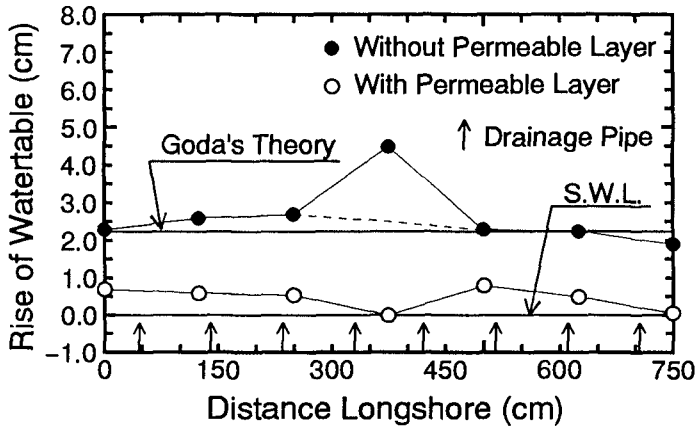


Figure 8 : Comparison of Groundwater Levels between on the Beaches with and without the Permeable Layer (three-dimensional experiment).

3.3 Seepage velocity in the Sand Layer and the Permeable Layer

Figure 9 shows the seepage velocity in the sand layer and the permeable layer. The top portion shows the values for the beach without the permeable layer, the bottom portion those for the GPL. The velocity in the profile without the permeable layer is smaller than 0.15 mm/min. The velocity in the sand layer located above the still water level is directed onshoreward, whereas the flow in the sand layer below the still water level is directed toward the offshore along the sea bottom. In the beach with the permeable layer, the seepage velocity is two to three times that in the beach without the permeable layer, with a offshoreward velocity of about 30 cm/min (about 1000 times the velocity in the sand layer; note that velocity vectors are in logarithmic expression in the figure). It must be noted that the flow in the permeable layer fluctuated with the same period as wave motions, but the time average velocity is shown in Figure 9.

A reason of the fast velocity in the permeable layer is studied. Firstly, a numerical simulation of two dimensional unsteady flow was conducted to evaluate the amount of water infiltration into the beach due to the wave run-up. The simulation was carried out for the entire model beach. The water infiltration into the beach in the portion from the shoreline to the run-up level was given, so that the calculated groundwater level agreed with the measured value. The rate of infiltration into the beach without the permeable layer was estimated to be $1.1 \text{ cm}^3/\text{min}/\text{cm}$. As for the beach with the permeable layer, if the same amount of water is assumed to infiltrate into the beach due to the wave swashing,

the seepage velocity in the permeable layer (10 cm thick) would be 0.37 cm/min, given the void ratio of 0.3. Thus, the fast velocity in the permeable layer cannot be explained solely by this infiltration. In the following consideration, therefore, the experimental fact that no wave set-up is observed on the beach with the permeable layer is taken into account.

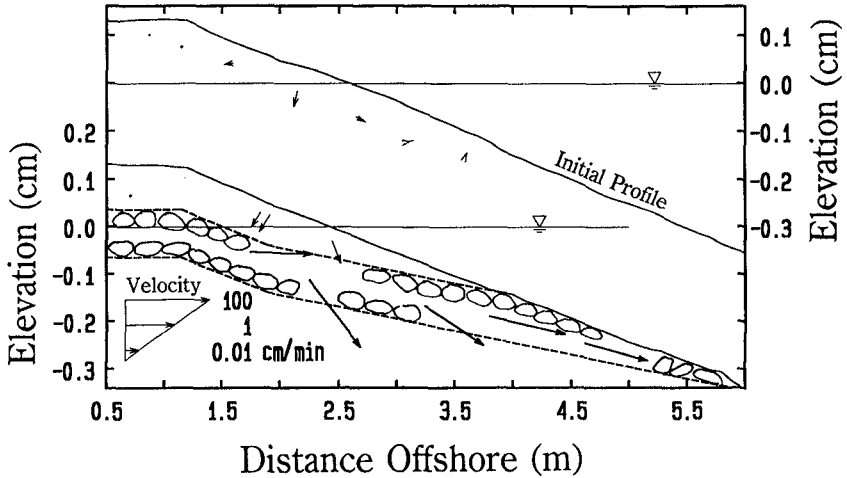


Figure 9 : Seepage Velocity in the Sand Layer and the Permeable Layer (two-dimensional experiment).

Assuming two-dimensional steady-state condition and ignoring the term of horizontal diffusion, the equation of motion in the breaker zone is

$$\frac{d}{dx} (\rho U^2 (h + \eta) + Sxx) = - \rho g (h + \eta) \frac{d \eta}{dx} - \tau_b \dots\dots\dots (1)$$

with the offshore direction taken along the positive x-axis, where U is the mean velocity, h water depth, η wave set-up, Sxx radiation stress and τ_b bottom shear stress. Since there is no wave set-up, $\eta = 0$. Then, by assuming $\tau_b = 0$, the equation (2) can be easily integrated.

From the radiation stress given by the equation below,

$$Sxx = - \frac{3}{16} \rho g \gamma^2 \tan^2 \beta \dots\dots\dots (2)$$

which is approximated by the linear shallow-water theory by assuming a uniform slope ($h = x \tan \beta$) and a constant proportionality between the wave height and depth ($\gamma = H / h$), then it holds:

$$U = -\frac{\gamma}{4} \sqrt{3 g x \tan^3 \beta} \dots\dots\dots (3)$$

If it is assumed that a flow which compensates the onshoreward discharge ($U \times h$) is generated in the permeable layer, then the velocity V_i in the permeable layer is

$$V_i = \frac{\gamma}{4 \lambda D} \sqrt{3 g x^3 \tan^3 \beta} \dots\dots\dots (4)$$

where λ is the porosity (=0.3) and D is the thickness of the permeable layer (=10 cm). By assuming $\gamma = 0.78$, V_i at a distance of 5 cm offshore ($h=0.5$ cm) from the shoreline is calculated to be 75 cm/min, which is almost 2.5 times larger than the value actually measured in the permeable layer. This is probably because the velocity is overestimated in equation (3). The calculated value would be much closer to the actual measurement if considerations are given to the factors that the onshore velocity in the surf zone is subject to the bottom shear stress, that any small rate of wave set-up would act to decelerate the velocity, and that there is the effect of the permeability coefficient in the sand layer above the permeable layer. It can be said that the fast velocity in the permeable layer is subject to the strong influence of the gradient of the radiation stress.

3.4 Profile changes

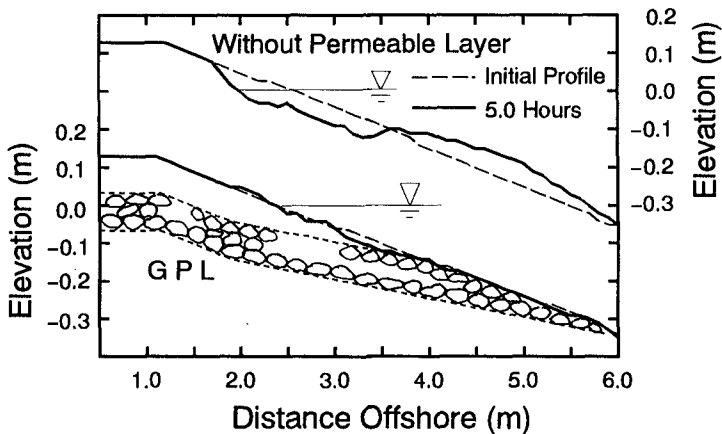


Figure 10 : Comparison of Profile Changes
(two-dimensional experiment : $H=8.4$ cm, $T=1.34$ s).

Figure 10 shows the profile changes on the beach without the permeable layer and with GPL, respectively acted with waves of 1.34 s in period and 8.4 cm in height for five hours. The profile without the permeable layer eroded in the range including the initial shoreline, and the sand deposited on the offshore forming a bar. The shoreline receded for about 0.5 m. On the beach with GPL, on the other hand, hardly any profile change is observed except for a small berm slightly on the onshore side of the shoreline. No change

in the shoreline position is observed. In this case, the permeable layer is effective in preventing erosion near the shoreline.

Figure 11 shows the profile changes acted with waves of 1.79 s in period and 15.0 cm in height for five hours. Because of severe wave conditions, the beach without the permeable layer eroded in the range from 1.3 m to 4.3 m. At a point about 4.1 m, there is formed a trough, of which on the offshore side a bar is formed. Although similar erosion is observed on the beach with GPL, no trough is formed since the erosion do not extend deeper than the permeable layer. Sand from the layer above the permeable layer is transported toward offshore direction and deposits on the outlet vent of the permeable layer. This phenomenon was observed from an early stage of wave action. The drainage capacity of the permeable layer was reduced by the clogging of the outlet vent. The erosion occurring at the initial stage of wave action was attributable to the insufficient drainage capacity of the permeable layer, but the eventual erosion similar to that occurring on the beach without the permeable layer was probably because the outlet vent was clogged.

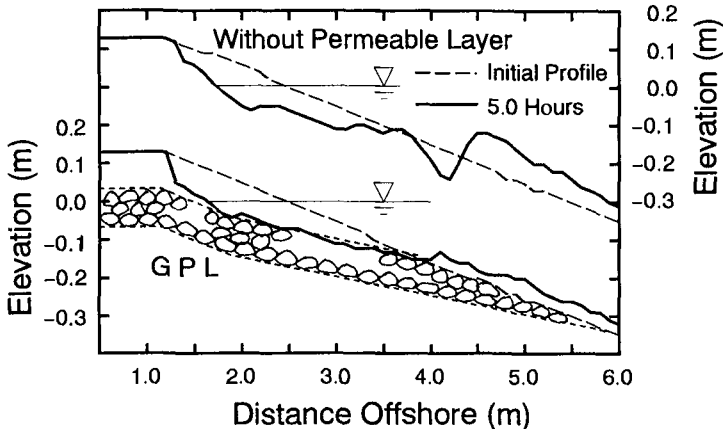


Figure 11 : Comparison of Profile Changes
(two-dimensional experiment : $H=15.0$ cm, $T=1.79$ s).

The top part of Figure 12 shows the topographical change on the beach with the permeable layer, PP-DP. Waves of 8.4 cm in height and 1.34 s in period were acted for one hour. The locations of drainage pipes are clearly shown in the figure, but as they were actually buried underground, only the outlet vents were visible. Because of the wave incident angle of 90° to the shoreline, the profile change is two dimensional and there is no three dimensional effect of draining the water offshore through the eight drainage pipes.

As for the changes in the cross-shore direction, the foreshore is eroded and a bar is formed offshore at about 4 m. The outlet vents of the drainage pipes was located on the immediately onshore side of the bar. However, the vents were not clogged by the sand because the terminal end of the drainage pipe was set slightly above the sea bottom (see Figure 1). Then, the groundwater controlling effect of the permeable pipes is included

even in this foreshore erosion. To demonstrate this point, we conducted a similar experiment using a beach without the permeable layer. The result is shown in the bottom part of Figure 12. On the beach without the permeable layer, erosion on the foreshore is extensive, with a substantial amount of deposition on the offshore bar.

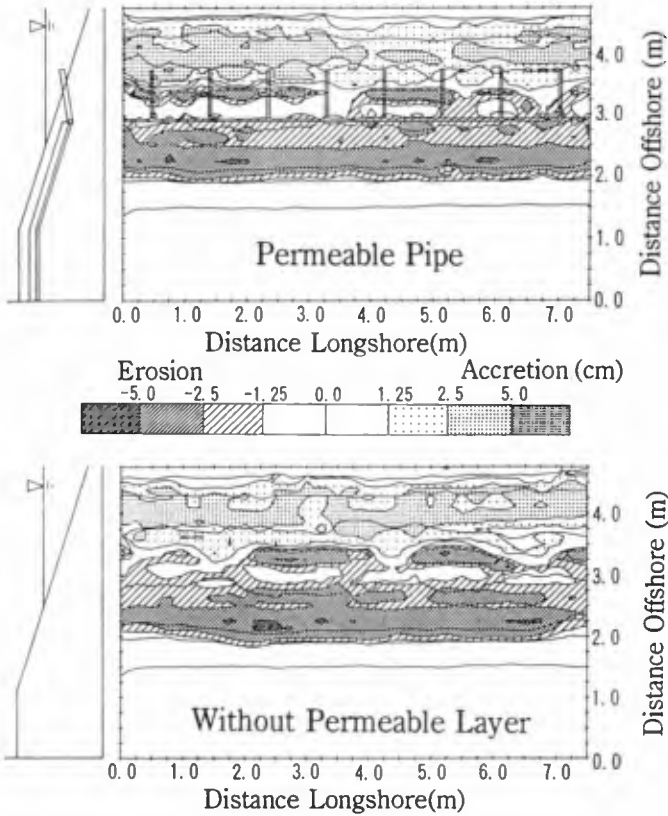


Figure 12 : Comparison of Topographical Changes
(three-dimensional experiments : $H=8.4$ cm, $T=1.34$ s).

As discussed above, in some cases erosion do occur on the beach with the permeable layer, although its extent is slightly less. To have quantitative understanding on the effect of permeable layer, we conduct an analysis using the constant C of the beach profile type classification (Sunamura and Horikawa, 1974) which is evaluated by the equation (5), in which an averaged profile is considered in each case.

$$C = (\tan \beta)^{0.27} \left(\frac{d}{L_0} \right)^{-0.67} \left(\frac{H_0}{L_0} \right) \dots\dots\dots (5)$$

According to Sunamura et al, profile changes can be classified into three types depending on the value C . Characteristic features of each type with regard to the change of the shoreline position can be described as follows:

- $C > 8$ Type I : Recession
 $8 > C > 4$ Type II : Stable
 $4 > C$ Type III : Advancement

The value C calculated by the equation (5) for each case is listed in the third column of Table 2. The value C is the same so long as the wave conditions are identical, without regarding to whether or not the permeable layer is employed. However, different types of shoreline changes are observed on the beaches with and without the permeable layer even if the value C is identical. The types of shoreline changes were investigated for all cases in the three-dimensional experiment. The results are listed in Table 2 and shown in Figure 13. Referring to Figure 13, it is noted that the value C in the case of experiment without the permeable layer is smaller than that of Sunamura et al. This is probably because of the following differences in the experimental conditions: the present experiment is the three-dimensional one (two-dimensional in Sunamura et al); the foreshore slope was 1/10 (many cases gentler than 1/10 are contained in Sunamura et al); and, waves were acted for one hour (more than 40 hours in Sunamura et al). Because of these differences, we evaluate the effect of permeable layer by comparing the results obtained for the beaches with and without the permeable layer instead of comparing with the results obtained by Sunamura et al. Referring to Figure 13, it is seen that the value C is larger on the beach with the permeable layer. In the case without a permeable layer, the mean value of C in the category of shoreline stable is 3.2, while in the case with the permeable layer it is 5.3. In short, the value of C is larger in the case with the permeable layer by a factor of 1.66.

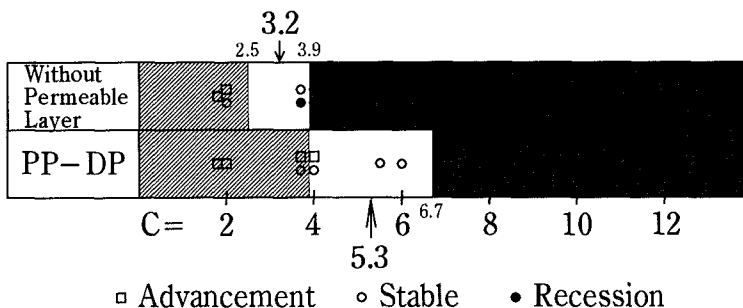


Figure 13 : Classification of Types of Shoreline Changes
in Three-Dimensional Experiment.

When the changes in the value C are viewed from a different angle, the following can be said. When a beach with the permeable layer is subjected to waves having a value C_a , shoreline changes of the beach will be the same as those observed in the natural

beach (without the permeable layer) subjected to waves of $C_a / 1.66$. In other words, the permeable layer is effective in reducing the value C_a to about 60 %. This effect can be achieved also by a wave controlling structure. Generally, a wave controlling structure can control the wave height and not the wave period. Thus, given a constant bottom gradient, grain size and wave length (period) in equation (5), the value C will be in direct proportion only to the wave height. This in turn means that reduction of the value C to about 60 % attained by the permeable layer is comparable to the effect of a structure which is capable of decreasing the wave height to about 60 %. This wave decreasing effect is achieved by a submerged breakwater with a slightly larger crown depth with slightly narrower crown width. It should be noted, however, that a permeable layer has additional effect in that hardly any wave set-up near the shoreline occurs, which is a function not obtained by a submerged breakwater.

4. Conclusion

Effects of the permeable layer are as follows:

- ① Substantially no wave set-up occurs at the shoreline.
- ② Rise in the groundwater level can be suppressed to a greater extent.
- ③ Erosion near the shoreline can be mitigated.
- ④ According to our experiment, combination of permeable pipe and drainage pipe is most effective.
- ⑤ Effect of permeable layer in respect of shoreline changes is comparable to that obtained by reducing the wave height by about 40 % .

It can be concluded that the effect of permeable layer is demonstrated by our laboratory model experiments. Presently, we are conducting filed experiments at a beach in order to complete the present technique. (Katoh and Yanagishima, 1996).

REFERENCES

- Yoshimi Goda(1975) : Deformation of Irregular Waves due to Depth-Controlled Wave Breaking, Rep.of PHRI, Vol.14, No.3, pp.59-106.
- Katoh, K. and S.Yanagishima(1992) : Berm Formation and Erosion, Proc.of 23rd ICCE. pp.2136-2149.
- Katoh, K. and S.Yanagishima(1993) : Beach Erosion in a Storm due to Infragravity Waves, Rep.of PHRI, Vol.31, No.5, pp.73-102.
- Katoh, K. and S.Yanagishima(1996) : Field Experiment on The Effect of Gravity Drainage System on Beach Stabilization, Proc of 25th ICCE.
- Sunamura, T. and K.Horikawa(1974) : Two-Dimensional Beach Transformation Due To Waves.Proc.of 14th Coastal Eng.Conf., ASCE, pp.920-937.
- Zienkiewicz, O.C.(1977) : The Finite Element Method Third Edition, McGraw-Hill, New York, 787p.

CHAPTER 205

Field Experiment on the Effect of Gravity Drainage System on Beach Stabilization

Kazumasa KATOH ¹ and Shin-ichi YANAGISHIMA ²

Abstract

To have a coastal protection work of high quality, we are developing a new beach protection system, that is a beach drainage system, in which the groundwater is naturally drained to the offshore through a permeable layer setting up under the beach. To examine the drainage function of the permeable layer and its effect on the beach stabilization, a field experiments have been conducted during storms. As a result, it is confirmed that the permeable layer drain the groundwater gravitationally into the surf zone and has a function of decreasing a speed of erosion in a storm, and the eroded foreshore is recovered quickly in a calm.

Introduction

As Japan has a long coastline and exposed to severe natural conditions, strong efforts on the coastal protection works such as detached breakwaters, jetties, seawalls are necessary to prevent the coastal disasters. However, these concrete hard structures keep the people away from the waterfront. The view of coastal regions are worse than they were. Over against this the demand for a better quality of protection gets greater, and multipurpose use of valuable coastal zone comes to be required.

In order to make the coasts what people currently desire to be, we started from the basic research on the changes of sandy beach in a storm because a sandy beach is fundamentally essential to create the desired coast. The series of researches have been reported in the ICCE (Katoh and Yanagishima, 1988,

Chief ¹ and member ² of Littoral Drift Laboratory, Port and Harbour Research Institute, Nagase 3-1-1, Yokosuka, 239, JAPAN

1990, 1992; Katoh, 1994). According to the results of basic researches, a shoreline rapidly recesses and a berm on the foreshore erodes in one or two days during a storm, which is due to the development of infragravity waves. When infragravity waves run up beyond the berm crest in the storm, the sea water stays for a good while on the horizontal area of berm, which accelerates infiltration of water into the beach. As a result, the water table becomes higher, and the water exfiltrate through the surface of foreshore. The seepage level of water corresponds to the critical level of berm erosion.

Taking these results into consideration, there are two kinds of measures for maintaining the sandy beach against the severe natural conditions. One is a construction of structure in the offshore such as detached breakwaters to diminish the wave energy and to suppress the wave run-up on the beach. Another is to lower the water table by some method. The system of lowering the level of water table by pumping, which is called the sub-sand filter system, has been tested in the laboratories and in a small scale field experiment in a calm (Chapell et al., 1979; Vestebey, 1991). There is a problem in this method, that is to say, a continuous pumping of the groundwater is required for lowering the water level. Then, an alternative drainage system is considered, in which the ground water is naturally drained to the offshore through a permeable layer setting up under the beach. We carried out an experiment on the function of permeable layer under the beach in a flume (Katayama et al., 1992), of which the final result is reported by Kanazawa et al. (1996). Davis et al. (1992) developed the prototype beach drainage system which incorporated an array of shore normal strip drains made of geotextile fabric enclosing a plastic core in an "egg-carton" configuration, and examined its function for lowering the water table and stabilizing the beach in the field. The results of these researches strongly suggest a possibility of gravity drainage system which enhances the stabilization of beach. If so it will be possible to maintain the beach of beautiful view without any artificial obstacles, because the whole system may be built under the ground.

To examine the drainage function of permeable layer under the foreshore and its effect on the beach stabilization, especially during a storm, a field experiment has been conducted.

Field experiment

1. Site of field experiment

The site of field experiment is an entirely natural sandy beach, being exposed to the full wave energy of the Pacific Ocean (see Figure 1). The foreshore slope is about 1/50, and the median diameter of sand on the beach is 0.18 mm which is nearly constant during the calm and storm conditions (Katoh and Yanagishima, 1995) . The tide range is about 1.5 m. According to the

analysis of shoreline locations which were read from eleven aerial photographs taken during a period from 1947 to 1984, the shoreline advanced about 50 m during a period from 1975 to 1979, which was due to the construction of Kashima in 1974. However, it has been stable since 1979. On this beach, Port and Harbour Research Institute, Ministry of Transport, has constructed the Hazaki

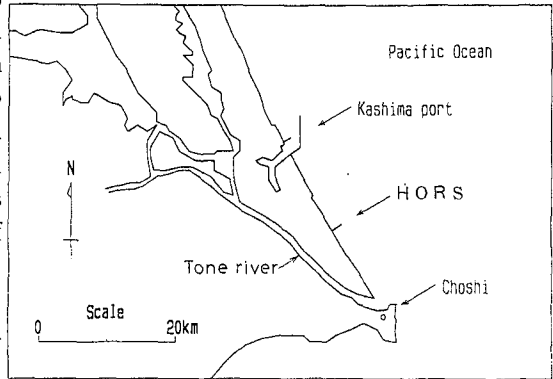


Figure 1 Site of Field Experiment.

Oceanographical Research Station (HORS) in 1986 for carrying out field observation in the surf zone even under the sever sea conditions. The research pier is a 427 meters long concrete structure supported by 0.8 meter diameter concrete-filled steel piles in a single line, at 15 meters interval. Although the beach is stable, the field experiment is being carried out on this beach because the basic data obtained in HORS have been accumulated since 1986.

2. Permeable layer and its execution

As the permeable material, the unit such as shown in Figure 2 is produced with the two sheets of corrosion-proof expanded metal in a factory, being wrapped with a geotextile fabric. A dimension of the unit is 1 meter wide, 2 meters long, and 20 centimeters thick. There is nothing inside the unit. The units can be connected by using couplers in the longitudinal direction. In August 1994 the permeable layer was set up under the beach in six columns from the foreshore to the backshore, being 30 meters apart in the longshore direction from the pier, as shown in Photo. 1. The elevation of permeable layer is about 3 meters below the beach surface, which is just below an envelope of the beach profiles overlapping for the last decade. The area is 88 meters in the cross-shore direction and 7.8 meters in width, which was enclosed by sheet piles when the permeable layer was being set. The pipe of 0.4 meter in

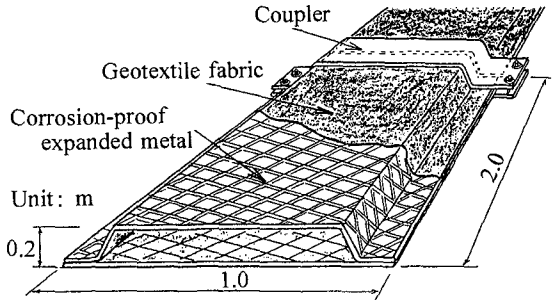


Figure 2 Permeable Layer.



Photo. 1 Execution of Permeable Layer.

diameter has been connected to the sea-side end of permeable layer to drain the ground water into the middle surf zone, 144 meters offshore from the shoreline. The pipe has been buried in the sea bottom with keeping the outlet in the sea. After setting, sand was put on the permeable layer so that we had the same profile as before. The sheet piles at the sea and land sides have been removed. The sheet piles along the longitudinal sides, however, were left without removing in order to make two-dimensional situation in the first experiment. In the second experiment, all the sheet piles were removed.

3.Items of measurements

In the first two-dimensional experiment, two representative measuring lines were taken into account in the cross-shore direction; one was coincided with the center line of the area where the permeable layer was buried, another was the line on the natural beach which was parallel to the first and 29 meters apart in the longshore direction. Along these lines, profiles of groundwater table and beach were surveyed once a day during a calm or every several hours in a storm, respectively. In the second three-dimensional experiment, a topography and plane distribution of water table were measured once a day in an area of 110 meters in the cross-shore direction and 75 meters in the longshore direction, including the area of permeable layer. The drained discharge through the pipe was continuously measured by a supersonic type discharge meter. Waves were measured near the shore line and the offshore.

Result of the first two-dimensional experiment

After about one month of setting up, on 18th September, 1994, a typhoon

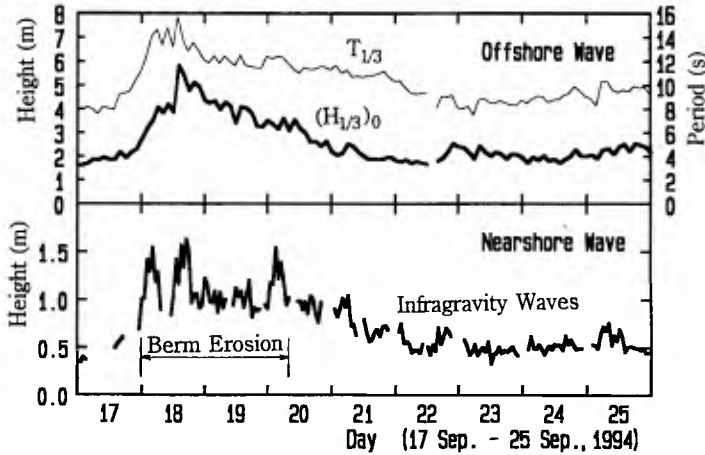


Figure 3 Waves in Typhoon No.9424.

attacked the experimental site. Waves at the offshore and infragravity waves near the shoreline are shown in Figure 3. The extreme value of significant wave height was 5.8 meters. The infragravity waves developed well, being about 1.5 meters in height near the shoreline, which run up to the backshore. The berm on the beach eroded during the days from 18 to 20, which is denoted in the Figure 3.

Photo. 2 was taken from the rooftop of laboratory at HORS on 19th September, on the second day of the storm, when an infragravity wave was running up on the drained beach. Small poles dug into the beach at the cross-shore intervals of 5 meters were arranged along a center line of the area where



Photo. 2 Infragravity Waves Running on the Drained Beach.



Photo. 3 Dried up Area on the Drained Beach.

the permeable layer was set up. Under this situation, sea-water infiltration into the beach was considered to be enhanced in the drained area, because on the drained beach we recognized a very interesting phenomenon that air bubbles came out actively from the ground through the surface of beach, which had never been seen in the laboratory. It is not difficult to infer the situation that the water was infiltrating into the beach because the effusion of air bubbles was a result of being replaced with the infiltrated water into the ground. Photo. 3 is a picture taken about one minute after the situation of Photo. 2, when the infragravity wave was running down to the sea. The beach surface of drained area, of which both sides were cut off by the sheet piles, was already dried up, while the surface of natural beach was still wetted.

Figure 4 is a comparison of profiles of water table between the natural beach and the drained beach, measured on the day of 18th September when the beach began to erode. Infragravity waves had already developed well, and run up to the high elevation denoted by an arrow which was higher than the usual H.W.L. of 1.4 meters. The elevation of groundwater table in the natural beach, which is denoted by triangles, rose up

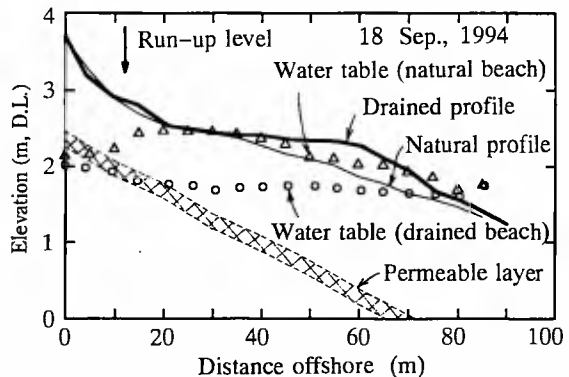


Figure 4 Comparison of Water Tables.

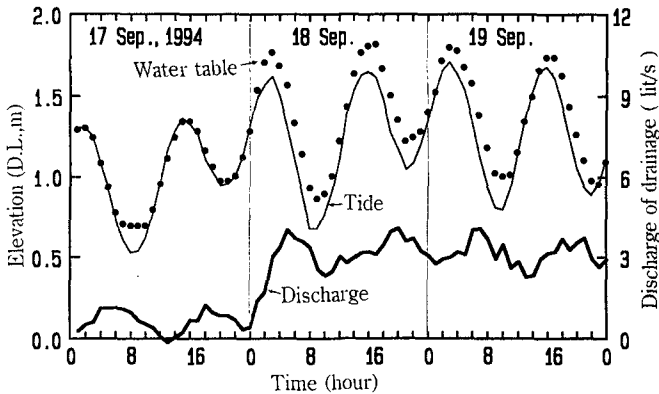


Figure 5 Changes of Tide Level, Water Table, and Drained Discharge.

to the beach surface. In other words, the ground was completely saturated with the water. On the other hand, that in the drained beach which is denoted by circles was 0.6 meter lower in maximum than the beach surface. The area between the beach surface and the water table in the drained beach was unsaturated, which means that the groundwater was gathered to the permeable layer and drained offshore through the drainage pipe.

Figure 5 shows the changes of a tide level at the outlet of drainage pipe, the water table at the point of -25m in the drained area, and a mean discharge in the drainage pipe for 20 minutes. On the day of 17th September, before the storm, the discharge was small. From the day of 18th September on, during the storm, The discharge was large, being about 30 lit/s. The groundwater level changed with a lag of about one hour behind the tidal change. As a result, the level difference between the groundwater table and the tide level became large during the ebb tide, which produced larger discharge.

Figure 6 shows the actual fluctuations of ground water level in the drained

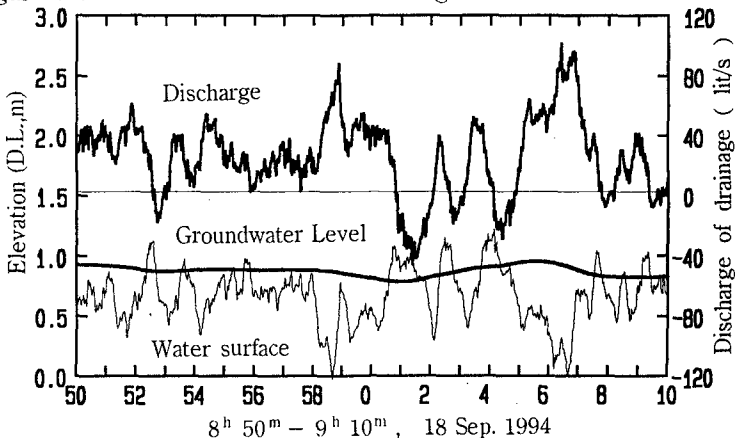


Figure 6 Fluctuations of Groundwater level, Water Surface, and Discharge.

beach and the drained discharge in the surf zone during the segment of twenty minutes in the storm. The level of water surface at the point of outlet in the surf zone, which is the result of running average with 10 seconds, is also presented in the same figure. These elevations were measured on the day of 18th September, the first day of storm. The fluctuation of groundwater level was smooth and small, while that of surface elevation was large, being 70 cm in amplitude and 1 to 2 minutes in period, which was due to the infragravity waves in the surf zone. As the surface level at the outlet was lower than the groundwater level in the better part of time, the water in the pipe usually flowed offshoreward with the discharge of 100 lit/s in maximum, which was equivalent to the mean velocity of 80 cm/s in the pipe. However, the surface level at the outlet was sometimes higher than the groundwater level when the crest of infragravity waves is passing over the point of outlet. When the surface level at the outlet was higher than the groundwater level, the water flows backward, or in the onshore direction.

In Figure 7, the mean discharges are plotted against the level difference between the ground water level and the surface level at the outlet. These values are the averaged ones for every 20 minutes before and during the storm. The averaged discharge was in roughly proportional to the difference of water level, which means that the water was gravitationally drained into the surf zone.

Figure 8 shows the successive comparisons of beach profiles on the natural beach and the drained beach. On the two day before the storm, the day of 16th September, berms were formed on the foreshores of both the natural and the drained beaches (Figure 8, top) due to the relatively calm wave conditions during the three weeks before the storm. The berm on the drained beach was developed better, which is considered to be the effect of drainage. On the first day of storm, the berm on the natural beach eroded to the constant slope as seen in the middle figure, while the berm existed on the drained beach. In the bottom figure, one hour after, the berm still existed on the drained beach, which gradually eroded with time. Around 16 h of 18th, September, which was 13 hours after the time of profiles shown in the bottom figure, the tide level became highest and the height of infragravity waves also became the largest. Under this severe condition, the berm on the drained beach eroded completely to be the same constant slope as that of natural beach. In short, the effect of

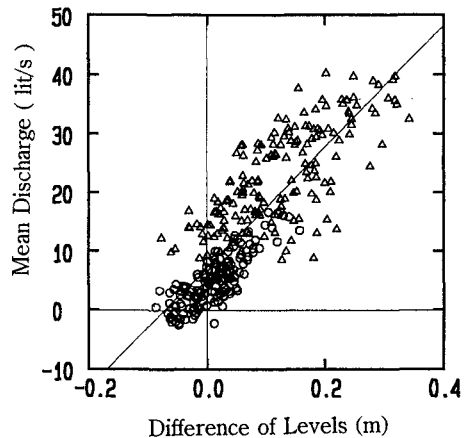


Figure 7 Relation between the Level Difference and the Drained Discharge.

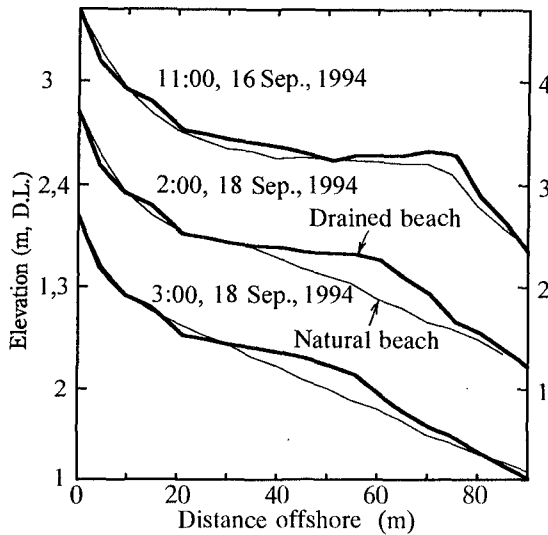


Figure 8 Comparisons of Profiles on the Natural and the Drained Beaches.

permeable layer is to decrease the speed of beach erosion in the storm.

Result of the second three-dimensional experiment

In the second field experiment, the sheet piles along the both sides of drained area had been removed. About one year after, on the day of 17 September 1995, a large typhoon No.9512 passed near the experimental site. Figure 9 shows the changes of the offshore significant waves and the height of infragravity waves near the shoreline. The extreme height of significant wave occurred at 14h on the day of 17th September, being 6.0 m. The height of infragravity waves near the shoreline increased from about 1.0m at 7th on the same day to 1.8m in maximum at 15h, which is the largest in the last 9 years

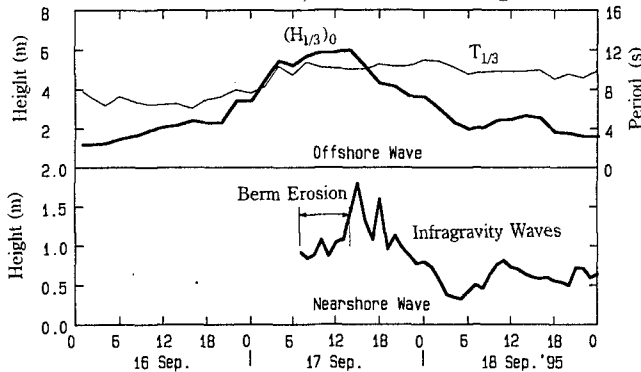


Figure 9 Waves in Typhoon 9512.

since the observation of infragravity waves have started at HORS in 1987.

Figure 10 shows a plane distribution of water table on the day of 16th, September. The water table above the permeable layer was lower than that of the circumference. Waves run up to the location of $y=0\text{m}$, where the water table was higher than 2.0 m in the areas apart from the permeable layer and lower than 1.5 m above the permeable layer.

Figure 11 shows the topography around the drained area, which was surveyed at 7h on the day of 17th, just before the storm. The slope is gentle in the area from $y=-50\text{m}$ to 0m , while it is steep in the area offshoreward from $y=0\text{m}$, because a berm is formed on the foreshore. At this time, waves run up to the location of $y=-55\text{m}$, which was observed visually during surveying.

In order to survey the wide area in a short time, nine researchers took part in surveying. During the time from 7h to 14h, on the day of 17th September, however, we could not succeed in obtaining the data of topography because it was very dangerous for us to survey due to the large run-up of infragravity waves and a strong wind velocity of 29 m/s in average.

Figure 12 shows the topography around the drained area which was surveyed after the extreme condition, at 14h on the day of 17th. The foreshore has almost completely eroded to be a plane beach of the two dimensional state of 1/40 in slope. A contour line of 2m has recessed by 30

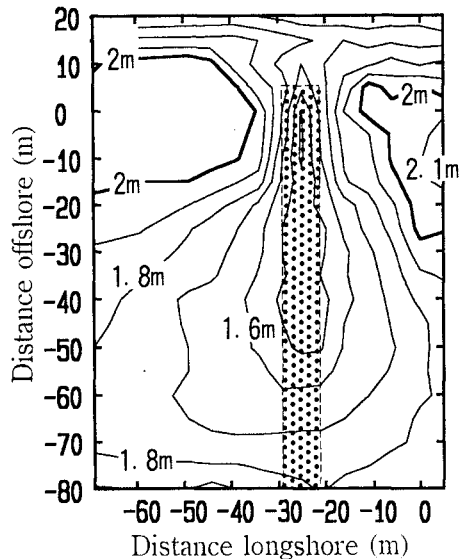


Figure 10 Water Table before the Storm (16th Sep., 1995).

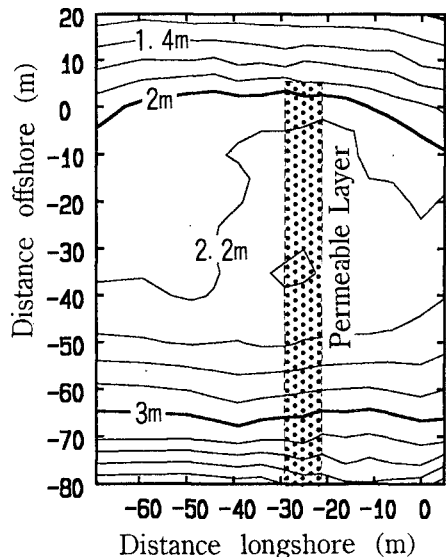


Figure 11 Foreshore Topography, just before the storm

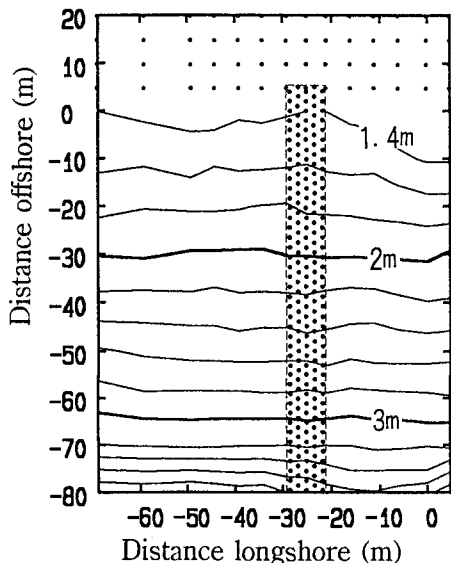


Figure 12 Foreshore Topography, after Erosion.

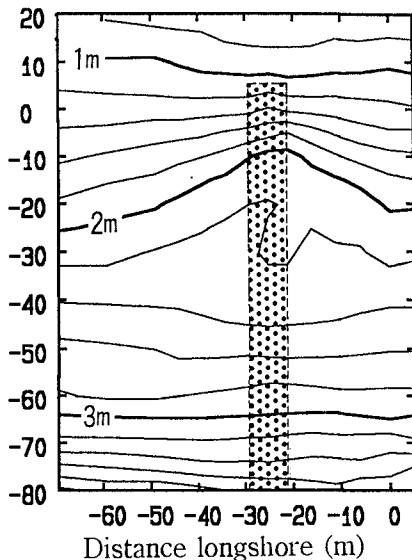


Figure 13 Foreshore Topography, One Week after the Storm.

meters from $y=0m$ (in Figure 11) to $y=-30m$. No effect of permeable layer is observed in this topography. It is considered to be due to the narrow width of drained area, 7.8 meters, and the attack of extreme large waves. As the interruption of surveying was 7 hours, the effect of permeable layer on decreasing the speed of beach erosion was not confirmed.

After the storm, it was continued to survey the topography in the same area once a day. Figure 13 shows the topography on the day of one week after the storm, 25th September. The contour lines of 1.4m to 2.2m advanced offshoreward, being convex in the area above the permeable layer. As a result, in the area above the permeable layer a slope was gentle in the area higher than 2m in elevation, while it

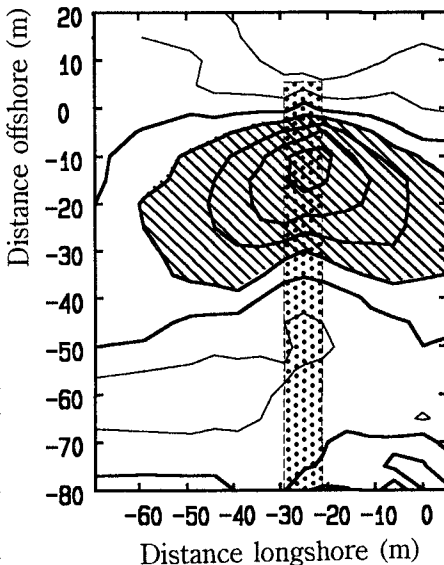


Figure 14 Change of Topography during one week.

was steep in the area lower than 2m. In short, a new berm was formed on the foreshore above the permeable layer.

The rate of sand accumulation during this one week has been calculated, of which result is shown in Figure 14. The area of sand accumulation more than 10 cm is hatched. In the middle of this area, on the drained beach, the thickness of accumulation is more than 40 cm. Then, it can be said that there was a quick recovery on the drained beach. The effect of permeable layer extended to the both lateral areas for about 20 meters, which suggests a possibility of beach protection by setting up the belts of permeable layers in stripes. On the lateral beaches where there was no permeable layer below, sand accumulated gradually and the berms were formed finally, being as the same topography as that before the storm (see Figure 11).

Conclusions

The effects of permeable layer set up under the beach are as follows:

- (1)The permeable layer can drain the groundwater gravitationally through the drainage pipe into the surf zone even in a storm.
- (2)It has a function of decreasing the speed of foreshore erosion in a storm.
- (3)On the drained beach, the eroded foreshore is recovered quickly after a storm.

References

- 1) Katoh,K. and S.Yanagishima(1988):Predictive model for daily changes of shoreline, Proc. of 21st ICCE, pp.1253–1264.
- 2) Katoh,K. and S.Yanagishima(1990):Berm erosion due to long period waves, Proc. of 22nd ICCE, pp.2073–2086.
- 3) Katoh,K. and S.Yanagishima(1992):Berm formation and berm erosion, Proc. of 23rd ICCE, pp.2136–2149.
- 4) Katoh,K.(1994):Difference between waves acting on steep and gentle beaches, Proc. of 24th ICCE, pp.315–329.
- 5) Chappell,J., I.G.Eliot, M.p.Bradshaw and E.Londsdale(1979):Experimental controle of beach face dynamics by watertable pumping, Eng. Geol., 14, pp.29–41.
- 6) Vesterby,H.(1991):Coastal drain system, Proc. Inter. Conf. Geotec. Eng. Coastal Development, pp.651–654.
- 7) Davis,G.A., D.J.Hanslow,K.Hibbert and P.Nielsen(1992):Gravity drainage:A new method of beach stabilization through drainage of the watertable, Proc. of 23rd ICCE, pp.1129–1141.
- 8) Katayama,T. et al.(1992) :Lowering of watertable with drainage layer under the foreshore, Proc. of Coastal Eng., Vol.39, JSCE, pp.871–875 (in Japanese).
- 9) Katoh,K. and S.Yanagishima(1995):Changes of sand grain distribution in the surf zone, Coastal Dynamics'95, pp.639–650.

CHAPTER 206

On the change of velocity field in nearshore zone due to coastal drain and the consequent beach transformation

Michio Sato¹, Tadahiro Fukushima², Ryuichiro Nishi³
and Masahiko Fukunaga⁴

ABSTRACT

It is essential to understand the details of the mechanisms by which a coastal drain works in order to build up the method which enables us to estimate discharge requirement for effective operation in field conditions. Some measurements on the changes of quantities which may be relevant to the function of coastal drain are discussed. Then, an attempt to implicate the current components produced by drainage in a numerical model of beach profile evolution is discussed.

INTRODUCTION

The coastal drain has been considered to be an effective soft approach to coastal erosion control and beach erosion. From the practical point of view, it is indispensable to know how to estimate discharge requirement for effective operation in field conditions. Small scale physical experiments give us qualitative information on some physical aspects related with the coastal drain. There seems, however, to be a difficulty in estimating discharge needed for a coastal drain system based on experimental results due to scale effects. Hence, when we consider the remarkable recent progress of numerical models on beach profile evolution, it will be a practical way to construct a numerical model which enables us to estimate beach profile change under the operation of a coastal drain system. To do this, it is essential to understand the details of the mechanisms by which the coastal drain works.

Authors have shown the following results on forced coastal drain experimentally(1994),

- 1) seaward area of a shoreline is most appropriate for the installation of a drain pipe
- 2) as the discharge increases, the drain system becomes effective even for storm wave conditions.

Figure 1 is an example of beach profiles under erosive wave condition. In this case, sediments on the initial shoreline moved mainly toward the upper beachface and the bottom level lowered. But, the erosion in the shoreward part of the drain pipe was

¹ Professor, Department of Ocean Civil Engineering, Kagoshima University, 1-21-40 Korimoto, Kagoshima-shi, 890 JAPAN

² Miyazaki prefectural government

³ Research Associate, Department of Ocean Civil Engineering, Kagoshima University

⁴ Kagoshima prefectural government

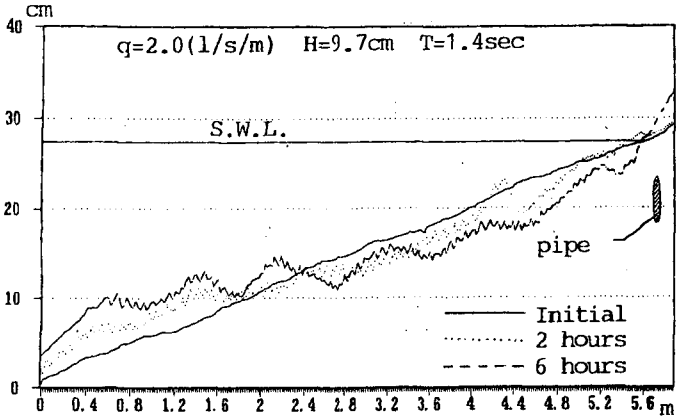


Figure 1 Beach profile change (1)

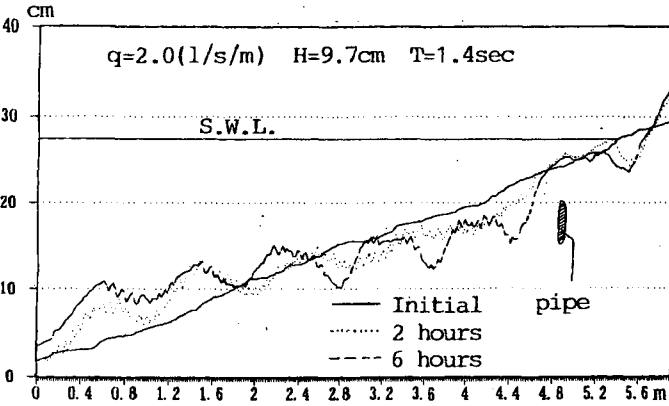


Figure 2 Beach profile change (2)

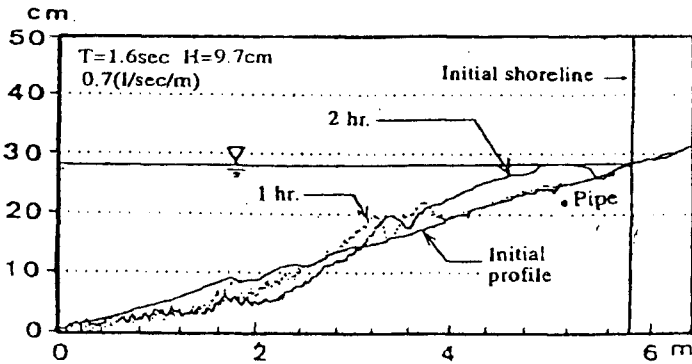


Figure 3 Beach profile change (3)

restrained on the whole. This example made us have expectation the landward area of a drain pipe to be protected at the worst, when the drain pipe was installed in seaward area of a shoreline.

Figure 2 shows an example of the case in which drain was done under the shoreline. Erosion due to erosive waves attained almost to the initial shoreline for the same drainage as the case mentioned above.

Figure 3 is the case which attracted our attention specially in that it showed remarkable accretion in the inshore area after wave action of two hours. The wave condition was less steeper compared with the cases in Figures 1 and 2, but it was not accretive one at all for the cases of without or smaller drainage. This result suggests that, when a storm passes by a shore, similar situation may occur in some stages of the storm passage according to wave condition and drainage. And the process which brought the accumulation of sediments is expected to retard erosion and accelerate restoration of an eroded beach. So, our main interest has been directed to determine under what conditions the accretion takes place.

Generally, the reason a coastal drain system works has been explained by relating effects of drainage to the net sediments carried due to runup-down wash processes of waves on a beachface. Our observation, however, showed that the changes of the hydraulic conditions in the nearshore zone were important. Especially, shoreward flow component induced by drainage in and out of a surf zone, which carried suspended sediments and migrated a bar toward the beachface, seemed to play the dominant role for the accretion when the drain pipe was installed in the seaward area of a shoreline.

In this paper, some measurements on the changes of quantities which may be relevant to the function of coastal drain are discussed. Then, an attempt to implicate the current components produced by drainage in a numerical model of beach profile evolution is discussed.

EXPERIMENTS

The changes of wave runup, wave setup and mean velocity fields due to coastal drain were investigated experimentally by using a wave flume of 13m long, 0.4m wide and 0.4m deep (Figure 4). Water elevation was measured by capacitance type wave gages and velocity fields were measured with an electromagnetic current meter. The measurements were limited in the range between the level about 1cm lower from wave trough and the level 2cm above the bottom.

RESULTS AND DISCUSSIONS

Wave set-up : In their experiments on the gravity drainage system which utilize permeable layer artificially placed under a beach, Kanazawa et.al.(1996) observed no wave set-up, the gradient of which in on-offshore direction provides one of the driving force of undertow. We also anticipated similar result for our cases in early stage. Our measurements of mean water level, however, did not show any definite change in the mean water level as shown in Figure 5. The difference may be considered to reflect the difference of mechanisms which make each system effective.

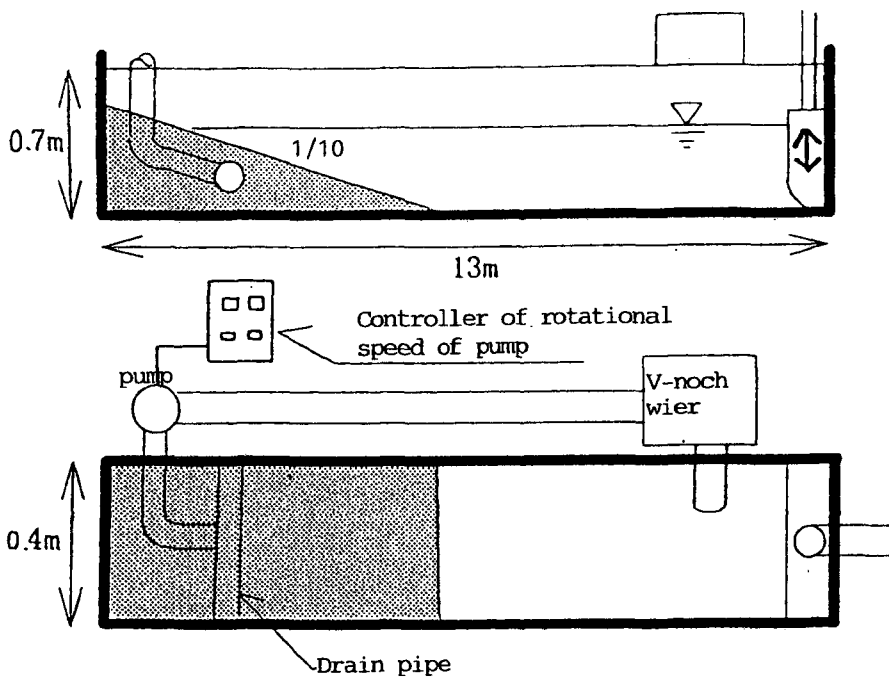


Figure 4 Experimental setup

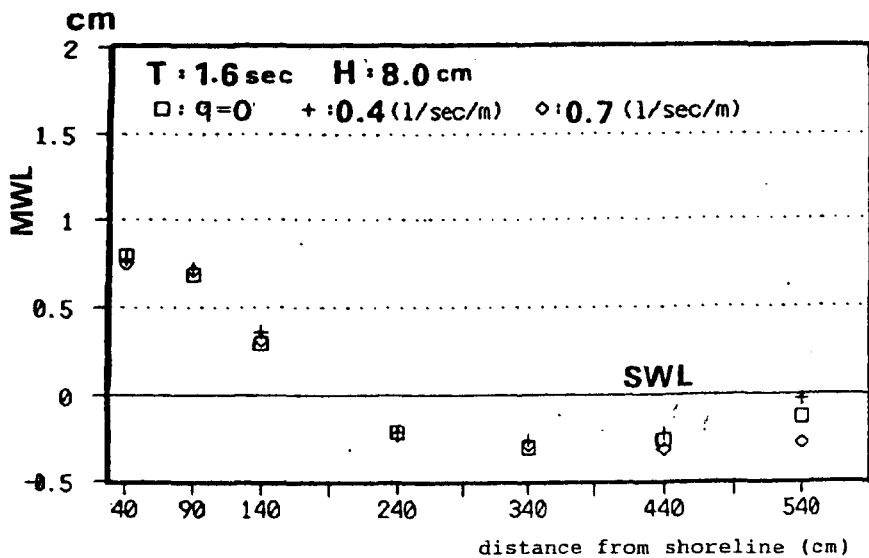


Figure 5 Wave setup

Wave runup : Wave runup was measured visually. The change of wave runup was small. This was supported by the numerical model of wave runup including the effects of coastal drain (Figure 6). These results reveals the change of runup-down wash process due to coastal drain is not necessarily the dominant mechanism when a drain pipe is buried in the seaward part of a shoreline.

Numerical computation was done based on the equations of continuity and motion for nonlinear shallow water waves implicating infiltrating flow from the bottom surface due to drain. The non-dimensional form of the equations are as follows.

$$\frac{\partial h}{\partial t} + \frac{\partial}{\partial x}(hu) = -v^* \quad (1)$$

$$\frac{\partial}{\partial t}(hu) + \frac{\partial}{\partial x}\left(hu^2 + \frac{h^2}{2}\right) + \theta h + f_w |u|u + uv^* = 0 \quad (2)$$

$$x = \frac{x'}{\sqrt{gh'T'}}, \quad t = \frac{t'}{T'}, \quad h = \frac{h'}{H'}, \quad u = \frac{u'}{\sqrt{gh'}} \quad , \quad v^* = \frac{v'}{H'/T'}$$

$$\theta = \frac{\tan \theta'}{H'/(\sqrt{gH'T'})}, \quad \tau_b = \frac{\tau'_b}{\rho g H'^2 / (\sqrt{gH'T'})}$$

where h is water depth, t is time, u is fluid velocity in x -direction, v^* is infiltration velocity, H is wave height, T is wave period, τ_b is shearing stress on the bottom, g is the gravitational acceleration and f_w is friction factor. Prime denotes the dimensional variables.

The infiltration velocity v^* was given as the velocity $-(a'q')/\{\pi(x'^2 + a'^2)\}$ of the flow induced along x' -axis by a source at $z' = i a'$ with the intensity of $-q'/2\pi$ and a sink at $z' = -i a'$ with the intensity of $q'/2\pi$ in z' -plane (Figure 7). The non-dimensional form of the velocity for the coordinate system in Figure 8 is given by the following equation.

$$v^* = -\frac{aq}{\pi\{(x-x_0)^2 + a^2\}} \quad (3)$$

In conducting the numerical computation, Kobayashi et al.(1987) was referred to.

Mean velocity : Measurements of the mean flow field over the beach in the wave channel were carried out. The beach was plane uniform one of 1/10 slope initially. Wave action of several minutes, however, changed the beach profile to the extent we could ignore. Then, the bed was flattened in every several minutes. Nevertheless, the measurements seems to contain the influence due to the bottom change in the course of measurement.

Figure 9-A shows the mean velocity distribution induced by waves without drain. Figure 9-B and C are the velocity field induced by drain without wave action. And Figure 9-D and E are the velocity field due to waves and drain.

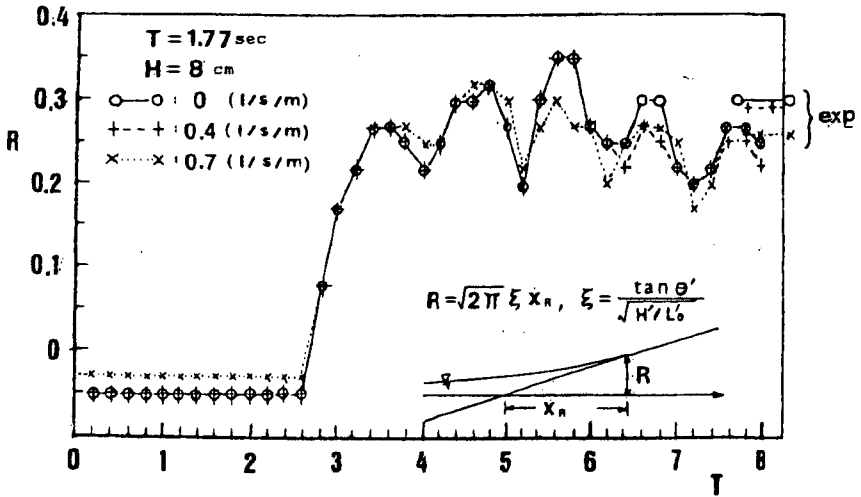


Figure 6 An example of measured and calculated runup

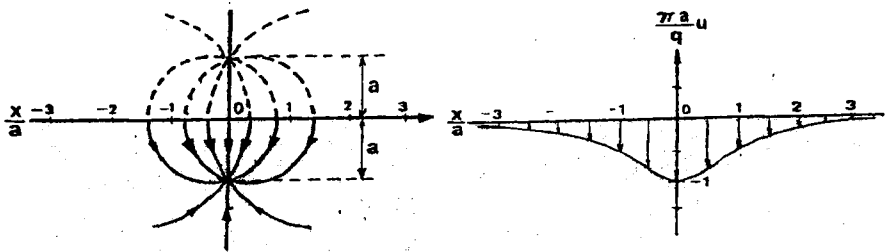


Figure 7 Infiltration velocity model used in the calculation of wave runup

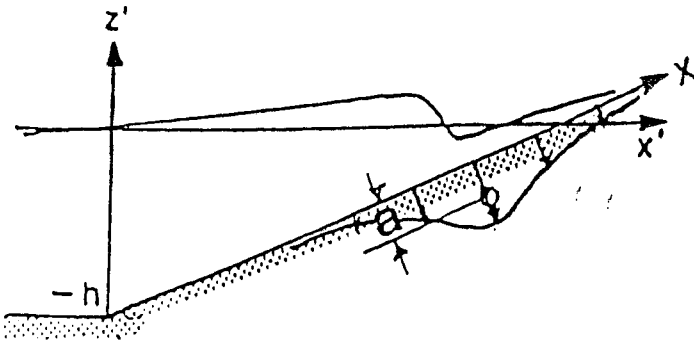


Figure 8 Definition sketch

From these measurements we can see that the flow in the direction of offshore decreases the intensity near the drain pipe. And the reverse of the flow direction was observed in close proximity to the pipe.

BEACH PROFILE EVOLUTION AND COASTAL DRAIN

In an attempt to know what changes in beach profile evolution will result when the following two effects are taken into consideration, numerical simulations of beach profile evolution based on a modified existing model (Dally and Dean(1984)) were done.

1. the horizontal velocity component of the flow produced by drainage reduces the wave induced offshore-directed mean current,
2. the vertical velocity component of the flow adds to the settling velocity of sediment particles and modify the vertical distribution of suspended sediments.

The flow components due to drain were simply modeled by the flow in a wedge shaped region produced by a point sink on a side of the wedge(Figure 10). The velocity components (u , v) are given by

$$u - iv = \frac{m\pi}{\theta} \cdot \frac{(z/a)^{\pi/\theta}}{z\{(z/a)^{\pi/\theta} - a\}} \quad (4)$$

where $z = x + iy$ and $i^2 = -1$. The calculated flow distributions are shown in Figure 11.

Sediment transport rate Q_{SS} was given by

$$\begin{aligned} Q_{SS} &= \int_{-h}^0 \bar{u}(z) \cdot C(z) dz \\ &= \int_{D_r-h}^0 \{u_1(z) + u_{Dx}(z)\} \cdot C(z) dz + \int_{-h}^{D_r-h} \{u_2(z) + u_3(z) + u_{Dx}(z)\} \cdot C(z) dz \end{aligned} \quad (5)$$

where \bar{u} is mean velocity, $C(z)$ is concentration of suspended sediments, u_{Dx} is x -component of the velocity induced by drain (Figure 12).

The concentration of suspended sediments was given by

$$C(z) = C_A \exp\left\{-1.5(w + u_{Dz}) \cdot (z - z_A) / (h\sqrt{\tau/\rho})\right\} \quad (6)$$

where C_A is reference concentration, w is the settling velocity of sediments, u_{Dz} is z -component of the velocity induced by drain.

Beach profile evolution was calculated by

$$\frac{dh}{dt} = \lambda \frac{dQ_{SS}}{dx} \quad (7)$$

Figure 13 shows the calculated results. For the case of without drain, specious results were obtained. Addition of the flow due to drain makes the sediment transport rates several times larger in magnitude and the sediment transport direction onshore over the whole beach area. And accretion of the shore-side area of the pipe was obtained.

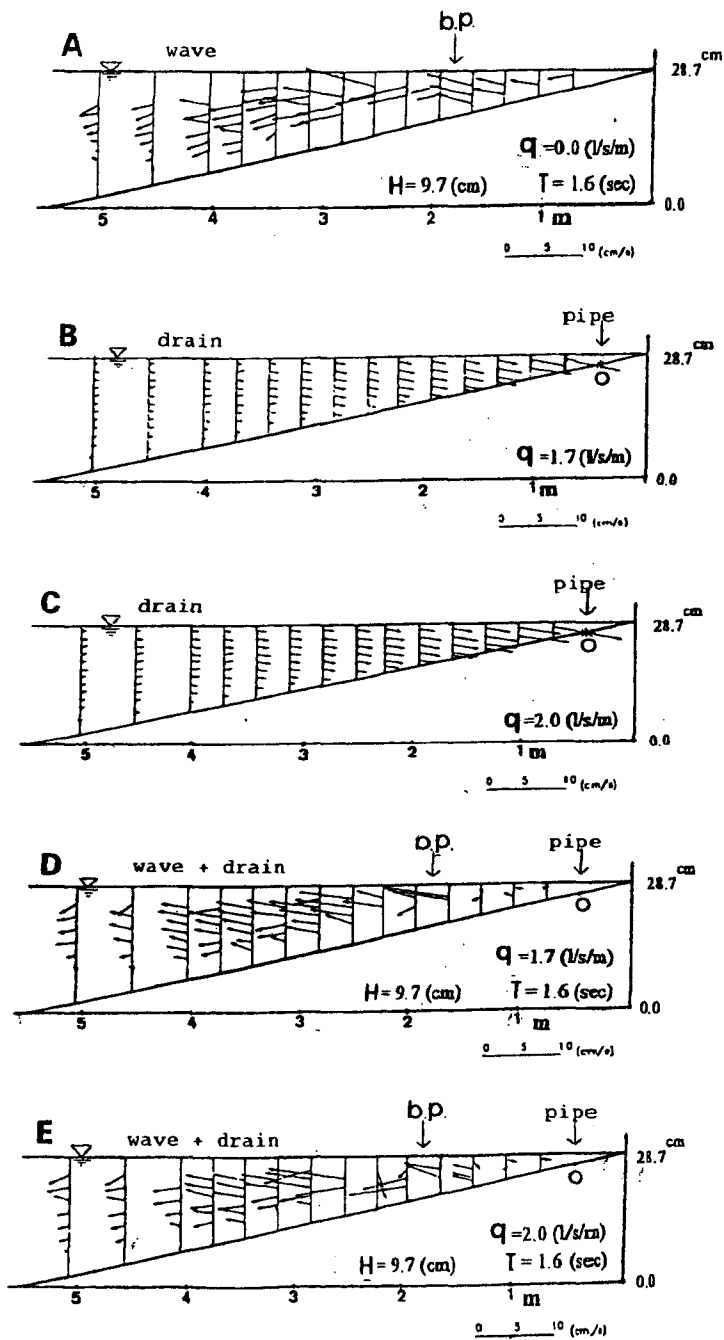


Figure 9 Measured mean velocity

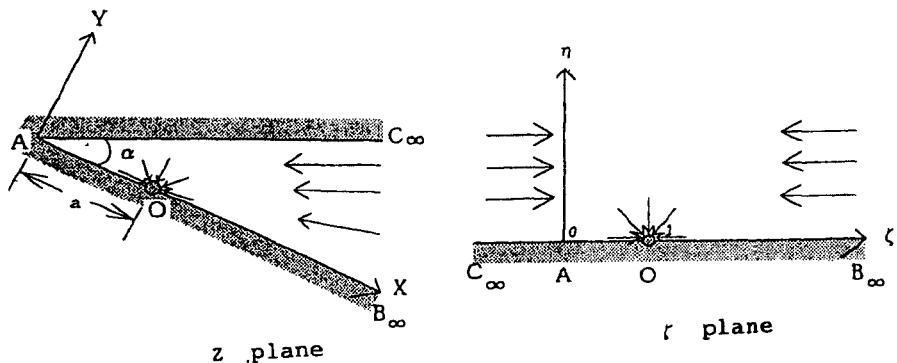


Figure 10 Model of the drain induced flow

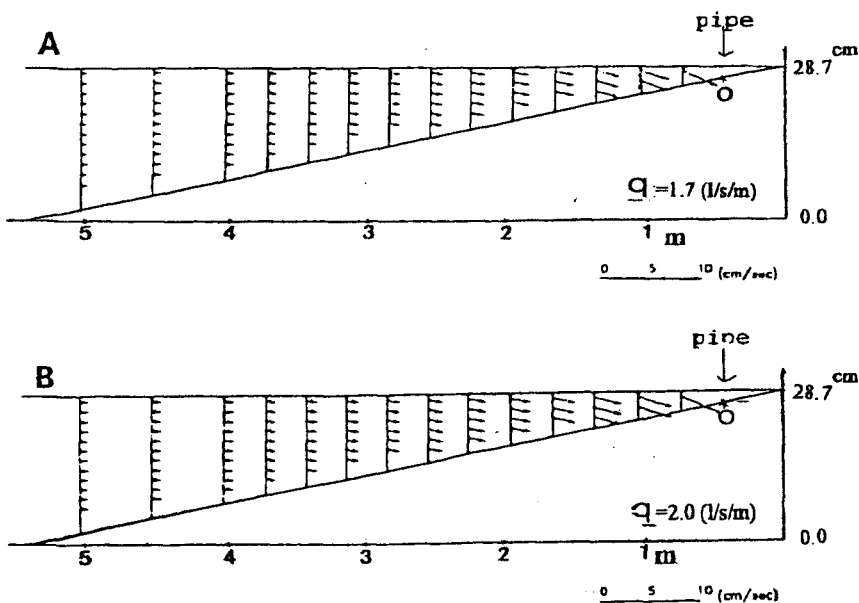
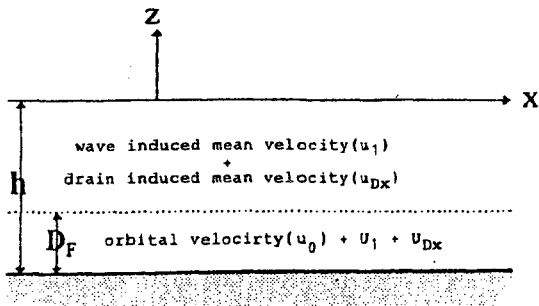


Figure 11 Examples of calculated velocity distribution

Figure 12 Definition of variables in Eq.(5)



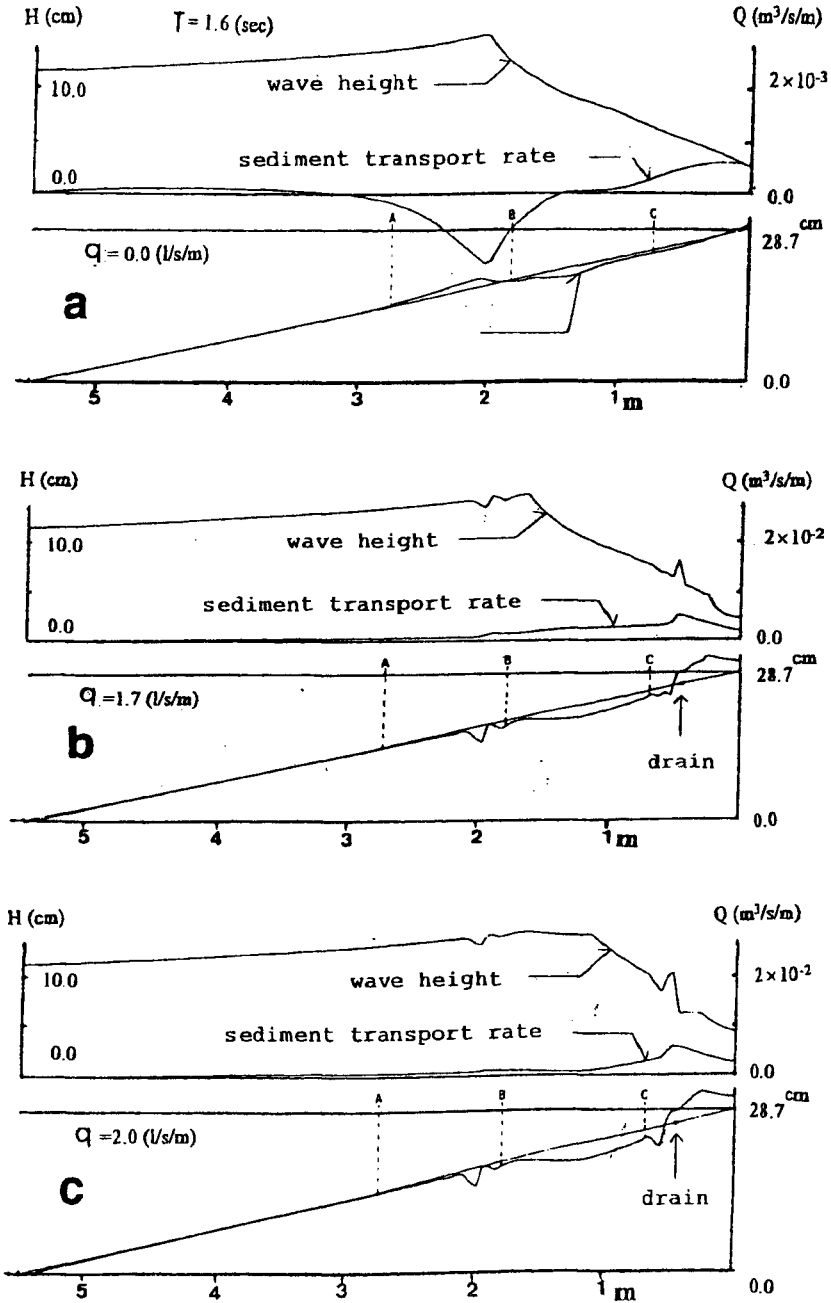


Figure 13 Calculated beach profile evolutions

Therefore, the calculated results show some features of beach profile evolution and they are considered to account for one of possible mechanisms how a coastal drain works though in a qualitative sense, when the pipe is installed under the bottom of the seaward area of a shoreline. The results, however, show fairly bumpy transformation of wave height and bottom topography. Some trials to improve the situation have been done. But, they are not successful so far. Besides, this model does not include bed load sediment transport.

To complete the numerical model for the coastal drain, it will be essential to take the bed load into consideration. However, there are some problems remained to be investigated on the bed load sediment transport under the operation of a coastal drain system like the change in flow within a wave bottom boundary layer over a drain pipe due to suction by forced drain and its effect on bed load sediment transport.

CONCLUSIONS

The following conclusions were drawn from the study:

When a drain pipe is installed in the seaward area of a shoreline,

1. the mean flow in the offshore direction over the whole beach area is reduced by the onshore current induced by drainage. This will result in the reduction of offshore suspended sediments transport in stormy conditions.
2. In this case, the changes in wave runup and wave setup, which are connected with the processes on a uprush zone, were small.

Then, an attempt to implicate the current components produced by drainage in a numerical model of beach profile evolution is discussed. To complete the numerical model, however, there are some problems remained to be investigated, especially on the effects of forced drain on bed load sediment transport.

REFERENCE

- Dally, W.R. and R.G. Dean (1984): Suspended sediment transport and beach profile evolution, *Jour. of ASCE, WW.*, Vol. 11. 110, No.1, pp. 15-35.
- Kanazawa, H., Matsukawa, F., Katoh, K. and I. Hasegawa (1996) : EXPERIMENTAL STUDY ON THE EFFECT OF GRAVITY DRAINAGE SYSTEM ON BEACH STABILIZATION, 25th ICCE, BOOK OF ABSTRACT, pp.632-633
- Kobayashi, N., Ota, A.K. and I. Roy (1987) : Wave reflection and run-up on rough slopes, *J. Waterway, Port, Coastal and Ocean Engineering*, ASCE, Vol. 113. No.3, pp.282-298
- Sato, M., Hata, S. and T. Fukushima (1994): An experimental study on beach transformation due to waves under the operation of coastal drain system., *Proc.24th ICCE.*,pp.2571-2582

CHAPTER 207

EVALUATION OF A BEACH DEWATERING SYSTEM: NANTUCKET, USA

William R. Curtis¹, Jack E. Davis², Ian L. Turner³

Abstract

A commercial multi-segmented beach dewatering system became operational December 1994 on the eastern shoreline of Nantucket Island, Massachusetts, USA. The objective of the installation was to cost-effectively stabilize a critically eroding reach of shoreline with minimal environmental impact. To assess the potential for wider use of beach dewatering in coastal erosion management, a comprehensive and independent monitoring program was developed and implemented to objectively evaluate the beach dewatering project. Observational methods and analyses are discussed relative to the ability to differentiate between the influence of the dewatering segments on beach response, in contrast to 'natural' shoreline response to coastal processes. Economics, measurement needs, measurement accuracy, and temporal and spatial resolution of data acquisition are discussed and evaluated.

Introduction

Nantucket Island is the eastern most member of the Elizabethan Island chain located 48 km southeast of the New England coast, USA (Figure 1). The eastern shoreline of the island is exposed to direct attack from the high-energy wave environment of the North Atlantic. Mean offshore significant wave heights are on the order of 2 m. However, offshore significant wave heights in excess of 5 m are frequently measured, particularly during winter storms. The maximum wave height offshore measured between 1984 and 1993 was 11.6 m (Hubertz, 1995). Historical charts and aerial photography indicate that, for at least the past 150 years, the beach face, dune line and bluff face have experienced episodic accretion and recession (Tiffney et al., 1991). Present estimated erosion rates along the eastern shoreline range from 0.8

¹Research Oceanographer, ²Research Hydraulic Engineer, USAE Waterways Experiment Station, Coastal and Hydraulics Laboratory, 3909 Halls Ferry Rd., Vicksburg, MS 39180, USA.

³Assistant Research Scientist, University of Maryland, Laboratory for Coastal Research, College Park, MD 20742, USA.

m/yr to 4.6 m/yr, depending on location. An analysis of wave refraction patterns suggested that episodic erosion events are due primarily to the focusing of storm wave energy by an offshore shoal complex along the south eastern shoreline of Nantucket (Weishar et al., 1991).

Bluff and dune recession are presently encroaching on private and public facilities of several Nantucket coastal communities. On the eastern shore of the island, where coastal storm damage has been catastrophic, increased coastal development has led to serious consideration of beach management and land use practices.

In 1990, the Siasconset Beach Preservation Fund (SBPF), a private organization of Nantucket homeowners, sponsored an evaluation of shoreline stabilization options. Results of the evaluation revealed that structural shoreline protection alternatives such as large stone revetments and cement seawalls are not economically feasible to construct at Nantucket. In addition, state and local regulatory agencies firmly restrict use of permanent shoreline structures. Beach nourishment was also evaluated, with a projected cost of \$20 million (US) with an annual maintenance cost of \$1 million (US) to protect approximately 4.27 km of shoreline. In light of these costs, the SBPF opted to privately fund the installation of three commercial beach dewatering-system segments. The dewatering-system segments cost \$1 million (US) to construct. Projected annual maintenance costs are approximately \$100,000 (US) for the three segments.

Installation

The three beach dewatering segments were developed and installed by Coastal Stabilization, Inc., under license to the Danish Geotechnical Institute (DGI) and became fully operational in December 1994. The project at Nantucket Island is the third commercial installation of beach dewatering technology in the United States, and one of several prototype or full scale facilities installed on North Atlantic coastlines by DGI or under license to DGI (Ovensen and Schuldt, 1992; Lenz, 1994).

Each STABEACH segment consists of buried, perforated drain pipes installed in a shore-parallel orientation below the beach face swash zone. The pipes slope toward wet wells located in the back shore region of the beach. Two dewatering segments drain by gravity, while drainage at the third segment is aided by a vacuum pump. Water collected in the wells is pumped offshore through a 35.5 cm discharge pipe by a 25 hp pump. The stated operational concept of the system is to induce continuous draw down of the watertable at the beach face, enhancing the depositional effect of wave uprush and reducing the erosive effect of wave backrush during natural accretionary periods.

In total, the project spans 9.8 km of shoreline (Figure 2). The northern most segment is referred to as Lighthouse North (*LHN*). The segment immediately to the south of *LHN* is referred to as Lighthouse South (*LHS*). The southern most segment is referred to as Codfish Park (*CFP*). The three systems are separated by stretches of beach outside the influence of groundwater draw down. Figure 3 illustrates the plan-view design of the *LHN* system. Constructed STABEACH segments at *LHS* and *CFP* are similar in concept. STABEACH system parameters are presented in Table 1. Each drain pipe connects to a 1.2 m diameter wet well.

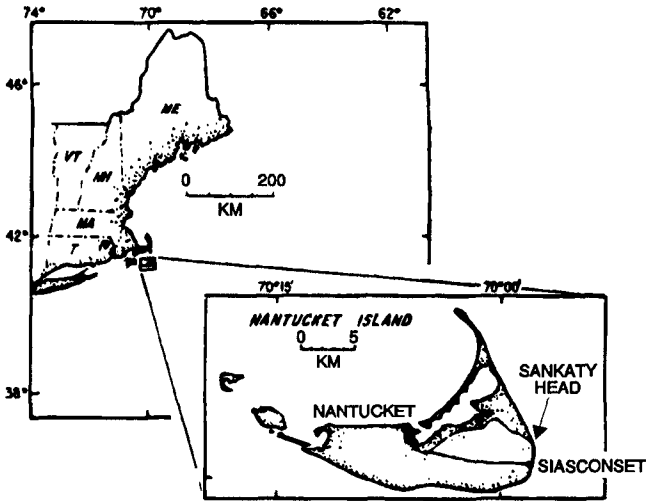


Figure 1. Location of Nantucket Island relative to New England mainland (after Oldale, 1987).

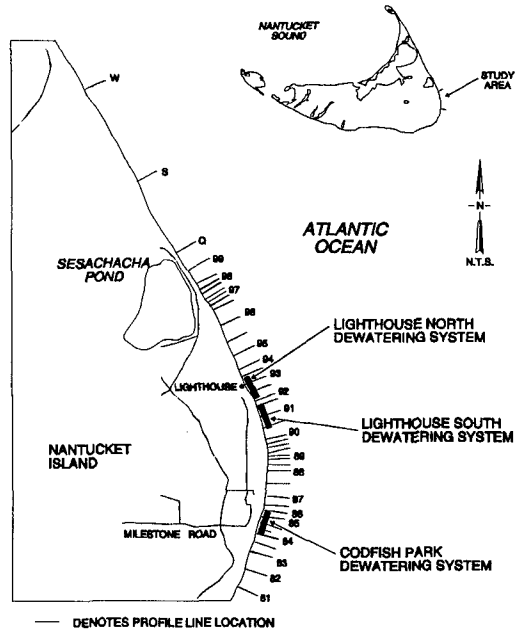


Figure 2. STABEACH segment and profile transect locations (after Coastal Planning and Engineering, Inc., 1996).

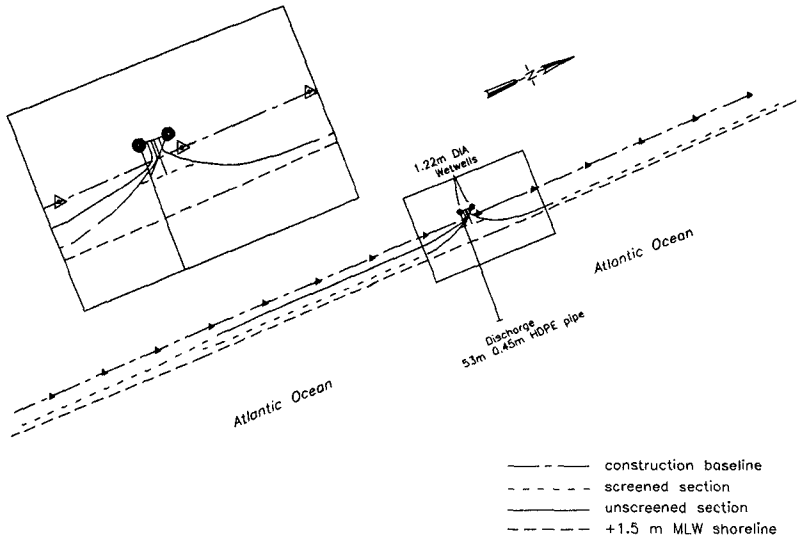


Figure 3. Plan-view schematic of Lighthouse North STABEACH segment.

Table 1. STABEACH Installation Parameters						
Segment	Drain Length	Drain Diameter	Drain Elev. (-MSL)	Drain Method	Pump Capacity	Initial Flow Rate
<i>LHN</i>	405 m	30.5 cm	2.4-3.6 m	gravity wet well	22716 lpm 6000 gpm	52 lpm/m 4.2 gpm/ft
<i>LHS</i>	309 m	30.5 cm	2.4-3.6 m	gravity wet well	22716 lpm 6000 gpm	30 lpm/m 2.45 gpm/ft
<i>CFP</i>	357 m	30.5 cm	2.4-3.0 m	low vac. wet well	11350 lpm 3000 gpm	28 lpm/m 2.25 gpm/ft

Note: gpm = gallons (US)/minute, lpm = liters/minute.

Prior to installation of the STABEACH segments, a series of tests were performed by Coastal Stabilization, Inc., to characterize hydrogeological properties of the project site. Subsurface borings identified vertical and horizontal variation of grain-size distributions. Hydraulic conductivity tests were used to optimize vertical and horizontal placement of drain lines and optimize discharge pump design. Table 2 presents average subsurface soil properties for each STABEACH location.

Location	Soil Type	Hydraulic Conductivity (calculated)
<i>CFP</i>	med-coarse sand, no fines clean, uniform	0.233 cm/s
<i>LHS</i>	fine-coarse sand, clean	0.089 cm/s
<i>LHN</i>	fine-med sand, silt/clay	0.2 cm/s

Monitoring Program

Laboratory and prototype field demonstration studies suggest that beach dewatering technology has the potential to stabilize a shoreline. However, the practical application of the technology as a viable means of coastal protection has yet to be adequately documented (Turner and Leatherman, 1996).

To assess the potential for the wider use of beach dewatering in coastal erosion management, a comprehensive and independent monitoring program was developed and implemented by the US Army Engineer Waterways Experiment Station (WES) to objectively evaluate the STABEACH project underway on Nantucket Island. The primary emphasis of the monitoring program is to evaluate whether observed beach changes can be attributed to the dewatering segments. If successful, data from the monitoring program will be used to address quantitative guidelines for the design, construction and operation of future beach dewatering-systems.

Elements of the monitoring program include measurements of beach profiles, bathymetry, hydrogeology, sediment characteristics, coastal processes and system parameters. System parameters such as discharge, operational period, and power requirements have been measured at each dewatering segment for the duration of the monitoring program. The elements of the monitoring program are described in more detail below.

Quarterly Beach Profiles

Beginning in November 1994 (pre-construction), forty-two transects have been established and surveyed on a quarterly basis (Figure 2). The project extends 9.8 km with survey transect 81 at the south end and transect W at the north end. Profile transects are regularly spaced at 305 m intervals, with the exception of 122 m intervals in the vicinity of system drain pipes. For reference, *CFP* system extends from 67 m south of transect 81 to 44 m north of transect 84; *LHS* system extends from 131 m south

of transect 91 to 83 m north of transect 91; *LHN* system extends from 46 m north of transect 92 to 122 m north of transect 93.

Each transect extends from the crest of the dune or base of the coastal bank to wading depth (-1.5 m MLW) and was surveyed with a total station and prism rod system. Elevations were surveyed at inflection points in the profile slope and at 6 m intervals from the baseline to wading depth.

To date, quarterly beach profile data have been analyzed for volume and shoreline change. Quarterly measurements document seasonal variability, and comparisons to the pre-construction surveys document the longer-term trends. Figures 4a and 4b present the variation in shoreline position (as defined by the 0.0 m MLW contour) for June 1996 data compared to pre-construction (November 1994) data. When considering profile transects 81-96.5, dewatered beaches have experienced an average shoreline recession of -5.2 m and non-dewatered beaches an average recession of -8.2 m between November 1994 and June 1996. North of transect 96.5, the averaged shoreline has accreted since project installation (0.1 m).

Figures 4a and 4b suggest that rates of recession generally decrease from south to north along the project area. Figure 5 confirms the inference as volumetric changes of the beach profiles between November 1994 and June 1996 range from -115 m³/m at profile 81 to +12.5 m³/m at profile W. The trends are consistent with longshore currents which are generally from south to north and dominated by tidal currents (Gutman et al., 1979).

Bi-Monthly Beach Profiles

Spatially and temporally dense data were acquired and are being analyzed to understand small scale variations in beach morphological dynamics as influenced by the system segments. Beach profiles were obtained at 15 day intervals for a six month period (June-November 1996) at eleven transect locations in the vicinity of and outside the influence of the *CFP* segment. Transect locations (82.6, 83.0, 83.5, 84.0, 84.3, 84.6, 85.0, 86.0, 86.4, 87.0, 87.4) were spaced at 122 m intervals in the longshore direction and had a cross-shore spatial resolution of 1.5 m from the dune to -0.9 m MLW. The objective of the high resolution profiling initiative is to correlate beach profile response with concurrent dewatered and non-dewatered groundwater elevation measurements. Through a statistical correlation of profile data with groundwater measurements, an assessment of the system-induced manipulation of beach groundwater on morphological response will be quantified.

Bathymetry

The forty-two transects established for beach profiles were extended offshore using a ship-mounted digital fathometer interfaced to the Coastal Oceanographic HYPAC program. Hydrographic surveys were conducted November 1994, December 1995 and September 1996 using standard fathometer techniques. In September 1995 and June 1996 Scanning Hydrographic Operational Airborne Lidar System (SHOALS) surveys were conducted (Lillycrop et al., 1996). Complete SHOALS surveys of the *LHN* and *LHS* offshore regions were obtained on both occasions, while surveys offshore

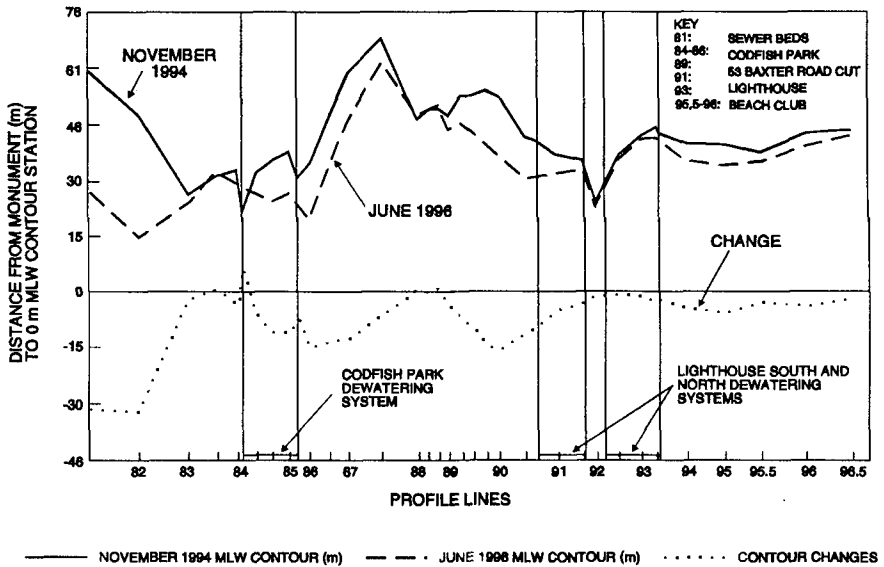


Figure 4a. Contour changes at elevation 0.0 m MLW: November 1994-June 1996 (after Coastal Planning and Engineering, Inc., 1996).

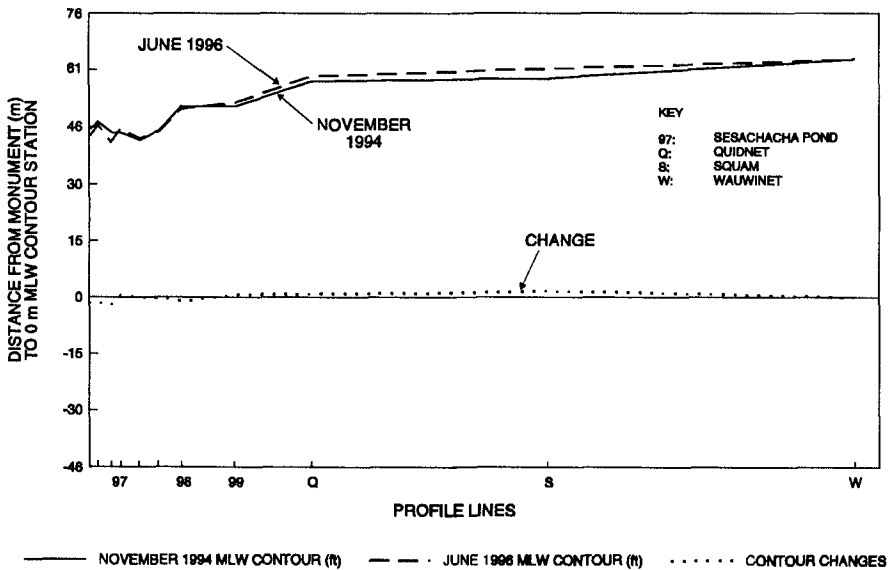
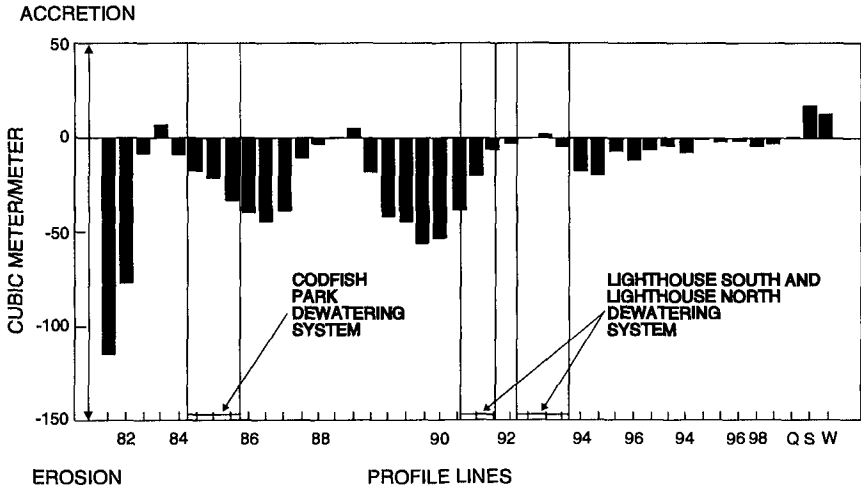


Figure 4b. Contour changes at elevation 0.0 m MLW (continued): November 1994-June 1996 (after Coastal Planning and Engineering, Inc., 1996).



PROFILE SPACING NOT TO SCALE

Figure 5 . Volumetric changes at -1.5 m MLW: November 1994-June 1996 (after Coastal Planning and Engineering, Inc., 1996).

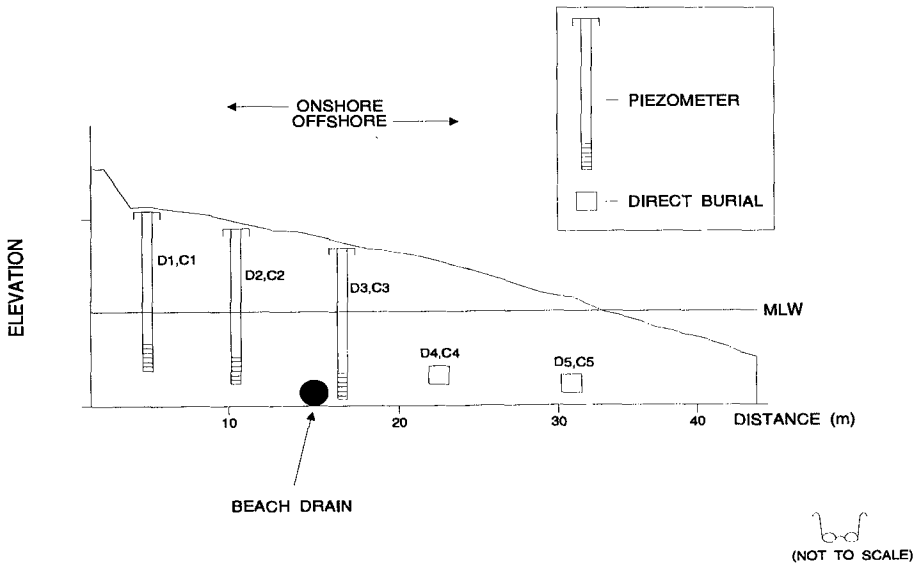


Figure 6 . Cross-sectional schematic of the groundwater monitoring installation at Codfish Park STABEACH segment and adjacent control beach.

CFP were unobtainable due to water clarity and weather limitations. Data obtained using standard fathometer and SHOALS methods will be used in combination with the beach profiles by comparative analysis to assess the response of morphological processes to the STABEACH segments.

Groundwater Elevation

Two cross-shore transects of buried pressure sensors were installed in December 1995 and re-installed in May 1996 following storm damage at the project site to monitor the variations of watertable elevation below a dewatered and non-dewatered beach (Figure 6). Groundwater monitoring transects are located at *CFP* and at the non-dewatered beach between *CFP* and *LHS*. Sensors are either directly buried or encased in screened wells and connected to recording instruments. Data loggers sample watertable fluctuations every 30 seconds and average them over 5 minutes at 15 minute intervals. A barometer and internal thermometers are used to correct absolute pressure measurements for low-frequency barometric and temperature fluctuations. The objective of the measurements is to determine the influence of a STABEACH segment on beach groundwater dynamics and address key issues such as the effect of dewatering on bed saturation characteristics at the beach face, the influence of dewatering during storms and during post-storm recovery of the beach profile, and the effect of dewatering on the local fresh groundwater supply. The second transect of pressure sensors outside the influence of the *CFP* system will be used as a control for comparative analysis.

Other Morphological Monitoring Elements

Additional WES-sponsored monitoring include quarterly controlled aerial photographic surveys and use of a video imaging system. Aerial photographic surveys will be used to compliment analyses of shoreline and coastal dune position for the project.

A digital imaging system was installed on a lighthouse located on the bluff above the *LHN* segment. The cameras were located approximately 55 m above the beach. Three cameras were needed to photograph the full extent of the beach within view of the lighthouse. The imaging system is capable of quantifying beach changes and patterns of incident wave breaking within the camera's field of view (Lippman and Holman, 1989). The system obtains instantaneous images of the beach (Figure 7) on the hour during daylight. In addition, the system produces a 10 minute time-averaged image (Figure 8). The time averaged image is produced by sampling at a rate of 3 Hz for 10 minutes and applying an averaging routine to produce a statistically stable image. Images will be used to analyze variations in foreshore morphology at a dewatered and adjacent non-dewatered beach.

Wind and Wave Parameters

Deep water wave parameters are measured on the continental shelf at approximately 500 km east and at 223 km southeast of Nantucket Island. The moored discus buoys are maintained by the National Data Buoy Center and provide directional wind spectra, non-directional wave spectra and climatic data. Unfortunately, no shallow



Figure 7. Instantaneous digital image of Lighthouse North dewatered swash zone.



Figure 8. Time-averaged digital image of Lighthouse North dewatered swash zone and adjacent non-dewatered shoreline to the north.

or intermediate depth wave parameters are measured in the nearshore region. However, given the NDBC buoy data, shallow or intermediate water depth equivalents can be estimated. In addition, the SBPF sponsors data collection of local climate variables (e.g., wind speed, direction and barometric pressure).

Monitoring Elements of Public Concern

The SBPF sponsors environmental impact monitoring of the STABEACH segments. Parameters of public concern are measured quarterly and include the impact of beach groundwater draw down on the public fresh water supply, on dune vegetation communities, on beach meiofauna, and on system discharge quality.

Discharge Quality

Salt water is discharged offshore from all three dewatering segments. Salinity of the discharged water ranges from 21-33 ppm and is comparable to nearshore ocean water (30-33 ppm). Bacteria levels of water discharged offshore are an order of magnitude below the standard acceptable for safe swimming. Measured nitrate levels are slightly higher at the *CFP* discharge (0.21-0.54 mg/l) than the *LHS* and *LHN* discharges (0.07-0.29 mg/l). The close proximity of residential septic systems to the dewatering segment is responsible for the higher nitrate measurements at *CFP*. Variations in the elevation of the public fresh water supply aquifer are monitored at 0 m, 70 m, 104 m, 453 m and 640 m landward of the *CFP* wet wells. Monitoring results follow the fluctuation trends in the elevation of the regional aquifer landward of the wet wells, as measured by the United States Geological Survey (USGS) (Figure 9).

Maritime Vegetation and Meiofauna

Monitoring transects were established at *CFP* and *LHS* for evaluation of the impact of groundwater elevation draw down on dune vegetation communities. Variations in the vegetative communities are not influenced by dewatering-system operation. Since project construction, variations in the vegetative communities are primarily due to vegetation lost during wave erosion events. Attempts to quantify dewatering effects on beach meiofauna are not definitive. Spatial and temporal variability in taxonomic richness, diversity, evenness and total number of organisms per sample was significant at dewatered and non-dewatered sample stations (Figure 10). The influence of the STABEACH system on local meiofauna communities is not detectable from the available monitoring data.

Summary

The objective of this paper is not to present definitive conclusions as to the effectiveness of the STABEACH installations at Nantucket Island. Rather, the emphasis has been to convey elements of an independent monitoring program which was established to evaluate beach dewatering technology as a means to stabilize sand on a receding shoreline in a high wave energy environment. Shoreline position of Nantucket Island is highly variable when considering temporal scales ranging from several hours to decades. Monitoring efforts were established to identify trends in shoreline

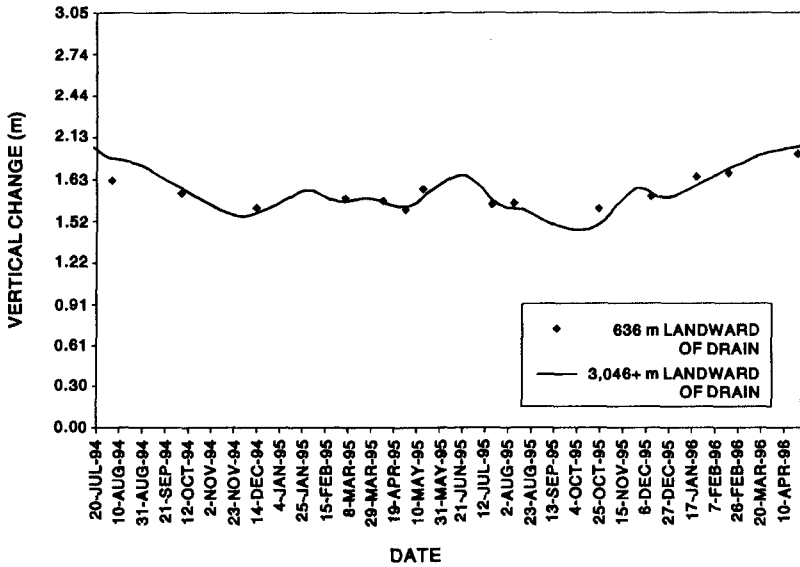


Figure 9. Vertical changes in groundwater elevation landward of Codfish Park STABEACH segment (after Fugro East, Inc., 1996).

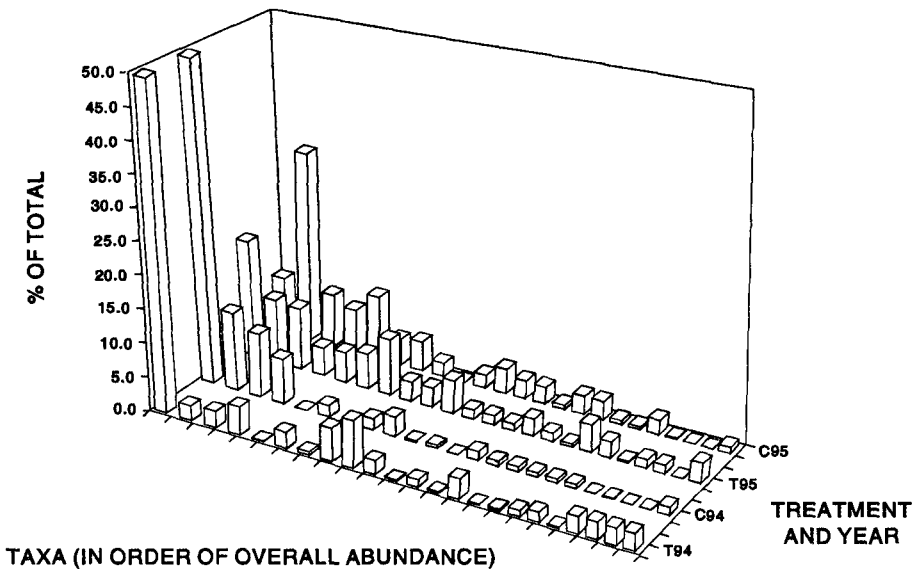


Figure 10. Meiofauna count for dewatered and non-dewatered beaches: 1994 and 1995 (after Fugro East, Inc., 1995).

morphodynamics on varying temporal scales as influenced by operational STABEACH segments.

WES-sponsored monitoring was initiated in June 1995 and is scheduled to terminate in May 1997. After the data collection is terminated, a comprehensive evaluation of use of the STABEACH system as a shoreline stabilization method at Nantucket Island will be presented in the literature.

Three STABEACH segments have been in operation at Nantucket Island for two years. Operation of the *LHN* segment has been nearly continuous since installation. Discharge pumps located at *LHS* were damaged during a storm in January 1996 and returned to operation at 70% capacity in July 1996 and 100% capacity in September 1996. The pump which draws water through the drains at the *CFP* segment was rendered inoperable February 1996. It is speculated that the *CFP* segment operated at 50% capacity under gravity drainage, until the pump returned to operation in August 1996.

Following 18 months of quarterly monitoring, visual and statistical analyses confirm that both dewatered and non-dewatered beaches have highly variable seasonal profile fluctuations. Quantification of the influence of drainage of the beach face on sand stabilization at the project site is presently under investigation.

SBPF-sponsored monitoring reveals that the quality of discharged water has negligible impact on water quality offshore of the dewatering-system segments. Groundwater draw down attributed to the STABEACH segments has had no discernable impact on local vegetative and meiofaunal communities. In addition, the drainage of the beach face has no adverse impact on the local public freshwater aquifer.

Acknowledgments

The Authors would like to acknowledge Coastal Planning and Engineering, Inc., Boca Raton, Florida, USA for providing shoreline analysis and beach profile volume change calculations and Fugro East, Inc., Sandwich, Massachusetts, USA for providing environmental analysis information. Results and information presented herein, unless otherwise noted, were obtained from research conducted under the Construction Productivity Research Program of the US Army Corps of Engineers by the US Army Engineer Waterways Experiment Station. Permission to publish this paper was granted by the Chief of Engineers.

References

- Coastal Planning and Engineering, Inc. (1996), "Coastal engineering analysis of the Siasconset, Nantucket Island erosion control project", *Sixth Qtr. Rpt: June 1996*, Coastal Planning and Engineering, Inc., Boca Raton, FL.
- Coastal Stabilization, Inc. (1994), "Geotechnical and hydrological investigation and design for the installation of a STABEACH system: Nantucket, Massachusetts", *Int. Doc.*, Coastal Stabilization, Inc., Rockaway, NJ, 11p.
- Fugro East, Inc. (1996), "Winter quarterly report (December 1995-February 1996): Siasconset erosion control project, Nantucket, Massachusetts", *Int. Doc.*, Fugro

- East, Inc., Sandwich, MA.
- Fugro East, Inc. (1995), "Summer quarterly report (June-August 1995): Siasconset erosion control project, Nantucket, Massachusetts", *Int. Doc.*, Fugro East, Inc., Sandwich, MA.
- Gutman, A.L., M.J. Goetz, F.D. Brown, J.F. Lentowski, and W.N. Tiffney (1979), "Nantucket shoreline survey: An analysis of Nantucket shoreline erosion and accretion trends since 1846", *MITSG 79-7*, Massachusetts Institute of Technology Sea Grant College Program, Cambridge, MA.
- Hubertz, J.M. (1995), "Variation of measured meteorologic and oceanic variables off the U.S. Atlantic coast: 1980-1994", *4th Int'l. Workshop on Wave Hindcasting and Forecasting*, Banff, Canada, October 16-20, 1995, 45-57.
- Lenz, R.G., (1994), "Beach face dewatering - a tool for coastal stabilization", *Proc. 1994 Nat'l Conf. on Beach Pres. Tech.*, 27-52.
- Lippman, T.C. and R.A. Holman (1989), "Quantification of sand bar morphology: A video based technique on wave dissipation", *J. Geophys. Res.*, 94(C1), 995-1011.
- Lillicrop, W.J., L.E. Parson and J.L. Irish (1996), "Development and operation of the SHOALS Airborne Lidar Hydrographic Survey System", SPIE: Laser Remote Sensing of Natural Waters: From Theory to Practice (unpublished).
- Oldale, R.N. (1987), "Wisconsinian and pre-Wisconsinian drift and Sangamonian marine deposits, Sankaty Head, Nantucket, Massachusetts", *Centennial Field Guide-Northeastern Section*, Geological Society of America, 221-224.
- Ovansen, N.K. and J.C. Schuldt (1992), "Beach Management System", *Int. Doc.*, Danish Geotechnical Institute, 20p.
- Tiffney, W.N., L.L. Weishar and J.C. Andrews (1991), "Nantucket Island's shifting shoals and moving shores: Nearshore bathymetry controls beach deposition and erosion", *Coastal Zone '91*, American Society Civil Engineers, N.Y., vol. 3, 2421-2433.
- Turner, I.L. and S.P. Leatherman (1996), "Beach dewatering as a 'soft' engineering solution to coastal erosion - a history and critical review", In press, *J. Coast. Res.*
- Weishar, L., W.N. Tiffney, N. Kempe and M. Fields (1991), "Shoreline response to offshore shoals and storms: Low Beach, Nantucket, MA", *Coastal Zone '91*, American Society Civil Engineers, N.Y., vol. 3, 2435-2449.

CHAPTER 208

SEDIMENT TRANSPORT PROCESSES AT OCEAN BEACH, SAN FRANCISCO, CALIFORNIA

Robert T. Battalio, P.E.¹ & Dilip Trivedi, Dr. Eng., P.E.¹

The San Francisco estuary inlet and tidal bar is a highly complex system that strongly influences littoral processes on adjacent beaches. Ocean Beach is about 4 miles long, located near the entrance to the estuary (Figures 1 and 2). The purpose of the study was to investigate the extent and causes of shoreline variability at Ocean Beach, and identify possible sand transport processes and directions based on available information (Moffatt & Nichol Engineers, 1994; 1995).

Geographic Description of Vicinity

Ocean Beach is a sandy beach on the west side of San Francisco, California, USA (Figures 1,2 and 3). A linear dune behind the beach forms an embankment covering the West Side Sewer Transport Box, supporting the Upper Great Highway, and protecting the urban residential area from the Pacific Ocean. Seawalls have been constructed where the embankment eroded frequently. These structures are the most obvious indications of impacts by man dating back to the late 1800's (O'Shaughnessy, 1924; Olmsted and Olmsted, 1979; Berrigan, 1985a; O'Doherty, 1994). Perpendicular to the Great Highway are a series of streets named alphabetically from north to south (eg. Noriega, Ortega, Pacheco, Quintara, etc.) which are often used as location references.

The offshore bathymetry and shoreline to the north and south are very irregular, affecting wave propagation and littoral sand transport (Figure 1). The Golden Gate is located to the north of Ocean Beach. This channel connects San Francisco Bay with the Pacific Ocean. The large tidal prism (2.3×10^9 cubic meters, m^3 for a typical tide range of 1.5 meters) and rocky shoreline results in a relatively constricted channel (0.084 square kilometer) and strong currents (typical peaks about 10 kilometers per hour) (USACE, 1990).

1) Civil/Coastal Engineer, Moffatt & Nichol Engineers, 131

Steuart Street, Suite 300, San Francisco, California, 94105

The San Francisco Bar is a horseshoe-shaped, sandy shoal with a radius of about 5 kilometers (3 miles). The Bar crest depths are as shallow as 7.3 meters (24 feet) at low tide. Every winter, larger storm seas and swells induce wave breaking along the crest of the Bar. There are several sand shoals just east of the Golden Gate in San Francisco Bay. Sand beaches exist along the south boundary of the Golden Gate.

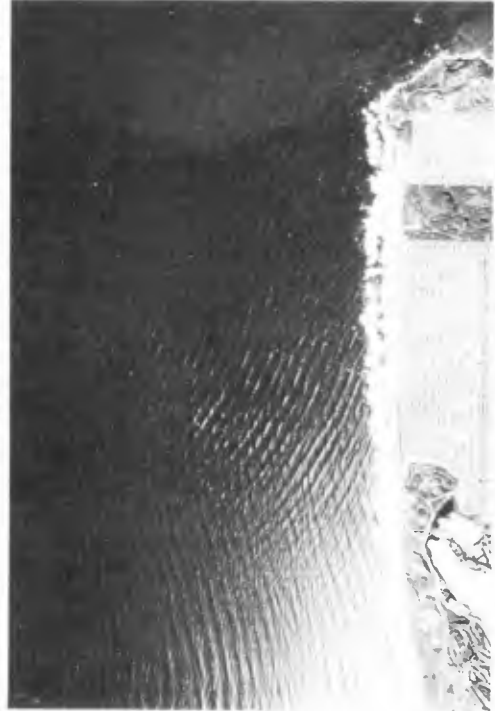
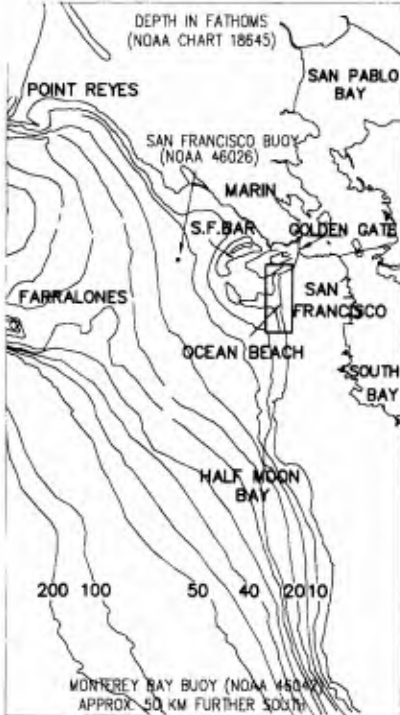
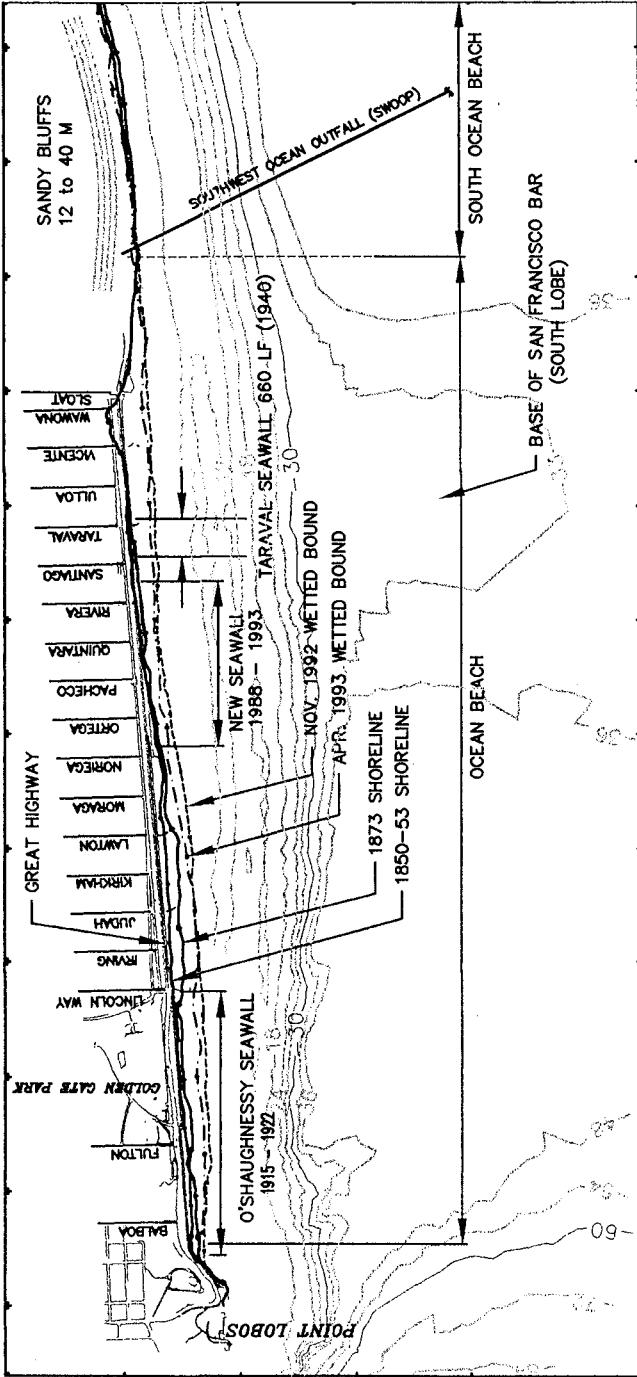


Figure 1: Site Location Figure 2: Aerial Photo of Site

Sediment Characteristics

Median grain sizes of sand samples from the vicinity were reported by Trask(1958), Moore(1965), Johnson(1971), USACE(1974;1993), Galvin(1979a), Woodward-Clyde Consultants (1979), Ecker(1980), and Noble(1985). At Ocean Beach, the median grain sizes were typically 0.2 to 0.6 millimeters (mm), but occasionally between 0.6 and 1.6 mm. Grain sizes vary significantly along the beach and seasonally, with larger grain sizes in the spring (Trask, 1958; Galvin,1979), especially near the base of the San Francisco Bar. Median grain sizes on the crest of the San Francisco bar are the smallest (0.1 to 0.2 mm), with coarser sizes inside the crest (0.2 to 0.7 mm). Median grain sizes inside the Golden Gate are similar.

Johnson (1971) summarizes mineralogy studies in the area.



NOTES:

1. DEPTH CONTOURS (FT) SHOWN BASED ON MEAN LOWER LOW WATER, FROM 1954 - 1956 HYDROGRAPHIC SURVEY.
2. PLANIMETRIC MAP OBTAINED FROM HAMMON, JENSEN & WALLEN, NOVEMBER 1992.

SCALE IN FEET



Figure 3: Study Area

Similar heavy mineral content in the sands were found at Ocean Beach and nearby areas (San Francisco Bar, Golden Gate, and beaches south to Pedro Point), but not for offshore areas or beaches to the north or farther south. Johnson(1971;1977) concluded that there was probably very little net sand transport at the boundary of the area defined by the San Francisco Bar and Entrance, and the beaches south to Pedro Point.

Currents

Detailed data regarding tidal currents and sediment grain sizes can be found in Enclosure 1 of USACE (1974). Tidal current charts show directions that "fan-out" to cross the San Francisco Bar roughly perpendicular to the crest. At Ocean Beach, ebb tide currents are roughly parallel to shore and southward. Flood tide currents are roughly northward. Due to the diurnal inequality, the strongest currents are associated with the larger ebb tides. Peak annual tide ranges are about 2.5 to 2.8 meters, with peak ebb currents between 2 and 4 kilometers per hour. During these strong flows, large eddies form near headlands, causing nearshore currents to flow in the opposite direction. Currents in the surf zone are strong, complex and variable. Detailed measurements are not available.

Waves

Ocean Beach is exposed to storm seas and swell generated in the Northern Pacific, and swell generated in the Southern Pacific. Large wave power is incident, with the greatest in the winter (Johnson,1977; Woodward-Clyde Consultants,1978; Cross,1980; Berrigan,1985b, Wiegel,1992). Wave refraction causes focusing of incident waves at Ocean Beach for most directions and especially for longer wave periods (Street, Mogel and Perry,1970; Woodward-Clyde Consultants,1978; USACE,1993). Long period waves begin to refract around the 200-fathom (360 meters) line noted on Figure 1. The complex bathymetry results in multiple wave travel paths incident to Ocean Beach, and exposure to waves incident from north of the geometric shadow formed by Point Reyes. Refraction over the San Francisco Bar contours causes a focusing of wave energy near the base of the Bar, even for relatively short wave periods (Figure 4). Figure 2 is a high-altitude photograph which shows wave crossings due to refraction (see also, Vincent et. al., 1994). The result is an amplified breaking wave height at the location of wave crossing, resulting in a very peaked wave form (Figure 5, Battalio, 1994).

Prior estimates of wave-induced alongshore sand transport do not agree in direction nor magnitude. Estimated rates are typically around 5×10^5 to 1.5×10^6 m³/yr (7×10^5 to 2×10^6 cubic yards/yr, yd³/yr) for the gross, and zero to 6×10^5

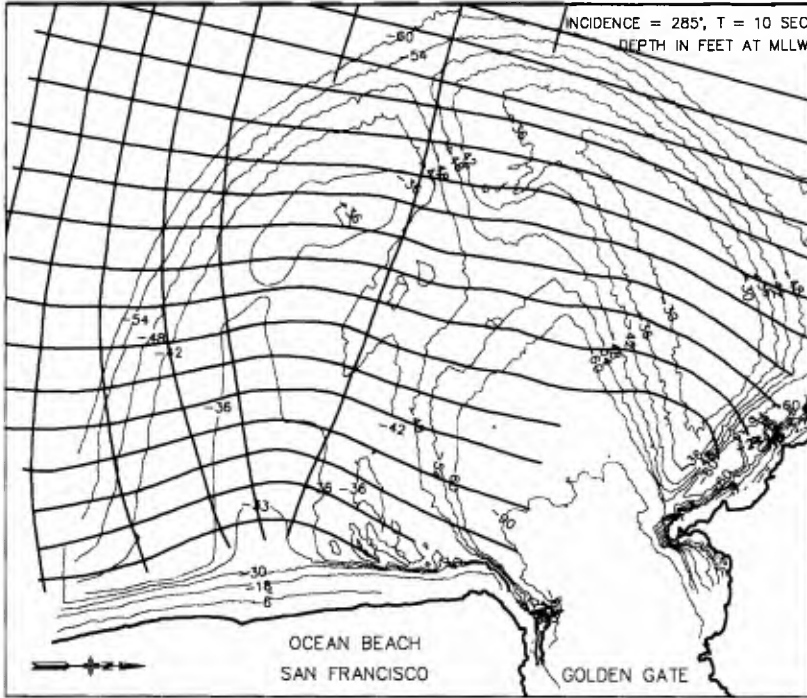


Figure 4: Wave Refraction Over San Francisco Bar
 (Source Woodward Clyde Consultants, 1978)



Figure 5: Grant Washburn Observes Breaking Wave Heights near Taraval Street, Ocean Beach, San Francisco, (Winter 1992).
 For scale, the surf board is 9 feet long. Photo: Tim Britton

m^3/yr ($8 \times 10^5 \text{ yd}^3/\text{yr}$) for the net (Street et. al., 1970; Kamel, 1962; Johnson, 1979; USACE, 1979; Galvin, 1979; Domurat, Pirie, and Sustar, 1979).

A five-year data set of daily visual observations of breaking wave heights was reviewed (Washburn, 1996). Table 1 summarizes the cumulative distribution of breaking wave heights from these data, which were observed near the base of the San Francisco Bar (Taraval Street). These observations were compared to deep water significant wave heights recorded by the San Francisco Buoy and the Monterey Bay Buoy (see Figure 1 for locations): A time series correlation analysis produced coefficients of 0.79 and 0.76, respectively, indicating a strong correlation (maximum coefficient is 1.0).

Table 1: Cumulative Distribution of Breaking Wave Heights, Taraval Street, Ocean Beach (1991-1996)

Breaking Wave Height		Frequency of Occurrence
Meters	(Feet)	Larger Waves (% of Daily observations)
1.8	(6)	50%
3.0	(10)	25%
4.6	(15)	10%
7.3	(24)	1%

The method of Hands & Allison (1991) was used to gage the potential for onshore sand transport from the Bar to Ocean Beach. An average wave period of 12 seconds, a depth of 9 meters, and the cumulative distribution given in Table 1 were used. Calculations show a strong potential for onshore sand transport, as concluded by others (Kamel, 1962; Galvin, 1979).

Wind

Strong onshore (mostly northwest) winds occur at Ocean Beach. Prior to major development in the 1900's, the area behind Ocean Beach was an extensive dune field (Olmsted and Olmsted, 1979). Sand losses due to inland transport by wind are estimated to be zero to $23 \times 10^3 \text{ m}^3/\text{yr}$ ($30 \times 10^3 \text{ yd}^3/\text{yr}$) prior to 1975, and zero to $7.6 \times 10^3 \text{ m}^3/\text{yr}$ ($10 \times 10^3 \text{ yd}^3/\text{yr}$) since then. The reduction is based on the City's practice of returning sand to the beach since 1975.

Man's Activities

Significant beach and dune fill occurred during the period 1882 to 1929, when the natural dunes were re-graded to form a straight embankment for the shore-parallel Great Highway (Olmsted and Olmsted, 1979). This resulted in a seaward shift of the shoreline of about 60 to 90 meters (200 to 300 feet) (Figures 3 and 6). The estimated net

volume changes to the beach and dunes by man since 1929 were summarized for the sediment budget (Table 3). Comparison of the shoreline data with the timing and location of sand placement indicates a northward littoral drift from the base of the Bar, which agrees with Johnson (1979).

The need for safe navigation to and from San Francisco Bay requires a dredged channel through the San Francisco Bar. The Bar Channel is authorized to a depth of 17 meters (55 feet) below mean lower low water. Since the Bar Channel was last deepened in 1975, annual dredging has totaled about $4.6 \times 10^5 \text{ m}^3$ ($6 \times 10^5 \text{ cy}$) of sand. The sand is dumped on the south part of the Bar (see Figure 10). Prior to 1971, the dredged sand was reportedly dumped about one mile southwest of the Bar Channel entrance in about 24 meters (80 feet) of water. The dump location was changed so that the sand would stay in the littoral zone (USACE, 1974).

Prior to 1971, at least 20 million m^3 (26 million yd^3) of sand was dredged. Since 1971, about 11 million m^3 (14 million yd^3) were dredged from the channel area and reportedly placed near the crest of the south side of the Bar. Of this total, about 4.6 million m^3 (6 million cy) was attributed to deepening of the channel.

Shoreline, Dunelines, and Related Volume Changes

Shorelines and toe-of-dune lines from historic maps and aerial photographs were used to investigate changes and as input to the sediment budget analysis. Five shorelines digitized from smooth sheets for the period 1850 to 1944, and eleven shorelines and toe of dune positions from aerial photographs for the period 1938 to 1993 were mapped (Moffatt & Nichol, 1994). The mean high water shoreline was used from the maps. The wetted bound visible in the aerial photos was used to estimate the shoreline position, which was found to approximate the Mean Higher High Water elevation of about +1.8 meters (6 feet) Mean Lower Low Water datum.

Time histories of the shoreline positions and beach widths for Ocean Beach and South Ocean Beach are shown in Figures 6 and 7. The Ocean Beach data show a large seaward offset between 1900 and 1929, while South Ocean Beach data do not. This is attributed to the construction of the embankment supporting the Great Highway, and related beach nourishment. The Ocean Beach data show large fluctuations about an accretion trend, while South Ocean Beach data show smaller fluctuations about a slow erosion trend. Both areas show erosion to the early 1970's, and a recovery in recent years.

Beach and shoreface volume changes were estimated by applying a conversion factor of volume change per beach area change. A range of 8 to 14 m³/m², (1.0 to 1.7 yd³/ft²)

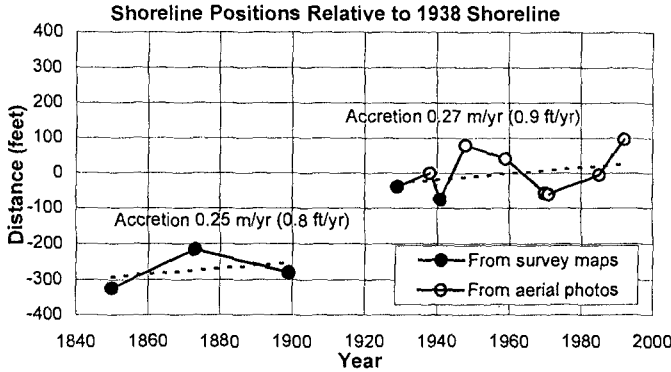


Figure 6: Shoreline Change Data Ocean Beach
Shoreline Positions Relative to 1938 Shoreline

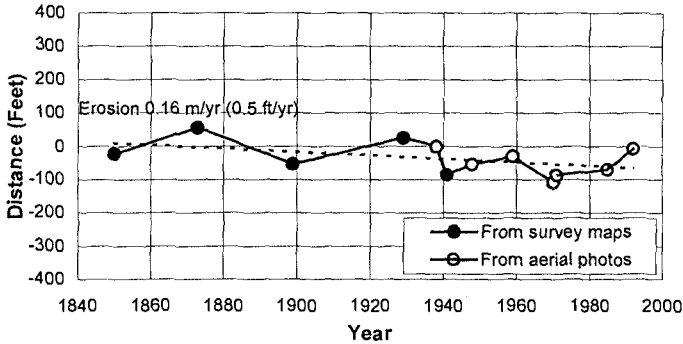


Figure 7: Shoreline Change Data So. Ocean Beach

due to erosion of sand placed by man on the upper beach and dune, per Galvin(1979) and Ecker (1980). Volume changes for the dune face were calculated using a conversion factor that ranged between zero and 6 m³/m² (0.74 yd³/ft²) of dune line change.

San Francisco Bar Depth Changes

Prior studies of historic changes to the San Francisco Bar have been identified by Gilbert(1917), Homan and Schultz(1963), and Johnson(1965). Figure 8 shows the depths surveyed in 1900. Figure 9 shows the depths surveyed in 1956, and major depth changes since 1900.

Prior to 1900, the Bar had a relatively consistent "cusplate" shape. By 1956, outer portions eroded and inner portions accreted. Significant changes include the dredged channel, which is deeper, the area closer to Ocean Beach, which is shallower, and the Bar crest, which

of beach change was used to calculate the values for Beach and Shoreface in Table 3. The higher value was developed based on a review of profile "closure" elevations and the assumption that the shoreface geometry remains essentially constant as the shoreline migrates. The minimum conversion factor was based on the assumption that shoreline changes were

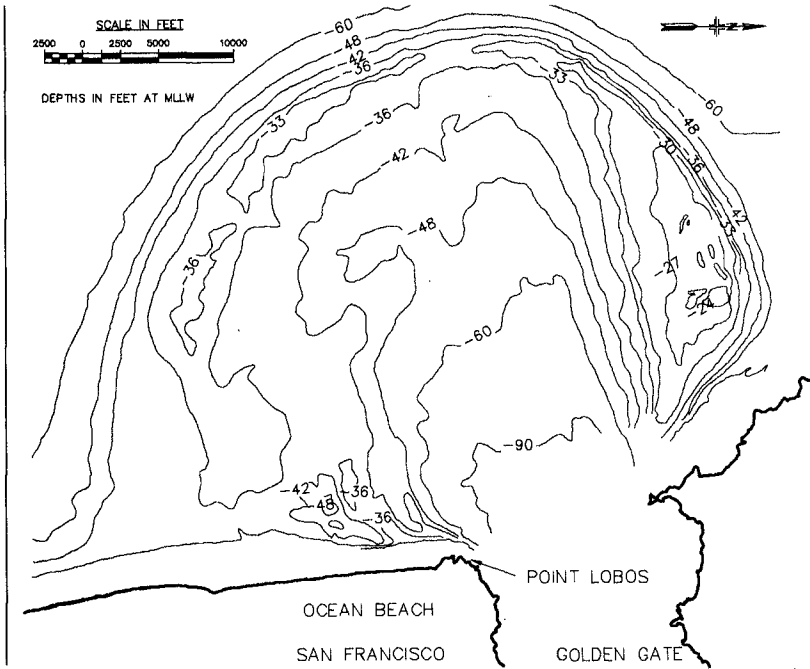


Figure 8: Bathymetry of San Francisco Bar, Circa 1900

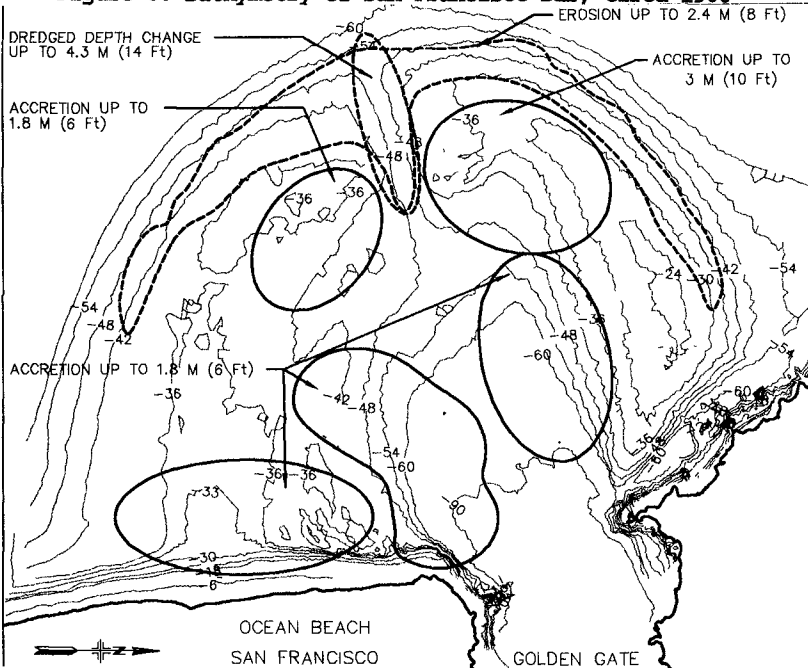


Figure 9: Bathymetry of San Francisco Bar, Circa 1956 and Major Depth Changes 1900 - 1956

generally shows a radial "shrinking."

Volume changes calculated for the San Francisco Bar by a comparison of the 1900 and 1956 survey maps are provided in Table 2. The Table includes volume changes adjusted for two arbitrary systematic elevation corrections.

Since no recent survey is available, and due to the sensitivity to vertical control, the Bar changes were not directly incorporated into the sediment budget.

TABLE 2: San Francisco Bar Volume Changes and Sensitivity to Systematic Elevation Corrections

LOCATION	VOLUME CHANGES FOR 1900-1956 TIME PERIOD		
	Million Cubic Meters		
	Calculated	0.09 m correction	0.12 m correction
Four Fathom Bank	4.5	0.0	-1.5
Channel	-10.2	-12.4	-13.2
South Bar	19.2	14.6	13.1
Net Change	13.5	2.2	-1.5
Average Rate (m3/year)	241,000	39,000	-28,000

Sediment Budget Analysis

The sediment budget was developed to best use the available data, as summarized in Table 3. A range of values were used to reflect the uncertainty of the available data, and to facilitate a sensitivity analysis. The sediment budget analysis was applied to the Ocean Beach shoreface, beach, and dune face.

Based primarily on the historic shoreline positions, the sediment budget analysis was applied to the time period of 1929 to 1971 and 1971 to 1992. By 1929, the shoreline and embankment had been established roughly in its present location. An erosion trend dominated to 1971, becoming an accretion trend to the present. Starting in 1971, sand dredged from the Bar Channel was disposed on the Bar offshore of Ocean Beach, and the Channel was deepened significantly. Starting in 1975, wind blown sand was returned to the beach by the City.

For 1929-1971, a net deficit of 1.3×10^4 to 1×10^3 m³/yr (1.7×10^4 to 1.4×10^3 yd³/yr) is calculated (**Subtotal (I-II)** in Table 3). This range is small, and within the possible range of wind-induced losses inland, so that it is possible to balance the budget for this time frame by assuming zero net sand transport at the area boundaries, or that net input at one boundary (onshore from the Bar), is balanced by losses past other boundaries (north past Point Lobos, and/or south past South Ocean Beach). Local

knowledge indicates erosion is occurring in the area south of Ocean Beach, while sand accumulation is a problem in several areas along the north waterfront of San Francisco. It is therefore considered more likely that losses from Ocean Beach are passing Point Lobos and migrating into San Francisco Bay.

TABLE 3: Sediment Budget for Ocean Beach, San Francisco (Annualized for Listed Time Periods)

No.	ITEM	RANGE OF SAND VOLUME CHANGES (Thousands of Cubic Meters per Year)					
		1929-1971		1971-1992		1929-1992	
		Low	High	Low	High	Low	High
I	VOLUME CHANGES						
1	Beach & Shoreface	(7.3)	(12.6)	103.4	175.9	29.6	50.2
2	Dune Face (data from 1938)	0.0	(3.1)	0.0	(10.9)	0.0	(5.7)
	Net Volume Changes	(7.3)	(15.7)	103.4	164.9	29.6	44.5
II	SAND INPUT (LOSSES)						
3	Net Beach/Dune Nourishment (+) Mining (-)	5.5	9.1	36.4	36.4	15.8	18.2
4	Wind Blown Loss to Inland	0.0	(23.7)	0.0	(7.3)	0.0	(18.2)
	Net Input (Losses)	5.5	(14.6)	36.4	29.1	15.8	0.0
	Subtotal (I - II)	(12.7)	(1.1)	67.0	135.8	13.8	44.5
III	Estimated to Balance Budget						
6	Minimum Northward Transport Past Point Lobos	(12.7)	(77.6)	(12.7)	(77.6)	(12.7)	(77.6)
7	Minimum Onshore Transport From San Francisco	0.0	76.5	79.7	213.4	26.6	122.1
	Subtotal	(12.7)	(1.1)	67.0	135.8	13.8	44.5
III	Total (I - II - III)	0	0	0	0	0	0

For 1971-1992, a net surplus of 6.7×10^4 to 1.4×10^5 m³/yr (8×10^4 to 1.8×10^5 yd³/yr) is calculated, which is a significant change from the previous period. This rate of input can only be explained by alongshore transport from the area south of Ocean beach, or onshore transport from the Bar. However, only the onshore transport potential from the Bar changed markedly around 1971, due to the change in dredging practices.

Postulated Rates to Balance Sediment Budget

The third part (III) of Table 3 shows one possible solution to the sediment budget. Assuming a range for onshore transport from the Bar during 1929-71 to be zero to 7.6×10^4 m³/yr (1×10^5 yd³/yr), the loss due to alongshore transport past Point Lobos is calculated to be about the same as the input from the Bar. For the period 1971-92, the rate of alongshore transport past Point Lobos is assumed to be the same as for 1929-71. The required onshore sand transport rate from the bar is then calculated to be 8×10^4 to 2.1×10^5 m³/yr (1×10^5 to 2.8×10^5 yd³/yr).

Figure 10 presents the 1971-92 rates and postulated sand transport for the Ocean Beach, Golden Gate cell. The net alongshore transport rate at Ocean Beach is estimated to

be northward. The rate decreases with distance north, with sand accumulating in the beach and dunes. South of the base of the Bar, the net alongshore transport rate is unknown, but expected to be near zero.

The sand that passes Point Lobos is believed to mostly continue alongshore through the Golden Gate. Some is lost to maintenance dredging and dunes. The remainder is speculated to return to Ocean Beach by ebb tide currents, probably diverting from shore at several locations. Some or most of the sand is believed to migrate back to the San Francisco Bar prior to returning to Ocean Beach.

These rates are presented as long-term, average annual rates that could be substantially different in any particular year. Further study is needed, including

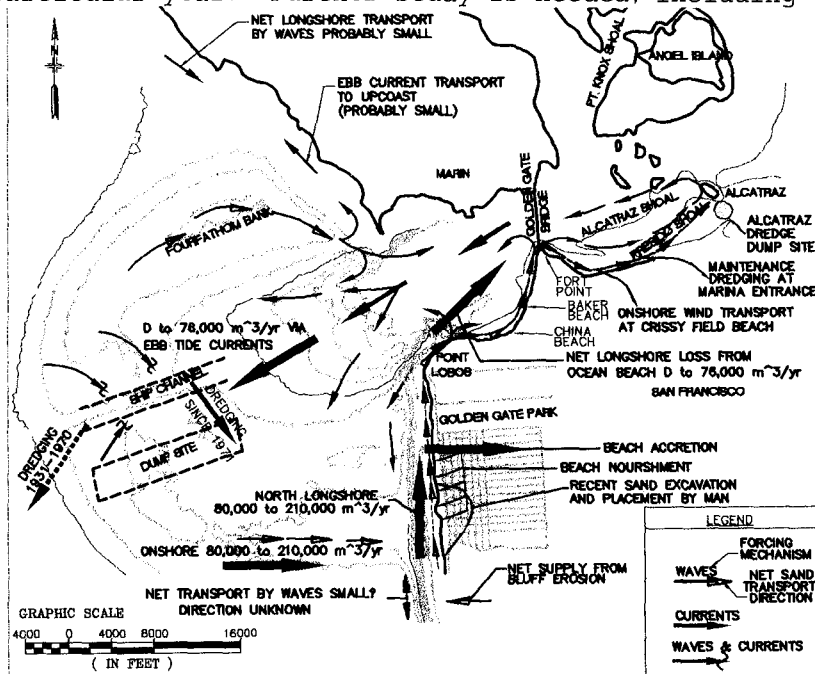


Figure 10: Residual Sediment Transport at Ocean Beach

recent Bar changes, sand transport and sediment budget in the Golden Gate area, and sand transport and sediment budget south of Ocean Beach to Pedro Point, Pacifica.

Acknowledgements

A Technical Review Panel reviewed the methodology and results, and provided guidance. Members included USACE (George Domurat, Tom Kendall and Len Madalon), City and County of San Francisco (Dave Jones), U.S. Geological Survey (John Dingler), Professors Robert Wiegel, Paul Komar and Ray Krone,

and individuals familiar with the area (Dr. James Walker and Dr. Philip Williams).

References

1. Battalio, R.T. (Oct 1994) "Estimating Breaking Wave Height at Ocean Beach, San Francisco," Shore and Beach, Vol. 62, No. 4, pp. 33-36.
2. Berrigan, P.D. (Apr 1985a) "Seasonal Beach Changes at the Taraval Seawall," Shore and Beach, Vol. 53, No. 2, pp. 3-9.
3. Berrigan, P.D. (Jan 1985b) "The Taraval Vertical Sea Wall," Shore and Beach, Vol. 53, No. 1, pp. 3-7.
4. Cross, R.H. (July 1980) "Ocean Wave Statistics for San Francisco," Shore and Beach, Vol. 48, No. 3, pp. 26-29.
5. Domurat, G.W., Pirie, D.M. and Sustar, J.F. (Oct 1979) "Beach Erosion Control Study, Ocean Beach, San Francisco, California," Shore and Beach, Vol. 47, No. 4, pp. 20-22.
6. Ecker, R.M. and Towill, Inc. (1980) Ocean Beach Sand Replenishment Program, prepared for City and County of San Francisco. October 1980
7. Galvin, C.G. (1979) Coastal Processes and Sediment Budget at Ocean Beach, San Francisco, prepared for the San Francisco Wastewater Program.
8. Gilbert, G.K. (1917), Hydraulic-Mining Debris in the Sierra Nevada, United States Geological Survey Professional Paper 105.
9. Hands, E.B. and Ellison, M.C. (1991) "Mound Migration in Deeper Water and Methods of Categorizing Active and Stable Berms," Coastal Sediments '91, Seattle WA, June 25-27, 1991.
10. Homan, W.J. and Schultz, E.A. (1963) Model Tests of Shoaling and of Dredge Spoil Disposal in San Francisco Bay, US Army Corps of Engineers, San Francisco District, California, January 28 - February 1, 1963.
11. Johnson, J.W. (Oct 1965) "Nearshore Sediment Movement- Central California Coast," presented at Coastal Engineering Specialty Conference, ASCE, Santa Barbara, CA, October 11-13, 1965.
12. Johnson, J. W. (1971) Bottom Sediment Characteristics Near Entrance to San Francisco Bay, University of California, Berkeley, Hydraulic Engineering Laboratory Technical Report HEL-24-3, April 1971.
13. Johnson, J.W. (May 1977) Shoreline Characteristics, Ocean Beach-San Francisco, Berkeley, California, May 10, 1977.
14. Johnson, J.W. (1979) Littoral Processes At Ocean Beach, San Francisco, California, November 28, 1978.
15. Kamel, A.M. (Jan 1962) Transportation of Coastal Sediments, University of California, Berkeley, IER, Series 185, Issue 1.
16. Moffatt & Nichol, Engineers (Jan 1994) Shoreline Mapping for Ocean Beach, San Francisco, California, Prepared for USACE San Francisco District.
17. Moffatt & Nichol, Engineers (July 1995) Sediment Transport Processes Study, Ocean Beach, San Francisco, California, Prepared for USACE San Francisco District.
18. Noble Coastal & Harbor Engineering and Dr. Per Bruun (July 1985)

- Great Highway - Ocean Beach, Coastal Engineering Report, Seawall Design, prepared for Clean Water Program - City and County of San Francisco, July 9, 1985.
19. O'Doherty, John, (October 1994), "Micheal Maurice O'Shaughnessy-San Francisco City Engineer, 1912-1932." Shore and Beach, Vol. 62 . No. 4, pp. 17-23.
 20. O'Shaughnessy, M.M. (1924) "Ocean Beach Esplanade, San Francisco, California, Paper No. 1539," Transactions, American Society of Civil Engineers Vol LXXVII 1924
 21. Olmsted, R. and Olmsted, N. (Feb. 1979) Ocean Beach Study: A Survey Of Historic Maps And Photographs, City of San Francisco, California, February 23, 1979.
 22. Street, R.L, Mogel, T. And Perry, B. (1970) "Computation of Alongshore Energy And Littoral Transport," Proceedings 12th Coastal Engineering Conference, Washington D.C., VII, Ch 57, ASCE, Sept 1970.
 23. Trask, P.D. (1958) Beaches Near San Francisco, California, 1956-1957, Technical Memorandum No. 110, Beach Erosion Board, Office of the Chief of Engineers, US Army Corps of Engineers.
 24. USACE (June, 1974) Dredge Disposal Study, San Francisco Bay and Estuary, Appendix A: Main Ship Channel (San Francisco Bar), US Army Corps of Engineers, San Francisco District, California.
 25. USACE (1979) Ocean Beach, San Francisco, California, Feasibility Report, Beach Erosion Control Study, US Army Corps of Engineers, San Francisco District, California, July 1979.
 26. USACE (December, 1990) Long Term Management Strategy for Dredged Material Disposal in the San Francisco Bay Region, Phase I: Evaluation of Existing Management Options, US Army Corps of Engineers, San Francisco District, California.
 27. USACE and City and County of San Francisco (Sept 1996) Final Report: Ocean Beach Storm Damage Reduction Study, US Army Corps of Engineers, San Francisco District, California.
 28. USACE (September, 1993). Wave Studies at Ocean Beach, San Francisco, US Army Corps of Engineers, San Francisco District, California.
 29. USACE (1995), Dredging Records for San Francisco Bar Dredging, Construction Operations Division, US Army Corps of Engineers, San Francisco District, California.
 30. Vincent, Charles L., Robert F. Jenson and Richard Goldstein, (Oct. 1994) "Wave-Current Interaction at an Inlet," Shore and Beach, Vol. 62, No. 4, pp. 13-15.
 31. Washburn, Grant (September, 1996), Daily Visual Observations (Aug 1991 - 1996) of Breaking Waves, Ocean Beach, San Francisco. Unpublished. Notes provided to Moffatt & Nichol Engineers for analyses.
 32. Wiegel, R. L. (January 1992), "Coastal Forum: Some Complexities of Coastal Waves, Currents, Sand and Structures," Shore and Beach, Vol. 60, No. 1, pp. 21-33.
 33. Woodward Clyde Consultants (Jan. 1978) Coastal Engineering Evaluation, Sub-Task 3-2, Southwest Ocean Outfall Project, City and County of San Francisco, prepared for PBQ & D, Inc. San Francisco, California, January 20, 1978.

CHAPTER 209

TWO TREATMENTS OF SHORE EROSION IN EXTREME FLOODS ON U.S. GREAT LAKES

Robert J. Hallermeier¹

Abstract

This investigation addresses empirical evidence on wave action and shore erosion during extreme floods on Great Lakes coasts. Historical information shows that record coastal floods on the Great Lakes usually involve moderately extreme storms during relatively brief intervals with overall lake level much above the long-term average. The 100-year flood on U.S. lakeshores appears most likely to be accompanied by coastal wave heights with recurrence interval of about: three years on the four upper Great Lakes; or one-half year on Lake Ontario. Shore changes during the 100-year flood seem susceptible only to a coarse statistical estimate because available studies reveal Great Lakes erosion to be extremely variable in onset and amount. Two simplified erosion treatments are outlined here, one applying average annual recession rate for a locality, and the second, an empirical relationship originally developed for seacoast storm effects. The latter treatment appears verified by evidence from a Lake Michigan study, and such estimates of episodic erosion cross section are much lower than for extreme events on U.S. seacoasts.

INTRODUCTION

Conclusions developed in the following material are intended for application in the U.S. National Flood Insurance Program (NFIP). The NFIP includes the generation of maps quantifying expected hazards for the local base flood, an event having average annual probability of one percent (or mean recurrence interval of 100 years). Suitable coastal assessments must take into account distinctive characteristics of extreme events along Great Lakes shores, reflecting the particular basin configurations along with the marked variations of mean water levels over long terms.

To demonstrate the distinctive circumstances on the Great Lakes, Figure 1 displays annual mean water levels since 1860 for Lake Huron, with very large oscillations apparent but no clear trend during this century. That behavior strongly differs from the historical sea levels on the Atlantic ocean, where a rising trend is the most notable feature and other variations appear relatively minor. These signals indicate a

¹ Senior Coastal Scientist, METS Division, Dewberry & Davis, 8401 Arlington Boulevard, Fairfax, Virginia 22031-4666, U.S.A.

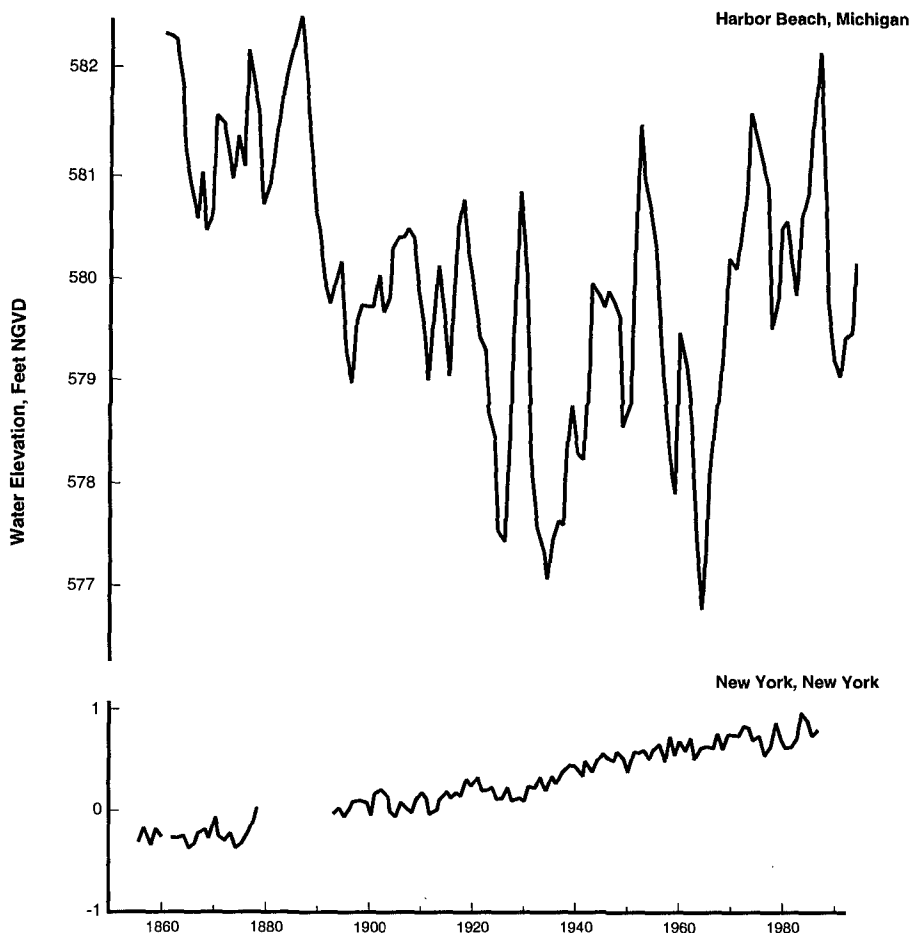


Figure 1. Annual mean water elevations on Lake Huron and Atlantic seacoast

markedly different context exists for coastal processes and extreme floods on the Great Lakes, in comparison to seacoasts.

Until recently, only stillwater inundation was considered in mapping coastal flood hazards for the Great Lakes, but documented flooding during the 1985-1987 highs clearly established the importance of additional wave effects. For NFIP treatments of U.S. Great Lakes shores, a full suite of methodologies for hazard assessment now addresses local stillwater flood elevations, shore erosion expected during the base flood, wave dimensions including growth or decay in coastal areas, and wave runup elevations at barriers to flooding. The U.S. Army Corps of Engineers (USACE) has documented conclusions on extreme local stillwater elevations from long-term records (USACE, 1988) and has provided a simplified treatment for wave runup at the most common types of shore barrier (USACE, 1989). This paper outlines the development of guidance on two other aspects of flood hazards: incident wave action

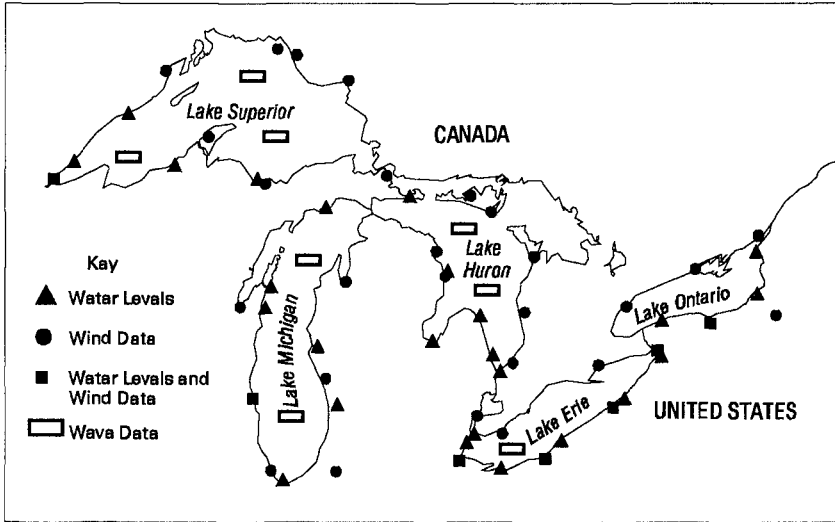


Figure 2. Pertinent data locations for Great Lakes investigations

and resultant shore erosion expected to accompany a base flood on the Great Lakes. These topics are interrelated, since shore erosion from wave action with flood waters alters the crucial boundary condition for storm impacts, thus controlling magnitude and penetration of wave effects over flooded land.

The following considerations are entirely empirical in basis, using best available information on recent extreme events. Quantitative analyses (Dewberry & Davis, 1995) have examined storm wave heights, flood elevations, and erosion magnitudes documented at about 100 varied sites on the U.S. Great Lakes. The necessary order of treatment begins with wave conditions during floods and proceeds to erosion considerations.

WAVE ACTION DURING FLOODS

Wave conditions during record Great Lakes floods have been computed in the recent USACE hindcast covering 1956 to 1987 (e.g., Hubertz and others, 1991). That interval includes 20th-century highs in mean lake levels during 1973-1975 and 1985-1987, along with record instantaneous elevations at many water-level gauges. Before combining this disparate information on waves and water levels for extreme events at particular sites, it is appropriate to examine the reliability of wave hindcast results. Figure 2 provides a map locating important data sites.

The USACE hindcast procedure applies measured winds at scattered land stations (Figure 2) to define wind fields over each lake, and then computes resultant wave action at many deep-water sites. Validation possibilities for hindcast computations are restricted to limited nearshore measurements and to several long-term buoy sites near the lake centers (Figure 2). The reported verifications of hindcast waves tend to

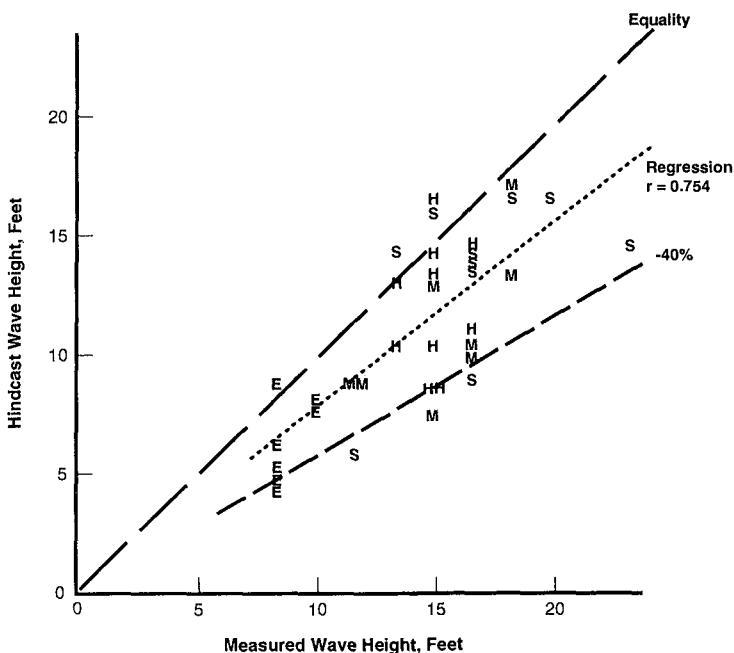


Figure 3. Hindcast versus measured extreme wave heights on four upper Great Lakes; separate lakes identified by initials used in plot.

focus on overall distributions of parameters, consistent with a comprehensive long-term hindcast. However, the present application utilizes brief intervals of storm winds, surges and waves, so the hindcast reliability for such extreme conditions merits evaluation. This is in line with the caveat stated by Hubertz and others (1991): "It is recommended that separate studies be done for specific storms at specific sites for more detailed information."

A convenient evaluation of the hindcast may be based on 35 extreme wave heights tabulated in a published summary of buoy data (Gilhousen and others, 1991). Those 1979-1987 measurements pertain to eight buoy sites on the four upper Great Lakes, and include all tabulated wave heights among the extreme 1% at each site. Hindcast wave height for each case is taken as the highest value during the same wind episode at a nearby computation point. This present selection yields a fairly balanced sample of extreme conditions, with separate lakes identified by the initial used in plotting results on Figure 3. Measured wave heights in this sample are typically on the order of 4.5 m (or 15 feet). Comparison of hindcast and measured wave heights yields a correlation coefficient sufficient to confirm a linear relationship with certainty. However, the hindcast does not accurately reproduce these measured conditions, being 20% low typically and having an error band of $\pm 20\%$. Part of the hindcast bias may be explained by a lower peak value with the three-hour hindcast interval versus hourly measurements, but the error band remains notable. That sizable random scatter of hindcast wave heights appears related to errors in interpolated winds at buoy sites, as shown in Figure 4 using measured windspeeds also tabulated for a typical 7 of the 35 cases (Gilhousen and others, 1991).

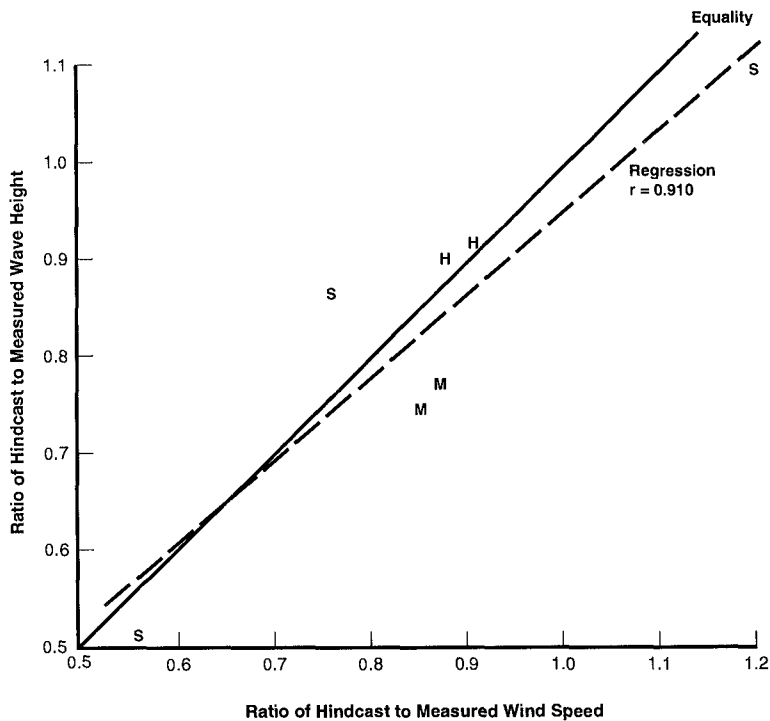


Figure 4. Relation of wave height and windspeed errors in Great Lakes hindcast.

According to this modest but objective selection of storm events, there are considerable errors in the USACE hindcast of extreme wave conditions on the Great Lakes. The data buoy sites may present a notable challenge for wave hindcasts, given relatively large separations from wind data locations. Hindcast results may generally be more reliable at nearshore sites, but appreciable variations in accuracy still seem likely in view of the scattered stations providing wind data. To apply USACE hindcast information in assessing wave action accompanying extreme floods, it seems advisable to maximize the variety of sites and events considered together, aiming at a simplified conclusion with generic pertinence to Great Lakes shores.

That program is carried out by considering in one group the record flood during 1956-1987 at each of 32 water-level gauges (Figure 2), along with wave hindcast results at a nearby computation point for the same episode. To use evident measures of extremity, both peak measured water elevation and largest computed wave height for each event are converted into recurrence intervals from the type of results shown in semi-logarithmic form on Figure 5. There, purely exponential recurrence relations as straight lines are fully defined by the medians of monthly and yearly highs, plotted at recurrence intervals of two months and two years, respectively. Such simplified analysis provides the advantages of a direct basis in annual probability along with a recurrence estimate for any value; note that results for relatively common flood elevations relate smoothly on Figure 5 to reported USACE conclusions on extremes. This example of recurrence relations is remarkable because each line has nearly

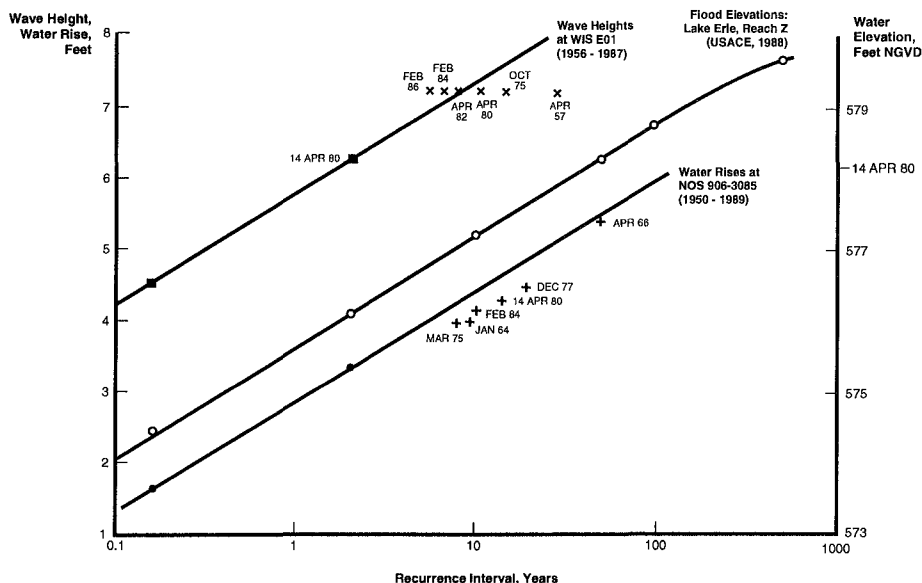


Figure 5. Summaries of extreme effects on Lake Erie at Toledo, Ohio

identical inclination. The inclination is representative of flood elevations on any of the Great Lakes except Lake Superior, where the line would tilt much less; for wave heights, the line has about the minimum inclination to be found on the Great Lakes, while water rises typically define a line with less inclination.

Figure 6 presents a logarithmic cross-plot of recurrence measures for the 32 extreme events, again distinguishing the separate Great Lakes by initial. Measured flood elevations for these cases typically have recurrence intervals on the order of 50 to 100 years. Immense scatter is evident among these results, in part reflecting the notable errors possible in hindcast wave heights and those recurrence intervals. The $\pm 20\%$ estimate based on Figure 3 converts to various sizable ranges in recurrence intervals for wave heights here, depending strongly on the hindcast result and the local recurrence relation; a usual error bar for representative results extends over a factor of ten. However, a very wide range in wave extremity certainly can be associated with a given flood elevation on the Great Lakes, considering that significant variables include mean lake level and lake seiches, in addition to storm winds.

From close inspection of available evidence, floods on Lake Ontario differ from effects on the four upper lakes in always being associated with very common hindcast wave conditions; in contrast, notably extreme waves occasionally occur during many floods on the other Great Lakes. Deleting the Lake Ontario floods in Figure 6, remaining results yield a sizable positive correlation between recurrence intervals for wave height and flood elevation. The regression result shown in Figure 6 has statistical significance at the 5% level (but not the 1% level; Sachs, 1984), and indicates wave height recurrence of about 1 year for the 100-year or base flood. Since the correlation has limited significance, this evidence may also be examined

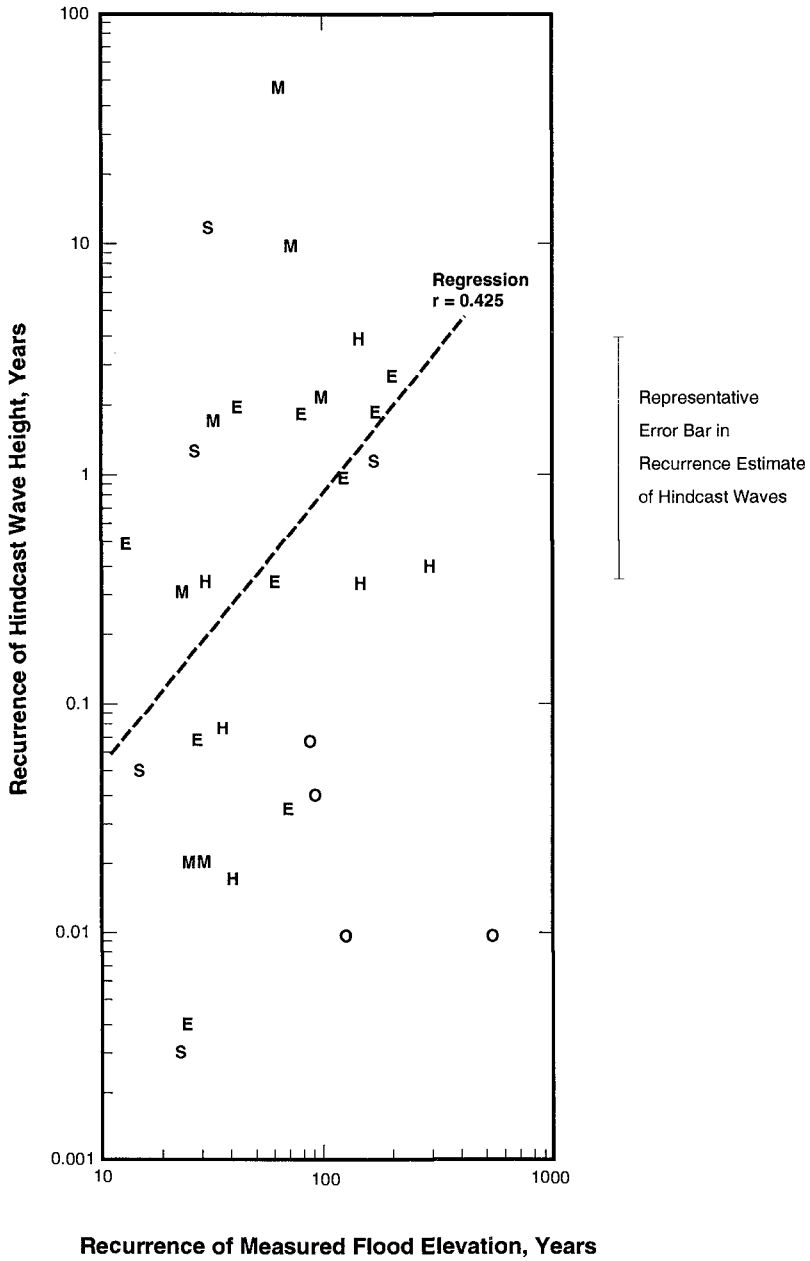


Figure 6. Parameters describing 32 recent extreme floods on Great Lakes; displayed regression result omits events on Lake Ontario (O).

without regard to trend: the most common condition with these record floods is about a 2-year wave height, according to the band of results in that vicinity. Such wave conditions occur during events from mid-November through mid-April, when storm winds can overwhelm the seasonal water levels least conducive to flooding. Taking into account the hindcast bias, these considerations indicate a prudent conclusion to be that a 3-year wave condition (as defined here by an exponential recurrence relation) accompanies the base flood at typical U.S. shore sites on Lake Erie, Huron, Michigan, or Superior.

Hourly water-level measurements demonstrate that lake seiches rather than storm surges are dominant in extreme flood elevations on the U.S. shore of Lake Ontario. There, the large seasonal excursion of mean lake level enhances flooding during the usual May-July high, when onshore storm winds rarely occur. An appropriate conclusion is found to be that wave height with a ½-year recurrence interval accompanies the base flood on U.S. shores of Lake Ontario.

Present conclusions must be recognized as highly generic regarding the likely wave action during extreme floods on the Great Lakes, and as somewhat tailored for routine NFIP application. Additional analysis or historical evidence may provide more appropriate estimates for specific shore sites.

EROSION EFFECTS AND TREATMENTS

Detailed measurements of shore changes pinpoint the apparent complexity of Great Lakes effects over space and time. A striking attribute is erosion variability over all but the longest terms, so that coastal changes during extreme conditions seem coherent only in a statistical sense over appreciable shore reaches. Many factors can be important in Great Lakes erosion processes, but the characteristic result appears to be quite intermittent progress in the fall and removal of dune or bluff sediments, yielding a markedly slowed or interrupted replica of typical seacoast storm effects. This discussion will address just a few erosion studies on sandy coasts of Lake Michigan, considered representative for various erodible lakeshores.

Two intensive studies, Hands (1979) and Birkemeier (1981), documented erosion along the eastern shore of Lake Michigan during the 1964-1973 interval when the increase in mean lake level was about 1.5 meters. Hands (1979) reported shoreline positions at irregular time intervals of a year or more, for a total of 30 transects spanning about 50 km near Pentwater, Michigan. Alongshore variability of retreat rate was extreme as lake level generally rose over 8 years, but the average or median rates over available transects were rather steady in time, regardless of mean lake level or storm climate variations. Those findings do not appear sensitive to the spatial or temporal frequency of measurements, or a later study area extension. As lake level declined over the last study year, shore accretion typically reversed about two years of retreat. The basic results might be summarized as indicating a lagging response to the increasing erosive stress with rising water, but only in an overall sense; changes on individual transects appear too variable in time for simple interpretation.

In the other study, Birkemeier (1981) summarized survey results at four-week intervals during 1970-1974, for 17 profiles roughly 20 km apart. Shore erosion appeared somewhat random in time and location: various numbers of profiles showed bluff or terrace retreat in greatly varying amounts over separate intervals. However, erosion was also clearly seasonal, in phase with the annual storm cycle but not with

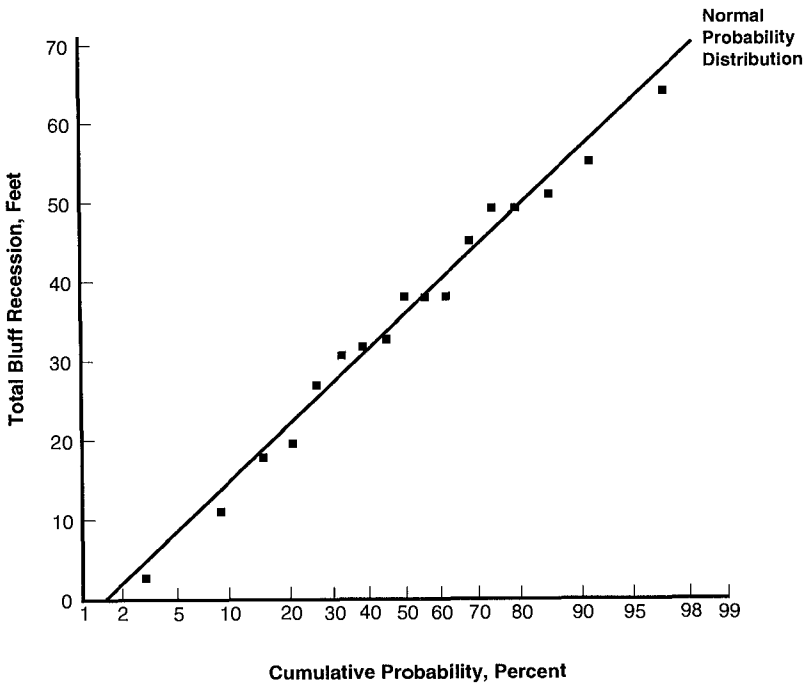


Figure 7. Bluff recessions during 1970-1974 on 17 Lake Michigan profiles.

the lake level cycle. Through the complete study term, changes accruing through sporadic episodes disclose some orderly variation over the entire data set: total recessions on individual profiles conform to a normal probability distribution with sizable dispersion, as shown in Figure 7. With no clear geographical trends, nor much correlation between adjacent profiles, the effectively random scatter of recorded erosion seems to result from the interplay of many independent factors, with insufficient time to develop an equilibrium response.

Even long-term changes on the Great Lakes can require careful interpretation due to the dependence of shore erosion on mean lake level, as revealed by results from two recent studies of Lake County, Illinois. Jibson and others (1994) addressed rates and processes of bluff erosion based on measurements for 1872-1937 and 1937-1987. Average retreat rate over the region showed no significant difference for the two periods, during which mean lake level or precipitation was nearly identical. However, Chrzastowski and others (1993) studied the same shore reach and timespan, but with three intervals isolating sizable elevation differences for Lake Michigan. Documented results reveal significant correlations between the mean lake level and representative movements of sandy shoreline or coastal bluff top, as demonstrated in Figure 8. Since differences from the long-term mean can be larger over briefer intervals, mean lake levels apparently contribute to sizable departures from an average erosion rate.

With this brief outline of factors and variabilities in Great Lakes erosion, it seems clear that statistical viewpoints can most conveniently provide useful summaries or projections. In turn, projections for short-term or storm erosion may be expected to

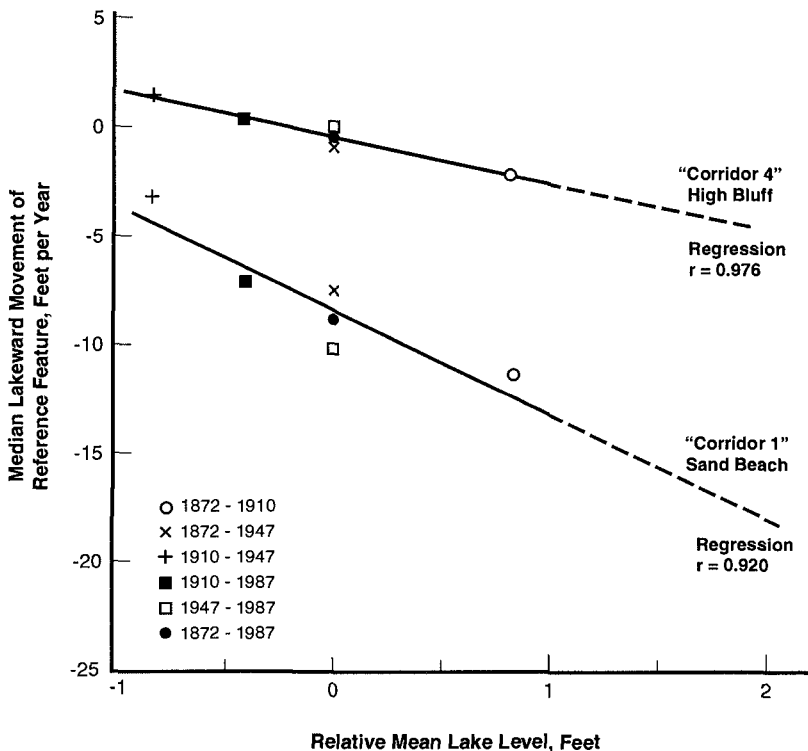


Figure 8. Representative erosion rates versus mean Lake Michigan levels.

attain only order-of-magnitude agreement with actual effects, but suitable procedures for erosion estimates might be rather simplified or generalized in basic character. Two treatments outlined here apply either average local recession rate, or storm erosion quantities from a generic database, the two evident alternatives. The independent treatments take into account distinctive attributes of the Great Lakes.

The first alternative applies the local value of A , average annual rate of shore recession over a long term. This development presumes available topography to be defined during usual lake levels, and addresses cumulative erosion until the base flood is likely to be encountered. As mean lake level rises to highs conducive for the base flood, shore recession is more rapid than the long-term average, and described as a rate of $(2.5 A)$. If that rate occurs over about one-third of a long term, it implies that $(0.25 A)$ is characteristic otherwise, and such a range of values appears appropriate according to available Great Lakes studies. Projected erosion before the base flood equals the accelerated rate times an expected waiting time of 4.8 years with high lake levels. That waiting time is supported by the normal probability distribution defined by data in Figure 9: actual intervals of high lake level before the record flood during 1972-1987, at 31 gauges on the four upper lakes. Given the notable storm waves likely to accompany an extreme flood on the four upper lakes, the additional allowance of $(3A)$ for storm erosion in the base flood appears appropriate. These considerations yield $(15A)$ as projected site erosion on Lake Erie, Huron, Michigan,

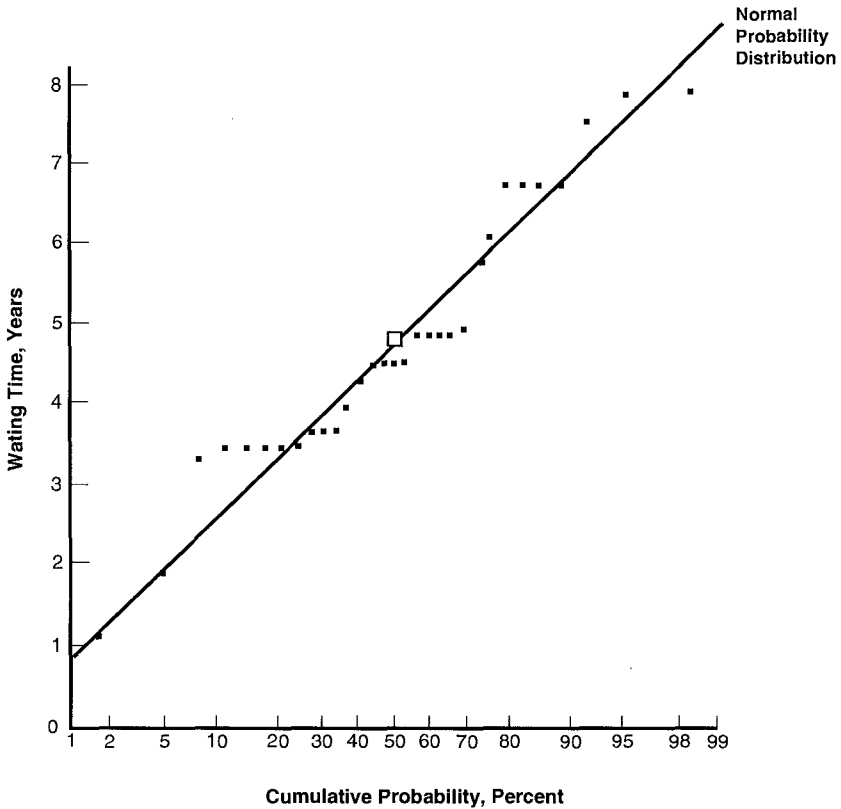


Figure 9. Waiting times for record floods at 31 sites on four upper Great Lakes, after onset of monthly mean levels higher than long-term mean.

or Superior; and (12A) on Lake Ontario. These recession distances describe a parallel retreat of the shore profile from the reference feature to which A pertains.

Such treatment seems relatively straightforward, but the result does not appear validated by measured Lake Michigan erosion reported by Birkemeier (1981). On 17 profiles in nine separate Michigan counties, total recessions over 4.3 years of high lake level show essentially no correlation with average long-term recession rates documented for the individual counties. Although no extreme flood occurred within the study area over this term, cumulative recessions make the present estimation method seem of dubious usefulness. This might be caused by the multiplication of two very uncertain quantities, in regard to short-term applicability at specific sites.

The second alternative considers only the storm effects likely to be associated with the base flood, using an empirical relationship for expected erosion in duneface retreat on U.S. Atlantic and Gulf coasts (Hallermeier and Rhodes, 1988). The relationship

expresses eroded cross section above flood elevation in terms of recurrence interval for the flood, amounting to 50 m² erosion in a 100-year event:

$$\text{Erosion [m}^2\text{]} = 8 (\text{Recurrence Interval [yr]})^{0.4} \quad (1)$$

This erosion treatment has proved to be suitable for NFIP applications in defining coastal flood hazards, and has been validated by effects recorded in more recent extreme events (e.g., Wolf and others, 1993).

Along U.S. seacoasts, wave condition and flood elevation generally may be expected to have comparable recurrence intervals for most episodes in a sizable sample of extreme events, but that is not the case for the base flood on the Great Lakes, as established by Figure 6. This application therefore employs a blend of individual erosion estimates for the wave and flood recurrences, using the geometric mean of cross sections defined by the basic relationship in Equation (1). Resultant erosion for the base flood, with a 1/2-year wave condition on Lake Ontario and a 3-year wave condition on the four upper lakes, is estimated as: 17 m² for Lake Ontario sites; and 25 m² on Lake Erie, Huron, Michigan, or Superior. These quantities are taken to be eroded amounts above local 100-year stillwater elevation.

Results from this erosion treatment appear consistent with storm erosion quantities documented in the Lake Michigan study by Birkemeier (1981). Erosion was recorded on a majority of the 17 profiles only during two intervals, covering notable storms in mid-December 1971 and in mid-March 1973. As defined by USACE hindcast wave heights and measured water elevations: the 1971 storm had 1/2-year waves and a 1-year flood, giving an erosion estimate of 7 m²; and the 1973 storm combined 4-year waves and a 1 1/2-year flood, for an erosion estimate of 11 m². Average bluff cross sections removed on the eroding profiles in those events were 8 m² during December 1971 (for 10 profiles) and 10 1/2 m² during March 1973 (11 profiles). The quantitative agreement of estimates with representative erosion magnitudes in these cases provides appreciable validation of the present viewpoint, since base flood estimates for the Great Lakes lie between these amounts and many documented seacoast episodes. However, serious uncertainties in predicting the onset and amount of short-term erosion at Great Lakes sites remain worth emphasizing.

CONCLUSIONS

Empirical evidence provides an extensive basis for simplified summaries of the wave action and erosion expected to accompany the base flood on U.S. shores. Lake Ontario sites may be expected to experience wave heights having recurrence interval of 1/2 year and eroded cross section of 17 m² above flood elevation. Wave heights having recurrence interval of 3 years and erosion of 25 m² are projected for sites on Lake Erie, Huron, Michigan, or Superior. These results pertain only to storm-induced flood episodes, and are intended for routine application in flood hazard assessments within the National Flood Insurance Program.

Acknowledgments. The reported investigation was performed by Dewberry & Davis as a technical evaluation contractor for the National Flood Insurance Program, Federal Emergency Management Agency. The conference presentation and preparation of this paper were supported jointly by Dewberry & Davis and the Federal Emergency Management Agency. Present summaries and interpretations represent views of the author. The author wishes to express thanks for extremely responsive assistance provided by Edward Hands, U.S. Army Coastal Engineering Research Center, Vicksburg, Mississippi, and by John Herron, Great Lakes Section, National Ocean Service, Silver Spring, Maryland.

REFERENCES

- Birkemeier, W. A., 1981. Coastal Changes, Eastern Lake Michigan, 1970-74, Miscellaneous Report No. 81-2, U.S. Army Corps of Engineers, Coastal Engineering Research Center, Fort Belvoir, Virginia.
- Chrzastowski, M. J., Erdman, A. L., Stohr, C. J., and Terpstra, P. D., 1993. Illinois Pilot Erosion-Rate Study. Open File Series 1993-3, Illinois State Geological Survey, Champaign, Illinois.
- Dewberry & Davis, 1995. Basic Analyses of Wave Action and Erosion With Extreme Floods on Great Lakes Shores. Fairfax, Virginia.
- Gilhausen, D. B., Meindl, E. A., Changery, M. J., Franks, P. L., Burgin, M. G., McKittrick, D. A., 1990. Climatic Summaries for NDBC Buoys and Stations, Update 1. U.S. Department of Commerce, National Oceanic and Atmospheric Administration, National Weather Service, National Data Buoy Center, NSTL, Mississippi.
- Hallermeier, R. J., and Rhodes, P. E., 1988. Generic Treatment of Dune Erosion for 100-year Event. Proceedings 21st Coastal Engineering Conference, ASCE, pp. 1197-1211.
- Hands, E. B., 1979. Changes in Rates of Shore Retreat, Lake Michigan, 1967-76. Technical Paper No. 79-4, U.S. Army Corps of Engineers, Coastal Engineering Research Center, Fort Belvoir, Virginia.
- Hubertz, J. M., Driver, D. B., Reinhard, R. D., 1991. Hindcast Wave Information for the Great Lakes: Lake Michigan. Wave Information Studies Report 24, U.S. Army Corps of Engineers, Coastal Engineering Research Center, Vicksburg, Mississippi.
- Jibson, R. W., Odum, J. K., and Stande, J. M., 1994. Rates and Processes of Bluff Recession along the Lake Michigan Shoreline in Illinois. Journal of Great Lakes Research, Vol. 20, pp. 135-152.
- Sachs, L., 1984. Applied Statistics, A Handbook of Techniques (2nd Edition). Springer-Verlag, New York.
- U.S. Army Corps of Engineers, Detroit District, 1988. Revised Report on Great Lakes Open-Coast Flood Levels. Detroit, Michigan.
- U.S. Army Corps of Engineers, Detroit District, 1989. Great Lakes Wave Runup Methodology Study. Detroit, Michigan.
- Wolf, Lisa J., Bowen, J. D., and Hickey, K. A., 1993. Dune Profiles Before and After Storm Events in Coastal Massachusetts. Proceedings Hydraulic Engineering '93 Conference, ASCE, pp. 269-274.

CHAPTER 210

LONG-TERM BEACH RESPONSE TO SHORE STABILIZATION STRUCTURES ON THE OREGON COAST

G.E. Hearon¹
W.G. McDougal²
P.D. Komar³

ABSTRACT

Increased development along the Oregon coast has led to heightened concern over beach erosion. As a result, more shore stabilization structures have been erected in recent years. A long-term field monitoring program, involving seven typical structures located on the central Oregon coast, was initiated in the spring of 1986 to quantify the effects of shore stabilization structures on the surrounding beach and adjacent properties. All structures are rip-rap revetments or seawalls. Volumetric changes of the subaerial beach at each site were examined at scales ranging from the entire beach surrounding the structure to the beach in the immediate vicinity of the structure. When the data coverage and site geometry permitted, a far field control section was utilized to compare the volumetric response of a portion of beach relatively uninfluenced by the presence of the structure with that of the beach on the two structure flanks. Measurements are presented for the seven structures over the observation period of ten years to document the long-term effects the structures are having on the fronting beach and adjacent unprotected properties. Ten years of monitoring has revealed that the structures at these seven sites are having no adverse impacts on the surrounding beach or adjacent properties. This can be attributed to the limited amount of wave attack that the structures have experienced. The structures are built high on the profile, and experience wave attack only during the most severe storms.

¹ Coastal Engineer, Coastal Frontiers Corp., 9420 Topanga Canyon Blvd., Suite. 101, Chatsworth, CA 91311, USA

² Professor, Civil Engineering Department, Oregon State University, Corvallis, OR 97331, USA

³ Professor, College of Oceanic and Atmospheric Sciences, Oregon State University, Corvallis, OR 97311, USA

INTRODUCTION

The structures selected for the monitoring program are located between Neskowin and Florence; spanning a distance of nearly 100 miles of the central Oregon coast. Structures were selected in locations such that the number of factors that could affect the long-term beach change were reduced primarily to the structure itself. As a result, the majority of the structures were chosen such that there were no headlands, jetties, or river mouths in the immediate vicinity, and the adjacent properties were unprotected for at least three structure lengths on either side of the structure. The structures are backed by dunes, sea cliffs, or bluffs; all common coastal environments in Oregon. Table 1 shows the characteristics and site codes

Table 1 Site and Structure Characteristics

Site	Site Code	Structure Type	D ₅₀ (mm)	Length (m)
Pacific Sands Motel	PSM	Timber Seawall	0.30	70
Gleneden	GE	Rip-Rap Revetment	0.53	40
Pacific Palisades	PP	Rip-Rap Revetment	0.31	300
Pacific Shores	PS	Rip-Rap Revetment	0.20	20
C&L Ranch	CL	Rip-Rap Revetment	0.20	25
San Marine	SM	Rip-Rap Revetment	0.22	150
Driftwood Shores	DS	Rip-Rap Revetment	0.21	30

(abbreviations) of the seven sites selected for the field monitoring program. The study was initiated to aid the Oregon State Parks Division and DLCD, which regulates the construction of coastal structures in their permit review process.

DATA COLLECTION

Field data, in the form of multiple beach profiles, were collected intermittently from the fall of 1986 to 1990, and resumed in the winter of 1995. On average, the database contains fifteen surveys per site. An effort was made to obtain at least a winter and summer survey for each year. Numerous transects were measured with an EDM in order to monitor the topography of the beach surrounding each structure. Weather permitting, the surveys provided coverage at least five structure lengths on either side of the structure, and seaward to the swash zone. Transects were spaced on the order of 20 m to 30 m on planar beaches with little three-dimensionality in the longshore direction. For more three-dimensional beaches displaying cusps, transects were spaced accordingly to achieve an accurate representation of the beach.

ANALYSIS METHODS

The beach profile data were analyzed using contour plots, surface plots, contour of difference plots, and results from sand volume calculations. The profile data were interpolated to a uniformly spaced rectangular grid using MatLab codes, from which the plots and sand volume calculations were generated. To obtain the maximum use from the gridded data and explore all aspects of the structures effect on the surrounding beach, several scales were examined. A large scale (Scale I) was examined by considering the largest common area of beach covered in the field monitoring program. To reduce seasonal contamination and noise in the analysis, an intermediate scale (Scale II) was employed, defined as two structure lengths to either side of the structure and one structure length seaward. Finally, to concentrate on effects in the immediate vicinity of the structure, a scale consisting of the two structure flanks and beach immediately fronting the structure (Scale III) was examined. Each scale was divided into three sections; north, center, and south. When possible, the north and south survey sections were defined with the same sizes, thereby allowing a direct comparison between the two sections.

This approach was used primarily for analyzing the changes in sand volume. The volume of sand on the beach was calculated in reference to the 1929 NGVD mean sea level. Volumetric response, or the magnitude to which the sand volume is changing due to erosion and accretion events, was examined with the results of the volumetric calculations. The flanks on either side of the structure are typically considered the most susceptible to erosion; therefore, the sand volume of the north and south flanks, and the volumetric changes of the sand at these flanks over the observation period were of particular interest. Comparison of the sand volumes at these flanks with a far field control section, relatively uninfluenced by the presence of the structure, was an important analysis tool. The far field section provides a baseline to which volumetric responses close to the structure can be compared. The location of the far field section was always taken at the same distance from the bluff and defined with the same plan area as the flank section.

Contour and surface plots provide a means to observe seasonal changes at the sites, such as profile slope or formation of a berm or rip current embayment, as well as an indication of how the beach changes or adjusts in the vicinity of the structure. Figure 1 shows a contour and surface plot from Gleneden, obtained in June 1989. Contour of difference plots were used to show the specific areas of erosion and accretion between two sequential sets of beach profile data. They are useful in determining the degree to which the beach in the vicinity of the structure was responding to erosion and accretion events. Used in conjunction, this array of tools, contour and surface plots, contour of difference plots, and sand volume calculations, provide a detailed account of the long-term changes at the sites.

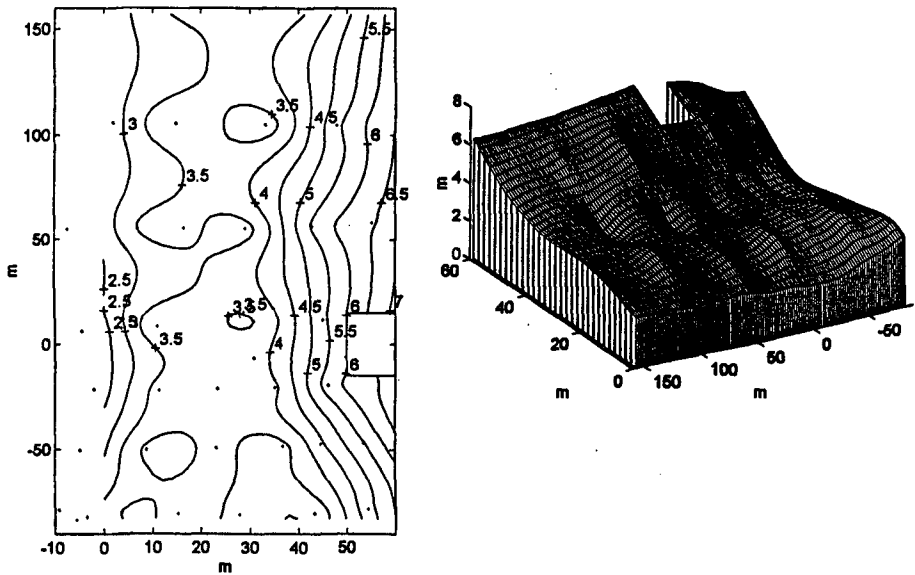


Figure 1 Contour and Surface Plot for Gleneden, June 1989

RESULTS

Analyses were undertaken by examining the contour and surface plots and the sand volume calculations for each site at of the aforementioned scales. One site will be analyzed in greater detail to illustrate the methodology and techniques used throughout the study to derive conclusions for all seven sites. A complete analysis of all sites is given in Heaton (1995) and Sturtevant (1987). Data for the remaining six sites will be presented in two forms, the volume of sand at Scale I over the observation period, and the results of the far field baseline comparison. Research has shown that the structure flanks are susceptible to erosion, therefore the results of the far field comparison are an effective indicator of structure induced impacts. The far field comparison data will be displayed in a normalized form, the volume of sand at the structure flank divided by the volume of sand in the far field control section ($V_{\text{flank}}/V_{\text{far field}}$). It is stressed that conclusions for each of the sites were derived by utilizing all analysis tools discussed in the previous section, and not solely from the data presented herein.

C&L Ranch (CL)

C&L Ranch provides an excellent open coast site. The structure is a 25-m long rubble mound revetment that protects and stabilizes the backing bluff. There are no headlands, jetties or river mouths in the vicinity. The bluff is shore parallel and unprotected for several structure lengths to either side. The land slide potential of

the bluff is high. Evidence of several recent localized slides was observed during the 1995 data collection. Aerial photographs indicate that the beach and bluff line at C&L Ranch has changed little from 1965 to 1983.

The complete series of contour and surface plots indicates that the beach at C&L Ranch is very flat and planar throughout the year, exhibiting very little three-dimensionality. A summer berm was not observed in any of the surveys. The flat, dissipative beach at C&L Ranch is common on the central Oregon coast. A slight increase in sand elevation in the vicinity of the structure was observed in the majority of the contour and surface plots. The increased sand elevation was generally at the beach face junction of the flanks or at the seaward corners of the structure. The increased sand elevation at the seaward corners would generally extend several meters seaward of the structure. However, it cannot be concluded from this slight increase in sand elevation that the structure was retaining sand in its vicinity.

Figure 2 shows the volumetric responses of the north, south, and center sections for Scale I. The north and south sides of the structure are of equal area, but the center section is not of comparable size. The three sections all responded similarly to each other and to the total volumetric of Scale I shown in Figure 3. It appears as though the beach on the north side of the structure responded less sensitively to major erosion and accretion events than the beach on the south side of the structure. Similar to the total volumetric response of Scale I, all three sections of beach shown in Figure 2 displayed a balanced volumetric response fluctuating seasonally about a nearly constant mean and experienced a negligible net change in sand volume over the observation period. The volumetric response at Scale II was nearly identical to that of Scale I, showing seasonal fluctuation about a nearly constant mean.

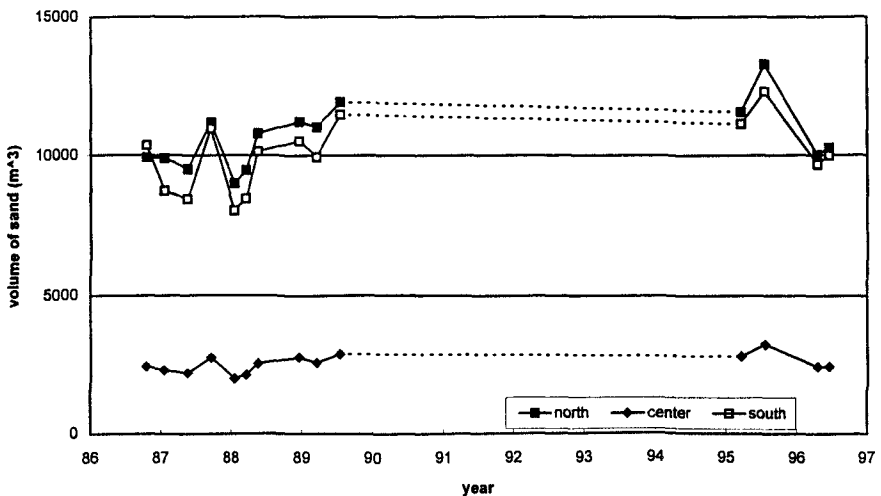


Figure 2 C&L Ranch Section Sand Volumes, Scale I

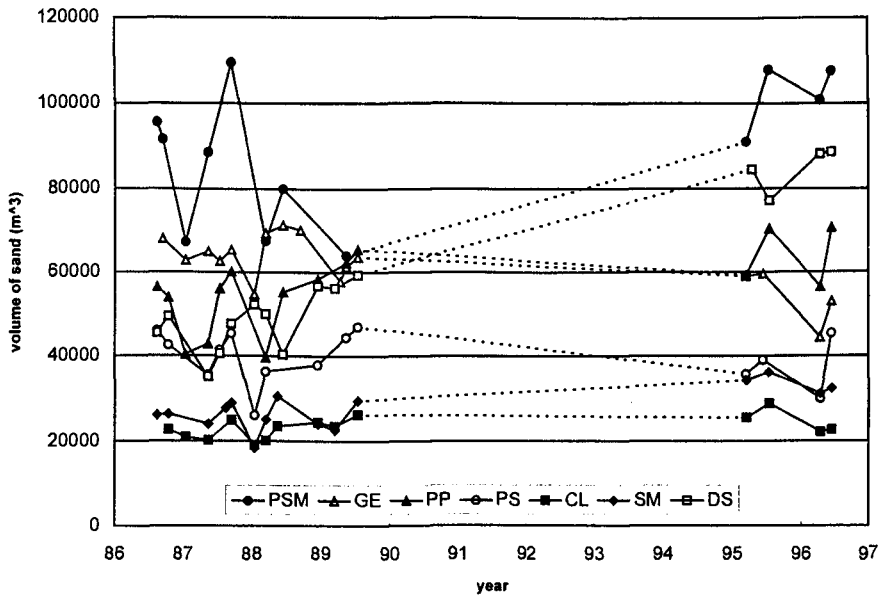


Figure 3 Total Sand Volumes at Each Site, Scale I

Far field sections were used both to the north and south of the structure. Figure 4 shows the comparison of the north far field and the north flank of the structure. The volumetric responses of the two areas were remarkably similar. The sensitivity to erosion and accretion events was approximately the same for both the north flank and the north far field. The north flank experienced a slight net gain in sand volume over the observation period, whereas the north far field section experienced a slight net loss. As Figure 5 indicates, the volumetric response of the south far field and the south flank of the structure were reasonably similar. The south far field section appeared to be slightly more sensitive to erosion and accretion events than the south flank. Both far field and the flank experienced a moderate net loss in sand volume over the observation period. Each of the structure flanks and corresponding far field volumes displayed a balanced volumetric response and negligible net change in sand volume over the ten year period.

The beach at C&L Ranch was very stable. The volumetric response of the beach followed a pattern of fluctuation between summer accretion and winter erosion. Erosion events were followed by periods of comparable recovery. The volumetric response of the beach was very similar for Scale I and Scale II, indicating the absence of seasonal features such as berms. The far field baseline comparison indicated that the structure flanks are responding similarly to the beach uninfluenced by the structures presence. The south flank appeared to be more stable than the south far field, and the north flank experienced a net gain in sand volume over the observation period, whereas both far field sections experienced a slight net loss.

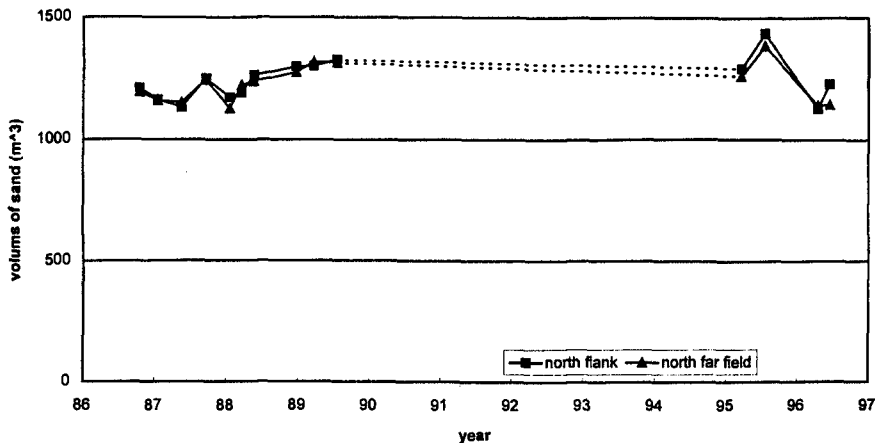


Figure 4 C&L Ranch North Far Field Comparison

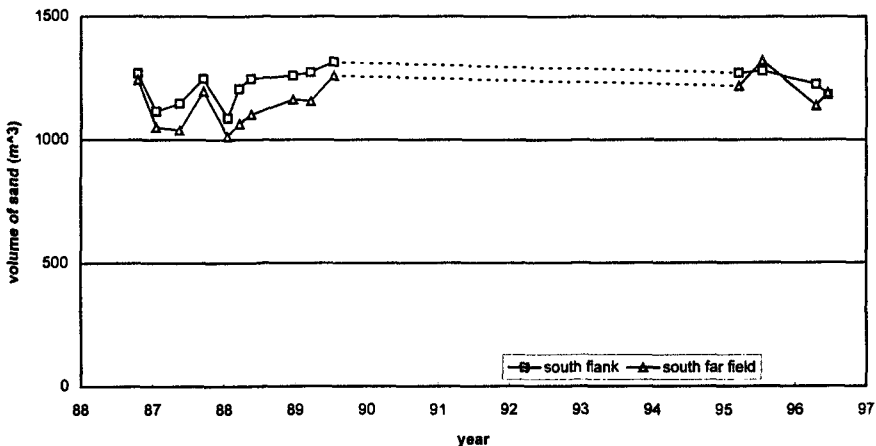


Figure 5 C&L Ranch South Far Field Comparison

Pacific Sands Motel (PSM)

Pacific Sands Motel, located in Neskowin, is the northern most site considered in this study. The structure is a timber seawall fronting the Pacific Sands Motel. The seawall is constructed of railroad ties with limited steel lateral supports and a 4 cm x 25 cm timber cap. The upper portion of the beach is characterized by low dunes with non-continuous low bluffs to the south of the structure. Proposal Rock, located to the south of the structure, is the predominate morphological feature

in the area. Evidence suggests that Proposal Rock has a considerable influence on the beach processes at the site, mainly in the formation of a rip current embayment. Concentrated foot traffic at the north end of the seawall results in lower a local dune elevation and sparse vegetation at the foot path, making it difficult to separate structure induced flank erosion from foot traffic induced erosion. Aerial photographs for Pacific Sands Motel show that the coastline has not changed much since the mid-1960's.

Examination of the contour and surface plots reveal that during the summer, generally May through September, when the beaches are subjected to low wave energy, the beach at PSM is characterized by a well defined berm and cusps. The berm is often altered by a rip current embayment formed by the presence of Proposal Rock. During periods of high wave energy, typically November through April, the beach becomes very flat in order to dissipate the increased wave energy. The seawall and dunes are most susceptible to wave attack during these periods.

Figure 3 gives the results of the sand volume calculations for Scale I. Profile data for January 1989 and February 1988 were not used in the Scale I calculations due to insufficient range of coverage. The volume of sand fluctuates between winter lows and summer highs about a slightly increasing mean. The beach experiences a sizable net gain in sand volume over the observation period. The volumetric response of Scale II was very similar to that of Scale I.

Comparison of the volume of sand at the structure flanks with far field control sections, in plots similar to Figures 4 and 5, indicates that the flanks responded less sensitively to seasonal erosion and accretion. This data is presented in a normalized form in Figures 6 and 7. The north flank contained a greater volume of sand than the far field section throughout the observation period. A portion of the north far field control section is located landward of the mean dune line. The dune line tends to migrate seasonally, and at the time of the April 1988 survey the dune line had receded several meters. This results in the +2.40 spike in the V_n/V_{aff} data indicating a much larger volume at the north flank in comparison to the north far field. As shown in Figure 7, the volume of sand at the south flank deviates only slightly from that of the south far field. Sand volumes at the south flank are greater than those of the south far field section over the vast majority of the observation period. The results of the far field baseline comparison indicate that the structure flanks appear to be more stable than far field control sections partially because the seawall tends to stabilize the position of the dune line at its flanks. Overall, the south side of the structure was very stable, and although the north side occasionally underwent large volumetric changes, it was fairly stable over the long-term.

Gleneden (GE)

The Gleneden site is located in the town of Gleneden. The structure is a rubble mound revetment approximately 40 m long. The beach is backed by bluffs approximately 10 m in height. The revetment has two well defined flanks as the structure extends several meters from the bluff. This site provides a good open coast

scenario, as the beach extends several miles in either direction without any significant obstructions. A beach access is located approximately 90 m to the south of the structure. A cut, several meters in width, was excavated through a low section of the bluff and partially paved to create this access. The access is significant to the site because a great deal of the storm water runoff from the neighborhood is discharged onto the beach at this point. Depending on the time of year, high flows associated with this runoff scour a creek through the beach face. A considerable volume of sand can be removed through this hydrologic process. Aerial photographs of Gleneden indicate that the coastline has changed little from 1963 to 1983.

The beach at Gleneden is characterized by a well defined berm and cusps in the low wave energy summer months (Komar and McDougal, 1988). A berm of some magnitude usually formed in the early spring and remained until October, however, a slight berm was often present through most of the year. A dominant reflective profile at Gleneden can be partially attributed to the presence of coarser sands on the beach (Shih and Komar, 1994).

The results of the sand volume calculations for Scale I are given in Figure 3. Profile data from January 1989 were not incorporated into the Scale I analysis due to lack of data range in the cross-shore direction. The volumetric response of the beach in Scale I shows the typical pattern of winter erosion followed by summer accretion or recovery. A sizable net loss in sand volume over the observation period had occurred primarily as a result of the severe erosion in May 1996. Recovery from this erosion event indicated from the July 1996 volume was significant, however, this data point probably does not represent full recovery. Oregon experienced a late summer in 1996, and beaches commonly experience accretion well into October.

Due to the drainage area located to the south of the structure, only a north far field control section was utilized for the baseline comparison. Normalized far field comparison data shown in Figures 6 and 7 indicate that the sand volume at the flanks was similar to that of the north far field section throughout the observation period. On average, both the north and south flanks of the structure contained greater volumes than the far field section. During the most severe erosion event recorded over the ten year monitoring period, May 1996, both flanks retained over 10% more sand than the north far field section. This is an indication that the flanks are more stable than the far field control section, and appear to be less sensitive to seasonal fluctuations. Although the beach at Scale I and the far field control section experienced significant net losses in sand volume, the north and south flanks of the structure were not impacted as severely by comparison. The north flank actually recorded a slight net gain in sand volume.

Pacific Palisades (PP)

Pacific Palisades is located just south of Lincoln Beach. The site is on the north side of Fishing Rock, a rocky point of land jutting out approximately 150 m into the ocean. Fishing Rock is not considered a littoral cell boundary, but it does inhibit longshore sediment transport and has a substantial effect on the beach

processes at the site. The bluff line north of Fishing Rock forms a crescent shape, indicative of a hooked beach. A rubble mound revetment follows the curve in the bluff for approximately 300 m. The rubble blends into the bluff face and there are no discernible flanks on either end of the structure. The south end of the structure essentially extends to the base of Fishing Rock. The analysis of Pacific Palisades was limited to investigations of Scale I and Scale II. A far field investigation was not feasible considering the crescent shaped backing bluff and the lack of identifiable flanks. Aerial photographs indicate relatively little change in the coastline from 1962 to 1983.

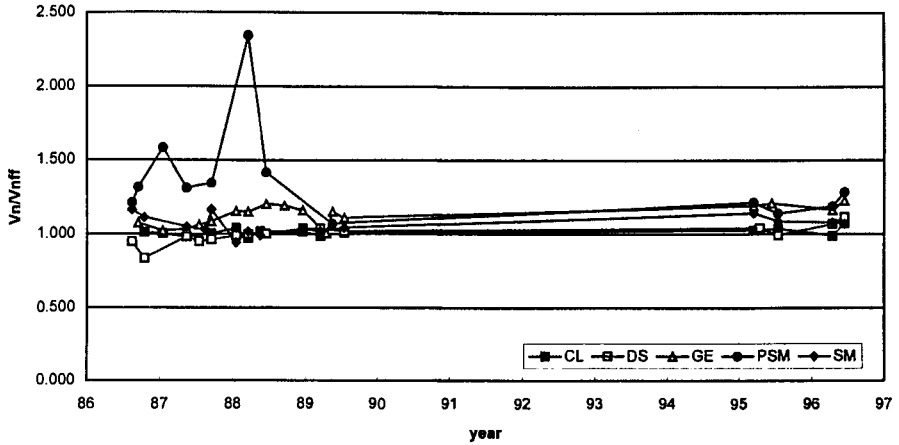


Figure 6 Normalized North Far Field Comparison

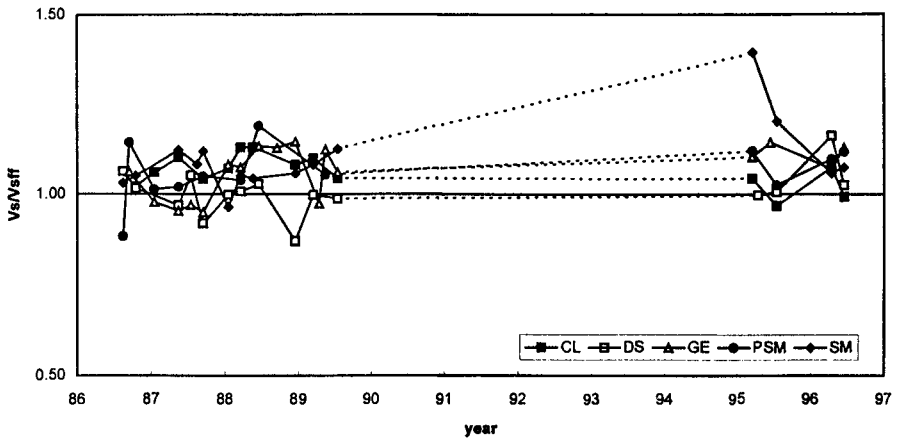


Figure 7 Normalized South Far Field Comparison

When the beach at Pacific Palisades was subjected to low energy waves, usually May through October, the beach was typified by a well defined berm, cusps,

and a rip current embayment. The rip current embayment, present throughout most of the year, was most likely caused by Fishing Rock. The sand volume of the beach at Scale I, shown in Figure 3, fluctuates seasonally about a nearly constant mean. The beach experienced a slight net gain in sand volume over the observation period.

Pacific Shores (PS)

Pacific Shores is a sea cliff backed site located approximately three miles south of Newport. The dominant morphological feature at the site is a section of the sea cliff that protrudes further seaward than the adjacent cliffs on either side. This protruding section of cliff, which is probably subjected to wave attack on a regular basis, is composed of an erosion resistant material. The cliff line south of the protrusion, where the structure is located, forms a crescent shape similar to that of Pacific Palisades. The original structure selected for the field monitoring program was a rubble mound revetment measuring approximately 20 m in length. However, since the initiation of the study in 1986, a new 140 m long rubble mound revetment has been constructed immediately north of the original structure. The newer structure was probably built in response to localized land slides which occur at the site. The two structures were not joined together, thus leaving a 15 m gap of unprotected sea cliff between them. The addition of this enormous new structure during the observation period and in such close proximity to the original, smaller, structure made for a complicated analysis. Aerial photographs show that parts of the southern portion of the protruding cliff have been eroded since 1965. It is also possible that parts of the cliff were removed as part of the construction of the newer structure.

The complete chronology of contour and surface plots suggests the beach at Pacific Shores was very flat and planar throughout the year. A summer berm was not present, and there was no evidence of a rip current in any of the surveys. The contour plots did not indicate a trend of sand accumulating in front of any part of the structure. The volumetric response of the beach at Scale I, shown in Figure 3, followed a typical pattern of summer accretion and winter erosion, with the exception of 1989 when the beach experienced a prolonged period of accretion. Ten years of monitoring yielded a negligible net change in sand volume. A far field comparison was not feasible due to the addition of the new structure and the geometric nature of the backing bluff.

San Marine (SM)

San Marine is located between Walport and Yachats. The beach is backed by a low bluff, which is very irregular, containing several indentations and moderately protruding areas along a lengthy front. These are rather small scale features on the bluff, which is essentially shore parallel. The structure is a rubble mound revetment that measures approximately 150 m in length. The bluff line position is several meters further seaward at the structure. The bluff appears to be fairly stable with

respect to slides. Aerial photographs for San Marine indicate that the coastline and the bluff were remarkably stable from 1962 to 1983. Several of the unique and irregular features in the bluff, which is composed of an erodable material, are present in both the 1965 and 1983 photos. This suggests that waves seldom reach the bluff line.

The beach at San Marine was very flat and dissipative throughout the year. The majority of the Scale I contour and surface plots indicate a slight rise in elevation near the structure flanks. This slight rise may be attributed to the fact that the bluff is recessed several meters on either side of the structure.

Seasonal fluctuations about a slightly increasing mean are apparent in the volumetric response of the beach at Scale I, Figure 3. The beach at San Marine experienced a considerable net gain in total sand volume over the observation period. This can be attributed to significant recovery following the winter erosion events.

Far field control sections were defined both to the north and south of the structure. Normalized results of the far field comparison, shown in Figures 6 and 7, indicate that the volume of sand at the north flank deviates little from the volume of sand at the far field control section. A trend of increasing volume in the south flank in comparison to the south far field is apparent in Figure 7. This trend can be attributed to a volumetric response about an increasing mean for the south flank, and a volumetric response about a nearly constant mean for the south far field section. Volumes for both the north flank and the north far field section fluctuated about an increasing mean. A gain in net volume over the observation period and the stability of the bluff indicated in the aerial photos suggest that the structure is having no adverse affect on the surrounding beach or adjacent properties.

Driftwood Shores (DS)

Driftwood Shores, the southern most site included in this study, is located at Heceta Beach just north of Florence. The structure is a low rubble mound revetment measuring approximately 30 m in length. There are large dunes to the south of the structure and the area north of the structure is more similar to low hills with heavy vegetation than dunes. The structure is located at a low point in the dune. The backshore area behind the dune is actually lower than the structure and many parts of the upper profile. A house is situated several meters behind the structure. The house is not built in the backshore depression, but is very low relative to the other houses in the vicinity.

The beach exhibits a great deal of local three-dimensionality. The small scale three-dimensionality of the upper portions of the beach appears to be aeolian dominated. The complete chronology of contour and surface plots indicates that the beach was reasonably flat and dissipative during much of the year. The dunes to the south were evident in several of the surveys, but absent in the majority. It was likely that the dunes migrated back and forth in the cross-shore direction during the observation period. There were no typical summer profile features evident in the

contour and surface plots, although it was generally in the summer months when the south dunes were present in the contour and surface plots.

The volumetric response of the beach at Scale I, contained in Figure 3, shows seasonal fluctuation about an increasing mean, and a dramatic net increase in sand volume over the observation period. Driftwood shores was the only site which experienced accretion during the May 1996 period. The beach appeared to be gaining sand volume during the active portion of the study, 1986 through 1990, but the most substantial net gain in sand volume occurred between 1990 and 1996. Results from plots similar to Figures 4 and 5 show that the flanks responded nearly identical to the far field section over the ten year period. As indicated in Figures 6 and 7, the flank volumes deviated little from the respective far field volumes throughout the study. Similar to the volumetric response at Scale I, both flanks experienced a considerable net gain in sand volume.

CONCLUSIONS

All seven sites on the Oregon coast behaved in a similar manner. The volumetric response of the beach at each of the sites fluctuated seasonally between low sand volumes in the winter and higher sand volumes in the summer. Considerable recovery following periods of erosion resulted in net gains in sand volume over the observation period at Scale I for three sites (PSM, PP, DS), negligible changes at three sites (PS, CL, SM), and a significant net loss in sand volume at only one site (GE).

The structure flanks at each site, including Gleneden, were stable over the observation period. Sand volumes at the structure flanks deviated little from those of the far field control sections used in the baseline comparison. The average $V_{\text{flank}}/V_{\text{far field}}$ value for all seven sites, regardless of north or south flank, was 1.094 with a coefficient of variance of 0.102. This indicates that the structure flanks were retaining greater volumes of sand over the observation period than the far field control sections. In general, the structure flanks experienced negligible net changes in sand volumes, and often slight net gains in sand volume over the observation period.

There were no significant negative effects caused by the structures at any of the seven sites. This can be attributed to the lack of wave attack that these structures experience (Ruggiero et. al., 1997) The structures were built high on the profile against the base of the bluff or dune. Each site has a wide buffer beach fronting the structure which dissipates the high wave energy found on the Oregon coast and prevents waves from reaching the structure or bluff except during the most severe storms. The structures tend to serve as bluff retention and stabilization structures as much as shore protection structures. Structures built against bluffs appear to be doing an excellent job supporting the bluff and preventing landslides, which can be brought about by undercutting of the bluff or cliff by wave action, but many other non-beach process related factors are also recognized (Komar and Shih, 1994).

When examining the long-term effects of seawalls on beaches, the analysis must be site specific. Susceptibility to wave attack should be considered when permitting or building a shore stabilization structure on the central Oregon coast.

REFERENCES

- Hearon, G.E. 1995. *Long-Term Beach Response to Shore Stabilization Structures*. M.S Engineering Report, Oregon State University.
- Komar, P.D., and McDougal, W.G. 1988. Coastal Erosion and Engineering Structures: The Oregon Experience. *Journal of Coastal Research*, Special Issue 4: 77-92.
- Komar, P.D., and Shih, S.M. 1991. Sea-Cliff Erosion Along The Oregon Coast. *Proceedings Coastal Sediments '91*, American Society of Civil Engineers, 1558-1570.
- Shih, S.M., and Komar, P.D. 1994. Sediment, Beach Morphology and Sea Cliff Erosion Within an Oregon Coast Littoral Cell. *Journal of Coastal Research*, 10(1): 144-157.
- Sturtevant, M.A., McDougal, W.G., and Komar, P.D. 1987. *The Impact of Shoreline Stabilization Structures on Beaches and Adjacent Properties*. Sea Grant Report, Oregon State University.
- Ruggiero, P., Komar, P.D., and McDougal, W.G. 1997. Extreme Water Levels, Wave Runup, and Coastal Erosion. *In these Proceedings*.

CHAPTER 211

Profile Volumes as a Measure of Erosion Vulnerability

Timothy W. Kana, Ph.D.,¹ and Ram Krishna Mohan, Ph.D., P.E.²

ABSTRACT

Profile volumes provide an indication of the condition of barrier islands and beaches. While site specific, they can be used along any littoral shoreline as a measure of the relative "health" of one section compared with another. Assuming shorelines develop an equilibrium profile around which the beach cycle and cross shore changes occur, profile volumes integrate small scale perturbations and provide a target sediment volume for the site between reference contours. Profile volumes may be considered for various parts of the profile as follows:

- *Dune volume above storm surge levels* (after FEMA) as a measure of the reservoir of sand required to prevent over topping.
- *Mean sea level (MSL) barrier cross-section* — the section that must be fully scoured to produce a full breach channel.
- *Inner beach profile* — the section that represents the condition of the recreational beach.
- *Inshore profile* — the section that represents the core "base" of the barrier island.

By comparing versions of these sections from site to site, especially where there have been known breaches and variations in beach erosion rates it is possible to develop systematic criteria for the health of the shoreline in question. Profile volumes provide a straight-forward technique for diagnosing barrier erosion problems. A case study from Westhampton Beach and Fire Island (New York) illustrate the application.

¹ Senior scientist, CSE-Baird, A Division of W.F. Baird & Associates, Ltd., PO Box 8056
Columbia SC 29202

² Senior engineer, Gahagan & Bryant Associates, 9008-O Yellow Brick Road, Baltimore, MD
21237

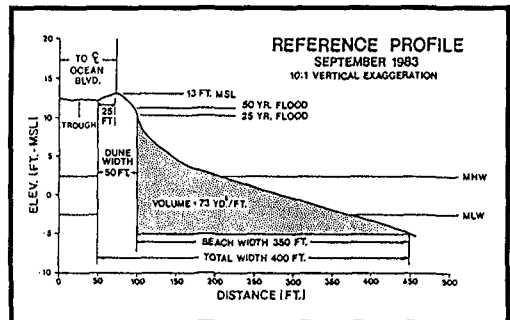
INTRODUCTION

Profile volumes, that is, the unit quantity of sediment contained between defined contour limits in the littoral zone, can be used as predictors of erosion vulnerability, breach vulnerability, and nourishment requirements. They are especially useful for analyzing sites with few data or sites where surveys are spaced widely in time. The profile volume for a site, ideally, should incorporate the foredune (or the entire backshore seaward of buildings where development is a concern), berm, intertidal beach, and lower foreshore to closure depth.

Multiple transects surveyed between common boundaries along shorelines having similar orientations and exposures provide a set of profile volumes that can be normalized and compared statistically by simple means (Fig. 1) (Kana et al., 1984; Kana, 1993). The unit volume of any one profile to closure integrates all small-scale perturbations in slope and bar formation, and becomes a reasonably pure measure of the littoral condition. Seasonal or beach-cycle-related variations are accounted for in the volume. Therefore, the phasing of surveys with storms or seasons is less critical. Where the setting is a narrow barrier beach, the profile volume method also provides a measure of vulnerability to breaches.

FIGURE 1.

The reference profile illustrates how average unit-width profile volumes can be developed on a site-specific basis for analyses of the condition of the beach from one section to another, as well as from one survey to the next (after Kana et al., 1984).



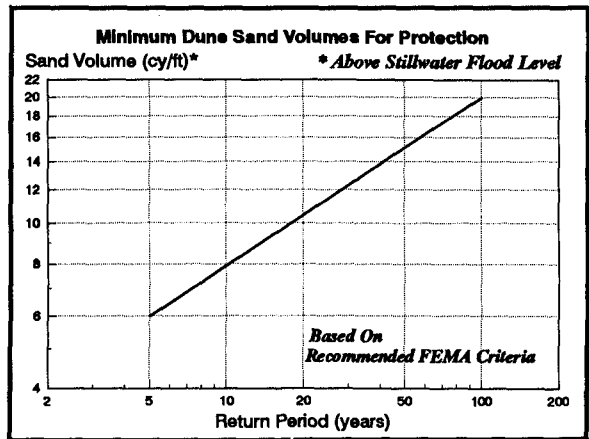
Barrier Sediment Volumes

There are no universally accepted criteria defining the condition of a barrier beach to withstand erosion and storm surges without breaching. In the United States, FEMA (Dewberry & Davis, 1989) has developed rough guidelines relating to dune preservation during storms. FEMA considers a particular volume of sand above the still-water flood level and seaward of the dune crest as being the minimum necessary to prevent overtopping and washovers for a particular return-period storm. Dutch coastal engineers (TAW, 1985; Van de Graaff, 1986) further consider the amount of freeboard above the still-water surge level needed to absorb wave runup without overtopping and breaching. These criteria are based on probabilities and are poorly documented because there are so few sites where all necessary data are available to quantify the relationship. In most cases, dunes either remain standing with considerable excess sediment landward of poststorm scarps, or they are washed out. Thus, establishing threshold minimum quantities to sustain surges without (dune) breaching is difficult.

The present criteria of FEMA are given in a rating curve (Fig. 2). The minimum cross-sectional areas recommended above the still-water surge elevation (for a particular return period) equate to unit volumes of sand (cubic yards per foot) as given on the graph. In simple terms, the 100-year storm would require about 20 cy/ft (50 m³/m) above its still-water surge level, whereas a 5-year storm would require about 6 cy/ft (15 m³/m) for protection. FEMA representatives emphasize these criteria are for guidance only and may not apply for certain dune configurations (R. Hallermeier, Dewberry & Davis, pers. comm., March 1994). In other words, the absolute quantity of sand above the surge level must be configured to absorb wave runup effectively; otherwise, breaching may still occur.

FIGURE 2.

FEMA minimum criteria for dune unit volumes above flood still-water level as a function of storm-return period (based on guidelines in Dewberry & Davis, 1989). Standard deviation for the 100-year storm is ± 10 cy/ft, confirming a wide range of "safe" values based on experience.



In the following example application, the authors have computed reference sand volumes above particular datums to relate the condition of a barrier to FEMA criteria. Unit-volume analysis is also useful for comparing the overall condition of the barrier island, including the underwater portion of the profile. By comparing barrier sections that have experienced breaches with unbreached sections, it is possible to develop site-specific criteria relating to the potential vulnerability of future breaches along nearby sites.

EXAMPLE APPLICATION

Winter storms (northeasters) on 11 December 1992 and 13 March 1993 caused widespread damage along the south shore of Long Island, New York (Fig. 3). In terms of beach erosion, structural damage, and mainland flooding, these two storms were the worst for this part of the coast since the well-known 4-6 March 1962 northeaster (USACE, 1963). Over 100 houses were lost along Pikes Beach (Westhampton, immediately downdrift of the groin field) as a result of continued erosion and a breach through the barrier in December. The 1992 breach was left open for over ten months and contributed to locally higher tides in Moriches Bay (J. Tanski, unpubl. data,

SUNY, Stony Brook, March, 1993) before it was closed by the U.S. Army Corps of Engineers by hydraulic dredge (contractor: Great Lakes Dredge & Dock Co.).

The breach at Westhampton demonstrated the problem of unstable inlets near development and the potential for increased flooding around the lagoon shoreline. Concerns over the possibility of a similar breach through Fire Island, the next barrier island downdrift of Westhampton Beach, and a possible increase in the tide range within Great South Bay led to a study funded by the New York Coastal Partnership (Kana and Krishnamohan, 1994). The purpose of the study was to assess the vulnerability of Fire Island to storm breaches and determine the likely physical impacts along Great South Bay (Fig. 3). The study was multidisciplinary and drew on historical shoreline data, developed an updated sediment budget for Westhampton and Fire Island, and used available predictive models of storm surges to evaluate flooding potential. One analysis (the subject of the present paper) evaluated profile volumes in an attempt to develop site-specific criteria for barrier sections that had breached in the past and to identify other potential sites for breaches.

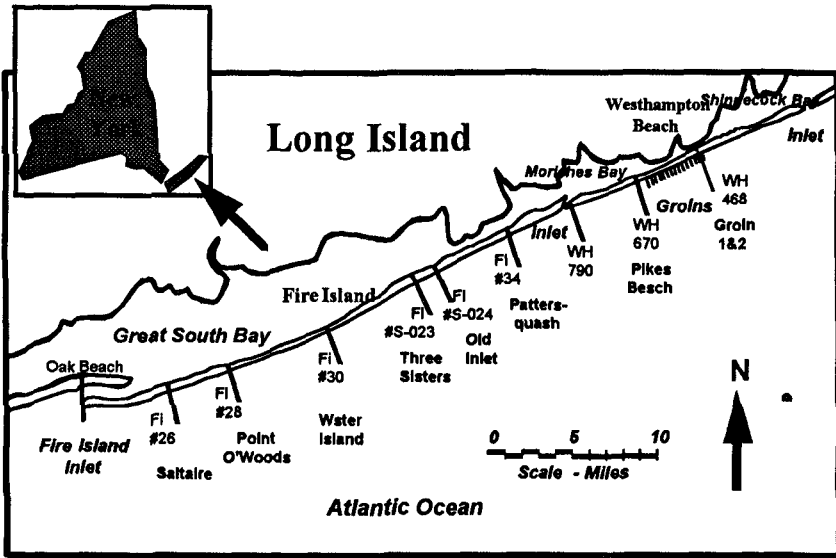


FIGURE 3. General location map of representative barrier-island cross-sections developed for the 1994 study (after Kana and Krishnamohan, 1994).

Methodology

Representative cross-sections through Westhampton Beach and Fire Island were developed from USACE profiles (RPI, 1985), unpublished surveys, and planimetric maps (see Fig. 3). These were selected to represent the range of conditions including physical dimensions of the barriers and historical erosion trends. The profiles extend

from the bay shoreline across the barrier and out to approximately -30 ft below MSL. Table 1 describes some of the cross-sections, localities, and significant features [see Kana and Krishnamohan (1994) for details].

TABLE 1. Representative barrier island cross-sections, relevant physical dimensions, and key distinguishing features. [* (1) Width at mean sea level. (2) Highest dune elevation. (3) Distance from MSL to -20 ft contour.]

USACE Transect ID	Locality	1979 Dimensions (ft)			Key Features
		(1)*	(2)*	(3)*	
WESTHAMPTON BEACH					
468+00	Between groins 1 and 2, east end of groin field	825	21	1,400	Rapid accretion and growth of a new foredune to 15 ft MSL between 1962 and 1979; continued accretion through 1993.
670+00	2,700 ft west of groin 15, compartment 143B	700	10	1,600	Rapid erosion between 1962 and 1979, loss of an 18-ft-high foredune within 1,000 ft of 1962 and 1992 breaches.
790+00	2,000 ft east of east jetty, Moriches Inlet	450	15	1,950	Situated btwn 1980 breach and east jetty; breach widening and easterly migration eroded the section btwn January and July 1980.
FIRE ISLAND					
34	6,700 ft east of Smith Point Park Pavilion, eastern Fire Island	1,225	18	1,350	Zone of washovers west of Moriches Inlet; high erosion rates; artificial dune (spoil area from bay dredging) constructed 400 ft landward of the shoreline.
~26	West walk at Saltaire, western Fire Island	2,050	15	1,375	Wide barrier section; highly erosional; first row of houses lost between 1967 and 1979; area of concentrated damage in 1992-93.

Westhampton Profiles

In 1962, Westhampton had sustained its worst storm since the 1938 hurricane (storm of record). The March northeaster breached the barrier along Pikes Beach and caused extensive structural damage. Prior to the storm, erosion had reduced the width of the barrier and chronic problems of overwash forced periodic sand scraping to clear Dune Road. The USACE (1958) had been developing a shore protection plan which proposed construction of 21 groins and concomitant nourishment. By December 1962, emergency repairs had closed the storm breach and had added almost one million cubic yards of additional sand to Westhampton Beach (USACE, 1963). Construction of a

portion of the groin field was initiated in 1964 and the final four of 15 groins were completed around 1969.

Two transacts illustrate dramatically different results along Westhampton Beach between 1962 and 1979--USACE station 468+00 (Fig. 4a) situated at the updrift end of the groin field between groins 1 and 2, and USACE station 670+00 (Fig. 4b) situated 2,700 ft downdrift of groin 15. In 1962, both transacts represented narrow sections of the barrier island. In fact, the updrift station (468+00) was barely 600 ft wide from the ocean to the bay shoreline and contained a single, well-developed foredune to 20 ft above sea level. The downdrift station (670+00) was slightly wider at about 725 ft with a smaller foredune reaching about 17 ft.

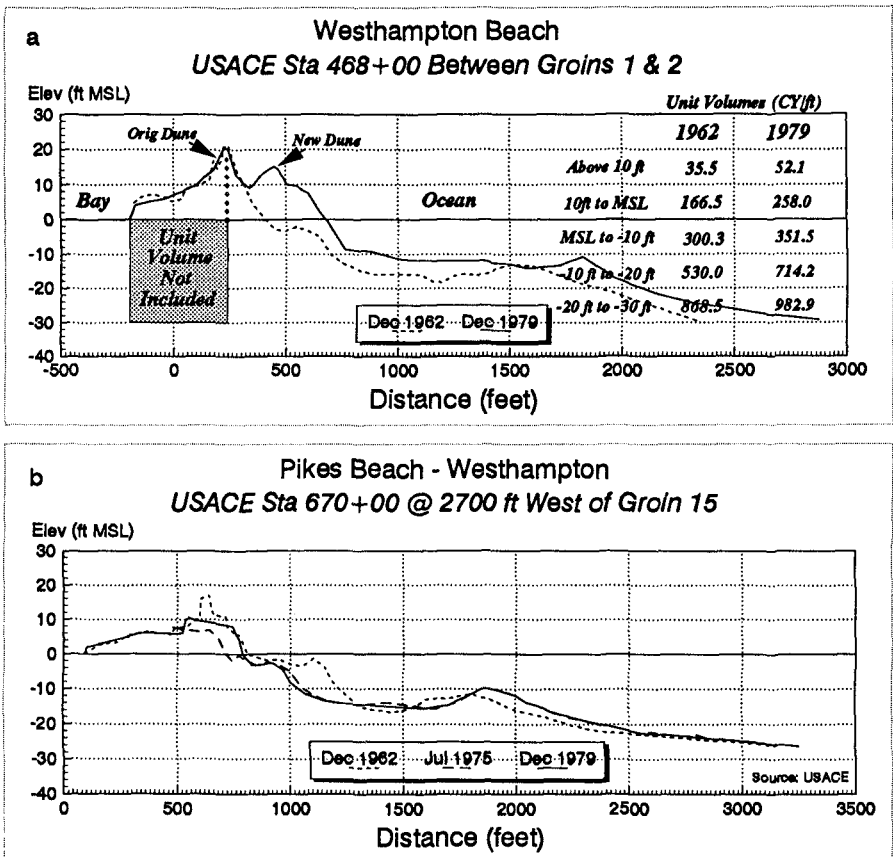


FIGURE 4. Representative, barrier-island cross-sections from the east end of the Westhampton groin field (a) and Pikes Beach (b), illustrating opposite trends in shoreline change between 1962 and 1979. Unit volumes refer to the profile areas between the indicated contours.

By 1979, station 468+00 had gained a second foredune and the shoreline built seaward, increasing the barrier width to about 825 ft (Fig. 4a). Associated with the dune and upper beach building was a large increase in sand volume below MSL. This trend of large-scale accretion has continued through 1993 as shown in nearby profile 461+25 at groin 1 (Fig. 5). By January 1994, groins 1 and 2 (500-ft-long structures when built) were completely buried.

In contrast, transect 670+00 lost dune elevation and width between 1962 and 1979. The trends shown in Figure 4b actually incorporate several beach fills during the period. By July 1975, the barrier had narrowed to about 600 ft and the maximum elevation at the transect was only 7 ft above sea level. Nourishment is believed to have restored part of the beach between 1975 and 1979, but the dune elevation remained no higher than 10 ft MSL. An aerial photo from August 1981 (Fig. 6) in the vicinity of station 670+00 shows the recession of the shoreline downdrift of the groin field and a number of houses left standing on the active beach.

The 1992 northeaster caused at least two breaches between transect 670+00 and groin 15. The easternmost breach immediately downdrift of groin 15 became the dominant and only channel and expanded from several hundred feet wide after the storm to over 2,000 ft wide by the summer of 1993 (Westhampton Fire Marshall's Office, unpubl. reports). Field observations by the authors in March 1993 and January 1994 confirmed deposition of a flood delta in Moriches Bay in connection with the breach channel. Around November 1993, the breach was closed by hydraulic dredge using a USACE-approved offshore borrow source ~1.5 miles south of the breach.

A third Westhampton Beach transect considered here is from USACE 790+00, ~2,000 ft east of the east jetty of Moriches Inlet. This undeveloped section of Cupsogue spit consists of a narrow barrier segment flanked on the landward side by the navigation channel to Moriches Inlet. During the 1960s, the bay channel meandered closer to Cupsogue spit and contributed to scour along the bay shoreline.

By 1979, portions of the spit about 0.5 mile north of the jetties had been reduced in width to 300 ft from ocean to bay. In January 1980, continued narrowing of the spit combined with higher-than-normal wave action breached the barrier (Kana et al., 1981). Between January and July, the breach channel widened and migrated west until it removed the last part of the spit and coalesced with the navigation channel between the jetties.

Transect 790+00 is situated between the January breach point and east jetty. At the time of the breach, section 790+00 had a width of about 450 ft and a dune elevation of 15 ft (Fig. 7). Much of this section was artificial, having been filled several times in connection with dredging projects in the bay. As the breach widened, it migrated through section 790+00, washing out the beach and depositing a large volume in the bay channel.

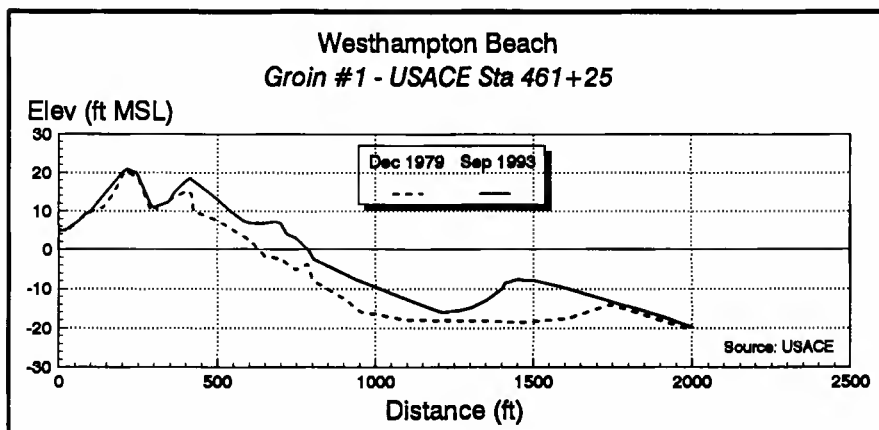


FIGURE 5. Comparative profiles at groin 1 (easternmost) for December 1979 and September 1993. Data courtesy of U.S. Army Corps of Engineers.



FIGURE 6. Pike's Beach and Westhampton Beach in August 1981, looking east. Groin field is at top of photo.

As Figure 7 shows, by July 1980, the elevation across 790+00 was about 4 ft below sea level. The breach was closed in January 1981 by hydraulic dredge, using barrier and littoral sediments that had accumulated in the bay channel, and by trucks using sand from an inland source.

Unit volumes were computed through each barrier cross-section by 10 ft contour intervals (example values given on Fig. 4a). Conveniently, the predicted 100-year still-water surge elevation along this microtidal coast nearly equals +10.0 ft MSL (FEMA, 1987).

Unit volumes above the +10 ft contour generally reflect the condition of the dunes. At Westhampton, the volumes above 10 ft are much greater at section 468+00 (groin field) than the sections near recent breaches. If 468+00 is typical of the groin field, dune unit volumes approached 50 cy/ft by 1979 and are higher today (see Fig. 5). In contrast, stations 670+00 and 790+00 yield an average volume of about 10 cy/ft with zero volume occurring in three of the six surveys used in the analysis.

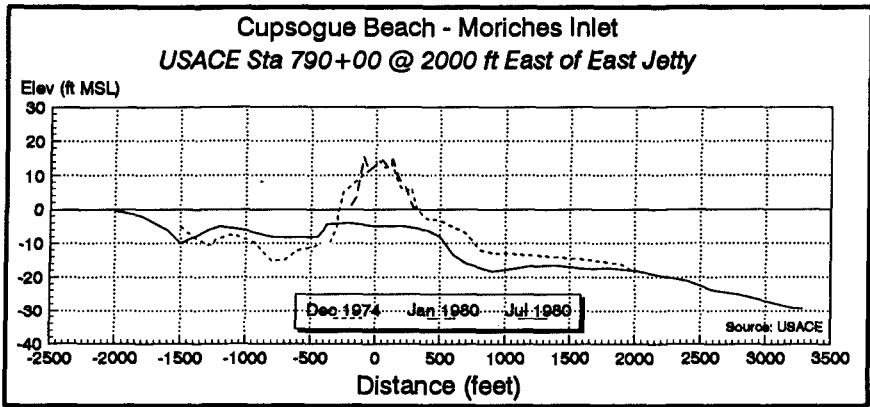


FIGURE 7. USACE station 790+00 situated ~2,000 ft east of Moriches Inlet. Erosion in 1980 occurred after the January 1980 breach to the east migrated through this section.

Between +10 ft and mean sea level, the barrier cross-section volume is largely a function of barrier width. Of the few surveys used for Westhampton, a typical section volume is about 160 cy/ft.

Relative to the total section volumes above MSL, the net changes for the three Westhampton stations generally represent a high percentage of the maximum section volume. For example, station 468+00 gained 108 cy/ft between 1962 and 1979, a volume which is 35 percent of the 1979 section volume (i.e., a gain of over 50 percent of the original unit volume). Station 790+00 lost 100 percent of its 1974 section volume due to the January 1980 breach; station 670+00 lost more than reflected (see Fig. 4) because of remedial nourishment between surveys.

Underwater sand volumes for Westhampton Beach stations similarly reflect the trends above sea level. Typical unit volumes from MSL to -10 ft seaward of the fore-dune are about 125 cy/ft and from -10 ft to -20 ft are about 425 cy/ft. The net change for 468+00 (groins) between MSL and -20 ft was 235 cy/ft, nearly 50 percent more sand than the 1962 volume. Assuming 461+25 (see Fig. 5) is similar, 468+00 has probably gained an additional 240 cy/ft in these lenses between 1979 and 1993.

Station 670+00 actually contained almost 20 percent more sand than 468+00 between MSL and -20 ft in 1962 before the groins were built. By 1979, this section contained about 75 percent of the unit volume at 468+00 (between MSL and -20 ft); a greater loss occurred between MSL and -10 ft; unit volumes between -10 ft and -20 ft increased by about 5 percent. Most likely, the change would have been much greater if there had been no beach fills.

Station 790 + 00 had a healthy underwater profile prior to the 1980 breach. As the breach widened and eroded the section, unit-volume losses between MSL and -20 ft were 260 cy/ft, an exceedingly rapid loss over the five-year survey interval. The upper lens from MSL to -10 ft was reduced to a section of about 50 cy/ft by July 1980, a volume representing the underwater sill through the breach. The lower shore-face (-10 ft to -20 ft) eroded severely, reducing the section volume to 330 cy/ft (about 80 percent of the same lens at station 670 + 00).

Based on the sand volume results in Table 2, typical Westhampton Beach values (rounded) are as follows:

Dune Volume	Mean (cy/ft)	Std. Dev. (cy/ft)	(No. of Surveys)
Above + 10 ft MSL	20	±20	(8)
+ 10 ft to MSL	150	±77	(8)
MSL to -10 ft*	125	±45	(7)
-10 ft to -20 ft*	425	±75	(7)

[*Seaward of dune crest of earliest survey]

The results show high standard deviation because one station built up rapidly and one incorporated breach conditions. Thus, the "healthy" profiles reflect volumes incorporating the additional volume indicated by the plus standard deviation. Unhealthy profiles vulnerable to breaching reflect mean volumes minus the standard deviation. These results provide benchmarks for comparison with Fire Island profiles.

TABLE 2. Barrier-island unit-profile volumes (cy/ft) from the bay to -30 ft NGVD (above MSL encompasses entire barrier width; below MSL extends from foredune seaward). [Numbers in parentheses represent number of surveys.]

	Above 10 ft	10 ft to MSL	MSL to -10 ft	-10 ft to -20 ft	-20 ft to -30 ft
WESTHAMPTON					
468 + 00 (avg)	43.8 (2)	212.2 (2)	154.4 (2)	450.6 (2)	754.2 (2)
Breach sections (avg)	12.6 (6)	139.6 (6)	115.6 (5)	420.6 (5)	811.2 (4)
FIRE ISLAND					
Minimum	3.1	210.0	90.7	310.9	665.5
Maximum	90.0	475.1	176.3	459.2	786.8
Mean	32.3 (11)	343.3 (11)	134.3 (10)	407.7 (10)	739.6 (9)

Fire Island Profiles

Six transects across Fire Island (two of which are shown in Figure 8) illustrate the typical range of conditions (see Table 1). Unit volumes have been computed for the same contour intervals and boundaries as Westhampton (Table 2). Some differences are immediately apparent. Above mean sea level, Fire Island profiles typically contain more sediment. The average unit volume above +10 ft is 32 cy/ft (± 27.7 cy/ft standard deviation) for 11 surveys. Point O' Woods (USACE-28) and Saltaire (near USACE-26) had the lowest dune volumes, ranging from 3.1 cy/ft for the 1993 Saltaire profile to 7.1 cy/ft for the 1967 Point O' Woods profile. Three Sisters dunes off Bellport represented the maximum with 90 cy/ft above +10 ft (1979). Between +10 ft and MSL, Fire Island sections averaged about 345 cy/ft (± 98.6 cy/ft standard deviation), much of which is due to the wider backshore. In fact, volumes in this lens

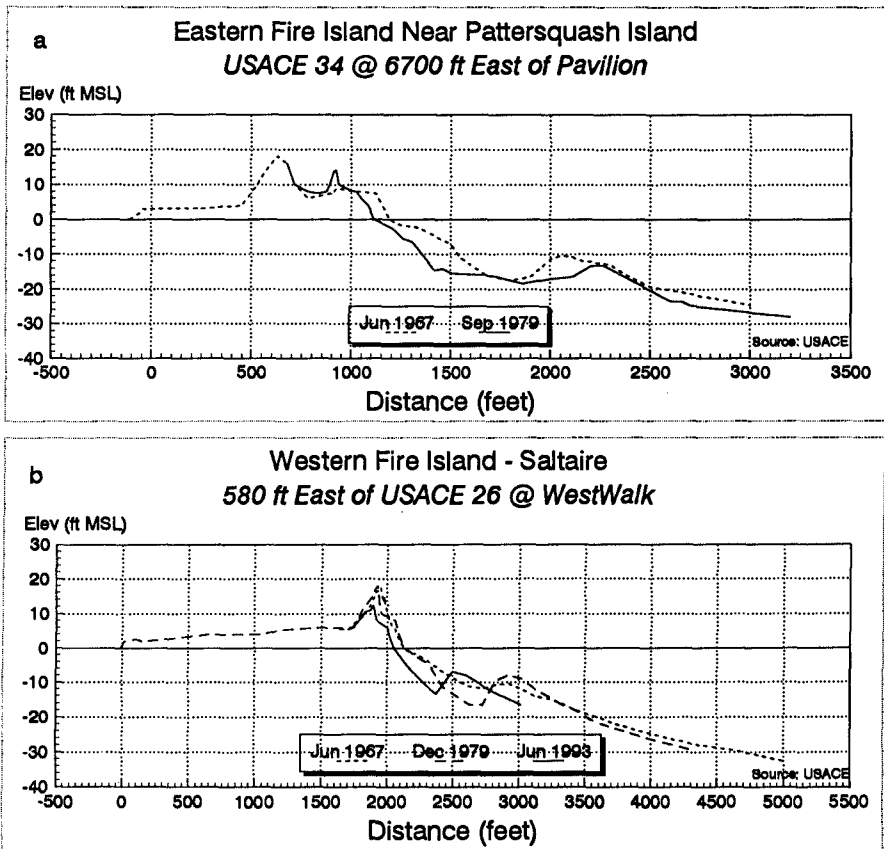


FIGURE 8. Representative, barrier-island cross-sections from (a) Pattersquash Island area east of Smith Point Park (locality for numerous washovers) and (b) west end of Saltaire, where major erosion of the underwater profile has accelerated erosion of the foredune.

are roughly double those of Westhampton (Table 2). Below mean sea level, unit volumes were very similar to Westhampton's, averaging -135 cy/ft between MSL and -10 ft, and ~400 cy/ft between -10 and -20 ft. This is expected because the landward computation boundary in each case is the dune crest.

Highest erosion rates were at the Pattersquash section (near USACE-34) and at Saltaire (near USACE-26) (see Fig. 8). The net change for these stations, respectively, ranged from about 10 cy/ft to 50 cy/ft above MSL and from 200 cy/ft to 150 cy/ft below MSL. In 1979, station USACE-34 was reduced to a volume of 415 cy/ft below MSL (to -20 ft) compared to an average of -550 cy/ft for other stations.

Aerial overflights by the authors and reports from officials of Suffolk County Department of Public Works (SCDPW) indicate the area around the Pattersquash Island transect continued to overwash through January 1994. But at this station, the setback of the artificial dune appears to have prevented a more landward shift of sediment. The artificial dune ends less than 1,000 ft to the east of transect 34, suggesting that more easterly areas are likely to experience deeper penetration of overwash along the back barrier. The authors observed a number of large washovers in that area during a January 1994 overflight. Officials at SCDPW confirmed these trends along eastern Fire Island over the past ten years. The results of the profile volume analysis suggest washovers will be more likely along Fire Island when the profile volumes between MSL and -20 ft go below 500 cy/ft relative to the foredune and when the foredune has negligible volume above +10 ft MSL.

The Saltaire section (near USACE-26) bears some similarities to USACE-34 because of its rapid erosion since 1967. While the barrier is much wider at Saltaire, its backshore elevations are low, averaging less than 5 ft above sea level (Fig. 8b). A single foredune has existed along the oceanfront. In 1967, the dune contained about 24 cy/ft above the +10 ft contour, about 75 percent of the average for the selected Fire Island transects. By June 1993, dune volume above +10 ft was reduced to only 3 cy/ft. This low volume is offset by over 450 cy/ft between +10 ft and MSL (a total approximately three times that of Westhampton sections). Below mean sea level, station 26 lost about 155 cy/ft between 1967 and 1993, reducing its volume seaward of the 1967 dune crest to 450 cy/ft. As discussed in a regional sediment budget analysis (Kana, 1995), rapid erosion in the western Fire Island area is believed the result of depletion of offshore shoals associated with an earlier position of Fire Island Inlet. This has left the foredune much more vulnerable to erosion. An ~80 ft recession of the foredune since 1967 has destroyed (or caused to be removed) the oceanfront structures at this site, leaving the second row buildings on the oceanfront in 1993.

On the basis of backshore volumes above mean sea level, the Saltaire section is less likely to breach than Pattersquash because it contains almost twice the volume. But the Saltaire foredune is more likely to recede than Pattersquash's artificial dune because of the low unit volumes seaward of it and the lesser setback. Pattersquash's artificial dune profile could be created at Saltaire, but to be stable under present offshore conditions, it would have to be set back at least 150 ft from the 1993 dune

crest. Planimetric maps indicate there are at least three rows of houses within 150 ft of the present dune crest at that locality.

SUMMARY — CASE STUDY

The remaining four sections along Fire Island represent intermediate conditions and are not discussed in this paper (see Kana and Krishnamohan, 1994, for details). By the measure of profile volumes through 1979, Fire Island cross-sections generally contain much more sand above MSL than Westhampton Beach sections. The difference in dune volumes between the two islands represents only a fraction of the total lens of sand comprising the barrier. The bulk of the subareal barrier is contained between MSL and +10 ft. Westhampton profiles contain roughly half the volume of Fire Island profiles above mean sea level. Transects that are breached along Westhampton typically contained less than 150 cy/ft above MSL before breaching.

While absolute volumes above mean sea level are not the only parameters to rank the condition of the barrier and establish vulnerability to breaching, they provide one quantitative measure to compare with historical breach areas.

REFERENCES

- Dewberry & Davis. 1989. Basis of assessment procedures for dune erosion in coastal flood insurance studies. Prepared for FEMA; Dewberry & Davis, Inc., Fairfax, VA, 57 pp. + appendices.
- FEMA. 1987. Flood Insurance Study, Village of Westhampton Beach, Suffolk County, New York. Federal Emergency Management Agency, Washington, DC (unpublished).
- Kana, T.W. 1993. The profile volume approach to beach nourishment. In D.K. Stauble and N.C. Kraus (eds.), *Beach Nourishment Engineering and Management Considerations*, ASCE, New York, NY, pp. 176-190.
- Kana, T.W. 1995. A mesoscale sediment budget for Long Island, New York. *Marine Geology*, Vol. 126, pp. 87-110.
- Kana, T.W., and R. Krishnamohan. 1994. Assessment of the vulnerability of the Great South Bay shoreline to tidal flooding. Final Report, New York Coastal Partnership, Babylon, NY; Coastal Science & Engineering, Columbia, SC, 153 pp. + appendix.
- Kana, T.W., M.O. Hayes, and S.A. Covell. 1981. Fire Island to Montauk Point, Long Island, New York, reformulation study: sediment budget — phase I, Moriches Inlet. Report for N.Y. District, USACE, Contr. DACW51-81-C-0030; Research Planning Inst., Inc., Columbia, SC, 82 pp.

- Kana, T.W., S.J. Siah, M.L. Williams, and W.J. Sexton. 1984. Analysis of historical erosion rates and prediction of future shoreline positions, Myrtle Beach, South Carolina. Project Report for City of Myrtle Beach; CSE (as subdivision of Research Planning Inst., Inc.), Columbia, SC, 130 pp.
- RPI. 1985. Fire Island Inlet to Montauk Point, Long Island, New York: sediment budget analysis. Summary Report for New York District, USACE; Research Planning Inst., Inc., Columbia, SC, 85 pp. + app.
- TAW. 1985. Guidelines for the evaluation of safety of dunes as coastal defense. Unauthorized translation of Leidraad voor de beoordeling van de verligheid van duinen als zeevering, Technical Advisory Committee on Sea Defenses (Technische Adviescommissie noor de water keringen), Dutch Government Printing Office, 16 pp.
- USACE. 1958. Atlantic Coast of Long Island, New York (Fire Island Inlet to Montauk Point). Cooperative Beach Erosion Control and Interim Hurricane Study. Appendices, U.S. Army Corps of Engineers, New York.
- USACE. 1963. Report on Operation Five High disaster recovery operations from 6-8 March 1962 storm. U.S. Army Corps of Engineers, North Atlantic Division, Civil Works Branch.
- Van de Graaff, J. 1986. Probabilistic design of dunes; an example from The Netherlands. Coastal Engineering, Vol. 9, pp. 479-500.

CHAPTER 212

BREACH GROWTH: EXPERIMENTS AND MODELLING

by

Harry de Looff ¹⁾, Henk J. Steetzel ²⁾, Arie W. Kraak ³⁾

ABSTRACT

Since 1989 research has been conducted in the Netherlands on the issue of breach growth. This contribution describes the set-up and results of wave basin experiments which had the aim to obtain insight into the process of growth of the width of a breach. From analysis of the recorded data (flow characteristics in the breach and the development of the breach) an empirical relation for breach width growth has been derived. This relation has been implemented into a (conceptual) numerical model which is briefly described in this document also.

1. INTRODUCTION

The Dutch Technical Advisory Committee on Water Defences (TAW) is aiming for a design method for water defences in which the optimal safety level of these defences is related to the risk of flooding. Risk is defined as the product of the probability of failure and the expected damage costs in case of failure. One of the key factors in the damage costs assessment is the speed and rate of inundation

-
- 1) Rijkswaterstaat, Department of Road and Hydraulic Engineering,
P.O.Box 5044, 2600 GA Delft, The Netherlands
 - 2) ALKYON Hydraulic Consultancy & Research bv, PO Box 248,
8300 AE Emmeloord, The Netherlands (formerly DELFT HYDRAULICS)
 - 3) Rijkswaterstaat, National Institute for Coastal and Marine
Management/RIKZ, P.O.Box 20907, 2500 EX The Hague,
The Netherlands

of a polder. The latter is predominantly determined by the discharge rate through the breach [Kraak et al., 1994].

Research regarding breach growth in a sandy dike-like structure started in 1989 with an exploratory field experiment. Further, flume experiments have been carried out for the initial phases of the breach erosion process (lowering of the dike crest) [Steezel & Visser, 1992]. More recently wave basin experiments were done to investigate the breach widening process. Finally a large scale field experiment has been carried out in order to investigate the three-dimensional aspects of breach growth i.e. widening of the breach in combination with the development of a scour hole [Visser et al., 1995].

One of the main instruments to predict inundation and damage costs assessment is a theoretical model for breach growth and inundation. Recently, as a first step towards that model, a conceptual numerical model for breach growth prediction in a sanddike has been developed.

The present contribution is focused on the wave basin experiments regarding the widening of the breach and the conceptual numerical model of the breach growth process.

2. WAVE BASIN EXPERIMENTS

2.1 Set-up of the experiments

The set-up of the experiments is similar to the experiments which have been carried out to investigate the initial phases of breach growth (lowering of the crest) as is described in [Steezel & Visser, 1992]. The cross-sections of the dike-structure are identical in both experiments. The only difference is the use of a wave basin instead of a wave flume, with the purpose of investigating the widening of the breach.

All model tests have been carried out at DELFT HYDRAULICS and started with a sandy dike-like structure situated transversely across the wave basin. Because a breach develops symmetrically to the centre of the breach, it was sufficient to investigate only one side of the breach. The breach development, originated from minor initial overflow through a small pilot channel in the crown of the dike, was recorded using three simultaneously operating video camera's and a large number of precise instruments to obtain time series of both the water levels and the velocities in the area next to the breach. By using a recirculating system with an optional pump capacity up to 1.0 m³/s, the upstream water level was kept as constant as possible. In this way the widening of the breach could be studied in detail until the major part of the dam was eroded.

In order to complete this description of the experiment set-up, in figure 1 a planview of the wave basin lay-out is shown.

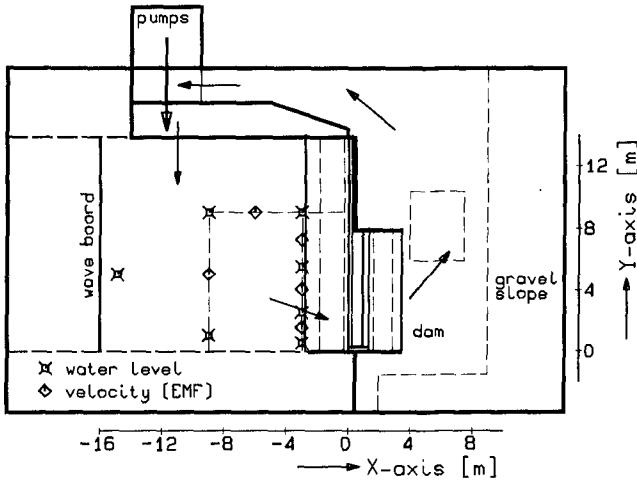


Figure 1: Planview of the wave basin lay-out

2.2. Description of the tests

The influence of several parameters on the breach erosion process has been investigated, viz. the width and height of the dike, the level of the foundation, the seaward bottom slope and the additional effect of (perpendicular) wave attack.

A total of 8 experiments have been performed in which the above mentioned parameters have been varied. Figure 2 gives an overview of the typical cross-sections used for the experiments. The focus lies here on the widening of the breach; in order to avoid effects of depth-growth, a treshold construction has been used for the experiments T1 .. T7 (as can be seen in figure 2). In the test T8 the treshold construction was absent; the only depth limitation is the floor of the basin. In this latter situation, a full three-dimensional experiment was conducted also.

In short the description of the experiments:

T4 = reference case

T1 = as T4, level of treshold is 0.1 m higher;

T2 = as T4, smaller crest width (0.7 m vs. 1.3 m);

T3 = as T4, lower (0.19 m) crest level

T5 = as T4, higher (0.2m) crest level

T6 = as T5, with wave attack (all other tests were without wave attack);

T7 = as T4, with a milder outer slope

T8 = as T7, treshold equals basin floor.

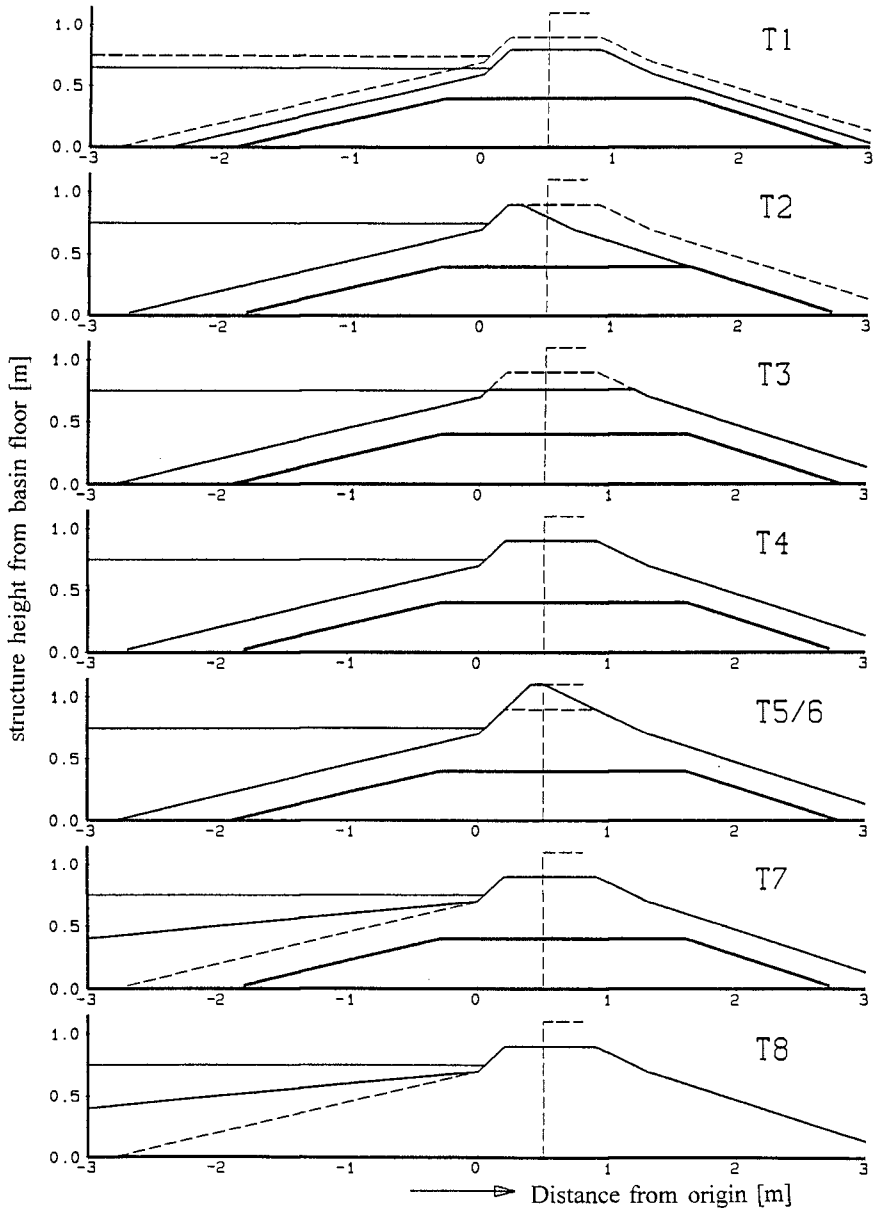


Figure 2: Overview of the cross-sections used for the tests T1 .. T8

2.3 Results of the experiments

The observed breach width development in time (B(t)) is presented in figure 3. It shows that the erosion of a dam having a narrow (T2) or low (T3) crest is more rapid than in case of a wider (T4) or a higher (T4, T5) crown. Relative to the case T5, additional wave attack (T6) yielded a larger breach width, whereas the opposite effect was present in the case of a less steep foreshore (T7, relative to reference case T4). The case without a threshold (T8) shows the slowest development of the breach width of all the tests due to the fact that a lot more sand has to be eroded in order to create the same breach width as for the other tests.

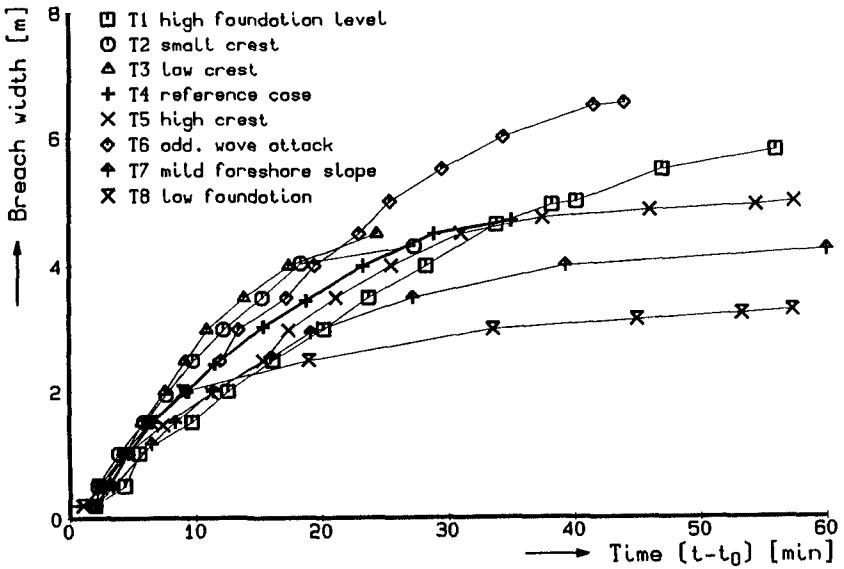


Figure 3: Overview of observed breach growth for all tests performed.

For modelling reasons a new parameter, the breach growth velocity, has been defined as:

$$\beta(t) = dB(t)/dt \quad [m/min] \tag{1}$$

To get an impression of this parameter, figure 4 gives its development as a function of time. It shows that a milder outer slope (case T7) yields a smaller breach growth velocity in respect to the reference case (T4).

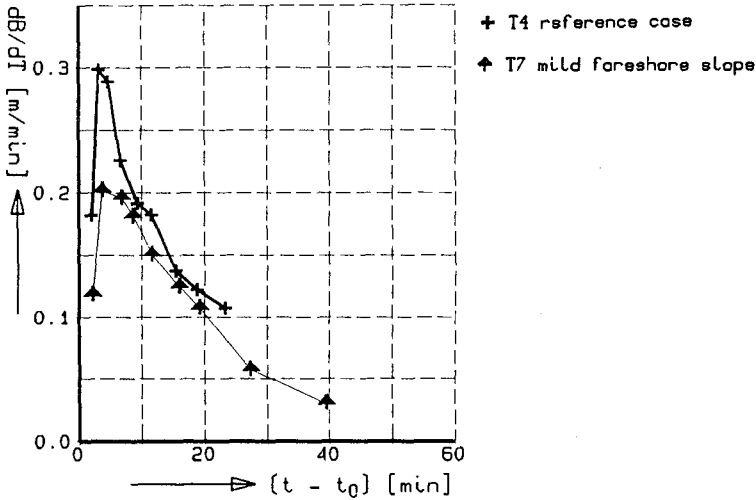


figure 4: development of the breach growth velocity as a function of time; shown is the effect of a mild foreshore slope

To get additional physical insight into the background of the breach growth velocity, this parameter is linked to the recorded flow characteristics in the breach.

Firstly, the relation with a characteristic water velocity in the breach ($v_{breach}(t)$), has been investigated. Figure 5 shows for the reference case (T4) and for the case T7 (milder outer slope) the breach growth velocity as a function of the water velocity in the breach. It can be seen that in order to obtain the same breach erosion velocity ($\frac{dB}{dt}$) as for the reference case, a higher water velocity in the breach (v_b) is required for case T7 (milder outer slope).

One of the conclusions is that breach width growth stops (and starts) when a certain critical water velocity in the breach is reached. From the experiments (laboratory and field) a critical value of 1.0 m/s can be derived

Secondly, the erodable volume is important. Therefore the volumetric breach growth velocity has been defined as:

$$\frac{dV}{dt} = \beta(t) \cdot A_d \quad [m^3/min] \tag{2}$$

in which A_d = eroded cross-section of the dam as is illustrated in figure 6.

Figure 7 shows the volumetric breach growth velocity as a function of the water discharge through the breach. In this figure all the tests performed are present, except for T6 (waves) and T8 (3D). A more or less linear relation can be derived.

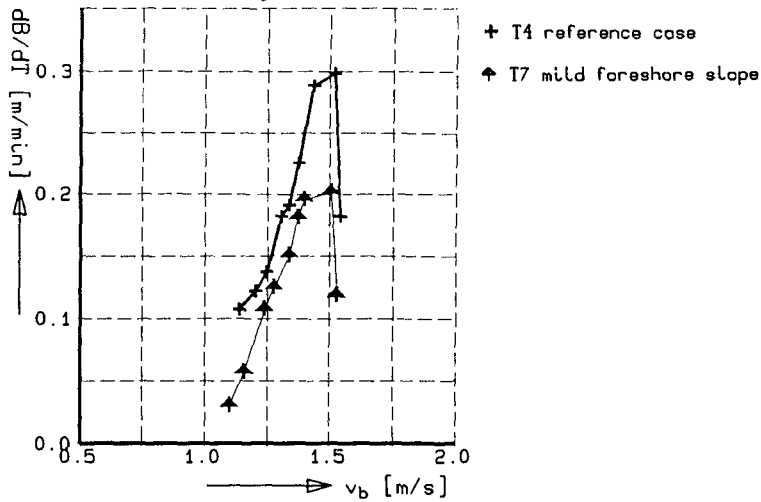


figure 5: development of the breach growth velocity as a function of the water velocity in the breach, shown is the effect of a mild foreshore slope

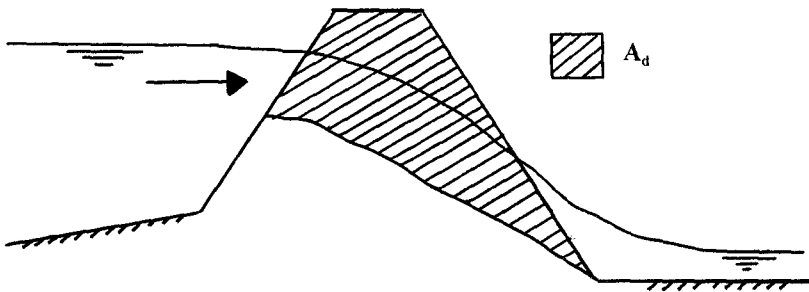


figure 6: definition of the eroded cross-section A_d

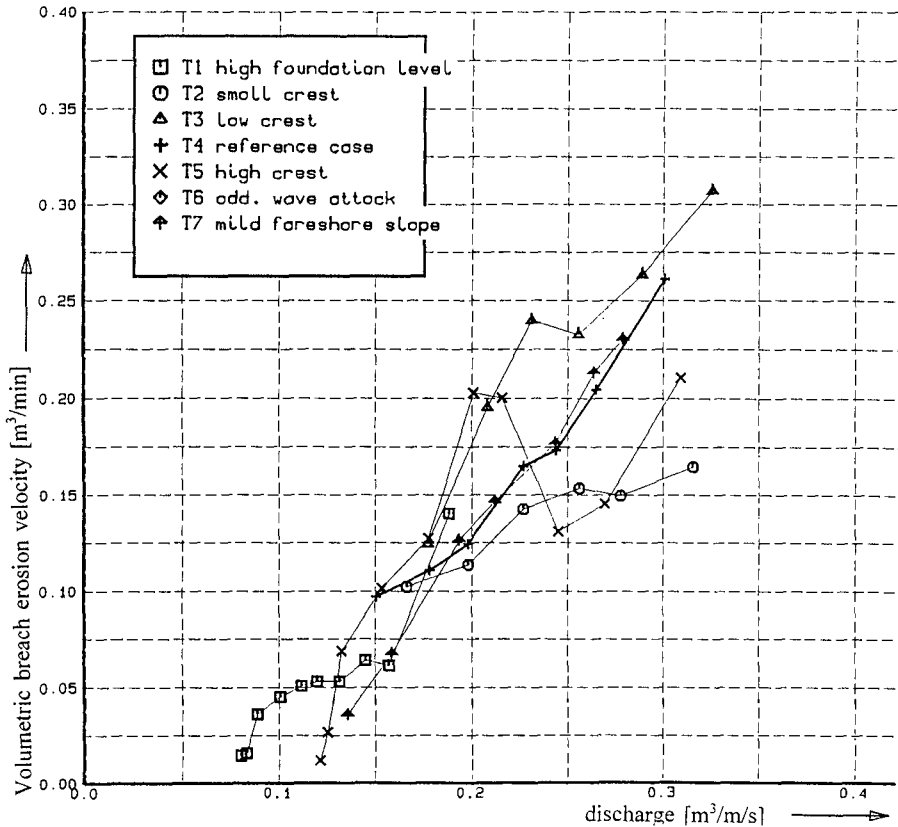


figure 7: volumetric breach erosion velocity as a function of the water discharge in the breach

3. NUMERICAL MODEL FOR BREACH GROWTH

The breach erosion process is characterized by a complex three dimensional behaviour in which low as well as very high velocities and thus erosion rates occur. The Froude number varies typically in the range of 0.03 to 3 and the Shields parameter varies from 0.03 - 50 [Visser et al., 1995]. In order to describe this complex process in a numerical model, five different phases in the breach erosion process have been distinguished [Visser, 1994]:

- Phase 1: steepening of the inner slope;
- Phase 2: narrowing of the dike crest;
- Phase 3: erosion of the dike crest;
- Phase 4: breach widening under super-critical flow and development of a scour hole;
- Phase 5: breach widening under sub-critical flow until velocities are under a critical value.

In every phase a characteristic set of discharge and transport formulae is used to calculate the development of the breach during each time step. In the first three phases the rate of erosion is described by a Visser-Bagnold equation in which the erosion rate is proportional to the kinetic energy of the flow. The modelling of the first three phases has been described in [Visser, 1994]. For the modelling of the phases 4 and 5, the results of the wave basin experiments have been used. With the parameters and relations mentioned in chapter 3 the following empirical relation for the breach width growth velocity has been derived.

$$\beta = C_b \cdot (d_b \cdot q_b) / A_d \quad [\text{m/s}] \quad (3)$$

where: q_b is the water discharge rate per unit breach width [$\text{m}^3/\text{m/s}$]; q_b is described by a weir formula.
 A_d is the eroded cross-section of the dam as defined in figure 6
 d_b is the water depth in the breach
 C_b is a coefficient, related to the sediment concentration near the edges of the breach

$$C_b = \bar{c} \cdot b_r / d_b \quad [-] \quad (4)$$

where: \bar{c} = depth averaged sediment concentration near the edges of the breach

b_r = width of the zone near the edges for which \bar{c} is defined

At present there is a test-version of the numerical model available. This model covers all the above mentioned phases of the breach growth process. The main input parameters of the model are:

- * cross-section of the sand-dike (array of (x,z) values):
 - erodable cross-section
 - cross-section with initial breach
 - ir-erodable cross-section (sill)
 - breach and material characteristics:
 - initial breach width
 - mean grain size diameter D_{50}
 - sediment fall velocity w

- porosity n
- bottom roughness r
- * outside boundary:
 - waterlevel as function of time (array of (z,t) values)
 - optional: in case of e.g. a lake: areas/volume of the outer basin
 - optional: in case of river: external input discharge
- * inside boundary (in the polder):
 - initial waterlevel
 - area of the polder that will be inundated

During 1996 and the first half of 1997 this model will be completed. The results of the large-scale field experiments (1989 and 1994) and findings of the 1953 and earlier flood disasters will be used to calibrate and verify the model.

REFERENCES

- Kraak, A.W., Bakker, W.T., Van de Graaff, J., Steetzel, H.J. and Visser, P.J., (1994). Breachgrowth and its place in damage assessment for a polder. *Proc. 24th ICCE*, Kobe, Japan.
- Steetzel, H.J. and P.J. Visser (1992), Profile development of dunes to overflow, *proc. 23rd ICCE*, Venice, Italy.
- Visser, P.J., (1994). A model for breach growth in sand-dikes. *Proc. 24th ICCE*, Kobe, Japan.
- Visser, P.J., Kraak, A.W., Bakker, W.T., Smit M.J., Snip W.D., Van de Graaff, J., Steetzel, H.J. (1995). A large-scale experiment on breaching in sand-dikes. *Proc. Coastal Dynamics'95*, Gdansk/Gdynia, Poland.

CHAPTER 213

THE IMPACT OF AN EXTREME EVENT ON THE SEDIMENT BUDGET: HURRICANE ANDREW IN THE LOUISIANA BARRIER ISLANDS

Jeffrey H. List¹, Mark E. Hansen², Asbury H. Sallenger, Jr.², and Bruce E. Jaffe³

Abstract

This paper examines the influence of Hurricane Andrew on the sediment budget of an 80-kilometer section of the Louisiana barrier islands west of the modern Mississippi delta. Because long-term bathymetric change has been extensively studied in this area, excellent baseline data are available for evaluating the impact of Hurricane Andrew. Results show that despite the high intensity of the storm and a storm track optimally positioned to impact the study area, the storm did not have an overwhelming influence on the sediment budget when compared to the changes occurring over the previous 50 years. For the Louisiana barrier islands, a 50-year record appears to be adequate for averaging the long-term contributions of both major and minor storm events to the sediment budget.

Introduction

The coastal sediment budget, i.e., the identification of sediment sources, sinks, and transport pathways, is essential information for predicting rates of shoreline erosion and for planning beach nourishment projects (e.g., Kana, 1995). Unfortunately, most investigators have had to assume that the sediment budget, derived from past measurements, is an adequate representation of future trends as well. This assumption is weakened by the commonly unknown influence of changing and difficult to predict processes, such as the impact of infrequent but high-energy storm events. Few studies have been able to assess their potentially important impact. In one exception, Morton et al. (1995) monitored changes in beach volume associated with a major hurricane along the Texas coast, concluding that large storms can

¹ Oceanographer, U.S. Geological Survey, 384 Woods Hole Rd., Woods Hole, MA 02543, USA.

² Oceanographer, U.S. Geological Survey, 600 4th St. S., St. Petersburg, FL 33701, USA.

³ Oceanographer, USGS, 345 Middlefield Rd. MS-999, Menlo Park, CA 94025, USA

significantly alter the long-term sediment budget and hence, shoreline evolution. They demonstrate that short term sediment budget data (< 10 yr) are inadequate for modeling and predicting future changes because of the variable influence of great storms. It remains unclear whether longer term data, which would potentially include the effects of many major storm events, would be more representative of future conditions.

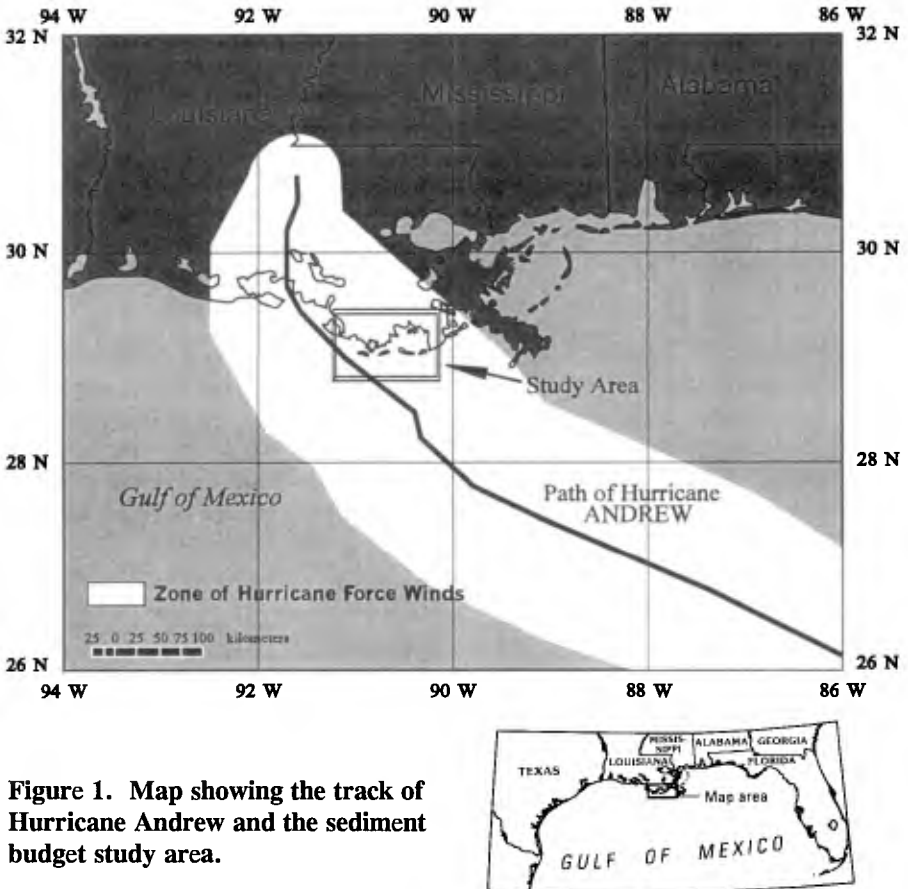


Figure 1. Map showing the track of Hurricane Andrew and the sediment budget study area.

A unique opportunity to address this issue was presented to us in 1992 when Hurricane Andrew impacted the Louisiana coast with wind speeds of more than 50 m/s (Grymes and Stone, 1995), offshore significant wave heights of more than 10 m (DiMarco et al., 1995; Stone et al., 1995), and a maximum storm surge of more than 2.5 m (Halford, 1995). This Class 3 storm on the Saffir-Simpson scale passed just west of a series of barrier islands (Figure 1) which had been the focus of an intensive study on the physical and geological processes responsible for the rapid erosion and disintegration of these islands (the Louisiana Barrier Island Erosion Study, Sallenger et al., 1987, 1991). In response to Hurricane Andrew, several components of the

original study were repeated, including measurements of shoreline position, nearshore profiles (Dingler, 1995), and near-island bathymetry. In this paper we compare the bathymetric changes in a six-year period including Hurricane Andrew with the bathymetric changes observed for the 50 years prior to the storm, and evaluate the impact of Hurricane Andrew on the sediment budget.

Data Sources and Processing Techniques

Bathymetric surveys from three time periods were used as the basic source of sediment budget information considered here. Two surveys, from the 1930's and 1980's, were processed or collected as part of the U.S. Geological Survey's Louisiana Barrier Island Erosion Study (1986-1991). The third bathymetric survey was conducted in 1993/1994 following Hurricane Andrew.

The data sources, processing techniques, and error assessment for the 1930's and 1980's surveys are described in detail by List et al. (1991, 1994), and will only be briefly summarized here. The 1930's survey consists of soundings obtained in digital form from the National Geophysical Data Center in Boulder, CO. Data were digitized by the National Ocean Service of the National Oceanic and Atmospheric Administration (NOAA) from U.S. Coast and Geodetic Survey (USCGS) hydrographic smooth sheets for the years 1933, 1934, 1935, and 1936. The 1980's bathymetry was constructed from soundings obtained in digital form from hydrographic surveys conducted in 1986, 1988, and 1989 by companies under contract to the USGS. In addition to bathymetric data, shoreline data were obtained for each of these time periods to provide a mean high water (MHW) line to constrain the bathymetry surrounding the study area's many small islands. Shorelines for the 1930's were digitized from USCGS topographic smooth sheets, while for the 1980's, shorelines were photo-interpreted and digitized from National Aeronautics and Space Administration (NASA) high-altitude photography. A detailed description and analysis of shoreline data for the Louisiana barrier islands are found in McBride et al. (1992).

The post-Andrew bathymetric data were collected by the U.S. Geological Survey in 1993 and 1994, using an Innerspace 448 echosounding fathometer and a Global Positioning System (GPS) for navigation. Although we originally intended to correct soundings for tide effects using post-processed differential GPS vertical measurements, processing difficulties resulted in unreliable depth values. Thus the data were corrected using the same methods as were used in the 1980's survey, i.e., by applying corrections based on local tide observations. Shoreline data assumed to represent the MHW line were also incorporated into the 1993/1994 data set; post-Andrew shorelines were digitized by the Louisiana State University in 1993 (Penland, pers. comm.). The 1993/1994 bathymetric survey was processed exactly as were the 1930's and 1980's surveys, as described by List et al. (1994). Figure 2 shows the 1993/1994 bathymetric coverage area; for comparative purposes, analysis of the 1930's and 1980's data is restricted to the same area.

1993/1994 Bathymetry (Post-Andrew)

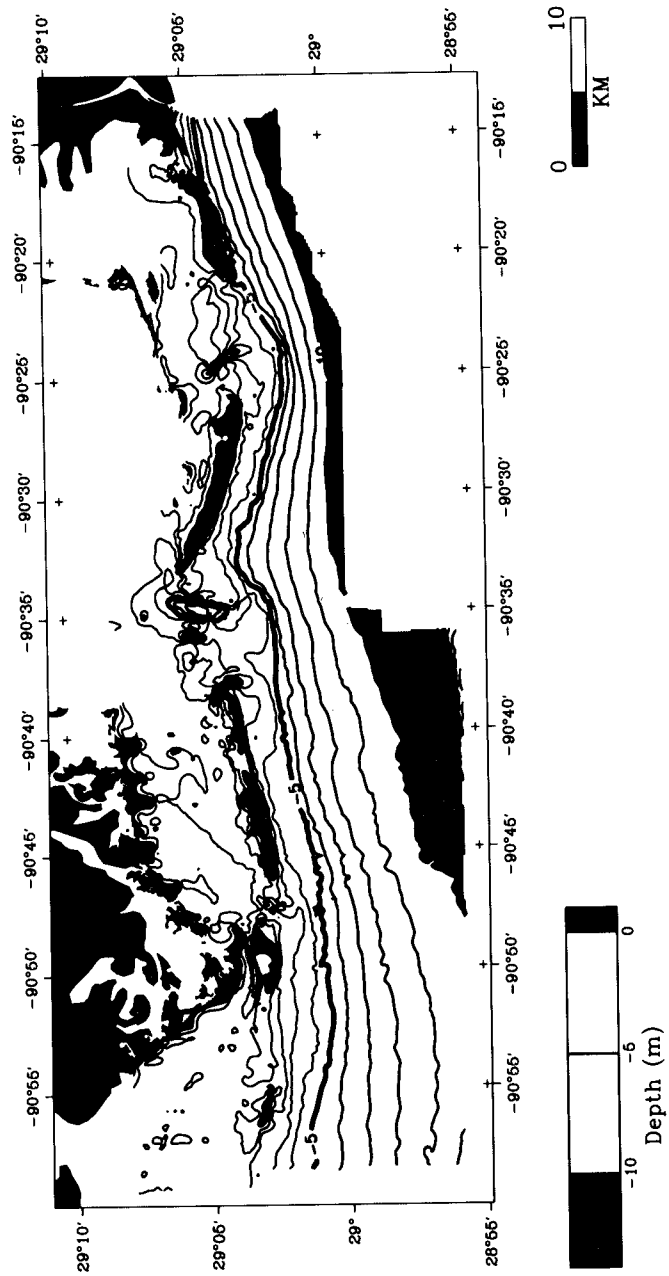


Figure 2. Post-Hurricane Andrew bathymetry collected in 1993 and 1994, showing the coverage area for this study. Depths are relative to Mean Low Water. For comparison purposes, data from the 1930's and 1980's data sets are analyzed within this same region.

After constructing surface models of each survey period's bathymetry using a minimum-tension gridding technique (Briggs, 1974; Dynamic Graphics, Inc.), we calculated bathymetric change grids for the 1930's to 1980's and 1980's to 1993/1994 periods. These change grids, with a spacing of 135 m (see List et al., 1994), form the basis for this study's comparison between long-term changes and changes occurring during a six-year period which included a major storm. Because of the approximate 1 cm/yr relative sea-level rise in the study region (Penland and Ramsey, 1990), a sea-level correction was necessary to prevent a strong bias toward erosion and to permit calculations of erosional and accretionary volumes. As continuous tide records were not available for the entire study period, we employed an alternate means of correcting for relative sea level using an area of sea floor which was judged to have minimal accretion or erosion (Jaffe et al., 1991). The error associated with this datum correction constitutes a large part of the overall data uncertainty.

The total error associated with sea-floor change calculations is a complex combination of many potential sources of error, including sounding measurement error, tidal correction problems, vertical and horizontal datum inconsistencies, computer gridding errors, and non-synoptic sources of data for each survey period. Although some errors can be quantitatively evaluated, others, such as the tidal datum correction problem mentioned above, could only be evaluated qualitatively. Therefore, a combination of quantitative and qualitative approaches were employed to assess the error in bathymetric comparisons (List et al., 1994). As a conservative estimate, a ± 0.5 m range of sea-floor change was designated as a zone of no significant change.

Results

Regional

Figures 3 and 4 show the patterns of erosion and accretion associated with the 1930's to 1980's and 1980's to 1993/1994 change periods respectively. Overall, the strikingly coherent and large-scale patterns of erosion and deposition observed in the 1930's to 1980's change period are lacking in the 1980's to 1993/1994 change period. (For a description and analysis of the changes occurring in the 1930's to 1980's change period, see List et al., 1991, 1994, 1997a, 1997b; Sallenger et al., 1992; Jaffe et al. 1989, 1997).

Figure 5 quantifies the total volumes of erosion and accretion within the area enclosed by the data limit polygon in Figure 4, excluding areas of no significant change. In Figure 5A, both erosional and depositional volumes are significantly smaller for the change period encompassing Hurricane Andrew, indicating that the storm did not have an overwhelming influence on the sediment budget of the study area.

However, as the 1980's to 1993/1994 change period represents only about six years compared to the 50 years in the 1930's to 1980's change period, a better comparison between these two periods may be the rates of volume change, as shown

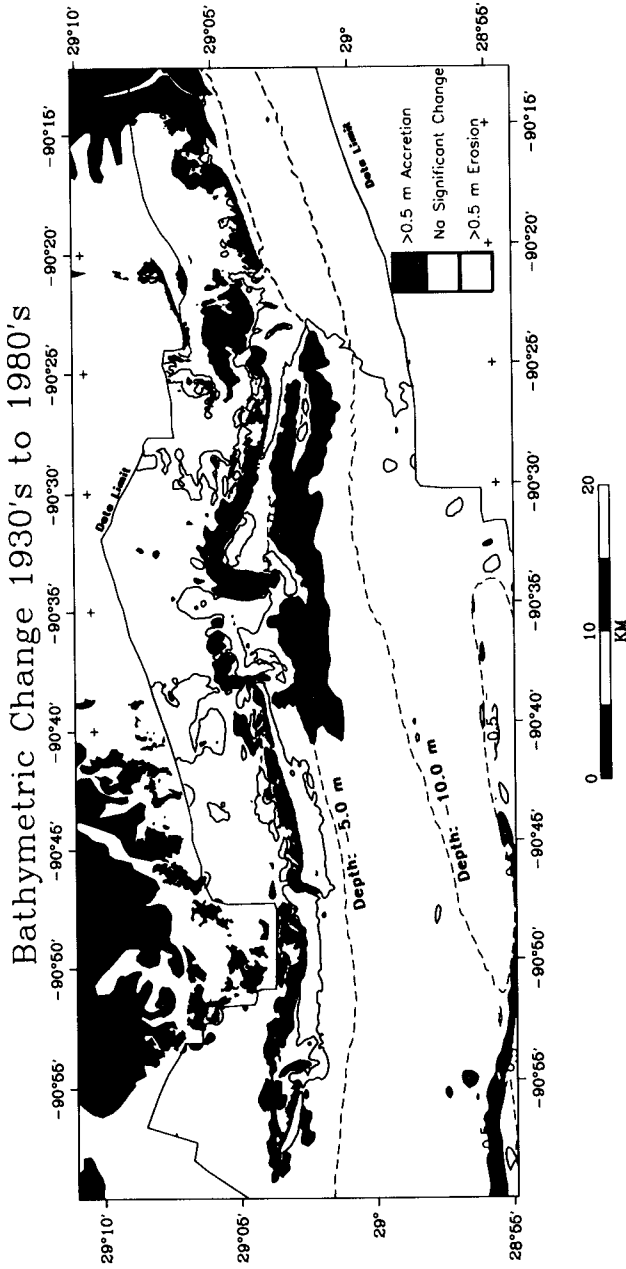


Figure 3. 1930's to 1980's bathymetric change within the complete study region. The -5.0 and -10.0 depth contours are from the 1980's bathymetry. The region encompassed by the line marked "data limit" is the area of overlap between the 1930's and 1980's bathymetries.

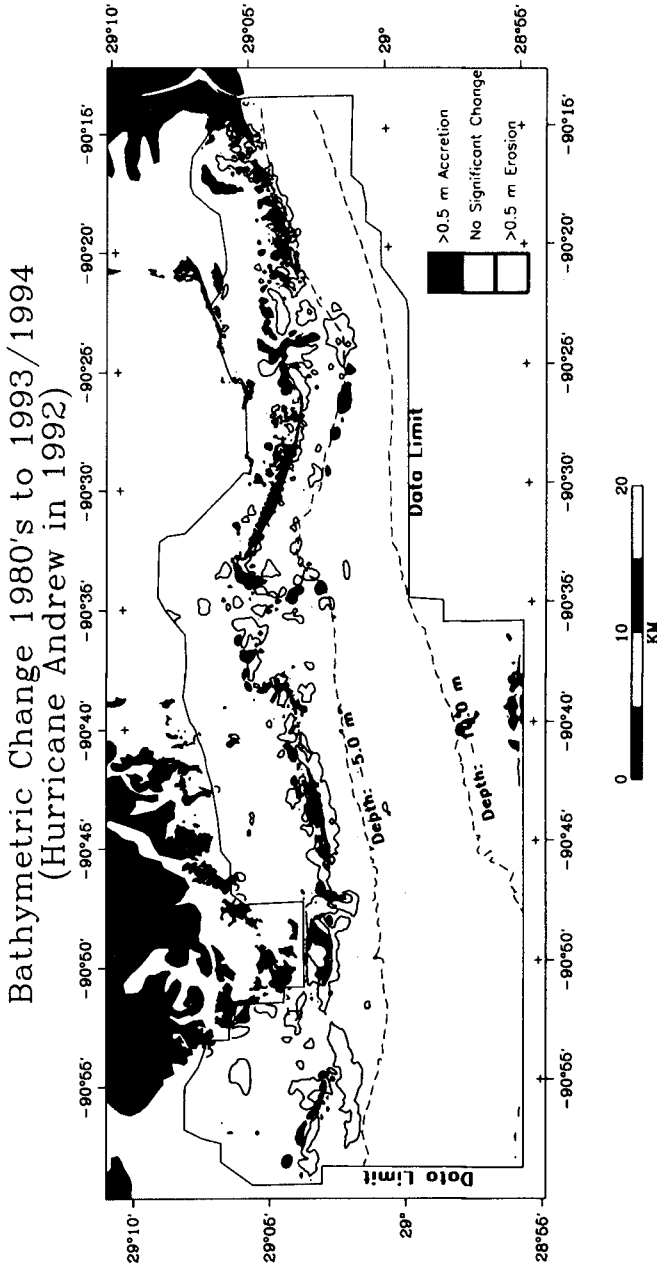


Figure 4. 1980's to 1993/1994 bathymetric change within the complete study region. The -5.0 and -10.0 m depth contours are from the 1993/1994 bathymetry. The region encompassed by the line marked "data limit" is the area of overlap between the 1980's and 1993/1994 bathymetries.

in Figure 5B. This figure shows that two change periods' erosional and deposition rates do not differ significantly, within the error bars resulting from the assumption of a ± 0.5 m zone of no-significant change (after List et al., 1994).

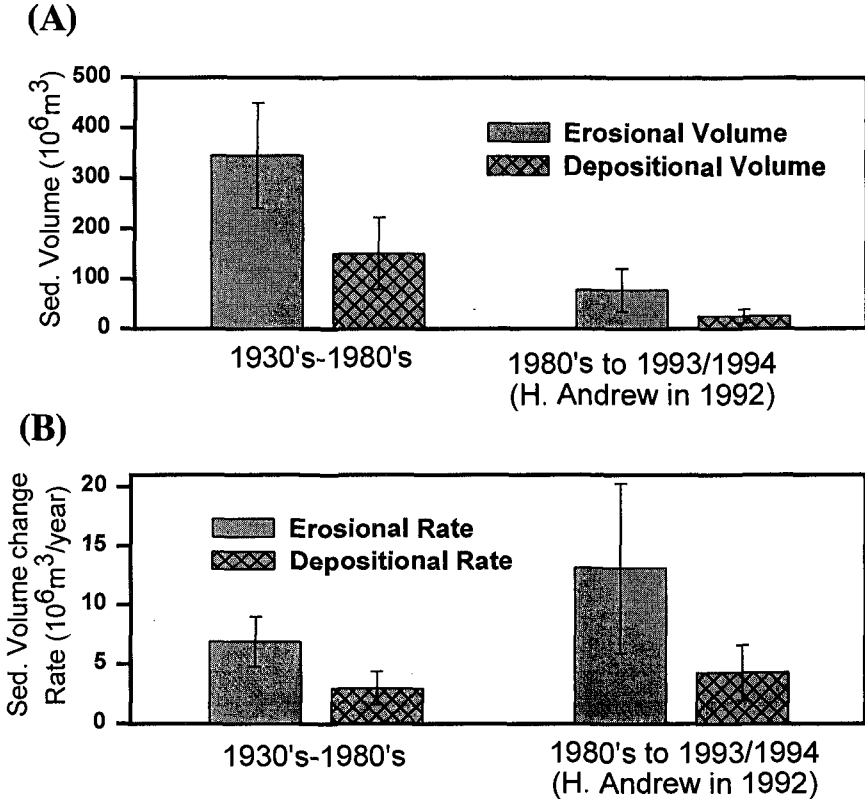


Figure 5. Volumes of sediment change within the area enclosed by the data limit region shown in Figure 4, excluding areas of no significant change. Error bars are based on the assumed ± 0.5 m range of no significant change following List (1994). For comparison purposes, the same data limit region is applied for calculating volumes within the 1930's to 1980's change period. (A) Total erosional and depositional volumes for the 1930's to 1980's and 1980's to 1993/1994 change periods. (B) Corresponding yearly rates of erosion and deposition, using intervals of 50 and 6 years for the 1930's-1980's and 1980's-1993/1994 change periods respectively.

Eastern Portion of the Study Area

Figures 6 and 7 focus on changes in the eastern portion of the study area. Again, the 1980's to 1993/1994 change period exhibits few of the large and coherent patterns of erosion and deposition observed in the 1930's to 1980's change period. Still, it is noteworthy that there are *any* coherent patterns of erosion and deposition in the 1980's to 1993/1994 period, given the short six year period of change and the ± 0.5 m range designated as no-significant change. While the extensive area of offshore erosion present in the 1930's to 1980's comparison is lacking in the 1980's to 1993/1994 period, many of the smaller patterns, especially in depositional areas, appear to duplicate the later change period, albeit at reduced magnitudes.

Four of these depositional areas in the 1930's to 1980's change period are labeled A through D in Figure 6, with 1980's to 1993/1994 deposits interpreted to be of the same origin similarly labeled in Figure 7. Area A represents a shoreface deposit that appears to extend from erosional areas to the east. In the 1930's to 1980's change period, this depositional area extends from the extensive area of shoreface erosion it adjoins to the east to the next chain of barrier islands to the west, suggesting a mode of sediment bypassing of a wide inlet complex (Figure 3 here, see also Jaffe et al., 1991, 1997). In the 1980's to 1993/1994 change period, deposit A is much less coherent, but still occupies approximately the same location along the 5 m depth contour. Erosion of an ebb-tidal delta to the east suggests a source for the deposit in this change period (compare the bathymetry in Figure 2 with the bathymetric change in Figure 4). Area B represents a bay-side deposit that seems to be associated with landward migration of small barrier islands within a large inlet complex (similarly, they may be, in part, migrating flood-tidal delta deposits). In the 1980's to 1993/1994 period, depositional area B comprises several small areas that are clearly associated with the landward migration (and submergence) of small barrier islands (the depositional area between the two parts of B is associated with inlet migration). Area C represents another bay-side region of accretion, similar in both change periods. This deposit takes the form of a flood-tidal delta, but arguably could also be related to strong landward-directed flows associated with storm surges. Finally, area D in both change periods is a result of inlet infilling at the terminus of a westward migrating barrier island.

Similar to Figure 5, Figure 8 gives the total volume and yearly rates of deposition within areas A-D for the 1930's to 1980's and 1980's to 1993/1994 change periods. Again, while the total volumes associated with the 1980's to 1993/1994 period are much less than in the 1930's to 1980's period (Figure 8A), the *rates* of accretion are not significantly different (Figure 8B).

Discussion

Because the average rates of change in the period bracketing Hurricane Andrew were not significantly different from the average rates of change in the previous 50 years, we cannot conclude with certainty that *any* of the bathymetric changes are

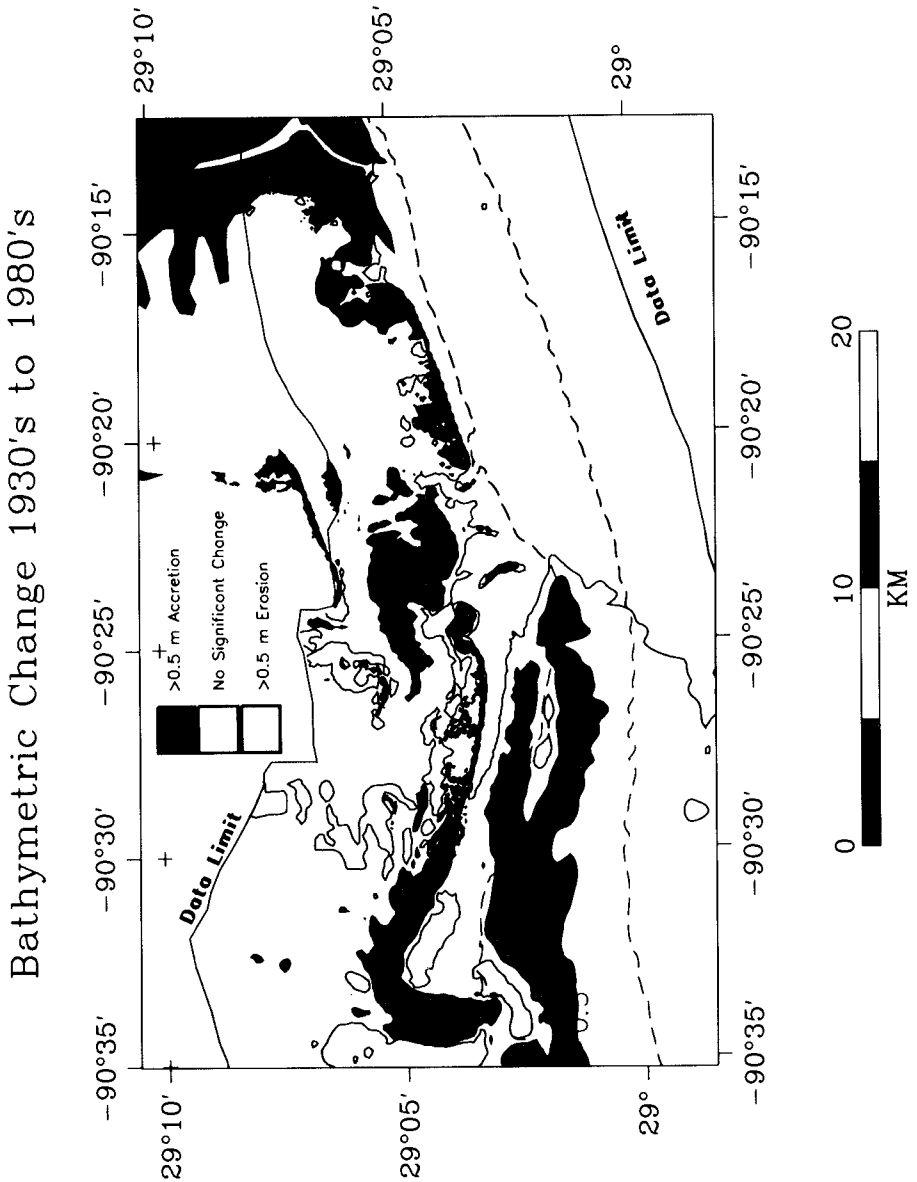


Figure 6. 1930's to 1980's bathymetric change within the eastern portion of the study region. The depth contours (unlabeled) and data limit boundary are the same as in Figure 3. Letters A through D represent areas of accretion for which volumes are shown in Figure 8. In the volume calculations shown in Figure 8, area A is limited to the area east of longitude $-90^{\circ}34'$, and Area D is limited to the area west of the adjoining barrier island.

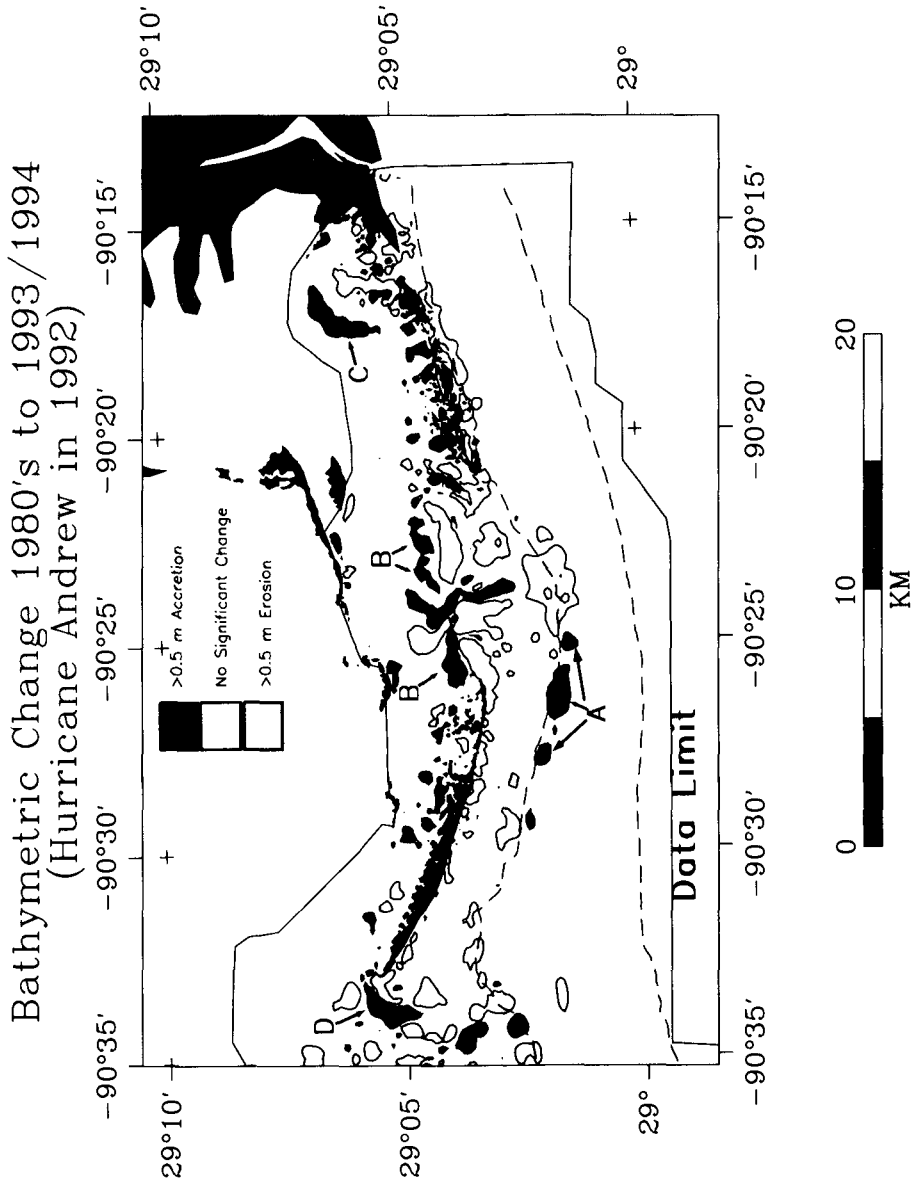


Figure 7. 1980's to 1993/1994 bathymetric change within the eastern portion of the study region. The depth contours (unlabeled) and data limit boundary are the same as in Figure 4. Letters A through D represent areas of accretion for which volumes are shown in Figure 8.

attributable to Hurricane Andrew, rather than typical storm conditions that occur much more frequently. However, as Hurricane Andrew was without doubt the largest storm in the 1980's to 1993/1994 change period, it is reasonable to assume that many of the changes are, in fact, due to this storm. With this assumption, we surmise that Hurricane Andrew had a moderate, through not overwhelming, contribution to the area's sediment budget.

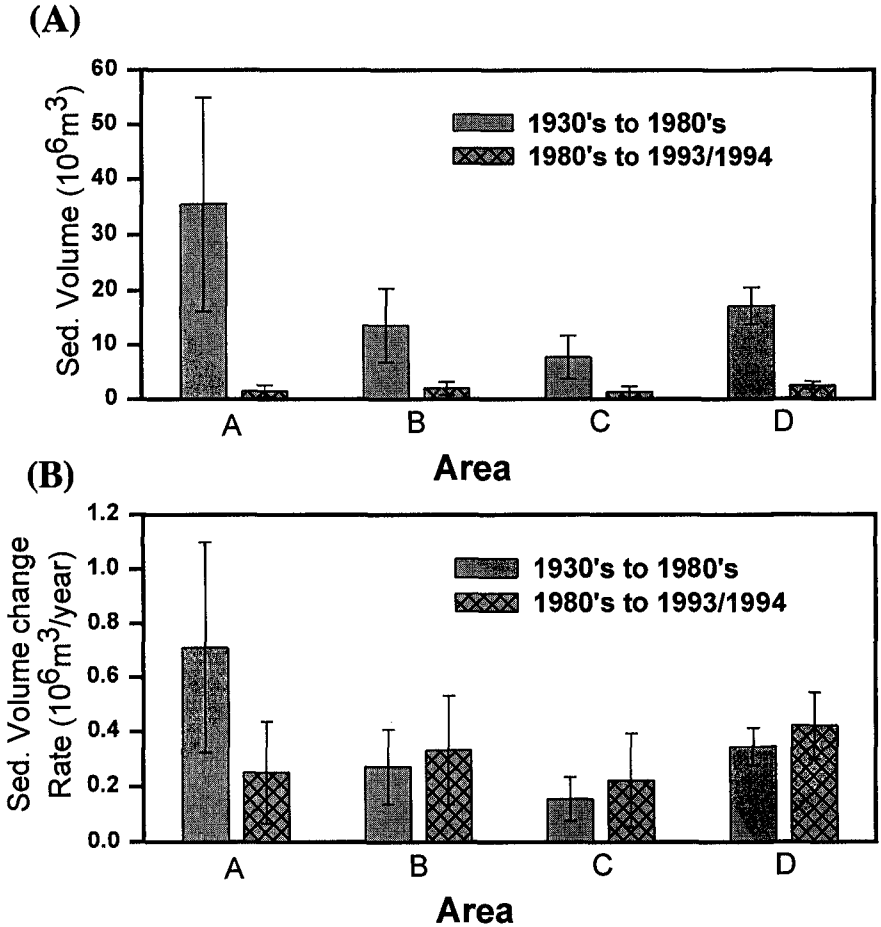


Figure 8. (A) Depositional volumes and (B) rates of deposition within the labeled deposits shown in Figures 6 and 7. Rates are found by dividing the depositional volumes for each region by the 50 and 6 year intervals for the 1930's to 1980's and 1980's to 1993/1994 change periods respectively. Error bars are found as in Figure 5.

Because the rates and patterns of change were similar in both change periods examined here, it seems likely that the processes were similar as well. An examination of the historical database of hurricane tracks (Jarvinen et al., 1984) shows that while Hurricane Andrew might have been the *most* intense storm experienced by the study area in the last 50 years (in terms of both magnitude and track), there were many other hurricanes that could have had a comparable impact. In terms of average rates of change, the 6-year period encompassing Hurricane Andrew (and many minor storms) appears to be representative of the long-term average of processes occurring in the previous 50 years.

Conclusions

Despite Hurricane Andrew's high intensity and a track that was near optimal for impacting the study area, the storm did not have an overwhelming influence on the sediment budget of an 80-km section of the Louisiana barrier islands when compared to the changes occurring over the previous 50 years. However, with the assumption that most of the bathymetric changes observed in the pre/post-Andrew survey were due to the storm, we conclude that the storm had a moderate impact on the sediment budget; however, other storms in the 50-year period prior to Andrew likely had a similar impact. For this study area, 50 years appears to be adequate for averaging the cumulative contributions of both major and minor storm events.

Acknowledgments

This work was conducted as part of the Hurricane Andrew in Louisiana Project and the Louisiana Barrier Island Study, cooperative studies between the U.S. Geological Survey, Coastal and Marine Program, and the Louisiana State University. We thank Shea Penland, Randy McBride and others at the Louisiana State University for providing shoreline-position data. The bathymetric data were collected and processed through the efforts of numerous people, including Greg Gabel, Thang Phi, Graig McKendrie, Rob Wertz, Todd Holland, Carolyn Degnan, Clint Steel, Tracy Logue, Dorothy Hopkins, Keith Dalziel, Lance Thornton, and Jennifer Bexley. Karen Morgan is thanked for contributions to the figures. Any use of trade names in this publication is for descriptive purposes only and does not imply endorsement by the USGS.

References

- Briggs, I. C., 1974. Machine contouring using minimum curvature. *Geophysics*, 39: 39-48.
- DiMarco, S. F., Kelly, F. J., Zhang, J., and Guinasso, N. L.Jr., 1995. Directional wave spectra on the Louisiana-Texas shelf during Hurricane Andrew. *Jour. Coastal Res.*, Special Issue No. 21, 217-233.
- Dingler, J. R. and Reiss, T. E., 1995. Beach erosion on Trinity Island, Louisiana caused by Hurricane Andrew. *Jour. Coastal Res.*, Special Issue No. 21, 254-264.

- Grymes, J. M. III and Stone, G. W., 1995. A review of key meteorological and hydrological aspects of Hurricane Andrew. *Jour. Coastal Res.*, Special Issue No. 21, 6-23.
- Halford, K. J., 1995. Estimating the dynamic water-level surfaces associated with Hurricane Andrew crossing the Louisiana coast. *Jour. Coastal Res.*, Special Issue No. 21, 265-279.
- Jaffe, B. E., List, J. H., and Sallenger, A. H., Jr., 1997. Massive sediment bypassing on the lower shoreface offshore of a wide tidal inlet; Cat Island Pass, Louisiana. *Marine Geology*,
- Jaffe, B.E., List, J.H., Sallenger, A.H., Jr., and Holland, T., 1991. Louisiana Barrier Island Erosion Study: correction for the effect of relative sea level change on historical bathymetric survey comparisons, Isles Dernieres, Louisiana. U.S. Geological Survey Open File Report 91-276, 33 pp.
- Jaffe, B. E., Sallenger, A. H., Jr., and List, J. H., 1989. Massive sediment bypassing of a wide tidal inlet: Cat Island Pass, Louisiana. *Transactions, Gulf Coast Assoc. Geol. Soc.*, 39: 403-411.
- Jarvinen, B.R., Neuman, C.J., and Davis, M.A.S., 1984. A tropical cyclone data tape for the North Atlantic basin, 1886-1983: contents, limitations, and uses. NOAA Technical Memorandum NWS NHC 22,
- Kana, T. W., 1995. A mesoscale sediment budget for Long Island, New York. *Marine Geology*, 126: 87-110.
- List, J. H., Jaffe, B. E., and Sallenger, A. H., Jr., 1991. Large-scale coastal evolution of Louisiana's barrier islands. *Proceed. Coastal Sediments '91*, Amer. Soc. Civil Eng., New York, pp. 1532-1546.
- List, J. H., Jaffe, B. E., Sallenger, A. H. Jr., and Hansen, M. E., 1997a. Bathymetric Comparisons in the Louisiana barrier islands: processes of large-scale change. *Jour. Coastal Res.*, in press.
- List, J.H., Jaffe, B.E., Sallenger, A.H., Jr., Williams, S.J., McBride, R.A., and Penland, S., 1994. Louisiana Barrier Island Erosion Study: atlas of sea-floor changes from 1878 to 1989. U.S. Geological Survey Misc. Invest. Series I-2150-B, 82 pp.
- List, J. H., Sallenger, A. H., Jr., Hansen, M. E., and Jaffe, B. E., 1997b. Accelerated relative sea-level rise and rapid coastal erosion: testing a causal relationship for the Louisiana barrier islands. *Marine Geology*,
- McBride, R. A., Penland, S., Hiland, M. W., Williams, S. J., Westphal, K. A., Jaffe, B. E., and Sallenger, A. H., Jr., 1992. Analysis of barrier shoreline changes in Louisiana from 1853 to 1989. In: S. J. Williams, S. Penland, and A. H. Sallenger, Jr. (Editors), Louisiana Barrier Island Erosion Study--Atlas of Barrier Shoreline Changes in Louisiana from 1853 to 1989. U.S. Geological Survey Misc. Invest. Series I-2150-A, pp. 36-97.
- Morton, R. A., Gibeaut, and J.C., Paine J. G., 1995. Meso-scale transfer of sand during and after storms: implications for prediction of shoreline movement. *Marine Geology*, 126: 161-179.
- Penland, S. and Ramsey, K. E., 1990. Relative sea-level rise in Louisiana and the Gulf of Mexico: 1908-1988. *Jour. Coastal Res.*, 6: 323-342.
- Sallenger, A. H., Jr., List, J. H., Jaffe, B. E., Penland, S., and Williams, S. J., 1992. Regional coastal erosion research and beach preservation. *Proceed. 5th Annual Nat. Conf. on Beach Preserv. Tech.*, Florida Shore and Beach Preserv. Assoc., pp. 115-134.
- Sallenger, A. H., Jr., Penland, S., Williams, S. J., Jaffe, B. E., and Suter, J., 1991. Louisiana Barrier Island Erosion Study: further results. *Proceed. Coastal Zone '89*, Am. Soc. Civ. Eng., New York, pp. 1503-1516.
- Sallenger, A. H., Jr., Penland, S., Williams, S. J., and Sutter, J. R., 1987. Louisiana Barrier Island Erosion Study. *Proceed. Coastal Sediments '87*, Am. Soc. Civ. Eng., New York, pp. 1503-1516.
- Stone, G. W., Xu, J. P., and Zhang, X., 1995. Estimation of the wave field during Hurricane Andrew and morphological change along the Louisiana coast. *Jour. Coastal Res.*, Special Issue No. 21, 234-253.

CHAPTER 214

BEACH MAINTENANCE STRATEGIES, A COMPARISON FOR A RECREATIONAL BEACH

M. Pluijm¹, G. Kant¹, R. Nolten², A.P. de Looff³

ABSTRACT

This paper describes the morphological and economical evaluation of the beach nourishment maintenance strategy of an eroding recreational beach at the Dutch coast. In addition to the results of this evaluation two alternative strategies were analysed. In order to assess the economical feasibility of the alternatives appeared to be essential to estimate the morphological effectiveness of the alternative strategies. Therefore, an extensive numerical modelling scheme was set up. The numerical modelling played a key role in the understanding of the existing morphological system and subsequently in the assessment of the effectiveness of the alternatives on a long term basis. The morphological effectiveness of the alternatives, being offshore breakwaters and a 450 m long groin, was calculated in terms of reduction of required beach nourishments. The objective of the study was not only to find an optimal coastal morphology strategy but also to find the best strategy which combines a sound beach protection with effects valuable for the specific recreational function of the beach, including an effective way to deal with eventual lee-side erosion. Possibilities were studied to shift the erosion to the dune area in the north which would allow a more flexible and dynamic way of maintenance.

¹ Frederic R. Harris B.V., Badhuisweg 11, P.O. Box 87875, 2508 DG The Hague, The Netherlands.

² Ministry of Transport, Water Management and Public Works (Rijkswaterstaat), Directorate Zuid-Holland, P.O. Box 556, 3000 AN Rotterdam, The Netherlands.

³ Ministry of Transport, Water Management and Public Works (Rijkswaterstaat), Road and Hydraulic Engineering Division, P.O. Box 5044 Delft, The Netherlands.

SITE DESCRIPTION

Scheveningen Beach (Figure 1) is located on the west coast of The Netherlands. Scheveningen Port is located just south of the beach with its breakwaters reaching 550 and 725 m into the sea. During the entire year but especially in summertime, the sandy beach attracts thousands of locals and holiday making tourists.

The beach consists of sand with a characteristic grainsize (D50) of about 200 µm. The slope of the beach is approximately 1:40. The -10 m MSL contour lies about 1300 m offshore. Scheveningen is also protected by a seawall with a length of 2.5 km. The beach level at the toe of the seawall is about +3 m MSL. North of Scheveningen the land is protected by a massive dune area.

Scheveningen Beach is eroding continuously. In the beginning of the century a system of 150 m long groins (spacing 500 m) was built but the erosion was not stopped. Up to now five beach nourishments were carried out starting in 1969 (see Table 1).

The Dutch west coast is known as a morphological dynamic system. The wave and current climate result in massive longshore sediment transports in northern as well as in southern direction. The average yearly sand transport is directed to the north and is estimated, for this part of the coastline, at 500,000 m³/year.

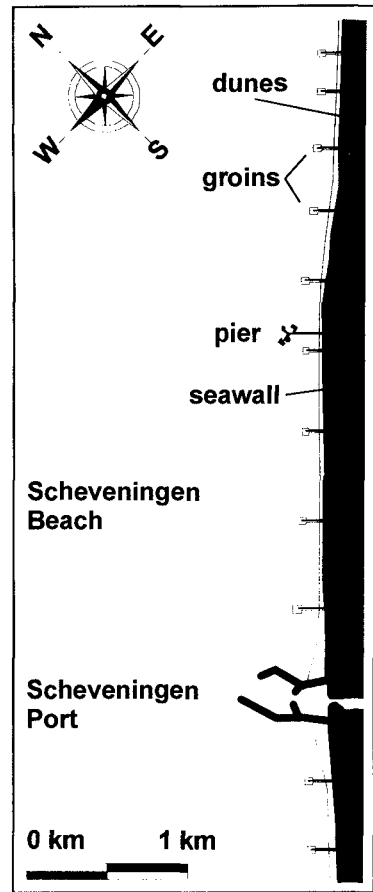


Figure 1 *Scheveningen Beach*

year	1969	1975	1985	1991	1996
volume [m ³]	45,000	700,000	330,000	1,000,000	850,000

Table 1 *Beach Nourishment Volumes at Scheveningen Beach*

HYDRAULIC BOUNDARY CONDITIONS

The average wave climate on the southern North Sea is presented as a wave rose diagram in Figure 2. The most persistent conditions develop from south-western directions whereas the highest extreme conditions are to be expected from north-western directions.

The average amplitude of the diurnal tide for this part of the Dutch Coast is 1.7 m. The tidal variation induces a significant tidal flow along the coast. Typical flood currents are in the order of 0.6 m/s, typical ebb currents are 0.4 m/s. Peak flood currents may reach up to 0.9 m/s and ebb currents to 0.75 m/s. However, during extreme south west storms (directed parallel along the shore) the wind-driven current can give a significant contribution to the flow especially in shallow areas (surf zone). Consequently, the longshore sediment transport along this part of the Dutch coast is dominated by the interaction between the waves (disturbance, wave-driven current) and the tidal current. The wind-driven current effect pays a minor but nevertheless a not to be neglected contribution.

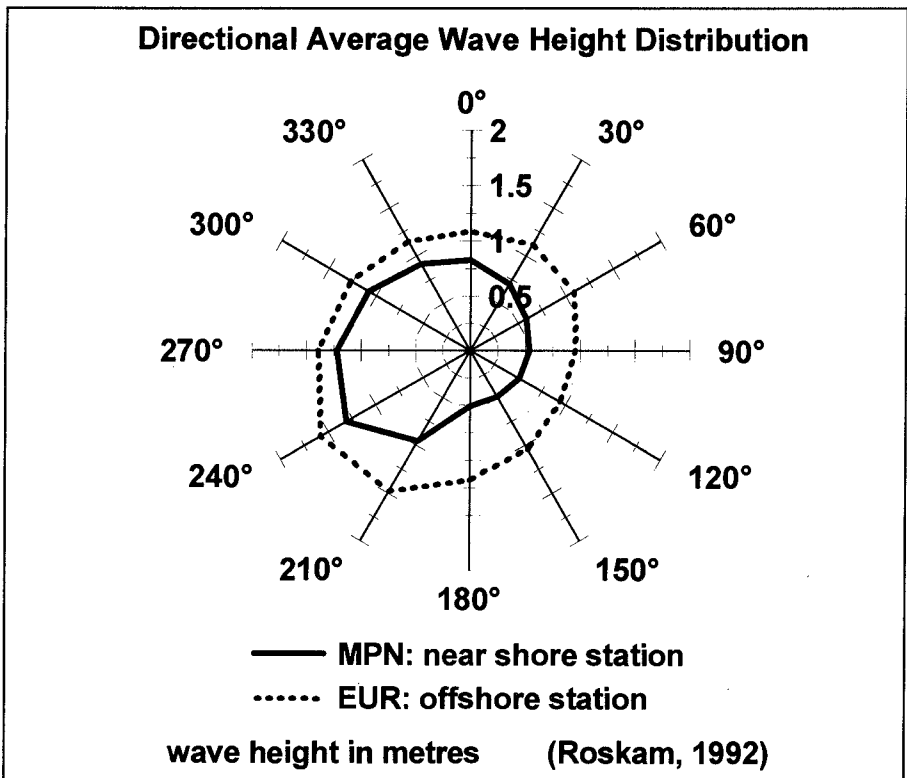


Figure 2 *Directional Average Wave Height Distribution*

EVALUATION PRESENT BEACH NOURISHMENT STRATEGY

The evaluation of the present beach nourishment strategy concentrated on the behaviour of the executed nourishments and the sand transports along the coast. Regular measurements of the Ministry of Transport, Water Management and Public Works were analysed giving insight in the behaviour of the beach nourishments. Based on the measurements and sediment transport calculations it was concluded that (i) especially the first nourishments were used as restoration of the steepened cross sectional profile, that (ii) the aims of the nourishments were initially met but (iii) that the lifetime of the nourishments was almost completely determined by extreme wave conditions, which resulted in a rather random nourishment behaviour. The characteristics of the morphological system do not allow a complete natural restoration of the beach after an erosion causing storm. The unpredictability of the wave conditions results in a capricious development of the beach. This has already led to an unexpected narrow beach in the summer having negative effects on the tourist industry.

NUMERICAL MODELLING ANALYSIS

Based on the conclusions of the beach development evaluation one- and two-dimensional wave, flow, and sediment transport models were applied (DHI, 1995 and DH, 1992). The well calibrated models of the wave- and flow climate were combined in sediment transport simulations using the Bijker sand transport formulae. The model results were used to understand the importance of the various sediment transport mechanisms and to finally formulate a well based hypothesis of the morphological system. After the formulation of the hypothesis simulations were made of alternative coastal protection structures. These were, among others, offshore breakwaters and a 450 m long groin perpendicular to the coastline. The effects of the structures were brought in relation with the hypothesis of the existing system in order to quantify the predicted impacts on the coastal development.

existing situation

The key questions after the evaluation of the nourishment strategy were (i) what are the physical reasons for the erosion and (ii) where is the sediment going to. It was clear that the position of the beach, the breakwaters of the port, the seawall and the geometry of the beach were essential elements in the morphological system. With the use of the mentioned numerical simulations the following conclusions (schematically presented in Figure 3) could be drawn:

- (1) The net north going longshore sediment transport is not blocked by the breakwaters of the port but is passing these obstacles. It was shown that under

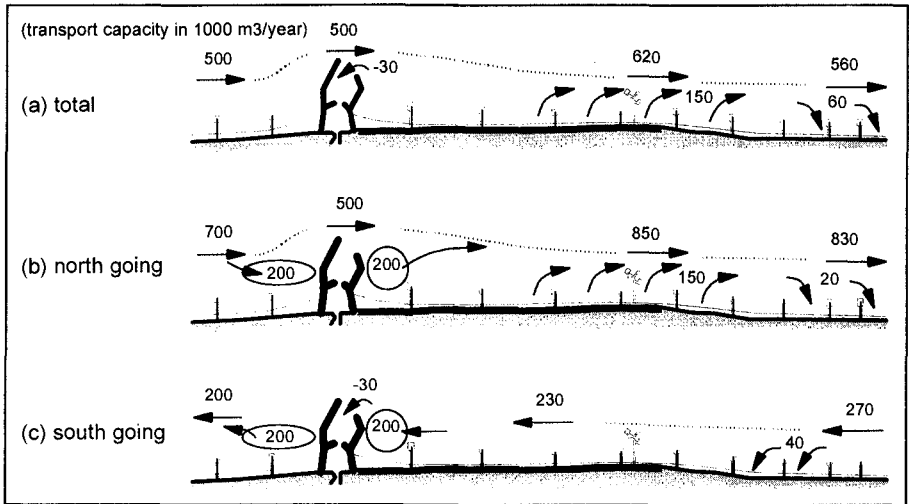


Figure 3 *Sediment Transport Capacities, Existing Situation*

south-western wave conditions the contracted current (tide-, wave- and wind-driven current) in combination with the orbital wave motion result in a substantial sediment transport in front of the breakwaters. This transport is developing in front of the breakwater tips in a water depth of -8 m MSL. Evidence that this process exists is the absence of a sedimentation zone south of the breakwaters. The passing of the net northern transport around the breakwaters is very important for the development of Scheveningen Beach. This transport is the main feeding mechanism of the beach.

- (2) It was found the sediment transport north of the port is about 10% higher than south of the port. The reason for this was found in the bathymetry of both areas. The beaches north of the port appear to be more gentle sloping. This results in a wider surf zone north of the port which in this case (transport driven by the combination of waves and tidal current) generates a higher sediment transport. This effect can be observed while standing on the breakwaters.
- (3) Because of the forced orientation of Scheveningen Beach by the seawall a strong local longshore transport gradient develops at the northern side of the beach.
- (4) The natural beach restoration after a north-western storm is distorted due to the presence of the breakwaters. The timescale of storm events is in the order of hours whereas the timescale of the restoration is weeks to months. In this part of the Netherlands the time averaged flow along the shore is directed to the

north. Sediment deposited on the foreshore during a storm event will therefore contribute to the beach restoration of a beach section somewhat to the north. The presence of the breakwaters of the port distorts this mechanism which results in an incomplete natural restoration of the beach or, in other words, erosion of the beach.

These four main conclusions are the basis of the hypothesis of the morphological system of Scheveningen Beach. The hypothesis is schematically presented in Figure 3. In the figure the annual yearly north going and south going transports are shown as well as the total average yearly transport.

offshore breakwaters

One of the alternative measures which was defined was offshore breakwaters. The impacts were studied on the basis of the developed hypothesis of the existing morphological system. The simulations were repeated for the schematized offshore breakwaters. The main result of the computational effort was that offshore breakwaters do not fit in the morphological system of Scheveningen Beach. Indeed the structure reduces the wave action and thus the sediment transport on the beach. But the structure also redirects the sediment which is transported past the port's breakwaters along the seaward side of the structure. This transport was found to be the most important feeding mechanism of the beach. It is therefore expected that the construction of offshore breakwaters as defined for this study will result in an even stronger erosion on the beach. The predicted sediment transport patterns after the construction of the offshore breakwaters are presented in Figure 4.

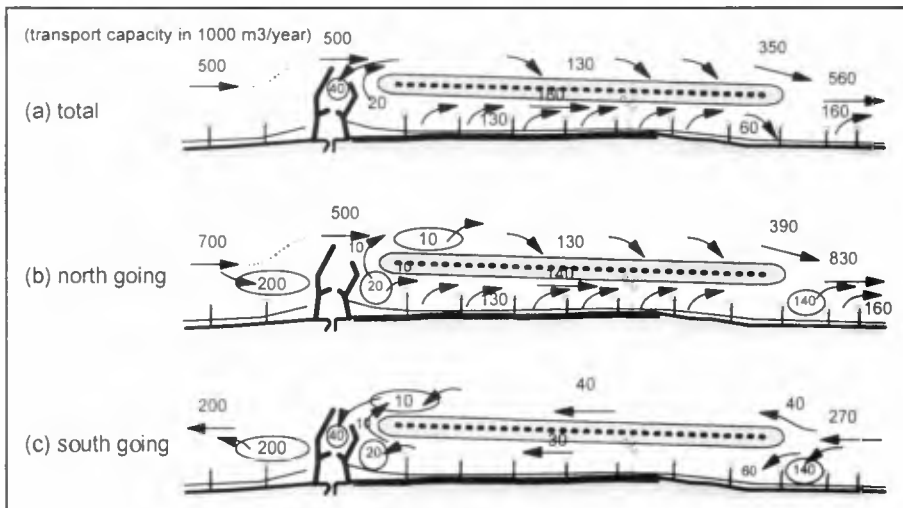


Figure 4 *Sediment Transport Capacities, Offshore Breakwaters*

450 m long groin

Another alternative was the construction of a 450 m long groin at the northern side of Scheveningen Beach. This would prevent the build up of the transport gradient due to the shoreline orientation. The simulations show (Figure 5) that indeed positive results for the beach development are to be expected. The redistribution of sediment due to the local gradient will be prevented and part of the erosion of Scheveningen Beach will be shifted towards the north. This was one of the objectives of the study. A relatively wide dune area is located north of the Beach. Here, the opportunity exists to handle the erosion in a more flexible dynamic way. The construction of a long groin would result in a less frequent nourishment need. This predicted effectiveness of the structure was used to compute the cash flow over a long term period. In this way an economical comparison could be made to the present nourishment strategy including maintenance and re-nourishment needs.

COST COMPARISON

The long term costs of investment of the various beach maintenance schemes were evaluated by means of a Nett Present Value (NPV) computation (Pluijm et al., 1994). In this calculation all the costs of an alternative are capitalized over a period of 50 years. Construction costs, interest, inflation, maintenance but also the nourishment need (the results of the morphological studies) are taken into account in this analysis. The results of the NPV cost comparison are presented in Figure 6. It can be seen that with the present rates for sand it is economically more attractive to proceed with the present nourishment strategy. However, when the prices of sand would increase the construction of a long groin would then become an attractive alternative.

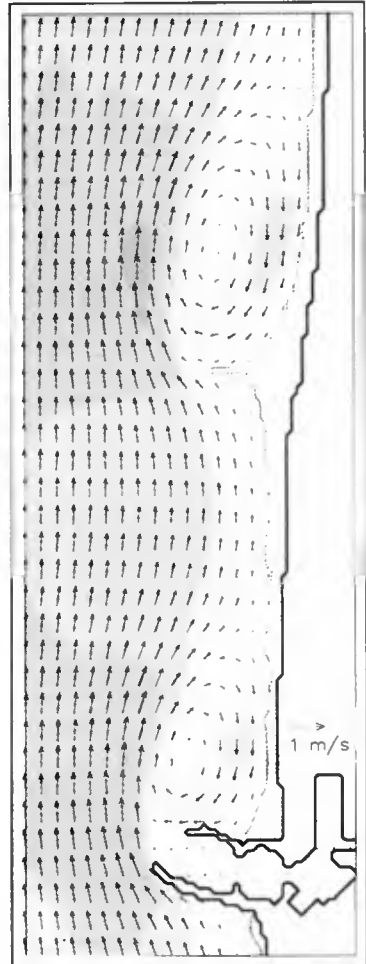


Figure 5 Flow model result
450 m long groin

For this cost comparison the extra benefits for the local tourism industry have not been taken into account. The construction of a groin would result into two advantages over the beach nourishment strategy being (i) a more predictable development of the beach

(coastline stability) and (ii) a wider beach. In view of the recreational function of the beach this is an important factor.

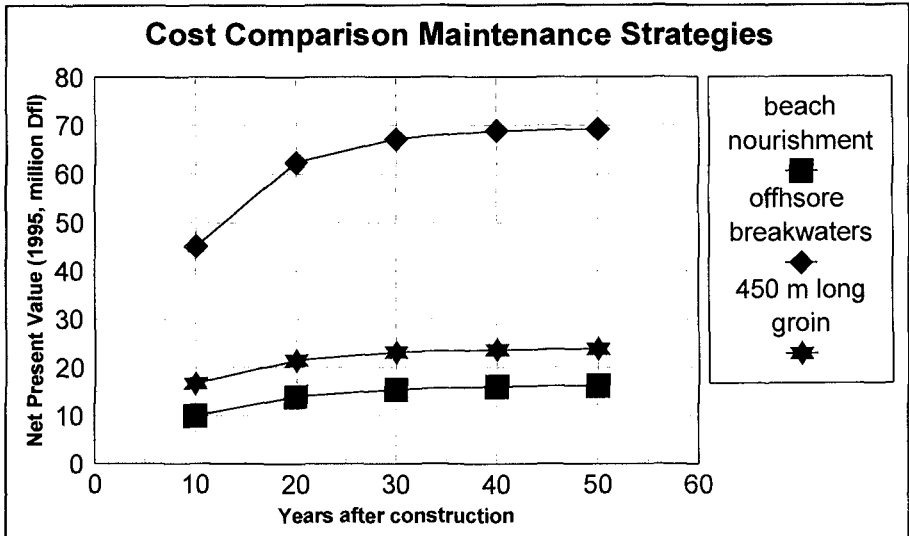


Figure 6 Cost Comparison Beach Maintenance Strategies Scheveningen Beach

CONCLUSIONS

Numerical models are of significant importance to develop insight and understanding of the role of each of the morphological processes. The models help to understand the development of a particular beach section, to define the governing processes and to indicate the beach developing sediment transport patterns. Based on this understanding of the morphological system a well-based assessment can be made of impacts of a structure on each of the processes. In many cases this comprehension will allow a reliable prediction of coastline development.

In this paper the methodology has been presented which was adopted to compare alternative beach maintenance strategies. A key element in this evaluation is the nourishment need which will be required when one of the strategies is implemented and which is an important factor in the long term costs. It has been described how numerical simulations models were adopted to assess the morphological effectiveness of the alternatives. These results were then used as input for the cost evaluation resulting in a well based comparison of various beach maintenance strategies.

ACKNOWLEDGEMENT

This study was executed with the full support of the Ministry of Transport, Water Management and Public Works, Directorate Zuid-Holland which is gratefully acknowledged..

REFERENCES

Danish Hydraulic Institute (1995); *Mike 21: A modelling suite for two dimensional simulation of flows, wave propagation and sediment transports*; Danish Hydraulic Institute; Denmark.

Delft Hydraulics (1992); *Unibest-LT, a software package for simulation of longshore sediment transport capacities*; Delft Hydraulics; The Netherlands.

Pluijm, M. (1994); *Offshore Breakwaters Versus Beach Nourishments, A Comparison*; Proceedings of the 24th International Conference on Coastal Engineering, 1994; pp3208-3222; Kobe; Japan.

Roskam, A.P. (1992); *Wave Measurements and Statistical Analyses, MeAO-92-26 and Correspondence (in Dutch)*; Ministry of Transport, Water Management and Public Works (Rijkswaterstaat); Tidal Water Division; The Netherlands.

CHAPTER 215

Littoral Impact of Ocean City Inlet, Maryland, USA

Julie Dean Rosati¹, M. ASCE, and Bruce A. Ebersole², M. ASCE

ABSTRACT

Ocean City Inlet, Maryland presents a data-rich site for evaluating the total littoral impact of an inlet system with a significant adjacent beach response. Analysis of adjacent beach and bay shoreline data, adjacent beach profiles, ebb and flood shoal evolution, and dredge/fill history provided a database with which the inlet's littoral impact to adjacent beaches was quantified. The even/odd method, which decomposes shoreline changes into their symmetric (even) and antisymmetric (odd) components about a point of significance, was applied to the volume change dataset. This analysis indicated a present-day (1996) alongshore impact distance of 8 to 13 km from the centerline of the inlet. A second method, which relates the total "inlet sink" volume to adjacent island (ocean and bay) volume change, was also applied. The total inlet sink volume ranged from 10.8 to 15.6 million m³, and reflects the volume of material captured by the inlet which is assumed to have been derived from adjacent beaches. The inlet sink method indicated that, at most, 10.8 million m³ can be realized within ± 14.2 km (data limit). The paper concludes that the alongshore impact of Ocean City Inlet most likely extends beyond ± 14.2 km.

1.0 EVOLUTION OF OCEAN CITY INLET

Ocean City Inlet is located on the Atlantic coast of the United States (Figure 1), and was created by a hurricane on 25 August 1933 which breached the outer barrier island. In 1922, groins were constructed on Fenwick Island (to the north) to stabilize this increasingly-popular beach resort. Assateague Island (to the south) remained in a natural state, and, in February 1920, Sinepuxent Inlet breached the island approximately 4.8 km south of the existing inlet, and had migrated southward about 0.8 km until it was closed by another storm in May 1928. After the hurricane of August 1933, jetty construction commenced in September and the inlet quickly scoured to 3 m depth and 76 m width (Underwood and Hiland 1995).

A study by Dean and Perlin (1977) and Dean, Perlin, and Dally (1978) documented sediment transport moving north along northern Assateague Island, which deposited in the inlet channel. As a result of the study, in 1985 the south jetty was raised and

¹Research Hydraulic Engineer, ²Supervisory Hydraulic Engineer, US Army Engineer Waterways Experiment Station, Coastal and Hydraulics Laboratory, CEWES-CR-P, 3909 Halls Ferry Road, Vicksburg, MS 39180-6199

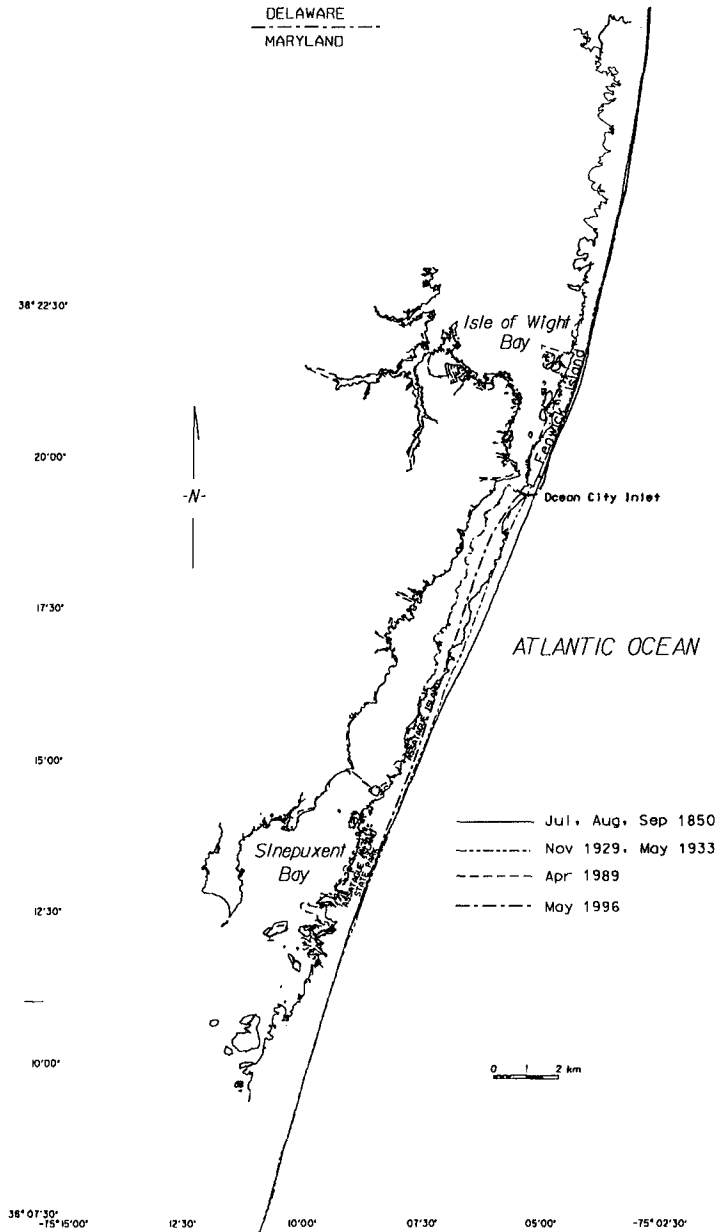


Figure 1. Historical shorelines, Ocean City Inlet, Maryland, USA

tightened, and the northern Assateague Island channel bank was stabilized with three detached breakwaters. The most recent significant engineering event affecting the littoral system has been the placement of approximately 7.4 million m³ of beach fill on Fenwick Island from June 1988 through April 1995, which extended from the just north of the inlet to the Maryland-Delaware state line.

2.0 DATA ANALYSIS

Shoreline position, adjacent beach profile, ebb shoal bathymetry, and flood shoal data sets as well as dredging events were analyzed and used to create a volume change database. A range of parameters which were applied in sensitivity evaluations were also defined, and are discussed below.

2.1 Variation of Shoreline Position with Time

Both ocean and bay shoreline position were recorded with respect to an alongshore coordinate, x , which was set to zero at the centerline of the inlet and used a right-handed coordinate convention (i.e., negative x indicates north; positive x indicates south). The shoreline position represents the high water line, and was calculated for each time period at a 50-m alongshore cell spacing. Results of the shoreline change analysis are presented in Table 1.

Time Period	Alongshore Extent: Ocean (km)	Alongshore Extent: Bay (km)	Fenwick Island		Assateague Island	
			Ocean	Bay	Ocean	Bay
1850-1929/33	-15.1 to 14.2 ¹	-13.7 to 3.3	-0.37 ± 0.98	~0 ²	-1.5 ± 1.7	2.8 ± 1.8
1929/33-1995/96	-15.1 to 14.2	Varies; range -13.5 to 16.6	0.44 ± 0.80 ³ -0.21 ± 0.91 ⁴	0.75 ⁵	-2.9 ± 2.2 ³ -2.9 ± 2.7 ⁴	2.5 ⁶

¹ Full extent was -19.4 to 23.5 km; the analysis was limited here to equal the alongshore extent for the post-inlet period.

² Calculated value was a small negative number. Because it is not likely that pre-inlet bay processes would erode the bay shoreline, a near-zero bayshore change rate was assumed for the pre-inlet time period.

³ Shoreline change rate reflects advancement due to beach fill.

⁴ Adjusted shoreline change rate to remove advancement due to beach fill.

⁵ Calculated by prorating 1929-1965 and 1965-1980 bay shoreline change rates. Standard deviation values are unavailable.

⁶ Calculated by prorating 1933-1965, 1965-1980, 1980-1989, and 1989-1995 bay shoreline change rates. Standard deviation values are unavailable.

Ocean shoreline change rates for Assateague Island extending 14.2 km south of the inlet nearly doubled from a pre-inlet (1850-1929/33) erosion rate averaging -1.5 ± 1.7 m/yr to an average post-inlet (1929/33-1996) erosion rate averaging -2.9 ± 2.7 m/yr (latter rate excludes shoreline advancement due to documented beach fill of 0.9 million m³). For both the pre- and post-inlet time periods, overwash processes were significant along Assateague Island, with bay shoreline change indicating accretion. For the Fenwick shoreline extending approximately 15.1 km north of the inlet, the ocean shoreline

responded to construction of the jetties by decreasing the pre-inlet erosion trend (-0.37 ± 0.98 m/yr for the pre-inlet time period to -0.21 ± 0.91 m/yr in the post-inlet time period (latter rate excludes shoreline advancement due to documented beach fill of 8.1 million m^3). For the pre-inlet time period, the bay portion of Fenwick Island was comparably stable. The post-inlet time period reflects some bay shoreline accretion, which occurred prior to 1980 (a majority of the Fenwick bay shoreline in the vicinity of the inlet has been developed since 1980).

2.2 Profile Data

Beach profile data were analyzed to provide a relationship to convert shoreline change rates into volumetric change rates. Shoreline change within a given alongshore cell is estimated to represent a horizontal translation of the profile over its active depth. The absolute sum of the berm elevation and the depth at which profile changes are insignificant, the closure depth, is one method of estimating the active profile depth. A second method relates the profile volume change to shoreline movement for a given time period. Sensitivity testing of values from both methods indicated that the difference was not significant (less than 2-percent difference in total volumes). Thus, the first method was applied herein. For Fenwick and Assateague Islands, ocean beach profile data were analyzed to estimate active depth. Fenwick Island pre- and post-fill profile data were also analyzed to estimate the percentage of Fenwick Island beach fill remaining in 1996, which was required to correctly account for alongshore movement of this material from Fenwick Island into other regions of the project.

In evaluating the initial performance of the Fenwick Island beach fill, Stauble et al (1993) estimated the depth of closure for Fenwick Island using profile data measured from the spring of 1988 through the winter of 1992, and concluded that 6.1 m relative to National Geodetic Vertical Datum (NGVD) was a representative value. Because coastal processes at this depth are most likely similar offshore of Fenwick and Assateague Islands, this depth was also assumed to be representative of Assateague Island. However, this active depth was not used for southern regions of Fenwick Island and northern region of Assateague Island which were sheltered by the ebb tidal shoal. For these regions, the depth at the shoreward edge of the ebb shoal was used in active depth calculations. Volume change within the ebb shoal was accounted for separately.

Stauble et al (1993) estimated the active berm elevation for Fenwick Island as 3.0 m NGVD, resulting in an estimate of active depth for regions of Fenwick Island outside the shelter of the ebb shoal equal to 9.1 m. For Assateague Island, the sensitivity of applying pre- versus post- rehabilitation jetty berm crest elevations was insignificant; therefore, post-rehabilitation jetty berm crest elevations were applied herein. The estimate of active depth for the regions of Assateague Island unaffected by the ebb tidal shoal (from 2 to 14 km south of the inlet) ranged from 8.3 to 8.5 m.

Seven profiles from June 1988 (immediately pre-fill) and May 1996 (present-day condition) were analyzed to determine the rate of beach fill "loss" from the profile.

Volume change for each profile was multiplied by an alongshore distance represented by that profile to properly “weight” results at each profile location. Results from this analysis indicated that approximately 17 percent of the placed material was lost over the active depth. An additional 10 percent of material was originally placed in a dune feature (above 3.0 m NGVD), and this entire volume was assumed to remain on the profile. Because the fill material was similar to or coarser than the native sediments, it was assumed that any fill loss moved alongshore rather than offshore. The portion of the 1988-1995 Fenwick Island beach fill that was assumed to move alongshore, totaling approximately 1.7 million m³, was assumed to deposit and remain within the inlet sink. Shoreline change calculations assumed a beach fill “loss” rate of approximately 2-percent per year.

Profile data for the bay shoreline were only available for the northwest corner of Assateague Island (Dean, Perlin, and Dally 1978), and represented conditions prior to sand-tightening and raising of the south jetty and construction of the detached breakwaters. These data extended into the channel, and reflect stronger current conditions than the rest of the bayshore. Based on estimates of bay active depth of approximately 4 m for this small, higher energy, region of the bayshore, the sensitivity of results to a range of slightly smaller bay shoreline active depths, thought to be more representative of conditions along the majority of the bay (1 m, 2 m, and 3 m) was evaluated. The sensitivity of volume calculations to the choice of bay active depth was found to be significant for certain cases (see Section 3.4).

2.3 Ebb Shoal Evolution

Bathymetric data from 1933, 1976, and 1995 were utilized to define the ebb shoal planform “footprint,” depth at the landward edge of the footprint (used in estimating active depth), and volume. Visual inspection of a bathymetric data set or a bathymetric contour plot to delineate an ebb shoal is rather subjective. For this study, the availability of a pre-inlet (1933) bathymetry enabled application of a more objective procedure, as modified from that discussed by Hicks and Hume (1996). First, an idealized “non-inlet” bathymetry was created by using the 1933 bathymetric data set, but replacing the 1933 shoreline and nearshore beach profile data along the northern region of Assateague Island with present-day shoreline and bathymetry which were typical of that found outside the influence of the ebb tidal shoal. Using this idealized non-inlet bathymetry, “residual” topographies were created by subtracting it from the subsequent time periods. Next, the ebb tidal shoal footprint for each residual topography was estimated by four different individuals, and residual ebb shoal volumes were calculated. Four independent estimates of the ebb shoal footprint gave an indication of the error associated with personal subjectivity.

Estimates 1, 2, and 4 applied similar methods of using the 1-m residual contour to delineate the ebb shoal footprint. This contour appeared to provide a planform shape of the ebb tidal shoal that reflected onshore and alongshore evolutionary trends of the shoal as evidenced from bathymetric data. Estimate 3 used the 0-m residual contour to

delineate the shoal, and therefore these volume and area estimates are higher. Estimate 3 chose the 0-m residual contour to fully capture bathymetric regions which may have accreted. These regions resulted in a footprint which included more of the areas reflecting growth and lengthening of finger shoals, and deposition in troughs, which are probably only partly represented by Estimates 1, 2, and 4. All residual volumes were calculated by using the selected footprint and determining the volume above a 0-m residual contour within this polygon. Bathymetric data from 1995 did not fully cover the ebb tidal shoal. Therefore, 1933-1976 residual ebb shoal data were used to complete coverage on the outer edges of the ebb tidal shoal for the 1933-1995 residual bathymetry. Results are presented in Table 2.

Estimate Number	Volume (million m³)	Area (million m²)	Volume Change Rate (m³/yr)
1, 2, 4	9.8, 9.9, 9.9	3.0, 3.0, 3.0	158,000, 159,000, 158,000
3	12.9	4.2	207,000

For estimates of total ebb shoal volume from 1933 to 1996, two ebb shoal volumes were used: a minimum value was obtained by extrapolating the average of Estimates 1, 2, and 4 to 1996 (approximately 10 million m³); and a maximum value was obtained by extrapolating Estimate 3 to 1996 (approximately 13 million m³). For each estimate, depths at the landward edge of the ebb tidal shoal footprint were applied in calculating active depth for regions of Fenwick and Assateague Islands sheltered by each ebb shoal. In sensitivity testing, the differences between active depths for the 10 and 13 million m³ ebb tidal shoal footprints were found to have an insignificant impact on final calculations. Therefore, results are presented herein for active depths as indicated by the 10 million m³ ebb shoal footprint.

2.4 Flood Shoal Evolution

Information about deposition in the bay is necessary to account for losses to the littoral system. Unfortunately, detailed bathymetric data provide only partial coverage for Isle of Wight and Sinepuxent Bays. For this study, the flood shoal/bay accretion rate calculated by Dean and Perlin (1977) and Dean, Perlin, and Dally (1978) using 1931 to 1972 bathymetry was used, 19,600 m³/yr. It is likely that the 1972 through 1996 flood shoal accretion rate has decreased somewhat, perhaps half this value, for a present-day estimate of total flood shoal/bay volume equal to 1 million m³. This estimate is based on the belief that flood shoal accretion would probably be greatest during the initial years after inlet formation, and would decrease with time. The sensitivity of calculations presented herein was evaluated with two other flood shoal/bay accretion estimates. A maximum estimate assumed that the original rate continued through the present, for a total flood shoal/bay volume of 1.2 million m³. A minimum volume of 0.76 million m³ was estimated by assuming that no additional bay/flood shoal accretion has occurred since 1972.

2.5 Dredging History

Various sources were culled to determine the dredging and placement history for Ocean City Inlet. A total of 24 dredging events between 1947 and 1995 indicated a channel shoaling rate of approximately 56,000 m³/yr, with many dredge placements on northern Assateague Island. For this study, a minimum channel shoaling volume between 1933 and 1996 was calculated by assuming that only the documented dredging events occurred (2.7 million m³). A maximum channel shoaling volume assumed that the 56,000 m³/yr rate continued from 1933 through 1996 (3.5 million m³). Adjacent beach placement of the dredged material was accounted for in the shoreline change database.

3.0 LITTORAL IMPACT OF OCEAN CITY INLET

3.1 Volume

The "inlet sink volume" captured by Ocean City Inlet is defined as the volume of material within the inlet which is assumed to have been derived from adjacent ocean and bay beaches. A range of volumes representing the Ocean City Inlet sink was calculated by summing the minimum and maximum estimates for ebb shoal volume, flood shoal volume, and channel shoaling volume, subtracting maximum and minimum estimates for the original 1933 Ocean City Inlet breach, and subtracting the volume of Fenwick Island beach fill which was assumed to move alongshore and deposit in the inlet. The initial loss of material due to the island breach in 1933 was estimated using typical ocean and bay profile shapes (best estimate: 0.53 million m³, with a range between 0.43 and 0.97 million m³).

The minimum inlet sink volume was estimated as 10.8 million m³ (ebb shoal: 10 million m³ + flood shoal: 0.76 million m³ + shoaling volume: 2.7 million m³ - initial breach: 0.97 million m³ - alongshore movement of Fenwick Island beach fill: 1.7 million m³). The maximum inlet sink volume totaled 15.6 million m³ (ebb shoal: 13 million m³ + flood shoal: 1.2 million m³ + shoaling volume: 3.5 million m³ - initial breach: 0.43 million m³ - alongshore movement of Fenwick Island beach fill: 1.7 million m³). Thus, **the total volume of material captured by Ocean City Inlet which can be attributed to adjacent beaches is estimated to be between 10.8 and 15.6 million m³.**

3.2 Alongshore Impact: Overview. Two methods were used to estimate the distance alongshore for which the inlet has affected adjacent beaches: the even/odd procedure (Section 3.3), and an examination of the inlet's net sink effect and adjacent island response (Section 3.4). Both methods accounted for a background erosion rate, and assumed that pre-inlet volume change trends would have continued through the present if the inlet had not been created. Thus, pre-inlet (1850-1929/33) volume change rates were subtracted from post-inlet (1929/33-1996) volume change rates. The effect of beach fill (which is reflected in the shoreline position) was removed from the signal by subtracting an estimate of the beach fill volume remaining from the volume in each 50-m shoreline calculation cell. An estimate of beach fill reflected in the shoreline position was

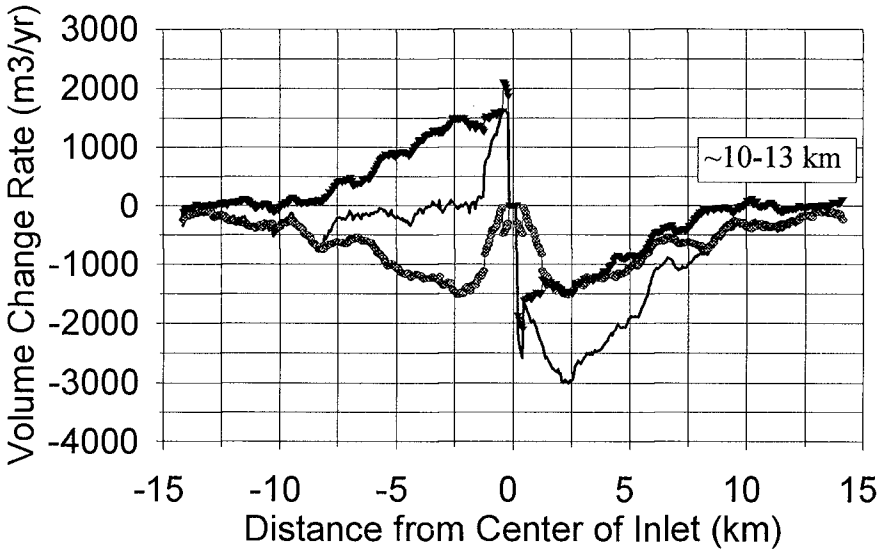
estimated by assuming a beach fill "loss" (or alongshore movement) rate of approximately 2-percent per year (discussed in Section 2.2).

The assumption of a background erosion rate is reasonable, as evidenced from the Fenwick Island shoreline change rates from 1929/33-1996 (Table 1 with beach fill advancement removed), and the trend for relative sea level rise in this region of the U.S. (1.1 mm/yr for Lewes, Delaware, north of Ocean City Inlet, Marine Board 1987). In addition, the 1850 to 1929/33 reorientation of the Fenwick-Assateague Island barrier island from a convex to a more "linear" shoreline orientation (see Figures 1 and 3a) most likely is a long-term, large-scale response which is continuing through the present.

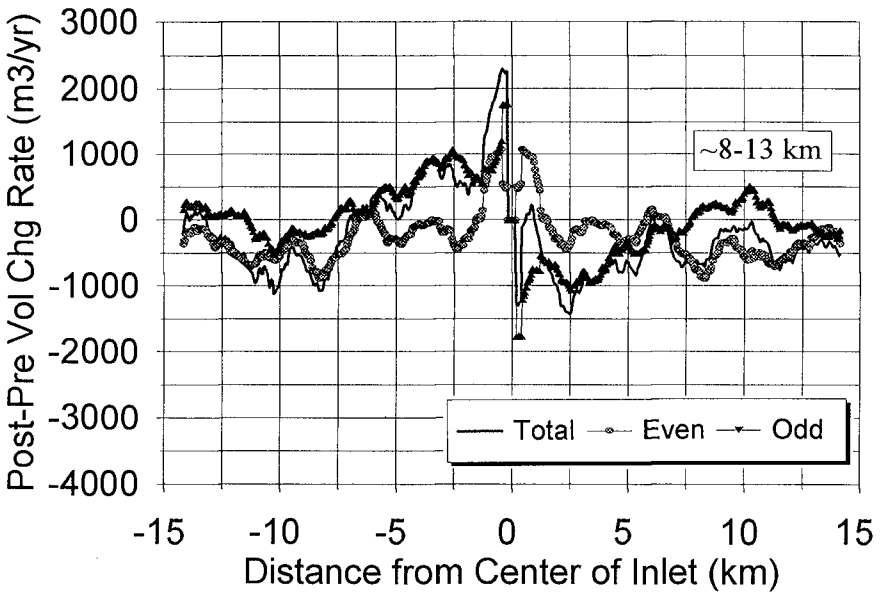
3.3 Alongshore Impact: Even/Odd Method. The even/odd method is a simple analytical procedure discussed and applied by Dean and Work (1993) and Bodge (in preparation) among others, and can be solved from the linearized treatment of shoreline evolution (Pelnard-Considere 1956). The method decomposes shoreline change (or, as applied in this case, volume change) data into their symmetric (even) and anti-symmetric (odd) components about a point of significance. For application at Ocean City Inlet, the center of the inlet was chosen as the point about which data were decomposed into even and odd components. Volumetric change data were used so that the effects of beach fill could be removed, and so that the alongshore variation in active depth could be incorporated. Due to space limitations herein, the reader is directed to Dean and Work (1993) or Bodge (in preparation) for a description of even/odd calculation procedures.

The even and odd functions are indicators of those shoreline or volumetric changes which have been symmetric or anti-symmetric, respectively, about the point of significance. For an inlet with the centerline chosen as the point of significance, the even function reflects changes in shoreline position (or volume change rate) which have occurred symmetrically about the inlet, such as shoreline retreat or advance due to cross-shore transport (due to storms and relative sea level change), and symmetric shoreline retreat due to sediment feeding the ebb and flood tidal shoals. An example of an anti-symmetric change common to stabilized inlets, which is reflected by the odd function, is impoundment on the updrift beach at the expense of the downdrift beach. The alongshore point at which the odd function returns to a zero value is an indicator of the alongshore distance influenced by the anti-symmetric effects, such as impoundment, which is a project-induced impact. The alongshore point at which the even function approaches a constant value is an indication of the alongshore distance influenced by symmetric inlet-induced effects such as shoreline retreat due to feeding the ebb and flood tidal shoals.

Figure 2a shows the post-inlet (1929/33-1996) even/odd analysis, and Figure 2b shows results for the post-inlet rate adjusted by the background erosion rate as defined by the pre-inlet (1850-1929/33) data set. Negative distances indicate shoreline to the north along Fenwick Island. For both Figures 2a and b, the "total" curve shows the updrift



(a)



(b)

Figure 2. Total volumetric change, even, and odd functions for (a) post-inlet volume change rates (1929/33-1996); and post-inlet minus pre-inlet (1850-1929/33) volume change rates

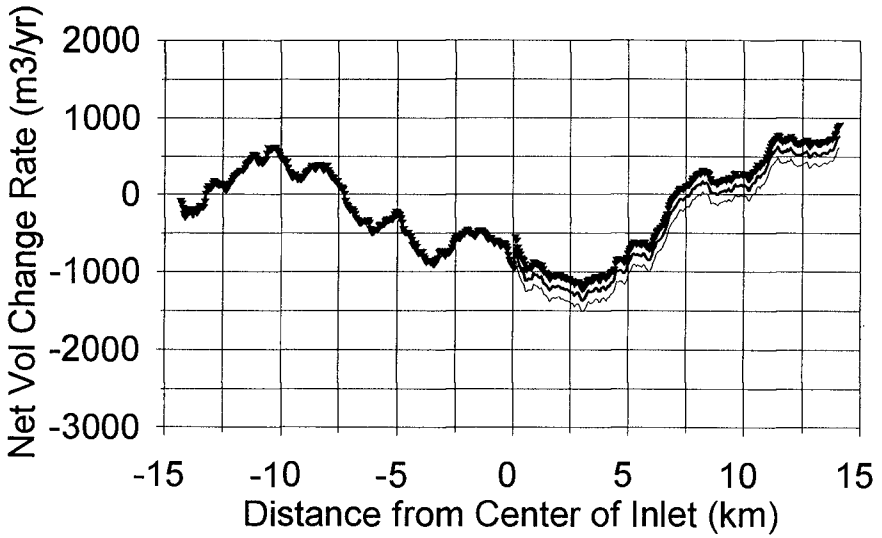
accretion that has occurred as a result of inlet stabilization and the groin field along Fenwick Island. It is interesting to note the erosional peak in the post-inlet volume change rate ("total" curve in Figure 2a) at approximately 8 km updrift of the inlet, which agrees in concept with a longshore sediment transport nodal point in the vicinity of York Beach, Delaware (approximately 18 km north of the inlet), with a variation of 10 km (Mann and Dalrymple 1986). For Assateague Island, except for a peak in the total adjusted volume change curve at approximately 1 km (Figure 2b), the entire shoreline response has been erosional. The peak at approximately 1 km in Figures 2a and b agrees well with the presently-observed bridging of the ebb tidal shoal to the downdrift beach. The "odd" function indicated in Figures 2a and b illustrates the strong alongshore impact that the inlet and Fenwick Island groin field have incurred on the adjacent beaches. This function returns to a zero value approximately 10 km from the inlet in Figure 2a, and at approximately 8 km in Figure 2b. The "even" function in Figure 2a returns to a near-constant value at approximately 13 km from the inlet, and approaches a constant value in this region for Figure 2b. If Figure 2a were taken to represent the inlet's impact (i.e., no background erosion existed from 1933 to 1996), then the alongshore impact distance would be interpreted as between 10 and 13 km. However, we have evidence that background erosion has occurred during the post-inlet time period. Thus, considering both the even and odd functions, **the alongshore impact distance of the inlet (and Fenwick Island groin field) is estimated to be between 8 and 13 km from the centerline of the inlet.**

3.3 Alongshore Impact: Net Sink Effect

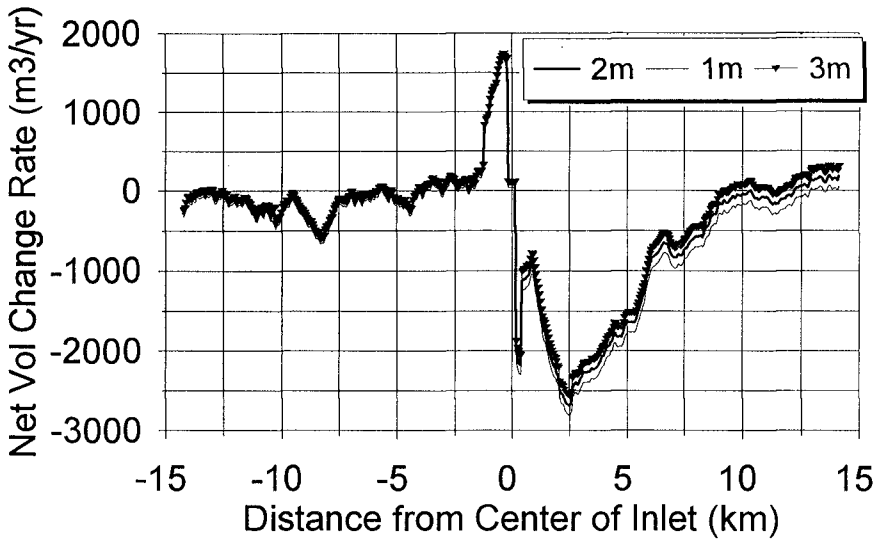
Overview. A second method of determining alongshore impact distance is discussed by Bodge (in preparation). This method calculates the alongshore variation in total volume change, and determines the alongshore distance for which the total inlet sink volume can be accounted. Alongshore impact distance as determined through application of this method is very sensitive to the total sink volume estimate, due to the fact that the alongshore volume changes due to the inlet will decrease with distance from the inlet.

Pre- and Post-Inlet Volumetric Change. Shoreline change from August/September 1850 to November 1929/May 1933 indicated that the pre-inlet Fenwick-Assateague barrier island in the region ± 7 km from the centerline of the existing inlet was in an erosive state (Figure 3a). The island (ocean and bay) cumulative volume change rate for what would become Fenwick Island (extending 14.2 km north of the inlet location) was $-42,500 \text{ m}^3/\text{yr}$ during this time period (independent of bay active depth; the bay shoreline change rate was approximately zero during this period, see Table 1). The cumulative island pre-inlet volume change for 14.2 km of Assateague Island ranged between $-137,700$ and $-59,300 \text{ m}^3/\text{yr}$, depending on bay active depth.

In the post-inlet (November 1929/May 1933 through March 1995/May 1996) time period, Fenwick Island stabilized with cumulative island volumetric change rates ranging from $-16,500$ to $+4,400 \text{ m}^3/\text{yr}$, depending on bay active depth. However, cumulative



(a)



(b)

Figure 3. (a) Pre-inlet (1850-1929/33) and (b) post-inlet (1929/33-1996) island (bay and ocean) volumetric change rates as a function of bay active depth (1, 2, or 3 m)

volumetric erosion rates along Assateague Island increased, ranging from -293,000 to -224,000 m³/yr depending on bay active depth (Figure 3b). The first four columns of Table 3 summarize these results.

Island	Bay Active Depth (m)	Net Island ¹ Volume Change Rate (m ³ /yr)		Present-Day Normalized ² Cumulative Volume (million m ³)
		Pre-Inlet (1850-1933)	Post-Inlet (1933-1996)	
Fenwick	1	-42,500	-16,500	+1.6
	2	-42,500	-6,000	+2.3
	3	-42,500	+4,400	+3.0
Assateague	1	-137,700	-293,000	-9.8
	2	-98,500	-259,000	-10.1
	3	-59,300	-224,000	-10.4

¹ Net ocean and bay volume change.
² Post-inlet minus pre-inlet rate multiplied by the number of years since inlet creation (1996-1933=63 years).

Present-Day Impact Accounting for Background Erosion. The fifth column of Table 3 presents the cumulative volume change, accounting for "background erosion" which was defined by the pre-inlet condition, at ± 14.2 km of the inlet. The degree to which the bay active depth assumption influences magnitudes of cumulative impact can be evaluated from these data. For Fenwick Island, the bay active depth assumption can alter the normalized cumulative volume by nearly a factor of two. For Assateague Island, ocean volumetric change dominates the volumetric impact and the influence of bay active depth is less significant.

Summing the Fenwick and Assateague Islands cumulative volumes for a given bay active depth gives *total adjacent beach impact volumes* which vary at most by 10-percent as a function of bay active depth (-8.2, -7.8, and -7.4 million m³ for 1, 2, and 3 m bay active depth, respectively). Note that only 0.9 million m³ of dredged material is documented as being placed on Assateague Island, whereas between 2.7 and 3.5 million m³ were dredged. If it is assumed that this entire dredged volume was placed on Assateague Island (as has been standard practice), and (to be conservative) that this entire volume moved alongshore or was lost to the profile and is not reflected in the shoreline data, then an additional loss of 1.8 to 2.6 million m³ can be assigned to the adjacent island losses. Using the upper value of 2.6 million m³, it can be

concluded that the volumetric impact of Ocean City Inlet realized on adjacent ocean and bay shores within 14.2 km from the inlet, is *at most* 10.8 million m³. This estimate approaches the minimum total inlet sink volume, which was estimated to range from 10.8 to 15.6 million m³. (However, note that the 10.8 million m³ adjacent island loss was developed with the *upper* dredge volume estimate, whereas the 10.8 million m³ sink volume was developed with the *lower* dredge volume estimate.) Thus, with a pre-existing background erosion rate which is defined by the pre-inlet condition, it is likely that the inlet's influence exceeds the available data limit (14.2 km).

4.0 SUMMARY AND CONCLUSIONS

A database representing 146 years of beach response in the vicinity of Ocean City Inlet, Maryland, was created to reflect adjacent beach, bay, and inlet volume change. Analyses were conducted to evaluate the total sink volume of the inlet, and the alongshore distance associated with this volumetric impact. The total inlet sink, defined as the volume captured by the inlet which can be attributed to the adjacent ocean and bay shorelines, was estimated to range between 10.8 and 15.6 million m³. The even/odd method was applied to ocean shoreline change (adjusted by a background erosion rate) since inlet formation, and indicated an alongshore impact distance (which includes the effects of the Fenwick Island groin field) of approximately 8 km from the centerline of the inlet. The inlet sink analysis, assuming that pre-inlet trends continued through the present, indicated, *at most*, that 10.8 million m³ can be realized along 14.2-km of up- and downdrift ocean and bay shorelines. This analysis indicated that the alongshore impact distance most likely exceeds the available data limit (± 14.2 km from the centerline of the inlet).

5.0 ACKNOWLEDGEMENTS

The research discussed herein was partially supported by the *Inlet Channels and Shorelines* work unit of the Coastal Inlets Research Program, Coastal and Hydraulics Laboratory, Waterways Experiment Station, US Army Corps of Engineers (USACE), and by the *Ocean City Water Resources Study* funded by the USACE District, Baltimore. Permission to publish this paper was granted by the Chief of Engineers. Thanks to reviewers Mark B. Gravens and Nicholas C. Kraus.

6.0 REFERENCES

Bodge, K. R. 1996 (in preparation). "Sediment Management at Inlets/Harbors," draft Coastal Engineering Manual Chapter V-6, USACE Waterways Experiment Station, Coastal and Hydraulics Laboratory, Vicksburg, MS (draft dated August 21, 1996).

Dean, R. G., and Perlin, M. 1977. "Coastal Engineering Study of Ocean City Inlet, Maryland," *Proceedings, Coastal Sediments '77*, American Society of Civil Engineers, pp. 520-540.

Dean, R. G., Perlin, M., and Dally, W. 1978. (March). "A Coastal Engineering Study of Shoaling in Ocean City Inlet," prepared for USAED, Baltimore, under contract with the University of Delaware, Newark, DE, 135 p.

Dean, R. G., and Work, P. A. 1993. "Interaction of Navigational Entrances with Adjacent Shorelines," *Journal of Coastal Research*, Vol 18, p. 91-110.

Hicks, D. M., and Hume, T. M. 1995. "Morphology and Size of Ebb Tidal Deltas at Natural Inlets on Open-sea and Pocket-bay Coasts, North Island, New Zealand," *Journal of Coastal Research*, Vol 12(1), pp 47-63.

Mann, D. W., and Dalrymple, R. A. 1986. "A Quantitative Approach to Delaware's Nodal Point," *Shore and Beach*, Vol 54, No. 2, pp 13-16.

Marine Board. 1987. "Responding to Changes in Sea Level: Engineering Implications," National Academy Press, Washington, D.C.

Pelnard-Considere, R. 1956. "Essai de theorie de l'evolution des formes de rivage en plages de sable et de galets," *4th Journees de l'Hydraulique: Les Energies de la Mer*, Question III, No. 1, pp. 289-300.

Stauble, D. K., Garcia, A. W., Kraus, N. C., Grosskopf, W. G., and Bass, G. P. 1993. "Beach Nourishment Project Response and Design Evaluation: Ocean City, Maryland, Report 1, 1988-1992," Technical Report CERC-93-13, USAE Waterways Experiment Station, Vicksburg, MS 39180-6199.

Underwood, S. G., and Hiland, M. W. 1995. "Historical Development of Ocean City Inlet Ebb Shoal and its Effect on Northern Assateague Island," final draft report prepared for the USACE Waterways Experiment Station under Work Order No. DACA39-92-M-198 and the US Department of the Interior, National Park Service under Inter-agency agreement IA4000-1-0022.

CHAPTER 216

EXTREME WATER LEVELS, WAVE RUNUP AND COASTAL EROSION

P. Ruggiero¹ , P.D. Komar² , W.G. McDougal¹ and R.A. Beach²

ABSTRACT

A probabilistic model has been developed to analyze the susceptibilities of coastal properties to wave attack. Using an empirical model for wave runup, long term data of measured tides and waves are combined with beach morphology characteristics to determine the frequency of occurrence of sea cliff and dune erosion along the Oregon coast. Extreme runup statistics have been characterized for the high energy dissipative conditions common in Oregon, and have been found to depend simply on the deep-water significant wave height. Utilizing this relationship, an extreme-value probability distribution has been constructed for a 15 year total water elevation time series, and recurrence intervals of potential erosion events are calculated. The model has been applied to several sites along the Oregon coast, and the results compare well with observations of erosional impacts.

INTRODUCTION

Much of the Oregon coast is characterized by wide, dissipative, sandy beaches, which are backed by either large sea cliffs or sand dunes. This dynamic coast typically experiences a very intense winter wave climate, and there have been many documented cases of dramatic, yet episodic, sea cliff and dune erosion (Komar and Shih, 1993). A typical response of property owners following such erosion events is to build large coastal protection structures. Often these structures are built after a single erosion event, which is followed by a long period with no significant wave attack. From a coastal management perspective, it is of interest to be able to predict the expected frequency and intensity of such erosion events to determine if a coastal structure is an appropriate response. Predicting the frequency and magnitude of the most extreme erosion conditions is also important for the establishment of setback lines for coastal developments.

Field studies have been undertaken along the Oregon coast to better understand the processes involved in wave-induced sea cliff and dune erosion. The

¹ Ocean Engineering Program, Civil Engineering Dept., Oregon State Univ., Corvallis, OR 97331

² College of Oceanic and Atmos. Sciences, Oregon State Univ., Corvallis, OR 97331

goal is to develop simple methods for estimating the susceptibilities of coastal properties to wave attack. Wave-induced property erosion generally occurs when wave runup reaches the junction between the beach face and the sea cliff or dune. However, depending on a number of wave, water level and morphological parameters, both the elevation attained by wave runup and the elevation of the beach-face junction are highly variable. This paper presents a simple probabilistic method for predicting the frequency of occurrence of cliff or dune erosion. The predicted frequencies are then compared with the observed shoreline stability for several beaches along the Oregon coast.

Other researchers have attempted to determine the risk of coastal properties to flooding using probabilistic techniques. For example, Gares (1990) demonstrates a method for using runup to determine flooding risk on the New Jersey shoreline. Runup is calculated using the composite slope technique presented in the *Shore Protection Manual* and probability curves are produced assuming that maximum runup occurs at times of maximum storm surge. In the current work, an attempt is made to characterize extreme runup statistics on the high energy, yet dissipative beaches common in Oregon where the storm surge is small. Extreme total water levels, hence erosion risks, are then predicted utilizing a long term data base consisting of both measured tides and measured wave characteristics.

MODEL DEVELOPMENT

There are two main components, in Figure 1, which combine to generate total water levels (Shih *et al.*, 1994). The first is the tide elevation, ζ ; all tidal and land elevations presented in this paper will be referenced to the U.S. National Geodetic Vertical Datum (NGVD) of 1929. Superimposed on the measured tide level is the vertical component of wave runup, R , which consists of both wave setup, $\bar{\eta}$ and the swash fluctuations, S , about the setup. Wave induced erosion of a sea cliff or dune will occur only when the total elevation of the water at times of maximum runup exceeds the elevation of the beach-face junction ($\zeta + R > E_j$). Once again, the objective of this study is to predict the frequency with which the total water level, E , reaches or exceeds the elevation E_j of the junction between sea cliff, dune or coastal protection structure and the beach face. To achieve this goal, we construct extreme-value probability distributions (e-v pdf) for water levels measured by tide gauges, water levels due to wave runup, and finally for the combined total water levels.

Extreme Water Levels

Measured tides are often greater than predicted due to the occurrence of a storm surge, or the effects of water temperatures, currents and atmospheric disturbances such as an El Niño. A 24 year time series of hourly measured tides taken from a tide gage in Yaquina Bay, Oregon, has been analyzed to investigate some of these processes. The yearly maxima have been fitted to a Fisher-Tippet Type I extreme-value probability distribution, commonly known as the Gumbel extreme value distribution, and return intervals have been computed for extreme tides. A

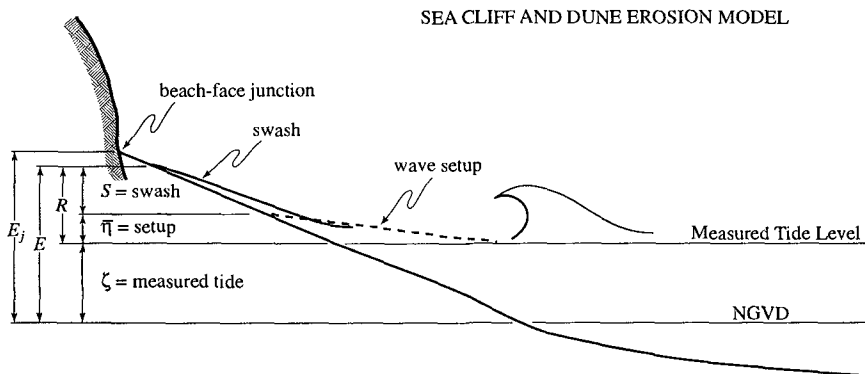


Figure 1: The basic model for the quantitative assessment of the susceptibilities of sea cliffs and dunes to wave-induced erosion.

predicted tide time series has been generated for the same 24 year period, and the predicted yearly maxima have also been fit to a Gumbel distribution. Shih *et al.* (1994) noted that for long return periods there are significant differences, on the order of 0.5 m, between predicted and observed extreme tides.

The difference between measured and predicted tides has been computed for the entire 24 year data set. The auto-correlation of this raw residual time series shows a roll off in correlation at a lag of approximately 48 hours. This lag corresponds well with the typical storm duration on the Oregon coast. The raw residuals were then filtered using a 48 hr low pass filter, eliminating measurement noise from the signal. The standard deviation of the low pass filtered residual time series is approximately 13 cm, giving a typical elevation for storm surge on the Oregon coast. Figure 2 shows the 24 year residual time series after applying a 1 month low pass filter in which single storms as well as spring and neap tides have been averaged out. Surprisingly, there is no distinct seasonal pattern in the figure. The extreme residuals evident in the smoothed time series, those in 1973, 1977, 1982-83, 1992 and 1993, all correspond to times of well-documented El Niño events. Although these events are usually associated with increased wave energy, both the residual and the measured tide are not significantly correlated with wave height throughout the period of overlap between the tide and wave data, a period of approximately 15 years. This observation, along with the relatively low contribution of storm surge to extreme total water levels on the Oregon coast, suggests that models such as that proposed by Gares (1990) may not be applicable to the Oregon coast. Models in which extreme measured water levels and extreme runup occur at the same time, although well suited for coastlines which experience hurricanes and Nor'Easters which generate significant storm surge, are not generally suitable to conditions typical of the Oregon coast.

Wave Runup

The second water-level component in the sea cliff and dune erosion model, superimposed on the measured tide, is wave runup. It is necessary to have the

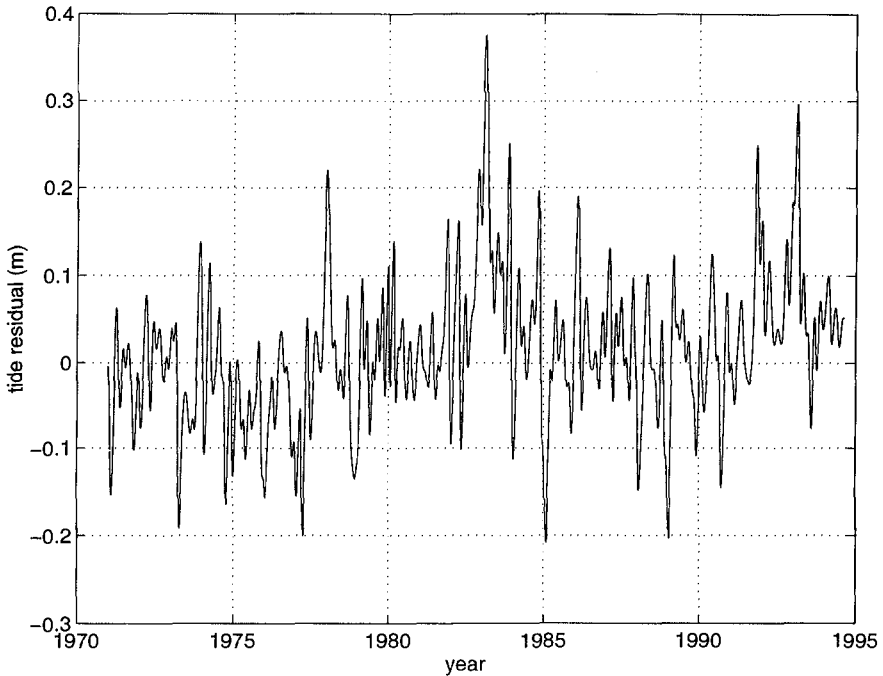


Figure 2: Thirty day low-pass filtered residual time series of measured minus predicted tides in Yaquina Bay, Oregon.

capability to predict extreme runup statistics utilizing measured wave parameters and beach morphology characteristics. Data bases containing a decade or more of measurements of wave heights and periods are now becoming readily available for use by engineers, scientists and planners, and much effort has been spent in finding simple relationships between deep-water wave parameters and runup on beaches. A well known data set of extreme runup statistics is that of Holman and Sallenger (1984) and Holman (1986), who measured wave runup using video techniques on the relatively steep beach of the Field Research Facility, Duck, North Carolina. Among other runup statistics, Holman (1986) examined the 2% exceedence elevation for runup maxima, non-dimensionalized by wave height, and found a dependence on the dimensionless surf similarity parameter, ξ_0 , commonly referred to as the Iribarren number, the ratio of the beach slope to the deep-water wave steepness. The resulting relationship is

$$R_{2\%}/H_S = C \xi_0 = C \beta / (H_S/L_0)^{(1/2)} \quad (1)$$

where C is an empirical constant determined by the measurements, β is the beach slope, H_S is the deep-water significant wave height, and L_0 is the deep water wave length given by $L_0 = (g/2\pi)T^2$ where g is the acceleration of gravity and T is the wave period. This result has been proposed by many researchers, including Battjes

(1971) and van der Meer and Stam (1992). In an attempt at further simplification, Holman's data were re-analyzed by Douglas (1992), who found that removing the beach slope term from Eq. (1) does not cause any reduction in the ability to predict runup on beaches. By analyzing a wide variety of Australian beaches, Neilson and Hanslow (1991) found that the relationship proposed by Holman explained results from field experiments on relatively steep beaches, $\beta > 1:10$, while for flatter more dissipative beaches with $\beta < 1:10$, runup depended only on the wave steepness. Many Oregon beaches are extremely dissipative with beach slopes much less than 1:10. The resulting Iribarren numbers are usually less than for beaches studied by other researchers, including the most dissipative in the Neilson and Hanslow (1991) study.

To test the dependence of extreme runup statistics on measured wave and beach morphology characteristics, video techniques were used to measure wave runup on several Oregon beaches over a broad range of dynamic conditions. Deep-water significant wave heights ranged from 1.9 to 4.6 m, periods from 7 to 17 seconds, and foreshore slopes from 1:100 to 1:20. This field program culminated in February 1996 at Agate Beach on the central Oregon coast, with a major investigation into the dynamics of high energy dissipative beaches. During this experiment, three video cameras were used to measure wave runup, and the overlap between the cameras allowed for continuous coverage of runup measurements over approximately 2 km of beach. Detailed analysis of the longshore variability of runup on dissipative beaches is underway. Runup elevation time series were extracted from all video data using image-processing techniques developed at the Coastal Imaging Lab of Oregon State University (Holman and Guza, 1984; Holland *et al.*, in press). For each data record, the tide has been removed and extreme runup statistics have been computed after identifying the local maxima of the shoreline elevation time series. Although there is a distinction in the processes which force wave setup and swash fluctuations, for most engineering applications the measure of interest is the extreme statistics associated with the total runup. Therefore, all runup statistics presented include both setup and swash.

The Oregon measurements of $R2\%$ are non-dimensionalized in the form of Eq. (1), and compared with the data of Holman (1986) in Figure 3. The Iribarren number distinguishes between the dynamically different nearshore systems from which the data were taken. The Oregon data falls in the extremely dissipative range of Iribarren numbers, while the FRF data range from dissipative to reflective. Although the Oregon data are of the expected order of magnitude, any linear predictive model such as Eq. (1), derived from Holman's data, would tend to under predict $R2\%$ on the flatter Oregon beaches, an observation noted earlier by Shih *et al.* (1994). The data from Oregon have been re-plotted in Figure 4a, which suggests that extreme runup statistics do not depend on the Iribarren number over this dissipative range. Figure 4b shows that the Oregon runup data has virtually no dependence on the beach slope, and Figure 4c shows a lack of dependence of $R2\%/H_s$ on the wave steepness. Although not shown, the extreme runup also does not depend on the wave period. This is surprising, as runup has a first order dependence on the wave

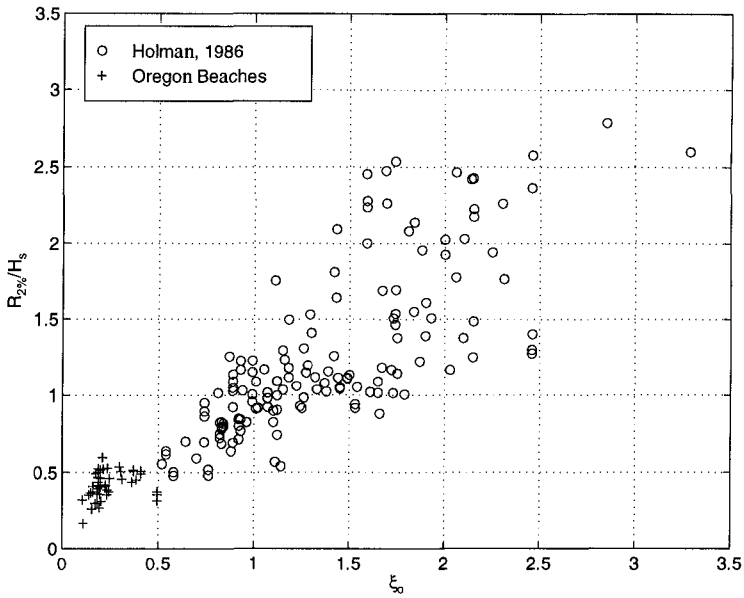


Figure 3: Comparison between non-dimensional extreme runup statistics obtained by Holman from the FRF and from Oregon beaches.

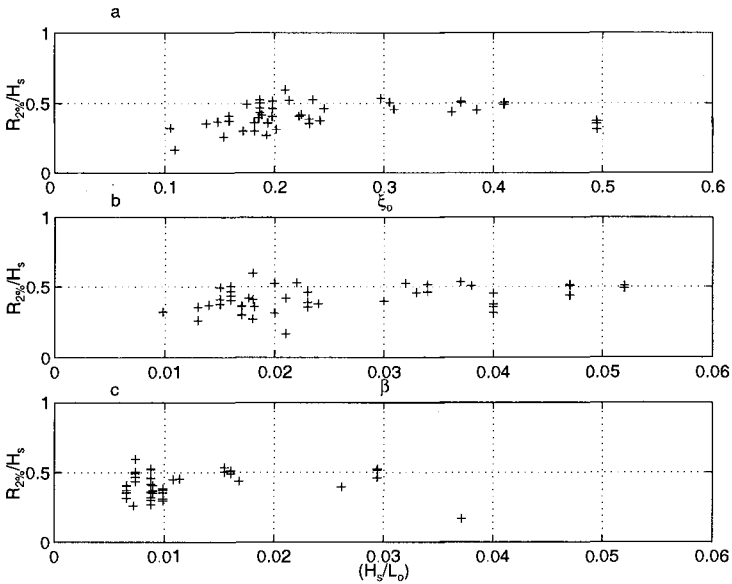


Figure 4: Relationships between non-dimensional extreme runup statistics and a) the Iribarren number, b) beach slope, and c) wave steepness.

period in the dimensional form of Eq. (1). The best parameterization of $R_{2\%}$ for the Oregon data is a simple dependence on the deep-water significant wave height as shown in Figure 5. The best-fit straight line matched to the Oregon data is

$$R_{2\%} = 0.5 H_s - 0.22 \text{ (m)} \quad (r^2 = 0.72) \quad (2)$$

A linear relationship between runup elevation and wave height on relatively low energy dissipative beaches was also found by Guza and Thornton (1982) in Southern California, and by Aagaard (1990) in Denmark and Australia. Guza and Thornton (1982) found that the significant vertical swash excursion, defined as 4σ , where σ^2 is the total variance of the runup elevation time series, was approximately 70% of the significant wave height, a slightly stronger dependence on wave height than found for the Oregon data and the results presented by Aagaard (1990). The FRF data of Holman (1986) are shown again in Figure 5 to emphasize the fact that the data are derived from dynamically very different systems as the Holman data clearly falls above the Oregon data. More research is needed to identify regimes where different models for extreme runup statistics are applicable.

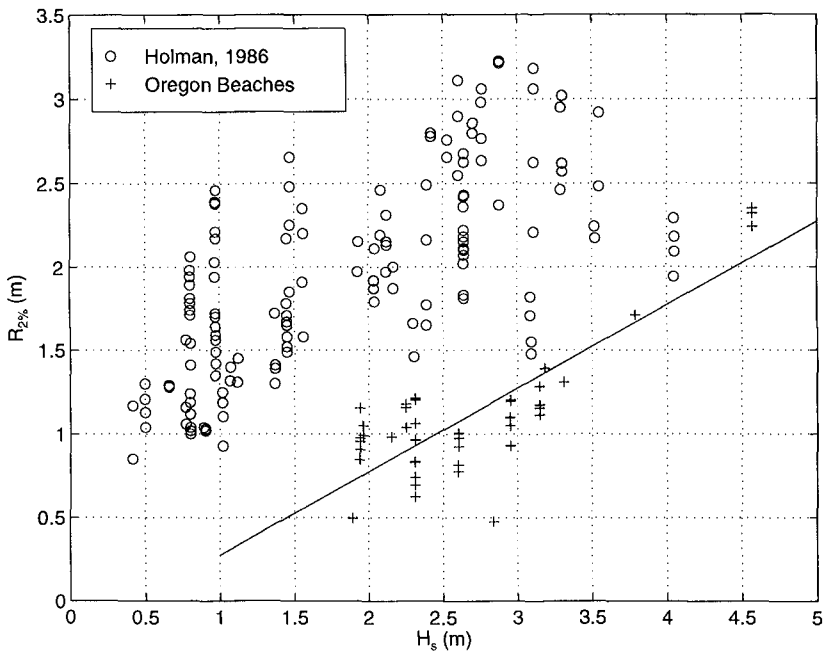


Figure 5: Dependence of extreme runup statistics on the deep-water significant wave height.

The extreme runup statistics presented here, as in the work done by other researchers, are monochromatic representations of spectral phenomena. In fact, all of the Oregon runup data, particularly that on the very low sloping Agate Beach, were dominated by infragravity energy ($f < 0.05$). Spectral peaks typically occurred at

periods ranging from approximately 100 seconds to 200 seconds, and usually more than 90% of the runup elevation variance fell in the infragravity band. This infragravity dominance helps explain why runup statistics are independent of the incident band wave period. The incident band energy was saturated for most data runs, and the dependence on wave height shown in Figure 5 can almost entirely be explained by the infragravity band energy and its dependence on the wave height. Again, this is a similar result to that found by Guza and Thornton (1982).

Waves and Total Water Levels

In the previous section we showed that the best predictor of extreme runup on dissipative Oregon beaches is simply the deep-water wave height. A 15-year wave data set from the Coastal Data Information Program buoy offshore from Bandon, Oregon, has been used to estimate the extreme wave climate of the Oregon coast. This irregularly spaced data set has been interpolated to hourly measurements to match the measurement interval of the Yaquina Bay tide measurements. A Gumbel extreme-value distribution has been fitted to this data, and the resulting recurrence intervals for extreme waves are shown in Figure 6. This extreme value pdf has been produced by using all of the wave data above 6.5 meters, rather than just the yearly maxima (Muir and El-Shaarawi, 1986).

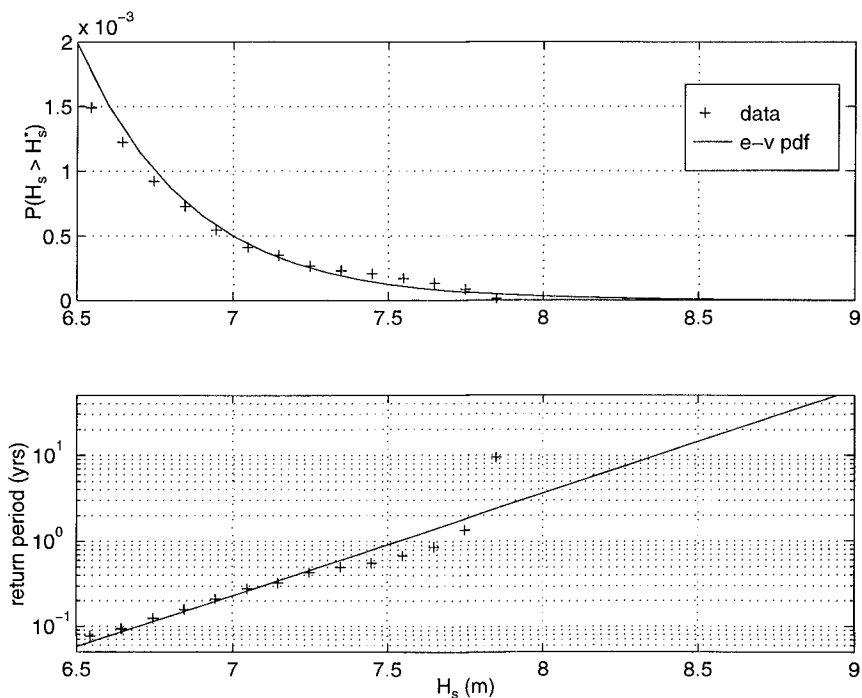


Figure 6: Extreme-value probability distribution and recurrence intervals constructed from 15 years of wave height data obtained by the CDIP buoy offshore from Bandon, Oregon.

Figure 6, as well as results presented by Tillotsen and Komar (in press), clearly demonstrate the intense nature of the wave climate experienced along the Oregon coast. The linear relationship between wave height and extreme runup statistics given in Eq. (2) can now serve as a transfer function to construct an extreme value distribution for $R_{2\%}$ from the distribution of wave heights, and is shown in Figure 7.

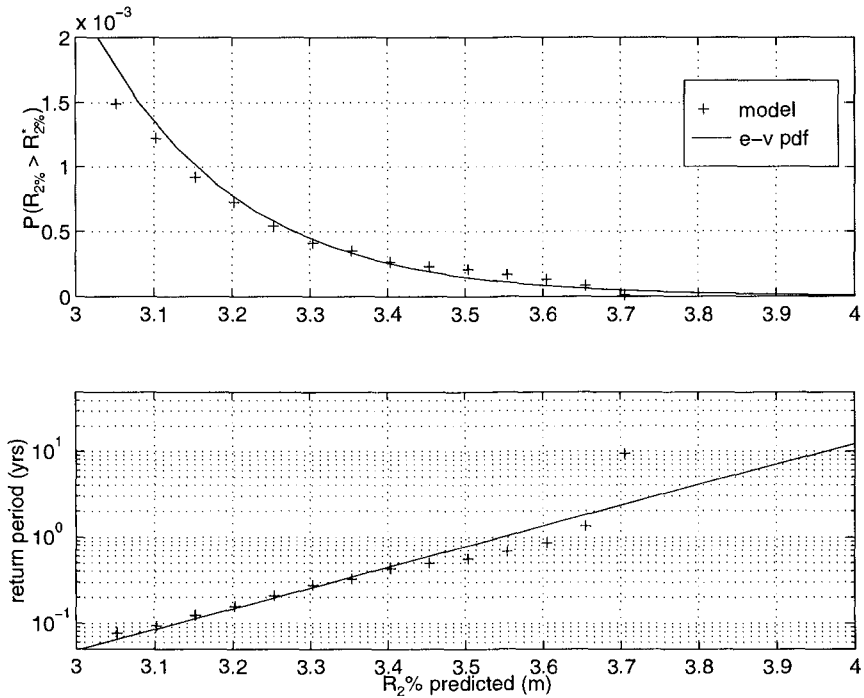


Figure 7: Extreme-value probability distribution and recurrence intervals for wave runup calculated from the wave height distribution in Figure 6.

Analytic probability density functions have been determined for both extreme measured tides and extreme wave runup, the two components of the sea cliff and dune erosion model. Assuming that runup and tides are statistically independent, the joint probability of tides and runup is easily calculated. This exercise has been completed, and contours of equal probability of occurrence have been generated. However, a more useful and direct method for determining the statistics of extreme total water levels is to apply the above model for wave runup to the wave component of the joint time series of waves and water levels. This joint time series is constructed from the time periods in which the wave data and tide data overlap. In doing this, we generate a runup time series which can be added to the measured tide to give a simulated total water level time series. An extreme value distribution is determined from this time series directly, using all total water levels above 2.8 m, and

is shown in Figure 8. The recurrence intervals of the total water level reaching or exceeding any elevation can now be determined.

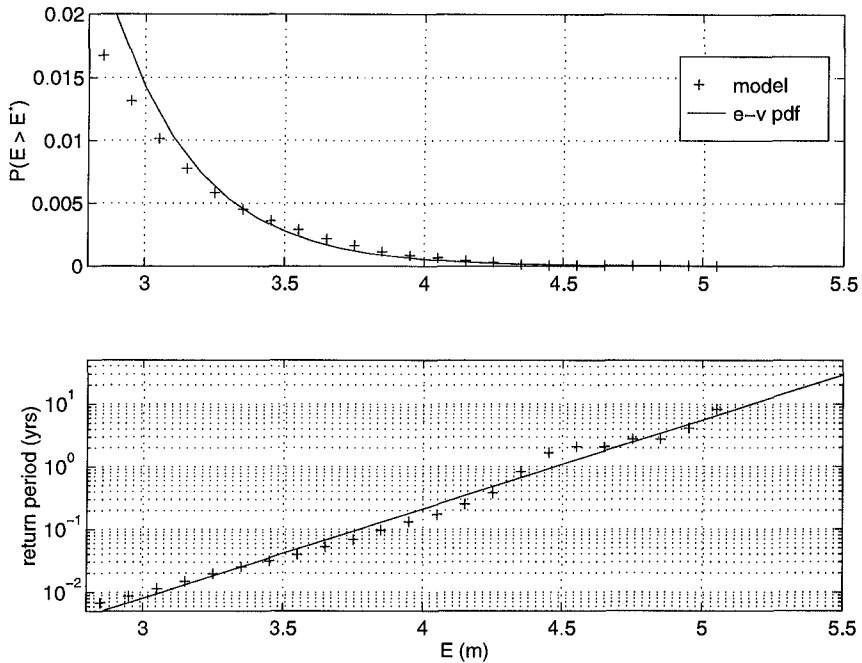


Figure 8: Extreme-value probability distribution and recurrence intervals for total water levels, measured tides plus wave runup.

MODEL APPLICATION

The Oregon coast is divided into a series of littoral cells, with beaches confined between large headlands. The elevation of the beach-face junction varies considerably between cells due to differences in sediment grain sizes, and the quantities of sand in a particular cell. This elevation can also vary within a cell due to local effects such as the lowering of the beach by rip current embayments (Shih and Komar, 1994). A number of beaches with varying morphologies are being monitored in Oregon to determine these elevations relative to NGVD, as well as to quantify typical summer and winter profiles and long term morphology changes. The model has been applied to 13 sites along the central Oregon coast, accounting for 9 of the 13 littoral cells. The beaches are backed by sea cliffs, dunes and shore protection structures and all have beach slopes within the range of applicability of the runup model. The model allows for the determination of the frequency with which the total water level exceeds the elevation of the beach-face junction, thus being a good indicator of potential erosion.

Table 1: Impacts per year as compared to beach stability observations.

Site	Backing Feature	β	E_j (m)	Impacts per year (hrs)	Observations
Jump off Joe	Sea Cliff	.034	2.90	173	severe erosion
Nye Beach	Sea Cliff	.034	3.70	13	stable
Beverly Beach	Sea Cliff	.043	4.02	4	erosion
Oceanside	Dune	.023	3.60	18	stable/erosion
South Beach	Dune	.026	4.12	3	accretion
Manzanita North	Dune	.025	4.20	2	stable/accretion
Manzanita South	Dune	.038	6.30	---	heavy accretion
Nestucca Spit	Dune	.046	6.50	---	heavy accretion
C&L Ranch	Sea Wall	.030	3.15	77	severe erosion
Pacific Shores	Sea Wall	.039	3.65	15	erosion
San Marine	Sea Wall	.030	3.75	11	erosion
Pacific Palisades	Sea Wall	.052	5.30	---	accretion
Driftwood Shores	Sea Wall	.033	7.50	---	heavy accretion

Table 1 summarizes the results as applied to the sites on the Oregon coast. The table lists the average winter beach slopes and the average elevations of the junction between the beach and the respective backing feature. The return interval, the fraction of time when the 2% exceedence elevation of runup maxima superimposed on the tide reaches or exceeds E_j has been calculated. However, since we have used all of the data above a threshold value from our simulated total water elevation time series to construct the extreme pdf shown in Figure 8, we can convert return intervals to the more convenient unit of hours of wave runup impact per year. This column in Table 1 gives an estimate of the number of hours per year in which $R_{2\%}$ exceeds E_j for a particular beach, thus being a reasonable proxy for potential erosion at the site. The final column in the table lists basic field observations concerning the morphologic stability of the particular site. The first site, Jump Off Joe, is backed by the remains of a massive landslide which protrudes out onto the active beach profile, hence the very low E_j . The toe of the landslide is actively eroding and is reached by swash during most higher high tides in the winter. Nye Beach, immediately to the south of Jump off Joe, is relatively stable and backed by a vegetated sea cliff. The model predicts that the sea cliff at Jump off Joe will be hit by wave runup much more often than any other site including the cliff at Nye Beach, agreeing well with observations.

SUMMARY AND DISCUSSION

With an appropriate model relating runup elevations to deep-water wave conditions, the frequency of occurrence of sea cliff or dune erosion can be predicted using historical wave and tide records. Coastal regulators, the anticipated users of the model, will have a quantitative method to determine the susceptibilities of properties to erosion and thus a rationale to establish setback distances for coastal developments. The model can also aid in the development of dune-management plans which balance the role of dunes in reducing future property losses versus the development pressure currently being experienced on the Oregon coast. For

example, from this data set it appears that shorelines subjected to less than 1 hour of attack per year tend to be stable, while those with more than 10 hours per year tend to experience erosion. In its present form the model may be used to evaluate the need for shore protection structures and may potentially assist in their design. Future model development will attempt to include impact forces in order to predict erosion rates of both sea cliff and dune backed shorelines. The major weakness of the model is the simple relationship between extreme runup statistics and wave height. The model takes no account of the possibility that the functional relationship between runup and wave height may change under more extreme conditions than those measured. The model also ignores large-scale morphology, including offshore bars and bathymetry, as well as large-scale alongshore variability. More runup data are needed on beaches between the dissipative extremes presented here, and the more intermediate to reflective systems to help identify appropriate runup models for a particular beach state.

ACKNOWLEDGMENTS

We would like to thank Rob Holman for the use of his extensive data set. This work is a result of research supported by the NOAA Office of Sea Grant, Department of Commerce. The Agate Beach field experiment and data analysis was supported by ONR Grant # N000-14-94-11196.

REFERENCES

- Aagaard, T., 1990, "Swash Oscillations on Dissipative Beaches - Implications for Beach Erosion," *Journal of Coastal Research*, Special Issue No. 9, pp. 738-752.
- Battjes, J.A., 1971, "Run-up Distributions of Waves Breaking on Slopes," *ASCE Journal of Waterways Harbor Coastal Engineering Division*, 92, pp. 91-114.
- Douglass, S.L., 1992, "Estimating Extreme Values of Run-up on Beaches," *Journal of Waterway, Port, Coastal, and Ocean Engineering*, Vol. 118, No. 2, pp. 220-224.
- Gares, P.A., 1990, "Predicting Flooding Probability for Beach/Dune Systems," *Environmental Management*, Vol. 14, No. 1, pp. 115-123.
- Guza, R.T. and Thornton, E.B., 1982, "Swash Oscillations on a Natural Beach," *Journal of Geophysical Research*, Vol. 87, No. C1, pp. 483-491.
- Holland, K.T., Holman, R.A., Lippman, T.C., Stanley, J. and Plant, N.G. (in press), "Practical use of Video Imagery in Nearshore Oceanographic Field Studies," *Journal of Oceanic Engineering*, Special Issue on Image Processing for Oceanic Applications.

- Holman, R.A. and Guza, R.T., 1984, "Measuring Runup on a Natural Beach," *Coastal Engineering*, Vol. 8, pp. 129-140.
- Holman, R.A. and Sallenger, A.H., 1985, "Setup and Swash on a Natural Beach," *Journal of Geophysical Research*, Vol. 90, No. C1, pp. 945-953.
- Holman, R.A., 1986, "Extreme Value Statistics for Wave Run-up on a Natural Beach," *Coastal Engineering*, 9, pp. 527-544.
- Komar, P.D. and Shih, S.-M., 1993, "Cliff Erosion Along the Oregon Coast: A Tectonic-Sea Level Imprint Plus Local Controls by Beach Processes," *Journal of Coastal Research*, Vol. 9, No. 3, pp. 747-765.
- Muir, L.R. and El-Shaarawi, A.H., 1986, "On the Calculation of Extreme Wave Heights: A Review," *Ocean Engineering*, Vol. 13, No. 1, pp. 93-118.
- Nielson, P. and Hanslow, D.J., 1991, "Wave Runup Distributions on Natural Beaches," *Journal of Coastal Research*, Vol. 7, No. 4, pp. 1139-1152.
- Shih, S.-M., Komar, P.D., Tillotsen, K.J., McDougal, W.G. and Ruggiero, P., 1994, "Wave Run-up and Sea-Cliff Erosion," *Proceedings 24th Coastal Engineering Conference, American Society of Civil Engineers*, pp. 2170-2184.
- Shih, S.-M. and Komar, P.D., 1994, "Sediments, Beach Morphology and Sea Cliff Erosion within an Oregon Coast Littoral Cell," *Journal of Coastal Research*, Vol. 10, No. 1, pp. 144-157.
- Tillotsen, K.J. and Komar, P.D., in press, "The Wave Climate of the Pacific Northwest (Oregon and Washington): A Comparison of Data Sources," *Journal of Coastal Research*.
- van der Meer, J.W., and C.-J. Stam, 1992, "Wave Runup on Smooth and Rock Slopes of Coastal Structures," *Journal of Waterway, Port, Coastal and Ocean Engineering*, American Society of Civil Engineers, vol. 118, pp. 534-550.

CHAPTER 217

A morphological “mixed-type” model for the Ebro delta coast

Agustín Sánchez-Arcilla and José A. Jiménez¹

Abstract

A conceptual model to explain and simulate the long-term (decadal) Ebro delta coast evolution is presented as well as the approach to be followed to convert this conceptual model into a numerical one able to quantitatively predict the deltaic coast behaviour. Moreover, a first running sub-model which simulates most of the changes suffered by the outer coast is described in details. This sub-model is a long-term scale version of a one-line coastal model in curvilinear coordinates. The developed model has been verified and predictions of coastline evolution under different scenarios are also presented.

Introduction

The impact assessment of management policies and/or climate change on coastal zones requires comparing the coastal evolution under the present management/climate scenario with respect to the evolution under a different (targetted) scenario. To do this, it is necessary to develop proper tools to predict coastal evolution at adequate temporal and spatial scales.

According to the analysis of scales in coastal morphology done by Sánchez-Arcilla and Jiménez, (1994a, 1996), the representative scale for this kind of tools must be the large spatial scale and the long-term temporal one. In this case, long-term refers to a temporal scale of decades and large scale refers to a length of tens of kilometres up to the entire littoral cell. This implies building models able to adequately reproduce/simulate coastal processes and the corresponding behaviour at this scale, *i.e.* long-term/large scale morphological models.

One of the main questions to solve in large scale coastal modelling is the level of accuracy in the description of the driving terms to be considered. This will determine the

¹ Laboratori d'Enginyeria Marítima (LIM), Catalonia University of Technology (UPC), c/Gran Capitá s/n, 08034 Barcelona, Spain (arcilla@etseccpb.upc.es, jimenez@etseccpb.upc.es).

aggregation level of the processes included in the model. According to deVriend *et al.* (1993) three main approaches exist in large scale modelling:

- (i) *input data reduction*, in which it is assumed that large scale processes can be modelled by using process-oriented-models (usually employed to characterise short-term morphological processes) fed by aggregated input data representative of the process to be modelled;
- (ii) *model reduction*, in which the model is re-formulated according to the scale of interest (and avoiding shorter scale processes or retaining its integrated effect) and;
- (iii) *behaviour-oriented models*, which describe coastal changes without considering the underlying physical processes.

The model here presented is a kind of combination of approaches (i) and (iii) and it is thus called “mixed-type” model. The concept *mixed-type* model refers to a morphological set of equations derived by combining two approaches: (i) the underlying physical processes, particularly at large time scales -*i.e.* subject to an averaging from which only the “residual” effect of small scale processes is retained- and (ii) the actually “observed” morphological evolution, which integrates all “driving” agents into an a priori assumed “predictable” behaviour -from which governing equations could also be derived in an heuristic manner-.

Thus, the aim of this work is to introduce a morphological *mixed-type* model developed for the Ebro delta coast to predict the large scale deltaic evolution. The model is based on the analysis of (i) the existing information on “driving” agents (basically river regime, wind-wave and meteorological climates and mean sea-level fluctuations) and associated physical processes (see *e.g.* Jiménez *et al.* 1996) and (ii) the observed Ebro delta coast evolution at different scales (Jiménez and Sánchez-Arcilla, 1993; Sánchez-Arcilla and Jiménez, 1994; Jiménez, 1996).

After introducing this model, a first sub-model is developed quantitatively. This sub-model deals with one of the main processes involved -the longshore sediment transport- and is used to predict the deltaic coastline behaviour for different scenarios.

Conceptual model

The term conceptual applied in this context refers to a model explaining all the processes governing the Ebro delta coastal behaviour at different temporal and spatial scales as well as their dependence with the acting driving terms and for a defined set of boundary conditions.

This means to develop a model for the Ebro delta coast evolution using all the available relevant information where the coastal response at the different scales is isolated and quantified and, moreover, integrated into a general framework able to explain the coastal evolution as a whole.

This model has been developed for the Ebro delta coast after a detailed analysis of forcing agents, induced processes and associated coastal responses at three main scales: medium-term (Jiménez and Sánchez-Arcilla, 1993), episodic events (Sánchez-Arcilla and Jiménez, 1994) and long-term (Jiménez *et al.* 1993). These components have been

integrated into a generic model in which the processes are linked through sediment fluxes (across- and alongshore) and the coastal response is aggregated (Jiménez, 1996).

Figure 1 shows a cross-shore section of the model in which the main considered processes are presented. The coast is thus divided alongshore into a series of cells, each one composed by different units linked by sediment fluxes.

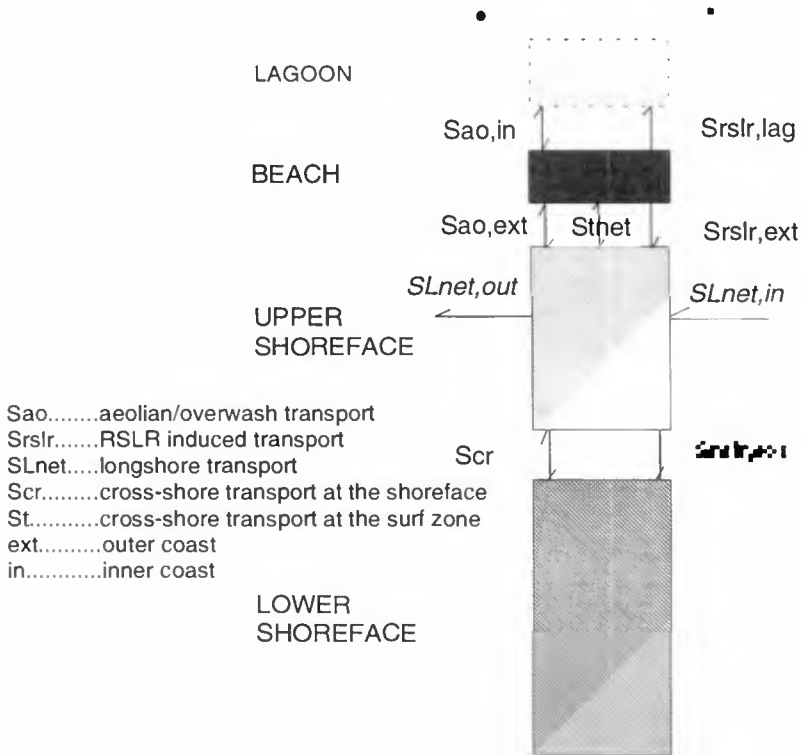


Figure 1. Cross-section of the conceptual model and considered sediment fluxes.

Full details on the conceptual model as well as on the way of quantifying the different sediment fluxes are given in Jiménez (1996).

As a sample description, the most apparent conclusions arising from the developed conceptual model is that, at present times, the Ebro delta coast is subject to a reshaping process in which the net longshore wave-induced sediment transport pattern is the main driving term. This longshore sediment transport pattern (fig. 2), although with a peak frequency located at the medium-term scale (*i.e.* over several years) has a very important residual effect at a longer time scale, since it can be shown that it is also one of the main agents responsible for the sediment redistribution along the coastline on the “long-term” scale (*i.e.* over decades). At this long-term scale, longshore transport will redistribute the sediment along the coast, whereas river sand supplies (severely limited at present), cross-

shore sediment exchanges at the shoreface, RSLR induced changes and aeolian and overwash transports (over the dune rows and subaerial coast) will determine the global sediment budget.

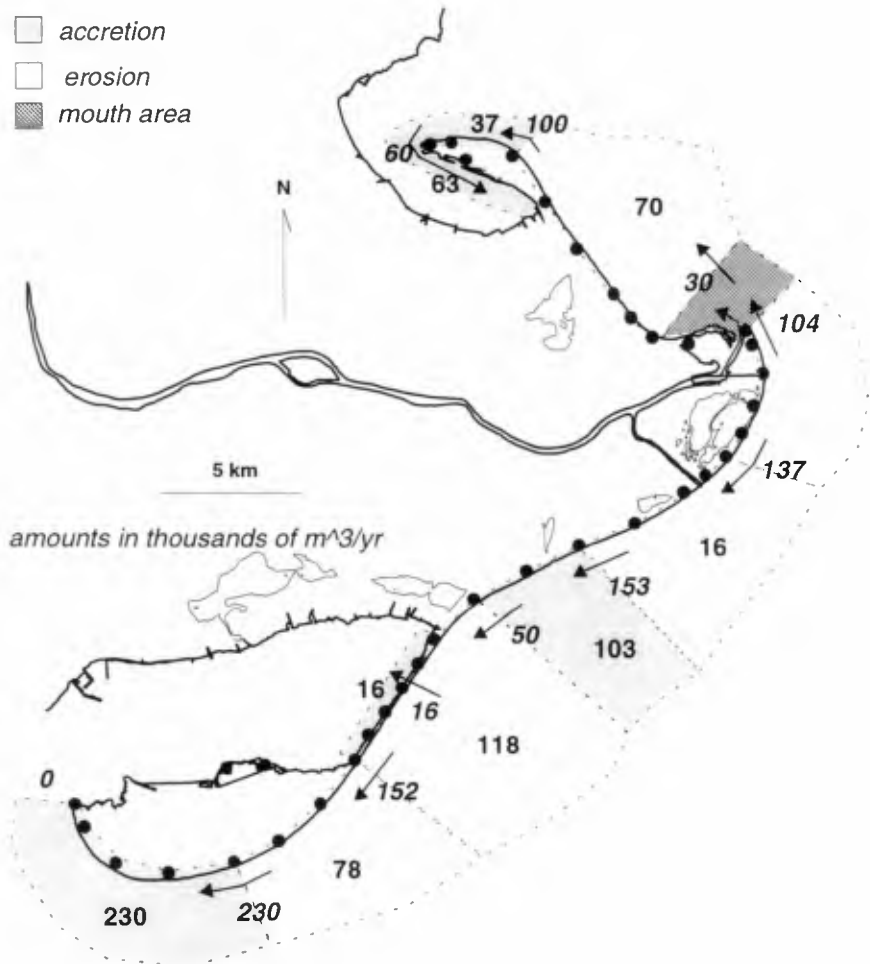


Figure 2. Net longshore sediment transport pattern and associated sediment budget at the medium-term scale (adapted from Jiménez and Sánchez-Arcilla, 1993).

The resulting morphological model has been developed using all the identified “transport mechanisms” relevant for the decadal scale. To estimate the “predictable” coastal evolution, a numerical “box-type model” (*i.e.* based on sediment budget considerations) is being built. This general model is composed by a series of sub-models considering the different processes to be afterwards coupled.

In what follows, the sub-model to predict the coastal "reshaping" due to the existence of a longshore sediment transport gradient (as the only driving term) along the coast is presented and used to simulate/predict the Ebro delta coastline evolution.

Longshore sediment transport parameterization

The net longshore sediment transport rate along any coast, $Sl_{net,i}$, can be expressed as the summatory of contributing transport rates induced by wave conditions acting on that coast,

$$Sl_{net,i} = \sum_{w=1}^{w=n} Sl_{w,ii} f_w \quad (1)$$

where $Sl_{w,i}$ is the local longshore transport rate induced by the w waves and f_w is the occurrence frequency of those waves, subscript i indicates the position along the coast.

Due to the selected approach - the model to be developed is a combination of *input data reduction* and behaviour oriented models which represent a kind of *result reduction*, equation (1) will be solved at the maximum aggregation level here considered. This approach implies to consider the net longshore sediment transport as the result of a *representative morphological wave*, i.e. integrating the effects of the existing wave climate on the Ebro delta coast from a longshore transport standpoint (see e.g. DeVriend *et al.*, 1993 for review of wave data reduction approaches).

The way of parametering sediment transport must be done considering the functional relationship between the type of transport to be modelled and the wave parameters controlling such transport. Since the net longshore sediment transport is the "object" to be parameterized and considering that, in previous studies, the CERC formula has proven to be simple while reasonably reproducing the obtained net longshore transport pattern (Jiménez and Sánchez-Arcilla, 1993; Jiménez, 1996), it has been selected to parameterize this transport.

Transport parameterization

Due to the above mentioned assumptions (maximum aggregation and functional relationship given by the CERC formula), the local net longshore sediment transport in each control point i can be represented by

$$Sl_{net,i} = C K_i H_{b,i}^{2.5} \sin[2(\alpha_{b,i} - \alpha_{s,i})] \quad (2)$$

where C groups all the constant terms of the CERC formula, K_i is the CERC calibration factor, $H_{b,i}$ is the "morphological wave height" at breaking in each point along the coast, $\alpha_{b,i}$ is the local wave angle at breaking and $\alpha_{s,i}$ is the local shoreline orientation.

In this approach, the CERC calibration factor, K_i , is permitted to vary alongshore to account for local factors which may influence the transport capacity such as differences in the sediment grain size, sediment availability, beach slope, etc.

Equation (2) is expressed in terms of breaking wave characteristics so that, offshore waves must be propagated towards the coast to evaluate wave parameters at breaking.

This would be equivalent to employing a short term evolution model coupled with a wave propagation model.

In order to obtain a simpler (parametric) formula to be included in a long term evolution model, it will be expressed as a function of deep water wave characteristics as

$$Sl_{net,i} = CK_i Kw_i H_o^{2.5} \sin[2(\alpha_o - \alpha_{s,i})] \quad (3)$$

where Kw_i is a local constant including wave propagation effects. For a "steady" incident wave climate and for coastal changes small enough not to affect wave propagation, the local values will be "steady" as the coast evolves.

Thus, the parameterized net longshore sediment transport rate will be composed by four components: (i) a global constant ($KI = CH_o^{2.5}$) including all the common terms such as "universal" constants and offshore morphological wave height; (ii) a local constant (K_i) -the calibration factor of the CERC formula- accounting for local effects such as sediment availability, grain size variations, beach slope, etc.; (iii) a local constant (Kw_i) representing the modifications of wave characteristics due to wave propagation and (iv) a sinusoidal function in which the argument varies as the coastline orientation does. In a compressed manner, the net longshore sediment transport rate is given by

$$Sl_{net,i} = Ksl_i \sin[2(\alpha_o - \alpha_{s,i})] \quad (4)$$

where $Ksl_i = KI K_i Kw_i$.

Transport constants

The application of equation (4) requires to know the net longshore sediment transport rates along the coast of study, Sl_{net} , the actual coastal orientation for which transport rates are estimated, α_s , and, a deep water "representative wave" angle, α_o .

Assuming that the first two variables, transport and orientation are known as it has been already pointed up in the previous section, it remains the problem of the selecting wave angle.

Fig. 3a shows the directional wave climate off the Ebro delta coast in which three main directional components can be seen. From these, the NW component is not relevant for morphological processes due to the coastline orientation since it will represent calm conditions for coastal dynamics (NW waves are generated by local winds blowing offshore). The other two components, E and S, have similar occurrence percentages being Eastern waves slightly more frequent.

In order to see the relative importance of each one of the two components, their energetic content was estimated through their respective offshore wave energy flux. This flux was calculated as the yearly-integrated value of $H_s^2 T_p$ -being H_s the significant wave height and T_p the peak period- (see Fig. 3b). The obtained pattern of wave energy flux indicates the effectiveness of waves acting on the Ebro delta coast. It is clear that, the "representative" morphological wave, must be close to the East component. This is clearly reflected in the Ebro delta coastal morphology, where the presence of the two spits

indicates a net longshore transport directed towards the north northwards of the river mouth, and towards the south southwards of the river mouth.

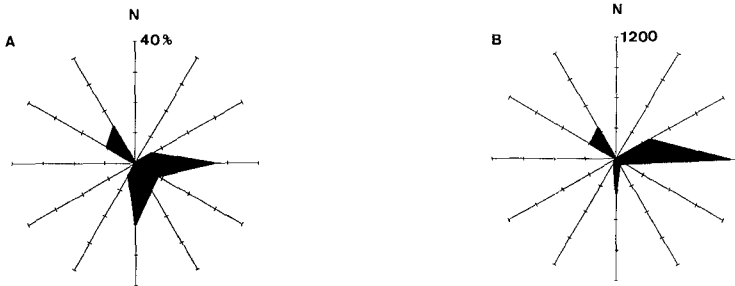


Figure 3. (a) Offshore directional wave distribution. (b) Offshore directional distribution of the yearly-integrated wave energy flux (calculated as $H_s^2 T_p f$) (Jiménez, 1996).

To select the *representative* long-term morphological wave angle the various wave energy fluxes associated with all effective wave directions (from N to S) were vectorially added, resulting in a "net" wave direction of 100° .

Once this *representative* wave angle was selected, the long-term transport coefficient, Ksl , was calculated using equation (4) fed by the estimated net longshore transport rates for the Ebro delta coast from measurements during the period 1988-1992 (Jiménez and Sánchez-Arcilla, 1993) and the coastal configuration for which these transport rates verify. The so obtained Ksl values along the Ebro delta coast will reflect all the terms affecting local net longshore sediment transport rates (such as the longshore variation in wave height and wave power along the coast, sediment grain size, etc). Fig. 4 shows the estimated long-term transport constants along the southern part of the Ebro delta coast and their variability as a function of the selected *representative* wave angle. As it can be seen, there are some stretches where the variability in Ksl values is high and, even, in some cases -such as the coastal stretch represented by profile 23- it presents a reversal in the transport direction for wave angles greater than the selected one (*i.e.* for waves arriving southwards of 100°).

This variability can also be reproduced by maintaining constant the *representative* wave angle but changing the local coastal orientation and, due to this, it can be used as a measurement of the sensitivity of the local longshore sediment transport to changes in effective wave angle (difference between *effective* wave angle and coastal orientation).

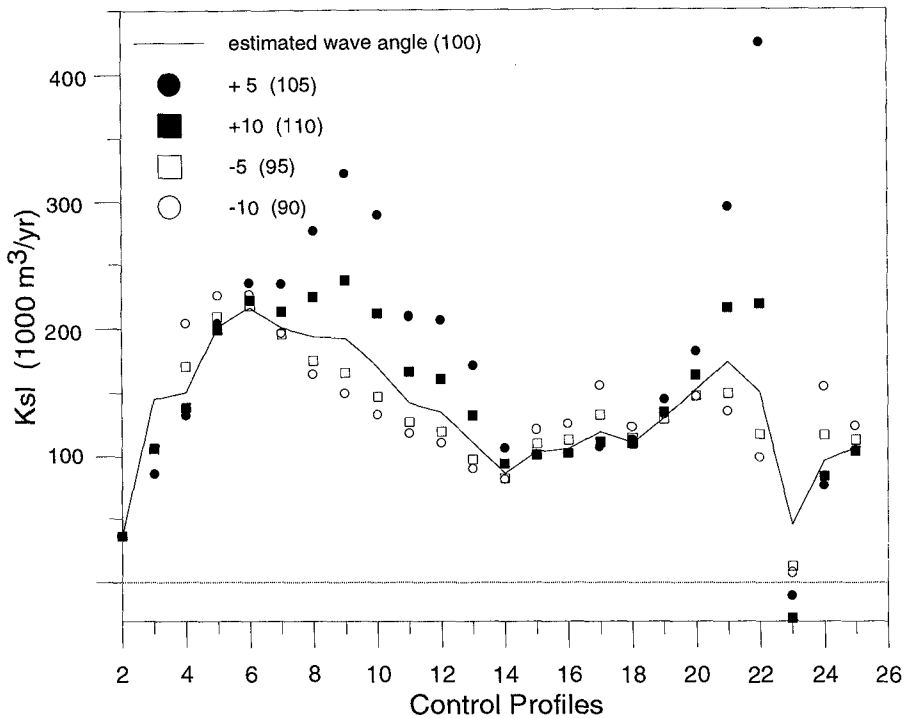


Figure 4. Long-term transport constant K_{sl} along the southern part of the Ebro delta coast as a function of the selected *representative* wave angle.

The coastline model

The effects induced by the net longshore sediment transport pattern along the Ebro delta coast have been modelled through a one-line coastal model.

This first sub-model of the generic conceptual one has been selected due to the good performance of this kind of models to reproduce such effects/changes (associated basically to a longshore sediment transport gradient). Moreover, this approach will permit to include other additional effects/processes to complete the ones already considered in the conceptual model by introducing them into the term representing local sediment sinks/sources and by expanding it to a kind of multi-line model.

Since the entire Ebro delta coastline can be considered as significantly curved (locally, with very strong curvatures as is the case of the apex of both spits), the use of an one-line model in Cartesian coordinates will not properly reproduce the coastline behaviour, specially for the most curved stretches. In order to solve this problem a curvilinear coordinate system (following to Le Blond (1972)) will be used. In this system the orientation of any point P of coordinates (x,y) can be written in terms of local coordinates (normal to and tangential to the shoreline), being θ the orientation between the local axes and the original ones (see Fig. 5).

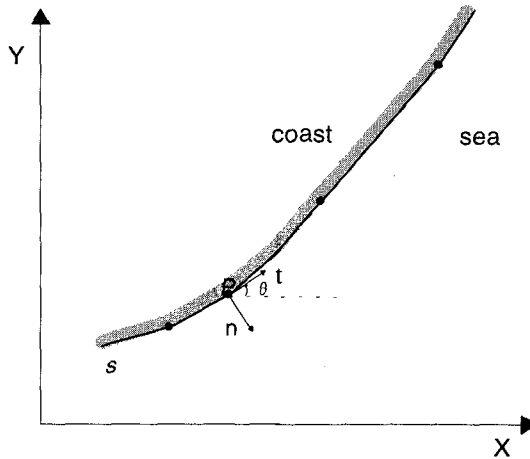


Figure 5. Curvilinear coordinate system.

Using the complex notation $P = x + iy$, in which $i = \sqrt{-1}$ and, assuming that the movement of any point $P(x,y)$ (induced by a longshore sediment transport gradient along the coast, s) will be perpendicular to the shoreline, the continuity equation can be expressed as (see *e.g.* Suh and Hardaway, 1994)

$$\frac{\partial P}{\partial t} = -\frac{1}{d_c} \left(\frac{\partial Sl}{\partial s} + q \right) \exp(i(\theta + \pi/2)) \quad (5)$$

in which d_c is the closure depth and q a term to include local sediment sources and/or sinks.

Numerical model

The equation (5) is numerically solved by means of an explicit finite-differences scheme using a staggered grid in which shoreline positions are defined in the centre of cells and longshore transport rates are evaluated at cell edges (see *e.g.* Kraus, 1988).

In the selected approach (local coordinates) the cell length, s , is or can be variable along the coast and, to obtain the direction normal to a local point i , an average local orientation is defined considering the orientation upcoast and downcoast of the point of interest.

The finite-differences version of equation (5) for point i along the coast is thus

$$P_{i,j+1} = P_{i,j} - \frac{\Delta t}{d_c} \left(\frac{Sl_{i+1,j} - Sl_{i,j}}{0.5(s_{i+1,j} + s_{i,j})} + q_i \right) \exp \left[i \left(\frac{\theta_{i+1,j} + \theta_{i,j}}{2} + \frac{\pi}{2} \right) \right] \quad (6)$$

where

$$s_i = \left[(x_{i+1} - x_i)^2 + (y_{i+1} - y_i)^2 \right]^{1/2}$$

The typical time step used in the simulations is of 1 year and the cell length is between 1 and 2 km. The selection of the time step will control the accuracy of the modelling, not only due to stability reasons, but also due to the fact that in any time step the transport rate is updated according to the final coastal orientation and it will be considered as steady during that time step. Thus, the longer the time step is, the smaller the capacity of transport updating will be.

The model requires boundary conditions at both limits of the domain, which in this specific case have been selected (based on the analysis of deltaic coastal behaviour) as *null* transport ($S_{net}=0$) in the southern boundary (apex of the spit) and *free beach* in the northern one.

Model verification

In order to verify the developed model, a hindcast of the Ebro delta coastal evolution has been performed. The selected time frame was from 1973 to 1989 in which detailed coastline configurations, obtained from aerial photographs, were available.

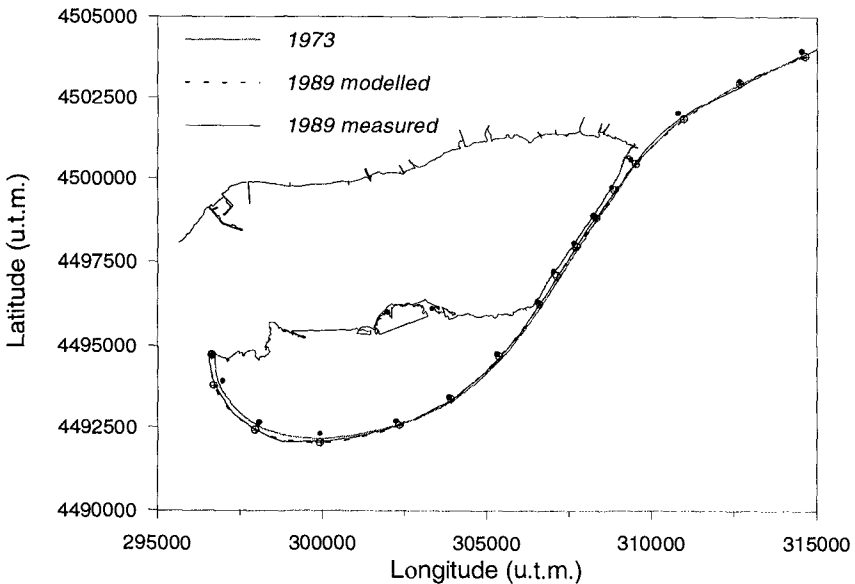


Figure 6. Comparison between modelled and measured coastline evolution between 1973 and 1989 (Jiménez, 1996).

The long-term coastal transport constant, Ksl , obtained from data measured during the period 1988-1992 were used together the Ebro delta coastal configuration corresponding to the year 1973. Fig. 6 shows the comparison between modelled and measured coastlines. As it can be seen, both coastlines are nearly coincident, with deviations measured in terms of the relative error ($|\Delta x_{\text{mes}} - \Delta x_{\text{mod}}| / |\Delta x_{\text{mes}}|$), giving an average relative error of about 15%. This magnitude can be considered as reasonable for the scale of modelled processes.

In any case, the comparison of measured and modelled deltaic coastlines cannot be considered as a model calibration in the sense that no parameter has been fitted. It should be stressed that, the values of the constant (Ksl) along the coast, have been obtained from the analysis of a period (1988-1992) not included in the verification interval (1973-1989).

This fact can be used as a clear indication that the net longshore transport pattern along the Ebro delta coast is the main driving term/process governing the outer coastal behaviour at this scale. The estimated net transport rates for a four year period, which according to the analysis of Jiménez and Sánchez-Arcilla (1993) are representative of the medium-term evolution (over a period of several years), will have a "residual" effect on the long-term/large scale coastal behaviour which is reflected in the observed coastal reshaping (although not contributing to the overall sediment budget). Thus, for the Ebro delta coast, if net longshore sediment transport rates at the medium-term scale are available, and the incident wave climate is steady, the large scale/long-term coastline behaviour can be reasonably predicted by considering the changes in coastal orientation.

Ebro delta coastline evolution under different scenarios

Fig. 7. shows the predicted coastline evolution for the southern part of the Ebro delta from 1989 to 2050 assuming that present conditions (river sediment supply and wave climate) are steady during all that period.

The predicted evolution, in which only longshore sediment transport is considered, shows a spit growth similar to the one observed under present conditions. Moreover, it also shows that the outer coast along the Trabucador Bar will shift landwards towards the present backbarrier coast. In this particular case, it must be taken into account that this implies that this barrier is "sandy rich", *i.e.* no breaching is considered and, in any case, it is assumed that behind the eroding barrier there is always enough sand available. Of course, this will only occur if the effects of overwash processes which permit the barrier rollover are included. Although in this sub-model overwash is not included, existing data on the Trabucador Bar evolution during the last decades, have shown a similar behaviour. Fig. 8 shows thus the barrier evolution from 1957 to 1989 where it can be seen that the barrier outer coast in 1989 occupies the position of the backbarrier corresponding to 1957.

Additionally, the model results can also be used to characterise the barrier as a high vulnerability area in the sense that, if overwash is prevented, the barrier will be prone to be breached due to the existing positive gradient in the net longshore sediment transport pattern.

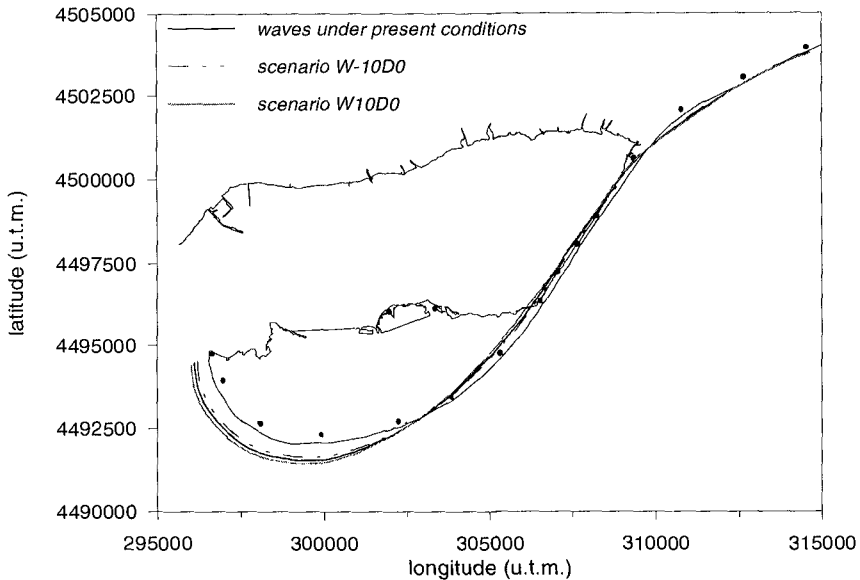


Figure 7. Prediction of the Ebro delta coastline evolution for the year 2050 under present conditions and assuming two scenarios of wave height change (*W10D0*: 10% increase in wave height, *W-10D0*: 10% decrease in wave height).

The potential of this kind of models to predict some climate effects on coastal evolution can be assessed from Fig. 7. Two climate scenarios, in terms of changes in wave height, have been defined: (i) scenario *W10D0* where an increase of 10% in wave height is assumed and (ii) scenario *W-10D0* with a decrease of 10% in wave height.

To account for these variations in wave height, the local transport constant, Ksl , has been modified for these two scenarios as follows:

$$Ksl_{(W10D0)} = Ksl (1.1)^{2.5}$$

$$Ksl_{(W-10D0)} = Ksl (0.9)^{2.5}$$

As it can be seen from Fig 7, the coastline evolution under both scenarios is similar same from a qualitative standpoint although differing in the magnitude of the predicted shoreline displacements according to the assumed variation in wave height (larger displacements for an increase in the wave height because it implies larger gradients in longshore sediment transport and viceversa).

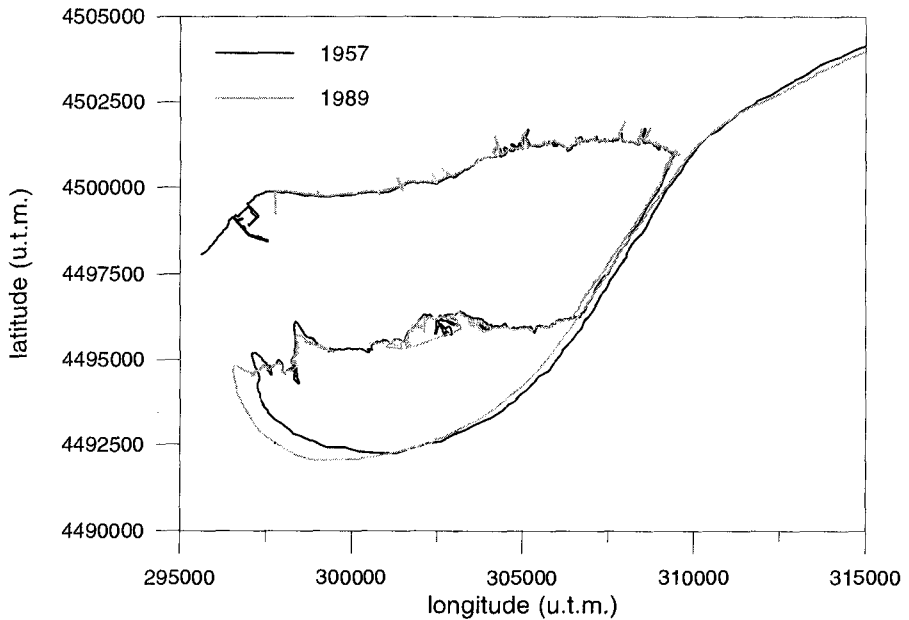


Figure 8. Evolution of the Trabucador Bar between 1957 and 1989 (modified from Sánchez-Arcilla and Jiménez, 1994b).

Summary and on-going works

A conceptual model to explain and simulate the long-term Ebro delta coast evolution has been presented as well as the approach to be followed to convert this conceptual model into a numerical one able to quantitatively predict the deltaic coast behaviour.

From all the considered modules, a first running sub-model which simulates most of the changes suffered by the outer coast of the Ebro delta, has been described in details. Although this sub-model only considers coastal changes induced by the existence of longshore sediment transport gradients, it has been proven to reproduce most of the observed changes along the Ebro delta coast. This is due to the fact that longshore sediment transport is the main process governing the evolution of the Ebro delta coast at the long-term scale. However, other processes are also important, specially for determined coastal stretches in order to fully explain the coastal behaviour and not only the coastline evolution (*e.g.* overwash processes to explain barrier rollover).

In this way, other different sub-models are being developed and included into a general model able to reproduce and simulate the large scale/long-term evolution of the Ebro delta coast. A first specific module to simulate the effects of overwash, which combined with the effects on the outer coast is able to reproduce different barrier behaviours is nearly operational. The inclusion of this process will permit to eliminate the assumption of a sandy-rich barrier (which in fact implies a quasi-infinity barrier width) as it has been used in the example shown here (Fig. 7). It will be then possible to simulate the

evolution of both barrier coastlines (outer and inner) and this will permit identifying the barrier vulnerability conditions (leading to a barrier prone to breaching).

At present, all other processes considered in the conceptual model have been included in a parametric way (*i.e.* including them in the model as sediment sinks and sources), although a process-oriented approach is being followed to describe these terms in a dynamical manner.

Acknowledgements

This work was carried out as part of the MEDDELT and PACE projects. It was supported by the EU Environment and Marine Science and Technology (MAST-III) Programmes, under Contracts No. EV5V-CT94-0465 and No. MAS3-CT95-0002 respectively. This work was also co-sponsored by the Spanish Ministry of Education and Research through DGICYT (UE95-0033). JAJ was partly supported by a travel grant given by the DPTOP (Generalitat de Catalunya) through the ETSECCPB (UPC). We also thank to Marcel Stive and Michele Capobianco earlier fruitful discussions on some parts of this work.

References

- De Vriend, H.J., Capobianco, M., Chesher, T., De Swart, H.E., Latteux, B. and Stive, M.J.F., 1993. Approaches to long-term modelling of coastal morphology: A review. *Coastal Engineering*, 21: 225-269.
- Jiménez, J.A. 1996. *Evolución costera en el Delta del Ebro. Un proceso a diferentes escalas de tiempo y espacio*. Ph.D. Thesis, Catalonia Univ. of Technology, 274 pp.
- Jiménez, J.A. and Sánchez-Arcilla, A., 1993. Medium-term coastal response at the Ebro delta, Spain. *Marine Geology*, 114: 105-118.
- Jiménez, J.A., Sánchez-Arcilla, A., Valdemoro, H.I., Gracia, V. and Nieto, F. 1996. Forcing terms controlling reduction processes in the Ebro delta. *Marine Geology* (in review).
- Kraus, N.C., 1988. Shoreline models. In: K. Horikawa (Ed.), *Nearshore dynamics and coastal processes*. Univ. of Tokyo Press, 321-366.
- LeBlond, P.H., 1972. On the formation of spiral beaches. *Proc. 13th ICCE*, ASCE, pp. 1331-1345.
- Sánchez-Arcilla, A. and Jiménez, J.A., 1994a. Ingeniería de playas (I): Conceptos de morfología costera. *Ingeniería del Agua*, 1(2): 97-114.
- Sánchez-Arcilla, A. and Jiménez, J.A., 1994b. Breaching in a wave-dominated barrier spit: The Trabucador Bar (NE Spanish coast). *Earth Surface Processes and Landforms*, 19, 483-498.
- Sánchez-Arcilla, A. and Jiménez, J.A., 1996. Physical impacts of climatic change on deltaic coastal systems (I): an approach. *Climatic Change*, (in press).
- Suh, K.D. and Hardaway, C.S. 1994. Calculation of tombolo in shoreline numerical model. *Proc. 24th ICCE*, ASCE, 2653-2667.

CHAPTER 218

SEA DIKE EROSION AND COASTAL RETREAT AT NAM HA PROVINCE, VIETNAM

Ton That Vinh¹, G. Kant², Dr. Nguyen Ngoc Huan³, Dr. Z. Pruszk⁴

ABSTRACT

Nam Ha Province is situated on the coast of the Red River Delta, immediately east of the mouth of the Red River. The coast of the delta is very dynamic in which large quantities of sediment are supplied by wet season run-off. However, in Nam Ha province the coast is retreating such that successive lines of dikes have been abandoned and a unique 'managed retreat' strategy is underway with double lines of dikes along large parts of the province's coast. This paper reviews and describes the possible causes of the erosion problem and highlights the unique way in which the local coastal engineers are adopting, out of necessity, the classical retreat strategy. Other impacts of the problem such as environmental and socio-economic impacts are also reviewed. Based on the qualitative first order analyses a strategy has been defined towards a sustainable development of this coastal area.

SITE DESCRIPTION

The Delta of the Red River is located in the northern part of Vietnam (Figure 1). The Thao River rises in the Dai Ly Lake in China. In Vietnam, near the town of

¹ Ministry of Agriculture and Rural Development, Department of Dike Management and Flood Control, 23 Hang Tri Street, Hanoi, Vietnam.

² Frederic R. Harris B.V., Badhuisweg 11, P.O. Box 87875, 2508 DG The Hague, The Netherlands.

³ Marine Hydrometeorological Centre of HMS, Lang Trung, Dong Da, Hanoi, Vietnam.

⁴ Polish Academy of Sciences, Institute of Hydroengineering, Kosciarska 7, 80-953 Gdansk, Poland.

Viet Tri, the Thao River becomes Red River and receives flow from two other major contributors: the Da River and the Lo River. The Red River Delta has the classical triangular form downstream of Viet Tri. East of the Red River the Thai Binh River flows onto the Red River Delta. The Red River catchment area is about 155000 km² and reaches into China and Laos, resulting in an average annual discharge of $137 * 10^9$ m³/year, and a total estimated sediment load of about $72 * 10^6$ t/year to the Gulf of Tongking (World Bank, 1994). The sediment is discharged through a large number of branches over a coastline with a length of some 165 km (as the crow flies). The enormous amount of sediment in general leads to accretion in the coastal areas for which the growth of the Red River Delta itself is the most outstanding proof and example.

However, despite this fact there are local stretches of coast on which serious erosion problems are reported. Two provinces where such erosion problems exist are the provinces Thai Binh and Nam Ha. Surprisingly both provinces are directly located at Cua Balat, the mouth of the main branch of the Delta: the Red River itself (Figure 2).

Nam Ha province is bound by the Red River in the north-east and by the Day River in the south west. The coast length is about 60 km and generally faces E to SE. The province has three coastal districts which are separated by branches of the Red River (Figures 2 and 3). One of the branches, Ngo Dong River was dammed in 1955. The middle district, Hai Hau district, experiences a serious consistent widespread erosion. About 75% of the total of 25 km coastline of Hai Hau district is retreating.

The coastline of Hai Hau district is being protected by dikes. In front of the dikes is a very gentle sloping beach. The slope of the beach varies along the coastline from 1:40 on eroding beaches to 1:200 in other places. The beaches consist of very fine sand with an average grainsize of about 80 μm. Measurements show an increase of the grainsize on the eroding sections of the coast.

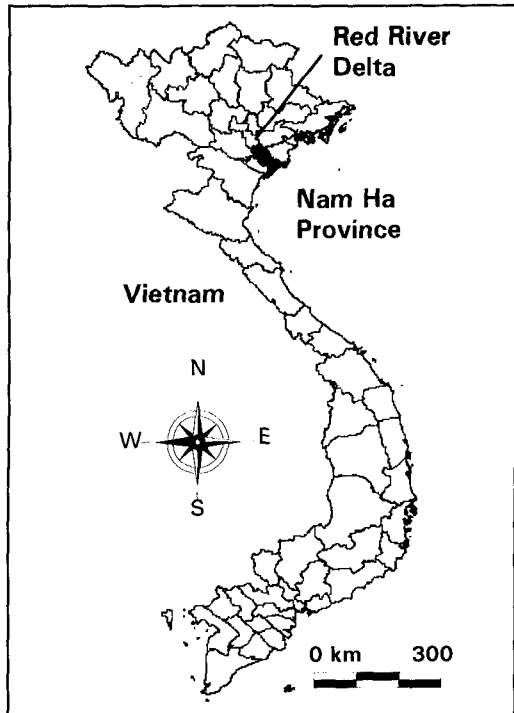


Figure 1 Vietnam

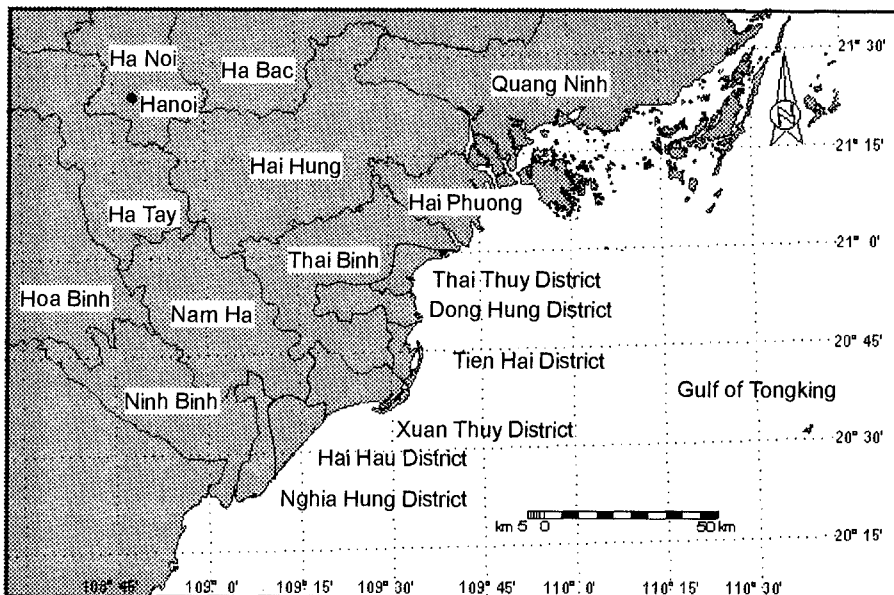


Figure 2 Red River Delta Provinces and Coastal Districts Nam Ha Province

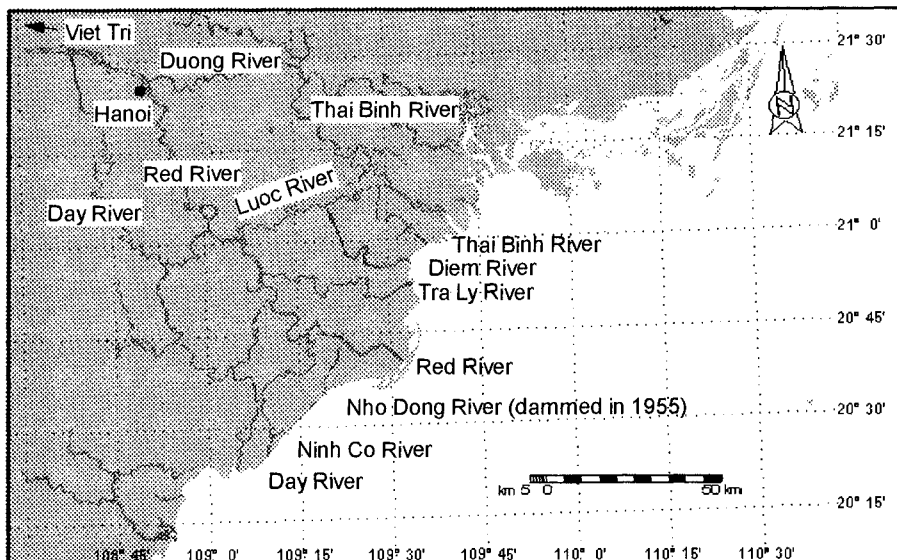


Figure 3 Red River Delta River Branches

HISTORIC SHORELINE DEVELOPMENT

The coastline development this century (from 1905 to 1992) in Nam Ha province is presented in Figure 4. It can be seen that the development of the coast is irregular. Near the mouths of the Red River (right hand side of the figure), the Ninh Co and the Day River (both on the left hand side of the figure) progressive sedimentation has led to accretion. This results in shoreline developments in these areas of 2.5 km to 6.5 km in seaward direction over the 87 year period. However, in Hai Hau district the development is just the opposite. Over the last 87 years a strip some 16 km long and about 2.5 km wide was lost to the sea. This is a time averaged shoreline retreat of about 29 m/year. It appears from this figure, which is based on maps, that the erosion at Hai Hau district started in the beginning of the century and seems to be slowing down after 1966. This indicates that the damming of the adjacent Ngo Dong River in 1955 is not the main reason of the consistent erosion problems.

LOCAL RESPONSE STRATEGY

The present coastal defence at Hai Hau district consists of a double dike system (Figure 5). These parallel dykes, with a separative distance of about 250 m, are constructed along 75 % of the Hai Hau coastline. The area between the dykes has been split into sections alongshore in the range of 500 to 3000 m long. The beach in front of the first dike reaches to about MSL. The slope of the dike is about 1:2 (v:h) and is protected by pitched limestone rock of about 30 cm diameter placed on a clay layer. The crest height is approximately 4 m above MSL. The dike body itself consists of clay and sand. On heavily attacked sections the toe of the dike is reinforced with cement grouting.

Since the erosion is progressing continuously the first defence line is becoming weaker every year. During extreme events the first dike is therefore at some points not strong enough to withstand the attack. In

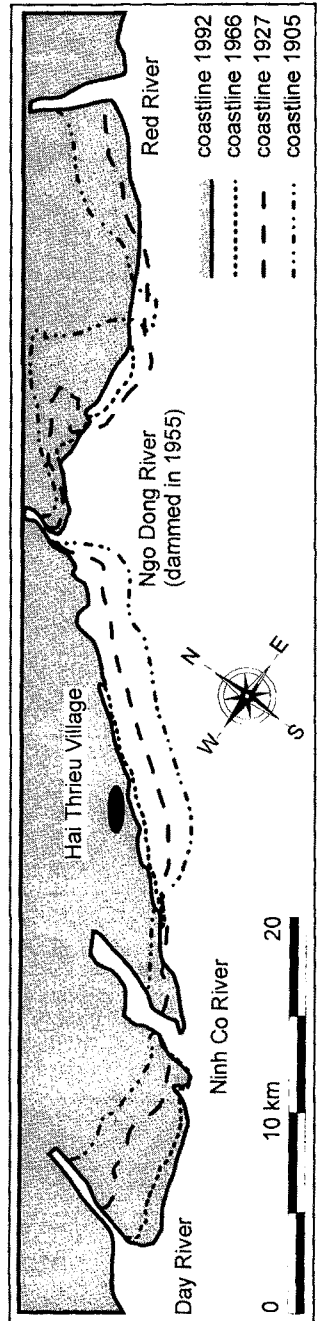


Figure 4 Shoreline Development

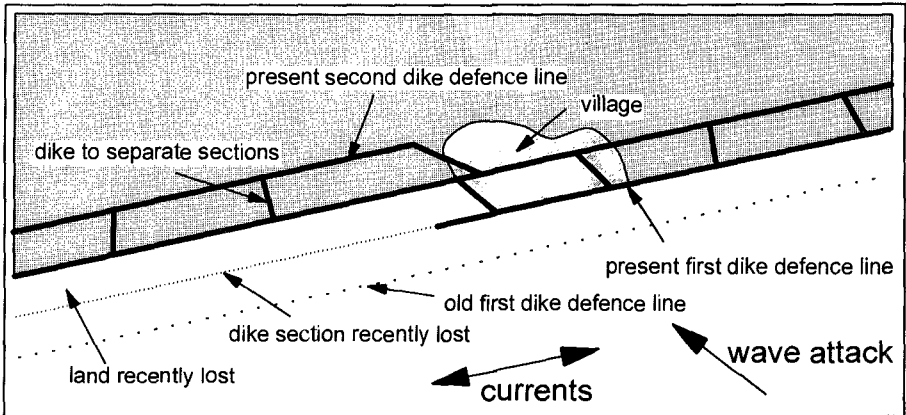


Figure 5 *Double Dike System*

order to prevent inundation the second defence line has been built. When the first dike fails the section behind the first dike is inundated and the second dike becomes the new first dike. Every time the first dike fails a section of land is lost to the sea since there are no resources to repair the old dike. In response to such a breakthrough a new second dike is built behind the new first defence line. On average every ten years a dike section is lost to the sea. This is a typical example of a managed retreat strategy although the Vietnamese authorities are forced by the circumstances. Beside the weakening of the dikes by the continuous erosion, the strength of the first defence line itself is in general insufficient due to problems such as funding and practical construction problems (such as accessibility of roads and availability of vehicles). This results in generally weak dykes, which are also too low, causing severe overtopping problems and revetment instabilities.

As the retreat of the coastline is known for many years evacuation plans are readily available. These plans are started on average every 2-3 years in case of high flooding risks. For maintenance and construction of the sea defences the authorities mobilise local inhabitants. As in the whole country the population has to invest a number of days per year in the community. The national average is about 10 workdays per year. In villages endangered by the erosion able bodied workers are required to work 40 days per year on dike repair, maintenance and construction.

ENVIRONMENTAL BOUNDARY CONDITIONS

The meteorological conditions of the area can clearly be divided into a summer (July and August) and winter (October to March) monsoon period. During the summer monsoon period moderate winds (average force: 3 Beaufort) from south western directions prevail. In winter the predominant wind direction is north east (average

wind force about 4 Beaufort). The summer monsoon period is also known as the 'wet season'. During this season 80% of the yearly run-off is discharged through the Red River system. Peak discharges are to be expected towards the end of the wet season or at extreme storm or typhoon events. On average two typhoons per year hit the coastline of the northern provinces of Vietnam. The typhoon season starts in May and lasts till October with the highest activity in the months July and August.

Similarly, the wave climate is also strongly influenced by the monsoon periods which is typical for this region of the world. The average deep water wave height in the summer months is about 1.5 m (coming from SW directions) whereas the average deep water wave height in winter is about 2 m (NE directions). However, during storms and typhoons the deep water significant wave height can develop to 10 m.

The characteristic range of the diurnal tide at spring tide is about 2.4 m. Currents along the coast are mainly tidally driven with a significant (seasonal) influence of wind and waves. During the last 30 years water levels (astronomic tide plus wind set-up) up to 3.00 m above MSL have been reported in bays and inlets along the shallow coast.

QUALITATIVE MORPHOLOGICAL ANALYSIS

The morphological system of the Red River Delta is very dynamic. During the wet summer monsoon season 80% of the annual sediment load is discharged to the Gulf of Tongking resulting in huge deposits near the River mouths. As the prevailing wave and wind direction is south west most of the sediment will be deposited on the eastern side of the river mouths (Figure 6). Wave conditions in the summer season can

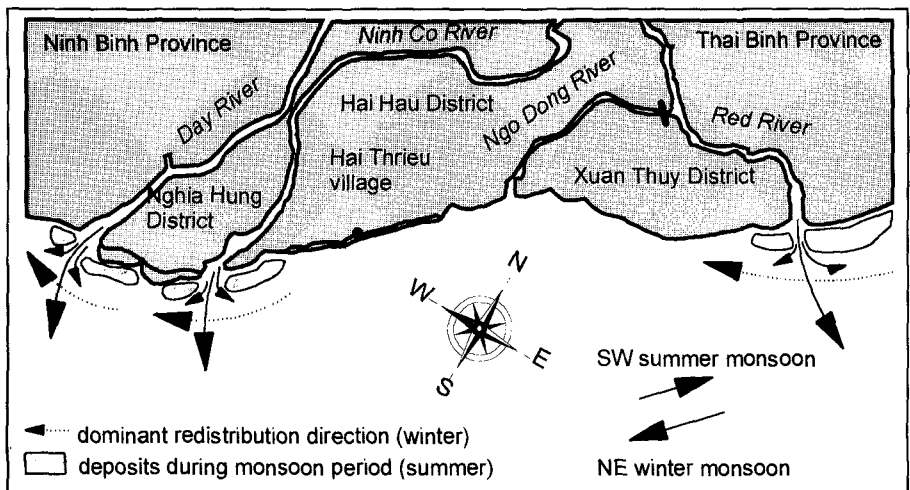


Figure 6 *Sediment Deposits and Redistribution Along the Shore*

be characterized as 'moderate' resulting in some redistribution of sediment in north-eastern direction. However, during the remainder of the year wind and wave conditions from north-eastern directions prevail. Compared to the summer monsoon the north-east monsoon is somewhat stronger and more persistent resulting in higher longshore sediment transports. During the winter season a substantial part of the fresh deposits will therefore be transported further offshore or be redistributed along the shore in south-western direction. The beach sections between the river mouths (beyond the direct influence of the river mouths) are therefore dependent on the redistribution mechanisms of deposited sediment from the nearest river branches.

Up to 1955 the Hai Hau district beaches were nourished by the Ngo Dong River in the north and the Ninh Co River in the south. The net sediment transport is directed to the south-west so the main source of sediment was the Ngo Dong River. With the damming of the Ngo Dong River the main sediment source was blocked resulting in erosion south of the River mouth. From then on the beaches of Hai Hau district had to be nourished from either the Red River or the Ninh Co River mouth (Figure 6). However, due to the shape of the Red River mouth hardly any nourishment took place from the north-east. Nourishment from the Ninh Co River could only develop during the summer months. From the coastline development graph (Figure 4) it can be seen that indeed some nourishment took place resulting in a stable or accreting development of the southern beaches of the Hai Hau district.

However, the erosion of the Hai Hau coastline did not start after the damming of the Ngo Dong River. The erosion started at the beginning of the century or even earlier. The reported erosion rates of 29 m/year over a length of 16 km indicate the Ngo Dong River must have been a major branch of the Red River. A possible explanation would be that at the end of the 19th century the Ngo Dong River lost its importance as a major branch of the Red River. This process, which can either be a natural development or a result of man made channelling works, redirected the discharge to, most probably, the present Red River mouth. The discharge through the Ngo Dong River diminished which allowed the damming in 1955. Damming would have never been possible when the Ngo Dong River was still a major branch of the Red River. This hypothesis of the historic development and importance of the Ngo Dong River is still under investigation.

QUALITATIVE PREDICTION OF THE SHORELINE DEVELOPMENT

Based on the above described hypothesis of the morphological system a prediction of the shoreline development can be made. When no action is taken the coastline will retreat at same pace for the coming years. On a longer timescale it is expected that the accreting coast of the Nghia Hung District will, due to the changing coastline orientation, develop an increasing nourishing effect on the Hai Hau coastline.

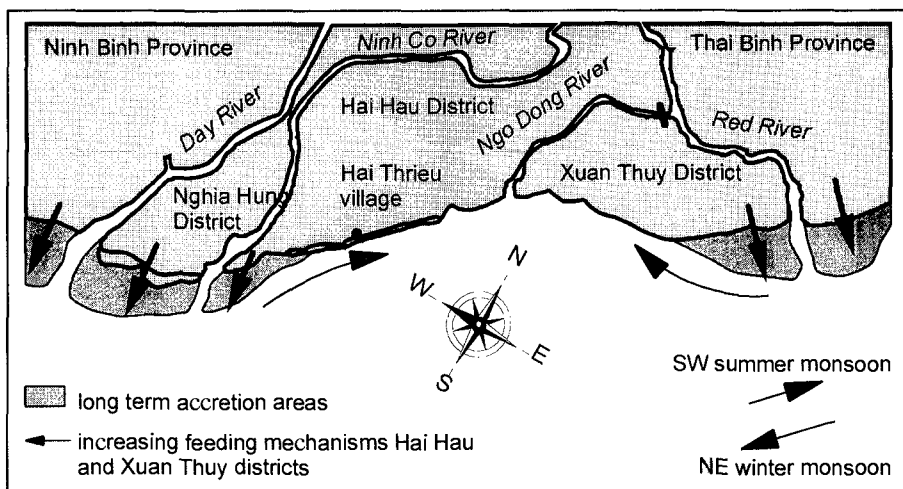


Figure 7 *Qualitative Prediction of Long Term Coastline Development*

The accretion near the mouths of the Ninh Co and Day River will slow down and the retreat at Hai Hau will decrease (Figure 7). This effect will develop along the coast starting in the south of the district.

SOCIO-ECONOMIC IMPACTS

Within Vietnam the Red River Delta (16,000 km²) is the most densely populated region with 1,700 inhabitants per square kilometre. This is also among the highest population densities on arable land in the world (VVA, 1996). The erosion at Hai Hau district causes significant socio-economic impacts. The land in the coastal strip is completely in use for agriculture, aquaculture and salt production. Further, because of the progressing retreat, a number of villages are at risk being located directly behind the sea defence. Hai Thrieu for instance is a commune of which part of the 8000 inhabitants live between the first and second sea defence. At present the second dike is being reinforced as the authority reluctantly have to abandon the first dike in case of a breakthrough. Moving this part of the village requires resources and will include a social problem since practically all the land is presently in use. A more general problem of the coastal region is salt intrusion via overtopping of dikes. In this way storms and typhoons can impact a strip of 750 m wide along the coast with salt (eg. typhoon Wayne, 1986). It takes years after such an event before the original crop yield can be reproduced.

STRATEGY TOWARDS SUSTAINABLE DEVELOPMENT

Based on this qualitative analysis of the erosion at Hai Hau district a number of measures and preliminary strategies can be defined. However, an integrated approach is recommended which includes not only technical aspects but also socio-economics, planning and institutional matters in order to achieve a sustainable development. This Coastal Zone Management approach needs to include more investigations and studies on the mentioned fields in collaboration with the responsible Vietnamese authorities and the local people. The key study would be, in succession on this first qualitative analysis, the extensive investigation of the morphological development. A sound understanding of the processes and developments will result in a quantitative prediction of the shoreline development. This will form the basis for all further strategy decision making.

ACKNOWLEDGEMENTS

The authors gratefully acknowledge the support of DGIS (Netherlands Ministry of Foreign Affairs), sponsors for this work and the Vietnamese Government (Hydrometeorological Services, the local host for this project and the Ministry of Agriculture and Rural Development), for permission to publish these findings.

REFERENCES

- VVA** (1996); *Vietnam Coastal Zone Vulnerability Assessment, various reports*; Government of the Netherlands; Ministry of Foreign Affairs; Government of the Socialist Republic of Vietnam, Hydrometeorological Services.
- World Bank** (1994); *Red River Delta Master Plan*; Ministry of Science, Technology and Environment; UNDP; World Bank.

CHAPTER 219

BEACH PROFILE ANALYSIS AROUND INDIAN RIVER INLET, DELAWARE, U.S.A.

Kirk F. Bosma¹ and Robert A. Dalrymple²

ABSTRACT: The purpose of this study is to examine the recent shoreline history at Indian River Inlet, Delaware using beach profile data. Indian River Inlet was stabilized in the late 1930's with two parallel rubble mound jetties. The stabilization resulted in considerable modifications to the surrounding beach environment, leading to the construction of a sand bypassing system in 1990. The profiles adjacent to the inlet are first examined with the standard tools, such as shoreline change, volume change, and sand budget. Then, details are given on the use of Principal Component Analysis (PCA) in the coastal field, an explanation of its function, and the differences between the complex and non-complex versions. Results are presented for areas north and south of the inlet in both 2-mode and 3-mode versions of Complex Principal Component Analysis (CPCA). The results illustrate the ability of CPCA to detect moving features within the profile data, including its direction and speed, as bypassed sand is seen moving to the north.

INTRODUCTION

The Delaware Atlantic coastline, a sandy shore that spans approximately 24 miles, is an area of constant transformation. Significant littoral drift rates, man-made structures, remediation efforts, and occasional battering by large storms all effect the coastline. Thus, the beach profiles are 'dynamic' in character, changing continuously. These profile variations occur in both the subaqueous and subaerial elements of each profile, as wave energies constantly move sand on, off, or alongshore. In effect, changes in profiles can reveal a vast amount of information, both long and short term, about the coastline.

The focus of this study is the profiles adjoining Indian River Inlet (as shown in Figure 1), which is one of the most unique features along the Atlantic Coast of Delaware. After several failed attempts to keep the Indian River Inlet open by dredging alone, a 152 meter (500 foot) wide inlet was constructed in the late 1930's. The goal being to establish a stable passage way from the inner bays (Rehoboth and Indian River) to the Atlantic Ocean, increase bay salinity, reduce stagnation, and increase the tide range (Thompson and Dalrymple, 1976). The

¹Graduate Student, Center for Applied Coastal Research, University of Delaware, Newark, DE 19716, USA.

²Professor and Director, Center for Applied Coastal Research, University of Delaware, Newark, DE 19716, USA.

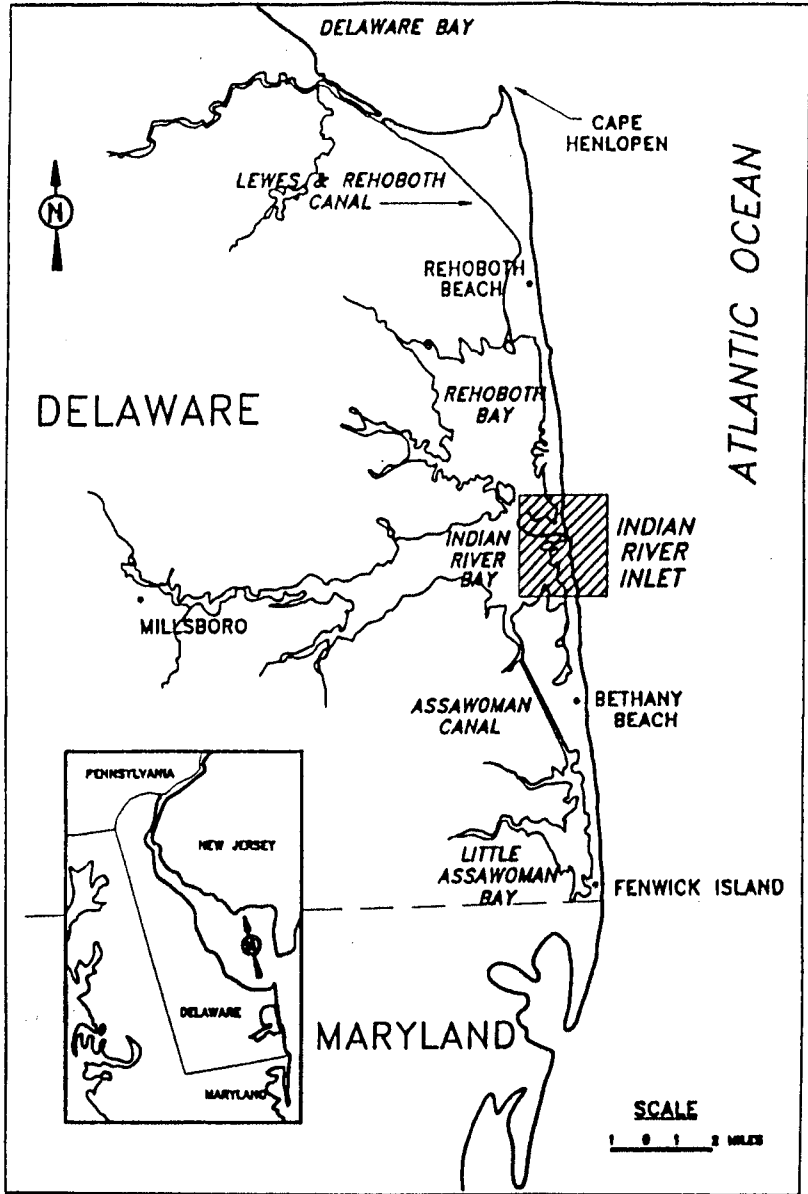


Figure 1: The Atlantic Coast of Delaware

inlet is stabilized by two parallel rubble mound jetties, originally extending a distance of 472 meters (1550 feet). 185 meters (600 feet) of this length extended seaward of the ocean shoreline at the time of construction. There have been significant problems with the engineered inlet over the years, including erosion of channel banks west of the jetties, accelerated scour along the jetties, and massive downdrift erosion, due to the predominant northward drift (Gebert *et al.*, 1992). The main concern related to the downdrift erosion is the threat it poses to the Route 1 highway traveling parallel to the shoreline. In fact, by 1954, a dune scarp had been created that was, in places, less than 60 meters (200 feet) from the roadway. From 1957 to 1990, mitigation of the beach erosion was accomplished by dredging of the flood tidal shoal and back barrier deposits. Approximately $380,000 \text{ m}^3$ ($49,700 \text{ yd}^3$) of sand was placed on the north beach approximately every five years. Since February of 1990, however, a fixed sand bypassing system was constructed to pump sand from the southern shore and "slurry" it across the inlet to the northern shore. The system mines the south accretional fill by using an eduction unit deployed by a crane. Through May of 1995, approximately $350,000 \text{ m}^3$ ($456,000 \text{ yd}^3$) have been pumped across the inlet at a cost of \$2.11 per m^3 (\$1.62 per yd^3). The system is performing well and is relatively inexpensive to run.

The objective of the present study is to investigate many aspects of the beach profile at Indian River Inlet through the use of the newest analytic methods and the most recent field data available. We want to determine what the profiles north and south of the inlet reveal about the region and to answer questions such as:

- What happens to the bypassed sand?
- Is enough sand being pumped?
- Can we identify moving forms or sandwaves?

To do this, we consider the early performance of the bypassing plant through shoreline changes, evaluation of littoral drift, and other standard analytical tools. We also explore the use of complex principal component analysis (CPCA), in both 2-mode and 3-mode versions, to evaluate propagating features that exist within a bathymetry.

FIELD DATA COLLECTION

Profile data sets are considered on both the north and south side of Indian River Inlet collected by the U.S. Army Corps of Engineers, Philadelphia District. The profiles span from 1984 to 1994, with an average of two surveys per year. 28 profile lines are taken in the range from 1524 meters (5000 ft) south of the inlet to 1524 meters (5000 ft) north of the inlet, as shown in Figure 2. 17 of the lines are located in the northern portion of the study area, while 11 are located in the south. As shown in Figure 2, some profile lines extend far offshore, while others only advance to the water line. The station numbers provided are the distance in hundreds of feet (30.5 m), from the respective jetty centerline. Survey points were taken randomly during each survey, thus requiring linear interpolation in both the alongshore and cross-shore directions for much of the analysis. Examples of the bathymetries north and south of the inlet are shown in Figure 3. Notice the scour hole that is evident at the tip of the northern jetty.

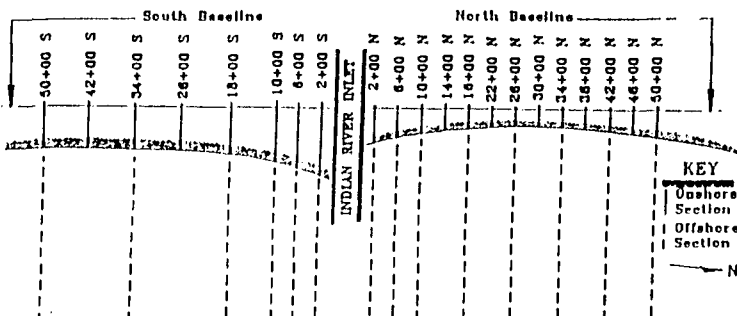


Figure 2: Profile lines north and south of Indian River Inlet

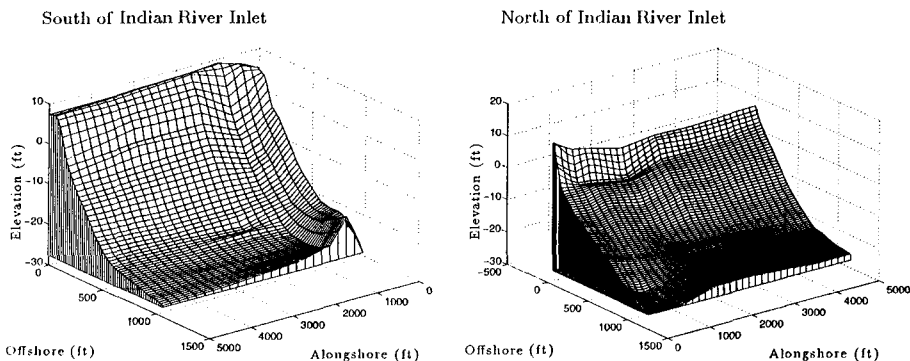


Figure 3: Sample bathymetries (October 1994) for north and south of Indian River Inlet. Offshore grid intervals are 152.4 meters (500 feet); alongshore, 304.8 meters (1000 feet); and elevation, 3.05 meters (10 feet).

SHORELINE CHANGE

The simplest way to examine what is occurring on a given region along the coast is to evaluate the change in shoreline position. This 1-line analysis quantifies beach behavior and allows for comparison of pre- and post-bypassing. Cumulative shoreline change plots for four profile stations in the range extending up to 305 meters (1000 feet) away from the inlet in both the north and south directions are shown in Figure 4. The figure illustrates the shoreline behavior at various stations through time. Watson *et al.* (1993) have computed similar results for a shorter interval of time. For this study, the pre-bypassing interval is from November of 1984 to October of 1989. The initial survey of November 1984 takes place after a large beach fill of 35,781 m³ was placed between stations 0+00 to 30+00. Surveys measured after October of 1989 are considered post-bypassing. Since we only have a total of four years of data after bypassing start-up, only the short-term performance of the system can be determined.

North of the inlet the trend had been towards progressive retreat, as expected due to the influence of the inlet and the northward littoral drift. Only once,

during the winter season from September 1987 to March 1988, did a substantial shoreline advance occur. This was most likely due to the net reversal of littoral drift in the winter months (response to “northeasters”) and thus the trapping of some sediment in the shadow of the jetty. The general shoreline retreat was evident until approximately 1035 meters (3400 feet) from the jetty. At this distance, the effect of the inlet was lessened and larger seasonal variations tended to dominate. The bypassing operation was started with the aid of a 133,800 m³ (175,000 yd³) fill (evident in the March 1990 survey) obtained from the flood shoal. The initial increase in beach width was not retained due to the spreading of the beach fill, but the shoreline for the stations just north of the inlet seems to have stabilized since bypassing initiation.

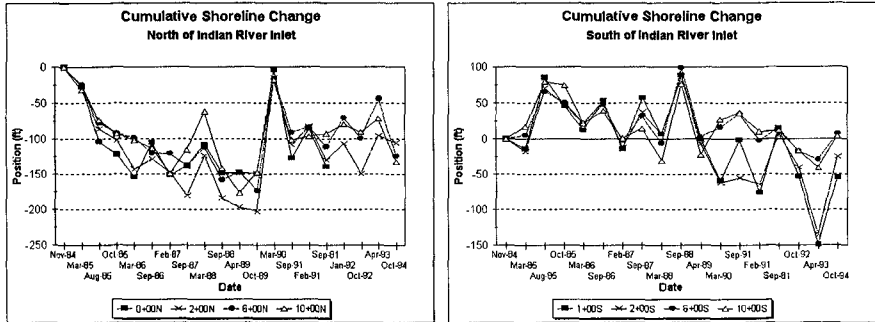


Figure 4: Cumulative shoreline plots showing relative distance from original shoreline position with time for the first four profile stations both north and south of Indian River Inlet.

South of the inlet, pre-bypassing, the trend had been overall stability with some slight accretion. The accretion, if any, was at a much lower rate than the erosion to the north. Again, at around 1035 meters (3400 feet), the effect of the inlet seemed to be minimized as the overall change in beach width was small. After bypassing start-up, Stations 1+00 and 2+00 exhibited immediate effects of the sand mining. Proceeding southward, the next two stations (6+00 and 10+00) show a slight lag in the response to the mining and a smaller shoreline retreat. Notice as well that all stations recover quickly from the effect of the mining. Sand bypassing influence is also typically seen to about 1035 meters (3400 feet) south of the inlet.

VOLUME CHANGE AND SAND BUDGET

Next, volume changes for the areas between profile stations were computed. From these volume changes, a standard sand budget analysis was calculated for the northern region by assuming that the only sediment entering the area was due to bypassing or beach fills. The results from this analysis, shown in Figure 5, yield a measure of the local transport rate. The littoral drift is found to be dominantly northward, as expected, at a rate of approximately 79,500 m³ (104,000 yd³) per year. This value was found to be consistent with values found in the past by other methods (Lanan and Dalrymple, 1977; U.S. Army Corps of Engineers, 1984).

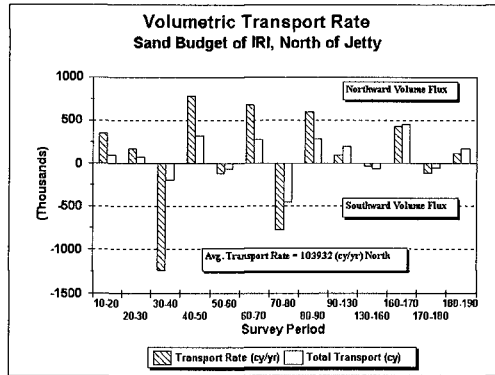


Figure 5: Local volumetric transport rate for north of Indian River Inlet.

THE HISTORY OF PRINCIPAL COMPONENT ANALYSIS

Many geophysical phenomena derive from interactions between traveling waves of different spatial scales and temporal frequencies. Principal component analysis (PCA) was developed to explore these spatial and temporal relations with the primary advantage of its ability to express the complicated variability of data into the fewest possible number of modes. Thus, applying this idea to beach profiles, beach changes can be described by linear combinations of space and time through the breakdown of data into spatial and temporal dependence (e.g. Winant *et al.*, 1975; Aubrey, 1979). Winant *et al.* (1975) found that most of the variation in a profile configuration is accounted for by the first three eigenfunctions, which corresponded to the "mean beach," "bar-berm," and "terrace" functions. However, PCA detects standing oscillations only, such as the standing phenomena of the shift from summer to winter profiles in seasonally sampled data (Winant *et al.*, 1975), not traveling waves. Therefore, PCA can not identify a coherent form moving through the data, such as a rapidly traveling bar as a sand wave alongshore.

Complex principal component analysis (CPCA) was developed for meteorological applications (e.g. Wallace and Dickinson, 1972; Barnett, 1983) and has been used to detect a fast moving sand bar by Liang and Seymour (1991). CPCA has also been shown to out-perform PCA by capturing more of the variance in fewer terms by Liang, White, and Seymour (1992). CPCA has considerable potential for being widely used to detect propagating features, yet its limitations as an analysis technique have not been well explored.

Both of the methods discussed above account for only one spatial direction when evaluating the temporal changes in the data set. This assumes the movement is directed in two independent directions and therefore, the analysis is limited to looking at only individual cross-shore or alongshore "lines." However, what if there is two dimensional movement of sand, as expected in response to a coastal structure or a beach nourishment? Then the 2-dimensional analysis may be rendered inadequate. So, in a further expansion of PCA, the analysis was carried into a third dimension allowing the break down of data into three separate components. This so-called 3-mode PCA was started for mathematical psychology applications, such as the evaluation of multiple personality patients

(Tucker, 1966; Kroonenberg and DeLeeuw, 1980). For the case of a coastal region, 3-mode PCA allows a bathymetric survey to be divided into two spatial directions (cross-shore and alongshore) and a temporal dependence. The technique was applied to a beach fill site in Spain by Medina *et al.* (1992).

In the next section, we apply the 2-mode CPCA tool to the beach profile data of Indian River Inlet and develop a 3-mode CPCA model to examine movement occurring in multiple directions within a bathymetry. The 2-mode CPCA is shown to not only detect the moving forms as well as standing forms, but also distinguish between them.

2-D COMPLEX PRINCIPAL COMPONENT ANALYSIS

To apply CPCA, the data field must first be augmented in a manner such that propagating features within it may be detected. This is done by deriving a complex data matrix, where the real part is simply the original data field and the imaginary part is the Hilbert transform, which represents a filtering operation upon the data in which the amplitude of each spectral component is unchanged, but each components phase is advanced by $\pi/2$. If $g(t)$ is a real-valued function of time, we can define an analytic function

$$z(t) = g(t) + ih(t)$$

where $h(t)$ is the Hilbert transform of $g(t)$ given as:

$$h(t) = \mathcal{H}(g(t)) = \frac{1}{\pi} \int_{-\infty}^{\infty} \frac{g(t')}{t' - t} dt' \quad (1)$$

Using the complex data, we can compute complex eigenvectors (functional decompositions of the data) and eigenvalues (portions of the variation represented by each eigenvector). The goal is to expand the data, $z(x, t)$, into two dimensions (in this case offshore and time) as:

$$z(x, t) = \sum_{i=1}^n a_i g_i(t) e_i(x) \quad (2)$$

n =number of desired modes

a_i =normalizing factors (eigenvalues)

g_i =temporal eigenfunctions

e_i =spatial eigenfunctions

This is done through computation of the correlations between the spatial locations to develop a complex correlation matrix, as shown in Equation 3, where n_t is the total number of surveys and the large brackets denote a time average. The eigenvalues and eigenvectors are then determined from the complex correlation matrix.

$$A_{ij} = \langle z_j(t)^* \cdot z_i(t) \rangle_{n_t} \quad (3)$$

The 2-mode CPCA is used to look at an alongshore profile lines north of Indian River Inlet in the hope of identifying migrating features. Because of the random sampling of the data, many profile lines had to be discarded for various reasons (e.g. did not extend far enough offshore, a given survey was missing,

etc.). The results shown below are for an alongshore profile line located approximately 76 meters (250 feet) from the baseline. The complex correlation between the complex time series at given alongshore grid points are shown in Figure 6a. Each complex correlation is plotted in vectorial format where the real portion (magnitude) is indicated in the vertical direction of the vector and the imaginary portion (phase) is indicated in the horizontal direction. A vector pointing upwards (downwards) indicates that the two time series are in-phase (out-of-phase). For example, a vector pointing to the right indicates a lag of 90 degrees. The complex correlation between the time series delineates the propagation of a moving "bump" through the domain. Figure 6b shows the resulting spatial eigenvectors for the alongshore line, plotted in vectorial format as in Figure 6a. The numbers correspond to the percent of variance retained by each eigenvector. The top panel is the first eigenvector which represents the mean alongshore profile and accounts for 98% of the variance. The eigenvector is almost entirely real valued, which signifies that no extensive movement is associated with it, and exhibits a depression in magnitude near the inlet entrance. The second eigenvector identifies a definite progressive feature, which represents 1% of the total variance. Imagine the movement as a spinning motion indicated by vectors "rotating" through space. The second eigenvector then represents a moving form that augments the mean alongshore profile. Similarly, the third eigenvector, which indicates no coherent movement, modifies the mean further.

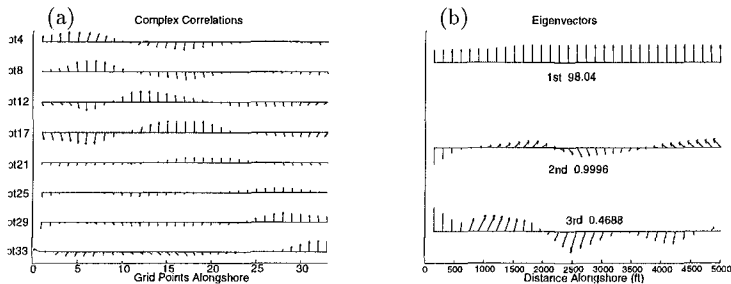


Figure 6: (a) Complex correlation between time series for alongshore grid points. Notice that the vector is normalized to one when a time series is correlated to itself; i.e. the time series of point 4 is perfectly related to itself. (b) Eigenvectors computed by CPCA for an alongshore profile line North of Indian River Inlet. Spacing intervals in the distance alongshore are 152.4 meters (500 feet).

Once the eigenvectors and eigenvalues have been determined, we are able to define both a spatial ($\theta_i(x)$) and temporal ($\phi_i(t)$) phase function as:

$$\theta_i(x) = \arctan \left[\frac{\text{Im}(e_i(x))}{\text{Re}(e_i(x))} \right] \quad \phi_i(t) = \arctan \left[\frac{\text{Im}(g_i(t))}{\text{Re}(g_i(t))} \right] \quad (4)$$

The spatial derivative of the spatial phase function then provides a measure of the "local" wavenumber. Similarly, the time derivative of the temporal phase function is directly proportional to the "instantaneous" frequency. Therefore, CPCA not only allows us to identify a moving form, but also determine the direction and the rate at which it is moving. The spatial and temporal phase functions for the same alongshore profile line, as presented in Figure 6, are shown in Figure 7. The numbers correspond to the approximate wavenumber

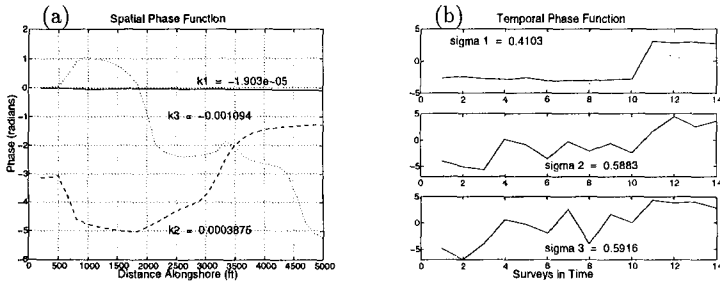


Figure 7: (a) Spatial phase function for alongshore location north of Indian River Inlet. Spacing intervals in alongshore distance are 152.4 meters (500 feet). (b) Temporal phase function for the same location.

and frequency of each eigenvector component. By using these values, the second eigenvector indicates a feature that is moving northward at the rate of around 1.68 meters (5.5 feet) per day. Therefore, over this time period, CPCA reveals that sand was relatively quickly moved out of the area to the north.

3-D COMPLEX PRINCIPAL COMPONENT ANALYSIS

The 2-mode CPCA appears to be very useful for many cases. However, what if 2-dimensional movement of sediment is expected, as mentioned earlier. The 3-mode CPCA is applied to the nearshore region, where significant movement is occurring, for both north and south sides of the inlet. In 3-mode CPCA, we begin with a set of data matrices or rather, a large 3 by 3 cube of data, which can also be thought of as a collection of 2-mode matrices (Figure 8).

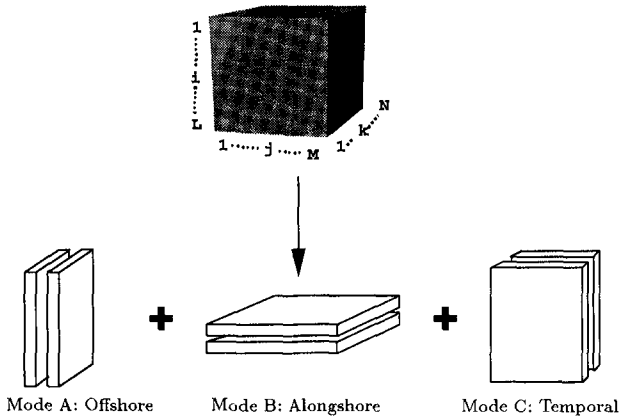


Figure 8: Schematic breakdown of a 3-mode data set into 2-mode submatrices.

Again, after Hilbert transforming the data in time to generate a complex

data set, we seek to expand the data in two spatial dimensions and time by:

$$z(x, y, t) = \sum_{m=1}^s \sum_{p=1}^u \sum_{q=1}^v e_m(x) f_p(y) g_q(t) C_{mpq} \tag{5}$$

where

s, u, v are the number of components in the 3 modes, respectively
 e, f, g are the offshore, alongshore, and temporal eigenfunctions, and
 C_{mpq} is the core matrix (normalizing factors)

Rewriting Equation 5 in matrix form we arrive at

$$Z(x \times yt) = E(x \times s)C(s \times uv)[F(y \times u)' \otimes G(t \times v)'] \tag{6}$$

where \otimes denotes the Kronecker product and the dimension of the matrices Z and C are augmented to be two dimensional arrays. The core matrix, C , is no longer a simple diagonal matrix of eigenvalues as in 2-mode analysis, but a complex combination of elements that describe the basic relations that exist between the various collections of variables as expressed through their components (Kroonenberg and DeLeeuw, 1980).

The cross-shore and alongshore eigenvectors for the nearshore region north of the inlet are presented in Figure 9. For simplicity, only the real part of each eigenvector is shown. To illustrate the relative importance between both the variables and components, the eigenvectors shown have been weighted. These eigenvectors can be thought of as the average form of all cross-shore or alongshore profile lines in the region. In the cross-shore direction, we see the mean is easily identifiable. The second component, typically referred to as the “bar-berm” function is significantly reduced in importance due to the larger fluctuations occurring in the alongshore direction. In the alongshore eigenvectors, the mean is characterized by a dramatic depression that occurs near the inlet. The second and third components highlight sizable changes in the alongshore direction.

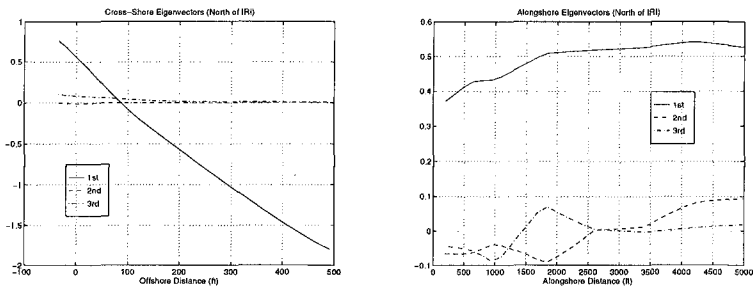


Figure 9: The real portion of cross-shore and alongshore eigenvectors computed from 3-mode CPCA. Offshore distance is spaced at 30.5 meters (100 feet), while the alongshore distance is spaced at 304.8 meters (1000 feet).

The eigenvector components can also be combined to represent various features of the bathymetry. These *eigenvector combinations* are products of the

different alongshore, cross-shore, and temporal components. Similar to a large puzzle, if we have three components in each variable, then there are 27 combinations that make up a complete bathymetry. The three combinations that capture the highest amount of variance are shown in Figure 10. The real part of each combination is shown on the left and the imaginary part of the combination on the right. The top panel shows the combination A1O1, which is defined as the product of the first eigenvector in the alongshore direction (A) and the first eigenvector in the cross-shore direction (O). This combination represents the mean bathymetry and the real part is characterized by the erosion located at nearshore region of the inlet entrance. The middle panel shows the A1O3 combination, corresponding to the product of the first alongshore eigenvector and the third cross-shore eigenvector. This combination modifies the mean bathymetry most notably in the shoreline area where bypassing has a significant effect. The lower panel, which contains the A3O3 combination (same nomenclature as before), is perhaps the most intriguing. A large "bump" appears on the real portion of the bathymetry, while the imaginary portion depicts a wave-like phase rotation. This imaginary "hot spot" of movement indicates that the feature is in motion. Notice that the magnitude of the imaginary bathymetry decreases as we proceed offshore. Therefore, the alongshore movement is strongest at the nearshore area and becomes less severe further offshore.

The eigenvector combinations for the region south of Indian River Inlet are shown in Figure 11. The nomenclature remains the same as for the combinations north of the inlet. Again, the top panel represents the mean bathymetry and shows a build up of sediment in the area adjacent to the southern jetty. The A2O3 and A2O1 combinations illustrate changes that are occurring once again in the neighborhood of the inlet entrance. The difference between the two is that the imaginary portion of A2O3 identifies more of a movement in the alongshore direction, while the imaginary portion of A2O1 identifies more of a movement in the cross-shore direction. This may mean that, after bypassing occurs, the large eduction hole that remains recovers by receiving sediment from both the alongshore and offshore elements of the bathymetry.

CONCLUSIONS AND SUMMARY

An in-depth analysis of the profiles at Indian River Inlet, Delaware has been accomplished by using standard analysis tools and Complex Principal Component Analysis. Early returns of the sand bypassing system seem to be positive. The shoreline analysis reveals that the north shore has been stabilized by the bypassing and the south shore recovers quickly from the eduction process. The littoral drift indicates sand is moving to the north and that a larger amount of sand could be pumped each season. Generally, sand moves quickly to the north as evident from both the shoreline variation and CPCA analysis. As shown, CPCA has considerable potential, but needs further investigation on a more finely sampled data set.

ACKNOWLEDGMENTS

Special thanks to the State of Delaware Department of Natural Resources and Environmental Control, Beach Preservation Section for support and providing the profile data. The program TUCKALS3 for 3-mode real PCA was provided by R. Medina of Universidad de Cantabria.

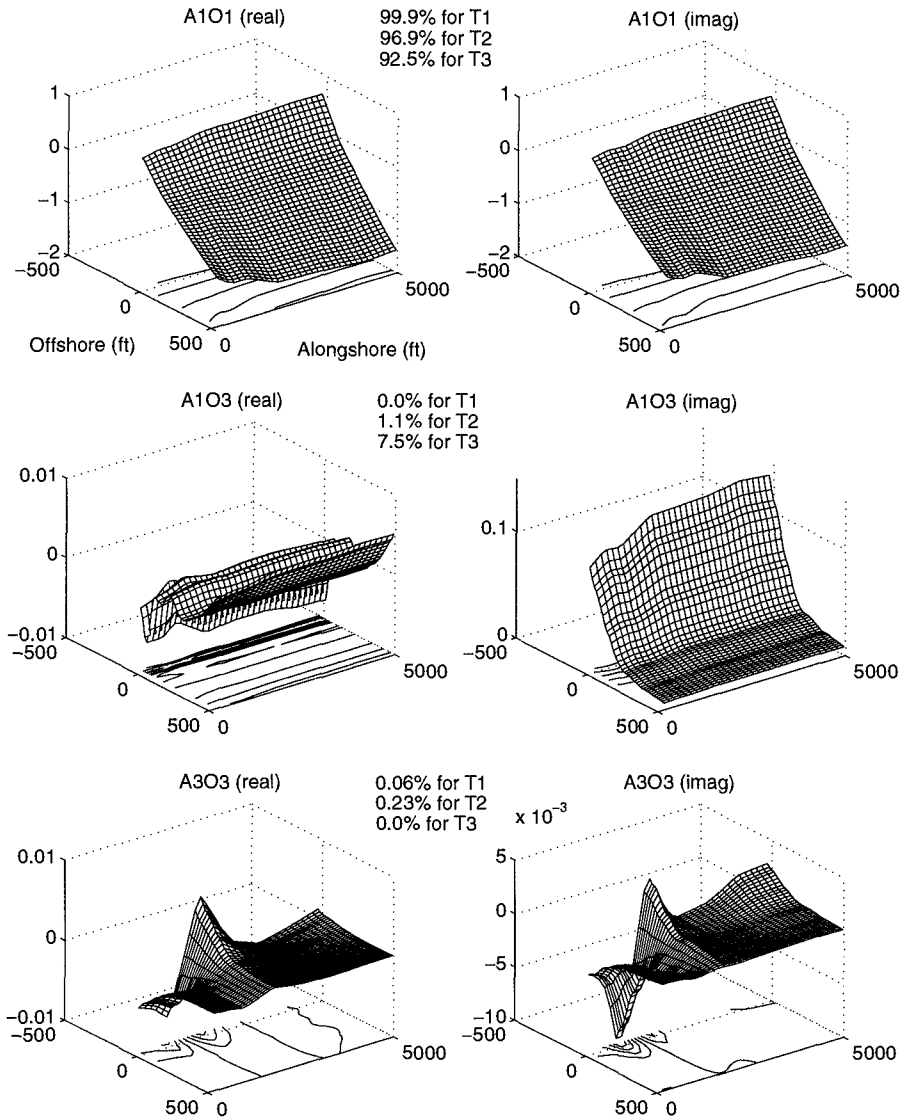


Figure 10: Eigenvector combinations north of Indian River Inlet. The numbers (or core matrix values) included represent the percent of variance captured by each eigenvector combination for a given temporal component. The offshore range is spaced at 152.4 meters (500 feet) and the alongshore range covers 1524 meters (5000 feet).

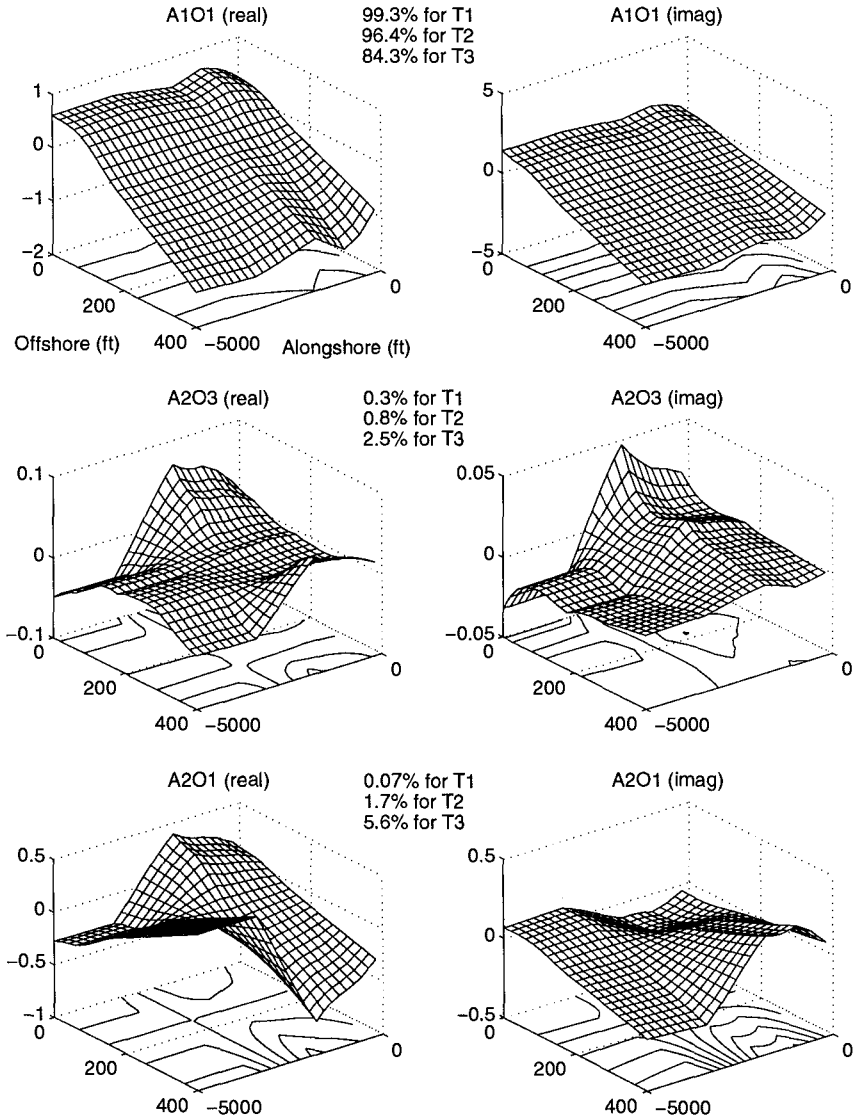


Figure 11: Eigenvector combinations south of Indian River Inlet. The numbers (or core matrix values) included represent the percent of variance captured by each eigenvector combination for a given temporal component. The offshore range is spaced at 61 meters (200 feet) and the alongshore range covers 1524 meters (5000 feet).

REFERENCES

- Aubrey, D. G. (1979). "Seasonal Patterns of Onshore/Offshore Sediment Movement." *J. of Geophys. Res.*, 84, 10, 6347-6354.
- Barnett, T. P. (1983). "Interaction of the Monsoon and Pacific Trade Wind Systems at Interannual Time Scale. Part I: The equatorial zone." *Mon. Weather Review*, 111, 756-773.
- Gebert, J., Watson, K., and A. Rambo (1992). "57 Years of Coastal Engineering Practice at a Problem Inlet: Indian River Inlet, Delaware." *Coastal Eng. Practice*, ASCE, 1-17.
- Kroonenberg, P. M., and J. DeLeeuw (1980). "Principal Components Analysis of Three-Mode Data by Means of Alternating Least Squares Algorithms." *Psychometrika*, 45, 69-97.
- Lanan G. A. and R. A. Dalrymple (1977). "A Coastal Engineering Study of Indian River Inlet, Delaware." University of Delaware, Newark Col. of Marine Studies, MD Sea Grant, Report No. DEL-SG-5-77.
- Liang, G. and R. J. Seymour (1991). "Complex Principal Component Analysis of Wave-like Sand Motions." *Coastal Sediments '91*, ASCE, 2175-2186.
- Liang, G., White T. E., and R. J. Seymour (1992). "Complex Principal Component Analysis of Seasonal Variation in Nearshore Bathymetry." *Coastal Eng.*, ASCE, 2242-2250.
- Medina, R. *et. al* (1992). "Three-Mode Principal Component Analysis of Bathymetric Data, Applied to 'Playa de Castilla' (Huelva, Spain)." *Coastal Eng.*, ASCE, 2265-2278.
- Thompson, W. W. and R. A. Dalrymple (1976). "A History of Indian River Inlet, Delaware." *Shore and Beach*, Vol. 7, 24-31.
- Tucker, L. R. (1966). "Some Mathematical Notes on Three-Mode Factor Analysis." *Psychometrika*, 31, 279-311.
- U.S. Army Corps of Engineers, Philadelphia District (1984). "General Design Memorandum Sand Bypass Plant: Indian River Inlet, Delaware." Philadelphia, Pa.
- Wallace, J. M. and R. E. Dickinson (1972). "Empirical Orthogonal Representation of Time Series in the Frequency Domain, Part I. Theoretical considerations." *J. Appl. Meteorology*, 11, 887-892.
- Watson, K. D., Clausner, J. E., and R. D. Henry (1993). "Beach Response to Sand Bypassing at Indian River Inlet, Delaware." *Coastal Technology*, ASCE, Hilton Head S.C.
- Winant, C. D., Inman, D. L., and C. E. Nordstrom (1975). "Description of Seasonal Beach Changes using Empirical Eigenfunctions." *J. Geophys. Res.*, 80, 15, 1979-1986.

CHAPTER 220

IMPROVED 3-D BEACH EVOLUTION MODEL COUPLED WITH THE SHORELINE MODEL (3D-SHORE)

Takuzo Shimizu ¹, Takahiro Kumagai ¹ and Akira Watanabe ²

ABSTRACT

An improved 3-D beach evolution model coupled with the shoreline model, named "3D-SHORE", was newly developed to estimate both the spatial bottom topography change and the shoreline change. In calculation of the shoreline change, the total longshore sediment transport rate is estimated by integrating the local sediment transport rate in the direction parallel to the shoreline from the breaking point to the run-up point. The applicabilities of the model were verified through comparisons with both the results of the movable bed laboratory experiment and the actual beach evolution.

INTRODUCTION

In recent years, the 3-D beach evolution model which treats only the sediment transport due to nearshore currents have been applied to many practical problems in Japan. This model, based on the depth-averaged nearshore current model, is called "Medium-term 2DH Coastal Area Model" according to de Vriend et al.(1993). The authors have presented a few attempts to quantitatively verify its field applicabilities through comparisons with the actual medium-term topographical changes around a harbor entrance during 1 to 5 years(e.g. Shimizu et al., 1990, 1994). This conventional 3-D beach evolution model have reached the stage of being applicable for engineering use to estimating the volume of maintenance dredging around a harbor entrance and to investigating an effective countermeasure against harbor shoaling. It is, however, difficult to estimate the shoreline change, especially shoreline retreat, because the shoreline is used to be

¹Penta-Ocean Construction Co., Ltd., 2-2-8 Koraku, Bunkyo-ku, Tokyo 112, Japan.

²Professor, Dept. of Civil Eng., Univ. of Tokyo, 7-3-1 Hongo, Bunkyo-ku, Tokyo 113, Japan.

treated as a fixed boundary in the model. Therefore, we cannot assess the impacts due to construction of a harbor on neighbouring beaches with good accuracy. In order to make the 3-D beach evolution model more practically useful, the model should be improved to treat the shoreline as a moving boundary and to properly estimate the shoreline change.

In this study, we developed an improved 3-D beach evolution model, named "3D-SHORE", which is coupled with the conventional shoreline model. The applicability of the model is verified through comparison with the result of movable bed laboratory experiment for the beach evolution around a detached breakwater. And we also tried to simulate the actual bottom topography changes around an offshore man-made island type fishing port during approximately a year.

IMPROVED BEACH EVOLUTION MODEL

Basic Model Concepts

Our interests are focussed on the impact assessment of neighbouring beaches due to construction of a maritime structure. It is demanded to evaluate long-term beach evolution during more than 10 years after the construction. For the beach evolution around a maritime structure, the sediment transport due to nearshore currents plays a predominant role and the contribution from cross-shore sediment transports due to waves and undertow is usually cancelled for a long period beyond approximately a year.

The shoreline model which describes only the longshore sediment transport is widely used in practise for such a case. We have recognized that the shoreline model is applicable to estimating beach evolution caused by the unbalance of sediment budget in the alongshore direction over long time scales and for broad spatial scales. However, in the vicinity of the harbor, where the nearshore circulations occur and the offshoreward sediment transport due to nearshore currents exist, the shoreline model approach has a limited applicability.

The 3-D beach evolution model which treats only the sediment transport due to depth-averaged nearshore currents, "Medium-term 2DH Coastal Area Model", is based on the same concept as that of the shoreline model. This medium-term predictive model can be, therefore, regarded as an improved version of the shoreline model, which has an advantage of estimating the spatial beach topography changes.

Another 3-D beach evolution model is a short-term predictive model which treat both longshore and cross-shore sediment transports. This model is based on the quasi-3D or fully 3D current model which can describe the vertical structure of nearshore current and undertow. In order to properly estimate the beach profile changes, the short interval iterations, probably every one or two hour repetitions are needed. The computations of the wave and current fields are, however, much time-consuming. At present, it is unrealistic to improve the short-term predictive model to properly estimate the shoreline change. We, therefore, tried to develop the 3D-SHORE for practical use by coupling the medium-term predictive model

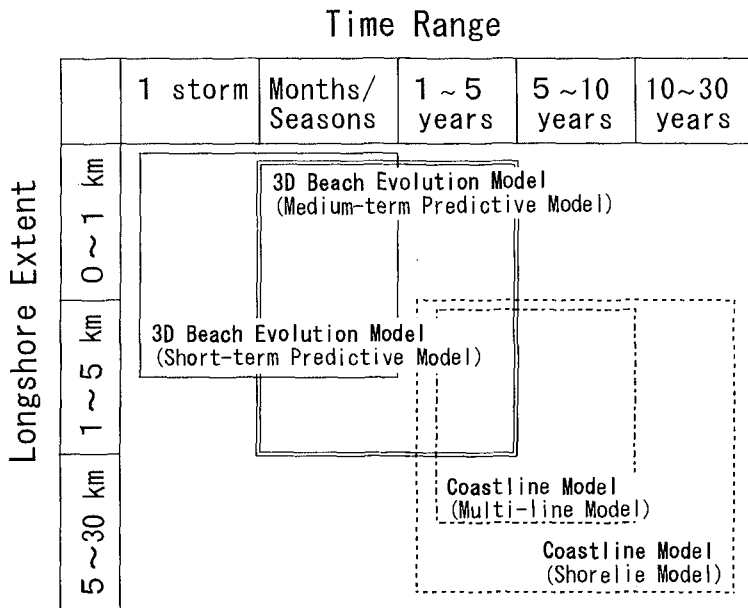


Fig. 1 Classification of numerical models of beach evolution.

Table 1 Comparisons of numerical models of beach evolution.

	Coastline Model	3D Beach Evolution Model (Coastal Area Model)	
	Shoreline Model/ Multi-line Model	Medium-term Predictive Model	Short-term Predictive Model
■ Spatial Scale Temporal Scale	5~10 km 1~30 years	1~5 km 1~5 years	1~3 km 1 storm~1 year
■ Current Calculation	×	2DH (Depth-averaged Nearshore Current)	• Quasi-3D : (Nearshore Current (2DH) +Undertow (1DVor2DV)) • Fully-3D
■ Sediment Transport • Longshore Transport (due to nearshore currents) • On-offshore Transport (net transport due to waves + offshore transport due to undertow)	○ ×	○ ×	○ ○

with the shoreline model.

Fig.1 shows the classification of numerical models of beach evolution by spatial and temporal scales. The comparisons of the models are briefly summarized in Table 1.

Structure of 3D-SHORE

The flow chart of the improved 3-D beach evolution model (3D-SHORE) is shown in Fig.2. The model consists of four submodels for calculating 1)nearshore waves, 2)nearshore currents, 3)local sediment transport rate and spatial beach change, and 4)total longshore sediment transport rate by integrating local sediment transport rate and shoreline change.

The new bottom topography can be calculated by coupling the calculation results of shoreline change and spatial beach evolution. The new bottom topography is, then, fed back into the wave-current computations with appropriate intervals.

Wave Model

The waves in the swash zone play important roles on the shoreline change. In the nearshore wave model, the run-up height is estimated by the Hunt's formula, assuming the beach-face slope determined by the empirical relationship incorporating wave height, period and sediment grain size proposed by Sunamura(1984). The wave set-up and set-down are estimated by the approximate expressions for a plane beach according to Longuet-Higgins and Stewart(1962). The water depth in the swash zone is given virtually by decreasing linearly from the wave set-up height at the still water level to zero at the run-up point as shown in Fig.3. This virtual water depth is also used for calculation of the nearshore current field. Although this treatment of swash zone is not correct in a strict sense, it is a simple and effective method for engineering use in order to save computational time and take an important factor into consideration.

The parabolic-type equation model proposed by Isobe(1987) is employed in this study to properly estimate the wave field behind the offshore breakwater and man-made island and so on where combined diffraction and refraction occur. This basic equation is derived from the mild slope equation by using the wave ray-front coordinates. The energy dissipation term due to wave breaking is included. Random waves are described as a superposition of component regular waves with different frequencies and directions. The applicabilities of the model to the actual wave field were verified through comparisons with field measurement data (e.g. Shimizu et al.,1992).

Nearshore Current Model

In most of the previous computation of nearshore currents, the friction term is expressed as the general nonlinear form and a constant value has been used for the frictional coefficient C_f in the calculation domain. Its value, however, affects the magnitude of the nearshore current velocity and the resultant sediment transport rate. We, therefore, tried to directly estimate the local values of bottom frictional

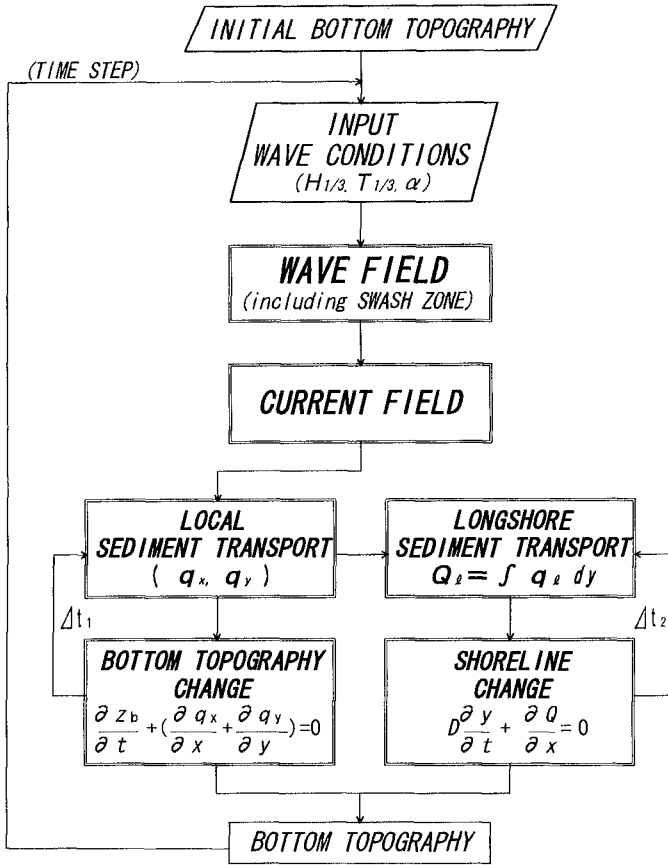
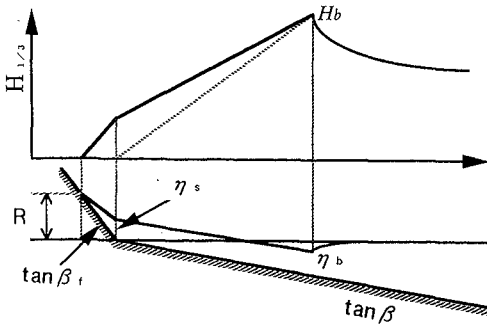


Fig. 2 Flow chart of the 3D-SHORE.



- R : Run-up Height
- η_s : Wave Set-up at the Shoreline
- η_b : Wave Set-down at the Breaking Point
- $\tan \beta$: Bottom Slope
- $\tan \beta_f$: Foreshore Slope

Sunamura (1984) :

$$\tan \beta_f = 0.12 (H_b / g^{1/2} T_d^{1/2})^{-1/2}$$

Fig. 3 Schematic illustration of the estimation method of the wave height and water level in the swash zone.

Table 2 Outline of the nearshore wave and current models.

【WAVE MODEL】
<p><i>Parabolic Equation Model</i> using the curvilinear coordinates (Isobe, 1987)</p> <ul style="list-style-type: none"> • Combined Refraction, Diffraction, Shoaling and Wave Breaking • Field verification : Shimizu et al. (1992, 1994)
【NEARSHORE CURRENT MODEL】
<p><i>Depth-averaged Current Model</i></p> <p>• Friction Term :</p> <p>① Conventional Expression</p> $\left. \begin{aligned} \tau_x &= \rho C_f \frac{(U+u_b)}{\sqrt{(U+u_b)^2 + (V+v_b)^2}} \\ \tau_y &= \rho C_f \frac{(V+v_b)}{\sqrt{(U+u_b)^2 + (V+v_b)^2}} \end{aligned} \right\} \quad (1)$ <p>where U, V: the mean currents, u_b, v_b: the orbital velocities, C_f: the friction coefficient.</p> <p>② Improved Expression <i>directly estimate the local friction term</i> in the mean current direction by using the friction law under combined wave and current action proposed by Tanaka and Thu(1994).</p> $\tau_c = \rho u_{c*}^2 = \rho \kappa \alpha \sqrt{\frac{f_{cw}}{2}} U_w^2 \quad (2)$ $\alpha = \begin{cases} \frac{1}{\ln(z_h/z_o) - 1} \frac{u_c}{U_w} & \text{: rough turbulent} \\ \frac{1}{\left[\ln(9.0 \frac{R_c}{u_c/U_w} \sqrt{\frac{f_{cw}}{2}}) - 1 \right]} \frac{u_c}{U_w} & \text{: smooth turbulent} \\ \frac{1}{\kappa} \sqrt{\frac{f_{c(L)}}{2}} & \text{: laminar} \end{cases} \quad (3)$ <p>where u_c: the mean current, U_w: the amplitude of near-bottom orbital velocity, z_h: the water depth, z_o: the roughness height, κ: the Karman constant, f_{cw}: the wave-current friction coefficient, $R_c = u_c z_h / \nu$, ν: the kinematic viscosity.</p> $\tau_c = f_2 [f_1 \tau_{c(L)} + (1 - f_1) \tau_{c(S)}] + (1 - f_2) \tau_{c(R)} \quad (4)$ <ul style="list-style-type: none"> • f_1, f_2: weight function [see Tanaka and Thu(1994)] • Subscripts L, S, R describe Laminar, Smooth turbulent and Rough turbulent flows respectively.

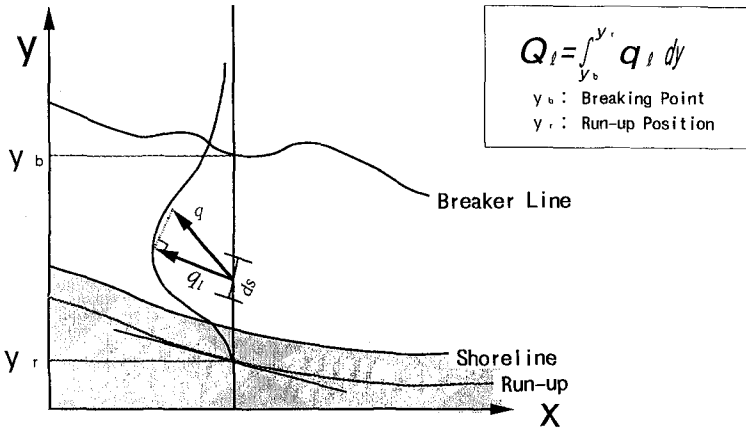


Fig. 4 Schematic illustration of the estimation method of the total longshore sediment transport rate by the cross-shore integration of the local sediment transport rate.

term by using the full-range explicit approximate expressions of frictional law for a wave-current coexistent system proposed by Tanaka and Thu(1994). The outline of the nearshore wave and current models is summarized in Table 2.

Sediment Transport and Beach Evolution Model

Fig.4 shows schematically the cross-shore integration of the local sediment transport rate in the direction parallel to the shoreline from the breaking point to the run-up point. The shoreline change is calculated using the mass conservation equation of the shoreline model based on the alongshore balance of the total longshore sediment transport rate.

In coupling the spatial bottom topography changes with the shoreline changes, both results are interpolated near the shoreline. In the area of shoreline retreat, the profile is determined by the smaller depth comparing between the profile extended offshoreward from the new shoreline position with the foreshore slope estimated by empirical formula by Sunamura(1984) and the profile extended onshoreward from the grid point adjacent to the old shoreline position with the local bottom slope. In the area of shoreline advance, in order to prevent the new shoreline calculated based on the mass conservation of total longshore sediment transport rate from advancing the new shoreline calculated by that of local sediment transport, the appropriate local sediment transport rate coefficient and duration of time-stepping are to be selected.

The local sediment transport rate is evaluated by the formula proposed by Watanabe et al.(1986). The outline of the model is shown in Table 3. The formula for local sediment transport rate under combined wave-current action was formulated so as to be consistent with previous studies on both longshore drift and cross-shore sediment transport. The total transport rate vector is divided

Table 3 Outline of the local sediment transport rate formula.

[LOCAL SEDIMENT TRANSPORT RATE FORMULA]

Watanabe Model (Watanabe et al., 1986)

- Seiment transport due to nearshore currentn q_c :

$$\vec{q}_c = A_c (\tau_m - \tau_c) \vec{u}_c / \rho g \quad (5)$$

- Seiment transport due to nearshore current q_w :

$$\vec{q}_w = A_w F_D (\tau_m - \tau_c) \vec{u}_b / \rho g \quad (6)$$

where τ_m : the maximum bottom shear stress under waves and currents,

τ_c : the critical shear stress,

u_c : the mean current, u_b : bottom orbital velocity

F_D : the direction function(+1 for onshore, -1 for offshore)

• Relationships among the coefficients

(Watanabe et al., 1991; Shimizu et al., 1994)

$$A_c = 10 A_w \quad (7)$$

$$A_w = w_o \sqrt{0.5 f_w / \{(1 - \lambda) s' \sqrt{s' g D}\}} B_w \quad (8)$$

where B_w : the nondimensional coefficient of the wave-induced sediment transport rate formula by Watanabe(1982),

f_w : the wave-current friction coefficient proposed by Tanaka and Shuto(1981),

w_o : the fall velocity, D : the grain diameter,

λ : the porosity, g : the gravity acceleration,

$s' (= \rho_s / \rho - 1)$ (ρ_s, ρ : the densities of sand and fluid).

• Determination of local coefficients

- ① Previous studies $\rightarrow B_w \begin{cases} = 3 \sim 5 & \text{for field} \\ = 7 & \text{for laboratory experiment} \end{cases}$
- ② $H, T, \theta, h, D, s' \rightarrow f_w \rightarrow A_w$ at each local point (eq. (8))
- ③ $A_w \rightarrow A_c$ (eq. (7))

into that due to mean currents including both nearshore current and undertow and that due to waves. This formula is based on the power model concept and assume that the sediments set in motion by the excess shear stress under combined wave-current action are transported with both mean currents and wave motion into the respective directions. In this study, only the sediment transport due to nearshore currents is taken into account. The value of the sediment transport rate coefficient is determined by using the empirical relations, according to the previous studies (Watanabe et al.,1991; Shimizu et al.,1994). The local transport rate coefficients depend on local wave conditions and properties of sea-bed material.

MODEL VERIFICATION

Outlines of Laboratory Experiment and Numerical Calculation

The applicability of the newly developed model is investigated on the basis of the movable bed laboratory experiment conducted by Mimura et al.(1983). The experiment was carried out using a wave basin 14m long and 7.5m wide. The sediment grain diameter was 0.2mm and the initial bottom slope was 1/20. After the initial beach was subjected to wave attack for approximately 12 hours, a 1.5m long detached breakwater was placed approximately at the breaker line. The incident wave height was 5.7cm and the period was 0.9s. The verification data used in this study are the beach topography change for about 6 hours after placement of the detached breakwater.

In the calculation of beach evolution, the new bottom topography is fed back into the hydrodynamic and sediment transport computations and the dynamic time-evolution of the seabed is calculated. The calculations of waves, currents and beach topography changes were repeated every 20 minutes and 18 time iterations in total were conducted. The change in the bottom shear stress caused by bottom elevation change is taken into account every 4 minutes in the calculation of beach evolution. The grid spacing is 15cm. The local sediment transport rate coefficient B_w is 7 and the depth of closure D is set to 10cm.

Calculation of Nearshore Wave and Current Fields

Fig.5 shows the alongshore distribution of breaking wave height. The calculations show good agreement with the measurements.

Fig.6(a) and (b) show the examples of the calculated depth-averaged nearshore currents. Fig.6(a) is for initial bottom topography and Fig.6(b) is for that after 5 hours and 40 minutes. The shoreline advance behind the detached breakwater and the strong and sharp nearshore circulations are simulated.

Calculation of Beach Evolution

Fig.7 shows comparisons between the calculated and the measured positions of the shoreline and the depth contours of 2cm and 4cm. The shoreline position calculated by the shoreline model is also plotted. The shoreline change is reproduced better by the shoreline model than by the 3D-SHORE, because the

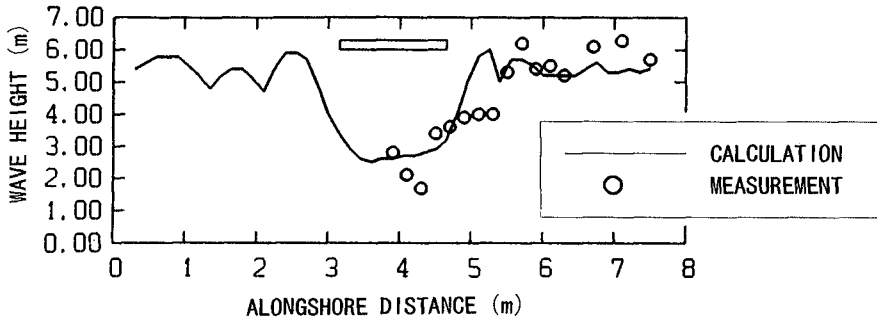


Fig. 5 Alongshore distribution of breaking wave height.

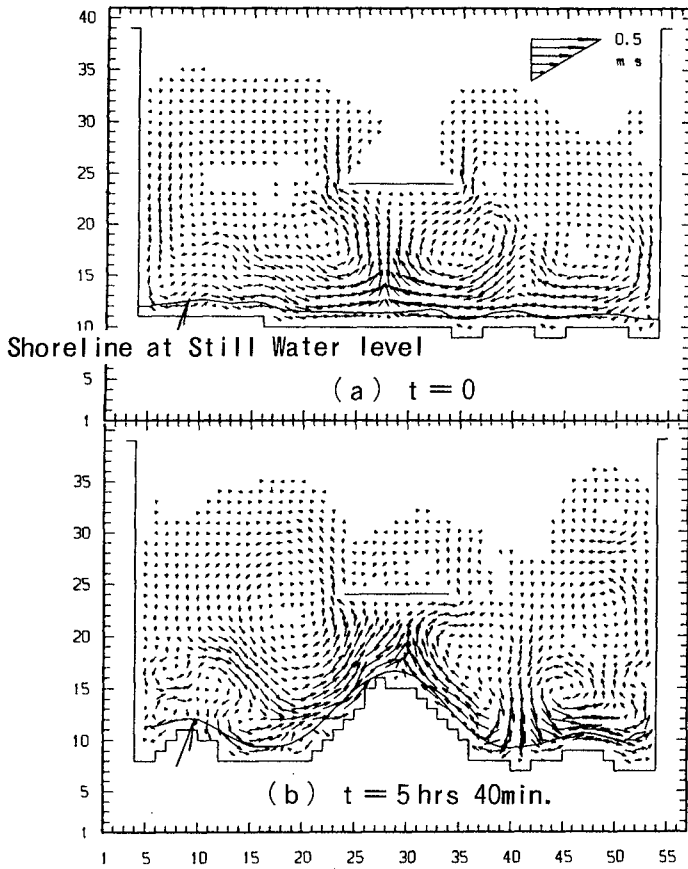


Fig. 6 Calculated nearshore current fields.

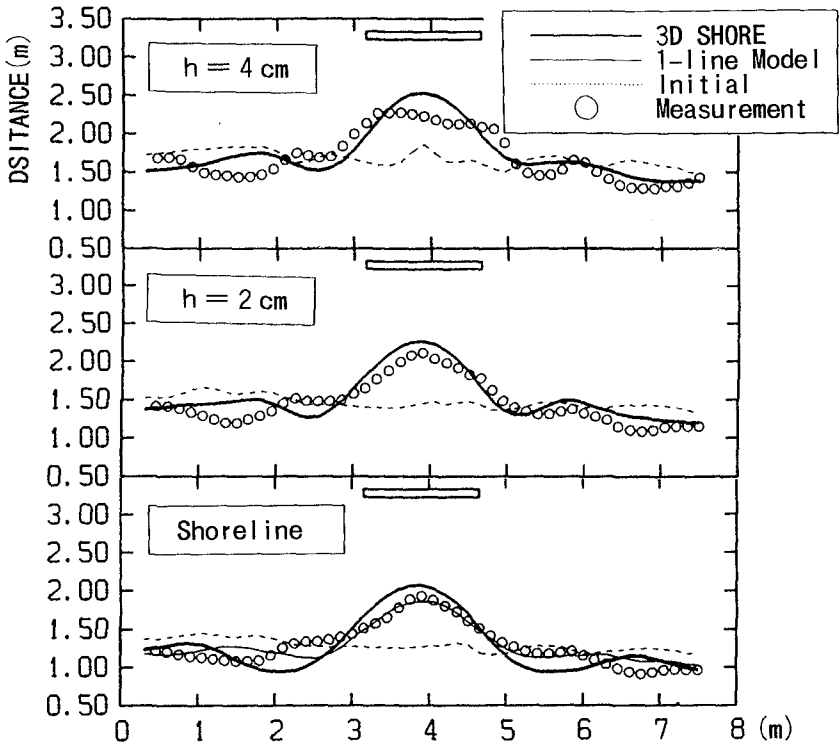


Fig. 7 Comparisons between the calculated and the measured positions of the shoreline and the depth contours of 2cm and 4cm.

computational time of the shoreline model is considerably shorter than that of the 3D-SHORE and it is, then, easy to adjust the parameters to agree with the measurement. The shoreline model, however, can calculate only the shoreline and cannot estimate the spatial bottom topography change. The present improved model, on the contrary, has good accuracy for estimating the changes in both the shoreline and the depth contours for approximately 6 hours.

Fig.8(a) and (b) show the time-evolutions of the shoreline and the 2cm depth contour calculated by the 3D-SHORE and (c) shows the time-evolution of the shoreline calculated by the shoreline model. The shoreline behind the detached breakwater advances gradually and reaches an equilibrium state after 5 hours according to the calculation result of the 3D-SHORE. The contour of 2cm advances faster than the shoreline.

According to the result calculated by the shoreline model, on the contrary, the shoreline advances rapidly and reaches an equilibrium state after only 3 hours. In the shoreline model, the longshore sediment transport rate becomes zero at the equilibrium state, because the breaking wave crest angle to the shoreline becomes zero. This shows that the shoreline model can describe only the static equilibrium. The improved 3-D beach evolution model, on the other hand, can describe

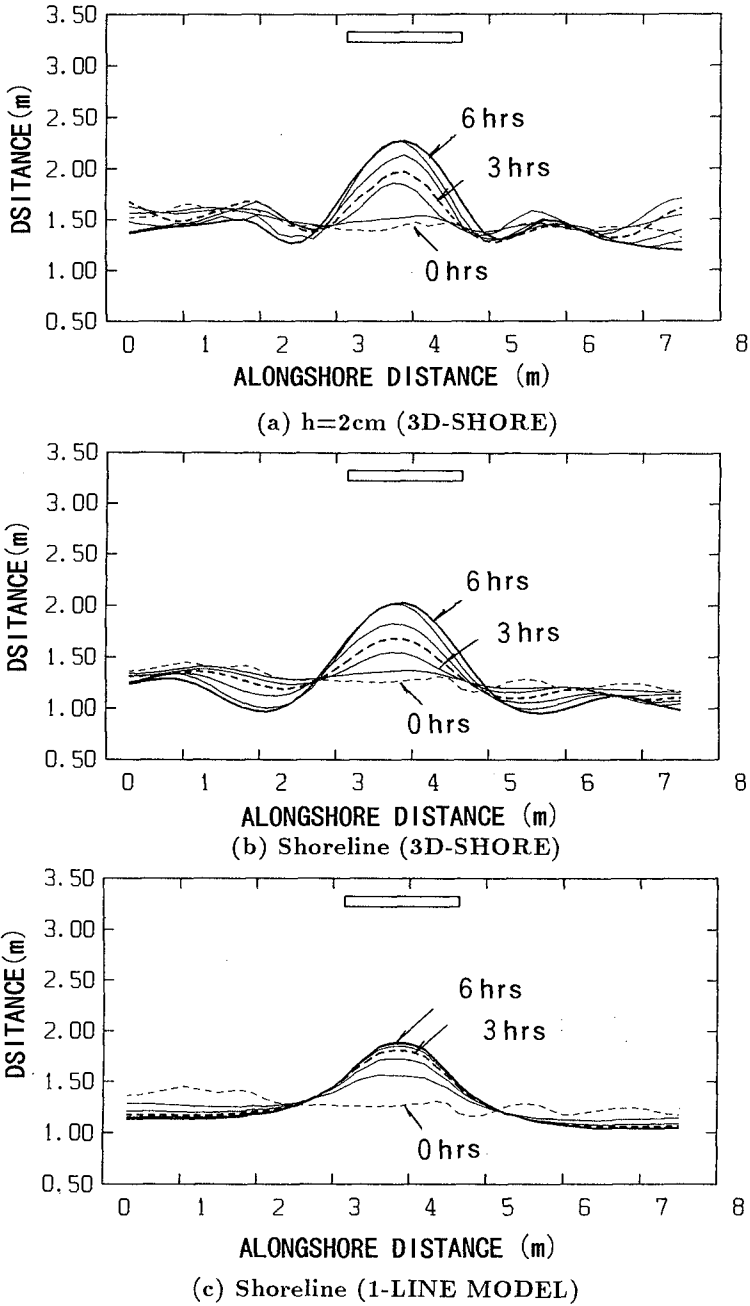


Fig. 8 Time-evolution of the calculated depth contours.

the dynamic equilibrium and is, therefore, more effective for properly predicting the time-evolution of bottom topography.

FIELD APPLICATION

In order to verify the field applicability, we try to simulate the beach evolution due to construction of the Kunnui Fishing Port, an offshore man-made island type fishing port, in Hokkaido, Japan (Kawaguchi et al., 1994). The man-made island is located about 200m offshore from the initial shoreline. The maximum width of the man-made island is about 180m, which approximately equals to the detached distance. Although the bottom contours are straight and parallel to the shoreline in 1985 before construction of the fishing port, they extend offshoreward like a tongue behind the fishing port owing to extreme accretion caused by nearshore circulations. The rapid and extreme beach evolution took place during only a year from 1989 to 1990 after the start of the construction of man-made island. At present, the tombolo is formed behind the fishing port.

The calculation was conducted with the area of 1.0km long in the alongshore direction and 0.8km long in the cross-shore direction. The grid spacing is 10m. The bottom slope is approximately 1/75. The grain diameter is about 0.2mm and the transport rate coefficient B_w is 4. The numerical simulation was performed under simply modelled two series of the storms by repeating the calculations of waves, mean currents and beach changes. The modelled series of waves have the same occurrence frequency in total as that of the observed wave climate data. The depth of closure D was expressed as a function of the incident wave conditions.

Fig.9 shows the comparisons between the calculated and the measured depth contours after a year from 1989 to 1990. The calculations show fairly good agreements with the measurements. The field applicability of the proposed model is also verified.

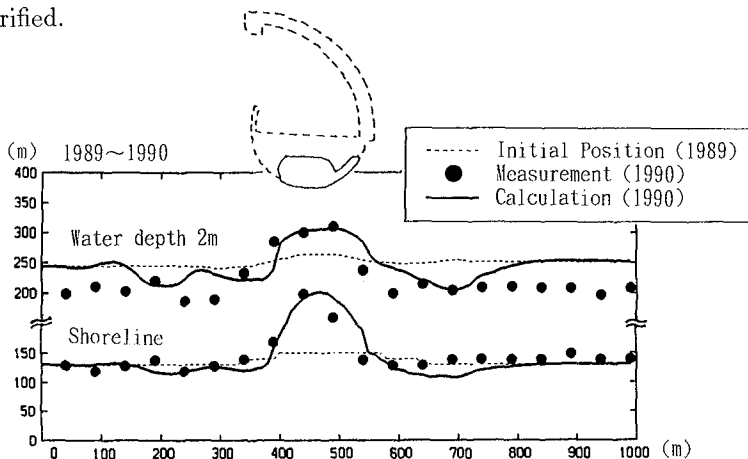


Fig. 9 Reproduction of the beach evolution around the Kunnui Fishing Port during a year.

CONCLUSIONS

In this study, an improved 3-D beach evolution model coupled with the shoreline model (3D-SHORE) is newly developed. And the applicabilities of the model were successfully verified through comparisons with both results of movable bed laboratory experiment and the actual beach evolution. The 3D-SHORE can describe the dynamic equilibrium of beach evolution and is, therefore, more effective for properly predicting the time-evolution of bottom topography than the conventional shoreline model which can only the static equilibrium. It is concluded that the 3D-SHORE has enough accuracy for practical use.

REFERENCES

- De Vriend, H.J., J. Zyserman, J. Nicholson, J.A. Roelvink, P. P  chon and H.N. Southgate, 1993: Medium-term 2DH coastal area modelling, *Coastal Eng.*, Vol.21, pp.193-224.
- Isobe, M., 1987: A parabolic equation model for transformation of irregular waves due to refraction, diffraction and breaking, *Coastal Eng. in Japan*, Vol. 30, No. 1, JSCE, pp.33-47.
- Kawaguchi, T., O. Hashimoto, T. Mizumoto and A. Kamata, 1994: Construction of offshore fishing port for prevention of coastal erosion, *Proc. 24th Int. Conf. on Coastal Eng.*, ASCE, pp.1197-1211.
- Longuet-Higgins, M.S. and R.W. Stewart, 1962: Radiation stress and mass transport in gravity waves, with application to 'surf beat', *J. Fluid Mech.*, Vol.13, pp.481-504.
- Mimura, N., T. Shimizu and K. Horikawa, 1983: Laboratory study on the influence of detached breakwater on coastal change, *Proc. Coastal Structure '83*, ASCE, pp.740-752.
- Shimizu, T., H. Nodani and K. Kondo, 1990: Practical application of the three-dimensional beach evolution model, *Proc. 22nd Int. Conf. on Coastal Eng.*, ASCE, pp.2481-2494.
- Shimizu, T., A. Ukai and M. Isobe 1992: Field verification of numerical models for calculation of nearshore wave field, *Proc. 23rd Int. Conf. on Coastal Eng.*, ASCE, pp.590-603.
- Shimizu, T., M. Tsuru and A. Watanabe, 1994: Field verification of a numerical model of beach topography change due to nearshore currents, undertow and waves, *Proc. 24th Int. Conf. on Coastal Eng.*, ASCE, pp.2610-2624.
- Sunamura, 1984: Quantitative predictions of beach-face slopes, *Geol. Soc. Am. Bull.*, Vol.95, pp.242-245.
- Tanaka, H. and N. Shuto, 1981: Friction coefficient for a wave-current coexistent system, *Coastal Eng. in Japan*, Vol.24, JSCE, pp.105-128.
- Tanaka, H. and A. Thu, 1994: Full-range equation of friction coefficient and phase difference in a wave-current boundary layer, *Coastal Eng.*, Vol.22, pp.237-254.
- Watanabe, A., 1982: Numerical models of nearshore currents and beach deformation, *Coastal Eng. in Japan*, Vol.25, JSCE, pp.147-161.
- Watanabe, A., K. Maruyama, T. Shimizu and T. Sakakiyama, 1986: Numerical prediction model of three-dimensional beach deformation around a structure, *Coastal Eng. in Japan*, Vol.29, JSCE, pp.179-194.
- Watanabe, A., T. Shimizu and K. Kondo, 1991: Field application of a numerical model of beach topography change, *Proc. of Coastal Sediments '91*, ASCE, pp.1814-1828.

CHAPTER 221

EVALUATION OF SHOREFACE NOURISHMENTS BY LINE MODELLING

Martin D. Groenewoud¹, Willem T. Bakker^{2,3}, Jan van de Graaff¹,
Ruud Spanhoff³ and Christian Lastrup⁴

ABSTRACT

Shoreface nourishments are sometimes used as an alternative for ordinary beach nourishments. Many aspects of the behaviour of shoreface nourishments are still unknown. Shoreface nourishments affect the morphological behaviour of a coast. Line modelling might be used to study and to predict the behaviour of shoreface nourishments after execution. Although not every detail of the real behaviour can be dealt with, line modelling is still a rather simple but powerful tool. The recent application is discussed of the line modelling technique to study several shoreface nourishments carried out in the NOURTEC framework.

INTRODUCTION

Coastal zone managers may fight undesired structural erosion of coasts either by 'hard' or by 'soft' measures.

With 'hard' measures the basic idea is to interfere in the sediment transports involved in such a manner that the erosion in the stretch of coast under consideration is stopped, or at least reduced. With a well-tuned system of groynes or a number of shore-parallel detached breakwaters this aim can in principle be achieved. That often the erosion problem is shifted to the adjacent lee side beaches is a serious draw-back of these types of countermeasures.

With 'soft' methods (e.g. a beach nourishment [further: BN]) this adverse lee side effect is avoided. The basic idea of artificial nourishments is to accept the losses as observed (no attempts to interfere in the processes which cause the erosion) but replenish from time to time the apparent losses. Often life times in the range of 5 till 10 years are striven after. Although artificial BN's have to be repeated, it often turns out to be a very cost effective method in comparison with 'hard' alternatives.

Structural erosion of a stretch of coast means that the stretch loses sediments at a regular basis. Often a gradient in the longshore sediment transports is the main cause of the erosion problem. In a cross-shore profile the volume of sediments (m^3/m) in that profile in a predefined (fixed) area, diminishes as a function of time. All parts of such a profile (dunes; beach; shoreface) suffer eventually from this type of

¹ Delft University of Technology; Stevinweg 1; 2628 CN Delft; the Netherlands

² Netherlands Center for Coastal Research; Delft University of Technology; Stevinweg 1; 2628 CN Delft; the Netherlands

³ Rijkswaterstaat, National Institute for Coastal and Marine Management; P.O. Box 20907; 2500 EX the Hague; the Netherlands

⁴ Kystinspektoratet; Høbovej 1; 7620 Lemvig; Denmark

erosion. However, the upper part of the profile (beach and dunes) is often considered as the most important part of the entire profile; many important functions of a coast to mankind are concentrated in just this part. Because structural erosion manifests itself most clearly in the upper part of the profile, artificial nourishments are often applied just there. With a BN the 'health' of a beach is directly improved; one clearly can notice the improvements for the time being; e.g. the beach is widened which is favourable for recreational use.

Many methods exist to execute artificial BN's [see e.g. CUR (1987)]; most of them are, however, rather cumbersome in practice. The handling of the sediments from borrow area to fill site is often complicated and thus costly. Because of the recreational use of beaches often the summer period is excluded as execution time.

Instead of applying (cumbersome) artificial BN's, nourishing just the shoreface seems an (easy) alternative. Sediment handling is quite simple; the dredge sails from the borrow area and dumps the load at the shoreface and starts with a new cycle. Because of no (or less) hindrance to the recreational use of the beaches also the summer time can be used for execution. Large cost savings are expected to be achieved with shoreface nourishments [further: SN] in comparison with classical BN's.

In the scope of the NOURTEC project [Mulder *et al.* (1994)] at 3 sites (Terschelling, the Netherlands; Norderney, Germany; and Torsminde, Denmark; see Fig.1) sand has been supplied on the shoreface. The NOURTEC project implies evaluation and comparison of the coastal behaviour at those sites after the SN's.

Bakker *et al.* (1994) made a prediction of the expected coastal behaviour after the SN at the Dutch Wadden island of Terschelling; furthermore the coastal behaviour after the supply at the German Wadden island of Norderney was evaluated. They used the 3-line modelling technique. Later on the nourishments in Denmark and Terschelling have been evaluated with the same technique (Groenewoud 1996a and 1996b). The study has been finished with an overall evaluation of the 3-line modelling technique as a design and evaluation tool (Groenewoud 1996c).

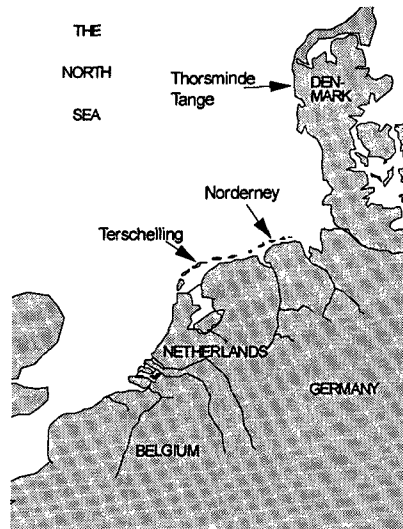


Fig.1 Location of the 3 NOURTEC test sites

In the present paper the application of the 3-line modelling technique in the 3 NOURTEC cases is discussed; strong and weak points of the method are revealed.

SHOREFACE NOURISHMENTS IN PRACTICE

Fig.2 shows in plan view a (shore parallel) SN along a sandy coast. Because a SN is meant to be a substitute of an ordinary BN it is expected that a part of the supplied volume is transported towards the coast. With the notion of the existence of equilibrium profiles one can indeed expect that because of cross-shore transports the extra volume of sand is eventually spread over the entire profile (in onshore as well in offshore direction). Consequently also a part of the supplied volume is thought to reach eventually the beach. For the judgment of the effectiveness of SN's in comparison to BN's it is of course important to know which part of the volume of SN's reaches the beaches, and which time scales are involved. With detailed cross-shore transport calculations these topics are to be evaluated.

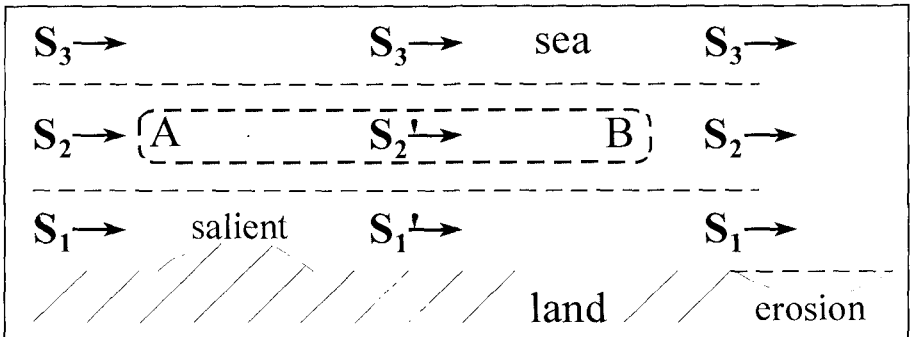


Fig.2 (Arbitrary) shoreface nourishment in plan view

In plan view (see Fig.2) a SN is limited; between points A and B the depths contours are just after the execution locally shifted in seaward direction. In the neighbourhood of the points A and B the orientation of the depth contours has changed. With a description of the (local) longshore transport depending on the orientation of the depth contours it is easily understood that near the points A and B a redistribution of the volume of sediments of the SN in longshore direction will take place. Also in the upper part of the profile, as soon as some sediment has reached that part of the profile by cross-shore transports, a similar reorientation of the local depth contours will occur with a consequent redistribution of sediments in longshore direction in the upper part of the profiles of the stretch of coast.

A SN acts, however, also as a (mobile) submerged breakwater. The presence of a SN will affect (reduce) the wave heights in the zone between the SN and the waterline. Consequently the longshore sediment transports in this zone are reduced compared to the original transports along the non-supplied coast at the left-hand side of A and at the right-hand side of B (see Fig.2). Assuming a net longshore transport in the zone behind the SN as indicated in Fig.2 from left to right, it is expected that behind the left side of the SN some accumulation of sediments will occur (salient formation). Right from B it is expected that (additional) erosion of the beaches will occur.

Especially the expected salient formation at the up-drift side behind the SN will confuse phenomenological studies based on bathymetric data. Is the observed

accumulation of sediments in this area because of cross-shore sediment transport effects or because of longshore transport effects?

If a SN is applied in a zone with water depths where in the non-supplied situation still substantial yearly net longshore sediment transports do occur (either wave or tide driven or due to a combination of waves and tidal currents), the mere sudden uplift of the bottom because of the presence of the SN will cause increased sediment transports above the SN (see Fig.2). Induced gradients in the local longshore transport will cause erosion of the SN just right of point A and accumulation of sediments just right of point B. It seems that the entire SN is moving (within the schematization of Fig.2) from left to right along the coast.

In the brief discussion of the different morphological effects of a SN it was presumed that the borrow material of the SN is equal to the native material. In practical applications, however, this presumption might not be true; the borrow material may differ from the native material. It is for sure that consequently the sediment transports involved, will change.

In the previous part 4 morphological effects of a SN have been briefly discussed, viz.:

- i) (straightforward) cross-shore redistribution of the volume of a SN over the entire cross-section;
- ii) longshore redistribution of the volume of a SN due to reorientation of the depth contours in the zone of the SN itself (starts immediately after execution) and in the upper part of the profile (starts when after some time sediments have reached the upper part of the profile);
- iii) salient formation at the up drift side (and erosion at the down drift side) in the zone between SN and waterline because of reduction of the yearly net longshore sediment transport in this zone;
- iv) integral movement of the SN in longshore direction because of yearly net longshore sediment transports in the SN zone.

In the next section the 3-line modelling technique is discussed. It will turn out that the effects i) and ii) can in principle be properly modelled with the present technique; the effects iii) and iv) cannot be accounted for with the present model set up. In the present 3-line modelling approach it is also assumed that borrow and native material are the same. Additional effects due to differences in borrow and native material are not accounted for.

3-LINE MODELLING TECHNIQUE

General

In the present study 3 lines have been used to represent a cross-shore profile. More, or only 2 lines are in principle also possible. The 3-line modelling technique is a rather simple technique which can be used to study the behaviour of a morphological system with time. The approach relies on the assumption that the actual behaviour of a morphological system can be considered as a linear superposition of different sub-systems. In the present application for instance, the autonomous behaviour of the system is assumed to be the same before and after a SN application. Only the additional effect of the SN is modelled. So if the behaviour of the SN with time is

modelled reliably, the eventual behaviour of the system with time is found by adding both sub-systems (autonomous behaviour + behaviour because of the SN).

Schematization of cross-shore profile and cross-shore transports

In a 3-line model the cross-shore profile is schematized by 3 zones with horizontal separation planes (see Fig.3). The volumes of sand in the zones (layers) are characterized by 3 lines which may, contrary to equilibrium profile approaches, develop 'freely' with time. It is assumed that in each zone the mutual distance between the upper and the lower limit remains the same and (thus) that the part of a profile coinciding with the zone moves only horizontally.

The characterizing lines each have a distance to an arbitrary vertical reference line which for L_1 can be defined as (see Fig.3):

$$L_1 = \frac{1}{h_1} \int_{-d_1}^0 y(z) dz \quad (1)$$

For lines L_2 and L_3 similar formulae can be derived.

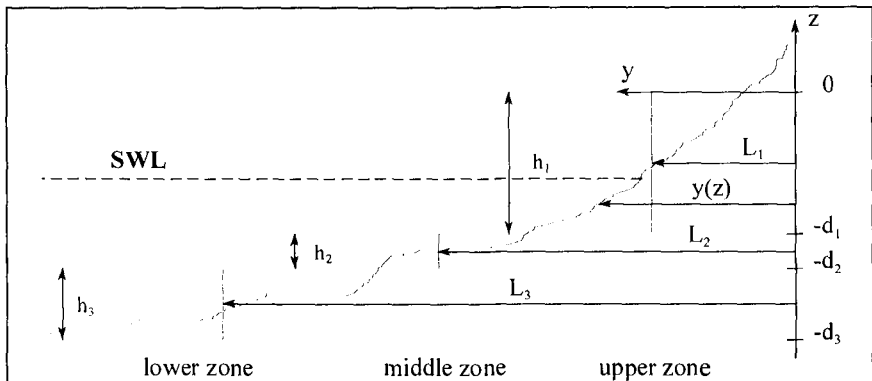


Fig.3 Schematization of cross-section

The parameters of Eq.1 and Fig.3 are:

- d_1, d_2 = depth of separation plane between zone 1 and 2; zone 2 and 3;
- d_3 = depth of lower limit of zone 3;
- h_1, h_2, h_3 = height of zone 1; zone 2; zone 3;
- L_1, L_2, L_3 = characterizing mean line of upper zone; middle zone; lower zone;
- $y(z)$ = distance of point of profile at depth z to a reference line;
- z = height above the y -axis.

The cross-shore sediment transport rate between the zones is assumed to be proportional to the difference between the actual distances and the equilibrium distance between the characterizing lines. This method of describing cross-shore

sediment transports was originally proposed by Bakker (1968) and further developed by Swart (1974).

Since in the present application the profiles before the SN application are assumed to be equilibrium profiles, the use of L_1 , L_2 and L_3 can be avoided; only perturbations from the initial equilibrium profile are considered. These perturbations are expressed as (see Fig.4) y_1 , y_2 and y_3 respectively.

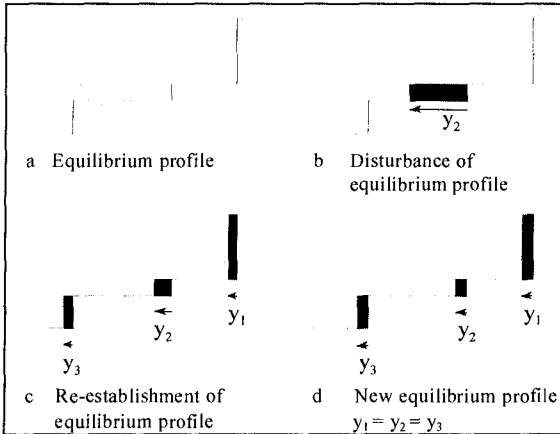


Fig.4 Schematized equilibrium profile (a); disturbance in middle layer (b) and behaviour (c and d)

If the transport rates S_{y1} [and S_{y2}] are assumed to be proportional to the differences ($y_1 - y_2$) for S_{y1} [and ($y_2 - y_3$) for S_{y2}], then the following equation for S_{y1} can be written:

$$S_{y1} = s_{y1} (y_1 - y_2) \quad (2)$$

(For S_{y2} similar formula.)

with: S_{y1} = cross-shore transport from the upper to the middle zone [$m^3/m/year$]
(positive in seaward direction)

s_{y1} = cross-shore coastal constant [$m/year$]

The description of the cross-shore sediment transport relies on a proper estimate of the cross-shore coastal constants. It can be proved that these coastal constants can be rewritten as:

$$s_{y1} = \frac{1}{T_{01}} * \left(\frac{h_1 * h_2}{h_1 + h_2} \right) \quad (3)$$

with: T_{01} = time constant for diffusivity between upper and middle zone (year)

(For the time constant for diffusivity between the middle and lower zone T_{02} a similar formula can be derived.)

The T_0 period is the lapse of time in which a certain value of deviation from the equilibrium distance will decrease with a factor e . The problem of estimating proper values for the cross-shore constants is now shifted to the proper estimate of the T_0 periods.

Schematization of longshore transport

In each zone of the schematized cross-shore profile longshore sediment transports will occur. These longshore transports are indicated by S_1 , S_2 and S_3 for the upper, middle and lower zone, respectively. In the following discussion S_x is generally used.

In the present Nourtec cases the total longshore transport, and the distribution over the different zones, is calculated with the CERC formula; the possible contribution of tidal currents is consequently ignored. The method can, however, also be used if tidal currents are taken into account; the preparatory calculations are only somewhat more complicated in that case.

A gradient in the longshore transport results in the following equation of continuity:

$$\frac{\partial S_x}{\partial x} + h \frac{\partial y}{\partial t} = 0 \quad (4)$$

with h being the thickness of the layer over which erosion or accumulation takes place. The gradient of the longshore sediment transport is due to changes in angle of wave approach.

The wave climate is assumed to be constant along the coast. With small changes of the angle, the longshore transport is assumed to depend linearly on the angle of wave approach.

$$\frac{\partial S_x}{\partial \phi} = s_x \quad (5)$$

with: s_x = longshore coastal constant

The chain rule gives:

$$\frac{\partial S_x}{\partial x} = \frac{\partial S_x}{\partial \phi} * \frac{\partial \phi}{\partial x} \quad (6)$$

Substitution of Eqs.5 and 6 in Eq.4 and assuming small angles ultimately yields:

$$-s_x \frac{\partial^2 y}{\partial x^2} + h \frac{\partial y}{\partial t} = 0 \quad (7)$$

The change of the position of the coastline ($\partial y/\partial t$) due to longshore transport is proportional to the curvature of the coastline. This also applies if the profile is divided into several zones. The equation for the upper zone then becomes:

$$\left[\frac{dy_1}{dt} \right]_{\text{long}} = \frac{s_1}{h_1} * \frac{\partial^2 y_1}{\partial x^2} \quad (8)$$

with: s_1 = longshore coastal constant

Combination of both cross-shore and longshore processes with linear addition gives:

$$\frac{dy_1}{dt} = \frac{s_1}{h_1} * \frac{\partial^2 y_1}{\partial x^2} - \frac{s_{y1}}{h_1} (y_1 - y_2) \quad (9)$$

$$\frac{dy_2}{dt} = \frac{s_2}{h_2} * \frac{\partial^2 y_2}{\partial x^2} + \frac{s_{y1}}{h_2} (y_1 - y_2) - \frac{s_{y2}}{h_2} (y_2 - y_3) \quad (10)$$

$$\frac{dy_3}{dt} = \frac{s_3}{h_3} * \frac{\partial^2 y_3}{\partial x^2} + \frac{s_{y2}}{h_3} (y_2 - y_3) \quad (11)$$

In these equations the longshore transport is determined by the constants s_1 , s_2 and s_3 and the direction of the coast. The cross-shore transport is determined by the constants s_{y1} and s_{y2} and the deviation from the equilibrium position.

These three equations determine the development of y_1 , y_2 and y_3 in time and position along the coast.

Numerical solution

The numerical method used to solve Eqs.9, 10 and 11 is the Euler Explicit Time Forward Central Space method. Time and space steps have to be carefully linked in order to fulfil the stability criterion.

Example

In Fig.5 the results of an arbitrary example are given. Along 2 km a shore-parallel SN is placed in the middle layer. The thicknesses of the layers are respectively: upper: 6 m; middle: 3 m and lower: 3 m. The cross-shore constants are $s_{y1} = 1.33$ m/year and $s_{y2} = 0.3$ m/year. The longshore coastal constants read: $s_1 = 2.65 * 10^6$ m³/year/rad; $s_2 = 0.22 * 10^6$ m³/year/rad and $s_3 = 0$ m³/year/rad. The volume as nourished is 300 m³/m; because of the nourishment just after the nourishment the y_2 values shifted with 100 m in seaward direction.

From Fig.5 it becomes clear that the SN diffuses in all directions. With the constants as used indeed a large part of the SN reaches the upper part of the profile.

The lower zone just seaward of the SN gets some sand directly from the middle zone because of cross-shore transports. In the adjacent lower zones also some sedimentation is noticed. Since the longshore coastal constant s_3 in the present

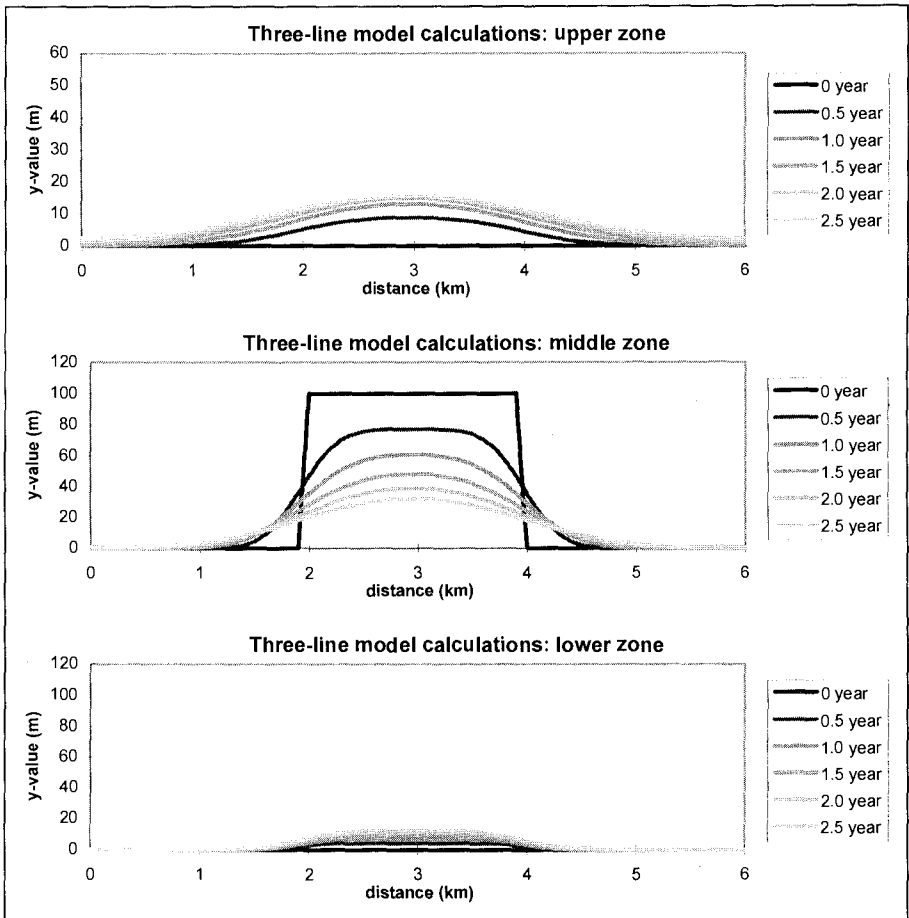


Fig.5 Development with time of a shoreface nourishment in middle layer

example is zero, this material has reached these zones first via the adjacent middle layers and next by cross-shore transport.

In the present example the autonomous behaviour of the coast is not taken into account; in real life problems the autonomous behaviour has to be added to the computation results. To determine the autonomous behaviour in real cases turns out to be a cumbersome task (see *NOURTEC* examples next section).

NOURTEC EXAMPLES

Torsminde

The Torsminde test side is located along the west coast of Denmark (see Fig.6). Fig.7 shows two typical cross-shore profiles; 1 to 3 offshore bars are present. The site is located in front of a sand dike. A typical value of D_{50} for the sand in the profile is 0.4 mm.

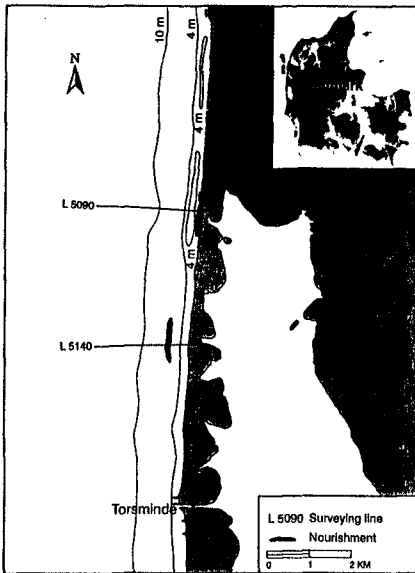


Fig. 6 Location Torsminde test site

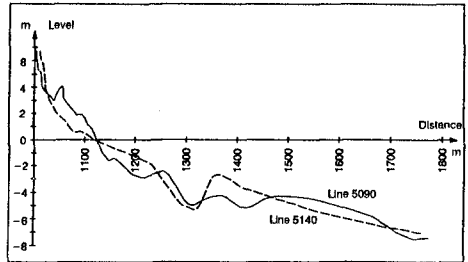


Fig. 7 Typical cross-shore profiles

Separate beach and shoreface nourishments took place in 1993. Over longshore stretches of one km each, approximately $250,000 \text{ m}^3$ sand has been nourished in both cases; so approximately $250 \text{ m}^3/\text{m}$. The D_{50} of the borrow sand ($D_{50} = 0.34 \text{ mm}$) for the BN was slightly less than the native sand; the borrow sand ($D_{50} = 0.58 \text{ mm}$) for the SN was coarser than the native material.

The BN was placed between DNN +4 m and DNN -1 m (DNN = Danish Normal Zero); the SN between DNN -4 m and DNN -6 m. The cross-shore profiles have been divided in 3 layers: upper: DNN +4 m to DNN -4 m; middle: DNN -4 m to DNN -6 m; lower DNN -6 m to DNN -10 m.

Estimates of the longshore coastal constants have been calculated using the CERC formula; the distribution of the transport over the different zones have been found by using the Svašek and Bijker (1969) method.

In the modelling the determination of the cross-shore coastal constants is a vital item. In the Torsminde case different sets have been tested using the observed behaviour as criterion. A reasonable set was eventually found.

To judge the quality of the computation, a comparison with the observed behaviour was made. The autonomous behaviour was set on an average coastline retreat of 6.7 m/year. This value was based on measurements in the period 1978 - 1988.

In the example case of Fig.5 y-values are computed for each 100 m along the coast. In the Torsminde case also a 100 m spacing was used in the computations. In order to facilitate comparison of measurements with computations, averaged values for stretches of coast of 1 km length (so-called boxes) have been used.

The fluctuations of the measured y -values turned out to be relatively large compared to the calculated development of the y -values. It is not expected that these large fluctuations are mainly due to the two nourishments.

Overall the comparison between the calculated and the observed development showed in some cases similarities and in some other cases considerable differences. One of the shortcomings of the present model is that the model can not cope with the effects of the different grain sizes on the morphological development.

Norderney

As already discussed by Bakker *et al.* (1994), the Norderney case is in fact too complicated to be modelled properly with a 3-line modelling technique. The complicated bottom topography in front of the test site and the presence of a number of groynes made this site in fact unsuitable for a simple line-modelling technique.

Terschelling

In the Terschelling case (see Figs.8 and 9) the shoreface was nourished in 1993 with a volume of 2.1 million m^3 over a length of 4.6 km at a depth of Datum -7m to -5m. In fact the most seaward trough of the bar system was filled. The SN was located in the middle part of a 12 km long study area.

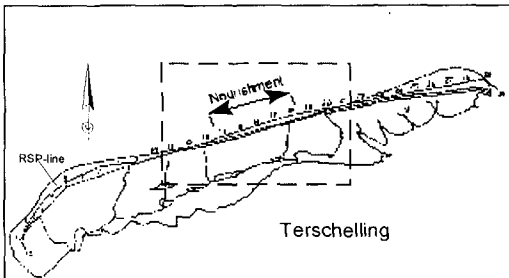


Fig. 8 Location Terschelling test site

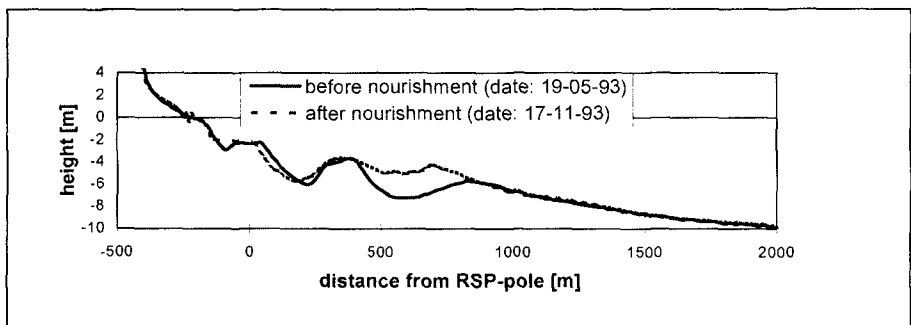


Fig. 9 Typical cross-shore profiles

The native bed material shows a typical distribution over the cross-shore profile: $D_{50} = 0.24$ mm at the beach and gradually decreasing to $D_{50} = 0.16$ mm at the deeper shoreface. The D_{50} value of the borrow material was 0.20 mm. Apart from the yearly profile measurements (since 1964; 200 m spacing), just before and after the execution of the SN many more profile measurements have been carried out. After the nourishment e.g. in a lapse of time of 2 years 11 series of measurements have been carried out.

The shape of the cross-shore profile was schematized in 3 layers. Normally (fixed) depth contours are chosen as layer limits. In the Terschelling case because of the bar system, the upper layer was defined from Datum +3 m to Datum -3 m (most landward contour); the lower layer was defined from Datum -6 m (most seaward contour) to Datum -9 m. All the sediment between the most landward Datum -3 m depth contour and the most seaward Datum -6 m depth contour was considered to belong to the middle layer. So even if a trough of the bar system is deeper than Datum -6 m or a crest is higher than Datum -3 m the sediments (or the lack of sediments) involved belong to the middle layer. With this procedure the entire (with time moving) bar system is confined in the middle layer.

The 3-line model is based on the hypothesis that an equilibrium profile exists in cross-shore direction. It might be questioned whether this concept holds as well in case of a bar system with a cyclic behaviour as for Terschelling.

The longshore coastal constants have been derived with the CERC formula. The cross-shore coastal constants have been derived by trial and error, taking the observed behaviour after the SN into account. Rather short T_0 (time constant for diffusivity) values had to be adopted ($T_{01} = 1.5$ years upper to middle zone; $T_{02} = 5$ years middle to lower zone). It is felt that the rather small value T_{01} of only 1.5 years is partly 'artificially'. As discussed in section 'Shoreface nourishments in practice' some salient formation landward of the SN is expected because of gradients in longshore transport. Although this phenomenon can not be properly modelled with the present technique, the effects are accounted for by the relatively small T_{01} value.

The study area was divided in several (8 in this case) boxes (1.2 km each). Prior to the SN the autonomous behaviour of each box could be determined since many profile measurements are available. In the final judgment of the observed and calculated behaviour of the coast, the calculated autonomous behaviour of each box was taken into account.

The calculated development of the y -values of the upper zones was very similar to the measured development after the application of the SN. The large observed volume increase in the upper zone is, in the present simulation, almost entirely caused by cross-shore transports from the middle zones. It might be questioned whether this is physically correct.

The simulation results for the middle zones were less good. E.g. the observed general movement of the SN in eastward direction could not be properly modelled. The differences between the measured and modelled behaviour of the lower zone were in some cases large.

ESTIMATES OF COEFFICIENTS

In the preceding section the modelling results of the 3 NOURTEC cases have been briefly discussed. The Torsminde and Terschelling cases could be modelled more or less successfully. The Norderney case has been reported by Bakker *et al.* (1994); the complexity of that problem was demonstrated.

The quality of the modelling results depends to a large extent on a proper choice of the coastal constants. Reliable longshore constants could be determined with the CERC formula. The proper choice of the cross-shore constants turned out to be more difficult. Till now a sound theoretical basis is lacking for the determination of these constants. By trial and error (using the observed behaviour after execution of the SN's) useful estimates have been found. With these estimates at least some essential characteristics of the behaviour could be modelled. This procedure makes it difficult to use the model in an *a priori* predictive mode in other cases.

In Table 1 the constants as used in the Torsminde and Terschelling cases have been summarized.

	Torsminde	Terschelling
T ₀₁	5.0 years ($s_{y1} = 0.32$ m/year)	1.5 years ($s_{y1} = 1.33$ m/year)
T ₀₂	5.0 years ($s_{y2} = 0.27$ m/year)	5.0 years ($s_{y2} = 0.30$ m/year)
s ₁	$2.65 * 10^6$ m ³ /year/rad	$3.63 * 10^6$ m ³ /year/rad
s ₂	$0.23 * 10^6$ m ³ /year/rad	$0.96 * 10^6$ m ³ /year/rad
s ₃	$0.00 * 10^6$ m ³ /year/rad	$0.00 * 10^6$ m ³ /year/rad

Table 1 Coastal constants Torsminde and Terschelling cases

The longshore constants for the upper zone for Torsminde and Terschelling are of the same order of magnitude; in the middle zone the constants for Torsminde are somewhat smaller than for Terschelling. This is partly caused by the difference of the height of the upper limit of the middle zone; DNN -4 m for Torsminde and Datum -3 m for Terschelling. Both in Torsminde and in Terschelling no longshore sediment transports are assumed to occur in the lower zone.

The time constants for diffusivity in cross-shore direction are generally 5 years, except for the Terschelling case between upper and middle zone (T₀₁ = 1.5 years). There is no reliable theory available yet to predict time constants. In the Terschelling case the observed cycle for the (offshore) movement of the bar system is 10 - 15 years. It is felt that the time constants should have the same order of magnitude; 5 years is in this respect not too strange. The rather small value of T₀₁ = 1.5 years for Terschelling is probably because in this value also the (not modelled) effects of longshore sediment transport gradients are accounted for.

With the use of mathematical cross-shore transport (and morphological) models in principle estimates of cross-shore constants could be derived. Although this procedure has not yet followed in the present NOURTEC cases, promising results have already been achieved in other Dutch research cases. [See Steetzel (1996).]

CONCLUSIONS

The 3-line modelling technique has proved to be a powerful method to represent the most important characteristics of the behaviour of SN's after placement. Different design alternatives can be easily compared. It is certainly not a technique to answer all questions which might be raised related to the application of SN's.

A serious problem in analyzing the behaviour of SN's after placement is the distinction between the SN-induced behaviour and the autonomous behaviour. Much of the observed differences between model results (added to the estimated autonomous behaviour) and the measured behaviour, is caused by uncertainties about the estimated autonomous behaviour.

The present 3-line modelling technique is not able to cope with differences between borrow and native material.

Although the modelling results were in some respects not fully successful, the study has revealed that modelling attempts can serve as a very fruitful focus point for better understanding of the complex behaviour of shoreface nourishments.

ACKNOWLEDGEMENTS

The study was sponsored by partners in the Nourtec project: Rijkswaterstaat, National Institute for Coastal and Marine Management/RIKZ; the Netherlands (Terschelling case), Coastal Research Station Norderney; Germany (Norderney case) and Danish Coastal Authority; Denmark (Torsminde case). The Nourtec project was co-sponsored by the Commission of the European Union, Directorate General XII, Marine Science and Technology (MaST II) Programme under contract MAS2-CT93-0049.

REFERENCES

- Bakker, W.T. (1968)** The dynamics of a coast with a groyne system. Proc. 11th Int. Conf. on Coastal Eng., London, UK.
- Bakker, W.T., N.F. Kersting and H.D. Niemeyer (1994)** Line-modeling of Shoreface Nourishment. Proc. 24th Int. Conf. on Coastal Eng., Kobe, Japan.
- CUR (Centre for Civil Engineering Research, codes and specifications) (1987)** Manual on Artificial Beach Nourishment. Report 130; Rijkswaterstaat and DELFT HYDRAULICS; Gouda, the Netherlands.
- Groenewoud, M.D. (1996a)** Three-line modelling of the Torsminde supplies. Delft University of Technology, Fac. of Civil Eng., May 1996.
- Groenewoud, M.D. (1996b)** Three-line modelling of the Terschelling supply. Delft University of Technology, Fac. of Civil Eng., October 1996.
- Groenewoud, M.D. (1996c)** Summary of the three-line modelling of the Nourtec supplies. Delft University of Technology, Fac. of Civil Eng., October 1996.
- Mulder, J.P.M., J. van der Kreeke and P. van Vessem (1994)** Experimental Shoreface Nourishment, Terschelling (NL). Proc. 24th Int. Conf. on Coastal Eng., Kobe, Japan.
- Steetzel, H.J. (1996)** Beach nourishment and rock structures; behaviour oriented modelling of the combination of beach nourishment and rigid shore parallel structures. DELFT HYDRAULICS, Delft (in preparation).
- Svašek, J.N. and E.W. Bijker (1969)** Two methods for determination of morphological changes induced by coastal structures, XXIInd Int. Nav. Congress Paris, section II, item 4.
- Swart, D.H. (1974)** Offshore sediment transport and equilibrium beach profiles. PhD thesis Delft University of Technology.

CHAPTER 222

BEACH MONITORING PROGRAM OF VALENCIA (SPAIN)

José Serra¹, and Josep R. Medina¹

Abstract

The littoral processes and long-term shore protection plans are analysed for the coast of Valencia (Spain). The breakwaters built during this century by the Port Authorities have greatly affected the most Southern beaches by interrupting the natural longshore sand transport. The monitoring program of the beaches of Valencia (Spain) has been established for a precise estimation of the evolution in time of the beaches to the North and South by the Port of Valencia. Periodic topographic surveys provide the basic time-dependent beach description of the area. The two main objectives are the following: **a)** 3-D description of the beach surface, including estimation of reliability and measurement errors of bathymetrics, and **b)** stochastic description of wave climate.

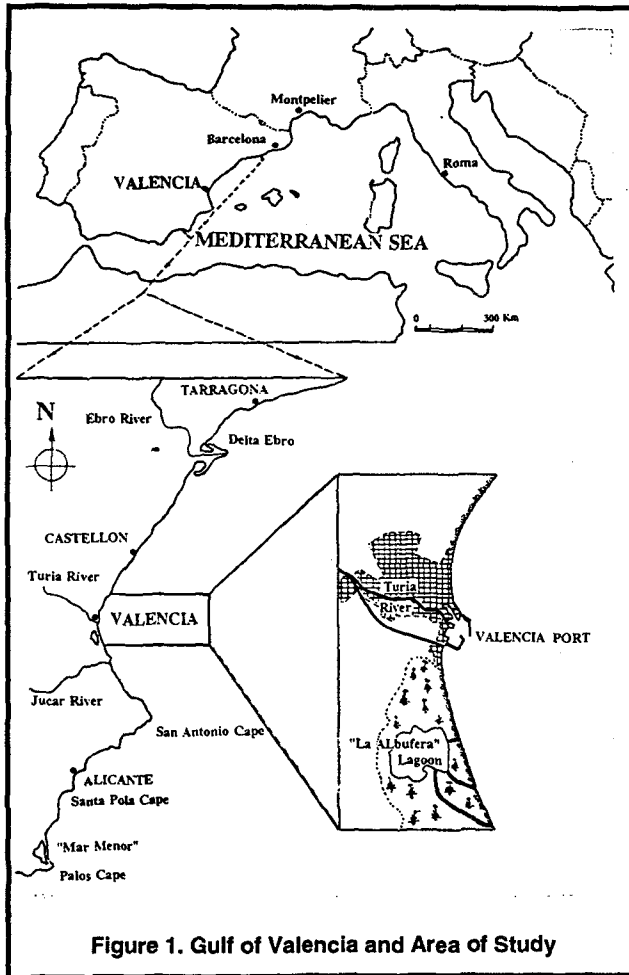
High precision and cost-efficient beach surveying techniques have been developed during the monitoring program of the beaches of Valencia (Spain). Beach profiles and zero-shorelines have been obtained with systems and errors similar to the terrestrial topography. The methods are simple enough to be applied by general land surveyors with a minimum training and may be extended to a variety of beaches for systematic and low-cost monitoring programs.

Introduction

Most beaches of the Gulf of Valencia in Spain suffer an erosion/acretion

¹ **Department of Transportation, Universidad Politécnica de Valencia, Camino de Vera s/n, 46022 Valencia, SPAIN.**

processes induced by inappropriate constructions and unadequate coastal policies. The rivers and the natural littoral sand drift created more than a hundred miles continuous natural sand beach which has been altered in several points by breakwaters, jetties, commercial ports and marinas. According to Yepes (1995), economic, social and political pressures and different kind of lobbies are interacting on the sand beaches, which are considered the most critical production factor of the touristic sector in Valencia (10% of the Spanish GNP).



Cost-efficient beach monitoring programs appears as key elements in developing appropriate shore protection and beach nourishment plans. A high precision low-cost beach profile system developed during the monitoring program of Valencia (see Medina and Serra, 1993) is being applied for beach

monitoring North and South of Valencia and may become a common low-cost system for autonomous and decentralized control of beaches along the Spanish Mediterranean coast

Environmental Characteristics

Figure 1 shows the location of the area of study in the Gulf of Valencia. Serra (1986) analysed the natural morphodynamic unit known as "Ovalo Valenciano" (Gulf of Valencia), located in the Western Mediterranean Sea, between the Delta Ebro (North), and the San Antonio Cape (South); it is almost a continuous sand beach of approximately 270 kilometers.

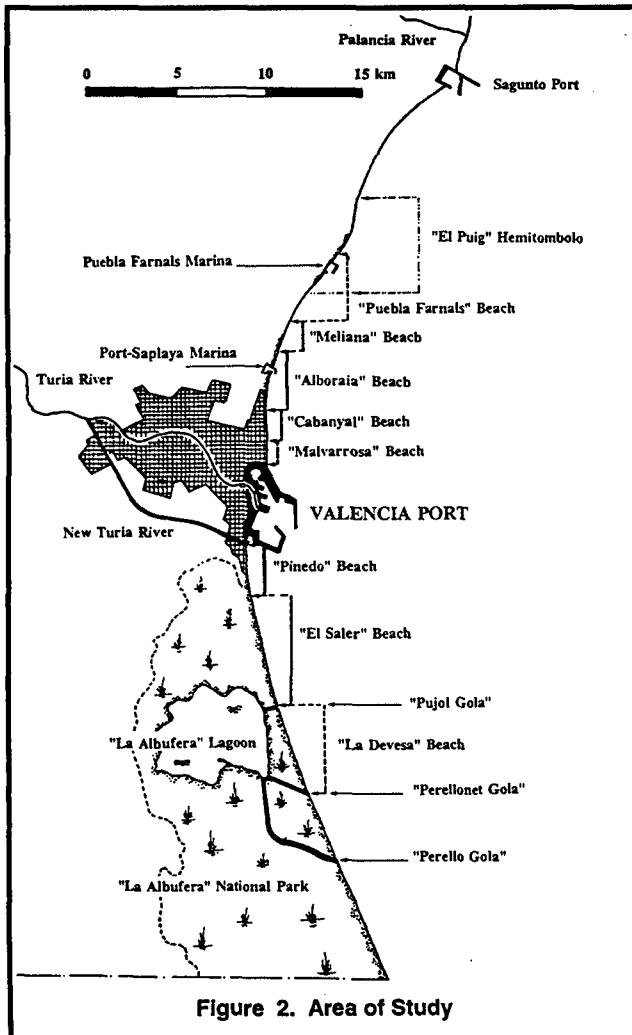
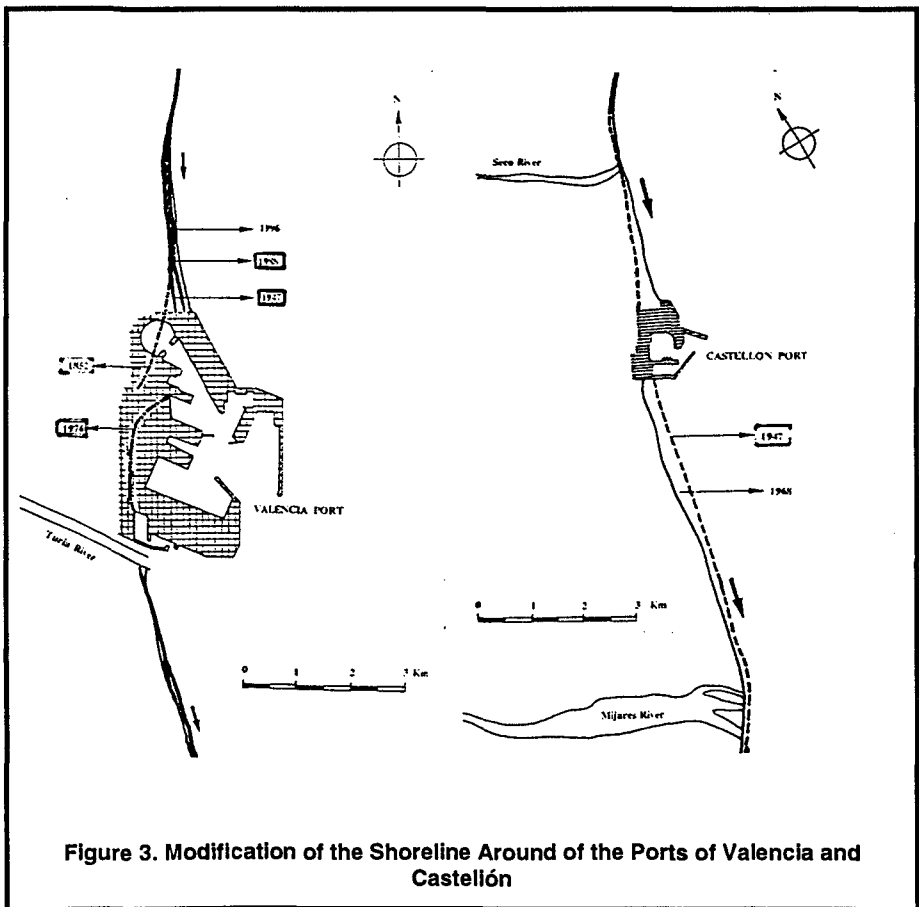


Figure 2. Area of Study

Figure 2 shows the monitorized area located in the "Ovalo Valenciano", between the "Puebla Famals" marina on the Northern limit and de inlet of the "La Albufera" lagoon, known as "Gola del Perellonet" on the Southern limit, littoral stretch length approximately 30 kilometers. The longshore transport of the coast of Valencia is about $500.000 \text{ m}^3/\text{yr}$ North to South and $200.000 \text{ m}^3/\text{yr}$ South to North.

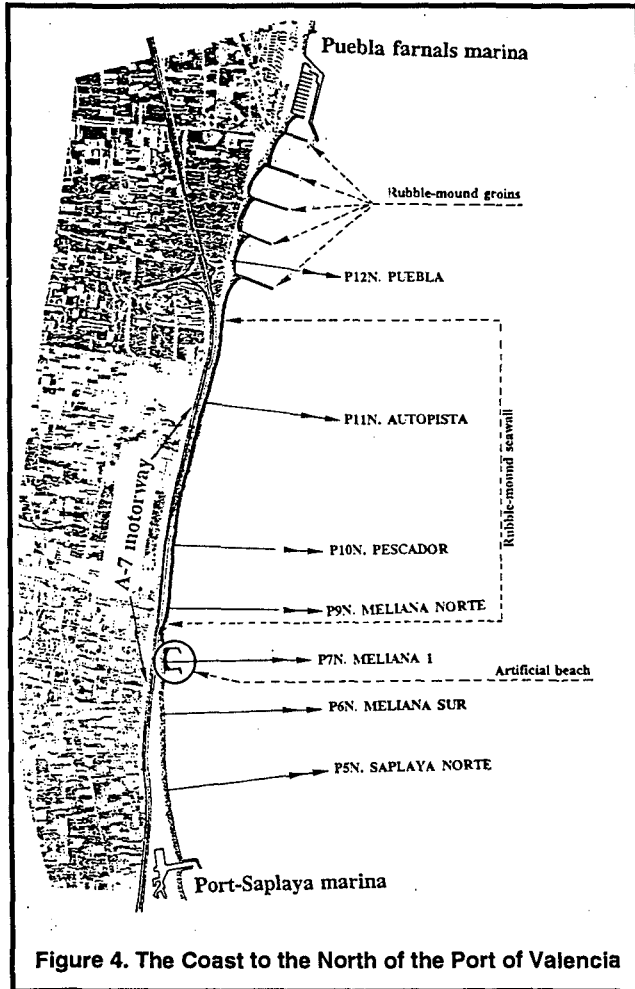
During centuries, there was not enough construction and dredging capacity to build up breakwaters and docks able to resist a sand current of half a million m^3/yr , and a variety of projects enlarging the ancient Port of Valencia failed because of the sand sedimentation processes. Nevertheless, modern construction techniques and the economic development of this century altered the traditional conditions.



A barrier to the littoral drift was established on the sandy coast and an

erosion process was generated since then on the beaches South of the harbor, where the shoreline is retreating about one meter per year. Not only the Port of Valencia, but also the dams built in the Turia river and marinas North of Valencia are contributing to the beach erosion process.

Unfortunately, neither the Port nor the dams are expected to be removed as barriers in the near future, because they are key elements to the economic development of the region. Additionally, the urban development of the Southern beaches (El Saler) has affected the natural mobility of dunes resulting in a significant retreat of the shoreline during the last three decades.



The case of the Port of Valencia and the accretion on the Northern

beaches and erosion of the Southern beaches is similar to other cases along the Gulf of Valencia. The figure 3 shows the modification of the shoreline during this century around of the Ports of Valencia and Castellón.

The coast South of the Valencian Port has two different stretches. The one next to the Port is under erosion and the furthest from the Port is stable. On the other hand, the coast North of The Port of Valencia, presents stretches in accretion and others in erosion. The erosion is located South of the barriers of the marinas; the areas in accretion are located North of the marinas, and on the beach North of the breakwater of the Port of Valencia.

The coast to the North, (figure 4), is characterized by the high number of constructions of coastal and nearshore works: the Puebla Farnals and Port-Saplaya marinas, and various coastal work fenders, emphasizing the longshore revetments which protect the A-7 motorway against direct action from strong waves.

Beach Monitoring Program of Valencia

The sand deposits at "El Saler" is in the order of dozens of millions of cubic meters, and short term problems of vital structures caused by erosion is not expected. However, the construction of a new container terminal in the Port of Valencia and the social and economic value of the beaches in the area of Valencia (1.300.000 inhabitants) has favored the establishment of a systematic beach monitoring program. This monitoring will be the basis of the long-term planning and shore protection works on the coast of Valencia.

The Valencia beach monitoring program focuses on two main points: 1) the topographic and bathymetric description of the beaches, and 2) the description of wave climate. Figure, shows the location of the wave recording equipment and in the twenty beach profiles that define the beach morphology to the North and to the South of the Valencia Port.

Bathymetric Survey

From the theoretical point of view, it is relatively simple to describe the beach erosion process. The aerial topography and bathymetry of the beach defines the surface of the sedimentary deposits or rocks along the coast.

The common equipment for systematic bathymetries are echosounders on boats with GPS which are affected by temperature, salinity, and calibration method. The bathymetries on boats must be related to a "zero level" which requires a high precision topographic network and a continuous measurement of the mean water level during the beach survey; it is a difficult to estimate the

error level of the survey because the high precision measurement techniques, when available, are low-efficient.

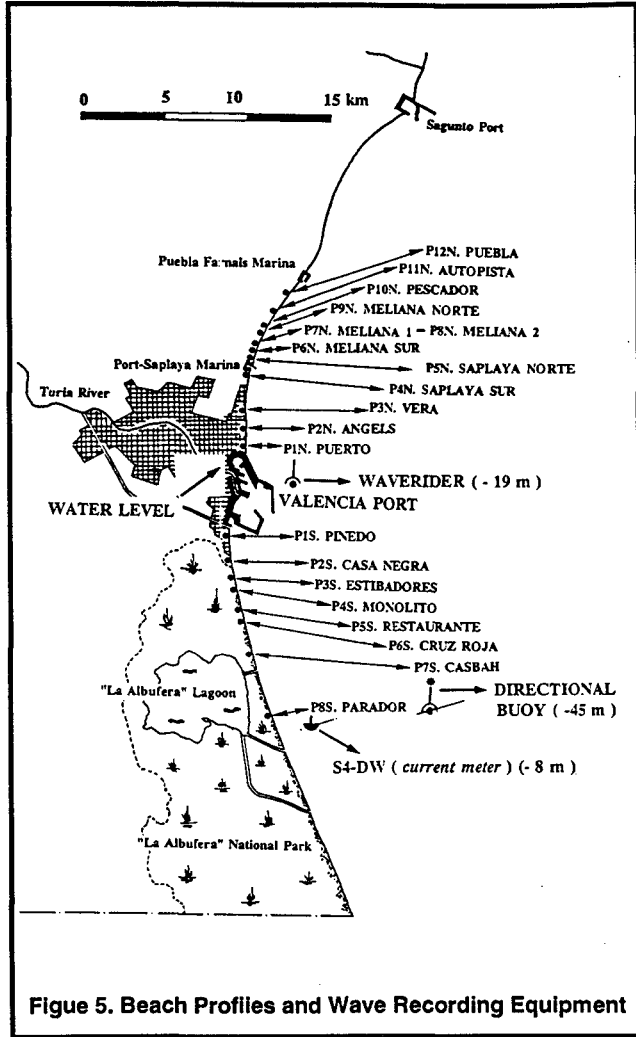
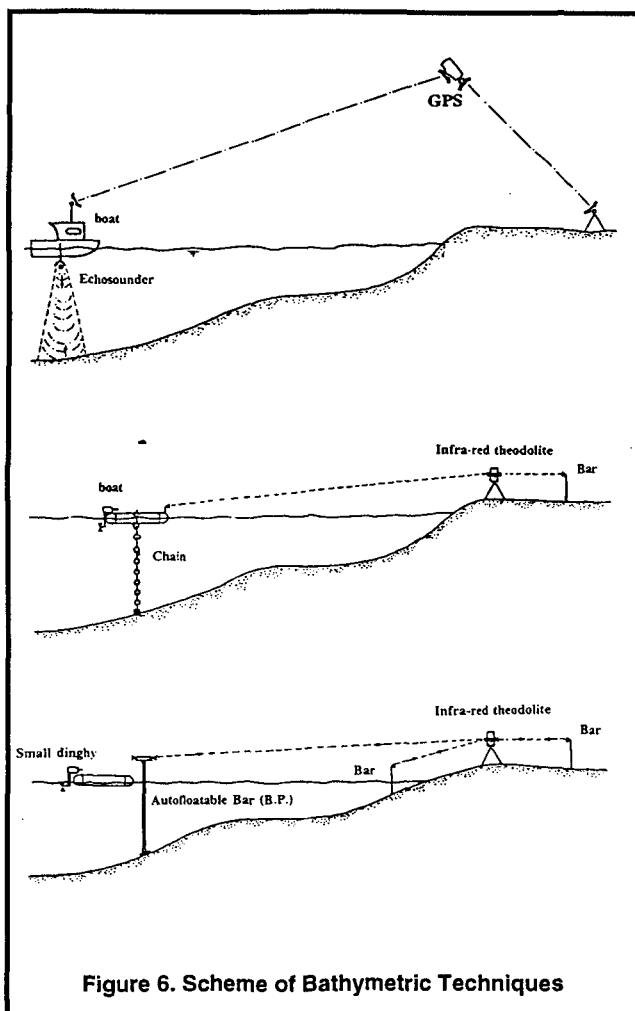


Figure 6 shows a scheme of the three different surveying techniques commonly used in the beach monitoring programs of Valencia. The first technique is a systematic automated method based on an echosounder boat mounted with GPS. The second technique is a manual method based on a small dinghy and chain; and the third technique is a manual method based on a land rod readapted for marine purposes, this technique is known as *Beach Profiler (BP)*.



The Beach Profiler (BP) Within the last decade new measuring systems for bathymetric survey with a common criteria of moving land topography to marine topography have been considered by different research groups. Following this research line the Laboratory of Ports and Coast of Univerisidad Politécnica de Valencia has developed the denominated Beach Profiler (BP) represented in Figure 7. The unit has proved its effectivity as a precise unit for beach profile measuring in beach monitoring. A basic idea is that, in the long-term, cost-efficient beach monitoring techniques appear to be key elements in developing apropiate shore protection and beach nourishment plans.

BP is a high precision and low-cost beach profiler system developed

during the first monitoring program of "El Saler" which is being also applied for monitoring the beaches North of Valencia, and may become a standard low-cost system for regional and decentralized control of beaches along the Spanish Mediterranean coast.

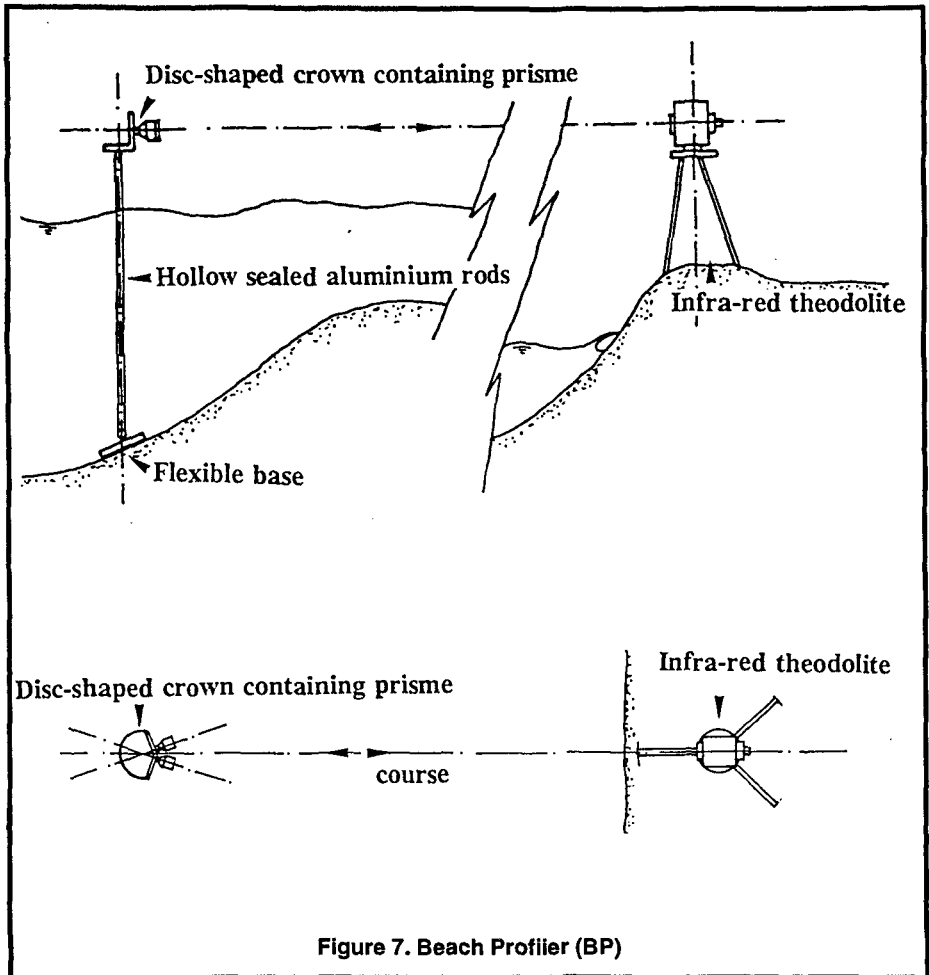


Figure 7. Beach Profiler (BP)

The BP system only requires a two man work team aboard to a small boat, and a land surveyor with a conventional infra-red equipment. The especial designed element to measure the level of the sea botton was a self-floatable aluminium bar, with a crow on the top on which the infra-red reflectors are fixed covering all directions and an articulated led plait in the botton. The BP shows the following characteristics: high precision (error < 2 cm), high efficiency (about 60 points/hour), low cost, and simplicity. Figure 8 shows a typical enveloped and standard deviation of the elevation of the measured profiles using BP.

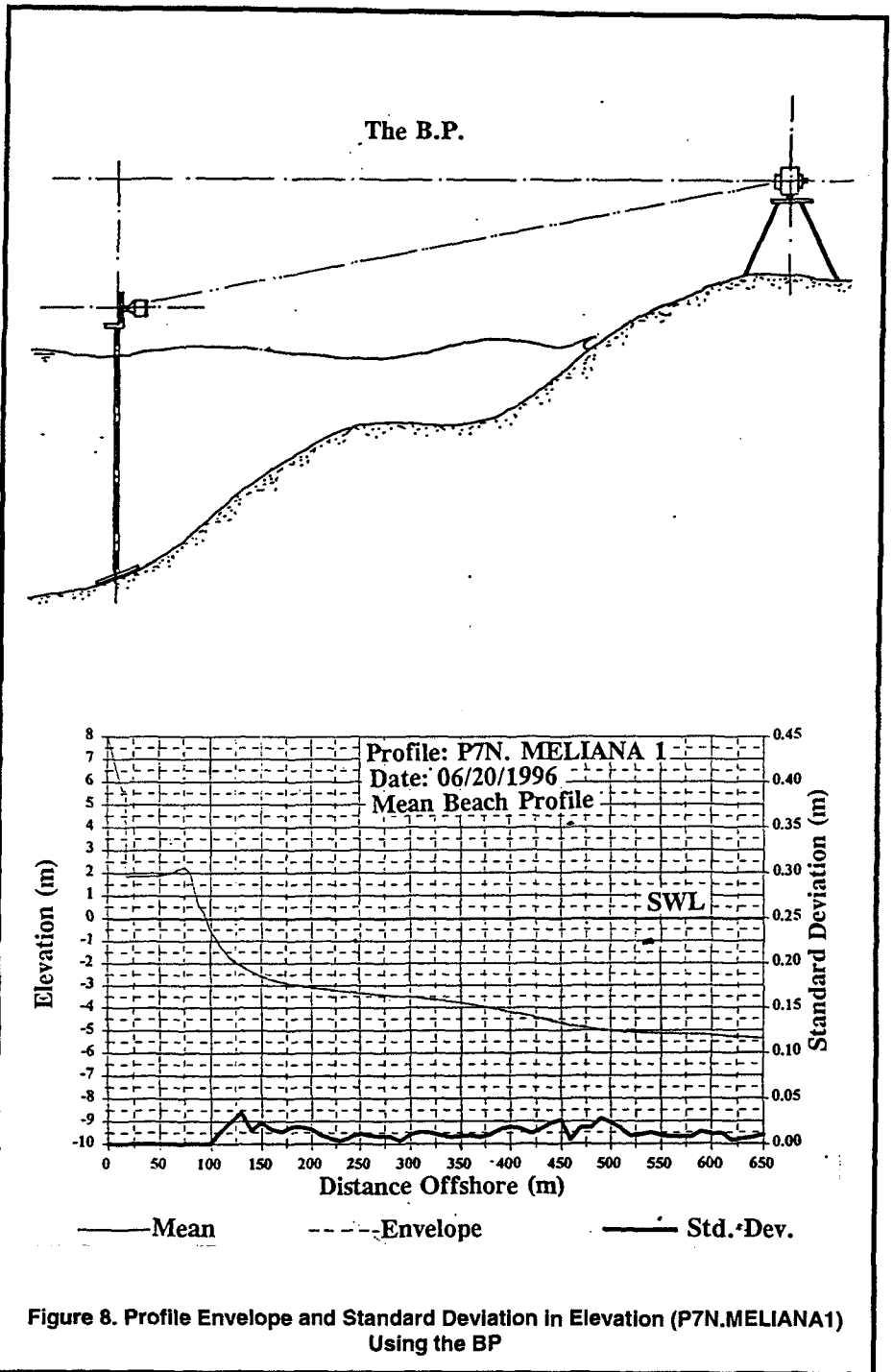


Figure 8. Profile Envelope and Standard Deviation in Elevation (P7N.MELIANA1) Using the BP

Beach Profiles: Errors

Esteban (1993) and Esteban et al. (1995) analysed the problems associated with the use of different bathymetric systems in beach monitoring. Table 1 shows a comparison of different bathymetric techniques, incorporating the results obtained by the BP.

Bathymetric Technique	Sources of Error	Estimated Error	Cost
ECHOSOUNDER	⇨ Mean water level: <i>Tides</i> <i>Strong surges,...</i> ⇨ Calibration: <i>Temperature (° C)</i> <i>Salinity (g/l).</i> ⇨ Boat movement: <i>Heave, Pitch, Roll.</i>	$\approx 10 \text{ cm}$ <i>(Mediterranean)</i>	High
CHAIN	⇨ Mean water level: <i>Tides</i> <i>Strong surges,...</i> ⇨ Manual operation	$\approx 20 \text{ cm}$ <i>(Mediterranean)</i>	Low
SLED <i>Stauble et al. (1993)</i>	⇨ Terrestrial topography ⇨ Positioning	$\sigma \approx 7 \text{ cm}$ (Atlantic)	High
CRAB <i>Birkemeier et al. (1993)</i>	⇨ Terrestrial topography ⇨ Positioning	$\sigma \approx 1 \text{ cm}$ (Atlantic)	Very High
BEACH PROFILER	⇨ Terrestrial topography ⇨ Positioning	$\sigma \approx 2 \text{ cm}$ (Mediterranean)	Low

Table 1. Sources of Error Corresponding to Different Bathymetric Techniques

Conclusions

High precision and cost-efficient beach surveying techniques have been developed during the monitoring program of the beaches of Valencia (Spain).

The BP method is simple enough to be applied by a general land surveyor with a minimum training and may be extended to a variety of beaches for systematic and low-cost monitoring programs. The technical characteristics are:

- 1.- *High precision (1 cm < error < 2 cm).*
- 2.- *High efficiency (about 60 points/hour).*
- 3.- *Maximum length profile: 1000 m.*
- 4.- *Maximum water depth: 10 m.*
- 5.- *It does not require specially trained personnel.*
- 6.- *The BP may be considered a simple terrestrial topography system adapted for monitoring beaches.*

Continuous mean water level measurements during surveys are unnecessary, neither is special equipment nor highly trained personnel required.

Therefore, the BP is adequate for manual beach monitoring and the problems of the BP are similar to terrestrial topography.

References

Esteban, V (1993). Sistemas de Información y Medición Batimétrica. Proc. *II Jornadas Españolas de Ingeniería de Costas y Puertos*, Gijón (Spain), 10-11 May 1993, 163-174.

Esteban, V., Aguilar, J., Serra, J., and Medina, J.R. (1995). Levantamientos y Seguimientos Topo-Batimétricos en Ingeniería de Costas (in Spanish). *Ingeniería del Agua*, Vol. 2 (April 1995): 181-200.

Lee, G. And Birkemeier, W.A. (1993). Beach and Nearshore Survey Data: 1985-1991 CERC Field Research Facility. *Technical Report CERC-93-3*. U.S. Army Corps of Engineers.

Medina, J.R. , and Serra, J. (1993). Beach monitoring Program of El Saler (Spain). *Spain-U.S. Workshop on Natural Hazards*, Barcelona, 8-1 June, 1993, 279-291.

Stauble, D.K., Garcia, A.W., Kraus, N.C., Grosskopf, W.G. and G.P. Bass (1993). Beach nourishment Project Response and Design Evaluation: Ocean City, Maryland. *Technical Report CERC-93-13*. U.S. Army Corps of Engineers.

Serra, J. (1986). Procesos Litorales en las Costas de Castellón. (in Spanish) *Ph.D. Thesis* presented at the Universidad Politécnica de Valencia, Spain.

Yepes, V. (1995). Gestión Integral de las Playas como Factor Productivo de la Industria Turística. El Caso de la Comunidad Valenciana. (in Spanish). *Proc. III Jornadas Españolas de Ingeniería de Costas y Puertos*. Valencia, 3-4, May, 1995, 958-976.

CHAPTER 223

BAR MIGRATION AND DUNEFACE OSCILLATION ON DECADAL SCALES

Marcel J.F. Stive^(1,2), Jorge Guillen^(1,3) and Michele Capobianco⁽⁴⁾

Abstract

While structural erosion or accretion of a coastal stretch is of primary concern to coastal management, knowledge of coastline oscillations on larger time scales relative to the erosional or accretional trend would allow for a more efficient management practice. Our analysis of more than thirty years of observations of dune, beach and nearshore evolution reveals some of the typical oscillatory behaviour in time and space on a decadal scale. We have focused on the behaviour of the duneface and analyzed the possible relation between the duneface behaviour and that of the nearshore morphology. Amongst our results are the findings that the demeaned oscillatory duneface evolution on a decadal scale is not only correlated with the recurrence frequency of the migratory bar system, but also with a cumulative measure of episodic wave events.

Introduction

Moderate rates of structural erosion or accretion only become apparent on larger time and space scales, because of the dominance of shorter scale oscillations caused by natural processes. Most evident is that due to episodic wave events, which can cause strong erosion and associated steepening of the duneface, while the eroded sediment is deposited on the beach and nearshore profile, resulting in a more weakly sloping and wider beach. After these events a

¹ Netherlands Centre for Coastal Research, Delft University of Technology, PO Box 5048, 2600 GA Delft, The Netherlands

² Delft Hydraulics, PO Box 177, 2600 MH Delft, The Netherlands

³ Instituto de Ciencias del Mar, Paseo Juan de Borbon, 08039 Barcelona, Spain

⁴ Tecnomare SpA, 3584 San Marco, 30124 Venezia, Italy

restoration may occur due to aeolian and hydrodynamic processes. Our interest is typically into the scales intermediate to the short term, event related, behaviour and the long term, structural trend of erosion or accretion associated with gradients in cross-shore and longshore directions over a coastal stretch.

These intermediate scales concern the temporal behaviour on decadal scales, leading to duneface amplitude oscillations of magnitudes comparable to those of the structural trend. Our objective has been to develop an understanding of the mechanisms behind this behaviour, based on the "working-hypothesis" that a relation may be expected between the bar dynamics and the duneface behaviour. The JARKUS data-set, comprising more than thirty years of field observations of the duneface, beach and nearshore profile along the central Netherlands coast, has revealed typical and unexpected properties of subaqueous bar morphodynamics on a decadal scale. Amongst the most recent analyses is that of Wijnberg and Terwindt (1995) pointing towards the existence of four distinct morphodynamic regimes, each characterized by their own particular bar dynamics. These regimes occur in four coastal stretches, each constrained by coastal engineering structures. While the precise physical interpretation and explanation remains to be resolved, our objective (stimulated by the findings of Guillen and Palanques, 1993) has been to investigate and explain the possible relation between the above described bar behaviour and the duneface dynamics.

It is clear that the dune system and the bar system interact through the dynamic processes of the coastal area; they are both subject to the same wave and tidal forcings and, at same time, they are part of an interconnected system. We recall the fact that not only tides have clearly defined astronomic cycles with a periodicity ranging from hours to decades, but also wave climate has at least a seasonal cycle and, on a long term basis, longer cycles linked to climate oscillations. These are still active subjects of investigation; think for instance to the so-called Bruckner cycles, basically consisting of the recurrence in northwestern Europe of periods of cold and damp alternating with warm and dry years, the average interval between successive maxima being 34.8 years (as calculated by Bruckner in 1890), though individual cycles vary from 25 to 50 years. However there is an increasing evidence that, when looking at large scale and long term evolution of the coastal system, we need to highlight the long term character of the forcing factors.

Study area

Our study area is the Holland coast (Fig. 1), bounded by Rotterdam harbour and the port of Den Helder. It is characterized by an almost uninterrupted dune system, without barrier islands and tidal inlets. The main human interventions along this stretch of 120 km are the harbourmoles of Scheveningen and IJmuiden, the sea dike of Petten and the dike of Den Helder.

During the last three hundred years this coast is erosive in the north (approx. 1 m/yr), and the south (approx. 0.3 m/yr) and accretive in the centre (approx. 0.2 m/yr). Sediment grain sizes are 200 to 250 microns in the dunes and 250 to 300 microns on the beach. The tide ranges from 1.7 m near Scheveningen to 1.4 m near Den Helder. Mean wave heights and periods are 1.2 m and 5 s respectively, with approaches from south-west and north-northwest mainly.

Foredunes are regressive, stable or progressive over the last decades, with widths ranging from 500 to 2500 m. The subaerial beach averages 43 m in width, with a mean slope of 1:15 (Short, 1991). The bar-beach system commonly consists of a beach-bar, attached to the beach as a ridge and runnel system, an outer bar, highly rhythmic and rip-dominated and a longshore bar (Short, 1992). Their temporal and spatial behaviour has been analyzed by Wijnberg (1995). A common characteristic is that of a cyclic two or three bar system, initiated

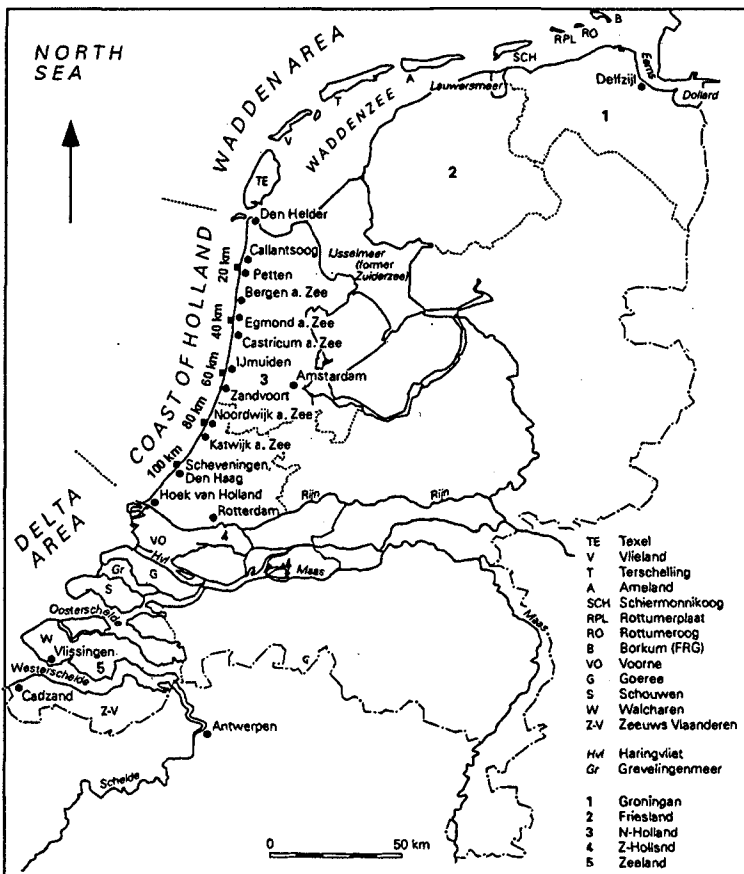


Figure 1 Study area

nearshore, migrating and growing through the surfzone and then decaying offshore. Apparent return periods range between 4 and 15 years.

Methodology

The medium-term dune, beach and nearshore profile evolutions were analyzed using the JARKUS data-set. It consists of (about 3,000) fixed measuring rays extending along the Dutch North Sea coast. The distance between the profiles is 200-250 m and yearly profiles approximately from the foredune to 1,000 m seaward are available since 1964. Profiles are usually surveyed between early April and late September. It is expected that the biased sampling does not affect a decadal analysis of the shapes of the profiles (Wijnberg and Terwindt, 1995).

Our morphometric analysis of the dune and beach system concerns first the determination of temporal and spatial oscillations on decadal scales in the dunefoot, and second the possible relation of this behaviour with the shoreface slope and the behaviour of bar and trough systems. Our parameters are the dunefoot position, the duneface slope and the beachface slope.

Qualitatively it is clear that the shoreface slope plays a fundamental role in the dynamics of the coastal system. Firstly, in the sense that in the steeper slope area, the bar system needs longer return period waves to be moved offshore. Second, in the steeper slope area, the dunefoot is subject to larger wave impact under storm conditions. In addition, residual tidal currents will determine a relatively larger speed of motion for the shallower part of the bar system with respect to the deeper part, which is a clear mechanism of introduction of a "structural modification" in the coastal system. If we consider two adjacent zones with different profile slope, this is clearly a mechanism for the introduction of a longshore mechanism of motion.

Following Wijnberg (1995) we distinguish four distinct spatial sectors (Fig. 1), viz. (I) km 8-20, (II) km 28-52, (III) km 63-95 and (IV) km 104-114. These sectors are bounded by structures, the Hondsbossche dike (km 23) and the harbours of IJmuiden (km 55) and Scheveningen (km 102), and have been found to exhibit a uniform bar behaviour within them. In our analysis we further concentrate on Zones (II) and (III), which contrary to (I) and (IV), are virtually without human interference.

Our initial effort has been to derive a representative duneface and dunefoot definition, such that it is not affected by local and instantaneous processes occurring immediately before the survey. A heuristic procedure, based on hydrodynamic and morphologic considerations, using two constant planar surfaces and a sediment volume balance was chosen (Fig. 2). By using this procedure the temporal changes in the calculated dunefoot position indicate the changes in the volume of sediment stored in the dune-beach system between +1 and +5 m NAP heights, allowing a comparison between all the profiles in a coherent way. The

choice of the +5 m NAP height as the upper boundary is based on the storm surge design level height for dune erosion in Holland.

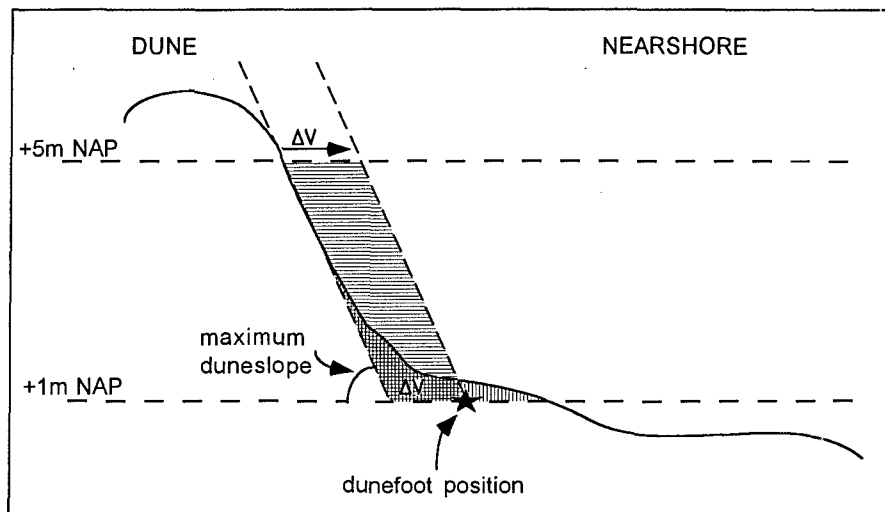


Figure 2 Dunefoot definition procedure

In the analysis the dunefoot and nearshore profile evolution has been based on space-time diagrams. Linear temporal trends were calculated in each profile and the "residuals" with respect to this trend were extracted. This approach has been complemented by application of Empirical Orthogonal Function (EOF) analysis techniques, the presentation of which has been omitted here because of space limitations. We have used the EOF's to derive periodicities more clearly.

In analyzing possible effects of wave forcing we have used a time history of 1,090 "storm events" during the period 1979-1991 (De Valk, 1994). They have been characterized by two parameters, viz.

$$A = H_{m0} * \text{SQRT}(t), \text{ and}$$

$$B = SL * \text{SQRT}(t),$$

where H_{m0} is the average significant wave height during the storm event, SL the average surge level and t the duration of the storm event. Furtheron we have summed these parameters over the period in between soundings to account for the cumulative effect of storm events.

Results and analysis

Dunefoot data

Following our derivation of a morphologically equivalent and stable duneface profile, we find that the average maximum duneface slope is nearly

constant along the different zones ($\tan b = 0.14$ to 0.15). The average beach slope between the + 1 m NAP and the - 1 m NAP ranges from 0.025 to 0.030, implying a mean beachface width of 70 to 80 m.

The linear trend of the dunefoot position shows a high longshore variability (Fig. 3), but the average over several kilometres is less than 1 m/yr, while the accretional and erosional character is not very different from that over the last few hundred years. Standard deviations relative to the trend also show a high longshore variability (Fig. 4), while the average over several kilometres is between 5 and 10 m.

We now describe the behaviour of Zones II and III, showing a general erosive and accretive trend respectively, which are relatively untouched by human intervention.

The evolution of the residual dunefoot position in Zone II exhibits longshore and temporal oscillations (Fig. 5). Spatially, alternating accretional and erosional stretches of 2 to 3 km are observed alongshore. Temporally, this longshore rhythmicity may be viewed as a shoreline wave propagating towards the south with a propagation velocity of 150 to 200 m/yr. The amplitude of the oscillation is approximately 20 m and its periodicity 15 years.

In contrast the evolution in Zone III shows virtually no longshore oscillations (Fig. 6). Temporally, periods of relative accretion and erosion alternate simultaneously along the coast.

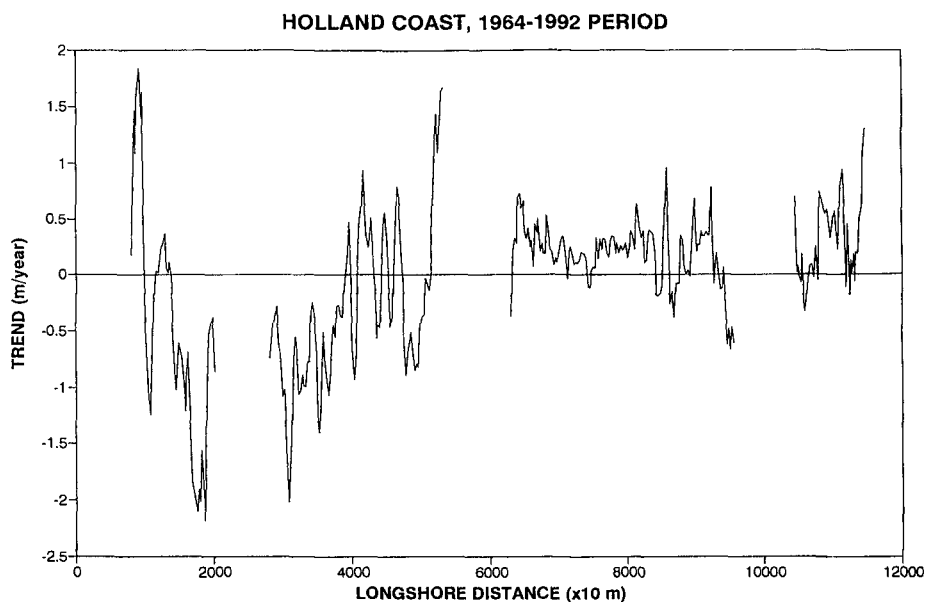


Figure 3 Trend in the dunefoot position (positive is seaward, negative is shoreward)

HOLLAND COAST, 1964-1992 PERIOD

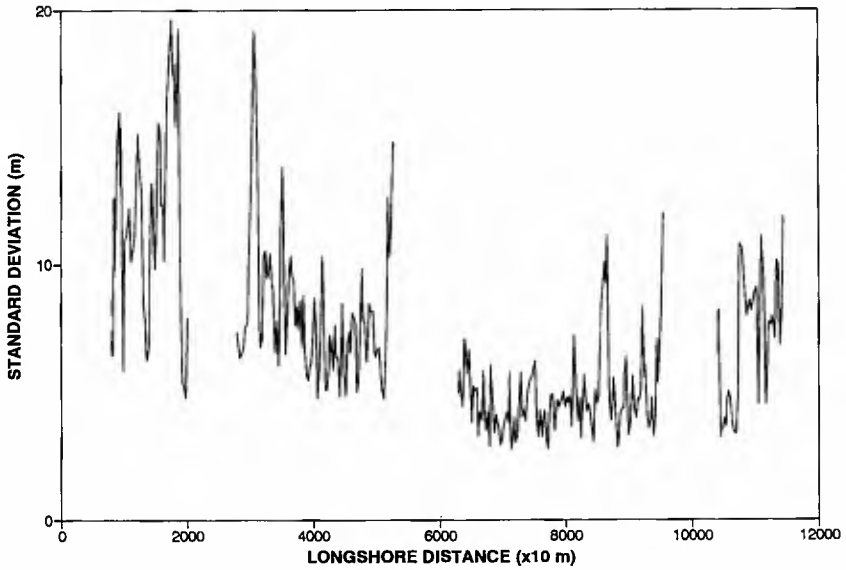


Figure 4 Standard deviation of the dunefoot position

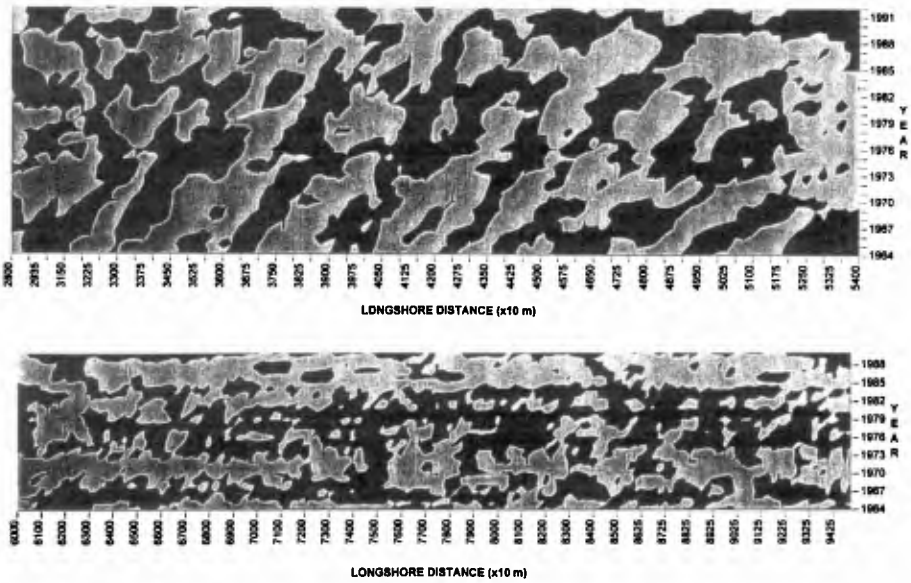


Figure 5 and 6 Residual dunefoot position relative to the trend for zones II and III respectively (dark shading is shoreward, grey shading is seaward)

Also, in spite of the above differences, inspection of Fig. 5 and 6 reveals some simultaneous occurrences of relative erosion and accretion. This may be more clear from Fig. 7, comparing the spatially averaged residual position over time in the two zones. Although our extreme event data only cover the period 1980 to 1991 (Fig 8), we note that we expect that these simultaneous occurrences are related to the decadal variation of the cumulative extreme events. For instance, the relative accretion between 1985 and 1988 appears to correspond to a relative minimum in the extreme events.

A preliminary analysis of the periodicity of the first empirical orthogonal function of the dunefoot position for the whole coast has also been performed. It consists of applying a simplified non-linear model as a reference concept. In practice the temporal evolution of the first and the second empirical orthogonal functions has been considered as determined by the sum of a linear (sinusoidal) term and two nonlinear terms related to the amplitude of the first one. Using empirical process-oriented considerations we assume that, under erosive conditions, the dunefoot is less mobile (composed by less mobile sediments), while under accretive conditions, the dunefoot is more mobile (composed by more mobile sediments). This way three fundamental periods have been identified: 51 years for the oscillation of the mean dunefoot position; 7.5 years for the oscillation of the dunefoot during erosive periods; 2 years for the oscillation of the dunefoot during the accretive periods. These results (see Figure 9) need to be further examined mainly because of the short duration of the dataset with respect to the longer period of oscillation. The results also need to be further examined with respect to the cycles in the forcing factors. We note that the dunefoot evolution is recovered by multiplying the "reconstructed" temporal orthogonal functions and the spatial temporal orthogonal functions. In case the results will be confirmed by further analyses, it is clear that, with a very simple modelling concept we are able to gain some predictive value.

Profile data

A main morphological feature of the profile along the Holland coast is the existence of migrating breaker bars. A comprehensive analysis of their behaviour was recently made by Wijnberg (1995), using EOF analysis. In each of the four coastal stretches the bar behaviour is found to be temporally and spatially different, but internally (i.e. within a particular stretch) coherent. The explanation of this is as yet undetermined.

Zone II and III both exhibit an offshore migratory behaviour of the bars. The average number of bars is constant in time, where the offshore decay of the outer bar is followed by the appearance of a new bar at the shoreline. The temporal behaviour is thus similar, only the recurrence frequency is different, viz. approximately 15 years in Zone II and 4 years in Zone III. Their spatial behaviour is significantly different, however. Whereas in Zone III the relative

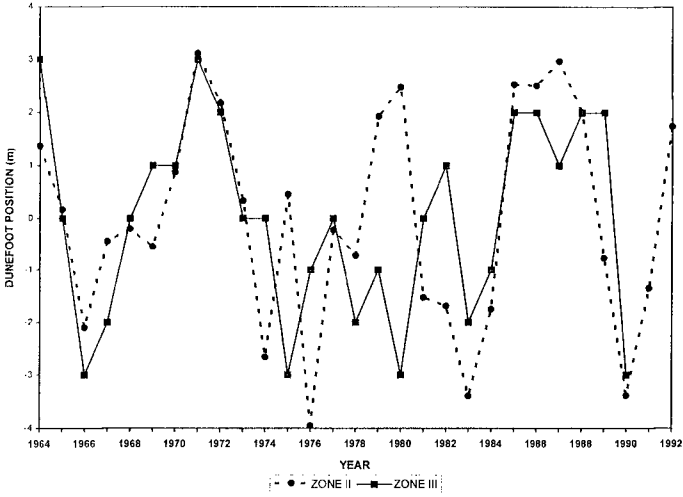


Figure 7 Longshore-averaged mean dunefoot position versus time

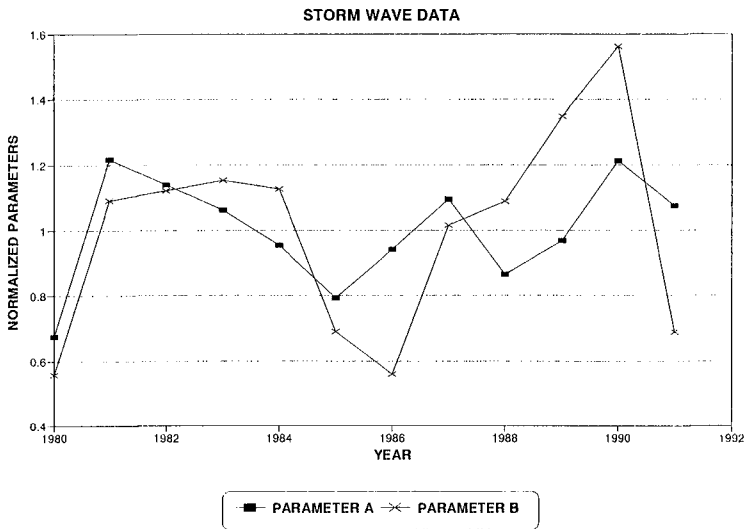


Figure 8 Normalized year-cumulative storm event parameters

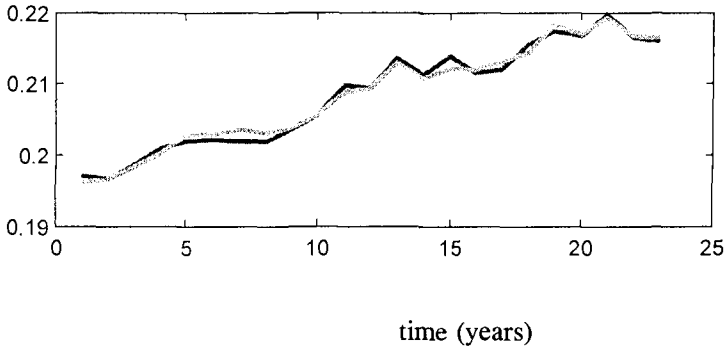


Figure 9 Normalized first temporal eigenfunction of the dunefoot displacement of all four zones (full line observed, grey line modelled)

position is homogenous alongshore, without any longshore rhythmicity, Zone II has two specific spatial features. First, at a large spatial scale, the bar migration is not in phase, exhibiting an obliquity relative to the shore. Apparently, the bar initiation first occurs in the south and this initiation propagates towards the north. The obliquity creates a discontinuity. Second, on a smaller spatial scale, longshore discontinuities (of a length of 2 to 3 km) in bar position exist, which are caused by the crescentic morphology of the bar systems here.

Discussion and conclusions

The standard deviation of the mean shoreline position has been termed beach mobility (Dolan et al., 1978). Short and Hesp (1982) found it to be a function of the morphodynamic beach state: dissipative, intermediate and reflective beaches correspond to low-moderate, moderate-high and low beach mobility respectively. On Australian shores beach mobility ranges between 5 and 14 m from data taken over 1 to 5 years. Shoreline mobility along the Holland coast, averaged over several km (as inferred from the + 1 m NAP depth contour) over the period 1964-1992 amounted to some 20 m, suggesting an increase of mobility over longer time scales. On the other hand, dunefoot mobility, such as defined here, is approximately half that of the shoreline. Apparently, the shoreline evolution exhibits more "noise" than that of the dunefoot. Further, it is noted that the dunefoot mobility on shorter time scales, e.g. due to extreme events, can be nearly an order-of-magnitude larger, i.e. 25 to 75 m of duneface retreat (Stetzel, 1993). While longer term erosive or accretive trends are relevant for long term nourishment policy, our findings of mobility are relevant to medium term (decadal) coastline management.

While the order-of-magnitude of dunefoot mobility has been found the same along the Holland coast, its spatial and temporal nature is quite different in the two, virtually unmanaged, Zones II and III. Our findings suggest that the dunefoot behaviour is strongly influenced by the subaqueous bar behaviour, confirming earlier suggestions by Bruun (1954).

In Zone III, both the dunefoot and the subaqueous bar behaviour behave spatially homogeneous alongshore. Erosional-accretive oscillations appear to correlate with the cumulative parameters describing the storm events.

The latter effect is also found in Zone II, but here most interestingly is the occurrence of the longshore rhythmicity and of the recurrence frequency. It exhibits spatially the same scale as that of the crescentic bar morphology (2 to 3 km) and temporally the same recurrence frequency as that of the migratory bar behaviour (15 yr). Clearly, there exists a strong signature of the bar dynamics in the shoreline and dunefoot behaviour.

A comparison of earlier observed temporal oscillations and -if present- their alongshore propagation speed is given in Table 1. We note the study of Verhagen (1989), who interpreted from long term shoreline observations the presence of 'sand waves' along the Holland coast, moving northwards.

Author	length (km)	migration rate (m/yr)	amplitude (m)	period (yr)
Bruun (1954)	0.5-3	0-1,000	60-80	-
Morton (1979)	5-7	-	-	-
	2.5-3	-	-	-
Dolan & Hayden (1981)	> 1	-	-	-
Davidson-Arnott (1988)	0.5-2.5	150-300	50-90	10
Verhagen (1989)	5.5	65	40-60	75-100
Pelczar et al. (1990)	5-9	100-200	70-110	50-60
This study	2-3	150-200	20	15

Table 1. Observed shoreline oscillations

Our final conclusion is that our interpretation of shoreline mobility on decadal scales for the Holland coast indicates that the dunefoot, according to our definition, shows an oscillatory amplitude of some 20 m. It is quite moderate compared to other studies, and its behaviour is clearly related to the dynamics of bar behaviour on the one hand and to the cumulative effect of extreme wave events on the other hand.

Acknowledgements

Part of this work is based on work in the PACE- and SAFE-projects, in the framework of the EU-sponsored Marine Science and Technology Programme (MAST-III), under contract no. MAS3-CT95-0002 and MAS3-CT95-0004. The second author would like to acknowledge his grant from the Ministerio de Educacion y Ciencia of Spain, allowing for his post-doctoral stay at Delft University of Technology in 1995. We thank Mark Voorendt of Delft University of Technology for his technical support.

References

- Bruckner E., Klimaschwankungen seit 1700 nebest Bemerkunge uber die Klimaschwankungen der Diluvialzeit, "Geographische Abhandlungen" B. IV. H. 2, Wien, 1890, pp. 153-184.
- Bruun, P., 1954. Migrating sand waves or sand humps, with special reference to investigations carried out on the Danish North Sea Coast. Proc. 5th Int. Conf. Coastal Engineering, New York, ASCE: 269-295.
- Davidson-Arnott, R.G.D., 1988. Temporal and spatial controls on beach/dune interaction, Long Point, Lake Erie. Journal of Coastal Research, Special Issue No 3: 131-136.
- De Valk, C.F., 1994. Selection of storm events and estimation of exceedance frequencies of significant wave height for five North Sea locations. Delft Hydraulics, Report H 1931, 54 pp.
- Dolan, R. and Hayden, B.P., 1981. Storms and shoreline configuration. Journal of Sedimentary Petrology, 51: 737-744.
- Dolan, R.; Hayden. B.P. and Heywood, J., 1978. Analysis of coastal erosion and storm surge hazards. Coastal Engineering, 2: 41-53.
- Guillen, J. and Palanques, A., 1993. Longshore bar and trough systems in a microtidal, storm-wave dominated coast: the Ebro Delta (NW Mediterranean). Marine Geology, 115: 239-252.
- Morton, R.A., 1979. Temporal and spatial variations in shoreline changes and their implications, examples from the Texas Gulf Coast. Journal Sedimentary Petrology, 49: 1101-1111.
- Pelczar, M.; Nejczew, P. and Mielczarski, A., 1990. Cartometric analysis of the shore-line changes on eastern part of the Polish Baltic coast in the last century (in Polish). Rozprawy Hydrotechniczne, 51.
- Short, A.D., 1991. Beach morphodynamic systems of the central Netherlands coast, Den Helder to Hoek van Holland. Rapport GEOPRO 1991.01, University of Utrecht: 106 pp.
- Short, A.D., 1992. Beach systems of the central Netherlands coast: Processes, morphology and structural impacts in a storm driven multi-bar system. Mar. Geol., 107: 103-137.

- Short, A.D. and Hesp, P., 1982. Wave, beach and dune interaction in southeastern Australia. *Marine Geology*, 48: 259-284.
- Steetzel, H.J., 1993. Cross-shore transport during storm surges. PhD. thesis, Delft University, The Netherlands: 242 pp.
- Verhagen, H.J., 1989. Sand waves along the Dutch coast. *Coastal Engineering*, 13: 129-147.
- Wijnberg, K.M., 1995. Morphologic behaviour of a barred coast over a period of decades. PhD. Thesis, University of Utrecht: 250 pp.
- Wijnberg, K.M. and Terwindt, J.H.J., 1995. Quantification of decadal morphological behaviour of the central Dutch coast. *Marine Geology*, 126: 301-330.

CHAPTER 224

Morphological development of the Terschelling shoreface nourishment in response to hydrodynamic and sediment transport processes

P.Hoekstra¹, K.T. Houwman¹, A. Kroon¹, B.G. Ruessink¹,
J.A. Roelvink² and R. Spanhoff³

Abstract

The Terschelling shoreface nourishment was studied over a period of about 2.5 years. The nourishment was originally designed to act as a feeder berm. Since its implementation, the nourishment has completely satisfied the design objectives. However, the nourishment only partly acts as a feeder berm and the actual success of the nourishment is also based on its breaker berm function. The creation of a wave shadow zone leads to an interception of part of the longshore drift and the development of a salient effect.

Introduction

The Dutch barrier island of Terschelling is part of the northern coastline of the Netherlands. The island is facing the North Sea and separates the North Sea from the backharrier system of the Wadden Sea (Fig. 1). The North coast of the island consists of a sandy shoreface, flanked by sandy beaches and dunes. In the last decades the central part of this coastline has chronically suffered from erosion. Over an alongshore distance of 5 km, the average annual coastal retreat was about 2-3 m/yr. This corresponds with an estimated, average annual loss of sand of 110.000 m³. In 1993 a shoreface nourishment was implemented along the Terschelling coast to stabilize the existing coastline. The main design objective of this nourishment was (and is) "to return the Transient Coastline to a position seaward of the Basal Coast Line (Dutch BKL concept; NOURTEC, 1995) and to ensure that this Transient Coast Line will not retreat landward of the Basal Coast Line during the next 8 years" (Biegel and Spanhoff, 1996). In terms of design dimensions in total 2.1 million m³ of sediment was involved and this sediment was supplied to the nearshore zone, filling up the trough between the middle and outer breaker bar (Fig. 1).

¹Institute for Marine and Atmospheric Research Utrecht, Utrecht University, P.O. Box 80115, 3508 TC Utrecht, The Netherlands.

tel: +31 302532753; fax: +31 302540604; e-mail: p.hoekstra@frw.ruu.nl

²Delft Hydraulics, P.O. Box 177, 2600 MH Delft, The Netherlands.

³National Institute for Coastal and Marine Management (RIKZ), P.O. Box 20907, 2500 EX 's-Gravenhage, The Netherlands.

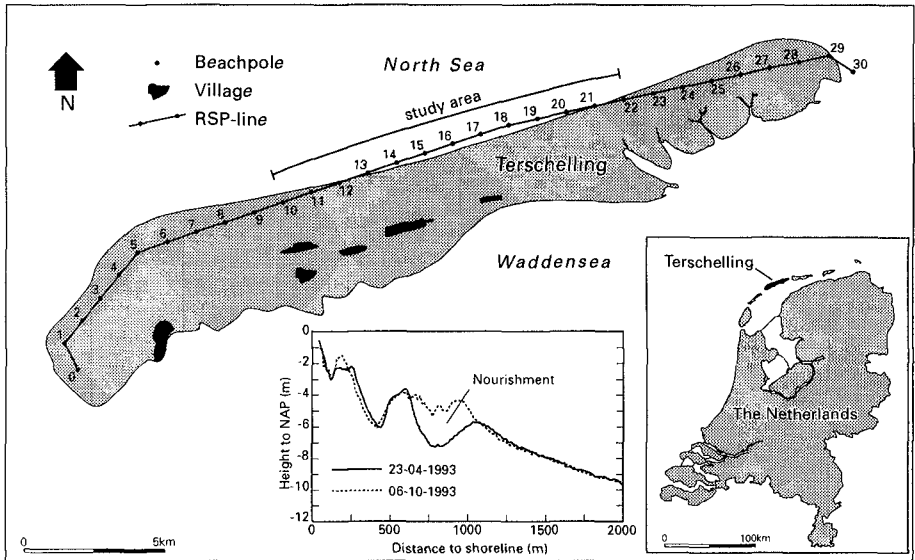


Figure 1. The North coast of the island of Terschelling with the study area. The beachpole (RSP)-line indicates the location of the cross-shore transects; the main measuring array is located in section 17

For the nourished zone, the amount of sediment supplied was equivalent to an average, vertical change in sea bed elevation of about 1 m and, in a longshore direction, the amount of nourished sediment per cross-section was in the order of 450 m³/m. The nourishment, with a total length of about 4.4 km and extending from km section 13.7 to 18.1 (Fig. 1), is located in the depth interval between -5 and -7 m below NAP (Dutch Ordnance Datum; the zero - NAP level approximately equals mean sea level).

In 1993 the EC-MAST2 programme NOURTEC was launched to study and explain the behaviour of shoreface nourishments in different European coastal environments (Hoekstra et al., 1994, Knaack et al, 1997 and Laustrup et al, 1997). The final objective of the NOURTEC programme is to study, determine and explain the feasibility, effectiveness and optimum design characteristics of shoreface nourishment techniques for different environmental conditions.

The basic assumption underlying the design and implementation of the Terschelling shoreface nourishment is that eventually sand will be carried to the shore. The nourishment is expected to act as a feeder berm. In case of a feeder berm there has to be a significant net onshore directed sediment transport due to the presence of the nourishment.

Apart from being a potential feeder berm, a shoreface nourishment may also start acting as an offshore located breaker berm or as a combination of these two features. A shoreface nourishment acting as a breaker berm is able to reduce the erosional power of the waves by increasing the degree of wave energy dissipation, in particular due to wave breaking. The nourishment creates a "wave-shadow zone" landward from the

nourishment which will locally reduce the strength of the wave-driven longshore current and the littoral drift.

This paper will focus on the developments at the Terschelling site in the first 30 months after the implementation of the nourishment. The aim of the present study is to analyse and evaluate the potential role as both a feeder berm and submerged breakwater. First of all, the bathymetric data set is used to determine the main morphological evolution in the nearshore zone and to compute changes in sediment volumes for specific horizontal and vertical control sections. The second way of addressing the problem is by analyzing the available process measurements and model computations on (suspended) sediment transport in the nearshore zone. It comprises an analysis of the dominant role of wave- and flow-driven processes in generating cross-shore (and landward-directed) and/or longshore fluxes of sediment.

Methods of research

Bathymetry

Bathymetric surveys were frequently carried out with varying time intervals and the total number of surveys until January 1996 is 12. After the nourishment the time interval varied from 53 to 182 days between two consecutive soundings. The surveyed area North of Terschelling covers approximately 25 km² and measurements were performed along survey lines perpendicular to the coast. Inside the nourished area the longshore spacing of these survey lines varied from 25 to 100 m; outside the nourished area the longshore spacing was about 200 m. The supra- and intertidal part of the cross-shore survey line, starting at the dunefoot, was done by leveling. The subtidal section until a depth of at least 10-12 m was measured by a Rijkswaterstaat survey vessel using a digital acoustic depth sounder (ATLAS DESO, 210 kHz), in combination with an accurate positioning system (Syledis and dGPS).

Hydrodynamics

The hydrodynamic field measuring programme of Terschelling consisted of two main activities: a long-term, continuously recording monitoring network and a series of process-oriented measuring campaigns (4). The monitoring network has been operational for about 2.5 years and almost all measurements were more or less concentrated around cross-sectional transect 17 (Fig. 1), covering the central part of the nourishment. Tidal water levels have been measured by a tide station, located in cross-section 14.60 and in a water depth of approximately 10 m. Every 10 minutes a mean value of the water level has been recorded. Offshore wave conditions were registered with a wave-directional buoy (WAVEC) positioned in the central measurement section in a water depth of about 15 m. The WAVEC measured continuously with a frequency of 1.28 Hz. Each block of 10 minutes was automatically processed using standard zero down-crossing and spectral methods. Information on the time-dependent variation in water levels (waves and tides) was also obtained from 2 measuring poles positioned in the surfzone (section 17.00; Fig.2). Both poles were equipped with a pressure transducer and a capacitance wire, measuring water levels for 40 minutes per hour with a frequency of 4 Hz. The fourth element of the monitoring network consisted of an instrumented tripod, equipped with 2 electro-magnetic flow meters at about 0.25 and 1.2 m. above the bed and with a pressure sensor. Occasionally, the tripod also carried two Optical Back Scatter (OBS) sensors to measure suspended sediment concentrations (0.15 and 0.25 m above the bed).

The instrumented tripod measured in a burst mode sampling scheme with a burst interval of one hour, a burst length of 2048 s. and a sampling frequency of 2 Hz. The tripod was located at the seaward margin of the nourishment, at a water depth of approximately 5.5 m.

During the process-oriented measuring campaigns the monitoring network was substantially expanded and consisted of the following configuration: 2 offshore located wave directional buoys, 6 instrumented tripods in the nearshore zone - including 3 tripods with OBS's - and 2 poles. Emphasis in the measuring programme was given to processes operating in a cross-shore direction and, consequently, a cross-shore array of instruments was installed in section 17 (Fig. 2). Four concentrated measuring campaigns were carried out in the period November 1993 until November 1995; each campaign lasted for approximately 5 to 6 weeks. Data calibration, validation and analysis is discussed in further detail by Houwman and Ruessink (1997) and Hoekstra et al (1996).

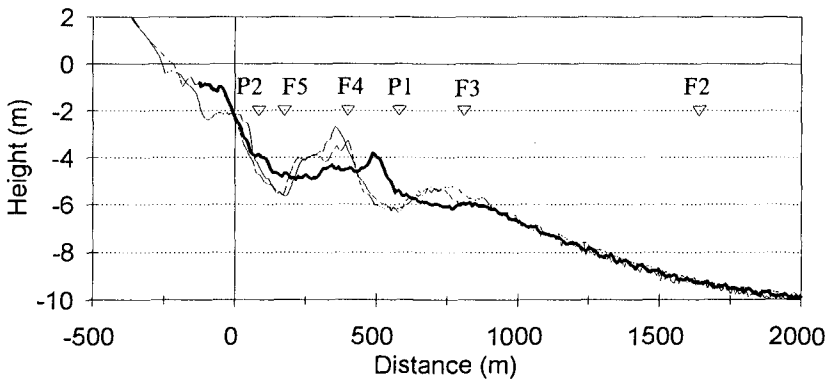


Figure 2. Measuring array in the cross-shore profile of section 17 (T2 campaign drawn line, T3 dashed line and T4 thick line); P = Poles and F = Frames or instrumented tripods

Hydrodynamic boundary conditions

Tidal conditions

Tides along the North coast of the island of Terschelling are semidiurnal and are characterized by a mixed micro- to mesotidal range. A maximum range of about 2.8 m is recorded at spring tide whereas the neap tide range is about 1.2 m. Associated tidal currents are basically flowing shore-parallel. The tidal flow during flood is in an ENE direction and the ebb tidal flow is directed towards the WSW. Especially at neap tide, the tidal ellipse is almost flat and rectilinear.

As expected, tidal flow is considerably modified by the presence of wind- and wave-driven currents (compare Whitford and Thornton, 1993). Earlier observations (Hoekstra et al., 1994) make clear that during moderate winds ($< 8 \text{ Bf}$) wind-driven flow has the same order of magnitude as the tidal flow. During storm and heavy storm conditions, the wind- and wave-driven longshore flow, in combination with cross-shore (mean) flow patterns, will even fully dominate the nearshore flow regime.

Wind and waves

The wind climate of Terschelling shows a clear predominance of westerly winds with a prevailing wind force of 4 to 5 Bf. In the period 1984-1994 the predominant wind direction for each year is in the sector between 210 and 300 degrees. This is more or less parallel to the coastline in the nourished zone (Kruyt, 1995). More than 12% of the total number of observations is in the sector 210-240 degrees. In addition, wind forces between 3 and 6 Bf make up 79% of the total number of observations in the data set. The year 1994, just following the nourishment, appears to be a year with a relatively large number of storms with a considerable duration (Kruyt, 1995).

The wave climate of Terschelling has been analysed by Van Beek (1995). Nearly 65% of the total number of wave observations is related to obliquely incident waves from the West to North (270-360 degrees; Fig. 3). The most energetic wave fields are incident from the NW to NNW. This almost coincides with a shore-normal direction (Fig. 3). The average annual significant wave height ($H_{1/3}$) and significant wave period ($T_{1/3}$) for 1994 are 1.08 m (st.dev. \pm 0.67 m) and 7.0 s (st.dev \pm 1.4 s), respectively. For only 2% of the total distribution, wave heights are higher than 3 m (Van Beek, 1995). However, as already mentioned before, in the first three months following the nourishment a number of significant storm events with high seas and swell have been recorded in the study area: November 15, 1993 ($H_{1/3}$ = 5.50 m; data correspond to peak of the storm), December 10, 1993 ($H_{1/3}$ = 5.50 m), December 20, 1993 ($H_{1/3}$ = 5.00 m), January 24, 1994 ($H_{1/3}$ = 4.25 m) and January 28-29, 1994 ($H_{1/3}$ = 8 m; all data based on WAVEC observations offshore).

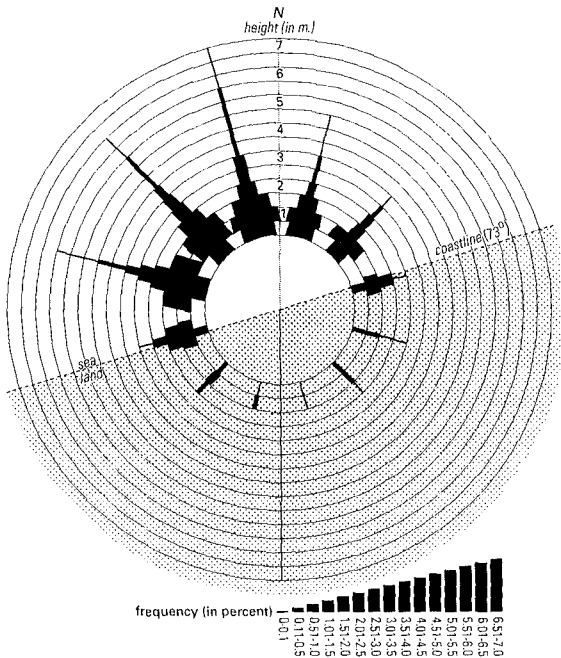


Figure 3. Offshore wave climate for the coast of Terschelling

Morphological evolution and sediment volumes

Coastal behaviour prior to the nourishment

The natural behaviour of the nearshore zone before the nourishment was studied in detail by Ruessink and Kroon (1994). Herein, both the alongshore and cross-shore tendencies of especially the long-term evolution of the nearshore breaker bars was discussed. In particular, the (geometrical) properties and dynamics of these bars, like their position and depth, were documented in time from 1965 to 1993. With the results of this study, the following conclusions were obtained:

- The cross-shore behaviour of bars is strongly influenced by an alongshore migration of bar attachment-points. Migration rates of these attachment-points are highly variable and can be in the order of $1200 \text{ m}\cdot\text{year}^{-1}$.
- The cross-shore behaviour of a bar is schematized in *three phases*:
 1) generation close to the shore; 2) seaward migration from 300 to 1300 m offshore and 3) bar degeneration when the crest of the bar is at a depth of about -5.5 m NAP. There is a coupling mechanism involved: as soon as the outer bar disappears the inner is triggered, leaves phase 1 and enters phase 2.

This typical cyclic behaviour, also found along other parts of the Dutch coast (see for example Wijnberg, 1995), has a total period of about 12-15 years (Ruessink and Kroon, 1994).

Morphological response of the nourishment

The morphological behaviour of the nearshore zone in the post-nourishment conditions has been studied and reported by e.g. Kroon et al (1995) and Westlake (1995) and summarizing their results indicates the following trends (Hoekstra et al, 1996):

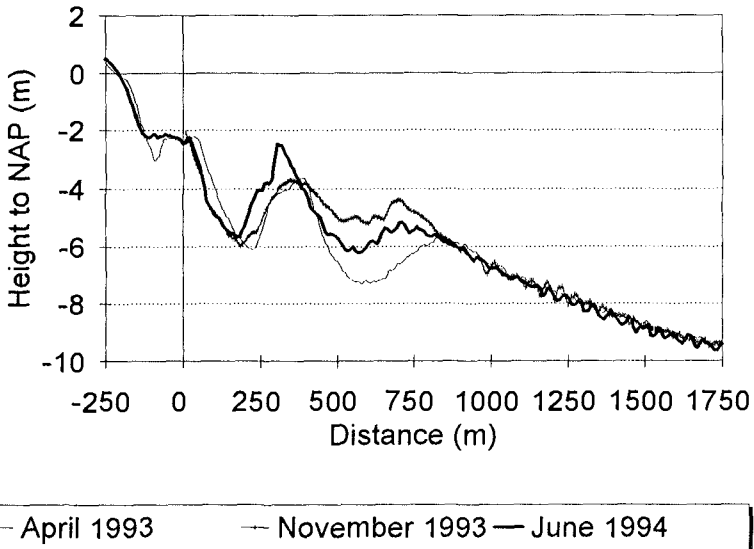


Figure 4. Morphological development of the cross-shore profile of section 17 after the nourishment

- the nearshore morphology inside and outside the nourished zone is becoming strongly 3-dimensional due to the presence of crescentic bars, the presence and migration of bar attachment points and drumstick-shaped nearshore breaker bars, separated by obliquely oriented rip channels. Such a pronounced development of a 3D morphological system has never been experienced in the past (Ruessink and Kroon, 1994);
- the disturbed bar-trough morphology caused by the nourishment is quickly adjusting itself and the former bar-trough pattern appears again (Fig. 4); the time of adjustment is rather short and the strongest response is visible in the first 150 days following the nourishment and the process slows down afterwards;
- the initial morphological response results in an extreme growth of the landward located middle bar and the adaptation of the profile is associated with a dominantly onshore movement of sediment (Fig.4);
- the western part of the nourishment is predominantly eroding whereas the eastern part shows accretion: the nourishment clearly migrates in an alongshore direction, towards the ENE (Fig. 1) at a variable rate of 280-320 m/yr (1994) or 400-420 m/yr (1995; Westlake, 1995).

As a matter of fact, (nourished) sediment is dominantly moving in an onshore and longshore (eastward) direction.

Sediment volumes

The consecutive bathymetric maps are now used in a more quantitative sense to identify areas of erosion and deposition and to compute the change in sediment volume in well-defined control sections. The computations have been reported previously by Westlake (1995). The selected control-sections are presented in Fig. 5 and are related to the nourished zone itself, areas landward and seaward of the nourishment and "reference" areas in both the East and West.

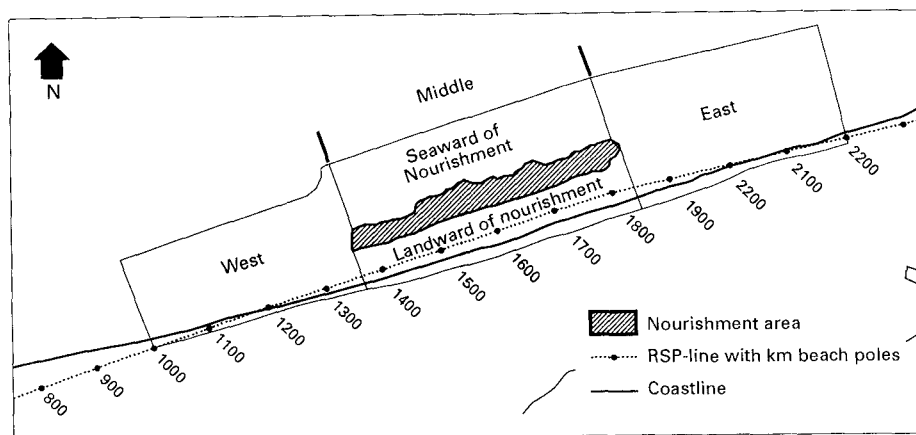


Figure 5. Control sections for volumetric computations of sediment budgets

The analysis of individual soundings occasionally shows the presence of systematic errors in the data sets and related bathymetric maps which may cause substantial inaccuracies in volume calculations. To reduce the effect of individual errors, results concerning the behaviour and effectiveness of the nourishment are based on the average linear trends in volumes, deduced from the total sequence of soundings, rather than the individual difference calculated for just two separate soundings (Westlake, 1995). In total, the nourished volume of sediment is about 2.0 million m^3 . In general it's rather difficult to assess whether there is an overall conservation of sediment volumes in the entire research area. For the most important sections though a number of trends are very consistent, as illustrated by Fig. 6. The nourishment area clearly shows erosion and the areas landward of the nourishment are definitely accreting. Remarkably though is the fact that the area landward of the nourishment is accreting at about twice the rate the nourishment is eroding. The nourished surface has lost about 560.000 m^3 of sediment. Part of this sediment - a conservative estimate is approximately 100.000 m^3 - is related to the alongshore migration of the nourishment. Meanwhile though, landward of the nourished zone a total gain of about 1.1 million m^3 of sediment is observed. And even if potential survey errors are taken into account, the order of magnitude of the difference suggests that the landward gain of sediment is not simply explained by a cross-shore redistribution of sediment. Significant longshore sediment transport gradients have to exist as well.

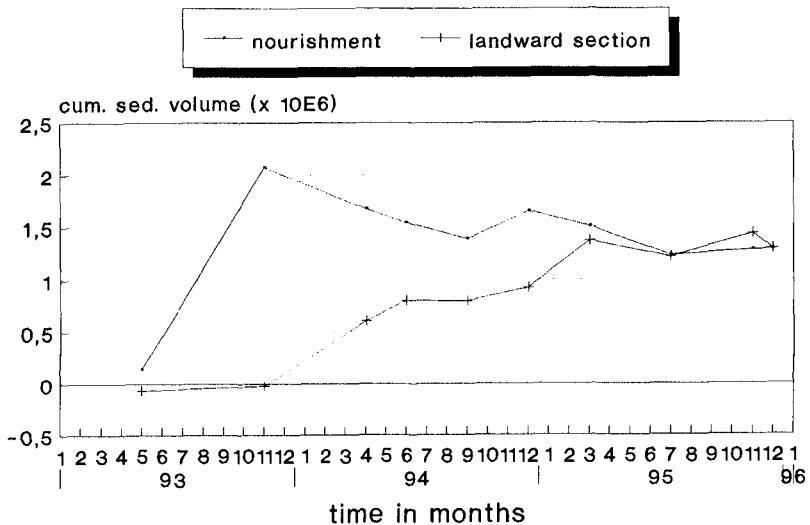


Figure 6. Cumulative sediment volumes for the nourished zone and the section landward of the nourishment

The frequent occurrence of storms and heavy storms in the period after the nourishment is predominantly held responsible for the relative rapid evolution of the nourished profiles and sediment volumes. This rapid response of the nearshore morphology is probably not fully representative for average conditions along the Terschelling coast.

The onshore directed redistribution of sediment certainly implies that the Terschelling shoreface nourishment has satisfied the design objective: the momentary or yearly computed coastline is estimated to have migrated seaward over a distance of about 16 m/yr (Biegel and Spanhoff, 1996). This totally reverses and exceeds the assumed retreat over the same period which should have been approximately 3 m/yr.

Based on the results of the present analysis, the Terschelling shoreface nourishment *only partly acts as a feeder berm*. Approximately 40% of the total gain of sediment in the inner nearshore can be explained by direct losses in the nourished zone. The success of the nourishment is not simply the result of the onshore movement of sediment from the nourishment. Accretionary processes in relation to longshore sediment transport gradients are probably equally important.

Cross-shore sediment transport processes

The partially, onshore-directed movement of sediment from the feeder berm has to be the result of cross-shore sediment transport processes. The transport study carried out in the framework of the Terschelling shoreface nourishment has focussed on both the dominant processes as well as dominant conditions that are mainly responsible for the onshore-directed fluxes of sediment. In this sediment transport analysis (Houwman and Ruessink, 1997) four main issues are addressed:

- 1) the contribution of oscillating and mean suspended transport to the net suspended transport;
- 2) the relative importance of high- and low-frequency suspended transport to the total oscillating suspended transport;
- 3) the ratio between bedload and suspended load;
- 4) the transport conditions under which most sediment is transported on the time scale of months to years.

Sediment transport measurements carried out in October and November 1995 (T4 campaign) at location F3 (Fig. 2) are selected to illustrate a number of features. Location F3 is one of the most interesting positions with respect to the hydrodynamic and sediment transport processes affecting the behaviour of the nourishment.

Some additional information is given here (Houwman and Ruessink, 1997):

- time series of u (cross-shore), v (longshore) and c (concentration) were divided in a mean and oscillating part; the net cross-shore suspended sediment transport, for example, is given by:

$$\langle u \cdot c \rangle = \langle \bar{u} \cdot \bar{c} \rangle + \langle u' \cdot c' \rangle$$

The net suspended sediment transport (left hand side) is based on the transport by mean currents (first term right hand side) and the oscillating transport (e.g the effect of wave asymmetry; 2nd term on the right). A positive cross-shore and longshore transport is onshore and eastward directed, respectively;

- the oscillating term is sub-divided into a high- and low-frequency part; the separation frequency between both was set to 0.04 Hz;
- cross-spectral analysis was applied to yield information about phase and coherence between u' and c' as a function of frequency.

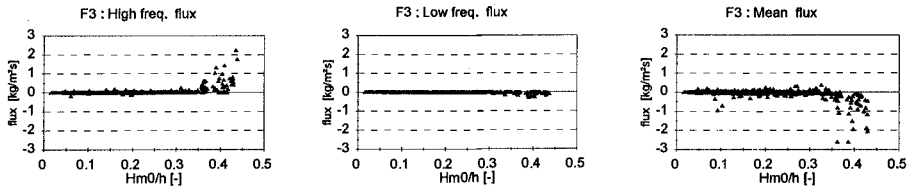


Figure 7. Cross-shore sediment fluxes measured at tripod F3 at 0.15 m above the bed (T4 campaign): high- and low-frequency ($f < 0.04$ Hz) fluxes and mean fluxes, respectively

Burst-averaged values (burst: measuring series of 34 minutes per hour with a sampling frequency of 2 Hz) of the high- and low-frequency oscillating fluxes in a cross-shore direction and at a height of 0.15 m above the bed are plotted in Fig. 7 as a function of local relative wave height ($Hm0/h$). The factor $Hm0/h$ accounts for both variations in wave climate as well as (tide-induced) fluctuations in water depth. Non-zero fluxes only occurred for $Hm0/h$ larger than about 0.30-0.35, in other words, during situations that were just outside, or inside the surfzone. High-frequency fluxes were in an onshore direction and were associated with the horizontal asymmetry of the incident short waves, i.e. the difference in magnitude between onshore and offshore orbital velocity. Low-frequency fluxes were seaward directed and were caused by the dominance of bound long waves in the total long wave field (Ruessink, 1996). For this sensor height, the low-frequency sediment flux was only about 16% of the high-frequency one, averaged over the entire campaign.

Burst-averaged values of the mean flux for the T4 campaign are shown in Fig.7 as well, again as a function of relative wave height $Hm0/h$. The largest fluxes, which were in a seaward direction, occurred for situations with the ratio $Hm0/h$ above 0.3-0.35. This indicates that these negative fluxes were associated with wave-driven undertows. The mean flux was larger than the total oscillating flux (i.e. the sum of high- and low-frequency flux) averaged over the entire campaign. Consequently, the net flux was in an offshore direction. In addition, it is also clear that the (high-frequency) oscillating fluxes can not be neglected.

To estimate the long-term bedload and suspended load transport in the surfzone, the sediment transport is calculated with the Bailard model (Bailard, 1981) and the adapted Van Rijn/Ribberink model (Van Rijn, 1993). The suspended load component of the Van Rijn model does not include the oscillating suspended load transport. For that reason, Houwman and Ruessink (1997) incorporated an oscillating suspended load term in the model in a parameterized way.

Summarizing all measurements and modelling results (Houwman and Ruessink, 1997) it becomes obvious that the measured and computed cross-shore sediment transport fluxes (for Terscheling) are reasonably related to a dimensionless wave height ($Hm0/h$). This term can also be interpreted as a breaker coefficient and it turns out that sediment fluxes increase with $Hm0/h$. By making use of a probability density function for the term $Hm0/h$, it appears that the suspended sediment transport on a time scale of months to years is typically related to breaking wave conditions ($Hm0/h > 0.33$); in other words is limited to situations inside the surfzone. It also supports the view that the relative rapid

evolution of the Terschelling shoreface nourishment is partly related to the frequent occurrence of storms in the period just following the nourishment.

Both measurements and modelling efforts also demonstrate that wave asymmetry is primarily responsible for the potential onshore movement of sediment; this sediment is mainly transported as suspended load by the oscillating flow related to seas and swell (high-frequency oscillating suspended load). Bedload, according to results obtained with the Van Rijn/Ribberink model, is of lesser importance.

However, the actual fate of the feeder berm is determined by a delicate balance of offshore directed mean fluxes and onshore directed oscillating fluxes. Paradoxically, in these conditions the contribution of some minor transport components, such as bedload and the effect of low-frequency waves, may eventually explain the success or failure of the nourishment. It's clear though that there is no significant and consistent net landward directed sediment transport in the nearshore zone. Therefore, it's not surprising that only part of the nourished sediment is moving in an onshore direction.

The observations make clear that it's not realistic to come up with a proper and reliable sediment balance for the area, based on sediment transport measurements and model computations.

Longshore sediment transport processes

Breaker berm and longshore sediment transport

The classic concept of a feeder berm is the idea that a cross-shore redistribution of sediment is mainly responsible for nourishing the upper part of the profile. Meanwhile, for the Terschelling coast, it's becoming quite evident that longshore processes are expected to be equally important. This is, for example, illustrated by the computations of sediment budgets inside and landward of the nourished zone, the longshore migration of the nourishment and the potential breaker berm function of the combination shoreface nourishment/nearshore breaker bar.

The breaker berm function is evaluated by using the UNIBEST-TC model. UNIBEST-TC is a morphodynamic coastal profile model (Roelvink et al, 1996). Application of the model required quite a lot of validation and calibration runs. During this process the model was further modified by using Terschelling data. Results of wave decay were obtained with the UNIBEST-TC model after considerable tuning of the model for wave heights using the breaker index (H/h) and the bottom friction factor f_w (Bakker, 1995 and Roelvink et al, 1996).

Model computations were carried out using measurements and conditions observed during the T2 campaign (May-June, 1994). The morphological boundary conditions are presented in Fig. 4. For all computations it is clear, that there commonly is a gradual reduction in wave heights across the seaward side of the profile and over the nourished zone. The wave dissipation is primarily due to bottom friction. A rapid decay in wave heights, though, is observed across the landward located middle bar (Fig. 1 and 4; Hoekstra et al, 1996). Here, wave breaking is the prime reason for a rapid decay in wave heights. In the landward located trough the wave field propagates without any major modifications. The model simulations definitely indicate that the design of the present shoreface nourishment not necessarily leads to an increase in wave energy dissipation: it is essentially the interaction of the shoreface nourishment with the nearshore breaker bars (Fig. 4) that is effective in reducing the landward propagating wave energy. Indirectly nourishing the middle bar is considered to be an effective method to construct or maintain

a natural breaker berm.

The longshore transport module of the UNIBEST-TC model is further applied to study to what extent longshore sediment transport rates and gradients in these rates are initially affected

by the presence of the nourishment. The influence of the nourishment on longshore sediment transport patterns was determined by computing the cumulative longshore transports for a profile with (T1-condition) and without (T0-condition) a nourishment (Fig. 8). The measured wave climate for approximately the first 160 days since the implementation of the nourishment was used as input for the model, in combination with the recorded (tidal) water levels. The effect of tidal currents, however, was omitted. Every 3 hours a longshore transport computation was carried out; results are given in Fig. 8.

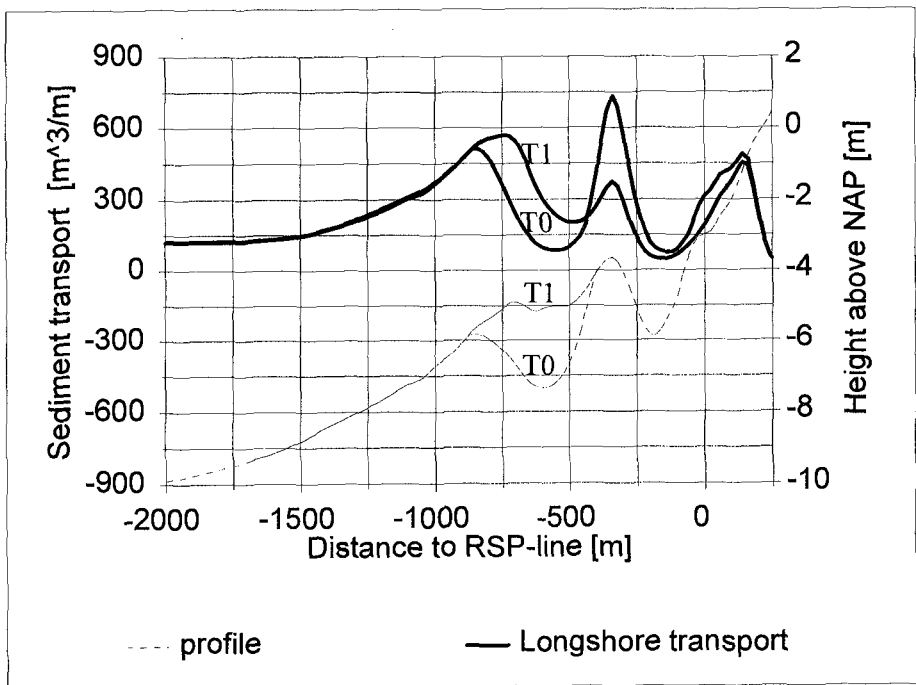


Figure 8. Cross-shore distribution of cumulative longshore sediment transport for conditions with and without a nourishment and for a period of about 160 days just following the nourishment

The net longshore sediment transport in the nearshore zone is predominantly towards the East (compare Fig. 3). Going from West to East - or from a non-nourished profile to a nourished one - longshore sediment transport in the trough is smaller than on the nourishment (Fig. 8). As a result, the West side of the nourishment will be eroding.

Sediment transport on the middle bar, by contrast, will be lower upon entering the nourished zone, which creates accretion on top of the bar (Fig. 8). On the nourished surface no transport gradients are expected to develop due to the longshore uniformity. On the downdrift side, however, longshore sediment transport patterns change again. The sediment transport on the nourished surface is larger than in the trough and the trough is gradually filled up with sediment. Simultaneously, the top of the middle bar shows erosion. The net effect is a gradual longshore migration of the nourishment towards the East, as observed for the Terschelling case.

The leeside deposition on the updrift side of the nourishment or breaker berm is commonly referred to as the salient effect. It probably partly explains the fact that the accretion in the cross-shore profiles landward of the nourished zone may exceed the losses from the nourishment. A salient is also frequently associated with erosion at a downdrift section of the coast. For the time being, no clear erosional patterns have developed yet.

In conclusion, longshore sediment transport gradients are important for understanding the behaviour of the nourishment. These gradients are responsible for the longshore migration of the nourishment and they can also partly explain the additional input of sediment in the inner nearshore zone.

Conclusions

The Terschelling shoreface nourishment has completely satisfied the design objectives in the first 2.5 years since the implementation. The nourishment not only compensates for the annual coastal retreat of about 3m/yr, but results in a net seaward migration of the momentary or yearly computed coastline of about 16 m/yr. The nourishment only partly acts as a feeder berm and the actual success of the nourishment is also based on the "interception" of longshore sediment transport due to the creation of a wave shadow zone and the salient effect. The combination of middle bar and shoreface nourishment effectively acts as a breaker berm.

Wave asymmetry is primarily responsible for the potential onshore movement of (nourished) sediment. This sediment is mainly transported in the form of a high-frequency oscillating suspended flux due to seas and swell. Bedload transport is of minor importance. In addition, the long-term suspended sediment transport from the nourished zone into an onshore direction is mainly related to breaking wave conditions ($H_m0/h > 0.33$). The net cross-shore suspended load flux, however, is determined by a very sensitive balance of two large components: a large offshore directed mean suspended flux due to currents is opposed by a large onshore directed oscillating flux due to waves. In these conditions the contributions of some minor transport components, such as bedload and the oscillating flux due to low-frequency waves, may eventually determine the behaviour of the nourishment.

Acknowledgements

This work was carried out as part of the project NOURTEC: Innovative Nourishment Techniques Evaluation. It was funded jointly by the Ministry of Transport, Public Works and Water Management in the Netherlands and by the Commission of the European Communities, Directorate General for Science, Research and Development under the Marine Science and Technology programme contract no. MAS2-CT93-0049.

References

- Bailard, J.A., 1981. An energetics total load sediment transport model for a plane sloping beach. *Journal of Geophysical Research*, 86 (C11), 10938-10954.
- Bakker, R., 1995. Verifications of the UNIBEST-TC model. Masters thesis Delft University of Technology / National Institute for Coastal and Marine Management (RIKZ), OS-95.133x, Delft, 76 pp. with app.
- Biegel, E.J. and Spanhoff, R., 1996. Effectivity of a shoreface nourishment, Terschelling, The Netherlands. National Institute for Coastal and Marine Management (RIKZ) and SEPRa bv.
- Hoekstra, P., Houwman, K.T., Kroon, A., Van Vessem, P. and Ruessink, B.G., 1994. The NOURTEC experiment of Terschelling: process-oriented monitoring of a shoreface nourishment (1993-1996). *Proc. Coastal Dynamics '94*, ASCE New York, 402-416.
- Hoekstra, P., Houwman, K.T., Kroon, A. and Ruessink, B.G., 1996. Morphodynamic Behaviour of the Terschelling Shoreface Nourishment. Institute for Marine and Atmospheric Research Utrecht (IMAU), Utrecht University, rep. R96.14, 64 pp. with appendix.
- Houwman, K.T. and Ruessink, B.G., 1997. Cross-shore sediment transport mechanisms in the surfzone. *Proc. 25th Int. Conf. Coast. Eng.*, ASCE New York (this volume).
- Knaack, H., Kaiser, R. and Niemeyer, H.D., 1997. Effectiveness of a combined beach and shoreface nourishment. *Proc. 25th Int. Conf. Coast. Eng.*, ASCE New York (this volume).
- Kroon, A., Hoekstra, P., Houwman, K.T. and Ruessink, B.G., 1995. Morphological monitoring of a shoreface nourishment - NOURTEC experiment at Terschelling, the Netherlands. *Proc. 24th Int. Conf. Coast. Eng.*, ASCE New York, 2222-2236.
- Kruyt, N.M., 1995. Wind Climate of Terschelling. Institute for Marine and Atmospheric Research (IMAU), Utrecht University, rep. R95.19, 57 pp. with app.
- Laustrup, C., Toxvig Madsen, H., Sørensen, P. and Brøker, I., 1997. Comparison of beach and shoreface nourishment Torsminde Tange, Denmark. *Proc. 25th Int. Conf. Coast. Eng.*, ASCE New York (this volume).
- NOURTEC, 1994. Design report of the three NOURTEC test sites. Coord. National Institute for Coastal and Marine Management (RIKZ), The Hague, The Netherlands.
- Roelvink, J.A., Meijer, Th.J.G.P., Houwman, K.T., Bakker, R. and Spanhoff, R., 1996. Field validation of a coastal profile model. *Proc. Coastal Dynamics '95*, ASCE New York, 818-828.
- Ruessink, B.G., 1996. On the origin of infragravity waves in the surf zone of a dissipative multiple bar system. *Proc. Coastal Dynamics '95*, ASCE New York, 93-104.
- Ruessink, B.G. and Kroon, A., 1994. The behaviour of a multiple bar system in the nearshore zone of Terschelling, The Netherlands: 1965-1993. *Marine Geology*, 121, 187-197.
- Van Beek, L.P.H., 1995. Wave climate of Terschelling. A statistical analysis for the NOURTEC project. Institute for Marine and Atmospheric Research (IMAU), Utrecht University, rep. R95.10, 48 pp. with app.
- Van Rijn, L.C., 1993. Principles of sediment transport in rivers, estuaries and coastal seas. Aqua Publications, Amsterdam, The Netherlands.
- Westlake, S.J., 1995. Behaviour of a Shoreface Nourishment, Terschelling, The Netherlands. Masters thesis International Institute for Infrastructural, Hydraulic and Environmental Engineering, Delft, the Netherlands, rep. HH249, 95 pp. with figs.
- Whitford, D.J. and Thornton, E.B., 1993. Comparison of wind and wave forcing of longshore currents. *Cont. Shelf Res.*, vol.13, 11, 1205-1218.
- Wijnberg, K.M., 1995. Morphologic Behaviour of a harred Coast over a Period of Decades. PhD thesis, Utrecht University, 245 pp.

CHAPTER 225

JUSTIFICATION FOR BEACH NOURISHMENT

by John G. Housley, PE, M.ASCE ¹

ABSTRACT

Sand balance of the littoral system determines whether erosion or recession will occur. Adding sand to the system is the only engineered way to restore the balance and prevent erosion or recession. Justification of beach nourishment as a shore protection measure depends on the benefits criteria used in the analysis, and societal goals will decide the criteria.

INTRODUCTION

Mankind, in its love affair with the coast, has often encroached on sandy areas which are basically unstable - at least as far as lines on a map are concerned. Sandy coasts are particularly attractive as recreation sites, and in the last half century they have been the target of intensive development. In the United States, about 50 percent of the population lives within 30 miles of a coast. Erosion of those shores has become a national concern.

THE EROSION PROBLEM

Sand is in constant motion along the shores of this country due to waves, currents, and wind. As long as the sand leaving a stretch of beach is balanced by the same quantity of sand arriving on the beach, there is no erosion or recession. But if the balance is not maintained (either by the arriving sand being interrupted by a structure such as a jetty or by a lack of sand on the updrift beach), erosion/recession will result.

When the user of a beach wants to construct some fixed structure in the immediate vicinity, such as a road or a house, then, if the shoreline moves in the direction of the fixed structure, that is called a problem.

¹Coastal Engineering Consultant, Michael Baker Corporation, Alexandria, VA 22304

There are three basic responses to an erosion threat: reduce the hazard, adjust human use, or accept the cost. Only the first one is amenable to an engineering approach; the others are either management options or the do-nothing alternative with its attendant increased costs. To reduce the hazard, the choices are to modify the physical process or to reduce the impact. From an engineering viewpoint, it is usual to pursue some combination of those hazard-reduction options.

A BEACH NOURISHMENT SOLUTION

For developed coasts, the serious problem of coastal erosion is caused by a deficit of sand in the littoral system. Adding sand to the system (beach nourishment) is the only engineering solution that remedies the basic problem. All other potential engineering solutions (groins, seawalls, breakwaters, etc.) may stop the erosion at a particular point, but the deficit of sand in the littoral system will cause erosion to occur at some other location. And the cost of mitigation of those adverse effects is one of the strong reasons for a beach nourishment approach.

When sand is first installed as part of a beach nourishment project, it is placed on the existing beach to raise it to a higher elevation and to widen the dry beach in the seaward direction; the seaward face is thus on a steep slope. The filling procedure is dictated by the least total cost of the operation. If the fill is made from the land side, say by truck haul, then the trucks dump near the waters edge and continually push that edge seaward. If the fill is by hydraulic dredge, then the pipes are positioned so that the effluent moves the edge of the fill seaward. If the fill is by offshore mounding, a split-hull hopper dredge or barge is maneuvered as close to shore as the draft of the vessel will allow, and the fill is placed in shallow water so that waves will move the sand toward the shore.

When first placed, the sand slope in the water is not at the equilibrium slope. As waves work on that slope, the sand tends toward the equilibrium position, that is, a slope which is stable under the wave regime present. Since the waves are not of constant height, period, or direction, each wave climate tries to put the beach slope in an equilibrium position for that instant. Seconds later, the regime has changed, thus the process of equilibration is continuous.

So as the sand pile is reshaped by waves, some of the dry beach sand is moved into the water to provide the material for a flatter equilibrium slope. And the perception that the beach was "lost" comes to those who only consider the subaerial beach. Without the subaqueous beach, surely the beach *is* lost.

BENEFITS

The recent study by a blue-ribbon committee of the Marine Board of the National Research Council found that, when used in appropriate situations, beach nourishment does indeed become a cost-effective measure to combat the effects of coastal erosion. The key is to determine what are the appropriate situations for the use of beach nourishment. First, a determination must be made of the benefits to be derived from such a project. Those benefits are not only in terms of dollars of increased revenues and decreased losses, but also social and environmental benefits. The costs associated with the project are not only the planning, design, construction, and maintenance costs, but also the social and environmental costs.

In an effort to stem what many consider unwise development on pristine shores in this country, the Coastal Barrier Resources Act precludes (with some exceptions) the federal government from expending funds on undeveloped coastal barriers. For developed shores, the rules for U.S. federal participation in shore protection projects are quite explicit about how and how much benefits can be claimed. The benefits in the category of storm damage reduction must be at least one half the costs of design and construction. After that benefit requirement is fulfilled, other benefits (such as recreation) can be added to bring the total benefits up to something greater than the total costs. However, these are not all the benefits that should be considered.

Justification usually has the connotation of financial break-even or better. Justification on the national, state, local, or personal levels uses different yardsticks and different elements of measure. Measures that would justify a project on the local level may not be counted on the national level, since benefit gains in one region may be offset by losses in another. And on the personal level, hard to quantify aesthetics may be the most important element for some people. And for environmentalists, the fill material as habitat for birds, turtles, and other creatures may be the important elements.

One of the major benefits not considered in beach nourishment cases involving federal participation are those benefits outside the project boundaries caused by sand being transported to property beyond those boundaries. In the recreation benefit category, the benefit to the non-federal sponsor is usually far greater than that allowable under U.S. federal rules. Those rules require the benefits to be national economic development (NED) benefits, but the local entities realize benefits in addition to NED benefits. An often overlooked cost is a navigation project that causes a sediment deficit in the littoral system by trapping sand in the channels and harbor areas, or in ebb-tide deltas that effectively divert sand away from a beach area.

CONSTRAINTS

The major problem with beach nourishment is not technical, but perception. The person who views a beach nourishment project has a certain expectation from that project. If it is a property owner in the vicinity, he looks for protection. If it is visitor, he looks for a recreation site. And if it is a taxpayer from a distant location, he looks for a return on his investment.

Beach nourishment mimics what nature does, so that sand is not held in one place but is allowed to move under the influence of the waves and current. Although beach nourishment is not appropriate for all locations, it is the preferred option in many problem areas. A beach nourishment project is sacrificial; that is, it is designed so that sand is removed from the beach rather than buildings being removed from the backshore. Sand replenishment restores the beach to the design dimensions upon which the benefits are derived, and if the project is well designed, constructed, and maintained, and if there is the political and financial will to continue the periodic renourishment program, the benefits will continue to accrue. While hard structures (groins, seawalls, etc.) require a large, up-front, construction-cost investment, beach nourishment involves a smaller, periodic expenditure for construction over the life of the project. In almost all cases, the benefits of beach nourishment outweigh those of hard structures.

It was once said that anyone could build a bridge, but it took an engineer to build one economically. The same can be said for beach fills.

Beach nourishment projects need to use state-of-the-art engineering principles, which includes a thorough understanding of shore processes. It is not enough that an adequate supply of sand is available to a project for it to be successful; there must also be an understanding of the goals of the project and the criteria for success. If the public does not understand how success is measured, and that beach nourishment is meant to be sacrificial, then when some of the subaerial beach is lost during a storm, the project may be labeled a failure, even when much of the sand is returned to the dry beach by natural processes in a few months, and the engineer has expected those results.

So beach nourishment (or renourishment) is the preferred solution to the sand deficit problem. To properly engineer the sand fill, the characteristics of the native sand and the proposed fill material must be known, as well as the forces acting on it, i.e., waves, current, wind, etc.

A recent (1995) legislative proposal by the Clinton administration would redefine the US Army Corps of Engineers' (the federal agency charged with

shore protection) mission as "nationally significant missions." If enacted, the cost sharing for federally-funded water resources projects would change to 25/75 (federal/non-federal), and the benefit/cost ratio would be at least 2. Federal participation in storm damage reduction projects would be eliminated on the basis that these projects are local (not national or interstate), and should be paid for by non-federal dollars. As of the date of this paper, the proposal has been rejected by the Congress, but the administration is using the budget process to put shore protection in a low priority position.

CONCLUSION

The expense of a nourishment program (initial plus subsequent re-nourishments) is not inconsequential. However, the loss of property during storms and loss of revenue from tourism on a neglected beach can be much greater.

BIBLIOGRAPHY

Adams, J.W.R., "Florida's Beach Program at the Crossroads", *Shore and Beach*, v 49, nr 2, Apr 81, pp 10-14.

Adams, J.W.R., "The Politics of Beach Nourishment", *Shore and Beach*, v 50, nr 1, Jan 82, pp 2-5.

Basco, D.R., "Boundary Conditions and Long-Term Shoreline Change Rates for the Southern Virginia Ocean Coastline", *Shore and Beach*, v 59, nr 4, Oct 91, pp 8-13. Discussion by E.R. Thieler, R.S. Young, and O.H. Pilkey in *Shore and Beach*, v 60, nr 4, Oct 92, pp 29-30. Closure by D.R. Basco in *Shore and Beach*, v 60, nr 4, Oct 92, pp 31-34.

Bodge, K.R., "Damage Benefits and Cost Sharing for Shore Protection Projects", *Shore and Beach*, v 59, nr 2, Apr 91, pp 11-18.

Camfield, F.E., "Different Views of Beachfill Performance", *Shore and Beach*, v 61, nr 4, Oct 93, pp 4-8.

Campbell, T.J. and R.H. Spadoni, "Beach Restoration - An Effective Way to Combat Erosion on the Southeast Coast of Florida", *Shore and Beach*, v 50, nr 1, Jan 82, pp 11-12.

Davison, A.T., C.P. Ulrich, and R.J. Nicholls, "Accreditation of Beach Nourishment Projects: An Issues Discussion", *Shore and Beach*, v 61, nr 4, Oct 93, pp 9-15.

Denison, P.S., "The North Carolina Experience", *Shore and Beach*, v 49, nr 2, Apr 81, pp 15-16.

Domurat, G.W., "Beach Nourishment - A Working Solution", *Shore and Beach*, v 55, nr 3-4, Jul-Oct 87, pp 87-91.

Herron, W.J., "Sand Replenishment in Southern California", *Shore and Beach*, v 55, nr 3-4, Jul-Oct 87, pp 87-91.

Houston, J.R., "Beachfill Performance", *Shore and Beach*, v 59, nr 2, Jul 91, pp 15-24.

Houston, J.R., "Beach Nourishment", *Shore and Beach*, v 63, nr 1, Jan 95, pp 21-24.

Magoon, O.T., "A Letter to President Bill Clinton", *Shore and Beach*, v 62, nr 2, Apr 94, pp 2-3.

O'Brien, M.P., "Beach Stabilization by Sand Replenishment", *Shore and Beach*, v 52, nr 4, Oct 84, p 19.

Pilkey, O.H., "Another View of Beachfill Performance", *Shore and Beach*, v 60, nr 2, Apr 92, pp 20-25.

Seymour, R.J., "An Introduction to the Marine Board Study on Beach Nourishment and Protection", *Shore and Beach*, v 64, nr 1, Jan 96, p 3.

Seymour, J.R. et al., "Beach Nourishment and Protection: Executive Summary", *Shore and Beach*, v 64, nr 1, Jan 96, pp 5-10.

Stone, K.E. and B. Kaufman, "Sand Rights: A Legal System to Protect the 'Shores of the Sea'", *Shore and Beach*, v 56, nr 3, Jul 88, pp 7-14.

Stronge, W.B., "Beaches, Tourism and Economic Development", *Shore and Beach*, v 62, nr 2, Apr 94, pp 6-8.

Stronge, W.B., "The Economics of Government Funding for Beach Nourishment Projects: The Florida Case", *Shore and Beach*, v 63, nr 3, Jul 95, pp 4-6.

Smith, A.W.S., "Beaches and Tourism - An Example of the Results of a Dramatic Beach Erosion Episode: Gold Coast, Queensland, Australia", *Shore and Beach*, v 63, nr 3, Jul 95, pp 7-8.

Smith, A.W.S. and L.A. Jackson, "The Siting of Beach Nourishment Placements", *Shore and Beach*, v 58, nr 1, Jan 90, pp 17-24.

Sudar, R.A. et al., "Shore Protection Projects of the U.S. Army Corps of Engineers", *Shore and Beach*, v 63, nr 2, Apr 95, pp 3-16.

Wiegel, R.L., "Beaches - Tourism - Jobs", *Shore and Beach*, v 62, nr 2, Apr 94, pp 4-5.

Wiegel, R.L., "Beach Nourishment, Sand By-Passing, Artificial Beaches: Bibliography of Articles in the ASBPA Journal *Shore and Beach*", *Shore and Beach*, v 60, nr 3, Jul 92, pp 3-5.

CHAPTER 226

BEACH NOURISHMENT VERSUS SHORE PROTECTION STRUCTURES

Alexander Khabidov¹, Yuri Bazhenov², Marina Glodenis², Nadya Ivanova¹,
Liya Kaskevitch¹, Oleg Rybak³, Valery Savkin², Anatoly Trizno²,
Grigory Zelensky², Veniamin Yedapin²

ABSTRACT

The problem of coastal erosion in Russia became especially urgent in 50th-60th during the extensive river damming, taking place mainly in the regions valuable for society. To prevent erosion, which spanned thousands of kilometres of new shoreline different shore protection techniques were used, including hard structures, shoreface and beach nourishment as well as hybrid methods. Most if not all of these techniques were previously applied on Novosibirsk Reservoir, one of the first Russian large man-made lakes. Long-term observations of structures state and recent studying of response of the coastal environment on the projects emplacing testify the greater efficiency of coastal stabilization by beach nourishment programs and hybrid structures.

INTRODUCTION

Novosibirsk Reservoir was created in Western Siberia in 1956 when the Ob River was dammed ca. 20 km upstream the city of Novosibirsk (latitude 55° N, longitude 83° E). It is a freezing reservoir which ice season lasts about 180-190 days from November till April or May. Like many man-made lakes seasonal changes in water level of Novosibirsk Reservoir occur because of the river flow fluctuations; they reach more than 5 m/yr in amplitude and include: (i) Water level rise in May-June: mean duration - ca. 50 at a rate of ca. 0.1 m per day, (ii) Water level stabilization: mean duration - ca. 120 days, and (iii) Water level subsidence in October-April: mean duration - ca. 195 days at a rate of ca. 0.02 m per day.

The fetch of Novosibirsk Reservoir is 220 km from northeast to southwest up to town of Kamen-on-Ob, its minimal, mean, and maximum width are 2, 10,

¹ Institute for Water and Environmental Problems, Siberian Branch of the Russian Academy of Sciences, 105, Papanintsev Street, 656099, Barnaul, Russia; e-mail: khabidov@iwep.altai.su

² Department of Natural Resources of Russian Federation; 19, Geroev Truda St., 630055 Novosibirsk, Russia

³ Scientific and Research Center of Marine Coasts; 1, Jan Fabritsius St., 354002 Sochy, Russia

and 22 km, respectively, water plane area is 1070 km², depth is up to 25 m, total storage is 8.8 km³, effective storage is 4.4 km³, and shoreline length is 550 km.

The principle basin morphometries of Novosibirsk Reservoir are: a shallow area in the south-western edge of the lake basin under fetch of about 60 km, an area of transitional depths, and a deep-water area with typical depths exceeding the average reservoir depth in the north-eastern part of the lake basin under fetch of 100-120 km. These areas correspond to main types of dynamical relief-forming and depositional sedimentary environments of the lake basin, namely: the deltaic/fluvial-dominated environment, the wave-dominated one with significant influence of the channel flows, and wave-dominated environment itself.

The wave heights are among the most significant features of dynamic relief-forming and depositional sedimentary environments of the reservoir. Within delta-like environment wave heights do not exceed 0.5 m even under severe storm. As for transitional zone the waves of up to 1.5-1.7 m height occur, while the waves of more than 3.5 m were observed in deep water area.

High rate of erosion of Novosibirsk reservoir coasts is primarily caused by wave. Two more factors contribute to erosion. First, the reservoir coasts are formed mainly of loose and soft grounds - sands, sandy loam, and loss-like loam. Second, like natural lakes and other man-made lakes, its beach berms are narrow or even absent at all. That is why the mean erosion rate reaches here 7-10 m/yr and more and the extension of eroding shores makes up 350 km.

Coastal erosion caused the most serious problems in wave-dominated area of Novosibirsk Reservoir. It is precisely here where the coast protection started before the reservoir filling. At present more than 40 km of its coasts have been protected already. As this takes place different shore protection techniques, including hard structures, shoreface and beach nourishment as well as hybrid methods were used.

Long-term observations of structures state showed considerably different reliability and effectiveness of hard structures, filled natural and artificial beaches as well as hybrid projects which combine a shoreface and/or beach nourishment with stabilization of sand by breakwaters, groins, artificial headlands, etc.

Recent studying of response of the coastal environment on the different projects emplacing allowed to reveal some causes of these phenomena.

METHODS

The work on the project began from the studying of data on long-term visual and tool supervision of seawalls, bulkheads, revetments, filled natural and artificial beaches as well as other coastal engineering sites of Novosibirsk Reservoir. This allowed to determine the key sites for special investigations. These investigations include repeated topographic surveys, continuous meteorological observations, synchronized with measurements of waves and studies of swash interactions by wire gauges, measurement of nearshore currents by omni-directional and two-component impeller current meters, measurement of bedload and suspended sediment concentration by *in-citu* samplers, sand tracers movement observations and piezometric studies of beach groundwater interactions.

For comprehensive evaluation of the affect of protective measures on coastal environment, all observations are conducted not only on the coastal engineering sites, but on the upcoast and downcoast areas as well. Investigations on the key sites started a year ago. In this connection only the preliminary results of the observations are presented here.

BEACH MORPHOLOGY AND NEARSHORE PROCESSES NEAR A SEAWALL

As development increases along the shoreline and property is lost, engineers, developers as well as planners need quantitative descriptions and models of how coastal processes affect the shoreline (Dean, 1987) and how the projects, emplaced to protect the threatened structures, affect the surrounding coastal environment. In recent years, many of the investigations were devoted to the studying of the nearshore processes near a seawall and the resultant beach morphology under marine conditions (Kraus, 1988; Tait and Griggs, 1990; Plant and Griggs, 1992, and others). The definite severity of the environment occur at the man-made lakes, because of the long-term water level fluctuations from weeks to months.

Just as the seawalls, so bulkheads and revetments were built at the Novosibirsk Reservoir; as this took place, the first hard structure was emplaced before its initial filling. The concrete curved-face seawalls, concrete combination inclined and curved-face seawalls and rubble-mound seawalls as well as concrete and rubble-mound revetments had common occurrence at the reservoir. Since 1956 more than 25 km of the seawalls were built here, but only about 12 km still persist to date.

For an understanding of the reasons of improper operation and destroying of the structures, beach morphology and nearshore processes were studied near seawalls of several types. The noted effects were both seasonal and long-term ones. According to observations, in the case typical for natural and man-made lakes, when a seawall is placed on the water edge or near it, and the adjacent beaches have a narrow berm or have not it at all, these effects are: (a) the bottom erosion rate increases after the seawall construction and on the fronting beach and its value is always higher than on the adjacent beaches without structures, (b) the bottom erosion in front of seawall before erosion on the protected beaches, (c) the coastal erosion increasing downcoast of seawalls. Near the seawall placed at the backshore, the erosion of beach berm in front of the structure had arised before equivalent erosion on the flanked beaches, because the erosion increses with the reflectivity of the seawall and the mobility of the fronting beach as the result of altering of the pattern of groundwater flux.

That is why, though under such sea-wall position the beach slows down the scour at the toe and ends of the structure, however as the result of the berm erosion the final response of the coastal environment will be equivalent to the first case.

In this manuscript the attention is focused on the effect of the nearshore currents on beach processes near a seawall that protrude into the surf zone. Dean (1976), Berkemeir (1980), and McDougal et al, (1987) noted, that structures of such type can effect longshore currents; trap sand upcurrent of wall and, perhaps, induce scour in front and downcoast of the seawall. However, the

observations, conducted by Plant and Griggs (1992) in Monterey Bay, did not reveal this effect neatly.

The study site on Novosibirsk Reservoir consisted of a gently curving shorelines and a 350 m concrete combination inclined and curved-face seawall flanked by the continuous natural beaches at the upcoast and a 200 m beach at the downcoast. The flanked beaches, all backed by 3-5 m escarpment, had the berm the slope of which is 1:35, the width from 3-5 m (downcoast) up to 10 m (upcoast) and initial bottom slope was of order 1:25. The seawall protrude into the surf zone by 2:1 sloping revetment at its toe. The present investigation involved the pre-storm, storm, and post-storm beach surveys to capture morphological changes as well as measurement of the longshore and cross-shore currents at 10 cm level above the bottom in front of the seawall and in the flanked beaches. The storm surveys were carried out under the waves of Hsig 0.5 m, 1.2 m, and 2.3 m; the angle between wave crest and shoreline varied from 35° to 42° in all three events.

The beach surveys in the upcoast, seawall-backed, and downcoast sections of the site showed that the behavior of morphological changes within these sections differs greatly. Total losses of the bottom sediment per one metre of the shoreline made up 0.15, 2.75, and 4.25 m³ within the upcoast section, 1.00, 5.14, and 8.00 m³ within the seawall-backed section and 2.5, 4.25, and 6.25 m³ for the 1st, 2nd, and 3rd storm events, respectively (Table 1).

Table 1.

Beach profile changes near the seawall and on the flanked beaches under different storm events

Beach profile area	Storm event	Net total volumetric changes in beach erosion and sediment accretion, m ³		
		Upcoast section	Seawall-backed section	Downcoast section
Beach Berm	1	+120	-	-150
Breaker Zone	1	-850	-1650	-1000
Offshore	1	+700	+1300	+1000
Beach Berm	2	-350	-	-450
Breaker Zone	2	-1500	-3900	-1900
Offshore	2	+1300	+2100	+1500
Beach Berm	3	-500	-	-650
Breaker Zone	3	-2450	-6700	-3400
Offshore	3	+2100	+3900	+2800

Note. Sign <+> corresponds to accretion, sign <-> corresponds to erosion

Measurements of the nearshore currents during the storms in the front of seawall and on the flanked natural beaches correlate with beach surveys data, and to all appearances, explain the observed morphological changes. The absolute values of time-averaged longshore and cross-shore current velocities at the seawall-backed and downcoast sections of the study site were higher

than the current velocities within the upcoast beach during the steady stage of all the storms (Table 2). Alongside, it is hard to state, that the observed rather higher rates of the nearshore currents at the downcoast beach are directly related to hydrodynamic processes in front of the seawall. It is stipulated by the fact that under small width of beach berm at the downcoast section, the backed cliff can induce nearshore processes, in principal similar to the processes caused by the seawall.

Table 2.

The range of the absolut values of time-averaged longshore (V) and cross-shore current (U) velocities near the seawall and on the flanked beaches during the steady stage of storms

Beach profile area	Storm event	Longshore and cross-shore current velocities, m/s		
		Upcoast section	Seawall-backed section	Downcoast section
Breacker Zone	1	0.08-0.22	0.12-0.31	0.10-0.25
V				
U		0.07-0.23	0.10-0.35	0.10-0.27
Offshore	1	0.02-0.11	0.02-0.12	0.02-0.12
V				
U		<0.03	<0.04	<0.04
Breacker Zone	2	0.10-0.27	0.12-0.38	0.12-0.32
V				
U		0.10-0.31	0.15-0.39	0.10-0.35
Offshore	2	0.02-0.14	0.02-0.15	0.02-0.15
V				
U		<0.05	<0.05	<0.05
Breacker Zone	3	0.18-0.50	0.20-0.65	0.17-0.58
V				
U		0.16-0.52	0.21-0.72	0.20-0.60
Offshore	3	0.05-0.18	0.05-0.21	0.04-0.20
V				
U		<0.10	<0.10	<0.10

Notes. 1) Time averaging interval by hardware is of 30 sec.
2) Time of continuous measurement is of 5 hours for all the storm events.

Visual observations of the seawall reliability started immediately after construction of Novosibirsk Reservoir. During the period of observation the most typical were the cases of seawalls destroy during several years or decades. At this time some events were noted, when the wall was completely destroyed under a prolonged severe storm with Hsig exceeding 3-3.5 m or under series of 2-3 such storms.

The survey of the walls destroyed showed that the main reasons of their destruction were not the construction failures but a scour at the toe and ends of the structures. No doubt, the scour was caused not only by the nearshore currents, but by wave reflection from a seawall, and the effect of groundwaters as well. However, in all cases of wall breakdown on the reservoir nearshore currents appeared to be of a prime consideration.

COASTAL ENVIRONMENT RESPONSE TO BEACH NOURISHMENT AND EMPLACING OF HYBRID PROJECTS

The first event of seawall damage on Novosibirsk Reservoir occurred in 1959 near the Novosibirsk Academic Center. This wall was constructed in an effort to protect the shore site associated with federal highway and railway as well. Thus at this site renovation of shore defence, wherein the combined shoreface and beach nourishment were used for the first time in Russia, began.

At Novosibirsk Academic Center stretching 3 km alongshore, approximately 5,000,000 m³ of sand have been nourished during three years. The constructed open artificial beach was located within the curved shoreline site where the longshore transport rate is not more than 20,000-25,000 m³/yr. Owing to appropriate location the beach provided a powerful shore protection for 25 years without renourishment.

In spite of reasonable results of shore protection by beach nourishment, this technology became widely used on Novosibirsk Reservoir only at the end of 70th . At present there are more than 7 km of the open artificial beaches on the man-made lake.

The continuous monitoring of the beach morphology changes showed that under the environmental conditions of Novosibirsk Reservoir the equilibrium beach profile has shapes of several years. The process of profile formation usually begins from intensification of beach face erosion and is followed by cross-shore sediment transport. Superimposed terrace is formed in consequence of the sediment accretion at the outer border of the beach profile. As development progress of the profile the terrace edge is shifting to the seaward direction and the beach profile becomes level out. When two-three years elapse the terrace edge position has become fairly stable and the longshore sediment transport begins to dominate among the nearshore processes (Table 3). It seems likely that profile formation is completed.

The occurrence of abnormal conditions with erosion of the accretive terrace at the outer border of the beach is mainly stipulated by severe storms effects during the lake's water level subsidence in autumn or water level rise in spring. It resulted in increasing of bottom slope (Table 3), that finally brought to intensification of berm beach erosion, cross-shore sediment transport and decreasing of longshore sediment rate.

Table 3.

Temporal morphological changes and prevailing trends in the nearshore processes on the nourished beach near the Novosibirsk Academic Center

Year	Total amount of the sediment losses			Total amount of the sediment accretion		Observed trends of the sediment transport
	Beach berm, m ³	Nearshore, m ³	Outer border of the beach, m ³	Near-shore, m ³	Outer border of the beach, m ³	
1	-82,000	-63,000	-	+21,000	+110,000	Cross-shore
2	-81,500	-52,000	-	+24,000	+97,000	Cross-shore
3	-78,000	-51,000	-	+54,000	+64,000	Cross-shore
4	-49,300	-51,000	- 5,000	+53,000	+35,000	Longshore
5	-46,500	-52,000	-35,000	+70,000	+15,000	Longshore
6	-54,500	-63,000	-	+38,000	+73,000	Cross-shore
7	-48,000	-54,000	-11,000	+49,000	+42,000	No clear trend
8	-46,700	-52,000	-27,000	+61,000	+21,000	Longshore
9	-39,200	-47,000	-	+34,000	+45,000	Cross-shore
10	-45,000	-54,000	- 4,000	+51,000	+34,000	Longshore
11	-40,500	-51,000	-31,000	+54,000	+19,000	Longshore
12	-46,100	-55,000	-23,000	+62,000	+20,000	Longshore
13	-59,200	-64,000	-16,000	+55,000	+49,000	No clear trend
14	-35,000	-40,000	-10,000	+54,000	+11,000	Longshore
15	-40,300	-53,000	-21,000	+59,000	+20,000	Longshore
16	-42,500	-55,000	-37,000	+53,000	+23,000	Longshore
17	-46,100	-57,000	-	+40,000	+47,000	Cross-shore
18	-45,400	-58,000	-9,000	+57,000	+25,000	Longshore
19	-45,500	-54,000	-10,000	+64,000	+18,000	Longshore
20	-53,000	-65,000	-23,000	+65,000	+30,000	Longshore
21	-62,500	-78,000	- 7,000	+68,000	+47,000	Longshore
22	-63,000	-83,000	-10,000	+64,000	+58,000	No clear trend
23	-70,300	-81,000	-14,000	+68,000	+62,000	No clear trend
24	-69,000	-86,000	-15,000	+71,000	+65,000	No clear trend

Within the wave-dominated region of Novosibirsk Reservoir the net longshore transport rate at the open shores varies from 25,000 m³/yr to 150,000-200,000 m³/yr. In term of this, the priorities in policy of beach nourishment are established as following:

1. Initial beach nourishment and periodic replenishment after ten and more years existence of protective beach.
2. The accomplishment of hybrid projects, which combine beach nourishment with the use of isolated groins, breakwaters or their systems.

Practically all attempts to prevent erosion along the Novosibirsk Reservoir shores by beach nourishment and hybrid structures were rather successful and these projects offer numerous benefits. Firstly, unlike the seawall and similar hard structures the main part of nourishment-based projects are in good condition (Table 4). Secondly, groin systems and/or detached breakwaters retain the desired shape of beach berm. Thirdly, the longshore transport of borrow material from filled beaches allowed tangibly to mitigate the coastal erosion at downcoast areas and the costs on shore protection were reduced by virtue of this phenomenon.

Table 4.

General results of the Novosibirsk Reservoir shore protection

Shore Protection Type	Length km	Modern condition		
		Destroyed km	Indamage, km	In good condition, km
Seawalls and similar hard structures	11.88	5.51	4.50	1.87
Beach nourishment	7.50	–	0.50	7.00
Hybrid projects:				
protective beach + groins	9.00	–	1.50	7.50
protective beach + segmented breakwaters	5.20	–	1.20	4.00
protective beach + segmented breakwaters + groins	3.30	–	–	3.30
protective beach + artificial headlands	5.00	–	–	5.00

CONCLUSION

Preliminary data based on over one year of observations provide some information that can assist in future efforts to mitigate shoreline erosion. The construction of hard structures like seawalls under a man-made lake's environmental conditions marked by strong storms and long-term water level fluctuations had failed measure. This type of shore protection structure presumably will be admissible only in case of feeder beach creation on the upcoast area.

Beach nourishment and fulfilling of hybrid projects are considered to be the most efficient ones. There are numerous benefits providing these measures, among which are the significant mitigation of the shoreline erosion, fair reliability, and improvement of coastal environment on adjacent shore sites. It resulted in serious changes in shore protection policy in Russia, because Novosibirsk Reservoir is a study site for a full-scale testing of various ideas in applied coastal engineering.

ACKNOWLEDGEMENTS

The portion of this research was conducted under the support of Russian Foundation of Basic Research, the project # 96-05-64448.

REFERENCES

- Birkemeier, W.A., 1980. The effect of structures and lake level on bluff and shore erosion in Berrigan County, Michigan, 1970-74. Coastal Eng. Research Center, Misc. Rept. No. 80-2, U.S. Army Corps of Engineers, 74p.
- Dean R.G., 1976. Beach erosion: causes, processes, and remedial measures. *CRS Critical Review Environmental Control*, 6 (3), 259-296.
- Dean R.G., 1987. Coastal sediment processes: Toward engineering solutions. *Coastal Sediments '87* (ASCE), pp. 1-24.
- Kraus, N.C., 1988. The effects of seawalls on the beach: An extended literature review. *Journal of Coastal Research*, Special Issue No. 4, 1-28.
- McDougal, W.G.; Sturtevant, M.A., and Komar, P.D., 1987. Laboratory and field investigations of shoreline stabilization structures on adjacent properties. In: Kraus, N.C. (ed.), *Proceedings of coastal sediments '87* (ASCE), pp. 961-973.
- Plant, N.G., Griggs, G.B., 1992. Interaction between nearshore processes and beach morphology near seawall. *Journal of Coastal Research*, 8 (1), 183-200
- Tait, J.F. and Griggs, G.B., 1990. Beach response to the presence of a seawall: A comparison of field observations. *Shore and Beach*, 58 (2), 11-28.

CHAPTER 227

COMPARISON OF BEACH AND SHOREFACE NOURISHMENT TORSMINDE TANGE, DENMARK

Christian Lastrup¹, Holger Toxvig Madsen², Per Sørensen³, Ida Brøker⁴

Abstract

Within the framework of the EU-sponsored programme Marine Science and Technology (MAST), a full-scale test was implemented in 1993 in Denmark, Germany and the Netherlands with the aim of evaluating the use of shoreface nourishment.

In this paper the background, the set-up and the results of the Danish part of the NOUR-TEC project are presented.

1. Introduction

Nourishment has been used by the Danish Coastal Authority (DCA) on the Danish North Sea coast since 1974. The volume of sand has been gradually increased and has now reached a level of about 3 mill. m³/year distributed along 150 km of the coast. Most of the nourishment has been beach nourishment but shoreface nourishment has also been used occasionally.

There has always been and there still is a considerable difference in the unit price of the two ways to protect the coast. The inevitable question is therefore which nourishment method has the best benefit/cost ratio.

Qualitatively, the following relative advantages are seen for the two nourishment methods:

Beach nourishment

– gives a better dune foot protection

1) Deputy Director, Danish Coastal Authority, Box 100, 7620 Lemvig, Denmark

2) Chief Engineer, Danish Coastal Authority, Box 100, 7620 Lemvig, Denmark

3) Project Engineer, Danish Coastal Authority, Box 100, 7620 Lemvig, Denmark

4) Chief Engineer, Danish Hydraulic Institute, Agern Allé 5, 2970 Hørsholm, Denmark

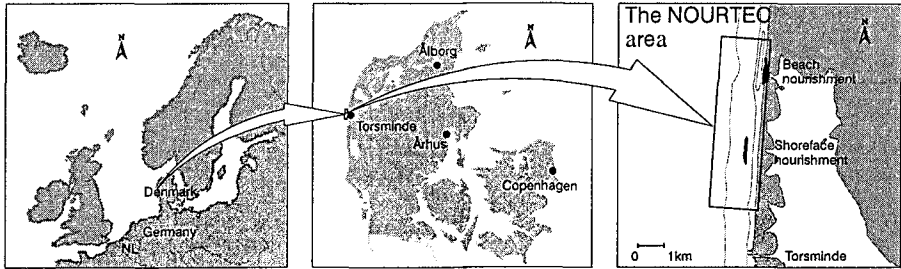


Fig. 1 Nourtec site, Torsminde Tange.

- gives a more well-defined local effect within the problem area
- is politically more attractive because a direct result of the nourishment can easily be seen

Shoreface nourishment

- is about 30% cheaper per m^3
- can be carried out without machinery on the beach
- is applicable to small nourishment projects because the mobilization costs are low

However, to our knowledge no quantitative methods exist which can be used to make a rational choice in the design situation. The design has been based on experience and on the use of rules of thumb.

The Danish Coastal Authority therefore decided to initiate a full-scale test on beach and shoreface nourishment, see Fig. 1. Together with similar projects in the Netherlands and Germany, the Danish project constitutes the NourTEC project.

2. Research questions

In the planning and design of the test nourishment projects, the three NourTEC partners agreed upon the following general design objectives [Niemeyer et al. 1995]:

- stabilization of the coastline
- coastal protection
- widening of the beach

Each of the design objectives is evaluated in terms of a corresponding design parameter, see section 4.2. The evaluation should end up giving the answers to these research questions:

- Does the nourishment fulfil the design objectives?

- What is the relative effect of the two nourishment projects? Here the benefit/cost ratio should be included.
- What is the importance of the grain size of the nourishment sand?

Besides, the project should give an improved understanding of the morphological changes induced by placing large volumes of sand in a coastal environment.

3. Experimental set-up

3.1 Test site description

Torsminde Tange is a 300 – 500 m wide barrier located north and south of Torsminde on the North Sea coast of Denmark, see Fig. 1. The barrier is a sand dune system on a clay layer. The top of the dunes is at +8 m DNN (Danish normal zero). The top of the clay layer is found at approximately –4 m DNN along the beach. The beach is 100 m wide and consists of sediment ranging from fine sand to pebbles. The beach slope is 1:20. A 2 – 3 bar system is found offshore and the sediment D_{50} range is from 0.3 to 0.8 mm. The closure depth is at –16 m DNN. The depth contours are straight and parallel to the coastline and the profile slope is 1:100. The average coastal retreat is 2.6 m/year.

3.2 Nourishment and survey programme

The shoreface nourishment is located on the outside of the outer bar in the southern sector and the beach nourishment is located from the dune foot to the shoreline in the northern sector. The nourishment volume in both nourishment projects was 250,000 m³ of sand distributed with 250 m³/m. Each of the stretches was 1 km long and 2 km apart from each other. The D_{50} of the beach nourishment sediment was 0.32 mm while the D_{50} of the shoreface nourishment was 0.57 mm. A red fluorescent tracer was mixed with the shoreface nourishment in a ratio of 1:100,000. Similarly, a blue tracer was mixed into the beach nourishment [Madsen et al. 1995].

The survey area is 7 km long and 1.5 km wide located symmetrically around the nourishment projects. The survey lines span from dune top to –12 m DNN with a mutual spacing of 100 m giving a total of 70 survey lines. A single beam echo sounder was used to survey the bathymetry and GPS was used to survey the topography and the zone from 0 to –2 m DNN. The survey accuracy was 0.04 m. A total of 17 survey campaigns were carried out during the 2–year *NOURTEC* period.

In every fifth of the survey lines 9 – 10 sediment samples were taken by hand on the beach and by a Van Veen grab offshore in predefined positions. All samples were sieved and analysed for content of tracer grains.

3.3 Boundary conditions

The water level is recorded at a groyne at Torsminde and at a groyne 5 km north of the survey area once every 15 min. The tidal range is 0.6 m and the 100 year water level

is 3.40 m DNN. Wind speed and direction are recorded at Torsminde once every 15 min. Wind from the north west is dominant and the 100-year wind speed is 33 m/s. Wave height and direction are recorded by a waverider just north of the survey area at 18 m depth. Wave characteristics have also been recorded by a current meter, at first placed at 14 m depth just seaward of the NOURTEC area. Later it was placed at 4 m depth on the shoreface nourishment. Waves were recorded once every 3 hours. The dominant deep water waves come from NW and the 100-year significant wave height is 8.1 m. Current has been measured at the above described locations once every 15 min. At both locations the current meter was placed 1 m above the bottom. At 14 m depth the dominant current is the tidal current with an amplitude of 0.2 m/s. At 4 m depth the current is also significantly influenced by waves but still the tidal current is dominant.

4. Effectiveness analysis

4.1 Introduction

The surveys showed that the beach nourishment was eroded after about 3/4 year while the shoreface nourishment only lost about 40% of its volume in the whole monitoring period. The morphological description and interpretation of the development in the monitoring area is presented in section 6.

Here the results are presented of a strictly mechanistic method to analyse the survey data. This so-called effectiveness analysis gives objective results easy to compare with the results produced by the other two partners in the NOURTEC project.

The analysis is based on the use of a number of common design parameters. The parameters are calculated for each bathymetry and the development of the parameters is compared to the estimated development of the parameters in the absence of the nourishment projects. The difference between this so-called autonomous development and the actual development represents the net effect of the nourishment. Here it is assumed that the autonomous development and the nourishment effect can be superimposed.

4.2 Definition of the design parameters

In section 2, the general design objectives were presented. Each of these objectives is evaluated by means of one of the following three common design parameters:

- position of the coastline
- position of the upper part of the profile
- beach width

In Fig. 2 it is shown how the design parameters are calculated. Apart from the “beach width” the parameters are calculated on the basis of a volume divided by the height of the zone used in the volume calculation. The result is a horizontal distance to the reference line. The level DNN +4 m is considered to be representative of the beach level at the dune foot.

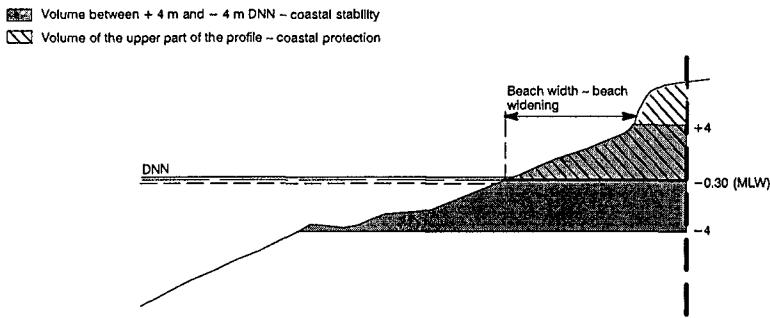


Fig. 2 Definition of the common design parameters.

4.3 The autonomous development

For practical reasons it was not possible to estimate the autonomous development in the monitoring area for the NOURTEC period 1993 – 95 from the development of a nearby reference stretch. So instead, historical data were used.

The wind rose for the monitoring period 1993 – 95 is nearly identical to the wind rose for the period 1985 – 92. This indicates that the meteorological boundary conditions are about the same for the two periods. On this basis it was decided to calculate the design parameters for the period 1985 – 92 and consider the slope of the corresponding trend lines as good estimates for the autonomous development in the monitoring period.

4.4 Results

The effect of the nourishment projects can be calculated for any section along the coast. Here it has been chosen to show the results for 3 km stretches located symmetrically around the two project areas. The reason for this choice is that the analyses have shown that the effect of the nourishment projects is not limited to the nourished 1 km stretches themselves.

The development of the three design parameters for the southern and the northern 3 km stretches is shown in Fig. 3. The autonomous development is shown as well.

From the figure it appears that in the 2-year monitoring period the beach nourishment stabilizes the coastline and improves the coastal protection level. On the other hand, the beach width has not been improved. For the shoreface nourishment there is a positive net effect on all three design parameters. Hence, the shoreface nourishment has fulfilled all the design objectives.

Quantitatively speaking the shoreface nourishment has an effect on the coastal stability of 10.4 m or 250,000 m³ for the 3 km stretch while the similar effect of the beach nourishment is 2.8 m or 67,000 m³. The effect on the coastal protection is 9.0 m or 189,000 m³ for the 3 km stretch for the shoreface nourishment and 5.4 m or 113,000 m³ for the beach nourishment.

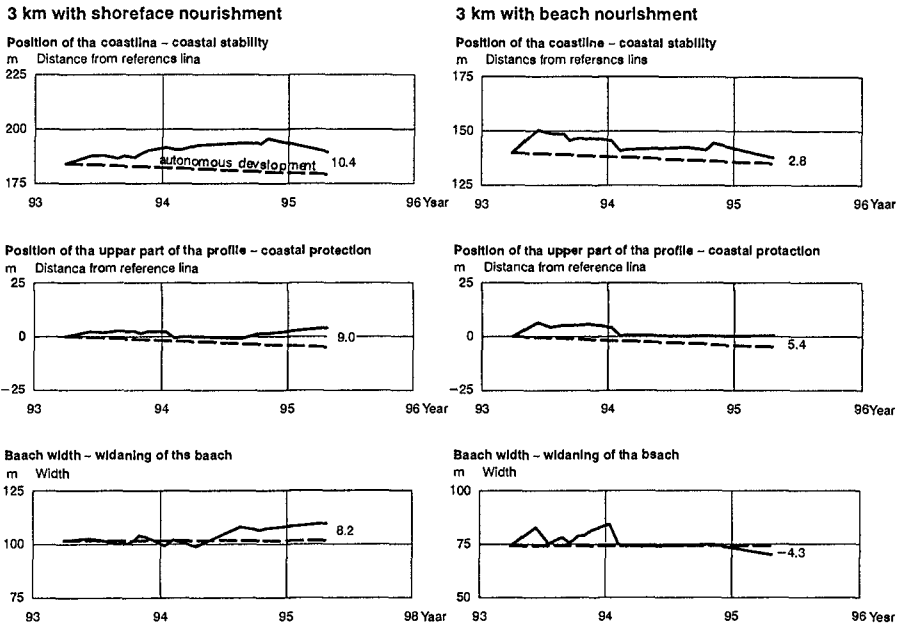


Fig. 3 Nourishment effect on the design parameters.

A direct comparison of the two nourishment projects is shown in Fig. 4. It appears that the shoreface nourishment gives the better stabilization of the coastline over the whole period. However, in the first 3/4 year the beach nourishment is the more effective. Concerning coastal protection the shoreface nourishment is the better option. Again the beach nourishment is the better option at the beginning of the period. For the beach width the result is similar. At the beginning, the beach nourishment is better but over the whole period the shoreface nourishment ends up being better.

Also in Fig. 4 the benefit/cost ratios are shown for the effect of the nourishment projects. Because it is about 30% cheaper to nourish on the shoreface than on the beach, the better relative effect of the shoreface nourishment mentioned before is increased when the costs are included in the evaluation.

5. Modelling

The 1-dimensional numerical model LITPACK and a 2-dimensional numerical model MIKE 21 have been used. Both models have been developed by the Danish Hydraulic Institute. The purpose of using the models is to analyse the effect of using coarse sand in the shoreface nourishment and to extrapolate the results to other boundary conditions.

5.1 1-dimensional modelling

LITPACK has been used to calculate the longshore sediment transport during the entire NOURTEC period and the results have been used in the calibration of MIKE 21. The

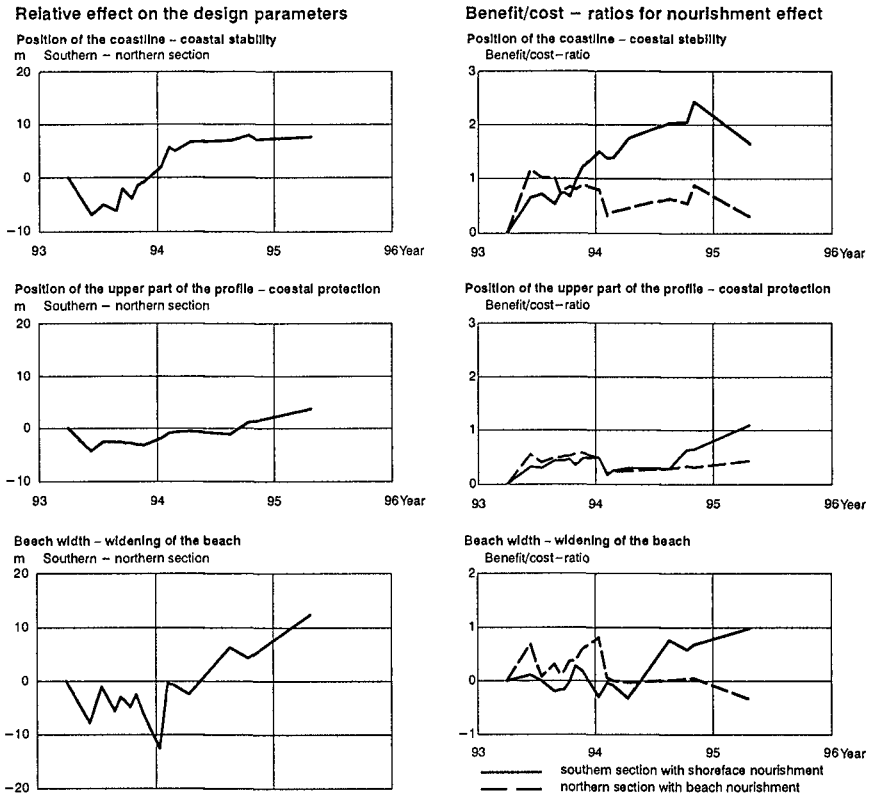


Fig. 4 Relative effect of the two nourishment methods and benefit/cost ratios for the nourishment effect.

nourishment projects are included in the two areas S(horeface nourishment) and B(each nourishment), see Fig. 5. For each area there is one survey line on both sides of the nourishment and 3 lines which include the nourishment.

First, LITPACK was calibrated to the annual littoral drift. The annual littoral drift has been calculated by accumulating the profile erosion from the nodal point for the littoral drift to the NOURTEC area by using three different approaches. Based on these calculations the south-going net littoral drift was estimated to be in the interval of 550,000 – 850,000 m³/year. Secondly, LITPACK was calibrated to the measured volume changes in the areas S and B in the entire NOURTEC period, including the variation intervals due to survey inaccuracy.

In LITPACK, uniformity of the coastal profiles is a basic assumption. The applicability of LITPACK for quantification of erosion/accretion along a coastline depends entirely on the fulfillment of this assumption. This assumption was not completely met, which

was confirmed by the 2-dimensional modelling, and must be taken into account when the results are analysed.

In Fig. 5 the results of the calibration are shown. It appears that the calibration is good for the area S and less good for the area B but still within the variation intervals which are given by the measured data. The problems with area B are caused by an extremely large erosion that took place during the winter of 1994 – 95 outside the beach nourishment.

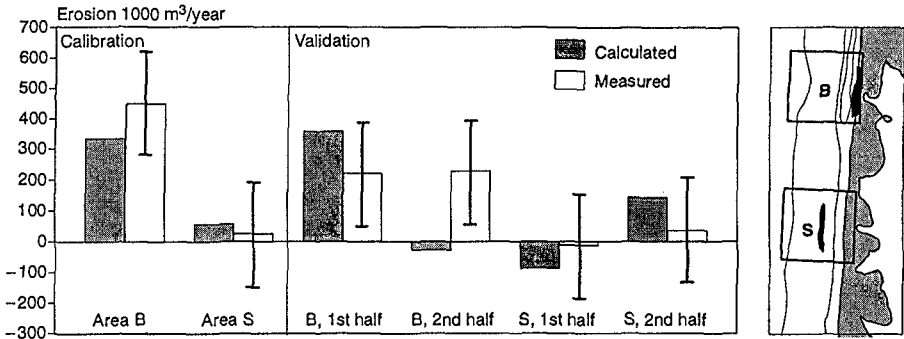


Fig. 5 Calibration and validation of LITPACK.

After the calibration, the model set-up has been verified for the two halves of the monitoring period, each about 1 year long. The results are also shown in Fig. 5. Again good agreement is seen for area S and for area B, less agreement is seen for the second half of the period. Although the results have not been quite perfect, the model set-up is assumed to be calibrated and validated as far as possible and the model set-up can be used in a descriptive and prognostic mode.

The cross-shore distribution of the longshore sediment transport in the NOURTEC period has been analysed and it is found to be very sensitive to the local shape of the shoreface nourishment on the outer bar. A decrease in the water depth above the nourishment causes extensive wave breaking and hence increased sediment transport on the bar and decreased transport near the coastline. The sediment transport distribution is not particularly affected by the the beach nourishment because only a small part of the nourishment is under influence of waves.

For both the shoreface and the beach nourishment area it is found that during the NOURTEC period waves with a significant wave height of 1 to 2 m cause most of the sediment transport and the net sediment transport direction is southward.

In order to quantify the effect of nourishment sediment characteristics on the sediment transport, the dependence of D_{50} is analysed. For the shoreface nourishment $D_{50} = 0.57$ mm and for the beach nourishment $D_{50} = 0.32$ mm. It is done by averaging the longshore sediment transport for the NOURTEC period in each of the areas S and B for each D_{50} . For the shoreface nourishment the ratio between $D_{50} = 0.32$ mm and $D_{50} = 0.57$ mm was found to be 2.3. Similarly for the beach nourishment, the ratio was found to be 1.2.

5.2 2-dimensional modelling

MIKE 21 is a 2-dimensional modelling complex. In the present case a parametrised wind wave model, a depth integrated hydrodynamic model and a deterministic, intra wave period sediment transport have been applied. The intention of using MIKE 21 is to calibrate the model so that it will reproduce the sediment transport in the NOURTEC period.

The simulated conditions had to be limited to 3 wave heights and corresponding water levels, 2 wave directions, 3 bathymetries and 4 different types of sediments due to computer time consumption and with that the costs. The wave heights are chosen from knowledge gained in the LITPACK study about which waves are significant for the sediment transport. Wave directions from south- and northwest were chosen as a minimum. Both are 40° off the coast normal. As a minimum, a bathymetry taken prior to the nourishing, one describing a "summer" bathymetry and one describing a "winter" bathymetry were chosen. Finally, the sediment range from natural sand to the coarse shoreface nourishment sand was described by the D_{50} parameter. The same sediment spreading was used to reduce the number of variables. These parameters were combined in 18 sets of data, each set representing a typical combination of boundary conditions.

The 2-dimensional modelling complex consists of a large wind wave model with a resolution of 20 by 100 m, which gives boundary conditions to the local model area. Here the resolution of the wave modelling is 4 by 20 m. The resolution of the hydrodynamic and sediment transport model is 20 by 20 m.

The results show that even small morphological changes are reflected in the sediment transport pattern so it was difficult to distinguish between the sediment transport caused by natural variations and the sediment transport caused by the nourishment volumes. An attempt has been made to eliminate all other changes but the ones caused by the nourishments by integrating the longshore transport in depth intervals of +4 m to -4 m ("coastline") and of -4 m to -8 m ("6 m depth"). It was found that the changes introduced by the nourishments are nearly insignificant compared to the natural variations both in space and time.

Fig. 6 shows examples of sediment transport fields calculated for 3 different bathymetries. Here the 2-dimensional effect of the nourishments are clearly seen. The longshore sediment transport components have been integrated within the intervals "coastline" and "6 m depth". The calculated integrated sediment transport rates are compared for a) the bathymetry just before nourishment and the "before nourishment bathymetry" supplemented with the "after nourishment bathymetry" within the area S and B, and b) for a "summer" bathymetry and a "winter" bathymetry.

Another result was that of migrating bed forms on deep water (15 – 20 m) influence the direction of the incoming waves and effect the longshore sediment transport. The effect is most pronounced in the most seaward part of the NOURTEC area.

The effect on the integrated longshore transport of using coarse sand for the shoreface nourishment was calculated. For the shoreface nourishment the ratio between the longshore sediment transport rates for $D_{50} = 0.32$ and 0.57 mm was found to be 1.17. Similarly for the beach nourishment, the ratio was found to be 1.11.

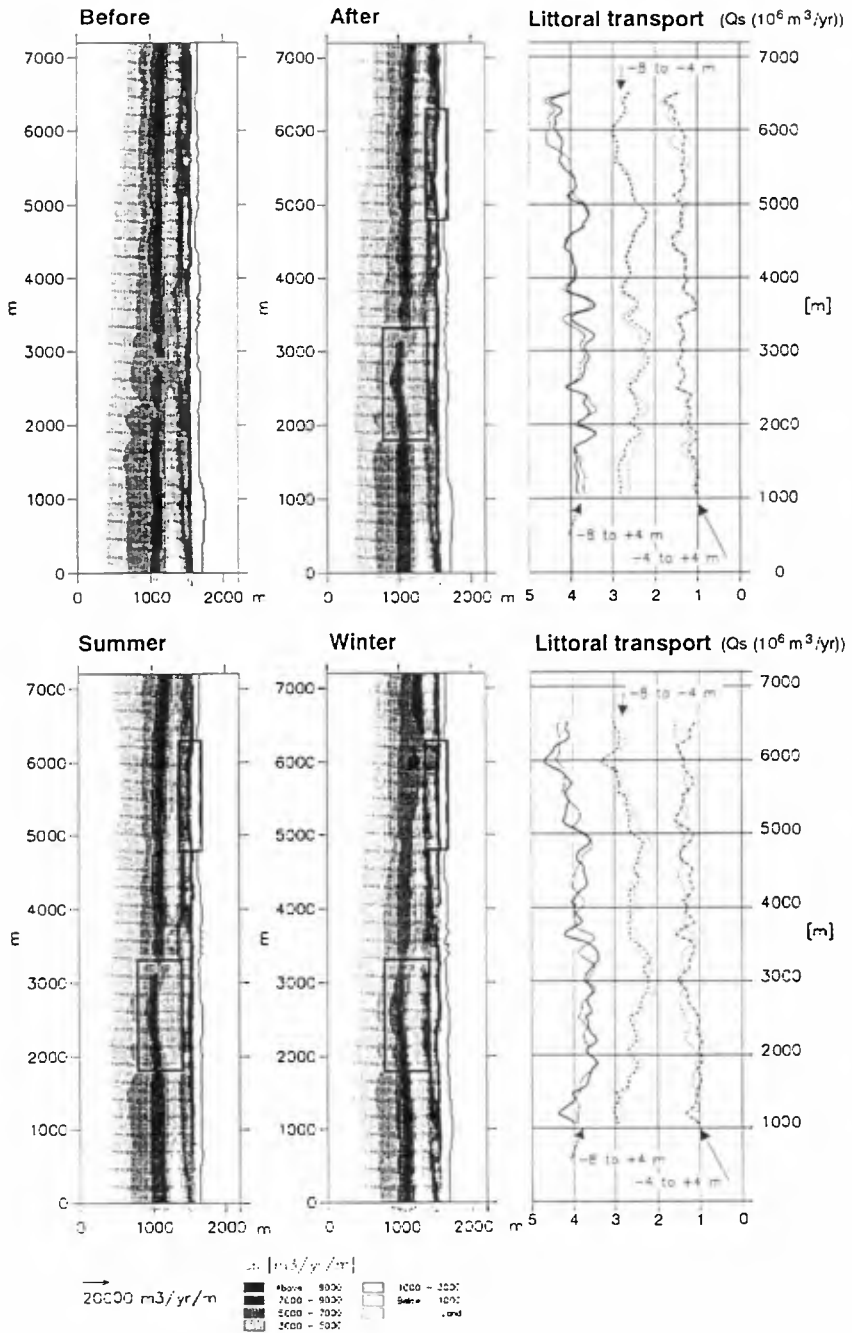


Fig. 6 Calculated, 2-dimensional sediment transport fields and integrated longshore sediment transport components for the intervals +4 m to -4 m, and -4 m to -8 m.

Finally, attempts were made to combine the MIKE 21 calculated volume changes in a system of 12 boxes by which the Nourtec area is described to reproduce the development in the Nourtec period. The longshore sediment transport variation with wave direction calculated by LITPACK was used to extrapolate the volume changes. The morphological changes were taken into account by using the "summer" or "winter" bathymetry. Fig. 7 shows the MIKE 21 weighted and measured accretion in 1 km long boxes. In 3 of the 6 boxes good agreement is seen but poor agreement is seen in the other boxes.

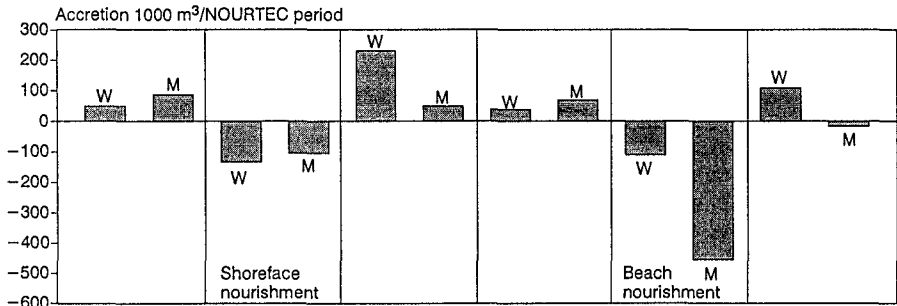


Fig. 7 Weighted Mike 21 and Measured volumes from south to north.

6. Morphological analysis

The volume changes in the monitoring area have been analysed by use of a system of cells with fixed horizontal boundaries. For each cell the volume development has been calculated.

In Fig. 8 the system of cells is shown together with the volume curves for selected cells and combinations of cells. The shoreface nourishment is located in cell H. For this cell there is a volume increase just after completion of the nourishment. From here the volume is stable with some fluctuations. In the cells A–B–C landward the shoreface nourishment there is a gradual volume increase over the whole monitoring period. For the beach nourishment in cell E a gradual volume decrease is seen over the monitoring period. After about 3/4 year the beach nourishment has been eroded. Tracer results indicate that part of this sand migrates towards south in the coastline zone.

Although the volume is constant in cell H, some morphological changes are seen. Over the monitoring period the nourishment migrates about 50 m onshore and the level of the top of the nourishment is reduced by about 0.5 m.

In Fig. 9 an overview is given of the horizontal development of the bar system. Just south of the shoreface nourishment the bar becomes continuous shortly after completion of the nourishment, probably because of the surplus of sand transported on the bar at the nourishment. It can also be seen that a weakening starts after a year at the northern end of the nourishment. Corings in the nourishment area show that about 60% of the nourishment sand is still in the initial position at the end of the monitoring period.

The 40% loss of the nourishment sand is only about 1/3 of the total accretion landward of the nourishment. It means that the accretion effect of the shoreface nourishment is

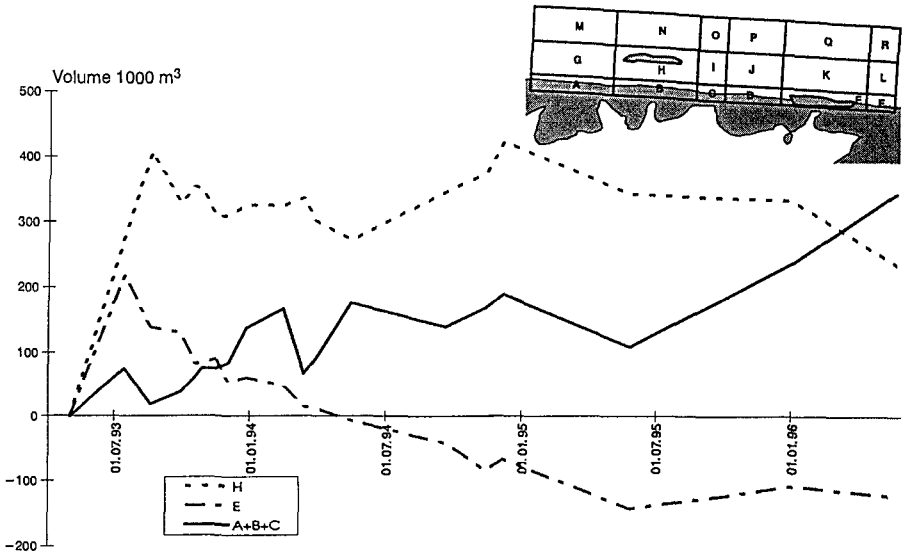


Fig. 8 Volume development in selected cells.

much larger than the nourishment volume itself. The reason is the breakwater effect of the nourishment. Like a breakwater, the nourishment reduces the longshore transport landward with an accretion as result.

An interesting result of this project is the better stability of the shoreface nourishment compared to the beach nourishment. Part of the explanation of this fact is the coarser sand in the shoreface nourishment. However, a reason which is even as important is the specific position of the shoreface nourishment. The position in the bar zone is a natural position for a perturbation so to say. Therefore the nourishment quickly becomes an integrated part of the bar system instead of being eroded away.

Outside the monitoring area migrating bed forms have been observed. However, it has not been possible to verify if the bed forms cause a longshore variation in the sand transport from the outer to the inner part of the profile.

7. Conclusions

The effects of a beach nourishment and a shoreface nourishment have been analysed and compared. Because the weather conditions in the monitoring period were about average, the results are considered to be valid for average weather conditions.

By use of a mechanistic analysis approach it has been determined if the nourishment projects fulfil three design objectives: stabilization of the coastline, coastal protection and widening of the beach. It was found that the beach nourishment stabilizes the coastline and improves the coastal protection but the beach width has not been improved. On the other hand, the shoreface nourishment fulfils all the design objectives.

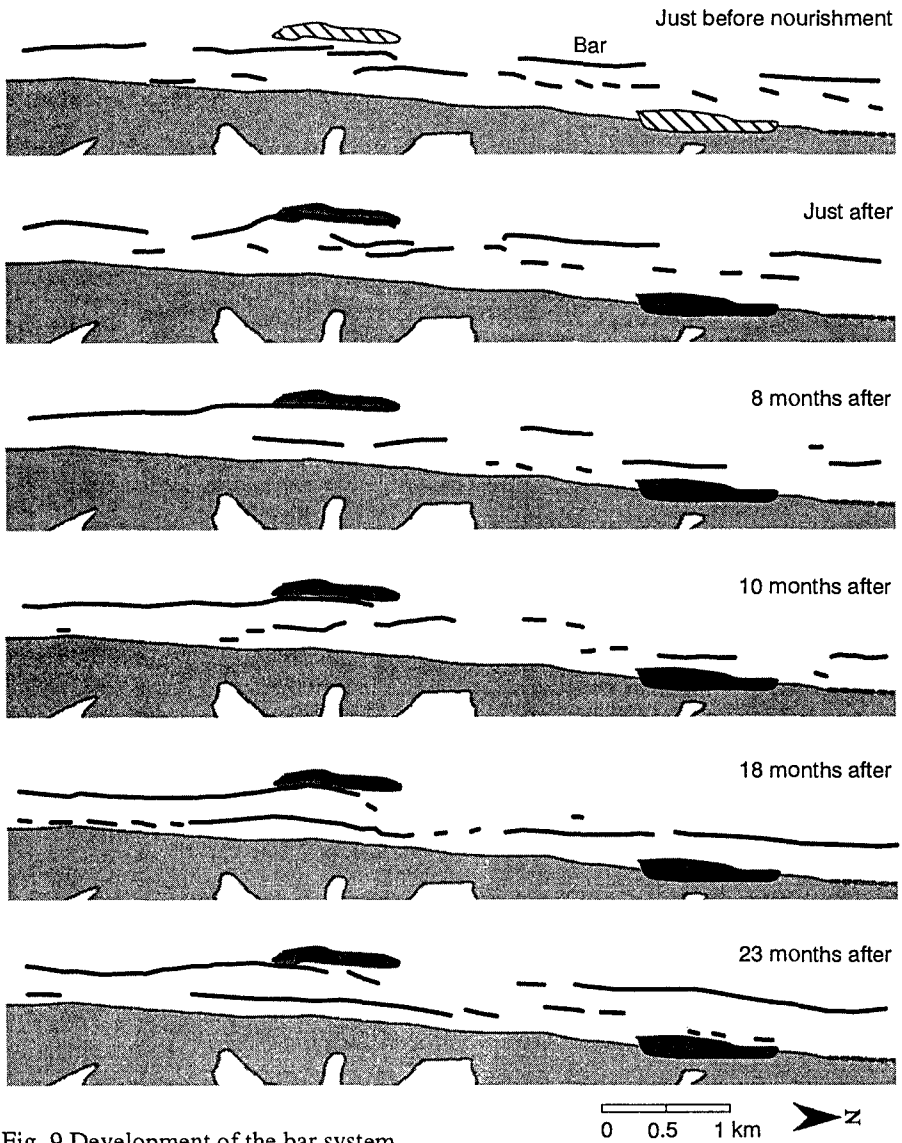


Fig. 9 Development of the bar system.

The relative effect of the two types of nourishment has also been analysed. For all three design objectives, shoreface nourishment is the better option at the end of the monitoring period but beach nourishment is the better option at the beginning. When the price of the nourishment sand is taken into account, the relative effect of the shoreface nourishment is improved because this nourishment type is cheaper.

The 1-dimensional model LITPACK has been calibrated and verified to the monitoring data. LITPACK was then used to calculate the sediment budget and the effect of grain size.

The 2-dimensional model MIKE 21 has shown that the processes in the surf zone are highly 3-dimensional and that the natural variations of the longshore transport are large compared to the changes introduced by the nourishment.

It was concluded that the 2-dimensional calculations of 6 wave conditions combined with 3 bathymetries have been helpful in understanding details of some of the processes which contribute to the natural re-shaping of the investigated area. However, partly due to a limited number of simulated conditions and partly due to the fact that the processes in the surf zone are highly three dimensional, the results cannot be combined in such a way that the observed losses and gains of sediment are reproduced.

The two nourishment volumes have shown a clear difference in stability. The beach nourishment was eroded after 3/4 year. For the shoreface nourishment about 60% of the sand was still in the initial position two years after completion of the nourishment. One reason for the stability is the coarser sand. It was found that the shoreface nourishment sand with $D_{50} = 0.57$ mm is about 2.3 times as stable as sand with $D_{50} = 0.32$ mm. However, a reason which is probably just as important is the position of the nourishment in the bar zone.

The accretion effect of the shoreface nourishment is much larger than the nourishment volume itself. The reason is the breakwater effect of the nourishment. Like a breakwater, the nourishment reduces the longshore transport landward resulting in an accretion.

Acknowledgement

This work was carried out as part of the NourTEC project. It was funded jointly by The Danish Coastal Authority and by The Commission of the European Communities, Directorate General for Science, Research and Development under Contract no. MAS2-CT93-0049.

References

- Madsen H.T., Laustrup C. and Soerensen P., 1995. A full scale comparison of beach and shoreface nourishment. COPEDEC IV Rio de Janeiro, Brazil 1995, 263-272.
- Niemeyer H.D., Biegel E., Kaiser R., Knaack H., Laustrup C., Mulder J.P.M., Spanhoff R. and Toxvig H., 1995. General aims of the NourTEC project- Effectiveness and execution of beach and shoreface nourishments, COPEDEC IV Rio de Janeiro, Brazil 1995, 311-325

CHAPTER 228

Mathematical and Physical Modeling of Beach Nourishment Projects

W. Erick Rogers¹ and Paul A. Work², Associate Member, ASCE

Abstract

This paper evaluates the utility of mathematical models for prediction of the planform movement of beach nourishment projects. The results of one-line models (analytical and numerical) are compared to the evolution of nine laboratory-scale model beachfills. Several methods of planform modeling are evaluated, varying in complexity. Comparison of planform modeling suggests that, in some circumstances, using a simple analytical treatment of refraction may be a feasible alternative to using more rigorous numerical wave modeling for shoreline modeling purposes. The relative ability with which different equations for net longshore sediment transport rate reproduce observed beachfill evolution is discussed. Information on the effect of wave climate and beachfill geometry on beachfill lifetime is extracted from the laboratory study. The observed effect of lower wave height, greater beachfill length, and the tapering of a beachfill is a greater beachfill lifetime, in agreement with conventional wisdom. Increasing beach slope and decreasing wave period are both observed to cause a slight decrease in beachfill lifetime.

Introduction

A beach nourishment project is an attempt to widen the dry portion of a beach and offer protection from storms to existing nearby structures by adding large quantities of sediment to some portion of the beach. They are sometimes appropriately referred to as "sacrificial beachfills." This emphasizes the fact that beach nourishment projects are rarely expected to stay in place for more than a decade without losing a large portion of the placed material. Any improvement in the ability to predict this redistribution of beachfill material, through the use of better modeling techniques, allows for more cost effective design and more efficient coastal zone management.

¹U.S. Nav. Res. Lab. Contractor (Planning Systems Inc.); MSAAP Bldg.9121 Stennis Space Center, MS 39529 USA; e-mail:rogers@lincoln.nrlssc.navy.mil

²Asst. Prof., Dept of Civil Eng., 110 Lowry Hall, Clemson Univ., Clemson, SC 29634-0911 USA; e-mail: pwork@ces.clemson.edu

Laboratory Study

A laboratory study was conducted, with two primary purposes in mind: 1) to observe in detail longshore sediment transport patterns in the presence of beach nourishment projects, and 2) to provide prototype beachfills for validation of mathematical shoreline models. Similar studies have been conducted. Kamphuis et al. (1986), Kamphuis (1991), and Nielsen (1988) studied longshore sediment transport in a laboratory setting. Kamphuis and Meyer (1976) studied beachfills using physical models. Dean and Yoo (1994) conducted a laboratory study of beach nourishment projects in front of seawalls and compared the results to mathematical models.

Nine laboratory beachfills were monitored. A paddle-type wave-maker was used to generate nominally shore-normal, monochromatic waves. A set of parameters were compiled which were expected to have an effect on beachfill lifetime: project length, degree of beachfill tapering, breaking wave height, wave period, and beach slope. In a laboratory setting these parameters are easily controlled; each case was assigned a different set of values for these parameters. For each case, a beachfill "lifetime" was calculated based on the amount of beachfill remaining in place, by volume, after wave attack. Lifetime is defined as the time period required for a significant percentage of material to be eroded; loss of 5% of beachfill volume was used. Beachfill material which was dispersed in the longshore direction, outside the original location of the beachfill, was considered "lost" sediment volume. Based on these calculations, the effect of each of the important parameters on beachfill lifetime was inferred (see Table I). Comparison is made to mathematical models employing the "CERC equation" for longshore sediment transport rate (U.S. Army Corps of Engineers 1984).

Table I
Effect of Parameters on Beachfill Lifetime

Parameter	Mathematical Models (with CERC formula)	Physical Model Observations
H_b , wave height at breaking \uparrow	Lifetime \downarrow	Lifetime \downarrow (significant effect)
T , wave period \uparrow	No effect	\uparrow (slight)
L , project length \uparrow	\uparrow	\uparrow (moderate)
m , beach slope \uparrow	No effect	\downarrow (slight)
Tapering of fill	\uparrow	\uparrow (moderate)

Figure 1 shows the location of two typical beach profiles from one of the laboratory cases. Figure 2 is a beach profile located at the "shoulder" of one of the beachfills; the profile experiences a net loss of sediment. Figure 3 shows a beach profile located in the adjacent, unnourished region; accretion occurs due to beachfill material deposited there via longshore transport.

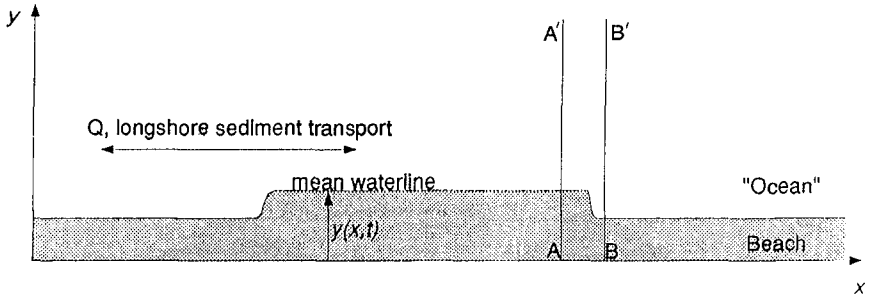


Figure 1. Locations of Laboratory Beach Profiles A and B

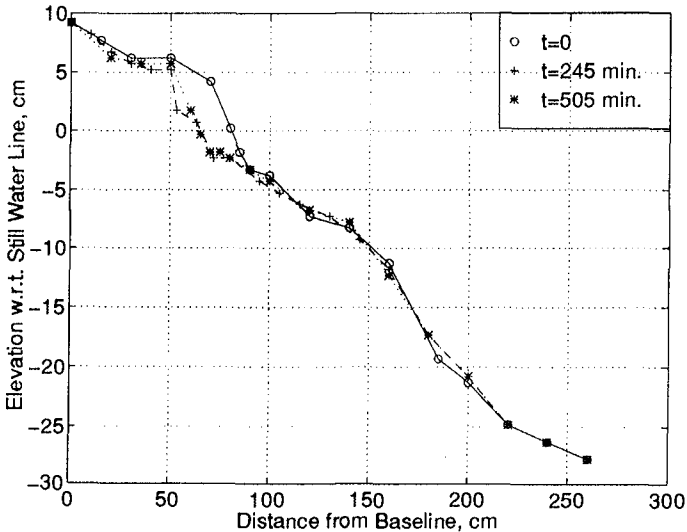


Figure 2. Laboratory Beach Profile A

With any physical model, scale effect is a major concern. Due to the relatively small scale of this laboratory study, it is unreasonable to expect accurate quantitative information. However, if the physical model behaves in a manner similar to full scale beachfills, useful qualitative information can be gained, like that shown in Table I. Figure 4 is a beach profile from the shoulder of a full-scale beach nourishment project (Perdido Key, FL). The similarity to Figure 2 is encouraging.

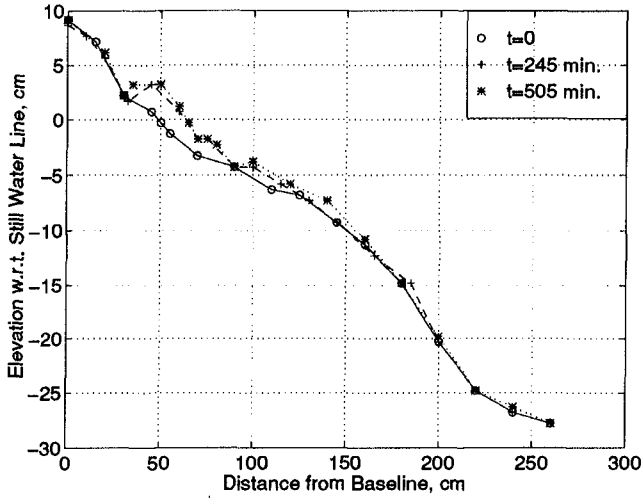


Figure 3. Laboratory Beach Profile B

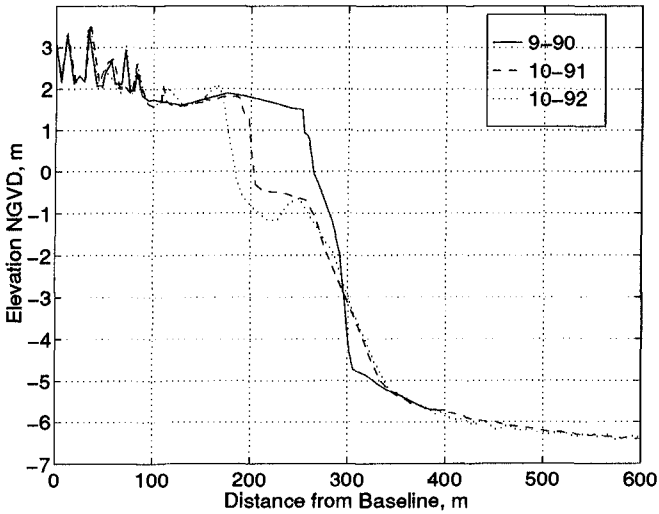


Figure 4. Beach Profile from Full-Scale Beachfill (Perdido, FL)

Shoreline Models

The shoreline model used in this study was a "one-line model", a tool which has been used extensively by researchers and engineers (e.g. Pelnard Considère 1956, Hansen and Kraus 1989). One-line models are used to predict the movement of a single elevation contour of a beach, typically the still water line. These models are governed by the sediment continuity equation,

$$\frac{\partial y}{\partial t} + \frac{1}{h_* + B} \frac{\partial Q}{\partial x} = 0, \tag{1}$$

and an equation for longshore sediment transport. In equation (1), $h_* + B$ defines the vertical extent of the active beach profile.

If a one-line model is used to provide the shoreline location, $y(x,t)$, the assumption must be made that the shape of a beach profile does not change, but that the profile only shifts onshore or offshore as erosion or accretion occurs (implying zero net cross-shore sediment transport over the time period of interest). However, a recently constructed beachfill typically has an overly steep beach slope, resulting in significant offshore sediment transport. Shoreline models were used to calculate longshore distributions of longshore sediment transport gradients, $\partial Q/\partial x$. A longshore sediment transport gradient can be directly compared to the time averaged rate of change of beach profile area $\partial A/\partial t$, which can be inferred from laboratory and field beach profile measurements:

$$\overline{\frac{\partial Q}{\partial x}} = \overline{\frac{\partial A}{\partial t}} = \frac{\Delta A}{\Delta t}. \tag{2}$$

Here, the overbar denotes time averaging. This method of comparison removes the effect of cross-shore sediment transport from calculations, provided that the entire "active" portion of the beach profile is included in area calculations.

Sediment Transport Equations used in Mathematical Shoreline Models

Three basic equations for longshore sediment transport were tested with the shoreline change models of the laboratory beachfills: the "CERC equation," the "Kamphuis equation" (Kamphuis 1991), and the "GENESIS equation" (Hansen and Kraus 1989). The CERC equation states that longshore sediment transport is proportional to the longshore component of wave energy flux:

$$Q = \frac{KH_{sb}^2 C_{gb} \sin 2\theta_b}{16(SG-1)g(1-p)}. \tag{3}$$

Here K is an empirical coefficient.

The GENESIS equation is a slight modification of the CERC formula, with an added term to account for longshore sediment transport driven by longshore gradients in wave height caused by the presence of structures or (less significantly) irregular bathymetry:

$$Q = (H^2 C_g)_b [a_1 \sin(2\theta_b) - a_2 \cos\theta_b \frac{\partial H}{\partial x}]_b, \quad (4)$$

where

$$a_1 = \frac{K_1}{16(SG-1)(1-p)(1.416)^{\frac{5}{2}}}, \quad (5)$$

and

$$a_2 = \frac{K_2}{8m(SG-1)(1-p)(1.416)^{\frac{7}{2}}}. \quad (6)$$

The Kamphuis equation is an empirically-based equation, developed by a power fit analysis using data from lab and field studies:

$$Q = KH_{ab}^2 T_p^{1.5} m_b^{0.75} D_{50}^{-0.25} \sin^{0.6}(2\theta_b). \quad (7)$$

Inclusion of Refraction in the Numerical Shoreline Model

Longshore sediment transport rate is generally accepted to be dependent on the angle between the wave orthogonal and the local shore normal. This suggests that the inclusion of refraction is requisite for any numerical modeling of irregular shorelines, such as a coastline with a trapezoidal beachfill. In most beach nourishment scenarios, inclusion of refraction will lead to a lower predicted rate of evolution, as it tends to decrease wave obliqueness at breaking.

The numerical wave transformation model REFRACT (Dalrymple 1988) was used to calculate breaking wave conditions for use in the shoreline model. This wave model includes shoaling and refraction (but not diffraction).

As an alternate method for including refraction in a numerical one-line model, a modified form of the CERC equation for longshore sediment transport (Work and Dean 1995) was employed. This equation is based on a two-line, analytical approach to wave transformation, which is much simpler than using a numerical wave model to supply breaking wave input data. The equation is a generalized form of an equation proposed by Dean and Yoo (1992). It can be stated as:

$$Q = K \frac{H_R^{2.4} g^{0.4} \cos^{1.2}(\beta_R - \alpha_R) C_{G_R}^{1.2}}{8(SG-1)(1-p)\kappa^{0.4} C_*} \left[\frac{C_* \sin(\beta_R - \alpha_R)}{C_R} - \beta_t \left(1 - \frac{C_*}{C_t}\right) + \beta_s - \beta_R \frac{C_*}{C_t} \right] \quad (8)$$

The notation is illustrated in Figure 5. Subscript *t* denotes the location of the "toe" of the beach nourishment.

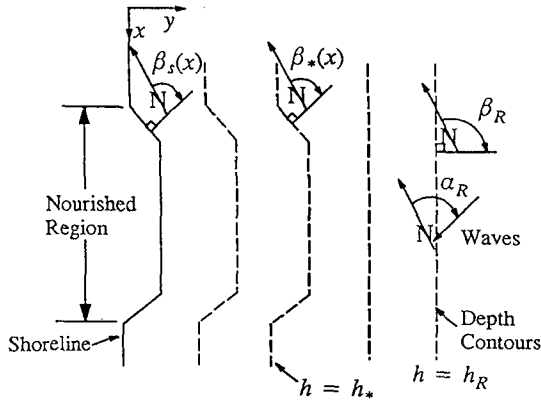


Figure 5. Notation used in Equation (8)

Inclusion of Diffraction in the Numerical Shoreline Model

Diffraction acts to reduce along-wave wave height gradients and thus tends to counter the effects of refraction. Without the inclusion of diffraction, a wave transformation model may tend to yield exaggerated focusing of wave energy near the "shoulders" of a beach nourishment project, which would compromise the predictive capability of the one-line model. The numerical wave model REF/DIF1 (Kirby and Dalrymple 1994) was used to generate breaking wave conditions (for use in the one-line model) including the effects of the shoaling, refraction, and diffraction of waves.

Comparison of One-Line Model Results to Laboratory Results

Laboratory data and numerical model results were compared based on longshore gradients of longshore sediment transport rate ($\partial Q/\partial x$), rather than shoreline evolution; thereby the effects of cross-shore sediment transport on shoreline movement were removed. Time-averaged longshore gradients of longshore sediment transport were inferred from beach profile measurements using equation (2).

Several shoreline modeling schemes were used, varying in complexity:

1. analytical calculation of shoaling (using conservation of wave energy flux), CERC equation for longshore sediment transport (equation (3));
2. analytical calculation of shoaling (using conservation of wave energy flux), Kamphuis equation for longshore sediment transport;
3. analytical treatment of the shoaling and refraction of waves in CERC equation (equation (8));
4. analytical treatment of shoaling and refraction in Kamphuis equation (analogous to equation (8));
5. shoaling and refraction determined by numerical wave model REFRACT, CERC equation for longshore sediment transport;
6. shoaling and refraction determined by numerical wave model REFRACT, GENESIS equation for longshore sediment transport; and
7. shoaling, refraction, and diffraction determined by numerical wave model REFDF1, CERC equation for longshore sediment transport.

Figure 6 shows the longshore gradients of longshore sediment transport calculated by the one-line model for one of the laboratory cases. Note the similarity between the results using the numerical and analytical treatment of refraction.

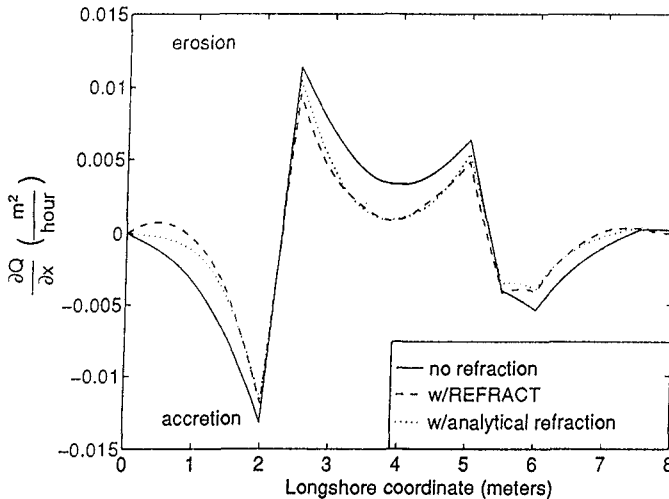


Figure 6. Comparison of Shoreline Modeling Schemes (1, 3, and 5)

Figure 7 compares longshore sediment transport gradients inferred from measurements for a laboratory beachfill to model output using option (1) above. This plot is representative of most comparisons of the one-line model results to lab results: though quantitative agreement is somewhat artificial due to calibration of the longshore sediment transport equation, qualitative agreement is good.

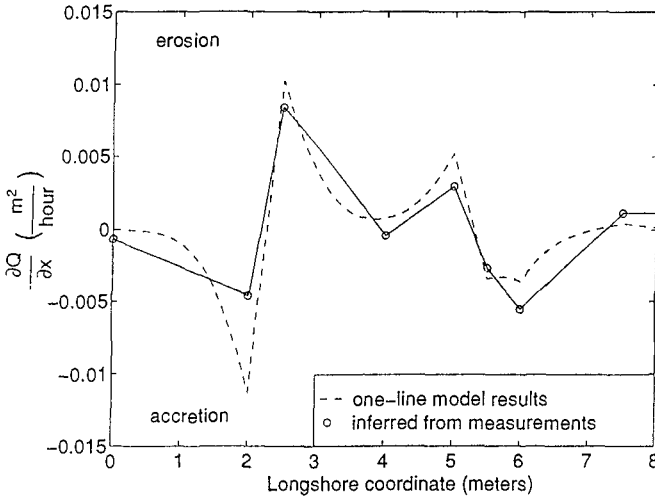


Figure 7. Comparison of Laboratory Results to One-Line Model Results

Using standard "field" values for coefficients of proportionality, none of the longshore sediment transport equations yielded good quantitative agreement. With standard coefficients, the equations typically greatly over-predicted longshore sediment transport. This is almost certainly due to scale effect, and has been observed by other researchers (e.g. Komar and Inman 1970).

The ability of the calibrated numerical one-line model to duplicate laboratory results was determined for each of the variations of the shoreline model. This comparison indicated that the use of the numerical wave models did not provide any added accuracy over method (1) above. On the other hand, use of the longshore sediment transport equation with an analytical treatment of refraction did yield a slight improvement in results.

In this comparison of methods, the Kamphuis equation yielded slightly better qualitative agreement than the other two basic equations for longshore sediment transport. The added term in the GENESIS equation did not result in any improvement over the CERC equation, probably because longshore gradients in wave height were not large in the laboratory.

Comparison to Field Data

Numerical one-line model results were compared to data from a well-monitored beach nourishment project at Folly Beach, South Carolina (Figure 8). The method for analytical treatment of refraction (method 3 above) was used with a standard calibration factor for the CERC equation ($K=0.77$ using H_{ms}). 2.1 million cubic meters of beachfill material were placed during the first four months of 1993 (Ebersole, et al., 1996). A 25-month period was investigated, from July, 1993 to August, 1995.

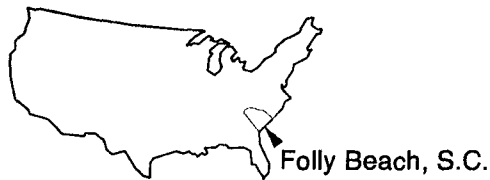


Figure 8. Location of Folly Beach

For the shoreline model initial condition, the "ad hoc transformation" method was used. This method is suggested by Dean and Yoo (1992) for situations "where substantial perturbations (human or natural) have placed the system out of balance." The initial planform used was simply the deviation from an assumed equilibrium planform caused by the placement of the beachfill.

Nine groins located northeast of the Holiday Inn (see Figure 9) were renovated at roughly the same time that the beachfill was placed. These groins were not included in the model results presented in this paper. For the time period modeled, the groins were thought to have a minor impact on shoreline movement; the groins are relatively short and were dry at low tide. Offshore wave data for 1993 and 1994 were obtained from a Wave Information Study (WIS) hindcast database (Brooks and Brandon 1995) for shoreline model input.

Comparison of the one-line model results to measured data is shown in Figure 10. The one-line model provides a reasonably good prediction of erosion and accretion, in both a quantitative and qualitative sense. Close inspection of Figure 10 suggests that the inclusion of the groins in the numerical model may have improved the model's accuracy--erosion was overpredicted by the model inside the groin field, and underpredicted downdrift (southwest) of the field.

Volume calculations indicate that 413,000 m³, or 19% of the beachfill volume which existed in July 1993 was lost from the nourished region by August, 1995. Volume calculations include both the subaerial and submarine portions of Folly Beach; beachfill material deposited immediately offshore of the beach (above

-3m to -4m NGVD) was not considered a sediment loss, even though, by some measures, this cross-shore sediment transport would decrease the value of the beach. A majority of the 413,000 m³ should therefore represent a loss of sediment due to longshore gradients in longshore sediment transport. However, other factors such as aeolian sediment transport, transport by tidal currents, and sand deposition well offshore of the beach could have contributed to the loss or gain of sediment. The shoreline model predicted a loss of 302,000 m³ for the same time period. Had a larger empirical sediment transport coefficient been used, to account for the relatively fine sand at Folly Beach, this volumetric prediction would have been more accurate.

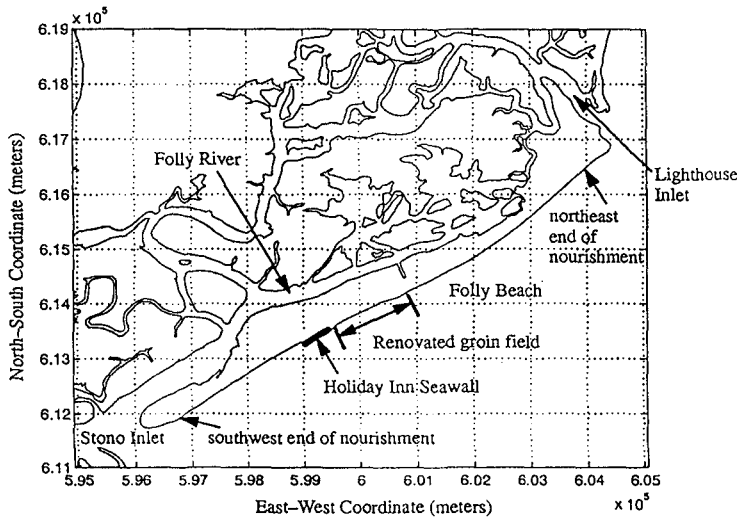


Figure 9. Map of Folly Island, S.C.

Conclusions

The laboratory observations regarding wave height and beachfill geometry shown in Table I agree with conventional wisdom on beach nourishment design. The observed weak dependence of sediment transport (and beachfill lifetime) on beach slope is not widely accepted, though it has been observed by other researchers, such as Kamphuis (1991). On the other hand, the observed positive correlation between wave period and beachfill lifetime is contrary to Kamphuis (1991). This discrepancy merits further study; though shorter waves impact on the shoreline with greater frequency, longer waves possess greater energy.

Results of the laboratory study suggest that relatively small-scale physical models of coastal sediment transport can yield useful qualitative information on shoreline and beach profile changes, though the magnitude of sediment transport rates may be greatly influenced by scale effects. The laboratory models cited in this study evolved similarly to prototype projects.

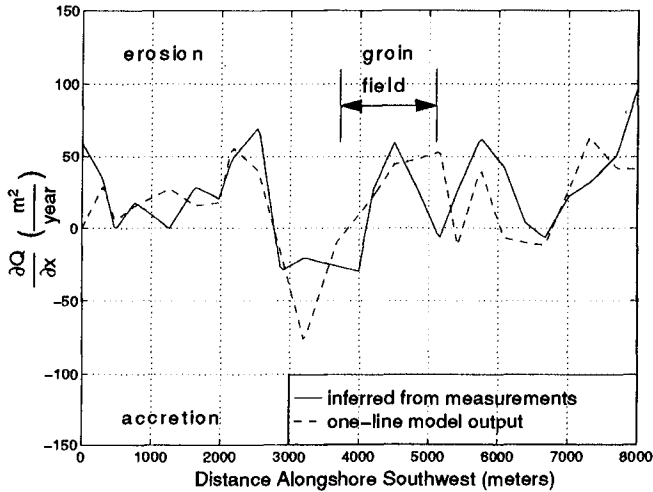


Figure 10. Comparison of One-Line Model Results to Field Measurements

The use of simple, one-line shoreline models in this study indicates that such models are adequate tools for predicting the volumetric redistribution of beachfill material. More rigorous, three-dimensional models of beachfill evolution are a worthy goal; however such models are equally, if not more, limited by present uncertainties in prediction of sediment transport.

The CERC equation for longshore sediment transport is adequate for predicting qualitatively the longshore trends of longshore sediment transport at both laboratory and field scale. The equation is a fair predictor of the magnitude of longshore sediment transport at field scale but requires calibration at small scales. Comparison to laboratory data suggests that the Kamphuis equation for longshore sediment transport is slightly more accurate than the CERC equation. Because of the possibilities of measurement error and scale effect with the laboratory study, this finding is inconclusive.

Based on limited laboratory and field-scale beach nourishment modeling, the analytical treatment of refraction seems to be an efficient method of including wave transformation in one-line models. This method may be considered by engineers for use in lieu of more rigorous, numerical approaches to wave transformation. However, in cases where a complex bathymetry exists (and accurate, high resolution survey data are available), a good numerical wave model is likely to give a better representation of the spatial variability of the wave climate. But again, the beachfill modeling as a whole is only as good as the "weakest link," so unless longshore sediment transport can be reliably predicted, extensive efforts at wave modeling may be unwarranted.

List of Symbols

The following symbols are used in this paper:

A =cross-sectional area of beach profile;
 B =berm height;
 C_g =wave group velocity;
 C_r =wave celerity at toe of beachfill;
 C_c =wave celerity at depth of closure;
 D_{50} =representative grain size;
 g =acceleration of gravity;
 H_s =significant wave height;
 h =depth to which longshore sediment transport affects beach profile;
 K =empirical longshore sediment transport coefficient;
 L =length of beach nourishment;
 m =beachface slope;
 p =sediment porosity;
 Q =volumetric longshore sediment transport rate;
 SG =sediment specific gravity;
 T =wave period;
 T_p =wave period at peak of frequency spectrum
 t =time;
 x =longshore coordinate;
 y =cross-shore location of shoreline;
 β =local contour or shoreline orientation, relative to North;
 κ =ratio of wave height to water depth at breaking;
 θ =angle between wave orthogonal and local shore normal.

References

- Brooks, R.M., and Brandon, W.A., 1995. *Hindcast Wave Information for the U.S. Atlantic Coast: Update 1976-1993 with Hurricanes*. U.S. Army Corps of Engineers. Waterways Experiment Station.
- Dalrymple, R.A., 1988. "Model for refraction of water waves." *J. Waterway, Port, Coastal, and Ocean Engineering*, 114(4), ASCE, New York, N.Y., 423-435.
- Dean, R.G., and Yoo, C., 1992. "Beach nourishment performance predictions." *J. Waterway, Port, Coastal, and Ocean Engineering* 118(6), ASCE, New York, N.Y.
- Dean, R.G., and Yoo, C., 1994. "Beach nourishment in presence of seawall." *J. Waterway, Port, Coastal, and Ocean Engineering* 120(32), ASCE, New York, N.Y.
- Ebersole, B.A., Neilans, P.J., Dowd, M.W. 1996. "Beach-fill performance at Folly

Beach, South Carolina (1 year after construction) and evaluation of design methods." *Shore and Beach*, Jan. 1996.

- Hansen, H., and Kraus, N.C., 1989. *GENESIS: Generalized Model for Simulating Shoreline Change*. Coastal Engineering Research Center Technical Report CERC-89-19, U.S. Army Corps of Engineers, Vicksburg, MS.
- Kamphuis, J.W., 1991 "Alongshore sediment transport rate." *J. Waterway, Port, Coastal, and Ocean Engineering*, 117(6), American Society of Civil Engineers, New York, NY, 624-640.
- Kamphuis, J.W., and Meyer, R.M., 1976. "Three dimensional tests on dynamic equilibrium and artificial nourishment." *Proc. 15th Coast. Engineering Conf.*, ASCE.
- Kamphuis, J.W., Davies, M.H., Nairn, R.B., and Sayao, O.J. (1986). "Calculation of littoral sand transport rate." *Coastal Engineering*, 10, 1-21.
- Kirby, J.T. and Dalrymple, R.A., 1994. *Combined Refraction/Diffraction Model: REF/DIF1*. Center for Applied Coastal Research. Department of Civil Engineering, University of Delaware, Newark, DE.
- Komar, P.D. and Inman, D.L. 1970, "Longshore sand transport on beaches, *Journal of Geophysical Research*, v.75, No. 30, Oct. 20, 1970.
- Nielsen, P., 1988. "Comparison of a numerical model for longshore sediment transport with measurements." *Computer Modeling in Ocean Engineering*. Schrefler & Zienkiewicz (eds.) Balkema, Rotterdam.
- Pelnaud-Considére, R., 1956. "Essai de théorie de l'évolution des formes de rivages en plage de sable et de galets." *4th Journées de la Hydraulique, les Energies de la Mer*, Question III, Rapport No. 1, pp.289-298 (in French).
- U.S. Army Corps of Engineers, 1984. *Shore Prot. Manual*, Coastal Eng. Res. Center, Vicksburg, MS.
- Work, P.A. and Dean, R.G. 1995, "Assessment and prediction of beach-nourishment evolution." *J. Waterway, Port, Coastal, and Ocean Engineering*, 121(3), ASCE, New York, N.Y., 182-189.

CHAPTER 229

COASTAL ZONE DYNAMICS DURING ARTIFICIAL NOURISHMENT

Elżbieta Zawadzka¹

Abstract

The nearshore zone of the Hel Peninsula has a hydro-geomorphological system which, together with the influence of the port at Władysławowo, causes permanent erosion of the basal and central part of the peninsula's sea coast. After a period during which traditional methods of coastal defence (seawalls, groynes) were used, a massive artificial nourishment of the dune and beach was realised in the years 1989-1995. The borrow material used was of lagoon and marine origin. The progress of morpho- and lithodynamic processes was evaluated basing on quantitative analyses of changes in topography and granulometry. In the land part of the coastal zone, accretion of deposits resulted in rebuilding of the dunes and beaches. In the nearshore zone, accretion occurred on the beach slope, and resulted in the development of shore terraces and breaker bars (especially the outer breaker bars). This was accompanied, by related with the accretion, processes of erosion in the form of U-shaped troughs. These processes proceeded at small changes in the erosion/accretion (e/a) system of the nearshore zone in the whole region. Smaller input of sandy material into the nearshore zone resulted in gradual return of the e/a system to initial state. If the safety of the peninsula is to be maintained, artificial nourishment must be executed every year. Frequency and volumes of renourishment will depend on the quality of used material. Therefore new sources of borrow material must be sought.

Introduction

Artificial beach nourishment, considered as one of the most environment friendly methods of coastal defence, was used in Poland several times (Basiński, 1992; Basiński & Szmytkiewicz, 1991; Mierzyński, 1985). However, these were experimental pilot projects, realized in small temporal and spatial scale, using rather small amounts of material. In this paper are discussed results of investigations of changes in the coastal environment caused by a large-volume nourishment project implemented on the Hel Peninsula coast (Fig. 1). The decision to use artificial nourishment resulted from the catastrophic state of the basal part of the peninsula, and from the imminent danger of flooding of the hinterland of the narrow and

¹Dr., Department of Maritime Hydrotechnics, Maritime Institute, Abrahama 1, 80-307 Gdańsk, Poland.

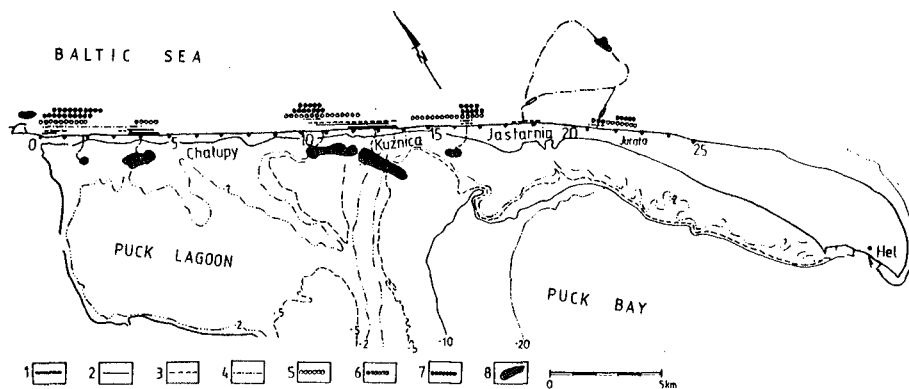


Fig. 1 Location of beach nourishment and borrow sites, Hel Peninsula 1989-1995. (1-7 - years of nourishment; 8 - borrow sites)

intensely eroded dune, at limited width of the spit. Strong storms in the autumn and winter of 1988/1989 resulted in a danger of breaking of the peninsula at 2-3 places.

The Hel Peninsula is an accumulative spit of 36 km length, which is an extension of the mainland to SE, and which shelters from the north the Gulf of Gdansk. In historical times it was broken several times. Analysis of maps from the period 1908-1978 (Zawadzka, 1994) has shown that the average rate of coastline retreat along the peninsula is -0.6 m/year (Fig. 2a). Processes of erosion in the period 1980-1987, directly preceding the nourishment project, are characterized by a similar spatial distribution as in the 70-year period 1908-1978 (Fig. 2b). The foredune became nearly completely eroded in the basal and central part of the peninsula along 17 km of coastline, resulting in a danger of breaking of the peninsula, especially at these stretches where the width of the spit did not exceed 100 m. In this situation, the decision was taken to use artificial nourishment as the most effective and least ingereventive method of coastal protection (Cieślak, 1994).

In the years 1989-1995 the largest project of artificial nourishment of a dune coast in Poland was realized. On the seaward coast of the Hel Peninsula, along a length of 23.4 km, 8 mln. m^3 of sand was supplied, gradually widening the range of sand suppletion works, which in total were executed along 14 km of the coastline. The material for nourishment was taken from the Puck Bay, from the sand trap at the port at Władysławowo, and from borrow sites at sea located to NE of the central part of the peninsula and to NE of Cape Rozewie (Zawadzka, 1993). In order to determine the effectiveness of the method, a comprehensive program of measurements and investigations was systematically realised. It included investigations of sediments and morphology of the seabed, beach and dune along the first 23 km of the peninsula's coastline. Each year 800-1000 sediment samples were analysed. Analyses of the variability of the dune, beach, beach slope, breaker bars, interbar troughs and of the deepwater slope to 10 m water depth were made. Comparison of maps of statistical grain size indicators (median diameter, sorting, skewness, steepness) on the background of proceeding changes in the shape of the nearshore bed and of its morphological forms, and taking into account the hydrodynamic conditions, has

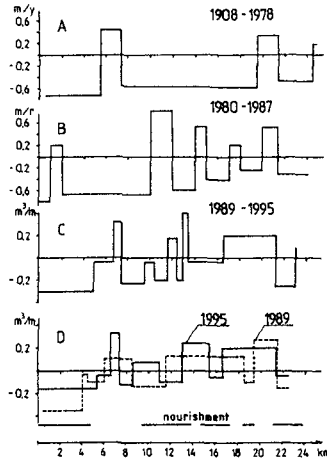


Fig. 2 Changes of coastline position, Hel Peninsula, 1908-1978, 1980-1987 and changes of the fill coefficient of the nearshore zone to -10 m MSL, 1989-1995. A-B - Zawadzka, 1990; C-D - Dubrawski, 1995.

shown that independently of the local short term changes connected with artificial sand supply, in the coastal zone there is a hydro-geomorphological system, which forms relatively stable erosion/accretion trends in the coastal zone - also in conditions of artificial nourishment. Nourishment works carried out for 7 years have not resulted in a basic change of the general trend within the erosion/accretion system in the Hel peninsula region. Generally erosion has decreased, but its spatial distribution remained almost the same (Figs. 2c, 2d).

Characteristics of supplied material

For the nourishment material dredged from the Puck Bay and from sea borrow sites located at sea was used (Fig. 1). Deposits accumulated in the Puck Bay consist of fine and medium sand, well and medium sorted, and the median diameter (M_d μm) ranged between 139 and 237 μm . Marine material consists of medium sand of M_d 290 μm , medium sorted. Comparative analysis of the "bay" borrow material and native material, using the R_j and R_A indicators (Manual, 1990), shows that these two sands do not fit satisfactorily. Highest stability of the supplied material may be attained when 2-3.5 larger quantities of material are nourished than the volumes resulting from calculations of deficiency of sand material in the basal part of the peninsula. In the central part, material borrowed from marine sources may be used in 1:1.5 (2) proportion. Grain size parameters of borrow material from the Puck Bay suggest that mass transport of that sand may proceed at speeds of 12-20 cm/s.

Nourishment started in 1989 at two sites: at Chałupy (km H3.5-4.5) and at Kuźnica (km H11.9-13.7). By 1993, about 5.85 mln. m^3 of sand were supplied, and the nourishment works were executed on 5 stretches of total length of 11.1 km. At the Chałupy nourishment field the resultant average volume of nourishment per metre of coastline was 510 m^3 , at Kuźnica it was 730 m^3 . On the other fields the average

volume of nourishment per metre of coastline ranged between 100 and 330 m³. In the next two years, until 1995, the length of directly nourished coastline grew to 14 km, and the total amount of sand supplied since 1989 increased to 8 mln. m³. Most intensive nourishment was still realized at Chałupy and Kuźnica due to the highest deficit of sediments in the nearshore zone, and because of the limited stability of the nourished material.

Morphodynamics and lithodynamics of the region

The shore and the nearshore zone of the Hel Peninsula are characterized by a semistable erosion/accretion system, with a strong predomination of erosional trend resulting from the hydrodynamic conditions in the region (Fig. 2).

The stable predisposition to erosion along given stretches of the coastline are caused by trough-like forms present in the sea bottom, which are obliquely oriented at an angle of 25-27° to the shoreline. In the western part of the peninsula they are of glacialfluvial origin (Tomczak, 1994), in the eastern part they are remnants of the Yoldia Sea coastal systems (Musielak, 1989). Location of these forms influences the occurrence of areas with permanent erosion of the sea bottom and shore. The stability of the erosion/accretion system is confirmed both by cartometric analysis of coastal change (Zawadzka 1990, 1994) and by means of modelling of hydrodynamic processes in the nearshore zone (Skaja & Szymkiewicz, 1995). When wind blows from the west and north sectors, dangerous to the west and central part of the peninsula wave and current systems are generated. In extreme conditions current velocity may reach 2 m/s. Wind from the east results in higher energy supply to the east and central parts.

The variability of sediment transport characteristics in natural conditions, in the different zones of bottom and shore, influences the intensity with which the artificially nourished material is displaced in given meteorological conditions, resulting in different reactions of the erosion/accretion system of the coastal zone.

Transformation of morphological forms of the coastal zone

The caused by artificial nourishment increase of volume of the beaches resulted in adaptive transformation of the adjoining forms of the shore and nearshore zone.

Accretion of nourished material on the beach and dunes was accompanied by an appearance of erosion along stretches east (downstream) of the nourishment fields. Gradually these phenomena moved also into the nearshore zone.

After the first season of nourishment, along 14% of the observed coastline well developed shore terraces were present, and their average width was 75 m (Dubrawski, 1995). After 4 years terraces occurred along 45%, and after 6 years - even along 76% of the coastline (Table 1).

The intensive development of inner and outer bars took place after four years of artificial nourishment, during which 5.8 mln. m³ of sand were supplied. One of the most significant features of the transforming during the artificial nourishment seabed was the generation of rarely occurring in the natural bottom profile U-shaped troughs. Maximum development of the interbar U-troughs also was observed after 4 years of

nourishment. The maximum number of shore U-troughs appeared after 6 years of nourishment, suggesting increased current velocities in the shallow part of the nearshore zone.

Table 1. Changes of parameters of morphological forms in the nearshore zone, 1989/1995 (Dubrawski, 1995)

Year	Shore terraces		Shore slope		shore U-trough		Inner bar lower class		interbar U-trough		Outer bar higher class	
	%	l [m]	l [m]	slope	%	l [m]	%	[m ²]	%	l [m]	%	[m ²]
1990	14	75	133	1:33	4	76	26	37	8	144	33	303
1993	45	76	141	1:37	11	80	12	43	21	108	52	332
1995	76	81	135	1:33	19	85	17	43	9	71	45	335

The decreased volumes of nourishment in the period 1994-1995 resulted in stronger erosion on the beach and in smaller differentiation of morphological forms in the nearshore zone and of grain size composition within these forms, which suggests a gradual return to the state before artificial nourishment (Dubrawski, 1995). Analysis of the average crossshore profile showed stabilisation of the volume of the inner bar after 4 years of nourishment, and a steady development of the outer bar where redeposition of fine sands occurs. The shore slope increased its volume by 4.8% of the volume of nourished material, attaining maximum after 4 years of nourishment. Similarly to shore terraces, in the next years it was subjected to gradual reduction.

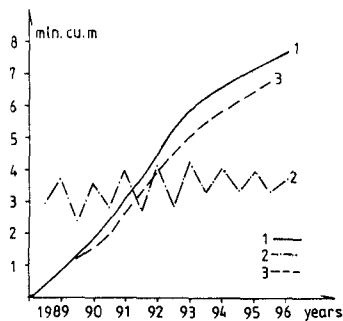


Fig. 3 Nourished stretches and net beach volume (1 - sum of annual suppletion; 2 - changes of dune and beach volume; 3 - sum of annual losses)

The balance of changes of the shore, evaluated basing on measurements carried out twice every year, shows that during the first 3.5 years, in spite of repeated nourishment, the volume of dunes and beaches remained at the level of 1989 (Fig. 3). When intense nourishment was carried out after strong storms of winter 1992/93, and after the relatively mild wind and wave conditions of the 1994/95 season with higher than average percentage of winds from the east, did result in stabilisation accretion on the beach and dune. After the annual amount of nourished material was reduced, the volume of material contained in the beach and dune decreased in spite of a

consecutive mild winter season. In effect of 6.5 years of artificial nourishment, the volume of the shore (beach and dune) increased by about 1 mln. m³.

Lithodynamics in conditions of artificial nourishment

Grain size analysis of bottom surface samples, taken each year from the seabed in the whole region before each annual nourishment works, show that the mean value of the median diameter has not changed significantly. Before the nourishment works began, the belt-like distribution of mean and fine sands was locally disturbed by zones of coarse sand and fine gravel, which indicated areas with higher wave and current activity. In these areas erosion of shore and bottom was observed (Fig. 4).

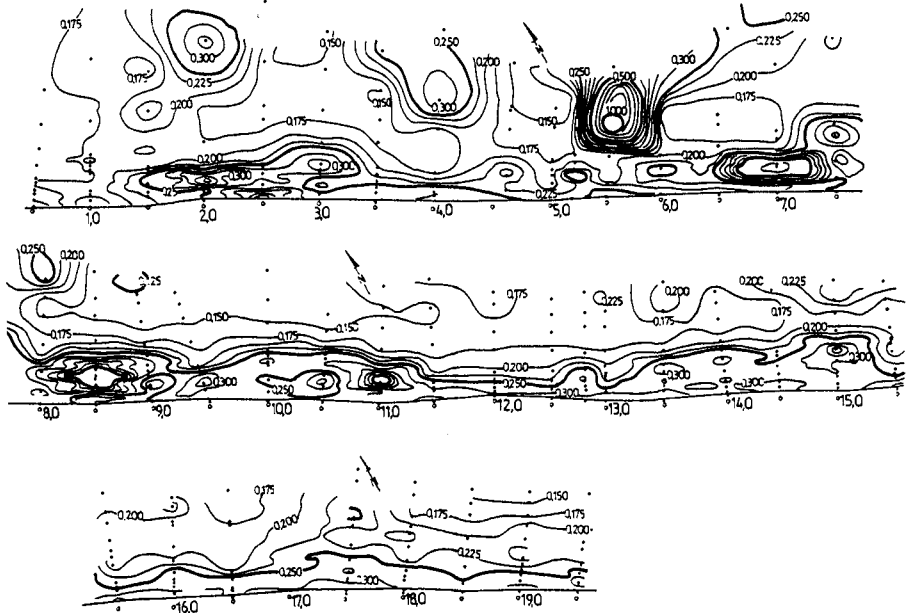


Fig. 4 Plan of median diameter (M_d mm) of bottom surface sediments in the coastal zone of Hel Peninsula, 1990

After 6 years of artificial nourishment, grain size composition shows changes of sediment parameters in the central part of the peninsula, which became supplemented with fine sands, at maintained erosional trend in the central part and at development of erosion along the basal part. The grain size composition of bottom surface sediments in the 10-12 m water depth zone was characterized, after 6 seasons of nourishment with sand from the Puck Lagoon (Puck Bay), by a slight decrease of the median diameter from 253 μm to 238 μm in 1993 and to 225 μm in 1995. The median diameter of beach deposits, which were successively supplemented with mean and fine sand, was after three years of artificial nourishment nearly the same as in prenourishment conditions.

The average grain size composition of deposits in the nearshore zone remained nearly unchanged through 3 years of nourishment. In the fourth year, due to erosion of nourishment fields during strong storms of the 1992/93 season, beach deposits

became slightly coarser and the nearshore zone was supplemented with large amounts of fine sand, and the median diameter of bottom surface deposits in the nearshore zone decreased to $206 \mu\text{m}$. It may be supposed that the stability of nearshore zone

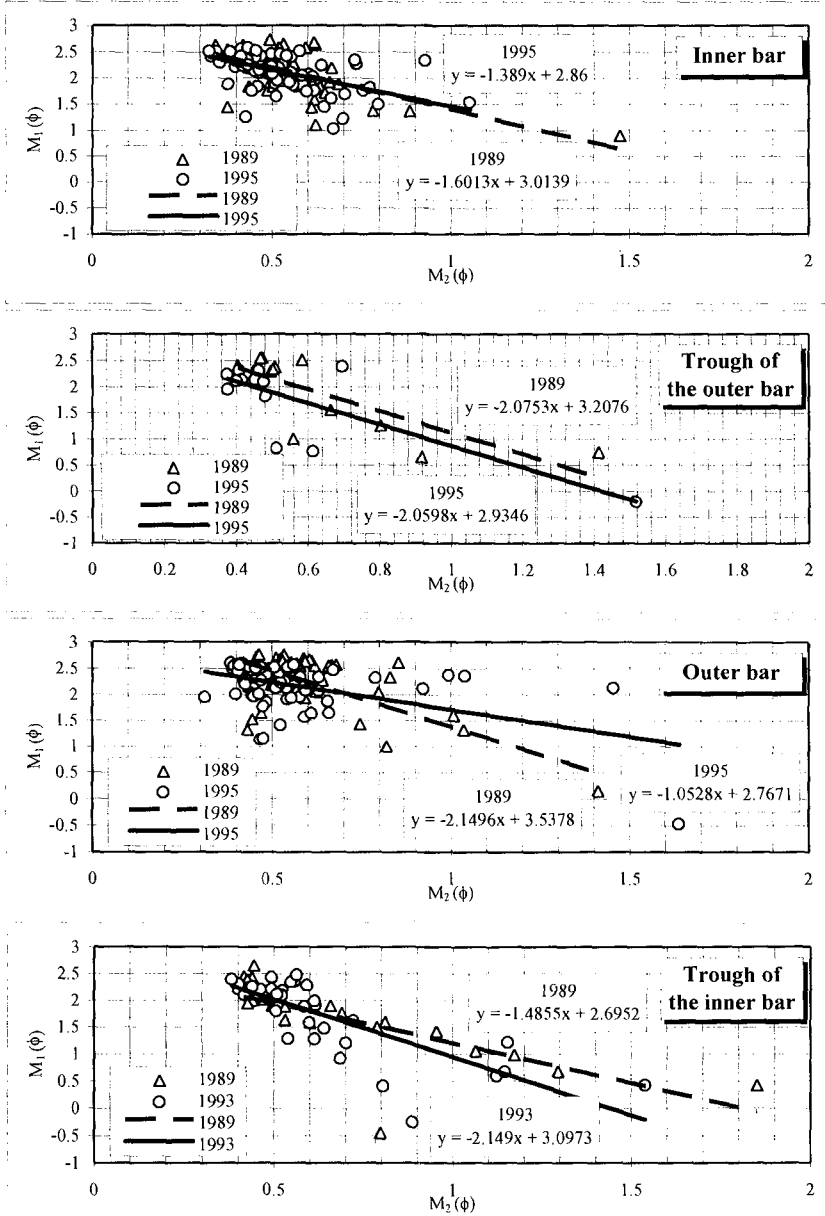


Fig. 5 Relationship between mean diameter (M_1) and standard deviation (M_2) of sediments in breaker bars and bar troughs, Hel Peninsula, 1989-1995

forms built of artificially supplied material, which was finer than the natural material, is smaller than in case forms built of material present before the nourishment project, and that they will quicker undergo transformation.

Small changes in the grain size (evaluated using mean parameters) of the nearshore forms during the nourishment are proof of an inner stability of the hydrogeomorphological system and that the finest particles are displaced outside the active zone. However, at the same time within each of the morphological forms in the nearshore zone proceeded distinct granulometric changes, indicating a different distribution in the wave and current field (Basiński & Szmytkiewicz, 1991). Development of the shore terraces and the breaker bar zone was accompanied by deepening and widening of the troughs. Increased nearbottom current velocities in the troughs, which increase is largest in the trough between the inner and outer bar, suggest a transformation of the erosion/accretion system (Fig. 5). The development of interbar troughs is connected with the existence of gradient currents (Pruszek & Zeidler, 1995). Probably gradient currents increased in the nourished areas, and in effect U-shaped troughs developed.

The median diameter in the interbar troughs increased by 150 μm , from 280 μm in 1989 to 430 μm in 1995, in spite of relatively mild hydrodynamic conditions in the last winter season. After the strongest storm season 1992/93 the median diameter in the troughs was even up to 480 μm . In areas of most distinct development of U-shaped troughs, the median diameter exceeded 1000 μm , which could be related with current velocities of over 1 m/s (current velocities require confirmation by field measurements).

The decrease from 260 μm to 220 μm of median diameter of sediments building the breaker bars indicates that the accumulated in them material will be moved at lower initial current velocities. This fact may be the reason of quicker transformation of the outer breaker bars.

In conditions of a growing amount of supplied artificially material, of steadily growing length of nourished stretches, and of variable hydrodynamic conditions, the lithodynamic system of the Hel Peninsula nearshore zone was characterized by a variable spatial distribution of fields of erosion and accretion. Basing on analysis of the changes of median diameter of sediments and their mean values, calculated for each of the morphological zones (beach, shore slope, interbar troughs, breaker bar zone and deepwater slope), areas with finer or coarser sand were determined. This allowed to draw plans of the surface erosion/accretion system of the nearshore zone, and to evaluate its dynamics.

Before artificial nourishment works started, there were 4 erosional areas along the basal part of the peninsula, covering all morphological zones: the shore slope, breaker bar zone and the deepwater slope. Along the central part of the peninsula, the shore slope and the breaker bar zone were eroded. Along the eastern part, alternately located zones of erosion and accretion occurred, indicating routes of sediment transport to the deepwater slope and then out of the observed area.

In spring 1990, after the first artificial nourishment campaign, the initial system of erosion/accretion areas did not change along the basal and central part of the peninsula, though local accretion of the supplied material in the breaker bar zone and

on the shore slope was observed. East of the fill field at Chałupy and Kuźnica (central part) the breaker bar zone was supplemented with fine sand material, at simultaneous erosion of the deepwater slope (Fig. 6). Influence of the fill material was observed in the interbar troughs and on the outer bar to 8 m water depth and up to 1.5 km from the fill field. On the other hand, segregation of the nourished material resulted in an increase of coarse sand and gravel on the beach and at the water line. No significant change of grain size was observed on the outer breaker bar.

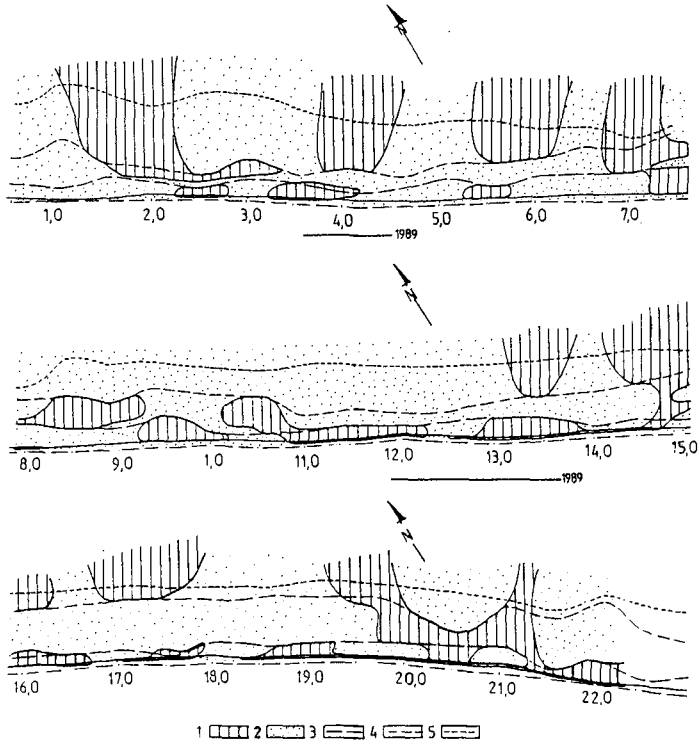


Fig. 6 Erosion/accretion system of surface sediments, Hel Peninsula, 1990
(1 - areas with erosive trend; 2 - areas with accretional trend; 3 - range of shore slope; 4 - range of breaker bar zone; 5 - 10m depth contour)

After two years of nourishment (in 1991), while distinct accretion occurred in the shallow water and breaker bar zones, also development of areas of erosion of the breaker bars and deepwater slope was observed east of the fill field located in the basal part of the peninsula. In the central part, zonal accretion on the shore slope and on the breaker bars was observed, accompanied by erosion in the same zones east and west of the fill field. Rhythmically occurring erosion/accretion surfaces, encompassing the breaker bar zone occurred in the eastern part, suggesting a development of circulation cells of 1 km order. In the Chałupy area, in effect of segregation of the material, the beach became saturated with mean and fine sand, while percentage of mean and coarse sand grew on the shore slope. The process of washing out of the shore slope proceeds at simultaneous enriching of the breaker bar zone and of the deepwater slope with fine sediments. The influence of the fill material was observed

in the breaker bar zone 2 to 3 km east of the fill field. Further migration of the fill material is limited by a convex bottom form at km H7.0-7.5, which is considered to be a natural boundary of a lithodynamic unit of the nearshore zone. Observations at Kuźnica showed that the fill material is transported over larger distances than in case of the Chałupy field. Within the shore slope and inner bar zones the material was transported 3 km, and in the outer bar zone - about 5 km to the east of the fill field. East of the Kuźnica fill field two independently occurring in 1990 areas of scour, one on the shore slope and the other on the deepwater slope, were transformed into an oblique to the coastline and cutting through the breaker bars zone of intense transport.

After the third year (in 1992) of artificial nourishment of the western stretch of coastline with material from the Puck Bay, supplemented with material from the sand trap at the port at Władysławowo, the inner bar and its inner trough became richer in fine sand. Deposition of sediments grew also locally in the outer bar zone. The large supply of material from the fill resulted in a shallowing of the interbar trough and in supplementing the balance of sediments up to about 1.5 km east of the fill field. Areas of bottom scour formed in 1991 became filled with sands of 225-250 μm diameter. Finer material (less than 150 μm) was deposited in the 8-10 m water depth zone about 3 km east of the fill field. Accretion in the area of transport of the fill material was always accompanied by erosion, which indicates a nonuniform character of the transport. In 1992, due to the continuing suppletion of the shore at Kuźnica, the system of shore terraces became distinctly developed, and the median diameter of sediments accumulated in them was 275-300 μm . The shallowing of the shore slope was accompanied by deepening of the trough before the inner bar and in its transformation from a V shape to a U shape. Suppletion of the inner bar occurred at a distance of 1 km and of the outer bar - at a distance of 2.5 km east of the fill field. The change of zones of wave energy dissipation resulted in a local rebuilding of the double bar profile into a single bar profile, which was built of medium sands. The new system of eroded and accreting bottom surfaces suggests a distinct stabilisation of lithodynamic processes over a stretch of 5-6 km east of the fill field at Kuźnica.

Intensive development of large erosive forms, encompassing nearly all the morphological zones appeared after 4 years of nourishment (1993), pointing to the development of oblique to the coastline routes of sediment transport. The field at Chałupy still supplemented the coastal zone to a distance of 2.5-3.0 km east of the field, and to a water depth of 6 m. In the nearshore zone a strip of 350 m width seaward of the water line, and reaching to 4 m water depth, was supplemented at a length of about 3.5 km. Predominance of wind from the NW sector in autumn and winter of 1992/93 resulted in the generation of distinct "upstream" zones and of new routes of sediment transport out of the nearshore zone. The obliquely situated erosive areas were characterized by larger grain sizes than the average values determined for the whole observed area, and crossed all analysed nearshore zones. The larger rates of loss of fill material over the deepwater slope occur, among others, along the defined routes of intensive transport (Fig. 7).

In the last year of observations (1995), in the nearshore zone of the basal part of the Hel Peninsula accretion occurred over large areas of the shallow water zone adjacent to the fill field. Locally in the central part erosive areas appeared, independently of the development of massive breaker bars, which are a transient zone

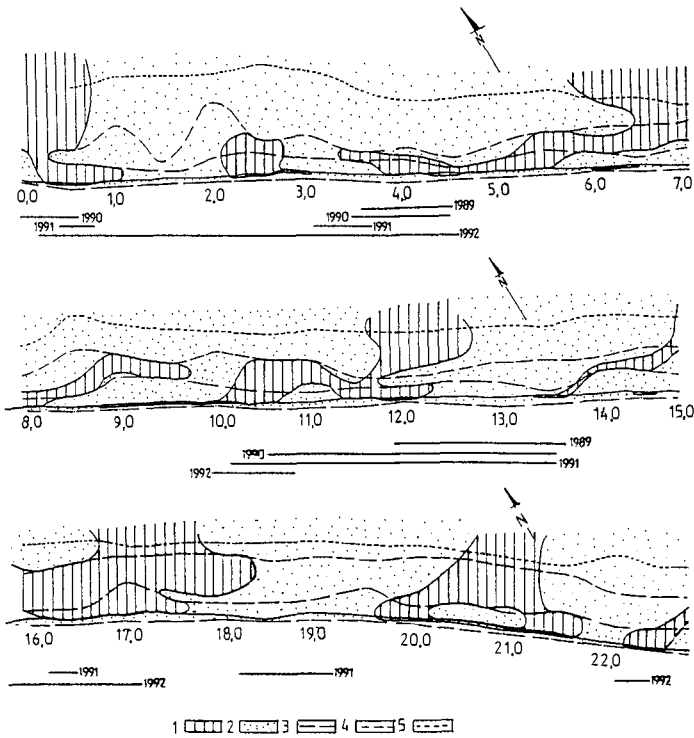


Fig. 7 Erosion/accretion system of surface sediments, Hel Peninsula, 1993 (explanations as in Fig. 6)

of deposition. Also distinct zones of higher energy appeared, which caused scouring of breaker bars east and west of the fill field at Kuźnica, formation of deep interbar troughs, and erosion on the deepwater slope. Hydrodynamic conditions at the break of 1994/95 resulted in the formation of two distinct circulation cells in the central and eastern region (Fig. 8). The direction of sediment transport out of the intensely artificially nourished region in the central part suggests an influence of a trough form situated obliquely to the coastline. A very similar arrangement of sediment transport routes (accretion in the central part of the system and erosion in the outer zones) was observed in the Jastarnia-Jurata region. The distribution of the eroded and accreting surfaces in the nearshore zone suggests that bottom forms farther offshore and deeper situated influence the nearshore zone, steering circulation at winds from the NW to NE sector.

The highest percentage of nearshore surface, subjected to processes of erosion in the breaker bar zone and on the shore slope, occurred before artificial nourishment began (Table 2). The area of redeposition of the sediments was located on the deepwater slope below the breaker bar zone. Accumulation on the beach, shore slope and in the breaker bar zone caused increased erosion of the deepwater slope. After a period of strong storms at the break of 1992/93, processes of erosion increased again in the shallow part of the nearshore zone (shore terraces and breaker bars), but weakened below the breaker bar zone due redeposition of the sediments.

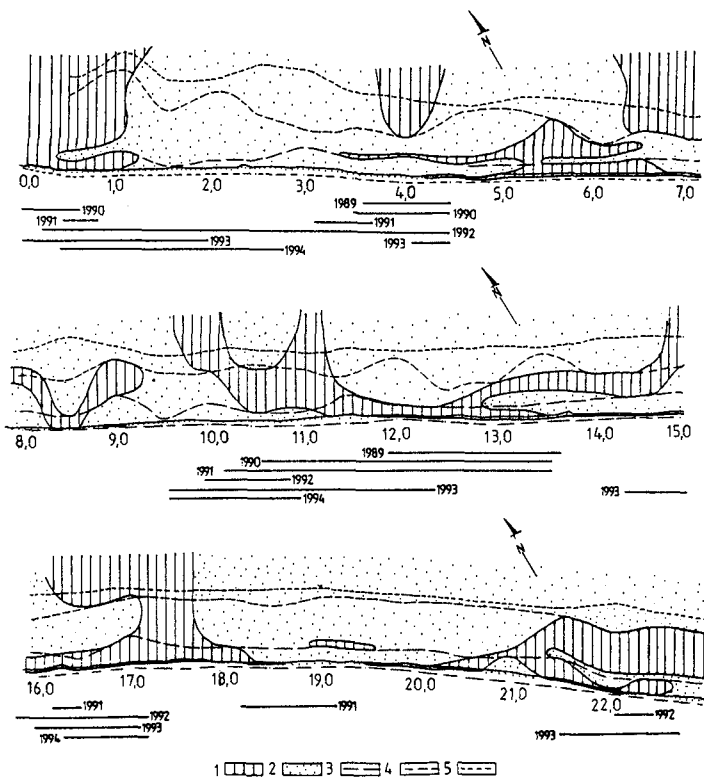


Fig. 8 Erosion/accretion system of surface sediments, Hel Peninsula, 1995 (explanations as in Fig. 6)

Table 2. Percentage of eroded nearshore zone surface, Hel Peninsula, period 1989-1995 (on the basis of granulometric parameters)

Year	Erosion (in %) of nearshore zone (to 10 m water depth)		
	Whole nearshore (0.0±-10.0 m MSL)	Shore slope & breaker bar zone	Deepwater slope
1989	35.2	46.5	20.5
1990	21.0	16.9	33.7
1991	22.0	21.1	27.5
1993	29.0	36.4	19.4
1995	23.4	22.6	27.9

Obtained results show that in intensive hydrodynamic conditions the shallow part of the nearshore zone and the breaker bar zone was being destroyed over 36 to 46 % of its surface. Stabilisation on the shore slope and breaker bars is connected with development of processes of erosion on the deepwater slope, indicating that in the erosion/accretion system proceed compensatory processes.

Summary

The six years of artificial nourishment along the Hel Peninsula, due to the restoration of dunes and to the improvement of sediment balance in the coastal zone, resulted in higher safety of the coast and its hinterland. The total volumetric change in the strip from dunes to breaker bars inclusive was over the whole period 1.8 mln. m³, i.e. about 28% of the total volume of the nourishment in the period 1989-1994 (Cieślak et al, 1995), in that about 12.5 % remained in the dunes and beach, and 15.5 % remained in the shore terraces and breaker bar zone. The rest was transported outside of the investigated area. Significant amounts of fill material were accumulated in the developing shore terraces, which at the end of the analysed period covered 3/4 of the length of the observed coastline. Terraces improve the stability of beaches and dunes because they dissipate wave energy.

Breaker bar height increased by 11.8%, and cross-section area by 22% in reference to the 1989 state. Formerly present stretches with no breaker bars disappeared. A decisive change in the shape and volume of breaker bars took place. Participation of small breaker bar forms decreased. Massive breaker bar forms developed, especially after the fourth year of artificial nourishment. During the last two years of suppletion, when volumes of supplied fill material were reduced, the percentage of breaker bars of each of the volumetric classes began to stabilise at the levels of the period preceding the nourishment works, indicating a predominant influence of hydrodynamic processes. The grain size composition of fill material indicated that it may nourish especially zones with lower hydrodynamic activity. Gradual reduction of massive breaker bars caused by reducing the volume of annual artificial nourishment will result in the future in higher levels of danger to the coast. Development of shore terraces and breaker bars was connected with local changes in the erosion/accretion system, which appeared especially through the generation of U-shaped troughs and areas of scour downstream of the fill fields and terraces.

Observed morpho- and lithodynamic changes of the coastal zone during artificial nourishment are of adaptative character and proceed within an existing, well established hydro-geomorphological system of the Hel Peninsula. Gradual reduction of the volume of artificially supplied to the erosion/accretion system material will result in a slow return of the shore and seabed forms to the state present before artificial nourishment began. In the conditions of prevailing winds from the west sector and of generated by them waves and currents, and of the system of macroformations of the outer part of the coastal zone and of the breaker bar zone, there is a natural predisposition to transport a part of the sediments of the dynamic layer to east and north. This requires repeated artificial nourishment in the west and central part of the peninsula, in order to ensure relative stability of permanently eroded stretches, especially when too fine fill material is used. In periods when prevail winds from the east, morphodynamic processes in the erosion/accretion system become stabilised.

The basic recommendation, resulting from grain size and sediment transport analyses, is that borrow sites with grain sizes better fitted to open sea hydrodynamics should be sought. Sand from the Puck Bay is very easily moved, and only for a short period supplement the areas with sediment deficit. Material with parameters ensuring 40-50% better stability in the whole strip from shore to outer bar than the

presently used sand should be used. Maintaining the present state of the coast requires annual nourishment of the order of 0.6-1.0 mln. m³.

The presented results show that artificial nourishment, as any other method, has a limited range of application, and - as any other technical ingerence into the coastal zone - causes changes in the wave and current system which result in a development of negative morpho- and lithodynamic effects.

References

- Basiński, T. 1992. Experience from shore protection of the Hel Peninsula. *Proc. Int. Coastal Congress*. Kiel, p.639-647.
- Basiński, T. & Szmytkiewicz M. 1991. Effectiveness of different artificial nearshore and beach nourishment technologies. *Proc. of the 3rd Int. Conf. on Coastal and Port Develop. Countries*, Mombasa.
- Cieślak, A. 1994. Concept of Hel Peninsula coast protection. *Symp. on Changes of Coastal Zones, Polish Coast '94*, Gdynia p.57-59.
- Cieślak, A., Semrau, I., Michowski, A. & Zawadzka, E 1989-1995 Stage. Complex protection of Hel Peninsula. (in Polish). Int. report IM WW4884, Gdańsk.
- Dubrawski, R. 1995. Analysis of shore and offshore of Hel Peninsula during beach nourishment in 1989-1995. (in Polish). Int. Rep. IM WW 4864, Gdańsk.
- Manual of artificial beach nourishment 1986. Center of Civ. Eng. Research. Codes and Specification, Report 130, Delft.
- Mierzyński, S. 1985. Experimental artificial nearshore zone nourishment of the Hel Peninsula. (in Polish). *Materiały na sesję naukową*, IM, Gdańsk.
- Musielak, S. 1989. Remarks on the Genesis of the Hel Peninsula in the Light of New Data. *Studia i Materiały Oceanologiczne* 56, p.311-322.
- Pruszek, Z. & Zeidler, R. 1995. Sediment Transport in Various Time Scales. *ICCE '94, 24th Int. Conf. on Coastal Eng.* Kobe, p.570-571.
- Skaja, M. & Szmytkiewicz, M. 1995. Calculations of waves and currents along the Hel Peninsula. (in Polish). Int Rep. of IBW-PAN, Gdańsk.
- Tomczak, A. 1994. Hel Peninsula - relief, geology, evolution. *Symp. on Changes of Coastal Zones, Polish Coast '94*, Gdynia, p.45-49.
- Zawadzka, E. 1990. Determination of coastline changes. (in Polish). Int. Rep. IM WW 4571, Gdańsk, pp.76.
- Zawadzka, E. 1993. Sedimentological investigation of material from borrow sites in the Puck Bay. Int. Rep IM WW 4799, Gdańsk
- Zawadzka, E. 1994. South Baltic coastal changes during the last 100 years. *ICCE'94 Int. Conf. on Coastal Eng.* Kobe. Book of Abstracts pp.568-569.

CHAPTER 230

Dune Damage Curves and Their Use to Estimate Dune Maintenance Costs

David R. Basco¹ and Cheol S. Shin²

Abstract

A beach profile numerical model is employed to calculate the change in dune cross-section for a wide range of increased, water level events. The volume loss in dune cross-section increases with relative increase in storm surge elevation above the design water level. These "damage curves" for dunes are analogous to rubble mound damage curves created by excessive wave energy above the design wave height.

The results are applied in the design of a protective, beach-dune structure (with buried seawall as a safety factor) at Dam Neck, Virginia for the US Navy. The damage curves are used to estimate annual dune maintenance costs and hence, total life-cycle costs for this "soft" alternative to shore protection. Interestingly, the dune-beach-buried seawall alternative costs less than a concrete structure using artificial units for armor.

Construction is complete and a three year monitoring project begun so that actual versus theoretical dune damage curves can be determined in the future.

1.0 Introduction

Dunes are "soft" coastal structures that quickly lose cross-sectional volume during elevated, storm surge events. Cross-shore sediment transport, beach profile models permit the development of dune "damage" curves showing the percent dune cross-sectional change, ΔV (damage) versus the relative storm surge level, S compared with the design storm surge, S_D . The dune damage curves can then be used in the classical, convolution integral method to compute annual dune maintenance costs. Life-cycle

¹ Professor of Civil & Environmental Engineering and Director, the Coastal Engineering Centre, Old Dominion University, Norfolk, Virginia 23529 USA

² Instructor, Department of Civil Engineering, Dongshin University, Daeho-Dong, Naju-City, Jeonranam-Do, 520-714 Korea

costs of the "soft" solution for coastal protection (dune-beach alternative) can then be compared with the "hard" alternatives (seawalls, dikes, etc.) on an equal, total annual cost per unit shoreline length basis.

The objective of this paper is to present the results of one analysis using the SBEACH model (Larsen and Kraus, 1989) for the design of a dune-beach restoration project to protect \$95 million of structures and property at the US Navy's, Fleet Combat Training Center (FCTC), Dam Neck, Virginia. Section 2 briefly reviews the available models and key independent variables. The dune damage curves are summarized in Section 3 including safety factors used in dune design. Maintenance costs are determined in Section 4 and a cost comparison with an armored seawall design presented in Section 5. Construction of the entire project has recently been completed and a three year, beach profile monitoring project begun so that the theoretical versus actual dune damage curves can be determined in the future.

2.0 Beach - Dune Erosion Models

Recently, ten cross-shore sediment transport models have been evaluated by Schoonees and Theron (1995). The model developed by Larsen and Kraus, 1989 called SBEACH was found to be "acceptable" on its theoretical basis and in the "best group" category based on the extent of verification with prototype data. It allows sand overwash during elevated water level events so that the total, cross-shore sectional volume is conserved.

The probabilistic design of dunes with examples from the Netherlands are presented by van de Graaff (1989) as illustrated in Figure 1. It was learned (Table 1) that storm surge elevation accounted for about 83 percent of the total variance associated with dune erosion. Wave height, particle size, initial profile shape, storm duration and other factors were far less important. The change in dune cross-sectional area (per unit width) was primarily related to elevated water levels during storm surge events.

Dune damage curves are thus analogous to rubble mound damage curves created by excessive *wave energy* above the design, wave height.

3.0 Dune Damage Curves for Dam Neck, Virginia

Figure 2 shows the location of the Navy's FCTC at Dam Neck, Virginia on the Atlantic Ocean below the City of Virginia Beach.

Using a 50 ft. (15.2m) crest width at elevation +22ft (6.7m) above the City of Virginia Beach datum and 2:1 side slopes produces a unit volume of 30cy per foot ($75\text{m}^3/\text{m}$) above the one percent chance, storm surge event (9.1 ft., 2.8m). This dune cross-sectional (Figure 3) is essentially that originally designed by Headland (1991) and contains fifty percent more sand than the minimum requirement of $540\text{ ft}^3/\text{ft}$ ($50\text{m}^3/\text{m}$) as established by the Federal Emergency Management Agency (FEMA) for breaching of natural dunes.

A nearshore survey taken in May, 1990 was considered representative for the existing bathymetric conditions in the model. The SBEACH model was run with eleven successively higher water level events to cover the return periods between 1

The objective of this paper is to present the results of one analysis using the SBEACH model (Larsen and Kraus, 1989) for the design of a dune-beach restoration project to protect \$95 million of structures and property at the US Navy's, Fleet Combat Training Center (FCTC), Dam Neck, Virginia. Section 2 briefly reviews the available models and key independent variables. The dune damage curves are summarized in Section 3 including safety factors used in dune design. Maintenance costs are determined in Section 4 and a cost comparison with an armored seawall design presented in Section 5. Construction of the entire project has recently been completed and a three year, beach profile monitoring project begun so that the theoretical versus actual dune damage curves can be determined in the future.

2.0 Beach - Dune Erosion Models

Recently, ten cross-shore sediment transport models have been evaluated by Schoonees and Theron (1995). The model developed by Larsen and Kraus, 1989 called SBEACH was found to be "acceptable" on its theoretical basis and in the "best group" category based on the extent of verification with prototype data. It allows sand overwash during elevated water level events so that the total, cross-shore sectional volume is conserved.

The probabilistic design of dunes with examples from the Netherlands are presented by van de Graaff (1989) as illustrated in Figure 1. It was learned (Table 1) that storm surge elevation accounted for about 83 percent of the total variance associated with dune erosion. Wave height, particle size, initial profile shape, storm duration and other factors were far less important. The change in dune cross-sectional area (per unit width) was primarily related to elevated water levels during storm surge events.

Dune damage curves are thus analogous to rubble mound damage curves created by excessive *wave energy* above the design, wave height.

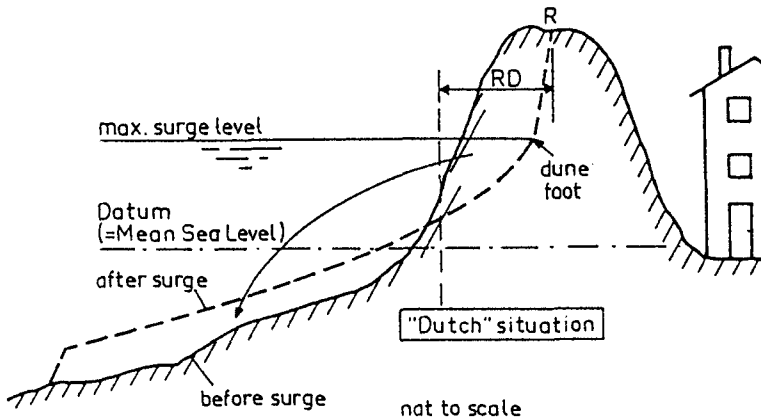


Figure 1 Schematic of Dune Erosion by Elevated Water Levels: Dutch Practice (from van de Graaff, 1986)

Table 1 Relative Importance of Independent Variables on Dune Erosion (from van de Graaff, 1986)

Contribution parameters to variance reliability function

Parameter	Contribution variance reliability function (%)
surge level	82.8
wave height	0.9
particle size	7.3
initial profile	1.3
surge duration	2.6
gust bump	0.0
accuracy computation	5.0

3.0 Dune Damage Curves for Dam Neck, Virginia

Figure 2 shows the location of the Navy's FCTC at Dam Neck, Virginia on the Atlantic Ocean below the City of Virginia Beach.

Using a 50 ft. (15.2m) crest width at elevation +22ft (6.7m) above the City of Virginia Beach datum and 2:1 side slopes produces a unit volume of 30cy per foot (75m³/m) above the one percent chance, storm surge event (9.1 ft., 2.8m). This dune cross-sectional (Figure 3) is essentially that originally designed by Headland (1991) and contains fifty percent more sand than the minimum requirement of 540 ft³/ft (50m³/m) as established by the Federal Emergency Management Agency (FEMA) for breaching of natural dunes.

A nearshore survey taken in May, 1990 was considered representative for the existing bathymetric conditions in the model. The SBEACH model was run with eleven successively higher water level events to cover the return periods between 1 on Southeastern Coastline, Atlantic Ocean and 1000 years (Table 2). Wave heights associated with these water levels were established from measured and extrapolated values at the Corps' FRF, Duck, NC. As illustrated in Figure 3, the original dune section was modified by sand moving offshore ΔV_3 , sand overwash ΔV_1 , and the dune volume ΔV_2 . Dune damage is the volume change (loss) ΔV_2 and here after simply ΔV as found in Table 2. The total volume change above mean low water (MLW) accounted for all but less than 1cy per foot which moved offshore.

Dune Volume loss in cy/ft (ΔV in Table 2) and the percent loss (damage) are plotted against the S/S_D ratio as shown in Figure 4a and 4b, respectively. These curves are conservative in that they do not include the renourished beach in front of the dune as discussed blow.

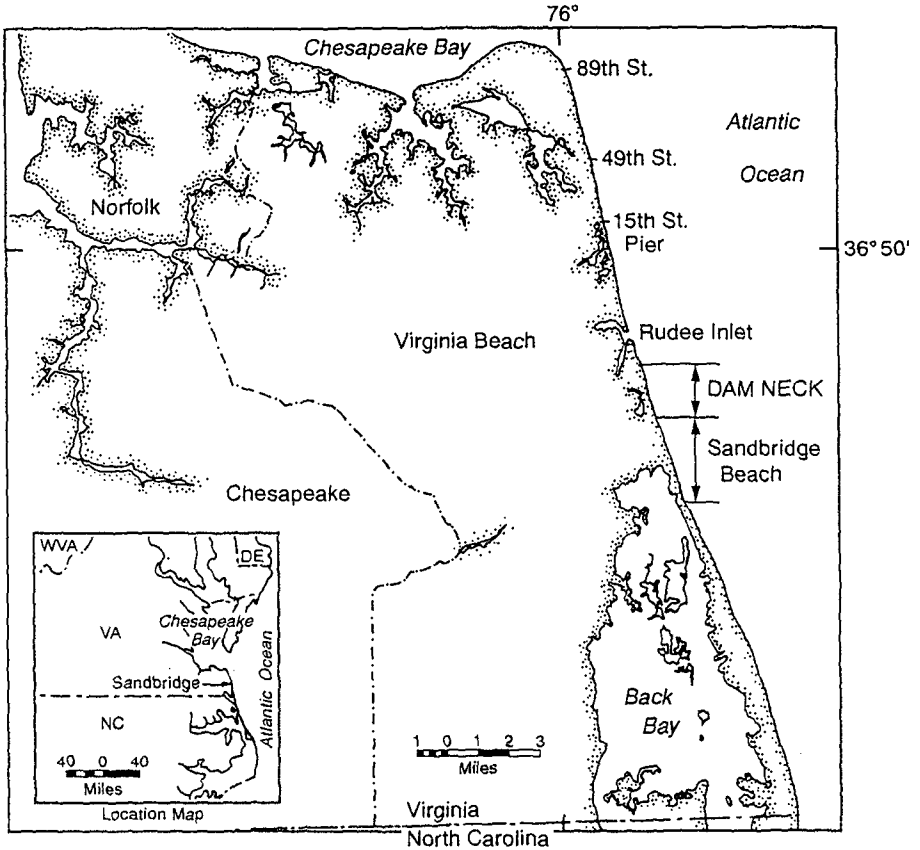


Figure 2 Location of US Navy, Fleet Combat Training Center, Dam Neck, Virginia on Southeastern Coastline, Atlantic Ocean

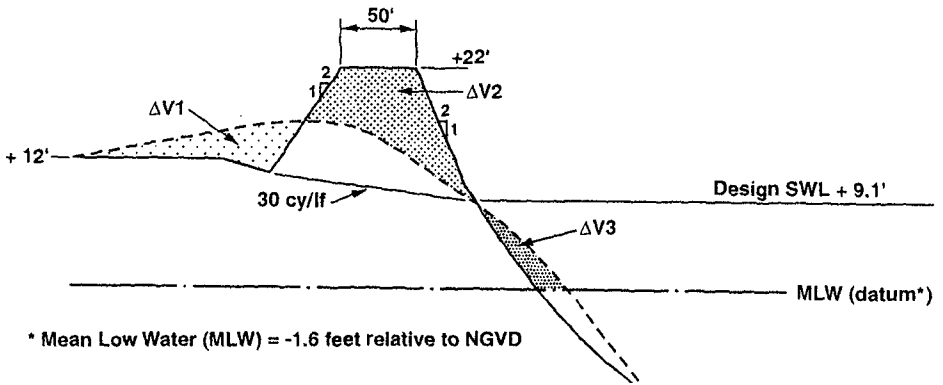


Figure 3 Dune Cross-Section Design for Dam Neck, Virginia and Definitions of Volume Change Regions, ΔV1, ΔV2 and ΔV3.

Table 2 Calculated ΔV Values for Various Water Elevations at Dam Neck, Virginia

Return Period in Year	Water Level, ft	S/S _D	H _{mo} , ft	T _p , sec	ΔV , cy/ft	ΔV_w , cy/ft	P, %	P _w , %
1	4.50	0.52	8.99	8.72	2.31	2.31	7.7	7.7
2	4.90	0.56	10.63	10.01	3.35	3.35	11.2	11.2
5	5.85	0.67	12.53	11.45	7.06	7.06	23.5	23.5
10	6.50	0.75	13.45	12.11	11.82	11.82	39.4	39.4
20	7.20	0.83	13.98	12.45	15.02	15.00	50.1	50.0
50	8.10	0.93	14.76	12.96	19.02	17.74	63.4	59.1
75	8.35	0.96	15.26	13.32	20.27	18.58	67.6	61.9
100	8.70	1.00	15.80	13.70	21.42	19.02	71.4	63.4
200	9.30	1.07	16.67	14.31	22.76	19.08	75.9	63.6
500	10.10	1.16	17.45	14.78	23.32	19.60	77.7	65.3
1000	10.70	1.23	18.18	15.25	23.40	19.68	78.0	65.6

ΔV = Volume Loss Without Seawall

ΔV_w = Volume Loss With Seawall

P = Percent Damage Without Seawall

P_w = Percent Damage With Seawall

(P, P_w) = 100*(ΔV , ΔV_w)/V, V=Total Volume of the Dune, 30 cy/ft

Dutch design practice for dunes (TAW, 1984) includes a safety factor or "remanent" dune volume remaining after a major storm event. Headland (1991) replaced this minimum remanent volume by an equivalent volume of rubble-mound seawall buried beneath the dune. Should a second major storm occur the same winter season, the buried seawall will be in place to protect the structures behind the dune. A similar buried seawall structure as shown in Figure 5 has been incorporated in the constructed project. Its effect on the damage curve is ΔV_w in Table 2 as illustrated in Figure 4b. The buried seawall acts to reduce dune volume loss at high water level events.

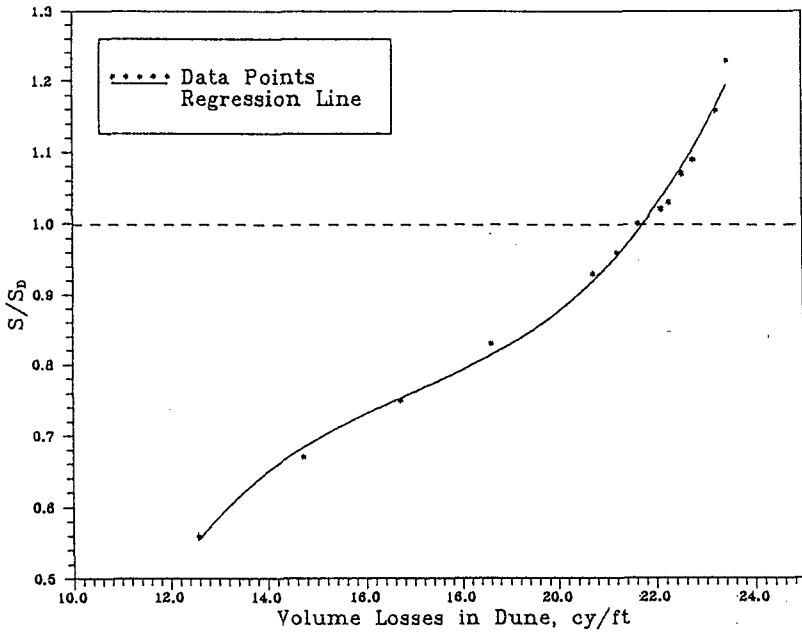


Figure 4a Dune Volume Loss (cy/ft) Versus S/S_D

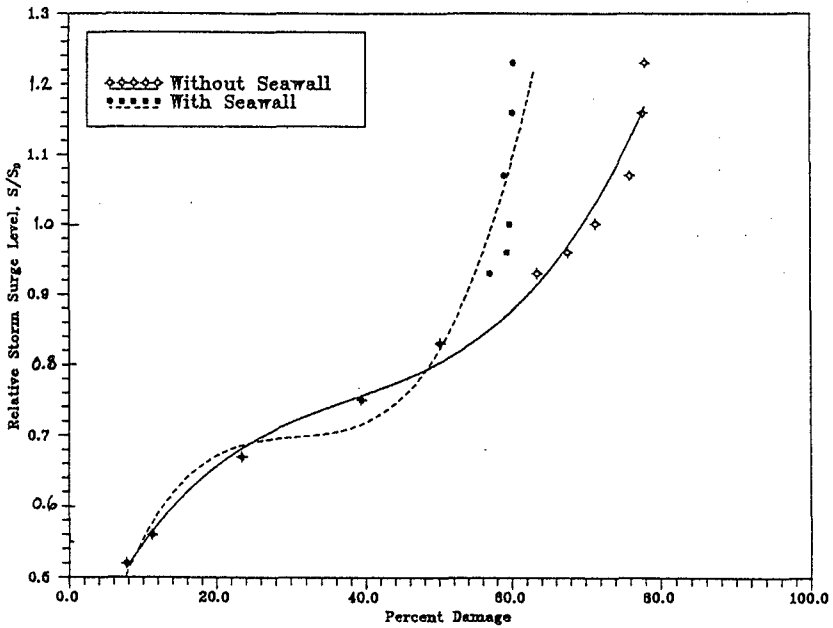


Figure 4b Dune Damage Curve: Percent Loss Versus S/S_D

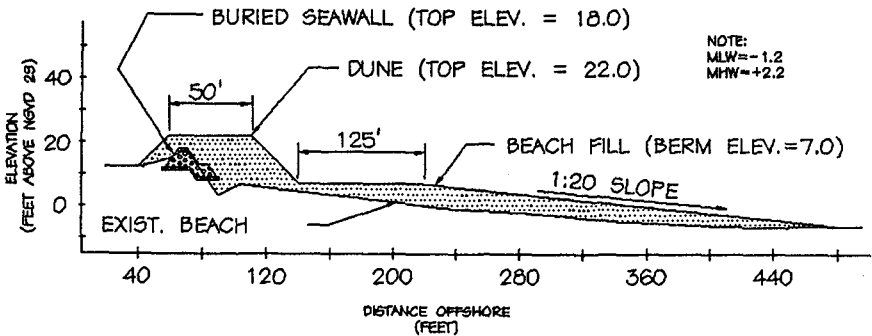


Figure 5 Dune-Beach-Buried Seawall Design for Dam Neck, VA

However, as illustrated in Figure 6, a major reduction in dune volume loss (percent damage) occurs when the beach is also renourished seaward of the dune. As an example, when the constructed beach width is 75ft (23m) damage curves for a design width after equilibration of 40 ft (12m) and with one-half life remaining of 20 ft (6m) are presented in Figure 6. Dune maintenance costs are obviously impacted by the volume of beach remaining over time to protect the dune system. The results of these computations are summarized in Table 3.

4.0 Dune Maintenance Costs

Simply stated, higher water elevations produce greater damage but have lower probabilities of occurrence each year. Annual dune maintenance costs are computed using the classical, convolution integral method of Kreeke and Paape, 1964 as illustrated in Figure 7. The dune damage curve was divided into eight subregions with damage greater than 70 percent requiring complete rebuilding of the dune structure. the storm surge probability curve was also divided into eight comparable subregions and then annual dune repair costs computed. As shown, subregion 2 for 10 - 20 percent damage from storms in the 0.2 - 0.35 probability of occurrence range accounted for the highest increment of maintenance expense. The total annual repair costs per unit foot of dune summed to about \$74 per foot (Table 4).

Using a 25 year design life and 9.5 percent interest rate in the present worth method of economic analysis resulted in annual dune maintenance costs of \$695 per foot. The value is conservative because the damage curve *without* the protective beach (Figure 4b) was used in the analysis. This can also be considered as a safety factor in the design and economic analysis.

Monitoring of the entire dune system and beach to closure depth will provide the requisite feedback information over a three year period to insure that dune maintenance is performed at appropriate intervals.

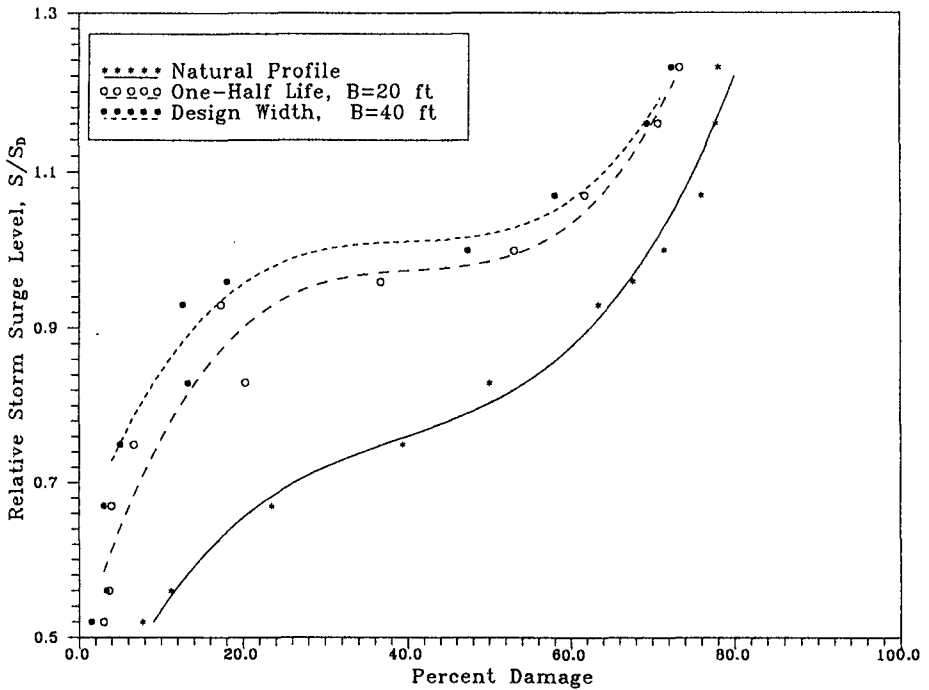


Figure 6 Effect of Beach Renourishment on Dune Damage Curves (Example for design beach width of 40 feet)

5.0 Cost Comparison With Armored Seawall

The dune damage curves used to compute dune repair costs permitted total, life-cycle cost estimates to be made for the dune-beach-buried seawall system (DBBS). Initial, unit costs for the dune of \$15/cy or \$450 per foot together with the maintenance costs of \$695 per foot produced a total cost of \$1145 per foot for the dune system. Using an offshore borrow area (Sandbridge shoal) for beach renourishment, one renourishment after 10-12 years and realistic, unit cost estimates for sand and rubble materials (buried seawall), the "soft" alternative system totalled about \$1820 per foot on an annual, life-cycle cost basis.

The original, engineering study (Cummings and Basco, 1995) also considered a conventional, large armor unit, revetment structure as the "hard" solution for storm damage mitigation.

Table 3 Summarized Computations of ΔV Values for Various Water Elevations at Dam Neck, Virginia

Return period in year	Water Level, ft	S/S _D	H _{ms} , ft	T _p , sec	Volume Loss, cy/ft					Percent Damage, %				
					ΔV	ΔV_{20}	ΔV_{30}	ΔV_{40}	ΔV_{65}	P	P ₂₀	P ₃₀	P ₄₀	P ₆₅
1	4.50	0.52	8.99	8.72	2.31	0.90	0.80	0.80	0.60	7.70	3.00	2.67	1.43	2.00
2	4.90	0.56	10.63	10.01	3.35	1.10	1.00	1.00	0.90	11.20	3.67	3.33	3.33	3.00
5	5.85	0.67	12.53	11.45	7.06	1.20	0.90	0.90	1.10	23.50	4.00	3.00	3.00	3.67
10	6.50	0.75	13.45	12:11	11.82	2.00	1.60	1.50	1.30	39.40	6.67	5.33	5.00	4.33
20	7.20	0.83	13.98	12.45	15.02	6.10	4.40	4.00	1.90	50.10	20.33	14.67	13.33	6.33
50	8.10	0.93	14.76	12.96	19.02	5.20	4.20	3.80	2.60	63.40	17.33	14.00	12.67	8.67
75	8.35	0.96	15.26	13.32	20.27	11.00	7.40	5.40	2.90	67.60	36.67	24.67	18.00	9.67
100	8.70	1.00	15.80	13.70	21.42	15.90	14.60	14.20	12.70	71.40	53.00	48.67	47.33	42.33
200	9.30	1.07	16.67	14.31	22.76	18.50	17.60	17.40	16.10	75.90	61.67	58.67	58.00	53.67
500	10.10	1.16	17.45	14.78	23.32	21.20	20.80	20.80	20.00	77.70	70.67	69.33	69.33	66.67
1,000	10.70	1.23	18.18	15.25	23.40	22.00	21.80	21.70	21.80	78.00	73.33	72.67	72.33	71.00

Notes :

- S_D = Design Storm Surge Level, ft
- S/S_D = Relative Storm Surge Level
- H_{ms} = Significant Wave Height, ft
- T_p = Spectral Peak Period, sec
- ΔV , P = Volume Loss and Percent Damage Without Any Beach Renourishment
- ΔV_{40} , P₄₀ = Volume Loss and Percent Damage on Design Beach Width, B=40 ft under 75 ft Construction Beach Width
- ΔV_{20} , P₂₀ = Volume Loss and Percent Damage on One-Half Life Width, B'=20 ft under 75 ft Construction Beach Width
- ΔV_{65} , P₆₅ = Volume Loss and Percent Damage on Design Beach Width, B=65 ft under 125 ft Construction Beach Width
- ΔV_{30} , P₃₀ = Volume Loss and Percent Damage on One-Half Life Width, B'=30 ft under 125 ft Construction Beach Width
- P=100 $\cdot\Delta V/V$, V=Total Volume of the Dune, \approx 30 cy/ft.

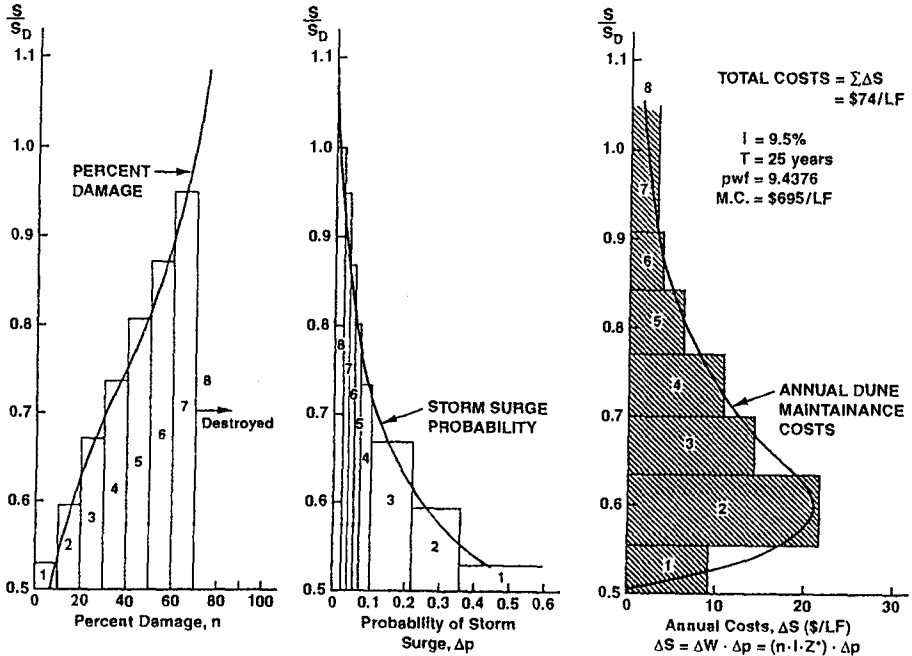


Figure 7 Probabilistic Design Method for Dune Maintenance Costs

Table 4 Dune Maintenance Costs

Region	Storm Surge Elev.*, S feet	Percent Damage (Average) n	Storm Probability Difference Δp	Dune Repair Costs $\Delta W = n.I.Z \$$	Annual Dune Maint. Costs, \$ $\Delta S = \Delta p . \Delta W$	
1	4.57	5	0.42	22.50	9.45	
2	5.18	15	0.32	67.50	21.60	
3	5.83	25	0.125	112.50	14.06	
4	6.39	35	0.068	157.50	10.71	
5	7.00	45	0.030	202.50	6.08	
6	7.57	55	0.015	247.50	3.71	
7	8.27	65	0.012	292.00	3.51	
8	> 8.7	> 100 destroyed	0.010	450.00 rebuild	4.50	
* ZERO DATUM (NGVD)					$\Sigma \Delta S$	73.62

Z = repair cost factor (say 1)

INITIAL COSTS, I.C.

$$IC = \$15/cy * 30 cy/LF = \$450/LF$$

MAINTENANCE COSTS, M.C.

$$i = 9.5\%$$

$$T = 25 \text{ yrs}$$

$$pwf = 9.4376$$

$$MC = \$73.62 * 9.4376 = \$695/LF$$

TOTAL COSTS, T.C.

$$TC = IC + MC$$

$$= \$450/LF + \$695/LF$$

$$TC = \$1145/LF$$

For a proper design study, the water depths at the toe of the stone revetment were estimated as those at the *end* of the 25 year design life. The historic, long term erosion rate, seasonal beach variations and toe scour during storms were all considered to determine the design water depth. In effect, at the end of 25 years, the beach would be gone in front of the seawall and the design water depth would be far different than today's conditions. The SBEACH model and others were used to calculate the surf zone wave conditions and design wave height for the armor layer. Artificial armor units (core-loc) were selected and resulted in total costs (minimal maintenance) of about \$2350 per foot.

Interestingly, the dune-beach-buried seawall alternative costs *less* than a concrete structure using artificial units for armor. This was primarily because the lowered beach elevations at the end of the design life permitted in large waves to directly attack the armor units with no beach remaining. Full details can be found in Cummings and Basco, 1997.

Costs are only one criteria in the decision matrix for choosing the "soft" or "hard" alternative for shore protection. Table 5 summarizes these decision criteria at Dam Neck. The only advantage of the armored revetment is lower annual maintenance costs. All others favored the dune-beach-buried seawall system. The primary benefits of this design are also that:

- a beach is present in the year 2020 at the end of the design life;
- the new sand spreads north and south to benefit all Dam Neck;
- the permitting agencies favor the "soft" alternative;
- the general public favors the "soft" alternative;
- the Navy's image will be enhanced by these efforts to protect/improve the environment.

6.0 Recommendations

Research is needed to develop generic damage curves and equations for use by coastal engineers for a wide range of practical applications. This dune design information could be developed through the systematic application of numerical models (e.g. SBEACH) plus confirmation of the results using large scale laboratory experiments and field data. The influence of the beach width should be quantified and design recommendations presented to aid the coastal engineer in dune design.

More case studies are needed comparing the life-cycle, costs of "soft" versus "hard" solutions for shore protection.

Table 5 "Soft" Versus "Hard" Alternatives for Storm Damage Mitigation

	ALTERNATIVE	
	"SOFT" Beach/Dune Buried Seawall	"HARD" Armored Revetment
● Shore Protection	✓	✓
● Economics - Initial Costs	✓	
Maintenance Costs		✓
Total Costs	✓	
● Environmental Consequences	✓	
● Recreation and Aesthetics	✓	
● Permit Application	✓	
● Public Perceptions	✓	
● Navy's Image	✓	
Combined Total	✓	

7.0 Acknowledgement

The authors wish to acknowledge the original contributions of John Headland (1991, 1992) for the buried seawall concept. Discussions with Professor van de Graaff, Delft Technical University are also appreciated. The project has been completed by Glenn and Sadler, consulting engineers, Norfolk, Virginia under the supervision of Mr. Robert E. Cummings, Jr.. The first author of this paper served as a special consultant on this project.

8.0 References

- Cummings, R.B. and D.R. Basco (1997) "A Beach-Dune-Buried Seawall Shore Protection System for the Fleet Combat Training Center, Atlantic, Dam Neck, Virginia Beach, Virginia" (10th Annual, National Beach Preservation Tech. Conf., St. Petersburg, January)
- Headland, J.R. (1991) "Erosion Study" Final Rept, NAVFAC, Alexandria, VA.
- Headland, J.R. (1992) "Design of Protection Dunes at Dam Neck, Virginia," *Proceedings*, Coastal Engineering Practice '92, Specialty Conference, ASCE, Long Beach, CA.
- Kreeke, J.v.d. and A. Paape (1964) "Europoort Breakwater Structures: A Cost Comparison," Ministry of Public Works (Rijkswaterstaat) and Delft Hydraulics, Final Rept W732M748.
- Larsen, M. and N.C. Kraus (1989) "SBEACH: Numerical Model for Simulating Storm Induced Beach Change," Rept 1, Empirical Foundation and Model Development, Tech Rept, CERC-89-9, CERC, Vicksburg, MS.
- Schoonees, J.S. and A.K. Theron (1995) Evaluation of Ten Cross-Shore Sediment Transport/Morphological Models," *Coastal Engineering*, Vol. 25, Nos. 1-2, pp.1-41.
- TAW (1989) "Guide to the Assessment of the Safety of Dunes as a Sea Defense," Rept 140, CUR (Centre for Civil Engineering Research and Codes), Gouda, the Netherlands.
- van de Graaff, J. (1986) "Probabilistic Design of Dunes: An Example from the Netherlands," *Coastal Engineering*, Vol. 9, pp.479-500.

CHAPTER 231

HURRICANE OPAL INDUCED CHANGES ON NATURAL AND NOURISHED BEACHES, WEST-CENTRAL FLORIDA

Richard A. Davis, Jr.¹ and Ping Wang²

ABSTRACT

Twenty-six beach profiles were surveyed immediately after the passage of storm conditions and were compared with pre-storm situations. They include 1) eleven locations spread throughout the entire 60 km reach of the Pinellas County coast including wide, narrow, natural and nourished sites, with and without seawalls; and 2) 15 locations confined to three adjacent nourishment projects along 14 km of Sand Key.

The overall behavior of the nourished and natural beaches along the 60 km reach of coast was similar, displaying a general trend of 1) shoreline erosion ranging from 2 to 10 m, 2) upward and landward migration of the nearshore bar, and 3) backbeach accumulation and increase in the berm height. Shoreline orientation and beach sand composition played no significant role in beach performance during the storm. The technique of dry beach replenishment using a dragline and conveyer belt may contribute to the more severe shoreline erosion at the Indian Shores nourishment project as compared to the traditional pumping technique used at Indian Rocks Beach and Redington Beach.

Temporary berm accumulation and shoreline accretion were recorded at two chronically eroding locations downdrift of structures. The shoreline accretion was caused by the landward sand transport induced by the storm waves. The storm accumulation was eroded by the normal-weather longshore sediment transport within three months after the storm.

The current version of SBEACH model (Larson and Kraus 1989) failed to reproduce the Opal-induced beach changes in the surf zone. The unsuccessful prediction was attributed to the uncertainties in offshore wave measurement, and morphological and computational complications caused by the exposure of hard bottom in the nearshore region.

-
- 1) Director and Distinguished Research Professor, Coastal Research Laboratory, Department of Geology, University of South Florida, Tampa, FL 33620, USA;
 - 2) Research Associate, Coastal Research Laboratory, Department of Geology, University of South Florida, Tampa, FL 33620, USA.

INTRODUCTION

Hurricane Opal passed about 250 km to the west of the west-central Florida coast in its northerly path toward the Florida panhandle in early October, 1995. The speed of the hurricane center (Fig. 1) in the central Gulf of Mexico was relatively slow. The slow speed generated abnormally long-period, high waves in the Gulf. A storm surge of about 1 m was measured in the study area along the west-central Florida coast (Fig. 2). The energetic conditions and the storm surge lasted for approximately two days during spring tide conditions.

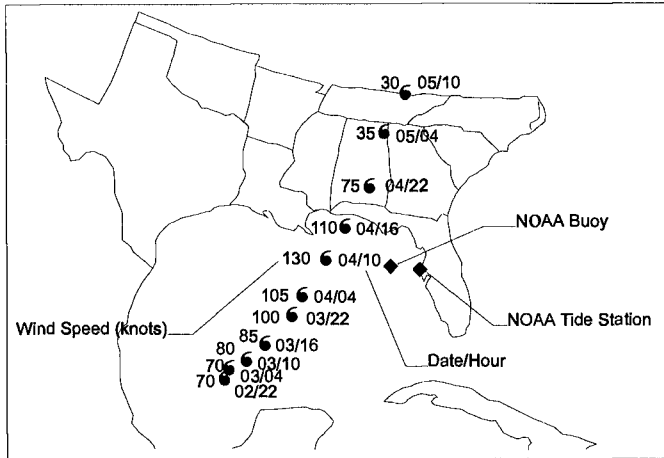


Figure 1. Storm track of Hurricane Opal and NOAA's wave buoy and tide gage.

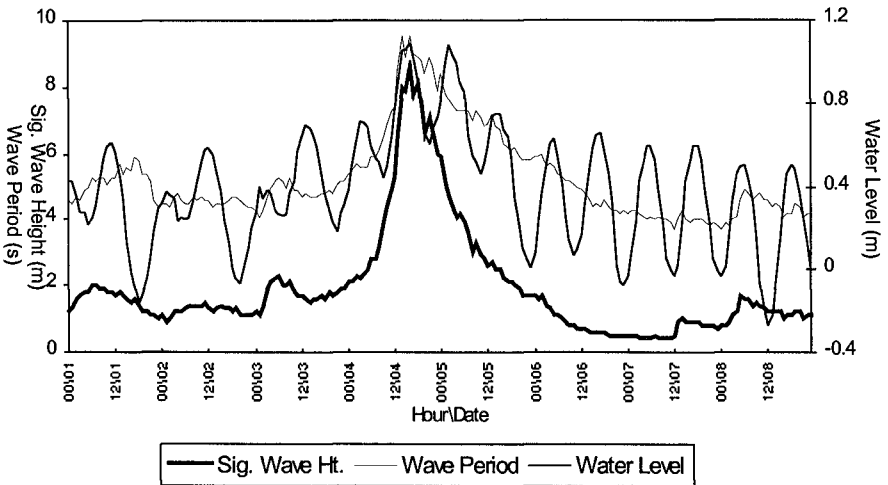


Figure 2. Measured significant wave height, average wave period, and storm surge by the NOAA buoy station 42036 and Clearwater tide station.

The significant wave height measured by the NOAA wave buoy (Fig. 1) reached a maximum over 9 m. Although the average wave period as shown in Figure 2 was less than 10 s, the dominant wave period reached 13 to 14 s during the peak of the storm. A storm surge of nearly 1 m was measured by the NOAA Clearwater tide station at the northern boundary of the study area (Fig. 2).

Twenty-six beach profiles were surveyed immediately after the passage of storm conditions and were compared with pre-storm profiles which were surveyed 1 to 2 months before the storm. Each profile was surveyed to a depth of 1.5 m below NGVD along a shore-normal transect. The 26 profiles are located along nearly 60 km of coast in Pinellas County, Florida and are part of an ongoing, long-term study of beach dynamics. Both natural and nourished beaches were included with construction ranging from 2 years old to nearly 10 years. The study area has a coastal orientation that ranges over about 40 degrees with a broad headland in the middle (Fig. 3). The shoreface gradient ranges from about 1:400 to 1:700 with the steepest being at the headland.

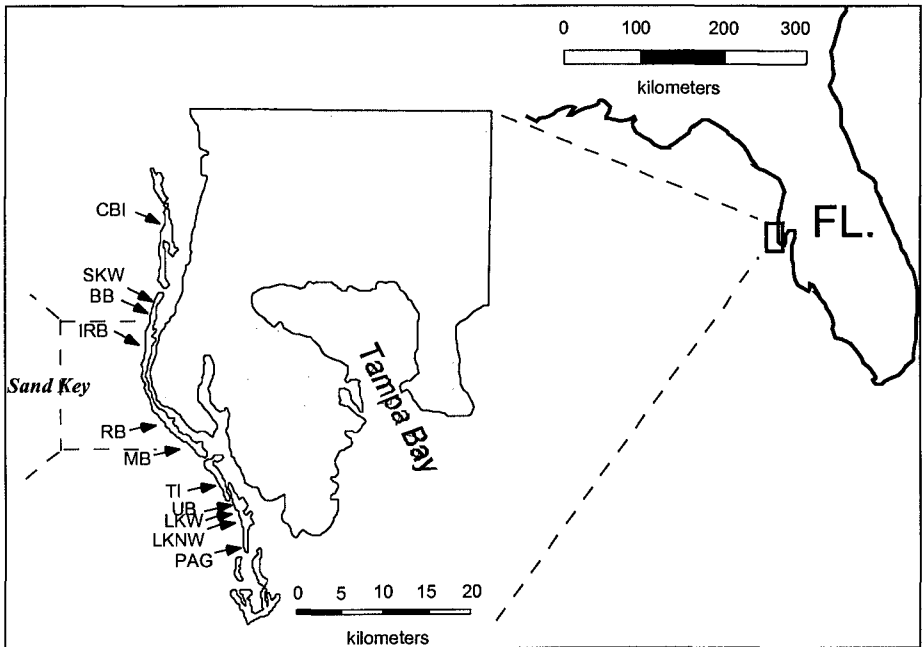


Figure 3. Study area in Pinellas County, Florida. The eleven sites are indicated by the lettered arrows. The 15 nourished locations are equally spaced at 300 m intervals on central Sand Key.

The objective of this study was to examine the hurricane-induced beach morphology changes through the comparison of profiles surveyed before, immediately after, and 4 to 8 months after Hurricane Opal. Different types of

beaches with different orientations and different degrees of human activities including natural and nourished, with and without seawalls, were examined and compared. Dominant direction of sediment transport during storm and normal-weather conditions is discussed. The application of the SBEACH model in predicting the storm induced beach changes along west-central Florida coast is also examined.

STUDY AREA

Two sets of profiles were surveyed: 1) eleven locations spread throughout the entire 60 km reach of coast including wide, narrow, natural and nourished beaches, with and without seawalls; and 2) 15 locations confined to three adjacent beach nourishment projects along 14 km of Sand Key (Fig. 3). The dominant longshore sediment transport along the entire coastal reach is toward the south, but there are local reversals. Two locations (SKW and UB), downdrift of structures, are experiencing severe beach erosion. SKW (Fig. 3) is currently protected by seawalls. The chronically eroding Upham Beach (UB in Fig. 3; Leonard et al. 1989, Dixon and Pilkey 1989) was protected by sand bags and renourished for the fifth time in the last 20 years in May, 1996.

Three adjacent beach nourishment projects were constructed on Sand Key. Five locations, R74, R75, R78, R80, and R81, were surveyed on Indian Rocks Beach which was nourished in 1990. The middle project at Indian Shores (R86, R87, R89, R91, and R92) which is located on the protruding headland was nourished in 1992 and the southern project at Redington Beach (R98, R99, R106, R107, and R108) was nourished in 1988. The nourishment at Indian Shores was constructed differently from the two adjacent projects. Instead of using the conventional pumping, the sand was replenished dry with a dragline and conveyer belt. The less expensive dry fill resulted in a looser packing than the wet pumping. The nearshore wave energy is usually higher at the Indian Shores headland due to the steeper shoreface gradient than at the adjacent Indian Rocks Beach and Redington Beach.

Sediment properties on natural beaches are different from those on the nourished beaches. Natural beaches or beaches that have not been nourished for the last decade or so are typically composed of well-sorted fine sand with less than 10% shell gravel. Nourished beaches, especially the two recently constructed at Indian Rocks Beach and Indian Shores, have significant amount of shell gravel, generally more than 20 %, inherited from the borrow material. Sediments in the swash zone have even higher shell-gravel concentration.

OPAL-INDUCED CHANGES ON NOURISHED BEACHES

All the nourished sites showed shoreline erosion of 2 to 10 m (Fig. 4A). The protruding 4-year old Indian Shores suffered the most shoreline loss, ranging from 8 m to over 10 m. The 8-year old Redington Beach lost the least shoreline, from 2 to 8 m. The 6-year old Indian Rocks Beach lost between 5 to nearly 10 m. The severe

shoreline erosion at Indian Shores headland is believed to be caused by a combination of high wave energy and loose packing.

The sand-volume change above the -1.5 m NGVD datum was generally small, ranging from 15 m³/m gain to 17 m³/m loss (Fig. 4B). Although most of the locations lost 2 to 17 m³/m sand, five of the 15 locations gained various amount of sand. The trend of volume change was not as apparent as the shoreline change. The reason for the less distinctive trend of volume change as compared to shoreline change was that the volume loss at the shoreline was compensated by the landward and upward migrations of the nearshore bar and the accumulation on the backbeach, forming a higher berm (Fig. 5).

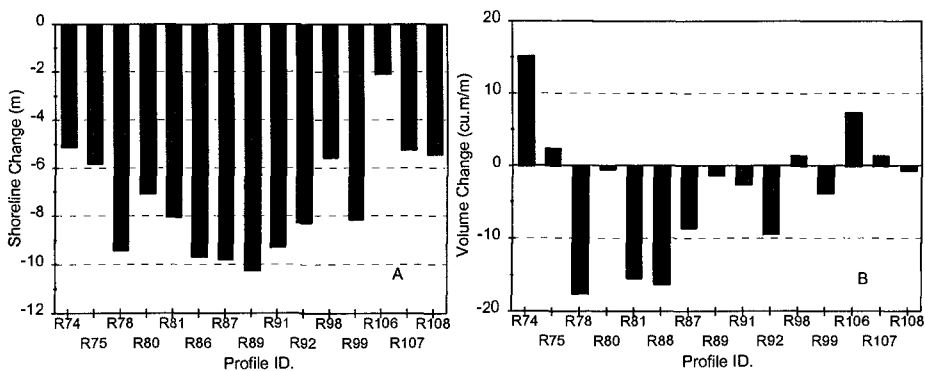


Figure 4. Shoreline (A) and volume (B) changes on the nourished beaches.

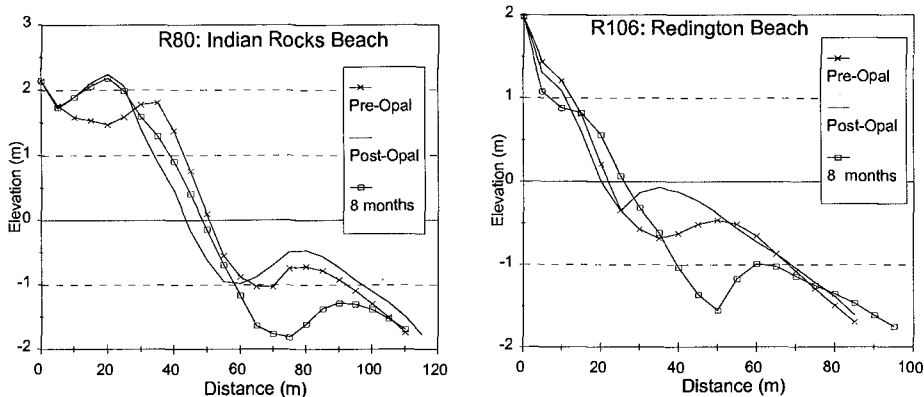


Figure 5. Beach profile changes: before, immediately after, and 8 months after.

It is generally assumed that large storm waves induce seaward migration of the breaker-point bar (e.g., Komar 1976, Dean 1995). This hypotheses which was developed from the original beach cycle study of Shepard (1950) has been used

broadly in shoreface-development studies (e.g., Pilkey et al. 1991). Larson and Kraus (1994) documented landward sediment transport during 3 of the 4 examined storms in 1989 and 1991 at Duck, North Carolina. Landward and upward migration of the nearshore bar induced by Hurricane Opal was measured on all the barred locations in the present study along the 60 km study area (Fig. 5). This landward migration of nearshore bar was also observed by Stone et al. (1996) on the Florida panhandle. Shoreline recovery and seaward migration of the nearshore bar was measured 4 and 8 months after Opal, indicating a seaward transport during the normal-weather conditions.

Seasonal beach cycles like those observed along the U.S. Pacific coast (e.g., Shepard 1950, Inman et al. 1993) are not observed along west-central Florida coasts. The landward migration of the nearshore bar observed in this study cannot be explained by the seaward shift of breaker point during high-energy storm wave conditions, which would result in seaward migration of the breaker-point bar. The unexpected upward and landward bar migration indicates that in addition to the wave steepness and the location of breaker point, the nearshore bar migration may be also controlled by other factors. Further study is needed to understand the mechanism of landward bar migration during storm conditions.

Another morphological change that was observed at all the profile locations except the "hot spot", R106 (Fig. 5B), was the accumulation on the backbeach. A large amount of sand was deposited landward of the previous berm crest. The berm crest was shifted landward and higher than before. The thickness of the wedge-shaped accumulation decreased landward and terminated, at most of the nourished locations, before the accumulation reached the seawalls. The backbeach accumulation was the thickest, up to 1 m thick at the storm-berm crest, on the high-energy Indian Shores headland, and the thinnest on the relatively low-energy Redington Beach.

Significant shoreline recovery and the seaward migration of the nearshore bar were observed 8 months after the storm (Fig. 5). The shoreline recovery resulted in more gentler beach than the storm beach, especially in the vicinity of the shoreline. The backbeach accumulation remained unchanged because the storm berm crest is beyond the reach of wave uprush under normal weather conditions.

Natural beaches or those that have not been nourished in the last decade or so (CBI, MB, TI, LKNW, and PAG in Fig. 3) showed a similar general trend, i.e., shoreline erosion, landward migration of nearshore bar, and backbeach accumulation, across the entire 60 km study area. The amount of shoreline retreat, ranging from 2 to 10 m, was similar to that measured on Indian Rocks Beach and Redington Beach and was less than that on Indian Shores (Fig. 6A) headland. Volume change above -1.5 m NGVD was generally small, mostly less than 15 m³/m, and showed similar trend (Fig. 6B) as that observed on nourished beaches in Sand Key.

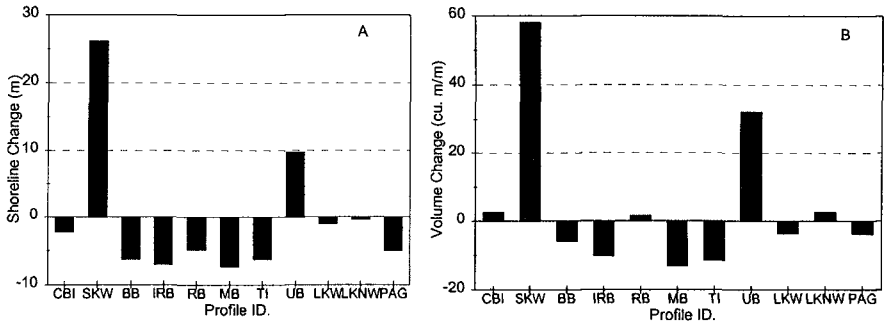


Figure 6. Shoreline (A) and volume (B) change of the 11 locations along Pinellas County, Florida.

OPAL INDUCED CHANGES ON THE CHRONICALLY ERODING STRUCTURED BEACHES

Two of the beaches that are historically erosional, SKW and UB (Fig. 3), are both downdrift of structures. Scour behind the seawall and damage to the adjacent residential buildings occurred due to storm wave over-topping at both locations. A significant amount of sand accumulation was measured in front of the seawall at SKW, and the sand bags at UB were buried by sand that was deposited on the beach (Figs. 6, 7). As much as 26 m of shoreline accretion with nearly 60 m³/m volume gain was measured at SKW immediately after the storm. Ten meters of shoreline accretion and 35 m³/m volume gain were measured at UB just south of the wave-dominated inlet, Blind Pass (Davis and Gibeaut 1990). Large carbonate rock fragments characteristic of the Tampa Limestone which is exposed offshore were found on the storm beach, indicating that the sediment was transported landward from offshore during the storm. It is believed that the seawalls and sand bags induced significant energy dissipation during the storm surge. The fast rate of energy dissipation resulted in backbeach accumulation above the normal wave uprush limit.

The temporary sediment accumulation induced by Opal was eroded completely within four months after the storm (Fig. 7). The longshore transport under normal weather and the lack of updrift sediment supply are believed to be responsible for the erosion. The southward transport is evident at Upham Beach (UB) from the most recent beach nourishment. A profile, LKW (Fig. 3), about 150 m south of the UB location, was surveyed as part of a long-term beach monitoring program. A large amount of sediment was replenished on the Upham Beach about 7 months after the storm. The LKW location was about 80 m south of the nourishment project. Significant shoreline erosion was measured at UB only 3 months after the nourishment (Fig. 8). Remarkable accumulation was measured at the LKW location during the same period. The shape and slope of the shoreface at Upham Beach

remained fairly constant, suggesting that the shoreline retreat was not caused by the cross-shore profile adjustment. It is evident that the southward longshore transport is the cause of the long-term beach erosion at Upham Beach as well as the erosion of the storm accumulation from Opal.

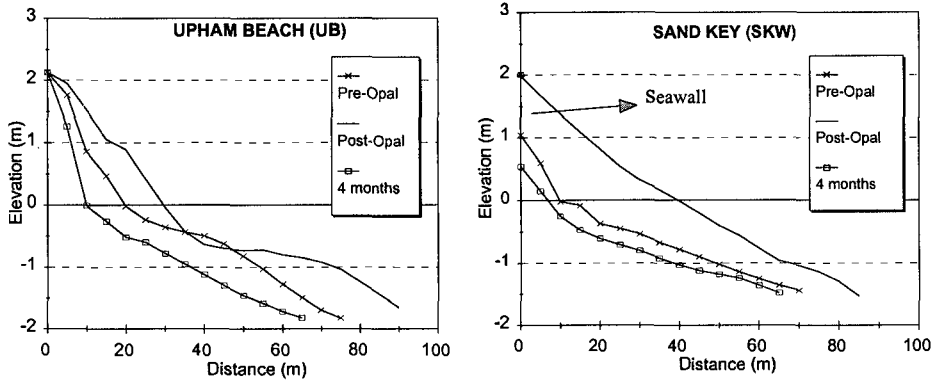


Figure 7. Temporary accumulation induced by Hurricane Opal on structured beaches.

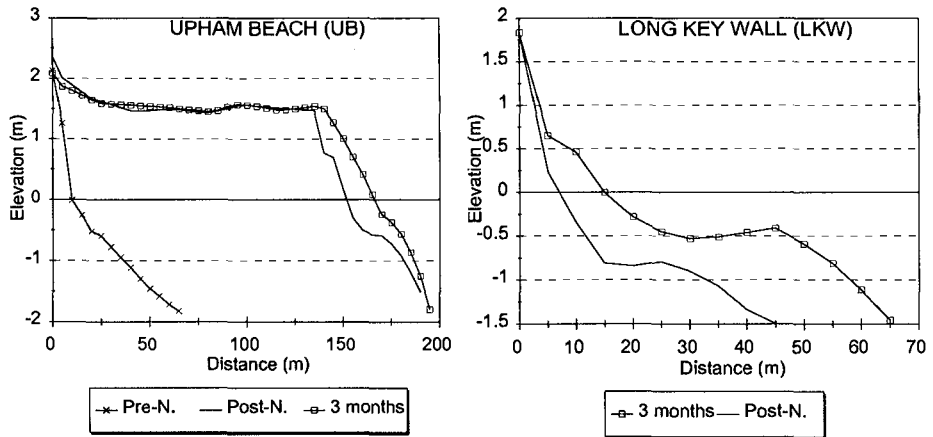


Figure 8. Shoreline erosion at the recently nourished Upham Beach and sand accumulation at the downdrift beach. Note the differences in scale.

The seawall and stabilizing sand bags effectively protected the coast and dissipated a significant amount of wave energy during Hurricane Opal. The structures are not capable of controlling regional and long-term beach changes caused by longshore sediment transport. Beach nourishment not only provides a

buffer for normal weather shoreline erosion caused mainly by longshore sediment transport but also protects the coasts against dramatic storm events.

SBEACH MODELLING OF THE BEACH PROFILE CHANGES

SBEACH, the numerical model for simulating storm-induced beach change (Larson and Kraus 1989), was applied to reproduce the Opal-induced beach profile changes along west-central Florida coast. The offshore wave condition measured at the NOAA's 42036 wave buoy and the water level measured at the NOAA's Clearwater tide station (Fig. 2) were used as the key hydrodynamic input data. The numerical modeling was applied to the 15 locations on Sand Key. An average grain size of 0.33 mm obtained from over 1100 samples was used to represent the sediment. The model was calibrated at two locations, one at the northern Indian Rocks Beach and one at the southern Redington Beach.

Examples of SBEACH modeling are illustrated in Figure 9. The trend of shoreline erosion induced by Hurricane Opal was successfully reproduced by the SBEACH model, although the magnitude of the shoreline erosion was over predicted. The backbeach accumulation and the unexpected upward and landward migration of the nearshore bar were not predicted. The bar/trough features were basically absent from the predicted profiles. The increased berm height and the wedge-shaped sediment accumulation on the backbeach were not predicted, on the contrary, significant berm erosion and a much gentler beach slope near the shoreline, as compared to the pre-storm situations, were predicted.

The unsatisfactory SBEACH modeling is believed to be caused by the uncertainties in input wave data and regional morphological and geological complications. A significant wave height of over 9 m with a relatively short wave period of less than 10 s was measured by the NOAA's 42036 wave buoy offshore west-central Florida. The 9 m significant wave height was much larger than that observed in the nearshore (3 to 4 m, as printed on the local newspaper). The over-predicted backbeach erosion is believed to be caused by the possibly exaggerated wave height. This assumption was proved by using an arbitrary smaller wave height of 3.5 m. Much less backbeach erosion was predicted with the smaller input wave height.

The nearly horizontal hard bottom composed of Tampa Limestone violated the bottom boundary condition of movable sand assumed in the current version of SBEACH. The depth of the hard bottom decreases from north to south. At northern Indian Rocks Beach, the hard bottom is exposed at 7 m, the depth decreases to about 3 m at the southern Redington Beach. Based on the wave breaking criterion used in the SBEACH model (Larson and Kraus 1989), the nearly horizontal hard bottom is within the breaker zone during the peak of the storm conditions with over 9-m waves. The current version of SBEACH is not capable of incorporating the non-erosible hard bottom, especially when the hard bottom is within the breaker zone. The above situation will be an ideal field test for the updated SBEACH model (N.C. Kraus, personal communication; available:

December 1996, Randy Wise, personal communication) which will incorporate the influences of non-erosible bottom.

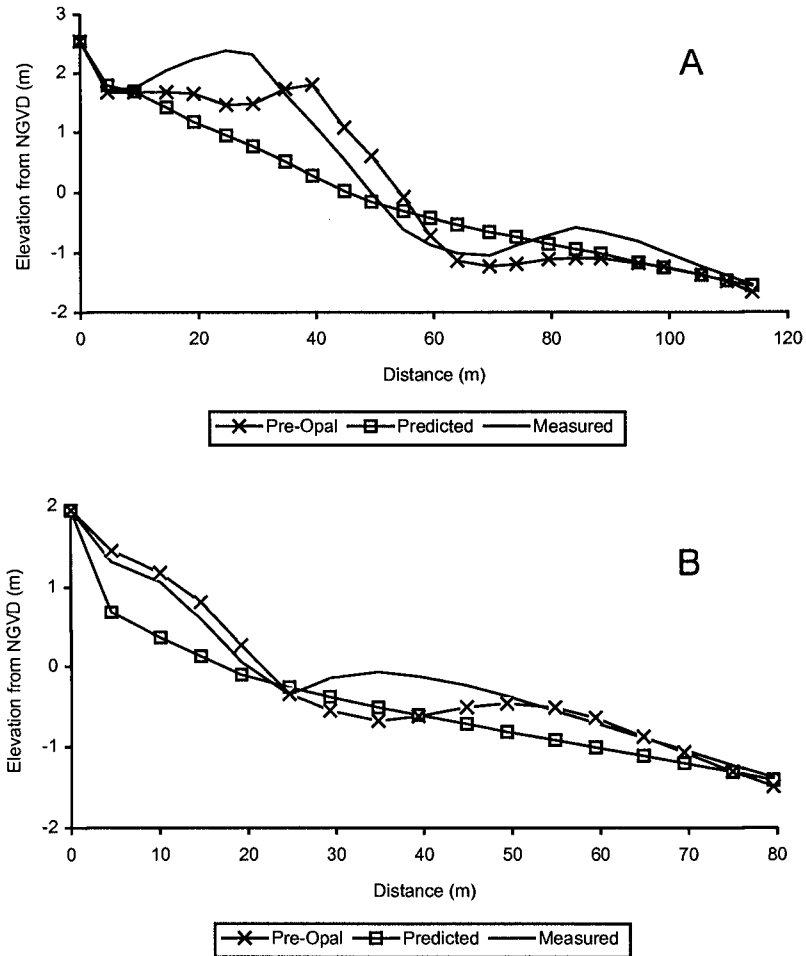


Figure 9. Measured and predicted beach profiles; A) R74, Indian Rocks Beach; and B) R106, Redington Beach.

SUMMARY AND CONCLUSIONS

The overall behavior of the nourished and natural beaches during the passage of Hurricane Opal is similar. All surveyed beaches along the 60 km reach of coast displayed a general trend of shoreline erosion, upward and landward migration of the nearshore bar, and accumulation on the backbeach resulting a higher berm. This

trend was observed on beaches with different orientations and different sediment compositions, ranging from less than 10% shell gravel on natural beaches to greater than 30% shell gravel on nourished beaches. This indicates that shoreline orientation and sand composition played no significant role in beach performance under storm conditions.

It is apparent from the data collected on the three adjacent and differently constructed nourishment projects on Sand Key that they behaved differently. The oldest showed least change and the most recent showed the most. The most recent project was also constructed without the benefit of dredging and pumping, thus creating a loosely compacted beach. The loose packing contributed to the greater rate of erosion.

The two chronically eroding locations downdrift of structures behaved differently from the nourished and natural beaches. Significant shoreline accretion was measured at the two locations, with one protected by seawalls and the other protected by sand bags, immediately after the storm. A large amount of sand accumulated on the beach in front of the structure resulting from the storm-induced landward transport. The temporary storm accumulation was eroded by the normal-weather longshore sediment transport within 3 months after the storm.

The current version of SBEACH model failed to reproduce the Opal-induced beach changes along west-central Florida coast. The unsuccessful prediction is attributed to uncertainties in input wave data and the model's limitation in incorporating the non-erosible hard bottom in the study area into the computation.

ACKNOWLEDGEMENTS

This study was supported by Pinellas County, Florida and Florida Department of Environmental Protection. The authors would like to thank the graduate students in the Coastal Research Laboratory at the University of South Florida for their assistance in the field work. The SBEACH model was kindly provided by Randy Wise at the Coastal Engineering Research Center.

REFERENCES

- Davis, R.A., Jr. and Gibeau, J.C. (1990). "Historical morphodynamics of inlets in Florida." Florida Sea Grant, 81p.
- Dean, R.D. (1995). "Cross-shore sediment transport processes." *Advances in coastal and ocean engineering*, P.L.-F., Liu, ed., World Scientific, New Jersey, 159-220.
- Dixon, K., and Pilkey, O.H. (1989). "Beach nourishment along the U.S. coast of the Gulf of Mexico." *Proceedings of Coastal Zone '89*, ASCE, 2007-2020.

- Inman, D.L., Elwany, M.H.S., and Jekins, S.A. (1993). "Shoreface and bar-berm profiles on ocean beaches." *Journal of Geophysical Research*, 98, 18,181-18,199.
- Komar, P.D. (1976). "*Beach processes and sedimentation.*" Prentice-Hall, Englewood Cliffs, New Jersey, 429p.
- Larson, M. and Kraus, N.C. (1989). "SBEACH: Numerical Model for Simulating Storm-Induced Beach Change." *Technical Report CERC-89-9*, U.S. Army Engineer Waterways Experiment Station, Vicksburg, MS.
- Larson, M. and Kraus, N.C. (1994). "Temporal and spatial scales of beach profile change, Duck, North Carolina." *Marine Geology*, 117, 75-94.
- Leonard, L., Clayton, T.D., Dixon, K., and Pilkey, O.H. (1989). "U.S. beach nourishment experience: a comparison of the Atlantic, Pacific, and Gulf coasts." *Proceedings of Coastal Zone '89*, ASCE, 1994-2006.
- Pilkey O.H., Young, R.S., Riggs, S.R., Smith, A.W.S., Wu, H., and Pilkey, W.D. (1991). "The concept of shoreface profile of equilibrium: A critical review." *Journal of Coastal Research*, v. 9, p. 255-278.
- Shepard, F.P. (1950). "*Beach cycles in southern California.*" U.S. Army Corps of Engineers, Beach Erosion Board, Technical Memo., n. 15, 26p.
- Stone, G.W., Grymes, J.M., Armbruster, C.K., Xu, J.P., and Oscar, K.H. (1996). "Researcher study impact of Hurricane Opal on Florida coast." EOS, May 7.

CHAPTER 232

Modelling Sand Transport and Profile Evolution on Macrotidal Beaches

Paul.R.Fisher¹ & Tim.J.O'Hare²

Abstract

An empirical model is presented which simulates the effect of tidal translation of cross-shore sediment flux patterns, in support of a hypothesis that wave height *and* tidal range are the key influences in the formation of characteristic macrotidal beach profiles. The energetics-based model is based upon field observations of cross shore currents and sediment fluxes from three high-energy macrotidal (tide range >4m) locations around the U.K, chosen as representations of dissipative, intermediate and reflective environments (after Wright and Short, 1984). The observed depth-dependant flux patterns are translated across linear beach profiles, with gradients modelled from sediment characteristics (Dean 1977, Kriebel et al 1991), the evolution of characteristic macrotidal beach profiles and the development of attendant features such as break-point bars, low tide terraces, and steepened foreshores are observed.

Introduction

The morphological significance of tidal translation of the swash, surf and shoaling wave zones across the beachface has received increasing attention over the last fifteen years (Wright et al (1982), Short (1991), Masselink (1993), Masselink and Short (1993)). It has been suggested that the continual variation in water depth by the tidal signal in a *macrotidal* environment is responsible for temporal variations in local dynamics. Furthermore, the intermittence of swash and surf processes in the high-tidal zone modifies the dynamics of that zone, whereas the mid and low-tidal zone dynamics are more similar to nearshore and offshore zones on micro-tidal beaches (Wright et al, 1982).

This contribution sets out to give some insight into the effects of asymmetric residence times of the water level on the beachface within macrotidal regimes.

¹Research student, ²Senior Lecturer, Institute of Marine Studies, University of Plymouth, Drake Circus, Plymouth, Devon, UK, PL4 8AA

According to the classification of Bird (1969) macrotidal regimes are those locations where the mean maximum tidal range during a month is greater than 4 metres, mesotidal regimes experience a mean maximum tidal range between 2 and 4 metres, and microtidal regimes are between 1 and 2 metres. While much work has been done relating the effects of a varying wave field on sediment transport processes in macrotidal regimes, (e.g. Wright et al (1982), Wright and Short (1984)), it is not clear how transport processes are modulated by a continual rise and fall of the water level by the tidal signal. This effect is pronounced within macrotidal environments where migration velocities and widths of swash, surf and wave shoaling zones are variant during the tidal cycle dependant on (a) the phase of

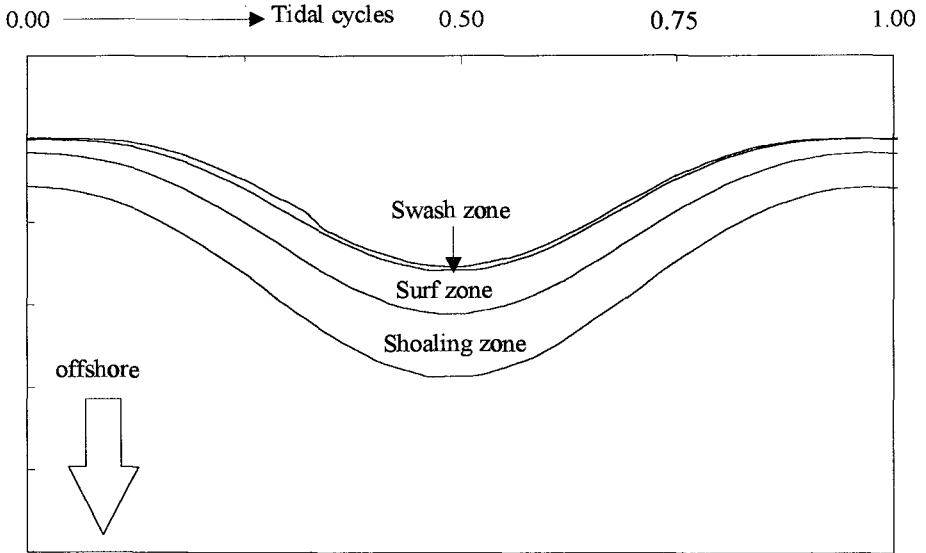
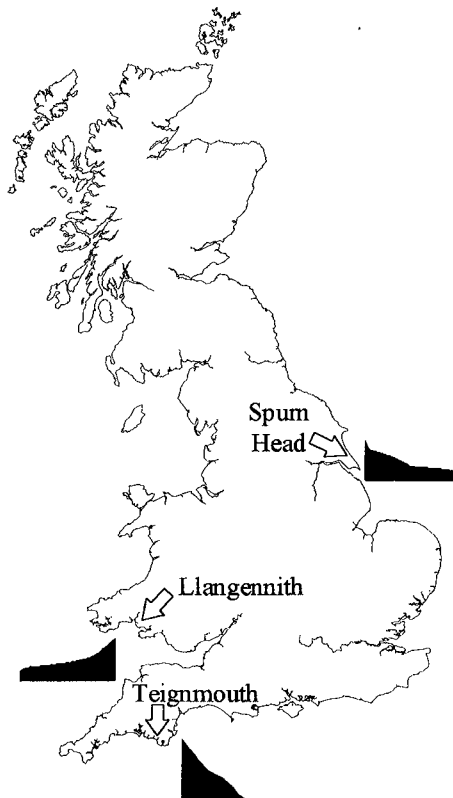


Figure 1. Tidal translation of swash, surf and shoaling zone processes across a beachface of exponential form. Because of the shoreward increasing beach gradient swash, surf and shoaling zones narrow significantly at high tide levels.

the tide and (b) the local gradient of the beach. The tidal variation in magnitude and position of these zones is illustrated in Figure 1 for the case of an exponential beachface. The approach taken in this study is to oscillate simple empirical models of cross-shore sediment transport across a beachface, allowing the profile to respond to the resulting patterns of erosion and deposition. The empirical model used is constructed from field observations of water and sediment dynamics at a variety of high energy macrotidal locations around the U.K during the British Beach and Nearshore Dynamics (B-BAND) experiment.

A useful overview of the B-BAND experiment is given by Davidson et al (1993). This three-year experiment investigated surf zone processes at three high

energy macrotidal locations around the UK. The sites were chosen to represent dissipative, intermediate and reflective beaches following the morphodynamic classifications of Wright and Short (1984). The locations are illustrated in Figure 2 along with typical beach profiles and are described briefly in turn.



Llangennith: A dissipative high energy beach with a shallow beach gradient (0.014-0.020) with fine to medium quartz sands ($D_{50}=0.21\text{mm}$). This beach is west facing, has a tide range up to 9 metres, and broad surf (up to 350m) and intertidal ($\sim 500\text{m}$) zones.

Spum Head: An intermediate beach located near the end of a 5km long spit facing the North Sea. The beach profile comprises a steep high tide beach ($\tan\beta \sim 0.0975$) and a low tide terrace ($\tan\beta \sim 0.023$, and $D_{50}=0.35\text{mm}$). This beach has a tide range up to 6m and experiences strong longshore tidal currents which have a significant effect on surf zone dynamics.

Teignmouth: A reflective beach site facing south-east into the English Channel sheltered from Atlantic swell. The beach is backed by a sea wall, and has a gradient of 0.067-0.142. Cross-shore variation of sediment size at this location is significant, with a D_{50} value of 0.24mm. Tidal range is 6 metres.

Figure 2. Location of B-BAND field sites around the UK, showing typical cross-sectional profiles.

Shape Function Approach To Sediment Transport

Foote (1994), Foote et al (1994), and Russell and Huntley (1996) examined field measurements of cross-shore sediment transport from these three locations. They calculated velocity moment contributions to sand transport, by assuming the instantaneous velocity field to be composed of the following contributions:

$$\bar{\mathbf{u}} = \bar{\mathbf{u}} + \mathbf{u}_S + \mathbf{u}_L \quad (1)$$

where \bar{u} is the mean flow, u_s is the incident wave component of velocity, and u_L is the long wave component. Using Bagnold's (1963, 1966) uni-directional stream flow total load sediment transport model, modified by Bailard (1981, 1987) for cross shore sediment transport under bi-directional flow, Guza and Thornton (1985) used field measurements to examine the relative importance of the velocity moment terms in Bailard's model, and found the transport significant terms to be (in normalised form):

$$\overline{|u|^2 u} / \left(\overline{u^2} \right)^{3/2} \quad \text{for bedload transport, and} \quad (2)$$

$$\overline{|u|^3} / \left(\overline{u^2} \right)^2 \quad \text{for suspended load transport} \quad (3)$$

Foote et al (1994) examined the cross-shore distribution of the significant moments for bedload and suspended load and found in both cases that the sum predicted a net onshore movement shoreward of the breakpoint and a net offshore movement seaward of the breakpoint. To clarify this pattern for each case they normalised the water depth by the depth of wave breaking. The position of wave breaking was determined from the position of maximum wave height from pressure transducer records and this was checked with visual observations in the field. Combining data from all three field sites they noted that not only was there a pattern of net onshore transport shoreward of wave breaking and a net offshore transport seaward of it, but that a curve could be reasonably fitted through the velocity moments calculated for the interim positions.

They subsequently proposed the existence of quasi-universal, cross-shore sediment transport spatial distribution curves for bed load and suspended load on high energy beaches. These sediment 'shape functions' are illustrated in Figure 3. Third order polynomials are fitted through each data set, with one root at $x=0$, $y=0$ (zero transport at the shoreline). O'Hare (1994) proposed that this 'shape function' approach be adopted to develop a tentative cross-shore sediment transport model, suggesting that the patterns observed in the B-BAND data are in fact required by the break-point bar hypothesis, and that characteristic macrotidal profiles may be constructed by the repeated tidal excursion of the shape function. This contribution presents the preliminary results from the development of such a model.

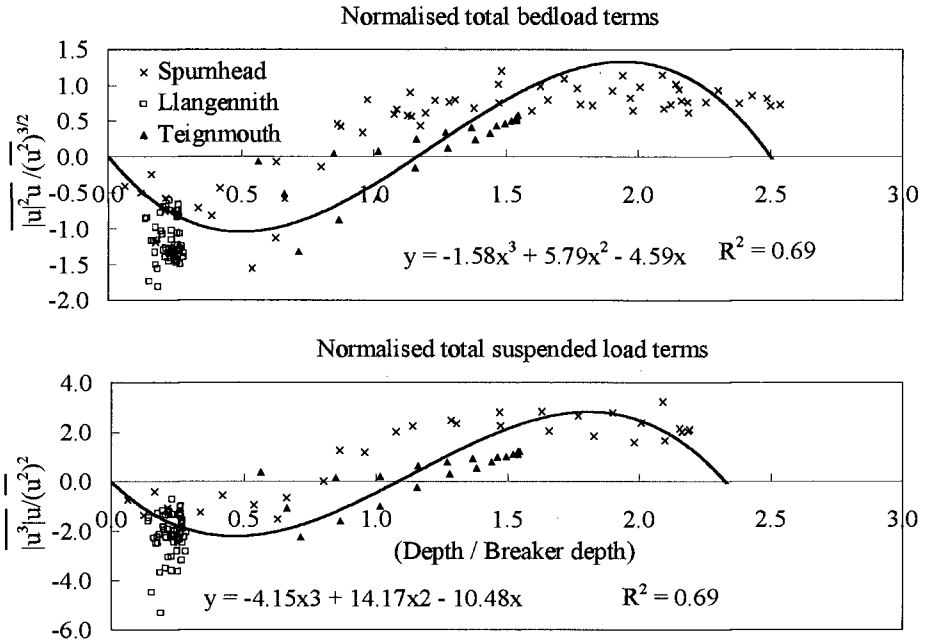


Figure 3. Sediment transport shape functions obtained from the B-BAND data.

Model Description

The simulation model migrates the proposed shape functions for bed and suspended load across a beachface. The input parameters for the model are breaker height H_b , grain diameter ϕ , tide range, wave period T , sediment and fluid densities ρ_s and ρ , gravity, kinematic fluid viscosity ν , bed drag coefficient C_d , and bed and suspended load efficiencies ϵ_b and ϵ_s . Related parameters such as sediment repose angle, $\tan\phi$, and sediment porosity, n , are evaluated using an empirical model (Allen, 1970).

The first stage for the simulation model is to evaluate the grain buoyancy and fall velocity of the beach sediment according to the CERC Shore Protection Manual procedures (US Army Corps of Coastal Engineers, 1984):

$$\text{Grain buoyancy (A): } \frac{(\rho_s - \rho) g D^3}{\rho \nu^2} \tag{4}$$

Sediment fall velocity (w):

$$w = \frac{1}{18} \frac{(\rho_s - \rho) g D^2}{\rho v} \quad \left\{ \frac{(\rho_s - \rho) g}{\rho} \right\}^{0.7} \cdot D^{1.1} \quad \left\{ \frac{(\rho_s - \rho) g D}{0.91 \rho} \right\}^{0.5} \quad (5)$$

(for $A < 39$) (for $39 < A < 10^4$) (for $A > 10^4$)

Breaking depth is then calculated iteratively according to the model of Le Mehaute (1961) using an initial estimated value for breaking depth (taken as 5m):

$$d_b = \left[\frac{H_b (g d_b T^2)^{0.5} g T^2}{0.12 \tanh 2\pi d_b} \right] \quad (6)$$

Next breaker coefficient (γ) and breaking wavelength (L_b) are evaluated from:

$$\gamma = \frac{H_b}{d_b} \quad (\text{from Galvin, 1972}) \quad (7)$$

$$L_b = \sqrt{g d_b T^2} \quad (\text{assuming shallow water}) \quad (8)$$

The preliminary (linear) gradient of the profile is evaluated at closure depth, d_c , (the outer root of the transport polynomial) from Dean (1977) and Kriebel et al (1991):

$$\tan \beta = \left(\frac{2.25 \left(\frac{w^2}{g} \right)^{\frac{1}{3}}}{d_c} \right)^{\frac{3}{2}} x_c^{-1} \quad \text{Where } x_c \text{ is the offshore distance to closure.} \quad (9)$$

The model starts at high tide with a vertical increment of 0.1 metres. Water depth is simply calculated by subtracting the profile level (initially linear) from the still water level. Next a simple model of shoaling wave height is used to determine velocity scales to apply to the polynomial coefficients. The model, again using shallow water approximations is linear from the shore to the breakpoint (depth = 0:gd), and offshore of the breakpoint, takes the form

$$H = \left(\frac{d_b}{d} \right)^{\frac{1}{4}} H_b \quad (10)$$

The shoaling wave heights are used to calculate cross-shore varying maximum orbital velocities from:

$$u_{\max} = \frac{H}{2} \sqrt{\frac{g}{d}} \quad (11)$$

u_{\max} is used to evaluate $\overline{u^2}$ by assuming a sinusoidal variation in u within the wave period. $\overline{u^2}$ is then used to scale the transport coefficients. Normalised depth, i.e. depth over breaking depth, is calculated cross-shore, so that bedload and suspended load velocity terms may be calculated from the B-BAND derived coefficients giving the $\overline{u^2|u|}$ term for bedload transport and $\overline{u^3|u|}$ for suspended load transport. The transport coefficients from the B-Band field data are then:

$$I_{\text{bed}}_{\text{coeff}} = \frac{\overline{|u^2|u}}{(\overline{u^2})^{3/2}} \left\{ -1.58 \left(\frac{d}{d_c} \right)^3 + 5.79 \left(\frac{d}{d_c} \right)^2 - 4.59 \left(\frac{d}{d_c} \right) \right\} \quad \text{bed load} \quad (12)$$

$$I_{\text{sus}}_{\text{coeff}} = \frac{\overline{|u^3|u}}{(\overline{u^2})^2} \left\{ -4.15 \left(\frac{d}{d_c} \right)^3 + 14.17 \left(\frac{d}{d_c} \right)^2 - 10.48 \left(\frac{d}{d_c} \right) \right\} \quad \text{suspended load} \quad (13)$$

The expression for bed and suspended load transport, i , from Bagnold (1966) and Bowen (1980) is:

$$i_{\text{bed}} = \frac{\varepsilon_b C_D \rho I_{\text{bed}}_{\text{coeff}}}{\tan \phi - \frac{u\beta}{|u|}} \quad (14)$$

$$i_{\text{suspended}} = \frac{\varepsilon_s C_D \rho I_{\text{sus}}_{\text{coeff}}}{W - u\beta} \quad (15)$$

where ε_b is a bedload efficiency factor, C_d is the drag coefficient for the bed, ρ the density of fluid, $\tan\phi$ is the angle of repose of sediment and $\tan\beta$ the beach slope. Similarly for suspended load transport ε_s is a suspended load efficiency factor, w is the sediment fall velocity and u is the instantaneous orbital velocity. Because our data provides a time averaged expression for $\overline{u^2|u|}$ and $\overline{u^3|u|}$ respectively, it is difficult to isolate the instantaneous orbital velocity to evaluate the slope terms in the denominator of the two expressions. In this contribution they are ignored (i.e. $u\beta$ is set to zero in the denominators).

The total cross-shore immersed weight sediment transport rate is the sum of expressions (14) and (15), and the total volumetric transport rate, Q , is thus determined by:

$$Q = \frac{i_{\text{bed}} + i_{\text{suspended}}}{(\rho_s - \rho_w)g(1-n)} \quad (16)$$

where ρ_s and ρ_w are the sediment and fluid densities, g is gravity and $(1-n)$ is the packing of settled grains (where n is the void ratio).

The sediment is then moved across the profile on the basis of the gradient of the volumetric transport rate, and the submerged part of the new profile is smoothed so that each point on the new profile is elevated or lowered to the mean of the height of its two neighbours. Having completed all these calculations for a particular tide level, the tide is moved at intervals of 1/100th of a tidal cycle through a simple sinusoid, and the process repeated.

Clearly the model works on several underlying assumptions, which may be summarised as follows:

1. The energetics model is valid.
2. Downslope and upslope transport are equal.
3. Airy wave theory is appropriate.
4. There is transmission of wave energy through bars.
5. Longshore transport is ignored.
6. Swash zone transport is ignored.
7. Sediment supply is unlimited.
8. No avalanching can occur.
9. There is a sinusoidal monochromatic tide signal.

Model Results and Discussion

Figure 4(a) shows the results of a model run with zero tidal range and a 2m breaking wave. Sediment is continually eroded at the shoreline and deposited offshore. The transport convergence point gradually moves offshore, the rate of movement being governed by the asymmetry of the transport profile in the surf zone, and the magnitude and asymmetry of the transport profile in the shoaling wave zone. As the profile evolves what started initially as an area of onshore erosion in the shoaling wave zone gets filled in by the offshore movement of sediment due to broadening of the surf zone. The plateau corresponds to the level of peak offshore transport, as modified by the wave energy profile. The onshore transport region quickly narrows into a spike as the beach gradient in the shoaling zone becomes steeper and steeper. Profile changes from cycle to cycle get smaller, suggesting that the model is approaching an equilibrium state.

Figure 4(b) shows what happens in the model when a tide range is introduced, so that the water surface is continually fluctuating and the transport zones migrate up and down the beachface. A pronounced high water bar forms, but

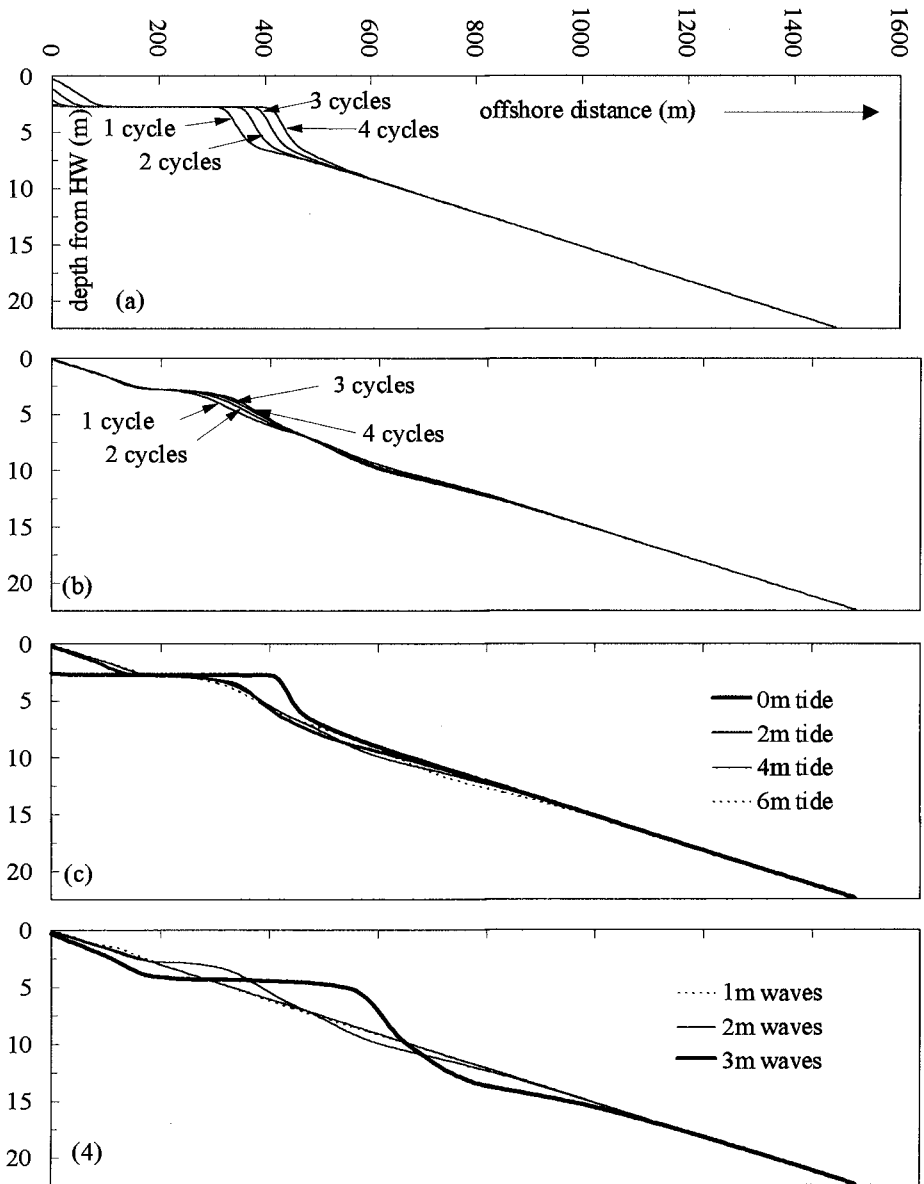


Figure 4. (a) Profile evolution through four tidal cycles with no tidal range and 2m wave height. (b) With 4m tidal range and 2m wave height. (c) Model sensitivity to tidal range 2, 4 and 6m tides (all with 2m waves). (d) Model sensitivity to wave height: 1, 2 and 3m breaking waves (all with 4m tide range).

the low water bar, corresponding to a depth from high water of approximately 6 metres, appears to be suppressed as a result of residence in both offshore and onshore transport zones. The area shoreward of the high water bar only ever resides in a zone of offshore erosion. Again the pattern of erosion and deposition is determined by the total effect of the transport profile, as modified by the shoaling wave energy profile. As the profile develops it appears to be approaching an equilibrium, and changes through time become progressively smaller. Because of the smoothing technique used, what is happening at the shoreline and in the offshore regions is that the elevation of cells outside of the transport zone is being modified by those inside, simulating a slumping effect. This model will only run for approximately 4 tidal cycles before it demands sediment from the very top, or very bottom of the profile, and fails a volume continuity test.

Figure 4(c) shows the evolution of the model profile under different tidal regimes after 4 tidal cycles, with 2 metre waves. The figure demonstrates the suppressing effect of larger tide ranges, with morphological change being the least for the 6m tidal range. In addition with the 6m range the high and low water bars become separated from each other. The position of the high water bar is similar for all cases except for the case of no tide range, where the amount of erosion has pushed it slightly further offshore.

Figure 4(d) shows the sensitivity of the model to wave height, it can be seen that the effect of increasing the wave height is similar to a reduction in tidal range - an increase in the magnitude of wave height leads to tendency for the profile to resemble the non-tidal case. 1m waves have a negligible effect on the profile even after 4 tidal cycles, while with 3m waves the erosion is so substantial, that, as with the zero tide case, the bar is moved offshore by the erosion, to the extent that it becomes indistinct from onshore accretion at low water.

Conclusion

At this stage in its development the model is not able to *quantitatively* simulate the cross-shore profile evolution on 2-dimensional beaches from a knowledge of the wave and tide regimes and sediment characteristics, although that is a possibility with further development. What has been shown is that, using quantitatively accurate flux profiles, the model produces realistic beach profiles within reasonable time-scales. Also, as has been observed by researchers examining field data from macrotidal beach sites (e.g. Wright et al (1982), Jago & Hardisty (1984), Short (1991), Masselink (1993), Masselink and Short (1993)), the model is able to confirm that wave height and tide range are the key influences on the form of the cross-shore profile.

The qualitative appearance of realistic features (offshore bar, intertidal terrace) indicates that the scale of macrotidal beach profile features can be predicted by the tidal translation of a transport shape function across the beachface. The

model will now be used to explore more complex scenarios such as profile response to tide & wave field variations, and examine the effect of spring/neap variations within the tidal cycle.

Acknowledgements

This work was supported through funding by the Environmental and Physical Sciences Research Council, research grant reference 94305086.

References

- Allen, J.R.L. (1970), *Physical Processes of Sedimentation*, George Allen and Unwin, London.
- Bagnold, R.A. (1963), Mechanics of marine sedimentation, In: *The Sea, Ideas and Observations*, Wiley-Interscience Publishers, New York, 3, 507-528.
- Bagnold, R.A. (1966), An approach to the sediment transport problem from general physics, *U.S. Geol. Surv. Prof. Paper* 422-1.
- Bailard, J.A. (1981), An energetics total load sediment transport model for a plane sloping beach, *Journal of Geophysical Research* 86, 10938-10954.
- Bailard, J.A. (1987), Surfzone wave velocity moments, *Proceedings of Coastal Hydrodynamics, ASCE*, 328-342.
- Bird, A.C.F. (1969), *Coasts*, Australian National University Press, Canberra.
- Bowen, A.J. (1980), Simple models of nearshore sedimentation; beach profiles and longshore bars, In: *The Coastline of Canada*, Ed. S.B. McCann, Geological Society of Canada, Paper 1-11.
- Davidson, M.A., Russell, P.E., Huntley, D.A. and Hardisty, J. (1993), Tidal asymmetry in suspended sand transport on a macrotidal intermediate beach, *Marine Geology* 110, 333-353.
- Dean, R.G. (1977), Equilibrium beach profiles: U.S. Atlantic and Gulf coasts, *Ocean Engineering Technical Report #12*, 45pp.
- Foote, Y.L.M. (1994), Waves, Currents and Sand Transport Predictors on a Macro-Tidal Beach, *Ph.D. Thesis*. Institute of Marine Studies, University of Plymouth.
- Foote, Y.L.M., Huntley, D.A. and O'Hare, T.J. (1994), Sand transport on macro-tidal beaches, *Proceedings of the Euromech 310 colloquium*, Le Havre, 360-374.
- Galvin, C.J. (1972), Waves breaking in shallow water, In: *Waves on Beaches*, Ed. R. Meyer, Academic Press, London, 413-455.
- Guza, R.B. and Thornton, E.B. (1985), Velocity moments in the nearshore zone, *Journal of Waterways, Port, Coastal and Ocean Engineering*, 111, 235-256.
- Jago, C.F. and Hardisty, J. (1984), Sedimentology and morphodynamics of a macrotidal beach, Pendine Sands, SW Wales, *Marine Geology* 60, 123-154.

- Kriebel, D.L., Kraus, N.C. and Larson, M. (1991), Engineering methods for predicting beach profile response, *Proceedings of Coastal Sediments '91*, 557-571.
- Le Mehaute, B. (1961), A theoretical study of waves breaking at an angle with a shoreline, *Journal of Geophysical Research* **66** no.2, 495-499.
- Masselink, G. (1993), Simulating the effects of tides on beach morphodynamics, *Journal of Coastal Research* **15**, 180-197.
- Masselink, G. and Short, A.D. (1993), The effect of tide range on beach morphodynamics and morphology: a conceptual model, *Journal of Coastal Research* **93**, 785-800.
- O'Hare, T.J. (1994), What is the origin of the macro-tidal beach profile? *Unpublished Report*, Institute of Marine Studies, University of Plymouth.
- Russell, P.R. and Huntley, D.A., (1996), The spatial distribution of cross-shore transport on high energy beaches, (*in prep.*) Institute of Marine Studies, University of Plymouth.
- Short, A.D. (1991), Macro-meso tidal beach morphodynamics - an overview, *Journal of Coastal Research* **72**, 417-436.
- U.S. Army Corps of Engineers, CERC (1984), *Shore Protection Manual*, 4th Ed, (2 vols), U.S. Printing Office, Washington DC.
- Wright, L.D., Nielsen, P., Short, A.D. and Green, M.O. (1982), Morphodynamics of a macrotidal beach, *Marine Geology* **50**, 97-128.
- Wright, L.D. and Short, A.D. (1984), Morphodynamic variability of surf zones and beaches: a synthesis, *Marine Geology* **56**, 93-111.

CHAPTER 233

BEACH EVOLUTION UNDER RANDOM WAVES.

Patrick Holmes¹, Thomas E. Baldock², Ray T. C. Chan³ and M. Ahmad L. Neshaei³

ABSTRACT

This paper considers the evolution of steep mobile sediment beaches under random waves and results from a new experimental investigation are presented. Both hydrodynamic data obtained over fixed beds and the resulting profile evolution of fine, coarse and bimodal sediment beaches are discussed. Wave heights and undertow in the inner surf zone are found to be poorly predicted by commonly used numerical solutions. In addition, the undertow appears to be strongly influenced by wave grouping in the nearshore. The behaviour of the fine, coarse and bimodal sediment beaches are compared and contrasted. The fine sand beaches tend to erode in the inner surf and swash zones, with the sediment moving predominantly offshore to form a bar. In contrast, onshore sediment transport dominates over the coarse sand beaches, resulting in the formation of a berm above the initial still water level. The bimodal beaches show a similar evolution to the fine sand beaches. However, considerable sediment sorting occurs, with the swash zone largely denuded of fines and the coarser sediment deposited between the still water line and the bar. The data suggests that the stability of the coarse material is significantly reduced by the presence of fines, with little evidence of armouring effects under high incident energy conditions.

1) INTRODUCTION

The hydrodynamics within the nearshore region and the subsequent evolution of beaches under wave attack are important elements governing the stability of the coastal zone. However, numerical modelling of these processes has yet to result in consistent and realistic predictions of beach behaviour. The present

1) Professor.

2) Research Associate.

3) Ph. D. student.

Dept. of Civil Engineering, Imperial College, London, SW7 2BU, UK.

study addresses this issue and considers two key aspects of the problem; the undertow and the sediment particle size. The time mean flow, or undertow, is considered one of the dominant mechanisms in the erosion of beaches (Svendsen, 1984). However, particularly under random waves, significant difficulties remain in the modelling of the undertow. This may in part be due to the difficulties in successfully predicting the wave motion in the inner surf zone (Hamm et al., 1993). In the present study, a comprehensive series of measurements of both the wave heights and near bed horizontal velocity are compared to a deterministic numerical model of nearshore processes (Southgate and Nairn, 1993).

Sediment size has a significant effect on both the magnitude and direction of sediment transport under wave action but the mechanics of the process are still poorly understood. Recent work by Work and Dean (1991) considered the effects of varying grain size on equilibrium beach profiles and showed that steeper profiles were found on beaches with larger grain sizes. However, most beaches exhibit a range of grain sizes, with frequent cross-shore sorting of sediment sizes. Moutzouris (1991) found that the coarsest sediments on a beach were generally found just seaward of the shoreline, while the finest sediments tended to be deposited on offshore bars. Mechanisms for this process have been considered by a number of authors (see Horn, 1991), but numerical models have so far resulted in little success.

Bimodal sediment transport under unbroken waves over a flat bed was considered by Mansell (1992). This work indicated a transient process, whereby the winnowing of fine grains from the bed surface led to the formation of a coarse armour layer. Using model beaches, Quick and Dyksterhuis (1994) found some evidence of an armouring process at low energy conditions. In contrast, at higher energy conditions the coarser sediment had little effect on the profile evolution and the fines controlled the beach steepness. The beach permeability therefore appeared to have a controlling influence on the beach behaviour. However, previous experimental work has not considered the sediment sorting process on beaches and, in particular, the cross-shore distribution of sediment sizes. The present study considers this process and identifies key features that appear consistent with field observations.

2) HYDRODYNAMICS

The experiments were carried out in a large wave flume in the Civil Engineering Department at Imperial College. This flume is 60m long, 3m wide and was used with a working depth of 0.9m. Waves are generated by a hydraulically driven bottom hinged paddle with the facility to absorb wave components reflected from the far end of the flume. The end of the flume is subdivided into three sections to minimise cross-tank motions and consists of a composite beach, with an initial slope of approximately 1/20, rising to 1/10 at the

shoreline. Jonswap spectra with three different significant wave heights and wave periods were used (table 1). Data was collected over 330s at 25Hz, giving 8192 points in each run. The water surface elevation was measured with standard surface piercing resistance type wave gauges and the wave heights calculated from the zeroth spectral moment ($H_{rms} = \sqrt{8m_0}$). The horizontal velocity 6mm above the fixed bed was measured using LDA and an acoustic Doppler velocimeter (ADV). The ADV was less sensitive than the LDA to noise from air bubbles generated by breaking waves, and allowed velocity data to be obtained in very shallow water.

Spectrum	H_{rms} (mm)	f_p (Hz)	T_z (s)
L	90	0.68	1.47
P	70	0.68	1.47
K	45	1.0	1.0

Table 1. Random wave spectral characteristics.

Wave heights

Figures 1a&b shows the H_{rms} wave height across the surf zone for cases P and K respectively. In the outer surf zone, the numerical solution (based on the Battjes and Janssen (1978) approach) gives good results. However, in the inner surf zone the variance and, consequently the wave height, does not decrease to zero at the shoreline. Indeed, the wave height only reduces to about half that of the initial offshore wave height. This is because the steep beach slope allows waves to travel close inshore before breaking and forming bores. The set-up just shoreward of the initial shoreline position is found to be small (of order 5mm) and this is therefore not the reason for the observed increase in wave height in the inner surf zone. It is interesting to note that calculations of the wave height based on the spectral approach and a zero crossing analysis give very similar results in the inner surf zone. This is despite the fact that the wave heights frequently exceed the water depth.

The measured spectra for case P are shown on figure 2, together with the smoothing interval and 95% confidence limits. Offshore of the breaker zone there is little energy in either the lower or higher harmonics, while just seaward of the initial shoreline the energy in the lower harmonics increases significantly. This is expected due to the generation of non-linearities by the shoaling process and the amplification of low frequency waves in shallow water. There is also a small frequency downshift of the spectral peak. However, the spectrum close to the shoreline is still dominated by energy close to the initial spectral peak frequency. The inner surf zone spectra are therefore significantly different from those observed on low slope beaches, where low frequency energy often dominates (e.g.

Holland et al., 1995). The present data are consistent with both the measured wave heights and the formation of bores with a frequency close to f_b .

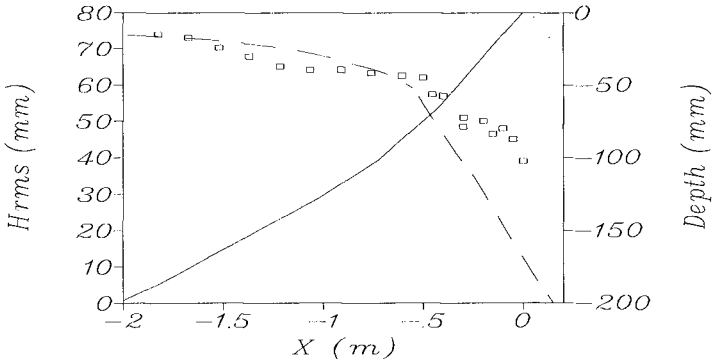


Figure 1a. RMS wave height across the surf zone, case P.
 ——— Depth, □□□□ Data points, — — — Numerical solution.

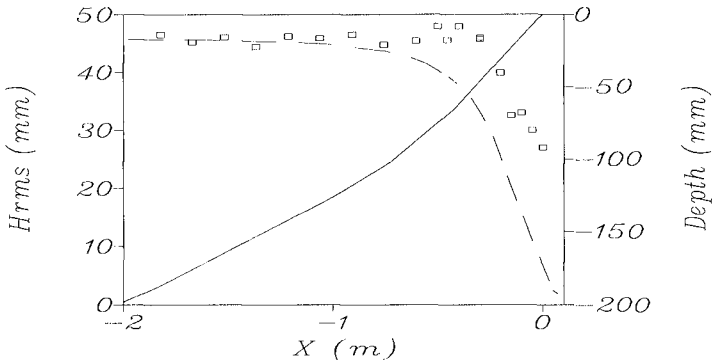


Figure 1b. RMS wave height across the surf zone, case K.
 ——— Depth, □□□□ Data points, — — — Numerical solution.

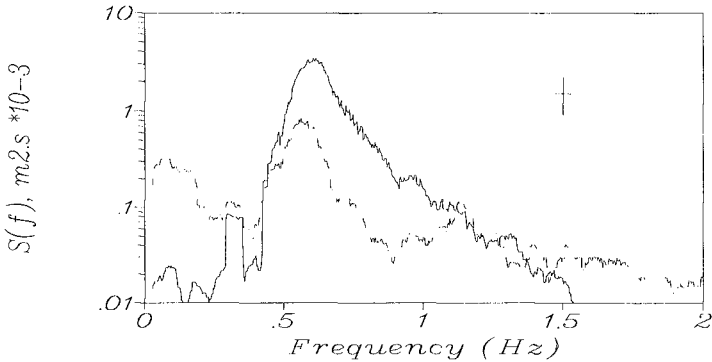


Figure 2. Wave spectra for case P outside the surf zone and close to the shoreline.
 ——— $x=-2\text{m}$ ($d=200\text{mm}$), - - - - $x=-0.05\text{m}$ ($d=10\text{mm}$).

Undertow

The time-mean flow, or undertow, averaged over the total run time is shown in figures 3a&b. For both cases P and K, the undertow in the outer surf zone is very well predicted. However, for case P, the maximum value of the undertow is over-estimated but the undertow close to the shoreline is under-predicted. The over-estimation of the maximum is probably due to the difficulty in determining the depth over which the forward mass flux should be averaged and the less well defined breakpoint (see figure 1a). In shallow water, and particularly with a significant degree of turbulence, it may be more realistic to average the mass flux over the mean water depth, rather than just below trough level as is usual (e.g. Svendsen, 1984). The under-estimation of the undertow in the inner surf zone is consistent with the presence of larger waves than predicted by the numerical solution. A similar effect may be observed for case K (figure 3b), where, in addition, the principal breakpoint is also closer to the shore than predicted (figure 1b). This is likely to increase both the maximum value of the undertow and the undertow close to the shoreline. It therefore appears that a more realistic model for the nearshore wave heights is required for beach slopes of this steepness.

Recent field measurements have suggested that suspended sand concentrations are strongly correlated with the occurrence of wave groups (e.g. Hay and Bowen, 1994). This prompted a closer examination of the velocity field beneath the random waves used in the present investigation. The measured Eulerian horizontal velocity, averaged over either one or three wave periods, shows significant variations in the "local mean" flow, which may be an order of magnitude greater than the long term mean. Figure 4 shows the velocity averaged over three wave periods, the wave height averaged over the same time period and the long term mean velocity.

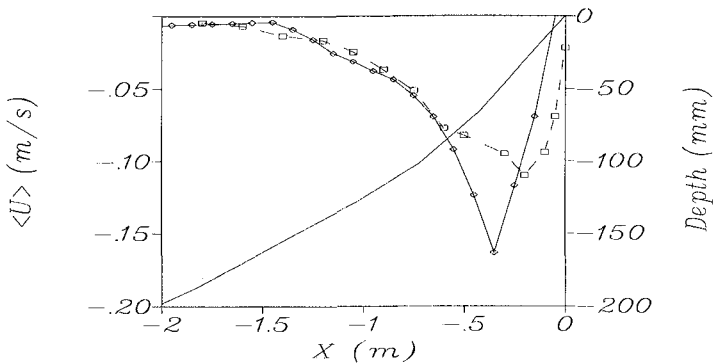


Figure 3a. Undertow. Case P.

— Depth, —□— data points, —◇— Numerical solution.

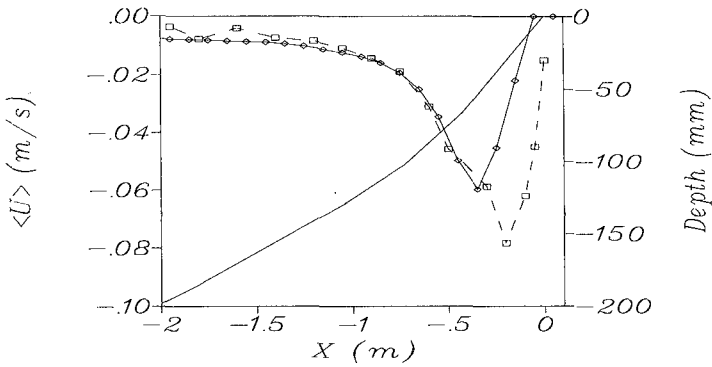


Figure 3b. Undertow. Case K.

— Depth, —□— data points, —◇— Numerical solution.

The variation in the “local mean” flow is strongly correlated with the occurrence of incident wave groups, which suggests that the groupiness of the wave field may be an important feature in suspended sediment transport. Note that the sign of the mean velocity has been inverted to show the correlation with wave height more clearly. The data show that large onshore mean velocities generally occur during the passage of smaller waves, while offshore mean velocities are found under the largest waves. If these variations in the mean flow are combined with coherent fluctuations in the concentration of suspended sediment, then a much large volume of sediment may be moved in suspension than a volume based on the product of the mean velocity and mean sediment concentration.

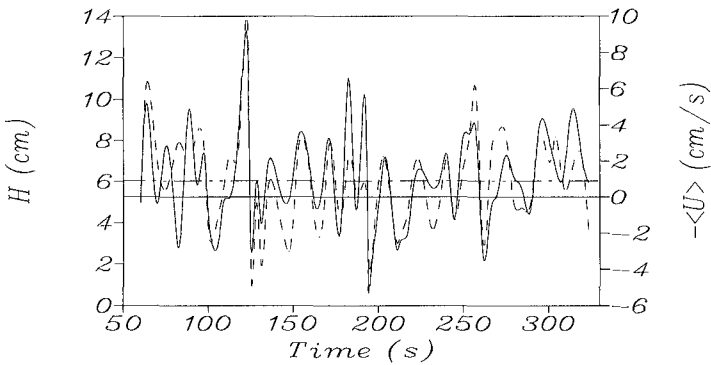


Figure 4. Temporal variations in the “local mean” flow. Case P.

— Wave height, - - - - “local mean” flow (inverted),
 — · — long term mean, $\langle U \rangle$ (inverted).

3) Beach evolution

Beach evolution experiments were carried out under random waves for a fine sand beach, a coarse sand beach and a bimodal sediment beach. In order to facilitate the experimental study, the sediment sizes needed to satisfy three criteria:

1. Both sediment sizes should be mobilised by the maximum velocity in the inner part of the surf zone.
2. The ratio of the two sizes should be large enough to result in significantly different profile evolution as well as allowing them to be readily separated from the bimodal mixture.
3. Each sediment should be well-sorted so as to produce the bimodal characteristics in the resulting grain size distribution of the mixture.

Using these criteria, the sediment size for the coarse and fine sand respectively were chosen to be $D_c = 1.5$ mm and $D_f = 0.5$ mm. The grading curves for the two sands and a 50:50 mix are shown in figure 5. Sediment beds with a thickness of 100 mm were laid over the existing solid beach and the water level in the flume raised by the same amount, resulting in the same initial beach profile as used while collecting the hydrodynamic data. The profile evolution experiments were conducted for a total duration of 240 minutes, using repeated 30 minute runs of the spectra shown in table 1. The flume was allowed to settle after each 30 minute run and there was no evidence of the build up of significant seiche due to wave reflections. The experiments were carried out on the coarse and fine grained beaches separately to serve as controls and to provide comparison with the evolution of the bimodal beach.

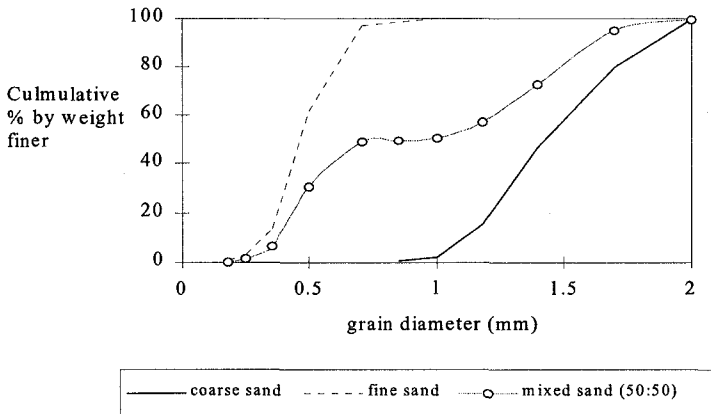
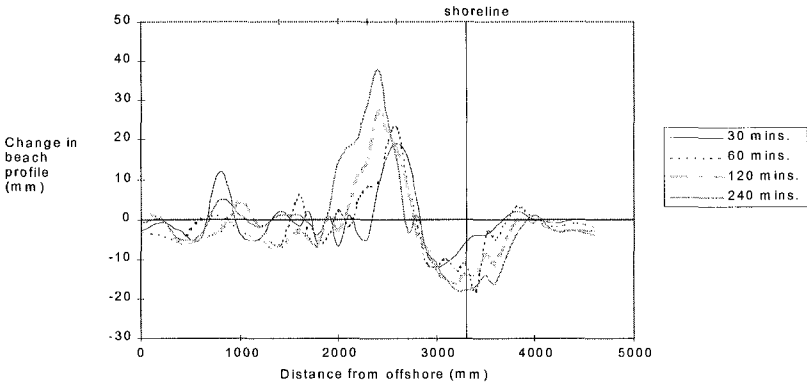


Figure 5. Grading curves.

Profile evolution with uniform sediment size

Several general observations apply to the beach profile evolution for each of the three spectra. Firstly, the coarse sand beaches tend to form a distinct berm shorewards of the initial SWL. The berm appears steepest for case P, which has the lowest deep water wave steepness. For the fine sand beaches, the formation a bar flattens the beach slope in the surf zone. Seaward migration of the bar was evident and the bar moves further offshore as the wave height increases. The SWL recedes shoreward in all cases, except for the coarse beach using case P. Examples of the cross-shore changes in bed level are shown on figures 6&7. A predominant onshore transport is observed in the case of coarse sand while the fine sand bed suffered much erosion around the shoreline, with sediment transported offshore to form a bar.

Fine sand



Coarse sand

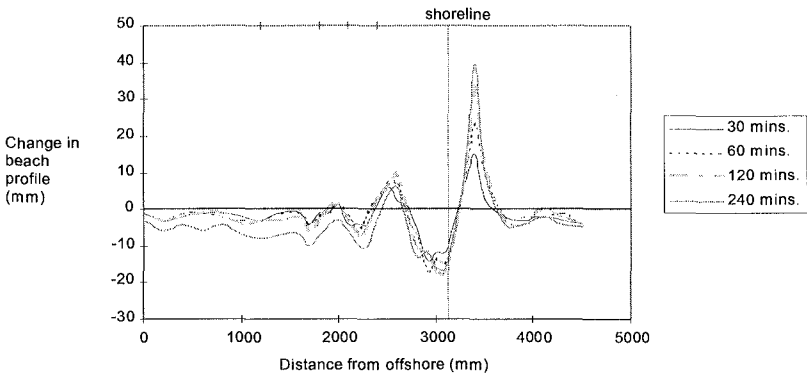


Figure 6. Change in bed elevation from original profile, case K.

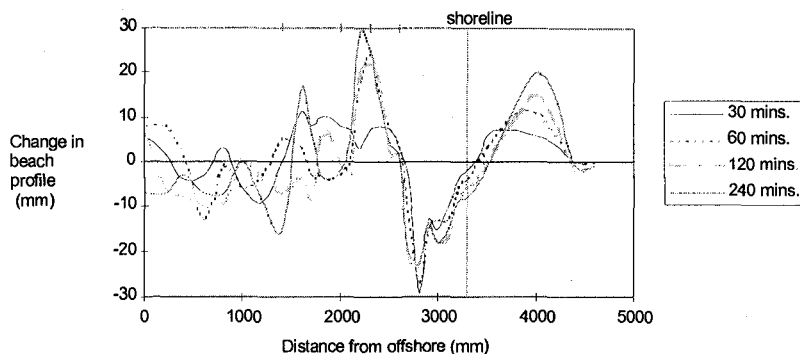
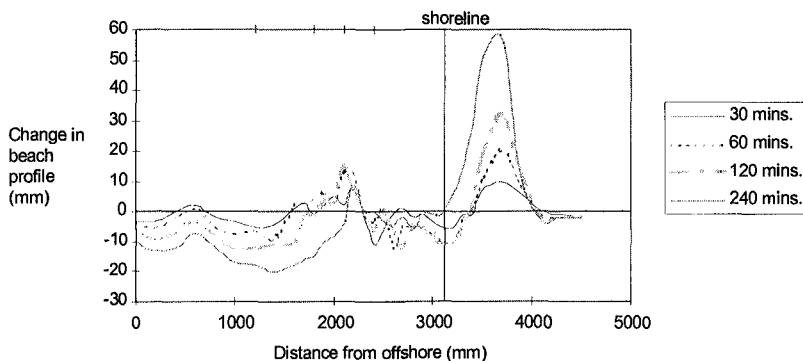
Fine sand**Coarse sand**

Figure 7. Change in bed elevation from original profile, case P.

Bimodal sediment sampling methods

A 50:50 mix of coarse and fine sand was chosen for the bimodal beach. Two sampling devices were used to determine the changes in the composition of the bimodal beach after wave action. The first was a 25mm square spot sampler, which was used to take sediment samples along the centre line of the bed. The second was an in-situ section sampler, placed in position before laying the beach and used to lift whole sections of the bed material from the beach. The section sampler allowed a section of the bed to be removed with minimal disturbance of the sample and enabled the vertical section of sediment sample to be analysed layer by layer (with layers as small as 5 mm). A calibrated fall tube was employed to sort the sampled material, allowing the change with depth in the mix ratio of the beach material to be ascertained. Further details of the sampling method will be available shortly in the Ph.D. thesis of R. T. C. Chan. In order to establish the

variability of initial bed composition a trial experiment was performed to sample the bimodal beach after it was laid. The sampling procedure included taking a section of the bed out (using the section sampler) at six different locations on the beach and 10 layers, each of 5 mm thick, were analysed at each location. The mean in-situ initial mix ratio was found to be 0.515 (coarse/total), with variations of less than 1% by volume between the different locations.

Profile evolution with bimodal sediment

Comparisons of the final beach profiles (after 240 minutes of wave action) for the fine, coarse and bimodal beaches are shown on figures 8a&9a for cases K and P respectively. The original profile in each case is also shown as a reference. The numbered circles at the top of each graph indicate the locations of the section samplers. Figures 8b&9b show the change in bed level from the original profile, where the positions of the section samplers are shown by the numbered triangles. The variation of the mix ratio (coarse/total) with depth at different sections of the beach is shown on figures 8c&9c. The experimental data show several features of particular interest.

In the inner surf zone and swash zone, the final profiles for the bimodal beach resemble the fine sand profiles much more closely than those for the coarse sand. This is the case for all three wave spectra and is confirmed by the bed level changes (figures 8b&9b). The bar positions on the bimodal beach are shoreward of those found in the fine sand beach. Recalling that a seaward migration of the bar was observed on the fine sand beach, it is apparent that there is a tendency for the coarse sand to curb the bar from migrating offshore. On the bimodal beach, the surface of the shoreward slope of the bar is dominated by coarse sediment (refer to section 4a on figures 8c and sections 4,5 and 6 on figure 9c). This is in marked contrast to the higher proportion of fines found on the seaward slope of the bar (section 4b on figure 8c, section 7 on figure 9c). Finally, the foreshore (just above the SWL in the lower swash zone) of the bimodal beach tends to be denuded of coarse sand (sections 2 and 3 on figures 8c&9c).

In summary, the results show that, although the bimodal sediment beach behaves in a similar fashion to the fine sand beach, in agreement with Quick and Dyksterhuis (1994), considerable sediment sorting has also been observed. The present data show that the region between the shoreline and the bar tends to be dominated by the coarse sediment. This appears consistent with the field data of Moutzouris (1990), which showed that the largest grain size often occurred just seaward of the shoreline. Within the swash zone, the fine sand within the mixture seems to destabilise the coarser sand. This facilitates the erosion of coarse sand on the foreshore, and is most conspicuous at the position of the steepest slope. A similar process is also evident on the seaward slope of the bar. This suggests that the mobility of the coarse sand in the mixture is substantially increased due to a

greater exposure and a reduction in friction in the presence of fines. This appears consistent with the results of Miller & Byrne (1966), who found that there is a reduction of the angle of repose when large grains sit on a bed of smaller grains.

The difference in the evolution of the fine and coarse sand beds may be due to a combination of factors. The most dominant are probably a different threshold condition and a difference in the permeability of the beach material. A higher threshold condition for the coarse sand will tend to result in a greater net shoreward transport of sediment. The high permeability of the coarse sediment is also likely to lead to greater infiltration within the swash zone, reducing the backwash and leading to or increasing the asymmetry in the swash zone velocities. This hypothesis is consistent with the much larger berm formation observed on the coarse beaches. In contrast, the bimodal beach permeability will be largely controlled by the finest 10% of sediment within the mix (e.g. Hazen, 1892). Consequently, both the fine sand beaches and the bimodal beaches have a similar permeability. Since both beaches evolve similarly, the permeability appears to be the dominant controlling factor, as suggested by Quick and Dyksterhuis (1994). This has important implications for both numerical modelling of swash processes and beach recharge schemes. For example, if the fines control the beach permeability, and as a consequence the beach behaviour, the addition of coarser supposedly more stable sediment may have little effect on the overall stability of the beach. On the other hand, if the permeability is a controlling factor, beach drainage should be an effective method of beach stabilisation, although some questions remain as to its effectiveness.

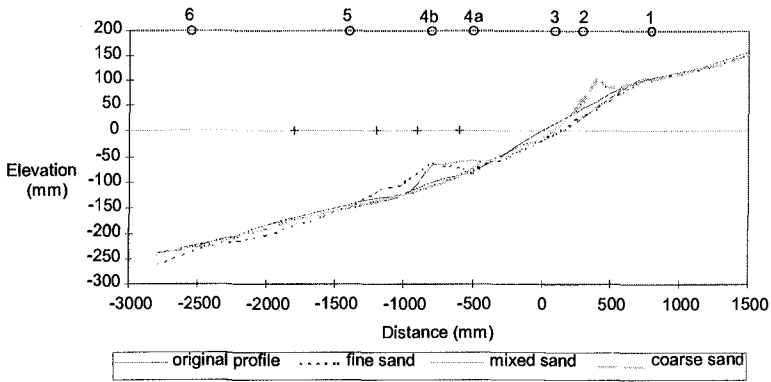


Figure 8a. Profile evolution after 240 minutes, case K.

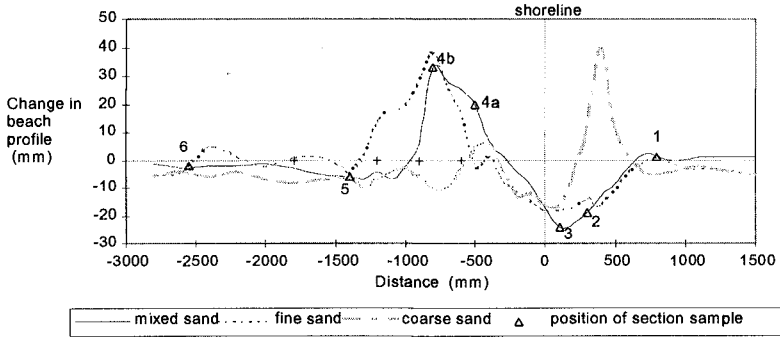


Figure 8b. Change in bed elevation from original profile, case K.

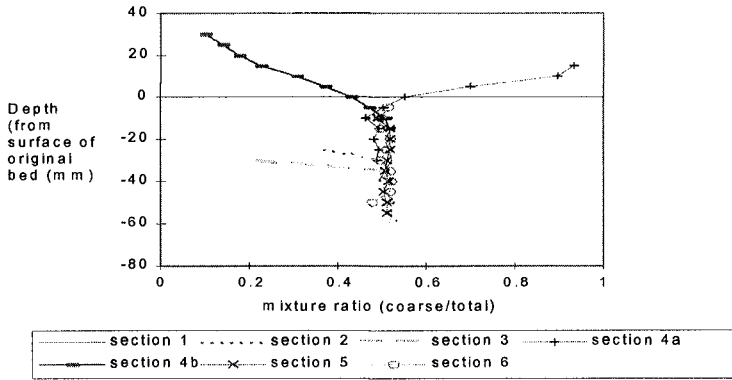


Figure 8c. Variation in mix ratio with depth at six cross-shore locations, case K.

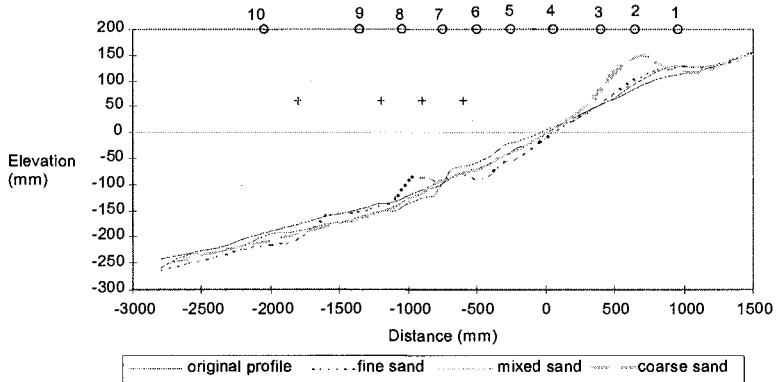


Figure 9a. Profile evolution after 240 minutes, case P

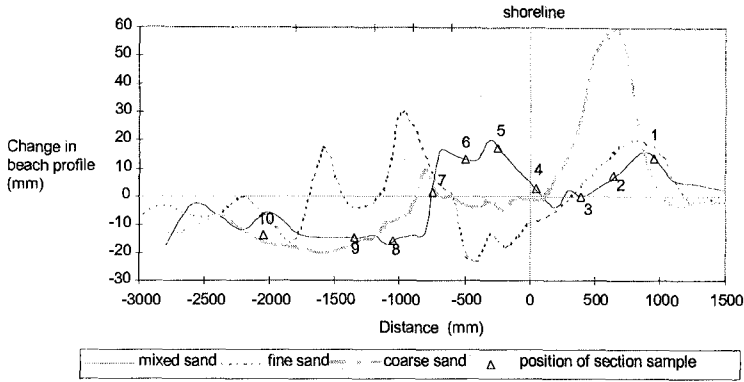


Figure 9b. Change in bed elevation from original profile, case P.

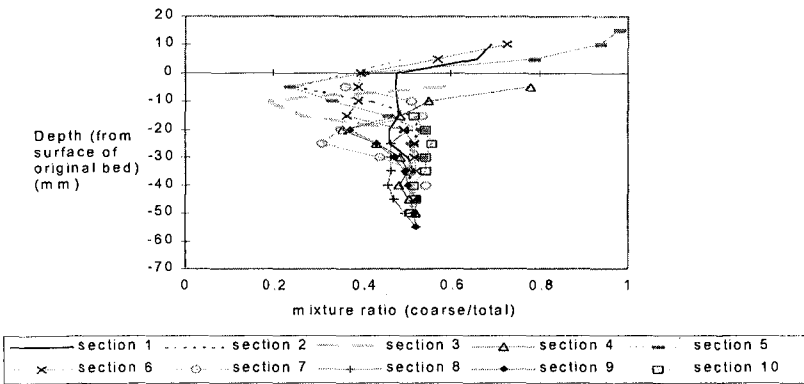


Figure 9c. Variation in mix ratio with depth at six cross-shore locations.

CONCLUSIONS

The results of a new experimental investigation have been presented. Hydrodynamic data obtained over a steep fixed beach show that the wave heights and undertow in the inner surf zone are under-estimated by the numerical solution. In particular, the wave heights in the inner surf zone are not depth limited to the expected degree. This is a consequence of the steep beach slope, with insufficient time for wave breaking fully to establish. Significant wave grouping is evident in the nearshore. This leads to large local fluctuations in the “mean flow”, which are strongly correlated with the wave groups. The profile evolutions of fine and coarse sediment beaches were found to be very different, with the fine sand beaches tending to erode to form a bar, while the coarser beaches generally accreted, resulting in the formation of a berm. The profile evolution of bimodal beaches

was found to be similar to that of fine sand beaches, although considerable sorting was observed. The data suggest that the permeability of beaches is of particular importance, in agreement with some previous studies. The presence of fines appeared to destabilise the coarser material within the bimodal beach, with little coarse material present on the bed surface in the swash zone and on the bar crest. In contrast, the coarse material appeared to have little effect on the movement of the fine sediment, with little evidence of armouring. Clearly there is a need further to investigate the influence of the fine/coarse ratio in bimodal sediments and to consider continuously-graded sediments.

REFERENCES

- Battjes, J. A. and Janssen, J. P. F. M., 1978. Energy loss and set-up due to breaking of random waves. *Proc. 16th Int. Conf. Coastal Eng.*, ASCE, **1**, 569-587.
- Hamm, L., Madsen, P. A. and Peregrine, D. H., 1993. Wave transformation in the nearshore: a review. *Coastal Engineering*, **21**, 5-39.
- Hay, A. E. and Bowen, A. J., 1994. Coherence scales of wave induced suspended sand concentration fluctuations. *J. Geo. Phys. Res.*, **99**, C6, 12749-765.
- Hazen, A., 1892. Discussion of : Dams in sand foundations, by A. C. Loenig. *Transactions ASCE*, **73**:199.
- Holland, K. T., Raubenheimer, B., Guza, R.T. and Holman, R. A., 1995. Run-up kinematics on a natural beach. *J. Geophys. Res.*, **100**, (C3), 4985-4993.
- Horn, D. P., 1991. Computer simulation of shore-normal variations in sediment size. *Proc. Coastal Sediments' 91*. ASCE, 874-889.
- Mansell, P., 1992. Transport of bimodal sediment, MSc. Dissertation, Department of Civil Engineering, Imperial College. London. pp 62.
- Miller, R. L. and Byrne, R. L., 1966. The angle of repose for a single grain on a fixed rough bed. *Sedimentology*, **6**, 303-314.
- Moutzouris, C. I., 1991. Beach profiles vs. cross-shore distributions of sediment grain sizes. *Proc. Coastal Sediments' 91*, ASCE, 860-874.
- Quick, M. C. and Dyksterhuis, P., 1994. Cross-shore transport for beach of mixed sand and gravel. *Int. Symp.: Waves - physical and numerical modelling*, IAHR, Vancouver, 1443-1452.
- Southgate, H. N. and Nairn, R. B., 1993. Deterministic profile modelling of nearshore processes. Part 1. *Coastal Engineering*, **19**, 27-56.
- Svendsen, I. A., 1984. Mass flux and undertow in a surf zone. *Coastal Engineering*, **8**, 347-65.
- Work, P. A. and Dean, R. G., 1991. Effect of varying sediment size on equilibrium beach profiles. *Proc. Coastal Sediments' 91*, ASCE, 890-904.

ACKNOWLEDGEMENTS

The authors gratefully acknowledge the support of the UK Engineering and Physical Sciences Research Council.

CHAPTER 234

BEACH PROFILE SURVEYS ALONG THE U.S. PACIFIC COAST 1945 – 1947

Nicholas C. Kraus¹, M. ASCE, Robert L. Wiegel², Hon. M. ASCE, Willard N. Bascom³

ABSTRACT: The Wave Project at the University of California at Berkeley was established in 1944 to develop a relationship between nearshore waves and the underlying topography for supporting amphibious military landings. The project was continued for scientific purposes until 1952 under the more general name of “Wave Observation and Beach Surveys,” including the Amphibious Oceanography Project. These early field observations are a central part of the genesis of coastal engineering in the United States. Beach profiles were surveyed by stadia and by amphibious vehicle along the coasts of Washington, Oregon, and California, and the results were documented in University of California, Fluid Mechanics Laboratory, reports in the HE-116 series. The profile survey measurements, now 50 years old, are still the only such data available for many beaches along the U.S. Pacific Coast. The data set thus comprises a valuable baseline for documenting change in the coast, and it is a resource on the morphology and grain size for high-energy beaches that are extremely difficult to survey. The profile survey plots in the limited-circulation reports have been digitized and are available for general access in the present study. This paper reviews the early measurement program and the available data set.

INTRODUCTION

The Wave Project of the University of California at Berkeley, sponsored by the Navy Department, was established in 1944 to develop a relationship between nearshore waves and the underlying topography for aiding in WWII beach landings. The project was continued for scientific purposes until 1952 under the more general name of “Wave Observation and Beach Surveys (WOBS),” including the Amphibious Oceanography Project. These early field observations are the genesis of coastal engineering in the United States, and a typical objective was “... to relate wave characteristics to beach changes and to collect sufficient data on surf, beach, and meteorological conditions to make a comparison with the results of

-
- 1) Research Physical Scientist, U.S. Army Engineer Waterways Experiment Station, Coastal and Hydraulics Laboratory, 3909 Halls Ferry Road, Vicksburg, MS 39180.
 - 2) Professor Emeritus, Department of Civil Engineering, University of California, Berkeley, 412 O'Brien Hall, Berkeley, CA 94720.
 - 3) Scientist-Explorer (geophysics and underwater archeology), 5137 Vista Hermosa, Long Beach, CA 90815.

existing forecasting procedures and general wave theory” (Stump and Bascom 1947). Beach profiles were surveyed by stadia and by amphibious vehicle (Dukw – pronounced “duck”) along the coasts of Washington, Oregon, and California, supplemented by measurement of numerous types of coastal processes. The Wave Project and WOBS are believed to have made the first systematic and comprehensive field measurements of the beach profile, sediment, waves, and water level. The results were documented in the HE-116 series of Laboratory Memorandums of the Fluid Mechanics Laboratory, Department of Civil Engineering, U. of California, Berkeley. In the early years, this pioneering program was planned, financed, and directed by Dean Morrough P. O’Brien (U. of California, Berkeley) and by John Isaacs (U. of California, San Diego). Isaacs (1947) made all the surveys in 1945, when he invented the system, and Willard Bascom made virtually all the rest, many at the risk of life. The profile survey measurements have been described authoritatively by Bascom (1964, 1980). The principals responsible for the work were M. P. O’Brien, J. D. Isaacs, W. N. Bascom, D. McAdam, D. Patrick, and R. L. Wiegel.

Surprisingly, the profile survey measurements, now 50 years old, are still the only data available for many beaches along North Pacific coast. In fact, Dean O’Brien had insisted that the northern beaches be surveyed in the winter when there was violent surf (see Bascom 1987 for further discussion), and it remains a challenge to repeat such measurements. The data set thus comprises a valuable baseline for documenting change in the beach that has occurred since that time, and it also serves as a rare resource on the morphology of high-energy beaches that are extremely difficult to survey. The data exist in limited circulation HE-116 reports as distance-elevation plots and have been little accessed, one exception being an article by Komar (1978), who discussed data from HE-116-229 (Isaacs 1947) and HE-116-247 (Bascom and McAdam 1947) for the Washington and Oregon coasts.

The objective of the present work was to capture and preserve the profile data taken on the U.S. West Coast over the period 1945-1952. However, only data for the period 1945-1947 could be recovered in the present effort. For our study, the available profile survey data were digitized manually from the original drawings and the information transferred to magnetic media. This paper presents an overview of the data set, including the institutions and personalities behind the WOBS projects. The paper was prepared as a contribution for the celebratory theme “Coastal Engineering Heritage” (Kraus 1996) of the Twenty-fifth International Coastal Engineering Conference. Further information about the history of coastal engineering in the United States can be found in Wiegel and Saville, Jr. (1996).

RESOURCES CONSULTED

For this study, the originals of ten HE-116 reports were borrowed from the Water Resources Center Library, Department of Civil Engineering, University of California, Berkeley. Of these, five reports contained beach profile survey data. Table A1 of the appendix lists by report the beaches, years, and ranges for which profile data are available from these reports. The data set developed in the present study contains 216 profile surveys from nine beaches in Washington, six in Oregon, and 16 in California.

Many of the reports contain black and white photographs, most taken from the ground, but with some from the air by military planes. HE-116-223 (Fluid Mechanics Laboratory 1946) includes pictures and captions with the location and date for “...various beaches which were not at the time subjects of intensive study.” In order to preserve the photographic record of west-coast beaches in the late 1940s and early 1950s, for the present project more than 100 photographs compiled from the different reports were scanned to create digital files.

After making three sets of copies of the reports, including the oversize plots of the profile plots, the originals were returned to the Water Resources Center Library. A complete set was sent to the Coastal Engineering Archive at the University of Florida, Gainesville, Florida; the University Library at Oregon State University, Corvallis, Oregon; and the Technical Library at the U.S. Army Engineer Waterways Experiment Station, Vicksburg, Mississippi.

Many of the profile surveys extended from the upper beach to a depth of approximately 10 m, although surveys to wading depth were also made. Bascom (1980) gives a vivid first-hand account of the surveys made by amphibious vehicle (Dukw, Fig. 1). Horizontal position was measured by triangulation, and measurement points were marked through radio communication when a lead-line was heaved overboard. The sum of the water depth measured beneath the trough of a wave and one-third of the estimated wave height were reported by radio to a recorder on shore as an estimate of total water depth. The depths were converted to mean lower low water tidal datum by reference to either a tide gauge or predictions. Komar (1978) has summarized the measurement procedures and cites primary documents and reports not discussed here.

Other measurements or observations routinely made by the field parties included visual "surf observations" of the wave height and period, breaking wave type, and the nearshore current – both the longshore and rip currents. Measurements were sometimes made of the water table. Sediment samples were taken, but the authors were not able to locate the substantial information that should have been compiled. Other interested parties should continue in that search. An interesting aspect was documentation of the depth of tire impressions in the beach sediment made by the field-reconnaissance vehicles. Both military applications and relation of compaction to beach change were of interest, as was operation of the Dukws in future data collection.

In remainder of this paper, we focus on the beach profile survey data.

DIGITIZATION PROCEDURE

The original reports were unbound to mount the individual plots of the beach profiles on a digitization table. At first, it was planned to trace the profile lines by cross hair sighting on a high-resolution electronic digitization tablet. However, most of the pages containing the plots had become warped, making standard digitization mapping on to electronic axes inaccurate.

As an alternative to rubber sheeting through software, which would have introduced or distributed errors, distance-elevation pairs on the plotted profiles were located manually by placing a straight edge parallel to the grid lines on the plots and reading corresponding intersection values on the two axes. The locations of actual survey points on the plots were almost always unambiguously evident by discontinuities in the lines joining the points. Because of the presence of the grid lines on the plots, errors that might have been introduced by warping of the paper are believed to be minimal.

After manual digitization of the profile survey data, the distance-elevation pairs were entered into the computer and plotted to the same scale as the original drawings. Plots of the digitized data drawn on transparent paper were laid on top of the original drawings and visually compared for discrepancies, which were corrected. The resultant quality-controlled data set is believed to be an accurate representation of the original measurements. These data are available as ASCII files. The data are in the original American customary units (feet), but in this paper results are presented in metric units for the international audience.



12845
0·00 at Halfmoon Bay Municipal Beach
April 29, 1947 - 0930
Halfmoon Bay, California



12846
0·00 at Halfmoon Bay Municipal Beach
April 29, 1947 - 0835
Halfmoon Bay, California

Fig. 1. Survey preparations (from Wiegel 1947).

EXAMPLE RESULTS

In this section we give examples from Washington, Oregon, and California, from the data set compiled. Locations of many of the sites encompassed by the total data set are shown in Fig. 2. Appendix A gives the locations of all the beaches for which survey data were compiled.

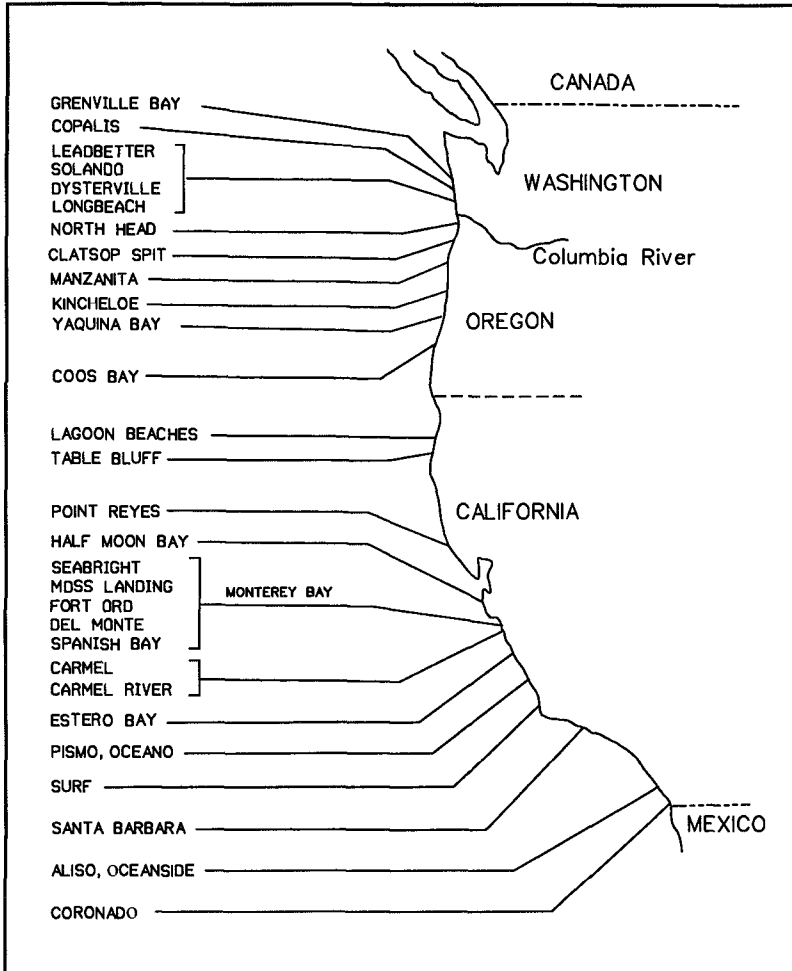


Fig. 2. Location of Pacific Coast beaches investigated (after Bascom 1951a).

Comparison to Echo Sounder

Depth soundings were typically made by lead line as described above, because echo sounders blanked out in the surf zone where air bubbles are present. Patrick and Bascom (1950) discuss technical details of the lead-line method and echo sounder measurement methods as applied in the Wave Project and subsequent studies. Many of the considerations are still valid today for making beach-profile surveys. As an example, we quote "After the ground control is established, the remaining field work is accomplished in two parts: water soundings during high tide and beach land profiles during low tide. The method gives *an overlap* (emphasis added here) of the data obtained and provides a check on the accuracy of the work." Lack of appreciation for the necessity of overlap of land and water surveys is found in some works today, which introduces ambiguity in collection of expensive data.

Patrick and Bascom (1950) compare the two methods "...made at Carmel (California, in 1947) and the results for one range line...", which is reproduced in Fig. 3 here. Although the lead-line method did not pick up detail of the bars on the profile, the comparison indicates remarkable skill in the lead-line survey that was consistent to almost 10-m depth, giving confidence in the reliability of the overall data set. The maximum difference in readings between the two methods is on the order of 1 m beyond the 6-m contour (MLLW).

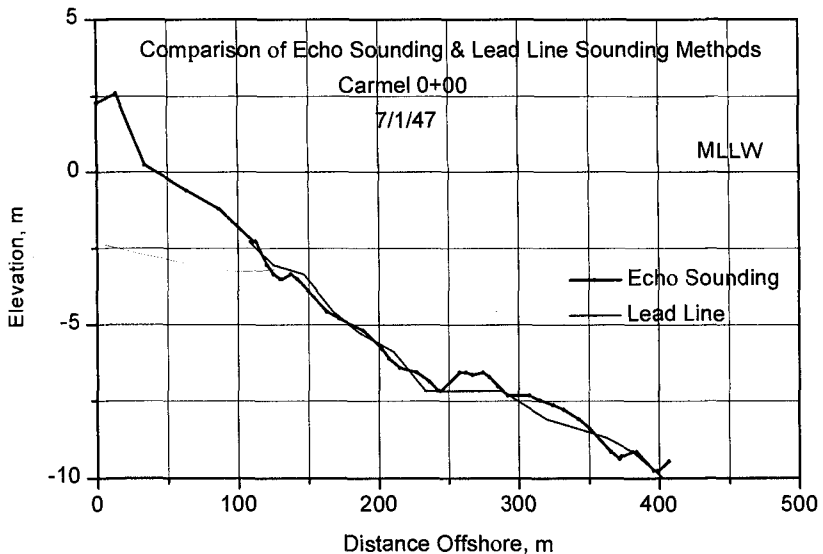


Fig. 3. Comparison of sounding methods (adapted from Patrick and Bascom 1950).

Point Grenville, Washington

This beach is located north of the mouth of the Columbia River and north of Grays Harbor, Washington. The two profiles plotted in Fig. 4 were surveyed approximately 1 year apart, with the 1945 survey made by a party led by Isaacs (1947) and the 1946 survey made by a party led by Bascom and McAdam (1947). Quoting from Isaacs: "(Between August 27 and September 27, 1945) ...the field party of the University of California Wave Investigation Project made surveys of the beach and surf characteristics at a number of beaches of the Pacific Northwest. These beaches are noted for their gentle slopes and fine grained materials." Further in the report, it is stated for the Point Grenville, South Station: "About 2 miles (3.2 km) south of the Cape (Cape Grenville) a section of the beach existed where the beach face was comparatively steep. No berm existed and it was apparent that high water reached the low clay banks in this region. The profile there showed a slope of beach face of about 1:20. The breaker zone was quite irregular but the bottom offshore was smooth and of gentle slope." This description fits Fig. 4 well. Wave breaker heights tabulated by Bascom and McAdam (1947) at the approximate time of the 1946 survey were approximately 1.5, 2, and 3 m for the inner, middle, and outer bars, respectively.

Grain-size information is not given for Point Grenville in the two aforementioned reports. However, Bascom (1951a) indicates that a representative median grain size might be on the order of 0.17 mm. As an example of a possible use of the profile data, we fit an equilibrium profile following a "distance to the 2/3 power law" (Dean 1991) to the 1945 profile survey. The grain size of 0.14 mm was inferred from the shape parameter (Moore 1982) of the equilibrium profile, which is seen to describe the survey measurements well from MLLW shoreline to the survey limit (7-m depth). This small exercise confirms the concept that profile shape is governed primarily by sediment grain size on an open-coast beach (see Bascom (1951a) for a conclusions about a wave-sheltered beach).

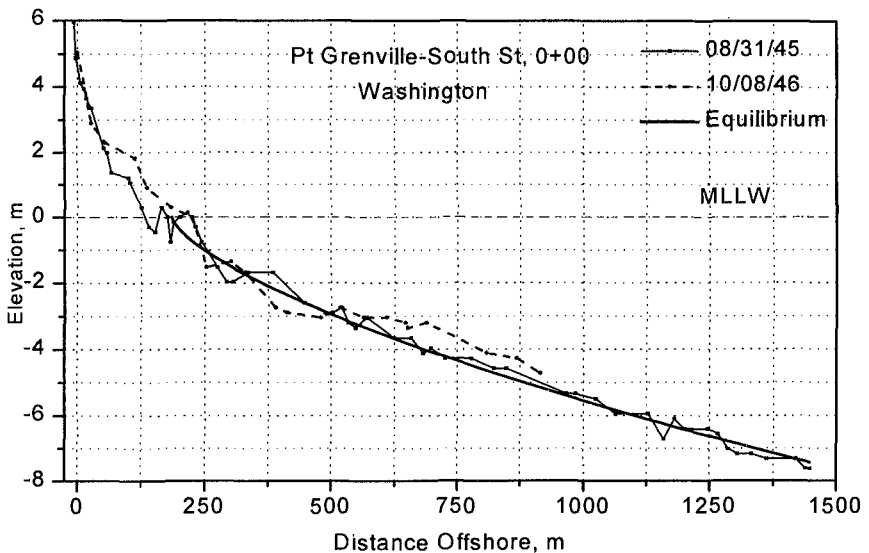


Fig. 4. Profile surveys approximately 1 year apart, Pt. Grenville, South Station, Washington.

Clatsop Spit Beach, Oregon

This beach is located south of the Columbia River, Oregon. The two profile surveys shown in Fig. 5 were taken only 3 days apart and within approximately 300 m of each other. A substantial bar-and-trough topography existed on the profiles. Komar (1978) speculated on mechanisms that might be responsible for the substantial trough. Clatsop Spit is presently experiencing moderate erosion, and data such as shown below will be useful for understanding the coastal processes acting at the site.

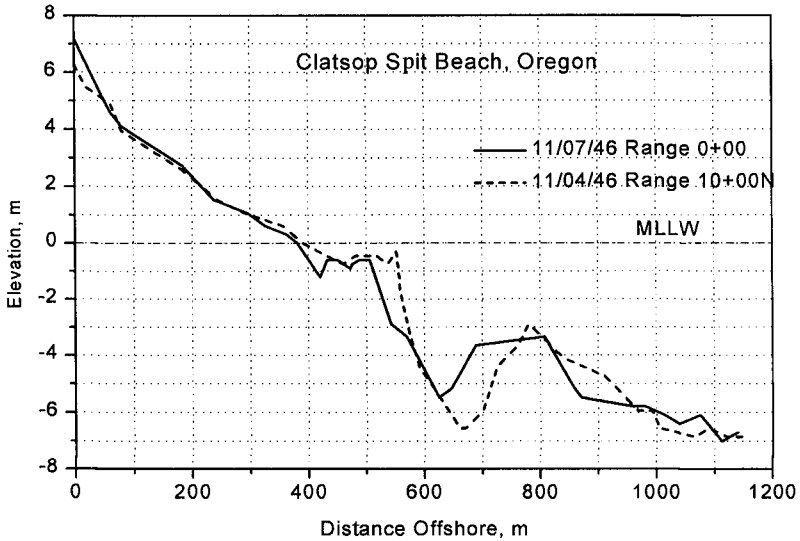


Fig. 5. Profile surveys on two range lines, Clatsop Spit Beach, Oregon.

Carmel Beach, California

The beach at Carmel, California, was studied intensively while the surveying parties "...would rest in the spring to recover from winter encounters with the northern surf" (Bascom 1980). Fig. 73 in Bascom (1980) illustrates seasonal shifts in the berm at Carmel, which were measured to be more than 60 m. Figs. 6 and 7, taken from data given by McAdam and Bascom (1947), reproduce some of the profiles in Bascom (1980) and display the remarkable seasonal changes at Carmel Beach. Bascom (1951a) indicates that a representative grain size for Carmel Beach is about 0.35 mm. This beach was one of those analyzed by Bascom (1951a) in a seminal paper on the relation between beach slope, grain size, and exposure to waves. In Fig. 6, it is interesting to note that little profile change occurs below approximately 4-m depth (MLLW) as compared to the elevation changes above that depth.

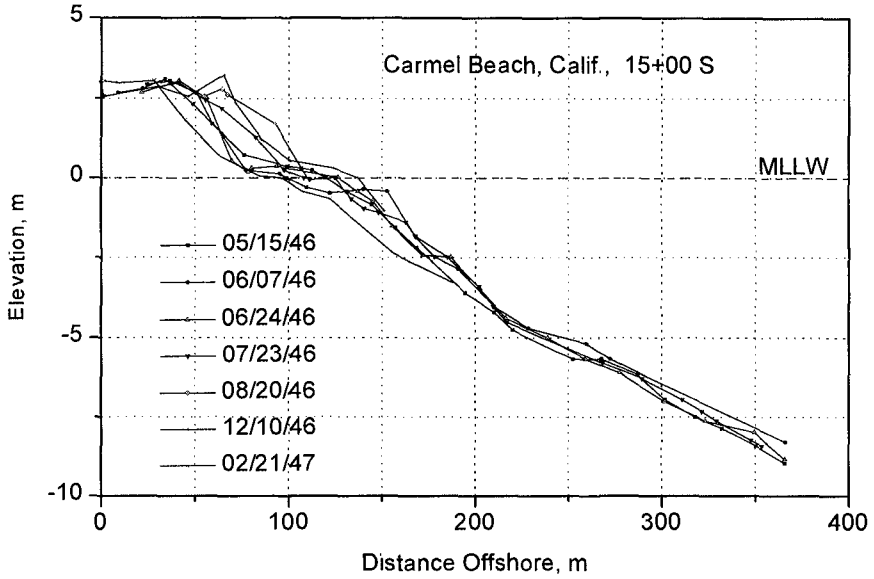


Fig. 6. Seasonal change in the berm and foreshore, Carmel Beach, California.

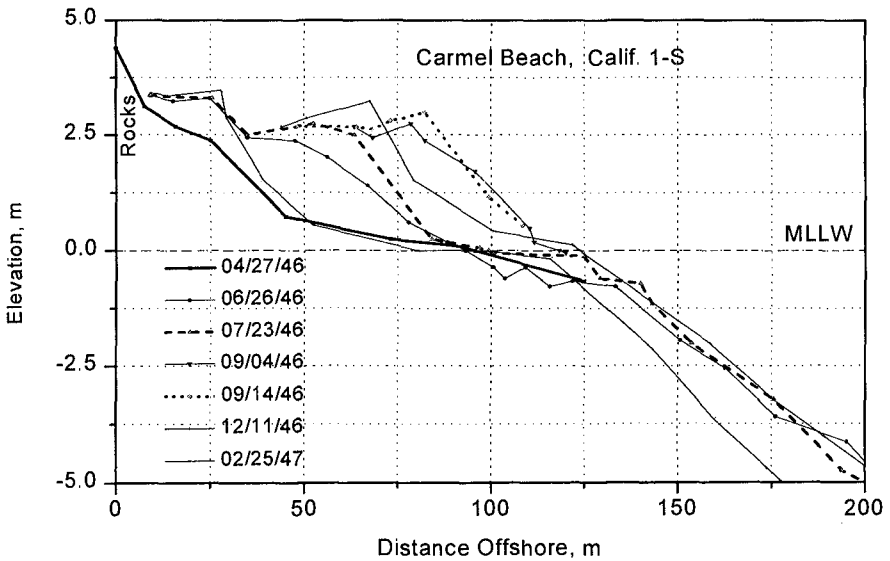


Fig. 7. Close-up view: seasonal change in the berm at Carmel Beach, California.

Miramar Beach, California

Discussion of the survey range lines along Halfmoon Bay, California, including Miramar Beach (Fig. 8) is given by Wiegel (1947). In the present study, it was originally intended to recover the locations of such range lines and reestablish survey monumentation. However, lack of funding prevented us from undertaking this task. Fig. 8 is provided to inform others that the HW-116 reports do contain information with which to reoccupy many of the survey ranges. Although recovery of the vertical datum may be impossible because of loss of benchmarks, location of many of the range lines along the beach will be straightforward because of the excellent photographic documentation.

CONCLUDING DISCUSSION

This study has attempted to capture and preserve, in digital form, beach profile survey data obtained on the Pacific Coast of the United States during the inception of the discipline of coastal engineering, the mid-1940s through mid-1950s. Ten original reports from that era were consulted, of which five contained plots of the survey data, which were digitized and quality checked. Approximately 100 photographs were also scanned to create digital copies. The basic product is a data base consisting of 216 profile surveys for 31 beaches in Washington, Oregon, and California, taken during the years 1945-1947.

The data set is expected to be valuable for coastal engineers, planners, and researchers because of its uniqueness – profile surveys extending to 10-m depth on high-energy beaches of various grain sizes. The data set allows study of fundamental aspects of beach morphology, including summer-winter profile change, time scales of profile change, bar size and movement, and beach slope versus grain size. Early analysis of the data (Bascom 1951a, 1951b) has yielded now-classic results on beach behavior. Many more insights and uses of the data can be expected.

The quest should not end for additional data from the WOBS project. Bascom (1951a) reports that approximately 500 beach profile surveys were made on some 40 beaches, so that the present study has located less than half of the available surveys. In addition, in this unfunded project we were not able to find much of the data for the approximately 600 sediment samples taken (see Bascom 1951a, 1951b for some data). Our goal of recovering all the beach profile survey ranges was not achieved, and we hope that this paper will serve as a stimulus for researchers to locate and preserve the remaining data, and for Federal, state, and local agencies in Washington, Oregon, and California, responsible for the coast to locate and reestablish the range lines.

ACKNOWLEDGEMENTS

This study would not have been possible without the cooperation of the Water Resources Center Library, Department of Civil Engineering, University of California, Berkeley, which permitted long-term loan of the HE-116 original reports. Digitization of the profile survey data was carried out at the Conrad Blucher Institute for Surveying and Science, Texas A&M University-Corpus Christi, while the first author served as Director of the Institute. The digitization and quality-control checks were performed by Ms. Karen Bridges and Ms. Margie Langely, both undergraduate students. The day-to-day work was supervised by Ms. Deidre Williams, graduate student in charge of the Blucher Institute Geographic Information Systems Laboratory. Permission was granted to N. C. Kraus by Headquarters, U.S. Army Corps of Engineers, to publish this information.



Fig. 8. Range lines at Miramar Beach, California (circa April 1947).

REFERENCES

- Bascom, W. 1946. Report of Field Studies at Monterey, April to August 1946. Tech. Rep. HE-116-224, Dept. of Engrg., Univ. of Calif., Berkeley.
- Bascom, W. N. 1951a. The Relationship Between Sand Size and Beach-Face Slope. *Trans. Am. Geophys. Union* 32(6): 866-874.
- Bascom, W. N. 1951b. The Relationship Between Sand Size and Beach Face Slope. Series 14, Issue 2, Dept. of Engrg., Univ. of Calif., Berkeley, Beach Erosion Board Contract W49-055-eng-2, April, 1951.
- Bascom, W. 1964. Revised and updated edition, 1980. *Waves and Beaches*. Anchor Books, Anchor Press/Doubleday, Garden City, New York, 367 pp.
- Bascom, W. 1987. The Waves Project – An Illustrated Letter to Morrrough P. O'Brien. *Shore & Beach* 55(3-4): 25-30.
- Bascom, W. and McAdam, D. 1947. Beach and Surf Conditions on the Beaches of the Oregon and Washington Coasts Between October 9, 1946 and November 18, 1946. Laboratory Memorandum HE-116-247, Dept. of Engrg., Univ. of Calif., Berkeley.
- Dean, R. G. 1991. Equilibrium Beach Profiles: Characteristics and Applications. *J. Coastal Res.*, 7(1): 53-84.
- Fluid Mechanics Laboratory. 1946. Reconnaissance of Miscellaneous Pacific Beaches. Laboratory Memorandum HE-116-223, Dept. of Engrg., Univ. of Calif., Berkeley.
- Isaacs, J. D. 1947. Beach and Surf Conditions on Beaches of the Oregon and Washington Coast Between August 27 and September 27, 1945. Laboratory Memorandum HE-116-229, Dept. of Engrg., Univ. of Calif., Berkeley.
- Komar, P. D. 1978. Beach Profiles on the Oregon and Washington Coasts Obtained with an Amphibious Dukw. *Shore & Beach* 46(3): 27-33.
- Kraus, N. C. (Editor). 1996. *History and Heritage of Coastal Engineering*. ASCE, N.Y., 603 pp.
- McAdam, D. and Bascom, W. N. 1947. WOBS Field Party at Monterey, Supplement. Laboratory Memorandum HE-116-224 Supplement, Dept. of Engrg., Univ. of Calif., Berkeley.
- Moore, B. 1982. Beach Profile Evolution Response to Changes in Water Level and Wave Height. M.S. Thesis, Dept. of Civil Engrg., Univ. of Delaware, Newark, Del.
- Patrick, D. A. and Bascom, W. N. 1950. Methods for Surveying and Plotting Beach Profiles. Tech. Rep. 155-21, Dept. of Engrg., Univ. of Calif., Berkeley.
- Stump, R. S. and Bascom, W. N. 1946 (revised 1947). Surf Observations and Photographic Data Obtained by Field Party and Comparison to Hindcasts: Table Bluff Station, December 1945 - January 1946. Laboratory Memorandum HE-116-205, Dept. of Engrg., Univ. of Calif., Berkeley.
- Wiegel, R. L. 1947. Beach and Surf Conditions at Halfmoon Bay, April 28, 29, 1947. Tech. Rep. HE-116-256, Dept. of Engrg., Univ. of Calif., Berkeley.
- Wiegel, R. L. and Saville, T., Jr. 1996. History of Coastal Engineering in the USA. In (N. C. Kraus, editor) *History and Heritage of Coastal Engineering*, ASCE, N.Y., 513-600.

APPENDIX A: DATA FOUND IN THIS STUDY

Table A1 lists profile data by source and state that was available for digitization in this study.

Table A1. Source and locations of available data			
Report No.	Surveyed Beaches	Range	Date
Washington			
HE-116-229	Grays Harbor to Columbia		
HE-116-229	Copalis to Cape Grenville		
HE-116-229	Longbeach to Leadbetter		
HE-116-229 HE-116-247	Point Grenville	0+00; 5+00S 10+00S	8/27/45, 10/8/46 8/28/45 8/31/45
HE-116-229 HE-116-247	Point Grenville, South St.	0+00	8/31/45, 10/8/46
HE-116-229 HE-116-247	Copalis Beach	0+00, 10+00N, 10+00S	8/28/45, 10/9/46
HE-116-229 HE-116-247	Ocean City	0+00	8/31/45, 10/11/46
HE-116-229 HE-116-247	Leadbetter Point	10+00S 20+00S 0+00 30+00S	8/31/45, 10/16/46 9/7/45, 10/16/46 9/8/45, 10/16/46 9/10/45, 10/16/46
HE-116-229 HE-116-247	Solando Wreck	0+00; 10+00N, 20+00N, 30+00N	10/16/46; 9/10/45, 10/16/46
HE-116-229 HE-116-247	Oysterville Beach	10+00S 0+00; 10+00N	9/14/45, 10/14/46, 10/17/46; 9/14/45, 10/17 - 11/18/46; 9/14/45, 10/14/46, 10/17/46
HE-116-229	Ocean Park	10+00N; 0+00; 10+00S	9/12/45; 9/14/45; 9/14/45
HE-116-229	Long Beach Portal	0+00	8/31/45
Oregon			
HE-116-229 HE-116-247	Clatsop Spit Beach	0+00; 10+00N; 10+00S	9/24/45, 11/7/46; 9/24/45, 11/4/46; 9/24/45, 11/7/46
HE-116-247	Manzanita	0+00, 8+00N, 8+00S	10/18/46, 11/6/46
HE-116-229 HE-116-247	Cape Lookout Station (Lookout Beach)	0+00, 10+00S	9/27/45, 10/28/46
HE-116-229 HE-116-247	Cape Merriweather Station	0+00	9/27/45, 10/26/46, 11/12/46
HE-116-229 HE-116-247	Sand Lake Station	0+00; 10+00S; 10+00N	9/27/45, 10/26/46, 11/5/46, 11/12/46; 9/27/45, 11/12/46; 10/26/46
HE-116-247	Coos Bay (Empire Beach)	0+00, 10+00S&N	11/15/46

California			
HE-116-205	Table Bluff		10/27/45 - 2/10/46 3/24/46 - 3/30/46
HE-116-224	Seabright Beach	0+00; 4+47N; 1+50N	6/5/46, 7/30/46, 2/4/47; 6/12/46, 7/30/46, 2/4/47; 6/21/46
HE-116-224	Seacliff Beach	0+00; 5+00N; 2+85N	6/5/46, 7/30/46, 2/4/47; 6/13/46, 7/30/46, 2/4/47; 6/21/46
HE-116-224	Moss Landing Beach, North	0+00, 5+00N	6/6/46, 6/12/46, 8/14/46, 3/6/47
HE-116-224	Moss Landing Beach, South	0+00, 5+00N, 5+00S	8/14/46, 8/15/46, 3/6/47
HE-116-256	Halfmoon Bay Municipal Beach	0+00, 10+00N	4/29/47
HE-116-256	Coast Guard Beach	0+00	4/28/47 & 4/29/47
HE-116-256	Princeton Beach	0+00, 10+00S	4/28/47 & 4/29/47
HE-116-256	Miramar Beach	0+00, 6+00S, 6+00N; 0+00; 6+00S; 6+00N	4/28/47 & 4/29/47; 7/17 & 18/45, 4/28 & 29/47; 7/17 & 18/45, 4/28 & 29/47; 7/17 & 18/45, 4/28 & 29/47
HE-116-224	Fort Ord (Soldier's Club)	0+00, 5+00S, 5+00N	6/13/46
HE-116-224	Fort Ord (Concrete Block)	0+00, 5+00S, 10+00S	6/13/46
HE-116-224	Fort Ord (Landing Barge)	0+00, 5+00S	6/13/46, 8/2/46, 2/24/47
HE-116-224	Spanish Bay	2+75N	5/24/46, 7/24/46
HE-116-224	Spanish Bay, South St.	2+75N	5/24/46, 7/24/46
HE-116-224	Carmel	1-S; 15+00S; 5+00S, 10+00S; 0+00 5+00N 10+00N 15+00N	4/27/46, 6/26/46, 7/23/46, 9/4/46, 9/14/46, 12/11/46, 2/25/47; 5/15/46, 6/7/46, 6/24/46, 7/23/46, 8/20/46, 12/10/46, 2/21/47; 5/15/46, 6/7/46, 6/24/46, 7/23/46, 8/20/46, 12/11/46, 2/21/47 4/24/46, 5/22/46, 6/24/46, 7/23/46, 8/21/46, 12/11/46, 2/21/47 5/15/46, 6/7/46, 6/24/46, 7/23/46, 8/21/46, 2/21/47 4/24/46, 5/15/46, 6/7/46, 7/23/46, 8/20/46, 2/21/47 5/15/46, 6/7/46, 6/26/46, 7/23/46, 8/20/46, 2/21/47
HE-116-224	Carmel River Bight	2+50N 0+00 2+50S 5+00S	6/11/46, 7/23/46, 2/25/47 6/11/46, 7/23/46, 2/25/47 6/11/46, 7/23/46, 2/25/47 6/11/46, 7/23/46, 2/25/47
HE-116-22	Point Sur	3+50S 0+00 5+00N	6/18/46, 7/31/46 6/18/46, 7/31/46 6/18/46, 7/31/46

CHAPTER 235

MECHANISM AND CALCULATION OF SAND DUNE EROSION BY STORMS

Ryuichiro Nishi¹ and Nicholas C. Kraus²

ABSTRACT: Dunes constitute a central element in shore-protection designs aimed at preventing inundation and erosion of the upland by storms. In the present study, the dune-erosion mechanism is investigated through field observations of the performance of sand dunes under storm action in Japan and in the United States. The observations are quantified by analysis of three test series carried out in the SUPERTANK project. The SUPERTANK data set includes tests on erosion of an uncompacted and a compacted near-vertical dune by random waves. The SBEACH numerical model of dune erosion and profile change is modified to erode dunes by the force of incident waves. This sediment can then supply the profile change model that demands offshore movement of sand in response to the occurrence of storm waves and elevated water level. The simulations show good agreement with the erosion measured at SUPERTANK for the uncompacted and the compacted dunes.

INTRODUCTION

Dune design is a central element in shore-protection projects aimed at preventing inundation and erosion of the upland by storms. In the United States and some other countries, the performance of protective dunes is often estimated with the Kriebel and Dean (1985) model or the Larson and Kraus (1989) (SBEACH) model of storm-induced beach erosion. These models operate under the assumption that erosion of the beach and dune complex is controlled by the demand for sand in the surf zone to satisfy establishment of an equilibrium profile under the impressed storm water level and waves. The demand, or, cross-shore sediment transport capacity, is estimated from the difference in wave energy dissipation between the existing profile and an assumed equilibrium profile shape. Conceptually, in such a demand-and-supply model (demand model), if a dune exists on an equilibrium beach profile for a given storm condition, little dune erosion is expected to occur. Clearly, however, a dune will erode if it is subjected to violent wave action almost independently of the equilibrium profile dynamics occurring offshore. Resolution of this problem is discussed here.

-
1. Assistant Professor, Department of Ocean Civil Engineering, Kagoshima University, 1-20-40 Korimoto, Kagoshima-shi 890, Japan.
 2. Research Physical Scientist, US Army Engineer Waterways Experiment Station, Coastal and Hydraulics Laboratory, 3909 Halls Ferry Road, Vicksburg, Mississippi 39180-6199, USA.

In the present study, the dune-erosion mechanism is investigated through field observations of the performance of sand dunes under storm action in Japan and the United States. These observations are quantified by analysis of test series from the SUPERTANK Data-Collection Project (Kraus et al. 1992, Kraus and Smith 1995, Smith and Kraus 1996). The data set includes two tests involving erosion by random waves of 0.8-m high, nearly vertical dunes composed of 0.23-mm median-diameter sand. One test involved an uncompacted dune (SUPERTANK Test ST_50) and the other a compacted dune (ST_60). Complete time series of the water-surface elevation are available from the offshore to the face of the dune, although only breaking waves were employed here to compute the impact parameter and related volume of dune erosion.

Dune erosion is calculated as a function of a wave-force parameter (Sunamura 1977, Fisher and Overton 1984). Material eroded from the dune is supplied to the nearshore where profile change is calculated through equilibrium-profile concepts. Therefore, we call the methodology a *supply-and-demand* dune erosion and profile change model. This paper describes different mechanisms of dune erosion and the new supply-and-demand model. The model is then tested to simulate dune erosion measured at SUPERTANK.

MECHANISM OF SAND DUNE EROSION BY STORMS

In this paper, we consider dune erosion produced by impact forces of waves incident nearly normal to the shore, a cross-shore transport process that is assumed to be two dimensional. This assumption is supported by the uniform dune recession commonly observed after large storms along kilometers of shore despite longshore variations in coastal structures and offshore bathymetry. However, we note the possibility of the action of shearing forces exerted on dunes by waves and associated currents passing tangentially to the shore. Such a situation occurs by waves generated by ships passing dunes in narrow channels. Shearing erosion is not considered further here.

Field Observations

Sunamura (1992) has described basal erosion and mass movement (failure or erosion) of cliffs on rocky coasts as four types: falls, topples, slides, and flows. In the present study, the authors have documented three types of erosion mechanisms of sand dunes by wave impacts during storms or strong wave action. The cross-shore dune-erosion mechanisms, schematized in Fig. 1, are classified as (a) layer separation, including layer separation and overturning, (b) notching and slumping, and (c) sliding and flowing.

Layer separation. Layer separation typically occurs if a near-vertical dune face is subjected to wave impact. Over the duration of a certain number of impacts, a vertical fault line (crack) develops, and this outer layer gradually separates (typically 30 to 50 cm thick) from the landward portion of the dune. As it separates, the outer layer detaches from the main body of the dune, becomes unstable, and either collapses suddenly (Fig. 1a) or tilts forward and overturns (Fig. 1a').

Notching and slumping. Severe notching tends to occur if a dune slope is nearly vertical, permeated by roots, highly compacted, or composed of rocks such as a rocky cliff. Notching is limited to the elevation of wave attack and, after the notch is cut sufficiently deep into the base of the dune, the overlying sand column collapses. (Some notching may also occur during layer separation, but it is not the dominant factor in the collapse of the separated layer.) The material from the collapsed dune face is deposited in front of the new dune face.

The width of sand deposition at the foot of the dune face is less than that of layer separation, which involves the overturning and sliding of a layer.

Sliding and flowing. Sliding and flowing occur on uncompacted gently sloping dunes that have a face slope close to the angle of repose of the sediments forming them. In this situation, modest wave impact at the base of the dune or even pelting by rain or exposure to strong wind can cause a thin layer of sand to run down the slope. It is expected that this mode of dune erosion does not cause severe dune recession in a short period of time; however, this mechanism tends to steepen the dune face and a resultant steeper dune slope will probably trigger layer separation or notching and slumping under storm conditions.

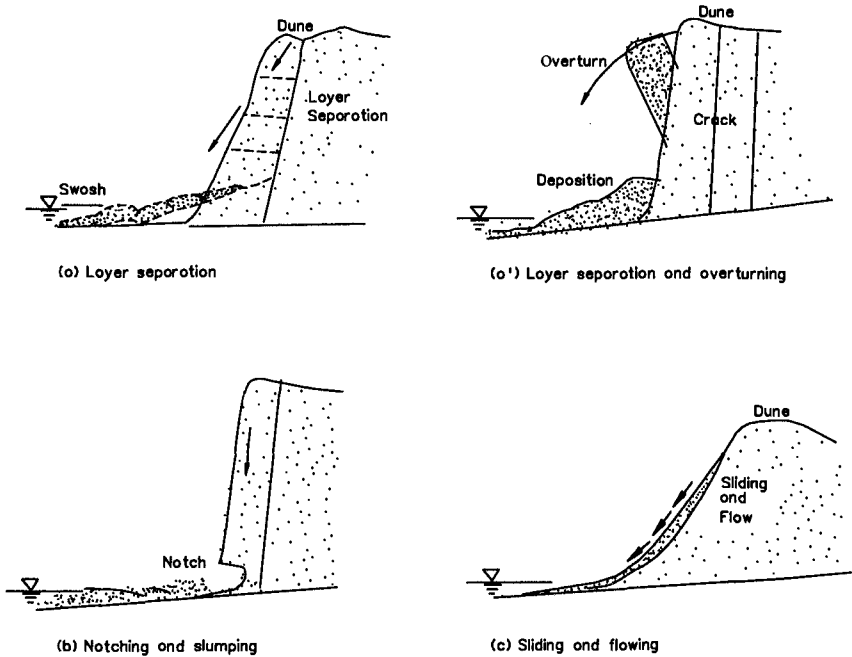


Fig. 1. Dune erosion mechanisms by cross-shore processes.

SUPERTANK Dune-Erosion Tests

The erosion mechanism was quantified by using profile response measurements made at the SUPERTANK project. The particular tests analyzed here concern profile steepening and dune erosion. These test series involved random wave incident to a near-equilibrium profile, and to uncompacted (loose sand) and compacted near-vertically faced dunes. Complete time series of the water surface elevation are available from the offshore to the dune face (Smith and Kraus 1995); however, in this study, as a preliminary and less computationally intensive step, only wave-related quantities calculated at the breaker line were used.

The three SUPERTANK tests discussed in the present study were ST_10 (erosion of an equilibrium profile), ST_50 (uncompacted dune), and ST_60 (compacted dune). The waves were run in bursts of 10-40 min, and conditions were sometimes changed between bursts, for which representative waves are as follows:

<u>Test Number</u>	<u>Significant Wave</u>	<u>Peak Spectral</u>
	<u>Height, m</u>	<u>Period, sec</u>
ST_10	0.8	3.0
ST_50	0.5 - 0.8	6.0 - 3.0
ST_60	0.5 - 0.7	6.0 - 3.0

Erosion above a near-equilibrium profile. For SUPERTANK Test ST_10, random waves and monochromatic waves were generated to act on an initial idealized sub-aqueous equilibrium beach profile. Evolution of the beach profile is shown in Fig. 2. Four series of slope steepening (scarping) events occurred in the test. The profile in the swash zone steepened and maintained a constant angle at the second through fourth wave-burst events, while the upper beach face receded. The slope of the upper beach face is $\tan\beta \approx 0.89$, slightly less than that of a one-to-one slope (45 deg) typically specified in the Kriebel and Dean (1985) model. The slope of the upper beach face appears to exert control on the speed and volume of upper beach erosion.

Fig. 3 shows the process of profile steepening and scarp generation at the first and second wave-burst events of the erosion processes shown in Fig. 2. The beach-face slope steepened, and the swash waves carried the sediment offshore while lowering the beach face. Once the slope of the upper beach face approached the angle of failure (avalanching), the upper portion of beach face collapsed and the sediment was deposited in front of the scarp. Thereafter, successive swash waves transported the sediment seaward that was supplied from the upper beach face. As the beach face was lowered by erosive swash waves, swash uprush intensely impacted the steep beach face, again causing avalanching. These erosion processes in the swash zone continued until the upper beach face was no longer vulnerable to swash waves. This test series demonstrates that the upper beach face behind a sub-aqueous near-equilibrium beach profile can be eroded by swash wave activity until it also achieves equilibrium with the water level and swash.

Dune erosion tests. Two dune-erosion tests were conducted at SUPERTANK, one for a dune formed of sand without compaction (ST_50) and the other for an artificially compacted dune (ST_60). The dune was compacted by applying a pavement vibrator for approximately 2 hr. Both dunes were subjected to short-period high waves. The water level was lower at the beginning of the tests and higher at the end of the tests (Kraus and Smith 1995, Smith and Kraus 1996). In the dune-erosion tests, the dune face tended to recede in parallel to itself, as shown in Fig. 4. Video records made during SUPERTANK indicate both the uncompacted and compacted dunes eroded primarily by layer separation. In all situations observed in the field and at SUPERTANK, dune faces tended to recede in parallel to themselves.

This coherent behavior of dune evolution illustrates the consistency and reproducibility of the dune-erosion mechanism. The sediment supply from the dune to the swash zone by either the layer-separation or notching-and-slumping erosion mechanisms was injected virtually instantaneously (order of one wave period) when a wave or backwash swept the eroded sediment toward the swash zone.

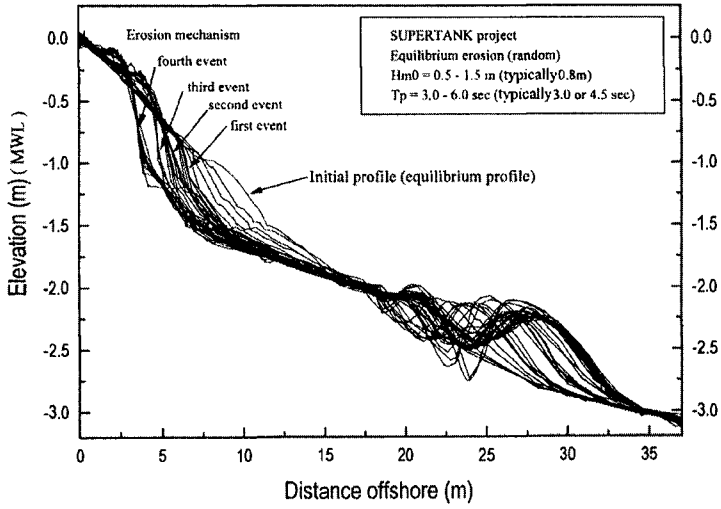


Fig. 2. Profile change on a near-equilibrium beach (ST_10).

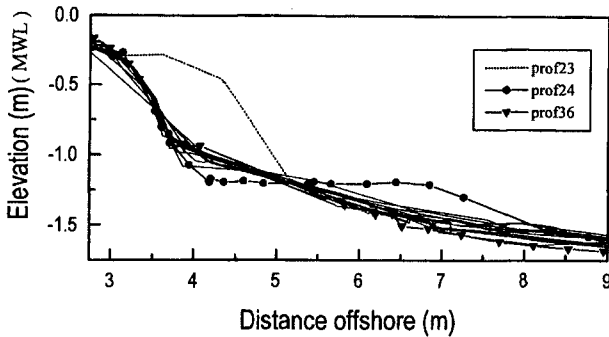
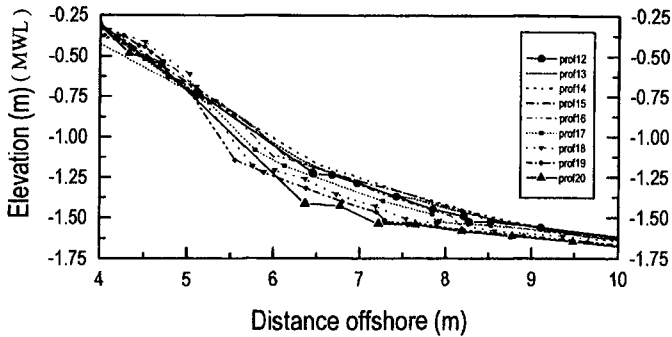


Fig. 3. Beach face steepening and scarp generation (ST_10).

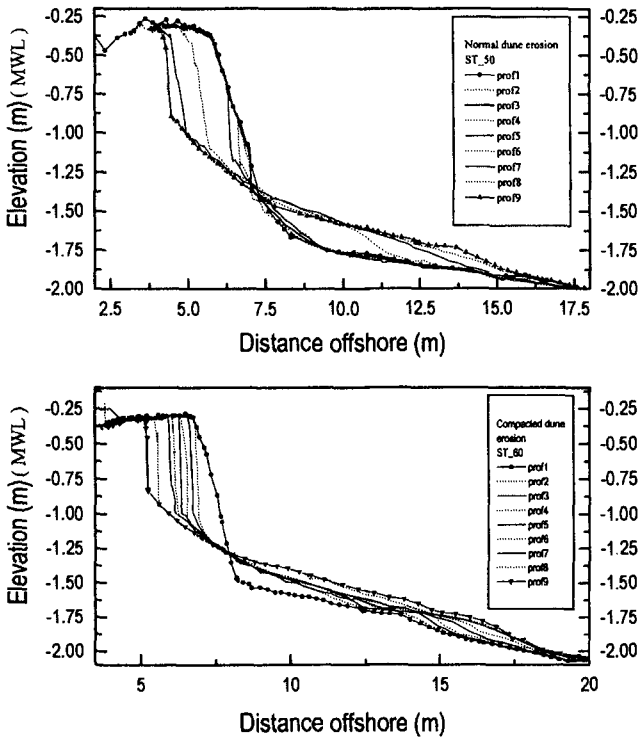


Fig. 4. Erosion of uncompacted (ST_50) and compacted (ST_60) dunes.

The volume of erosion of the compacted dune was less than that of the uncompacted dune, despite the slope of the compacted dune being steeper than that of the uncompacted dune during the erosion, as shown in Fig. 4. Compaction altered the strength of the dune and the volume of eroded material, thickness of layer separation, and angle of slope failure. It is clear that a compaction coefficient should be introduced in future studies of profile evolution.

DUNE EROSION MODEL

A numerical model of dune erosion was developed in the present study that simulates the impact force of individual waves on the dune face. Research conducted at Tuskuba University, Japan, for cliff erosion (see Sunamura 1977, 1992) and at North Carolina State University for sand dunes (see Fisher and Overton 1984, Fisher et al. 1986, and Overton et al. 1994) has advanced this approach. The impact-force and dune-erosion model was incorporated as a sub-model of SBEACH (Larson and Kraus 1989, Nishi et al. 1991) and employs the wave model of SBEACH supplemented by a swash model that includes bore velocity and height to estimate the impact parameter. The total model consists of a wave transformation model, cross-shore sediment transport model in the surf zone, and a sediment supply model from the dune.

In SBEACH, wave transformation in the surf zone is computed based on the Dally et al. (1985) model. For describing random wave incidence, it was assumed that the heights of individual waves follow a Rayleigh distribution and the wave period for an individual wave corresponds to an average wave period. The wave height of individual waves was computed by a Monte Carlo method (Larson and Kraus 1991).

Profile Zonation

Because the model computes the sediment transport in the surf zone and sediment supply and transport from the dune by different mechanisms, the beach and dune systems were divided into three zones as the (a) dune, (b) swash zone, and (c) surf zone (Fig. 5). This profile zonation modifies that of the original SBEACH model at the dune. The maximum runup or swash elevation Z_r is defined as a function of the surf-similarity parameter as given by Eq. (1) (Larson and Kraus 1989)

$$\frac{Z_r}{H_o} = 1.47 \left(\frac{\tan \beta}{\sqrt{H_o / L_o}} \right)^{0.79} \quad (1)$$

where H_o = deep-water wave height, and L_o = deep-water wavelength by linear-wave theory.

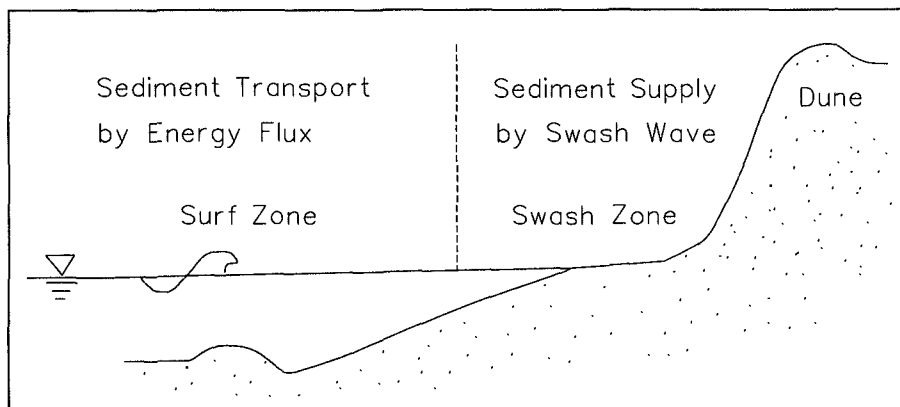


Fig. 5. Schematic diagram of dune and beach system.

Calculation of Sediment Supply from Dune

As storm waves approach the beach, bores impact the dune face and cause erosion. Thus, the volume of dune erosion during a storm or by waves that reach the dune face during times of elevated water level should be related to the force of wave impact. Sunamura (1977) parameterized this impact wave force by the incident wave height in study of rocky cliff erosion. A strong correlation between wave impact force and sand dune erosion was found by Fisher et al. (1986) for artificially constructed sand dunes in the field and by Overton et al. (1994), who obtained a correlation between the force of impacting waves and volume of dune erosion for the compacted dune at SUPERTANK.

The wave-force impact parameter is derived heuristically by considering the situation shown in Fig. 6 and the rate of change of wave momentum. The mass m of water per unit length of crest in a bore of height H and length L moving in shallow water of average depth h over the length of the wave is given by

$$m \approx \frac{1}{2} \rho_w HL = \frac{1}{2} \rho_w HT \sqrt{gh} \quad (2)$$

where ρ_w = density of water, T = wave period, g = gravitational acceleration, and $(gh)^{1/2}$ is the celerity of the wave. The wave impact force per unit length of dune is estimated by multiplying the mass m by the deceleration $(gh)^{1/2}/T$ resulting from the wave striking the dune and stopping in the time interval of the wave period T . This derivation suggests consideration of a cumulative wave-force impact parameter I defined by

$$I \equiv \rho_w gh H \frac{\Delta t}{T} \quad (3)$$

where Δt is the time interval or duration over which the waves impact, and the ratio $\Delta t/T$ is the number of waves. The ratio $\Delta t/T$ can be easily modified to describe random waves by summing the contributions of the individual waves of different height, period, and speed. The impact parameter has the dimensions of Newtons per unit wave crest or dune width.

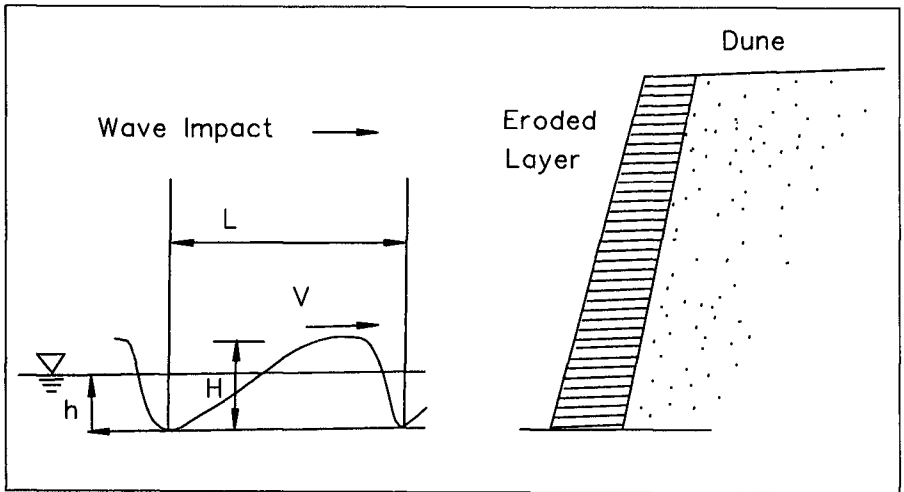


Fig. 6. Schematic diagram for the wave impact parameter.

For dimensional homogeneity it is convenient to work with the weight per unit width alongshore of the eroded material $W_E = \rho_s (1 - p) g V_E$, where ρ_s = density of the sand comprising the dune, p is the porosity of the sand (0.4 for uncompacted sand, 0.2 estimated for the compacted sand dune), and V_E is the volume of material eroded from the dune. The density and, therefore, the porosity, of the uncompacted and compacted dunes should be different.

Analysis of the data computed from the average of the impact forces indicated a linear relationship as shown in Fig. 7 and resulted in the empirical equation for the weight per unit width $(W_E)_U$

$$(W_E)_U = 0.81(I - I_{crit}) \quad (4)$$

for the uncompacted dune, and the weight $(W_E)_C$

$$(W_E)_C = 0.50(I - I_{crit}) \quad (5)$$

for the compacted dune. In the above, the critical wave impact parameter for inception of erosion I_{crit} is set to zero at the present time because of uncertainty in its value.

These equations and Fig. 7 show that waves with the same impact parameter erode a compacted dune less than a uncompacted or unconsolidated dune. An engineering lesson from this result indicates that greater erosion protection would be gained through construction of dunes by wetting the sand for consolidation and compacting them with vibrating compactors, rollers, and other heavy equipment. The above result was obtained from a limited number of tests available from the SUPERTANK project, and further verification needs to be done to refine the result.

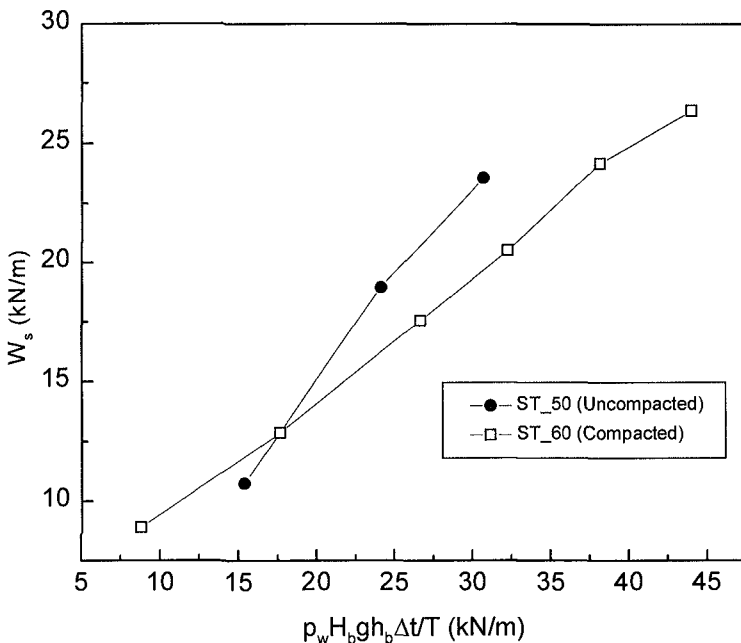


Fig. 7. Impact parameters for uncompacted and compacted dunes at SUPERTANK.

NUMERICAL MODEL OF DUNE EROSION

From the above discussion, the volume of sand eroded from a dune can be calculated as a function of time through knowledge of the incident waves and the wave-force impact parameter. Thus, the amount of sand supplied to the profile by the dune is known. As the next step, an assumption must be made as to how the sediment enters the swash zone or surf zone where other transporting mechanisms are operating. Here, it is assumed that sediment is introduced to the swash zone at a uniform rate within each time step of the model according to the supply available from the dune at that time step. A typical calculation time step in the model is 1 min, and the grid cell size on the foreshore is 0.1 m. Uniform distribution of sediment supply agrees with visual observations made at SUPERTANK and inferences from field observations, and it is also reasonable in a time-average sense. The structure of the numerical model does not preclude a more detailed description of the sediment-supply procedure to the swash zone and can be modified as understanding improves.

Dune Erosion Model (Supply)

We found above that a dune face recedes with a certain angle in accordance with the amount of compaction. Nearly vertical dune faces produced by erosion during storms are commonly observed in the field, in particular for well-established dunes presumably compacted by natural settling and wetting. In the SUPERTANK project, the angles of the dune face were approximately 68 deg for the uncompacted dune and 87 deg for the artificially compacted dune, as shown in Fig. 8. The irregularity in dune-face angle through time for the compacted dune may have been caused by uneven compaction close to the initial dune face. In the model simulations described below, it is assumed that the slope of the dune face is 68 or 87 deg depending on the amount of compaction.

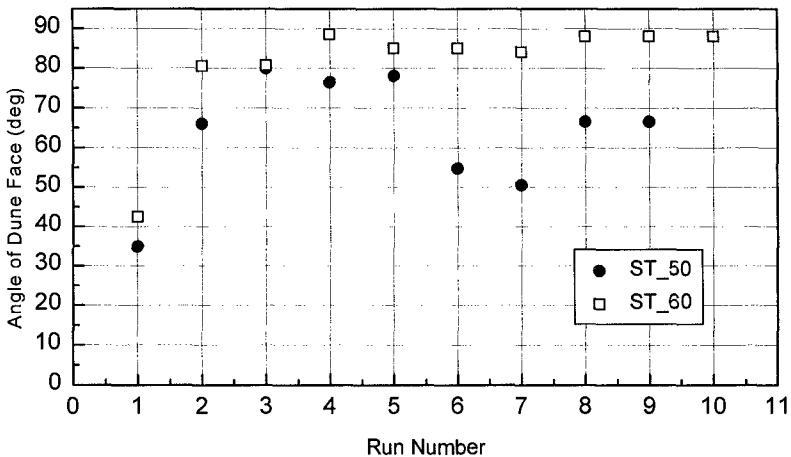


Fig. 8. Angle of dune face for uncompacted and compacted dunes at SUPERTANK.

As determined from the SUPERTANK data, the volume of dune erosion can be estimated by the duration and intensity of wave impact, which yields an eroded volume ΔV_E per unit longshore width of dune. A corresponding recession distance can be computed by assuming the dune face retreats a certain distance and at a certain angle to a baseline. The baseline is a vertical datum located at the toe of the dune. In the model, the volume of sand eroded from the dune is distributed uniformly as a thickness Δh_s over a distance X_s , which is taken to be an effective distance of the swash zone extending from the toe of the dune at the present time step to some depth defining the seaward limit of the swash zone, arbitrarily set to 0.3 m or a comparable value (Larson and Kraus 1989). Then we have

$$\Delta h_s = \frac{\Delta V_E}{X_s} \quad (6)$$

for the thickness of the sand layer.

Profile Change Model (Demand)

In the SBEACH model, sediment demand or the potential transport rate in the surf zone is calculated based on the dissipation of wave energy flux originally derived by Dean (1977) and implemented by Kriebel and Dean (1985) in dune-erosion modeling. In the surf zone, SBEACH computes the cross-shore sediment transport rate as

$$q = K \left(D - D_{eq} + \frac{\varepsilon}{K} \frac{\partial h}{\partial x} \right) \quad (7)$$

where K = empirical transport rate coefficient, ε = empirical coefficient controlling the strength of the slope-dependent transport rate term, and the energy dissipation per unit water volume D is

$$D = \frac{1}{h} \frac{\partial F}{\partial x} \quad (8)$$

in which F is the wave-energy flux. The dissipation for a profile in equilibrium with the existing waves and water level D_{eq} is given by (Dean 1977)

$$D_{eq} = \frac{5}{24} \rho_w g^{3/2} \left(\frac{H_b}{h_b} \right)^2 A^{3/2} \quad (9)$$

where A is an empirical "shape" parameter related to the form of the equilibrium profile and the grain size of the beach (Moore 1982).

In SBEACH, the transport rate in the surf zone as given by Eq. (7) is only calculated if $D > D_{eq} - \varepsilon/K \partial h/\partial x$, and the transport direction as onshore or offshore is determined by a separate function (Kraus et al. 1991). As originally developed (Larson and Kraus 1989), SBEACH calculates cross-shore transport rates in four zones, with a linear rate employed in the swash zone and a magnitude as determined by matching with Eq. (7) at the swash zone and surf zone interface. Material moved from the dune to the swash zone by the supply dune-erosion model is then moved offshore by the swash and surf zone transport.

Numerical Simulation of Dune Erosion at SUPERTANK

A numerical simulation was conducted to calculate dune erosion for Test ST_60 (compacted dune). The empirical dune-erosion predictor incorporated in the model was developed based on the SUPERTANK data and impact parameter, as described above. Therefore, the simulation is not a verification of the model; rather, it demonstrates the validity of the numerical scheme and behavior of the supply-and-demand procedure that connects the dune to the profile.

Fig. 9 shows the profile change simulated by applying the (standard) demand model, which can be compared to the profile change simulated by applying the supply-and-demand model, Fig. 10. The demand model underestimates the dune erosion for which the compacted dune is located on a beach profile in near equilibrium with the impressed waves.

We note in this paragraph independent contemporaneous work involving SUPERTANK Tests ST_10, ST_50, and ST_60. Wise et al. (1996) report comparisons of SUPERTANK measurements (and field measurements) and calculations performed with the most recent version of SBEACH operated by the US Army Engineer Waterways Experiment Station (WES), for which default calibration parameters (K and ϵ) were specified (the calibration parameters were not optimized for the individual tests). The most recent WES version of SBEACH incorporates sophisticated random-wave and cross-shore sediment transport models not applied in the version used in the present study. The WES version is still a demand model. For equilibrium Test ST_10, erosion of the foreshore was obtained by Wise et al. for random waves with the new WES version of SBEACH. For the dune erosion tests, the WES version well reproduced erosion of the uncompacted dune (ST_50) and overpredicted dune erosion for the compacted dune (ST_60). Wise et al. comment that "The difference in model predictions between the two dune cases might be expected due to greater erosion resistance associated with the compacted sediment which is not accounted for in SBEACH." This comment was verified in the present work.

CONCLUDING DISCUSSION

Three types of dune erosion mechanisms were identified through field observations as: (a) layer separation, (b) notching and slumping, and (c) sliding and flowing. The layer-separation mechanism was quantified by analysis of the SUPERTANK dune erosion tests by which the eroded volume could be related to the cumulative wave impact force. The degree of compaction was found to be a significant parameter that decreases the potential for dunes to erode. Therefore, an economic benefit might be gained by compacting artificially placed dunes to improve their performance as shore protection. The supply-and-demand model developed can simulate dune erosion and beach profile change based on representations of the hydrodynamics and sediment transport acting in each region and provides, in principle, a more accurate representation than existing demand models, especially in applications where the beach profile is approximately in equilibrium with the impressed storm waves and water level. The present study suggests ways through which geotechnical considerations might be incorporated in dune erosion modeling to both account for compaction and introduce supply and demand considerations.

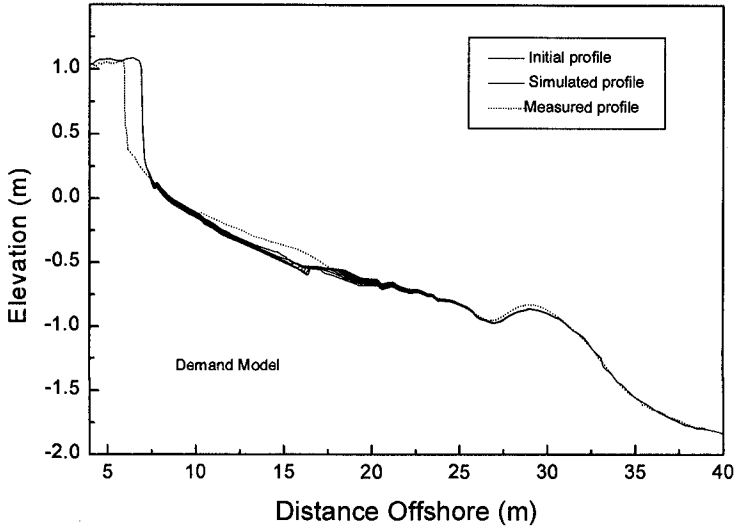


Fig. 9. Simulation for compacted dune (ST_60) by demand model.

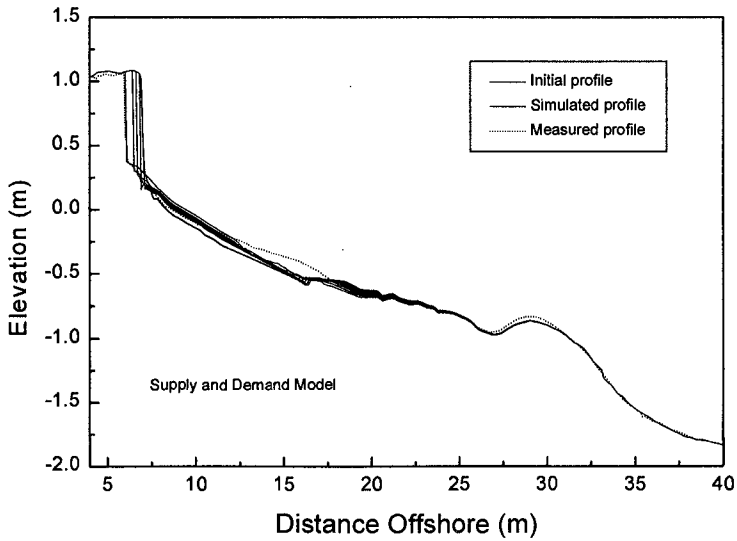


Fig. 10. Simulation for compacted dune (ST_60) by the supply-and-demand model.

ACKNOWLEDGEMENTS

Appreciation is expressed to all the individuals who participated in SUPERTANK and created the valuable data set. Bill McDougal, Oregon State University, compacted the dune for ST_60. Jane Smith, WES, Coastal and Hydraulics Laboratory (CHL), provided the SUPERTANK wave data used in this study. Randy Wise, CHL, reviewed an early draft of this paper. The second author received permission by Headquarters, U.S. Army Corps of Engineers, to publish this information.

REFERENCES

- Dally, W. R., Dean, R. G., and Dalrymple, R. A. 1985. Wave height variation across beaches of arbitrary profile. *J. Geophys. Res.* 90(C6): 11917-11927.
- Dean, R. G. 1977. Equilibrium beach profiles: U.S. Atlantic and Gulf Coasts. Dept. of Civil Engrg., Univ. of Delaware, Newark, Del.
- Fisher, J. S. and Overton, M. F. 1984. Numerical model for dune erosion due to wave uprush. *Proc. 19th Coastal Engrg. Conf.*, ASCE, 1553-1558.
- Fisher, J. S., Overton, M. F., and Chisholm, T. 1986. Field measurements of dune erosion. *Proc. 20th Coastal Engrg. Conf.*, ASCE, 1107-1115.
- Kraus, N. C., Larson, M., and Kriebel, D. L. 1991. Evaluation of beach erosion and accretion predictors. *Proc. Coastal Sediments '91*, ASCE, 572-587.
- Kraus, N. C. and Smith, J. M. 1994. SUPERTANK laboratory data collection project, Volume I: main text, Tech. Rep. CERC-94-3, US Army Engineer Waterways Experiment Station, Coastal Engrg. Research Center, Vicksburg, Miss.
- Kraus, N. C., and Smith, J. M., and Sollitt, C. K. 1992. SUPERTANK laboratory data collection project. *Proc. 23rd Coastal Engrg. Conf.*, ASCE, 2191-2204.
- Kriebel D. L. and Dean, R. G. 1985. Numerical simulation of time dependent beach and dune erosion. *Coastal Engrg.* 9: 221-245.
- Larson M. and Kraus N. C. 1989. SBEACH: Numerical model for simulating storm-induced beach change, Report 1, empirical foundation and model development. Technical Report CERC-89-9, US Army Engineering Waterways Experiment Station, Coastal Engrg. Research Center, Vicksburg, Miss.
- Larson, M., and Kraus, N. C. 1991. Numerical model of longshore current over bar and trough beaches. *J. Waterway, Port, Coastal and Ocean Engrg.*, 117(4): 326-347.
- Moore B. 1982. Beach profile evolution in response to changes in water level and wave height. Unpub. MS Thesis, Dept. of Civil Engrg., Univ. of Delaware, Newark, Del.
- Nishi, R., Sato, M. and Wang, H. 1994. Field observation and numerical simulation of dune and beach scarping. *Proc. 24th Coastal Engrg. Conf.*, ASCE, 2434-2448.
- Overton M. F., Fisher, J. S., and Hwang, K. 1994. Development of a dune erosion model using SUPERTANK data. *Proc. 24th Coastal Engrg. Conf.*, ASCE, 2488-2502.
- Smith, J. M. and Kraus, N. C. 1995. SUPERTANK laboratory data collection project, Volume II. Appendices A-I, Tech. Rep. CERC-94-3, US Army Engr. Waterways Experiment Station, Coastal Engrg. Research Center, Vicksburg, Miss.
- Sunamura, T. 1977. A relationship between wave-induced cliff erosion and erosive force of waves. *J. Geol.*, 85: 613-618.
- Sunamura, T. 1992. *Geomorphology of Rocky Coasts*. John Wiley & Sons, N.Y., 302 pp.
- Wise, R. A., Smith, S. J., and Larson, M. 1996. SBEACH: Numerical model for simulating storm-induced beach change, Report 4: cross-shore transport under random waves and model validation with SUPERTANK and field data. Tech. Rep. CERC-89-9, US Army Engr. Waterways Experiment Station, Coastal Engrg. Research Center, Vicksburg, Miss.

CHAPTER 236

SIMULATION OF COASTAL PROFILE DEVELOPMENT USING A BOUSSINESQ WAVE MODEL

K.A. Rakha¹, R. Deigaard², P.A. Madsen¹, I. Brøker³, and J.K. Rønberg³

ABSTRACT

A phase-resolving wave transformation module is combined with an intra-wave sediment transport module to calculate the on/offshore sediment transport rates. The wave module is based on the Boussinesq equations extended into the surf zone. The vertical variation of the instantaneous currents and concentrations are calculated. The net sediment transport rates are calculated, and the equation for conservation of sediment is solved to predict the beach profile evolution. The results of the present paper showed that the undertow contribution to the sediment transport rates dominated only at local areas even for eroding beaches, suggesting that other contributions should not be neglected.

1. INTRODUCTION

The study of beach profile evolution includes a large range of time and space scales. Process based morphology models (Roelvink and Brøker, 1993) usually include some averaging of the different space and time scales. This averaging is applied to either the hydrodynamic or the sediment transport calculations or both. The sediment transport calculations used in most of the present morphology models are based on phase-averaged calculations of the sediment concentrations or on the 'energetics approach'. Although models based on the energetics approach account for the intra-wave sediment transport rates, the intra-wave variation of the eddy viscosities and sediment concentrations are not calculated. Such models may be classified as semi-intra-wave sediment transport models. The model developed by Fredsøe et al. (1985) represents an example of a detailed intra-wave model for the sediment concentrations. Watanabe (1994) combined a wave model based on the Boussinesq equations with a semi-intra-wave sediment transport model. Such a model neglects a large part of the information provided by the wave module, and will require some approximations for irregular waves. The model described by Brøker et al. (1991) combines a detailed intra-wave sediment transport module with a phase-averaged wave module, where a wave theory is required to describe the intra-wave water motion. The extension of such a model to irregular waves will also require some approximations. In the present study a phase-resolving wave module is combined with a detailed intra-wave sediment transport module to study in more detail the process of sediment transport and morphological evolution.

¹International Research Center for Computational Hydrodynamics (ICCH)

Danish Hydraulic Institute (DHI), Agern Allé 5, DK-2970 Horsholm, Denmark.

* Currently at Department of Irrigation and Hydraulics, Faculty of Eng., Cairo University, Egypt.

²Institute of Hydrodynamics and Hydraulic Eng. (ISVA), Technical University of Denmark, DK-2800 Lyngby, Denmark.

³Danish Hydraulic Institute (DHI), Agern Allé 5, DK-2970 Horsholm, Denmark.

2. MODEL DESCRIPTION

The morphological calculations are performed by updating the beach profile over the morphological time step Δt_{\max} . For each morphological update the simulations are performed by four modules; a wave module, a hydrodynamic module, a sediment transport module and a bathymetry updating module.

2.1 Wave Module

The wave module simulates the wave conditions across the beach profile by a phase-resolving model based on the Boussinesq equations, with improved linear dispersion characteristics as explained in Madsen et al. (1991), and Madsen and Sørensen (1992). The effect of wave breaking is included by using the surface roller concept (Schäffer et al., 1993). Figure (1A) shows a sketch of the assumed velocity field under a wave with a surface roller. An extra term is included in the momentum equation to represent the momentum flux due to the rollers. This term extracts energy from the wave motion. Breaking is initiated when the local water surface slope exceeds the initial value of ϕ_b . The roller is defined as the water above the tangent slope $\tan(\phi)$. Initially ϕ is equal to ϕ_b for each roller, which then decreases exponentially to ϕ_o , and breaking is assumed to cease when the maximum of the local slope becomes less than $\tan(\phi)$. The resulting roller thickness δ is finally multiplied by the roller shape factor f_δ to compensate for the simple method of separating the roller from the rest of the flow.

The calculation proceeds into the swash zone using the slot-technique (Madsen et al. 1994), by extending the computational domain into an artificial permeable beach. Near the moving shoreline the water surface will intersect with the sea bed and continue into the porous beach. The instantaneous position of the shoreline is simply determined by this intersection.

2.2 Hydrodynamic Module

The hydrodynamic module consists of two parts, an oscillatory boundary layer model (Figure, 1B) and an undertow model (Figure, 1C). The boundary layer model calculates the vertical velocity distribution for the oscillatory wave motion u_o inside the boundary layer. The undertow model determines the vertical distribution of the mean undertow \bar{U}_o .

2.2.1 Boundary Layer Calculations

The oscillatory flow near the bottom is modelled by the momentum integral method developed by Fredsoe (1984). The shear stress is assumed to be zero at the top of the boundary layer, and the velocity distribution u inside the boundary layer is assumed to follow a logarithmic distribution. The boundary layer thickness is assumed to develop from zero at every zero-crossing of u_o outside the boundary layer. The values of the shear velocity U and the boundary layer thickness ζ are calculated for each time step. The streaming in the boundary layer and the wave asymmetry causes the time averaged bed shear stress to deviate from zero. To obtain this mean shear stress a constant drift velocity V_{st} is added to the near bed orbital velocity. The magnitude of V_{st} is found by iteration requiring that the time averaged bed shear stress in the boundary layer model is equal to the shear stress determined by the streaming.

2.2.2 Eddy Viscosity Calculations

The eddy viscosities are calculated by assuming that the total kinetic energy can be determined as the sum of three contributions (Brøker et al., 1991),

$$\epsilon = \sqrt{\epsilon_w^2 + \epsilon_b^2 + \epsilon_U^2} \quad (1)$$

where, ϵ_w , ϵ_b , and ϵ_U are the eddy viscosities due to the bottom boundary layer, wave breaking, and the undertow, respectively. The eddy viscosity ϵ_w is calculated based on the variables calculated in

the boundary layer, assuming a parabolic distribution inside the bottom boundary layer (Fredsøe et al., 1985). The eddy viscosity ϵ_v is calculated from the undertow velocity profile using a simple mixing length formulation. The eddy viscosity ϵ_b is calculated from the turbulent kinetic energy induced by wave breaking calculated from a one-equation turbulence model (Deigaard et al. 1991). The instantaneous production of turbulence due to wave breaking is calculated from the following equation proposed by Deigaard (1989),

$$P_r = \alpha_p Diss = \alpha_p \rho g c \delta \tan \phi_o \quad (2)$$

where, Diss is the instantaneous energy dissipation due to wave breaking, and α_p is the fraction of the energy that is not dissipated immediately in the shear layer beneath the roller. α_p is assumed to be 0.33 as suggested by Deigaard et al. (1991). The production of turbulence is assumed to have a parabolic distribution over a distance of half the wave height ($H/2$) below the mean water depth as shown in Figure (2).

2.2.3 Undertow Calculation

The undertow is calculated by the following approximate equation,

$$\frac{\partial U_c}{\partial y} = \frac{1}{\rho \epsilon} \bar{\tau} \quad (3)$$

where an overbar denotes time averaging over a single wave. The time averaged shear stress distribution is assumed to vary linearly over the water depth as shown in Figure (2). The shear stress at the surface (mean water level, MWL) is calculated from the following formula,

$$\bar{\tau}_s = \frac{Diss}{c} \quad (4)$$

Eqn. (3) is solved with the no slip condition imposed at the bed, and the condition that the total flux compensates the wave drift (determined from the Boussinesq model) and the velocity V_{st} determined by the boundary layer model.

2.3 Sediment Transport Module

2.3.1 Bed Load and Sediment Concentrations

The instantaneous near bed concentration C_b is calculated from the formulation suggested by Zyserman and Fredsøe (1994). The value of C_b depends on the instantaneous value of the Shield's parameter. The instantaneous bed load q_b is calculated using the formulation by Engelund and Fredsøe (1976).

Neglecting the convective terms, the distribution of the sediment concentration C can be calculated from the diffusion equation,

$$\frac{\partial C}{\partial t} = w_f \frac{\partial C}{\partial y} + \frac{\partial}{\partial y} \left(\epsilon_s \frac{\partial C}{\partial y} \right) \quad (5)$$

where, ϵ_s is the sediment diffusion coefficient assumed to be the same as the flow eddy viscosity ϵ , and w_f is the fall velocity. Eqn. (5) is solved with the boundary conditions $C = C_b$ at the bed ($y = 2D_{50}$), and zero sediment flux through the water surface.

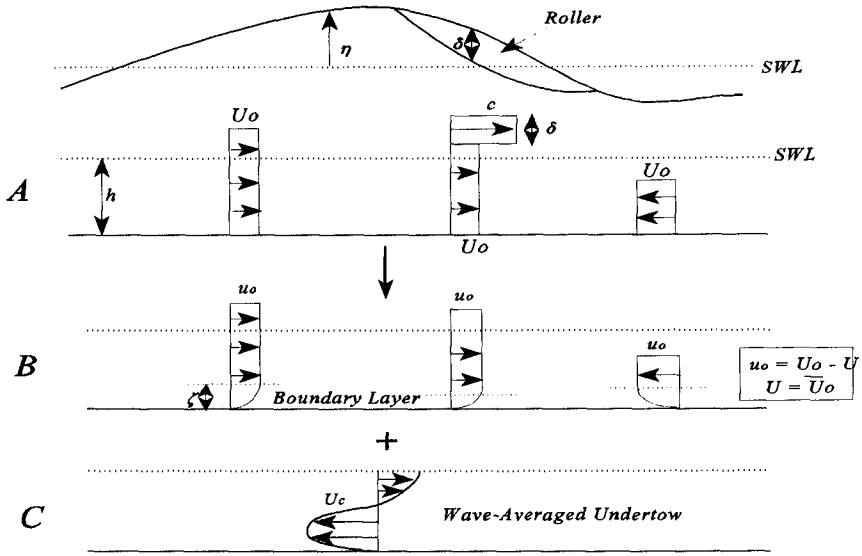


Figure (1): The elements of the hydrodynamic module; A- The wave description. B- The oscillatory current. C- The undertow.

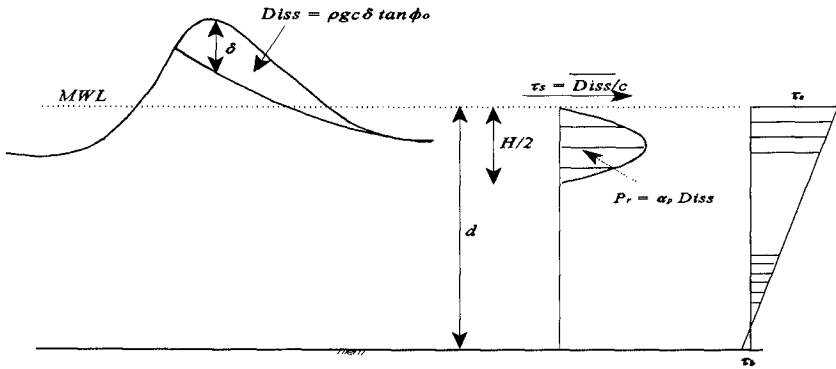


Figure (2): Vertical distribution of production of turbulence and shear stresses due to wave breaking.

2.3.2 Lagrangian Drift

For an Eulerian calculation a contribution due to the Lagrangian drift should be added as an approximation for the wave drift of suspended sediment (Brøker et al., 1991). This approximation is required because the convective terms were not included in the calculations for the sediment concentrations. The Lagrangian drift velocity U_l results from the fact that the water particles do not follow a closed path, but a net forward displacement exists. As an approximation it is assumed that the sediment on average follows the fluid motion. The drift current for each wave is calculated from,

$$U_l = \frac{1}{c} \left(\overline{u^2} - (\bar{u})^2 \right) \quad (6)$$

where an overbar again denotes time averaging over a single wave.

2.3.3 Total Sediment Transport Rates

The total instantaneous sediment transport rates are obtained from,

$$q'_s = q_b + q_{sw} + q_{su} + q_{sl} \quad (7)$$

where the sediment transport rates due to the oscillatory motion q_{sw} are evaluated by integrating uC over the water depth. The contributions due to the undertow q_{su} and the Lagrangian drift q_l are evaluated by integrating $U_c C$ and $U_l C$ over the water depth respectively. The swash zone was included in an approximate manner by assuming that q'_s varies linearly from the last grid point to the location of the water line for each time step. Time averaging of q'_s over the time series provides the time averaged sediment transport rates q_s . Figure (3) shows the instantaneous sediment transport rates calculated for a regular and irregular wave of the same deep water rms wave height for Test 1c explained later. As shown in Figure (3) the time variation of the sediment transport rates under an irregular wave are quite different from a "representative" regular wave.

2.4 MORPHOLOGY MODULE

The bathymetry is updated by solving the conservation of sediment equation,

$$\frac{\partial Z_b}{\partial t} = -\frac{1}{(1-n)} \frac{\partial q_s}{\partial x} \quad (8)$$

where Z_b is the bed level, and n is the porosity of the sediment assumed to be 0.4. A Forward in Time Central in Space (FTCS) finite difference scheme was used to solve Eqn. (8), with an additional diffusive term for the numerical stability (Abbott and Basco, 1989). The resulting finite difference equation would correspond to the following differential equation,

$$\frac{\partial Z_b}{\partial t} + \frac{1}{(1-n)} \frac{\partial q_s}{\partial Z_b} \frac{\partial Z_b}{\partial x} = K \frac{\partial^2 Z_b}{\partial x^2} \quad (9)$$

where, K is a diffusion coefficient assumed to be proportional to q_s ,

$$K = \epsilon_s |q_s| \quad (10)$$

which is similar to the additional gravitational term included by De Vriend et al. (1993) and

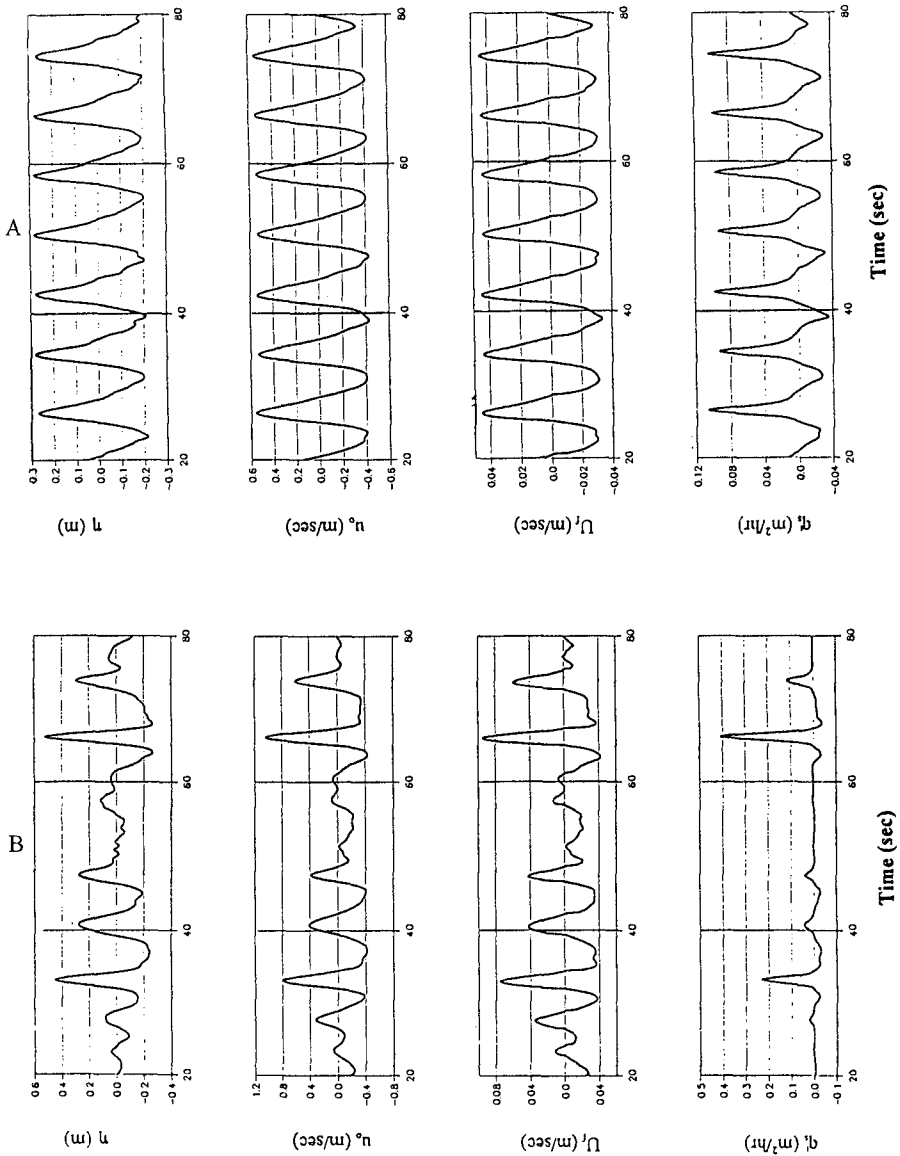


Figure (3): A- Time series of η , u_o , U_r , and q_o of Test 1c (regular wave).
 B- Time series of η , u_o , U_r , and q_o of Test 1c (irregular wave).

Horikawa (1988). ϵ_s is an empirical coefficient. The following constraint on the morphological time step Δt must be satisfied (Abbott and Basco, 1989),

$$D_{cr} \leq \frac{1}{2} ; D_{cr} = \frac{K\Delta t}{\Delta x^2} \tag{11}$$

where, Δx is the spatial grid spacing. In the present study two time steps are used; the first is called the inner time step Δt_i and the second the outer time step Δt_{max} . The maximum value of Δt_i is chosen to satisfy Eqn. (11). Eqn. (8) is solved over the duration Δt_{max} with the values of q assumed constant (Horikawa, 1988, and Rakha and Kamphuis, 1996). The value of Δt_{max} was specified to the model together with a criterion limiting the maximum change in bed level to 10% of the deep water average wave height (Rakha et al., 1996). A modified Lax-Scheme (Abbott, 1979) with no inner times steps was also tested.

Figure (4) shows a long term simulation for a highly erosive beach with a specified outer time step $\Delta t_{max} = 0.2$ hr. The actual time step was less than 0.1 hr resulting in nearly 80 wave field updates. As shown in Figure (4) the bars tended to move offshore with the depth over their crests increasing with time. Onshore of the previous bar, new bars also developed with time.

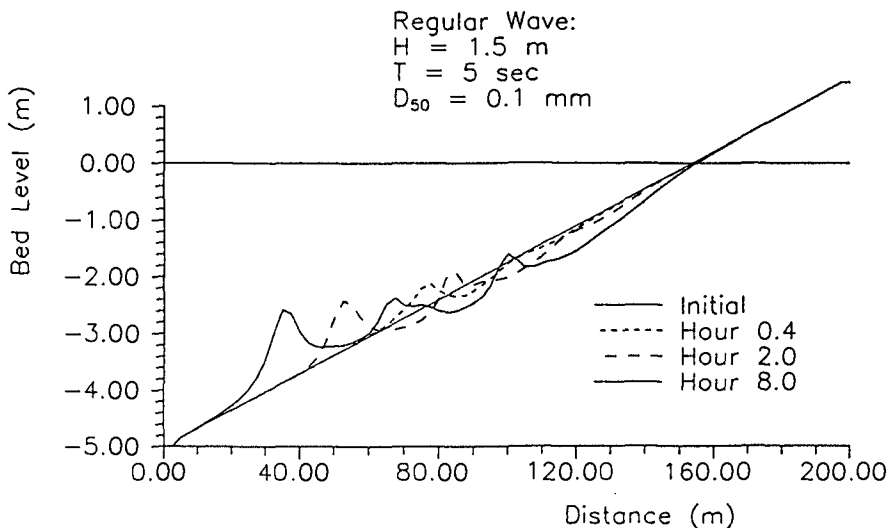


Figure (4): Long term morphology simulation for a regular wave.

3. MODEL VALIDATION

3.1 LIP 11D Delta Flume Tests

The Delta Flume '93 tests were performed at the Delft Hydraulics large-scale wave flume. These tests were supported by the "Large Installations Plan" (LIP) of the European Union. The main purpose of the tests was to provide high quality data to validate/calibrate numerical beach profile models. The details of the tests performed can be found in Arcilla et al. (1993) and Roelvink and Reniers (1995). Two tests (Tests 1b and 1c) were selected for the model verification. Test 1b represents a highly erosive wave condition, and Test 1c a strongly accretive wave condition. Table (1) provides a summary of the test conditions used in this paper.

Table (1): Summary of Test Conditions.

Test	H_{m0} (m)	T_p (sec)	D_{s0} (mm)	Type
LIP 11D: Test 1c	0.60	8.0	0.2	Irregular
LIP 11D: Test 1b	1.40	5.0	0.2	Irregular
Shimizu et al. (1985): Test 3-2	1.05	6.0	0.27	Regular

The prediction of the characteristic wave height H_{m0} variation over the initial bathymetry for Tests 1c and 1b is shown in Figures (5) and (6) respectively. The Boussinesq model predicted the wave heights well for both Tests. It appears that the wave heights are slightly overpredicted inside the surf zone for Test 1c (Figure, 5). The results obtained using a phase-averaged wave model based on the Battjes and Janssen (1978) model are also shown in both figures, which shows that such a model provides a good estimate for H_{m0} .

Figures (7) and (8) show the time-averaged undertow for Tests 1c and 1b. At some locations measurements were performed twice at different hours of the test. Figures (7) and (8) show that the undertow is predicted well for most sections. The undertow however is overpredicted just before the bar ($x = 138$) for Test 1c and underpredicted in the trough of the bar ($x = 145$) for both Tests 1b and 1c.

The predicted on/offshore sediment transport rates for Test 1c are shown in Figure (5). Very good results are obtained outside the surf zone showing that the calculation of the sediment transport rates due to the oscillatory current is well predicted. Over the bar, the overestimation of the undertow (Figure, 8) results in the underestimation of the onshore sediment transport rates. Good predictions of the sediment transport rates for Test 1b are also shown in Figure (6), where the model follows the measured sediment transport rates well. The onshore sediment transport rates are overestimated inside the trough of the bar ($x = 145$) due to the underestimation of the undertow as explained earlier (Figure, 8). The use of the Boussinesq model provided much better results than the use of a phase-averaged wave model (Figures, 5 & 6). Linear wave theory was used with the rms wave height assumed to be the representative wave for the phase-averaged wave model calculations.

Figure (9) shows a decomposition of the time averaged sediment transport rates into three of the four calculated components. The three contributions plotted are the Lagrangian drift, the integral of uC , and the contribution due to the undertow. The bed load was not included since it gives only a small contribution for these tests. From Figure (9) it can be seen that for Test 1c just before the bar where some of the waves start breaking, the undertow contribution increases rapidly. The measurements suggest that the drop in the sediment transport rates is delayed and occurs on the top of the bar. Figure (9) shows that for eroding beaches (Test 1b) the contributions due to the oscillatory current and the Lagrangian drift are important. The undertow contribution dominates only at the locations where a high percentage of waves are breaking.

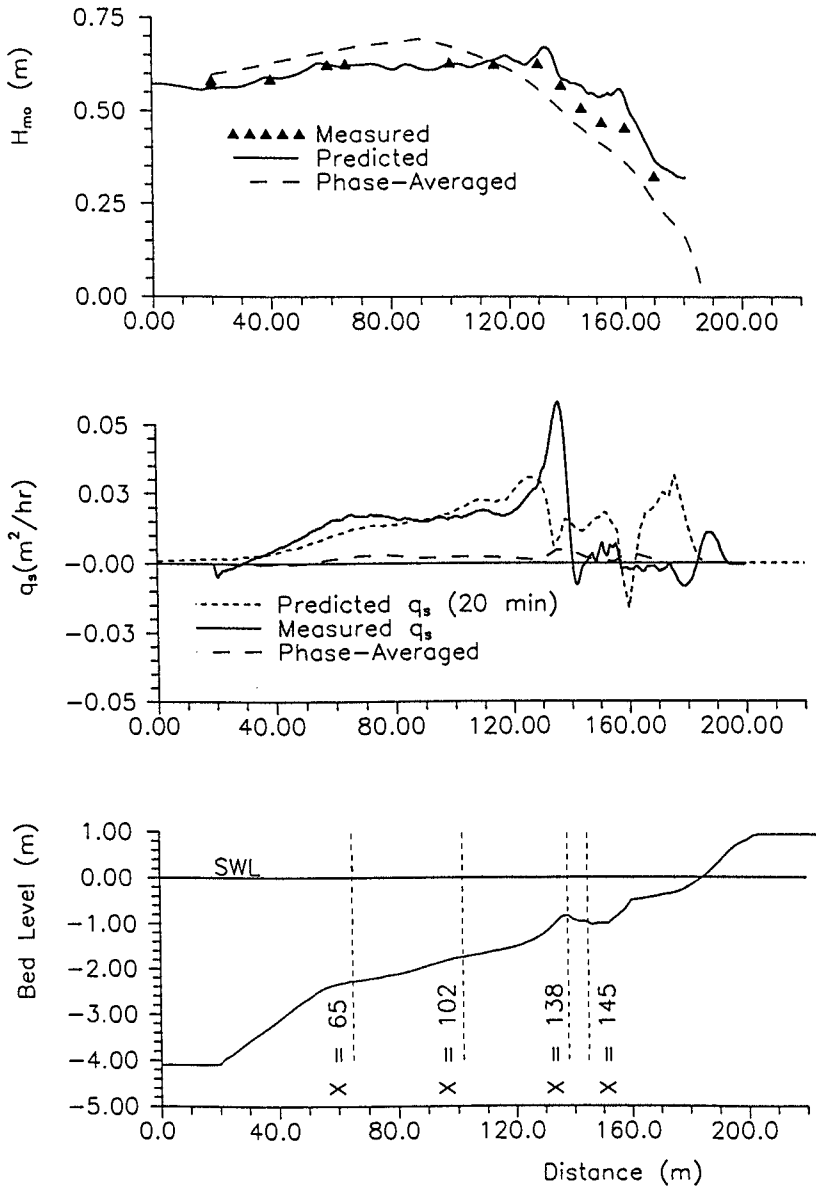


Figure (5): Model results for H_{mo} and q_s of Test 1c (LIP 11D).

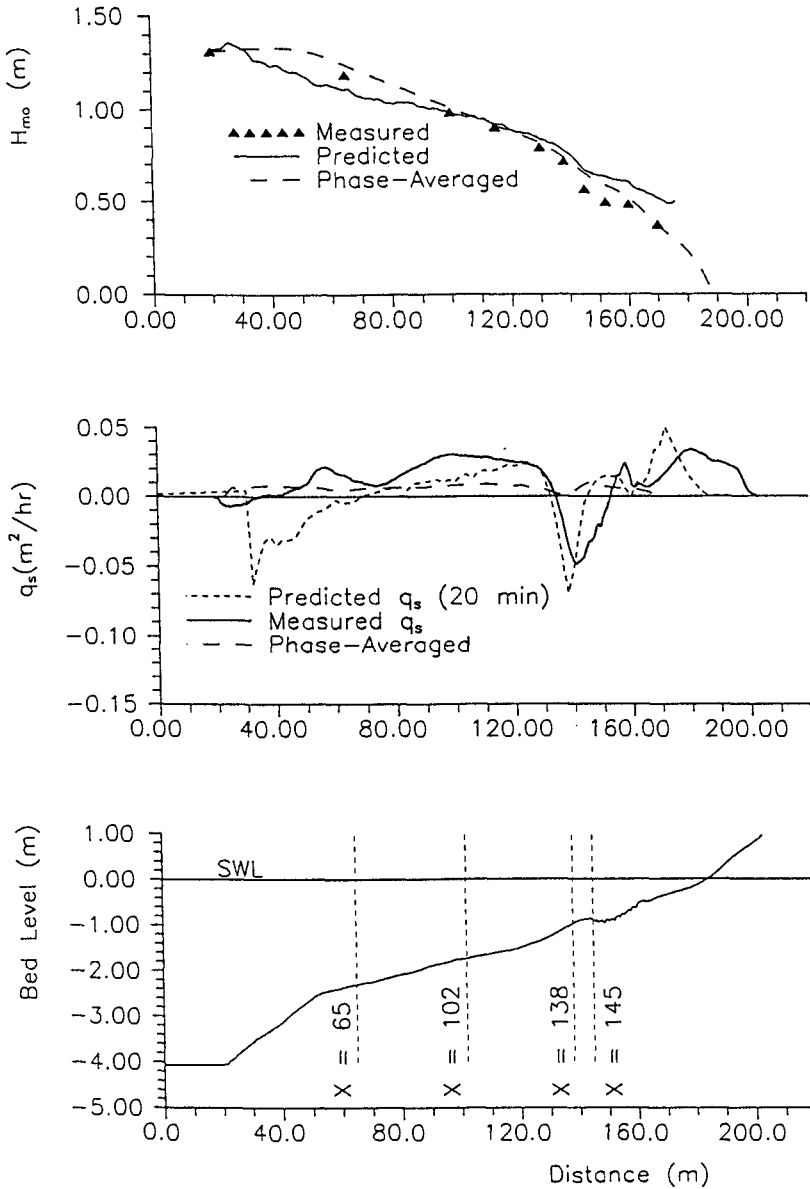


Figure (6): Model results for H_{mo} and q_s of Test Ib (LIP IID).

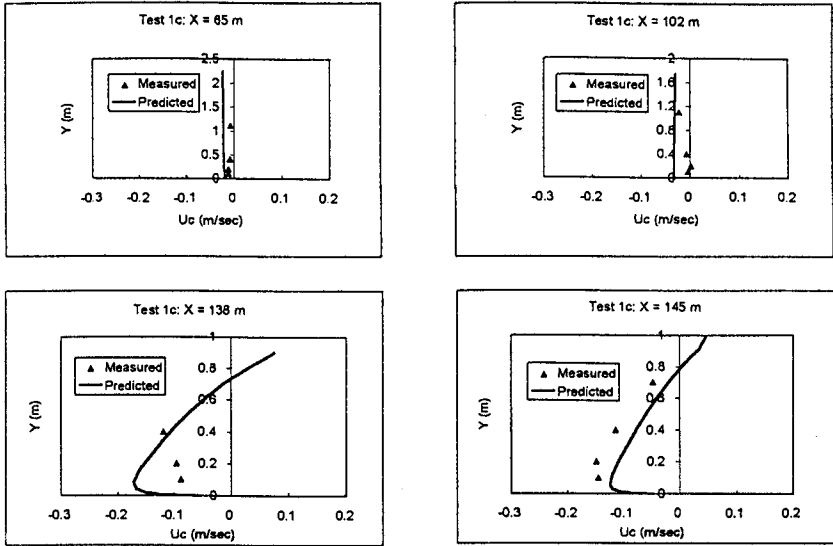


Figure (7): Model results for Undertow of Test 1c (LIP 11D).

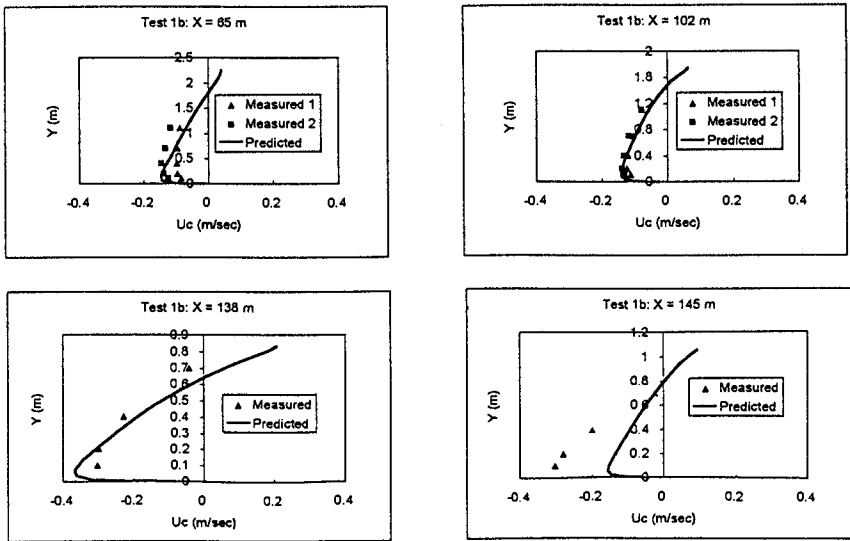


Figure (8): Model results for Undertow of Test 1b (LIP 11D).

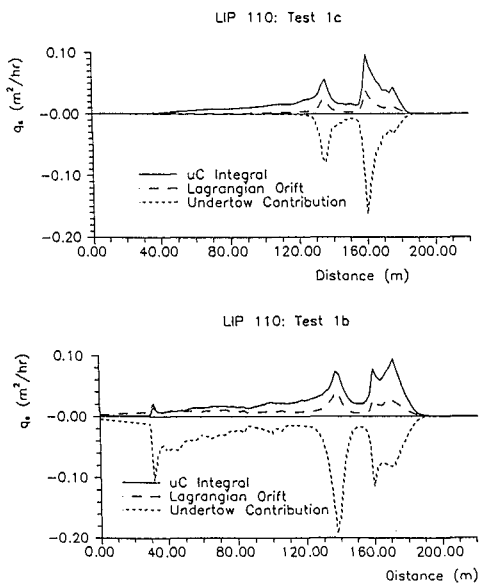


Figure (9): Sediment transport rate contributions for Tests 1c and 1b (LIP 11D).

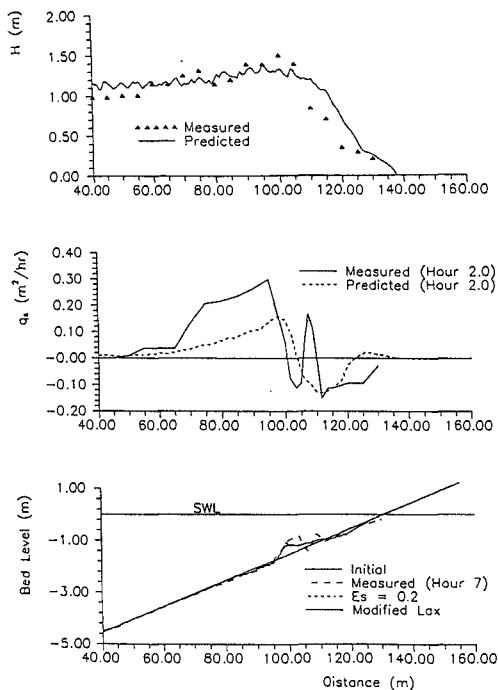


Figure (10): Model results for Test 3-2 (Shimizu et al., 1985).

3.2 Validation of Morphology Model

Figure (10) shows the morphology model predictions for Test 3-2 of Shimizu et al. (1985) with the test conditions provided in Table (1). Good results were obtained for the bar formation as shown in Figure (10) although the numerical model underpredicted the bar development due to the underprediction of the sediment transport rates outside the surf zone. Figure (10) shows that the Boussinesq model underpredicts the shoaling of the waves outside the surf zone. This underprediction of the wave shoaling could be responsible for the underprediction of the sediment transport rates. As shown in Figure (10) the modified Lax-scheme and the FTCS scheme with $\epsilon_s = 0.2$ gave similar results. A sensitivity analysis on the effect of using a value of $\epsilon_s = 2.0$ (as suggested by Watanabe, 1994) showed that the model was not sensitive to the value of ϵ_s for this case.

CONCLUSIONS

A phase-resolving wave transformation module was combined with an intra-wave sediment transport module to predict the on/offshore sediment transport rates and the resulting beach evolution. The roller geometry was used to determine the instantaneous production of turbulence and a mean shear stress at the water surface. The instantaneous sediment transport rates due to the oscillatory wave induced currents (bed load and suspended load), the undertow, and the Lagrangian drift were calculated.

The present model was verified against a few test conditions. The model predicted the undertow and the sediment transport rates well for both erosive and accretive conditions. The onshore sediment transport rates for accretive beaches were underpredicted before the bar due to the overprediction of the undertow, and the underprediction of wave shoaling.

The results of the present paper showed that even for eroding beaches the undertow contribution to the sediment transport rates dominated only at local areas, suggesting that other contributions should not be neglected for eroding beaches.

ACKNOWLEDGMENT

The Danish National Research Foundation financed the first and third authors and the Danish Technical Research Council under the program 'Marin Teknik' financed the fourth author, their support is greatly appreciated. The assistance of Ole Sørensen with the Boussinesq model is also appreciated. Dano Roelvink (Delft Hydraulics) helped in providing the data for the LIP experiments.

REFERENCES

- Abbott, M.B. (1979). Computational Hydraulics. Pitman Books Ltd.
- Abbott, M.B. and Basco, D.R. (1989). Computational Fluid Dynamics. John Wiley and Sons, Inc., New York. 425p.
- Arcilla, A.S., Roelvink, J.A., O'Conner, B.A., Reniers, A., and Jimenez, J.A. (1994). The Delta Flume '93 experiment. Coastal Dynamics 1994, ASCE, Barcelona, pp. 488-502.
- Battjes, J.A. and Janssen, J.P.F.M. (1978). Energy loss and set-up due to breaking of random waves. Proc. 16th Int. Conf. Coastal Eng., ASCE, Vol. 1, pp. 569-589.
- Brøker, H.I., Deigaard, R., and Fredsøe, J. (1991). On/offshore sediment transport and morphological modelling of coastal profiles. Proc. ASCE Specialty Conf. Coastal Sediments' 91, Seattle, WA, pp. 643-657.
- Deigaard, R., (1989). Mathematical modelling of waves in the surf zone. Progress Report 69, ISVA, Technical University, Lyngby, Denmark, pp. 47-59.
- Deigaard, R., Justesen P., and Fredsøe, J. (1991). Modelling of undertow by a one-equation turbulence model. Coast. Eng., Vol.15, pp.431-458.

- De Vriend, H.J., Zyserman, J., Nicholson, J., Roelvink, J.A., Péchon, P., and Southgate, H.N. (1993). Medium-term 2DH coastal area modelling. *Coast. Eng.*, Vol.21, pp.193-224.
- Engelund, F., and Fredsøe, J. (1976). A sediment transport model for straight alluvial channels. *Nordic Hydrology*, Vol. 7, pp. 293-306.
- Fredsøe, J. (1984). The turbulent boundary layer in combined wave current motion. *Journal of Hydraulic Eng.*, ASCE, Vol. 110, No.HY8, pp. 1103-1120.
- Fredsøe, J., Andersen, O.H., and Silberg, S. (1985). Distribution of suspended sediment in large waves. *Journal of Waterway, Port, Coastal and Ocean Eng.*, ASCE, Vol. 111, No. 6, pp. 1041-1059.
- Fredsøe, J., and Deigaard, R. (1992). *Mechanics of Coastal Sediment Transport*. World Scientific, 369p.
- Horikawa, K. (1988). *Nearshore dynamics and coastal processes*. University of Tokyo Press.
- Madsen, P.A., Murray, R., and Sørensen (1991). A new form of the Boussinesq equations with improved linear dispersion characteristics. *Coast. Eng.*, Vol.15, pp.371-389.
- Madsen, P.A., Sørensen O.R. (1992). A new form of the Boussinesq equations with improved linear dispersion characteristics. Part 2. A slowly-varying bathymetry. *Coast. Eng.*, Vol.18, pp.183-204.
- Madsen, P.A., Sørensen O.R., Schäffer, H.A. (1994). Time domain modelling of wave breaking, runup, and surf beats. 24th Int. Conf. on coastal Eng., pp. 399-411.
- Rakha, K.A., and Kamphuis, J.W. (1996). A morphology model for an eroding beach backed by a seawall. Submitted to *Coastal Eng.*
- Rakha, K.A., Deigaard, R., Brøker, I. (1996). A phase-resolving cross shore sediment transport model for beach profile evolution. Submitted to *Coastal Eng.*
- Roelvink, J.A. and Brøker, I. (1993). Cross-shore profile models. *Coast. Eng.*, ASCE, Vol.21, pp.163-191.
- Roelvink, J.A. and Reniers, A.J.H.M. (1995). LIP 11D delta flume experiments. Data Report, Delft Hydraulics, H 2130.
- Schäffer, H.A., Madsen, P.A., and Deigaard, R. (1993). A Boussinesq model for waves breaking in shallow water. *Coastal Eng.*, Vol. 20: 185-202.
- Shimizu, T., Sato, S., Maruyama, K., Hasegawa, H., and Kajima, R. (1985). Modeling of cross-shore sediment transport rate distributions in a large wave flume, Report of Central Res. Inst. for Electric Power Industry, Rep. No. 384028, 60 p. (in Japanese).
- Watanabe, A. (1994). A mathematical model of beach processes under sheet-flow condition using nonlinear wave theory. *International Symposium Waves - Physical and Numerical Modelling*, Vancouver, Canada, pp.1520-1529.
- Zyserman, J.A. and Fredsøe, J. (1994). Data analysis of bed concentration of suspended sediment. *Journal of Hydr. Engng.*, ASCE, 120(9).

CHAPTER 237

Cross-shore Sediment Transport and Beach Deformation Model

Rattanapitikon Winyu ¹

Tomoya Shibayama ²

Abstract

Based on a large amount of published laboratory results, reliable model is developed for computing beach profiles under regular wave actions. The sediment transport is separated into suspended load and bed load. The suspended load is computed as the product of the time-averaged suspended concentration and the time-averaged velocity. The bed load is developed following the similar step as Watanabe (1983) but the applied area is different. The wave model of Dally et al. (1985) is modified and used to compute wave height transformation. The beach profile change is computed from the conservation of sediment mass. The beach deformation model is verified with small scale and large scale experiments. Reasonably good agreement is obtained between measured and computed beach profiles.

I. Introduction

In the previous research works, most of the models were developed based on data with the limited experimental conditions. Therefore their validity is limited according to the range of experimental conditions which were employed in the calibration or examination. The evidence is that there are so many models exist. At this moment, the experimental results obtained by many researchers have been accumulated and a large number of experimental results have become available. It is a good time to develop a model based on the large amount and wide range of experimental results. The present model is developed based on 1138 data sets of 24 sources of published experimental results covering both small and large scale experiments, as shown in table 1.

¹ D. Eng., Dept. of Civil Engineering, Sripatum University, 61 Phahonyothin Rd., Jatujak, Bangkok, 10900, Thailand.

² D. Eng., Assoc. Prof., Dept. of Civil Engineering, Yokohama National University, Hodogaya-ku, 240, Yokohama, Japan.

Table 1. Sources and number of collected data for present sediment transport study.

Sources	$c(z)$	$u(z)$	H	$h(x,t)$	Others	Experiment
Bosman and Steetzel (1986)	3					SE
Deigaard et al. (1986)	6					SE
Dette and Uliczka (1986)	11					LE
Duncan (1981)					A,12	SE
Hansen and Svendsen (1984)		4	1			SE
Hayakawa et al. (1983)	4					SE
Horikawa and Kuo (1966)			213			SE
Horikawa et al. (1982)	7					SE
Irie et al. (1985)	27					SE
Kajima et al. (1983)	149	219	79	91		LE
Kraus and Larson (1988)				69		LE
Nadaoka et al. (1982)		11	2		$h_{ot},2$	SE
Nagayama (1983)			12			SE
Nakato et al. (1977)	3					SE
Nielsen (1979)	44					SE
Okayasu et al.(1988)		44	9		$h_{ot},9$	SE
Okayasu et al.(1989)					$h_{ot},47$	SE
Sato et al. (1988, 1989)			5			SE
Sato et al. (1990)	14					SE
Sawamoto et al. (1981)	4					SE
Shibayama and Horikawa (1985)			10	11		SE
Skafel and Krishnappan (1984)	8					SE
Sleath (1982)	4					SE
Vongvisessomjai (1986)	4					SE
Total	288	278	331	171	70	

where $c(z)$ is the time-averaged sediment concentration, $u(z)$ is the time-averaged fluid velocity, H is the wave height, $h(x,t)$ is the beach profile, A is the cross section area of surface roller, h_{ot} is the still water depth at transition point, SE is the small scale experiment, and LE is the large scale experiment.

1.1 Governing equation

The cross-shore change in local water depth, h , can be calculated by solving the conservation of sediment mass as the following

$$\frac{\partial h}{\partial t} = \frac{1}{(1-\Lambda)} \frac{\partial q_t}{\partial x} \dots\dots\dots (1)$$

where t is the time, x is the horizontal coordinate in cross-shore direction, Λ is the porosity, and q_t is the total transport rate per unit width.

The sediment transport rate is usually expressed as

$$q_t = \int_{-s}^h c(z)u(z) dz \dots\dots\dots (2)$$

where δ is the level above which there is no effective movement of sand particles, z is the vertical coordinate measured upward from the bed, $c(z)$ is the time-averaged sediment concentration, and $u(z)$ is the time-averaged fluid velocity.

In order to compute the transport rate, q_s , the sediment concentration and fluid velocity should be known first. The sediment concentration profile was described in Shibayama and Rattanapitikon (1993). The following sections will describe about velocity profile, sediment transport, wave model, and beach deformation model, respectively.

II. Time-Averaged Velocity Profiles

Following Okayasu et al. (1988, pp. 93-94), the vertical distribution of time-averaged velocity profile is calculated based on the assumption of eddy viscosity model. By considering time-averaged values, the eddy viscosity model can be expressed as

$$\tau = \rho \nu_t \frac{\partial u}{\partial z} \dots\dots\dots (3)$$

where τ is the time averaged shear stress, ρ is the fluid density, ν_t is the time-averaged eddy viscosity coefficient, u is the time-averaged velocity, and z is the upward vertical coordinate from the bed.

To solve the eddy viscosity model, one boundary condition of velocity should be given and the expression of τ / ν_t should also be known. In this study, the vertical-averaged value of velocity, u_m , is used as the boundary condition for Eq. 3 and will be described in the following subsection.

2.1 Vertically averaged velocity

Using the concept of Svendsen (1984), the vertically averaged velocity, from bed to wave trough, u_m , consists of two components. One is caused by the wave motion, u_w , and the other is caused by the surface roller, u_r .

$$u_m = u_w + u_r \dots\dots\dots (4)$$

Various formulas for computing u_w and u_r have been suggested by the previous researchers. From the previous studies, of Duncan (1981), Svendsen (1984), Stive and Wind (1986), Deigaard et al. (1991), and Fredsoe and Deigaard (1992), we can conclude that there are three formulas for computing u_w and three formulas for computing u_r (see in table 2).

Table 2. Formulas for computing u_m and u_r

	Formula 1	Formula 2	Formula 3
u_w	$\frac{B_o \sigma H^2 \coth(kh)}{h}$	$\frac{B_o c_w H^2}{h^2}$	$\frac{c_w H}{h}$
u_r	$\frac{H^3}{(0.7Th^2)}$	$\frac{0.9H^2}{(Th)}$	$\frac{0.1c_w H}{h}$

where $B_o = (1/T) \int_0^T (\xi/H) dt$, c_w is the phase velocity, H is the wave height, h is the mean water depth, T is the wave period, and ξ is the water surface elevation measured from mean water level.

The general form of u_m may be written as

$$u_m = au_w + bu_r \dots\dots\dots (5)$$

where a and b are the constants.

The proper combination of u_w and u_r and the constants a, b can be found from multi-regression analysis with the observed u_m .

After the regression analysis and include the effect of transition zone, the final equation for computing u_m can be written as

$$u_m = 0.77 \frac{B_o \sigma H^2 \coth(kh)}{h} + b_1 0.1 \frac{c_w H}{h} \dots\dots\dots (6)$$

where b_1 is the constant and expressed as

$$b_1 = \begin{cases} 0 & \text{offshore zone} \\ (1/\sqrt{H} - 1/\sqrt{H_b}) / (1/\sqrt{H_t} - 1/\sqrt{H_b}) & \text{transition zone} \\ 1 & \text{inner zone} \end{cases}$$

where H_b and H_t is the wave height at breaking point and transition point.

Example of examination results of u_m along the cross-shore direction are shown in Fig. 1.

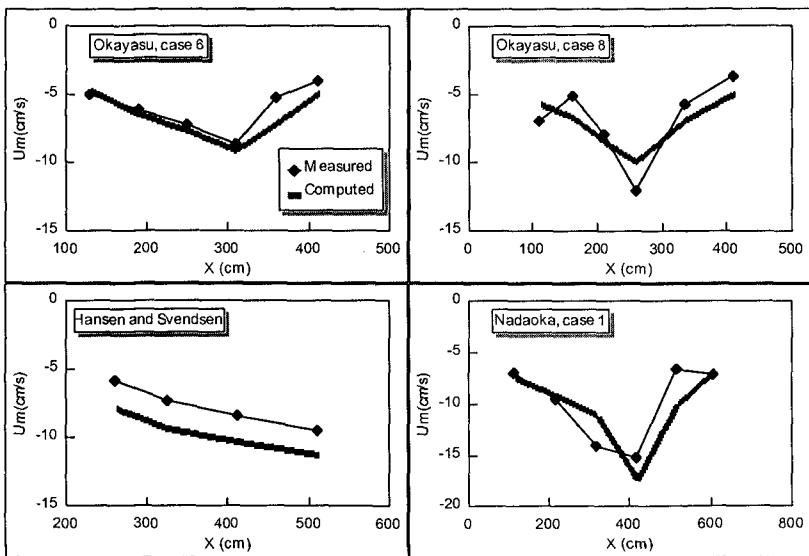


Figure 1. Example of cross-shore variations of measured and computed vertical averaged velocity, u_m .

2.2 Vertical distribution of shear stress and eddy viscosity coefficient

Based on dimensional analysis, Okayasu (1989, pp. 93-94) proposed a formulas for computing τ / ν_t as follows

$$\frac{\tau}{\nu_t} = \rho^{1/3} D_B^{1/3} \left[\frac{k_3}{d_t} + \frac{k_4}{z} \right] \dots\dots\dots (7)$$

where k_3 and k_4 are the constants, d_t is the water depth at wave trough, and D_B is the energy dissipation. From the bore model (Thornton and Guza, 1983),

$$D_B = \frac{\rho g H^3}{47h} \dots\dots\dots (8)$$

By inserting Eq. 7 into Eq. 3 and then, after an integration of Eq. 3 and use u_m as the boundary condition, the analytical solution of u can be expressed as

$$u = \rho^{1/3} D_B^{1/3} \left[k_3 \left(\frac{z}{d_t} - \frac{1}{2} \right) + k_4 \left(\ln \frac{z}{d_t} - 1 \right) \right] + u_m \dots\dots\dots (9)$$

As mentioned in previous research works, the energy dissipation process at the breaking point is not in the same manner as in the inner zone (e.g., Okayasu, 1989). To incorporate this process, Eq. 9 may be written as follows

$$u = k_5 \rho^{1/3} D_B^{1/3} \left[k_3 \left(\frac{z}{d_t} - \frac{1}{2} \right) + k_4 \left(\ln \frac{z}{d_t} - 1 \right) \right] + u_m \dots\dots\dots (10)$$

where k_5 is the constant and equal to 1 at the inner zone.

From the multi-regression analysis and assume linear distribution of energy dissipation in the transition zone, Eq. 10 become

$$u = b_2 \rho^{1/3} D_B^{1/3} \left[b_3 \left(\frac{z}{d_t} - \frac{1}{2} \right) - 0.22 \left(\ln \frac{z}{d_t} - 1 \right) \right] + u_m \dots\dots\dots (11)$$

where b_2 and b_3 are the constants and expressed as,

$$b_2 = \begin{cases} 0.3 + 0.7(x_b - x) / (x_b - x_t) & \text{transition zone} \\ 1.0 & \text{inner zone} \end{cases}$$

$$b_3 = \begin{cases} (x_b - x) / (x_b - x_t) & \text{transition zone} \\ 1.0 & \text{inner zone} \end{cases}$$

where x is the position in cross-shore direction, x_b is the position at the breaking point, and x_t is the position of the transition point.

The comparison between measured u and computed u from Eq. 11, using measured u_m , are shown in Fig. 2. From Fig. 2 we can judge that the form of τ / ν_t in Eq. 7 are accurate enough to be used for computing the velocity profiles. Examples of measured and computed velocity are shown in Fig. 3.

2.3 Formula verification

The prototype scale experiment of Kajima et al. (1983) is used to examine the validity of present formula. By using the same formula as that used for small scale wave flume (Eq. 11), Fig. 4 shows examples of verification results in the term of averaged velocity of each section along the cross-shore direction.

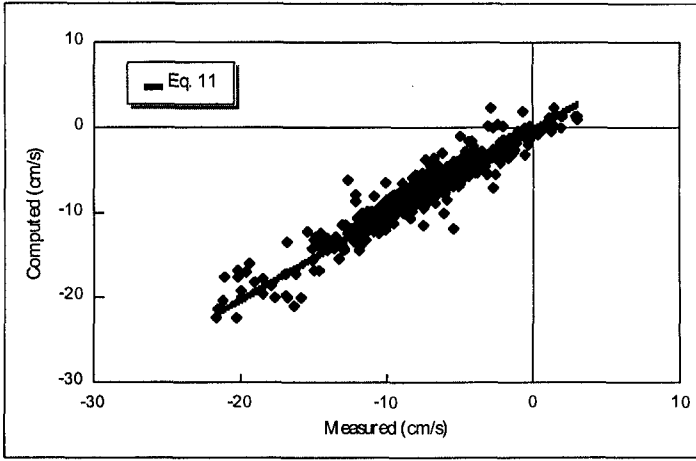


Figure 2. Comparison between measured and computed u (using measured u_m).

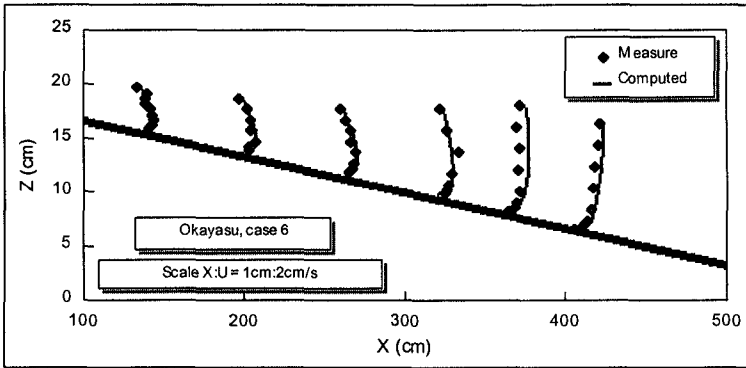


Figure 3. Comparison between measured and computed velocity profiles (laboratory data from Okayasu et al., 1988, case 6).

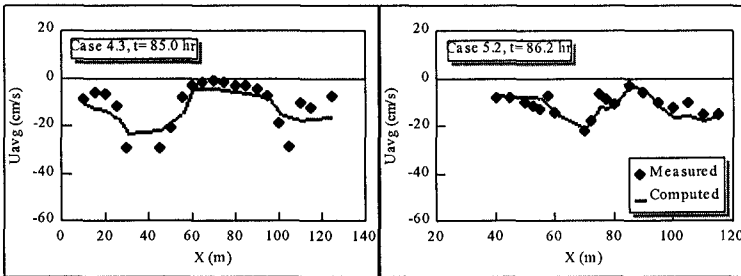


Figure 4. Example of verification results in term of averaged velocity along the cross-shore direction (laboratory data from Kajima et al., 1983).

III. Sediment Transport Rate

The sediment transport rate is separated into bed load and suspended load. The suspended load is expressed as the product of sediment concentration and fluid velocity. The bed load formula is derived in the similar procedure as Watanabe (1983) but the assumption on the time level and region of application are not the same. After calibrate the coefficient of bed load, the total load can be written as

$$q_t = \int_{\delta_s}^{d_s} c(z)u(z) dz + 2.0(\psi - \psi_c)\sqrt{\psi} w_s d \quad \dots\dots\dots (12)$$

where ψ is the Shields parameter, ψ_c is the critical Shields parameter, w_s is the falling velocity, and δ_s is the bottom boundary layer which computed from Jonsson (1966) formula.

The comparison of computed suspended load, bed load and total load and the measured total load are shown in Fig. 5. It should be note that the separated equation for computing transport direction is not necessary in the present model. The transport direction is depended on the combination of bed load and suspended load. In the present model, bed load is the dominant transport for accretion beach (on-shore directed transport), and suspended load is the dominant transport for erosion beach (off-shore directed transport). These transport directions correspond well with the measured total load transport as shown in Fig. 5.

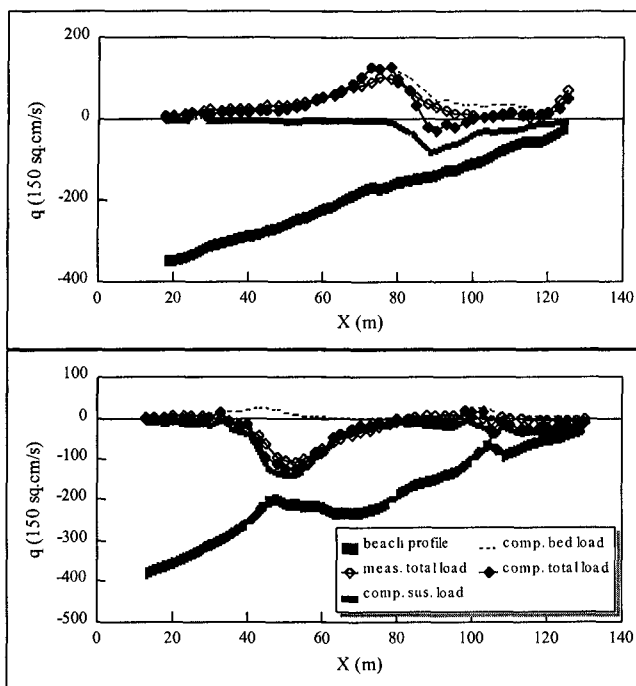


Figure 5. Comparisons between measured and computed sediment transport (laboratory data from Kajima et al., 1983, case 2.2, and 4.3).

IV. Wave Model

For computing beach transformation, the wave model should be kept as simple as possible because of the frequent updating of wave field for accounting the variability of mean water surface and the change of bottom profiles. In the present study, wave height transformation in cross-shore direction will be computed from the energy flux conservation.

$$\frac{\partial Ec_g}{\partial x} = -D_B \dots\dots\dots (13)$$

where E is the wave energy density, c_g is the group velocity, and D_B is the energy dissipation rate which is zero outside the surf zone.

4.1 Energy dissipation rate

Widely used formulas for computing energy dissipation rate are Bore model and Dally et al. (1985) model. The Bore model is shown in Eq. 8, and Dally model is

$$D_B = \frac{0.15c_g \rho g}{8h} [H^2 - (\Gamma h)^2] \dots\dots\dots (14)$$

The advantage of Dally model is that it is able to reproduce the pause (or stop breaking) in the wave breaking process at a finite wave height on a horizontal bed or in the recovery zone while the Bore model gives a continuous dissipation due to wave breaking. However, for the condition when waves continuously break both two models give nearly the same result of energy dissipation rates (for example see Fig. 6). Based on the above considerations, Dally model is selected for calculation in the present research.

The published experimental results of wave height transformation inside the surf zone have been collected to test the ability of Dally model as shown in the first column of table 3. Total 9 sources of published experimental results, covering 331 data sets, are used in this section. The experiments cover wide range of wave and bottom topography conditions, including both small scale and large scale wave flume experiments. Most of the experiments were performed under fixed bed conditions, except data of Kajima et al. (1983) and Shibayama and Horikawa (1985) which were performed under movable bed conditions.

The verification results are presented in term of error function, ER , as used by Dally et al. (1985), which is defined as

$$ER = 100 \sqrt{\frac{\sum_{i=1}^{tn} (H_{ci} - H_{mi})^2}{\sum_{i=1}^{tn} H_{mi}^2}} \dots\dots\dots (15)$$

where i is the wave height number, H_{ci} is the computed wave height of number i , H_{mi} is the measured wave height of number i , and tn is the total number of measured wave height. Small value of ER expresses a good prediction.

The verification results of Dally model are shown in the third column of table 3. From the third column of table 3, we can see that Dally model gives quite good estimation of wave height inside the surf zone.

Although, Dally model gives good estimation to the experimental results, it still has some error. We may be able to improve Dally model.

Considering Dally model, the measured Γ can be computed from the measured wave height and water depth by using the following formula (rewriting Eq. 14).

$$\Gamma = \frac{1}{h} \sqrt{H^2 - \frac{\partial(Ec_g)}{\partial x} \frac{8h}{0.15c_g \rho g}} \dots\dots\dots (16)$$

The right hand side term of Eq. 16, RS , can be computed if we have the profile of wave height transformation. If we plot RS with any wave parameters, it will show a horizontal line (since Γ is constant).

Fig. 7 shows the relation between RS and the various dimensionless parameters, i.e., h/L_o , h/L , h/\sqrt{LH} . From Fig. 7 we can see that the parameter Γ is not a constant. Comparison among Fig. 7a-7c, the relation between Γ and h/\sqrt{LH} , in Fig. 7c, shows more consistent results than the others. A formula for parameter Γ , from Fig. 7c, can be expressed as

$$\Gamma = \exp\left[-0.36 - 1.25 \frac{h}{\sqrt{LH}}\right] \dots\dots\dots (17)$$

The next question is how much difference of computed wave height is resulted when we compare the results calculated by using constant Γ and calculated by using Γ from Eq. 17. Table 3 shows the error function, ER , when wave height is computed from Dally model by using either constant Γ or Γ from Eq. 17.

From table 3 we can see that the computed results show not much difference, but for most cases the results of computed wave height are improved. The selection of any type of model depends on each researcher. In the present study, the better estimation formula (Eq. 17) will be used.

Table 3. Verification results in term of error function parameter, ER .

Sources	No. of data sets	$\Gamma = 0.4$	Γ from Eq. 17
Hansen and Svendsen (1984)	1	16.12	6.95
Horikawa and Kuo (1966),slope=0	101	13.30	11.65
Horikawa and Kuo (1966),slope=1/80-1/20	112	20.58	17.67
Nagayama (1983)	12	9.19	8.62
Kajima et al. (1983)	79	18.36	16.37
Nadaoka et al. (1982)	2	11.97	10.81
Okayasu et al. (1988)	10	14.18	11.3
Sato et al. (1988)	3	11.36	7.74
Sato et al. (1989)	2	31.83	19.78
Shibayama and Horikawa (1986)	10	16.23	17.69

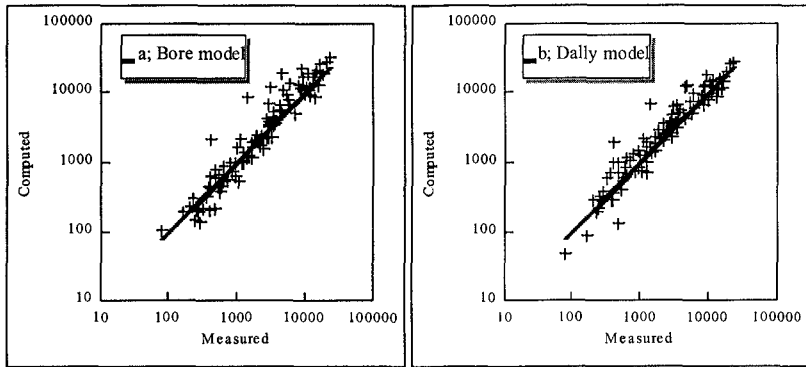


Figure 6. Comparison between measured and computed energy dissipation rate from a: Bore model, b: Dally model (laboratory data from Hansen and Svendsen, 1984, Okayasu et al., 1988, and Sato et al., 1988 and 1989).

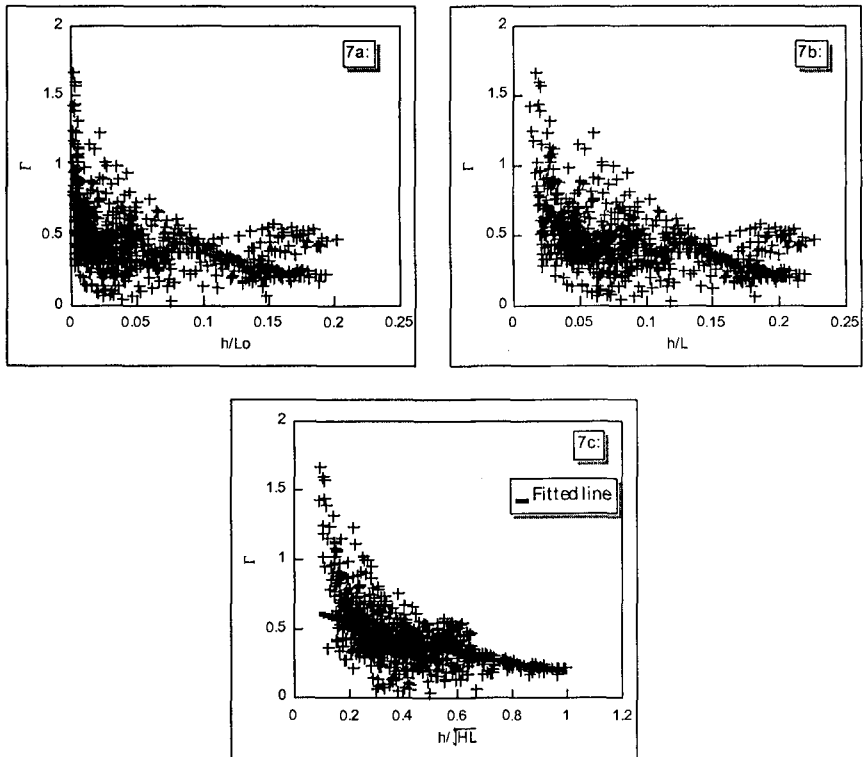


Figure 7. Relations between Γ and a: h/L_0 , b: h/L , c: h/\sqrt{LH} (laboratory data from Kajima et al., 1983).

V. Beach Deformation Model

Wave model is used to compute wave transformation from offshore boundary to shoreline boundary. From the computed wave height, sediment transport rate can be computed. Then new beach profile can be computed from the mass conservation equation (Eq. 1). The new beach profile will feed-back into the wave model and causes wave height changes. This yields the loop of dynamic beach deformation and the beach profile at any desired time can be computed.

The shoreward boundary is defined at the wave runup height. Following Larson and Kraus (1989, pp. 170-172), the sediment transport inside the swash zone is assumed to decrease linearly from the end of surf zone to zero at the runup limit. If the local beach slope exceeded the repose angle, avalanching concept will be used.

5.1 Model verification

A number of simulations are performed in order to examine the capability of the present model. All coefficients in the model are kept to be constant for all cases in the verification. Model results are compared with laboratory data of small scale experiment of Shibayama and Horikawa (1985) and large scale experiment of Kajima et al. (1983) and Kraus and Larson (1988).

The verification is performed for all cases, total 45 cases. The verification of these independent data sources and wide range of experiment conditions are expected to clearly demonstrate the accuracy, and stability of present model. The main input data of the model is the incident wave dimensions and initial beach profile. The model was run on workstations (HP 9000 series 700 computers); the total CPU time for simulation about 1000 hr (45 cases) is about 6 min. Examples of examination results are shown in Figs. 8-10. The examination results of all cases, including four profiles per case, are shown in Rattanapitikon (1995, pp. 173-196). Interesting points of the comparison results are described as follows

1. The global shapes of measured profiles are generally well predicted by the model. The predicted profiles are smoother than the measured ones. Small fluctuation of measured profiles can not be predicted by the present model (see Kajima, case 3.1 and Kraus, case 510 in Fig. 8).
2. The agreements of predicted beach profiles of the prototype scale are better than those of small scale wave flume. The fluctuation of measured beach profiles in small scale experiment are more than the prototype scale experiment and the present model can not predict those fluctuations.
3. The model is able to simulate a breaker bar of either the growth of breaker bar (see case 5.2 in Fig. 10) or the reduction of breaker bar (see case 1.2 in Fig. 9).

VI. Conclusions

Cross-shore beach deformation model is developed based on a large amount of published laboratory results. The model contains description of time-averaged concentration profile, velocity profile, sediment transport, wave height, and beach deformation. The validity of model is confirmed by small scale and large scale experiments. The main merit of this model is that it requires very short CPU time and the results are reasonably well.

Acknowledgment

The authors wish to express their gratitude to Prof. Yoshimi Goda of the Yokohama National University for his comments and fruitful discussions.

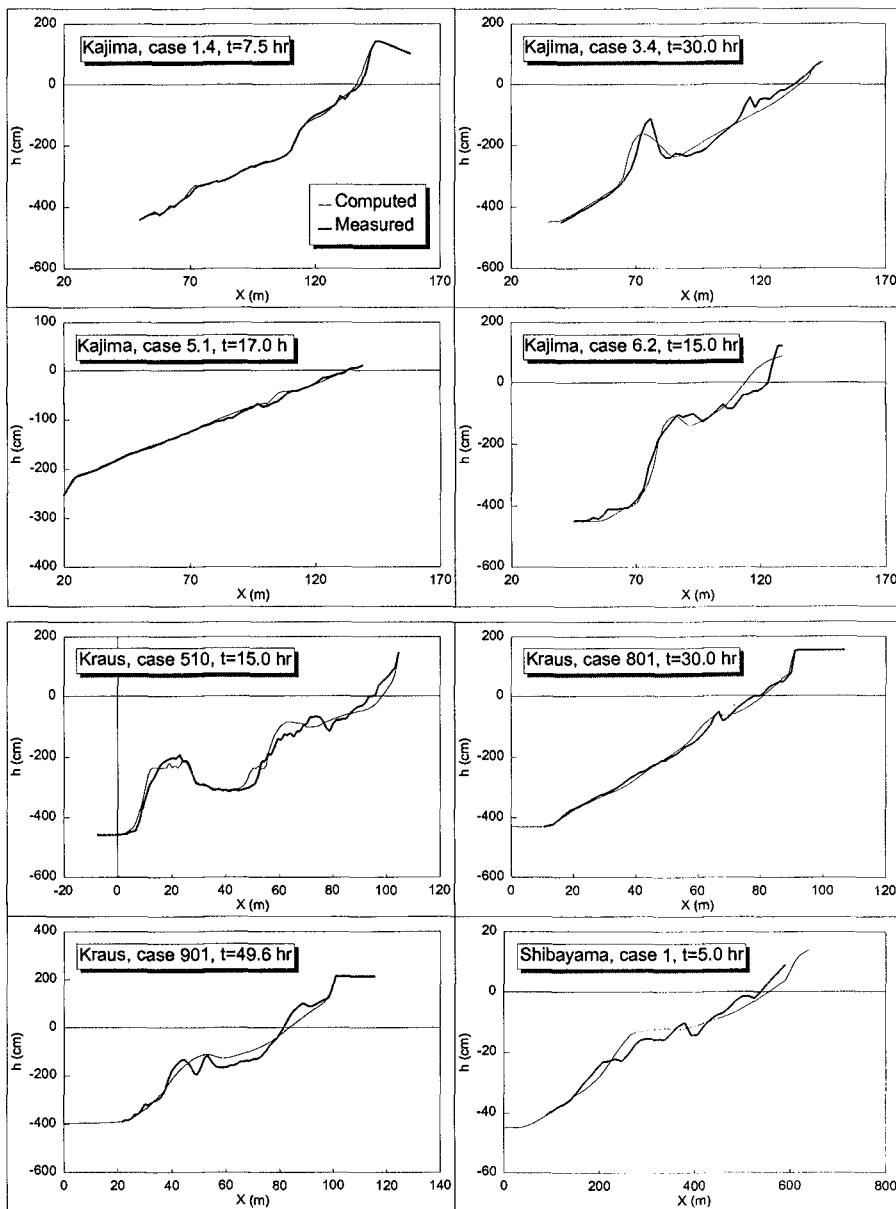


Figure 8. Examples of comparison between measured and computed beach deformation (laboratory data from Kajima et al., 1983, Kraus and Larson, 1988, and Shibayama and Horikawa, 1985).

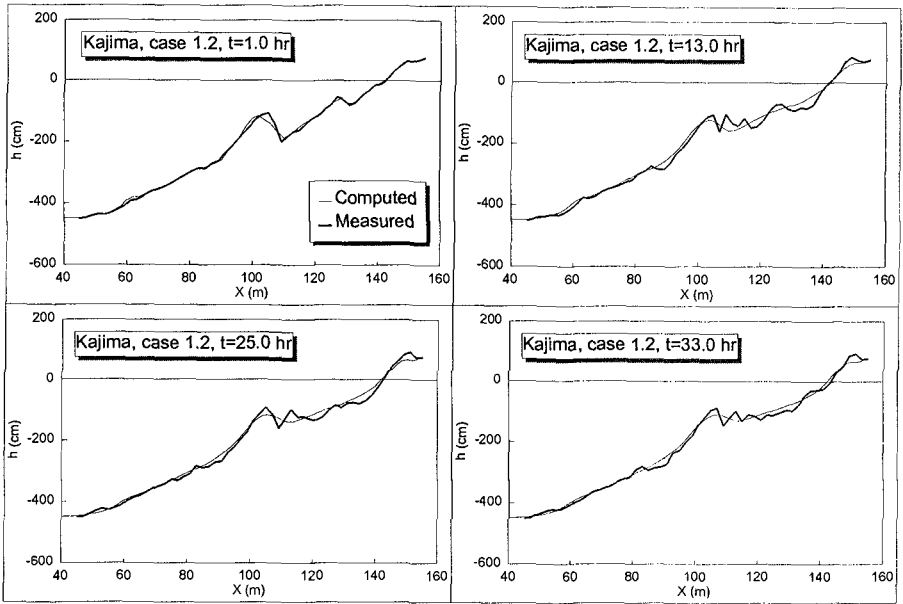


Figure 9. Comparison between measured and computed beach deformation (laboratory data from Kajima et al., 1983, case 1.2).

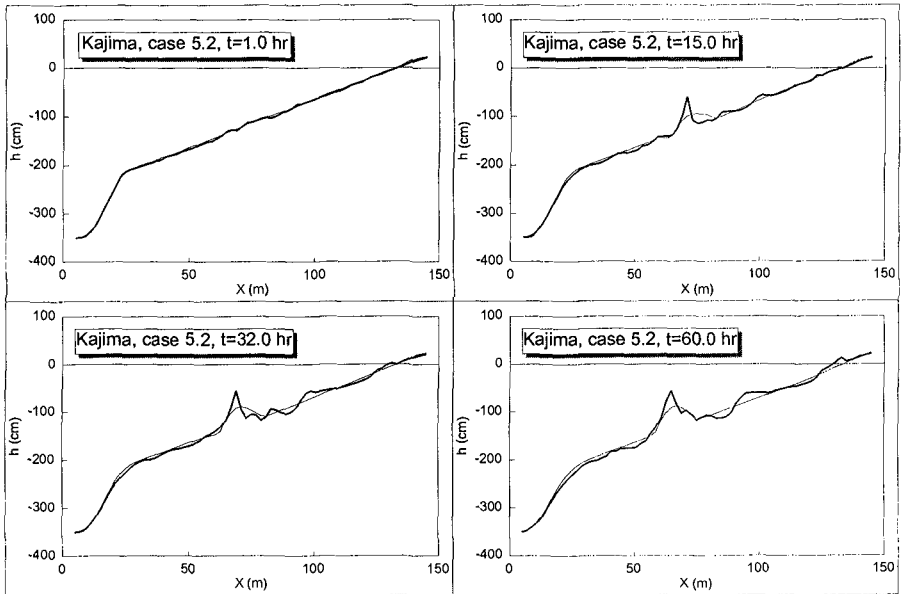


Figure 10. Comparison between measured and computed beach deformation (laboratory data from Kajima et al., 1983, case 5.2).

References

- Dally, W.R., Dean, R.G., and Dalrymple, R.A. (1985): Wave height variation across beaches of arbitrary profile, *J. of Geo. Res.*, Vol. 90, No. C6, pp. 11917-11927.
- Deigaard, R., and Fredsoe, J. (1991): Modelling of undertow by a one-equation turbulence model, *Coastal Engineering*, No. 15, pp. 431-458.
- Duncan J.H. (1981): An experimental investigation of breaking waves produced by a towed hydrofoil, *Proc. R. Soc. London, Ser. A* 377, pp. 331-348.
- Horikawa, K., and Kuo, C.T. (1966): A study of wave transformation inside surf zone, *Proc. 10th Coastal Engineering Conf., ASCE*, pp. 217-233.
- Kajima, R., Shimizu, T., Maruyama, K., and Saito, S. (1983): On-offshore sediment transport experiment by using large scale wave flume, Collected data No. 1-8, Central Research Institute of Electric Power Industry, Japan (in Japanese).
- Kraus, N.C., and Larson, M (1988): Beach profile change measured in the tank of large waves, 1956-1957 and 1962., Technical Report CERC-88-6, Coastal engineering research center, US Army Eng. Waterways Exp. Station.
- Larson, M. and Kraus, N.C. (1989): SBEACH: Numerical model for simulating storm-induced beach change, Report 1, Technical Report CERC-89-9, Coastal engineering research center, US Army Eng. Waterways Exp. Station.
- Nadaoka, K., Kondoh, T., and Tanaka, N. (1982): The structure of velocity field within the surf zone revealed by means of laser-doppler anemometry, Report of The Port and Harbour Research Institute, Vol. 21, No. 2, pp. 50-102 (in Japanese).
- Okayasu, A., Shibayama, T., and Horikawa, K. (1988): Vertical variation of undertow in the surf zone, *Proc. 21st Coastal Eng. Conf., ASCE*, pp. 478-491.
- Okayasu, A. (1989): Characteristics of Turbulence Structure and Undertow in Surf Zone, D. Eng. Dissertation, Civil Eng., University of Tokyo, Japan.
- Rattanapitikon, W. (1995): Cross-shore Sediment Transport and Beach Deformation Model, D. Eng. Dissertation, Civil Eng., Yokohama National University, Yokohama, Japan.
- Sato, S., Isayama, T., and Shibayama, T. (1989): Long-wave component in near-bottom velocity under random waves on a gentle slope, *Coastal Engineering in Japan, JSCE*, Vol. 32, No. 2, pp. 149-159.
- Shibayama, T., Horikawa, K. (1985): Numerical model for two-dimensional beach transformation, *Proc. of JSCE*, No. 357/II-3, pp. 167-176.
- Shibayama, T., and Rattanapitikon, W. (1993): Vertical distribution of suspended sediment concentration in and outside surf zone, *Coastal Engineering in Japan, JSCE*, Vol. 36, No. 1, pp. 49-65.
- Stive, M.J.F., and Wind, H.G. (1986): Cross-shore mean flow in the surf zone, *Coastal Engineering*, No. 10, pp. 325-340.
- Svendsen, I.A. (1984): Mass flux and undertow in surf zone, *Coastal Engineering*, No. 8, pp. 347-365.
- Thornton, E.B. and Guza, R.T. (1983): Transformation of wave height distribution, *J. Geophys. Res.*, Vol. 88, pp. 5925-5983.
- Watanabe, A. (1983): Lecture-1; Fundamental of littoral transport, Seminar on Sediment Problems in Beachs and Estuaries, Manila and Jakarta.

CHAPTER 238

Experimental Study on Sediment Transport in Surf and Swash Zones Using Large Wave Flume

Takao Shimizu¹, Masaaki Ikeno²

Abstract

In the present study, experiments were conducted using CRIEPI's Large Wave Flume (205m long, 3.4m wide and 6m deep) to investigate cross-shore hydrodynamics, sediment transport and beach change processes. On the experiments, suspended sediment transport in the surf and swash zones was directly measured under the condition of random waves. Moreover, the long wave effect to sediment transport was also investigated.

Introduction

Suspended sediment transport rate must be evaluated accurately to predict beach change, especially in a calm basin behind an artificial island, because suspended sediment in a surf zone is transported into the calm basin by circulating nearshore current. Recently, it was mentioned that low frequency component in a wave group influences remarkably suspended sediment transport(Sato et al.;1993). Sediment transport rate in a swash zone has to be estimated correctly to expect shoreline change, because erosion and accretion in a swash zone causes shoreline change directly. Ogawa et al.(1981) and Katori(1983) observed sediment transport in a swash zone by using sand traps.

In this study, large scale experiments on beach profile changes due to irregular waves were performed in the Large Wave Flume. Suspended sediment transport and sediment transport rate in a swash zone were measured directly. Effects of irregularity of waves on a sediment transport and influences of low frequency component in a wave group were discussed.

Experimental method

Uniform slopes of sand were piled up in the Large Wave Flume(Kajima et al; 1982) as shown in Fig.1. The bottom of offshore side 90m length of the flume is 1/15 slope. Horizontal coordinate X was defined as an seaward distance from the onshore side end of the flume. An origin of a vertical coordinate Z was defined on a still water level. Still water depth was 4m in cases of 1/10 and 1/20 slope of sand and 3.2m in a case of 1/50 slope of sand. A toe of the sand slope of 1/50 was cut

-
- 1) Research Fellow, Central Research Institute of Electric Power Industry, 1646 Abiko, Abiko-city, Chiba 270-11, JAPAN.
 - 2) Senior Research Engineer, Central Research Institute of Electric Power Industry, 1646 Abiko, Abiko-city, Chiba 270-11, JAPAN.

off by a 1/10 slope, because the still water level can't be smaller than 3.2m for wave generating and the sand volume was limited.

A measuring vehicle that runs on the flume onshore-offshore was used for measurement in a surf zone. The measuring vehicle is equipped with a capacitance type wave gauge(W) and an installing arm going up and down just beside each other. Two sets of an electromagnetic current meter(C), an optical turbidity meter(T) and a pumping tube(P) for water sampling were assembled to the installing arm. Vertical distance between two sets is 40cm. Water sample including suspended sediment was sucked up by an engine pump, and a volume of sampled water was measured by a water counter. Between the pump and the counter, the suspended sediment was filtered out by a 97μ mesh plankton net and weighed. Median diameter of the sand was 1mm, and the grain size distributed from 0.2mm to 1.3mm as shown in Figure 2. Output of turbidity meter was calibrated individually by the time averaged sediment concentration based on the water sampling data. A wheel type sand surface profiler was loaded on a trolley dragged by the measuring vehicle. The profiler can trace the beach profile under the still water and in the air continuously, accurately and speedy.

In some cases, sediment transport due to uprush and sediment transport due to downrush of individual waves were measured respectively by sand traps(S) in a swash zone. The sand traps are original hand made with metal frame and 97μ mesh plankton net as shown in Photo 1. A mouth of the trap is 5cm wide and 20cm high. The length of the trap is 1m. Fifty traps were prepared and numbered. Two footings was built up in a swash zone, and sediment transport was trapped by three persons on the footings as shown in Photo 2. Right one of this side in the photo is trapping sediment transport due to downrush pressing the under edge of the mouth of the trap against the sand surface. Right one of back side is taking a trap away from the one of this side and going to stack it in a bucket. Left one is preparing the next trap. Trappings of sediment transport due to uprush were continued for fifty waves, and after the collection of trapped sand, sediment transport due to fifty downrushes were trapped. A trapping of sediment transport due to uprush was started when a front edge of an uprush reached the trapping point, and was finished when the water started to flow down. But if the front edge of the next uprush reached the trapping point before the water started to flow down, the trap was changed quickly to the next trap. A trapping of sediment transport due to downrush

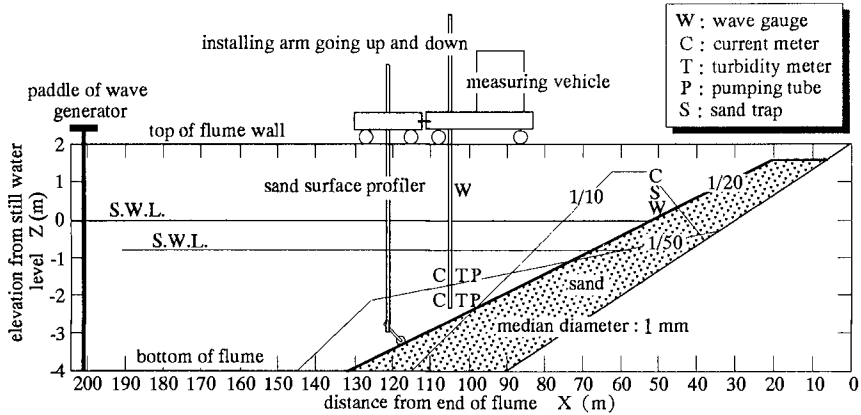


Figure 1. Arrangement of experiments

was started when the water started to flow down, and was finished when the front edge of the next uprush reached the trapping point or the down flow of the water sank into the sand. A wave gauge and a current meter was set up just beside the sand trapping. Bottom end of the wave gauge was stuck in a sand. Head of the current meter was set 1 or 2cm above the sand surface. The wave gauge on the measuring vehicle was set 8m offshore the trapping point. Outputs of wave gauges and a current meter were recorded in a memory of a personal computer and on a chart of linear-corder with trap numbers called by the trapper.

Irregular waves were generated by piston type wave generator. The wave train was repeated every hundred waves. Sampling of outputs of a wave gauge, current meters, turbidity meters and sampling water were continued for one hundred waves at every measuring points in a surf zone. Trappings of sediment transport in a swash zone was performed in the first half of the wave train and in the second half separately. In some cases, the free long wave generated at the paddle of the wave generator was canceled by the method after Ikeno et al.(1996).

Experimental cases and conditions

Table 1 shows experimental cases and conditions. In the case L1, sand slope " $\tan\beta$ " was 1/20 and regular waves were generated. Offshore wave height " H_o " was 1m and wave period " T_o " was 5s. In the case L2, irregular waves were generated using JONSWAP spectrum. Significant wave height and significant wave period was same to the case L1. Sharpness parameter " γ " is 1 according to the wind wave condition. Conditions of the case L3 were same to the case L2 except for the sharpness parameter is 7 according to the swell condition. In the case L4, free long wave cancel method was adopted to the condition of the case L2, but the significant wave height had to be reduced to 0.6m because the stroke of the paddle of wave generator is limited up to 2.1m. Conditions of the case L5 were same to the case L3 except for the sand slope and the wave was steeper than the case L3. Condition of the case L6 was same to the case L5 except for the free long wave was canceled. Conditions of the case L7 was same to the case L3 except for the sand slope and the wave was more gentle than the case L3.



Photo 1. Sand trap

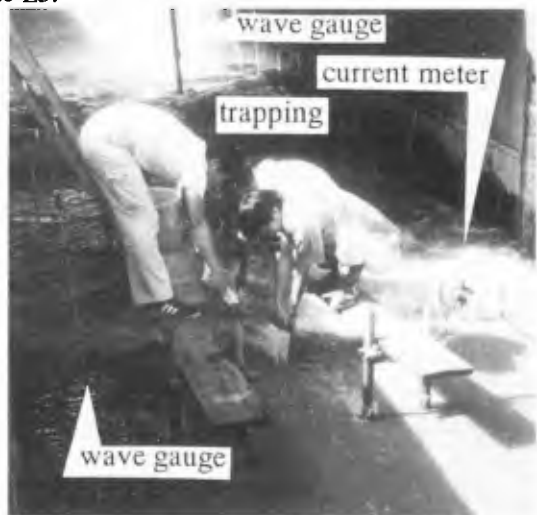


Photo 2. Observation in the swash zone

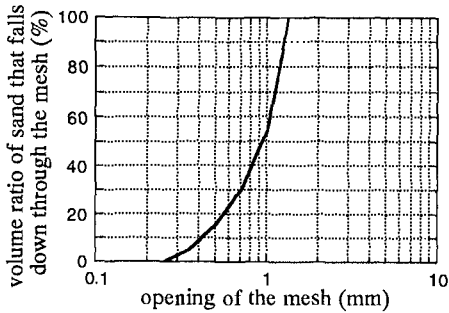


Figure 2. Sand particle diameter distribution

Table 1. Experimental cases and conditions

case	$\tan \beta$	H_0 (m)	T_0 (s)	γ	wave generation
L1	1/20	1.0 m	5.0 s	r.w.	p.m.
L2	1/20	1.0 m	5.0 s	1	p.m.
L3	1/20	1.0 m	5.0 s	7	p.m.
L4	1/20	0.6 m	5.0 s	1	f.l.w.c.m.
L5	1/10	1.2 m	3.0 s	7	p.m.
L6	1/10	1.2 m	3.0 s	7	f.l.w.c.m.
L7	1/50	0.5 m	8.0 s	7	p.m.

γ : sharpness parameter of JONSWAP spectrum

r.w.: regular wave

p.m.: previous method

f.l.w.c.m.: free long wave cancel method

Experimental results

Figure 3 shows the initial beach profiles of each cases as dotted lines and final profiles as solid lines. Profile changes of the cases L1, L2 and L3 are bar and berm system. Profile change pattern is decided by significant wave characteristics, not by sharpness of spectrum or irregularity. Profile change due to swell is more rapid than due to wind waves of the same significant wave characteristics. Profile changes of the cases L5 and L6 are typical erosional pattern with remarkably developed bar. Profile change in the case L7 is accretional pattern with sediment transport from offshore zone to surf zone.

Figure 4 shows fluctuation of suspended sand concentration "c" due to wave motion near the breaking point in the cases L1 and L6 together with horizontal velocity "u" and water surface elevation " η ". Suspension of sediment due to regular wave motion takes place at the phase when the horizontal velocity changes from onshore to offshore. Sediment is suspended due to irregular wave motion at the phase when horizontal velocity changes not only from onshore to offshore, but also from offshore to onshore.

Figure 5 to 8 show vertical distributions of suspended sediment transport flux in the cases. The graph at the top is cross-shore distribution of significant wave height and beach profiles. The graphs in the second row are vertical distributions of time averaged suspended sediment concentration. The graphs in the third row are vertical distributions of time averaged horizontal velocity. The graphs at the bottom is vertical distributions of time averaged product of suspended sediment concentration and horizontal velocity namely suspended sediment transport flux. In the cases L5 and L6, suspended sediment concentrations are higher than the other cases. In the almost cases, suspended sediment transport fluxes near the bottom are directed offshore, even in the accretional case L7.

Figure 9 shows low and high frequency components of suspended sediment transport flux in the cases L5 and L6. In the case L6 where the free long wave is canceled, long wave components of suspended sediment transport fluxes are directed offshore when the sort wave components are directed onshore. In the case L5, the above mentioned property is not clear.

Figure 10 shows synchronized data observed at the point A in a swash zone and at the point B in a surf zone of the case L5. The graph at the top of four is volume of sand per unit width trapped at the point A. Length of right side of each triangle is trapped volume. Left vertex points to the starting moment of trapping. Right

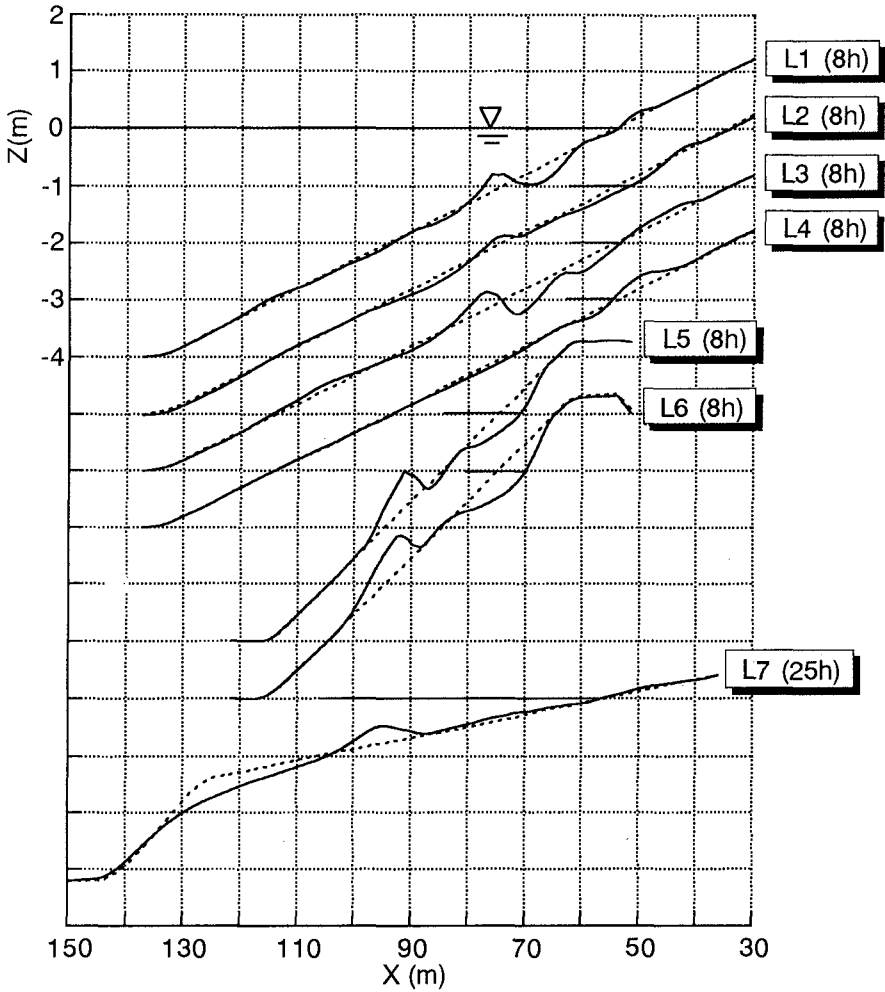


Figure 3. Beach profile change

vertices point to the finishing moment of trapping. For convenience' sake, sediment transport due to uprush and downrush are shown in one graph. The second graph is horizontal velocity 1 or 2cm above the sand surface at the point A. The curve is interrupted in the middle of downrush, because the head of current meter is exposed in the air. The third and the bottom graphs are water surface elevation at the points A and B. The waves corresponding to each other are connected by dotted lines. Number of waves reduces by half propagating from the point A to B. Waves in a swash zone are apt to be grouped and uprush velocity due to the first wave of the group is strong and uprush sediment transport is remarkable under the action of the first wave. Crest level of the last wave of the group in a swash zone is highest and downrush velocity due to the last wave is strong and the downrush sediment transport due to the last wave is striking and drags on.

Table 2 shows the uprush and downrush data of individual waves in a surf zone of the case L5. "H" is crest height measured from the trough just before the crest. "h" is water depth under the trough. "Uu" is horizontal velocity under the crest. Positive data is onshore velocity. Three data are negative, because the bottom velocity remains offshore when the front of the next uprush reached the trapping point. "Qu" is trapped volume of sediment transport due to uprush par unit width. "Ud" is trapped volume of sediment transport due to downrush par unit width. Total volume of Qu is 65.7 litter par meter and total volume of Qd is -84.4 litter par meter. Net volume of sediment transport during one hundred waves is -18.7 litter par meter. It is converted to the net sediment transport rate $-6.2 \times 10^{-5} \text{ m}^3/\text{m/s}$.

Figure 11 shows sand transport rate counted back from profile change in the case L5. The net sediment transport rate at the trapping point $-6.3 \times 10^{-5} \text{ m}^3/\text{m/s}$ is read

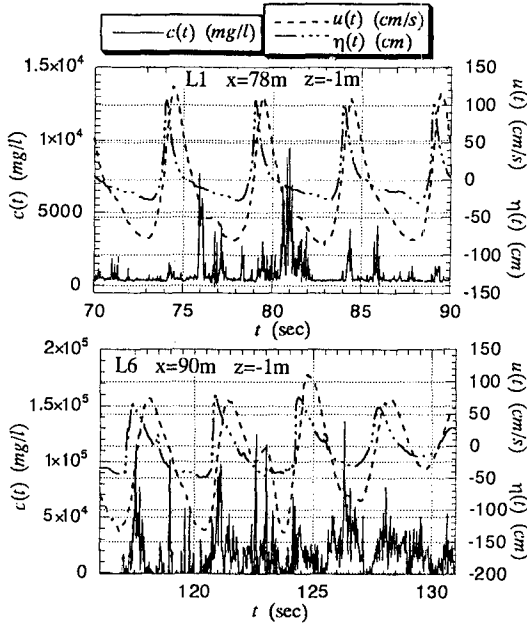


Figure 4. Fluctuation of suspended sand concentration due to wave motion in the case L1 and L6

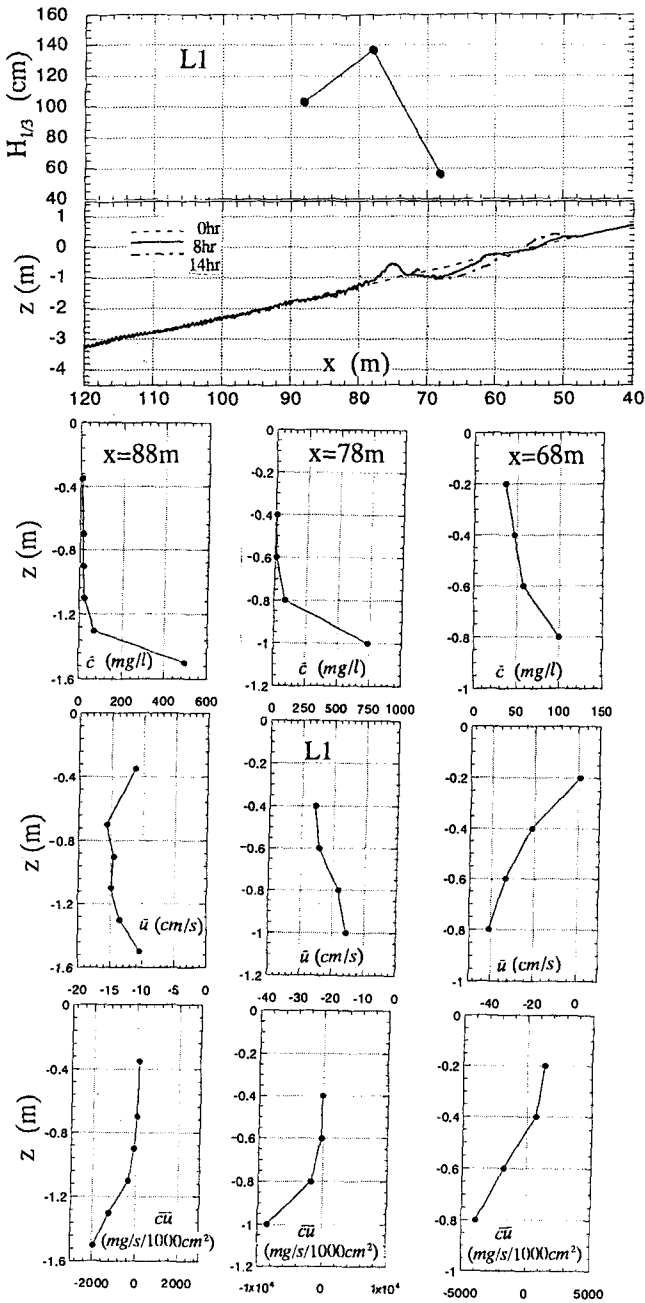


Figure 5. Vertical distribution of suspended sand transport flux in the case L1

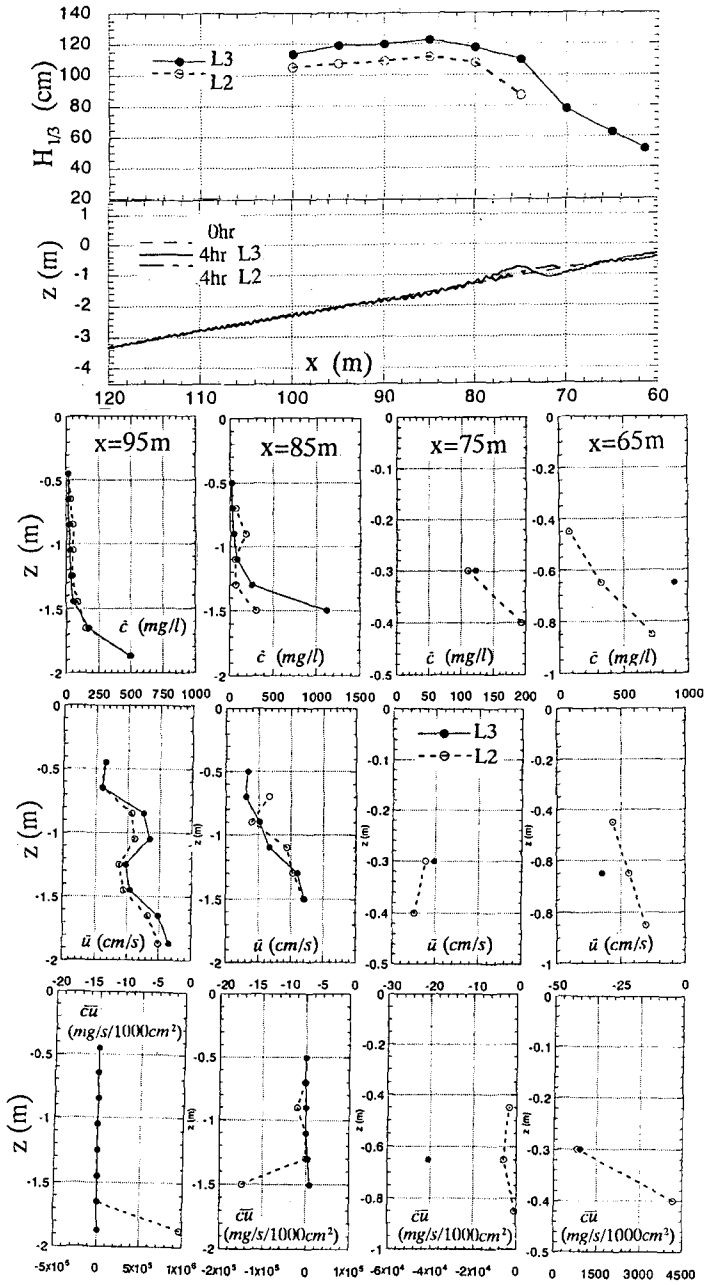


Figure 6. Vertical distribution of suspended sand transport flux in the cases L2 and L3

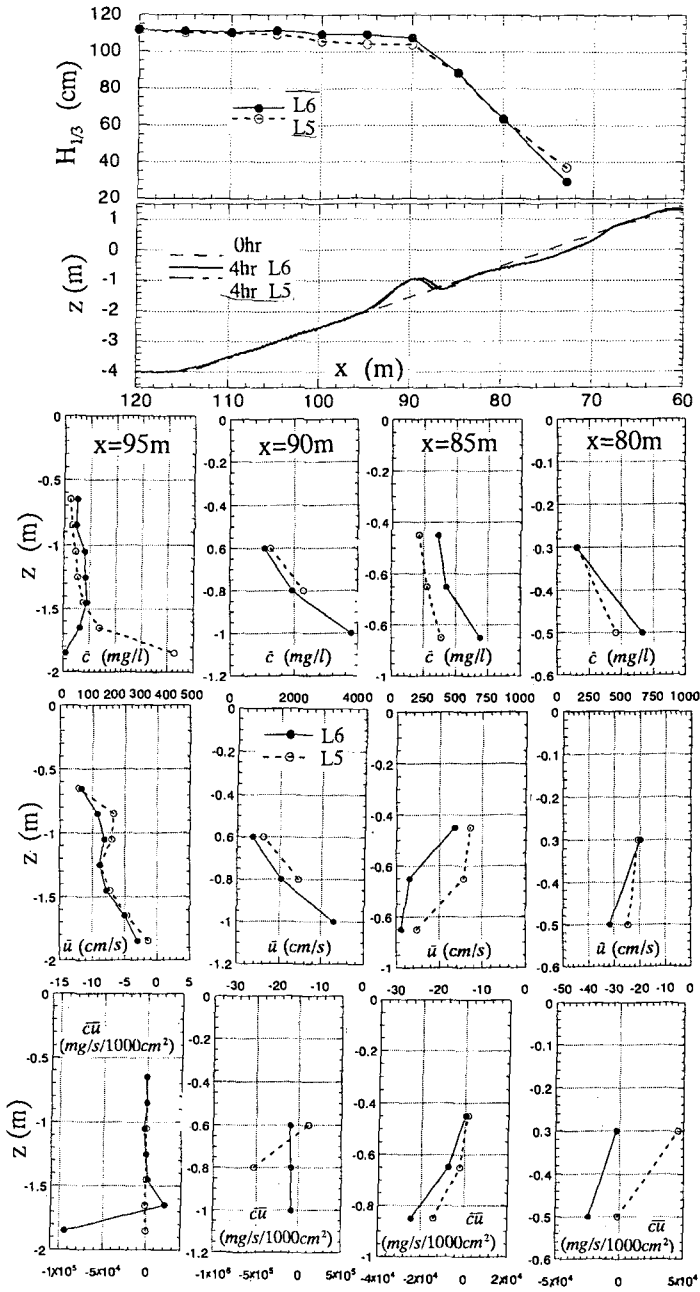


Figure 7. Vertical distribution of suspended sand transport flux in the cases L5 and L6

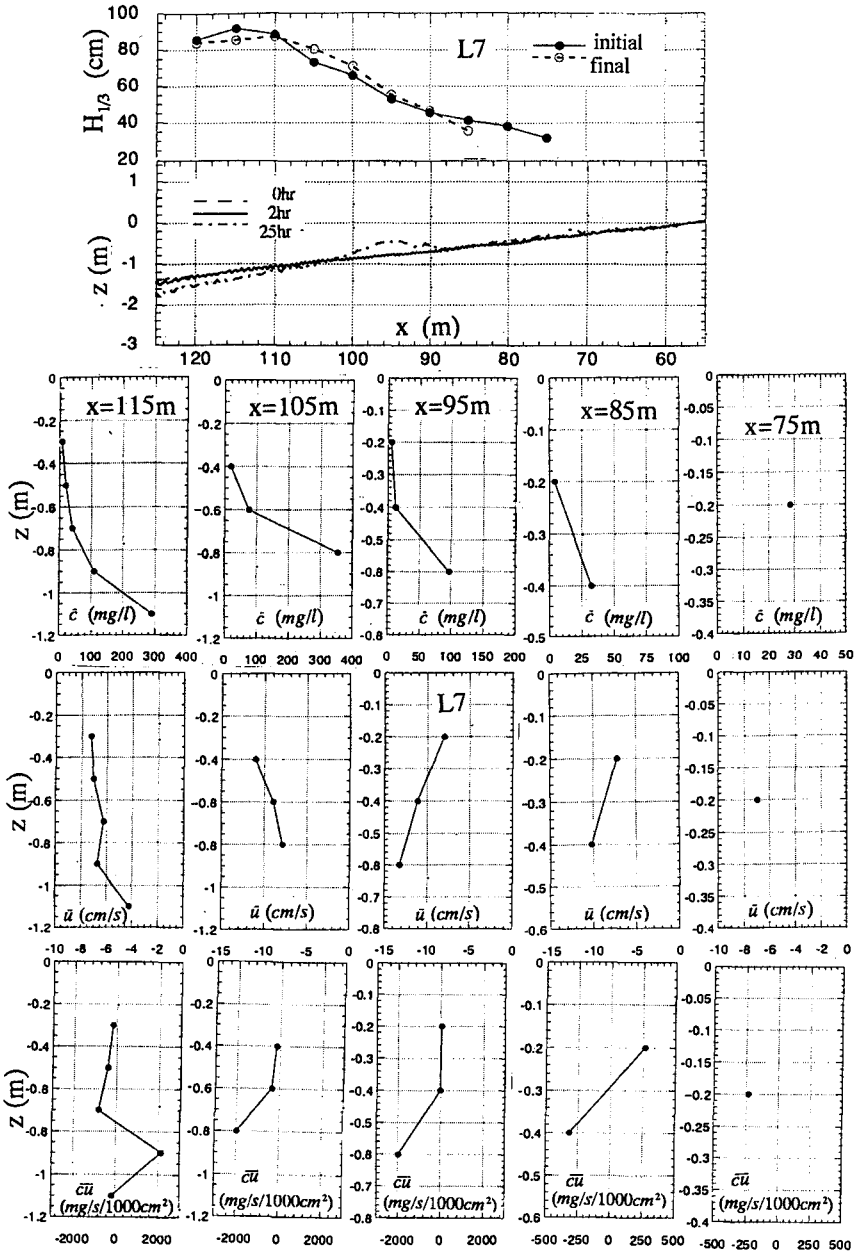


Figure 8. Vertical distribution of suspended sand transport flux in the case L7

from the figure. Good agreement of two independent values indicates high accuracy of the sand trapping method.

Figure 12 shows relationship between nondimensional sediment transport rate Φ' due to individual downrush and nondimensional bottom friction Ψ' . Φ' and Ψ' is defined by the following equations;

$$\Phi' = Q / (wD) \tag{1}$$

$$\Psi' = U^2 / (s'gD) \tag{2}$$

where Q is sediment transport rate in the half period of wave, w is settling velocity of sand particle, D is median diameter of sand, U is amplitude of bottom velocity, s' is submerged specific gravity of sand and g is gravity acceleration. Sediment transport rate due to downrush is modeled by following equation;

$$\Phi' = -0.037 \Psi'^{1.29} \tag{3}$$

Figure 13 shows relationship between nondimensional sediment transport rate Φ'

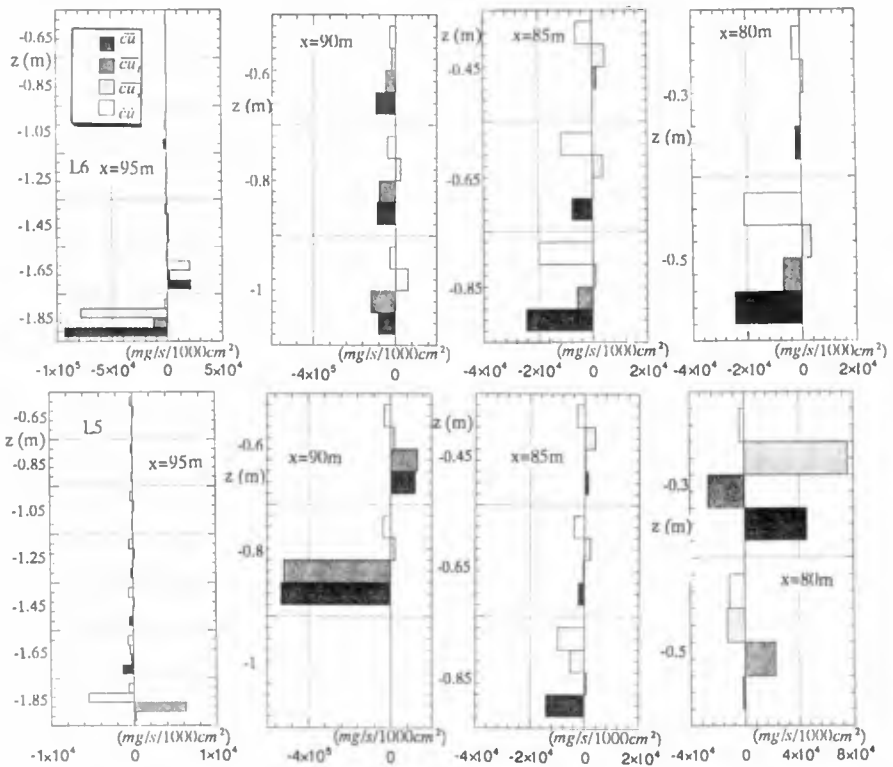


Figure 9. Low and high frequency components of suspended sand transport flux in the case L5 and L6

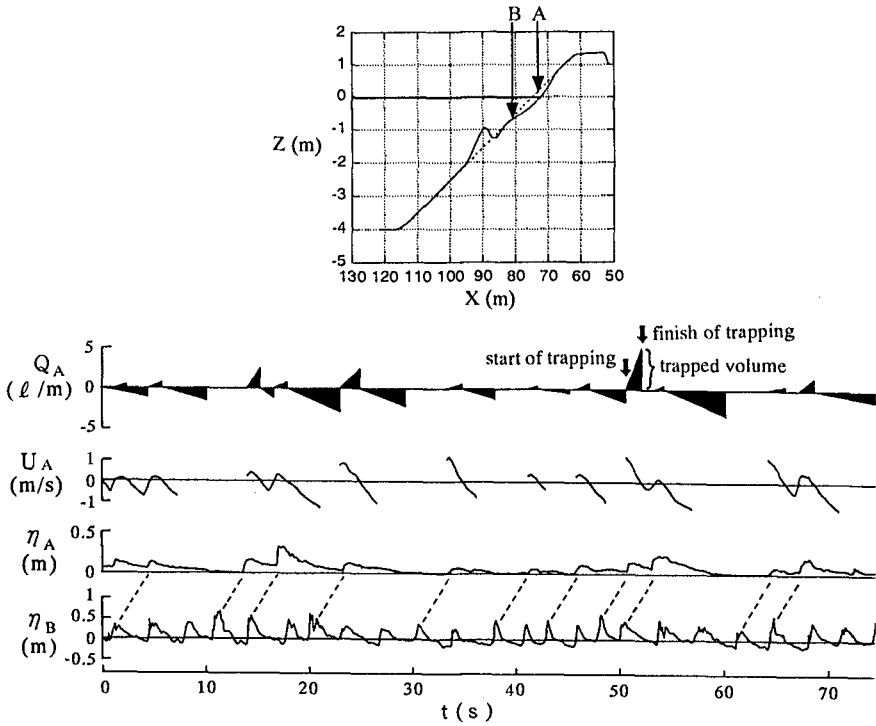


Figure 10. Synchronized data observed in the swash zone and the surf zone

Table 2. Uprush and downrush data of individual waves in the swash zone of case L5

H (m)	h (m)	Uu (m/s)	Qu (l/m)	Ud (m/s)	Qd (l/m)
0.225	0.000	0.90	3.15	-1.15	-2.74
0.150	0.000	0.90	1.43	-0.60	-0.23
0.100	0.025	0.40	0.29	-0.80	-0.70
0.175	0.013	0.65	1.69		
0.225	0.112	0.20	0.70	-1.30	-3.03
0.100	0.050	0.25	2.45	-1.00	-1.89
0.062	0.013	0.70	0.23	-0.60	-0.33
0.150	0.000	0.50	1.40	-1.00	-0.87
0.213	0.050	0.60	9.30		
0.200	0.125	0.35	0.23	-1.10	-3.21
0.138	0.000	0.60	1.05		
0.150	0.062	0.60	0.31	-1.00	-1.13
0.100	0.112	0.50	0.29	-0.60	-0.47
0.062	0.000	0.50	0.17	-0.30	-0.21
0.162	0.038	0.60	0.58		
0.213	0.087	0.00	0.64	-0.90	-1.54
0.150	0.000	0.60	2.45		
0.200	0.038	0.45	0.65		
0.125	0.138	-0.20	0.12	-0.80	-2.74
0.075	0.000	0.90	0.30		
0.138	0.038	-0.10	0.24	-0.50	-0.73

0.200	0.000	0.85	2.81	-1.10	-3.26
0.200	0.025	0.90	2.52	-1.10	-0.61
0.150	0.075	-0.20	0.45		
0.125	0.025	0.60	1.11	-0.90	-0.23
0.175	0.038	0.60	4.31	-1.20	-2.51
0.200	0.000	0.60	5.48		
0.138	0.100	0.00	0.12	-1.40	-1.07
0.062	0.000	0.80	0.27		
0.250	0.062	0.60	0.64	-1.30	-3.73
0.075	0.000	0.90	0.82	-1.20	-0.90
0.125	0.000	0.90	1.63	-1.20	-2.04
0.150	0.000	0.70	2.02	-1.00	-1.14
0.200	0.050	0.80	2.45		
0.350	0.125	0.90	3.21	-2.00	-15.51
0.087	0.000	0.85	0.97		
0.213	0.050	0.30	1.19	-1.30	-3.50
0.087	0.000	0.75	0.17		
0.125	0.000	1.25	0.58	-1.30	-3.11
0.200	0.025	0.90	0.12		
0.225	0.150	0.80	3.73	-1.80	-17.49
0.075	0.000	0.60	0.22		
0.275	0.050	0.70	1.14	-1.40	-4.90
0.125	0.000	1.00	1.35		
0.250	0.050	0.70	0.73	-1.35	-4.57
		Qu total	65.7	Qd total	-84.4

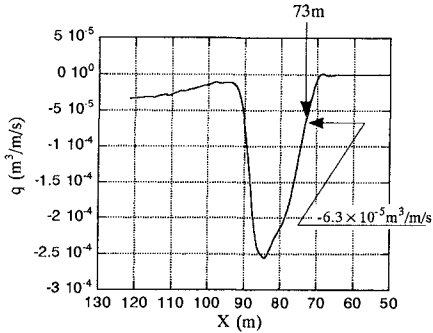


Figure 11. Sand transport rate counted back from profile change

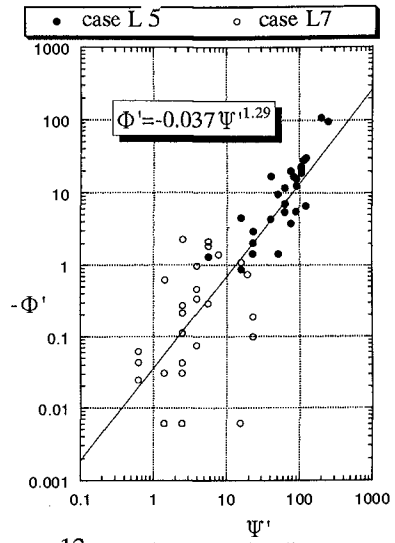


Figure 12. Nondimensional sediment transport rate Φ' due to individual downrush and non dimensional bottom friction Ψ'

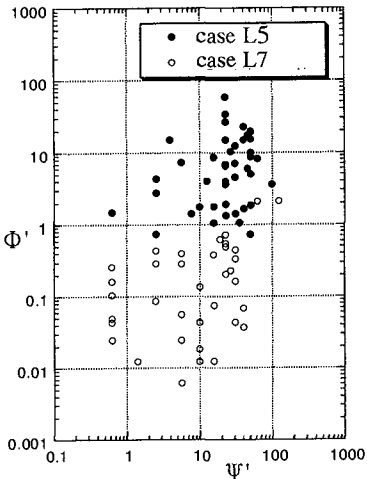


Figure 13. Φ' due to individual uprush and Ψ'

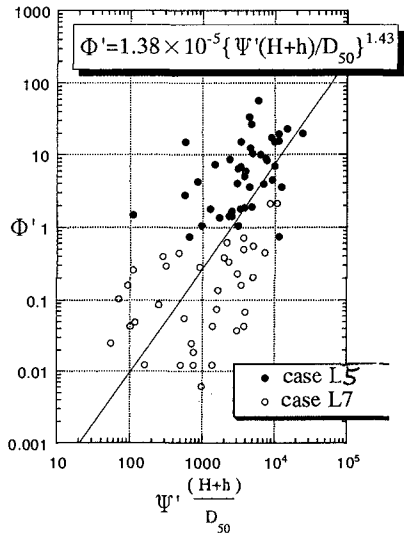


Figure 14. Φ' due to individual uprush and $\Psi'(H+h)/D_{50}$

due to individual uprush and nondimensional bottom friction Ψ' . Relationship between Φ' and Ψ' is bad, because uprushing bore involves suspended sediment according to not only bottom friction but also thickness of the bore.

Figure 14 shows relationship between nondimensional sediment transport rate Φ' due to individual uprush and product of nondimensional bottom friction Ψ' and nondimensional thickness of the front bore of uprush. Sediment transport rate due to uprush is modeled by following equation;

$$\Phi' = 1.38 \times 10^{-5} \{ \Psi' (H+h)/D \}^{1.43} \quad (4)$$

Conclusions

- ① Beach profile change due to swells is more rapidly than that due to wind waves.
- ② Around the breaking point, there is the case that low frequency component of suspended sediment transport due to long waves is offshore, and high frequency one is onshore.
- ③ The number of waves decreases immediately in the swash zone, because a downrush prevents runoff of the next wave in trough phases of long wave.
- ④ Waves in a swash zone are apt to be grouped and uprushing bottom flow due to the first wave of the group is strong. Hence, uprush sediment transport is remarkable under the action of the first wave.
- ⑤ Crest level of the last wave of the group in the swash zone is highest and downrush bottom flow due to the last wave is strong. So, downrush sediment transport due to the last wave is striking and drags on.
- ⑥ Sediment transport rate due to uprush and downrush in a swash zone was modeled relating to bottom friction and thickness of uprushing bore.

References

- Ikano, M. and Tanaka, H.(1996): A new experimental system for reproduction of infragravity waves bounded by irregular wave groups and their wave deformation, Report of Central Research Institute of Electric Power Industry, No.U95042.(in Japanese)
- Kajima, R., Shimizu, T., Maruyama, K. and Saito, S.(1982): Experiments on beach profile change with a large wave flume, Proc. 18th Coastal Eng. Conf., ASCE, pp.1385-1404.
- Katori, S.(1983): Measurement of sediment transport by streamer sand trap, NERC, Rep. No. 17, TR-82-1, pp.110-117.(in Japanese)
- Ogawa, Y. and Shuto, N.(1981): Field measurements of hydraulics and sediment movements in a swash zone, Proc. 28th Japanese Conf. on Coastal Eng., JSCE, pp.212-216.(in Japanese)
- Sato, S., Shimatani, M. and Shimura, T.(1993): Analysis of suspended sediment transport rate in a surf zone of irregular waves, Proc. 40th Japanese Conf. on Coastal Eng., JSCE, pp.321-325.

CHAPTER 239

The Influence of Long Waves on Macrotidal Beach Morphology

David J. Simmonds¹, Tim J. O'Hare² & David A. Huntley³

Abstract

The aim of the following paper is to demonstrate that standing long waves can generate intertidal morphological features in a dissipative macrotidal setting. In this environment the tidal excursion can exceed the length scales associated with long waves. This extends the work of Simmonds et al (1995) in which it was shown that monochromatic long waves could generate sediment convergence patterns that bore a good similarity to observed topographic features, namely ridges and runnels from a field site on the Belgian coast. The simulation is modified to include a band of long waves and it is found that a good correspondence with real topography can still be achieved on a tidally averaged basis by allowing for a degree of uncertainty in the breaking criterion. It is also argued why the observed scales are more likely to correspond with the shorter end of the long wave spectrum. The simulation helps to shed light on the conditions in which such features are known to form.

Introduction

This paper examines the question “can a spectrum of long waves be capable of creating intertidal bedforms on a macrotidal beach?”

Despite the abundance of macrotidal coastlines Short (1991) has been led to remark that the “study of macro-tidal beaches has lagged considerably” in relation to the published material on micro- and meso-tidal coasts. Whilst numerical modellers are beginning to recognise the importance of long wave processes in the modeling of coastal morphology (Roelvink & Broker, 1993) very few of these models, even though applied to macrotidal coastal regions, appear to consider the further complication of a tidally modulated boundary. Although the concept of an equilibrium cross-shore profile is useful in a microtidal setting, the interpretation of equilibrium profile is questionable in the macrotidal setting when considered with

¹ Res. Fellow, School Civil Eng., Univ. Plymouth, Palace Court, Plymouth, UK PL1 2DE

² Senior Lecturer, Inst. Marine Studies, Univ. Plymouth, Drake Circus, Plymouth, UK PL4 8AA

³ Reader, Inst. Marine Studies, Univ. Plymouth, Drake Circus, Plymouth, UK PL4 8AA

respect to timescales of the order of days, even when tidally averaged quantities are considered. The cross shore tidal excursion on a dissipative macrotidal beach is measured in hundreds of meters and is further modulated by the Spring-Neap cycle. The boundary is neither steady nor varying by the same amount from day to day. It seems more appropriate to speak of a dynamic equilibrium whereby the profile is constantly adjusting from minute to minute within limits determined by the tidal level and variations in the wave climate.

Standing long wave motion at the shoreline is often associated with the formation of submerged bars (Short, 1991, Sallenger & Holman, 1987) and support for this has been provided by field observations (e.g. Bauer & Greenwood, 1990). But what of the intertidal bedforms such as the bar-like features, referred to as ridges and runnels, that are evident on some macrotidal coastlines?

Wright et al (1982) suggested that macrotidal beach profiles are due to the combination of swash, surf and deeper water processes that operate over different regions of the beach face for different periods of time. It was also suggested that some wave-lain features may survive swash & surf zone excursion in low energy conditions — but that in high energy conditions any bedforms are erased by the more energetic processes.

These studies have been predominantly based on high energy exposed shorelines. In the European context, many dissipative macrotidal shorelines are to be found sheltering in fetch limited environments well away from the continental shelf breaks. In these situations, more subtle, lower energy mechanisms might be more evident.

It is tempting to suggest that standing long waves might be somehow responsible for the development of intertidal features such as ridges and runnels as the length scales of both are comparable. In addition it is widely recognised by field workers that long wave energy is present, to some degree, on all shorelines. In the simplest analysis, topographic features are believed to be generated under a stationary standing long wave. However on a macrotidal dissipative coast the reflection point of the long waves (whether considered at the shoreline or in the surfzone) can move cross-shore by several long wave wavelengths.

Simmonds et al (1995) showed how standing long waves might form bar-like features in the intertidal zone of a linear beach dominated by cross-shore long wave processes. They based their analysis upon a simple transport mechanism resulting from the correlation of the long waves with the incoming wave groups to demonstrate how intertidal bedform development might be initiated through a "tidal bar hypothesis". Using a monochromatic long wave envelope, a pattern for the *potential for erosion* across the beach face was shown to correspond well with observed scales of ridge and runnel morphology even around the mid-tide region, despite the inclusion of tidal modulation of the transport envelope across the beach face.

However, long waves observed in the field are generally broad-banded in nature (Huntley et al, 1993) and it might be predicted that the result of including of a realistic bandwidth of long waves would smear over the effect of the individual waves. This effect combined with tidal modulation of the reflection point would surely destroy any “memory” that the beach retains of the long wave structure – although Bowen and Huntley (1983) suggested that feedback, in the form of erosion of the bed and subsequent modification of long wave structure might result in a narrowing of the effective spectrum that shapes the beach through resonance.

A further criticism of the hypothesis is that given that there is a band of long waves why does there appear to be a stronger correlation at the shorter wavelength end of the measured band than at the longer scales?

We will investigate these criticisms by reference to an improved version of the original simulation outlined in Simmonds et al. (1995). It will be shown that under conditions recognised as precursory to ridge and runnel formation, rhythmic intertidal features are indeed predicted. We draw upon the geometry and field measurements of a particular example of ridge and runnel morphology. The aim is not to present a full sediment and hydrodynamic coupled model, but instead to show that the mechanism for forming intertidal bedforms involving standing long waves is feasible.

A Field Example of Rhythmic Intertidal Morphology

First of all it is useful to reintroduce the field example of ridge and runnel features (Simmonds et al, 1995). The macrotidal beach profile is shown in Figure 1 and is taken from a field site at Nieuwpoort on the Belgian coastline which was the

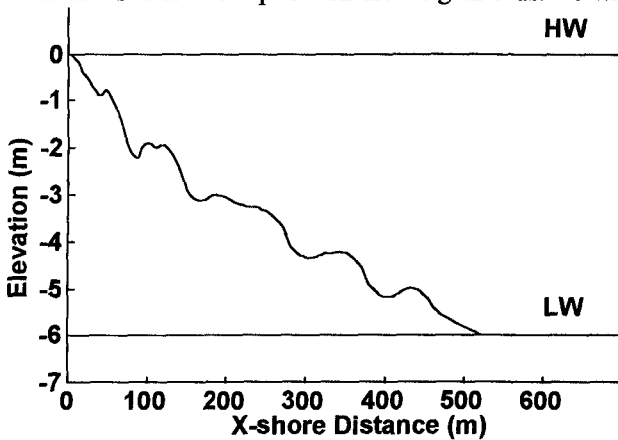


Figure 1. Ridge & Runnel profile at Nieuwpoort, Belgium

focus of the recent *MAST* project *Circulation and Sediment Transport Around Banks* (CSTAB —O'Connor et al, 1996). This illustrates the kind of intertidal features that are expected to be associated with long waves by virtue of their length scales. These ridges exist as low lying, shore-parallel bodies of sand with cross-shore scales of the

order of 50m separated by runnels. Their longshore extent is interrupted by shore-normal channels spaced every 500m or so, down which water is drained from the runnels on the ebb of the tide. They are exclusive to dissipative macrotidal beaches of medium sand sized material and fetch limited wave climate.

It is hard to justify that these particular features are merely swash bars formed at low and high still stands at Spring and Neap tide levels (King & Williams, 1949). Five bars are clearly visible. Other documented cases of ridge and runnel beaches exhibit even greater numbers of ridges (Mulrennan et al, 1992). Indeed the number and spacing of these particular features on low energy beaches is reported to be strongly related to the beach slope and this is more reminiscent of long wave structure where the node-anti-node spacings are also dictated by the beach slope β . Therefore this swash bar hypothesis should be rejected.

The scales involved are certainly too large for comparison with gravity wavelengths. So the question "Could long waves be responsible?" arises. Simmonds et al (1995) previously reported the identification of standing long wave activity, even during low energy conditions at this particular beach in the frequency band of 0.01-0.04Hz (100s to 25s wave period). The scale of the features was shown to be consistent with shortest of these long wave scales (0.04Hz) measured at the beach which had a slope of around 1%. It therefore seems likely that long waves are indeed responsible.

Long Wave Transport Mechanisms

The mechanism by which a memory of the structure of a standing long wave can come to be imprinted upon a beach is now discussed. The cartoon (Figure 2) illustrates two mechanisms that can be considered.

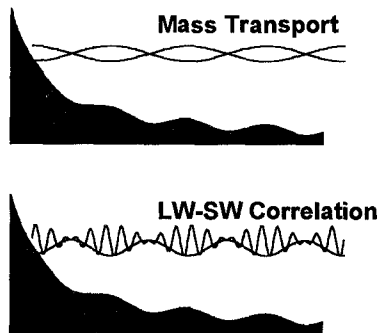


Figure 2 Transport mechanisms

The first involves sediment movement in response to the mass transport induced under a standing wave. This has been investigated in associated with sub-tidal bar formation (e.g. Carter et al. 1973). In this, the sediment is assumed to move in response to the drift velocities induced by the standing long wave structure. Sediment accumulates either at the nodes or anti-nodes according to different

investigators though there is no general agreement as to which, although the answer is thought to depend upon the sediment grain size.

The second is a mechanism based upon the correlation of short-wave groups with a bound long wave. O'Hare & Huntley (1994) have discussed a model that furthers the concept of short waves acting as sediment stirrers and correlated long waves acting as transporters (pseudo-steady currents). In the case of a bound long wave the long wave is generated through the radiation stress variation under wave groups so that the largest short waves occur around the long wave troughs and the smaller at the long wave crests. Such a correlation creates a net offshore transport when integrated over a long wave cycle.

If a planar beach face is considered, in the absence of any other processes, this offshore sediment flux would be predominantly modulated by the simple depth dependence of the short wave orbital velocity. The inclusion of a phase-locked reflected long wave, however, introduces a rhythmic cross-shore spatial variability in the sediment flux. The function which is the gradient of this can be interpreted as regions of net erosion or accretion.

Both of these two mechanisms would produce an erosion pattern that would predict features of the same scale. However, the efficiencies of the two in transporting sediment will have different magnitudes. We argue here that the correlation mechanism is likely to be more important.

In the first case the transport mechanism is related through a power law to the "drift velocity". This second order parameter arises from the non-linearity in orbital motion under the standing waves. In the case of long waves this is likely to be very small in relation to the orbital velocity of the long waves.

In the second, the net transport is the result of averaging the correlation between the square of the heights of the (stirring) short wave and the velocity of the (transporting) long waves. Again, it is difficult to estimate the relative importance of this quantity since the resulting transport over a long wave cycle will depend upon, amongst other factors, the amplitude of the long wave orbital velocity and the groupiness of the short waves — that is, the net effect depends upon the difference between the onshore and offshore directed correlation's.

However, the magnitudes of the latter velocities are much greater than those of the drift velocities, and so the second mechanism has the potential to be significantly greater.

Bias to Shorter Scales

If it is accepted that there is a process for the imprinting of long wave scales on the beach face the next question to address is "why is a stronger correspondence with the shorter end of long wave spectrum observed in the field?" As we stated earlier, the observed correlation between the measured long wave spectrum and the observed morphological scales at Nieuwpoort indicated a good agreement but only at

the shorter (0.04Hz) end of the long wave spectrum. This bias can be understood by considering the following arguments.

First, we should define what we understand by the description “broad banded” in relation to the long wave spectrum. If we take the naïve interpretation of “broad-bandedness” as implying equal wave heights at all frequencies in the spectrum, quite clearly the velocity (transporting) spectrum will be biased towards higher frequencies. This is because the velocity is obtained as the gradient of the time series. Put another way, a “white” amplitude spectrum corresponds to a “blue” velocity spectrum (predominance of higher frequencies).

We can also argue, on a geometric basis, that shorter long wave scales grow more rapidly. This is because the work done on the bed in changing from a flat to an undular bed is less if the undulations are of shorter wavelength (Figure 3). The distance that the centroid of sand has to move in order to create a depression and an adjacent hole is less for the shorter wavelength feature than the longer, although the

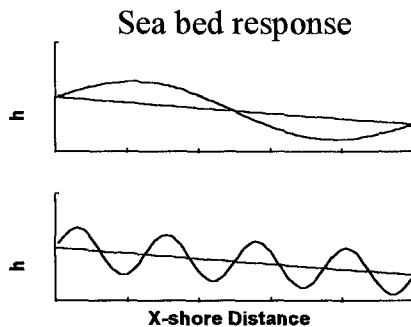


Figure 3 Geometric argument: mass centroid in (a) moves further than in (b)

amount of material that has moved is the same. It is therefore likely that the shorter scales are quicker to develop upon the beach and can be concluded that there is an inherent bias to short scales forming. This is especially important for a system in a state of dynamic equilibrium where features that require longer timescales in order to establish themselves will be discriminated against.

Simulation

Attention is now turned to the simulation reported in Simmonds et al. (1995). The simulation is used to predict the spatial cross-shore profile development. The basis for this is the assumption that the sediment transport is everywhere offshore directed due to the correlation mechanism outlined above. Obviously this is unrealistic—beaches do not simply disappear off-shore, (at least, in the short term), but this assumption is made so that the potential of this mechanism can be investigated in isolation. As such, other processes such as surf-zone and swash processes are not represented.

A bound long wave is assumed to interfere with a reflected free long wave to give a shallow water standing long wave. The sediment transport rate is assumed to be proportional to the product of the magnitude of the standing long wave orbital velocity and of the square of the short-wave envelope.

It is further assumed that the short wave envelope that stirs the sediment can be described by simple shoaling waves which break with a linear decrease in waveheight to the shoreline. The standing long wave envelope, calculated from the bessel function solutions of Lamb (op cite Kirby et al, 1981) defines the magnitude of the offshore flow. The product of these two represents an expression of the uncalibrated offshore sediment flux whose spatial representation is the sediment flux function. The gradient of this is the quantity that is of interest, and is referred to here as the *sediment flux convergence* (SFC). This is interpreted as an indication of zones of sediment accretion or erosion across the profile.

The bias to higher frequencies is incorporated in the model in terms of a "blue shift" of the velocity spectrum. This is generated by assuming uniform amplitude spectrum and hence a velocity spectrum biased linearly towards the high end of the frequency band.

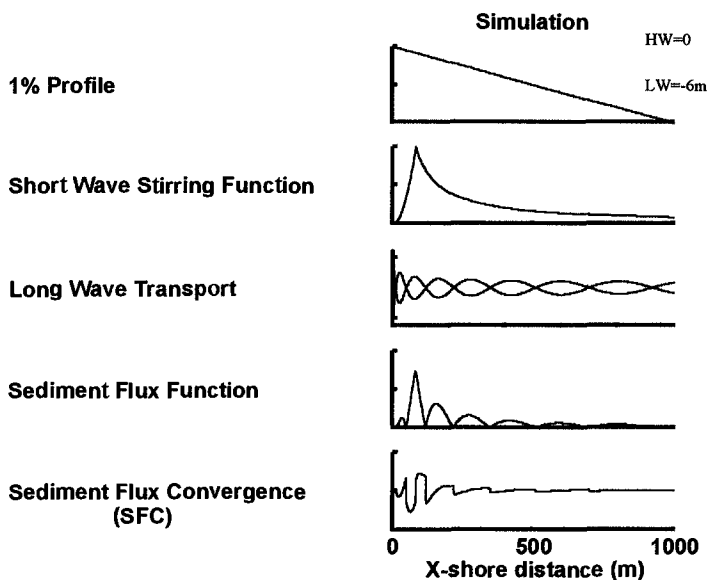


Figure 4. Components of the simulation

Taking parameters similar to those observed at the site at Nieuwpoort beach, a Spring tidal modulation of 6m height is introduced over a planar beach of 1% slope. Figure 4 shows how the simulation is constructed. This was implemented in the MATLAB language on a PC.

The simulation is also represented by the flow diagram (Figure 5). The model parameters specified include the short-wave height, the breaking depth, the long wave spectral amplitudes and the beach slope. From this information the standing long wave envelope (SLW env) is calculated and the short wave envelope (SW env). Multiplied together, these give the sediment flux function for a particular long wave frequency and reflection point on the profile.

The simulation has then been adapted to permit the summation of the sediment flux functions over a suitable spectrum of standing long waves at each position of the tide. The summation of the calculated sediment flux convergence functions is then performed to calculate the tidal average.

It is also possible to modify the short-wave envelope to allow for a degree of uncertainty in the short wave height and breaking criterion. This is desirable because, firstly, groupy waves do not all break at the same position, and, secondly, breaking is believed to be influenced by instabilities which determine that the nature of this process is chaotic (Longuet-Higgins, 1994).

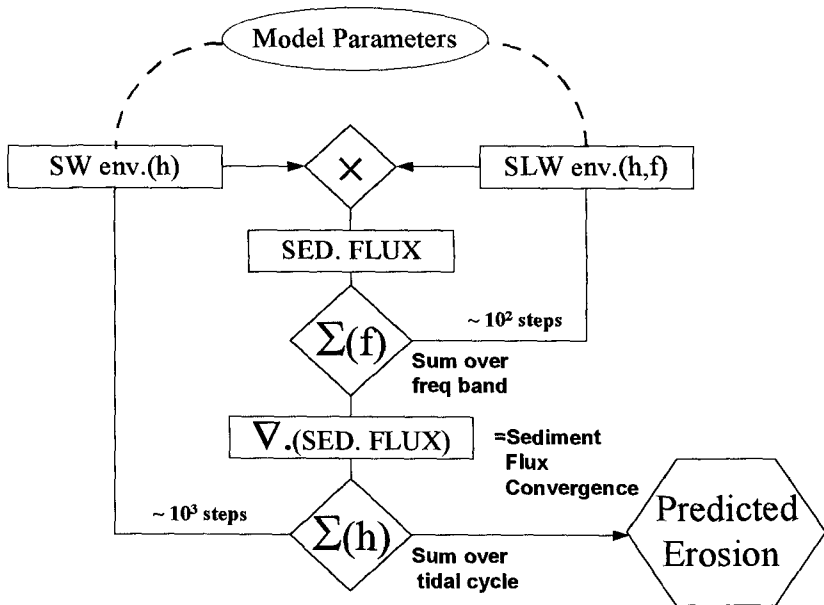


Figure 5 Flow-chart for improved simulation

As mentioned, the simulation involves two summations. Summation over frequency band and summation over all tidal amplitudes. An appropriate indication of the magnitude of the number of steps for these two summations is indicated in the figure. These have been selected to optimise processing time against numerical "noise".

It should also be pointed out that at each position of the tide the sum of the superimposed velocities is being calculated. It is therefore being assumed that all the different standing long wave modes occur simultaneously and, further, that their respective correlations with the short waves also all occur together. Whether this is realistic is a matter for debate. Usually the statistical analysis of a wave record is interpreted to mean that the spectrum of frequencies is stationary. It may be that, in reality, there is a "wandering" of the peak band of frequencies from long wave to long wave.

The present simulation is not sensitive to the order in which the two summations are calculated. However to develop the model further, feedback, in the form of bed evolution, is to be introduced before summing over the next tidal

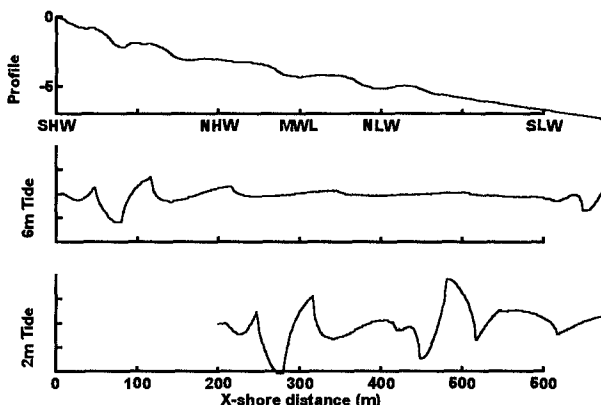


Figure 6(a) Ridge & runnel profile. Monochromatic calculations of the SFC for (b) 6m tide & (c) 2m tide.

amplitude after the summation over frequency bandwidth.

Tidally averaged runs for Spring & Neap tides using values for these parameters obtained from the Nieuwpoort beach produces the results in figure 6(b) & (c) for monochromatic long waves (0.04Hz). As can be seen the predicted SFC shows good correspondence with the actual topography, Figure 6(a), in terms of scale.

A Realistic Bandwidth of Long waves

The main query regarding the above simulation is: "what effect does a realistic, broad long wave bandwidth have on these predictions?" This question will now be addressed and the sensitivity of this simple model to other parameters will also be discussed.

At first sight, Figure 7 indicates that calculating the SFC for a band of long waves destroys the intertidal undulations, except in the case of a very narrow bandwidth indeed. However this can be shown to be misleading by studying the

sediment flux functions. Figure 8(a) indicates that the flux function (the offshore transport) is dominated by the position of the breakpoint. This creates two relatively sharp peaks in the SFC near high and low water throwing the remaining details in to the shadows. The convergence here is emphasised by the fact that the breakpoint dwells at these two positions for the longest. As mentioned above, in reality the breaking of the short waves has a statistical variation caused by variations in the waveheight due to groupiness, return flows, interactions with preceding waves and an inherent chaotic instability in the breaking process.

To study the effect of this, an uncertainty in the breakpoint was modeled assuming a gaussian description of wave height and the breaking criterion. This was included in the description of the short wave envelope or "stirring function". The effect in the sediment flux function is evident in Figure 8(b). The breakpoint is rounded off and de-emphasised, allowing detail of the long wave structure to emerge. Figure 9(b) shows the effect of this in the predicted SFC which displays once again some undular detail across the profile, more obviously than in Figure 9(a). Again the scales correspond well with those observed in the field.

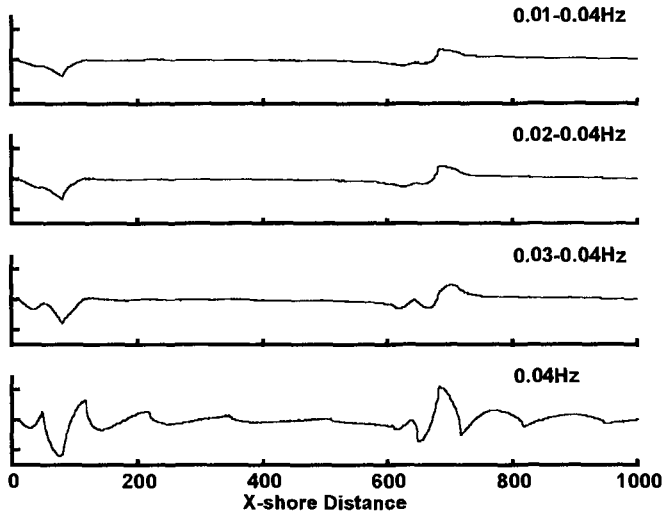


Figure 7 SFC calculated for different long wave bandwidths

The uncertainty in the breakpoint acts to widen the surf zone. Another way this can be achieved is to consider short waves with larger waveheight. As can be seen in Figures 8(c) and 9(c), the effect of this is to smooth off the breakpoint further and to bring out more intertidal profile detail. This remarkable result shows that despite summing over a band of long waves and averaging over a tide, the predicted SFC still shows details that correspond to the observed topography even in the mid tidal region. However, although larger wave heights are helpful in this model it is probably true, as Wright (1982) indicates, that in very high energy events other

processes will dominate and the surf zone “bulldozer” will mask the effects of this subtle mechanism.

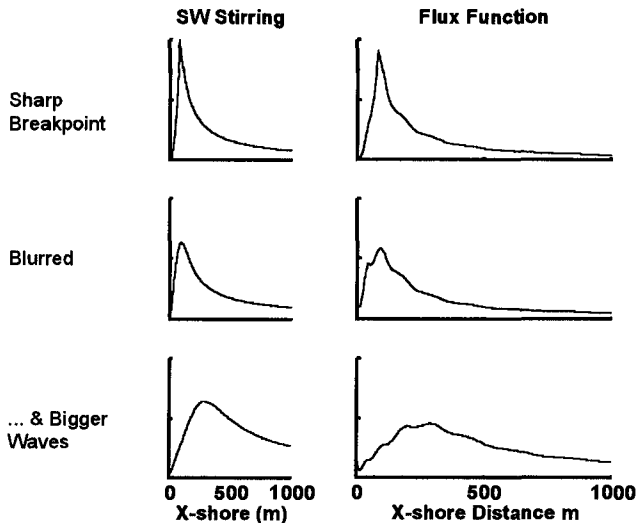


Figure 8 Short wave envelopes and sediment flux functions for (a) sudden breaking, (b) uncertain breaking, (c) uncertain breaking & larger wave height

Further Investigations

The simulation was also used to investigate other parameters, including shape of the tidal curve and of the spectrum. These predictably showed that a flatter tidal curve de-emphasised erosion at the high and low water marks, and that a “blue” long wave amplitude spectrum brought out even more detail in the undulations of the sediment flux convergence.

Time-scales

The results so far have all been calculated as averages over the tidal cycle. Figure 10 shows the sediment flux convergences calculated for averages over shorter fractions of a tide ($1/6$ ths). As can be seen, the tidally averaged result shows no indication of some of the features that can develop during the middle of the tide. Two features at 200m and 500m are clearly visible in the mid tide SFC but these are cancelled by the SFCs approaching high and low water.

It is likely that the bed will respond over shorter time-scales than that of a tide. If the bed is modified, the long and short wave field are changed accordingly

and the erosion patterns will be changed. It may be that the erosion pattern is capable of “tuning in” with the topography to favour growth of certain scales.

Southgate (1995) has remarked that since the interaction between hydrodynamics and the transport of sediment is non-linear, the chronology or sequencing of wave events is of direct influence. Further, in the macrotidal case, the erosion of the beach face will be dependent upon both the temporal variation of the long wave transport functions and the tidal variation.

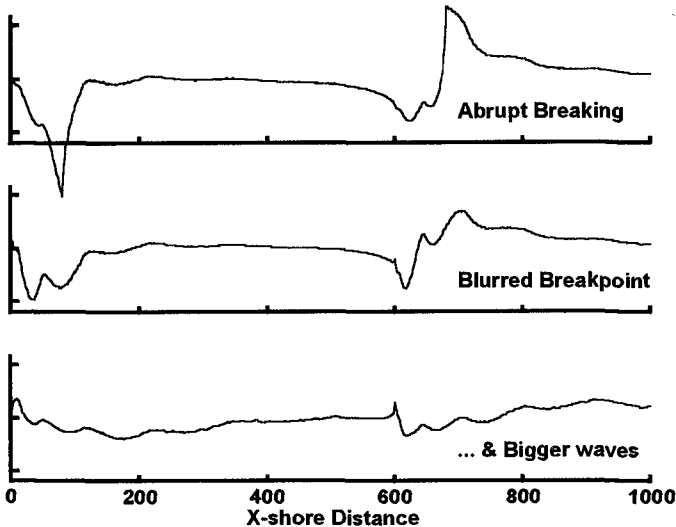


Figure 9(a) SFC for a band of long waves (0.01–0.04Hz), (b) inclusion of uncertain breaking & (c) bigger short waves.

Summary & Discussion

Simmonds et al (1995) demonstrated that a standing long wave mechanism such as the bound long wave–short-wave correlation is capable of generating intertidal bedforms at scales observed in nature. This idea has been extended in this paper to the consideration of a band of long waves. It has been argued that there exists an inherent bias towards the quicker development of shorter scales. It has been shown that a band of longwaves will still generate undular intertidal topography, even in the mid–tide region so long as a smoothing of the breakpoint and hence a widening of the surfzone is introduced. This was necessary to de-emphasize the erosion at the high and low water levels caused by the constancy of the breaking at these places. The smoothing is justified by considering the uncertainty in the breaking process. The resulting predicted regions of sediment convergence agree remarkably well with the observed topography.

It has also been suggested that the current approach to integrating results over tidal timescales needs re-examining since it is that the bed will respond over much shorter timescales.

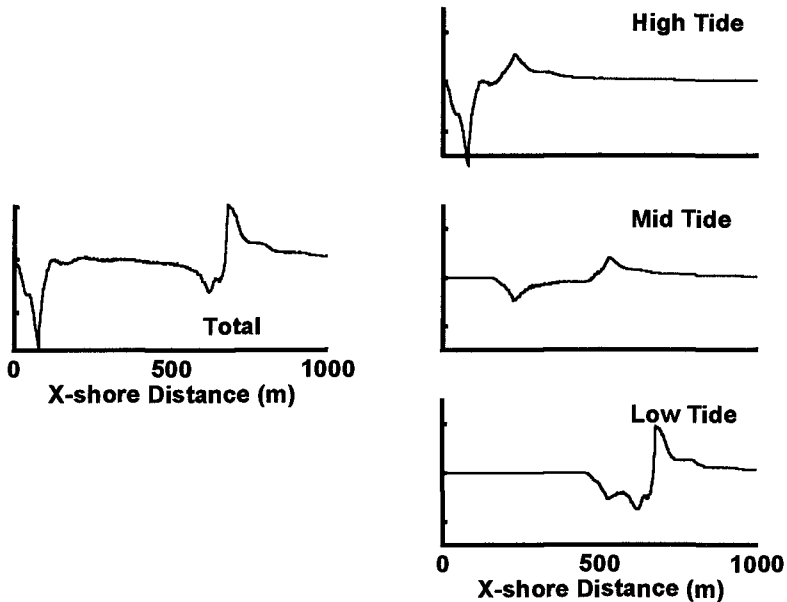


Figure 10 SFCs calculated for different sixths of the tide

The model helps us to explain the environment in which ridge and runnel features are found. For the mechanism to work, the cross shore tidal excursion must exceed the scale of the shorter long wave wavelengths otherwise no intertidal structure can be created. Broad, dissipative macrotidal beaches are ideal for this. The mechanism is, however relatively subtle, depending upon the long wave orbital velocities to carry out the transporting of the sediment, and would probably be masked by other processes in a more energetic environment. This might explain why these features are only found on fetch limited macrotidal coastlines.

Future developments of the model are envisaged that allow erosion of the bed as a feedback mechanism which perturbs the structure of the sediment flux function. It is hoped that such a coupled sediment transport and hydrodynamic model can be used to study the parameters that control the behaviour of these intertidal features and the time-scales of their development.

Acknowledgments

This work was supported through funding by the European community under the Marine Science and Technology programme (EC contract MAS2-CT92-0024)

The authors would also like to acknowledge the contribution of those who assisted with collection of the original field data, especially Mike Wilkin, formerly of Southampton University, Dept. Oceanography.

References

- Bauer, B.O. & Greenwood, B., (1990). Modification of a linear bar-trough system by a standing edge wave, *Marine Geology*, **92** :177–204.
- Carter, T.G., Liu, P.L-F., Mei, C.C., (1973). Mass transport by waves and offshore sand bedforms, *J.Waterways Harbours and Coastal Eng.* **WW2** May 1973, :165–184.
- Huntley, D.A., Davidson, M., Russell, P., Foote, Y., & Hardisty, J., (1993). Long waves and sediment movement on beaches: recent observations and implications for modeling, *J.Coastal.Res*, **SI 15**, :215–229
- King C.A.M. and Williams W.W., (1949). The Formation and Movement of Sand Bars by Wave Action, *Geographical J.* **113**:70–85.
- Kirby, J.T.,Jr, Dalrymple, R.A. and Liu, L.-F , (1981). Modification of edge waves by barred beach topography, *Coastal Engineering*, **5**: 35–49.
- List, J.H., (1992). A model for the generation of two-dimensional surf beat, *J.Geophysical Research*, **97 C4**:5623–5635.
- Longuet-Higgins, M.S., (1994). A fractal approach to breaking waves *J.Phys.Oceanog*, **24**: 1834–1838.
- Mulrennan, M.E., (1992). Ridge and runnel beach morphodynamics: An example from the Central East Coast of Ireland, *J. Coastal Research* **8**(4): 906–918.
- O'Connor *et al*, (1995). Circulation and sediment transport around banks —CSTAB final report. (held by MAST office, Brussels.)
- O'Hare, T.J. and Huntley, D.A., (1994). Bar formation due to wave groups and associated long waves, *Marine Geology*, **116**: 313–325
- Roelvink, J.A. & Broker, I, (1993). Cross-shore Profile Models. *Coastal Eng.*, **21**:163–191
- Sallenger, A.H., Jr, and Holman, R.A., (1987). Infragravity waves over a natural barred profile. *J.Geophysical Res.*, **92**, C9: 9531–9540.
- Short, A.D., (1991). Macro-meso tidal beach morphodynamics– an overview. *J.Coastal.Res.* **7**(2): 417–436
- Simmonds, D.J., Voulgaris, G. & Huntley, D.A., (1995). Dynamic processes on a ridge and runnel beach. Paper presented at *Coastal Dynamics '95, Gdansk, ASCE*
- Southgate, H.N., (1995). The effects of wave chronology on medium and long term coastal morphology *Coastal Engineering*, **26**: 251–270.
- Wright, L.D., Nielsen, P., Short, A.D., Green, M.O. (1982). Morphodynamics of a macrotidal beach, *Marine Geology*, **50** :97–128

CHAPTER 240

MATHEMATICAL MODELS FOR WAVES AND BEACH PROFILES IN SURF AND SWASH ZONES

Akira Watanabe¹ and Mohammad Dibajnia²

Abstract

The paper presents mathematical models for wave deformation and for beach profile change in the surf and swash zones. Boussinesq-type equations including a breaker-induced energy dissipation term (Watanabe *et al.*, 1994) is extended to the swash zone by introducing a periodically moving shoreward boundary. Computation is made on the wave deformation on constant slope beaches, particularly on the runup and run-down heights as well as the wave heights at the still water shoreline, which are compared with existing formulas. Beach profile change is computed with the sediment transport rate formula proposed by Dibajnia and Watanabe (1992) after a further generalization, together with Lagrangian treatment for the sediment motion in the swash zone, using the near-bottom velocity obtained from the wave computation. The validity of the models is examined through comparisons with measurement data obtained in large wave flume experiments.

Introduction

The authors have presented a numerical model for profile change of sheet-flow dominated beaches based on Boussinesq-type wave equations and a sediment transport rate formula proposed by themselves (Watanabe *et al.*, 1994). It has been demonstrated that the model can predict well the cross-shore distributions of the wave height and the transport rate as well as the beach profile change in and around the surf zone. However, the model has a crucial limitation of the incapability of computing the wave behavior and the beach evolution in the surf zone, both of which are generally very important in practical applications and fundamental studies regarding

¹ Professor, Department of Civil Engineering, University of Tokyo, Hongo-7, Bunkyo-ku, Tokyo, 113, Japan.

² Associate Professor, ditto.

the coastal processes. A major effort in the present study is thus focused on the treatment of the swash zone dynamics both for waves and for sediment transport. Mathematical models are proposed for wave deformation and beach profile change and their validity is examined by comparing computations with measurements.

Mathematical Model for Wave Deformation

Watanabe *et al.* (1994) have presented a set of one-dimensional Boussinesq-type equations including a breaker-induced energy dissipation term as follows:

$$\frac{\partial \zeta}{\partial t} + \frac{\partial Q}{\partial x} = 0, \quad \zeta = \zeta(x,t), \quad Q(x,t) = \int_{-h}^{\zeta} u(x,z,t) dz \tag{1}$$

$$\frac{\partial Q}{\partial t} + \frac{\partial}{\partial x} \left(\frac{Q^2}{D} \right) + gD \frac{\partial \zeta}{\partial x} - \frac{1}{3} \bar{D}^2 \frac{\partial^3 Q}{\partial t \partial x^2} - M_D = 0 \tag{2}$$

where

$$D(x,t) = h + \zeta, \quad \bar{D}(x) = h + \bar{\zeta},$$

u is the horizontal velocity, and M_D corresponds to the momentum diffusion in the surf zone and has been expressed by Sato and Suzuki (1990) (See also Sato and Kabiling, 1994a, b) as

$$M_D = \frac{g\bar{D}}{\sigma^2} f_D \frac{\partial^2 Q}{\partial x^2} \tag{3}$$

in which σ is the angular frequency, and f_D is the following energy dissipation coefficient proposed by Watanabe and Dibajnia (1988).

$$f_D = \alpha_D \tan \beta \sqrt{\frac{g}{D}} \cdot \sqrt{\frac{\hat{Q} - Q_r}{Q_s - Q_r}} \tag{4}$$

where $\alpha_D = 2.5$, $\tan \beta$ is the bottom slope around the breaking point, \hat{Q} is the amplitude of the flow rate Q , and Q_s and Q_r correspond to \hat{Q} in the dissipation zone on a uniform slope and in the recovery zone of constant depth, respectively, defined in this study by

$$Q_s = 0.4(0.57 + 5.3 \tan \beta) C \bar{D}, \quad Q_r = \gamma_B \cdot C \bar{D} \tag{5}$$

where C is the wave celerity, and γ_B is a coefficient proportional to the ratio of the wave amplitude to the total mean depth. In the present model, we don't use any breaking criterion that determines the location of the breaking point *a priori* as employed in most previous models. Instead, by setting an appropriate value of γ_B and by equating f_D to zero in regions where $\hat{Q} \leq Q_r$, the model can automatically handle the problem of determining the breaking point and the dissipation zone as well as the recovery zone. This also makes it unnecessary to use the factitious increase of the value of α_D from 0 to 2.5 around the breaking point that is otherwise needed to avoid numerical wave reflection from there.

The Sommerfeld radiation condition is imposed on the offshore boundary of a computation domain in the same way as in the previous model (Watanabe *et al.*, 1994). On the other hand, the treatment of the shoreward boundary in the present model is completely different from the previous one that assumes the presence of a fictitious shoreward zone of constant depth and neglects the swash wave behavior. Here we adopt a periodically moving shoreward boundary (swash wave front) on which the condition $Q = 0$ is imposed all through the period of uprush and backwash.

Numerical computation is conducted by a finite difference method with a staggered grid scheme of the central difference except for the convection term that is treated with the upwind difference for the sake of stability.

Application of the Wave Model

Figure 1 shows one example of a time-series of wave profiles for one wave period in and near the swash zone computed by using the present model. The bottom consists of a uniform slope of 1/20 and a horizontal bed with a depth of 2 m. The time history of incident waves ($H_I = 0.45$ m, $T = 8$ s) has been calculated by the second-order cnoidal wave theory and given on the seaward boundary ($x = 0$ m). The swash wave behavior or runoff/run-down process seems to be simulated reasonably.

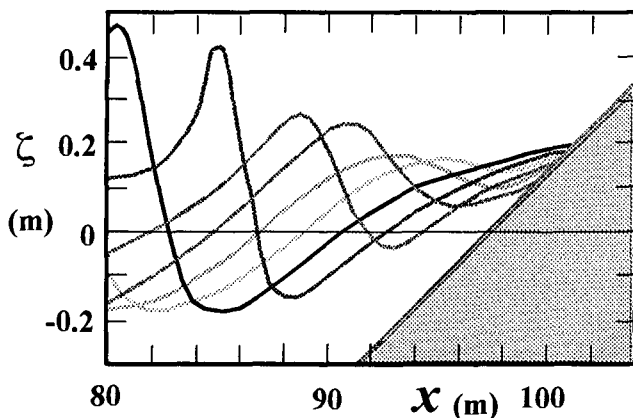


Fig. 1 Wave behavior near the shoreline; Runup and run-down.
($H_I = 0.45$ m, $T = 8$ s, $\tan \beta = 1/20$)

In order to examine the validity of the present wave model more quantitatively, swash-related parameters are computed and compared with existing formulas. Regarding the runup height R_u , Hunt (1959) proposed the following formula:

$$R_u / H_0 = \tan \beta / \sqrt{H_0 / L_0} \quad (6)$$

On the other hand, Ogawa and Shuto (1984) formulated the runup height R_u , on mild

slope solid beds as the summation of the rundown height R_d and the swash zone height S_h as follows (See their paper for details):

$$R_u / H_0 = R_d / H_0 + S_h / H_0 \tag{7}$$

Comparisons of the runup height R_u are shown in **Fig. 2** between the computations by the present model and the above formulas. The agreement of the computations with Ogawa and Shuto's formula is remarkably good.

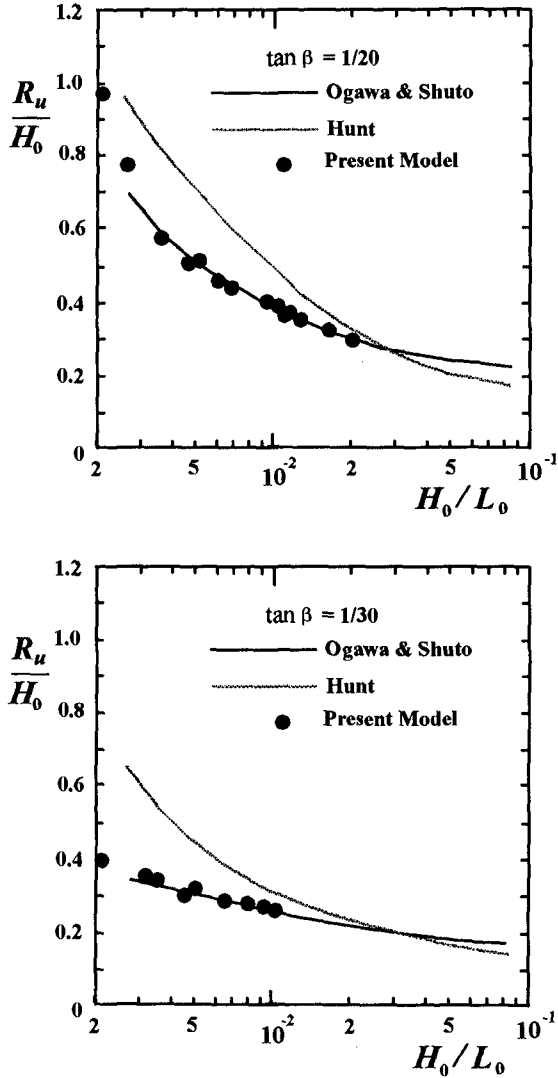


Fig. 2 Runup height R_u .

Similar comparisons are made in Fig. 3 for the rundown height R_d and the vertical length of the swash zone S_h . The agreement with Ogawa and Shuto's formula is worse for R_d and thus for S_h than for R_u in particular for the small deepwater wave steepness, but still fairly good.

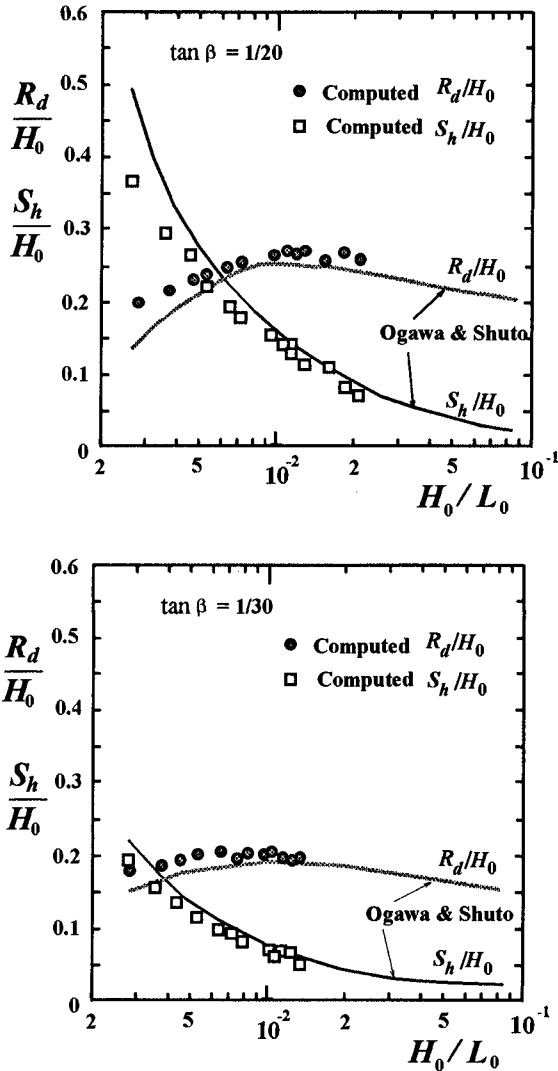


Fig. 3 Rundown height R_d and swash zone height S_h .

Now we will discuss the accuracy of the present model for evaluating the wave height H_S at the still water shoreline. Sunamura (1984) has reported the following

empirical formula for H_S based on wide-range experimental data.

$$H_S / H_B = 2.5 \tan \beta \tag{8}$$

where H_B is the breaker height, which, according to Sunamura and Horikawa (1974), is related to the deepwater wave height H_0 , wavelength L_0 and the bottom slope as

$$H_B / H_0 = (\tan \beta)^{1/5} (H_0 / L_0)^{-1/4} \tag{9}$$

Substituting Eq. (9) into Eq. (8), we obtain

$$H_S / H_0 = 2.5 (\tan \beta)^{6/5} (H_0 / L_0)^{-1/4} \tag{10}$$

Figure 4 compares H_S between the computations and Eq. (10), also demonstrating the applicability of the present model to simulating the swash wave dynamics.

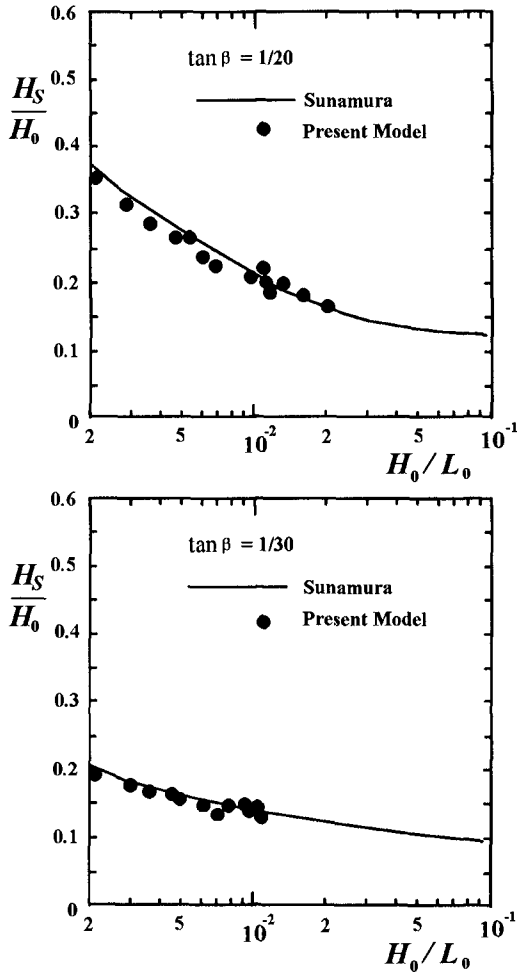


Fig. 4 Wave height H_S at the still water shoreline.

Mathematical Model for Beach Profile Change

The sediment transport rate formula proposed by Dibajnia and Watanabe (1992) is for the sheet flow in asymmetric oscillatory flow with superimposed steady flow, and has already been generalized by them for the bedload as well as for the suspended load over ripples (Dibajnia *et al.*, 1994). After a further slight modification, Dibajnia and Watanabe's sediment transport rate formula reads as follows:

$$\Phi = \frac{q_{\text{net}}(1 - \lambda_v)}{w_0 d} = 0.001 \cdot \text{sign}(\Gamma) \cdot |\Gamma|^{0.5} \quad (11)$$

where q_{net} is the net transport rate, and w_0 , d , and λ_v are the settling velocity, grain diameter, and porosity of the sediment, respectively. The quantity Γ is defined by

$$\Gamma = \frac{u_c T_c (\Omega_c^3 + \Omega_t^3) - u_t T_t (\Omega_t^3 + \Omega_c^3)}{(u_c + u_t) T} \quad (12)$$

in which u_c and u_t are the equivalent root-mean-square amplitudes and T_c and T_t are the periods of the onshore and offshore velocity, respectively, and $T (= T_c + T_t)$ is the wave period, namely,

$$u_c^2 = \frac{2}{T_c} \int_0^{T_c} (u_w + U)^2 dt, \quad u_t^2 = \frac{2}{T_t} \int_{T_c}^T (u_w + U)^2 dt \quad (13)$$

where u_w is the near-bottom orbital velocity and U is the steady flow velocity. Values of Ω_j are determined as follows:

$$\left\{ \begin{array}{l} \text{if } \omega_j \leq \omega_{\text{cr}} \\ \text{if } \omega_j > \omega_{\text{cr}} \end{array} \right\} \left\{ \begin{array}{l} \Omega_j = \omega_j \cdot \frac{2w_0 T_j}{d} \\ \Omega'_j = 0 \\ \Omega_j = \omega_{\text{cr}} \cdot \frac{2w_0 T_j}{d} \\ \Omega'_j = (\omega_j - \omega_{\text{cr}}) \cdot \frac{2w_0 T_j}{d} \end{array} \right. \quad (14)$$

where the subscript j is to be replaced by either c or t , and

$$\omega_j = \frac{1}{2} \cdot \frac{u_j^2}{sgw_0 T_j}, \quad s = \frac{\rho_s - \rho}{\rho} \quad (15)$$

$$\omega_{\text{cr}} = 1 - 0.97 \cdot \sqrt{\Lambda}, \quad \Lambda = \{1 - [(\Psi_{\text{rms}} - 0.2) / 0.4]^2\} \cdot \min(1, 2\lambda / d_0) \quad (16)$$

in which ρ and ρ_s are the densities of the water and sediment, respectively, Ψ_{rms} is the Shields number estimated in terms u_c and d , λ is the pitch length of ripples if any, and d_0 is the near-bottom orbital diameter.

Now one very important issue is how to apply this generalized formula to computing the sediment transport rate in the swash zone reasonably, where the wave-induced orbital velocity drastically varies over a distance of the periodical movement of sediment mass. In the present model for beach profile change, we will adopt a Lagrangian method, namely, assuming that the velocity of every sediment mass in

motion is given by the concurrent flow velocity, we trace the motion of a sediment mass over every wave period, memorize the velocity variation experienced by it, determine its mean position by taking the time-average, and evaluate its net transport rate at this position from the above formula with the velocity variation.

The undertow velocity, which is particularly large near the breaking point in the surf zone, is also incorporated in the computation of the transport rate (For details, readers are referred to Watanabe *et al.*, 1994). Change in beach profiles is obtained from the following conservation equation of sediment mass including the effect of local bottom slope (Watanabe *et al.*, 1986) through alternate computation of the wave deformation, the net transport rate, and the beach transformation itself.

$$\frac{\partial z_b}{\partial t} = -\frac{\partial h}{\partial t} = -\frac{\partial}{\partial x} \left(q_{\text{net}} - \varepsilon_s |q_{\text{net}}| \frac{\partial z_b}{\partial x} \right) \quad (17)$$

where z_b is the bottom elevation, and a value of the coefficient ε_s is set equal to 2.0 in consideration of the repose angle of sand.

Application of Beach Profile Model

Now we will examine the validity of the model for the beach profile change. **Figures 5 and 6** show examples of comparisons of the wave height distribution and of the beach profile change between the computations and measurements. The measurement data are those obtained in large-wave-flume experiments by Shimizu *et al.* (1985). Figure 5 corresponds to an erosional condition, whereas Fig. 6 to a depositional case. For both the cases, the computed wave height distributions agree very well with the measurements except for the under-estimation near breaking points, which is attributable to the weak nonlinearity of Boussinesq-type equations. It is seen in Fig. 5 that the present model properly reproduces not only the formation of a bar but also the recession of the shoreline. Figure 6 also indicates high capability of the model in reproducing both the accretion near the shoreline and the berm formation.

Concluding Remarks

Mathematical models have been proposed in this paper both for the nearshore wave deformation and for the beach profile change in the surf and swash zones. The wave model is based on a Boussinesq-type equations including the breaker-induced energy dissipation and adopts a periodically moving shoreline boundary for the treatment of the swash zone dynamics. In the beach profile model, a Lagrangian method has been employed to evaluate the net rate of sediment transport in and near the swash zone. The validity and applicability of the proposed models have been verified through comparisons with the existing formulas and the experimental data both for the wave deformation and the beach profile change. Improvement of the computational efficiency and application to longer-term and H-2D conditions are left for future study.

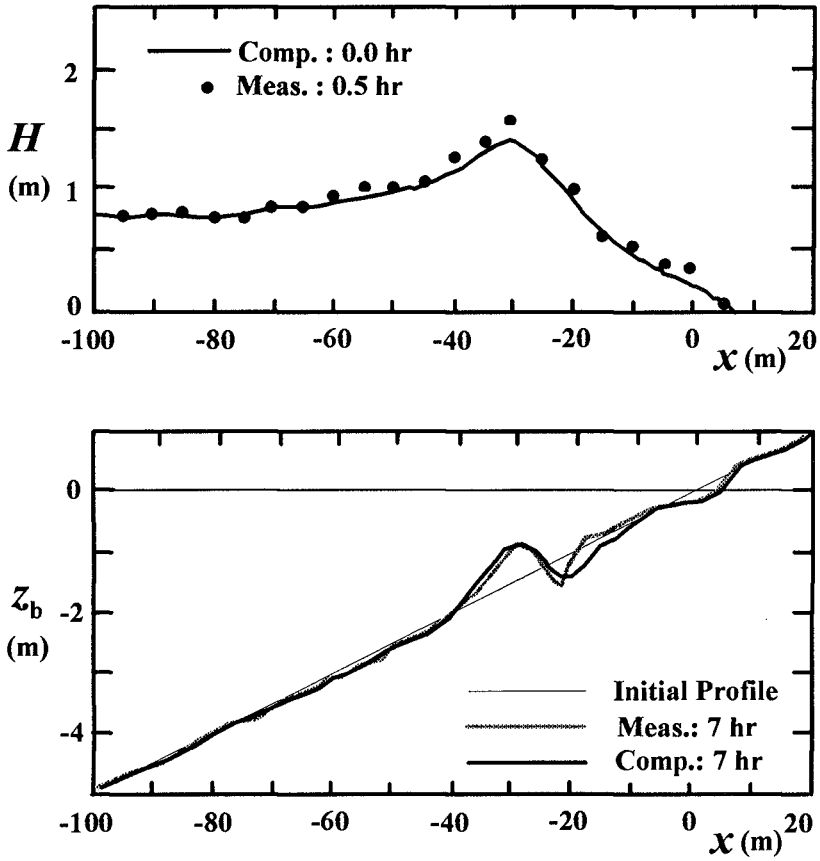


Fig. 5 Wave height distribution and beach profile change.
 ($H_0 = 0.81$ m, $T = 12$ s, $d = 0.27$ mm)

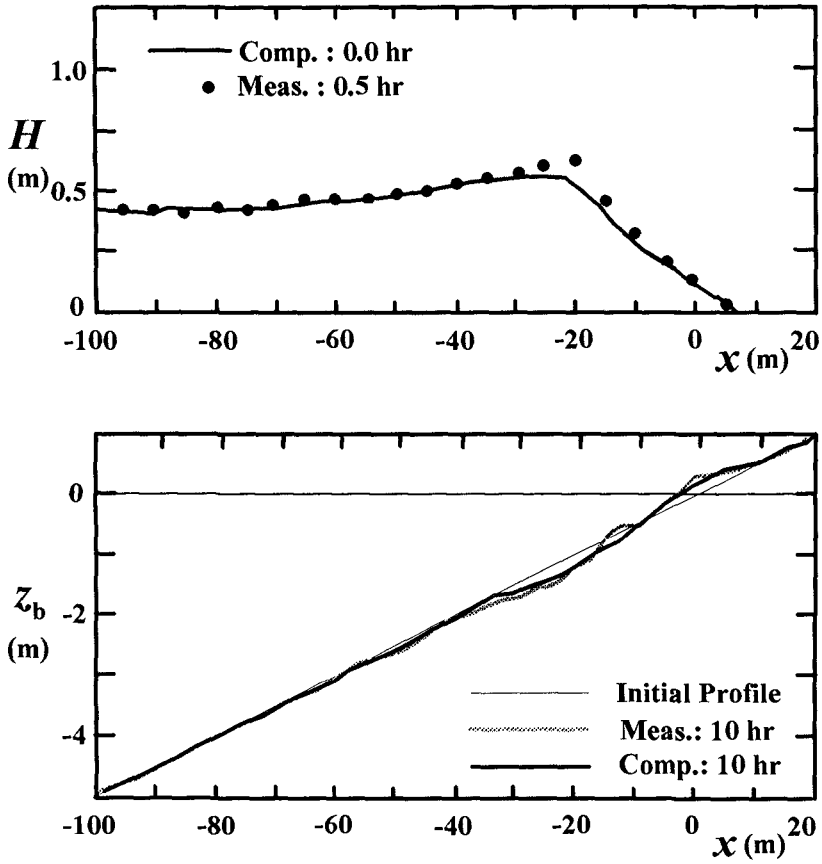


Fig. 6 Wave height distribution and beach profile change.
 ($H_0 = 0.46$ m, $T = 6$ s, $d = 0.27$ mm)

References

- Dibajnia, M., T. Shimizu and A. Watanabe (1994): Profile change of a sheet flow dominated beach, *Proc. 24th Int. Conf. on Coastal Eng.*, ASCE, pp. 1946-1960.
- Dibajnia, M. and A. Watanabe (1992): Sheet flow under nonlinear waves and currents, *Proc. 23rd Int. Conf on Coastal Eng.*, ASCE, pp. 2015-2028.
- Hunt, A.I. (1959): Design of seawalls and breakwaters, *Proc. ASCE*, Vol. 94, No. WW1, pp. 72-92.
- Ogawa, Y. and N. Shuto (1984): Runup of periodic waves on beaches of non-uniform slope, *Proc. 19th Int. Conf. on Coastal Eng.*, ASCE, pp. 198-205.
- Sato, S. and M.B. Kabiling (1994a): A numerical model for three-dimensional beach evolution including the swash zone, *Proc. of Coastal Eng.*, JSCE, Vol. 41, pp. 401-405. (in Japanese)
- Sato, S. and M.B. Kabiling (1994b): A numerical simulation of beach evolution based on a nonlinear dispersive wave-current model, *Proc. 24th Int. Conf. on Coastal Eng.*, ASCE, pp. 2557-2570.
- Sato, S. and H. Suzuki (1990): Estimation method for near-bottom orbital velocities in the surf zone, *Proc. 37th Japanese Conf. on Coastal Eng.*, JSCE, pp. 51-55.
- Shimizu, T., S. Saito, K. Maruyama, H. Hasegawa and R. Kajima (1985): Modeling of cross-shore sediment transport rate distributions in a large wave flume, *Rep. of Central Res. Inst. for Electric Power Industry*, No. 384028, 60 p. (in Japanese)
- Sunamura, T. (1984): Onshore-offshore sediment transport rate in the swash zone of laboratory beaches, *Coastal Eng. in Japan*, JSCE, Vol. 27, pp. 205-212.
- Sunamura, T. and K. Horikawa (1974): Two-dimensional beach transformation due to waves, *Proc. 14th Int. Conf. on Coastal Eng.*, ASCE, pp. 920-938.
- Watanabe, A. and M. Dibajnia (1988): A numerical model of wave deformation in surf zone, *Proc. 21st Int. Conf. on Coastal Eng.*, ASCE, pp. 578-587.
- Watanabe, A., K. Maruyama, T. Shimizu and T. Sakakiyama (1986): Numerical prediction model of three-dimensional beach deformation around a structure, *Coastal Eng. in Japan*, JSCE, Vol. 29, pp. 179-194.
- Watanabe, A., K. Shiba & M. Isobe (1994): A numerical model of beach change due to sheet-flow, *Proc. 24th Int. Conf. on Coastal Eng.*, ASCE, pp. 2785-2798.

CHAPTER 241

Comparisons of Erosion Models For Storms at Ocean City, MD

Jie Zheng¹ and Robert G. Dean²

Abstract

A new non-linear cross-shore sediment transport model called CROSS is developed based on equilibrium beach profile concepts and scaling relationships. CROSS and three other existing models, CCCL (Chiu and Dean 1984), EDUNE (Kriebel 1989) and two versions of SBEACH (version 2.0, Larson and Kraus 1989, and version 3.0, undocumented) are investigated by comparing erosion occurring from November 1991 to January 1992, at Ocean City, Maryland, the site of a major beach fill placed by the State of Maryland and Federal Government in 1988, 1990 and 1991. Among the four models, CCCL is the only one which overpredicts average dune erosion; the other three underpredict it. Overall CROSS and EDUNE yield better predictions than the other two models.

Introduction

Ocean City, Maryland, is located on Fenwick Island, a north-south oriented barrier island of the central Delaware-Maryland-Virginia coast. The Ocean City beach was nourished by the State of Maryland in 1988, and the Federal Government in 1990 and 1991 to protect the city against storm damage (Stauble et al. 1993). The project layout is shown in Figure 1. The entire project was finished in August 1991.

After the project, a series of storms occurred in late 1991 and early 1992. Among these 1991-1992 winter storms, the January 4, 1992 storm was very severe with a peak storm surge of 2 meters (Jensen and Garcia 1993). The initial pre-storm beach profiles were surveyed on November 2-4, 1991, and the post-storm profiles were surveyed on January 11, 1992. In this period, an additional storm occurred on November 11, 1991. For consistency with the measured pre-storm and post-storm profiles, both the November 1991 and January 1992 storms are included in the numerical simulations. A total of seven survey lines located from the southern (37th

¹ Coastal Engineer, Coastal Technology Corporation, 3625 20th St., Vero Beach, FL, 32960, USA.

² Professor, University of Florida, 336 Weil Hall, Gainesville, FL 32611, USA.

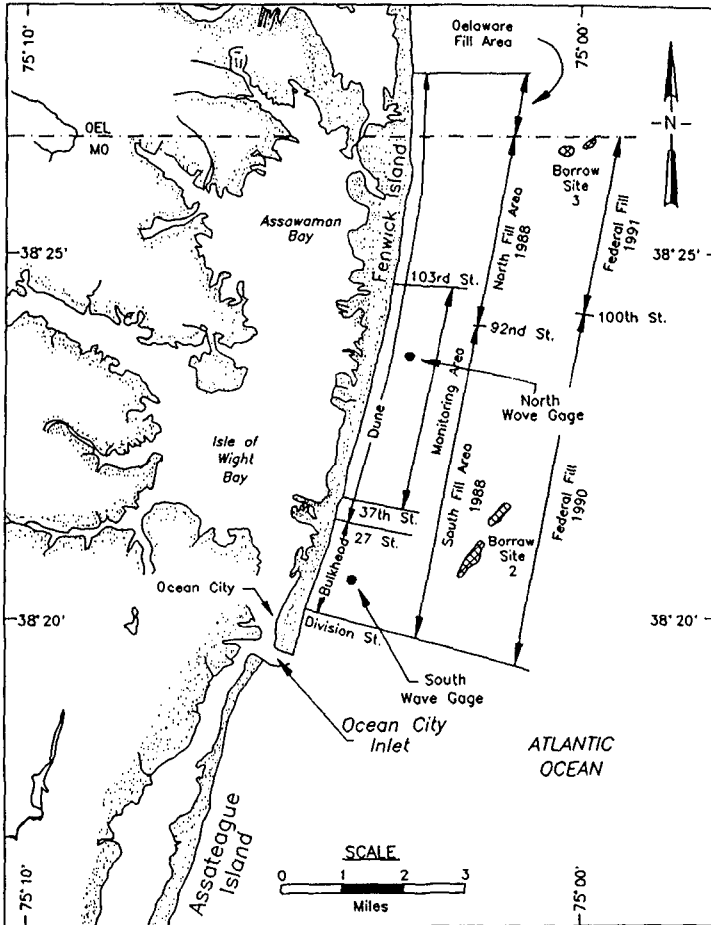


Figure 1. The Ocean City beach nourishment project layout.

Street) to northern (124th Street) portion of the project are available for both pre and post-storm surveys (Stauble et al. 1993, and Kraus and Wise 1993).

Four cross-shore sediment transport models are compared for the simulations of beach erosion at Ocean City during the November 1991 and January 1992 storms. These models are

- CCCL (Chiu and Dean 1984, 1986)
- EDUNE (Kriebel and Dean 1985, Kriebel 1986)
- SBEACH (Larson and Kraus 1989, Larson et al. 1989)
- CROSS (Zheng 1996, Zheng and Dean 1996)

Two versions (2.0 and 3.0) of SBEACH models will be included in the following comparisons. Version 3.0 was released in September 1994 by the U.S. Army Corps of Engineers after a study of storm erosion at Ocean City during the 1991-1992 winter storms. Three measures are presented for comparison of quantitative model performance.

Brief Description of Four Models

All four models discussed here are of the "closed loop" type and based on equilibrium beach profile concepts, which consider beach profile changes to be caused by deviations of a profile from its equilibrium. An equilibrium beach profile represents a dynamic balance of constructive and destructive forces acting on the beach. A change in the two competing types of forces will result in a disequilibrium. Considering wave energy dissipation per unit volume to represent the dominant destructive force, Dean (1977) proposed that a sediment of given size will be stable in the presence of a particular level of wave energy dissipation per unit volume, D_* , which is expressed as

$$D_* = \frac{1}{h} \frac{d(Ec_g)}{dy} \quad (1)$$

where h is the water depth, y is the shore-normal coordinate directed offshore, E is the wave energy density, and c_g is the wave group velocity. As a first approximation, D_* is assumed to dependent only on sediment size (Moore, 1982). With linear wave theory and shallow water assumptions, Eq (1) is integrated to

$$h = \left(\frac{24D_*}{5\rho g\sqrt{g}\kappa^2} \right)^{2/3} y^{2/3} = A y^{2/3} \quad (2)$$

where κ is the ratio of breaking wave height to water depth, and A is defined as a profile scale parameter.

CCCL Model

Under erosive water level and wave conditions, the time dependent beach recession, $R(t)$ is given by

$$R(t) = R_\infty (1 - e^{-K_R t}) \quad (3)$$

where R_∞ is equilibrium recession and K_R is a reciprocal time scale. At each time step, the equilibrium profile and recession are calculated by considering Eq. (3) and sand conservation. After the final computational time step, a factor of 2.5 is applied to the recession, in part to incorporate the alongshore variability of beach erosion.

EDUNE Model

The cross-shore sediment transport rate per unit beach width, Q , is considered as linearly proportional to the deviation of local wave energy dissipation per unit volume from the equilibrium,

$$Q = K_e(D - D_*) \quad (4)$$

where K_e is an empirical transport parameter and D is the local wave energy dissipation per unit volume. A beach steeper or milder than the equilibrium at a given depth will cause sediment transport offshore or onshore, respectively. Since the transport (Eq. (4)) has two variables, a continuity equation is used to close the system.

SBEACH Model

The cross-shore sediment transport rate is determined by

$$\begin{aligned} Q &= \pm K_s \left| D - D_* + \frac{\epsilon}{K_s} \frac{\partial h}{\partial x} \right|, & D > D_* - \frac{\epsilon}{K_s} \frac{\partial h}{\partial x} \\ &= 0, & D \leq D_* - \frac{\epsilon}{K_s} \end{aligned} \quad (5)$$

where ϵ is an empirical constant and K_s is a transport coefficient. This relationship is similar to EDUNE except for the last term which incorporates the effect of local slope. The beach profile evolution is solved by combining the transport relationship with the continuity equation. The direction of transport (\pm in Eq. (5)) is determined according to

$$\begin{aligned} \frac{H_0}{L_0} - 0.00070 \left(\frac{H_0}{w_f T} \right)^3 &< 0, + \\ \frac{H_0}{L_0} - 0.00070 \left(\frac{H_0}{w_f T} \right)^3 &> 0, - \end{aligned} \quad (6)$$

CROSS Model

Based on scale analysis and the Froude relationship, the cross-shore sediment transport rate per unit beach width, Q , should scale as

$$Q_r = L_r^2 / T_r = L_r^{3/2} \quad (7)$$

where L_r and T_r are length and time scales, respectively. To satisfy this scale relationship (7) and ensure convergence to the equilibrium beach profile, the following sediment transport relationship is proposed

$$Q = K_c (D - D_*)^3 \quad (8)$$

where K_c is a dimensional constant. Time dependent profile response is determined by solving the transport equation (8) and sand conservation equation.

Storm and Beach Profile Characteristics

Water depth and profile elevations used here are referenced to NGVD (National Geodetic Vertical Datum), which lies 2 cm below mean water level for Ocean City. The wave height, wave period and storm surge time histories during the two storms were measured by two gages located directly offshore of Ocean City in a water depth of 10 meters. The measured significant wave height, peak spectral wave period and storm surge are shown in Figure 2 for the January 4, 1992 storm (Stauble et al. 1993).

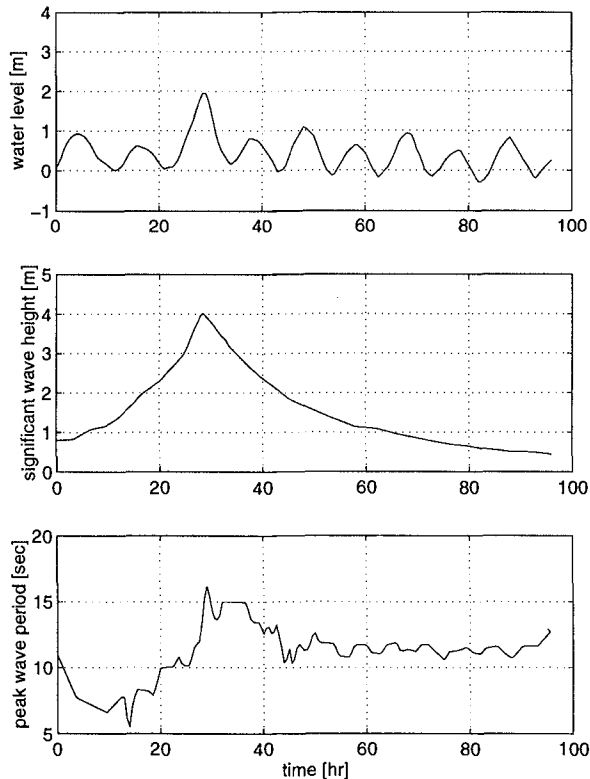


Figure 2. Water level, significant wave height and peak spectral wave period time history for the January 4, 1992 storm at Ocean City, MD (From Stauble et al. 1993).

Seven survey lines located at 37th, 45th, 56th, 74th, 103rd and 124th Streets (Stauble et al. 1993, Kraus and Wise, 1993) have both pre-storm and post-storm measured profiles available and are simulated. The mean grain sizes within each of 11 cross-shore morphologic zones are presented in Table 1. The seven measured pre- and post-storm profiles are shown in Figure 3 for the two surveys taken on November 2, 1991 and January 11, 1992, respectively. It appears that the storm-caused erosion is

Table 1 Average mean grain size in millimeters.

Sample Location	37 th St.	45 th St.	56 th St.	63 rd St.	74 th St.	103 rd St.	124 th St.
Dune base	0.35	0.34	0.33	0.39	0.39	0.44	0.44
Berm crest	0.29	0.31	0.34	0.35	0.35	0.38	0.38
Mean-tide line	0.32	0.30	0.27	0.27	0.29	0.38	0.38
Swash zone	0.34	0.38	0.44	0.47	0.48	0.39	0.39
Nearshore trough	0.31	0.33	0.36	0.45	0.47	0.81	0.81
Nearshore bar	0.29	0.36	0.46	0.44	0.46	0.34	0.34
- 1.52 m contour	0.29	0.26	0.21	0.26	0.32	0.23	0.23
- 3.05 m contour	0.21	0.21	0.22	0.22	0.21	0.21	0.21
- 4.57 m contour	0.20	0.22	0.24	0.21	0.22	0.21	0.21
- 6.10 m contour	0.29	0.23	0.14	0.15	0.28	0.17	0.17
- 7.62 m contour	0.34	0.25	0.13	0.12	0.17	0.16	0.16

quite different for profiles at different locations. After two storms, the profiles at 37th and 56th Streets had almost no erosion, whereas the other profiles experienced quite severe losses in the dune area. Based on the measured profiles, the net volume changes are calculated for each profile and presented in Table 2. It appears that the net volume changes during the two storms are quite different from zero for most profiles due to the gradients in longshore sediment transport. To remove this effect, each post-storm profile is adjusted by shifting the profile horizontally a distance Δy to yield zero net volume change. The value of Δy is calculated by

$$\Delta y = \frac{1}{h_{total}} \int_{y_0}^{y_*} (h_{mb} - h_{ma}) dy \quad (9)$$

where subscripts *mb* and *ma* denote profile elevation measured before and after storms, respectively, y_0 and y_* are offshore directed coordinates at the baseline and the limit of offshore profile change, respectively, and h_{total} represents the total elevation of the active storm profile. The sign of Δy is positive for a seaward translation. The profile retreat at the 3 meter contour and the eroded volume with and without the shifting adjustments are shown in Table 3. These parameters will be used as measures of the storm erosion and the performance of the numerical models.

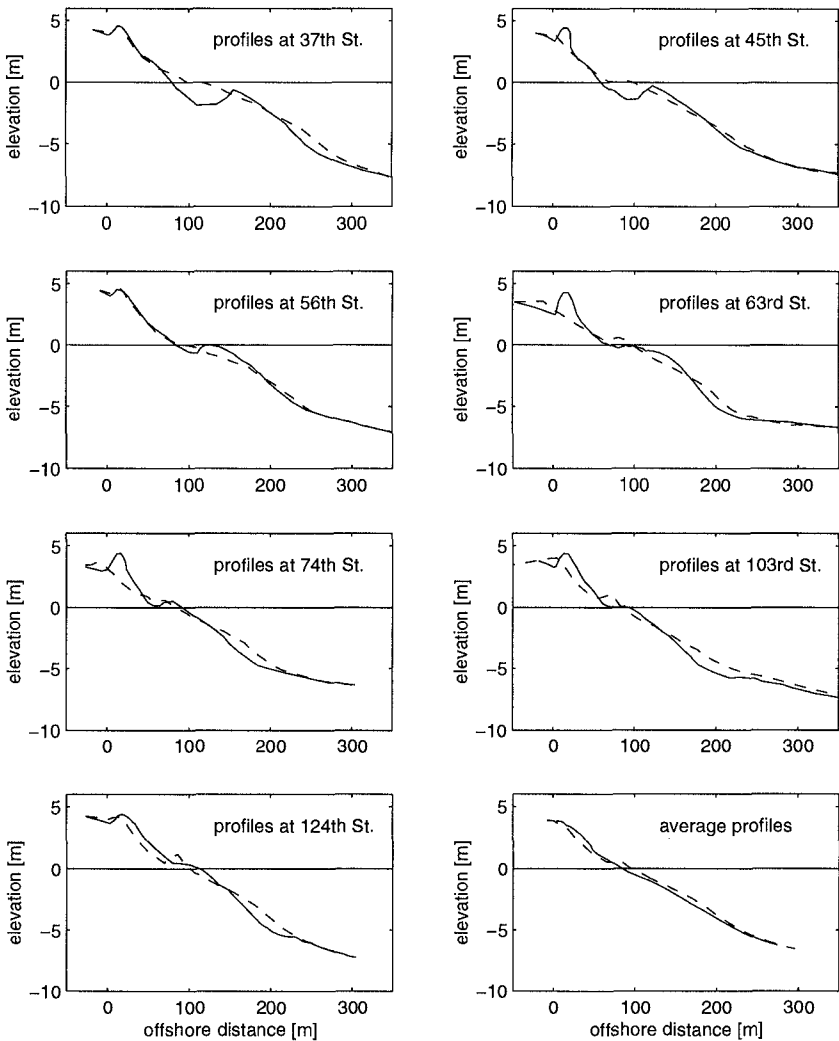


Figure 3 Measured pre-storm (solid line) and post-storm (dashed line) profiles.

Input Conditions for Each Model

The predictions of the four models are compared with the storm erosion measured at Ocean City, Maryland. The input parameters for each model in this study are selected to represent the conditions for which each model was calibrated. Among the four models, CROSS is the only one which can incorporate variable sediment size along a profile. The conditions run for each model are described briefly as follows.

Table 2 Measured volume change during the storm and adjustment Δy .

Street	Volume change (m ³ / m)			Adjustment Δy (m)	h_{total} (m)
	Gain	Loss	Net		
37 th	158.77	20.78	137.99	-11.29	12.22
45 th	81.01	49.42	31.59	-2.83	11.16
56 th	27.71	47.96	-20.25	1.97	10.28
63 rd	82.34	83.99	-1.65	0.16	10.31
74 th	80.53	59.61	20.92	-2.19	9.55
103 rd	136.06	56.33	79.73	-7.09	11.25
124 th	75.74	56.10	19.64	-1.80	10.91
Average	55.71	24.97	30.74	-3.04	10.11

CCCL Model

This model has been used in establishment of the Coastal Construction Control Line (CCCL) in Florida. The CCCL is a line which depicts the landward limit of impact of a 100 year period storm event. The default dune slope is set to 1. Since this model cannot represent variable sediment size along a profile, a uniform grain size of 0.35 mm is applied. At each time, the significant wave height is used as the input wave height. The set-up at the shoreline is calculated based on linear wave theory as 0.23 times the incoming wave height. No wave run-up is included in the model. After running the storms, consistent with model calibration, a factor of 2.5 is applied to those contours which receded. This model does not incorporate a transport equation, but rather considers the profile to approach equilibrium with a folding time scale of 13 hours.

EDUNE Model

The default input dune slope is set to 1 and the input shoreline slope is taken as 0.05 which is the average shoreline slope of the measured pre-storm profiles. For the same reason as described for the CCCL model, a sediment size of 0.35 mm is used. The significant wave height is input at each time step. In EDUNE, the wave run-up is an input parameter held constant throughout the erosion simulation, and is used to control the location of the dune scarp above the peak water flood level. For the Ocean City storm erosion simulations, the run-up was fixed as 0.91 meters and 1.52 meters for the November 1991 and January 1992 storms, respectively, and was based on a combination of matching elevation of dune scarps and Hunt's equation (1958)

$$R = F_R H_b \frac{m}{\sqrt{H_b/L_0}} \quad (10)$$

where R is the run-up height measured vertically upward from the storm water level, F_R is a non-dimensional coefficient and is approximately 1, m is the average bed slope

from the run-up limit to the breaking point, and L_0 is the deep water wave length. In the application here, it was found that the best agreement was provided by using the maximum significant wave height of each storm in Eq. (10). The transport coefficient, K_e , for this application is the program default value of $8.73 \times 10^{-6} \text{ m}^4/\text{N}$.

SBEACH Model

Both versions (2.0 and 3.0) of SBEACH model are believed to incorporate wave run-up and set-up. The maximum slope that a predicted profile is allowed to achieve is required and is set to 17.5° as a default condition; this corresponds to a beach slope of 0.32. A constant sediment size of 0.35 mm is applied here, which was recommended by Kraus and Wise (1993) in their study. Both versions of the SBEACH model provide a choice of wave type (monochromatic or irregular). The option of irregular waves which requires an input of time history of significant wave height was chosen for this study. The default value for the transport coefficient, K_s , in both version is $1.50 \times 10^{-6} \text{ m}^4/\text{N}$.

CROSS Model

The dune slope and the offshore slope are set equal to 1 and 0.5, respectively, as default conditions, and the shoreline slope is set to the average shoreline slope of the measured pre-storm profiles (0.05). Two different sediment size distributions are compared in this model. First, along each measured profile, the variable sand size listed in Table 1 is applied. Second, as a basis for comparison with the other three models, a uniform grain size of 0.35 mm is used. During each storm, a random wave series is generated according to the time history of the measured significant wave height and spectral peak wave period. The wave-by-wave set-up is calculated based on linear wave theory, and the wave run-up limit is established from Hunt’s Equation (10). A transport coefficient value, K_c , of $7.14 \times 10^{-10} \text{ m}^8 \text{ s}^2/\text{N}^3$ is used for this field application.

Numerical Results and Comparisons

The numerical results from the four models are quantified in terms of several parameters. A comparison of measured and predicted entire active profile changes is provided by the residual parameter, Res, defined in non-dimensional form as:

$$Res = \frac{\sum_{i=1}^n (h_{pi} - h_{mai})^2}{\sum_{i=1}^n (h_{mbi} - h_{mai})^2} \tag{11}$$

where h is the profile elevation, the subscripts “p” and “m” denote predicted and measured, respectively, “b” and “a” indicate before and after storm conditions, respectively, “i” represents the i^{th} location on the profile, and the sums extend across the entire active profile. The minimum possible value of Res is zero, which would correspond to a perfect simulation. If the numerical simulation predicts no changes, the value of Res is 1, which therefore should represent an upper limit of Res.

The dune erosion agreement between calculated and measured values is quantified by the eroded volume and the beach retreat at the 3 meter contour. To provided a measure of erosion and retreat, two different errors are presented: the mean square error, ERR_{ms} , and the algebraic average error, ERR_{ave} . These are expressed as

$$ERR_{ms} = \frac{\sum_{j=1}^n (S_{pj} - S_{mj})^2}{\sum_{j=1}^n S_{mj}^2} \quad (12)$$

$$ERR_{ave} = \frac{\sum_{j=1}^n S_{pj} - S_{mj}}{\sum_{j=1}^n S_{mj}}$$

where S is an eroded volume or beach retreat, the subscripts "p" and "m" again represent the predicted and measured values, respectively, and "j" means the j^{th} beach profile. ERR_{ms} represents a factor of simulation accuracy and ERR_{ave} provides a measure of over or under-prediction of erosion. Compared with the measure, Res , which is based on local differences across the entire active profile, ERR_{ms} and ERR_{ave} are based on average differences of eroded volume or beach retreat at a particular elevation.

Comparisons between predictions and measurements for the profiles at 45th Street are presented in Figure 4. The ridge features presented on the measured post-storm profiles suggest that there was some beach recovery even though the post-storm profiles were measured only a week after the second storm. The predictions of CROSS with both variable and uniform sand size are presented. It appears that the results predicted with variable sand size provide more reasonable simulations for dune erosion while the predictions with the uniform sand size fit the entire profile better. After applying the factor of 2.5 to those contours which receded, the CCCL model tends to overpredict erosion for most profiles. Since the application purpose of CCCL is to establish the Coastal Construction Control Line, the 2.5 factor is included to incorporate the variability of beach erosion at different locations. As mentioned above for EDUNE, the wave run-up is determined, in part, according to measured post-storm profiles used throughout the entire time of numerical simulation. Since beach erosion is quite sensitive to water level, the numerical results of EDUNE will depend greatly on the storm duration time and the input of wave run-up. Among all four models, SBEACH version 2.0 is the only model which represents the offshore bar feature. The newly modified version 3.0 of SBEACH presents substantially better agreement than version 2.0.

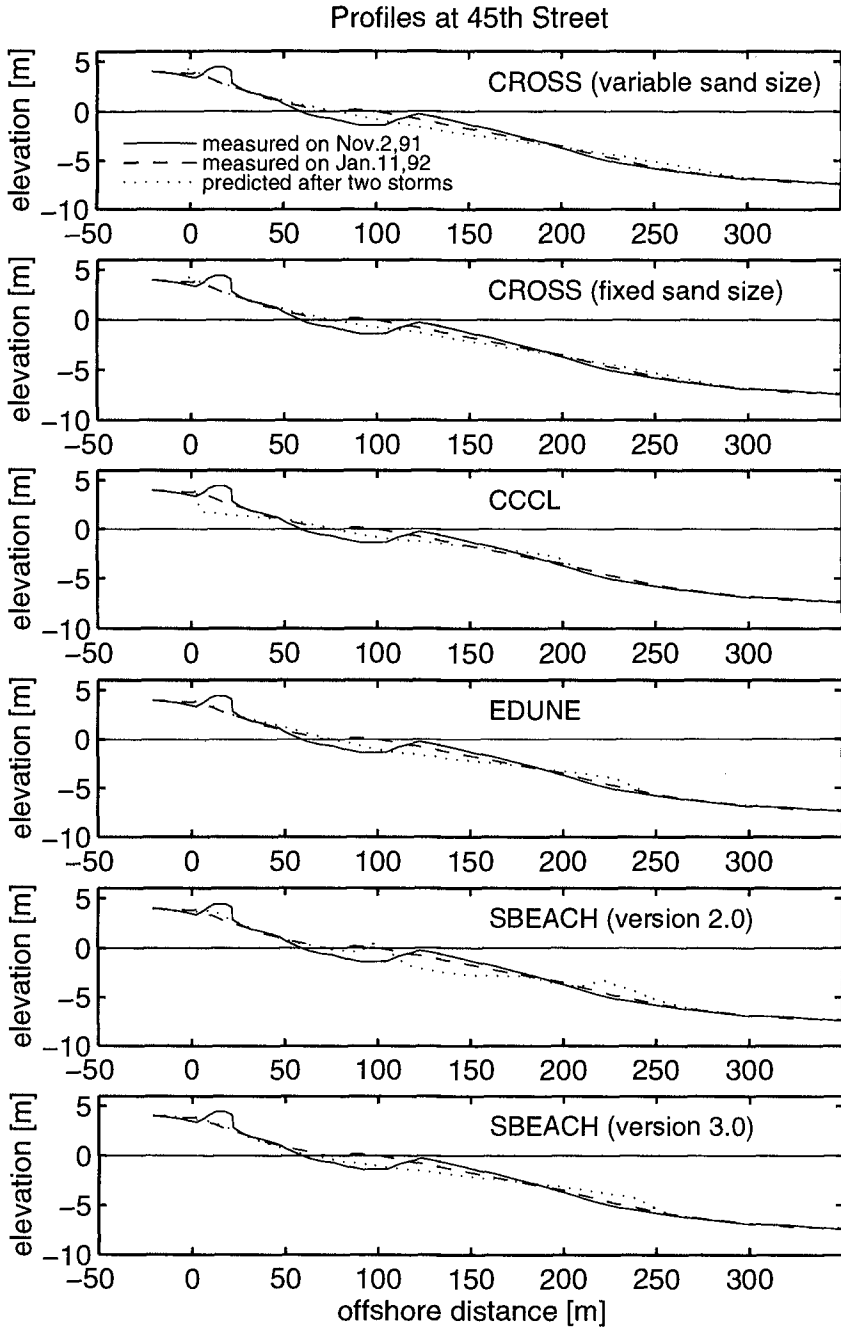


Figure 4. Comparisons of predicted and measured profiles at 45th Street.

The corresponding residuals, eroded volumes and beach retreat at the 3 meter contour for each individual profile were calculated. Two examples of profiles at 45th and 103rd Streets are shown in Table 4. Because the net volume changes between measured pre-storm and post-storm profiles are quite different from zero due to gradients of longshore sediment transport, in addition to the measured profiles, results are included based on shifting each post-storm profile the horizontal distance, Δy , to yield zero net volume change. In the table, "without adjustment" means data given by the original measured post-storm profiles, while "with adjustment" means data resulting from horizontally shifted post-storm profiles. Since all four models discussed here included only cross-shore sediment transport, the data presented "with adjustment" are considered to be more appropriate.

Table 4 The residuals, eroded volumes and beach retreat at the 3-meter contour.

Profile	Model	Residual		Eroded vol. (m ²)	Retreat at 3-m contour (m)
		w/o adjust.	With adjust.		
45 th St.	CROSS(var. sand size)	0.525	0.496	20.13	8.71
	CROSS(fixed sand size)	0.287	0.280	19.39	8.36
	CCCL	1.067	0.851	60.56	18.34
	EDUNE	0.624	0.604	18.30	6.51
	SBEACH (ver. 2.0)	1.018	0.971	15.21	2.96
	SBEACH (ver. 3.0)	0.736	0.713	23.34	6.79
103 rd St.	CROSS(var. sand size)	0.329	0.274	35.18	15.23
	CROSS(fixed sand size)	0.261	0.251	28.88	13.41
	CCCL	2.233	1.499	123.05	28.92
	EDUNE	0.548	0.413	54.66	20.04
	SBEACH (ver. 2.0)	0.596	0.590	19.54	7.03
	SBEACH (ver. 3.0)	0.510	0.433	35.20	10.61

The residuals averaged over the seven measured profiles and the two errors defined in Eq. (11) for eroded volume and beach retreat at the 3-m contour with respect to the horizontal shifted profiles are presented in Table 5. Overall, CCCL overpredicts the dune erosion during the two storms, whereas the other three models underpredict it. It appears that CROSS with fixed sand size results in significantly less average residual than the others. The dune erosion errors of CROSS with variable sand size, EDUNE and SBEACH version 3.0 are comparable. It is noticed that dune overwash occurred during the January 1992 storm. Among the four models, only EDUNE and SBEACH incorporate dune overwash processes. In the CROSS model, the profile shoreward of the dune crest is treated as a horizontal beach with the same elevation as

the dune crest. Therefore, the numerical simulations of CROSS do not include the dune erosion part caused by overwash. It is expected that the underpredictions of CROSS could be improved by incorporating dune overwash processes in the model.

Table 5 The average residuals and errors of eroded volume and beach retreat at the 3-meter contour with respect to the horizontally shifted measured profiles.

Model	Averaged residual	Error of eroded volume		Error of retreat	
		ERR _{ms}	ERR _{ave}	ERR _{ms}	ERR _{ave}
CROSS (variable sand size)	0.725	0.227	-0.401	0.283	-0.359
CROSS (fixed sand size)	0.458	0.319	-0.511	0.327	-0.444
CCCL	1.331	0.707	0.847	0.480	0.561
EDUNE	0.792	0.182	-0.328	0.260	-0.324
SBEACH (ver. 2.0)	1.211	0.470	-0.663	0.623	-0.749
SBEACH (ver. 3.0)	0.752	0.183	-0.399	0.259	-0.479

Summary

This paper has presented comparisons of the predictions of the CROSS model and three other commonly used closed loop models (CCCL, EDUNE and SBEACH) for storm erosion at Ocean City, Maryland during the November 1991 and January 1992 storms. The "2.5" factor was applied in the CCCL model in this comparison. The wave run-up parameters used in the EDUNE model are determined according to the measured post-storm profiles and the maximum significant wave heights during two storms. Seven survey lines located from the southern (37th Street) to northern (124th Street) portions of the project are selected for evaluation of the four models. In most locations, the net volume changes in profiles are quite different from zero due to gradients in longshore transport. An adjustment is made by shifting the whole profile horizontally a distance Δy to yield a zero net volume change for each profile.

A non-dimensional mean square residual parameter is provided to evaluate the agreement between the entire measured and predicted profiles (including subaerial and subaqueous parts). Two kinds of error averaged with different methods (mean square and algebraic average) are provided to evaluate the prediction of dune erosion. It appears that the residuals are less affected by the shifting adjustment, while eroded volumes and beach retreat are affected more significantly by the shift. Among the four models, the CCCL model is the only one which overpredicts average dune erosion. CROSS yields the least average residual and presents the best prediction for an entire profile (including both subaerial and subaqueous parts). For errors of eroded volume and beach retreat, CROSS with variable sand size, EDUNE and SBEACH (version 3.0) provide reasonably comparable predictions. It is anticipated that by incorporating dune overwash, the under prediction of dune erosion by CROSS can be reduced.

References

- Chiu, T.Y. and Dean, R. G. 1984. "Methodology on coastal construction control line establishment," *Tech. and Design Memorandum 84-6*, Beaches and Shores Resource Center, Florida State University, Tallahassee, FL.
- Chiu, T.Y. and Dean, R. G. 1986. "Additional comparisons between computed and measured erosion by hurricanes," *Technical Report*, Beaches and Shores Resource Center, Florida State University, Tallahassee, FL.
- Dean, R.G. 1977. "Equilibrium beach profiles: U.S. Atlantic and Gulf Coasts," *Ocean Engineering Report No. 12*, Department of Civil Engineering, University of Delaware.
- Hunt, I.A. Jr. 1958. "Design of seawalls and breakwaters," *U.S. Lake Survey*, Corps of Engineers, U.S. Army, January 1958.
- Kraus, N.C. and Wise R.A. 1993. "Simulation of January 4, 1992 storm erosion at Ocean City, Maryland," *Shore and Beach*, Vol. 61 No. 1, pp. 13-22.
- Kriebel, D.L. 1989. "Users manual for dune erosion model EDUNE."
- Kriebel, D.L. 1986. "Verification study of dune erosion model," *Shore and Beach*, Vol. 54, No. 3, pp13-21.
- Kriebel, D.L. and Dean, R.G. 1985. "Numerical simulation of time-dependent beach and dune erosion," *Coastal Engineering*, Vol. 9, pp. 221-245.
- Larson, M. and Kraus, N.C. 1989. "SBEACH: Numerical model for simulating storm-induced beach change, Report 1: Theory and model foundation," *Tech. Report CERC 89-9*, CERC, US Army WES, Vicksburg, MS.
- Larson, M., Kraus, N.C. and Byrnes M.R. 1989. "SBEACH: Numerical model for simulating storm-induced beach change, Report 2: Numerical formulation and model tests," *Tech. Report CERC 89-9*, CERC, US Army WES, Vicksburg, MS.
- Stauble, D.K., Garcia A.W. and Kraus N.C. 1993. "Beach nourishment project response and design evaluation: Ocean City, Maryland. Report 1, 1988– 1992," *Tech. Report CERC 93-13*, CERC, US Army WES, Vicksburg, MS.
- Zheng, J. 1996. "Improved cross-shore sediment transport relationship and model," *Ph.D. Dissertation*, University of Florida, Gainesville, Florida, U.S.A.
- Zheng, J. and Dean, R.G. "Numerical modeling and intercomparisons of beach profile evolution," to appear in *Coastal Engineering*.

CHAPTER 242

Measurements of Wave Generated Bedforms

Christopher D. Jetté¹ and Daniel M. Hanes²

Abstract

A 5 MHz multiple transducer array was used to measure wave generated bedforms near Duck, NC. The transducer array consists of 37 transducers with a center to center spacing of 1.2 centimeters. Seabed measurements were made with approximately 1 millimeter vertical and 2 centimeter horizontal resolution. Measured ripple dimensions are compared to three popular ripple prediction models. It is shown that errors of over 100 percent were found between measured and predicted ripple heights and lengths for all ripple models compared. Errors in predicting ripple steepness ranged from 37 to 55 percent.

Description Of Experiment

Field measurements of bedforms were made during an experiment at the Army Corps of Engineers Field Research Facility in Duck, NC during August 23-25, 1995. The instruments were deployed using a Sensor Insertion System (SIS) on the research pier. The SIS was positioned at multiple locations along the cross-shore profile during the experiment.

Bedform measurements were made using a multiple transducer array (MTA) developed at the University of Florida. The MTA consists of 37 ultra-sonic transducers operating at a frequency of 5 MHz. The center-to-center spacing of the transducers is 12 mm. Such configuration allows for O(1 mm) vertical resolution and O(2 cm) horizontal resolution. The MTA can scan a profile in approximately 4 seconds. The distance to the seabed is calculated from the elapsed time between the pulsing of the transducer and the time at which the return exceeds a software selectable threshold.

-
- 1) Research Assistant, Department of Coastal and Oceanographic Engineering, University of Florida, PO Box 116590, Gainesville, FL 32611, USA.
 - 2) Associate Professor, Department of Coastal and Oceanographic Engineering, University of Florida, PO Box 116590, Gainesville, FL 32611, USA.

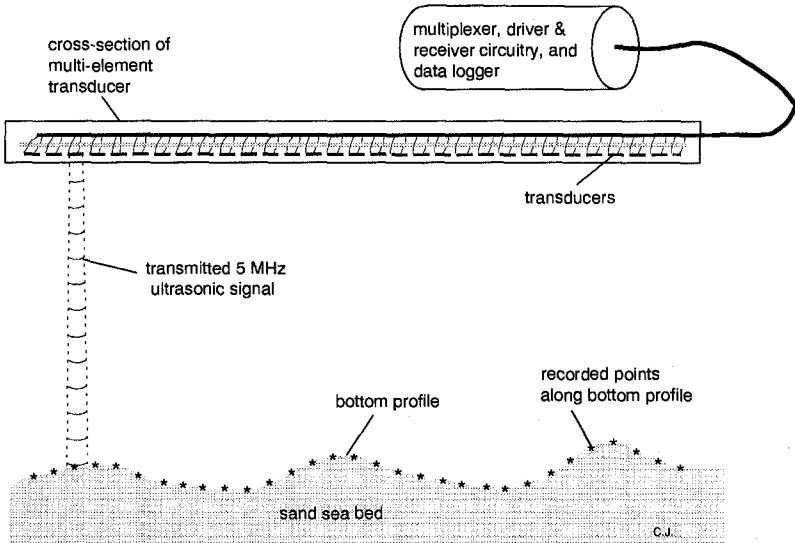


Figure 1. Schematic of the MTA

In addition to the MTA, an under-water video camera was deployed in order to document bedform orientation. Electro-magnetic current meters and pressure transducers were deployed to measure the wave and current conditions. Measurements of the vertical distribution of suspended sediment by acoustical backscatter methods were also made.

The data was collected in 13 minute bursts. Each burst contained 131 profiles taken with the MTA. Current, pressure, and concentration profile data were collected at 4 Hz.

Conditions During Experiment

Exploiting the mobility of the SIS, measurements were made under a variety of wave and sediment conditions. During the experiment, an off-shore bar was present at approximately 210 meters from the high water line. Measurements were made at 8 separate cross-shore locations in the regions offshore of the bar, on the bar, in the trough, and on the nearshore beach-face. Depths where measurements were made ranged from 1.6 to 6.8 meters. The vertical lines in figure 2 indicate cross-shore locations where measurements were obtained.

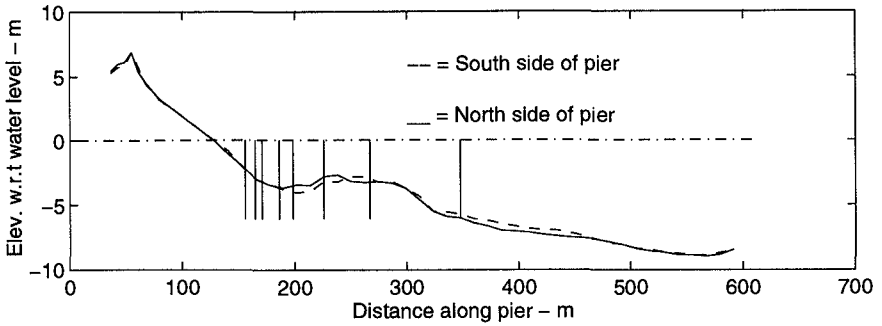


Figure 2. Cross-shore profiles from North and South sides of pier during experiment.

The sediment characteristics varied greatly over the cross-shore profile. D_{50} values of the mostly quartz sediment ranged from 0.19 to 1.67 mm. The range of D_{50} values versus run number are plotted in Figure (3) along with H_{m0} (a), peak wave period (b), and water depth (c).

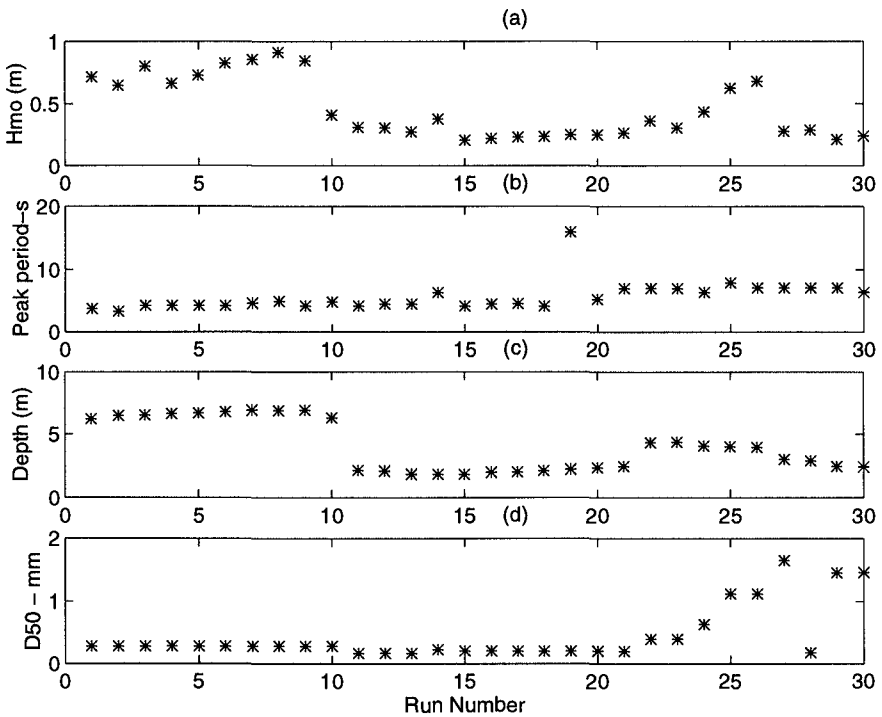


Figure 3. H_{m0} (a), peak wave period (b), water depth (c), and D_{50} (d) vs. Run number for SIS experiment

Most of the wave data taken over the three day period contained at least two, if not three frequency peaks in the surface elevation spectrum. For many of the runs there was a low frequency component (12-15 sec. period) generated from hurricane Felix, which was several hundred miles off-shore, as well as a moderate frequency component (6-8 sec. period), and generally in the afternoon, a higher frequency (4-5 sec. period) locally generated component. H_{m0} wave heights varied from 0.2 to 0.9 meters. During most of the experiment the predominate wave direction at the experiment site was directly on-shore.

For most of the runs measurements were made offshore of the breakpoint, however during runs 11 through 21 some waves were noted to break in the vicinity of the instruments. It is also noted that, after transforming the pressure spectrums into surface elevation spectrums, in the majority of cases the higher frequency component became the peak frequency. Consequently, the wave period used in model prediction was the lowest period component in the wave profile.

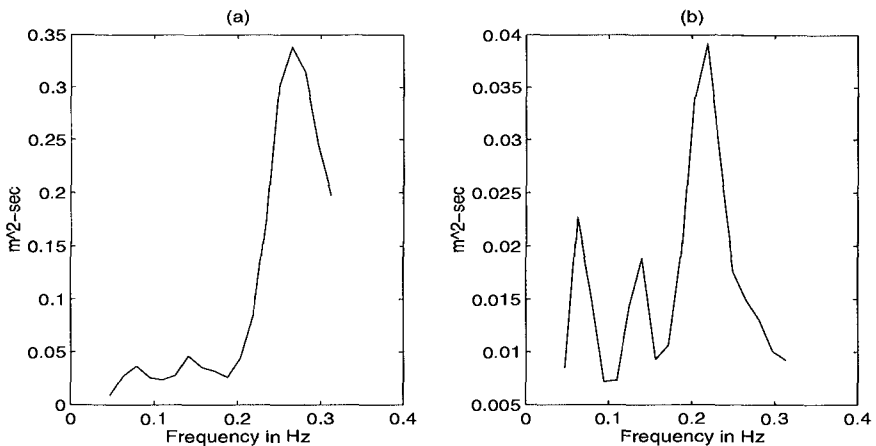


Figure 4. Representative corrected surface elevation spectrums from SIS experiment for runs 1 (a) and 13 (b) with H_{m0} wave heights of 0.72 and 0.28 meters respectively

Measurements

Bedforms were present throughout the experiment, however their geometries varied greatly over the beach profile. Measured bedform heights ranged from 7 to 50 mm, and bedform lengths ranged from 80 to 1000 mm. Active ripple conditions were observed during all times of data collection. For most of the files under-water video was available to document near-bed sediment motion and ripple orientation. Significant ripple migration was not observed during any of the 13 minute runs.

Bedform profiles were collected at a rate of ten profiles per minute. For the measurements presented herein, a single representative profile was found for each minute of data (10 scans). An example of the thirteen representative profiles for an entire run is shown in figure 5 (a-c). In these figures, each profile has been offset by -3 mm from the previous profile for comparative display. The top profile represents the first minute of data and contains circles at each of the 37 measured data points.

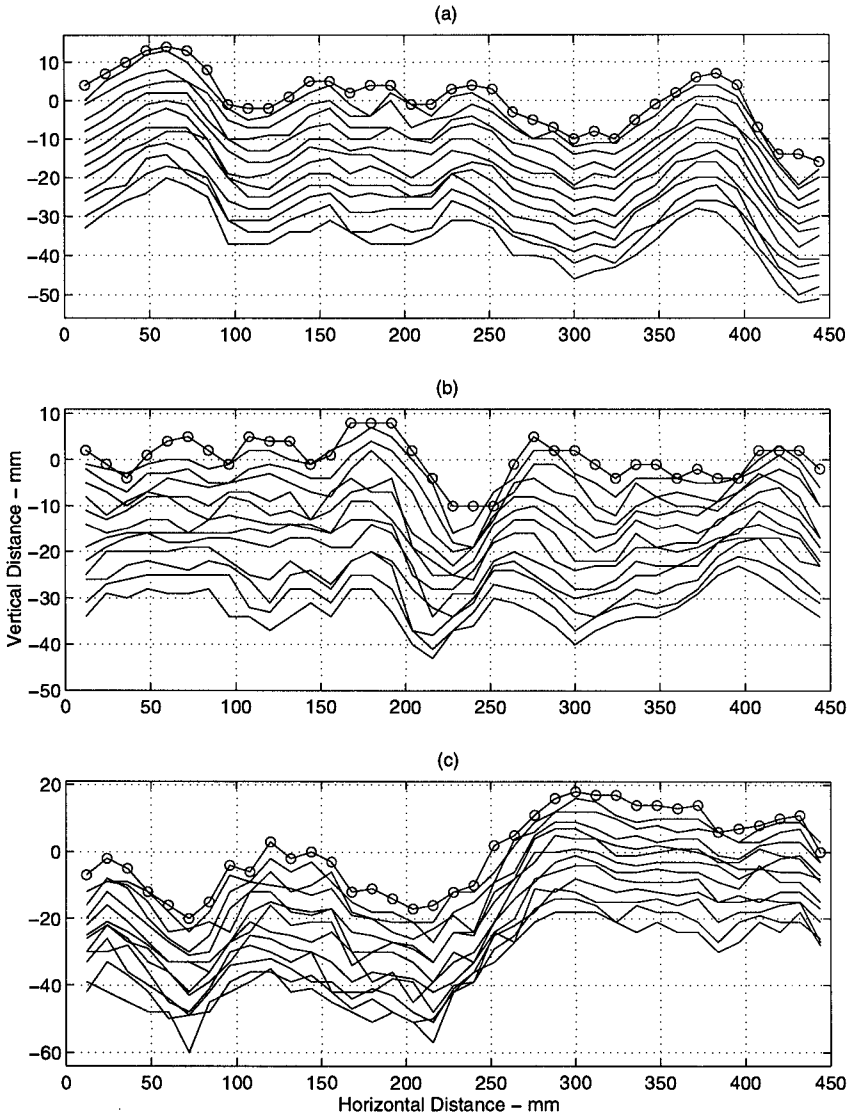


Figure 5. Representative profiles for each minute of a 13 minute run from runs 1(a), 13(b), and 26(c). Data from first minute of run is plotted with circles.

In order to compare these data to models, the bedforms need to be characterized in terms of a wavelength and height. In previous work this has typically been accomplished by visual inspection. We therefore chose a threshold method to determine ripple height and length dimensions for each representative ripple profile. This method first found the peaks and troughs along a profile. Then, if the distance between adjacent peaks and troughs met a certain threshold criterion, they were recorded. From these peaks and troughs average ripple heights and lengths were found. The threshold was chosen conservatively, that is, to maximize ripple heights and lengths. Figure (6) is an example of a representative profile with the threshold ripple crests and troughs marked.

Table 1. Measured hydrodynamic parameters and ripple dimensions for field experiment.

run	loc. (m)	depth (m)	Hmo (m)	Tp (s)	D50 (mm)	ltm(1) (mm)	ltm(4) (mm)	ltm(8) (mm)	ltm(13) (mm)	h _m (1) (mm)	h _m (4) (mm)	h _m (8) (mm)	h _m (13) (mm)
1	347	6.10	0.71	3.76	0.28	103	81	103	107	13	11	13	14
2	347	6.33	0.65	3.76	0.28	103	103	82	105	13	13	12	13
3	347	6.42	0.80	4.27	0.28	100	106	101	106	14	14	12	16
4	347	6.53	0.66	4.27	0.28	108	107	101	154	13	13	14	19
5	347	6.58	0.73	4.27	0.28	107	103	101	105	14	14	15	14
6	347	6.69	0.83	4.27	0.28	152	150	147	149	18	19	16	17
7	347	6.78	0.85	4.57	0.28	103	146	144	105	12	16	16	12
8	347	6.79	0.92	4.92	0.28	98	136	95	104	12	14	10	12
9	347	6.82	0.85	4.27	0.28	158	164	154	152	18	17	17	17
10	347	6.16	0.41	4.92	0.28	102	102	101	102	14	14	15	14
11	267	1.94	0.31	4.27	0.18	112	112	113	115	10	10	9	11
12	267	1.90	0.31	4.57	0.18	117	86	89	113	10	11	10	12
13	267	1.62	0.27	4.57	0.18	84	110	110	105	10	11	14	13
14	267	1.65	0.38	6.40	0.24	1000	1000	1000	1000	50	50	50	50
15	226	1.63	0.21	4.27	0.21	77	101	97	94	8	9	11	10
16	226	1.76	0.22	4.57	0.21	102	99	106	124	13	13	14	16
17	226	1.82	0.23	4.57	0.21	94	90	88	113	11	12	11	11
18	226	1.91	0.24	4.27	0.21	107	139	97	113	8	11	10	12
19	226	1.99	0.26	16.00	0.21	70	86	84	82	9	10	8	10
20	226	2.14	0.25	5.33	0.21	83	83	83	83	7	7	7	7
21	226	2.25	0.27	7.11	0.21	101	101	101	101	11	11	11	11
22	198	4.19	0.37	7.11	0.40	275	275	275	275	40	40	40	40
23	198	4.21	0.31	7.11	0.40	275	275	275	275	40	40	40	40
24	186	3.90	0.44	6.40	0.64	240	232	224	240	26	28	28	26
25	186	3.86	0.63	8.00	1.12	136	134	138	131	23	20	22	20
26	186	3.80	0.69	7.11	1.12	146	147	154	154	23	25	23	23
27	171	2.80	0.28	7.11	1.66	144	136	127	139	15	15	16	15
28	165	2.72	0.29	7.11	0.18	500	500	500	500	45	45	45	45
29	155	2.25	0.22	7.11	1.47	197	108	103	120	27	17	17	17
30	155	2.20	0.24	6.40	1.47	117	128	106	125	18	17	16	17

For model comparisons, each run of data was summarized into four profiles. These profiles were from minutes 1, 4, 8, and 13 of each 13 minute run. The reasons for this were to minimize the amount of clutter in model comparisons, while at the

same time retain the range of ripple geometries present during each run. Measured ripple length (ltm) and height (htm) along with summaries of hydrodynamic and sediment conditions are presented in table 1 for each run.

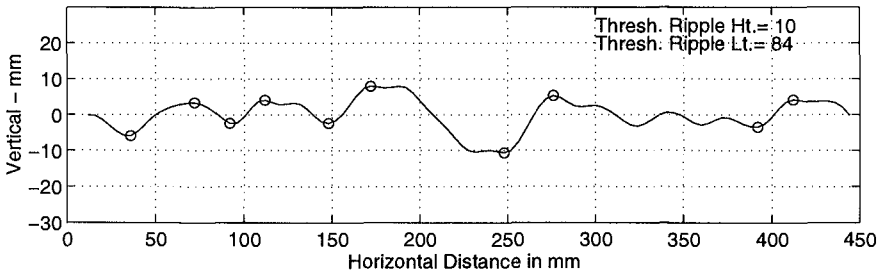


Figure 6. Representative ripple profile with threshold method results for first minute of data from run number 13.

Model Comparisons

Measured bedform dimensions were compared to three predictive models; Nielsen (1981), Wiberg and Harris (1994), and Grant and Madsen (1981). For each run measured values of water depth, Hmo wave height, peak period, and sediment properties were entered into the predictive models. Measured bedform dimensions were plotted with the model curves, if possible, in order to better illustrate the relationships between measured values and predicted values.

Nielsen (1981) derived different predictive models for regular (laboratory) and irregular (field) conditions. Comparisons included herein refer to the irregular or field ripple models. The Nielsen (1981) bedform model characterizes flow conditions using sediment mobility number (Ψ), grain roughness Shield’s parameter ($\theta_{2.5}$), and the wave friction factor “ $f_{2.5}$ ” given by Swart (1974). These parameters are defined as follows

$$\theta_{2.5} = 0.5 f_{2.5} \psi \tag{equation 1}$$

$$f_{2.5} = \exp \left[5.213 \left(\frac{2.5 D_{50}}{A} \right)^{0.194} - 5.977 \right] \tag{equation 2}$$

$$\psi = \frac{(a \omega)^2}{(s - 1) g D} \tag{equation 3}$$

where “D” is the mean grain diameter, “a” is the near-bed wave semi-excursion, “s” is the sediment specific gravity, “g” is the acceleration of gravity, and ω is the

angular frequency of the waves. The Nielsen (1981) irregular wave model for non-dimensional ripple steepness, height, and length are respectively

$$\eta/\lambda=0.342-0.34(\theta_{2.5})^{0.25} \quad \text{equation 4}$$

$$\eta/a=21\Psi^{-1.85} \quad \text{for } \Psi>10 \quad \text{equation 5}$$

$$\eta/a=0.275 - 0.022\Psi^{0.5} \quad \text{for } \Psi<10 \quad \text{equation 6}$$

$$\lambda/a = \exp\left[\frac{693 - 0.37\ln^8\Psi}{1000 + 0.75\ln^7\Psi}\right] \quad \text{equation 7}$$

where η and λ represent ripple height and length respectively.

Relationships between measured ripple dimensions and the Nielsen (1981) model curves are illustrated in figure (8). As can be seen in figure 8(a), for all but 5 out of the 30 runs the Nielsen (1981) irregular wave ripple model over-predicted ripple height. The largest amount of over-prediction was found to occur at low values of sediment mobility number ($\Psi<20$). The Nielsen (1981) ripple length model agreed best with measured dimensions for higher values of mobility number ($\Psi>12$), however for lower values of mobility number ($\Psi<12$), the model over-predicted ripple length for all runs. Measurements of ripple steepness had better agreement with the Nielsen (1981) model curves than did ripple height or ripple length. Best agreement was found at higher values of the grain roughness Shield's parameter ($\theta_{2.5}>0.08$). For lower values of the Shield's parameter the Nielsen (1981) model over-predicted ripple steepness.

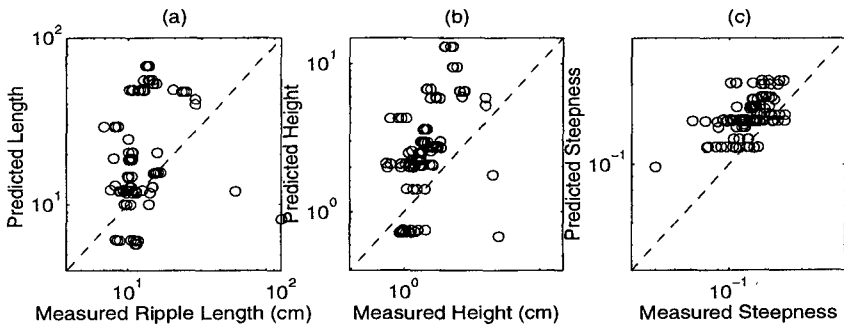


Figure 7. Nielsen (1981) irregular wave ripple comparison with measurements

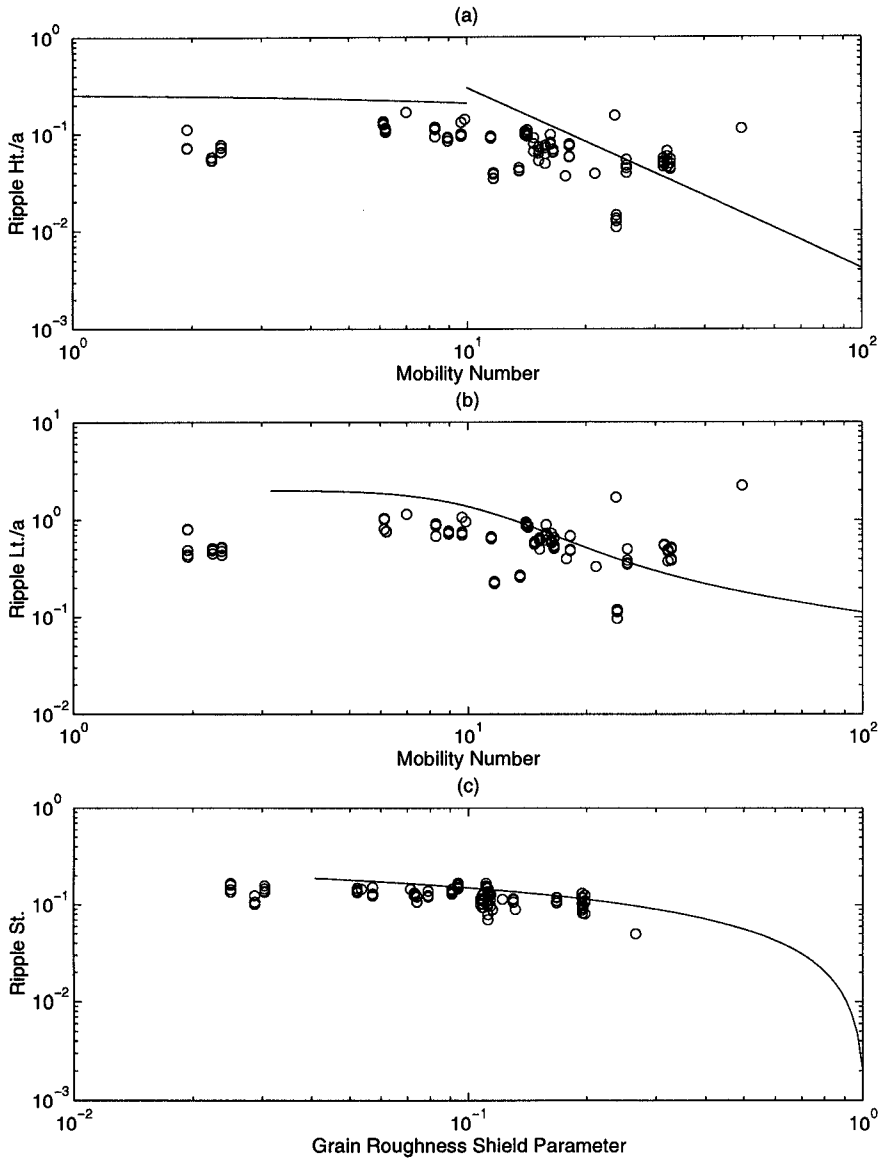


Figure 8. Comparison of measured field ripple dimensions and Nielsen (1981) model curves for height (a), length (b), and steepness (c).

Wiberg and Harris (1994) reexamined existing ripple data from oscillatory flows in both flume and field studies to construct a model to predict ripple geometry for all types of oscillatory flow environments. Wiberg and Harris (1994) classified

bedforms according to the ratio of the wave boundary layer thickness and ripple height (d_o/η). From this ratio, the ripples were classified as orbital, anorbital, or suborbital by the following criteria

Table 2. Wiberg and Harris (1994) ripple classification

flow conditions	ripple classification
$d_o/\eta_{ano} < 20$	orbital ripples
$20 < d_o/\eta_{ano} < 100$	suborbital ripples
$d_o/\eta_{ano} > 100$	anorbital ripples

The Wiberg and Harris (1994) equations for ripple length and steepness for orbital ripples are:

$$\lambda_{orb} = 0.62d_o \quad \text{equation 8}$$

$$(\eta/\lambda)_{orb} = 0.17 \quad \text{equation 9}$$

for anorbital ripples

$$\lambda_{ano} = 535 D \quad \text{equation 10}$$

$$\frac{\eta}{\lambda} = \exp \left[-0.095 \left(\ln \frac{d_o}{\eta} \right)^2 + 0.442 \ln \frac{d_o}{\eta} - 2.28 \right] \quad \text{for } d_o/\eta > 10 \quad \text{equation 11}$$

and for suborbital ripples

$$\lambda_{sub} = \exp \left[\left[\frac{\ln \left(\frac{d_o}{\eta_{ano}} \right) - \ln 100}{\ln 20 - \ln 100} \right] \left(\ln \lambda_{orb} - \ln \lambda_{ano} \right) + \ln \lambda_{ano} \right] \quad \text{equation 12}$$

where “ d_o ” is the near bottom orbital diameter, and “ D ” is the mean sediment size.

In figure (9), measured non-dimensional ripple dimensions are plotted versus the parameters used in the Wiberg and Harris (1994) ripple model. Where possible, the model curves were included. It is noted that in figure (9d) the x-axis is near bottom orbital diameter divided by measured ripple height. For these plots, the dashed and solid curves refer to the orbital and anorbital ripple models respectively. The data in figure (9) is also plotted according to the Wiberg and Harris (1994) ripple classification scheme. Each data point is plotted as an “o”, “+”, or “*” indicating ripple types of orbital, suborbital, or anorbital ripples, respectively. The Wiberg and Harris (1994) model also over-predicted ripple length and height for most of the runs. It is also interesting to note that only 2 of the 30 runs were classified as anorbital ripples.

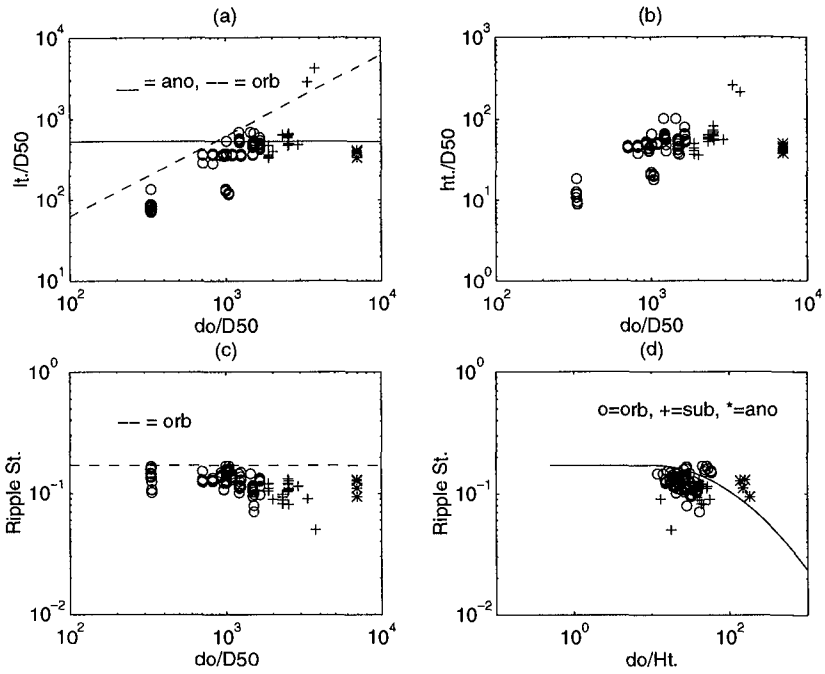


Figure 9. Wiberg and Harris (1994) ripple models with measured values.

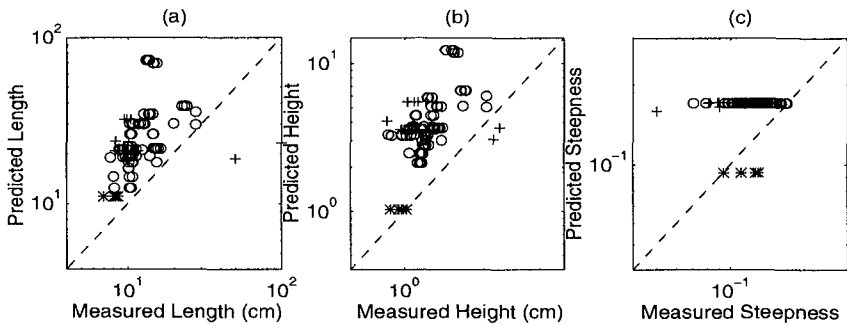


Figure 10. Wiberg and Harris (1994) model ripple comparison with measurements

The Grant and Madsen (1982) ripple model uses the ratio of the maximum value of the skin friction (shear stress) under the wave (τ_{*sf}) to the critical value of shear stress for the initiation of sediment motion (τ_{*cr}). Also a dimensionless sediment parameter (S_*) is used. This ripple model was based primarily on the Carstens et al. (1969) laboratory oscillatory ripple study.

Two separate regions of transport stages were used in the Grant and Madsen (1982) model. The first stage, when the flow conditions are less than the breakoff point defined by equation (18), is known as the equilibrium stage. Within the equilibrium range, ripple steepness is a maximum and the ripple length is said to scale with the near-bottom excursion amplitude. When flow conditions exceed the breakoff point, conditions are said to be in the breakoff region; the ripple length is said to no longer be in equilibrium and a decorrelation between ripple length and near-bottom excursion amplitude occurs (Grant and Madsen (1982)). As the flow intensity increases within the breakoff region, ripple steepness continues to decrease to a point where ripples are no longer present.

The Grant and Madsen (1982) ripple prediction model is as follows:
when the transport stage is less than the breakoff point

$$\eta/\lambda = 0.16 \left(\tau_{*sf} / (\tau_*)_{cr} \right)^{-0.04} \quad \text{equation 13}$$

$$\eta / a_o = 0.22 \left(\tau_{*sf} / (\tau_*)_{cr} \right)^{-0.16} \quad \text{equation 14}$$

and at higher transport stages, above the breakoff range

$$\eta/\lambda = 0.28 S_*^{0.6} \left(\tau_{*sf} / (\tau_*)_{cr} \right)^{-1.0} \quad \text{equation 15}$$

$$\eta / a_o = 0.48 S_*^{0.8} \left(\tau_{*sf} / (\tau_*)_{cr} \right)^{-1.5} \quad \text{equation 16}$$

where

$$S_* = (d / 4\nu) [(S - 1)gD]^{0.5} \quad \text{equation 17}$$

and the breakoff point is defined as

$$\left[\tau_{*sf} / (\tau_*)_{cr} \right]_B = 1.8 S_*^{0.6} \quad \text{equation 18.}$$

where 'v' is the kinematic viscosity of water, 'D' is the grain diameter, 'S' is the specific gravity of the sediment, and 'g' is the acceleration of gravity.

A comparison of Grant and Madsen (1982) predicted ripple heights and lengths versus measured values is shown in figure 11. It can be seen that the Grant and Madsen (1982) model over-predicted ripple length and height for almost every run.

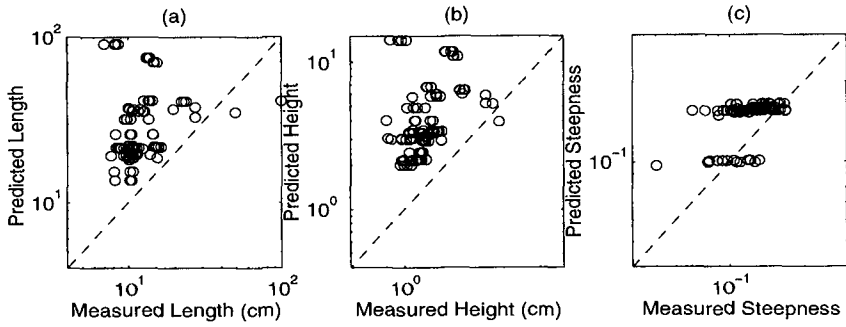


Figure 11. Grant and Madsen (1982) model ripple comparison with measurements

In order to evaluate the performance of the predictive models, the relative error was computed between measured and predicted values. The relative error is defined as:

$$\Delta = \exp \left\{ \left[\frac{1}{n} \sum_1^n (\ln(y) - \ln(\hat{y}))^2 \right]^{1/2} \right\} \quad \text{equation 19}$$

where y is the measured value and \hat{y} is the predicted value. This quantity is a multiplicative factor that indicates the possible variation about the predicted value (Wikramanayake, 1993). For example if Δ equals 1.34, the average error is equal to 34 percent.

Table 3 contains values of the relative error for each of the different predictive models. It can be seen that the predictive models performed much better at predicting ripple steepness than ripple height or length independently. The Nielsen (1981) and Grant and Madsen (1982) ripple steepness models performed the best at predicting ripple steepness with an average error of 37 percent, the Wiberg and Harris (1994) model had an average error of 55 percent. The Nielsen (1981) model predicted ripple height the best, however the average error was found to be 153 percent. The Wiberg and Harris (1994) and Grant and Madsen (1982) models had even greater error. Ripple length comparisons showed the Wiberg and Harris (1994) model having the least error with an average error of 125 percent. The Nielsen (1981) and Grant and Madsen (1982) ripple length models had slightly higher relative errors with 150 and 154 percent respectively.

TABLE 3. Relative Error for model predictions and measured values.

	Ripple Length	Ripple Height	Ripple Steepness
Nielsen (1981) Field	2.50	2.53	1.37
Wiberg & Harris (1994)	2.25	2.84	1.55
Grant and Madsen (1982)	2.54	3.03	1.37

Conclusions

The multiple transducer array (MTA) has proven the ability to measure bedforms in the field environment with $O(1 \text{ mm})$ vertical and $O(2 \text{ cm})$ horizontal resolution. Comparisons of oscillatory field ripple data collected with the MTA and the most popular predictive models show errors of over 100 percent for all models in predicting ripple heights and lengths. Average errors of 37 to 55 percent were found in predicting ripple steepness. Such errors could be due to errors in the previously collected data sets used to construct these models, or to the current understanding of the mechanics of ripple formation and geometric equilibrium with the flow field. More investigation is necessary in this field in order to improve bedform prediction models.

Acknowledgments

The authors wish to acknowledge the financial support of the U.S. Office of Naval Research, Coastal Sciences Program, the field assistance provided by the Field Research Facility, U.S. Army Corps of Engineers, and the help of Chuck Broward, Eric Thosteson, Mike Krecic, and Carl Miller.

References

- Bagnold, R. A., Motion of waves in shallow water: Interaction between waves and sand bottoms, Proc. R. Soc. London Ser. A, 187, 1-15, 1946.
- Carstens, M. R., R. M. Neilson, and H. D. Altinbilek, Bed forms generated in the laboratory under oscillatory flow: Analytical and experimental study, Tech. Memo. 28, U.S. Army Corps of Eng., Coastal Eng. Res. Center, June 1969.
- Dingler, J. R., and Inman D. L., Wave-formed ripples in near-shore sands, Proc. Fifteenth Conf. Coastal Engng., Amer. Soc. Civil Eng., 1976.
- Grant, W. D., and O. S. Madsen, Movable bed roughness in unsteady oscillatory flow, J. Geophys. Res., 87, 469-481, 1982.
- Nielsen, P., Dynamics and geometry of wave-generated ripples, J. Geophys. Res., 86, 6467-6472, 1981.
- Nielsen, P., Field measurements of the time-averaged suspended sediment concentration under waves. Coastal Engn., 8, 51-72, 1984.
- Sleath, J. F. A., Sea bed mechanics, Wiley Interscience, New York, 1984.
- Swart, D. H., Offshore sediment transport and equilibrium beach profiles. Delft Hydr. Lab. Publ. No. 131, 1974.
- Vincent, C. E., and P. D. Osbourne, Bedform dimensions and migration rates under shoaling and breaking waves, Unpublished manuscript (1992).
- Wiberg, P.L., and C. K. Harris, Ripple geometry in wave dominated environments, J. Geophys. Res., 99, 775-789, 1994.
- Wikramanayake, P. N., Velocity profiles and suspended sediment transport in wave-current flows. Ph.D. Thesis. Dept. of Civil Eng., MIT, Cambridge, Mass., 1993.

CHAPTER 243

Field Measurement of Bed Roughness for Waves on an Off-Shore Reef

Raymond C. Nelson¹

Abstract

This paper takes advantage of fortuitous, near ideal conditions which existed for a subset of field data, to obtain the hydraulic roughness of the surface of a coral reef platform. This was accomplished by observing the transformation of natural, unbroken, oscillatory wave trains, propagating over the reef top in water of constant depth, where wave bed friction damping was the only active wave transformation process. The paper also demonstrates that while coral reefs may be perceived as being much rougher than sandy beds, they may in fact be no rougher in hydraulic terms, than many sandy beds experiencing the same wave and water depth conditions.

Introduction

The bed friction factor (f) associated with wave motion, is a function of a Reynolds number and a relative roughness.

$$f = \phi_1 \left(R_e, \frac{r}{a} \right) \quad (1)$$

R_e is the Reynolds number associated with the oscillatory water movements at the bed as estimated from linear wave theory.

$$R_e = \frac{aU}{\nu} \quad (2)$$

a is the amplitude of the oscillatory bed movements, U is the amplitude of the periodic bed velocity, and ν is the kinematic viscosity of the fluid. r/a is the relative roughness where r is the hydraulic roughness. For all turbulent flow conditions, the friction factor can be expressed in the form of Eq. 1. However,

¹ Senior Lecturer, School of Civil Engineering, University of New South Wales, University College, Australian Defence Force Academy, Canberra, ACT, 2600, Australia

for all prototype wave conditions of engineering significance, the oscillatory flow at the bed is always fully developed rough turbulent flow (Jonsson, 1963 and 1966; Swart, 1974). In this regime the friction factor is independent of Reynolds number, reducing Eq. 1 to Eq. 3 for field conditions.

$$f = \phi_2 \left(\frac{r}{a} \right) \quad (3)$$

On a movable bed, both r and a are variables, depending on the wave and water depth conditions, the changes in r being caused by the variability of bed form (Nelson, 1989 and 1995).

On fixed beds, such as coral reef platforms, a still varies with wave and water depth conditions, but r remains constant. A measured value of this fixed roughness is far more useful than a measured value of friction factor. The latter is only applicable to wave and water depth conditions that produce the same value of a existing when the measurement was made, while the hydraulic roughness value can be used to obtain wave friction factors for all wave and water depth conditions.

This paper presents values of reef top hydraulic roughness derived from the observed transformation of natural random waves, propagating in water of constant depth, over the fixed bed of a platform coral reef. The resulting values are to some extent site specific. However, from an engineering viewpoint, the use of a measured roughness that can be varied by visual comparisons and reasoning, is far more desirable than the use of a *guesstimate*.

Experiment Description

The experimental data were collected from John Brewer Reef, located inside the line of the Barrier Reef approximately 70 km north east of Townsville, Australia. The reef is elliptical in shape (6 km by 3 km - see Fig. 1) with a major axis approximately normal to the prevailing south easterly winds. The windward reef platform is a continuous reef flat 200m to 300m wide and uniform in elevation at a level approximating Lowest Astronomical Tide. High tide water depths over the reef platform seldom exceed 3m. Seaward of the windward edge, the reef drops rapidly to a depth of about 50m below the reef platform, while the lagoon enclosed by the whole of John Brewer Reef averages about 10m in depth.

Wave and current measuring instruments were deployed on the windward side of the reef (Fig. 1). WR1 was a Waverider buoy located about 500m seaward of the reef front and transmitted incident wave data to a receiver located in the floating hotel. ZP1, ZP2, ZP3 and ZP4 were 6m high, surface piercing wave transducers known as Zwarts Poles (Zwarts, 1974). These were aligned normal to the reef front and parallel to the prevailing south east winds. ZP1 and ZP4 are of special interest to this study. ZP1 was 27m from the reef front while ZP4 was located at a further interval of 141m. Most of the time the line of Zwarts Poles was located along the line of the reef top wave orthogonal but there were some exceptions at high tide during incident wave events with very low energy.

Each wave sample collected from WR1 contained 2048 readings at intervals of 0.391 seconds (sample length about 14 minutes). Each wave sample from each Zwarts pole contained 4800 readings at an interval of 0.25 seconds (sample length about 20 minutes). Data sets consisted of wave samples collected concurrently

from all 5 wave instruments with the recording commencement times for each instrument being identical. The interval at which data sets were recorded was sometimes 1 hour and at other times 2 hours.

CM1 was an S4 electromagnetic XY current meter that measured reef top currents. Every 10 minutes it took 120 readings at 0.5 second intervals of both the easterly and northerly velocity components and logged the average.

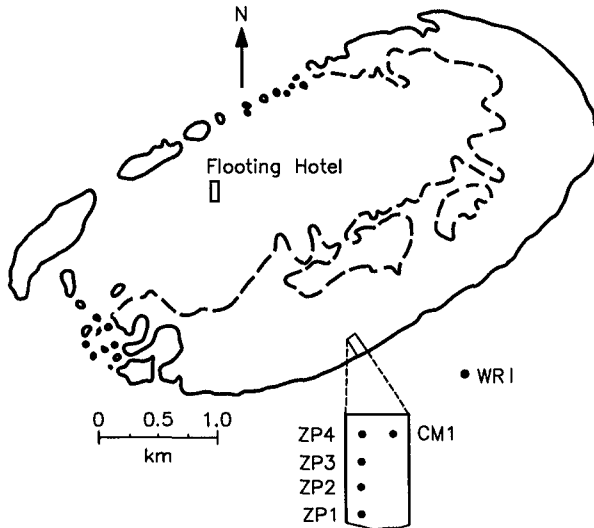


Fig. 1 John Brewer Reef and Instrument Locations

Data Selection

The extraction of bed friction effects from other interacting sub-processes, increases the uncertainties incorporated in the results, the preferred option being to have a prototype location and wave motion where bed friction damping is the only active sub-process. Some of the John Brewer Reef Zwart's Pole data conformed with this requirement. The water depths were, for all practical purposes, uniform eliminating the effects of shoaling and refraction. There were no barriers around which diffraction could occur, and careful selection of data sets ensured that the effects of wave breaking were all but eliminated.

The data base used in this study contained 72 consecutive data sets, some times recorded at one hourly intervals, and at other times, two hourly intervals. They spanned a sustained period of high incident wave energy and some periods of low incident wave energy, both coupled with large tide ranges. This provided a wide range of reef top wave and water depth combinations. These data are presented as a time series in Fig. 2.

Incident high wave energy events were dominated by sea states with peak energy periods of between 4 and 6 seconds with direction determined by the

dominant south east wind. During low energy events, when the sea state was minimal, longer peak energy periods were observed when small amounts of wave energy from distant sources became significant relative to the local sea state. The direction of this longer period wave energy was unknown and it was necessary to eliminate it from the data records. All characteristic spectral wave parameters have been restricted to the wind wave component by only considering wave frequencies greater than or equal to 0.16 Hz.

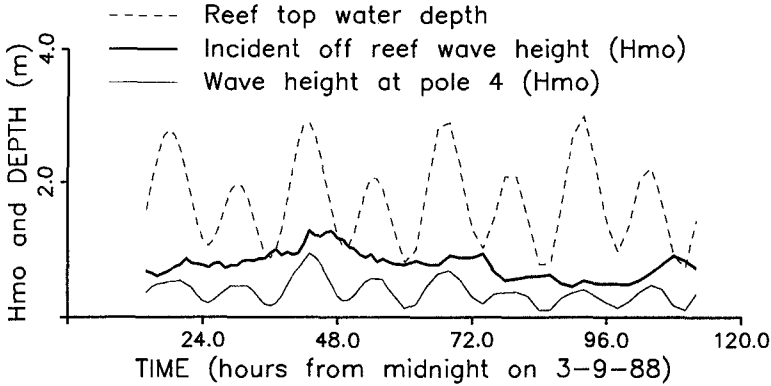


Fig. 2 Wave and Tide Summary

The selected subset of wave records were to be free of wave breaking influences, with the wave energy dissipation over the flat bed between ZP1 and ZP4 (Fig. 1) due only to bed friction damping. However, for most data sets at John Brewer Reef, waves broke at the reef edge due to depth limiting effects and dissipated energy, primarily through the turbulence associated with the breaking process, until stable wave heights compatible with reef top water depths were attained. The waves then reformed into stable oscillatory waves. It was established that even the largest waves in any of the recorded incident wave trains, reformed into oscillatory waves before reaching ZP4 (Nelson, 1994). However, this was not the case at ZP1 making it necessary to delineate which data sets were largely free of breaking waves at this station. These will obviously be those biased towards lower incident wave energy and larger reef top water depths.

This screening was made using the criterion of Nelson (1994) for the maximum stable oscillatory wave heights sustainable over horizontal beds, namely Eq. 4, and the fact that this criterion was shown to be applicable to the individual waves of a naturally occurring random wave train.

$$\frac{H}{h} = \frac{F_c}{22 + 1.82F_c} \quad (4)$$

F_c is a non-linearity parameter after Swart and Loubser (1979), as defined in Eq. 5. F_c values less than 10 indicate deep water waves, those between 10 and 500 indicate transitional water depth waves, and values greater than 500, shallow

water waves when H/h approaches a value of 0.55.

$$F_c = \frac{g^{1.25} H^{0.50} T^{2.50}}{h^{1.75}} \quad (5)$$

Waves with larger H/h ratios can exist on horizontal beds but these would be turbulent breaking waves losing height rapidly by the turbulent dissipation of energy.

A wave by wave analysis of all 72 wave records at ZP1 determined the H/h population for each record and the value of F_c associated with each H/h value. This took into account the effect of tide and infragravity wave activity in varying the effective water depth on which the wind waves were superimposed, since the maximum wave height that could be sustained varied with time because local water depth was time dependent. The F_c value assigned was based on the wave height and water depth associated with each wave and the wave period equal to the lapsed time between the crest of this wave and the crest of the previous wave (see Nelson, 1994 for greater detail).

The results for all 72 wave records were compared with the criterion of Eq. 4. Wave records with little or no wave breaking were those for which none (or at least very few) of the observed values of H/h exceeded the value given by Eq. 4 when using the observed value of F_c . Based on this criterion 20 wave records were available for further consideration.

A further 6 of these 20 records were rejected because the reef top wave orthogonal was not sufficiently aligned to the line of wave poles. There remained 14 acceptable data sets.

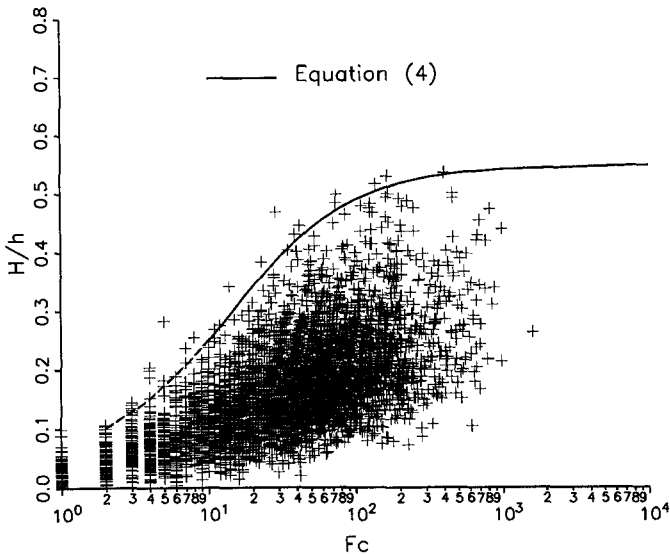


Fig. 3 ZP1: H/h versus F_c for all Waves in all 14 Data Sets

Fig. 3 shows the results for all waves in all 14 data sets plotted on the H/h versus F_c plain. The solid line is Eq. 4 and the dotted line is the deep water wave steepness limit at F_c values less than 10. The average number of waves per wave record is 357, and on average, only 1 or 2 waves per record significantly exceeded the envelope curve. While it is possible some waves did break at H/h values less than the envelope curve (Nelson 1987), it is reasonable to assume that this impact was slight, and that for the 14 selected data sets, all wave energy dissipation between ZP1 and ZP4 was due to bed friction damping only.

Table 1 summarises the characteristic parameters associated with the adopted 14 data sets. The data set number is the location of the data set within the consecutive order of the original 72 data sets. The day and time indicate the common instrument commencement time for the recording of each data set. H_1 and H_4 are respectively the spectral estimates of significant wave height (H_{mo}) of the wind wave component at ZP1 and ZP4 and H is the mean of these two values. T_p is the mean of the four peak energy periods at ZP1, ZP2, ZP3, and ZP4 for the wind wave component. h is the mean, reef top water depth during the data set.

Table 1
Observed Reef Top Parameters - September 1988

Data set	Day	Time (hrs)	* H_1 (m)	* H_4 (m)	H (m)	* T_p (s)	h (m)
02	4	1500	0.544	0.418	0.481	4.280	1.865
03	4	1600	0.536	0.446	0.491	3.443	2.273
04	4	1700	0.521	0.461	0.491	4.455	2.555
07	4	2000	0.570	0.496	0.533	4.265	2.343
17	5	0600	0.559	0.429	0.494	4.025	1.843
49	6	1800	0.625	0.582	0.604	3.975	2.693
50	6	2000	0.641	0.599	0.620	4.265	2.758
55	7	0600	0.379	0.319	0.349	4.932	1.948
56	7	0800	0.361	0.315	0.338	5.200	1.935
60	7	1600	0.337	0.257	0.297	3.880	1.505
65	8	0200	0.253	0.125	0.189	4.020	0.828
66	8	0400	0.323	0.210	0.266	4.265	1.208
67	8	0600	0.407	0.349	0.378	3.595	1.905
68	8	0800	0.539	0.456	0.498	3.710	2.078

* Based on all frequencies ≥ 0.16 Hz

Reef Top Wave Energy Dissipation Factors

Two wave related friction factors are in common use. The wave friction factor (f_w) is defined by Eq. 6.

$$\tau_{max} = 0.5\rho f_w U^2 \quad (6)$$

τ_{max} is the maximum bed shear stress due the horizontal oscillatory water particle velocities at the bed and ρ is the water density. The determination of f_w requires the direct or indirect measurement of bed shear. The wave energy dissipation

factor (f_e) is defined in terms of the time averaged rate of wave energy dissipation due to bed friction as given in Eq. 7.

$$\frac{dE_f}{dx} = (\tau u)_{mean} = \frac{2}{3\pi} \rho f_e U^3 \quad (7)$$

E_f is the wave energy flux, τ is the instantaneous bed shear stress, u is the instantaneous bed velocity, and U is the amplitude of the of the bed velocity variations. The determination of f_e requires the measurement of wave energy loss over a known distance.

The second of the above procedures was adopted at John Brewer Reef, but in so doing it is important to note the following. The two wave related friction factors are different according to how they are defined and measured. However, it has been shown that for fully developed rough turbulent oscillatory flows, $f_w \approx f_e$ (Jonsson, 1963; Swart, 1974; Nielsen, 1992; Raudkivi, 1988). The oscillatory flow at the bed is fully developed rough turbulent flow for all prototype wave conditions of engineering significance. Therefore, for all practical purposes, the field estimates of f_e can be interchanged with f_w . This will be important when estimates of the reef top hydraulic roughness are made.

f_e can be evaluated two ways. The first considers the attenuation of the total energy using only characteristic spectral parameters. The second considers the attenuation of individual frequency components in the spectrum, based on the assumption that these components travel independently of all other spectral components and that there are no non-linear interactions. Experimental limitations dictated the use of the first method. Despite the difficult and hostile environment, the field measurements of small total energy deficits between poles 1 and 4 displayed good consistency and trends. To deal with still smaller energy deficits within individual frequency components introduces anomalies due to the lesser confidence associated with these components relative to that of the total wave energy measurement.

In water of constant depth, the loss rate of wave energy per unit surface area (left hand side of Eq. 7) can be expressed as,

$$\frac{dE_f}{dx} = \frac{\rho g C_g}{8} \frac{dH^2}{dx} \quad (8)$$

where C_g is the group velocity and g is the acceleration due to gravity. The right hand sides of Eqs. 7 and 8 can be equated, integrated, and re-arranged to yield the solution for f_e shown in Eq. 9, and can be applied directly to the John Brewer Reef data shown in Table 1. Δx is the distance between ZP1 and ZP4 namely 141m.

$$f_e = \frac{3g}{8\pi^2} \frac{(H_1 - H_4)}{H_1 H_4} \frac{C_g}{\Delta x} (T_p \sinh(kh))^3 \quad (9)$$

The resulting values of f_e are shown in Table 2. Also shown are the associated values of a , U , and R_e obtained using the values of H , h , and T_p given in Table 1.

A plot of f_e versus R_e is shown in Fig. 4. At first glance the scatter appears considerable with f_e values of between 0.1 and 0.2 over a Reynolds number range

Table 2
Derived Reef Top Parameters - September 1988

Data set	Day	Time (hrs)	a (m)	U (m/s)	R_e (-)	f_e (-)
02	4	1500	0.323	0.474	153000	0.164
03	4	1600	0.206	0.376	77000	0.218
04	4	1700	0.281	0.396	111000	0.150
07	4	2000	0.304	0.449	137000	0.132
17	5	0600	0.308	0.480	148000	0.162
49	6	1800	0.279	0.441	123000	0.090
50	6	2000	0.314	0.463	145000	0.082
55	7	0600	0.273	0.348	95000	0.152
56	7	0800	0.283	0.342	97000	0.120
60	7	1600	0.202	0.327	66000	0.177
65	8	0200	0.194	0.303	59000	0.207
66	8	0400	0.234	0.344	80000	0.190
67	8	0600	0.196	0.342	67000	0.144
68	8	0800	0.253	0.428	108000	0.143

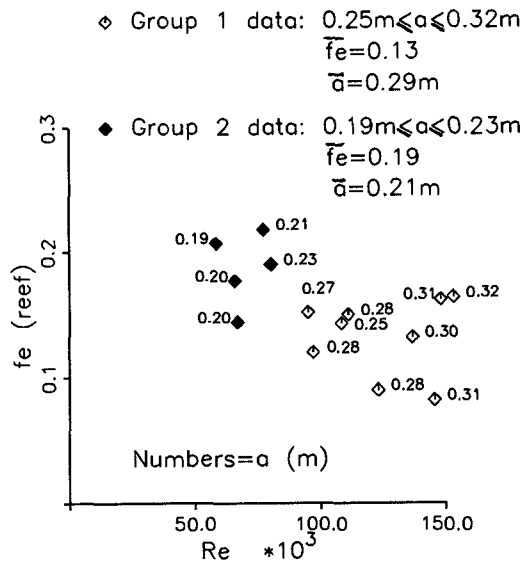


Fig. 4 f_e versus R_e - Reef Data

of between 50000 to 150000. To some extent, the perceived scatter is more apparent than real, accentuated by the linear scales. More common practice is to use log log axes for such plots (e.g. see Fig. 5), masking the extent of the scatter. While much of the scatter must remain unexplained, some can be attributed to

the different characteristic values of relative roughness associated with each data set, and the dependence of f_e on that value (see Eq. 3). The values shown beside each point are the a values given in Table 2. These alone are an indicator of relative roughness ($= r/a$) because the reef top roughness remains unchanged for all data sets. Based on this indirect measure of relative roughness the results can be divided into two groups. Group 1 data has a values between 0.25m and 0.32m (mean=0.29m) and a mean f_e value of 0.13. Group 2 data has a values between 0.19m and 0.23m (mean=0.21m) and a mean f_e value of 0.19.

Analyses demonstrated that the small prevailing pole line current that existed on the reef (average value of 0.06 m/s for the 14 data sets) would have had little influence on the computed values of f_e shown in Table 1.

Reef Top Hydraulic Roughness

Kamphuis (1975) used an oscillating water tunnel to measure the maximum shear stresses on a smooth bed and 5 different artificially roughened beds. The shear stress values, measured using a shear plate incorporated in the bed, enabled the computation of wave friction factor, f_w (Eq. 6). Kamphuis summarised the results in a friction factor diagram reproduced here in Fig. 5. The results are consistent with the friction factor being independent of Reynolds number for fully rough turbulent flow. In this region, f_w and f_e (the wave energy dissipation factor) are for all practical purposes, interchangeable as indicated on the vertical axis of Fig. 5. The John Brewer Reef data in Fig. 4 fall well within the fully rough turbulent region of Fig. 5 ($0.1 < f_e < 0.2$ and $50000 < R_e < 150000$) and can be used to estimate values of reef top hydraulic roughness in conjunction with Fig. 5.

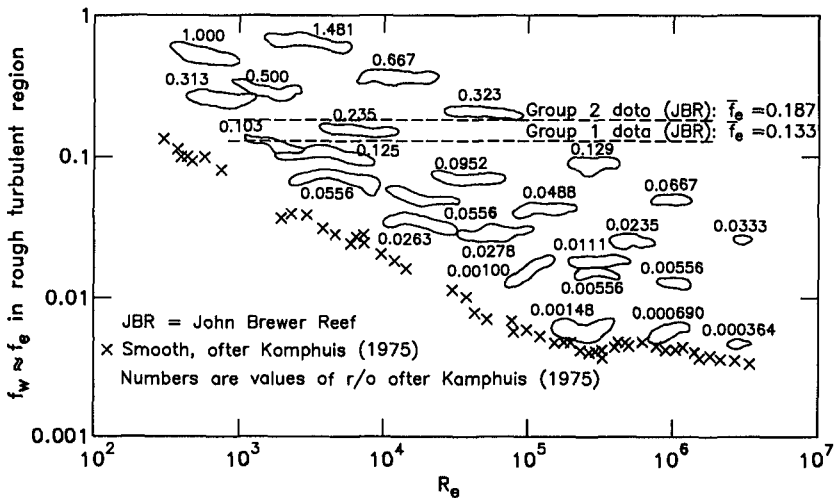


Fig. 5 f_e versus R_e (after Kamphuis, 1975)

The group 1 data has a mean f_e value of 0.130, corresponding to a relative roughness (r/a) value in Fig. 5 of about 0.2. Based on the mean a value of 0.29m

for the group 1 data, the hydraulic roughness (r) of the reef top is estimated as $0.2 \times 0.29 = 0.06\text{m}$. Similarly for group 2 data, the mean values of $f_e = 0.183$ and $a = 0.21\text{m}$ lead to values of $r/a \approx 0.3$ and $r = 0.3 \times 0.21 = 0.06\text{m}$. Hence, one estimate of the reef top roughness is 0.06m .

A second independent estimate of hydraulic roughness can be made using the work of Jonsson (1963) who developed the following implicit equation for fully rough turbulent oscillatory flow over a fixed immobile bed.

$$\frac{1}{4f_w} + \log\left(\frac{1}{4\sqrt{f_w}}\right) = -0.08 + \log\left(\frac{a}{r}\right) \tag{10}$$

Swart (1974) presented Eq. 11 as an explicit alternative to Eq. 10. The author has replaced f_w in Swart's equation with f_e as has been previously justified in this paper for fully rough turbulent flow.

$$f_e = \exp\left(5.213\left(\frac{r}{a}\right)^{0.194} - 5.977\right) \tag{11}$$

Fig. 6 shows the John Brewer Reef data over-plotted with curves corresponding to fixed values of r computed from Eq. 11. These show that the best estimate of reef top hydraulic roughness is 0.07 m , and this closely approximates the previous estimate of 0.06m .

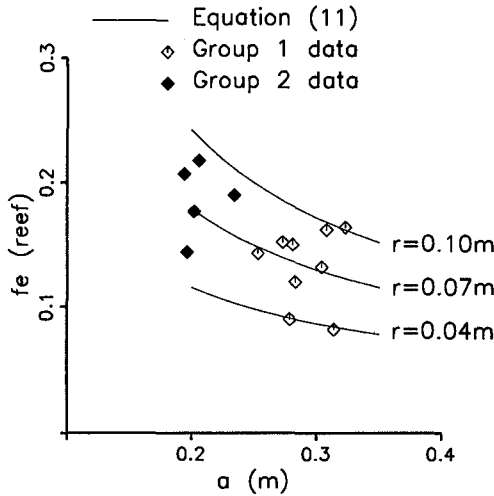


Fig. 6 f_e versus a - Reef Data

Movable Sand Bed Equivalents

An interesting comparison has been made between the influence of this fixed reef surface on wave damping and that of a movable bed of sand using the dimensionless function of Nelson (1995). This expresses the wave energy dissipation

factor (f_c) and the physical state of a movable bed as a function of two dimensionless parameters namely $T_c = T\sqrt{g/D}$ and $D_c = D/a$. A range of bed particle sizes were used in the function for each reef top wave and water depth condition listed in Table 1. It was found that movable bed f_e values, comparable with the observed fixed bed reef top values, occurred most consistently when the bed particle size was equal to 0.6 mm. The comparative results are shown in Fig. 7.

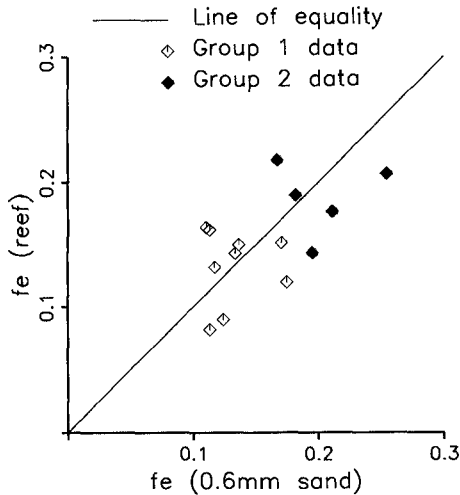


Fig. 7 Movable Bed versus Reef Top Friction Factors

The scatter in the plot results from the fact that a movable bed of given particle size no longer has a constant roughness because the bed form varies with the prevailing wave and water depth conditions. Nevertheless, the comparison demonstrates that while coral reefs may be perceived as being much *rougher* than sandy beds, they may in fact be no rougher, in hydraulic terms, than many sandy beds.

Comments and Conclusions

Field observations have enabled the hydraulic roughness for the fixed bed of a coral reef platform to be determined. In so doing, advantage has been taken of fortuitous and near ideal conditions, where natural trains of random, stable and unbroken oscillatory waves were propagating in water of constant depth, such that wave bed friction damping was the only active wave transformation process present. The roughness estimate of 60mm to 70mm was based on small total energy deficits measured over a known length of wave orthogonal.

The measured fixed bed roughness value is of more use to wave transformation modelers than any of the measured values of wave friction factor. The latter change with wave and water depth conditions while the former remains unchanged, so that the applicable relative roughness and wave friction factor can be determined no matter what wave and water depth conditions prevail.

The measured hydraulic roughness value is transferable to other similar reefs. If differences between reefs are perceived, the measured roughness is a datum value that can be varied based on visual comparisons and reasoning.

The paper has demonstrated that, while coral reefs may be perceived as being much rougher than sandy beds, they may in fact be no rougher in hydraulic terms than many sandy beds experiencing the same wave and water depth conditions.

Acknowledgements

The author wishes to acknowledge the efforts of Dr T. Hardy (James Cook University, Queensland) during the field data collection program.

Appendix 1. References

- Jonsson, I.G., 1963. Measurements in the turbulent wave boundary layer. In: Proc. 10th IAHR Congress, London, Vol. 1, pp. 85-92.
- Jonsson, I.G., 1966. Wave boundary layers and friction factors. In: Proc. 10th Coastal Eng. Conf., Tokyo. ASCE, New York, Vol. 1, pp. 127-148.
- Kamphuis, J.W., 1975. Friction factors under oscillatory waves. J. Waterways Harbors and Coastal Eng., ASCE, Vol. 101, pp. 135-144.
- Nelson, R.C., 1987. Design wave heights on very mild slopes. Civil Eng. Trans., Inst. Eng. Australia, Vol. CE29, pp. 157-161.
- Nelson, R.C., 1989. A simplified function for wave energy dissipation factor over mobile beds. Coastal Engineering, Vol. 13, pp. 149-159.
- Nelson, R.C., 1994. Depth limited design wave heights in very flat regions. Coastal Engineering, Vol. 23, pp. 43-59.
- Nelson, R.C., 1995. Wave bed friction damping over shoaling movable beds. Coastal Engineering, Vol. 25, pp. 65-80.
- Nielsen, P., 1992. Coastal bottom boundary layers and sediment transport. World Scientific, Singapore.
- Raudkivi, A.J., 1988. The roughness height under waves. J. Hydraulic Research, IAHR, Vol. 26, pp. 569-584.
- Swart, D.H., 1974. Offshore sediment transport and equilibrium beach profiles. Delft Hydr. Lab., Publication No. 131.
- Swart, D.H. and Loubser, C.C., 1979. Vocoidal wave theory. Vol. 2: verification. CSIR (South Africa), NRIO, Research Report No. 360.
- Zwarts, C.M.G., 1974. Transmission line wave height transducer. In: Proc. Symp. on Ocean Wave Measurement and Analysis, New Orleans. ASCE, New York, Vol. 1, pp. 605-620.

CHAPTER 244

Effect of Wave-Induced-Pressure on Seabed Configuration

Tetsuo Sakai¹, M. ASCE and Hitoshi Gotoh²

Abstract

In almost all of the previous studies on the seabed configuration, the seabed configuration is classified based on the bottom shear stress, or Shields number. While, in the wave field, the wave-induced-water-pressure change can have a secondary effect on the sediment transport. The laboratory experiment on the seabed configuration under the coexistence of the oscillatory flow and the water-pressure change is conducted in this study, to investigate the effect of water-pressure change on the seabed regime classification.

The existing region of various bed configurations, such as no-motion, bed-lad, suspension over ripple and sheet flow, changes with the change of the amplitude of water-pressure change. The ripple geometry, or flatness of ripple, are also affected by the water-pressure change. The mechanism of these changes are discussed related to the lift force due to the porewater-pressure distribution in sand layer.

Introduction

Seabed configuration, which is formed as the result of sediment transport, is quite different under the various conditions of wave and current. On the other hand, the mode of sediment transport depends on the seabed configuration.

Although there is an interactive structure among the wave-current field, the sediment transport and the seabed configuration, the time scale of the development of seabed configuration is sufficiently longer than that of others. Therefore, to describe

¹ Professor, Department of Civil Engineering., Kyoto University
Yoshida Honmachi, Sakyo-ku, Kyoto, 606, Japan

² Lecturer, Department of Civil Engineering., Kyoto University

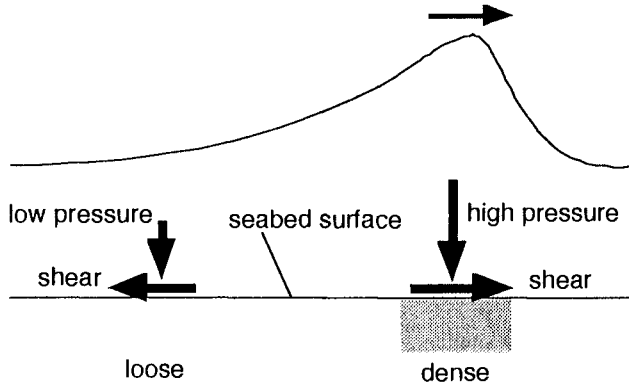


Figure 1. Forces acting on seabed under the wave propagation

the sediment transport process based on the mechanics of the motion of sediment particles, it is essential to know the relation between the seabed configuration and the bottom shear stress, or Shields number, due to wave and current.

These relation has been investigated through some experimental studies; while the effect of wave-induced-water-pressure change on the seabed configuration was not examined in detail. Fig. 1 shows the schematic expression of external forces acting on seabed due to the wave propagation. High water pressure acts on the seabed under the crest of a wave, then the particle density of the bed becomes to be dense. On the other hand, low water pressure acts on the seabed under the trough of a wave, then the particle density of the bed becomes to be loose. In both situations, the bottom shear stress is the dominant driving force of sediment motion. To discuss the additional effect due to the water-pressure change by wave propagation in detail, porewater pressure distribution should be investigated.

In this study, the experiment on the seabed configuration under the coexistence of the oscillatory flow and the water-pressure change is performed by using an oscillating water tunnel with cylinder system for the control of the water pressure.

Laboratory experiment

experimental apparatus

Figure 2 shows the oscillating water tunnel with the water-pressure-control system. Both sides of the rectangular water tank are connected to the water circulating pipe, at the top of which a water-circulating-propeller system, or an oscillatory-flow generator,

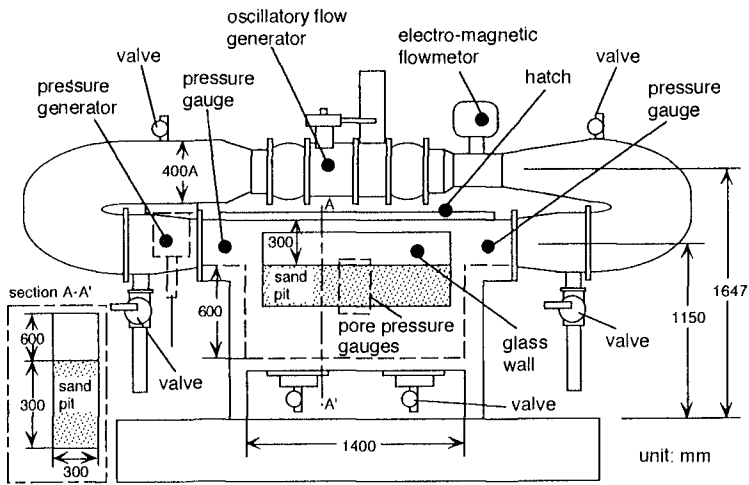


Figure 2. Oscillating water tunnel with water-pressure-changing system

is installed. Lower part of the water tank is a sand pit, the depth of which is 600 mm. The front and back sides of the water tank is made by glass wall for the observation of the motion of sediment particles. In the back side wall, porewater-pressure sensors are flash mounted. In order to generate the water-pressure change, a oil-hydraulic-pressure-driven piston system is connected to the water-circulating pipe. The electromagnetic current meter and the water-pressure sensors are equipped to monitor the discharge of current and the changing water pressure, which are used as the feedback signal of the personal-computer based current-water-pressure control system. Although various kinds of the time series of current-velocity and water-pressure can be generated by using this apparatus, the in-phase sinusoidal time series of current-velocity and water-pressure, which correspond to the condition of a progressive small amplitude wave, are generated.

procedure of experiment and experimental conditions

The transition of bed configuration occurs with the increase of the bottom shear stress in the following order: (i) no motion; [critical state for sediment movement]; (ii) bed-load motion; (iii) suspended load over ripples; and sediment transport in sheetflow regime. In the experiment, the flow-velocity amplitude is gradually increased with keeping the amplitude of water-pressure change, to observe the transition of bottom

Table 1. Experimental conditions

	oscillatory flow	oscillatory flow and pressure
velocity amplitude u_b (cm/s)	3.0 - 78.0	3.0 - 78.0
total pressure amplitude p_0 (m)	0.0	0.5, 1.0, 1.5
period T (s)	6.0	6.0

configuration mentioned above. The series of the experiment were conducted with changing the magnitude of the amplitude of the water-pressure change, to investigate the effect of the water-pressure change on the transition of the bed configuration.

The ripple geometry affected by the amplitude of water-pressure change is examined based on the detailed observation of sediment motion over ripples, and the mechanism to determine the ripple geometry is considered.

Table 1 shows the experimental conditions. The test particle are the two kinds of the uniform sand, the diameter of which are $d=0.025$ cm and $d=0.035$ cm. The specific density of the sand is 2.65.

Classification of the seabed configuration

Figure 3 shows the experimental results of the bed configuration under the action of oscillatory flow for the cases of $d=0.025$ cm and $d=0.035$ cm. The lines in this figure shows the division of the bed configuration proposed by Shibayama and Horikawa (1982). In the figure, u_b =amplitude of the flow velocity in the neighbourhood of the bottom; w =terminal fall velocity of sediment particle; and Ψ =Shields number defined as $\Psi = f_w u_b^2 / 2(\sigma / \rho - 1)gd$ (f_w =friction coefficient proposed by Jonsson (1966); σ =density of sediment; ρ = density of water; and g =gravitational acceleration). The flow velocity in the neighborhood of the bottom is estimated by extrapolating the measured velocity near-bottom-wall region by supposing the logarithmic velocity profile. The friction coefficient was calculated by using the explicit expression proposed by Tanaka (1990). The thresholds of four modes, such as no motion, bed-load motion, suspension over ripples and sheetflow, estimated from the present experiment show fairly good agreement with the empirical relation proposed by Shibayama and Horikawa, which was determined based on the existing experimental results.

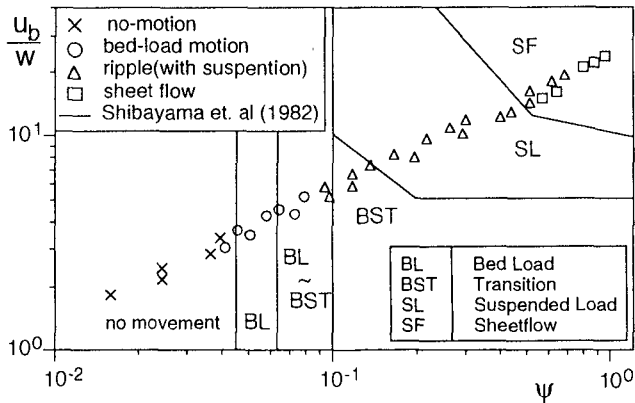


Figure 3. Classification of seabed

Figure 4 shows the classification of the bed configuration, namely, no motion, bed-load, suspension over ripple and sheetflow, under the various combination of flow-velocity amplitude, u_b , and total water-pressure-change amplitude, p . In this figure, the experimental results of the cases of the particle diameter $d=0.025$ cm are shown. The critical shear stress of the sediment movement decreases with the increase of the amplitude of water-pressure change. In other words, the no-motion region decrease with the increase of the amplitude of water-pressure change. The suppression of the ripple generation increases with the increase of the amplitude of water-pressure change, consequently, the be-load region increase with the increase of the amplitude of water-pressure change. In contrast with the ripple generation, the generation of the sheetflow is promoted by the increase of the amplitude of water-pressure change.

The changing porewater pressure is induced in the sandy bed constituted by fine sediment under the action of water-pressure change on the bed surface. Because of the phase lag between the porewater pressure and the water-pressure acting on the sand surface, an additional lift force acts on the sediment layer near the sand surface. This additional lift force depends on the porewater-pressure profile, and the positive lift force acts on the sediment layer when the changing water-pressure is smaller than the average, namely in wave-trough phase. The decrease of the critical bottom shear stress of sediment movement is caused by the action of this additional lift force.

Figure 5 shows the classification of the bed configuration under the various combination of flow-velocity amplitude, u_b , and water-pressure-change amplitude, p ,

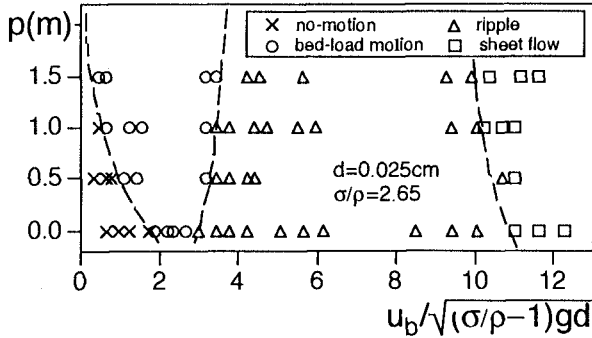


Figure 4. Classification of the bed configuration ($d=0.025$ cm)

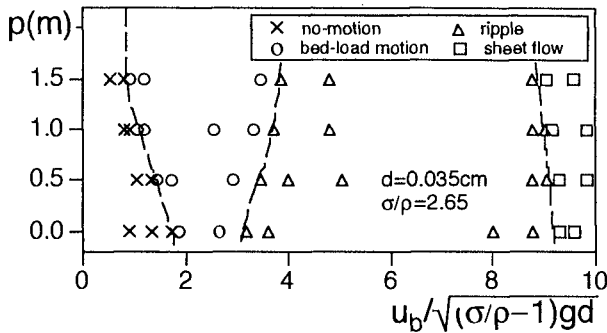


Figure 5. Classification of the bed configuration ($d=0.035$ cm)

for the particle diameter $d=0.035$ cm. Although the tendency of the transition of bed configuration shown in Fig. 5 is the same as in Fig. 4, the effect of the amplitude of the water-pressure change to the transition of the bed configuration is stronger in Fig. 4 than that in Fig. 5. To clarify this point, the bottom neighboring flow velocities, u_{cp} , at three threshold such as the transition point from no motion to bed load, from bed-load to suspension and from suspension to sheetflow for the change of the amplitude of water-pressure change are shown in Fig. 6. The bottom neighboring flow velocities, u_{cp} , are normalized by that of oscillatory flow condition, u_c . Fig. 6 shows that the transition points of the bed configuration clearly depend on the magnitude of the

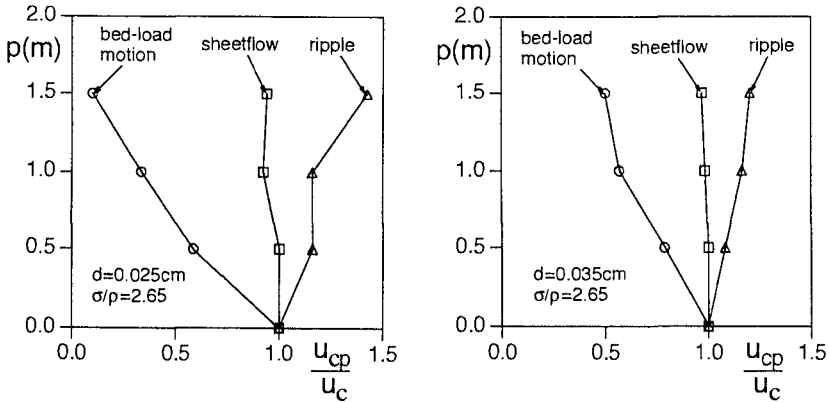


Figure 6. Transition points of the bed configuration

amplitude of water-pressure change. This tendency is most clearly detected in the transition point from no motion to bed load. By comparing the cases of $d=0.025$ cm and the cases of $d=0.035$ cm, the change of the threshold of bed configuration against the change of the amplitude of water-pressure change in small size sediment is more significant than that in large size sediment.

Under the action of critical bottom shear stress of sediment movement, hydrodynamic force, or driving force, acting on the sediment particle balances with the bottom frictional force, or resistant force. Therefore the sediment motion is keenly affected by the additional lift force due to the changing porewater pressure in sand layer. While, in the cases of the transition from suspension to sheetflow, the amplitude of the bottom shear stress are sufficiently larger than that of no-motion-bed-load transition. Hence the bottom shear stress plays a significant role in the transition from suspension to sheetflow, and the change of the threshold from suspension to sheetflow against the change of the water-pressure amplitude is smaller than that from no motion to bed load.

Geometry of ripples under coexistence of shear and water-pressure changes

The geometry of ripples in suspension mode is also affected by the change of the amplitude of water-pressure change. Maeno et al. (1989) conducted the experiment on the ripple geometry under the action of porewater pressure in sandy bed. They mainly discussed the energy dissipation due to the ripples based on the measurement of the porewater pressure change. While in this study, the role of the porewater pressure

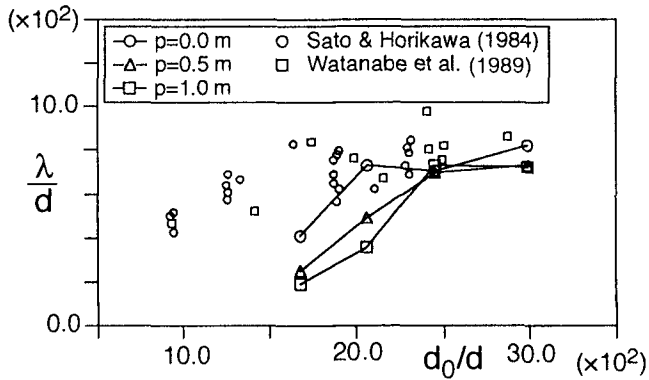


Figure 7. Relation between ripple wave length and excursion length of water particle

change in sandy bed is investigated as a part of the mechanism to determine the ripple geometry.

Figure 7 shows the relation between ripple wave length, λ , and excursion length of water particle, d_0 . In this figure, the cases of three kinds of total water-pressure amplitude, $p=0.0, 0.5$ and 1.0 m are shown with the experimental result by Sato et al. (1984) and Watanabe et al. (1989). In the region of $15.0 < d_0/d < 25.0$, the ripple wave length decreases with the increase of amplitude of water-pressure change; while, in the region of $25.0 < d_0/d$, the dependence of ripple wave length on the amplitude of water-pressure change becomes less significant, and the ripple wave length is regarded to be constant.

Figure 8 shows the relation between ripple wave steepness, η/λ , and Shields number, Ψ (η =ripple wave height). In this figure, the cases of three kinds of total water-pressure amplitude, $p=0.0, 0.5$ and 1.0 m are shown with the experimental result by Sato et al. (1984) and Watanabe et al. (1989). In the region of small Shields number, or in the region of ripple generation, the ripple wave length decreases with the increase of amplitude of water-pressure change. In other words, ripples become flatter with the increase of amplitude of water-pressure change. This tendency becomes less significant with the increase of Shields number. In the neighborhood of $\Psi=0.3$, the dependence of the ripple wave length on the amplitude of water-pressure change is not clear.

Figure 9 shows the change of the transition from two-dimensional ripples to three-dimensional ripples with the change of the amplitude of water-pressure change. The dashed lines in this figure shows the threshold of two- and three-dimensional

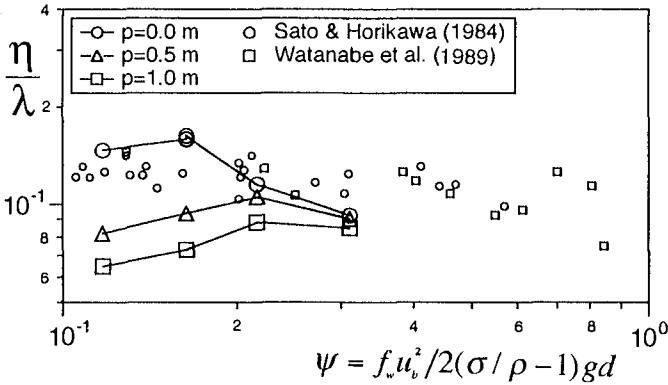


Figure 8. Relation between ripple wave steepness and Shields number

ripples proposed by Watanabe et al. (1989). In the pure oscillatory cases, $p=0.0$ m, the experimental results agree fairly well with the proposal by Watanabe et al. The transition point from two-dimensional ripple to three-dimensional one gradually decreases with the increase of d_0/d . In the coexistence cases of oscillatory flow and water-pressure change, the transition point from two-dimensional ripple to three-dimensional one shifts upward, and the dependence of the transition point to the excursion length of water particle becomes smaller.

Two-dimensional ripples are dominantly observed when the ripple wave length and the ripple wave steepness is affected by water-pressure change. The motion of sediment in the neighborhood of the crest of ripple was recorded by a CCD video camera, to investigate the flattening process of ripple due to the water-pressure change in detail. Table 2 shows the experimental condition. Figure 10 shows the behavior of sediment at every $3/\pi$ intervals on the symmetric ripple, which is generated in the pure oscillatory flow condition, $p=0.0$ m. On the other hand, Fig. 11 shows the behavior of sediment on the asymmetric ripple, which is generated in the oscillatory flow and water-pressure change coexisting condition ($p=1.0$ m).

For the simplicity, direction of the current from left to right is taken positive, and the opposite one is taken negative. In this study, the oscillating flow is in phase with the water-pressure change, hence the pressure difference from the average is positive when the current direction is positive; while the pressure difference from the average is negative when the current direction is negative.

In the pure oscillatory flow case, the time series of the current velocity follows the sinusoidal curve, then the flow velocity is symmetric between the positive-current phase and negative-current phase. Two ripple geometry with the phase lag π are

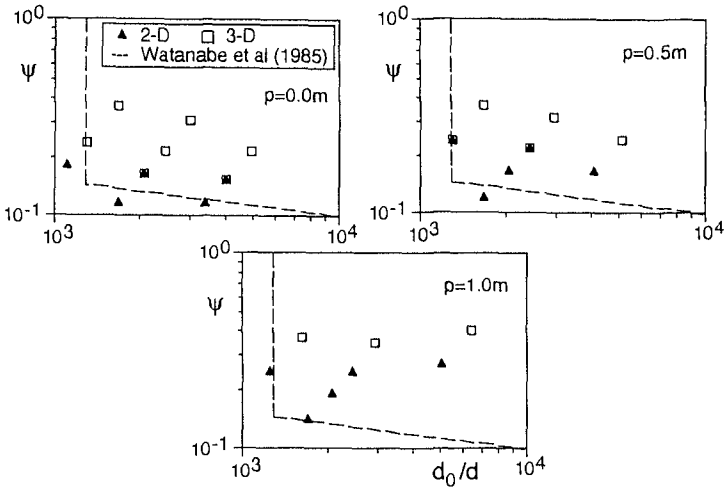


Figure 9. Transition from two-dimensional ripples to three-dimensional ripples

Table 2. Experimental conditions of the visualization

	oscillatory flow	oscillatory flow and pressure
velocity amplitude u_b (cm/s)	29.0	29.0
total pressure amplitude p_0 (m)	0.0	1.0
period T (s)	6.0	6.0
diameter of sand d (cm)	0.025	
specific density of sand σ/ρ	2.65	
ripple wave length λ (cm)	20.0	23.0
ripple wave height η (cm)	2.5	2.0

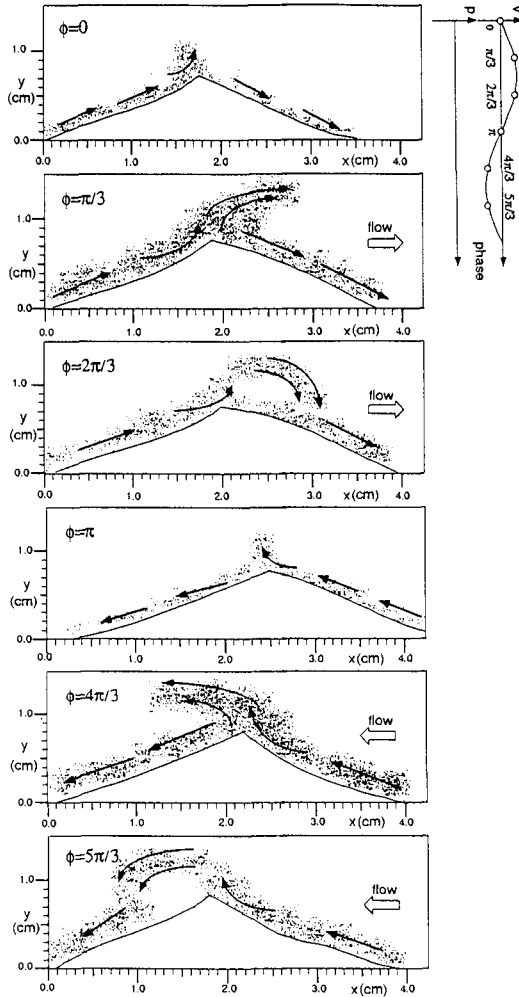


Figure 10. Behavior of sediment at every $3/\pi$ intervals on the symmetric ripple

symmetric. On the contrary, under the coexistence of oscillatory flow and water-pressure change, a significant asymmetric ripple geometry is detected between the positive-current phase and the negative-current phase. Suspended sediment transported along a backward slope of the ripple in the negative-current direction at the phase $\phi=4\pi/3$ is significantly larger than that in the positive-current direction at the phase

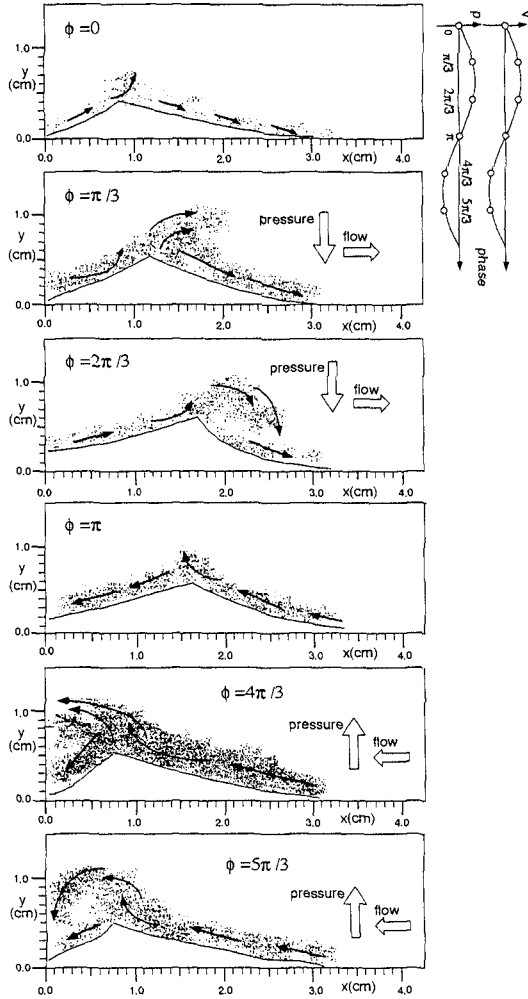


Figure 11. Behavior of sediment at every $3/\pi$ intervals on the asymmetric ripple

$\phi = \pi/3$. When the pressure difference from the average is negative, or the current direction is negative, the additional lift force due to the porewater pressure in sand layer acts on the sediment particles near the surface of sand layer. Because of this additional lift force, sediment particles are promoted to be dislodged, consequently the sediment transport rate increases. On the other hand, when the pressure difference

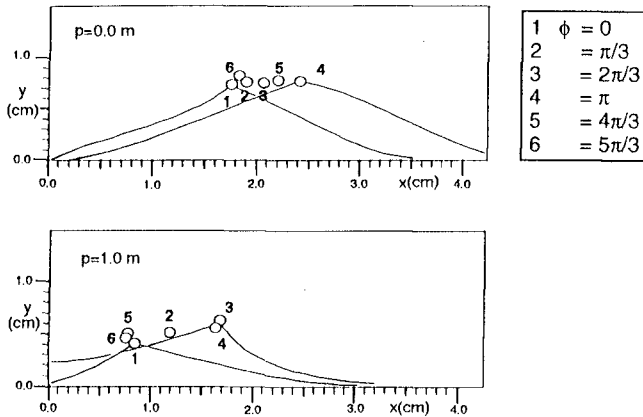


Figure 12. Movement of the crest of ripple

from the average is positive, or the current direction is positive, the negative lift force, or the additional force acting in downward direction, due to the porewater pressure in sand layer acts on the sediment particles near the surface of sand layer. This force increases the resistance of the sediment particle against the dislodgment and, consequently the sediment transport rate decreases.

Figure 12 shows the movement of the crest of ripple during one oscillating cycle. In the symmetric ripple, which is generated under the pure oscillating flow ($p=0.0$ m), the moving path of the crest toward right and that toward left overlap with each other. In other word, the vertical displacement of the crest of ripple is sufficiently small compared with the horizontal motion of the crest of ripple. On the contrary, in the case of the coexistence of the oscillatory flow and water-pressure change, the moving path of the crest during the positive-current-direction phase and that during the negative-current direction phase is significantly different. The moving velocity of the crest is slower during the positive-current-direction phase (1-3 in Fig. 12) than during the negative-current-direction phase (4-6 in Fig. 12). The crest of ripple moves upward during the positive-current-direction phase and moves downward during the negative-current-direction phase. Because the ripple wave length is approximately constant in all phases, this characteristics of the ripple wave height, or the movement of the crest in vertical direction, are interpreted as the change of the ripple wave steepness. The ripple wave steepness is larger during the positive-current-direction phase than during the negative-current-direction phase. The additional force due to porewater pressure induced by water-pressure change acts in upward direction during the negative-current-direction phase. This additional force brings the decrease in the apparent angle of

repose of sand, and the resultant flattening of ripple geometry.

Conclusion

In this study, the experiment on the seabed configuration under the coexistence of the oscillatory flow and the water-pressure change is performed by the oscillating water tunnel with cylinder system for the control of the water pressure.

The existing region of various bed configurations, such as no-motion flat bed mode, bed-load mode, suspension over ripple bed and sheet flow, changes with the change of the amplitude of water-pressure change. Furthermore, the ripple geometry, such as ripple wave length and wave steepness, or flatness of ripple, are also affected by the amplitude of water-pressure change.

Lift force due to the porewater-pressure distribution in sand layer acts in both upward and downward direction. The upward lift force promotes a sediment motion; while the downward force, or negative lift force, suppress a sediment motion. These difference of the sediment motion is the reason of the change of the existing region of the dominant bed configuration and the asymmetric characteristics of ripple geometry.

References

- Jonsson, I. G.(1966): Wave boundary layer and friction factors, Proc. of 10th Conf. on Coastal Eng., pp.127-148.
- Maeno, Y, Matsuoka, Y, Hayashida, H. and Mase, H.(1989): Effects of ripple geometry on wave-induced pore pressure, Proc. of Coastal Eng., JSCE, Vol. 36, pp. 789-793(in Japanese).
- Sato, S. and Horikawa, K.(1984): Laboratory study on sand transport over ripples due to asymmetrical oscillatory flows, Proc. of Coastal Eng., JSCE, Vol. 31, pp. 286-290(in Japanese).
- Shibayama, T. and Horikawa, K.(1982): Sediment transport and beach transformation, Proc. 18th ICCE, pp.1439-1458.
- Tanaka, H.(1990): An explicit expression of a friction coefficient for a wave-current coexisting motion, Proc. of JSCE, No. 417/II-13, 285-288 (in Japanese).
- Watanabe, A., Sakinada, M. and Isobe, M.(1989): Ripple formation and sand transport rate in a wave-current coexistent system, Proc. of Coastal Eng., JSCE, Vol. 36, pp. 299-303(in Japanese).

CHAPTER 245

The Measurement of Bed Form Shapes in Hydraulic Models

Ian E Shepherd¹

Abstract

Mobile bed hydraulic models have been used in the laboratory for a very long time. Attempts to predict the consequences of river engineering works, dams and barrages, flood protection schemes and dredging methods have led to wide ranging scientific research in material scaling. The design of breakwaters, beach protection systems and sea walls have long been studied in physical models. All of these require a method for measuring the effects of water movements and the resultant erosion, deposition and scouring of materials. This paper reviews some methods that have been used on laboratory models, and attempts to suggest ways forward in the future.

Introduction

Laboratory models of mobile bed properties require measurements of the topography resulting from water moving over the surfaces. This ranges from sedimentation effects in rivers to wave action on beaches. Measurements can be on the macro scale (ie, methods for producing 3D contours over the complete surface) or local 2D tracks of surface elevation (eg, scour around pile structures). It is a difficult measurement, as a wide range of materials and circumstances is encountered. Many experimental laboratories have developed specific techniques to suit particular projects, so it has always been difficult to design equipment and methods that are easily transportable between investigations.

¹HR Wallingford Ltd, Howbery Park, Wallingford, Oxon, OX10 8BA, UK

The durability of this style of investigation is confirmed by the fact that they still occur, and the long history (Hydraulic Models, 1942). In this reference, a description is given of a mechanical system for lowering a small probe onto the surface of the bed from a bridge over the model, and a scale to indicate its elevation. It is a source of surprise and regret that little real progress has been made in the last 50 years. This is partly due to the reluctance of civil engineering laboratories in all areas (government, private and university) to adequately invest in instrumentation development. Recent work by Jetté (1996) has shown what can be achieved by individual innovation, in this case to solve a specific field measurement problem.

This paper reviews some options, but concludes that a simple, adaptable, universal method has still only been possible using old technology, with the advantage of PC control. There must be better ways but time and resources have not permitted their development, underlining the comments above about lack of investment.

In recent years there has been a continuing interest at HR Wallingford in the effects of flowing water and waves over mobile beds. The range of work has included:

- (a) Under-mining of sea walls
- (b) Loss of sand from amenity beaches
- (c) Prevention of siltation in navigation channels
- (d) Research on the combined effects of waves and currents on bed load transport
- (e) Embankment erosion and protection
- (f) Scour around bed mounted structures

Most of this work requires the measurement of bed form disturbance to assess the effects of the existing regime and the consequences of engineering changes to the environment. Some researchers have used remote optical techniques (for example Oesch et.al., 1985) but most of these are time consuming to set-up, require sophisticated and expensive equipment, and cannot record what is happening underwater.

To overcome these objections a number of different mobile probe measurement methods have been developed by several laboratories.

Sensor Method	Use in Air	Use Under Water	Typical min. depth mm	Use in Air-Water Transition	Typical horizontal resolution at the bed mm	Typical vertical resolution mm
Conductivity	X	✓	20	X	5	0.2
Optical retro-reflective	✓	✓	10	X	10	0.2
Ultrasonic	✓	✓	100	X	20	1
Laser distance sensor	✓	✓	60	X	2	<0.1
Touch Sensitive	✓	✓	Zero	✓	2	0.1
Remote photographic	✓	X	(Surface reflection)	X	?	?
Image analysis	✓	?	?	?	?	?

TABLE 1 - COMPARISON OF METHODS

Table 1 shows some sensing methods that have been used and typical performance comparisons. There is only one universally applicable method, that of the touch sensitive, incremental technique. HR Wallingford has used optical servo probes for many years (HRS 1968), and the Delft conductivity probe has been popular (Delft 1985, and Villanueva, 1989). They are all subject to the limitations in the table. Models in flumes, for example, can be measured either by draining the water out or by flooding; it is always inconvenient, and a method which will traverse the (shallow) air-water boundary is better, even if the measurement process itself is slower. Early designs of touch probe were used by SOGREAH (Limnidyn, 1985) for a mobile bed river model, and by KENEK in Japan. The design requirements for an instrument include:

- (a) Must operate in air, underwater, and through the air-water boundary in both directions.
- (b) Must be suitable for sand, mud, coal dust, rocks, plastics, saw dust and in fresh or saline water.
- (c) Vertical resolution to be better than 1mm, horizontal resolution to be better than 5mm in a working range of 10m. Horizontal range ideally unlimited.
- (d) Options for use in flowing water to be available.
- (e) Should be easy to move from one location to another, and be cheap to build.

- (f) Expandable from 2D to 3D operation.
- (g) Must be able to operate over steep rock faces.
- (h) Automatic pc control and data logging.
- (i) Good vertical range.
- (j) Remote control options

There is an obvious choice of sensor operation, either

- (a) Remote sensing probe with a large gap between the probe tip and the bed, or
- (b) Servo operated probe following the bed surface with a small gap.

Option (a) is ideal for flowing water (to prevent scour around the probe tip) but has a poorly defined horizontal "footprint".

Option (b) provides good horizontal and vertical resolution but is unsuitable for use in flowing water or under waves.

The well-equipped experimental hydraulic laboratory should have the capability to use any of the techniques described above, so that the varied demands of different experiments can be accommodated. Each method is described in more detail below.

Methods Available

Most of the techniques depend on a probe that is servo-driven so that its tip is near to the measured surface. The error between a reference value and the value of the measured variable is used to maintain a 'constant' following distance of the probe above the surface. Exceptions to this are the photographic, laser distance and image analysis methods.

Conductivity

This option has been available for a long time (Wilkie, 1954), and had been used even earlier using the water surface as a reference (Anon 1952). Essentially it consists of a probe that can measure the bulk conductivity of the water surrounding a probe tip, and variations that depend on the proximity of non-conducting surfaces. Figure 1 (a) shows the principle. Since the water properties affect the measured values, some method must be used to eliminate the problems caused by water conductivity variations.

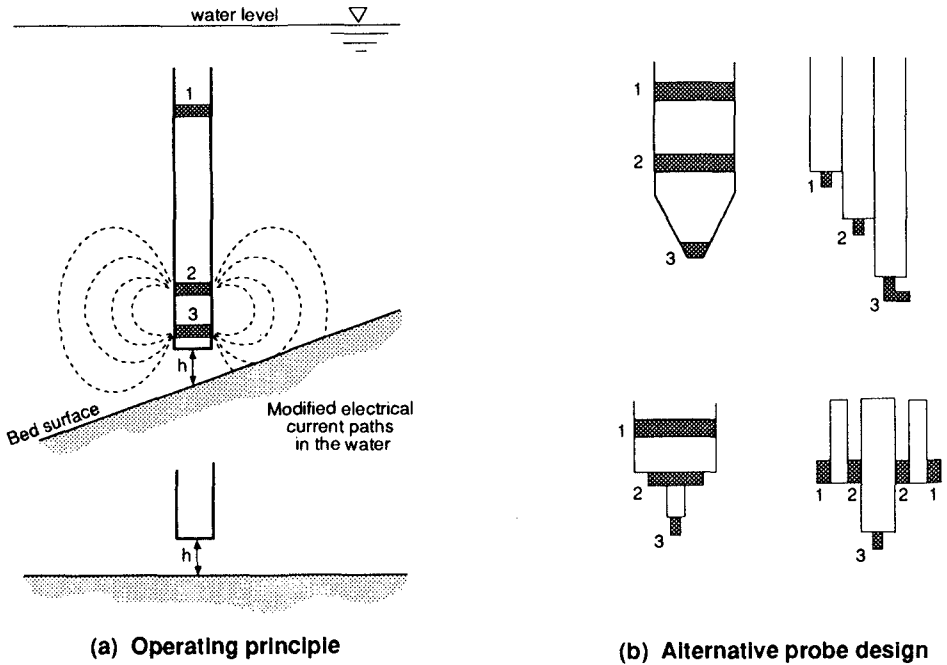


Figure 1 Conductivity Probes

The usual approach is to use an additional electrode (1) which is not affected by the surface proximity, and to use the bulk conductance measured between (1) and (2) as a form of compensation in a 'bridge'-type of arrangement.

At HR Wallingford we have experimented with a range of different probe tip designs, some of which are shown in figure 1(b). We have found that the following height H in 1(a) varies depending on the steepness of the surface. This would, of course, be expected, as the modification to the conductive path depends on the shape of the surface as well as the spacing. This is a very subjective problem, and care must be taken in the interpretation of results. The retro-reflective optical probe also has the same problem.

Optical retro-reflection

Again, this method has been used for a very long time (HRS 1968). It can be used in air (whereas the conductivity method cannot) but must be carefully optimised for the type of material over which it is working. It is also independent of water conductivity variations. The basic principle is to shine pulsed (infra-red) light on to the surface and detect the back scattered light. A convenient way to make a small diameter probe without active electronics

in the water is to use fibre optic guides so that the source and detector are above water level, as in figure 2 (a).

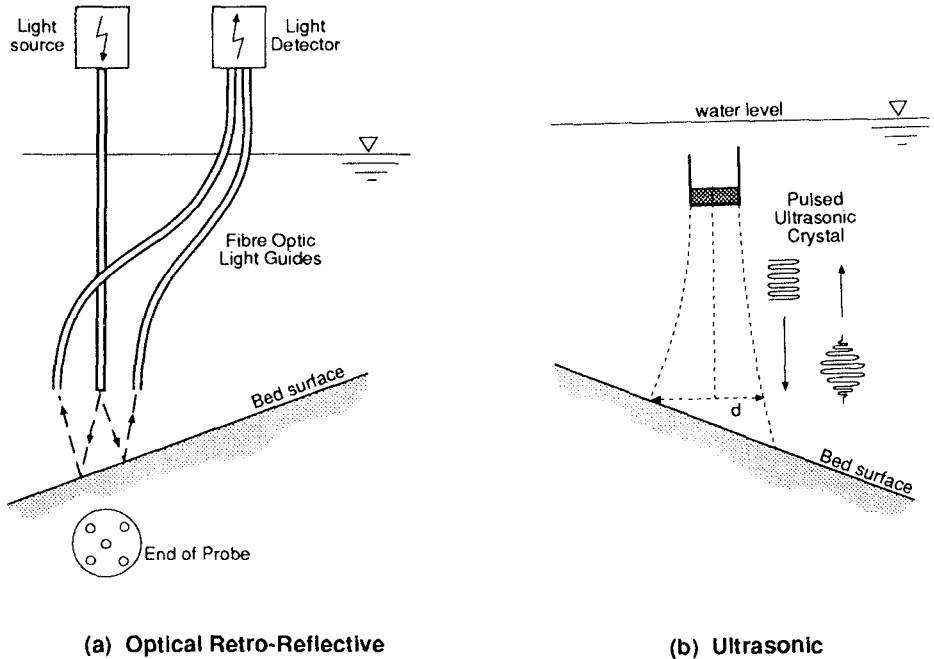


Figure 2 Optical and ultrasonic methods

The use of pulsed infra-red and synchronous detection helps to minimise the effects of ambient lighting. For effective operation, the surface must be a good homogeneous reflector such as sand or light plastics. It will not work satisfactorily over coal or gravel of mixed size and colour. Although it will operate in air or in water, the following height is different due to changes of refractive index. It can be adjusted to operate through the air-water boundary (with a step change of level at the boundary), but not the other way round. We have found that the probe collects water droplets at its tip as it emerges from the water, and this causes internal light reflections.

During some experiments, where the water has been drained away from a rippled sand bed, problems again occur even though the probe is always in air. This is because small pools of water are trapped between the ripples and cause surface reflection. The optical probe method has been used successfully over an eroded mud bed in a greenhouse to measure the effects of irrigation sprays.

Both the conductivity probe and the optical probe can also be adjusted

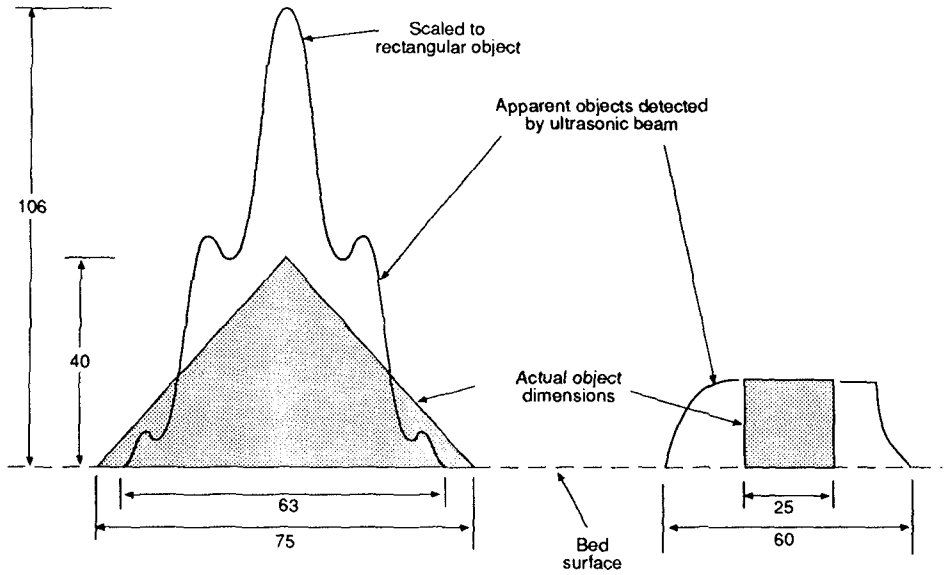
to detect the water surface location, which is useful for datum location. The HR optical probe has been mounted on a reversible carriage and used to traverse a rippled sand bed by ourselves for many projects, and also by others (Richards, 1986), using computer based logging.

Ultrasonic

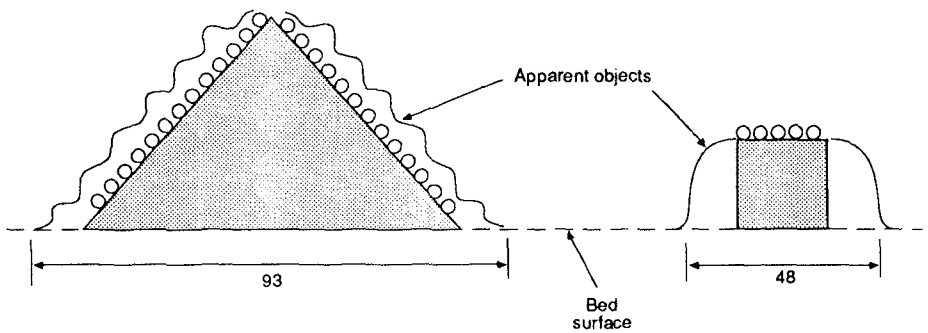
The use of ultrasonics for hydrographic survey work in the field has been developed to an extremely sophisticated level, and impressive imaging is achieved with side scan sonar. Sensors have also been used for sand ripple measurements (Jetté, 1996). Hydraulic modelling is not in the same price/performance environment, so the same intense development has not occurred.

Some laboratories have used ultrasonic probes, but there is a minimum water depth for satisfactory operation. This depends on the sensor frequency (hence the transmitted wavelength) and the accuracy of the time resolution of the returned pulse within the electronics. Figure 2 (b) shows the usual principle. It is clear that there must be enough time for the transmitted pulse to be detected back at the source before the next pulse is transmitted. Theoretically, bed slope could be measured by driving the probe at a constant horizontal speed, and then detecting the Doppler shift of the backscattered acoustic signal.

A potentially more important limitation is the transmitted beam width. The beam pattern of an acoustic source is complex, and the reader is referred to Stansfield for information. Simply, if the beam angle is 10° , then at a distance of 160mm above the bed, the horizontal projection 'd' will be about 28mm. A narrowed beam angle will improve this, but a larger spacing will degrade it. This sort of horizontal resolution is often inadequate for ripple measurements in models. A typical result is shown in figure 3. Steep ripples and edges of small stones are not measured accurately. This performance has been achieved with a 2.5 MHz probe mounted about 160mm above the bed. Ideally, a vertically driven servo probe (as with the HR systems) would be used, but has not yet been tried. In addition, the vertical resolution is limited by the wave length (0.6mm at 2.5 MHz).



(a) Result from 'shiny' surfaces (mm)



(b) Objects as (a) covered with fine coal dust (mm)

Figure 3

Objects detected by a 10° ultrasonic beam with a source 160mm above the bed $f = 2.5$ MHz

Laser distance sensors

A wide range of solid state laser displacement sensors have become available in recent years. Some of these have been described by Shepherd (1994). At HR we have used the 'Keyence' type of sensor for bed measurements. The probe was packaged in a waterproof perspex housing and used on a fixed support underwater. A great advantage of this type of sensor is that it can be used with a good "stand off" (distance between the probe and the surface) so that flowing water does not cause scour of the bed. Used in this way, it is not necessary to operate the probe on a vertical servo drive unless the total range required is beyond the range of the sensor.

The method again relies on scattered reflected infra-red light, and will work well on sand but generally requires a good homogeneous light scattering surface. It is not satisfactory on shiny reflecting surfaces. The typical optical path is shown in figure 4, and the calibration is different in water than in air. The horizontal resolution is very good as the projected light spot has a diameter of less than 1mm. Calibration in air was linear but underwater it was non-linear.

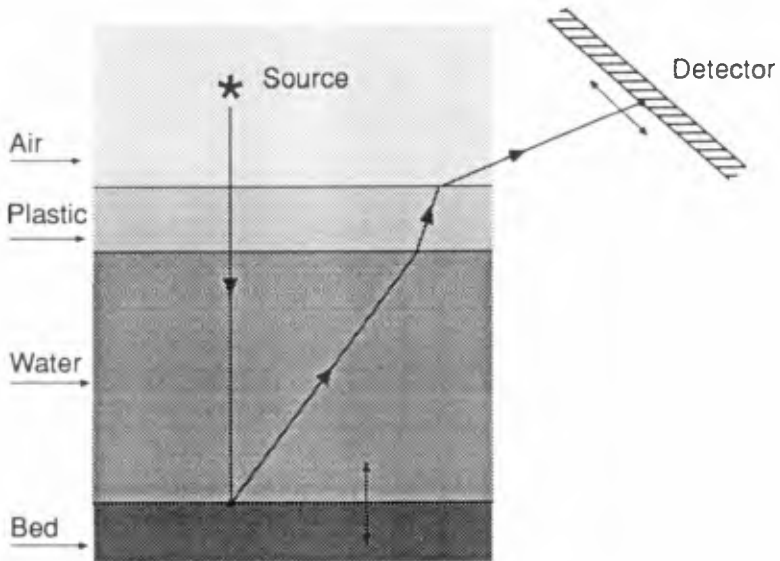


Figure 4 Laser Position Detector

There are other longer range optical 'time-of-flight' laser distance detectors and scanners that are potentially useful, but we have not yet investigated these. They are generally much more expensive than the short range distance detectors.

Touch sensitive detector

This is an extension of the retro-reflective probe described above, and as can be seen from Table 1, the only universal technique. This relies on the use of a 'diving bell' type of attachment as shown in figure 5, attached to the bottom of the optical probe. The very light weight (< 5g) piston has a good reflecting surface on its top, so that the intensity of the collected light is independent of the type of bed material.

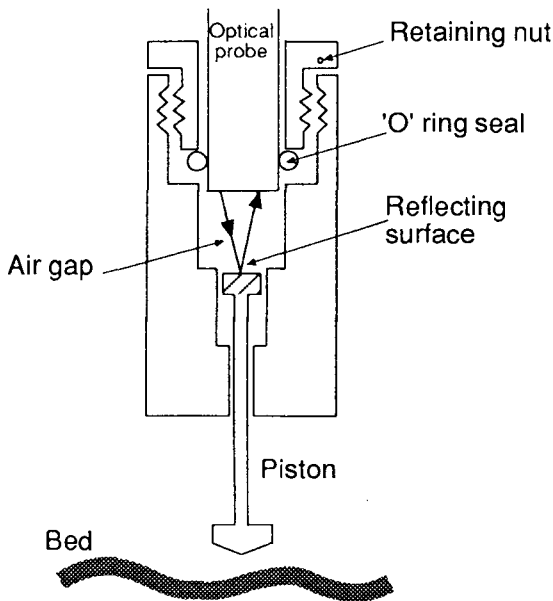


Figure 5 Universal Touch Probe

In operation, the probe is driven down to the bed, the piston tip contacts the bed and deflects by an amount which produces a repeatable level of light reflection at its top. The light level is compared with a fixed threshold which generates the error signal for the probe drive. The air gap is retained when the probe is underwater, so that the optical detection path is unchanged. Use through the air-water boundary has no effect on

operation, and any type of bed material can be detected. The weight of the piston does not produce significant bed deformation.

Remote photography

An early example of remote measurements used Moiré fringe techniques (Oesch et al 1985), and a method used for height detection has potential for bed profiling (Nagle et al ca 1988). Early attempts to use digital image analysis on a rock beach at HR was not very successful due to the variations of surface reflection from wet and dry rock faces.

More recently Lowe and Steele at HR have been developing a method suitable for wide area beach contour measurement.

In principle, it consists of arranging suitable lighting to illuminate the edge of the water at the beach so that it produces adequate contrast to provide a good photographic image from an overhead camera. The water level is changed in known increments, and successive photographic images of the water edge produced, which can then be digitised as two coordinates. The values are then subject to numerical calibration based on the location of the data point and the measured projections of vertical calibration rods located at known positions on the model. Future plans include automatic image analysis of the photographic or video based images. Image processing has already been used for surface float tracking in hydraulic models, and it is probable that these techniques will be adopted for beach movement measurement.

Typical Equipment and Results

Application examples were presented at the Conference, together with results. Figure 6 shows a typical result of a changing profile resulting from wave action. We have used profile measuring equipment for beach erosion studies, sea wall armour research, sediment transport, sand ripple propagation and mud erosion measurements. It is difficult to design universally applicable equipment, as detailed requirements vary with the type of experiment. However, it is possible to make available a range of methods that can be adopted for differing needs.

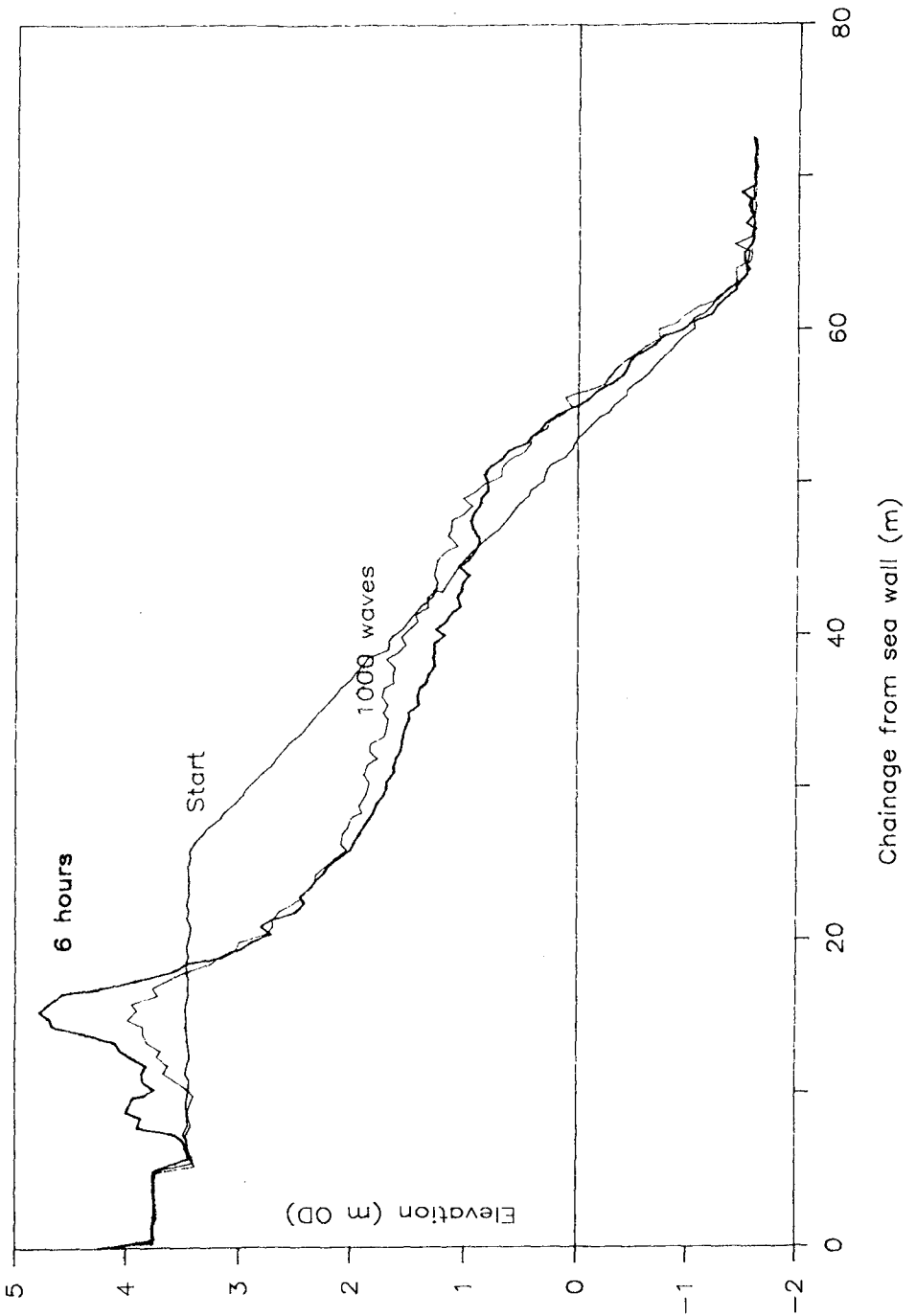


Figure 6 Profile Measurements on a Model Beach

Typical problems include the sag of instrument beam supports, either due to the weight of a moving carriage, or due to the weight of the beam itself. This can be remedied in several ways, for example:

- (a) Use of a water surface datum location
- (b) Software correction for measured values which are dependent on carriage position
- (c) Overhead fixed datum reference compensation.

In most of our applications adequate support for traversing beams can be provided so that vertical errors due to sag effects are less than 1mm.

Conclusions

Measurements of bed profiles in hydraulic modelling have been very popular in recent years. Project specific studies and basic research both demand this type of measurement. The advances in numerical techniques also require experimental data to help prove computational models. Various methods have been used, but we have found that the touch sensitive technique is the only method completely independent of bed material, slope steepness and air-water boundaries. Photographic and image analysis methods are still in development, and solid state lasers will be important in the future.

Acknowledgements

I am greatly indebted to all my colleagues at HR Wallingford, many of whom have contributed to the successful instrument developments. In particular I want to thank Les Smith and Ian Payne.

APPENDIX

References

Anon. Houille Blanche, 7, p 289, 1952.

Delft Hydraulics. PV-07 Profile Indicator, 1985.

Hydraulic Models. ASCE Manual of Engineering Practice No 25, p53, 1942.

Hydraulics Research Station. The Bed Level Plotter. 1968.

Jetté, C.D., Hanes, D. M. Measurements and Model Comparisons of Wave Generated Bedforms. Paper No 196, 25th Int. Conference on Coastal Eng. ASCE, 1996.

Limnidyn. SOGREAH, 1985.

Nagle, T. J., Lindenmuth, W. T., Baldwin, B. M., Snyder, G. I. Measurement of the wave pattern generated by a ship model in a towing basin using close range photogrammetry. David Taylor Naval Ship Research and Development Center Bethesda, Maryland, USA.

Oesch, S., Burry, J-M., Schneiter, L. Moiré Topography of Hydraulic Models. IAHR 21st Congress Vol 5, pp 41-46. Melbourne, August 1985.

Richards, K. S., Robert, A. Laboratory Experiments with the HR Multipurpose Profile Follower on a Rippled Sand bed. Dept. of Geography, University of Cambridge, 1986.

Shepherd, I. E. Optical methods for movement measurements (To be published).

Stansfield, D. Underwater Electroacoustics Transducers. Pub. Bath University Press and the Institute of Acoustics. 1991.

Villanueva, L. F. A Novel Technique of Automatic Beach Profile Measurements. IAHR Workshop on Instrumentation for Hydraulics Laboratories. pp 267-275. Canada, August 1989.

Wilkie, M. J., King, R. F. J. A bed level indicator for detecting the boundary of a body of water. Jnl.Sci.Inst. Vol 31, pp 8-9, January 1954.

CHAPTER 246

Asymmetric boundary layer flow above sand ripples under progressive waves

Takao Toue¹, Kazuo Nadaoka² and Hidehiro Katsui³

Abstract

Boundary layer flow above sand ripples under both oscillatory flow and progressive waves is examined by two dimensional numerical simulation. The simulation shows the difference of the flow between under an oscillatory flow and progressive waves. The boundary layer flow under oscillatory flow is symmetric, on the other hand, the flow under progressive waves is asymmetric. The mechanism of the asymmetric flow is explained by the convection effects of progressive waves.

Introduction

To understand the boundary layer flow above sand ripples is important for the mass transport rate and the sediment transport. The boundary layer flow above sand ripples is characterized by vortices which are generated at ripple crests. The generation, development, movement and dissipation of the vortices should be carefully examined for the understanding of the boundary layer flow.

Many experimental and numerical studies for the boundary layer flow above ripples have been carried out. There are several types of numerical simulation such as the vortex method, the turbulent simulation by $k-\epsilon$ and the direct numerical simulation (DNS). The discrete vortex method is performed by Longuet-Higgins (1981), Smith and Stansby (1985) and Ismail and Syuto (1985). Sato, Uehara and Watanabe (1985) simulated the boundary layer flow using the $k-\epsilon$ model, and Penasantana, Watanabe and Isobe (1990) examined the accuracy of the three types of $k-\epsilon$ turbulent model. Both Blondeaux and Vittori (1990) and Hamanaka and Sato (1992) simulate the boundary layer flow by DNS using the spectral method or the pseudo spectral method, and examine the characteristics of the vorticity.

In most of the numerical studies, the main flow, i.e., the flow above boundary layer, is an oscillatory flow. Nadaoka and Yagi (1988) report the difference of the

1 M.S, Senior Research Engineer, Dep. of Coastal and Hydraulics Eng., Tech. Res. Center, Taisei Corp.

2 Dr. of Eng., Professor, Department of Mechanical and Environmental Informatics, Graduate School of Information Science and Engineering, Tokyo Institute of Technology

3 Dr., Manager Dep. of Coastal and Hydraulics Eng., Tech. Res. Center, Taisei Corp.

boundary layer flow between under an oscillatory flow and progressive waves over a horizontal bed. Takigawa, Kim and Gonotani (1989), and Toue, Nadaoka and Katsui (1993) also show the differences above ripple beds. According to Nadaoka et al (1988), the difference are caused by the vertical convective effects of progressive waves. Takigawa et al (1990) showed the differences of the vortex formation between at left side of a ripple and at right under progressive waves, but the shape of the ripples is asymmetric.

The vertical convective effects also exist above symmetric ripples, and the boundary layer flow can be asymmetric under progressive waves. In this report, the boundary layer flow under progressive wave above symmetric ripples is numerically simulated, and then the difference of the flow under an oscillatory flow and progressive waves are shown, and finally the mechanism of the asymmetry is also stated.

Methodology of Numerical Simulation

The method of the numerical simulation used is based on the method of Blondeaux et al (1990) or Hamanaka et al (1992). The basic equations are followings.

$$\omega_t = \{-\Psi_\eta \omega_\xi + \Psi_\xi \omega_\eta + v(\omega_{\xi\xi} + \omega_{\eta\eta})\} / J \quad (1)$$

$$\Psi_{\xi\xi} + \Psi_{\eta\eta} = -J\omega \quad (2)$$

where ω is the vorticity, Ψ is the stream function, t is the time, ξ and η are the boundary fitted coordinate system and J is the Jacobian. Sub-scripts denote the differentiation. ξ , η and J are expressed as below.

$$x = \xi + ae^{-\eta} \cos \xi \quad (3)$$

$$y = \eta - ae^{-\eta} \sin \xi$$

$$J = 1 - 2ae^{-\eta} \cos \xi + a^2 e^{-2\eta} \quad (4)$$

where x and y are the horizontal and vertical coordinate in Cartesian coordinate system and a is the ripple height. All variables are non-dimensionalized by the ripple wave number, $k^* = 2\pi/l^*$ and σ^* is the angular frequency, where l^* is the ripple length. Furthermore, to generate finer meshes near the bottom, the new variables, ζ , is introduced as below.

$$\eta = \eta_r \frac{e^{b\zeta} - 1}{e^b - 1} \quad (5)$$

where η_r is the non-dimensional height of the calculation region, and b is the coefficient to adjust the mesh size.

The lateral boundary condition is the periodic condition, and at the top of the boundary,

$$\omega = 0 \quad (6)$$

$$\Psi = u_{\infty} n_r \sinh \frac{\eta_r}{n_r} \sin\left(\frac{\xi}{n_r} - t\right) \quad \text{for progressive waves} \quad (7)$$

$$\frac{d\Psi}{d\xi} = u_{\infty} \sin(t) \quad \text{for an oscillatory flow} \quad (8)$$

where u_{∞} is the horizontal velocity amplitude at the top of the boundary layer and n_r is the number of ripples in one wave length. At the bottom, the following boundary conditions are used ;

$$\Psi = 0 \quad (9)$$

$$\omega = -J^{-1} \left(\frac{\partial \xi}{\partial \eta} \right)^2 \frac{2\Psi(\Delta \xi)}{\Delta \xi^2} \quad (10)$$

Toue et al (1992) analyze the boundary layer flow by this method. They apply the method to high-Reynolds number flows ($Re=3400$). The calculation can not reach the steady condition, and the time-averaged flow can not be symmetric under an oscillatory flow above a symmetric ripple. Exact two dimensional simulation can express the two dimensional high Reynolds-number flow, but not the three dimensional flow that we usually observe. The method, however, can simulate the boundary layer flow exactly as long as the Reynolds number is small, around 600, and is quite useful to understand the difference of the boundary layer.

In this study the calculation condition is limited to the low Reynolds number, but the flow has vortex sheddings. According to Hamanaka et al (1992), the phenomena are controlled by the non-dimensional ripple height, a , Reynolds number, Re , and Strohal's number, S_t , being expressed as below.

$$Re = 2\pi \frac{u_{\infty}}{\nu} \quad (11)$$

$$S_t = \frac{2\pi}{u_{\infty}} \quad (12)$$

where ν is the non-dimensional viscous coefficient.

Nadaoka et al (1988) showed the ratio of the representative horizontal velocity, u , to wave celerity, C , u/C , is another control parameter for progressive waves. If u/C is large, the vertical convective effects is large. u/C is also expressed as

$$u/C = u_{\infty} / n_r \quad (13)$$

in our formulation. The calculation condition is listed in Table-1.

Table-1 Condition of Calculation(p-1 and p-2 are for verification)

O.F=Oscillatory Flow,P.W=Progressive Waves

	a	u_{∞}	b	ν	η_T	Re	St	Ψ_o	nr	u/C	
case p-1	0.00	5.0	3.0	0.05	5.0	628					O.F
case p-2	0.00	0.08	3.0	0.0023	5.0	221		0.37	10	0.01	P.W
case 1-0	0.50	5.0	3.0	0.05	5.0	628	1.26				O.F
case 1-1	0.50	5.0	3.0	0.05	5.0	628	1.26	23.11	10	0.50	P.W
case 1-2	0.50	5.0	3.0	0.05	5.0	628	1.26	19.04	5	1.00	P.W
case 1-3	0.50	5.0	3.0	0.05	5.0	628	1.26	24.11	15	0.33	P.W
case 2	0.80	8.0	3.0	0.05	5.0	1005	0.79				O.F
case 3	0.70	7.0	3.0	0.05	5.0	880	0.90				O.F
case 4	0.60	5.0	3.0	0.05	5.0	628	1.26				O.F
case 5	0.75	3.0	3.0	0.03	5.0	628	2.09				O.F

$$\Psi = \Psi_o \sin\left(\frac{\xi}{n_t} - t\right)$$

Verification of Method

To verify the the numerical method, the boundary layer flow above a flat bed are calculated. Fig.1 is the velocity distribution under oscillatory flow. The theoretical value is the 1st order solution. The agreement is quite well. Fig.2 shows the distribution of the vorticity under progressive waves. Fig.2 (a) is the analytical value

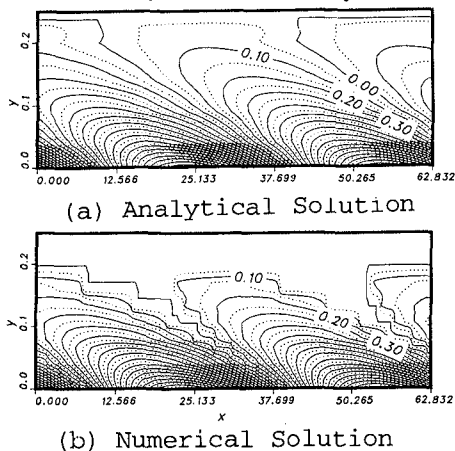
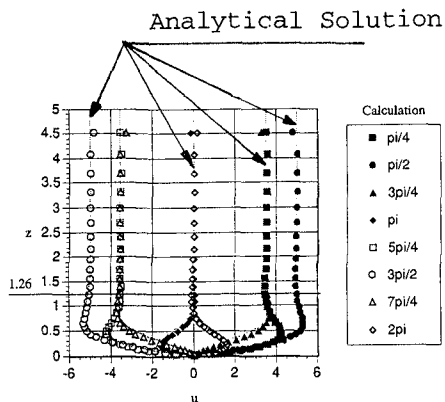


Fig.1 Comparison of Vertical Velocity Profile in Laminar Oscillatory Boundary Layer over Flat Bed between Numerical Simulation and Analytical solution.

Fig.2 Comparison of Vorticity Profile in Laminar Wave Boundary Layer over Flat Bed between Numerical Simulation and Analytical solution.

, and Fig.2 (b) is the numerical one . Both have quite good agreements.

Time Averaged Vorticity and Stream Function

The time averaged vorticity is shown in Fig.3. A pair of the symmetric vorticity cell can be seen in the case of oscillatory flow, i.e. case1-0, case4 and case5. On the other hand, the profile of the vorticity is asymmetric in case1-1, case1-2 and case1-3 which are the cases of progressive waves. When the flow become high Reynolds number, the calculation could not obtain steady state. Those cases are case2 and case3, and they are not analyzed further.

Asymmetry of the time averaged vorticity means the existence of the residual components of the circulation in a ripple, and the residual components cause steady currents. Fig.4 is the time averaged stream function in case 1-1. The profile of the stream function above all ripples should have been the same for each ripple, but since the calculation has not reached the complete steady condition, there are small differences among the stream functions. In spite of the minor differences, unidirectional and uniform steady currents can be seen near the top boundary.

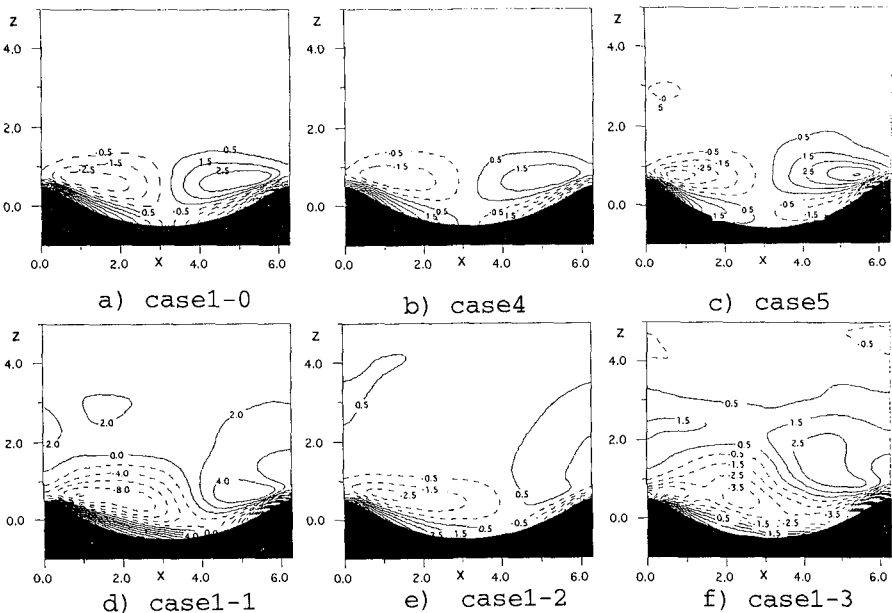


Fig.3 Time Averaged Vorticity (a) case1-0 b) case4 c) case5 d) case1-1 e) case1-2 f) case 1-3)

General Feature of Vorticity Development under Progressive Waves

Fig.5, Fig.6 and Fig.7 are the instant vorticity and the stream function for case1-1, case1-2 and case1-3 respectively in one wave length for $t = \pi/4$. In the figures, waves propagate from the left to the right, and when $t=0$, the horizontal

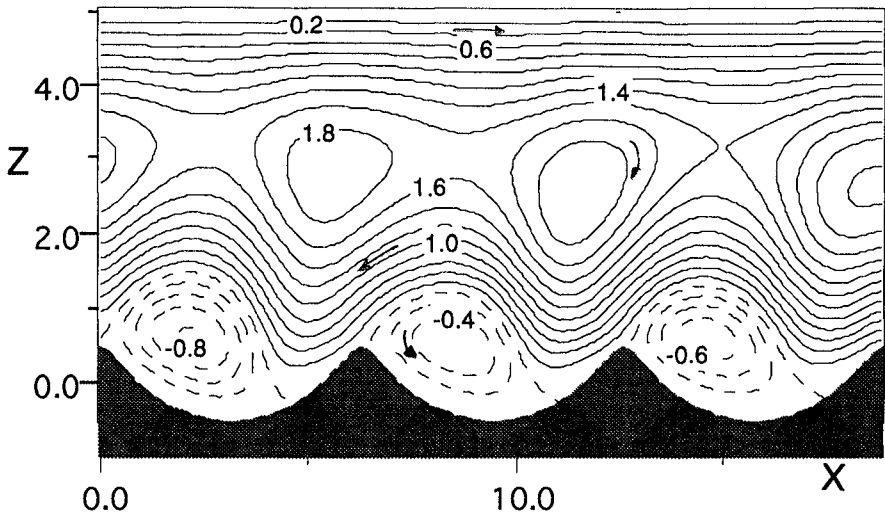


Fig.4 Time Averaged Stream Function for case 1-1

velocity and the vertical velocity on the top boundary are 0 and maximum at the center respectively. Since the calculation has reached almost a steady condition after the third cycle, the figure can be regarded as the time evolution of both vorticity and stream function at every $\pi/5$ for case 1-1, $2\pi/5$ for case 1-2 and $2\pi/15$ for case 1-3 when they are looked from the right to the left. It is clear that the dynamics of the vorticity are quite different between the positive vorticity and negative one.

The positive vorticity, denoted by A, is generated at Ripple 9 in Fig.5 where the horizontal velocity is negative. The vorticity A is convected upward by the vertical velocity of waves, and finally disperse during a half period of the waves. On the contrary, the negative vorticity, denoted by B, is generated at Ripple 5 in Fig.5 where the horizontal velocity is positive. The vorticity B is pressed down to the bottom also by the vertical velocity of waves. The another positive vorticity can be found at Ripple 3 on the bottom. That is generated by the velocity of the vortex which consists of vorticity B. The vorticity B and the positive vorticity on the bottom interact and then diminished each other. In other word, the vorticity B is diminished by the bottom friction. The positive vorticity convected upward is at far from the bottom, thus, they can not be affected by the bottom friction so much.

The differences mentioned above is related to the phase of the vorticity developing and the direction of the velocity of the main flow. When the positive vorticity is developing, the horizontal velocity is negative and the vertical velocity being directed upward. On other hand, the negative vorticity is developing, the horizontal velocity is positive and the vertical velocity being directed downward.

The phase when the vorticity stop developing is not clear, but it would be the phase during the velocity decreasing in its amplitude. These processes seem to occur at the phase between ripple 2 and 3 for the positive velocity, and 7 to 8 for the negative velocity.

The similar phenomena can be seen in case 1-2 and 1-3 in Fig.6 and 7. In case 1-2, the convection is stronger than case 1-1 and case 1-3. Thus, the positive vorticity A disperse and the negative vorticity B dissipate more quickly. In case 1-3, the

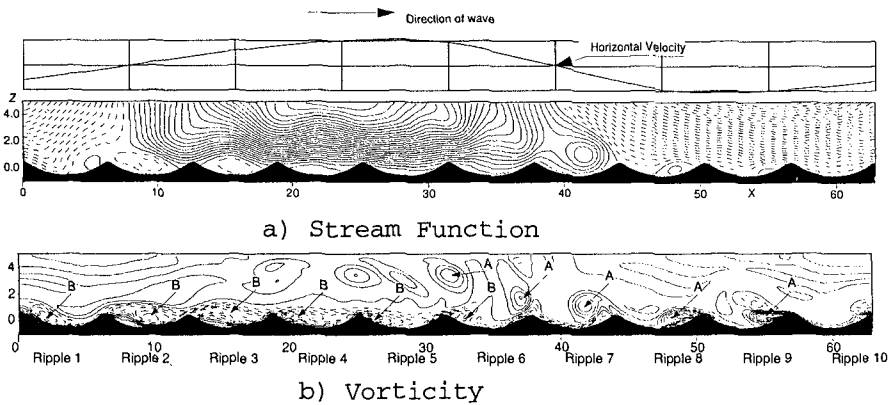


Fig.5 Instantaneous Stream Function and Vorticity in One Wave Length at $t = \pi/4$ for case 1-1 (a) Stream Function $\Delta \psi = 1.0$ b) Vorticity $\Delta \omega = 2.0$, Top Figure shows the phase of the horizontal velocity on the top boundary)

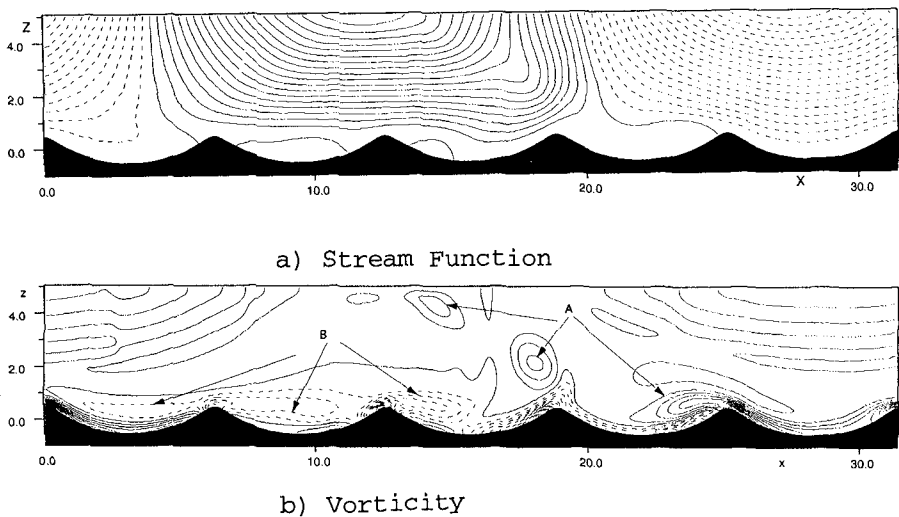


Fig.6 Instantaneous Stream Function and Vorticity in One Wave Length at $t = \pi/4$ for case 1-2 (a) Stream Function $\Delta \psi = 1.0$ b) Vorticity $\Delta \omega = 2.0$, Top Figure shows the phase of the horizontal velocity on the top boundary)

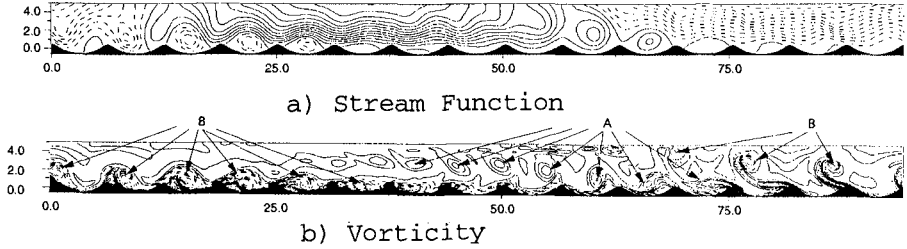
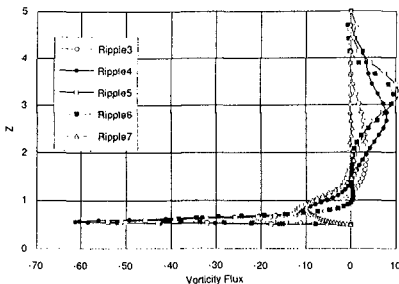


Fig.7 Instantaneous Stream Function and Vorticity in One Wave Length at $t = \pi/4$ for case1-3 (a) Stream Function $\Delta \psi = 1.0$ b) Vorticity $\Delta \omega = 2.0$, Top Figure shows the phase of the horizontal velocity on the top boundary)

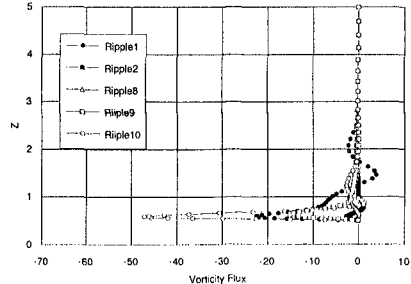
convection effects is weak, thus, the negative vorticity B still remain when the positive velocity change the direction. The survived negative vorticity B and the part of the generating positive vorticity interact, and then they goes upward by their own self-propelling velocity.

Vorticity Flux over Ripple Crest

To examine this more quantitatively, the vorticity flux, $u\omega$, in case1-1 that goes across a ripple crest is examined next. In Fig.8, the vertical profiles of $u\omega$ at the left crests of ripples are shown. Fig.8 (a) is the vorticity flux when the velocity is positive, and (b) is for negative velocity. From Fig.8 (a) , when the horizontal velocity is positive, the negative vorticity enters near the bottom and the positive vorticity enters near the top boundary. On the contrary, in the case of the negative velocity, the positive vorticity goes into near the bottom. By comparing the strength of the vorticity flux between the positive and the negative, it is clear that $u\omega$ which goes across a ripple crest is also quite asymmetric.



a) Horizontal velocity is positive



b) Horizontal velocity is negative

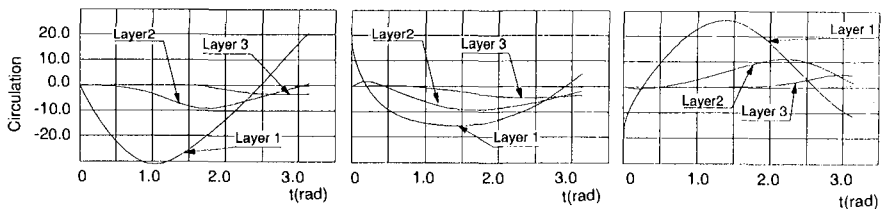
Fig.8 Vertical Distribution of Vorticity Flux at Ripple Crests (a) The horizontal velocity is positive, b) The horizontal velocity is negative.)

Circulation in A Ripple

The time evolution of the circulation that a ripple obtain for case1-1 is shown in Fig.9 from $t=0$ to $t=\pi$ of the first wave cycle. The time evolution of the circulation for case 1-0 is also shown in Fig.9. The reason why the results of the first cycle is examined is to eliminate the effect of the vortex that is formed at a half cycle before and the effects of the steady currents. The circulation are divided into four layers which are shown in Fig.10 to understand how the vorticity which is generated at the bottom transfer to upward. The circulation of Fig.9 (b) is the value for Ripple 6 in Fig.5, and that of Fig.9 (c) is the value for Ripple 1. Fig.9 (a) is the circulation under an oscillatory flow, (b) and (c) are the circulation under progressing waves. In Fig.9 (a) and (b), the horizontal velocity is positive, and the horizontal velocity is negative in Fig.9 (c).

In Fig.9 (b) and (c), the circulation in the lowest layer (Layer 1) has some value from the beginning, because even though the main flow is exactly zero at $t=0$ at the crest, the velocity is not zero above the other part of the ripple. The circulation in Layer 1 develop first since the source of the vorticity exists on the bottom. The value of circulation monotonously decreases in (b) and that monotonously increase in (c). The value has a peak before $\pi/2$, since the opposite sign of vorticity is generated on the bottom beneath a vortex. This opposite sign of vorticity is caused by the velocity of the vortex that has oppsite sign to the main flow. Before the peak of the circulation in Layer 1, the circulation in Layer 2 and Layer 3 start to develop, because the vorticity near the bottom disperses and the vortex at a ripple begins to form. The characteristics of the circulation mentioned above are common in Fig.9 (a) to (c).

The circulations of (b) and (c) in Layer 1 are the same up to around $t=0.5$, though the sign is different. After this stage, the differences between (b) and (c) can be seen. The circulation of (c) develops more than that of (b), because the negative vorticity remains near the bottom, thus, the positive vorticity beneath the negative vorticity develops. In Fig.9 (c), the positive vorticity is conected upward



a) Under Oscillatory Flow(case1-0) b) Under Progressive Waves; Horizontal Velocity is positive(case 1-1) c) Under Progressive Waves; Horizontal Velocity is negative(case 1-1)

Fig.9 Evolution of Circulation in a Ripple (a) under Oscillatory Flow b)under Progressive Waves and Positive Horizontal Velocity c) under Progressive Waves and Negative Horizontal Velocity)

, thus, the negative vorticity on the bottom beneath the vortex is small. Also comparing the circulation in Layer 2 and 3 between (b) and (c), the circulation in (b) has a peak earlier than (c) has a peak, and the peak value of (b) is smaller than that of (c). This means that the positive vorticity goes upward more easily than the negative vorticity as mentioned before.

Difference of Phase in Separation

From the difference of the time development of the circulation among Fig.9 (a), (b) and (c), there might be a phase difference in vorticity separation. Fig.11 is the vorticity distribution at $t = \pi/4$ of Ripple 5 and 1 in case1-1 in the first cycle. When the velocity is negative, the vorticity forms along the bottom topography, but the vorticity starts to separate when the velocity is positive. The separation time (phase) of the vorticity is earliest when the velocity is positive under progressive waves (see the right side of the bottom figure of Fig.11). The separation time under oscillatory flow is next and that is latest when the velocity is negative under progressive waves. This is caused by the difference of the attack angle of the velocity against the ripple crest. In the vortex evolution, i.e., $t=0$ or $\pi/2$, the positive velocity of the progressive waves attack with a steep angle, and the angle becomes milder in oscillatory flow, and much milder for negative velocity. This is also effects of the vertical velocity.

Concluding Remarks

Boundary layer flow above ripples under both an oscillatory flow and progressive waves is examined by two dimensional numerical simulation. The simulation shows the differences between the flow under an oscillatory flow and progressive waves. The boundary layer flow under an oscillatory flow is symmetric, on the other hand, the flow under progressive waves is asymmetric. The mechanism of the asymmetric flow is explained by the vertical convection of waves. Furthermore, there are the differences of the phase of the vortex separation.

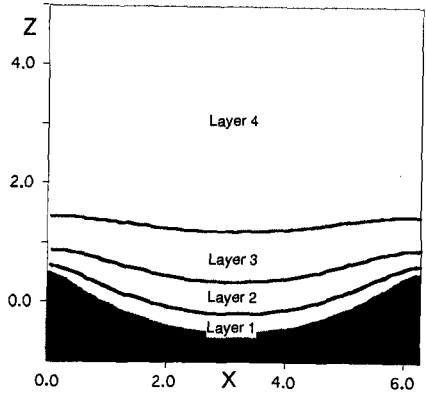


Fig.10 Explanation of Layers

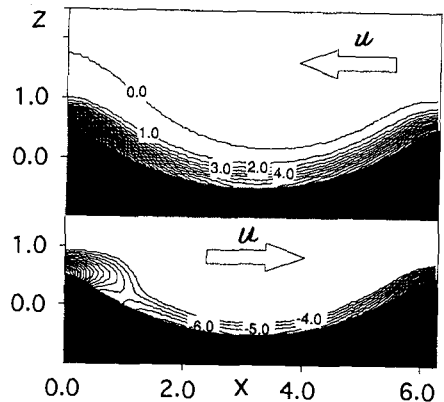


Fig.11 Instantaneous Vorticity Distribution at $t = \pi/4$ of The First Wave Cycle in case1-1 (Top figure is for Ripple 5 where the horizontal velocity is negative and the bottom is for Ripple 1 where the horizontal velocity is positive.

The Reynolds number of the flow is small and the relation of main flow and the dimension of ripples are neglected in this simulation because this calculation is to examine the mechanism of the asymmetric flow. It is necessary to calculate the high Reynolds number flow by including the appropriate turbulent model for further quantitative discussion.

References

- Blondeaux, P. and G. Vittori (1991) : Vorticity dynamics in an oscillatory flow over a rippled bed, *J. Fluid Mech.*, Vol. 226, pp. 257-289
- Ismail Aydin and Nobuo Shuto (1988) : Flow field over sand ripples due to combined wave-current motion, *Proceeding of Coastal Eng. in Japan*, Vol. 32, pp. 278-282 (in Japanese)
- Nadaoka, K., and H. Yagi (1988) : Numerical Simulation of Wave Boundary Layer by Vortex Method, *Proceedings of Coastal Eng. in Japan*, Vol. 35, pp. 16-20 (in Japanese) .
- P. G. Pena-Santana, A. Watanabe and M. Isobe (1990) : Numerical Simulation of Oscillatory Turbulent Boundary Layer Flow and Suspended Sediment Movement, *Proceedings of Coastal Eng. in Japan*, Vol. 37, pp. 264-268 (in Japanese)
- Sato, S., H. Uehara and A. Watanabe (1986) : Numerical simulation of the oscillatory boundary layer flow over sand ripples by a k- ϵ turbulence model, *Coastal Eng. in Japan*, Vol. 29, pp. 65-78
- Smith, P. A. and Stansby, P. K. (1985) : Wave-induced bed flows by a Lagrangian vortex scheme. *J. Comput. Phys.* 60, 489-516
- Takigawa, K., N. H. Kim and S. Gonotani (1989) : Numerical Analysis of Turbulent Boundary Layer Flow over Arbitrary bottom Topography under Wave Motion, *Proceedings of Coastal Eng. in Japan*, Vol. 36, pp. 1-5 (in Japanese) .
- Toue, T., K. Nadaoka and H. Katsui and K. Ito (1993) : Two dimensional boundary layer flow under progressive waves above sand ripple, *Proceedings of Coastal Eng. in Japan*, Vol. 40, pp. 1-5 (in Japanese) .

CHAPTER 247

Undertow Profiles in the Bottom Boundary Layer under Breaking Waves

Daniel T. Cox¹ and Nobuhisa Kobayashi²

ABSTRACT: The vertical distribution of the mean shear stress inside the surf zone is compared to the terms in the time-averaged horizontal momentum equation using one set of laboratory measurements of the free surface elevations and fluid velocities u and w induced by regular waves spilling on a plane slope. The vertical distribution of the eddy viscosity is estimated directly from the measured mean shear stress and velocity. The shear stress distribution in the surf zone is shown to vary linearly with depth until the bottom boundary layer where it reached a nearly constant, negative value. The shear stress variation in the transition region differs distinctly from the inner surf zone. The vertical variation of \overline{uw} is shown to be small outside the surf zone except near the bottom. Inside the surf zone, it is shown that the \overline{uw} term of the horizontal momentum equation is likely to be important in the transition region and that its importance diminishes in the inner surf zone. The vertical distribution of the eddy viscosity has a form which is small near trough level, increases to a maximum value about one-third of the depth below trough level, and then decreases toward the bottom. The eddy viscosity in the middle of the bottom boundary layer is two orders of magnitude less than the eddy viscosity in the interior.

INTRODUCTION

Detailed cross-shore sediment transport models require accurate prediction of near-shore currents, particularly an accurate description of the flow in the bottom boundary layer under breaking waves. The horizontal component of the mean cross-shore flow, or undertow, is driven by the vertical imbalance of the depth-varying momentum flux and the depth-uniform pressure gradient due to the setup (Dyhr-Nielsen and Sørensen, 1970). In the last decade, several undertow models have been developed based on this concept and vary in the degree of empiricism, choice of boundary conditions, specification of eddy viscosity, and treatment of the bottom boundary layer (e.g., Dally and Dean, 1984; Svendsen, 1984; Stive and Wind, 1986; Svendsen *et al.*, 1987; Deigaard *et al.*, 1991; Stive and de Vriend, 1994). Cox *et al.* (1994) presented for the first time detailed laboratory measurements of the instantaneous velocities and shear stresses in the bottom boundary layer of about 1 cm thickness under breaking waves. In the present paper, these measurements are used to compare the vertical distribution of the mean shear stress to the terms of the time-averaged horizontal momentum equation and to estimate the vertical distribution of the eddy viscosity used to express the mean shear stress in terms of the mean horizontal velocity.

The time-averaged horizontal momentum equation may be written

$$\frac{\partial}{\partial z} \left(\frac{\bar{\tau}}{\rho} \right) = g \frac{\partial \bar{\eta}}{\partial x} + \frac{\partial}{\partial x} (\overline{u^2} - \overline{w^2}) + \frac{\partial \overline{uw}}{\partial z} = \alpha(x, z) \quad (1)$$

¹Asst. Prof., Ocean Engrg. Prog., Dept. of Civil Engrg., Texas A&M Univ., College Station, TX 77843-3136, USA; Email: dtc@arlo.tamu.edu; Tel: +1 409 862 3627; Fax: +1 409 862 1542.

²Prof. and Assoc. Dir., Center for Applied Coastal Res., Univ. of Delaware, Newark, DE 19716, USA; Email: nk@coastal.udel.edu; Tel: +1 302 831 8044; Fax: +1 302 831 1228.

where x is the horizontal coordinate, positive onshore; z is the vertical coordinate, positive upward with $z = 0$ at the still water level (SWL); τ is the shear stress; ρ is the fluid density; η is the free surface elevation; u and w are the horizontal and vertical components of the fluid velocity; g is the gravitational acceleration; α is the vertical gradient of $\bar{\tau}/\rho$; and the overbar denotes time-averaging over the wave period. The subscripts x and z are used later to denote differentiation with respect to the horizontal and vertical coordinates. The mean shear stress $\bar{\tau}$ is generally related to the vertical gradient of the mean horizontal velocity \bar{u} through an eddy viscosity ν_t in the following form:

$$\frac{\bar{\tau}}{\rho} = \nu_t \frac{\partial \bar{u}}{\partial z} \tag{2}$$

In this paper, each of the terms in (1) are analyzed using the laboratory measurements of Cox *et al.* (1994). The eddy viscosity is estimated using (2) with the measured values of $\bar{\tau}/\rho$ and \bar{u} .

The data of Cox *et al.* (1994) consists of free surface and velocity measurements for the case of regular waves spilling on a rough, impermeable 1:35 slope. The roughness consisted of a single layer of sand grains glued on the plane slope. The median diameter of the sand grains is $d_{50} = 0.10$ cm. The velocity profiles were measured at six vertical lines in the cross-shore direction to include the shoaling region seaward of breaking (denoted L1), the break point (L2), the transition region (L3) and the inner surf zone (L4, L5, and L6). Each of the measuring lines include measuring points at a fraction of the grain height above the rough, fixed bottom. Table 1 lists basic statistics of the data set where x is the cross-shore coordinate with $x = 0$ at L1 and $x = 980$ cm at the still water shoreline, H is the wave height, \bar{h} is the local water depth including the setup, k is the wavenumber, η_{min} is the trough level, and $\bar{\eta}$ is the setup. The wave period is $T = 2.2$ s, and the free surface statistics are based on the phase-average of 50 waves.

Table 1: Measuring line locations and free surface statistics for L1 to L6.

Line No.	x (cm)	H (cm)	\bar{h} (cm)	$k\bar{h}$	η_{min} (cm)	$\bar{\eta}$ (cm)	$[\bar{\eta}_x]_m$ $\times 10^3$	$[\bar{\eta}_x]_B$ $\times 10^3$	Q_s (cm ² /s)
L1	0	13.22	27.60	0.4982	-3.88	-0.30	-0.6	-0.5	-88
L2	240	17.10	20.64	0.4265	-3.60	-0.44	0.0	—	-99
L3	360	12.71	17.56	0.3917	-2.82	-0.05	3.3	4.6	-148
L4	480	8.24	14.38	0.3529	-2.33	0.20	3.3	3.1	-114
L5	600	7.08	11.51	0.3144	-1.60	0.75	3.3	3.3	-70
L6	720	5.05	8.50	0.2690	-0.82	1.13	3.3	3.5	-45

ANALYSIS OF HORIZONTAL MOMENTUM EQUATION

The shear stress appearing in (1) is estimated from the measurements assuming $\bar{\tau}/\rho = -\bar{\sigma}_{uw}$ where $\bar{\sigma}_{uw}$ is the time-average of the phase-averaged covariance of the measured horizontal and vertical velocity components (Cox *et al.*, 1995). Fig. 1 shows the vertical variation of $\bar{\tau}/\rho$ below trough level at the four measuring lines inside the surf zone. Outside the surf zone, $\bar{\tau}/\rho \simeq 0$ even in the bottom boundary layer (Cox *et al.*, 1995).

The mean water level and trough level corresponding to $\bar{\eta}$ and η_{min} of Table 1 are indicated in the figure with the long and short horizontal lines, respectively. The vertical variation of $\bar{\tau}/\rho$ below trough level increases from the transition region (L3) to the inner surf zone (L4). For the three measuring lines in the inner surf zone, the vertical variation of $\bar{\tau}/\rho$ is fairly linear and decreases with depth, as shown in Okayasu *et al.* (1988); but $\bar{\tau}/\rho$ is negative and almost constant in the bottom boundary layer. In the transition region, $\bar{\tau}/\rho$ also decreases linearly with depth, but the thickness for which $\bar{\tau}/\rho$ is negative is much larger.

The variations of $\bar{\tau}/\rho$ in the bottom boundary layer are shown in detail in the bottom panel of Fig. 1. A second vertical coordinate z_b is introduced and is related to the vertical coordinate z by $z = (z_b - d)$ where d is the depth below the SWL. This figure clearly shows that $\bar{\tau}/\rho$ is non-zero and negative near the bottom in the inner surf zone and could be modeled as depth-invariant near the bottom. The solid circle at $z_b = 0$ indicates $\bar{\tau}_b/\rho$ computed by a linear regression analysis assuming a logarithmic profile of the mean velocity in the bottom boundary layer (Cox and Kobayashi, 1996). The thick line indicates the 95% confidence interval from the regression analysis. These points are added as a check of the $\bar{\tau}/\rho$ estimates near the bottom. The temporal variations of the bottom shear stress τ_b were discussed in Cox *et al.* (1996).

The solid line in the upper and lower panels is a piecewise continuous line approximated by a constant shear stress in the bottom boundary layer and a linear best-fit line through the interior points. The constant shear stress was computed using a number of measured points, j , above the bottom as listed in Table 2. The number j was determined at each measuring line by choosing all of measured values for which $\bar{\tau}/\rho < 0$ near the bottom. The best-fit line through the interior points was estimated using the interior points from the j th point to the trough level. Because of the large scatter in $\bar{\tau}/\rho$ in the interior and because of a regression analysis minimizing the squared error, it was necessary to use a weighting function which emphasized the j th point by counting it ten times. The j th point is indicated in the figure with an open circle.

Table 2 lists the average shear stress in the bottom boundary layer, denoted $\bar{\tau}_b$. These values are reasonably close to the values obtained by Cox and Kobayashi (1996) as indicated in Fig. 1. Table 2 lists the vertical gradient of $\bar{\tau}/\rho$, denoted α , for the interior points using the weighted best-fit line. The uncertainty using a 95% confidence interval is indicated in parenthesis. The value of α without the weighting, denoted α_* , is also indicated in Table 2 with the 95% confidence interval. The values of α and α_* are similar, and the effect of the weighting is to change the intercept of the best-fit line rather than its slope. The confidence intervals, however, were affected since the weighting function effectively doubled the number of points in the regression analysis; hence, the uncertainties based on the unweighted regression analysis are adopted hereafter as realistic estimates. For completeness, Table 2 lists an estimate of the boundary layer thickness δ defined here as the location where the shear stress changes sign from negative to positive. The boundary layer thickness is approximately $\delta \simeq 0.9$ cm in the inner surf zone, similar to the values obtained by Cox *et al.* (1996). At L3, the shear stress changes sign at a much higher elevation, $\delta \simeq 5$ cm, which may not give a good indication of the actual boundary layer thickness in the transition region.

The setup gradient $\bar{\eta}_x$ is the dominant term on the right-hand-side of (1) in the surf

Table 2: Shear stress estimates and gradients for L3 to L6.

Line. No.	j	$\bar{\tau}_b/\rho$ (cm^2/s^2)	α (cm/s^2)	α_* (cm/s^2)	δ (cm)
L3	14	-1.1	1.1 (0.2)	1.1 (0.6)	4.5
L4	10	-0.8	2.6 (0.5)	2.3 (1.0)	1.0
L5	9	-0.5	1.9 (0.3)	1.7 (0.5)	0.7
L6	8	-0.6	2.8 (0.3)	2.6 (0.5)	0.8

zone. The estimates of $\bar{\eta}_x$ are listed in Table 1, where the m subscript is used to denote the gradient estimated from the measured $\bar{\eta}$. For L1, $\bar{\eta}_x$ is estimated by a forward difference of the measured values at L1 and L2. For L2, no estimate is given, although $\bar{\eta}_x \simeq 0$ at the break point (e.g., Bowen *et al.*, 1968). For L3 to L6, $\bar{\eta}_x$ is estimated using a linear regression which includes an additional measuring value of $\bar{\eta} = 1.45$ cm at $x = 840$ cm (Cox *et al.*, 1995). The regression analysis indicated

$$\bar{\eta}_x = (3.3 \pm 0.6) \times 10^{-3}, \quad \gamma_{xy}^2 = 0.988$$

where the uncertainty is estimated by a 95% confidence interval and γ_{xy}^2 is the square of the correlation coefficient. To check the accuracy of $\bar{\eta}_x$ estimated from the measurements, comparisons were made with $\bar{\eta}_x$ estimated using the analytical expression in Bowen *et al.* (1968). These analytical values are listed in Table 1 and are indicated with the B subscript. The agreement is good except at L3 where the analytical $\bar{\eta}_x$ may be overpredicted.

The second term on the right-hand-side of (1) involves the horizontal and vertical velocities, u and w , which can be expressed as the sum of the orbital velocity, denoted with a tilde, and the mean velocity, denoted with an overbar,

$$u = \tilde{u} + \bar{u} \quad \text{and} \quad w = \tilde{w} + \bar{w} \tag{3}$$

The time-average of the squared velocities may be written

$$\overline{u^2} = \overline{\tilde{u}^2} + \bar{u}^2 \quad \text{and} \quad \overline{w^2} = \overline{\tilde{w}^2} + \bar{w}^2 \tag{4}$$

Undertow models based on (1) generally assume that $u \simeq \tilde{u}$ and $w \simeq \tilde{w}$. As a further simplification, it is often assumed that $\overline{u^2}$ is depth-invariant and that $\overline{\tilde{w}^2}/\overline{u^2} \ll 1$. Fig. 2 shows the vertical variation of $\overline{u^2}$, $\overline{\tilde{u}^2}$, and $\overline{w^2}$ for L1 to L6. This figure indicates that $\overline{u^2}$ is nearly constant over depth, except very near the bottom and that $\overline{\tilde{w}^2}/\overline{u^2} \ll 1$ is a reasonable assumption, except near the trough level. Outside the surf zone, the approximation of $u \simeq \tilde{u}$ is also quite good since $\bar{u}^2 \simeq 0$ everywhere below trough level. Inside the surf zone, however, the magnitude of \bar{u}^2 is sufficiently large compared to $\overline{u^2}$. Table 3 lists the depth-averaged values of $\overline{u^2}$, $\overline{\tilde{u}^2}$, and \bar{u}^2 where the a subscript denotes averaging from the trough level to the bottom. Outside the surf zone, $[\overline{\tilde{u}^2}]_a/[\overline{u^2}]_a \simeq 0.05$, and inside the surf zone, $[\overline{\tilde{u}^2}]_a/[\overline{u^2}]_a \simeq 0.25$. Table 3 also indicates that the vertical velocity component is negligible both outside and inside the surf zone, $[\overline{w^2}]_a/[\overline{u^2}]_a \simeq 0.05$, except near trough level where $[\overline{w^2}]_{tr}/[\overline{u^2}]_{tr} \simeq 0.15$.

Table 3: Depth-averaged values and horizontal gradients of $\overline{u^2}$, $\overline{\tilde{u}^2}$, and $\overline{u^2}$ for L1 to L6.

Line	$[\overline{u^2}]_a$	$[\overline{\tilde{u}^2}]_a$	$[\overline{u^2}]_a$	$\frac{\partial}{\partial x} [\overline{u^2}]_a$	$\frac{\partial}{\partial x} [\overline{\tilde{u}^2}]_a$	$\frac{\partial}{\partial x} [\overline{u^2}]_a$	$\frac{[\overline{w^2}]_a}{[\overline{u^2}]_a}$	$\frac{[\overline{w^2}]_{tr}}{[\overline{u^2}]_{tr}}$
No.	(cm/s) ²	(cm/s) ²	(cm/s) ²	(cm/s ²)	(cm/s ²)	(cm/s ²)		
L1	473	460	13	0.09	0.01	0.07	0.080	0.20
L2	494	464	30	-0.4	-0.9	0.4	0.071	0.19
L3	410	307	103	-0.8	-1.0	0.2	0.054	0.16
L4	309	220	89	-0.5	-0.4	-0.2	0.036	0.11
L5	260	202	58	-0.5	-0.4	-0.2	0.031	0.09
L6	183	135	48	-0.5	-0.4	-0.2	0.022	0.07

Fig. 3 shows the cross-shore variation of the depth-averaged values of $\overline{u^2}$, $\overline{\tilde{u}^2}$, and $\overline{u^2}$ with the horizontal gradients. The estimates of the horizontal gradients are listed in Table 3. At L1, L2 and L3, the gradients were computed using finite differences as follows: L1, forward difference with $(L2 - L1)/(\Delta x)$ with $\Delta x = 240$ cm from Table 1; L2, central difference with $(-L1 - 3L2 + 4L3)/(6\Delta x)$ with $\Delta x = 120$ cm; and L3, central difference with $(L4 - L2)/(2\Delta x)$ with $\Delta x = 120$ cm. The horizontal step size is large given that the vertical resolution of the measuring points is only a few centimeters in the interior and a few millimeters near the bottom. The gradients for L4, L5 and L6 were computed using linear regression which gave

$$\begin{aligned}(\overline{u^2})_x &= -0.5 \pm 0.3 \text{ cm/s}^2, & \gamma_{xy}^2 &= 0.98 \\(\overline{\tilde{u}^2})_x &= -0.4 \pm 0.5 \text{ cm/s}^2, & \gamma_{xy}^2 &= 0.90 \\(\overline{u^2})_x &= -0.2 \pm 0.2 \text{ cm/s}^2, & \gamma_{xy}^2 &= 0.93\end{aligned}$$

Although there is large uncertainty in the horizontal gradient estimates, the analysis based on the depth-averaged values of $\overline{u^2}$, $\overline{\tilde{u}^2}$, and $\overline{u^2}$ indicates that the approximation of $u \simeq \tilde{u}$ is reasonable for estimating the horizontal gradient of the $\overline{u^2}$ term in (1) in the surf zone.

Deigaard and Fredsøe (1989) indicated the importance of \overline{uw} appearing in the third term on the right-hand-side of (1). Fig. 4 shows the temporal variation of uw with u and w at five elevations $z = -7.9, -15.9, -23.9, -26.9,$ and -27.8 cm, indicated (a) to (e), respectively, for L1. In this figure, uw is reduced by a factor of 10 to facilitate plotting, and the phases have been adjusted such that the zero upcrossing of the free surface elevation is at $t = T/4 = 0.55$ s. The figure shows that the variation in uw is large, especially in the upper portion of the water column $z = -7.9$ cm (a) where uw reaches a maximum value of $uw \simeq 500 \text{ cm}^2/\text{s}^2$. Near the bottom at $z = -27.8$ cm (e), uw is small since the vertical velocity component is approximately zero.

Fig. 5 shows the vertical variation of the time-averaged value of \overline{uw} below trough level for L1 to L6. The time-averaged values for the five elevations in Fig. 4 are indicated by a solid circle for L1. The magnitude of \overline{uw} is $10 \text{ cm}^2/\text{s}^2$ which is an order of

magnitude less than the fluctuations of uw shown in Fig. 4. Outside the surf zone, $\overline{w\overline{w}}$ is nearly depth-invariant except near the bottom. Inside the surf zone, the variation of $\overline{w\overline{w}}$ is noisy. Nevertheless, crude estimates of the vertical gradients of the $\overline{w\overline{w}}$ at L3 and L4 may be made. At L3, $(\overline{w\overline{w}})_z \sim (-2.7) \text{ cm/s}^2$ in the lower portion of the water column, and $(\overline{w\overline{w}})_z \sim 2.3 \text{ cm/s}^2$ in the upper portion. These estimates were made "by eye" using the curves of Fig. 5 re-plotted on a separate sheet of graph paper. The uncertainties are roughly $\pm 50\%$. For L4, $(\overline{w\overline{w}})_z \sim (-2.5) \text{ cm/s}^2$ in the lower portion of the water column. In the upper portion, $(\overline{w\overline{w}})_z$ is approximately zero. For L5 and L6, $(\overline{w\overline{w}})_z$ is small. Again, these are very crude estimates based on time-averaged quantities that are an order of magnitude less than the fluctuating quantities.

Considering (3), the $\overline{w\overline{w}}$ term can be expressed as

$$\overline{w\overline{w}} = \overline{\overline{w\overline{w}}} + (\overline{u\overline{w}}) \tag{5}$$

and the assumption of a weak current gives $\overline{w\overline{w}} \simeq \overline{\overline{w\overline{w}}}$. Fig. 5 indicates that the $(\overline{u\overline{w}})$ term is indeed small below trough level and in the bottom boundary layer outside the surf zone. Inside the surf zone, the $(\overline{u\overline{w}})$ term appears to give a substantial contribution to the $\overline{w\overline{w}}$ term.

Table 4 summarizes the quantification of the terms in the horizontal momentum equation (1) based on the measurements of Cox *et al.* (1994) inside the surf zone. The uncertainties are indicated in parenthesis. The table indicates that for L4 and L6 in the inner surf zone, the shear stress gradient is balanced by the sum of the first two terms on the right-hand-side of (1). The relative error is less than 5% for both L4 and L6 which is well within the uncertainty of the estimates. For L5, the measured shear stress gradient is smaller than for L4 and L6, but the gradient is still balanced by the first two terms within the uncertainties of the measurements. At L3 however, the measured shear stress gradient is smaller than the sum of the first two term by a factor of two. Therefore, it is likely that the $\overline{w\overline{w}}$ term plays an important role in the transition region and that its importance decreases in the inner surf zone. Outside the surf zone, the gradient of $\overline{w\overline{w}}$ is small, except in the bottom boundary layer.

Table 4: Summary of terms in horizontal momentum equation for L3 to L6.

Line. No.	$(\overline{\tau}/\rho)_z$ (cm/s ²)	$g \overline{\eta}_x$ (cm/s ²)	$\left(\left[\overline{u^2}\right]_a\right)_x$ (cm/s ²)	$(\overline{w\overline{w}})_z$ (cm/s ²)
L3	1.1 (0.6)	3.2 (0.6)	-0.8 (0.5)	-2.7 to 2.3
L4	2.6 (1.0)	3.2 (0.6)	-0.5 (0.3)	-2.5 to 0
L5	1.9 (0.5)	3.2 (0.6)	-0.5 (0.3)	small
L6	2.8 (0.5)	3.2 (0.6)	-0.5 (0.3)	small

ESTIMATE OF EDDY VISCOSITY

The use of (2) in undertow models requires the specification of an eddy viscosity, ν_t . Several forms have been proposed including depth-invariant, two-layer, parabolic, and piecewise continuous. The eddy viscosity is specified empirically, with a velocity scale related to the wave celerity or to the local turbulent kinetic energy and a length scale related to the local water depth.

In this paper, ν_t is estimated from (2) using the measured values of $\bar{\tau}/\rho$ and \bar{u} . The left panel of Fig. 6 shows the vertical variation of the measured \bar{u} with a best-fit cubic spline at L4. The values of the seaward volume flux, Q_s , per unit width listed in Table 1 were calculated by integrating this curve from the bottom where $\bar{u} = 0$ to just above trough level where again $\bar{u} = 0$. The middle panel of Fig. 6 shows the measured values of $\bar{\tau}/\rho$ below trough level and is the same as that plotted at L4 in Fig. 1. The right panel shows the eddy viscosity at L4 estimated from

$$\nu_t = \frac{\bar{\tau}/\rho}{(\bar{u})_z} \quad (6)$$

where $\bar{\tau}/\rho$ is given by the piecewise continuous best fit curve and the vertical gradient of the horizontal velocity is estimated from the best-fit cubic spline using a finite difference approximation with a vertical resolution of $\Delta z = 0.01$ cm. The figure shows that from trough level, the eddy viscosity increases downward to a maximum value about one-third of the depth below trough level and then decreases. The variation in the eddy viscosity is unrealistically large as the velocity gradient approaches zero at $z \simeq (-12)$ cm. This is the major limitation of the eddy viscosity approach. Near the bottom, the eddy viscosity is small as the velocity gradient becomes large.

Fig. 7 shows the vertical variation of the measured eddy viscosity at the four measuring lines inside the surf zone similar to the right panel of Fig 6. Only those portions for which (6) gave reasonable estimates are shown. The vertical distribution of the eddy viscosity is qualitatively similar for L4, L5, and L6 in the inner surf zone. For L3, reasonable estimates could not be obtained over most of the depth. The magnitude of ν_t in the bottom boundary layer for the four measuring lines is

$$\nu_t = 0.10 \pm 0.05 \text{ cm}^2/\text{s} \quad \text{at } z_b = 0.5 \text{ cm}$$

and is about two order of magnitude smaller than ν_t estimated in the interior. This large decrease is consistent with the assumption made by Svendsen *et al.* (1987).

CONCLUSIONS

The following conclusions are supported in this paper based on the analysis of one set of laboratory measurements of regular wave spilling on a rough, plane slope.

- The mean shear stress distribution in the inner surf zone varies linearly with depth until the bottom boundary layer where it reaches a nearly constant, negative value. The bottom shear stress is also negative. The shear stress variation in the transition region differs distinctly from the inner surf zone in that the negative shear stress extends much higher in the water column.

- The $\overline{w^2}$ term is negligible compared to $\overline{u^2}$ except near the trough level.
- Outside the surf zone, $\overline{u^2}/\overline{u^2} \ll 1$. Inside the surf zone, $\overline{u^2}$ contributes significantly to $\overline{u^2}$. The approximation of $u \simeq \tilde{u}$, however, is reasonable for estimating the horizontal gradient of $\overline{u^2}$ inside the surf zone.
- The vertical variation of \overline{uw} is small outside the surf zone except near the bottom.
- The shear stress gradient can be balanced by the first two terms of the horizontal momentum equation (1) in the inner surf zone.
- The \overline{uw} term is likely to be important in the transition region and its importance diminishes in the inner surf zone.
- The vertical distribution of the eddy viscosity in the surf zone estimated from the measured mean shear stress and horizontal velocity has a form which is small near trough level, increases to a maximum value about one-third of the depth below trough level, and then decreases toward the bottom.
- The eddy viscosity in the middle of the bottom boundary layer is two orders of magnitude less than the eddy viscosity in the interior.

Dynamic undertow models based on (1) and (2) are difficult to apply with confidence because of the many uncertainties involved in estimating the terms in (1) and the eddy viscosity in (2). An alternative kinematic model is proposed by Cox and Kobayashi (1996). This model relates the horizontal velocity, bottom shear stress, and boundary layer thickness in a simple but general manner.

ACKNOWLEDGMENTS

This work was sponsored by the U.S. Army Research Office, University Research Initiative under contract No. DAAL03-92-G-0116 and by the National Science Foundation under grant No. CTS-9407827.

REFERENCES

- Bowen, A., Inman, D., and Simmons, V. (1968) "Wave 'set-down' and setup." *J. Geophys. Res.*, 73, 2569-2577.
- Cox, D.T. and Kobayashi, N. (1996) "A kinematic undertow model with a logarithmic boundary layer." *J. Waterway, Port, Coastal, and Ocean Engrg.*, (submitted).
- Cox, D. T., Kobayashi, N., and Okayasu, A. (1994) "Vertical variations of fluid velocities and shear stress in surf zones." *Proc. 24th Coast. Engrg. Conf.*, ASCE, 1, 98-112.
- Cox, D.T., Kobayashi, N., and Okayasu, A. (1995) "Experimental and numerical modeling of surf zone hydrodynamics." *Rpt. No. CACR-95-07*, Center for Applied Coastal Research, University of Delaware, Newark, Delaware, 293 p.

- Cox, D.T., Kobayashi, N., and Okayasu, A. (1996). "Bottom shear stress in the surf zone." *J. Geophys. Res.*, 111 (C6), 14337-14348.
- Dally, W.B. and Dean, R.G. (1984). "Suspended sediment transport and beach evolution." *J. Waterway, Port, Coastal, and Ocean Engrg.*, 110 (1), 15-33.
- Deigaard R. and Fredsøe, J. (1989). "Shear stress distribution in dissipative water waves." *Coast. Engrg.*, 13, 357-378.
- Deigaard, R., Justesen, P., and Fredsøe, J. (1991). "Modeling of undertow by a one-equation turbulence model." *Coast. Engrg.*, 15, 431-458.
- Dyhr-Nielsen, M. and Sørensen, T. (1970). "Sand transport phenomena on coasts with bars." *Proc. 12th Coast. Engrg. Conf.*, ASCE, 182-192.
- Okayasu, A., Shibayama, T., and Horikawa, K. (1988) "Vertical variation of undertow in the surf zone." *Proc. 21rd Coast. Engrg. Conf.*, ASCE, 478-491.
- Stive, M. J. F. and de Vriend, H. J. (1994) "Shear stresses and mean flow in shoaling and breaking waves." *Proc. 24th Coast. Engrg. Conf.*, ASCE, 1, 594-608.
- Stive, M.J.F. and Wind, H.G. (1986) "Cross-shore mean flow in the surf zone." *Coast. Engrg.*, 10, 325-340.
- Svendsen, I. A. (1984) "Mass flux and undertow in a surf zone." *Coast. Engrg.*, 8, 247-365.
- Svendsen, I. A., Schäffer, H. A., and Hansen J. B. (1987) "The interaction between the undertow and the boundary layer flow on a beach." *J. Geophys. Res.*, 92(C11), 11845-11856.

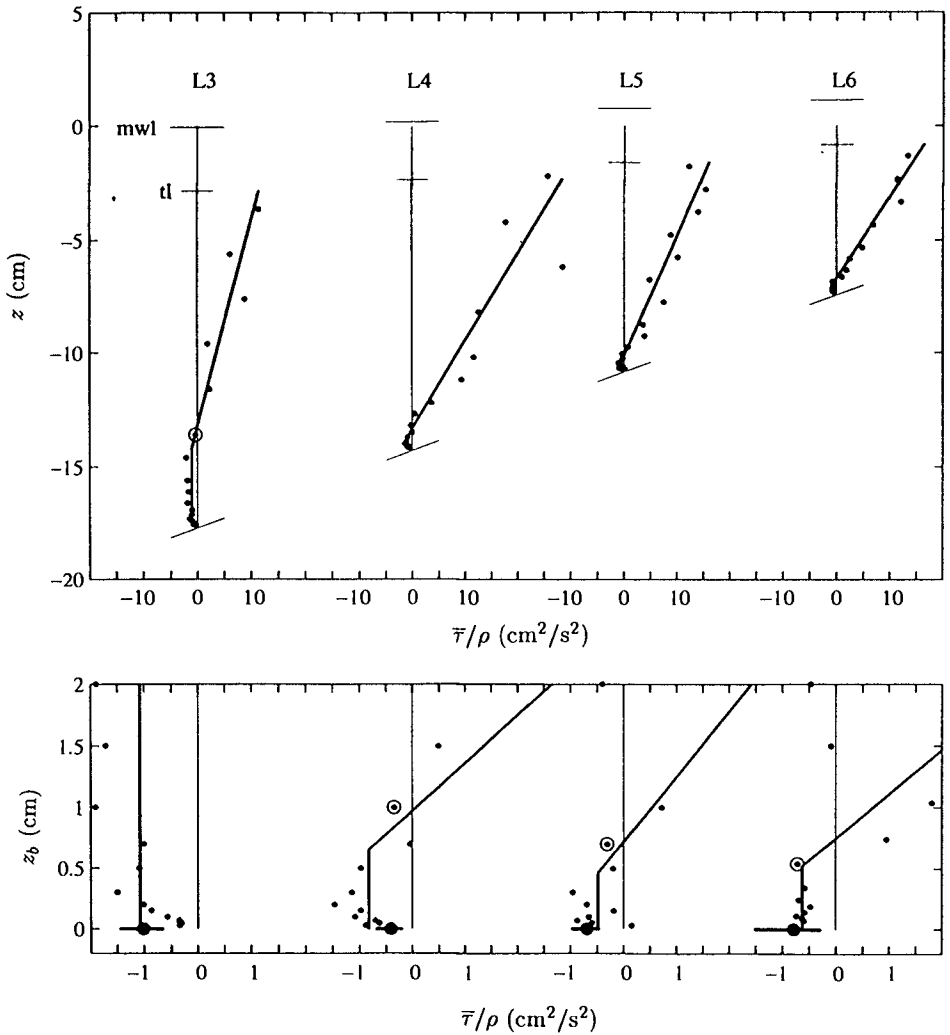


Figure 1: Vertical variation of measured shear stress $\bar{\tau}/\rho$ (\bullet) with piecewise continuous best-fit line (—) (top) and detail in bottom boundary layer with $\bar{\tau}_b$ from linear regression (\bullet) and 95% confidence interval (—) for L3 to L6. Circle indicates j th elevation listed in Table 2.

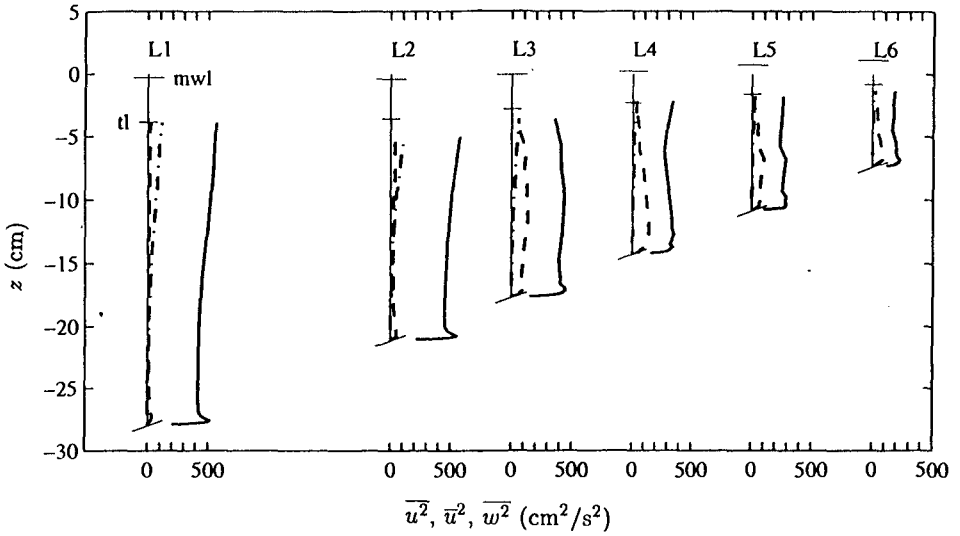


Figure 2: Vertical variation of $\overline{u^2}$ (—), $\overline{u^2}$ (---), and $\overline{w^2}$ (-.-) for L1-L6.

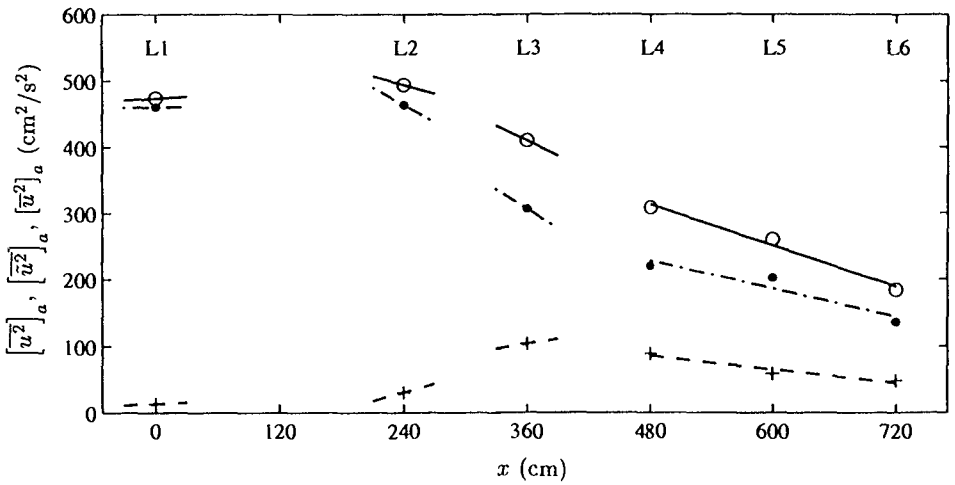


Figure 3: Cross-shore variation of $[\overline{u^2}]_a$ (\circ —), $[\overline{u^2}]_a$ (\bullet -.-), and $[\overline{u^2}]_a$ (+ -.-) with gradients for L1-L6.

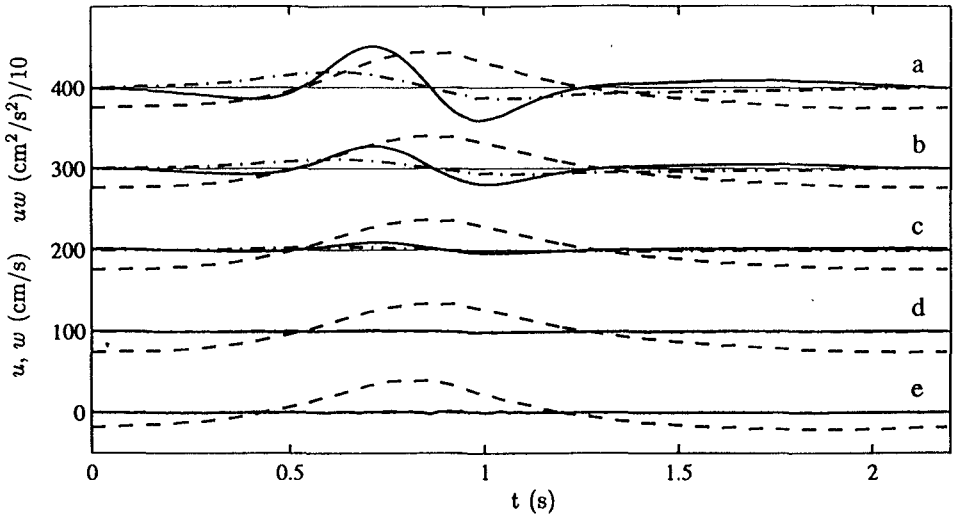


Figure 4: Temporal variation of u (---), w (-·-·), and uw (—) at five elevations for L1. To facilitate plotting, uw is reduced by a factor of 10, and there is an offset of a factor of 100 in the ordinate.

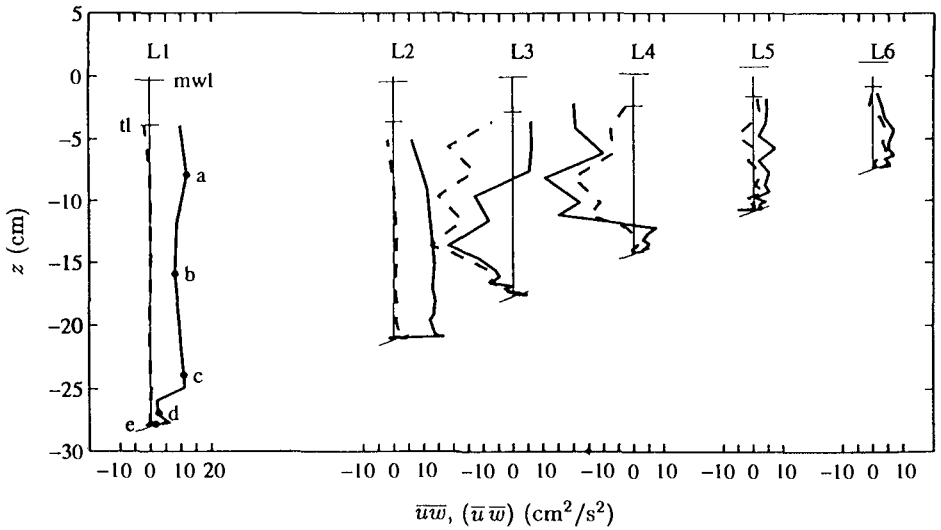


Figure 5: Vertical variation of \overline{uw} (—) and $(\overline{u} \overline{w})$ (- -), for L1-L6. Five elevations of Fig. 4 at L1 indicated by solid circle (•).

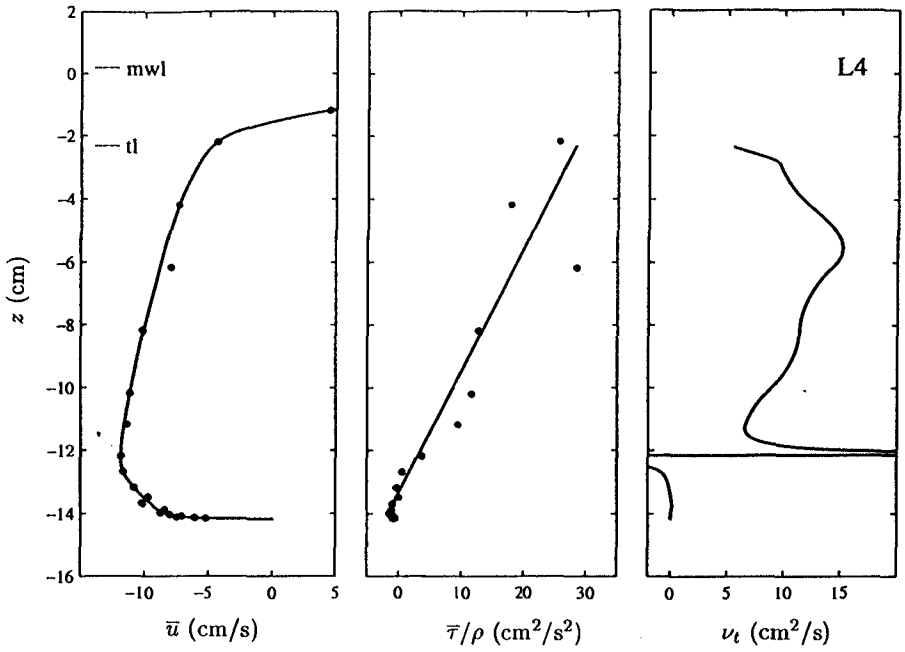


Figure 6: Vertical variation of measured \bar{u} (•) with cubic spline (—) (left); measured shear stress $\bar{\tau}/\rho$ (•) with best-fit curve (—) (middle); kinematic viscosity ν_t (—) (right) for L4.

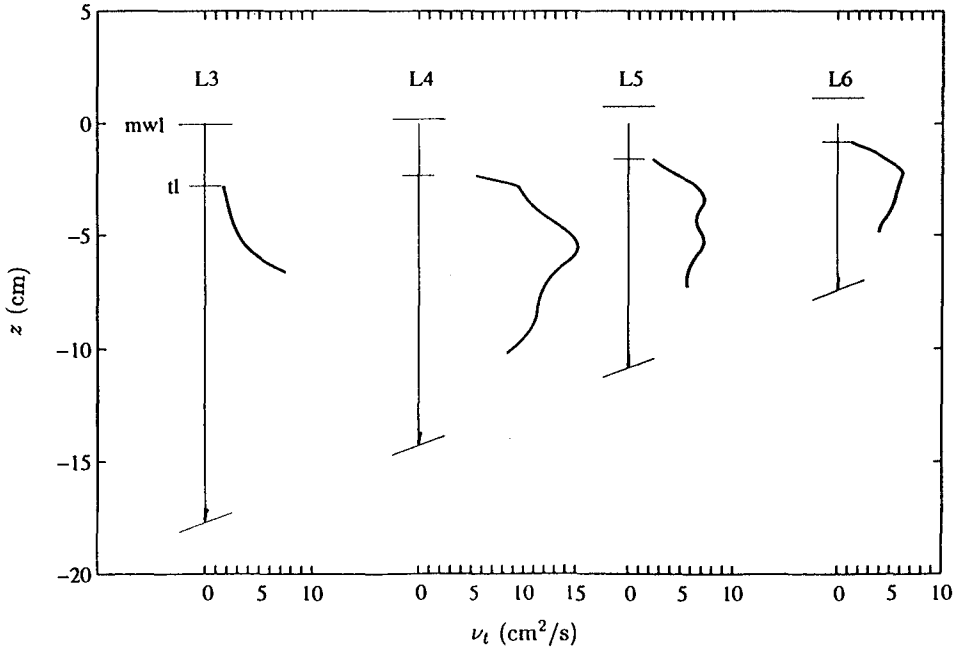


Figure 7: Vertical variation of measured eddy viscosity ν_t (—) for L3 to L6.

CHAPTER 248

A Comparison of Field Observations and Quasi-Steady Linear Shear Instabilities of the Wave Bottom Boundary Layer

D. L. Foster¹, A. J. Bowen¹, R. A. Beach² and R.A. Holman²

Abstract:

Field observations of near-bed high frequency velocity fluctuations and suspended sediment are compared with predictions of momentary flow stability by a quasi-steady linear instability model. Field observations were made as part of the Duck94 cooperative field experiment and consisted of a vertical array of four hot-film anemometers and 19 fiber-optic backscatter sensors located within the wave bottom boundary layer. Predicted instabilities for the quasi-steady model occur over length scales ranging from 2 cm to 1 m and therefore may be assumed to be a plausible mechanism for the generation of turbulence and suspension of sediment. However with the quasi-steady model, the instabilities are at the same phase as the sediment suspension events, but are occurring too late in the wave phase for them to be generating the observed turbulence.

¹ Department of Oceanography, Dalhousie University, Halifax, Nova Scotia, Canada, B3H 4J1.
internet: diane.foster@dal.ca

² Department of Oceanography, Oregon State University, Ocean Admin Bldg 104, Corvallis, Oregon, USA 97331.

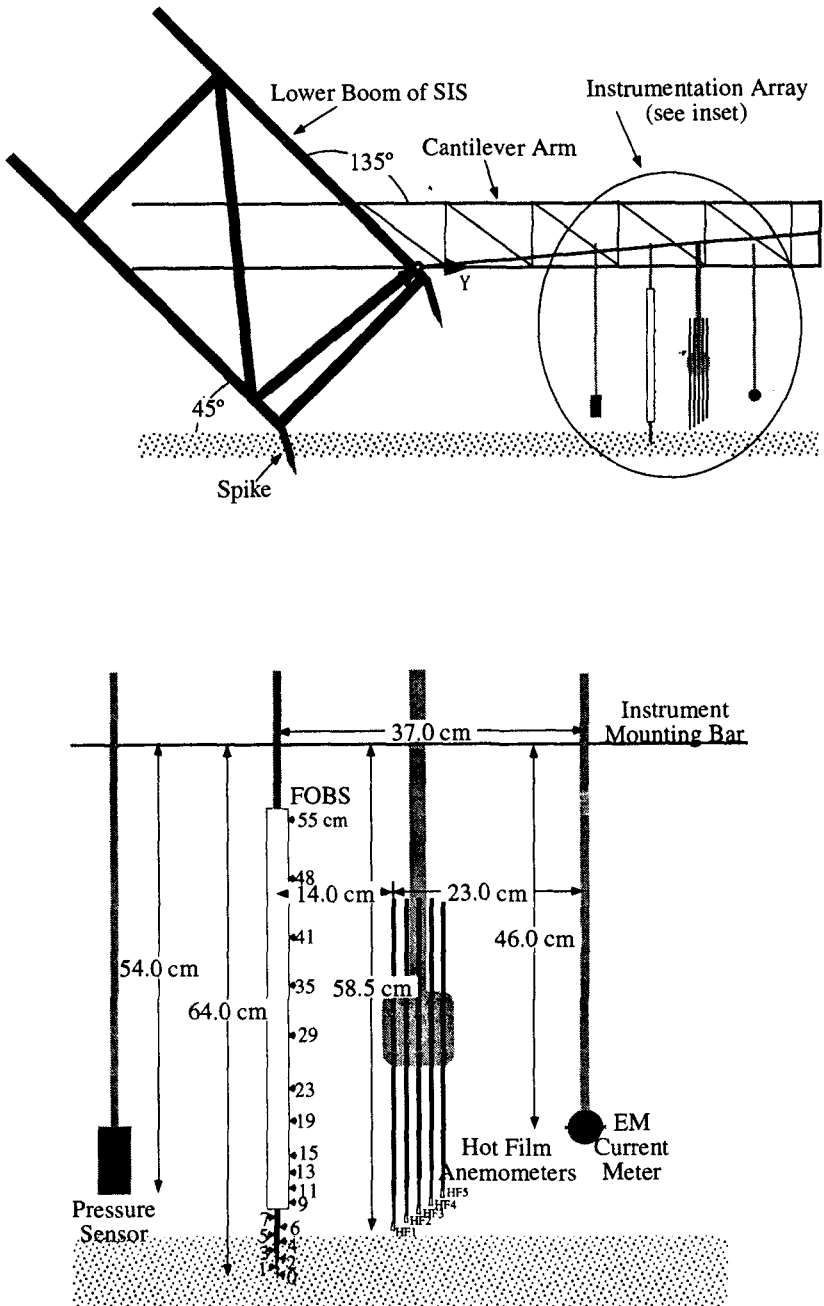


Figure 1: A schematic showing the instrument cantilever as deployed from the Sensor Insertion System on the FRF pier (top panel) and positions of the pressure sensor, FOBS probe, hot film anemometer array, and electromagnetic current meter (bottom panel) (Foster, et al., 1996).

1 Introduction

The seemingly random occurrence of sediment suspension events in the surf zone has long been the topic of research for coastal oceanographers and engineers. These short-lived events are the first step in morphologic evolution and consequently hold significance in our understanding of coastal dynamics. Intuition suggests that suspension events are a result of rapid increases of turbulence levels in the near-bed region. The wave bottom boundary layer is the region of fluid bounding the seabed which responds to the oscillatory surface waves. Within this relatively small region ($\delta \sim O(5 \text{ cm})$), the velocity transitions from the free stream value ($u \sim O(100 \text{ cm/s})$) to zero. Thus far, most of the previous research on the introduction of turbulence to the wave bottom boundary layer has focussed on bottom shear generation. An additional and equally plausible mechanism is the generation of turbulence from within the wave bottom boundary layer through a shear instability. Using a piecewise continuous linear instability model, Foster, et al. (1994) showed that at particular wave phases, the high shears in this region may lead to shear instabilities. With laboratory observations of oscillatory boundary layer flow, Hino et al. (1983) concluded that increased levels of turbulence during the decelerating phase of the flow were triggered by a shear instability.

The objective of this paper is to compare Duck94 field observations of near-bed high frequency velocity fluctuations and suspended sediment with predictions of momentary flow stability by a quasi-steady linear instability model. This paper is organized in the following manner. An overview of the field experiment and data collection technique is given in section 2. The theoretical formulation and solution method of the shear instability problem is presented in section 3. Comparisons between the theory and observations are made in section 4. Finally, the conclusions are given in section 5.

2 Observations

The experiment was conducted at the Army Corps of Engineers, Field Research Facility (FRF) in Duck, NC (Figure 1) on August 17, 1994, as part of the Duck94 field experiment. The significant offshore wave height, angle, and period measured in 8 m water depth were 0.83 m, 50 from the southeast, and 4.54 s, respectively. The observations were made in 2 m water depth on the crest of the bar over flat bed conditions. The instruments were deployed from a cantilever arm attached to the lower boom of the sensor insertion system on the FRF pier, see Figure 1. Near bed velocity observations were made with an array of 5 hot-film anemometers, sampled at 256 Hz, separated with a 1 cm vertical spacing, Figure 1. The velocity outside the wave bottom boundary layer was measured with an electromagnetic current meter. The bed elevation and suspended sediment were measured with a vertical stack of 19 fiber-optic backscatter sensor probe (FOBS), sampled at 16 Hz. The bed elevation is determined by examining each independent sensor for burial. A thorough presentation of field techniques and instrument calibration may be found in Foster et al. (1996).

3 Theoretical Formulation

As formulated in Foster, et al. (1994), let the total velocity be partitioned into perturbation and wave components and given by

$$\begin{aligned} u^T(x, z, t) &= u(x, z, t) + U(z, t) \\ w^T(x, z, t) &= w(x, z, t), \end{aligned} \quad (1)$$

where x and z are the horizontal coordinates (x being positive offshore from the shoreline and z being positive up from the seabed), t is time, u and w are the perturbation velocities, and U is the known horizontal oscillatory background velocity. In a linear instability analysis, it is assumed that perturbation velocities are significantly smaller than the background velocity, simply $u, w \ll U$. Substituting (1) into the continuity equation, subtracting the linearized wave bottom boundary layer equation and neglecting terms of $O(u^2)$, we obtain the governing equation:

$$\begin{aligned} u_t + Uu_x + wU_z &= -\frac{1}{\rho}P_x + \nu(u_{xx} + u_{zz}) \\ w_t + Uw_x &= -\frac{1}{\rho}P_z + \nu(w_{xx} + w_{zz}), \end{aligned} \quad (2)$$

where P is the pressure and ν is the kinematic viscosity. By assuming conservation of mass and two-dimensional flow, it is possible to represent u and w in terms of the stream function, Ψ , such that

$$\begin{aligned} u &= \Psi_z \\ w &= -\Psi_x. \end{aligned} \quad (3)$$

Substitute the stream function definitions into (2), cross differentiate, and subtract to eliminate the pressure reducing to one equation

$$\left(\frac{\partial}{\partial t} + U \frac{\partial}{\partial x} + \nu \nabla^2 \right) (\nabla^2 \Psi) - U_{zz} \Psi = 0. \quad (4)$$

For this investigation, we neglect the effect of viscosity.

The quasi-steady model assumes that the time-varying background profile may be represented with a series of time-independent profiles, such that $U(z, t) \equiv U_n(z)$. At each instant in time, t_n , we assume a solution of the form

$$\Psi_n(x, z, t_n) = \phi_n(z) e^{i(k_n x - \sigma_n t_n)} \quad (5)$$

where k is the real wavenumber and $\sigma = \sigma_r + i\sigma_i$ is the complex frequency. The substitution of (5) into (4) results in the well known Rayleigh equation

$$(U_n - c_n) (\phi_{nzz} - k_n^2 \phi_n) = U_{nzz} \phi_n. \quad (6)$$

The boundary conditions are specified by assuming that there is no mass flow through the bottom and that the perturbation must decay as $z \Rightarrow H$, where H is the water depth, and

are given by

$$\begin{aligned}\phi(z = z_o) &= 0 \\ \phi_z(z = \delta) &= -k\phi(z = \delta).\end{aligned}\tag{7}$$

(6) may be solved with a finite centered difference approximation scheme. For this model, we assume that the background flow may be approximated with a time- and depth-dependent eddy viscosity model (Foster, 1996). The wave bottom boundary layer background flow model was forced with a 256 second record of velocity measured at 13 cm above the bed. The system is discretized into 100 nodal points and solved numerically as an eigenvalue problem (Dodd, et al., 1992), where the wave celerity, $c = \sigma/k$, is the eigenvalue and the stream function, Ψ , is the eigenfunction. The momentary flow stability is examined by searching for the fastest growing mode at each instant in time over a given wavenumber range of interest.

The concept of momentary stability (Shen, 1961) implies that when $\sigma_i > 0$ the disturbances are growing relative to the background flow and the flow may be considered to be "momentarily unstable". Conversely, when $\sigma_i < 0$ the disturbances are decaying relative to the background flow and the flow may be considered to be "momentarily stable".

4 Results

Flow stability was determined at 1/8 second intervals using the eddy viscosity model-generated background velocity profile, $U(z, t)$. An example of this can be seen in Figure 2. Notice that at times a and d the flow is stable and that at times b and c, when the free stream flow is decelerating and there exists an inflection point in the profile, the flow is unstable. The peak growth rate occurs prior to flow reversal when the near-bed internal shear is largest. The oscillatory perturbation frequency, σ_r , is nearly zero in the two unstable cases, b and c, indicating that there will exist a fixed spatial pattern which grows exponentially in time. This may be a possible explanation for ephemeral ripples which form over a wave phase following a suspension event. An example of the eigenfunction amplitude and phase structures for 3 wavenumbers is given in Figure 3. For cases b and c, the peak phase shift is as large as $\pi/2$.

A 60 second time series of near bed cross shore velocity, turbulent variance, concentration, and predicted growth rates is given in Figure 4. The perturbation growth rates, concentration, and turbulent variance all have 'event-like' structures. Although instabilities are predicted during each 1/2 wave and more often than concentration or turbulent variance events, the larger perturbation growth rates are correlated to the highly correlated concentration and turbulent variance events. The concentration (increasing with increasing proximity to the bed) and turbulent variance (decreasing with increasing proximity to the bed) magnitudes vary over the vertical (Foster, 1996), however the temporal event-like structure is uniform throughout this near-bed region. For further comparisons, we use one FOBS sensor located at 3 cm above the bed and the vertically averaged turbulent variance.

To examine the evolution of the growth rates, concentration, and turbulent variance

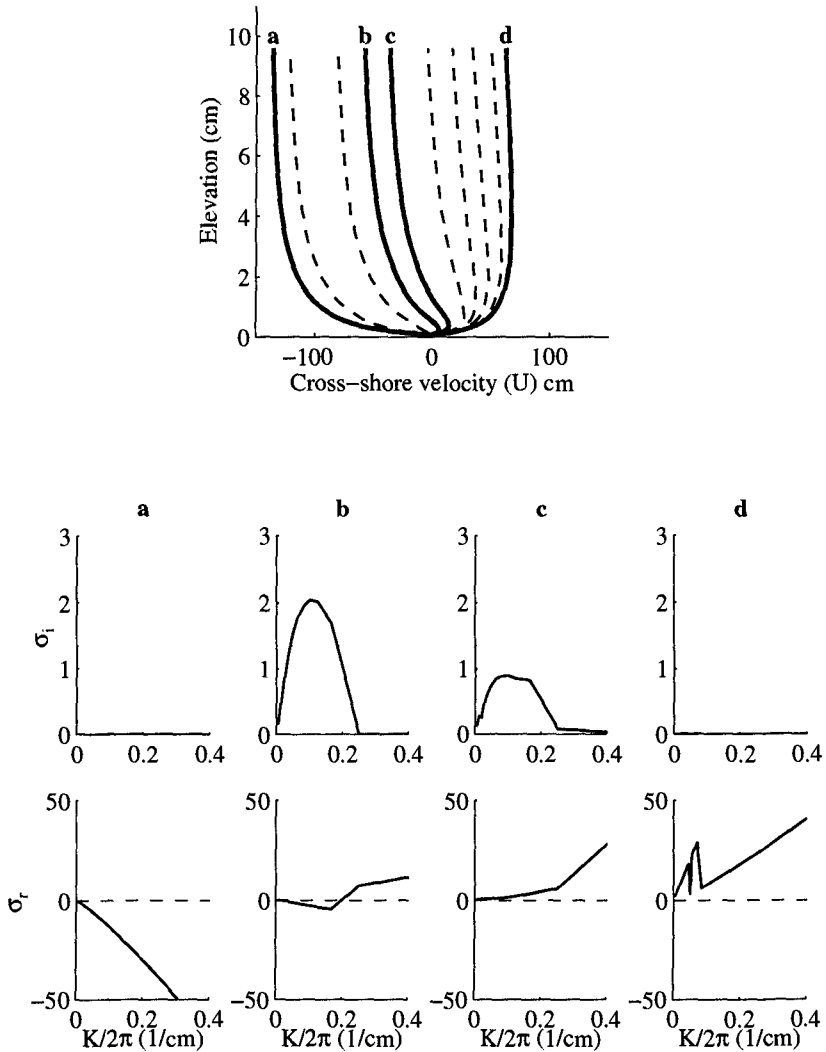


Figure 2: The top panels shows the vertical structure of $U(z, t)$ at 1/4 sec intervals over a 2.5 second record. At 4 of these times, a-d, we have shown the predicted perturbation growth rates, $\sigma_i(k)$ (Hz) (middle panels), and the real frequencies, $\sigma_r(k)$ (Hz) (bottom panels).

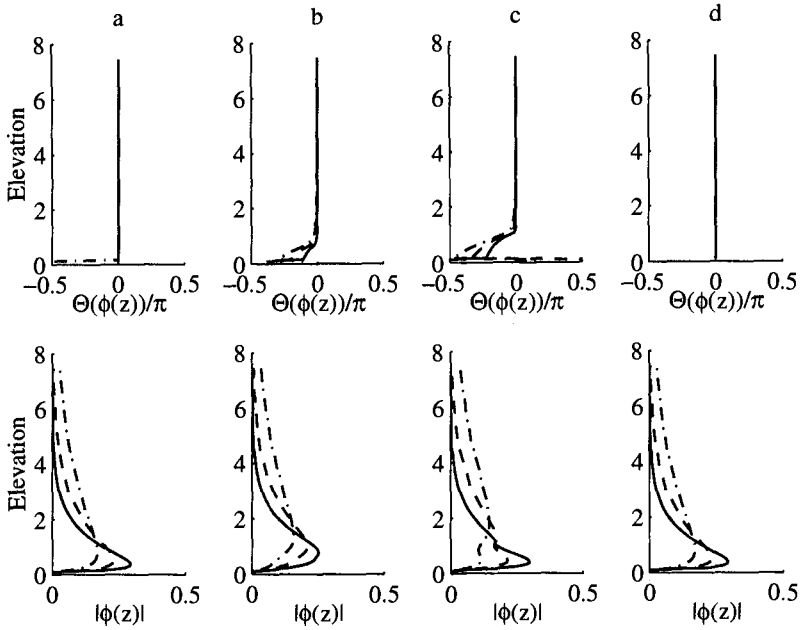


Figure 3: The top panels show the eigenfunction phase, $\Theta\phi(z)$, and the bottom panels show the amplitude, $|\phi(z)|$, for each of the 4 cases (a-d) for 3 selected wavelengths (straight line, 4 cm; dashed line, 10 cm; and dashed-dotted line, 20 cm).

over the course of the wave, we use a phase space averaging (PSA) technique. The PSA technique averages quantities of similar velocity and accelerations bins over a 256 second record. The acceleration is determined in the frequency domain with a tapered 1 Hz low pass cutoff frequency. This technique allows us to evaluate the phase averaged temporal event structure as it corresponds to the magnitude and phase of the background wave. The PSA for the growth rates, concentration, and turbulent variance are given in Figures 5, 6, and 7, respectively. The growth rate PSA shows two peaks, one prior to each of the flow reversal on the larger waves (the outer part of the wave ellipse), with the largest peak occurring after the wave crest when the internal shears are largest. The concentration PSA shows one peak during the flow reversal period following the wave crest prior to flow reversal at relatively the same phase as the growth rate. This peak also occurs at the outer part of the wave ellipse, indicating, not surprisingly, that concentration events are closely associated with the larger waves. The second peak in the concentration PSA occurs following the flow reversal and may be a result of the sediment plumes being advected back through the instrument array. The turbulent variance PSA shows a peak intensity at and following the large wave crest, leading to the concentration and predicted growth rates peaks. This indicates that the turbulence is occurring too early in the wave phase for it to be a result from the instabilities predicted here.

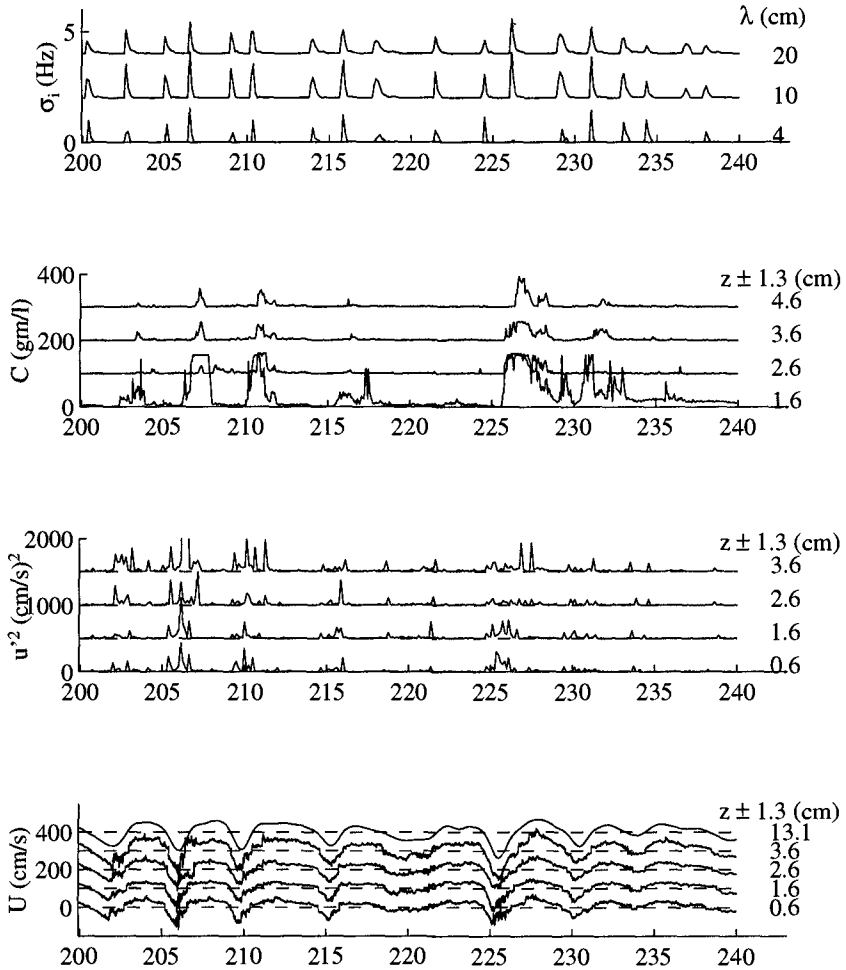


Figure 4: This example 60 sec time series shows near bed velocity as measured by four hot film anemometers and the free stream velocity as measured by an EMCM (bottom panel); high frequency VITA velocity variance at four elevations above the bed (lower middle panel); and concentration at 4 elevations above the bed (upper middle panel). The average distance of each sensor as measured by the FOBS is listed in the right column. The predicted growth rates at three wavelengths (4, 10, 20 cm) listed in the right column are given in the upper panel. Each velocity, variance, concentration, and predicted growth rate time series is offset by 100 cm/s, 500 (cm^2/s^2), 100 g/l, and 2 Hz, respectively. Offshore directed flow is defined with positive velocities.

5 Conclusions

Predicted instabilities for this quasi steady model occur over the appropriate length scales for them to be a plausible mechanism for the generation of turbulence and suspension of sediment. With this quasi-steady model, the instabilities are at the same phase as the sediment suspension events, but are occurring too late in the wave phase for them to be generating the observed turbulence. Work in progress indicates that considering the time-dependent nature of the background flow may yield growth rates which are larger and earlier in the wave phase.

Acknowledgments

This work was graciously funded by the Office of Naval Research, Coastal Sciences Program, and the Andrew Mellon Foundation. The first author wishes to thank Keith Thompson for his insight into the numerical computations world.

References

- Dodd, N., J. Oltman-Shay, and E.B. Thornton (1992), *Shear Instabilities in the longshore current: a comparison of observation and theory*, Journal of Physical Oceanography, 22.
- Foster, D.L., R.A. Beach, and R.A. Holman (1994), *Correlation sediment suspension events and shear instabilities in the bottom boundary layer of the surf zone*, Coastal Dynamics '94, ASCE, Barcelona, Spain.
- Foster, D.L., R.A. Beach, and R.A. Holman (1996), *Field Observations of the Wave Bottom Boundary Layer*, submitted to Journal of Geophysical Research.
- Foster, D.L. (1996), *Dynamics of the nearshore wave bottom boundary layer*, Ph.D. thesis, Oregon State University.
- Hino, M., M. Kashiwayanagi, A. Nakayama, and T. Hara (1983), *Experiments on the turbulent statistics and the structure of a reciprocating oscillatory flow*, Journal of Fluid Mechanics, 131, 363-400, .
- Rayleigh, L., and J.W. Strutt (1880), *On the stability, or instability of certain motions*, Proceedings of the London Mathematical Society, 11, 57-70.
- Shen, S.F.(1961), *Some Considerations on the laminar stability of incompressible time-dependent basic flows*, Journal of Aerospace Science, 28, 397-404 and 417.

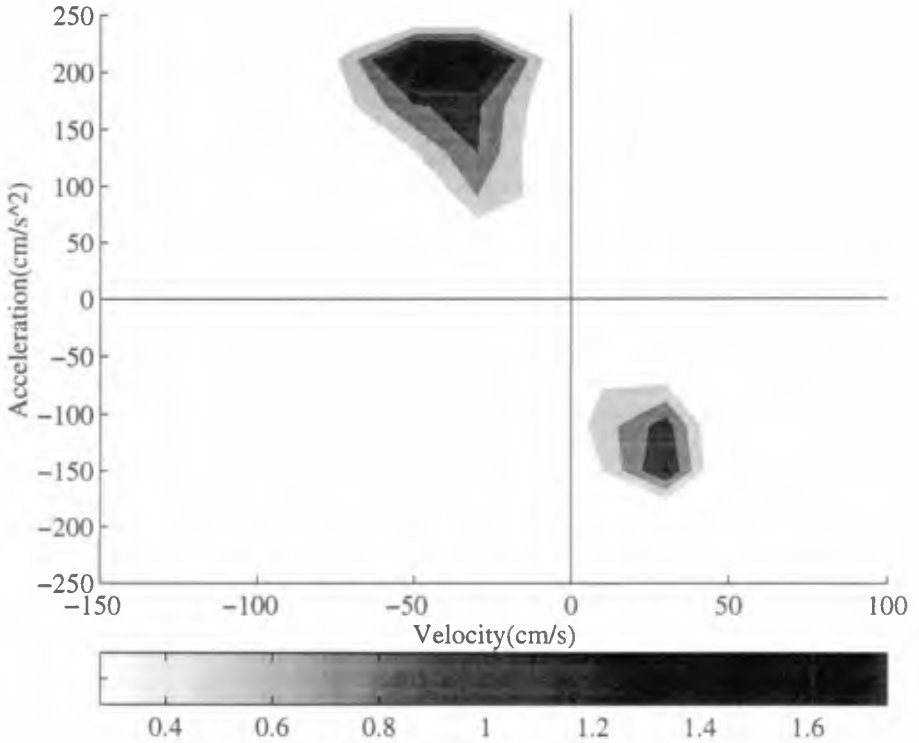


Figure 5: The phase space average of perturbation growth rate shows the background flow phases where the flow is momentarily unstable. The velocity and acceleration are binned at 20 cm/sec and 40 cm/sec² intervals, respectively. Note that the flow moves clockwise around the figure, and that zero acceleration and maximum negative velocity corresponds to the wave crest. The units of the grayscale colorbar are in Hz.

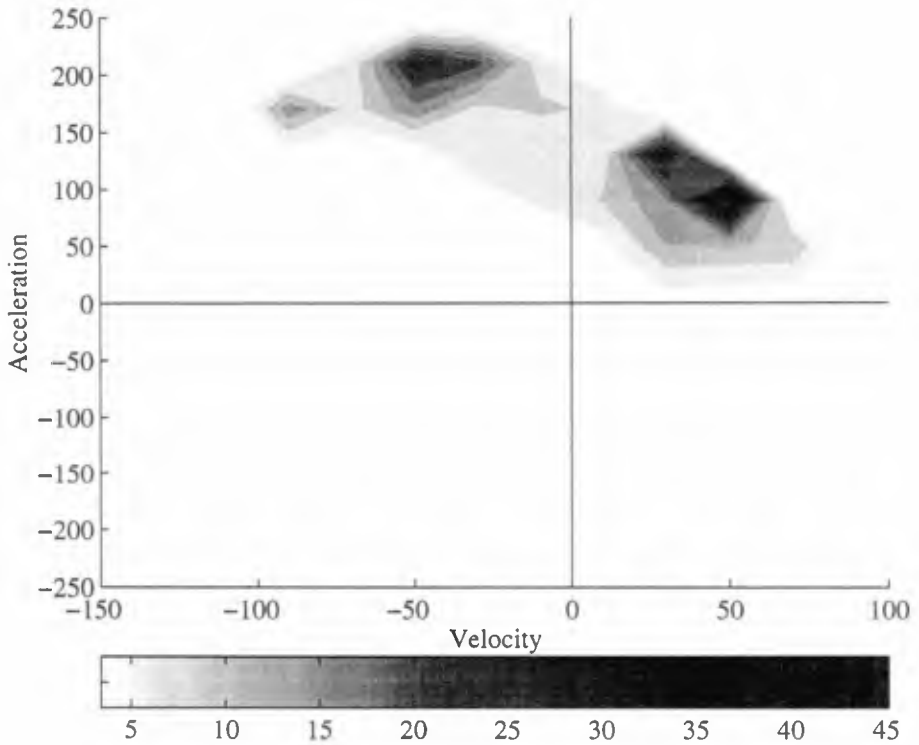


Figure 6: The phase space average of concentration at 3 cm above the bed shows the background flow phases where the suspension events occur. The velocity and acceleration are binned at 20 cm/sec and 40 cm/sec² intervals, respectively. Note that the flow moves clockwise around the figure, and that zero acceleration and maximum negative velocity corresponds to the wave crest. The units of the grayscale colorbar are in Hz.

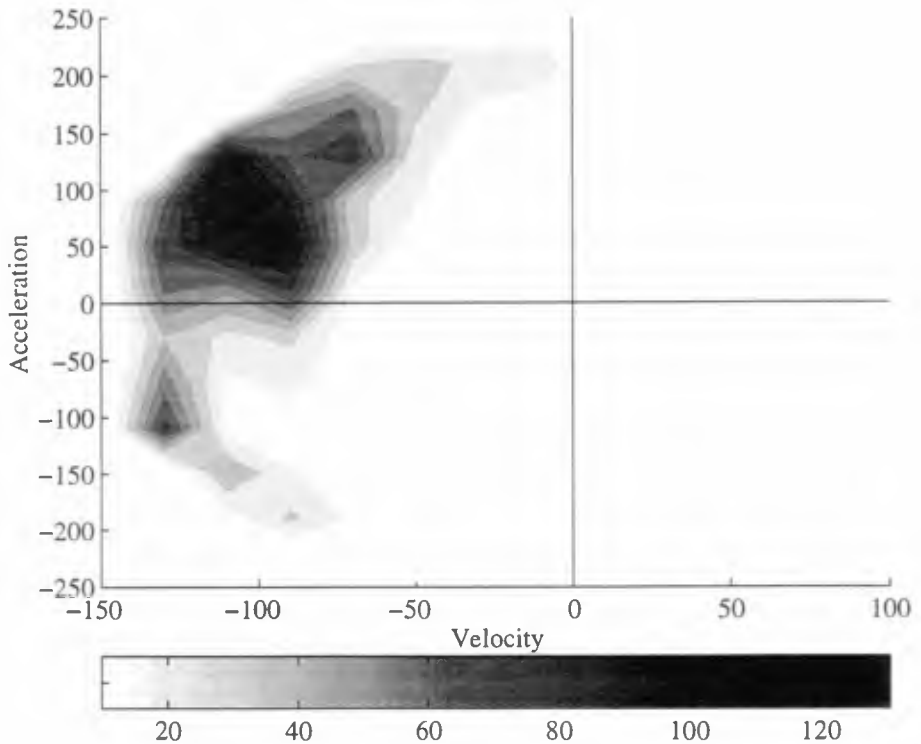


Figure 7: The phase space average of average turbulent variance over the 4 hot-film sensors shows background flow phases where the turbulent variance events occur. The velocity and acceleration are binned at 20 cm/sec and 40 cm/sec² intervals, respectively. Note that the flow moves clockwise around the figure, and that zero acceleration and maximum negative velocity corresponds to the wave crest. The units of the grayscale colorbar are in Hz.

CHAPTER 249

Wave Boundary Layer Flows and Pore Pressures in Permeable Beds

H. H. Hwung¹ K. S. Hwang² B. H. Lee³

Abstract

The boundary layer flows and wave-induced pore pressures inside porous beds are both investigated in wave tank. Two kinds of porous beds are composed of two different grades of quartz sands which the porosities are 0.437 and 0.472 respectively. According to the experimental results, it is found that the larger pore pressure in permeable bed is induced by the longer wave period, and the pore pressure has an exponential attenuation with the wave steepness increasing.

From the elaborate measurements in the boundary layer, the overshooting induced by wave motion is effected by bed porosity and it becomes smooth. In the experimental cases, the maximum horizontal overshooting occurs at $\tilde{z}/\delta \approx 1.2$, which is lower than the impermeable case of $\tilde{z}/\delta \approx 2.7$ obtained by Hwung and Lin (1989). Furthermore, the vertical overshooting has also been found in our experiments.

Introduction

The natural sea beds are usually permeable, however, most investigations about the bottom wave boundary layer flow were conducted on rigid impermeable beds. Longuet-Higgins (1953, 1958), Collins (1963), Jonsson (1966), Kajiura (1968) and so on, analyzed the characteristics of boundary layer flows with linear or nonlinear wave theory in uniform water depth. Furthermore, Du Toit and Sleath (1981), Sleath (1982, 1984, 1987), Hwung and Lin (1989) and other investigators detected the velocity profile of boundary layer on rigid bottom.

¹ Professor of Hydraulic and Ocean Engineering Department, Director of Tainan Hydraulic Laboratory, National Cheng Kung University, Tainan, Taiwan

² Associate Researcher of Tainan Hydraulic Laboratory, National Cheng Kung University, Taiwan

³ Graduate Student of Hydraulic and Ocean Engineering Department, National Cheng Kung University, Taiwan

Concerning the pore pressure induced by wave motion in permeable bed, many researchers have paid more attention on the theoretical studies, such as Putnam (1949), Sleath (1970), Liu (1973) and so on. However, only a few of experimental studies has been done in the past years. Therefore, the elaborate experiments including the pore pressure and boundary layer flow in permeable beds have been carried out in this paper.

Experimental set-up

Two different grade of quartz sand of which the porosities are 0.437 and 0.472 respectively, are used in the experiments. The wave flume and related facilities are schematically illustrated in Figure 1. Within the wave flume, a section which 120 cm x 30 cm x 26 cm is filled with quartz sands as the testing section. Four pore pressure transducers are buried inside the porous bed to measure the pore pressure, while a Laser-Doppler velocimetry is used to detect the velocities above the porous bed. The enlargement testing section with the experimental installation are shown in Figure 2.

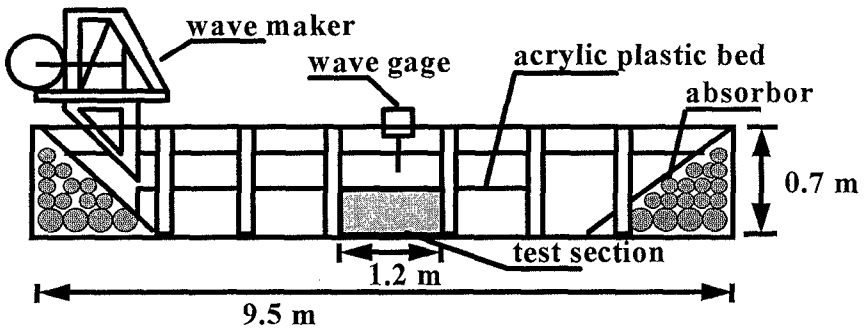


Fig. 1 The layout of wave flume

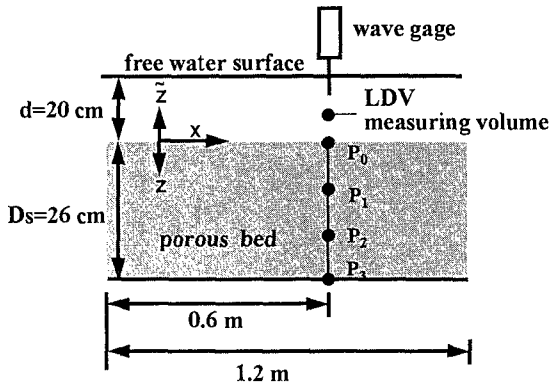


Fig. 2 The installation of test section

Herein, there are three kinds of experimental wave conditions listed in Table-1.

Table-1 The experimental wave conditions

Test Cases	T (sec)	d (cm)	H (cm)	H/L
Case 1	1.00	20	5.0	0.041
Case 2	0.95	20	7.0	0.062
Case 3	1.20	20	5.0	0.033

Results and Discussions

According to the experimental results, Figure 3 shows the original measurements of water surface elevation and horizontal, vertical velocities. Due to the wave reflection and boundary turbulent effect, we can see the fluctuations are existed in the velocity measurements. And Figure 4 is the original measurements of water surface elevation and the corresponding dynamic pore pressure. It is obviously to see that the dynamic pore pressure is decreasing from surface to bottom.

From the above original measurements, it shows that the length of each wave cycle in wave flume is not exactly the same due to wave reflection. This phenomena will lead to phase time shifting and create a false image of wave component by the phase average method. Therefore, according to the modified phase average method proposed by Hwung *et al.* (1988), the quantities of phase average can be express as

$$\langle Q \rangle = \frac{1}{N} \sum_{j=1}^N \tilde{Q} \left(\frac{T_j}{T} \cdot t_i \right) + \bar{Q} \quad i=1 \sim M$$

where $\langle Q \rangle$: the quantities of phase average,
 \tilde{Q} : the quantities of wave component,
 \bar{Q} : the quantities of time average,
 N : numbers of testing wave cycle,
 M : numbers of phase time within one wave cycle.

After using the modified phase average method, the water surface elevation, velocities and dynamic pore pressure measurements are shown in Figure 5 and Figure 6 respectively, and the quantities of velocities and dynamic pore pressure at any phase time can be calculated from the above figures.

From the above measurements and analysis, we obtained the relationship between dimensionless pore pressure attenuation and wave period for the two different quartz sands in Figure 7. It shows that the pore pressure increases linearly as

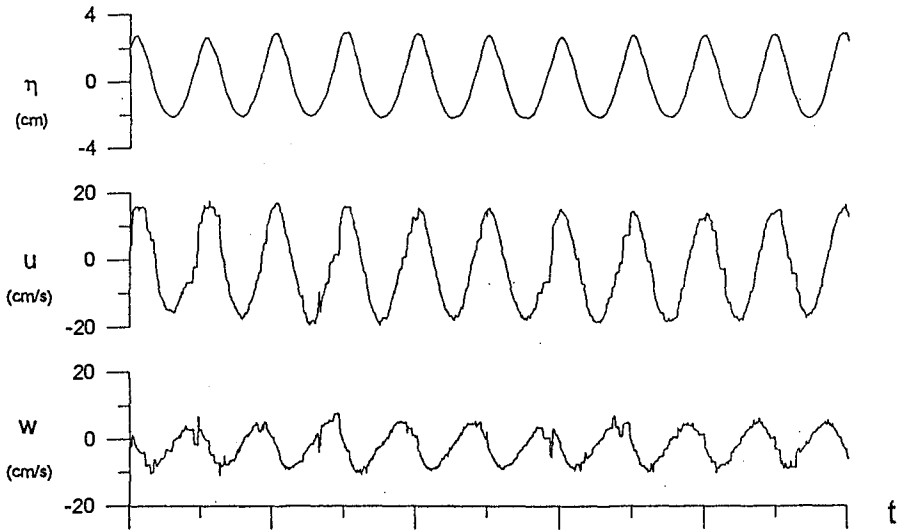


Fig. 3 The surface elevation and velocity measurements

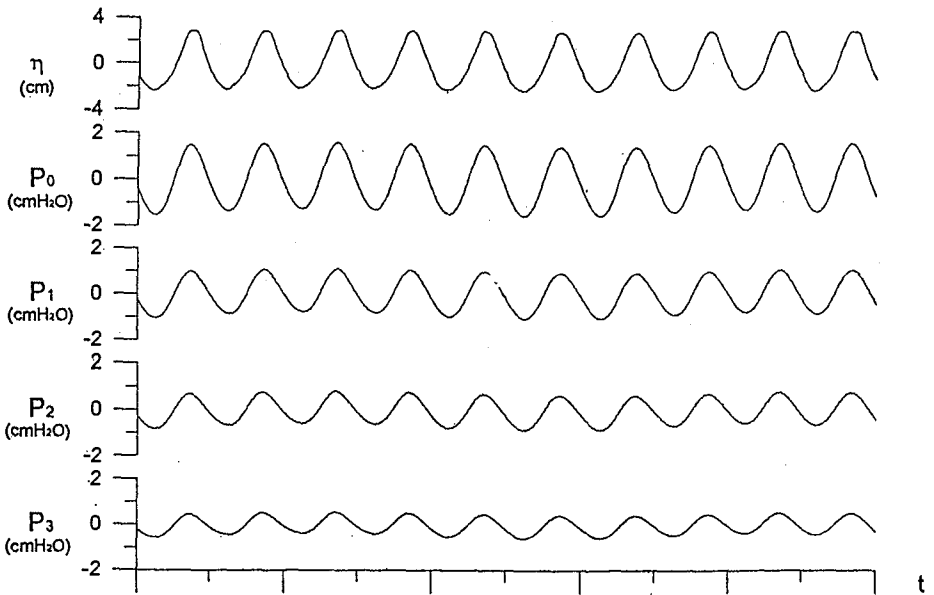


Fig. 4 The surface elevation and pore pressure measurements

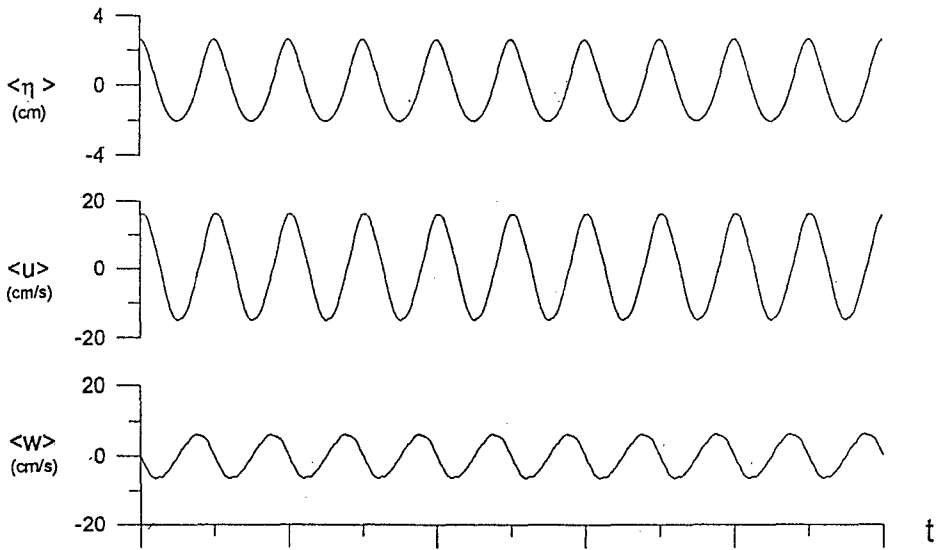


Fig. 5 The surface elevation and velocity measurements of the modified phase average

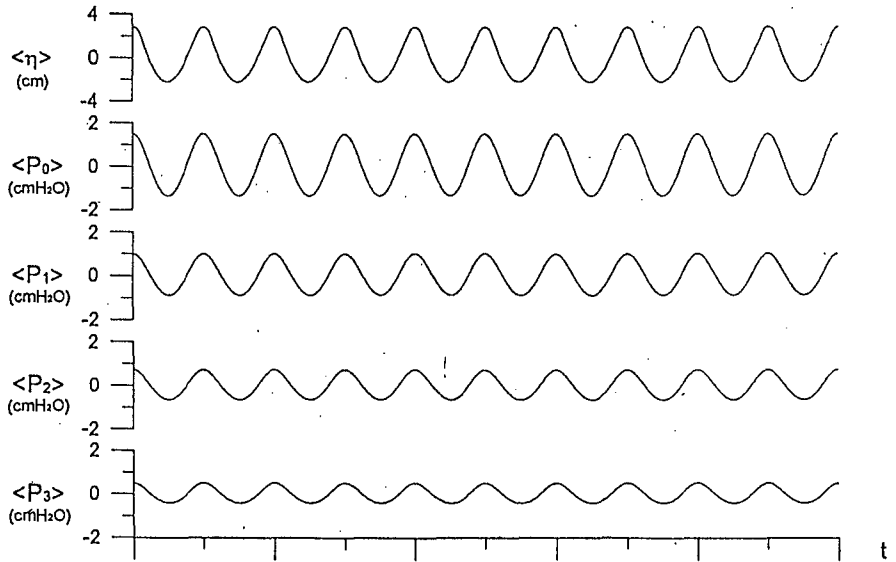


Fig. 6 The surface elevation and pore pressure measurements of the modified phase average

wave periods increasing, and the larger porosity bed has larger pore pressure at the same permeable depth. Besides, Figure 8 shows the relationship between dimensionless pore pressure attenuation and wave steepness. From the results, we found that the pore pressure decreases as wave steepness increasing, and it seems to have an exponential attenuation in this figure.

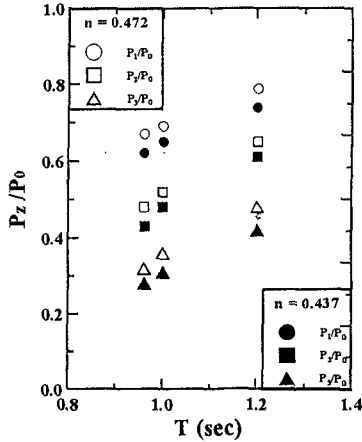


Fig. 7 The relationship between pore pressure attenuation and wave period

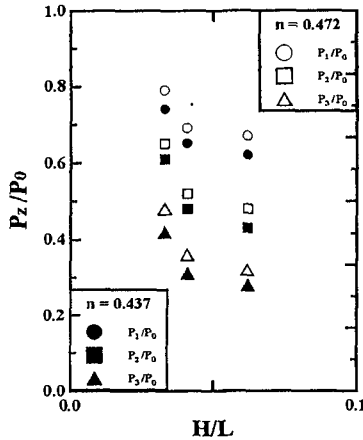


Fig. 8 The relationship between pore pressure attenuation and wave steepness

In addition, we also made the comparison between the dynamic pore pressure and previous theoretical studies as shown in Figure 9. We see that it has similar variation for the measurements and theoretical values, however, there is a little difference at the bottom, due to the reflection of rigid bed.

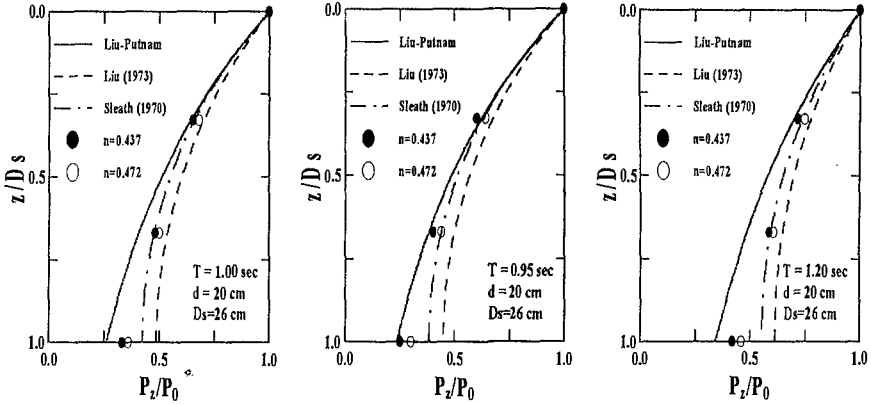


Fig. 9 The comparison between pore pressure measurements and theoretical values

In order to understand the boundary flows on permeable beds, a two-dimensional LDV system was employed to detect the horizontal and vertical velocities simultaneously. Figure 10 shows the horizontal velocity distributions on the permeable bed of porosity is 0.437 at seven different time phases. We can see that it also has overshooting in the boundary layer at $\tilde{z}/\delta \approx 1.2$, and it is less than on rigid smooth bottom which the overshooting is at $\tilde{z}/\delta \approx 2.7$ obtained by Hwung and Lin (1989). Figure 11 shows the horizontal velocity distributions on the permeable bed of porosity is 0.472 at different time phases. And the overshooting phenomena disappears in this larger porosity case.

Further, the extreme horizontal velocity distributions of all experiments are plotted in Figure 12, we can see that the overshooting phenomena in the boundary layer is clearer in shorter wave period and the overshooting disappears in longer wave period. The another cases of the extreme horizontal velocity distributions on the permeable bed of porosity is 0.472 as shown in Figure 13. From the comparison with Figure 12, we see that the boundary layer flows are more uniform in larger porosity bed.

Finally, the extreme vertical velocity distributions in bottom boundary layer on the permeable beds are shown in Figure 14 and Figure 15 respectively. It is interesting to see that the velocity in lower layer are larger than in upper layer within the boundary layer, and the velocities are more scattering due to the effect of vertical low passing through the porous material. From the vertical velocity distribution, we found the overshooting phenomena also occurs in porous bottom boundary layer.

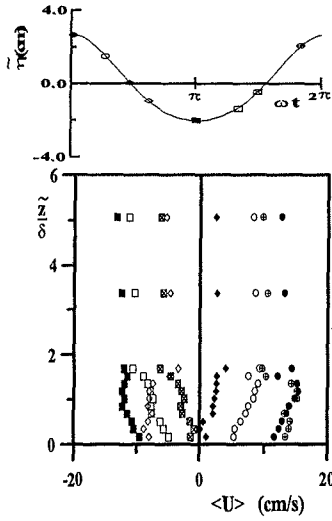


Fig. 10 Case 1, The horizontal velocity distributions on permeable bed of $n=0.437$

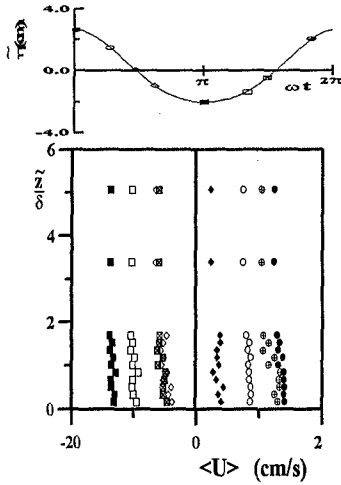


Fig. 11 Case 1, The horizontal velocity distributions on permeable bed of $n=0.472$

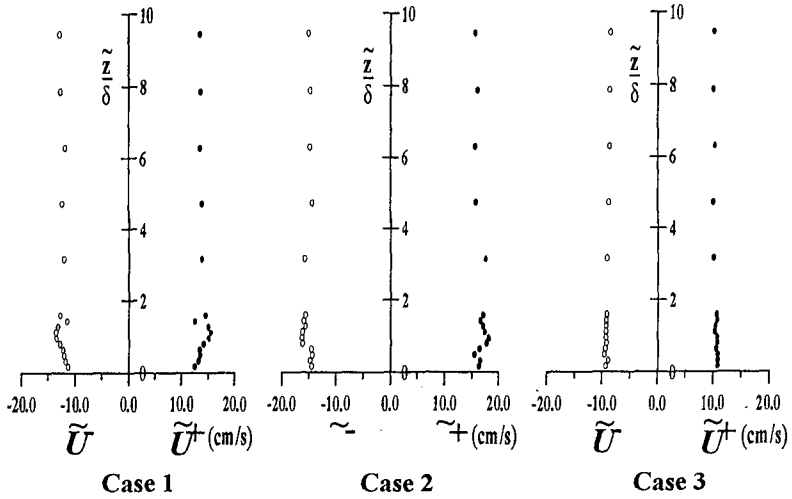


Fig. 12 The extreme horizontal velocity distributions on permeable bed of $n=0.437$

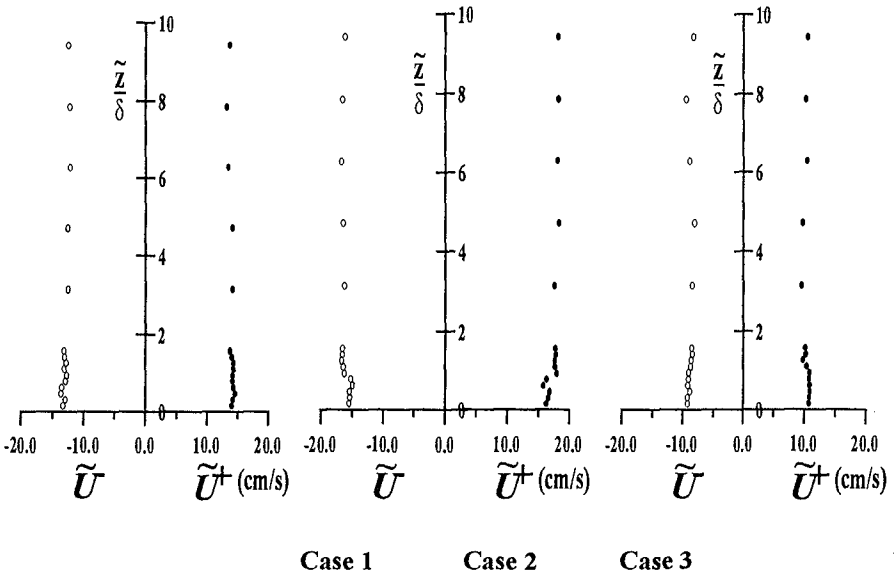


Fig. 13 The extreme horizontal velocity distributions on permeable bed of $n=0.472$

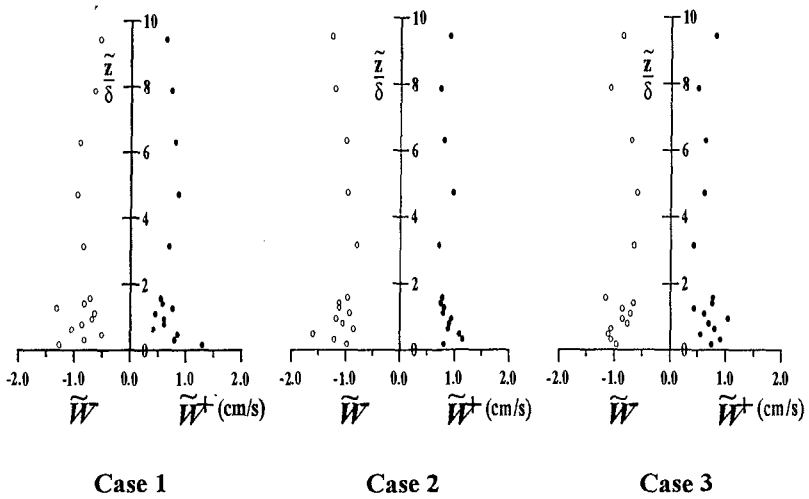


Fig. 14 The extreme vertical velocity distributions on permeable bed of $n=0.437$

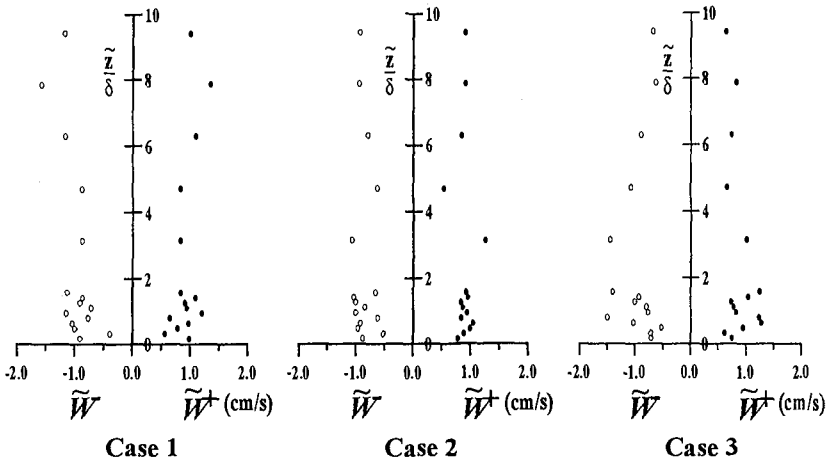


Fig. 15 The extreme vertical velocity distributions on permeable bed of $n=0.472$

Conclusions

The results summarized above indicate that the permeability of the bottom would result in interesting phenomena in wave boundary flows and dynamic pore pressure. Some remarkable conclusions would be described as follows:

1. In permeable beds, the larger pore pressure is induced by the larger wave period, and the dynamic pore pressure decreases exponential with the wave steepness increasing.
2. On the same wave condition, the larger porosity bed has larger dynamic pore pressure.
3. In the boundary layer, the horizontal overshooting induced by wave motion is influenced by bed porosity and becomes smoother. In our experimental cases, the maximum horizontal overshooting occurs at $\bar{Z} / \delta \approx 1.2$, which is lower than the impermeable case of obtained by Hwung and Lin (1989).
4. From the vertical velocities measurements, we found that the vertical overshooting phenomena also occurs within bottom boundary layer.

References

1. Longuet-Higgins, M.S. (1953): Mass transport in water waves, Phil. Trans. Royal Society of London, Series A, No. 903 Vol. 245, pp. 535-581.
2. Longuet-Higgins, M.S. (1958): The mechanics of the boundary-layer near the bottom in a progressive waves, Proceedings of the 6th International Conference of Coastal Engineering, pp. 184-193.
3. Collins, J.I. (1963): Inception of turbulence at the bed under periodic gravity waves, J. Geophysical Research, Vol. 68, pp. 6007-6014.
4. Jonsson, I.G. (1966): Wave boundary layers and friction factors, Proceedings of the 10th International Conference of Coastal Engineering, pp. 127-148.
5. Kajiura, K. (1968): A model of the bottom boundary layer in water waves, Bull. Earthquake Research Inst., Vol. 46, pp. 75-123.
6. Du Toit and J.F.A. Sleath (1981): Velocity measurements close to rippled beds in oscillatory flow. Journal of Fluid Mechanics, Vol. 112, pp.77-96.
7. Putnam, J.A. (1949): Loss of wave energy due to percolation in a permeable seabed, Trans. Am. Geo. Un., 30, pp. 349-356.
8. Sleath, J.F.A. (1970): Wave-induced pressure in beds of sand. J. Hyd. Div., ASCE, 96, HY2. pp.367-378.
9. Liu, P.L.F. (1973): Damping of water waves over porous beds. J. Hyd., Div., ASCE, 99, HY12, pp.2263-2271.

10. Sleath, J.F.A. (1984): *Sea Bed Mechanics*. John Wiley & Sons, Inc. Press.
11. Hwung H.H., S.C. Wang and C. Lin (1988): The investigation of turbulent characteristics in the surf zone by LDV, Proceedings of the 10th Conference on Ocean Engineering in Republic of China, pp. 17-34.
12. Hwung, H.H. and C. Lin (1989): The experimental study on the boundary layer flow of waves propagating on a sloping bottom, The Chinese Journal of Mechanics, Vol.5, No.1, pp.67-76. (in Chinese)

CHAPTER 250

Backfilling Of Trenches Exposed to Waves

Jacob Hjelmager Jensen¹ and Jørgen Fredsøe²

Abstract

This paper treats the numerical prediction of initial and long-term morphology of small pipeline trenches. For this purpose a refined flow and sediment transport description is applied such that the entire mathematical problem is formulated and solved on a curvilinear grid using a $k - \epsilon$ turbulence-closure.

The backfilling process of trenches exposed to either waves or a steady current is of importance in relation to the implementation of pipelines in the marine environment. With respect to the sedimentation of trenches, the non-dimensional Trench-Keulegan-Carpenter number, $KC = a/L$, where a is the excursion length of a particle in waves and L the trench length, is investigated in detail, and an optimal KC -number for the backfilling rate is found. Coherent structures in the non-uniform unsteady trench-flow are shown to dominate the deposition rate when present.

The importance of a detailed description of the flow is further justified by comparing predictions of a very simple flow-model neglecting convective terms with the sophisticated flow-model.

Introduction

The morphodynamics of trenches or other man-made excavations in the marine environment involves the process of natural backfilling. In some cases backfilling is intended, as is the case with pipeline trenches, yet, in other cases, such as navigation channels, self-maintenance is striven for. For scientific as well as for economic reasons it is desirable to fully understand and control the mechanisms responsible for this specific morphological process.

A number of investigations of flow and sediment transport processes in a trench or a navigation channel have been conducted during the years. Bijker (1980), van Rijn (1986) and the analytical work of Fredsøe (1979) focus on the sediment transport processes. Other papers such as Alfrink's (1983) and Basara's (1995) focus on the sophisticated modelling of the hydrodynamics. These papers are all confined to the steady current case, and treat waves, if modelled, as a stirring mechanism for sediment only.

¹Ph.D.-student, ISVA, Tech. Univ. of Denmark, DK-2800 Lyngby, Denmark.

²Professor, ISVA, Tech. Univ. of Denmark, DK-2800 Lyngby, Denmark.

Deposition of sediment takes place whenever a suspended particle advected by the flow starts adapting to an environment with less capacity. This might happen when the velocity or the turbulent kinetic energy level of the fluid decreases. A change in fluid capacity is exactly what a particle travelling with the flow across a trench will experience. A net deposition of sediment within the boundaries of the trench may therefore take place. On top of that the bottom concentration of the suspended sediment decreases, which means that less sediment will erode from the bed. Another important contribution to the backfilling process is the action of gravity on bed-load particles moving on a sloping bed that makes particles go downhill more easily than uphill.

For particles carried by a steady stream past a trench the maximum change in capacity (depth-averaged velocity for instance) is obviously some function of the maximum expansion in depth. However, in the case of an oscillatory flow crossing the trench a suspended particle might not experience the maximum expansion in depth. For a given wave situation the expansion felt by a particle advected with the flow generally becomes a function of both the Trench-Keulegan-Carpenter-number and the maximum expansion in depth.

Problem

The trench is initially sinusoidal and characterized by a length, L , and a depth, h , see figure (1). The water depth is called D .

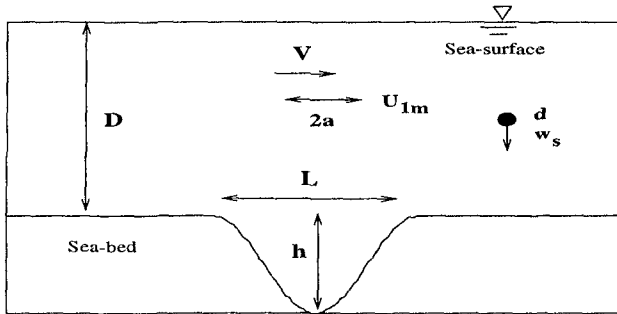


Figure 1: Sketch defining some of the key parameters used in the text.

The bed sediment is characterized by a fall velocity, w_s , and a diameter, d . The flow is generally combined by waves and currents (co-directional) and these are separately characterized by the fluxes, V and U_{1m} . The excursion length for a particle in a wave motion is symbolized by a . The wave is simulated by an oscillating pressure gradient neglecting any deformations of the water surface.

The initial backfilling rate is generally a function, Π , of all above-mentioned quantities, i.e.:

$$\Delta q = \Pi(L, h, D, d, w_s, a, V, U_{1m}, g)$$

where Δq is the amount of trapped sediment. A natural selection of non-dimensional

parameters from these quantities become:

$$\Delta\phi = \Psi\left(\frac{h}{L}, \frac{h}{D}, \theta, Z, KC, \frac{V}{V + U_{1m}}, \frac{k_N}{D}\right)$$

The parameters are in order of appearance referred to as: steepness, expansion, Shields, ($\theta = U_f^2/((s-1)gd)$) and Rouse parameter ($Z = U_f/(\kappa w_s)$), Trench-Keulegan-Carpenter number (a/L) and the wave/current parameter, where U_f is the friction velocity at a reference point far from the trench. The spatial coordinates, x (horizontal) and z (vertical), are non-dimensionalized by D and the time, t , by $(U_{1m} + V)/D$. For the present case the wave/current parameter is either 0 or 1, that is for waves and currents, respectively. All intermediate points define a combined wave/current flow. Furthermore, we will confine ourselves to an analysis based on the expansion parameter and the KC -number.

Solution of flow and sediment-transport equations

The finite volume concept (see Patankar (1980)) formulated in curvilinear orthogonal multi-block coordinates is applied, solving the transformed continuity equation and the fully 2D transformed Reynolds-averaged Navier-Stokes equations employing the standard $k - \epsilon$ closure of turbulence. A thorough description of the present model is reported by Tjerry (1997).

The partial differential equations of the turbulence model in Cartesian form, i.e. turbulent kinetic energy, k , and dissipation of turbulent kinetic energy, ϵ , are given by:

$$\frac{\partial k}{\partial t} + \frac{\partial u_j k}{\partial x_j} - \frac{\partial}{\partial x_j} \left(\frac{\nu_T}{\sigma_k} \frac{\partial k}{\partial x_j} \right) = \nu_T \frac{\partial u_i}{\partial x_j} \left(\frac{\partial u_j}{\partial x_j} + \frac{\partial u_j}{\partial x_i} \right) - \epsilon \quad (1)$$

$$\frac{\partial \epsilon}{\partial t} + \frac{\partial u_j \epsilon}{\partial x_j} - \frac{\partial}{\partial x_j} \left(\frac{\nu_T}{\sigma_\epsilon} \frac{\partial \epsilon}{\partial x_j} \right) = C_{\epsilon 1} \frac{\epsilon}{k} \nu_T \frac{\partial u_i}{\partial x_j} \left(\frac{\partial u_j}{\partial x_j} + \frac{\partial u_j}{\partial x_i} \right) - C_{\epsilon 2} \frac{\epsilon^2}{k} \quad (2)$$

Here, t is time, x_i the spatial coordinates, u_i the velocities and ν_T is the eddy-viscosity, calculated from:

$$\nu_T = C_\mu \frac{k^2}{\epsilon} \quad (3)$$

The set of constants that appears in the $k - \epsilon$ model is standard choice and originally proposed by Launder (1974):

C_μ	σ_k	σ_ϵ	$C_{\epsilon 1}$	$C_{\epsilon 2}$
0.09	1.0	1.3	1.44	1.92

The transport of sediment, q , is divided into a bed and a suspended load contribution and corrected with the porosity, n , implicitly. The non-dimensional bed load, ϕ_B , is calculated using the Meyer-Peter formula modifying tractive stresses with slope effects as suggested by Fredsøe (1978):

$$\phi_B = \frac{q_B/(1-n)}{\sqrt{(s-1)gd^3}} = \frac{8}{(1-n)} (\theta - \theta_c - 0.1 \frac{\partial h}{\partial x})^{3/2} \quad (4)$$

where q_B is the bed load, $\partial h/\partial x$ the slope of the bed, g the acceleration of gravity, s the relative density and θ_c the critical Shields parameter (~ 0.05).

The concentration of suspended sediment is derived by solving the transport equation:

$$\frac{\partial c}{\partial t} + u \frac{\partial c}{\partial x} + v \frac{\partial c}{\partial z} = w_s \frac{\partial c}{\partial z} + \frac{\partial}{\partial x}(\nu_T \frac{\partial c}{\partial x}) + \frac{\partial}{\partial z}(\nu_T \frac{\partial c}{\partial z}) \quad (5)$$

The non-dimensional suspended transport, ϕ_S , is found as:

$$\phi_S = \frac{q_S/(1-n)}{\sqrt{(s-1)gd^3}} = \frac{\int_{-h}^1 cudz/(1-n)}{\sqrt{(s-1)gd^3}} \quad (6)$$

where q_S is the suspended transport, and u and v are the longitudinal and vertical velocities, respectively.

Intra-wave calculation is applied for the sediment-transport model in order to take into account non-linear and phase-lag effects.

In the present model the water surface is taken to be plane, and the waves are introduced as an oscillatory motion caused by an oscillatory pressure gradient. At the water surface the flow equations apply symmetry conditions while the c -equation applies a no-flux condition. At the bed boundary a no-slip condition is used for the momentum equations, and a Dirichlet condition is used for the c -equation as the Engelund-Fredsoe formula (1976) is applied, i.e. $c_b = c_b(\theta)$, where c_b is the concentration at bed level.

Furthermore the k -equation uses a no-flux condition at the bed, and the bed condition for the ϵ -equation reads: $\epsilon = (30C_\mu^{0.75})/(\kappa k_N/D)k^3/2$, where k_N/D is the relative roughness of the sea-bed and κ the von Karman mixing length constant. On the in- and outlets Dirichlet and Neumann are applied, respectively, if not, periodic conditions are used.

The total flux of sediment is used in a continuity equation, which governs the morphodynamics. This reads:

$$\frac{\partial h}{\partial t} + \frac{\partial q}{\partial x} = 0 \quad (7)$$

stating that the divergence of depth-integrated sediment flux, $q = q_B + q_S$, is equal to the rate of change in bed elevation, h . This equation is discretized with a second order accurate scheme minimizing numerical diffusion. This is crucial when predicting diffusive processes such as backfilling of trenches.

If the entire flow, sediment, and morphological modules are run together, the dynamics of a mobile bed can be described and the backfilling tracked.

Backfilling in currents

In addition to the $k - \epsilon$ model an alternative flow description of the depth-averaged type is employed for the steady state case to emphasize the effect of including a more refined flow description. The depth-averaged approach uses a prescribed logarithmic velocity profile matched by the flux of water and a parabolic eddy-viscosity distribution

scaled with the friction velocity. This is identical to a flow solution where convective terms have been ignored, i.e. local equilibrium.

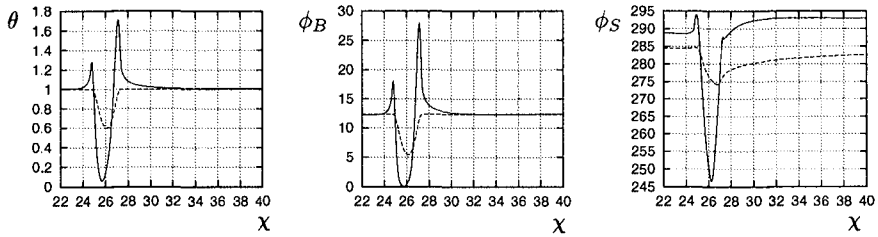


Figure 2: The Shields parameter along with the non-dimensional bed and suspended load distributions across a trench with the deepest section of the trench at $x = 26$ predicted by a $k - \epsilon$ model and a depth-averaged model. Reference flow: \rightarrow . Parameters are: $L/h=10$, $\theta=1$, $h/D = 0.25$ and $Z=0.6$. $k - \epsilon$ model: —, Depth-averaged model: - - -.

The depth-averaged approach has earlier been applied in the field of sediment transport for analytical purposes, and it is therefore of interest to compare the performance of these flow models with respect to morphology (cf. e.g. Fredsøe (1979)).

The shear stress along with the non-dimensional bed and suspended load predicted by the two flow models typically vary as illustrated in figure (2). It is obvious from the shear-stress variation (i.e. $\theta(x)$) that the depth-averaged approach cannot in detail capture the complex behaviour of flow over a negative bump, which involves separation (or retardation), a phase shift between shear stress and bed form, speed-up and the relaxation of speed-up.

It is seen from figure (2) that both models predict erosion and deposition on the down- and upstream trench side, respectively. The additional shear stress features uncovered by the $k - \epsilon$ model relate in a morphological sense to a faster migration, a slower backfill (partly due to the above mentioned phase shift) and a more violent downstream deformation. The progressing asymmetrical shape of the bed, $h(x)$, is captured with both models as seen in figure (3), where bed forms at $T = tV/D=3000$, 9000, 18000 and 28000 are shown.

It is surprising how well the depth-averaged flow model performs in general and with respect to backfilling in particular. One reason for this is that the sediment transport mechanics such as the response length of suspended sediment is the governing parameter for the backfilling, and that very detailed flow mechanics to some extent is unnecessary. However, for $h/D \rightarrow 0$ (deep-water case) the depth-averaged model must fail since the gradient in capacity as well as in bottom concentration approaches zero in the limit. In this case the depth-averaged mechanism is not capable of explaining the deposition process, and a detailed description of the flow past a trench, including separation or even flow retardation, becomes necessary.

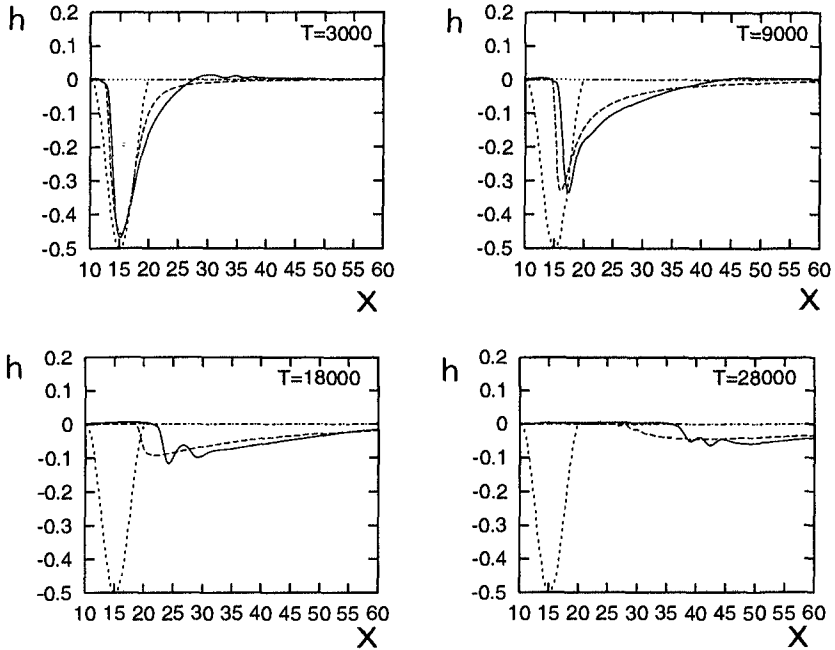


Figure 3: Shape of trench at four stages of its morphological evolution, for $k_N/D = 0.001$, $w_s/V = 0.02$ and $\theta = 0.25$. Reference flow (current alone): \rightarrow . $k - \epsilon$ model: --- , Depth-averaged model: - - - , Initial trench shape:

Backfilling in waves

If wave effects are included matters become more complicated. The waves introduce an additional parameter that in non-dimensional form is described by a KC -number. This is the Keulegan-Carpenter number well-known from the offshore hydrodynamics where it is defined as:

$$KC = \frac{2\pi a}{D_c}$$

in which D_c = the diameter of the cylinder. For small KC -numbers ($< 1-2$) flow separation will not occur, while at larger KC -numbers ($> 10-20$), the flow is fully separated. In trenches, the flow may also separate if the slope is steep enough, and the equivalent KC -number is sufficiently large. In the following we define this number by:

$$KC = a/L$$

With respect to the sedimentation of trenches the KC -number involves at least one important aspect other than flow-separation. For $KC \sim 1$ it is seen that a sand particle picked up on the plane bed may reach the deepest part of the trench where it may settle due to a reduced capacity. The capacity is reduced on the upstream slope as the depth increases (non-uniformity) and as the flow decelerates (unsteadiness), which

gives rise to smaller flow velocities as well as a decrease in intensity of turbulent kinetic energy.

So this is what happens: As suspended particles adapt to the local flow capacity by settling, they might get trapped in the separation bubble growing simultaneously on the upstream slope. If the vortex (former separation bubble) maintains its rotation and is able to keep the particles 'alive' when ejected at flow reversal, particles will be convected out of the trench and into the outer flow with the vortex.

The situation described is captured in figure (4) where time series of contours of concentration and turbulent kinetic energy are shown side by side for a short span of time around flow reversal. The phase in the wave period is symbolized as a dot on the sine-curve (positive values indicate left- to right-going flow).

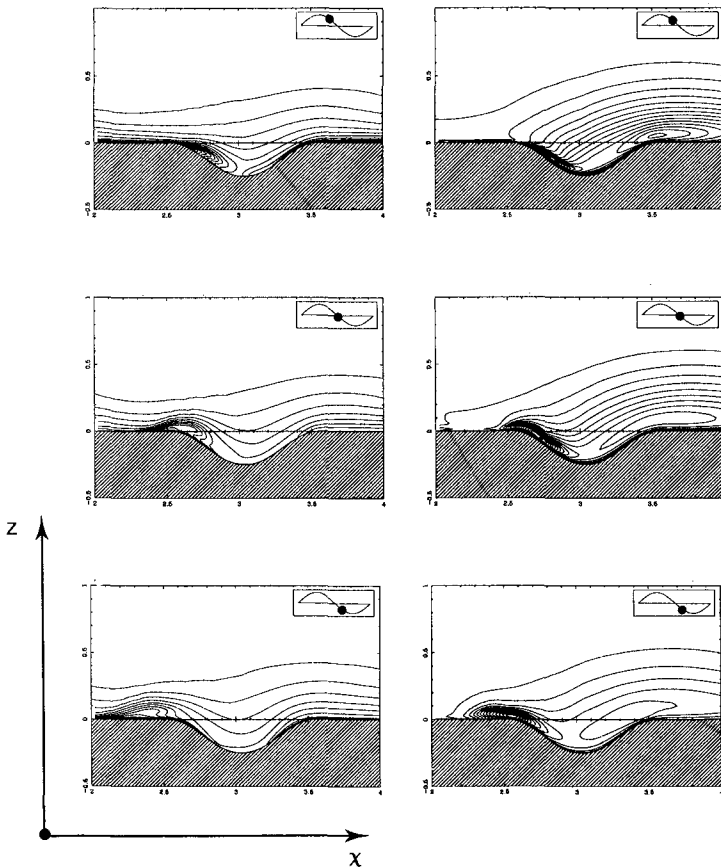


Figure 4: Time series of contours of concentration (left hand side of figure) and turbulent kinetic energy (right hand side of figure) around flow reversal. For $L/h=5$, $\theta=1$, $h/D=0.25$, $w_s/U_{1m}=0.02$ and $KC=1$.

While the separation develops on the upstream slope, the speed-up of fluid on the downstream trench-shoulder creates high shear-stress levels, which causes a large amount of sediment to suspend. This is seen in figure (5) where time series of profiles for horizontal velocities and contours of concentration are placed side by side at a phase close to flow reversal. The speed-up process in the converging section is visualised by sediment being bursted off the sloping trench bed. This results in an overloaded cloud of sediment that returns with the reversing flow to deeper parts of the trench where it most likely will be deposited. This process, captured in figure (5), may intensify the backfilling.

The time series of concentration contours shown in figure (5) are created by shutting off the bed erosion shortly before the reversal of the flow occurs.

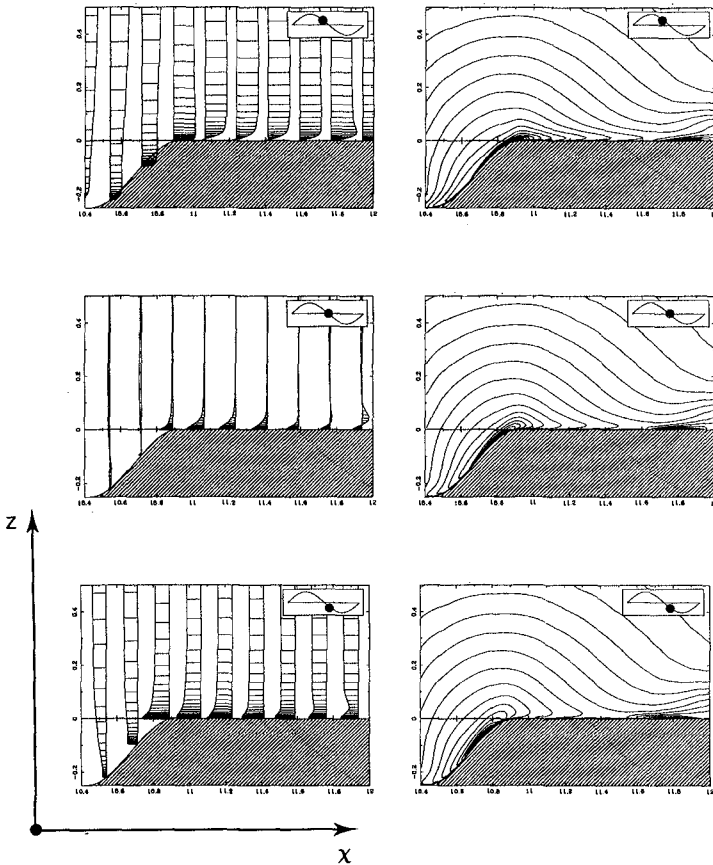


Figure 5: Time series of profiles of horizontal velocities (left hand side of figure) and contours of concentration (right hand side of figure). For $L/h=5$, $\theta=1$, $h/D=0.25$, $w_s/U_{1m}=0.02$ and $KC=1$.

The non-uniform and unsteady flow separates and will speed-up succeedingly, which in the period-averaged sense will create a near bed flow directed towards the banks. A return flow, required for reasons of continuity, is therefore directed towards the centre of the trench so that the time-averaged streamline pattern, depicted in figure (6), shows two cells rotating clock- and anti-clockwise on the left and right hand side, respectively. It is also worth noticing that two additional rotating cells will develop on the shoulders of the trench.

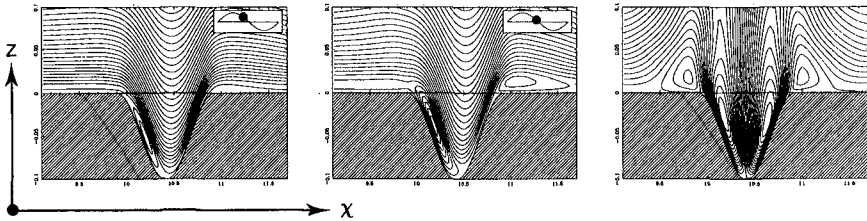


Figure 6: Two patterns of instant streamlines just before flow reversal occurs (in both cases the direction of main flow: \rightarrow) along with the corresponding period-averaged streamline pattern. $KC=0.5$, $h/D=0.1$, $L/h=10$, $k_N/D=0.001$.

The result seen on the right hand side of figure (6) is a time-integrated effect from using a detailed flow-description.

Distributions of the time-averaged bed and suspended loads are shown in figure (7). With the streaming pattern in mind it is interesting to study the period-averaged bed load distribution in the neighbourhood of the trench. The resulting transport rate is an outcome of a battle between the action of gravity and the time-averaged shear stress. It is seen that the gradient, $\partial q_B/\partial x$, which determines whether the sinusoidal trench is being eroded (positive) or sediment is being deposited (negative) in some cases may shift sign at the centre of the trench, such that the deepest regions of the trench is eroded. The cases where the deepest regions are eroded are, for this particular span of parameters, found (see left hand side of figure (7)) as the KC -number is increased and the steepness parameter decreased, thus the time-averaged hydrodynamical forces are strengthened and the gravitational forces weakened.

The period-averaged rotating cells which appear on top of the shoulders are reflected in the bed transport, $\bar{\phi}_B$, at that particular location. This is shown on the left hand side of figure (7). The bed transport here are, however, damped by the vortices (increases in strength with the KC -number) which pass through the shoulder region shortly after flow reversal.

The influence of the vortex on $\bar{\phi}_B$ and $\bar{\phi}_S$ at a given location on the flat bed is recognized as a departure from $\bar{\phi}_B = 0$ and $\bar{\phi}_S = 0$. The vortex disturbs the flat bed region at a distance which is of the same order as the excursion length and is for obvious reasons amplified as h/L is increased. On the flat bed the sediment transport is, in the time-averaged sense, directed away from the trench by the strength of the advected vortex.

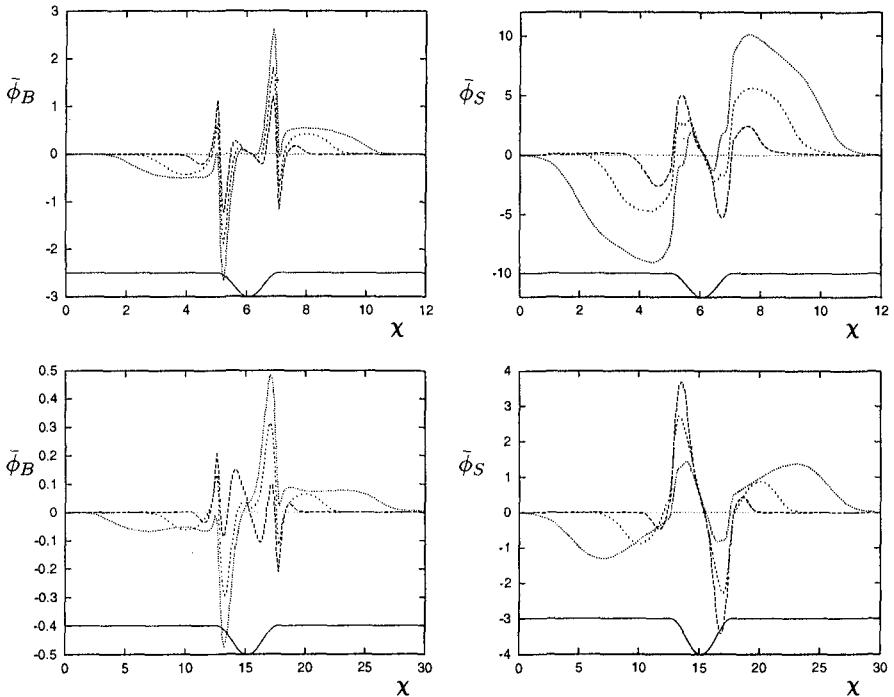


Figure 7: Distribution of period-averaged bed (left-hand side) and suspended sediment transport (right hand side) for a steep ($L/h = 4$ for the top of figure) and a moderate trench slope ($L/h = 10$ for the bottom of figure). $KC = 1.0$: \cdots , $KC = 0.5$: $---$, $KC = 0.25$: $- \cdot -$, with $h/D = 0.5$, $\theta = 0.65$ and $w_s/U_{1m} = 0.02$. The trench height depicted is highly distorted.

At the deeper regions of the trench the suspended sediment transport, $\bar{\phi}_S$, is directed towards the centre (see right hand side of figure (7)), implying that suspended material will be deposited here as opposed to erosion of the shoulder region.

More generally the backfilling process can be analysed by looking at period-averaged trapped sediment within control boxes (CB). Figure (8) shows the amount of trapped sediment as a function of the KC -number for three expansion parameters in two control boxes; an inner and an outer. The outer control box surrounds the entire trench from shoulder to shoulder, and the inner control box is bounded by the two steepest sections of the trench.

The trapped sediment is furthermore divided into contributions from bed and suspended load and where deposition is assigned with positive values. The Shields parameter in these calculations are: $\theta = 1$, and the steepness: $h/L = 0.1$.

An interesting feature of figure (8) is that an optimal backfilling rate takes place at $KC \sim 0.2$ for the suspended sediment. This is before the vortex mechanism becomes dominant. At this point the backfilling rate drops as the separation bubble grows in size

and strength. However, beyond a certain KC -number the strength of the separation bubble will not increase any more, which is evident in figure (8) where a small increase in deposition of suspended sediment is seen for large KC -numbers.

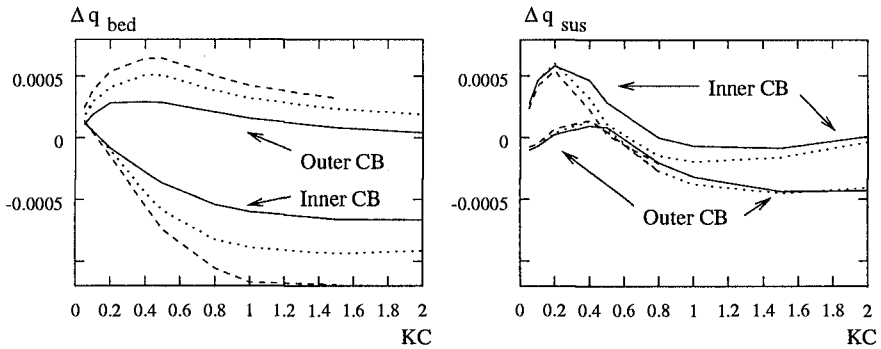


Figure 8: Trapped bed, (left hand side) and suspended load (right hand side) within control boxes (CB) for $h/D = 0.05$: - - -, $h/D = 0.10$: ····· and $h/D=0.25$: ———, and $L/h = 10$, $\theta = 1$, $Z = 0.6$.

The trapped sediment originating from bed load is of the same order of magnitude but negative as the trapped suspended load (at least when $\theta = 1$ and $L/h = 10$) even though $q_{S,max} \gg q_{B,max}$. It is seen from the left hand side of figure (8) (inner CB) that the action of gravity for this particular steepness parameter is merely capable of reducing the forces from the time-averaged shear-stress.

The time-averaged rotating cells on the shoulders are also seen to affect the in-fill of bed load through the outer box. This in-fill rate decreases as the KC -number increases because the separation bubble is washed over the shoulder thus counteracting this time-averaged motion.

It is clear from figure (8) that the typical morphological evolution is a net erosion of the trench shoulders together with a deposition in the centre of the trench. This is, however, exactly the way a diffusion process works.

The morphological development of a trench exposed to waves has been calculated using both flow models discussed previously. Four selected results are shown in figure (9), which clearly demonstrates the diffusion-like process.

As opposed to the steady current case, the depth-averaged model performs poorly in the pure wave case. This is not surprising since a detailed flow description is required to resolve the significant effect from the separation bubble dynamics on the backfilling process in waves. This causes the depth-averaged model to predict a faster backfill.

One interesting, but not surprising, consequence of the change in bed shape was the slow vanishing of the separation bubble as the trench slope becomes gentler. This involves a similar decrease in the vortex mechanism. One would immediately guess that this would lead to an increase in the backfilling rate. However, the trench widens and with this a decrease in the effective KC -number was found. After $T = tU_{1m}/D=1000$ the change in bed form was extremely weak.

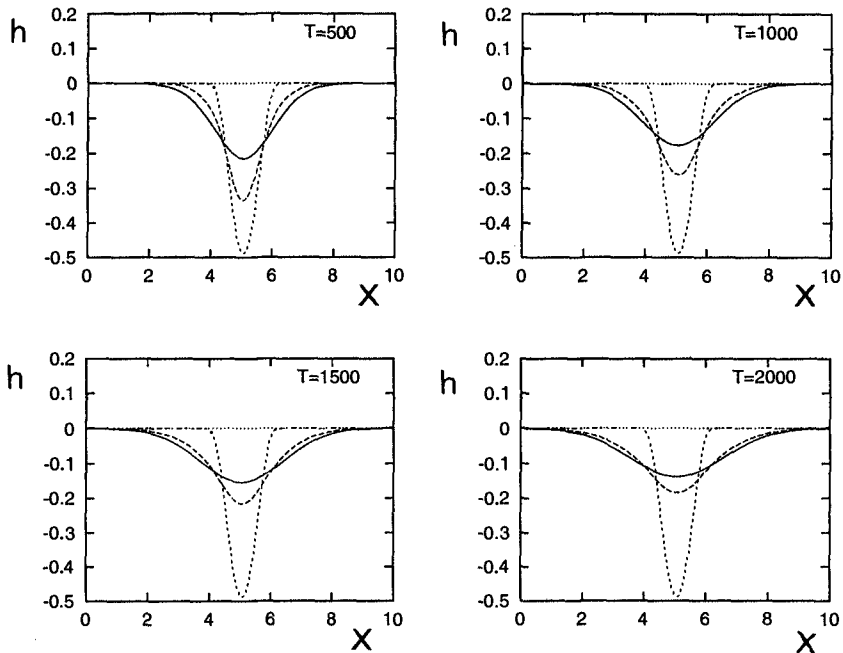


Figure 9: Shape of trench at four stages of its morphological evolution, for $k_N/D = 0.001$, $w_s/U_{1m} = 0.02$, $\theta = 0.25$ and $KC = 0.2$. $k-\epsilon$ model: - - -, Depth-averaged model: —, Initial trench shape: - - - -.

Conclusion

The dynamics of vortices originally born as separation bubbles seem to dominate the backfilling process in waves whenever they are present. This is because the separation bubble traps incoming sediment particles on the upstream slope and keeps some of these 'alive' by the massive level of turbulent kinetic energy found in separating regions. When it detaches from the surface at flow reversal, a cloud of sediment will be advected out of the trench with the vortex.

It has been shown that the vortex mechanism is important and that models which neglect this process may over-predict the backfilling rate.

The optimal backfilling rate in waves was found to be $KC \sim 0.2$.

Furthermore, depth-averaged steady state flow models give good results when applied in morphological calculations particularly in shallow waters which include navigation channels etc.. However, these simple flow models fail to describe more complicated KC -effects found in waves as the effect of separation and vortex shedding is not taken into account.

Acknowledgments.

The computer-code applied in the present investigation is originally developed at ISVA by Ph.D. Søren Tjerry.

This work is jointly supported by "Numerical and Experimental Fluid Mechanics" and "Marine Technique" both funded by the Danish Technical Research Council (STVF).

References

- Alfrink, B.J., and van Rijn, L.C. (1983). Two-equation turbulence model for flow over trenches. *Journal of Hydraulic Engineering (ASCE)*, Vol. 109, No.7, pp. 941-958.
- Basara, B. and Younis B.A. (1995). Prediction of turbulent flows in dredged trenches. *Journal of Hydraulic Research*, Vol. 33, No. 6.
- Bijker, E.W. (1980). Sedimentation in channels and trenches. Proc., 17'th ICCE'80, Vol 2. pp. 1708-1718, Sydney, Australia.
- Engelund, F. and Fredsøe J. (1976). A sediment transport model for straight alluvial channels. *Nordic Hydrology* 7:293-306.
- Fredsøe, J. (1978). Sedimentation of river navigation channels. *Journal of the Hydraulics Division (ASCE)*, Vol. 104, No. HY2, pp.223-236.
- Fredsøe, J. (1979). Natural backfilling of pipeline trenches. *Journal of Petroleum Techn. Vol. 31*, pp. 1223-1230.
- Lauder, B.E. and Spalding, D.B. (1974). The numerical computation of turbulent flows. *Comput. Meths. Appl. Mech. Eng.*, 3:269-289.
- Patankar, S.V. (1980). *Numerical Heat Transfer and Fluid Flows*. Hemisphere, New York.
- Tjerry, S. (1997). *Morphological Calculations of Dunes in Alluvial Rivers*. Ph.D.-thesis ISVA, Technical University of Denmark. (In print).
- van Rijn, L.C. (1986). *Sedimentation of Dredged Channels by Currents and Waves*. Delft Hydraulics Laboratory. Delft Hydraulics Communication No. 369.

CHAPTER 251

A CLOSED-FORM SOLUTION FOR TURBULENT WAVE BOUNDARY LAYERS

Magnus Larson¹

ABSTRACT: A general, closed-form solution is presented to the linearized equation describing the velocity in a turbulent boundary layer. The solution is valid for any type of time-varying free-stream velocity, although the focus of the paper is on oscillatory flows generated by surface waves propagating over the sea bottom. A primary objective is to employ the solution for waves with an asymmetric velocity field, where nonlinear effects are small enough to be neglected in the linearized turbulent boundary layer equation. The general solution is developed to more convenient forms for a few special cases, including a sinusoidally varying free-stream velocity and a velocity given by stream function theory. The solution is tested against two different data sets from oscillatory tunnels; one set involves a sinusoidal and the other set a cnoidal free-stream velocity.

INTRODUCTION

The oscillatory boundary layer that develops when surface waves propagate over the sea bottom has many important implications for flow-dependent phenomena in the coastal zone. Examples of such phenomena are wave energy dissipation due to bottom friction and the initiation and transport of sediment (Grant and Madsen 1986). The velocity changes with elevation at a high rate in the wave boundary layer, which typically causes large shear stresses, high dissipation rates, and strong turbulence intensities. An oscillatory free-stream velocity generates a boundary layer with a characteristic thickness that is much smaller than the corresponding boundary layer under a uni-directional current. Thus, the near-bottom velocity gradients and the associated shear stresses are much larger under oscillatory waves than under a uni-directional current, which suggests that the waves dominate the flow close to the

¹ Associate Professor, Department of Water Resources Engineering, University of Lund, Box 118, S-221 00 Lund, SWEDEN. (Email: magnus.larson@tvrl.lth.se)

bottom in many cases. However, because the oscillatory wave motion often does not give rise to any net transport of for example sediment, but primarily has a stirring effect, a superimposed current may have a marked influence on the net transport rate, although the current itself may be too weak to mobilize and transport the sediment on its own.

In nature the boundary layer under waves will almost always be turbulent (Nielsen 1992). Most simple approaches to calculate the velocity in the wave boundary layer employ the eddy viscosity concept to model the turbulence, where the viscosity is taken to be a function of the elevation above the bottom (Kajiura 1968, Grant and Madsen 1979, Brevik 1981, Myrhaug 1982). These models mainly differ in the formulation of how the eddy viscosity ν varies with the elevation z ; the most simple models are based on a linear variation in ν with z (Grant and Madsen 1979), whereas more complex models assume several different layers, each having a separate equation to relate ν and z (Kajiura 1968). In reality, ν should also depend on time and Trowbridge and Madsen (1984a) developed a model where a time-varying eddy viscosity was employed. However, in most models the prediction of the velocity in the wave boundary layer is not overly sensitive to the formulation of ν , and a simple model such as the one suggested by Grant and Madsen (1979) often yields satisfactory results. This is especially true if the velocity calculations are performed with the aim of computing sediment transport rates; existing equations for calculating the sediment transport rate include large uncertainties that do not warrant excessively detailed flow computations (Madsen and Wikramanayake 1991).

The main objective of the present study is to develop a simple, analytical model of the flow in an oscillatory boundary layer under rough turbulent conditions that may be employed for situations where the free-stream velocity is not purely sinusoidal. Such velocity fields are generated by nonlinear shoaling waves, which could produce a net transport of sediment due to the asymmetry in the wave velocity. In deriving the analytical model, it will be assumed that the effects of the nonlinear terms in the momentum equations are negligible, implying that the linearized boundary layer equation may be used (Nielsen 1992). A simple eddy viscosity formulation in accordance with Grant and Madsen (1979) is employed to model the turbulent stresses. The proposed model is tested with data from Jonsson (1980) for a sinusoidal free-stream velocity and with data from Nadaoka et al. (1994) for an asymmetrical free-stream velocity of cnoidal type.

The present study focusses on boundary layer development under oscillatory waves, but the general solution presented for the velocity profile in the boundary layer is valid for any time-varying free-stream velocity. A first-order approach is taken (Grant and Madsen 1979) where the governing equation is linearized in order to obtain a closed-form solution. Thus, for cases where the free-stream velocity is generated by nonlinear waves second-order effects, such as the mass transport in the boundary layer (Trowbridge and Madsen 1984b), are not included in the solution.

Even though the mass transport may be small it could still be of significance for calculating the sediment transport.

THEORETICAL CONSIDERATIONS

General Solution

Employing the simple eddy viscosity model by Grant and Madsen (1979), the linearized turbulent boundary layer (TBL) equation may be written (Nielsen 1992),

$$\frac{\partial}{\partial t}(u_w - u_b) = \frac{\partial}{\partial z} \left\{ \kappa u_{*m} z \frac{\partial}{\partial z} (u_w - u_b) \right\} \quad (1)$$

where $u_w(z, t)$ is the velocity in the TBL, $u_b(t)$ the free-stream (wave) velocity, t time, z a vertical coordinate, κ von Karman's constant ($=0.40$), and u_{*m} a constant, representative bottom shear velocity. With the boundary conditions $u_w = 0$ for $z = z_o$, where z_o is the characteristic height of the bottom roughness, and $u_w = u_b$ for $z \rightarrow \infty$, Equation 1 has the following general solution,

$$u_w = \int_0^t \frac{\partial}{\partial t} (u_b(t - \xi)) I_u(\xi, z) d\xi + u_{bo} I_u(t, z) \quad (2)$$

where u_{bo} denotes u_b at $t=0$ and,

$$I_u(t, z) = \frac{2}{\pi} \int_0^\infty e^{-\frac{1}{4} y^2 \kappa u_{*m} t} \frac{J_0(y\sqrt{z_o}) Y_0(y\sqrt{z}) - J_0(y\sqrt{z}) Y_0(y\sqrt{z_o})}{J_0^2(y\sqrt{z_o}) + Y_0^2(y\sqrt{z_o})} \frac{dy}{y} \quad (3)$$

in which J_0 and Y_0 are zero-order Bessel functions of the first and second kind, respectively, and y is a dummy integration variable. Equation 3 corresponds to the solution for a time-independent free-stream velocity employed at $t=0$ (that is, $u_b(t) = u_{bo} = \text{constant}$); thus, the solution for any $u_b(t)$ is obtained through the superposition of the response from an infinite number of temporal changes in u_b , as expressed by the convolution integral in Equation 2. Figure 1 illustrates I_u in non-dimensional form, and the curves may be interpreted as velocity profiles at different times indicating the TBL growth through the water column.

The shear stress at any elevation z may be derived from,

$$\frac{\tau}{\rho} = \kappa u_{*m} z \frac{\partial u_w}{\partial z} = \kappa u_{*m} z \left\{ \int_0^t \frac{\partial}{\partial t} (u_b(t - \xi)) I_s(\xi, z) d\xi + u_{bo} I_s(t, z) \right\} \quad (4)$$

where,

$$I_s(t,z) = \frac{1}{\pi\sqrt{z}} \int_0^\infty e^{-\frac{1}{4}y^2\kappa u_* t} \frac{-J_0(y\sqrt{z_0})Y_1(y\sqrt{z}) + J_1(y\sqrt{z})Y_0(y\sqrt{z_0})}{J_0^2(y\sqrt{z_0}) + Y_0^2(y\sqrt{z_0})} dy \quad (5)$$

in which J_1 and Y_1 are first-order Bessel functions of the first and second kind, respectively. The integral $I_s \rightarrow \infty$ as $t \rightarrow 0$, but the approach towards infinity is slow and the singularity is easy to handle within the convolution integral in Equation 4. However, if $u_{b0} \neq 0$ an infinite shear stress will be obtained at $t=0$, because $u_w=0$ at $z=z_0$ simultaneously as $u_w=u_{b0}$ an infinitesimal distance above. The integrals in Equations 3 and 5 are time-consuming to evaluate, so in order to speed up the calculation of u_w and τ in Equations 2 and 4, respectively, it is convenient to derive look-up tables for I_u and I_s .

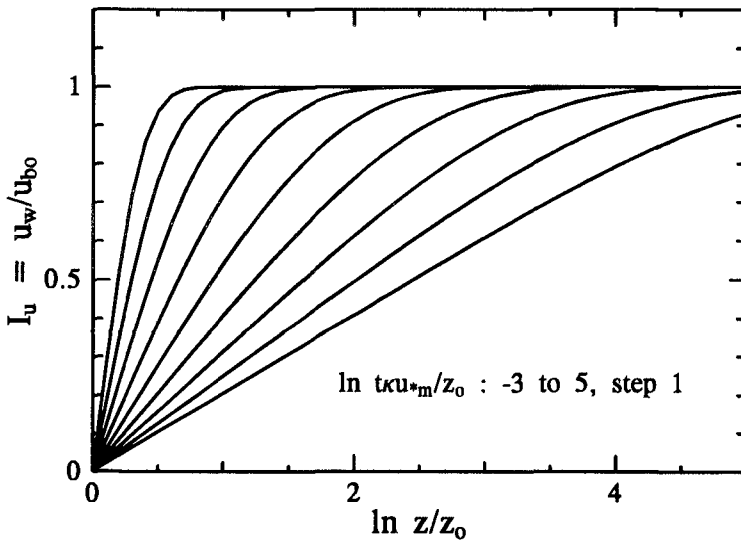


Figure 1. The integral I_u as a function of non-dimensional distance and time.

Equation 2 is a general solution of Equation 1 for any type of free-stream velocity, although from a physical point of view the solution only makes sense for a wave boundary layer where the assumptions behind Equation 1 are applicable. There is only one free parameter in the solution, namely the roughness length scale z_0 , which in the case of rough turbulent flow over a flat bed is typically set to $k_n/30$, where k_n is the equivalent Nikuradse sand grain roughness (Grant and Madsen 1979). After it has been defined, the representative shear velocity u_{*m} may be obtained implicitly from the solution. Grant and Madsen (1979) studied the TBL under a sinusoidal free-stream velocity and used the maximum bottom shear stress τ_{bmax} during a wave period to define $u_{*m} = (\tau_{bmax}/\rho)^{1/2}$, where ρ is the water density. For

more complex variations in the free-stream velocity other choices to define u_{*m} may be more appropriate, such as the mean absolute value of the bottom shear stress during a cycle (τ_{bav}).

Sinusoidal Free-Stream Velocity

Equation 2 was derived using Laplace transform technique and for elementary $u_b(t)$ more convenient forms than Equation 2 may be obtained. If the free-stream velocity is sinusoidal and described by $u_b = u_o \cos \omega t$, where u_o is the velocity amplitude at the bottom and ω is the angular frequency, the following solution satisfies Equation 1 and the boundary conditions,

$$u_w = u_o \cos \omega t - u_o \frac{N_o(2\sqrt{\frac{fz}{z_o}})}{N_o(2\sqrt{f})} \cos \left(\omega t + \Phi_o(2\sqrt{\frac{fz}{z_o}}) - \Phi_o(2\sqrt{f}) \right) - \frac{2u_o}{\pi} \int_0^{\infty} e^{-\frac{1}{4}\frac{\omega t}{f}y^2} \frac{y^3}{y^4 + (4f)^2} \frac{J_o(y\sqrt{\frac{z}{z_o}})Y_o(y) - Y_o(y\sqrt{\frac{z}{z_o}})J_o(y)}{J_o^2(y) + Y_o^2(y)} dy \quad (6)$$

where N_o and Φ_o is the modulus and phase, respectively, of the zero-order Kelvin function $ker_{\sigma}x + i kei_{\sigma}x$, and $f = \omega z_o / \kappa u_{*m}$. The second term in Equation 6 is a transient that is dampened out quickly for small values on f ; in most cases this term is negligible already after a wave period. The shear stress at steady-state conditions is given by (see first part of Equation 4),

$$\frac{\tau}{\rho} = -\kappa u_o u_{*m} \sqrt{\frac{fz}{z_o}} \frac{N_1(2\sqrt{\frac{fz}{z_o}})}{N_o(2\sqrt{f})} \cos \left(\omega t - \frac{\pi}{4} + \Phi_1(2\sqrt{\frac{fz}{z_o}}) - \Phi_o(2\sqrt{f}) \right) \quad (7)$$

where N_1 and Φ_1 is the modulus and phase, respectively, of the first-order Kelvin function. Grant and Madsen (1979) previously derived the steady-state part of the solution for a sinusoidal free-stream velocity (see also Kajjura 1968).

To permit rapid evaluation of the maximum bottom shear stress it is convenient to define a wave friction factor f_w from $\tau_{bmax} = 0.5 \rho f_w \mu_o^2$ (Jonsson 1966, 1980). In accordance with Grant and Madsen (1979), who defined u_{*m} based on τ_{bmax} , f_w may be obtained through the expression for τ_{bmax} given by Equation 7. An alternative approach would be to use τ_{bav} in u_{*m} instead. This would yield a smaller τ_{bmax} , because the turbulent mixing is less if τ_{bav} is used to define u_{*m} , also implying that f_w is smaller than if the conventional definition of u_{*m} is employed. Figure 2 displays f_w as a function of the bottom excursion amplitude A_b ($= u_o / \omega$) over the grain size k_n for a u_{*m} defined based on τ_{bmax} and τ_{bav} .

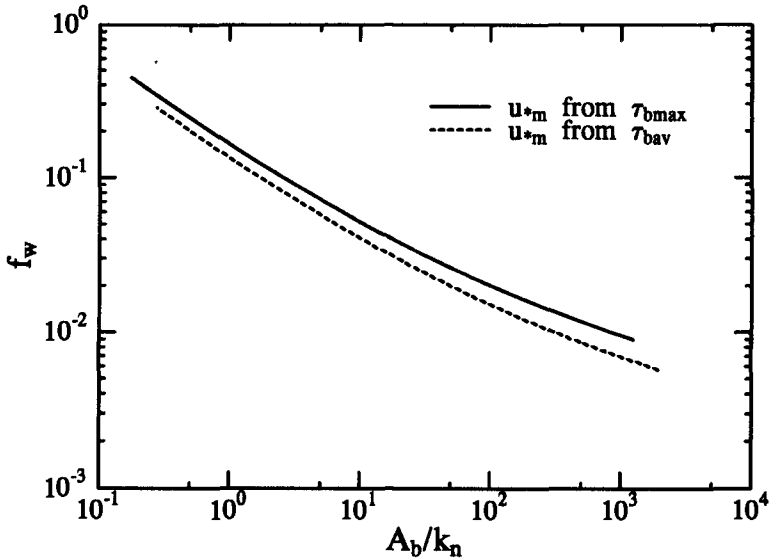


Figure 2. Friction factors for a sinusoidal wave velocity, where the friction velocity is defined based on τ_{bmax} respective τ_{bav} .

Free-Stream Velocity from Stream Function Theory

Stream function theory (Dean 1965) is convenient for describing nonlinear wave properties, because the theory is valid from deep water up to wave breaking. The bottom orbital velocity at a point under a wave described by stream function theory may be expressed as,

$$u_b = -\frac{2\pi}{L} \sum_{n=1}^N nX(n) \cos(n\omega t) \tag{8}$$

where L is the wavelength, $X(n)$ stream function coefficients, and N the order of the theory employed. The velocity given by Equation 8 is a sum of sinusoidal components and the steady-state solution to Equation 1 with this u_b is,

$$u_w = \sum_{n=1}^N u_n \left\{ \frac{N_o(2\sqrt{\frac{nfz}{z_o}})}{N_o(2\sqrt{nf})} \cos\left(n\omega t + \Phi_o(2\sqrt{\frac{nfz}{z_o}}) - \Phi_o(2\sqrt{nf})\right) - \cos(n\omega t) \right\} \tag{9}$$

where $u_n = 2\pi nX(n)/L$. The corresponding shear stress is given by,

$$\frac{\tau}{\rho} = \kappa u_{*m} \sqrt{\frac{f_w z}{z_o}} \sum_{n=1}^N u_n \sqrt{n} \frac{N_1(2\sqrt{\frac{nf_w z}{z_o}})}{N_o(2\sqrt{nf_w})} \cos\left(n\omega t - \frac{\pi}{4} + \Phi_1(2\sqrt{\frac{nf_w z}{z_o}}) - \Phi_o(2\sqrt{nf_w})\right) \quad (10)$$

A wave described by stream function theory is uniquely defined by the two ratios h/L_o and H/L_o (Dean 1990), where h is water depth, H wave height, and the subscript o denotes deepwater conditions. Waves with identical values on h/L_o and H/L_o yield the same dimensionless velocity $u_b/(H/T)$; thus, the quantity H/T appears as a normalizing "velocity". A friction factor derived for a stream function wave will depend not only on the normalized roughness k_n/H , but also on h/L_o and H/L_o . The friction velocity may be computed by using τ_{bav} , which is obtained from time integration of the absolute shear stress over a wave period T .

RESULTS

Data From Jonsson (1980)

Measurements by Jonsson (1980) of u_w in a water tunnel for a sinusoidally varying u_b with the amplitude u_o was employed as a first step to validate Equation 1 for describing the velocity in the TBL. It was verified that Equation 2 produced identical results to Equation 6, and the steady-state portion of the solution was used for the comparison with the data. Jonsson (1980) presented data for two cases: 1) $u_o = 2.11$ m/s, $T = 8.39$ s, $k_n = 2.3$ cm, and 2) $u_o = 1.53$ m/s, $T = 7.20$ s, $k_n = 6.3$ cm. Comparison between the analytical solution and the measurements was performed for the phases $t/T = 1/2, 5/8, 3/4, 7/8$, and 1 . The Reynolds number Re for Cases 1 and 2 were $6.0 \cdot 10^6$ and $2.7 \cdot 10^6$, respectively, based on A_b and u_o . The roughness values given by Jonsson were employed and there were no free calibration parameters. Two different definitions of u_{*m} were used in the comparison, namely $u_{*m} = (\tau_{bmax}/\rho)^{1/2}$ and $u_{*m} = (\tau_{bav}/\rho)^{1/2}$.

Figures 3 and 4 display the comparison between the analytical solution and the measurements for Cases 1 and 2, respectively. In general, the difference between the two formulations for u_{*m} is small, although using τ_{bav} seems to consistently produce somewhat better agreement with the data. Some of the overshoot effect in the data is not entirely captured by the analytical solution, especially for Case 2. The computed wave friction factors f_w for Cases 1 and 2 were 0.019 and 0.033, respectively, when τ_{bmax} was employed, and 0.014 and 0.025 when τ_{bav} was used. Using different formulations for u_{*m} will not change u_w as much as it will affect the calculation of the shear stress.

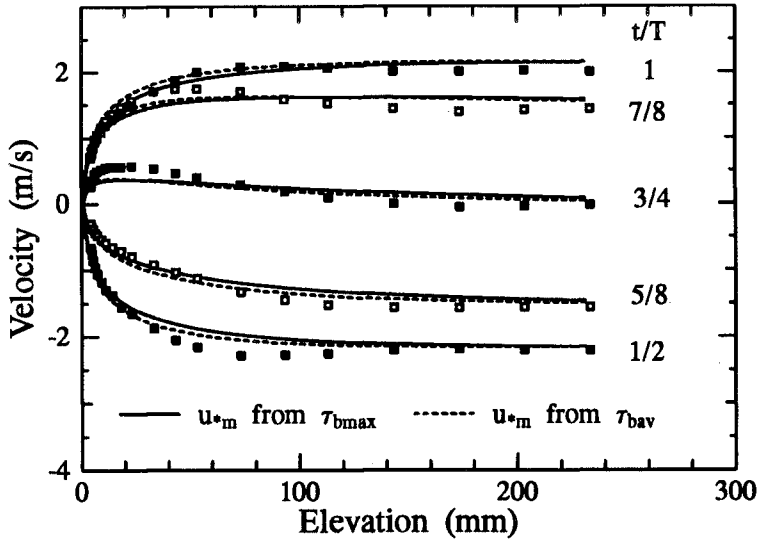


Figure 3. Calculated and measured velocity in the turbulent boundary layer for Case 1 from the data by Jonsson (1980).

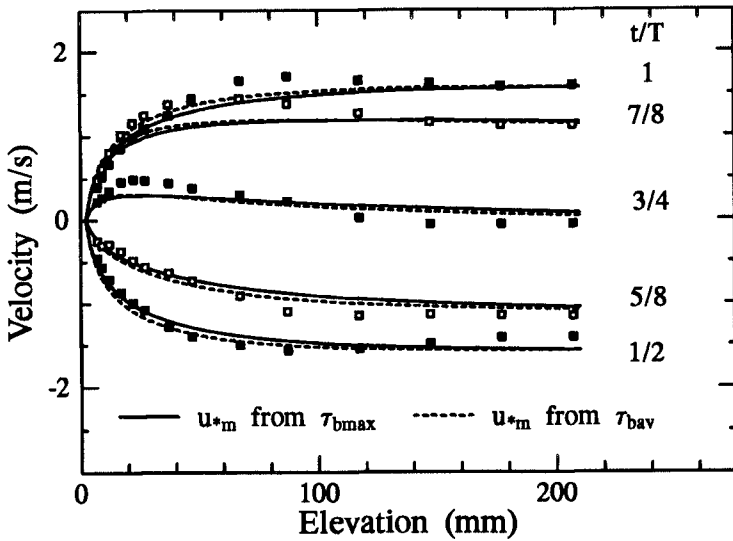


Figure 4. Calculated and measured velocity in the turbulent boundary layer for Case 2 from the data by Jonsson (1980).

Data From Nadaoka et al. (1994)

Nadaoka et al. (1994) measured u_w in an oscillatory tunnel using air for a free-stream velocity that was asymmetric. The measurements used here to evaluate the TBL model involved a velocity u_b that was of cnoidal type with a positive peak velocity of 2.50 m/s, a negative peak velocity of 1.05 m/s, and a period of 5 s. A cnoidal wave producing a non-dimensional time variation in u_b corresponding to the experimental conditions implies an Ursell number of $U_r=57.8$, although during the experiment u_b was generated to agree with the velocity induced by a hyperbolic wave. In general, such a strongly nonlinear wave provides a severe test for the linearized TBL equation; neglecting the nonlinear terms in the governing equation assumes that the particle velocity is small compared to the wave phase speed (Madsen and Wikramanayake 1991), which may not be the case for strongly nonlinear waves. However, for data obtained in oscillatory tunnels the spatial gradients should be small enough to permit that the nonlinear terms are neglected.

Instead of using a cnoidal or hyperbolic wave to describe u_b in the solution given by Equation 2, u_b was approximated using a wave described by 20-order stream function theory ($H=5.26$ m, $T=10.3$ sec, and $h=8.22$ m; the resulting velocity as a function of non-dimensional time is shown in Figure 5 together with the generated hyperbolic velocity variation during the experiment). Stream function, cnoidal, and hyperbolic theory produced essentially identical variation in u_b with time, but the former theory allows direct calculation of u_w from Equation 9 for steady-state conditions without having to compute for the transient phase, which is necessary if the general solution in Equation 2 is employed. The bed consisted of spray-painted aluminum and was judged to be hydraulically smooth during the experiments. Thus, the length scale z_o is independent of the boundary roughness and may be calculated from $z_o=(3.3\nu_a/u_{*m})/30$ (Madsen and Wikramanayake 1991), where ν_a is the kinematic viscosity for air. The air temperature was about 10 deg during the experiment and the corresponding Reynolds number was $Re=2.8 \cdot 10^5$. The origin of the vertical axis in the measurements was assumed to approximately coincide with z_o .

Since smooth turbulent flow prevailed during the experiment, z_o could be obtained from ν and u_{*m} and no calibration was needed to estimate the bed roughness. The representative shear velocity was based on τ_{bav} , which was determined through time integration over T . A value of $u_{*m}=0.065$ m/s was thus calculated implying $z_o=0.024$ mm. Figure 6 displays measured and calculated velocity profiles for selected phase values of t/T . The maximum positive peak in u_b occurred at about $0.18t/T$, the maximum negative peak at $0.68t/T$, and zero velocity at $0.36t/T$. The model captures the overall features of the velocity variation in the boundary layer, but the overshoot effect is not well predicted by the model, especially during the phase of flow reversal in the boundary layer in connection with large gradients in the wave velocity. The simple eddy viscosity model employed in the linearized TBL equation is most likely the reason for the disagreement between

the model and the measurements (Sleath 1987), although lack of detailed information on z_o and the use of stream function theory to describe u_b may also contribute to the discrepancy.

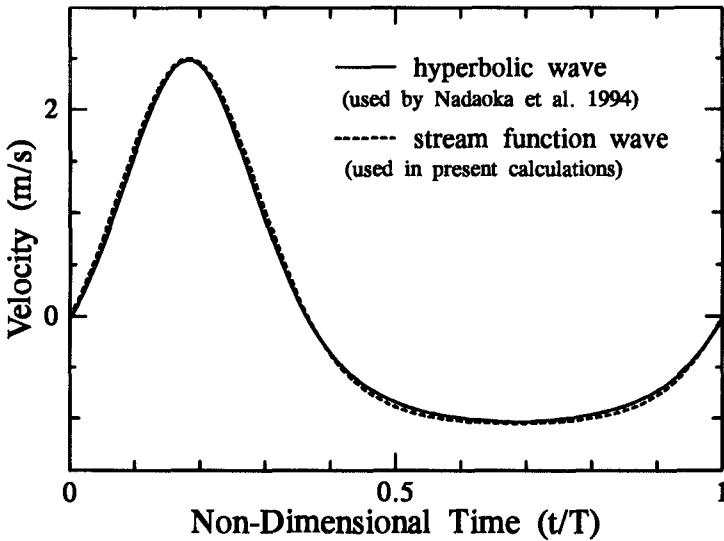


Figure 5. Hyperbolic wave velocity generated by Nadaoka et al. (1994) in their experiment on turbulent boundary layers and the velocity from a stream function wave that approximates the hyperbolic wave.

Figure 7 shows the computed normalized shear stress as a function of time at selected elevations based on the experimental conditions from Nadaoka et al. (1994). The time variation in the shear stress differs significantly from u_b and τ is completely asymmetric. This feature of the shear stress under nonlinear waves is important to include in for example detailed sediment transport calculations that employ the instantaneous shear stress to compute the transport rate.

CONCLUDING REMARKS

The analytical solution presented in Equation 2 is valid for any time-varying free-stream velocity, although from a physical point of view the solution is only interesting when the conditions underlying the linearized TBL equation are fulfilled. For example, the solution will describe the temporal growth of a TBL under a unidirectional current (compare Figure 1); however, the boundary layer will grow infinitely large and at some time the assumption that the layer thickness is small compared to the water depth will be violated and the solution lacks physical meaning. Also, for strongly nonlinear waves where the convective terms in the momentum equations are significant, the linearized TBL equation will yield results that are not

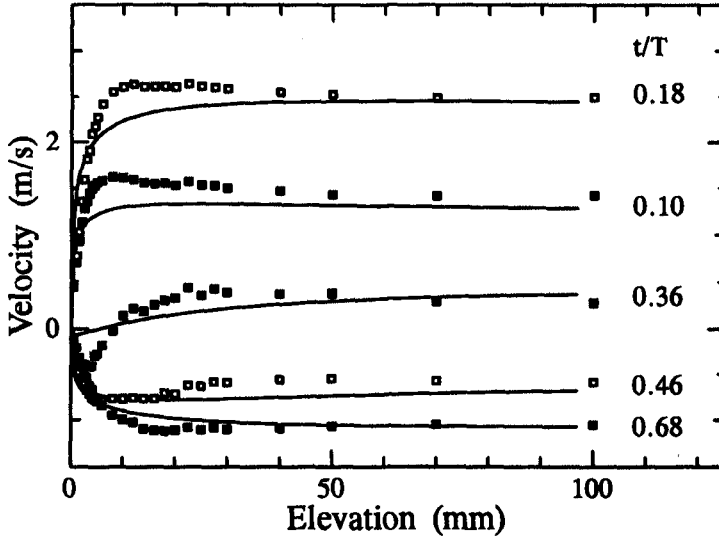


Figure 6. Calculated and measured velocity in the turbulent boundary layer using the asymmetric velocity case from Nadaoka et al. (1994).

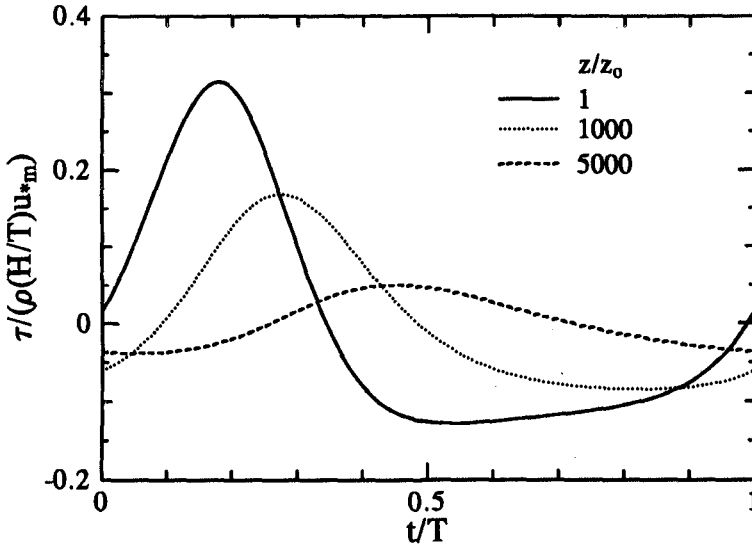


Figure 7. Calculated time variation in the shear stress at selected elevations for the experimental conditions given by Nadaoka et al. (1994).

reliable. For the case tested from the data by Nadaoka et al. (1994) the linearized equation failed to produce accurate predictions, especially during the phase of flow reversal in the boundary layer in connection with large gradients in the wave velocity. This is mainly attributed to the simple eddy viscosity model approach employed which fails to realistically capture the variation in the turbulence during a wave cycle (Sleath 1987). A time-varying eddy viscosity would most likely improve the agreement with the data, but such a formulation would not permit an analytical solution of the governing equations.

However, the simple eddy viscosity model of Grant and Madsen (1979) seemed to produce acceptable results for a sinusoidal wave velocity, even if ν increases without limit with distance from the boundary. This observation pertains mainly to the velocity profile, whereas the shear stress is more sensitive to the eddy viscosity formulation because of the dependence on the velocity gradient. Similarly, the velocity profile is not overly sensitive to the choice of representative friction velocity, in contrast to τ which is more affected by the u_{*m} used. It was found in the present study that a u_{*m} based on the mean absolute shear stress during a wave cycle produced somewhat better agreement with data for a sinusoidal wave than using the maximum absolute shear stress.

ACKNOWLEDGEMENTS

The author is grateful to Professor Akira Watanabe, University of Tokyo, for valuable comments on the paper. Professor Masahiko Isobe, University of Tokyo, developed the program for calculating waves by stream function theory. Professor Kazuo Nadaoka and his coworkers at Tokyo Institute of Technology kindly provided the data from their experiments. The support from the Japan Society for the Promotion of Science for the research visit of the author to the University of Tokyo is gratefully acknowledged, as well as the assistance from all members of the Coastal Engineering Laboratory during his stay.

The research presented in this paper was partly conducted under the SAFE Project of the Marine Science and Technology Program (Contract No. MAS3-CT95-0004) funded by the Commission of the European Communities, Directorate for Science, Research, and Development.

REFERENCES

- Brevik, I. 1981. "Oscillatory Rough Turbulent Boundary Layers," Journal of Waterways, Port, Coastal and Ocean Engineering, Vol 103, pp 175-188.
- Dean, R.G. 1965. "Stream Function Representation of Nonlinear Ocean Waves," Journal of Geophysical Research, Vol 70, No. 18, pp 4561-4572.

- Dean, R.G. 1990. "Stream Function Wave Theory and Applications," In: Handbook of Coastal and Ocean Engineering, Herbich, J.B (ed), Gulf Publishing Company, Vol 1, pp 63-94.
- Grant, W.D. and Madsen, O.S. 1979. "Combined Wave and Current Interaction with a Rough Bottom," Journal of Geophysical Research, Vol 84, No. C4, pp 1797-1808.
- Grant, W.D. and Madsen, O.S. 1986. "The Continental-Shelf Bottom Boundary Layer," Annual Review of Fluid Mechanics, Vol 18, pp 265-305.
- Jonsson, I. 1966. "Wave Boundary Layers and Friction Factors," Proceedings of the 10th Coastal Engineering Conference, American Society of Civil Engineers, pp 127-148.
- Jonsson, I. 1980. "A New Approach to Oscillatory Rough Turbulent Boundary Layers," Ocean Engineering, Vol 7, pp 109-152.
- Kajiura, K. 1968. "A Model of the Bottom Boundary Layer in Water Waves," Bulletin of the Earthquake Research Institute, Vol 46, pp 75-123.
- Madsen, O.S. and Wikramanayake, P.N. 1991. "Simple Models for Turbulent Wave-Current Bottom Boundary Layer Flow," DRP-91-1, Coastal Engineering Research Center, US Army Waterways Experiment Station, Vicksburg, MS.
- Myrhaug, D. 1982. "On a Theoretical Model of Rough Turbulent Wave Boundary Layers," Ocean Engineering, Vol 9, No. 6, pp 547-565.
- Nadaoka, K., Yagi, H., Nihei, Y., and Nomoto, K. 1994. "Characteristics of the Structure of Turbulence Under Asymmetrical Oscillatory Flow," Proceedings of the Japanese Coastal Engineering Conference, Japan Society of Civil Engineers, pp 141-145. (in Japanese)
- Nielsen, P. 1992. "Coastal Bottom Boundary Layers and Sediment Transport," World Scientific, Singapore.
- Sleath, J.F.A. 1987. "Turbulent Oscillatory Flow Over Rough Beds," Journal of Fluid Mechanics, Vol 182, pp 369-409.
- Trowbridge, J. and Madsen, O.S. 1984a. "Turbulent Wave Boundary Layers. 1. Model Formulation and First-Order Solution," Journal of Geophysical Research, Vol 89, No. C5, pp 7989-7997.
- Trowbridge, J. and Madsen, O.S. 1984b. "Turbulent Wave Boundary Layers. 2. Second-Order Theory and Mass Transport," Journal of Geophysical Research, Vol 89, No. C5, pp 7999-8007.

CHAPTER 252

Observed Suspended Sediments in Storm Conditions

J.J. Williams¹, C.P. Rose², P.D. Thorne¹, L.E. Coates², J. R. West²,
P.J. Harcastle¹, J.D. Humphery¹, S.P. Moores¹ & D. J. Wilson¹

Abstract

High resolution synchronous measurements of turbulence, waves and vertical suspended sediment (S_{sed}) concentration profiles have been obtained during a storm above a rippled bed comprising coarse/medium sand located close to the end of a large offshore sand bank in a water depth of approximately 20m. These data are utilised to study the temporal characteristics of sediments in suspension. Sediment resuspension 'events', exhibiting vertical coherence up to approximately 30cm above the sea bed, are observed to span a range of temporal scales encompassing half wave, wave and wave group periods. The vertical concentration of S_{sed} is shown to be enhanced significantly by wave groups. Average S_{sed} profiles are described using a simple Rouse-type and an new 'convective' model.

Introduction

At the most fundamental level, a fluid motion directed away from the bed with a velocity exceeding the *in situ* grain settling velocity is the basic requirement for the suspension of sediments. In marine situations, such fluid motion can arise in three ways (Pykhov *et al.*, 1995): (a) turbulent fluid 'bursting' (Kline *et al.*, 1967; Hino *et al.*, 1983; Sleath, 1987); (b) vortices formed by interactions between waves, currents and the bed (Mogridge & Kamphuis, 1972; Kaneko, 1981); and (c) vortices formed under breaking waves which penetrate to the bed (Nadaoka & Kondoh, 1989). Spatial and temporal scales determined by the hydrodynamics and the physical properties of the sediment makes simple descriptions of the instantaneous physical characteristics of suspended sediment difficult and most approaches consider only time-average conditions. Further, in field situations, waves at angles to tidal currents frequently lead to the generation of complex and interacting bedform assemblages (Sleath, 1984) adding further complexity to the modelling of sediment dynamics.

¹ Proudman Oceanographic Laboratory, Bidston Observatory, Birkenhead, Merseyside, L43 7RA, UK, (jjw@pol.ac.uk).

² School of Civil Engineering, The University of Birmingham, Edgbaston, Birmingham, B15 2TT, UK.

Recently, the use of acoustic instruments has enabled acquisition of high temporal resolution data pertaining to the vertical distribution of suspended sediment in marine conditions (e.g. *Thorne et al., 1993*; *Lee & Hanes, 1996*) and progress has been made in understanding and modelling of sediment resuspension and suspension dynamics. However, the majority of experiments examining sediment processes in marine situations have been conducted just outside the breaker zone in moderate conditions (e.g. *Osborne et al., 1994*) and few field data relate to the mobilisation of sediments during storm conditions at offshore locations (e.g. *Green et al., 1995*). As a consequence, data necessary for validation of numerical models of sediment transport in extreme conditions remains scarce. The present paper presents field observations of suspended sediments and hydrodynamic conditions in the first metre of the water column above a rippled coarse/medium sandy bed in a water depth of 20m during a moderate storm.

Field site and measurements

The study site was located close to the northern end of Middelkerke Bank in the Flemish sand banks, southern North Sea, Europe (*Figure 1a*). Middelkerke Bank is approximately 10km long, 1-2km wide and is located approximately 10km offshore. Bottom sediments consisted of medium/coarse sand ($D_{50} = 450\mu\text{m}$). Approximately 15% of the sediment by weight was composed of platy angular shell fragments ($D_{50} = 650\mu\text{m}$). Data relating to hydrodynamic conditions (turbulence and waves) and vertical suspended sediment concentration (S_{sed}) profiles have been obtained using the autonomous benthic lander *STABLE* (*Figure 1b, Humphery & Moores, 1994*).

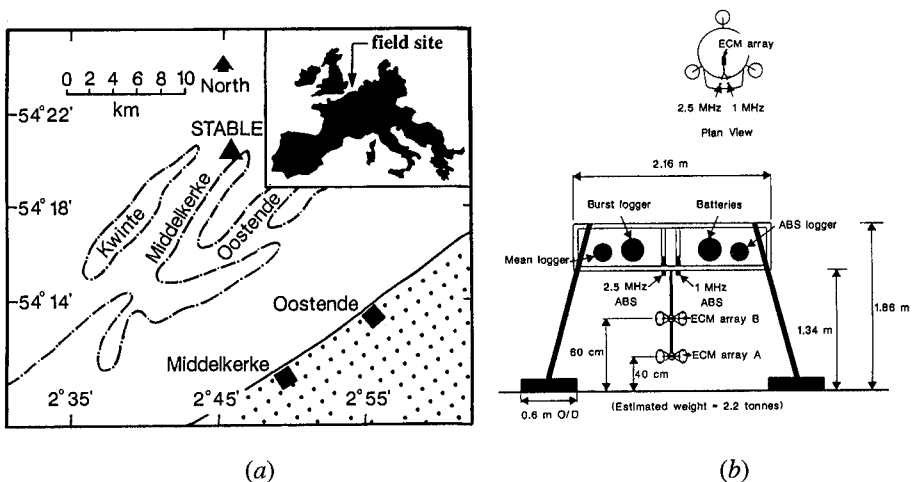


Figure 1. (a) Location of the field site at Middelkerke Bank, Belgium; (b) *STABLE* (Sediment Transport And Boundary Layer Equipment).

Instantaneous near-bed flow in orthogonal vertical planes (x - z , y - z) was measured using pairs of electromagnetic current meters (*ECM*, diameter 10cm) at heights (z) of approximately 36cm and 76cm above the sea bed (*Figure 1b*). A pressure sensor at $z = 1.63$ m was used to measure waves. *ECM* and wave data were sampled at 8Hz for approximately 19 minutes every hour in 'burst' mode. The analysis methods used to obtain hydrodynamic parameters referred to below are described by *Hannay et al., (1994)*. A vertical profile of S_{sed} perpendicular to the *ECM*'s over the range $1\text{cm} < z < 100\text{cm}$ with a vertical resolution of 1cm was derived from two acoustic backscatter sensors (*ABS*) operating at 1.0MHz (*ABS1*) and 2.5MHz (*ABS2*), (*Thorne et al., 1993*). These sensors were separated horizontally by a distance of 10cm along a line normal to the *ECM* axis (*Figure 1b*) and were synchronised precisely with *ECM* and pressure sensor data. *ABS* data were recorded independently in burst mode at 4Hz for approximately 9 minutes every hour. *ABS* data were calibrated in the laboratory using samples of the bed sediments from the *STABLE* deployment site (*Wylie et al., 1994*). For the range of instantaneous and average S_{sed} values observed in the present study ($\approx 10^{-4} - 10^1 \text{g/l}$), close agreement was found between *ABS1* and *ABS2*. Estimates of ripple wavelength ($\lambda \approx 50\text{cm}$) were obtained in the field using the *ABS* instruments and ripple height (a) was estimated using an empirical relationship between ripple steepness and grain Shields number (*Nielsen, 1981*) and approximated to 7cm. The physical roughness (k_s) of the ripples was calculated using $k_s = 8a^2/\lambda$, (*Nielsen, 1992*).

Experimental conditions

In total 50 burst records encompassing calm and storm conditions were obtained. A detailed description of the hydrodynamic conditions occurring during the periods preceding and following the storm is given by *Williams et al., (1996)*. In the present paper attention is focused upon a period of 5 hours spanning the peak of storm activity (*bursts* 34-39) when the average S_{sed} value reached a maximum. *Burst* average hydrodynamic conditions and S_{sed} values observed during this period are summarised in *Figure 2*.

During *bursts* 34-39, wave direction ($\psi_w \approx 330^\circ$) and current direction ($\psi_c \approx 200^\circ$) remained approximately constant and *burst* average S_{sed} values increased in response to increasing tidal current speed and wave orbital speed (*Figure 2*). Following *burst* 38, S_{sed} values decreased as the storm subsided. During the storm, waves were observed to be long-crested and groupy in nature and the vertical position of the bed was observed to change relative to *ABS* sensors. Since the motion sensors on *STABLE* indicated that the rig remained static during the experiment it is considered likely that the observed changes in bed elevation are attributable to the migration of bedforms beneath *STABLE*.

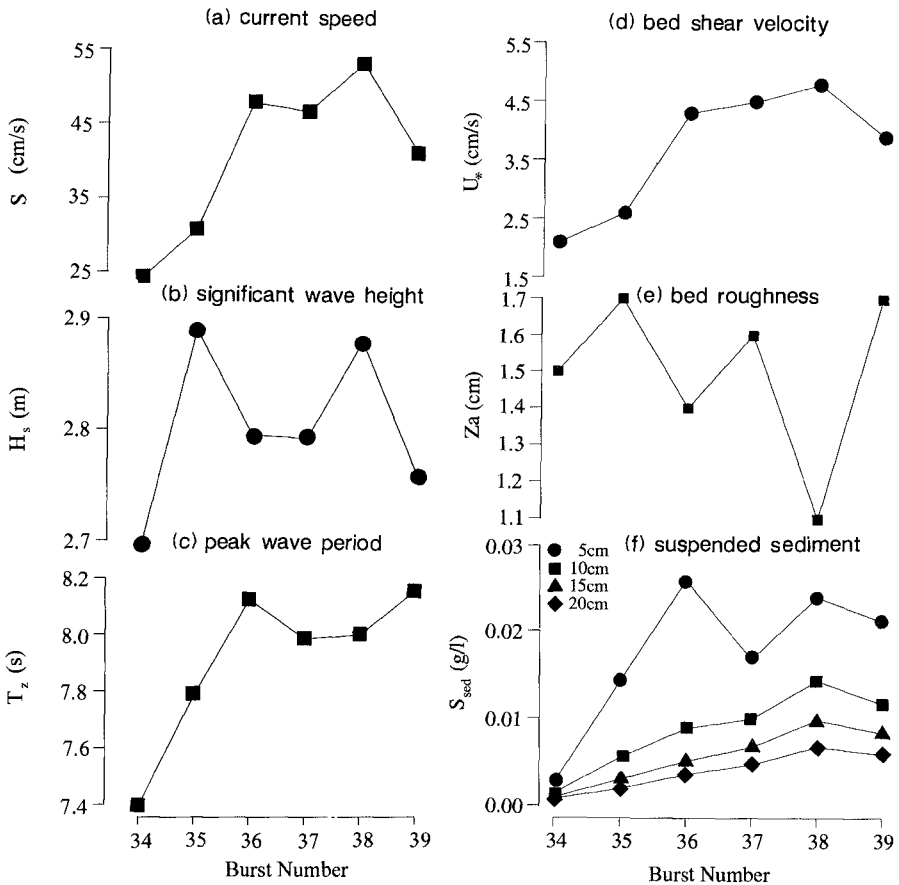


Figure 2. (a) burst average current speed (S) at $z = 76\text{cm}$; (b) significant wave height (H_s); (c) peak wave period (T_p); (d) burst average bed shear velocity (currents) obtained using the turbulent kinetic energy (t.k.e.) method (cf. Hannay et al., 1994); (e) apparent bed roughness (z_a); and (f) S_{sed} at $z = 5\text{-}20\text{ cm}$.

Results and discussion

Observed temporal and spatial structure of sediment resuspension events

Typical time series measurements of S_{sed} at $z = 4\text{cm}$, 6cm , 10cm and 40cm and surface wave amplitude are shown in Figure 3. S_{sed} time series in this figure comprise a 'background' population of suspended material ($\approx 0.02\text{g/l}$ at $z = 4\text{cm}$) and

discrete resuspension *events* in which instantaneous S_{sed} peaks frequently exceed 1.0g/l. Whilst *Figure 3* shows strong visual correlation between waves and S_{sed} *events* and marked vertical coherence in S_{sed} , coherent vertical fluid motion necessary to suspend sediment was not detected by the *ECM* sensors. This is attributed to the dissipation of coherent vertical fluid motion by $z = 40$ cm and to the physical size of the *ECM* measuring volume.

When examining *Figure 3* it is important to remember that during the storm, long-crested waves were approximately normal to the tidal currents and that the location of the *ABS* sensors changed in relation to ripple crests through time as ripples migrated. However, if it is assumed that resuspension *events* occurred along a significant length of the rippled bed parallel to the wave crests, (i.e. vortices formed by wave action are also long-crested), then material in suspension will be advected past the *ABS* sensors by the combined action of waves and the tidal current as coherent clouds approximately in phase with the waves.

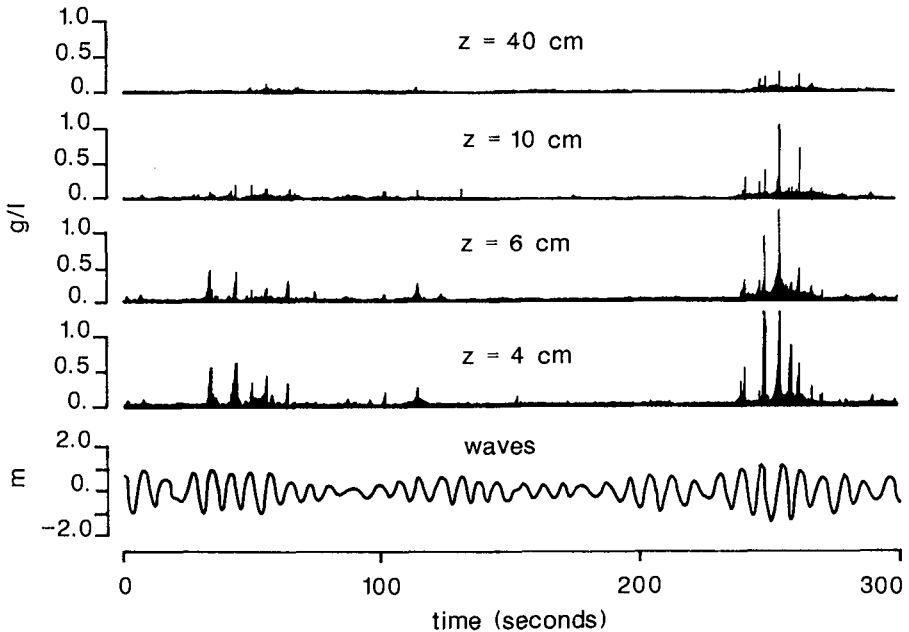


Figure 3. Time series of observed suspended sediments and waves.

Surprisingly, given the strong visual correlation between waves and resuspension *events* illustrated in *Figure 3*, periodic components at wave frequencies were not identified in power spectra of S_{sed} time series irrespective of the observation height above the sea bed. This is attributed to two problems: (i) the S_{sed} time series are 'spiky' in nature; and (ii) the temporal changes in spatial location between *ABS*

sensors and resuspension *event* sources (i.e. ripple crestlines) and spatial variation in horizontal S_{sed} values combine with advected populations of suspended material to results in complex phase relationships between observed surface waves and S_{sed} time series. However, velocity²-sediment cospectra (Figure 4) show statistically significant correlation's between the horizontal flow components squared (u^2 and v^2) and S_{sed} .

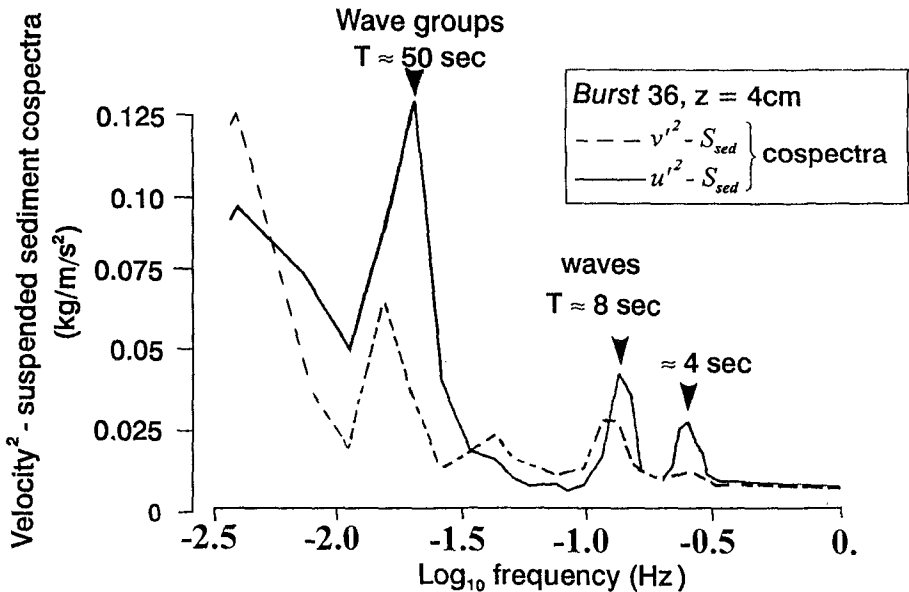


Figure 4. Velocity²-sediment cospectra, burst 38.

Figure 4 shows correlation's between u^2 and S_{sed} and between v^2 and S_{sed} at half wave ($\approx 0.25\text{Hz}$), wave ($\approx 0.125\text{Hz}$), wave group ($\approx 0.01\text{Hz}$) and lower frequencies (in the range $0.01 - 0.003\text{Hz}$). In all cases examined during the storm, wave groups dominate the cospectra. This is also illustrated visually in Figure 3. Although low frequency fluid motion is recorded by *ECM* sensors, it is unclear whether or not the low frequency peak in the velocity²-sediment cospectra is a real phenomenon or simply an artefact of the analysis method. If shown to be real, further work is then required to quantify the role of this low frequency component in suspended sediment transport.

Waves recorded during *bursts* 34-39 exhibited well developed groupy structure (Figure 3). Initial visual inspection of correlation's between the wave groups and modulation in suspended sediment concentration indicated strongly that successive waves in a group resulted in a progressive increase in average S_{sed} values up to $z \approx 30\text{ cm}$ consistent with the idea of *wave pumping*. It was also determined that average

S_{sed} values associated with the last wave in a given group of more than 6 waves were a factor of approximately 2 times larger than values associated with the first wave in the same group. Following passage of a group, average S_{sed} values were observed quickly to decline to their former value.

In order to investigate further the wave-by-wave ‘pumping’ effect, the Goda run-length was utilised (Goda, 1985). Here, the start of a wave group was defined by the passage of a wave of height (h_j) that was observed to mobilise bottom sediments. For the group to continue, successive waves must be equal to or exceed h_j . In all cases an observed linear increase in average S_{sed} values with j demonstrated the enhancement of the sediment resuspension process by the passage of a successive series of larger than average waves (Figure 5). At present suspended sediment transport formulae do not include explicitly this important effect and thus are likely to underestimate the sediment transport rate in combined wave-current situations.

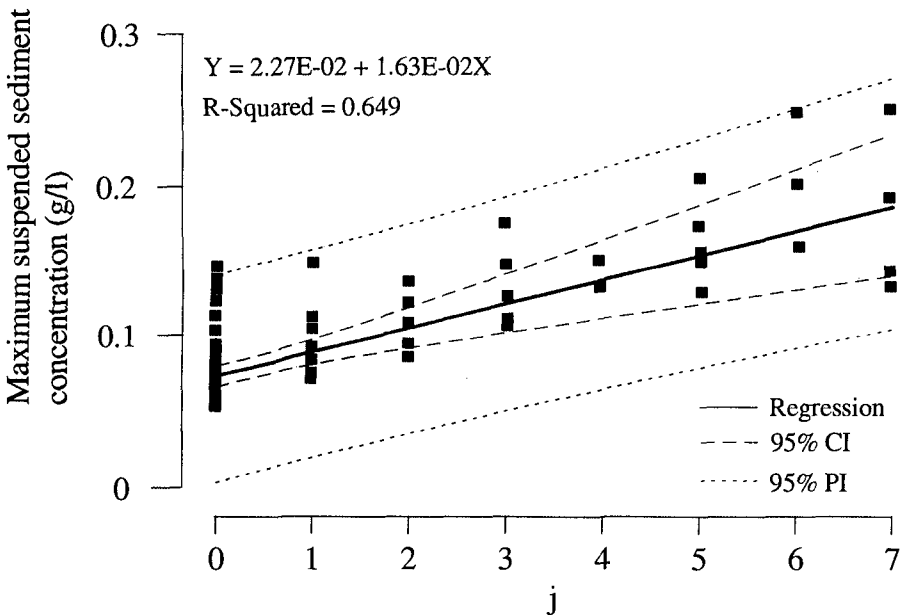


Figure 5. Goda wave group run length (j) versus observed suspended sediments.

Burst average suspended sediment concentration profiles

Burst average suspended sediment concentration profiles observed over the range $1\text{cm} < z < 50\text{cm}$ are shown in Figure 6. Since ripples are observed to migrate beneath the ABS sensors during a burst measurement period, these profiles also represent horizontally spatially averaged S_{sed} values in the direction of ripple migration. The observed profiles show a progressive increase in the burst average

suspended sediment concentration over the range $1\text{cm} < z < 50\text{cm}$ from a minimum during *burst* 34 to a maximum during *burst* 38. At $z > 50\text{cm}$, S_{sed} values are small (0.001g/l to 0.005g/l) and slowly decay with height above the bed. In all cases the profiles are smooth, continuous and are Rouse-like above $z \approx 20\text{cm}$. In the bottom 10cm , S_{sed} profiles for *bursts* 37-39 exhibits a significant concave curvature which develops through the storm.

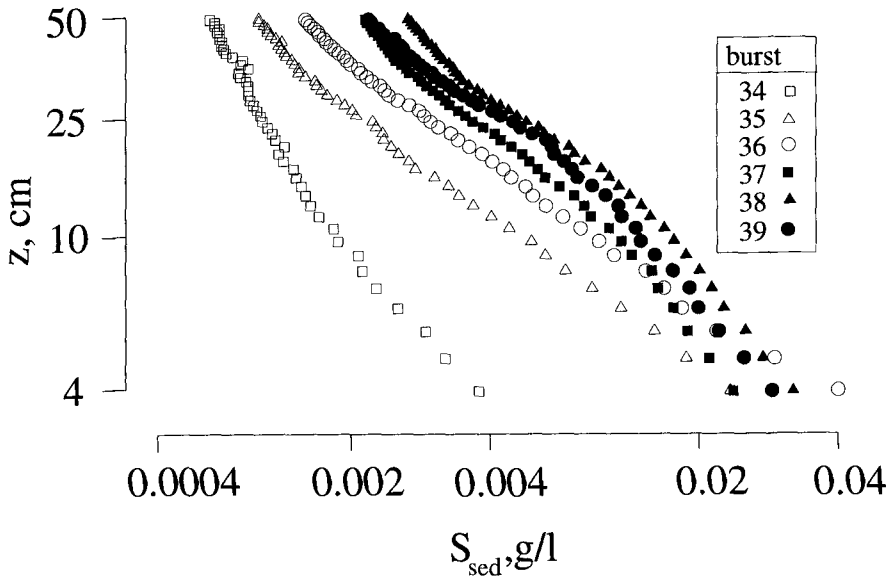


Figure 6. Suspended sediment concentration profiles, *bursts* 34-39.

During the period of increasing wave height preceding the peak storm activity, S_{sed} profiles in the range $3\text{cm} < z < 40\text{cm}$ for *bursts* 34-36 were found to follow approximately Rouse-type profiles defined by *Smith (1977)* as

$$C(z) = C(a)(z/a)^{-\alpha} \quad (1)$$

where α is the Rouse parameter (i.e. $\alpha = w_s / \beta \kappa U_{*wc-max}$), $C(z)$ and $C(a)$ are S_{sed} values at heights z and a , respectively, above the sea bed, w_s is the settling velocity (estimated to be 3.5 cm/s , *van Rijn, 1989*), β is the ratio of the eddy diffusion coefficients for the fluid and the sediment (assumed to be 1.0), κ is the von Kármán coefficient (0.4) and $U_{*wc-max}$ is the maximum wave-current bed shear velocity.

Using a least squares fit to the straight line portion of the observed S_{sed} profiles, values for α were obtained from the gradient of the straight line fit, (Table 1).

Burst	S (cm/s)	σ_w (cm/s)	α	$U_{*wc-max}$ (cm/s)
34	24.2	15.5	1.27	-
35	30.9	20.7	1.32	6.6
36	47.8	22.7	1.33	6.6

Table 1. S , RMS wave orbital speed σ_w , α and $U_{*wc-max}$, values derived from observed S_{sed} profiles (Eq. 1), bursts 34-36.

Utilisation of the observed α values in Eq. 1 gave predicted S_{sed} values that matched well observed S_{sed} values for bursts 34-36 ($R^2 > 0.95$). $U_{*wc-max}$ values for bursts 35 and 36 agree broadly with values predicted by a number of wave-current models (e.g. Soulsby, 1994). Although S and σ_w values measured during burst 34 are significantly lower than those pertaining during bursts 35 and 36, a larger than expected value for $U_{*wc-max}$ was obtained from the burst 34 S_{sed} profile data (6.8cm/s). This may imply that the assumed settling velocity of 3.5 cm/s is incorrect for this burst and for this reason the value for $U_{*wc-max}$ for burst 34 is not included in Table 1.

In the case of bursts 37, 38 and 39 a new expression is required to simulate the concave curvature in the bottom 10cm of the observed profiles (Figure 6). In these cases it was found that the whole S_{sed} profile for $1\text{ cm} < z < 40\text{ cm}$ could be matched closely to the "convective" empirical profile proposed by Nielsen (1992) for natural sand ripples composed of coarse grains in oscillatory flows. Thus

$$C(z) = C(0) \left(\frac{z}{L} + 1 \right)^{-\alpha'} \quad (2)$$

where L is a characteristic length scale. Nielsen (1992) suggests a value of 2 for α' . In contrast to Eq. 1, Eq. 2 tends towards a Rouse-type profile when $z/L \gg 1$ and also tends toward $C(0)$ at the bed. The gradients of S_{sed} profiles depart from the form of Eq. 2 at $z > 30\text{-}40\text{cm}$ where finer material in suspension might be anticipated. Present data indicates that the vertical distribution of S_{sed} in the range $35\text{cm} < z < 100\text{cm}$ can be modelled well using a second Rouse-type profile with a smaller α value. However, for $z > 50\text{cm}$, S_{sed} values are observed to be 3-4 orders of magnitude

less than those observed at $z < 10\text{cm}$ and can therefore be neglected for practical purposes when estimating rates of sediment transport.

In the present study, *Eq. 2* was obtained using a semi-analytical approach by assuming that the total wave-current sediment diffusivity is the sum of the Rouse-type diffusivity defined in *Smith (1977)* and a constant diffusivity (ϵ_c) found in oscillatory only flow over ripples (*Nielsen, 1992*). This gives

$$-w_s C = (\kappa U_{*wc-max} z + \epsilon_c) \frac{\partial C}{\partial z} \quad (3)$$

and hence

$$C(z) = C(a) \left(\frac{z+L}{a+L} \right)^{-\alpha'} \quad (4)$$

where α' is a Rouse-type parameter and $L = \epsilon_c / \kappa U_{*wc-max}$. When $a = 0$, this profile is identical to *Eq. 2*.

The values of the parameters used in *Eq. 4* to obtain the best fit between observed and predicted S_{sed} profiles for *bursts 37-39* are shown in *Table 2*. These were obtained by firstly estimating the gradient of the straight line portion of a given S_{sed} profile (α') on log-log axes (typically this fell within the range $15\text{cm} < z < 25\text{cm}$). Using the suspended sediment concentration values at $z = 4\text{cm}$ as a 'reference' concentration, values of L were obtained using $C(z)$ values up to $z = 25\text{cm}$. Finally, taking the average value of L (*Table 2*), $C(0)$ was calculated using observed concentration values at $z = 4\text{cm}$ and $U_{*wc-max}$ values were derived from α' assuming $w_s = 3.5\text{cm/s}$ (*van Rijn, 1989*). A comparison between computed and observed S_{sed} profiles is illustrated in *Figure 7*. In all cases the fit between observed and predicted S_{sed} profiles is statistically significant ($R^2 > 0.97$).

<i>Burst</i>	S (cm/s)	σ_w (cm/s)	$C(0)$ (g/l)	α' -	L (cm)	k_s (cm)	$U_{*wc-max}$ (cm/s)
37	46.6	21.8	0.058	1.27	4.2	7.3	6.9
38	53.1	22.1	0.090	1.48	5.6	10.1	5.9
39	41.0	23.5	0.079	1.29	3.7	13.3	6.8

Table 2. S , σ_w and *Eq. 4* parameter values derived from observed hydrodynamics and S_{sed} profile data, *bursts 37-39*.

Table 2 shows that values for α' are lower than the value suggested by Nielsen (1992) and are similar to the α values shown in Table 1 suggesting α' may be the same parameter. Values of the parameter L in the range 3.7-5.6 are only a factor of two to four times lower than k_s values. A relationship between these two parameters is therefore suggested. Work to improve the fit between observed and predicted S_{sed} profiles for these and other field observations of suspended sediment profiles in marine situations is currently being undertaken by the authors.

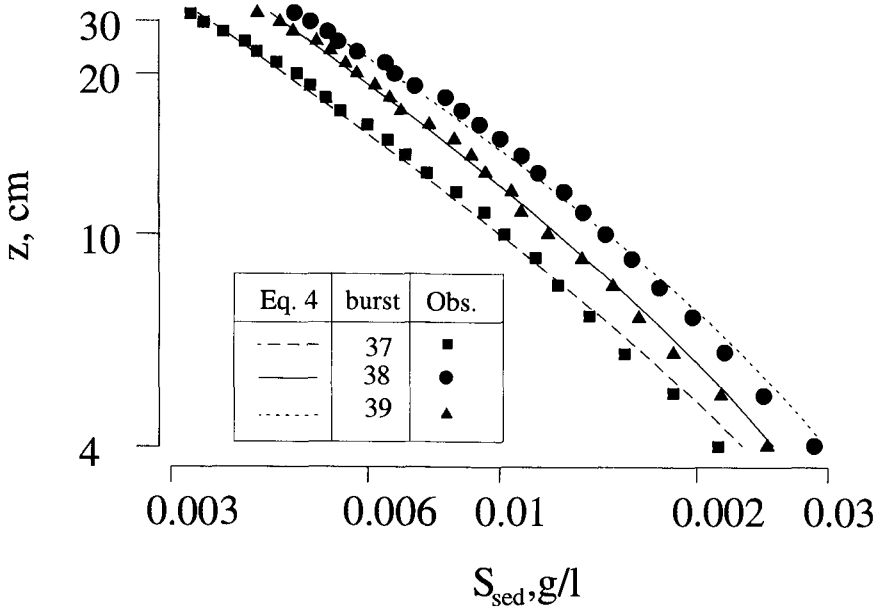


Figure 7. Comparison between and computed S_{sed} profiles, bursts 37-39.

Conclusions

- (i) Field data have been obtained in the bottom 1m of the water column during a storm.
- (ii) Present analysis has examined the temporal response of medium/coarse sandy sediments to waves and tidal currents.
- (iii) Sediment resuspension has been shown to be enhanced significantly by the passage of groups of waves.
- (iv) Average S_{sed} profiles observed during storm conditions have been represented using a 'simple' Rouse-type profile (Smith, 1977) and a new wave-current profile based upon the "convective" empirical profile proposed by Nielsen (1992). The new profile allows accurate determination of $C(0)$.

Acknowledgements

This work was funded jointly by NERC and by The Commission of the European Communities Directorate General for Science and Education, Research and Development under contract number MAS2-CT-0024 (CSTAB).

References

- GODA Y (1985) Random sea and design of maritime structures. University of Tokyo Press.
- GREEN M.O., VINCENT C.E., McCAVE I.N., DICKSON R.R., REES J.M. & PEARSON N.D. (1995) Storm sediment transport: observations from the British North Sea shelf. *Continental Shelf Research*, **15**, 889-912.
- HANNAY A., WILLIAMS J.J., WEST J.R. & COATES L.E. (1994). A field study of wave:current interactions over a rippled sandy bed. *EUROMECH 310: Sediment Transport Mechanisms in Coastal Environments and Rivers*, M. Belorgey, R.D. Rajaona & J.A.F. Sleath (editors), World Scientific, 345-359.
- HINO M., KASHIWAYANAGI M. & NAKAYAMA A. (1983) Experiment on the turbulence statistics and the structure of a reciprocating oscillatory flow. *Journal of Fluid Mechanics*, **131**, 363-400.
- HUMPHERY J.D. & MOORES S.P. (1994) STABLE II - An improved benthic lander for the study of turbulent wave-current-bed interactions and associated sediment transport. *Electronic Engineering in Oceanography*, IEE Conference Publication No. **394**, 170-174.
- KANEKO A. (1981) Oscillation sand ripples in viscous fluids. *Proceedings of the Japanese Society of Civil Engineering*, **307**, 113-124.
- KLINE S.J., REYNOLDS W.C., SCHRAUB F.A. & RUNDSTADLER P.W. (1967) The structure of turbulent boundary layers. *Journal of Fluid Mechanics*, **30**, 741-773.
- LEE T.H. & HANES D.M. (1996) Comparison of field observations of the vertical distribution of suspended sand and its prediction by models. *Journal of Geophysical Research*, **101**, 3561-3572.
- MOGRIDGE G.R. & KAMPHUIS J.W. (1972) Experiments on bedform generation by wave action. *Proceedings 13th. Conference on Coastal Engineering*, Vancouver, Canada, 1123-1142.
- NADAOKA K. & KONDOH T. (1989) Turbulent flow field structure of breaking waves in the surf zone. *Journal of Fluid Mechanics*, **204**, 359-387.
- NIELSEN P. (1981) Dynamics and geometry of wave-generated ripples. *Journal of Geophysical Research*, **86**, 6467-6472.
- NIELSEN P. (1992) *Coastal bottom boundary layers and sediment transport*, World Scientific Publishing Co., River Edge, N.J, USA.
- OSBORNE P.D., VINCENT C.E. & GREENWOOD B. (1994) Measurement of suspended sand concentrations in the nearshore: field intercomparisons of

- optical and acoustic backscatter sensors. *Continental Shelf Research*, **14**, 159-174.
- PYKHOV N.V., KOS'YAN R.D. & KUZNETSOV S. YU. (1995) Time scales of sand suspending by irregular waves. *Proceedings of the Second International Conference on the Mediterranean Coastal Environment*, Tarragona, Spain, Vol. 2, 1073-1092.
- SLEATH J.P.A. (1984) *Sea Bed Mechanics*. John Wiley & Sons, 335 pp.
- SLEATH J.P.A. (1987) Turbulent oscillatory flow over rough beds. *Journal of Fluid Mechanics*, **182**, 369-400.
- SMITH J.D. (1977) Modelling of sediment transport on continental shelves. In: *The Sea*, 6, E.D Goldberg, I.N. McCave, J.J. O'Brien & J.H. Steele (Eds.), Wiley, New York, pp. 539-578.
- SOULSBY R.L. (1994) *Manual of Marine Sands*. Report **SR 351**, HR Wallingford, UK, 70pp.
- THORNE P.D., HARDCASTLE P.J & SOULSBY R.L. (1993) Analysis of acoustic measurements of suspended sediments. *Journal of Geophysical Research*, **98**, 899-910.
- VAN RIJN L.C. (1989) *Handbook Sediment Transport by Currents and Waves*. Delft Hydraulics, Report **H 461** (2nd. edition).
- WILLIAMS J.J., THORNE P.D., O'CONNOR B.A., HUMPHERY J.D., HARDCASTLE P.J., MOORES S.P. & COOKE J.A. (1996) Interactions between currents, waves and sediments in calm and storm conditions. *Continental Shelf Research*, (submitted).
- WYLIE T., TAYLOR K. & BORN A. J. (1994) Design and calibration of the sediment tower. *POL Internal Document Number 60*, 15pp, (*unpublished manuscript*).

CHAPTER 253

EBB TIDAL DELTA EVOLUTION OF COASTAL INLETS

Michael R. Dombrowski¹, Associate Member, ASCE
Ashish J. Mehta, Ph.D², Member, ASCE

ABSTRACT

Previous investigations have established the dependence of ebb delta volumes on wave energy and tidal energy at sandy inlets. In this study, this dependence was examined with respect to the rate of delta growth and the final equilibrium delta volume starting with the opening of a new inlet when no delta is present. A diagnostic model was developed for examining the influence of the ratio of wave energy to tidal energy on delta growth. Model sensitivity tests showed that increasing the suspended sediment concentration in the littoral zone caused the delta to approach equilibrium faster, but did not affect the equilibrium volume. Increasing the wave height increased the time of approach to equilibrium but decreased the volume. Finally, increasing the sand size increased the growth rate as well as the equilibrium volume. The model was applied to five Florida inlets. It was shown that the delta may never attain a true equilibrium volume, and the actual volume may fluctuate about a "quasi"-equilibrium volume consistent a wave energy to tidal energy ratio representative of the long-term wave and tidal conditions at the entrance.

INTRODUCTION

At the seafloor in the immediate vicinity of a coastal inlet the interrupted littoral sediment tends to accumulate and raise the floor, leading to the formation of an ebb delta. The ebb tidal delta grows due to the supply of littoral sediment and ultimately reaches an equilibrium volume when the condition of no net deposition is attained. At new inlets, or ones which have been closed for a period of time, the rate at which the seafloor is modified by deltaic formation depends on the prevailing physical

1) Coastal Engineer, Coastal Tech, 1234 Airport Road, Suite 104, Destin, Florida 32541, USA.

2) Professor, Coastal & Oceanographic Engineering, 336 Weil Hall, University of Florida, Gainesville, Florida 32611, USA.

conditions, availability of littoral sediment, and geologic setting. Previous investigations have established the dependence of the delta volume on wave energy and tidal energy at sandy inlets. In this study, this dependence was examined with respect to the rate of delta growth and final equilibrium delta volume starting with the opening of a new inlet when no delta is present. The aim of this study was therefore to examine the inter-dependence between significant physical parameters governing sediment transport and the rate of delta formation at coastal inlets.

PROCEDURE

To examine the influence of the effects of current and waves on the growth rate of ebb deltas, a diagnostic approach is developed. The growth process of the delta will have an initial condition of a new inlet with no delta present (Figure I.A). The opening of an inlet the ebb delta volume increases as the inlet tidal current deposits material derived from the littoral system and ultimately reaches an equilibrium volume when the condition of no net deposition is attained. Delta accumulation height will be simulated by modeling tidal currents and superimposed waves to determine the combined shear stress, τ_b (Pa). The seafloor will continue to rise on the condition that the combined shear stress is smaller than the critical shear stress, τ_{cr} (Pa), for deposition (Figure I.B). The model must then determine the delta volume when the seafloor reaches an equilibrium elevation (Figure I.C) due to a balance of shear stresses (ie. $\tau_b = \tau_{cr}$), and the estimate the time for the equilibrium to occur.

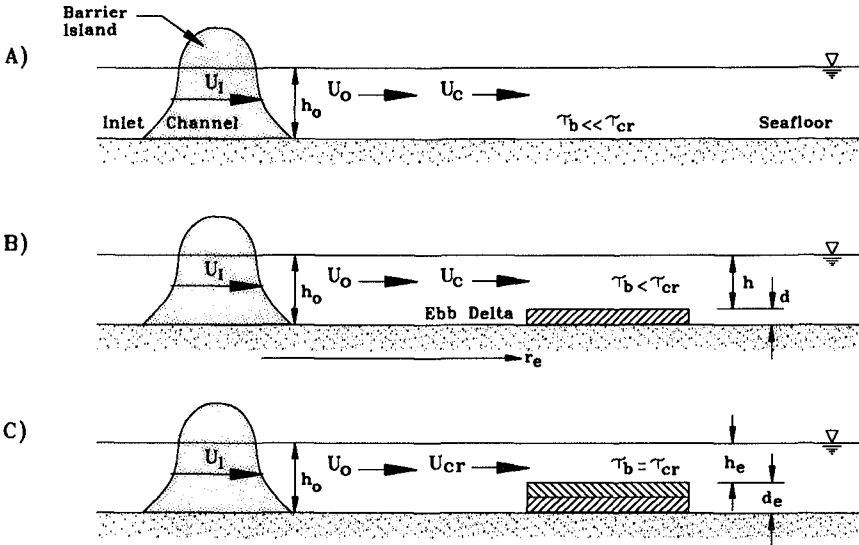


Figure I. Idealized ebb delta growth: A) initial condition; B) growth period; and, C) equilibrium condition

DIAGNOSTIC EXAMINATION OF SEAFLOOR EVOLUTION

The net decrease of suspended sediment mass per unit delta bed area, m , with respect to time, t (s), is related to sediment settling flux by

$$\frac{dm}{dt} = F_s \quad (1)$$

Substituting $F_s = -pW_sC_s$, where W_s = particle settling velocity (m/s), C_s = depth-averaged suspended sediment concentration (kg/m³), and p = probability of deposition which is given as $p = (1 - \tau_b/\tau_{cr})$ (Krone, 1962) which can range between 1 (total deposition) and 0 (no deposition). The settling velocity can be expressed as $W_s = [(4gd_{50}/3C_D)(\rho_s - \rho_w/\rho_w)]^{1/2}$, where ρ_s = particle density (kg/m³), ρ_w = seawater density (kg/m³), d_{50} = median particle size (mm), g = acceleration due to gravity (m/s²), and C_D = drag coefficient (Schiller and Naumann, 1933). The value of C_D outside the Stokes range (Reynolds number < 1) decreases rapidly then levels off and becomes nearly constant (e.g., 0.43 for spheres) in the fully turbulent flow regime considered.

Equation 1 can thus be expressed as

$$\frac{dm}{dt} = -H_f \left(1 - \frac{\tau_b}{\tau_{cr}} \right) W_s C_s \quad (2)$$

where $H_f[x]$ = heavyside function such that $H_f[x > 0] = x$, and $H_f[x \leq 0] = 0$. Next, $\rho_d = A_D m/V$, where ρ_d = dry bed density, A_D = ebb delta deposition area (m²), m = mass (kg), and V = delta volume (m³). Furthermore, $dV = dhA_D = d(d)A_D$, where dh = change in water depth and $d(d)$ = change in ebb delta height. Substituting these relations into Equation 1 results in an expression for the change of ebb delta height over time:

$$\frac{d(d)}{dt} = -H_f \left(1 - \frac{\tau_b}{\tau_{cr}} \right) \frac{W_s C_s}{\rho_d} \quad (3)$$

Given W_s , C_s , and ρ_d , Equation 3 can be solved provided τ_b and τ_{cr} are determined. Komar and Miller (1974) found that data for sediment threshold under oscillatory flows closely agreed with Shields' (1936) relationship for incipient grain motion under unidirectional flows. Thus, $\tau_{cr} = 0.058(\rho_s - \rho_w)gd_{50}$, can be used to determine the critical shear stress for waves and currents. Grant and Madsen (1978) prescribed the following relationship for shear stress due to both current and waves, $\tau_b = 0.5\rho_w f_{cw} U_i^2$, where f_{cw} is the wave-current friction factor, and the combined wave-current velocity near the bottom, $U_i = (U_{wb}^2 + U_{cb}^2 + 2U_{cb}U_{wb}\cos\phi)^{1/2}$. The quantity, U_{cb} , is the near-bed current velocity over the bottom, U_{wb} = near-bed orbital velocity due to waves (m/s), and ϕ = angle between the current and wave direction. During flood flow, when $\phi = 0$, the waves are able to penetrate over the shoal and into the

inlet channel thereby causing more bottom scour at the delta during flood flow than ebb. Therefore, $\phi = 0$ will be assumed for this study.

For calculating the bottom stress, τ_b , the friction factor due to the combined current and waves is given by $f_{cw} = (|U_{cb}| f_c + |U_{wb}| f_w) / (|U_{cb}| + |U_{wb}|)$, where f_c = friction factor due to current, and f_w = friction factor due to waves. The near-bed orbital velocity due to waves can be obtained from linear wave theory, $U_{wb} = [H\pi \cosh(kh)/T \sinh(kh)]$ (Dean and Dalrymple, 1984), where k = wave number equal to $2\pi/L$ (1/m), L = wave length (m), T = wave period (s), and h = water depth at the delta (m). As a wave train propagates from offshore into shallower water, the wave height changes as the depth changes. According to linear wave theory, the shoaled wave height (m), $H = [H_o(C_o/2C)^{1/2}(b_o/b_s)^{1/2}]$, where b_o = distance between two adjacent deep water wave rays (m), b_s = distance between two adjacent nearshore wave rays (m), C_o = deep water wave celerity (m/s) equal to $gT/2\pi$, C = shallow water wave velocity (m/s) equal to $(gh)^{1/2}$, and H_o = deep water wave height (m). The model assumes the contours are to remain straight and parallel. Thus, the refraction coefficient, $(b_o/b_s)^{1/2} = 1$.

The initial step to determine the near-bed current velocity over the delta, U_{cb} , is to obtain the maximum velocity (m/s) through the inlet for a spring tide is given by $U_{max} = (0.86\pi P / T_i A_c)$, where P = spring tidal prism (m^3), T_i = tidal period (s), and A_c = throat cross-sectional area of the inlet (m^2) (O'Brien, 1969). The average inlet velocity at the mouth of the inlet channel over one-half tidal cycle (m/s), $U_I = (2U_{max}/\pi)$. As the flow exits the inlet channel it is considered to spread out from the inlet mouth. To obtain a characteristic velocity (m/s), U_o , at the shoreward end of the deposition area, this velocity is assumed to occur along an arc, one-half the distance (m), r_e (Figure I.B), from the entrance mouth to the outer edge of the tidal prism based ebb delta area (m^2), A_p , where $r_e = (2A_p/\pi)^{1/2}$ is obtained from continuity. Thus, $U_o = (2U_I w / \pi r_e)$, where w = width of the entrance (m).

As the seafloor rises, the water depth decreases with respect to the initial water depth (m), h_o , whereby to maintain the continuity of flow, the current velocity over the delta (m/s), U_c , must increase. The current velocity, U_c , decreases with distance from the entrance as the flow spreads out over the delta from its inner to outer limit. For this study, U_c will be defined as its value at the inner limit of the delta. It should also be noted that the velocity profile of U_c is vertically uniform, it is therefore necessary to apply a correction factor to obtain the near-bed velocity (m/s), U_{cb} .

From the logarithmic velocity profile (Mehta, 1978), the ratio of the near-bed velocity to the depth averaged current velocity, $U_{cb}/U_c = \ln(z_b/z_o)/\ln(h/z_o) - 1$, in which z_o = theoretical origin of the logarithmic profile (m), and z_b = distance above profile origin (m) and is set here equal to 0.05 m. The virtual origin of the profile is obtained from the Manning-Strickler formula, $z_o = 10^7 n^6$.

Mehta and Özsoy (1978) noted that a representative Manning's n value of 0.028 can be used for sandy inlets with a typical initial water depth of 4.0 m. Thus, the current velocity obtained by continuity is multiplied by a correction factor of 0.40, $U_{cb} = 0.40U_o(h_o/h)$. Note that when the equilibrium delta volume is attained, $U_c = U_{cr}$, hence $U_{cb} = U_{cr} = 0.40U_o(h_o/h_e)$, where h_e = equilibrium water depth (m).

Inserting equations above into Equation 3 results in the governing equation for ebb delta height variation with time, and is expressed as

$$\frac{d(d)}{dt} = -\frac{W_s C_s}{\rho_d} \left[1 - \frac{\rho_w f_{cw}}{2\tau_{cr}} \left[\frac{(H\sigma)^2 \cosh^2 kh}{4 \sinh^2 kh} + 0.16 \left[\frac{U_o h_o}{h} \right]^2 + \frac{H\sigma \cosh kh}{2.5 \sinh kh} \frac{U_o h_o}{h} \right] \right] \quad (4)$$

In the finite difference form, the left hand side of Equation 4 becomes $\Delta d/\Delta t$, and was solved using the fourth order Runge-Kutta iteration method for the incremental change in delta accumulation, Δd , for $\Delta t = T_t$ (tidal period). The incremental change in delta accumulation, Δd , can then be multiplied by the depositional area, A_D , to obtain the incremental ebb delta volume, ΔV . The cumulative volume change is then plotted to illustrate the effects of waves and currents on ebb delta growth rate and estimate the duration to achieve an equilibrium volume.

MODEL PARAMETERS

Ebb delta area, A_D . It is necessary to identify the ebb delta depositional area, A_D , over which deposition occurs. This was achieved by empirically correlating the tidal prism based ebb delta area, A_p , with A_D using measurements of 21 ebb delta areas of Florida's lower Gulf Coast inlets (Davis and Gibeau, 1990). The equation of the regression line relating the tidal prism based delta surface area and the delta depositional area, $A_D = 2.34A_p^{0.81}$, corresponds to the coefficient of regression of $r^2 = 0.65$ which shows an acceptable relationship. The surface area, $A_p = P/2a_{os}$, is characterized by spring tidal prism, P and spring sea tidal amplitude (m), a_{os} .

Suspended sediment concentration, C_s . Downing (1984) presented a time-series of sediment concentrations at three locations across the surf zone at Twin Harbor Beach, Washington. The investigator found two distinct types of vertical concentration profiles. The first occurred between resuspension events ranged from 0.0002 to 0.0004 kg/m³, when the sediment concentration had vertical uniformity. While during resuspension events a concentration gradient, 0.0015 to 0.0100 kg/m³, occurred within 0.10 m above the bed in a total column water depth of 0.25 m. These concentration ranges will be assumed to apply for this study.

Sediment grain size diameter, d_{50} . Mehta and Özsoy (1978) noted that for sandy inlets the median grain size at most inlets range between 0.2 and 0.4 mm. This range will be considered in the present study.

Deep water wave height and period, H_o . The deep water wave height has a significant effect on the growth rate of the ebb delta and its equilibrium volume. By adjusting the wave height, the model generated delta volume-time curve can be made to pass through the appropriate smallest and largest measured delta volumes at a given inlet. A characteristic wave period of 8 seconds will be used for all model runs.

Friction factors, f_w, f_c . The friction factor due to current, $f_c = 8gn^2/h^{1/3}$, where Manning's n and h = water depth (Mehta, 1978). Mehta and Özsoy (1978) noted that a typical mean Manning's n value of 0.028 can be used for sandy inlets. The initial water depth used to model the evolution of the ebb deltas averaged 4 m (Dombrowski, 1994), resulted in a characteristic friction factor due to current of 0.039. It should be noted that Mehta (1978) determined friction factors for three inlets on the Gulf Coast of Florida ranging between 0.021 to 0.050.

The friction factor due to waves, f_w , was obtained from the wave friction factor diagram developed by Jonsson (1965) which plots the friction factor against the wave Reynolds number. Given, $h = 4$ m, $H_o = 0.4$ m, and wave period of 8 seconds, $R_e = 1.7 \times 10^4$, corresponds to the fully turbulent flow range (Figure 6 in Jonsson, 1965). Given the typical variation of R_e in the present study, a representative value of $f_w = 0.005$ in the fully turbulent flow range was chosen.

Tidal inlet characteristics. The tidal inlet characteristics used in the analysis are derived from the database found in Dombrowski (1994). The characteristics include: inlet throat width, throat depth, tidal prism, and spring tidal range.

EFFECTS OF IMPORTANT PARAMETERS ON DELTA GROWTH

The effects of important parameters on the rate of delta formation at coastal inlets is examined. The three selected parameters are 1) suspended sediment concentration, C_s ; 2) median sediment grain size, d_{50} ; and 3) deep water wave height, H_o . The influence of varying these parameters on the volume growth curves are shown in plots of ebb delta volume versus time, beginning with a new inlet with no delta. The range of values of these three parameters are found in Dombrowski (1994).

Suspended sediment concentration, C_s . In the Equation 4 for the change rate of ebb delta height, $d(d)/dt$, is proportional to the suspended sediment concentration, C_s . Figure II plots the ebb delta volume, $V = A_D(h_o-h)$, versus time (years) for three suspended sediment concentrations. A characteristic that is evident from the growth curves is that the equilibrium ebb delta volumes are the equal (1.4×10^6 m³) for the three concentrations. However, it is evident that as C_s increases the rate of deposition becomes more rapid.

Sediment grain size diameter, d_{50} . Two physical parameters are dependent on the median grain size diameter, d_{50} , the settling velocity, W_s , and the critical shear stress

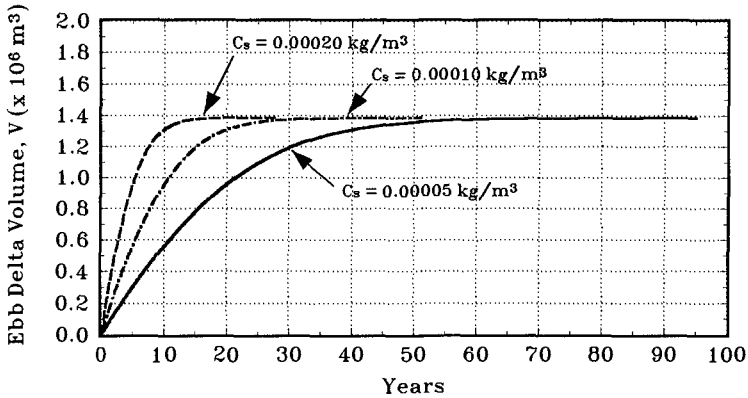


Figure II. An illustration of the influence of suspended sediment concentrations on calculated delta growth rate.

for sediment transport, τ_{cr} . The ebb delta volume versus time plot for varying sediment diameters (Figure III) is characterized by three different growth rates and equilibrium volumes. The increase in the sediment diameter increases the rate of deposition, due to the dependence of particle fall velocity on sediment size. An increase in the sediment size also increases the critical shear stress, allowing the sediment bed to remain more stable as compared to a bed composed of smaller grain size under the same flow conditions. This effect results in an increase in the equilibrium volume for increasing grain diameters.

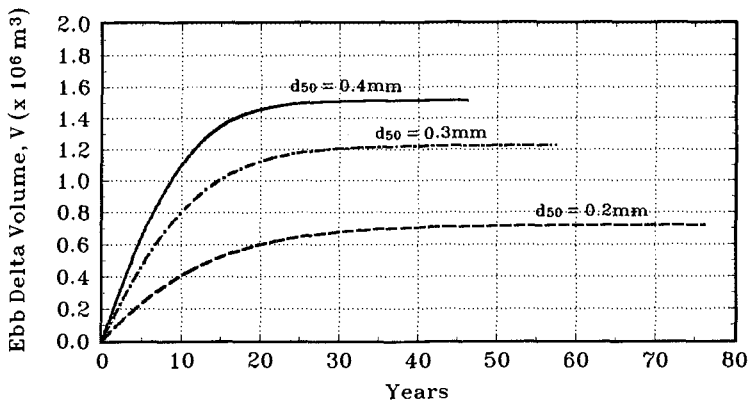


Figure III. An illustration of the influence of sediment grain size diameters on calculated delta growth rate.

Deep water wave height, H_o . As the waves approach the shoreline, its height increases as the water depth decreases. This increase in wave height in turn increases the near-bed orbital velocity, U_{wb} , hence reduces the rate of deposition. Figure IV plots the ebb delta volume versus time illustrating delta growth due to current alone, 0.0 m wave height, and two additional deep water wave heights of 0.4 and 0.8 m. During sea conditions when the deep water wave height is equal to 0.0 m, the rate of deposition is observed to be relatively rapid compared to the other two wave conditions. Note the drastic decrease in the equilibrium volume with increasing H_o .

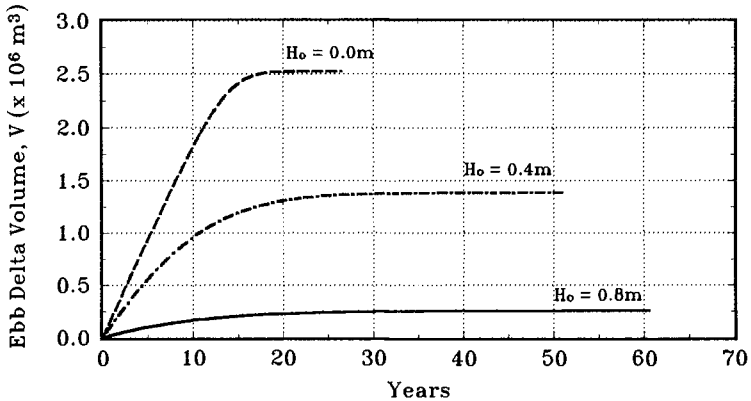


Figure IV. An illustration of the influence of deep water waves on calculated delta growth rate.

Model sensitivity tests showed that increasing the suspended sediment concentration in the littoral zone caused the delta to approach equilibrium at a greater rate, but did not affect the equilibrium volume. Increasing the wave height increased the time the delta approached equilibrium but decreased the equilibrium volume. Finally, increasing the sand size increased the growth rate as well as the equilibrium volume.

TIME-EVOLUTION OF DELTA VOLUMES

The time-evolution of sand volumes of five selected deltas along the east coast of Florida including those at 1) Jupiter Inlet; 2) South Lake Worth Inlet; 3) Boca Raton Inlet; 4) Bakers Haulover Inlet; and 5) Sebastian Inlet were analyzed. These inlets were chosen because 1) the date when each inlet was opened was available, and 2) four or more data points were available per inlet to represent the time-variation of ebb delta volumes. A plot of the measured delta volumes versus date of survey with the corresponding volume ranges for Jupiter Inlet obtained from the model is presented. The theoretical volume curves were derived from the model using the specific characteristics of the respective inlet. These data including 1) spring tidal prism, P ; 2) inlet throat width, w ; 3) inlet depth, h_o ; and 4) spring tidal range, $2a_{os}$

are summarized in Dombrowski (1994). By adjusting the deep water wave height, H_o , and the suspended sediment concentration, C_s , the delta volume-time curves were made to pass through the appropriate smallest and largest measured delta volumes.

Wave energy to tidal energy ratio, α . The inlet stability parameter, α , was introduced by O'Brien (1971) and was later expanded by Mehta and Hou (1974) to provide an indicator of the stability of inlets. An inlet in equilibrium is due to a balance between the wave energy which tends to close an inlet and the tidal energy which maintains the opening. For the present study, the (non-dimensional) stability coefficient, α , defined as the ratio of longshore wave energy to the tidal energy is used to provide an indication of the relative effect of waves and tidal current in governing the rate of growth of the ebb delta. In a reduced form for a representative deep water wave height H_o , the relationship can be expressed as:

$$\alpha = \frac{H_o^2 T_w T_t}{64 \pi a_{os} P} \quad (5)$$

where T = wave period (s), T_t = tidal period, a_{os} = spring tidal range, and P = spring tidal prism).

As the deep water wave height is increased at a given inlet, α increases and reflects a tendency to drive material toward the inlet and the nearshore area, thus limiting the delta volume. Conversely, if the deep water wave was set to zero, the corresponding α would equal zero indicating a current-determined delta. This condition results in a larger ebb delta volume as compared to a higher α -value for the same inlet when waves are present.

Jupiter Inlet. Nine delta volumes were available for Jupiter Inlet since this entrance was re-opened for navigation in 1947 (Figure V). The near linear delta growth rate from 1947 to 1967 is characteristic of the high initial growth of the delta following the opening of the inlet. This high growth rate is consistent with the occurrence of a deep sea floor at the time of the entrance opening when the incipient influence of wave action is low. The non-zero delta volumes range between $0.23 \times 10^6 \text{ m}^3$ and $0.77 \times 10^6 \text{ m}^3$, for the years 1981 and 1993, respectively. This variability may, in part, be due to the method used in estimating the volumes which could be on the order of 15% for Jupiter Inlet. We infer that this variability is primarily influenced by wave action and its seasonal as well as year-to-year variation.

The model was used to simulate the growth curves matching the volume range. The α -value of 0.17 resulting from a $H_o = 0.54 \text{ m}$ yielded a volume of $0.77 \times 10^6 \text{ m}^3$ in 1993. The higher α -value of 0.27 was calculated for a $H_o = 0.68 \text{ m}$ to modify the growth curve to achieve a volume of $0.23 \times 10^6 \text{ m}^3$ in 1981. It is therefore surmised that the relative wide range in the delta volumes between the two curves is the result of waves relative to current. Larger delta volumes correspond to lower values of α and vice versa. The maximum range of α being 0.17 to 0.27 for this inlet.

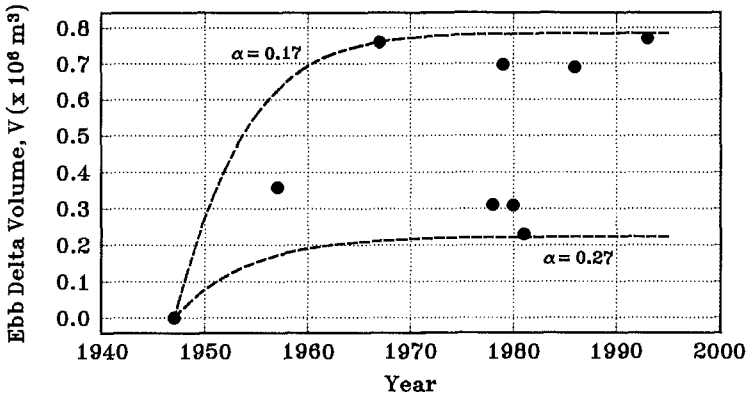


Figure V. Ebb delta volume versus year with model-calculated volume ranges for Jupiter Inlet.

INFLUENCE OF α ON DELTA GROWTH

A comparison of the ebb delta volume ranges and the corresponding wave to tidal energy ratio, α , for each of the five inlets is illustrated in Figure VI.

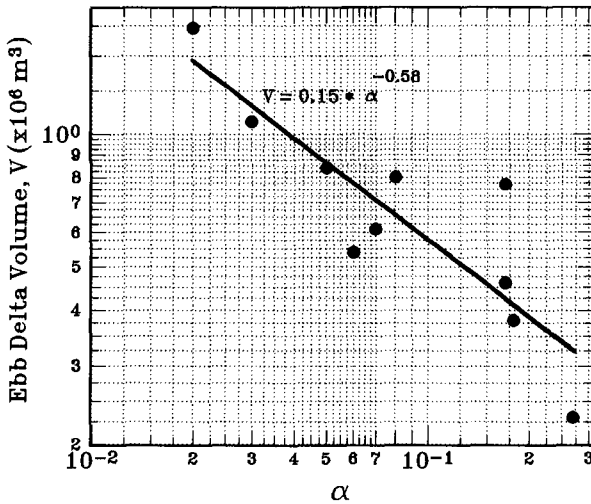


Figure VI. Ebb delta volume against wave to tidal energy ratio, α

As α increases, the ebb delta volume has a tendency to decrease, and vice versa. Although there is data scatter and a r^2 -value of 0.58, which is low, the regression line does show that there is an inverse relationship between the delta volume to α .

The equation of the regression line relating α and V is

$$V = 0.15\alpha^{-0.58} \quad (6)$$

Note that V (delta volume) in this case may not represent the actual equilibrium value, but may be close to it, given the manner in which the curve fitting was conducted.

DELTA VOLUME VERSUS MAXIMUM WAVE HEIGHT

Devine (1996) related historical ebb delta volumes with episodic extreme sea conditions. The calculated delta volumes for three inlets were plotted against the corresponding maximum WIS (Hubertz *et al.*, 1993) wave height of the preceding year which showed an inverse relationship between the volumes and wave heights. For one inlet, there was no distinct relationship presumably because the ebb delta has not reached a equilibrium condition.

For this study, 13 surveys performed between 1974 and 1995 of Sebastian Inlet ebb delta were estimated and plotted versus the maximum WIS (Hubertz *et al.*, 1993 and Brooks, unpublished) wave height of the preceding year (Figure VII). A "best-fit" line through the data shows an inverse relationship of wave conditions on the ebb delta volumes. The average ebb delta volume for this time period, based on the available data, is $1.48 \times 10^6 \text{ m}^3$. The inlet has not undergone any major modification since before 1974, therefore the only one parameter controlling the delta volume is the changing sea conditions. The fluctuation of data about the average may be indicative of the ebb delta being in a "quasi"-equilibrium condition due to: 1) the variation of sea conditions; and, 2) the sink not available to accumulate more sand.

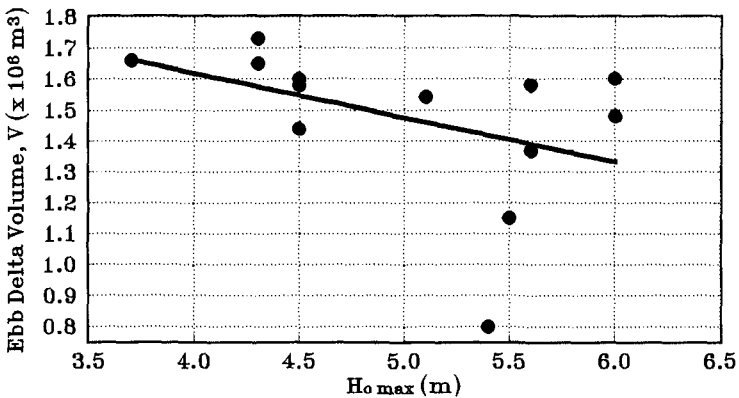


Figure VII. Ebb delta volume versus maximum WIS wave height for Sebastian Inlet.

CONCLUSIONS

Effects of Significant Physical Parameters on Delta Growth. Three parameters, namely the suspended sediment concentration, sediment grain size, and the deep water wave height, were varied in the diagnostic model developed for delta growth to determine their effects on the rate of delta formation at coastal inlets. It was found that an increase in the suspended sediment concentration increases the rate of approach to equilibrium, but does not result in a change in the equilibrium volume. On the other hand, a change in the sediment grain size and the deep water wave height effect both the rate of growth and the equilibrium volume. Thus, an increase in the sediment diameter increases the rate of growth due to the dependence of the particle fall velocity on sediment size, and increases the critical shear stress resulting in an increase in the equilibrium volume. An increase in the deep water wave height increases the near-bed orbital velocity at the site of the delta, hence decreases the rate of growth. The equilibrium delta volume likewise decreases.

Effects of α on Equilibrium Delta Volumes. It was shown through the application of the model to five Florida inlets that there is a dependence between the ebb delta volume and the wave to tidal energy ratio, α . The growth of the delta is determined by the rate at which the sand, supplied by the littoral system, is deposited by the ebb tidal flow. As wave action increases, thus increasing α -value, the delta growth rate decreases as wave and current induced bottom shear stresses scour sand deposited on the delta.

The dependence of delta volume on α partly explains the observed fluctuations in the delta volume at many inlets, since α tends to vary seasonally as well as annually. This relationship was further illustrated by plotting the ebb delta volume of Sebastian Inlet versus the maximum wave height of the preceding year. Another cause of variation of the delta volume at a given inlet is that even under constant sea conditions, the equilibrium volume often occurs after several decades following the opening of an inlet. Thus the delta volumes measured during the early years of evolution will be lower than the equilibrium volume. It was shown that the delta may never attain a true equilibrium volume, and the actual volume may fluctuate about a "quasi"-equilibrium condition. This would be consistent with a value of the wave energy to tidal energy ratio representative of the long-term wave and tidal conditions at the entrance.

ACKNOWLEDGMENTS

The authors would like to extend their appreciation to Rebecca Brooks of CERC for processing the additional wave information and to Ray LaRoux and Kathy FitzPatrick of the Sebastian Inlet Taxing District for providing the historic survey data of the inlet.

REFERENCES

- Brooks, R.M., unpublished. Maximum WIS wave heights 1994 to 1995.
- Davis, R.A. and Gibeaut, J.C., 1990. Historical morphodynamics of inlets in Florida: models for coastal zone planning, *Florida Sea Grant College Technical Paper 55*. University of South Florida, Department of Geology, Tampa, Florida, 81p.
- Dean, R.G. and Dalrymple, R.A., 1984. *Water Wave Mechanics for Engineers and Scientists*, P.L. Liu (ed.), World Scientific Publishing Company, Singapore.
- Devine, P.T., 1996. Modulation of inlet tidal deltas by severe sea. *M.S. Thesis, UFL/COEL-96/010*, University of Florida, Coastal and Oceanographic Engineering Department, Gainesville, Florida, 113p.
- Dombrowski, M.R., 1994. Ebb tidal delta evolution and navigability in the vicinity of coastal inlets. *M.S. Thesis, UFL/COEL-94/010*, University of Florida, Coastal and Oceanographic Engineering Department, Gainesville, Florida, 95p.
- Downing, J.P., 1984. Suspended sand transport on a dissipative beach. *Proceedings of the 19th Coastal Engineering Conference*, Houston, Texas, pp. 1765-1781.
- Grant W.D. and Madsen, O.S., 1978. Bottom friction under waves in the presence of a weak current. *NOAA Technical Report ERL-MESA*, National Oceanographic and Atmospheric Administration, Washington D.C., 150p.
- Hubertz, J.M., Brooks, R.M., Brandan, W.A. and Tracy, B.A., 1993. Hindcast wave information for the U.S. Atlantic Coast. *WIS Report No. 30*, Coastal Engineering Research Center, U.S. Army Engineer Waterways Experiment Station, Vicksburg, Mississippi, 20p., plus appendices.
- Jonsson, I.G., 1965. Friction factor diagrams for oscillatory boundary layers. *Basic Research Report No. 10*, Coastal Engineering Laboratory, Technical University of Denmark, Copenhagen, pp. 10-21.
- Komar, P.D. and Miller, M.C., 1974. Sediment threshold under oscillatory waves. *Proceedings of the 14th Coastal Engineering Conference*, Copenhagen, Denmark, pp.756-775.
- Krone, R.B., 1962. Flume studies of the transport of sediment in estuarial shoaling processes. *Final Report*, Submitted to the U.S. Army Corps of Engineers, San Francisco District. Hydraulic Engineering Laboratory, University of California, Berkeley, California, 110p.

- Mehta, A.J., 1978. Bed friction characteristics of three tidal inlets, *In: Coastal Engineering*, Elsevier Scientific Publishing Company, Amsterdam, The Netherlands, pp. 69-83.
- Mehta, A.J. and Hou, H.S., 1974. Hydraulic constants of tidal entrances II: stability of Long Island inlets. *Technical Report No. 23*, University of Florida, Coastal and Oceanographic Engineering Department, Gainesville, Florida, 88p.
- Mehta, A.J. and Özsoy E., 1978. Inlet hydraulics. *In: Stability of Tidal Inlets*, P. Bruun (ed.), Elsevier Scientific Publishing Company, Amsterdam, The Netherlands, pp. 83-161.
- Mehta, A.J., Dombrowski, M.R., and Devine, P.T., 1996. Role of waves in inlet ebb delta growth and some research needs related to site selection for delta mining. *Journal of Coastal Research*, Special Issue 23, Winter 1996, Fort Lauderdale, Florida, pp. 121-136.
- O'Brien, M.P., 1969. Equilibrium flow areas of inlets on sandy coasts. *Journal of Waterways and Harbors Division*, American Society of Civil Engineers, 95(1), pp. 43-52.
- Schiller, L. and Naumann, A., 1933. Über die grundlegenden Berechnungen bei der Schwerkraftaufbereitung, *Z. VDI*, Volume 77.
- Shields, A., 1936. Anwendung der Ähnlichkeitsmechanik und der Turbulenzforschung auf die Geschiebebewegung, *Versuchsanstalt für Wasserbau und Schiffbau*.

CHAPTER 254

Adjustments toward Equilibrium of a Large Flood-Tidal Delta after a Major Dredging Program, Tauranga Harbour, New Zealand

Terry Healy, Joseph Mathew, Willem de Lange, and Kerry Black*

Abstract

The Port of Tauranga is located within a tidal inlet estuarine lagoon system which has been dredged to improve navigation for shipping since 1968. In 1992 a major dredging program deepened the entrance navigation channel through the ebb-tidal delta from 10 to 14 m, and the inner harbor channels to ~13 m. As a condition of the consent to dredge a detailed monitoring program was required which included annual hydrographic surveys over the flood and ebb-tidal delta as well as recording current meter records from morphodynamically sensitive locations to compare with records taken before the dredging. Results of the hydrographic surveys showed significant morphodynamic change of the flood-tidal delta had occurred essentially by the time the 6 month dredging program was completed. Comparison of the S4 current meter recordings showed current changes consistent with expectations of the EIA. Changes on the ebb-tidal delta were not expected but have occurred although not as rapidly, and seem to be ongoing.

Introduction: The Pre-dredging Assessment of Impacts

The Port of Tauranga was established last century within a meso-tidal estuarine lagoon enclosed by a Holocene barrier island and tombolo system (Fig.1). The inlet exhibits many morphological features typical of a meso-tidal inlet as presented by Boothroyd (1985), including a flood and ebb-tidal delta system and a narrow inlet gorge. Prior to dredging, channel depths reached 7-8 m through the delta systems with the narrow inlet gorge attaining 30 m.

* Coastal Marine Group, Department of Earth Sciences, University of Waikato, Hamilton, New Zealand. Email: trh@waikato.ac.nz

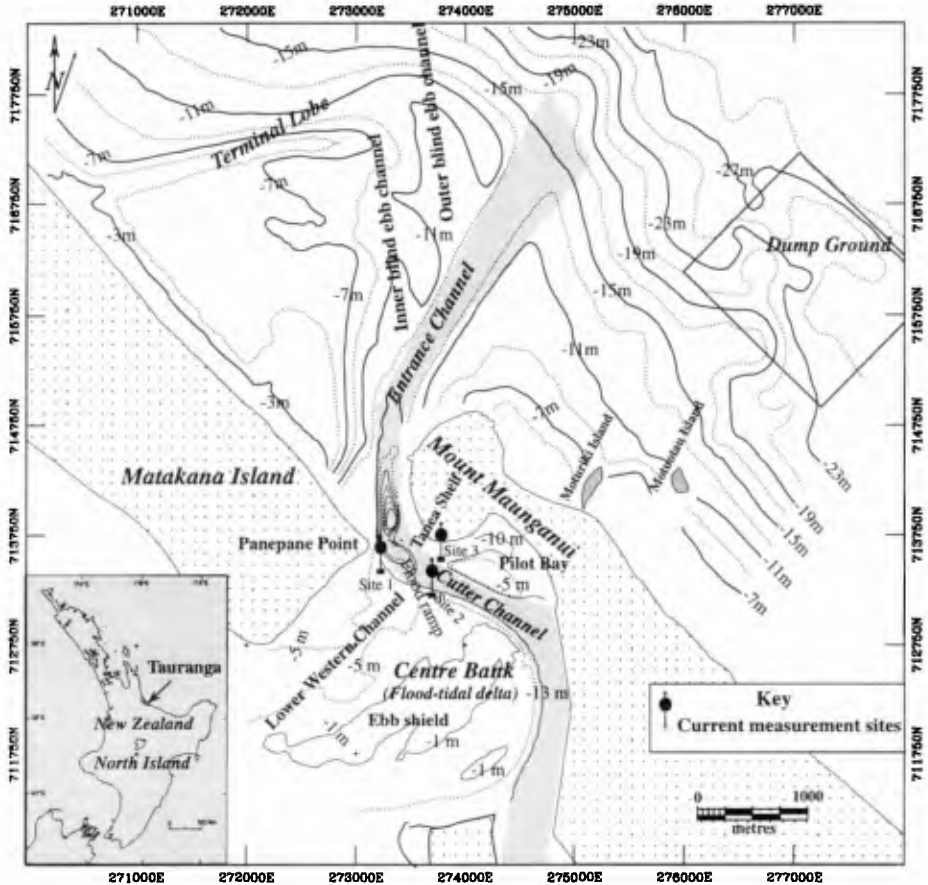


Fig. 1. Location map of Tauranga Harbour flood and ebb-tidal deltas and dredged shipping channels.

The port was expanded in the 1950s, and in the 1960s Wallingford Hydraulics Laboratory of the UK was commissioned to undertake a study investigating improvements for navigation approaches to the port. To improve port operations for ocean-going vessels, dredging of a navigation channel to depths of 10 m through both the flood and ebb-tidal deltas was carried out in the late 1960s. As was to be expected in a high current flow sandy tidal inlet located on a littoral drift shoreline, the navigation channels required significant maintenance dredging. Since the initial navigation channel construction through the tidal delta system, the average maintenance dredging has been $\sim 70,000 \text{ m}^3$ per year, which was taken primarily from specific zones of channel deposition located either side of the inlet gorge, i.e., in the Entrance Channel through the ebb-tidal delta, and in the Cutter Channel which transects the flood-tidal delta.

In 1992, as part of further port expansion, a major shipping channel deepening and widening program was undertaken to deepen the channels from 10 to 13 m within the harbor, and to 14 m outside of the entrance. This involved dredging some 5.5 million m³ of predominantly sandy material with some shell gravel (Healy et al., 1991).

A condition of the consent permitting the development, required the port company *"to monitor all aspects of the dredging programme and its impact upon the environment, and take such action as necessary to mitigate adverse effects that the dredging shall have."* Accordingly, monitoring included annual full hydrographic surveys over the flood-tidal delta and adjacent channels, pre- and post-dredging measurement of current flows using RCMs, and surveys of barrier island shoreline change, in conjunction with biological monitoring. The monitoring continued until the end of 1995, some 4 years after the dredging.

The aims of this paper are to report on the morphodynamic changes that occurred after the dredging in this large tidal inlet and delta system, and make an assessment of the time it took for the inlet-tidal delta system to readjust to changed hydraulic conditions.

Morphodynamic Change

Morphodynamic change refers to change in bathymetry or landform created by the actions of the formative processes, in this case the currents and waves. Changing the conditions of the tidal inlet dynamic equilibrium, such as by inducing current flow hydraulic change will likely change the sediment transport pathways, and therefore lead to morphological change. The most sensitive areas are the ebb and flood-tidal deltas and the associated channels.

The projected impact on morpho- and hydrodynamics was studied at the EIA stage using 2-dimensional hydrodynamic modelling (Bell, 1991). The modelling indicated a substantial alteration to the current flow regime over the flood-tidal delta and shipping channel (the Cutter Channel), but no detectable impact on tidal currents over the ebb-tidal delta. Within the harbor the major impact predicted was that the shipping channel of ~13 m depth (c.f. original natural pre-dredged depths of 5-6 m) would act as a tidal "sink" on the ebb flow which would substantially alter the tidal cycle residual flow vectors over the flood-tidal delta (Fig.2). Accordingly, Healy et al. (1991; 1993) predicted as a result of the dredging that parts of the flood-tidal delta sediment transport pathways would be subject to change which would likely induce some morphodynamic change. What was not known was how long it would take for the flood-tidal delta to come to equilibrium after the dredging.

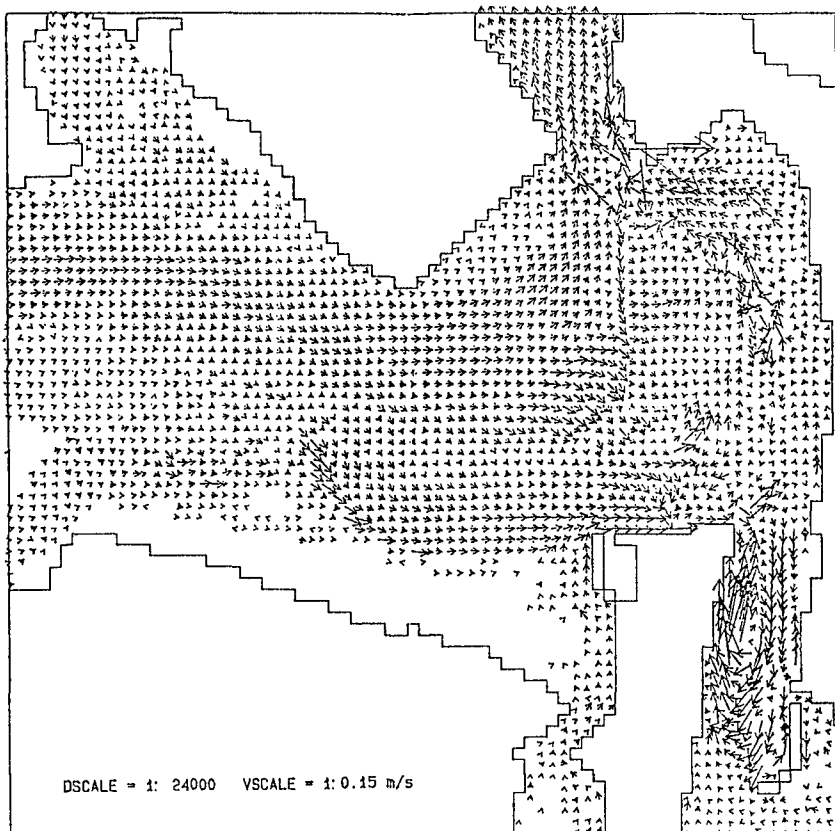


Fig. 2. Residual velocity vector differences showing the changes due solely to the deepened shipping channel in a spring tide (after Bell, 1991).

Sedimentation Within The Dredged Channels

Deepening an entrance channel to an inlet creates a greater hindrance to littoral drift and a more effective sediment trap. The long term effectiveness of the sediment trap is measured by the maintenance dredging requirement. For this case, since the channel deepening of 1992, the maintenance dredging has increased from a long term average of $\sim 70,000 \text{ m}^3$ per year to $\sim 110,000 \text{ m}^3$ per year for each of 1993, 1994, and 1995. An increase of this magnitude was expected, and to date has been remarkably uniform in amount per year. The sediment has accumulated on both the seaward and the harbor side of the inlet gorge.

The Flood-Tidal Delta (Centre Bank)

The flood-tidal delta is perhaps the most sensitive to morphodynamic change because it is formed largely as an interplay between the tidal current hydraulics and

sediment supply, whereas the ebb-tidal delta may also be influenced by wave action. Centre Bank shows some features typical of the Boothroyd (1985) "horseshoe crab" morphological model of flood-tidal delta, but is distorted by alignment of the harbour in relation to the inlet entrance, and the consequent predominant ebb-tidal discharge flowing laterally across the feature rather than being diverted by the ebb shield around the delta. For Centre Bank the EIA showed that deepening of the shipping channels within the harbor would be expected to induce a much greater west-to-east component of flow across Centre Bank, and this would likely have an impact on the sediment transport pathways.

The availability of earlier hydrographic surveys over Centre Bank, and the regular soundings since 1989, allow a close monitoring of the changes. The changes in tidal channel and bank outline bathymetry for the 1 m and 5 m depths relative to chart datum (extreme low water spring tide level) are presented in Fig.3. The plots show that between 1982 and 1989 the Lower Western Channel where it crossed the flood-tidal delta, markedly reduced in depth with a greater proportion of the tidal flow being diverted around and to the south of Centre Bank, at which time the disparate, shallower small southern shoals were scoured away. In July 1992 the major dredging program was just being completed, and as a result of the greater west-to-east tidal flows across Centre Bank, the Lower Western Channel was already opening up again. By September 1993, the Lower Western Channel had re-established itself, coincident with shallow shoals also redeveloping on the southeastern margins, and increased area of shoaling on the eastern margin adjacent to the shipping channel. Since 1993 the flood-tidal delta morphology has not changed in broad outline (Mathew et al., 1995).

The net bathymetric differences exceeding 0.5 m between April 1990 and April 1994 are presented in Fig. 4. A broad zone of scour is evident along the Lower Western Channel, resultant upon the deepening of the channel. A zone of minor scour occurred along the outer ebb shield, with a parallel band of minor accretion, indicating a relocation of the distal ebb shield. Minor scour also occurred along the southeastern flank of Matakana barrier island. Accretion was marked on the flood ramp due to channel realignment, as well as an additional capping on the highest part of the inner ebb shield, and along the northeastern rim of the Centre Bank adjacent to the shipping channel.

J. Mathew (in prep.) has undertaken detailed analysis of the sounding data including detailed cross sections. The profiles showing the most change are presented in Fig 5. The sounding sections show post-dredging infilling and scour of parts of the Lower Western Channel, with only minor change on the other parts of the Centre Bank. In particular the shallowing of the ebb shield, interpreted as a strong possibility in the EIA (Healy et al., 1991), has partly occurred, but only up to 0.5 m vertical accretion over an area of $\sim 600 \times 300 \text{ m}^2$, and this change likewise occurred rapidly after the 1992 dredging.

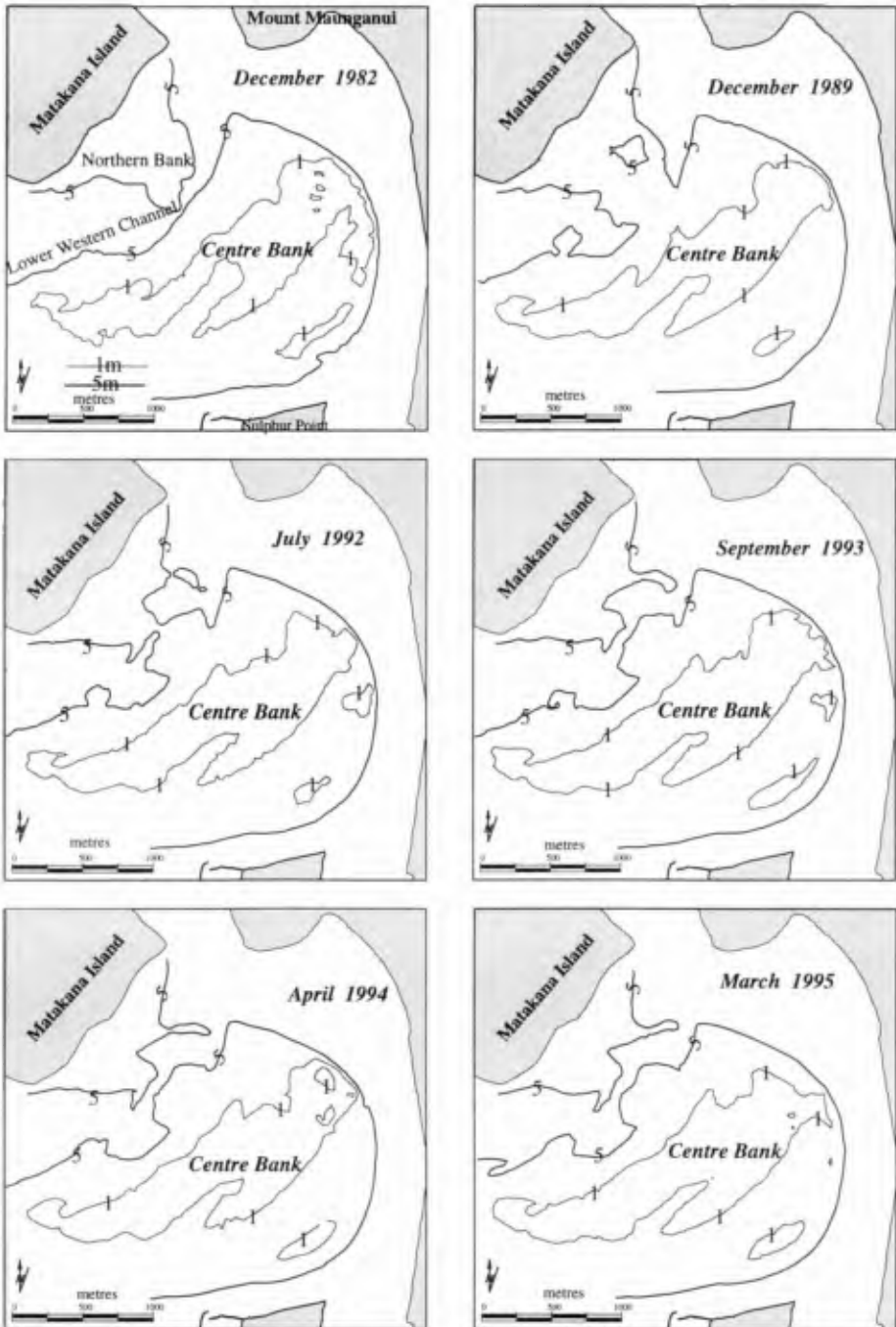


Fig. 3. Bathymetric changes in the Lower Western Channel between December 1982 and March 1995.

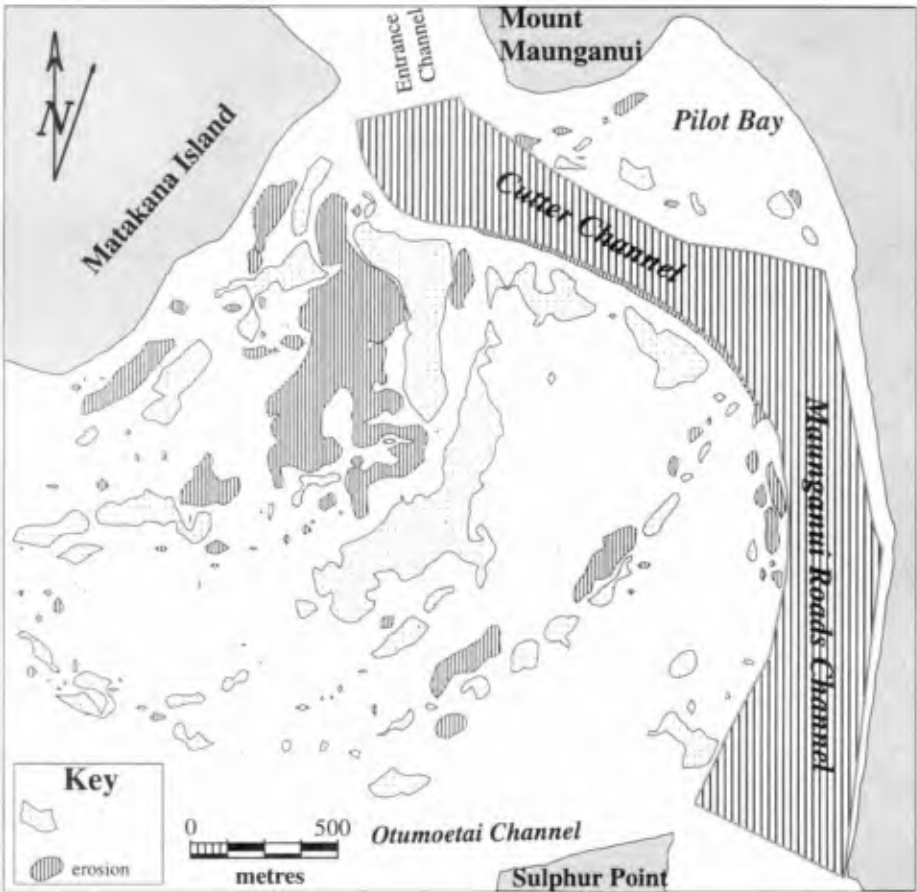


Fig. 4. Bathymetric differences on the flood tidal delta exceeding 0.5 m vertical extent between April 1990 and April 1994.

Air Photo Record

The annual vertical air photos flown since the major dredging have shown realignment of the direction of the sand waves which cap the topographical high of Centre Bank, geomorphically the ebb shield. Noticeable on the eastern sector of the ebb shield the sand wave bedforms have shown an easterly movement. The air photos also show a response of the flood ramp to the dredging and removal of part of a rocky shelf which had been protruding into the inlet gorge and was considered a hazard to navigation. This resulted in an expanded flood jet onto the flood ramp, and created a new area of scoured shell-gravel lag. Expansion of the flood jet was consistent with the higher current flows recorded after dredging by the S4 current meters, discussed below.

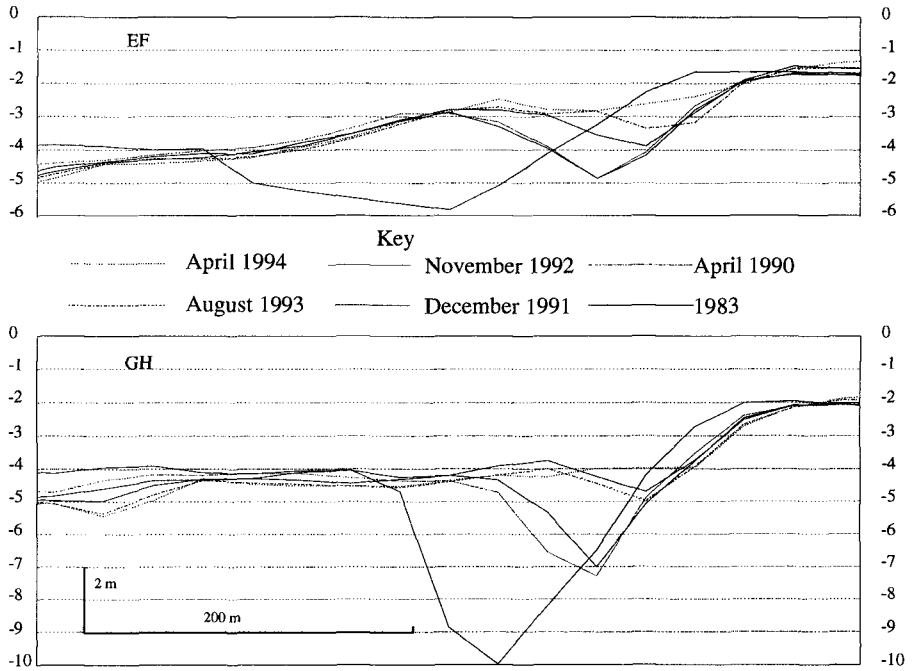


Fig. 5. Cross-sections across Western Channel showing deposition of up to 3 m in Lower Western Channel (EF) and up to 6 m in the blind flood channel (GH) between 1983 and 1994.

Changes in Current Flows Near Panepane Point

Current flows were monitored at 3 locations adjacent to the barrier island side of the inlet using S4 electromagnetic current meters. These were located in the Lower Western Channel, Pilot Bay Channel and on the edge of the Cutter Channel. The resulting data (Figs 6a-b) show some changes in velocities for the Cutter Channel site with greater flood tide dominance rising from 0.85 m/s to 1.20 m/s after the 1992 major dredging. In the Lower Western Channel near Panepane Point there was an increase in current magnitude from 1.00 m/s peak flood flow and 0.75 m/s peak ebb flow before the dredging to 1.25 m/s peak flood flow and 1.10 m/s peak ebb coincident with a directional change after the dredging. However a later deployment at the same site in 1994 showed that the current direction had resumed its pre - 1992 dredging alignment.

The observed increase in current speed at points measured is consistent with a re-aligned and laterally extended tidal jet as a result of removal of the Tanea Shelf from the inlet gorge. That, as expected, has induced some change in the affected sea floor, in particular the Lower Western Channel and flood ramp area.

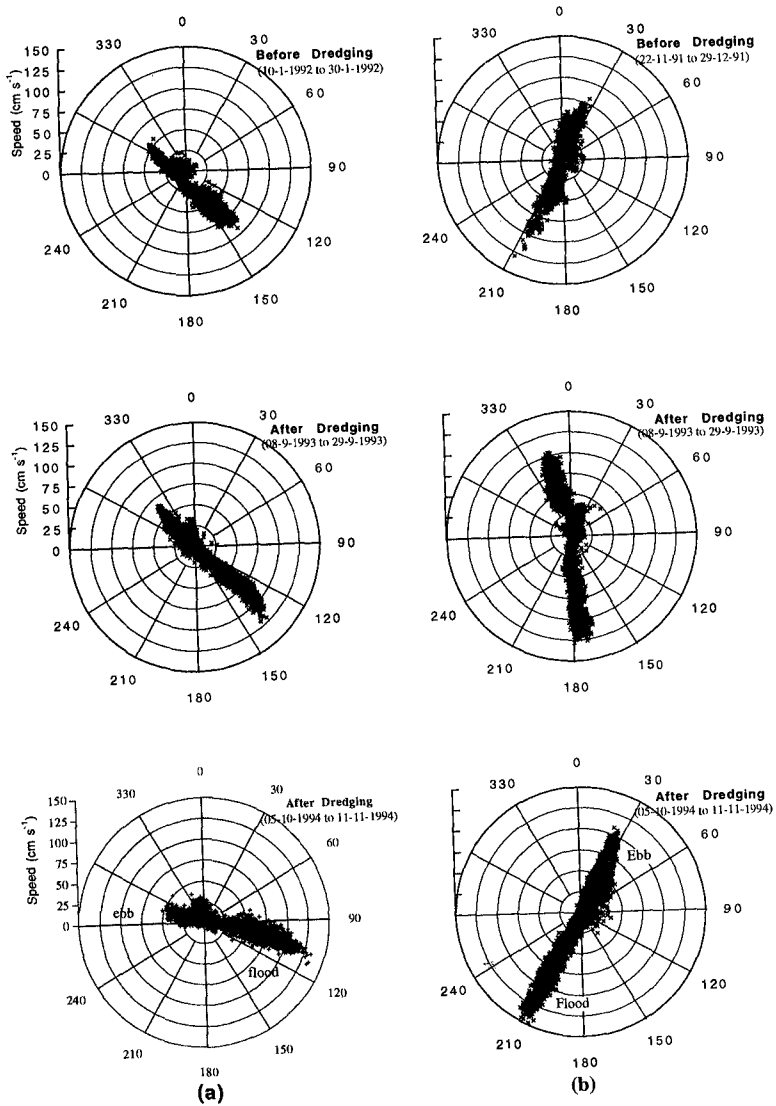


Fig. 6. Current velocities at 1 m above the bed before and after dredging at: (a) the edge of Cutter Channel and (b) at Lower Western Channel near Panepane Point.

The Ebb-Tidal Delta

Annual bathymetric surveys were also carried out over the ebb-tidal delta since 1989. Comparison of the surveys indicates that the ebb delta has been largely stable in terms of its gross morphology, for example the terminal lobe has not changed in location between 1989 and 1995 (Fig.7). The major identifiable change has been that a proximal (inner) blind ebb channel northwest of Mount Maunganui has tended to infill from about 13 m depth in 1989 to 10 m depth in 1995. A distal (outer) blind ebb channel has increased in size.

Overall there has been no sudden or substantial change to the ebb delta morphology which can obviously be linked to the entrance shipping channel deepening in 1992. This is consistent with the numerical model residual vector patterns carried out in the EIA which showed that there was unlikely to be identifiable difference from deepening the Entrance navigation channel from 11 m to 14 m.

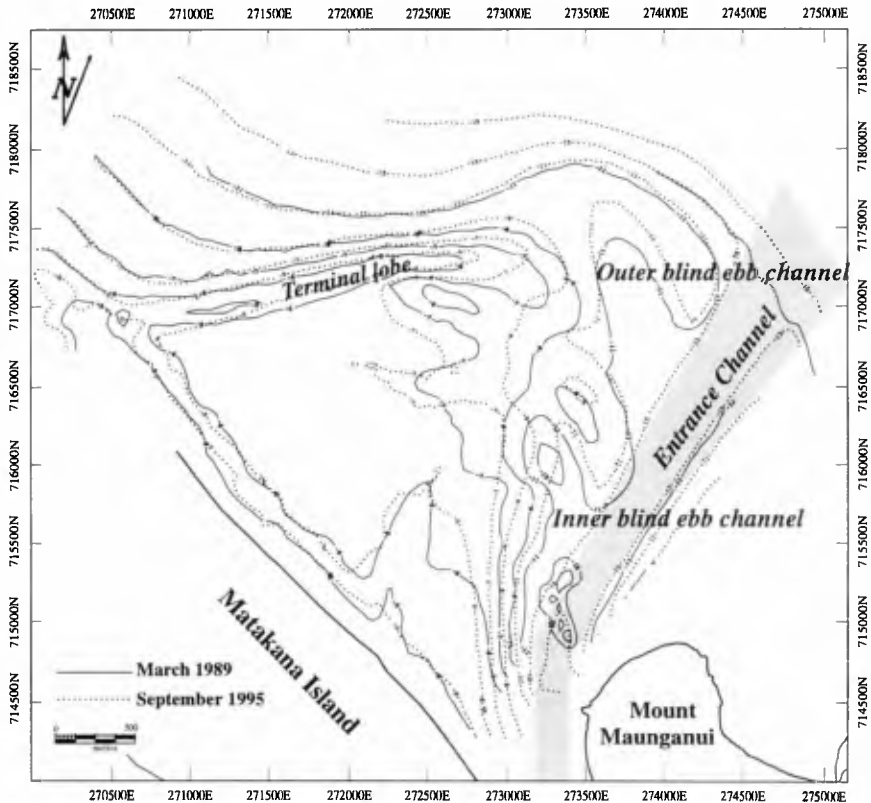


Fig. 7. Bathymetric differences on the ebb-tidal delta between March 1989 and September 1995.

Conclusions

Since the 1992 major channel dredging, the hydrographic surveys have shown that some areas of the flood ramp have accreted by up to 3 m in vertical extent while up to 2.5 m of scour associated with increased currents have occurred in the non-dredged semi-major Western Channel. Alignment of large 'dune' bedforms on the topographic high of the flood delta, morphologically the ebb shield, has changed significantly, but the depths have changed only by about 0.5 m, and overall the broadscale morphology of the flood-tidal delta has retained its coherency.

In terms of how rapidly the tidal inlet and delta system has adjusted to new conditions after the substantial hydraulic change to the tidal delta system consequent upon the 1992 dredging, it is clear that major readjustment for the flood-tidal delta was very rapid, and essentially occurred by the time the dredging was completed - over a 6 month period. On the other hand, the ebb-tidal delta adjustment has been much slower and seems to be ongoing.

References

- Bell, R.G., (1991). Port of Tauranga Model Study (Deepened Shipping Channel Proposal). DSIR Water Quality Centre Consultancy Report No 6127/1. 22p.
- Boothroyd, J. (1985). Tidal inlets and tidal deltas, chapter 7 in R.A.Davis Jnr.(ed.): *Coastal Sedimentary Environments*, Springer-Verlag, pp 445-532.
- Healy, T., McCabe, B., and Thompson, G., (1991). Port of Tauranga Ltd. Channel Deepening and Widening dredging Programme 1991-92 Environmental Impact Assessment. 122p.
- Healy, T., Bell, R., and de Lange, W., (1993). Predicting morphodynamic change from tidal residual vectors at a large tidal inlet, Tauranga Harbour, New Zealand. In List, G.H., ed., *Large Scale Coastal Behaviour - 1993*, U.S. Geological Survey Open File Report 93 - 381, pp64-67.
- Mathew, J., Healy, T.R. and W.P. de Lange, (1995). Changes to a large flood-tidal delta system following major channel dredging, Tauranga Harbour, New Zealand. Proc. Fourth International Conference on Coastal and Port Engineering in Developing Countries, Rio de Janeiro, Brazil, September 1995. pp 1464-1478.
- Mathew, J. (in prep.) Morphodynamic change in response to dredging and dumping, Tauranga, New Zealand. D.Phil. Thesis, University of Waikato.

CHAPTER 255

LABORATORY MOBILE BED MODEL STUDIES ON EBB TIDAL SHOAL EVOLUTION

Xu Wang¹, Lihwa Lin² and Hsiang Wang³

Abstract

Laboratory mobile bed experiments were conducted to study the ebb tidal shoal evolution process under storm wave conditions. An idealized inlet configuration was chosen for the experiment representing a typical median-sized inlet on the east coast of Florida, USA. Six different cases were tested including a natural inlet and a jettied inlet with different jetty length and jetty type. Formation of ebb tidal shoal was observed in all cases; the rate of growth and location of ebb tidal shoal were different for the cases. Inlet channel shoaling and beach erosion next to the inlet are far more severe in the case of natural inlet than that in the case of jettied inlet. In general, the established tidal shoal tends to grow during the ebb cycles and deteriorate during flood cycles. And partial removal of ebb tidal shoal has shown to increase downdrift beach erosion and reduce the rate of ebb shoal growth, though the rate of change of the mined case rapidly approached that of the case without mining.

1. Introduction

Ebb tidal shoal is a common feature associated with tidal inlets in coastal area. It is created by the combined deposition of littoral material diverted from adjacent beaches together with the alluvial material carried out from inlet by the tidal current. When inlets are stabilized with training structures, ebb tidal shoal can become more prominent as littoral material is diverted further offshore into deeper water. As a consequence, the ebb shoal volume also increases. This causes additional disruption of the normal longshore sediment transport and often results in severe downdrift shoreline recession. In Florida, over 85% of the shoreline erosion is considered to be related to inlets, particularly to those with training structures.

¹Engineer I, Division of Natural Resources Management of Lee County, FL 33902,
²Research Scientist, ³Professor, Coastal and Oceanographic Engineering Department,
Univeristy of Florida, Gainesville, FL 32611,USA.

Since ebb tidal shoal is formed mainly by material diverted from the updrift beach it is a tempting source, and reasonably so, to tap for downdrift beach nourishment. However, such practice is not common because the formation of ebb tidal shoal is part of the natural process and disturbing an ebb tidal shoal environment so close to shoreline without knowing clearly its effects is unsettling.

This paper is aimed at investigating the evolution process of ebb tidal shoal on one hand and finding the possibility of utilizing the sand from ebb tidal shoal on beach nourishment on the other by means of movable-bed physical modeling in the laboratory. To achieve this goal, an inlet model testing is designed and carried out to investigate ebb tidal shoal evolution process and corresponding shoreline responses for a natural and unimproved inlet, an inlet with jetty structures and with the ebb tidal shoal partial removal.

2. Design Of Inlet Model Experiments

The inlet-beach physical model was designed with considerations on experimental constraints and modeling laws. The model was tested under simulated storm wave conditions to insure turbulent flow and suspended sediment transport mode. The modeling law adopted in the present study is shown in Table 1, which is for an inlet-beach system based on the analyses of the experimental results of a series of 2-D and 3-D laboratory model study (Wang, *et al.*, 1994; Wang, *et al.*, 1995).

Table 1: Modeling Law

Geometric Distortion*	Wave Height Distortion	Hydrodynamic Time Scale	Morphological Time Scale
$N_\delta = N_w^{0.4} N_\lambda^{0.8}$	$N_H = \sqrt{N_\lambda}$	$N_T = \sqrt{N_\lambda}$	$N_t = \sqrt{N_\lambda}$

* N_w, N_δ, N_λ are fall velocity, vertical and horizontal length ratios, respectively.

The model experiments were carried out in a wave basin located in Coastal and Oceanographic Engineering Laboratory at the University of Florida. The wave basin has a physical size of 25m wide, 30m long, and 1m deep as shown on Figure 1. The inlet-beach model and a wave maker were located at two long ends of the basin. An ideal inlet, of straight, rectangular channel, with uniform width and depth of 1.75m and 0.2m, respectively, was constructed cutting through a plane beach made of a natural quartz sand ($D_{50}=0.19\text{mm}$). The overall length of the beach from updrift to downdrift ends is 19m. The model is laterally bounded on two wave guides formed by concrete blocks. The wave guides are perforated to allow flows in and out of the test section. The downdrift wave guide is open at the beach end to allow downdrift littoral transport to leave the test section and to be collected in the catch channel. The plane beach consists of a flat back shore segment, a steep-slope

foreshore segment, and a mild-slope offshore profile which extends seaward to about 7m from the shoreline beach face before merging with the concrete floor. The beach profile approximates an equilibrium shape of $h = Ax^{0.8}$, which h is water depth, x is seaward distance from shoreline, A is a scale factor.

A schematic of experiment setup

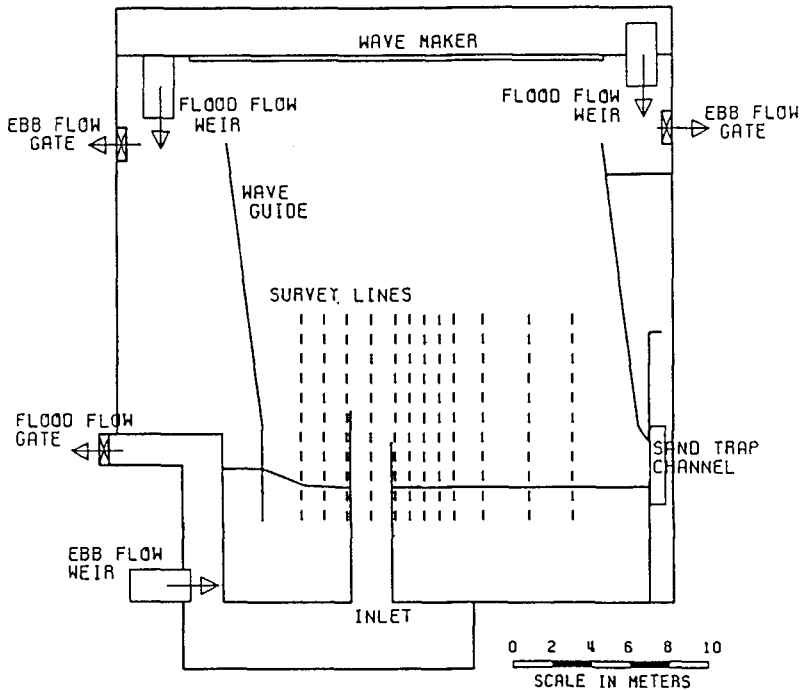


Figure 1: The Schematic Setup for Movable-Bed Inlet Physical Model.

The inlet is offset from the center towards the updrift with the updrift beach length of 5m and downdrift beach length of 12m. The wave generator is located about 27m from the shoreline based on an average water depth about 0.35m. Tidal currents are generated by recirculating water through the circulation channels connected with the wave basin. The flow discharge is controlled by the flood and ebb flow weir boxes. Water is supplied from the upper basin weir boxes (flood flow weirs) for flood current and from the lower basin weir box (ebb flow weir) for ebb current. A curved feeder beach section at the updrift end allows for continuous and

more uniform sediment supply to the downdrift which is purely due to wave-induced transport.

3. Experimental Conditions

Six different experimental cases and associated conditions are summarized in Table 2. Tidal currents are simulated in the experiment by alternating ebb and flood cycles at equal interval of 40 minutes, which is equivalent to a semi-diurnal tidal period at 1:80 geometrical scale ratio according to Froud number criterion. A constant discharge of $0.04 \text{ m}^3/\text{sec}$ is used for both ebb and flood cycles. The cross-sectional averaged currents in the inlet are maintained to be 0.12 m/s and 0.14 m/s for the flood and ebb cycles, respectively. The tidal range is 3 cm in the experiment.

Table 2: Test Conditions of Inlet-Beach System Experiment.

Case	Wave height	Incident wave condition (Wave period: 1sec) Wave angle	Beach slope		Jetties (type) e: even length u:uneven length	Model time (min)
			Foreshore	Offshore		
C1	8 cm	15 deg	1:2.4	1:14.5	none	480
C2	8 cm	15 deg	1:2.9	1:14.5	Riprap(u)	1600
C3	8 cm	7.5 deg	1:2.9	1:14.5	Caisson (u)	3200
C4	7 cm	7.5 deg	1:2.9	1:14.5	Caisson (e)	3200
EC1	7 cm	7.5 deg	1:2.9	1:14.5	Caisson (e)	3200
EC2	7 cm	7.5 deg	1:2.9	1:14.5	ebb shoal mining	3200

Experiment C1 is to simulate a natural inlet; C2 is to simulate a jettied inlet with riprap type jetties; C3 and C4 are to simulate a jettied inlet with caisson type jetties. In Case C2 and C3, the inlet consists of an updrift jetty of 1.5m and a downdrift jetty of 0.7m, both straight and perpendicular to initial shoreline. The uneven updrift and downdrift jetty geometry of an inlet is common in Florida. In C4, the updrift and downdrift jetty jetties have the same length of 1m. Experiment EC1 and EC2 were conducted to investigate the effects of ebb tidal shoal removal. Experiment EC1 is the case without removal of ebb tidal shoal and EC2 is the case with removal of ebb tidal shoal. Both experiments have the same test conditions as that of C4, except C4 has a slight larger width of the inlet. The jetty elevation is about 5cm above the flood tide water surface and jetty width is 20cm. Figure 2 shows the initial bathymetry for natural inlet case. Also, the major difference between riprap and caisson type jetties is that the riprap is porous and not sand tight whereas the caisson is impervious.

4. Experimental Procedures

The model experiments is conducted according to the following procedures: (1) Prepare initial inlet model bathymetry, (2) Conduct initial profile survey at selected cross-sections as shown in Figure 1, (3) Adjust water level and discharge to

the specified ebb conditions, (4) Start wave maker to generate storm waves, (5) Run the ebb cycle experiment for 40 minutes, (6) Readjust water level and tidal flow for the flood condition, (7) Start wave generator and run the flood cycle for 40 minutes, (8) Repeat steps from (3) to (7) until an prominent ebb tidal shoal is established, and (9) Reshape the model to its initial bathymetry for the next experiment. Eleven bottom profile surveys were conducted at irregular time intervals, shorter in the early stage and longer later in the experiment. Sediment accumulated inside the inlet and outside of the downdrift boundary was collected at the same time when bottom surveys were conducted. Both dye and sand tracer studies were conducted from time to time. The dye study was for current pattern observation and was documented by video recordings. Sand tracers were used for visual examination on sediment transport pattern. No quantitative measure of sand tracer movement was attempted.

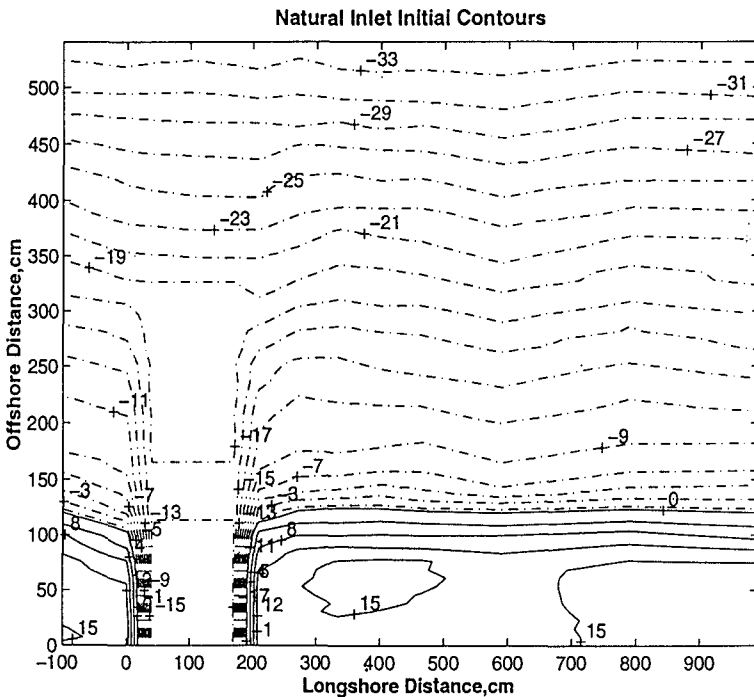


Figure 2: Initial Topographic Contours for Natural Inlet Experiment

The initial topography of Case EC2 was prepared by modifying the final topography (3200 min) of EC1, which included mining of ebb tidal shoal and downdrift beach nourishment. Sand was removed from the ebb shoal and inlet channel areas which is indicated by the dashed rectangle in Figure ?. This sand was used in all for the downdrift beach nourishment in the preparation of initial topography of EC2.

5. Experimental Results

Formation of ebb tidal shoal was observed in all cases; the location of ebb tidal shoal and the rate of growth were different. In the laboratory, + 2cm above the initial bottom profile was chosen as the reference plane to present the results of ebb tidal shoal growth.

In the natural inlet experiment, a small shoal formed immediately near the entrance in the first ebb and flood cycles as the beach material was rapidly carried seaward to form nearshore breaking bars. Inside the breaking line, sediment from the updrift beach was seen to move towards the inlet by strong wave action. Outside the breaking line, sediment was carried across the channel and deposited at downdrift side of the channel outside the surf zone. Beach erosion was severe at both sides of the inlet from the beginning of the experiment. In the following ebb and flood cycles, the initial shoal built near the inlet entrance continued to grow and expand to form channel shoal and ebb tidal shoal. The experiment was stopped at 480 minutes or six complete tidal cycles as both channel shoaling and beach erosion became excessively severe. The shoreline erosion pattern was nearly symmetrical with respect to the inlet center. The generation and growth of the ebb tidal shoal and also the shoreline patterns in Experiment C1 using the net +2cm as the base contour are exhibited in Figure 3. It is seen that shoaling began at the channel entrance and grew in both directions towards offshore and into the channel. At 120 minutes, channel shoal and ebb tidal shoal can be separately identified. The ebb shoal began to shift towards downdrift after 120 minutes. At the end of 480 minutes, a drastic ebb tidal shoal was established while the channel shoaling was seen to extend and reconnect with the ebb shoal.

In the jettied inlet experiments, general sediment transport patterns were similar in the beginning ebb and flood cycles. Accretion of sediment occurred at the tips of both updrift and downdrift jetties. Generation of ebb shoal was not evident in this early stage. In subsequent time, the sediment transport patterns became different, which then influenced the development of the ebb tidal shoal. In C2, the updrift jetty tended to attract sediment owing to the structural porosity. Accordingly, sediment was heavily deposited on both sides of the updrift jetty around its tip. In C3 and C4, on the other hand, more updrift sediment was seen to bypass the jetty. In these jettied inlet experiments, beach erosion was significant only at the downdrift side, particularly in C2 owing to the larger incident wave angle. In C4, the ebb tidal shoal was generated more closer to the inlet than in C2 and C3 due to the small incident wave height. Compared with C4, EC1 had more centered ebb tidal shoal and much less channel shoaling because of the smaller width of the inlet which tended to transport more sediment bypassing the jetties.

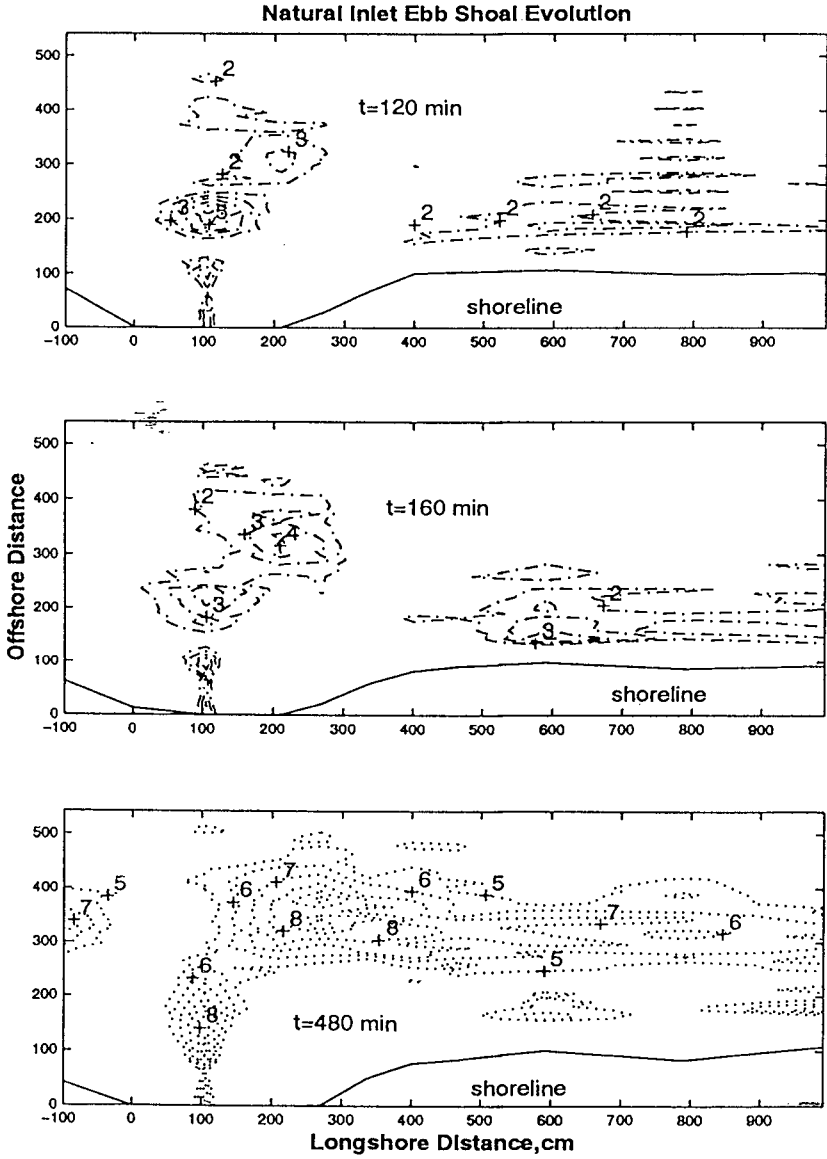


Figure 3: Ebb Tidal Shoal Evolution in Experiment C1.

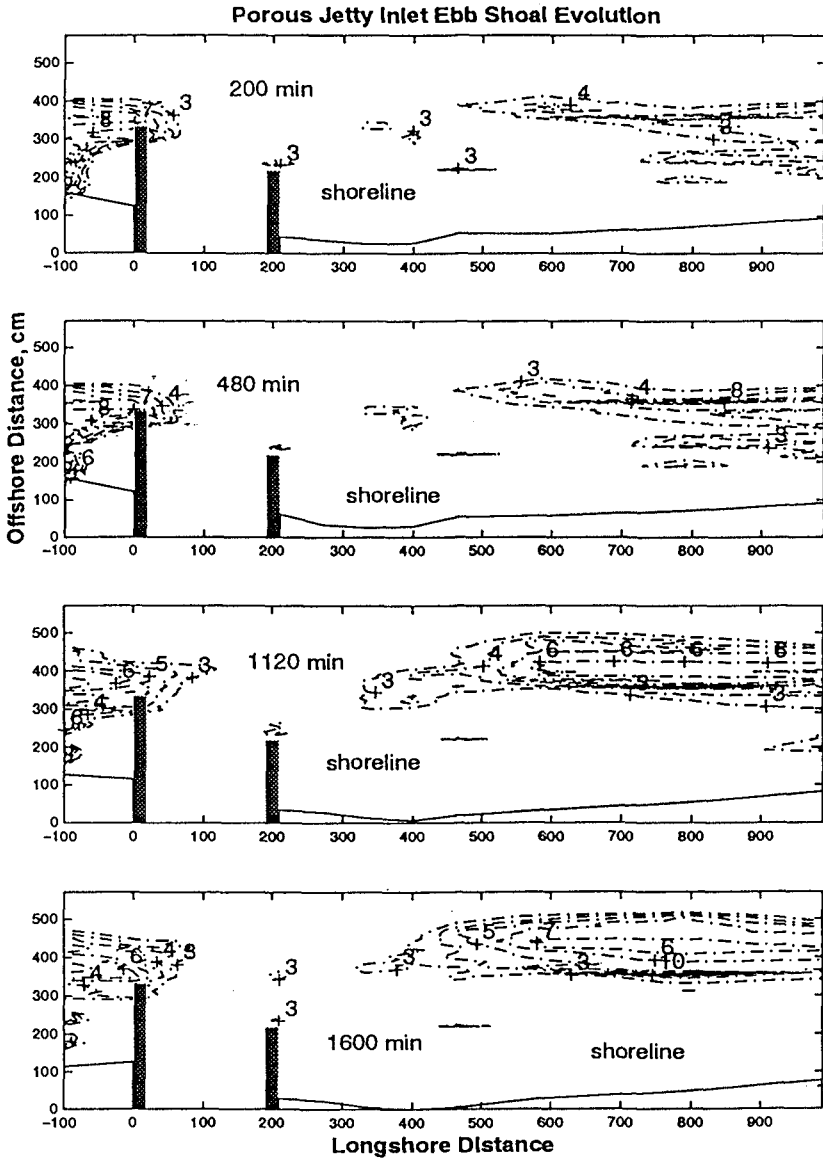


Figure 4: Ebb Tidal Shoal Evolution in Experiment C2.

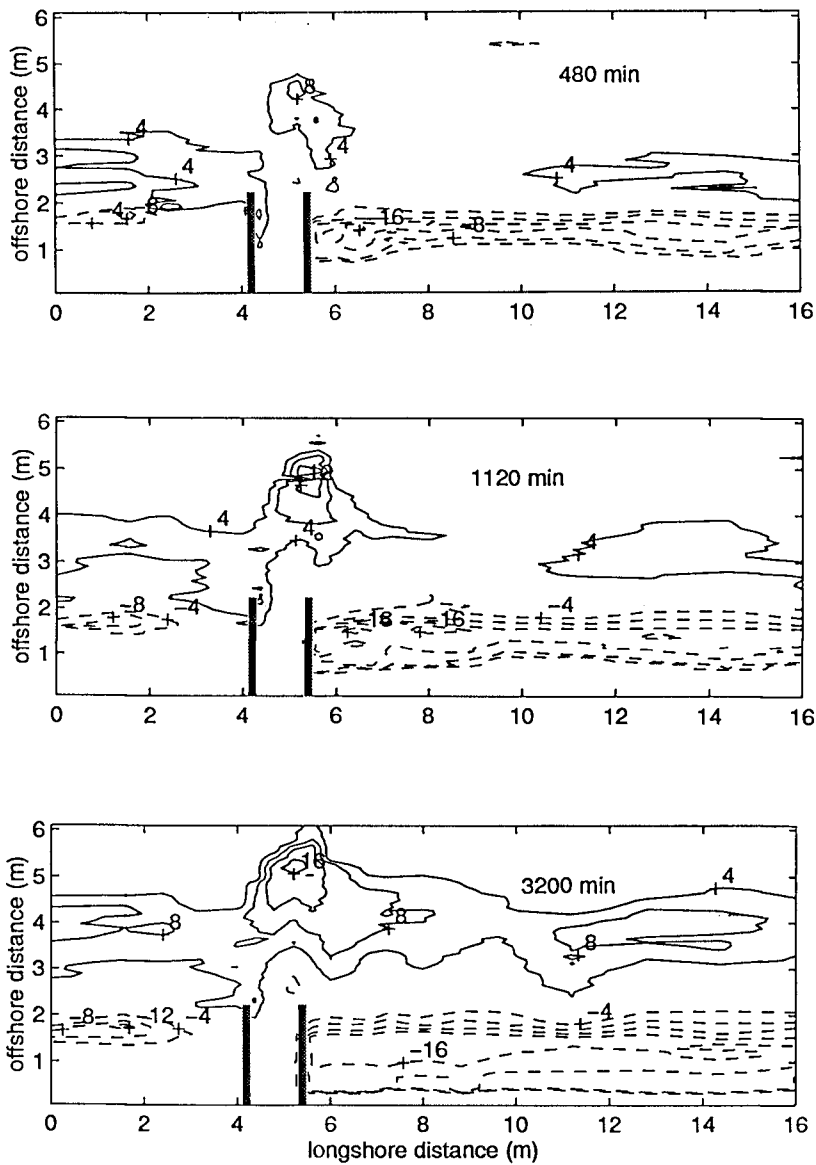


Figure 5: Ebb Tidal Shoal Evolution in Experiment EC1.

Figure 4 to 5 present the evolution pattern of ebb tidal shoal in C2 and C3 , respectively. Figure 6 compares the ebb tidal shoal volume for C1,C2, C3 and EC1. It is seen that the growth of ebb tidal shoal was unsteady in the early stage in these cases. The ebb shoal simply grew during ebb cycles but shrunk during flood cycles. After the first few cycles, the ebb tidal shoal began to grow steadily, almost in a linear fashion. The process was much rapid in the case of the natural inlet than the jettied inlet. The rate of growth apparently slowed down at a later stage of the experiment.

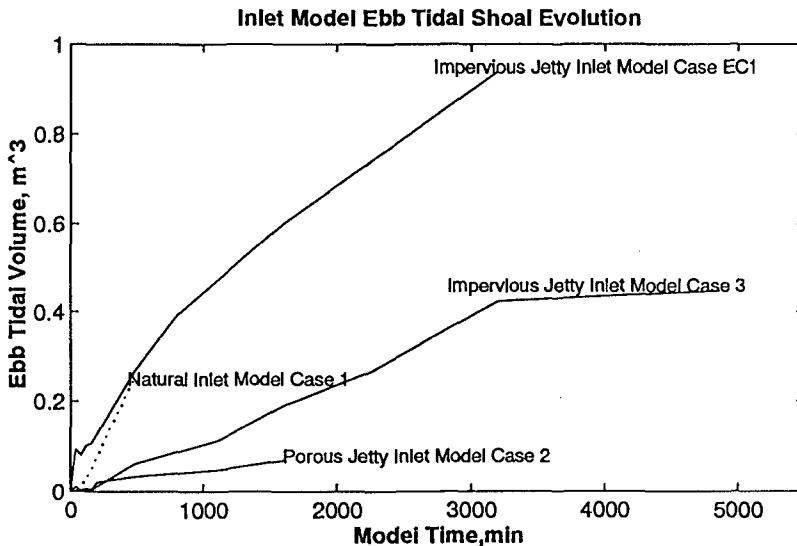


Figure 6: Comparison of Ebb Tidal Shoal Volume Changes for C1, C2, C3 and EC1

Experiments EC1 and EC2 were conducted to study the effect of the partial ebb tidal shoal removal. Figure 7 shows the ebb tidal shoal evolution process after part of the ebb tidal shoal sand was removed and used as the downdrift beach nourishment in EC2.

The effects of ebb tidal shoal removal on downdrift beach were evaluated by comparing the total volume of sand eroded from the beach between the downdrift

jetty and downdrift boundary in experiments EC1 and EC2. This comparison of downdrift beach erosion and erosion rate versus the elapsed time is shown in Figure 8. It is seen that the downdrift beach erosion is overall significant in EC1 and EC2, with a greater erosive rate in EC2 than in EC1, though at the later stage, this difference became much smaller.

The degree of restoration of the ebb tidal shoal was evaluated by comparing the volumes of the ebb shoal in EC1 and EC2 as shown in Figure 9. At 800 min, the ebb tidal shoal in EC2 has less volume than the shoal in EC1 implying a slower rate of growth in EC2. However, from 800 min to 1600 min, the ebb shoal growth approaches a steady rate in both experiments. The rate of growth fluctuates greatly in the first 160 min reflecting the effects of the short time intervals corresponding to individual ebb and flood tides.

6. Conclusion

Based on the experimental results, inlet channel shoaling and beach erosion in the cases of jettied inlet experiment were not as severe as compared to the case of the natural inlet. Apparently, the presence of jetties slows down the inlet shoaling and beach erosion near the inlet. It is evident that jetty structures are necessary for tidal inlets under strong wave environment.

Formation and growth of ebb tidal shoal were observed in all the inlet experiments. The location and rate of growth of ebb shoal were different, though. The ebb tidal shoal were created and expanded during ebb cycles but deteriorated and diffused during flood cycles. The porous jetty tended to attract sediment deposition near the inlet entrance whereas impervious jetty caused more sediment by passing the inlet.

Mining an ebb tidal shoal has shown to increase downdrift beach erosion and reduce the rate of ebb shoal growth at certain degree. However, the rate of change of the mined case rapidly approached that of the case without mining, which implies the feasibility of using sediment from ebb tidal shoal in downdrift beach nourishment. The experiment was successful in reproducing ebb tidal shoals observed in nature.

However, more research work is needed to gain the insight of dynamics of the system.

Acknowledgement

The work is partially supported by the Coastal Engineering Research Center, US Army Waterway Experimental Station under Contract: DACW39-95-K-0084. Mr. Jack Davis of CERC is the project monitor. Both their financial support and personnel assistance are sincerely acknowledged here.

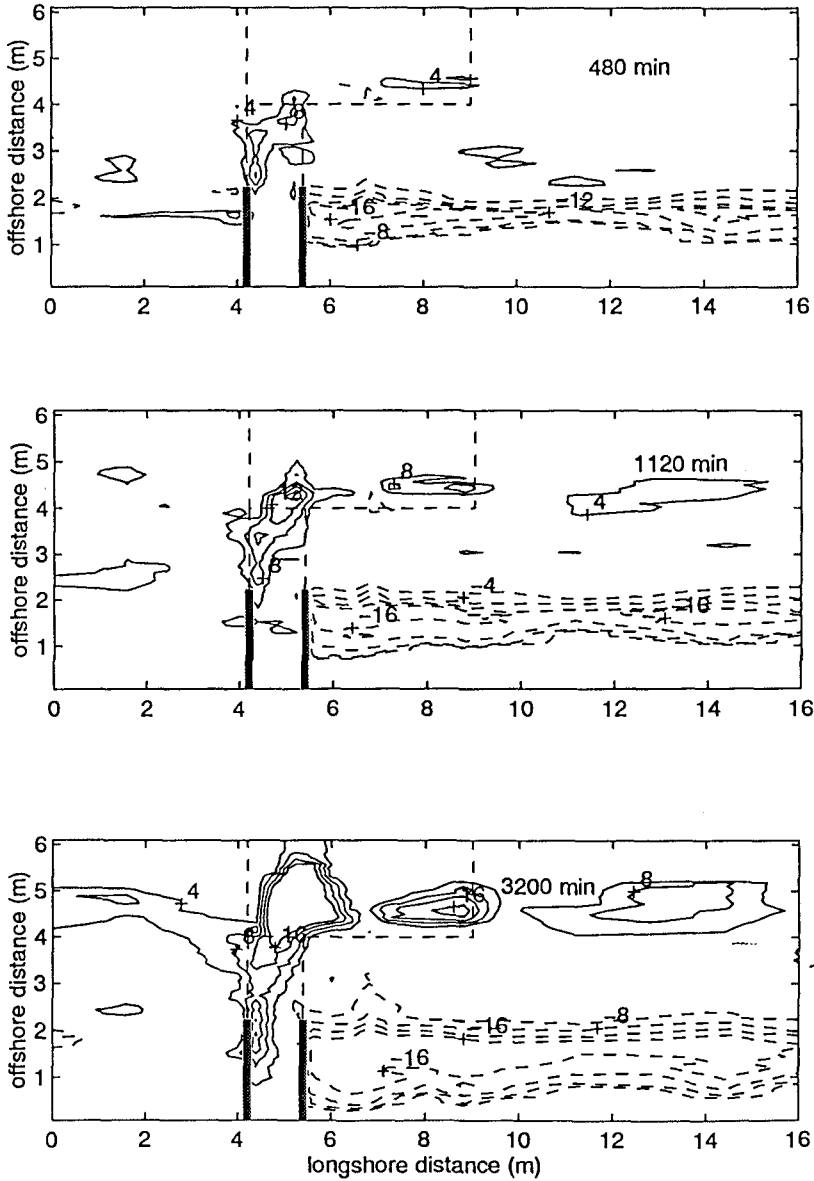


Figure 7: Ebb Tidal Shoal Evolution in Experiment EC2.

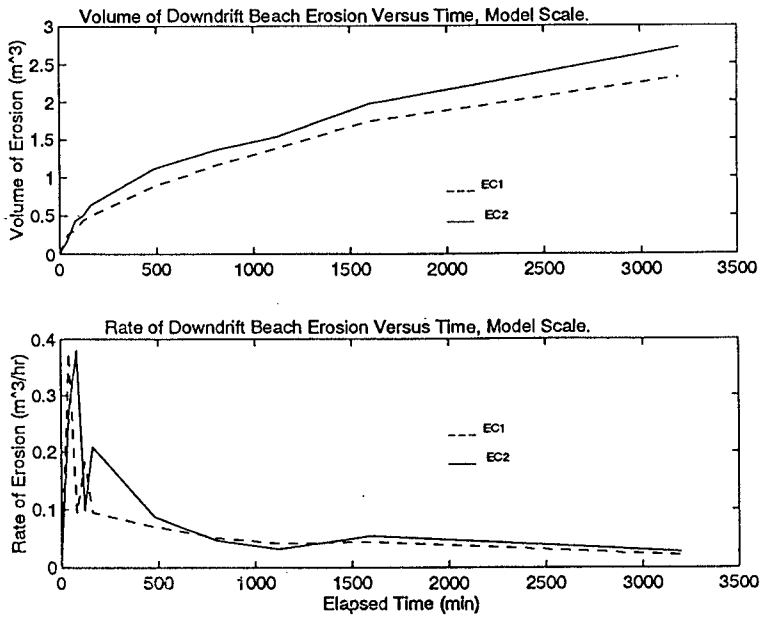


Figure 8: Comparison of Downtdrift Beach Erosion in Experiments EC1 and EC2.

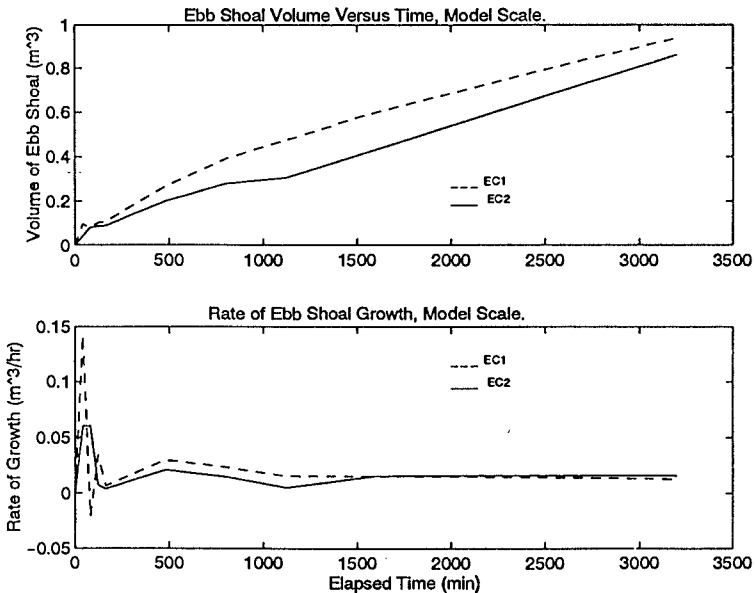


Figure 9: Comparison of Ebb Tidal Shoal Evolution in Experiments EC1 and EC2.

REFERENCE

1. U.S. Army Corps of Engineers, 1984. "Shore Protection Manual," Waterways Experiment Station, Coastal Engineering Research Center. Vicksburg, Mississippi.
2. X. Wang, L.Lin, and H. Wang, 1994. "Scaling Effects on Beach Response Physical Model," Proceedings of the 24th Coastal Engineering Conference, ASCE, Kobe, Japan.
2. Wang, H, L.Lin, and X. Wang, 1995. "Laboratory Mobil Bed Model Studies on Inlet,," UFL/95-021, Coast and Oceanographic Engineering Dept., University of Florida.

CHAPTER 256

INTERACTION OF THE COLORADO RIVER PROJECT, TEXAS, WITH LONGSHORE SEDIMENT TRANSPORT

Daniel J. Heilman¹, M. ASCE and Billy L. Edge², M. ASCE

ABSTRACT

In 1985, a weir jetty system was constructed at the mouth of the Colorado River, Texas, and river discharge was diverted from this mouth in 1992. An evaluation of project impacts on longshore sediment transport was performed to determine the effectiveness of the project at preserving an open, navigable channel while preventing excessive erosion along adjacent beaches. This evaluation included both physical and numerical analysis of pre- and post-project conditions at the Colorado River mouth. Analysis of site data revealed that under the dredging and mechanical bypassing schedule followed during the first 8 years after jetty construction, the project resulted in significant trapping and sorting of sediment transported alongshore. Numerical modeling of the design maintenance dredging plan confirmed the plan to be sufficient for achieving project objectives. However, the entrance channel has continued to shoal considerably more rapidly than was anticipated during the project design.

INTRODUCTION

General Setting

The Colorado River discharges into the Gulf of Mexico through Matagorda Peninsula on the Texas Gulf Coast about midway between Galveston and Corpus Christi (Fig. 1). With a generally linear WSW-ENE orientation, the Matagorda Peninsula outer shoreline is dominated primarily by Gulf waves from the northeast (Fig. 2), and it is subjected to a resulting longshore current that transports sediment in a southwestward direction (McGowen and Brewton 1975). The peninsula ranges in width from about 1.2 to 1.6 km with an average elevation of approximately 2 m and faces the Gulf with a moderately wide sandy beach. The tide is diurnal with a range on the order of 0.6 m (U.S. Army Corps of Engineers (USACE) 1977). As reported by Morton *et al.* (1976), the beach varies in composition and texture from fine sand to shell and rock-fragment gravel.

-
- 1) Research Scientist, Conrad Blucher Instit. for Surveying and Science, Texas A&M Univ.-Corpus Christi, 6300 Ocean Drive, Corpus Christi, TX 78412. Formerly M.S. student, Ocean Eng. Program, Dept. of Civil Eng., Texas A&M Univ., College Station, TX 77843.
 - 2) Head, Ocean Eng. Program, Dept. of Civil Eng., Texas A&M Univ., College Station, TX 77843.

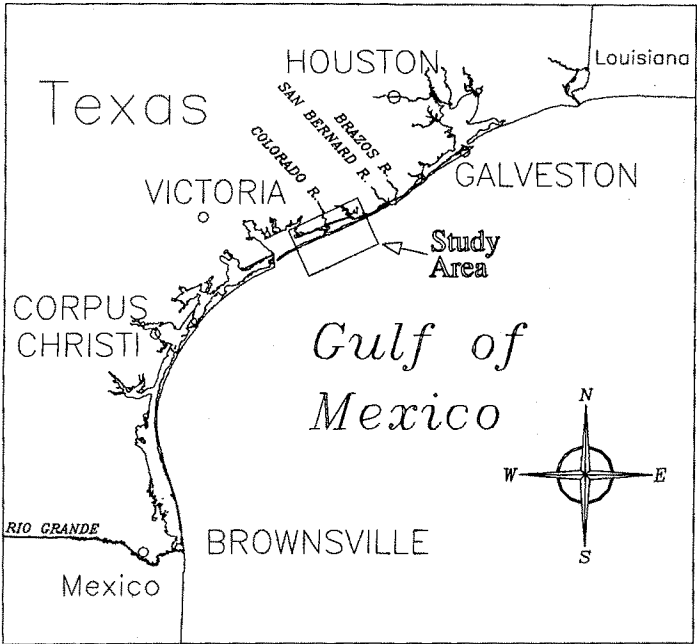


Figure 1. Site location map.

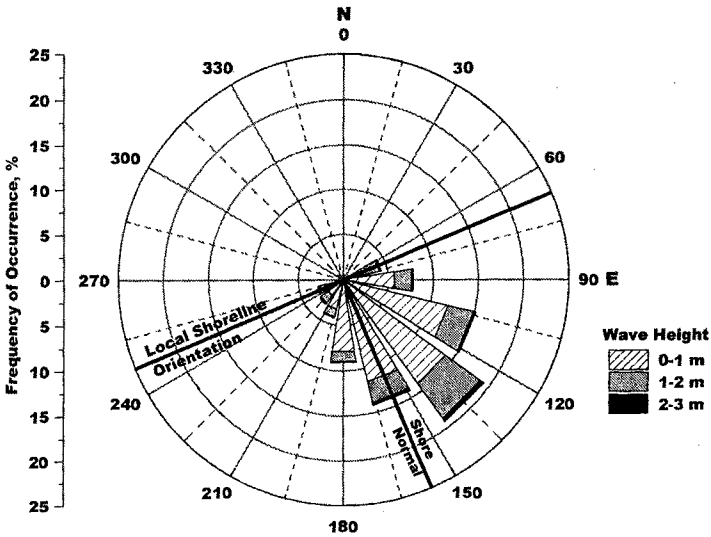


Figure 2. Wave rose for study site (data collected by USACE, CERC, May, 1990 - August, 1992).

The Colorado River Mouth

Originally discharging into a large estuary shared with the nearby Brazos River, the Colorado River began discharging into Matagorda Bay near the mainland shore at Matagorda, Texas, around 1,000 years ago (McGowen and Brewton 1975). Sediment transported by the river to the bay was restricted in the mid and late 1800s by a jam consisting of tangled masses of logs and brush embedded in silt, which was characteristic of the Lower Colorado River (Morton *et al.* 1976). By 1926, the log mass backed up in the river 74 km above Matagorda and created a lake, further restricting river sediment discharge by impounding coarse sediment. As shown in Fig. 3, which is a digitized rendering of a survey map prepared in January, 1839, the lake and log mass effectively prevented the river from creating a delta in the bay. In the late 1920s, a channel was dredged through the log mass, resulting in the release of trapped sediment and the rapid growth of the Colorado River delta into Matagorda Bay (Fig. 4) (Bouma and Bryant 1969). By 1935, the delta extended across Matagorda Bay to Matagorda Peninsula. In search of a direct path connecting the river to the Gulf, the Matagorda County and Reclamation District dredged a straight channel from one of the river outlets in the delta, across the bay, and through Matagorda Peninsula to the Gulf of Mexico (Morton *et al.* 1976, Ralston 1987).

The Colorado River Project

The Gulf entrance of the Colorado River has historically been subject to heavy shoaling, primarily due to longshore transport, and was often restricted enough to prevent the passage of small boats or flood flows. The major portion of the bed load material transported by the river was deposited above the GIWW in a silting basin (USACE 1977). The inlet was occasionally re-opened by high river discharges and by periodic maintenance dredging (Ralston 1987).

The shoaling which occurred at the Gulf entrance of the river continued to interrupt the capability of the river to serve as a dependable small-craft channel. In 1968, federal authorization was given for the USACE Mouth of the Colorado River Project in response to a need for a dependable, navigable channel connecting the Gulf Intracoastal Waterway (GIWW) to the Gulf of Mexico near the town of Matagorda, Texas. The project included a jettied entrance at the Gulf of Mexico, a navigation channel along the existing Colorado River through the delta, a harbor and turning basin, recreational facilities, and full, uncontrolled diversion of the Colorado River into Matagorda Bay (Fig. 5) (USACE 1977). The primary benefit from the project was dependable navigation between the Gulf and the GIWW.

The jetty system for the project was completed in 1985 and included a weir jetty on the northeast side of the inlet and an impoundment basin adjacent to the weir to accumulate southwesterly moving longshore sediment. The river diversion was completed in 1992, and construction of a 4.6-m deep and 61-m wide entrance channel and a 3.7-m deep and 30.5-m wide navigation channel extending to the GIWW

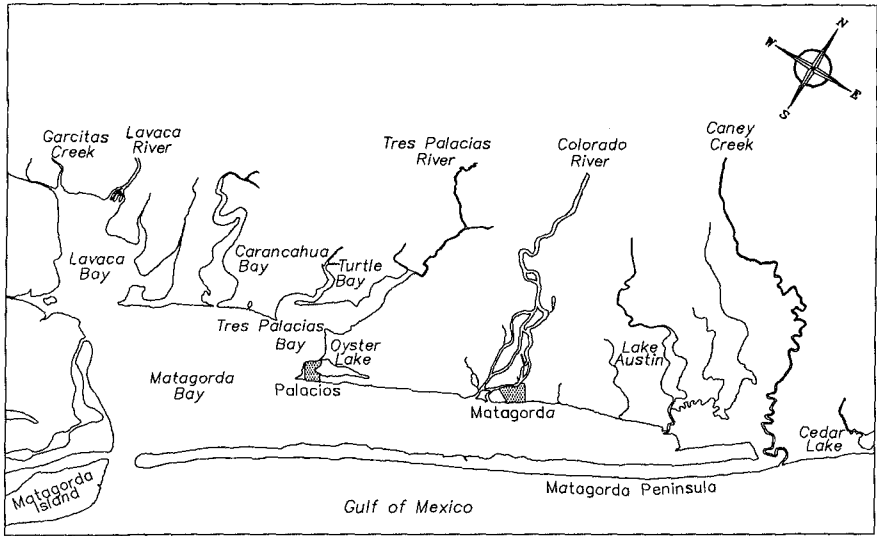


Figure 3. Survey map of Matagorda Bay, dated January 16, 1839 (original map archived by the Texas General Land Office).

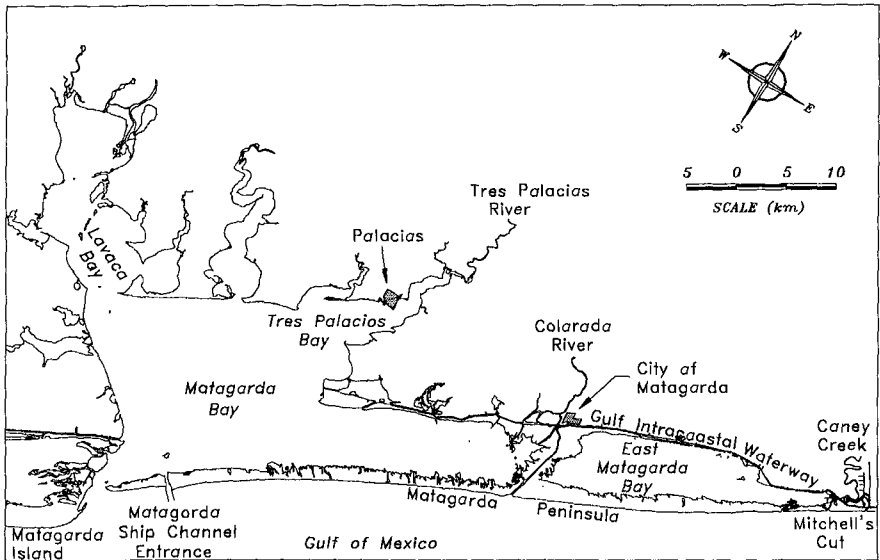


Figure 4. Map showing Colorado River delta which extended across Matagorda Bay to Matagorda Peninsula by 1935.

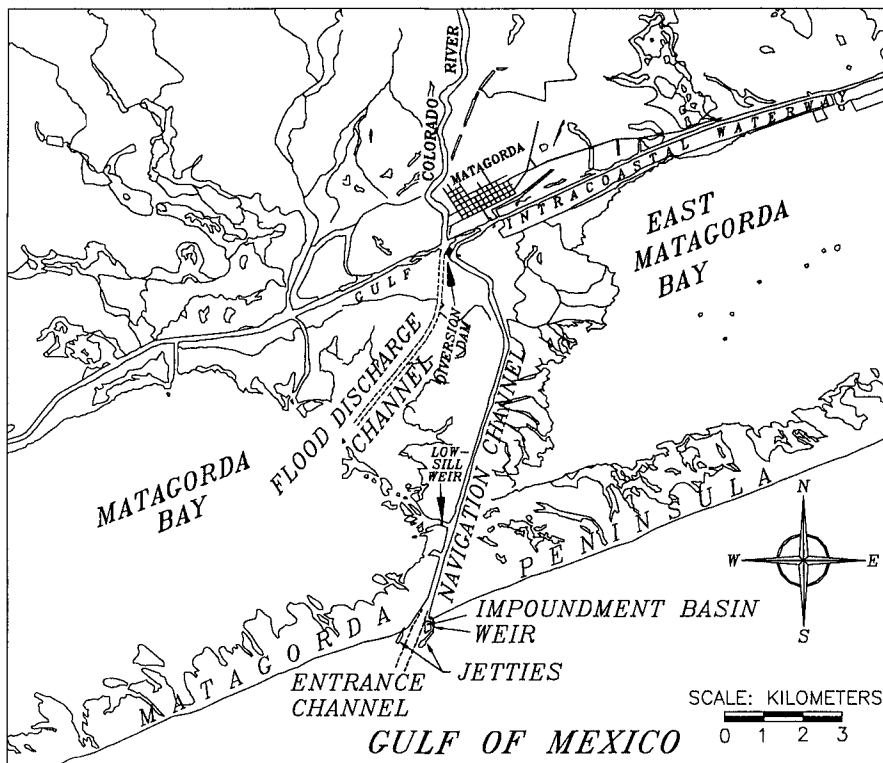


Figure 5. Features of the USACE Colorado River Project.

near Matagorda was completed by 1990 (USACE 1977). The jetties and entrance channel were aligned along the pre-existing flood discharge channel into the Gulf, with the seaward ends of the jetties spaced about 400-m apart. The weir section in the northeast jetty extended 305-m seaward from the shoreline at a crown elevation of 0 mean low tide (MLT). Past the weir section the jetty extended to the 3.7-m depth contour and was aligned to serve as a breakwater for the impoundment basin and entrance channel. The southwest jetty extended seaward to the 1.5-m depth contour.

The impoundment basin was initially designed to hold approximately 460,000 m³ of littoral sediment (USACE 1977). Based on estimated rates of longshore sediment transport, it was assumed the basin would require dredging on average once every two years. Material dredged from the basin was to be mechanically bypassed by pipeline and discharged in the surf zone approximately 610 m downdrift of the southwest jetty (Fig. 6).

STUDY OBJECTIVES

Because the entrance to the navigation channel and the impoundment basin have accumulated sediment more rapidly than was anticipated, assumptions made about the



Figure 6. Colorado River mouth, December 12, 1992.

sediment transport rate at the mouth of the Colorado River have been in question since completion of the jetties (Rozsypal 1994). The frequent maintenance that has been required to retain an open, navigable channel has suggested the need for modification of the jetties or bypassing system. However, improvements cannot be made without accurate understanding of the interaction between the project and sediment transport processes.

To evaluate the influence of the project on longshore sediment transport, a coastal processes analysis was conducted using historical and recent data, and numerical analysis was conducted using the GENESIS shoreline change model (Hanson and Kraus 1989). The updrift and downdrift limits of inlet impact on shoreline migration were estimated, a summary of predicted longshore sediment transport rates was developed, and pre- and post-project beach profiles were used along with dredging records to quantify sediment trapping. Present and future project impacts on shoreline stability and longshore sediment transport were estimated through the use of GENESIS. Future project effectiveness was tested based on the anticipated pre-project maintenance dredging plan.

PROCEDURE

Historic Inlet Impact on Adjacent Shorelines

An evaluation of historical volumetric shoreline changes along Matagorda Peninsula was conducted using shoreline position data obtained from the University of Texas, Bureau of Economic Geology (Morton *et al.* 1976, Paine and Morton 1989). The data were compiled from topographic charts and aerial photographs and cover the period from 1855 to 1982. Based on these data, Morton *et al.* (1976) and Paine and Morton (1989) concluded that the Matagorda Peninsula Gulf shoreline is historically erosional.

Beach volume change trends were estimated by application of the equilibrium beach profile concept as presented by Moore (1982) and Dean (1991). The beach volume change trends were evaluated to a distance of 33.6 km downdrift and 11.5 km updrift. Using methods developed by Bodge (1995), whereby shoreline change data representing pre- and post-introduction of a potential sediment sink are compared, the differences between the average of the pre- and post-inlet beach volume change rates were considered to identify the net effects of the inlet (which was cut in 1935) on the adjacent beaches. In the method, all beach volume change updrift and downdrift of the inlet is attributed to the interruption of the longshore sediment transport by the inlet (i.e., the effects of hurricanes, cross-shore transport, wind-blown sand transport, etc., are neglected). Based on this assumption, the maxima in a curve plotting the difference between the averages of the pre- and post inlet volume change rates, calculated cumulatively as a function of the distance from the inlet, represents the alongshore terminus of the beach segment within which the inlet influences beach volume change. As plotted in Figs. 7 and 8, the un-jettied Colorado River mouth (as existed from 1935 to 1982) may have impacted shoreline stability as far downdrift as 18.4 km and as far updrift as 5.4 km along the Gulf-facing shoreline of Matagorda Peninsula.

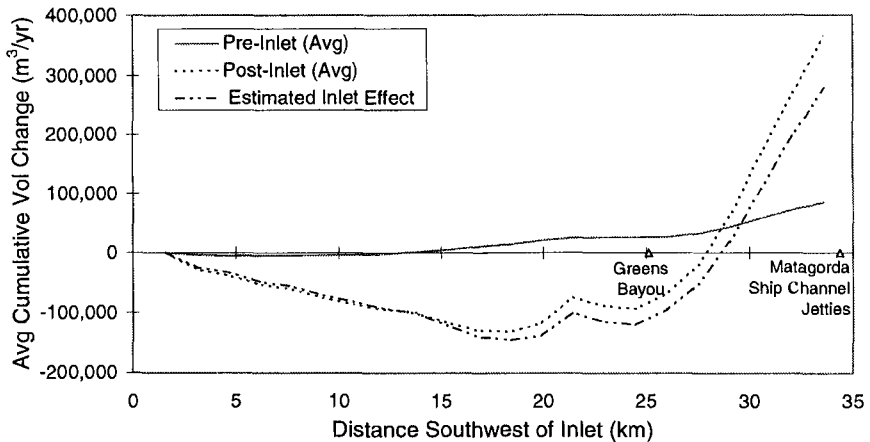


Figure 7. Cumulative annualized volume changes downdrift of the un-jettied Colorado River mouth. The pre-inlet average is based on 1855 to 1937 shoreline position data, and the post-inlet average is based on 1937 to 1982 shoreline position data.

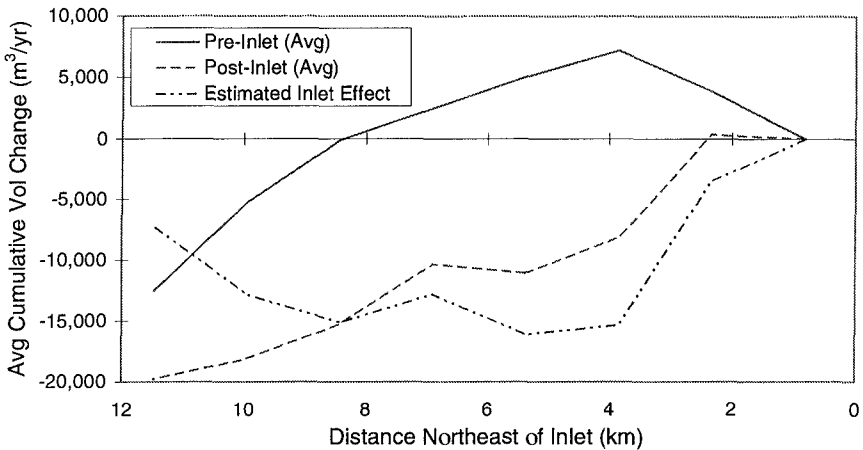


Figure 8. Cumulative annualized volume changes updrift of the un-jetticed Colorado River mouth. The pre-inlet average is based on 1855 to 1937 shoreline position data, and the post-inlet average is based on 1937 to 1982 shoreline position data.

Sediment Transport

As outlined by USACE (1984), four methods of estimating longshore sediment transport exist, including (in order of decreasing preference) calculations based on: (1) A known rate at a nearby site; (2) Measured historical changes in bathymetry or topography; (3) Wave height and direction data; (4) Only wave height data. These prediction methods can be combined to compare estimated rates or to supplement a lack of data that precludes the complete application of any one method. The traditional methods outlined by the USACE were applied to the study area, and the results are summarized in Table 1.

Calculated net longshore transport rates for the Texas Gulf Coast which are in excess of 200,000 m³/yr appear to the authors to represent over-estimates, particularly if comparison is made to other calculations of net transport documented for harsher wave climates. For example, Bodge (1995) determined the net average longshore transport rate to be about 184,000 m³/yr for a beach on the north Florida coast facing the Atlantic Ocean; the transport rate along Texas beaches should be less because the average wave climate is less severe. Heilman and Kraus (1995) calculated the net average transport rate along South Padre Island, Texas, to be 115,000 m³/yr based on a sediment budget, and Kraus *et al.* (1996) calculated the net rate along Mustang and north Padre Islands to be 34,000 m³/yr and the gross rate to be 150,000 m³/yr based on 8 years of wave hindcast data. Also, as noted by Mason (1971), Mason and Sorensen (1971), and Kraus and Militello (1996), small cuts have historically existed near the eastern end of East Matagorda Bay. These cuts, which are not subjected to strong tidal flows, would be expected to rapidly close under a strong longshore transport rate.

Method	Rate (m³/yr)
1. Estimate based on hindcast wave data, spit growth, and beach erosion at Brown Cedar Cut, Matagorda Peninsula (Mason and Sorensen 1971).	38,000 <i>net</i> 460,000 <i>gross</i>
2. Estimation derived from sediment budget developed for nearby Sargent Beach (Seelig and Sorensen 1973).	31,000 <i>net</i>
3. Average rate based on 47 years of historical shoreline position data (Heilman 1995).	152,000 <i>net</i>
4. Estimation derived from evaluation of sediment impoundment at nearby Matagorda Ship Channel jetties (USACE 1977).	150,000 <i>net</i>
5. Estimation based on inspection of historic data at the project site, including survey data, aerial photography, and dredging records (USACE 1977).	170,000 <i>net</i>
6. Design rate used for the project based on combination of methods 2 and 3 above (USACE 1977).	230,000 <i>net</i>
7. Post-project rate based on inspection of beach profile survey data and dredging records (revised after Heilman 1995) (data obtained from USACE).	250,000 <i>net</i> 420,000 <i>gross</i>
8. Potential rate calculated from a 22-month time series of directional wave data using $K = 0.77$ (Heilman 1995) (data obtained from USACE, CERC).	310,000 <i>net</i> 580,000 <i>gross</i>

Over-prediction of sediment transport rates based on bathymetric changes at the study site may be due to use of the assumption that sediments are predominantly introduced to the system from alongshore. A significant volume of sand may be transported onshore as the historic Colorado River ebb delta (if it exists) is eroded by waves (Kraus 1995). The cause of the suspected over-prediction of the longshore transport rate based on collected directional wave data is unknown, but may have occurred if the sampling period (May, 1990 to August, 1992) was not representative of the typical, long-term wave climate. A comparison between wave and wind data for the study site indicated that the measured wave directions were accurate, with the predominant direction being from the southeast and sediment transport reversals occurring only 20% of the year. The average mean wave height at a depth of 5.2 m was 0.77 m, the average wave period was 5.3 sec, and the average incident wave angle was 84 deg measured clockwise from the local shoreline orientation.

Inspection of aerial photographs and observations made at the site indicate that wind-blown sand also plays a significant role in channel infilling, as sand along the beach is transported across and around the jetties to constrict the channel opening.

This process has been noted to play an important role at other jettied Texas inlets (Kieslich 1977, Kraus and Heilman 1996).

Sediment Sorting and Trapping

Sediment grain-size data collected in August, 1994, and October, 1995, by the USACE, Galveston District, were examined to determine that finer sand (0.02 to 0.04 mm) collects in the impoundment basin than in the portion of the entrance channel adjacent to the basin (0.14 to 0.18 mm). The existence of finer sand in the impoundment basin is probably a result of: 1) the sorting of suspended-load sediments from bed-load sediments by the weir; 2) the lack of sediment sorting by currents in the deep (low-energy) basin; and 3) the transport of fluvial silts and clays to the inlet from the navigation channel during ebb flows (these fine sediments may be trapped in the basin). Analysis of survey data collected by the USACE revealed that the channel and impoundment basin fill from the weir side in a southwestward direction and that the heaviest shoaling occurs close to the shoreline.

As shown in Table 2, a comparison was made between pre- and post-project beach volume change rates near the jetties. The change from pre-project beach erosion to post-project beach accretion was considered to represent a reduction in the net longshore transport of sand past the inlet. The comparison indicated an average increase in the beach volume change rate of about 53,700 m³/yr (the difference between -9,700 m³/yr and +44,000 m³/yr) between 1984 and 1992 along 3.9 km of shoreline updrift and downdrift of the channel. Based on a longshore transport rate of approximately 230,000 m³/yr, this impoundment of sand at the inlet is equivalent to a 23% reduction in the transport of sand to beaches downdrift of the inlet.

Period (Years)	Rate of Beach Volume Change (m ³ /yr)		
	Uprift Beach (from 0.8 to 3.6 km from inlet)	Downdrift Beach (from 1.6 to 2.7 km from inlet)	Total (along 3.9 km of shoreline)
1857-1935 (Pre-Inlet)	6,700	-2,800	3,900
1935-1956	13,800	22,000	35,800
1956-1965	-58,000	60,400	2,400
1965-1974	-15,400	-109,000	-124,400
1974-1982	8,100	-13,000	-4,900
1935-1982 (Average)	-7,100	-2,600	-9,700
1984-1992	31,000	13,000	44,000

Numerical Simulation of Shoreline Change

As a means of supplementing knowledge gained through evaluation of field data collected at the project site, numerical modeling was conducted to simulate shoreline change based on theory and approximation. The GENESIS model, developed by the USACE, Coastal Engineering Research Center (CERC) (Hanson and Kraus 1989) was applied to the study site to test the effectiveness of the design maintenance dredging schedule at preventing channel shoaling. Shoreline reaches updrift and downdrift of the jettied inlet were modeled separately. Details of the model setup, input, and calibration are presented in Heilman (1995).

Model results indicated that the design maintenance dredging volume of 460,000 m³ consistently bypassed every other year is sufficient for preserving the transport of sand past the inlet and for minimizing channel shoaling. However, the model results also suggested that accelerated shoreline erosion will occur updrift of the weir due to the unidirectional transport of sediment over the weir. Based on inspection of aerial photography and visits to the site, this shoreline recession has not distinctly occurred updrift of the weir, although a series of beach profile surveys conducted by the USACE, CERC indicate beach erosion occurred within about 500 m updrift of the weir between 1984 and 1992 (Liang 1995). Model results also revealed a tendency for sediments to be temporarily stockpiled in the dredged material discharge zone (approximately 600 m downdrift) due to wave sheltering by the jetties. The sediment stockpiling process may increase rates of channel shoaling as the effective length of the downdrift jetty is reduced and northeastward-flowing sand enters the channel.

CONCLUSIONS

The Colorado River Project was a response to the need for a dependable, navigable channel connecting the GIWW to the Gulf of Mexico. Jetties were constructed in 1985 including provisions for the mechanical bypassing of littoral sediments past the entrance from an impoundment basin filled by functioning of an innovative weir. Through utilization of the bypassing system, whereby sediments are regularly dredged from the impoundment basin and discharged into the surf along the downdrift beach, the potential for accelerated beach erosion has been reduced. However, the efficiency of the system has been decreased by the unexpectedly-high infilling of the impoundment basin and resulting excessive channel shoaling, and by the sorting of littoral sediments.

Possible causes for the rapid shoaling which occurs at the Colorado River mouth include:

1. A higher than anticipated net longshore transport rate.
2. The breakup of an assumed historic Colorado River shoal.
3. The reduction in effective length of the downdrift jetty (which originally extended only to the 1.5-m depth contour) by the growth of a shoreline fillet; this process results in a nearly unimpeded transport of sediment around the jetty during longshore transport reversals.

4. The diversion of river discharge to Matagorda Bay and associated reduction in flushing of channel sediments from the channel entrance.
5. The growth of shoals across the channel adjacent to open, unvegetated areas of the beach by wind-blown sand.

Main results of this study are:

1. Historical records indicate that the un-jettied Colorado River inlet influenced migration of the Matagorda Peninsula Gulf shoreline as far updrift as 5.4 km and as far downdrift as 18.4 km. The Colorado River jetties and channel are expected to exert control on long-term shoreline migration at least as far as these extents.
2. The Colorado River jetties trap sediment despite mechanical bypassing. Some sorting occurs as the weir separates suspended and bed-load sediments.
3. A varying degree of sediment is lost from the mechanical bypassing process when more sediment reaches the impoundment basin than can be stored. Overflowing sediment may be either lost to shoals (causing navigation hazards) or transported farther downshore (starving the local beach). Numerical simulation indicates that this sediment overflow can be reduced with a consistent bypassing schedule.
4. Numerical simulation predicts that a unidirectional transport of sediment occurs across the weir, resulting in a sediment deficit directly northeast of the weir during periods when waves arrive from the southwest. The effects of this process have not been observed at the study site.

ACKNOWLEDGEMENTS

Special thanks is given to Dr. Nicholas Kraus of the Coastal Engineering Research Center (CERC) for providing technical review of this report. The authors also give thanks to Mr. T. Neil McLellan at the U.S. Army Corps of Engineers, Galveston District and to Dr. David King and Dr. Tom White, both of CERC, for providing technical assistance and data. Recognition is given to Dr. Robert Morton at the University of Texas, Bureau of Economic Geology, and Dr. Richard Seymour at Texas A&M, College Station, for their patience and cooperation in providing other needed information.

REFERENCES

- Bodge, K.R. 1995. The Extent of Inlet Impacts Upon Adjacent Shorelines. *Proc. 24th International Conf. Coastal Engin.*, ASCE, 2943-2957.
- Bouma, A. H., and Bryant, W. R. 1969. Rapid Delta Growth in Matagorda Bay, Texas, Lagunas Costeros Un Sinposio, Nov., 1967, 171-189.
- Dean, R. G. 1991. Equilibrium Beach Profiles: Characteristics and Applications. *J. Coastal Res.*, 7(1): 53-84.

- Hanson, H. and Kraus, N. C. 1989. GENESIS: Generalized Model for Simulating Shoreline Change, Report 1: Tech. Ref. Technical Report CERC-89-19. U.S. Army Coastal Eng. Res. Center, Vicksburg, Mississippi.
- Heilman, D. J. 1995. The Effects of the Colorado River Project on Longshore Sediment Transport at Matagorda Peninsula, Texas. Unpublished M.S. thesis, Texas A&M Univ., Dept of Civil Eng., College Station, Texas, 105 p.
- Heilman, D. J., and Kraus, N. C. 1995. Beach Fill Functional Design, Town of South Padre Island, Texas. Tech. Rep. TAMU-CC-CBI-95-14, Conrad Blucher Instit. for Surveying and Science, Texas A&M Univ.-Corpus Christi, Corpus Christi, Texas, 35 p.
- Kieslich, J. M. 1977. A Case History of Port Mansfield Entrance Channel, Texas. GITI Report 12. U.S. Army Coastal Eng. Res. Center, Vicksburg, Mississippi, 66 p.
- Kraus, N. C. 1995. *Personal Communication*. Director, Conrad Blucher Instit. for Surveying and Science, Texas A&M Univ.-Corpus Christi, Corpus Christi, Texas.
- Kraus, N. C., Heilman. 1996. Packery Channel Feasibility Study: Inlet Functional Design and Sand Management, Report 1 of a Two-Part Series. Tech. Rep. TAMU-CC-CBI-96-06, Conrad Blucher Instit. for Surveying and Science, Texas A&M Univ.-Corpus Christi, Corpus Christi, Texas, 112 p.
- Kraus, N. C., and Militello, A. 1996. Hydraulic Feasibility of Proposed Southwest Cut, East Matagorda Bay, Texas. Tech. Rep. TAMU-CC-CBI-96-03, Conrad Blucher Instit. for Surveying and Science, Texas A&M Univ.-Corpus Christi, Corpus Christi, Texas, 80 p.
- Liang, G. 1995. Shoreline and Sediment Volume Changes at the Colorado River Mouth, Texas. Contract Report CERC-95-2, U.S. Army Coastal Eng. Res. Center, Vicksburg, Mississippi, 31 p.
- Mason, C. 1971. Properties and Stability of a Texas Barrier Beach Inlet. M.S. thesis, Texas A&M Univ., Dept. of Oceanography, College Station, Texas, 105 p.
- Mason, C. and Sorensen, R. M. 1971. Properties and Stability of a Texas Barrier Beach Inlet. TAMU-SG-71-217, COE No. 146, Depts. of Oceanography and Civil Eng., Texas A&M Univ., College Station, Texas.
- McGowen, J.H. and Brewton J.L. 1975. *Historical Changes and Related Coastal Processes, Gulf and Mainland Shorelines, Matagorda Bay Area, Texas*. The Univ. of Texas at Austin: Bureau of Economic Geology, in Cooperation with The General Land Office of Texas, 72 p.
- Moore, B. D. 1982. Beach Profile Evolution in Response to Changes in Water Level and Wave Height. Unpub. M.S. thesis, Univ. of Del., Newark, Delaware.

- Morton, R. A., Peiper, M. J., and McGowen, J. H. 1976. Shoreline Changes on Matagorda Peninsula (Brown Cedar Cut to Pass Cavallo): An Analysis of Historical Changes of the Texas Gulf Shoreline. *Geological Circular 76-6*. The Univ. of Texas at Austin: Bureau of Economic Geology, 37 p.
- Paine, J.G. and Morton, R.A. 1989. Shoreline and Vegetation-Line Movement, Texas Gulf Coast, (1974-1982). *Geological Circular 89-1*. The Univ. of Texas at Austin: Bureau of Economic Geology, 50 p.
- Ralston, D. O. 1987. *Summary for Mouth of Colorado River*. 47th Meeting of the Coastal Eng. Res. Board, Corpus Christi, Texas, 19-20 May, 1987, U.S. Army Eng. District, Galveston, Texas.
- Rozsypal, J. 1994. *Personal Communication*. Area Engineer, Fort Point Area Office, U.S. Army Eng. District, Galveston, Texas.
- Seelig, W. N., and Sorensen, R. M. 1973. Investigation of Shoreline Changes at Sargent Beach, Texas. TAMU-SG-73-212, COE No. 169, Department of Civil Engineering, Texas A&M Univ., College Station, Texas.
- U.S. Army Corps of Engineers. 1977. *General Design Memorandum (Navigation Features), Mouth of Colorado River, Texas, Phase I*. U.S Army Eng. Distriet, Galveston, Texas, 122 p.
- _____. 1984. *Shore Protection Manual*. (4th ed), 2 vols, Coastal Eng. Res. Center, U.S.A.E. Waterways Expt. Sta., U.S. Govt. Printing Office, Washington, D.C.

CHAPTER 257

A Comprehensive Field Study of Tidal Inlet Processes at Ponce de Leon Inlet, Florida

Gary L. Howell¹

1 Introduction

Traditional coastal engineering concerns at tidal inlets include navigation and channel maintenance. Today coastal engineers are faced with new concerns such as adjacent shoreline impacts, water quality, and wetlands preservation. The development of new engineering tools to address these problems depends on improved understanding of tidal inlet processes. A necessary component of this research is comprehensive field measurement of the complex hydrodynamic and sedimentation processes at tidal inlets (Mehta, 1995).

The field measurement work unit of the Coastal Inlets Research Program (CIRP) of the US Army Corps of Engineers is a coordinated effort to acquire a comprehensive data set of physical inlet processes. The measurements will be used to evaluate and refine existing process models and motivate new predictive methods. A wide range of approaches must be served by common measurements. These include physical, numerical, analytical, empirical, semi-empirical, and hybrid models. Field data are required for development, calibration, and validation.

This paper describes the planning, site selection, and design of the study. Preliminary results from the first year of data collection are presented. It is intended as a reference for investigators using the data. Problems as well as successes are described so that future studies will hopefully improve on the efforts described here.

2 Planning

2.1 Measurements

The Ponce study is the first major long term field study of a tidal inlet since the General Investigations of Tidal Inlets program (G.I.T.I.) of the 1970s. It is also the first to benefit from the major improvements in instrumentation and computer technology since that time. However a tidal inlet remains a difficult environment for field studies. The same conditions that cause hazardous navigation impact the installation and survivability of instrumentation. Rapid changes in bedforms

¹Research Engineer, US Army Engineer Waterways Experiment Station, Coastal and Hydraulics Laboratory, 3909 Halls Ferry Road, Vicksburg, Mississippi 39180-6199 USA.

make siting of in-situ gages difficult and mandate frequent surveys. The variety of measurements required to describe all of the interacting processes still exceeds today's measurement capabilities.

Careful planning of field experiments is required to match limited resources with conflicting needs. Approaches to field experiments are affected by the technical discipline and research interests of various investigators. For example, there is not a consensus on whether it's best to study a single inlet intensively or study several inlets with limited measurements. The planning of the Ponce experiment reflects the evolution of research from traditional tidal hydraulics problems to problems of decadal or longer time scales such as impacts on adjacent shorelines from dredging and other engineering activities. Today there is more emphasis on these longterm geomorphologic responses and the sediment transport processes that drive them. Measurement technology has improved in the areas of hydrodynamics but unfortunately, progress in sediment transport measurements has been much slower.

The approach which led to the Ponce study was based on applying an engineering design method to the field studies. Study proposals and measurement requirements documents were developed by each investigator. The requirements focussed on the end use of the data, rather than specific gages or surveys. Based on requirements, experiment plans were developed which attempted to meet as many requirements as possible. Gages and surveys were prioritized by the number and technical value of requirements they satisfied. The decision to initially concentrate on comprehensive measurements at a single inlet was based on cost/benefit analysis. There remains a need to examine variability between different types of inlets, but this will be left to future studies. The planning resulted in the following types of measurements:

- Water levels at the open coast, outer throat, inner throat, and back bay open boundaries.
- Directional wave measurements in the offshore, ebb shoal, and throat areas.
- Current measurements in the throat and on the ebb shoal.
- Wind velocity and barometric pressure.
- Bathymetry
- Beach profiles on the ocean side
- Sediment samples
- Long term monitoring of shoreline, breaker lines, and the shoals.
- Regular and post-storm aerial photography.

2.2 Site selection

Since the CIRP is a national program, there were many possible field study sites. The selection was based on technical merit by using a formal analysis that matched technical and operational requirements with the characteristics of candidate inlet field sites. Each investigator developed requirements for hydrodynamic and sedimentary characteristics of the study inlet. Operational and cost factors were also considered for each inlet.

The set of all U.S. inlets was reduced to 12 candidate inlets by establishing minimum requirements. From the research viewpoint, availability of historical data was a major factor. Relevance as demonstrated by real world problems representative of those faced by the Corps was important. Finally the inlet should have a manageable physical size for field operations.

A weighted requirements matrix analysis was employed to compute separate metrics for technical and operational characteristics of the candidate inlets. In the case of the technical requirements, the field study requirements were used to compute the weights. For operational and cost factors, weights were assigned based on a consensus of senior field technicians and project engineers.

The candidate inlets were ranked by operational score, technical score, and a combined score which was normalized to provide equal weight to the operational and technical factors. Separately each candidate inlet was evaluated to determine its suitability for physical modeling. The major factor in this evaluation was the scale factor necessary to represent the inlet in available facilities. For some inlets, factors such as tide range and wave generation requirements were also important.

The results of the formal analysis ranked Ponce de Leon Inlet, Fl. highest. The recommendation was reviewed and accepted by all investigators, program managers, and sponsors. Experience during the first year of the field study has supported the selection. Ponce is a tidal inlet typical of the east coast of the U.S. It has a jettied entrance with a visible north jetty and a south jetty covered with sand. The design channel is 5m deep and 70m wide. Historically, the inlet has undergone significant evolution due to engineering activity and natural response. A substantial set of historic data is available (USAE Jacksonville District, 1993). Present engineering problems include dangerous navigation, potential breach locations, severe scour along the inside of the north jetty, inner bank erosion, and jetty sand bypassing problems. Many unique operational advantages at Ponce have been important in achieving a successful monitoring effort. These include undeveloped land south of the inlet, the Coast Guard Station close by, and a single tall condominium building near the inlet which was ideally sited for video monitoring. Ponce is a dynamic inlet which can be expected to undergo measureable changes during the lifetime of the study.

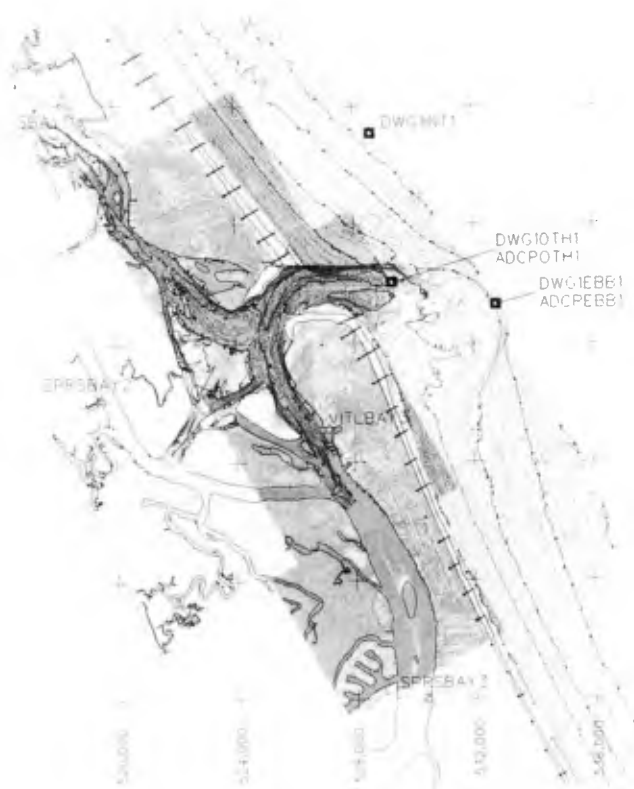


Figure 1: Ponce Inlet long term field measurements.

3 Instrumentation

3.1 Hydronamic gages

Figure 1 shows the layout of the long term instrumentation at Ponce. There are directional wave gages at three sites on the ocean side of the inlet. The site **DWG1INT1** is intended as a reference for incident waves. The gage is located in 14m of water north of the inlet in an area where the bottom contours are relatively parallel. The site **DWG1EBB1** is located on the face of the ebb shoal in approximately 7m of water. The site in the outer throat of the inlet is **DWG1OTH1**. Each of these sites has a DWG-1 (Howell, 1992) directional wave gage. The DWG-1 is a short-baseline pressure gage array. The pressure gages are Paros Digiquartz which provide accurate water level information. *PUV* type directional wave gages using electro-magnetic current meters were not used because of the high cost and difficulty of the regular cleaning. The Ponce area is regularly visited by shrimp trawlers, making the trawler resistant design of the

DWG1EBB1	Ebb Shoal	29deg 04.565min N, 80deg 53.902min W
DWG1INT1	North of Inlet	29deg 05.462min N, 80deg 54.620min W
DWG1OTH1	Outer Inlet Throat	29deg 04.605min N, 80deg 54.489min W
SPRSBAY1	Deepwater Marina	29deg 05.453min N, 80deg 56.432min W
SPRSBAY2	Utility Company (W)	29deg 03.944min N, 80deg 56.332min W
SPRSBAY3	Riverview Restaurant (S)	29deg 02.266min N, 80deg 54.299min W
VITLBAY3	Coast Guard Station	29deg 03.776min N, 80deg 54.909min W

Table 1: Map coordinates of the principle gage sites.

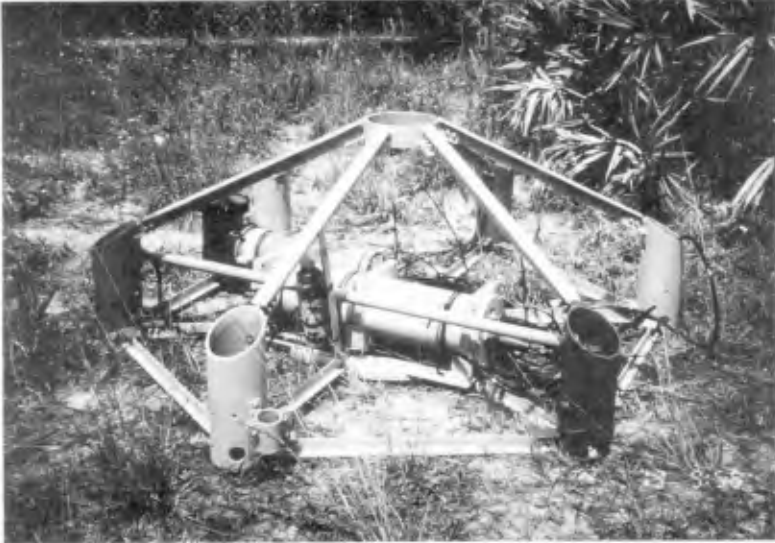


Figure 2: DWG-1 directional wave gage modified with a colocated ADCP (top right). Continuous digital time series data from both instruments are transmitted on a single cable.

Gage type	Sample period	Resolution
Directional Wave Gages	0.2-sec	2-mm
Current Profiler	1-sec	1 - <i>cm/sec</i>
Bay Water Levels	360-sec	1-cm

Table 2: Sampling periods for the hydrodynamic measurements. Record lengths are approximately continuous.

DWG-1 advantageous.

The ebb shoal site and the inlet throat site also have RDI ² broadband 1200kHz Acoustic Doppler Current Profilers (ADCP) located on the same mounting pod as the DWG-1. Figure 2 shows the right angle upward looking style ADCP used. The ADCP is configured for continuous real time output at a 1Hz sample rate and 1m vertical bins. The combined DWG-1 and ADCP share the same cable for both power and data output. All data recording is continuous, real-time via the cable. The internal recording modes of the instruments are not used.

Water level data in the inner bay is provided by Paros Digiquartz pressure sensors. The sensors are mounted in a steel protective sleeve are attached to a fixed length pipe which is used to mount the sensors to a pile. The top of the pipe has a reference mark which can be surveyed to establish the datum for the water levels. Both the offshore water levels (from the DWG-1) and the inner bay water levels use absolute pressure sensors which require compensation for barometric pressure. Another Paros sensor is used as the principle barometric pressure measurement and is recorded simultaneously with the water level sensors. A backup barometric measurement is available from the meteorological station installed on the north beach³The meteorological station is provided by the Battelle institute. A standard stilling well tide gage is located at the Coast Guard Station (**VITLBAY3** in Figure 1). This gage uses an air acoustic sensor and provides a check on the air pressure corrections and datums for the pressure water level sensors.

Datums for the offshore water levels obtained from the DWG-1 wave gages were not surveyed like the inner bay gages. Instead data analysis of six months of data was used to estimate the datums. The technique is based on an iterative minimization of the residuals between the Coast Guard Station tide gage (**VITLBAY3**) and the offshore water levels. The technique selects data windows at slack water when the inner and outer water levels approach equality. The method produces accuracies comparable to that obtained with conventional surveys. Details of the method will be provided in a future publication.

Table 1 lists the locations of the principle measurement sites.

²RD Instruments, see <http://www.adcp.com/> for additional information.

³.

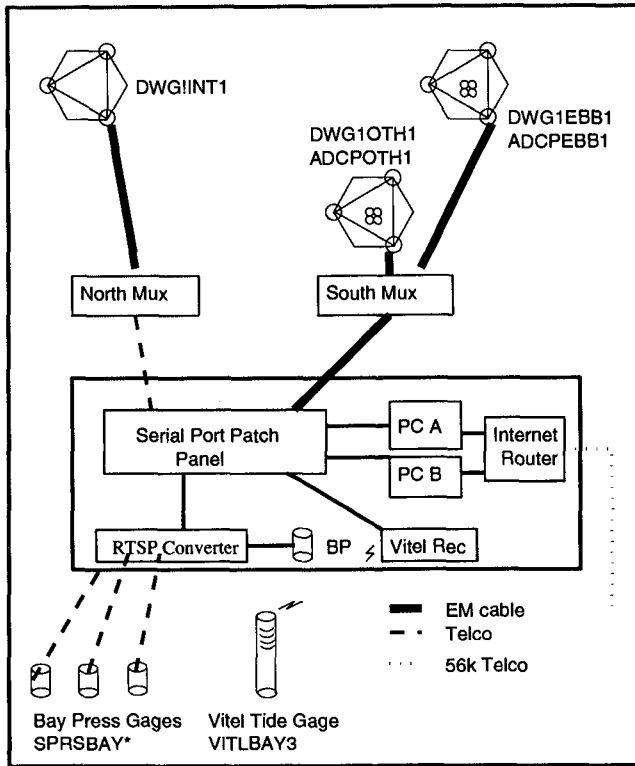


Figure 3: Diagram of the Ponce hydrodynamic gage data acquisition system.

3.2 Time series data acquisition

Table 2 gives the sample rates and resolution of the measurements. All data are acquired continuously. However some of the routine analysis use shorter record lengths. For example directional wave spectra are computed using 34 minute records windowed from the available 59 minute records.⁴ All data analyses are performed at least hourly. Data from all of the time series gages are logged by a single computer located in a leased trailer at the Coast Guard Station. The trailer is connected to the Internet via a 56k Band leased line to the Jacksonville COE District office in Jacksonville. Figure 3 shows the layout of the connections from the gages to the central logging computer. Most of the connections are through

⁴A variety of analysis products are produced from the Ponce data. Users should check the analyses parameters used for the particular product rather than relying on the general description here.

cable installed for the experiment or local leased telephone lines. This design was used instead of radio telemetry because experience in previous projects has shown that wireline installations provide higher data return at a lower maintenance cost than telemetry. Another reason for use of a central computer facility was the desire to preposition the infrastructure that would be required for a larger short term experiment. Without this requirement a design based on several outdoor Remote Transmission Units (RTUs) could have been used.

All of the data logged by the central computer are acquired through serial ports. The computer is a standard industrial rackmount PC computer. A multiport serial card is installed to provide extra ports. There are three identical computers installed. Two of the computers are operational all of the time and have the serial data arriving continuously. Logged data from one of the computers is transferred over the Internet link to a computer in Vicksburg which is configured with a standard data acquisition, analysis and storage system known internally as PMAS (McKinney and Howell, 1996). Should a failure of the principal computer occur, data are automatically acquired from the backup computer. The third computer is installed and tested, but disconnected from power, network, and serial lines. It can be manually configured to replace either of the two operating computers. This mode is used to protect this machine from lightning surges which overpower the surge protection devices.

The software for the PC compatible computers logs the data from each serial port to files. The Posix compliant Linux⁵ operating system provided most of the building blocks for the system. Customized code was implemented primarily with shell scripts. Procedures too complex for shell scripts were implemented as Ada programs using the freely available GNAT Ada compiler⁶. The software is configured to operate completely unattended. Status information is available at any time on-site or remotely using the *finger* command. Automated email messages are sent to advise of any unusual situation or error. A status monitor implemented as a shell script runs continuously on the computer in Vicksburg. It uses a combination of the *finger* and *traceroute* commands to detect problems at the site and network outages. Automated email messages are also sent by the Vicksburg monitor computer to warn of problems.

3.3 Problems and performance

The general performance of the hydrodynamic monitoring system has been very good. The data acquisition system has achieved over 99% reliability. The ebb shoal directional wave gage and ADCP experienced a cable failure during the March 1996 storm. The failure was caused by incomplete disassembly of the instrument by unauthorized divers. The instrument located in the throat of the

⁵A freely available Unix like operating system which runs on PCs. See <http://www.li.org/> for additional information.

⁶GNAT is a the Free Software Foundation Ada 95 compiler. See <http://www.gnat.com/> for additional information.



Figure 4: The SHOALS helicopter Lidar bathymetric system. The Pod on the bottom of the helicopter contains the laser, scanner, and optics. The computers and operator's consoles are located inside the helicopter.

inlet has experienced periodic burial by sand. The directional wave gage continued to yield useful data. However the sand cover which ranged from 1-2m rendered the ADCP data unuseable. Relocation of these instruments is under consideration. Some problems have been encountered with the Vitel tide gage in setting its range to accomodate the extreme highs and lows of the water levels. These problems have been easily corrected but compromise the peak tide data until correction. After an initial period of working with the telephone company to debug the leased telephone lines, the bay pressure tide gages have been very reliable.

Data analysis of the wave and water level gages has been generally routine. However the Ponce system is our first experience with continuous time series data from multiple ADCPs. Automated analysis and quality control software was not available at the beginning of the study. Development of this software is underway, but will require extensive effort before its performance is comparable with existing wave and tide measurement software. ADCPs have the potential to provide details of both mean and orbital velocities, as well as suspended sediment concentrations. As better analysis tools become available these measurements should become feasible.

4 Spatial monitoring and surveys

4.1 Bathymetry

The Ponce study is fortunate to have available a powerful new tool for coastal engineering work, the helicopter Lidar bathymetric system. The system developed by the Corps of Engineers is known as SHOALS. Irish *et al.*(1996) in this Proceedings provides a detailed description of the SHOALS system and its use for monitoring volume changes at inlets. Figure 1 shows bathymetry obtained from the SHOALS system. The detailed and rapid coverage provided by the laser system allow the details of the complex bottom topography of the inlet system.

A Lidar system operates by measuring the time difference between the reflection of a laser light pulse from the water surface and the bottom. Scanning the laser allows coverage of a 100m swath as the helicopter moves across the survey area. Figure 4 shows a photograph of the SHOALS system mounted on the survey helicopter. The accuracy of SHOALS is continually being evaluated and improved. Experience at Ponce shows that accuracies are already comparable with that of traditional fathometer surveys. Improved GPS technology now allows SHOALS to survey the above water portions of the beach profile. The accuracies of this capability are currently under evaluation.

The main limitation of Lidar technology is dependence on water clarity. At Ponce there have been periods where surveys could not be performed because the water was too turbid. Turbidity problems were most severe near the throat and in the back bay. Turbidity can be caused by a variety of weather conditions. These include storms which suspend large quantities of sediment. The rapid survey capability of SHOALS makes it ideal as a post-storm survey tool, however turbidity will prevent its use during the storm and the recovery period immediately afterwards.

4.2 Shoreline response

Monitoring of the long term shoreline response is performed using previously developed techniques. Data are acquired from

- Color digital aerial photography
- Wading beach profiles
- Continuous video monitoring

The aerial photography and beach profiles are combined with the SHOALS bathymetry in a Geographic Information System (GIS) database. Once in the GIS, standard tools such as differencing and volume change mapping are applied. As longer records become available, the GIS will be used as a tool to help manage the spatial data and facilitate correlations with the hydrodynamic forcing.



Figure 5: Video photo looking out from the top of the condominium toward the inlet channel and jetties. The photo is a result of a timed exposure which causes the breaker lines to appear as white streaks.

Potential development of inlet response models require long term data of shoreline position that is sampled more frequently than annual or semiannual beach surveys. One approach that has been applied to beaches on the open coast is video monitoring. Konicki and Holman (1996) describe the technique in a paper in this Proceedings. For the Ponce experiment, five video cameras were mounted on top of a condominium on the south side of the inlet. The cameras provide views of the up and down coast beach, the throat, ebb shoal, and flood shoal. Figure 5 shows an unrectified view from one camera of the channel and jetties. The photo is the result of a six minute time averaged exposure. Averaging highlights wave breaking zones as white bands. By processing many such photos, shoreline, bar, and shoal positions may be tracked.

The usefulness of the video data has not yet been demonstrated. Long term records and substantial efforts in data analysis are required. If successful, results from this monitoring will appear in future publications.

5 Sample storm data

Figure 6 shows waves from both the offshore gage and the wave gage in the throat of the inlet. This storm occurred in March 1996 and was unusual in that the wind

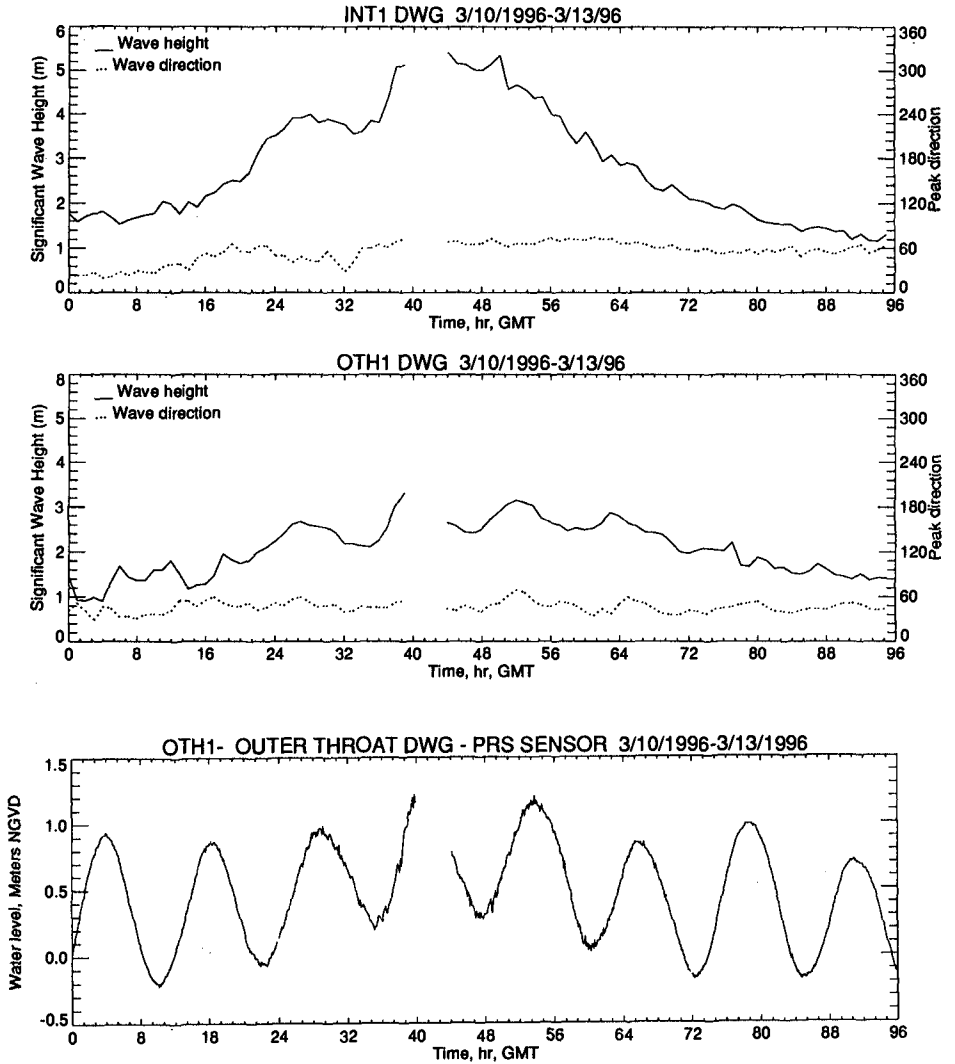


Figure 6: Inlet wave shoaling during a large storm. Note the modulation of wave height by water level in the throat (OTH1).

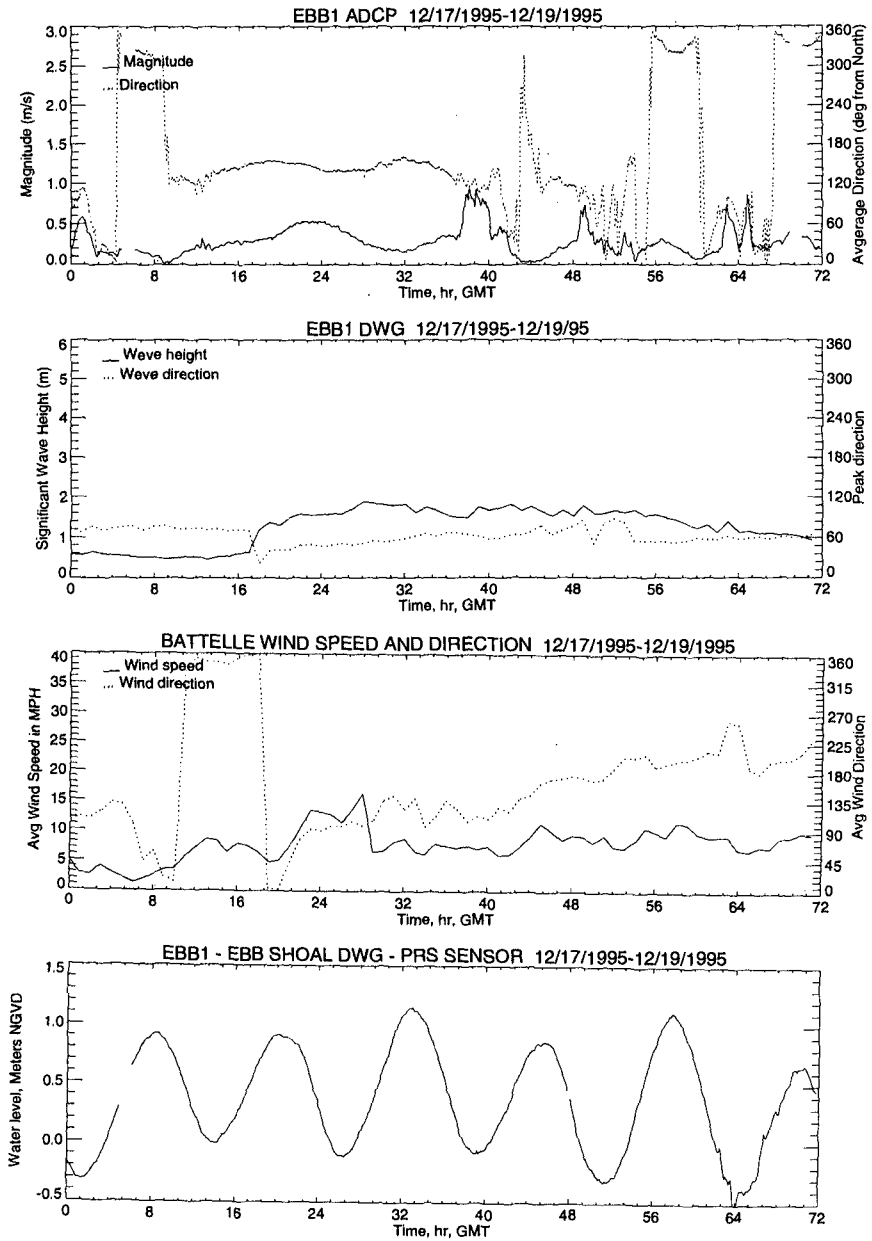


Figure 7: Ebb shoal waves and currents. Note the wind and waves driven currents as well as tidal currents.

direction stayed fairly constant as can be seen by the wave direction. The throat waves show both the effects of shoaling and the sheltering of the north jetty. The modulation of the wave height by the tide confirms the importance of water levels and tidal currents in predicting waves in inlets.

Figure 7 shows vertically averaged mean currents on the ebb shoal during a moderate Nor'easter. The beginning and end of the record show tidal currents dominant as is the ambient condition. As the wind and wave directions change, the tidal component of the mean current is strongly influenced.

Additional data analysis is currently underway and will be reported by the program investigators. The data already acquired provide confirmation of the complexity of the hydrodynamic and sedimentary processes at Ponce inlet.

6 Acknowledgements

Many people made important contributions to this study. Bill Grogg, Trap Puckette, Sam Corson, Pat McKinney, Rhonda Lofton, Kent Hathaway, Jeff Lillycrop, and Tom Martin all played key roles. The U.S. Coast Guard Station, the Inlet Condominium, the Battelle Paint testing facility, and many other public and private land owners made their property and facilities available. This work was supported by the Coastal Inlets Research Program of the US Army Corps of Engineers. Permission for publication was granted by the Chief of Engineers.

References

- Howell, G.L.** "A New Nearshore Directional Wave Gage," Proc. 23rd ICCE, Venice, Italy, ASCE, October, 1992.
- Irish, J.L., Lillycrop, W.J., and Parson, L.E.** "Accuracy of Sand Volumes as a Function of Survey Density," Proc. 25th ICCE, Orlando, FL, ASCE, September, 1996.
- Konicki, K.M. and Holman, R.A.** "Transverse Bars in Duck, North Carolina," Proc. 25th ICCE, Orlando, FL, ASCE, September, 1996.
- McKinney, J.P. and Howell, G.L.** "A Data Acquisition and Analysis System for Coastal Ocean Measurements," Proc. Oceans 96, Ft. Lauderdale, FL, IEEE, September, 1996.
- Mehta, A.J. ed.** "Understanding Physical Processes at Tidal Inlets," SI 23 *Journal of Coastal Research*, Winter 1996.
- USAE Jacksonville District** "Navigation Study for Ponce de Leon Inlet, Reconnaissance Report," U.S. Army Corps of Engineers, Jacksonville District, Jacksonville, FL, January 1993.

Transport of Fluid Mud generated by Waves on Inclined Beds

Thijs van Kessel*, C. Kranenburg† and J.A. Battjes‡

Abstract

Liquefaction of a freshly deposited mud bed may occur if shear stresses in the bed, generated by wave-induced pressure gradients, locally exceed the yield strength. In this way fluid mud is generated, which has a concentration close to the original bed concentration (generally a few hundreds kg m^{-3}). If fluid mud is displaced, very high transport rates are to be expected. This may be an explanation for rapid mud accumulations often observed in navigation channels after storm periods. In this paper wave-induced liquefaction of a sloping mud bed is investigated with laboratory experiments. A yield strength profile of the bed is obtained with a small-scale sounding test. Rheological properties of the mud after liquefaction are determined with independent rheological experiments. It is shown that calculated shear stresses in the bed at the onset of liquefaction just exceed the measured yield strength. The combination of waves and a slope turns out to be very effective for the transport of fluid mud.

1 Introduction

Harbours and coastal areas are affected by the accumulation of mud in several respects. Resulting bathymetric changes often hamper navigation and make expensive dredging operations unavoidable in order to maintain navigable depth. Moreover, mud is often heavily polluted as it easily adsorbs many pollutants such as heavy metals and pesticides because of its high specific area and surface properties. This negatively affects water and sea bed quality and makes disposal of dredged material expensive. In order to prevent the undesired accumulation of mud, the relevant transport mechanisms have to be identified, thus providing a tool for coastal management.

*PhD Student, Hydromechanics Group, Dept. of Civ. Engrg., Delft Univ. of Technol., P.O. Box 5048, 2600 GA Delft, The Netherlands. E-mail: T.vanKessel@ct.tudelft.nl

†Assoc. Prof., Hydromechanics Group, Dept. of Civ. Engrg., Delft Univ. of Technol., P.O. Box 5048, 2600 GA Delft, The Netherlands.

‡Prof., Hydromechanics Group, Dept. of Civ. Engrg., Delft Univ. of Technol., P.O. Box 5048, 2600 GA Delft, The Netherlands.

Mud may accumulate gradually by sedimentation from the water column during slack tide. This is a slow process, as the sediment concentration in the water column generally does not exceed 1 g l^{-1} , and the settling velocity of the mud particles is low. The freshly deposited sediments may also be resuspended during ebb and flood tides, which reduces the net accumulation rate during a tidal cycle.

Another transport mechanism is the transport of concentrated, near-bottom mud layers—often referred to as 'fluid mud'—under the influence of waves and gravity. This may result in very high transport rates during a short period of time, as sediment concentrations in fluid mud may be up to a few hundreds kg m^{-3} . This transport mechanism may be an explanation for the rapid, event-like mud accumulations often observed after storm periods.

In this paper the latter mechanism is studied by means of laboratory experiments. In §2 the theory underlying the generation and transport of concentrated mud layers is discussed in greater detail; in §3 the experimental results are presented and discussed. Conclusions are drawn in §4.

2 Theory

2.1 Generation of fluid mud

Several erosion mechanisms of mud are possible. Surface erosion will occur if the bed shear stress exerted by the orbital motion of water under waves or by current, exceeds the critical shear strength for erosion (Mehta et al. 1989). Bulk erosion will occur if the shear stress inside the bed generated by wave-induced pressure gradients on the bed surface, exceeds the yield strength of the bed. For the experiments reported in this paper the latter mechanism prevailed, as the frictional bed shear stress remained small because of the absence of current.

Because of the very low permeability of a mud bed, water flow inside the bed caused by wave-induced pressure gradients is negligible (undrained conditions). Erosion caused by fluidisation or swell will not occur in this case. The behaviour during and after undrained failure of a mud layer will depend on its state of consolidation. Freshly deposited and consolidated beds tend to decrease in volume when subjected to shear, as they are loosely packed. A (positive) excess pore water pressure is generated, resulting in decreases in effective stress and strength. As the bed liquifies without the flow of water, sediment particles become mainly supported by the pore water instead of the grain skeleton. A liquified bed is easily transported if net forces are acting on it (De Wit 1995).

However, if the bed is closely packed because it has been exposed to high effective stresses in the past—by burial and subsequent exposure, for example—it tends to expand under shear, resulting in the generation of negative pore pressures. No liquefaction occurs in this case; on the contrary, the bed 'breaks'. Shear stresses needed for this type of failure to occur are generally much higher

than those for the liquefaction of loosely packed mud beds.

The sediment beds used in the experiments described in the present paper were freshly consolidated and loosely packed. Therefore, a positive excess pore water pressure generated upon failure, and liquefaction of the bed are to be expected.

The yield stress of the sediment bed is the key parameter for possible bed failure for the present experiments. It is essential that yield strength is measured *in situ*, as remoulded yield strength tends to be much lower than *in situ* strength. Measurements with a rheometer using a standard geometry in which a bed sample is injected gives erroneous results. A better option would be to use a vane geometry that inserted into the undisturbed bed, as the shear surface during insertion is different from the shear surface when measuring yield strength.

Another technique, which has been applied to the beds used in this study, is a sounding test, during which the force exerted on a small geometry slowly penetrating into the sediment bed is measured with a sensitive balance. With bearing capacity theory (Terzaghi 1943) the yield strength profile can be calculated from the force as a function of vertical position (Van Kessel 1996b).

As was remarked before, undrained failure occurs if the wave-induced shear stresses inside the mud bed exceed the local yield strength. Shear stresses in the bed generated by the pressure gradients caused by waves can be calculated from prescribed boundary conditions assuming a certain constitutive behaviour of the bed. For stresses well below the yield stress the bed will behave as an elastic material, whereas for stresses close to the yield stress the bed will behave as a visco-elastic material. Stresses beyond the yield stress result in liquefaction and concurrently viscous behaviour. If the constitutive behaviour of the bed is purely elastic, then the applied shear stress and the resulting strain are in phase. If the behaviour is purely viscous, then the shear stress and shear rate are in phase.

The wave-induced shear stresses in the bed during the present experiments were calculated assuming an elastic constitutive behaviour, which is in accordance with the concept of a yield strength as long as it is not exceeded. Horizontal and vertical displacements at the interface between sediment bed and fixed bottom were assumed to be zero (no-slip condition), whereas at the interface between sediment bed and overlying water the shear stress was assumed to be zero. The latter boundary condition can be justified if the stresses inside the bed caused by the pressure gradients are much larger than the frictional shear stress on the bed surface caused by the orbital motion of water under waves, which is shown to be true in §3.2. The final boundary condition needed to obtain a closed set of equations is the wave-induced pressure gradient exerted on the bed surface, which can be calculated from linear surface wave theory, for example. Details of the calculations are not presented herein for reasons of brevity. An analytical solution can be obtained (Van Kessel et al. 1997), which is a special case of the Yamamoto et al. (1978) model.

2.2 Transport of fluid mud

After the yield strength has been exceeded, the liquified bed starts to flow if subjected to a net force, which is the gravity force in the present study. As failure of the bed is undrained, the sediment concentration in the liquified layer equals the original bed concentration, which generally is a few hundreds kg m^{-3} . Because of the high viscosity, the flow of these layers tends to be laminar. Mixing with overlying water hardly occurs, because of the large density gradient stabilizing the interface.

In order to predict the flow of fluid mud layers, it is essential to know their rheological behaviour. The rheology of concentrated suspensions of cohesive sediment particles is quite complex; for a detailed discussion the reader is referred to Van Kessel (1996a), Toorman (1993), James et al. (1987) and Williams (1984). Fluid mud subjected to simple shear flow can be rheologically characterized by a (residual) yield strength and a shear rate dependent viscosity (non-Newtonian behaviour). A complication is that the viscosity is a function of the shear rate history rather than the actual shear rate, because structural changes that take place within fluid mud if the shear rate is changed, need time to reach an equilibrium situation. The constitutive model used to describe the fluid mud flow in the present experiments includes thixotropic behaviour (Toorman 1997):

$$\tau_{xz} = \lambda \tau_y + \left(\eta_\infty + \frac{c_1}{1 + \beta |\dot{\gamma}|} \right) \dot{\gamma} \quad (\tau_{xz} > \lambda \tau_y) \quad (1)$$

where τ_{xz} is the shear stress parallel to the bed, $\dot{\gamma}$ is the shear rate, τ_y is the yield stress, η_∞ is the viscosity as infinite shear rate and c_1 and β are coefficients incorporating shear-thinning behaviour. The structure parameter λ decreases with time from 1 to 0 as a result of structural break-up of the sediment caused by wave action (Moore 1959):

$$\frac{d\lambda}{dt} = -c_2 \lambda |\dot{\gamma}| \quad (2)$$

Structural recovery is not taken into account for the present experiments, because the time scale of recovery is much larger than that of the experiments. In §3.3 the calibration of the model coefficients τ_y , η_∞ , c_1 , β and c_2 for the sediment type and concentration used is discussed.

The equation of motion for the fluid mud layer can be solved together with the rheological model and boundary conditions. The equation of motion can be simplified into:

$$\rho \frac{\partial u}{\partial t} = -\frac{\partial p}{\partial x} + \frac{\partial \tau_{xz}}{\partial z} + (\rho - \rho_w) g \sin \theta \quad (3)$$

where ρ is the density of fluid mud, ρ_w is the density of water, u the local velocity, t is time, $\partial p / \partial x$ is the the wave-induced pressure gradient, z the coordinate normal to the bed, g is the acceleration of gravity and θ is the angle of the slope

to the horizontal. The convective terms that should appear in (3) have been neglected, as for the present experiments they are very small compared to the other terms. Additionally, it has been assumed that the motion of the overlying water layer is not influenced by the mud layer, and that the slope is small. The pressure gradient at the bed caused by wave action is expressed by:

$$-\frac{\partial p}{\partial x} = -k \frac{\rho_w g a}{\cosh kh} \cos(\omega t - kx) \quad (4)$$

where k is the wave number, a is the wave amplitude, h is the water depth, ω is the circular wave frequency and x the coordinate parallel to the water surface.

Boundary conditions are:

$$\left. \begin{array}{l} z = D_1 : u = 0 \\ z = 0 : \dot{\gamma} = 0 \end{array} \right\} \quad (5)$$

Here $z = D_1$ is the elevation of the interface between non-liquified and liquified mud determined from observations and $z = 0$ is the interface between liquified mud and water. Initial conditions are:

$$t = 0 : u = 0 \text{ for all } z \quad (6)$$

These equations, which describe the motion of the mud layer after liquefaction, were solved numerically.

3 Experimental results and discussion

3.1 Experimental methods

An experimental setup was built to study wave-induced liquefaction and transport on a slope experimentally (Figure 1). Sediment beds were prepared by sedimentation and consolidation of a suspension of China clay in tap water in which 0.5% NaCl was dissolved. The initial sediment concentration was 275 kg m^{-3} . The suspension was mixed for 2 weeks in order to reach physicochemical equilibrium. China clay—mainly consisting of kaolinite—was used as an artificial mud because of its reproducible properties and easy handling. After 1 week of consolidation the bed height remained constant and the bed was tilted to its desired angle (0.05 rad). The bed height after consolidation was 0.12 m, its width 0.65 and its length 4.67 m.

At $z = 0, 0.02, 0.06$ and 0.10 m from the bed surface pore pressure transducers were mounted to observe the liquefaction behaviour. These transducers were located at measuring station 3. The sediment concentration profile in the bed was measured with a conductivity probe. Velocities both in the bed (after liquefaction) and above the bed were measured with two electromagnetic flow meters (EMF) mounted on traversing units to obtain vertical profiles. These traversing units were located at measuring stations 1, 2 and 3. Sediment concentrations in

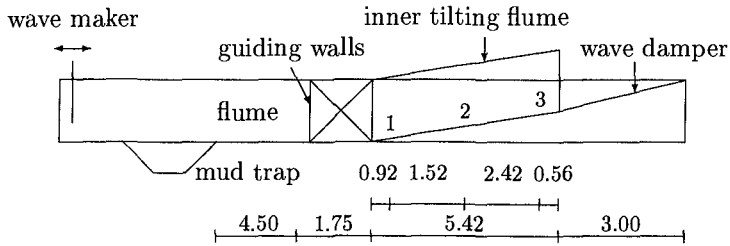


Figure 1: Experimental set-up (not to scale); measuring stations 1, 2 and 3 are indicated; lengths in m

the water column were measured with turbidity meters in order to estimate the importance of interfacial mixing. Also three wave height meters were installed. The signals of these instruments were logged onto a PC.

3.2 Wave-induced liquefaction

The experiments were started by generating sinusoidal waves with a period of 1.65 s and an initial wave amplitude of 0.005 m. During the experiments the wave amplitude was increased in steps to 0.008, 0.010, 0.013, 0.016, 0.021, 0.027, 0.036 and finally 0.042 m and the pore pressure response was measured (Figure 2). Initially no changes in the wave-averaged pore pressure were observed. However, after an increase in wave-height from $a = 0.005$ to $a = 0.008$ m, suddenly excess pore pressures were generated and the bed started to liquefy. Bed flow does not yet occur at this wave-height, as is illustrated in Figure 3, where the velocity histories at several levels inside and above the bed are shown.

The bed did flow if the wave amplitude was increased to 0.010 m. This can be derived from Figure 2, where a sudden drop in pore pressure can be attributed to the removal of the liquified mud layer. The thickness of this layer can be calculated from the observed pore pressure drop (approximately 150 Pa at $z = 0.06$ m), as the initial sediment concentration is known from the conductivity probe measurements ($\rho = 1340 \text{ kg m}^{-3}$). The thickness thus estimated is 0.045 m. This result is consistent with Figure 4, where the velocity histories shown indicate that the bed is eroded up to the level $z = 0.065$ m.

A comparison of the wave-induced stresses in the bed—calculated from the elastic model—with the yield strength profile obtained with the sounding test (§2) is shown in Figure 5. At $a = 0.005$ m, when no liquefaction is observed, wave-induced shear stresses just remain below the yield strength. At $a = 0.008$ m, however, onset of liquefaction was observed, which is consistent with Figure 5, where, for this wave amplitude, the shear stress exceeds the yield strength in the

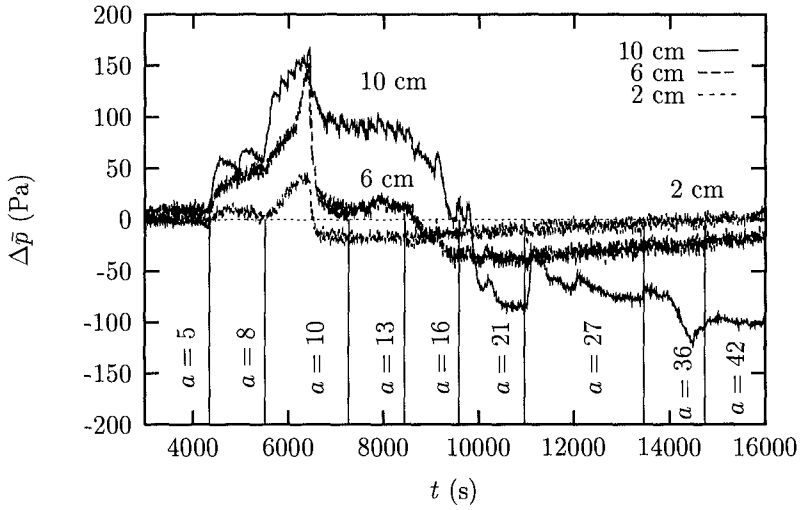


Figure 2: Changes in wave-averaged pore pressure $\Delta\bar{p}$; wave amplitudes in mm

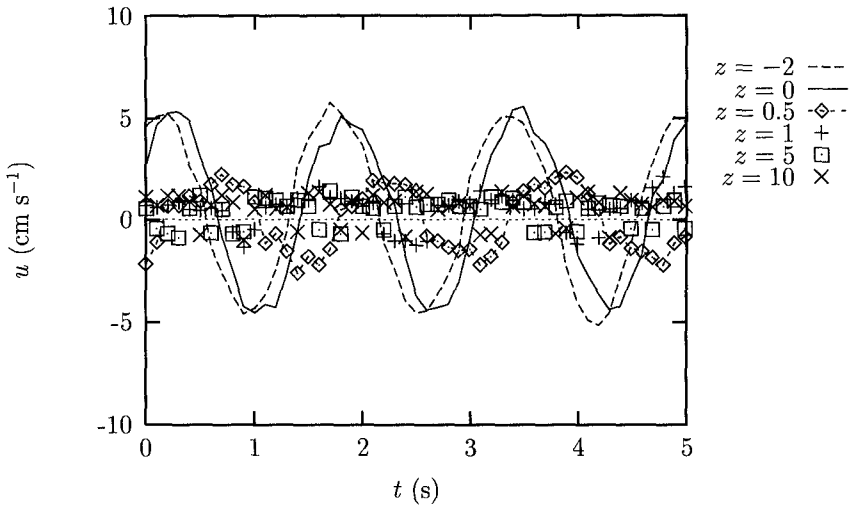


Figure 3: Velocities versus time for $a = 5$ mm; z in mm; station 3

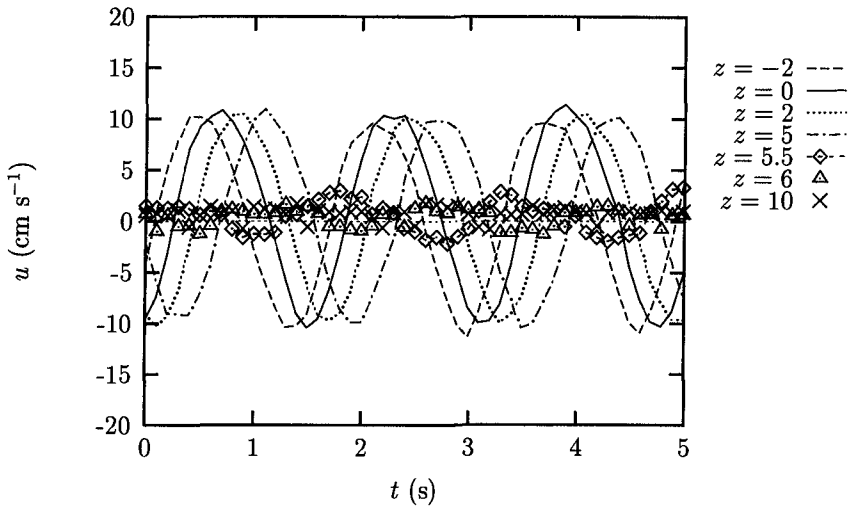


Figure 4: Velocities versus time for $a = 26$ mm; z in mm; station 3

upper 8 cm of the bed. The onset of liquefaction can therefore be well predicted if the yield strength profile of the bed is known. The yield strength of the bed increased with depth in a similar fashion as the effective stress, which was also observed by Bowden (1988).

3.3 Fluid mud flow

After liquefaction the fluid mud starts to flow. Rheological properties of China clay have been investigated independently to calibrate the rheological model applied (§2). In Figure 6 the equilibrium flow curve of China clay with $C = 467$ kg m^{-3} suspended in tap water with 0.5% NaCl is shown. It was measured with a Carrimed controlled stress rheometer equipped with a cone-plate geometry. This flow curve has been used to calibrate the Toorman (1997) model. In addition to measuring the flow curve, also thixotropic experiments have to be performed to measure the time-scales of structural break-up. These measurements are not discussed herein, the reader is referred to Van Kessel (1996a). Values for the model parameters used are listed in Table 1.

With the rheological model and the equation of motion presented in §2 fluid mud flow can be calculated numerically. Results of these calculations are shown in Figure 7. Peak velocities are approximately 0.02 m s^{-1} and increase in time because of structural break-up of fluid mud. Plug flow can be explained by the residual yield strength of the bed; negative velocities do not occur for the conditions during the experiments because of the finite yield stress. The model shows that the combination of wave-loading and the shear-thinning behaviour of mud results in a decrease in its effective viscosity, which markedly enhances

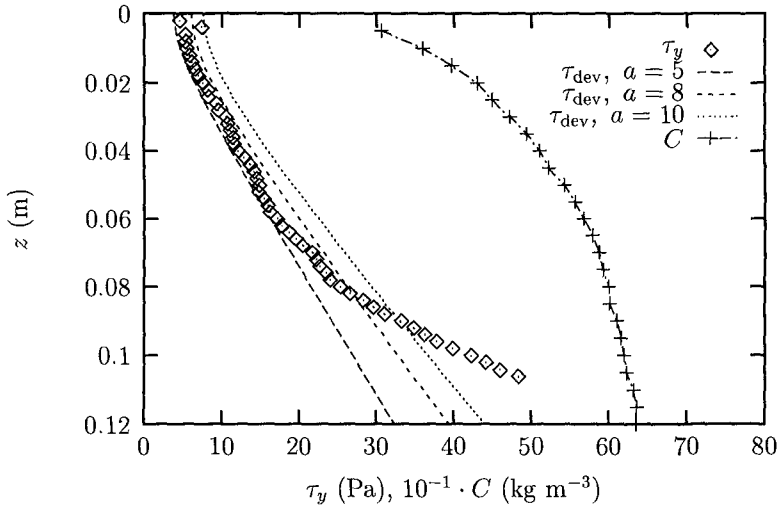


Figure 5: Yield strength, deviator stress and concentration profiles of a bed of China clay, obtained from sedimentation of a suspension of 275 kg m^{-3}

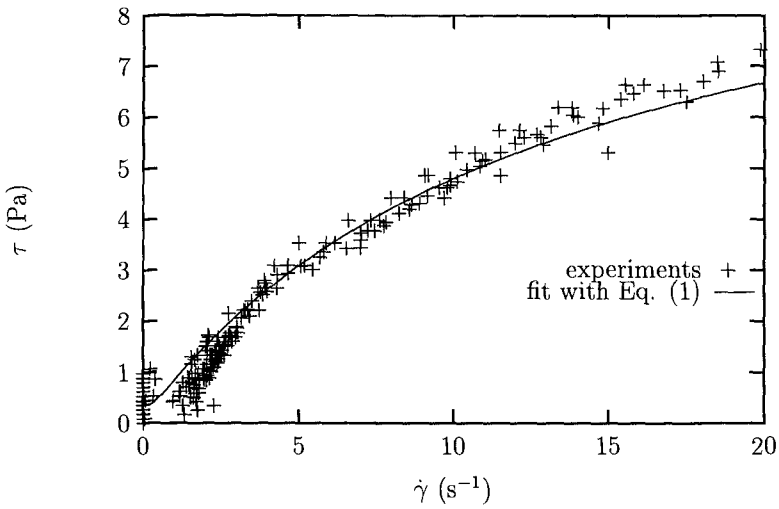


Figure 6: Equilibrium flow curve for China clay; $C = 467 \text{ kg m}^{-3}$, with Carrimed controlled stress rheometer; cone-plate configuration used

Table 1: Calibrated values of the parameters in (1) based on Figure 6 and τ_y shown in Figure 5

parameter	value	dimension
τ_y	$3.4 + 235z$	Pa (z in m)
η_∞	0.0066	Pa s
c_1	0.86	Pa s
β	0.081	s
c_2	10^{-2}	-

transport under the influence of net forces, such as gravity.

A displacement of 5 m (approximately the length of the test section) is reached within a few minutes, therefore fluid mud flow can be observed only for a short period of time, which is confirmed by visual observations. However, quantitative comparison between the flow model and measured velocities proved difficult. The accuracy of the flow meters in the velocity range of 0.01 m s^{-1} is low, too.

After removal of the fluid mud layer, a new non-liquefied layer became exposed, which would only liquefy if the wave amplitude was increased. At $a = 0.027 \text{ m}$, when the bed is clearly completely eroded at $z = 0.06 \text{ m}$, a pore pressure increase at $z = 0.10 \text{ m}$ was observed. Erosion of this layer occurred at $a = 0.027$ and 0.036 m .

Even at the largest wave amplitude, $a = 0.042 \text{ m}$, not all sediment was liquefied. After the experiments a layer of $0.02\text{--}0.03 \text{ m}$ was still present in the upper part of the tilting flume, which is not influenced by the sill at the lower end. This can be explained by two factors. First, the yield strength close to to the fixed bottom is the highest as the mud has been most compacted by the weight of the overlying sediment, and secondly, the (high) pressure gradients at the end of the experiments are much less effective, as the bed becomes thinner and thinner, which leads to lower shear stresses inside the bed.

4 Conclusions

Undrained failure of freshly deposited mud layers may be caused by pressure gradients on the bed surface, if the resulting shear stresses inside the layer locally exceed the yield strength. If the yield strength profile is known, failure can be well predicted using an elastic model to calculated shear stresses in the mud layer. For loosely packed layers, which have not yet been subjected to higher effective stresses than the actual effective stress, positive excess pore pressure are generated upon failure and liquefaction occurs. The strength of the layer is then much reduced, and a transition from predominantly elastic to predominantly viscous behaviour takes place.

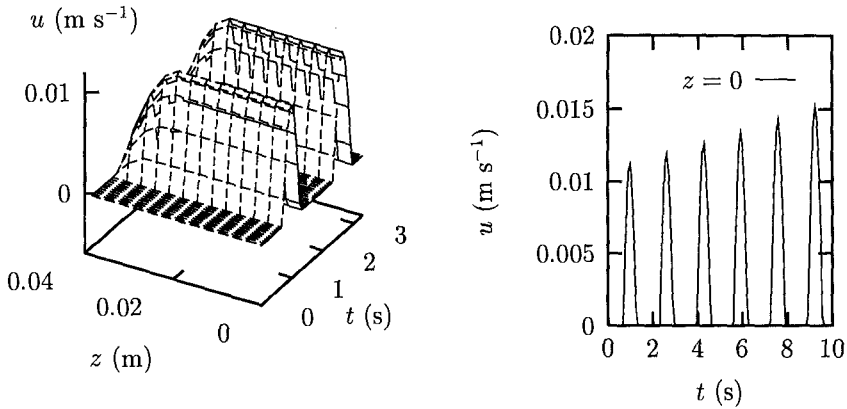


Figure 7: Velocity profile $u(z, t)$ resulting from wave-induced liquefaction on a slope. $D_1 = 0.04$ m, $\rho = 1346$ kg m $^{-3}$, $\theta = 0.05$ rad, $h = 0.30$ m, $a = 10$ mm, $k = 2.49$ m $^{-1}$, $\omega = 3.93$ s $^{-1}$; rheological coefficients used are listed in Table 1

If the fluid mud layer generated by liquefaction starts to flow under the influence of a net force, e.g. gravity, very high transport rates in a short period of time are possible, as the concentration of the liquified mud equals the original bed concentration (generally a few hundreds kg m $^{-3}$). This may partly explain the large mud accumulations often observed in the field after a storm period. In order to model fluid mud flow, its rheological properties have to be studied first, taking into account shear rate dependent and thixotropic behaviour.

The transport mechanism described in this paper may be important for the redistribution of cohesive sediments in depositional areas, where layers of freshly deposited, still consolidating mud are present. In erosional areas, however, the surface layer has generally been buried in the past and is therefore more compacted. Also ageing effects will contribute to the strength which tends to be much higher than for surface layers in depositional areas. Liquefaction of these old layers is therefore unlikely.

Acknowledgments

This work was carried out as part of the G8 Coastal Morphodynamics program. It was funded jointly by the Delft University of Technology and the Commission of the European Communities, Directorate General for Science, Research and Development under contract no. MAS2-CT-92-0027. It was carried out in the framework of the Dutch Center for Coastal Research. Special thanks go to

M. Reijnders, who assisted in the measurements reported.

References

- Bowden, R. (1988). *Compression behaviour and shear strength characteristics of a natural silty clay sedimented in the laboratory*. Ph. D. thesis, Oxford University.
- De Wit, P. (1995). *Liquefaction of Cohesive Sediments caused by Waves*. Ph. D. thesis, Delft University of Technology, the Netherlands.
- James, A., D. Williams, and P. Williams (1987). Direct measurement of static yield properties of cohesive suspensions. *Rheol. Acta* 26, 437–446.
- Mehta, A., E. Hayter, W. Parker, R. Krone, and A. Teeter (1989). Cohesive sediment transport. I: Process description. *J. Hydraul. Eng.* 115(8), 1076–1093.
- Moore, F. (1959). The rheology of ceramic slips and bodies. *Trans. Brit. Ceram. Soc.* 58, 470–494.
- Terzaghi, K. (1943). *Theoretical Soil Mechanics*. John Wiley and Sons, New York.
- Toorman, E. (1993). *Rheological properties*. In: On the methodology and accuracy of measuring physico-chemical properties to characterize Cohesive Sediments. MAST-I Report. pp. 79–123.
- Toorman, E. (1997). Modelling the thixotropic behaviour of dense cohesive sediment suspensions. *Rheologica Acta*, (to be publ.).
- Van Kessel, T. (1996a). Rheological properties of cohesive sediment suspensions. Report 1–96, Hydromechanics Group, Delft University of Technology, the Netherlands.
- Van Kessel, T. (1996b). Small-scale sounding tests on soft saturated cohesive soils. Report 7–96, Hydromechanics Group, Delft University of Technology, the Netherlands.
- Van Kessel, T., C. Kranenburg, and J. Battjes (1997). Wave-induced liquefaction and transport of mud on inclined beds. (to be publ.).
- Williams, D. (1984). *Rheology of cohesive suspensions*, Volume 14 of *Lecture notes on coastal and estuarine studies*.
- Yamamoto, T., H. Koning, H. Sellmeijer, and E. Van Hijum (1978). On the reponse of a poro-elastic bed to water waves. *Journal of Fluid Mechanics* 87(1), 193–206.

CHAPTER 259

Wave on pebble beach and deformation of pebble beach

Ichiro Deguchi¹⁾, Masanobu ONO¹⁾ and Toru SAWARAGI²⁾

Abstract

Hydraulic function of pebble are investigated by carrying out 2-D experiments in laboratory. Numerical model for predicting wave height and wave run-up are developed by applying a Boussinesq type equation and a non-linear unsteady Darcy's law for the fluid motion on the pebble beach and in the pebble layer. The applicability of the model are examined using experimental results. Deformation of pebble beach are also measured in the field and laboratory to investigate the applicability of Dean's profile and to examine the shoreline change by a single-line theory.

Introduction

Urban coastal region in Japan have been developed in various ways for various purposes. Especially, after the World War II, through the post-war industrial reconstruction, Japan experienced a rapid and high economic growth. During that period, a large part of natural shoreline around big cities in Japan disappeared by the reclamation for heavy industries. As a result, public access to the shoreline decreased and natural coastal environment was lost. Recently, there are strong demands for restraining lost natural coastal environment and creating new pro-water front structures to increase public access to the coast and coastal amenity.

Target structure of this study is the pebble beach constructed as a permeable gentle slope seawall to increase public access and improve coastal view. It is usually permitted for such kind of pebble beaches to deform their profiles until they lose their originally expected function. The aims of this study are to examine hydraulic function of pebble beach and to establish numerical model for predicting wave transformation and run-up on pebble beach through carrying out two dimensional experiments. Characteristics of deformation of pebble beach is also investigated by using experimental results and field data.

2-D experiments on the hydraulic function of pebble beach

Experimental set-up and conditions:

Hydraulic function of pebble beach was examined by carrying out two-dimensional experiments in a laboratory. Figure 1 shows a rough sketch of the experimental set-up.

-
- 1) Department of Civil Engineering, Osaka University, Suita-city, Osaka 565, Japan
 - 2) Department of Civil Engineering, Osaka Sangyo University, Daito-city Osaka, Japan

We examined two slopes 1/10 and 1/5 constructed by pebbles of different sizes in a wave tank of 27m long, 1,9m high and 1,5m wide. To investigate the effect of permeability of the slope on incident wave, wave run-up, reflection, we also conducted the same measurements on the impermeable slope. The mean diameter D of the larger one was about 4.1cm and that of smaller one was 1.8cm. Table 1 shows the permeability k_p , turbulent drag coefficient C_f , added mass coefficient C_m and void ratio λ of these two pebbles obtained from the unsteady permeability tests. Depth at the horizontal bottom was varied from 25cm to 55cm and incident wave height was in the region of 6cm to 14cm with the period of 1.2s to 2.0s.

Surface displacement was measured between 0.5m landward from the shoreline and horizontal bottom. When deformation of pebble beach took place, we recorded the profile.

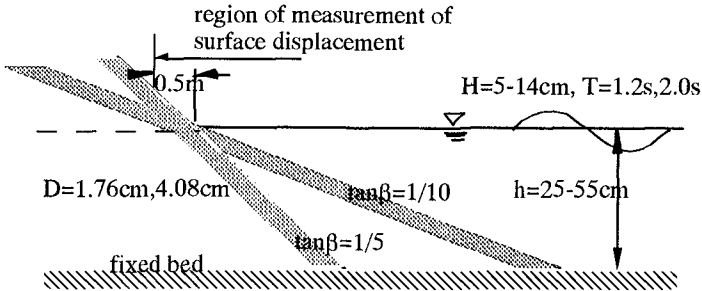


Figure 1 Experimental set-up

Table 1 Characteristics of pebbles

D (cm)	k_p (cm ²)	C_f	C_m	λ
4.08	0.0038	0.151	1.0	0.47
1.76	0.0015	0.255	1.0	0.46

Wave height distribution on pebble beach:

Figures 2 and 3 show measured cross-shore distribution of wave height on pebble beach and on impermeable slope of the slope 1/5 and 1/10. Incident wave period and height on horizontal bottom in both figure are 1.6s and 14cm and water depth at horizontal bottom was 50cm. Closed and open circles are the wave height and set-up measured on the impermeable slope and another symbols are the results obtained on the pebble beaches.

Wave height on pebble beach decreases significantly when compared with that on the impermeable slope. Especially the decay of wave height on the slope of 1/10 is large because incident waves have to travel for long distance on the permeable layer when compared with the case of the slope 1/5. On the other hand, there is little difference between the wave height measured on the pebble beaches of different sizes.

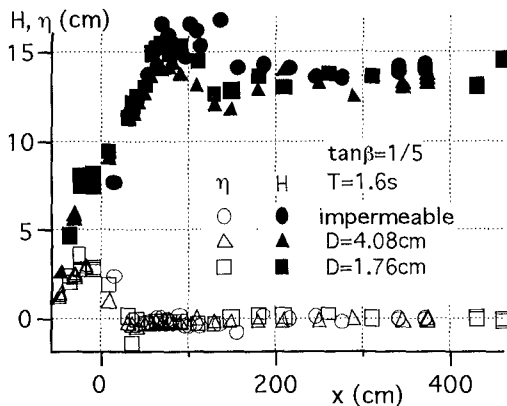


Figure 2 Wave height distribution on 1/5 slope

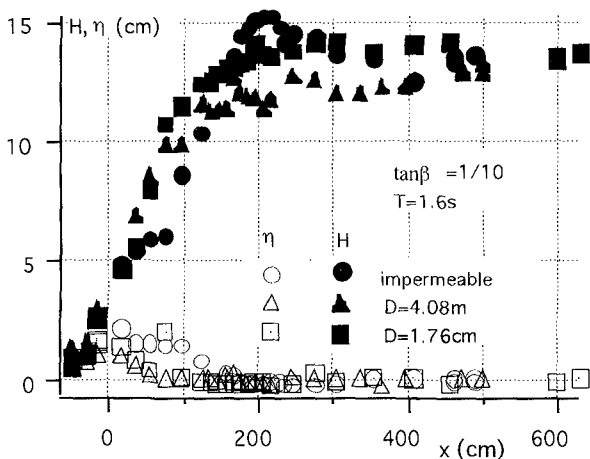


Figure 3 Wave height distribution of 1/10 slope

Wave run-up and reflection coefficient:

Figure 4 shows the non-dimensional run-up height normalized by the incident wave height R/H . The horizontal axis is the surf similarity parameter. Measured run-up height on pebble beaches shown by closed triangle and rectangle are 40 to 50% smaller than that measured on impermeable slope shown by the closed circles. Solid line in the figure show the relation $R/H = \xi$ that is usually applied to the run-up height on impermeable slope. Broken line in the figure is the empirical result for the non-dimensional run-up height on rubble mound breakwater obtained by Losada and Kurto(1981).

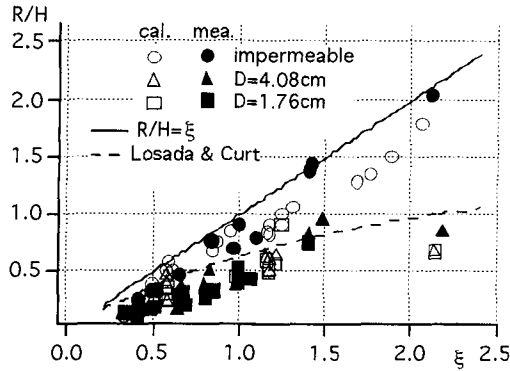


Figure 4 Wave run-up height

Figure 5 illustrates measured reflection coefficient K_r by Goda's method using two time series of measured surface displacements on the horizontal bottom. Horizontal axis is the incident wave steepness. The value of K_r in all cases are less than 30% and significant difference between the value of K_r measured on impermeable slope and pebble beaches can not be seen. K_r plotted in the region of wave steepness smaller than 0.005 is the result of long wave generated by a bichromatic waves.

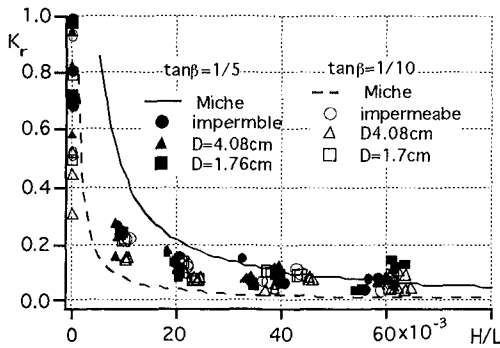


Figure 5 Reflection coefficient

Solid and broken line in the figure are the reflection coefficient on the impermeable slope of 1/5 and 1/10 evaluated by the Mich's formulae.

Numerical model for predicting wave height distribution on pebble beach

We have already proposed a simple model for estimating wave height on the permeable slope (Deguchi et al., 1995). Definition of variables and coordinate system used in the model is illustrated in Fig.6. h is the depth on pebble beach and d is the thickness of the pebble layer. For evaluating wave height on the sloping beach, we apply nonlinear shoaling model proposed by Shuto(1974) with the energy dissipation

after wave breaking E_b , energy loss in the permeable layer E_p and surface drag on the pebble beach E_{fb} . These expressions are shown below:

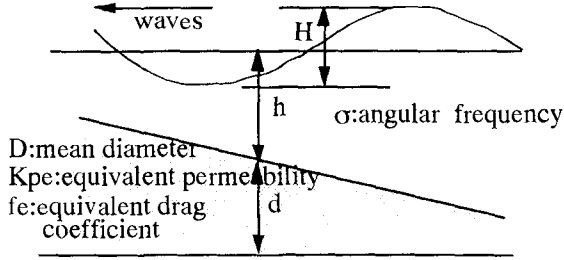


Figure 6 Definition of variables

In the calculation, wave height on the sloping beach was firstly calculated from Eq.(1) by giving incident wave height at offshore. When the wave height became greater than wave breaking height, wave height was reduced according to the energy loss by wave breaking that is given by Eq.(2) (Sawaragi, et al., 1984).

$$\begin{aligned}
 gHT^2/h^2 \leq 30: & \text{small amplitude wave theory} \\
 30 \leq gHT^2/h^2 \leq 50: & Hh^{2.7} = \text{const.} \\
 50 \leq gHT^2/h^2: & Hh^{5/2}(\sqrt{gHT^2/h^2} - 2\sqrt{3}) = \text{const.}
 \end{aligned}
 \tag{1}$$

$$E_b = \alpha_1 \left(5.3 - 3.3 I_r - \frac{0.07}{\tan \beta} \right) \left(\frac{(\rho g H^2 / 8)^3}{\rho h^3} \right)^{1/2}
 \tag{2}$$

where ρ is the density of water, g is the gravitational acceleration, β is the slope, ξ is the surf similarity parameter and α_1 is the empirical constant of the order of one.

When waves propagate on pebble beach, wave height is also reduced by energy dissipation on the permeability and the surface drag that are expressed by Eqs.(3) and (4) (Sawaragi et al., 1992).

$$E_p = \frac{\rho g H^2}{4} C_g k_i
 \tag{3}$$

$$E_{fb} = \frac{2}{3} \pi^2 \frac{\rho f_w H^3}{T^3 \sinh^3 kh} (1 - \lambda)
 \tag{4}$$

where C_g is the group velocity, f is Jonsson's friction factor, and k_i is the imaginary wave number determined by the following dispersion relation on the permeable layer:

$$\sigma^2 = gk \frac{(S/f_e + i) \sinh kh \cosh kd + (1/f_e) \cosh kh \sinh kd}{(S/f_e + i) \cosh kh \cosh kd + (1/f_e) \sinh kh \sinh kd}
 \tag{5}$$

in which k is the complex wavenumber and f_e is the equivalent drag coefficient defined by using equivalent permeability k_{pe} as follow:

$$1/f_e = K_{pe} \sigma / \nu, f_e = 0.1 + 1.8(u/\sigma D_m)
 \tag{6}$$

Figure 7 is the comparisons of measured and calculated wave height and set-up on permeable and impermeable slope of 1/10. The mean diameter of the pebble on the permeable slope was $D=1.76\text{cm}$. Shift of the location of breaking point and decrease in wave height are reproduced well by the model.

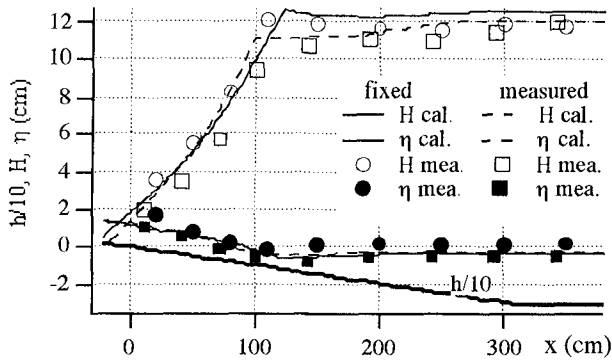


Figure 7 Comparison of measured and calculated wave height

Numerical model for predicting wave run-up on pebble beach

Some numerical model have already developed to predict wave run-up on the permeable slope (for example, Kobayashi and Wurjanto, 1990). However, it is not sufficient to explain various non-linear phenomena including wave breaking, wave propagation into the permeable layer, wave run-up on the slope and so on. Here, we developed a numerical procedure for predicting surface displacement on the slope in a coordinate system shown in Fig.8. To construct numerical model, we neglected a vertical water particle velocity and applied Boussinesq type equation and a non-linear unsteady Darcy's law for the fluid motion on and in the pebble beach. Driving force of the fluid motion on and in the pebble beach is the pressure gradient. Although pressure on the pebble beach calculated from the Boussinesq equation is not hydrostatic, driving force on fluid motion in the pebble layer is assumed to be determined by the gradient of surface displacement. Definition of variables are shown in Fig.8.

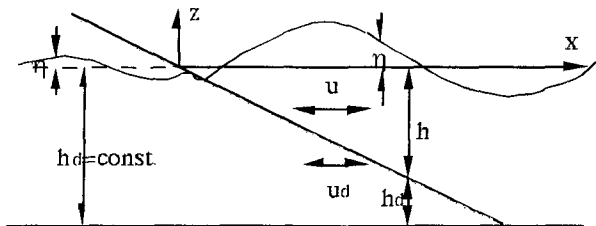


Figure 8 Coordinate system and definition of variables

Equation of motion of water particles on and in the pebble beach are expressed as follows:

$$\frac{\partial u}{\partial t} + u \frac{\partial u}{\partial x} + g \frac{\partial \eta}{\partial x} = \frac{h}{2} \frac{\partial}{\partial x} \left[\frac{\partial}{\partial x} \left(h \frac{\partial u}{\partial t} \right) \right] - \frac{h^2}{6} \frac{\partial}{\partial x} \left[\frac{\partial}{\partial x} \frac{\partial u}{\partial t} \right] - D_1 \quad (7)$$

$$D_1 = \alpha_2 \frac{\partial}{\partial x} \left[\kappa g (h + \eta) \left(\frac{u}{h} \right)^2 \right] + \frac{\alpha_3}{h + \eta} f u |u| \quad (8)$$

$$S \frac{\partial u_d}{\partial t} + u_d \frac{\partial u_d}{\partial x} + g \frac{\partial \eta}{\partial x} = - \frac{\nu}{K_p} u_d - \frac{C_f}{\sqrt{K_p}} u_d |u_d| \quad (9)$$

$$S = \{1 + (1 - \lambda) C_m\} / \lambda$$

where u and u_d are the water particle velocity on the pebble beach and in the pebble layer, ρD_1 is the momentum dissipation, κ is Karman's constant, α_2 and α_3 are the empirical constants.

Equation of continuity of the fluid motion on the horizontal bottom and on the pebble beach are expressed by the following two equations.

$$\frac{\partial \eta}{\partial t} + \frac{\partial}{\partial x} [(\eta + h)u] = 0 \quad (10)$$

$$\frac{\partial \eta}{\partial t} + \frac{\partial}{\partial x} [(\eta + h)u + h_d u_d] = 0 \quad (11)$$

In the region shoreward of the wave front on pebble beach, h in Eq(11) becomes zero.

These equations are transformed into finite difference equations and are solved by giving time variations of surface displacement and water particle velocity at the offshore boundary. Continuity condition of surface displacement inside and on the pebble beach is imposed. A so-called moving boundary condition is used to determine the location of wave front on the pebble beach.

Figure 9 illustrates a comparison of calculated and measured surface displacements in the breaker zone on the pebble beach of the slope 1/5 of large grain size.

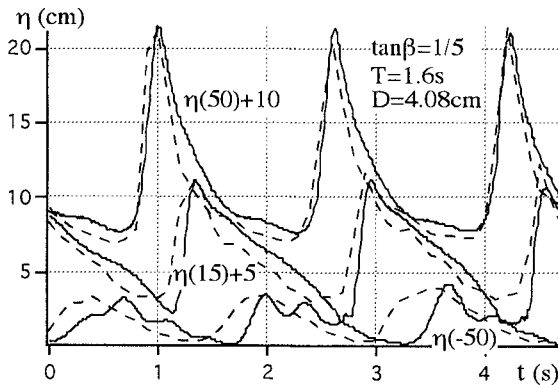


Figure 9 Comparison of calculated and measured time variation of surface displacement

In the figure, $\eta(-50)$, $\eta(15)$ and $\eta(50)$ are the surface displacements at -50m , 15m and 50m from the initial shoreline, solid and broken lines are the calculated and measured surface displacement. Calculated and measured surface displacements in front of the pebble beach, $\eta(15)$ and $\eta(50)$, coincide well with each other. Calculated amplitude of the surface displacement in pebble beach, $\eta(-50)$, also reproduces the measured one. However, the time variation of measured surface displacement is smooth when compared with the calculated result and there is a small phase lag between them. Until now, we can not explain the reason of these discrepancy.

Figure 10 is an example of calculated surface profiles drawn at time interval of 0.2s on impermeable slope of $1/5$. Incident wave period is 2.0s .

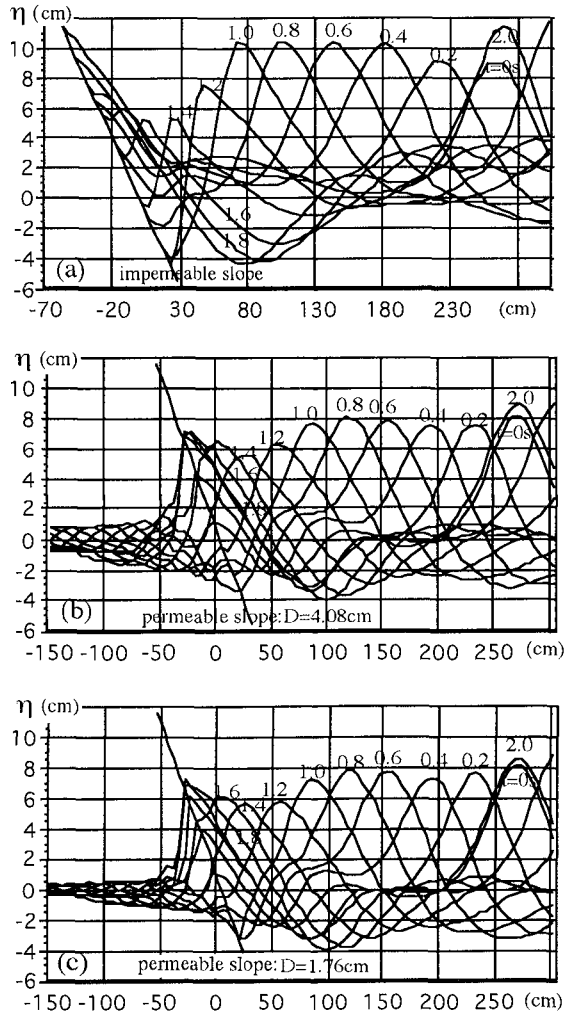


Figure 10 Surface profile in front of impermeable slope and pebble beach

Figure(a) is the result on the impermeable slope and Figures(b) and (c) are the results on the pebble beach of different materials. The maximum run-up height on the impermeable slope is almost the same as the incident wave height. Run-up height on the pebble beach of large materials under the same wave conditions shown in Fig.(b) is smaller than the incident wave height and even in the permeable layer, surface displacement of the amplitude of more than 1cm exists. Run-up height on the pebble beach of small materials shown in Fig.(c) is almost the same as that in the former case but the amplitude of the surface displacement in the permeable layer is smaller than the former case.

Open symbols in Fig.4 are the run-up height determined from the calculated surface profiles examples of which are shown in Fig.10. Although the predicted run-up height on both pebble beach and impermeable slope are a little bit smaller than those of the measured results, the decrease in the run-up height on a pebble beach is expressed by the numerical model.

Characteristics of topography change of pebble beach

Field and laboratory experiments:

We examined the characteristics of the deformation of the pebble beach based on the bottom topographies measured in two dimensional experiments and field measurements. In the experiments, significant deformation took place only in the case of pebble beach of small materials of the slope of 1/5. Field measurement were carried out on the artificial pebble beach constructed as a gentle slope seawall of the reclamation just landward of the Kansai International Airport in Osaka Bay as shown in Fig.11. The total length of the beach is about 3km and we measured bottom topography in one section of the beach surrounded by two groins. The length of the section is 300m. Construction of the beach finished in March 1992. In this paper, characteristics of the deformation are discussed based on the measured results on October 1995 about 3.5years after the construction of the beach.

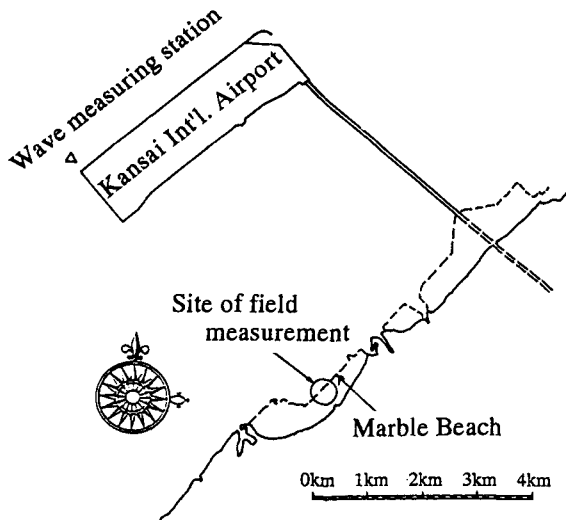


Figure 11 Location of field measurement

The representative planned cross-section of the beach is shown in Fig. 12. Average depth at the toe is about 5m and the slope of the beach is 1/15. The surface of the beach is covered by pebbles of marble of the diameter 4-10cm. The thickness of the cover layer is 1m. We call this beach as Marble Beach.

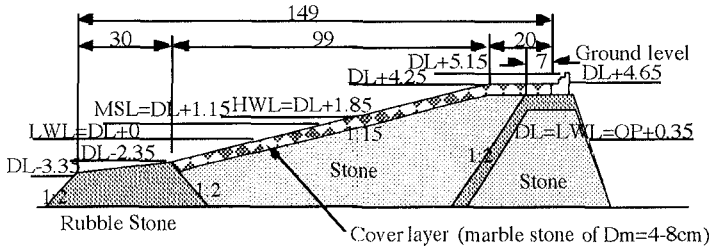


Figure 12 Representative cross-section of the Marble beach

Bottom topography was measured along 15 measuring lines set at an interval of 20m. Figure 13 illustrates the bottom topography when we see the beach from the land. There are groins at both side of this section.

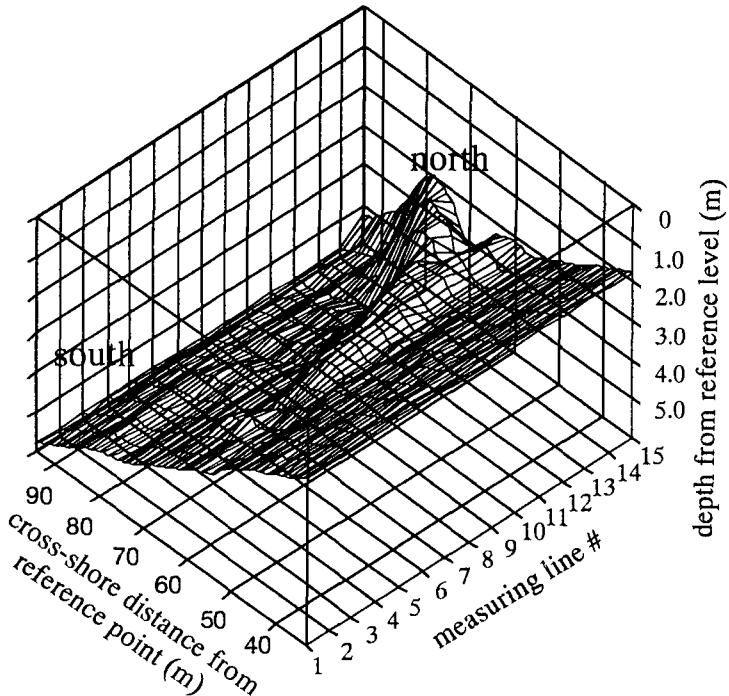


Figure 13 Measured topography of Marble Beach

Characteristics of topography change took place on Marble Beach:

In Fig.13, two berm crests can be seen at the north side of the beach and it is easy to imagine that pebbles were transported landward to form landward berm at first stage of the deformation and then they were transported from south to north to form the

second berm. According to the empirical eigenfunction analysis, it is found that about 60% of the total deformation was caused by the longshore pebble transport and about 30% was caused by the net onshore pebble transport. Measuring line #15 is the north end of the beach and #8 is almost the neutral section for the topography change due to longshore transport.

Applicability of 2/3-power law:

Figures 14 and 15 are the representative cross-sections measured on the Marble Beach and in the laboratory.

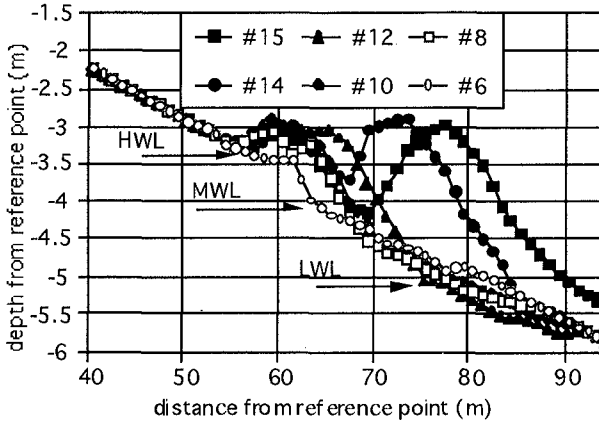


Figure 14 Representative measured cross-sections of Marble Beach

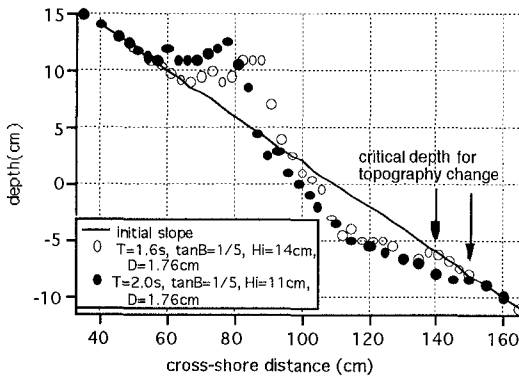


Figure 15 Measured cross-sections in experiments

Both sections shown in the figure, as well as those shown in Fig.14, are the typical accretion-type profile. We examined the applicability of the 2/3-power-law to these sections. Bruun(1962) and Dean(1991) proposed the equilibrium beach profile that is expressed by Eq.(12).

$$h = Ax^{2/3} \tag{12}$$

where h is the depth of the equilibrium beach profile, x is the cross-shore distance and A is the empirical constant.

Dean (1991) gave physical meaning to Eq.(12) from the view point of energy dissipation in the surf zone and proposed the following empirical expression for the value of A as a function of settling velocity of the bed material W_f .

$$A = 0.067W_f^{0.44} \quad (13)$$

We examined the applicability of the expression of Eq.(12) to the measured profile of pebble beach in the laboratory and in the Marble Beach. Figures 16 and 17 are the results. Profiles of both laboratory and field roughly coincide with the predicted profiles with the value of A 0.34 and 0.4, respectively.

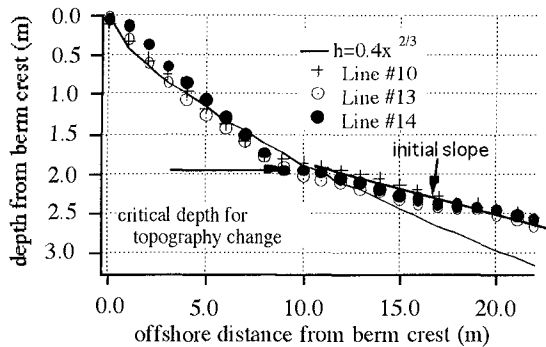


Figure 16 Comparison of Dean's profile and that measured on Marble Beach

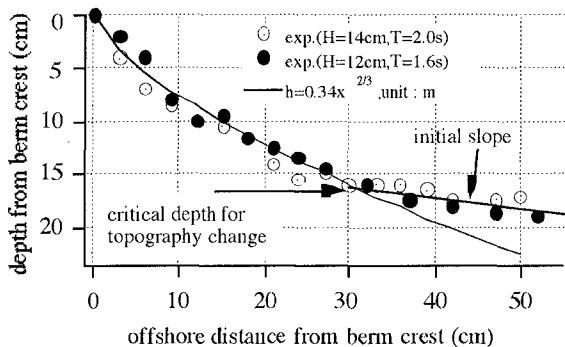


Figure 17 Comparison of Dean's profile and that measured in experiments

Shoreline change:

To evaluate total energy flux to the beach, we used wave records measured at observation station near the Kansai International Airport where various quantities concerning with the sea state are measured at one hour interval.

The total incident wave energy flux are evaluated from south to north and from north to south separately. The result is shown in Table 2. Energy flux from south to north is larger than that from north to south. Using this result together with the calculated volume of pebbles that were transported from south to north, we determined

the longshore pebble transport rate and one representative wave to calculate location of contour line by a so-called one line theory.

Table 2 Incident wave energy flux in longshore direction (ton)

	1992	1993	1994	1995	total
from south to north	107280	178740	136656	68076	490752
from north to south	45720	61128	56988	32580	196416

It is found that the total longshore pebble transport rate Q_y is related to the longshore energy flux of incident waves in deep water by the following relation:

$$Q_y (m^3 / day) = 0.036(EC_g)_o \sin \theta \cos \theta (t / m / day) \tag{14}$$

where $(EC_g)_o$ is the incident wave energy flux in deep water and θ is the incident wave direction.

Figure 18 is the comparison of the calculated shift of the -4m contour line and measured location of the same contour line. As can be seen from the figure, -4m contour line almost becomes equilibrium 4 years after the construction and the measured location coincides calculated location fairly well. The measured contour line locates a little shoreward than the location of the calculated contour line. This is because the advancement of the contour line caused by the net onshore pebble transport is not taken into account in the calculated location of the -4m contour line.

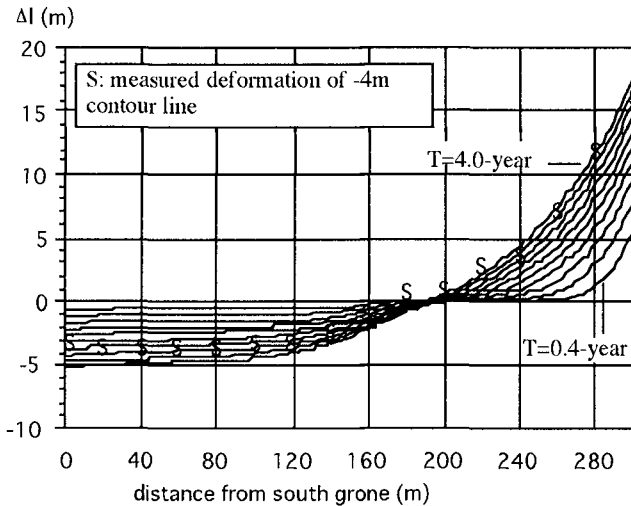


Figure 18 Comparison of measured and calculated deformation of -4m contour line

Conclusions

In this paper, numerical models for predicting wave height and run-up on pebble beach are proposed and the applicability of the model are examined through the laboratory experiments. Although the proposed model is too simple to reproduce the phenomena perfectly, we can predict rough figure of the wave tun -up on pebble beach.

Characteristics of the deformation of the pebble beach are also investigated using measured bottom topography in the field and laboratory. It is found that we can apply a so-called $2/3$ -power law and a single line theory for the cross-sectional profile and shoreline change of pebble beach.

Acknowledgment

This study was carried out by as a part of the research sponsored by the Grant-in-Aid for Scientific Research of the Ministry of Science, Culture and Education to DI (0605065)

Reference

- Bruun, P., 1962, Sea level rise as a cause of shore erosion, *J. Waterways and Harbor Div.*, ASCE, 88(WW1), pp.117-130
- Dean, R. G., 1991, Equilibrium beach profiles, Characteristics and applications, *J. Coastal Res.*, 7(1), pp.53-84.
- Deguchi, I. and K. Moriwaki, 1995, Wave transformation on pebble beach, *Proc. Coastal Engineering, JSCE*, Vol.41, pp.41-45.
- Kobayashi, N. and A. Wurjanto, 1990, Numerical model for waves on rough permeable slopes, *J. Coastal Res.*, No.7, pp.149-166.
- Losada, M. and L. Gimenez-Kurto, 1981, Flow characteristics on rough, permeable slopes under wave action, *Coastal Engineering*, 4, pp.187-206
- Sawaragi, T., I. Deguchi and K. Kim, 1984, Energy loss and wave set-up due to breaking waves, *Tech. Rept.*, Osaka University, Vol.34, No.,1779, pp.329-338.
- Sawaragi, T. and I. Deguchi, 1992, Waves on permeable layer, *Proc. 23rd ICCE*, pp.1531-1544.
- Shuto, N., 1974, Nonlinear long waves in a channel of variable section, *Coastal Eng. in Japan*, Vol.17, pp.1-12.

CHAPTER 260

Wind-Induced Waves and Currents in a Nearshore Zone

Nobuhiro Matsunaga¹, Misao Hashida² and Hiroshi Kawakami³

Abstract

Characteristics of waves and currents induced when a strong wind blows shoreward in a nearshore zone have been investigated experimentally. The drag coefficient of wavy surface has been related to the ratio u_{*a}/c_p , where u_{*a} is the air friction velocity on the water surface and c_p the phase velocity of the predominant wind waves. Though the relation between the frequencies of the predominant waves and fetch is very similar to that for deep water, the fetch-relation of the wave energy is a little complicated because of the wave shoaling and the wave breaking. The dependence of the energy spectra on the frequency f changes from f^{-5} to f^{-3} in the high frequency region with increase of the wind velocity. A strong onshore drift current forms along a thin layer near the water surface and the compensating offshore current is induced under this layer. As the wind velocity increases, the offshore current velocity increases and becomes much larger than the wave-induced mass transport velocity which is calculated from Longuet-Higgins' theoretical solution.

1. Introduction

When a nearshore zone is under swell weather conditions, the

1 Associate Professor, Department of Earth System Science and Technology, Kyushu University, Kasuga 816, Japan.

2 Professor, Department of Civil Engineering, Nippon Bunri University, Oita 870-03, Japan.

3 Graduate student, Department of Earth System Science and Technology, Kyushu University, Kasuga 816, Japan.

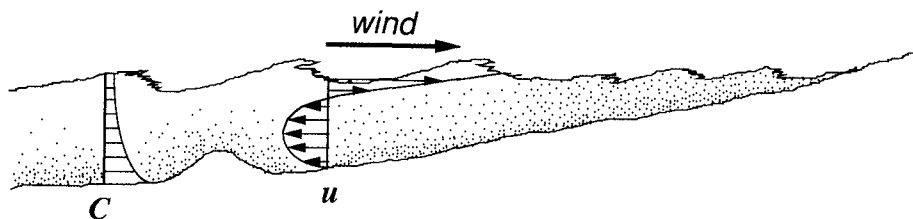


Fig.1 Sketch of sediment transport process in a nearshore zone under a storm.

sediment transport process depends strongly on the wave-induced mass transport velocity. The process is relatively slow. On the other hand, a large amount of sediment is suspended and transported under a storm. The transport process under storm weather conditions is very different from that under swell weather conditions. Shepard (1950) observed the change of beach profiles along Scripps Pier, La Jolla, California. He revealed that a beach profile with longshore bars forms under storm weather conditions and a profile with pronounced berms develops under swell weather conditions. The former has been referred to as the winter profile, and the latter as the summer profile. Komer (1976) claims the use of terms 'storm profile' and 'swell profile' to be preferable.

Many researchers (e.g., Johnson (1949), Rector (1954), Iwagaki and Noda (1963)) investigated seasonal variations of beach profiles and obtained a critical wave steepness at which they change from the storm profile to the swell one. In their studies, the steepness of storm waves was regarded as the most important factor to determine the beach profile. However, it seems to be difficult to explain the sediment transport process under storm weather conditions without considering the wind effect. In the case when a strong wind blows shoreward, a strong onshore wind-driven current forms along a thin layer near the water surface, and the compensating offshore current along the bed (see figure 1). The offshore current may transport a large amount of sediment seaward because the concentration of suspended sediment increases to the seabed. After a storm, in fact, we can often see a beach being eroded remarkably and floating matters such as seaweeds and pieces of wood being cast ashore.

In this study, waves and currents formed in a nearshore zone under storm weather conditions have been investigated experimentally in order to understand the wind effect on the onshore-offshore sediment transport.

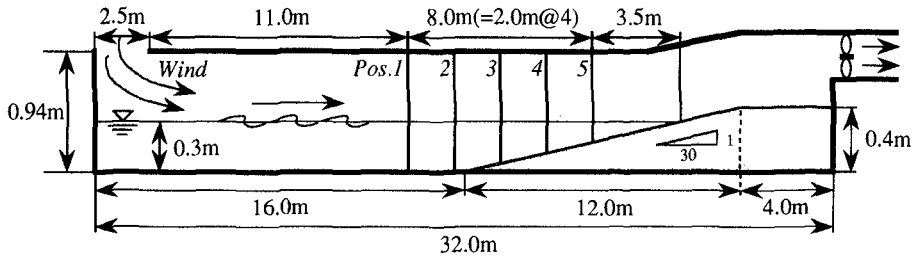


Fig.2 Experimental apparatus.

2. Experimental set-up

Experiments were carried out by using a water tank equipped with an inhalation-type wind tunnel. Figure 2 shows a schematic diagram of the experimental apparatus. The tank was 32 m long, 0.6 m wide and 0.94 m high. A sloping bed was attached to the end of the tank as a beach model. Its gradient was fixed at 1/30. The mean water depth was 0.3 m at the horizontal bed section. Wind waves were generated by the shoreward wind. Measurements of the wind velocity, wave height and wind-induced current velocity were made at positions 1 to 5. The distance from the intake of the wind to Position 1 was 11 m. The intervals between the adjacent measuring positions were 2.0 m. Positions 1 and 2 were in the horizontal bed section and positions 3 to 5 on the sloping bed. The wind velocity was measured by using a propeller-type current meter. In the wave height measurements, two capacitance-type wave gauges were used in order to obtain the phase velocity. They were set 28 cm away. The wave signals were digitized at the intervals of 1/50 s and 16,384 data were sampled. Horizontal and vertical components of the wind-induced currents were obtained by using an electromagnetic current meter. The sampling rate of the velocity signals was 1/20 s and the number of sampled data was 2,048.

Table 1 shows the wind parameters and the wave ones. Five tests in all were carried out by varying the wind velocity. The cross-sectionally averaged wind velocity U_m was varied from 7.60 m/s to 21.8 m/s. F is the fetch and h the mean water depth. The air friction velocity on the wavy surface is denoted by u_{*a} and the mean wind velocity at a 10 m height by U_{10} . H is the mean wave height. The periods, lengths and phase velocities of predominant waves are

Table 1 Experimental parameters.

U_m (m/s)	Pos.	F (m)	h (cm)	u_{*a} (m/s)	U_{10} (m/s)	H (cm)	T_p (s)	L_p (m)	c_p (m/s)	E (cm ²)	u_{*a}/c_p	C_D	U_r
7.60	1	11.0	30.0	0.335	10.9	2.20	0.467	0.400	0.856	0.688	0.391	9.45E-4	0.130
	2	13.0	30.0	0.259	10.4	2.43	0.467	0.417	0.893	0.836	0.290	6.20E-4	0.157
	3	15.0	25.0	0.274	10.4	2.63	0.474	0.433	0.914	0.977	0.300	6.94E-4	0.316
	4	17.0	18.4	0.238	10.7	2.83	0.515	0.493	0.956	1.17	0.249	4.95E-4	1.10
	5	19.0	11.9	0.294	11.1	2.99	0.535	0.483	0.903	1.26	0.326	7.02E-4	4.14
11.6	1	11.0	30.4	0.682	18.1	4.68	0.585	0.637	1.09	2.88	0.626	1.42E-3	0.676
	2	13.0	30.2	0.568	17.3	5.06	0.595	0.685	1.15	3.31	0.494	1.08E-3	0.862
	3	15.0	25.2	0.723	19.1	5.30	0.658	0.743	1.13	3.53	0.640	1.44E-3	1.83
	4	17.0	18.7	0.823	20.6	5.33	0.662	0.834	1.26	3.59	0.653	1.60E-3	5.67
	5	19.0	12.4	0.658	19.1	4.46	0.699	0.741	1.06	2.57	0.621	1.19E-3	12.8
15.5	1	11.0	29.9	1.18	26.4	5.58	0.662	0.768	1.16	4.01	1.02	2.00E-3	1.23
	2	13.0	30.1	1.29	28.0	6.41	0.714	0.971	1.36	5.07	0.949	2.10E-3	2.22
	3	15.0	25.5	1.19	27.3	6.55	0.709	0.851	1.20	5.26	0.992	1.91E-3	2.86
	4	17.0	19.3	1.32	29.1	6.11	0.746	0.896	1.20	4.86	1.10	2.06E-3	6.82
	5	19.0	13.4	1.49	31.1	4.55	0.775	0.791	1.02	3.01	1.46	2.30E-3	11.8
18.9	1	11.0	28.5	1.10	29.0	6.05	0.699	0.881	1.26	4.71	0.873	1.45E-3	2.03
	2	13.0	30.0	1.63	34.8	6.39	0.719	0.971	1.35	5.45	1.21	2.20E-3	2.23
	3	15.0	25.6	1.82	36.9	6.69	0.746	0.955	1.28	6.06	1.42	2.44E-3	3.64
	4	17.0	19.6	2.10	40.3	5.87	0.787	1.00	1.27	4.95	1.65	2.72E-3	7.80
	5	19.0	14.0	2.57	45.6	4.81	0.840	0.830	0.988	3.43	2.60	3.19E-3	12.1
21.8	1	11.0	27.8	1.99	39.4	6.30	0.719	0.971	1.35	5.38	1.47	2.54E-3	2.76
	2	13.0	28.1	2.04	43.3	6.49	0.741	1.02	1.38	5.92	1.48	2.21E-3	3.04
	3	15.0	24.1	2.02	42.9	6.91	0.794	1.04	1.31	6.41	1.54	2.21E-3	5.34
	4	17.0	18.2	2.19	45.1	5.76	0.794	1.02	1.28	4.64	1.71	2.36E-3	9.94
	5	19.0	13.5	2.40	45.9	4.19	0.885	1.04	1.18	3.09	2.03	2.72E-3	18.4

represented by T_p , L_p and c_p , respectively. E denotes the total wave energy. The drag coefficient C_D is defined by $(u_{*a}/U_{10})^2$, and U_r is an Ursell parameter defined by HL_p^2/h^3 .

3. Experimental results and discussion

3.1 Drag coefficient of wavy surface

Vertical profiles of the mean wind velocity U in the case of $U_m = 15.5$ m/s are shown in figure 3, where z is the vertical coordinate taken upward from the mean water level. Though the wind velocity near the ceiling of the wind tunnel decreases due to the boundary layer, a logarithmic profile is formed near the water surface. The wind set-up increases the wind velocity and the velocity gradient near the water surface in the leeward direction. The values of u_{*a} were calculated by

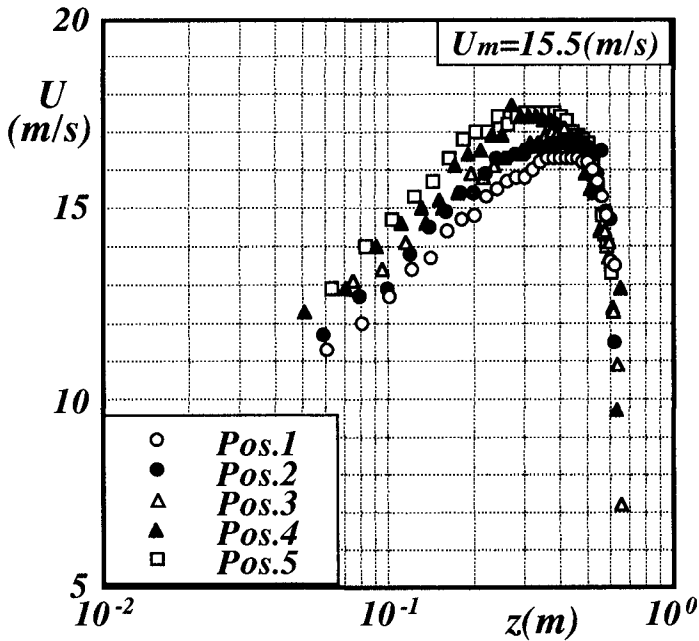


Fig.3 Vertical profiles of mean wind velocity.

fitting the logarithmic law

$$U = \frac{u_* a}{\kappa} \ln \frac{z}{z_0} \quad (1)$$

to the wind velocity profiles, where κ ($= 0.4$) is von Karman's constant. It is read from table 1 that the values of $u_* a$ increase with increase of U_m and with increase of F . The drag coefficient C_D is defined by

$$C_D = \left(\frac{u_* a}{U_{10}} \right)^2 \quad (2)$$

The relation between C_D and U_{10} has been investigated until now by many researchers. Some of the empirical expressions and our experimental data are shown in figure 4. The data include ones obtained through other experiments in which the wind blew on swells made by a wavemaker. Though the U_{10} -dependence for the wind waves is different from that for the swell and wind waves, the data approach gradually to Kondo's empirical curve when $U_{10} \geq 25$ m/s. Some of our data are under the values to which the empirical curves

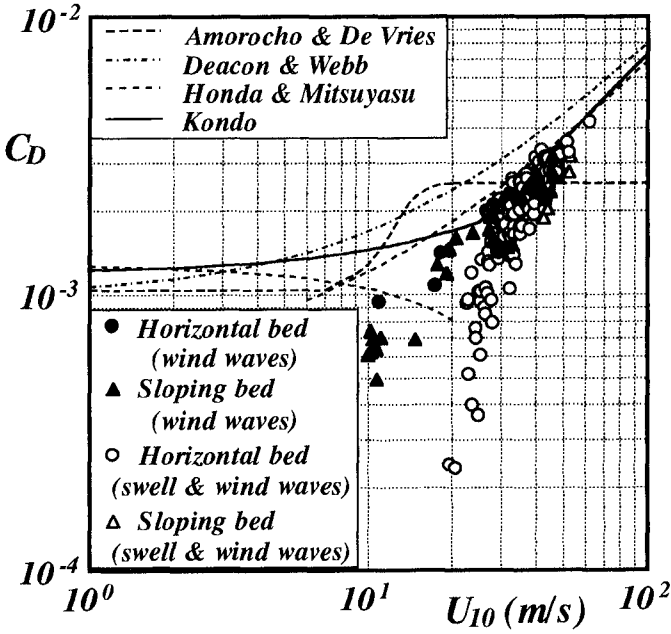


Fig.4 U_{10} -dependence of C_D .

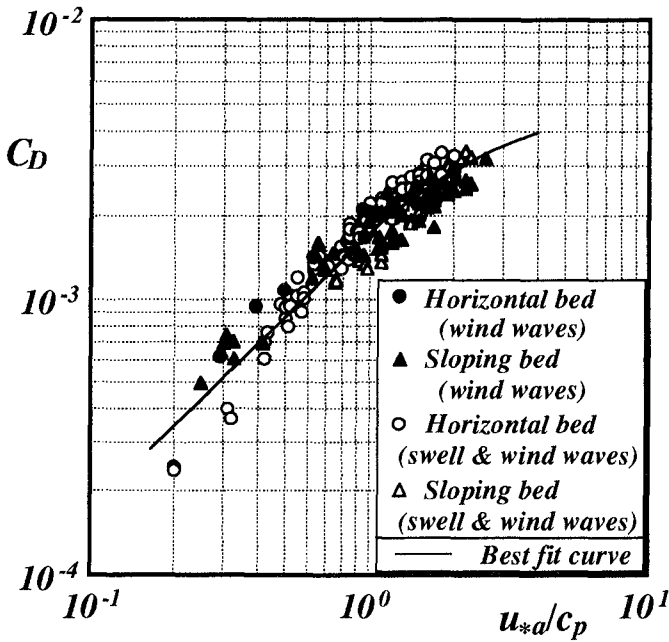


Fig.5 Relation between C_D and u_{*a}/c_p .

approach with increase of U_{10} . The validity of these data remains to be proved.

The relation of C_D and U_{10} has been investigated from the standpoint of practicality. However, if we try to obtain a universal form for C_D , relations between C_D and dimensionless parameters should be examined. Figure 5 shows a relation between C_D and u_{*a}/c_p . The solid line is drawn by the least-square fit method. The discrepancy between the data for the wind waves and ones for the swell and wind waves becomes much smaller than that shown in figure 4. Increasing linearly with u_{*a}/c_p when $u_{*a}/c_p \leq 1$, C_D becomes constant for a large value of u_{*a}/c_p .

3.2 Wind waves in shallow water

It is well-known that the energy of wind waves in deep water and the periods of the predominant wind waves increase with increase of u_{*a} and F . The empirical fetch-relations proposed by Mitsuyasu (1968) are

$$\frac{gE^{1/2}}{u_{*a}^2} = 1.31 \times 10^{-2} \left(\frac{gF}{u_{*a}^2} \right)^{0.504} \quad (3)$$

and

$$\frac{u_{*a} f_p}{g} = 1.00 \left(\frac{gF}{u_{*a}^2} \right)^{-0.330} \quad (4)$$

where $f_p = 2\pi/T_p$. As read from table 1, the values of T_p in shallow water increase with increase of F but the values of E do not increase monotonically with F because of the wave breaking. We can also read that the increase of F corresponds to that of U_r . It means that the wind waves progress into a shallow region with increase of F . If equations (3) and (4) are rewritten by using the wave energy E_0 and the frequency f_{p0} at a standard point,

$$\frac{E}{E_0} = \left(\frac{F}{F_0} \right)^{1.008} \quad (5)$$

and

$$\frac{f_p}{f_{p0}} = \left(\frac{F}{F_0} \right)^{-0.330} \quad (6)$$

are obtained, where F_0 is fetch at the standard point. Equations (5) and (6) give the increasing rate of the wave energy to E_0 and the decreasing rate of the predominant wave frequency to f_{p0} , respectively. The

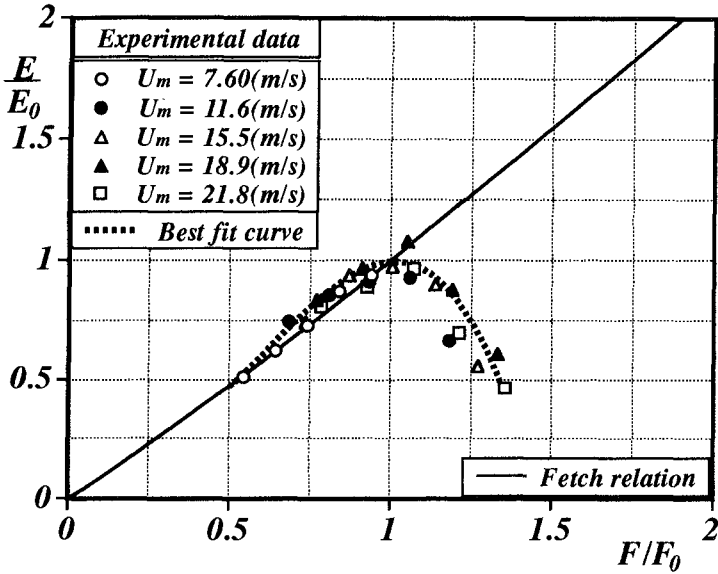


Fig.6 Comparison of fetch relation of E in shallow water with that in deep water.

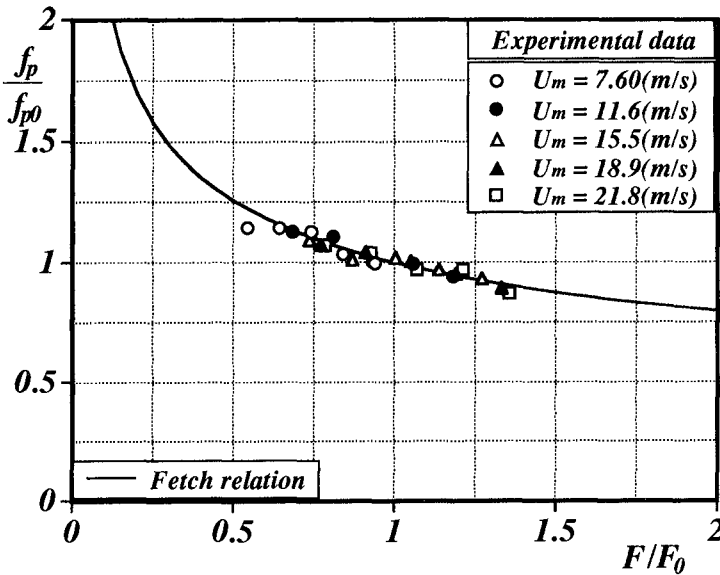


Fig.7 Comparison of fetch relation of f_p in shallow water with that in deep water.

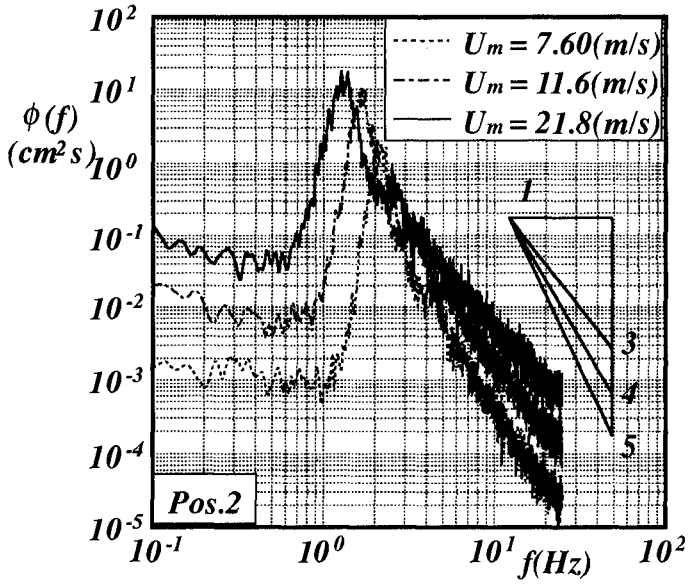


Fig.8 Variation of energy spectra of wind waves with increase of U_m .

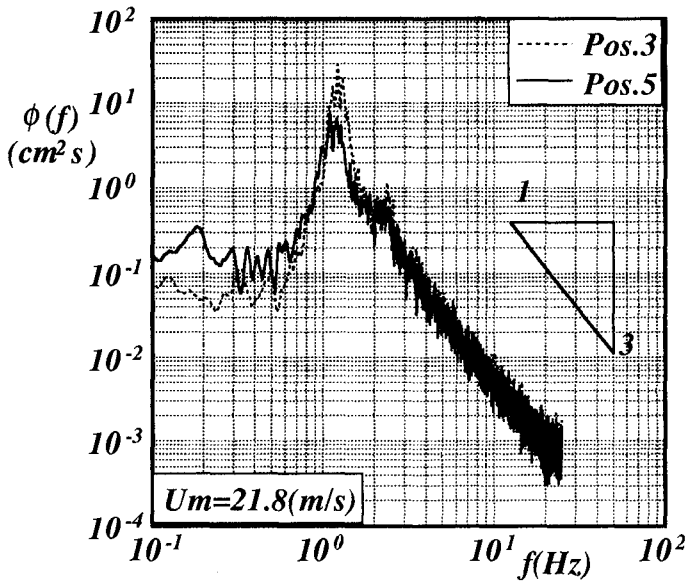


Fig.9 Comparison between energy spectra before and behind breaking point.

values of E/E_0 are plotted against F/F_0 in figure 6, where the fetch to the breaking point is selected as F_0 . The breaking point of the wind waves is defined as a position at which E becomes maximum. The solid line expresses the relation given by equation (5). The dashed line is the best fit curve based on the data. In the offshore side from the breaking point ($F/F_0 < 1$), the increasing rate of E is a little larger than that in deep water. It may be caused by the wave shoaling. On the other hand, in the onshore side ($F/F_0 > 1$), the increasing rate decreases rapidly with fetch because of the wave breaking. Figure 7 shows the relation between f_p/f_{p0} and F/F_0 . The data collapse well onto the curve given by equation (6). It means that the decreasing rate of f_p in shallow water agrees well with that in deep water.

Figure 8 shows energy spectra $\phi(f)$ of wind waves measured at Position 2. The total energy increases with increase of U_m because no wave breaking occurs at Position 2. The values of $\phi(f_p)$ become large with the U_m -increase and the values of f_p become small. These are the same features as in deep water waves. The f -dependence of $\phi(f)$ in the high frequency region changes from f^{-5} to f^{-3} as the wind velocity increases. The spectral form in an equilibrium region is given by

$$\phi(f) \propto g^\alpha u_* a^{2-\alpha} f^{-3-\alpha} \quad (7)$$

with the aid of a dimensional analysis, where g is the gravity acceleration and α an arbitrary constant. In the case when the effect of the gravity is much larger than the wind effect, α takes 2. At that time, $\phi(f)$ is proportional to f^{-5} in the high frequency region. On the other hand, as the wind velocity increases, it can be guessed that the effect of the gravity becomes small and $\phi(f) \propto f^{-3}$ in the limit. These dimensional considerations are supported by the results shown in figure 8.

Figure 9 shows the energy spectra of wind waves at positions 1 to 5. It is seen that the energy of the predominant waves decays remarkably due to the wave breaking.

3.3 Wind-induced currents

Figures 10 (a) to (e) show vertical profiles of wind-induced currents. Here, u is the horizontal component of the current velocity and the negative value indicates that the current is offshore. The vertical axis z is normalized using the local water depth h . Offshore wind-induced currents are formed in the range of $-1.0 \leq z/h \leq -0.1$. This suggests that an onshore strong current is generated in a thin layer near the water surface. As a natural result, the offshore currents

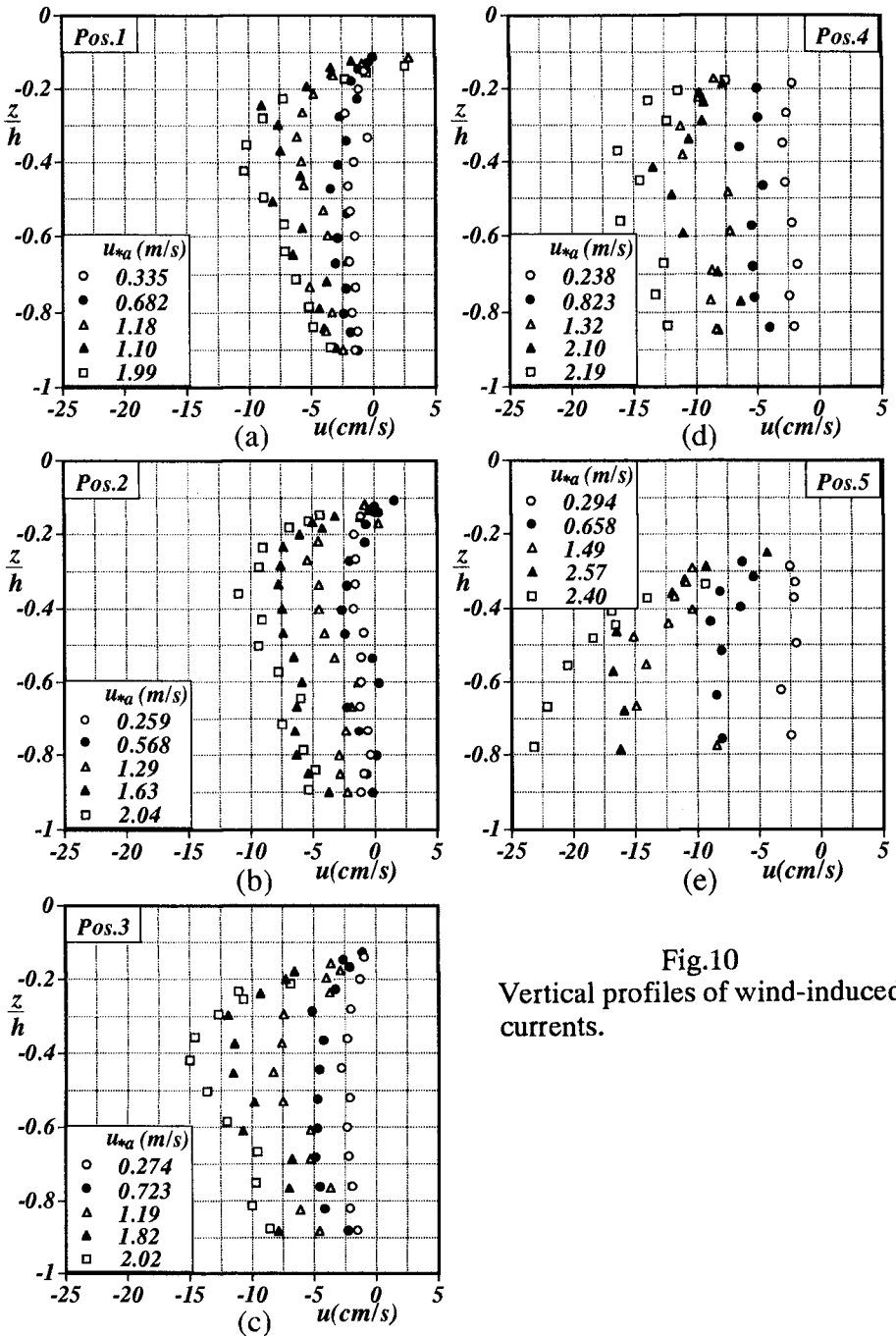


Fig.10
Vertical profiles of wind-induced currents.

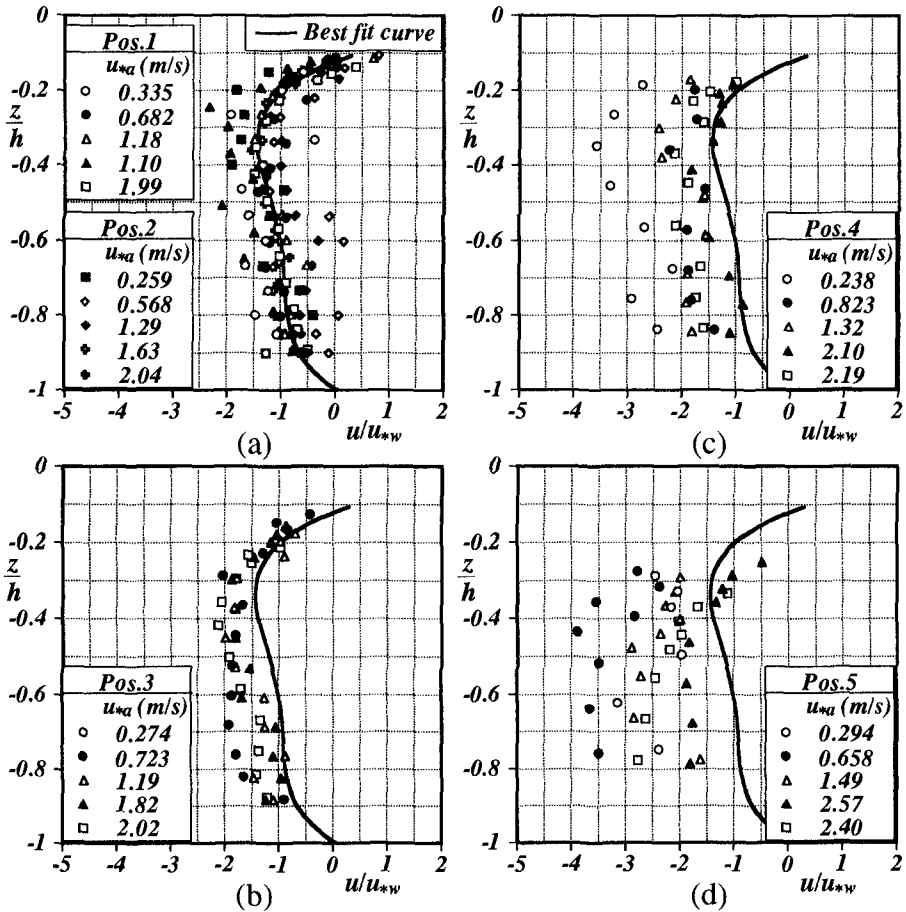


Fig.11 Normalized vertical profiles of wind-induced currents.

become stronger as u_{*a} increases and as the water depth decreases.

In figures 11 (a) to (d), the values of u are normalized by using the water friction velocity u_{*w} calculated from $(\rho_a/\rho_w)^{1/2}u_{*a}$. Here ρ_a and ρ_w are the densities of air and water, respectively. The values of u/u_{*w} at positions 1 and 2 are expressed approximately by the solid line (see figure 11 (a)). It may be due to that the wind-induced currents on a horizontal bed are uniform in the flow direction and the current velocity increases in proportion to u_{*a} . The maximum velocity of the offshore currents takes about $1.5u_{*w}$ at $z/h = -0.3$. Figures 11 (b) to (d) show the normalized vertical profiles for positions 3 to 5, respectively. The solid lines in these figures are the one drawn in figure 11 (a). It is

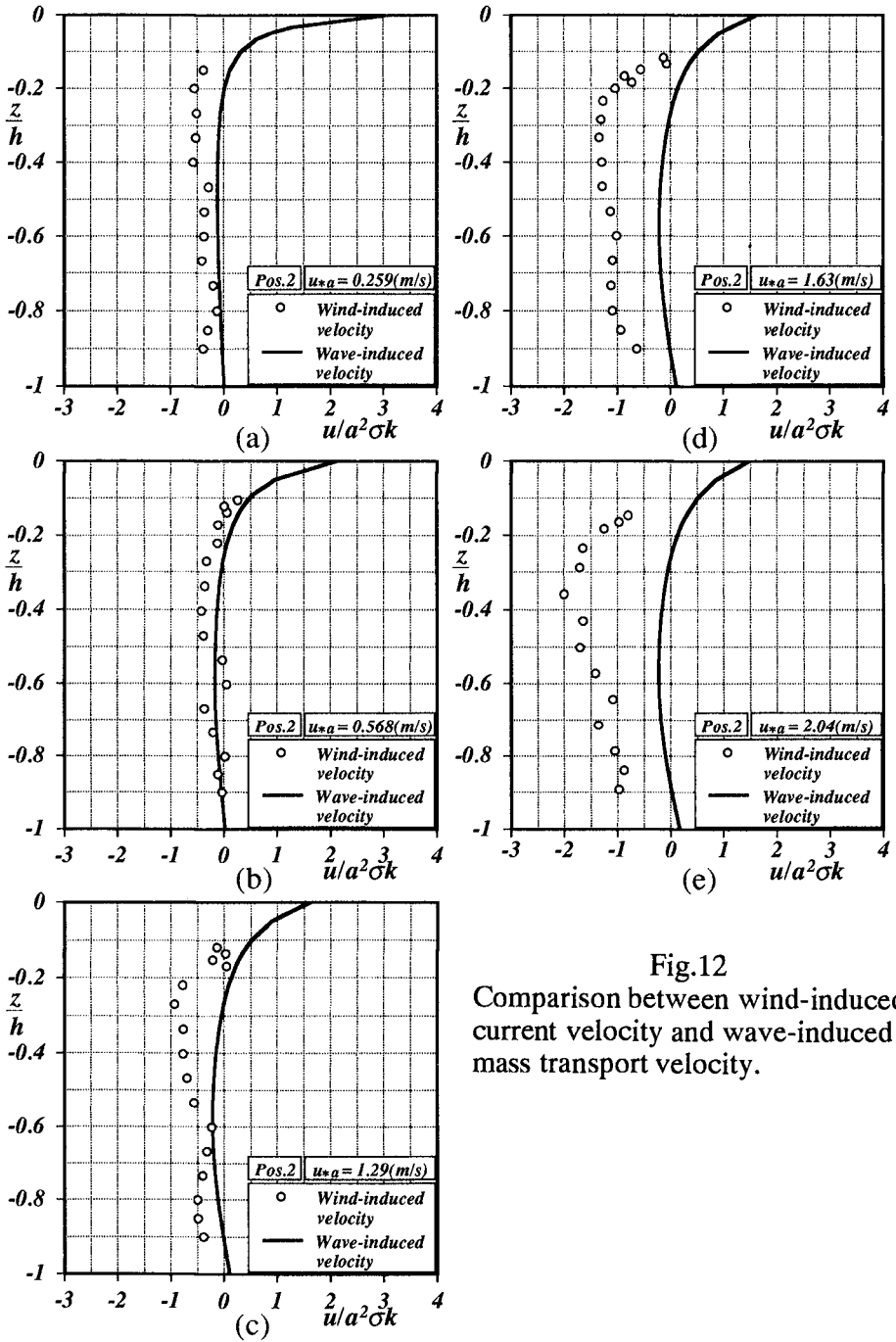


Fig.12
Comparison between wind-induced current velocity and wave-induced mass transport velocity.

difficult to express universally the vertical profiles on the sloping bed by using u_{*w} and h , because even if u_{*w} is uniform in the leeward direction, the water depth variation makes the offshore currents accelerate. In fact, the values of u/u_{*w} increase in the leeward direction.

Dimensionless velocity profiles of the wind-induced currents at Position 2 and the wave-induced currents are compared in figures 12 (a) to (e). The wave-induced velocity is estimated by using Longuet-Higgins' theoretical solution (Longuet-Higgins (1953)) and the measured values at Position 2. The theoretical results are drawn by the solid lines. The wave amplitude a , frequency σ and wave number k are given by $H/2$, $2\pi/T_p$ and $2\pi/L_p$, respectively. From these figures, it is seen that the wind-induced currents become much larger than the wave-induced currents as the values of u_{*w} increase. This suggests that the wind effect on the sediment transport under storm weather conditions is very important rather than the increase of wave steepness.

4. Conclusions

In this study, the characteristics of waves and currents formed in a nearshore zone under storm weather conditions have been investigated experimentally. The obtained main results are as follows.

- 1) The drag coefficient of wavy surface C_D is related to u_{*a}/c_p . The values of C_D increase monotonically with increase of u_{*a}/c_p but become constant for a large value of u_{*a}/c_p .
- 2) In the offshore side from the breaking point, the increasing rate of the total wave energy in shallow water is a little larger than that in deep water because of the wave shoaling. However, the increasing rate reduces remarkably in the onshore side from the breaking point due to the wave breaking. The decreasing rate of the predominant wave frequency in shallow water agree well with that in deep water.
- 3) The wind-induced current velocity increases with the wind velocity and becomes much larger than the wave-induced current velocity. Therefore, the wind effect is very important in the sediment transport process under storm weather conditions.

The authors are grateful for a grant from the Ministry of Education, Science and Culture.

References

- Iwagaki, Y. and Noda, H. (1963) Laboratory study of scale effects in two-dimensional beach processes, Proc. 8th Conf. on Coastal Eng., ASCE, 194 - 210.
- Johnson, J.W. (1949) Scale effects in hydraulic models involving wave motion, Trans. Am. Geophys. Union **30**, 517 - 525.
- Komar, P.D. (1976) Beach processes and sedimentation, Prentice-Hall, Englewood Cliffs, N.J., 288 - 300.
- Longuet-Higgins, M.S. (1953) Mass transport in water waves, Phil. Trans. Roy. Soc. (London), series A, **245**, 535 - 581.
- Rector, R.L. (1954) Laboratory study of the equilibrium profiles of beaches, U.S. Army Corps of Engrs., Beach Erosion Board Tech. Memo., **41**.
- Shepard, F.P. (1950) Beach cycles in Southern California, U.S. Army Corps of Engrs., Beach Erosion Board Tech. Memo., **20**.

CHAPTER 261

PREDICTING LARGE-SCALE, CROSS-SHORE SEDIMENT MOVEMENT FROM ORBITAL SPEEDS

Edward B. Hands¹, John P. Ahrens², and Donald T. Resio³

ABSTRACT: The ratio U of near-bed peak orbital speed to grain threshold speed should express the competence of coastal waves to agitate loose seafloor sediments. Using Stream Function Wave Theory, U can be evaluated separately under the wave crest U_C and trough U_T to produce a pair of parameters whose relative magnitudes indicate the direction of the displacing force. The authors tested this simple parametrization in two distinctly different, large-scale coastal transport situations. One situation involved relative stabilities and displacements of submerged dredged-material mounds outside the normal surf zone. These mounds contained 10s to 100s of thousands of cubic meters of sandy material. Predicted wave responses match well with measurements made over months and years at 11 such mounds widely scattered around the United States. The second situation involved predicting whether beaches accrete or erode during single storms. Comparison between U -based predictions and 99 beach responses, compiled from the published literature, provided good confirmation in the second situation.

Critical values of U are surprisingly skillful in predicting both types of cross-shore movement. Where extreme U_C 's exceeded U_T 's by more than about 5, mounds migrated shoreward; where waves were more linear, mounds remained stationary. Beaches eroded significantly where $U_T < -2$; and accreted otherwise regardless of the degree of wave linearity.

Research Phy Scientist ¹ and Senior Scientist ³ USAE Waterways Experiment Station,
Coastal and Hydraulics Laboratory, 3909 Halls Ferry Road, Vicksburg, MS 39180

Specialist ², Coastal Processes, NOAA, Sea Grant, 1335 East-West Highway, Silver
Spring, MD 20910

INTRODUCTION

Purpose

Two very simple critical conditions “explain” different types of coastal sediment dispersion. Either the tested large-scale laboratory and field studies fail to capture some significant class of conditions or the relative speed of bottom wave oscillations and sediment thresholds is the dominant factor controlling coastal profile response from the shoreline to well offshore. Broad-scale predictors, even if not precise, are useful to engineers who must often work with limited input data. Accordingly, the profile adjustment predictors developed here depend on the height and period of the wave, size and density of the sediment, and depth and density of the water.

Background

Artificial beach nourishment is a widely popular form of storm damage reduction. Good uses for dredged sands that improve cost-to-benefit ratios of inlet channel maintenance are of keen interest to coastal managers. Much of the sand dredged continually to maintain navigation can be used to reduce coastal storm damages. Several new uses involve designing submerged mounds to either shelter adjacent shorelines from erosive waves or cost-effectively augment the natural sediment supply to the coast (Bodge 1994 a 1994b; Foster, Healy, and de Lange 1996; Hands and Resio 1994; Landin, Davis, and Hands 1995; Stive et al. 1992). Motivated by the need for an easy method to determine which conditions move sand onshore and offshore, we found two velocity parameters to be effective predictors in widely disparate transport situations.

DEFINITION OF PARAMETERS

Both parameters are ratios of near-bed oscillatory peak speeds (NOPS) to the sediment threshold speed, i.e., $U \equiv u_{d \max} \div u_{\text{crit}}$, where $u_{d \max}$ is the NOPS and u_{crit} is the threshold speed required to initiate motion of selected grain sizes. As waves approach shore, orbital speeds increase under narrowing crests while decreasing under widening troughs. A pair of parameters results if a nonlinear theory is used to evaluate U separately under the wave crest (U_c) and trough (U_T). Differences ($U_c - U_T$) may be crucial especially in contrasting nearshore transport effects of steep storm waves versus gentle swell.

METHODS OF APPLICATION

NOPS were determined from Dean's (1974) Stream Function Wave Theory (SFWT). SFWT contains the crucial nonlinearities and is easy to apply because extremely accurate regression equations were developed in this study for a suitably wide range of conditions ($0.002 \leq d/L_0 \leq 0.20$ and $H_b/4 \leq H \leq H_b$, where d is water depth, L_0 is the deepwater wave length, H is local wave height, and H_b is the breaking wave height).

Under the wave crest,

$$u_{-d \max c} = \left(\frac{H}{T} \right) \left(\frac{d}{L} \right)^{-0.579} e^{0.289 - 0.491(H/d) - 2.97(d/L_o)} \quad (1)$$

where T is the wave period and L is the local wave length. Under the trough,

$$u_{-d \max t} = - \left(\frac{H}{T} \right) e^{1.996 - 1.73(H/d) - 8.70(d/L_o) + 5.58(H/L_o)} \quad (2)$$

More information on fitting near-bed speeds to Stream Function Wave Theory will be provided in Ahrens and Hands 1997.

If the representative grain size $d_{50} \leq 2 \text{ mm}$, threshold speeds come from Hallermeier (1980)

$$u_{crit} = \sqrt{8 \gamma g d_{50}} \quad (3)$$

where γg is the grain to fluid ratio of unit submerged weights. If $d_{50} > 2 \text{ mm}$, threshold speeds come from Komar and Miller (1974)

$$u_{crit} = \left[0.47 \gamma g T^{1/4} (\pi d_{50})^{3/4} \right]^{4/7} \quad (4)$$

For application to long-term fates of submerged mounds, where wave conditions fluctuated over a wide range, NOPS were calculated for an arbitrary, but common representation for wave extremes: the 12-hr/year exceedance value. Threshold speeds were calculated based on median grain sizes as sampled soon after mound placements.

For discrimination between beach erosion and accretion, the threshold speeds were calculated for the reported typical beach grain sizes. The breaker depth was selected as a reasonable standard location at which threshold ratios (U_c and U_T) are compared. This reference depth was obtained by fitting a breaker depth index to the SFWT data to obtain

$$d_b = 0.68 \left(\frac{L_o}{2\pi} \right) \ln \left(\frac{1+s}{1-s} \right) \quad (5)$$

where $s = H_b / 0.171 L_o$ and H_b comes from Kaminski and Kraus's (1993) expression for the breaker height index

$$\frac{H_b}{H_o} = 0.46 \left(\frac{H_o}{L_o} \right)^{-0.26} \quad (6)$$

RESULTS

The skill of these new U parameters is determined by applying them to a number of published laboratory and field studies. The single parameter U_T shows considerable and unsuspected skill in predicting erosion or accretion of beaches. Surprisingly, the seaward-directed component better discriminates between eroding and accreting beaches. Combining both parameters, U_C and U_T , explains observed movement of the 11 test mounds.

Response of Shore Profiles from Large Wave Tank Tests

Larson and Kraus (1989) published results from two sets of large-scale wave tank tests. One set was run with monochromatic waves at the Coastal Engineering Research Center (CERC) (Saville 1957). The other set was run at the Central Research Institute of Electric Power Industry in Japan (CRIEPI) (Kajima et al. 1982). Deep-water wave heights were in the range of $0.30 < H_o < 1.78$ m, wave periods were in the range of $3.0 < T < 16.0$ sec., and sediment sizes were in the range of $0.22 < d_{50} < 0.47$. These laboratory conditions thus cover a wide range of prototype conditions.

Erosional profiles had no berm above uprush and at least one pronounced bar offshore; *accretional* profiles had a prominent berm and no bar formations. Kraus et al. (1991) has shown that H_o/L_o and $H_b/w_f T$, where w_f is the sediment fall velocity, correctly categorize these two types of storm profile changes. Dalrymple (1992) combined Kraus's two variables into a single profile change predictor.

Figure 1 shows *accretional* (A) and *erosional* (E) profile responses as functions of U_C and U_T . Profile transitions during the storms were *erosional* if U_T was less than a critical value near -2. In other words, if magnitude of NOPS under the trough was greater than twice the grain threshold speed, the storms ended with *erosional* profiles. Otherwise profiles became *accretional*. Even events with high U_C values remained *erosional* so long as the critical value of U_T remained less than -2.

Skill is a simple statistical measure for quantifying the performance of a categorical predictor on a given set of data (Seymour and Castel 1989). *Skill* equals the ratio of correct predictions to total observations. Using $U_T = 1.8$ as a threshold level, there is one miscategorized erosion and one miscategorized accretion in the 32 tank results, for a predictive skill of 0.94.

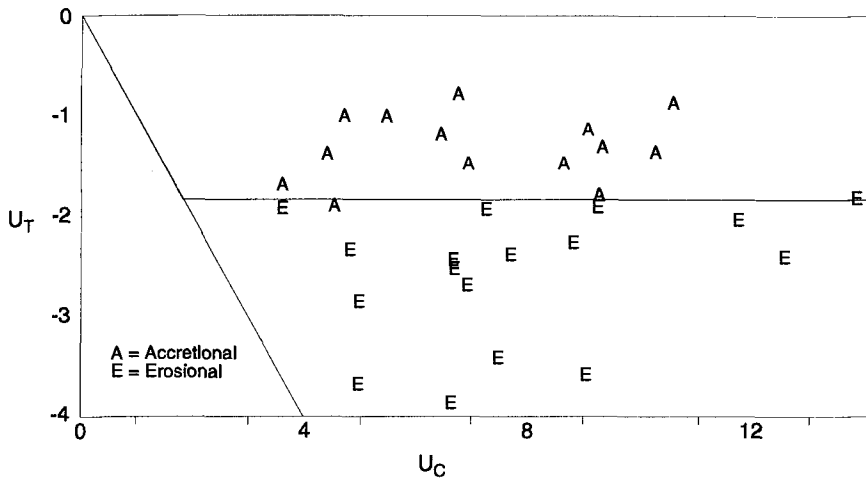


Figure 1 Large wave tank data

Storm Response of Shore Profiles from Field Measurements

Kraus and Mason (1991) compiled and standardized 99 cases of storm profile change from field studies published by many researchers worldwide. Seventy-two cases were *erosional*. Twenty-seven were *accretional*. To qualify as *accretional* the storm had to have resulted in a notable seaward advance of the shoreline, a buildup of the subaerial berm, or a landward movement of the longshore bar. Kraus et al. (1991) used this data set, along with the previously presented results from large wave tank tests, to develop discriminators between *erosional* and *accretional* storms. In the field data set, deepwater significant wave heights ranged from 0.08 to 7.90 m, wave periods from 2.0 to 15.3 sec, and sediment sizes from 0.17 to 3.5 mm. Wave periods were associated with either deepwater significant wave height or the spectral peak.

Accretional and *erosional* type profiles are denoted in Figure 2 as functions of U_C and U_T . U_T discriminates well between *erosional* and *accretional* profiles at a value around -2, just as for the laboratory data. And if $U_T < -2$, *erosional* profiles occur even if U_C is quite large.

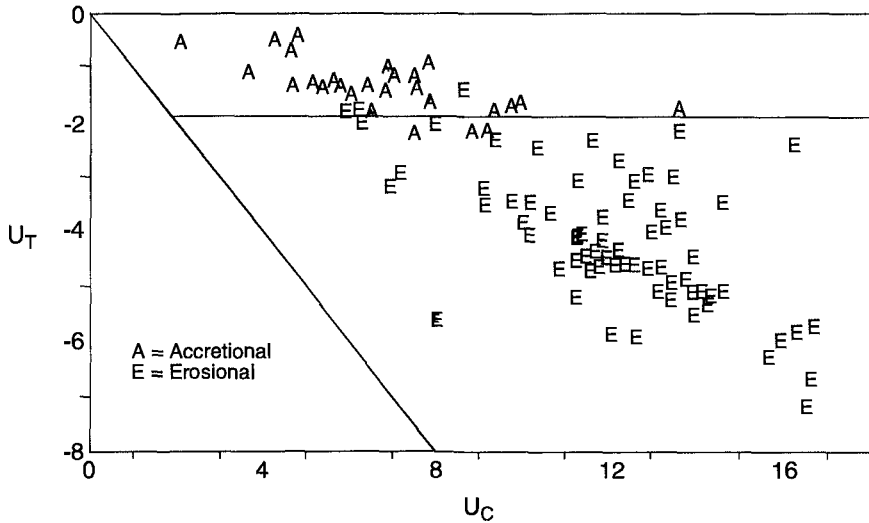


Figure 2 Field beach profile data

Using $U_T = -1.90$ as the discriminator, three cases are miscategorized as *erosional* and three are miscategorized as *accretional* in this field data set of 99, for a predictive skill (0.94) similar to that of previously proposed criteria. The skill of Dalrymple's (1992) criterion on this field data is 0.94 and the favored pair one of eight criteria examined by Kraus et al. (1991) had a skill of 0.91. Largely by coincidence, the skill of U_T on field and laboratory data are identical. More importantly, the critical U_T threshold levels are essentially equal for both field and large wave tank results.

Long-Term Response of Submerged Mounds

Nearshore placement of feeder deposits is an increasingly attractive form of erosion protection offering a variety of environmental, social, and economic benefits (Bodge 1994a and b; Bruun 1988; de Lange and Healy 1994; Foster, Healy, and de Lange 1994; Foster, Healy, 1996; Mulder, van de Kreeke, and van Vessem 1995; Roelvink and Stive, 1988; Russell, Robinson, and Soward 1994; Uda, Naito, and Kanda 1991; Zenkovich and Schwartz 1987). Hands and Allison (1991) compiled results from feeder mound tests and developed criteria to distinguish between stable nearshore deposits and others that moved promptly shoreward. Those mound criteria were used to identify conditions where dredged material mounded outside the surf zone acts not only as a temporary wave dissipator, but also gets pushed shoreward to nourish the surf zone.

Eleven reference mounds monitored in the United States have been categorized as *active* or *stable* depending on whether repeated surveys indicated significant loss of material from the placement area. All but one of the *active* cases showed clear shoreward displacement of mound centroids. Evidence of change was always identifiable within months. *Stable* mounds remained stationary without evidence of dispersion or displacement for years (Hands 1991). Wave forces appear to be the dominant factor in moving mounds landward (Hands and Resio 1994, Douglass, Resio, and Hands, 1995). There has never been strong evidence of any seaward movement at the test sites.

Table 1 lists the locations of all 11 field test mounds, pre-mound water depths, median grain sizes of placed material (d_{50}), wave parameters, and indicators of which mounds were *active* (A) and which *stable* (S).

Table 1 Dredged Mound Data

Site Location	Mound Depth (m)	Smaller of $H_{99.863}$ or H_b (m)	\bar{T}_A (sec)	Grain Size d_{50} (mm)	Stable or Active	U_C	U_T
Long Island, NY	4.6	2.4	8.0	0.40	A	7.20	-3.27
Long Branch, NJ	11.6	2.9	8.0	0.23	S	6.25	-5.38
Atlantic City, NJ	5.8	2.5	8.0	0.35	S	7.16	-3.98
Dam Neck, VA	10.4	3.4	10.0	0.08	S	15.39	-10.06
Dam Neck, VA (crest)	7.6	3.1	10.0	0.08	A	16.97	-9.36
New River, NC	2.1	1.6*	7.0	0.50	A	6.62	-1.63
Sand Island, AL (berm)	5.8	2.2	9.1	0.20	A	8.96	-4.63
Sand Island, AL (mound)	5.6	2.2	9.1	0.22	A	8.63	-4.34
Brazos, TX	8.1	2.8	10.0	0.13	A	11.88	-6.79
Silver Strand, CA	5.8	2.3	16.7	0.22	A	10.70	-2.82
Santa Barbara, CA	6.7	1.4	15.0	0.20	S	6.66	-2.65
Humboldt, CA	15.8	7.6	14.3	0.23	A	16.29	-8.01

* = only case with $H_b > H_{99.863}$

To test the velocity ratios, the full time series of waves were transformed to each mound from the nearest offshore Wave Information Study hindcast site. Velocity ratios were evaluated using transformed spectral peak heights and average associated peak periods, T_A , i.e., the average period of all waves having a height within 0.1 m of the 99.863 percentile nonexceedance wave height ($H_{99.863}$). This wave height was chosen

to match Hallermeier's (1980) selection of the 12-hr/ year exceedance wave height as the determinate for beach profile zonation. Use of $H_{99.863}$ to calculate the velocity ratio is also consistent with its use in the Empirical BERM model (Hands and Resio 1994). In only one case would this extreme wave have broken before passing over the mound. It seems reasonable in such a case to use the H_b estimated from SFWT. Both approaches gave identical results, however, to within the two significant figures used here.

Mound responses are denoted in Figure 3 as functions of U_C and U_T . In the mound situation, U_T alone is a poor discriminator. U_C and U_T are both needed. *Stable* mounds have smaller values of U_C than active mounds for approximately equivalent values of U_T . The $U_C = U_T$ line indicates the limiting condition for NOPS which is reached only by linear waves. Above this line a curve follows the trend between *active* and *stable* mounds.

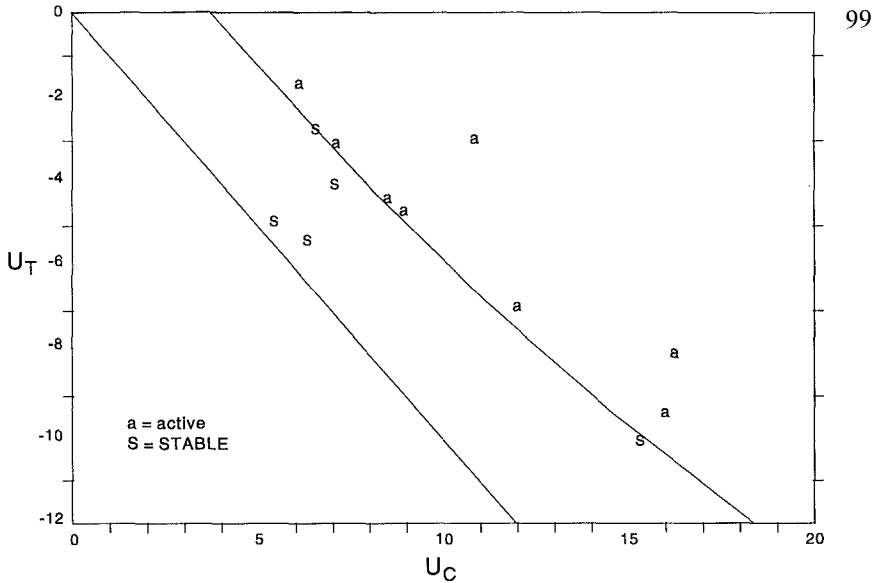


Figure 3 Field mound response data

Bivariate classification of the reference mounds does not imply one should expect unambiguous behavior at future mounds. An ill-defined zone of uncertainty separates the two classes. Occurrence of a severe storm or extended periods of unusual calm will affect a mound's response and the accuracy of any climatological-based prediction. And the role of unusual storms should be most critical for the mounds in the transition zone separating expected *stable* and *active* regions.

Earlier Approach for Mound Predictions

Hallermeier (1977) proposed a sediment entrainment parameter to characterize fluid motion at the onset of intense bed agitation. This parameter had the form of a Froude number which Hallermeier (1980) simplified using linear wave theory to obtain his two profile zonation limits. Hands (1991) used dimensionless ratios of these profile limits to mound depths as feeder-berm citing criteria. Linear theory was also used to show that the distributions of predicted near-bed oscillatory speeds from hindcasted waves could be used to distinguish between *active* and *stable* mound sites (ibid.). The new approach, presented here, is the first attempt we know to improve mound predictions by advancing beyond linear wave theory.

Revised Approach for Evaluation of Nonlinear Oscillatory Speeds

Threshold ratios presented here are very much works in progress. The form of the threshold ratios, the theory and procedure for evaluating oscillatory speeds, and alternative methods for summarizing distributions have not been thoroughly explored. We briefly examined the impact of basing the criteria on deepwater, local, and breaking wave heights; fitting $u_{-d \max}$ instead of U to SFWT, and optimizing fit in terms of U_T instead of to both U_T and U_C because only the single criterion seems necessary for erosion prediction. These variations led to considerable differences in the spread of U_T and U_C values, yet, each of these versions support the same conclusions except for small adjustments as to the best critical values. With different versions, the critical U_T for beach erosion field data ranged from -1.8 to -2.3. Present uncertainties about sediment transport and the limited available prototype data do not support refinement of details. Fortunately threshold ratios seem to be robust with respect to tested methods of evaluation.

SUMMARY

Simple threshold ratios indicate tendencies for waves to drive cross-shore sediment fluxes. These ratios combine oscillatory peak speeds with initiation of movement criteria. The given equations are applicable over a wide range of indicated wave conditions and sediment sizes. Results from testing these ratios against known laboratory and field data produce trends consistent with present understandings of onshore and offshore sediment movement under waves.

The single parameter U_T shows considerable and unexpected skill (0.94) in distinguishing between beach erosion and accretion. Surprisingly, the speed under the trough is more diagnostic than under the crest. In fact U_C seems to be unimportant for predicting the shore profile change. Both parameters, U_T and U_C , are necessary, however, to predict responses of nearshore mounds built of sand- to silt-sized dredged material. While experiences with mounds is limited and many cases cluster close to the discrimination boundary, the present approach has an advantage over previous methods given by Hands (1991), because U captures the inherent nonlinearity of waves nearshore

and provides a logical explanation for the noted preferential shoreward movement of *active* mounds.

CONCLUSIONS

Admittedly, this presentation does not investigate the mechanics of sediment motion and thus does not offer a general solution to cross-shore coastal transport. Nevertheless, we hope our results focus more attention on what certainly seems to be the dominant effect of nonlinear wave motion in some important coastal situations. The success of U criteria over the demonstrated range of wave conditions, water depths, and grain sizes seems to justify their adoption as simple decision criteria needed now to help manage coastal sediment resources. For long-term mound movement, the option of using a more encompassing parameter to represent ranges of near-bed fluid motion seems promising as an easy improvement that should characterize the net effect of the range of waves impacting mounds over their months and years of migration. On a spatial scale, some broader measure of surf conditions may offer improvements over the simple default to breaker conditions tested first.

Obviously, however, wave effects are more complex than can be represented by peak bottom speed and many other factors affect sediment motion (e.g., bottom slope, bed forms, cohesive particle forces, and other currents). Net effects of wave groupiness, undertow, grain inertia, and intra-wave phase lags between stress and sediment concentration and a time-varying eddy viscosity are simply lumped in a single critical ratio. The fact that such a simple characterization as U , even with reduction of NOPS distributions to a default percentile, produced a more than acceptable correlation with laboratory and field data, will hopefully spark theoretically based improvements.

ACKNOWLEDGMENTS

Support from the NOAA Sea Grant Office and the U.S. Army Engineer Waterways Experiment Station is acknowledged, especially the recently concluded Dredging Research Program for collecting mound response data and the new Dredging Operations and Environmental Research Program for follow-on analyses. Comments and suggestions from Mr. Thomas W. Richardson and Drs. Nicholas C. Kraus and Andrew Morang were very helpful and are greatly appreciated. The first author received permission from Headquarters, U.S. Army Corps of Engineers, to publish this information.

REFERENCES

Ahrens, J. P., and Hands, E. B. 1997. "Velocity Parameters, for Predicting Cross-Shore Sediment Movement," in preparation for *Journal of Waterway, Port, Coastal and Ocean Engineering*, ASCE, NY.

- Bodge, K. R. 1994a. "Performance of Nearshore Berm Disposal at Port Canaveral, Florida," *Proceedings 2nd International Conference Dredging and Dredged Material Placement, Dredging '94*, ASCE, NY, 1182-1191.
- Bodge, K. R. 1994b. "Performance Of 1992/93 Nearshore Berm Disposal At Port Canaveral, Florida," *Proceedings Beach Preservation Technology 1994*, L.S. Tait, ed., Florida Shore & Beach Preservation Association, Tallahassee, FL, 285-301.
- Bruun, P. 1988. "Profile Nourishment: Its Background And Economic Advantages," *Journal of Coastal Research*, 4 (2) 219-288.
- Dalrymple, R. A. 1992. "Prediction of Storm/Normal Beach Profiles," *Journal of Waterway, Port, Coastal, and Ocean Engineering*, 118 (2) 193-199.
- Dean, R. G. 1974. "Evaluation and Development of Water Wave Theories for Engineering Application," Volumes I and II, Coastal Engineering Research Center Special Report No.1, Fort Belvoir, VA.
- de Lange, W., and Healy, T. 1994. "Assessing The Stability Of Inner Shelf Dredge Spoil Mounds Using Spreadsheet Applications On Personal Computers," *Journal of Coastal Research* 10 (4) 946-958.
- Douglass, S. L., Resio, D. T., Hands, E. B. 1995. "Impact of Near-Bottom Currents on Dredged Material Mounds Near Mobile Bay," Dredging Research Program Technical Report DRP-95-6, U.S. Army Engineer Waterways Experiment Station, Vicksburg, MS.
- Foster, G. A., Healy, T. R., and de Lange, W. P. 1996. "Presaging Beach Renourishment from a Nearshore Dredge Dump Mound, Mt. Maunganui Beach, New Zealand," *Journal of Coastal Research* 12 (2) 395-504.
- Foster, G. A., Healy, T. R., and de Lange, W. P. 1994. "Sediment Budget and Equilibrium Beach Profiles Applied To Renourishment of an Ebb Tidal Delta Adjacent Beach, Mt-Maunganui, New Zealand," *Journal of Coastal Research* 10 (3) 564-575.
- Hallermeier, R. J. 1977. "Calculation of a Yearly Limit Depth to the Active Beach Profile," Technical Paper 77-9, U.S. Army Engineer Coastal Engineering Research Center, Ft. Belvoir, VA.
- Hallermeier, R. J. 1980. "Sand Motion Initiation by Water Waves: Two Asymptotes," *Journal of Waterway, Port, Coastal, and Ocean Engineering* 106 WW3 299-318.
- Hands, E. B., and Resio, D. T. 1994. "Empirical Guidance for Siting Berms to Promote Stability or Nourishment Benefits," *Proceedings 2nd International Conference*,

Dredging and Dredged Material Placement, Dredging '94, Buena Vista, FL, ASCE, NY, 220-228.

Hands, E. B. 1991. "Unprecedented Migration Of a Submerged Mound Off the Alabama Coast," *Proceedings 12th Conference Western Dredging Association and 24th Annual Texas A&M Dredging Seminar.*, ed., Center for Dredging Studies, College Station, TX, 245-269.

Hands, E. B., and Allison, M. C. 1991. "Mound Migration in Deeper Water and Methods of Categorizing Active and Stable Depths," *Proceedings Specialty Conference on Quantitative Approaches to Coastal Sediment Processes, SEDIMENTS '91*, Seattle, WA, ASCE, NY, 2, 1985-1999.

Kajima, R., Shimizu, T., Maruyama, K., and Saito, S. 1982. "Experiments of Beach Profile Change with a Large Wave Flume," *Proceedings 18th International Coastal Engineering Conference*, ASCE, NY, 1385-1404.

Kaminski, G. M., and Kraus, N. C. 1993. "Evaluation of Depth-limited Wave Breaking Criteria," *Proceedings Ocean Wave Measurement and Analysis Conference*, New Orleans, LA, ASCE, NY, 180-193.

Komar, P. D., and Miller, M. C. 1974. "Sediment Threshold under Oscillatory Waves," *Proceedings 14th International Coastal Engineering Conference*, ASCE, NY, 756-775.

Kraus, N. C., Larson, M., and Kriebel, D. L. 1991. "Evaluation of Beach Erosion and Accretion Predictors," *Proceedings Coastal Sediments '91*. N. C. Kraus, K. J. Gingerich, and D. L. Kriebel, eds., ASCE, NY, 572-587.

Kraus, N. C., and Mason, J. G. 1991. "Field Data Set for Testing Beach Erosion and Accretion predictive Criteria," Memorandum for Record, Coastal and Hydraulics Laboratory, U.S. Army Engineer Waterways Experiment Station, Vicksburg, MS.

Larson, M., and Kraus, N. C. 1989. "SBEACH: Numerical Model for Simulating Storm-Induced Beach Change," Report 1: Empirical Foundation and Model Development, TR CERC 89-9. U.S. Army Engineer Waterways Experiment Station, Vicksburg, MS.

Landin, M. C., Davis, J. E., and Hands, E. B. 1995. "Wetland Restoration, Underwater Features, and Other Beneficial Uses, A Phase I Report on the Delaware Bay Deepening Project," U.S. Army Engineer District, Philadelphia, PA.

- Mulder, J. P. M., van de Kreeke, J., and van Vessem, P. 1995. "Experimental Shoreface Nourishment, Terschelling (NL)," *Proceedings 24th International Coastal Engineering Conference*, B.L. Edge, ed., ASCE, NY, 2886-2899.
- Roelvink, J. A., and Stive, M. J. F. 1988. "Large Scale Tests of Cross-Shore Sediment Transport on the Upper Shoreface," *Proceedings of the Symposium on Mathematical Modelling of Sediment Transport in the Coastal Zone*, Copenhagen, Denmark, IAHS, Washington, DC, 137-147.
- Russell, R. J., Robinson, D. A., and Soward, C. L. 1994. "Southern Gold Coast Beach Nourishment Project: Implementation, Results, Effectiveness," *Terra et Aqua* 66, 12-23.
- Saville, T. 1957. "Scale Effects in Two Dimensional Beach Studies," *Transactions 7th General Meeting International Association of Hydraulic Researchers*, 1 A3.1-A3.10, IAHS, Washington, DC.
- Stive, M. J., de Vriend, H. J., Nicholls, R. J., and Capobianco, M. 1992. "Shore Nourishment and the Active Zone: a Time Scale Dependent View," *Proceedings 23rd International Conference Coastal Engineering*, B. L. Edge, ed., ASCE, NY, 2464-2473.
- Uda, T., Naito, K., and Kanda, Y. 1991. "Field Experiment On Sand Bypass Off the Iioka Coast," *Coastal Engineering in Japan* 34 (2) 205-221.
- Zenkovich, V. P., and Schwartz, M. L. 1987. "Protecting the Black Sea-Georgian SSR Gravel Coast," *Journal of Coastal Research* 3 (2) 201-209.

CHAPTER 262

Small-scale Morphology Related to Wave and Current Parameters Over a Barred Beach

A.F. Garcez Faria¹, E.B. Thornton¹, T.P. Stanton¹

ABSTRACT: Small-scale morphology (< 5 m horizontal wavelength) was measured by combining CRAB surveys with bed elevations acquired from a 1 MHz sonic altimeter mounted on the CRAB during the DUCK94 experiment in October 1994. Bedform plan views were recorded simultaneously using a 500 KHz side-scan sonar mounted on the CRAB. Waves and currents were measured at the same time. Three cases are examined in detail: mild waves and weak longshore currents resulting in wave ripples throughout the study area; narrow-band, normally incident waves with a strong rip current resulting in a planar bed except in the throat of the rip where mega-ripples were measured; and storm waves with strong longshore currents resulting in lunate and straight-crested mega-ripples in the trough of the barred beach. During these strong current days, bed shear stresses calculated from logarithmic velocity profiles are equated to a quadratic bottom shear stress formulation. The associated bed shear stress coefficients vary by more than an order of magnitude across the surf zone (0.0006-0.012). Bottom roughness was obtained by calculating the wavenumber spectra of the bed. The bed shear stress coefficients are positively correlated with bottom roughness (linear correlation coefficient, 0.68). A higher linear correlation coefficient (0.80) is obtained by subtracting skin friction from the total bed shear stress.

INTRODUCTION

The nearshore bed on a barred beach is composed of complex bedforms caused by varying wave and current regimes. With the exception of wave ripples in deeper water, few quantitative observations of bedforms are available, especially in the nearshore, and simultaneous quantitative wave and current measurements are almost non-existent. The lack of data is due to difficulties in making measurements in the nearshore. Observations historically have been made by divers who are limited by visibility and the harsh nearshore environment, which can become unfavorable for observations even in the mildest of storms.

Earlier field measurements were reported by Dingler and Inman (1976), which profiled wave ripples using a moveable acoustic altimeter placed on a track on the bottom outside the surf zone, but were limited to a single track of approximately 2 m in length. Other methods have included using waxed combs pushed into the bed by divers to record ripple profiles. Miller and Komar (1980) found ripple wavelength to be related to the orbital diameter of the waves.

The measurements described in this paper were made in shallow water (< 8 m) where shoaling and breaking waves are typically asymmetric, resulting in asymmetric bedforms. A conceptual view of wave-induced small-scale morphology on a barred beach is summarized by Clifton (1976) based on diver observations, which describes the asymmetric transition of bedforms with increasing velocity from long-crested

¹Oceanography Department, Naval Postgraduate School, Monterey, CA, 93943-5000, USA; E-mail: faria@oc.nps.navy.mil; Tel: +1 408 656 2379; Fax: +1 408 656 2712.

ripples, to irregular ripples, to cross-ripples, to lunate mega-ripples on the seaward slope of the bar, to a planar bar crest where the waves break, and to wave ripples again in the trough where wave intensity decreases after waves cross the bar. These are the least observed nearshore bedforms owing to difficulties in obtaining quantitative measurements.

The objective of this paper is to correlate small-scale morphology measured over a barred beach with waves and currents. In the following sections, a description of the DUCK94 experiment, the methodology of the data analysis, the description of the small-scale morphology observed on Oct. 8, 12, and 20, and the relationship between measured bottom roughness and bed shear stress are presented.

DUCK94 EXPERIMENT

The measurements described here are part of the comprehensive nearshore DUCK94 experiment conducted during October 1994 at the U.S. Army Corps of Engineers Field Research Facility (FRF), Duck, North Carolina. The weather during October was climatologically characterized by three distinct phases: weak currents and winds from the north (4-9 Oct.), relatively strong currents from the north (0.6-1.0 m/s) caused by a storm with predominant winds and waves from the north (10-12 Oct.), and variable currents and winds from the north/south (13-21 Oct.).

The morphology of the bottom (bathymetry) was measured at various scales using the Coastal Research Amphibious Buggy (CRAB). The surveys were performed daily during the experiment by driving the CRAB in a series of cross-shore survey lines with alongshore separation of 25 to 30m. Large-scale variations of bathymetry were obtained by recording the CRAB position using a laser ranging/auto-tracking system approximately every meter (order 3 cm rms vertical and horizontal accuracy). Three-dimensional, large-scale morphology mapped by the CRAB during the three periods of interest (8, 12, and 20 Oct.) are shown in Fig. 1.

Small-scale vertical bottom variations relative to the CRAB, including ripples and megaripples, were measured with a 1 MHz sonic altimeter mounted on the CRAB 70 cm from the bed. The altimeter has a nominal sampling rate of 25 Hz, which resulted in a sample spacing of 2-4 cm (dependent on CRAB speed) with mm vertical resolution and accuracy less than 2 cm (Gallagher *et al.*, 1995). The decrease in accuracy relative to resolution is due to the changing reflective surface owing to the bed dialating or sediment transported along the bed as waves pass overhead. The CRAB survey and altimeter measurements were combined to obtain a high resolution description of the bottom (Thornton *et al.*, 1996).

A 500 KHz side-scan sonar suspended in the center of the CRAB approximately 1.25 m from the bed generates high-resolution plan views of the morphology. The nominal horizontal range of the sonar was approximately 10 to 15 m to each side of the sonar, which allowed overlap of sonar data from adjacent survey lines, giving a relatively complete view of the geometry and spatial representation of the ripple features.

Corroborating wave and current data were acquired using an instrumented sled. A vertical stack of eight Marsh-McBirney two-component electromagnetic

current meters (cm's, hereafter) with 2.5 cm diameter spherical probes were mounted on a 2.5 m mast to measure vertical profiles of longshore and cross-shore currents. The sled was oriented with the vertical stack of current meters placed on the up-current side to prevent the sled structure from contaminating flow measurements. Waves and mean water level were measured using an array of five pressure sensors configured in a 3 m square with sensors at the corners and one at the center. For data collection, each morning the sled was towed by the CRAB to its furthest position offshore, dependent upon wave conditions, for the first data run. A forklift on the beach pulled the sled shoreward approximately 10 to 30 m for each subsequent run. Data were acquired at each location for approximately one hour at four to eight locations. Additionally, directional wave spectra were acquired using a linear array of 10 pressure sensors in 8 m depth offshore of the survey area.

METHODOLOGY

The bottom roughness is examined by calculating wavenumber spectra of the bed. To calculate wavenumber spectra, the unevenly spaced data from the combined CRAB surveys and altimeter measurements are linearly interpolated to evenly spaced 2 cm increments of the cross-shore distance. The small-scale morphology in general shows large cross-shore variation; as a consequence, the condition of spatial homogeneity (stationarity) required for calculating averaged spectra is not met. Therefore, continuous wavenumber spectra are calculated for 20 m cross-shore segments at increments of 1 m across the surf zone. Lowest wave numbers are filtered by subtracting a third-order polynomial best-fit curve from each 20 m section. A 10 percent eosine-taper data window is applied. The spectra are summed over three wavelength bands (0.4 - 0.83 m, 0.83 - 1.67 m, and 1.67 - 5 m) plus the total band (0.4 - 5 m), resulting in 52, 24, 16, and 92 degrees of freedom for each band respectively. The wavelength bands chosen are based on examination of individual spectra that were generally broad, indicating that several ripple wavelengths coexisted as a result of newly formed ripples combining with residual ripples from the past to form a complex series of ripple patterns. The *rms* height of each band is calculated as the square root of the variance within each band. The general trend is that the bottom was smoothest offshore and over the bar where wave ripples were planed-off due to higher near-bottom velocities, with increased roughness within the trough associated with mega-ripples (see Thornton, *et al.*, 1996, for details).

Linear shear stress gradients occur in flows driven by constant hydrostatic pressure gradients, such as in steady open channel flows, are well described by a logarithmic velocity profile. Therefore it is hypothesized that a steady, uniform, turbulent boundary layer flow over a rough surface in the alongshore direction can be described by a logarithmic profile:

$$V(z) = \frac{v_*}{\kappa} \ln \left(\frac{z + h}{z_o} \right) \quad (1)$$

where z is positive upwards from the surface, h is the mean water depth, κ is the Von Karman constant (0.4), v_* is the alongshore shear stress velocity and z_o is the physical roughness height, determined by bottom topography and sediment grain size. When waves are present, nonlinear interactions between waves and currents within the bottom boundary layer increase the bottom shear stress. Following Grant and Madsen (1979), this additional stress can be modeled by an apparent roughness height z_a , that is analogous to, but larger than z_o . Logarithmic profiles are fit to the data based on a linear-regression least-squares method. The value of z_a is calculated from the z intercept of the linear-regression on a semi-log plot of z versus $V(z)$, and the shear stress velocity v_* is calculated from the slope.

Mean along shore bottom shear stress ($\overline{\tau_y(-h)}$) is related to the alongshore shear stress velocity (v_*) through (overbar indicates time averaging)

$$\overline{\tau_y(-h)} = \rho v_*^2 \quad (2)$$

where ρ is water density. In addition, the bed shear stress coefficient, C_f , can be calculated assuming a quadratic bed shear stress relationship

$$\overline{\tau_y(-h)} = \rho C_f \overline{(u^2 + v^2)^{1/2} v} \quad (3)$$

and combining with (2), gives

$$C_f = \frac{v_*^2}{\overline{(u^2 + v^2)^{1/2} v}} \quad (4)$$

C_f values are calculated using measured velocities (u, v) at the elevation of 1 m above the bed, with v_* determined by least-squares log fit (Garcez Faria *et al.*, 1996).

DISCUSSION

October 8 Morphology

The large-scale morphology on Oct. 8 at first glance appears to be relatively homogeneous. The offshore bar is nearly parallel to the shore and is located approximately 230-250 m offshore (Fig. 1). Therefore, it would be expected that the small-scale morphology would also be homogenous alongshore throughout the survey area given the same wave and current conditions. However, close examination shows that the small-scale morphology is not homogeneous and that ripple patterns vary both in the cross-shore and alongshore directions.

Two representative lines (710 and 940 m along shore coordinate) of cross-shore combined CRAB and altimeter profiles are selected to depict the differences present in the small-scale morphology for the survey area (Fig. 2). The primary differences in the ripple dimensions between the two representative lines are observed in the trough and the seaward slope of the bar. The small-scale morphology in the trough of line 940 is predominantly long wavelength mega-ripples (1.67-5 m)

with shorter wavelength wave ripples superimposed on them. The trough region of line 710 has a more homogeneous ripple pattern in which no wavelength band predominates. The seaward slope of the bar on line 940 shows the ripple wavelength bands of 0.83-1.67 m and 1.67-5 m are dominant and the rms height is on the order of 3 cm. The seaward slope of the bar on line 710 shows relatively homogeneous ripple wavelengths with rms heights of approximately 2 cm.

October 20 Morphology

The most striking observation on the 20th is the hole in the bar with the bar bowed seaward due to the rip current between 800 and 1100 m in alongshore coordinates (Fig. 1). The bar is parallel to the beach and is located approximately 210-225 m offshore north of the rip area, shifting to greater than 300 m offshore in the rip area. The narrow trough, north of the rip area, acts as a rip-feeder channel and has the same small-scale morphological features as the rip area. The dominant small-scale morphology observed in the rip area are seaward-facing lunate and straight-crested mega-ripples. The mega-ripples were generally asymmetric with the steep slope facing seaward indicating the ripples were formed primarily as a result of the rip current. However, some ripples were symmetric while others were asymmetric facing toward the beach, which may infer a more complex formation due to a combination current and wave interactions. The area immediately north and south of the rip current is void of any discernable small-scale morphology with the exception of the rip-feeder channel. Typical rms roughness values in the rip area range from 5 to 15 cm, which are an order of magnitude larger than rms roughness values away from the rip. A contour plot of rms roughness values for the survey area is shown in Fig. 3, which displays the extreme variability of roughness in the rip current area compared with that of the area away from the rip current. The rip current, as qualitatively observed with dye on the 20th, is superimposed on the accompanying contour plot of the macro-scale bathymetry. The bed is essentially smooth away from the rip current with rms roughness values being less than 2 cm, which appears to be the result of planing action of the long-period swell.

October 12 Morphology

The large-scale morphology of Oct. 12 is similar to that of Oct. 8. The offshore bar is nearly parallel to the beach, but migrated 30 m offshore to approximately 260-280 m offshore (Fig. 1). Although the large-scale morphology is similar for the two days, the small-scale morphology is dramatically different owing to differences in the wave and current conditions associated with the arrival of a storm on Oct. 10. Large amplitude mega-ripples are now present in the trough and no regular bedform patterns are observed seaward of the bar for the entire survey area. The strong longshore current that appeared on the 10th is believed to be the dominant process that formed the small-scale morphology observed in the trough on the 12th.

The small-scale morphology across the surf zone is relatively homogeneous alongshore, and therefore, the survey area is represented by the rms roughness from the combined CRAB and altimeter profile for line 940 (Fig. 4, lower panel), which

is close to the position occupied by the sled. The small-scale morphology in the trough compared with the region seaward of the bar crest are distinctly different. Seaward of the bar the bed is essentially plane, due to intense breaking associated with large waves. In the trough, the rms roughness is primarily associated with the larger ripple wavelengths of 1.67-5 m. Side scan plots showed the mega-ripples in the outer trough to be lunate, facing in the direction of the longshore current; while straight crested in the inner trough.

Bottom Roughness and Bed Shear Stress

The more energetic period (Oct 10-12) is used to relate small-scale morphology to wave and current forcing. The data are qualitatively sorted by location into the two regions of over the bar and in the trough. This sorting allows a better identification of the possible correlations among variables, as wave breaking which is a major controlling factor within the surf zone is significantly different for these regions.

All 22 vertical profiles of longshore currents obtained during these three days are analyzed. The profiles are based on the measurements by three to seven em's over the vertical. The em closest to the sea bed was not used because of malfunction. The observed and logarithmic predicted velocity profiles at successive offshore positions (runs) that the sled occupied during 12 Oct. is shown in the upper panel of Fig 4. The data agree well with the model.

A high correlation coefficient for the linear regression, is commonly accepted as an indicator of the validity of the logarithmic approach (Gross *et al.*, 1994; Li, 1994). The linear correlation coefficients for all profiles ranged from 0.95 to 0.99, with an average value of 0.98, and the largest deviations occurring over the bar, where wave breaking was strong. This can be related to the increase of turbulent mixing due to wave breaking producing a more uniform vertical profile of the current for a given shear stress, compared with profiles in the absence of breaking. Therefore, larger discrepancies between observations and logarithmic profile predictions (lower correlation coefficients) would be expected for increased turbulent mixing caused by wave breaking, as the logarithmic profile presumes no surface turbulence source.

The bottom shear stress coefficient (C_f) varied by an order of magnitude across the surf zone, with the values offshore and over the bar in the order of 10^{-3} , while the values in the trough were in the order of 10^{-2} . An attempt was made to find empirical relationships between C_f with measured physical parameters commonly used throughout the literature such as $|\vec{u}_b| / V$ (ratio of near-bottom wave velocity magnitude to mean current speed), and the rms bottom roughness (r). Surprisingly, no statistically significant correlation was found between C_f and $|\vec{u}_b| / V$. The strongest correlation was found between C_f and the bottom roughness, with C_f increasing with bottom roughness (Fig. 5, upper panel), with a linear correlation coefficient of 0.68, which is statistically significant at the 99.75 percent confidence level. Theoretically this is expected as larger roughness implies larger bottom stress due to form drag, and consequently larger C_f values.

The scatter of data observed in Fig. 5 (upper panel) may be due to correlating the non-synoptic velocity measurements with bottom roughness measured once in the

morning, prior to the positioning of the sled for the first station. Wave forcing changed during the period of observation due to both wind and tidal variations. Changes in wave forcing have a direct effect in the measured velocities and an indirect effect in bottom roughness due to modification of wave ripples associated with variations in wave height.

Another reason for scatter of data arises from C_f values being calculated from the total bottom shear stress, which has stress contributions from skin friction related to sediment grains, waves-current nonlinear interactions within the bottom boundary layer as well as form drag related to bed forms. Smith and McLean (1977) linearly partitioned the total bed shear stress into skin friction and form drag and found good agreement with the data from the Columbia River. Extending this concept to the surf zone environment requires adding a component due to non-linear interactions between waves and currents within the bottom boundary layer to the total bed shear stress. Assuming that the linear stress partition is valid within the surf zone, the skin friction contribution can be removed from the total bottom stress and a new bed shear stress coefficient C_f' is defined

$$C_f' = \frac{v_{*d}^2 + v_{*wc}^2}{(u^2 + v^2)^{1/2} \nu} \quad (5)$$

where v_{*d} and v_{*wc} are the form drag and waves-current interactions shear stress velocities. The relationship between C_f' and the total bed shear stress coefficient (C_f) can be determined from (4) and (5)

$$C_f' = \left[1 - \left(\frac{v_*}{v_*'} \right)^2 \right] C_f \quad (6)$$

where v_* is the skin friction related shear stress velocity. As skin friction was not measured during the DUCK94 experiment, an attempt is made to isolate its contribution from the total bottom shear stress by applying a stress partitioning model. The probabilistic approach used to quantify bottom roughness does not allow the adjustment of the two empirical coefficients C_D and a_1 necessary to apply the Smith and McLean (1977) model. Therefore, the empirical relationships obtained by Li (1994) are used to estimate skin friction shear stress velocity from the total shear stress velocity obtained from the logarithmic profile

$$\frac{v_*'}{v_*} = 0.125 \left(\frac{v_*}{R} \right) + 0.373 \quad \text{for} \quad \frac{v_*}{R} < 2.3 \text{ s}^{-1} \quad (7)$$

$$\frac{v_{*s}}{v_*} = 0.107 \left(\frac{v_*}{R} \right) + 0.266 \quad \text{for} \quad \frac{v_*}{R} \geq 2.3 \text{ s}^{-1} \quad (8)$$

where R is ripple height, assumed here to be equal to the measured *rms* bottom roughness ($R = r$). The recalculated bed shear stress coefficients C_f' (Equation 6) are also positively correlated with bottom roughness (Fig. 5, lower panel), but show a higher linear correlation coefficient (0.80). Theoretically this is expected as the removal of the skin friction component from the total stress should enhance the form drag contribution, and consequently increase the correlation between bed shear stress and bottom roughness.

CONCLUSIONS

Quantitative measurements of small-scale morphology on a barred beach were acquired during the DUCK94 experiment. Three separate sequences are examined in which distinctly different ripple dimensions and bedform types were observed owing to varying wave and current regimes.

The measurements of small-scale morphology on Oct. 8, when mild waves and weak longshore currents prevailed, shows surprising differences within the survey area. The absence of significant variation associated with wave and current forcing suggests that the mega-ripples in the trough of line 940 may be residual from some earlier time of formation, such as on Oct. 3 when a strong longshore current was present.

Oct. 20 is characterized by a rip current with two distinct areas of small-scale morphology. In the throat of the rip current, straight-crested and lunate mega-ripples were observed. The area away from the rip current was void of any ripple patterns as a result of the planing action of the long-period swell.

Oct. 12 is characterized by the occurrence of a strong longshore current. The small-scale morphology of the inner trough region is characterized by relatively straight-crested mega-ripples (1.67-5 m) generated by the waves, superimposed by smaller wavelength ripples $O(1 \text{ m})$. In the outer trough, lunate mega-ripples in the direction of the longshore current predominated. Seaward of the bar, the bed was essentially void of ripples.

The wavenumber spectral results infer a spatial and temporal variability of ripple dimensions in both the cross-shore and alongshore directions. The wavenumber spectra were generally broad, indicating that several ripple wavelengths coexisted as a result of newly formed ripples combined possibly with residual ripples from the past to form a complex series of ripple patterns. This broadening is also due to non-cross-shore (cross-track) orientation of the morphological features.

The vertical structure of mean longshore currents on a barred beach is well described by a logarithmic profile for the three strong longshore current days examined. This hypothesis works better in the trough where turbulent bottom boundary layer processes are more dominant than over the bar, where breaking-wave induced turbulence generated at the surface modifies the profile.

A relationship between bed shear stress coefficients (C_f) and bottom roughness was found. While the relatively small amount of data used (three days) are not enough to establish a definitive empirical relation from the available data, it can be concluded that C_f is directly proportional to bottom roughness, and therefore, the latter is an important parameter to characterize the bottom boundary layer. Surprisingly, only poor correlations of C_f and z_a were found with wave parameters.

The empirical relationships obtained by Li (1994) were used to remove the skin friction contribution from the total bottom shear stress. The improved correlation between bottom shear stress and bottom roughness obtained, although not conclusive to validate these simple expressions, indicates that the linear stress partition concept introduced by Smith and McLean (1977) can be extended to the surf zone environment.

ACKNOWLEDGMENTS

This research was funded by the Office of Naval Research, Coastal Sciences Program, under contract N00114-95-AF-002. The authors wish to express their appreciation to all those who participated in DUCK94 experiment, particularly the staff of the U.S. Army Field Research Facility. In addition, special appreciation is expressed to R. Wyland, Jim Stockel, and Mary Bristow, Naval Postgraduate School, for their role in the acquisition and processing of wave and current data.

REFERENCES

- Clifton, H.E. (1976) "Wave-formed sedimentary structures- A conceptual model." *Beach and Nearshore Sedim., SEPM, Special Publication*, 24, 126-148.
- Dingler, J.R., and Inman, D.L. (1976) "Wave formed ripples in the seashore sands." *Proceedings 15th Coastal Engineering Conference, ASCE*, pp. 2109-2126.
- Gallagher, E.L., Boyd, W., Elgar, S., Guza, R.T., and Woodward, B. (1996). "A performance of a sonar altimeter in the nearshore." *Marine Geology*, 133, 241-248.
- Garcez Faria, A.F., Thornton, E.B., Stanton, T. P., and Soares, C.M.C.V. (1996) "Vertical profiles of longshore currents and related bed shear stress and bottom roughness." *J. of Geophysical Research*, (submitted).
- Grant, W.D., and Madsen, O.S. (1979) "Combined wave and current interaction with a rough bottom." *J. of Geophysical Research*, 84 (C4), 1797-1808.
- Gross, T.F., Williams III, A.J., and Terray, E.A. (1994) "Bottom boundary layer spectral estimates in the presence of wave motions." *Continental Shelf Research*, 14, 1239-1256.
- Li, M.Z. (1994) "Direct skin friction measurements and stress partitioning over movable sand ripples." *Journal of Geophysical Research*, 99(C1), 791-799.
- Miller, M.C., and Komar, P.D. (1980) "A field investigation between oscillation ripple spacing and the near-bottom water orbital motions." *J. Sedimentary Petrology*, 50, 180-191.
- Smith, J.D., and McLean, S.R. (1977) "Spatially averaged flow over a wavy surface." *Journal of Geophysical Research*, 82(C12), 1735-1746.
- Thornton, E.B., Swayne, J.L., and Dingler, J.R. (1996) "Small-scale morphology related to waves and currents across the surf zone." *Mar. Geology* (accepted).

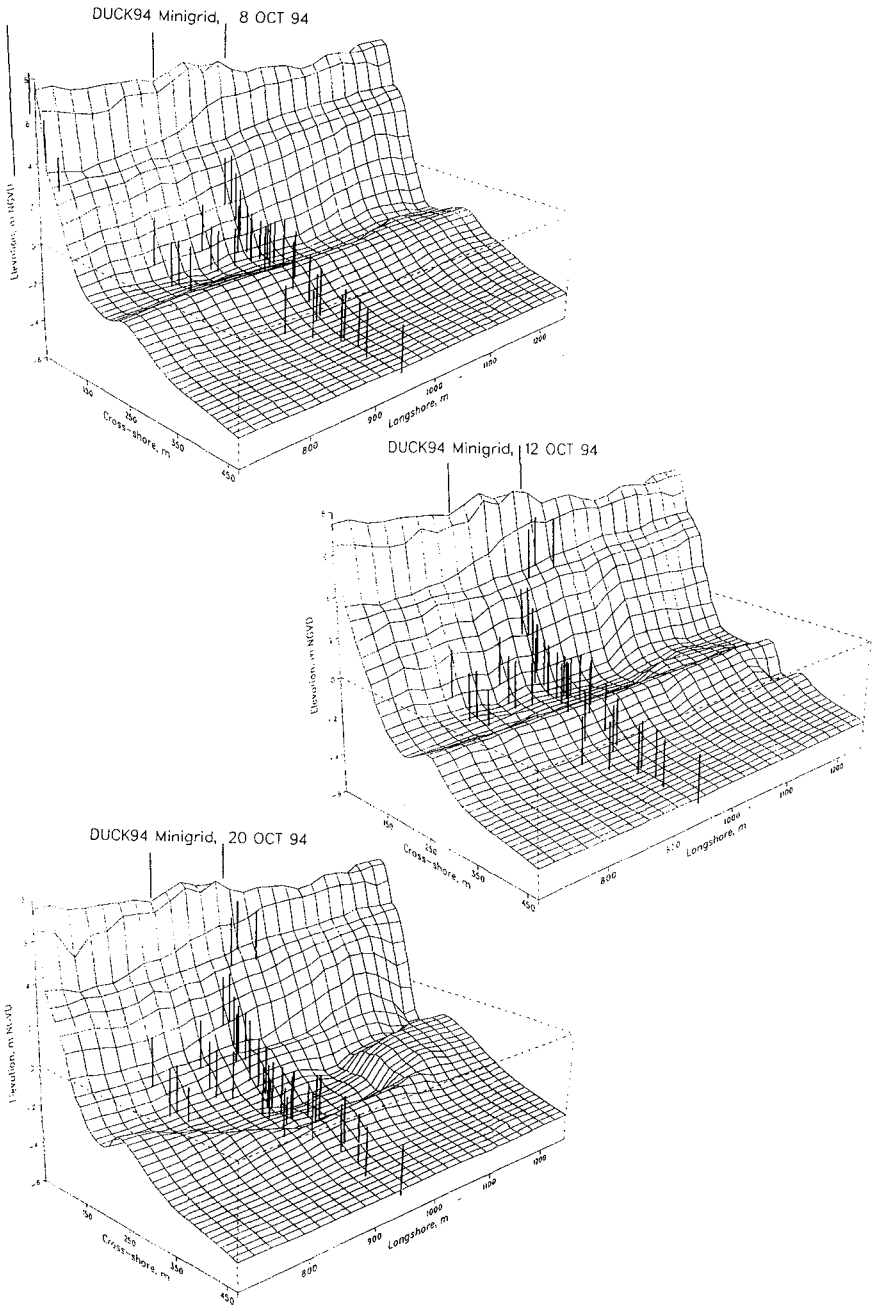


Figure 1. Three-dimensional bathymetry profiles of the survey area as mapped by the CRAB for the three days considered (Oct. 8, 12, and 20).

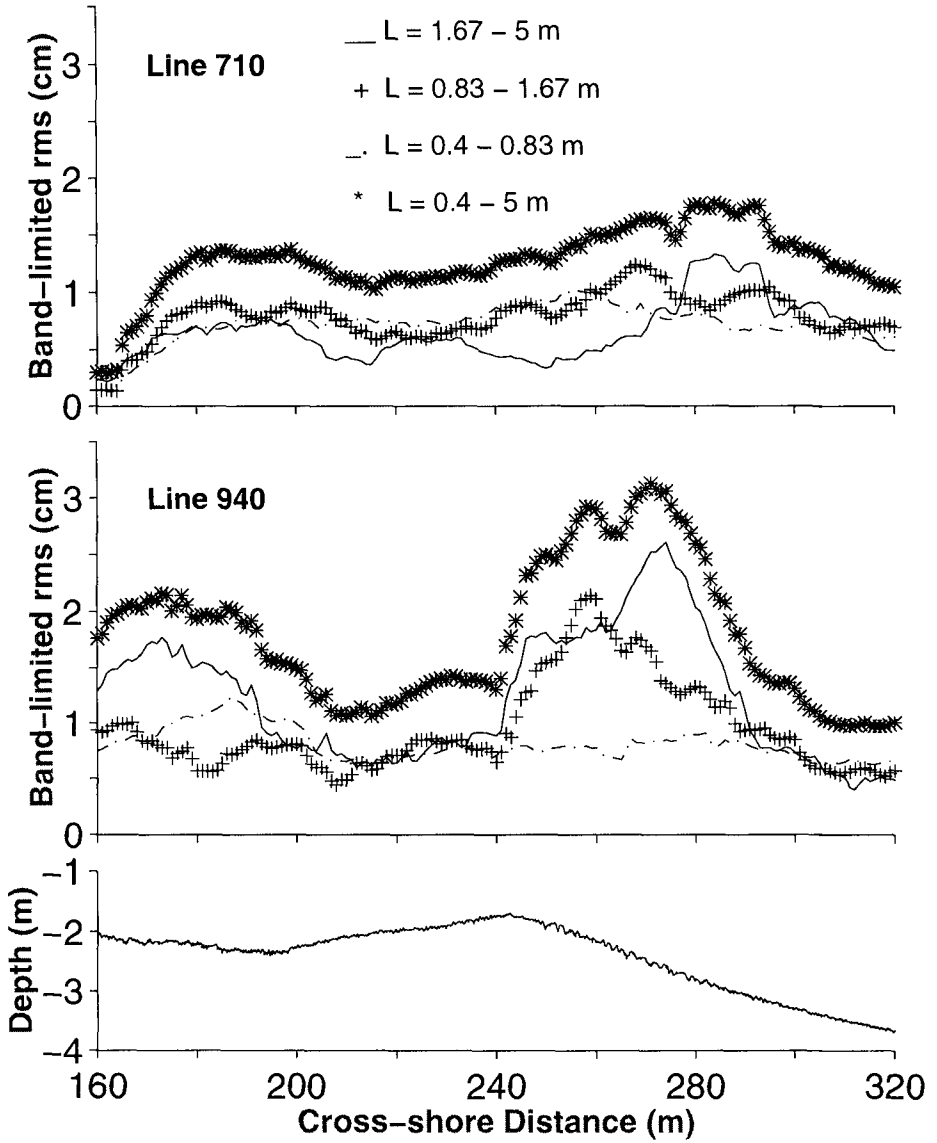


Figure 2. Band limited rms heights calculated across lines 710 (upper panel) and 940 (middle panel) for Oct. 8. Combined CRAB and altimeter bathymetry profile of line 940 for Oct. 8 (lower panel).

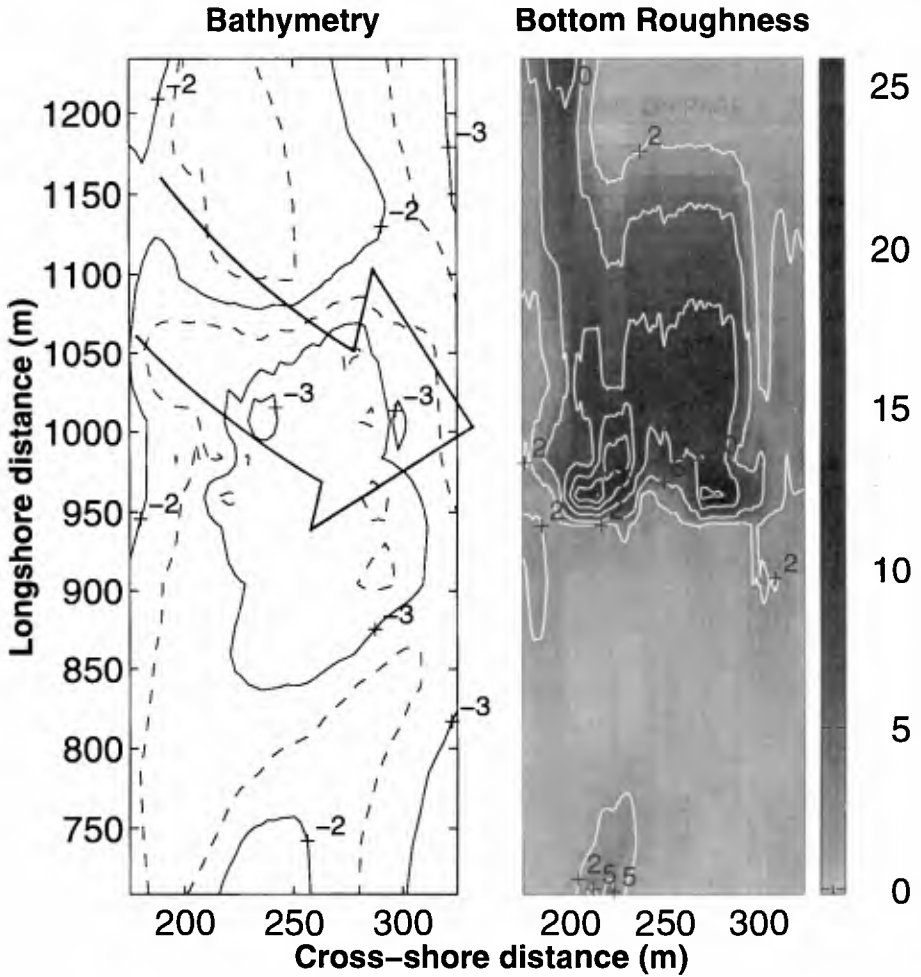


Figure 3. Bathymetry contour plot of DUCK94 survey area for Oct. 20 (left plot). Contour levels are in meters. Rip current is qualitatively indicated based on dye observations. Bottom rms roughness contour plot of survey area for Oct. 20 (right plot). Contour levels are in centimeters.

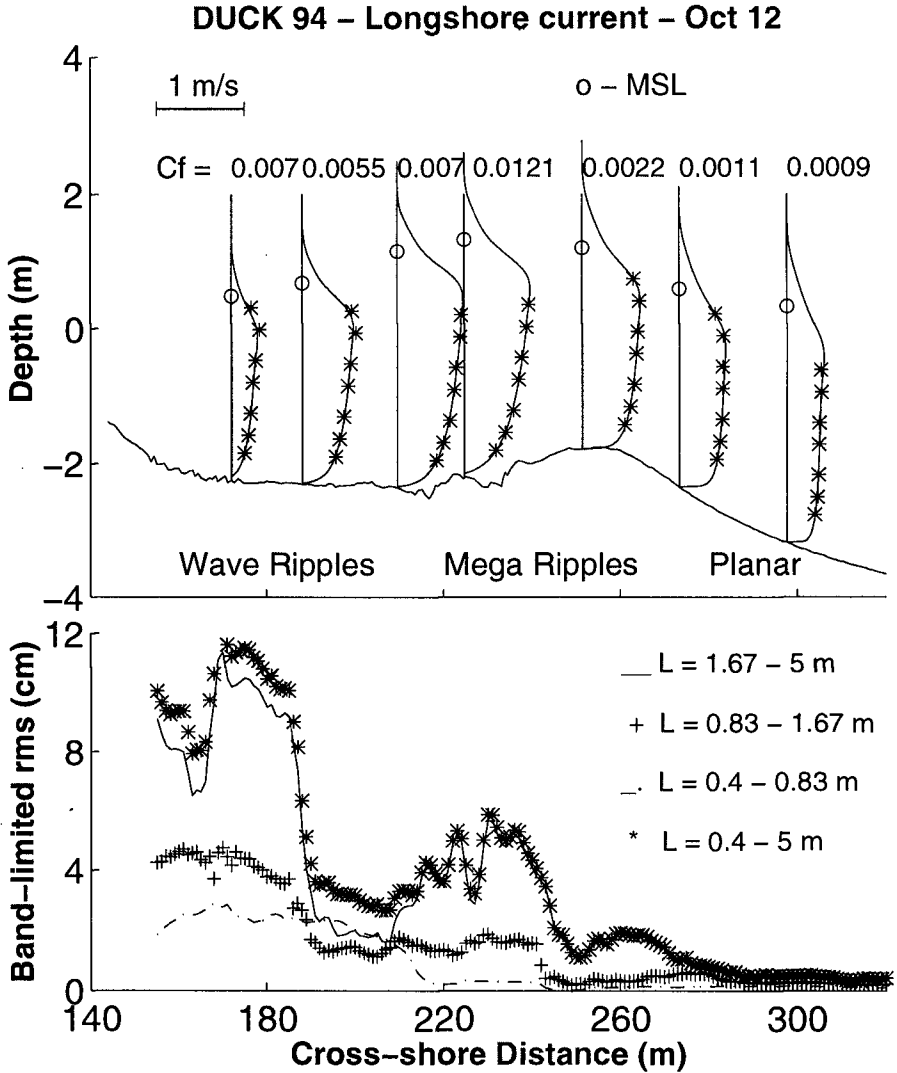


Figure 4. Vertical profiles of mean longshore currents superposed on bottom profile with tide elevation indicated by (o) and measured C_f values (upper panel). Variation of band-limited rms bottom roughness with the cross-shore distance for Oct. 12 (lower panel).

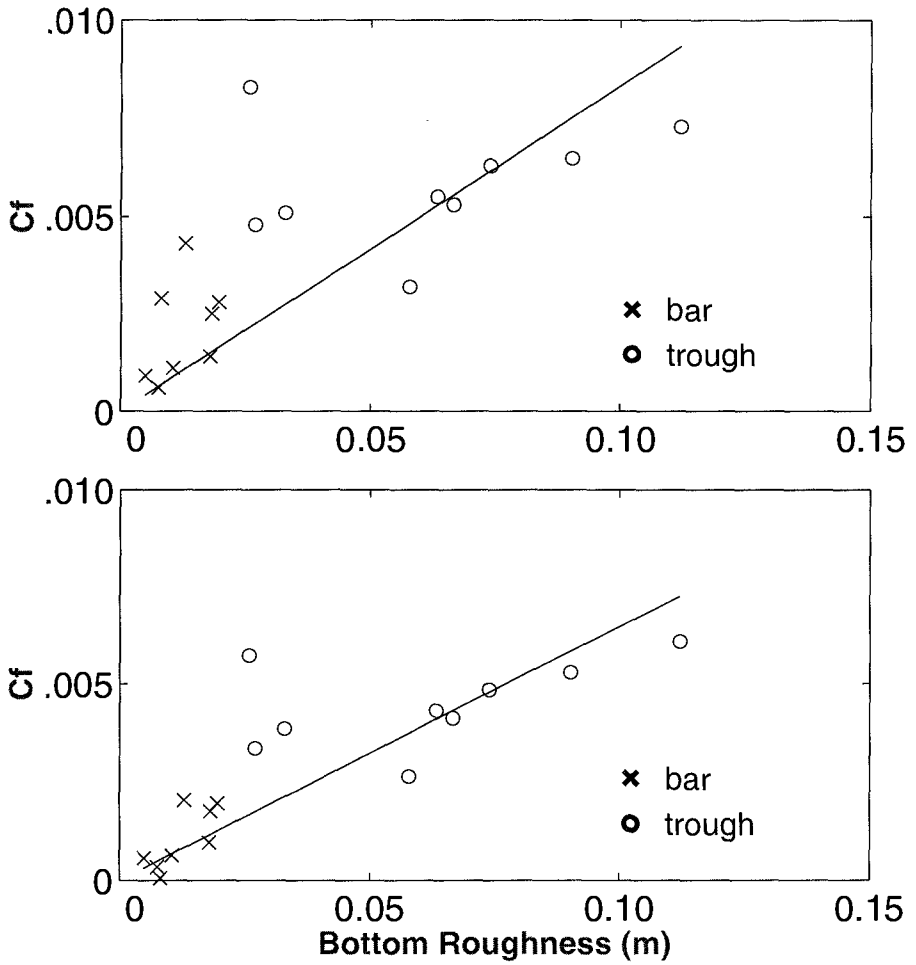


Figure 5. Total bed shear stress (C_f) versus bottom roughness (upper panel). The line represents a linear regression with a regression coefficient of 0.68. Bed shear stress coefficient without skin friction contribution (C_f') versus bottom roughness (lower panel). The line represents a linear regression with a regression coefficient of 0.80.

CHAPTER 263

PREDICTION OF SHORELINE CHANGE CONSIDERING CROSS-SHORE SEDIMENT TRANSPORT

Yoshimichi Yamamoto¹, Kiyoshi Horikawa², Katsutoshi Tanimoto³

ABSTRACT

Relations of cross-shore sediment transport rate with the grain size of sediment, the sea bottom slope in a surf zone and others were investigated by using data of field observation and large scale model experiments. The results are as follows :

- (1) the coefficient of a cross-shore sediment transport rate varies inversely as the 1.31th power of the grain size. Then, the steeper a initial bottom slope is, the faster a beach profile reaches a state of equilibrium.
- (2) The amount of a shoreline change is roughly proportional to the square root of the cross-shore sediment transport rate.
- (3) The stabilized bottom slope in the surf zone increases with the grain size and the wave period, and it decreases as the breaking wave height increases.

Then, new equations to predict a beach profile change induced by cross-shore sediment transport were introduced from this investigation. Moreover, the adequate applicability of these equations to actual coasts was confirmed.

1. INTRODUCTION

As practical models for predicting long-term transformation of long beaches, a shoreline change model and Uda et al.'s contour change model (1991, 1996) were proposed. However, these numerical models do not take cross-shore sediment transport rate into consideration.

In designing measures to control coastal erosion and wave overtopping, it is necessary to take account of short-term beach transformation under stormy weather condition in addition to the long-term transformation as shown in Figure 1. The short-term transformation, which cannot be

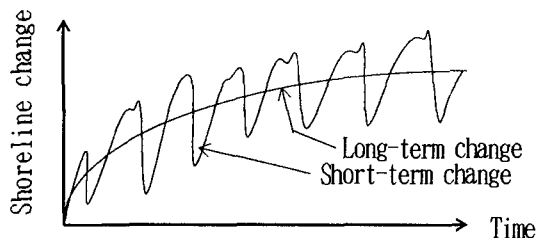


Figure 1 Transformation of a beach with time.

¹ Dr.-Eng., Coastal Eng. Dept., INA Corporation, 1-44-10 Sekiguchi Bunkyo-ku, Tokyo, 112, Japan.

² Dr.-Eng., President, Saitama University, 255 Shimo-okubo, Urawa, 338, Japan.

³ Dr.-Eng., Professor, Ditto.

determined without considering the cross-shore sediment transport, can be predicted by means of 2 or 3 - dimensional beach transformation models combined with the computation of waves and currents (e.g., Horikawa, 1988; Sato, 1994; Shibayama et al., 1994). However, it is difficult to apply these models to long-term prediction of long beaches, because long computational time is required and numerous coefficients introduced in sand transport rate formulas have not yet been generalized.

In this study, an attempt was made to generalize the coefficient of cross-shore sediment transport rate formulas. Moreover, a convenient beach evolution model using this result was proposed and applied to actual coasts.

2. CROSS-SHORE SEDIMENT TRANSPORT NEAR SHORELINE

Sunamura (1984) proposed the following formula for calculating cross-shore sediment transport rate, Q near the shoreline per unit time and unit beach width :

$$Q = K U_r^{0.2} \phi (\phi - 0.13 U_r) w \bar{d} \tag{1}$$

where K : a coefficient of sediment transport rate, U_r : Ursell parameter $[= g H T^2 / h^3]$, ϕ : Hallermeier parameter $[= H^2 / s h \bar{d}]$, w : the settling velocity of sediment, \bar{d} : the median grain size of sediment, g : the acceleration of gravity, h : the wave setup height at shoreline against the still water level $[= (1.63 \tan \alpha + 0.048) H_b]$, Sasaki and Saeki (1974), H : the wave height at shoreline against the still water level $[= 2.4 (\tan \alpha)^{0.3} h]$ Yamamoto(1988), T : the wave period, s : the specific gravity of sediment in water, $\tan \alpha$: the initial bottom slope in the surf zone, H_b : the breaker height.

Now, let us generalize the coefficient K of Eq. (1). As long as external forces remain constant, the rate of cross-shore sediment transport decreases with the lapse of time, and the beach profile approaches the equilibrium state. Therefore the coefficient K can be expressed by the following equation with the elapsed time t :

$$K = A \cdot e^{-Bt/T} \tag{2}$$

where A and B are coefficients. Then, we assume that the coefficients A and B are dominated by $\tan \alpha$ and \bar{d}/H_b (H_b is the wave height in deep water), and investigate relations of these coefficients with $\tan \alpha$

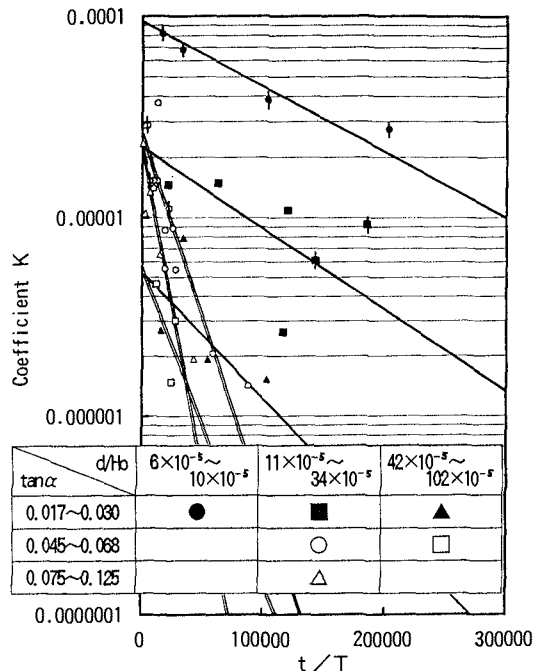


Figure 2 Relationship of the coefficient K with t/T .

and d/H_0 by using data of field observation and large scale model experiments given in Tables 1 ~ 4 in the appendix.

Figure 2 is a semilogarithmic graph of the relationship between K and t/T based on these data. Symbols with a vertical segment mean field data and other symbols mean experimental data. Then, average values of significant waves are used for the wave height and the wave period of irregular waves, because data of significant waves are used in many countries. However, experimental data of regular waves are used in order to supplement lack of data. Each straight line in this figure shows a tendency of data of each group. When t/T is 0, $K (= A)$ varies greatly depending on the value of d/H_0 , but changes very little by d/H_0 . Moreover, the slope of the straight lines in this figure varies widely depending on the value of $\tan\alpha$, while it is little affected by the value of d/H_0 . This means that the coefficient B is strongly dominated by $\tan\alpha$.

$\tan\alpha$ \ d/H_0	$6 \times 10^{-5} \sim 10 \times 10^{-5}$	$11 \times 10^{-5} \sim 34 \times 10^{-5}$	$42 \times 10^{-5} \sim 102 \times 10^{-5}$
0.017~0.030	●	■	▲
0.045~0.068		○	□
0.075~0.125		△	

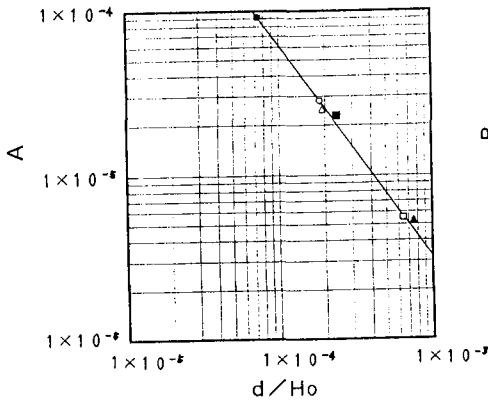


Figure 3 Relationship of A with d/H_0 .

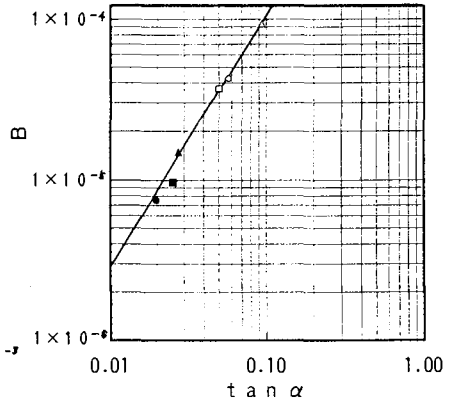


Figure 4 Relationship of B with $\tan\alpha$.

Figure 3 illustrates the relationship of the coefficient A with d/H_0 and Figure 4 shows the relationship of the coefficient B with $\tan\alpha$. As these figures indicate clearly that the coefficient A increases as d/H_0 falls and the coefficient B increases with $\tan\alpha$. Namely, the smaller the grain size of sediment is the larger the coefficient A is and the steeper the sea bottom slope is the faster the beach profile reaches the equilibrium state. These relations can be expressed by the following equations :

$$\left. \begin{aligned} A &= 3.61 \times 10^{-10} (d/H_0)^{-1.31}, & B &= 4.20 \times 10^{-3} (\tan\alpha)^{1.57} \\ &[\tan\alpha = 0.017 \sim 0.125, & d/H_0 &= 0.00006 \sim 0.00102] \end{aligned} \right\} \quad (3)$$

The rate of cross-shore sediment transport near the shoreline can be obtained from Eqs. (1), (2), and (3). Figure 5 shows the comparison between

measured values and calculated values obtained from data shown in Tables 2 and 4. This figure shows that the calculated values agree fairly well with the measured values.

3. SHORELINE CHANGE DUE TO CROSS-SHORE SEDIMENT TRANSPORT

Let us consider a simplified pattern of beach profile change, as shown in Figure 6, due to cross-shore sediment transport. Transforming slightly the continuity equation of cross-shore sediment transport, we can obtain the shoreline displacement as $\Delta y \propto (\int_0^t Q dt)^{0.5}$. Moreover, by using the data shown in Tables 2 and 4, the following equation can be obtained:

$$\Delta y = 2.7 (\int_0^t Q dt)^{0.5} \quad (4)$$

Therefore, the shoreline displacement due to cross-shore sediment transport can be calculated by using Eq. (4).

Figure 7 compares the measured values shown in Tables 2 and 4 with the calculated values given by Eq. (4). The data marked with + mean cases that initial bottom slopes above the still water level are steep by cliffs or steps. This figure shows that the calculated values agree well with the measured values. However, since Eq. (4) is intended for the simple beach profile change due to cross-shore sediment transport, Application of Eq. (4) to shores undergone complex beach changes should be preceded by careful study.

By combining the above equations with a formula for calculating the stable slopes of sea bottoms, the beach pro-

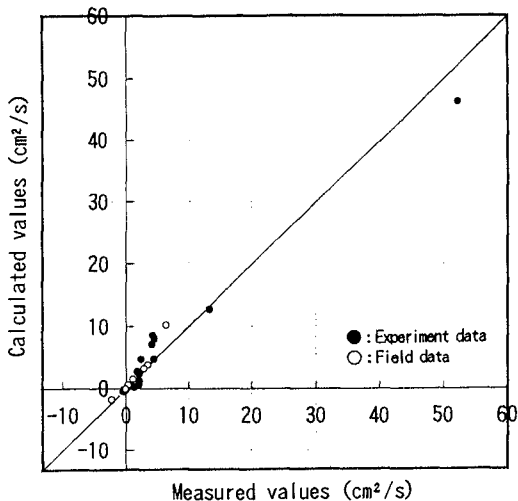


Figure 5 Measured vs. calculated values of cross-shore sediment transport rate.

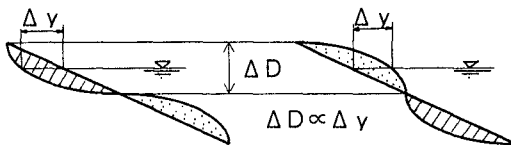


Figure 6 Patterns of beach change due to cross-shore sediment transport.

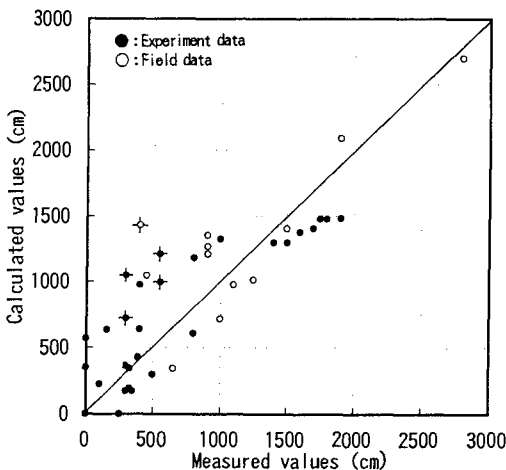


Figure 7 Measured vs. calculated values of Δy .

files after transformation can be determined.

From Eq. (1), when the beach profile reaches the equilibrium state, the following relation can be obtained:

$$\phi = 0.13 U_r \quad (5)$$

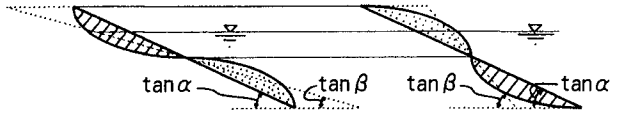


Figure 8 Image of $\tan \beta$ (sea bottom slope under equilibrium state in the surf zone).

Substituting Hallermeier parameter, Ursell parameter and Eq. (6) (Yamamoto, 1988) to Eq. (5), and transforming slightly, we can obtain Eq. (7).

$$H = 2.4(\tan \beta)^{0.3} h = 1.9(\tan \beta)^{0.3} H_b \quad (6)$$

$$\tan \beta = \left(\frac{0.0864 s g d T^2}{H_b^2} \right)^{2/3} \quad (7)$$

where $\tan \beta$ is the sea bottom slope under the equilibrium state in the surf zone, and H_b is the breaking wave height.

Then, assuming that the rate of time change of the sea bottom slope equals $e^{-Bt/T}$, the sea bottom slope of the arbitrary elapsed time t in the surf zone, $\tan \theta$, can be expressed by the following equation:

$$\tan \theta = \tan \beta + \frac{\tan \alpha - \tan \beta}{e^{-Bt/T}} \quad (8)$$

Moreover, substituting the data shown in Tables 5 and 6 in the appendix, we can obtain Figure 9. The figure indicates that the calculated values agree well with the measured values.

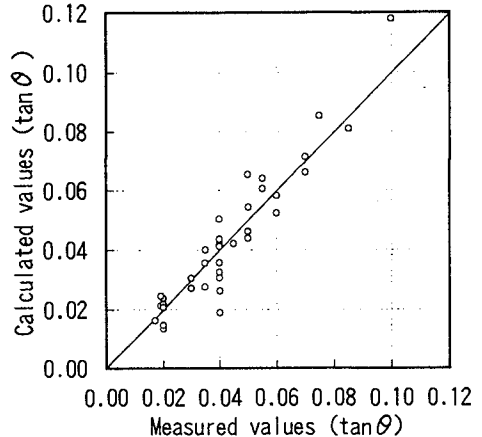


Figure 9 Measured vs. calculated values of $\tan \theta$.

4. APPLICATION OF THE PROPOSED

EQUATIONS TO ACTUAL COASTS

We performed the following two beach change simulations.

(1) SHORELINE CHANGE AT HAZAKI COAST

The first one is the time series hindcast for 18 days at Hazaki coast in Ibaragi Prefecture, Japan, based on the data given in Katoh and Yanagishima's paper (1988). In their paper, time series data of the daily mean wave energy flux, and limited data of the maximum significant wave height $[(H_{1/3})_{max}]$ and period on stormy days were given. Therefore, time series data of the significant wave height $(H_{1/3})$ from the data of the square root of the daily mean wave energy flux $(E^{1/2})$ were calculated by using the following empirical relations:

$$H_{1/3} = (H_{1/3})_{\max} / 1.5 \quad (9), \quad E^{1/2} = (H_{1/3})_{\max} \quad (10)$$

Equation (10) can be obtained from Figure 10 drawn by limited data under stormy weather. However, as the offshore bars exist and the mean water depth at the bar crown is about 2.9 m, the significant wave height of waves acting on the shoreline is less than approximately 2.2 m due to wave breaking. Therefore, the breaking wave height higher than 2.2 m is reduced to 2.1 m. Then, the time series data of the wave period are calculated by using Eq. (11) obtained empirically in their paper.

$$H_{1/3} / L^{1/3} = 0.25 \times E^{0.37} \quad (11)$$

where L is the wavelength.

However, as larger waves are diminished in this case, the breaking wave height is cut down, the wave period in this case should be shortened by using the following equation based on Bretschneider's formula [$T = 3.86 (H_{1/3})^{0.5}$]:

$$T_a / T_b = C (2.1 / H_{1/3b})^{0.5} \quad (12)$$

where the suffix a means the values after wave breaking, while the suffix b means the values before wave breaking, and C is a proportional coefficient ($= 1.1$ from a few field observation data).

Because the shoreline of Hazaki coast is straight and no coastal structure like a groin exists along this coast, the shoreline change due to longshore sediment transport can be neglected. Therefore, the shoreline change on this coast can be simulated by using Eqs. (1) ~ (4), (7), and (8). The calculated result of shoreline change agrees well with the measured result as shown in Figure 11.

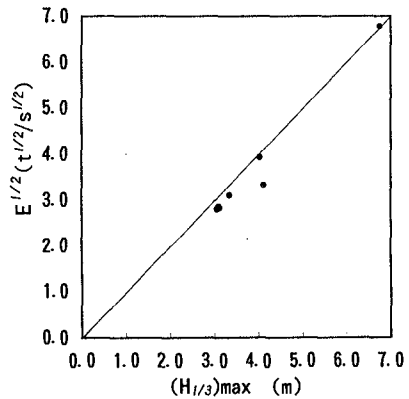


Figure 10 Relation between maximum significant wave height and square root of daily mean wave energy flux.

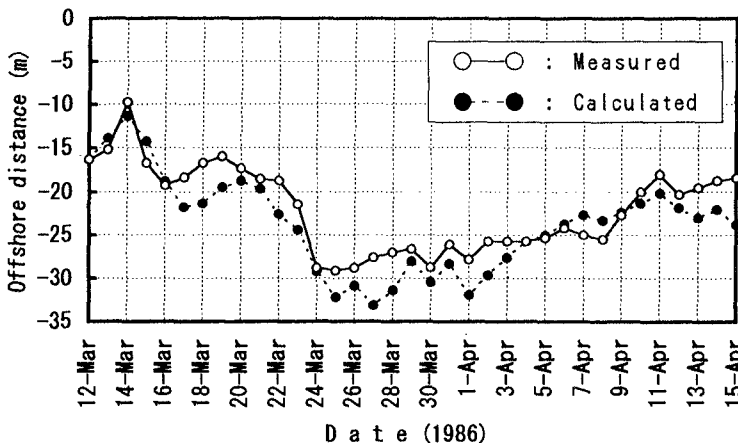


Figure 11 On-offshore changes of shoreline position (D.L. + 1.4 m).

(2) SHORELINE CHANGE AT MISAWA PORT COAST

Another example is the simulation for one year at Misawa Port coast in Aomori Prefecture, Japan, based on data of Hashimoto and Uda's paper (1979).

A remarkable shoreline change occurred during the period of one year from 1976 to 1977, when the off-shore breakwater at Misawa Port became long enough to bring about remarkable diffraction effect (refer to Figure 12).

It is likely that the diffraction effect of the breakwater made the wave height small in the water area sheltered by the breakwater, thereby the rate of onshore sediment transport increased in this area as shown in Figure 13. Hashimoto and Uda applied an empirical eigenfunction expansion method to predict shore transformation at and around Misawa Port and pointed out the existence of cross-shore sediment transport.

Thus, the probable mechanism of this shoreline change was that alongshore transport sediment entered the port area due to influence of the diffraction effect of the breakwater, then the waves in the port transported the sediment onshore, therefore the shoreline advancement occurred.

The hindcast of the shoreline change in this area was performed by combining Eqs. (1) ~ (4) with the shoreline change model.

First, the shoreline change model was applied under the following conditions on the basis of the Hashimoto and Uda's paper :

- (a) The height of the longshore sediment transport zone was 11 m.
- (b) Ozasa and Brampton's formula (1979) was used to calculate the longshore sediment transport rate, and the figure 0.2 was selected as a coefficient in

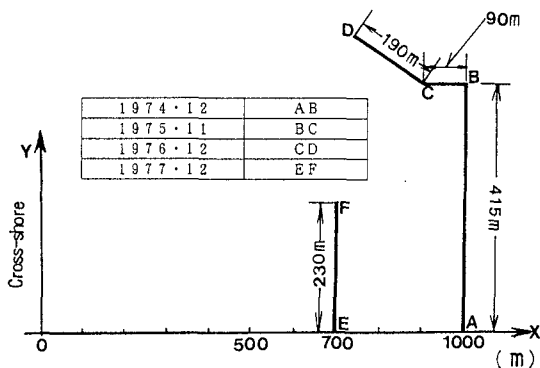


Figure 12 Configuration of breakwaters at Misawa port.

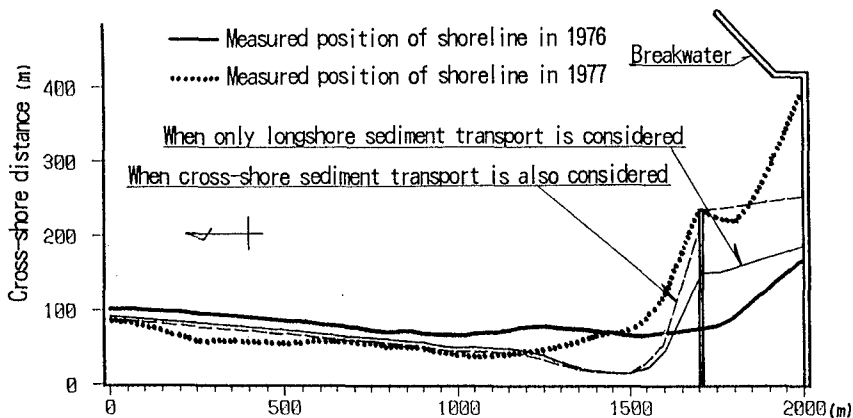


Figure 13 Result of shoreline change simulation.

the formula.

- (c) The wave height, period and direction are shown in Table 7 in the appendix.
- (d) The sea bottom slope was $1/50$.

The result of this simulation was plotted in Figure 13 by a solid line. This result, which was the same as that calculated by Hashimoto and Uda, did not agree with the measured result shown as a dotted line.

Then, the shoreline change due to the cross-shore sediment transport was taken into account by using Eqs. (1) ~ (4). The influence of the wave hysteresis on the shore transformation seems to be great. However, the available data were not the time series data of waves but the statistical data shown in Table 7. Therefore, we adjusted the median grain size of sediment so as to obtain reasonable shoreline displacement. Because the natural beach change after one year induced by cross-shore sediment transport is regarded as small, the shoreline change due to the cross-shore sediment transport near the 0 m point, which is far from the breakwater, can be deemed small. Namely, the median grain size of sediment must be selected so as to obtain a small shoreline change due to the cross-shore sediment transport near the 0 m point. When the figure 0.43 mm was selected as the median grain size from usual grain size at Misawa Port coast, the shoreline displacement near the 0 m point became small as shown in Table 7. Therefore, the calculation by Eqs. (1) ~ (4) was performed under the condition of the median grain size 0.43 mm. By combining this result with the result obtained by the shoreline change model, the significantly improved shoreline displacement was obtained as shown in Figure 13 by a broken line.

5. CONCLUSIONS

Main conclusions are as follows :

- (1) The relations among $\tan\alpha$, d/H_0 and the coefficient K of cross-shore sediment transport rate (in Sunamura's formula) can be expressed by Eqs. (2), (3) based on the analyses of data obtained by field observation and large scale experiments.
- (2) The formulas [Eqs. (4), (7) and (8)] were proposed for calculating the shoreline displacement and the bottom slope change in the surf zone due to the cross-shore sediment transport. Then the effectiveness of these formulas against actual coasts was demonstrated by the simulation results of shoreline change on two actual coasts.

REFERENCES

- Hashimoto, H. and Uda, T. (1979). "The application of empirical shoreline change model to Ogawarako coast", Proc. 26th Japanese Conf. on Coastal Eng., JSCE, pp.215-219 (in Japanese).
- Horikawa, K. (1988). "Nearshore Dynamics and Coastal Processes" Univ. of Tokyo Press, 522pp.
- Katoh, K. and Yanagishima, S. (1988). "Predictive model for daily changes of shoreline", Proc. 21st International Conf. on Coastal Eng., ASCE, pp.1253-1264.
- Ozasa, H. and Brampton, A. H. (1979). "Models for predicting the shoreline evolution of beaches backed by seawalls", Report of The Port and Harbour Research Institute, Vol.18 - no.4, Ministry of Transport, pp.77-104.
- Sasaki, M. and Saeki, K. (1974). "Study on wave transformation after wave breaking (2)", Proc. 21st Japanese Conf. on Coastal Eng., JSCE, pp.39-44 (in Japanese).

- Sato, S. and Kabling, M. B. (1994). "Numerical model of 3-dimensional shore transformation including swash zone", Proc. 41st Japanese Conf. on Coastal Eng., JSCE, pp.401-405 (in Japanese).
- Shibayama, T., Yamada, M. and Kobayashi, A. (1994). "Shore transformation model around mouth of a river and its verification", Proc. 41st Japanese Conf. on Coastal Eng., JSCE, pp.466-470 (in Japanese).
- Sunamura, T. (1984). "Study on cross-shore sediment transport in surf zone including swash zone", Proc. 31st Japanese Conf. on Coastal Eng., JSCE, pp. 316-320 (in Japanese).
- Uda, T., Yamamoto, K., and Kouno, S. (1991). "Prediction method of 3-dimensional shore transformation due to longshore sediment transport", Proc. 38th Japanese Conf. on Coastal Eng., JSCE, pp.386-390 (in Japanese).
- Uda, T., Yamamoto, Y., Itabashi, N., and Yamaji, K. (1996). "Field observation of movement of sand body due to waves and verification of its mechanism by numerical model", Proc. 25th International Conf. on Coastal Eng., ASCE, pp. 774-775.
- Yamamoto, Y. (1988). "On the wave run-up height after wave breaking on a complicated nearshore profile", Proc. of Civil Engineering in the Ocean, Vol.4. JSCE, pp.295-300 (in Japanese).

APPENDIX

- H_o : significant wave height in deep water.
 T : wave period.
 L_o : wavelength in deep water.
 H_o/L_o : wave steepness in deep water.
 $\tan\alpha$: initial mean bottom slope in the surf zone.
 H_b : breaking wave height.
 h : wave setup on shoreline against the still water level.
 H : wave height on shoreline against the still water level.
 d : median grain size of sediment.
 ϕ : Hallermeier parameter.
 U_r : Ursell parameter.
 A_r : cross sectional area of erosion part near shoreline.
 t : observation time.
 Q : rate of cross-shore sediment transport.
 w : settling velocity of sediment.
 K : coefficient in the cross-shore sediment transport rate formula.
 Δy : shoreline displacement due to cross-shore sediment transport.
 $\tan\beta$: mean bottom slope under the equilibrium state in the surf zone.
 $\tan\theta$: mean bottom slope of the arbitrary elapsed time in the surf zone.
 α : wave direction.
 T_p : frequency of incoming waves.

Suffix c means the calculated value.

Table 1 Field observation data (No1).

h/c	T(s)	Lo(cm)	Ho/Lo	tan α	h/c	h(cm)	h(cm)	d(cm)	Φ	Ur	Ar(cm ²)	t(s)	Researcher	
100	13.5	28431	0.004	0.040	216	24.4	22.3	0.030	440	6584	-200000	88620	Sonu, 1960	
170	6.0	5616	0.030	0.045	219	26.6	25.2	0.030	515	1256	150000	133260	Sonu, 1960	
120	8.5	11271	0.011	0.025	179	15.9	12.6	0.030	216	3544	-270000	1209600	Uda, 1982	
250	9.0	12636	0.020	0.020	305	24.6	18.2	0.020	439	2398		172800	Sunamura et al., 1983	
250	9.0	12636	0.020	0.020	305	24.6	18.2	0.027	325	2398		172800	Sunamura et al., 1983	
300	10.0	15600	0.019					0.076			280000		1036800	Takeda et al., 1985
280	9.5	14079	0.020					0.026			130000		259200	Takeda et al., 1985
290	10.0	15600	0.019	0.017	346	26.0	18.3	0.018	463	2646	380000		1036800	Kuriyama, 1991
180	8.5	11271	0.016	0.017	223	16.8	11.8	0.018	298	2965	-220000		1728000	Kuriyama, 1991
130	7.0	7644	0.017	0.017	159	11.9	8.4	0.018	212	2828	-70000		1296000	Kuriyama, 1991
230	9.0	12636	0.018	0.045	337	40.9	38.7	0.026	913	1839	275000		43200	Nairn, 1991
300	10.5	17199	0.017	0.023	388	33.2	25.7	0.020	644	2520	600000		172800	Katoh et al., 1992
300	10.5	17199	0.017	0.023	388	33.2	25.7	0.020	644	2520	1000000		345600	Katoh et al., 1992

Table 2 Field observation data (No2).

Q(cm ² /s)	H(cm/s)	K	d/h ₀	t/T	Kc	Qc(cm ² /s)	Δyc(cm)	Δy(cm)	Researcher
-2.257	4.490	0.000153	0.00030	6564	0.000125	-1.846	1207	900	Sonu, 1960
1.126	4.490	0.0000111	0.00018	22210	0.000146	1.479	1046	450	Sonu, 1960
0.223	4.490	0.0000061	0.00025	142306	0.000030	-0.111	1403	1500	Uda, 1982
	2.178		0.00008	19200	0.000707	0.812	1011	1250	Sunamura et al., 1983
0.270	3.558		0.00011	19200	0.0000477	0.093	342	650	Sunamura et al., 1983
0.502	14.793		0.00025	103680			1429	400	Takeda et al., 1985
0.367	3.087		0.00009	27284			973	1100	Takeda et al., 1985
-0.127	2.008	0.000382	0.00006	103680	0.000580	0.556	1664		Kuriyama, 1991
-0.054	2.008	0.0000274	0.00010	203294	0.000158	-0.074	1266	900	Kuriyama, 1991
6.366	2.008	0.000092	0.00014	185143	0.0000117	-0.068	714	1000	Kuriyama, 1991
3.472	2.178	0.0000287	0.00011	4800	0.000458	10.158	1416		Nairn, 1991
2.894	2.178	0.0000816	0.00007	16457	0.0000887	3.773	2091	1900	Katoh et al., 1992
	2.178	0.0000680	0.00007	32914	0.0000737	3.136	2700	2800	Katoh et al., 1992

Sunamura et al.'s Δy is the calculated value by using Qc.
Nairn's data is based on information by Kriebel and Dean's paper.

Table 3 Experimental data in large wave tanks (No.1).

llo(cm)	T(s)	Lo(cm)	llo/Lo	tan α	Hb(cm)	h(cm)	ll(cm)	d(cm)	ϕ	Ur	Ar(Cm ²)	t(s)	Rescarcher
141	11.3	19920	0.007	0.066	200	31.1	33.0	0.022	1034	4270	300000	144000	Saville, 1957
108	11.3	19920	0.005	0.066	170	26.4	28.1	0.022	879	5024	300000	144000	Saville, 1957
48	11.3	19920	0.002	0.070	110	17.8	19.3	0.022	614	7585	0	144000	Saville, 1957
171	5.6	4892	0.035	0.066	220	34.2	36.3	0.022	1137	953	300000	144000	Saville, 1957
46	6.0	5616	0.008	0.050	100	13.0	12.7	0.047	170	2662	-18000	72000	Simizu et al., 1984
95	9.0	12636	0.008	0.050	128	16.6	16.2	0.047	218	4679	-130000	250200	Simizu et al., 1984
85	3.0	1404	0.061	0.050	88	11.4	11.1	0.047	150	756	0	75600	Simizu et al., 1984
176	6.0	5616	0.031	0.030	199	19.3	16.2	0.047	187	1534	-7000	126000	Simizu et al., 1984
73	9.0	12636	0.006	0.030	147	14.2	11.9	0.047	138	4671	-50000	140400	Simizu et al., 1984
71	3.1	1499	0.047	0.030	82	7.9	6.7	0.047	77	993	-5000	105840	Simizu et al., 1984
96	9.1	12918	0.007	0.050	190	24.6	24.0	0.027	564	3222	55000	255600	Simizu et al., 1984
110	6.0	5616	0.020	0.050	180	23.3	22.8	0.027	534	1479	55000	353160	Simizu et al., 1984
65	12.0	22464	0.003	0.050	160	20.7	20.2	0.027	475	6654	-44000	288000	Simizu et al., 1984
162	3.1	1499	0.108	0.050	160	20.7	20.2	0.027	475	444	25000	273960	Simizu et al., 1984
34	3.5	1911	0.118	0.030	47	4.6	3.8	0.027	77	2209	-4000	360000	Simizu et al., 1984
106	4.5	3159	0.034	0.030	132	12.8	10.7	0.027	216	1300	17000	280800	Simizu et al., 1984
161	3.1	1499	0.107	0.030	159	15.4	12.9	0.027	260	512	16000	360000	Simizu et al., 1984
30	5.8	5248	0.006	0.020	62	5.0	3.7	0.027	66	4896	-12000	313920	Simizu et al., 1984
80	3.1	1499	0.053	0.020	91	7.3	5.4	0.027	97	953	-4000	370800	Simizu et al., 1984
178	5.0	3900	0.046	0.100	191	40.3	48.5	0.027	1400	731	270000	212400	Simizu et al., 1984
110	7.5	8775	0.013	0.100	137	28.9	34.8	0.027	1004	2294	230000	109800	Simizu et al., 1984
150	6.0	5616	0.027	0.075	221	37.6	41.5	0.033	900	1035	70000	15480	Dette et al., 1986
151	5.4	4549	0.033	0.075	211	35.9	39.6	0.023	1258	879	150000	36000	Vellinga, 1986
200	5.6	4892	0.041	0.068	230	36.5	39.1	0.022	1235	901	230000	54000	Kraus et al., 1988
200	5.6	4892	0.041	0.068	230	36.5	39.1	0.022	1235	901	260000	108000	Kraus et al., 1988
200	5.6	4892	0.041	0.064	230	35.0	36.9	0.040	628	923	240000	54000	Kraus et al., 1988
200	5.6	4892	0.041	0.064	230	35.0	36.9	0.040	628	923	190000	108000	Kraus et al., 1988
140	6.0	5616	0.025	0.085	215	40.1	46.0	0.022	1552	1007	200000	15120	Nairn, 1991
150	6.0	5616	0.027	0.125	245	61.6	79.3	0.033	2002	736	135000	2590	Southgate, 1991

Wave heights of Saville's, Simizu et al's, Dette et al's, Kraus et al's, and Southgate's data are not significant values but mean values, because of experiments carried out by using regular waves.

Table 4 Experimental data in large wave tanks (No2).

$Q_c(\text{cm}^2/\text{s})$	$W(\text{cm}/\text{s})$	K	d/llo	t/T	Kc	$Q_c(\text{cm}^2/\text{s})$	$\Delta y(\text{cm})$	$\Delta y(\text{cm})$	Researcher
2.08	2.354	0.0000153	0.00016	12743	0.0000165	2.25	1479	1750	Saville, 1957
2.08	2.354	0.0000369	0.00020	12743	0.0000117	0.66	1479	1900	Saville, 1957
0.00	2.354	0.0000000	0.00046	12743	0.0000037	-0.26	0	250	Saville, 1957
2.08	2.354	0.0000089	0.00013	25714	0.0000099	2.33	1479	1800	Saville, 1957
-0.25	7.947	0.0000046	0.00102	12000	0.0000019	-0.10	362	300	Simizu et al., 1984
-0.52	7.947	0.0000030	0.00049	27800	0.0000027	-0.46	973	400	Simizu et al., 1984
0.00	7.947	0.0000000	0.00055	25200	0.0000026	0.03	0	0	Simizu et al., 1984
-0.06	7.947	0.0000146	0.00027	21000	0.0000121	-0.05	226	100	Simizu et al., 1984
-0.36	7.947	0.0000027	0.00064	15600	0.0000042	-0.55	604	800	Simizu et al., 1984
-0.05	7.947	0.0000079	0.00066	34142	0.0000029	-0.02	191	330	Simizu et al., 1984
0.22	3.558	0.0000055	0.00028	28088	0.0000056	0.22	633	400	Simizu et al., 1984
0.16	3.558	0.0000021	0.00025	58860	0.0000021	0.16	633	150	Simizu et al., 1984
-0.15	3.558	0.0000015	0.00042	24000	0.0000039	-0.40	566	0	Simizu et al., 1984
0.09	3.558	0.0000014	0.00017	88374	0.0000011	0.07	427	390	Simizu et al., 1984
-0.01	3.558	0.0000015	0.00079	102857	0.0000007	-0.01	171	300	Simizu et al., 1984
0.06	3.558	0.0000149	0.00025	62400	0.0000064	0.03	352	0	Simizu et al., 1984
0.04	3.558	0.0000026	0.00017	116129	0.0000044	0.07	342	330	Simizu et al., 1984
-0.04	3.558	0.0000019	0.00090	54124	0.0000022	-0.04	296	500	Simizu et al., 1984
-0.01	3.558	0.0000109	0.00034	119613	0.0000043	0.00	171	350	Simizu et al., 1984
1.27	3.558	0.0000019	0.00015	42480	0.0000003	0.20	1403	1700	Simizu et al., 1984
2.09	3.558	0.0000065	0.00025	14640	0.0000037	1.18	1295	1500	Simizu et al., 1984
4.52	4.709	0.0000105	0.00022	2580	0.0000185	7.95	714	300	Dette et al., 1986
4.17	2.459	0.0000135	0.00015	6667	0.0000230	7.11	1046	300	Vellinga, 1986
4.26	2.354	0.0000153	0.00011	9643	0.0000305	8.52	1295	1400	Kraus et al., 1988
2.41	2.354	0.0000086	0.00011	19286	0.0000168	4.70	1377	1600	Kraus et al., 1988
4.44	6.349	0.0000140	0.00020	9643	0.0000147	4.68	1323	1000	Kraus et al., 1988
1.76	6.349	0.0000055	0.00020	19286	0.0000086	2.73	1177	800	Kraus et al., 1988
13.23	2.354	0.0000290	0.00016	2520	0.0000278	12.68	1207	550	Nairn, 1991
52.12	4.709	0.0000235	0.00022	432	0.0000208	46.27	992	550	Southgate, 1991

Table 5 Field observation data (No3).

$\tan \beta (-)$	$\tan \theta c (-)$	$\tan \theta (-)$	Researcher
0.062	0.044	0.040	Sonu
0.021	0.032	0.040	Sonu
0.043	0.040	0.035	Uda
0.017	0.020		Sunamura et al.
0.021	0.020		Sunamura et al.
			Takeda et al.
			Takeda et al.
0.016	0.016	0.017	Kuriyama
0.023	0.021	0.019	Kuriyama
0.028	0.024	0.019	Kuriyama
0.018	0.041	0.040	Nairn
0.015	0.022	0.020	Katoh et al.
0.015	0.021	0.020	Katoh et al.

Table 6 Experimental data in large wave tanks (No3).

$\tan \beta (-)$	$\tan \theta c (-)$	$\tan \theta (-)$	Researcher
0.044	0.054	0.050	Saville
0.054	0.060		Saville
0.097	0.085	0.075	Saville
0.015	0.026	0.040	Saville
0.079	0.061	0.055	Simizu et al.
0.097	0.081	0.085	Simizu et al.
0.037	0.042	0.045	Simizu et al.
0.031	0.030	0.030	Simizu et al.
0.081	0.042	0.040	Simizu et al.
0.043	0.036	0.035	Simizu et al.
0.040	0.044	0.040	Simizu et al.
0.025	0.028	0.035	Simizu et al.
0.073	0.064	0.055	Simizu et al.
0.012	0.013	0.020	Simizu et al.
0.073	0.065	0.050	Simizu et al.
0.026	0.027	0.030	Simizu et al.
0.012	0.015	0.020	Simizu et al.
0.098	0.050	0.040	Simizu et al.
0.026	0.024	0.020	Simizu et al.
0.018	0.019	0.040	Simizu et al.
0.048	0.058	0.060	Simizu et al.
0.022	0.066	0.070	Dette et al.
0.016	0.052	0.060	Vellinga
0.014	0.044	0.050	Kraus et al.
0.014	0.031	0.040	Kraus et al.
0.021	0.046	0.050	Kraus et al.
0.021	0.036	0.040	Kraus et al.
0.017	0.072	0.070	Nairn
0.019	0.118	0.100	Southgate

Table 7 Calculated shoreline position at Misawa Port coast.

α	$l_{lo}(cm)$	$T(s)$	$l_{Lo}(cm)$	l_{lo}/L_0	$Tp(\%)$	$t(s)$	t/T	$\tan \alpha$	$l_{fb}(cm)$	$l_{fb}(cm)$	$l_{fb}(cm)$	Φ	l_{tr}	d/l_{fo}	k_c	$W(cm/s)$	$Q_c(cm/s)$	$\Delta Y_c(cm)$	
ENE 150	9.0	12636	0.012	25.0	7884000	876000	0.020	0.020	208	16.7	12.4	0.043	139	3517	0.00029	0.000000006	7.689	-0.00043	158
ENE 250	9.0	12636	0.020	7.0	2207520	245280	0.020	0.020	305	24.6	18.2	0.043	204	2398	0.00017	0.000003362	7.689	-0.11586	1365
ENE 350	9.0	12636	0.028	2.8	883008	98112	0.020	0.020	392	31.6	23.5	0.043	263	1863	0.00012	0.000019746	7.689	0.15718	-1006
ENE 450	9.0	12636	0.036	0.2	63072	7008	0.020	0.020	474	38.2	28.3	0.043	317	1543	0.00010	0.000062500	7.689	3.31069	-1234
E 150	9.0	12636	0.012	28.0	8830080	981120	0.020	0.020	208	16.7	12.4	0.043	139	3517	0.00029	0.000000002	7.689	-0.00017	104
E 250	9.0	12636	0.020	6.0	1892160	210240	0.020	0.020	305	24.6	18.2	0.043	204	2398	0.00017	0.000004615	7.689	-0.15901	1481
E 350	9.0	12636	0.028	1.9	599184	66576	0.020	0.020	392	31.6	23.5	0.043	263	1863	0.00012	0.000026254	7.689	0.20899	-955
E 450	9.0	12636	0.036	0.1	31536	3504	0.020	0.020	474	38.2	28.3	0.043	317	1543	0.00010	0.000064510	7.689	3.41716	-886
ESE 150	7.5	8775	0.017	20.0	6307200	840960	0.020	0.020	190	15.3	11.3	0.043	127	2676	0.00029	0.000000008	7.689	-0.00036	128
ESE 250	7.5	8775	0.028	3.0	946080	126144	0.020	0.020	278	22.4	16.6	0.043	186	1824	0.00017	0.000009864	7.689	-0.13885	979
ESE 350	7.5	8775	0.040	0.1	31536	4205	0.020	0.020	358	28.9	21.4	0.043	240	1417	0.00012	0.000046121	7.689	0.86454	-446
																		Σ	-313

CHAPTER 264

THE INFLUENCE OF ROLLERS ON LONGSHORE CURRENTS

Daniel A. Osiecki¹ and William R. Dally²

Abstract

A computational model is developed for depth-averaged cross-shore and longshore currents which includes the effects of the surface roller generated by wave breaking. The creation and evolution of the roller itself is modeled explicitly (Dally and Brown, 1995), and convective acceleration terms are included in both the cross-shore and longshore momentum equations. Lateral mixing is parameterized in terms of the local cross-shore current and a turbulent eddy viscosity, as proposed by Svendsen and Putrevu (1994); however, a new model for eddy viscosity is proposed which contains contributions from both the roller-induced and bed-induced turbulence. The laboratory measurements of quasi-uniform longshore currents reported by Visser (1991) are used to calibrate and verify the model. For driving the model, it is shown that using stream function wave theory produces significantly better results than linear wave theory. Also, comparisons of longshore current distributions with and without the roller terms included show that the roller plays an essential role in faithfully modeling the longshore current. The calibrated model also produces accurate results for the set-up/set-down using stream function theory, for the limited data available from Visser (1991).

Introduction

Recent investigations of the roller have demonstrated its importance in mean cross-shore currents (undertow); e.g., see Svendsen (1984b), Okayasu et al. (1988), Deigaard et al. (1991), and Dally and Brown (1995). We now focus attention on

¹ Research Engineer and ²Associate Professor, Ocean Engineering Program, Florida Institute of Technology, 150 W. University Blvd., Melbourne FL 32901, USA.

the potentially important influence of the aerated roller on longshore currents, both in driving longshore flows as well as in cross-shore mixing.

For shore normal waves, Dally and Brown (1995) showed that the roller momentum flux (R_{xx}) was comparable to the Radiation Stress (S_{xx}) associated with the organized wave motion, and that their gradients tend to balance in the outer surf zone. This balance is responsible for the landward shift in the initiation of setup, as well as the landward shift in the location of the peak of the undertow, that have been observed in laboratory data (Bowen, et al., 1968; Nadaoka and Kondoh, 1982). In the present study it will be shown that with obliquely incident waves, the gradients of the cross-product momentum terms (R_{xy} and S_{xy}) also tend to balance in the outer surf zone. This results in a landward shift in the peak of the longshore current, which is also evident in laboratory data (Visser, 1991).

Although lateral mixing of the longshore current has been an important modeling issue since the 1970's, it was not until recently that a physically realistic mechanism for observed cross-shore mixing, i.e. residual convective acceleration induced by the vertical structure of the cross-shore and longshore currents, was proposed by Svendsen and Putrevu (1994). In the present study the influence of the roller, which enhances vertical mixing and consequently *reduces* lateral mixing, will also be modeled and explored.

General Governing Equations for Longshore and Cross-shore Currents

Assuming steady currents, longshore uniformity, and no flow through the shoreline, a simple equation for the mean, depth-integrated, period-averaged, cross-shore current below the mean water level (U) is developed by integrating the conservation of mass equation. This relation is given by

$$U = \frac{-(Q_{wx} + Q_{rx})}{(h + \bar{\eta})} \quad (1)$$

The Stokes Drift term (Q_{wx}) is provided by the wave theory selected to drive the model, the roller volume flux (Q_{rx}) is provided by an energy-based roller model, and the still water depth (h) is known. The elevation of the mean water level ($\bar{\eta}$) is as yet unknown.

Again, assuming steady state conditions, applying longshore uniformity, and neglecting wind stress, the period-averaged, depth-averaged momentum equations for the cross-shore and longshore directions are

$$-\frac{\partial}{\partial x} [U^2(h + \bar{\eta})] + \frac{1}{\rho} \left(\frac{\partial}{\partial x} S_{xx} + \frac{\partial}{\partial x} R_{xx} \right) + g(h + \bar{\eta}) \frac{\partial \bar{\eta}}{\partial x} = \frac{1}{\rho} \left(\overline{\tau_{zx}} \Big|_{-h} \right) \quad (2)$$

and

$$\frac{\partial}{\partial x} \left(D_c h \frac{\partial V}{\partial x} \right) - \frac{1}{\rho} \left(\frac{\partial}{\partial x} S_{xy} + \frac{\partial}{\partial x} R_{xy} \right) = \frac{1}{\rho} \left(\overline{\tau_{zy}} \Big|_{-h} \right) \tag{3}$$

where S is the Radiation Stress, R is the roller momentum flux, D_c characterizes a horizontal mixing mechanism, τ is the time-averaged bed stress, and V is the depth-averaged longshore current. The first term in Eq. 3 represents a lateral mixing mechanism due to the vertical structure of the cross-shore and longshore currents (Svendsen and Putrevu, 1994) with D_c approximated by,

$$D_c = \frac{0.5 h^2 U^2}{\nu_t} \tag{4}$$

where ν_t is a turbulent eddy viscosity. The eddy viscosity model developed herein contains vertical mixing introduced by both the aerated surface roller and the bottom, as described below.

A quadratic bed stress model is adopted:

$$\overline{\tau_{zx}} \Big|_{-h} = \rho \frac{c_f}{8} \overline{u_b (u_b^2 + v_b^2)^{\frac{1}{2}}} \tag{5}$$

$$\overline{\tau_{zy}} \Big|_{-h} = \rho \frac{c_f}{8} \overline{v_b (u_b^2 + v_b^2)^{\frac{1}{2}}} \tag{6}$$

where u_b and v_b are the total instantaneous velocities at the bed. Following Smith et al. (1993) c_f is the Darcy-Weisbach friction factor, related to Manning's n_m and the total water depth by

$$c_f = \frac{8 g n_m^2}{(h + \overline{\eta})^{\frac{1}{3}}} \tag{7}$$

Manning's resistance coefficient has units of ($s \cdot m^{-1/3}$) and was determined experimentally by Chow (1959) for a wide variety of channels.

To solve the system of equations, the initial conditions of wave height, wave angle, and bottom topography must be specified. The selected wave theory is then used to determine the mass and momentum fluxes while shoaling and refracting the wave to the next grid. The cross-shore mass and momentum equations are next solved for the undertow and the wave induced set-up/set-down. By iterating between the mass equation, the cross-shore momentum equation, and the roller model, the undertow and the set-up/set-down are determined across the entire transect. The present model employs the wave height decay model of Dally, Dean, and Dalrymple (1985), hereafter referred to as the D^3 model.

Once the cross-shore hydrodynamics are computed, the longshore momentum equation is solved with a forward difference scheme. The longshore momentum equation is solved from onshore to offshore because the boundary condition of $V=0$ must be applied at the shoreline. Equation (3) is solved across the entire transect using an implicit tridiagonal solution method. Because there is a quadratic dependence on V in the longshore mean bed stress, the longshore momentum equation is iterated until V converges to a selected tolerance for all points across the

transect. The solution method outlined in this section is the same regardless of the wave theory used to drive the model.

The Roller Model

The roller model recently developed by Dally and Brown (1995) is used to predict the development and decay of the aerated surface roller in the surf zone, and is based on a depth-integrated and period-averaged energy balance equation. For obliquely incident waves, the roller model, under the condition of longshore uniformity, is expressed by

$$\frac{\partial \overline{F}_w \cos \theta}{\partial x} + \frac{\partial}{\partial x} \left(\frac{1}{2} M_R c^2 \cos^2 \theta \right) = -M_R g \beta_d \cos \theta \quad (8)$$

where \overline{F}_w is the depth-integrated, time-averaged, wave-induced energy flux, x is the cross-shore coordinate positive in the shoreward direction, M_R is the roller mass flux, θ is the local wave angle (computed from Snell's law), g is gravity, and β_d is the roller dissipation coefficient. β_d was calibrated by Dally and Brown (1995) using a number of laboratory data sets, and a value of 0.1 yields good agreement when stream function theory is used to compute the driving terms. The volume flux of the roller, used in the conservation of mass equation (Eq. 1), is calculated from

$$Q_{rx} = \frac{M_R}{\rho} \cos \theta \quad (9a)$$

$$Q_{ry} = \frac{M_R}{\rho} \sin \theta \quad (9b)$$

The momentum flux terms for the roller in used in Eqs. 2 and 3 are calculated from

$$R_{xx} = \rho Q_{rx} c \cos \theta \quad (10a)$$

$$R_{xy} = \rho Q_{rx} c \sin \theta = \rho Q_{ry} c \cos \theta \quad (10b)$$

The Eddy Viscosity Model

It is suggested that two sources of turbulence, i.e. roller-induced turbulence and bottom-induced turbulence, should be accounted for in the eddy viscosity model. The measurements of Battjes and Sakai (1981) and Nadaoka and Kondoh (1982) suggest that as a wave dissipates across the surf zone, the turbulence it creates and leaves behind is similar to a turbulent wake. Consequently, an analogy is made that the turbulent wake produced by the roller of a breaking wave is similar to the turbulent wake produced by a cylinder submerged in a moving fluid. From the

theory of turbulent wakes, the eddy viscosity in a turbulent wake (v_T) can be described by (Tennekes and Lumley, 1977)

$$v_T = \frac{\kappa}{R_T} U_o \Theta \tag{11}$$

where κ is Von Karman's constant (equal to 0.4), R_T is the turbulent Reynolds number (equal to 12.5 based on experimental observations), U_o is the free stream velocity, and Θ is the momentum thickness of the wake. For a coordinate system moving with the breaking wave, it would seem that the wave celerity (c) is analogous to U_o . Tennekes and Lumley (1977) show that the momentum thickness for a circular cylinder is approximately half the frontal height of the cylinder, for Reynolds numbers between 10^3 and 3×10^5 . Thus, if the roller is equated to a cylinder, a logical estimate of the momentum thickness, or 'radius', of the roller (Θ_R) is given by

$$\Theta_R = \frac{1}{\sqrt{\pi}} \sqrt{M_R \frac{T}{\rho}} \tag{12}$$

Completing the cylinder analogy, the roller contribution to the eddy viscosity is given by

$$v_R = \frac{0.4}{12.5} c \Theta_R \tag{13}$$

where v_R is uniform over depth, which also follows from turbulent wake theory.

With the upper layer turbulence represented, the bottom-induced turbulent eddy viscosity is now developed. Nielsen (1985) suggests that the length scale of the near-bed eddies should be that of the oscillatory water particle excursion, whereas the velocity scale should be that of a friction velocity. We also suggest that the friction velocity is well-represented by the maximum water particle velocity multiplied by a friction factor. Consequently, it appears that the turbulent eddy viscosity contribution from the bed might be modeled by

$$v_B = \sqrt{\frac{c_f}{2}} |u_{max}| \xi_{max} \tag{14}$$

$$u_{max} = \frac{H\sigma}{2 \sinh kh} \tag{15}$$

$$\xi_{max} = \frac{H}{2} \frac{1}{\sinh kh} \tag{16}$$

where, c_f is the friction factor discussed in the previous section, u_{max} is the maximum orbital velocity given by linear wave theory in equation (15), ξ_{max} is the maximum water particle displacement given by linear wave theory in equation (16), H is wave height, σ is angular frequency, and k is wave number. With the bottom-induced eddy viscosity component modeled, the combination of mixing induced by the roller of the breaking wave and mixing induced by bottom turbulence is given by

$$v_T = \left(v_R^2 + v_B^2 \right)^{\frac{1}{2}} \tag{17}$$

A comparison of the new eddy viscosity model with the eddy viscosity model proposed by Svendsen and Putrevu (1994) (Figure 1) shows an order of magnitude agreement. The new eddy viscosity model does provide a better behaved transition across the breakpoint, with the point of maximum turbulence located inside the surf zone, whereas the Svendsen and Putrevu (1994) eddy viscosity model has a maximum at the breakpoint.

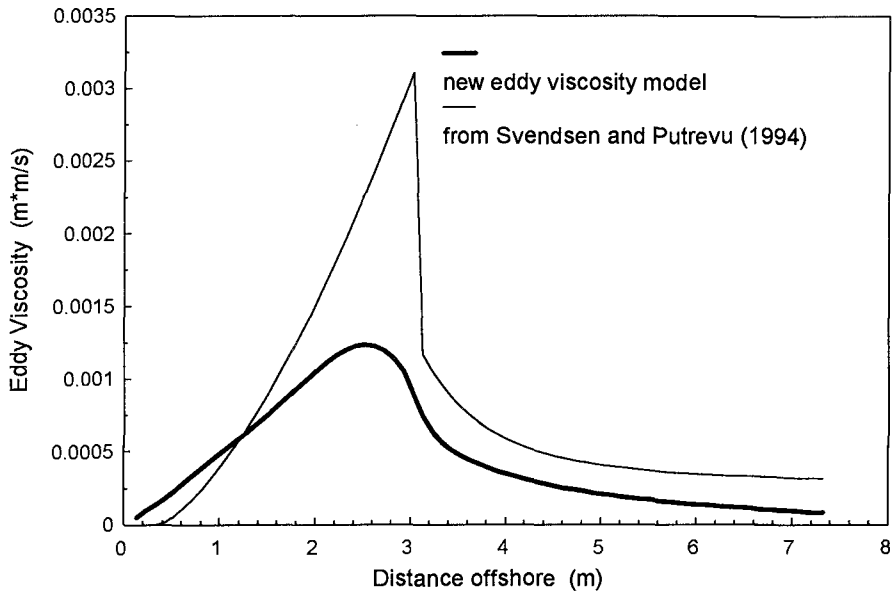


Figure 1 Comparison of the new eddy viscosity model to Svendsen and Putrevu's (1994) eddy viscosity model for Visser's (1991) Case 4 conditions.

Calibration

The numerical model presented here is compared to the laboratory data set of Visser (1991) for calibration and verification. This data set is unique because it is the only experiment to minimize the recirculation present in enclosed basins by utilizing a longshore pumping method, to develop a uniform longshore current. Calibration of the longshore current model entailed the selection of a Manning's friction factor from a range of values presented by Chow (1959) for open channel flow conditions. The empirical decay coefficient (κ) and the stable wave height coefficient (Γ), in the D^3 wave decay model are also calibrated to minimize the error in wave height prediction. Manning's friction factor and the D^3 coefficients are

selected based on their relative least squares error to the measured data defined by equation (18) where B represents the variable in question:

$$E_v = \left(\frac{\sum (B_{meas} - B_{calc})^2}{\sum (B_{meas})^2} \right)^{\frac{1}{2}} \tag{18}$$

Calibration results for the longshore current model are presented for two wave theories in tables 1 and 2. The numerical model results with stream function theory are presented in contrast to the model results for linear wave theory.

Case #	D ³ Coefficients		Least squares error in wave height	
	κ	Γ	<i>Stream Function Theory</i>	<i>Linear wave theory</i>
4	0.15	0.2	7.89 %	5.80 %
5	0.15	0.4	12.45 %	16.70 %
6	0.2	0.3	4.09 %	4.51 %
7	0.2	0.2	9.06 %	7.03 %

Table 1 Selected D³ wave decay model coefficients and relative least squares error from Visser’s (1991) measured data.

Least squares error in longshore current velocity			
Case #	n _m = 0.01	n _m = 0.011	n _m = 0.013
<i>Stream Function Theory</i>			
4	9.42 %	6.85 %	17.13 %
5	19.10 %	13.05 %	16.92 %
6	25.35 %	26.65 %	31.92 %
<i>Linear Theory</i>			
4	19.02 %	20.16 %	25.29 %
5	10.85 %	8.84 %	16.71 %
6	33.13 %	34.97 %	39.59 %

Least squares error in longshore current velocity			
Case #	n _m = 0.015	n _m = 0.017	n _m = 0.02
<i>Stream Function Theory</i>			
7	59.32 %	43.89 %	25.75 %
<i>Linear Theory</i>			
7	43.27 %	31.35 %	17.01 %

Table 2 Least squares percent error for the range of Manning’s friction coefficients (n_m) from Chow (1959) for Visser’s (1991) cases 4 through 7.

Because Visser did not measure the cross-shore current distribution, it is impossible to assess the validity of the cross-shore velocity predictions. However, based on the work of Dally and Brown (1995), the cross-shore current is expected to be reasonably represented. Sensitivity testing of the longshore current model shows that the magnitude of the longshore current is not overly dependent on Manning's friction factor. For the smooth bottom, cases 4-6, the normal friction factor value provides accurate results; however, for the gravel bottom in case 7 a value larger than Chow's (1959) suggested maximum provides better results.

Visser's experiments 1-3 were performed on a beach with a slope of 1/10. Because stream function theory is limited by the breaker height to water depth ratio of 0.78, cases 1-3 were not investigated because the breaking waves in these experiments exceeded this ratio. Because case 8 was reported without wave height measurements, this case was also discarded.

Results and Discussion

The most obvious way to assess the effect of the roller on the longshore current is to contrast the results to a model without the roller term. Figure 2 shows the calibrated longshore current model results for Case 4, with and without the roller term in the cross-shore and longshore momentum equations. It is noted that the roller contribution to turbulence is still included. The model that neglects the roller term in the momentum equations shows a dramatic decrease in the longshore current velocity inside the surf zone and the location of the maximum current is shifted offshore. A similar effect occurs in the model predictions for all the cases studied.

To assess the importance of the roller contribution to turbulence in the surf zone, results are presented that neglect the roller contribution to the eddy viscosity model. It is noted that the roller contribution to the longshore momentum equation is included in this comparison so that the effect of the roller turbulence on lateral mixing may be examined exclusively. Figure 3 clearly shows that the roller-induced turbulence has a significant effect on the overall longshore current distribution. The absence of the roller turbulence in the eddy viscosity model decreases the maximum velocity in the longshore current and shifts this point landward. Also, outside the breakpoint, a slight increase in the longshore current is produced without the roller-induced turbulence included.

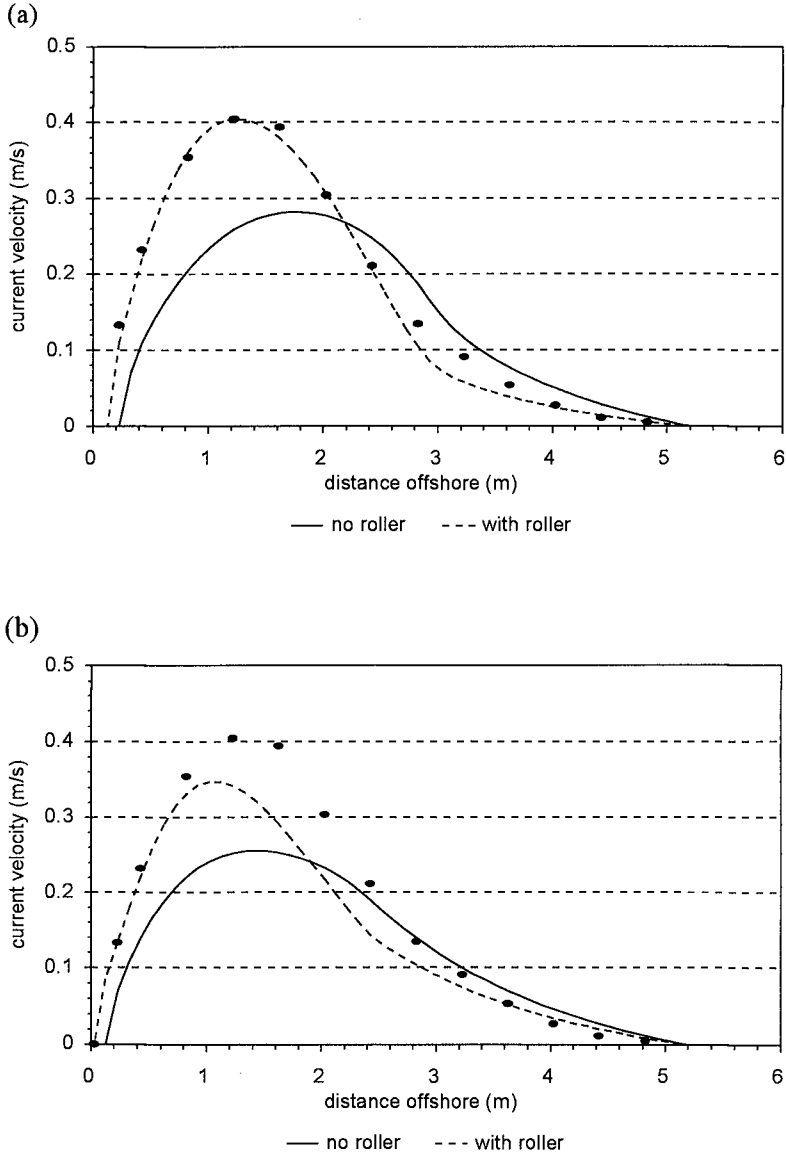


Figure 2 Visser's (1991) Case 4 model comparisons with and without the roller contribution to the longshore momentum equation for (a) Stream Function theory and (b) Linear Wave theory.

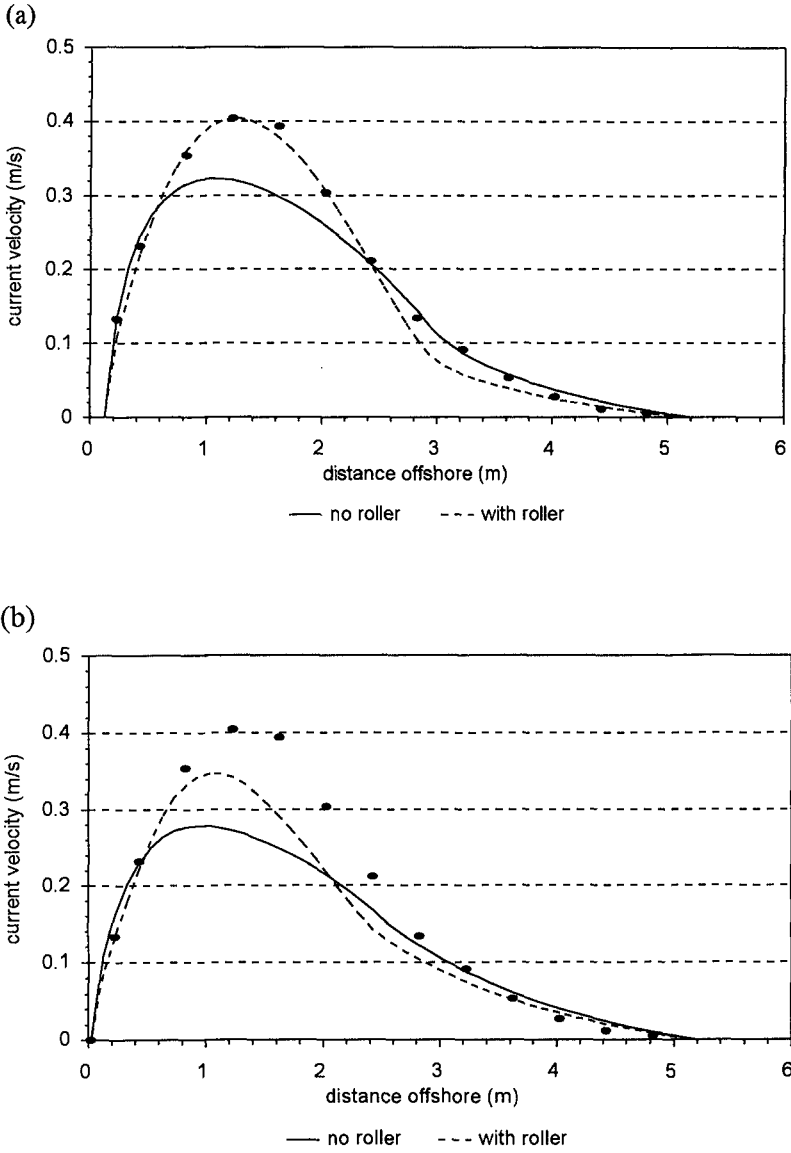


Figure 3 Visser's (1991) Case 4 model comparisons with and without the roller contribution to the eddy viscosity model for (a) Stream Function theory and (b) Linear Wave theory.

It is important to note that the predicted cross-shore current driven by linear wave theory is much greater than the stream function theory cross-shore current. According to Dally and Brown (1995) linear theory in general overpredicts the Stokes drift, whereas stream function theory provides a better prediction of this wave-induced mass transport. Although Visser (1991) did not measure the cross-shore velocity component, it is reasonable to conclude that the hydrodynamic model that uses stream function theory is the better model for calculating the cross-shore and longshore currents.

Conclusions

The major findings of this investigation are as follows: (1) The nonlinear mixing term described by Svendsen and Putrevu (1994) provides an adequate amount of lateral mixing, with realistic eddy viscosity values, in comparison to the laboratory data for longshore currents collected by Visser (1991). (2) The addition of roller momentum to the longshore equation of motion is necessary for accurate longshore velocity predictions. (3) The contribution of turbulence from the roller is an important aspect of realistically modeling the turbulent eddy viscosity. These findings affirm the premise that the roller plays a significant role in driving the longshore current and in shifting the maximum longshore velocity inside the breakpoint.

Acknowledgments

Funding for this research was provided in part by the Sebastian Inlet Tax District Commission.

References

- Battjes, J.A., and T. Sakai, Velocity field in a steady breaker, *J. Fluid Mech.*, 111, 421-437, 1981.
- Bowen, A.J., D.L. Inman, and V.P. Simmons, Wave 'set-down' and set-up, *J. Geophys. Res.*, 73(8), 2569-2577, 1968.
- Chow, V.T., *Open channel hydraulics*, McGraw-Hill, New York, 1959.

- Dally, W.R. and C.A. Brown, A modelling investigation of the breaking wave roller with application to cross-shore currents, subm. to *J. Geophys. Res.*, 100(C12), 24,873-24,883, 1995.
- Dally, W.R., R.G. Dean, and R.A. Dalrymple, Wave height variation across beaches of arbitrary profile, *J. Geophys. Res.*, 90(C6), 11917-11927, 1985.
- Dean, R.G., Evaluation and development of water wave theories for engineering applications, Special Report No. 1, U.S. Army Waterw. Exp. Stn., Vicksburg, Miss., 1974.
- Deigaard, R., P. Justesen, and J. Fredsøe, Modeling of undertow by a one-equation turbulence model, *Coastal Eng.*, 15, 431-458, 1991.
- Nadaoka, K. and T. Kondoh, Laboratory measurements of velocity field structure in the surf zone by LDV, *Coastal Eng. Jpn.*, 25, 125-145, 1982.
- Nielsen, P., A short manual of coastal bottom boundary layers and sediment transport, Public Works Dept. of New South Wales, TM 85/1, 1985.
- Okayasu, A., T. Shibayama, and K. Horikawa, Vertical variation of undertow in the surf zone, *Proc. 21st Conf. Coast. Engr.*, 478-491, 1988.
- Putrevu, U., and I.A. Svendsen, A mixing mechanism in the nearshore region, *Proc. 23rd Conf. Coast. Engr.*, 2758-2771, 1992.
- Smith, J.M., M. Larson, and N. Kraus, Longshore current on a barred beach: field measurements and calculation, *J. Geophys. Res.*, 98(C12), 22,717-22,731, 1993.
- Svendsen, I.A., Mass flux and undertow in a surf zone, *Coastal Eng.*, 8: 347-365, 1984b.
- Svendsen, I.A. and U. Putrevu, Nearshore mixing and dispersion, *Proc. R. Soc. Lon.*, 445, 561-576, 1994.
- Tennekes, H., and J.L. Lumley, *A first course in turbulence*, MIT Press, 1977.
- Visser, P.J., Laboratory measurements of uniform longshore currents, *Coastal Eng.*, 15, 563-593, 1991.
- Visser, P.J., Uniform longshore current measurements and calculations, *Proc. 19th Conf Coast. Eng.*, 2192-2207, 1984.

CHAPTER 265

Velocity Field Measurements in a "Coastal Buffer Zone"

Hiroshi Yagi¹, Hirofumi Hinata¹ and Kazuo Nadaoka²

Abstract

To investigate the characteristics of flow field in the coastal buffer zone (C.B.Z.), velocity measurements in a field were performed both in non-stratified and stratified conditions. The results of the data analysis have shown that in the non-stratified condition wind action, together with tidal motion, may induce unexpectedly large velocity even near the bottom with the magnitude beyond the threshold of the sediment movement, suggesting that the appreciable sediment transport may be caused by these wind-driven currents in C.B.Z.. In the stratified condition, it is revealed that internal tides with baroclinic velocity fluctuation may dominate the cross-shore exchanging motion of water mass.

INTRODUCTION

In coastal current system, the surf zone and the far-offshore region may be regarded as two extremes in a sense that the former is dominated exclusively by nearshore currents, while the latter is governed mostly by the ocean currents (Fig.1). The intermediate-depth zone, on the other hand, may be affected by both the factors as well as tidal currents, wind-driven currents, density currents, river flow, and hence may be called "coastal buffer zone (C.B.Z.)". Therefore for developing a reliable tool to describe the flow field in this zone, more integrated knowledge on these factors and, if any, the interactions among them are necessary. However, still limited parts

¹ Department of Civil Engineering, Tokyo Institute of Technology, 2-12-1, O-okayama, Meguro-ku, Tokyo 152, Japan.

² Department of Mechanical and Environmental Informatics, Graduate School of Information Science and Engineering, Tokyo Institute of Technology, 2-12-1, O-okayama, Meguro-ku, Tokyo 152, Japan.

of the actual physical process of these factors are known for this purpose (Sato,1995; Yasuda et al.,1995). Hence, in the present study, field measurements in a C.B.Z. have been performed to clarify the fundamental characteristics of its velocity field.

OUTLINE OF FIELD OBSERVATION

The observation was carried out in the Kashima coast, as a typical open coast in Japan, which has a straight sandy beach facing the Pacific Ocean (Fig.2(a)). To clarify the characteristics of the current system in the C.B.Z. both in the non-stratified and stratified conditions, field observations were performed in the periods from Nov. 6 to 28 in 1994 and from July 19 to Aug. 20 in 1995.

In the field measurements, three observation stations (St.1-3) were set to be aligned in the cross-shore direction as shown in Fig.2(b). At these stations electromagnetic current meters, pressure-type wave gauges and thermometer were installed. The location of observation stations and the arrangement of measuring instruments were slightly changed between the observations in the non-stratified and stratified conditions as shown in Fig.2(b).

RESULTS AND DISCUSSTION

Non-stratified condition

Figure 3 shows the time histories, at the three stations, of the mean water surface elevation and the shore-parallel component of the mean velocity close to the bottom (0.7-1.7m above the bottom). These mean values were obtained by a moving time averaging over one hour. The regular diurnal tidal fluctuations appear in the mean surface elevation. On the other hand, the shore-parallel bottom velocity shows appreciable irregularity and its maximum magnitude attains almost 40cm/s at St.1. This is an unexpectedly large value, and such a large near-bottom velocity is observed also by Sato (1995) at the Ishikawa coast facing the Sea of Japan. The velocity of 40cm/s is beyond the threshold for the sediment movement, which is estimated as about 25cm/s by the Shields experimental curve for the sand with the mean diameter of 0.2mm. This fact suggests that in C.B.Z. appreciable sediment transport may be caused by these currents, although conventionally significant sediment transport has been believed to occur mostly in the surf zone and its vicinities.

To find the causes of the large velocities near the bottom, the non-tidal irregular components were extracted from the near bottom velocity data by a moving time average over 24 hours. The results are shown in Fig.4, in which the long-period fluctuations with the period of 6 or 7 days appear at each station. Although the velocity amplitude at St.1 in the shallower region is larger than that at St.3 in the deeper region, their fluctuation patterns are very similar each other. This fact suggests that there exists a common mechanism to cause these long-period velocity fluctuations in the C.B.Z.. To find the mechanism, the wind speed, which is indicated with a thick line in Fig.4 (wind-speed data are partly lacked because of trouble in the measurement), is compared with these long-period velocities.

Obviously there is a close correlation among them. Hence, it is suggested that the wind may induce the long-period fluctuating currents with an appreciable magnitude even near the bottom.

To obtain more quantitative understanding of the wind-driven currents in the C.B.Z., its numerical simulation has been done. The governing equations of the computations are 2-DV momentum equations with the coriolis force and the continuity equation. The k - ε model described below has been employed to evaluate the vertical eddy viscosity ν_t .

$$\frac{\partial k}{\partial t} + u \frac{\partial k}{\partial x} + w \frac{\partial k}{\partial z} = \frac{\partial}{\partial z} \left(\frac{\nu_t}{\sigma_k} \frac{\partial k}{\partial z} \right) + P_k - \varepsilon, \quad (1)$$

$$\frac{\partial \varepsilon}{\partial t} + u \frac{\partial \varepsilon}{\partial x} + w \frac{\partial \varepsilon}{\partial z} = \frac{\partial}{\partial z} \left(\frac{\nu_t}{\sigma_\varepsilon} \frac{\partial \varepsilon}{\partial z} \right) + C_{\varepsilon 1} \frac{\varepsilon}{k} P_k - C_{\varepsilon 2} \frac{\varepsilon^2}{k}, \quad (2)$$

$$\nu_t = C_\mu \frac{k^2}{\varepsilon}, \quad (3)$$

where x and z represent the cross-shore and vertical coordinate, u and w the velocity components in the x - and z -direction, k the kinetic energy of turbulence, ε the dissipation rate of the turbulence kinetic energy, and P_k the production rate of k . C_μ , $C_{\varepsilon 1}$, $C_{\varepsilon 2}$, σ_k and σ_ε are the turbulence model parameters, for which the standard values ($C_\mu=0.09$, $C_{\varepsilon 1}=1.44$, $C_{\varepsilon 2}=1.92$ and $\sigma_k=\sigma_\varepsilon=1.0$) are adopted here. In the present computation, the shore-parallel uniformity is assumed and the topography of the computational area is simplified as shown in Fig.5. The spatially uniform wind shear stress at the water surface was given, being based on the wind data obtained at the nearshore observation station (as shown in Fig.4) and the friction factor at the water surface ($C_d=0.002$).

Figure 6 shows the computed vertical profiles of the shore-parallel velocity for the three cases of the water depth; i.e. $h=20, 60, 100$ m. The indicated results are those after 9.5 days from the beginning of the computation. In the case of $h=100$ m, the vertical gradient is relatively large in the surface layer, while it becomes small beneath it. This fact suggests that the effect of wind shear stress is limited to the surface boundary layer, and the geostrophic current under the balance between the coriolis force and the cross-shore gradient of the water surface elevation is formed beneath the surface layer. On the other hand, in the case of $h=20$ m, the influence of wind shear stress reaches the bottom so that the large vertical gradient of velocity is induced through the entire depth. This means that in the present observation area, because of its shallow water depth less than 20m, the large bottom velocity may be induced by the wind shear stress. These facts indicate that the ratio between the surface Ekman boundary layer width δ_E and the local water depth h , δ_E/h , is one of

the principal factors for the overall understanding of the velocity field of a C.B.Z..

Figure 7 represents the computed time histories of shore-parallel bottom velocities at St.1 to 3, which show the long-period fluctuation similar to those found in Fig.4. However, the magnitude of the computed velocity, except for St.3, is smaller than that of the measured, and the velocity differences among the three stations are not well reproduced. One of the possible causes of these discrepancies is the difference between actual and simulated turbulence structure of the wind-driven currents. Besides the offshore wave breaking due to wind may act to augment the bottom velocity (Yasuda et al., 1995).

Stratified condition

Figure 8 (a) and (b) show respectively the shore-parallel and cross-shore components of the bottom velocity fluctuation in the case of the stratified condition at St.2, where the water depth is 13m and the distance from the shoreline is 1.5km. The long-period fluctuation as found in the non-stratified condition does not appear in this case. However, more conspicuous feature in the time variation characteristics can be found; namely, as compared with those in the non-stratified condition, these velocity data show high frequency fluctuation with appreciable irregularity, especially in the cross-shore component. To examine the frequency characteristics of these velocity fluctuations, the frequency spectra have been computed as shown in Fig.9, which indicate that in the shore-parallel component the diurnal tidal fluctuation has dominant contribution to the spectrum both in the surface and bottom velocities. In the cross-shore velocity component, on the other hand, the diurnal tidal fluctuation prevails in the surface velocity, while in the bottom velocity the semi-diurnal fluctuation arises with appreciable magnitude.

These diurnal and semi-diurnal velocity fluctuations were further examined with the water surface tidal fluctuation by extracting them from the raw data by applying a band-pass filtering. The results are shown in Fig.10 and indicate that the diurnal components of the shore-parallel velocity in the surface and bottom layer are nearly in phase. This means that the shore-parallel velocity is governed mainly by the *barotropic* tidal motion. On the other hand, the semi-diurnal components of the cross-shore velocity in the surface and bottom layer are mutually 180 degrees out of phase. These facts suggest that the *baroclinic* tidal motion is dominant in the cross-shore direction.

To examine the cross-shore barotropic motion in more detail, the water temperature variations both in time and space has been investigated. The field data for this purpose was obtained with the vertical arrays of several thermometers at the three stations. Figure 11 represents a typical example of the time sequence of the spatial distribution of the water temperature. It can be seen that the bottom water body with relatively low temperature runs up and down on the sloping sea bottom with the excursion length of about 1 km for the front movement. Corresponding to this bottom water motion, the upper water body with higher temperature shows cross-shore oscillating motion in the opposite phase from the bottom water motion.

From these results, the velocity field of the C.B.Z. in the stratified condition may

be summarized as follows; i.e., in the shore-parallel direction, the barotropic tidal motion is dominant, while in the cross-shore direction the baroclinic tidal fluctuation is significant. This difference may be explained by the role of the shore boundary; i.e. it prevents the barotropic tidal motion exclusively in the cross-shore direction. However, the baroclinic cross-shore tidal motion appears as running up and down motion near the shore with large excursion length. Since this baroclinic tidal motion results in appreciable cross-shore exchange of water mass, it may have a dominant role in the cross-shore mass transfer in C.B.Z..

CONCLUSIONS

The major conclusions obtained in the present study for C.B.Z. are summarized as follows:

1. In the non-stratified condition, wind action may induce unexpectedly large velocity even near the bottom with the magnitude beyond the threshold of the sediment movement. This fact suggests that the wind-driven current may cause appreciable sediment transport in the C.B.Z..
2. The ratio between the surface Ekman boundary layer width δ_E and the local water depth h is one of the principal factors for overall understanding of the velocity field in C.B.Z..
3. In the stratified condition, internal tide with baroclinic velocity fluctuation may dominate the cross-shore exchanging motion of water mass.

References

- Sato, S. (1995): Characteristics of wave and current induced by low pressures in Japan Sea, *Journal of Hydraulic, Coastal and Environmental Engineering*, JSCE, No.521, 113-122. (*in Japanese*)
- Yasuda, T., Mori, N., Kato, S. and Sato, S. (1995): Currents off the Ishikawa coast and their breaker effects, *Proc. of Coastal Engineering*, JSCE, Vol.42, 431-435. (*in Japanese*)

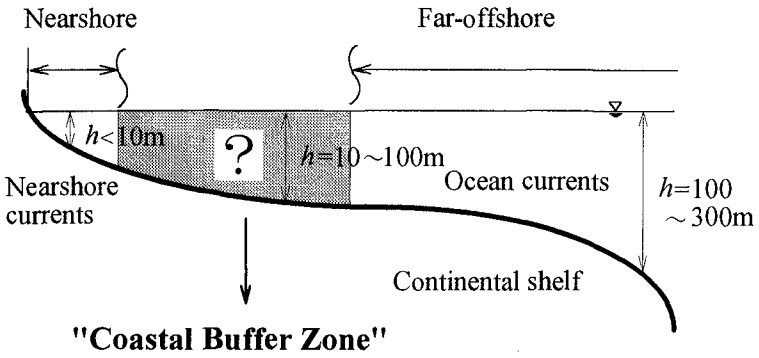


Fig.1 Conceptual illustration of coastal buffer zone in an open coast.

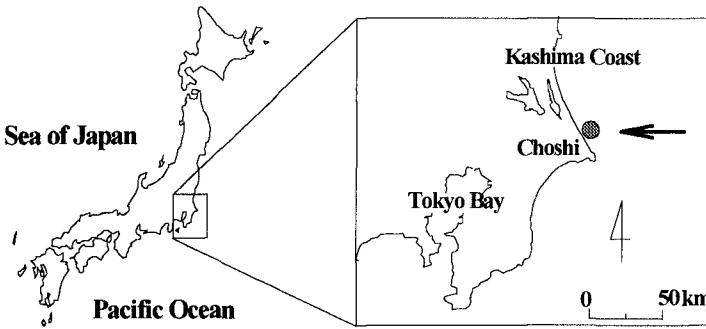


Fig.2(a) Location of study.

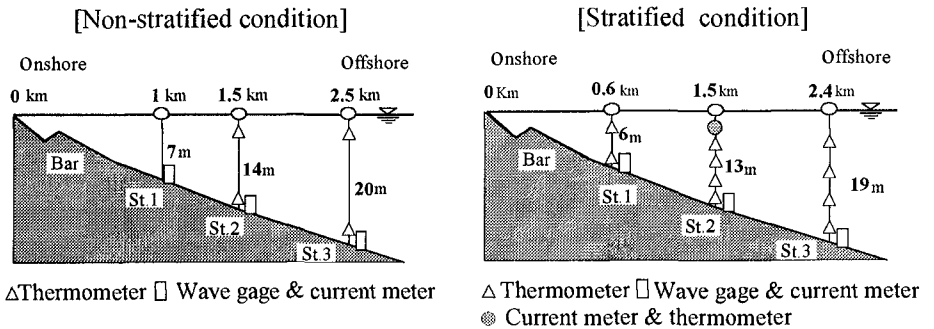


Fig.2(b) Location of observation stations and arrangement of measuring instruments.

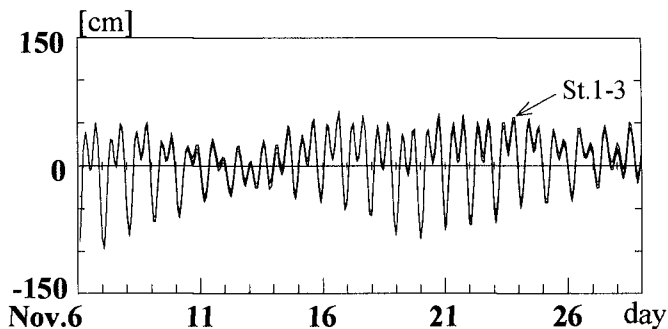


Fig.3 (a) Mean water surface elevations.

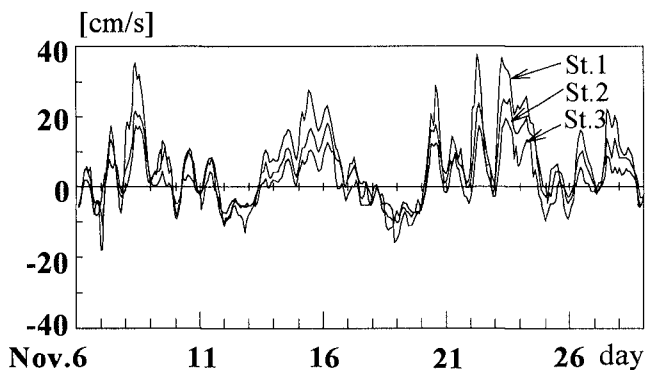


Fig.3 (b) Shore-parallel component of bottom velocities.

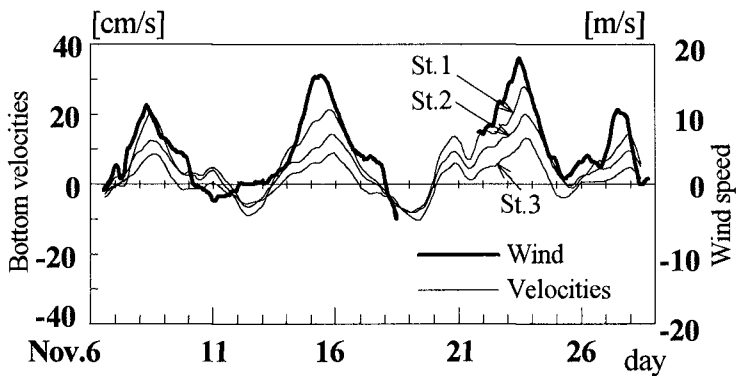


Fig. 4 Long-period fluctuating components of shore-parallel bottom velocities and wind speed.

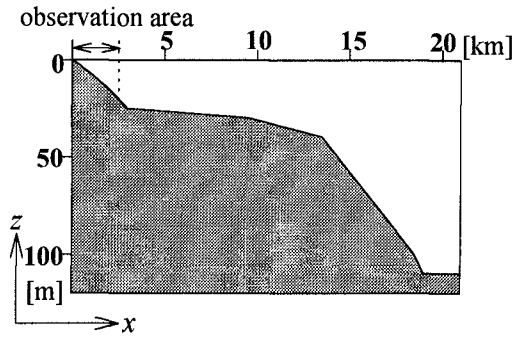


Fig.5 Computational area.

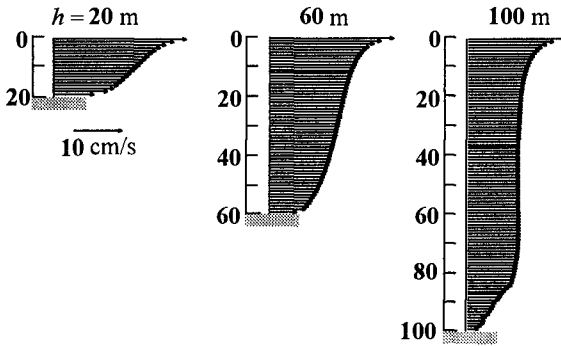


Fig.6 Computed vertical profiles of shore parallel velocity.

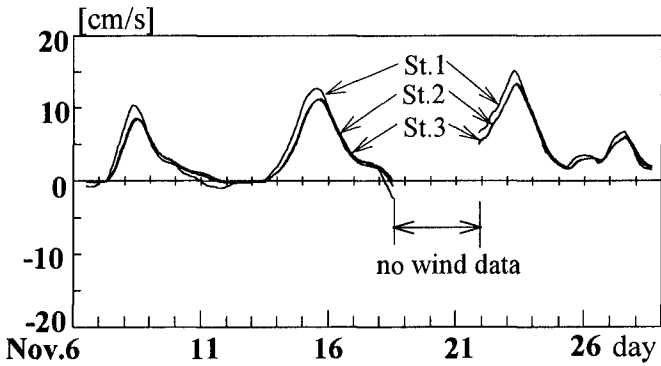


Fig.7 Computed shore-parallel velocities at St.1 to 3.

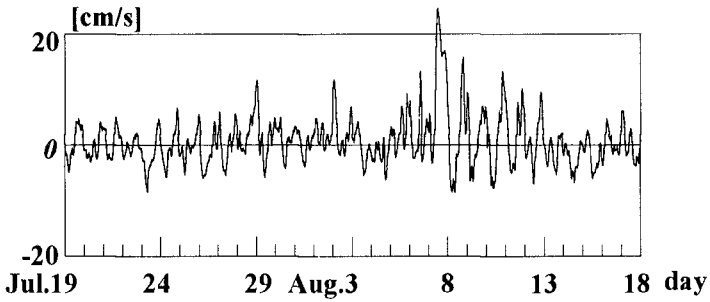


Fig.8(a) Shore-parallel component of bottom velocity at St.2.

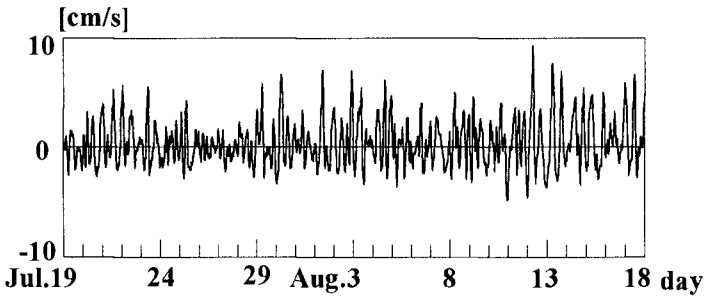
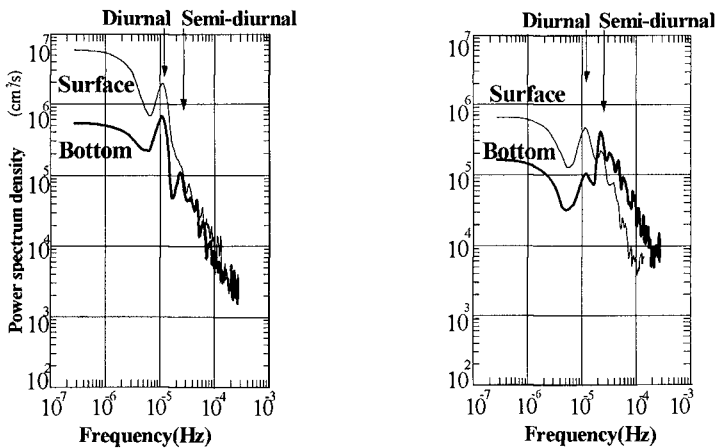


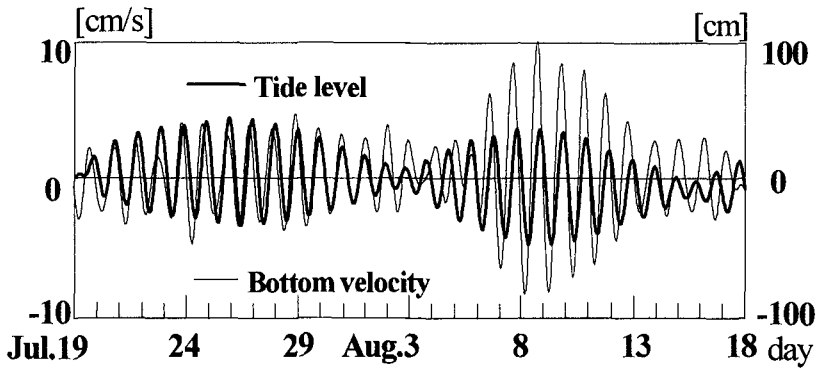
Fig.8(b) Cross-shore component of bottom velocity at St.2.



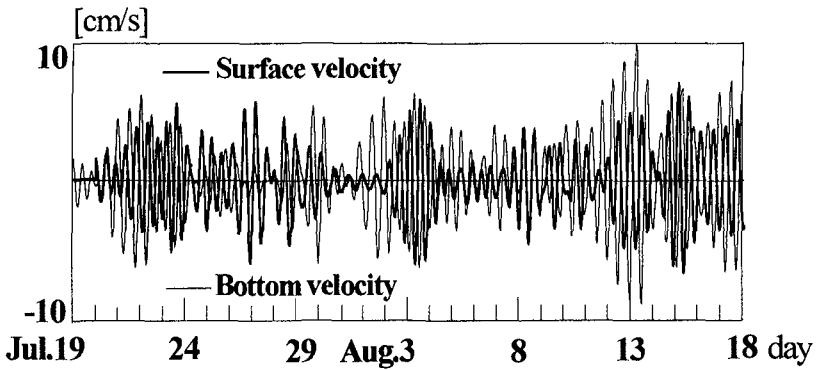
(a) Shore-parallel component.

(b) Cross-shore component.

Fig.9 Power spectra of velocity fluctuations at St.2.



(a) Diurnal component of shore-parallel bottom velocity and tide level at St.2.



(b) Semi-diurnal component of cross-shore bottom velocity and tide level at St.2.

Fig.10 Band-pass filtered velocities.

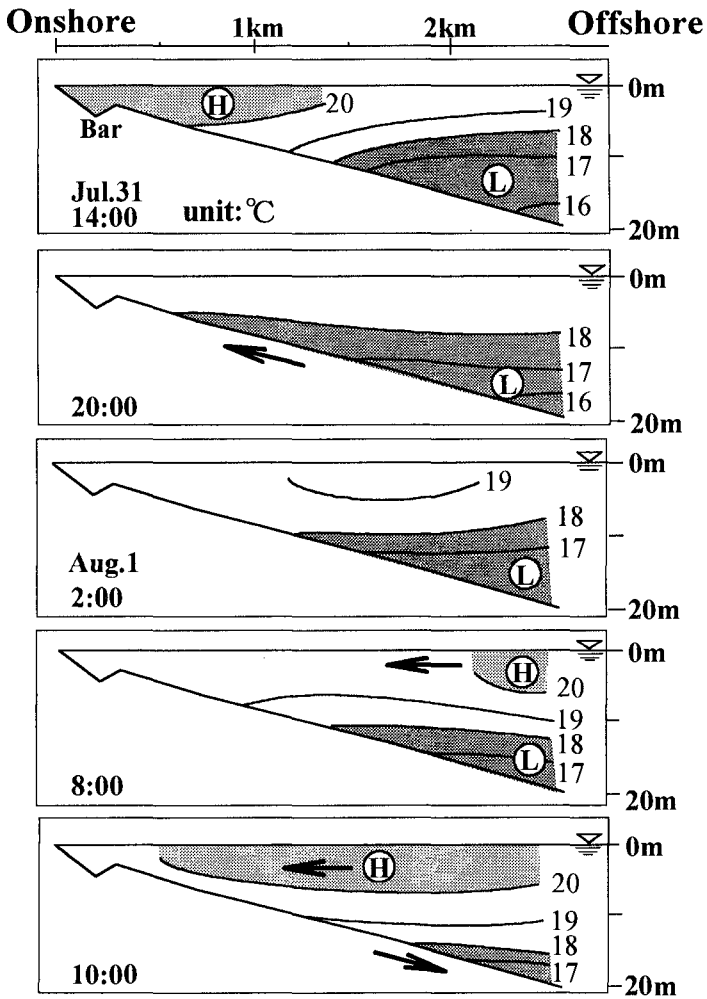


Fig. 11 Time sequence of spatial distribution of water temperature in diurnal time scale.

CHAPTER 266

DEVELOPMENT OF UNDERWATER BEACH PROFILE BY MONOCHROMATIC AND RANDOM WAVES

Karsten Peters¹, Jürgen Neue¹ and Hans-H. Dette², M.ASCE

ABSTRACT: Central to all problems involving alluvial coasts is the response of the underwater profile to given wave conditions. It has been demonstrated in laboratory tests that a constant wave pattern leads to an equilibrium profile. BRUUN (1954) defined this profile by a parabolic equation and various refinements have been proposed since. Applications to field data show, however, that the fit is frequently less than satisfactory. Noteworthy is also that profiles generated in the large wave flumes tend to have significantly narrower surf zones than similar sand beaches in the nature. To answer this and other questions a series of experiments were carried out in the Large Wave Flume (LWF) in Hannover.

INTRODUCTION

The Large Wave Flume in Hannover is 324 m long, 5 m wide and has a depth of 7 m and is capable of generating waves up to 2 m height. These waves are generated by an electronically controlled hydraulic system, which drives a piston-type wave board. A wave absorption device allows the minimization of wave reflections during the tests.

The main objective in the 1993 experiments was the investigation of beach profile response under erosional and accretional wave conditions. The experiments included tests with monochromatic waves and spectral waves at constant water level and spectral waves with superimposed tidal simulation with 1m tidal range.

¹) Research Assistant ²) Academic Director, Department of Hydrodynamics and Coastal Engineering, Leichtweiss-Institute for Hydraulics, Technical University Braunschweig, Beethovenstr. 51a, 38106 Braunschweig, Germany.

EXPERIMENTAL SET-UP

The initial profile geometry consisted of a dune, a 1:30 beach slope and a 70 m long toe berm (Fig. 1). A sand volume of 1.700 m³ was necessary to build up the initial profile. The used sand had a grain diameter of $D_{50} = 330 \mu\text{m}$ with a fairly narrow grading. This is representatively for the beaches along the west coast of the high energy coast of the Island of Sylt/North Sea. Data were collected on bed profile development, water levels and waves, wave energy dissipation, velocity distributions and suspended sediment distributions, only aspects relating to profile development will be discussed here.

The experiments in the Large Wave Flume can be divided into three major parts:

- In part I monochromatic waves were used to generate an equilibrium profile under erosional conditions (Test Series 0 and 2) and accretional conditions (Test Series 1), while the water level was kept constant.
- In part II (Test series 3 and 4) random waves (TMA-Spectra) were used to investigate the profile response under erosional and accretional test conditions with a constant water level.
- In part III (Test Series 5 and 6) random waves (TMA-Spectra) were run together with water level variations in order to simulate a profile development under tidal conditions. The tide had a range of 1 m with the previous constant water depth of 4.50 m representing the high water level. The 12 hours 'sinusoidal' tide is simulated as step function in 25 cm steps of 60 minutes, except high and low water phases with 90 minutes duration.

Table 1 summarizes information on wave parameters, water level, test duration and profile response for the Test Series' 0 to 6. The final profile of each single Test Series was used as initial profile for the following series.

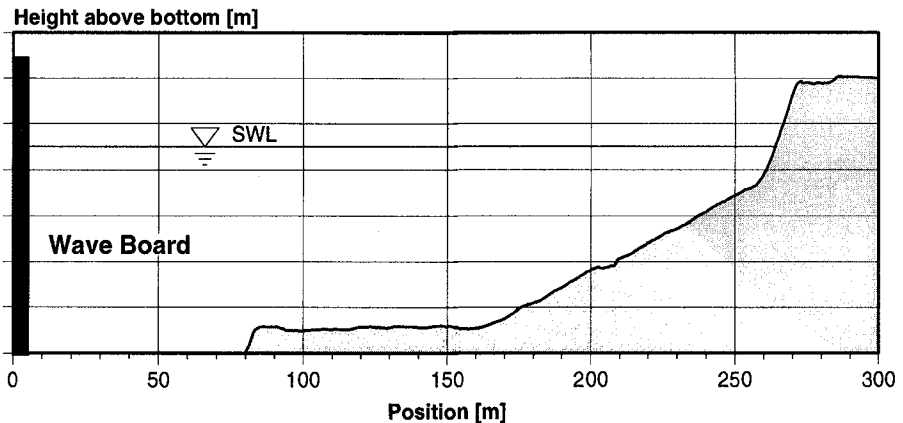


Figure 1. Initial profile built up in the Large Wave Flume in Hannover.

Table 1: Test conditions for the flume experiments 1993.

Test Series	Initial Geometry	Wave Parameters			Water Level [m]	Duration [hrs]	Profile Response
		Type	H, H_{m0} [m]	T, T_p [sec]			
0	1:30 slope	M	1.20	5	4.50	17:00	Erosion
1	result of 0	M	1.20	10	4.50	15:45	Accretion
2	result of 1	M	1.20	5	4.50	07:20	Erosion
3	result of 2	S	1.20	5	4.50	15:00	Erosion
4	result of 3	S	1.20	10	4.50	10:30	Accretion
5	result of 4	S+T	1.10	5	3.5 - 4.5	45:00	Erosion
6	result of 5	S+T	1.05	10	3.5 - 4.5	39:00	Accretion

with M - monochromatic waves with H and T

S - TMA-spectrum with H_{m0} and T_p

S+T - TMA-spectrum with water level variations (tidal simulation)

RESULTS AND DISCUSSION

Profile Shape

- In part I monochromatic waves in Test Series 0 with a height of 1.2 m and a period of 5 sec. were used to generate an equilibrium profile under erosional conditions. The initial 1:30 beach slope and the dune (Fig. 2a) were transformed during 17 hours of erosion in Test Series 1 (Fig. 2b) into a typical bar-trough-profile, which can be characterized by the relatively steep and narrow bar and the following trough. The slope of the seaward bar face had a magnitude of 1:5. Arrows in Fig. 2 indicate the direction of the bar movement.

The final profile form in Test Series 0 was stabilized under 16 hours of accretional waves with a period of 10 sec. in the following Test Series 1 (Fig. 2c), where ripple structures were formed seaward and landward of the widened bar. The surf zone has been filled with sand so that the profile level inside the surf zone raised.

Additional 7 hours of erosional wave conditions in Test Series 2 (Fig. 2d) widened the surf zone and formed a steeper bar. The inner surf zone was raised again and rebuild like a foreshore terrace, while the ripple structures at the sea floor disappeared.

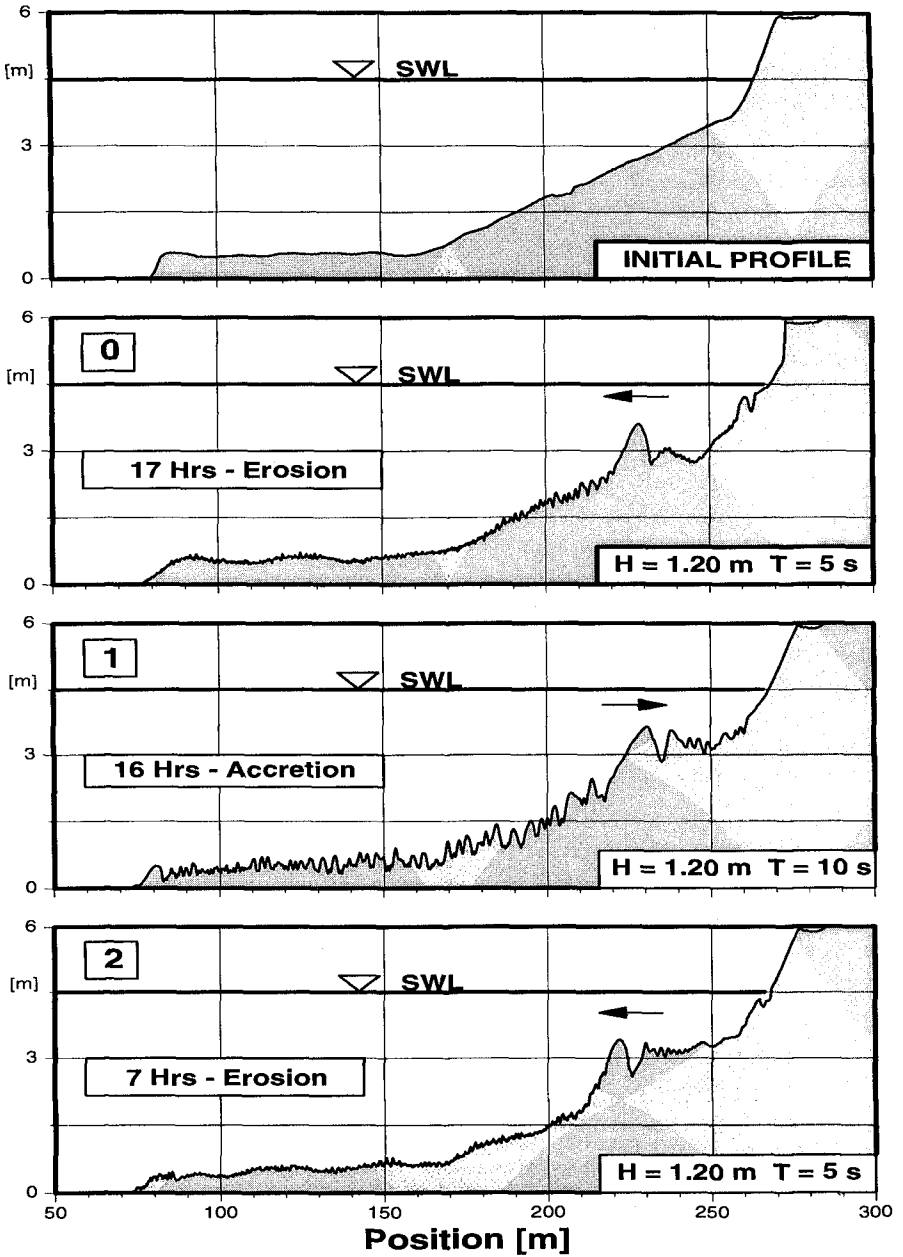


Figure 2. Initial and final beach profiles under monochromatic waves and constant water level (Test Series 0 - 2).

- In part II (Test series 3 and 4) irregular waves (TMA-Spectra) were used in order to investigate the profile response under erosional and accretional waves. In 15 hours of erosion the profile has smoothed inside and outside the surf zone and the seaward slope of the foreshore terrace has moved further offshore (Fig. 3a).

11 hours of accretional wave conditions formed ripple structures at the profile bottom (compare with Test Series 1) and rounded the foreshore terrace (Fig. 3b). In comparison to the monochromatic case the bar is much lower and broader.

- In part III (Test Series 5 and 6) random waves (TMA-Spectra) were run together with water level variations in order to simulate the profile development under tidal conditions. Caused by different water levels and spatially moving zones of energy dissipation an equilibrium profile developed in the surf zone area. The final profile of Test Series 5 (Fig. 3c) shows how the inner surf zone has been smoothed, while the seaward front face of the surf zone moved further offshore indicated by an arrow.

39 hours of accretional wave conditions in Test Series 6 flattened the bar profile in the surf zone area and a short terrace could develop (Fig. 3d). The wet beach remained the original shape over the whole Test Series' 5 and 6.

2D/3D Profile Development

In order to illustrate the morphological processes caused by the spectral waves and superimposed tidal simulation more in detail the single profiles of Test Series 5 have been joint together into time-dependent profile evolution diagrams. The upper diagram in Fig. 4 shows the profile evolution under erosional wave conditions over the time of $3\frac{1}{2}$ tidal cycles. Two arrows indicate the starting and the final position of the bar crest. In the lower graph (Fig. 4), which shows the top view of the profile evolution, the phases after low and high water level conditions are marked.

It is significant to see in both graphs how the bar profile changed into a smoothed foreshore terrace, while the seaward face of the terrace moved in rhythmic manner further offshore. The offshore movement of the bar, which is caused by erosional wave conditions, is overlapped by the rhythmic bar movement over the tidal cycles. This morphological rhythm, which can be observed between position 200 m and 220 m in the upper diagram with the help of the contour lines, shows the profile response on the tidal simulation.

At low water level zones of energy dissipation are spatially placed further offshore, which results in a higher erosion potential because the profile in that tidal phase is not in equilibrium with the incoming waves. At high water level the zones of energy dissipation are shifted further onshore and the waves do not break at the front face of the foreshore terrace as at low water levels. The front face of the foreshore terrace moves onshore, by which means the crest height of the bar is increased.

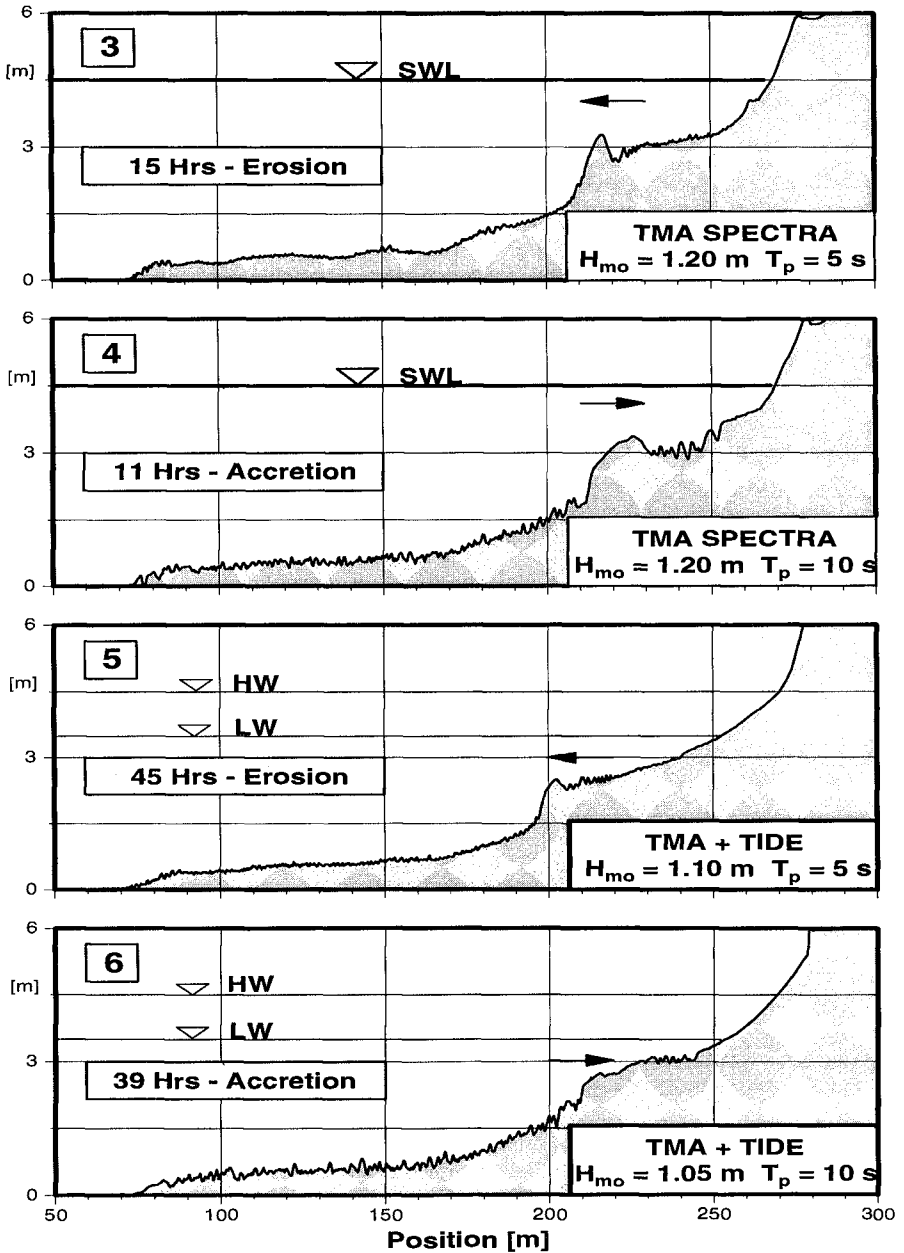


Figure 3. Initial and final beach profiles under spectral waves with constant water level (Test Series 3 and 4) and spectral waves with superimposed tidal simulation (Test Series 5 and 6)

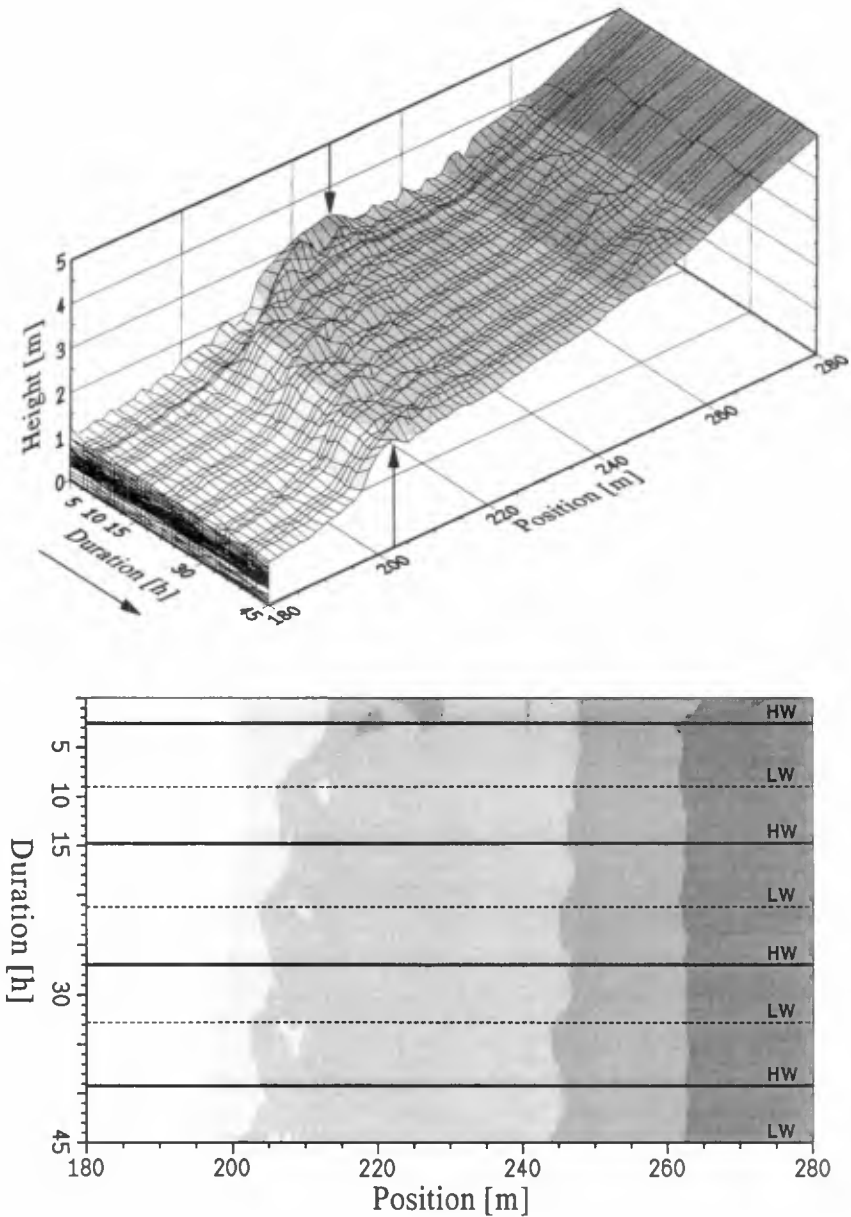


Figure 4. Profile evolution under erosional wave conditions (TMA spectra) with superimposed tide as a 3D-diagram (above) and as a top view (2D diagram below).

By tidal simulation the bar movement has been intensified. This was also observed for Test Series 6 (not illustrated here) under accretional wave conditions, where the rhythmic bar movement caused by the tide overlapped the onshore movement of the bar system.

Bar Position and Bar Height

All profile data for each wave condition can be analysed as a time history over the whole test duration. In the upper graph of Fig. 5 the definitions of the bar height, the bar position and the surf zone width are shown. The bar crest in this case is defined as crest height of the seaward shore face.

In the lower graph of Fig. 5 the surf zone and the enclosed beach with the adjacent shoreline is shown as a top view and the bar height with the corresponding water level as a side view. It can be seen how the bar position at the seaward end of the surf zone developed, and how the crest height of the bar corresponds to this. Additionally the water level is indicated. For Test Series 5 and 6 the manner of tidal simulation is illustrated.

For the Test Series' 1 to 6 it can be summarized that erosional wave conditions (marked with 'E' in the graph) widen the surf zone and lower the crest of the bar, while accretional wave conditions (marked with 'A' in the graph) cause a reduction of the surf zone width and connected with an increase of the bar crest level. The superimposed tide and the tidal range intensify the bar movement, compared to the Test Series with constant water level. These two components, the bar movement at a constant water level and the tidal cycles itself, lead to a rhythmic bar movement. After 2-3 tides the morphological changes during each tide became stable, which means that the morphological changes on the profile over one tidal cycle reached already a minimum.

Ripple Structures

Accretional monochromatic waves (see Test Series 1) have caused large bed forms at the profile bottom. This is demonstrated in Fig. 3b. As a time history the plotted profiles in Fig. 6 show a considerable ripple movement seaward of the bar. Starting with the initial profile at the bottom the intermediate profiles are plotted above in temporal order. It can be seen how the bed forms grow and develop at the seafloor and how they propagate in landward direction until they reach the toe of the bar. The bed forms were not able to propagate into the surf zone, so that they stopped at the toe of the bar and increased the width of the bar. Because the bar crest remained nearly at its position the seaward slope of the bar became flatter.

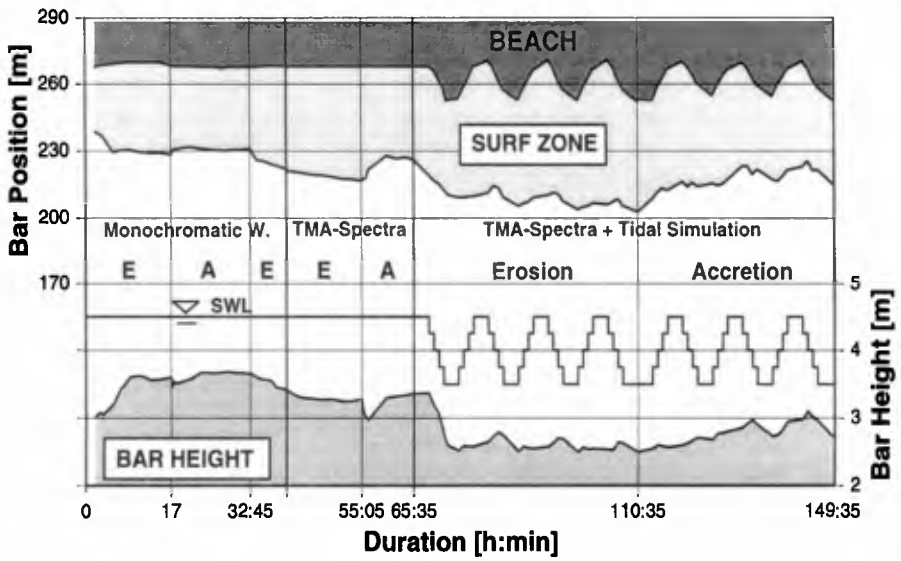
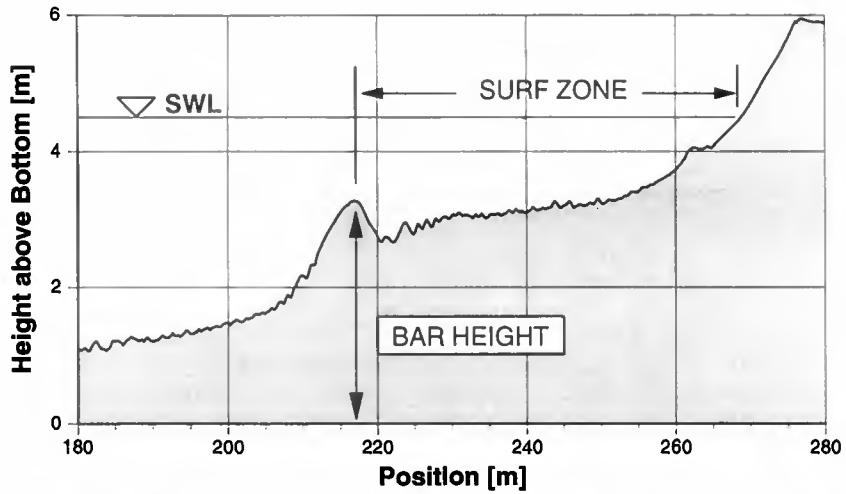


Figure 5. Definition of the surf zone (above) and position and height of bar over all Test Series' (below)

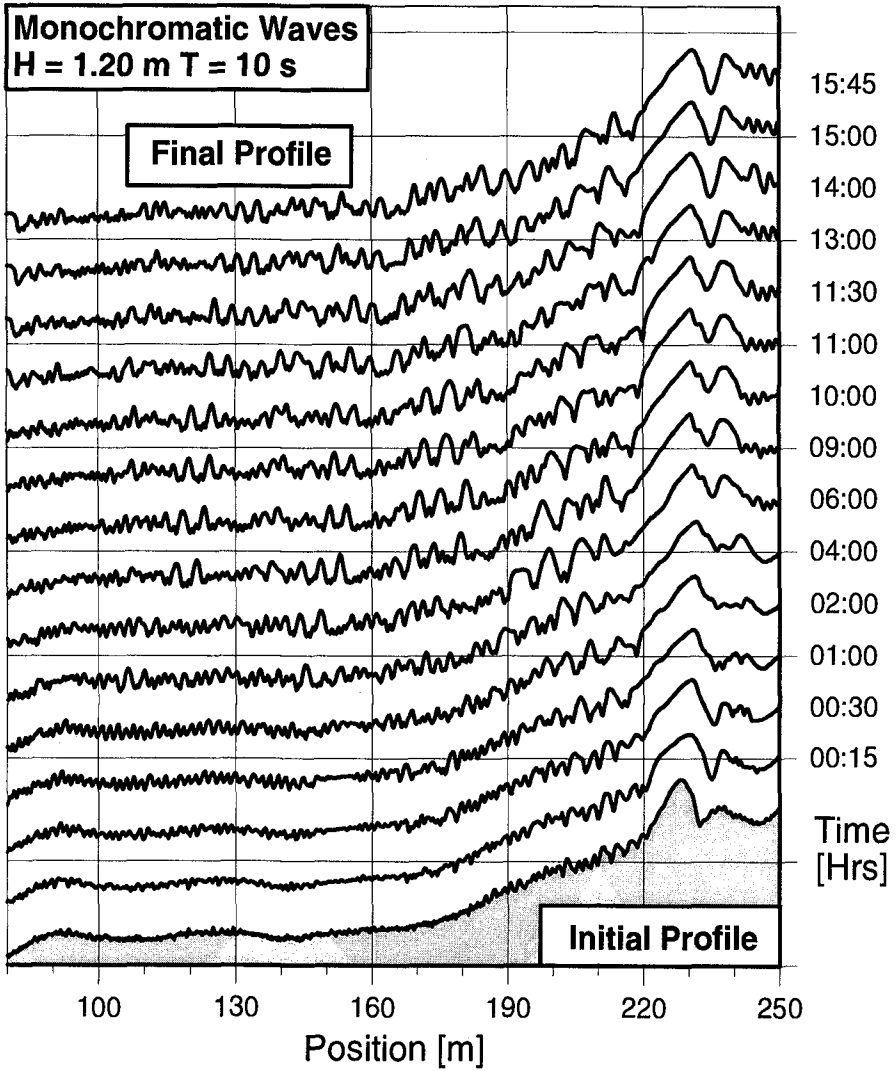


Figure 6. Development of bed forms during accretional wave conditions (Test Series 1).

CONCLUSIONS

The flume experiments in 1996 showed that beach profiles reached their equilibrium state under erosional and accretional wave conditions in small timescales. For a constant water level the profiles have been transformed into quasi-equilibrium profiles after 10 to 15 hours of test duration. In the case of a varying water level 2-3 tidal cycles were only necessary to develop a state, where the profile changes during one tidal cycle reached a minimum.

The experiments for accretional conditions were affected by a steep seaward slope, what is not naturelike. Further tests are necessary to investigate this question.

ACKNOWLEDGEMENT

This work was carried out as a part of the research project "Untersuchungen zur Ausbildung von Gleichgewichtsprofilen auf der Grundlage von Experimenten im Großen Wellenkanal" ("Investigation in the development of equilibrium profiles based on experiments in the Large Wave Flume") funded by the German Ministry of Education, Science, Research and Technology under contract no. 515-3892-MTK 0559.

REFERENCES

- BRUUN, P. (1954) "Coast Erosion and Development of Beach Profiles", U.S. Army Corps of Engineers, Beach Erosion Board., Tech. Memo. No. 44.
- DETTE, H.H.; NEWE, J. and PETERS, K. (1995) "Large Wave Flume Experiments '93. Volume I: Data Report - Wave Data and Beach Profile Surveys", Report No. 787, Leichtweiss-Institute, Technical University Braunschweig (unpublished).

CHAPTER 267

TURBULENT STRESSES IN THE SURF-ZONE: WHICH WAY IS UP?

John W. Haines¹ and Guy Gelfenbaum¹

Abstract

Velocity observations from a vertical stack of three-component Acoustic Doppler Velocimeters (ADV) within the energetic surf-zone are presented. Rapid temporal sampling and small sampling volume provide observations suitable for investigation of the role of turbulent fluctuations in surf-zone dynamics. While sensor performance was good, failure to recover reliable measures of tilt from the vertical compromise the data value.

We will present some cursory observations supporting the ADV performance, and examine the sensitivity of stress estimates to uncertainty in the sensor orientation. It is well known that turbulent stress estimates are highly sensitive to orientation relative to vertical when wave motions are dominant. Analyses presented examine the potential to use observed flow-field characteristics to constrain sensor orientation. Results show that such an approach may provide a consistent orientation to a fraction of a degree, but the inherent sensitivity of stress estimates requires a still more restrictive constraint. Regardless, the observations indicate the degree to which stress estimates are dependent on orientation, and provide some indication of the temporal variability in time-averaged stress estimates.

Introduction

Few observations of turbulent stresses in energetic surf-zone conditions exist. This observational void is in marked contrast to modeling efforts describing surf-zone circulation. Published models include details of the stress distribution which have yet to be constrained by field observations (*Svendson et al.*, 1987, *Deigaard et al.*, 1991). Moreover, investigations of nearshore circulation have suggested that simpler (constant eddy viscosity) models of the stress distribution may be inconsistent with field observations of the mean flow field (*Haines and Sallenger*, 1994).

¹U.S. Geological Survey, Center for Coastal Geology, 600 4th St. South, St. Petersburg, FL, 33701

In an attempt to better constrain modeling efforts, a field program was designed to collect data on the vertical and temporal distribution of turbulent stresses within the surf-zone. As part of the Duck94 field program a vertical array of SonTek Acoustic Doppler Velocimeters (ADV) was deployed and 24 days of nearly continuous data collected (Figure 1). The principle aim of the deployment was to return observations of the high-frequency intermittent phenomena associated with bottom and surface boundary-layer processes. The objective was to accurately describe the turbulent statistics of the flow-field adjacent to both boundaries under breaking and non-breaking wave conditions.

A critical requirement for the calculation of stress estimates is the precise definition of an appropriate coordinate system. Because of the relatively large horizontal flows associated with shallow-water incident waves, stress estimates are inherently sensitive to the choice of a vertical coordinate. Previous work has suggested that, under representative incident wave conditions, a precision of 0.03 degrees is required in definition of the tilt angle to assure stress estimates are correct within $1\text{cm}^2\text{s}^{-2}$ (Lohrmann *et al.*, 1995). The appropriate coordinate system may depend on the modeling approach taken. For example, a gravitational coordinate system may produce results significantly different than a coordinate system aligned with the local bed slope. In the absence of field observations of the magnitude and variability of the stresses, the precision required for array design is speculative. Observed variability also provides an indication of the sensitivity of results to the choice of coordinate frame.

The ADV array deployed was instrumented with a continuously recording tilt-meter. Subsequent analyses suggest that the tilt-meter lacked the required accuracy for definition of a reliable coordinate system. Given the shortcomings of the tilt measurements, and the sensitivity of stress estimates to tilt, we are investigating the potential for using the flow data itself to determine an appropriate coordinate system. Regardless of the success of this effort, the data also provides a means for investigating the sensitivity of field observations to deviations from the vertical. The observations will also provide some indication of the magnitude of the temporal and spatial variability of surf-zone stresses.

Data

As part of the Duck94 experimental program, a vertical stack of Sontek ADVs was deployed at the US Army Corps of Engineers (ACOE) Field Research Facility (FRF) in Duck, NC. The deployment consisted of 7 ADV sensors in a vertical array, with supplementary observations of water level, optical backscatterance, array tilt and rotation, and bed elevation from a sonic altimeter (Figure 1). All sensor outputs were digitized *in situ*, synchronized via GPS clock, and written to shore-based storage via a fiber optic cable. The ADVs were sampled at 25 Hz. All other sensors were sampled continuously at 64Hz. The ADV distribution was intended to span the bulk of the water column and return observations of near-bed and near-surface turbulent fluctuations.

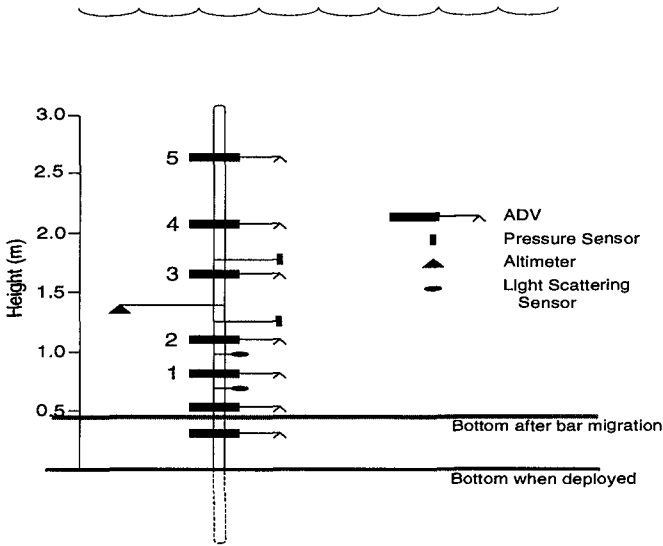


Figure 1: Array configuration. Bed height determined from altimeter is approximately 1m from ADV position. ADV sensing volumes are 15cm below the sensor heads shown.

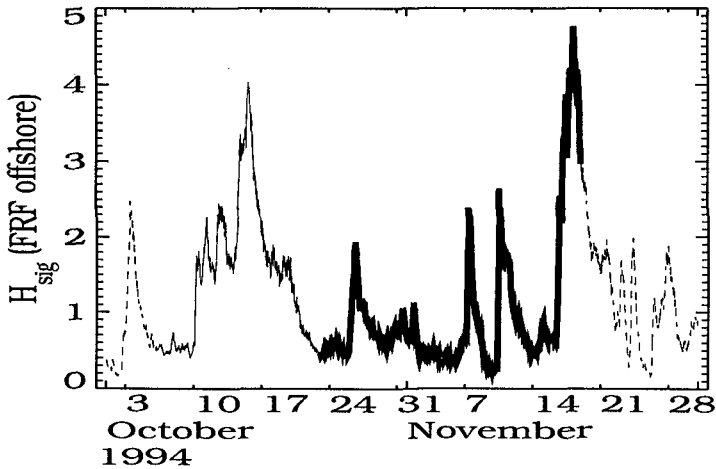


Figure 2: Offshore significant wave heights from the Field Research Facility pressure array in 8m water depth. Solid lines indicate period of sensor deployment, thick solid line shows period of data recovery.

The array was initially deployed in approximately 4.5m water depth, outside the primary bar normally present at the Duck site. Subsequent to deployment, an energetic storm event (October 16-18th, Figure 2) resulted in substantial bar migration, burying the lowermost ADV and obscuring the sampling volume of the next highest sensor. The following weeks saw a slow erosion of the bar, and the upper impacted sensor eventually began to return data. Figure 2 shows the off-shore wave conditions present throughout the deployment. The deployment spans 3 substantial storm events, and only data from these events, where the array was within the surf zone, are discussed in the following. Discussion is further limited to those 5 sensors which were continuously operational. The deployment was violently terminated by surf-zone debris associated with the passage of Hurricane Gordon.

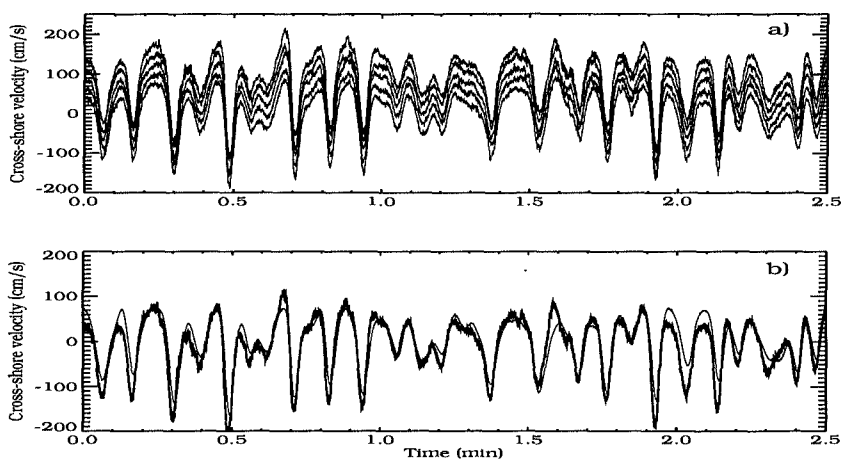


Figure 3: a) Time series from ADV sensors, offset to indicate increasing height above the bed. b) Time series from uppermost ADV and pressure sensor (normalized by velocity variance).

The data quality from the ADV sensors appears to be uniformly good. Figure 3a shows representative data from the 5 operational ADV's, demonstrating extremely high coherence between sensors across the incident wave band. Independent verification of sensor performance is given by comparison to the water level data (as shown in Figure 3b.) Depth decay of the incident-band velocities are consistent with linear theory, supporting the overall data quality. Visual inspection of the data suggests that high-frequency variance "events" occur with greater frequency high in the water column. This may be suggestive of breaking-produced turbulence, and is an area for further investigation.

The data are further described in Figure 4a, showing cross-shore, u , and vertical, w , velocity spectra (Figure 4a). Above incident-band frequencies the

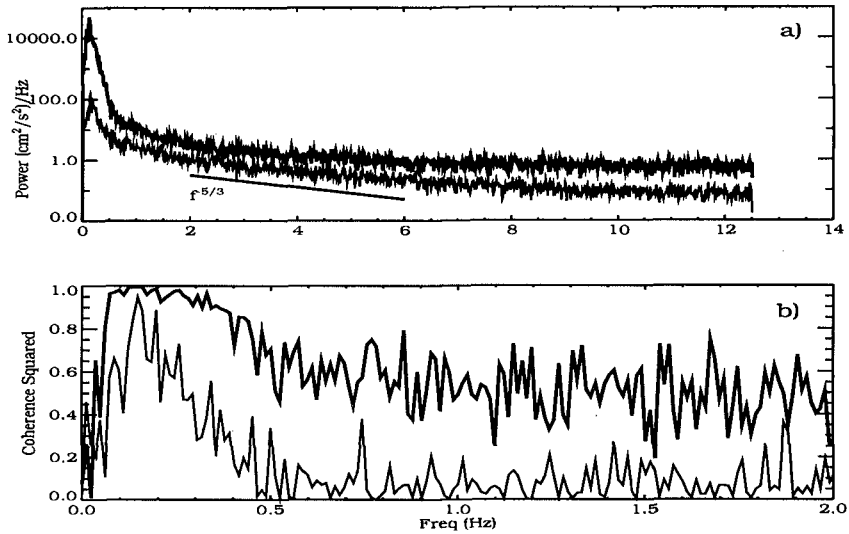


Figure 4: a) u (higher energy) and w spectra. b) pu (thick line) and pw squared coherences. Frequency scales are not equivalent for the two panels. Data shown are post-rotation as determined by the analysis described herein.

spectra show an $f^{-5/3}$ decay. The horizontal velocities generally show enhanced energy levels relative to the vertical velocities at all frequencies. The leveling of spectral energy at high frequencies for the horizontal velocity is due to the noise-floor of the sensor, which is substantially reduced for the vertical component. Coherences between pressure observations, p , and horizontal velocities are high across the incident band and uniformly higher than pw coherences.

Analysis

While the data appear reliable, calculation of the turbulent stresses requires accurate constraint of the coordinate frame. In the following we will attempt to determine the sensor orientation from the observed flow characteristics. In order to maximize the signal-to-noise ratio of the data, further analysis is restricted to high-energy conditions. Selected one-hour data segments, described in Table 1, were analyzed.

The underlying assumption for the following analysis is that the flow field, as described by the observations, contains information about the sensor orientation. A plausible first assumption might be that, following linear wave theory over a horizontal bed, within the incident-wave band, vertical and horizontal velocities are in quadrature. It follows that the time-averaged stress, $\langle uw \rangle$, should be zero. We might then choose to rotate the observations into a coordinate frame where this criteria is met. For a sloping bed, the result is rotation into a bed-normal

Run #	Date	Time UTC	Depth <i>m</i>	H_{rms} <i>m</i>	T_p <i>s</i>	bed ht. <i>m</i>
0	10/26	13:00	4.49	.81	4.9	.25
1	10/26	15:00	4.78	.92	5.3	.26
2	10/26	19:00	4.54	1.21	6.1	.27
3	10/26	21:00	4.20	1.21	6.4	.26
4	11/7	08:00	3.50	.55	12.8	.35
5	11/7	09:00	3.65	.68	11.6	.36
6	11/7	10:00	3.77	.79	11.6	.37
7	11/7	11:00	4.18	1.14	11.6	.38
8	11/7	12:00	4.52	1.29	11.6	.39
9	11/7	13:00	4.80	1.38	6.4	.41
10	11/7	16:00	4.90	1.60	7.5	.42
11	11/7	17:00	4.69	1.35	7.5	.37
12	11/7	22:00	3.80	.99	11.6	.38
13	11/8	14:00	4.73	.62	11.6	.48

Table 1: Summary statistics for analyzed runs. All quantities are from array observations of surface water level and bed elevation. Bed height is distance beneath lowermost operational sensor. Sensor height for remaining sensors are, relative to lowermost sensor, 20.8 *cm*, 86.4 *cm*, 130.1 *cm*, 189.4 *cm*.

coordinate system, or more correctly, rotation into a wave-defined coordinate system. Alternative criteria for determination of the coordinate system might include rotation to zero mean vertical velocity, $\langle w \rangle = 0$, or minimization of the vertical variance, $\langle ww \rangle$. The $\langle w \rangle$ criteria would follow on assuming that mean flows were constrained to be bed-parallel. The validity of this assumption may vary with distance from the bed. In all cases the resulting coordinate frame may be expected to reflect the influence of a sloping bed. It is of interest to examine whether variations on the order of the bed slope significantly change the estimated stress quantities.

The rather simplified view outlined supports a variety of approaches for determining a best rotation. The assumption that relevant information is contained in the wave-driven flow requires application of any methodology across some subset of the entire frequency range sampled. Any of the above criteria might be applied, singularly or in a weighted combination. The assumption of uw -quadrature further supports minimization of a number of co-spectral quantities across the frequency band of interest. In fact, any of the variance properties ($\langle uw \rangle$, $\langle ww \rangle$) may be minimized as band-averaged quantities, or minimized frequency band-by-band in a least-squares sense across the entire frequency range of interest.

A number of candidate criteria were tested. The "best" criteria were determined by the consistency of the resulting coordinate system. This is based on

the necessary assumption that the array was stationary throughout the data examined. Here the deposition of approximately 50cm of sand associated with the bar migration may be viewed as a benefit. This deposition, we presume, further stabilized the array, reinforcing the stability properties provided by a deep central jetted pipe and three anchored guy wires. A further assumption is that the coordinate frame, as defined by the flow, is stationary. This assumption is invalidated by any significant change in the underlying bed topography.

Among all the criteria tested the most consistent results were achieved by constraining the mean vertical velocity to be zero ($\langle w \rangle = 0$) and minimizing the vertical variance subject to this constraint. The minimization requires selection of a frequency band of interest, and it is the band-averaged variance which is ultimately minimized. Variations arising from this selection will be discussed in the following.

The constraint of $\langle w \rangle = 0$ defines a functional relationship between the two tilt angles given by $\gamma = f(\beta)$, where γ is the tilt angle in the alongshore/vertical (yz) plane, and β is the tilt angle in the cross-shore/vertical (xz) plane. The search for $\langle ww \rangle = \min$ may then be restricted to the line in $\gamma\beta$ space defined by the $\langle w \rangle$ constraint.

The shore-normal horizontal coordinate frame chosen approaches, for the nearly shore-normal wave conditions examined here, a frame oriented with the principle component of the wave velocities. As a result, as will be shown, the tilt angle, β , in the shore-normal direction is strongly constrained by the energetic wave motions, while the γ solution, subject to less energetic wave motions, is less well defined. Conversely, small variations in β have a large (relative to γ) impact on the estimated stresses. The alongshore component of the system is dominated by the strong alongshore currents present during most of the runs analyzed. The mean currents influence the rotation through the $\langle w \rangle = 0$ constraint.

This approach to determining a coordinate frame implies a further, less obvious constraint. The minimization procedure ($\langle w \rangle = 0$, $\langle uw \rangle = \min$) is equivalent to constraining the stress terms, $\langle uw \rangle$, to be zero. We do not expect this constraint to be strictly valid, due to system noise and the influence of "non-wave" motions. Nonetheless, the results provide the greatest consistency in determination of sensor tilt. While it might be hoped that averaging the results over several data segments might reduce the effects of such contamination, it is equally (or more) likely that this procedure has a systematic bias in the tilts determined.

The minimization procedure was applied to the data subsets described in Table 1. Stable estimates resulted only when conditions were energetic, suggesting the wave signal must exceed some "noise" level in the data (where noise may include a variety of non-wave motions as well as system or random noise). Further examination indicated that the stability of the estimates was enhanced when the incident wave field was narrow-banded in direction. The stability of the tilt estimates was determined from the variance of the estimates from segmented runs. While variability in the results increased with decreasing wave height,

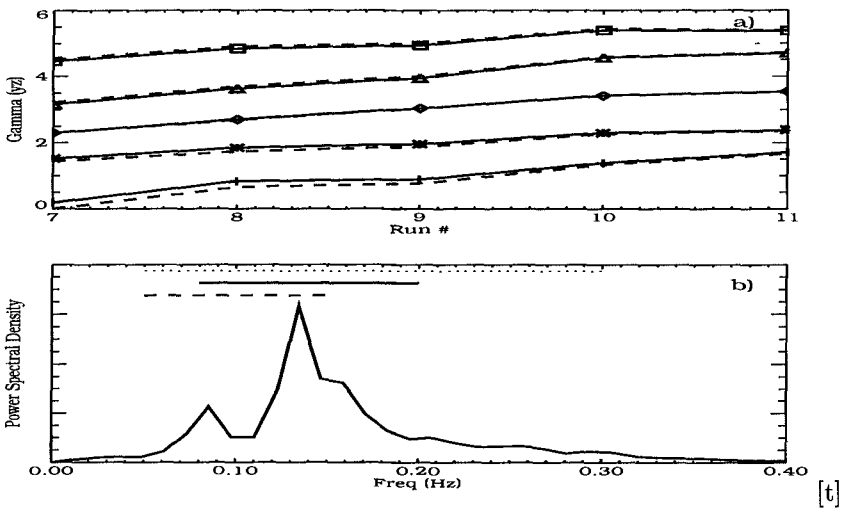


Figure 5: a) Resulting best γ (tilt in yz plane) values for 1 hour data runs. Values offset to indicate sensor location. Line types indicate the frequency range of the solution. b) Representative cross-shore velocity spectrum and frequency range of solutions (shown by horizontal lines).

there was no significant change in the mean values determined. The final values determined are consistent with the data from the tilt sensor, though this provides constraint within only a few degrees.

Determination of the best rotation in the following is restricted to data Runs 7 – 11 (Table 1) which are relatively continuous in time and subject to energetic incident wave conditions. In fact, all runs listed are well within the surf-zone. Only beneath breaking waves were conditions energetic enough to result in stable estimates. The impact of breaking wave conditions on the approach can not be assessed as non-breaking conditions with large waves were not observed.

Results

Results for the γ (yz plane) tilt determination are shown in Figure 5a. The minimization was applied over three separate frequency bands as shown in Figure 5b. For determination of γ the results are insensitive to the frequency band chosen. The best γ values resulting show significant variance and a marked trend with time. While the variance in γ is large, the relatively modest amounts of incident wave energy in the along-shore direction results in little effect on calculated stress quantities.

Determination of β , in the plane of maximum wave orbital motions, has a far greater impact on stress calculations. Figure 6 shows that while the overall variance in the estimated orientation is reduced relative to γ , the sensitivity to

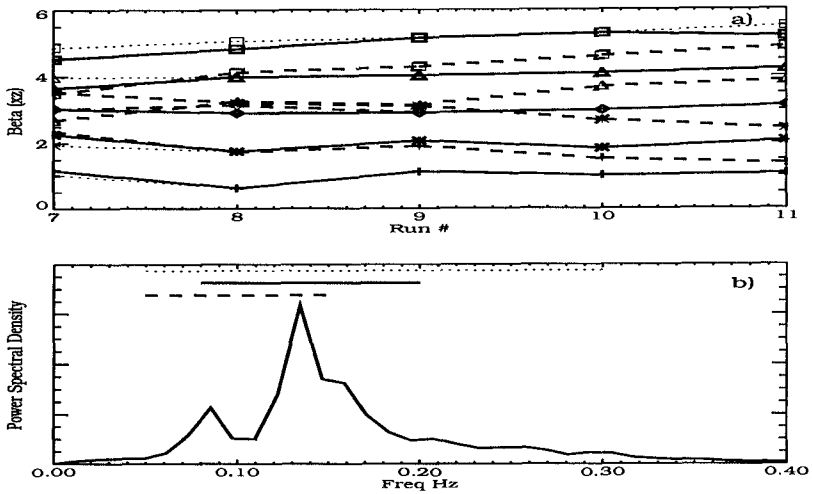


Figure 6: a) Resulting best β (tilt in xz plane) values for 1 hour data runs. Values offset to indicate sensor location. Line types indicate frequency range of solution. b) Representative cross-shore velocity spectrum and frequency range of solutions (shown by horizontal line).

frequency band selection is increased. Stable estimates require a choice which encompasses the entire incident band, and stability is further enhanced by inclusion of the higher harmonics. This is a somewhat problematic finding. Ideally we would like to determine orientation using an approach independent of information in the higher turbulent frequencies.

The standard deviations of the β values found for the 5 runs are shown in Table 2. The variance reduction with increasing frequency range is clear. There is also an indication that the upper and lower sensors are less well constrained. This is consistent with enhanced turbulence generation at the boundaries (reducing the wave signal relative to other motions) or may suggest some deviation from linear-wave behavior near the free-surface and bed. Overall, consistent tilt estimates are found to within half a degree (2 standard deviations) for all sensors.

Discussion

The mean tilt values from the 5 runs described were applied to correct all the data. The resulting vertical velocity spectra and uw coherences are shown in Figure 4. Vertical velocity variances are substantially reduced relative to the unrotated data, as are uw coherences; suggesting a removal of wave fluctuations from the vertical component. The data still show marked spectral and coherence peaks in the incident wave band. The method applied minimizes the w -variance across the entire band. Peak removal is somewhat enhanced if the variance mini-

Sensor #	Std. deviation β (degrees)		
	Low Freq.	Incident	Broad band
5	.53	.32	.23
4	.47	.29	.10
3	.10	.09	.09
2	.44	.20	.14
1	.38	.22	.20

Table 2: Standard deviation of β values determined over 5 runs analyzed. Values are shown (in degrees) for frequency ranges indicated in Figure 5b.

mization is applied in a least-squares sense, band-by-band, across the frequency range selected. Results from this approach are comparable, though somewhat more variable.

The approach followed here is based on some general assumptions about the frequency contribution to the stress. Figure 7 describes this contribution, and the effect of rotation. The figure shows the cumulative stress as higher frequencies are included in the stress calculation. Shown are the results for the best orientation determined previously (averaged over 5 runs), and rotations representative of ± 0.2 and ± 0.4 degrees in γ and β . The solid horizontal line shows the frequency range for which the tilt angles are determined. The best rotation for this run (as opposed to the best average rotation) would result in the intersection of the cumulative stress curve and the high-frequency end of the frequency range. The case shown is a worst case result, serving to illustrate the sensitivity of the stress to relatively small changes in tilt.

The total stress is given by the high-frequency end of the cumulative stress curve (flat beyond the limits shown). It is clear that the resulting estimates are highly sensitive to the tilt. Furthermore, the stress is completely specified to a high degree by frequencies lower than 0.5Hz . This result is independent of uncertainties in the orientation. Also of note, the resultant stresses change in a near-linear fashion with orientation, with the rate of change fairly constant for all sensors. This implies that, though absolute values of the stress may be highly sensitive to orientation, temporal and spatial trends (between-sensor variability) may be more amenable to observation.

For the sensor and data run shown the "best" average rotation results in a flattening of the cumulative stress curve across the incident band. In contrast, the best solution specific to this run and sensor (approximated by the lowermost cumulative stress curve) shows stress contributions which cancel within the incident band. This cancellation of regions (in frequency) of opposing stress is common to all the runs examined. A more rigorous approach will require a more complete consideration of this structure and the indicated physics of incident-band motions.

Overall the message from Figure 7 is rather disheartening. The suggestion

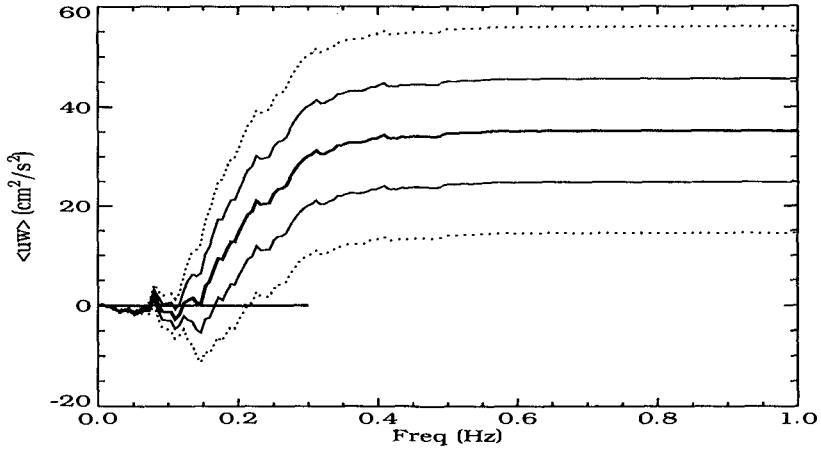


Figure 7: Cumulative stress plots for representative time series. Results from best rotation (thick line), plus (minus) 0.2 degrees in γ and β are given by upper (lower) solid lines, plus (minus) 0.4 degrees in γ and β are given by upper (lower) dotted lines.

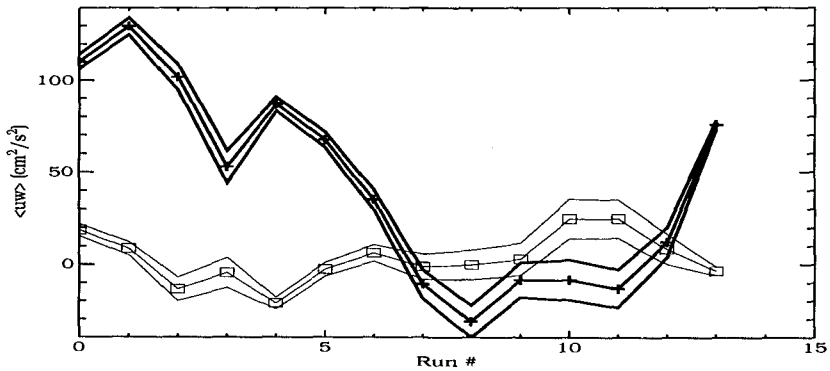


Figure 8: Stress estimates for all runs for uppermost (thin) and lowermost (thick) sensors. Error bounds indicated represent ± 2 standard deviations in γ and β .

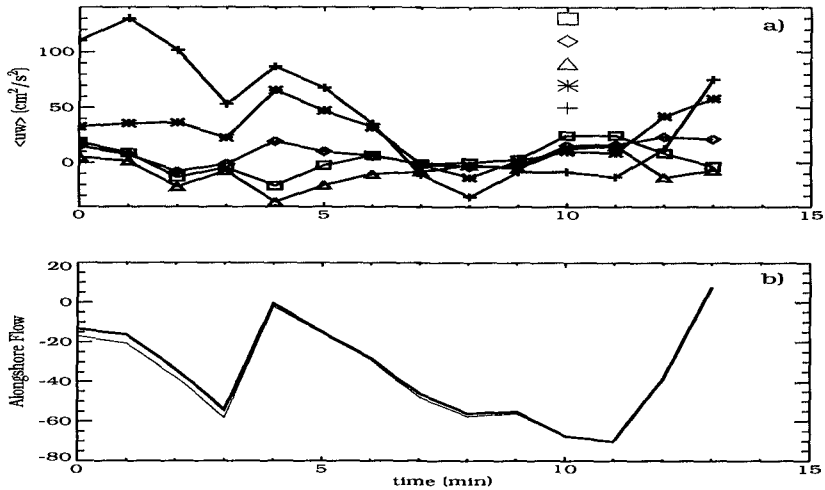


Figure 9: a) Estimated stresses for all sensors. Sensor location indicated by symbols. b) Variation in alongshore mean current for uppermost (thin line) and lowermost (thick line) sensors.

is that the most consistent results require utilization of flow information across the entire frequency band responsible for the observed stresses. There is no clear indication that the wave band is, in fact, independent of some turbulence band which contributes significantly to the stress.

The stresses resulting from the top and bottom sensors are shown in Figure 8. Calculations have been extended to incorporate all the data from Table 1, applying the best rotation as found for the 5 runs (7 – 11) previously discussed. While we believe the array was stationary across the entire period, we can not demonstrate this to the level required and the data must be viewed with some skepticism. Indications are that the near surface stress is much less variable than that near the bed. The effects of significant changes in bed elevation may be contributory. Estimates show changes in sign for both sensors, and changes in relative sign between sensors. The degree of temporal variability is large near the bed and suggests that observational efforts, with orientation precision of order 0.2 degrees are feasible. Some credibility is added to these results as both the bottom two sensors show marked temporal variability relative to the uppermost sensors (Figure 9a).

The temporal variability noted may be related to both changes in bed elevation and changes in the fluid forcing. The mean alongshore flow was highly variable across the runs examined. Figure 11b shows this variability, which is qualitatively similar to that observed for the stress estimates in the lower water column. The temporal trend in γ previously shown (Figure 5) is strongly correlated with the

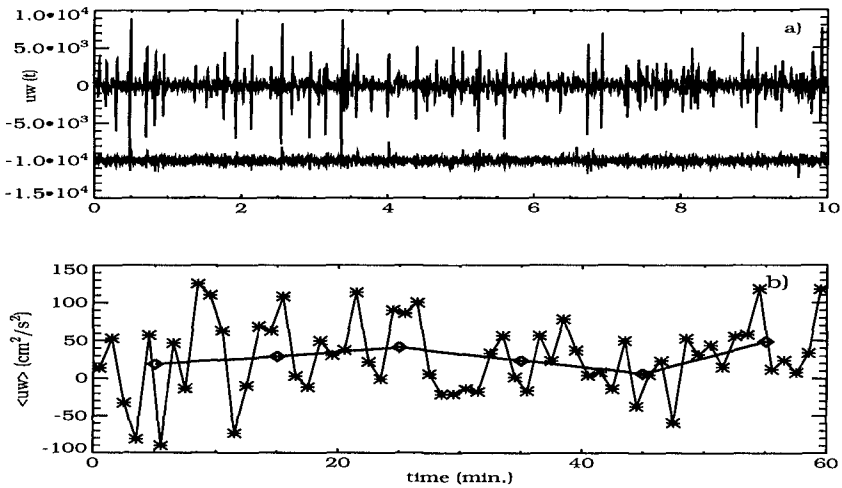


Figure 10: a) Instantaneous stress (uw) for uppermost and lowermost (offset by -10^{-4}). b) One and ten minute averages of stress from uppermost sensor.

variability in the alongshore current.

As a final note we leave the rotation problem behind to examine the variability of the stress estimates on short time scales. Figure 10a shows time series of stress from the uppermost and lowermost (offset by -10^{-4}) sensors. The degree of variability in the instantaneous stresses is elevated near the free surface, in contrast to the behaviour previously shown for time-averaged values. Averaged values (1 and 10 minute averages, Figure 10c) from the uppermost sensor clearly show that, over 10 minute periods, the stress estimates display substantial temporal variation.

Conclusions

First and foremost, precise sensor orientation is critical to estimating the absolute magnitude of turbulent stresses. Observed sensitivity to variations in tilt suggests that a precision of order 0.1 degrees in the vertical is required. Flow derived orientations are consistent to roughly 0.4 degrees. This level of precision appears to be sufficient for investigations of the temporal and spatial variability in stress estimates in at least some cases. The lack of a clear physical underpinning for the resulting coordinate frame limits further application of the results. The sensitivity of the results to orientation further suggests that consideration of bed slope effects may be required.

The observations demonstrate that stress estimates are highly variable across a variety of temporal scales. The bulk of the stress is generated by motions at frequencies approaching the incident band fundamental and harmonic frequencies.

The separation of motions into turbulent and wave-driven components is dubious when based solely on the frequency characteristics of the data.

Acknowledgements

This work was funded through the Coastal and Marine Program of the U.S. Geological Survey, and benefited from the cooperative support of the Duck94 field experiment provided by the U.S. Army Corps of Engineers, the U.S. Geological Survey, and the Office of Naval Research. Special thanks are due to the many USGS personnel who supported us in preparation and deployment and to the entire staff of the Field Research Facility (FRF) in Duck, NC. Any use of trade names in this publication is for descriptive purposes only and does not imply endorsement by the USGS.

References

- Deigaard, R., P. Justesen, and J. Fredsoe, Modelling of undertow by a one-equation turbulence model, *Coastal Eng.*, 11, 565–602, 1987.
- Haines, J. and A. H. Sallenger, Vertical structure of mean cross-shore currents across a barred surf zone, *J. Geophys. Res.*, 99, 14,223–14,342, 1994.
- Lohrman, A., R. Cabrera, G. Gelfenbaum, and J. Haines, Direct measurements of Reynolds stress with an acoustic doppler velocimeter, *Proceedings IEEE Fifth Workshop on Current Measurements*, 205–210, 1995.
- Svendsen, I., A. Hemming, and J. Buhr Hansen, The interaction between the undertow and the boundary layer flow on a beach, *J. Geophys. Res.*, 93, 11,845–11,856, 1987.

CHAPTER 268

Asymmetric and Irregular Wave Effects on Bedload: Theory versus Laboratory and Field Experiments

Leszek M. Kaczmarek & Rafał Ostrowski¹

1. INTRODUCTION

To parameterise the sediment transport in terms of the wave spectrum and a few other parameters, it is necessary to start from the surface elevation spectrum which can be transformed into orbital velocities at the bed and then to bed shear stress. The bed shear stress so derived is used in a new sediment transport formula put forth by the Authors. The problem is highly non-linear and at a few points in the process it is necessary to make non-linear transformations. This route: surface elevation - sediment transport and the importance of the non-linearity are central to this study.

The theoretical model is based on the concept proposed by Kaczmarek & O'Connor (1993) who used the procedure for matching the solutions of equation of motion in the turbulent flow above the theoretical bed level and in the collision-dominated granular-fluid region. This concept, first used for regular linear waves, has recently been developed for random waves by Kaczmarek et al. (1994) and for non-linear waves by Kaczmarek (1995).

Then, on the above basis, the first attempt was made by Kaczmarek et al. (1995) to formulate bedload theory and verify it using available laboratory data and IBW PAN radio-tracer field results.

This paper presents the results of experiment carried out at IBW PAN laboratory. The verification of the theory for regular and irregular waves using own experimental data is the major goal of this study. There are few experimental data sets for ripple regime, especially in the range $\theta_{2.5}=0.1-0.4$. Therefore the laboratory survey covered this range, particularly taking account of the identification of non-linear effects. This range of small $\theta_{2.5}$ is extremely important as one can expect the equivalence of bedload and total sediment transport in this regime (small suspended load rate). Thus,

¹ both Polish Academy of Sciences' Institute of Hydro-Engineering, *IBW PAN*,
7 Kościarska, 80-953 Gdańsk, Poland

only in this regime bedload theory can be precisely verified while in more severe hydrodynamic conditions bedload is a minor part of total sediment transport.

The various aspects of the non-linearity in respect to moveable bed roughness including the asymmetry of waves (described by 2nd and 3rd Stokes theory) and the wave-current interactions as well as wave irregularity are also discussed. A methodology for predicting the bed shear stress time series for irregular waves is applied to a large number of data sets of bottom velocity, some of which are simulated from field free surface elevation spectrum and some taken from IBW PAN laboratory data. The resulting bed shear stress is used in the bedload transport formula to predict sediment transport rate series for each data set. Hence, some questions concerning the equivalent regular waves generating the same shear stress root-mean-square values and the same bedload root-mean-square values as the irregular waves are answered.

2. MOVEABLE BED BOUNDARY LAYER THEORY

2.1. FORMULATION OF THE PROBLEM

The nearbed dynamics is examined and modelled for the flow regions above and beneath the original static bed line, see Figure 1. The collision-dominated granular-fluid region I stretches below the nominal static bed while the wall-bounded turbulent fluid region II extends above it. Since both water and sand grains are assumed to move in both regions, there must be a certain transition zone between I and II, in which the velocity profiles of I and II would merge and preserve continuity of shape.

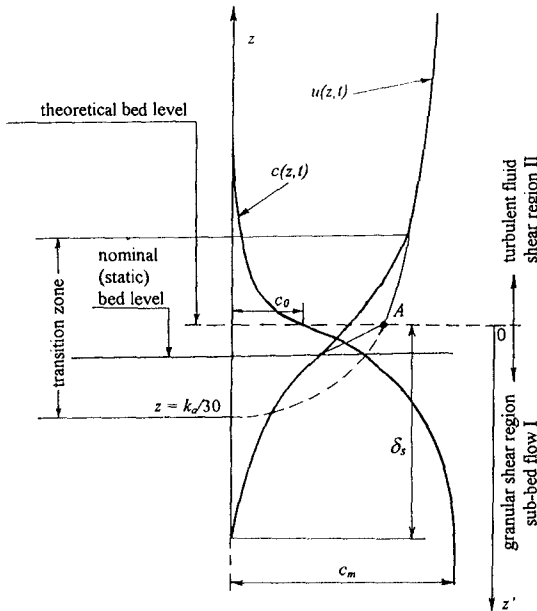


Figure 1. Definition sketch

The velocity distribution about a porous rough bed is controlled by various features of roughness and bed permeability. At first it is assumed that the velocity is determined by roughness geometry and outer flow parameters, such as the free-stream wave velocity.

The iteration procedure permits matching of velocities in the regions I and II. The velocity profile in the upper turbulent layer, which is linked with identification of roughness k_a , is determined first and then passed to the lower collision-dominated layer. The intersection of the two velocity profiles is marked as point *A* in Figure 1.

2.2. BASIC EQUATIONS

The flow in the turbulent upper region for regular waves is described by the integral momentum model based on the solution proposed by Fredsøe (1984):

$$\frac{dz_1}{d(\omega t)} = \frac{30\kappa^2 U}{k_a \omega e^{z_1} (z_1 - 1) + 1} - \frac{z_1 (e^{z_1} - z_1 - 1)}{e^{z_1} (z_1 - 1) + 1} \frac{1}{U} \frac{dU}{d(\omega t)} \quad (1)$$

$$\frac{dz_1}{d(\omega t)} = \frac{30z_1^2 \left[\left(\frac{\kappa U}{z_1} \mp u_{f0} \right) \left(\frac{\kappa U}{z_1} \pm u_{f0} \right) \pm u_{f0}^2 \right]}{k_a \omega U \left[e^{z_1} (z_1 - 1) + 1 \right]} - \frac{z_1 (e^{z_1} - z_1 - 1)}{e^{z_1} (z_1 - 1) + 1} \frac{1}{U} \frac{dU}{d(\omega t)} \quad (2)$$

for pure wave motion and wave with/against current, respectively.

The solutions of Equations (1) and (2) are achieved by the Runge-Kutta second-order method. As a result for a particular case, the function $z_1(t)$ is obtained and the time distributions of the friction velocity $u_f(t)$ and boundary layer thickness $\delta(t)$ are calculated thereafter using the following equations:

$$z_1 = \frac{U\kappa}{u_f \mp u_{f0}} \quad (3)$$

$$\delta = \frac{k_a}{30} (e^{z_1} - 1) \quad (4)$$

It should be emphasised that the free stream velocity $U(t)$ can be described as linear or nonlinear, thus Fredsøe's model can be adapted to nonlinear (asymmetric) wave motion, cf. Kaczmarek & Ostrowski (1992).

The solutions of Equations (1) and (2) enable the values of $u_{f\max}$ to be determined, if the quantities k_a are specified. To evaluate the roughness parameter k_a an iterative procedure is proposed for finding the matching point *A*.

The approach for irregular waves incorporates a time-invariant, two-layer eddy viscosity and bottom boundary layer thickness. Bed roughness is calculated using the iteration procedure taking account of the reduction of this parameter due to irregularity of wave motion. More detailed discussion on modelling of bed roughness is given in section 3.1.

In the sub-bed flow region, the sediment concentration is high and chaotic collisions of grains are the predominant mechanism. Particle interactions are assumed to produce two distinct types of behaviour. The Coulomb friction between particles give rise to rate-independent stresses (of the plastic type) and the particle collisions bring

about stresses that are rate-dependent (of the viscous type). The use of the mathematical description by Sayed & Savage (1983) for determination of the stress tensor was made and the balance of linear momentum according to Kaczmarek & O'Connor (1993) leads to the following equations:

$$\alpha^0 \left(\frac{c - c_0}{c_m - c} \right) \sin \varphi \sin 2\psi + \mu_1 \left(\frac{\partial u}{\partial z'} \right)^2 = \rho u_f^2 \quad (5)$$

$$\alpha^0 \left(\frac{c - c_0}{c_m - c} \right) (1 - \sin \varphi \sin 2\psi) + (\mu_0 + \mu_2) \left(\frac{\partial u}{\partial z'} \right)^2 = \left(\frac{\mu_0 + \mu_2}{\mu_1} \right) \Big|_{c=c_0} \rho u_f^2 + (\rho_s - \rho) g \int_0^{z'} c dz' \quad (6)$$

in which:

ρ_s and ρ are the densities of the solid and fluid, respectively;

α^0 is a constant;

c_0 and c_m are the solid concentrations corresponding to fluidity and the closest packing, respectively;

μ_0 , μ_1 and μ_2 are functions of the solid concentration c :

$$\frac{\mu_1}{\rho_s d^2} = \frac{0.03}{(c_m - c)^{1.5}} \quad (7)$$

$$\frac{\mu_0 + \mu_2}{\rho_s d^2} = \frac{0.02}{(c_m - c)^{1.75}} \quad (8)$$

The value φ in Equations (5) and (6) is the quasi-static angle of internal friction, while the quantity ψ is equal to:

$$\psi = \frac{\pi}{4} - \frac{\varphi}{2} \quad (9)$$

For the calculations the following numerical values are recommended:

$$\frac{\alpha^0}{\rho_s g d} = 1 \quad c_0 = 0.32 \quad c_m = 0.32 \quad \varphi = 24.4^\circ \quad (10)$$

where d denotes the diameter of grains.

3. MODELLING OF BEDLOAD UNDER IRREGULAR WAVES

3.1. BED ROUGHNESS

The apparent bed roughness parameter k_a is a central quantity in the theoretical model. Both the turbulent and sub-bed velocity profiles depend on k_a , which is not known a priori. Therefore an iteration procedure is proposed for finding the matching point A between these profiles. The matching is assumed to take place at the phase of maximum shear stress, although at any other phase of oscillatory motion there must be some transition between the two profiles. Under monochromatic waves the maximum shear stress is the maximum value of shear stress during a wave period, while for spectral waves it becomes the maximum value of the random shear stress

time series. To calculate this value it is proposed to use, the following simple relation, Kaczmarek et al. (1994):

$$\tau_{\max} = \frac{3\tau_{rms}}{\sqrt{2}} = 3\delta_{\tau} \quad (11)$$

The choice is fairly arbitrary, however, as it was shown by Kaczmarek et al. (1994), it yields the best agreement of the calculations of wave friction using Madsen et al.'s (1990) data.

For engineering purposes it is useful to approximate the theoretical results by a curve expressed in terms of skin friction. To determine the skin friction one can follow Nielsen's (1992) description:

$$\theta_{2.5} = \frac{1}{2} f_{2.5} \psi_1 = \frac{1}{2} f_{2.5} \frac{(a_{1m}\omega)^2}{(s-1)gd} \quad (12)$$

$$f_{2.5} = \exp \left[5.213 \left(\frac{2.5d_{50}}{a_{1m}} \right)^{0.194} - 5.977 \right] \quad (13)$$

in which $s = \rho_s/\rho$.

The iteration procedure proposed for finding the matching point A between the velocity profiles (Fig. 1) was run for a wide range of small and large scale conditions and for a few diameters of sandy bed. Then the results were approximated yielding the following formulae for regular and irregular waves, respectively:

$$\frac{k_a}{d} = 47.03\theta_{2.5}^{-0.66} \quad (14)$$

$$\frac{k_a}{d} = 26.64\theta_{2.5}^{-0.71} \quad (15)$$

For irregular waves k_a is calculated using Eq. (15) taking root-mean-square wave height (or free-stream velocity) and peak period for determination of $\theta_{2.5}$.

The moveable bed roughness under sinusoidal and asymmetric waves with/versus a steady current has also been considered. The numerical solution of Eq. (2) is used with the free stream velocity $U(\omega, t)$ expressed using linear or nonlinear approximation. The considerations on nonlinearity have been limited to the 2nd Stokes wave propagating without current and with/against weak and strong currents. For wave-current motion the ratio U_{mean}/U_{1m} was kept constant and amounted to 0.2 and 0.5 for weak and strong current, respectively. The quantity U_{mean} is the steady current, known as an input, averaged over water depth in the outer region (outside the bed boundary layer). The mean slip velocity (at the top of the bed boundary layer) is calculated from U_{mean} with the assumption of the logarithmic velocity profile in the outer region, using the model of Kaczmarek & Ostrowski (1992). This model also provides the value of shear stress $u_{\tau 0}$ resulting from the presence of steady current.

Figure 2 depicts the relative differences in roughness computed for regular waves (linear and nonlinear) and currents, as well as irregular wave motion, with respect to pure sinusoidal cases. The results imply that the greatest reduction of the roughness

parameter k_a (about 40%) is observed when the waves are irregular and in a certain range of Shields parameter - when the nonlinear waves are accompanied by a steady current. Smaller reductions of k_a occur for sinusoidal waves superimposed on currents. It can be seen that for nonlinear cases the reduction of k_a is more distinct for waves propagating with the current than for waves versus the current.

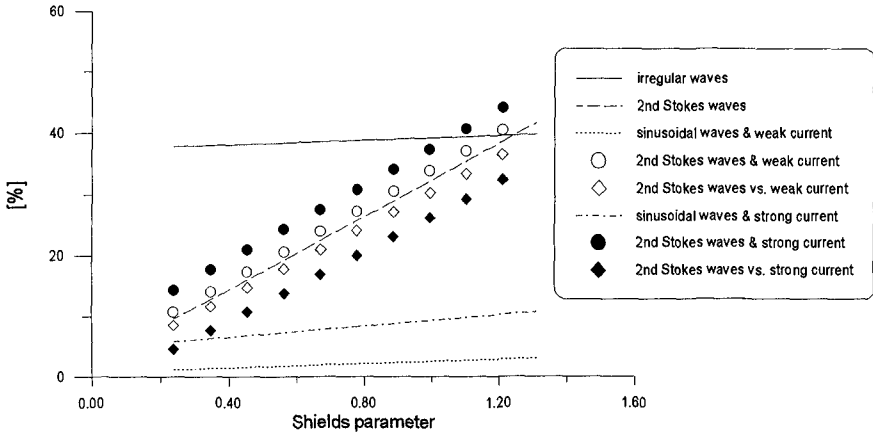


Figure 2. Relative differences (smoothed values) in k_a with respect to sinusoidal case Hence, the irregularity of waves is the most important factor causing the reduction of moveable bed roughness.

3.2. SHEAR STRESS AND BEDLOAD

It is convenient to introduce complex notation which determines the dependence of velocity on time and will ensure the analytical solution of the equation of motion. The free stream velocity will be written as $U(t)=U\exp(i\omega t)$, in which U = real velocity amplitude. Similarly, one may write:

$$u(z,t) = u(z)e^{i\omega t} \quad \text{and} \quad u_d(z,t) = u_d(z)e^{i\omega t} \tag{16}$$

in which $u(z)$ and $u_d(z)$ are in general complex due to the phase shift relative to the free stream velocity. The equation of motion may now be written as:

$$\frac{d}{dz} \left[\nu_t(z) \frac{du_d(z)}{dz} \right] - i\omega u_d(z) = 0 \tag{17}$$

It is fortunate that this equation is explicitly solvable both when $\nu_t(z)$ varies linearly with z and when it is a constant. Thus, following Brevik (1981), the two-layer eddy viscosity model is proposed:

$$\nu_t(z) = \kappa u_{fr} z \quad \text{for} \quad \frac{k_a}{30} < z \leq \frac{\delta_r}{4} + \frac{k_a}{30} \tag{18}$$

$$\nu_t(z) = \kappa u_{fr} \left(\frac{\delta_r}{4} + \frac{k_a}{30} \right) \quad \text{for} \quad z > \frac{\delta_r}{4} + \frac{k_a}{30} \tag{19}$$

where $u_{fr} = \sqrt{\tau_r / \rho}$ and δ_r are the representative friction velocity and representative bottom boundary layer thickness, respectively.

To solve the Eq. (17) the free stream velocity is specified as that associated with a wave spectrum, i.e.:

$$U(t) = \sum_n U_n e^{i\omega_n t} \quad (20)$$

in which the index n denotes summation over frequencies. With such a representation of $U(t)$ the velocity amplitudes U_n are related to the near-bottom orbital velocity spectrum and to the surface amplitude spectrum through:

$$U_n = \sqrt{2S_U(\omega_n)d\omega} = \frac{\omega_n}{\sinh(k_n h)} \sqrt{2S_\eta(\omega_n)d\omega} \quad (21)$$

in which ω_n and k_n are related to each other by linear dispersion relationship.

The linearity of Eq. (17) combined with the assumed time-invariant eddy viscosity concept (Equations (18) and (19)) suggests a solution in the form of:

$$u(z, t) = \sum_n u_n(z) e^{i\omega_n t} \quad (22)$$

in which $u_n(z)$ represents the complex velocity component amplitudes and only the real part of Eq. (22) constitutes the solution sought.

Introducing Equations (18) and (19) into Equation (17), one can obtain the equation for each velocity component n . Introducing the dimensionless variable:

$$\xi_n = \left(4\omega_n \frac{z}{\kappa u_{fr}} \right)^{\frac{1}{2}} \quad (23)$$

Eq. (17) reduces to the standard differential equation for the Kelvin functions of zeroth order, with ξ_n as the independent variable.

On the basis of the velocity solution one can obtain the shear stress at $z=z_0$ (complex value) which can be expressed as:

$$\tau(t) = \tau_n \exp[i(\omega_n t + \varphi_{\tau_n})] \quad (24)$$

where τ_n and φ_n are the bed shear stress amplitude and phase, respectively, corresponding to n th harmonic component U_n of the input free stream velocity random series $U(t)$.

The solution obtained for the turbulent flow in the wave boundary layer involves the representative friction velocity u_{fr} and the representative thickness of the boundary layer δ_r , which are yet to be specified. Although each harmonic component of wave motion is described by the same equation, i.e. Equation (17), there is a coupling between the components incorporated in the eddy viscosity. This appears in the modelling of the representative values u_{fr} and δ_r by iterative procedure which is schematically shown in Figure 3. The quantities u_{fr} and δ_r are determined by using Eq. (1) and specified as:

$$u_{fr} = u_{f \max} \quad (25)$$

$$\delta_r = \delta_m = \max(\delta_1, \delta_2) \quad (26)$$

where u_{fmax} is the maximum value of bed shear velocity during the wave period, that is $\max[u_f(\omega t)]$ and δ_1 and δ_2 the boundary layer thicknesses at the moments corresponding to maximum and minimum velocity at the top of the turbulent boundary layer. For a given by free stream irregular series the iterative procedure of Fig. 3 is used to determine the representative period T_r , friction velocity u_{fr} and the boundary layer thickness δ . The exemplary shear stress results vs. Gdańsk lab data, collected by Ostrowski (1993), are shown in Figure 4.

< 1 >	Fourier decomposition of the free stream velocity input $U(t)$ $U(t) = \sum_n U_n \sin(n\omega t + \varphi_n) + \frac{1}{2}U_0$
< 1a >	Alternatively Fourier decomposition of the water surface elevation input $\eta(t)$ $U(t) = \sum_n \eta_n \frac{n\omega}{\sinh(k_n h)} \sin(n\omega t + \varphi_n) + \frac{1}{2}U_0$
< 2 >	Calculation of the input root mean square value: $U_{rms} = \sqrt{\sum_n U_n^2}$
< 3 >	Computation of bed roughness for irregular waves
< 4 >	Assumption of representative period T_r
< 5 >	Determination of parameters of representative eddy viscosity distribution: u_{fr} & δ_r (running Fredsøe's (1981) model with U_{rms} & T_r as an input)
< 6 >	Computation of representative shear stress amplitude ρu_{fB}^2 (using Brevik's (1981) approach with U_{rms} , T_r & eddy viscosity distribution from step < 5 > as an input)
< 7 >	Computation of bed shear stress components τ_n & $\varphi_{\tau n}$ using Brevik's approach with U_n , $n\omega$ (from step < 1 > or < 1a >) and representative eddy viscosity (determined in step < 5 >) as an input
< 8 >	Calculation of bed shear stress root mean square value: $\tau_{rms} = \sqrt{\sum_n \tau_n^2}$
< 9 >	Checking whether ρu_{fB}^2 (step < 6 >) = τ_{rms} (step < 7 >) if NO \rightarrow correction of T_r and going to step < 5 > if YES \rightarrow going to step < 10 >
< 10 >	Calculation of output time series (bed shear stress): $\rho u_f^2(t) = \tau(t) = \sum_n \tau_n \sin(n\omega t + \varphi_n + \varphi_{\tau n})$
< 11 >	Calculation of bedload time series using present model with the boundary conditions $u_f _{z=0} = u_f(t)$

Figure 3. Computation of bed shear stress and bedload under irregular waves

Once the bed shear stress is determined the velocity distributions can be computed for the regions I and II (Fig. 1), as well as the concentration of grains in bedload layer. Basing on Bagnold's (1956) definition, according to which the bedload is a part of sediment transport subject to inter-granular forces, the bedload layer can be

represented as the region II. Knowing the instantaneous shear stress one can calculate the instantaneous bedload rate from velocity and concentration profiles in this layer:

$$Q_B = \int_0^{\delta_s} u(z', t) \cdot c(z', t) dz' \quad (27)$$

and the dimensionless bedload rate defined as:

$$\phi_B = \frac{Q_B}{d\sqrt{(s-1)gd}} \quad (28)$$

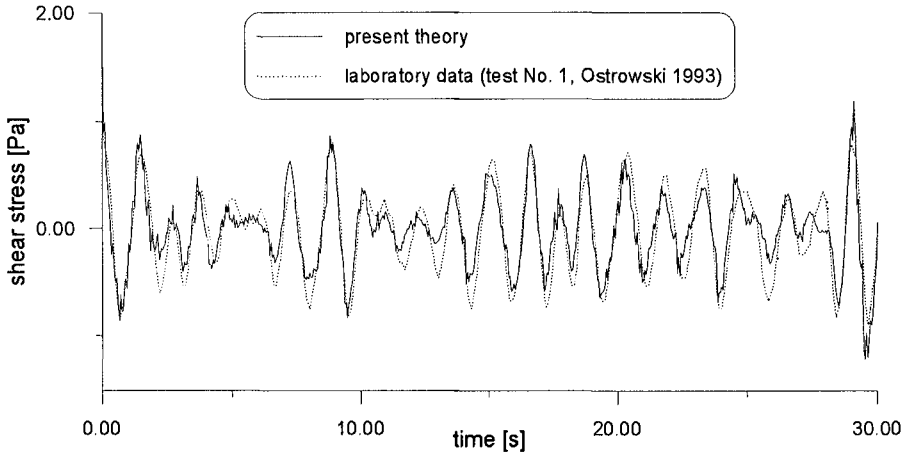


Figure 4. Theoretical and experimental irregular shear stress

The methodology for predicting the bedload time series for irregular waves was applied to a number of laboratory data sets. These results are discussed in the next section. The presented concept was also used for modelling of the bedload series for the field free surface elevation series taken at IBW PAN Coastal Research Facility in Lubiato. The exemplary results of the bedload simulation are given in Figures 5 and 6.

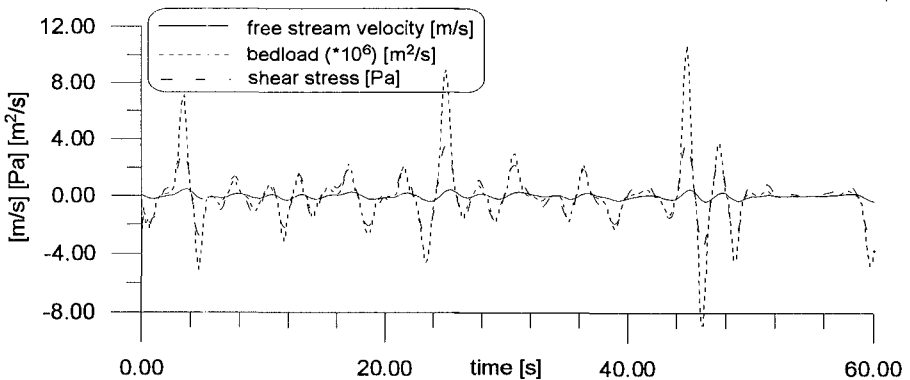


Figure 5. Time series of shear stress and bedload simulated for field wave input

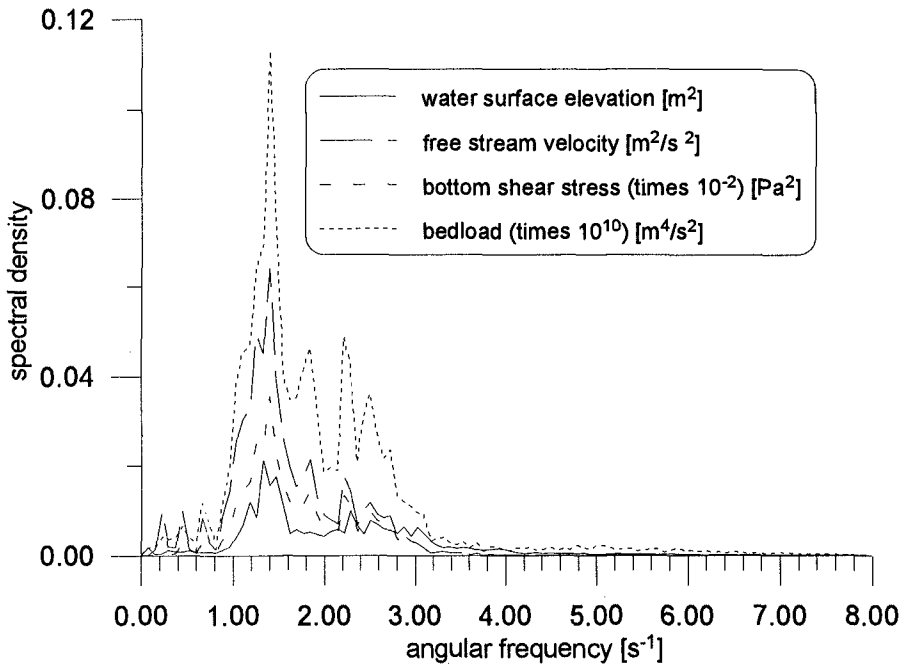


Figure 6. Spectra of shear stress and bedload simulated for field wave input

4. LABORATORY BEDLOAD SURVEY

4.1. EXPERIMENTAL SETUP

The measurements were carried out in the IBW PAN wave flume. The wave flume, 0.5 m wide and 22.5 m long, is equipped with a programmable wave maker and can be filled with water up to 0.7 m. Reinforced concrete slabs 8 cm thick were placed on the bottom with a sandy measuring section (also 8 cm thick) 7 m long situated about the middle of the flume. Natural sand was used in the experiments with a grain diameter $d_{50}=0.22$ mm.

For each test, free surface elevation was registered at three points along the flume. The horizontal component of free stream velocity was measured at one point in the measuring section, using a micro-propeller, together with one of the wave gauges which was located above the sand trap. The other two wave gauges were spaced $1/4*L$ from each other (L being a wave length) to estimate the reflection effects in the flume. Experimental setup, together with the sand trap, is shown in Figure 7.

The sand trap was covered by a lid and buried in the sandy section before each test. Then the waves were generated until bed ripples were fully formed, which took 25-60 minutes. The lid, suspended on four strings, was removed thereafter, together with a thin layer of sand on it. Then the wave action was continued for 1.2-15 minutes and

sediment grains were being accumulated in the sand trap. Finally, the grains were siphoned from the trap and weighed to determine the sedimentation quantity.

The sand trap had two cells to ensure the determination of onshore and offshore bedload components.

Together with the sedimentation, bed forms geometry was measured and their shape was assessed after each test.

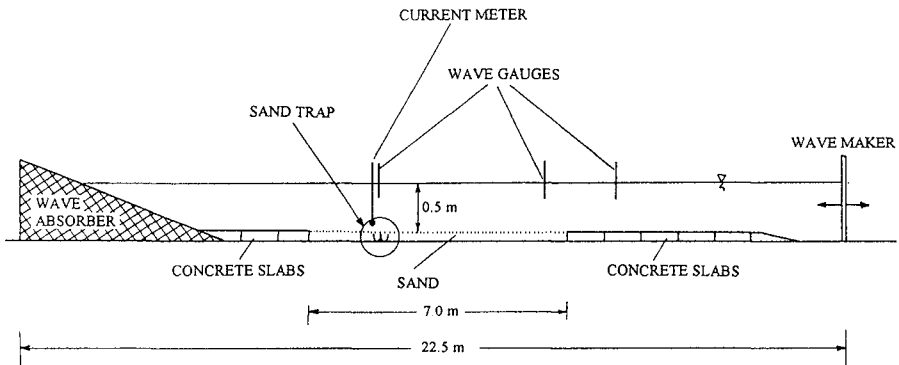


Figure 7. Experimental setup

A constant water depth of $h = 0.5$ m above the measuring section was maintained during each test. The experiments were carried out for six sets of parameters for regular waves (Tests 1, 2, 3, 4, 11 and 12) and for six irregular wave series (Tests 5, 7, 8 for JONSWAP and Tests 6, 9, 10 for Pierson-Moskowitz spectrum generated by the wave maker). As a total, 141 series were run, among which 103 ones were regular.

The conditions expressed in terms of $\theta_{2.5}$ varied roughly from 0.1 in Test 3 to 0.4 in Test 12. This range of rippled bed (cf. Fig. 4b) is extremely important as one can expect the equivalence of bedload and total sediment transport in this regime (small suspended load rate). Thus, only in this regime bedload theory can be precisely verified while in more severe hydrodynamic conditions bedload is a minor part of total sediment transport.

4.2. RESULTS OF MEASUREMENTS VS. PRESENT THEORY

The experimental bedload data in comparison with theoretical results obtained by using present theoretical linear approach are shown in Figure 8.

The waves registered in the flume had a slightly asymmetric shape. Therefore, for better representation of actual laboratory conditions, the theoretical results have been produced using present approach adapted for non-linear waves. The free stream velocity in Equation (1) was described using 2nd order Stokes theory, as indicated by Kaczmarek & Ostrowski (1992). Then, for known distributions of u_f in time, the instantaneous bedload transport rate has been found from Equations (5) and (6) for

the entire wave period, integrated over time and averaged over wave period. These results are also shown in Figure 8.

The conformity of theoretical evaluations and experimental data can be seen in Figure 8, especially while using non-linear approach (except for Test 2). It should be pointed out that for long and highly asymmetric waves, represented by Test 11 (Ursell parameter of 40), the experimental data fit the present non-linear theory while they differ significantly from the linear approach. The most severe shear stress conditions generated in the flume without wave breaking had a $\theta_{2.5}=0.4$ and were achieved in Test 12. However, the Ursell number (equalled to 31) was less than in Test 11. In Test 12, a very distinct concentration of suspended sediment was observed which could result in increased accumulation in the sand trap, bigger than theoretically modelled, using both linear and non-linear theory.

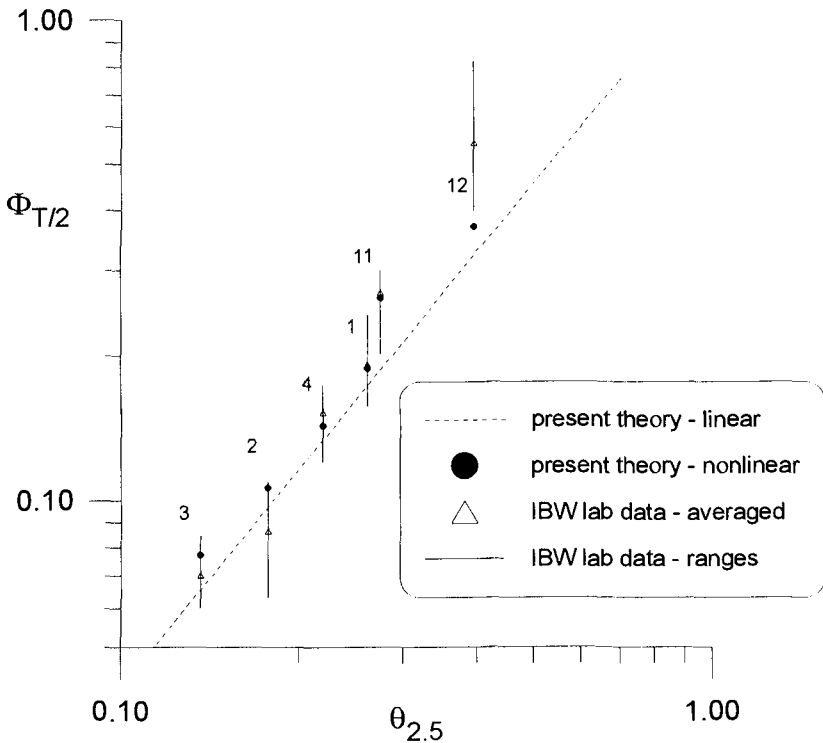


Figure 8. Regular bedload IBW PAN lab data vs. present linear and non-linear theory

The laboratory bedload data for irregular waves in comparison with theoretical results are depicted in Figure 9. Computed values have been modelled using the present computational procedure (Fig. 3) for the full-time (15 minutes) water surface elevation series registered at the measuring section. The agreement between theoretical and experimental results appears to be very good.

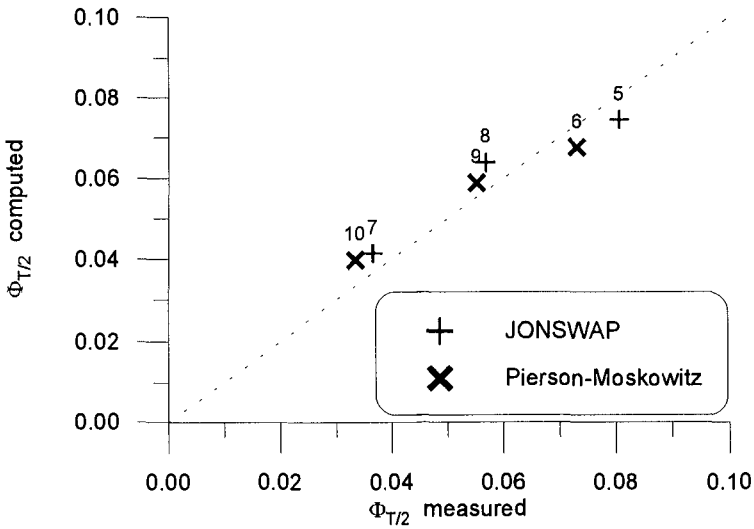


Figure 9. Bedload IBW PAN lab data vs. present theory for irregular waves

For the sake of full comparison the laboratory bedload data for regular and irregular waves are plotted together in Figure 10, against linear theory. Additionally, the bedload results simulated for field-recorded waves are included in Fig. 10. All results for irregular waves are presented as a function of dimensionless stress $\theta_{2.5}$, calculated using root-mean-square wave height and representative wave period T_r .

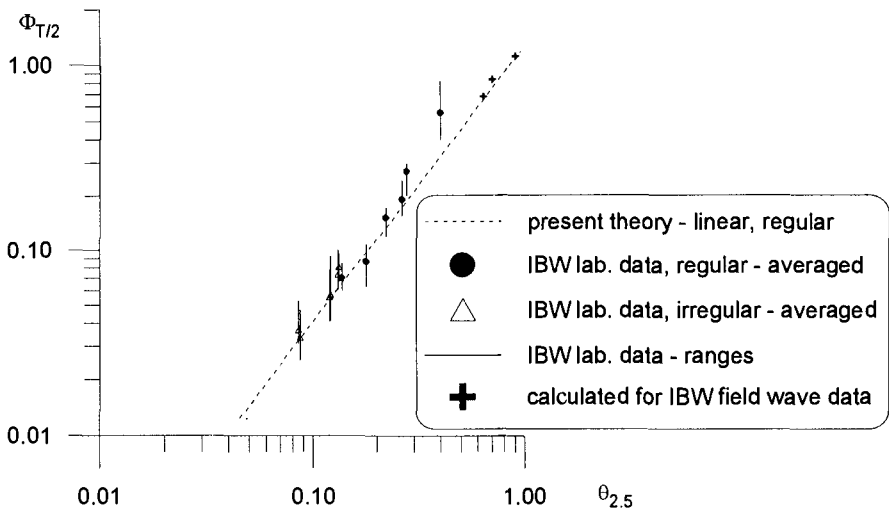


Figure 10. Bedload under regular and irregular waves vs. present linear theory

Figure 10 implies that the bedload rate for irregular cases can be successfully modelled with the use of present linear theory taking root-mean-square wave height

H_{rms} and representative wave period T_r as an input. It should be noted that in analysed cases the computed values of T_r are close to those of peak period, thus the peak period (T_p) can be used as representative. However, further studies are necessary to find out whether this conclusion is valid for all types of spectra.

It can also be seen from Figure 10 that for weak and moderate shear stress conditions the regular laboratory bedload data lie slightly above the results obtained using linear theory, thus for precise determination of bedload rate under regular-asymmetric waves the non-linear approach should be used. Finally, it can be concluded that for high shear stresses the present linear theory underestimates bedload rate, most probably - due to significant concentration of suspended sediment.

REFERENCES

- Bagnold, R.A. (1956). The flow of cohesionless grains in fluids, *Phil. Trans., R. Soc., London, Ser. A*, 249 (964), 235-297
- Brevik, I. (1981). Oscillatory Rough Turbulent Boundary Layers, *J. Watrway., Port, Coast. and Oc. Eng.*, ASCE, Vol. 107, No. 3, 175-187
- Fredsøe, J. (1984). Turbulent boundary layer in combined wave-current motion, *J. Hydraulic Eng.*, ASCE, Vol. 110, No. HY8, 1103-1120
- Kaczmarek, L.M. (1995). Nonlinear Effects of Waves and Currents on Moveable Bed Roughness and Friction, *Archives of Hydro-Engineering and Environmental Mechanics*, Vol. 42, No. 1-2, pp. 3-27
- Kaczmarek, L.M., J.M. Harris & B.A. O'Connor (1994). Modelling moveable bed roughness and friction for spectral waves, *Proc. 24th ICCE*, 300-314, ASCE, New York
- Kaczmarek, L.M. and B.A. O'Connor (1993a, b). A new theoretical approach for predictive evaluation of wavy roughness on a moveable flat/rippled bed, Parts I/II, *Reps. CE/14-15/93*, Dept. Civ. Engng., Univ. Liverpool
- Kaczmarek, L.M. and Ostrowski, R. (1992). Modelling of wave-current boundary layer in the coastal zone, *Proc. 23rd Intern. Conf. Coast. Eng.*, ASCE, 350-363
- Kaczmarek, L.M., R. Ostrowski & R.B. Zeidler (1995). Boundary Layer Theory and Field Bedload, *Proc. International Conf. Coast. Res. in Terms of Large Scale Experiments (Coast. Dynamics '95)*, ASCE, 664-675
- Madsen, O.S., P.P. Mathison & M.M. Rosengaus (1990). Moveable bed friction factors for spectral waves, *Proc. 22nd Intern. Conf. Coast. Engng.*, 420-429, ASCE, New York
- Nielsen, P. (1992). Coastal bottom boundary layers and sediment transport. *Advanced Series on Ocean Engineering*, Vol. 4, World Scientific, Singapore
- Ostrowski, R. (1993). Bottom friction induced by surface waves and currents with nonlinear effects (in Polish), *Ph. D. thesis*, IBW PAN, Gdańsk
- Sayed, M. and Savage, S.B. (1983). Rapid gravity flow of cohesionless granular materials down inclined chutes, *J. Applied Mathematics and Physics (ZAMP)*, Vol. 34, 84-100

CHAPTER 269

KINEMATICS AND SHEAR STRESSES FROM COMBINED WAVES AND LONGSHORE CURRENTS IN THE UK COASTAL RESEARCH FACILITY

Richard R.Simons¹, Ruairi D.MacIver², Wameidh M.Saleh²

Abstract

The paper describes a series of experiments involving regular and random waves propagating over an orthogonal longshore current in the UK Coastal Research Facility at Wallingford. Mean and wave-induced velocities have been measured above a horizontal fixed rough bed using three acoustic velocimeters, and simultaneous measurements of mean and oscillatory bottom shear stress have been made with a UCL shear cell. Wave-induced shear stresses have been expressed as friction factors and compared with widely used empirical formulae. Other results have been compared with predictions for shear stress and apparent bed roughness from eight wave-current theories. The predicted enhancement of these parameters is judged against the relative strengths of the waves and currents tested, and against the practical range of conditions achievable in such laboratory basins.

Introduction

In trying to understand the effects of waves and currents on the coastal environment it is important to be able to predict the forces exerted on the seabed by the fluid motion and, conversely, what effect the seabed has on that motion. Such boundary layer processes are included in the wave-current interaction elements of the new generation of coastal numerical models, but there remains insufficient reliable data against which predictions from these models can be validated. Researchers at UCL are involved in a number of projects aimed at filling this gap.

In an earlier series of tests performed by the UCL group [Simons *et al.* (1992), (1994)], bottom shear stresses were measured directly using a novel shear cell device under conditions including regular and random waves propagating across an orthogonal current. This work suggested that waves have a significant effect on the current-induced mean shear stresses but that an additional current makes little difference to the wave-induced stresses. However, the relatively small basin used for those tests meant that the flows were not all fully rough turbulent. To produce

1) Senior Lecturer, Civil & Environmental Engineering Department, UCL
2) Research Assistant, Civil & Environmental Engineering Department, UCL
University College London, Gower Street, London WC1E 6BT, UK

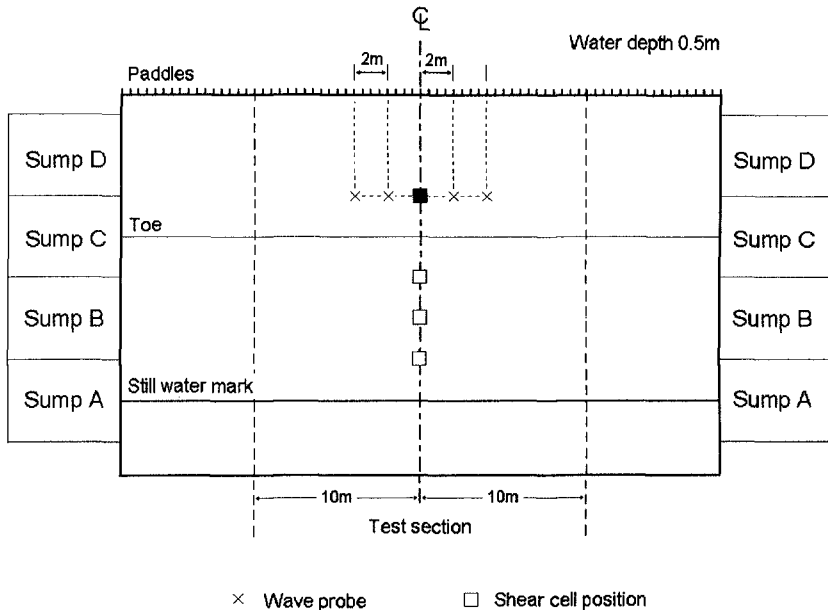


Figure 1 Schematic layout of UK Coastal Research Facility

results which can be applied to field-scale conditions and provide a valid test for the models, the experiments reported here have been carried out in the UK Coastal Research Facility (UKCRF) at Reynolds numbers well beyond transition and over a large fixed bed roughness.

The number of models in the literature which offer possible solutions to the problem of wave-current interaction in a turbulent coastal flow field is too extensive for detailed consideration here. All such models require empirical assumptions about the physical structure of the combined flow, and many also lead to difficult calculations in achieving a solution. In their review of the subject, Soulsby *et al.* (1993) put forward a simplified method for applying these theories using a set of standard formulae to relate the significant parameters. Each model is characterised by a unique set of 26 coefficients - found by fitting curves through model solutions for a wide range of input parameters - and these are used in the standard formulae to determine mean and maximum shear stresses. These "parameterised" versions of certain models are compared with the present experimental data later in this paper, both in terms of the enhanced bottom shear stress and also the apparent increase in bed roughness when waves are superimposed.

UK Coastal Research Facility

The UKCRF has been designed to provide a controlled environment in which various coastal processes can be simulated at relatively large scale. It measures 54m by 27m overall, with a central test region 20m by 15m (**fig.1**), and is designed for

water depths between 0.3m and 0.8m - although the present tests have been performed with 0.5m depth. The wave generation system consists of 72 individually controlled wave boards (each 0.5m wide) mounted along one wall of the basin. This can produce orthogonal or oblique-incidence regular or random waves up to 30° from shore-normal, with periods between 0.8s and 3.5s and heights up to 0.25 metres.

Currents are circulated by 4 independent reversible flow pumps and are introduced into the basin through 40 inlet flumes, each controlled by its own undershoot weir, with a matching set of flumes at the outlet end. One of the novelties of the UKCRF is that this system allows wave-driven currents to be circulated and at the same time allows for simulated wind- or tidally-driven longshore currents to be superimposed. Another is that the pumps act under programmable control, thus allowing time-varying (tidal) longshore currents with a user-defined period to be superimposed onto a controlled sequence of waves.

The facility is equipped with a wide range of instrumentation. For the present tests, a UCL shear cell was used to make direct measurements of the wave- and current-induced bottom shear stresses on the horizontal region of the basin. Briefly, the shear cell consists of a thin 250mm diameter plate supported level with the bed on four thin needles and deflecting laterally under the action of any horizontally applied shear stress at the bed. The movement (less than 0.5 mm) is recorded by two orthogonal eddy-current sensors and converted into an analogue voltage - as described in Grass *et al.* (1995).

A 3-d fibre-optic laser Doppler velocimeter (restricted here to 2-d operation only) provided detailed information within the bottom boundary layer; three Sontek 3-d acoustic Doppler velocimeters (ADV) were mounted, one above the other (**fig.2**), on the z-axis of the instrument deployment bridge, thereby speeding up the process of measuring full vertical profiles of mean and wave-induced velocities; and 4 wave probes were deployed close to the shear cell to provide measurements of wave height and period.

To control the ADV's when they are operating near the centre of the basin, it is necessary to deploy a dedicated computer on the instrument carriage. The system is then operated from the control room via long cables linking the keyboard, screen and data logger to the remote processor.

For the present set of tests, the bed was roughened with nominal 10mm diameter granite chippings stuck to the concrete base of the basin and also to the surface of the UCL shear cell (**fig.3**). The bottom roughness was stuck as a single layer, with a thin coating of adhesive painted onto the bed, the chippings rolled into it and left to set, and the surplus swept off some time later. The observed Nikuradse roughness was 18.7 mm.

Long-crested waves were generated in the offshore region and propagated across

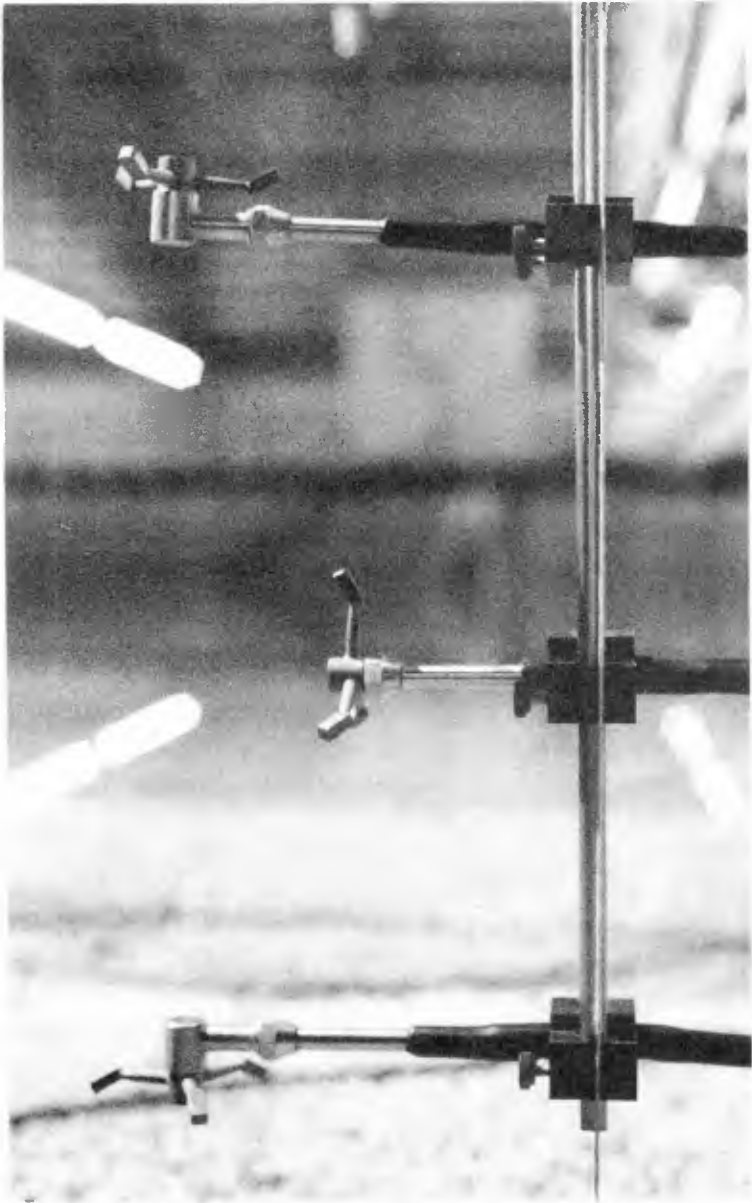


Figure 2 **Photograph of the three Sontek acoustic velocimeter probes**



Figure 3 Granite roughness on the surface of the UCL shear cell

the horizontal bed before moving on to a 1-in-20 sloping plane beach. The general design and capabilities of the basin are described by Simons *et al.* (1995).

Experiments

The experiments reported here were performed with waves propagating orthogonally across a turbulent current above a fixed bed roughness. They involved:

- a) 2 wave sequences generated from Jonswap spectra with peak frequencies of 0.4 Hz and significant wave heights of 0.15m and 0.18m; and
- b) 5 regular wave conditions, with periods in the range 1.7s to 3s and heights between 0.18m and 0.26m.

Each test condition was repeated with the velocity measuring system positioned at different heights above the bed to allow vertical velocity profiles to be determined. For the tests on regular waves, between 150 and 200 wave cycles were recorded at each position - from which ensemble averages were processed; for the random waves, the sequences lasted 20 minutes.

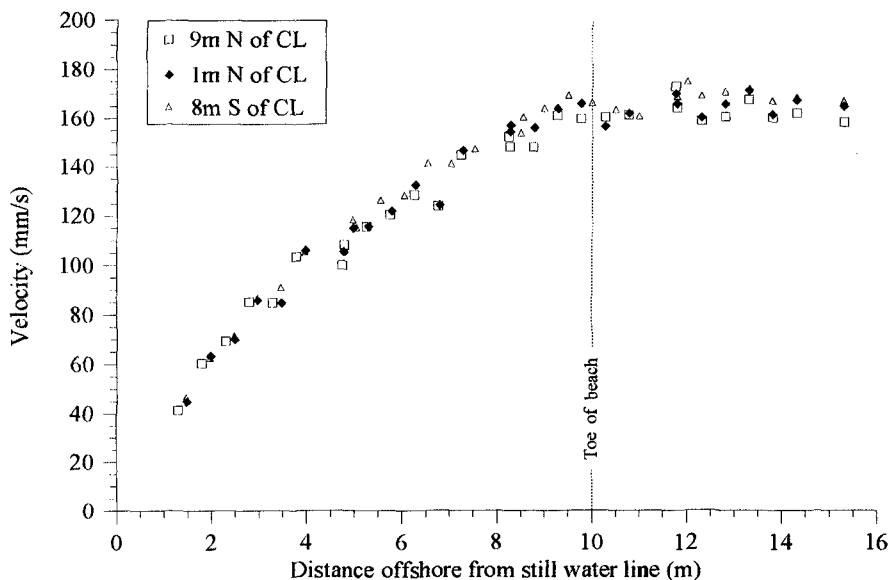


Figure 4 Graph showing the distribution of longshore current across the beach in the central test region of the basin.

The longshore current superimposed on the waves had a maximum velocity in the deep water region of approximately 0.14 m/s, reducing parabolically up the plane beach - see **fig.4**. At each position on the basin centreline, the vertical profile was logarithmic and demonstrated that the boundary layer was fully developed. This particular current setting is one of the standard reproducible conditions for the UKCRF established during initial evaluation work on the Facility. Test conditions and results are listed in **Table 1**.

MEAN CURRENT PARAMETERS

Current Alone			U_{bed}^c	Z_0^d	τ_c (N/m ²)	
TEST	T (s) ^a	H (m) ^b	(m/s)	(m)	Log layer	Shear cell
0410953	--	--	0.119	6.24 E-4	0.086	0.079

Regular Waves & Current

Regular Waves & Current			U_{bar}^c	Z_a^d	τ_m (N/m ²)		WCI ^k parameter y =
TEST	T (s) ^a	H (m) ^b	(m/s)	(m)	Log layer	Shear cell	$\tau_m/(\tau_c+\tau_w)$
0310951	1.70	0.213	0.122	3.33 E-3	0.254	--	0.047
0610953	2.10	0.219	0.125	4.52 E-3	0.364	0.264	0.057
0210951	2.45	0.256	0.119	6.19 E-3	0.395	0.365	0.064
0610951	2.70	0.262	0.121	3.48 E-3	0.258	0.263	0.058
0410951	3.00	0.260	0.116	4.73 E-3	0.284	--	0.064

WAVE PARAMETERS**Regular Waves Alone**

Regular Waves Alone			Crest				Trough			
			U_{bed}^c	a/Z_0^f	τ_w^g	WCI ^k parameter x =	U_{bed}^c	a/Z_0^f	τ_w^g	WCI ^k parameter x =
TEST	T (s) ^a	H (m) ^b	(m/s)		(N/m ²)	$\tau_c/(\tau_c+\tau_w)$	(m/s)		(N/m ²)	$\tau_c/(\tau_c+\tau_w)$
0310952	1.70	0.199	0.331	131	6.41	0.013	0.253	100	5.31	0.016
0610954	2.10	0.177	0.409	204	7.34	0.012	0.326	162	6.30	0.013
0210952	2.45	0.275	0.406	194	7.52	0.011	0.233	111	6.09	0.014
0610952	2.70	0.254	0.435	203	9.45	0.009	0.228	107	4.36	0.019
0310953	2.99	0.243	0.451	220	10.01	0.008	0.269	131	4.38	0.019

Irregular Waves Alone

Irregular Waves Alone			U_{bed}^h	a/Z_0^i	τ_w^h
TEST	T (s) ^a	H (m) ^b	(m/s)		(N/m ²)
2909952	2.24	0.152	0.130	74	1.98
2809951	2.19	0.187	0.149	83	2.32

Regular Waves & Current

Regular Waves & Current			Crest				Trough			
			U_{bed}^c	a/Z_0^f	τ_{max}^g	WCI ^k parameter Y =	U_{bed}^c	a/Z_0^f	τ_{max}^g	WCI ^k parameter Y =
TFST	T (s) ^a	H (m) ^b	(m/s)		(N/m ²)	$\tau_{max}/(\tau_c+\tau_w)$	(m/s)		(N/m ²)	$\tau_{max}/(\tau_c+\tau_w)$
0310951	1.70	0.213	0.310	124	6.08	0.937	0.237	94	4.97	0.921
0610953	2.10	0.219	0.358	176	5.70	0.768	0.290	142	5.86	0.919
0210951	2.45	0.256	0.416	187	7.97	1.048	0.187	84	4.78	0.774
0610951	2.70	0.262	0.439	197	8.76	0.919	0.210	94	4.14	0.930
0410951	3.00	0.260	0.464	237	9.69	0.960	0.266	136	4.09	0.916

Irregular Waves & Current

Irregular Waves & Current			U_{bed}^h	a/Z_0^i	τ_w^h
TEST	T (s) ^a	H (m) ^b	(m/s)		(N/m ²)
2909953	2.23	0.153	0.128	73	1.97
2909951	2.20	0.186	0.156	88	2.37

^a T₁₃, established from phase locking wave probe 3. (Data file B)^b H₁₃, established from wave probes 2 & 3. (Data file B)^c Depth averaged velocity.^d At z=35mm. (Ensemble average data file C)^e Established from shear cell.^f a calculated as $U_{bed}/(2\pi/\text{wave period})$.^d Established from log layer.^e a calculated as $U_{bed}/(\pi/\text{half period})$.^h RMS of time series. (Data file A)^k WCI parameters from Soulsby *et al.* (1993)

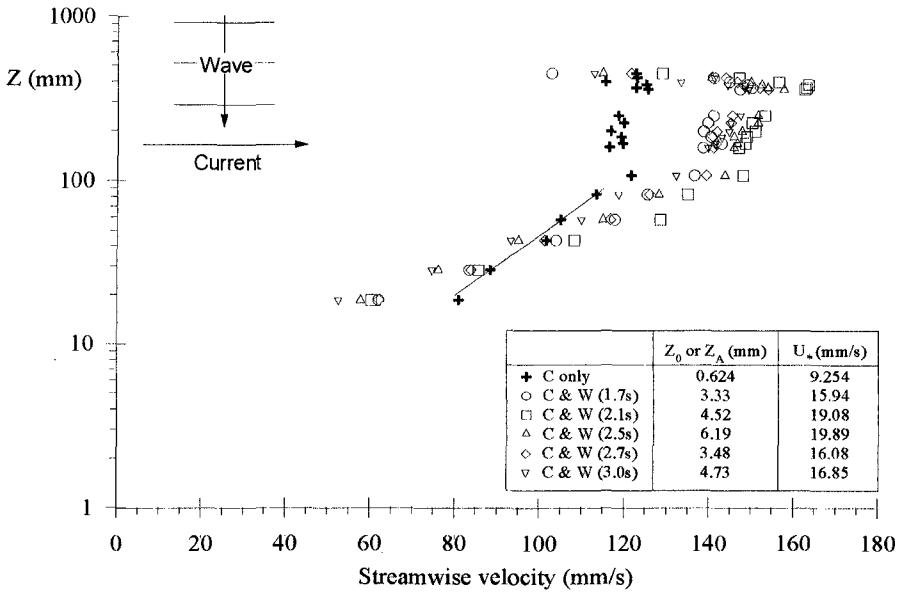


Figure 5 Longshore current mean velocity profiles: $u \ v \ \log z$
Current alone and with waves superimposed.

Results

Analysis of the logarithmic mean velocity profiles for the current alone suggested a bed roughness, k_s , of 18.7mm. When orthogonal (or oblique) waves were superimposed, the logarithmic profiles (**fig.5**) showed the expected increases in mean shear stress and apparent bed roughness from their values for current alone. It was also noted that the average-over-depth flow rate was slightly higher at the offshore measuring position when the waves were present. This was attributed to the non-linear wave-current enhancement of mean shear stress being greater in shallow water than in the deep water region, thereby producing a greater resistance to the longshore current inshore on the 1-in-20 beach and thus redirecting the flow out towards the deeper water - where the present measurements were made.

Table 2 shows a comparison between the observed mean longshore shear

Test Data			Model predictions for τ_{wc} Nm^{-2}							
T s	τ_c Nm^{-2}	τ_{wc} Nm^{-2}	F 84	MS 90	HTT 91	DSK 88	OY 88	CN 86	S 91	N 92
1.7	0.09	0.25	0.16	0.14	0.22	0.16	0.15	0.20	0.20	0.20
2.1	0.09	0.36	0.19	0.17	0.26	0.18	0.15	0.22	0.25	0.23
2.5	0.09	0.39	0.17	0.16	0.23	0.17	0.14	0.19	0.22	0.20
2.7	0.09	0.26	0.18	0.17	0.24	0.17	0.13	0.19	0.23	0.21
3.0	0.09	0.28	0.19	0.18	0.25	0.19	0.13	0.20	0.24	0.18

Table 2: Mean bed shear stress τ_m : comparison of measurements from regular wave tests with predictions from 8 theories.

stresses τ_{wc} deduced from the logarithmic velocity profiles and predictions from a number of wave-current models. τ_c was measured for the current on its own. The values from Davies *et al.* (1988), Fredsoe (1984), Huynh-Thanh & Temperville (1991), Myrhaug & Slaattelid (1990), and O'Connor & Yoo (1988) were all deduced from the parameterised versions of those models presented by Soulsby *et al.* (1993) and discussed above; this was particularly helpful for the fully numerical models which would otherwise have been inaccessible. The values from Coffey & Nielsen (1986), Sleath (1991), and Nielsen (1992) were calculated (more-or-less) directly.

Test data			Model predictions for z_a							
T s	z_0 mm	z_a mm	F 84	MS 90	HTT 91	DSK 88	OY 88	CN 86	S 91	N 92
1.7	.63	4.73	3.82	3.09	6.92	3.65	3.45	6.04	9.12	5.7
2.1	.63	3.48	4.63	3.81	8.29	4.43	3.04	6.47	12.3	6.68
2.5	.63	6.19	4.96	4.35	8.13	4.75	3.13	5.55	11.7	6.24
2.7	.63	4.52	4.92	4.35	8.00	4.71	2.81	5.40	12.4	6.34
3.0	.63	3.33	6.31	5.67	9.89	6.06	3.20	5.93	14.5	6.97

Table 3: Apparent bed roughness k_s : comparison of measurements from regular wave tests with predictions from 8 theories.

However, these three models are intended primarily to predict the enhanced bed roughness assuming an appropriate value for wave-current shear stress. To deduce the predicted shear stress in these cases, it has been assumed that the mean-over-depth velocity is as measured for the wave-current tests, and also that the velocity profile remains logarithmic across the full flow depth. Then, starting with an initial guess for shear stress, it is possible to calculate a first estimate for apparent bed roughness from an integrated form of the logarithmic boundary layer equation. An improved estimate for shear stress can then be found, and repeated iteration used to produce solutions both for apparent roughness and for mean shear stress.

Table 3 gives a similar comparison to that described above, but now looking at the apparent bed roughness. The predictions have been calculated, again assuming fully logarithmic velocity profiles and also that the mean-over-depth velocity is as measured in the combined wave-current flow. This was done to allow flows to be compared "like-for-like" and to overcome the problem of the local flow rate having been altered by the redirection of the longshore current (as discussed above). In order to obtain these data for each case, it was necessary to integrate the velocity profiles manually - taking into account the additional Eulerian mean flow taking place above Still Water Level through the wave crest. A typical example, showing a curve-fit through the scattered ADV data from which the mean-over-depth velocity was calculated, is shown in **fig.6**.

The first thing to note from these two tables is that the apparent bed roughness and mean shear stress have, as the models all predict, both increased when the waves are superimposed. That there is not a steady increase with relative wave strength can be attributed to the observation that the longer period waves have become non-linear with significant secondary crests. However, even when looking at the 1.7s and 2.1s period tests, it can be seen that there is a wide range of predictions and that no single model stands out as ideal.

Turning to the wave-induced stresses, friction factors for the regular wave tests calculated from ensemble averaged wave-induced velocities and shear stresses showed no visible change when the current was superimposed, so confirming UCL's earlier results.

Continuous time-series of velocities and shear stresses from the random wave tests were analysed half a wave cycle at a time to produce some hundreds of independent values of friction factor through each sequence of irregular waves (**fig.7**). Values were calculated for a specific half-wave period, determining the amplitude between consecutive trough and crest - of wave-induced shear stress from the shear cell, and of velocity from ADV measurements outside the wave boundary layer.

Again, these showed that for the range of test conditions possible in the UKCRF

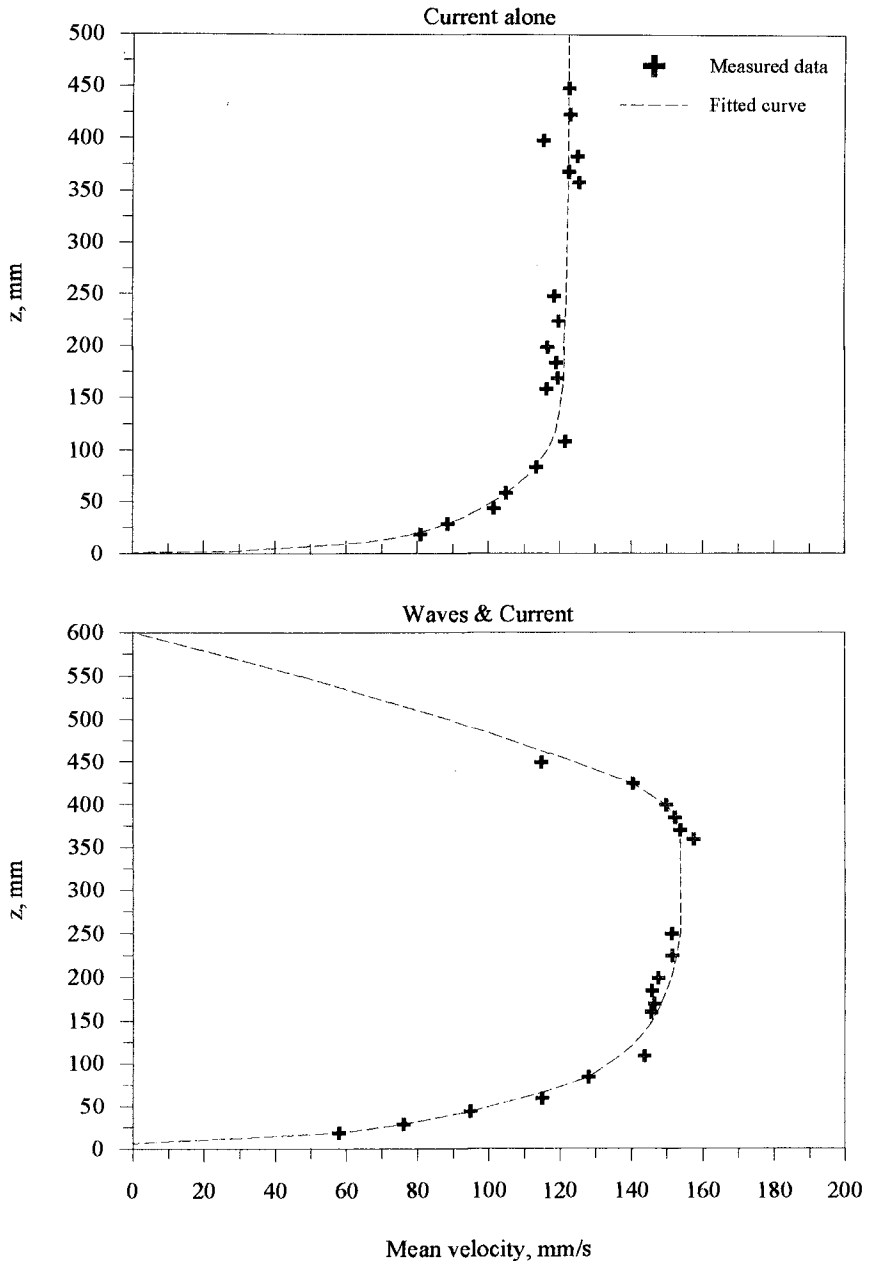


Figure 6 Mean velocity profiles for:
 a) current alone, b) current + wave ($T=2.5s, H=0.2m$)

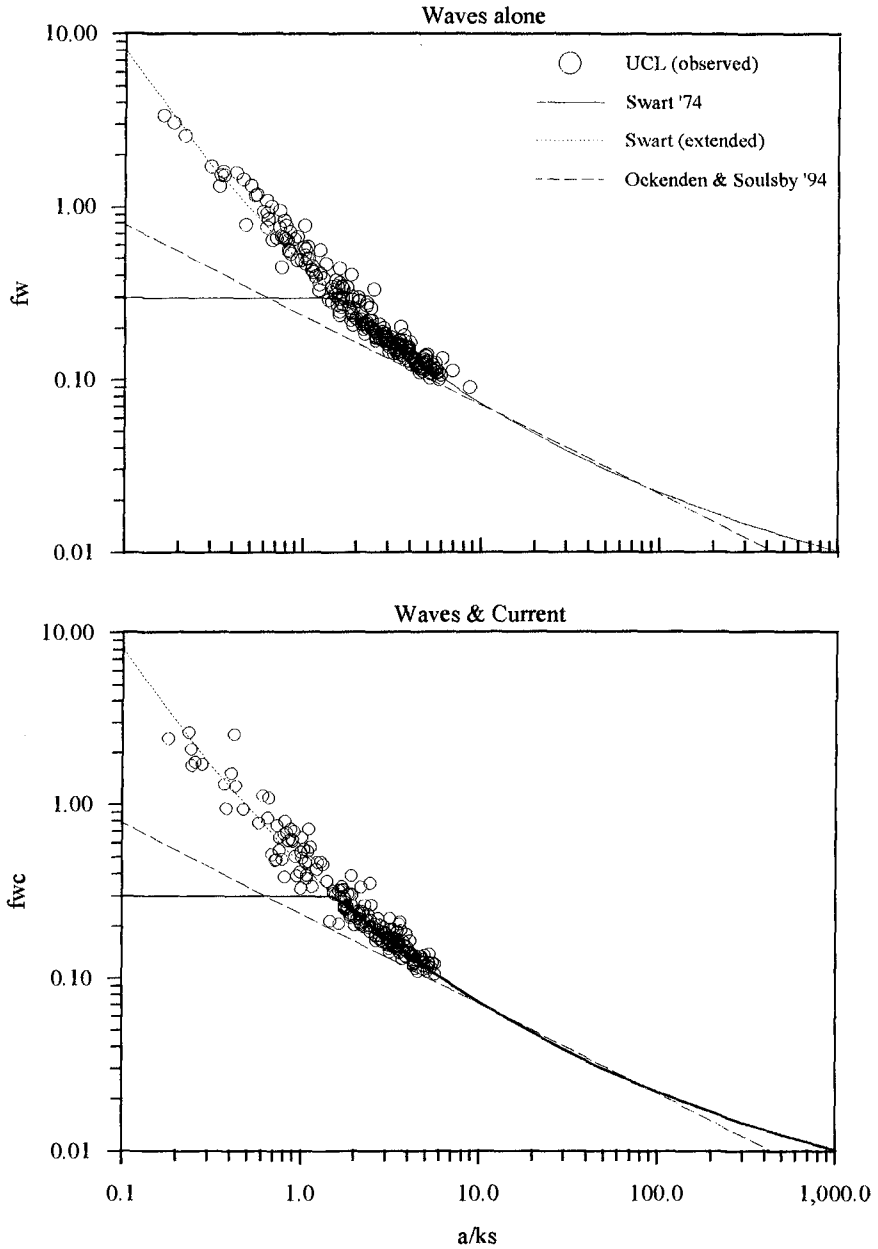


Figure 7 Friction factor calculated from each half wave cycle:
 Random wave sequence: $T_p=2.5s$, $H_s=0.15m$

there is no discernable increase in friction factor (and hence no effect on the wave-induced bottom shear stress) when a current is superimposed. However, they did confirm that Swart's (1974) formula for friction factor gives a good estimate, for waves alone or with an orthogonal current added, even at very low a/k where a constant value has sometimes been proposed. Comparison with the power law approximation proposed in Ockenden and Soulsby (1994) is also encouraging for the practical range $5 < a/k < 100$ although this appears less accurate at low values of a/k and cannot be correct at high a/k where the friction factor should tend to a constant value for a quasi-steady current.

If we now consider what enhancement of wave-induced shear stress (or friction factor) is to be expected when a current is superimposed, it seems that none of the models actually predicts any significant enhancement under the conditions being investigated. This is because the wave boundary layer only starts to be modified when the current-induced mean shear stress is of a similar magnitude to the wave-induced stress, and this can only be achieved in the laboratory if mean flow velocities are impractically high or the waves are so small as to be dominated by viscosity and surface tension. So the consistent behaviour of the waves whether with and without the longshore current is indicating that this aspect of wave-current theory is valid.

Conclusions

For a longshore current, mean shear stress and apparent bed roughness are both increased significantly by the addition of relatively strong orthogonal waves. Predictions from the wave-current models vary significantly, although the Davies *et al.* (1988) and Fredsoe (1984) theories appear most consistent with the present data.

Swart's (1974) formula for wave friction factor gives excellent agreement with the values measured by the shear cell for both regular and irregular waves.

The addition of a relatively weak longshore current has no effect on the bottom shear stress generated by waves on a rough bed.

The UCL shear cell is capable of measuring mean and oscillatory bottom shear stresses in a large-scale three-dimensional flow field.

Acknowledgements

The authors would like to express their gratitude to the UK Engineering and Physical Sciences Research Council for their financial support of this project, and also to HR Wallingford Ltd for their co-sponsorship of the UKCRF.

References:

- Coffey, F.C. and Nielsen, P. 1986 The influence of waves on current profiles. Proc. 20th Int. Conf. on Coastal Engng., Taipei, pp.82-96
- Davies, A.G., Soulsby, R.L. and King, H.L. 1988 A numerical model of the combined wave and current bottom boundary layer. J.Geophysical Res., 93(C1), pp.491-508
- Fredsoe, J. 1984 Turbulent boundary layer in wave-current motion. J.Hydraulic Engng., ASCE 110: pp.1103-1120
- Grass, A.J., Simons, R.R., Maclver, R.D., Kalopedis, A. 1995 Shear cell Proc.IARH Congress, London, 11-15 Sept. 1995, Vol.1, 1C8, pp.415-420
- Huynh-Thanh, S. and Temperville, A. 1991 A numerical model of the rough turbulent boundary layer in combined wave and current interaction. In: R.L.Soulsby and R.Bettess (Editors), Sand Transport in Rivers, Estuaries and the Sea. Balkema, Rotterdam, pp.93-100
- Myrhaug, D. and Slaattelid, O.H. 1990 A rational approach to wave-current friction coefficients for rough, smooth and transitional turbulent flow. Coastal Engineering, 14, pp.265-293
- Nielsen, P. 1992 Coastal bottom boundary layers and sediment transport. Advanced series on Coastal Engineering, Vol.4. World Scientific Publishing Co., Singapore.
- O'Connor, B.A. and Yoo, D. (1988) Mean bed friction calculation of combined wave-current flow. Coastal Engineering, 12, pp. 1-21.
- Ockenden, M.C. and Soulsby, R.L. 1994 Sediment transport by currents plus irregular waves. HR Wallingford Report SR 376, February 1994.
- Simons R.R., Whitehouse R.J.S., Maclver R.D., Pearson J., Sayers P., Zhao Y. and Channell A. 1995 Evaluation of the UK Coastal Research Facility. Coastal Dynamics '95. Proc. Int. Conf. - Large Scale Experiments, Gdansk, Poland, 4-8 September 1995, pp.161-172
- Simons, R.R., Grass, A.J., Saleh, W.M. and Mansour-Tehrani, M. (1994) Bottom shear stresses under random waves with a currents superimposed. Proc. 24th Int. Conf. on Coastal Engng, Kobe, Japan, Ch.42, pp.565-578
- Simons, R.R., Grass, A.J. and Mansour-Tehrani, M. (1992) Bottom shear stresses in the boundary layer under waves and currents at right angles. Proc. 23rd Int. Conf. on Coastal Engng, Venice, Italy, Ch.45, pp.604-617
- Sleath, J.F.A. 1991 Velocities and shear-stresses in wave-current flows. J.Geophysical Res., Vol.96 (C8), pp.15237-15244
- Soulsby, R.L., Hamm, L., Klopman, G., Myrhaug, D., Simons, R.R., and Thomas, G.P. (1993) Wave-Current Interaction within and outside the bottom boundary layer. Coastal Engineering, 21, pp.41-69.

CHAPTER 270

Movable Bed Roughness in the Flow of Irregular Waves and Currents over Movable Beds

Zai-Jin You¹ Peter Nielsen²

Abstract

The bed roughness k_s in the flow of irregular waves and currents over a movable bed is studied on the basis of measured current profiles and the model of You (1994). It is found that the movable bed roughness k_s is affected by both waves and currents and that the existing formulae derived in purely oscillatory flow generally fail to predict k_s in the flow of waves and currents. A new formula is proposed to calculate k_s in the flow of irregular waves and currents over a movable bed. The present bed roughness formula together with You's (1994) model gives better prediction of current shear velocity \bar{u}_{cw}^* and especially apparent roughness z_1 than the existing formulae derived in purely oscillatory flow.

Introduction

The bed roughness k_s is an important input parameter in the modelling of coastal processes, but usually unknown in the coastal zone where the seabed is often movable owing to irregular waves and currents. The movable bed roughness k_s in purely oscillatory flow has been studied by many investigators (Van Rijn, 1982, Grant and Madsen, 1982; Nielsen, 1983; Raudkivi, 1988), but little investigated in the flow of irregular waves and currents. Consequently, the formulae derived in purely oscillatory flow have been often applied to estimate the movable bed roughness k_s in

¹Victorian Institute of Marine Sciences, Locked Bag 7, Collins Street East Post Office, Melbourne 8003, AUSTRALIA.

²Department of Civil Engineering, University of Queensland, Brisbane 4072, AUSTRALIA.

in the flow of irregular waves and currents. For example, Coffey (1987) used the formulae of Nielsen (1983), Van Rijn (1982), and Grant and Madsen (1982) to calculate k_s at $\theta = 0^\circ$, 90° and 180° , but did not explain why the different formulae were applied for the different angles, where θ is the angle between the wave propagation and a current.

Van Kampen and Nap (1988) found that the movable bed roughness k_s , estimated at $\theta = 0^\circ$ or 180° from their experimental data was very large and could not be predicted by the existing formulae. In the sequential experiment of Havinga (1992), however, k_s estimated at $\theta = 60^\circ$ or 120° was found to be very small and could not be predicted by the existing formulae either.

Drake *et al.* (1992) used the model of Grant and Madsen (1979) to study the movable bed roughness k_s in the flow of irregular waves and currents on the basis of measured current profiles. A simple empirical formula was suggested to be $k_s = 28\eta^2 / \lambda - 0.14\theta$, where $0 \leq \theta \leq 90^\circ$. Unfortunately, the model of Grant and Madsen (1979) together with the empirical formula still failed to predict the apparent roughness z_1 as shown in Figure 4 of Drake *et al.* (1992).

More recently, Mathisen and Madsen (1996) studied the fixed bed roughness in steady flow, oscillatory flow and combined wave-current flow, respectively. It was found that k_s experienced by a pure current was equal to that by waves alone or by waves and currents. However, this is not valid for a movable bed simply because the movable bed form, which is suggested to a main contributor to k_s , is found to be quite different in steady flow compared to that in a combined wave-current flow (Arnot and Southard, 1990; Havinga, 1992).

In the present study, the movable bed roughness k_s in the flow of irregular waves and currents over a movable bed is studied on the basis of measured current profiles and the calibrated model of You (1994). A practical application is also given to calculate k_s in the coastal zone.

Model of Wave-Current Flows over Fixed Beds

In steady flow over a fully rough fixed bed, the current profile is logarithmic

$$\bar{u} = \frac{\bar{u}_c^*}{\kappa} \ln \frac{z}{z_0} \quad (1)$$

in which \bar{u}_c^* is the current shear velocity, κ is the von Karman constant, $k_s = 30z_0$ and k_s is the bed roughness. When waves are superimposed on a current, a logarithmic current profile near the bed can still be found and similarly expressed as

$$\bar{u} = \frac{\bar{u}_{cw}^*}{\kappa} \ln \frac{z}{z_1} \quad (2)$$

but with $\bar{u}_{cw}^* > \bar{u}_c^*$ and $z_1 > z_o$ as first studied experimentally by Bijker (1967) and recently by Havinga (1992) and Klopman (1994).

Many models of combined wave-current flows over fixed beds have been developed to calculate the current shear velocity \bar{u}_{cw}^* and the apparent roughness z_1 in Eq.(2). A review of existing models of combined wave-current flows refers to You (1992). You (1994, 95a) compared the four analytical models of Christoffersen and Jonsson (1985), Coffey and Nielsen (1986), Sleath (1991) and You (1994) with the laboratory measurements of van Doorn (1991, 82) and Kemp and Simons (1982). It was concluded that the model of You (1994) was simpler and gave better agreement with the experimental data than the others. In the present study, the model of You (1994) is chosen to study the movable bed roughness k_s in the flow of irregular waves and currents.

In the model of You (1994), the input parameters were chosen to be the wave parameters (A , ω), a reference current velocity \bar{u}_r at an arbitrary level, and the bed roughness k_s . For irregular waves, significant wave height H_s and period T_s were suggested to calculate A and ω using linear wave theory. The current shear velocity \bar{u}_{cw}^* in Eq.(2) was explicitly calculated by

$$\bar{u}_{cw}^* = 0.5u_w^* \left\{ \log_a^b + \left[(\log_a^b)^2 + 1.6 \frac{\bar{u}_r}{u_w^*} \log_a^a \right]^{0.5} \right\} \quad (3)$$

in which the wave shear velocity u_w^* was evaluated as

$$u_w^* = \sqrt{0.5f_w} A \omega \quad \text{and} \quad f_w = 0.108 \left(\frac{k_s}{A} \right)^{0.343} \quad (4)$$

and the parameters a and b were defined by

$$a = \frac{30e\delta_1}{k_s}, \quad b = \frac{2\delta_1}{z_r} \quad \text{and} \quad \delta_1 = \frac{0.5\kappa u_w^*}{\omega} + 0.2z_o. \quad (5)$$

The apparent roughness z_1 in Eq.(2) was also calculated explicitly by

$$z_1 = 2\delta_1 \left(\frac{30e\delta_1}{k_s} \right)^{\frac{\bar{u}_{cw}^*}{u_w^*}}. \quad (6)$$

The derivations of Eqs.(3)-(6) refer to You (1994). Alternatively, when the current shear velocity \bar{u}_{cw}^* and the apparent roughness z_1 are measured, the movable bed roughness k_s in the flow of waves and currents can be determined by the model.

Movable Bed Roughness

The formulae derived in purely oscillatory flow have been often used to calculate the movable bed roughness k_s in the flow of waves and currents (Grant Williams, 1984; Coffey, 1987; Drake et al, 1992)

$$k_s = C \eta^2 / \lambda + f(\Theta) \quad (7)$$

in which η and λ are the ripple height and length, $f(\Theta)$ is an additional bed roughness owing to the near-bed sediment transport, and C is constant and was chosen to be 8, 16 and 28 by Nielsen (1983), Raudkivi (1988) and Grant and Madsen (1982), respectively. Since no direct measurements of k_s are available in the flow of waves and currents over movable beds, a direct comparison of Eq.(7) with experimental data on k_s becomes impossible. When the current shear velocity \bar{u}_{cw}^* and apparent roughness z_1 are measured, however, Eq.(7) may be verified indirectly by using a calibrated model of combined wave-current flows. That is, if the calibrated model together with Eq.(7) can agree well with the measured \bar{u}_{cw}^* and z_1 , it may be concluded that Eq.(7) gives good estimation of k_s .

In the present study, the laboratory experimental data from Kaaij and Nieuwjaar (1987), Van Kampen and Nap (1988) and Havinga (1992) are used to study the movable bed roughness k_s in the flow of irregular waves and currents. The irregular waves in the three sequential experiments were generated by a directional wave generator. The wave spectrum was JONSWAP. The significant wave heights H_s ranged from 7.5 to 18cm, the peak wave period T_p was about 2.5s, and the depth-averaged current velocity $\langle \bar{u} \rangle$ varied from 10 to 40cm/s. The current profiles and bed forms in the absence and presence of irregular waves were measured. The movable roughness k_s calculated from Eq.(7) was found to be generally dominated by the first term in Eq.(7).

In Figure 1, the models of Sleath (1991) and You (1994) together with Grant and Madsen's (1982) formula of $k_s = 28\eta^2 / \lambda$ are used to calculate the apparent roughness z_1 and compared with the experimental data. It can be seen that the models generally underestimate z_1 at $\theta = 0^\circ$ and 180° , but overpredict z_1 at $\theta = 60^\circ$ and 120° . This indicates that the bed roughness k_s used in the models has been underestimated at $\theta = 0^\circ$ and 180° , but overcalculated at $\theta = 60^\circ$ and 120° . The models would not give better prediction of z_1 by adjusting the constant C or the second term in Eq.(7).

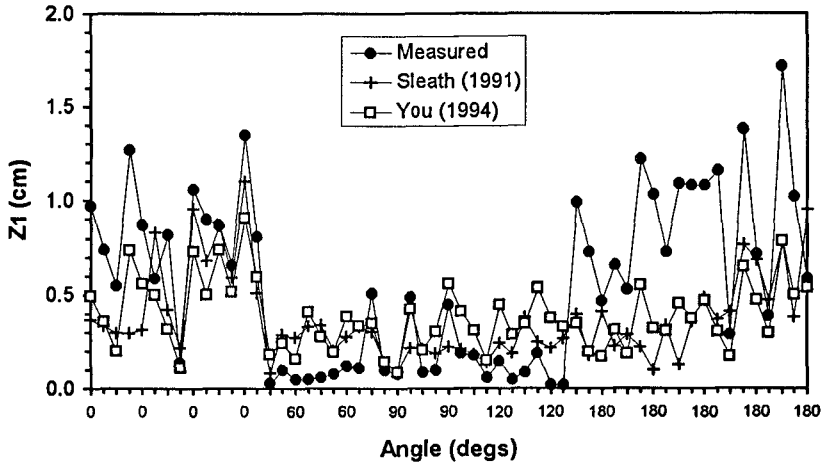


Figure 1. Comparison of the apparent roughness z_1 measured by Kaaij and Nieuwjaar (1987), Van Kampen and Nap (1988) and Havinga (1992) with those calculated by the models of Sleath (1991) and You (1994) with $k_s = 28\eta^2 / \lambda$. The ripple height η and length λ were directly measured in the experiments.

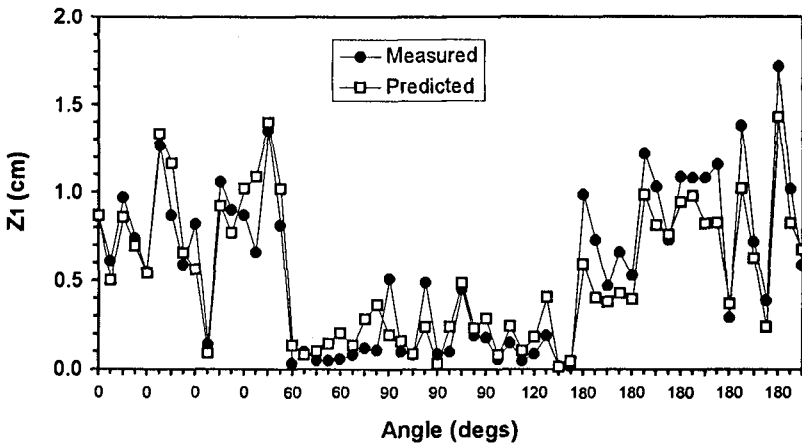


Figure 2. Comparison of the apparent roughness z_1 measured by Kaaij and Nieuwjaar (1987), Van Kampen and Nap (1988) and Havinga (1992) with those calculated by You's (1994) model with the input of k_s estimated from Eq.(8). The bed roughness z_0 in steady flow alone, the depth-averaged current velocity $\langle \bar{u} \rangle$ and the nearbed wave velocity amplitude $A\omega$ in Eq.(8) were measured in the experiments.

In other words, the use of the other former formulae (eg Nielsen, 1983; Raudkivi, 1988) in the models would not give better prediction of z_1 in Figure 1.

As a first approximation, the movable bed roughness k_s in the flow of irregular waves and current flow may be simply structured as

$$k_s = 30z_o \left(1 + \frac{A\omega}{\langle \bar{u} \rangle} \right) \quad (8)$$

in which A is the nearbed semi-excursion of wave orbital motion, ω is the angular frequency, $\langle \bar{u} \rangle$ is the depth-averaged current velocity, and z_o is the movable bed roughness in steady flow alone. In the field, a current velocity \bar{u}_A averaged from the bed to a level h_A is suggested to replace $\langle \bar{u} \rangle$ in Eq.(8). It can be seen from Eq.(8) that the movable bed roughness k_s in the flow of waves and currents is larger than that in steady flow alone. The increase of k_s in the presence of waves may be understood to result from the appearance of wave-generated sand ripples and the increase of the nearbed sediment transport. It is shown in Figure 2 that the model of You (1994) together with Eq.(8) gives satisfactory agreement with the measured apparent roughness z_1 . The three variables z_o , $\langle \bar{u} \rangle$ and $A\omega$ in Eq.(8) were directly measured in the experiments. It may be concluded here that the new formula expressed by Eq.(8) gives good estimation of k_s in the flow of waves and currents.

It should be mentioned here that the formula suggested by Eq.(8) is only valid for a movable bed. For a fixed bed, it is often assumed that the bed roughness in steady flow is equal to that in oscillatory flow alone or in a combined wave-current flow. This has also been studied quantitatively by Mathisen and Madsen (1996).

Practical Applications

The bed roughness in the flow of waves and currents can't be obtained from Eq.(8) unless all the variables in Eq.(8) are known. The movable bed roughness k_s in the field can be determined from Eq.(8) when \bar{u}_{cw}^* , z_1 and $A\omega$ are measured.

The current velocity \bar{u}_A , which is depth averaged from z_o to a level h_A in steady flow alone, can be calculated by

$$\bar{u}_A = \frac{\bar{u}_c^*}{\kappa} \ln \frac{h_A}{e z_o}. \quad (9)$$

In the presence of waves, \bar{u}_A can also be approximately estimated from

$$\bar{u}_A = \frac{\bar{u}_{cw}^*}{\kappa} \ln \frac{h_A}{e z_1} \quad (10)$$

in which h_A is an arbitrary level and is chosen to be about 1.0m above the seabed in the present study. On the other hand, the relationship between \bar{u}_c^* and \bar{u}_{cw}^* was derived by You (1995b) as

$$\bar{u}_{cw}^* = \bar{u}_c^* + K \times A \omega \quad (11)$$

in which K is constant and was determined to be 0.026 and 0.020 for the laboratory and field data, respectively. For irregular waves, significant wave height H_s and period T_s were suggested to calculate $A \omega$ in Eq.(11) using linear wave theory. The comparison of Eq.(11) with available experimental data is shown in Figure 3. Therefore, the movable bed roughness k_s in the coastal zone can be explicitly calculated from Eqs.(8)-(11). The depth-averaged current velocity $\langle \bar{u} \rangle$ in Eq.(8) should be replaced by \bar{u}_A in Eq.(10).

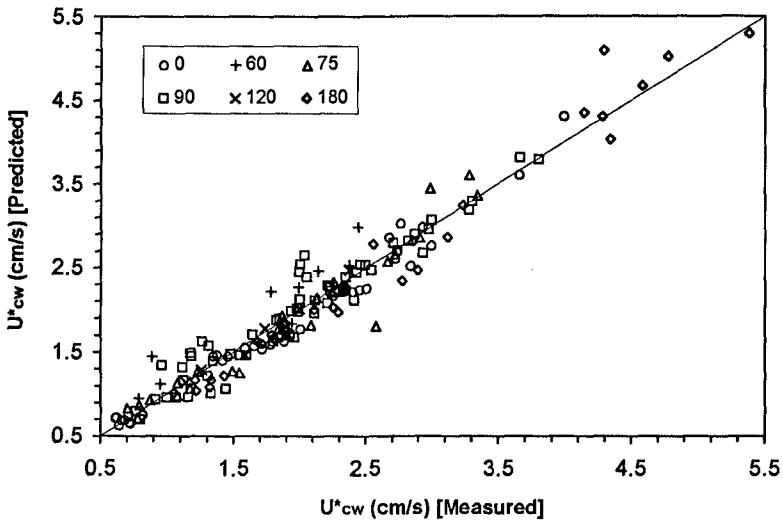


Figure 3. Comparison of Eq.(11) with the available experimental data from Bijker (1967) [$\theta = 75^\circ$ and 90° , regular waves], Kemp and Simons (1982, 1983) [$\theta = 0^\circ$ and 180° , regular waves], Visser (1986) [$\theta = 90^\circ$, regular waves], Kaaij and Nieuwjaar (1987) [$\theta = 0^\circ$ and 180° , irregular waves], Van Kampen and Nap (1988) [$\theta = 0^\circ$ and 180° , irregular waves], Simons *et al.* (1988) [$\theta = 0^\circ$, regular waves], and Havinga (1992) [$\theta = 60^\circ$, 90° and 120° , irregular waves]. After You (1995b).

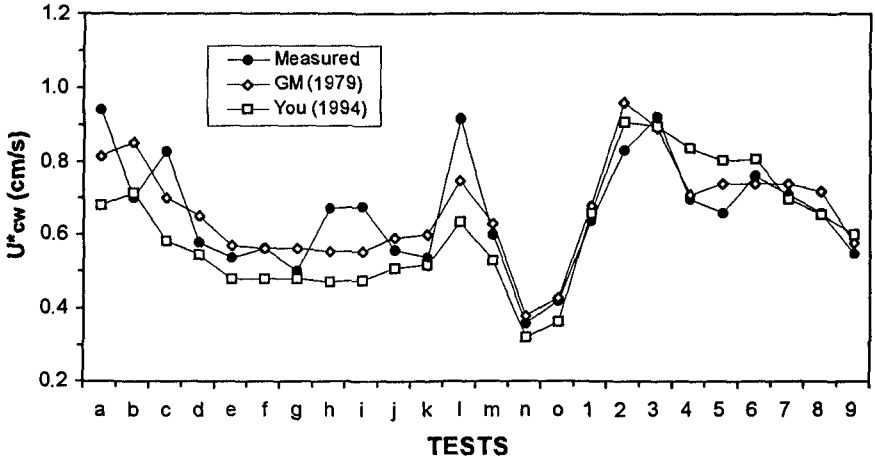


Figure 4. Comparison of the current shear velocities \bar{u}_{cw}^* calculated by the models of Grant and Madsen (1979) and You (1994) with the field measurements of Grant and Williams (1984, 85). The movable bed roughness of $k_s=6.0\text{cm}$ used in the models was calculated from Grant and Madsen's (1982) formula by Grant and Williams (1984, 85).

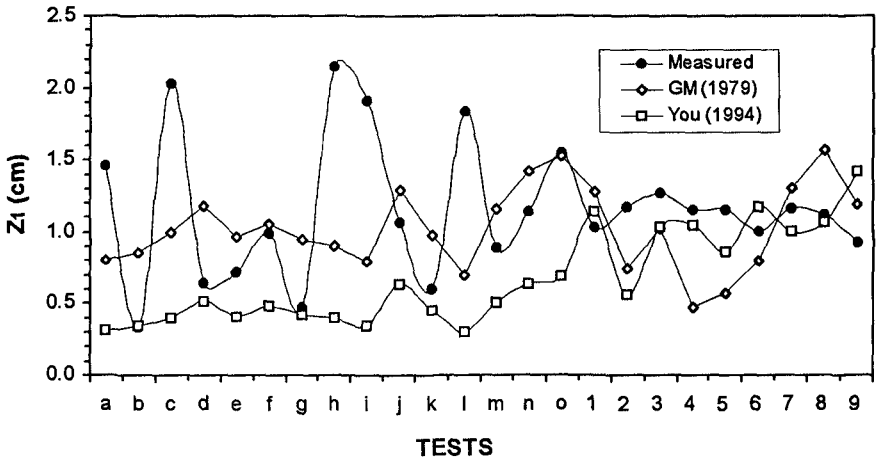


Figure 5. Comparison of the apparent roughness z_1 calculated by the models of Grant and Madsen (1979) and You (1994) with the field measurements of Grant and Williams (1984, 85). The bed roughness of $k_s=6.0\text{cm}$ used in the modes was estimated from Grant and Madsen's (1982) formula by Grant and Williams (1984, 85).

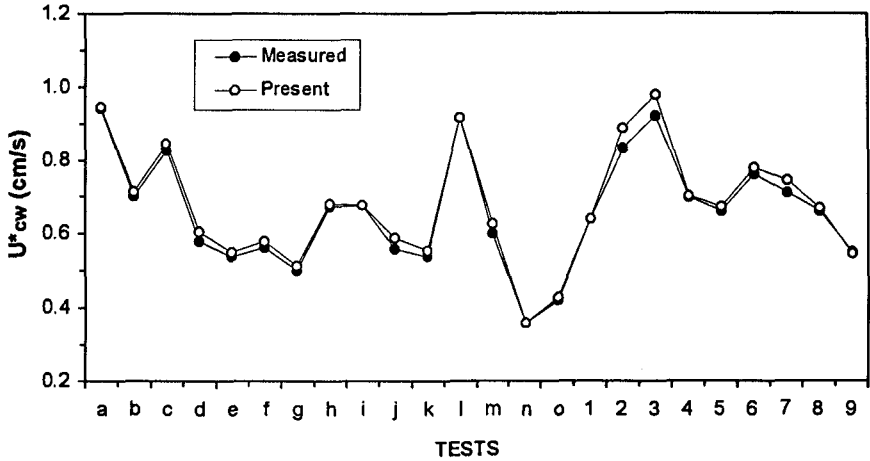


Figure 6. Comparison of the current shear velocities calculated by the model of You (1994) with the field measurements of Grant and Williams (1984, 85). The bed roughness k_s used in the model is calculated from Eqs.(8)-(11).

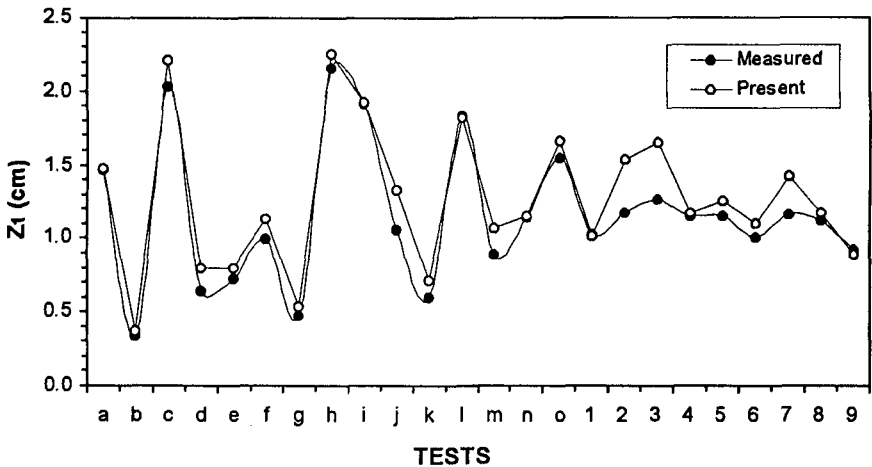


Figure 7. Comparison of the apparent roughness z_1 calculated by the model of You (1994) with the field measurements of Grant and Williams (1984, 85). The bed roughness k_s used in the mode is calculated from Eqs.(8)-(11).

Grant and Williams (1984, 85) provided high-quality field measurements of current profiles of combined wave-current flows over a movable seabed. In Figures 5 and 6, the models of Grant and Madsen (1979) and You (1994) are used to calculate the current shear velocity \bar{u}_{cw}^* and apparent roughness z_1 and compared with the field measurements. The bed roughness of $k_s = 6.0\text{cm}$ used in the two models was estimated from Grant and Madsen's (1982) formula by Grant and Williams (1984, 85). It can be seen that the two models generally fail to predict the apparent roughness z_1 even though the models give good agreement with the measured current shear velocities \bar{u}_{cw}^* . In Figures 6 and 7, however, the model of You (1994) gives satisfactory agreement with the measured \bar{u}_{cw}^* and z_1 when the bed roughness k_s is calculated from Eqs.(8)-(11). The depth-averaged current velocity $\langle \bar{u} \rangle$ in Eq.(8) should be replaced by \bar{u}_A in Eq.(10), and $h_A = 1.0\text{m}$.

Conclusions

The movable bed roughness in the flow of irregular waves and currents are studied based on the simple model of You (1994) and measured current profiles. A new formula expressed by Eq.(8) is proposed to calculate k_s in the flow of irregular waves and current. The present bed roughness formula together with the model of You (1994) gives better agreement with the measured apparent roughness z_1 than the former formulae derived in purely oscillatory flow. The field measurements of current profiles in the presence of irregular waves can be also predicted well with the model of You (1994) and the new bed roughness formula.

References

- Arnot, R. W and Southard, J. B (1990). Exporatory flow duct experiments on combined flow bed configurations and some implications for interpreting storm even stratification. *Sedimentary Petrology*, 60: 211-219.
- Bijker, E. W (1967). Some considerations about scales for coastal models with movable beds. Delft Hydraulics Lab, Pub No. 50.
- Christoffersen, J. B and Jonsson, I. G (1985). Bed friction and dissipation in a combined current and wave motion. *Ocean Eng.*, 12: 387-423.
- Coffey, F. C (1987). Current profiles in the presence of waves and the hydraulics roughness of natural sand beaches. Ph.D thesis, Dept of Geography, University of Sydney, Australia.
- Coffey, F. C and Nielsen, P (1986). The influence of waves on current profiles, *Proc 20th Int Conf Coastal Eng.*, Taipei, p. 82-96.
- Drake, D. E, Cacchinone, D. A and Grant, W. D (1992). Shear stress and bed roughness estimates for combined wave and current flows over a rippled bed. *J Geophys Res.*, 97: 2319-2326.

- Grant, W. D and Madsen, O. S (1979). Combined wave current interaction with a rough bottom. *J Geophys Res.*, 84: 1797-1808.
- Grant, W.D and Madsen, O.S (1982). Movable bed roughness in unsteady oscillatory flow. *J Geophys Res.*, 87: 469-481.
- Grant, W. D and Williams, A. J (1984). Bottom stress estimates and their prediction on the Northern California Continental Shelf during CODE-1: the importance of wave-current interaction. *J Phys Oceanogr.*, 14: 506-727.
- Grant, W. D and Williams, A. J (1985). Reply to Huntley's Comments. *J Phys Oceanogr.*, 15: 1219-1228.
- Havinga, F. J (1992). Sediment concentrations and sediment transport in case of irregular non-breaking waves with a current. Draft Thesis, Faculty of Civil Engineering, Delft University of Technology.
- Kemp, P. H and Simons, R. R (1982). The interaction between waves and a current: waves propagating with the current. *J Fluid Mech.*, 116: 227-250.
- Kemp, P. H and Simons, R. R (1983). The interaction between waves and a current: waves propagating against the current. *J Fluid Mech.*, 130: 73-89.
- Klopman, G (1994). Vertical structure of the flow due to waves and currents, Delft Hydraulics Laboratory, Report H840, Part II.
- Mathisen, P. P and Madsen, O. S (1996). Waves and currents over a fixed rippled bed: 1. Bottom roughness experienced by waves in the presence and absence of currents. *J Geophys Res.*, 101: 16,533-16,542.
- Mathisen, P. P and Madsen, O. S (1996). Waves and currents over a fixed rippled bed: 2. Bottom and apparent roughness experienced by currents in the presence of waves. *J Geophys Res.*, 101: 16,543-16,550.
- Raudkivi, A, J (1989). The roughness height under waves. *J. Hydraulic Res*, 26: 569-584.
- Simons, R. R, Kyriacou, A, Soulsby, R. L, Davis, A. G (1988). Predicting the nearbed turbulent flow in waves and currents. *IAHR Symp Mah Modelling of Sediment Transport in the Coastal Zone*, Copenhagen, pp.33-47.
- Nielsen, P (1983). Analytical determination of nearshore wave height variation due to refraction, shoaling and friction. *Coastal Eng.*, 7: 233-251.
- Sleath, J. D (1991). Velocities and shear stress in wave-current flows. *J Geophys Res.*, 96: 15237-15244.
- van Doorn, Th (1981). Experimental investigation of near-bottom velocities in water waves without and with a current. Delft Hydraulics Laboratory, Report No M143.
- van Doorn, Th (1982). Experimental investigation of the velocity field in the turbulent bottom boundary layer in an oscillatory water tunnel. Delft Hydraulics Laboratory, Report No M1562-b (in Dutch).

- van Kampen, H. F. A and Nap, E. N (1988). Sediment concentrations and sediment transport in case of irregular non-breaking waves with a current. Faculty of Civil Engineering, Delft University of Technology.
- van Rijn, L.C (1982). The prediction of bedforms and alluvial roughness. *In Mechanics of Sediments Transport*, Proc Euromech 156, pp. 133-135.
- You, Z. J (1992). Oscillatory boundary layers with and without currents. Ph.D thesis. School of Civil Engineering, University of New South Wales.
- You, Z. J (1994). A simple model for current velocity profiles in combined wave-current flows. *Coastal Eng.*, 23: 289-304.
- You, Z. J (1995a). A simple model for current velocity profiles in combined wave-current flows: reply to the comments by P. Nielsen. *Coastal Eng.*, 26: 101-104.
- You, Z. J (1995b). Increase of current bottom shear stress due to waves. *Coastal Eng.*, 26: 291-295.

CHAPTER 271

Seabed and Foundation Response to Wave Loading

Michael H. Davies¹

Abstract

The interactions between wave loading and soil response in both open waters and around the foundations of coastal structures are observed experimentally. Experimental results for wave action over sand beds are compared to analytical predictions based on both Sleath's porous bed model and on Biot's consolidation theory. Experiments on wave action in the vicinity of a rigid caisson, in conjunction with Mei's boundary layer theory, allow for the development of guidelines for interpreting the relative importance of drainage on the effective stress response of foundations to wave action.

Introduction

The geotechnical response of seabeds and foundations to wave loading can be a critical factor in evaluating the stability of proposed coastal and offshore structures. This paper reviews some of the techniques available for analysis of seabed response to wave action and presents a new heuristic approach for evaluating the relative importance of soil drainage in the response of coastal foundations.

Bea and Aurora (1981) and Wright and Dunham (1972) proposed total stress analysis for seabeds under wave loading. These techniques view the seabed loading as a harmonic tractive stress on the upper boundary, total stress analysis is used to calculate seabed response. Such analysis can use elastic, elasto-plastic or visco-elastic constitutive models and is commonly undertaken within a finite element framework. These approaches are particularly suitable to conditions where the soil is relatively soft and impermeable. These techniques have been successfully applied in analyzing the behaviour of soft soils such as Mississippi Delta muds in the Gulf of Mexico.

The pore pressure response within a seabed was originally explored by Putnam (1949) and later expanded by Sleath (1970). This analysis assumes that pore fluid flows are independent of soil stresses. This assumption is generally valid for stiff, permeable beds such as coarse sands and gravels. Yamamoto (1978) and Madsen (1978) independently proposed the use of 'poro-elastic' analysis for seabed response to wave action using Biot's (1941) linearized equations of consolidation. This allows the treatment of the coupled response to wave-seabed interactions, that is the porous

¹ Canadian Hydraulics Centre, Bldg.M-32, National Research Council, Ottawa, Canada, K1A 0R6 (e-mail: Michael.Davies@NRC.CA)

media response coupled with the elastic soil response. This provides a technique suitable for a wide range of soil and wave conditions ranging from soft, impermeable silts and clays through to stiff sands. Since the initial work by Madsen and Yamamoto, a wide range of papers has been written proposing expansions and adaptations of the work, e.g. Finn et al (1983) and Okusa (1985). The development of full finite element solutions of time-dependent effective stress problems has provided another analysis tool. Models such as those of Shen et al (1986) provide a finite element framework within which the coupled effective stress response of soils can be investigated.

In experimental studies of soil-wave-structure interaction, measurements of soil stress or strain are difficult. Pore pressure response is, however, readily measured and is thereby often used as the main indicator of soil behaviour. Other techniques tend to be highly intrusive and fail to provide a time history of soil response (e.g. cone penetration testing). One promising technique for measurement of soil response is measurement of the acoustic emissions from the soil mass (AE). This technique was successfully employed in this research program and was described in Davies, et al (1990). The present paper focuses on the use of pore pressure response as a measure of soil behaviour.

Pore pressure in seabeds

In a porous seabed under harmonic wave loading (wave frequency, ω) the pore pressure, U of a fluid with unit weight, γ , has three components:

$$U = \gamma z + \gamma P(\cos \omega t) + u_r \quad (1)$$

Where γz is the hydrostatic component of the pore pressure at depth z below the free surface, P is the wave-induced component of the pore pressure fluctuation (expressed as a piezometric head), and u_r is the residual component of the pore pressure (due to consolidation and or shearing action). It is important to draw the distinction between the wave-induced fluctuation in the pore pressure, P and u_r , the residual pore pressure in excess of hydrostatic. The wave-induced pore pressure fluctuation is an indicator of the steady-state harmonic fluctuations in the effective stress state of the soil caused by wave loading. The residual pore pressure, u_r is a more gradual change in the pore pressure (non-harmonic) possibly caused by shearing action of the soil which results in soil volume change and consequent changes in the residual pore pressure.

Experimental Set-up—Flat Bed Testing

A series of flume tests was conducted on a sand bed consisting of 15 m^3 of a fine Ottawa sand ($D_{50}=0.07\text{mm}$). The sand was hydraulically placed using a positive displacement slurry pump. The resulting berm had a uniform crest height of 0.91m over a 10 m width. This uniform section was flanked by 1:10 side slopes. A vertical array of pore pressure transducers had been installed in the flume prior to construction of the berm. This consisted of 14 Druck PDCR81 pore pressure transducers (7 kPa capacity) at 10 cm vertical spacing. A capacitance-type wave gauge was located directly above the pressure transducers.

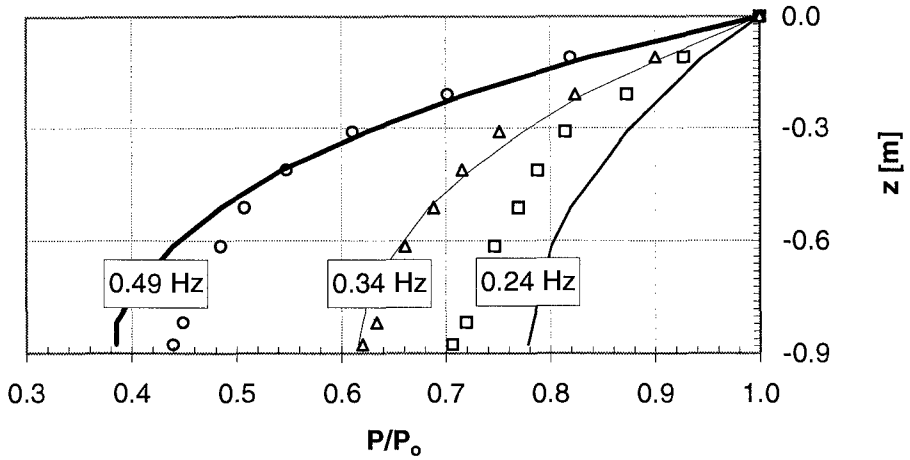


Figure 1 Vertical distribution of pore pressure as per Sleath (1970) for $k_x=1.8k_z$

Sand densities were determined using a 12 cm diameter brass sampling tube. Soil relative density was determined to be 47% (soil unit weight was 15.5 kN/m^3). Constant head permeability tests yielded a coefficient of permeability of $k=5.0 \times 10^{-5} \text{ m/s}$. The experimental setup is described in detail in Davies (1992).

Steady-state harmonic response

The pore pressure response measured in these experiments was compared to Sleath's rigid, porous bed model and to that predicted by poro-elastic theory as per Yamamoto, and Finn.

In general, the Sleath formulation was seen to provide a good estimate of the vertical distribution of the magnitude of the pore pressure fluctuation if the effects of anisotropic permeability are considered (see Figure 1). Here the amplitude of the harmonic pore pressure, P is normalized by P_0 , the pressure at the top of the seabed. Since Sleath's model assumes a porous media flow within a rigid bed, this solution provides no information about the stress response of the soil. Poro-elastic analysis is required to examine the coupled response of the soil and the pore fluid.

In comparing the pore pressure response to that predicted by poro-elastic theory, initial comparisons were made to the model of Yamamoto, 1978. This formulation does not consider the effect of anisotropic permeability and it was not possible to obtain good agreement between the model and theory. To match the observed vertical attenuation of the pressure magnitude, the predicted phase lags were far too large – on the order of 30° . Measured phase lags in the model were not seen to exceed 15° . Consequently, Finn's Stabmax routine was employed since it allows for anisotropic permeability. Using Stabmax, good agreement could be obtained for both the amplitude and phase of the pore pressure response. This agreement is shown in Figures 2 and 3. It should be noted here that the poro-elastic models were seen to be extremely sensitive to the volumetric degree of soil saturation, S_r . Sensitivity tests showed that varying the soil saturation ratio from 98% to 99.8%

resulted in predicted phase lags at the bottom of the bed varying from 28° down to 3° , the trend being that phase lag reduces with reducing air content. These findings are described in more detail in Davies (1992).

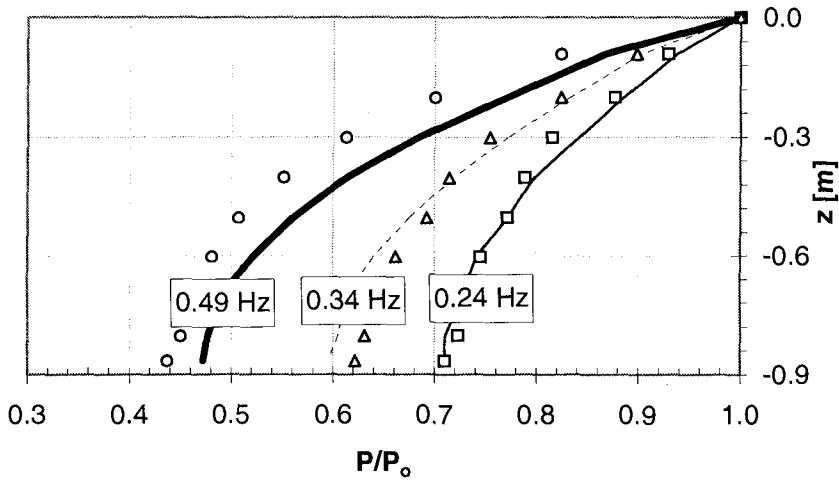


Figure 2 Measured pore pressure response vs poro-elastic theory (Stabmax, Finn, 1982)

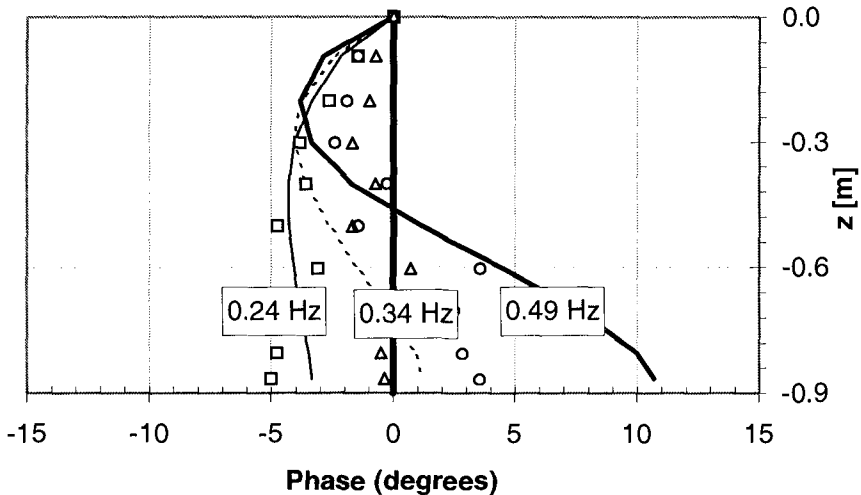


Figure 3 Phase lag of pore pressure response vs poro-elastic theory (Stabmax, Finn, 1982).

Experimental Set-up—Caisson Testing

The second experimental test program in this study was designed to examine the interactions between seabeds and rigid coastal structures under the influence of wave action. Large-scale flume tests were undertaken to study the effective stress response

of seabeds beneath caissons, and to examine the combined effective stress, pore pressure and scour response of the toes of caisson-type coastal structures. This experimental study was also used to explore the validity of the Tsai et al (1990) analytical poro-elastic approach for the prediction of foundation response.

The Coastal Wave Basin of the National Research Council in Ottawa was used for the caisson testing. This basin is 85m long and 14m wide. The maximum water depth available for testing is 1.2m (allowing 0.3m of freeboard for waves). Two parallel 2.4m wide channels were built within the basin. This layout enabled the simultaneous testing of two different caisson foundations. Berms were built in each of these channels to serve as foundations for two identical steel caissons (see Figure 4). The berms were composed of two different sands; a coarse sand with $D_{50}=0.38\text{mm}$, and a fine sand, with $D_{50}=0.10\text{mm}$. Due to the large amount of fill required to build the foundations for the caisson (roughly 25 tonnes of sand in each flume) it was not possible to rebuild the berm between tests. The test sequence employed gradually exposed the caissons to irregular waves of increasing amplitude and period in a manner simulating the building of a storm. For all tests, the hydrodynamics acting on the structure and the response of both the soil and the caisson were measured in detail.

One of the results of the test program was a series of measurements of the pore pressure response within the foundations beneath the leading edge of the caissons. The following section gives a review of some of these pore pressure measurements.

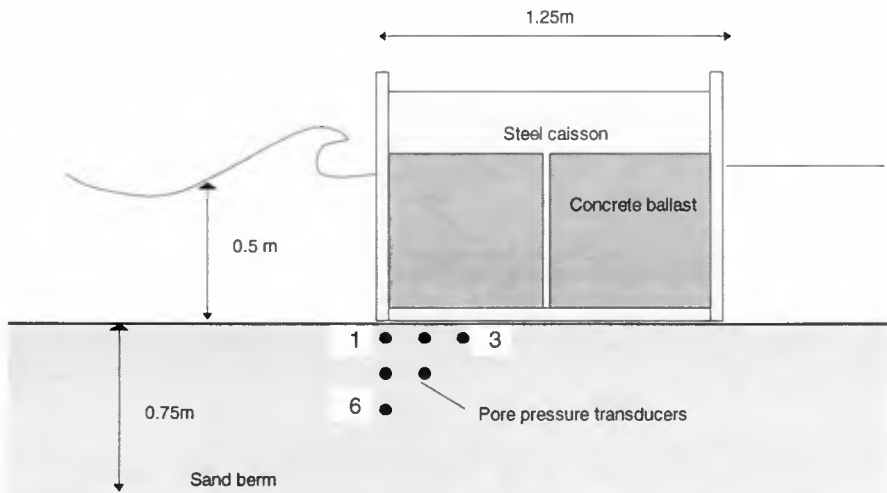


Figure 4 Schematic cross-section of caisson tests.

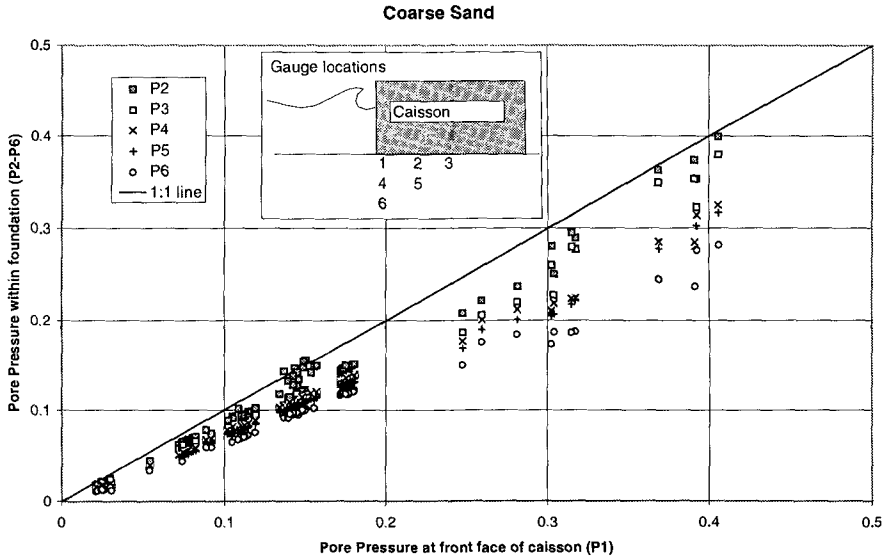


Figure 5 Pore pressure response - coarse sand.

Pore pressure response within coastal foundations

Figure 5 shows how the pore pressure response measured beneath the caisson compared to that at the outside front corner of the caisson (at the mudline) for the coarse sand foundation. This plot shows the amplitude of the pressure fluctuations measured by each of six pore pressure transducers installed beneath the caisson. These transducers are denoted as P1 through P6 and their locations are shown schematically in the inset in Figure 5. The measured pore pressure at each of gauges P2 through P6 is plotted against the pore pressure measured at the front corner (P1). There is a general trend that the pore pressure diminishes with depth into the seabed and with distance beneath the caisson, i.e. P3 and P6 are significantly lower than P1.

Figure 6 shows a similar plot for the fine sand test. The general pattern of diminishing pressure amplitude with depth and with distance from the front edge of the caisson still exists with one exception: for test conditions generating a pore pressure at the front face of the caisson (gauge P1) of around 0.1 m, the pressures along the underside of the caisson were significantly increased. This trend was not observed for the coarse sand caisson when exposed to the same wave conditions with the same caisson geometry and caisson ballast. This suggests that, under this combination of wave conditions, the finer sand caisson was experiencing complex wave-soil-structure interactions which were not observed with the coarser sand. The following sections describe a boundary layer approach to provide some insight to these interactions.

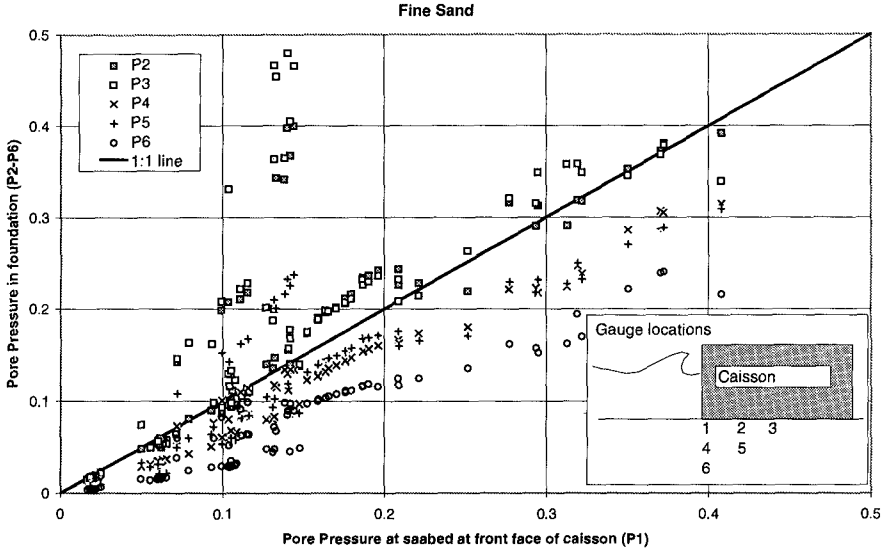


Figure 6 Pore pressure response - fine sand

The Boundary Layer Approach

The boundary layer approach of Mei and Foda (1981) shows that, in the treatment of a poro-elastic solid using Biot's linearized theory of consolidation, for the frequencies of typical ocean waves, a Stokes' type of boundary layer exists near the top of the bed. The soil and fluid move together as a single phase in the region below this boundary layer. Within the boundary layer, the effects of the free draining upper boundary are evident. This allows a greatly simplified analysis where the outer region (far below the mudline) can be treated as a single phase elastic solid for which analytical solutions to the soil's behaviour are readily found. Mei and Foda show that in the boundary layer, a one-dimensional analysis using Terzaghi's theory of consolidation can be applied (provided that the boundary layer thickness is small relative to wavelength). Solutions to a variety of poro-elastic problems using this boundary layer technique have been presented in the literature (see Mei and Foda, 1981 and Mei, 1982)

Intuitively, one would expect that for a soil of permeability, k , which is small relative to the frequency of loading, $\omega=2\pi f$, there is little fluid motion relative to the soil skeleton. For such a case the soil and fluid move together and the medium can be treated as a single phase as described by the equations of elastic dynamics. Near the seabed there will be a free-draining region extending to some depth, δ . For $\delta/L \ll 1$, where L is the wavelength, then the upper boundary region becomes essentially one-dimensional. Mei and Foda show that the first order approximation of the boundary layer is the Terzaghi equation for one-dimensional consolidation.

In the boundary layer $\partial/\partial z \gg \partial/\partial x$. The thickness of the boundary layer, δ is given by

$$\delta = \sqrt{\frac{c'_v}{\omega}} \quad (2)$$

where c'_v is the soil consolidation coefficient

$$c'_v = \frac{k \gamma}{m'_v} \quad (3)$$

Here k is the soil's coefficient of permeability, γ is the unit weight of water, and m'_v is the effective modulus of volume compressibility for soil with a partially saturated pore fluid.

$$m'_v = n\beta' + \frac{1-2\nu}{2(1-\nu)G} \quad (4)$$

Here the stiffness of the soil matrix is characterized by the bulk shear modulus, G , and Poisson's ratio, ν . The soil porosity is n and the stiffness of a partially saturated fluid is β' (as per Verruijt, 1969),

$$\beta' = \beta + \frac{1-S_r}{P_{\text{tot}}} \quad (5)$$

Here β is the compressibility of pure water ($\beta=4.3 \times 10^{-10} \text{ Pa}^{-1}$), and S_r is the volumetric degree of saturation of the soil. P_{tot} is the absolute pressure at the point of interest.

The exact total solution for dynamic stresses and pore pressures is determined through the solution of the dynamic elastic equations governing the outer region and subsequent application of a boundary layer correction:

$$()_{\text{exact}} = ()^o + ()^b \quad (6)$$

where the superscripts o and b denote outer region and boundary layer region terms, respectively.

The boundary layer formulation provides an accessible and heuristically appealing treatment of the soil-wave interaction problem. The boundary layer thickness, δ quantifies the relative depth of influence of wave action in a seabed.

Foundations - Drained vs Undrained

The problem of wave action in the vicinity of coastal structures can be considered in terms of the permeability and stiffness of the soil mass relative to the size of the structure. Wave loading on a rigid coastal structure such as a caisson causes wave stresses to be transferred from the caisson to the seabed. At the same time wave-induced pressure fluctuations at the seabed cause uplift pressures along the underside of the structure. The complex interactions between a rigid structure and the seabed under wave loading have been examined in the literature by Lee and Focht (1985), Lindenberg et al, (1982) and Tsai et al (1990). Analytic solutions of the wave-soil-structure interaction problem have been formulated by Mei (1982) as well as by Tsai et al (1990). These analytic solutions use elastic solutions for a rigid block resting on

a flexible base to solve the total stress state in the foundation. A boundary layer correction is then applied to take account of the presence of the free-draining upper boundary. These solutions rely on an assumption that the boundary layer thickness, δ is small relative to the wavelength, L and furthermore that the boundary layer thickness is small relative to the caisson size, C (for some solutions the half-width of the caisson is used as the representative caisson dimension).

These calculations are quite complex but yield some interesting insight into the behaviour of wave-soil-structure interactions. For practical problems, a finite element effective stress model is more adaptable (e.g. Shen, 1990).

One of the insights provided by boundary layer theory is the concept of relative boundary layer thickness. In assessing the appropriate analysis to be undertaken for a specific structure, simple calculations of boundary layer thickness relative to wavelength and relative to caisson geometry can allow the classification of the problem in terms of the influence of pore fluid flow on soil response.

There are two bounding conditions often considered in analysing foundation response. These are **undrained** and **drained** behaviour:

- 1) For **undrained** analysis, it is assumed that the rate of application of loading is rapid relative to the soil's permeability. Consequently the pore fluid and soil matrix move together. At a lower bound, for example, the case of a structure resting on clay, the role of pore pressures in generating uplift forces is negligible. For undrained analysis the total stress state is used, and the concept of effective stresses is not applicable.
- 2) For **drained** analysis, it is assumed that the rate of application of loading is slow relative to the soil's permeability. Consequently, the pore fluid is free to move relative to the soil matrix. At an upper bound, the Shore Protection Manual (1984) and Goda's models of wave-induced uplift pressures are reasonable, (a triangular pressure distribution acting along the underside of the structure). For drained analysis, an effective stress approach is employed.

In reality, these limiting cases rarely exist. The true soil response lies somewhere between fully undrained and fully drained. What is needed is a set of practical guidelines to evaluate the relative importance of drainage to the structure.

Foundation response guidelines

When the boundary layer thickness, δ is small, free-drainage occurs only close to the mudline. When δ is large the free-drainage zone extends further into the seabed.

The pore pressure response within the seabed in the vicinity of a caisson will be related to two dimensionless parameters:

1. f/f_n - describes the frequency response of the system and how close the loading frequency, f is to the natural frequency of the caisson, f_n . For a single degree of freedom oscillator (such as the caisson response in pure pitch motion), the natural frequency of the caisson-soil system is related

to the foundation stiffness and the polar mass moment of inertia of the caisson as follows:

$$f_n = \frac{1}{2\pi} \sqrt{\frac{E'B^3}{12I_p}} \quad (7)$$

Here, E' is the equivalent foundation stiffness, and B is the caisson width.

2. δ/C - the thickness of the boundary layer, δ relative to the caisson size gives a measure of how large the free-draining boundary is relative to the size of the caisson.

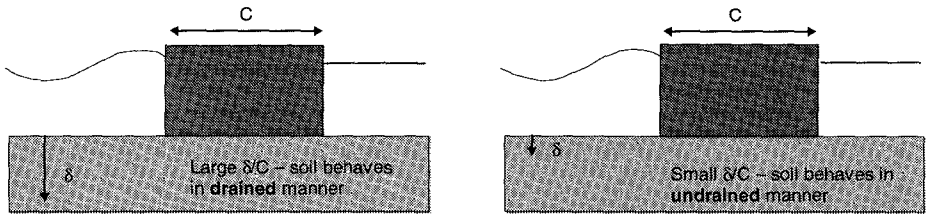


Figure 7 Illustration of boundary layer thickness concept for caissons

For a given caisson geometry (and hence given f/f_n), the pore pressure response could be expressed as a function of the ratio of boundary layer thickness to caisson width alone:

$$\frac{P}{P_0} = \phi\left(\frac{\delta}{C}\right) \quad (8)$$

Three conditions can then exist:

- 1) If $\delta \ll C$ then the boundary layer effect will be small, uplift pressures will only exist very close to the outer edge of the caisson and undrained analysis will be sufficient.
- 2) If $\delta \gg C$ then the entire caisson will lie within the boundary layer, uplift pressures will be large and drained analysis will be appropriate. Here solution of the pore pressure response (and uplift) can be 'de-coupled' from the soil stress response.
- 3) Where δ is of the order of C , the response will be partially drained – the interactions between the pore fluid and soil matrix must be considered. Figure 7 provides a schematic of these concepts.

Consider the behaviour of the two caisson test series shown in Figure 5 and Figure 6. The major differences between these two caissons were the soil's coefficients of consolidation. This is reflected in different boundary layer thicknesses for the two caisson datasets. Figure 8 shows a plot of the relative amplitude of the pore pressure response beneath the caisson (normalized by P_1) against the ratio of boundary layer

thickness to caisson size, δ/C . This figure shows that for test conditions corresponding to δ/C around 0.1, amplification of the pore pressure response beneath the caisson is observed (e.g. P3 in caisson 1). This trend is not observed for sensors mounted deep in the bed at the front face of the caisson (vis P6). For test conditions of δ/C much greater than 0.5, the amplitude of the pore pressure response starts to approach the linear distribution suggested by Goda and others for caissons resting on very coarse rubble beds.

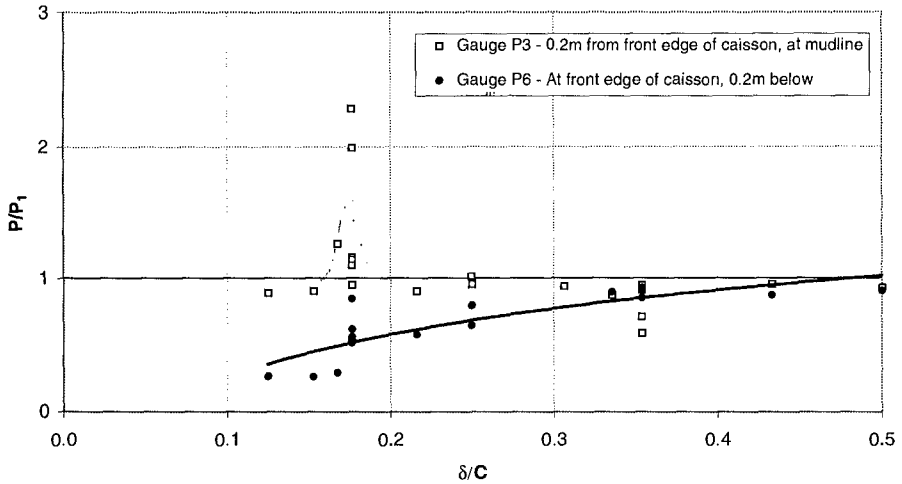


Figure 8 Pore pressure response vs drainage ratio, δ/C (combined results for both coarse and fine sands).

Table 1 shows typical ranges of foundation conditions and wave conditions for some typical coastal structure geometries

Wave period, $T = 15$ s		$\omega = 2\pi/T = 0.42$		
Influence of foundation type	c_v (m ² /s)	δ [m]	C [m]	δ/C
Rubble fill	1000	48.86	15	3.26
Hard sand	100	15.45	15	1.03
Soft sand	10	4.89	15	0.33
Stiff clay	0.1	0.49	15	0.03
Soft clay	0.001	0.05	15	0.00
Influence of caisson size	c_v (m ² /s)	δ [m]	C [m]	δ/C
Rubble fill	1000	48.86	3	16.287
Rubble fill	1000	48.86	10	4.886
Rubble fill	1000	48.86	100	0.489
Soft clay	0.001	0.05	3	0.016
Soft clay	0.001	0.05	10	0.005
Soft clay	0.001	0.05	100	0.000

Table 1 Relative boundary layer thickness for typical field conditions

For cases where the foundation material is stiff and permeable (such as rubble fill), Table 1 shows that, except in the case of exceptionally wide structures, the ratio δ/C

is large and the free-draining condition can be expected to be observed along the entire underside of the structure. This is in accordance with the design techniques presented by Goda and the Shore Protection Manual where, for caissons resting on rubble foundations, a triangular uplift pressure distribution is assumed along the underside. For cases where either the foundation material is soft and impermeable (soft clay) or where the structure is very large (large C), the ratio δ/C can be seen to be quite small. In these cases, the uplift pressures due to wave action will be negligible and the undrained analysis is most appropriate (e.g. as described by Lee and Focht). In cases such as this, skirts are sometimes installed around the base of the structure to act as cut-off walls to further reduce the likelihood of uplift pressures existing. The structures are then designed for a no-uplift condition. The ratio δ/C serves to delineate how foundations in intermediate conditions may behave. For example if a structure rests on soft sand or stiff clay, the ratio δ/C becomes useful in combining the effects of wave period, consolidation coefficient and structure size to give a sense of the relative size of the drainage path, δ .

Conclusions

The pore pressure response of a seabed exposed to wave loading can be reasonably well described by the rigid, porous bed solution of Sleath (1970). To obtain information about the effective stress state in the soil, however, it is better to use a poro-elastic seabed response model such as that of Finn (1982).

Often the response of a coastal structure is neither fully drained nor fully undrained but somewhere in between. For engineering analysis, practical guidelines are needed to delineate the extent of influence of the free-draining boundary. Through boundary layer theory, it is possible to interpret this influence through δ , the boundary layer thickness. Preliminary analysis of test results indicates that the ratio, δ/C might be useful here. For small values of δ/C (less than 0.05, say), the soil can be treated as fully undrained and a total stress analysis can be used. As δ/C becomes large (greater than 0.3, say), soil behaviour starts to become fully drained and analysis techniques such as those proposed by Goda and the Shore Protection Manual become more appropriate. Soil conditions in the intermediate range ($0.05 < \delta/C < .3$) require particularly close attention since the response of the soil and pore fluid is closely coupled.

The idea of using the relative boundary layer thickness, δ/C as a predictor of seabed response is hypothetical at this stage. Further verification and extension of this idea requires examination of a wider range of experimental conditions. Variation of the ratio of f/f_n (the frequency of wave loading relative to the natural frequency of the system) should also be further explored.

Acknowledgements

This work was made possible by funding from Program on Energy Research and Development of Natural Resources Canada and the National Research Council of Canada. The continuing support of my colleagues at CHC greatly appreciated, in particular the technical assistance of Dave Watson.

References

- Bea, R.G. and Aurora, R.P. (1981): *A simplified evaluation of seafloor stability*. Proc. Offshore Technology Conference, paper no. 3975, pp. 223-240.
- Been, K., and Jefferies, M.G. (1985): *A state parameter for sands*. Geotechnique, Vol. 35, No. 2, pp. 99-112.
- Biot, M.A. (1941): *General theory of three-dimensional consolidation*. Journal of Applied Physics, Vol. 12, pp. 155-164.
- Davies, M.H. (1986): *Wave-induced liquefaction of sands*. Proc. of the Ocean Structure Dynamics Symposium, Oregon State University, Corvallis, Ore.
- Davies, M.H., Chichibu, A., and Garga, V.K. (1990): *Study of AE response of coastal structures under storm wave loading*. Proc. of the 10th International Acoustic Emission Symposium, Sendai, Japan, Publ. by the Japanese Society for Non-Destructive Testing, pp. 153-159.
- Davies, M.H. (1992): *Soil-wave-structure interaction in coastal engineering*, Ph.D. thesis, Queen's University at Kingston, January, 1992, 301 pp.
- Finn, W.D.L., Siddhartan, R., and Martin, G.R., (1983): *Response of seafloor to ocean waves*. J. of Geotechnical Engg., ASCE, Vol.109, No.4, April 1983, pp.556-573.
- Goda, Y. (1985): *Random seas and design of maritime structures*. University of Tokyo Press, Japan 323 pp.
- Lee, K.L., and Focht, J.A.. (1985): *Liquefaction potential at Ekofisk tank in North Sea*. Journal of Geotechnical Engg., ASCE, Vol. 101, No. GT1, pp. 1-18.
- Lindenberg, J., Swart, D.H., Kenter, L., and den Boer, W. (1982): *Wave-induced pressures beneath caisson: Comparison between theory and large scale tests*. BOSS '82, Cambridge, Mass., pp. 337-357.
- Madsen, O.S. (1978): *Wave-induced pore pressures and effective stresses in a porous bed*. Geotechnique, Vol. 28, No. 4, pp. 377-393.
- Mei, C.C. (1982) *Analytical theories for the interaction of offshore structures with a poro-elastic seabed*. Proc. of BOSS '82, Cambridge, Mass., August 1982, Published by Hemisphere Publishing, Washington, D.C., USA pp. 358-370.
- Mei, C.C. and Foda, M.A. (1981): *Wave-induced responses in a fluid-filled poro-elastic solid with a free surface – A boundary layer theory*. Geophysical Journal of the Royal Astronomical Society, Vol. 66, pp. 597-631.
- Okusa, S. (1985): *Wave-induced stresses in unsaturated submarine sediments*. Geotechnique, Vol. 35, No. 4, pp. 517-532.
- Putnam, J.A. (1949): *Loss of wave energy due to percolation in a permeable sea bottom*. Transactions of the American Geophysical Union, Vol. 30, No. 3.
- Seed, B.H., and Rahman, M.S. (1978): *Wave-induced pore pressures in relation to ocean floor stability in cohesionless soils*. Marine Geotechnology, Vol. 3, pp.123-150.

- Seed, B.H., Idriss, I.M., and Arango, I. (1983): *Evaluation of liquefaction potential using field performance data*. Proc. J. of Geotechnical Engg., ASCE, Vol. 109, No. 3, March 1983, pp. 458-482.
- Shen, C.K., Wang, Z.L., and Herrmann, L.R. (1986) *Final report on ocean wave - induced effective stresses in an elasto-plastic seafloor*. Calif Sea Grant College Program Proj. No. R/OT-13, Dept. of Civil Engg., University of California, Davis, November 1986, 52 pp.
- Sleath, J.F.A. (1970): *Wave-induced pressures in beds of sand*. Journal of Hydraulics Division, ASCE, Vol. 96, No. HY2, pp. 367-378.
- SPM (1984) *Shore Protection Manual*, Coastal Engineering Research Centre, U.S. Army Corps of Engineers, 3 volumes.
- Tsai, Y.T., McDougal, W.G., and Sollitt, C. (1990) *Response of finite depth seabed to wave and caisson motion*. J. of Waterway, Port, Coastal and Ocean Engg., ASCE, Vol. 116, No. 1, January 1990, pp. 1-20.
- Wright, S.G., and Dunham, R.S. (1972): *Bottom stability under wave-induced loading*. Proc. Offshore Technology Conference, Paper no. 1603, pp. 853-862.
- Yamamoto, T., Koning, H.L., Sellmeijer, J., and van Hijum, E. (1978): *On the response of a poro-elastic bed to water waves*. J. Fluid Mechanics, Vol. 87, Part 1, pp. 193-206.

CHAPTER 272

Interannual Shoreline Variations at Duck, NC, USA

Nathaniel Plant and Rob Holman

ABSTRACT

We have analyzed 3 years of daily observations of the shoreline position along a 2 km segment of the coast at Duck, NC. Shoreline variations were found to be dominated by length scales of order 1 kilometer, with an amplitude that was modulated by a seasonal cycle, and a spatial structure that progressed alongshore at an average rate of 1 m/day. Surprisingly, the alongshore-averaged shoreline position did not display an annual cycle. Instead, the most pronounced alongshore-averaged shoreline changes occurred over several years. The dominance of large spatial and temporal scales suggests that short scale studies at Duck (typical duration < 1 month and lengths < 500 m) seriously under-resolve an important component of shoreline variability.

INTRODUCTION

To describe general beach behavior, we have often referred to a "summer-winter" conceptual model (e.g. Komar, 1974), in which beaches erode and sand bars form or move offshore during large storms (winter), followed by beach accretion and onshore bar movement during calm periods (summer). Recently, however, observations of nearshore bathymetry have revealed interannual and decadal morphologic behavior, which are not described by a seasonal model. Examples include offshore progressive sand bars at Duck, NC, USA (Birkemeier, 1985; Lippmann and Holman, 1990; Kraus and Larson, 1992) and along the Holland Coast (Ruessink and Kroon, 1994; Wijnberg and Terwindt, 1995) over periods of several years to over a decade. In addition, there is evidence that beach response over these long time periods is not alongshore-uniform. Wijnberg and Terwindt (1995) showed examples of alongshore progressive variations at the shoreline, with an alongshore wavelength of about 2 km and periodicity matching that of the bars. It appears likely that, with increasing time scales, beach variability may be dominated by large length scales. Quantifying the contribution of various alongshore length scales to beach variability, and determining characteristic time scales associated with each length scale are clearly important to understanding (or simply describing) the long term behavior of beaches.

In this paper, we focus on the behavior of a particular beach elevation contour near the shoreline at Duck, NC. One reason to focus on the shoreline is that it

delineates the width of the subaerial beach, which is of practical significance to those who live on or visit the beach. Also, the shoreline is a morphologically active (and therefore interesting) region of the beach, which responds to variations in wave conditions, tides, and (perhaps) interannual forcing. We seek to determine the relative contribution of different length scales to shoreline variability, and to describe the relationships between length and time scales. First, we will describe observations of the cross-shore position of a particular shoreline contour, obtained from analysis of video images. Then, we will present an analysis of the spatial and temporal variability of this data set. Since the dominant variability is associated with large length scales, we quantify this variability by focusing on two scales: (1) the alongshore-averaged shoreline position and (2) variability with a wavelength of about 1 km. The observed variability is partitioned into amplitude time series for both scales, as well as a time series of the spatial phase shift of the 1 km scale, which describes alongshore propagation. Finally, we describe the correlation between the shoreline variability and the wave field.

DATA COLLECTION

Video images of the surf zone at Duck, NC have been collected since 1986. Originally, the images were obtained once per day; however, they have been obtained every hour since 1993. The type of images that we will use in this study are time exposures (Lippmann and Holman, 1989, 1990). A time exposure (Figure 1) represents the average image brightness over, in this case, a 10 minute period. In relatively shallow regions where waves tend to break (e.g. over sand bars and at the shoreline), the average brightness is relatively high (white) due to the persistent production of foam, hence, morphologic features are often easily identified. At Duck, time exposures have been used successfully to locate the position of sand bars as well as the shoreline (Lippmann and Holman, 1989, 1990).

Plant and Holman (in press) described the methods that we used to locate and map the shoreline position. To summarize: we assumed that the shore-parallel band of high image intensity at the shoreline, also called the shoreline intensity maximum (SLIM), visually marked the still water level shoreline. The SLIM was identified in each image and its cross-shore position at a series of alongshore sample locations was determined from simple photogrammetric relationships (Lippmann and Holman, 1989). Since the cross-shore position of the SLIM varied with tidal elevation, we selected images corresponding to tidal elevations within 0.25 m of the 0.50 m level. We attempted to locate the shoreline once per day, within a 2 km long region, sampling every 2 m. The shoreline position is overlain on each image in Figure 1, and is plotted in map coordinates on the adjacent panels.

This shoreline estimation technique ought to be most accurate when applied to simple intertidal bathymetry (i.e. slowly varying in both alongshore and cross-shore directions) and when the wave height is low, so that the SLIM is a narrow band located near to the still water shoreline. The beach slope and wave height at the shoreline scale the errors in the estimates of the cross-shore position of the shoreline. For a barred beach, the error is approximately $\frac{1}{2} \frac{H}{\beta}$, where H is the (potentially depth-limited) rms wave height shoreward of the sand bar and β is the beach slope at the shoreline. The intertidal beach slope at Duck is typically about 0.1 and the shoreline wave height is limited by breaking over the bar to 1.0 m, resulting in a maximum error of about 5 m. Finite resolution of the digital images also contributed to measurement errors that

ranged from 0.50 m nearest to the camera to 2.0 m farthest from the camera. The alongshore resolution of the shoreline position estimates varied from 1 m to 50 m .

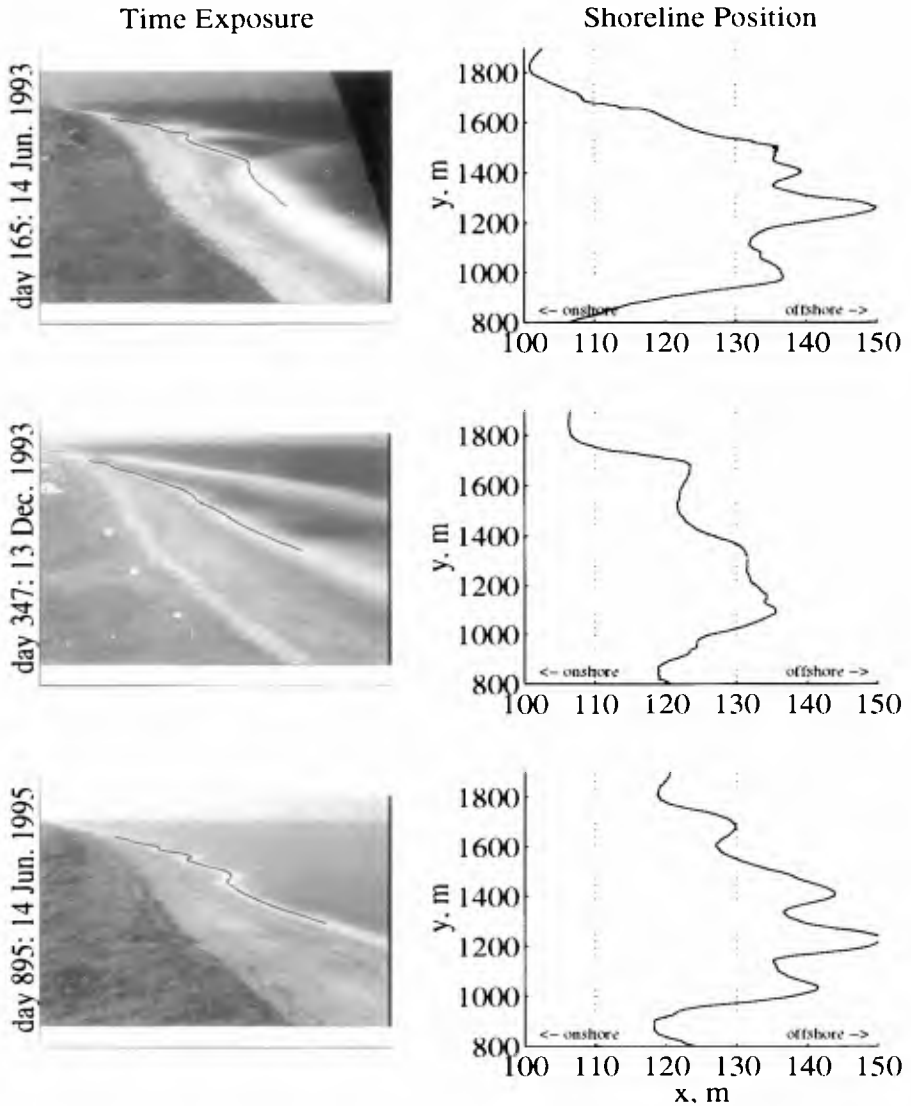


Figure 1. Examples of time exposure images, from Duck, NC. The location of the shoreline intensity maximum (SLIM) line is identified on each image and the map projection of that line is shown adjacent to each image. On the map projection, the ordinate is the alongshore range; positive is to the north (away from the camera). The cross-shore scale is exaggerated 20x.

RESULTS

Of the 980 days in the study period, 748 images fell within the desired tidal level range ($0.25 \leq \text{tide} \leq 0.75$). Due to problems with image quality (rain on the lens, fog, equipment failure, and very small wave heights that did not produce a SLIM), only 578 images yielded shoreline positions. Of these, some shoreline position estimates did not cover the entire 2 km sample region. Only 336 images yielded data fully spanning a 1 km subset of the sample region ($900 \text{ m} \leq y \leq 1900 \text{ m}$). This subregion was sampled at an average rate of about 1 sample/3 days. We will focus much of the analysis on the 1 km sub region.

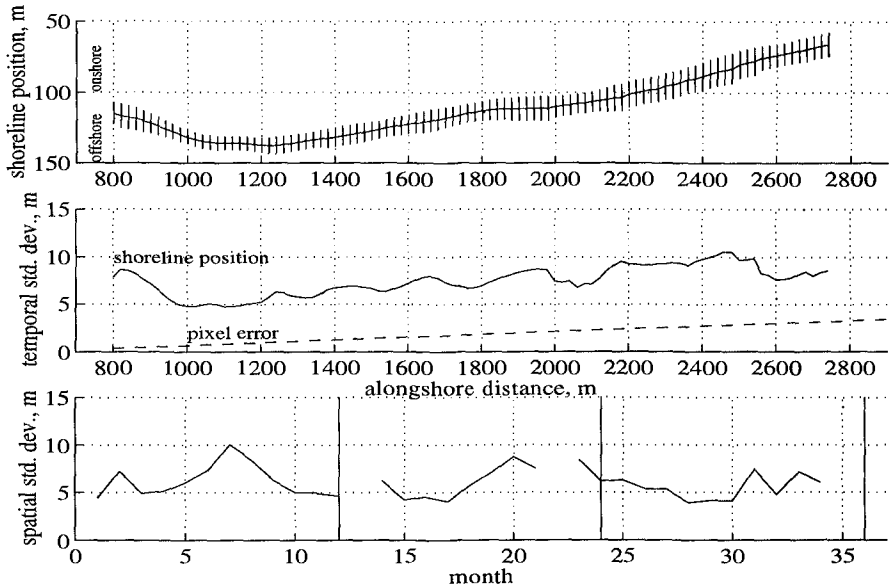


Figure 2. Mean and standard deviation of the shoreline position. The time-averaged shoreline position is shown in the upper panel, where error bars are the standard deviation, plotted at 20 m intervals. In the second panel, the standard deviation is plotted again, along with the cross-shore error due to the pixel footprint dimensions (dashed line). The third panel shows monthly-averaged spatial variability. January of each year is marked by a vertical line.

Shoreline Mean and Variance

Over the 3 year study period, the observed shoreline position varied by as much as 45 m. The spatial structures of the shoreline and its variability are summarized by plots of the mean and standard deviation as a function of alongshore location, shown in Figure 2. The mean shoreline position was not straight, but curved smoothly through the entire study area. The bend in the mean shoreline likely stems from geologic constraints. The temporal variability of the shoreline, indicated by its standard deviation, was not uniform either. The minimum variance occurred near the most seaward protrusion of the mean shoreline ($y = 1100$). The observed shoreline variance increased with distance from the camera, which may be due, in part, to the increasing size of the pixel footprint. The expected cross-shore pixel error is plotted for reference. Our choice of coordinate system was not shore-normal everywhere, which also contributed to increased apparent variability.

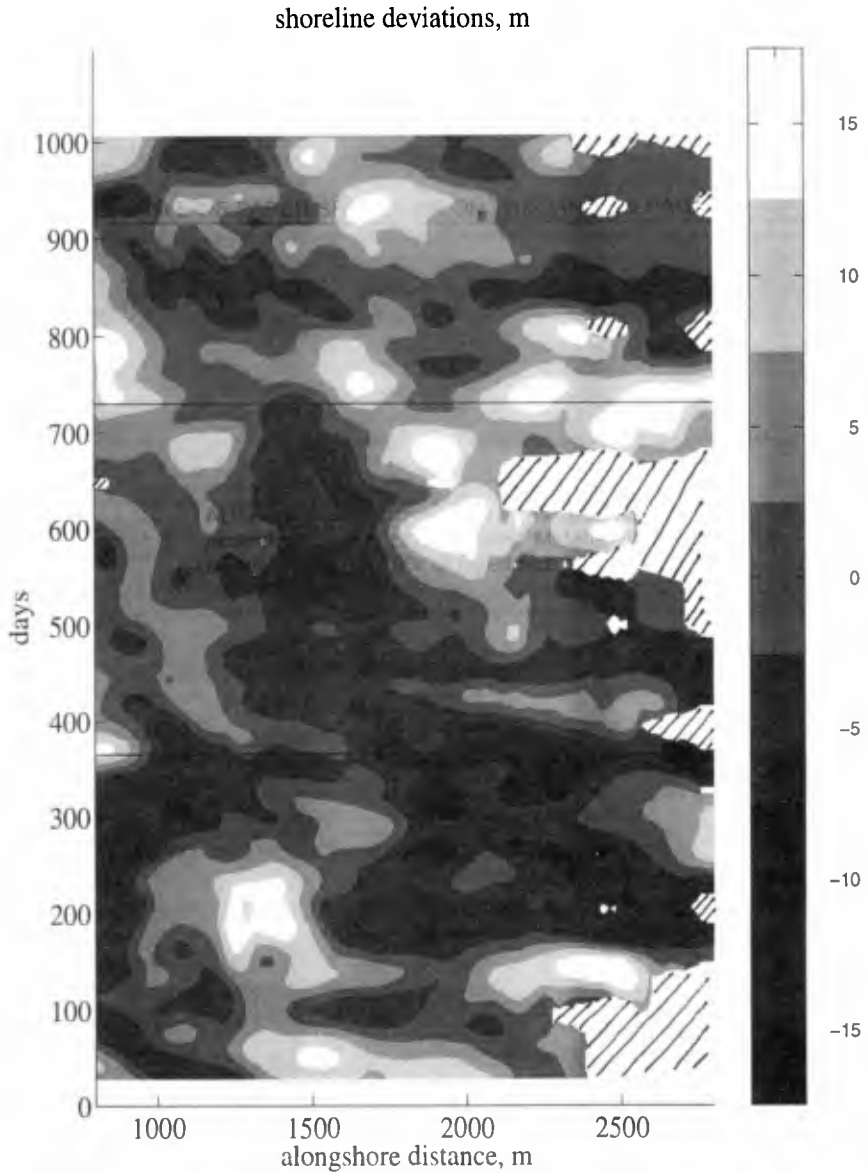


Figure 3. Gray scale plot of shoreline deviations. The scale bar is in meters. Positive deviations (whiter) correspond to displacement of the shoreline seaward of its mean position. Missing data are filled by hatching, and January 01 of each year is marked by a horizontal line.

Time series of shoreline deviations were obtained by subtracting the mean shoreline position from each observation, at each alongshore location. The final panel in Figure 2 shows the monthly-averaged, spatial variation from the mean shoreline position, as a function of time. In order to visualize the variation of the Duck shoreline, Figure 3 displays low-pass-filtered deviations of the shoreline position at each alongshore location and each time. Positive deviations (light shades) indicate that the shoreline was seaward of its mean position. The low pass filter (Ooyama, 1989) damped variations with time scales less than 1-2 months, and interpolated missing data if the time gaps were shorter than the filter cutoff. The remaining missing data values are filled with hatching.

In Figure 3, the most striking features are lineations that generally trend obliquely from the lower right towards the upper left (traveling toward the south) and have length scales of about 1 km. The behavior of these large scale features was not always characterized by simple southward propagation. For example, their direction reversed at times (e.g. day 200 to day 300). Also, shorter scales contributed to prominent coherent behavior. For example, between days 850 to 900, megacusps with approximately 200 m wavelengths were well developed. The megacusps appeared to propagate at the same speed as the large scale features. An annual cycle is not particularly apparent in Figure 3. We turn now to quantitative descriptions of these shoreline deviations, partitioned into an alongshore-averaged component and a component with an alongshore length scale of 1 km.

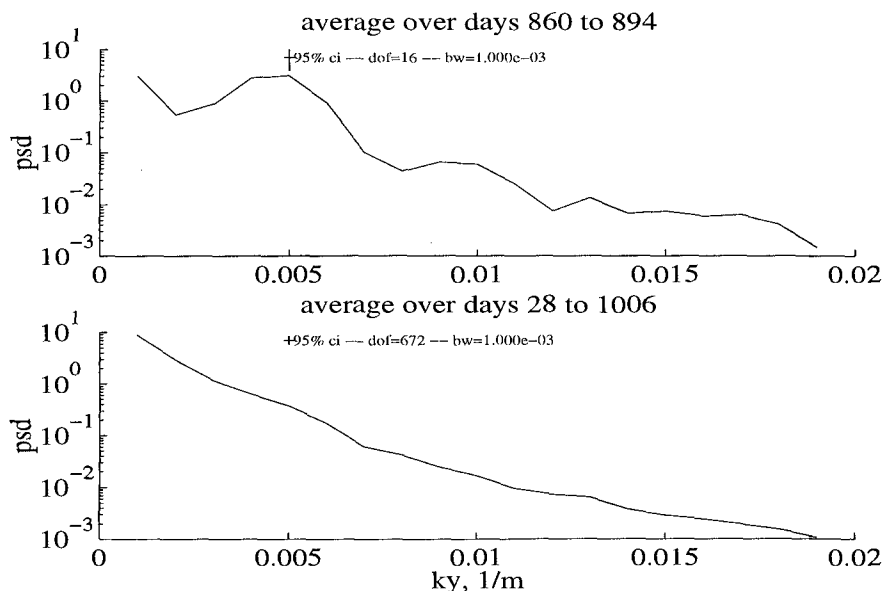


Figure 4. Shoreline variance spectra as a function of alongshore wavenumber. The upper panel shows sample spectral estimates averaged over a 34 day period (containing only 8 images) when megacusps were present with 200 m wavelengths. The lower panel is the spectrum averaged over the entire 3 year study period.

Length Scales

The contribution of different length scales to the observed shoreline variability was quantified using wavenumber spectra of the shoreline deviations. A discrete spectrum was estimated on each day, using data within the 1 km subregion, $900 \leq y \leq 1900$ m. Spectral estimates corresponded to the Fourier wavenumbers, $k_y = 0, \pm \frac{1}{1000}, \pm \frac{2}{1000}, \dots$, and $\frac{250}{1000} \text{ m}^{-1}$. The alongshore-averaged shoreline position was removed at each time before estimating the spectra, and was the estimate of the first component, $k_y = 0$. The variance spectrum, $S(k_y)$, on any particular day describes the contribution of each length scale to the spatial variability on that day. As an example, we show several spectra, averaged over time to improve the reliability of the spectral estimates (Figure 4). For instance, megacusps, which were obvious in the space-time map of deviations (days 850 to 900), also appeared as a well defined and significant spectral peak. However, the dominance of large length scales (low wavenumbers) was the most typical characteristic of these spectra. The spectrum averaged over the entire 3 year study period (Figure 4) emphasizes this point. In fact, the first two Fourier components, which are the alongshore-averaged shoreline position ($k_y = 0$) and the 1 km wavelength ($k_y = \frac{1}{1000} \text{ m}^{-1}$), explain nearly 80% of the total shoreline variance. We will focus the remaining analysis on these two components.

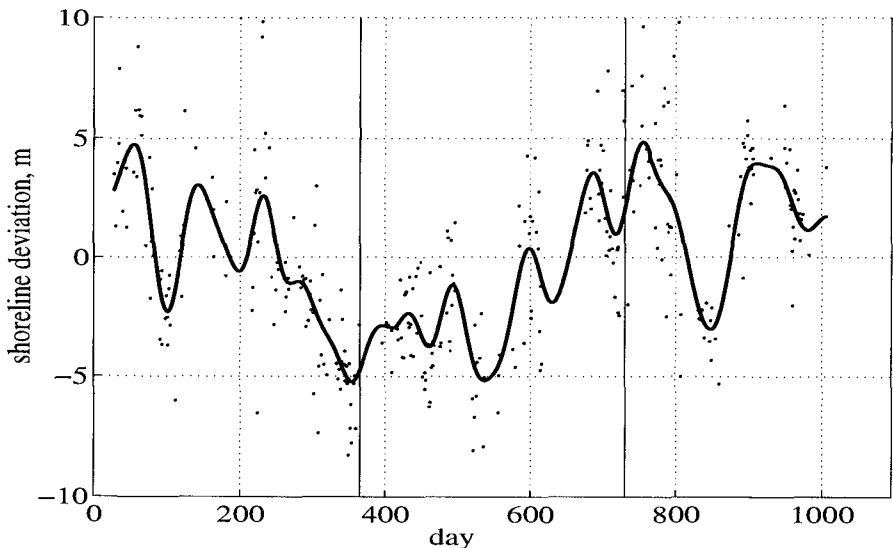


Figure 5. Time series of the alongshore-averaged shoreline position over the 1 km subregion ($900 \text{ m} \leq y \leq 1900 \text{ m}$). The dots correspond to the actual samples, while the solid line is the filtered time series. January 01 of each year is marked by a vertical line.

Alongshore-averaged shoreline variability explained 36% of the total, observed shoreline variance. This component represented net onshore or offshore change of the shoreline (Figure 5). Apparent, high frequency fluctuations due to measurement errors associated with rapid variation of the wave height were removed by filtering using a 30-60 day cutoff. The filtered time series of the alongshore-averaged shoreline deviations

shows that dominant variability occurred over time periods greater than one year (inter-annual behavior). More rapid variations likely corresponded to storm/calm cycles. The absence of an annual cycle, as might be predicted with the summer/winter model, is conspicuous.

The second component that we will consider corresponds to the 1 km wave length ($k_y = \frac{1}{1000} \text{ m}^{-1}$), and accounted for 40% of the total shoreline variance. This component may be represented by time series of both amplitude, A , and phase, ϕ .

$$A(k_y, t) = |a(k_y, t) + i b(k_y, t)| \quad (1)$$

and

$$\phi(k_y, t) = \text{Tan}^{-1}[-b(k_y, t)/a(k_y, t)], \quad (2)$$

where $a(k_y, t)$ and $b(k_y, t)$ are the real and imaginary parts of the Fourier amplitudes. The amplitude time series had a strong annual cycle (Figure 6). This is the quantitative representation of typical observations that the shoreline is relatively straight during the winter (largest waves) and develops increased alongshore variation during calmer periods, also evident in Figure 2. The phase time series describes alongshore shifts of a coherent morphological structure. A simple phase ramp (constant slope) is indicative of a progressive wave form, while phase jumps of 180° suggest standing motions. The net phase shift over the study period corresponded to an average southward propagation of about 1 m/day. The estimated celerities are shown in the lower panel of Figure 6. We expect the amplitude and celerity for this component to be correlated to wave height and direction.

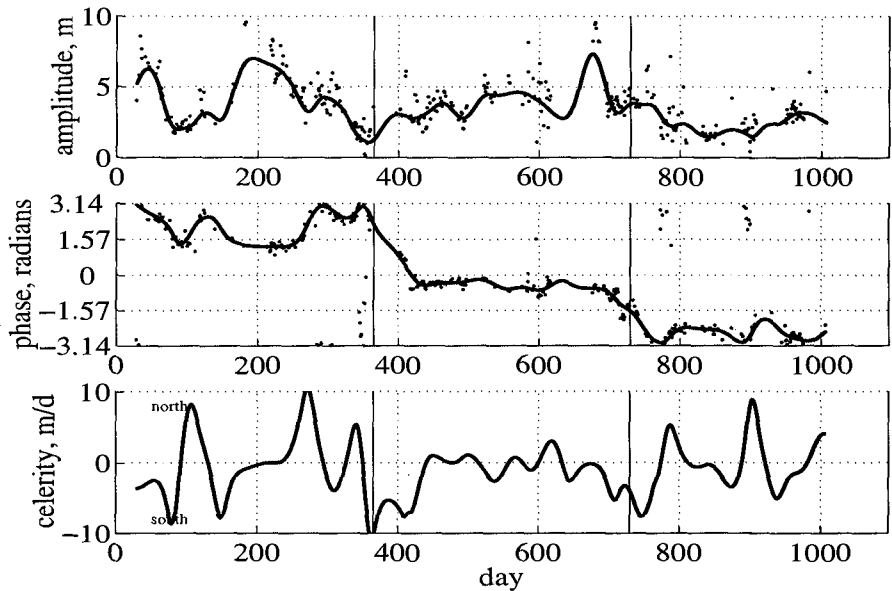


Figure 6. Time series of the amplitude (upper panel), phase (middle panel), and celerity (lower panel) of the 1 km wavelength component. The trend in the phase (ramp) corresponds to an average alongshore celerity of -0.95 m/day .

Correlation to Waves

We move now to determining how the two components of variability ($k_y = 0$, $\frac{1}{1000} \text{ m}^{-1}$) were related to variations in the wave field. In particular, we expect that the amplitudes of the two components should be correlated to the wave height, while we expect that the alongshore propagation of morphologic features should be related to the product of the wave height and angle of incidence. The alongshore component of wave energy flux ($Pl \sim H_s^2 \sin[-2\alpha]$) will be used to test this hypothesis. Figure 7 shows a time series of the wave height, wave angle, and wave energy flux over the study period. The wave directions are relative to shore normal and positive wave angles correspond to waves approaching from the north, consequently driving sediment transport to the south. High frequency fluctuations dominate the wave time series, so time series were low-pass filtered with a 30-60 day filter cutoff. The filtered time series contain seasonal cycles in which wave heights tended to be high in the winter months and low in the summer months. Waves tended to approach from the north during winter and south during summer. Comparing the filtered wave time series to the filtered morphologic time series allows us to test for correlation between low-pass variations.

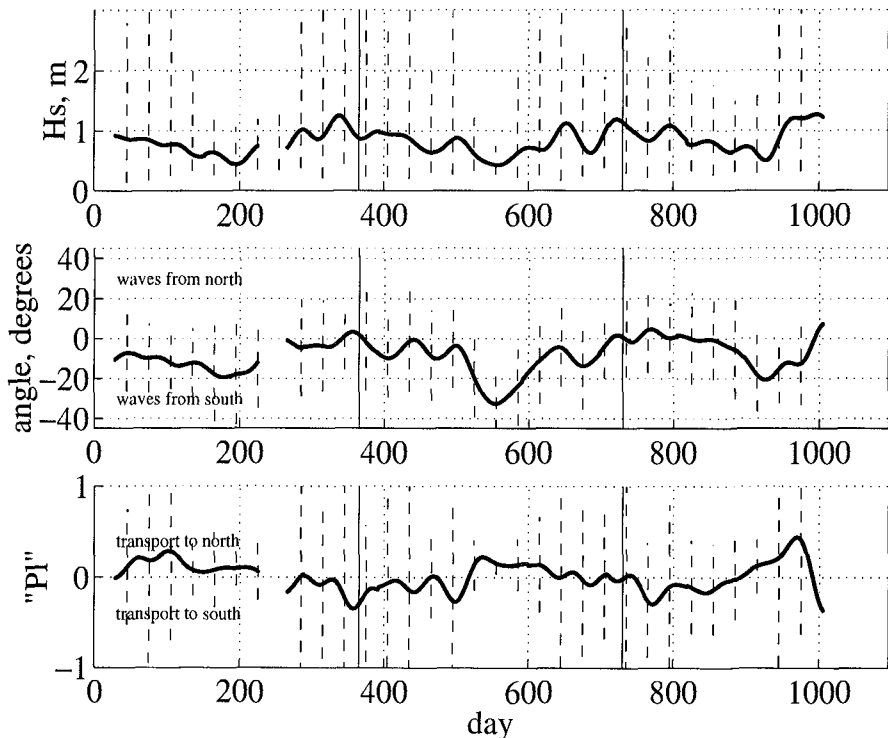


Figure 7. Time series of significant wave height (upper panel), wave direction (middle panel), and alongshore wave energy flux (lower panel). Dashed lines show the monthly wave height range. Wave angles are relative to a shore-normal coordinate system, positive from the north, while a positive alongshore wave energy flux corresponds to expected sediment transport to the north. Dashed lines in the two lower panels correspond to monthly standard deviations.

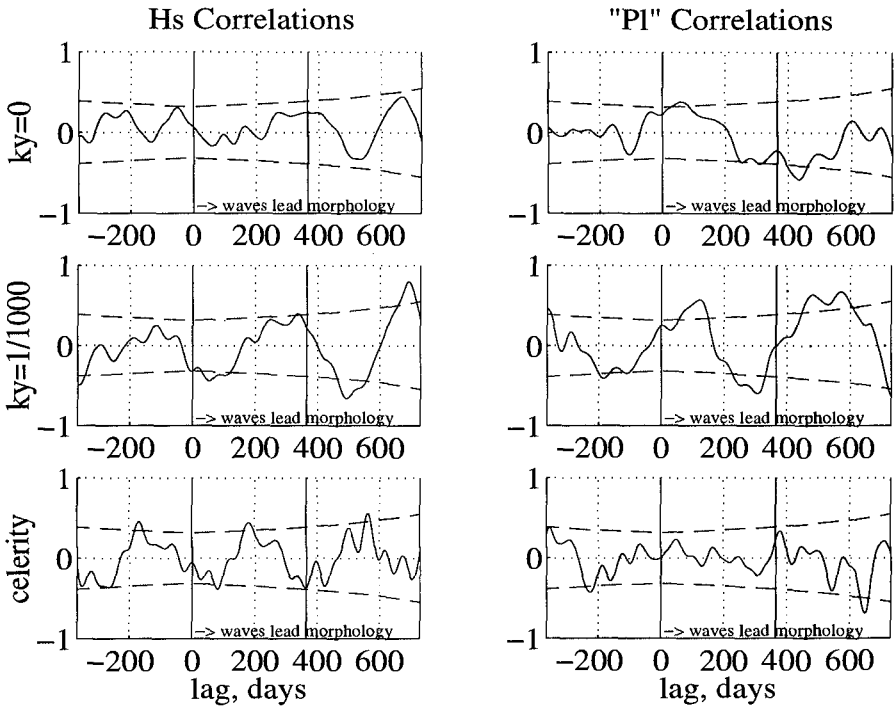


Figure 8. Cross-correlations between wave parameters and morphologic parameters. The wave parameters (H_s and PI) are labeled at the top of the figure and the morphologic parameters ($k_y=0$, $k_y=1/1000$ amplitude, and celerity) are labeled to the left of each pair of figures. In each plot, dashed lines mark the 95% significance level of the correlation and vertical lines mark lags of ± 1 year. Positive lags correspond to the wave time series leading the morphology.

The time-lagged, cross-correlations between the morphologic time series and both wave height and the alongshore wave energy flux are shown in Figure 8. The lag range is defined such that positive lags correspond to the wave time series leading (forcing) the morphologic response. Time lags between -1 and +2 years are shown in all the correlation plots. The first panel shows the correlations between alongshore-averaged shoreline position and wave height, which were less than the 95% significance level at nearly all lags. In the adjacent panel, the correlation to the wave energy flux was most significant at a lag of about 60 days. The positive correlation suggests that periods of northward sediment transport lead to increased beach width. Both results are surprising, since we expected a correlation to wave height but did not expect the alongshore-averaged response to be a function of wave direction.

The cross-correlations of both the amplitude and celerity of the 1 km wavelength component with the wave parameters contained strong seasonal signatures. The amplitude of the 1 km wavelength component was significantly and negatively correlated to the wave height, at a lag of about 60-90 days. We infer from this that increasing wave heights reduced the amplitude of the 1 km scale features and the response of the morphology lagged behind the change in wave conditions. The amplitude time series was also, surprisingly, correlated to the wave energy flux. This

may stem from the strong correlation between wave height and direction, rather than a direct forcing-response relationship of wave direction on these amplitudes.

The celerity and wave height were correlated significantly at a lag of about 90 days. The negative correlation indicates that when the wave height increased, the celerity increased towards the south. Surprisingly, the correlation between the celerity and wave energy flux was relatively poor, which was not expected. Interpretation of cause and effect relationships between the wave field and morphology is potentially impeded by the possibility that the celerity of the 1 km features was partly a function of their amplitude, which was modulated by the wave height.

DISCUSSION

Source of alongshore propagating waves

Sand waves with various amplitudes and celerities have been observed in several nearshore environments (e.g. Sonu, 1969). Clearly, large scale, progressive, morphologic features exist at Duck. We can suggest a few explanations for the existence of these features. We can also reject some possible explanations, based on characteristic time scales. For example, oblique sand ridges are large scale features, recently discussed by Trowbridge (1995). These features extend to deep water (~10 m), and have characteristic, long-term, alongshore celerities of $O(10^{-2}$ to $10^{-1})$ m/day. The forcing mechanism for them is probably storm driven currents, which, as Trowbridge showed, may cause an initially alongshore uniform coastline and bathymetry to become unstable. Hulscher (1996) presents theoretical descriptions of another type of sand wave, which is an instability driven by tidal currents. However, both oblique sand ridges and tidal sand waves, which are $O(0.1$ to $1)$ km in length, have much slower celerities than those observed at Duck. Since the length scale of these deeper water features matches the scales we have observed, it is possible that there is some interaction between the two.

Another sand wave formation mechanism, treated recently by Thevenot and Kraus (1995), is ejection of sand plugs from tidal inlets. These plugs may weld to the shore and perturb the longshore current field. Then, they are expected to propagate alongshore in the direction of the longshore current. Thevenot and Kraus observed sand waves with wavelengths of about 1 km and celerities of order 1 m/day. The alongshore-progressive behavior was modeled by Thevenot and Kraus. However, the modeled sand waves tended to diffuse more rapidly than those observed in the field. The addition of wave refraction in the model reduced the tendency of the modeled waves to dissipate, and appears to be an important sand wave maintenance mechanism. Although there are no nearby inlets at the Duck field site to allow formation of sand waves as ejected sand plugs, the kinematics of the features we have observed seem consistent with the Thevenot-Kraus model.

Potential Pier Effects

A possibly important physical characteristic of our study site is the presence of a pier, which extends 500 m offshore (6 m depth). Since we observed the shoreline behavior only north of the pier, we have no information about what happens near to and south of the pier. If sand waves propagate past the pier, how are they affected by its presence? Does the pier generate sand waves? We hope to extend analysis to observations from both sides of the pier, as there is an extensive collection of surveyed profiles at Duck, spanning over a decade.

CONCLUSIONS

Observations of the shoreline position at Duck, NC indicated that alongshore progressive features with a length scale of order 1 km were responsible for a large portion (40%) of shoreline variability at this site. The amplitude of these features (~10 m) was modulated by the annual variations in wave height. The amplitude was reduced during periods of increased wave height (winter) and the amplitude increases during calm conditions (summer). Although these features propagated to the south, variations in celerities were not well correlated to the direction of expected wave-driven sediment transport, and were more correlated to changes in the wave height. Surprisingly, the alongshore-averaged shoreline behavior was not well correlated to wave height. Although the wave field varied on an annual cycle, the alongshore-averaged shoreline position did not, in contrast to expectations from a simple conceptual model of summer-winter behavior. Instead, this component varied most dominantly over an interannual period, in which one cycle was completed in about two years.

The observations and analysis presented here describe the contribution of various alongshore length scales to beach variability at Duck, NC. The results of this analysis indicated the importance of large length and time scales to observed nearshore variability. Extending analysis to observations that cover larger lengths and longer time periods will improve our resolution of the phenomena presented here.

ACKNOWLEDGMENTS

The data used here comes from a large image database collected as part of an ever expanding research program called ARGUS. If John Stanley had not organized all the data so well, the pilot study for this project would not have been completed in the two days available to do so and the first author's scientific career would have been ruined. The research staff at the Army corps of Engineers Field Research Facility are similarly appreciated for their maintenance of the wave data. Thanks, also, to those people who discussed this work with us at the ICCE '96 meeting. This work was funded by the Office of Naval Research, Coastal Dynamics Program (grant # N00014-960237).

REFERENCES

- Birkemeier, W.A., Time scales of nearshore profile change, in 19th International Conference on Coastal Engineering, pp. 1507-1521, ASCE, New York, 1985.
- Hulscher, S.J.M.H., Tidal-induced large-scale regular bed form patterns in a three-dimensional shallow water model, *Journal of Geophysical Research*, 101 (C9), 20,727-20,744, 1996.
- Komar, P.D., *Beach processes and sedimentation*, 429 pp., Prentice-Hall, Englewood Cliffs, N.J., 1974.
- Larson, M. and N.C. Kraus, Dynamics of longshore bars, in 23rd International Conference on Coastal Engineering, pp. 2219-2232, ASCE, New York, 1992.
- Lippmann, T.C., and R.A. Holman, Quantification of sand bar morphology: A video technique based on wave dissipation, *Journal of Geophysical Research*, 94 (C1), 995-1011, 1989.
- Lippmann, T.C., and R.A. Holman, The spatial and temporal variability of sand bar morphology, *Journal of Geophysical Research*, 95 (C7), 11,575-11,590, 1990.
- Ooyama, K.V, Scale-controlled objective analysis. *Monthly Weather Review* 115(10): 2479-2506, 1987.
- Plant N.G. and R.A. Holman, Intertidal beach profile estimation using video images. *Marine Geology*, in press.

- Ruessink, B.G., and A. Kroon, The behavior of a multiple bar system in the nearshore zone of Terschelling, the Netherlands, 1965-1993, *Marine Geology*, 121, 187-197, 1994.
- Sonu, C.J., Collective movement of sediment in the littoral environment, in *Proc. of the 11th Conference of Coastal Engineering*, pp. 373-400, ASCE, 1969.
- Thevanot M.M. and N.C. Kraus, Longshore sand waves at Southampton Beach, New York; observations and numerical simulation of their movement. *Marine Geology*, 126(1-4), 249-269, 1995.
- Trowbridge, J.H., A mechanism for the formation and maintenance of shore-oblique sand ridges on storm-dominated shelves, *Journal of Geophysical Research*, 100 (C8), 16,071-16,086, 1995.
- Wijnberg, K.M., and J.H.J. Terwindt, Extracting decadal morphological behavior from high-resolution, long-term bathymetric surveys along the Holland coast using eigenfunction analysis, *Marine Geology*, 126, 1995.

CHAPTER 273

LONG TERM BEHAVIOUR OF THE SEDIMENT VOLUME INSIDE A TIDAL BASIN AFTER POLDERING

Ernst Schroeder¹, Roland Goldenbogen², Hans Kunz³

ABSTRACT

The development of morphological reactions over time as a result of polderings has been investigated for the Dithmarscher Bucht (Bay of Dithmarsch), a tidal basin which is located in the North Sea/Germany. Two methods of parametrization have been used: the first method is based on volume-differences and the second one refers to the vertical differences of the topography. The results have been used for an estimation of the stability of the tidal basin with respect to an accelerated rise of the relative sea level.

INTRODUCTION

Tidal basins are transition areas between the mainland and the sea. They exist under special hydrological and sedimentological boundary conditions. On account of these special conditions, tidal basins have been formed along the Southern North Sea coast during the last 10,000 years (Bantelmann 1966 and Streif 1990). In most of the areas, the actual situation has been substantially influenced by human interferences, especially by land reclamation.

Besides coastal engineering aspects the Wadden Sea areas are an unique ecological system, which is essential as breeding and feeding ground for migratory birds on their East Atlantic Flyway (Lozán et al. 1994).

¹ Dipl.-Ing., Coastal Research Station (CRS) of the Lower Saxonian Central State Board for Ecology, An der Mühle 5, D-26548 Norderney/Germany

² Dipl.-Ing., Coastal Research Station

³ Director Dr., Coastal Research Station

An accelerated rise of the relative sea level is a realistic prospective; therefore the question about its effects on the long term behaviour of the Wadden Sea-tidal basins along the North Sea coast is important. Only if the morphology of the tidal basin is able to adapt to the changing hydrological conditions, is it ensured, that the whole system keeps its stability.

A tidal basin is a feed-back system which tends towards an equilibrium stage, determined by the hydrological and morphological boundary conditions. Changes in the relation between these boundary conditions lead to reactions of the morphology. The morphology compensates the non-equilibrium stage by more or less intensive accumulation or erosion processes. These adjustments proceed with a phase lag, depending on the quantity of the disturbance in relation to the system itself.

Comparable processes occur after cutting off (poldering) parts of a tidal basin. The daming reduces the catchment area of the tidal basin and alters the relationships between the hydrological and the morphological boundary conditions. Investigations of the morphological development after cutting off parts from a tidal basin led to calculations over time of the adjustment-ability.

The morphological reaction of a tidal basin, forced into a non-equilibrium stage by cutting off parts, can be compared with the effects of the changing hydrological boundary conditions as a result of sea level rise. Thus, the adaptability can be estimated qualitatively for different values of sea level rise.

PARAMETRIZATION

The description of the morphological development has been based on two different methods for the parametrization. The parameters for the first method has been determined by calculating the difference between volumes. The second method is based on the averaged heights difference between bathymetric surveys of the morphology for successive stages. The introduced parameters are named "transpose-rates", for the first method as h_t and for the second one as h_A or h_E , with the dimension m/a . The transpose-rates which are presented and discussed in the paper represent mean yearly values.

Method N^o. 1

The sediment volume V_1 has been calculated above a fixed datum as horizontal reference level (Fig. 1). The reference level has been set below the deepest point of the topography for which morphological changes are recorded. For the total tidal basin

Dithmarscher Bucht, the reference level has been fixed at -22.0 m NN⁴ and for the defined subareas at -12.0 m NN. The upper limit is 2.0 m NN⁵. The volume difference ΔV_I (Fig. 2) of two successive surveys are divided by the time period between the surveys Δt and by the area of the cross section A_I (Schroeder et al.1995b). This parameter is named "transpose rate h_t " (m/a):

$$h_t = \Delta V_I / (\Delta t_i \cdot A_{I,i+1}) = (V_{I,i+1} - V_{I,i}) / ((t_{i+1} - t_i) \cdot A_{I,i+1}). \quad (1)$$

The division by the cross section A_I provides a standardization of the parameter, which allows the comparison of catchment areas A_c with different sizes.

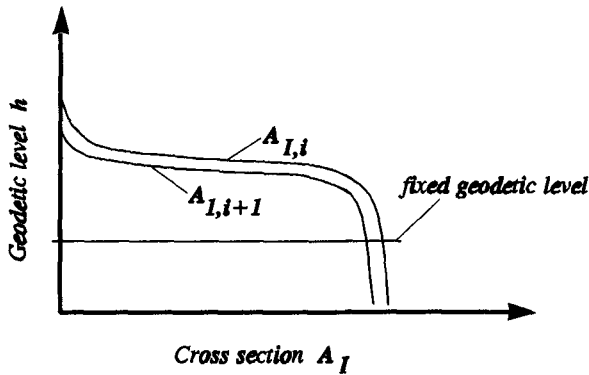


Figure 1. Idealized graphs of the geodetic level h over the cross section A_I

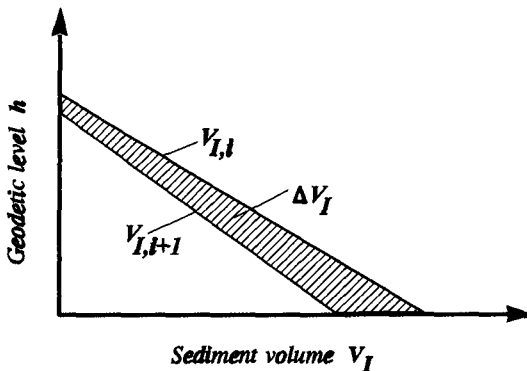


Figure 2. Idealized graphs of the geodetic level h over the sediment volume V_I

⁴ NN = Normal Null = German ordnance-datum (app. MSL)

⁵ MHW app. 1.55 m NN (min. HW/max. HW = 1.46/1.63 m NN; 1942 - 1990) at the tide-gauge Büsum (Fig. 6)

Method N°. 2

The second method leads to "transpose-rates" which have been determined separately for accumulation as " h_A " and for erosion " h_E ". The calculation of these parameters is based on the heights of a standardized area-element (vertical difference). Therefore, the topography has been transformed into square grids (Fig. 3). The resolution of the grid has been fixed as 25 m in x- and y-direction, hence, one grid-element covers an area of 625 m².

The horizontal reference level of one grid yields as mean value of the "average node" H_i (mNN) of the heights of each grid node (see A, B, C and D in Fig. 4):

$$H_i = (A+B+C+D)/4. \quad (2)$$

The difference of the parameter H of two successive surveys (H_i, H_{i+1}) is the accumulation or erosion-rate ΔH_i in m for each grid element:

$$\Delta H_i = H_{i+1} - H_i. \quad (3)$$

This rate, divided by the time interval between the successive surveys, leads to the yearly transpose-rate of each grid element, either as accumulation ($\Delta H_{A,i}$) or as erosion ($\Delta H_{E,i}$). The sum of all elements with accumulation or erosion inside the defined investigation areas (total basin or subarea) yields to the "transpose-rate", which is indicated as h_A (accumulation) and h_E (erosion) with the dimension m/a:

$$\sum \Delta H_{A,i} / \Delta t = h_A \quad (4)$$

$$\sum \Delta H_{E,i} / \Delta t = h_E. \quad (5)$$

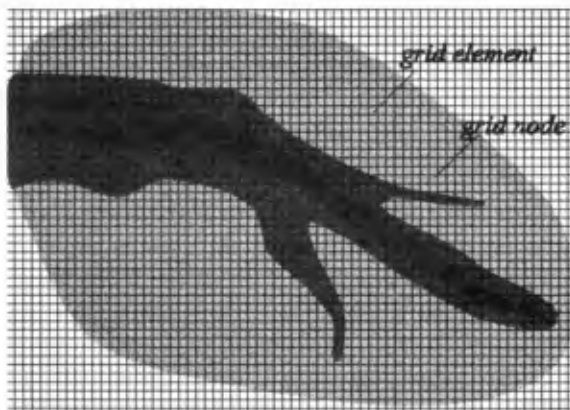


Figure 3. Idealized investigation area with grid

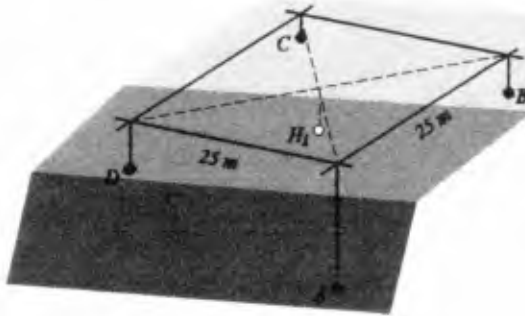


Figure 4. Idealized grid element with the grid nodes A, B, C and D and the average node H_i

INVESTIGATION AREA

The investigation area is called the *Dithmarscher Bucht* (Bay of Dithmarsch). It is located on the German North Sea coast on the West side of the German federal state of *Schleswig-Holstein* (Fig. 5).

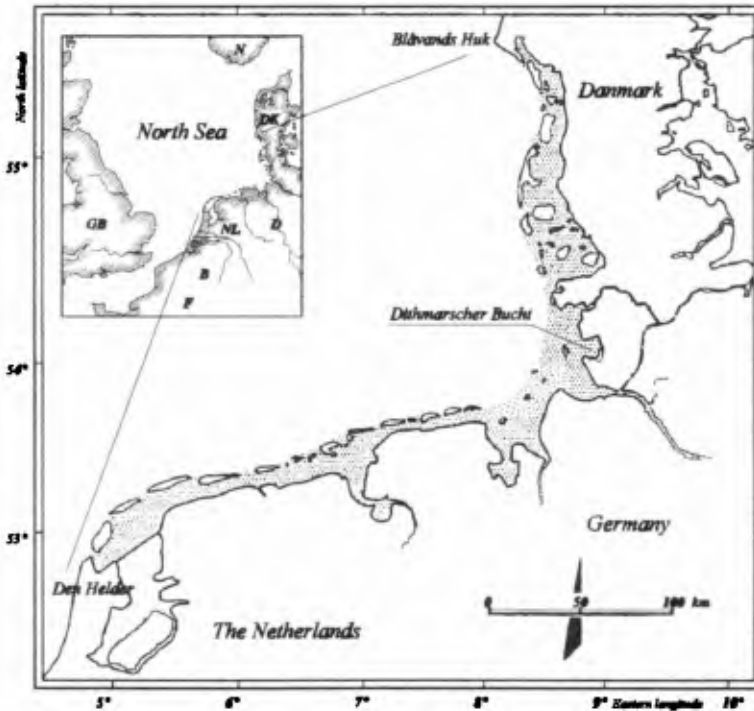


Figure 5. Location of the investigation area

The shape represents a single bay which opens towards the main wind- and wave direction. Inside the bay, the mean tidal range (semidiurnal tides) is 3.25 m (1942-1990); the dominate wind direction scatters around West. The mean offshore waveheight is about 1.00 m. The geological structure of the bay, developed during the Holozän-time-period, consists mainly of marine sediments (Fischer 1955).

The tidal basin had been reclaimed two times by poldering. The bay covered an area of approximately 157 km² before the polderings had been carried out. The first poldering (1972) reduced the bay-area (A_b) by about 16 km² and the second one (1978) by 26 km² (see dotted lines in Fig. 6).

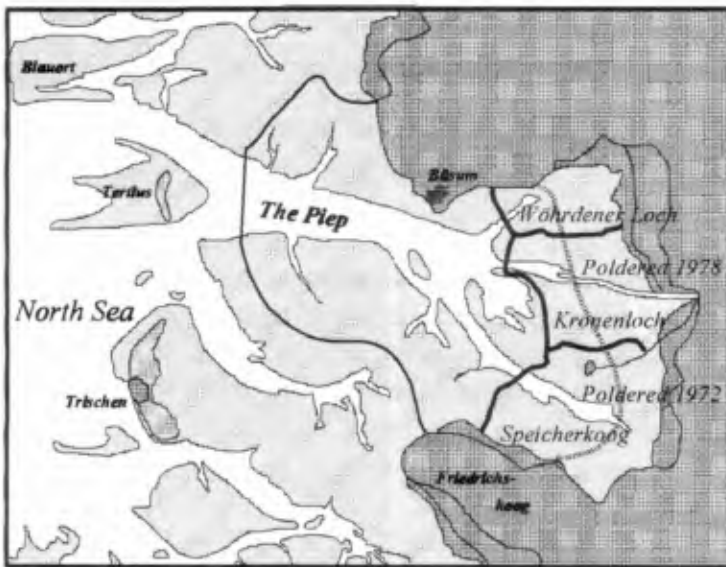


Figure 6. Investigation area *Dithmarscher Bucht* with poldered areas and the investigated subareas

With regard to the reaction of the bay as result of the polderings, the tidal basin has been split up into subareas according to the application of an applied empirical model (Goldenbogen 1994, Niemeyer et al. 1995 and Schroeder et al. 1995a). The subareas which include the poldered parts are shown on fig. 6: *Speicherkoog*, *Kronenloch* and *Währdener Loch*. The total bay-area is represented by *The Piep*. During the investigation period from 1942 up to 1990 the *Dithmarscher Bucht* had been surveyed 9 times (1942, 1956, 1969, 1973, 1976, 1979, 1982, 1985 and 1990). The bathymetric surveys of 1942, 1956 and 1969 describe an undisturbed topography. The surveys after the year 1973 are influenced by the poldering-means.

The morphological data for the *Dithmarscher Bucht* and parametrizations for "equilibrium stages" have been described by Schroeder 1994.

RESULTS

The following diagrams show the calculated transpose-rates h_i . The data (ordinate) has been plotted over the half period of an investigation intervall Δt_i (abscissa, Fig. 7).

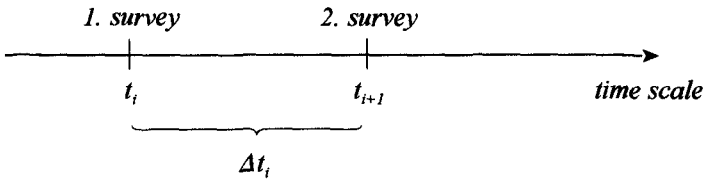


Figure 7. Definition of the investigation intervall Δt_i

Figure 8 shows data which are based on the the total difference of the sediment volume in accordance with the first method. During the period from 1942 up to 1969 the anthropogenic influences are negligible. The scattering of the results can be explained by natural effects and, additionally, in the case of the year 1956, by the quality of the bathymetric survey.

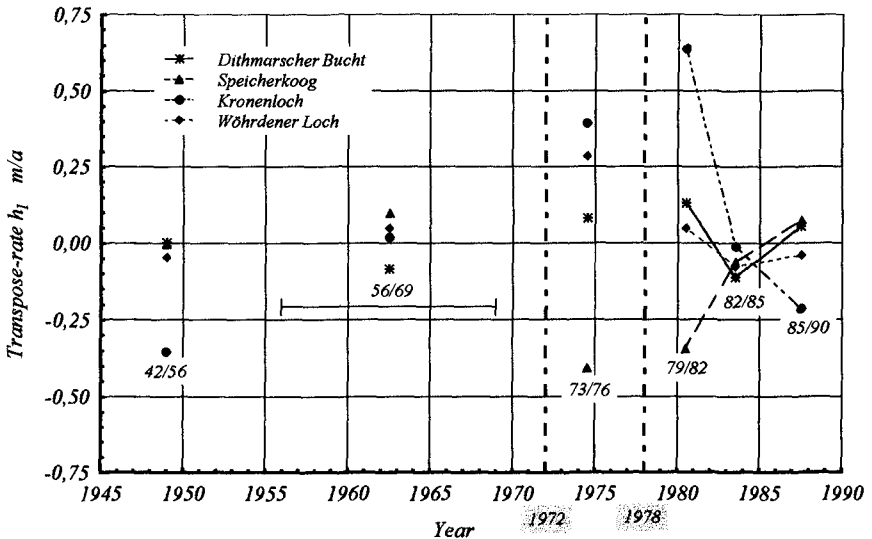


Figure 8. Transpose-rate h_i versus investigation intervall Δt_i

The first poldering was carried out inside the subarea *Speicherkoog* in 1972 (Fig. 6). The value of the subarea *Speicherkoog* shows a distinct tendency of erosion as a result of the first poldering, whereas the other subareas, as well as the total tidal basin, are characterized by accumulation.

The second poldering was carried out in 1978. This poldering extends over the subareas *Kronenloch* and *Wöhrdener Loch* (Fig. 6). After the second poldering, the tendency of erosion continued inside the subarea *Speicherkoog*. The transpose-rate inside the subarea *Wöhrdener Loch* decreased in the range of the average values, as monitored during the undisturbed period before 1969. Only the transpose-rates of the subarea *Kronenloch* increased significantly. However, already during the second investigation interval from 1982 to 1985, the values for this subarea also decreased. All values indicate a low erosion-tendency. The erosion effects continue for the subarea *Kronenloch* during the last interval (1985 to 1990). The results for the last interval scatter within a range which is comparable to the values during the undisturbed investigation period before 1969.

A similar development display the results for the accumulation rate h_E gained by the second method (Fig. 9).

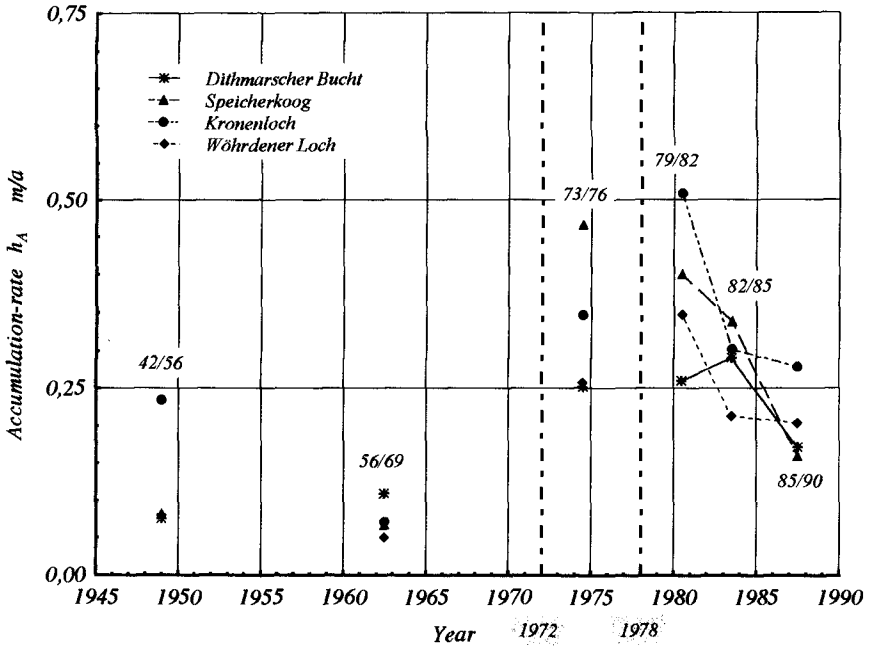


Figure 9. Transpose-rate h_A versus investigation interval Δt .

The value increased after the first poldering. The subarea *Speicherkoog*, where the poldering was carried out, shows the highest value. This value decreased after the second poldering, whereas the transpose-rates of the subarea *Kronenloch* and *Wöhrdener Loch* increase. The next investigation-interval indicates a reduction of the values for all subareas. During the following interval, this tendency continued for the subarea *Speicherkoog* and also for the whole tidal basin, whereas the subareas *Kronenloch* and *Wöhrdener Loch* show more or less constant accumulation-rates.

The data of the erosion rate also indicate clear trends (Fig. 10). The undisturbed period is followed by an increase of the values except for *Kronenloch*. Over the last two investigation intervals the values decrease, including those for the *Kronenloch*. During the last interval (1985-1990), the value scatter already in the range of the undisturbed period before 1969.

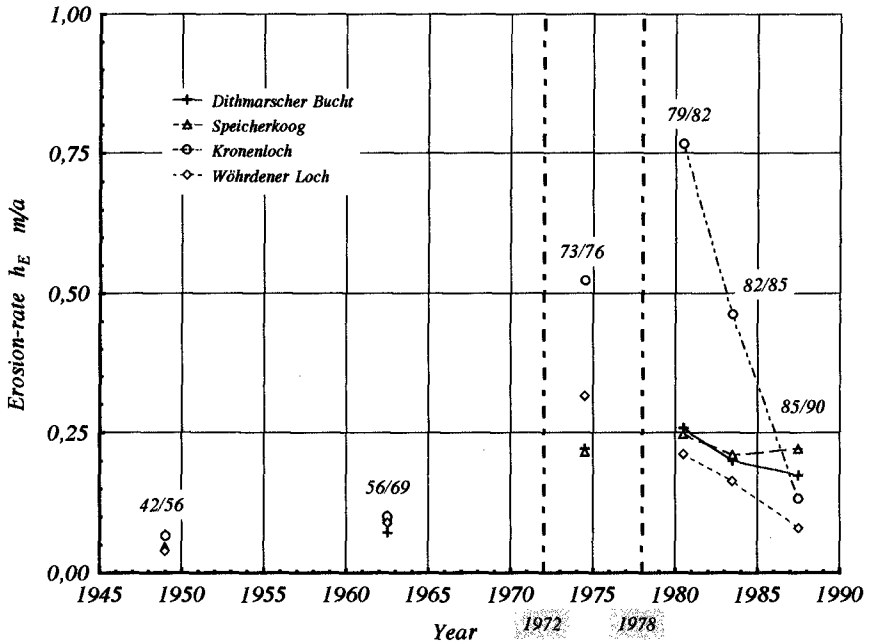


Figure 10. Transpose-rate h_E versus investigation interval Δt_i

CONCLUSIONS

The results allow estimations concerning the morphological reactions of a tidal basin on the changes of geographic boundaries by poldering (reduction of the bay-area leading to a disturbance of the equilibrium condition with respect to the tidal volume

as hydrographical boundary condition and the cross-section/area-size as morphological boundary condition). The discussed results show comparable reactions of the described parameters over the whole investigation-period from 1942 to 1990.

The results concerning the development of the *Dithmarscher Bucht* over the last three investigation intervals from 1979 up to 1990 (time period after the polderings) showed, that after approximately 5 years, the parameter-values had decreased, in part, more than 50% of the maximum values after the polderings. The assumption can be drawn that after 5 more years there will be no significant distinction between the anthropogenic and the natural influences of the transpose-rates. With respect to the strongly decreasing tendency of the investigated transpose-rates, the prediction seems to be reliable, that after one to two decades, the influences of the anthropogenic impacts (disturbance of the "equilibrium stage" by poldering) will fade away and the adaptation to the anthropogenically-created new boundary conditions will reach the new equilibrium.

The results indicate the *Dithmarscher Bucht* as an area with strong accumulation. Comparable investigations, described in literature, came up with similar results (Wieland 1984, Siefert 1987, Niedoroda et al. 1994), and Unsöld 1974 with respect to the regeneration after dredging.

With regard to a transfer of the described results to other tidal basin-areas, the available sediment capacity of the area is one of the main restricting factors that has to be taken into account.

The investigation have shown that, for the tidal basin *Dithmarscher Bucht*, there will be no danger concerning the stability of the morphology with respect to changes of the forecasted or feared hydrological boundary conditions, even if the acceleration of the relative mean sea level rise should reach the IPCC-best-estimate-values (IPCC 1990) of about 60 cm in hundred years.

ACKNOWLEDGEMENT

The findings result from the German-Dutch research project *Wadden Sea Morphological Development - WADE* (Niemeyer et al. 1995). The German part has been funded by the Federal Ministry for Science, Education, Research and Technology (BMBF), Bonn under contract MTK 0508.

REFERENCES

- Bantelmann, A.** (1966): Die Landschaftsentwicklung an der schleswig - holsteinischen Westküste, eine Funktionschronik durch fünf Jahrtausende. Die Küste, Heft 2, KFKI, Boyens & Co., Heide i. Holst., (in German).
- Fischer, O.** (1955): Landgewinnung und Landerhaltung in Schleswig-Holstein. Teil III: Das Festland. Bel. 5: Dithmarschen. Verlag Dietrich Reimer, Berlin, (in German).
- Goldenbogen, R.** (1994): Erste Ergebnisse empirischer Modellierung der Morphodynamik eines Wateinzugsgebiet am Beispiel der Dithmarscher Bucht. Die Küste, Heft 56, KFKI, Boyens & Co., Heide i. Holst., (in German).
- IPCC** (1990): Strategies for adaption to sea level rise. Intergovernmental Panel on Climate Change (IPCC), Response Strategies Working Group. Edit. Dutch Ministry of Transport and Public Works, Rijkswaterstaat, Tidal Water Division, Den Haag.
- Lozán, J.L.; Rachor, E.; Reise, K.; Westernhagen, H. v. & Lenz, W. (Ed.)** (1994): Warnsignale aus dem Wattenmeer. Blackwell Wissenschaftsverlag, Berlin, (in German).
- Nedoroda, A.W.; Reed, Chr.W.; Swift, D.J.P.; Arato, H. & Hoyanagi, K.** (1994): Modeling shore-normal large-scale coastal evolution. In: Mulder, J.P.M.; Vriend, H.J. de & Heeming, A.W. (Ed.): Validation on large scale morphological models. Nederlands Centrum voor Kustonderzoek, Workshop, Noordwijk.
- Niemeyer, H.D.; Goldenbogen, R.; Schroeder, E. & Kunz, H.** (1995): Untersuchungen zur Morphodynamik des Wattenmeeres im Forschungsvorhaben WADE. Die Küste, Heft 57, KFKI, Boyens & Co., Heide i. Holst., (in German).
- Schroeder, E.** (1994): Parametrisierungen morphodynamischer Strukturen von Wateinzugsgebieten für empirisch-konzeptionelle Modellierungen. Die Küste, Heft 56, KFKI, Boyens & Co., Heide i. Holst., (in German).
- Schroeder, E.; Goldenbogen, R. & Kunz, H.** (1995a): Parametrization for conceptual morphodynamic models of the Wadden Sea areas. Proc. 24th Int. Conf. Coast. Eng. (1994), Kobe/Japan, ASCE, New York.
- Schroeder, E.; Goldenbogen, R. & Kunz, H.** (1995b): Parametrization of intertidal areas and volumes. Proc. 4th Int. Conf. on Coast. and Port Eng. Develop. Countr. - COPEDEC IV, Rio de Janeiro/Brazil, Brazilian Water Resources Association (ABRH), Rio de Janeiro.
- Siefert, W.** (1987): Umsatz- und Bilanz-Analysen für das Küstenvorfeld der Deutschen Bucht.Grundlagen und erste Auswertungen (Teil 1). Die Küste, Heft 45, KFKI, Boyens & Co., Heide i. Holst., (in German).

- Streif, H.** (1990): Das ostfriesische Küstengebiet - Nordsee, Inseln, Watten und Marschen. Sammlung Geologischer Führer 57, Gebr. Borntraeger, Berlin/Stuttgart, (in German).
- Unsöld, G.** (1974): Jahreslagen und Aufwachsdaten in Schlicksedimenten eines künstlichen, gezeitenoffenen Sedimentationsbeckens (Wattgebiet südlich Nordstrand/Nordfriesland). Meyniana, Bd. 26, (in German).
- Wieland, P.** (1984): Untersuchungen über geomorphologische Veränderungen in der Dithmarscher Bucht. Die Küste, Heft 40, KFKI, Boyens & Co., Heide i. Holst., (in German).

CHAPTER 274

WAVE GROUPS IN A BARRED NEARSHORE

B. Boczar-Karakiewicz¹, W. Romańczyk¹, J.L. Bona² and B. Greenwood³

ABSTRACT

Observations of waves and sediment movement in coastal zones have shown evidence of groupiness in the wave field associated with episodic events of high sediment concentration above the sandy bed. These observations raised the question about the role of wave groups on large-scale coastal sand bars. The present study addresses this question. Analysis is based on data from a lacustrine experimental study site located in Nottawasaga Bay, Lake Huron, Ontario, Canada. The results of field measurements provided initial and boundary conditions for numerical simulations of wave-seabed interactions under waves and wave-groups. Model predictions are compared with observations. The conclusions suggest that nonlinearly modulated wave trains may potentially form and modify sand bars in coastal zones due to large-scale spatial variation in the nonlinear structure of these waves. However, strong irregularities in observed wave groups and related episodic sediment concentration events suggest that these groups do not represent an effective factor in the 'slow' process of sand bar formation.

1. INTRODUCTION

In deep ocean, with limited breaking, wave groups can be described by superposition of linear wave components or by applying nonlinear modulation instabilities. Medina and Hutspeth (1990) have shown that linear algorithms describe observed wave groups in a water depth greater than 10 m with satisfactory agreement. Battjes and Vledder (1984) supported this conclusion for the surf zone.

¹INRS-Océanologie (Université du Québec), Rimouski, Québec, Canada

²University of Texas, Applied Math, Austin, Texas, USA

³Scarborough College Coastal Research Group, University of Toronto, Toronto, Ontario, Canada

However, in the linear approach, waves are assumed to be a Gaussian process, with independent components of the wave field. In earlier studies, it also has been assumed that upon initial breaking, wave groups vanish, except for a small zone surrounding the mean breakpoint.

These assumptions were shown not to be valid in shallow coastal zones. List's quantitative study (1991, 1992), using the concept of wave group envelope, has confirmed that groupiness decreases rapidly through the surf zone, and is sensitive to initial wave breaking. However, he also proved that the degree of groupiness does not become negligible, even in a saturated surf zone. His analysis revealed that groupiness of unbroken waves remains constant over a wide range of incident wave conditions from fairweather swells to storm seas. That observation contradicts the intuitive concept of groupiness resulting from the superposition of sinusoidal waves of similar frequency. According to the linear concept, an increase of spectral bandwidth should result in decreased groupiness.

Laboratory tests and numerical simulations carried out with wave shoaling over a beach of constant slope allowed experimentations with nonlinear wave groups in a simpler environment than a natural coast. A set of such experiments has been conducted in the wave basin of the Hydraulics Laboratory of the National Research Council of Canada (Nwogu 1993). Bichromatic linear waves were generated at the deep-water end of a 1:25 sloping concrete beach. The time series of water surface elevation were measured at two locations: at the toe of the slope and at the initial breaking location. A numerical model based on Boussinesq equations simulated hydrodynamics in the experiment. Comparisons of model results and observations showed good agreement and explained the nature of nonlinear transformations in the initial modulated train composed of sinusoidal waves. When these waves approach shallow water, their shape changes into a complex nonlinear form. The nonlinearity in an individual wave profile increases with decreasing water depth, due to a transfer of energy from the two fundamental frequencies of the incident biharmonic wave train into respective higher harmonic modes. A small amount of energy is also transferred to a low-frequency group-bound wave. That energy increases with decreasing water depth.

The results of a similar numerical study based on a KdV equation with variable coefficients describe the nonlinear evolution of a single group of modulated sinusoidal waves propagating over a gently-sloping beach (Talipova *et al* 1995). Nonlinear and dispersive effects in this group lead to recurrent energy transfer between the fundamental and the higher harmonic components. The initial wave group evolves with increasing distance into a strongly nonlinear wave packet. At a distance of several tens of wavelengths from the deep-water end, the initial modulation changes shape. Higher waves are shifted to the front of the packet due to frequency dispersion. Nonlinearity causes the appearance of secondary crests in the individual waves of the packet. Therefore, it is not

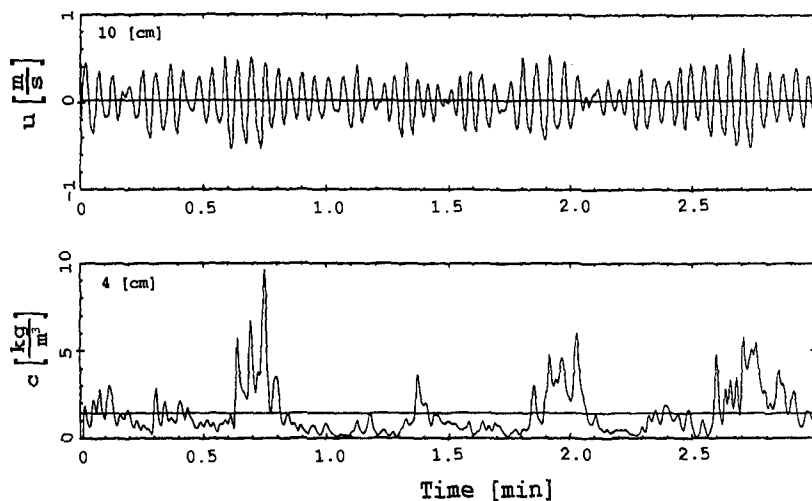


Figure 1: (a) Cross-shore velocity (at 0.10 m above the bed), (b) suspended sediment concentration (at 0.04 m above the bed).

clear how to relate the number and position of waves in the packet with the number of sinusoidal waves in the initial group.

Examples of numerical simulations and laboratory experiments with idealized wave groups show how their properties result from nonlinearity and dispersion of the shallow-water environment. On a natural coast, wave group behaviour is even more complex because of the presence of several flow components.

Observations of waves and sediment movement in coastal sites (Greenwood *et al.* 1992) show evidence of groupiness in the wave field associated with episodic events of high sediment concentration above the sandy bed. A typical record of nearbed velocities and suspended sediment concentration is shown in Figure 1. These observations raised the question about the role of wave groups on large-scale coastal sand bars.

The present study addresses this question and concentrates on the role of wave groups in sand bar formation and dynamics. Our analysis is based on observations from an experimental study site presented in Section 2. Numerical simulations of wave-seabed interactions under waves and wave-groups are presented in Section 3. Model calculations are carried out with initial data from the field experiment. Predictions are compared with observations from the experimental site. The conclusions are formulated in Section. 4.

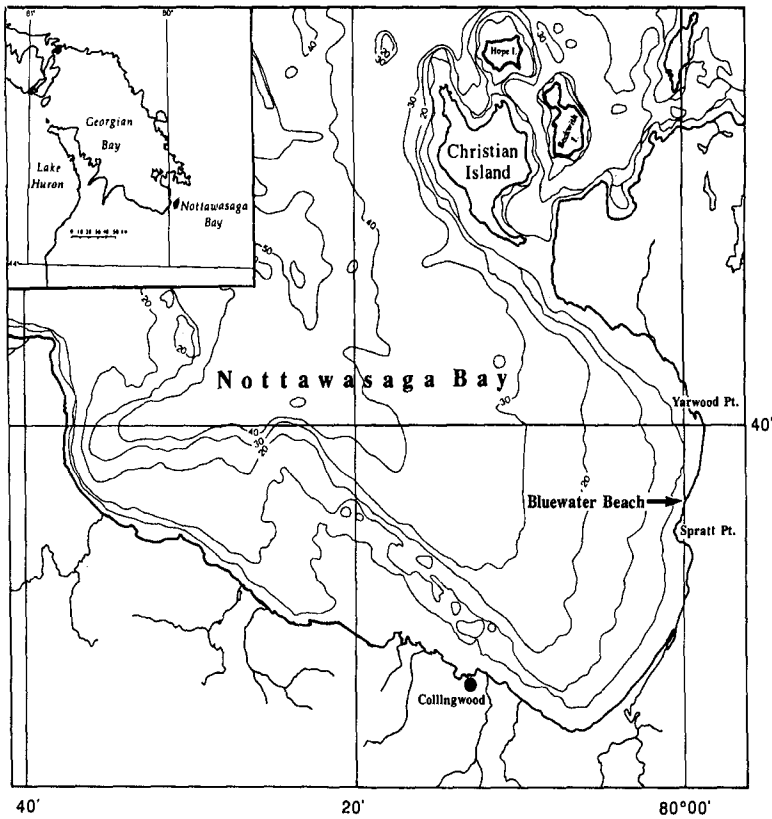


Figure 2: Field site, Bluewater Beach, Nottawasaga Bay, Ontario, Canada.

2. THE EXPERIMENTAL SITE AND FIELD OBSERVATIONS

The study site (Bluewater Beach, Nottawasaga Bay, Lake Huron, Ontario, Canada) is located in a narrow bay, as shown in Figure 2. Incident wind-generated storm waves arrive to the nearshore zone from a narrow window and impinge on the beach from the shore-normal direction. Under such conditions, we may apply our two-dimensional morphological model in calculations presented in Section 3. In the chosen site, surface hydrodynamics are simpler than on ocean coasts as they are not affected by tidal flows.

The study site has a barred shoreface (see Fig. 3 for the location of sensors used in measurements). The typical multibar shoreface from Figure 3 is not static. In 1987, a beach survey revealed a one-bar profile (Fig. 4a), which transformed into a multi-bar profile in the following year (Fig. 4b).

Field measurements of waves and sediment concentrations at Bluewater Beach analyzed by Osborne and Greenwood (1992) have shown that the lo-

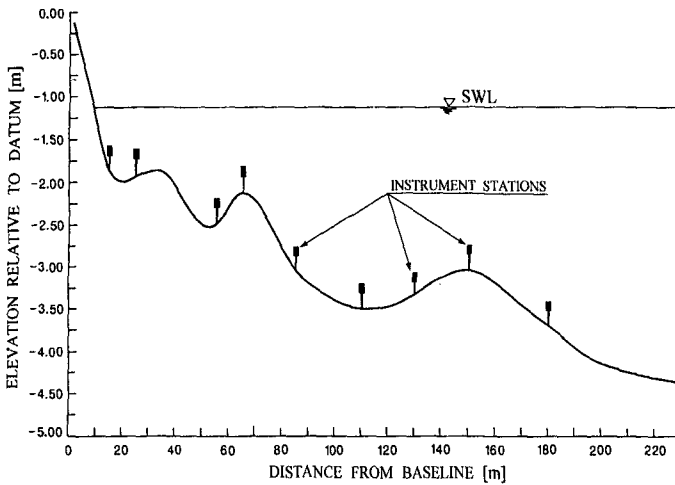


Figure 3: Typical shoreface profile and sensor deployment (pressure sensors, electromagnetic current meters, optical backscatter sensors (OBS)).

cal time-varying suspended sediment flux is a response to high-frequency wind-wave oscillatory currents, low-frequency waves and quasi-steady currents (undertow). The relative importance of these transport components varies spatially and temporally in association with variability in incident wave energy. In contrast to a non barred shoreface, where variations of transport components are strongly controlled by monotonically-decreasing local water depth, across a barred shoreface sediment fluxes are constrained by position with respect to the bars.

Co-spectral analyses of cross-shore velocities and sediment concentrations reveal that grouped, nonlinear shoaling waves induce large onshore sediment transport rates at wind-wave frequencies. However, simultaneously, net offshore-directed transport at low frequencies was also observed. This offshore sediment flux compensates onshore currents induced by grouped waves. During extreme storms, the group-bound long wave could potentially dominate the net oscillatory component of suspended sediment transport and, consequently, displace sediment in the offshore direction.

Additional complexity at a barred foreshore results from waves breaking over a bar crest and waves reforming in the bar trough. Observations show that, typically, outside the surf zone, the re-suspension of sediment under groups of large waves is coherent with the offshore phase of low-frequency modulation of the velocity field due to the presence of wave groups and the group-bound, forced long wave.

However, landward of the zone of wave breaking, on the bar crest and on the upper lakeward slope, the wave-group structure was observed to be diminished.

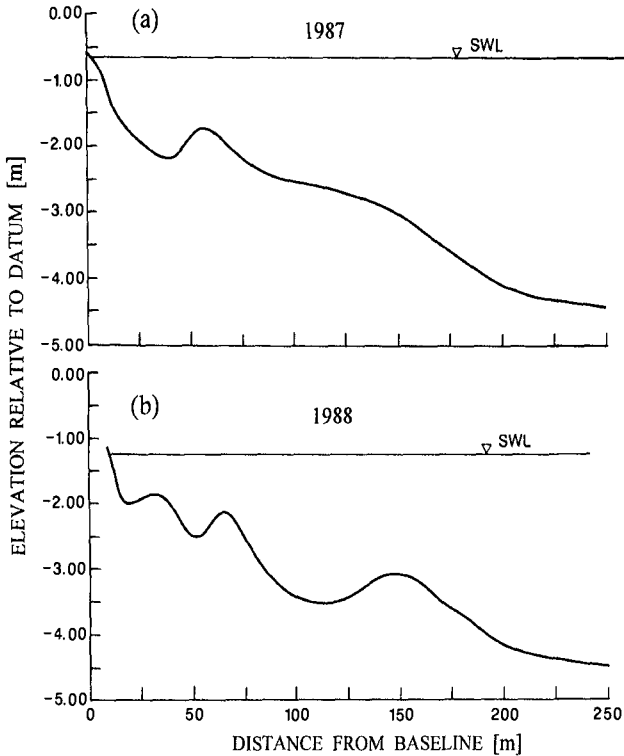


Figure 4: Shoreface profiles at Bluewater Beach in 1987 and 1988.

Here, low-frequency waves were still evident, which suggests the presence of edge waves or reflected long waves. These waves may contribute to observed high sediment concentrations and to the observed morphodynamic response under highly energetic conditions.

Observations have also shown that bar topography exerts an important constraint on both the magnitude and direction of transport by oscillatory and mean currents. The bar crests experienced the largest oscillatory currents and greatest levels of turbulence induced by wave breaking. Surprisingly, however, the net suspended sediment transport rates were minimal, near balance, between the mean transport rate directed offshore by undertow and the net on-shore oscillatory transport rate controlled by asymmetric waves at or close to breaking. The oscillatory transport rates at wind-wave frequencies decreased with increasing water depth both landward and lakeward of the bar crest.

According to the interpretation of reported spatial changes in suspended transport rates, it has been concluded that spatial variation in sediment transport does concur with bar morphodynamics that resulted from the monitored storm event. After the storm, the inner bar migrated landwards. However,

the lower lakeward slope did not show any erosion despite large and persistent sediment flux gradients and net offshore transport.

The reported results of observations analyzed by Osborne and Greenwood (1992) were concluded by a statement that the net oscillatory sediment transport rate induced by low-frequency waves increases both landward and lakeward of the breaker zone on the bar crest, as does the mean sediment transport rate. Additionally, it was shown that the low-frequency group-bound wave transports sediment offshore. However, it could only be inferred that the secondary low-frequency wave may transport sediment onshore because observations did not provide quantitative data on the structure of the low-frequency wave and about its role in the maintenance of the bar form.

The results of field data analysis presented above show that surface hydrodynamics and related sediment fluxes are extremely complex in a barred foreshore. With available technology and analytical methods applied in the study of Osborne and Greenwood (1992), it is, at present, impossible to discriminate between the contribution of wave groups to sediment transport from the contribution of the remaining transport components active in the nearshore. In their conclusion, Osborne and Greenwood also pointed out that the spatial variation of suspended sediment transport rates correlated only partially with observed changes in bar morphology.

The numerical modeling presented in Section 3 allowed us to investigate the influence of wave groupiness on bar dynamics in idealized, simple conditions. Wave and topography data from field measurements at Bluewater Beach were used in initial and boundary conditions required in the model, and in the experimental verifications of model predictions.

3. METHODOLOGY OF NUMERICAL SIMULATIONS

We present three sets of numerical experiments investigating wave-bed interactions in a coastal environment. In these experiments, surface hydrodynamics are induced by wave trains at wind-wave frequencies characterizing the wave climate at Bluewater Beach. In the first set of calculations, model predictions were carried out with incident nonlinear waves without any group-like modulation. In the remaining calculations (set 2 and set 3), wave-bed interactions were induced by modulated wave trains with some properties of groupiness observed in the coastal wave field.

In the analysis presented, quasi-steady flows (undertow) and low-frequency group-bound waves are not considered. The first simplification is sustained by observations from Bluewater Beach (Osborne and Greenwood 1992). The results of these observations show that despite evidence of steady flow contribution to sediment transport, the changes seen in bar morphology correlated only partially with measured transport rates. The second assumption is based on conclusions from the DUCK'85 field experiment. In this experiment, low-frequency group-bound waves and other secondary, low-frequency flows were

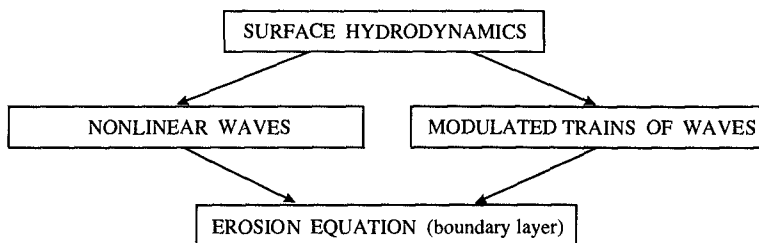


Figure 5: Schematic presentation of modeling non-modulated and modulated wave trains.

shown to contain lower energy levels than oscillations at wind-wave-induced frequencies (List 1991).

To predict the spatial and temporal evolution of the bed morphology under waves, we applied our two-dimensional morphological model (see, e. g., Boczar-Karakiewicz *et al.* 1995). In this modular model, the surface wave induces a nearbed flux of sediment, resulting in a deformation of the underlying seabed. For nonlinear incident, non grouped waves, surface hydrodynamics are described by a simplified Bussinesq equation (Boczar-Karakiewicz *et al.* 1987). To simulate incident trains of wave groups we have modified the original description of the surface wave. In this simulation, group-like modulations in the incident wave train result from superposition of two waves of similar frequency. The original and modified approaches are shown schematically in Figure 5. In all calculations, incident wave conditions are given at the deep-water end of a two-dimensional coastal zone. The initial topography, a uniform featureless slope, corresponds to mean slopes observed at Bluewater Beach (broken line in Fig. 6c).

In the first set of calculations, we analyzed the morphological response to incident nonlinear waves without any group-like modulation (Fig. 6). The spatial evolution of the surface wave (Fig. 6a and 6b) and the temporal change of the underlying bed from the initial featureless slope (broken line in Fig. 6c) to a final multibar profile (heavy line in Fig. 6c) are predicted for an extreme storm event. This event is simulated in the model by a train of regular waves with period T ($T = T_p = 6.9$ s), where T_p denotes the peak period of extreme storms at Bluewater Beach. (In the results presented, the amplitudes of harmonic wave components are non-dimensionalized by the amplitude of the incident wave.)

The temporal evolution of waves and morphology is shown in more detail in Figure 7. The morphological time scale τ (Fig. 7a) characterizing the formation of a multibar morphology from an initially featureless slope is of the order of hundreds of thousands of wave periods. The comparisons presented in Figure 7b show satisfactory agreement between the predicted and observed number of bars and bar-crest locations.

For a sequence of incident waves simulating a typical season (extreme winter

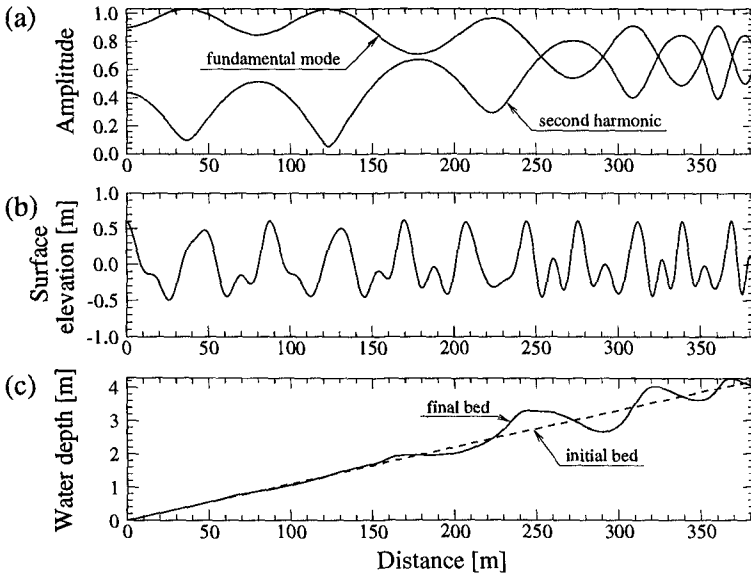


Figure 6: Prediction of wave and morphology evolution under nonlinear waves without group-like modulation (simulation of an extreme storm event with $T_p = 6.9$ s): (a) amplitude of the two first harmonic modes, (b) free-surface elevation, (c) initial and final bed.

storms followed by moderate summer wave conditions, with $T_p = 6.9$ s and $T_p = 3.5$ s, respectively), the model correctly reproduces the observed seasonal variability of the shoreface morphology that transforms from a multiple bar profile into a single bar, as observed at Bluewater Beach (Fig. 3; see also Boczar-Karakiewicz and Jackson 1991, Boczar-Karakiewicz *et al.* 1995).

In the second set of calculations, we simulated the linear effects of groupiness on coastal morphology. In this calculation presented in Figure 8, the group-like modulated wave train (Fig. 8a) propagates over the featureless mean slope of Bluewater Beach (Fig. 8b) without interacting with the underlying bed. A similar result is obtained for an initial multibar bed profile which remains unchanged under a train of linear wave groups (see again Fig. 8b). The amplitude modulation in the train of linear wave groups at $x = 100$ m is shown in Figure 9. Modulation results from a superposition of two waves of similar frequency, derived from the peak period, $T_p = 6.9$ s, of extreme storm events observed at Bluewater Beach.

In the third set of calculations shown in Figure 10, surface hydrodynamics are again induced by a group-like modulation (in the frequency band of extreme storms at Bluewater Beach). In contrast to previous experiments with linear wave groups (set 2), we have imposed spatial, nonlinear energy flow between

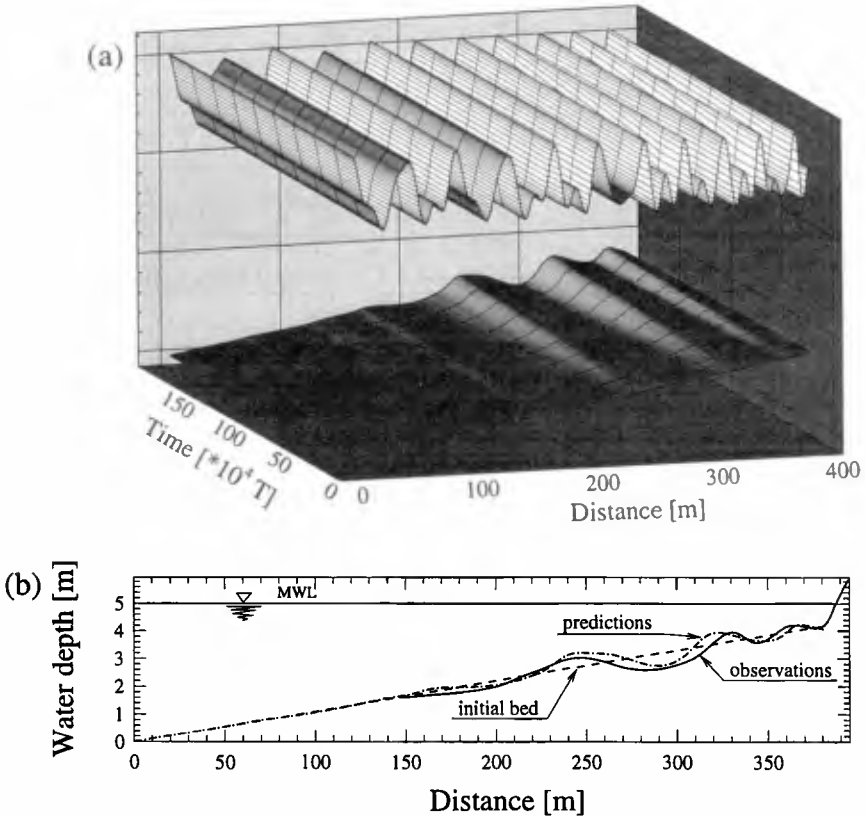


Figure 7: Prediction of morphology evolution under nonlinear waves without group-like modulation (simulation of an extreme storm event with $T_p = 6.9\text{s}$): (a) temporal evolution of waves and morphology, (b) predicted and observed multibar morphology.

fundamental modes of the incident wave train in the present simulation (see Fig. 10a). This pattern results from the solution of approximated Boussinesq equations (Fig. 5; Boczar-Karakiewicz *et al.* 1987). The spatial view of the resulting surface elevation is shown in Figure 10b. The velocity field of simulated wave groups generates nearbed sediment fluxes that gradually deform the underlying bed. Eventually, at time τ ($\tau = 10^4 T_p$), the initially-featureless, uniform slope (broken line in Fig. 10c), evolves into an equilibrium configuration (solid line in Fig. 10c). In the deeper part of the shoreface (at 0-260 m, Fig. 10c), the initial featureless slope remains nearly intact. In the shallower part (at 260-380 m in Fig. 10c), the initial bed deforms into multibar morphology. The spatial distribution of bar crests correlates with the nonlinear pattern of the imposed energy exchange among fundamental modes of the wave group

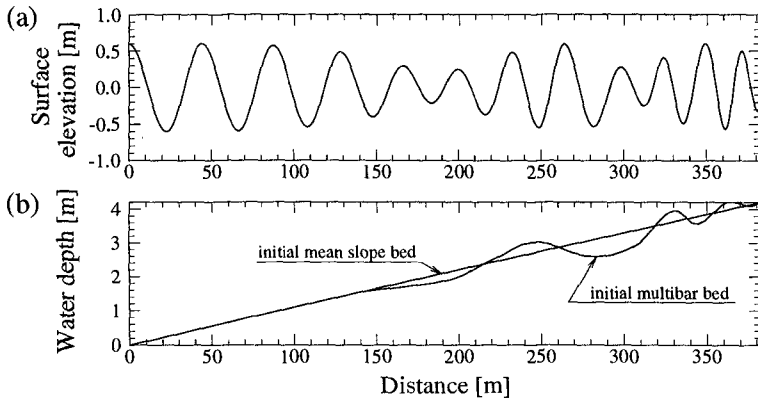


Figure 8: Evolution of waves and morphology under group-like modulated wave train (linear case): (a) free-surface elevation, and (b) shoreface morphology.

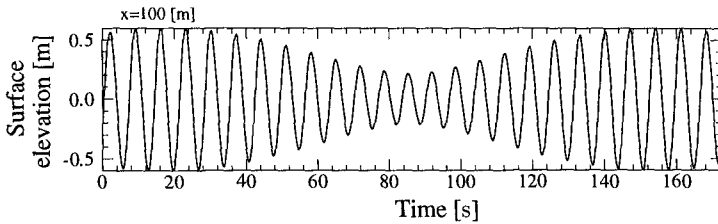


Figure 9: Time history of the incident bimodal wave train (linear case)

(Fig. 10a).

Figure 11 shows, at three chosen locations indicated in Figure 10c, the time history of surface elevation in nonlinear simulation. These records indicate strict periodicity in the time domain, T . In contrast, velocity records from field measurements show evidence of pronounced temporal irregularity in observed wave groups (see again Fig. 1a). The reported results of model calculations suggest that large-scale morphology in coastal zones responds to the passage of nonlinear waves. In both nonlinear cases considered (set 1 and set 3), a rhythmical bed configuration is generated by waves characterized by large-scale nonlinear modulation in their amplitudes. The process of bar formation (Fig. 6 and Fig. 10) and bar transformation (Fig. 4) lasts over time denoted by τ in Figure 6. This morphological time scale τ is several orders of magnitude lower than the hydrodynamical scale T , characterized by the wave period of the incident wind wave.

In contrast, the large-scale coastal morphology (featureless uniform slope and a multibar profile) does not respond to the passage of trains of linear wave groups. This conclusion explains observations reported from the study

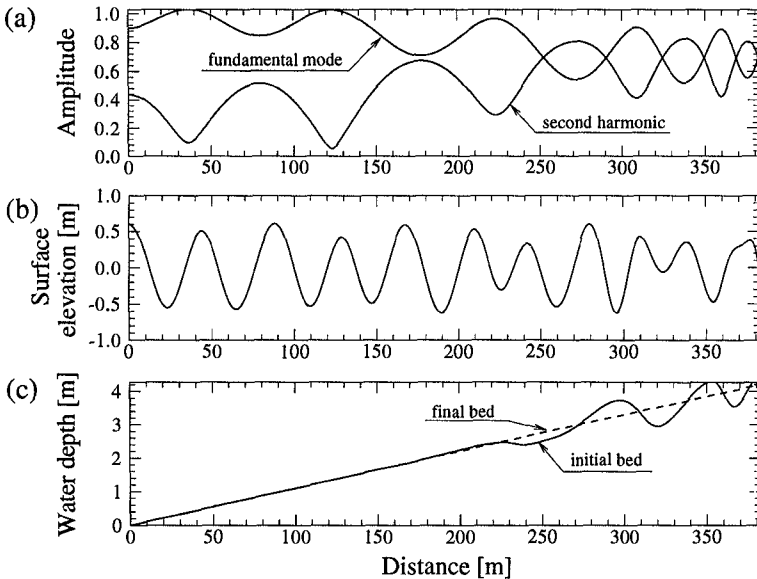


Figure 10: Evolution of waves and morphology under a group-like modulated wave train (nonlinear case): (a) initial spatial modulation of wave amplitudes, (b) free-surface elevation, and (c) shoreface morphology.

site according to which the deeper lying outer bar and the lakeward slope of the inner bar were unaltered during the monitored moderate summer storm (with peak period waves $T_p = 3.5$ s). During this storm, part of the unaltered underwater beach was located in a deep-water region for both the incident peak period wave and for observed wave groups related to summer wave conditions (see, e.g., Fig. 8).

4. CONCLUSION

1. Model predictions show that nonlinearly-modulated wave trains may potentially form and modify sand bars in coastal zones. These morphological changes are correlated with large-scale spatial variation in the nonlinear structure of these waves.
2. The predictions presented with strictly periodic nonlinearly-modulated waves suggest that sand bars are formed over time scales in the order of hundreds of thousands of wave periods. Velocity records from Bluewater Beach reveal strong irregularities in observed wave groups and related episodic sediment concentration events. Therefore, on natural coasts, these irregular wave groups do not represent an effective factor in sand bar generation.

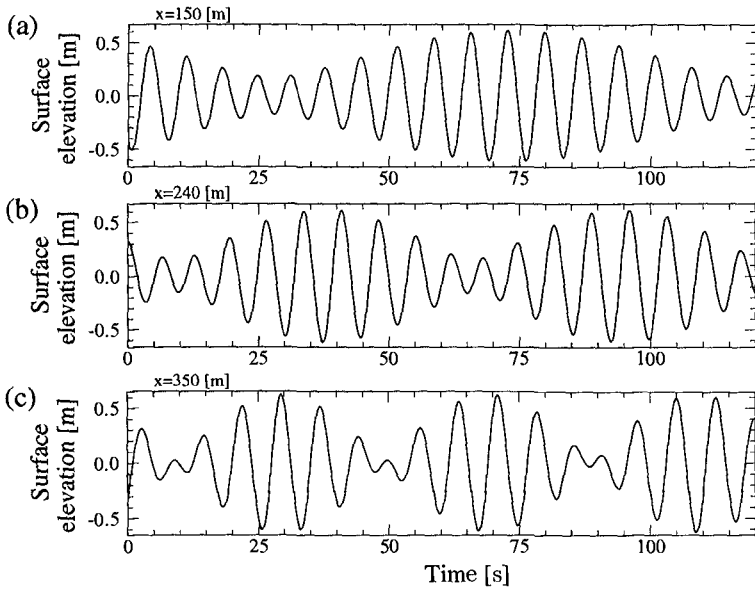


Figure 11: Time history of the shoaling group-like modulated wave train (in three chosen cross sections of the shoreface indicated in Fig. 10).

- Predictions and observations show that trains of linear wave groups do not interact with the large-scale nearshore morphology.

5. REFERENCES

- Battjes, J.A. and V. Vledder. 1984. Verification of Kimura's theory for wave group statistics. *Proceedings of the 19th International Conference of Coastal Engineering, American Society of Civil Engineers, Cape Town* : 642-648.
- Boczar-Karakiewicz, B., D.L. Cohen and J.L. Bona. 1987. Interaction of shallow water waves and bottom topography. *Dynamical problems in continuum physics. Mathematics and its applications*. J.L.Bona, ed., Springer Verlag, New York, NY, 4: 131-176.
- Boczar-Karakiewicz, B., D.L. Forbes and G. Drapeau. 1995. Formation and stability of coastal bars in the Gulf of St. Lawrence. *J. Waterways, Port, Coastal and Ocean Eng.* American Society of Civil Engineers, 129 : 49-60.
- Boczar-Karakiewicz, B. and L.A. Jackson. 1991. On the protection of a beach system, Gold Coast, Queensland, Australia. *Proceedings 22nd International Conference of Coastal Engineering, American Society of Civil Engineers, Delft*: 2265-2278.

- List, J.H. 1991. Wave groupiness variations in the nearshore. *Coastal Engineering*, 15: 475-496.
- List, J.H. 1992. A model for the generation of two-dimensional surf beat. *J. Geophys. Res.*, 97, (C4): 5623-5635.
- Medina, J.R. and R.T. Hudspeth. 1990. A review of the analyses of ocean wave groups. *Coastal Engineering*, 14: 515-542.
- Nwogu, O. 1993. Alternative form of Boussinesq equations for nearshore wave propagation. *J. Waterways, Port, Coastal and Ocean Eng.* American Society of Civil Engineers, 129 : 618-638.
- Osborne, P.D. and B. Greenwood. 1992. Frequency dependent cross-shore suspended sediment transport. 2. A barred shoreface. *Marine Geol.*, 106: 45-51.
- Talipova, T., E. Pelinovsky and E. Kit. 1995. Wind wave simulation in coastal zone. *Proceedings of the International Conference Coastal Dynamics'95*, American Society of Civil Engineers, Gdańsk, Poland: 105-127.

CHAPTER 275

COASTAL MORPHODYNAMIC INSTABILITIES

Albert Falqués, Amadeu Montoto and Vicente Iranzo ¹

Abstract

An initially plane beach is considered with waves incoming obliquely. For this basic steady state the Longuet-Higgins solution is used to give set-up and longshore current. The beach is assumed to be erodible. Then, a stability analysis is performed considering infinitesimal disturbances in the current, the free surface and the sea bottom. The basic undisturbed state is found to be unstable giving rise to topographic features similar to oblique or transverse bars and to a meandering in the longshore current. Some comparison with the earlier work by Christensen et al., 1994, is made.

1. Introduction

Beach topography often show tridimensional patterns with some kind of recurrence or rhythmicity in the alongshore direction. Typical examples are oblique/transverse bar systems, crescentic longshore bars, ridge and runnel systems, etc. The explanation for rhythmic topography has followed to main theoretical approaches: i) the infragravity wave influence on sediment transport and distribution (see for instance, Holman and Bowen, 1982) and ii) the morphodynamic instability of the surf-zone under the action of the incoming waves and the longshore current (see Hino, 1974 and Christensen et al., 1994). The basic idea in this latter approach is as follows. Given an initial beach topography, the incoming waves produce some currents. This currents carry sediments and this sediment transport can produce changes in the topography which in turn affects the incoming wave field and the current. In this way there is a feedback and if some perturbation within this loop produces a positive feedback the perturbation will start to grow. Then an instability arises leading to topographic features. In earlier works (Falqués et al., 1996a, Falqués et al., 1996b) the instability of the current-sea bed system

¹ Departament de Física Aplicada, Universitat Politècnica de Catalunya, 08034 Barcelona, Spain

keeping fixed the incoming wave field was analyzed (bed-flow instability). The aim of the present contribution is to include the effect of the perturbations in the incoming wave field. In this way we reproduce and extend the results of Hino, 1974, and Christensen et al., 1994, with a different numerical model. Special attention is paid to the bar shape and orientation, the systematic trends with respect to bottom friction and other parameters and the influence of lateral momentum diffusion.

2. Model equations

Since our aim is to look at large 2D horizontal patterns in the near shore, a 2D shallow water model with time-average over incoming wave period is considered. As governing equations we take the momentum equations:

$$\frac{\partial \vec{v}}{\partial t} + \vec{v} \cdot \nabla \vec{v} + g \nabla z_s - \frac{\vec{\tau}_b}{\rho \zeta} - \vec{\mathcal{V}} = \frac{1}{\rho \zeta} \nabla \cdot S \quad (1)$$

the mass conservation equation

$$\frac{\partial \zeta}{\partial t} + \nabla \cdot (\zeta \vec{v}) = 0 \quad (2)$$

and the sediment conservation equation

$$\frac{\partial z_b}{\partial t} + \nabla \cdot \vec{q} = 0 \quad (3)$$

A cartesian coordinate system is assumed with x cross-shore, y alongshore and z vertical upwards (see Fig.1). $\zeta = z_s - z_b$ is the total depth, $\vec{\tau}_b$ the bottom friction and S is the radiation stress tensor. The lateral momentum diffusion terms read:

$$v_i = \frac{1}{\zeta} \sum_{j=1}^2 \frac{\partial}{\partial x_j} [\nu_t \zeta (\frac{\partial v_i}{\partial x_j} + \frac{\partial v_j}{\partial x_i})] \quad i = 1, 2 \quad (4)$$

Here, $x_1 = x$ and $x_2 = y$. The sand transport is parametrized by the formula:

$$\vec{q} = \nu |\vec{v}|^m (\frac{\vec{v}}{|\vec{v}|} - \gamma \nabla h) \quad (5)$$

where h is any bottom perturbation with respect to equilibrium and where the term $\gamma \nabla h$ takes account of the tendency of the sand to move downslope. The exponent m has been set to 3 which is suitable for bed-load transport and $\gamma \sim 1$. Now we are going to perform a linear stability analysis for the system of equations 1, 2, 3. First, let us consider a basic steady equilibrium. In this state we assume waves incoming obliquely on the beach (see Fig. 2). The equilibrium consists of a set-up/down in the mean water level and a longshore current. For simplicity so that to be able to use analytical expressions, we will use the Longuet-Higgins solution (Horikawa, 1988). Thus, we assume a saturated surf zone, $H = \gamma_b \zeta$, $x \leq X_b$. The bottom friction (weak current and small angle) is given by

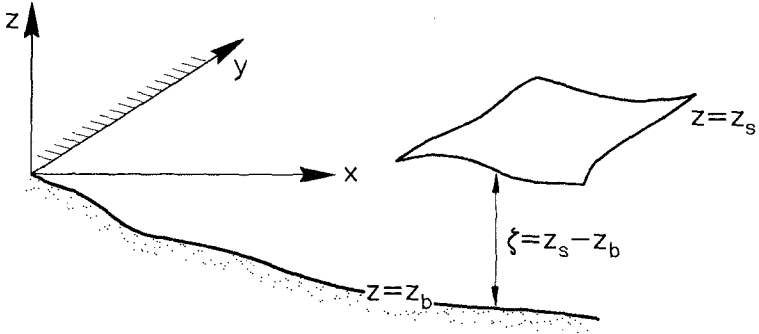


Figure 1: coordinate system.

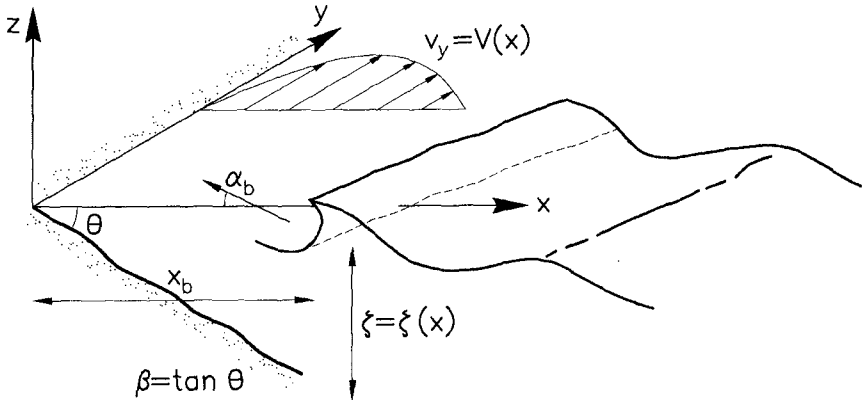


Figure 2: basic steady equilibrium.

$$\tau_{bx} = -\frac{4}{\pi} \rho c_f u_0 v_x \quad , \quad \tau_{by} = -\frac{2}{\pi} \rho c_f u_0 v_y \quad (6)$$

and the eddy viscosity reads $\nu_t = Nx\sqrt{g\xi}$.

Consider now a small perturbation on the basic equilibrium of the form:

$$\begin{aligned} \vec{v} &= (0, V(x)) + (\hat{u}(x), \hat{v}(x))e^{\sigma t +iky} \\ z_s &= z_s^0(x) + \hat{\eta}(x)e^{\sigma t +iky} \\ z_b &= z_b^0(x) + \hat{h}(x)e^{\sigma t +iky} \end{aligned}$$

where $\lambda = 2\pi/k$ is the wavelength or the alongshore spacing of the growing bedforms. Then, by linearizing equations 1, 2, 3 we obtain:

$$\frac{\partial u}{\partial t} + V \frac{\partial u}{\partial y} + g \frac{\partial \eta}{\partial x} = \left[\frac{\tau_{bx}}{\rho \zeta} \right]^{\mathcal{L}} + [\mathcal{V}_x]^{\mathcal{L}} + \left[\frac{1}{\rho \zeta} \left(\frac{\partial S_{xx}}{\partial x} + \frac{\partial S_{xy}}{\partial y} \right) \right]^{\mathcal{L}} \quad (7)$$

$$\frac{\partial v}{\partial t} + V \frac{\partial v}{\partial y} + \frac{dV}{dx} u + g \frac{\partial \eta}{\partial y} = \left[\frac{\tau_{by}}{\rho \zeta} \right]^{\mathcal{L}} + [\mathcal{V}_y]^{\mathcal{L}} + \left[\frac{1}{\rho \zeta} \left(\frac{\partial S_{yx}}{\partial x} + \frac{\partial S_{yy}}{\partial y} \right) \right]^{\mathcal{L}} \quad (8)$$

$$\frac{\partial \eta}{\partial t} - \frac{\partial h}{\partial t} + [\nabla \cdot (\zeta \vec{v})]^{\mathcal{L}} = 0 \quad (9)$$

$$\frac{\partial h}{\partial t} + [\nabla \cdot \vec{q}]^{\mathcal{L}} = 0 \quad (10)$$

These equations are too long to be written here in detail in such a way that we abbreviate 'linear part of' by

$$[\cdot]^{\mathcal{L}}$$

The perturbation in the radiation stress terms will be called bed-surf terms since they describe the perturbation in the incoming wave field due to growing bedforms. The perturbation in the wave refraction should be also included in the bed-surf terms but this has not been done in the present work. The remaining terms in the linearized equations if bed-surf effect is neglected will be called bed-flow terms since they describe the perturbation in the current due to the growing bedforms if the forcing by the waves is kept fixed.

Before solving the linear problem, a scaling and some non-dimensional parameters will be introduced. As horizontal lengthscale, the width of the surf zone, $L_H = X_b$, is chosen and $L_V = \beta X_b$ will be the vertical scale where β is the beach slope (see Fig.3). The velocity scale is the scale for the Longuet-Higgins model,

$$U = \frac{5\pi}{16} \frac{\gamma_b}{c_f} \sqrt{g \zeta_b} \beta' \sin \alpha_b$$

where β' is the effective beach slope including set-up and α_b is the wave angle with respect to the cross-shore at breaking. Two time scales appear, $T_h = L_H/U$, $T_m = L_H L_V/Q$, where $Q = \nu U^m$ is the scale for sediment transport. The second one arises in a natural way from the sediment conservation equation (10) and will be called morphological time scale. It is the scale at which bedforms are expected to grow. The first one will be called hydrodynamical time scale and it is much shorter than the other one.

The variables are made nondimensional by means of:

$$(x, y) = L_H(x', y') \quad , \quad z_b = L_V z'_b \quad , \quad z_s = \frac{U^2}{g} z'_s$$

$$(u, v) = U(u', v') \quad , \quad t = T_m t'$$

Then, we deal with non-dimensional linear equations with the following dimensionless parameters. First a nondimensional wavenumber and growth rate, $k' = kL_H, \sigma' = \sigma T_m$. Also, the breaking index, γ_b , the wave angle at breaking, α_b and the viscosity parameter, N , appear. The parameter related to the tendency of the sediment to go downslope now become $\gamma' = \gamma\beta$. An important parameter is the characteristic Froude number of the longshore current, $F = U/\sqrt{gL_V}$ and the frictional parameter, $r = c_f/\beta$. Finally, the ratio between both time scales, $\epsilon = T_h/T_m$, is very small but not set to 0 (which is usually called quasi-steady hypothesis. See 'response time concept' in Christensen et al, 1994). In this way, the model allows for the computation of purely hydrodynamic instabilities like shear waves or even for the possible interaction between both kind of instabilities. However, we have focussed only in morphological instabilities for the present contribution. Hereinafter, nondimensional quantities will be handled dropping accents for simplicity.

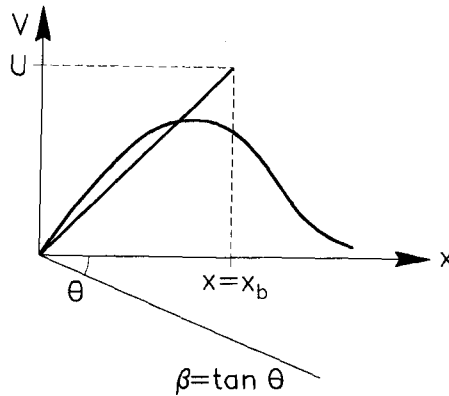


Figure 3: scaling.

Finally, equations (7),(8),(9) and (10) result in an eigenproblem where the eigenvalue is the growthrate, σ , and the eigenfunctions the perturbations $(\hat{u}(x), \hat{v}(x), \hat{\eta}(x), \hat{h}(x))$. This problem is discretized by a numerical spectral method. In the next section, an indication is given of the solution procedure.

3. Numerical method

For simplicity, we will illustrate the numerical method by means of a simpler eigenproblem than (7)-(10). Consider the differential equation

$$p(x)u''(x) + q(x)u'(x) + r(x)u(x) = \sigma u(x) \quad 0 < x < \infty \quad (11)$$

with boundary conditions $u(0) = u(\infty) = 0$. Here, σ is the eigenvalue and $u(x)$ the eigenfunction.

The method uses an expansion in Chebyshev polynomials and a

transformation from $[0, \infty)$ to $[-1, 1)$. First, this map is given by

$$x = \phi(z) = l \frac{1 - z}{1 + z} \tag{12}$$

(see Falqués and Iranzo, 1994).

Second, an expansion in Chebyshev polynomials is assumed:

$$u(x) = \sum_{n=0}^N \hat{u}_n T_n(z) = \sum_{n=0}^N \hat{u}_n T_n(\phi^{-1}(x)) \tag{13}$$

The following step is to find a combination of Chebyshev polynomials which verify the boundary conditions. The $N-1$ functions which satisfy this requirement are:

$$g_n(x) = T_n(\phi^{-1}(x)) - \frac{1}{2}(1 + (-1)^n)T_0(\phi^{-1}(x)) - \frac{1}{2}(1 + (-1)^{n+1})T_1(\phi^{-1}(x)) \tag{14}$$

where $n = 2, 3, \dots, N$. Then, expansion (13) is substituted by

$$u(x) = \sum_{n=2}^N \hat{u}_n g_n(x) \tag{14}$$

where the unknowns (eigenvector) are the $N - 1$ coefficients $\hat{u}_2, \dots, \hat{u}_N$.

Now, to discretize equation (11) we will apply collocation at the Gauss-Lobatto nodes $z_i = \cos(\pi i/N)$ transformed by the map (12) (Falqués and Iranzo, 1994). For this purpose, the first step is to know the values of g_n at the nodes. This is given by the matrix $G_{ij} = g_j(x_i)$, so that

$$u(x_i) = \sum_{n=2}^N G_{in} \hat{u}_n$$

In a similar way, the first derivative of u will be given by a matrix G' :

$$u'(x_i) = \sum_{n=2}^N G'_{in} \hat{u}_n$$

where $G'_{in} = g'_n(x_i)$ can be computed by using the derivatives of the Chebyshev polynomials and the map (12). Similarly, the second derivative will be computed by

$$u''(x_i) = \sum_{n=2}^N G''_{in} \hat{u}_n$$

where $G''_{in} = g''_n(x_i)$ can also be computed by means of the derivatives of the Chebyshev polynomials and the map (12). Explicit expressions of the

derivatives of Chebyshev polynomials combined with (12) can be found in Falqués and Iranzo, 1994.

Finally, after performing collocation at x_i , $i = 1 \dots N - 1$ the discretized eigenproblem reads:

$$p(x_i) \sum_{k=2}^N G''_{ik} \hat{u}_k + q(x_i) \sum_{k=2}^N G'_{ik} \hat{u}_k + r(x_i) \sum_{k=2}^N G_{ik} \hat{u}_k = \sigma \sum_{k=2}^N G_{ik} \hat{u}_k$$

where the eigenvector is $(\hat{u}_2 \dots \hat{u}_N)$.

4. Results

One of the drawbacks of Hino model, 1974, without the quasisteady hypothesis, i.e., hydrodynamic instabilities out of control, has been solved. All hydrodynamic instabilities could be identified as shear waves with a clear maximum in the $\sigma - k$ curve. Shear waves have growth rates an order ϵ^{-1} larger than bed wave growth rates. By comparison with other models (Falqués and Iranzo, 1994) they could be recognized. Usually, however, when a realistic friction and viscosity parameters are chosen, no hydrodynamic instabilities appear. Figure 4 shows the nondimensional growth rate $Re(\sigma)$ as a function of the wavenumber k , for three different cases. In one set of curves only bed-flow terms were kept in the equations while in the other set the full equations (bed-flow + bed-surf) were considered. It can be seen that bed-surf, that is, the effect of the wave field perturbation enhances significantly the instability. This was also found by Christensen et al., 1994. Also, bed-surf gives shorter spacing between the bedforms. The imaginary part of σ is not shown here. It is negative and of order one. This means that the topographic waves migrate downcurrent with a speed of the order L_H/T_m .

Regarding the shape of the topographic features, two kind of bedforms were found. First what we call current dominated bedforms. In this case, the shape of the bars looks very similar when only bed-flow terms were taken or when bed-flow and bed-surf were considered. The bars are upcurrent rotated, very oblique (a small angle with the shoreline of the order of 10°). These topographic waves come out in the case of a relatively high characteristic Froude number, say $F > 0.6$ (note that this is not the maximum local Froude number which can be smaller). According to

$$F = \frac{U}{\sqrt{g\zeta_b}} = \frac{5\pi}{16} \frac{\gamma_b}{\sqrt{1 + 0.375\gamma_b^2}} \frac{\sin \alpha_b}{r} \quad (15)$$

this corresponds to small frictional parameter, r , and large angle, α_b . Figure 5 shows how the bottom perturbations with only bed-flow and with bed-flow and bed-surf look quite similar. Figure 7 shows the full equation bedform when the basic slope is added to the perturbation.

Second, we found what we call wave-dominated bedforms. In this case the shape of the bars with only bed-flow or with bed-flow and bed-surf looks

quite different. With only bed-flow they are similar to alternate bars in a river and in the other case they are similar to transverse bars slightly upcurrent rotated (see Fig.6). Figure 8 shows, in this case, the total topography with bed-flow and bed-surf. Wave-dominated bedforms appear for small Froude number, say $F < 0.6$, that is, for large frictional parameter and small angle.

An important issue of morphological models for rhythmic features is the alongshore spacing or wavelength. This is found by looking at the fastest growing wavenumber, i.e., the maxima in the σ_r, k curves for different values of the parameters. From experimental data (usually from the spacing between rip currents assumed to be related to rhythmic topography) the wavelength to surf zone width ratio is in the order $\lambda/X_b \sim 1.5 - 8$. The mean value is between 3 and 4 (Sasaki and Horikawa, 1975). Christensen et al., 1994 found a ratio about 6. In our modelling this ratio ranges between 1 and 7, depending on the frictional parameter, r , and on the wave angle, α_b . It decreases with increasing r and with decreasing α_b (see Fig. 9).

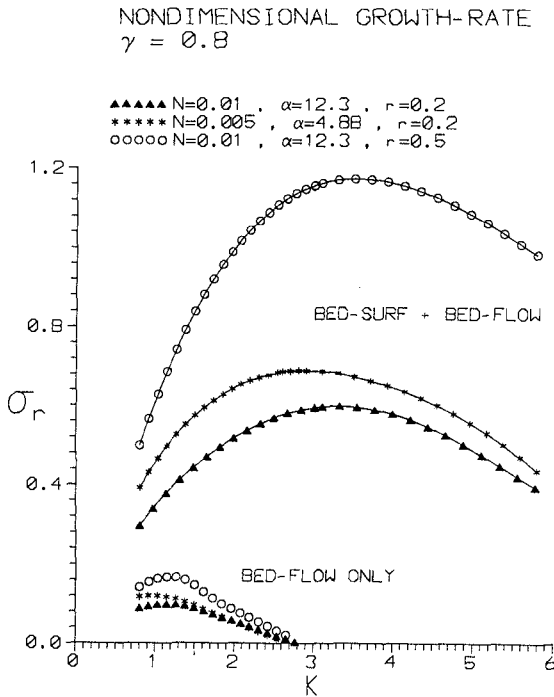


Figure 4: growthrate as a function of wavenumber for three sets of parameters. $F = 0.3, \epsilon = 0.001, \gamma = 0.01$.

The growing bedforms produce a meandering in the longshore current. According to our simulation, the current is deflected offshore over the shoals

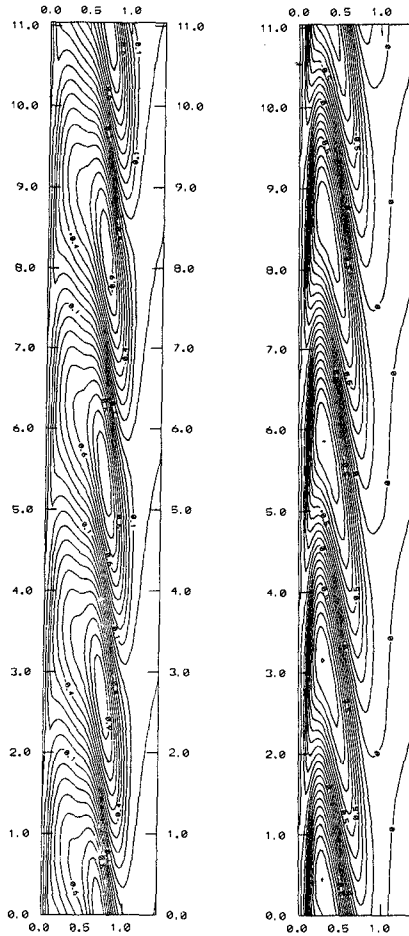


Figure 5: perturbation in the bottom for $r = 0.1$, $\alpha_b = 12.3^\circ$, $F = 0.8$, $N = 0.005$, $\gamma_b = 0.4$, $k = 1.14$. Right: only bed-flow, left= bed-flow and bed-surf. In this plot the current runs from the bottom to the top.

and inshore over the pools (see Fig.10). Thinking of rip currents, this is in contrast with many observed rip currents. But two things have to be taken into account. First this is the initial growth. It could be that for finite amplitude features this behaviour would be reversed leading to a non-linear saturation of the growth. Second, these are not exactly rip currents but just the

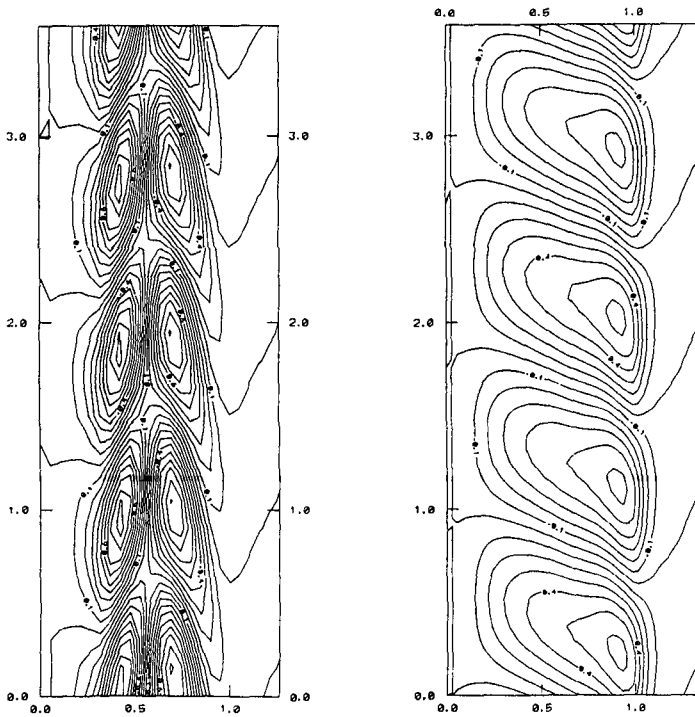


Figure 6: perturbation in the bottom for $r = 0.5$, $\alpha_b = 12.3^\circ$, $F = 0.16$, $N = 0.005$, $\gamma_b = 0.4$, $k = 3.5$. Right: only bed-flow, left= bed-flow and bed-surf. In this plot the current runs from the bottom to the top.

deflection of the longshore current. Also Christensen et al., 1994, found the same behaviour.

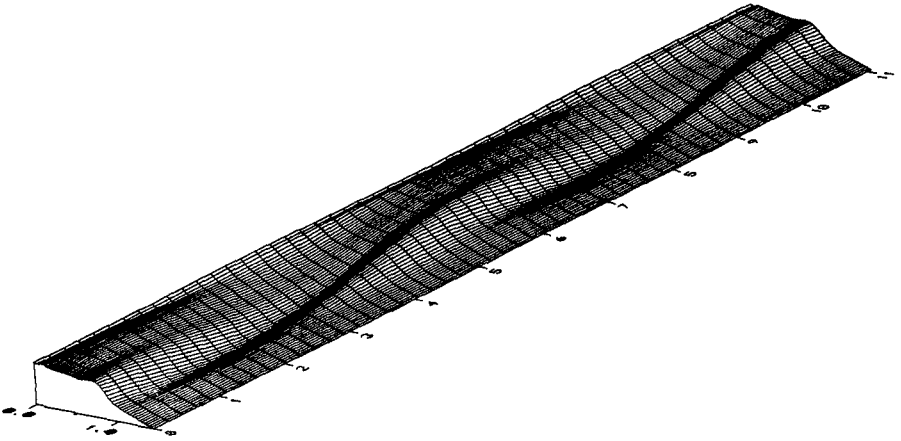


Figure 7: bottom topography for $r = 0.1$, $\alpha_b = 12.3^\circ$, $F = 0.8$, $N = 0.005$, $\gamma_b = 0.4$, $k = 1.14$. Basic slope plus perturbation (with arbitrary amplitude since we are dealing with a linear problem). Current running from left to right.

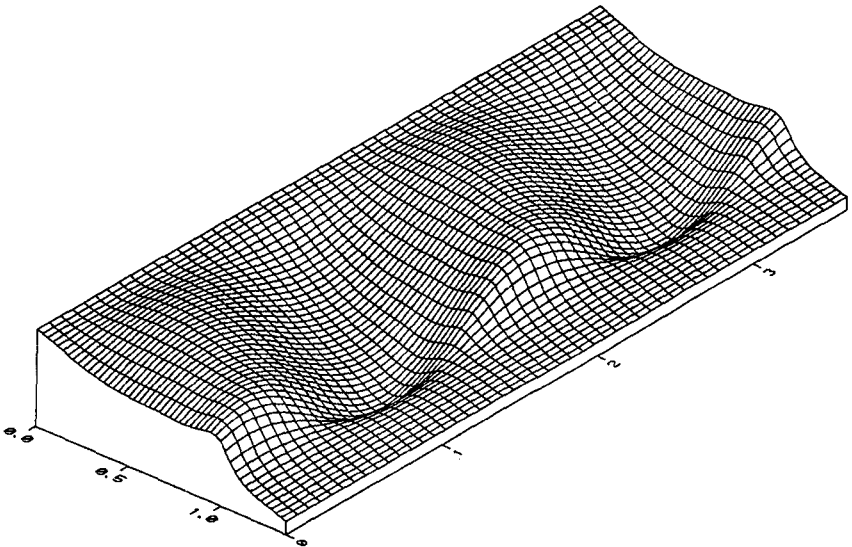


Figure 8: bottom topography for $r = 0.5$, $\alpha_b = 12.3^\circ$, $F = 0.16$, $N = 0.005$, $\gamma_b = 0.4$, $k = 3.5$. Basic slope plus perturbation. Current running from left to right.

5. Conclusions

It has been shown that the topography of a plane beach can be unstable due to the interaction with the incoming waves and the longshore current. The effect of the perturbation on the waves (bed-surf) turns out to be the most de-stabilizing. This is in line with Christensen et al., 1994. The instability produces the growth of upcurrent rotated bars which is also in agreement with the earlier work of Christensen et al. However, as these authors pointed out, this is sometimes in agreement with the observed bars in the field and sometimes is in contrast. We found two kind of topographic features: i) 'current dominated' (large angle, small friction) and ii) 'wave dominated' (small angle, large friction). Instead of fixed values of the alongshore spacing

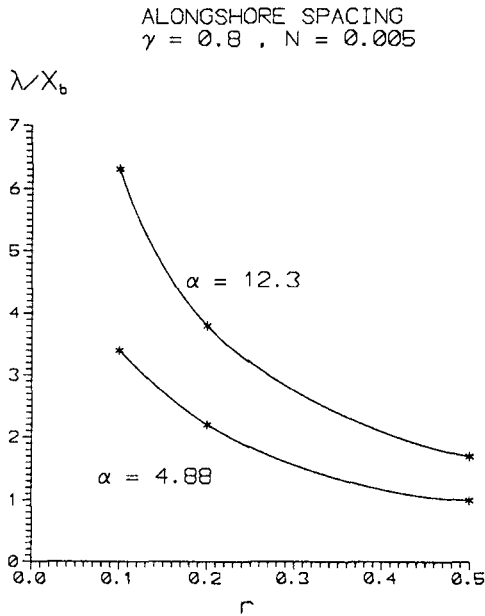


Figure 9: Alongshore spacing of the topographic waves.

λ/X_b (4 in the case of Hino and 6 in the case of Christensen et al.,) our alongshore spacing ratio ranges from 1 to 7, decreasing for increasing r , and depending on α_b and N . Finally, the growing bedforms produce a small meandering of the longshore current with an offshore deflection over the shoals. This can be a little surprising but it is also in line with earlier results of Christensen et al. Clearly, more research is needed to clarify the mechanism which produces this perturbed flow in combination with the perturbation in the set-up.

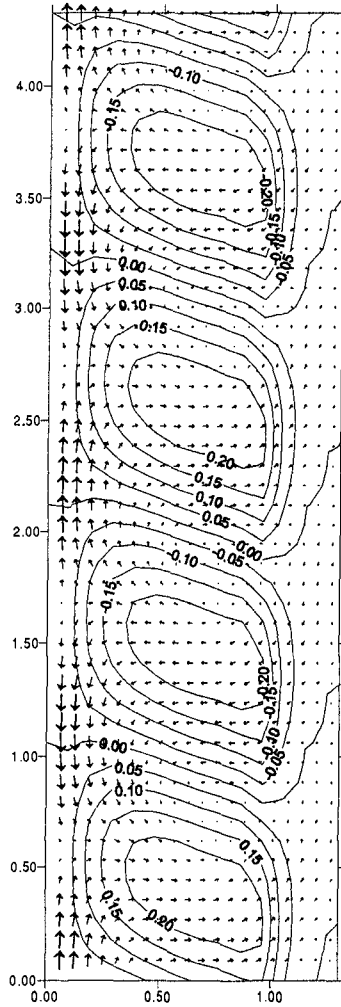


Figure 10: wave-dominated bedform and the perturbation produced on the current. Note the offshore deflection over the shoals. $r = 0.2$, $\alpha_b = 4.88^\circ$, $F^2 = 0.3$, $N = 0.005$, $\gamma_b = 0.8$. Basic current running from bottom to top.

Acknowledgements

This work has been funded by the Spanish government (DGICYT) under contract PB93-0948. Part of the work of A.Falqués has been done in Utrecht University (IMAU) funded by RIKZ (Netherlands Institute of Coastal Management).

References

- Christensen,E.,Deigaard,R.and Fredsoe,J.,1994. Sea bed stability on a long straight coast 24th Int. Conf. Coastal Engineering, 1865-1879.
- Falqués,A. and Iranzo,V.,1994. Numerical simulation of vorticity waves in the nearshore. J.Geophys. Res., 99, 825-841.
- A.Falqués, A.Montoto and V.Iranzo, 1996a. Bed-Flow instability of the longshore current. Cont.Shelf Res. (in press).
- A.Falqués, A.Montoto, V.Iranzo, 1996b. Bed-flow instability of longshore currents. XXI European Geophysical Society General Assembly, The Hague, 6-10 May 1996.
- Hino,M.,1974. Theory on formation of rip-current and cuspidal coast 14th Int. Conf. Coastal Engineering, 901-919.
- Holman,R.and Bowen,A.,1982. Bars, bumps, and holes: models for the generation of complex beach topography J.Geophys. Res.,87,457-468.
- K.Horikawa(editor), 1988. Nearshore Dynamics and Coastal Processes. University of Tokio Press.
- Sasaki,T. and Horikawa,K., 1975. Nearshore current system on a gently sloping bottom. Coastal Eng. in Japan, 18, 123-143.

CHAPTER 276

On validation of a sand waves and sand banks model

S. J. M. H. Hulscher *

Abstract

A morphological model is described for the interaction between tidal motion and an erodible bed. This model is able to distinguish between a flat bed, and the generation of tidal sand banks and/or sand waves, based on physical parameters. The physical meaning of the turbulence parameters A_v and S , as used in this model is subject of discussion in the present paper, therefore a simpler system is investigated. A simple flow is described by a logarithmic profile model (a generally accepted turbulence model), as well as by a partial slip model, using A_v and S . It is shown that the two models can be calibrated such that they produce the same bed shear stress, depth-averaged velocity and depth-averaged eddy viscosity. This leads to expressions for A_v and S as function of the roughness height and a shape parameter in the logarithmic profile model. Application of this information to two locations shows that the bed form prediction model gives encouraging results.

1 Introduction

The offshore seabed of shallow seas is covered with rhythmic patterns on a large scale, see e.g. *Off* [1963]. Tidal sand banks have wavelengths of about five kilometers and reach heights up to 40 meters. Sand waves, see figure 1 are smaller, wavelengths of 500 meters, heights up to 10 meters. Both patterns are shown in a schematic way in figure 2. When these two patterns overlap, the crests are oriented differently (angle between 60° - 90°), which suggests that these two patterns

*Civil Engineering & Management, University of Twente, P.O. box 217, 7500 AE, Enschede, The Netherlands.

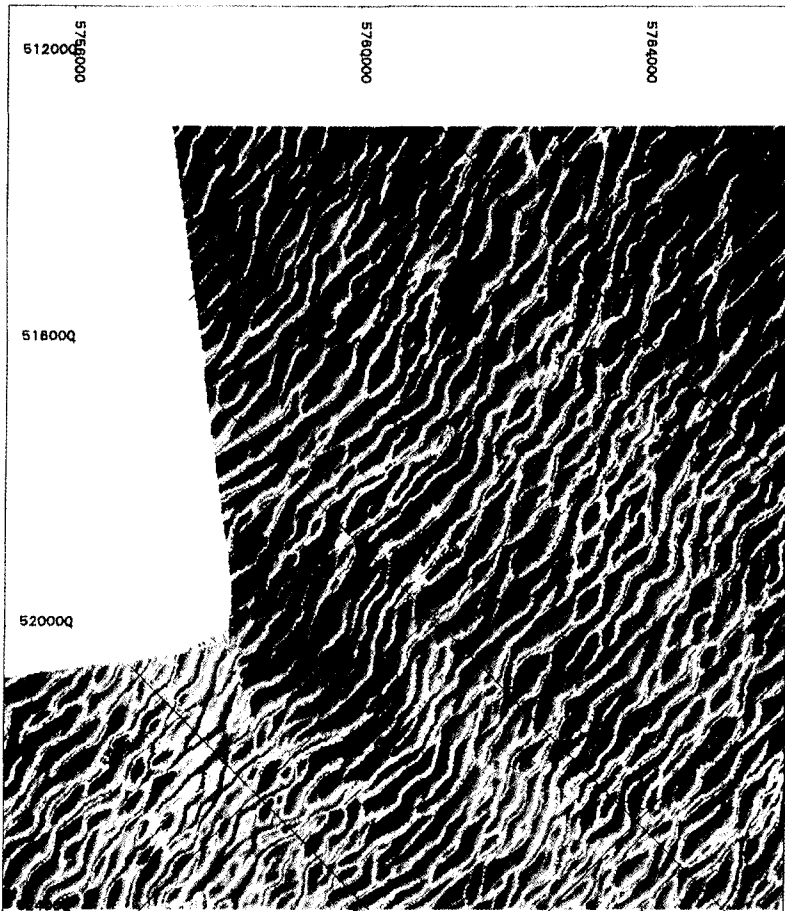


Figure 1: *Visualization of the North Sea bed near the Eurogeul, from Van Goor & Andorka Gal, 1996.*

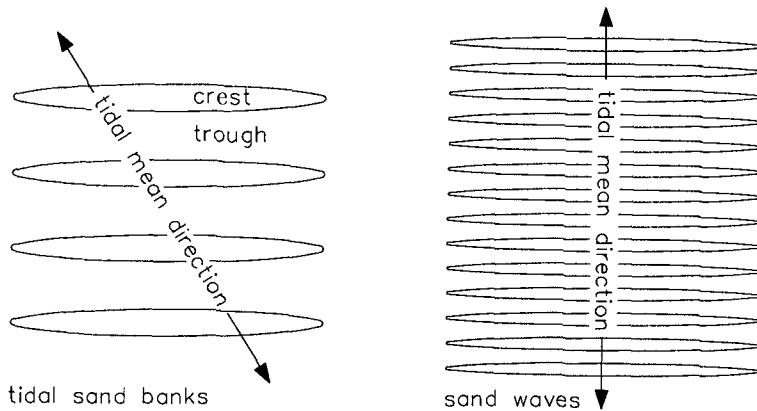


Figure 2: Sketch of tidal sand banks and sand waves, the relation to the main tidal current axis is indicated.

are different. Therefore different mechanisms are responsible for their formation and behavior.

A model to describe formation of these large-scale sea-bed patterns due to tide-topography interactions is given in *Hulscher* [1996]. In this model the tide is described by a three-dimensional shallow water model. This model uses a very simple turbulence closure scheme, see also *Engelund* [1970]: constant eddy viscosity A_v in combination with a partial slip parameter at the bottom. The latter introduces a so-called resistance parameter S .

Application of this turbulence model often raises questions how these results compare with more realistic turbulence-closure schemes. Unfortunately it is not completely known how turbulence should be modeled, therefore the answer to this question can never be definite. A further, even more important question is how these, rather abstract, parameters can be determined from observations. Illustrative issue is whether observations are to be collected either on the top and in the trough of the bank or at the adjacent sides.

A start to answer the first question is made studying a simplified system: a two-dimensional horizontal model without Coriolis force and neglecting inertia effects. This system is analyzed in two ways: using a realistic turbulence closure scheme and the simple scheme based on eddy viscosity and the resistance parameter. By comparing the results of these two methods one finds explicit relations between at one hand more accepted model parameters and at the other hand, the eddy viscosity A_v and the resistance parameter S . Furthermore this enables to investigate how the latter two variables are connected, and if they represent two degrees of freedom.

These results can be used to make estimates for the three dimensional model in which Coriolis effects and inertia effects are included. These lead to choices for the parameters which are following *Hulscher* [1996] crucial to determine the

bed structure: a flat bed or sand waves or tidal sand banks or a combination of the latter two patterns. This procedure enables the estimate of these parameters without analyzing an network of current meter recordings. For two cases explicit estimates are given: an average North Sea location and the Middelkerke bank.

The outline of this note is as follows. A short description of the three-dimensional bed form model is given in section 2. Next, the simplified system and subsequent modeling is given in section 3. The analyses in particular for the logarithmic profile and the $A_v - \hat{S}$ model are given in sections 3.3 and 3.4, respectively. Matching of these two models is discussed in section 3.5. These results are transferred to the three dimensional model, which is shown and discussed in section 4. In this section two physical locations are treated as examples. Lastly, conclusions are presented in section 5.

2 Model for sand waves and tidal sand banks

The generation of large-scale bed form patterns is studied based on the idea that these structures might be free instabilities of the coupled morphological system: sea water and sea bed. Therefore a suitable model of this system is formulated and use for analysis.

The morphological shallow water is based on tidal flow described by three-dimensional shallow water equations, bed load transport and conservation of sediment. Tidal averaging and application of a linear stability analysis lead to prediction of the dominant bottom mode starting from a flat bottom. Translating the measures of these fastest growing sinusoidal sea bed waves into physical quantities shows that the pattern is similar to either similar to sand waves or to tidal sand banks; patterns which are significantly different, see figure 2. This leads to the qualitative result in figure 3; the derivation of this figure is described in detail in *Hulscher* [1996].

Figure 3 shows that the bed structure prediction depends strongly on the Stokes number E_v of the tidal flow and the bed resistance parameter \hat{S} . These are defined as

$$E_v = \frac{2A_v}{H^2\sigma} \quad \text{and} \quad \hat{S} = \frac{2S}{H\sigma}, \quad (1)$$

in which H is the local mean depth and σ the frequency of the tidal motion. The constant turbulent eddy-viscosity, A_v (m^2s^{-1}), quantifies the way in which horizontal momentum is transferred in vertical direction. The quantity S (ms^{-1}) is used to model the partial slip near the bed boundary. This overcomes the problem that the constant eddy viscosity is near the bottom too simple to model both velocity and shear stress in a realistic way. After *Engelund* [1970] here A_v and S are considered as two constants which describe together the vertical profile of the vertical flow profile.

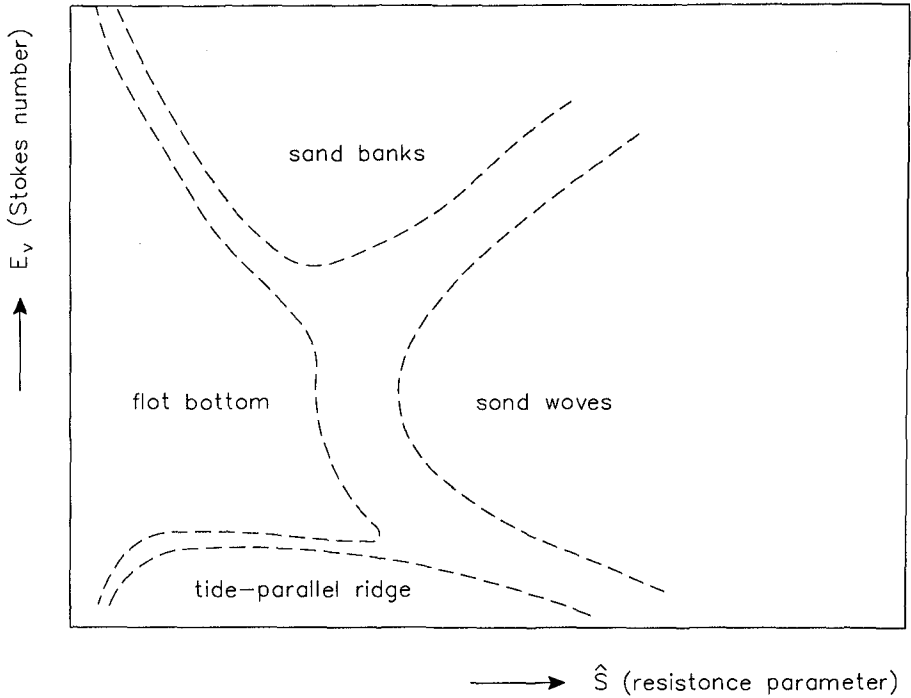


Figure 3: *Characteristic bed forms predicted by the three-dimensional shallow water model as a function of the bottom slip parameter \hat{S} and the Stokes number E_v . Quantification depends on values of the Coriolis parameter, local depth, bed-slope effects on sediment transport and the nonlinearity in the bedload transport formula.*

3 Modelparameter derivation

3.1 Simplified situation model

To illustrate the procedure a very simplified model and model-situation is sufficient. Starting from the three-dimensional shallow water model as in *Hulscher* [1996] the simplifications are as follows:

- Coriolis effects are neglected
- tidal flow, $\tilde{u}(z, t)$, is horizontally uniform
- friction dominates inertia effects: the eddy turn-over scale is much smaller than the scale on which the flow varies, such that eddies can reach a statistical equilibrium

Here the tidal flow is driven by pressure gradient, oscillating at the tidal frequency σ and having amplitude P_x . The flow is opposite the pressure gradient; the equation of motion becomes

$$0 = -\frac{P_x}{\rho} \sin \sigma t + \frac{\partial}{\partial z} \left[\nu_t(z, t) \frac{\partial \tilde{u}}{\partial z} \right], \quad (2)$$

in which ν_t is the turbulent eddy viscosity coefficient. The boundary conditions near the sea bed and surface are as follows

$$\begin{aligned} \tilde{u} &= 0 & \text{at } z &= z_0, & (3) \\ \nu_t(z, t) \frac{\partial \tilde{u}}{\partial z} &= 0 & \text{at } z &= H, & (4) \end{aligned}$$

in which z_0 is the roughness height. The z -axis is here directed upwards, from the sea bottom $z = 0$ till the sea surface $z = H$. Here the surface stress component is chosen zero. The bottom shear stress is denoted by $\tilde{\tau}_b(t)$ and is time-dependent:

$$\tilde{\tau}_b = \rho \nu_t(z) \frac{\partial \tilde{u}}{\partial z} \equiv \rho |\tilde{u}_*| \tilde{u}_* \quad \text{at } z = 0, \quad (5)$$

where \tilde{u}_* is the time-dependent friction velocity.

3.1.1 Linearization of the shear stresses

Definition (5) shows that, in general, the friction velocity \tilde{u}_* depends on time, so that the momentum equation is difficult to solve. To deal with this one usually replaces one friction velocity factor \tilde{u}_* by a representative constant \bar{u}_* . Now the bed shear stress condition becomes

$$\tilde{\tau}_b = \rho \nu_t(z) \frac{\partial \tilde{u}}{\partial z} \equiv \rho \bar{u}_* \tilde{u}_* \quad \text{at } z = 0, \quad (6)$$

A possible way to derive such a representative value for \bar{u}_* is requiring that the tidal-averaged shear stresses of both formulations are equal:

$$\rho \langle \tilde{u}_* \tilde{u}_*^2 \rangle = \rho \langle \bar{u}_* \bar{u}_*^2 \rangle, \quad (7)$$

in which $\langle \rangle$ denotes the tidal averaging. Further assuming that the friction velocity oscillates with the tidal frequency σ (like the forcing pressure gradient) and that it has an amplitude \hat{u}_* , the searched constant becomes [Zimmerman, 1981, and Mei, 1989]

$$\bar{u}_* = \frac{8}{3\pi} \hat{u}_*. \quad (8)$$

3.2 Model analysis: general part

In this model the tidal flow is forced by the pressure gradient and as the latter oscillates at frequency σ , so in absence of inertia effects the tidal flow can simply be decomposed as follows

$$\tilde{u}(z, t) = u(z) \sin(\sigma t). \quad (9)$$

Substitution of (9) into the equation (2) leads to the following equation of motion for $u(z)$:

$$0 = -\frac{P_x}{\rho} + \frac{\partial}{\partial z} \left[\nu_t(z) \frac{\partial u}{\partial z} \right]. \quad (10)$$

By integration of (10) using the upper boundary condition (4) and the lower as given in (6), the following equality is obtained

$$\frac{P_x}{\rho} H = \bar{u}_* \hat{u}_* = \frac{8}{3\pi} \hat{u}_*^2. \quad (11)$$

Up till this point no simplifications are made regarding the choice of a specific turbulence closure scheme. In the next two sections equation (10) will be solved using two different turbulence closure schemes.

3.3 Logarithmic profile model and analysis

Viscosity parametrization From turbulence modelling is known that the turbulent eddy viscosity increases from the boundaries in which the distance to the boundary is a measure for the length scale of the turbulent eddies. So at the fixed sea bottom the eddy viscosity equals zero and it increases with the distance from the bottom z :

$$\nu_t(z) \sim z. \quad (12)$$

The sea surface can act as a less stringent boundary. Many physical processes lead to a more effective mixing in the upper part of the water column, e.g. action

of wind waves, swell, stratification. Here this fact is parametrized by a parameter ϵ , which value is here between the limits 1/2 (little influence of surface on turbulence) and 1 (rigid surface). This is chosen such that the viscosity at the sea surface is:

$$\nu_t(H) \sim H(1 - \epsilon). \quad (13)$$

And near the surface $H - \zeta$ (in which ζ positive) the length scale of the turbulent eddies increases following

$$\nu_t(H - \zeta) \sim \nu_t(H) + \zeta(2\epsilon - 1). \quad (14)$$

The previous considerations motivate a parabolic function as parametrization for the dimensional turbulent eddy viscosity ν_t

$$\nu_t(z) = k\hat{u}_*z \left(1 - \epsilon \frac{z}{H}\right), \quad (15)$$

in which κ is the Von Karman constant $\kappa \simeq 0.41$.

Velocity profile Solving equation (10), using boundary conditions (3), (4) and expressing it in terms of \bar{u}_* using (6) yields

$$u(z) = \frac{\bar{u}_*}{\kappa} \left[\ln\left(\frac{z}{z_0}\right) + \frac{(1 - \epsilon)}{\epsilon} \ln\left(\frac{1 - \epsilon \frac{z}{H}}{1 - \epsilon \frac{z_0}{H}}\right) \right]. \quad (16)$$

Depth-averaged quantities The depth-average value of the turbulent eddy viscosity can easily be computed from equation (15) and yields

$$\bar{\nu}_t = k\hat{u}_*H \frac{(3 - 2\epsilon)}{6}. \quad (17)$$

In figure 4 the normalized viscosity profile is shown. The depth-averaged velocity follows from equation (16) and is given by

$$\bar{u} = \frac{\bar{u}_*}{\kappa} \left[\ln\left(\frac{H}{z_0}\right) - \frac{1}{\epsilon} + \frac{1 - \epsilon}{\epsilon} \ln\left(\frac{1 - \epsilon}{1 - \epsilon \frac{z_0}{H}}\right) + \frac{\epsilon - 1}{\epsilon^2} \ln(1 - \epsilon) \right]. \quad (18)$$

3.4 $A_v - S$ model

In this section the highly simplified turbulence model is chosen, here called S and A_v model, which is applied in *Hulscher* [1996]). The model has a vertically constant eddy viscosity, here denoted by A_v . This constant eddy viscosity model lacks variations which lead to describe the correct velocity and shear stress both in the interior as well as at the bottom. However, the aim here is to use this model for studying sediment transport, therefore it has to produce the correct bed shear stress, rather than the exact horizontal velocity near the sea bed. This can be achieved by choosing a partial slip condition, instead of condition (3), at the sea bed. In this context the partial slip condition is formulated as follows

$$\bar{u}_* \hat{u}_* = Su \quad \text{at} \quad z = 0, \quad (19)$$

in which S is the so-called resistance parameter.

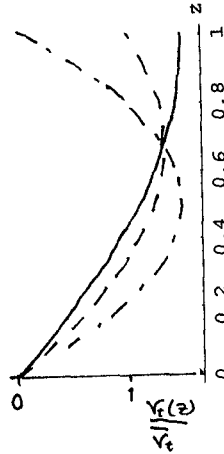


Figure 4: The dimensionless viscosity profile $\nu_t(z)/\bar{\nu}_t$ for three values of ϵ (straight $\epsilon = 0.5$, dashed/dotted $\epsilon = 0.75$, dashed $\epsilon = 1.0$).

Velocity profile The solution of equation (2), using (4) and (19) becomes

$$u(z) = \bar{u}_* \hat{u}_* \left[\frac{z}{A_v} \left(1 - \frac{z}{2H} \right) + \frac{1}{S} \right]. \quad (20)$$

Depth-averaged quantities The depth-averaged viscosity in this model is simply the constant

$$\bar{\nu}_t = A_v. \quad (21)$$

The depth-averaged velocity \bar{u} in this model yields

$$\bar{u} = \bar{u}_* \hat{u}_* \left(\frac{H}{3A_v} + \frac{1}{S} \right). \quad (22)$$

3.5 Matching

Now the models, discussed in the previous two sections, section 3.3 and section 3.4, will be matched by appropriate requirements. First remark is that sediment transport is a function of the bed shear stress. This motivates the first requirement: the $A_v - S$ model has to produce the same bottom shear stress as in the logarithmic model. Based on this, the bottom boundary condition in the $A_v - S$ model has already been adapted such that expression (6) is valid in both models.

The second condition is that the water discharge is equal in both models. This condition is here transferred into the requirement of equal depth-averaged velocities resulting from both turbulence formulations. Using equations (18) and (22) this means

$$\ln \left(\frac{H}{z_0} \right) - \frac{1}{\epsilon} + \frac{1-\epsilon}{\epsilon} \ln \left(\frac{1-\epsilon}{1-\epsilon \frac{z_0}{H}} \right) + \frac{\epsilon-1}{\epsilon^2} \ln(1-\epsilon) = \kappa \hat{u}_* \left(\frac{H}{3A_v} + \frac{1}{S} \right). \quad (23)$$

The third condition is that the depth-averaged value of the eddy viscosity $\bar{\nu}_t$ equals the constant eddy viscosity A_v . Using equation (17) this leads to

$$A_v = k\hat{u}_*H\frac{(3-2\epsilon)}{6}. \quad (24)$$

4 Discussion

Before the discussion here starts, it is worthwhile to remark that all values for turbulent eddy viscosity coefficients and bottom shear stress are results of the application of a turbulence closure scheme. The logarithmic model, used as a reference here, is often applied and produces satisfactory results. Therefore this model is generally accepted.

In the present model this leads to the following Stokes number E_v by using equations (11) and (24)

$$E_v = \frac{\kappa\sqrt{\frac{3\pi P_x H}{8\rho}}}{H\sigma} \left(1 - \frac{2}{3}\epsilon\right). \quad (25)$$

So if P_x, H, σ are already determined, the value of E_v is still a function of ϵ .

Using equations (11), (24) and the matching condition (23) the following relation for \hat{S} and E_v is obtained

$$\frac{E_v}{\hat{S}} = \frac{3-2\epsilon}{6} \left[\ln\left(\frac{H}{z_0}\right) - \frac{1}{\epsilon} + \frac{1-\epsilon}{\epsilon} \ln\left(\frac{1-\epsilon}{1-\epsilon\frac{z_0}{H}}\right) + \frac{\epsilon-1}{\epsilon^2} \ln(1-\epsilon) \right] - \frac{1}{3} \quad (26)$$

This relation shows that \hat{S} is a function of the roughness height z_0 , if the other parameters are specified. As z_0 usually is between $5 \cdot 10^{-5}$ m and $2 \cdot 10^{-1}$ m and $\frac{1}{2} \leq \epsilon \leq 1$, this will restrict the values of E_v, \hat{S} which are physically relevant.

4.1 Physical discussion

In general, the pressure gradient P_x can be determined from observations. Here the pressure gradient P_x is roughly estimated from the M_2 tidal (spring) range Δ , following

$$P_x = \rho * g * \frac{2\Delta}{L}, \quad (27)$$

in which L is the tidal wavelength and g the gravity acceleration. Assuming that Δ is 2 meters and the tidal wave follows from shallow water theory (so $L=770$ kilometers on a depth of 30 meters) one derives $P_x = \rho * 5.1 \cdot 10^{-5} \text{ms}^{-2}$; the tidal frequency is $\sigma = 1.4 \cdot 10^{-4} \text{s}^{-1}$.

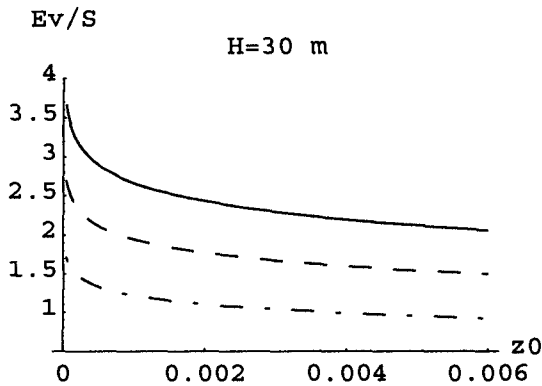


Figure 5: (a) The ratio E_v/\hat{S} and (b) \hat{S} for three values of ϵ (straight $\epsilon = 0.5$, dashed/dotted $\epsilon = 0.75$, dashed $\epsilon = 1.0$). Here average North Sea conditions are chosen, the depth $H = 30$ meters.

Offshore North Sea A suitable North Sea average depth is 30 m. Using equation (25) gives that $1.4 \leq E_v \leq 2.8$ due to the range of $0.5 \leq \epsilon \leq 1$. The correct value of ϵ has to be estimated based on current profiles. Using many field measurements *Sousby* [1990] has found that the roughness height z_0 in the North sea usually is between $5 \cdot 10^{-5}$ m and $6 \cdot 10^{-3}$ m, in which the larger values are found for rippled sand. Using (26) the ratio E_v/\hat{S} and subsequently the resistance parameter itself can be evaluated. Figure 5(a) shows the ratio E_v/\hat{S} and in figure 5(b) the resistance parameter \hat{S} is shown.

Middelkerke Bank The Middelkerke Bank is part of the Flemish Banks system; these large tidal sand banks are partly covered with sand waves. At the Middelkerke Bank the mean depth is significantly smaller, being about 15 meters. So here the expected range for the Stokes number becomes $2.0 \leq E_v \leq 3.9$. *Vincent & Stolk* [1993], p 217, reported that the roughness height z_0 at two stations around the Middelkerke Bank is between $9 \cdot 10^{-4}$ m and $3.3 \cdot 10^{-2}$ m. For these values the ratio E_v/\hat{S} and the resistance parameter \hat{S} are shown in figure 6.

General The areas in parameter space of both discussed locations are shown in figure 7. In this figure also the expected bed structure based on the bed form prediction model *Hulscher* [1996] is also indicated. For the offshore North Sea bed a part of the possible parameter combinations predict a flat sea bed, also a part of these combinations predicts tidal sand banks. Around the Middelkerke bank a part of the parameter combinations predicts tidal sand banks, for a different part the slowly growing tidal sand banks are dominated by sand waves, which grow faster. Comparison between prediction and the actual bed structure show that these results are not unrealistic. So the ranges in the parameters E_v and \hat{S}

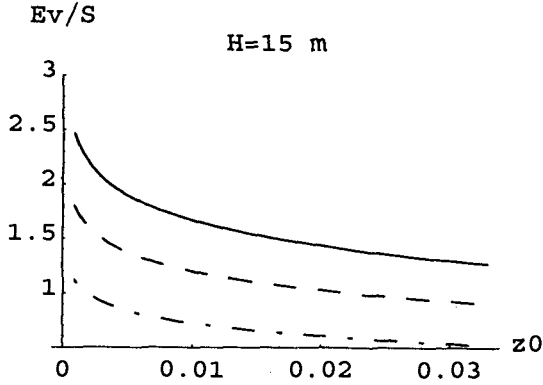


Figure 6: (a) The ratio E_v/\hat{S} and (b) \hat{S} for three values of ϵ (straight $\epsilon = 0.5$, dashed/dotted $\epsilon = 0.75$, dashed $\epsilon = 1.0$). Here Middelkerke Bank conditions are chosen, the depth $H = 15$ meters.

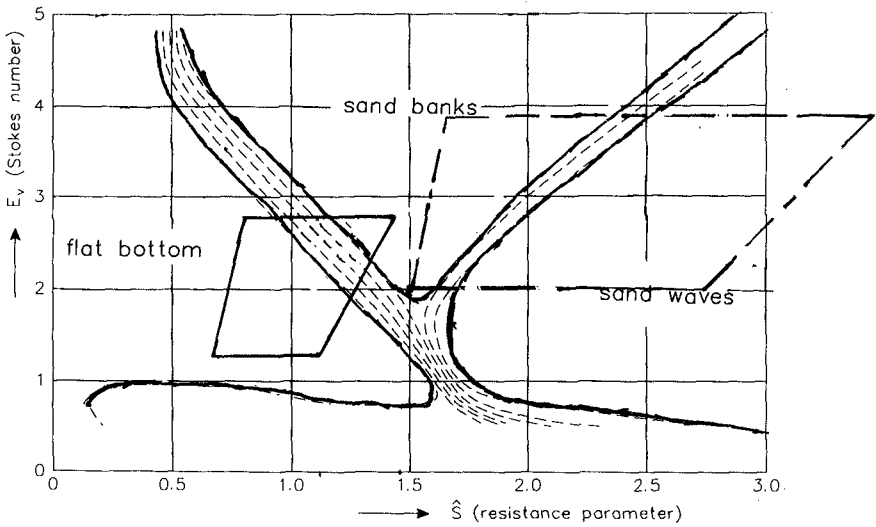


Figure 7: Parts of the parameter space E_v and \hat{S} possible in the offshore North Sea bed and around the Middelkerke bank. Also the expected bed behavior as found by Hulscher [1996] is indicated.

based on natural variations in the quantities roughness height z_0 and turbulence characteristics ϵ cover different bed structures. These results show that it will be worthwhile to determine the value of z_0 and ϵ more precise and subsequently compare the model prediction with the observed local bed structure, for several locations in the North Sea.

5 Conclusions

A way to investigate the implication of a potential sea-bed prediction model is presented. To quantify the parameters which describe the turbulence processes, first a simpler system, based on steady flow, is analyzed.

In the simpler system is shown that the S, A_v -turbulence model is able to produce the same bed shear stress as the accepted logarithmic model. The comparison between these models gives expressions for S and A_v in terms of the model parameters in the logarithmic model: ϵ and z_0 . So based on this comparison between the logarithmic model and the S, A_v model can furthermore be concluded that there are two basic degrees of freedom to choose S and A_v left, here expressed as ϵ and z_0 . One might argue that these two degrees of freedom are restricted, however these restrictions are the result of a calibration of the S, A_v -model with a logarithmic model. Boundaries limiting the physical realistic values of \hat{S}, E_v will certainly be different if the S, A_v -model is calibrated using another turbulence closure scheme than the one used in this note.

The results of the steady flow case are used to estimate the model parameters in the tidal morphological model. For two cases the prediction of the model and the local bed structure are compared and show good agreement. This indicates that it is worthwhile to continue this line of validation.

Acknowledgements The author thanks H.J. De Vriend and H.E. De Swart for the ideas and discussions which have led to this paper. This note is based on work both in the PACE-project, in the framework of the EU-sponsored Marine Science and Technology Programme (MAST-III), under contract no. MAS3-CT95-0002, as well as the project of The UK Ministry of Agriculture, Fisheries and Food under contract no. CSA3051-Offshore sand banks: Basic processes and effects on long-term coastal morphodynamics.

References

- Hulscher, S. J. M. H., Tidal-induced large-scale regular bed form patterns in a three-dimensional shallow water model, *Journ. of Geoph. Res* Vol 101 No C9, 20,727-20,744, 1996.
- Mei, C.C., *The applied dynamics of ocean surface waves*. World Scientific, 740pp, 1989.

- Off, T., Rhythmic linear sand bodies caused by tidal currents, *Bull. of the Am. Ass. of Petroleum Geologists* 47, 324-341, 1963.
- Soulsby, R. L., Tidal-current boundary layers, in *The Sea, Vol. 9. Part A*, edited by le Mehaute, B. and Hanes, D. M., pp 523- 566, Ocean Engineering Science, John Wiley and Sons, New York, 1990.
- Van Goor, S. and Andorka Gal, J.H., Bodem (in Dutch), document RIKZ/OS-96.109X, 28 pp, 1996.
- Vincent, C. and Stolk, A., Hydrodynamics and suspended load: measurements by total sediment-load sampler and acoustic backscatter, in *Sediment Mobility and Morphodynamics of the Middelkerke Bank*, edited by De Moor, G., and Lanckneus, J., pp 211-227, Final Report MAST Project, Gent, 1993.
- Zimmerman, J.T.F., On the Lorentz linearization of a quadratically damped forced oscillator, *Phys. Lett.* 89A, 123-124, 1982.

CHAPTER 277

Transverse Bars in Duck, North Carolina

Kathryn M. Konicki¹ and Rob A. Holman¹

Abstract

In 1985, unusual streaks were first seen in time exposure images of nearshore wave breaking. These features were persistent from image to image and ran perpendicular or oblique to the shoreline. They have been observed both between the shoreline and inner bar and offshore of the inner bar, and have a typical longshore wavelength of ~40-130 m, substantially shorter than normal sand bar length scales. Comparison with bathymetric data collected by the CRAB showed the bands to be bathymetric ridges with a relief of 0.3-0.5 m.

Both intensity transects as well as geometrically rectified images were used to determine the length scales of the bars. Longshore length scales of offshore bars (mean spacing of 131 m) were typically three times the spacing of trough bars (mean spacing of 41 m). The offshore limit of the visible features in the trough varied from as short as 5 m to a maximum of 35 m.

Frequency of occurrence statistics for the bars were determined by viewing Argus data from 1987-1995. Trough bars appeared in the images an average of 62 days/year while offshore bars appeared 41 days/year although there was substantial interannual variability. Offshore bar occurrence is more frequent in the winter, and trough bar occurrence is more frequent in the summer.

Introduction

The classic model of a sandbar is a large-scale feature aligned parallel to the shoreline. Sandbars that are oriented slightly oblique to the shoreline have also been observed and are called welded bars. In 1952, Shephard described a feature oriented perpendicular or at a high angle to the shoreline with a relatively short length scale that he called a transverse bar. Only a few studies have been done on these transverse bars, including Barcilon and Lau's (1973) and Niedoroda and Tanner's (1970) work on transverse bars off the coast of Florida.

In 1985, similar features were first observed in time exposure images off the coast of Duck, North Carolina. Figure 1a shows an oblique snapshot from January 10, 1994. The vegetated dunes, dry beach, and shoreline are evident, as is the pattern of breaking waves in the nearshore. By contrast, Figure 1b shows an oblique ten-minute time exposure. The time-averaged breaking waves now show up as smooth bands, clearly delineating the shoreline (from the shorebreak) and the

¹ College of Oceanic and Atmospheric Sciences, Oregon State University, Oregon State University, Corvallis, OR 97331



Figure 1. Images from Duck, NC. a). Snapshot from January 10, 1994. b). 10-minute time exposure from January 10, 1994. Transverse features are evident in the trough as well as offshore of the shore-parallel bar. Box shows area rectified in Figure 2.

offshore bar (Lippmann and Holman 1989). Intermediate-scale white bands, oblique to the shoreline, are also obvious in the trough, as well as offshore of the shore-parallel bar. Research has been carried out on these features to first determine whether or not the oblique bands in the video images are real bathymetric features or simply an artifact of the imaging technique. Statistics of the features, such as their frequency of occurrence and longshore and cross-shore lengths were then calculated.

Methodology

The data were taken at the Field Research Facility (FRF) at Duck. Duck is a dune-backed beach located on one of the barrier islands of the Outer Banks. It is a low-energy, intermediate to reflective beach that is barred. An inner bar is located at ~125 m offshore and an outer bar is also present at times. The spring tide range is 1.6 meters and the mean water level is 0.35 m above NGVD. The average annual breaker height is 88 cm (Birkemeier 1981). The study area for our research was a 1700 meter stretch along the beach.

The data were collected automatically as part of the Argus program. An Argus station is a video camera operated by a personal computer. Every hour, both a snapshot and a ten-minute time expose are taken of the nearshore region. These images are sent back to the Coastal Imaging Lab at Oregon State University every night. A data set of images sampled with Argus is available for Duck spanning 10 years (1986-1996).

A great deal of information can be extracted from time exposures such as the one shown in Figure 1b. Since the geometries of the video camera are known, the exact location on the ground for each pixel in the image is also known. The coordinate system that is used for the images is the FRF coordinate system. The video camera is located at $x=32.54$, $y=585.78$, with x and y increasing positively offshore and away from the camera, respectively.

One method of determining length scales and positions of the features is to use geometrically rectified images (plan views) of the study area. Knowledge of the camera geometries allows a rectification of a region on an oblique image to be made. (Figure 2). Measurements such as longshore length spacing, cross-shore position and cross-shore length can be manually made from such rectifications. Transects can also be taken along the rectification, or along the oblique images, to measure intensity. Intensity data were compared with bathymetric data that were collected using the FRF's Coastal Research Amphibious Buggy (CRAB) to determine if the features have a bathymetric nature.

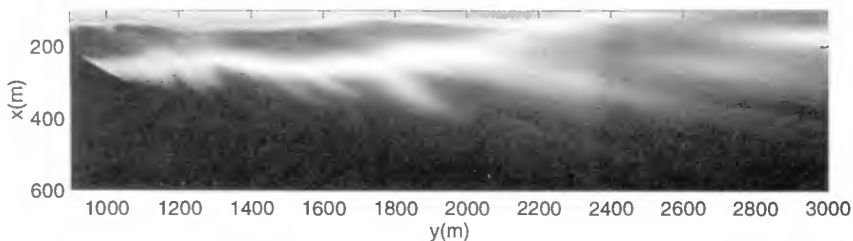


Figure 2. Rectification of boxed area in Figure 1b. Measurements can be made manually from the rectification.

In order to determine the frequency of occurrence of the bars, 8 years of Argus images (1987-1994) were viewed. One image from each day was studied for a total of 2600 images. There were some days when no data was available due to equipment failure, bad weather, or other reasons that an image could not be obtained. In order to quantify the presence/absence of transverse bars, each image was given a rating on a scale of 0-5, with 0 being no evidence of transverse bars and 5 being a clear indication of multiple transverse bars. A rating was given both for the *trough bars* (transverse bars found in the trough) as well as *offshore bars* (transverse bars found offshore of the shore-parallel bar). Figure 3 shows examples of images that were given ratings of 1, 3, and 5.

All the images were separated into two categories. An image that was given a rating of 3, 4, or 5 was considered a day in which bars were present. Images that received a rating of 0, 1, or 2 were considered as days in which bars were not present.

Results

The first objective of this study was to determine the persistence of the intensity streak features to insure that they are not random processing features. Longshore intensity transects were taken along a line at $x=145$ m, from $y=790$ to 1060 m, for a series of 4 hours (5 images) for January 10, 1994 (Figure 4a). From Figure 4b, it is evident that there was a peak in intensity where there was a white band in the time exposure. This figure also shows that intensity peaks were persistent over substantial periods, including tidal variations, suggesting that these features are not a random artifact of the image processing. Figure 5 shows intensity transects that were taken across a set of offshore transverse bands for 3 consecutive days in November of 1993. Transects were taken at $x=300$ m, from $y=1200$ m to 1700 m. The intensity maxima and corresponding white bands in the video images persisted for a period of days, supporting the fact that these features are real, not artifacts.

On July 18, 1995, a detailed CRAB survey was carried out to determine if the white bands in the images are real bathymetric features. Figure 6a shows a transect along which intensity data were taken and also shows the transect along which bathymetric data were collected. Intensity and depth along the transects in Figure 6a are shown in Figure 6b. It is evident that intensity maxima correspond to bathymetric highs and intensity minima correspond to bathymetric lows, proving that the oblique bands in the video images are ridges. The bathymetric data showed the relief of these bars to range from 0.3-0.5 m.

Length scales and positions for both the trough and offshore bars were calculated from intensity plots and rectified images. The mean longshore length spacing (distance between two consecutive bars), distance offshore (offshore extent of bars as measured from the shoreline), and cross-shore length of the bars, were determined. Longshore length spacing was determined using 18 images for trough transverse bars and 33 images for offshore transverse bars. Five images (up to 3 bars per image) were used to determine the distance offshore and cross-shore length for trough bars, and 7 images (up to 3 bars per image) were used to calculate those statistics for the offshore bars. These data are summarized in Tables 1 and 2 for trough and offshore bars, respectively.



Figure 3. Examples of ratings on a scale of 0-5 that were given to images. a). Time exposure from November 13, 1993. Trough bars were given a rating of 1. b). Time exposure from November 11, 1994. Trough bars were given a rating of 3. c). Time exposure from February 9, 1993. Both trough and offshore bars were given a rating of 5.

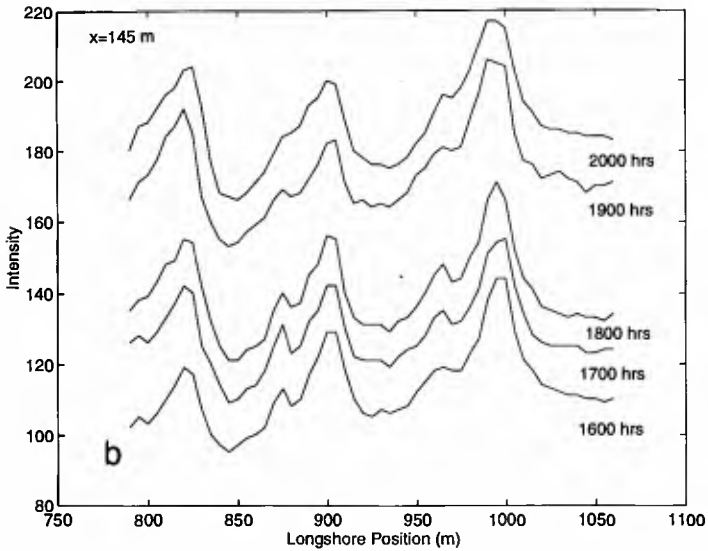


Figure 4. a). Time exposure from January 10, 1994 showing transverse bars in the trough. Transects along which intensity data were collected for 5 consecutive images are also shown. b). Intensity vs. longshore length from 1600-2000 hours along transect shown in a). This graph shows that the bars remain fixed over a period of 4 hours.

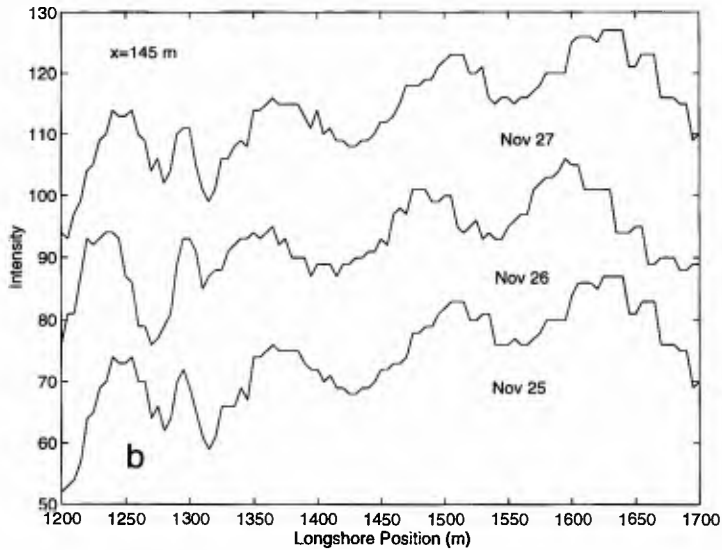


Figure 5. a). Time exposure from November 27, 1993 showing transverse bars offshore of the inner bar. Transects along which intensity data were collected are also shown. b). Intensity vs. longshore position for November 25, 26, and 27, 1993 along transects shown in a). This graph shows that most of the bars remain fixed over a period of days.

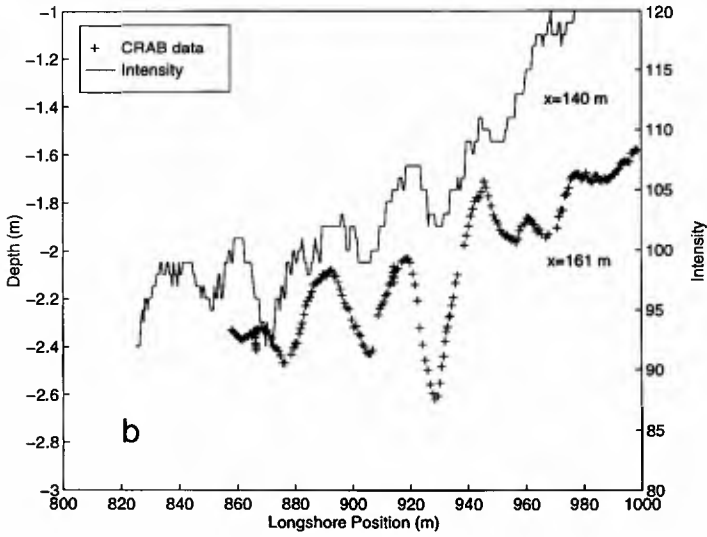


Figure 6. a). Time exposure from July 18, 1995 showing transverse bars in the trough. Transects along which intensity and bathymetric data were collected are shown. b). Comparison between intensity vs. longshore position and depth vs. longshore position for transects in a). This figure clearly shows that there is a correlation between the high pixel intensity in the video images and topographic highs.

Table 1. Length scales and locations for **trough bars**.

	<i>longshore length spacing (m)</i>	<i>distance offshore (m)</i>	<i>cross-shore length (m)</i>
mean	45.0	20.0	23.8
std dev.	21.4	9.2	15.5
range	12-87	5-35	5-50

Table 1. Length scales and locations for **offshore bars**.

	<i>longshore length spacing (m)</i>	<i>distance offshore (m)</i>	<i>cross-shore length (m)</i>
mean	130.7	249.1	180.0
std dev.	62.9	37.4	117.9
range	45-325	175-300	75-400

Offshore transverse bars are larger scale features than trough transverse bars. Their longshore length spacing is almost 3 times as large and their cross-shore length is up to an order of magnitude longer than the trough bars.

From the extensive Argus database, presence/absence data for the transverse bars were determined. We calculated the number of days transverse bars were observed annually and the average number of days transverse bars were observed per month. One problem that was encountered when calculating the statistics was the fact that there were many days for which no image was available. Taking this into consideration, the frequency of occurrence of transverse bars was determined as follows:

$$\text{For annual statistics: } N_{\text{annual}} = \frac{N_{\text{obs}}(\text{yr})}{N_{\text{images}}(\text{yr})} * 365$$

$$\text{For monthly statistics: } \bar{N}_{\text{month}} = \frac{N_{\text{obs}}(\text{month})}{N_{\text{images}}(\text{month})} * N_{\text{days}}(\text{month})$$

where N_{obs} is the number of images in a year or month in which transverse bars were present, N_{images} is the number of images available for that month or year, N_{annual} is the number of days transverse bars were observed annually, and \bar{N}_{month}

is the average number of days transverse bars were observed per month. If less than 20 images were available for a given month, that month was excluded from the monthly statistics because a representative average could not be determined.

The average number of days trough and offshore transverse bars appeared in the video images each month for the 8 years varies greatly (Figure 7). Trough bars were observed from 3 to 7 days/month and offshore bars were observed less frequently (~1 to 5 days/month). Trough bars were most frequently observed in the summer while offshore bars seem to follow a seasonal cycle, appearing in the video images more frequently in the winter than in the summer.

Each year, trough bars were observed more frequently than offshore bars (an average of 62 and 41 days/year, respectively), and there was an interannual variability in the statistics as well (Figure 8). There is a positive correlation between trough and offshore bars for most years and there seems to be an increasing trend for both sets of bars.

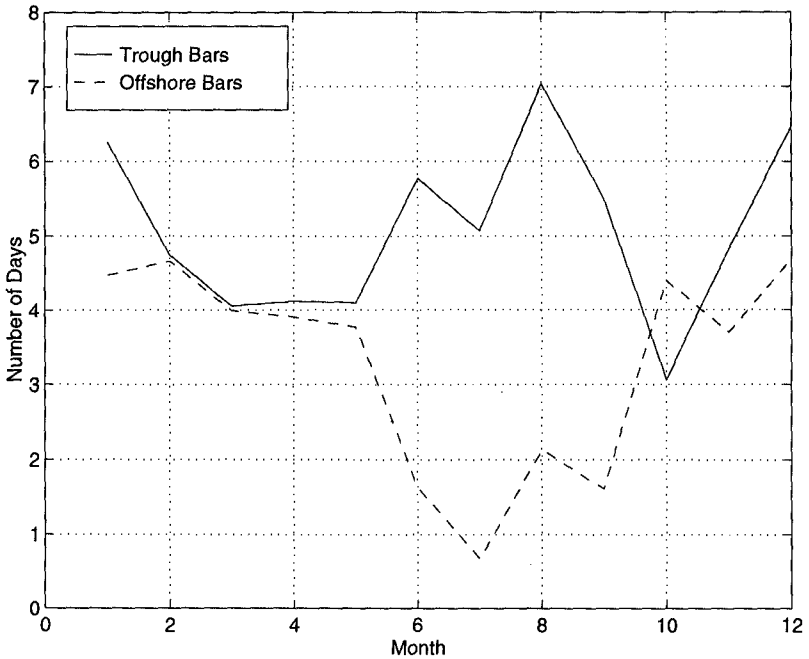


Figure 7. Average number of days transverse bars are observed per month.

Discussion

Transverse bars seem to be a common feature in the nearshore at Duck. They persist in the video images for periods up to days. There were, however, many instances when they were seen for consecutive days, "disappeared" from the images for a few days and then returned to what seems to be the exact location in which they

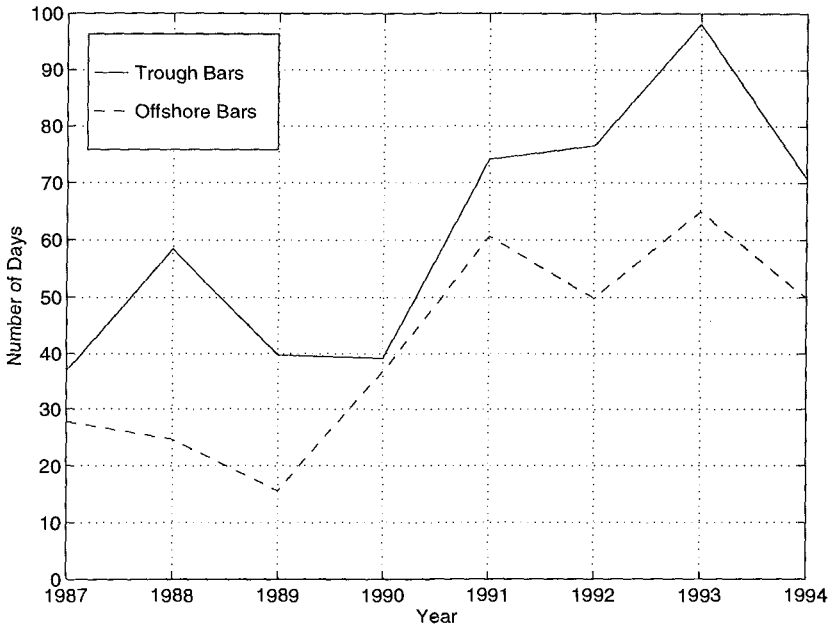


Figure 8. Number of days transverse bars are observed annually. Trough bars are observed more frequently than offshore bars.

were previously seen. This appearance/disappearance may be due to fluctuations in wave height. The bars are only seen in the images on days in which the waves are high enough to be breaking. Although they may “disappear” from the images when the wave height is lower and no breaking is taking place, they may still be present, but not observable. Wave height has not yet been taken into consideration in the calculation of bar statistics. Images in which no bars were seen were given a rating of 0 even when wave height was low. Wave height data from 1987-1995 will be studied to determine whether or not bars were always present during conditions of high wave height. This information will be used to better determine the statistics of the bars, as only days in which waves are breaking will be included in the statistics.

The mechanism for transverse bar formation is unclear. Their presence may be attributed to strong longshore currents and they may be formed in the same way that bedforms in a river are created. While longshore currents could perhaps be the mechanism for trough bar formation, it is not clear that they will be strong enough to locally form offshore bars.

Research will continue on the transverse bars at Duck. More complete statistics will be calculated for bar lengths and positions, and images from 1995 and 1996 will be viewed to augment the existing database. The movement, if any, of the bars will be determined, and an attempt will be made to understand the environmental conditions that are conducive to transverse bar formation. Finally, the Argus database for other beaches will be searched to determine if this process is unique to Duck.

Conclusions

Time exposures from Duck frequently show white bands perpendicular or oblique to the shoreline. These bands, which have been observed both in the trough and offshore of the shore parallel bar, persist for periods of hours up to days. Ground truthing has shown that they are transverse ridges with a relief of 0.3-0.5 m. Trough transverse bars (ridges in the trough) are a smaller scale feature than offshore transverse bars (ridges offshore of the shore-parallel bar). Their mean longshore length spacing is 3 times smaller than that of the offshore bars (44 m and 131 m, respectively). Trough bars obliquely extend up to 35 m from the shoreline while their actual cross-shore lengths may be up to 50 m. Offshore bars obliquely extend up to 300 meters from the shoreline with actual lengths up to 400 m. It appears that the cross-shore length of trough bars is constrained by the shore-parallel bar.

Trough transverse bars appear in the video images an average of 62 days/year and offshore transverse bars appear in the images an average of 41 days/year. There is an interannual variability in the statistics and a seasonal cycle. Offshore bars appear more frequently in the winter and trough bars appear most often from June-August and in December and January.

ACKNOWLEDGMENTS

We would like to thank Mike Leffler and Bill Birkemeir of the FRF for carrying out the CRAB survey. Thanks also to John Stanley for help with the wave data, and Eric Gilbert, Hilary Stockdon, Nathaniel Plant, and Peter Ruggiero for their continual help. Funding for this research is made available from The Office of Naval Research, Coastal Dynamics Program (grant number N00014-95-10753).

REFERENCES

- Barcilon, A.I. and J.P. Lau (1973). A model for formation of transverse bars: *Journal of Geophysical Research*, 78 (15): 2656-2664.
- Birkemeier, W.A. *et al.* (1981). A User's Guide to CERC's Field Research Facility US Army Corps of Engineers, CERC, Miscellaneous Report No. 81-7, p. 36.
- Lippmann, T.C. and R.A. Holman (1989). Quantification of sand bar morphology: A video technique based on wave dissipation: *Journal of Geophysical Research*, 94: 995-1011
- Niedoroda, A.W. and W.F. Tanner (1970). Preliminary study of transverse bars: *Marine Geology*, 9:41-62.
- Shephard, F.P. (1952). Revised nomenclature for depositional coastal features: *Bull. Am. Assos. Petrol. Geologists*, 36 (10): 1902-1912.

CHAPTER 278

On the systematic offshore decay of breaker bars

Kathelijne M. Wijnberg ^{1,2}

ABSTRACT

Multiple breaker bar systems along the Holland coast exhibit long term cyclic behaviour. Over periods of many years, all bars migrate in a net seaward direction; the outer bar decays offshore, and a new bar is generated near the shoreline. This behaviour is essentially a cross-shore redistribution of sediment; the sediment of the offshore decaying outer bar is transported back onshore.

This paper presents a tentative evaluation of a part of the hypothesis formulated by Wijnberg (1995) to explain the cyclic bar system behaviour. The systematic offshore decay of the outer bar is considered to be the key to explaining the cyclicity in this behaviour. The offshore decay is assumed to occur due to a change in the long term balance of bar maintaining conditions (breaking waves) and bar diminishing conditions (very asymmetric waves). This balance will change as a result of offshore migration of the outer bar to deeper water during single storm events.

The calculations presented in this paper support the hypothesis, but field observations of the hydrodynamic conditions during the process of bar decay are required for a more rigorous verification.

1. INTRODUCTION

Along the Dutch coast, multiple bar systems of nearshore breaker bars exist that exhibit systematic, cyclic behaviour on a time scale of many years (Edelman, 1974; Bakker and De Vroeg, 1988; Ruessink and Kroon, 1994; Wijnberg and Terwindt, 1995). This behaviour consists of a net seaward migration of all bars, with the outer bar decaying offshore and a new bar being generated near the shoreline (Fig. 1). This

¹ Dept. of Physical Geography, Institute for Marine and Atmospheric research Utrecht, Utrecht University, P.O. Box 80115, 3508 TC Utrecht, The Netherlands.

² College of Oceanic and Atmospheric Sciences, Oregon State University, Ocean Admin Bldg # 104, Corvallis, OR 97331-5503, USA.

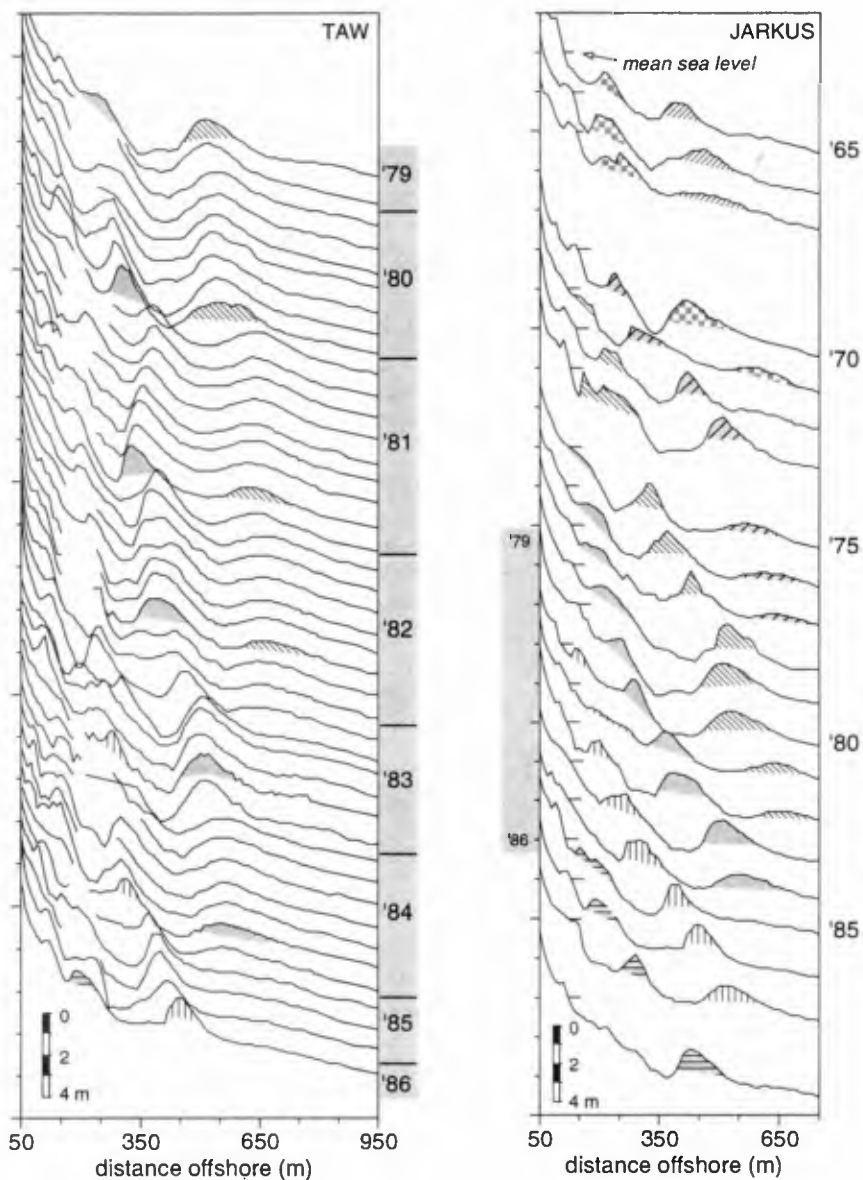


Fig. 1: Illustration of the offshore progression cycle for one profile line (line 8425). Left-hand figure based on TAW data base (several surveys per year, 1979-1986); right-hand figure based on JARKUS data base (one survey per year, 1965-1989). Bars are shaded to emphasise the offshore progression cycle; each bar has its own shading pattern through time.

behaviour implies that every so many years the same general cross-shore bar system configuration re-appears (i.e. when one offshore progression cycle has been completed). The time scale for the offshore progression cycle varies between bar systems, but seems to be quite constant for a given bar system (Wijnberg and Terwindt, 1995; Ruessink and Kroon, 1994).

Sediment budget considerations (Wijnberg, 1995; Wijnberg, in prep.) revealed that this cyclic morphologic behaviour is essentially a redistribution of sediment within the nearshore zone. So, although bar shapes are progressing in a net offshore direction, they are not representing a net offshore directed sediment transport. This implies that the sediment of the offshore decaying bar is transported back onshore.

The observed long term cyclic behaviour of multiple breaker bar systems is very intriguing in its own right, but may also have implications for the application and design of shoreface nourishments. For example, what is the best location and timing of a shoreface nourishment on a barred coastal profile? (eg. Hoekstra et al., 1994). Therefore, the identification of the mechanism that drives this systematic behaviour deserves further attention.

Wijnberg (1995) formulated a hypothesis to explain the cyclic bar system behaviour. In this hypothesis, which is briefly summarized in section 3, morphologic feedback in the coastal system is identified as the cause for the cyclicity in the bar behaviour rather than a cyclicity in the external forcing. The key to explaining the cyclic nature of the bar system behaviour is sought in the systematic offshore decay of the outer bar. In this paper, the part of the hypothesis dealing with the systematic offshore decay of the outer bar will be tentatively evaluated by studying the relation between the development stage of the outer bar and a wave climate integrated 'decay parameter'.

2. THE STUDY AREA

The hypothesis on the systematic decay of the outer bar will be evaluated for two multiple bar systems that exhibit similar cyclic behaviour but on a different time scale. The two multiple bar systems are located along the Holland coast (Fig. 2). These two bar systems have very different cycle times, viz. the bar system north of the IJmuiden breakwaters exhibits an approximately 15 year cycle, whereas the bar system south of the breakwaters has a typical cycle time of about 4 years. The alongshore change in the cycle times is rather abrupt, and coincides with the breakwaters (Wijnberg and Terwindt, 1995).

The northern bar system consist of 2 to 3 bars, depending on the phase in the offshore progression cycle (i.e. either 2 well developed bars or, in the case of 3 bars, a gentle outer bar and a small new inner bar, with a well developed middle bar in between). The whole bar system extents about 30 km alongshore.

In the southern bar system the number of bars changes alongshore: in the very south the number varies between 1 and 2, going north this changes into 2 to 3 bars, then 3 to 4 bars, and finally in the very north back to 2 to 3 bars. This bar system has a total length of about 40 km. The alongshore change in the number of bars has no obvious effect on the time span of the offshore progression cycle (Wijnberg and Terwindt, 1995).

Along the Holland coast, the mean wave height (H_{m0}) is about 1.2 m and the mean wave period (T_{m01}) is about 5 s; the mean tidal range is about 1.6 m. The grain size of the sediment in the breaker bar zone is generally in the fine sand range. There seems to be no significant difference in grain size between the two bar systems (Wijnberg, 1995)

Except for the large breakwaters that separate the two studied bar systems, the considered coastal stretch is almost free from engineering structures. In the northern bar system groins are present along about 5 km of beach at the northern end of the region (so still 25 km of beach has no groins). In the southern bar system a small discharging sluice is present (Fig. 2) which discharges some fresh water into the North Sea.

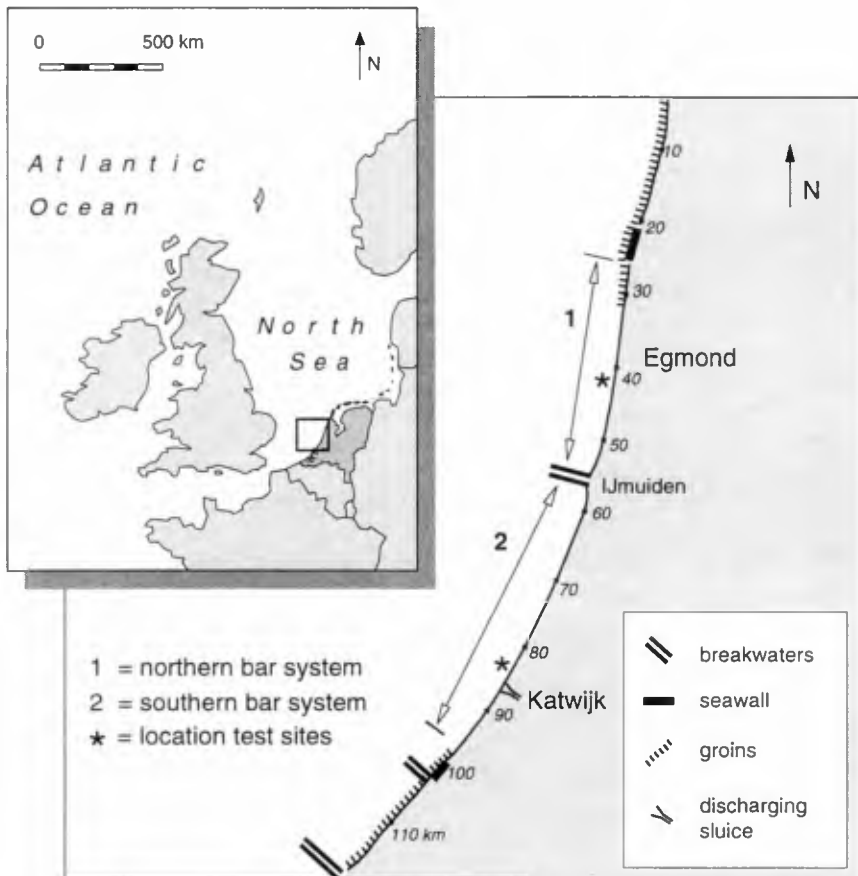


Fig. 2: Location of the study area

3. A CONCEPTUAL MORPHODYNAMIC MODEL

The multi-year cyclic behaviour of breaker bar systems can not readily be explained by existing theories on bar behaviour. These theories focus on the formation and maintenance of bar topography and pay little attention to the degeneration of bars. Our lack of understanding of the decay of bar features is illustrated by one of the findings of Roelvink et al. (1995) who mimicked long term cyclic bar behaviour with a cross-shore profile model. Roelvink et al. had to prescribe a reduced angle of repose for the sediment in the outer nearshore zone to force the outer bar to decay offshore.

According to Wijnberg (1995; in prep.), the cyclicality in the long term bar behaviour is most likely explained by morphologic feedback in the breaker bar system rather than by cyclicality in the external forcing. To explain the observed cyclic bar system behaviour, a central role was attributed to the behaviour of the outer bar. As long as the outer bar remains well developed at a certain position, the inner bar(s) do not move net offshore and will only move to and fro within a limited cross-shore range. Only as the outer bar disappears can the inner bar migrate net offshore (cf. Lippmann et al., 1993). This key role of the outer bar is plausible because the outer bar will obviously affect the hydrodynamic conditions in a down-wave direction, and therefore systematically affects the wave and current climate in the inner nearshore zone. Therefore, attention is further focused on mechanisms that may explain the systematic decay of the outer bar.

It was hypothesized by Wijnberg (1995; in prep.) that the systematic decay of the outer bar occurs due to a changing balance in the occurrence of conditions that favour decay of the outer bar topography (%DCA) and the occurrence of conditions that favour maintenance of the bar topography (%MAIN). The bar-maintaining conditions were identified as those with breaking waves across the bar, favouring the occurrence of break-point or long-wave mechanisms for the formation and maintenance of bar features. The bar-diminishing conditions were identified as those with very asymmetric waves across the bar (so the highest waves in the wave field will just start to break), allowing for an onshore directed sediment transport. A more complete justification for the choice of these two process 'regimes' can be found in Wijnberg (1995) or Wijnberg (in prep.)

The change in balance between the two types of conditions is induced by the offshore migration of the outer bar on a seaward sloping bed. The latter happens when the bar is migrating into deeper water during individual storm events, i.e. when waves are breaking on the outer bar. The deeper the bar gets, the less likely that bar-maintaining conditions occur. Consequently, the relative dominance of bar-diminishing conditions will increase. The rate of increase will depend on the characteristics of the wave climate.

4. METHODS

To evaluate the proposed mechanism for the systematic offshore decay of the nearshore bars, the balance of %DCAY and %MAIN will be calculated for various development stages of the outer bar (Fig. 3). The balance is expressed in terms of the decay parameter I_{decay} :

$$I_{\text{decay}} = \frac{\%DCAY}{\%DCAY + \%MAIN} = \frac{\%DCAY}{\%ACT} \quad (1)$$

%DCAY = mean annual percentage of occurrence of bar-diminishing conditions on the outer bar

%MAIN = mean annual percentage of occurrence of bar-maintaining conditions on the outer bar.

%ACT = mean annual percentage of occurrence of morphologically active conditions on the outer bar.

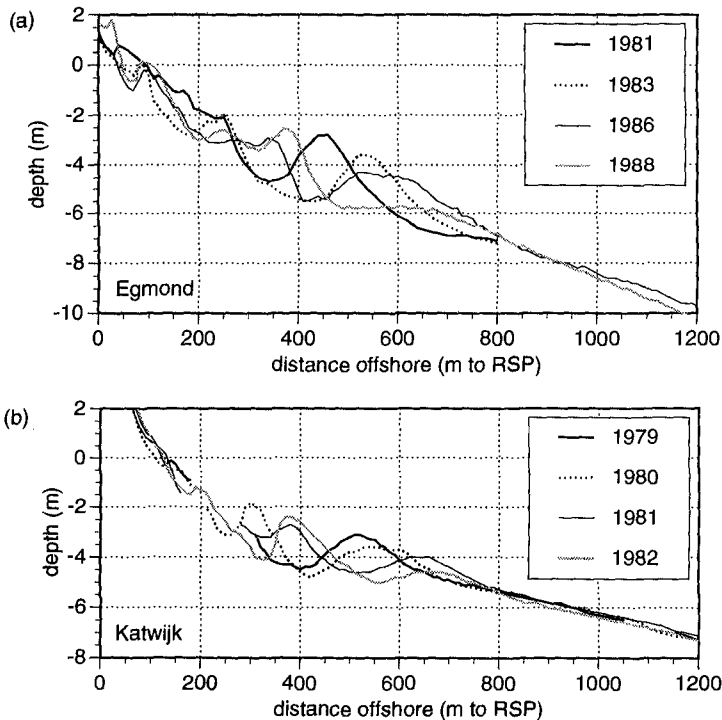


Fig. 3: Nearshore profiles used in the model computations at (a) the Egmond site, and (b) the Katwijk site. (All profiles extend down to about 20 m water depth.)

'Morphologically active conditions' (%ACT) are those conditions during which the outer bar is changing its morphology. This does not necessarily imply that during morphologically *inactive* conditions the sediment is completely immobile; it is just so that any sediment transport under those conditions does not result in noticeable morphological change. The outer bar has been observed to be morphologically inactive during the calm summer months (Wijnberg, 1995).

Bar-maintaining conditions are defined (Wijnberg, 1995; Wijnberg, in prep.a) as those conditions that produce more than 5% of breaking waves on the bar. Bar-diminishing conditions are defined as those which produce only 0.1% to 5% of breaking waves on the bar. %DCAY and %MAIN are estimated from the mean annual offshore wave climate.

The data on the offshore hydrodynamic climate along the Holland coast are of the following type: a mean annual percentage of occurrence, $P(H_{m0}, \alpha)$, and a mean water level elevation, $h(H_{m0}, \alpha)$, are available, with wave height bands of 0.5 m and wave direction bands of 15 degrees. The mean water level represents the average set-up or set-down that occurs during given wave conditions. H_{m0} and α are the central values of the wave height class respectively wave directional class that they represent.

To estimate %DCAY and %MAIN one needs to know the percentage of breaking waves occurring on the outer bar for each of the wave climate 'cells' (H_{m0}, α). Adding all $P(H_{m0}, \alpha)$ for all (H_{m0}, α) cells that produce more than 5% of breaking waves gives %MAIN; adding all $P(H_{m0}, \alpha)$ for all (H_{m0}, α) cells that produce between 0.1% and 5% of breaking waves gives %DCAY. The WAVIS model (Van Rijn and Wijnberg, 1996) was used to calculate the percentages of breaking waves for each (H_{m0}, α) cell.

Since WAVIS is a probabilistic type of wave model, a representative wave field (H_i, T_i, p_i, α_i) was generated for each (H_{m0}, α)-cell, where: H_i is the central value of the i^{th} (0.25 m wide) wave height class; T_i is an empirically determined wave period that goes on average with H_i ($T_i = 6 * H_i^{0.333}$ (Wijnberg, 1995)); p_i is the probability of occurrence of the i^{th} wave height class assuming the wave heights are Rayleigh distributed; α_i was chosen constant for all wave height classes, viz. equalling α .

The values of %DCAY and %MAIN are calculated for the outer bars at two locations, viz. near Katwijk and near Egmond. The Katwijk site is located in the southern bar system, and the Egmond site in the northern bar system (Fig. 2).

5. RESULTS

5.1 The decay parameter and the development stage of the outer bar

The values of %ACT, %DCAY, %MAIN, and I_{decay} in relation to the depth of the outer bar crest are shown in Fig. 4, for both the Katwijk site and the Egmond site. The depth of the outer bar crest represents the development stage of the outer bar (Fig. 3). The depth of the bar crest is given relative to the Dutch ordnance datum NAP which approximates mean sea level.

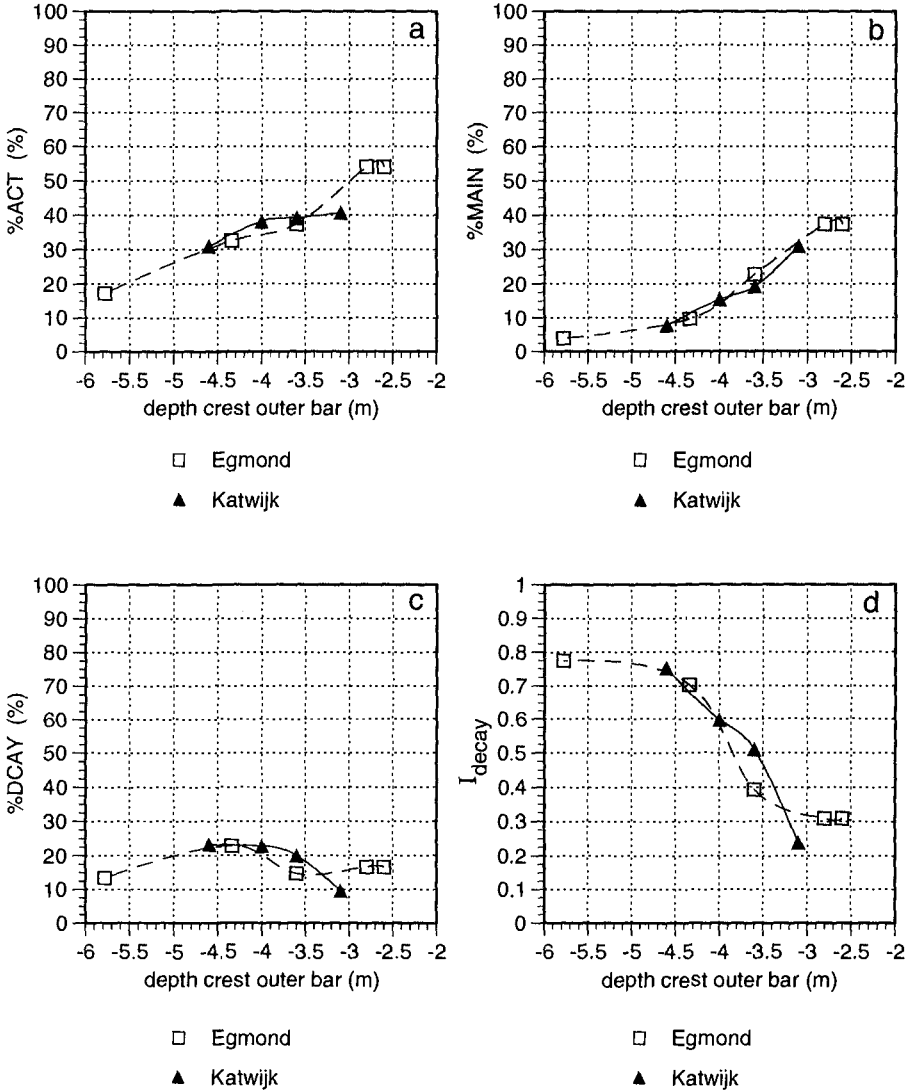


Fig. 4: Nearshore wave climate parameters as a function of the development stage of the outer bar. (a) %ACT, (b) %MAIN, (c) %DCAY, and (d) I_{decay} .

As expected, the percentage of time that morphologically active conditions occur on the outer bar decreases with the increase of depth of the bar crest (Fig. 4a). The percentage of time that bar-maintaining conditions occur on the outer bar decreases steadily with the increase of depth of the bar crest as well (Fig. 4b). The percentage of time that conditions occur that favour decay of the outer bar appears to vary between about 15% and 25% (Fig. 4c). %DCAY seems to reach a maximum around 4 to 4.5 m water depth. The balance between bar-diminishing conditions and bar-maintaining conditions, expressed by I_{decay} , changes with the depth of the crest of the outer bar. The deeper the bar crest, the larger the relative importance of conditions that favour bar decay (Fig. 4d).

The explanation for the fact that %DCAY does not steadily decrease with depth like %ACT and %MAIN, is the following. As the outer bar gets to deeper water, wave conditions that previously (i.e. when the bar was located shallower) produced just over 0.1% of breaking waves, will now produce less than 0.1% of breaking waves. Those wave climate classes will no longer add to the value of %DCAY. However, some of the wave climate classes that previously produced more than 5% of breaking waves on the outer bar will now produce between 0.1% and 5% of breaking waves, and consequently will add to the value of %DCAY.

5.2 Sensitivity of the decay parameter to the definition of %DCAY and %MAIN

The decay parameter I_{decay} reflects the relative importance of %DCAY vs. %MAIN and therefore depends on the definition of the two process regimes in terms of the fraction of breaking waves on the outer bar (Q_b). In this section, the extent to which the results shown in Fig. 4 are sensitive to the choice of the boundaries will be evaluated.

The sensitivity of the values of %DCAY and %MAIN, and consequently %ACT and I_{decay} , to the definition of the process regimes is analysed by plotting the cumulative percentage of occurrence of wave conditions with increasingly higher fractions of breaking (Q_b) waves on the outer bar (Fig. 5). These plots will reveal whether the values of %DCAY and %MAIN are sensitive to the choice of the boundaries between the process regimes in a reasonably close range around the previously defined values of $Q_b=0.001$ and $Q_b=0.05$. For the boundary between %DCAY and %MAIN a value of Q_b between 0.04 and 0.06 is considered, and for the lower boundary of %DCAY a value of Q_b between 0.001 and 0.01

The cumulation in the plots in Fig. 5 starts at a fraction of breaking waves of 0.001. Therefore, the cumulative percentage in Fig. 4 only refers to wave conditions that produce at least 0.1% of breaking waves on the outer bar. For example, on the bar crest at 3.1 m -NAP (Fig. 5a) about 22.5% of the mean annual wave conditions will produce between 0.1% and 8.3% of breaking waves on the outer bar (near Katwijk).

It appears that for the bar crest at 3.1 m -NAP, the variables %DCAY and %MAIN will be quite sensitive to the location of the boundary at $Q_b=0.05$. For the bar crest at 3.1 m -NAP about 11 % of the wave climate is enclosed in the discretely defined wave climate cells that produce a fraction of breaking waves of 0.055 on the outer bar (Fig. 5a). The value of %ACT will be hardly affected at this position of the bar crest.

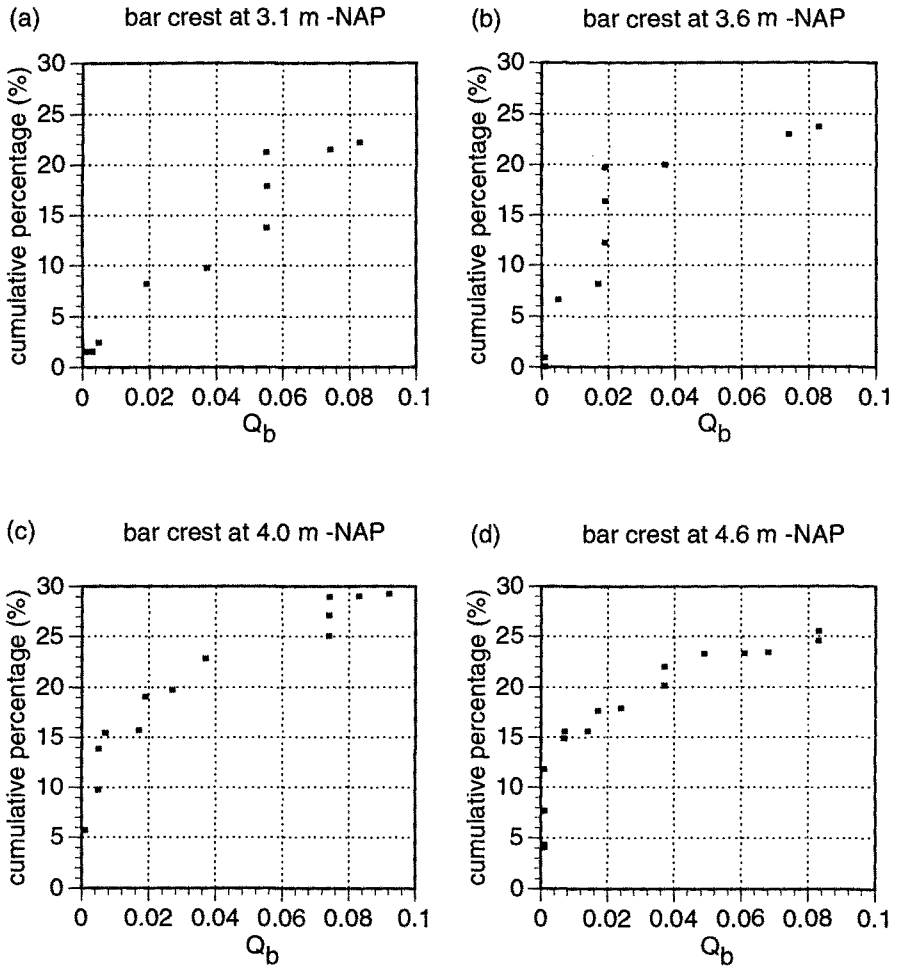


Fig. 5: Cumulative percentage of occurrence of wave conditions with increasingly higher fraction of breaking waves on the outer bar, for $Q_b \geq 0.001$ (Katwijk site). (a) Bar crest at 3.1 m -NAP, (b) bar crest at 3.6 m -NAP, (c) bar crest at 4.0 m -NAP, (d) bar crest at 4.6 m -NAP

A comparable sensitivity to the $Q_b=0.05$ boundary exists at the Egmond site for the bar crests at 2.6 m depth and 2.8 m depth (not shown).

The values of %DCAY and %MAIN on the bar crest located at 3.6 m -NAP will be insensitive to a shift between $Q_b=0.04$ and $Q_b=0.06$ (Fig. 5b). However, %DCAY will be somewhat affected by a raise of the lower boundary to $Q_b=0.01$.

For the positions of the bar crest at 4 m -NAP and 4.6 m -NAP, about 15% of the wave climate appears to be enclosed in wave climate cells that produce a fraction of breaking waves between 0.001 and 0.01 (Fig. 5c,d). Consequently, for these deeper bars the choice of the boundary between morphologically inactive conditions and morphologically active conditions is quite important for the values of %ACT and %DCAY.

The sensitivity of %DCAY and %MAIN - and consequently of %ACT and I_{decay} - to the choice of the boundaries is related to the stepwise increase of cumulative "curves" shown in Fig. 4. This shape is probably related to the discrete description of the wave climate and the discrete description of the input wave fields in the WAVIS model. Only a limited set of combinations of wave heights and wave directions is used for the wave climate description. Each single wave height represents an interval of wave heights and each single wave direction represents a sector of wave directions. In addition, the discrete description of the wave field input in the WAVIS model allows the value of Q_b to change in discrete steps only.

The effect of the discrete description of the wave climate and wave field on Fig.4 can be smoothed by averaging over a set of calculations where the lower boundary of %DCAY was varied between $Q_b=0.01$ and $Q_b=0.001$, and the boundary between %DCAY and %MAIN was varied between $Q_b=0.04$ and $Q_b=0.06$. The result of the averaging is shown in Fig. 6. This figure appears to be very similar to Fig. 4. The smoothed figures, however, reveal more clearly the similarities and differences between the Egmond site and the Katwijk site.

5.3 Differences between the Katwijk and Egmond site

To discuss differences between the Katwijk and Egmond site the smoothed results are analysed (Fig. 6), because these are less affected by the discrete representation of the wave information (see section 5.2).

A difference between the Egmond site and the Katwijk site in the occurrence of morphologically active conditions (Fig. 6a) only occurs for the shallower positions of the outer bar (bar crests shallower than 3.5 m -NAP). At both sites, those shallower outer bars are still in the non-decaying stage of their development. In that non-decaying stage, the percentage of time that morphologically active conditions occur on the outer bar seems to be slightly larger at the Egmond site than at the Katwijk site.

The bar-maintaining conditions occur about equally often at both sites for the deeper positions of the outer bar (Fig. 6b). However, for bar crest positions shallower than 4 m -NAP the bar-maintaining conditions occur somewhat more often near Egmond than near Katwijk.

Regarding the bar-diminishing conditions (Fig. 6c), an obvious difference only occurs for the bar crest position at 3.6 m -NAP, where the bar-diminishing conditions occur more frequently near Katwijk than near Egmond.

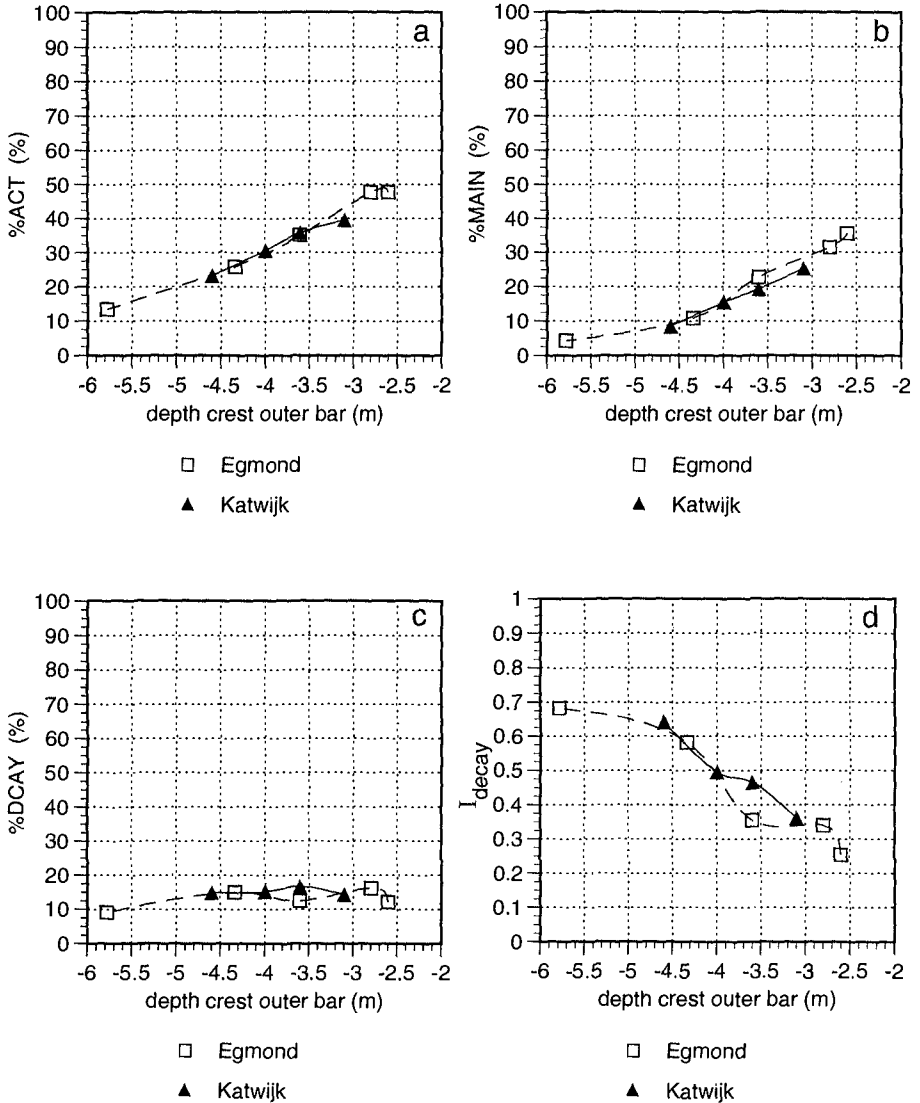


Fig. 6: Smoothed values of the nearshore wave climate parameters as a function of the development stage of the outer bar.
 (a) %ACT, (b) %MAIN, (c) %DCAY, and (d) I_{decay}

The slight differences between the %MAIN and %DCAY 'curves' for Egmond and Katwijk result in I_{decay} 'curves' for Egmond and Katwijk that clearly deviate for the bar crest position at 3.6 m -NAP. This discrepancy was consistently present irrespective of the exact definitions of the boundaries between the process regimes in terms of Q_b (Wijnberg, 1995). The relatively frequent occurrence of bar-diminishing conditions near Katwijk around 3.6 m -NAP coincides with the onset of bar decay at this location. Near Egmond, an outer bar with its crest at 3.6 m -NAP is still in a non-decaying stage.

6. DISCUSSION AND CONCLUSIONS

The relationship found between the decay parameter and the development stage of the outer bar, as shown in Fig. 4d and 6d, supports the concept that the balance between bar-diminishing conditions (very asymmetric waves) and bar-maintaining conditions (breaking waves) is important for the fate of the outer bar. These results support the bar-decay hypothesis for two reasons. Firstly, the value of the decay parameter increases with the depth of the outer bar crest. This indicates an increase in the relative importance of the bar-diminishing conditions with depth, as was expected from the formulated hypothesis. Secondly, the difference between the Egmond and Katwijk site in the depth of onset of bar decay is well indicated by the decay parameter.

The results presented in Section 5 further indicate that the chosen definitions of the two process regimes in terms of the fraction of breaking waves (Q_b) enclose the relevant processes for respectively maintaining bar topography and diminishing bar topography. It is emphasized that no choice is made here for a particular mechanism that maintains the bar topography other than that this mechanism is directly or indirectly related to the occurrence of wave breaking. Long-wave mechanisms are therefore not excluded here (eg. bound long waves can be released in the surfzone by the breaking of the short waves).

The suggested mechanism for the systematic decay of the outer bar could not directly be verified with field observations. The currently existing bathymetric surveys in the studied area are too widely spaced in time to pinpoint the hydrodynamic conditions responsible for the observed (net) changes in the outer bar topography. The relatively wide spacing of the surveys is due to the fact that ships can only survey the nearshore bathymetry during relatively calm conditions, and consequently cannot survey during the conditions that are hypothesized to be important for the behaviour of the outer bar. Remote-sensing systems like the video-monitoring system introduced by Lippmann and Holman (1989) might be a valuable tool for obtaining the required high resolution morphologic information during the more severe wave conditions.

To conclude, the presented conceptual model for the systematic offshore decay of breaker bars seems viable. However, the results presented in this paper are considered to be supporting evidence for the hypothesis rather than a real proof of it. For a more rigorous verification of the conceptual model field observations are needed of the process of bar decay itself.

ACKNOWLEDGEMENTS

This paper is based on work in the PACE-project, in the framework of the EU-sponsored Marine Science and Technology Programme (MAST-III), under contract number MAS3-CT95-0002. The work was co-sponsored by the Andrew Mellon Foundation.

The *Rijkswaterstaat* (Dutch Ministry of Transport, Public Works and Water Management) is thanked for providing the wave climate data and the bathymetry data.

REFERENCES

- Bakker, W.T., and H.J. De Vroeg, 1988. Is de kust veilig? Analyse van het gedrag van de Hollandse kust in de laatste 20 jaar. Nota GWAO 88.017, Rijkswaterstaat, Den Haag, The Netherlands, 42 p.
- Edelman, T., 1974. Bijdrage tot de historische geografie van de Nederalndse kuststrook. Rijkswaterstaat / Directie Waterhuishouding en Waterbeweging, Den Haag, The Netherlands, 84 p.
- Hoekstra, P., K.T. Houwman, A.Kroon, P. van Vessem, and B.G. Ruessink, 1994. The Nourtec experiment of Terschelling: process-oriented monitoring of a shoreface nourishment (1993-1996). Proceedings Coastal Dynamics '94, Barcelona, ASCE: 402-416.
- Lippmann, T.C., and R.A. Holman, 1989. Quantification of sand bar morphology: a video technique based on wave dissipation. Journal of Geophysical Research 94 (C1): 995-1011.
- Lippmann, T.C., R.A. Holman, and K.K. Hathaway, 1993. Episodic, nonstationary behaviour of a double bar system at Duck, North Carolina, U.S.A., 1986-1991. Journal of Coastal Research 15 Special Issue: 49-75.
- Roelvink, J.A., Th.J.G.P. Meijer, K. Houwman, R. Bakker, and R.Spanhoff, 1995. Field validation and application of a coastal profile model. Proceedings Coastal Dynamics '95, Gdansk, ASCE: 818-828.
- Ruessink, B.G. and A. Kroon, 1994. The behaviour of a multiple bar system in the nearshore zone of Terschelling, the Netherlands: 1965-1993. Marine Geology 121: 187-197.
- Van Rijn, L.C. and K.M. Wijnberg, 1996. One-dimensional modelling of individual waves and wave-induced longshore currents in the surf zone. Coastal Engineering 28: 121-146.
- Wijnberg, K.M., 1995. Morphologic behaviour of a barred caost over a period of decades. PhD thesis Utrecht University, The Netherlands. Netherlands Geographical Studies 195, KNAG, 245 p.
- Wijnberg, K.M., in prep. Long term behaviour of multiple breaker bar systems along the Holland coast.
- Wijnberg, K.M., and J.H.J. Terwindt, 1995. Extracting decadal morphological behaviour from high-resolution, long-term bathymetric surveys along the Holland coast using eigenfunction analysis. Marine Geology 126: 301-330.

CHAPTER 279

LONGSHORE BED-LOAD TRANSPORT

Jesper S. Damgaard ¹ and Richard L. Soulsby ¹

Abstract.

An analytical formula for longshore bed-load sediment transport is derived. The derivation is based on sediment physics and the formula is therefore less dependent on calibration. The formula is compared to the CERC formula, a numerical model and field data.

1 Introduction.

Around the UK coastline shingle and gravel beaches are common and considerable resources are spent on preserving and/or predicting the behavior of these beaches. Therefore, it is important for coastal engineers to have an easily applicable tool with which to predict the littoral drift of sediments consisting of larger grain sizes.

The most widely used longshore sediment transport formula is probably the CERC -formula (Coastal Engineering Research Center, 1977) which is based on the concept that the longshore sediment transport rate is dependent on the longshore component of wave energy flux $E_b(C_g)_b \cos(\alpha_b) \sin(\alpha_b)$, where subscript 'b' denotes values at the breaking point, E is the wave energy, C_g is the group velocity and α is the angle of wave incidence. There exist numerous extensions and variations of the CERC formula. Despite its popularity there are three major shortcomings of this type of formulae: i) it relies heavily on calibration, ii) it does not contain a threshold term, iii) it contains no dependence on grain or beach properties. The necessity of a calibration limits the predictive quality of the formula. Furthermore the calibrations of CERC type formulae are often performed using field data sets with different levels of variance within those data sets and with considerable systematic errors (Greer and Madsen, 1978). The inclusion of a threshold term is especially important for the determination of transport rates for large grain size sediments, as will be shown in the present paper.

¹Marine Sediments Group, HR Wallingford Ltd., Wallingford, Oxon OX10 8BA, UK.

2 The present study

It is the purpose of the present study to derive an analytical cross-shore integrated bed-load transport formula. The derivation is based on a bed-load transport formula for combined waves and currents developed by Soulsby (1996), which relates the wave-averaged value $\langle \dots \rangle$ of the non-dimensional bed-load transport rate vector $\vec{\Phi}$

$$\vec{\Phi} = \frac{\vec{q}_b}{\sqrt{(s-1)gd^3}} \tag{1}$$

to the non-dimensional bottom shear-stress vector due to skin friction induced by waves plus currents (Shields parameter) $\vec{\theta}$

$$\vec{\theta} = \frac{\vec{\tau}'_b}{\rho g(s-1)d} \tag{2}$$

where q_b is the volumetric bed-load transport rate per unit width and time, s is the relative density of the sediment, g is the acceleration of gravity, d is the grain size and τ'_b is the skin friction at the bed. The bed-load transport formula is based on a separation of the shear stress vector into a mean and an oscillatory part:

$$\vec{\theta}(\omega t) = \vec{\theta}_m + \vec{\theta}_w \cos(\omega t) \tag{3}$$

where ω is the frequency of the incoming waves. The coordinate system (x, y) is chosen such that $\vec{\theta}_m$ is parallel to the x -axis (see figure 1).

The formula has been extended to cover asymmetric waves (Damgaard *et al*, 1996) but since the asymmetry will have no significant impact on long-shore sediment transport calculations all higher order harmonics are set to zero for the present application. The bed-load transport formula of Soulsby (1996) reads:

$$\langle \vec{\Phi} \rangle = \begin{pmatrix} \Phi_x \\ \Phi_y \end{pmatrix} \tag{4}$$

with the components given as

$$\Phi_x = \text{sign}\{\Phi_{x1}, \Phi_{x2}\} \max\{\Phi_{x1}, |\Phi_{x2}|, |\}\tag{5}$$

$$\Phi_{x1} = \begin{cases} 12\sqrt{\theta_m}(\theta_m - \theta_{cr}) & \text{for } \theta_m > \theta_{cr} \\ 0 & \text{for } \theta_m \leq \theta_{cr} \end{cases} \tag{6}$$

$$\Phi_{x2} = 12(0.95 + 0.19 \cos 2\varphi)\theta_m\sqrt{\theta_w} \tag{7}$$

$$\Phi_y = \frac{12(0.19\theta_m\theta_w^2 \sin 2\varphi)}{\theta_w^{3/2} + 1.5\theta_m^{3/2}} \tag{8}$$

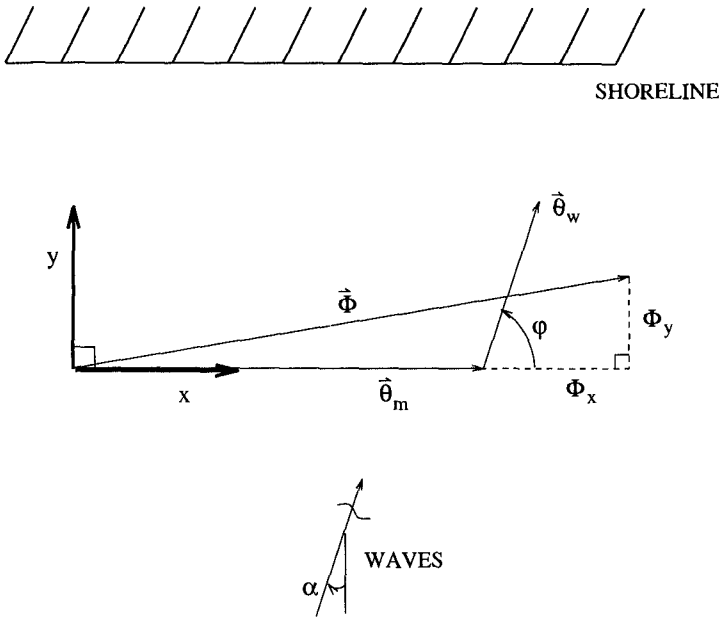


Figure 1: Definitions.

subject to the threshold condition

$$\Phi_x = \Phi_y = 0 \text{ for } \theta_{max} \leq \theta_{cr} \quad (9)$$

where φ is the angle between $\vec{\theta}_m$ and $\vec{\theta}_w$ and θ_{max} is the maximum Shields parameter for waves + currents within a wave cycle. Current dominated conditions correspond to Φ_{x1} and wave-dominated conditions to Φ_{x2} . The threshold condition is necessary as no threshold term appears explicitly in the formula for Φ_{x2} . It is important to note the fact that the formula is based on dimensionless parameters which makes it applicable to model as well as prototype scale.

The procedure of derivation for the analytical formula is as follows: Approximate expressions for the mean bottom shear-stresses, required as input to the bed-load transport formula are derived directly from the depth-integrated momentum equation. This avoids the need to calculate the speed of the longshore current. In order to solve the momentum equation analytically a number of assumptions have been made.

- (i) The ratio of wave-height, H_b , and water depth, h_b , at the breaker point is constant, $H_b/h_b = \gamma_b = 0.8$.
- (ii) After breaking the 1 decays linearly, so that $H = \gamma_b h$.
- (iii) No further refraction takes place beyond the breaking point, i.e. the angle of wave incidence, α , is constant in the surf zone, $\alpha(y) = \alpha_b$.
- (iv) All waves break at the same location.

- (v) Shallow-water linear wave theory is used in the surf zone.
 (vi) The effect of a lateral bed slope on the sediment transport is neglected.
 (vii) The effect of cross-shore currents (e.g. undertow) on the longshore transport is neglected.

Furthermore the variation in mean water level (set-down and set-up) is ignored and the beach is assumed to be plane with a constant slope, $\tan\beta$. Ignoring the lateral transfer of turbulent momentum the depth-integrated momentum equation for a longshore uniform beach reduces to a balance between the cross-shore gradient of the shear component of the radiation stress and the bottom friction:

$$\frac{\partial S_{xy}}{\partial y} = -\tau_{b,x} \quad (10)$$

where S_{xy} is the shear component of the radiation stress and $\tau_{b,x}$ is the x -component of the bed shear stress. The (x, y) -coordinate system used here is chosen such that the x -axis is parallel to the coast, and y is directed on-shore with origin shoreward of the breaker line. The relation between φ and α_b is $\varphi = \frac{\pi}{2} - \alpha_b$. The radiation stress can be expressed in terms of the momentum flux, F_m , in the direction of wave propagation:

$$S_{xy} = F_m \cos(\alpha) \sin(\alpha) \quad (11)$$

in which α is the angle of wave incidence and F_m is determined according to linear wave theory as:

$$F_m = \frac{1}{8} \rho g H^2 \quad (12)$$

Combining equations (10), (11) and (12) yields an expression for τ_b

$$\tau_b = -\frac{1}{16} \rho g \frac{\partial}{\partial y} (\sin(2\alpha) H^2) \quad (13)$$

According to the assumptions employed regarding refraction and wave height decay, (13) reduces to:

$$\begin{aligned} \tau_b &= -\frac{1}{16} \rho g \sin(2\alpha_b) 2H \frac{\partial H}{\partial y} \\ &= \frac{\gamma_b}{8} \rho g H \sin(2\alpha_b) \tan\beta \end{aligned} \quad (14)$$

in which h is the depth and γ_b is the constant ratio between wave height and depth in the surf zone. Thus the shore parallel component of the mean Shields parameter can be expressed as:

$$\theta_{m,x} = \frac{\gamma_b H \sin(2\alpha_b) \tan\beta}{8(s-1)d} \quad (15)$$

The amplitude of the oscillatory component of the bottom friction is calculated using a quadratic friction law

$$\tau_w = \frac{1}{2} \rho f_w U_w^2 \quad (16)$$

where f_w is the wave friction coefficient. The wave orbital velocity is estimated using shallow water linear wave theory i.e. $kh \ll 1$, $c = \sqrt{gh}$:

$$\begin{aligned} U_w &= \frac{\pi H}{T} \frac{1}{\sinh(kh)} \\ &\simeq \frac{1}{2} \sqrt{\frac{g}{h}} H = \frac{1}{2} \sqrt{g\gamma_b H} \end{aligned} \quad (17)$$

where T is wave period and k is the wavenumber. Two different friction factors were used. For rough turbulent flows Soulsby (1994) obtained an expression for the wave friction factor $f_{w,r}$ based on the analysis of a large data set:

$$\begin{aligned} f_{w,r} &= 1.39 \left(\frac{A}{z_0} \right)^{-0.52} \\ &\simeq \sqrt{\frac{d}{U_w T}} \\ &\simeq (g\gamma_b H)^{-1/4} \sqrt{\frac{2d}{T}} \end{aligned} \quad (18)$$

in which A is the amplitude of the near bed orbital motion, and the roughness length $z_0 = d/12$. The above equation is valid for weak sediment motion or immobile beds. For sheet flow conditions ($\theta > \text{say } 1$) Wilson (1989) derived a friction coefficient, $f_{w,sf}$:

$$\begin{aligned} f_{w,sf} &= 0.114 \left(\frac{A}{g(s-1)T^2} \right)^{2/5} \\ &\simeq 0.0655 \left(\frac{\gamma_b H}{g} \right)^{1/5} (\pi(s-1)T)^{-2/5} \end{aligned} \quad (19)$$

The actual friction coefficient for a particular wave condition was taken as the maximum of $f_{w,r}$ or $f_{w,sf}$. In accord with experimental observations (Simons *et al.*, 1994), the friction factor for the waves is not enhanced by the presence of a near-normal incidence current.

The oscillatory component of the Shields parameter can be expressed using equations (2), (16), (17) and (18) and (19) respectively

$$\theta_{w,r} = \frac{\sqrt{2}}{8} g^{-1/4} \frac{(\gamma_b H)^{3/4}}{(s-1)\sqrt{dT}} \quad (20)$$

and

$$\theta_{w,sf} = 8.187 \cdot 10^{-3} g^{-1/5} (\pi(s-1)T)^{-2/5} \frac{(\gamma_b H)^{6/5}}{(s-1)d} \quad (21)$$

Now the current-dominated case of the dimensionless bed-load transport rate is calculated by inserting equation (15) into equation (6)

$$\Phi_{x1} = 0.530 \left(\frac{\gamma_b H \tan \beta}{(s-1)d} \right)^{3/2} (\sin(2\alpha_b) - \theta_{cr}^*) \sqrt{|\sin(2\alpha_b)|} \quad (22)$$

where

$$\theta_{cr}^* = \theta_{cr} \frac{8(s-1)d}{\gamma_b H \tan \beta} \tag{23}$$

and the wave-dominated case (subject to flow regime) is determined by inserting equation (15) and (20) or (21) into equation (7)

$$\Phi_{x2,r} = (0.602 + 0.120 \cos(2\varphi)) \frac{(\gamma_b H)^{11/8} \tan \beta \sin(2\alpha_b)}{g^{1/8} d^{5/4} T^{1/4} (s-1)^{3/2}} \tag{24}$$

or

$$\Phi_{x2,sf} = (0.129 + 0.0259 \cos(2\varphi)) \frac{(\gamma_b H)^{8/5} \tan \beta \sin(2\alpha_b)}{g^{1/10} d^{3/2} (\pi T)^{1/5} (s-1)^{17/10}} \tag{25}$$

In order to transform to a bulk transport formula, equations (22), (24) and (25) are integrated across the surf zone, using assumptions (i) and (ii) above:

$$\int_{\text{surf zone}} \Phi_x dy = \int_{H_b}^0 \Phi_x \frac{1}{dH/dy} dH = \frac{-1}{\gamma_b \tan \beta} \int_{H_b}^0 \Phi_x dH \tag{26}$$

The cross-shore integrated volumetric sediment transport rate $Q'_{b,l}$ [m^3/s] is given as

$$Q'_{b,l} = \sqrt{g(s-1)d^3} \int_{\text{surf zone}} \Phi dy \tag{27}$$

and the resulting analytical formula for $Q_{b,l}$ is expressed as a combination of a current dominated transport (Q_{x1}) and a wave dominated transport (Q_{x2}):

$$Q'_{b,l} = \text{sign}\{\alpha_b\} \max\{|Q_{x1}|, |Q_{x2}|\} \tag{28}$$

$$Q_{x1} = \begin{cases} 0.21 \frac{\sqrt{g\gamma_b \tan \beta} H_b^{5/2}}{(s-1)} \left(\sin(2\alpha_b) - \frac{5}{3} \theta_{cr}^* \right) \sqrt{|\sin(2\alpha_b)|} & \text{for } \sin(2\alpha_b) > \frac{5}{3} \theta_{cr}^* \\ 0 & \text{for } \sin(2\alpha_b) \leq \frac{5}{3} \theta_{cr}^* \end{cases} \tag{29}$$

$$Q_{x2} = \begin{cases} (0.25 + 0.051 \cos(2\varphi)) \frac{g^{3/8} d^{1/4} \gamma_b^{3/8} H_b^{19/8}}{T^{1/4} (s-1)} \sin(2\alpha_b) & \text{for } f_{w,r}/f_{w,sf} > 1 \\ (0.050 + 0.010 \cos(2\varphi)) \frac{g^{2/5} \gamma_b^{3/5} H_b^{13/5}}{(\pi T)^{1/5} (s-1)^{6/5}} \sin(2\alpha_b) & \text{for } f_{w,r}/f_{w,sf} \leq 1 \end{cases} \tag{30}$$

subject to the threshold condition

$$Q'_{b,l} = 0 \text{ for } \theta_{max} \leq \theta_{cr} \quad (31)$$

where

$$\theta_{max} = \sqrt{(\theta_m + \theta_w \cos \varphi)^2 + (\theta_w \sin \varphi)^2} \quad (32)$$

In general the current dominated term, Q_{x1} , is used for large wave heights, small grain sizes and large beach slopes. In most cases $f_{w,r} > f_{w,sf}$. This is especially true for larger grain sizes which are rarely transported as sheet flow. A study of a field data set with approximately 25000 wave conditions sampled throughout a 4 year period (see section 4) showed that Q_{x1} was applied for approximately 60 % of the wave conditions, Q_{x2} with $f_{w,r}$ for the remaining 40 % of the conditions and Q_{x2} with $f_{w,sf}$ was not applied at all for that particular data set.

3 Comparison with the CERC formula.

The CERC-formula is probably the most widely used longshore sediment transport formula. In the course of the time since the CERC-formula was derived, several 'mutations' have emerged; only some of them will be mentioned here. Van Hijum and Pilarczyk (1982) analysed laboratory experiments on shingle transport and, using dimensional analysis, came up with an expression for littoral shingle drift. Their expression did contain a threshold term. Bailard (1987) derived an energetics based sediment transport formula which had the ratio of amplitude of orbital velocity to fall velocity of the sediment as an additional parameter. Kamphuis (1991) derived a longshore sediment transport formula based on dimensional analysis. The formula was calibrated using laboratory results obtained by Kamphuis and co-workers at Queens University. The drawback of these formulations is that they are not founded on sediment transport physics but on a relation between overall dissipation of wave energy and transport of sediments in a heuristic way.

Since the present formula (equations (28) to (32)) claims to be an improvement compared to the CERC- formula it is relevant to compare them. Using linear shallow-water wave theory and a constant breaking criterion the CERC-formula can be written as

$$Q_{CERC} = \frac{K_{CERC}}{16} \sqrt{\frac{g}{\gamma_b}} \frac{H_b^{\frac{5}{2}} \sin(2\alpha_b)}{(s-1)} \quad (33)$$

in which Q_{CERC} is the longshore sediment transport rate in solid volume per second. The constant K_{CERC} is equal to 0.77 for regular waves and for irregular waves with $H = H_{rms}$. Figure 2 shows a comparison between the analytical model (equations (28) to (32)) and the CERC formula (equation (33)). Figures 2(a) to

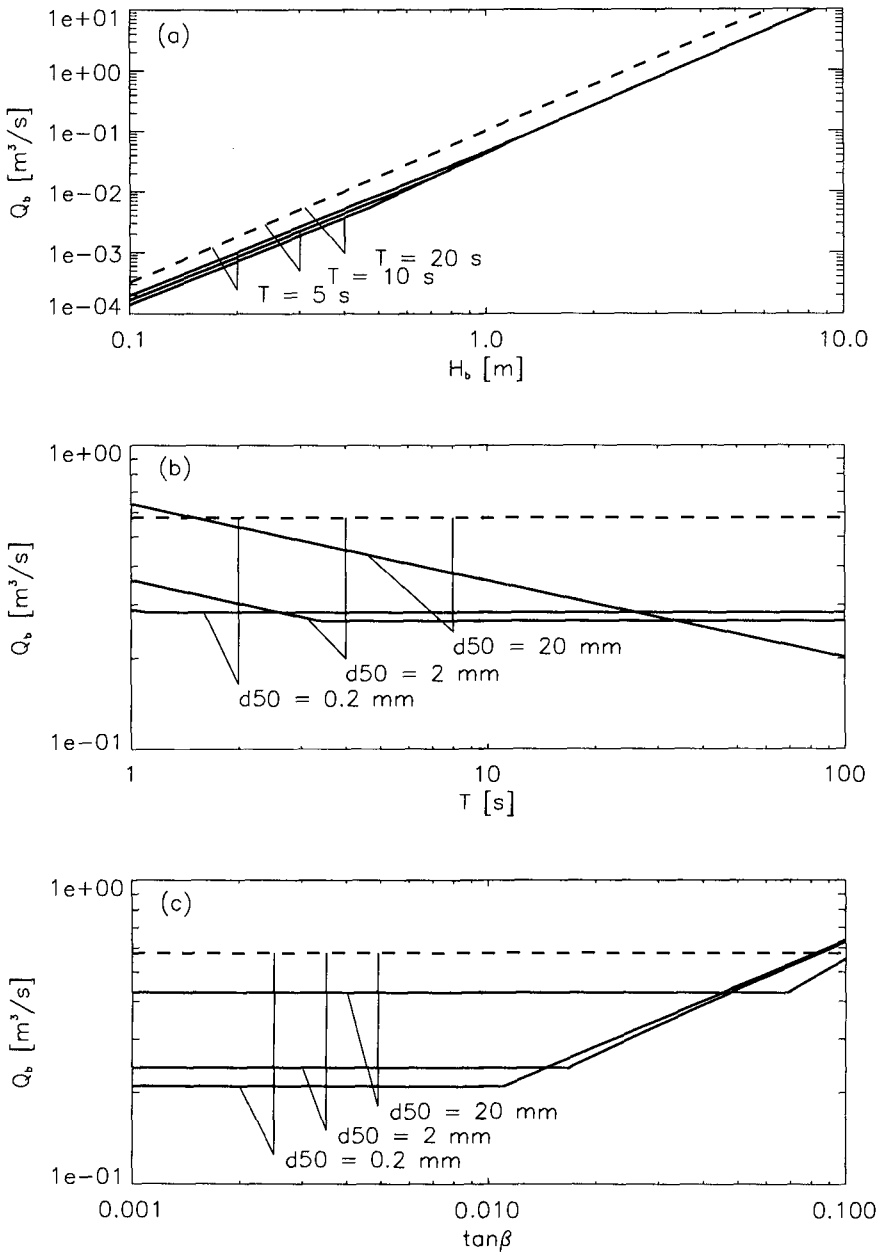
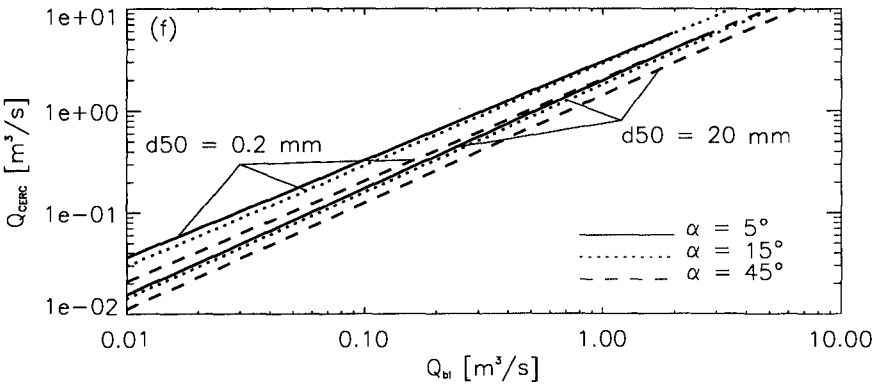
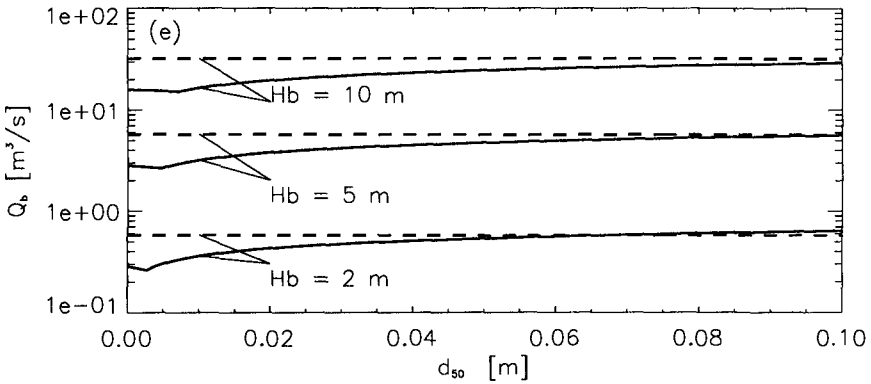
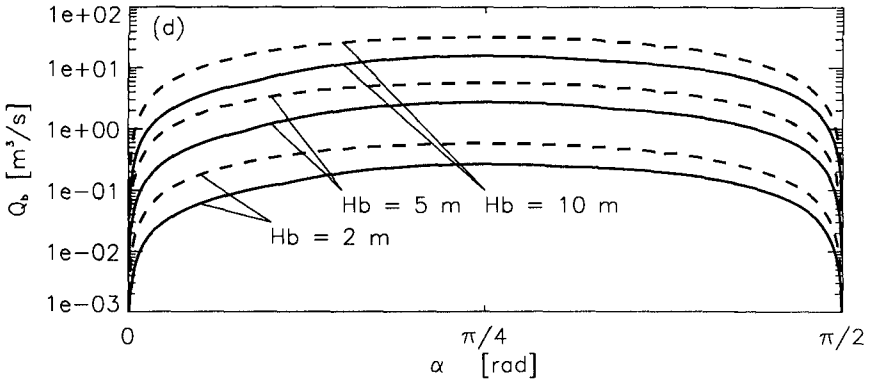


Figure 2: Comparison between the CERC formula (dashed line) and the analytical model (solid lines).



2(e) depicts the respective values of the littoral drift for the parameter range of the governing variables. The basic values of the parameters are: $H_b = 2.0m$, $T = 5s$, $d_{50} = 2.0mm$, $\tan\beta = 1/50$, $\alpha_b = 45$ and $\theta_{cr} = 0.05$. Each plot uses mainly the basic values, and varies the values of two parameters over a range. The parameter ranges are supposed to represent realistic values plus a bit more at each end of the range. Figure 2(f) shows a direct comparison between the analytical model and the CERC formula. The new method follows a broadly similar pattern to the CERC formula, but differs by up to a factor of 3 (generally smaller), depending on the value of T , d_{50} , $\tan\beta$, and α .

One of the shortcomings of the CERC formula is its lack of a grain size dependency. The sediment transport rate might actually not be so sensitive to modest changes in grain size but since the grain size on natural beaches can easily vary by two orders of magnitude (from fine sand $\simeq 100\mu m$ to gravel $\simeq 10mm$) the grain size dependency can be important. Thus, when it is taken into account that the CERC formula was calibrated using data from sandy beaches with values of d_{50} less than $500\mu m$, it is not surprising that it does not perform well for large grain sizes. For use on shingle or gravel beaches it is customary to multiply the CERC formula with a factor $\simeq \frac{1}{18}$ (see Brampton and Motyka, 1984) however, it is not clear what the procedure is for grain sizes in the intermediate range and this highlights one of the shortcomings of the CERC formula *viz.* the CERC-constant is not constant throughout the range of naturally existent grain sizes.

4 Comparison with data.

In order to quantify the deviation caused by the hydrodynamic assumptions employed, the results of the analytical formula were compared to the results of a numerical profile model using a state-of-the-art hydrodynamic module to propagate the waves inshore and calculate the bed shear-stress distribution (Southgate and Nairn, 1993). Bed-load transport was predicted by the formula of Soulsby (1996) given by equations (4) to (9) at a number of grid points across the profile and then cross-shore integrated numerically. The field data were provided by an extensive field observation programme of shingle beach re-nourishment at Seaford Beach on the south coast of England including more than three years of wave and sediment data. The wave data were obtained by a buoy located offshore at 10 m depth. Data were sampled every third hour and from the spectra the significant wave height, $H_s = \sqrt{2}H_{rms}$, the peak period, T_p , and the direction, α , were derived. For the analytical model and the CERC formula, the waves were propagated to the breaking point using Snel's law. Shingle transport volumes were determined through analysis of the beach profile surveys taken every 2-3 months during the period in question, at transects positioned along the beach at approximately 100m intervals. The results of the comparison are shown in figure 3, for the analytical model (equations (28) to (32)), the numerical model and the CERC formula. The full numerical model in conjunction with the bed-load trans-

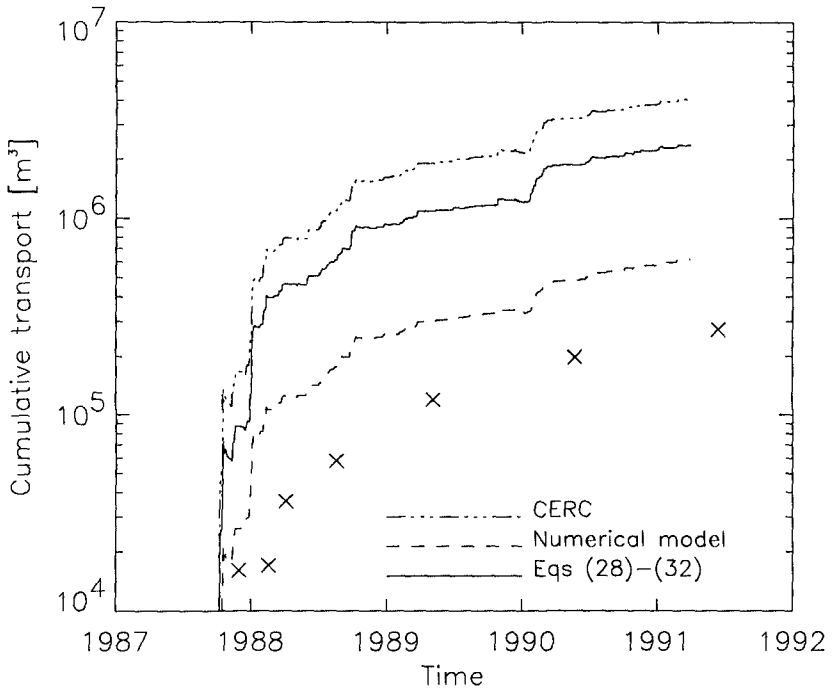


Figure 3: Comparison between the CERC formula, the numerical model, and the analytical model (equations (28) to (32)) for the Seaford data.

port formula gave relatively good results: it predicted the littoral drift within a factor 3, whereas the analytical model consistently over predicted by a factor 12, and the CERC formula over predicted by a factor 20. The fact that the hydrodynamically more advanced numerical model performed better was taken as an expression of the relevance of the sediment transport formulation and the factor 12 was interpreted as a quantitative representation of the errors made in applying the before mentioned hydrodynamic assumptions to the analytical model. The formula has therefore been corrected through dividing by this constant factor. Thus the corrected analytical formula gives the longshore transport rate, $Q_{b,l}$, as $Q_{b,l} = \frac{1}{12} Q'_{b,l}$ with $Q'_{b,l}$ given by equations (28) to (32).

The existence of a threshold term is very important particularly for larger grain sizes. The study of the Seaford data showed that a decrease in θ_{cr} from 0.05 to zero, increased the shingle transport by a factor 3.

The corrected analytical formula has been applied to a number of shingle field and laboratory data sets: Van Hijum and Pilarczyk (1982) did laboratory experiments at Delft Hydraulics (DH) with shingle transport under the action

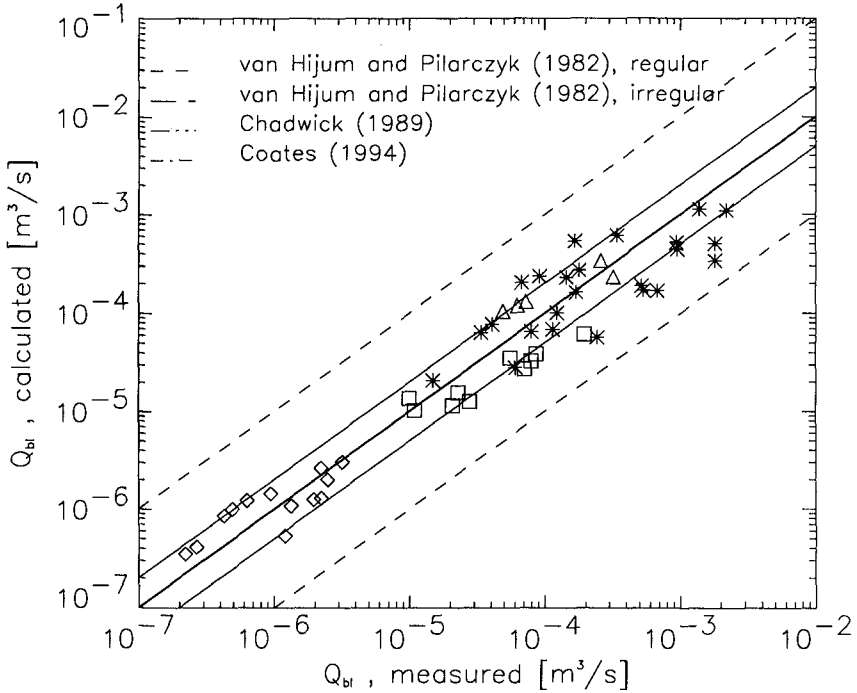


Figure 4: Comparison of the corrected analytical formula with existing field and laboratory data.

of regular and irregular waves, Chadwick (1989) collected field data of longshore shingle transport near Brighton, UK, and Coates (1994) did physical model studies of shingle transport at HR Wallingford. The results are shown in figure 4: Most transport rates are predicted within a factor 2 and all data sets are predicted within a factor 10.

5 Conclusions.

An analytical longshore bed-load transport formula has been developed from a bed-load transport formula developed at HR. Thus, the analytical formula is based on sediment transport physics and has been verified against a state-of-the-art numerical model and field data. This indicated the need to introduce a correction factor arising from grossly simplified assumptions about the hydrodynamics in the analytical model.

A major improvement on the CERC formula is dependencies on the grain size, beach slope and wave period, and the inclusion of a threshold term, which

has proven to be very important for the quantitative prediction of littoral shingle drift.

Acknowledgements.

The UK Ministry of Agriculture, Fisheries and Food provided the financial support for this work.

The authors would like to thank Stuart Stripling, Marine Sediments Group, HR Wallingford for running the numerical model.

References

- [1] J.A. Bailard. A simplified model for longshore sediment transport. In *Proc. 19th Int. Conf. Coastal Eng.*, pages 1454–1470, Houston, 1984.
- [2] A.H. Brampton and J.M. Motyka. Modelling the plan shape of shingle beaches. In *POLYMODEL7 Conference*, pages 219–233, Sunderland Polytechnic, 1984.
- [3] Coastal Engineering Research Center. Shore protection manual. Technical report, U.S.Army Corps of Engineers, Washington, 1977.
- [4] A.J. Chadwick. Measurements and numerical model verification of coastal shingle transport. In Palmer M.H., editor, *Advances in Water Modelling and Measurement*. British Hydromechanics Research Association, Cranfield, 1989.
- [5] T.T. Coates. Effectiveness of control structures on shingle beaches. Report SR 387, HR Wallingford, Wallingford, 1994.
- [6] J.S. Damgaard, S. Stripling, and R.L. Soulsby. Numerical modelling of coastal shingle transport. Report TR 4, HR Wallingford, Wallingford, 1996.
- [7] M.N. Greer and O.S. Madsen. Longshore sediment transport data: A review. In *Proc. 16th Int. Conf. Coastal Eng.*, pages 1563–1576, Hamburg, 1978.
- [8] J.W. Kamphuis. Alongshore sediment transport rate. *J. Waterway, Port, Coastal and Ocean Eng.*, 117(6):624–640, 1991.
- [9] R.R. Simons, A.J. Grass, W.M. Saleh, and M.M. Tehrani. Bottom shear stress under random waves with a current superimposed. In *Proc. 24th Int. Conf. Coastal Eng.*, pages 565–578, Kobe, 1994.
- [10] R.L. Soulsby. Manual of marine sands. Report SR 466, HR Wallingford, Wallingford, 1996.

- [11] H.N. Southgate and R.B. Nairn. Deterministic profile modeling of nearshore processes. *Coastal Eng.*, 19:27–56, 1993.
- [12] E. van Hijum and K.W.Pilarczyk. Equilibrium profile and longshore transport of coarse material under regular and irregular wave attack. Publication no. 274, Delft Hydraulics, Delft, 1982.
- [13] K.C. Wilson. Friction of wave induced sheet flow. *Coastal Eng.*, 12:371–379, 1989.

CHAPTER 280

Design Capacity of a Longshore Current Recirculation System for a Longshore Sediment Transport Laboratory Facility

David G. Hamilton¹, Julie D. Rosati², Jimmy E. Fowler², and Jane M. Smith²

ABSTRACT

A new longshore sediment transport laboratory facility for conducting three-dimensional moveable-bed experiments is being developed by the U.S. Army Engineer Waterways Experiment Station, Coastal and Hydraulics Laboratory. This paper focuses on the problem of designing the pumping capacity for an external longshore current recirculation system, designed to minimize adverse laboratory effects created by the updrift and downdrift lateral boundaries of the new facility. A review of longshore current recirculation systems used in other laboratory facilities is presented. The numerical model NMLONG is used to predict the magnitude and cross-shore distribution of the wave-driven longshore current that will be generated during experiments in the new facility. This paper concludes with a performance curve that defines the required pumping capacity of each of the individual pumps in the longshore current recirculation system.

1. INTRODUCTION

In performing its mission to maintain navigable waterways along U.S. coasts, the U.S. Army Corps of Engineers (USACE) regularly applies analytical and numerical models to estimate the total longshore sediment transport (LST) rate. Accurate prediction of LST rate is essential when predicting beach response in the vicinity of coastal structures, designing artificial beach nourishment projects, and approximating sedimentation rates in navigation channels. For design applications with adequate field measurements, the commonly used CERC formula (Shore Protection Manual, 1984) can be calibrated and applied to estimate total LST rates with reasonable confidence. However, for design applications without calibration data, the CERC formula provides only order-of-magnitude accuracy.

The present work is part of a research program intended to improve the USACE's capabilities to predict local and total LST rates and to evaluate errors associated with these predictions. The first goal of this research is to develop a world-class Longshore Sediment Transport Facility (LSTF) for conducting three-dimensional moveable-bed experiments. The LSTF will simulate nearshore hydrodynamic and sediment transport processes at a relatively large geometric scale. Further information on the objectives of this research program and general planning and design considerations for this new laboratory facility can be found in Rosati et al. (1995).

¹ Coastal Engineer, CS-310 Cain Ridge Rd., Vicksburg, Mississippi, USA, 39180.

Tel: 601 634-3029, Fax: 601 634-4314, Email: D.Hamilton@CERC.WES.ARMY.MIL

² Research Hydraulic Engineer, USAE Waterways Experiment Station, Coastal and Hydraulic Laboratory, 3909 Halls Ferry Road, Vicksburg, Mississippi, USA, 39180-6199

This paper focuses on the problem of calculating the required pumping capacity of a longshore current (LSC) recirculation system being designed to minimize the adverse laboratory effects created by the updrift and downdrift lateral boundaries of the LSTF.

The following sections review other LSC recirculation systems, provide a brief description of the LSTF, and discuss results obtained using the numerical model NMLONG to estimate the magnitude and cross-shore distribution of LSC that will be generated in the LSTF. Subsequent sections discuss limitations of the numerical analysis and other design parameters required to determine the design capacity of the LSC recirculation system. The final section provides a performance curve that defines the required pumping capacity for each of the individual pumps in the LSC recirculation system.

2. REVIEW OF OTHER LSC RECIRCULATION SYSTEMS

Early longshore current laboratory experiments were conducted without a LSC recirculation system that would have minimized the adverse laboratory effects created by the updrift and downdrift boundaries of each facility. Putman, Munk and Taylor (1949) used the sidewalls of the tank as wave guides to train the waves onto the beach. The LSC generated on the beach became part of the internal circulation pattern in the wave basin, which is considerably different than the situation on a long straight coast. Brebner and Kamphuis (1963) terminated the wave guides near the break point allowing the LSC to passively enter and exit the beach. Galvin and Eagleson (1965) and Mizuguchi and Horikawa (1978) terminated the downdrift wave guide at the break point, and completely closed the updrift wave guide. Apparently the longshore flux, in both of these experiments, was entering the test area underneath the wave generator, which would cause a non-uniform LSC distribution along the beach. Galvin and Eagleson (1965) were the first to measure the cross-shore distribution of LSC at several transects along the beach. Their data revealed the adverse effects created by the updrift and downdrift boundaries of the facility, in that the LSC was not able to reach its equilibrium magnitude and cross-shore distribution.

Visser (1982) conducted what appears to be the most detailed LSC experiments conducted to date. The wave basin was relatively large with a beach length between the wave guides of approximately 20 m. Visser's experiments were the first to use a LSC recirculation system to recirculate water from the downdrift to the updrift end of the beach. For most of Visser's experiments, the cross-shore distribution at the updrift boundary was controlled using 12 flow channels and control gates. Each flow channel was 0.2 and 0.4 m wide for tests with beach slopes of 1:10 and 1:20, respectively. Visser found it impossible to optimize the recirculation procedure from measurements of the mean water level in the longshore direction. He developed an alternative method where the optimum rate of external recirculation was determined by minimizing the internal circulation between the wave guides.

Simons et al. (1995) described some of the evaluation tests conducted in the recently developed Coastal Research Facility at HR Wallingford, in the United Kingdom. This facility was constructed in a large wave basin (27 x 54 m) and has a 36-m long directional wave generator. The most impressive component of the facility is the LSC recirculation system that has 4 independent reversible axial flow pumps with a total pumping capacity of

1.2 m³/s. Currents are introduced into the basin at the updrift boundary through 40 flow channels, each controlled by its own undershoot weir, with a matching set of flow channels at the downdrift end of the facility. All of the flow channels are 0.5 m in width and the fixed-bed beach has a slope of 1:20. This system allows the wave-driven LSC to be externally recirculated to establish longshore uniformity of waves and wave-driven currents. Some technical specifications on the facility were found in HR Wallingford (1994).

3. PHYSICAL DESCRIPTION OF THE NEW LABORATORY FACILITY

The LSTF occupies a 30-m cross-shore by 50-m longshore by 1.4 m deep wave basin (Figure 1). Monochromatic and random waves can be generated with four digitally controlled, piston-type, servo-electric wave generators. The wave generators are synchronized to create unidirectional long-crested waves up to 0.5 m in height for wave periods up to 3.0 s, and can be oriented at various angles ranging from 0 to 20 deg with respect to shore normal. For oblique angles of wave attack, the wave generators are phase-shifted to maximize the cross-shore dimension of the testing area. End-baffles, located between two adjacent wave boards, are used to guide the waves and prevent the formation of spurious waves caused from wave diffraction from the ends of each wave board and from wave energy reflected from the wave absorber located behind the wave generators. Wave guides that follow the refracted wave ray will be designed to facilitate current and sediment input and output at the lateral boundaries of the beach. Wave, current, and bathymetric data will be collected using a suite of sensors located on a custom-designed instrumentation bridge, as described by Rosati et al. (1995).

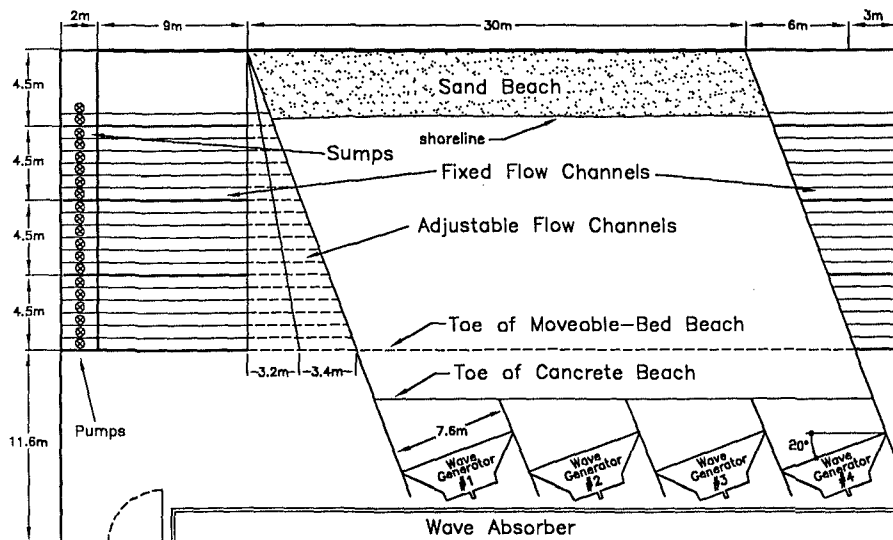


Figure 1: Plan View of the Longshore Sediment Transport Facility

The fixed-bed (concrete) beach has a longshore dimension of 30 m and a cross-shore dimension of 21 m, and was accurately constructed (tolerance of ± 2.0 mm) with parallel contours. The main section of the concrete beach has a constant slope of 1:30, and the toe

of the beach slopes down to the basin floor at a slope of 1:18. During future LST experiments, a 0.3 m thick moveable-bed of quartz sand will be placed on top of the fixed-bed beach and will extend 18.0 m offshore (see toe of moveable-bed beach in Figure 1). The toe of the beach will taper down to the basin floor at a slope of 1:6.5.

A LSC recirculation system is being designed to minimize the adverse laboratory effects resulting from the updrift and downdrift boundaries, and to maximize the length of beach over which longshore uniformity of waves and wave-driven currents exist in the facility. A LSC recirculation system creates a closed-loop system that continuously recirculates LSC from the downdrift to the updrift lateral boundary of the beach, while waves are being generated. As shown in Figure 1, the LSC recirculation system will extend 18.0 m offshore corresponding to the offshore limit of the moveable-bed beach which will be constructed for future LST experiments. A series of pumps will be located at the downdrift end of the facility and will recirculate the wave-driven LSC back to the updrift end of the facility through a series of pipes.

4. NUMERICAL SIMULATIONS OF LSC

The first part of this section provides a description of the numerical model used to estimate the magnitude and cross-shore distribution of the longshore current that will be generated in the LSTF. Subsequent sections describe the setup of the numerical model, validate the results obtained from the numerical model with dye measurements in the LSTF, and show the influence of wave height, period and direction on the estimated magnitude and cross-shore distribution of the longshore current.

4.1 Description of the Numerical Model

Kraus and Larson's (1991) numerical model NMLONG (Numerical Model of the LONGshore current) was used to estimate the wave-driven longshore current in the LSTF. NMLONG is a PC-based model that calculates wave transformation, mean water surface elevation, and longshore current for a 1-D cross-section of beach. The major assumptions in NMLONG are longshore homogeneity and linear wave theory.

Wave transformation in NMLONG includes shoaling, refraction, breaking with energy dissipation, and wave reformation. Random wave transformation is simulated by assuming a Rayleigh distribution of wave heights offshore (waves are assumed to be narrow banded in frequency and direction, so randomness enters only in variability in wave height). NMLONG randomly selects wave heights from the Rayleigh distribution and transforms them as individual waves. The individual wave heights are used to calculate root-mean-square wave height at each point across the profile. This approach neglects wave-wave interactions. The mean water surface elevation (setup and setdown) produced by waves is calculated from the cross-shore momentum balance. The wave forcing (radiation stress) is calculated from linear wave theory.

Wave-driven longshore current is calculated from the longshore momentum balance. The model includes wave forcing (gradients in radiation stress), lateral mixing, and bottom friction. Lateral mixing is modeled with an eddy viscosity approach. Bottom friction is

nonlinear (in the unknown current velocity) and requires time-averaging of nonlinear terms over the wave period. The offshore boundary condition for the current is zero wave-driven velocity. For random wave simulation, longshore currents from individual waves are averaged at each profile point.

Using the data from Visser (1982), Kraus and Larson (1991) illustrated that NMLONG can be calibrated to reproduce the LSC measured in the laboratory with reasonable success. In particular, the magnitude and cross-shore location of the peak of the LSC distribution was reproduced with reasonable accuracy. This suggests that NMLONG can be used to provide a reasonable estimate of the magnitude and cross-shore distribution of LSC that can be generated in the LSTF. However, in the Visser cases, NMLONG predicted that the magnitude of the offshore tail of the LSC distribution was higher than measured by Visser, even after the numerical model had been calibrated.

4.2 Numerical Model Setup

NMLONG requires the following input parameters: offshore wave height, period, and direction, specification of regular or random waves, offshore water depth, and beach profile elevation relative to mean water level. Random waves are characterized in NMLONG using the root-mean-square wave height, H_{rms} . Values of H_{rms} were converted to significant wave height, H_s assuming $H_s = 1.414 \times H_{rms}$. Nonlinear bottom friction with a friction coefficient equal to 0.01 was used in the LSTF simulations. For one wave condition, the sensitivity of results to this value was evaluated by reducing and increasing the coefficient to 0.005 and 0.02, respectively. All other empirical parameters were set to the default values: incipient breaking-wave-height-to-water-depth-ratio equal to 0.8, stable wave-height-to-water-depth-ratio equal to 0.4, energy flux dissipation rate equal to 0.15, and lateral mixing coefficient equal to 0.3.

NMLONG was set up to calculate the depth-averaged LSC velocities at each cell spaced 1 m across the beach profile. These depth-averaged velocities were multiplied by the corresponding mean water depth and integrated across the entire profile to estimate the total longshore volume flux for each wave condition.

Two series of numerical simulations were conducted to represent two different experimental configurations planned for the LSTF. The first series was conducted with an offshore water depth equal to 0.6 m and represents the configuration that will be used in the LSTF during the hydrodynamic testing phase. The second series was conducted with a water depth equal to 0.9 m and represents the configuration that will be used for the moveable-bed LST experiments. In this configuration a 0.3 m thick uniform layer of sand will be placed on top of the existing concrete beach. Increasing the water level from 0.6 to 0.9 m translates the shoreline directly upwards (i.e., there is no cross-shore translation of the nearshore zone). However, the resulting magnitude and cross-shore distribution of the LSC is slightly different for the two different configurations, due to the slight difference in wave transformation caused by the steeper toe of the beach in the case with the moveable-bed.

Numerical simulations in both test series covered the following range of hydrodynamic conditions: significant wave height, $H_s = 0.1$ to 0.4 m, peak wave period, $T_p = 1.0$ to 2.5 s, and angle of wave incidence, $\theta = 5$ to 20 deg relative to shore normal. For these test conditions total longshore volume flux ranged from 0.04 m³/s for $H_s = 0.1$ m, $T_p = 2.5$ s, and $\theta = 20$ deg to 1.3 m³/s for $H_s = 0.4$ m, $T_p = 2.5$ s, and $\theta = 20$ deg.

The sensitivity of the bottom friction coefficient was evaluated for a relatively energetic wave condition; namely $H_s = 0.3$ m, $T_p = 2.5$ s and $\theta = 20$ deg. The bottom friction coefficient was varied over a range of two times the default value of 0.01 (i.e., from 0.005 to 0.02). Results obtained using the lower friction coefficient (0.005) resulted in a total longshore volume flux of 1.1 and 1.2 m³/s for the 0.6 and 0.9 m water depth cases, respectively. The higher friction coefficient (0.02) reduced the total longshore volume flux to 0.4 m³/s for both water depth cases. Therefore, the results obtained using NMLONG to predict the total longshore volume flux in the LSTF are sensitive to the value of the bottom friction coefficient.

4.3 Validation with Dye Measurements in the LSTF

Preliminary estimates of the magnitude of the LSC were obtained in the LSTF by injecting dye into the surf zone while generating monochromatic waves. These measurements were then used to assess the validity of the numerical simulations. However, the following facility components had not been installed in the LSTF at the time these measurements were required: (1) lateral wave guides were not available to train the incident waves from the wave generators to the surf zone, (2) none of the LSC recirculation system components were available to minimize the laboratory effects caused by the lateral boundaries of the facility (i.e., pumps and flow channels), and (3) only monochromatic waves could be generated with the wave makers. As a result, strong adverse reflection patterns (from the vertical walls at the two ends of the basin) and circulation cells developed throughout the facility as the first 5-10 waves were generated. In addition, no flow velocity measurement sensors were available to accurately measure the wave driven LSC in the surf zone.

Three conclusions were made based on these limited dye measurements. First, NMLONG produced reasonable estimates of the peak LSC magnitude and cross-shore location, using the default bottom friction coefficient of 0.01 . However, insufficient data were collected to calibrate this coefficient. Secondly, we were unable to verify the cross-shore distribution of the LSC predicted using NMLONG due to the physical limitations and resulting adverse laboratory effects discussed above. Therefore, the default lateral mixing coefficient (0.30) was used. Thirdly, observations made while these dye measurements were being carried out strongly reinforced the expectation that a properly designed external LSC recirculation system would be required to maintain longshore uniformity of waves and wave-driven currents in the facility, especially for energetic wave conditions.

4.4 Influence of Hydrodynamic Variables

The influence of wave height, period and direction on the magnitude and cross-shore distribution of the LSC was investigated. All numerical simulations were conducted using

random waves. Figure 2 shows the LSC distribution for $H_s = 0.2, 0.3,$ and 0.4 m, with $T_p = 2.5$ s and $\theta = 20$ deg at the wave generator. Three general trends can be seen in this figure. First, as H_s increases, the magnitude of the LSC at the peak of the distribution significantly increases. The magnitude of the peak LSC equals $0.21, 0.28$ and 0.36 m/s for $H_s = 0.2, 0.3$ and 0.4 m, respectively. This is a relative increase of approximately 30% for each 0.1 m increase in wave height. Secondly, the peak of the LSC distribution moves offshore as H_s increases, because the incident waves begin to break further offshore. Thirdly, the width of the LSC distribution increases as the H_s increases, since the width of the surf zone increases.

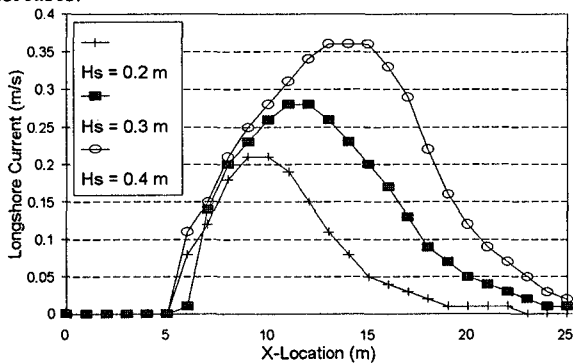


Figure 2: Influence of Significant Wave Height

Figure 3 shows the LSC distribution for $T_p = 1.0, 1.5, 2.0$ and 2.5 s with $H_s = 0.3$ m and $\theta = 20$ deg at the wave generator. Three general trends can be seen in this figure. First, as T_p increases, the magnitude of the LSC at the peak of the distribution increases slightly. The magnitude of the peak LSC equals $0.25, 0.26, 0.27$ and 0.28 m/s for $T_p = 1.0, 1.5, 2.0$ and 2.5 s, respectively. This is a relative increase of only 4% for each 0.5 s increase in T_p . Secondly, the peak of the LSC distribution moves slightly further offshore as T_p increases, since the incident waves begin to break slightly further offshore. Thirdly, the width of the LSC distribution increases slightly as T_p increases, since the width of the surf-zone increases slightly.

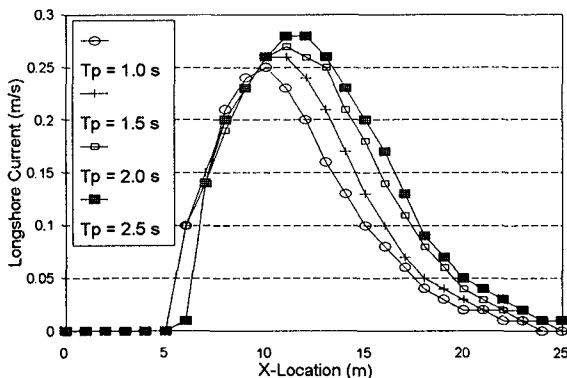


Figure 3: Influence of Peak Wave Period

Figure 4 shows the LSC distribution for $\theta = 5, 10, 15$ and 20 deg with $H_s = 0.3$ m and $T_p = 2.5$ s. Three general trends can be seen in this figure. First, as θ increases, the magnitude of the LSC at the peak of the distribution significantly increases. The magnitude of the peak LSC equals $0.10, 0.18, 0.23$ and 0.28 m/s for $\theta = 5, 10, 15$ and 20 deg, respectively. This is a relative increase of about $80\%, 28\%$, and 22% , for each consecutive increase in θ . Secondly, the cross-shore location of the peak of the LSC distribution remains constant as θ increases. Thirdly, the width of the LSC distribution remains reasonably constant as θ increases.

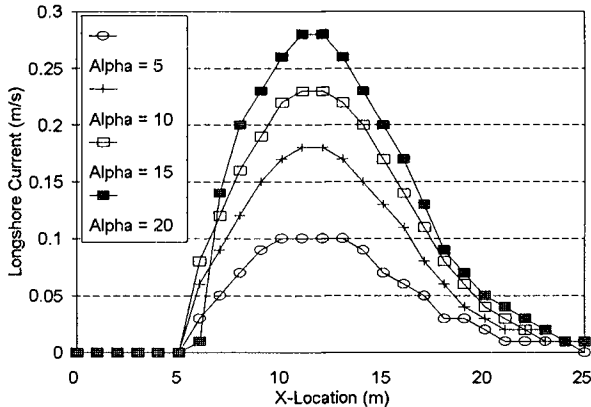


Figure 4: Influence of Incident Wave Direction

In summary, increasing H_s has a strong influence on increasing the magnitude and cross-shore location of the peak of the LSC distribution, whereas, increasing T_p has a much milder effect. Increasing θ has a very strong influence on increasing the peak magnitude, but no influence on the cross-shore location of the peak of the LSC distribution.

5. DESIGN PARAMETERS FOR THE LSC RECIRCULATION SYSTEM

The first part of this section describes the design wave condition used to determine the required pumping capacity of the LSC recirculation system. Subsequent sections discuss a factor of safety applied to the numerical modeling results, and incorporate the requirements of a moveable-bed beach and a variable operating water level into the design.

5.1 Design Wave Condition

To determine the design capacity of a LSC recirculation for the LSTF, a maximum design wave condition was selected. After observing the location of the break point for a number of different wave height and period combinations in the LSTF (and comparing these results with the numerical simulations), it was decided that $H_s = 0.3$ m and $T_p = 2.5$ s is probably the most energetic wave condition that will be generated during the moveable-bed LST experiments. As mentioned previously, the maximum angle of wave incidence (measured at the wave generators) to be tested in the LSTF is 20 deg. Therefore, the “design wave condition” used to determine the maximum required pumping capacity of the LSC

recirculation system was characterized by $H_s = 0.30$ m, $T_p = 2.5$ s and $\theta = 20$ deg with an offshore water depth of 0.9 m. This is the LSC distribution shown previously in Figure 2 (middle curve) and Figure 3 and 4 (upper curve). Results obtained using NMLONG to predict the magnitude and cross-shore distribution of LSC for this "design wave condition" indicated a total longshore flux of 0.76 m³/s within the surf zone.

5.2 Determining a Factor of Safety

A factor of safety was incorporated into the design to compensate for inaccuracies in calculating the magnitude and cross-shore distribution of LSC that will be generated in the LSTF. Our concerns included: (1) having inadequate data to calibrate the bottom friction coefficient and the lateral mixing coefficient in the numerical model, and (2) changes in the bottom roughness between the initial hydrodynamic tests on a fixed-bed concrete beach and multiple grain sizes used for the moveable-bed beach for the LST experiments. The surface of the concrete beach was broom-finished to simulate the roughness of a coarse grained sand. However, because bed-forms will develop in the LST experiments it is likely that the moveable-bed beach will have a higher friction coefficient for a given wave condition. Due to these uncertainties, the magnitude of the LSC at each cross-shore location was increased by 10% (i.e., a Factor of Safety = 1.1) for the purpose of determining the required pumping capacity of the LSC recirculation system.

5.3 Allowance for Maximum Depth of Erosion of the Moveable-Bed Beach

At this point in the design process, predictions of the LSC magnitude and cross-shore distribution to be generated in the LSTF are based on a 1:30 plane sloping fixed-bed beach having parallel contours. However, for future moveable-bed experiments in the LSTF, the beach profile will respond to incident wave conditions, creating a shore-parallel bar and trough feature near the location of initial wave breaking. Assuming longshore uniformity in the beach bathymetry, the capacity of the LSC recirculation system must be increased wherever the beach profile erodes, due to the increased longshore flux at the cross-shore location. For example, in the trough located shoreward of the offshore bar.

To investigate this problem, 2-D flume tests were conducted to estimate the maximum depth of erosion during future moveable-bed LST experiments in the LSTF. Each test started with a 1:30 plane sloping sand beach, with $D_{50} = 0.11$ mm. This is the same initial beach slope and sediment size to be used for the fine-grained sediment test series in the LSTF. In each experiment, the maximum depth of erosion was located just offshore of the still-water shoreline. For the design wave condition the maximum depth of erosion did not exceed 0.1 m, however, this conclusion is based on 2-D flume tests, and not 3-D tests in the LSTF.

For design purposes, it was assumed that the entire 18-m width of the moveable-bed beach will erode by 0.1 m. This is a fairly crude assumption, although it is conservative in that it allows for the maximum scour depth to occur at any location across the beach profile. In particular, this is a very conservative assumption near the offshore end of the beach where accretion should occur (as opposed to erosion) as the offshore bar develops. However, future plans for the LSTF include a test with a terminal groyne located at the downdrift end

of the moveable-bed beach. If this physical model behaves as expected, a scour hole will develop at the head of the groyne and the longshore flux (shoreward of the offshore end of the groyne) will be deflected offshore and bypass the end of the groyne. Therefore, over designing the LSC recirculation system near the offshore region of the beach will give the system more flexibility in the future when conducting experiments with coastal structures.

Note that this analysis assumes that the depth-averaged LSC at any cross-shore location does not change substantially (from the case with a plane sloping fixed-bed beach) as the offshore bar and trough feature develop in the moveable-bed experiments. Although this may not be the case, we feel that changes to the depth-averaged LSC (as the beach profile develops) will be relatively small since the initial beach slope is relatively gentle (1:30) and the total profile adjustment should be relatively small. Therefore, this assumption should be adequate for design purposes.

5.4 Allowance for Variable Operating Water Levels in the Facility

The design of the LSC recirculation system also accounted for the requirement to conduct experiments with variable water levels in the facility. As mentioned previously, we plan to conduct the majority of the moveable-bed LST experiments with an offshore water depth of 0.9 m. However, if we decide to increase the water level in the future, the LSC distribution will be translated shoreward on the beach.

A number of physical constraints in the vertical dimension of the facility dictate that the maximum operating water level in the facility will not exceed 1.0 m (at least for energetic wave conditions). Lower water levels can be used, however, the wave generation capability of the wave makers will decrease with decreasing water level. Therefore, the critical design parameter is the maximum operating water level in the facility. The first curve in Figure 5 shows the longshore flux distribution for the design wave condition, with an offshore water depth of 0.9 m. This curve includes the increased capacity required by using a factor of safety of 1.1 and assuming the moveable-bed erodes 0.1 m across the entire width of the beach. The abrupt change in cross-shore gradient at $X = 18$ and 21 m is caused by the sudden change in beach slope at these locations. The second curve was obtained by increasing the offshore water depth to 1.0 m, for the same design wave condition. Essentially, this 0.1 m increase in operating water level translates the LSC distribution 3.0 m shoreward, because the slope of the concrete beach is 1:30. The third curve in the figure encompasses both the first and second curve, and represents the required pumping capacity of the LSC recirculation system for water levels ranging from 0.9 to 1.0 m. As shown in the figure, incorporating a variable water level into the design essentially broadens the width of the LSC distribution that needs to be recirculated within the facility.

6. OTHER DESIGN CONSIDERATIONS

The following sections describe uncertainties related to how far the LSC distribution extends offshore, the magnitude of the longshore flux of water flowing in the swash zone, and the issue of what percentage of the wave-driven LSC needs to be recirculated.

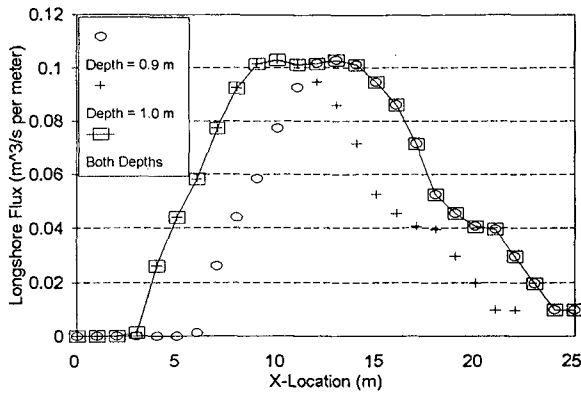


Figure 5: Influence of Offshore Water Depth

6.1 Offshore Tail of the LSC Distribution

Another design consideration is the possibility that a small longshore flux may exist offshore of the toe of the moveable-bed beach ($X > 18.0$ m), for very energetic wave conditions. Approximately 17% of the area under the curve in Figure 5 is offshore of $X = 18$ m, which is the location of the offshore end of the recirculation system, as shown in Figure 1. In Section 4.1, it was discussed that NMLONG may over predict how far the LSC distribution extends offshore. Unfortunately, this was impossible to verify due to problems encountered making dye measurements in the partially constructed LSTF, as discussed in Section 4.3. If the numerical simulations are correct, this offshore tail of the LSC distribution may cause adverse internal circulation patterns within the facility.

If this problem exists in the future, there are a number of possible solutions. First, we could decrease the magnitude of the maximum wave condition that is generated in the facility. Second, we could increase the offshore water depth to 1.0 m for very energetic wave conditions, which would shift the LSC distribution 3.0 m shoreward. The area under the curve (offshore of $X = 18$ m) associated with an offshore water depth of 1.0 m, is only 9% of the total area. Third, it may be possible to oversize the furthest offshore pump, and use the additional capacity to recirculate some of the LSC which exists offshore of $X = 18$ m. Based on these considerations, it was decided that the LSC recirculation system would initially be constructed to extend offshore to $X = 18.0$ m. If the numerical predictions turn out to be correct, one or more of the options discussed above will be employed.

6.2 Longshore Flux of Water in the Swash Zone

Another design feature to be considered is the longshore flux of water flowing downdrift within the swash zone. The swash zone was defined as the area between the still-water shoreline and the maximum point of wave uprush, including any setup in the mean water level. Unfortunately, it is impossible to accurately calculate the longshore flux in the swash zone due to our limited understanding of swash zone processes. One of the interesting

results obtained from the 2-D moveable-bed tests, discussed previously in Section 5.3, is that the swash zone was approximately 4 m in width for the design wave condition. Therefore, it is believed that it will be necessary to recirculate the longshore flux in the swash zone, due to the physical size of the swash zone that develops at this relatively large geometric scale.

Figure 5 indicates that at $X = 5.0$ m, the longshore flux of water will be approximately $0.045 \text{ m}^3/\text{s}$ per meter width of beach. In addition, we know that the longshore flux of water at the landward boundary of the swash zone will be zero. Therefore, we can make a somewhat crude assumption and draw a straight line between these two points to represent the time-averaged longshore flux of water flowing downdrift in the swash zone. Although we expect the longshore flux of water to have a nonlinear distribution across the swash zone, this assumption provides a first-order estimate for design purposes.

6.3 Percentage of Longshore Flux to be Externally Recirculated

Intuitively one would expect that 100% of the longshore flux within the surf zone should be externally recirculated back to the updrift end of the facility with a LSC recirculation system. However, laboratory facilities are not ideal systems and in many cases an internal circulation pattern may exist, in which case it may not be necessary (or possible) to externally recirculate 100% of the wave-driven longshore flux without adding too much momentum into the system. Visser (1982) developed a method to obtain a uniform LSC distribution along the finite length of a straight beach in a 3-D wave basin. Visser determined the “proper” rate of external recirculation by adjusting the pumping rate and inflow distribution until the internal circulation between the wave guides was minimized. However, after reviewing Visser’s work, Svendsen (1991) concluded that in some of Visser’s experiments the internal circulation was still disturbingly large (as much as 40-50% of the wave-driven longshore flux within the surf zone), even though Visser’s data indicate that he was able to establish a LSC distribution that was relatively uniform alongshore.

Based on Svendsen’s conclusion and the principle of continuity, Visser’s external recirculation flow rate must have been substantially less than the total longshore flux in the surf zone. This indicates that it may not be necessary to recirculate 100% of the longshore flux in the LSTF, to obtain longshore uniformity. This problem will be investigated in the LSTF during the initial hydrodynamic experiments on a fixed-bed beach. However, for the purpose of estimating the required pumping capacity of the LSC recirculation system, it was prudent to assume that 100% of the longshore flux will need to be externally recirculated.

7. DESIGN CAPACITY FOR EACH INDIVIDUAL PUMP

The last step in this phase of the design process was to determine the design capacity of each of the individual pumps that make up the LSC recirculation system. Required pump capacity is a function of the width of the flow channels at the downdrift end of the facility, which is directly related to the cross-shore resolution of the LSC recirculation system. Intuitively, one would expect that the higher the cross-shore resolution, the longer the “working beach region” where longshore uniformity of waves and wave-driven LSC’s exist. After reviewing the design of LSC recirculation systems used in other laboratory facilities

(see Section 2) it was decided that the flow channels at the downdrift and updrift end of the LSTF should be 0.75 m in width. This was a compromise between cross-shore resolution and the estimated cost of construction of the entire LSC recirculation system.

Knowing the required pumping capacity of the LSC recirculation system, shown in Figure 5 (third curve), and given a flow channel width of 0.75 m, the capacity of each individual pump could be readily calculated. Figure 6 shows a bar graph expressed in m^3/s for every 0.75 m of beach width, and the magnitude of each bar represents the required pumping capacity of each individual pump. This figure also includes the required pumping capacity to recirculate the longshore flux in the swash zone (see Section 6.2). Figure 6 shows 23 pump capacities. However, to reduce the number of pumps near the shoreline, where the longshore flux is relatively small, one large pump will be used as opposed to four smaller pumps, as illustrate in Figure 1. Therefore, there will be a total of 20 pumps in the system.

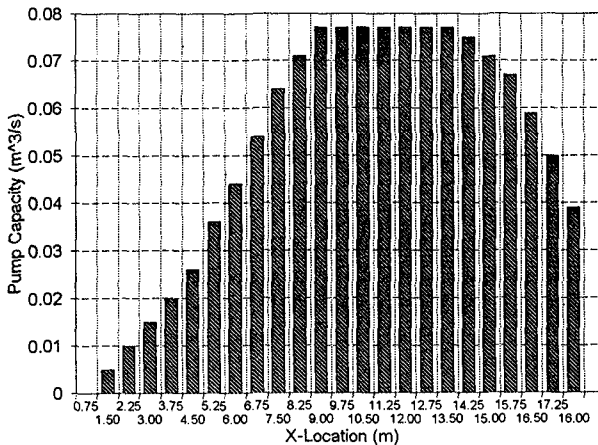


Figure 6: Design Capacity of the LSC Recirculation System

The total design capacity of the LSC recirculation system was calculated to be approximately $1.25 \text{ m}^3/\text{s}$. To put this pumping capacity into perspective, HR Wallingford (1994) states that the LSC recirculation system in the Coastal Research Facility has a design capacity of $1.2 \text{ m}^3/\text{s}$ (i.e., four axial flow pumps each with a capacity of $0.3 \text{ m}^3/\text{s}$). The LSC recirculation system in the Coastal Research Facility is used to generate not only wave-driven LSC within the surf zone, but also tidal currents offshore of the toe of the concrete beach. Therefore, although the purpose of the two systems is not exactly the same, the total design pumping capacities are very similar.

8. SUMMARY

This paper documents the design process used to determine the required pumping capacity of an external longshore current recirculation system for the development of a longshore sediment transport laboratory facility. A design wave condition of $H_s = 0.3 \text{ m}$, $T_p = 2.5 \text{ s}$, and $\theta = 20 \text{ deg}$, with an offshore water depth of 0.9 m was used to estimate the magnitude and cross-shore distribution of the longshore current that will be generated in the new

facility. By including a factor of safety and considering a number of functional design requirements, the total required design pumping capacity was determined to be 1.25 m³/s. It was estimated that twenty independent pumps and flow channels would be required to provide adequate cross-shore resolution for the system and to provide the required capability to recirculate a broad range of LSC distributions for a wide range of incident wave conditions, water levels and moveable-bed beach profiles.

9. ACKNOWLEDGEMENTS

The authors would like to thank the staff at HR Wallingford, in the United Kingdom for generously providing technical information about the Coastal Research Facility. This paper benefited from the review comments of Bruce A. Ebersole. This research is funded by the "Large-Scale Laboratory Investigation of Longshore Sediment Transport" work unit of the Coastal Sediment and Dredging Program, under the Coastal Navigation and Flood Damage Reduction Research Area. Permission to publish this paper was granted by the Chief of Engineers, U.S. Army Corps of Engineers.

10. REFERENCES

- Brebner, A., and Kamphuis, J.W. 1963.** Model Tests on the Relationship Between Deep-Water Wave Characteristics and Longshore Currents. Report No. 31, Department of Civil Engineering, Queen's University at Kingston, Canada.
- Galvin, C.J., and Eagleson, P.S. 1965.** Experimental Study of Longshore Currents on a Plane Beach. Technical Memorandum No. 10, US Army Waterways Experiment Station, Coastal Engineering Research Center, Vicksburg, MS, USA.
- HR Wallingford (1994).** Understanding the Nearshore Environment. A publication describing the Coastal Research Facility at HR Wallingford, 4 p.
- Kraus, N.C., and Larson, M. 1991.** NMLONG: Numerical Model for Simulating the Longshore Current, Report 1: Model Development and Tests. Technical Report DRP-91-1, US Army Engineer Waterways Experiment Stations, Vicksburg, MS.
- Mizuguchi, M. And Horikawa, K. 1978.** Experimental Study on Longshore Current Velocity Distribution, Bulletin 21, pp 123-150, Facul. Sci. & Eng., Chuo University.
- Putnam, J.A., Munk, W.H., and Taylor, M.A., 1949.** The Prediction of Longshore Currents. Transactions of the American Geophysical Union, Vol. 30 (3), pp 337- 345.
- Rosati, J.D., Hamilton, D.G., Fowler, J.E. and Smith, J.M. 1995.** Design of a Laboratory Facility for Longshore Sediment Transport Research. Proc. of Coastal Dynamics '95, pp 771-782, Gdansk, Poland.
- Shore Protection Manual 1984.** USACE Waterways Experiment Station, Coastal Engineering Research Center, Vicksburg, MS, 2 Vols.
- Simons, R.R., Whitehouse, R. JS., Maclver, R.D., Pearson, J., Sayers, P.B., Zhao, Y., and Channell, A.R. 1995.** Evaluation of the UK Coastal Research Facility. Proc. of Coastal Dynamics '95, pp 161-172, Gdansk, Poland.
- Svendsen, I.A. 1991.** Development of a Comprehensive Plan for Modeling Longshore Current Generation in the Laboratory. Unpublished Contract Report for the Waterways Experiment Station, Coastal Engineering Research Center, Vicksburg, MS.
- Visser, P.J. 1982.** The Proper Longshore Current in a Wave Basin. Report No. 82-1, Department of Civil Engineering, Delft University of Technology, The Netherlands.

CHAPTER 281

INFLUENCE OF NEARSHORE HARDBOTTOM ON REGIONAL SEDIMENT TRANSPORT

Paul C.-P. Lin, Ph.D., P.E.¹ and R. Harvey Sasso, P.E.²

ABSTRACT

The influence of nearshore hardbottom on longshore and cross-shore sand movement along a 21.2 km long southeast Florida coastline is evaluated. This study correlates a variation of longshore sediment transport rate within the region with the extent of nearshore hardbottom. The nearshore sand movement within this region was determined based on analysis of the hydrographic survey data over a 15-year period. The study area includes three major beach renourishment sites, which were renourished a combined total of seven (7) times with 5.5 million cubic meters of sand. The objectives of this study are to obtain a greater understanding of the causes of severe beach erosion and a more accurate estimate of nearshore sand movement in the region, thus providing a better design tool for future beach nourishment projects and inlet sand bypassing practices.

INTRODUCTION

The area of study extends from Port Everglades Inlet in Broward County to Bakers Haulover Inlet in Dade County. This region of coastline encompasses six (6) municipalities including, from north to south, John U. Lloyd, Dania, Hollywood/Hallandale, Golden Beach, Sunny Isles, and Bakers Haulover Park, with their major beach nourishment projects illustrated in Figure 1.

This study region is bounded by Port Everglades Inlet to the north and Bakers Haulover Inlet to the south. Port Everglades Inlet was opened in 1926 and stabilized by north and south jetties in 1931. Its 190-meter wide and 15 m deep inlet channel acted as a complete sand barrier and allowed no sediment bypassing

¹Senior Engineer, Coastal Systems International, Inc., 464 South Dixie Highway, Coral Gables, Florida

²President, Coastal Systems International, Inc.

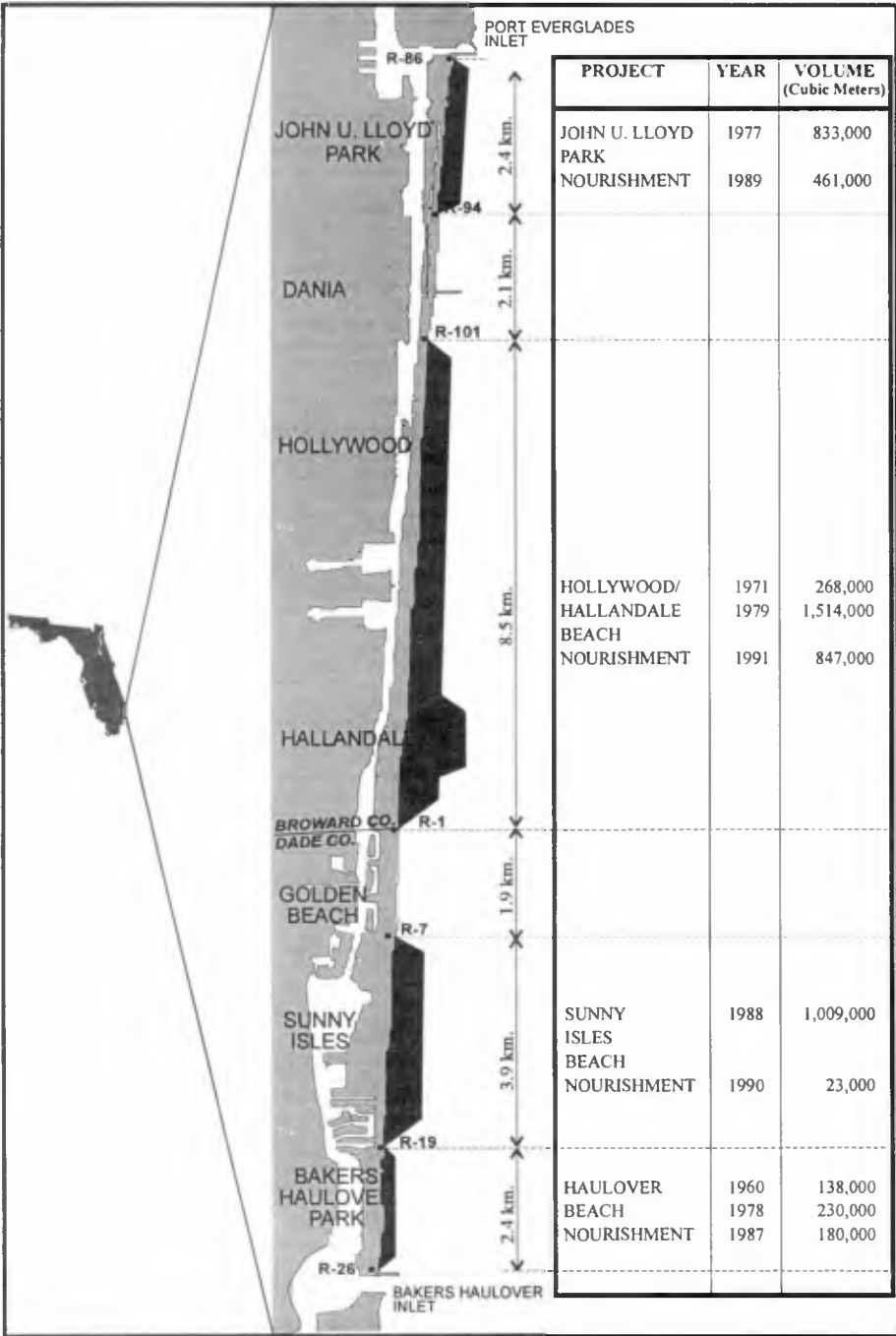


Figure 1. Study Area and Historic Beach Nourishment Projects

across the inlet (Coastal Tech, 1994). The Bakers Haulover Inlet is a man-made improved inlet measuring approximately 90 m wide and 5 m deep. This Inlet was opened in 1925 (CP&E, 1992a).

In the region, John U. Lloyd, Hollywood/Hallandale, and Sunny Isles have been periodically renourished. Some small-scale beach fill activities were also conducted in the Bakers Haulover Park. Meanwhile, Dania and Golden Beach have been accreting as a result of adjacent beach renourishment projects. The 2.4 km beach of John U. Lloyd Park was nourished in 1977 and 1989 with placement of approximately 0.83 million and 0.46 million cubic meters of sand, respectively. An estimated 0.27, 1.5, and 0.85 million cubic meters of sand were placed along the 8.5 km of Hollywood/Hallandale beach in 1971, 1979 and 1991, respectively. A major beach nourishment project took place along the 3.9 km of Sunny Isles beach in 1988 with placement of 1.0 million cubic meters of sand. Other small-scale beach fill projects within this region were detailed in the Sunny Isles report (Coastal Tech, 1993).

Extensive nearshore hardbottom was found within this study area, which aligned in a shore-parallel direction with an offshore distance between the hardbottom and shoreline increasing from north to south. Specifically, the nearshore hardbottom is located approximately 200 m offshore at the north end of the region and increases to 900 m offshore at the south end. The average width of the nearshore hardbottom area is 2,400 m.

REGIONAL SEDIMENT TRANSPORT

The overall sand movement within the study region is evaluated by examining volumetric changes at each DEP (formerly DNR) monument. The volumetric changes occurring above and below the -2 m National Geodetic Vertical Datum (NGVD) elevation are calculated. The depth of closure for sand movement in this region varies from approximately -4 m NGVD to -6 m NGVD, depending on the location of nearshore hardbottom. A detailed variation of volumetric changes along the region is illustrated in Figure 2.

Table 1 summarizes the average and total volumetric changes within each coastal municipality. In general, long-term hydrographic data for two consecutive beach nourishment projects were used to obtain an average volumetric change rate after a beach renourishment project. In the area of Sunny Isles and Bakers Haulover Park, relatively short-term data (approximately a three-year time period) was used due to the lack of accurate and extensive hydrographic survey data.

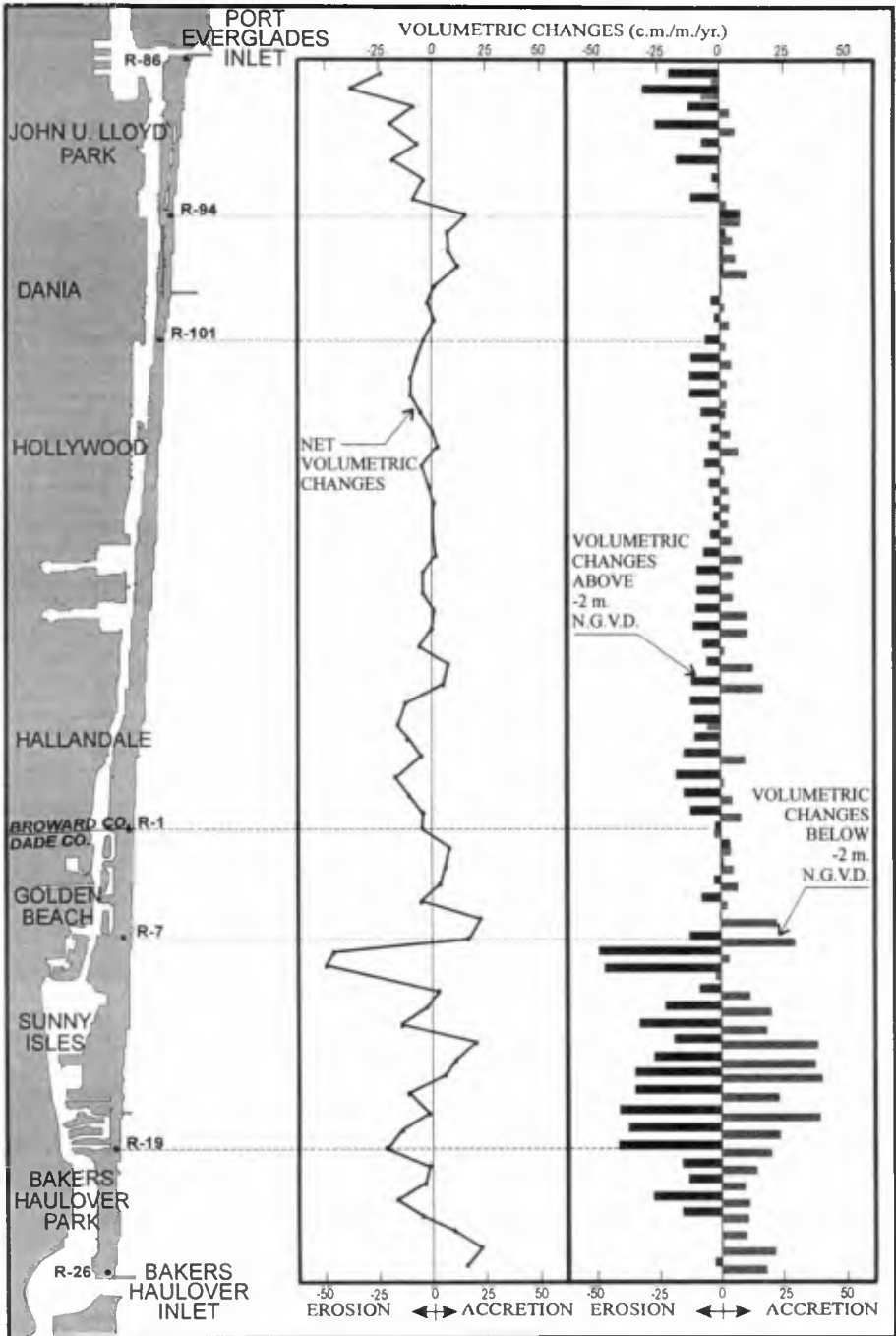


Figure 2. Net Volumetric Changes and Cross Shore Sand Movement

TABLE 1

VOLUMETRIC CHANGES WITHIN EACH COASTAL MUNICIPALITY

Coastal Municipality	Distance (km)	Survey Period	Volumetric Changes (c.m./m/yr)			Total Volumetric Changes (c.m./yr)
			Above -2 m NGVD	Below -2 m NGVD	Total	
John U. Lloyd State Park	2.4	1978-1989	-14.5	1.0	-13.5	-33,000
Dania	2.1	1978-1993	0.8	4.3	5.1	11,000
Hollywood/Hallandale	8.5	1979-1991	-8.0	4.0	-4.0	-34,000
Golden Beach	1.9	1980-1991	-2.3	9.5	7.2	14,000
Sunny Isles	3.9	1989-1991	-30.6	22.1	-8.5	-34,000
Bakers Haulover Park	2.4	1989-1991	-8.8	14.0	5.2	13,000
Total	21.2	—	—	—	—	-63,000

The nourished beach at John U. Lloyd, Hollywood/Hallandale (CP&E, 1992b) and Sunny Isles was found to be eroding at similar rates of 33,000, 34,000 and 34,000 cubic meters per year, respectively. The erosion rate per meter of shoreline decreased with increasing length of the renourishment project. For instance, Hollywood/Hallandale, having the greatest project length of 8.5 km, was found to have the least erosion rate per linear meter of shoreline at 4.0 cubic meters per meter per year. The greatest erosion of 13.5 cubic meters per meter per year occurred at John U. Lloyd Park. This high erosion rate is mainly due to the downdrift impacts associated with Port Everglades Inlet.

Non-nourished areas adjacent to the renourished beaches were accreting, as illustrated in Table 1. Dania, Golden Beach and Bakers Haulover Park were accreting at a rate of 11,000, 14,000 and 13,000 cubic meters per year, respectively. The accretion rates in these areas were relatively uniform, ranging from 5.1 to 7.2 cubic meters per meter per year.

A sediment budget, as illustrated in Figure 3, is developed for the region based on a known boundary condition and the results of the above volumetric changes. This sediment budget encompasses a region that extends beyond the area that is conventionally studied under inlet management plans and beach renourishment projects. The well-defined northern boundary condition of Port Everglades Inlet has improved the accuracy in the derivation of this regional sediment budget. A number of studies have reported that Port Everglades Inlet has interrupted 100 percent of longshore sediment transport and resulted in no sediment being naturally bypassed from north of the inlet to John U. Lloyd Park (COE, 1990; Coastal Tech, 1988 and 1994).

The regional sediment budget indicates that the longshore sediment transport rate at the north end of the region is less than the rate at the south end. This is contradictory to the trend experienced along the east coast of Florida, where longshore sediment transport rates usually decrease toward the south. The wave-induced longshore transport rate is found to be 33,000 cubic meters per year at John U. Lloyd/Dania, as compared to 76,000 cubic meters per year at Sunny Isles/Bakers Haulover Park. A net southern longshore transport rate of 77,000 cubic meters per year at Bakers Haulover Park was predicted by COE (1995) using the GENESIS numerical model.

The results of volumetric changes show that beach erosion generally occurred above the -2 m NGVD elevation and accretion occurred below the -2 m NGVD. Among all the beach renourishment projects, the amount of erosion that occurred above -2 m NGVD elevation was greater than the accretion in the area below -2 m NGVD.

Substantial beach erosion occurred above -2 m NGVD elevation in Sunny Isles, where a great amount of sand that was placed on the beach moved offshore. More substantial cross-shore sand movement occurred in Sunny Isles than that in other areas, as illustrated in Figure 2. This is due to the nearshore hardbottom in these other areas that have restricted sand movement in a cross-shore direction.

IMPACTS OF HARDBOTTOM ON SAND MOVEMENT

The relationship between the net longshore sediment transport rate and offshore location of hardbottom is presented in Figure 4. In general, the longshore sediment transport rate increases from north to south, as does the offshore

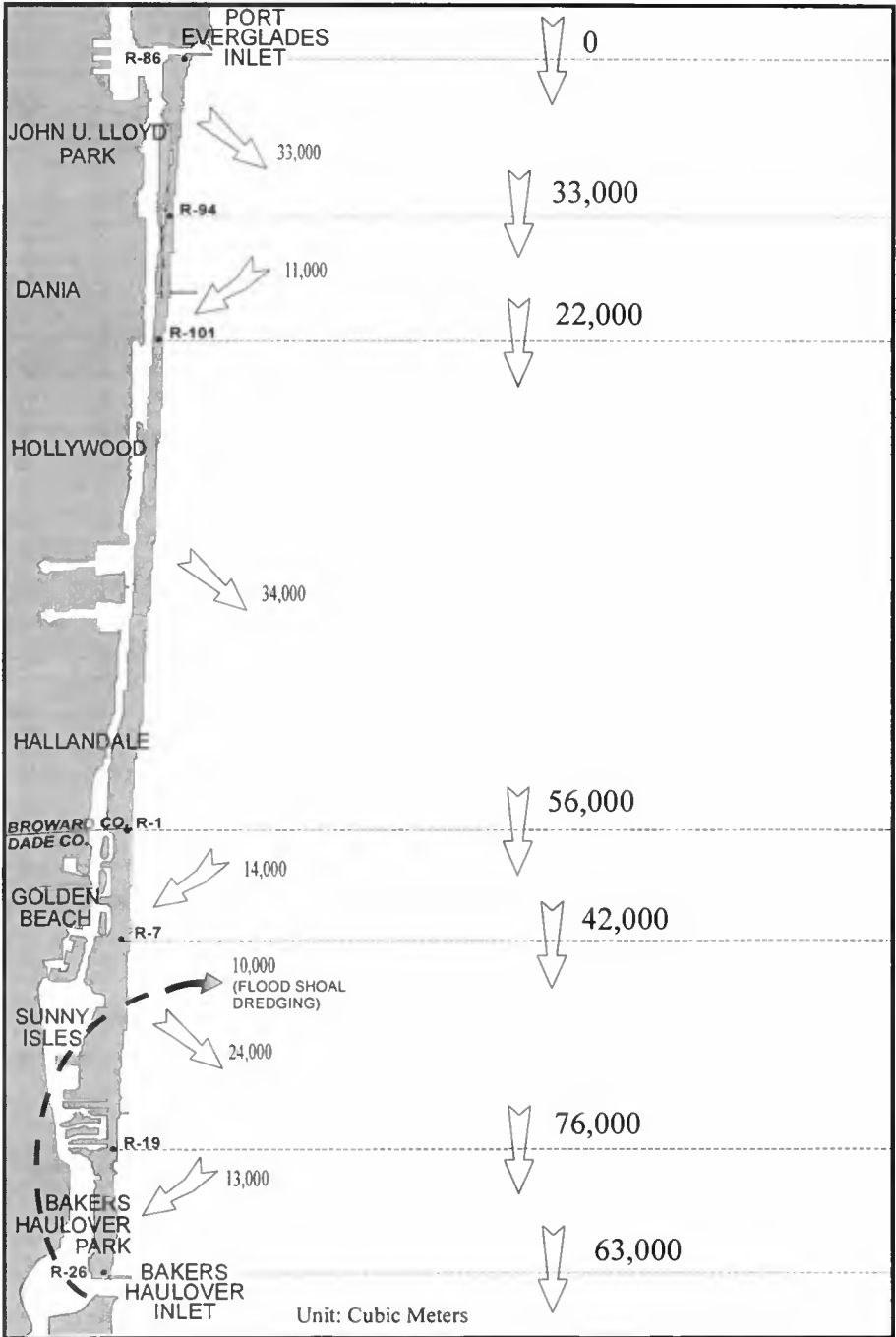


Figure 3. Regional Sediment Budget

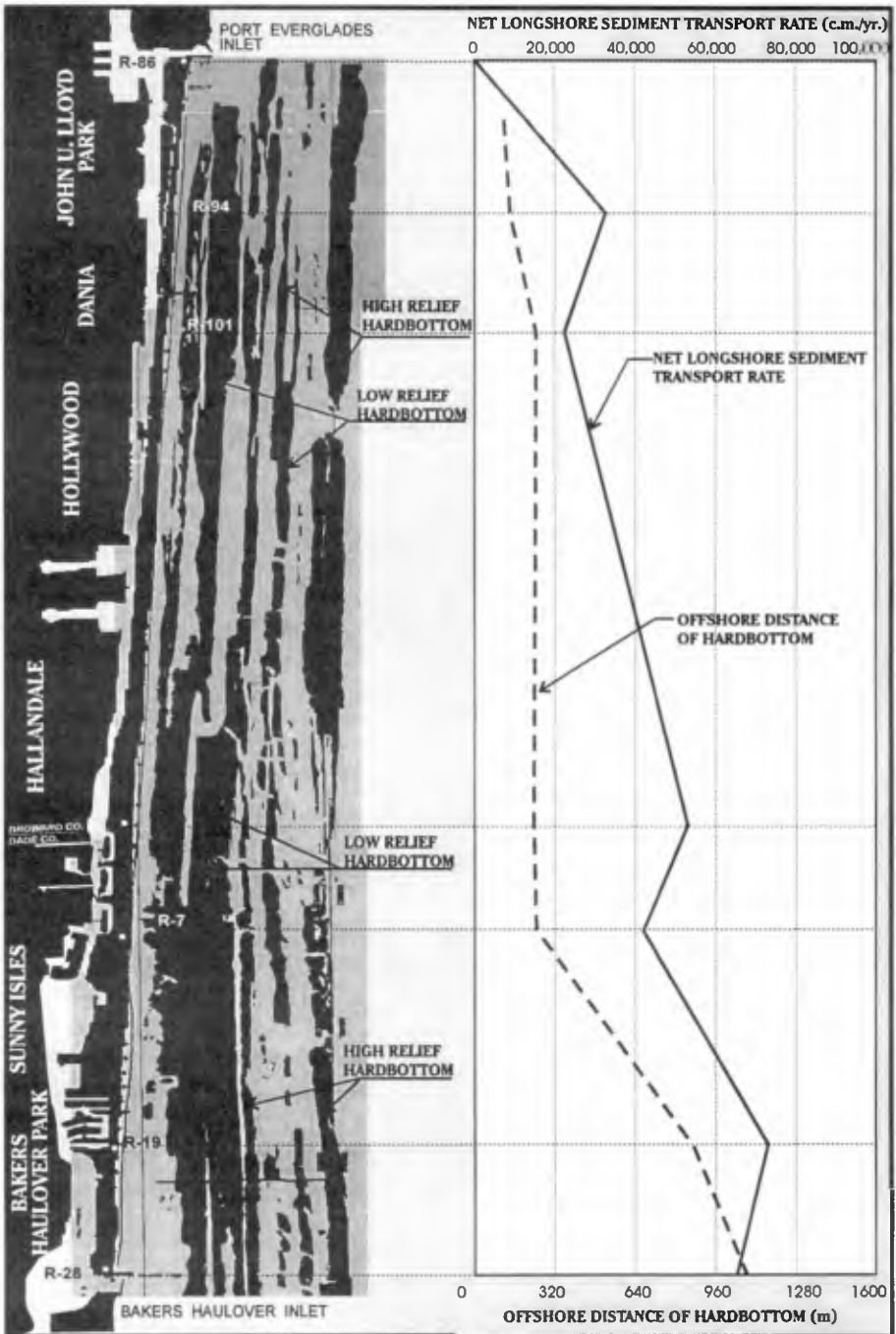


Figure 4. Longshore Sediment Transport Rate vs. Offshore distance of Hardbottom

distance of hardbottom.

Offshore wave climates along this study area are generally similar (Stauble, 1993). Along the north end, nearshore hardbottom has reduced wave energy and resulted in less longshore sand movement. In the northern half of the region, the hardbottom is located between 120 m and 300 m offshore, while the net longshore sediment transport rate ranged from 22,000 to 33,000 cubic meters per year. However, the hardbottom was located further offshore along the southern half of the area with the offshore distance between 300 m to 1,000 m, while the annual net longshore sediment transport rate ranged from 42,000 to 76,000 cubic meters.

Due to the differential sediment transport rate, there is an inherent sediment supply deficit within the region that would result in beach erosion. This may explain historically the need for beach renourishment projects for a combined total of 14.8 km of shoreline within the region.

CONCLUSIONS

The results of this study indicate that the existence of nearshore hardbottom has a significant impact on longshore and cross-shore sand movement within the region between Port Everglades and Bakers Haulover Inlet. Specifically, the net longshore sediment transport rate within the study area increased from north to south as the nearshore hardbottom aligned further offshore at the southern part of the area. The annual net longshore sediment transport rate increased from 33,000 cubic meters at John U. Lloyd State Park to 63,000 cubic meters at Bakers Haulover Inlet with a maximum of 76,000 cubic meters at the area between Sunny Isles and Bakers Haulover Park.

The hardbottom remains relatively close to the shore at approximately 120 m offshore at John U. Lloyd, then increases to 300 m offshore at Dania, Hollywood, Hallandale and Golden Beach, 600 m offshore at Sunny Isles, and 1,000 m offshore at Bakers Haulover Park. It is evident that the longshore sediment transport rate increases as the protection of nearshore hardbottom is diminished. At the southern end of the region, the net longshore sediment rate is consistent with that predicted by the COE using the GENESIS numerical model without consideration of hardbottom effect. Hence, the offshore hardbottom at Sunny Isles and Bakers Haulover Park has little or no effect on reducing wave energy and subsequently on the sand movement.

The effect of nearshore hardbottom on cross-shore sand movement is also evident. By examining the volumetric changes above and below -2.0 m NGVD as illustrated in Figure 2, less active offshore sand movement was observed in the area from John U. Lloyd to Hallandale. It suggests that the nearshore hardbottom may act as a perch structure preventing sand from moving offshore.

The use of the GENESIS numerical model to predict shoreline changes and sediment transport, may not provide reasonable results in regions with extensive nearshore hardbottom, such as occurs in southeast Florida. The effects of these nearshore hardbottom areas on longshore and cross-shore sand movement should be considered in developing a sediment budget for inlet or beach management plans.

ACKNOWLEDGEMENT

Assistance from the Department of Natural Resources Protection (DNRP) in Broward County, Florida, in providing valuable data is greatly appreciated.

REFERENCES

- Coastal Planning and Engineering, Inc. (CP&E) , "Bakers Haulover Inlet Management Plan," Interim Report No.1, Dade County, Florida, 1992a.
- Coastal Planning and Engineering (CP&E), Inc., "Hollywood/Hallandale First Periodic Beach Renourishment Project," One-year Beach Monitoring Study and Post-Storm (Hurricane Andrew) Analysis, 1992b.
- Coastal Technology Corporation, "Port Everglades Inlet Management Plan," Department of Natural Resources Protection, Broward County, Florida, 1994.
- Coastal Technology Corporation, "Sunny Isles Beach Restoration Project, 18-month Monitoring Study," Department of Environmental Resources Management, Dade County, Florida, November, 1993.
- Coastal Technology Corporation, "Port Everglades Sand Bypassing Study," Department of Natural Resources Protection, Broward County, Florida, 1988.
- Stable, D.K., "An Overview of Southeast Florida Inlet Morphodynamics," Beach/Inlet Processes and Management: A Florida Prospective, Journal of Coastal Research, Special Issue No. 18, Fall, 1993.
- U.S. Army Corps of Engineers (COE), "Broward County, Florida, Port Everglades to the South County Line (Segment III), Shore Protection Project Reevaluation Report, Section 934 study with environmental assessment," Jacksonville District South Atlantic Division, 1990.
- U.S. Army Corps of Engineers (COE), "Coast of Florida Erosion and Storm Effects Study, Region III" May, 1995.

CHAPTER 282

IMPROVEMENT OF THE MOST ACCURATE LONGSHORE TRANSPORT FORMULA

by
J S Schoonees¹ and A K Theron¹

ABSTRACT

The ability to predict the longshore sediment transport rate accurately is essential for many coastal engineering applications. Because of the existence of a large number of existing longshore transport formulae, it is important to know which formula to use/apply. Thus, the most universally applicable formula was identified and tested against a comprehensive data set. This formula (Kamphuis formula) was also re-calibrated and guidance is given regarding its use.

INTRODUCTION

The ability to predict the time-averaged longshore sediment transport rate accurately is essential for the design of breakwaters at harbour entrances, navigation channels and their dredging requirements, beach improvement schemes incorporating groynes, detached breakwaters and beach fill as well as for the determination of the stability of inlets and estuary mouths.

Because of the large number of existing longshore transport formula it is important to know which formula to apply in practice. The aim of this paper is therefore to identify the most universally applicable formula and to test this formula against a comprehensive field data database. Finally, this formula is re-calibrated and guidance is given regarding its use.

The data considered in this paper are only for particulate (non-cohesive) sediment (including sand, gravel and shingle) being transported alongshore from the swash zone across the surf zone to deep water. Bulk (total rate calculated perpendicular to the shoreline) as well as local (at a specific point)

¹Research Engineers, CSIR, P O Box 320, Stellenbosch, 7599, South Africa

point) transport rates are considered. These bulk rates include both the bedload and the suspended load. Only field data are used because laboratory investigations often contain possible scale effects and/or use regular waves. Furthermore, the ultimate aim is to be able to predict longshore transport accurately in the *field* (Komar, 1988).

It is assumed that if a longshore transport formula is capable of predicting transport rates accurately for the wide ranging data sets described herein, it can be used with reasonable confidence at similar sites to determine the long-term longshore sediment transport budget if representative wave and other input parameter data are available. It would of course be preferable to have site-specific calibration data before calculating average long-term transport rates at a specific site.

Previous studies where longshore transport formulae have been tested against data include Swart (1976), Fleming *et al.* (1986) and Kamphuis *et al.* (1986). These studies entailed a relatively small number of formulae and limited data. Schoonees (1996) evaluated 52 formulae against an extensive data base. This paper reports some of the findings of the above-mentioned study, with specific regard to the Kamphuis formula (Kamphuis, 1991).

FIELD DATA ANALYSIS

Schoonees and Theron (1993) compiled and reviewed almost all the available field data on longshore transport (as recorded up to 1993).

The data were collected at a wide variety of sites around the world, yielding a large number of data-points, of which 273 points give bulk transport rates. (This is considerably more than the 41 data points used in the Shore Protection Manual by US Army, Corps of Engineers, 1984). Included in the database are also 184 points which give local transport rates.

A point rating system was devised whereby the quality of the data could be assessed. The recording method and the accuracy thereof as well as the representativeness of the data were taken into account. It was found that this evaluation was done reasonably objectively and consistently (Schoonees and Theron, 1993).

According to this evaluation, the data sets were assigned to three categories, namely, the lower, middle and higher quality categories. Most of the data sets fell in the middle category which exhibited a very gradual increase in the overall accuracy of the data within this category. Distinguishing between short- and long-term bulk transport data yielded similar trends in the accuracy of the data. The highest score achieved in the data evaluation was only 71%, thus reflecting the difficulty of measuring longshore transport accurately.

EVALUATION OF LONGSHORE TRANSPORT FORMULAE

The method used in this study to evaluate the longshore transport formulae, was to compare the predicted longshore transport rates to the measured rates and to calculate the relative standard error of estimate (σ). (For a definition of σ , see Schoonees and Theron (1994)). The lower σ is, the better the predictions by the particular formula. In addition the residuals (e_i = measured transport rate - predicted rate) and the distribution of the discrepancy ratio (r_d = predicted/measured rate) were also determined. (The residuals were plotted against the predicted rates to check whether there are systematic trends in the residuals - these are not shown here (Schoonees, 1996)). The longshore transport formulae were also tested under as many different conditions and at as many sites as possible.

From the above-mentioned field data database, Data Set 1 containing 123 points was extracted (see Schoonees and Theron, 1994 for a full description of Data Set 1). In Data Set 1 all the parameters required for testing the transport formulae are available. This same data set was used to evaluate existing longshore transport formulae as well as a newly derived formula (Schoonees, 1996) based on the applied wave power concept.

It is important to note that the data ranges of Data Set 1 are:

0,058	< H_{bs} (significant breaker height, m)	< 3,400
2,32	< T_p (peak wave period, s)	< 16,60
0,30	< θ_b (breaking wave angle, °)	< 35,00
0,007 (=1/143)	< beach slope	< 0,138 (=1/7,2)
0,154	< D_{50} (median grain size, mm)	< 15,000
600	< S (longshore transport rate, m ³ /year)	< 14 793 000

From the above values it is clear that the data ranges of this data set are quite wide. Most conditions encountered on natural beaches are covered and the data were collected on beaches from a variety of sites from around the world. These factors give credibility to the conclusions drawn in this comparison of predicted versus measured transport rates.

In total, 52 different longshore transport formulae were evaluated (Schoonees, 1996). These formulae were classified into different categories with regard to the theories on which they are based. The following three formulae were found to be the most accurate as tested against Data Set 1:

Order of accuracy	Name of the formula	Relative standard error of estimate (σ)	Category
1	Kamphuis (1991)	0,393	Dimensional analysis
2	Van Hijum, Pilarczyk and Chadwick (1989)	0,417	Energetics (energy flux)
3	Van der Meer (1990)	0,447	Empirical

These formulae are all bulk (total rate) as opposed to detailed predictors. Figures 1, 2 and 3 illustrate the fit of the predicted transport rates against the measured rates (log-log scales).

The formulae were also ranked according to the highest percentage of discrepancy ratios (r_d) between 0,5 and 2 (i.e. under or over prediction by a factor of 2; $r_d = 1$ indicates perfect agreement). A similar ranking of the "best" five formulae was found. However, it was found that σ provides a better way to judge the accuracy of a formula than using the percentage of r_d between 0,5 and 2. This is because, when applying a transport formula to determine a longshore transport budget at a site, a single badly predicted transport rate can distort the calculated budget greatly. At the same time, however, the above-mentioned percentage of r_d can still be very high compared to σ which would be affected greatly by a single badly predicted rate. Therefore σ is a better yardstick.

Dimensional analysis incorporating all relevant variables ensured that the Kamphuis formula contains the most important parameters. The three top formulae (Kamphuis; Van Hijum, Pilarczyk and Chadwick and Van der Meer) are relatively simple. These "simpler" methods performed well probably because a lower degree of inaccuracy is or can be introduced by having fewer (but all the most important) parameters. It is very difficult to acquire accurate input data; and the more parameters incorporated in a formula, the more input data is required (thereby potentially increasing the noise).

It is common practice to compare the predictions from different longshore transport formulae when computing the annual longshore transport regime at a site. Swart and Fleming (1980) advocated the use of a so-called package deal approach. In this approach, the highest and lowest transport rates predicted by six formulae were ignored and the median of the remaining values was determined. The question then remains whether better results can be achieved by means of this or a related method. Three approaches were tried

(Schoonees, 1996). Firstly, by considering the median of the predictions by the five best formulae; secondly, by determining the mean of the three middle values after discarding the highest and lowest predictions; and thirdly, by computing a weighted mean transport of the five predictions. The variation in the transport rates predicted by the five best formulae was investigated. It was found (Schoonees, 1996) that these predictions are reasonably consistent; that is, the individual formulae do not yield excessive outliers. It can therefore be concluded that none of the package deal approaches yield better answers than the best formula (the Kamphuis method) and as such, are not worth pursuing if the above-mentioned five best formulae are used. The reason for this probably lies in the consistency (reliability) of the five best formulae.

RECALIBRATION OF THE KAMPHUIS FORMULA

The Kamphuis formula can be written as follows:

$$\begin{aligned} S &= (31\ 557\ 600.1.3.10^{-3}) x_{Kamphuis} \\ &= 41\ 024,88 x_{Kamphuis} \text{ (m}^3/\text{yr)} \end{aligned} \quad (1)$$

$$\begin{aligned} x_{Kamphuis} = & \frac{1}{(1 - \rho) \rho_s} \cdot (\rho / T_p) L_o^{1,25} H_{bs}^2 (\tan \alpha_k)^{0,75} \\ & \cdot (1/D_{50})^{0,25} (\sin 2\theta_b)^{0,6} \end{aligned} \quad (2)$$

where ρ = porosity
 ρ_s = density of the sediment grains
 ρ = density of sea water
 L_o = deep-water wavelength
 $\tan \alpha_k$ = beach slope to the breaker line

See Kamphuis (1991) for a more comprehensive definition of all the parameters.

Equation (1), the original Kamphuis formula, is plotted *on linear scales* in Figure 4a and b. Note that Figure 4b shows the detail of Figure 4a for $x_{Kamphuis}$ values up to 80 (instead of 200). The 80%, 90% and 95% confidence intervals for the predicted responses of the original Kamphuis formula are also shown in Figures 4a and b. Despite the fact that the Kamphuis formula fares the best of the 52 formulae tested, it is immediately apparent that the confidence intervals are very wide. For example, at the 80% confidence level, the predicted transport rate for $x_{Kamphuis} = 8,7$ varies between -1 290 000 m³/year and + 2 004 000 m³/year (predicted rate = +357 000 m³/year) - Figure 4b. The coefficient of determination (R^2) is 0,284.

Illustrated in Figure 5 is the best-fit straight line through all the data (called S_{Kamphuis} recalibrated, 1):

$$S = 88\,248 + 61\,892 x_{\text{Kamphuis}} \text{ (m}^3\text{/year)} \quad (3)$$

If Equation (3) is used, it is evident that the lowest transport rate that can be predicted, is 88 248 m³/year, which is when $x_{\text{Kamphuis}} = 0$. This is clearly unacceptable, because the transport rate must be zero if $x_{\text{Kamphuis}} = 0$. Furthermore, it can be seen from Figure 4a that there are three main outliers (which fall beyond the 95% confidence limit) and that Equation (3) fits the higher transport rates better than the original Kamphuis formula. Therefore, disregarding the three main outliers and fitting the line through the origin, the following equation is found:

$$S = 75\,549 x_{\text{Kamphuis}} \text{ (m}^3\text{/year)} \quad (4)$$

This relationship, S_{Kamphuis} recalibrated 2, is shown in Figure 5a and b (the latter Figure 5b again presents the detail of Figure 5a). Although this formula fits the high transport rates well, it over predicts significantly for x_{Kamphuis} values below 10 (Figure 5b). This is caused by two influential points where transport rates higher than 3×10^6 m³/year were measured (Figures 5a and b). (Remember that the three main outliers, although shown, have not been used in this regression).

To eliminate this problem all the data points (123) were again considered to yield the third regression line, the S_{Kamphuis} recalibrated, 3:

$$S = 63\,433 x_{\text{Kamphuis}} \text{ (m}^3\text{/year)} \quad (5)$$

This formula fits the data reasonably well over the whole range (Figures 5a and b). It gives virtually the same answers at high x_{Kamphuis} values than the first recalibrated formula Equation (3). It also fits the data at lower transport rates quite well. R^2 is 0,620 and thus Equation (5) explains 62% of the variance in the data (which is a 118% improvement compared with Equation (1)). However, the standard error of estimate (σ) for this formulation is 0,405, which is slightly poorer than the 0,393 of the original Kamphuis equation. The reasons for this apparent contradiction are:

- The least squares approach (Equations (3), (4) and (5)) minimizes $\sum (S_{m,i} - S_{p,i})^2$ while the standard error of estimate (σ) uses $(\log S_{p,i} - \log S_{m,i})^2$. (Subscripts m and p denote "measured" and "predicted" respectively while i is the number of the data point).
- The effect of a few data points with high transport rates act as influential points in the least squares approach. On the other hand, the number of data points at low transport rates play an important role in the value of the standard error of estimate (σ).

To investigate the effect of such low rates on the standard error of estimate, certain data points below a cut-off transport rate were temporarily disregarded and σ re-calculated. The result was the following:

Cut-off measured transport rate (m ³ /year)	Number of data points	σ for $S = 63433 x_{\text{Kamphuis}}$ (Equation 5)	σ for the original Kamphuis formula (Equation 1)
0	123	0,405	0,393
5 000	115	0,392	0,393
10 000	106	0,368	0,380
25 000	103	0,365	0,383
50 000	87	0,324	0,377
100 000	68	0,299	0,374

These values have been plotted in Figure 6. It is clear from the above table that except when very low transport rates of less than 5 000 m³/year are included, Equation (5) is superior to the original Kamphuis formulation. Figure 6 shows that the original Kamphuis formula is relatively insensitive to the cut-off transport rate. On the other hand, the standard error of estimate decreases significantly (to only 0,299 compared to 0,374 of the original formula, which is a 20% improvement) for Equation (5), if the cut-off transport rate increases. If a cut-off rate of 50 000 m³/year is applied, σ reduces from 0,377 to 0,324, a 14% improvement. This finding is important because relatively few storm conditions at any site usually contribute the major part of the longshore sediment transport budget. It is therefore important that the higher transport rates are predicted accurately.

In order to obtain an indication of which wave conditions would cause such cut-off transport rates, the following typical values were chosen:

$T_p = 10s$, $\theta_b = 2^\circ$, $D_{50} = 0,3 \text{ mm}$ and $\tan \alpha = 1/25 (= 0,04)$. It was also assumed that these wave conditions will occur throughout the year.

Using the *original* Kamphuis formula, the longshore transport was then computed for a range of wave heights:

H_{bs} (m)	Longshore transport rate ($S_{Kamphuis}$) ($m^3/year$)
0,1	2 007
0,3	18 067
0,5	50 187
0,7	98 366

For this particular (typical) case, it is clear that relatively low wave heights of about 0,5 m and 0,7 m will already cause transport rates of about 50 000 $m^3/year$ and 100 000 $m^3/year$ respectively. For these cut-off rates, the standard errors of estimate are 0,299 and 0,324 respectively (Figure 6). Equation (5) is therefore judged to be "good".

Instead of using the least squares approach, the question may also be asked: What value of K will cause the minimum standard error of estimate (σ) when using *all* the data points? That is, K in:

$$S = Kx_{Kamphuis} (m^3/year) \quad (6)$$

Computations with different K values yielded the following:

K	σ
30 000	0,438
41 025 (Equation (1))	0,393
45 000	0,388
48 000	0,387
49 000	0,387
50 000	0,387
55 000	0,391
64 433 (Equation (5))	0,405
70 000	0,420

These data have been plotted in Figure 7. From this figure it is evident that the minimum standard error of estimate(s) is 0,387. It can also be seen that σ is not very sensitive with regard to the value of K near the turning point: $\sigma = 0,387$ even if K varies from 48 000 to 50 000. Taking the accuracy of predicted transport rates during storms into account, the preferred (rounded off) equation is:

$$\begin{aligned} S &= 50\,000 \times x_{\text{Kamphuis}} \text{ (m}^3\text{/year)} & (7) \\ \text{with } R^2 &= 0,397 \end{aligned}$$

FINAL RECOMMENDATIONS

The least squares as well as the minimum standard error of estimate approaches were used to recalibrate the Kamphuis formula, yielding Equations (5) and (7) respectively. Finally the recommended procedure for calculating longshore sediment transport is as follows:

For obtaining bulk longshore transport rates, it is recommended that **Equation (5)** be applied at sites where the significant wave heights normally exceed say, 0,3 m and where the sediment grain size is usually less than 1 mm; that is, at partially protected and exposed sites (i.e. relatively high transport rates). Only at sites where very calm conditions prevail and/or where the sediment is coarse, is **Equation (7)** expected to yield better answers. The considerably higher R^2 for Equation (5) compared with the corresponding value for Equation (7) supports the preference for Equation (5). A significant improvement of 118% according to R^2 and up to 20% in σ in the predicted transport rates was obtained.

REFERENCES

- Chadwick, A J (1989). Field measurements and numerical model verification of coastal shingle transport. *Advances in Water Modelling and Measurement*, Palmer, M H (ed), BHRA, Cranfield, Bedford.
- Fleming, C A, Pinchin, B M and Nairn R B (1986). Evaluation of models of nearshore processes. *20 Intern. Conf. on Coastal Eng.*, ASCE, Taipei, Taiwan, Vol 2: 1116-1131.
- Kamphuis, J W (1991). Alongshore sediment transport rate. *J. Waterways, Port, Coastal and Ocean Eng.*, ASCE, Vol. 117(6): 624-640.
- Kamphuis, J W, Davies, M H, Nairn, R B and Sayao, O J (1986). Calculation of littoral sand transport rate. *Coastal Engineering*, Vol 10: 1-21.
- Komar, P D (1988). Environmental controls on littoral sand transport. *21st Intern. Conf. on Coastal Eng.*, ASCE, Malaga. Vol 2: 1238-1252.
- Schoonees, J S (1996). Longshore sediment transport in terms of the applied wave power concept. *PhD thesis*, University of Stellenbosch, Stellenbosch (in preparation).
- Schoonees, J S and Theron, A K (1993). Review of the field data base for longshore sediment transport. *Coastal Engineering* Vol. 19: 1-25.
- Schoonees J S and Theron, A K (1994). Accuracy and applicability of the SPM longshore transport formula. *24 Intern. Conf. on Coastal - Eng.* ASCE, Kobe, Japan. Vol 3: 2595-2609.
- Swart, D H (1976). Predictive equations regarding coastal transports. *15th Intern. Conf on Coastal Eng.* ASCE, Honolulu, Hawaii. Vol 2: 1113-1132.
- Swart, D H and Fleming, C A (1980). Longshore water and sediment movement. *17th Intern. Conf. on Coastal Eng.*, ASCE, Sydney. Vol 2: 1275-1294.
- U S Army, Corps of Engineers (1984). *Shore Protection Manual*, Volumes I and II, Coastal Engineering Research Center, Vicksburg.
- Van der Meer, J A W (1990). Static and dynamic stability of loose materials. In: *Coastal protection*, Pilarczyk K W (ed), Balkema, Rotterdam.

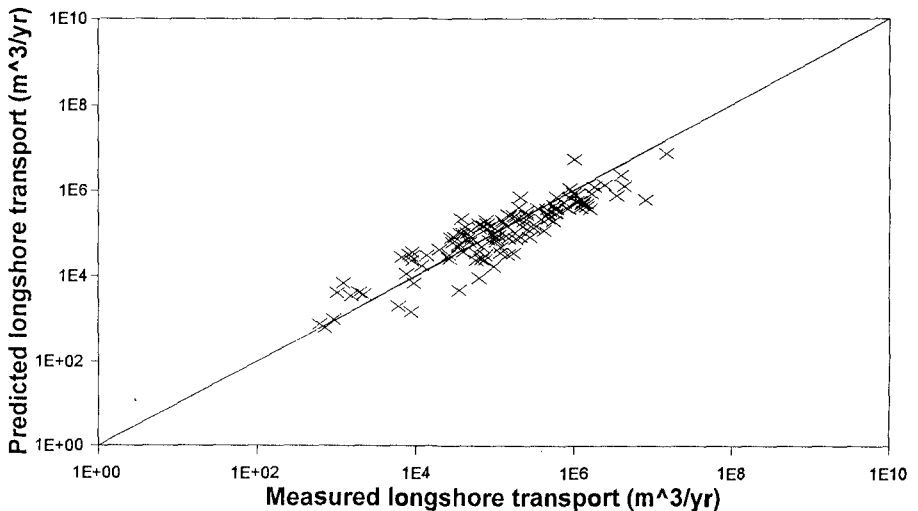


Figure 1: Predicted versus measured longshore transport rates for the Kamphuis formula

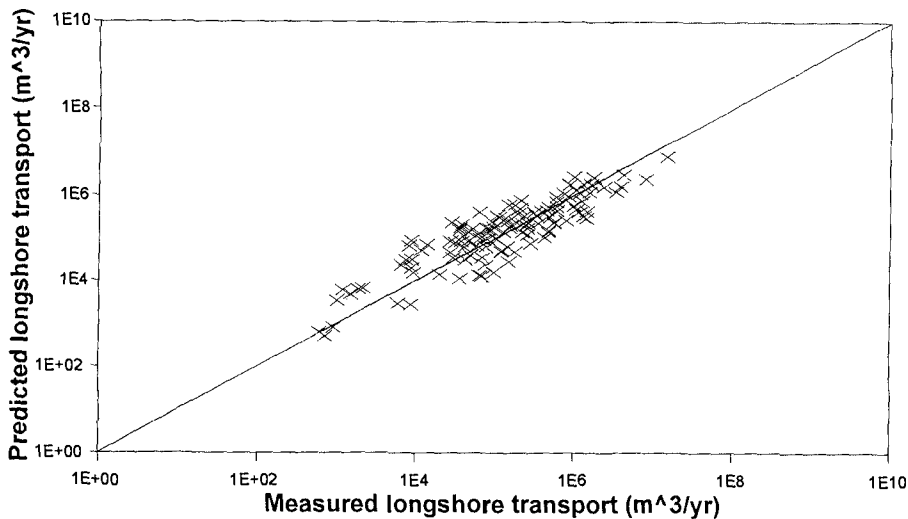


Figure 2: Predicted versus measured longshore transport rates for the Van Hljum, Pilarczyk and Chadwick formula

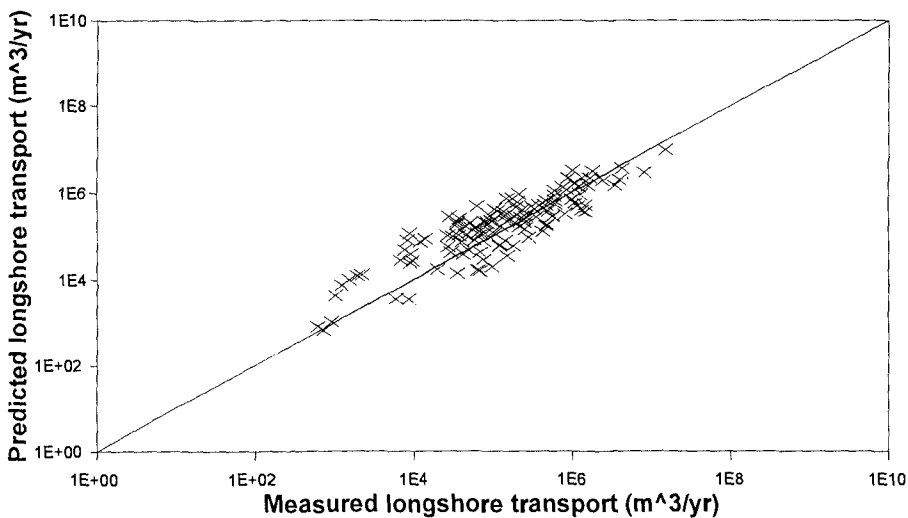


Figure 3: Predicted versus measured longshore transport rates for the Van der Meer formula

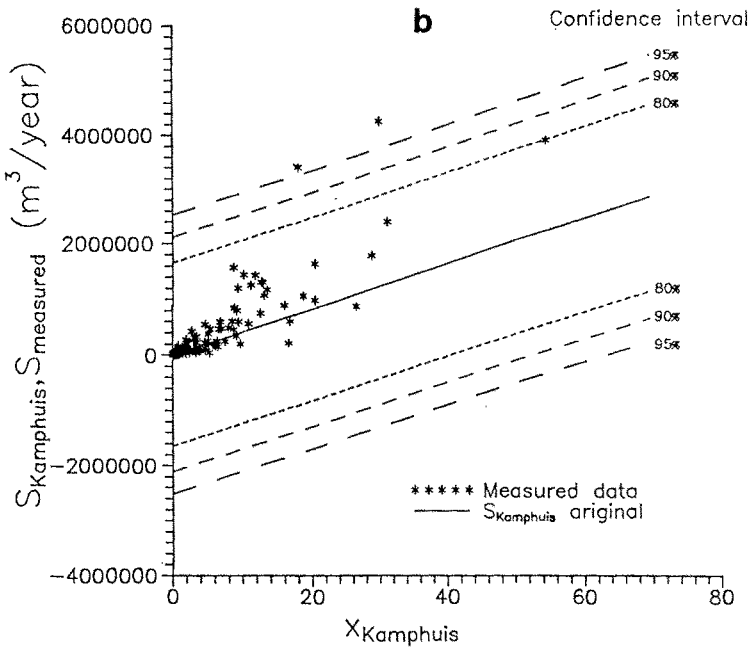
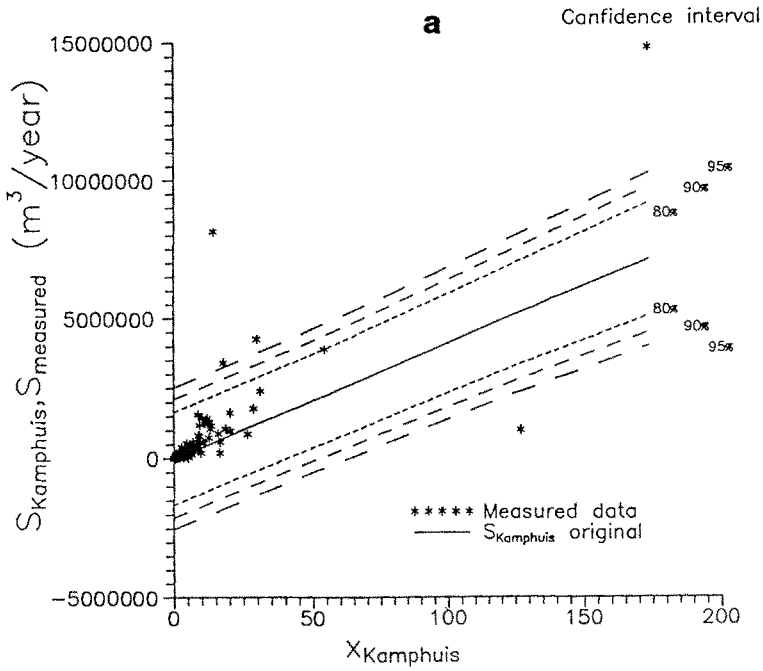


Figure 4: Confidence intervals for the original Kamphuis Formula

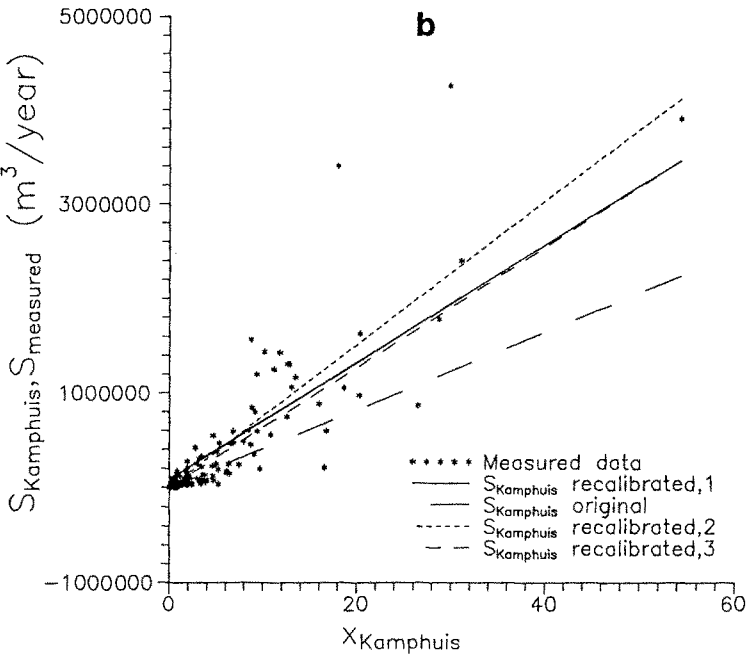
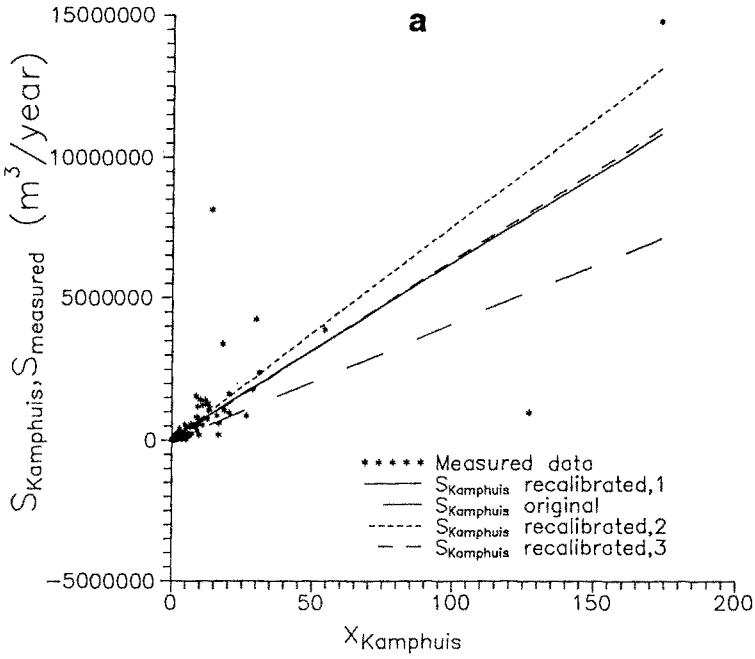


Figure 5: Recalibration of the kamphuis formula

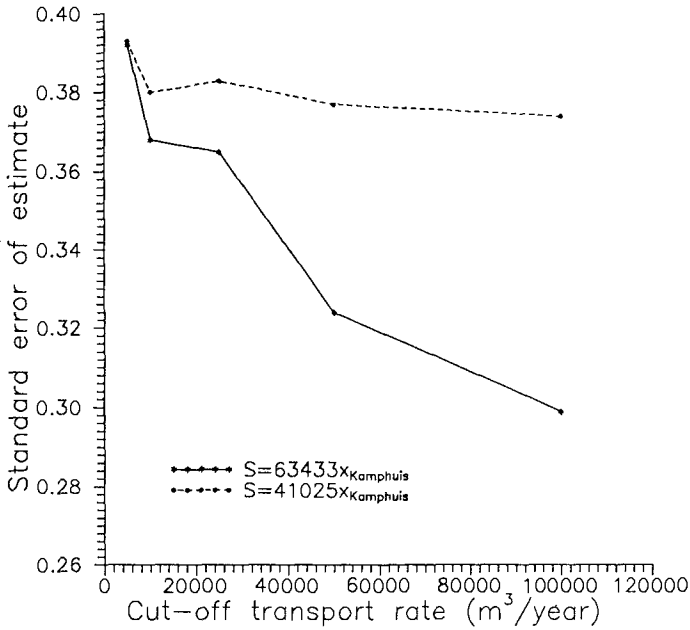


Figure 6: Standard error of the estimate for different cut-off rates

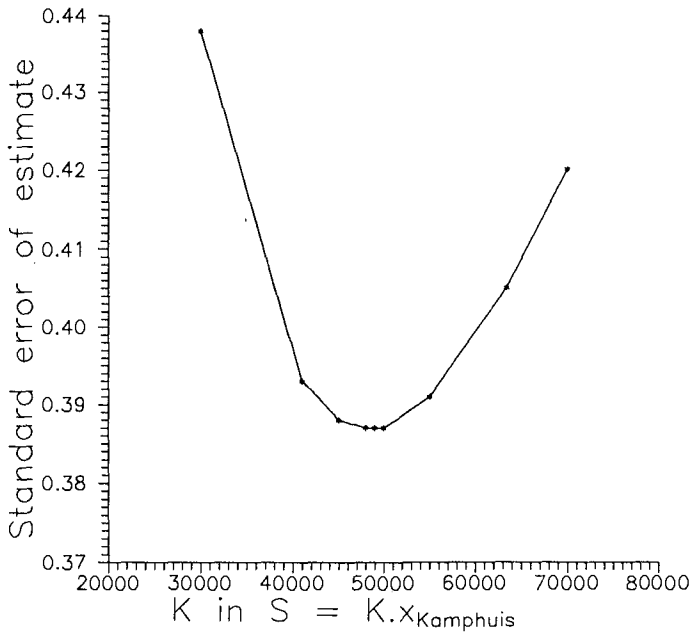


Figure 7: Minimizing the standard error of estimate for the Kamphuis formula

CHAPTER 283

Cross-shore Structure of Longshore Currents during Duck94

Falk Feddersen¹, R.T. Guza², Steve Elgar³, and
T.H.C Herbers⁴

Abstract

The cross-shore structure of the mean longshore current on a barred beach is investigated with observations from the Duck94 field experiment. Maxima of the hourly-averaged longshore current are most frequently located either slightly inshore of the bar crest or near the shoreline. At low tide the longshore current maxima are located closer to the bar crest, and the current is stronger and narrower than at high tide. The tidal cross-shore displacement of the longshore current maximum is qualitatively consistent with the observed radiation stress, S_{xy} , although the maximum currents are displaced shoreward of the maximum S_{xy} gradients at both high and low tide. This spatial lag suggests that some mechanism (such as wave rollers) delays the transfer of momentum from waves to the mean flow. Bathymetric longshore inhomogeneities may also affect the cross-shore structure of the longshore current.

Introduction

Selected observations from the DELILAH field experiment at Duck N.C. suggest that the maximum of the mean longshore current, \bar{v} , occurs between the crest of the sand bar and the trough between the bar and the shoreline (Figures 8-11 of *Church and Thornton*, (1993)), and that longshore current variability is coherent with the approximately 1 m semidiurnal tidal fluctuations in water level (*Thornton and Kim*, 1993). However, the generality of these results over the wide range of wave (*Long*, 1996), wind, and bathymetric (e.g. pronounced sandbars and alongshore inhomogeneities (*Lippmann and Holman*, 1990; *Gallagher*, 1996)) conditions observed at Duck is unknown. Here the cross-shore structure of \bar{v} is further explored with observations from the Duck94 field experiment.

¹ Graduate Student, Scripps Institution of Oceanography, 0209, La Jolla Ca, 92037-0209, falk@coast.ucsd.edu

² Professor, Scripps Institution of Oceanography, 0209, La Jolla Ca, 92037-0209, rguza@ucsd.edu

³ Professor, Washington State University, Pullman Wa, 99164-2752, elgar@eecs.wsu.edu

⁴ Assistant Professor, Naval Postgraduate School, Monterey Ca, 93943, herbers@zee.oc.nps.navy.mil

Duck94 Observations

The experiment site is located on a long straight barrier island exposed to the Atlantic Ocean. Directional properties of sea and swell (including the wave radiation stresses, S_{xy}) were estimated with data from a 2-dimensional array of 15 bottom-pressure sensors located in 8 m water depth operated by the Field Research Facility (FRF) of the U.S. Army Corps of Engineers (Long, 1996). Longshore currents, wave-induced bottom pressures, and the location of the sea floor were observed with colocated bidirectional electromagnetic current meters, pressure sensors, and sonar altimeters (Gallagher *et al.*, 1996) deployed on a cross-shore transect extending 750 m from the shoreline to 8 m water depth (Figure 1). The sensors were sampled at 2 Hz for approximately two months. At each pressure sensor-current meter pair, hourly values of S_{xy} were crudely estimated using linear theory.

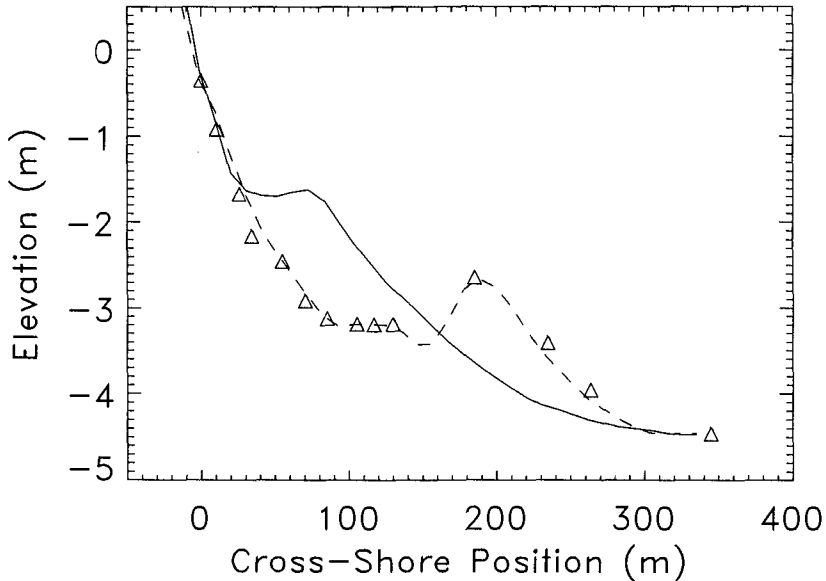


Figure 1. The cross-shore location of current meters (Δ), and measured bathymetry relative to sea level on August 25 (solid line) and October 26 (dashed line). An additional current meter at cross-shore location 749 m in 8 m water depth is not shown.

Conditions during Duck94 are shown in Figure 2. In 8 m water depth, the significant wave height (H_{sig}) ranged between 0.2 m to 4 m and the mean wave angle between $\pm 50^\circ$, so that the total (e.g. frequency-integrated) incident wave radiation stress S_{xy}/ρ (where ρ is the water density) in 8 m depth ranged from -0.7 to 0.5 m^3/s^2 (figures 2a-c). The mean (e.g. centroidal) wave frequency ranged from about 0.08 to 0.2 Hz (not shown). Maximum mean longshore currents (in each hour-long record, \bar{v}_{max}) ranged from 0.1 to 1.4 m/s (Figure 2d). The bar crest, originally located 80 m from the mean shoreline, gradually migrated 120 m offshore (Figure 2e, after *Gallagher*, 1996). Fluctuations in mean water level were about 1 m at spring tide. The slope of the beach foreshore is about 1/10 (Figure 1), so tidal fluctuations in the location of the mean shoreline are about 10 m. Tidal currents in depths less than 8 m are less than 0.03 m/s (S. Lentz, personal communication 1996).

Results

The sand bar is expected to strongly effect the longshore current, so a normalized cross-shore coordinate is defined as,

$$x' = \frac{x - x_{02}}{x_{bar} - x_{02}}$$

where x is the cross-shore coordinate, x_{bar} is the cross-shore location of the bar crest, and x_{02} is the cross-shore location of the most nearshore sensor uv02. The distance from sensor uv02 to the mean shoreline was typically less than 10 m. Depths at uv02 ($x'=0$) ranged from about 0.2 to 1.2 m. In this coordinate system, the bar crest is always located at $x'=1$, but the location of the trough is not constant because of variability in the shape of the cross-shore seafloor profile (e.g. Figure 1).

The location of the longshore current maximum, \bar{v}_{max} , is broadly distributed and roughly bimodal in the normalized coordinate system (1) (Figure 3, after *Gallagher*, 1996). Maxima most often occur either slightly inshore of the bar crest ($0.65 \leq x' \leq 1.2$) or near the shoreline ($x' < 0.3$). Rarely does \bar{v}_{max} occur seaward of the bar crest, even when large waves were breaking well seaward of the bar ($x' > 2$). The few maxima located well seaward of the bar crest typically are weak ($\bar{v}_{max} \sim 0.3 - 0.4$ m/s) and approximately correspond to times of strong buoyancy driven flows (Rennie and Largier, personal communication 1996). The stronger longshore currents ($\bar{v}_{max} > 0.8$ m/s) are associated with large offshore S_{xy} (Figures 2c and 2d) and occur near the bar crest ($0.65 < x' < 1.2$). Weaker maxima (0.25 - 0.7 m/s) occur typically near the shoreline ($0 < x' < 0.3$) or near the bar crest, with few maxima in the region in between. Many of the larger \bar{v}_{max} (0.4 - 0.6 m/s) in the region $0 < x' < 0.3$ occur after the sandbar migrated far offshore in mid-October (Figure 2e).

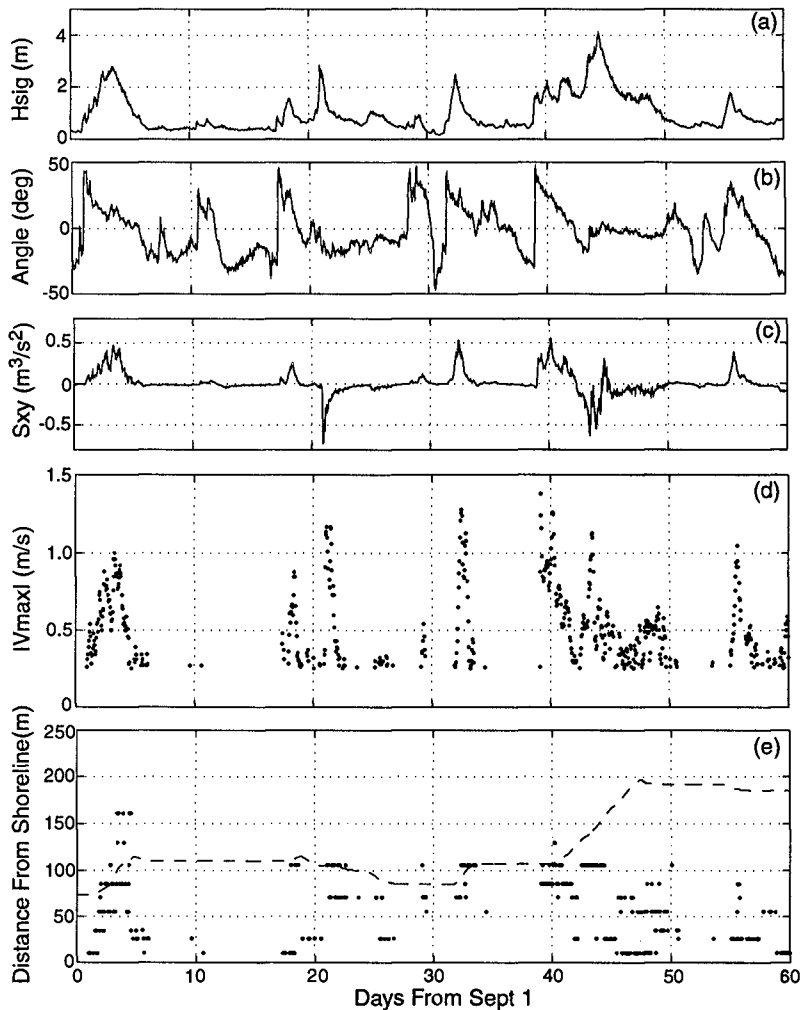


Figure 2. Hourly values of (a) significant wave height H_{sig} in 8 m depth (b) deviation of the mean incident wave angle from shore normal (positive angles correspond to waves from the northern quadrant) (c) S_{xy}/ρ in 8 m depth (d) maximum hour-averaged longshore current \bar{v}_{max} (e) bar crest location (dashed) and the cross-shore location of \bar{v}_{max} . \bar{v}_{max} is plotted only if there were at least five active current meters and $\bar{v}_{max} \geq 0.25$ m/s. Out of 1464 possible values, 572 hourly maxima pass these criteria. The few maxima occurring more than 250 m from shore are not shown in (e).

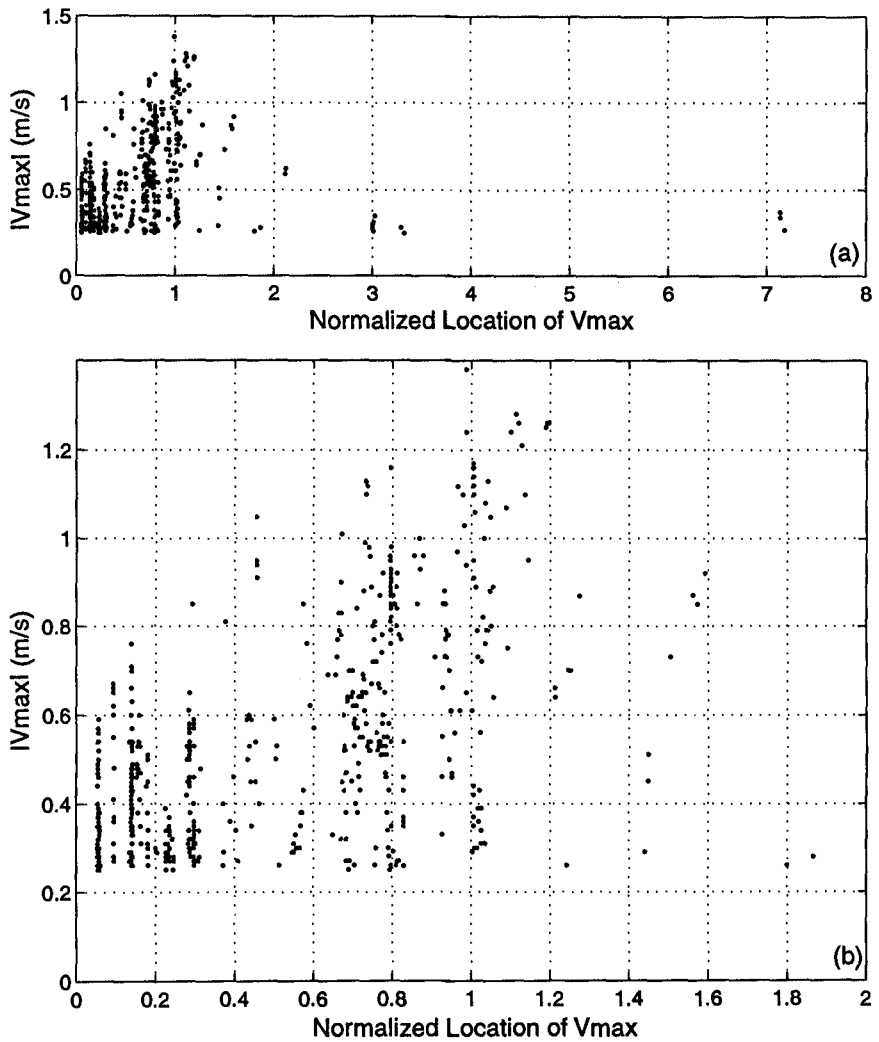


Figure 3. Magnitude of the maximum of the hourly averaged longshore current in normalized cross-shore coordinate, x' (1). the upper panel shows the entire cross-shore region. The region $0 < x' < 2$ is enlarged in the lower panel.

Tides dominate the variability of the local water depth, and thus affect wave shoaling, breaking, and the longshore current. When \bar{v}_{max} is near the bar crest ($0.65 \leq x' \leq 1.2$), the location of \bar{v}_{max} is tidally modulated (Figure 4). At high tide, \bar{v}_{max} is rarely located seaward of $x' = 0.8$, whereas at low tide \bar{v}_{max} is near $x' = 1$. Tidal effects on the location of \bar{v}_{max} are smaller when \bar{v}_{max} is near the shoreline ($x' < 0.3$). Tidal differences in the cross-shore structure of \bar{v} are further illustrated in Figure 5. The current profiles at low tide exhibit a number of similar features; \bar{v}_{max} is located close to $x' = 1$, and the current falls off rapidly shoreward of the maximum. Close to the beach, \bar{v} is approximately 1/4 of \bar{v}_{max} . In contrast, at high tide \bar{v}_{max} is farther shoreward (around $x' = 0.7$, consistent with Figure 4) and weaker. The current profile is broader, and near the shoreline \bar{v} is about 1/2-2/3 of \bar{v}_{max} . The observed \bar{v} tidal variation is consistent with the phase relationships between \bar{v} and sea-level at tidal frequencies found by *Thornton and Kim* (1993). Wave-breaking induced gradients in significant wave heights are greater during low tide than high tide ($0.8 < x' < 1.5$ in Figure 6), resulting in smaller waves shoreward of the sandbar at low tide ($H_{sig} \sim 0.7$ m) relative to high tide ($H_{sig} \sim 1.0$ m).

The differences within the low (Figure 5a) and high (Figure 5b) tide cross-shore structure of \bar{v} are primarily owing to differences in the conditions over the two days spanned by the observations. The bar was relatively stationary moving 7 m, H_{sig} in 8 m depth ranged from 1 to 2 m (Figure 6), the mean incident wave angle from 15 to 45 degrees, and S_{xy}/ρ from 0.2 to 0.5 m³/s². Similar qualitative features in the tidal variation of \bar{v} were observed at other times when the longshore current was strong for several tidal cycles (e.g. Sept 2-5 and Oct 10-16).

The modeled tidal variation of H_{sig} and \bar{v} , for waves and bathymetry representative of Figures 5 and 6, are shown in Figure 7. The wave heights are modeled using *Church and Thornton* (1993), with free model parameters selected to best fit the observed wave heights. The qualitative features of the observed H_{sig} distributions (Figure 6) are reproduced by the model (Figure 7a), except close to the shoreline. The longshore current predictions are made using the modeled H_{sig} variation and observed (in 8 m depth) directional wave properties in the *Thornton and Guza* (1986) longshore current model. A drag coefficient of 0.015 results in similar magnitudes for the modeled (Figure 7b) and observed (Figure 5) currents. Similar to previous results (e.g. *Church and Thornton*, 1993 and others), the modeled longshore currents have the familiar problem of predicting a flow with two maxima, one seaward of the bar crest and one near the shoreline, with no flow in the bar trough. The modeled low and high tide maxima occur at $x' = 1.25$ and $x' = 1.1$ respectively, farther offshore than observed (Figure 5). In physical units, the displacement of the maximum is about 30 m.

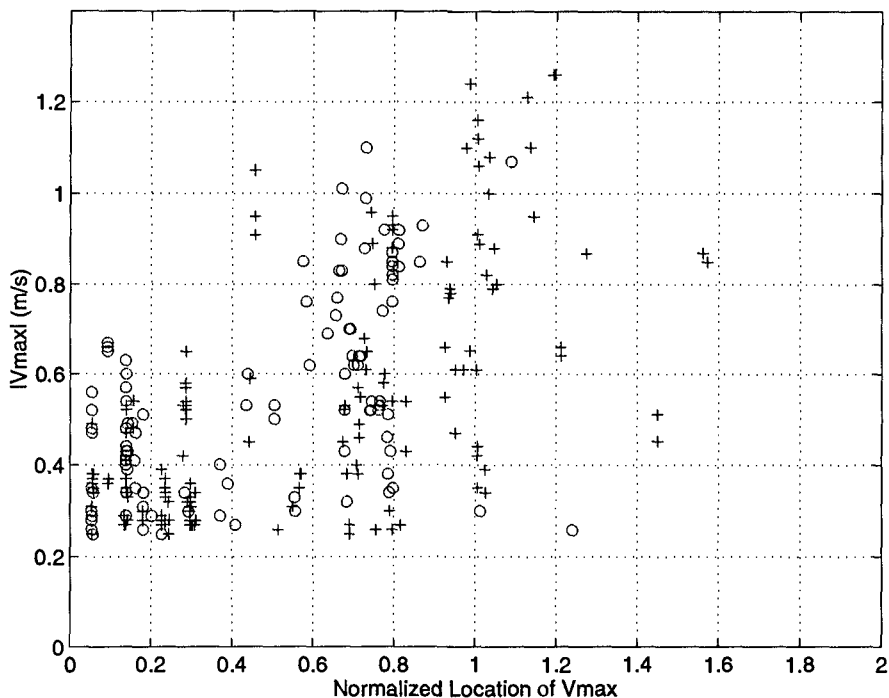


Figure 4. Location and magnitude of \bar{v}_{max} , observed within about 1.5 hours of tidal extrema in normalized cross-shore coordinate. There are 157 low tide (+) and 108 high tide (o) values.

Two commonly given reasons (among many) for the model failure are: (1) There may be a spatial lag in the transfer of momentum from the waves to the mean flow, possibly associated with wave rollers (Svendsen, 1984; Dally and Brown, 1995; and many others). (2) Longshore inhomogeneities in the bathymetry and wave field may result in nonlinear terms or longshore pressure gradient terms in the longshore momentum equation (e.g. Putrevu et al., 1995). Some of the observations are consistent with the lag hypothesis, and there are other examples where alongshore inhomogeneities are likely dominant.

The cross-shore variation of S_{xy} for the successive low and high tide cases (Figure 5 and 6) is shown in Figure 8. At low tide, strong S_{xy} gradients are observed seaward of the bar ($1 \leq x' \leq 1.5$, Figure 8a), whereas shoreward of the bar crest, S_{xy} is relatively constant. The shoreward displacement of the observed longshore current maxima (Figure 5a) relative to strong S_{xy} gradients (Figure 8a) is consistent with a spatial lag in the transfer of momentum to the mean longshore current. At high tide, the region of strong S_{xy} gradients is

slightly seaward of the bar crest ($0.9 \leq x' \leq 1.25$, Figure 8b), and seaward of the location of \bar{v}_{max} ($x' \sim 0.7$) again indicating a spatial lag in the transfer of momentum to the mean flow. The tidal differences in the cross-shore structure of \bar{v} (i.e. the the broadening of \bar{v} at high tide, Figure 5) may be related to tidal variations in the lagging mechanism.

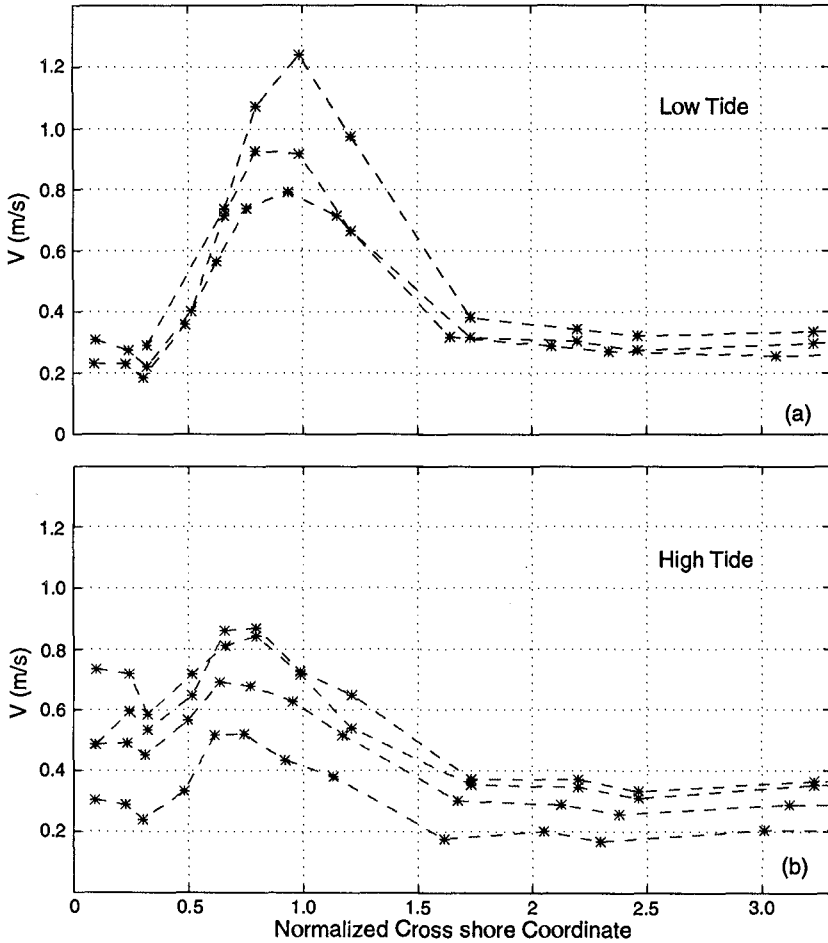


Figure 5. Mean longshore currents in the normalized cross-shore coordinate x' (1) during October 10 and 11. (a) 3 low tides (b) 4 high tides.

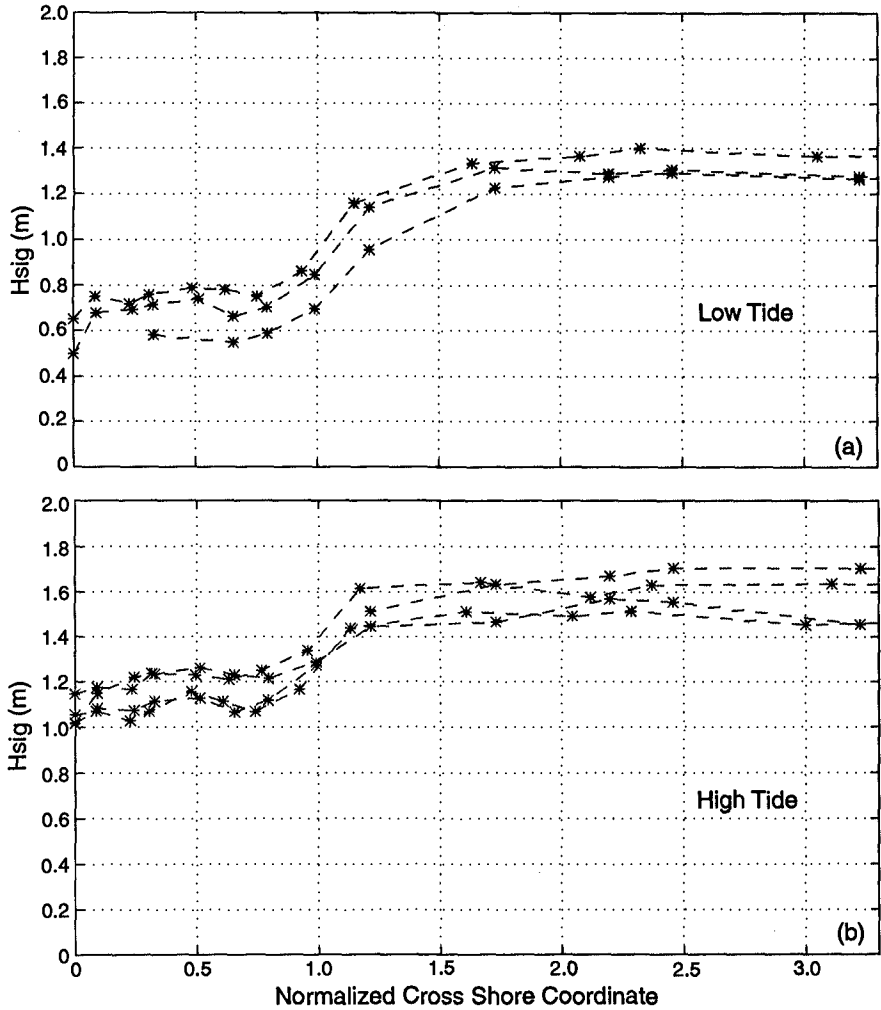


Figure 6. Significant wave height in the normalized cross-shore coordinate x' (1) during October 10 and 11. (a) 3 low tides (b) 4 high tides.

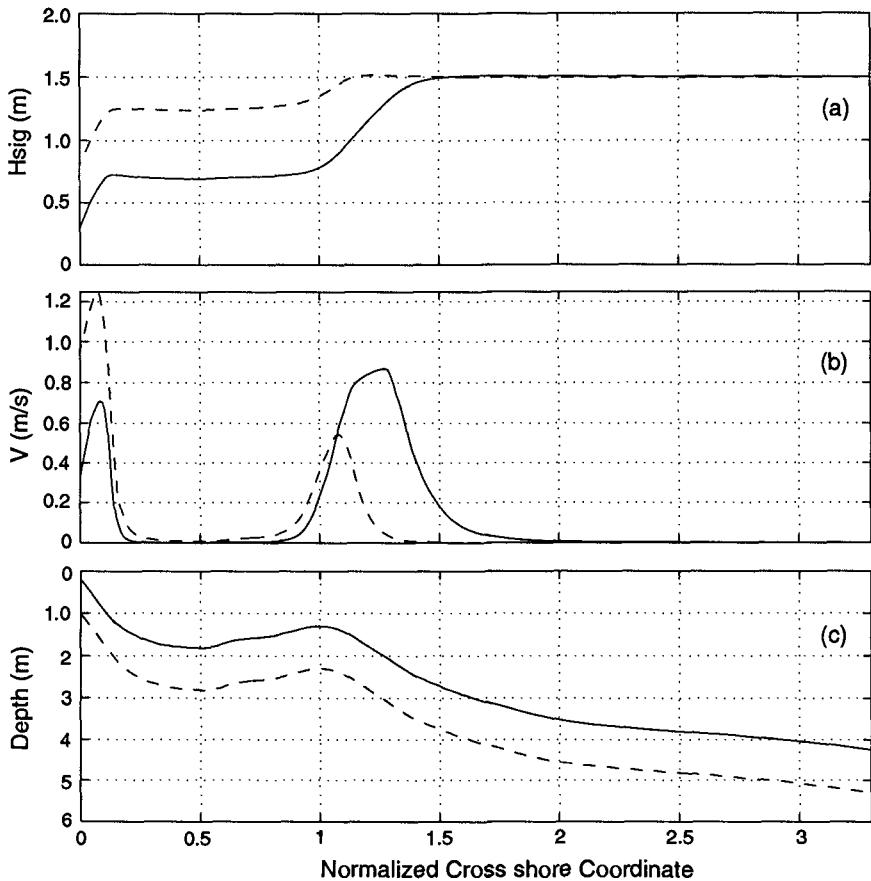


Figure 7. Modeled (a) significant wave heights (b) mean longshore currents (c) model bathymetry in normalized cross-shore coordinate (1). Solid curves represent low tide and dashed curves are high tide. The incident wave parameters are representative of conditions in Figure 5 and 6: $H_{sig} = 1.5$ m and $\theta = 25^\circ$.

An example of longshore currents likely affected by longshore bathymetric inhomogeneities is shown in Figure 9. Although the waves were energetic ($H_{sig} = 3$ m in 8 m depth), they were nearly normally incident (the mean incident wave angle in 8 m depth was 2°) and thus S_{xy} in 8 m depth was small (about 0.1 of S_{xy} with less energetic but more obliquely incident waves in Figure 8). The observations suggest that S_{xy} and S_{xy} gradients are small everywhere (Figure 9b), and that wave breaking began ($x > 200$ m, Figure 9a) far

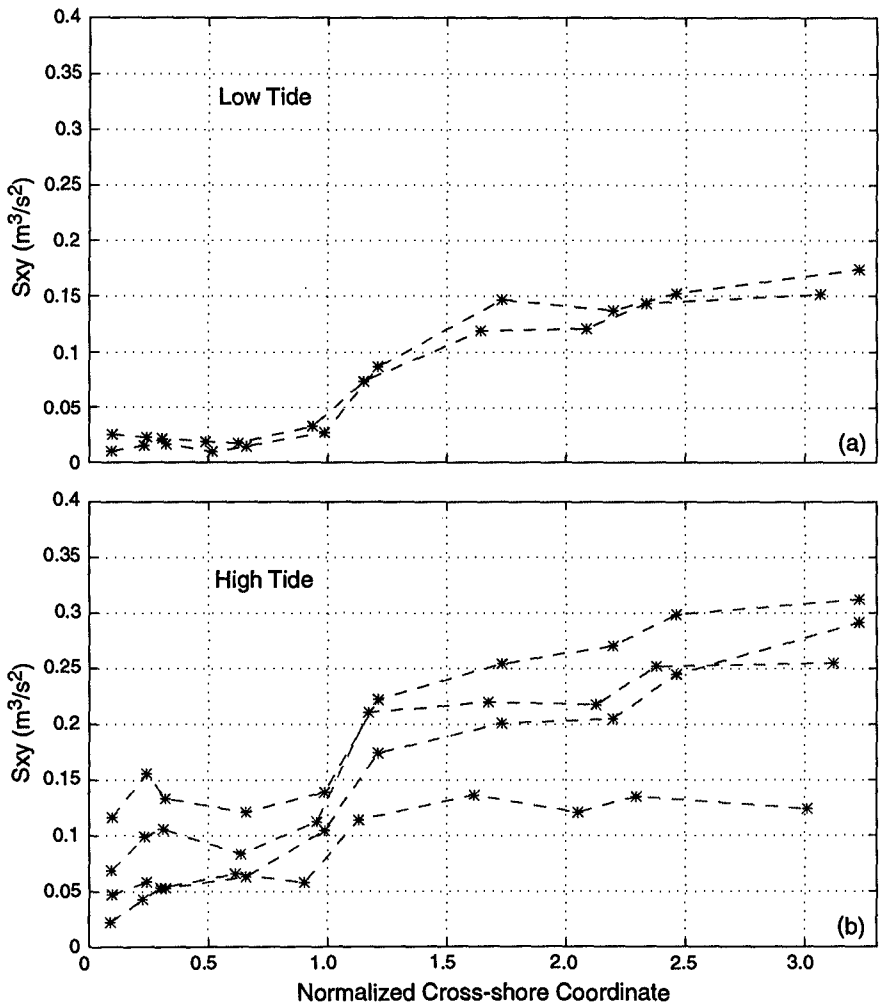


Figure 8. S_{xy}/ρ for the cases (October 10 and 11) shown in Figures 5 and 6 in the normalized cross-shore coordinate $x'(1)$. (a) low tide (b) high tide. The accuracy of S_{xy} estimates is limited because of uncertainties in current meter response and orientation, and because errors in linear theory may be significant in the surfzone. Only two low tide profiles are shown because of unavailable data.

offshore of the location of \bar{v}_{max} ($x \approx 25$ m, Figure 9c). The observed longshore current jet (Figure 9c) near the shoreline is inconsistent with model predictions (based on *Thornton and Guza, 1986*) of negligibly small currents (not shown). Time elapsed video images (R.A. Holman, personal communication, 1996) suggest that the bathymetry was longshore inhomogeneous. Three dimensional bathymetric surveys were not available because of the stormy conditions, however, the first post-storm survey (October 20) did reveal strong longshore inhomogeneity. *Sancho et al. (1996)* demonstrated that this inhomogeneous bathymetry can cause pressure gradients and nonlinear terms to become important in the longshore momentum balance.

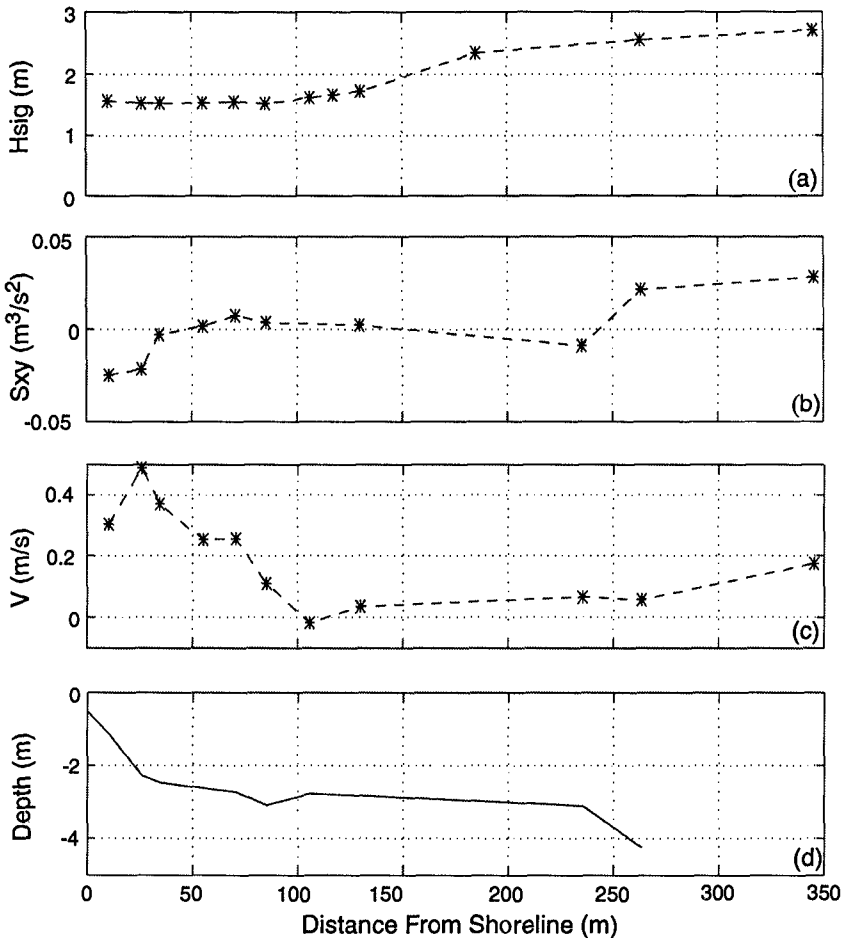


Figure 9. Observed cross-shore variation of (a) significant wave height (b) S_{xy}/ρ (c) longshore current \bar{v} (d) bathymetry on 0500 October 10.

Conclusions

Observations spanning a wide range of bathymetric and wave conditions show that the probability distribution of cross-shore location of longshore current maxima is bimodal. Maxima typically occur near the crest of the sand bar or near the shoreline (Figure 3). At both high and low tide, the observed currents (Figure 5) are qualitatively consistent with the observed S_{xy} (Figure 8), although with a spatial lag, perhaps associated with wave rollers. The 1 m tidal fluctuations in sea level affect the cross-shore structure of the longshore current (Figure 4). At low tide, the current jet is stronger, narrower, and located closer to the bar crest than at high tide (Figure 5). The reason for the tidal changes in the longshore current structure is unknown, however tidal changes in the wave forcing are surely important. Clearly more quantitative work is necessary. The observed variation in the cross-shore structure of the longshore current across a tidal cycle is a robust feature (see also Figure 12 of *Thornton and Kim*, (1993)), and one step in the verification of a roller model would be to reproduce qualitatively the observed tidal variation of the longshore current. Finally, although the magnitude of the effects of longshore bathymetric inhomogeneities is not known, there are cases where they dominate the longshore current (Figure 9).

Acknowledgments

The array of current meters, sonar altimeters, and pressure sensors was deployed and maintained by staff from the Center for Coastal Studies. Britt Raubenheimer and Edith Gallagher helped collect the data. Excellent logistical support was provided by the FRF. We thank Edith Gallagher for providing sonar-altimeter based depth profiles and Rob Holman for providing the video images. This research was supported by ONR and the NSF CoOP program. Falk Feddersen received trainee support from the National Sea Grant College Program, NOAA, U.S. Department of Commerce.

References

- Church, J.C. and E.B. Thornton, Effects of breaking wave induced turbulence within a longshore current model, *Coastal Eng.*, 20, 1-28, 1993.
- Dally, W.R. and C.A. Brown, A modeling investigation of the breaking wave roller with application to cross-shore currents, *J. Geophys. Res.*, 100, 24,873-24,883, 1995.
- Gallagher, E.L., Observation of sea oor evolution on a natural barred beach. SIO PhD thesis, 62pp. 1996.
- Gallagher, E.L., W. Boyd, S. Elgar, R.T. Guza, B. Woodward, Performance of a sonic altimeter in the nearshore, *Marine Geology*, 133, 3, 241-248, 1996.

- Lippmann, T.C., and R.A. Holman, The spatial and temporal variability of sand bar morphology, *J. Geophys. Res.*, 95, 11,575-11,590, 1990.
- Long, C.E., Index and bulk parameters for frequency-direction spectra measured at CERC Field Research Facility, June 1994 to August 1995, *Miscellaneous Paper CERC-96-6*, U.S. Army Engineer Waterways Experiment Station, Vicksburg, MS, 1996.
- Putrevu, U., J. Oltman-Shay, and I.A. Svendsen, Effect of alongshore nonuniformities on longshore current predictions, *J. Geophys. Res.*, 100, 16,119-16,130, 1995.
- Sancho, F.E., I.A. Svendsen, A.R. Van Dongeren, and U. Putrevu, Longshore nonuniformities of nearshore currents, *Coastal Dynamics 1995*, 425-436, 1996.
- Svendsen, I.A., Wave heights and set-up in a surf zone, *Coastal Eng.*, 8, 303-329, 1984.
- Thornton, E.B. and R.T. Guza, Surf zone longshore currents and random waves: field data and models, *J. Phys. Oceanogr.*, 16, 1165-1178, 1986.
- Thornton, E.B., and C.S. Kim, Longshore current and wave height modulation at tidal frequency inside the surf zone, *J. Geophys. Res.*, 98, 16,509-16,519, 1993.

CHAPTER 284

THREE-DIMENSIONAL HYDRODYNAMICS ON A BARRED BEACH

Tae-Myoung Oh¹ and Robert G. Dean²

ABSTRACT

Results are described from fixed bed wave tank tests to examine the generation and existence of three-dimensional flows on a barred beach. All tests were carried out with the use of two-dimensional and three-dimensional bar, which represented periodic forms parallel to the coast superimposed on a linear sloping beach. For these tests, wave heights and wave direction fields within and adjacent to the surf zone were documented to calculate the wave-induced horizontal torque based on mean vorticity and momentum equations. The circulation pattern clearly demonstrated that rip currents were stable on a three-dimensionally barred beach. It was found that the individual component including the depth gradients in the longshore direction, i.e., the effects of the bar morphology, tended to stabilize the bar-induced cellular circulation on the three-dimensional beach morphology although increased momentum fluxes of waves in the area with opposing currents induced by the bar tended to exert a counter force against them. It appeared that the mass transport over the more elevated portions of the bar tended to return to offshore through the deeper portions of the bar, where the depth gradients in the longshore direction existed. The cause is believed to be due to the greater hydraulic efficiency of flows through deeper portions of the profile.

¹Research Director, Woobo Space Co., Ltd., Seongkok Bldg. 7FL., #823-22 Yeoksam-Dong, Kangnam-Ku, Seoul, Korea, Zip-Code 135-080

²Professor, Coastal and Oceanographic Engineering Department, University of Florida, Gainesville, Fl 32611

INTRODUCTION

There are several proposed mechanisms to explain the presence of three-dimensional forms that are fairly regular and generally associated with rip currents, which range from the relatively simple to the complex, including: (1) Instability between the hydrodynamics and sedimentary systems (Hino, 1974; Deigaard, 1990), (2) Interaction between waves and currents (Dalrymple and Losano, 1978), (3) Interaction between synchronous edge waves and incident waves (Bowen, 1969; Bowen and Inman, 1969), (4) Intersecting wave trains (Dalrymple, 1975), and (5) Structural controls by natural and/or constructed features (Gourlay, 1976; Wind and Vreugdenhil, 1986). Some of those mechanisms (Hino, 1974; Dalrymple and Losano, 1978) contended that rip currents in nature could be explained by the reinforcement of three-dimensional flows over two-dimensional morphology. However, previous laboratory investigations (Dean and Oh, 1994) suggested that rip currents were neither self-reinforcing nor stable on two-dimensional topography due to the stabilizing wave-induced torque associated with the increased momentum fluxes in the vicinity of seaward mass return flow; hence, substantial rip currents could not occur without the presence of a rip channel.

This paper comprises the results of a series of fixed bed wave tank experiments conducted on a barred beach to examine the effects of three-dimensional bar morphology on the tendency for cellular circulation inside the surf zone, thus discussing the questions including: (1) Rip currents of significant strength can form on a barred beach, and (2) Whether the interaction between rips and incident waves causes increased or decreased wave heights at the location of the rip current with the presence of the rip channel.

Before presenting the experiments, it is helpful to discuss theoretical background governing three-dimensional circulation inside the surf zone. Primary emphasis is focused on the driving forces (torques) of the three-dimensional flows rather than the details of the hydrodynamics.

DRIVING FORCES OF THE THREE-DIMENSIONAL FLOWS

Consider a Cartesian coordinate system, where the y -axis is located at the still water line and the x -axis is directed seaward. Assuming horizontal flows, wave-induced circulation inside the surf zone is usually formulated based on depth-integrated, time-averaged continuity and momentum equations (Phillips, 1977). After neglecting the lateral shear stress coupling,

Continuity Equation

$$\frac{\partial \bar{\eta}}{\partial t} + \frac{\partial}{\partial x}[U(h + \bar{\eta})] + \frac{\partial}{\partial y}[V(h + \bar{\eta})] = 0 \quad (1)$$

Momentum Equations

$$\frac{\partial U}{\partial t} + U \frac{\partial U}{\partial x} + V \frac{\partial U}{\partial y} = -g \frac{\partial \bar{\eta}}{\partial x} + D_x + B_x \quad (2)$$

$$\frac{\partial V}{\partial t} + U \frac{\partial V}{\partial x} + V \frac{\partial V}{\partial y} = -g \frac{\partial \bar{\eta}}{\partial y} + D_y + B_y \quad (3)$$

where, t is the time, (U, V) the mean horizontal velocity components in the x - and y -direction respectively, $\bar{\eta}$ the mean water level measured from the still water level, h the still water depth, g the gravitational acceleration, and (B_x, B_y) are the shear stress components. The driving force components (D_x, D_y) are expressed in terms of the gradients of the radiation stresses.

$$D_x = -\frac{1}{\rho(h + \bar{\eta})} \left(\frac{\partial S_{xx}}{\partial x} + \frac{\partial S_{xy}}{\partial y} \right) \quad (4)$$

$$D_y = -\frac{1}{\rho(h + \bar{\eta})} \left(\frac{\partial S_{xy}}{\partial x} + \frac{\partial S_{yy}}{\partial y} \right) \quad (5)$$

in which,

$$S_{xx} = E[n(\cos^2 \theta + 1) - \frac{1}{2}] \quad (6)$$

$$S_{xy} = E n \sin \theta \cos \theta \quad (7)$$

$$S_{yy} = E[n(\sin^2 \theta + 1) - \frac{1}{2}] \quad (8)$$

where, E is the total wave energy per unit surface area and n is the ratio of the group velocity C_g to the wave celerity C .

Mean Vorticity Equations

Mean vorticity equation is obtained by cross-differentiating Equations (2) and (3) such that the set-up terms are eliminated.

$$\frac{\partial \bar{\omega}}{\partial t} + \frac{\partial}{\partial x}(U\bar{\omega}) + \frac{\partial}{\partial y}(V\bar{\omega}) = \frac{\partial D_y}{\partial x} - \frac{\partial D_x}{\partial y} + \frac{\partial B_y}{\partial x} - \frac{\partial B_x}{\partial y} \quad (9)$$

where, the mean vorticity, $\bar{\omega}$, is defined as

$$\bar{\omega} \equiv \frac{\partial V}{\partial x} - \frac{\partial U}{\partial y} \quad (10)$$

Sometimes, this time-averaged and depth-integrated vorticity equation is helpful since the contribution of set-up term to wave-induced current system is considered only indirectly through the total mean water depth $(h + \bar{\eta})$, thus making it possible to neglect $\bar{\eta}$ by assuming that $\bar{\eta}$ is small relative to the still water depth.

Vorticity Driving Torque based on Mean Vorticity Equation

The local vorticity driving torque, T_V , can be obtained directly from the mean vorticity equation presented in Equation (9):

$$T_V = \frac{\partial D_y}{\partial x} - \frac{\partial D_x}{\partial y} \tag{11}$$

in which D_x and D_y are given in Equations (4) and (5). Since D_x and D_y include the contributions by S_{xx} , S_{yy} and S_{xy} , the local torque T_V can also be expressed as the sum of three contributions: (1) $(T_V)_1$ by S_{xx} , (2) $(T_V)_2$ by S_{yy} , and (3) $(T_V)_3$ by S_{xy} .

$$T_V = (T_V)_1 + (T_V)_2 + (T_V)_3 \tag{12}$$

where,

$$(T_V)_1 = -\frac{1}{\rho(h + \bar{\eta})^2} \frac{\partial(h + \bar{\eta})}{\partial y} \frac{\partial S_{xx}}{\partial x} + \frac{1}{\rho(h + \bar{\eta})} \frac{\partial^2 S_{xx}}{\partial x \partial y} \tag{13}$$

$$(T_V)_2 = \frac{1}{\rho(h + \bar{\eta})^2} \frac{\partial(h + \bar{\eta})}{\partial x} \frac{\partial S_{yy}}{\partial y} - \frac{1}{\rho(h + \bar{\eta})} \frac{\partial^2 S_{yy}}{\partial x \partial y} \tag{14}$$

$$(T_V)_3 = \frac{1}{\rho(h + \bar{\eta})^2} \left[\frac{\partial(h + \bar{\eta})}{\partial x} \frac{\partial S_{xy}}{\partial x} - \frac{\partial(h + \bar{\eta})}{\partial y} \frac{\partial S_{xy}}{\partial y} \right] - \frac{1}{\rho(h + \bar{\eta})} \left[\frac{\partial^2 S_{xy}}{\partial x^2} - \frac{\partial^2 S_{xy}}{\partial y^2} \right] \tag{15}$$

Assuming that waves encounter the coast with nearly normal incidence (i.e., $\theta \cong \pi$), and using the shallow water asymptotes ($n = 1$), then the radiation stress terms can be written as

$$\begin{aligned} S_{xx} &= \frac{3}{16} \rho g H^2 \\ S_{xy} &= \frac{1}{8} \rho g H^2 (\theta - \pi) \\ S_{yy} &= \frac{1}{16} \rho g H^2 \end{aligned} \tag{16}$$

Assuming further that $\bar{\eta}$ is small relative to still water depth, i.e., $(h + \bar{\eta}) \rightarrow h$ (this assumption will not be valid near the still water shoreline where $h = 0$), then vorticity driving torque components $(T_V)_1$, $(T_V)_2$ and $(T_V)_3$ can be written as follows:

$$(T_V)_1 = \frac{g}{16h} \left[-\frac{3}{h} \frac{\partial h}{\partial y} \frac{\partial H^2}{\partial x} + 3 \frac{\partial^2 H^2}{\partial x \partial y} \right] \quad (17)$$

$$(T_V)_2 = \frac{g}{16h} \left[\frac{1}{h} \frac{\partial h}{\partial x} \frac{\partial H^2}{\partial y} - \frac{\partial^2 H^2}{\partial x \partial y} \right] \quad (18)$$

$$(T_V)_3 = \frac{g(\theta - \pi)}{8h} \left[\frac{1}{h} \frac{\partial h}{\partial x} \frac{\partial H^2}{\partial x} - \left(\frac{\partial^2 H^2}{\partial x^2} - \frac{\partial^2 H^2}{\partial y^2} \right) \right] + \quad (19)$$

$$\frac{g}{8h} \left[\frac{1}{h} \frac{\partial h}{\partial x} H^2 \frac{\partial \theta}{\partial x} - H^2 \left(\frac{\partial^2 \theta}{\partial x^2} - \frac{\partial^2 \theta}{\partial y^2} \right) \right] - \frac{g}{4h} \left[\frac{\partial \theta}{\partial x} \frac{\partial H^2}{\partial x} - \frac{\partial \theta}{\partial y} \frac{\partial H^2}{\partial y} \right]$$

Hence, if the distributions of wave height and local wave directions are known, the local vorticity driving torque induced on the surf zone can be calculated. It should be noted here that the torque T_V has dimensions of $[1/sec^2]$, which is not actual dimensions of torque, $[\text{force} \times \text{length}]$.

Vorticity Driving Torque based on Momentum Equations

Another expression for the vorticity driving torque, T_M , can be obtained by integrating local torque about a reference point over the entire surf zone.

$$T_M = \iint \rho(h + \bar{\eta}) [(x - x_o)D_y - (y - y_o)D_x] dx dy \quad (20)$$

where, (x_o, y_o) represent the coordinate of the reference point about which the total driving torque is to be calculated. Here, T_M has dimensions of torque, $[\text{force} \times \text{length}]$.

Using the radiation stress expressions given in Equation (16) with the assumption that $\bar{\eta}$ is small, T_M also can be written as the sum of three contributions: (1) $(T_M)_1$ by S_{xx} , (2) $(T_M)_2$ by S_{yy} , and (3) $(T_M)_3$ by S_{xy} , as follows:

$$T_M = (T_M)_1 + (T_M)_2 + (T_M)_3 \quad (21)$$

where,

$$(T_M)_1 = \iint (y - y_o) \frac{\partial S_{xx}}{\partial x} dx dy = \frac{3\rho g}{16} \iint (y - y_o) \frac{\partial H^2}{\partial x} dx dy \quad (22)$$

$$(T_M)_2 = -\iint (x - x_o) \frac{\partial S_{yy}}{\partial y} dx dy = -\frac{\rho g}{16} \iint (x - x_o) \frac{\partial H^2}{\partial y} dx dy \quad (23)$$

$$(T_M)_3 = \iint [-(x - x_o) \frac{\partial S_{xy}}{\partial y} + (y - y_o) \frac{\partial S_{xy}}{\partial x}] dx dy \quad (24)$$

$$= \frac{\rho g}{8} \iint [(y - y_o) \frac{\partial \{H^2(\theta - \pi)\}}{\partial y} - (x - x_o) \frac{\partial \{H^2(\theta - \pi)\}}{\partial x}] dx dy$$

Hence, T_M also can be calculated if the distributions of the radiation stresses, i.e., the distributions of wave heights and wave incidence angle, are known.

EXPERIMENTS

All experiments were conducted in a wave tank of the Coastal and Oceanographic Engineering Laboratory of the University of Florida. This tank is approximately 20 m long, 1.5 m high and 0.6 m wide, and is equipped with a piston type wavemaker and has glass panels on both sides of the tank. The water depth was 0.40 m in the horizontal section of the tank. Two types of regular waves of 3 cm and 9 cm heights were used while the wave period was fixed at 1.43 sec during the experiments. The bathymetry was configured to represent a bar morphology by superimposing two-dimensional and three-dimensional wood bars parallel to the coast on a uniform slope of 1:20. The two-dimensional bar extended to the whole width of the tank, while the three-dimensional bar extended from one wall to two-thirds of the tank width. These bars were installed approximately at the surf line, which depends on wave height condition. All four tests (two waves and two bars) were carried out to document the wave heights and wave direction distribution within and adjacent to the surf zone. The details are described in Oh (1994).

Wave heights and direction fields were measured to document and interpret the interaction of the waves and bar-induced currents. Figures 1 and 2 present the isolines of wave heights in the presence of the three-dimensional bar for the small waves and for the large waves, respectively. For the small waves, as shown in Figure 1, wave crest lines were almost uniform in the longshore direction even in the presence of the three-dimensional bar, which implied that the return flow due to the three-dimensional bar was weak to modify the wave fields. It is seen from Figure 2 that waves were much higher in the vicinity of the seaward return flow than those near the bar area. Much higher waves appeared to be caused by increased return current induced by the three-dimensional bar. However, it should be noted that the breakerline was not significantly influenced by the return flow. [It was observed by Dean and Oh (1994) that the breakerline was significantly displaced seaward near the return current during the circulation tests with the jet present on a prismatic beach.] Uniform breakerline with the three-dimensional bar morphology appeared to be due to both relatively weak return current induced by the three-dimensional bar and deeper water depth at the return current area than the area over the bar, and it was agreed with the field observations by Sonu (1972).

RESULTS AND DISCUSSIONS

Vorticity Driving Torque based on Mean Vorticity Equation

Considering that waves encounters the coast with normal incidence ($\theta = \pi$), Equations (17), (18), and (19) can be expressed as the combinations of different individual components depending on the wave height gradients and water depth near the bar area, as follows:

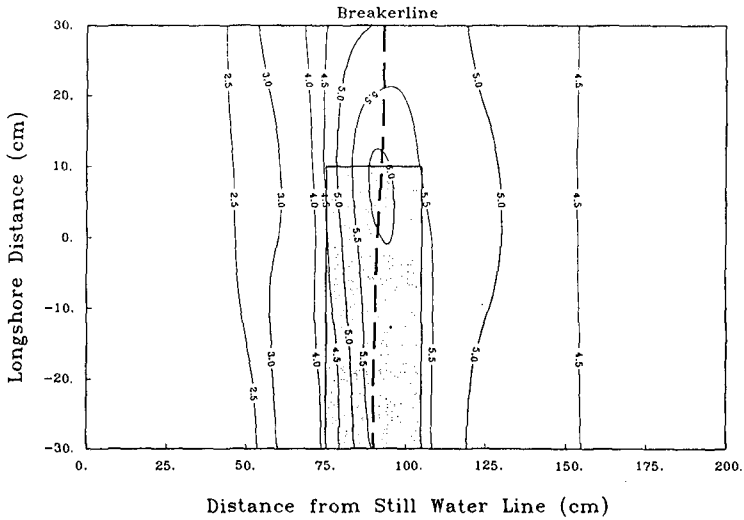


Figure 1: Wave Height Distributions in the Presence of Three-Dimensional Bar when $H_o = 3\text{ cm}$. Wave heights are given in cm . A dark area represents the area covered by the three-dimensional bar. Note that wave fields are not greatly influenced by the return flow induced due to the presence of the three-dimensional bar, resulting in more or less uniform breakerline.

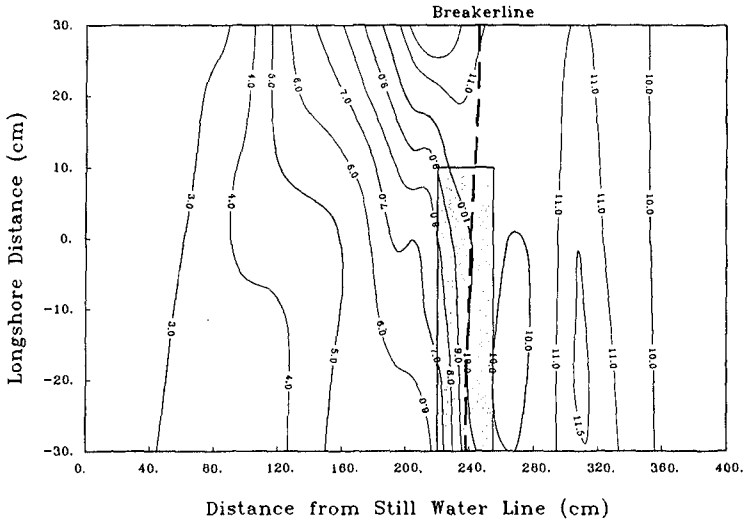


Figure 2: Wave Height Distributions in the Presence of Three-Dimensional Bar when $H_o = 9\text{ cm}$. Wave heights are given in cm . A dark area represents the area covered by the three-dimensional bar. Note that wave fields are substantially influenced by the return flow induced due to the presence of the three-dimensional bar. Note also almost uniform breakerline due to deeper water depth at the area of return flow than the area over the bar.

$$\begin{aligned}
 (T_V)_1 &= 3 (II - VI) \\
 (T_V)_2 &= I - II \\
 (T_V)_3 &= 0
 \end{aligned}
 \tag{25}$$

where,

$$I = \frac{g}{16h^2} \frac{\partial h}{\partial x} \frac{\partial H^2}{\partial y} \tag{26}$$

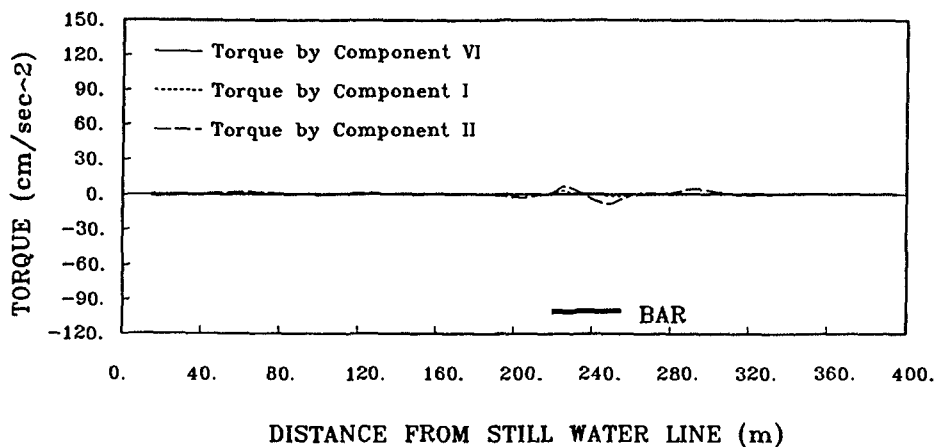
$$II = \frac{g}{16h} \frac{\partial^2 H^2}{\partial x \partial y} \tag{27}$$

$$VI = \frac{g}{16h^2} \frac{\partial h}{\partial y} \frac{\partial H^2}{\partial x} \tag{28}$$

The marginal distributions of individual components are presented in Figure 3 for the large waves. When the three-dimensional bar is installed, the vorticity driving torque is mainly contributed by Component VI, which includes the gradients of water depth in the y -direction, $\frac{\partial h}{\partial y}$, and is confined in the vicinity of the three-dimensional bar area. With the two-dimensional bar present, in which case $\frac{\partial h}{\partial y}$ is zero, the magnitude of the Components I and II are negligible. It is noted for the large wave tests in the presence of the three-dimensional bar that Component I increases up to a comparable magnitude to Component VI, as shown in Figure 3(b). This effect might be due to the increase in the gradients of wave heights in the y -direction. Due to space limitations, the results for the small wave condition will not be presented here; however, it was found that the results were consistent with those for the large waves.

The marginal distributions of the total torque are shown in Figure 4 for the large wave condition in the presence of the three-dimensional bar. Positive circulations occur within the surf zone and in the area seaward of the bar region but the magnitudes of these circulations are smaller than and overshadowed by the negative circulation near the bar area. Hence, it would be necessary for future experiments to simulate the more realistic and smooth bar morphology which could avoid these exaggerated effects of the depth gradients in the y -direction. However, these results clearly demonstrate that rip currents are stable on a three-dimensional barred beach although increased momentum fluxes of waves in the area with opposing currents induced by the bar tend to work against rip currents. It appeared that the water mass transported over the bar tended to return to offshore through deeper area in the bar morphology.

(a) Components I, II and VI with 2-D Bar



(b) Components I, II and VI with 3-D Bar

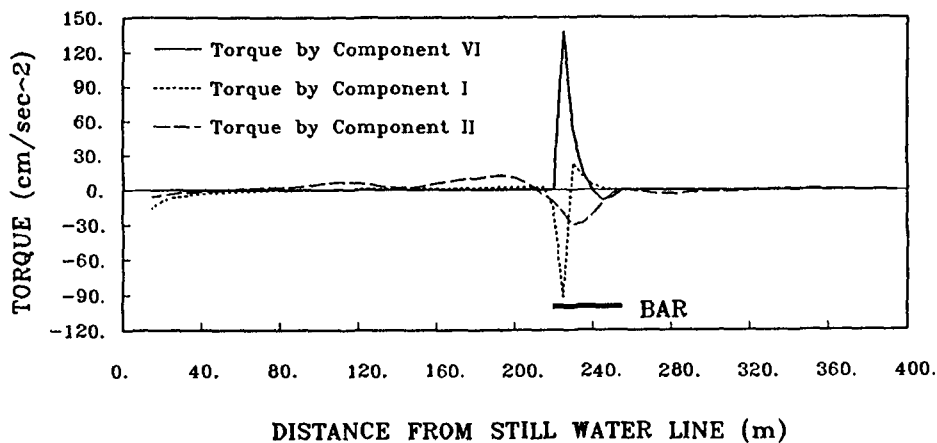


Figure 3: Marginal Distributions of Individual Components along x -axis in cm/sec^2 when $H_o = 9\text{cm}$: (a) Components I, II and VI in the presence of the two-dimensional (2-D) bar and (b) Components I, II and VI in the presence of the three-dimensional (3-D) bar

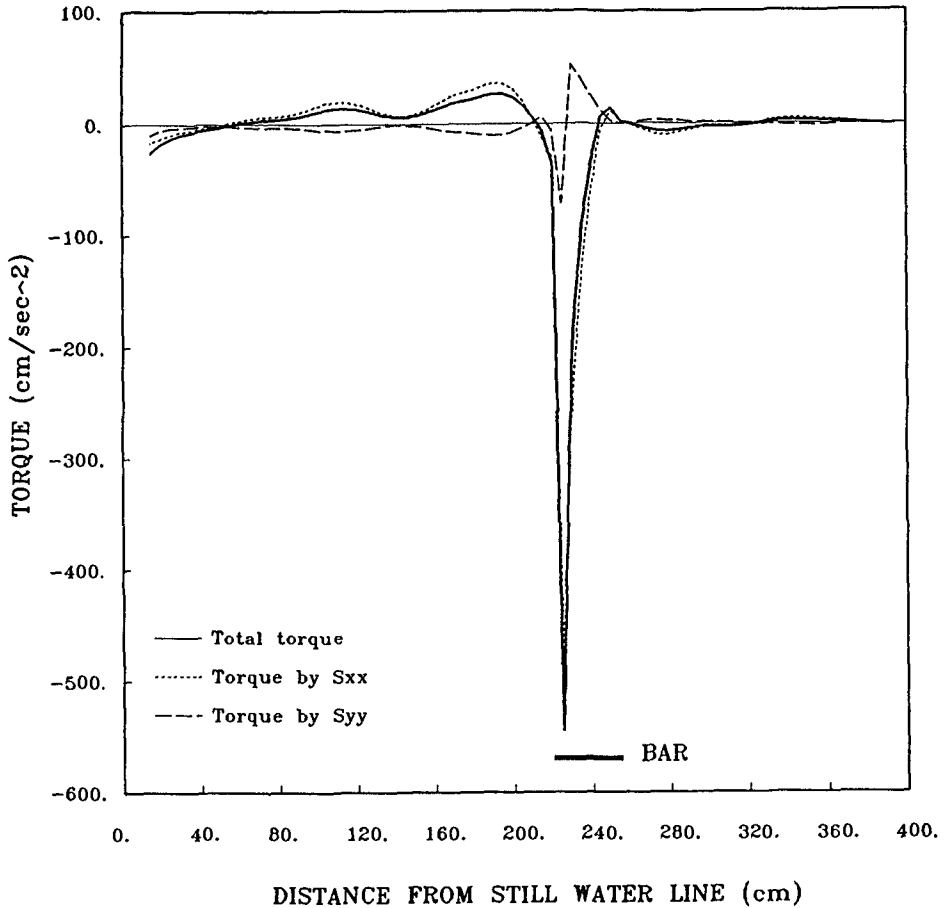


Figure 4: Marginal Distributions of Total Torque and the Contributions of Radiation Stresses Components along x -axis in cm/sec^2 when $H_o = 9cm$ in the Presence of the Three-Dimensional Bar. Note that torque by S_{xx} is dominant over the torque contributed by S_{yy} . Note also the positive values within the surf zone and in the area seaward of the bar. Hence, positive circulation occurs within the surf zone, which tends to suppress the bar-induced circulation.

Vorticity Driving Torque based on Momentum Equation

Marginal distributions of the total torque and the contributions by S_{xx} and S_{yy} were calculated based on the momentum equations, as presented in Equations (21) to (24), and the results are presented in Figure 5 for the large waves ($H_o = 9cm$) in the presence of the three-dimensional bar. For these calculations, the reference point was selected as the centerline point at the same x -location as the location of the bar crest. The contribution by S_{yy} dominates over the contribution by S_{xx} within the whole area of interest except the area over the bar, where the contribution by S_{xx} is dominant since $(x - x_o)$ is small in this area. The total torque changes from negative values near the shoreline to positive values within the surf zone and again to negative values over the bar, and demonstrates oscillating patterns beyond the breakerline. This figure clearly exhibits the opposing effects of waves to the bar-induced circulation, thus tending to stabilize the surf zone.

Table 1 summarizes the total torque induced on the area of interest from the shoreline to offshore. The positive values of the total torque T_M demonstrate that the wave-induced torque is in opposition to the three-dimensional bar-induced circulation (flowing from the bar area, i.e. shoals, to the base of return current, i.e. the embayments). The opposing wave effects appeared to be due to the increased momentum fluxes associated with higher waves in the vicinity of the return flow.

Table 1: Summary of Total Vorticity Driving Torque based on the Momentum Equation.

Item	Unit	$H_o = 3cm$		$H_o = 9cm$	
		2-D Bar	3-D Bar	2-D Bar	3-D Bar
$\sum \sum D_x$	N	-0.98	-1.29	-8.08	-8.40
$\sum \sum D_y$	N	0.049	0.011	0.23	-4.04
$(T_M)_1$ by S_{xx}	$N - m$	-0.002	-0.005	-0.001	0.035
$(T_M)_2$ by S_{yy}	$N - m$	0.015	0.036	0.376	1.103
Total torque, T_M	$N - m$	0.013	0.031	0.375	1.138

SUMMARY AND CONCLUSIONS

A series of fixed bed tests was carried out to investigate the generation and existence of three-dimensional flows on a barred beach. The bar morphology represented periodic forms parallel to the coast superimposed on a linear sloping beach. For these tests, wave heights and wave direction fields within and adjacent to the surf zone were documented to calculate the wave-induced horizontal torque.

It was found for the large wave condition ($H_o = 9cm$) that three-dimensional circulations occurred due to the effect of the three-dimensional bar morphology and flowed from the bar area (shoals) to the return channel (embayments), thus

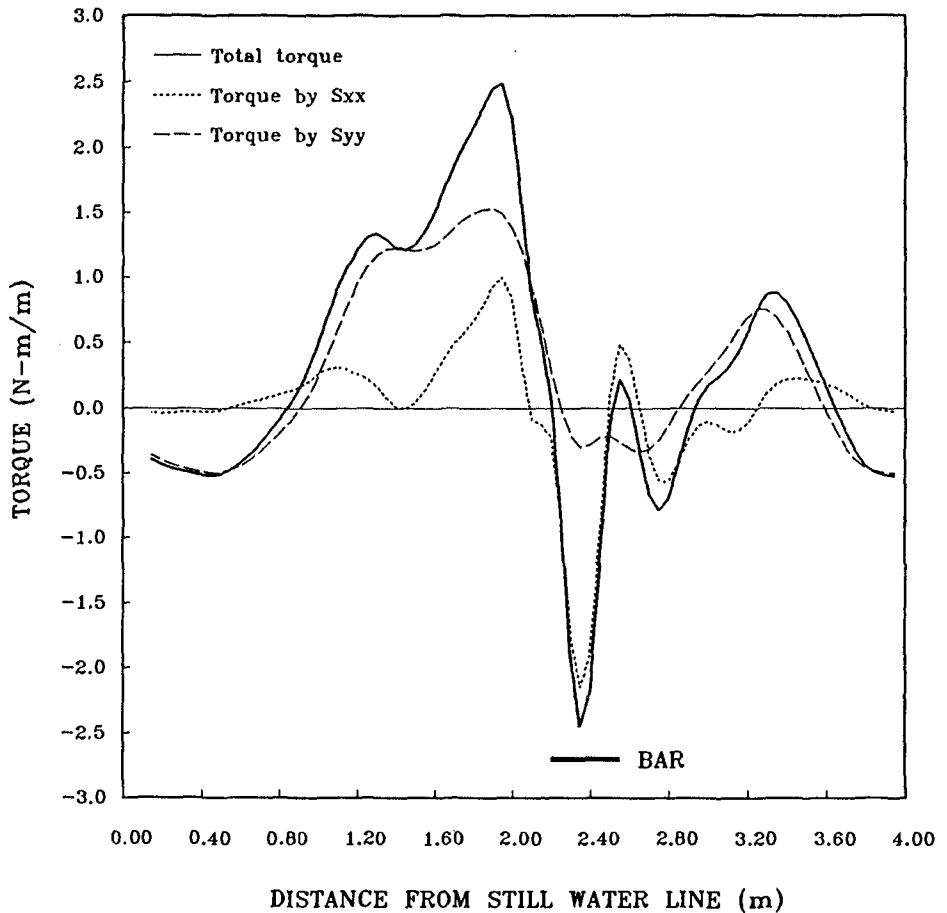


Figure 5: Marginal Distributions of Total Torque and the Contributions of Radiation Stresses Components based on Momentum Equations along x -axis in $N-m/m$ when $H_o = 9\text{ cm}$ with the Three-Dimensional Bar. Note that the contribution by S_{yy} is dominant term over the whole area of interest except over the bar area, where the contribution by S_{xx} is dominant. Positive circulation occurs within the surf zone, resulting in opposing effects of waves on the three-dimensional bar-induced circulation.

modifying the wave fields such that waves were higher in the vicinity of the return current. However, the breakerline was not significantly influenced by the return flow since the return current induced by the three-dimensional bar was weak and the water depth in the vicinity of the return current was deeper than that in the area over the bar, which was agreed with the field observations.

When waves were small ($H_o = 3m$), the resulting circulation pattern was the same as that for the large waves; however, the circulation was too weak to modify the wave fields. These results could indicate that rip currents need the wave height larger than a lower limit to form even with the bar morphology, which was observed in the field.

When individual components of the vorticity driving torque was calculated based on the mean vorticity equation, the component which included the depth gradients in the longshore direction demonstrated the largest contribution.

The marginal distributions of the total torque for the large wave tests with the three-dimensional bar present show positive circulations within the surf zone and in the area seaward of the bar region; hence, these results clearly demonstrated that rip currents were stable on three-dimensionally barred beach although increased momentum fluxes of waves in the area with opposing currents induced by the bar tended to exert a counter force against them. It appeared that the water mass transported over the bar tended to return to offshore through deeper area in the bar morphology, where the depth gradients in the longshore direction existed.

When the vorticity driving torque was calculated based on the momentum equations for the large wave condition tests in the presence of the three-dimensional bar, the contribution by S_{yy} dominated over the contribution by S_{xx} within the whole area of interest except the area over the bar. The total torque changed from negative values near the shoreline to positive values within the surf zone, which clearly demonstrated the opposing effects of waves to the bar-induced circulation, thus tending to stabilize the surf zone. The opposing wave effects appeared to be due to the increased momentum fluxes associated with higher waves in the vicinity of the return flow.

In aggregate, these studies suggest that rip currents are stable on three-dimensionally barred beach although increased momentum fluxes of waves in the area with opposing currents induced by the bar tended to exert a counter force against them. It appeared that the water mass transported over the bar tended to return to sea through deeper area in the bar morphology. This cause is believed to be due to the greater hydraulic efficiency of flows through deeper portions of the profile, which leads to a hydraulic/sedimentary instability which causes development of a vestigial channel.

REFERENCES

- Bowen, A.J. (1969), "Rip Currents. Part 1: Theoretical Investigation", *J. of Geophysical Research*, Vol. 74, No. 23, pp. 5467-5478.
- Bowen, A.J. and D.L. Inman (1969), "Rip Currents. Part 2: Laboratory and Field Observations", *J. of Geophysical Research*, Vol. 74, No. 23, pp. 5479-5490.
- Dalrymple, R.A. (1975), "A Mechanism for Rip Current Generation on an Open Coast", *J. of Geophysical Research*, Vol. 80, No. 24, pp. 3485-3487.
- Dalrymple, R.A. and C.J. Lozano (1978), "Wave-Current Interaction Models for Rip Currents", *J. of Geophysical Research*, Vol. 83, No. C12, Paper No. 8C0556, pp. 6063-6071.
- Dean, R.G. and T.M. Oh (1994), "Three-Dimensional Morphology in a Narrow Wave Tank: Measurement and Theory", *Proc. 24th Int. Conf. on Coastal Eng.*, Kobe, Japan, ASCE
- Deigaard, R. (1990), "The Formation of Rip Channels on a Barred Coast", *Progress Report No. 72*, Institute of Hydrodynamics and Hydraulic Eng., ISVA, Tech. Univ. Denmark, pp. 65-74.
- Gourlay, M. R. (1976), "Non-Uniform Alongshore Currents", *Proc. 15th Int. Conf. on Coastal Eng.*, Honolulu, Hawaii, ASCE, pp. 701-720.
- Hino, M. (1974), "Theory on Formation of Rip-Current and Cuspical Coast", *Proc. 14th Int. Conf. on Coastal Eng.*, Copenhagen, Denmark, ASCE, pp. 901-919.
- Oh, T.M. (1994), "Three-Dimensional Hydrodynamics and Morphology Associated with Rip Currents", Ph.D. Dissertation, Dept. of Coastal and Oceanographic Eng., Univ. of Florida, Gainesville, Florida, 210 pp.
- Phillips, O.M. (1977), "The Dynamics of the Upper Ocean", Cambridge Univ. Press, New York, 363 pp.
- Sonu, C.J. (1972), "Field Observation of Nearshore Circulation and Meandering Currents", *J. of Geophysical Research*, Vol. 77, No. 18, pp. 3232-3247.
- Wind, H.G. and C.B. Vreugdenhil (1986), "Rip-Current Generation near Structures", *J. of Fluid Mech.*, Vol. 171, pp. 459-476.

CHAPTER 285

Rip Current Generation on a Plane Beach

D.A. Suriamihardja¹ and Yoshito Tsuchiya², Member, ASCE

ABSTRACT: In order to establish a wave-current interaction model for rip currents, a set of first-order linearized governing equations describing the 2-D nearshore circulation is derived from the equations of nearshore currents by the perturbation method. Wave refraction induced by the generated currents is fully considered. The solutions to the field equations of rip currents both in the surf zone and shoaling zone are obtained, and expressed in the form of Gaussian hypergeometric functions and modified Bessel functions, respectively. The matching condition of the solutions at the breaking point determines the spacing of the rip currents. Comparison of the computed rip current spacing, circulation pattern, and rip current discharge, with laboratory and field data shows a satisfactory agreement especially in the so-called instability region of the surf similarity parameter.

INTRODUCTION

The change in momentum flux of incoming waves can be described by the offshore and longshore gradients of the radiation stresses which act as the driving forces in the nearshore circulation system. Therefore to formulate the driving forces in the momentum equations for the generation of nearshore currents is of importance (Dingemans, Radder and De Vriend, 1987). Two main causes of the driving forces are the so-called wave-current interaction, and structural interaction (Dalrymple and Lozano, 1978).

The first investigation of nearshore currents as 2-D horizontal circulation generated by the interaction between the incoming waves and the resulting rip currents was by Le Blond and Tang (1974), whose theory applies to a plane beach and normally incident waves. Similar to their work, Iwata (1976) developed a theory which assumed the nonuniformity of bottom friction between surf and shoaling zones. However, these two theories still failed in obtaining the nondimensional alongshore spacing of rip currents as an eigenvalue of the governing equations. Iwata further attempted to find

¹Lecturer, Department of Physics, Faculty of Mathematics and Natural Sciences, Hasanuddin University, Ujung Pandang 90245, Indonesia.

²Professor Emeritus, Kyoto University, and Professor, Meijo University, Kani 509-02, Japan.

currents as an eigenvalue of the governing equations. Iwata further attempted to find an asymptotic solution for both the surf and shoaling zones. Finally, he obtained the real eigenvalue from the characteristic equation which is derived by matching conditions at the breaking point, and found that its value is a function of a parameter determined by the bottom friction coefficient, the surf zone width and the breaker height.

Mizuguchi (1976) also attempted to obtain the eigenvalues from the characteristic equation without using any approximation such as asymptotic solution as in Iwata's work, by considering both the uniformity and nonuniformity of the bottom friction. However, no eigenvalue was obtained. He concluded that this failure occurred due to the exclusion of lateral mixing in the governing equation, and because the contribution of the bottom friction was not sufficient to represent the dissipative effect in the nearshore current. Consequently, he reformulated the bottom friction term to be a function of the distance from the shoreline, similar to the lateral mixing. Dalrymple and Lozano (1978) argued that no reason exists to justify this formulation, so that the real eigenvalue obtained as a function of a parameter proportional to the so-called surf zone similarity parameter and inversely proportional to the bottom friction was invalid.

Dalrymple and Lozano (1978) presented two wave-current interaction models. One was similar to the theory of Le Blond and Tang (1974), in which changes in local wave length due to currents were considered. However, their assumption of an extremely small refraction angle, which implied that no longshore variation in wave orthogonals was allowed, resulted in no rip-current formation. In the second model, the wave-current interaction effect was considered through wave refraction due to current, and the formation of longshore periodic nearshore circulation cells was calculated numerically. The obtained eigenvalue was a function of a parameter expressed by the ratio of beach slope to bottom-friction coefficient. The relationship between the eigenvalue and this parameter showed that the rip-current spacing increases as the parameter increases and vice-versa. Comparison with the rip current spacing of Balsillie (1975) obtained by field measurement showed a good agreement in the region of small values of the parameter, which implied that the theoretical eigenvalue of Dalrymple and Lozano was partly suitable for the prediction of rip-current spacings generated by the incidence of infragravity waves, as it was stated by Balsillie that almost all of the data are categorized into this type of waves. However, when compared with the field measurements collected by Sasaki (1977), which were made in wider regions such as the regions of instability and edge waves, the theoretical spacing showed a lower value than that of field measurements.

The present study investigates the steady-state nearshore circulation on a plane beach based on the interaction between normally-incident waves and the resulting rip currents. A mathematical formulation of the governing field equations for rip currents on a plane beach is made by means of the wave-current interaction model, including the formulation of the driving forces. The governing equations of 2-D nearshore currents on the plane beach are first established by employing the conservation laws for mass, momentum and wave action. The so-called mild slope equation (MSE), which is able to calculate wave transformation due to interaction with the nearshore currents, such as wave refraction, is applied to formulate the driving forces in the momentum equations. Nevertheless, to simplify the analysis without sacrificing the

generality of the theory, the lateral mixing terms are omitted. Using a perturbation method for a small parameter of beach slope, the field equations of rip currents are formulated. At the first order of approximation, the field equations of rip currents are obtained in both the surf and shoaling zones, where the wave refraction due to currents is fully considered. With some additional assumptions, solutions to the field equations are obtained both in the surf and shoaling zones in terms of the Gaussian hypergeometric function and the modified Bessel function, respectively. The matching condition for these solutions at the breaking point makes it possible to determine the eigenvalues of the characteristic equation of the derived field equations.

The theoretical results of the rip current characteristics such as the rip current spacing and flow patterns, are compared with both the previous theoretical results, laboratory and field data. The comparison of the theoretical rip current spacings and those of field data showed a satisfactory agreement. Current patterns in a nearshore circulation cell are also calculated numerically through the determination of integration constants in the stream function based on energy budgeting at the breaking point, which resulted in a reasonable value of rip discharge, both at laboratory and field scales.

THE BASIC EQUATIONS OF NEARSHORE CURRENTS

The MSE derived by Kirby (1984) which includes an additional wave energy dissipation term, $i\omega_r W\Phi$, is employed to formulate the driving forces. The terms in the MSE of Kirby are as follows: W is the ratio of the wave energy dissipation rate D to the total wave energy E , C is the wave celerity, C_g is the group velocity, where both values are assumed to be nearly equal due to the shallow water approximation, and D/Dt is the Lagrangian derivative. By introducing velocity potential of linear wave theory, $\Phi = \phi \exp(-i\omega t)$, and $\phi = (ga/i\omega_r) \exp(iS)$, where S is the phase function, into the MSE of Kirby in the steady state condition, the MSE is written as:

$$\left\{ \frac{\partial}{\partial x_j} \left(C C_g \frac{\partial}{\partial x_j} \right) + 2i\omega U_j \frac{\partial}{\partial x_j} \right\} \phi = - \left\{ i \left(\omega \frac{\partial U_j}{\partial x_j} + \omega_r W \right) + \left(\omega^2 + k^2 C C_g - \omega_r^2 \right) \right\} \phi \quad (1)$$

Following lengthy algebraic procedures using the expressions for the radiation stresses by Dingemans, Radder and De Vriend (1987), and for the depth-integrated mass transport by Crapper (1984) (see Tsuchiya and Suriamihardja, 1989), the driving force F_i can be obtained as:

$$F_i = \frac{\rho \omega_r}{2g} \frac{\partial S}{\partial x_i} W \phi \phi^* - \frac{\rho}{4g} d \frac{\partial}{\partial x_i} \left(\phi \phi^* \frac{\omega_r^2}{d} \right) + \frac{\rho \omega_r}{2g} \phi \phi^* \frac{\partial S}{\partial x_j} \left(\frac{\partial U_i}{\partial x_j} - \frac{\partial U_j}{\partial x_i} \right) - \frac{\rho}{4g} C C_g \frac{\partial}{\partial x_i} \left(\frac{\phi \phi^* \partial^2 A}{A \partial x_j^2} \right) \quad (2)$$

where ϕ^* is the complex conjugate of ϕ . The first term in the right side of (2) is the rotational term, and is the contribution from the dissipation of wave energy. The second is the irrotational term, and the third term describes the interaction between wave-induced mass transport and currents. The fourth term represents the additional effect resulting from the diffraction of waves. Dingemans, Radder and De Vriend (1987) demonstrated that only these rotational terms are able to generate non-zero depth-averaged current velocities. For simplicity, the horizontal components of the nearshore current are assumed to be independent of depth. Therefore the conservation laws to be employed in this study are presented in depth-integrated form (For example, Phillips, 1966; Dolata and Rosenthal, 1984; and Crapper, 1984). Neglecting the wave diffraction effect and assuming the shallow water condition, the steady state mass and momentum equations can finally be reduced to

$$\frac{\partial}{\partial x_j}(\rho U_j d) = 0 \tag{3}$$

$$U_j \frac{\partial U_i}{\partial x_j} + R_i = -g \delta_{ij} \frac{\partial \bar{\eta}}{\partial x_j} + \frac{D}{\rho \omega_r d} \frac{\partial S}{\partial x_i} - \frac{\partial}{\partial x_i} \left(\frac{E}{2\rho d} \right) + \frac{E}{\rho \omega_r d} \frac{\partial S}{\partial x_i} \left(\frac{\partial U_i}{\partial x_i} - \frac{\partial U_i}{\partial x_j} \right) \tag{4}$$

where $R_i = \frac{1}{\rho d} \left\{ \frac{\partial}{\partial x_j} (\rho d \tau_{ij}) + f_{ij} U_j \right\}$ $E = \frac{1}{2} \rho g \omega_r^2 \phi \phi^*$

in which U_i are the vertically-averaged horizontal current velocity components, τ_{ij} are the lateral mixing terms, η is the mean water level, ρ is the density of water, d is the water depth, g is the acceleration of gravity, t is time, x_j are the horizontal coordinates x and y for $j = 1$ and 2 , and f_{ij} are the bottom friction coefficients following Iwata's (1976) formulation in the case of normal incidence and are written as

$$\left. \begin{aligned} \begin{pmatrix} f_{xx} & 0 \\ 0 & f_{yy} \end{pmatrix} \begin{pmatrix} U \\ V \end{pmatrix} &= \frac{2}{\pi} K_* \sqrt{gd} \begin{pmatrix} 2 & 0 \\ 0 & 1 \end{pmatrix} \begin{pmatrix} U \\ V \end{pmatrix}, & x \leq x_B \\ \begin{pmatrix} f_{xx} & 0 \\ 0 & f_{yy} \end{pmatrix} \begin{pmatrix} U \\ V \end{pmatrix} &= \frac{2}{\pi} K_* \sqrt{gd_B} \begin{pmatrix} 2 & 0 \\ 0 & 1 \end{pmatrix} \begin{pmatrix} U \\ V \end{pmatrix}, & x \geq x_B \end{aligned} \right\} \tag{5}$$

where $K_* = 1.41 (\gamma / k \cdot k_e)^{2/3}$ in which k_e is the bottom roughness, k is the wave number and γ is the ratio of wave amplitude to local water depth, and suffix B stands for the position of wave breaking and indices x and y represent the seaward x and alongshore y directions. The conservation of wave action, which can be derived directly from (1), and wave number conservation which is equivalent to the irrotationality condition for wave number, are written as:

$$\frac{\partial}{\partial x_j} \left\{ \frac{E}{\omega_r} (U_j + C_j) \right\} + \frac{D}{\omega_r} = 0; \quad \frac{\partial k_j}{\partial x_i} = \frac{\partial k_i}{\partial x_j} \tag{6}$$

THE FIELD EQUATION OF RIP CURRENT

Perturbation Scheme

Before ordering the equations using the perturbation method, it is convenient to nondimensionalize them. The water depth d_B at the breaking point is selected as the representative length to facilitate the nondimensionalization. The process is defined as:

$$\left. \begin{aligned} (x, y, \bar{\eta}, d) &= d_B(x^*, y^*, \bar{\eta}^*, d^*) & (U, V, C) &= \sqrt{gd_B}(U^*, V^*, C^*) \\ (\omega, \omega_r) &= \sqrt{g/d_B}(\omega^*, \omega_r^*) & (k, k_x, k_y) &= d_B^{-1/2}(k^*, k_x^*, k_y^*) \end{aligned} \right\} \quad (7)$$

where an asterisk represents the dimensionless quantities.

The beach slope s is selected as a parameter of perturbation in ordering the equations, and the series expansion, in which asterisks have been dropped for convenience, are given as:

$$d = s(d_0 + s\zeta_1 + s^2\zeta_2 + \dots) \quad ; \quad a = s(a_0 + sa_1 + s^2a_2 + \dots) \quad (8a)$$

$$U = s^{1/2}(0 + sU_1 + s^2U_2 + \dots) \quad ; \quad V = s^{1/2}(0 + sV_1 + s^2V_2 + \dots) \quad (8b)$$

$$\mathbf{k} = (k_{0x} + sk_{1x} + s^2k_{2x} + \dots) \mathbf{i} + (0 + sk_{1y} + s^2k_{2y} + \dots) \mathbf{j} \quad (8c)$$

$$\omega_r = s^{1/2}\{k_{0x}C_0 + s(k_{1x}C_0 + k_{0x}C_1) + \dots\}; \quad S = (S_0 + sS_1 + s^2S_2 + \dots) \quad (8d)$$

$$C = s^{1/2}(d_0 + s\zeta_1 + s^2\zeta_2 + \dots)^{1/2} \sqrt{(\tanh kd_B)/(kd_B)} \quad (8e)$$

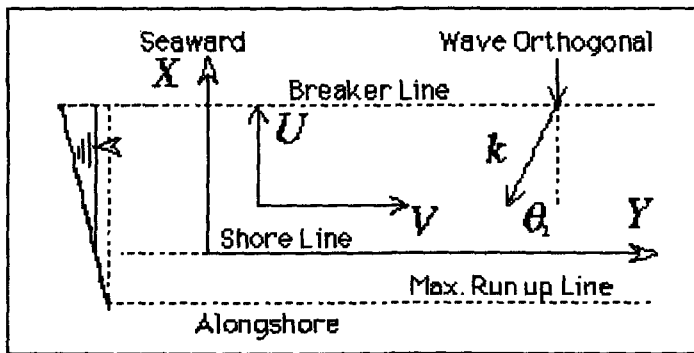


Figure-1 The coordinate system and geometry for nearshore current vectors U , V , and wave number k .

The Conservation of Wave Number

The normally-incident waves refract due to their interaction with rip currents. This may mean that the wave number direction intersects the beach obliquely. Therefore, based on Figure 1 the wave number can be given as:

$$\mathbf{k} = -(|\mathbf{k}| \cos \theta) \mathbf{i} - (|\mathbf{k}| \sin \theta) \mathbf{j} \quad (9)$$

where $|\mathbf{k}|$ is the magnitude of vector \mathbf{k} . Equation (9) can be expanded with respect to

the perturbation parameter ϵ , and as was mentioned above that the group velocity is to be nearly equal to the wave celerity in the surf zone, it was assumed to be in the same direction as the wave number vector. Consequently, it can also be expanded by the perturbation parameter. The conservation equation for the wave number is finally formulated for each order of the perturbation parameter (see Tsuchiya and Suriamihardja, 1989) as:

$$\left. \begin{aligned} O(s^0) &\equiv \frac{\partial k_{0x}}{\partial \bar{y}} = 0 \\ O(s^1) &\equiv \frac{\partial k_{1x}}{\partial \bar{y}} = \frac{\partial k_{1y}}{\partial \bar{x}} \Rightarrow \frac{\partial}{\partial \bar{y}}(C_1 - U_1) = -\frac{\partial}{\partial \bar{x}}(V_1) + \frac{1}{\bar{x}} V_1 \end{aligned} \right\} \quad (10)$$

where $\bar{x} = m(x + x_s) = d_0$; $\bar{y} = my$; $m = (1 + d\zeta_0/d\bar{x})$

m is the slope of mean water level, and x_s is the maximum run-up position.

Zeroth-order equations and their solutions

The leading terms of the governing equations produced by the perturbation expansion are given for the surf zone and shoaling zone, respectively. In the surf zone, the zeroth order equations of momentum and wave action conservation are given respectively as:

$$d_0 \left(\frac{d\zeta_0}{dx} \right) = \frac{D_0}{\omega_{0r}} \frac{dS_0}{dx} - d_0 \frac{d}{dx} \left(\frac{E_0}{2d_0} \right); \quad -\frac{d}{dx}(E_0 C_0) + D_0 = 0 \quad (11)$$

In order to solve the above equations, the wave amplitude a_0 in the surf zone is assumed to be proportional to the local depth to leading order: $a_0 = \gamma d_0$ where γ is an empirical constant. This formulation is employed in surf zone models. The wave energy dissipation term D is hypothesized as:

$$D = (5\gamma^2/4) \left\{ md_0^{\frac{3}{2}} + s \left(3md_0^{\frac{1}{2}} \zeta_1 / 2 + d_0^{\frac{3}{2}} (\partial \zeta_1 / \partial x) + \dots \right) \right\} \quad (12)$$

where D_0 in (11) is equal to $(5\gamma^2 m/4) d_0^{3/2}$

The wave amplitude in the shoaling zone is obtained from the leading order of the equation of wave action conservation as $a_0 = B_0^{1/2} d_0^{-1/4}$, where B_0 is an integration constant. The wave set-up is obtained from (11) (see Tsuchiya and Suriamihardja, 1989) as:

$$\zeta_0(x) = -\left\{ \left(\frac{3}{2} \gamma^2 \right) x + x_s \right\} m \quad (13)$$

where $m = (1 + \frac{3}{2} \gamma^2)^{-1}$; $x_s = \gamma^2 \left\{ \frac{3}{2} - \frac{1}{4} \left(1 + \frac{3}{2} \gamma^2 \right) / \left(1 - \frac{3}{2} \gamma_B^2 \right) \right\} x_B$, and $\gamma_B = B_0 x_B^{-3/4}$ and x_B is the distance from the shoreline to the breaking point.

The first-order equations of rip currents in the surf zone

The mass conservation equation is given from the first equation of (3), considering (8)

for its expansion and using variables defined from mass conservation, of which the stream function can be defined as follows:

$$\frac{\partial}{\partial \tilde{x}}(\tilde{x} U_1) + \frac{\partial}{\partial \tilde{y}}(\tilde{x} V_1) = 0 \Rightarrow (\tilde{x} U_1) = \frac{\partial}{\partial \tilde{y}}(\Psi) \text{ and } (\tilde{x} V_1) = -\frac{\partial}{\partial \tilde{x}}(\Psi) \quad (14)$$

The approximation may be made to the wave dispersion relation, to evaluate C_1 . It is necessary, of course, to obtain a simple relation between C_1 and ζ_1 in order to reduce higher-order differentiation terms. The simple relation can be derived from the established set of four equations. In order to approximate the relation along with the four equations, however, the x-direction of the first order of momentum equation (4) can be used by considering the most effective terms, thus:

$$C_1 = q\tilde{x}^{-\frac{1}{2}}\zeta_1; \quad q = \frac{1}{2}\sqrt{(\tanh kd_B)/(kd_B)} \quad (15)$$

if the other non-leading terms are neglected, q may equal to 1/2 which is equivalent to that of Darlymple and Lozano's approximation. However, based on this approximation, the value of q might be somewhat less than 1/2.

When the horizontal mixing terms remain in (4), the field equation of rip currents may become a fourth-order partial differential equation. Without loss of generality in the formation of rip currents, as previously treated in theoretical approaches to the formation of rip currents, the horizontal mixing terms are neglected, but the bottom friction terms are included. By use of the four equations using (15) to replace C_1 the first-order equation of momentum can finally be obtained (see Tsuchiya and Suriamihardja, 1989 for the detailed reduction) as:

$$\begin{pmatrix} M_{xx}^{\kappa} & 0 \\ 0 & M_{yy}^{\kappa} \end{pmatrix} \Psi = \begin{pmatrix} \beta & 0 \\ 0 & \alpha \end{pmatrix} \frac{\partial^2}{\partial \tilde{x} \partial \tilde{y}} (\tilde{x}^{\frac{3}{2}} \zeta_1) - \frac{5\gamma^2}{4} \begin{pmatrix} (1+2q) & 0 \\ 0 & q\kappa \end{pmatrix} \frac{\partial}{\partial \tilde{y}} (\tilde{x}^{\frac{1}{2}} \zeta_1) \quad (16)$$

where

$$\begin{cases} M_{xx}^{\kappa} = \left\{ \frac{1}{4} \gamma^2 \frac{\partial}{\partial \tilde{x}} \left(\tilde{x} \frac{\partial^2}{\partial \tilde{y}^2} \right) - \frac{15}{8} \gamma^2 (1-\kappa) \tilde{x}^{-1} \frac{\partial}{\partial \tilde{x}} - \frac{7}{8} \gamma^2 \left(1 + \frac{20\kappa}{7} \right) \frac{\partial^2}{\partial \tilde{y}^2} \right\} \\ M_{yy}^{\kappa} = \left\{ \frac{1}{4} \gamma^2 \frac{\partial}{\partial \tilde{x}} \left(\tilde{x} \frac{\partial^2}{\partial \tilde{y}^2} \right) - \frac{5}{2} \gamma^2 (1-\kappa) \tilde{x}^{-1} \frac{\partial}{\partial \tilde{x}} + \frac{3}{8} \gamma^2 \left(1 - \frac{10\kappa}{3} \right) \frac{\partial^2}{\partial \tilde{y}^2} \right\} \end{cases}$$

and $\alpha = \left\{ 1 + \left(\frac{3}{8} + \frac{1}{4}q \right) \gamma^2 \right\}; \quad \beta = \left\{ 1 + \left(\frac{13}{8} + \frac{1}{4}q \right) \gamma^2 \right\}; \quad \kappa = \frac{4K}{5\gamma^2 ms}$

By eliminating ζ_1 from (16), the first-order field equation of rip currents can finally be obtained as:

$$\left(\hat{P} \frac{\partial^2}{\partial \tilde{x}^2} - \hat{Q} \frac{\partial^2}{\partial \tilde{x}^2} \frac{\partial^2}{\partial \tilde{y}^2} - \hat{R} \frac{1}{\tilde{x}} \frac{\partial}{\partial \tilde{x}} - \hat{S} \tilde{x} \frac{\partial}{\partial \tilde{x}} \frac{\partial^2}{\partial \tilde{y}^2} - \hat{T} \frac{\partial^2}{\partial \tilde{y}^2} \right) \Psi = 0 \quad (17)$$

where

$$\hat{P} = \left\{ 1 + 2q \left(1 - \frac{\beta\kappa}{2\alpha} \right) \right\} \left\{ q(1-\kappa) + \left(q - \frac{1}{2} \right) \right\} + \frac{3q}{2} \left(\frac{4\beta}{3\alpha} - 1 \right) (1-\kappa)$$

$$\hat{Q} = \frac{q}{5} \left(\frac{\beta}{\alpha} - 1 \right)$$

$$\hat{R} = \left\{ 1 + 2q \left(1 - \frac{\beta\kappa}{2\alpha} \right) \right\} \left\{ 2 \left(q - \frac{1}{2} \right) + \frac{3q}{2} (1-\kappa) \right\} + \frac{9q}{4} \left(\frac{4\beta}{3\alpha} - 1 \right) (1-\kappa)$$

$$\hat{S} = \frac{3q}{5} \left(\frac{2}{3} + \frac{\beta}{\alpha} \right) + 2\kappa q \left(1 - \frac{\beta}{2\alpha} \right)$$

$$\hat{T} = \left\{ 1 + 2q \left(1 - \frac{\beta\kappa}{2\alpha} \right) \right\} \left\{ q(1-2\kappa) - \frac{1}{2} \right\} + \frac{q}{4} \left(1 + \frac{\beta}{\alpha} \right) + q\kappa \left(1 - \frac{\beta}{2\alpha} \right)$$

The first-order equation of rip currents in the shoaling zone

In the shoaling zone the governing equations differ from the surf zone equations principally in the wave energy dissipation term and in the formulation of the bottom-friction stresses. In this zone, the driving forces are presented in irrotational form, which may be incapable of generating currents of the first order. The remaining terms in the cross-differentiated equations originate from the friction terms. Consequently, the momentum equations in the shoaling zone play an important role in the decay of currents produced in the surf zone. As was previously indicated in (14), a stream function in the shoaling zone can be equally defined. The momentum equations in the x and y directions and cross-differentiated momentum equations are given respectively by

$$\begin{pmatrix} \frac{2\kappa}{s^2 \tilde{x}} & 0 \\ 0 & \frac{2\kappa}{s^2 \tilde{x}} \end{pmatrix} \begin{pmatrix} U_1 \\ V_1 \end{pmatrix} = - \left(1 - \frac{3\gamma_B^2}{8} \right) \begin{pmatrix} \frac{\partial}{\partial \tilde{x}} \\ \frac{\partial}{\partial \tilde{y}} \end{pmatrix} \left(\zeta_1 - \frac{B_0}{4} \tilde{x}^{-\frac{1}{2}} \zeta_1 + \frac{B_0^{\frac{1}{2}}}{2} \tilde{x}^{-\frac{1}{2}} a_1 \right) \quad (18)$$

$$\left(2 \frac{\partial^2}{\partial \tilde{y}^2} + \frac{\partial^2}{\partial \tilde{x}^2} - \frac{2}{\tilde{x}} \frac{\partial}{\partial \tilde{x}} \right) \Psi = 0 \quad (19)$$

THE SOLUTIONS OF THE FIELD EQUATIONS OF RIP CURRENTS

The solution in the surf zone

The solutions to (17) for the surf zone and (19) for the shoaling zone can be obtained by means of the method of separation of variables. The stream function Ψ to be solved for can be expressed by $\Psi(\tilde{x}, \tilde{y}) = \Xi(\tilde{x})Y(\tilde{y})$. Substituting this expression into

(17), the equation can be transformed into two equations as

$$\left\{ \begin{aligned} & \left[\left\{ 1 + \frac{\hat{Q}}{\hat{P}} (\lambda \tilde{x}^c)^2 \right\} \frac{d^2}{d\tilde{x}^2} + \left\{ \frac{\hat{S}}{\hat{P}} (\lambda \tilde{x}^c)^2 - \frac{\hat{R}}{\hat{P}} \right\} \frac{1}{\tilde{x}} \frac{d}{d\tilde{x}} - \frac{\hat{T}}{\hat{P}} \lambda^2 \right] \Xi(\tilde{x}) = 0 \\ & \left(\frac{d^2}{d\tilde{y}^2} + \lambda^2 \right) Y(\tilde{y}) = 0 \end{aligned} \right. \quad (20)$$

where λ is the separation constant which is the eigenvalue corresponding to the number of rip currents. Introducing the new variable

$$\xi = \{1 + \widehat{Q}(\lambda \tilde{x})^2 / \widehat{P}\}^{-1} \tag{21}$$

into the first equation of (20) yields

$$\left[\xi^2(1-\xi) \frac{d^2}{d\xi^2} - \{(\hat{a} + \hat{b} - 1)\xi + (2 - \hat{c})\xi^2\} \frac{d}{d\xi} + \hat{a}\hat{b} \right] \Xi(\xi) = 0 \tag{22}$$

where $(\hat{a}, \hat{b}) = \left\{ (\widehat{S}/\widehat{Q} - 1) \pm \sqrt{(\widehat{S}/\widehat{Q} - 1)^2 + 4\widehat{T}/\widehat{Q}} \right\} / 4$; $\hat{c} = (\widehat{S}/\widehat{Q} + \widehat{R}/\widehat{P})$

The general solution of this equation can be expressed as a Gaussian hypergeometric function in the form

$$\Xi_{\text{surf}} = A_1 \xi^{\hat{a}} \widehat{F}(\hat{a}, 1 + \hat{a} - \hat{c}; 1 + \hat{a} - \hat{b}; \xi) + A_2 \xi^{\hat{b}} \widehat{F}(\hat{b}, 1 + \hat{b} - \hat{c}; 1 + \hat{b} - \hat{a}; \xi) \tag{23}$$

where A_1 and A_2 are the integration constants to be determined, and the suffix "surf" represents the surf zone. To solve for regular rip-current spacing as an eigenvalue problem of the equation, a maximum point for (23) must exist in the surf zone. The solutions should have a finite value and a maximum point within $0 < \xi < 1$.

This behaviour can be examined through the following conditions:

$$\Xi(\xi) \Big|_{\xi=0} = 0 \quad ; \quad \frac{\partial}{\partial \xi} \Xi(\xi) \Big|_{\xi_B \leq (\xi - \xi_m) \leq 1} = 0 \quad ; \quad \frac{\partial^2}{\partial \xi^2} \Xi(\xi) \Big|_{\xi_B \leq (\xi - \xi_m) \leq 1} < 0 \tag{24}$$

where B indicates the breaking point. It is also confirmed by numerical calculation, that for $A_2=0$, the conditions will be fulfilled.

The solution in the shoaling zone

The solution in the shoaling zone can be obtained by solving (19) using the method of separation of variables. Introducing the new variables

$$\varphi(\tilde{x}) = \tilde{x}^{-\frac{3}{2}} \Xi(\tilde{x}) \quad ; \quad \tilde{x} = \lambda \tilde{x} \sqrt{2} \tag{25}$$

Equation (19) is reduced to

$$\left\{ \frac{\partial^2}{\partial \tilde{x}^2} + \frac{1}{\tilde{x}} \frac{\partial}{\partial \tilde{x}} - \left(1 + \frac{9}{4\tilde{x}^2} \right) \right\} \varphi(\tilde{x}) = 0 \quad ; \quad \left(\frac{\partial^2}{\partial \tilde{y}^2} + \lambda^2 \right) Y(\tilde{y}) = 0 \tag{26}$$

The solution to (26) can be expressed using modified Bessel functions of the first and second kinds. By use of (25) the solution can finally be written as

$$\Xi_{\text{shoal}}(\tilde{x}) = B_1 \tilde{x}^{\frac{1}{2}} I(\lambda \tilde{x} \sqrt{2}) + B_2 \tilde{x}^{\frac{1}{2}} K(\lambda \tilde{x} \sqrt{2}) \tag{27}$$

where B_1 and B_2 are integration constants to be determined, and the suffix "shoal" represents the shoaling zone. To fulfill the condition that $\Xi_{\text{shoal}} \rightarrow 0$ far offshore,

therefore, B_1 should be zero.

The boundary conditions and characteristic equation

The eigenvalues can be determined by the matching condition at the breaking point, that is:

$$\frac{d}{dx} \Xi_{\text{surf}}(x) \Big|_{\tilde{x}=\tilde{x}_B} = \frac{d}{dx} \Xi_{\text{shoal}}(x) \Big|_{\tilde{x}=\tilde{x}_B} ; \quad \Xi_{\text{surf}}(x) \Big|_{\tilde{x}=\tilde{x}_B} = \Xi_{\text{shoal}}(x) \Big|_{\tilde{x}=\tilde{x}_B} \quad (28)$$

where B indicates the breaking point.

The real and positive eigenvalues λ which satisfy the matching conditions (28) can be determined if the stream functions in both the surf and shoaling zones are decreasing monotonically in the offshore direction, the characteristic equation is given by

$$\frac{\hat{F}(-\hat{b}, \hat{c} - \hat{b}; 1 + \hat{a} - \hat{b}; \hat{\xi}_B)}{\hat{F}(1 - \hat{b}, \hat{c} - \hat{b}; 1 + \hat{a} - \hat{b}; \hat{\xi}_B)} = \left(\frac{\hat{P}}{\hat{a}\hat{Q}} \right) \left\{ \frac{(1 - \hat{\xi}_B)/\hat{\xi}_B}{1 + \sqrt{2\hat{P}(1 - \hat{\xi}_B)/\hat{Q}\hat{\xi}_B}} \right\} \quad (29)$$

By numerical solution of this characteristic equation, the eigenvalues λ can be determined. The eigenvalues λ directly correspond to rip spacing along the shore line.

Determination of the integration constants in the stream functions

The integration constant of the stream function A_{surf} in the surf zone can be determined from the steady-state wave power conservation in the shoaling and surf zones. The wave energy dissipation rate immediately after breaking is different from that in the inner region. This is revealed by the different wave-elevation decay rates. Therefore, the ratio of wave amplitude to local water depth should be taken into consideration in wave energy budgeting. This difference in the rate of wave energy dissipation is responsible for the structure of the nearshore current. Consequently, the wave power contribution to the generation of the nearshore current initiates at the breaking point. The change in wave power occurring in the region from just before to just after the breaking point can be expressed by:

$$\left(\frac{1}{2\pi} \right)^{\frac{1}{2}} \left(\frac{H'_{\infty}}{d_B} \right)^{\frac{1}{2}} \left(\frac{L'_{\infty}}{d_B} \right)^{\frac{1}{2}} \left(\frac{d_B}{d_{0B}} \right)^{\frac{1}{2}} = s^{\frac{1}{2}} [H_{0B}^{*2} C_{0B}^* + s \{ 2H_{0B}^* H_{1B}^* C_{0B}^* + H_{0B}^{*2} (C_{1B}^* - U_{1B}^*) \} + \dots]^{\frac{1}{2}} \quad (30)$$

Kimura, Goto, and Seyama's (1988) experimental work suggests the condition $\gamma_B > \gamma$.

Based on this fact, the first-order approximation of (30) is reduced to:

$$\frac{1}{s} \left(\frac{\gamma_B}{\gamma} - 1 \right) x_B \cong \left\{ \frac{a_{1B}}{\gamma} + \frac{1}{2} (C_{1B} - U_{1B}) x_B \right\} \Rightarrow \gamma_B = \frac{1}{2} \left(\frac{1}{2\pi} \right)^{\frac{1}{2}} \left(\frac{H'_{\infty}}{d_B} \right)^{\frac{1}{2}} \left(\frac{L'_{\infty}}{d_B} \right)^{\frac{1}{2}} \quad (31)$$

Using (31), the integration constant A_{surf} can immediately be evaluated, and the stream function Ψ can finally be expressed as

$$\left. \begin{aligned} \Psi(\xi, y^*) &= A_{\text{surf}} \xi^{\hat{a}} \hat{F}(\hat{a}, 1 + \hat{a} - \hat{c}; 1 + \hat{a} - \hat{b}; \xi) \cos(\lambda y^*) \\ \Psi(x^*, y^*) &= \text{Re} \left\{ (-1)^{-\hat{a}} \frac{\Gamma(\hat{c}) \Gamma(\hat{b} - \hat{a})}{\Gamma(\hat{c} - \hat{a}) \Gamma(\hat{b})} \Psi(\xi, y^*) \right\} \end{aligned} \right\} \quad (32)$$

The depth-integrated rip current velocity at first-order is now ready to be expressed numerically as:

$$Q(\bar{x}, \bar{y}) = \bar{i} dU(\bar{x}, \bar{y}) = \bar{i} (s\bar{x})s^{\frac{1}{2}} \{0 + sU_1(\bar{x}, \bar{y}) + s^2U_2(\bar{x}, \bar{y}) + \dots\} \quad (33)$$

Theoretical Results And Comparison With Field Data

A theory of the steady nearshore horizontal circulation cells induced by normally-incident waves on a plane beach has been proposed in this paper. The theoretical results predict two main characteristics of rip currents, i.e. the alongshore spacing and the depth-integrated velocity distribution in the seaward direction. The obtained rip current spacing is compared with the theoretical curve of Dalrymple and Lozano (1978) and the field data of Sasaki (1977) and other investigators where the surf similarity of the waves are categorized into instability region. To compare the theoretical results with the field data of Sasaki (1977) and other investigators, their values of the parameter q at the breaking point should be evaluated using their wave characteristics data, and their values of κ should be evaluated using bottom roughness k_e , bottom slope s , and wave length data at the breaking point, then the results are plotted over the theoretical curves. In the evaluation of κ , Kajiura's expression for bottom friction coefficient was used, as Dalrymple and Lozano used and assumed the bottom roughness as $k_e = 0.4$ mm.

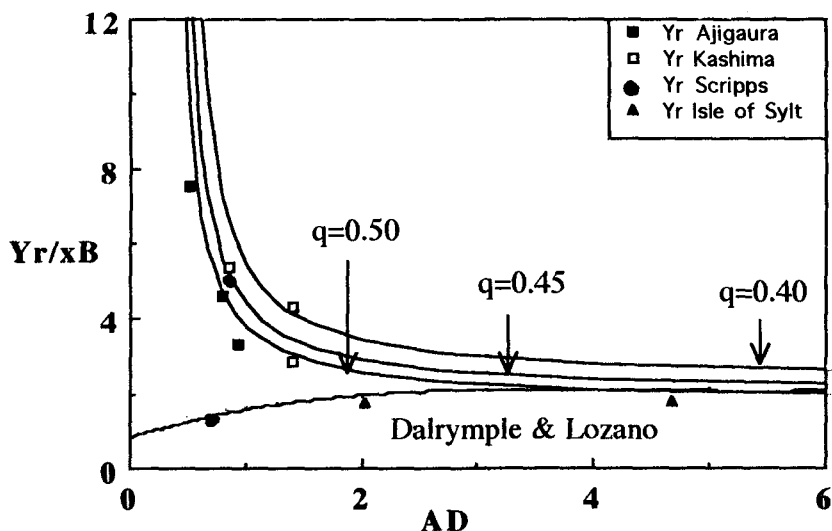


Figure 2. Theoretical curves of dimensionless rip spacing (Y_r/x_B) in terms of Dalrymple number A_D for q -values of 0.40, 0.45, and 0.50 including Dalrymple & Lozano's curve (1978) and rearranged field data of rip currents generated by waves having surf similarity parameter of the instability region.

In comparing the results of this study with those of Dalrymple and Lozano, the parameter κ , which has been previously defined, is transformed into Dalrymple and Lozano's number $A_D = 0.4 / \kappa$. Figure 2 shows the curve of dimensionless rip spacing as a function of Dalrymple parameter A_D . The present curves ($q=0.5, 0.4, \text{ and } 0.3$) rapidly increase as A_D becomes less than 1, while Dalrymple's curve decreases as A_D goes to 0. The present theoretical results and those of Dalrymple and Lozano differ particularly at small values of A_D . In the course of deriving the characteristics equation in the present eigenvalue problem, the dimensionless rip spacing depends on the values of κ and q . It was defined that q corresponds to wave characteristics and beach slope s , and κ depends on the bottom roughness and wave length at the breaking point. Therefore, we conclude that the dimensionless rip spacing is determined by incoming wave characteristics, i.e. wave height H and wave length L , and morphological characteristics, i.e. beach slope s and bottom surface roughness k_e .

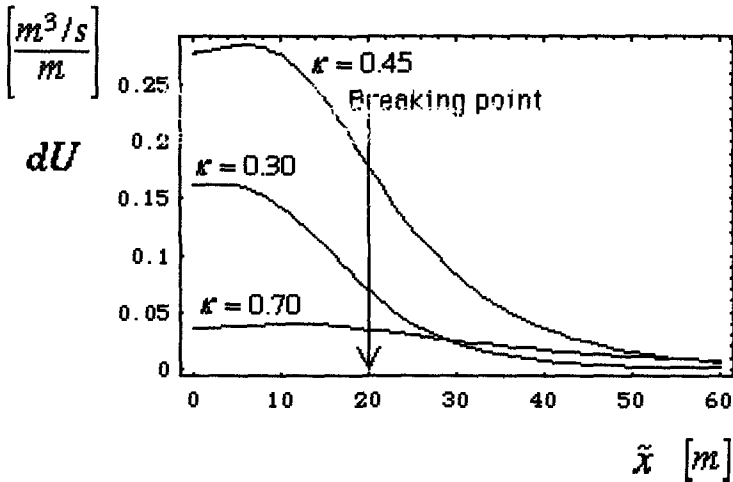


Figure 3. Seaward distribution of rip discharge, where beach slope $s = 0.05$ and dimensionless rip spacings of 3.12 ($\kappa = 0.30$), 4.21 ($\kappa = 0.45$), and 7.70 ($\kappa = 0.70$) are used.

Figures 3 illustrate the distribution of depth-integrated rip current velocity or seaward rip discharge as a function of seaward distance. The illustrations have dimensionless rip spacings of 7.70, 4.21, and 3.12, a beach slope of 0.05, and q of 0.50. The breaking point is located at 20 meters from run-up line. By using γ_B of 0.50, the numerical value of A_{surf} gives values of rip discharges with reasonable values at both laboratory and field scales.

CONCLUSIONS

In this study a new mathematical model for steady-state horizontal nearshore circulation has been developed, in which the wave-current interaction is taken into consideration. The basic equations consist of the depth-integrated equations for conservation of mass, momentum, wave action, and wave number. The wave-current interaction includes not only wave refraction due to currents but also the work done by radiation stresses against the mean current.

The basic equations are decomposed into the leading order and the instability order using the beach slope as a perturbation parameter. The leading order gave the solution for wave set-up in the surf zone and wave set-down in the shoaling zone. The instability order gave linearized field equations of nearshore currents. It is found that the nearshore circulations were generated by the rotational driving forces in the momentum equation. The solutions were characterized by boundary conditions at a shore line, a breaking line, and far offshore. In the surf zone, the solution was represented by the Gaussian hypergeometric function. In the shoaling zone, the solution was represented by the modified Bessel function. The eigenvalues which correspond to the dimensionless rip spacing are obtained from the characteristics equation extracted from the matching condition at the breaking point.

The present theoretical results for the dimensionless rip spacing were consistent with the scatter of the field data of Sasaki in terms of surf similarity parameter of the region of instability. The curves suddenly increase in the range $A_D < 1.0$, and tend to be a constant value for larger values of A_D . The field data on dimensionless rip spacings caused by infragravity waves are difficult to predict by this theory. Outside of this range, the theory gives reasonable predictions for rip spacing caused by wave-current interactions.

Rip discharge is illustrated with exact numerical values, using an integration constant which is obtained from energy budgeting at the breaking point. This budgeting was applied at the suggestion of Kimura et.al, that the wave energy dissipation rate immediately after breaking is larger than the dissipation rate in the inner region. The resulting value is within the range of data at both laboratory and field scales.

Acknowledgments

This work was completed while the first author was a fellow at the Coastal Disaster Section, Disaster Prevention Research Institute, Kyoto University, Japan. Most of this work was completed while the first author was a postgraduate student under the supervision of the second author at the same university. The authors' appreciations are expressed to Professor T. Takayama, Head of the Section, for his support in executing this work, Associate Professor T. Yamashita for his crucial advice and arrangement to make this work possible, Dr. Gary Watson, Visiting Research Fellow, for his kindness in critical correction of the draft, and Dr. H. Yoshioka for his cooperation during the execution this work at the Institute.

References

- Balsillie, J.H.(1975)." Surf observation and longshore current prediction", Technical Memorandum no.58, CERC, 39.
- Bowen, A.J.(1969)."Rip currents,I, Theoretical investigation", Jour. Geophys. Res.,74, 5479-5490.
- Bowen, A.J. and Inman, D.L.(1969)." Rip currents, II, Laboratory and field observation", Jour. Geophys. Res., 74, 5479-5490.
- Crapper, G.D.(1984)." Introduction to water waves". John Wiley & Sons, New York, 93-106.
- Dalrymple, R.A., and Lozano, C.J. (1978)." Wave-current interaction model for rip currents", Jour. Geophys. Res., 83, C12, 6063-6071.
- Dingemans, M.W., Radder, A.C. and De Vriend, H.J. (1987)." Computation of the driving forces of wave induced currents", Coastal Engineering,11, 539-563.
- Dolata, J.B., and Rosenthal, W. (1984)." Wave set-up wave-induced currents in coastal zones", Jour. Geophys. Res., 82, C2, 1973-1982.
- Horikawa, K., and Mizuguchi, M. (1975)." Experiment on nearshore currents on a plane beach", Proc. 22nd Japanese conf. on Coast. Eng., 141-153.(in Japanese).
- Iwata, N. (1976)." Rip Current Spacing", Jour. of the Ocean. Soc. Japan, 32, 1-10.
- Kimura, A., Goto, K., and Soyama, A. (1988)." On the wave height variation of irregular waves in shallow water", Proc. 33th Japanese conf. on Coast. Eng., 168-172. (in Japanese).
- Kirby, J. T. (1984)." A note on linear surface wave-current interaction over slowly varying topography", Jour. Geophys. Res., 89, C1, pp. 745-747.
- LeBlond, P.H., and Tang, C.L.(1974)."On energy coupling between wave and currents", Jour. Geophys. Res., 79, 6, 811-816.
- Noda, E.K.(1974)." Wave-induced Nearshore Circulation", Jour. Geophys. Res.,79, 27, 4097-4106.
- Phillips, O.M. (1977)." The dynamics of the upper ocean", second edition, Cambridge University Press, 23-81.
- Sasaki, T. (1977)." Field Investigation of nearshore currents on gently sloping bottom", PhD Disertation, NERC, Tokyo University, Japan.
- Sonu, C.J. (1972)." Field observation of nearshore circulation and meandering currents", Jour. Geophys. Res., 77, 18, 3232-3247.
- Tsuchiya, Y., Kawata, K., Shibano, T., Suriamihardja, D.A., and Shishikura, T.(1986). "Generation of rip currents on a plane beach with reflective boundaries", Proc.33rd Japanese conf. on Coast. Eng., 36-40. (in Japanese).
- Tsuchiya, Y., and Suriamihardja, D.A. (1989)." Nearshore circulation: Theory of rip current generation on a plane beach", Ann. DPRI, Kyoto Univ., 32, B-2. (in Japanese).

CHAPTER 286

NEARSHORE PLACEMENT OF SAND

By Scott L. Douglass¹, Member ASCE

ABSTRACT:

A methodology that evaluates the influence of depth on the rate of onshore migration of sand placed in the nearshore is presented. The results appear appropriate for the Atlantic and Gulf coasts of the United States. Migration rate is found to be extremely dependent, to the 4th or 5th power, on the water depth. This implies that doubling the rate of migration requires placement in only about 15% less depth. It is argued that accounting for the net shoreward bottom stress due to the velocity asymmetry under finite-amplitude waves is the appropriate way to model the fate of nearshore placed sands.

BACKGROUND

Nearshore placement of sand is becoming a more popular option in two related types of coastal engineering projects; beach nourishment and inlet dredging. "Nearshore" is defined rather loosely here as beyond the day-to-day surf zone but within the depths that are disturbed by storm waves. Nearshore placement is an alternative to direct placement on the beach that has been called "profile nourishment" or "shoreface nourishment" since the placement is farther out on the beach profile than the dry beach.

¹

Associate Professor, Civil Engineering Department, University of South Alabama, Mobile, Alabama, USA (334) 460-6174

Placing the sand in the nearshore instead of directly on the beach can reduce costs and improve the overall cost-benefit ratio of a beach nourishment project (Lastrup, et al. 1996). There may also be a perception that construction-related aesthetic and environmental impacts to the beaches are improved with nearshore placement instead of direct beachfill because the sand moves ashore in the form of migrating sand bars instead of being placed there by construction equipment.

Nearshore placement of sand is also an option in navigation dredging projects for similar reasons. First, it may be less expensive than other dredged material disposal options such as hauling to offshore disposal. Second, there may be a recognition that inlet sand transfer is required for the long-term maintenance of the downdrift beaches. The goal of nearshore placement of sand in this case would be to keep the sand resource in the littoral system for the least cost.

The primary question is, "what is the fate of sands placed in the nearshore?" More specific questions are:

1. does the sand move?
2. If so, which way does it move?
3. How fast does it move?
4. What is the influence of depth on this fate?

Depth is one of the primary parameters that the design engineer can specify.

Several tools to answer these questions have been developed in the United States as part of the Corps of Engineers Dredging Research Program in the last decade. Hands and Allison (1991) and Hands (1991) developed an empirically based answer to the first question concerning movement. The stability of bathymetric features (mounds or bars) constructed with dredged sands at eleven locations discussed in the American literature is summarized. A method based on combining extreme wave statistics and Hallermeier's estimates of the limits of sand movement successfully discriminates between mounds that moved and mounds that did not move.

Larson and Kraus (1992) suggest using empirical estimates of surf zone sand bar migration and beachface accretion/recession for estimating the direction of movement of sand placed in the nearshore. A design option is to place the sand in a long, linear, shore-parallel bathymetric feature that is similar to natural sand bars. They validate their method by comparison to the onshore migration of a constructed bar feature at Silver Strand, California (Andrassy 1991).

Scheffner (1991, 1996) suggests combining a hydrodynamic model with a

sediment transport model for evaluating the fate of sand placed in the nearshore. The influence of waves on the bottom friction factor is considered, but mean currents provide the transport mechanism for the sand movement. The migration of a mound south of Dauphin Island, Alabama (Hands and Allison 1991) is used for validation.

The answer to the primary question concerning the fate of sands placed in the nearshore is tied to a broader, underlying question that has been the focus of much research in the nearshore oceanography community for the past decade: "What moves sand in these depths beyond the day-to-day surf zone but within the influence of storm waves?" Considering the rich variations in sediment transport processes such as bed and suspended load, ripple and dune migration, sheetflow, and bed-ventilation; combined with the varying time-scales of the hydrodynamic forcing conditions and our limited understanding of the near-bottom boundary layer of the fluid column under real waves, the answer is only marginally understood at this time. Solving applied problems requires the use of that part of the available science that is considered to be the most important of the geophysical processes for the problem.

One concept for modeling surf zone sand bars is a balance between the cross-shore movement of sand due to the velocity asymmetry of waves and the undertow (Stive 1986, Roelvink and Stive 1989). Simplistically, the waves drive the sand bar landward and the undertow drives it seaward. Considering that the location of constructed mounds is offshore of the location of the typical sand bar, the undertow should be reduced and the wave asymmetry mechanism should dominate. This is the fundamental concept used in this paper.

Douglass (1995) briefly proposed a model for estimating migration of sand mounds constructed in the nearshore. The model assumes that landward migration is due primarily to the net landward transport by the velocity asymmetry of finite-amplitude waves. Conservation of sand considerations in the cross-shore direction lead to the classical convection-diffusion model equation. The "convection" and "diffusion" coefficients are functions of the wave conditions and depth and are based on the wave and transport theory, not traditional concepts of convection and diffusion. The model produced results which were in reasonable agreement with measured migration directions and rates at both Silver Strand and Dauphin Island. The implication of the diffusion is that mounds should spread out while moving landward. This type of behavior has been noticed to different degrees in many of the monitoring reports on mounds (Hands and Allison 1991; Andrassy 1991; Bodge 1994; Foster, et al. 1996; Mesa 1996) and is shown schematically in Figure 1.

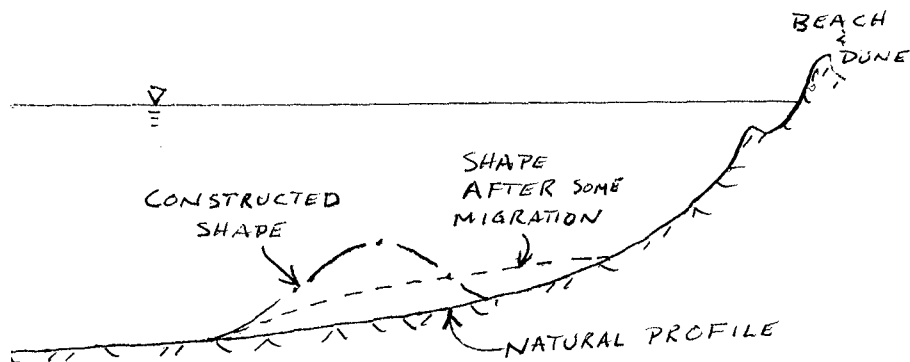


Figure 1. "Typical" migration of sand placed in the nearshore.

This present paper briefly discusses the results and implications of a study of the near-bottom current field at a nearshore sand placement site. The Douglass (1995) model is further developed. Modifications include the use of a calibration coefficient and a simple adjustment for wave breaking when using WIS wave climatology data as input. Results for a few locations on the Atlantic and Gulf coasts of the United States are presented. The implications of the dependence of migration on depth of placement are discussed. Some of the practical limitations of the model as well as the theoretical problems are briefly discussed. The implications concerning the important geophysics dominating the problem are discussed. The conclusion is that some form of modeling based on the influence of wave asymmetry is probably appropriate concerning the fate of sand placed in the nearshore.

DAUPHIN ISLAND, ALABAMA NEAR-BOTTOM CURRENT STUDY

The fate of sand mounds constructed in about 6 m depths south of Dauphin Island, Alabama in 1987 was monitored extensively by the US Army Corps of Engineers. A number of reports by Mr. Edward Hands and other co-authors documented the movement of these nearshore mounds (e.g. Hands and Bradley 1989, Hands and Allison 1991). Repetitive bathymetric surveys showed that the mounds moved landward.

Instantaneous, near-bottom currents were measured, along with waves, at the site. These near-bottom currents were examined in detail by Douglass, et al. (1995).

A number of possible mechanisms for mound migration; including mean currents, large wave correlation with mean currents, and mound-induced differences in current fields; were not able to satisfactorily explain the observed shoreward direction of mound migration. Douglass, et al. (1995) concluded that some unknown mechanism that moves the bottom back towards its equilibrium shape may be responsible for the landward migration of mounds and that the velocity asymmetry of storm waves might be part of such a mechanism. These finding played a role in the development of this work.

WAVE-BASED MODEL OF MOUND MIGRATION RATE

Assuming that wave-induced near bottom velocity asymmetries are the dominant mechanism for the net transport of sand in the depths of interest, net sand transport can be expressed as (Douglass 1995),

$$Q = \frac{9\pi^2}{64} \frac{\rho g C_f \epsilon_b}{(\rho_s - \rho) a' \tan^2 \phi} (\tan \phi - \tan \beta) \frac{H^4 T}{L^3} \operatorname{sech}^2 \left(\frac{2\pi h}{L} \right) \operatorname{csch}^4 \left(\frac{2\pi h}{L} \right)$$

where Q =net volumetric transport rate, ρ = density of water, ρ_s =sand density, C_f =a friction coefficient, ϵ_b = Bagnold's efficiency of transport coefficient, ϕ = angle of internal friction of the sediment, β = angle of slope of the bottom, a' =ratio of total volume to volume of solids, H =wave height, T =wave period, L = wave length, and h =water depth. This is an expression for cross-shore bedload transport rate using Stokes wave theory in Bailard and Inman's (1981) form of Bagnold's (1963) bedload transport equation assuming all motion is in the cross-shore direction.

It can be assumed that transport due to irregular waves with a spectral significant wave height, H_{m0} , with a period corresponding to the peak of the energy density spectrum, T_p , will be proportional to transport due to the corresponding monochromatic conditions. Also, given that several of the empirical coefficients, in particular ϵ_b , have typical values based on limited tests, it seems logical to modify this transport equation with an empirical coefficient that can be used to fit the results to observed data specific to the migration problem. Therefore another empirical coefficient, A , has been added to

the above transport equation modified to use the spectral estimates of wave climate:

$$Q = A \frac{9\pi^2}{64} \frac{\rho g C_f \epsilon_b}{(\rho_s - \rho) a' \tan^2 \phi} (\tan \phi - \tan \beta) \frac{H_{mo}^4 T_p}{L_p^3} \operatorname{sech}^2 \left(\frac{2\pi h}{L} \right) \operatorname{csch}^4 \left(\frac{2\pi h}{L} \right)$$

where L_p = wave length corresponding to T_p computed with linear wave theory. The A will be used to fit the results to observed migration rate data below.

Considering conservation of sand in the cross-shore direction,

$$\frac{\partial h}{\partial t} - \frac{\partial Q}{\partial x} = 0$$

where t = time and x = the cross-shore direction.

Substitution of the above transport equation into the conservation equation results in a form of the convection-diffusion equation (Douglass 1995):

$$\frac{\partial h}{\partial t} + C \frac{\partial h}{\partial x} - D \frac{\partial^2 h}{\partial x^2} = 0$$

where

$$C = A \frac{9\pi^3}{16} \frac{\rho g C_f \epsilon_b}{(\rho_s - \rho) a' \tan^2 \phi} \frac{H_{mo}^4 T_p}{L_p^4} \left\{ 2 \operatorname{csch}^5 \left(\frac{2\pi h}{L} \right) \operatorname{sech} \left(\frac{2\pi h}{L} \right) + \operatorname{csch}^3 \left(\frac{2\pi h}{L} \right) \operatorname{sech}^3 \left(\frac{2\pi h}{L} \right) \right\}$$

$$D = A \frac{9\pi^2}{64} \frac{\rho g C_f \epsilon_b}{(\rho_s - \rho) a' \tan^2 \phi} \frac{H_{mo}^4 T_p}{L_p^3} \operatorname{sech}^2 \left(\frac{2\pi h}{L} \right) \operatorname{csch}^4 \left(\frac{2\pi h}{L} \right)$$

C has the role of the "convection" coefficient and D has the role of the "diffusion"

coefficient. The expressions for C and D originated from the consideration of conservation of sand with the wave theory and transport model and not on physical concepts of convection or diffusion. The equation implies that the form of a submerged mound will "convect" or move at speed C while it diffuses. Similar behavior of constructed bottom mounds has been observed (Hands 1991, Bodge 1994, Foster et al. 1996, Mesa 1996).

The equations outlined above can be used as a planning and design tool when combined with an estimate of wave climate at a specific site. The equations predict the behavior of a mound under a given, specified sea state. To apply it to a non-constant sea state, either the time history of sea must be estimated or a statistically valid estimate of the overall wave climate must be evaluated in terms of an "expected value of migration." Given a tabular estimate of the onshore portion of the wave climate, the expected value of mound movement in any given depth, $E[C(h)]$, can be estimated with C, the "convection" coefficient as

$$E[C(h)] = \sum p(H, T) C(H, T, h)$$

where the summation is across all (H,T) bins, $p(H,T)$ = probability or percentage of time that the wave height and period is of that magnitude.

APPLICATION

The migration rate equation above can be roughly calibrated by matching the predictions to the observed migration of constructed mounds. The "expected value" of the migration rate can be estimated with an estimate of the "expected" wave climate such as the US Army Corps of Engineers Wave Information Study (WIS) wave hindcast data for the Atlantic and Gulf coasts of the United States (Hubertz, et al. 1993). Using WIS data provides a consistent estimate of wave climatology when comparing different locations.

WIS data is given at specific depths. Since this methodology evaluates migration rate at varying depths, some form of transformation of wave climatology is needed. For the purposes of this study, a very simple, depth-induced, wave height reduction was used. It was assumed that the maximum spectral significant wave height in any depth of water was half of the water depth, i.e. $(H_{m0})_{max} = 0.5 h$. Wave heights were reduced to

that level to evaluate migration for the shallower depths. A more sophisticated wave transformation scheme could be used.

The first comparison is for the mounds constructed in around 6 m depth off the Alabama coast in 1987-88. Hands and Allison (1991) showed survey data that indicated the mounds moved roughly 30 m/yr initially. The methodology outlined above with the WIS climatology for that location matches this expected value when the calibration coefficient is $A=0.5$.

The second comparison is for a disposal mound created in about 6 m depth off Cocoa Beach in the Cape Canaveral area in 1992. Bodge (1994) found that mound moved roughly 30 m to 45 m landward in the first six months. Most of this movement occurred during and immediately after construction. By the time of the second post-construction survey at six months, the peak of the constructed mound had been flattened to the extent that there was not a clear crest, i.e. the bottom elevation profile had no significant decrease in depth in the offshore direction. Apparently the top of the mound moved about 60 m/yr to 100 m/yr during the first 6 months and then slowed down as the mound or bar-like feature was lost. The methodology presented here with the WIS data for Cape Canaveral, matches this expected migration rate when the calibration coefficient is $A=0.2$ to 0.33 .

Based on these two comparisons, A (using WIS data) can be set to roughly $A=0.3$ with a reasonable expectation that it may vary from $0.1 < A < 1$. The use of observed migration rates for comparison to expected migration rates is not optimum since the observations are based on much less time than the overall WIS estimate of wave climate, 20 years. The waves would be expected to be larger or smaller than typical for any 6-month to one-year time spans because of the natural variability in wave climate. The observed migration rates were due to the actual waves for that time period and not the long-term wave climate.

Any calibration of this methodology is probably dependent on the wave climatology estimate used. For example, wave climatology based on long-term, in-situ wave gages will probably have different calibration coefficients.

Figure 2 shows the results of this methodology at three locations with very different wave climates. The calibration coefficient was set to $A=0.3$ for Figure 2. Alabama is on the Gulf of Mexico and has a relatively mild wave climate. Cape Canaveral on the Atlantic coast of Florida has a moderate wave climate. Cape Hatteras has one of the more severe wave climates on the Atlantic coast of the United States. Figure 2 shows that the model estimates migration rates that vary significantly, up to an order of magnitude, for these three locations. For a given depth, migration rate estimates

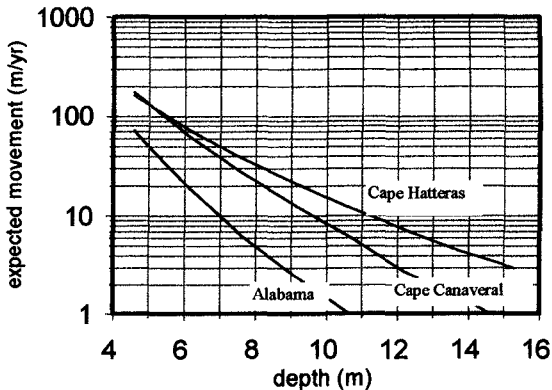


Figure 2. Expected migration rate at three U.S. locations

are higher for the Atlantic sites than for Alabama. Such variation would be expected for any process based on wave climate. In particular, wave lengths are typically significantly longer for the Atlantic Ocean than the Gulf of Mexico. For deeper depths, Cape Hatteras migration rates are higher than Cape Canaveral. The estimates for the two Atlantic sites become close to each other in shallower depths. This closeness is due to the depth-induced, wave height reduction employed to transform the data into shallower water as discussed above. The infrequent, largest waves at Hatteras are more influential in the deeper depths but are less so after breaking as the depths decrease.

Interestingly, Figure 2 shows a similar general shape and dependence with depth at the three locations. This similar shape apparently is a function of the model equations. The same general shape has been found using wave climatology based on wave gages for the Santa Anna River, California nearshore placement of sand (Mesa, personal communication, 1996). This dependence with depth has practical value for planning and design. The results shown on figure 2 can be fit to a simple power relation:

$$E[C] = ah^{-b}$$

where $E[C]$ = expected value of migration rate (m/yr), a =coefficient, b =exponent, and h =depth (m). For most of Figure 2 and all of the deeper depths at each location, the best fit for the exponent is $b=5$. These are the depths where the wave height decay due

to depth ($(H_{mo})_{max} = 0.5 h$) was small. This was all of the depths shown for the Alabama site, most of the depths for Cape Canaveral, and the deeper depths for Cape Hatteras. In the portion of Figure 2 where the depth reduced the largest waves in the climatology, the depth dependence exponent is $b=4$. Thus, this methodology implies that migration rate is dependent on depth to the 4th or 5th power.

DISCUSSION

Implications of influence of depth on migration

The depth dependence of migration rate outlined above provides some useful concepts for planning and design of nearshore placement. The above equation implies that migration is extremely sensitive to depth at any specific site. Doubling the depth of placement will decrease the rate of migration by a factor of 16 to 32. Considering it another way, to double the migration rate, it is necessary to place the sand in only 13-16% shallower depth. This guidance should be of value in evaluating the cost vs. depth-of-placement issues typical of nearshore placement of sand.

The extreme sensitivity to depth implied by this methodology has not been verified by observations. Verification would require placement at different depths at the same general location and time with adequate monitoring.

Theoretical limitations

There are a number of theoretical limitations to the methodology presented here. First, many of the physical mechanisms that influence sediment transport in these depths including the effects of suspended sediment load, wave groups, ripple and dune migration, sheetflow, bed-ventilation, wave grouping, undertow, wind, bottom streaming and other bottom boundary layer complexities have been ignored. Second, the one physical mechanism modeled, the influence of wave asymmetry on net bedload sand transport could be modeled in a more sophisticated manner. A primary limitation is the use of Stokes 2nd order theory - particularly in shallow water. It was used because it is the lowest order theory with asymmetry. Better representations of the actual velocities should be used. Thus, this methodology can be considered as a rough first attempt at applying such a model to the problem at hand. Its abilities, in spite of this serious limitation, are encouraging in that they indicate the proper physics may be included.

Practical limitations

One serious practical limitation of this methodology is the use of a single depth

for modeling migration rate. Nearshore placement in a mound-like feature implies that different parts of the feature are in different depths. More importantly, the equations given above are extremely sensitive to depth. This presents a practical problem in specifying the single, appropriate depth for the use of this model. For this work, that single depth was chosen as the pre-existing depth at the middle of the feature. Conceptually, the top, or shallower portion, of the feature should move fastest and be flattened out by landward movement of sand into the deeper depth shoreward. There is evidence at many observed mounds that this has occurred (Bodge 1994, Mesa 1996, Hands and Bradley 1990, Foster et al. 1996).

Appropriate physics for modeling migration

The implication of the observations and the results presented here is that a net sand transport equation that is dependent on depth could be used with the conservation of sand equation to model the fate of nearshore disposed sands. More specifically, the use of a model that accounts for the influence of velocity asymmetry on sand transport is recommended for modeling the fate of nearshore placed material. Such models have been proposed by Stive (1986) and several of the investigators in the European Nourtec project (Houwman and Ruessink 1996, Roelvink, et al. 1996, Hoekstra, et al. 1996). The results presented in this paper and the detailed simulation of the behavior of the Silver Strand, California mound shown in Douglass (1995) imply that such modeling is an appropriate approach. The use of some form of Bailard's model (Bailard and Inman 1981) is common to all of these approaches. This present work does not endorse the use of Bailard's model specifically. Other approaches that explicitly account for the effect of net onshore bottom stress due to wave asymmetry should also be considered.

Other existing American methods

The other existing American methods for estimating the fate of nearshore placed sand are not explicitly based on this physical mechanism (wave asymmetry) although it may be implicitly included through the empiricism. The Hands and Allison (1991) method for movement or non-movement is essentially empirical and does not attempt to explain migration direction. The Hands and Allison method is based on extreme wave heights and a sand movement initiation criterion, and thus is really is not incompatible with the wave asymmetry mechanism proposed here. The Hands and Allison method may be successful because it adequately captures the wave asymmetry mechanism through the empiricism.

The Larson and Kraus (1994) method is purely empirical so the same argument could be made. However, that method is based on empirical expressions for surf zone sand bars and beaches. It does not seem likely that the dominant physical mechanisms in the inner surf zone occur in the same relative proportions in the offshore depths for a number of obvious reasons. Any skill shown by methods based on inner surf zone empiricism may be due to fortune as much as physics.

The physical mechanism modeled by Scheffner (1991, 1996), the sediment response to the mean currents with transport rate modified by the presence of waves, seems relatively unimportant to the migration of nearshore placed sand. The evidence from the Mobile, Alabama site demonstrates the fundamental problem with a model based on mean currents. Douglass, et al. (1995) found that the measured mean near-bottom currents in the area were shore-parallel during the time that the mounds migrated shoreward. Shore-parallel mean currents are consistent with expectations for tidal currents near the coast, i.e. along the bathymetric contours. The cross-shore component of the mean near-bottom current was offshore during the time the mounds migrated landward! This offshore dominance was more pronounced during times of large waves, presumably due to downwelling due to onshore wind stress during storms. It appears that Scheffner (1991, 1996) was only able to verify his model at the Mobile, Alabama site by the explicit specification of shoreward mean currents. This was apparently based on a numerical, tidal simulation of a selected seven month period. Given that the actual measured, mean near-bottom currents at the site were in the other direction, Scheffner's method seems incorrect.

Diffusion concept

The diffusion coefficient, D , presented above has also been investigated. It is notable that the diffusion coefficient does not have any free parameters. It has the same coefficient, A , that is in the C equation. No results are presented here for two reasons. One, the methodology estimated more diffusion was observed at Cape Canaveral. Other mounds; such as Mobile, Alabama and Perdido Pass, Florida; have shown less diffusion than the one at Cape Canaveral. The primary reason for not focussing on the diffusion portion of the model is conceptual. The "diffusion" term results directly from the way that bottom slope, $\tan \beta$, is included in the Bagnold/Inman and Bailard formulation for quasi-instantaneous transport. It accounts for influence of gravitational effects to pull sand down-slope. None of the observed mounds have shown a tendency for sand to move offshore down the slope, only onshore down the slope.

CONCLUSIONS

A design and planning tool for the nearshore placement of sand that estimates the expected onshore migration rate is presented. The results appear appropriate for the Atlantic and Gulf coasts of the United States. For any specific wave climate, the results indicate an appropriate way to evaluate the influence of depth on migration rate. Specifically, doubling the depth of placement will decrease the rate of migration by a factor of 16 to 32. Doubling the rate of migration requires placement in 13-16% shallower depths.

The physical basis for the model is the velocity asymmetry of large waves. This is consistent with observations reported in the literature and the findings of a field study off the Alabama coast that eliminated several other potential physical mechanisms for controlling mound migration. This model is limited by several theoretical and practical shortcomings. Its abilities, however, indicate that a wave-based model that accounts for the net onshore transport or shear stress under finite-amplitude wave is the appropriate way to model the fate of nearshore placed sands.

REFERENCES

- Aldrassy, C. J. (1991). "Monitoring of a nearshore disposal mound at Silver Strand State Park." *Proc., Coast. Sediments 91 Conf.*, ASCE, New York, N.Y., Vol 2, 1970-1984.
- Bagnold, R. A. (1963) "Mechanics of marine sedimentation," in *The Sea*, vol. 3, Interscience, New York.
- Bailard, J.A. and Inman, D. L. 1981 "An Energetics Bedload Model for a Plane Sloping Beach: Local Transport" *J. Geophysical Res.*, 86(C3):2035-2043.
- Bodge, K. R. (1994) "Performance of 1992 nearshore berm disposal at Port Canaveral, Florida." Olsen Associates, Inc. report to the Canaveral Port Authority, Jacksonville, FL, 55 p.
- Douglass, S. L. (1995) "Estimating Landward Migration of Nearshore, Constructed, Sand Mounds," *J. Wtrwy, Port, Coast. and Oc. Engrg.*, ASCE, 121:5:247-250.
- Douglass, S. L., Resio, D. T., and Hands, E. B. (1995) "Impact of near-bottom currents on dredged material mounds near Mobile Bay," *Tech. Rep. DRP-95-6*, US Army Engrs. Wtwys. Exper. Sta., Vicksburg, MS.
- Foster, G. A., Healy, T. R., and DeLange, W. P. (1996) "Presaging beach renourishment from a nearshore dredge dump mound, Mt. Maunganui Beach, New Zealand." *J. Coastal Res.*, 12:2:395-405.
- Hands, E. B. (1991) "Unprecedented migration of a submerged mound off the Alabama coast." *Proc., 12th Annu. Conf. Western Dredging Assoc. And 24th Annu. Texas A&M Dredging Seminar, Oc.Engr. Program, Texas A&M Univ., College Station, Tx.*
- Hands, E. B. and Allison, M. C. (1991) "Mound migration in deeper water and methods of categorizing active and stable berms," *Proc. Coast. Sediments 91*, ASCE, 2:1985-1999.
- Hands, E. B. and Bradley, K. P. (1990) "Results of monitoring the disposal berm at Sand Island, Alabama; report 1: construction and first year's response." *Tech. Rep. DRP-90-2*, US Army Engrs. Wtwys. Exper. Sta., Vicksburg, MS.
- Hoekstra, P., Houwman, K. T., Kroon, A., Ruessink, B. G., Roelvink, J. A., and Spanhoff, R. (1996) "Morphological Development of the Terschelling shoreface nourishment in response to hydrodynamic and sediment transport processes," *Pre-Conf. Paper Summaries, 25th Inter. Coastal Engrg. Conf.*, Orlando, Fl., Amer. Soc. of Civil Engrs., pp. 548-549.

- Hubertz, J. M., Brooks, R. M., Brandon, W. A., and Tracy, B. A. (1993) "Hindcast Wave information for the US Atlantic coast," *WIS Report 30*, US Army Corps of Engrs. Wtwys. Exper. Sta., Vicksburg, MS, 502 p.
- Larson, M. and Kraus, N. C. (1992) "Analysis of cross-shore movement of natural longshore bars and material placed to create longshore bars," *Tech. Rep. DRP-92-5*, US Army Engrs. Wtwys. Exper. Sta., Vicksburg, MS, 115 p.
- Lastrup, C., Madsen, H. T., Sorensen, P., and Broker, I. (1996) "Comparison of Beach and Shoreface Nourishment Torsminde Tange, Denmark" *Pre-Conf. Paper Summaries, 25th Inter. Coastal Engrg. Conf.*, Orlando, Fl., Amer. Soc. of Civil Engrs., pp. 550-551.
- Mesa, C. 1996. Paper presented at 25th Inter. Coastal Engineering Conf., Orlando, Fl.
- Roelvink, J. A., and Stive, M. J. F. (1989) "Bar generating cross-shore flow mechanisms on a beach," *J. Geophysical Res.*, 94:C4:4785-4800.
- Roelvink, J. A., Meijer, Th., Spanhoff, R., and Hoekstra, P. (1996) "Process-based modelling of the behavior of barred coastal profiles" *Pre-Conf. Paper Summaries, 25th Inter. Coastal Engrg. Conf.*, Orlando, Fl., Amer. Soc. of Civil Engrs., pp. 546-547.
- Scheffner, N. W. (1991) "A systematic analysis of disposal site stability." *Proc., Coast. Sediments 91 Conf.*, ASCE, New York, N.Y., Vol. 2, 2012-2025.
- Scheffner, N. W. (1996) "Systematic analysis of long-term fate of disposed dredged material." *J. Wtrwy, Port, Coast. and Oc. Engrg.*, ASCE, 122:3:127-133.
- Stive, M. J. F. (1986) "A model for cross-shore sediment transport." *Proc., 20th Inter. Coastal Engrg. Conf.*, ASCE, New York, N. Y., pp. 1550-1564.

CHAPTER 287

Influence of Nearshore Berm on Beach Nourishment

Paul A. Work¹, A.M. ASCE, and Emre N. Otay²

Abstract

The influence of a large ($3.0 \times 10^6 \text{ m}^3$) nearshore berm on a large ($4.1 \times 10^6 \text{ m}^3$) beach nourishment project at Perdido Key, FL, is addressed via a monochromatic, numerical wave transformation model. Two years of post-placement survey data indicate that the nearshore berm, placed at a depth of 6 m with a relief of 1-1/2 m, did not migrate during this time period. Wave model results suggest that the berm influences the beach nourishment project via refraction, but breaking and diffraction effects are not significant. The berm causes wave transformation and leads to zones of wave energy focusing (and corresponding de-focusing) that affect longshore sediment transport rates in the lee of the berm. For a typical wave condition, predicted high-energy regions correlate well with observed erosional areas. The findings indicate the relative importance of project-induced wave transformation that should be considered during the design process for nearshore berm projects.

Project Background

The beach nourishment project at Perdido Key, FL, adjacent to Pensacola Pass, was initiated in late 1989. Pensacola Pass serves as an access channel to a major naval port; the beach nourishment material was generated by dredging of the entrance channel to 19 m. The region is characterized by diurnal tides with a very small range (mean tide range = 34 cm; spring range = 58 cm) and a relatively mild wave climate. The mean value of the significant wave height measured over 4 years

¹ Asst. Prof., Dept. of Civil Eng., 110 Lowry Hall, Clemson University, Clemson, SC 29634-0911. (864) 656-3000. pwork@eng.clemson.edu.

² Asst. Prof., Civil Eng., Boğaziçi Univ., Bebek 80815 Istanbul, Turkey. otay@boun.edu.tr.

as a part of this study near the 6 m contour is 0.6 m. The mean value of the wave period at which the peak of the energy spectrum is found is 6 sec for the same time interval.

The beach nourishment aspect of the project involved widening the dry beach by 140 m over a length of 7 km and required a volume of 4.1 million m^3 . This was completed in September, 1990. Construction of an offshore berm then commenced. The offshore berm was completed in 1991. The placed berm was 4 km (longshore) by 300-800 m (cross-shore) and included 3.0 million m^3 of sand. The bathymetry in the region where the berm was placed was quite flat (slope of 1:1000). Water depth averaged 6 m, and the berm relief is nominally 1.5 m, leaving 4.5 m of water above the berm. Figure 1 indicates the site location, and Figure 2 shows cross-sections through the berm at different times.

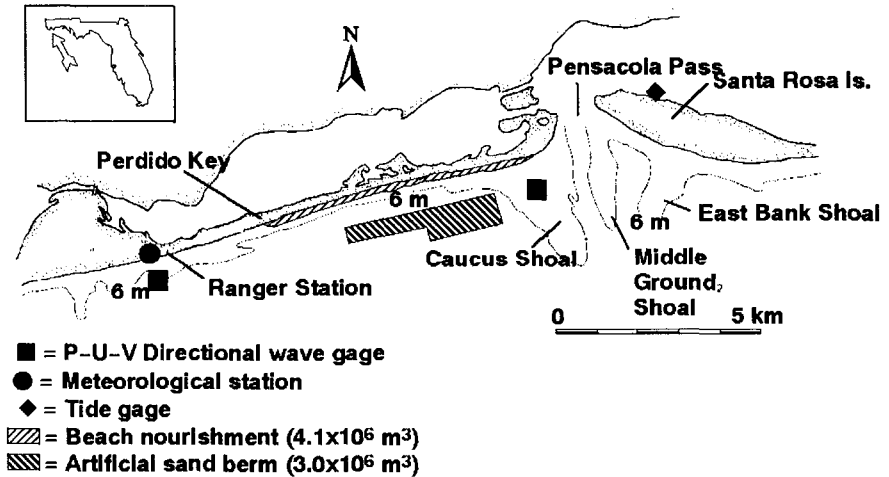


Figure 1. Site location and monitoring plan.

A monitoring program from 1989-1994 yielded a data set that is useful for assessment of hydrodynamics and sediment transport at Perdido Key, including annual bathymetric survey data and long-term wave and current data. Details of the monitoring program may be found in Work (1992), Otay (1994), and Work and Dean (1995).

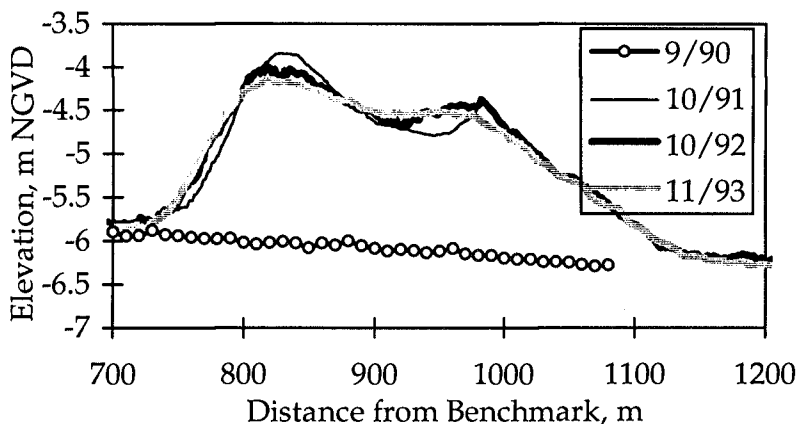


Figure 2. Cross-section through berm near midpoint.

Survey data indicate that the berm has not migrated since placement, although it has been smoothed slightly (Figure 2). But due to the 25% reduction in water depth that it introduces over a large area, it is expected that the berm will exert some influence on the waves that pass over it, and therefore modify nearshore sediment transport. The purpose of this paper is to investigate this effect and assess its significance.

A nearshore berm can provide at least two benefits, depending on its behavior:

- 1) Nourish the beach as sediment moves onshore.
- 2) Shelter the beach in the lee of the berm.

Berms are sometimes favored over beach nourishment because of the reduction in cost due to the relative ease of placement. But correct assessment of the benefits requires accurate prediction of both any migrational tendency and any effect on adjoining areas.

Bathymetry

A numerical grid of depths at the site was created for wave modeling. The grid represents a combination of measurements taken as a part of the monitoring study and digitized nautical charts. Depths at the offshore boundary are not uniform and the grid does not extend to deep water, posing some problems for wave modeling that are addressed below.

A second grid was created by artificially stripping out the berm from the first grid. A detail of the two grid files is shown in Figure 3. Some “scalping” of the nearshore contours is evident in the no-berm plot. This is due to limitations of the contouring routine when there are “stripes” of data (in this case due to surveying beach profiles at 300 or 600 m intervals along the beach), a common problem. This will lead to some overestimation of the effects of wave transformation.

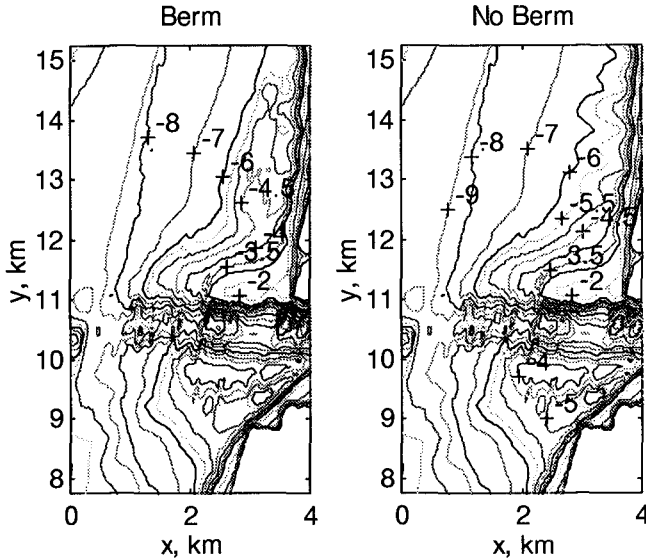


Figure 3. Bathymetry with and without offshore berm. Contour interval 1 m, with the addition of 3.5, 4.5, and 5.5 m depth contours. x -axis points onshore, y -axis in longshore direction. Pensacola Pass at right near $y = 10$ km.

Hydrodynamic Modeling

Measurements of wave energy spectra and mean currents are available at two locations at the site (Figure 1). A finite element hydrodynamic model (RMA-2, Norton, King, and Orlob, 1973, Thomas and McAnally, 1990) was employed to predict tidal currents. The friction factor in the model was adjusted until modeled currents agreed with published values for predicted tidal currents in the inlet throat (U.S. Dept. of Commerce, 1994). Results were then compared to measurements at the two wave gage locations for maximum ebb and maximum flood conditions. The model typically underpredicted currents slightly, not surprising due to the omission of wind- and wave-driven currents in the model. Figure 4 illustrates the results for maximum ebb tide.

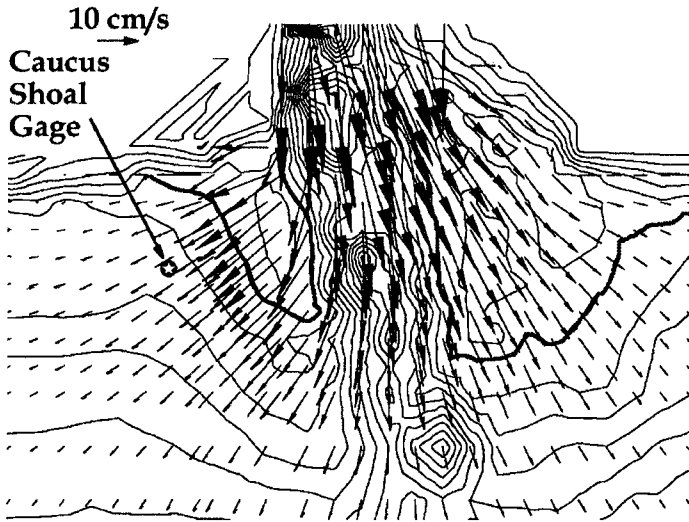


Figure 4. Predicted tidal currents (from RMA-2 model) for maximum ebb tide through Pensacola Pass. Note that flow is concentrated between shoals to either side of navigation channel.

Wave Modeling

A monochromatic, finite difference wave transformation model (REF/DIF 1, Kirby and Dalrymple, 1994) was used to investigate wave transformation at the site. The monochromatic model was selected for two reasons: 1) ease of use, compared to a spectral model, and 2) to assess the viability of a monochromatic model for such a situation. Ease and speed of use become major factors when long-term simulations (years) will be performed.

Since neither bathymetry grid extended to deep water for most of the wave conditions to be modeled, an iterative procedure was developed to estimate wave conditions at the offshore boundary, given wave conditions at the western wave gage, where the bathymetric contours are relatively straight and parallel (Work and Kaihatu, in press). This allows one to drive the model with data from one nearshore wave gage (a common situation) and predict wave conditions anywhere else in the domain.

A large number of model runs have been performed with the real (berm) bathymetry at the site, using data from the western wave gage to drive the model. The monochromatic model, on average, yields a reasonable prediction of wave height at the other gage, although there is a large amount of scatter (the average value of the ratio of model to measured wave heights is 0.99; standard deviation of this

ratio is 0.34). The model is not a good predictor of wave direction at the other gage, in part because of the fact that the contours run nearly perpendicular to the nominal shoreline orientation at the eastern wave gage, which sits near a shoal. Figure 5 shows results for one simulation near this shoal.

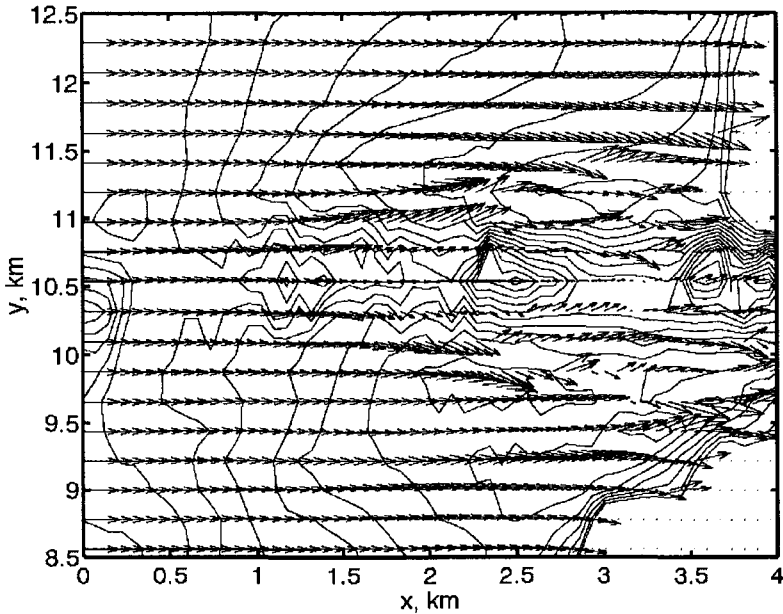


Figure 5. Wave vectors near Caucus Shoal, immediately west of Pensacola Pass. Conditions at western wave gage: $H_{mo} = 0.6$ m, $T_p = 6$ sec, shore-normal incidence.

Wave model results indicate that tidal currents at the site do not exert any significant influence on wave conditions outside of the inlet channel. Thus bathymetric gradients are the primary cause of wave transformation. This simplifies modeling efforts substantially.

Hypothetical cases were simulated to isolate the influence of wave period, tide stage, and incident wave height and direction, on wave conditions in the lee of the nearshore berm. Figure 6 compares the wave heights for the two bathymetric grids for the “typical” case ($T_p = 6$ sec, shore-normal waves with height $H_{mo} = 0.6$ m at western wave gage). Figure 7 shows the difference between the two results, normalized by the incident wave height. Some findings:

- Tide stage has minimal influence on the wave height differences (berm vs. no berm). This is largely due to the very small tide range at the site.

- Dependence on wave period is as expected: as period increases, refraction becomes more pronounced, and differences between the two results increase.
- Dependence on wave height is weak until the incident wave height is increased to the point where waves begin to break on the nearshore berm ($H_{mo} > 3.5$ m). The largest significant wave height measured during the 4-year wave monitoring program was 2.9 m, in August, 1992, while Hurricane Andrew was in the Gulf of Mexico. This event also yielded the largest measured wave period ($T_p = 13$ seconds). In summary, wave breaking on the berm has occurred rarely, if at all.
- Dependence on incident wave direction is relatively strong. Greatest differences between the berm and no-berm cases were observed for nearly shore-normal waves.

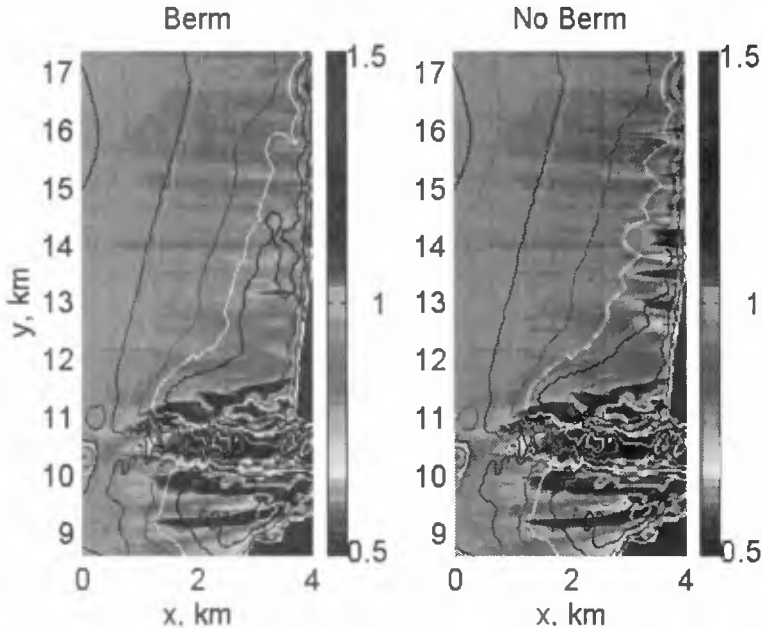


Figure 6. Wave model results with typical wave conditions ($H_{mo} = 0.6$ m, $T_p = 6$ sec, shore-normal incidence, at western wave gage), with and without berm. Contours indicate depth at 1 m intervals. Shade indicates wave height relative to wave height at western wave gage.

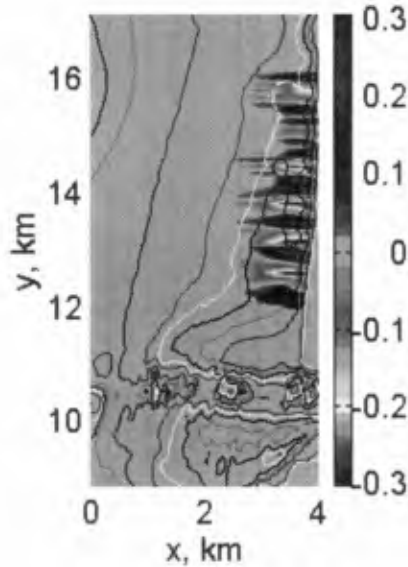


Figure 7. Difference between no-berm and berm wave model results shown in Figure 6. Normalized by no-berm results. Shade indicates percent difference in wave height. Positive values indicate percent increase in wave height in absence of berm, negative indicate percent reduction.

The maximum difference between the berm and no berm wave height fields, for the region behind the berm, is 30%. Because there is typically a minimal difference in energy dissipation between the berm and no berm cases, the total energy reaching the shoreline is the same whether or not the berm is present. The berm acts to redirect energy and leads to zones of focusing and de-focusing. If depths over the berm were less, breaking would occur on the berm and the shoreline behind the berm would be more sheltered. Figure 8 compares the wave height fields for large vs. small incident wave heights, both over the berm bathymetry, to illustrate this effect.

Limited tests were also performed with a spectral version of the same wave model (REF/DIF S, Ozkan and Kirby, 1993). This model essentially consists of superimposing many results from the monochromatic model for different frequencies. Results with the spectral model were similar to the monochromatic model results, but more muted. The presence of additional frequency components leads to less pronounced focusing of wave energy. One example is provided in Figure 9.

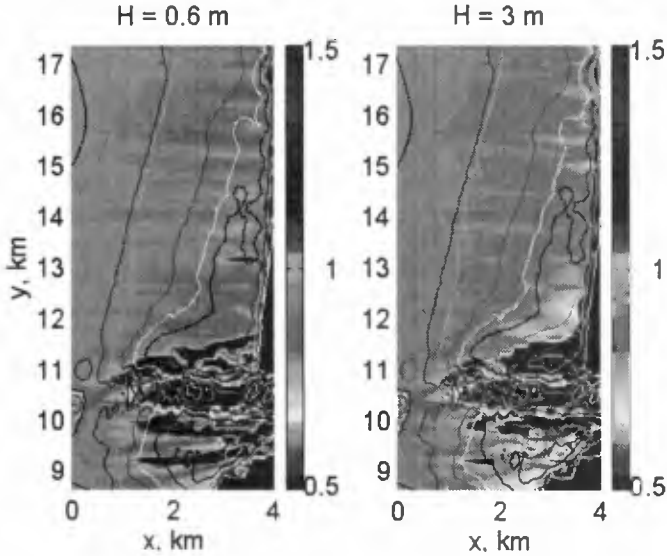


Figure 8. Small wave height ($H_{mo} = 0.6$ m, $T_p = 6$ sec, shore-normal at western wave gage) vs. large ($H_{mo} = 3.0$ m) wave height results over berm bathymetry. Shade indicates wave amplification. Contours indicate depth at 1 m intervals.

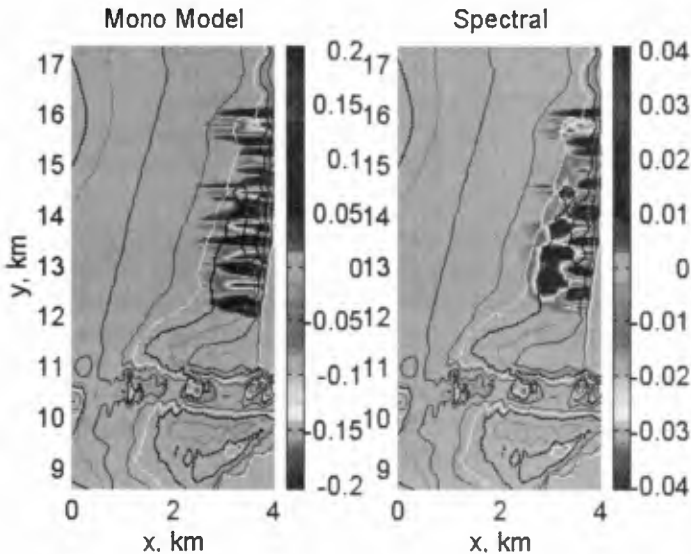


Figure 9. Monochromatic model (REF/DIF 1) vs. spectral model (REF/DIF S) results for conditions corresponding to Figure 6. Shade indicates percent difference in wave height. Positive values indicate percent increase in wave height in absence of berm, negative indicate percent reduction.

Shoreline Change

Redistribution or reduction of wave energy reaching the shoreline will affect sediment transport. Figure 9 shows the measured changes in shoreline planform, relative to the pre-nourishment condition. This is a classic signature for a beach nourishment project: the waterline moves back, rapidly at first, due to cross-shore sediment transport, since the as-built beach profile slope is much steeper than natural slopes. The “shoulders” (ends) of the project erode more rapidly due to the high rate of sediment diffusion in the longshore direction induced by strong planform gradients.

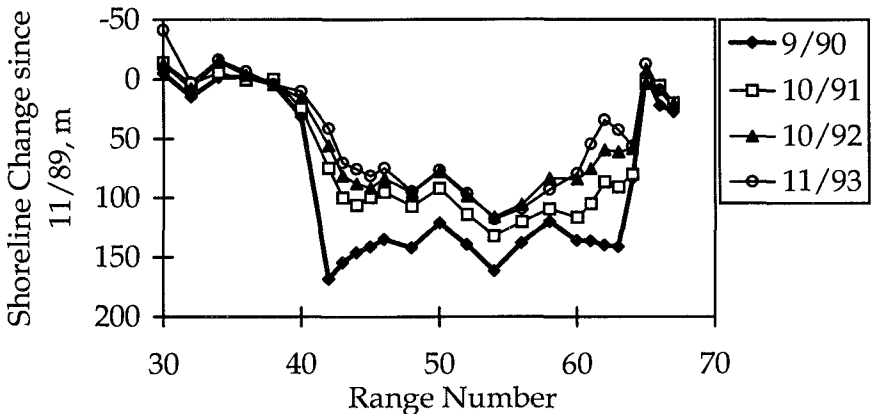


Figure 10. Measured change in shoreline position, relative to pre-nourishment condition. Nominal distance between survey ranges is 300 m, Pensacola Pass at right limit of figure.

Another means of investigating the evolution of a nourishment project is to calculate the volumetric changes per unit length of beach, i.e. the change in the cross-sectional area of the beach profile. Doing so allows one to integrate out the effects of cross-shore sediment transport: all observed changes are due to longshore redistribution of sediment arising from longshore gradients of longshore sediment transport. This requires assumption of a depth beyond which there is no cross-shore sediment transport. For the Perdido Key beach nourishment project, it is quite clear that there is negligible sediment transport beyond the 5.5 m contour (Work and Dean 1995).

Figure 11 shows the computed longshore gradient of longshore sediment transport, which is equal in magnitude (but opposite in sign) to the change in cross-sectional area of the beach profile per unit time. Positive values indicate erosion and

negative indicate accretion. The question is then whether these zones of erosion and accretion can be predicted by the numerical wave model. A definitive answer to this question would require that the wave model be run for every measured wave event to calculate a four-year time series of breaking wave height and direction. These time series could then be used to drive a shoreline change model.

Unfortunately it is not possible to model wave transformation for every measured wave event. There are many measured wave directions which are highly oblique (> 45 degrees) to the shoreline. The chosen wave model (and any other similar model which employs a parabolic approximation to the elliptic governing equation) has a limitation on the incident wave angle. If the incident wave angle exceeds a certain value (the value of which depends on details of the model formulation), the model will yield erroneous results or no results at all. In addition, the method developed to estimate wave conditions at the offshore boundary of the grid, given wave conditions at one nearshore wave gage, similarly will not work for highly oblique waves. In practice, it was possible to model only about one-half of the measured wave conditions.

A “typical” wave condition was therefore chosen for comparison of wave height fields and observed shoreline changes. Noteworthy regions are indicated by the arrows on Figure 11. Several features stand out:

- There is consistent focusing predicted (both with and without the berm, for nearly all wave conditions) at the eastern limit of the nourishment project. This is indicated by the arrow at the extreme right of Figure 11. A strong erosional trend is also observed there. This is erosion of the end of the beach nourishment project, enhanced by the focusing of wave energy.
- Placement of the berm reduced, for the “typical” wave condition, the wave heights near the midpoint of the beach nourishment project, where a switch from erosional to stable behavior is observed (middle arrow in Figure 11). A similar switch occurred near the western end of the nourishment project, where placement of the berm reduced wave heights, and a switch from a stable shoreline to accretion occurred (left arrow).

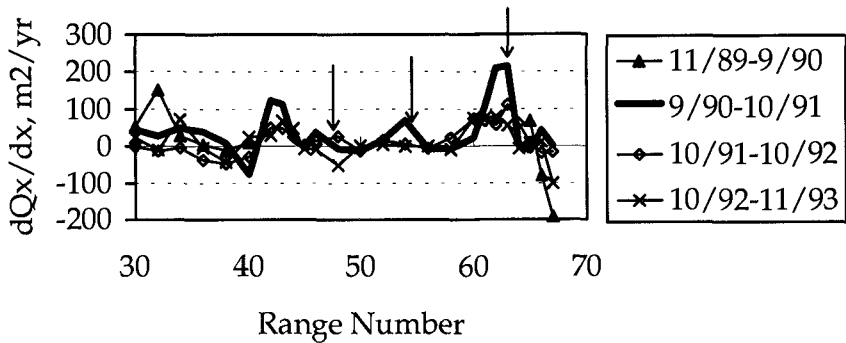


Figure 11. Longshore gradient of longshore sediment transport, calculated from surveyed beach profiles. Equivalent in magnitude to change in cross-sectional area of beach profile. Nominal spacing between ranges is 300 m, Pensacola Pass to right.

Project Performance

Volume of sand remaining within the nourished region was computed as a measure of project performance. Three years after placement of the beach nourishment material, 84% of the initial volume remains (Figure 12). If the entire monitored area is considered, the value is 82%. Some of the nourishment material has been deposited into the inlet, and some has moved westward due to the predominant wave conditions.

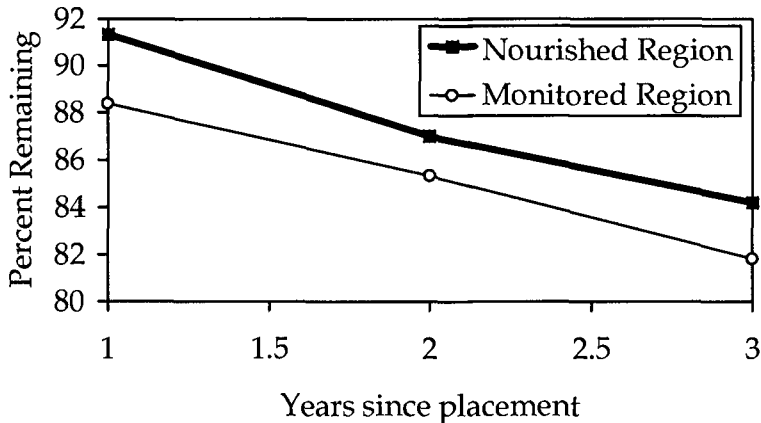


Figure 12. Volume changes for project. Nourished region is a subset of the monitored region.

Conclusions

Nearshore berms can and have been placed with the goal of gradual beach nourishment through onshore migration. Existing predictive capability with regard to rate and even direction of migration (onshore or offshore) is still limited. A berm can also exert a sheltering effect on the beach in its lee. The presence of the berm can either merely redistribute wave energy, or, if it induces additional dissipation through breaking over the crest of the berm, reduce wave energy reaching the shoreline. The effect of the berm on the shoreline behind it should be considered as part of the design process.

Data for two years after placement of a berm at Perdido Key, FL, indicate the berm did not migrate during this time. It has been slightly smoothed but its volume unchanged. Numerical wave model results indicate that the berm does exert some influence on the breaking wave climate by redistributing energy alongshore. This occurs even in the absence of waves breaking on the berm. Changes in nearshore wave heights which occur as a result of the berm are reflected in the measured shoreline signature, for a typical incident wave.

It was not possible to model all wave events with the chosen numerical wave transformation model. Waves which deviate significantly from shore-normal occur frequently at the site but could not be modeled. Improvements in wave modeling techniques will eventually remove this constraint.

References

- Kirby, J.T., and Dalrymple, R.A., 1994. REF/DIF 1: Combined refraction/diffraction model. Documentation and user's manual. CACR Report No. 94-22, Dept. of Civil Eng., Univ. of Delaware, Newark, DE.
- Norton, W.R., King, I.P., and Orlob, G.T., 1973. A finite element model for Lower Granite Reservoir. Water Resources Engineers, Inc., Walnut Creek, CA.
- Otay, E.N., 1994. Long-term evolution of nearshore disposal berms. Ph.D. Dissertation, Coastal and Oceanographic Eng. Dept., Univ. of Florida, Gainesville, FL.
- Ozkan, H.T., and Kirby, J.T. 1993. Evolution of breaking directional spectral waves in the nearshore zone. Proc. Ocean Wave Measurement and Analysis, New Orleans, LA, ASCE, 849-863.

Thomas, W.A., and McAnally, W.H., Jr., 1990. Users manual for the generalized computer program system: Open-channel flow and sedimentation, TABS-2. U.S. Army Engineer Waterways Expt. Station, Vicksburg, MS.

U.S. Department of Commerce, 1994. *Tidal Current Tables, 1995, Atlantic Coast of North America*. Natl. Oceanic and Atmos. Admin., Natl. Ocean Serv., Silver Spring, MD.

Work, P.A., and Dean, R.G., 1995. Assessment and prediction of beach-nourishment evolution. *J. Wtrwy, Port, Coast., and Ocean Eng.* 121(3), ASCE, 182-189.

Work, P.A., and Kaihatu, J.M., in press. Wave transformation at Pensacola Pass, FL. Accepted for *J. Wtrwy, Port, Coast., and Ocean Eng.*, ASCE.

CHAPTER 288

ACCURACY OF SAND VOLUMES AS A FUNCTION OF SURVEY DENSITY

Jennifer L. Irish¹, W. Jeff Lillycrop², and Larry E. Parson³

ABSTRACT

Hydrographic surveys are the primary tool for calculating beach nourishment project volumes. With costs for beach-quality sand as high as \$30 US per cubic meter, miscalculating project design volumes can result in significant cost differentials. Because conventional bathymetry and topography of beach projects are collected along shore-normal profile lines spaced anywhere from 30 m to 300 m, calculation of project volumes relies heavily on the assumption that there is little along-shore variability from one profile to another. In most cases, however, the beach and nearshore are highly irregular and this assumption is violated. With the development of high-resolution bathymeters, such as the SHOALS airborne lidar system, it is now feasible to collect accurate, high-density beach surveys. These types of data sets create a highly accurate, quantitative measurement of beach and nearshore conditions. This paper describes the SHOALS system and lidar technology and presents a comparison of volumes calculated using high-density lidar data and conventional nearshore profile surveys. Volumes are calculated to compare differences for beaches on the Atlantic Ocean, the Gulf of Mexico, and the Great Lakes.

1.0 INTRODUCTION

Cost for a cubic meter of sand placed on a beach ranges from \$5 US to \$30 US, depending on many geographic and engineering factors. Beach nourishment projects range in size from several thousands of cubic meters, such as the 1993 project at St. Joseph, Michigan of 39,000 m³, to millions of cubic meters, such as the project at Miami Beach, Florida of 12 million m³. Underestimated project design volumes can result in cost overruns or a reduced amount of sand being placed on the beach, while overestimated project design volumes can result in excessive budgeting and planning. Hydrographic surveys are the primary tool for calculating project

1) Hydraulic Engineer, 2) Research Physical Scientist, 3) Research Hydraulic Engineer, US Army Engineer Waterways Experiment Station, Coastal and Hydraulics Laboratory, 3909 Halls Ferry Road, Vicksburg, MS 39180-6199, USA

volumes. Conventional survey techniques use shore-normal wading depth surveys matched with offshore acoustic surveys, spaced at intervals along the beach ranging from 30 m to 300 m.

Calculation of project volumes relies on the assumption that there is little topographic or bathymetric variability from one profile line to the next, or that if there is variability, it averages out over the project limits. However, beach and nearshore topography are highly three-dimensional as a result of sub-aerial sand dunes, nearshore bars, hard-bottom outcrops, seawalls, and groins. At profile spacings typically on the order of 300 m, these assumptions are often violated. With the development of lidar (LIght Detection And Ranging) hydrographic systems, such as the US Army Corps of Engineer's (USACE) Scanning Hydrographic Operational Airborne Lidar Survey (SHOALS) system, it is now economically feasible to collect accurate, high-resolution beach and nearshore surveys.

The following discusses the SHOALS system and its technology and discusses the benefits of high-resolution bathymetry and topography. Four beach projects surveyed with SHOALS are presented and analyzed to determine sand volume computation sensitivity to survey density.

2.0 SHOALS SYSTEM

In 1994, the USACE introduced a new airborne hydrographic survey system capable of remotely collecting high-resolution, accurate bathymetry. The SHOALS system is an airborne-lidar system operating from a Bell 212 helicopter (Figure 2.1). The system uses state-of-the-art lidar technology to measure water depths (Guenther, 1996). A laser-transmitter/receiver is housed inside a pod mounted underneath the aircraft. As the laser pulses at 200 Hz, it is scanned in an arc producing a swath width equal to approximately one-half the aircraft altitude. This yields a uniform sounding spacing, nominally 4-m by 4-m. The laser pulse travels from the airborne platform to the water surface where part of the energy reflects back to the receiver (Figure 2.2). The remaining energy penetrates the water column and reflects off the sea bottom. The time differential between these two returns indicates the water depth (Lillycrop et al., 1996).



Figure 2.1 The SHOALS system

Table 2.1 gives SHOALS current performance specifications. SHOALS has a vertical accuracy of ± 15 cm and a horizontal accuracy of ± 3 m and meets the USACE Class I, dredge payment, performance specifications (Riley, 1995). Operating at a nominal speed and altitude of 30 m/s and 200 m, SHOALS surveys 8 km² per hour. In optically clear water, SHOALS records to depths of 40 m. Since early 1995, SHOALS also records accurate topographic

Table 2.1 SHOALS performance

maximum depth	40 m
minimum depth	< 1 m
vertical accuracy	± 15 cm
horizontal accuracy	± 3 m
sounding density	4 m
operating speed	30 m/s
swath width	110 m

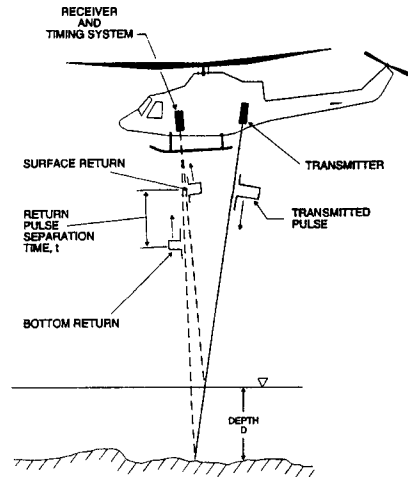


Figure 2.2 SHOALS operating principle

elevations of adjacent beaches allowing full mapping of both the beach and nearshore. To date, SHOALS surveyed over 80 USACE projects totaling 2,000 km².

3.0 SITE DESCRIPTIONS

Because SHOALS collects very dense bathymetry, typically 120,000 soundings per square kilometer, it is an ideal tool for monitoring the beach and nearshore in dynamic, irregular areas. For a particular stretch of beach, SHOALS data provides detailed bathymetry and adjacent beach topography allowing accurate identification of high-erosion areas and complex nearshore features. The four data sets presented herein include Longboat Key on the Gulf of Mexico, Island Beach State Park on the Atlantic, and St. Joseph and Presque Isle on the Great Lakes. Each of these sites is characterized by irregular cross-shore and/or along-shore variation in topography.

3.1 Longboat Key

Longboat Key, Florida is on the east shore of the Gulf of Mexico and is situated between Longboat Pass, to the north, and New Pass, to the south. Over 2 million cubic meters of beach-quality sand were placed on the southern-most 8.5 km of the key in 1993 to protect the shoreline from further erosion. SHOALS surveyed the area 5 times since March 1994 to monitor the nourishment project (Irish and Truitt, 1995). The high-resolution SHOALS bathymetry collected in November 1995 reveal a complex sand-bar system in the nearshore (Figure 3.1). The dual-bar system merges together and separates as it parallels the shoreline. At the southern end of the key, the seaward bar diverges into the ebb shoal of New Pass. Conventional profile data are regularly collected along profiles spaced 300 m apart and outline the dual-bar system; however,

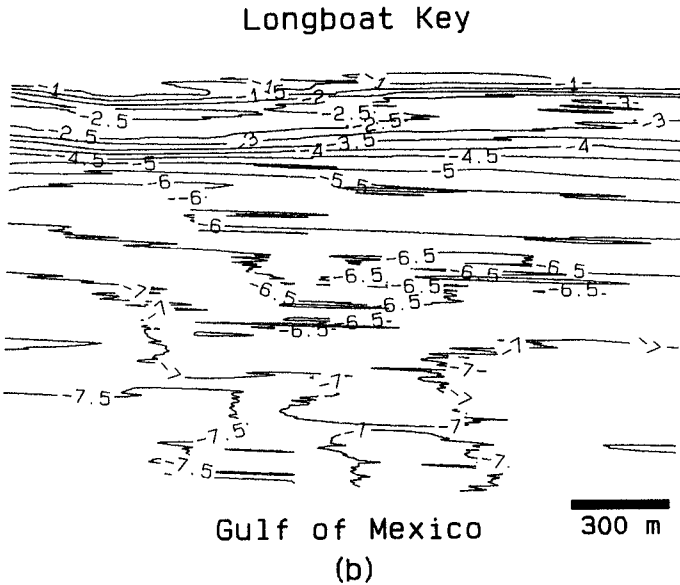
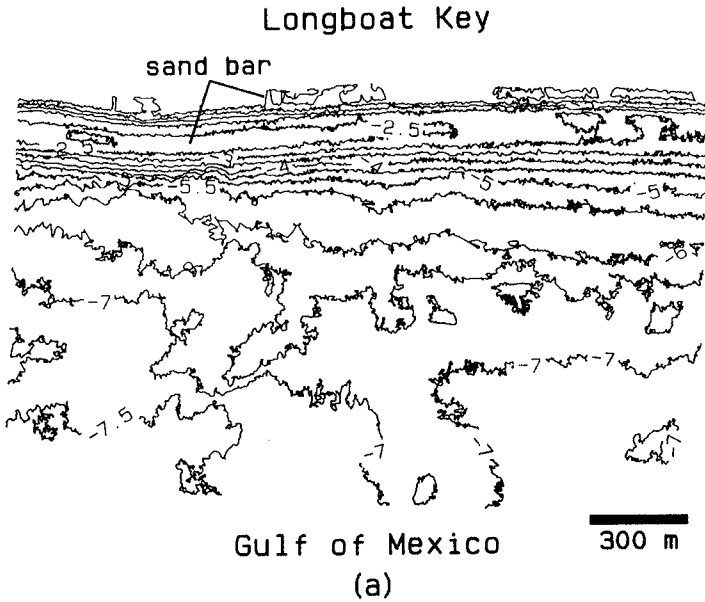


Figure 3.1 Longboat Key, Florida, November 1995: a) representative section of SHOALS bathymetry, b) simulated profile bathymetry at 300-m spacing. All depths are in meters referenced to NGVD.

these data sets do not reflect local complexities in the nearshore. The southern-most 3.4 km were analyzed in this investigation.

3.2 Island Beach State Park

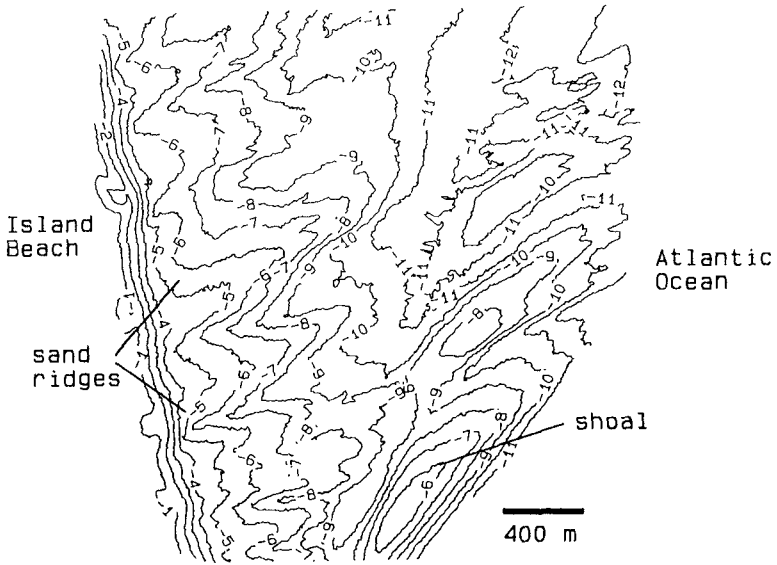
A 2.5-km stretch of Island Beach State Park, New Jersey, just north of Barnegat inlet was surveyed with SHOALS in 1994. The park is directly exposed to the Atlantic Ocean and is characterized by shore-perpendicular sand ridges stretching from the dry beach through the nearshore. Because the area is a state park, no man-made alterations are permitted. However, Barnegat inlet, which is jettied on both its north and south sides, does impact Island Beach. SHOALS surveyed the southern-most 2.5 km of Island Beach in June 1994 (Figure 3.2). The survey details the beach's three-dimensionality quantifying the sand formations and the shoaled areas formed by inlet processes.

3.3 St. Joseph

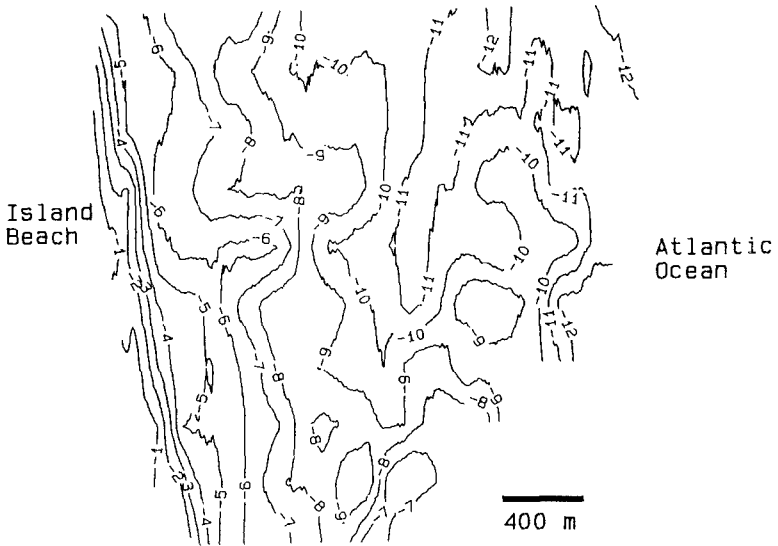
St. Joseph, on the southeastern shore of Lake Michigan, was authorized as a Federal beach nourishment project in 1976. In 1903, two jetties were constructed to stabilize the St. Joseph River entrance. These jetties interrupt the natural southerly longshore transport of 84,000 m³ per year, and as a consequence, the downdrift beach experienced erosion and the lake bed suffered downcutting (Parson and Smith, 1995). Since 1976, the USACE annually places dredged material from the maintenance dredging of St. Joseph Harbor south of the entrance to form a feeder beach to replenish 6 km of shoreline. Additionally, coarser material from an upland source is periodically placed. Typically, bathymetric and topographic data are collected along survey lines spaced 152 m apart through the fill area and 800 m apart south of the fill area. In August 1995, SHOALS surveyed the project collecting nearly 400,000 soundings (Figure 3.3). The SHOALS data quantify areas of severe lake-bed downcutting and identified a previously undiscovered headland feature with a 2-m relief. The entire 6-km project was analyzed in this investigation.

3.4 Presque Isle

Presque Isle Peninsula is on the south shore of Lake Erie at Erie, Pennsylvania. The peninsula historically tends to migrate easterly causing erosion of the lake-side beach. Occasionally the area breaches causing dangerous navigation conditions in Erie Harbor, situated between the peninsula and the mainland. The USACE has taken several measures to prevent erosion including beach nourishment and the construction of groins (Grace, 1989). In 1992, the USACE installed 55 breakwaters offshore of Presque Isle. Each breakwater is 47.5-m long and is separated by a 106.7-m gap. Additionally, 285,000 m³ of beach fill material were placed initially and renourishment occurs annually (Mohr, 1994). Ongoing project monitoring of the performance of the breakwater system includes bathymetry and topography collected annually along profiles spaced 300 m to 600 m apart. In August 1995, SHOALS surveyed this breakwater system detailing the salient and tombolo formations shoreward of the structures and the fairly uniform bottom seaward of the structures (Figure 3.4). The entire 9.9-km long project was used in this investigation.



(a)



(b)

Figure 3.2 Island Beach State Park, New Jersey, June 1994: a) SHOALS bathymetry, b) simulated profile bathymetry at 300-m spacing. All depths are in meters referenced to NGVD.

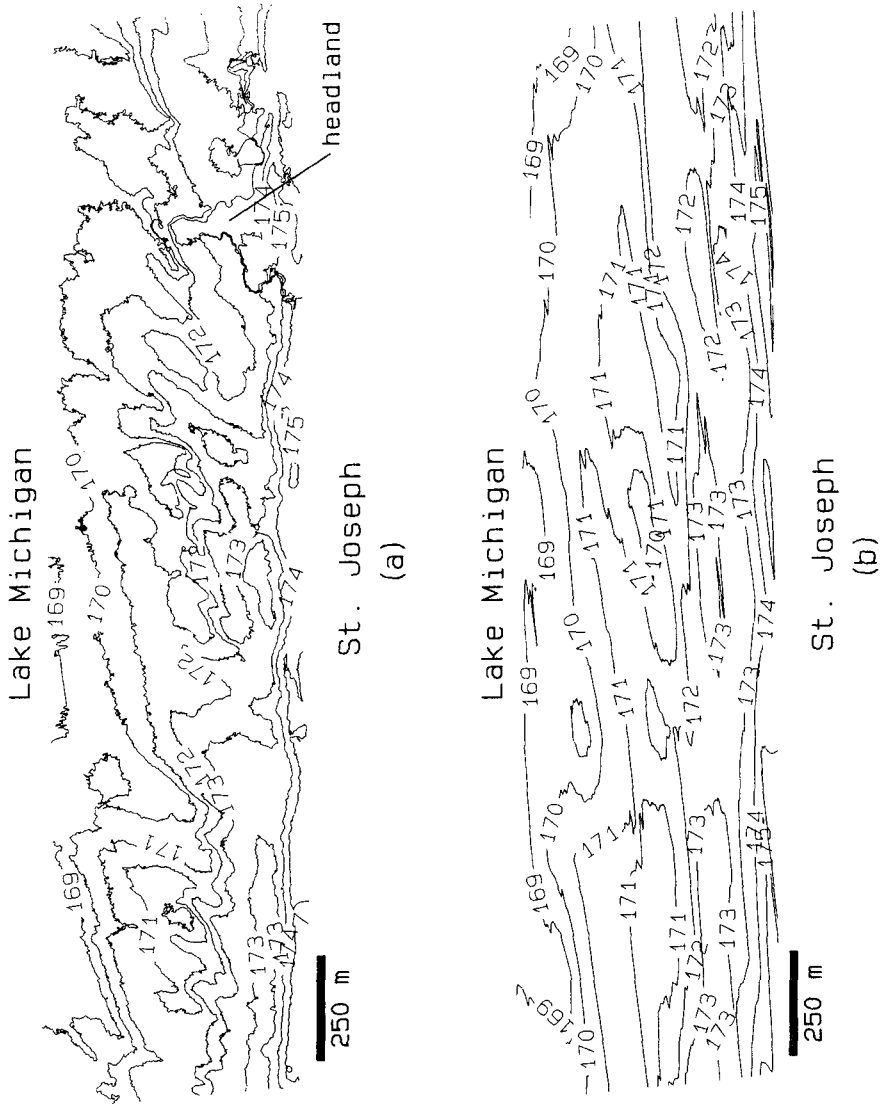


Figure 3.3 St. Joseph, Michigan, August, 1995: a) representative section of SHOALS bathymetry, b) simulated profile bathymetry at 300-m spacing. All depths are in meters referenced to IGLD.

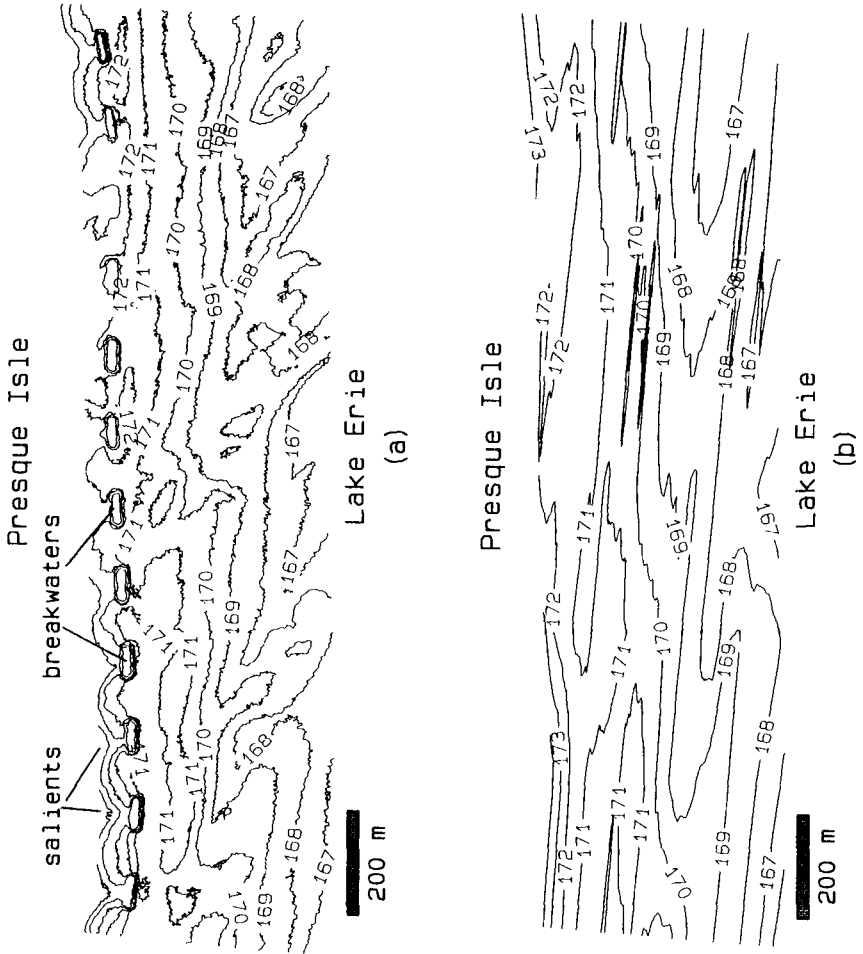


Figure 3.4 Presque Isle, Pennsylvania, August, 1995: a) representative section of SHOALS bathymetry, b) simulated profile bathymetry at 300-m spacing. All depths are in meters referenced to IGLD.

4.0 COMPARISON PROCEDURE

To evaluate the importance of data density on beach nourishment volume calculations, profile data along spacings varying from 5 m to 300 m were simulated from the SHOALS bathymetry using a commercially available CAD and engineering package, TERRAMODEL™. First, profile alignments spaced every 5 m were created along the project length. A digital terrain model (DTM) of the SHOALS data was created to represent it mathematically. The SHOALS depths, as represented by the DTM, were then projected onto the profile lines at 4-m intervals. The resulting bathymetric contours for the simulated profiles at 300-m spacing are in Figures 3.1b, 3.2b, 3.3b, and 3.4b illustrating the loss of detail with such a wide spacing.

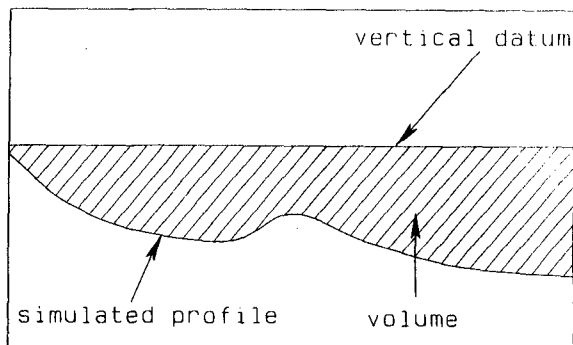


Figure 4.1 Cross-sectional area

To simplify calculations, volumes were computed between the horizontal plane representing a mean water vertical datum and the bottom topography as represented by the simulated profiles (Figure 4.1). Volumes were computed using the well-known area-end method for each profile spacing. When employing the area-end method, the cross-sectional area between the bathymetry and mean water at

each profile location was first calculated. (Only the area below the mean water vertical datum was computed.) The calculated area at one profile location (A_1) is then averaged with that of the next consecutive profile (A_2). The product of this averaged area and the length between the two consecutive profiles (L) gives the volume (V) between the profiles:

$$V = \frac{A_1 + A_2}{2} \cdot L$$

The total volume for the entire project is then equal to the summation of the volumes. The computed results are presented in Table 4.1 as volume difference between the highest resolution set, 5-m spacing, and the stated spacing, in cubic meters per meter length of beach. Positive differences indicate that the stated spacing resulted in a volume larger than the 5-m spacing volume while negative differences indicate a smaller volume.

5.0 DISCUSSION

The results, in general, show that as the spacing between survey profiles increases, so too does the error in computed volumes. Figure 5.1 gives a plot of

Table 4.1 Computed volume differences

Profile spacing	Volume difference (m ³ /m)			
	Longboat Key	Island Beach	St. Joseph	Presque Isle
5	0.0	0.0	0.0	0.0
10	-0.4	0.1	0.0	1.2
25	0.0	-0.1	-0.4	1.9
30	-1.8	0.1	0.2	0.8
50	0.2	-0.3	-1.7	3.3
60	-3.1	0.2	2.3	0.9
100	-1.6	-1.9	-3.3	6.1
150	-0.7	-0.3	-6.5	-10.4
200	2.2	5.3	-18.5	0.8
250	-6.6	-15.9	8.4	4.2
300	12.3	-19.8	-5.3	-9.8

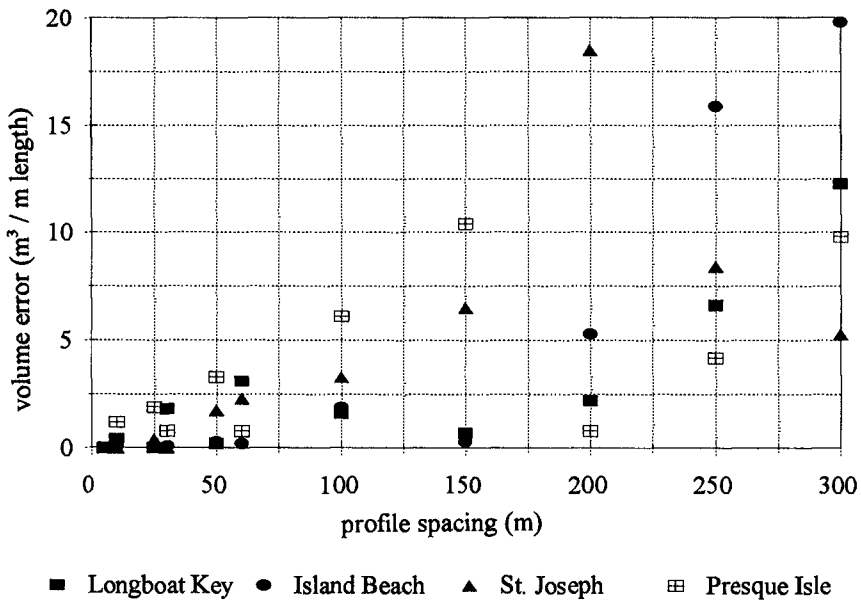


Figure 5.1 Measured volume error

absolute deviation from the 5-m volume (volume error) versus profile spacing for all four sites. In general, the volume error becomes more random and larger in magnitude as profile spacing increases. This is consistent with the findings of Saville and Caldwell (1952). In their investigation, the use of average profiles at spacings varying from 120 m to 2,800 m to represent lengths of a fairly uniform beach were analyzed for accuracy in evaluating engineering volumes. The spacing error, defined as the accuracy measurement of a particular profile in representing a section of beach, was evaluated by comparing the selected profile with the average profile for that section. The spacing error was then translated into a volume error, defined as the total volume difference over the project length. Their conclusions state that the volume error increases nearly linearly as profile spacing increases. Saville and Caldwell's results do not indicate a randomness in volume error; however, the results from this investigation do. This is most probably attributed to the irregularities in the bathymetry evaluated herein.

Of the four sites, the bathymetry at Longboat Key shows the least along-shore variation. This is reflected in the results where the volume error at Longboat Key is within $5 \text{ m}^3/\text{m}$ for profile spacings as great as 200 m. However the area is still highly three-dimensional, and the volume error when using 200-m, 250-m, and 300-m spacings continually increases and is as much as $12.3 \text{ m}^3/\text{m}$. The calculations for Island Beach indicated similar findings. Here, the volume error is small for profile spacings less than 200 m, and as the spacing increases beyond 200 m, the measured volume error increases. In contrast to Longboat Key, the bathymetry at Island Beach is highly variable along-shore with shore-normal sand ridges occurring every 400 m to 500 m. This investigation indicates that bathymetric variations associated with these large features do not impact volume computations until the profile spacing exceeds 200 m.

The analysis at St. Joseph shows that profile spacings larger than 100 m result in significant volume error. Differing from Longboat Key and Island Beach, as the profile spacing is increased at St. Joseph, the volume error does not continually increase. The measured volume error at St. Joseph when a 250-m spacing is used is significantly lower than that measured when a 200-m spacing is used. However, all spacings greater than 100 m result in volume errors larger than $5 \text{ m}^3/\text{m}$.

Of the four projects, Presque Isle is most affected by survey spacing changes between 5 m and 50 m, and volume computations deviate significantly with spacings greater than 50 m. Of the spacings evaluated at Presque Isle, the volumes computed using 150-m spacing yielded the largest error, $10.4 \text{ m}^3/\text{m}$. When the spacing is increased to 200 m, the volume error dramatically decreases. Because of the uniform repetition of salient formations every 155 m corresponding to the breakwater field, it is probable this decrease in volume error is a result of these features. By chance, the profile locations at the 200-m spacing were such that the volume error between consecutive profiles averaged out over the project length.

The economic impact of profile spacing is evident in Figure 5.2 where the cost error, or absolute cost difference per cubic meter per unit length of beach, for the Presque Isle project is displayed. The lower and upper cost error boundaries were calculated using a cost per cubic meter of beach-quality sand equal to \$5 US and \$30 US, respectively. Even at profile spacings as small as 50-m, the cost error is as great as \$100 US/m. As the profile spacing increase to 100 m or greater, the cost error

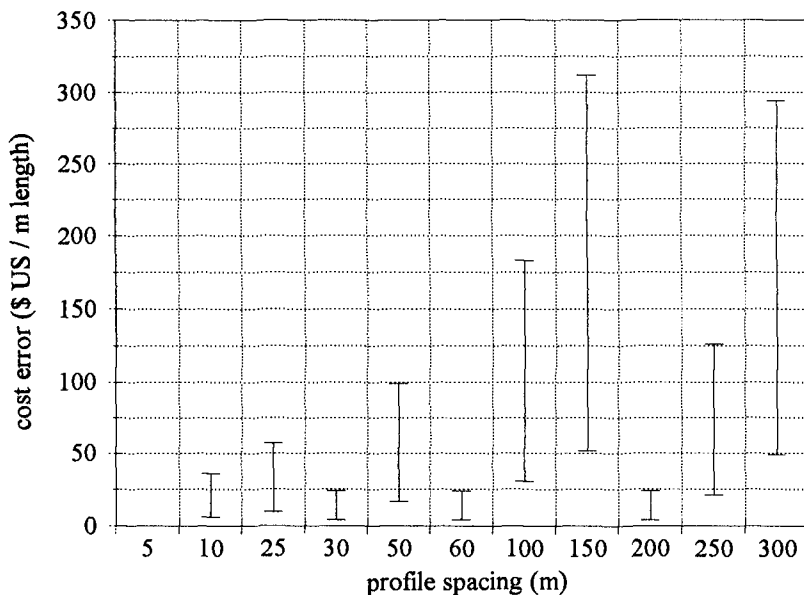


Figure 5.2 Cost error at Presque Isle, Pennsylvania

becomes as great as \$325 US/m, translating to a total project cost difference well over \$3 million US. With renourishment at \$22 US to \$26 US per cubic meter occurring annually at Presque Isle, higher density surveys are certainly warranted. Typical monitoring at profile spacings of 300 m or greater may result in cost differentials around \$2.5 million US over the project length.

Similar cost impacts may be observed at the other three projects. At Longboat Key, a 300-m profile spacing results in cost differentials between \$ 200,000 US and \$1.2 million US over the 8.5-km project length. At Island Beach and St. Joseph, profile spacings greater than 150 m may result in cost errors in excess of \$75 US/m. At all four projects, the economic benefits of higher density bathymetry are obvious.

Hydrographic surveys serve as the base for engineering planning and design of beach nourishment projects. Usually, a fixed budget for a particular project is developed from volume calculations between the design profile and the collected bathymetry. If design volumes were computed using sparse data, a fixed budget may result in too little, or too much, sand placement at the site. Ultimately, project performance is affected: an under-designed project will not adequately protect against further shoreline erosion.

6.0 CONCLUSIONS

This investigation clearly indicates the economic and planning benefits of high-resolution bathymetry for beach nourishment along irregular beaches. Low density data may result in gross miscalculation of fill volumes ultimately impacting project performance and financial management. The conclusions of this analysis are based on

engineering volumes computed with respect to the below-water portion of the profile and only reflect underwater bathymetric irregularities. However, initial design, maintenance, and monitoring of beach nourishment projects also encompasses the above-water portion of the profile. There are commonly occurring irregularities on the above-water portion as well including sand dunes and features associated with man-made structures. Based on the findings herein, inclusion of the above-water portion of the profile should result in even greater inaccuracies in engineering volumes when wide profile spacings are used.

Data density for a particular hydrographic survey mission should be governed by the degree of along-shore variability and the intended engineering application of the data set rather than the capability of the survey instrument. For example, high-density data may not be required when monitoring long-term regional coastal evolution; however, high-density data are required when preparing plans and specifications for a beach nourishment project in an area with irregular bathymetry. High-density bathymetry are also valuable when evaluating the performance of erosion-control structures such as groins or detached breakwaters.

The findings herein prompted several new investigations including the expansion of this study to include the above-water portion of the project. Furthermore, studies are ongoing to optimize profile locations to best represent a project while minimizing data collection requirements. Finally, similar investigations are evaluating the impacts of data density on other engineering computations, such as dredging volumes.

With complete coverage, accurate bathymetry now available at costs nearly two-thirds that of conventional methods, engineers can more accurately and cost-effectively plan, design and monitor beach nourishment projects. Furthermore, future research will provide new guidance for determining necessary survey densities for accurate engineering computations.

ACKNOWLEDGMENTS

The authors would like to thank Ms. Jennifer McClung and Mr. Wesley McCleese for their help in the analysis of these data. Results and information, unless otherwise noted, are based on work funded by Headquarters, US Army Corps of Engineers. The use of trade names does not constitute an endorsement in these products by the US government. Permission to publish this paper was granted by the Chief of Engineers.

REFERENCES

- Grace, P.J., 1989. "Investigation of Breakwater Stability at Presque Isle Pennsylvania Erie, Pennsylvania", TR-CERC-89-3. US Army Corps of Engineers, Vicksburg, MS.
- Guenther, G.C., Thomas, W.L., and LaRoque, P.E., 1996. "Design Considerations for Achieving High Accuracy with the SHOALS Bathymetric Lidar System," *SPIE Laser Remote Sensing of Natural Waters: From Theory to Practice*. Feigels, V.I. and Kopilevich, Ed. SPIE, Bellingham, WA, Vol. 2964, pp. 54-71.
- Irish, J.L. and Truitt, C.L., 1995. "Beach Fill Response at Longboat Key, Florida," *Proc. National Conference on Beach Preservation Technology*. Florida Shore

- and Beach Preservation Association, Tallahassee, FL.
- Lillicrop, W.J., Parson, L.E., and Irish, J.L., 1996. "Development and Operation of the SHOALS Airborne Lidar Hydrographic Survey System," *SPIE Laser Remote Sensing of Natural Waters: From Theory to Practice*. Feigels, V.I. and Kopilevich, Ed. SPIE, Bellingham, WA, Vol. 2964, pp. 26-37.
- Mohr, M.C., 1994. "Presque Isle Shoreline Erosion Control Project," *Shore and Beach*. American Shore and Beach Preservation Association, Berkeley, CA, Vol. 62, pp.23-28.
- Parson, L.E., and Smith, J.B., 1995. *Assessment of Native Beach Characteristics for St. Joseph, Michigan -Southeastern Lake Michigan*. US Army Corps of Engineers, Washington, DC.
- Riley, J.L., 1995. "Evaluating SHOALS Bathymetry Using NOAA Hydrographic Survey Data," *Proc. 24th Joint Meeting of UINR Sea Bottom Survey Panel*. Tokyo, Japan.
- Saville, T., and Caldwell, J.M., 1952. "Accuracy of Hydrographic Surveying In and Near the Surf Zone," *Proc. 1952 Coastal Engineering Conference*. American Society of Civil Engineers, New York, NY.

CHAPTER 289

Shoreline Analysis Using Digital Photogrammetry

Margery F. Overton¹
John S. Fisher²

Abstract

This paper discusses the application of digital photogrammetry to the analysis of shoreline change with examples from Holden Beach, NC. Beach cross sections are generated from a three dimensional stereo image. These profiles are then used to determine shoreline position and erosion rates. The paper compares these rates of shoreline change with those determined from the more traditional methodology based on the two dimensional interpretation of the wet-dry line. The paper also illustrates the improved accuracy obtained by using survey grade GPS as opposed to USGS topographic maps to establish ground control.

Introduction

Coastal engineers are always seeking better tools to analyze shoreline changes. These changes include the result of long-term erosion or accretion and short-term impacts of severe storms. The two most frequently used methods to record shoreline change are directly from field surveys and remotely from aerial photographs. Both methods have advantages and disadvantages.

¹ Associate Professor, NCSU-Kenan Natural Hazards Mapping Program, Department of Civil Engineering, NCSU, Raleigh, NC, USA, 27695.

² Professor, NCSU-Kenan Natural Hazards Mapping Program

Field surveys provide detailed information regarding the topography and bathymetry of the beach and shoreline. These surveys are relatively expensive. In addition, they can not be used to determine long-term change if no historical surveys have been conducted.

Alternatively, the interpretation of shoreline change from aerial photographs permits one to perform a historical analysis when such photographs are available. Unlike field surveys, traditional methods for analyzing shoreline change from aerial photographs do not generally furnish the three dimensional data provided by a field survey. Three dimensional data can be obtained from aerial photographs, however, if one utilizes photogrammetric techniques including the analysis of pairs of overlapping photographs.

Until recently, few coastal engineering projects have included the application of three dimensional photogrammetric techniques to analyze shoreline change, simply because traditional photogrammetry relies upon complex analytical stereoplotters. These devices do not lend themselves to routine use outside of the highly specialized photogrammetry laboratory.

The difficulties of using photogrammetry for shoreline change analysis have been significantly reduced by the introduction of the new computer based digital techniques. Digital photogrammetry replaces the analytical stereoplotter with a three dimensional image that has been generated by a computer coupled with a high resolution scanner. A pair of photographs is scanned, the two images merged and viewed on the terminal as a single three dimensional image with the use of special glasses worn by the operator. In addition to reducing the difficulty in generating a three dimensional image, the technique supplies an image in digital format. This greatly expands the opportunities for data manipulation and analysis.

This paper describes our experience with the application of digital photogrammetry to the analysis of shoreline change along the coast of North Carolina. While we are still learning, it is already clear that this technology has greatly expanded our abilities to make accurate measurements of erosion rates and the impacts of severe storms on the beach.

Project Study Area

The Holden Beach project described in the paper is located in Brunswick County, on the southernmost portion of the North Carolina coast, Figure 1. The study area is a typical barrier island separated from the mainland by a narrow estuary (the Intracoastal Waterway). Most of the beaches in Brunswick County are developed with low density single family houses as is typical for the mid-Atlantic coast. Long-term shore erosion is on the order of 2 to 4 ft/yr. The occasional severe storm, including both hurricanes and northeasters, coupled with the effects of long-term erosion has led to the loss of oceanfront houses and a general need to be able to make reasonable estimates for the future changes in shoreline position.

The analysis of the rates of shoreline change at Holden Beach is part of a larger study of the area being undertaken for the North Carolina Department of Emergency Management through a grant from the Federal Emergency Management Agency. The larger study is intended to develop new techniques for natural hazard identification through the use of digital photogrammetry.

Project Description

The analysis presented in this paper focuses on the measurement of the change in position of the shoreline. In this context the shoreline is defined as the interface between the wet and dry beach as seen from aerial photographs. This interface has been used by many investigators (e.g., Dolan, et al. 1978) as the shoreline, and is often referred to as the high water line in the literature. Strictly speaking it is not the high water line, but rather a time average of this line. This line is not fixed in space; it moves up and down the beach face depending upon the tide, beach slope, and to some extent the wave climate (Fisher and Overton, 1994).

Our laboratory utilizes both hardware and software developed by Intergraph Corporation. The photogrammetric grade scanner with a maximum scanning capability of 3386 dpi is a key feature of the system. It provides the digital resolution needed to achieve the accuracy desired in the data analysis. Figure 2 illustrates a typical digital photogrammetric project work flow. Two or more photographs are scanned (at a typical scanning resolution of 1693 dpi) and used to build a stereo image.

Standard photogrammetric procedures including interior and relative orientation correct for camera distortion and tilt.

One of the most important steps in this work flow is to establish an accurate set of ground control points. These points determine the absolute position of objects seen on the photographs. In order to maximize the ultimate accuracy of the project we have elected to use survey grade GPS equipment for this ground control.

Ideally the ground control should be established at the time of the aerial photographs. However, in many cases this is not possible, and we frequently have to establish ground control after the fact. For example, control points can be established from features that are visible in the photography and which can be surveyed accurately. Using photography from the last five years, this procedure has allowed us to establish control points with approximately 3 ft accuracy.

Once the control has been established, the computer can then generate a three dimension image of the beach. As noted above, the operator must be wearing a special set of glasses to view this image, much like one would do in a theater when viewing a 3-D movie.

The operator, using the stereo image, can next proceed to create a digital terrain model, or DTM. This model is developed by the operator "placing" the computer cursor on ground at multiple locations. This process requires a certain amount of training and experience, and therefore the quality of the DTM depends upon the skill of the photo analyst. Once the DTM has been created, a number of different digital products can be produced, depending upon the specific application and interest. Examples include orthophotos, triangulated irregular networks (TINs), grids, and draped images.

Shoreline Change Measurements

Figure 3 is a digital orthophoto for a portion of the study area for June 1992. A digital orthophoto is a computer generated 2-dimensional image which has been corrected for distortion. Accurate measurements can be made directly from this orthophoto. Because of the digital format it is possible to zoom in on a portion of the photo as shown by the inset in this figure. The shoreline (wet-dry line) has been identified by the operator as indicated by the line drawn on the beach. As noted above,

this shoreline is dependent upon the waves and tide at the site at the instant in time when the photograph was taken.

When analyzing shoreline change it is necessary to look at two dates. In addition to the 1992 date shown in Figure 3, we chose a set of photographs taken in 1955 as the second date. Figure 4 shows a pair of orthophotos at the same site for 1992 and 1955. The development that has taken place between these dates is clearly evident. In addition, the 1955 orthophoto was taken less than 12 months after Hurricane Hazel struck this coastline. Hazel (prior to Hurricane Fran in 1996) was the most severe storm to impact this shoreline in memory. The extremely wide overwash penetration shown on this photograph is due to that single storm. It is important to note that the absence on the 1955 photograph of most of the man-made features shown on the 1992 photograph makes it difficult to establish reasonable control for the earlier date.

Once we have identified the wet/dry line for the two different dates it is a relatively easy task to determine shoreline change. We use a technique developed by Dr. Robert Dolan (Dolan, et al. 1978). This technique uses an imaginary, shore parallel off-shore baseline as a reference line. The distance from this baseline to the shoreline is measured along an orthogonal drawn between the shoreline and the baseline. In our work we set these orthogonals at 150 ft intervals. Once the distance between the baseline and the shoreline is known for the two dates in question, it is a simple matter to compute the erosion/accretion rate.

Prior to our use of the digital orthophotos we used the more widely practiced techniques described by Dolan and others which depend upon less accurate corrections for the aerial photographs. In this prior method, ground control points for the photographs were identified using USGS topographic maps. Figure 5 illustrates the difference in erosion rates we found between these two methods at the study site. The difference is about 1 ft/yr. At this site, where the average erosion rate is about 3 ft/yr, this is a significant difference. Depending upon the site, this difference can be important when one attempts to use these data for shoreline management and construction permit programs.

The method to determine shoreline change described above is an essentially 2-dimensional technique. Since the digital image is stored in the computer as an 3-dimensional object, it is interesting to consider how one could determine shoreline change from this latter data. In this case

we work from a computer generated TIN. The TIN is a three dimensional wire diagram of the stereo image, as shown in Figure 6. The triangles connect points of known elevation.

From the TIN the software can generate cross-sections normal to the shoreline at any location. Figure 7 illustrates two such profiles, for 1955 and 1992. As an alternative to measuring the change in position in the wet/dry line, one can now measure the change in position of a specific elevation contour. For comparison, the wet/dry lines are also shown on this figure. Of course, the use of beach profiles to determine rates of shoreline change is not new. This is the normal procedure when working from field survey data. However, the ability to generate these profiles from digital historical aerial photographs is a relatively new procedure, and one worthy of future development.

Figure 8 illustrates the difference in erosion rates determined by these two methods. For this site the change in position of the wet/dry line between 1955 and 1992 yields a higher erosion rate than the method which is based upon the change in position for the 3 ft contour for these same dates. Note that the general trend in the data is consistent between the two methods. All things being equal, we feel that the erosion rate based upon the contour is preferable because it reduces the influence of the waves and tides on the data.

We are continuing to explore the pros and cons of the two methods to measure shoreline change. A rigorous test with field survey data is needed prior to making any conclusions regarding the preference of one over the other.

Draped Images

The discussion above has focused on the use of digital photogrammetry for measuring shoreline change. Another important use for this technology is the ability to generate realistic looking computer images of the beach. One way to generate such an image is to "drape" the orthophoto over the TIN, as shown in Figure 9. This image (shown here with a 5x vertical distortion) enables us to visualize the topography and see clearly the dunes, roads, houses, and vegetation. Such pictures are valuable both to the analyst as well as the general public. In the latter case these images can be used to help explain a problem, proposed solution, or probable impact. Again, since this is a digital image, it is

possible to easily change the scale, angle of viewing, and distortion as needed. We are currently working with these draped images to prepare a report which identifies areas most vulnerable to damage from severe storms.

Conclusions

While the application of digital photogrammetry to coastal engineering is new, it is already clear that this technology will provide important improvements to the field. In particular, the ability to generate orthophotos from historical aerial photographs will allow us to make more accurate determinations of rates of shoreline change. In addition, the computer generated images will create new tools for both shoreline managers as well as the general public to understand the nature of shoreline change.

Acknowledgments

The authors are greatly for the support this research has received from the Kenan Institute for Science and Technology, the NC Division of Emergency Management, the NC Division of Coastal Management, the NC Department of Transportation, the Federal Emergency Management Agency, and the Intergraph Corporation. In addition, we greatly appreciate the help from our research support staff, including Cheryl Hapke, Roger Grenier, Rob Hardy, Brian Joyner, and Beth Judge. Dr. Robert Dolan at the University of Virginia has been a valuable colleague in our work on this and related projects.

References

- Anders, F. J. and Byrnes, M. R., 1991. Accuracy of shoreline change rates as determined from maps and aerial photographs. Shore and Beach, 59 (1), 17-26.
- Dolan, R., Hayden, B. and Heywood, J., 1978. A new photogrammetric method for determining shoreline erosion. Coastal Engineering, 2:21-39.
- Fisher, J. S. and Overton, M. F., 1994. Interpretation of shoreline position from aerial photographs. Coastal Engineering 1994: Proceedings of the twenty-fourth international conference. Vol. 2, 1998-2003.

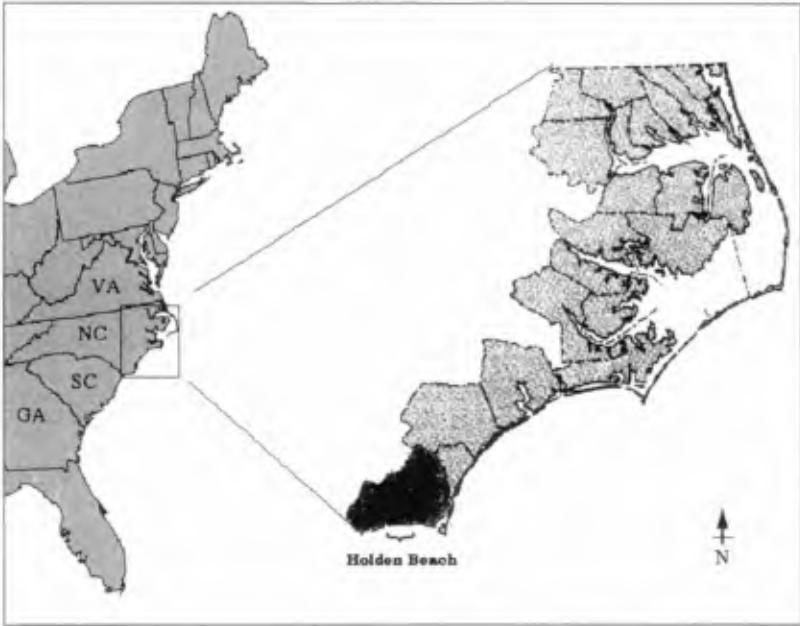


Figure 1. Project Study Area

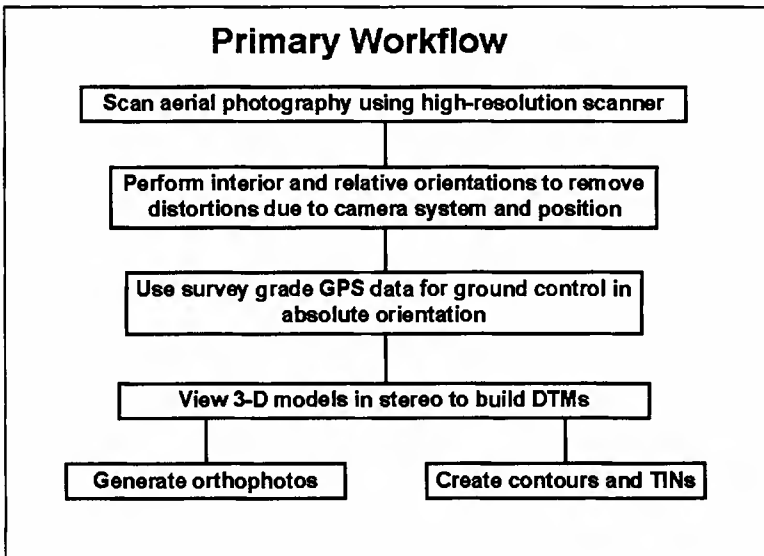


Figure 2. Project Workflow

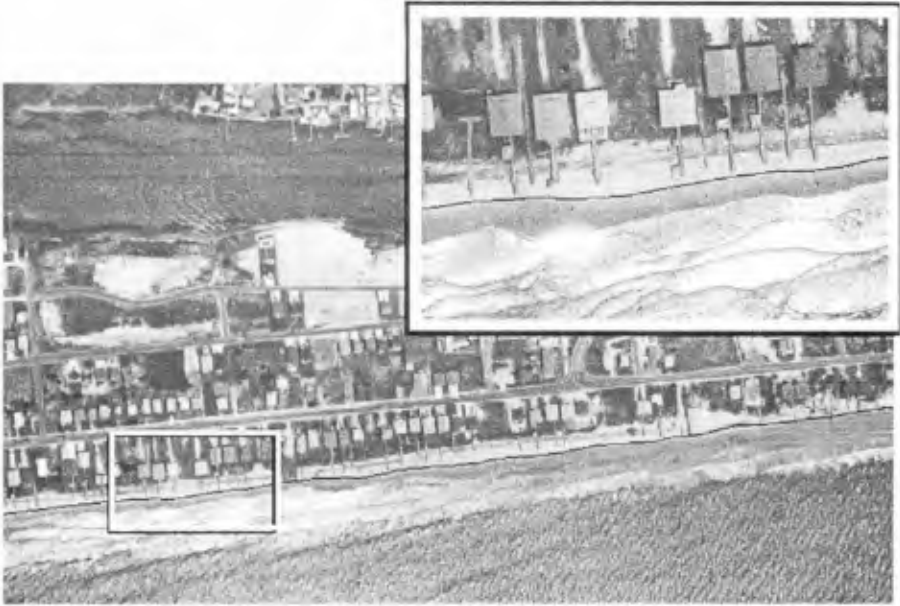


Figure 3. Holden Beach Orthophoto

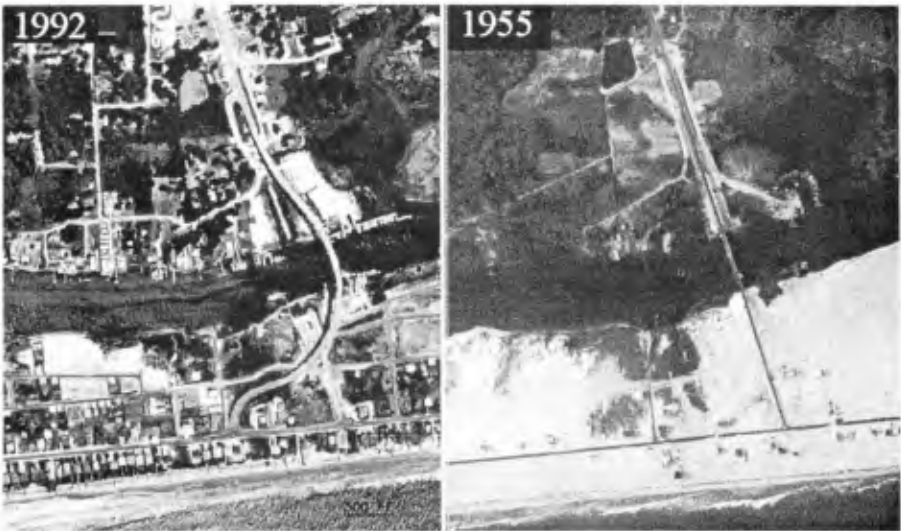


Figure 4. Holden Beach Orthophotos for 1992 and 1955

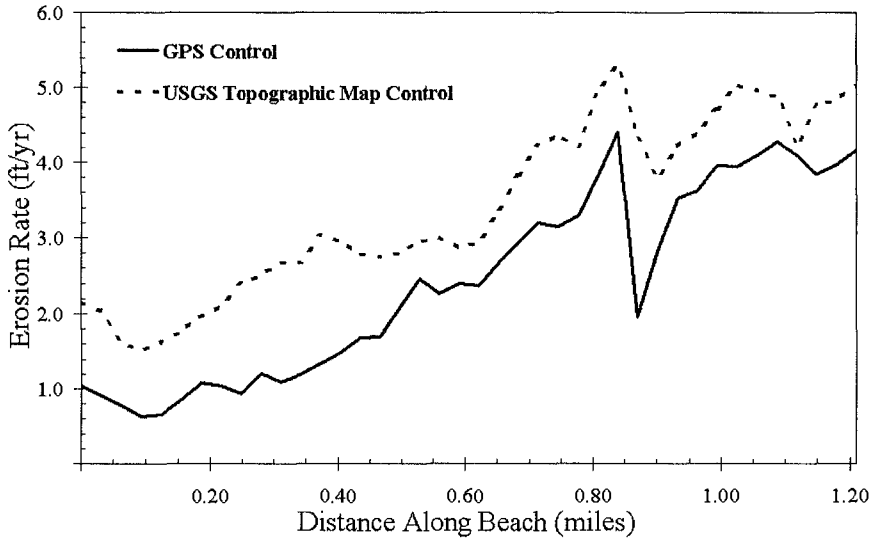


Figure 5. Comparison of Erosion Rates: Mapping Error

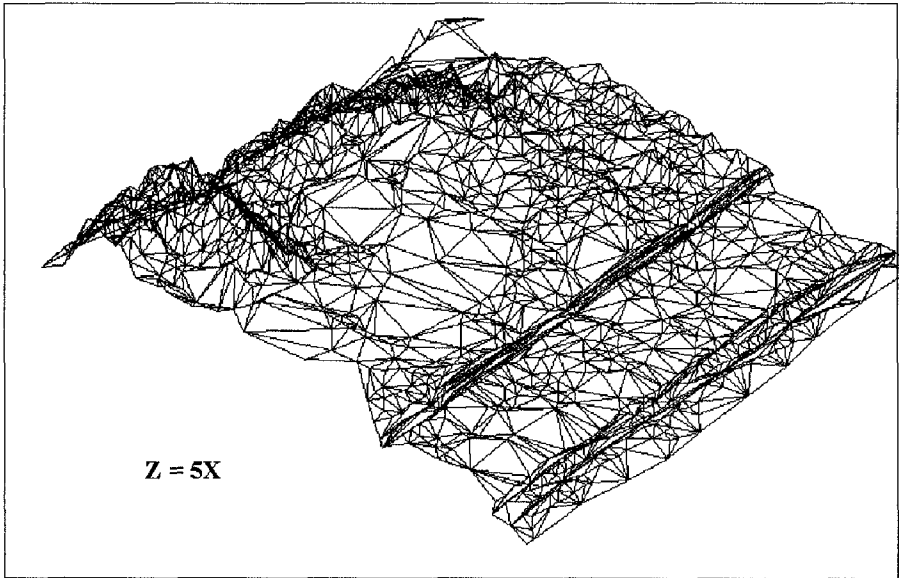


Figure 6. 1955 TIN for Study Site

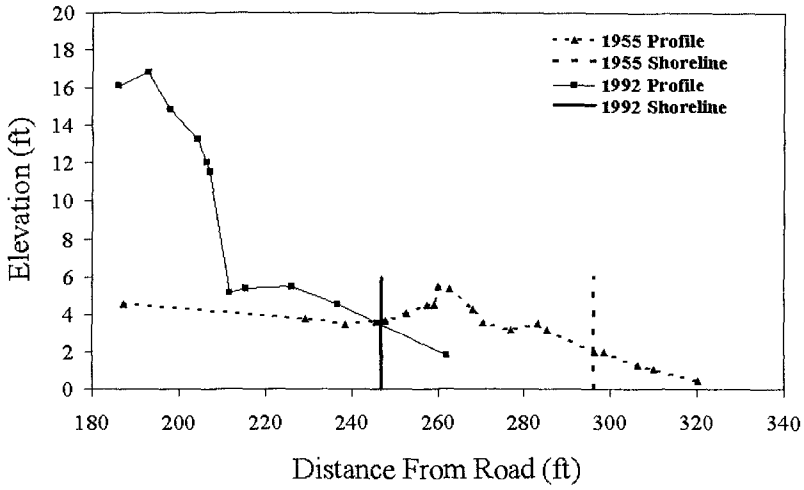


Figure 7. Computer Generated Shoreline Profiles

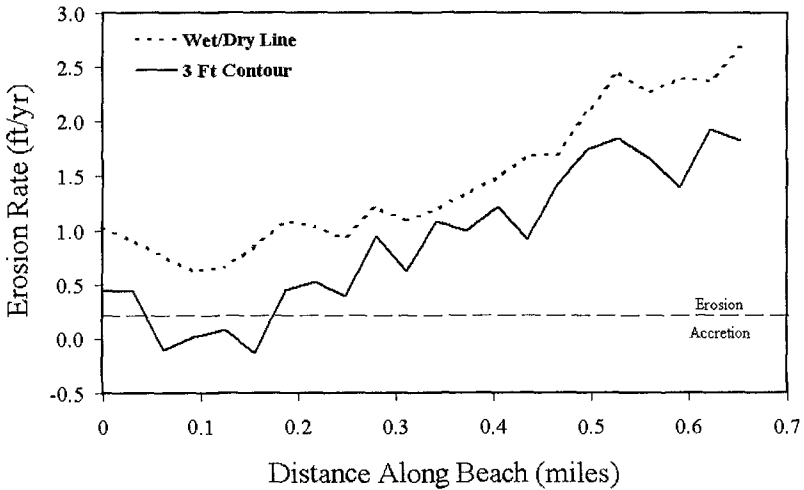


Figure 8. Comparison of Methods for Determining Erosion Rate

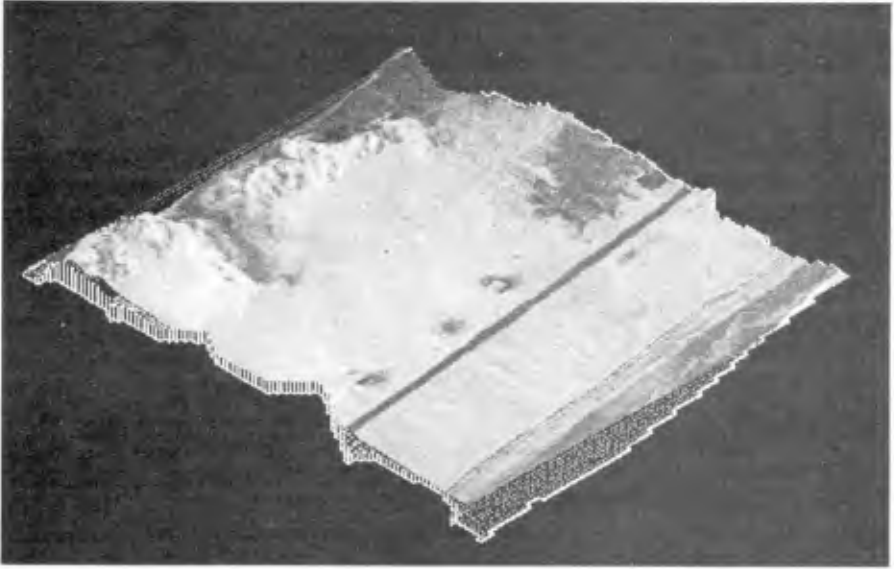


Figure 9. 1955 Orthophoto Draped Over Computer Generated Grid

CHAPTER 290

Application of Satellite Images to the Detection of Coastal Topography

Ji Wu¹ and Jea Tzyy Juang²

Abstract

Taking advantage of the high resolution visible images from the remotely sensed data of SPOT, the phenomenon of waves in the coastal area of Taichung was analyzed and its changing characteristics were studied. Changes of wave direction are affected by coastal topography; therefore, the changes of water depth can be detected by waves characters. In this study, the P band image data of SPOT of Taichung coast taken on 8th December 1993 was used. After dividing the area from deep to shallow into several blocks, each with 128x128 pixels, the wave images were transformed into two dimensional wave number spectra by ways of Fourier Transform. After that, the wave direction and the wave length were calculated. Results show that the shallower the water depth, the shorter the wave length; and the wave rays tend to approach shore normally. The phenomenon coincides with the theorem of wave dispersion. At last, based on the Snell's Law and the theory of shoaling, the average depth of each block was calculated. The results are encouraging.

Introduction

Remote sensing techniques have been developing rapidly since 1970. Since then, the LANDSAT, SEASAT and the SPOT satellites, have been launched and operated. The earth resources satellite receiving station in Taiwan was also installed in 1993.

¹ Assistant Researcher, Institute of Harbour & Marine Technology
No.83, Lin-Hai Rd., Wuchi, Taichung District, Taiwan, R.O.C.

² Deputy Director, Institute of Harbour & Marine Technology
No.83, Lin-Hai Rd., Wuchi, Taichung District, Taiwan, R.O.C.

In recent years, many researchers are using this new techniques to solve problems in the field of Oceanography, J. Populus (1991) used SPOT data to do the wave analysis. P.N. Bierwrith (1993) tried to detect depths on shallow water by studying the radiance of sea bottom reflectance. SPOT satellite is a sun-synchronous satellite with an average orbit height of 832 km. It passes Taiwan at 10:45 A.M. and reappears at the same track every 26 days. Since SPOT has the ability of inclined scan, we are able to get information of the same area every 3~5 days. The XS band image has a spatial resolution of 20 meters, and P band image has a spatial resolution of 10 meters. This study try to detect water depth at intermediate depth zone by using the characteristics of wave propagation.

Background Theory

The Dispersion equation states that

$$C^2 = \frac{g}{k} \tanh kh \quad (1)$$

where C : wave celerity
 σ : the angular frequency
 k : wave number
 g : gravitational acceleration
 h : depth

During the propagation of waves from deep sea to shallow water zone, wave height, wavelength and wave direction undergo changes due to changes of water depth. In region with intermediate water depth, we have

$$L = L_0 \tanh kh \quad ; \quad C = C_0 \tanh kh \quad (2)$$

where L_0, C_0 = wavelength & wave celerity in deep water

The irrotationality condition of wave number k yields

$$\frac{\partial(k \sin \theta)}{\partial x} - \frac{\partial(k \cos \theta)}{\partial y} = 0 \quad (3)$$

where θ is the angle between wave ray and the normal of coastline.

For a coast with straight and parallel contours, the changes of the wave direction obey the Snell's law :

$$\frac{\sin \theta}{c} = \frac{\sin \theta_0}{c_0} \quad (4)$$

By using all the above equations and the data from satellite image, the variations of the water depths at different locations can be estimated.

Techniques Used

Although the wave patterns are visible roughly in the satellite image, its real direction and wavelength can not be measured by eyes. Therefore, certain techniques of wave-number spectrum analysis using the two-dimensional Fourier transform are required. From the satellite image, we obtained the wave-number spectrum $S(k) = S(k_x, k_y)$. If $I(x, y)$ stands for the spatial intensity of the image, then the wave-number spectrum can be obtained by using the two-dimensional Fourier transform as

$$S(k_x, k_y) = \iint I(x, y) e^{-jk_x x - jk_y y} dx dy \quad (5)$$

When the spectrum peak was calculated, the wavelength and wave direction in each subregion can be determined as follows :

$$\frac{2\pi}{L} = k = \sqrt{k_x^2 + k_y^2} \quad ; \quad \theta = \tan^{-1}(k_x / k_y) \quad (6)$$

where k_x, k_y = the wave number components of the peak position on the spectrum diagram; θ = the angle between the wave direction and the Y-axis.

The above method is suitable for cases where wave phenomenon is simple and significant. If there is noise on the image scene, for example, a boundary of different water colors exists. We'll get a confused spectrum. In such cases we have to use special techniques, such as top-hat transform, to reduce the influence of noise. Fig.1 & Fig.2 show the comparison of the original image scene and the image after using Top-hat transformation, a detail flow chart of processing is shown in Fig.3.

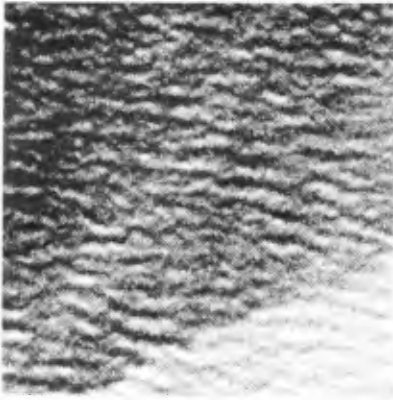


Fig. 1 Original image scene of the sea

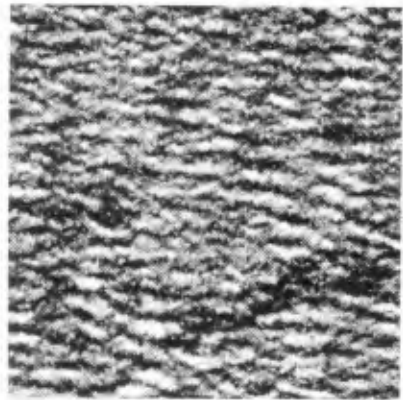


Fig. 2 Image scene after using Top-hat transformation

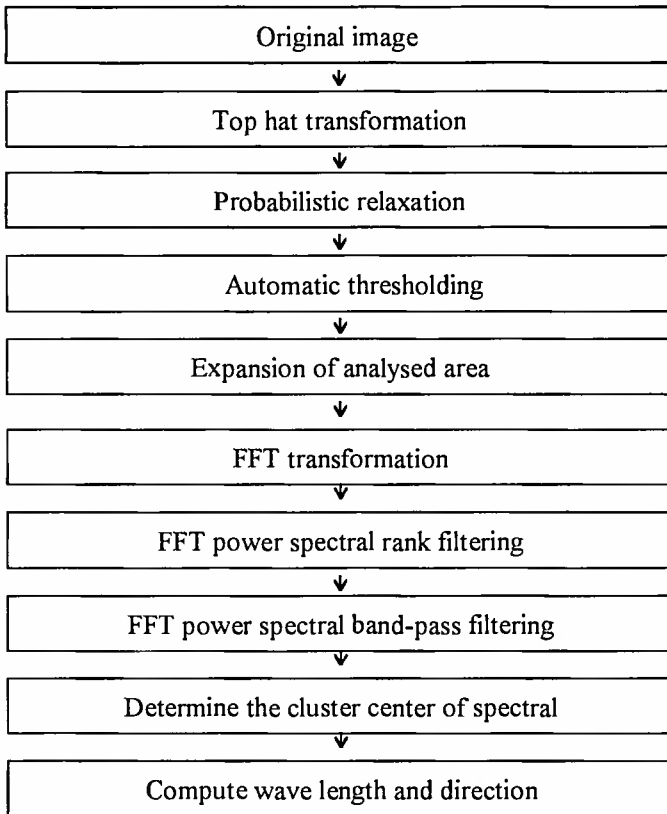


Fig. 3 Detail flow chart of processing



Fig. 4 Satellite images off Taichung Coast

Results

In this study, the Pan Band image data off Taichung Harbour on 8th December, 1993 were used (Fig.4), it covers an area of 18km x 12.5km. Taichung Harbour was built on 1970's, locate at the central western coast of Taiwan. From September to March, the winter monsoon season, the strong wind always blows from north. Therefore, the waves travel from the upper to the lower in Fig.4. The upper left corner is 9 kms away from coast and the depth is about 50 meters. The lower left corner is the outlet of Da-Du River and is quite shallow. Therefore we can observe the phenomenon of waves shoaling. After selecting and dividing some scope in the left part area from deep to shallow water and labelling them as A, B, ... S, with each block having 128x128 pixels, the wave image is then transformed into the wave-number spectrum.

Two example diagrams of the wave-number spectrum at block E (in deep water) and S (in shallow water) are shown in Fig.5 and Fig.6 respectively. In these figures, the longer the distance of the bright spot to the original point, the larger the wave number, which means shorter the wavelength.

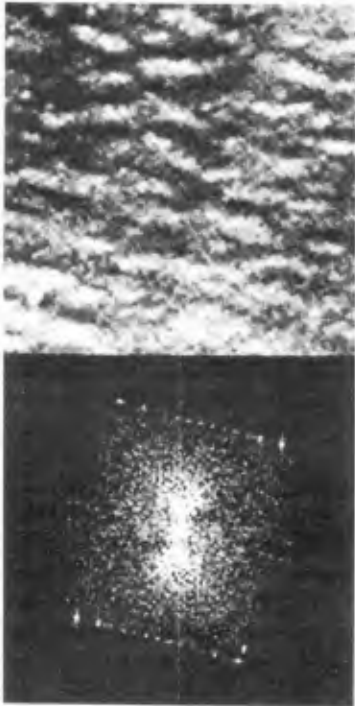


Fig. 5 Wave image & wave number spectrum at block E

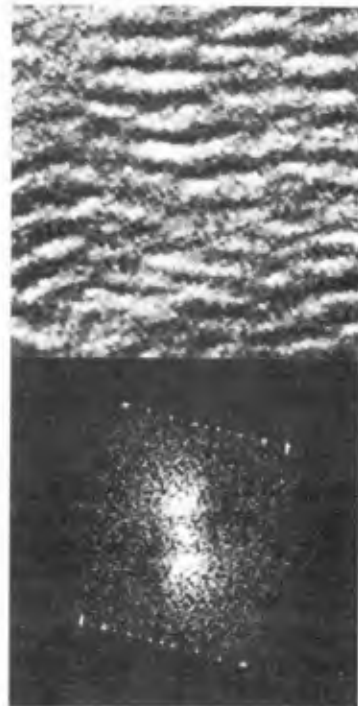


Fig. 6 Wave image & wave number spectrum at block S

From Table 1, we can see that the wavelength is decreasing and wave direction changes from 15° at block E to 350° at block S also. Fig.7 shows the variation of wavelength with wave direction from block E to block S.

Table 1 Results of water depth computation

Block	Wavelength	Wave direction 0° for N: clockwise	c/c_0	k	dp(m)	dr(m)
C	107	16	0.99	0.059	44	---
E	101	15	0.98	0.062	41	43
G	101	14	0.97	0.062	40	46
I	92	6	0.94	0.068	26	30
K	88	3	0.92	0.071	22	20
M	83	0	0.90	0.076	19	19
O	81	356	0.86	0.078	17	17
Q	75	353	0.83	0.083	14	15
S	68	350	0.80	0.092	12	10

Finally, the Snell's law of wave refraction and the small amplitude wave formula were used to compute the ratio of wave celerity from deep to shallow water and to predict the water depth at each block individually. Comparison of the predicted water depth (dp) and the measure's (dr) was also shown in Table 1 and Fig.8. The results are encouraging.

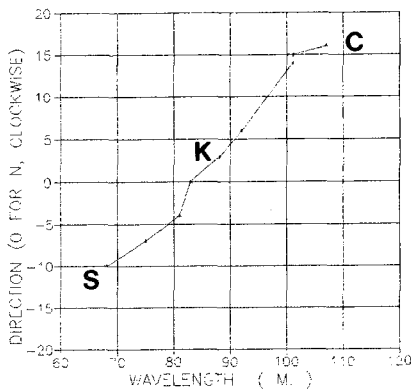


Fig. 7 Variation of wavelength with wave direction

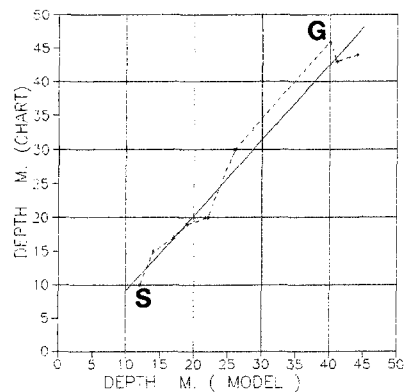


Fig. 8 Comparison of the predicted water depth and the measure's

Conclusions and Discussions

1. From the satellite image of the sea, we can get direct information of wave propagating from deep to shallow water, such as refraction, diffraction and reflection. It has the advantages of wide spatial information and lower cost, when compared to traditional field survey.
2. By combining Snell's law, dispersion relationship and spectral results, the bottom topography are easily derived. The results are encouraging.
3. The method used here takes the assumption of straight and parallel offshore contours; therefore the range of water depths can be estimated is within intermediate depth, i.e., from $L/2$ to $L/20$, where L is the wave length.
4. Block size influences the analyses. Larger block size provides better spectral resolution while causing more uncertainty due to shoaling effect. On the other hand, small block size has the problem of insufficient details. The present study uses a 128x128 pixel block size.
5. Effects of water color on the image may yield confusing in the detection of spectra. The top-hat transformation is used to reduce the influence of this factor.
6. SPOT Pan band images are used in the present spectral analyses. In comparison with most of the earlier works where SAR images were used, these images generally provides higher space resolution and lesser non-linear effects.

References

1. Bierwirth P. N., Lee T. J., and Burne R. V. "Shallow Sea-Floor Reflectance and Water Depth Derived by Unmixing Multispectral Imagery", Photogrammetric Engineering & Remote Sensing, Vol.59, No.3, pp.331-338, 1993.
2. J. Populus, C. Aristaghes, L. Jonsson, J. M. Augustin, and E. Pouliquen (1991) "The Use of SPOT Data for Wave Analysis", Remote Sens. Environ. 36:55-65.
3. J. Serra, "Image Analysts and Mathematical Morphology", London, Academic, 1982.

CHAPTER 291

SEDIMENT TRANSPORT IN SWASH ZONE UNDER OBLIQUELY INCIDENT WAVES

Toshiyuki Asano¹

ABSTRACT

Time dependent calculations on two-dimensional sediment transport are carried out. The swash wave front is treated as a moving boundary which can reproduce non-vanishing sediment transport rate even for landward region of the still water shoreline. Meanwhile, experimental investigations on this subject are conducted by florescent sand tracer method. By comparing the present and existing experimental results with the numerical ones, the sediment transport mechanism in the swash zone is discussed.

1. INTRODUCTION

Recently, swash zone has received much attention because the sediment process in this zone provides an important boundary condition for the entire beach evolution. And also, recent studies have reported that the alongshore sand transport takes bimodal distribution with maxima at the swash zone as well as near the breaking point(White-Inman (1986), Bodge-Dean (1987)). Under obliquely incident waves, sediment near shoreline moves in a zig-zag way which results in the inherent alongshore transport in the swash zone. Intensive turbulence generated in uprush and backwash waves causes a large volume of sediment in suspension. However, these mechanisms have not been sufficiently understood.

The author proposed a horizontally two-dimensional shallow water wave model for predicting the free surface elevation and fluid velocities in the swash and surf zone under obliquely incident waves (Asano, 1994). The

¹ Associate Professor, Dept. of Ocean Civil Engrg., Kagoshima Univ., 1-21-40, Korimoto, Kagoshima, 890, JAPAN

sediment movement in swash zone should be described in a time dependent way because the bed is immersed and dried alternatively corresponding to run-up and run-down motion. The objective of this work is to improve the understanding of sediment transport in the swash zone by numerical analysis as well as experimental investigations focusing on the alongshore transport rate.

2. NUMERICAL ANALYSIS

(a) Two dimensional velocity fields in swash zone

The author has presented the numerical model for the two-dimensional velocity field in a swash zone (Asano, 1994). The outline of the calculations is as follows:

Two dimensional coordinate system is considered where x- and y- axis is chosen to be in the normal and the parallel direction to the shoreline, respectively. The z-axis is taken positive upward with z=0 at the still water shoreline. The beach slope *S* is herein restricted to be uniform and its contour is straight and parallel to the shoreline. The incident monochromatic waves with straight parallel crests are assumed to arrive at the seaward boundary with an angle θ_B .

The basic equations are two-dimensional shallow water equations with a moving boundary at the front of wave runup. Ryrie's(1983) method is applied in order to obtain simplified equations. That is, the wave crest is straight parallel and bottom topography does not vary in y-direction, the observed wave motion moving along the alongshore direction at the speed $C/\sin\theta$ becomes independent in the y-direction. By introducing pseudo-time $\hat{t} = t - (\sin\theta_B / C_B)y$ to unify two independent variable t and y, and assuming the incident wave angle θ_B is small enough to be used as a small parameter, the basic equations are decoupled into independent equations both for longshore motion and cross shore motion.

(b) Particle trajectory in swash zone

Instantaneous behavior of a single spherical particle placed on a uniform slope is simulated under two-dimensional swash motion calculated in the above mentioned model. The momentum equation for the particle is given by

$$\begin{aligned}
 (\rho_s/\rho + C_A)A_3d^3\dot{u}_s = & \frac{1}{2}C_D A_2 d^2 |\mathbf{u} - \mathbf{u}_s| (\mathbf{u} - \mathbf{u}_s) \\
 & + (1 + C_A)A_3d^3\dot{u} - (\rho_s/\rho - 1)A_3gd^3 \sin S \\
 & - (\rho_s/\rho - 1)A_3gd^3 \tan \phi \cos S \dots\dots\dots (1)
 \end{aligned}$$

in which, *g*: gravitational acceleration, ρ and ρ_s : specific gravity of water and sediment, *d*: sediment particle diameter, A_2, A_3 : 2- and 3- dimensional shape factor of sediment particle, ϕ : internal friction angel, C_A, C_D : added

mass and drag coefficient, u , u_s : fluid and sediment particle velocity vector, respectively.

Since the fluid velocity u has been obtained at every calculation grid, interpolation is needed to calculate u at the point sediment particle locates. The instantaneous position of the particle can be calculated by integrating sediment particle velocity u_s with a time increment of $1/1000$ of the wave period.

Fig. 1 shows one example of the calculated trajectories of a single particle placed on a relatively steep slope $S=0.4$ to emphasize the gravitational effect. Here, x - and y - axis is chosen to be in the normal and parallel direction to the shoreline, respectively. The results reproduce the zig-zag transport under which a particle is conveyed onshore with a certain angle to the shoreline, then transported offshore with greater angle due to the gravity.

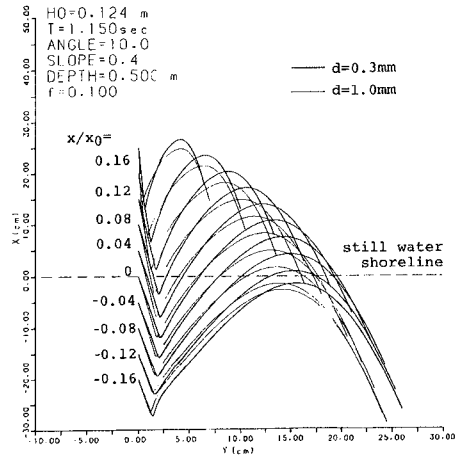


Fig. 1

Trajectories of a sediment particle
in a swash zone

(c) Sediment Transport Rate

Instantaneous sediment transport rate was calculated based on Kobayashi's (1982) bed load formula, which accounts for the effect of a slope explicitly. In the model, the composing forces acting on a spherical particle are the submerged weight, frictional force, fluid drag and lift forces. An inertia force acting on the particle was neglected in the model for simplicity.

To illustrate the external force of a sediment particle, the temporal variations of on-offshore velocity at the still water shoreline $x=0$ are shown in Fig. 2. The parameter of Fig. 2 (a) and (b) is the wave period T and the slope steepness S , respectively. The results show that each velocity fluctuation in swash zone rapidly increases at a passage of bore-like crest, and has long lasting backwash motion. Even though the incident wave height is same in the figures, the breaking wave height H_b will change by the parameter T and S , and that leads to different set-up height at the still water shoreline. The magnitude of the backwash flow is found to be large because the precedent onshore mass flux should be returned through a thin backwash flow. These figures show greater integrated areas in the offshore direction than those in the onshore direction.

The variations of sediment transport rate reflect the velocity variations shown above. Fig. 3(a),(b) illustrates the instantaneous on-offshore transport rates q_s/wd (w : sediment fall velocity) at the still water shoreline $x=0$. At the limit of horizontal bed, Kobayashi's formula yields that the sediment

transport rate is proportional to the Shields number $\Psi(t)$ to the power of 1.5 (3rd power of the instantaneous fluid velocity). As a result, the curves of sediment transport rate in Fig. 3 show steeper peaks than those in Fig. 2. Fig. 3(b) shows the results with a slope steepness S as a parameter. The steeper the bottom slope, the sharper the onshore transport fluctuations and the greater and the longer the offshore transport fluctuations.

Fig. 4 depicts the instantaneous alongshore transport rate q_y . The alongshore transport is generated mainly during wave up-rush under mild slope condition. Meanwhile, under steep slope condition, a large amount of alongshore transport is observed during down-rush.

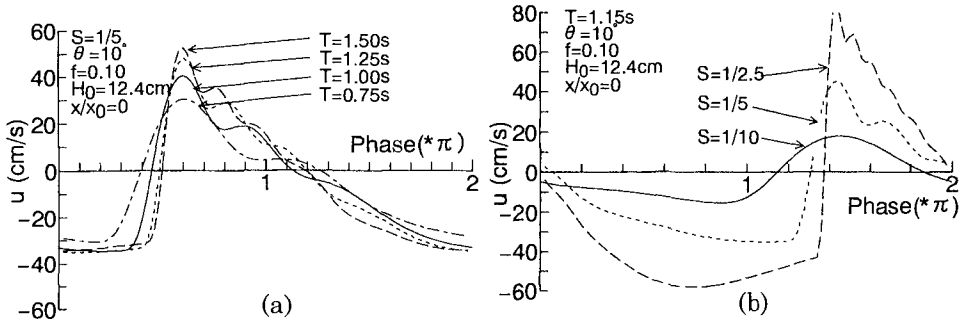


Fig. 2 Temporal variations of on-offshore velocity at $x/x_0 = 0$

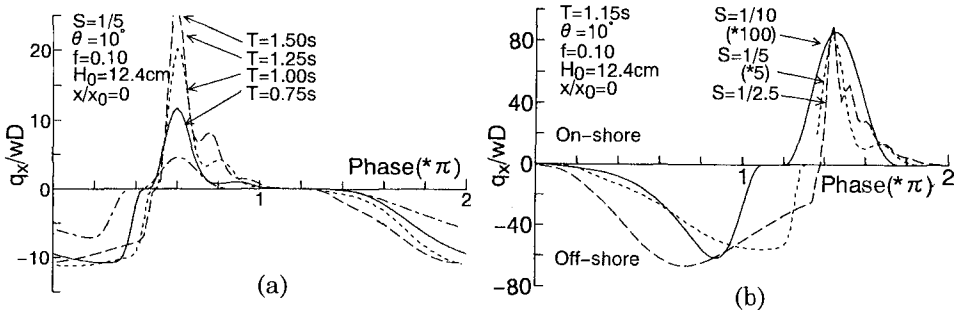


Fig. 3 Temporal variations of on-offshore sediment transport rate at $x/x_0 = 0$

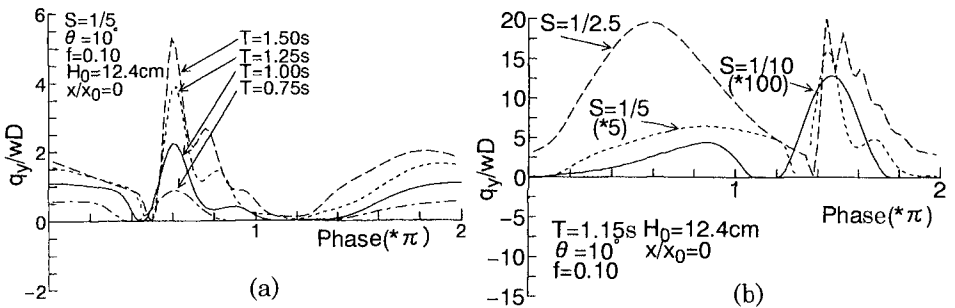


Fig. 4 Temporal variations of alongshore sediment transport rate at $x/x_0 = 0$

Fig. 5 and Fig. 6 depicts spatial variations of time averaged on-offshore and alongshore sediment transport rates Q_x, Q_y , respectively. The positive direction of the abscissa is taken in the onshore direction from S.W.S.L.. It is recognized that substantial values both for Q_x and Q_y are observed even in the onshore region of the shoreline. The time dependent calculation treating the swash wave front as a moving boundary is able to reproduce non-vanishing transport rates both Q_x and Q_y in the region $x/x_0 > 0$. These figures show that Q_x are offshore direction except for the mildest case $S=1/20$, and Q_y decreases monotonously toward the onshore direction, hence, no bi-modal peak around the shoreline is obtained.

(d) Comparison with Conventional Experimental Data

Kamphuis(1990) conducted three-dimensional mobile bed experiments, and investigated alongshore sediment transport rate in swash zone as well as surf zone. Most distributions of his data exhibited bimodal with one peak close to the breaking zone and another in the swash zone. One example of his data is shown in Fig. 7. The ratio of suspended load and bed load throughout his tests showed roughly constant for the entire region, even near the breaking point where suspend load is expected to be predominant.

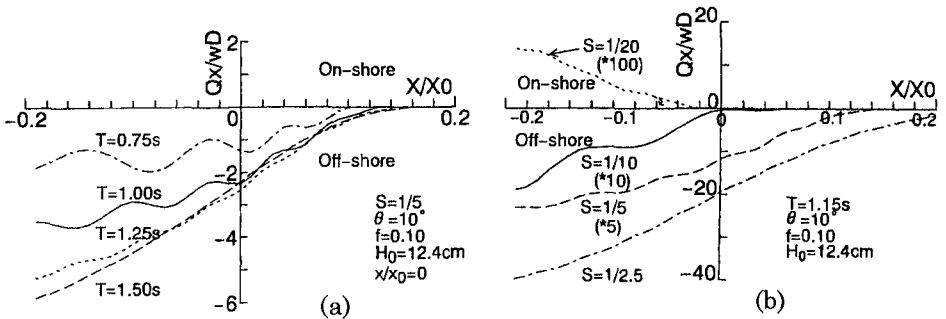


Fig. 5 Spatial variations of time averaged on-offshore sediment transport rate

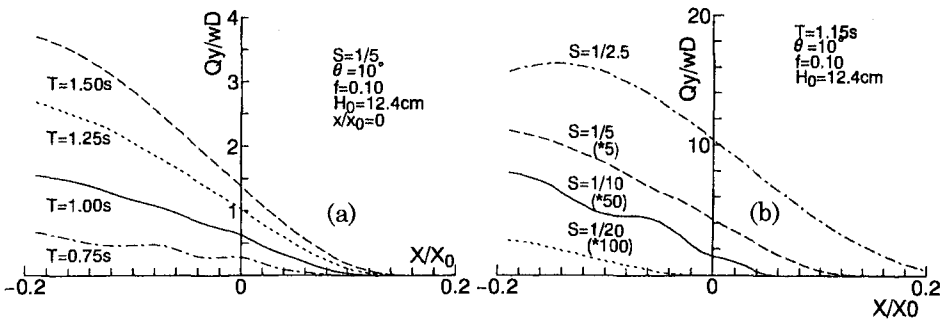


Fig. 6 Spatial variations of time averaged alongshore sediment transport rate

Comparisons with the present calculation under the same input condition of Kamphuis's experiment have revealed that his results were 2 order greater than the calculated results. Fig. 7 shows one of the results where the transport rate Q_y at still water shore line $x=0$ for the bed load was around 17kg/m/hr in its immersed weight. Converting into a non-dimensional transport rate Q_y/wd , this amount corresponds to 1.06, while the calculated rate is 0.029.

Sunamura(1984) measured on-offshore sediment transport rate focusing on the swash zone in a two-dimensional wave tank. Based on the results, he proposed a transport rate formula for the swash zone. Comparisons between the calculated on-offshore sediment transport rates Q_x at $x=0$ with those of Sunamura's empirical formula are shown in Fig. 8, in which the parameter H_0, T, d is the incident wave height, wave period and sediment diameter, respectively.

Qualitative agreements are fairly good in all the figures, but some discrepancies are found. In Fig. 8(a), Sunamura's formula predicts positive Q_x values for small wave height, which implies onshore sediment transport corresponding accretional beach formation. Meanwhile the calculated Q_x also decreases to zero with decreasing of wave tractive force but the direction is still offshoreward.

The present calculations deal only with bed load transport under non-breaking waves. Large amount of sediment will be suspended by the vortex when the backwash collides with the incoming bore. The discrepancy from the empirical formula suggests the significant contribution of the generated vortex.

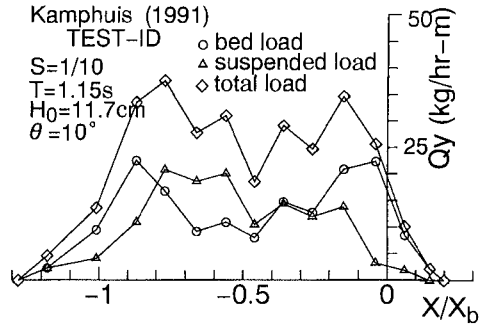


Fig. 7 Distributions of alongshore sediment transport rate (Kamphuis, 1991)

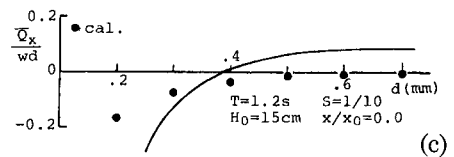
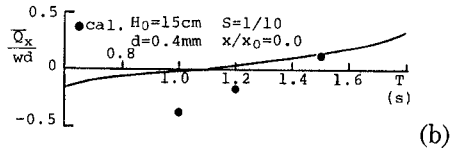
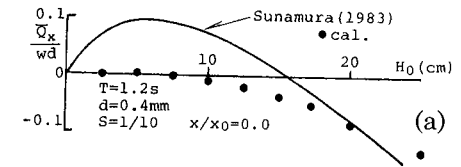


Fig. 8 Comparison of calculated on-offshore sediment transport rate with Sunamura's(1984) formula

3. EXPERIMENTAL STUDY

(a) Experimental Apparatus

The wave tank used here was 26.7m long, 13m wide and 1.2m deep wave basin in Dept. of Ocean Civil Engrg., Kagoshima Univ.(Fig. 8). In this section, the x-axis is taken positive in the offshore direction with the origin $x=0$ at the still water shoreline. The y-axis is taken in the alongshore direction. A uniform concrete slope of gradient $S=1/7.5$ was set up at an angle $\theta=15^\circ$ with a wave generator equipped at the other end of the basin. The uniform water depth in the offshore region was kept at constant 79cm throughout the experiments.

Ten capacitance type wave gauges were used, one for the offshore waves, and nine were set in an array on the slope from 210cm offshore to 40cm onshore of the still water shoreline(S.W.S.L.), which covered the surf and swash zone. The wave gauges were inserted into slit holes, which were ditched in order to maintain small water depth even when the bed was dried up at the downrush phase.

A 10mm thick sand layer extending 1.0m width by 3.2m length was laid on the mortar bed. The sand used here was clastic sediment particle originated from igneous rock, of which diameter d was 0.9mm and specific gravity s was 2.96.

Table-1 Test conditions

	H_i (cm)	T (s)	x_b (cm)	W_w (cm)	ξ
CASE-5	6.4	2.5	-70	85	1.65
CASE-6	7.9	2.0	-60	70	1.19
CASE-7	3.3	3.0	-70	100	2.75
CASE-8	7.5	1.5	-65	65	0.91

(b) Experimental Procedures

Measurements using the florescent sand tracer were conducted at 16 points with 15cm intervals in the range between $x=150$ cm offshore and $x=-75$ cm onshore of S.W.S.L. First, natural undyed sand was laid and leveled its surface accurately. Then, using a core sampler of 36mm inner-diameter and a thin spatula, a cylindrical sand mass was removed. Instead of this, a cylindrical plug of florescent colored sand was buried. After one minute wave action on the sand bed, core samples were collected at 16 points each for two concentric circles of 20cm and 40cm radius.

The samples were evaporated in a drying oven, then, weighed on a precision balance. Meanwhile, the weight

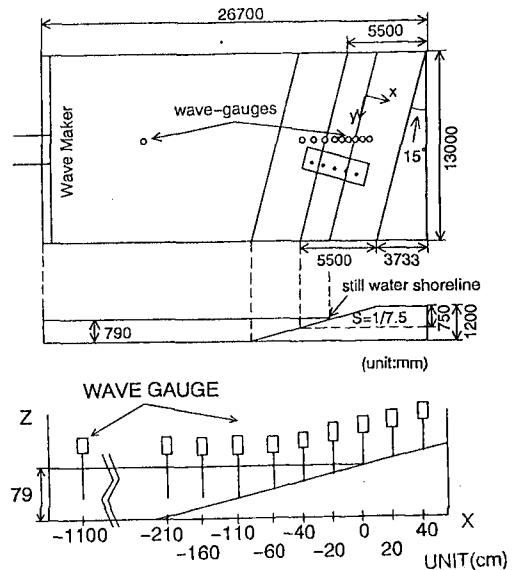


Fig. 8 Wave tank

of dyed sand was estimated by the number which was determined by visual counting under ultraviolet illumination. For this conversion, a calibration curve between the number of particles and its weight was determined beforehand. The final results were arranged in volumetric concentration; the occupation ratio of dyed sand against the whole sand.

Assuming advection is predominant, the sediment transport velocity was estimated in the following way. If a particle initially located at the center moves to the position (r, θ) after Δt time, the traveling velocity for on-offshore and alongshore direction u_s, v_s will be given by $r \cos \theta / \Delta t, r \sin \theta / \Delta t$, respectively. The representative sediment transport velocity was estimated by spatial averaging as follows:

$$\begin{aligned}
 u_s &= \frac{\iint c(r, \theta) \frac{r \cos \theta}{\Delta t} dS}{\iint c(r, \theta) dS} = \frac{\int_0^\infty \int_0^{2\pi} c(r, \theta) \frac{r \cos \theta}{\Delta t} r d\theta dr}{\int_0^\infty \int_0^{2\pi} c(r, \theta) r d\theta dr} \\
 v_s &= \frac{\iint c(r, \theta) \frac{r \sin \theta}{\Delta t} dS}{\iint c(r, \theta) dS} = \frac{\int_0^\infty \int_0^{2\pi} c(r, \theta) \frac{r \sin \theta}{\Delta t} r d\theta dr}{\int_0^\infty \int_0^{2\pi} c(r, \theta) r d\theta dr} \quad (2)
 \end{aligned}$$

However, the number of the measuring points was restricted as 16 for each concentric circle, 32 in total, thus the estimation for u_s, v_s was actually carried out by the following equations.

$$\begin{aligned}
 u_s &= \frac{\sum_{i=1}^{16} c_i \frac{r_1^2 \cos \theta}{\Delta t} + \sum_{j=1}^{16} c_j \frac{r_2^2 \cos \theta}{\Delta t}}{\left(\sum_{i=1}^{16} c_i \right) r_1 + \left(\sum_{j=1}^{16} c_j \right) r_2} \\
 v_s &= \frac{\sum_{i=1}^{16} c_i \frac{r_1^2 \sin \theta}{\Delta t} + \sum_{j=1}^{16} c_j \frac{r_2^2 \sin \theta}{\Delta t}}{\left(\sum_{i=1}^{16} c_i \right) r_1 + \left(\sum_{j=1}^{16} c_j \right) r_2} \quad (3)
 \end{aligned}$$

The test conditions are summarized in Table-1, in which H_i is the incident wave height in uniform depth region, x_b is the location of breaking wave, and W_u is the maximum run-up distance on the slope obtained by eye-measurements.

(c) Wave characteristics on a slope

Fig.9 shows the water surface fluctuations at each measuring point from offshore to onshore. From the fluctuation records, the following parameters were defined to describe the sediment transport; wave height, skewness (asymmetry in respect of horizontal level), asymmetry (asymmetry in respect of center line).

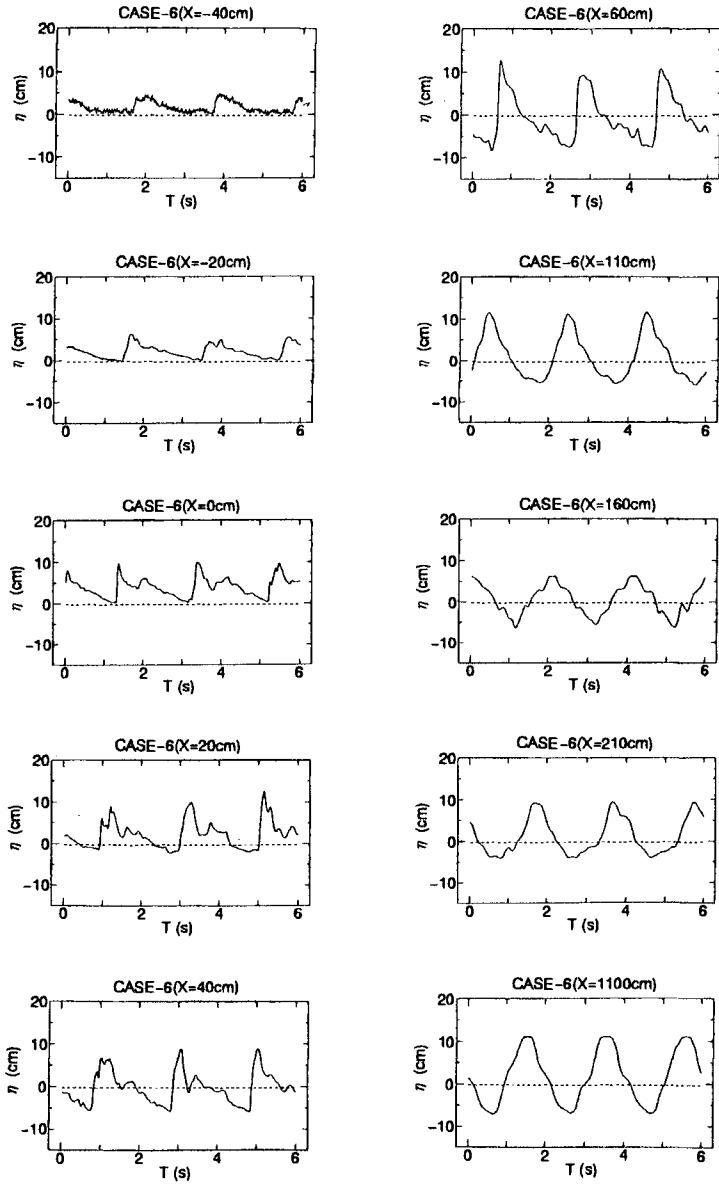


Fig. 9 Measured water surface fluctuations

The definitions of skewness $H(\text{cm})$ and asymmetry are given by

$$\text{skewness} = \frac{1}{\eta_{rms}^3} \overline{(\eta - \bar{\eta})^3}$$

$$\text{asymmetry} = (t_{peak} - t_0) / T$$

in which, η : water surface fluctuation, η_{rms} : root mean square of η , t_0 : time at the lowest water surface fluctuation, t_{peak} : time at the succeeding fluctuation peak.

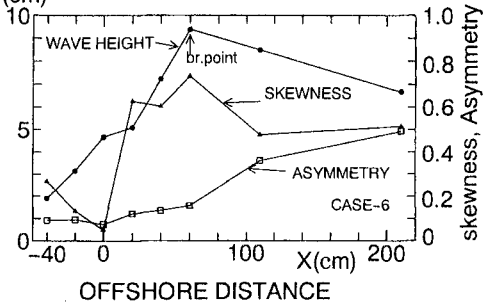


Fig. 10 Spatial variations of wave profile properties

Fig. 10 illustrates that *skewness* becomes small in the swash zone where the water surface fluctuation shows bore-like variation. Meanwhile, *asymmetry* monotonously decreases toward onshore. This sudden increase of wave profile will cause significant onshore-ward sediment transport in the swash region.

(d)Transport velocity determined by tracers

Fig. 11 shows an example of directional distribution of florescent sand concentration. Onshore transport predominance in the offshore region of the breaking point(in this case;x=70cm), alongshore transport in the surf region, and onshore transport around still water shoreline (x=0) are observed. Large scattering was found in the surf zone, where not only advection but diffusion contributes the tracer transport.

The sediment transport velocities estimated from Eq. (3) are plotted in a vector form(Fig. 12). In the figure, the solid vector indicates the data where more than 10 florescent sands were sampled, the dotted vector points out the data where 6 ~ 10 florescent sands were found (less reliable). Following characteristics are obtained:

In the offshore region of the breaking point(B.P) sediment is transported onshore because the velocity fluctuations are skewed in the onshore direction.

In the region between the breaking point and still water shoreline, alongshore transport is predominant. This is due to generated longshore current in this region. For on-offshore transport, the onward sediment transport due to the skewness of velocity fluctuation may be almost canceled by offshore transport due to an undertow generated near the bottom.

In the swash zone, the transport direction is offshore (except for CASE-7). Since water mass running up on a slope will be returned in a thin layer flow, the velocity of the return flow becomes large enough to transport the sediment offshore in averaging over a period.

The result of CASE-7 is slightly different from others especially in the swash zone, it could be because the wave period was the longest among all the cases, so the breaking type became collapsing (surf similarity parameter in this case $\xi = 2.75$) which breaks suddenly close to the shoreline.

(e) Comparison with the calculated transport velocity

In order to check the validity of the experimental results, calculations based on Kobayashi's formula are performed under the same input condition as the experiments. The results are illustrated in Fig. 13. All of the on-offshore components of transport velocity vector direct offshore. This directional property agrees with the experiment in the swash zone, but disagree in the surf zone and offshore zone.

The comparison also shows the discrepancy in the magnitude of transport velocity. For the experiment, most of the results ranges 0.3 ~ 0.4cm/s, and maximum is 0.66cm/s, which is so small compared to the calculation. In terms of a ratio to the generated longshore current velocity, the data were not so small, but agreed with existing field data. Nadaoka et al.(1981) reported that the sand transport velocity was less than 1.0cm/s, which corresponded to 1 ~ 2 % of the observed longshore velocity.

Several reasons can be considered to explain the difference. One would be due to the large grain size. In this experiment, relatively coarse sand $d=0.9\text{mm}$ was used. This might be beyond the applicability of Kobayashi formula which calibrated with existing data using medium and fine sand. The run-up waves propagate on a slope with generating much turbulence at the front. In the numerical model, the velocity field is treated as uniform and no-turbulence, the predictability of sediment transport in the swash zone is severely restricted.

4. CONCLUSIONS

- (1) Analysis on single particle trajectory reproduces the zig-zag sediment movement, which is inherent transport mechanism in the swash zone.
- (2) The time dependent analysis treating the swash wave front as a moving boundary enable the calculation to reproduce the swash zone sediment transport. Non-vanishing transport rates both for on-offshore and alongshore directions have been obtained even for the onshore region of the still water shoreline.
- (3) From the experiments using florescent sand tracers, the sediment transport in the swash zone is comparable in the magnitude with those in the surf zone, and to be directed generally offshore. The offshore transport can be explained due to the strong backwash flow prevailing over the onshore flow generated at a passage of bore-like front.

- (4) The present model postulates uniform velocity distribution and no turbulence. Quantitatively, the model could not reproduce the sediment transport rate in the existing and present experiments. For improving model to describe sediment transport in a swash zone, vortex and turbulence roles for sediment stirring up mechanism should be included.

REFERENCES

- Asano, T. H. Suetomi and J. Hoshikura(1994): Measurements of current velocity generated in swash zone by obliquely incident waves, Coastal Engrg., in Japan, Vol. 37, No. 2, pp.125-136.
- Asano, T. (1994): Swash motion due to obliquely incident waves, Proc. of 24 th I.C.C.E., ASCE, Vol.1, pp.27-41.
- Bodge, K. R. and R. G. Dean(1987): Short-term impoundment of longshore transport, Proc. of Coastal Sediment '87, pp.468-483.
- Kamphuis, J.W. (1991): Alongshore sediment transport rate distribution, Proc. of Coastal Sediment'91, pp.170-183.
- Kobayashi, N. (1982): Sediment transport on a gentle slope due to waves, J. Waterways, Port, Coastal and Ocean Div., Vol. 108, No. WW3, pp.254-271.
- Ryrie, S. C. (1983): Longshore motion generated on beaches by obliquely incident bores, J. Fluid Mech., Vol. 129, pp.193-212.
- Sunamura, T. (1984): Onshore-offshore sediment transport rate in the swash zone of a steeply inclined laboratory beach, Ann. Rep., Inst. Geosci., Univ. Tsukuba, No.10, p.69-72.
- White, T.E. and D. L. Inman(1989): Measuring alongshore transport with tracers, Nearshore Sediment Transport, Edited by R. J. Seymore, Plenum Press, pp.287-312.

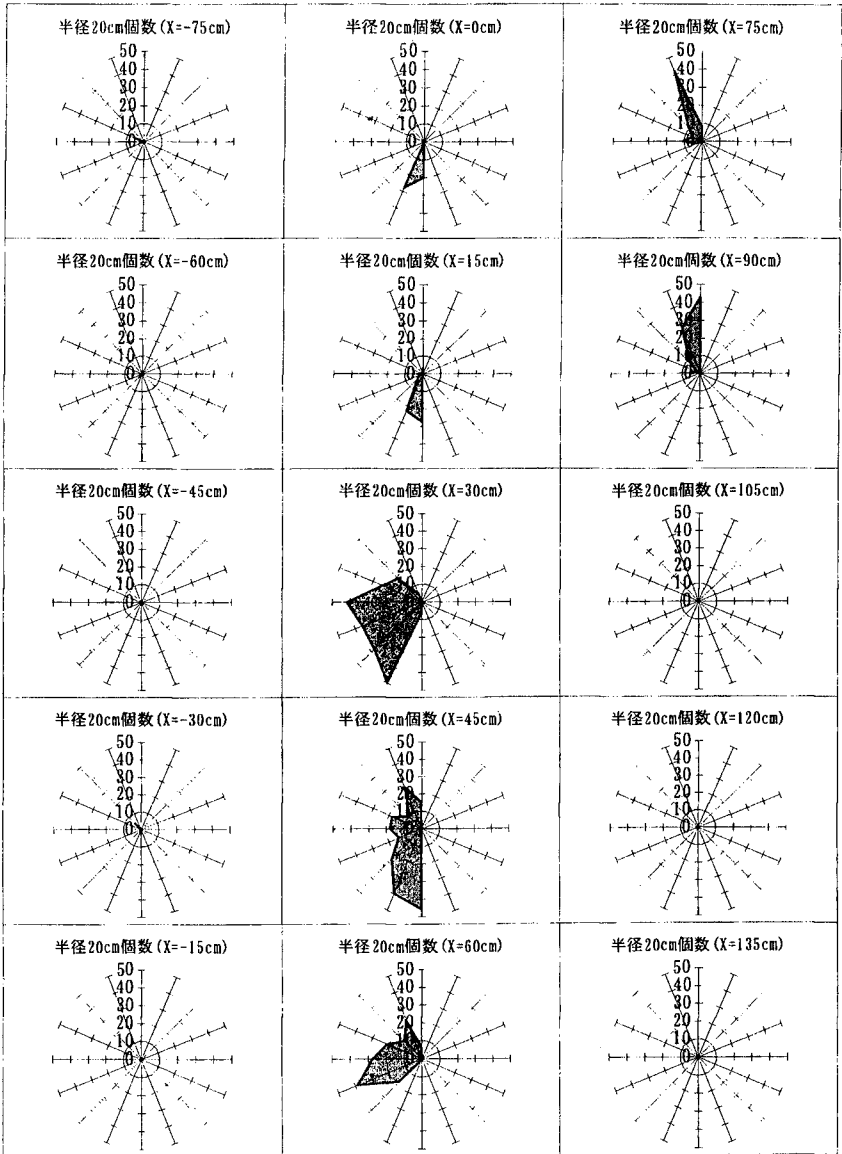


Fig. 11 Directional distributions of florescent sand tracers

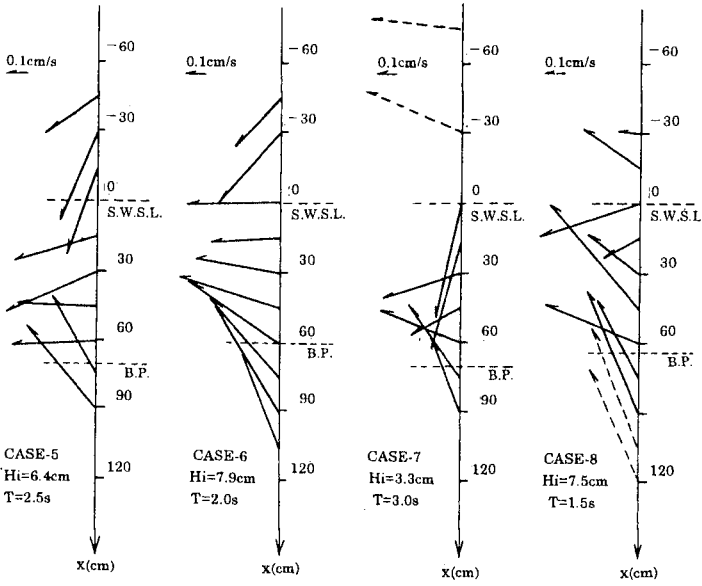


Fig. 12 Measured sediment transport velocity vectors

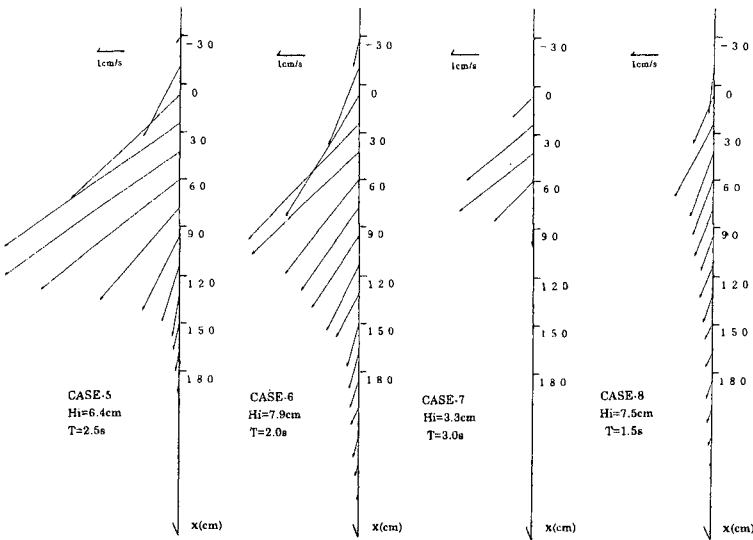


Fig. 13 Calculated sediment transport velocity vectors

CHAPTER 292

Sheet Flow Modelled as Pure Convection

Stephen Clark¹
Peter Nielsen²

Abstract

A considerable amount of experimental data regarding the transport of sand under violent wave conditions (specifically the sheet flow regime) has been gathered in recent years. Historically, modelling of the concentration distributions of the suspended sediments immediately above the sheet flow layer has been undertaken using the diffusion equation. A physically more appropriate model is the combined convection diffusion approach. However, analysis of the experimental results to date indicate that a pure convection which is far simpler than either of the other two is adequate.

Introduction

The transport of sand under violent wave conditions with Shield's parameter values greater than one is often described by the term sheet flow because no bedforms survive through the wave cycles and a layer (sheet) of sand, many grain diameters thick, can be seen to move back and forth with the wave motion.

A considerable amount of experimental details of the process have been gathered in recent years by Ribberink and co-workers (1992). However, modelling of the process is still inadequate. This paper concentrates on the "upper" or suspended part of the sediment distribution. Traditionally, concentration distributions have been modelled using forms of the diffusion equation. As will be presented below, analysis of experimental results indicates that a combined

¹ Senior Engineer, Lawson & Treloar, PO Box 115, Ashgrove, Queensland, Australia 4060.

² Reader, Dept of Civil Engineering, University of Queensland, Australia, 4072.

convection diffusion model or in some cases a pure convection model appears to be adequate.

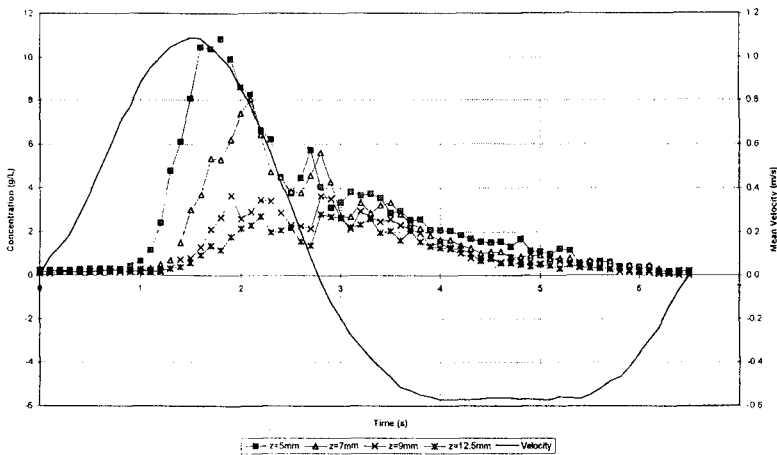
Experimental Data

A series of experiments have been conducted in the Large Oscillating Water Tunnel (LOWT) of Delft Hydraulics which have focussed on both time averaged and time dependant near bed and within bed sediment concentrations and sediment transport rates.

Flow conditions investigated have ranged from purely sinusoidal to regular, asymmetric waves over both rippled and plane beds. Sediments investigated have been predominantly sands with a $D_{50} = 0.2$ mm. An additional set of experiments have been conducted using a finer sand $D_{50} = 0.12$ mm.

Figure 1 provides an example of the results obtained through this procedure (Ribberink et al, 1992).

Figure 1: Experiment C8 Results

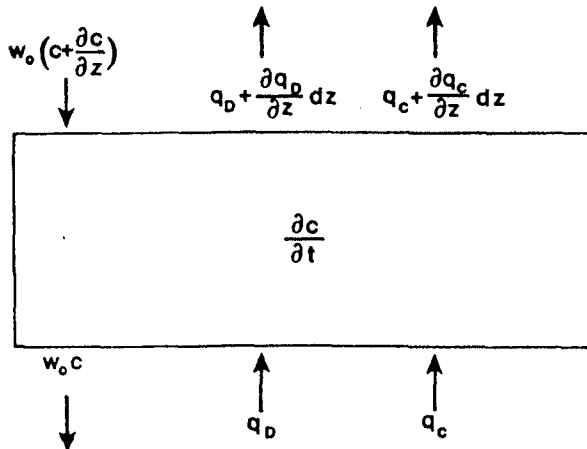


Suspended Sediment Distribution Models

Natural suspended sediment processes are a combination of both convective and diffusive processes. The process by which sediment (heavier than water) is driven upward has traditionally been described in terms of pure gradient diffusion. This process is due to driven by vertical mixing and consists of a large number of small, random vertical steps. Alternatively, the scale over which this mixing takes place is much smaller than the scale of the concentration profile.

Analysis of recent experimental data indicates that the pure gradient diffusion model is inadequate and that in many cases, a larger scale or convective process is reflected by many suspensions as well. These results reflect a process whereby the mixing scale is of the same order as the concentration profile.

Considering a horizontally uniform sediment concentration field $c = c(z, t)$ and a correspondingly uniform sediment velocity field $u_s = u_s(z, t)$, the vertical sediment flux $q = c u_s$ is considered to consist of three components. These components are a downward component $-w_0 c$ due to gravitational settling and an upward flux which can be of convective (subscript C) or diffusive (subscript D) nature or a combination of both. This process is illustrated in Figure 2 (Nielsen, 1992).



The total vertical flux is thus written as:

$$q_z = -w_0 c + q_D + q_C$$

enabling the conservation equation to be written as

$$\frac{\partial c}{\partial t} = w_0 \frac{\partial c}{\partial z} - \frac{\partial q_D}{\partial z} - \frac{\partial q_C}{\partial z}$$

The forms of convective and diffusive functions considered for this paper are as below:

$$\text{Convective Flux, } q_c(z, t) = p\left(t - \frac{z}{w_c}\right)F(z)$$

$$\text{Diffusive Flux, } q_D(z, t) = -\epsilon_s \frac{\partial c}{\partial z}$$

The pickup function $p(t)$ is a non-negative function describing the instantaneous pick up rate at the bed and the dimensionless convective distribution function $F(z)$ determines the fraction of the entrained sand which travels (convectively) beyond the level z above the bed.

Analytical Solution - Pure Convection

The vertical convective sediment flux, q_c is generally written in the following form

$$q_c(z, t) = p\left(t - \frac{z}{w_c}\right)F(z)$$

where w_c is the average vertical velocity with which the sand is convected upwards.

Assuming that the distribution function $F(z)$ is an exponential of the form

$$F(z) = e^{-z/L}$$

the general form of the time dependant sediment concentration equation may be expressed in terms of periodic functions as:

$$c_n(z, t) = C_n f(z) e^{im\omega t}$$

becoming

$$c_n(z, t) = C_n e^{-\beta_n z/L} e^{im\omega t}$$

where

$$C_n = \frac{P_n}{w_0} \frac{1 + im\omega L / w_c}{1 + im\omega L / w_c + im\omega L / w_0}$$

and

$$\beta_n = 1 + \frac{im\omega L}{w_c}$$

If the real portion of c_n is considered, have

$$\text{Re}\{c_n(z, t)\} = \text{Re}\{C_n\} e^{-z/L}$$

Analytical Solution - Pure Gradient Diffusion

As with the pure convection description, with the general form of the time dependant sediment concentration equation as

$$c_n(z, t) = C_n f(z) e^{in\omega t}$$

for the pure gradient diffusion solution, this becomes

$$c_n(z, t) = C_n e^{-\alpha_n z w_0 / \epsilon_s} e^{in\omega t}$$

where

$$C_n = \frac{P_n}{w_0 \alpha_n}$$

and

$$\alpha_n = \frac{1}{2} + \sqrt{\frac{1}{4} + \frac{in\omega \epsilon_s}{w_0^2}}$$

Note that for the pure gradient diffusion solution, the length scale, L of the convective solution is replaced by the sediment diffusivity over the still water settling velocity ϵ_s / w_0 .

There are two important differences between the analytical solutions for pure gradient diffusion and pure convection. Firstly, all the harmonic concentration components decay as $e^{-z/L}$ for the convective solution and secondly, the phase lag relative to the pick up function grows at the same rate for all frequencies. This indicates that in a process dominated by convection, defined concentration peaks will travel upwards through the water column at a constant rate. However, for a process dominated by diffusion, the phase lags will grow with elevation above the bed, leading to "blurring" of successive peaks.

Data Analysis

The experimental results previously illustrated may be expressed in terms of simple periodic functions via a Fourier Analysis. This has been carried out on the available data to the tenth harmonic. It has been found to date that six harmonics provide an appropriate level of accuracy.

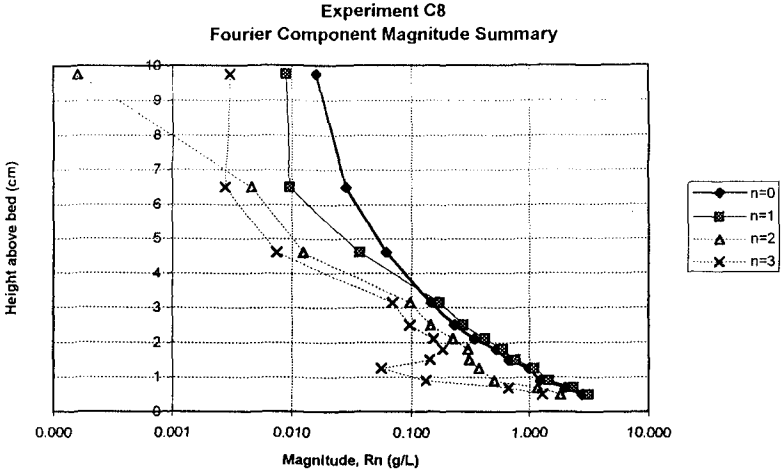


Figure 3 provides an example of the relative magnitudes of the primary harmonics obtained for the data set presented in Figure 1. From these results, parameters representing the mixing length (pure convection solution) and diffusivity (pure gradient diffusion solution) can be derived.

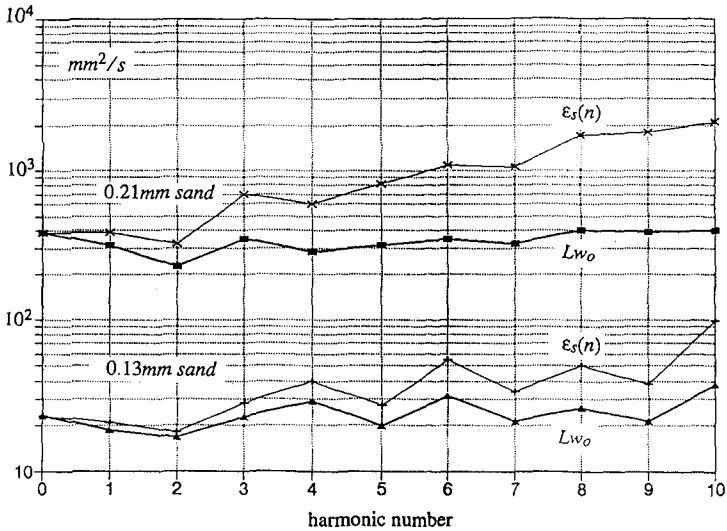


Figure 4 presents the results of this process. Note that the length scale (corresponding to pure convection) is approximately constant across all harmonics. However, the diffusivities show an increasing “drift” as the harmonic number increases. As could be expected, this is more pronounced for the sand of larger grain size.

Conclusions

The primary conclusion which may be drawn from this analysis is that the experimental results analysed are more appropriately represented by a purely convective model. This is convenient as computationally, the solution of the equations corresponding to pure convection is much more straightforward than for the second order partial DE for the pure diffusion (and combined convection diffusion) equation.

References

1. AA Al-Salem (1993), "Sediment transport in oscillating boundary layers under sheet flow conditions", Delft Hydraulics.
2. Katepodi, I et al (1994) "Intra-wave sediment transport in an oscillatory flow superimposed on a mean current", Delft Hydraulics Technical Report no. 1684 Part III
3. Nielsen, P (1992), "Coastal Bottom Boundary Layers and Sediment Transport", Advanced Series on Ocean Engineering, World Scientific, Singapore.
4. Nielsen, P (1991), "Combined Convection and Diffusion: A new framework for suspended sediment modelling", Proc Coastal Sediments '91", Seattle, pp 418-431.
5. Ribberink, JS & A Al-Salem (1992), "Time dependent sediment transport phenomena in oscillatory boundary layer flow" Delft Hydraulics Technical Report no 840.20 Part VI.
6. Ribberink, JS & Z Shen (1993), "Sediment transport of fine sand under asymmetric oscillatory flow", Delft Hydraulics Technical Report no. 840.20 Part VII.

CHAPTER 293

A TRANSPORT RATE FORMULA FOR MIXED-SIZE SANDS

Mohammad Dibajnia¹ and Akira Watanabe²

Abstract

Experiments were conducted on the transport of mixed grain size sands due to nonlinear waves, over both rippled and flat beds. The sand mixture was composed of a fine sand with median diameter of 0.2 mm and a coarse sand with median diameter of 0.87 mm. Conditions for the initiation of sheet flow were investigated and transport rates were measured. It was found that the transport rate of fine sand is significantly reduced by the existence of the coarse sand, whereas the coarse sand behaved almost as if there were no other sand present. A transport rate formula for mixed sands was presented and verified by using the measured data.

1. Introduction

Sandy beaches are the focus of many attentions because of their role in preserving the coastal environment, their ability in reducing disasters, and their attractiveness for recreational activities. They are, however, subjected to erosion problems due to the action of natural forces or artificial impacts. As a counter-measure, beach nourishment is one of the most acceptable methods for protecting sandy beaches. The grain size of the sand used for filling the beach is, however, decided by the available sources of material and in many cases does not coincide with the grain size of the native sand. Also, using a sand coarser than the native sand is in general more desirable because it can better stabilize the beach.

¹Associate Professor, Dept. of Civil Eng., Univ. of Tokyo, Bunkyo-ku, Tokyo 113, Japan.

²Professor, ditto.

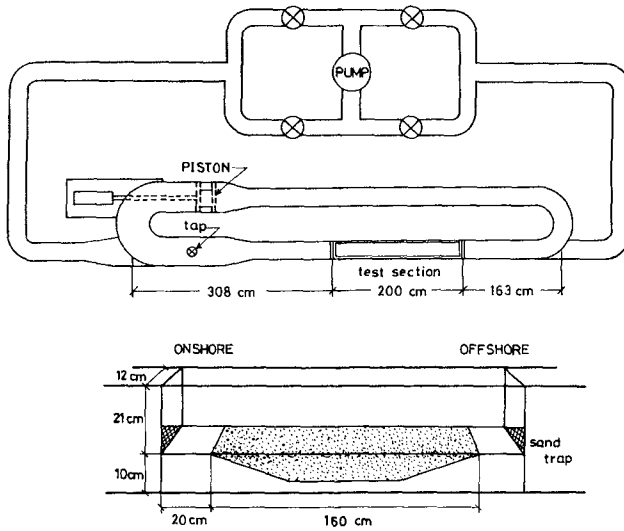


Figure 1: Oscillatory/steady flow water tunnel and its test section.

Needless to mention that even the grain size of the native sand itself may be nonuniform. Therefore, estimation of the transport rates of mixed-size sands is of crucial importance in predicting the behavior of both natural and artificial beaches.

In this study experiments were conducted on the transport of mixed grain size sands due to nonlinear waves over rippled and flat beds. The transport rate formula of Dibajnia and Watanabe (1992), which has originally been derived for 0.2 mm sand, was first generalized to cover the transport of granular sediments with other grain sizes and densities. A method was then presented to apply this formula to estimating the transport rate of mixed size sands. Conditions for the initiation of sheet flow were also investigated.

2. Experiments

The present experiments were carried out in a loop-shape oscillatory flow water tunnel at the University of Tokyo. The tunnel and its test section are shown in Fig. 1. Two kinds of sand, fine and coarse, were mixed together. The fine sand had a median grain size of 0.2 mm and the fall velocity of 2.3 cm/s. For the coarse sand these values were 0.87 mm and 8.7 cm/s, respectively. The percentage of the weight of each sand in the total weight of a mixed sample was defined as the percentage of that sand, P_i . Three types of mixed sands with percentages of fine sand, $P_{0.2}$, equal to 25%, 50%, and 75% were prepared. The oscillatory velocity profiles generated in the tunnel were calculated by the first

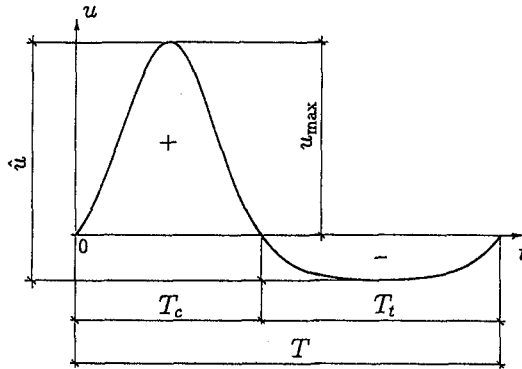


Figure 2: Typical velocity profile in the experiments.

Table 1: Experimental conditions for transport rate measurements.

T (s)	3	3	3	3	3	3	3	3	3	5	5	5
d_0 (cm)	23	28	35	38	43	48	50	55	71	62	78	98
$P_{0.2} = 100\%$				⊙	⊙						⊙	
$P_{0.2} = 75\%$	⊙	⊙	⊙	⊙	⊙		⊙	⊙	⊙			
$P_{0.2} = 50\%$	⊙	⊙	⊙	⊙	⊙	⊙	⊙	⊙		⊙	⊙	⊙
$P_{0.2} = 25\%$	⊙	⊙	⊙		⊙		⊙		⊙			
$P_{0.2} = 0\%$				⊙		⊙						

⊙ : Points where transport rate is measured.

order Cnoidal wave theory. Two wave periods, $T = 3$ and 5 s and one nonlinearity index $u_{max}/\hat{u} = 0.7$ (see Fig. 2) were selected. By changing the velocity amplitude, transport of sands over rippled beds as well as under sheet flow conditions were observed and net transport rates were measured. The experimental conditions for which transport rates were measured are summarized in Table 1. In this table, d_0 and T are the excursion length of water particle and the period of oscillation, respectively. Conditions for initiation of sheet flow were also investigated. The present experimental data have originally been reported in Suzuki *et. al* (1994) and Inui *et. al* (1995).

3. Initiation of Sheet Flow

For a uniform sand, the transport mode usually changes from the bedload transport over an initial flat bed to the suspended load transport over the ripples and, as the velocity amplitude continue to increase, to the sheet flow transport over the reflattened bed. Several experiments were performed to observe the

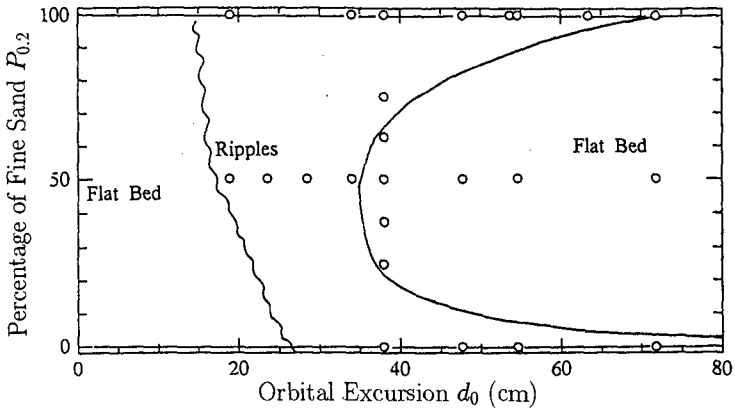


Figure 3: Occurrence of different transport modes.

behavior of mixed sand beds. The procedure was to start each experiment from a flat bed and see whether ripples appear or not. The results for $T = 3$ s were summarized in Fig. 3. It is interesting to see that for mixed sands, sheet flow occurs under lower velocities than those required for uniform sands. However, this was the case when the bed has initially been flat. Additional few experiments were performed with an initially rippled bed. As shown in Fig. 4, it was found that a higher velocity than that in the case of uniform sand is required to wash out the ripples from the mixed sand bed. It was thus concluded that the mixture of fine and coarse sand provides a firm structure which is not deformed as easily as uniform sands are.

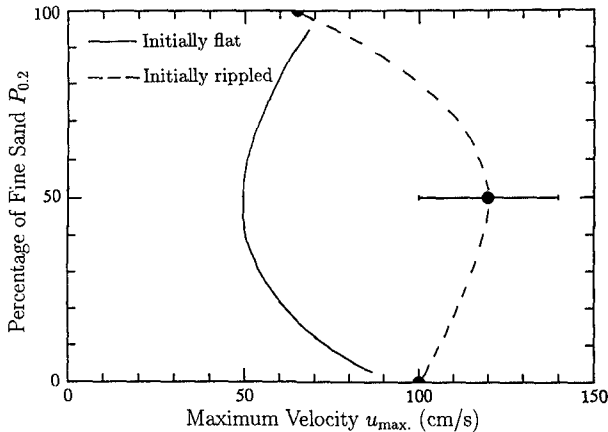


Figure 4: Dependence of the initiation of sheet flow on the initial bed form.

4. Generalized Transport Rate Formula

A transport rate formula involving unsteady aspects of the sand transport phenomenon has been presented by Dibajnia and Watanabe (1992) for estimating the sheet flow sand transport rates. The formula has later been extended by them (Dibajnia *et. al*, 1994) to cover suspended load over ripples as well as bed load transports. Their formula, however, is based on the experimental data obtained by using a sand with median grain size of 0.2 mm only, and needs further verification for sands of other sizes before it is applied to the transport of mixed sands.

In their experiments on sheet flow, Dibajnia and Watanabe (1992) noticed that once there was a positive velocity (Fig. 2) large enough to raise up sand particles to such a level that they could not reach the bottom before the negative velocity occurred, then these particles tended to be carried to the negative direction. Dibajnia and Watanabe (1992), therefore, defined a dimensionless parameter, Γ , as

$$\Gamma = \frac{u_c T_c (\Omega_c^3 + \Omega_t^3) - u_t T_t (\Omega_t^3 + \Omega_c^3)}{(u_c + u_t) T} \quad (1)$$

and assumed the net transport rate to be a function of Γ . For the dimensionless net transport rate, Φ , Dibajnia (1995) proposed

$$\Phi = \frac{q_{\text{net}}(1 - \epsilon)}{Wd} = 0.0023 \cdot \text{sign}(\Gamma) \cdot |\Gamma|^{0.5} \quad (2)$$

In the above relations q_{net} is the net volumetric transport rate, ϵ the sediment porosity, d the sediment grain size, W the sediment fall velocity, and u_c and u_t are representative velocity amplitudes for the positive and negative portions of the velocity profile, respectively, as

$$u_c^2 = \frac{2}{T_c} \int_0^{T_c} u^2 dt, \quad u_t^2 = \frac{2}{T_t} \int_{T_c}^T u^2 dt \quad (3)$$

In Eq. (1) Ω_c' represents the amount of suspended sand remaining from the positive half cycle, to be carried by the negative velocity. Similarly Ω_t' stands for the amount of sand still in suspension after the negative half cycle, which will be transported to the positive direction. On the other hand, Ω_c represents that amount of sand which is entrained and carried only by the positive velocity; and Ω_t indicates the amount of sand entrained, transported, and settled during the negative half cycle. Values of Ω were estimated in terms of another parameter, ω , equal to the ratio of the time required for a sand particle, suspended during a half cycle, to reach the bottom to the time duration of that half cycle. The reader is referred to the original paper for more details.

Now consider the simple case of sheet flow sand transport under half of a sinusoidal cycle. In this condition, Eq. (1) reduces to

Table 2: Transport rate data of Sawamoto and Yamashita (1986)

sediment type	specific gravity	d (cm)	W (cm/s)	T (s)	u_{\max} (cm/s)	Q (cm ² /s)
sand A	1.65	0.02	2.5	3.8	125.3	2.013
sand A	1.65	0.02	2.5	3.8	114.6	1.575
sand A	1.65	0.02	2.5	3.8	101.5	1.180
sand A	1.65	0.02	2.5	3.8	88.7	0.876
sand A	1.65	0.02	2.5	3.8	74.4	0.642
sand B	1.65	0.07	10.5	3.8	125.3	1.308
sand B	1.65	0.07	10.5	3.8	114.6	1.063
sand B	1.65	0.07	10.5	3.8	101.5	0.641
sand B	1.65	0.07	10.5	3.8	88.7	0.500
sand B	1.65	0.07	10.5	3.8	74.4	0.353
sand C	1.65	0.16	22.5	3.8	125.3	1.240
sand C	1.65	0.16	22.5	3.8	114.6	1.001
sand C	1.65	0.16	22.5	3.8	101.5	0.587
sand C	1.65	0.16	22.5	3.8	88.7	0.357
sand C	1.65	0.16	22.5	3.8	74.4	0.271
coal dust	0.58	0.15	7.6	3.8	125.3	4.750
coal dust	0.58	0.15	7.6	3.8	114.6	3.215
coal dust	0.58	0.15	7.6	3.8	101.5	2.405
coal dust	0.58	0.15	7.6	3.8	88.7	1.835
coal dust	0.58	0.15	7.6	3.8	74.4	1.080
coal dust	0.58	0.15	7.6	3.8	56.2	0.441
coal dust	0.58	0.15	7.6	3.8	44.3	0.158

$$\Gamma = \Omega^3 \quad (4)$$

which means that a method to evaluate Ω can best be verified by using averaged transport rates measured under half cycle of sinusoidal oscillations. Such data have been reported by Sawamoto and Yamashita (1986) for sheet flow sand transport, and are shown here in Table 2. The data are for quartz sands of three different sizes (0.2, 0.7, and 1.8 mm) and for coal dust with density of 1.58. According to Dibajnia and Watanabe (1992), Ω may be evaluated as

$$\begin{aligned} \Omega_j &= \omega_j \cdot \frac{WT_j}{d} = \frac{1}{2} \frac{u_j^2}{sgWT_j} \cdot \frac{WT_j}{d} \\ &= \frac{1}{2} \frac{u_j^2}{sgd} = \Theta \quad : \quad \text{Mobility number} \end{aligned} \quad (5)$$

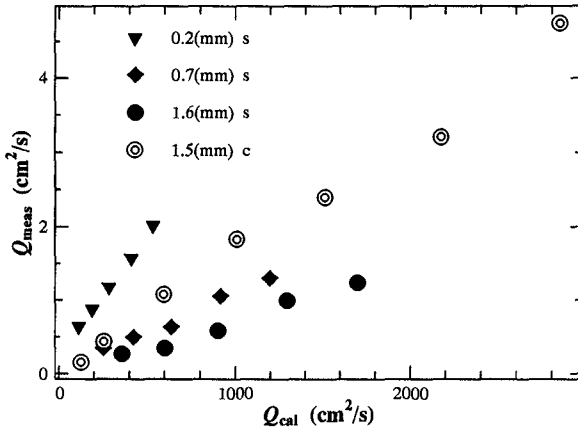


Figure 5: Comparison of calculated half cycle averaged transport rates with measurements (previous method).

where $s = (\rho_s - \rho) / \rho$ in which ρ and ρ_s are the densities of water and sediment, respectively, g is the acceleration of gravity, and the subscript j should be replaced by either c or t . Figure 5 shows the comparison between measured and calculated transport rates when Eq. (5) was applied. In this figure $Q = q(1 - \epsilon)$ where q is the half cycle averaged transport rate. The proportionality coefficient in Eq. (2) is not considered. It is seen that each sediment type defines a different line of agreement. This indicates that the proportionality coefficient should depend on the grain size and density of sediment whenever the transport rate is assumed to be a function of either Mobility or Shields numbers.

Sawamoto and Yamashita (1986) found that the half cycle averaged sheet flow transport rate is proportional to the third power of the ratio of the friction velocity to the sediment fall velocity. Considering this, a new way to evaluate Ω is as follows.

$$\begin{aligned} \Omega_j &= \omega_j \cdot T_j \sqrt{\frac{sg}{d}} = \frac{1}{2} \frac{u_j^2}{sgWT_j} \cdot T_j \sqrt{\frac{sg}{d}} \\ &= \frac{1}{2} \frac{u_j^2}{W \sqrt{sgd}} \propto \left(\frac{u_j}{W}\right)^2 \end{aligned} \tag{6}$$

Figure 6 shows the results after applying Eq. (6). All the data follow the same line of agreement, indicating that the new method for calculating Ω is valid for granular sediments with different grain sizes as well as different densities. The proportionality constant in Fig. 6 is about 0.0035, and is valid for half cycle averaged transport rates. For the net transport rate, original data of Dibajnia and Watanabe (1992) were used ($d = 0.2$ mm) to obtain the value of the constant.

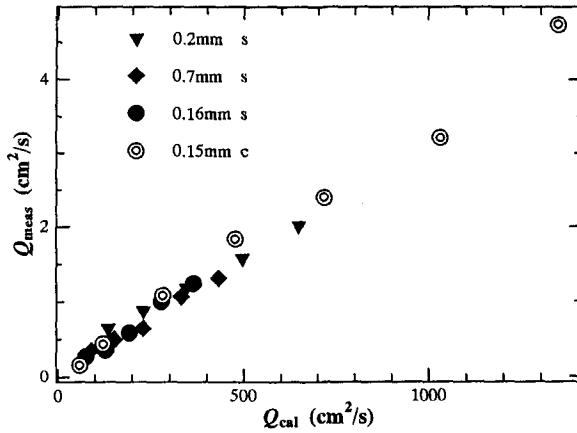


Figure 6: Comparison of calculated half cycle averaged transport rates with measurements (new method).

The generalized transport formula was thus obtained (Takasawa *et. al*, 1996) as

$$\Phi = \frac{q_{net}(1 - \epsilon)}{Wd} = 0.0015 \cdot \text{sign}(\Gamma) \cdot |\Gamma|^{0.5} \quad (7)$$

$$\left\{ \begin{array}{l} \text{if } \omega_j \leq \omega_{cr} \\ \text{if } \omega_j > \omega_{cr} \end{array} \right\} \left\{ \begin{array}{l} \Omega_j = \omega_j \cdot T_j \sqrt{\frac{sg}{d}} \\ \Omega'_j = 0 \\ \Omega_j = \omega_{cr} \cdot T_j \sqrt{\frac{sg}{d}} \\ \Omega'_j = (\omega_j - \omega_{cr}) \cdot T_j \sqrt{\frac{sg}{d}} \end{array} \right. \quad (8)$$

$$\omega_j = \frac{1}{2} \frac{u_j^2}{sgWT_j} \quad (9)$$

where Γ should be obtained as before from Eq. 1. In order to verify the above formulation, net sand transport rate data for grain sizes other than 0.2 mm are required. The only such a data set available to the authors was that reported by Watanabe and Isobe (1990), giving the net sand transport rate over ripples under nonlinear waves for sands of 0.2 and 0.87 mm median diameter. Value of ω_{cr} in Eq. (8) is equal to 1 for sheet flow. In presence of ripples, ω_{cr} is equal to 0.03 for 0.2 mm sand and equal to 0.05 for 0.87 mm sand. Threshold velocity should also be considered. Comparison between measured and calculated nondimensional net transport rates for the experiments of Watanabe and Isobe (1990) is shown in Fig. 7. In this figure, the transport rates of the 0.87 mm sand are multiplied by a factor of ten to be more visible. Satisfactory agreement is observed.

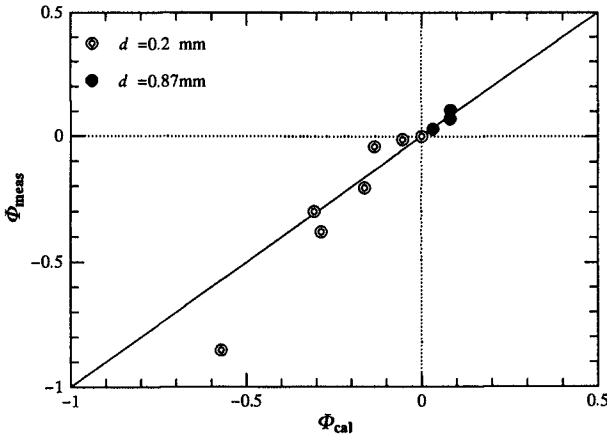


Figure 7: Comparison of calculated net transport rates over ripples with measurements.

5. Transport Rate of Mixed Sands

Let us first assume that the transport of each of the sands in a mixture, is not affected by the existence of the other sand. Then the transport rate of each sand could be obtained by using the following formulation.

$$\Phi_i = \frac{M_i}{(\rho_s - \rho)W_i d_i} = 0.0015 \text{ sign}(\Gamma) \cdot |\Gamma|^{0.5} \cdot P_i \tag{10}$$

$$\left\{ \begin{array}{l} \text{if } \omega_j \leq \omega_{cr} \\ \text{if } \omega_j > \omega_{cr} \end{array} \right\} \left\{ \begin{array}{l} \Omega_j = \omega_j \cdot T_j \sqrt{\frac{sg}{d_i}} \\ \Omega'_j = 0 \\ \Omega_j = \omega_{cr} \cdot T_j \sqrt{\frac{sg}{d_i}} \\ \Omega'_j = (\omega_j - \omega_{cr}) \cdot T_j \sqrt{\frac{sg}{d_i}} \end{array} \right. \tag{11}$$

$$\omega_j = \frac{1}{2} \frac{u_j^2}{sgW_i T_j} \tag{12}$$

In the above relations M is the immersed weight of sand corresponding to Φ , subscript i is to address each grain size, and it is assumed that sands have the same density ρ_s . The above formulation was applied to the present experimental data. The results were compared with the measurements as shown in Fig. 8. The dash line in this figure is to separate sheet flow data from those obtained over ripples, and the solid line is the line of perfect agreement. The coarse sand data are again multiplied by a factor of ten for clarity. It is noticed that the fine sand

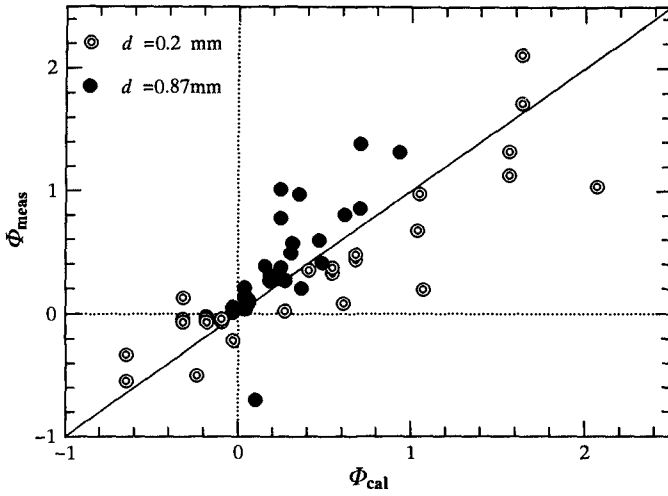


Figure 8: Calculated net transport rates of mixed sand (Eq. 10) compared with measurements.

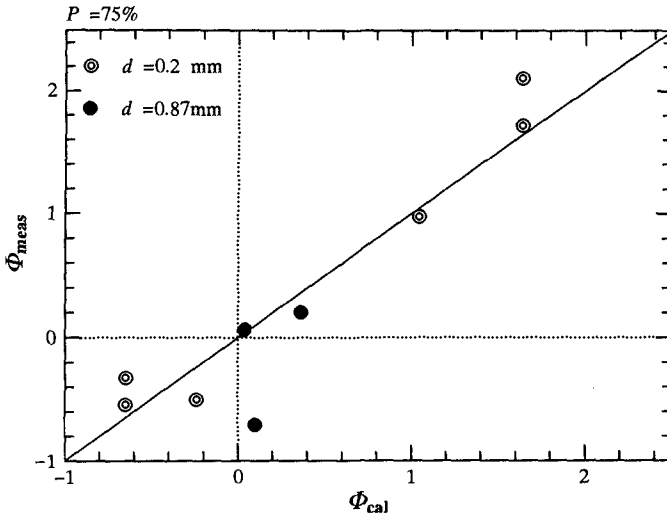


Figure 9: Calculated net transport rates of mixed sand (Eq. 10) compared with measurements for $P = 0.75\%$.

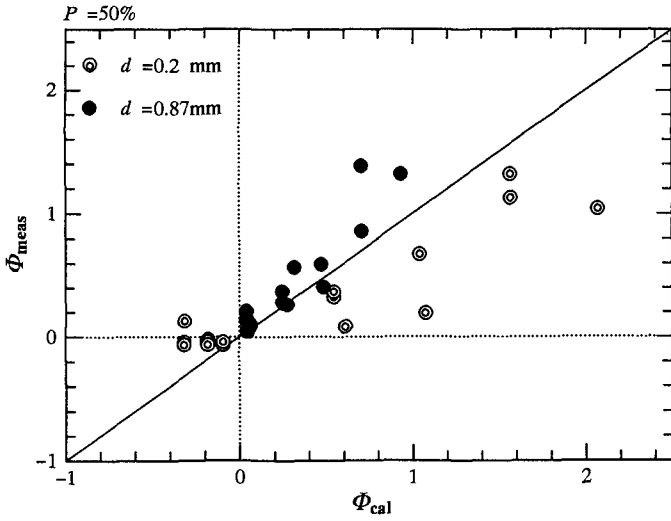


Figure 10: Calculated net transport rates of mixed sand (Eq. 10) compared with measurements for $P = 0.50\%$.

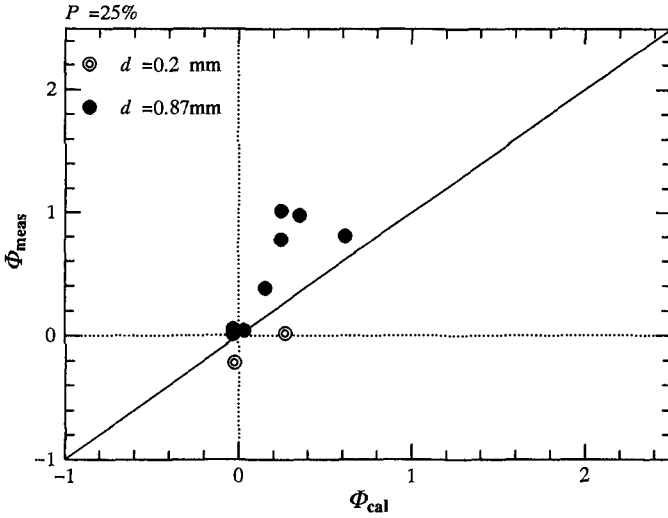


Figure 11: Calculated net transport rates of mixed sand (Eq. 10) compared with measurements for $P = 0.25\%$.

data lay below the solid line, whereas the data for coarse sand are located above this line. This simply means that while the transport rate of fine sand has in fact been reduced, the coarse sand has kept its activity. The data were separated according to the percentage of sand and plotted again in Figs. 9, 10, and 11. For $P = 75\%$, *i.e.* when each sand has occupied the major part of the mixture, the data more or less follow the solid line of agreement. Interesting results are observed for $P = 25\%$, where measured transport rates of coarse sand show much larger values than those estimated. Despite the fact that coarse sand amounted only to 25% of the mixture, it has behaved as if it were alone; a clear indication of the armouring phenomenon.

The reduction in the transport rate of fine sand was explained by assuming that a percentage of the total flow energy equal to the percentage of fine sand is consumed to carry the fine sand. In the present formulation, ω is the parameter involving the flow kinetic energy. In general, Eqs. (10) and (12) may be rewritten as

$$\Phi_i = \frac{M_i}{(\rho_s - \rho)W_i d_i} = 0.0015 \operatorname{sign}(\Gamma) \cdot |\Gamma|^{0.5} \quad (13)$$

$$\omega_j = \frac{1}{2} \frac{u_j^2}{sgW_i T_j} \cdot P_i^{\frac{1}{\alpha_i}} \quad (14)$$

where α is expected to depend on the ratio of the mean diameter of each sand to that of the other sand. For the present sand mixture it was found that $\alpha_{0,2} = 1$

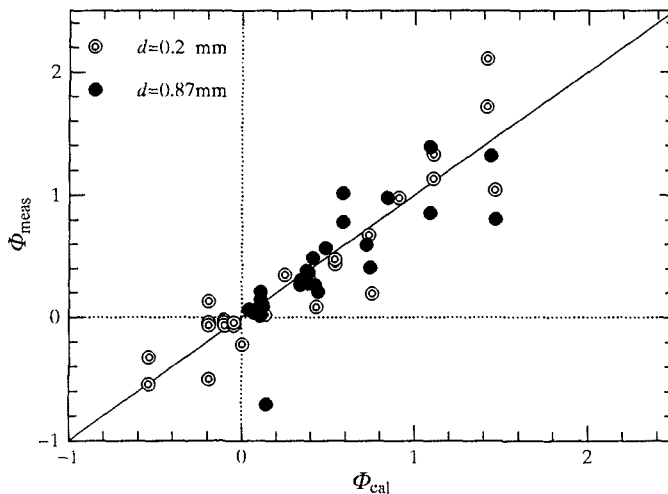


Figure 12: Comparison of net transport rates of mixed sand, calculated by the presented method, with measurements.

and $\alpha_{0.87} = 4$ are appropriate. Equations (1), (3), (11), (13), and (14) were thus applied to estimating the net transport rates of the present experiments. Calculated transport rates reasonably agreed with the measurements as shown in Fig. 12.

6. Concluding Remarks

The transport rate formula of Dibajnia and Watanabe (1992) was generalized to cover the transport of uniform granular sediments of any size and density.

Experiments were performed on transport of mixed-size sands. It was shown that fine and coarse sands when mixed together may make a firm structure and thus the bed may not be deformed as easily as in the case of uniform sands. Measurements of transport rate showed that armouring of fine sand by the coarse sand causes a significant reduction in the transport rate of the fine sand. But the transport rates of the coarse sand itself were almost unaffected by the presence of the fine sand. A method to apply the above generalized transport formula to estimating the transport rate of mixed sands was presented. Application of this method to beach profile simulation will be presented in a separate paper.

In the present experiments, the oscillatory velocity amplitude had to be limited because of the limited length of the test section (maximum velocity was about 95 cm/s) and higher velocities could not be tried. Therefore, further experiments under sheet flow conditions but with higher velocities are required to confirm whether the armouring function of the coarse sand will persist or not.

References

- Dibajnia, M. (1995): Sheet flow transport formula extended and applied to horizontal plane problems, *Coastal Eng. in Japan*, Vol. 38, No. 2, pp. 179-194.
- Dibajnia, M. and A. Watanabe (1992): Sheet flow under nonlinear waves and currents, *Proc. 23rd Int. Conf. on Coastal Eng., ASCE*, pp. 2015-2028.
- Dibajnia, M., T. Shimizu and A. Watanabe (1994): Profile change of a sheet flow dominated beach, *Proc. 24th Int. Conf. on Coastal Eng., ASCE*, pp. 1946-1960.
- Inui, T., M. Dibajnia, M. Isobe and A. Watanabe (1995): A transport rate formula for mixed-size sands and its application, *Proc. 42nd Japanese Annual Conf. on Coastal Eng., JSCE*, to be published (in Japanese).

- Sawamoto, M. and T. Yamashita (1986): Sediment transport rate due to wave action, *J. Hydrosoc. Hydraul. Eng.*, Vol. 4, No. 1, pp. 1-15.
- Suzuki, K., A. Watanabe, M. Isobe and M. Dibajnia (1994): Experimental study on transport of sediment with mixed-grain size due to oscillatory flow, *Proc. 41st Japanese Annual Conf. on Coastal Eng., JSCE*, pp. 356-360 (in Japanese).
- Takasawa, S., M. Dibajnia, and A. Watanabe (1996): A generalized sheet flow transport formula, *Proc. 51st Annual Civil Eng. Conf., JSCE*, Vol. B2, pp. 124-125 (in Japanese).
- Watanabe, A. and M. Isobe (1990): Sand transport rate under wave-current action, *Proc. 22nd Int. Conf. on Coastal Eng., ASCE*, pp. 2495-2507.

SUBJECT INDEX

Page number refers to the first page of paper

- Abrasives, 2166
Absorption, 55
Accretion, 2955, 4038
Accuracy, 2, 4770
Acoustic measurement, 275
Advection, 4024
Aeolian sands, 4214
Aerial surveys, 1944
Aging, 1888
Alaska, 1293
Algorithms, 914
Analytical techniques, 575, 1762, 1985
Anchorage, 1631
Anemometers, 602
Aquatic habitats, 4300
Armor units, 1542, 1583, 1617, 1640, 1665, 1679, 1721, 1735, 1748, 1789, 1803, 1862, 1944, 2377, 2418, 2522, 3006, 3791, 4228
Artificial islands, 754, 1862, 2298
Asymmetry, 3183, 3467
Australia, 4200, 4390

Backfills, 3231, 4261
Baltic Sea, 2142
Barrier beaches, 247, 2732, 3391, 3546
Barrier islands, 2128, 2732, 2756, 2897, 4621
Barriers, 2087, 2352, 2470, 4505, 4601
Bars, 3680, 4289
Bars, riverine, 2884, 2897, 3546, 3588, 3600, 3666, 4491
Bathymetry, 731, 3521, 4376

Bays, 4242, 4531
Beach erosion, 1349, 1985, 2352, 2666, 2691, 2705, 2718, 2732, 2756, 2770, 2820, 2857, 2871, 2884, 2911, 2918, 2955, 2982, 3115, 3295, 3378, 3442, 3521, 3874, 3976, 3986, 4038, 4583, 4613, 4650, 4717, 4744, 4756
Beach nourishment, 2746, 2770, 2857, 2897, 2911, 2918, 2927, 2941, 2955, 2982, 3115, 3642, 3708, 3722, 4014, 4390, 4440, 4613, 4621, 4650, 4730, 4756
Beaches, 151, 233, 261, 275, 602, 616, 717, 889, 955, 981, 1130, 2036, 2050, 2128, 2142, 2152, 2284, 2612, 2640, 2654, 2677, 2779, 2829, 2843, 2969, 2994, 3006, 3020, 3062, 3090, 3104, 3169, 3349, 3405, 3442, 3560, 3666, 3680, 3736, 3750, 3770, 3888, 3921, 3948, 3962, 3986, 4000, 4079, 4088, 4120, 4161, 4188, 4228, 4353, 4376, 4477
Bed load, 3467, 3913
Bed load movement, 3614
Bed movements, 3495
Bed ripples, 3129, 3183, 4079
Bed roughness, 3143
Bedforms, 3129, 3169, 3391, 3784
Belgium, 836
Benefit cost ratios, 2927, 4717
Berms, 1528, 1542, 1617, 1693, 1735, 1826, 1930, 2192, 2897, 2982, 3708, 3722, 4636
Blocks, 1888

Volume 1 1-1254, Volume 2 1255-2572, Volume 3 2573-3804, Volume 4 3805-4832

- Boundary conditions, 3770, 4120, 4134
- Boundary element method, 165, 1516, 2377, 2548
- Boundary layer, 3194, 3207, 3818
- Boundary layer flow, 3183, 3219, 4779
- Boussinesq equations, 95, 109, 123, 493, 589, 955, 1060, 1116, 1144, 1178, 1192, 1491, 3048, 3349, 4807
- Breaking, 1876
- Breaking waves, 2, 109, 151, 186, 200, 214, 233, 247, 261, 275, 286, 403, 527, 551, 602, 657, 754, 1144, 1156, 1178, 1192, 1219, 1321, 1403, 1803, 1826, 2216, 2244, 2298, 2338, 2366, 2442, 2456, 2484, 2598, 3104, 3194, 3588, 3805, 4228, 4793, 4807
- Breakwaters, 137, 186, 300, 767, 1280, 1528, 1542, 1589, 1640, 1652, 1665, 1693, 1707, 1721, 1735, 1789, 1803, 1816, 1826, 1852, 1930, 1998, 2008, 2022, 2036, 2050, 2063, 2178, 2192, 2216, 2312, 2324, 2352, 2366, 2377, 2391, 2404, 2428, 2470, 2494, 2508, 2522, 2534, 2584, 2770, 2871, 3830, 3976, 3986, 4664, 4676, 4689, 4744
- Bridges, piers, 2230
- Buoyant jets, 4325, 4569
- Buoys, 616, 743, 2087
- Caissons, 1516, 1902, 2008, 2584, 4583
- Calibration, 247, 1102, 3614
- California, 4214, 4636
- Canada, 2230
- Case reports, 1293, 2404, 2732, 3986, 4717
- Channel flow, 4491
- Channel improvements, 3323
- Channels, waterways, 1074, 4531, 4703
- Chaos, 864
- China, People's Republic of, 354
- Climatic changes, 314, 1349, 4364
- Climatic data, 81
- Closed form solutions, 3244
- Cnoidal waves, 2598
- Coastal engineering, 2, 67, 109, 286, 314, 328, 340, 354, 457, 465, 616, 1034, 1465, 1707, 2114, 3652, 3680, 4431
- Coastal environment, 314, 689, 794, 836, 1022, 1478, 2244, 3270, 3363, 3962, 4300, 4807
- Coastal management, 864, 1008, 1375, 2666, 2677, 2793, 2820, 2884, 2911, 2927, 3020, 3431, 4000, 4014, 4253, 4339, 4418, 4440, 4636, 4703, 4744
- Coastal morphology, 1349, 1417, 2770, 2806, 2829, 2897, 2955, 3048, 3090, 3391, 3521, 3534, 3560, 3574, 3600, 3750, 3762, 3830, 3913, 4024, 4038, 4079, 4477, 4517
- Coastal processes, 214, 2022, 2036, 2691, 2779, 2871, 3295, 3378, 3481, 3495, 3600, 3614, 3642, 3666, 3708, 3750, 3805, 3874, 3888, 4052, 4200, 4364, 4464, 4477, 4545, 4583, 4703, 4821
- Coastal structures, 43, 55, 214, 221, 314, 380, 389, 403, 616, 743, 981, 1452, 1569, 1735, 1852, 1862, 1876, 1957, 1971, 2008, 2114, 2128, 2142, 2152, 2166, 2178,

- 2206, 2216, 2258, 2272, 2284,
2338, 2352, 2391, 2404, 2418,
2456, 2560, 2573, 2718, 2918,
2969, 3507, 4397, 4440, 4531
- Coefficients, 1516
- Cohesive sediment, 3337
- Cold weather construction, 4397
- Colorado River, 3309
- Composite structures, 1707
- Computation, 537, 1102, 1130
- Computer aided design, 4650
- Computer aided drafting (CAD),
4650
- Computer networks, 1443
- Concrete blocks, 1652, 1665
- Concrete structures, 1556
- Configuration, 1735, 1816, 3155,
4636
- Construction, 4689
- Control, 493, 1998
- Control systems, 55
- Convection, 3784, 4098
- Coral reefs, 3143, 4261
- Core, 1735
- Corrosion, 2166
- Cost effectiveness, 2114, 4583
- Costs, 1735
- Cracks, 4411
- Crossflow, 175, 3378, 3405, 3666
- Currents, 30, 67, 95, 354, 629, 1060,
1219, 1247, 2391, 3363, 3431,
4066, 4079, 4569, 4730, 4807,
4821
- Curtain walls, 2470, 2484
- Cylinders, 380, 415
- Damage, 1233, 1789, 2969, 4261,
4676
- Damping, 2298, 2626, 3143, 4174
- Dams, 1233
- Dams, earth, 2101
- Data banks, 3652
- Data collection, 81, 137, 368, 629,
643, 677, 1916, 3722, 4200
- Data processing, 4770
- Databases, 81, 2418
- Decay, 300
- Decks, 2573
- Deep water, 2494
- Deflection, 2456
- Deformation, 261, 2338, 3062, 4411
- Deltas, 2806, 2820, 3270, 3284,
3976, 4505, 4545
- Denmark, 2927, 4703
- Density stratification, 4557
- Design, 314, 616, 1280, 1403, 1617,
1631, 1640, 1665, 1748, 1776,
1826, 1971, 2036, 2114, 2128,
2508, 2584, 2897, 2927, 3034,
3628, 4261, 4440, 4451, 4689,
4717
- Design criteria, 221, 354, 2352,
2534, 4397, 4431, 4591
- Design improvements, 2101
- Design waves, 328, 1233, 2494,
2560
- Dewatering, 2677
- Diffusers, 4325
- Diffusion, 3784, 4098
- Digital techniques, 657
- Dikes, 994, 1008, 1233, 1876, 1888,
2746, 2820
- Discharge, 3309
- Docks, 1293
- Documentation, 1443
- Dolos, 4664
- Doppler systems, 527, 629, 1060
- Drag, 3846
- Drag coefficient, 3363
- Drainage, 3507
- Drainage systems, 2640, 2654
- Drains, 2666, 2677
- Dredge spoil, 3708

- Dredging, 3284, 3708, 4274, 4289, 4390
Ducts, 3913
Dunes, 2793, 2884, 2955, 2969, 3034, 3115, 4148
Dynamic response, 2456, 2584
Dynamic stability, 1930, 2534
Dynamics, 1178, 2955, 3560, 3805, 3846, 3921, 4052, 4364, 4601
- Earthfill, 2101
Earthquakes, 1478
Ecology, 4274
Eddy viscosity, 200, 3194, 3419
Education, 1443, 4431
Effluents, 4325
Egypt, 3976
Eigenvalues, 1074, 2470
Eigenvectors, 2829, 4730
Embankments, 1707, 4188
Energy conversion, 4591
Energy dissipation, 261, 836, 1088, 1192, 1247, 2626, 3062
Engineers, 4431
Entropy, 643
Environmental impact statements, 4274
Equations of motion, 3846
Equipment, 4591
Erosion, 214, 1693, 2230, 2404, 3034, 4052, 4148, 4353, 4397, 4451, 4557, 4621, 4703
Erosion control, 2666, 2677, 2820, 4038
Estimates, 328, 3453
Estimating, 16, 43, 2508
Estimation, 30, 689, 794, 900, 981, 1389, 1503
Estuaries, 2691, 4289, 4491, 4557
Europe, 1375
Evaluation, 340, 2036, 2677, 2857, 3652
- Experimentation, 443, 479, 516, 1617, 1840, 2640, 2746
Extraction procedures, 4583
- Failure modes, 1902
Failures, 1542, 1589
Fatigue, 4664
Feasibility studies, 4591
Field investigations, 137, 994, 1652, 1876, 3600, 3901, 4000, 4491
Field tests, 516, 689, 2077, 2612, 2654, 3257, 3323, 3962, 4052, 4111, 4591
Finite element method, 2548
Finite elements, 465
Fisheries, 4253
Floating breakwaters, 1631
Floating structures, 2548
Flood control, 2820, 4253, 4339, 4505
Flood plain insurance, 4339
Flooding, 1349, 2244, 2746, 4314, 4339, 4418
Floods, 2258, 2705, 3284, 4491
Florida, 2312, 3323, 3642, 4242, 4613
Flow characteristics, 67
Flow patterns, 4134
Fluid flow, 3546
Fluidizing, 4161
Flumes, 300, 493, 575, 968, 1542, 1816, 1826, 1902, 2428, 3076, 3442
Forecasting, 340, 743, 864
Foundation performance, 3507
Fourier analysis, 968, 1034
Fourier transform, 3762
Fractures, 4411
Free surfaces, 389
Frequency analysis, 123, 1144
Frequency distribution, 16

- Friction, 836
Friction factor, 3143, 3495
- Gaging stations, 1465
Geographic information systems, 4650
Geometry, 1280
Georgia, 4314
Geotextiles, 1902, 2114
Germany, 2128, 3534, 4621
Gradient, 4161
Grain size, 4756, 4779
Gravel, 981
Gravity, 2640, 2654
Gravity waves, 1335
Great Lakes, 2705, 4289
Groins, structures, 2128, 2142, 2770, 3976, 4024, 4517, 4744
Ground water, 2152, 2654, 4120, 4601
Ground-water flow, 2640
Guidelines, 1748, 4188, 4253
Gulf of Mexico, 4770
- Harbors, 864, 889, 1256, 1268, 1280, 1491, 1816, 3284, 3986, 4014, 4451, 4744
Head loss, 1776
History, 457
Human factors, 275
Hurricanes, 781, 2756, 2982
Hydraulic design, 4314
Hydraulic models, 221, 443, 3169
Hydraulic performance, 1721
Hydraulic roughness, 3143
Hydraulics, 1679, 4531, 4545
Hydrodynamics, 109, 415, 668, 3419, 3546, 3680, 3948, 4289, 4491
Hydrology, 4274
- Ice forces, 4397
Ice loads, 4397
Ice sheets, 4411
Impact, 1640, 2022, 2442, 2573, 2779
Impact forces, 2456
Impact loads, 2508, 2522, 2534, 2584
Incipient motion, 1803
Indonesia, 1443
Infiltration, 2654
Inlets, waterways, 1219, 2258, 2779, 3270, 3284, 3295, 3323, 3642, 4464, 4477, 4517, 4531
Installation, 1631
Interactions, 1060, 1219, 2377, 2548, 3694, 4120, 4821
Ireland, 4557
Islands, 1452
Italy, 2404
- Japan, 137, 794, 1349, 1389, 1465, 1491, 4000, 4038, 4545, 4676
Jets, 4451
Jetties, 1852, 2573, 3295, 3309, 4531
- Kinematics, 502, 537, 565, 1034, 1247, 1776, 2442, 3481
- Laboratory tests, 43, 493, 927, 1022, 1307, 1321, 1583, 1631, 2077, 2626, 2746, 3295, 3628
Lagrangian functions, 4569
Landslides, 1293, 1478
Large structures, 380
Lasers, 527, 602
Leakage, 1556
Limit analysis, 3874
Liquefaction, 1902, 3860
Littoral currents, 175, 233, 602, 1361, 3391, 3419, 3481, 3560, 3628, 3666, 3860

- Littoral deposits, 2779
Littoral drift, 1998, 2871, 2897,
3270, 3309, 3628, 3652, 3830,
4390, 4464, 4545
Loading, 3507
Long waves, 151, 493, 1307, 1321,
1431, 1452, 1478, 3076, 3090
Louisiana, 2756
- Maintenance, 1852, 2770
Maintenance costs, 2969
Mass transport, 4174
Mathematical models, 589, 2941,
3104
Measurement, 286, 1762, 1916,
3129, 3169, 3391, 3431, 3588,
4079, 4098, 4161, 4569
Measuring instruments, 643
Mechanics, 4300
Membranes, 2087
Meteorology, 703, 822, 4200
Mixing, 175, 3419, 4098, 4325, 4569
Model studies, 1748, 4242
Model tests, 1431, 1528, 1693, 1971,
2428, 2484, 2534, 4689
Model verification, 2806, 4730
Modeling, 109, 186, 286, 565, 889,
1205, 1247, 1375, 2036, 2230,
2857, 2982, 2994, 3805, 3913,
4120, 4464, 4477, 4621, 4821
Models, 2, 81, 123, 165, 247, 403,
429, 502, 703, 767, 781, 794,
1048, 1060, 1116, 1144, 1168,
1192, 1307, 1335, 1417, 1589,
2008, 2022, 2178, 2298, 2456,
2494, 3062, 3115, 3207, 3257,
3405, 3419, 3467, 3574, 3784,
3935, 4066, 4214, 4569, 4756,
4770, 4779
Momentum transfer, 175
Monitoring, 889, 1944, 2312, 2871,
4014, 4664, 4689, 4730
- Monte Carlo method, 822, 900, 1665
Morphology, 3231
Movable bed models, 1998, 2258,
2428, 3169, 3295, 3495, 3628
Mud, 3337, 4174
- Navier-Stokes equations, 200
Navigation, 1074, 3231, 3284, 3323,
4390, 4531
Nearshore circulation, 808, 822, 878,
1205, 1335, 1361, 1417, 2391,
2843, 3020, 3694, 3722, 3830,
4000, 4052, 4242
Netherlands, 1876, 3600
Networks, 616
New Zealand, 3284
Noise measurement, 275
Nomographs, 781
Nonlinear analysis, 165, 589
Nonlinear response, 95, 717, 731,
767, 850, 927, 955, 1034, 1048,
1088, 1130, 1156, 1178
Nonlinear systems, 657, 1491
North Carolina, 3521, 3588, 3666,
4517
Numerical analysis, 575, 754, 927,
1130, 1361, 1516, 2548
Numerical models, 30, 95, 137, 200,
233, 300, 340, 389, 465, 551, 668,
941, 1074, 1219, 1256, 1268,
1876, 1930, 2050, 2324, 2338,
2666, 2746, 2770, 2969, 3614,
3722, 3736, 3818, 3830, 3888,
3962, 4174, 4289, 4601, 4807
- Ocean engineering, 457, 565
Ocean waves, 16, 1465, 1789
Oceanography, 3090
Offshore structures, 1603
Optimal design, 1589
Optimization, 479
Oregon, 2718

- Oscillations, 1268, 1491, 2884
Oscillatory flow, 3183, 3244, 3495,
4353, 4779
Outfall sewers, 4228
Outflows, 4120
Outwash, 4148
Overtopping, 1721, 1816, 1840,
1862, 2178, 2192, 2206, 2216,
2598
Oxygen transfer, 403
- Parks, 4274
Particle motion, 3846
Peak values, 900, 2484
Performance, 1852, 4636
Performance evaluation, 2087
Permeability, 2142
Photogrammetry, 3750, 4664
Piers, 2573
Piles, 2142
Pipelines, 3231, 4228
Planning, 3986
Plunging flow, 2442
Polynomials, 1130
Ponding, 2312
Pore pressure, 1916, 3219, 3860
Porosity, 2366
Porous materials, 2063
Porous media, 2377
Ports, 1707, 4376, 4676
Predictions, 123, 314, 429, 502, 703,
743, 864, 878, 941, 1321, 1417,
2077, 2230, 2338, 2806, 2941,
3231, 3378, 3405, 3574, 3652,
4650, 4807, 4821
Pressure measurement, 429, 1034
Pressures, 4161
Probabilistic methods, 2793, 4717
Probabilistic models, 808
Probability, 2560, 4418, 4440
Probability density functions, 368,
850, 4793
- Probability distribution, 328, 2272
Professional development, 4431
Profiles, 2829, 2982, 2994, 3006,
3020, 3048, 3104, 3169, 3194,
3349, 3405, 3442, 3736, 3750,
3784, 3901, 3921, 4052, 4650,
4756
Programs, 4613
Progressive waves, 3183
Projects, 1375, 2941
Propellers, 4451
Protective structures, 1403
Prototypes, 1762
Public land, 4418
Public opinion, 4253
Pumps, 4591
- Quality control, 643
Quays, 4451
- Radioactive tracers, 3901
Random waves, 2, 16, 30, 43, 261,
415, 537, 657, 754, 850, 914, 927,
1144, 1247, 2272, 3006, 3034,
3076, 3442
Ratings, 1852
Rayleigh waves, 914, 2272
Reaeration, 403
Recirculation, 3628
Recreational facilities, 2770
Reefs, 2298
Regulation, 2391
Reliability, 1589
Remote sensing, 1944
Repairing, 4689
Research, 286, 994, 1375, 1876,
1888, 3481
Reservoirs, 1233, 1748, 2101, 2918
Resonance, 1583
Resonators, 1280
Restoration, 4261

- Revetments, 1008, 1556, 1583, 1888,
2206, 2718
Reynolds stress, 200, 4079
Rheological properties, 4174
Rip currents, 1361, 2142, 3391,
3680, 3694, 4000
Riprap, 1233, 1748, 2101
Risk analysis, 4339, 4440, 4717
River flow, 4505
River systems, 2244
Rivers, 1349, 4545, 4557
Rock structures, 2077
Rocks, 1957
Rotational flow, 2178
Roughness, 3129, 3495
Rubble-mound breakwaters, 1516,
1569, 1589, 1603, 1617, 1679,
1776, 1916, 1944, 1957, 1971,
2418
Russia, 2918
- Salt water, 1022
Salt water intrusion, 4601
Sand, 981, 1876, 2050, 2166, 2927,
3034, 3219, 3600, 3642, 3770,
3874, 3888, 3962, 4353, 4390,
4505, 4613
Sand transport, 137, 2284, 2829,
2871, 2911, 2994, 3708, 3736,
3784, 3791, 3846, 3948, 4111,
4148, 4188, 4214, 4464, 4779
Sand waves, 3183, 3521, 3574, 4024
Satellite mapping, 81
Satellite photography, 3762
Scale effect, 403, 1762, 2152, 2192,
2522
Scale models, 1762, 1888, 2101,
2152, 2941
Scattering, 941
Scour, 2152, 2230, 2258, 4397, 4517
Scouring, 1652, 4451, 4676
Screens, 1762
- Sea cliffs, 2793
Sea floor, 941, 955, 2230, 3129,
3155, 3207, 3378, 3507, 3860,
4376
Sea level, 1349, 1503, 3860, 4364,
4418, 4583
Sea state, 703
Sea walls, 1022, 1403, 1840, 1862,
1902, 1985, 2192, 2216, 2442,
2456, 2508, 2612, 2718, 4621
Sea water, 354
Sediment, 2152, 2732, 4161
Sediment concentration, 3901, 3935,
4088
Sediment deposits, 4200, 4214
Sediment transport, 214, 1321, 2022,
2612, 2691, 2756, 2843, 2941,
2994, 3006, 3048, 3062, 3076,
3104, 3115, 3155, 3194, 3231,
3309, 3337, 3349, 3363, 3378,
3405, 3467, 3534, 3546, 3560,
3614, 3628, 3642, 3652, 3736,
3770, 3791, 3805, 3818, 3860,
3888, 3901, 3913, 3921, 4014,
4289, 4300, 4376, 4545, 4744,
4793
Sediment yield, 2391
Sedimentation, 3231
Sedimentology, 2050
Sensitivity analysis, 2746
Sensors, 3453
Settlement analysis, 1902
Sewage disposal, 4325
Shallow water, 95, 109, 123, 221,
465, 502, 551, 589, 602, 668, 878,
889, 955, 1088, 1452, 1930, 2192
Shape, 1957
Shear, 175, 3207
Shear stress, 1168, 3155, 3194, 3337,
3467, 3481, 3913, 4325
Shellfish, 4300, 4353
Ship motion, 1268

- Ships, 4261
- Shoaling, 2, 95, 151, 247, 537, 717,
754, 955, 1130, 3295, 4517
- Shore protection, 2063, 2114, 2128,
2206, 2312, 2352, 2391, 2404,
2418, 2428, 2470, 2640, 2654,
2705, 2718, 2911, 2918, 3034,
3976, 4440
- Shoreline changes, 1985, 2404, 2732,
2756, 2779, 2820, 2829, 2843,
2857, 2884, 2927, 3405, 3521,
3588, 3750, 3770, 3874, 3921,
4000, 4024, 4038, 4364, 4376,
4464, 4613, 4744
- Simulation, 16, 389, 657, 900, 914,
1431, 1789, 3442, 3560, 3818,
3976, 4024, 4242
- Simulation models, 67, 731, 2806
- Slope stability, 1556, 1603
- Slopes, 941, 3913
- Small structures, 380
- Soil mechanics, 1603
- Soil-structure interaction, 3507
- Solitary wave, 1156
- Sonar, 1944
- South Africa, 340
- Spain, 1816, 2806, 2871, 4014, 4418,
4730, 4744
- Spectral analysis, 43, 175
- Spraying, 994, 1022, 1840
- Sri Lanka, 4200
- Stability, 1583, 1617, 1640, 1652,
1665, 1679, 1721, 1748, 1776,
1789, 1803, 1826, 1862, 1888,
1957, 1971, 3534, 4161, 4228,
4664, 4756
- Stabilization, 2640, 2654, 2718,
2829, 3986
- Standing waves, 151, 3090
- Statistical analysis, 900, 914, 1985,
2560
- Statistical models, 1088
- Statistics, 123, 794, 808, 822, 1375,
1503
- Steel pipe piles, 2166
- Stochastic models, 1389, 4300
- Stochastic processes, 878
- Stones, 1583, 1640, 1693
- Storm surges, 822, 994, 1268, 1389,
1403, 1417, 4397
- Storms, 703, 743, 781, 1789, 2982,
3034, 3115, 3257, 3874, 3921,
4300, 4339, 4703
- Stratified flow, 4557
- Streams, 3183
- Stress, 3453
- Stress analysis, 4274
- Structural elements, 4261
- Structural response, 1617
- Submerged flow, 927
- Surf zone, 109, 151, 200, 214, 233,
286, 537, 551, 602, 1178, 1321,
1361, 1431, 3048, 3076, 3104,
3431, 3453, 3694, 3805, 3901,
4066, 4088, 4098, 4111, 4228,
4793
- Surface dynamics, 389
- Surface waves, 565, 1048, 3244,
3935
- Surveys, 2114, 3020
- Suspended sediments, 2612, 3076,
3207, 3257, 3736, 3784, 3791,
3888, 3935, 3948, 3962, 4088,
4098, 4111, 4793
- Tests, 30, 221, 286, 968, 1542, 1816,
3442, 3680
- Texas, 3736
- Theories, 443, 864, 3962
- Three-dimensional analysis, 1102
- Three-dimensional models, 233,
2843
- Tidal currents, 2691, 3722, 4491
- Tidal effects, 2994, 3090, 3574

- Tidal energy, 1478
 Tidal flats, 994
 Tidal waters, 3270, 3284, 3295,
 3323, 3534, 3948, 4242, 4314,
 4477, 4491
 Tides, 629, 1603, 1707, 3431, 3442
 Time studies, 1307
 Toe aprons, 1971
 Topography, 1349, 1417, 1452, 1998,
 3534, 3560, 3762, 4545
 Transducers, 3129
 Trenches, 3231, 4188
 Tributaries, 4289
 Tsunamis, 1443, 1465, 1478, 1707,
 4676
 Turbidity, 4088
 Turbulence, 186, 200, 214, 3207,
 3818, 3935, 4111, 4228, 4325
 Turbulent boundary layers, 3244
 Turbulent diffusion, 4066
 Turbulent flow, 200, 3453
 Two-dimensional models, 3846
 Typhoons, 1389, 1417, 1491

 Uncertainty analysis, 1256, 2560
 Undertow, 3006, 3048, 3062, 3194,
 3419, 3830
 Underwater structures, 380, 927,
 1998, 2312, 2324
 Uniformity, 479
 United Kingdom, 286, 3614, 4253,
 4339
 United States, 3020, 3708
 Uplift pressure, 2008

 Validation, 551, 794, 1256, 3574
 Vegetation, 2626, 3935, 4188
 Velocity, 629, 677, 1116, 1168, 1803,
 2666, 3244, 3431, 3453, 3818,
 4066, 4353, 4793
 Velocity distribution, 565, 1569
 Velocity profile, 109, 527, 551

 Vietnam, 2820
 Virginia, 1985
 Viscosity, 2178
 Vortices, 186, 1168, 3183, 3888,
 3935, 4111, 4821

 Waste disposal, 4274
 Water depth, 516, 677, 878, 1116,
 2324, 3257
 Water levels, 1205, 1826, 2244,
 2793, 4148
 Water pressure, 1603, 3155
 Water quality, 403, 2677, 4557
 Water surface, 850
 Water surface profiles, 629
 Water table, 3860, 4120, 4601
 Water waves, 55, 81, 186, 275, 340,
 457, 465, 502, 516, 527, 589, 657,
 677, 717, 731, 878, 889, 1022,
 1034, 1074, 1088, 1156, 1168,
 1205, 1219, 1256, 1268, 1280,
 1375, 1417, 1478, 1528, 1542,
 1776, 1862, 2063, 2087, 2166,
 2178, 2192, 2377, 2470, 2573,
 3020, 3155, 3363, 4174, 4353,
 4411
 Wave action, 137, 175, 221, 380,
 389, 415, 1603, 1679, 1693, 1930,
 3048, 3337, 3507, 3784, 3791,
 3948, 4038, 4088
 Wave attenuation, 1022, 1916, 3349
 Wave climatology, 314, 328, 575,
 689, 808, 864, 1008, 1233, 1503,
 1789, 2022, 2312, 4464, 4517,
 4621
 Wave diffraction, 2, 731, 754, 1048,
 1862, 2063, 2366
 Wave dispersion, 95, 300, 668, 767,
 836, 941, 1048, 1060, 1116, 1144,
 1631, 1652, 1665, 1840, 2077,
 2298

- Wave energy, 261, 731, 767, 836,
1156, 1205, 2484, 2598, 2626,
3270, 4583, 4591
- Wave equations, 1452, 2324, 2366
- Wave forces, 415, 1168, 1528, 2008,
2050, 2377, 2494, 2508, 2522,
2534, 2548, 2573, 2584, 3129,
3155, 3467, 3481, 3495, 3507,
3694, 4676
- Wave generation, 55, 165, 443, 479,
493, 668, 677, 1293, 1307, 1321,
1335, 2338
- Wave groups, 151, 165, 493, 677,
1178, 1307, 1335, 1491, 1503,
3006, 3143, 3257, 3546
- Wave height, 67, 221, 247, 261, 300,
328, 368, 537, 689, 717, 743, 767,
794, 808, 850, 900, 1192, 1205,
1389, 1431, 1583, 1679, 2272,
2298, 2560, 2640, 2705, 3270,
4770
- Wave measurement, 354, 368, 429,
527, 537, 565, 616, 629, 643, 689,
703, 781, 1034, 1465, 4636, 4770
- Wave pressure, 575, 1403, 1556,
1762, 2442, 2484, 2522
- Wave propagation, 123, 165, 457,
589, 668, 878, 889, 1074, 1102,
1130, 1156, 1335, 1569, 1998,
2626, 3244, 4134, 4411, 4807
- Wave reflection, 43, 55, 443, 955,
968, 1516, 2077, 2284, 2338,
2366, 2418, 2470, 2598, 2612
- Wave refraction, 2, 754, 1048, 2324,
2366, 2691, 3762, 4505
- Wave runup, 233, 551, 981, 994,
1008, 1431, 1452, 1556, 1916,
2206, 2244, 2793, 3104, 3349,
3770, 4120, 4134, 4601
- Wave spectra, 16, 30, 43, 175, 368,
516, 629, 643, 689, 781, 822, 914,
927, 968, 1247, 2272, 3762
- Wave tanks, 479, 717, 1840, 2428,
3034, 3219, 3680, 3830
- Wave velocity, 502, 1569, 1776
- Waves, 3207, 3219, 3378, 3560,
3722, 4066, 4079, 4148, 4569,
4821
- Weibull density functions, 2272
- Weirs, 3309
- Wetlands, 4314
- Wildlife habitats, 4314
- Wind, 354, 1233
- Wind forces, 781, 2206, 2216, 3363,
4188, 4200, 4214, 4364
- Wind speed, 429, 4770
- Wind velocity, 2705
- Wind waves, 30, 429, 1088, 3363
- Yield strength, 3337

AUTHOR INDEX

Page number refers to the first page of paper

- Ahn, Kyungmo, 657
Ahn, Sung Mo., 1516
Ahrens, John P., 981, 3378
Akeda, Sadamitsu, 4353
Akiyama, Yoshinobu, 3860
Alikhani, A., 1528
Alikhani, Amir, 1693
Allsop, N. W. H., 2508, 2522
Allsop, N. William H., 389
Aminti, P., 1542
Andersen, Henning, 968, 1679
Anglin, C. D., 2230
Annandale, G. W., 2230
Aono, Toshio, 2298
Appleton, William S., 4664
Araki, Hideo, 275
Archetti, Renata, 1693
Arès, Raymond, 2101
Arntsen, Øivind A., 565
Asano, Toshiyuki, 3770
Axe, Philip, 2036
Azarinsa, Seyed Ali, 2442
- Baird, Andrew J., 4120
Bakker, Willem T., 1876, 2857
Baldock, Thomas E., 3006, 4161
Bando, Kozo, 3860
Banijamali, B., 95
Barker, Christopher H., 1034
Barnes, T. C. D., 186, 214
Bartels, A., 4689
Basco, David R., 1060, 1985, 2969
Bascom, Willard N., 3020
Battalio, Robert T., P.E., 2691
Battjes, J. A., 109, 1088, 3337
Battjes, Jurjen A., 175
Bauer, Bernard O., 4214
- Bazhenov, Yuri, 2918
Beach, R. A., 2793, 3207
Beachler, Kim E., P.E., 4613
Beale, Robert G., 389
Beccq, Françoise, 465
Bedford, Keith W., 4289
Beji, Serdar, 1048
Benoit, Michel, 465, 1617
Berlamont, Jean, 836
Bian, J., 354
Bird, Paul A. D., 2077
Birkemeier, William A., 3874, 4052
Black, Kerry, 3284
Boczar-Karakiewicz, B., 3546
Bodge, Kevin R., P.E., 4261
Bollmann, Chad A., 2470
Bona, J. L., 3546
Booij, N., 668, 743
Bos, K. J., 2022
Bosboom, J., 109
Bosma, Kirk F., 2829
Bowen, A. J., 3207
Breeding, J. Ernest, Jr., 677
Breteler, M. Klein, 1556
Breteler, Mark Klein, 1888
Briggs, Michael, 1631
Briggs, Michael J., 1219
Brocchini, M., 186, 4134
Brodie, R. P. (Jock), 4390
Brøker, I., 3048, 4703
Brøker, Ida, 2927, 3805
Browder, Albert E., 2312
Brunone, Bruno, 1569
Bullock, Geoff N., 2077
Bullock, Geoffrey N., 2584
Burcharth, H. F., 1589, 1640

- Burcharth, Hans F., 2560
Burger, G., 1957
- Cadevall, Cristina, 1816
Caires, S., 743
Camfield, Fred E., 1583
Capobianco, Michele, 2884
Caron, Octave, 1233, 1748
Castañeda, A. M., 4014
Chadwick, Andrew, 2036
Chae, J. W., 1268
Chakrabarti, Subrata K., 380
Chakrabarti, Sumita, 380
Chan, Ray T. C., 3006
Chang, Kuang-An, 527
Chawla, Arun, 2
Chen, Qin, 1060
Chen, Renjie, 2312
Cho, Yong-Sik, 955
Christiani, E., 1589
Christopoulos, Spiros, 689
Cialone, Mary A., 3921, 4531
Cieślakiewicz, Witold, 703, 1375
Cinotto, Charles M., 2206
Claessen, Edward W. M., 2428
Clark, Stephen, 3784
Coates, L. E., 3257
Collins, Michael B., 3948
Cook, Benjamin, 1443
Cornett, A. M., 2230
Cox, Daniel T., 551, 3194
Craig, Kenneth R., II, 602
Creed, Christopher G., 4464
Cruz, Eric C., 2298
Curtis, William R., 2677
- Dally, W. R., 808
Dally, William R., 3419
Dalrymple, Robert A., 731, 1074,
2829
Damgaard, Jesper S., 3614, 3913
d'Angremond, Kees, 1971, 2418
- Davidson, Mark A., 2077
Davies, Michael H., 1679, 1748,
3507
Davies, P., 214
Davis, J. P., 2522
Davis, Jack E., 2677
Davis, Justin, 4242
Davis, Richard A., Jr., 2982
de Haas, Paul, 165
de Jong, Rutger J., 2418
de la Peña, Jose M., 889
de Lange, Willem, 3284
de Looff, A. P., 2770
de Looff, Harry, 2746
de Rouck, Julien, 1603, 1916, 1944
de Somer, Marc, 1916
de Vries, J. M., 4274
de Waal, Johannes P., 2216
Dean, Robert G., 2312, 3115, 3680
Deguchi, Ichiro, 3349, 3888
Deigaard, R., 3048
Deigaard, Rolf, 3805
Demirbilek, Zeki, 1219, 1256
Dennis, John M., 389
Dennis, William A., 4517
Dette, Hans-H., 3442
Diaz Rato, J. L., 1762
Dibajnia, Mohammad, 3104, 3791
DiCastro, Dan, 4376
Dingemans, M. W., 1156, 2022, 4821
Dingemans, Maarten, 165
Dombrowski, Michael R., 3270
Dong, Lifen, 2324
Dong, Ping, 4717
Donnars, Philippe, 1617
Douglass, Scott L., 3708
Dubi, Alfonse, 2626
Dunaszegi, L., 2230
Dupuis, Pierre, 1233, 2101
Duy, Nguyen The, 200

- Ebersole, Bruce A., 2779
Edge, B. L., 2087
Edge, Billy L., 941, 3309
Elbahrawy, Ali, 3976
Eldeberky, Y., 1088
Elfiky, Abd-Elfattah, 3976
Elfrink, Berry, 3805
Elgar, Steve, 3666
Elmongy, Abd-Elmohsen, 3976
Elsaeed, Gamal, 3976
Elwany, M. Hany S., 314
Escartín, F. Javier, 4014, 4744
- Falqués, Albert, 3560
Faria, A. F. Garcez, 3391
Feddersen, Falk, 3666
Fenton, J. D., 1130
Fenton, John D., 575, 1102
Fernández, A. J., 4418
Fisher, John S., 3750
Fisher, Paul R., 2994
Fleming, Chris, 4339
Fontijn, Henri L., 4228
Foster, D. L., 3207
Fowler, Jimmy, 1631
Fowler, Jimmy E., 3628
Franco, Claudio, 2008
Franco, Leopoldo, 2008
Fredsoe, Jørgen, 3231
Frigaard, P., 1640
Fujiwara, Ryuichi, 16, 1516
Fukumoto, Tadashi, 300
Fukunaga, Masahiko, 2666
Fukushima, Tadahiro, 2666
- Gadd, Peter E., 4397
Galofré, J., 4730
Galofré, Jordi, 4744
García, Cristina, 1816
Gares, Paul A., 4214
Gelfenbaum, Guy, 3453
Glodenis, Marina, 2918
- Gobbi, Maurício F., 1116
Goda, Yoshimi, 261, 629
Golan, Arik, 4376
Goldenbogen, Roland, 3534
Golik, Abraham, 4376
Gomyoh, Michio, 1652
Göricke, Frank, 2142
Gotoh, Hitoshi, 3155, 4300
Gouloumis, Spiros M., 429
Gracia, Vicente, 4098
Graff, Jerzy, 703, 1375
Grant, Geoffrey T., 2152
Gravens, Mark B., 4477
Greated, C. A., 214
Green, Debra R., 1219
Greenwood, B., 3546
Grilli, Stéphan T., 717
Groenewoud, Martin D., 2428, 2857
Grønbech, John, 968, 1679
Grüne, Joachim, 994, 1008
Guillen, Jorge, 2884
Guo, Lulin, 731
Guza, R. T., 3666
- Haines, John W., 3453
Hald, T., 1640
Hallermeier, Robert J., 2705, 3874
Hamill, G. A., 4451, 4557
Hamilton, David G., 3628
Hamm, Luc, 537
Hands, Edward B., 3378
Hanes, Daniel M., 3129, 3846
Hann, D. B., 214
Hansen, Erik Asp, 3805
Hansen, Mark E., 2756
Hanslow, David J., 2244
Hanson, Hans, 4024
Hanzawa, Minoru, 479, 1665
Harari, Pinkhas, 4376
Harcastle, P. J., 3257
Hasegawa, Iwao, 2640
Hashida, Misao, 1022, 3363

- Hashimoto, Noriaki, 30, 629, 1465
Hatada, Yoshio, 1389
Hathaway, Kent K., 4052
Hattori, Masatato, 2456
Haydon, T. R., 214
Healy, Terry, 3284
Hearon, G. E., 2718
Heilman, Daniel J., 3309
Hemsley, J. Michael, P.E., 616
Herbers, T. H. C., 3666
Herbich, John B., 3976
Hewson, Peter J., 2584
Hibbert, Kevin, 2244
Hinata, Hirofumi, 3431
Hoekstra, P., 2897
Holman, R. A., 3207
Holman, Rob, 3521
Holman, Rob A., 3588
Holmes, Patrick, 3006, 4161
Holthuijsen, L. H., 668, 743, 1247
Horikawa, Kiyoshi, 3405, 4188
Horn, Diane P., 4120
Horrillo, Juan, 717
Hosoi, Yoshihiko, 275
Hotta, Shintaro, 4188
Housley, John G., P.E., 2911
Houwman, K. T., 2897
Houwman, Klaas T., 4793
Howarth, M. W., 2522
Howell, Gary L., 3323
Hsu, John R. C., 3986
Huan, Nguyen Ngoc, 2820
Hubertz, Jon M., 4770
Hughes, Steven A., 2258
Hulscher, S. J. M. H., 3574
Humphery, J. D., 3257
Huntley, David A., 2077, 2612, 3090
Hwang, Ching-Her, 4088
Hwang, K. S., 3219
Hwang, H. H., 3219
Ikeno, Masaaki, 3076
Ilic, Suzana, 2036
Inman, Douglas L., 314
Iranzo, Vicente, 3560
Irie, I., 1840
Irie, Isao, 1022, 1998, 2391
Irish, Jennifer L., 3736
Ishii, Toshimasa, 754
Ishikawa, Motoyasu, 3860
Isobe, Masahiko, 16, 43, 443, 754, 767, 2324
Itabashi, Naoki, 137
Ito, Kazunori, 443
Ito, Shinichi, 2166
Itoh, Sadahiko, 275
Ivanova, Nadya, 2918
Iwata, Koichiro, 2338
Izumiyama, Koh, 4411
Jackson, Derek W. T., 4214
Jaffe, Bruce E., 2756
Jakobsen, Per Roed, 4703
Janssen, C. Marjolein, 4779
Jenkins, Scott A., 314
Jensen, Jacob Hjelmager, 3231
Jensen, Robert E., 781
Jensen, Thomas, 968, 1679
Jeong, W. M., 1268
Jervis, M., 2192
Jetté, Christopher D., 3129
Jeuken, Claire, 4491
Jiang, Qin, 4174
Jiménez, José A., 2806, 4098
Johanson, Hans, 1888
Johnson, Bradley D., 551
Johnston, H. T., 4557
Jones, Bryan N., 1985
Jones, R. J., 2522
Juang, Jea Tzyy, 3762
Juhl, J., 1528
Juhl, Jørgen, 1693

- Jung, K. T., 1268
Justesen, Peter, 3805
- Kaczmarek, Jarka, 4364
Kaczmarek, Leszek M., 3467
Kaihatu, James M., 123, 1144
Kaiser, Ralf, 4621
Kajima, R., 1862
Kakuno, Shohachi, 1516
Kamikubo, Y., 1840
Kamphuis, J. William, 221, 1431,
2258
Kana, Timothy W., 2732, 4314, 4756
Kanada, Shigeo, 4411
Kanazawa, Hiroshi, 2640
Kang, Hong-Yoon, 4601
Kânog`lu, Utku, 1452
Kant, G., 2770, 2820
Kariyazono, Yoshihisa, 2166
Karjadi, Entin A., 233
Karlsson, Robert I., 2152
Kaskevitch, Liya, 2918
Katmarian, R. Eric, 4314
Kato, Hajime, 794, 2391
Katoh, Kazumasa, 2640, 2654
Katori, Sadakazu, 3818
Katsui, Hidehiro, 443, 3183
Kawaguchi, Eiichi, 1349
Kawakami, Hiroshi, 3363
Kawamori, Akira, 1707
Kawanakajima, Y., 4000
Kawasaki, Koji, 2338
Kee, S. T., 2087
Kendall, Thomas, 4664
Kennedy, A. B., 1130
Kennedy, Andrew B., 1102
Khabidov, Alexander, 2918
Kim, Do-Sam, 2338
Kim, M. H., 2087
Kim, Taerim, 3830
Kimura, Akira, 864, 1776, 2272,
2366
Kimura, Katsutoshi, 4676
Kimura, Yoshiaki, 1707
Kioka, Wataru, 1491
Kirby, James T., 2, 123, 1116, 1144,
1361
Kitamura, Fujio, 1465
Klammer, P., 2534
Klopman, G., 109
Klopman, Gert, 165
Knaack, Heiko, 4621
Kobayashi, N., 1721, 1803
Kobayashi, Nobuhisa, 233, 551,
3194, 4148
Kojima, Haruyuki, 927
Komar, P. D., 2718, 2793
Kondo, Hideo, 1707, 4583, 4591
Konicki, Kathryn M., 3588
Kortenhaus, A., 1403, 2534
Kos'yan, R. D., 4111
Koyabu, Tsuyoshi, 275
Kraak, Arie W., 2746
Kranenburg, C., 3337
Kraus, Nicholas C., 3020, 3034,
4024
Krecic, Michael R., 3846
Kriebel, David L., 2470
Kroon, A., 2897
Krylenko, M. V., 4111
Kudale, M. D., 1721
Kumagai, Takahiro, 2843
Kunz, H., 4111
Kunz, Hans, 2128, 3534
Kurata, Katsuhiko, 1516
Kuriyama, Yoshiaki, 247
Kuwabara, Shinji, 1707
Kuznetsov, S. Yu., 4111
Kwan, K. H., 4569
Kweon, Hyuck-Min, 261
- Lai, M.-Y., 914
Lamberti, A., 1542
Lamberti, Alberto, 2352

- Larson, Magnus, 3244
Lastrup, Christian, 2857, 2927
Lee, B. H., 3219
Lee, Jiin Jen, 1293
Lee, Jiin-Jen, 2178, 4325
Lee, Jong-In, 955
Lee, Jong-Kyu, 955
Leidersdorf, Craig B., 4397
Lesnik, John, 1852
Leyden, V. M., 808
Li, Li, 1074
Liaw, S.-R., 2494
Lillycrop, W. Jeff, 3736
Lin, Lihwa, 643, 3295
Lin, Paul C.-P., P.E., 3642
Lin, Po-Ching, 4088
Lissev, Nikolay, 1735
List, Jeffrey H., 2756
Liu, Paul C., 457
Liu, Philip L.-F., 527, 589
Liu, Xiaodong, 2548, 4411
Liu, Zhou, 2560
Long, Charles E., 4052
Losada, I. J., 4418
Losada, M. A., 1762
Loveless, John H., 2152
Lozano, José, 889
Lu, Chia-Chi, 822
Luo, Weimin, 836
Lupón, Nuria, 4014, 4744
- MacIver, Ruairi D., 3481
Maddrell, Roger, 4339
Madsen, Holger Toxvig, 2927
Madsen, P. A., 95, 1178, 3048
Madsen, Per A., 1060
Maeno, Yoshihiko, 3860
Mancinelli, Alessandro, 2352
Mann, Douglas W., P.E., 4613
Mano, Akira, 4505
Mansard, Etienne P. D., 1679, 1748
Manzenrieder, H. A., 4274
- Marcos, Frédéric, 465
Marinski, Jordan, 2484
Martens, Jean-Pierre, 1916
Martin, F. L., 1762
Mase, Hajime, 2366
Mason, Travis, 3948
Mason, Travis E., 4120
Masselink, Gerhard, 4200
Mathew, Joseph, 3284
Matsukawa, Fumihiko, 2640
Matsumi, Yoshiharu, 1776
Matsumoto, Akira, 479
Matsumoto, Teruki, 1321
Matsunaga, Hiroshi, 1516
Matsunaga, Nobuhiro, 1022, 3363
Matsuoka, Gaku, 2166, 4353
McClarty, A., 4689
McDougal, W. G., 2377, 2718, 2793
McGarvey, J. A., 4451
McKee, Philip A., 4314
McKenna, J. E., 2508
Medina, Josep R., 328, 1789, 2871
Medina, R., 4418, 4730
Mehta, Ashish J., 3270
Melby, J. A., 1803
Melby, Jeffrey A., 4664
Méndez, F., 4418
Mesa, Chuck, 4636
Miles, Jonathon R., 2612
Miller, C., 1403
Miller, Herman C., 4517
Mimura, Nobuo, 1349, 2391
Mitsui, Masao, 629
Mizuguchi, M., 493
Mizuguchi, Masaru, 1307, 2598,
3818
Mizuno, Yuzo, 4591, 4676
Mizutani, N., 2377
Mlynarski, Jeffrey M., 1074
Mochizuki, Hitoshi, 1280
Mochizuki, Masashi, 443
Mocke, G. P., 1205

- Moe, Geir, 565
 Mohan, Ram K., P.E., 4756
 Mohan, Ram Krishna, P.E., 2732
 Monbaliu, Jaak, 836
 Monsó, José Luis, 1816
 Montoto, Amadeu, 3560
 Montoya, F. J., 4730
 Moores, S. P., 3257
 Mori, Nobuhito, 850
 Morita, Satoshi, 1280
 Moriya, Yoichi, 2598
 Mostafa, A. M., 2377
 Mounsey, Chris, 4339
 Moutzouris, C. I., 403, 1826
 Murakami, Hitoshi, 275
 Murakami, Keisuke, 927, 1840
 Murray, Russell J., 4390
 Mutsuda, Hidemi, 300, 2442
- Nadaoka, Kazuo, 1048, 3183, 3431
 Nagai, Toshihiko, 629, 1465
 Nagase, Satoru, 1307
 Naim, R. B., 2230
 Nakagawa, Yasuyuki, 30, 4676
 Nakamura, Satoshi, 1503
 Nakamura, Takayuki, 1280
 Nelson, Raymond C., 3143
 Neshaei, M. Ahmad L., 3006
 Neue, Jürgen, 3442
 Nicholls, Robert J., 3874
 Nielsen, Peter, 2244, 3495, 3784,
 4066, 4601
 Niemeyer, Hanz D., 4621
 Nishi, Ryuichiro, 2666, 3034
 Nobuoka, Hisamichi, 794, 2391
 Nolten, R., 2770
 Nwogu, Okey George, 4807
- Ochi, Michel K., 878
 O'Donoghue, Tom, 2284
 Oh, Tae-Myoung, 3680
 Ohara, S., 4000
- O'Hare, Tim J., 2994, 3090
 Ohno, Kenichi, 1776
 Ohta, Takao, 864, 2272
 Okayasu, Akio, 200, 1321
 Oliver, John, 1852
 O'Neil, Sean, 4289
 Ono, Masanobu, 3349, 3888
 Osanai, Senji, 4591
 Osiecki, Daniel A., 3419
 Ostrowski, Rafaxl, 3467
 Otay, Emre N., 3722
 Otta, A. K., 1156
 Oumeraci, H., 1403, 2534
 Overton, Margery F., 3750
 Owczarczyk, Andrzej, 3901
 Oya, Atsushi, 300
 Özkan-Haller, H. Tuba, 2, 1361
- Palao, Ian M., 368
 Panchang, Vijay, 1256
 Panchang, Vijay G., 81
 Park, W. S., 1268
 Parson, Larry E., 3736
 Pattiaratchi, Charitha, 4200
 Péchon, Philippe, 2050
 Peregrine, D. H., 186, 2192, 2573,
 4134
 Peters, Karsten, 3442
 Petroff, Catherine, 1293, 1443
 Phelp, D., 340, 4689
 Pilarczyk, K. W., 1556
 Pilarczyk, Krystian W., 2114
 Pirie, Douglas, 1852
 Plant, Nathaniel, 3521
 Plotkin, Don, 1852
 Pluijm, M., 2770
 Podber, David P., 4289
 Pollock, Cheryl, 1631
 Polnikov, V., 1088
 Porter, Mark, 4390
 Pruszek, Z., 2820
 Pruszek, Zbigniew, 3901

- Purnell, Reg, 4253
Pykhov, N. V., 4111
- Radder, A. C., 1156, 4821
Raichlen, Fredric, 1293
Rakha, K. A., 3048
Raudkivi, Arved J., 2142
Reniers, Ad, 175
Resio, Donald, 1631
Resio, Donald T., 3378
Ribberink, Jan S., 4779
Riddell, Keith J., 4717
Ris, R. C., 668, 1247
Rivero, Francisco J., 1168, 4098
Robillard, David J., 878
Robinson, David A., 4390
Rodríguez, Andrés, 4098
Roelvink, J. A., 109, 2022, 2897
Rogers, W. Erick, 2941
Romańczyk, W., 3546
Rønberg, J. K., 3048
Rosati, Julie D., 3628
Rosati, Julie Dean, 2779
Rose, C. P., 3257
Rosen, Dov S., 4376
Rossouw, Jan, 328
Rossouw, M., 340
Róz'yiński, Grzegorz, 4364
Ruessink, B. G., 2897
Ruessink, Gerben, 4793
Ruggiero, P., 2793
Russell, Paul E., 2612
Ryan, Joseph A., P.E., 4650
Rybak, Oleg, 2918
- Sabeur, Zoheir A., 389
Saeki, Hiroshi, 2166
Saito, K., 4000
Sakai, Kazuhiko, 1652
Sakai, Shigeki, 2548, 4411
Sakai, Tetsuo, 3155, 4300
Sakakibara, Hiroshi, 2366
- Sakakiyama, T., 1862
Saleh, Wameidh M., 3481
Sallenger, Asbury H., Jr., 2756
Sánchez-Arcilla, Agustín, 2806, 4098
Sancho, F. E., 1335
Santás, José C., 889
S.-Arcilla, Agustín, 1168
Sasamoto, Makoto, 4411
Sasso, R. Harvey, P.E., 3642
Sato, Hirokazu, 1665
Sato, Koichi, 2166
Sato, Michio, 2666
Savkin, Valery, 2918
Sawamoto, Masaki, 4505
Sawaragi, Toru, 3349, 3888
Schäffer, H. A., 95, 1178
Schäffer, Hemming A., 55
Scheffner, Norman W., 4440
Schiereck, Gerrit J., 1971, 4228
Schofield, Sidney, 643
Schoonees, J. S., 3652
Schroeder, Ernst, 3534
Seabergh, William C., 4531
Seaman, Roy C., 2284
Seelig, William N., 981
Serra, José, 2871
Shah, Adam M., 1431
Shak, Arthur T., P.E., 4650
Sharma, Jagat N., 354
Sheng, Y. Peter, 4242
Shepherd, Ian E., 3169
Sherman, Douglas J., 4214
Shibayama, Tomoya, 200, 3062
Shimizu, Kazuyoshi, 1465
Shimizu, Takao, 3076
Shimizu, Takuzo, 2843
Shimosako, Kenichiro, 1665
Shimosako, Ken-ichiro, 1902
Shin, Cheol S., 2969
Shoshany, Maxim, 4376
Siddabathula, M., 81
Sigurdarson, Sigurdur, 1640

- Silvester, Richard, 3986
Simmonds, David J., 3090
Simons, Richard R., 3481
Skaja, Marek, 4364
Skourup, Jesper, 55
Sloth, Peter, 1693
Smit, F., 1205
Smith, Jane M., 3628
Smith, Susan, 502
Soares, C. Guedes, 743
Sobey, Rodney J., 67, 1034
Solomonidis, Christos, 689
Somers, Christel, 1876
Sørensen, J. Dalsgaard, 1589
Sørensen, O. R., 95, 1178
Sørensen, Ole R., 1060
Sørensen, Per, 2927
Soulsby, Richard L., 3614, 3913
Southgate, Howard N., 286
Spanhoff, R., 2897
Spanhoff, Ruud, 2857
Stansby, P. K., 186
Stanton, T. P., 3391
Stanton, Timothy P., 4079
Stauble, Donald K., 3921, 4531
Steetzel, Henk J., 2746
Stelling, Guus S., 1876
Stive, Marcel J. F., 2884
Stoutjesdijk, Theo, 1888
Strange, R. Rea, III, 822
Stripling, Stuart, 286
Suriamihardja, D. A., 3694
Suzuki, Kojiro, 1652, 1902
Suzuki, Yasuyuki, 1321
Svendsen, I. A., 151, 1192, 1335
Swan, C., 4569
Swan, Christopher, 502
Synolakis, Costas Emmanuel, 1452, 1478

Tada, Akihide, 300
Tadepalli, Srinivas, 1478

Takahashi, Atsushi, 4545
Takahashi, Fumihiko, 4545
Takahashi, Shigeo, 1652, 1665, 1902
Takahashi, Tomoharu, 629
Takayama, Tomotsuka, 1665
Takayama, Tomotuka, 1652
Takewaka, Satoshi, 1998
Tanaka, Hitoshi, 4545
Tanimoto, Katsutoshi, 1665, 3405
Tega, Yukiko, 4148
Teisson, Charles, 2050
Teng, Chung-Chu, 368
Theron, A. K., 3652
Thevenot, Michelle M., 4024
Thieke, Robert J., 602
Thompson, Edward F., 4440
Thorne, P. D., 3257
Thornton, E. B., 3391
Thornton, Edward B., 4079
Togashi, Hiroyoshi, 2063
Toita, H., 493
Tokubuchi, Katsumasa, 1902
Tomasicchio, G. R., 1528
Tomasicchio, Giuseppe R., 1569
Tomasicchio, Ugo, 2404
Tönjes, Patrick, 2216
Tørum, Alf, 1735, 2626
Toue, Takao, 3183
Tournier, Jean-Pierre, 1233, 2101
Townsend, Murray, 575
Trampenau, Thomas, 2142
Trivedi, Dilip, P.E., 2691
Trizno, Anatoly, 2918
Troch, Peter, 1916
Tryggestad, S., 354
Tsai, Chin-Chi, 4088
Tsai, Li-Hung, 4088
Tsay, Ting-Kuei, 589
Tsoukala, V. K., 403
Tsuchiya, Yoshito, 3694, 4038
Tsujiimoto, Gozo, 3935
Tsujioka, Nobuaki, 2456

- Tsuruya, Hiroichi, 30, 4676
Turner, Ian L., 2677
Turnham, J., 2230
Tutuarima, W. H., 1957
Tzang, S.-Y., 2494
- Uchida, K., 4000
Uda, T., 4000
Uda, Takaaki, 137
Uittenbogaard, R. E., 4821
- van Damme, Luc, 1603, 1916, 1944
van de Graaff, Jan, 2428, 2857
van der Biezen, Stephan C., 2428
van der Meer, Jentsje W., 1957,
2008, 2216, 2418
van der Meulen, Ton, 1971
Van Dongeren, A. R., 1335
van Endt, M., 743
van Gent, Marcel R. A., 1930
van Hove, Conan, 1916
van Kessel, Thijs, 3337
van Kester, J. A. Th. M., 4821
van Kuik, Christine, 1876
Vann, A. M., 2522
Vaudrey, Kennon D., 4397
Veeramony, J., 151, 1192
Verhagen, Henk Jan, 4431
Verhagen, L. A., 516
Vermeir, Dierik, 1916
Vicinanza, D., 2508
Vidal, C., 1762
Vidaor, Alfonso, 1816, 4014, 4744
Vincent, Charles L., 781
Vinh, Ton That, 2820
Voulgaris, George, 3948
- Wada, Akira, 4353
Walkden, Michael J. A., 2584
Walker, S. A., 4557
Walstra, D. J. R., 1205
Wang, Hsiang, 643, 3295, 3830
Wang, Ping, 2982
Wang, Xu, 3295
Wang, Zeya, 1008
Ward, Donald L., 2206
Watabe, Tomiji, 4591
Watanabe, Akira, 754, 767, 2324,
2843, 3104, 3791, 3818, 4174
Watson, Gary, 1417
Watts, Philip, 1293
West, J. R., 3257
White, Thomas E., 3962
Whitehouse, Richard J. S., 3913
Whittaker, T. T. J., 2508
Wibner, Christopher G., 2206
Wiegel, Robert L., 3020
Wierzchnicki, Ryszard, 3901
Wijnberg, Kathelijne M., 3600
Williams, J. J., 3257
Wilson, D. J., 3257
Winyu, Rattanapitikon, 3062
Wood, D. J., 2573
Work, Paul A., 2941, 3722
Wu, Ji, 3762
Wu, Lilun, 4325
Wu, Nan-Jing, 589
Wutkowski, Michael, 4440
Wutkowski, Michael J., 4517
- Xu, Bingyi, 1256
Xu, Jianlu, 67
- Yabe, Kouichi, 3860
Yagi, Hiroshi, 3431
Yamaguchi, Masataka, 900, 1389
Yamaji, Kosuke, 137
Yamamoto, Shogo, 767
Yamamoto, Yoshimichi, 137, 3405
Yamashiro, Masaru, 927
Yamashita, Takao, 1417
Yamashita, Toshihiko, 2166, 4353
Yanagishima, Shin-ichi, 2654
Yano, Kenji, 4353

- Yasuda, Takashi, 300, 850, 2442
Yedapin, Veniamin, 2918
Yim, John Z., 914
Yokoki, Hiromune, 43
Yokota, K., 4000
Yoshida, Akinori, 927
You, Zai-Jin, 3495, 4066
Young, I. R., 516
Yu, Ke, 1192
Yu, Xiping, 2063
Yu, Yu-xiu, 415
Zawadzka, Elz'bieta, 2955
Zeidler, Ryszard B., 3901, 4364
Zelensky, Grigory, 2918
Zhang, Jun, 2206
Zhang, L., 2087
Zhang, Libang, 941
Zhang, Ning-chuan, 415
Zhao, Qun, 415
Zheng, Jie, 3115
Zhuang, Fei, 2178
Zyserman, J. A., 4703

Volume 4

BRIGGS

Coastal Engineering 1996

Proceedings of the
twenty-fifth international conference

September 2-6, 1996
The Peabody Hotel
Orlando, Florida

Held under the auspices of the
Coastal Engineering Research Council of the
American Society of Civil Engineers

Edited by Billy L. Edge

Published by the

ASCE *American Society
of Civil Engineers*

345 East 47th Street
New York, New York 10017-2398

Abstract:

This proceedings contains over 370 papers presented at the 25th International Conference on Coastal Engineering which was held in Orlando, Florida, 2-6 September, 1996. The book is divided into six parts: 1) Characteristics of coastal waves and currents; 2) long waves and storm surges; 3) coastal structures; 4) coastal processes and sediment transport; 5) coastal, estuarine and environmental problems; and 6) case studies. The individual papers include such topics as the effects of wind, waves, storms and currents as well as the study of sedimentation, erosion and beach nourishment. Special emphasis is given to case studies of completed engineering projects. With the inclusion of both theoretical and practical information, these papers provide the civil engineer and professionals in related fields with a broad range of information on coastal engineering.

Library of Congress Cataloging-in-Publication Data

Coastal engineering 1996 : proceedings of the twenty-fifth international conference, September 2-6, 1996, The Peabody Hotel, Orlando, Florida / edited by Billy L. Edge.

p. cm.

"Held under the auspices of the Coastal Engineering Research Council of the American Society of Civil Engineers."

ISBN 0-7844-0242-6

I. Coastal engineering--Congresses. 2. Ocean waves--Congresses. I. Edge, Billy L. II. Coastal Engineering Research Council (U.S.) III. International Conference on Coastal Engineering (25th : 1996 : Orlando, Fla.)

TC203.5.C6184 1997

97-10664

627.58--dc21

CIP

The Society is not responsible for any statements made or opinions expressed in its publications.

Photocopies. Authorization to photocopy material for internal or personal use under circumstances not falling within the fair use provisions of the Copyright Act is granted by ASCE to libraries and other users registered with the Copyright Clearance Center (CCC) Transactional Reporting Service, provided that the base fee of \$4.00 per article plus \$.25 per page is paid directly to CCC, 222 Rosewood, Drive, Danvers, MA 01923. The identification for ASCE Books is 0-7844-0242-6/97/\$4.00 + \$.25 per copy. Requests for special permission or bulk copying should be addressed to Permissions & Copyright Dept., ASCE.

Copyright © 1997 by the American Society of Civil Engineers,
All Rights Reserved.

Library of Congress Catalog Card No: 97-10664

ISBN 0-7844-0242-6

Manufactured in the United States of America.

Cover: One year after nourishment at Palm Beach, Florida. Photo courtesy of Applied Technology & Management, Inc. and Aerial Photography, Inc.

CONTENTS

Part I Characteristics of Coastal Waves and Currents

CHAPTER 1	
Experimental Study of Breaking Waves over a Shoal	2
<i>Arun Chawla, H. Tuba Ozkan-Haller, James T. Kirby</i>	
CHAPTER 2	
A Method for Estimating Standardized Bimodal Directional Spectra	16
<i>Ryuichi Fujiwara, Masahiko Isobe</i>	
CHAPTER 3	
The Effects of Currents on Estimations of Directional Wave Spectra	30
<i>Yasuyuki Nakagawa, Hiroichi Tsuruya, Noriaki Hashimoto</i>	
CHAPTER 4	
A Method for Estimating Directional Spectra in a Field of Incident and Reflected Waves	43
<i>Hiromune Yokoki, Masahiko Isobe</i>	
CHAPTER 5	
Active Absorption of Multidirectional Waves	55
<i>Hemming A. Schaffer, Jesper Skourup</i>	
CHAPTER 6	
Time-Averaged Wave Field Evolution in Coastal Zone	67
<i>Jianlu Xu, Rodney J. Sobey</i>	
CHAPTER 7	
Quality Control of GEOSAT Wave Data for Engineering Applications	81
<i>M. Siddabathula, Vijay G. Panchang</i>	
CHAPTER 8	
Boussinesq Type Equations with High Accuracy in Dispersion and Nonlinearity	95
<i>P.A. Madsen, B. Banijamali, H.A. Schaffer, O.R. Sorensen</i>	
CHAPTER 9	
Wave Kinematics Computations Using Boussinesq Models	109
<i>J. Bosboom, G. Klopman, J.A. Roelvink, J.A. Battjes</i>	
CHAPTER 10	
Effects of Mode Truncation and Dissipation on Predictions of Higher Order Statistics ..	123
<i>James M. Kaihatu, James T. Kirby</i>	
CHAPTER 11	
Field Observation of Movement of Sand Body Due to Waves and Verification of Its Mechanism by Numerical Model	137
<i>Takaaki Uda, Yoshimichi Yamamoto, Naoki Itabashi, Kosuke Yamaji</i>	

CHAPTER 12	
Wave Groups in the Surf-Zone: Model & Experiments	151
<i>J. Veeramony, I. A. Svendsen</i>	
CHAPTER 13	
Simulation of Propagating Nonlinear Wave Groups	165
<i>Paul de Haas, Maarten Dingemans, Gert Klopman</i>	
CHAPTER 14	
Cross-Shore Momentum Flux Due to Shear Instabilities	175
<i>Ad Reniers, Jurjen A. Battjes</i>	
CHAPTER 15	
Modelling Post-Wave Breaking Turbulence and Vorticity	186
<i>T.C.D. Barnes, M. Brocchini, D.H. Peregrine, P.K. Stansby</i>	
CHAPTER 16	
A Turbulent Flow Model for Breaking Waves	200
<i>Nguyen The Duy, Tomoya Shibayama, Akio Okayasu</i>	
CHAPTER 17	
Turbulence Structures in the Surf Zone	214
<i>T.R. Haydon, D.B. Hann, P. Davies, C.A. Greated, T.C.D. Barnes</i>	
CHAPTER 18	
Experiments on Design Wave Height in Shallow Water	221
<i>J. William Kamphuis</i>	
CHAPTER 19	
Time-Dependent Quasi-3D Modeling of Breaking Waves on Beaches	233
<i>Entin A. Karjadi, Nobuhisa Kobayashi</i>	
CHAPTER 20	
Models of Wave Height and Fraction of Breaking Waves on a Barred Beach	247
<i>Yoshiaki Kuriyama</i>	
CHAPTER 21	
A Parametric Model for Random Wave Deformation by Breaking on Arbitrary Beach Profiles	261
<i>Hyuck-Min Kweon, Yoshimi Goda</i>	
CHAPTER 22	
Generation Characteristics of Wave Sounds as a Factor of Beach Amenity	275
<i>Hitoshi Murakami, Sadahiko Itoh, Yoshihiko Hosoi, Hideo Araki and Tsuyoshi Koyabu</i>	
CHAPTER 23	
Measurements of Wave Breaking in the UK Coastal Research Facility	286
<i>Howard N. Southgate, Stuart Stripling</i>	
CHAPTER 24	
A New Type Breaker Forming a Giant Jet and Its Decaying Properties	300

CHAPTER 25	
Wave Climate Cycles and Coastal Engineering Practice	314
<i>Douglas L. Inman, Scott A. Jenkins, M. Hany S. Elwany</i>	
CHAPTER 26	
Stability of Design Wave Estimates	328
<i>Jan Rossouw, Josep R. Medina</i>	
CHAPTER 27	
An Evaluation of Two Wave Forecast Models for the South African Region	340
<i>M. Rossouw, D. Phelp</i>	
CHAPTER 28	
A Comprehensive Wind, Wave, and Current Measurement Program in the South China Sea	354
<i>Jagat N. Sharma, S. Tryggestad, J. Bian</i>	
CHAPTER 29	
Wave Height and Period Distributions from Long-Term Wave Measurement	368
<i>Chung-Chu Teng, Ian M. Palao</i>	
CHAPTER 30	
Interference of Small Structures in the Vicinity of Large Structures	380
<i>Subrata K. Chakrabarti, Sumita Chakrabarti</i>	
CHAPTER 31	
Wave Dynamics at Coastal Structures: Development of a Numerical Model for Free Surface Flow	389
<i>Zoheir A. Sabeur, N. William H. Allsop, Robert G. Beale, John M. Dennis</i>	
CHAPTER 32	
Scale Effects in Oxygenation in the Breaker Zone of Coastal Structures	403
<i>V.K. Tsoukala, C.I. Moutzouris</i>	
CHAPTER 33	
Wave Actions on a Vertical Cylinder in Multi-Directional Random Waves	415
<i>Yu-xiu Yu, Ning-chuan Zhang, Qun Zhao</i>	
CHAPTER 34	
Wind/Wave Relation and the Pressure Gradient Effect	429
<i>Spiros M. Gouloumis</i>	
CHAPTER 35	
Non-Reflected Multi Directional Wave Maker Theory and Experiments of Verification ..	443
<i>Kazunori Ito, Hidehiro Katsui, Masashi Mochizuki, Masahiko Isobe</i>	
CHAPTER 36	
Fifty Years of Wave Growth Curves	457
<i>Paul C. Liu</i>	

CHAPTER 37	
Development of a Third Generation Shallow-Water Wave Model with Unstructured Spatial Meshing	465
<i>Michel Benoit, Frederic Marcos, Francoise Becq</i>	
CHAPTER 38	
New Optimization Method for Paddle Motion of Multi-Directional Wavemaker	479
<i>Akira Matsumoto, Minoru Hanzawa</i>	
CHAPTER 39	
Generation of Second-Order Long Waves by a Wave Group in a Laboratory Flume and Its Control	493
<i>M. Mizuguchi, H. Toita</i>	
CHAPTER 40	
Kinematic Predictions in Large Shallow Water Waves	502
<i>Susan Smith, Christopher Swan</i>	
CHAPTER 41	
Fetch Limited Spectral Evolution in Finite Depth Water	516
<i>I.R. Young, L.A. Verhagen</i>	
CHAPTER 42	
Measurement of Breaking Waves Using Particle Image Velocimetry	527
<i>Kuang-An Chang, Philip L.-F. Liu</i>	
CHAPTER 43	
Computation of the Near-Bottom Kinematics of Shoaling Waves	537
<i>Luc Hamm</i>	
CHAPTER 44	
Formulation and Validation of Vertically 2-D Shallow-Water Wave Model	551
<i>Bradley D. Johnson, Nobuhisa Kobayashi, Daniel T. Cox</i>	
CHAPTER 45	
Particle Velocity Distribution in Surface Waves	565
<i>Geir Moe, Oivind A. Arntsen</i>	
CHAPTER 46	
A Comparison of Analysis Methods for Wave Pressure Data	575
<i>Murray Townsend, John D. Fenton</i>	
CHAPTER 47	
A Nonlinear Model for Wave Propagation	589
<i>Ting-Kuei Tsay, Philip L.-F. Liu, Nan-Jing Wu</i>	
CHAPTER 48	
Application of a Digital Particle Image Velocimetry (DPIV) System to Breaking Waves in the Surf Zone	602
<i>Kenneth R. Craig, Robert J. Thieke</i>	

CHAPTER 49	
Wave Gauging Networks Worldwide - An Overview616
<i>J. Michael Hemsley</i>	
CHAPTER 50	
Improvement of Submerged Doppler-Type Directional Wave Meter and its Application to Field Observations629
<i>Noriaki Hashimoto, Masao Mitsui, Yoshimi Goda, Toshihiko Nagai, Tomoharu Takahashi</i>	
CHAPTER 51	
Comparison of Directional Wave Data Quality from Two Different Monitoring Systems ..	.643
<i>Lihwa Lin, Sidney Schofield, Hsiang Wang</i>	
CHAPTER 52	
The Digital Simulation of Non-Linear Random Waves657
<i>Kyungmo Ahn</i>	
CHAPTER 53	
The “SWAN” Wave Model for Shallow Water668
<i>N. Booij, L.H. Holthuijsen, R.C. Ris</i>	
CHAPTER 54	
Generation Depths from Water Wave Data677
<i>J. Ernest Breeding, Jr.</i>	
CHAPTER 55	
Wave Climate Assessment in the South Aegean Shelf689
<i>Spiros Christopoulos, Christos Solomonidis</i>	
CHAPTER 56	
Sea State Parameterisation Using Empirical Orthogonal Functions703
<i>Witold Cieslikiewicz, Jerzy Graff</i>	
CHAPTER 57	
Fully Nonlinear Properties of Periodic Waves Shoaling over Slopes717
<i>Stephan T. Grilli, Juan Horrillo</i>	
CHAPTER 58	
Water Wave Fluctuations Induced by Irregular Bathymetry731
<i>Lulin Guo, Robert A. Dalrymple</i>	
CHAPTER 59	
Integral Control Data Assimilation in Wave Predictions743
<i>L.H. Holthuijsen, N. Booij, M. van Endt, S. Caires, C. Guedes Soares</i>	
CHAPTER 60	
Two-Dimensional Analysis of Wave Transformation by Rational-Approximation-Based, Time-Dependent Mild-Slope Equation for Random Waves754
<i>Toshimasa Ishii, Masahiko Isobe, Akira Watanabe</i>	

CHAPTER 61	
Nonlinear Wave Transformation Due to a Submerged Breakwater	767
<i>Masahiko Isobe, Akira Watanabe, Shogo Yamamoto</i>	
CHAPTER 62	
Observed and Modeled Wave Results from Near-Stationary Hurricanes	781
<i>Charles L. Vincent, Robert E. Jensen</i>	
CHAPTER 63	
Estimation of Persistence Statistics of the Waves Observed on Japanese Coast in the Light of Recent Studies	794
<i>Hajime Kato, Hisamichi Nobuoka</i>	
CHAPTER 64	
Probabilistic Modeling of Long-Term Wave Climate	808
<i>V.M. Leyden, W.R. Dally</i>	
CHAPTER 65	
Monte Carlo Simulation for Nearshore Wave Statistics in Southern California	822
<i>Chia-Chi Lu, R. Rea Strange III</i>	
CHAPTER 66	
Bottom Friction Dissipation in the Belgian Coastal Regions	836
<i>Weimin Luo, Jaak Monbaliu, Jean Berlamont</i>	
CHAPTER 67	
Weakly non-Gaussian Model of Wave Height Distribution for Nonlinear Random Waves ..	850
<i>Nobuhito Mori, Takashi Yasuda</i>	
CHAPTER 68	
An Attempt at Applying the Chaos Theory to Wave Forecasting	864
<i>Takao Ohta, Akira Kimura</i>	
CHAPTER 69	
Transition of Stochastic Characteristics of Waves in the Nearshore Zone	878
<i>David J. Robillard, Michel K. Ochi</i>	
CHAPTER 70	
Monitoring and Modelling on Shallow Water Wave Propagations in “El Saler” Beach ..	889
<i>Jose C. Santos, Jose M. de la Pena, Jose Lozano</i>	
CHAPTER 71	
Intercomparison of Parameter Estimation Methods in Extremal Wave Analysis	900
<i>Masataka Yamaguchi</i>	
CHAPTER 72	
Influences of Spectral Shapes on the Statistical Properties of Simulated Random Waves ..	914
<i>John Z. Yim, M.-Y. Lai</i>	
CHAPTER 73	
Second-Order Interaction between Random Wave and Submerged Obstacle	927

CHAPTER 74	
A Uniform Mild-Slope Model for Waves over Varying Bottom	941
<i>Libang Zhang, Billy L. Edge</i>	
CHAPTER 75	
Bragg Reflection of Shallow-Water Waves on a Sloping Beach	955
<i>Yong-Sik Cho, Jong-In Lee, Jong-Kyu Lee</i>	
CHAPTER 76	
Reflection Analysis with Separation of Cross Modes	968
<i>John Gronbech, Thomas Jensen, Henning Andersen</i>	
CHAPTER 77	
Wave Runup on Beaches	981
<i>John P. Ahrens, William N. Seelig</i>	
CHAPTER 78	
Field Study on Wave Run-Up on Seadykes	994
<i>Joachim Grune</i>	
CHAPTER 79	
Wave Run-Up on Revetments with Composite Slopes	1008
<i>Zeya Wang, Joachim Grune</i>	
CHAPTER 80	
Landward Transport of Spray Generated from a Wave Absorbing Sea Wall	1022
<i>Misao Hashida, Nobuhiro Matsunaga, Isao Irie</i>	
CHAPTER 81	
Irregular Wave Kinematics from a Pressure Record	1034
<i>Christopher H. Barker, Rodney J. Sobey</i>	
CHAPTER 82	
Nonlinear Refraction-Diffraction of Surface Waves over Arbitrary Depths	1048
<i>Serdar Beji, Kazuo Nadaoka</i>	
CHAPTER 83	
Boussinesq Equations with Improved Doppler Shift and Dispersion for Wave/Current Interaction	1060
<i>Qin Chen, Per A. Madsen, Ole R. Sorensen, David R. Basco</i>	
CHAPTER 84	
The Propagation of Water Waves in Prismatic Channels	1074
<i>Li Li, Robert A. Dalrymple, Jeffrey M. Mlynarski</i>	
CHAPTER 85	
A Statistical Approach for Modeling Triad Interactions in Dispersive Waves	1088
<i>Y. Eldeberky, V. Polnikov, J. A. Battjes</i>	

CHAPTER 86	
A Fully Nonlinear 3D Method for the Computation of Wave Propagation	1102
<i>Andrew B. Kennedy, John D. Fenton</i>	
CHAPTER 87	
A Fourth Order Boussinesq-Type Wave Model	1116
<i>Mauricio F. Gobbi, James T. Kirby</i>	
CHAPTER 88	
Fast Methods for Computing the Shoaling of Nonlinear Waves	1130
<i>J.D. Fenton, A.B. Kennedy</i>	
CHAPTER 89	
Structure of Frequency Domain Models for Random Wave Breaking	1144
<i>James T. Kirby, James M. Kaihatu</i>	
CHAPTER 90	
A Hamiltonian Model for Nonlinear Water Waves and Its Applications	1156
<i>A.K. Otta, M.W. Dingemans, A.C. Radder</i>	
CHAPTER 91	
The Role of Wave-Induced Shear Stresses in the Momentum Balance Equations	1168
<i>Francisco J. Rivero, Agustin S.-Arcilla</i>	
CHAPTER 92	
Nonlinear Wave Dynamics in the Surf Zone	1178
<i>O.R. Sorensen, P.A. Madsen, H.A. Schaffer</i>	
CHAPTER 93	
A Boussinesq Breaking Wave Model with Vorticity	1192
<i>I.A. Svendsen, Ke Yu, J. Veeramony</i>	
CHAPTER 94	
Roller Contributions as Inferred from Inverse Modelling Techniques	1205
<i>D.J.R. Walstra, G.P. Mocke, F. Smit</i>	
CHAPTER 95	
Wave-Current Interaction in Inlets	1219
<i>Michael J. Briggs, Zeki Demirebilek, Debra R. Green</i>	
CHAPTER 96	
Wave Climate of Large Reservoirs and a Revised Wave Hindcast Formula	1233
<i>Pierre Dupuis, Jean-Pierre Tournier, Octave Caron</i>	
CHAPTER 97	
Spectral Modelling of Current Induced Wave-Blocking	1247
<i>R.C. Ris, L.H. Holthuijsen</i>	

Part II Long Period Waves, Storm Surges and Wave Groups

CHAPTER 98	
Uncertainties in the Validation of Harbor Wave Models	1256
<i>Zeki Demirbilek, Bingyi Xu, Vijay Panchang</i>	
CHAPTER 99	
Field Measurements and Numerical Modeling of Harbor Oscillations During Storm Waves	1268
<i>W.M. Jeong, J.W. Chae, W.S. Park, K.T. Jung</i>	
CHAPTER 100	
Performance of a Resonator Designed by the Wave Filter Theory - Applicability to a Harbor	1280
<i>Takayuki Nakamura, Hitoshi Mochizuki, Satoshi Morita</i>	
CHAPTER 101	
The Generation of Waves by a Landslide: Skagway, Alaska - A Case Study	1293
<i>Fredric Raichlen, Jiin Jen Lee, Catherine Petroff, Philip Watts</i>	
CHAPTER 102	
Laboratory Experiment on Long Wave Generation by Time-Varying Breakpoint	1307
<i>Satoru Nagase, Masaru Mizuguchi</i>	
CHAPTER 103	
Laboratory Experiments on Generation of Long Waves in the Surf Zone	1321
<i>Akio Okayasu, Teruki Matsumoto, Yasuyuki Suzuki</i>	
CHAPTER 104	
Generation of Infragravity Waves	1335
<i>A. R. van Dongeren, I.A. Svendsen, F.E. Sancho</i>	
CHAPTER 105	
Responses of Coastal Topography to Sea-Level Rise	1349
<i>Nobuo Mimura, Eiichi Kawaguchi</i>	
CHAPTER 106	
Numerical Study of Low Frequency Surf Zone Motions	1361
<i>H. Tuba Ozkan-Haller, James T. Kirby</i>	
CHAPTER 107	
Neptune - An Integrated Approach to Determining NW European Coastal Extremes ...	1375
<i>Jerzy Graff, Witold Cieslikiewicz</i>	
CHAPTER 108	
A Stochastic Typhoon Model and Its Application to the Estimation of Extremes of Storm Surge and Wave Height	1389
<i>Yoshio Hatada, Masataka Yamaguchi</i>	

CHAPTER 109	
Design of Vertical Walls Against Storm Surge	1403
<i>A. Kortenhaus, C. Miller, H. Oumeraci</i>	
CHAPTER 110	
Nearshore, Wave and Topographic Effects in Storm Surges	1417
<i>Gary Watson, Takao Yamashita</i>	
CHAPTER 111	
The Swash Zone: A Focus on Low Frequency Motion	1431
<i>Adam M. Shah, J. William Kamphuis</i>	
CHAPTER 112	
The Development of an On-Line, Interactive, Tsunami-Information Resource	1443
<i>Benjamin Cook, Catherine Petroff</i>	
CHAPTER 113	
Long Wave Runup on Coastal Structures	1452
<i>Utku Kanoglu, Costas Emmanuel Synolakis</i>	
CHAPTER 114	
Offshore Tsunami Profiles Observed at the Coastal Wave Stations	1465
<i>Toshihiko Nagai, Noriaki Hashimoto, Kazuyoshi Shimizu, Fujio Kitamura</i>	
CHAPTER 115	
A Realistic Model for the 1992-96 Tidal Waves	1478
<i>Srinivas Tadepalli, Costas Emmanuel Synolakis</i>	
CHAPTER 116	
Long-Period Oscillations in a Harbour Caused by Typhoon	1491
<i>Wataru Kioka</i>	
CHAPTER 117	
Estimation of Wave Groups Parameter from Wave Climate Statistics	1503
<i>Satoshi Nakamura</i>	

Part III Coastal Structures

CHAPTER 118	
Reflection Coefficients of the Step-Shaped Slit Caisson on the Rubble Mound	1516
<i>Sung Mo Ahn, Ryuichi Fujiwara, Hiroshi Matsunaga, Katsuhiko Kurata, Shohachi Kakuno</i>	
CHAPTER 119	
Berm Breakwater Trunk Exposed to Oblique Waves	1528
<i>A. Alikhani, G.R. Tomasicchio, J. Juhl</i>	
CHAPTER 120	
Interaction Between Main Armour and Toe Berm Damage	1542
<i>P. Aminti, A. Lamberti</i>	

CHAPTER 121	
Stability of Artificial Roughness Elements and Run-Up Reduction	1556
<i>M. Klein Breteler, K.W. Pilarczyk</i>	
CHAPTER 122	
Wave Induced Velocities at a Rubble Mound Breakwater	1569
<i>Bruno Brunone, Giuseppe R. Tomasicchio</i>	
CHAPTER 123	
Natural Periods of Armor Stones	1583
<i>Fred E. Camfield</i>	
CHAPTER 124	
Reliability Based Optimal Design of Vertical Breakwaters Modelled as a Series System of Failure	1589
<i>E. Christiani, H.F. Burcharth, J. Dalsgaard Sorensen</i>	
CHAPTER 125	
Overall Slope Stability Analysis of Rubble Mound Breakwaters	1603
<i>Julien De Rouck, Luc Van Damme</i>	
CHAPTER 126	
Interactions in the Stability of Toe-Berm and Main-Armour for Rubble-Mound Breakwaters: An Experimental Study	1617
<i>Philippe Donnars, Michel Benoit</i>	
CHAPTER 127	
Potential Uses for the Rapidly Installed Breakwater System	1631
<i>Jimmy Fowler, Donald Resio, Michael Briggs, Cheryl Pollock</i>	
CHAPTER 128	
Stability of Reshaping Breakwaters with Special Reference to Stone Durability	1640
<i>P. Frigaard, T. Hald, H.F. Burcharth, Sigurdur Sigurdarson</i>	
CHAPTER 129	
Field Investigations on Wave-Dissipating Concrete Blocks Covering Vertical Wall Breakwater	1652
<i>Michio Gomyoh, Kazuhiko Sakai, Tomotuka Takayama, Kojiro Suzuki, Shigeo Takahashi</i>	
CHAPTER 130	
New Stability Formula for Wave-Dissipating Concrete Blocks Covering Horizontally Composite Breakwaters	1665
<i>Minoru Hanzawa, Hirokazu Sato, Shigeo Takahashi, Kenichiro Shimosako, Tomotsuka Takayama, Katsutoshi Tanimoto</i>	
CHAPTER 131	
Breakwater Stability under Regular and Irregular Wave Attack	1679
<i>Thomas Jensen, Henning Andersen, John Gronbech, Etienne P.D. Mansard, Michael H. Davies</i>	
CHAPTER 132	
Roundhead Stability of Berm Breakwaters	1693

CHAPTER 133	
Improvement of Composite Breakwater on Solid Bottom Against Severe Tsunamis1707
<i>Yoshiaki Kimura, Hideo Kondo, Shinji Kuwabara, Akira Kawamori</i>	
CHAPTER 134	
Hydraulic Stability Analysis of Leaside Slopes of Overtopped Breakwaters1721
<i>M.D. Kudale, N. Kobayashi</i>	
CHAPTER 135	
Influence of the Core Configuration on the Stability of Berm Breakwaters1735
<i>Nikolay Lissev, Alf Torum</i>	
CHAPTER 136	
Model Study of Reservoir Riprap Stability1748
<i>Etienne P. D. Mansard, Michael H. Davies, Octave Caron</i>	
CHAPTER 137	
Prototype Measurements of Wave Pressures on a Wave Screen: Comparison to Physical and Analytical Models1762
<i>F.L. Martin, M. A. Losada, C. Vidal, J.L. Diaz Rato</i>	
CHAPTER 138	
Velocity Field Measurements over Breakwater Heads under 3D Waves1776
<i>Yoshiharu Matsumi, Akira Kimura, Kenichi Ohno</i>	
CHAPTER 139	
Wave Climate Simulation and Breakwater Stability1789
<i>Josep R. Medina</i>	
CHAPTER 140	
Incipient Motion of Breakwater Armor Units1803
<i>J. A. Melby, N. Kobayashi</i>	
CHAPTER 141	
Overtopping Reduction in Crownwall Design1816
<i>Jose Luis Monso, Alfonso Vidaor, Cristina Cadevall, Cristina Garcia</i>	
CHAPTER 142	
Stable Profiles of Reshaping Breakwaters with a Berm Below the Water Level1826
<i>C.I. Moutzouris</i>	
CHAPTER 143	
Experiments on a Non-Wave Overtopping Type Seawall1840
<i>Keisuke Murakami, I. Irie, Y. Kamikubo</i>	
CHAPTER 144	
A Condition and Performance Rating System for Breakwaters and Jetties1852
<i>John Oliver, Don Plotkin, John Lesnik, Douglas Pirie</i>	

CHAPTER 145	
Wave Overtopping and Stability of Armor Units under Multidirectional Waves	1862
<i>T. Sakakiyama, R. Kajima</i>	
CHAPTER 146	
Numerical Modeling of Breach Growth in a Sanddike	1876
<i>Gaus S. Stelling, Willem T. Bakker, Christine van Kuik, Christel Somers</i>	
CHAPTER 147	
Aging and Stability of Placed Block Revetments	1888
<i>Theo Stoutjesdijk, Hans Johanson, Mark Klein Breteler</i>	
CHAPTER 148	
Experimental Analysis of the Settlement Failure Mechanism Shown by Caisson-Type Seawalls	1902
<i>Shigeo Takahashi, Kojiro Suzuki, Katsumasa Tokubuchi, Ken-ichiro Shimosako</i>	
CHAPTER 149	
Full Scale Measurements of Wave Attenuation Inside a Rubble Mound Breakwater ...	1916
<i>Peter Troch, Marc De Somer, Julien De Rouck, Luc van Damme, Dierik Vermeir, Jean-Pierre Martens, Conan van Hove</i>	
CHAPTER 150	
Numerical Modelling of Wave Interaction with Dynamically Stable Structures	1930
<i>Marcel R.A. van Gent</i>	
CHAPTER 151	
Monitoring of Zeebrugge Breakwaters	1944
<i>Luc van Damme, Julien de Rouck</i>	
CHAPTER 152	
Influence of Rock Shape and Grading on Stability of Low-Crested Structures	1957
<i>Jentsje W. van der Meer, W.H. Tutuarima, G. Burger</i>	
CHAPTER 153	
Toe Stability of Rubble Mound Breakwaters	1971
<i>Ton van der Meulen, Gerrit J. Schiereck, Kees d'Angremond</i>	
CHAPTER 154	
Seawall Effects on Historically Receding Shorelines	1985
<i>Bryan N. Jones, David R. Basco</i>	
CHAPTER 155	
Control of Wave Propagation Angle by Tapered-Submerged Breakwater	1998
<i>Satoshi Takewaka, Isao Irie</i>	
CHAPTER 156	
Multidirectional Wave Loads on Vertical Breakwaters	2008
<i>Claudio Franco, Jentsie W. Van der Meer, Leopoldo Franco</i>	

CHAPTER 157	
Modelling the Impact of Detached Breakwaters on the Coast	2022
<i>K.J. Bos, J.A. Roelvink, M.W. Dingemans</i>	
CHAPTER 158	
Evaluation of Beach Modelling Techniques Behind Detached Breakwaters	2036
<i>Philip Axe, Suzana Ilic, Andrew Chadwick</i>	
CHAPTER 159	
Numerical Modelling of Bed Evolution Behind a Detached Breakwater	2050
<i>Philippe Pechon, Charles Teisson</i>	
CHAPTER 160	
Combined Diffraction and Transmission of Water Waves around a Porous Breakwater	
Gap	2063
<i>Xiping Yu, Hiroyoshi Togashi</i>	
CHAPTER 161	
Prediction of Wave Reflection from Rock Structures: An Integration of	
Field & Laboratory Data	2077
<i>Mark A. Davidson, Paul A.D. Bird, David A. Huntley, Geoff N. Bullock</i>	
CHAPTER 162	
Performance Evaluation of Buoy-Membrane Wave Barriers	2087
<i>M.H. Kim, B. L. Edge, S.T. Kee, L. Zhang</i>	
CHAPTER 163	
An Improved Design Method for the Riprap of Earthfill Dams of Large Reservoirs ...	2101
<i>Jean-Pierre Tournier, Pierre Dupuis, Raymond Ares</i>	
CHAPTER 164	
Geotextile Systems in Coastal Engineering - An Overview -	2114
<i>Krzysztof W. Pilarczyk</i>	
CHAPTER 165	
Groynes on the East Frisian Islands: History and Experiences	2128
<i>Hans Kunz</i>	
CHAPTER 166	
Permeable Pile Groins	2142
<i>Thomas Trampenau, Frank Goricke, Arved J. Raudkivi</i>	
CHAPTER 167	
The Effect of Groundwater on Scour Near Structures	2152
<i>John H. Loveless, Geoffrey T. Grant, Robert I. Karlsson</i>	
CHAPTER 168	
Abrasion of Steel Pipe Piles by Sediment Motion in Coastal Zones	2166
<i>Gaku Matsuoka, Shinichi Ito, Toshihiko Yamashita, Hiroshi Saeki, Yoshihisa Kariyazono, Koichi Sato</i>	

CHAPTER 169	
A Viscous Rotational Model for Wave Overtopping over Marine Structure	2178
<i>Fei Zhuang, Jiin-Jen Lee</i>	
CHAPTER 170	
Overtopping of Waves at a Wall: A Theoretical Approach	2192
<i>M. Jervis, D.H. Peregrine</i>	
CHAPTER 171	
Wind Effects on Runup and Overtopping of Coastal Structures	2206
<i>Donald L. Ward, Jun Zhang, Christopher G. Wibner, Charles M. Cinotto</i>	
CHAPTER 172	
Wave Overtopping of Vertical Structures Including Wind Effect	2216
<i>Johannes P. de Waal, Patrick Tonjes, Jentsje W. van der Meer</i>	
CHAPTER 173	
Bridge Pier Scour Assessment for the Northumberland Strait Crossing	2230
<i>C.D. Anglin, R.B. Nairn, A.M. Cornett, L. Dunaszegi, J. Turnham, G.W. Annandale</i>	
CHAPTER 174	
Wave Setup at River Entrances	2244
<i>David J. Hanslow, Peter Nielsen, Kevin Hibbert</i>	
CHAPTER 175	
Scour at Coastal Inlet Structures	2258
<i>Steven A. Hughes, J. William Kamphuis</i>	
CHAPTER 176	
Probability Distribution of the Maximum Wave Height along a Sea Wall with Finite Width	2272
<i>Akira Kimura, Takao Ohta</i>	
CHAPTER 177	
Beach Response in Front of Wave-Reflecting Structures	2284
<i>Roy C. Seaman, Tom O'Donoghue</i>	
CHAPTER 178	
Fundamental Characteristics of Wave Transformation around Artificial Reefs	2298
<i>Toshio Aono, Eric C. Cruz</i>	
CHAPTER 179	
Performance of a Submerged Breakwater for Shore Protection	2312
<i>Albert E. Browder, Robert G. Dean, Renjie Chen</i>	
CHAPTER 180	
Nonlinear Wave Transformation over a Submerged Triangular Breakwater	2324
<i>Lifen Dong, Akira Watanabe, Masahiko Isobe</i>	
CHAPTER 181	
Breaking Limit, Breaking and Post-Breaking Wave Deformation Due to Submerged	

Structures	2338
<i>Koichiro Iwata, Koji Kawasaki, Do-Sam Kim</i>	
CHAPTER 182	
Italian Experience on Submerged Barriers as Beach Defence Structures	2352
<i>Alberto Lamberti, Alessandro Mancinelli</i>	
CHAPTER 183	
Resonant Reflection and Refraction-Diffraction of Surface Waves Due to Porous Submerged Breakwaters	2366
<i>Hajime Mase, Akira Kimura, Hiroshi Sakakibara</i>	
CHAPTER 184	
BEM-FEM Combined Analysis of Nonlinear Interaction between Wave and Submerged Breakwater	2377
<i>N. Mizutani, W.G. McDougal, A.M. Mostafa</i>	
CHAPTER 185	
Regulation of Nearshore Circulation by Submerged Breakwater for Shore Protection ..	2391
<i>Hisamichi Nobuoka, Isao Irie, Hajime Kato, Nobuo Mimura</i>	
CHAPTER 186	
Submerged Breakwaters for the Defence of the Shoreline at Ostia - Field Experiences, Comparison	2404
<i>Ugo Tomasicchio</i>	
CHAPTER 187	
Wave Transmission of Low-Crested Structures	2418
<i>Kees d'Angremond, Jentsje W. van der Meer, Rutger J. De Jong</i>	
CHAPTER 188	
Effect of Submerged Breakwater on Profile Development	2428
<i>Martin D. Groenewoud, Jan van de Graaff, Edward W.M. Claessen, Stephan C. van der Biezen</i>	
CHAPTER 189	
Cause and Characteristics of Impact Pressure Exerted by Spilling and Plunging Breakers on a Vertical Wall	2442
<i>Seyed Ali Azarmsa, Takashi Yasuda, Hidemi Mutsuda</i>	
CHAPTER 190	
Dynamic Response of Vertical Elastic Walls to Breaking Wave Impact	2456
<i>Masatato Hattori, Nobuaki Tsujioka</i>	
CHAPTER 191	
Wave Transmission Past Vertical Wave Barriers	2470
<i>David L. Kriebel, Chad A. Bollmann</i>	
CHAPTER 192	
Physical Study of the Nature of High Peak Wave Pressures	2484
<i>Jordan Marinski</i>	

CHAPTER 193	
A Design Short-Crested Wave Force Model for Vertical Deep-Water Breakwaters	2494
	<i>S.-Y. Tzang, S.-R. Liaw</i>
CHAPTER 194	
New Design Methods for Wave Impact Loadings on Vertical Breakwaters and Seawalls . .	2508
	<i>N.W.H. Allsop, J.E. McKenna, D. Vicinanza, T.T.J. Whitaker</i>
CHAPTER 195	
Scale Effects of Wave Impact Pressures on Cob Armour Units	2522
	<i>M.W. Howarth, N.W.H. Allsop, A.M. Vann, R.J. Jones, J.P. Davis</i>
CHAPTER 196	
Wave Impact Loading of Vertical Face Structures for Dynamic Stability	
Analysis - Prediction Formulae -	2534
	<i>P. Klammer, A. Kortenhaus, H. Oumeraci</i>
CHAPTER 197	
Analysis on the Interaction of Waves with Flexible Floating Structure	
by BE-FE Combined Method	2548
	<i>Xiaodong Liu, Shigeki Sakai</i>
CHAPTER 198	
Design Wave Height Related to Structure Lifetime	2560
	<i>Zhou Liu, Hans F. Burcharth</i>
CHAPTER 199	
Wave Impact Beneath a Horizontal Surface	2573
	<i>D.J. Wood, D.H. Peregrine</i>
CHAPTER 200	
Wave Impulse Prediction for Caisson Design	2584
	<i>Michael J.A. Walkden, Peter J. Hewson, Geoffrey N. Bullock</i>
CHAPTER 201	
Wave Overtopping Rate and Reflection Coefficient for Obliquely Incident Waves	2598
	<i>Yoichi Moriya, Masaru Mizuguchi</i>
CHAPTER 202	
Sediment Transport and Wave Reflection near a Seawall	2612
	<i>Jonathon R. Miles, Paul E. Russell, David A. Huntley</i>

Part IV Coastal Processes and Sediment Transport

CHAPTER 203	
Wave Energy Dissipation in Kelp Vegetation	2626
	<i>Alfonse Dubi, Alf Torum</i>
CHAPTER 204	
Experimental Study on the Effect of Gravity Drainage System on Beach Stabilization . .	2640
	<i>Hiroi Kanazawa, Fumihiko Matsukawa, Kazumasa Katoh, Iwao Hasegawa</i>

CHAPTER 205	
Field Experiment on the Effect of Gravity Drainage System on Beach Stabilization . . .	2654
	<i>Kazumasa Katoh, Shin-ichi Yanagishima</i>
CHAPTER 206	
On the Change of Velocity Field in Nearshore Zone Due to Coastal Drain and the Consequent Beach Transformation	2666
	<i>Michio Sato, Tadahiro Fukushima, Ryuichiro Nishi, Masahiko Fukunaga</i>
CHAPTER 207	
Evaluation of a Beach Dewatering System: Nantucket, USA	2677
	<i>William R. Curtis, Jack E. Davis, Ian L. Turner</i>
CHAPTER 208	
Sediment Transport Processes at Ocean Beach, San Francisco, California	2691
	<i>Robert T. Battalio, Dilip Trivedi</i>
CHAPTER 209	
Two Treatments of Shore Erosion in Extreme Floods on U.S. Great Lakes	2705
	<i>Robert J. Hallermeier</i>
CHAPTER 210	
Long-Term Beach Response to Shore Stabilization Structures on the Oregon Coast . . .	2718
	<i>G.E. Hearon, W.G. McDougal, P.D. Komar</i>
CHAPTER 211	
Profile Volumes as a Measure of Erosion Vulnerability	2732
	<i>Timothy W. Kana, Ram Krishna Mohan</i>
CHAPTER 212	
Breach Growth: Experiments and Modelling	2746
	<i>Harry de Looff, Henk J. Steetzel, Arie W. Kraak</i>
CHAPTER 213	
The Impact of an Extreme Event on the Sediment Budget: Hurricane Andrew in the Louisiana Barrier Islands	2756
	<i>Jeffrey H. List, Mark E. Hansen, Asbury H. Sallenger, Jr., Bruce E. Jaffe</i>
CHAPTER 214	
Beach Maintenance Strategies, a Comparison for a Recreational Beach	2770
	<i>M. Pluijm, G. Kant, R. Noltén, A.P. de Looff</i>
CHAPTER 215	
Littoral Impact of Ocean City Inlet, Maryland, USA	2779
	<i>Julie Dean Rosati, Bruce A. Ebersole</i>
CHAPTER 216	
Extreme Water Levels, Wave Runup and Coastal Erosion	2793
	<i>P. Ruggiero, P.D. Komar, W.G. McDougal, R.A. Beach</i>

CHAPTER 217	
A Morphological “Mixed-Type” Model for the Ebro Delta Coast	2806
<i>Agustin Sanchez-Arcilla, Jose A. Jimenez</i>	
CHAPTER 218	
Sea Dike Erosion and Coastal Retreat at Nam Ha Province, Vietnam	2820
<i>Ton That Vinh, G. Kant, Nguyen Ngoc Huan, Z. Pruszk</i>	
CHAPTER 219	
Beach Profile Analysis around Indian River Inlet, Delaware, U.S.A	2829
<i>Kirk F. Bosma, Robert A. Dalrymple</i>	
CHAPTER 220	
Improved 3-D Beach Evolution Model Coupled with the Shoreline Model (3D-SHORE)	2843
<i>Takuzo Shimizu, Takahiro Kumagai, Akira Watanabe</i>	
CHAPTER 221	
Evaluation of Shoreface Nourishments by Line Modelling	2857
<i>Martin D. Groenewoud, Willem T. Bakker, Jan van de Graaff, Ruud Spanhoff, Christian Laustrup</i>	
CHAPTER 222	
Beach Monitoring Program of Valencia (Spain)	2871
<i>Jose Serra, Josep R. Medina</i>	
CHAPTER 223	
Bar Migration and Duneface Oscillation on Decadal Scales	2884
<i>Marcel J.F. Stive, Jorge Guillen, Michele Capobianco</i>	
CHAPTER 224	
Morphological Development of the Terschelling Shoreface Nourishment in Response to Hydrodynamic and Sediment Transport Processes	2897
<i>P. Hoekstra, K.T. Houwman, A. Kroon, B.G. Ruessink, J.A. Roelvink, R. Spanhoff</i>	
CHAPTER 225	
Justification for Beach Nourishment	2911
<i>John G. Housley</i>	
CHAPTER 226	
Beach Nourishment Versus Shore Protection Structures	2918
<i>Alexander Khabidov, Yuri Bazhenov, Marina Glodenis, Nadya Ivanova, Liya Kaskevitch, Oleg Rybak, Valery Savkin, Anatoly Trizno, Grigory Zelensky, Veniamin Yedapin</i>	
CHAPTER 227	
Comparison of Beach and Shoreface Nourishment Torsminde Tange, Denmark	2927
<i>Christian Laustrup, Holger Toxvig Madsen, Per Sorensen, Ida Broker</i>	
CHAPTER 228	
Mathematical and Physical Modeling of Beach Nourishment Projects	2941
<i>W. Eric Rogers, Paul A. Work</i>	

CHAPTER 229	
Coastal Zone Dynamics during Artificial Nourishment	2955
<i>Elzbieta Zawadzka</i>	
CHAPTER 230	
Dune Damage Curves and Their Use to Estimate Dune Maintenance Costs	2969
<i>David R. Basco, Cheol S. Shin</i>	
CHAPTER 231	
Hurricane Opal Induced Changes on Natural and Nourished Beaches, West-Central Florida	2982
<i>Richard A. Davis, Jr., Ping Wang</i>	
CHAPTER 232	
Modelling Sand Transport and Profile Evolution on Macrotidal Beaches	2994
<i>Paul R. Fisher, Tim J. O'Hare</i>	
CHAPTER 233	
Beach Evolution Under Random Waves	3006
<i>Patrick Holmes, Thomas E. Baldock, Ray T.C. Chan, M. Ahmad L. Neshaei</i>	
CHAPTER 234	
Beach Profile Surveys Along the U.S. Pacific Coast 1945-1947	3020
<i>Nicholas C. Kraus, Robert L. Wiegel, Willard N. Bascom</i>	
CHAPTER 235	
Mechanism and Calculation of Sand Dune Erosion by Storms	3034
<i>Ryuichiro Nishi, Nicholas C. Kraus</i>	
CHAPTER 236	
Simulation of Coastal Profile Development Using a Boussinesq Wave Model	3048
<i>K.A. Rakha, R. Deigaard, P.A. Madsen, I. Broker, J.K. Ronberg</i>	
CHAPTER 237	
Cross-shore Sediment Transport and Beach Deformation Model	3062
<i>RattanapitikonWinyu , Tomoya Shibayama</i>	
CHAPTER 238	
Experimental Study on Sediment Transport in Surf and Swash Zones Using Large Wave Flume	3076
<i>Takao Shimizu, Masaaki Ikeno</i>	
CHAPTER 239	
The Influence of Long Waves on Macrotidal Beach Morphology	3090
<i>David J. Simmonds, Tim J. O'Hare, David A. Huntley</i>	
CHAPTER 240	
Mathematical Models for Waves and Beach Profiles in Surf and Swash Zones	3104
<i>Akira Watanabe, Mohammad Dibajnia</i>	

CHAPTER 241
Comparisons of Erosion Models for Storms at Ocean City, Maryland3115
Jie Zheng, Robert G. Dean

CHAPTER 242
Measurements of Wave Generated Bedforms3129
Christopher D. Jette, Daniel M. Hanes

CHAPTER 243
Field Measurement of Bed Roughness for Waves on an Offshore Reef3143
Raymond C. Nelson

CHAPTER 244
Effect of Wave-Induced-Pressure on Seabed Configuration3155
Tetsuo Sakai, Hitoshi Gotoh

CHAPTER 245
The Measurement of Bed Form Shapes in Hydraulic Models3169
Ian E. Shepherd

CHAPTER 246
Asymmetric Boundary Layer Flow above Sand Ripples under Progressive Waves3183
Takao Toue, Kazuo Nadaoka, Hidehiro Katsui

CHAPTER 247
Undertow Profiles in the Bottom Boundary Layer under Breaking Waves3194
Daniel T. Cox, Nobuhisa Kobayashi

CHAPTER 248
A Comparison of Field Observations and Quasi-Steady Linear Shear Instabilities of the Wave Bottom Boundary Layer3207
D.L. Foster, A.J. Bowen, R.A. Beach, R.A. Holman

CHAPTER 249
Wave Boundary Layer Flows and Pore Pressures in Permeable Beds3219
H.H. Hwang, K.S. Hwang, B.H. Lee

CHAPTER 250
Backfilling of Trenches Exposed to Waves3231
Jacob Hjelmager Jensen, Jorgen Fredsoe

CHAPTER 251
A Closed-Form Solution for Turbulent Wave Boundary Layers3244
Magnus Larson

CHAPTER 252
Observed Suspended Sediments in Storm Conditions3257
J.J. Williams, C.P. Rose, P.D. Thorne, L.E. Coates, J.R. West, P.J. Harcastle, J.D. Humphery, S.P. Moores, D.J. Wilson

CHAPTER 253	
Ebb Tidal Delta Evolution of Coastal Inlets	3270
<i>Michael R. Dombrowski, Ashish J. Mehta</i>	
CHAPTER 254	
Adjustments toward Equilibrium of a Large Flood -Tidal Delta after a Major Dredging Program, Tauranga Harbour, New Zealand	3284
<i>Terry Healy, Joseph Mathew, Willem de Lange, Kerry Black</i>	
CHAPTER 255	
Laboratory Mobile Bed Model Studies on Ebb Tidal Shoal Evolution	3295
<i>Xu Wang, Lihwa Lin, Hsiang Wang</i>	
CHAPTER 256	
Interaction of the Colorado River Project, Texas, with Longshore Sediment Transport ..	3309
<i>Daniel J. Heilman, Billy L. Edge</i>	
CHAPTER 257	
A Comprehensive Field Study of Tidal Inlet Processes at Ponce de Leon Inlet, Florida ..	3323
<i>Gary L. Howell</i>	
CHAPTER 258	
Transport of Fluid Mud Generated by Waves on Inclined Beds	3337
<i>Thijs van Kessel, C. Kranenburg, J.A. Battjes</i>	
CHAPTER 259	
Wave on Pebble Beach and Deformation of Pebble Beach	3349
<i>Ichiro Deguchi, Masanobu Ono, Toru Sawaragi</i>	
CHAPTER 260	
Wind-Induced Waves and Currents in a Nearshore Zone	3363
<i>Nobuhiro Matsunaga, Misao Hashida, Hiroshi Kawakami</i>	
CHAPTER 261	
Predicting Large-Scale, Cross-Shore Sediment Movement from Orbital Speeds	3378
<i>Edward B. Hands, John P. Ahrens, Donald T. Resio</i>	
CHAPTER 262	
Small-scale Morphology Related to Wave and Current Parameters Over a Barred Beach	3391
<i>A.F. Garcez Faria, E.B. Thornton, T.P. Stanton</i>	
CHAPTER 263	
Prediction of Shoreline Change Considering Cross-Shore Sediment Transport	3405
<i>Yoshimichi Yamamoto, Kiyoshi Horikawa, Katsutoshi Tanimoto</i>	
CHAPTER 264	
The Influence of Rollers on Longshore Currents	3419
<i>Daniel A. Osiecki, William R. Dally</i>	

CHAPTER 265	
Velocity Field Measurements in a “Coastal Buffer Zone”	3431
<i>Hiroshi Yagi, Hirofumi Hinata, Kazuo Nadaoka</i>	
CHAPTER 266	
Development of Underwater Beach Profile by Monochromatic and Random Waves . . .	3442
<i>Karsten Peters, Jurgen Neue, Hans-H. Dette</i>	
CHAPTER 267	
Turbulent Stresses in the Surf-Zone: Which Way Is Up?	3453
<i>John W. Haines, Guy Gelfenbaum</i>	
CHAPTER 268	
Asymmetric and Irregular Wave Effects on Bedload: Theory Versus Laboratory and Field Experiments	3467
<i>Leszek M. Kaczmarek, Rafal Ostrowski</i>	
CHAPTER 269	
Kinematics and Shear Stresses from Combined Waves and Longshore Currents in the UK Coastal Research Facility	3481
<i>Richard R. Simons, Ruairi D. MacIver, Wameidh M. Saleh</i>	
CHAPTER 270	
Movable Bed Roughness in the Flow of Irregular Waves and Currents Over Movable Beds	3495
<i>Zai-Jin You, Peter Nielsen</i>	
CHAPTER 271	
Seabed and Foundation Response to Wave Loading	3507
<i>Michael H. Davies</i>	
CHAPTER 272	
Interannual Shoreline Variations at Duck, NC, USA	3521
<i>Nathaniel Plant, Rob Holman</i>	
CHAPTER 273	
Long Term Behaviour of the Sediment Volume inside a Tidal Basin after Poldering . . .	3534
<i>Ernst Schroeder, Roland Goldenbogen, Hans Kunz</i>	
CHAPTER 274	
Wave Groups in a Barred Nearshore	3546
<i>B. Boczar-Karakiewicz, W. Romanczyk, J.L. Bona, B. Greenwood</i>	
CHAPTER 275	
Coastal Morphodynamic Instabilities	3560
<i>Albert Falques, Amadeu Montoto, Vicente Iranzo</i>	
CHAPTER 276	
On Validation of a Sand Waves and Sand Banks Model	3574
<i>Suzanne J.M.H. Hulscher</i>	

CHAPTER 277	
Transverse Bars in Duck, North Carolina	3588
<i>Kathryn M. Konicki, Rob A. Holman</i>	
CHAPTER 278	
On the Systematic Offshore Decay of Breaker Bars	3600
<i>Kathelijne M. Wijnberg</i>	
CHAPTER 279	
Longshore Bed-Load Transport	3614
<i>Jesper S. Damgaard, Richard L. Soulsby</i>	
CHAPTER 280	
Design Capacity of a Longshore Current Recirculation System for a Longshore Sediment Transport Laboratory Facility	3628
<i>David G. Hamilton, Julie D. Rosati, Jimmy E. Fowler, Jane M. Smith</i>	
CHAPTER 281	
Influence of Nearshore Hardbottom on Regional Sediment Transport	3642
<i>Paul C.-P. Lin, R. Harvey Sasso</i>	
CHAPTER 282	
Improvement of the Most Accurate Longshore Transport Formula	3652
<i>J.S. Schoonees, A.K. Theron</i>	
CHAPTER 283	
Cross-shore Structure of Longshore Currents during Duck94	3666
<i>Falk Feddersen, R.T. Guza, Steve Elgar, T.H.C. Herbers</i>	
CHAPTER 284	
Three-Dimensional Hydrodynamics on a Barred Beach	3680
<i>Tae-Myoung Oh, Robert G. Dean</i>	
CHAPTER 285	
Rip Current Generation on a Plane Beach	3694
<i>D.A. Suriamihardja, Yoshito Tsuchiya</i>	
CHAPTER 286	
Nearshore Placement of Sand	3708
<i>Scott L. Douglass</i>	
CHAPTER 287	
Influence of Nearshore Berm on Beach Nourishment	3722
<i>Paul A. Work, Emre N. Otay</i>	
CHAPTER 288	
Accuracy of Sand Volumes as a Function of Survey Density	3736
<i>Jennifer L. Irish, W. Jeff Lillycrop, Larry E. Parson</i>	
CHAPTER 289	
Shoreline Analysis Using Digital Photogrammetry	3750

CHAPTER 290	
Application of Satellite Images to the Detection of Coastal Topography	3762
<i>Ji Wu, Jea Tzyy Juang</i>	
CHAPTER 291	
Sediment Transport in Swash Zone under Obliquely Incident Waves	3770
<i>Toshiyuki Asano</i>	
CHAPTER 292	
Sheet Flow Modelled As Pure Convection	3784
<i>Stephen Clark, Peter Nielsen</i>	
CHAPTER 293	
A Transport Rate Formula for Mixed-Size Sands	3791
<i>Mohammad Dibajnia, Akira Watanabe</i>	
CHAPTER 294	
Modelling of 3D Sediment Transport in the Surf Zone	3805
<i>Berry Elfrink, Ida Broker, Rolf Deigaard, Erik Asp Hansen, Peter Justesen</i>	
CHAPTER 295	
A Numerical Model of Sheet Flow Sediment Transport	3818
<i>Sadakazu Katori, Masaru Mizuguchi, Akira Watanabe</i>	
CHAPTER 296	
Numerical Modeling of Nearshore Morphological Changes under a Current-Wave Field	3830
<i>Taerim Kim, Hsiang Wang</i>	
CHAPTER 297	
An Analysis of Particle Saltation Dynamics	3846
<i>Michael R. Krecic, Daniel M. Hanes</i>	
CHAPTER 298	
Sediment Movement and Stress Condition in Sea Bed	3860
<i>Yoshihiko Maeno, Motoyasu Ishikawa, Koza Bando, Yoshinobu Akiyama, Kouichi Yabe</i>	
CHAPTER 299	
Application of the Depth of Closure Concept	3874
<i>Robert J. Nicholls, William A. Birkemeier, Robert J. Hallermeier</i>	
CHAPTER 300	
Numerical Modeling of Sediment Transport for Various Mode	3888
<i>Masanobu Ono, Ichiro Deguchi, Toru Sawaragi</i>	
CHAPTER 301	
Nearbed Sediment Concentration from Tracer Studies	3901
<i>Zbigniew Pruszk, Ryszard Wierzchnicki, Andrzej Owczarczyk, Ryszard B. Zeidler</i>	

CHAPTER 302	
A Sloping Duct for the Study of Sediment Transport	3913
<i>Jesper S. Damgaard, Richard J.S. Whitehouse, Richard L. Soulsby</i>	
CHAPTER 303	
Sediment Dynamics and Profile Interactions: DUCK94	3921
<i>Donald K. Stauble, Mary A. Cialone</i>	
CHAPTER 304	
A Study on Flow Structure and Suspended Sediment Concentration over Seaweed Bed ..	3935
<i>Gozo Tsujimoto</i>	
CHAPTER 305	
An Energetics Approach for Suspended Sand Transport on Macrotidal Ridge and Runnel Beaches	3948
<i>George Voulgaris, Travis Mason, Michael B. Collins</i>	
CHAPTER 306	
Field Tests of Suspended-Load Transport Theories Used in Numerical Models	3962
<i>Thomas E. White</i>	
CHAPTER 307	
Shore Protection Studies for Ras-Elbar Area, Egypt	3976
<i>John B. Herbich, Abd-Elfattah Elfiky, Abd-Elmohsen Elmongy; Ali Elbahrawy, Gamal Elsaeed</i>	
CHAPTER 308	
Stabilizing Beaches Downcoast of Harbor Extensions	3986
<i>John R.C. Hsu, Richard Silvester</i>	
CHAPTER 309	
Observation of Nearshore Currents and Beach Changes around Headlands Built on the Kashimanada Coast, Japan	4000
<i>K. Saito, T. Uda, K. Yokota, S. Ohara, Y. Kawanakajima, K. Uchida</i>	
CHAPTER 310	
Nourished Beach Control Between Balis and Arenys Harbours (Spain)	4014
<i>F. Javier Escartin, Alfonso Vidaor, A.M. Castaneda, Nuria Lupon</i>	
CHAPTER 311	
Numerical Simulation of Shoreline Change with Longshore Sand Waves at Groins	4024
<i>Hans Hanson, Michelle M. Thevenot, Nicholas C. Kraus</i>	
CHAPTER 312	
Erosive Waves in Shoreline Change Due to the Reduction of a River Delta	4038
<i>Yoshito Tsuchiya</i>	
CHAPTER 313	
DELILAH, DUCK94 & SandyDuck: Three Nearshore Field Experiments	4052
<i>William A. Birkemeier, Charles E. Long, Kent K. Hathaway</i>	

CHAPTER 314	
Eulerian Mean Velocities under Non-Breaking Waves on Horizontal Bottoms	4066
	<i>Peter Nielsen, Zai-Jin You</i>
CHAPTER 315	
Reynolds Stress and Small-Scale Morphology Measurements during DUCK94	4079
	<i>Timothy P. Stanton, Edward B. Thornton</i>
CHAPTER 316	
Studies on the Suspended Concentration in the Surf Zone	4088
	<i>Ching-Her Hwang, Li-Hung Tsai, Po-Ching Lin, Chin-Chi Tsai</i>
CHAPTER 317	
Suspended Sediment Mixing in the Surf Zone	4098
	<i>Jose A. Jimenez, Francisco J. Rivero, Agustin Sanchez-Arcilla, Vicente Gracia, Andres Rodriguez</i>
CHAPTER 318	
Sand Suspension Events and Intermittence of Turbulence in the Surf Zone	4111
	<i>R.D. Kos'yan, H. Kunz, S.Yu. Kuznetsov, N.V. Pykhov, M.V. Krylenko</i>
CHAPTER 319	
Mechanisms of Beach Ground Water and Swash Interaction	4120
	<i>Andrew J. Baird, Travis E. Mason, Diane P. Horn</i>
CHAPTER 320	
The Equations for Integral and Mean Flow Properties in the Swash Zone	4134
	<i>M. Brocchini, D.H. Peregrine</i>
CHAPTER 321	
Wave Overwash of Subaerial Dunes	4148
	<i>Yukiko Tega, Nobuhisa Kobayashi</i>
CHAPTER 322	
Pressure Gradients Within Sediment Beds	4161
	<i>Thomas E. Baldock, Patrick Holmes</i>
CHAPTER 323	
Analysis of Mud Mass Transport under Waves Using an Empirical Rheological Model . .	4174
	<i>Qin Jiang, Akira Watanabe</i>
CHAPTER 324	
Countermeasures Against Wind-Blown Sand on Beaches	4188
	<i>Shintaro Hotta, Kiyoshi Horikawa</i>
CHAPTER 325	
Sea Breeze Effects on Nearshore Coastal Processes	4200
	<i>Charitha Pattiaratchi, Gerhard Masselink</i>
CHAPTER 326	
Wind Blown Sand at Castroville, California	4214
	<i>Douglas J. Sherman, Bernard O. Bauer, Paul A. Gares, Derek W.T. Jackson</i>

Part V Coastal, Estuarine and Environmental Problems

CHAPTER 327	
Pipeline Protection in the Surf Zone	4228
<i>Gerrit J. Schiereck, Henri L. Fontijn</i>	
CHAPTER 328	
Modeling Tidal Circulation in Florida Bay	4242
<i>Y. Peter Sheng, Justin Davis</i>	
CHAPTER 329	
Recent Developments in Coastal Defence Policy and Guidance in England	4253
<i>Reg Purnell</i>	
CHAPTER 330	
Structural Restoration of Coral Reefs Damaged by Vessel Groundings	4261
<i>Kevin R. Bodge</i>	
CHAPTER 331	
Dredging and Disposal within the Limits of a National Park	4274
<i>H. A. Manzenrieder, J.M. de Vries</i>	
CHAPTER 332	
Storm-Derived Bar/Sill Dynamics in a Dredged Channel	4289
<i>Sean O'Neil, Keith W. Bedford, David P. Podber</i>	
CHAPTER 333	
Bivalve Habitat Based on Sediment-Transport Mechanics	4300
<i>Hitoshi Gotoh, Tetsuo Sakai</i>	
CHAPTER 334	
Hydraulic Controls on Tidal Wetlands	4314
<i>R. Eric Katmarian, Philip A. McKee, Timothy W. Kana</i>	
CHAPTER 335	
Enhanced Mixing Through Perforated Discs on Round Buoyant Jet	4325
<i>Lilun Wu, Jiin-Jen Lee</i>	
CHAPTER 336	
Assessing Coastal Flood Risks	4339
<i>Roger Maddrell, Chris Fleming, Chris Mounsey</i>	
CHAPTER 337	
Experimental Study on the Behavior of Bivalves by Oscillatory Flow	4353
<i>Toshihiko Yamashita, Akira Wada, Gaku Matsuoka, Kenji Yano, Sadamitsu Akeda</i>	
CHAPTER 338	
Wind- and Sea Level-Induced Shore Evolution in Poland	4364
<i>Ryszard B. Zeidler, Marek Skaja, Grzegorz Rozynski, Jarka Kaczmarek</i>	

CHAPTER 339	
Ashdod Port's Effect on the Shoreline, Seabed and Sediment	4376
<i>Abraham Golik, Dov S. Rosen, Arik Golan, Maxim Shoshany Dan DiCastro, Pinkhas Harari</i>	
CHAPTER 340	
Tweed River Sand Bypass: Concepts and Progress	4390
<i>Russell J. Murray, R.P. (Jock) Brodie, Mark Porter, David A. Robinson</i>	
CHAPTER 341	
Design Considerations for Coastal Projects in Cold Regions	4397
<i>Craig B. Leidersdorf, Peter E. Gadd, Kennon D. Vaudrey</i>	
CHAPTER 342	
Experimental Study on Deformation and Fracture of Ice Sheet by Propagating Water Wave	4411
<i>Shigeki Sakai, Xiaodong Liu, Makoto Sasamoto, Shigeo Kanada and Koh Izumiyama</i>	
CHAPTER 343	
An Attempt to Determine the Spanish Public Domain Border	4418
<i>R. Medina, I.J. Losada, F. Mendez, A.J. Fernandez</i>	
CHAPTER 344	
Education of Coastal Engineers for the 50th ICCE	4431
<i>Henk Jan Verhagen</i>	
CHAPTER 345	
Risk-Based Analysis of Coastal Projects	4440
<i>Edward F. Thompson, Michael Wutkowski, Norman W. Scheffner</i>	
CHAPTER 346	
Designing for Propeller Action in Harbours	4451
<i>G.A. Hamill, J.A. McGarvey</i>	
CHAPTER 347	
Modeling Inlet Sand Bypassing	4464
<i>Christopher G. Creed</i>	
CHAPTER 348	
An Approach to Modeling Inlet and Beach Evolution	4477
<i>Mark B. Gravens</i>	
CHAPTER 349	
Hydrodynamics of a Bar in a Flood Channel - the Westerschelde Estuary	4491
<i>Claire Jeuken</i>	
CHAPTER 350	
Interactions between a Sand Barrier and Flood Terrace at the Abukuma River Mouth ..	4505
<i>Akira Mano, Masaki Sawamoto</i>	
CHAPTER 351	
A Unique Look at Oregon Inlet, NC USA	4517

CHAPTER 352	
Impacts of Inlet Structures on Channel Location	4531
<i>William C. Seabergh, Mary A. Cialone, Donald K. Stauble</i>	
CHAPTER 353	
Complete Closure of the Nanakita River Mouth in 1994	4545
<i>Hitoshi Tanaka, Fumihiko Takahashi, Atsushi Takahashi</i>	
CHAPTER 354	
The Erosion of a Salt Wedge Trapped Behind a Barrage Across An Estuary	4557
<i>S.A. Walker, G.A. Hamill, H.T. Johnston</i>	
CHAPTER 355	
Near-Field Measurements of a Buoyant Jet in Waves and Currents	4569
<i>K.H. Kwan, C. Swan</i>	
CHAPTER 356	
Cost Effectiveness of Wave Power Extraction at Erosive Coasts	4583
<i>Hideo Kondo</i>	
CHAPTER 357	
Feasibility Tests of New Pendular-Type Wave Energy Conversion Apparatus	4591
<i>Senji Osanai, Hideo Kondo, Yuzo Mizuno and Tomiji Watabe</i>	
CHAPTER 358	
Watertable Dynamics in Coastal Areas	4601
<i>Hong-Yoon Kang, Peter Nielsen</i>	
CHAPTER 359	
Long Range Positive Effects of the Delray Beach Nourishment Program	4613
<i>Kim E. Beachler, Douglas W. Mann</i>	
CHAPTER 360	
Effectiveness of a Combined Beach and Shoreface Nourishment on the Island of Norderney/East Frisia, Germany	4621
<i>Hanz D. Niemeyer, Ralf Kaiser, Heiko Knaack</i>	

Part VI Case Studies

CHAPTER 361	
Nearshore Berm Performance at Newport Beach, California, USA	4636
<i>Chuck Mesa</i>	
CHAPTER 362	
San Gabriel River to Newport Bay Erosion Control Project, Orange County, California—30 Years of Periodic Beach Replenishment	4650
<i>Arthur T. Shak, Joseph A. Ryan</i>	

CHAPTER 363
A Ten-Year History of Dolos Monitoring at Crescent City4664
William S. Appleton, Thomas Kendall, Jeffrey A. Melby

CHAPTER 364
Breakwater Damage in Okushiri Port Due to the Hokkaido Nansei-oki Earthquake Tsunami4676
Katsutoshi Kimura, Yuzo Mizuno, Hiroichi Tsuruya, Yasuyuki Nakagawa

CHAPTER 365
Richards Bay North Breakwater - Repair of a Roundhead: Monitoring, Model Testing, Design and Construction4689
D. Phelp, A. McClarty, A. Bartels

CHAPTER 366
Thyboron Coastal Investigations 1995: New Lessons from an Old Coastal Problem ... 4703
I. Broker, J.A. Zyserman, Per Roed Jakobsen

CHAPTER 367
Probabilistic Risk Assessment of Beach Erosion at Pevensey Bay in England4717
Ping Dong, Keith J. Riddell

CHAPTER 368
Beach Nourishment in Altafulla, Spain: Verification of Theoretical Models4730
J. Galofre, F.J. Montoya, R. Medina

CHAPTER 369
Alternatives to Beach Stabilization: Cambrils Coast Case Study (Spain)4744
Nuria Lupon, Alfonso Vidaor, Jordi Galofre, F. Javier Escartin

CHAPTER 370
The Effect of Grain Sorting on Profile Stability of Nourished Beaches4756
Ram K. Mohan, Timothy W. Kana

CHAPTER 371
The Use of Data Assimilation to Improve Wave Hindcast Results4770
Jon M. Hubertz

CHAPTER 372
Grain-Size Influence on Sand Transport in Oscillatory Sheet Flow4779
C. Marjolein Janssen and Jan S. Ribberink

CHAPTER 373
Cross-Shore Sediment Transport Mechanisms in the Surfzone on a Timescale of Month to Years4793
Klaas T. Houwman and Gerben Ruessink

CHAPTER 374
Numerical Prediction of Breaking Waves and Currents with a Boussinesq Model4807
Okey George Nwogu

CHAPTER 375

The Effect of the CL-Vortex Force in 3D Wave-Current Interaction4821

M. W. Dingemans, J. A. Th. M. van Kester, A. C. Radder and R. E. Uittenbogaard

Subject Index4833

Author Index4847

CHAPTER 294

MODELLING OF 3D SEDIMENT TRANSPORT IN THE SURF ZONE

by

Berry Elfrink¹, Ida Brøker¹, Rolf Deigaard², Erik Asp Hansen¹ and Peter Justesen¹

ABSTRACT

The three-dimensional sediment transport in the surf zone has been investigated using two different approaches for modelling of the flow pattern. The first approach is based on the integrated momentum concept for the turbulent wave-current boundary layer, see Fredsøe (1984), the second approach is based on the k-model, as described in Deigaard et al. (1991). The k-model allows for a more consistent description of the time and space varying eddy viscosity than the integrated momentum approach, but demands considerably more computation effort. The driving forces are calculated according to the formulations of Deigaard et al. (1991) and Deigaard (1993). The model based on the integrated momentum equation is able to reproduce the details of the flow satisfactorily. The presence of a longshore current increases the turbulence near the bed. This results in a decreased offshore directed flow velocity near the bed and an increase in the sediment concentration. Comparisons with field measurements show good agreement.

INTRODUCTION

When waves break turbulent kinetic energy is produced at the water surface. This energy is partly dissipated in the surface roller and partly transported downwards into the water column. The radiation stress gradients, associated with the wave breaking, are balanced by the pressure gradient originating from the wave setup and the mean bed shear stress.

In case of uniform conditions along the shore, the net discharge in the mean cross shore flow must balance the fluid mass transported in the surface roller and the discharge associated with the asymmetric wave motion and streaming in the bottom boundary layer. The zero mass flux in the cross shore direction is achieved by a slope of the mean water level. The vertical variation of the cross shore flow velocity is therefore characterized by offshore directed velocities near the bed (the undertow) and onshore velocities further away from the bed.

¹ Danish Hydraulic Institute, Agern Allé 5, DK-2970 Hørsholm, Denmark

² Institute of Hydrodynamics and Hydraulic Engineering, Technical University of Denmark, 2800 Lyngby, Denmark

In the longshore direction, the forces associated with the wave breaking can only be balanced by a mean bed shear stress which drives the wave induced longshore current.

The interaction of the turbulence originating from wave breaking with the turbulence generated in the bottom boundary layer is of great importance in the description of the sediment transport in the surf zone, see Justesen et al. (1986). Due to the higher level of turbulence more sediment can be kept into suspension under breaking waves than under non-breaking waves.

In the present work, the flow conditions along the shore are assumed to be uniform, see figure 1. The waves approach the coast under an angle α and are assumed to be long crested and monochromatic.

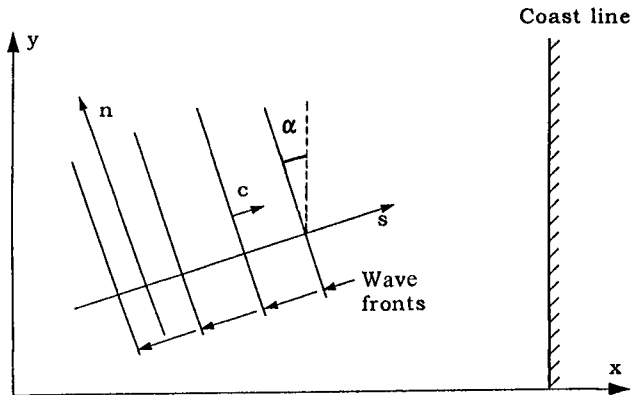


Figure 1 : plan view

VERTICAL VARIATION OF THE DRIVING FORCE

Deigaard and Fredsøe (1989) determined the time mean shear stress in normally incident breaking waves. It was found that the vertical transfer of horizontal momentum gives a significant contribution to the momentum balance. Deigaard (1993) derived expressions for the time mean shear stress in case of oblique waves by considering the momentum balance for the surface rollers. The surface shear stress is given as :

$$\overline{\tau_s} = \left(-\frac{g}{8c} \frac{dH^2c}{ds} - \frac{dAc}{ds} \frac{1}{T} \right) \begin{pmatrix} \cos\alpha \\ \sin\alpha \end{pmatrix} \quad (1)$$

where H=wave height, s=direction of wave propagation, A=surface roller cross section, c=wave celerity, α =wave angle, g=gravitational acceleration and T=wave period.

The cross shore and longshore components of the time mean bed shear stress are determined by the gradients in the radiation stress and the mean water surface slope, the wave set-up, in the cross shore direction, Justesen et al. (1994) :

$$\frac{\bar{\tau}_{b,x}}{\rho} = -\frac{g}{8} \frac{dH^2}{dx} \cos^2 \alpha - \frac{g}{16} \frac{dH^2}{dx} - \frac{d}{dx} \left(\frac{Ac}{T} \right) \cos^2 \alpha - gDs_s \tag{2}$$

$$\frac{\bar{\tau}_{b,y}}{\rho} = -\frac{g}{8} \frac{dH^2}{dx} \cos \alpha \sin \alpha - \frac{d}{dx} \left(\frac{Ac}{T} \right) \cos \alpha \sin \alpha \tag{3}$$

Here, s_s is the slope of the water surface, and x and y are the cross shore and longshore coordinate, respectively. The shear stress varies linearly across the water column. The vertical distribution of the time mean shear stress is illustrated in figure 2.

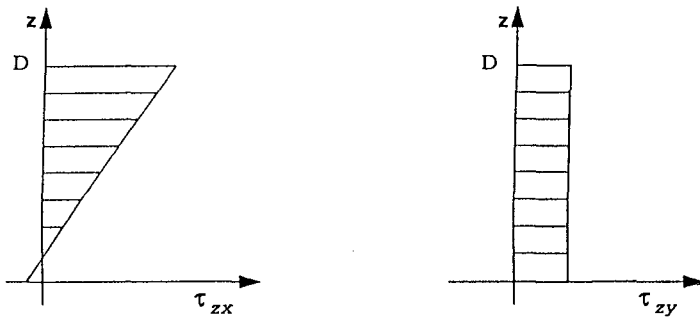


Figure 2 : Illustration of the time mean shear stress in the cross shore and longshore direction.

In both models, the wave orbital motion was calculated from linear wave theory, but any potential wave theory could be used here. If a non-linear wave description is used, the mean bed shear stress associated with the wave motion is non-zero. In the model based on the integrated momentum equation, the wave motion outside the boundary layer is described by potential theory. In order to fulfil the requirements of potential theory, the mean bed shear stress due to the wave motion must be zero. Brøker-Hedegaard et al. (1991) showed that a perfect force balance can be obtained by adding a small constant velocity to the orbital motion. This additional velocity is found iteratively by the requirement of zero mean bed shear stress, see Elfrink et al. (1993). In the K-model, this velocity is found automatically.

In case of progressive waves, a small net shear stress is generated due to the non-uniformity of the wave boundary layer. Brøker-Hedegaard (1985) showed that this streaming induced shear stress at the bed can be expressed as :

$$\tau_{str.} = \frac{\rho}{c} \overline{U_o U_f} |U_f| \quad (4)$$

where U_o = wave orbital velocity and U_f = instantaneous friction velocity.

THE INTEGRATED MOMENTUM APPROACH

In this model the instantaneous velocity profiles and eddy viscosity profiles inside the boundary layer are assumed to be given by a logarithmic and a parabolic distribution, respectively. The interaction of the undertow, the longshore current and the waves is taken into account by superposing the wave by a steady current and solving the turbulent boundary layer for the combined wave/current motion. The total mean eddy viscosity has contributions from the wave breaking, from the bottom layer and from the mean current. The eddy viscosity due to the mean current outside the boundary layer is calculated by applying the mixing length concept. The equations are solved by the assumption that the net flux perpendicular to the shoreline is zero. It is noted that the integrated momentum approach is by far the most computationally efficient.

The time-averaged flow velocity distribution is calculated from the vertical distribution of the driving forces (eq. 1 - 4) and the mean eddy viscosity :

$$\frac{d\bar{U}}{dz} = \frac{\bar{\tau}}{\rho\nu_t} \quad (5)$$

The three contributions to the eddy viscosity are calculated independently from each other. The contribution from the wave boundary layer is calculated from the boundary layer model of Fredsøe (1984). The contribution from the mean flow is modelled by applying a mixing length concept, see Justesen et al. (1994) and the eddy viscosity due to wave breaking is calculated from the transport equation for turbulent kinetic energy, see Deigaard et al. (1986).

THE K-EQUATION MODEL

The k-model approach in the present work is an extension of the model developed by Deigaard et al. (1991) for the case of normally incident waves.

The driving force in the unsteady motion is composed of a steady part as given in eqs. 1 - 4 and an oscillatory part which is given by the periodically varying horizontal pressure gradient associated with the wave motion. The flow equations, neglecting convective terms, read :

$$\frac{\partial u}{\partial t} = -\frac{1}{\rho} \frac{\partial p}{\partial x} + \frac{1}{\rho} \left[\frac{\partial \tau_{zx}}{\partial z} - \frac{\partial \bar{\tau}_{zx}}{\partial z} \right] \quad (6)$$

$$\frac{\partial v}{\partial t} = -\frac{1}{\rho} \frac{\partial p}{\partial y} + \frac{1}{\rho} \left[\frac{\partial \tau_{zy}}{\partial z} - \frac{\partial \bar{\tau}_{zy}}{\partial z} \right] \quad (7)$$

where u =cross shore flow velocity, v =longshore flow velocity, x =cross shore coordinate, y =longshore coordinate, z =vertical coordinate, p =pressure gradient associated with the wave motion, ρ =density of water, τ_{zx} and τ_{zy} = cross shore and longshore components of the shear stress respectively, t = time.

$$\tau_{zx} = \rho \nu_t \frac{\partial u}{\partial z} ; \quad \frac{1}{\rho} \frac{\partial p}{\partial x} = -\frac{\partial U_o}{\partial t} \quad (8)$$

$$\tau_{zy} = \rho \nu_t \frac{\partial v}{\partial z} ; \quad \frac{1}{\rho} \frac{\partial p}{\partial y} = -\frac{\partial V_o}{\partial t} \quad (9)$$

The eddy viscosity, ν_t , is calculated from the diffusion equation for turbulent kinetic energy, see Justesen et al. (1994) :

$$\nu_t = l\sqrt{k} ; \quad \frac{\partial k}{\partial t} = -\frac{\partial}{\partial z} \left(\nu_t \frac{\partial k}{\partial z} \right) + \frac{1}{\rho} PROD - c_l \frac{k^{3/2}}{l} \quad (10)$$

PROD = production term, which consists of contributions from wave breaking , as expressed through the gradient in wave energy flux, E_f , and from the shear stress in the model.

$$PROD = \tau_{zx} \frac{\partial u}{\partial z} + \tau_{zy} \frac{\partial v}{\partial z} - \frac{\partial E_f}{\partial x} \quad (11)$$

SEDIMENT TRANSPORT

The sediment transport is calculated according to Fredsøe et al. (1985) and Deigaard et al. (1986). Here the bed load transport model of Engelund and Fredsøe (1976) is used, where the bedload transport is calculated from the instantaneous bed shear stress. The vertical variation of the suspended sediment concentration is calculated from the vertical diffusion equation for suspended sediment.

The omission of the convective terms in the diffusion equation is alleviated by adding the lagrangian flow velocity times the mean concentration to the time averaged product of instantaneous velocity and concentrations.

COMPARISON OF THE 2 MODELS

Figs 3 and 4 show the mean cross shore and longshore flow velocities for the 2 models for varying wave angles. The wave height in this example was taken as 0.6 m and the period as 6 s. The water depth was 1 m and the bed roughness 0.5 mm. The energy dissipation, the surface roller volume and the cross shore gradient of the surface roller were calculated by using a wave height gradient of -0.015 and a bed slope of 0.033. The sediment grain size was taken as 0.2 mm.

It can be seen that the agreement between the two models is good. In the lower part of the water column, the gradients in the velocity profiles are somewhat steeper for the k-model than for the integrated momentum approach, which indicates slightly higher values of the eddy viscosity for the latter.

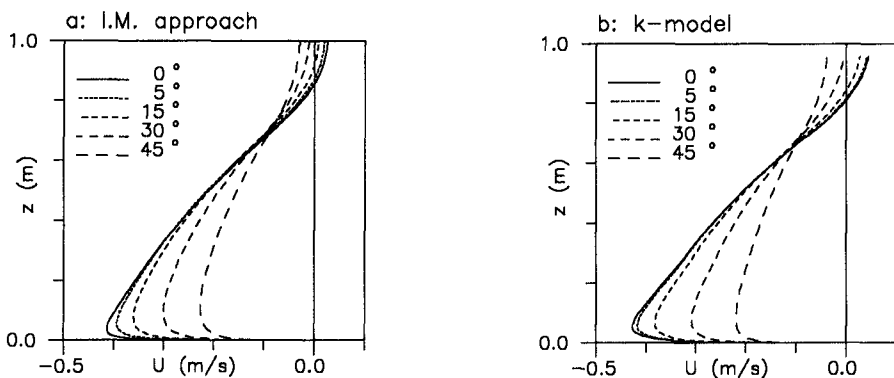


Figure 3 : Time averaged cross shore flow velocities for the two models.
 a = integrated momentum approach , b = k-model.

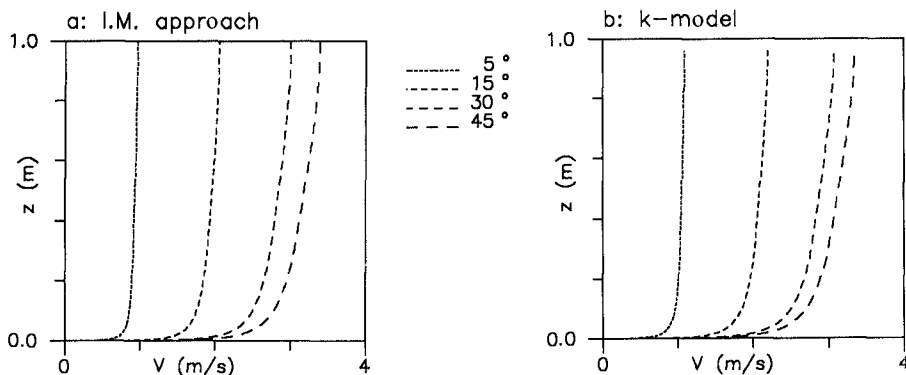


Figure 4 : Time averaged longshore flow velocities for the two models.
 a = integrated momentum approach , b = k-model.

The time variation of the cross shore and longshore components of the friction velocity are shown in figs. 5 and 6. For low angles of wave incidence, the cross shore friction velocities are slightly lower under the wave crest for the integrated momentum approach than for the k-model, but generally the agreement is good.

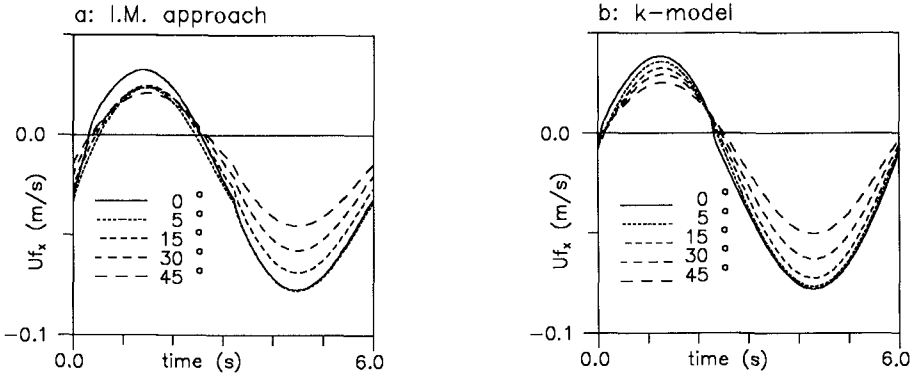


Figure 5 : Time variation of the cross shore component of the shear velocity. a = integrated momentum approach, b = k-model.

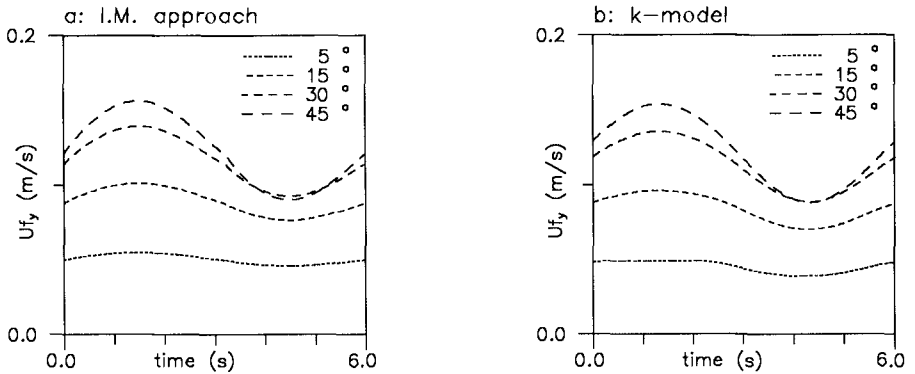


Figure 6 : Time variation of the longshore component of the shear velocity. a = Integrated momentum approach, b = k-model.

In this example, the cross momentum exchange of horizontal momentum, associated with the gradients in the longshore current velocity across the shore has been neglected. This causes unrealistically high values of the calculated longshore current velocities and friction velocities. Usually, the mean bed shear stress is calculated from a surf zone model which

includes this momentum exchange. However, this has no importance in the context of intercomparing the two different models.

In both models, the suspended sediment transport is calculated as the product of the instantaneous flow velocities and the instantaneous sediment concentration :

$$q_s = \frac{I}{T} \int_0^D \int_0^D (uc) dz dt \quad (12)$$

In the calculation of the sediment transport in the surf zone, the vertical variation of the suspended sediment concentration is important. Deviations in the time averaged suspended sediment concentrations may occur due the phase difference between the flow in the wave boundary layer and the outer flow. In the k-model, this phase difference is included, whereas the boundary layer in the integrated momentum approach is assumed to be in phase with the outer flow. Figs. 7 and 8 show the time averaged vertical variation of the suspended sediment fluxes for the two models in the cross shore and longshore direction. The agreement is seen to be good for all examined wave angles.

A number of comparisons were performed where the hydrodynamic parameters (e.g the wave height, period, angle of incidence and energy dissipation) were varied systematically. Also different grain sizes were analyzed. The integrated momentum approach tends to give slightly higher transport rates for high levels of turbulence, associated with wave breaking. This is due to the different techniques in determining the turbulence originating from the boundary layer, the mean flow and wave breaking. Generally the agreement is good.

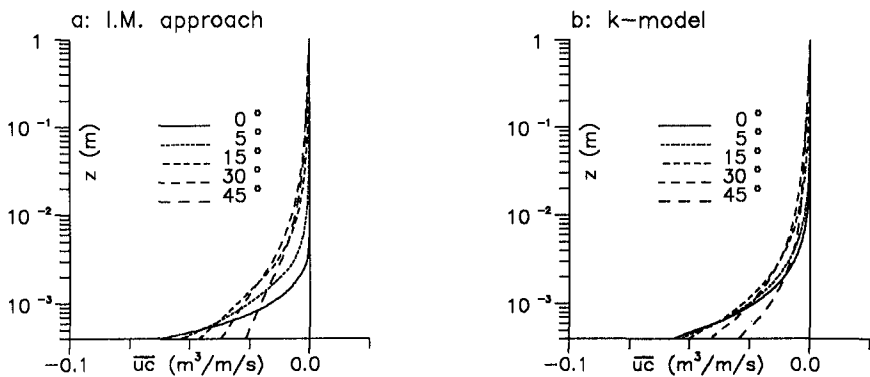


Figure 7 : Vertical variation of the time averaged cross shore sediment flux.
a = Integrated momentum approach, b = k-model.

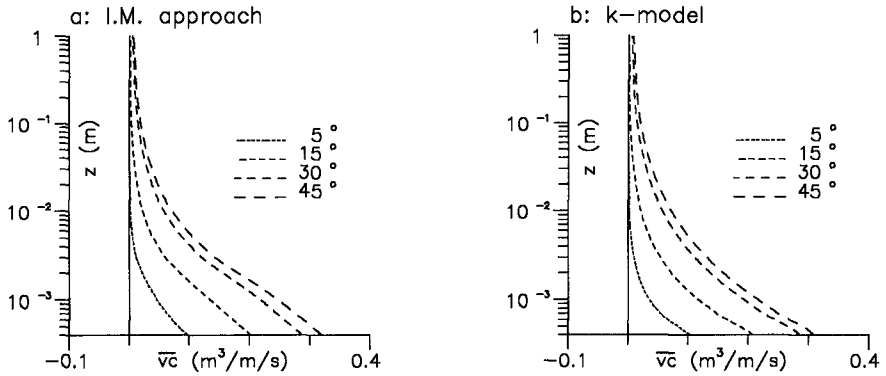


Figure 8 : Vertical variation of the time averaged longshore sediment flux.
 a = Integrated momentum approach, b = k-model.

It can be concluded that the integrated momentum approach gives results very similar to the more complete k-model in determining the mean flow, the time variation of the bed shear stress and the sediment transport.

THE INTERACTION OF UNDERTOW AND LONGSHORE CURRENT

The presence of a longshore current will affect the undertow and the resulting cross shore sediment transport. The interaction of the longshore current with the undertow is important in the determination of the cross shore profile evolution. The longshore current causes higher levels of turbulence near the sea bed, this affects the vertical shape of the cross shore velocity as the vertical velocity gradients decrease due to the higher eddy viscosity. This results in a reduction of the near bed cross shore flow velocity. At the same time, the higher levels of turbulence allow higher concentrations of suspended sediment.

A test was performed with the model based on the integrated momentum equation for a situation with and without the presence of a longshore current of 0.5 m/s. In the present example, a wave height of 0.7 m and a period of 5 s was used. The water depth is 1.5 m and the energy dissipation corresponds to the energy loss in a hydraulic jump. Figure 9a shows the simulated time averaged cross shore velocity profile with and without a longshore current. In both cases, the mean flow under the wave crest balances the mass transport in the surface roller and the wave drift. It can be seen that the near bed offshore directed velocities are lower in case of a longshore current. Consequently, the velocities in the vicinity of the water surface are slightly higher.

The bed concentrations for both cases are shown in figure 9b. The main difference is that the bed concentration does not vanish at the flow reversal ($t/T \approx 0.05$, and $t/T \approx 0.45$) in case of a longshore current. The bed concentrations are lower under the wave crest ($t/T < 0.5$) than under the trough ($t/T > 0.5$) because the wave orbital motion and the undertow counteract each other, whereas they both are directed offshore under the wave trough. The maximal bed concentration is slightly higher in case of a longshore current. The vertical variations of the time-mean sediment concentration for the two examples are shown in figure 9c. The increased eddy viscosity and the higher mean bed concentration result in a higher mean concentration in case of a longshore current. The combined effect of lower offshore velocities near the bed and the higher sediment concentrations result in an increased cross shore sediment transport in case of a longshore current in this example as shown in figure 9d.

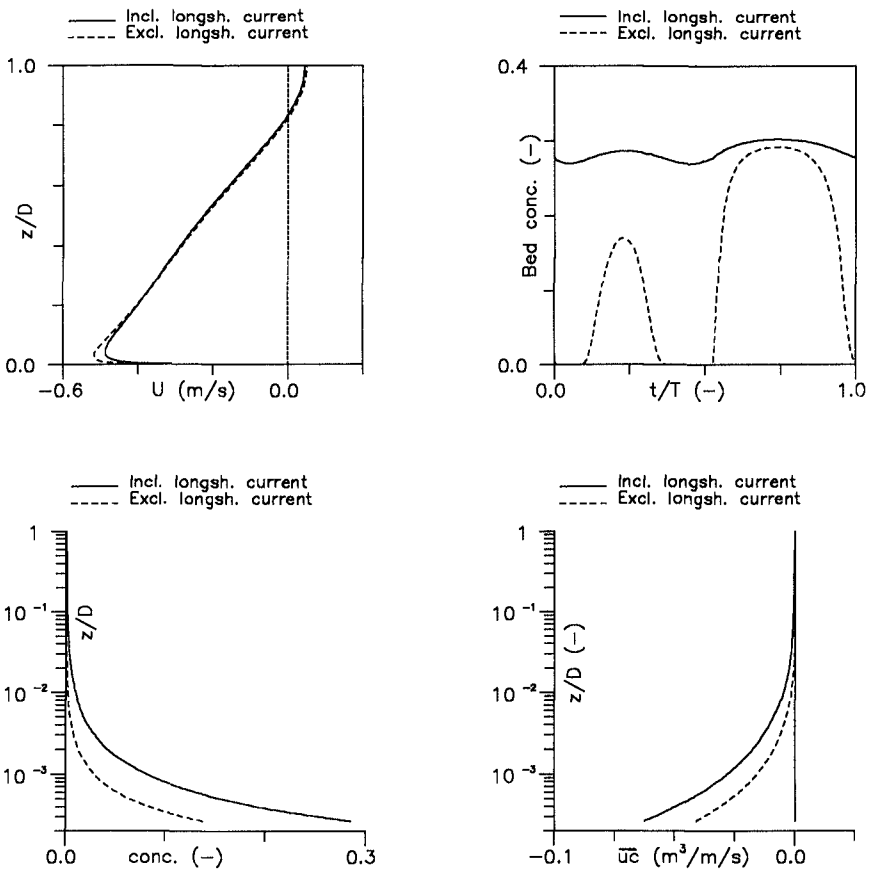


Figure 9 : Interaction of the undertow with a longshore current. a: Mean cross shore flow, b: time variation of the bed concentration, c: time-mean sediment concentration d: time-mean sediment flux.

COMPARISON WITH FIELD MEASUREMENTS

A comparison was made with measured flow velocity profiles at the Ebro delta, Spain, which were reported in Rodriguez et al. (1994). The comparison was made for three levels of calibration. First, the mean cross shore flow velocities were calculated without any calibration. In these simulations, a fully developed roller, where the associated energy dissipation corresponds to the energy loss in a stationary hydraulic jump was assumed.

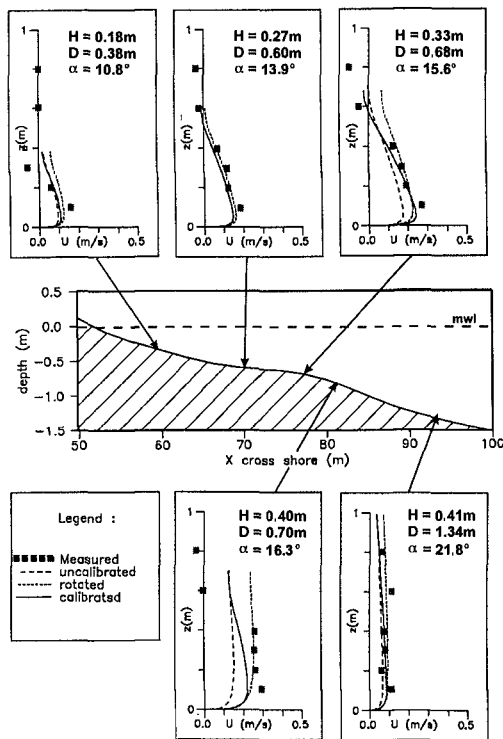


Figure 10 : Comparison of the present model with field measurements from Rodriguez et al. (1994). Three levels of calibration were applied :
 1 - uncalibrated, 2 - rotated, 3 - adjusted roller volume.

secondly, the uncalibrated flow velocity profiles were rotated such that the calculated depth averaged velocity matched the measured values. This adjustment accounts for possible 2D

effects, e.g. the coast is not perfectly uniform in the longshore direction. Thirdly, a calibration was performed by determining the volume of the surface rollers from the measured mean cross shore flow velocity and the estimated wave drift, which was calculated from sinusoidal wave theory. In all cases the waves were assumed to be unidirectional and regular. The wave orbital motion was calculated by using 1st order Stokes theory. The results for the mean cross shore flow are shown in figure 10. Generally the agreement is satisfactorily. The uncalibrated model underestimates the measured velocities near the bed slightly. The rotation of the coordinate system improves the agreement to a limited degree. The agreement is worst for the sample point located at a cross shore coordinate of approximately 80 m. For the present test, this corresponds to the outer surf zone. The calibrated velocity profiles match the velocity gradients better than the uncalibrated model.

CONCLUSIONS

A numerical model was developed for the flow and the sediment transport under oblique incident waves in the surf zone. The model is based on the integrated momentum equation for the wave boundary layer of Fredsøe (1984). The eddy viscosity consists of contributions from the wave boundary layer, the mean flow and wave breaking. These contributions are calculated separately.

The model based on the integrated momentum equation gives very similar results compared to a more complete turbulence model. For engineering purposes, the integrated momentum approach is recommended because it is able to reproduce the details of the flow and the sediment transport and is very efficient in computing time.

In case of a longshore current the level of turbulence near the bed is increased compared to a situation without current. This results in lower near bed velocities of the undertow and an increased concentration of suspended sediment.

Comparison of the simulated mean cross shore and longshore flow velocities show good agreement with field measurements.

ACKNOWLEDGEMENT

This work was supported by the Danish Technical Research Council (STVF) under the program "Marin Teknik".

The authors would like to express their gratitude to Andres Rodriquez for supplying the data of the field measurements at the Ebro delta.

REFERENCES

- Brøker Hedegaard, I. (1985). Wave generated Ripples and resulting Sediment Transport in Waves. Series paper no 36. Institute of Hydrodynamics and Hydraulic Engineering (ISVA). Technical University of Denmark.
- Brøker Hedegaard, I., R. Deigaard, and J. Fredsøe (1991). Onshore/Offshore sediment transport and morphological modelling of coastal profiles. Proc. Coastal Sediments '91, ASCE, Seattle, pp. 643-657
- Deigaard, R., J. Fredsøe and I. Brøker Hedegaard (1986). Suspended sediment in the surf zone. J. Waterway, Port, Coastal and Ocean Engineering, ASCE, vol. 112 (1), pp 115-128
- Deigaard, R and J. Fredsøe (1989). Shear stress distribution in dissipative water waves. Coastal Engineering, ASCE, vol. 13, pp 357-378
- Deigaard, R. (1993). A note on the 3-dimensional shear stress distribution in a surf zone. Coastal Engineering, vol. 20, pp 157-171.
- Deigaard, R., P. Justesen, J. Fredsøe (1991). Modelling of the undertow by a one equation turbulence model. Coastal Engineering, vol. 15, pp 431-458.
- Elfrink, B., I.Brøker Hedegaard, R. Deigaard and J. Fredsøe. (1993). Net sediment transport in non-breaking waves. Progress report no 74. Institute of Hydrodynamics and Hydraulic Engineering (ISVA). Technical University of Denmark. pp 1-10.
- Engelund, F and J. Fredsøe (1976). A sediment transport model for straight alluvial channels. Nordic Hydrology, vol 7, pp 293 - 306
- Fredsøe, J. (1984). Turbulent boundary layers in wave-current motion. Journal of Hydraulic Engineering, ASCE, vol. 110 (HY8), pp 1103-1120.
- Fredsøe, J., O.H. Andersen and S. Silberg. (1985) . Distribution of suspended sediment in large waves. J. of Waterways, Port, Coastal and Ocean Engineering, ASCE, vol. 111 (6), pp 1041 - 1059.
- Justesen, P., J. Fredsøe and R. Deigaard. (1986). The bottleneck problem for turbulence in relation to suspended sediment in the surf zone. Proc. 20th Coastal Engineering Conference, Taipei, Vol 2, pp 1225 - 1239.
- Justesen, P., E.A. Hansen, I. Brøker and R. Deigaard. (1994). Longshore and cross shore velocity profiles in spilling breakers with an oblique angle of incidence. Progress report no 75. Institute of Hydrodynamics and Hydraulic Engineering (ISVA). Technical University of Denmark. pp 41-54.
- Rodriguez A., A. Sánchez-Arcilla, F.R. Collado, V. Gracia, M.G. Coussirat, J. Prieto. Waves and currents at the Ebro delta surf zone: Measurements and modelling. Proc. 24th Int. Conf. on Coastal Eng. 1994. pp. 268-269

CHAPTER 295

A Numerical Model of Sheet Flow Sediment Transport

Sadakazu Katori,¹ Masaru Mizuguchi² and Akira Watanabe³

Abstract

Governing equations are derived for a numerical model to simulate the sediment motion under sheet flow condition. They consist of equations for the conservation of the horizontal momentum, the turbulence energy and the sediment mass. Values of coefficients in the governing equations are determined using the experimental results of Horikawa *et al.* (1982). The mean sediment transport rates during half a period of sinusoidally oscillatory flow are calculated and the computed values agree well with the experimental results of Sawamoto and Yamashita (1986). Computations are also made for the net transport rate in unsinusoidally oscillatory flow with and without superposed steady flow, showing a good agreement with the measurements of Dibajnia and Watanabe (1992). Finally the thickness of the sheet flow moving layers is computed and related to grain-flow parameters.

Introduction

The first author conducted a detailed experiment on the sheet flow sediment transport in an oscillatory flow tank with sinusoidal velocity variations, measured the velocity as well as concentration of the sediment, and evaluated the mean transport rate during half a period of sinusoidal flow (Horikawa *et al.*, 1982). After this experiment that remarkably advanced our understanding of the sheet flow transport, many studies have been performed until now. According to recent studies on the sediment transport, it has been widely recognized that the sheet flow predominates in the surf zone not only during storms but also even under moderate waves in the field (e.g., Watanabe *et al.*, 1991, Dibajnia *et al.*, 1994).

¹Director, Coastal Engineering Consultants Co., Ltd., Tamura Bldg., 5-23-13, Hongo, Bunkyo-ku, Tokyo, 113 Japan.

²Professor, Department of Civil Engineering, Chuo University.

³Professor, Department of Civil Engineering, University of Tokyo.

Hence not a few numerical models for the sheet flow sediment movement have been presented so far, but the validity and applicability of most of them are not sufficient enough.

This study aims to develop governing equations and a numerical model that can reproduce time-space changes in the velocity and concentration of the sediment as well as the net transport rate under the sheet flow condition.

Governing Equations Derived for A Numerical Model

Equations (1) to (3) are newly proposed to describe the sheet flow sediment motion.

For the conservation of the horizontal momentum:

$$\begin{aligned} \partial u / \partial t &= (\rho_w / \rho) [\partial U / \partial t + \partial (K_u \partial u / \partial z) / \partial z] & (1) \\ K_u &= \begin{cases} \nu + \kappa_{ul} d k^{1/2} + \kappa_{uc} \nu F(c) & (-\infty < z < z_5) \\ \nu + [\kappa_{ul} d + \kappa_{uh} (z - z_5)] k^{1/2} + \kappa_{uc} \nu F(c) & (z_5 < z < \infty) \end{cases} \\ F(c) &= [1 + 0.183c / (1 - 0.878c)]^2 \text{ - - - - - (Eilers, 1941)} \end{aligned}$$

For the conservation of the turbulence energy:

$$\begin{aligned} \partial k / \partial t &= K_{kp} (\partial u / \partial z)^2 + \partial (K_{kd} \partial k / \partial z) / \partial z - \varepsilon & (2) \\ K_{kp} &= \begin{cases} 0 & (-\infty < z < z_5) \\ [\nu + \kappa_{kp} (z - z_5) k^{1/2}] (c_5 - c) & (z_5 < z < \infty) \end{cases} \\ K_{kd} &= \begin{cases} 0 & (-\infty < z < z_{10}) \\ (\nu + \kappa_{kd} d k^{1/2}) (1 - c) & (z_{10} < z < z_5) \\ \{ \nu + [\kappa_{kd} d + \kappa_{kdh} (z - z_5)] k^{1/2} \} (1 - c) & (z_5 < z < \infty) \end{cases} \\ \varepsilon &= \kappa_{ke} g F(c) k^{1/2} \end{aligned}$$

For the conservation of the sediment mass:

$$\begin{aligned} \partial c / \partial t &= \partial (K_c \partial c / \partial z) / \partial z + \partial (w c) / \partial z & (3) \\ K_c &= \begin{cases} \nu + \kappa_{cl} d k^{1/2} |_{z=z_5} & (-\infty < z < z_5) \\ \nu + [\kappa_{cl} d + \kappa_{ch} (z - z_5)] k^{1/2} & (z_5 < z < \infty) \end{cases} \\ w &= w_0 (1 - c) \end{aligned}$$

Here U is the main flow velocity, u the velocity of the fluid-sediment mixture, k the turbulence energy, c the volumetric sediment concentration ($0 \leq c \leq 1.0$), t the time, z the vertical distance measured upward from an initial bed surface, ρ_w the fluid density, ρ the density of the fluid-sediment mixture, ν the fluid kinematic viscosity, d the sediment grain size, w_0 the free fall velocity of sediment particles, z_5 and z_{10} are z where $c = c_5 = 0.5$ and $c = 0.99$, respectively, and g is the acceleration of gravity. All the coefficients κ with subscripts are constants.

Equation (1) is a turbulence model for the conservation of the horizontal momentum in the bottom boundary layer. Here it is assumed that the fluid and sediment move together with the same horizontal velocity u . The density of the fluid-sediment mixture $\rho(z, t)$ is defined as

$$\rho = (1-\lambda)c\rho_s + [1-(1-\lambda)c]\rho_w \tag{4}$$

where λ is the porosity of the fluid-sediment mixture at $c=1.0$, ρ_s the density of the sediment particles. A main point of Eq. (1) is how to express the eddy viscosity K_u . According to Kolmogorov (1941) and Prandtl (1945), K_u is determined as $K_u \sim \ell k^{1/2}$, where ℓ is the length scale of turbulence and k is the turbulence energy. As observed in one of the experimental results of Horikawa *et al.* (1982) in Fig. 1, the vertical distribution of concentration has an inflection point around the vertical distance z_5 where concentration c is c_5 . This implies that the length scale in the inner layer is very different from that in the outer layer. Then we assume that the length scale in the inner layer is governed by the grain size d , because the concentration in this layer is very high. On the other hand, the length scale in the outer layer will be set as $z - z_5$, because more free turbulence field is formed in this layer. The grain size d , $z - z_5$, and the turbulence energy k are thus included in the expression of the eddy viscosity K_u . In addition, we employ an equation proposed by Eilers (1941) to describe the chaotic collision of grains.

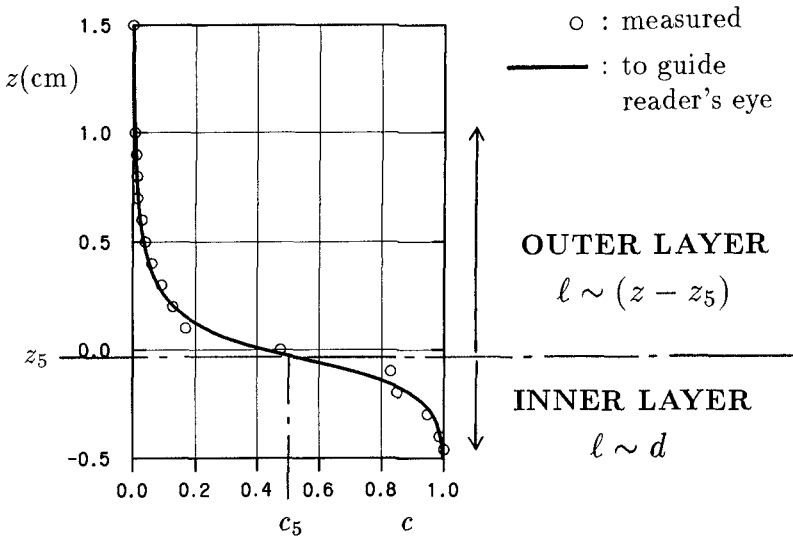


Fig. 1 Distribution of sediment concentration.

($d=0.2\text{mm}$, $T=3.64\text{s}$, $\hat{U}=127\text{cm/s}$, $\theta = 90^\circ$, i.e., $U=\hat{U}$)

Equation (2) shows that time change in the turbulence energy k is determined by three terms; the production, diffusion and dissipation. Regarding coefficients K_{kp} and K_{kd} in Eq. (2), similar formation is made in terms of $\nu, z - z_5, k$ and d for the same reasons mentioned above. A main difference is that there are layers where no production or diffusion of the turbulence energy takes place. This assumption is acceptable, because the concentration in the vicinity of the bed surface is very high and it is nearly impossible for the fluid-sediment mixture with high concentration to form the strong turbulence field. Another point is that the effect of concentration is simply expressed by $(c_5 - c)$ or $(1 - c)$ and that the dissipation rate ε is described in a very simple way. On these assumptions, Eq. (2) becomes a one-equation model of the turbulence energy which is much simpler to solve than two-equation models such as $k-\varepsilon$ models.

Equation (3) for the conservation of sediment mass takes similar formulation except that the diffusion coefficient K_c for the inner layer is determined by the turbulence energy k at $z = z_5$, because sediment particles are expected to diffuse even in the inner layer where the magnitude of turbulence energy is very small. In other words, the reduction of concentration in the inner layer is assumed to take place at the phase of acceleration of the main flow through loosening of the grain arrangement due to shear stresses around $z = z_5$. The reduction rate of fall velocity w with the increase of sediment concentration can be approximately expressed as $(1 - c)$ according to Katori and Homma (1984).

Boundary conditions are

$$\left. \begin{array}{l} u = 0 \\ k = 0 \\ c = 1 \end{array} \right\} \quad \text{at } z < z_{10} \quad \left. \begin{array}{l} u = U \\ k = 0 \\ c = 0 \end{array} \right\} \quad \text{at } z = z_{\infty} \quad (5)$$

Here z_{10} is the vertical distance where $c = 0.99$, and z_{∞} is that of the outer edge of the bottom boundary layer. It has been reported that the thickness of the bottom boundary layer becomes much larger when fluid contains granular sediment particles. For this reason, z_{∞} should be set as large as possible in computation. According to trial and error, $z_{\infty} = 5\text{cm}$ is large enough for grain diameter smaller than several millimeters. In addition it has been found that the concentration around $z = z_{10}$ sometimes exceeds 1.0 at the phase of sediment falling and in the worst cases the computation fails by oscillation or divergence of solutions. We employ the following procedure to avoid such computational failure. At each time step of calculation of the sediment concentration by Eq. (3), we detect the top vertical distance z_B where the concentration becomes or exceeds 1.0 by searching downward from z_{∞} , set the concentration below z_B as 1.0, and make the following adjustment for the upper region so as to maintain the conservation of total sediment mass.

$$c \leftarrow c [(V_o - z_B)/(V_i - z_B)] \quad \text{at } z > z_B \quad (6)$$

$$V_i = \int_{z_{-\infty}}^{z_{\infty}} c \, dz$$

where V_0 is the volume of sediment per unit horizontal area at the beginning of calculation, and $z_{-\infty}$ is the vertical distance of the lower boundary of a calculation domain.

Determination of Coefficients κ

In the governing equations, there are several coefficients κ with subscripts to be determined. These coefficients are determined using the experimental data presented by Horikawa *et al.* (1982). Figure 2 shows another example of their measurements. The experimental conditions are: $d=0.2\text{mm}$, $\rho_s=2.66$, $T=3.64\text{s}$ and $\hat{U}=127\text{cm/s}$. In Fig. 2 the phase θ of the main flow is defined as $\theta = 0^\circ$ for $U = 0$ and $\theta = 90^\circ$ for $U=\hat{U}$. Open circles in Fig. 2 are the measurement data of the horizontal velocity u and concentration c . As for the experimental data of the turbulence energy k , Yamashita *et al.* (1985) measured the velocity by

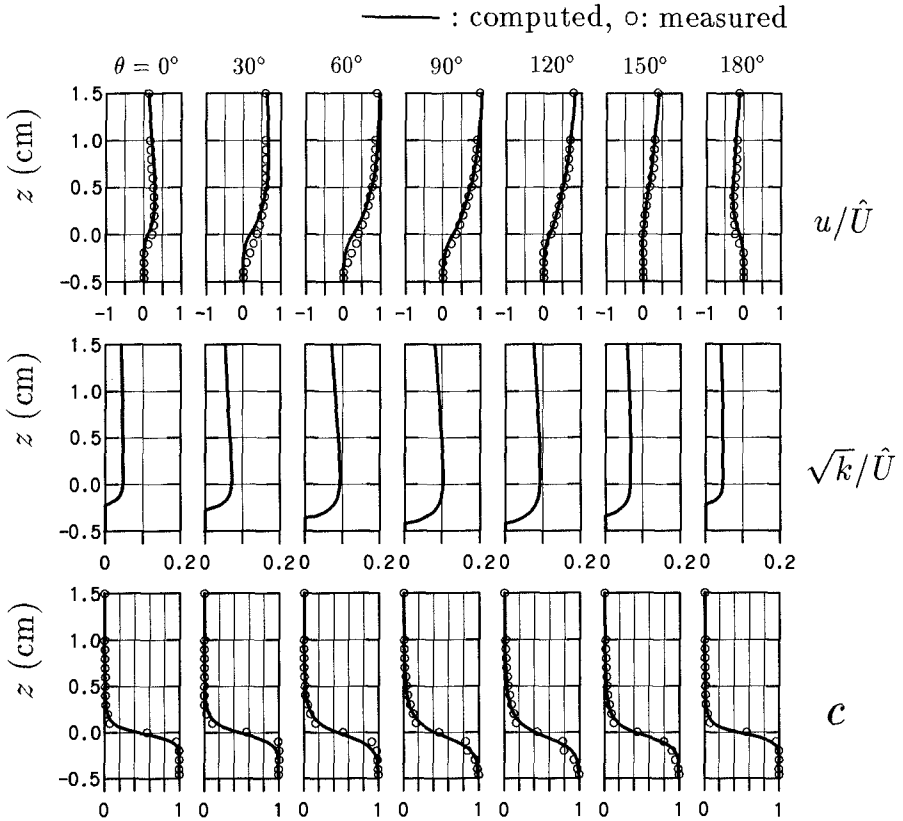


Fig. 2 Comparison of the horizontal velocity u and concentration c between the measurements and the computations.

using an optic fiber velocity meter and reported that the maximum magnitude of square root of the turbulence energy is about 1/10 of the main flow velocity. The computations shown by solid lines in Fig. 2 show a remarkably good agreement with the measurements when we set values of the coefficients κ as follows:

$$\begin{aligned} \kappa_{ul} &= 1.8, & \kappa_{uh} &= 0.045, & \kappa_{uc} &= 10.0 \\ \kappa_{kp} &= 0.984, & \kappa_{kdl} &= 45.0, & \kappa_{kdh} &= 18.0, & \kappa_{ke} &= 0.006 \\ \kappa_{cl} &= 0.833, & \kappa_{ch} &= 0.09 \end{aligned} \quad (7)$$

It should be emphasized that these constants have given a good agreement between the computations and the measurements also for all the other cases of Horikawa *et al.* (1982), and that they will be commonly used in the following calculations.

In the numerical computation the initial conditions are $u=0$, $k=0$, and

$$\begin{aligned} c=0 & & z > 0 \\ c=1 & & z \leq 0 \end{aligned} \quad (8)$$

The time interval Δt and the vertical grid interval Δz are set as follows:

$$\begin{aligned} \Delta t &= T/2400 \\ \Delta z &= \min(\sqrt{2q\Delta t}, d) \end{aligned} \quad (9)$$

where q is the mean sediment transport rate during half a period estimated by the following formulas presented by Sawamoto and Yamashita (1986).

$$\Phi \equiv (1 - \lambda)q/w_0d = 2.2 (u_*/w_0)^3 \quad (10)$$

in which Φ is the nondimensional mean transport rate, u_* the friction velocity, and w_0 the free fall velocity. To estimate the friction velocity u_* , we employ the following wave friction factor f_w proposed by Jonsson (1966).

$$\begin{aligned} \frac{1}{4\sqrt{f_w}} + \log \frac{1}{4\sqrt{f_w}} &= -0.08 + \log(a_m/\xi) & (a_m/\xi > 1.57) \\ f_w &= 0.3 & (a_m/\xi < 1.57) \end{aligned} \quad (11)$$

where a_m is the amplitude of main flow orbital movement, and ξ is the bottom roughness, which is set as $\xi=d$ in this study.

Sediment Transport Rate

Computations of the sediment transport rate are conducted to verify the validity and applicability of the present model. Sawamoto and Yamashita (1986) have carried out a series of experiments in a U-shape tube with a rectangular cross section. In the tube, quasi-sinusoidal flow is generated by releasing the initial imbalance of water heads between the tube ends. The period of the oscillatory flow is fixed to be 3.8s owing to the natural frequency of the fluid motion in the

tube. The range of the amplitude of main flow velocity is 44.3-125.3 cm/s. They have used three kinds of quartz sands and a coal powder as the bed materials to measure their transport rates. Imitation pearl pellets have also been used to observe the sediment motion through a side glass wall. Figure 3 shows the comparison between Φ_{cal} and Φ_{meas} , where Φ_{cal} is the calculated nondimensional mean transport rate during half a period and Φ_{meas} is that of the measurement data by Sawamoto and Yamashita (1986), Horikawa *et al.* (1982) and Abou-Seida (1965). Although a little scatter is observed especially for the case of Abou-Seida, the overall agreement between Φ_{cal} and Φ_{meas} is fairly good.

In addition Sawamoto and Yamashita (1986) proposed a mean transport rate formula during half a period of sinusoidal flow as already shown by Eq. (10). Figure 4 shows that the computed values of Φ shown by symbols agree well with thier formula except for the range of small u_* / w_0 , where the sediment movement approaches to its threshold of sediment motion. Here the computation conditions are almost the same with those of Sawamoto and Yamashita, while the range of main flow velocity amplitude \hat{U} has been extended to 0.2-4.0m/s.

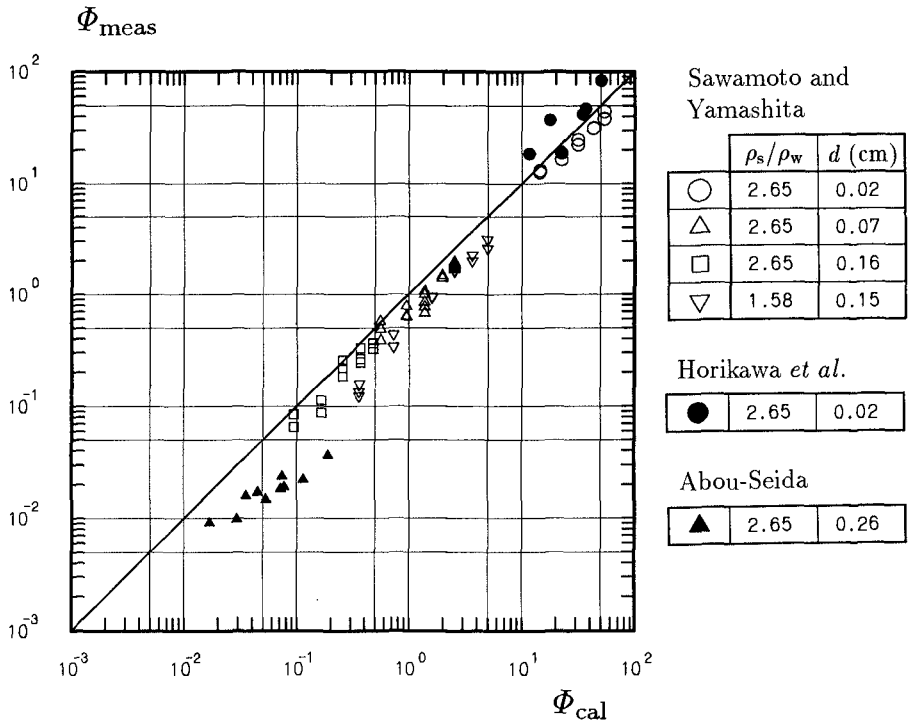


Fig. 3 Comparison between Φ_{cal} and Φ_{meas} in sinusoidally oscillatory flow.

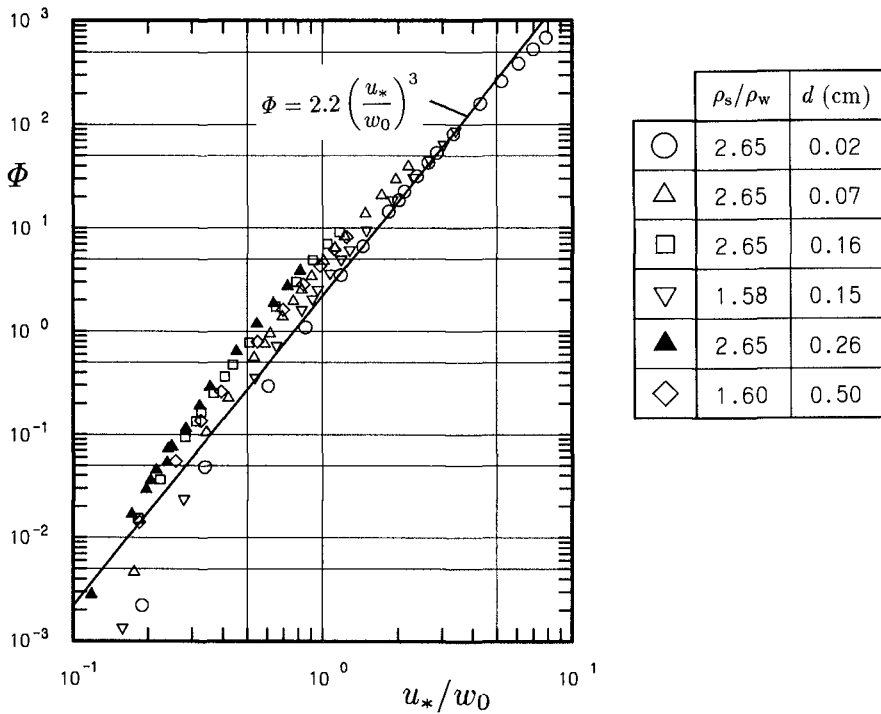


Fig. 4 Relation between Φ_{cal} and u_*/w_0 in sinusoidally oscillatory flow.

Dibajnia and Watanabe (1992) have measured the net rate of sheet flow sediment transport in unisusoidally oscillatory flow with and without superposed steady flow. The experiments have been carried out in a loop-shape oscillatory/steady flow water tunnel. The flow is driven by a piston to be oscillation with arbitrary temporal variations and by a pump to superpose a steady current on the oscillation. The bet material is the sand with a grain diameter of 0.2mm. They have selected five oscillation periods ranging from 1s to 4s and four conditions of the asymmetry index $U_{\text{max}}/\hat{U}=0.5$ to 0.8, where U_{max} is the maximum value of the oscillatory flow velocity U and \hat{U} is the total amplitude of U . In addition the steady flow with four velocities ($\bar{V} \simeq -20, -10, 10, 20\text{cm/s}$) have been superposed on each of the oscillations. In Fig. 5 their data are compared with computations, which shows a good agreement for both the positive and the negative transport rate. Here the results are plotted for the two oscillation periods of 3s and 4s, because the other experimental results for $T=1.0\text{s}, 1.5\text{s}$ and 2.0s show large scatter. The reason for such large scatter is to that Dibajnia and Watanabe have not measured the flow velocities directly in coexistent oscillatory

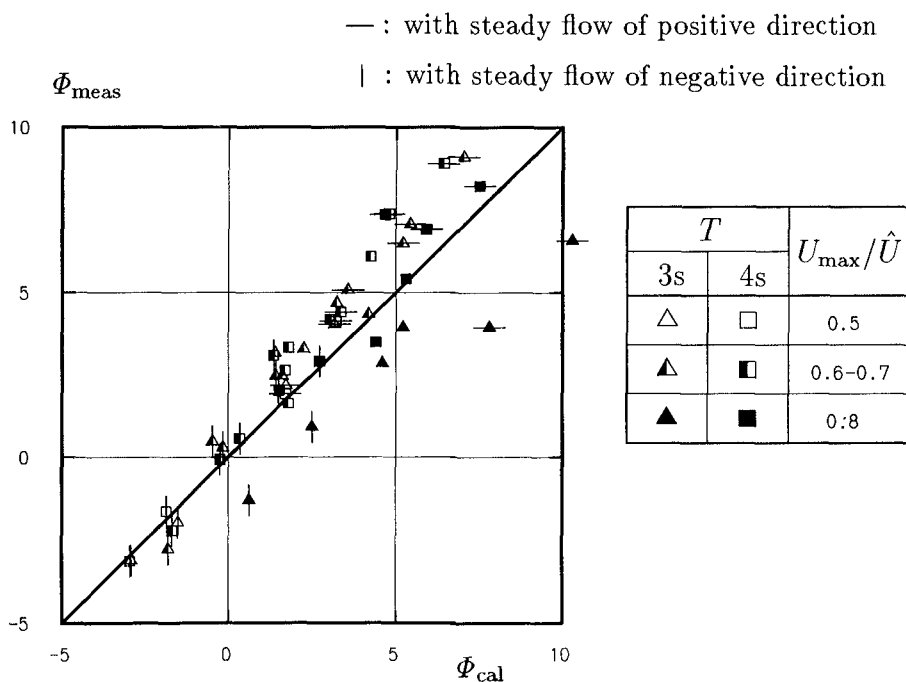


Fig. 5 Comparison between Φ_{cal} and Φ_{meas} in unsinusoidally oscillatory flow with and without superposed steady flow.

and steady flow. The expected flow conditions may not have been obtained when the period of oscillatory flow is short and the interaction between oscillatory flow and steady flow becomes significant in their water tunnel.

Thickness of Moving Layers

The thickness of moving layers is another major concern about the sheet flow sediment transport. In this study, the moving layer thickness δ_B is defined as the maximum change in the elevation of the bed surface, where the sediment particles never move during the whole period of the oscillatory flow. The quantity δ_B is not only important to be used as a boundary condition for analytical treatment of the sheet flow transport but also useful for rough evaluation of the transport rate. It is possible to make such evaluation by multiplying δ_B by the mean concentration and the mean near-bed velocity. Although experimental studies on δ_B have been performed (e.g., Li *et al.*, 1993, Yamashita *et al.*, 1993), most of them are observations through side glass walls where the movement of sediment particles is greatly affected by the side boundary layer. For this reason, we only

show computations without comparison with the measurements. Figure 6 shows the computed results, indicating a high correlation with grain-flow parameters. The solid line fitted for the computations reads

$$\delta_B / \sqrt{d\nu / \hat{U}} = 230 \Psi^{0.891} \quad (12)$$

where d is the grain size, ν the fluid kinematic viscosity, \hat{U} the amplitude of main flow velocity, $\Psi (=u_*^2 / s d g)$ is the Shield number, and $s = (\rho_s / \rho_w - 1)$ is the immersed specific gravity of sediment.

Conclusions

This paper has presented a numerical model for the sheet flow sediment transport. The model consists of governing equations for the conservation of horizontal momentum, the turbulence energy and the sediment mass. Comparisons have been made between the computations and laboratory measurements for vertical distributions of the horizontal velocity and sediment concentration as well as the

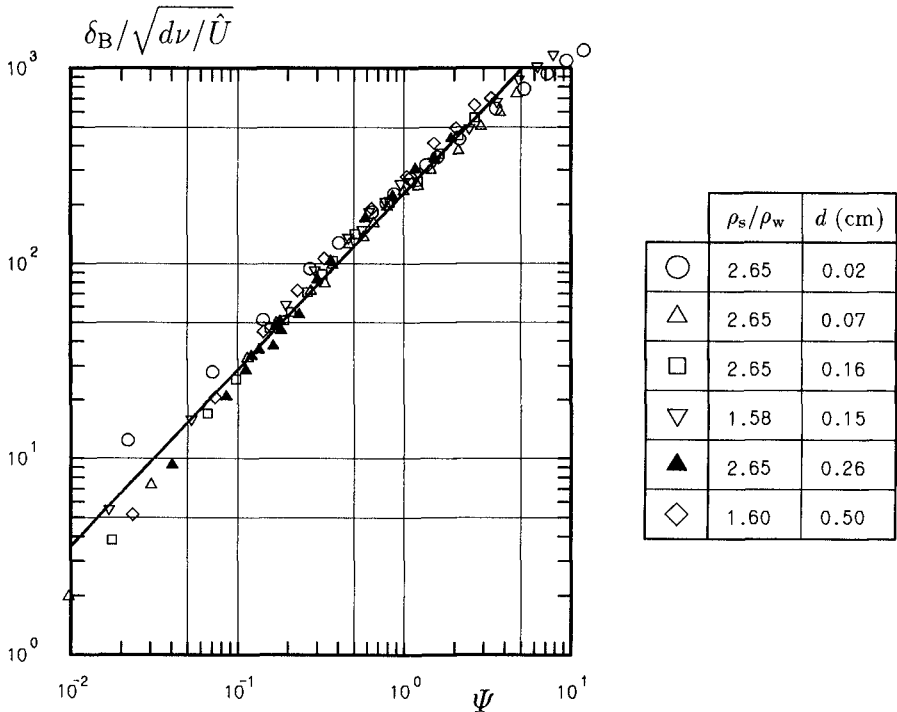


Fig. 6 Relation between $\delta_B / \sqrt{d\nu / \hat{U}}$ and Ψ in sinusoidally oscillatory flow.

sediment transport rate under a variety of main flow conditions, showing a remarkably good agreement for any of them. It should be emphasized that every coefficient in the governing equations has been set to be a constant respectively common for all the computations. These results indicate the validity and applicability of the present model for estimating the net transport rate of the sheet flow as well as time-space changes in its velocity and concentration over a very wide range of conditions.

Acknowledgement

The authors would like to express their appreciation to Assoc. Profs. M. Dibajnia and Y. Kawahara of University of Tokyo, Japan for their helpful discussion and to Assoc. Prof. T. Yamashita of Hokkaido University, Japan for his greatful kindness to provide us with his experimental data.

References

- Abou-Seida, M. M. (1965): Bed load function due to wave action, Univ. Calif., Hydraulic Eng. Lab. Rep., HEL-2-11, 78pp.
- Dibajnia, M. and A. Watanabe (1992): Sheet flow under nonlinear waves and currents, Proc. 23rd Int. Conf. on Coastal Eng., ASCE, Venice, Italy, pp. 2015-2028.
- Dibajnia, M., T. Shimizu and A. Watanabe (1994): Profile change of a sheet flow dominated beach, Proc. 24th Int. Conf. on Coastal Eng., ASCE, Kobe, Japan, pp. 1946-1960.
- Eilers, H. (1941): Die Viskositat von Emulsionen hochviskoser Stoffe als Funktion der Konsentration, Koloid. Z.: 97, pp. 313-321.
- Horikawa, K., A. Watanabe and S. Katori (1982): Sediment transport under sheet flow condotions, Proc. 18th Int. Conf. on Coastal Eng., ASCE, Cape Town, South Africa, pp. 1335-1352.
- Jonsson, I.G. (1966): Wave boundary layers and friction factors, Proc. 10th Int. Conf. on Coastal Eng., ASCE, Tokyo, Japan, pp. 127-148.
- Katori, S. and M. Homma (1984): Fall velocity of sediment in high concentrations, Proc. 28th Japanese Conf. on Hydr., JSCE, pp. 641-646 (in Japanese).
- Kolmogorov, A. N. (1941): The local structure of turbulence in incompressible viscous fluid for very large Reynolds numbers, C.R. Acad. Sci., U.R.S.S., 30, pp. 301-305.

Li, L., M. Sawamoto and T. Sato (1993): Experimental study on sediment transport in sheet flow regime, Proc. 40th Japanese Conf. on Coastal Eng., JSCE, pp. 341-345 (in Japanese).

Prandtl, L. (1945): Über ein neues formelsystem der ausgebildeten turbulenz, Nachr. Akad. Wisis, Göttingen, pp. 6-19.

Sawamoto, M. and T. Yamashita (1986): Sediment transport rate due to wave action, Jour. Hydroscience and Hydr. Eng., Vol. 4, No. 1, April, pp. 1-15.

Watanabe, A., T. Shimizu and K. Kondo (1991): Field application of a numerical model of beach topography change, Proc. Coastal Sediment '91, pp. 1814-1828.

Yamashita, T., M. Sawamoto, H. Takeda and G. Yokomari (1985): A study on oscillatory flow and sediment transport at sheet-flow condition, Proc. 32nd Japanese Conf. on Coastal Eng., JSCE, pp. 297-301 (in Japanese).

Yamashita, T., T. Someya and K. Nozaki (1993): The effect of unsteadiness of oscillatory flow and specific gravity of sediment on the mechanism of sheet flow motion, Proc. 40th Japanese Conf. on Coastal Eng., JSCE, pp. 331-335 (in Japanese).

CHAPTER 296

Numerical Modeling of Nearshore Morphological Changes under a Current-Wave Field

Taerim Kim¹ and Hsiang Wang²

Abstract

This paper presents a time-dependent 3-D nearshore morphological response numerical model which includes the slope effect, undertow current, wave-borne transport, and transition zone effect. These effects are very important but often not estimated in other sediment transport models. By including the cushioning effect in the water column, which prevents the advection of turbulence generated by wave breaking from the surface to the bottom, this model is shown to be able to approach an equilibrium state of sediment transport. The computed cross-shore and longshore sediment transport rates are calibrated based on the large wave tank data, 3-D basin experiments, and available sediment transport formulas. The predicted changes of bottom topography near structures and inlet in physical model are compared for model verification.

Introduction

Prediction of beach response to the engineering activities is important for assessing the impact of coastal structures and to improve their design. It is also useful for evaluating remedial and mitigation measures. Numerical modeling is clearly an attractive alternative for this purpose and is becoming increasingly viable with the advancement of computational facilities and improved understanding on wave mechanics and sediment transport processes.

There have been two types of approach to predict the 3- dimensional morphological changes in the nearshore zone. The so called 3DBEACH (3-dimensional decoupled model of beach change) by Larson et al. (1989) utilizes the profile change model, SBEACH, for calculating storm-induced beach erosion and recovery and the shoreline change model, GENESIS, for calculating long-term change in shoreline position. Since the profile model is based on equilibrium profile, the combined model also maintains

1 Senior Research Engineer, Ocean Engineering Division, KORDI, Ansan, P.O. Box 29, SEOUL 425-600, KOREA

2 Professor, Department of Coastal and Oceanographic Engineering, University of Florida, Gainesville, FL 32611, USA

the ability to approach an equilibrium bottom configuration under steady wave condition. This is difficult to attain in the models of other type. However, since the submodels are all wave driven, combined current wave effect can not be directly addressed. The other approach computes nearshore topographic change based on local sediment flux balance. This approach usually links a hydrodynamic submodel with a sediment transport submodel. Models of this kind with varying degrees of sophistication have been developed. van Rijn et al. (1989) estimated the sediment transport rate by multiplying the wave-averaged mean vertical sediment concentration by the wave-averaged local horizontal velocity. In their model, the wave-borne transport mechanism is not directly addressed. A model developed by Ohnaka and Watanabe (1990), on the other hand, computes the flow field with considerations of current and wave interaction based on coupled mild-slope wave equation and depth-averaged circulation equations. It calculates the rate of sediment transport as the summation of two energetic mechanisms, one due to the mean current and the other due to waves (Watanabe et al., 1986). Recently, the nearshore circulation model was improved by a 3-D approach, which employed a combined depth-integrated current model and a vertical profile model (De Vriend and Stive, 1987). This improvement when incorporated into the sediment transport model enables one to more realistically

represent the 3-D nature both inside and outside the surfzone. Briand and Kamphuis (1993) multiplied the time averaged quasi-3D velocities to a time averaged exponential sediment concentration profile to achieve a 3-D sediment flux. This technique of combining a quasi-3D velocity profile with a vertical distribution of suspended sediment concentrations is a promising step to lead to full 3-D models in the future.

The model developed in this study consists of three submodels for calculation of waves, nearshore currents, and beach changes. At the first step, the initial beach topography and the geometry of the structures for the study area are given as input data. Next, the wave model determines the spatial

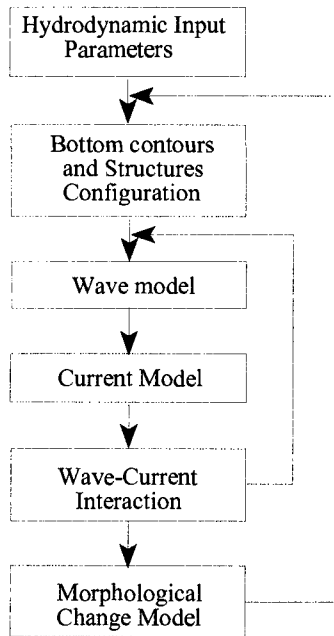


Figure 1 Structure of Nearshore Morphodynamic Model.

distributions of radiation stresses and near-bottom orbital velocities for a given incident wave condition. Then, the circulation model computes the mean water surface level and the depth-averaged mean currents using depth-averaged momentum and continuity equations. Inside the surf zone, mean undertow current, transition zone length, and cushioning effect are calculated based on the wave-current model results. Spatial distribution of sediment transport fluxes are computed in the domain of interest. Finally, bottom topography changes are computed based on sediment mass conservation. The change in bottom topography will modify the flow field. Therefore the hydrodynamic model needs to be updated from time to time. Figure 1 shows the computational flow chart of the model.

Wave and Circulation Models

The flow field in the nearshore is computed by depth integrated 2-D hydrodynamic model developed by Winer(1988). The hydrodynamic model consists of wave and circulation models which are fully coupled through interaction terms. First, the wave model determines the spatial distributions of radiation stresses and near-bottom orbital velocities based on the following parabolic wave equation,

$$\begin{aligned} (C_g \cos\theta + U)A_x + \frac{\sigma}{2} \left(\frac{C_g \cos\theta + U}{\sigma} \right)_x A + VA_y + \frac{\sigma}{2} \left(\frac{V}{\sigma} \right)_y A \\ - \frac{i}{2} k C_g (1 - \cos^2\theta) A - \frac{i}{2} \left[CC_g \left(\frac{A}{\sigma} \right)_y \right] + \frac{W}{2} A = 0 \end{aligned} \quad (1)$$

where, U and V are the depth averaged horizontal velocities in the x (cross-shore) direction and y (longshore) direction, respectively, C is the phase velocity, C_g is the group velocity, σ is the intrinsic angular frequency, A is the complex amplitude, θ is the angle of the wave propagation relative to the x axis, the subscripts x and y denote derivatives in the x and y directions, respectively, W is the energy dissipation coefficient. The coefficient W is related to the energy dissipation due to wave breaking following the work of Dally et al., (1984).

$$D_E = \frac{K}{D} [(E - E_s) C_g] \quad (2)$$

where, D_E is the energy dissipation rate, D is water depth, K is empirical parameter ($K=0.17$), E is the local wave energy density, E_s is the local stable wave energy density that the breaker is striving to attain.

The circulation model computes the mean water surface level and the depth averaged mean currents using depth averaged momentum and continuity equations with the radiation stresses imported from the wave model as the driving force.

The governing equations are given by (Ebersole and Dalrymple, 1979)

$$\begin{aligned} \frac{\partial U}{\partial t} + U \frac{\partial U}{\partial x} + V \frac{\partial U}{\partial y} + g \frac{\partial \bar{\eta}}{\partial x} + \frac{1}{\rho D} \tau_{bx} - \frac{1}{\rho D} \tau_{sx} \\ + \frac{1}{\rho D} \left(\frac{\partial S_{xx}}{\partial x} + V \frac{\partial S_{xy}}{\partial y} \right) + \frac{1}{\rho} \frac{\partial \tau_l}{\partial y} = 0 \\ \frac{\partial V}{\partial t} + U \frac{\partial V}{\partial x} + V \frac{\partial V}{\partial y} + g \frac{\partial \bar{\eta}}{\partial y} + \frac{1}{\rho D} \tau_{by} - \frac{1}{\rho D} \tau_{sy} \\ + \frac{1}{\rho D} \left(\frac{\partial S_{xy}}{\partial x} + V \frac{\partial S_{yy}}{\partial y} \right) + \frac{1}{\rho} \frac{\partial \tau_l}{\partial x} = 0 \end{aligned} \quad (3)$$

and the continuity equation

$$\frac{\partial \bar{\eta}}{\partial t} + \frac{\partial}{\partial x}(UD) + \frac{\partial}{\partial y}(VD) = 0 \quad (4)$$

where, t is the time; x and y are the Cartesian coordinates in a horizontal plane; U and V are the corresponding velocity components of the nearshore current; $D = h + \bar{\eta}$; h is the still water depth; $\bar{\eta}$ is the elevation of the mean water level due to wave set up/set down; τ_l is the lateral shear stress due to turbulent mixing; τ_{bx} and τ_{by} are the bottom shear stresses; τ_{sx} and τ_{sy} are the surface shear stresses; and S_{xx} , S_{xy} , and S_{yy} are the radiation stress components which arise from the excess momentum flux due to waves. These equations are obtained by integrating the local x and y momentum equations and the continuity equation over the depth of the water column and then time-averaging the results. The governing equations in the circulation model are solved by a matrix analysis using the alternating direction implicit (ADI) scheme (Winer, 1988). In order to treat the wave-current interaction, waves and currents are calculated alternatively.

Inside the surf zone, the 2-D model is inadequate as the model will yield null current in the cross-shore direction, consequently, zero net cross-shore transport. In reality, the current inside the surfzone is highly three dimensional. Field and laboratory observations of surf zone flow show the existence of current that is directed offshore on the bottom, balanced with the onshore flow of water carried by the breaking waves. This offshore-directed steady current near the bed, commonly referred to as undertow, is known to be the most important mechanism causing profile erosion and bar. The depth-integrated discharge of x component by undertow current, Q_u is expressed as

$$Q_u = \frac{\rho g H^2 k_x}{8\sigma} \quad (5)$$

The mean undertow velocity is simply estimated as $\bar{u} = Q_u / (\eta_c + h)$, which is directed offshore.

Sediment Transport Model

The computed current-wave field is used to drive the sediment model which, in turn, computes the morphological changes by utilizing the equation of conservation of sediment material. In the present study, the sediment transport formula contains two parts, bed load and suspended load. The bed load transport is based on an energetic approach driven by mean current and bottom wave orbital velocity. Owing to the asymmetric wave bottom orbital velocity in a wave cycle, this bed load transport by wave orbital velocity has a net onshore component. The suspended load transport which dominates in surfzone is built upon an undertow current. Here, the suspended sediment concentration is related to breaking wave energy dissipation and the transport velocity is the mean undertow current. This component is always directed offshore. The total transport Q is the sum of bed and suspended loads as followings

$$\begin{aligned} Q &= q_b + q_s \\ q_b &= A_{bc}(\tau_m - \tau_{cr})U_c/\rho g + A_{bw}(\tau_m - \tau_{cr})U_w/\rho g \\ q_s &= A_s \tau_{urb} Q_u \end{aligned} \quad (6)$$

, where ρ is the density of water, g is gravity coefficient, U_c is the integrated depth mean wave induced-current, U_w is the maximum orbital velocity at the bottom, Q_u is the discharge by the undertow, τ_m is the maximum bottom shear stress generated by wave and current, τ_{urb} is the turbulent shear stress generated by waves and mean current, τ_{cr} is the critical shear stress under waves and mean current, A_{bc} , A_{bw} , and A_s are calibrated coefficients.

Sediment transport is influenced by the bottom slope as downslope reduces resistance and upslope increases resistance. The down-slope gravitational transport is the most important mechanism to keep the bed from growing indefinitely and, to enable the coastal profile to reach a dynamic equilibrium state. A basic formulation to express the slope gravitational transport component proposed by Horikawa (1988) assumes the following functional form,

$$\begin{aligned} q_x &= q_x^1 + \epsilon_x |q_x^1| \frac{\partial h}{\partial x} \\ q_y &= q_y^1 + \epsilon_y |q_y^1| \frac{\partial h}{\partial y} \end{aligned} \quad (7)$$

and in which q_x and q_y are the transport components in x and y directions, respectively, q_x^1 and q_y^1 are their equivalents for horizontal bed, h is the water depth and ϵ are empirical coefficients

The zone between the incipient breaking and the plunging point is defined as

transition zone. The transition zone effect on the wave setup, undertow current, and sediment transport is a subject of increased research over recent years. It showed that the inclusion of the transition zone in profile modeling has an important effect on the predicted profiles, particularly for the bar features. Several approaches have been proposed to evaluate the distance and influence of the transition zone based on wave tank experiments (Galvin (1969)). The present model uses the following formula analyzed from the experimental data (O'Shea et al. (1991)).

$$l_t = 0.556 \tan\beta L_b \xi^{-1.465} \quad (8)$$

in which, $\tan\beta$ and L_b are respectively the bed slope and wave length at breaking, and ξ is the surfzone parameter.

Cushioning Effect

Most of the laboratory results as well as field evidence seems to support the concept of beach equilibrium. The profile equilibrium can be reached either when the tangential thrust by fluid is not strong enough to overcome the sand resistance or when the local landward sediment transport is balanced by the local seaward sediment transport. In the latter case, although there could be active sediment movement, the profile remains stable. Including this feature into the model is a difficult subject. One popular approach is to predesignate an equilibrium profile shape. The sediment transport formulas should then be consistent to lead the profile evolution to this equilibrium profile. Kriebel's (1985) storm profile model was of this kind. This type of models can be classified as closed loop model. On the other hand, most sediment transport models do not have a targeted equilibrium profile therefore often fail to reach an equilibrium state. This type of models is known as open loop model. For the open loop model to reach equilibrium, mechanisms must be devised to locally balance the on/offshore transport. The present model is an open loop model. In the formulas presented earlier, inside the surf zone the offshore transport is much too strong to be balanced by the onshore transport component. The reason is that in the formulation, once wave breaks wave breaking-induced turbulence immediately produces a strong bottom stress and the resulting offshore transport is much larger than the onshore transport computed by the bed load transport equation. Clearly, the offshore transport equation needs to be modified. Dally and Dean (1984) pointed out that the expression developed for the sediment concentration profile apparently lacks the "cushioning" effect which the water column provides in reducing the amount of sediment entrainment as breaking wave form and trough evolve. This cushioning effect is especially important in the stabilization of the bar and trough formation. Almost no work has been done for this cushioning effect. The present model attempted to incorporate this cushioning effect into the model based on the ratio of the depth and wave height at the plunging point as follows,

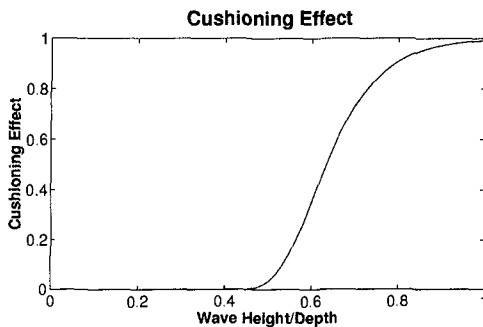
$$C_{us} = \tanh\left(7\frac{H}{D}\right)^{700} \quad (9)$$

where, C_{us} is the cushioning effect, H is the wave height, D is the water depth. Figure 2(a) plots this cushioning coefficient and its effect on sediment transport. As can be seen, when relative water depth increases, the cushioning equation limits the turbulence penetration to the bottom. When wave height is larger than water depth, there is no cushioning effect. However, as the water depth at the trough zone becomes larger, cushioning effect becomes stronger. Finally when water depth reaches 2.5 times the wave height breaking induced turbulence will not reach the bottom. This equation is, of course, purely empirical at this stage with no supporting data. Figure 2(b) shows the effect on sediment transport rate. With the inclusion of this effect, the open loop model presented in this study could reach profile equilibrium without a predetermined profile shape.

Calibration of Sediment Transport Rate

The nearshore sediment transport characteristics under storm wave conditions as predicted by the model are illustrated here. In order to validate the 3-D morphological response model, cross-shore transport rate and longshore transport rate are calibrated separately by using available experiment data or empirical formulas.

a)



b)

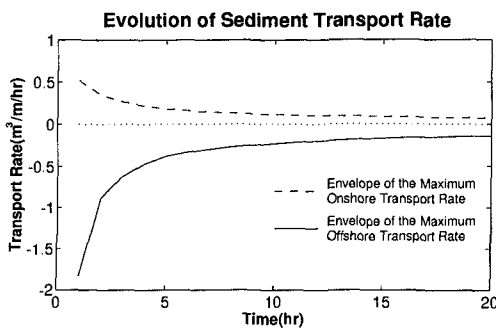


Figure 2 a) Distribution of Cushioning Effect.
b) Evolution of Sediment Transport Rate.

Cross-Shore Transport Rate

For the calibration of cross-shore transport rate, two sets of 2-D tank experiment data were used. These included the case of a sand beach backed by a sloping dike tested in the German Big Wave Flume (GWK) and case CE 400 from Saville's large wave tank tests (CE). Comparisons were made between computed values and experimental results both in profile changes and transport rates.

The GWK experiment (Dette and Uliczka, 1986) used sand with a median diameter of 0.33 mm and the test profile was subjected to regular wave attack ($H=1.5$ m, $T=6$ sec). Figure 3 shows the comparison between the predicted profiles and the experimental results at run times of 62, 111, and 273 minutes, respectively. The computed wave height distribution across shore

is also shown. The waves cut back the foreshore to produce a vertical scarp and a bar formed shoreward of the breaking point which grew and moved offshore with continued wave action. The numerical model satisfactorily reproduced the observed foreshore erosion and main breakpoint bar development. Simulated shoreline retreat and bar growth were initially rapid and gradually slowed as the bar moved offshore to reach a location close to that of the observed bar at the end of the run (20 hr). However, the bar trough is less well reproduced. All smaller features inshore of the main breakpoint bar were not reproduced in the simulations. Figure 4 shows the comparison of the cross-shore transport rate between the profile changes in Figure 3. Initially, a high peak appears near the shoreline as beach material slumps down slope into the foreshore zone in this experiment. These material was transported offshore to form the bar. The seaward changes of the peak transport rate explain the offshore movement of the bar. With the exception at the initial stage, the predicted transport rate distribution is in good agreement with the laboratory data. At the initial stage the experimental values were larger than predicted. There are many factors that could contribute to the difference such as slumping effect mentioned earlier. It was also found later in small scale experiments conducted at UF that the profile erosion particularly in the dune region was much more severe in the initial stage if the beach is dry and loosely compacted as opposed to wet and well compacted. The best overall fit of both profile

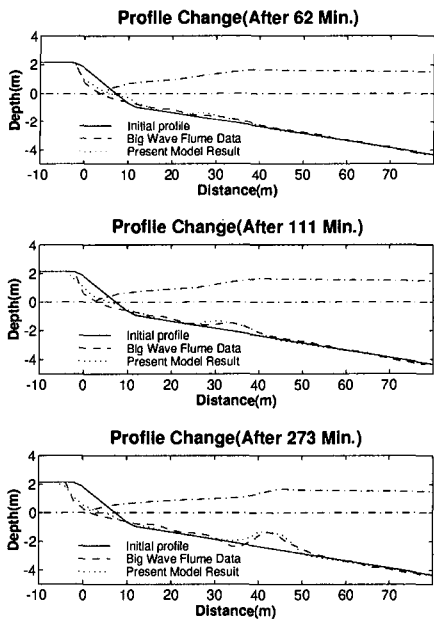


Figure 3 Comparison between Computed and Measured Beach Profiles for $t=62, 111, 273$ minutes. Data from Dette and Uliczka (1986).

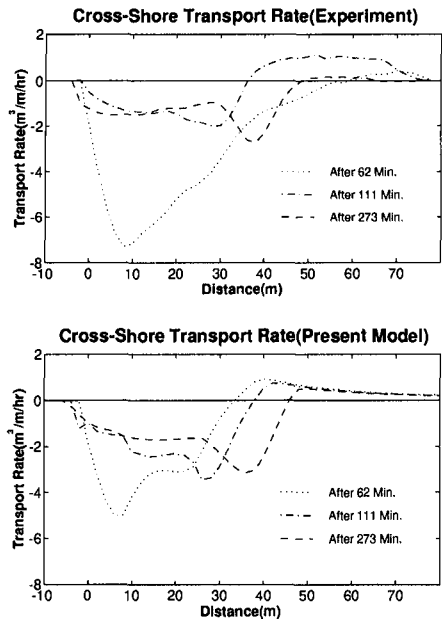


Figure 4 Comparison of Cross-Shore Transport Rates between Experiment and Present Model for $t=62, 111, 273$ minutes. Data from Dette and Uliczka(1986)

and transport rate was obtained by using A_{bw}

in a range from 0.05 to 0.07 and A_s from $1.0 \times 10^{-5} (m^2/N)$ to $1.5 \times 10^{-5} (m^2/N)$. With these determined A_{bw} and A_s values, the model was used to simulate the CE case CE400. Figure 5 shows the comparison of measured and calculated profiles. The test conditions were: initial uniform slope = 1/15; grain size = 0.22 mm; wave height and period of 1.62 m and 5.6 sec. The numerical and test results are shown for simulation times of 1, 3, and 5 hours. In this case, the bar development was also well predicted except at the initial stage. However, the profile change near the shoreline shows very different results between the experiment and the model. In experiment, there was strong erosion at the foreshore region above the water level, but this erosion was limited near the shoreline in the numerical model. The spatial distribution of the transport rate from the CE tests were very different from that of the GWK tests. Here in the CE case, peak transport initially occurred near the breaking point and did not show any onshore transport outside the breaking point (The numerical model results did show a very small onshore transport component). Also, in the CE experiments, the transport in swash zone apparently played an important role to cause shore face erosion. The numerical model does not have an appropriate swash zone transport mechanism. Therefore, it was unable to reproduce the large erosion near the shoreline in the experiment.

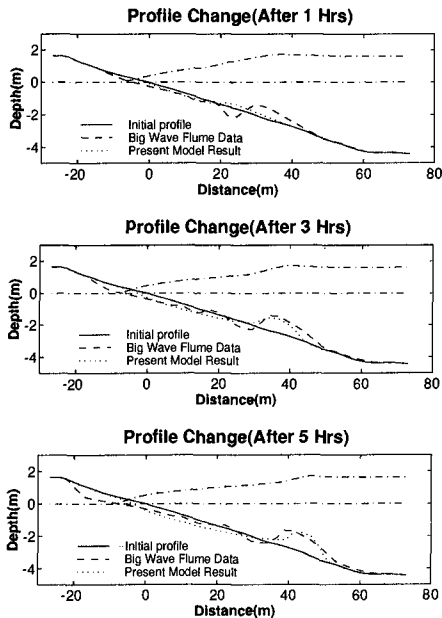


Figure 5 Comparison between Calculated and Measured Beach Profiles for $t = 1, 3, 5$ hours. Data from Saville(1957).

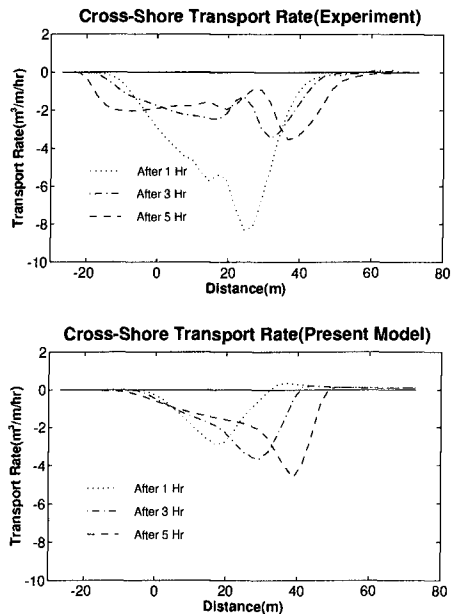


Figure 6 Comparison of Cross-Shore Transport Rates between Experiment and Present Model for $t = 1, 3, 5$ hours. Data from Saville(1957)

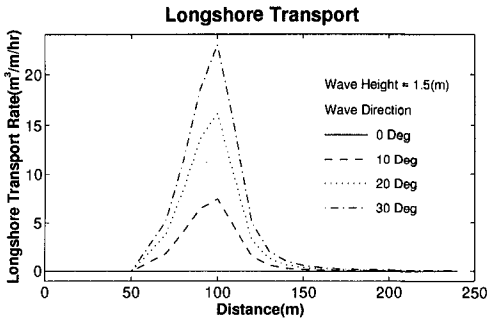
Longshore Transport Rate

Longshore sediment transport plays a very important role particularly in long term beach evolution. The longterm evolution of many coastlines is the result of slight gradients in the longshore transport rate. Available data suitable for calibration and verification of longshore transport rate are scarce and mostly limited to 2-D cases. The 2-D data will not yield information on A_{bc} . In this section, the characteristics of longshore transport rate are investigated by comparing with CERC formula and the coefficient A_{bc} was calibrated based on a 3-D basin experiment. The CERC's littoral drift formula (Shore Protection Manual, 1984) has the following form as,

$$Q = \frac{K(EC_g \cos\theta \sin\theta)_b}{\rho g(s-1)(1-p)} \quad (10)$$

where Q is the volumetric longshore transport rate, E is wave energy, C_g is group velocity, s is specific gravity, p is porosity and K is an empirical transport coefficient.

a)



b)

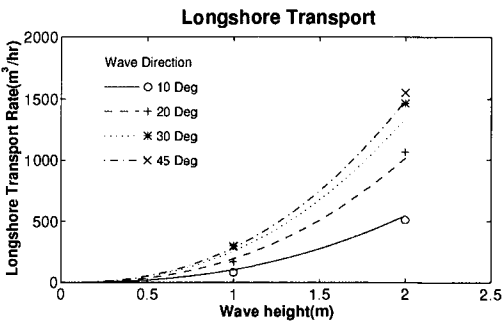


Figure 7 a) Distributions of Longshore Transport Rate in Different Wave Directions
b) Comparison of Longshore Transport Rates between CERC Formula and Present Model in Different Wave Directions.

The formula is based on energetic concept with empirically determined coefficient based on field evidence.

In the present model, the sediment transport formulas as presented are of very different nature. However, for lack of laboratory and/or field data for verification, CERC's formula is used here as a bench mark to test the model. A case of 2-D beach that has an initial profile of a uniform slope (1/20) was used here to compare the characteristics of the present model and CERC's formula. Figure 7(a) shows the longshore transport distribution across the surf zone as calculated by the model at different wave angles under the same wave height of 1.5 m. The transport patterns are all bell-shaped with a uni-modal peak inside the breaking point. This shape is consistent with observations on beaches of more or less uniform slopes excluding the swash zone (dual peaks were common if swash zone is included). It is also shown that the longshore transport rate increases drastically as

wave angle increases. The total transport rate is obtained by integrating the volume under the curves. These total transport rates are compared with the CERC's formula in Figure 7(b) which plots the transport rate vs. wave height for different wave angles. The comparisons are good for wave up to 20° . For larger wave angles, the model yields values slightly higher than the CERC's formula. The coefficient A_{bc} in the transport equation given by Equation (6) is equal to unity and 0.77 was used for the K value of CERC formula in this comparisons. As discussed earlier, most experiments and field measurements were conducted for cross-shore transport, and there is very little information on longshore transport rate. Therefore, a plain beach movable bed physical model was constructed in a wave basin to investigate the sediment transport patterns, specially longshore transport rate. The experiments were performed in the 16x23 m 3-D wave basin of the Coastal Engineering Laboratory of the Department of Coastal and Oceanographic Engineering at University of Florida. The designed initial beach profile consists of a flat backshore, a steep-sloped foreshore, and a mild-sloped offshore, and has simple straight shoreline and parallel offshore contours.

After 80 minutes run time, a total of $0.28 m^3$ sand was collected at the sediment trap channel located in the downdrift boundary. This longshore transported material was used to calibrate the A_{bc} value in the numerical model and to check the K value in CERC's formula. By applying wave height, and angle used in the experiment to the CERC's formula, it was found that $K=0.23$ from the results. This value of the proportionality coefficient obtained in this study is smaller than 0.77 in Komar and Inman's formula and is rather close to the value in Sato and Tanaka (1966)'s formula. It is noted here that many one line models utilizing CERC's formula the K coefficient was adjusted downward to the range of 0.05 - 0.4 based on model calibrations with physical experiment data. Here, the numerical longshore sediment transport is calibrated with measured total longshore transport quantitatively. The best fitting value was found to be $A_{bc} = 0.1$. This value is also smaller than the previous value which gave good agreement with CERC's formula.

Performance Test

The model performance is demonstrated here with two types of man-made structures including shore perpendicular structures (groins) and offshore breakwaters. The purpose is not for model calibration or verification as there is no available data in hand. Rather, model utilizations are illustrated with realistic coastal structures.

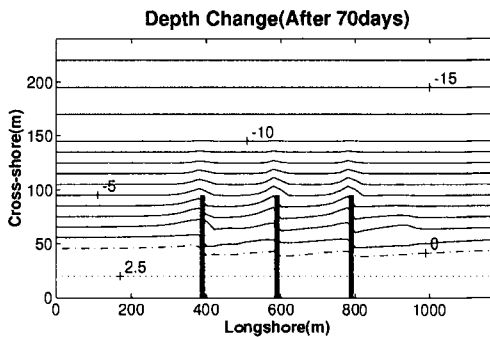
Groins

Groins are shore perpendicular structures which are built to intercept littoral transport from updrift. They are used to trap sand locally or as end structures to stabilize sand placed in conjunction with beach nourishment projects. For trapping sand, a series of groins is often used. The presence of groins is generally known to cause accretion on the updrift end and erosion on the downdrift end. The ability to be able to predict morphological changes associated with groin structure is undoubtedly useful in coastal engineering. Perlín and Dean (1985) developed an N-line model using a simple

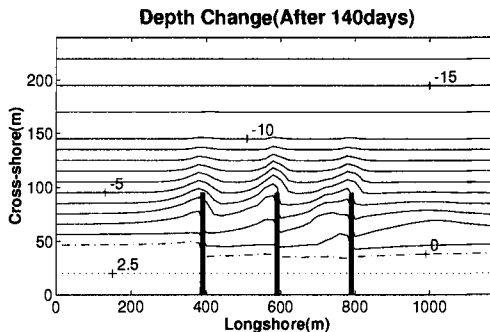
wave refraction and diffraction scheme and longshore sediment transport equation to modify the topography. Kraus et al.(1994) investigated parameters governing beach response to groins and incorporated them into the so-called GENESIS model that can be used to predict shoreline changes in the presence of groins. In the present model, the presence of a groin is reflected in the boundary conditions. The boundary conditions for the groin in the sediment transport model are given as,

$$\begin{aligned} q_y(I, J_{groin} + 1) &= 0, & \text{if } q_y(I, J_{groin} + 1) > 0 \\ q_y(I, J_{groin} - 1) &= 0, & \text{if } q_y(I, J_{groin} - 1) < 0 \end{aligned} \quad (11)$$

a)



b)



where q_y is the transport rate in y direction and J_{groin} is the J th grid column which has the groin.

Figure 8 shows the morphological changes for the case of a three-groin after 70 days and 140 days, respectively, when wave of 0.5 m, 6 sec approaches the beach at 15 degree angle. It is shown that shoreline and bottom contours advances at the updrift of first groin and retreats at the down drift of the last groin. In each compartment, erosion occurs at the updrift end and accretion takes place at the downdrift end. At present, there is a lack of reliable data especially on the morphological effects of groins to compare with numerical results.

Figure 8 Depth Changes after a)70 days, and b)140 days on the Plain Beach with Three Groins for 0.5 m, 8 sec, and 10 degree Incident Waves.

Breakwater

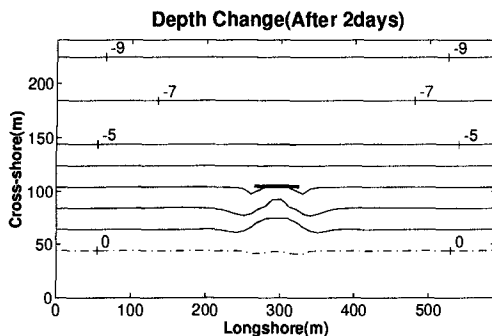
An offshore breakwater is generally a shore parallel structure designed to protect the beach behind the structure against severe erosion. Behind the breakwater wave

height is reduced and circulation cells are generated which draw sediment into the sheltered area. A salient feature soon appears which grows into a tombolo and sometimes becomes attached to the breakwater. Many numerical models, some based on rather artificial mechanisms are able to produce the described topographic changes. Hanson and Kraus (1990) employed a numerical model (GENESIS) to investigate the various depositional types in the lee of a single detached breakwater. Suh and Hardway (1994) developed a one-line numerical model for predicting shoreline change in the vicinity of multiple breakwaters and compared with the field data. The boundary condition for the breakwater in the present sediment transport model is as follows,

$$\begin{aligned} q_x(I_{break} + 1, J) &= 0, & \text{if } q_x(I_{break} + 1, J) > 0 \\ q_x(I_{break} - 1, J) &= 0, & \text{if } q_x(I_{break} - 1, J) < 0 \end{aligned} \quad (12)$$

where q_x is the transport rate in x direction and I_{break} is the I th grid row which has the breakwater. Figure 9 shows the topographic changes after 2 days and 7 days under the normal incident wave condition with 1 m height and 8 sec period. It is clear that salient

a)



b)

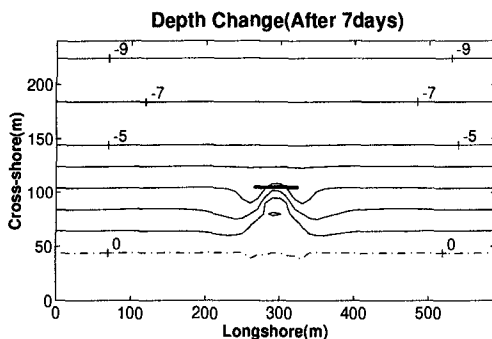


Figure 9 Depth Changes after a) 2 days, and b) 7 days on the Plain Beach with Breakwater for 1 m, 6 sec, and Normal Incident Waves.

feature grows rather rapidly. Shoreline, on the other hand, changes only slightly. The absence of swash transport mechanism might be one of the reasons that shoreline change is so slight.

Inlet Experiment

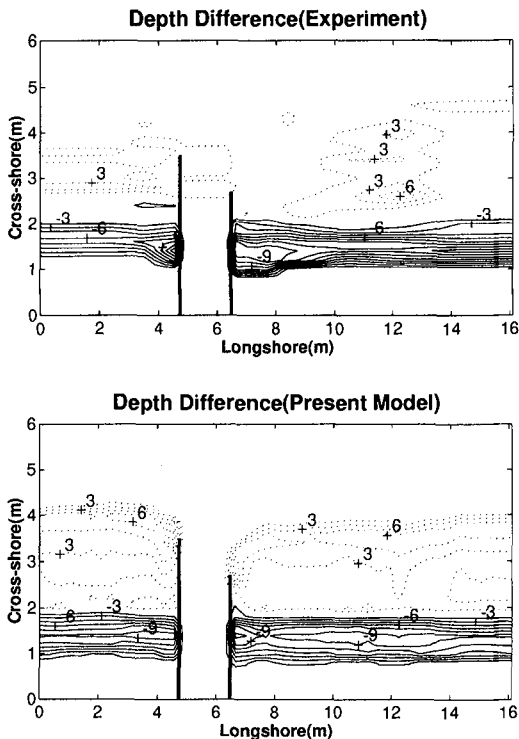
The sedimentary processes in the vicinity of a tidal inlet present a complex dynamic interaction problem between fluid and sediment motion. There exist water level changes at the shoreline by tide and periodical tidal currents in and out of the inlet. This tidal current interacts with wave and wave induced longshore current. Under the combined effects of waves, longshore current, tidal current and coastal structures, the behavior of the sediment movement and morphological evolution in the inlet region is a very complicated process and the current knowledge is extremely limited. Laboratory

modeling using movable bed-material is still a viable tool despite its limitations such as expensive cost, time consuming, and scale effects (Wang et al., 1992). Numerical model on inlet morphology is at its infancy. An attempt is made here to apply the present model to an inlet beach system. On a separate study(Wang et al., 1995), an inlet-beach physical model was constructed in the wave basin facility in the Coastal and Oceanographic Engineering Laboratory at the University of Florida. The inlet beach model consists of an idealized inlet on a plain beach with profile identical to that in the plain beach model. The inlet has two parallel jetties extending offshore with the updrift jetty twice as long as the downdrift jetty. These jetties are made of concrete blocks and impervious to sediment transport. The experiments were carried out under the condition of 7.5 degree oblique waves. The test conditions are as follows:

Wave condition: 8 cm wave height, 1 sec wave period, 7.5° wave direction

Current condition: 0.14 m/sec ebb current, 0.1 m/sec flood current

Tidal range(between flood and ebb): 3 cm



The flood and ebb tidal conditions were simulated alternatively in the model at every 40 minute intervals by holding the high and low water levels, respectively, and reversing tidal currents in the inlet. Figure 10 shows the changes of the topographies by plotting the difference between the initial contours and the contours after 160 minutes. The numerical model appears to be able to reproduce reasonably well some of the general features found in the physical model, as the locations of erosion and accretion, the position and size of breakpoint bars and the shoreline offset. Detailed topographic comparisons are still difficult and may not be too meaningful owing partly the three dimensional effects produced in the physical model.

Figure 10 Comparison of Bathymetric Changes after 160 minutes between Experiment and Numerical Model for 8 cm, 1 sec, and Oblique Incident Waves.

Results

- 1) The prediction of cross-shore transport from model was compared to the evolution of beach profiles and sediment transport rate distributions in the 2-D German's Big Wave Flume tests and CERC's large tank tests. The model is capable of predicting the growth and movement of main breakpoint bars and beach processes with reasonable reliability.
- 2) The comparison of longshore transport rates between present model and CERC formula shows close agreement for different wave angles when the coefficient $A_{bc} = 1$ is adopted in the model as compatible with $K=0.77$ in CERC's formula. A different calibration using 3-D basin experiments yields $A_{bc} = 0.1$ and $K=0.23$.
- 3) An application of the model to different coastal structures including groins and breakwaters shows the model is capable of producing the general scouring, accretion and erosion features found in nature. The model was tested with inlet beach movable bed physical model experiment. The comparison of depth changes shows reasonable agreement between numerical model and physical experiment.

References

- Briand, M.-H.G. and Kamphuis, J.W., 1993a. "Waves and currents on natural beaches: a quasi 3-D numerical model", *Coastal Eng.*, 20:101-134.
- Briand, M.-H.G. and Kamphuis, J.W., 1993b. "Sediment transport in the surf zone: a quasi 3-D numerical model", *Coastal Eng.*, 20:135-156.
- Dally, W. R. and Dean, R. G., 1984. "Suspended sediment transport and beach profile evolution", *Journal of Waterway, Port, Coastal and Ocean Engineering*, Vol.109, No. 4. pp.401-405.
- Dally, W. R., Dean, R. G. and Dalrymple, R. A., 1984. "A model for breaker decay on beaches", *Proc. 19th Coastal Eng. Conf.*, Houston, pp.82-98.
- Detle, H.H. and Uliczka, K., 1986. "Seegangserzeugte Wechselwirkung Zwischen Vorland und Vorstrand und Kustenschutzbauwerk", *Technischer Bericht SFB 205/TPA6*, University Hannover.
- De Vriend, H.J. and Stive, M.J.F., 1987. "Quasi-3D modeling of nearshore currents", *Coastal Eng.*, 11;pp.565-601.
- Ebersole, B.A. and Dalrymple, R.A., 1979. "A numerical model for nearshore circulation including convective accelerations and lateral mixing", *Ocean Engineering Report No. 21*, Dept. of Civil Eng., Univ. of Delaware, Newark, Delaware.
- Glavin, C.J., 1969. "Breaker travel and choice of design wave height", *Journal of Waterway, Port, Coastal and Ocean Engineering*, ASCE, Vol.95, No. 2. pp.175-200.
- Hanson, H. and Kraus, N.C. 1990. "Shoreline response to a single transmissive detached breakwater", *Proc. 22th, ICCE*, ASCE pp. 2034-2046.
- Horikawa, K., 1988., "Nearshore dynamics and coastal processes ", *University of Tokyo Press*, pp. 522.
- Kraus, N.C., Hanson, H., and Blomgren, S.H. 1994., "Modern functional design of

groin systems", Proc. 24th, ICCE, ASCE, pp.1327-1342.

Kriebel, D. L., 1985. "Numerical simulation of time-dependent beach and dune erosion", Coastal Eng., Vol 9, pp. 221-245.

Larson, M., Kraus, N. C. and Byrnes, M. R., 1989. "SBEACH: Numerical Model for Simulating Storm-Induced Beach Change", Technical Report CERC-89-9, Coastal Engineering Research Center, US Army Corps of Engineers.

Ohnaka, S. and Watanabe, A., 1990. "Modeling of Wave-Current Interaction and Beach Change", Proc. 22nd Coastal Eng. Conf., Delft, The Netherlands, pp. 2443-2456.

O'Shea, K.F., Nicholson, J. and O'Connor, B.A., 1991., "Analysis of existing laboratory data to find expression for the transition zone length", Report MCE/1, Dept. Civil Eng., University of Liverpool, UK.

Perlin, M., and Dean, R.G., 1985. "3-D model of bathymetric response to structures," Journal of Waterway, port, coastal and ocean engineering. Vol.111, No.2, pp.153-170.

Sato, S. and Tanaka, N., 1966. "Field investigation on sand drift at Port Kashima facing the Pacific Ocean", Proc. 10th Coastal Eng. Conf., pp. 595-614.

Saville, T., 1957. "Scale Relationship for Equilibrium Profiles", Int. Assoc. of Hydraulic Research, 1957

Shore Protection Manual, 1984(4th edition). Coastal Engineering Research Center, U.S. Army Corps of Engineers, Vicksburg.

Suh, K.D. and Hardaway C.S. 1994., "Calculation of Tombolo in Shoreline Numerical Model", Proc. 24th, ICCE, ASCE, pp. 2653-2667.

van Rijn, L.C. and Meijer, K., 1989. "Three dimensional mathematical modeling of suspended sediment transport in currents and waves", IAHR Symp., Copenhagen, Denmark.

Watanabe, A., Maruyama, K., Shimizu, T., Sakakiyama, T., 1986. "Numerical prediction model of three dimensional beach deformation around a structure", Coastal Eng. in Japan. 29, pp.179-194.

Wang, H., Lin, L., Zhong, H., and Miao, G., 1992, "Sebastian Inlet Physical Model Studies, Part II --- Movable Bed Model", Coastal and Oceanographic Engineering Department, University of Florida. UFL/COEL--91/014.

Wang, H., Lin, L., Zhong, H., and Wang Xu, 1995, "Laboratory Mobile Bed Model Studies on Inlet , Part II---Ebb Tidal Shoal Evolution Process", Coastal and Oceanographic Engineering Department, University of Florida. UFL/COEL--95/021.

Winer, H.S., 1988. "Numerical Modeling of Wave-Induced Currents Using a Parabolic Wave Equation", Ph.D. Dissertation, Coastal and Oceanographic Engineering Dept. Univ. of Florida.

CHAPTER 297

An Analysis of Particle Saltation Dynamics

Michael R. Krecic¹ and Daniel M. Hanes²

Abstract

A two-dimensional particle saltation model for unidirectional flow is applied to simulate the motion of single particles. The equations of motion include added mass, gravity, drag, shear lift, Basset history, and Magnus or spin lift forces. A sensitivity analysis is performed on the forces, initial lift-off speeds and angles, and for different size particles. The Magnus lift force is found to have a significant effect on a particle's trajectory for coarse sand sized and larger particles. The shear lift and Basset history forces cause particles to saltate farther. Most of the forces vary with particle size. The model predictions compare favorably to observations if appropriate initial conditions are assumed.

Introduction

The term saltation was first used by Gilbert (1914) and comes from the Latin word "saltare" meaning to leap or dance. Saltation is analogous to a ballistic trajectory in the sense that trajectories are smooth and not strongly influenced by turbulent fluctuations. However, hydrodynamic forces such as lift and drag significantly influence the particles' trajectory (Nino, Garcia, and Ayala, 1992).

Fernandez Luque and van Beek (1976) performed experiments in a flume with different bed slopes. They were able to measure the mean critical bed shear stress for the initiation of motion, rate of bedload transport, average particle velocity, and the average length of individual saltations. This was accomplished through the use of high speed photography. Two different sediment types, gravel and magnetite, were studied. When they compared their model results, they concluded that a lift force was needed to explain the observed saltation characteristics.

¹ Research Assistant, Coastal and Oceanographic Engineering Department, University of Florida, Gainesville, FL 32611

² Associate Professor, Coastal and Oceanographic Engineering Department, University of Florida, Gainesville, FL 32611

There is some debate as to what angles the saltating particles leave the bed. Owen (1964) examined particle saltation in air. Owen suggested that those particles that leave the bed nearly vertically with a certain initial speed will saltate to a higher elevation than those with other initial angles. White and Schulz (1977), in contrast, observed that particles in air eject at angles ranging from 30 to 70 degrees.

Other researchers such as Murphy and Hooshiari (1982), van Rijn (1984), Wiberg and Smith (1985), Nino and Garcia (1992), and Lee and Hsu (1994) have tried to derive a set of equations to describe the motion of a particle in saltation from bed ejection to bed impact based on the fluid forces. This paper focuses on developing a complete equation of motion from a Lagrangian perspective and provides a detailed analysis of the model parameters.

Particle Saltation Model

This model simulates the trajectory of a single saltating sphere in a steady state, unidirectional flow. An equation of motion is developed and evaluated using previous experimental observations. Models based on only drag and gravity proved insufficient, so other forces have been included, as will be described below. Some of these other forces are found to be significant while others can be ignored in certain situations. What follows is a brief description of the relevant forces.

The effect of gravity is usually written as a submerged weight,

$$\mathbf{F}_G = (\rho_s - \rho)gV \quad (1)$$

where V is the volume of the particle. Obviously, this force increases with increasing particle size because of its dependence on the volume of a particle.

The added mass force arises from the relative accelerations of the particle and the fluid. A submerged body induces accelerations on a fluid if the body is moving with an acceleration relative to the surrounding fluid. The particle can be thought of as having an 'added mass' of fluid attached to its own mass when it accelerates relative to the surrounding fluid (Patel, 1989). The added mass force is given by Auton et al. (1988) as

$$\mathbf{F}_A = -\rho C_M V \left(\frac{d\mathbf{u}}{dt} - \frac{Du_f}{Dt} \right) \quad (2)$$

where \mathbf{u} is the particle velocity, u_f is the fluid velocity, and C_M is the added mass coefficient. The added mass coefficient is defined as a ratio of the additional mass of fluid that is accelerated with the particle to the mass of the displaced fluid by the particle. For a sphere, C_M equals 0.5.

A drag force is a net force in the direction of the fluid relative to the body due to pressure and viscous forces on the body. The drag force on a particle may be written as

$$F_D = C_D A \frac{1}{2} \rho V_r^2 \quad (3)$$

where C_D is the coefficient of drag, A is the cross-sectional area of the particle normal to the force, and V_r is the relative velocity (Fredsoe and Deigaard, 1992). The drag coefficient is a strong function of Reynolds number and shape; thus, it is generally not constant. There have been many empirical formulas for C_D such as those found by Graf (1984) and Morsi and Alexander (1972) which provide C_D as a function of particle Reynolds number. The following formula is used for this analysis:

$$C_D = \frac{24}{Re} + \frac{7.3}{1 + \sqrt{Re}} + 0.25 \quad (4)$$

where Re is the Reynolds number, $Re = \frac{V_r d}{\nu}$

In shear flow the particle develops a pressure gradient across it which results in a lift force, which is commonly called the shear lift force. This phenomenon can be attributed to the Bernoulli effect where the lift force acts in the direction of the velocity gradient. The shear lift force may be written as

$$F_L(\text{shear}) = C_L A \frac{1}{2} \rho (u_{\Delta Top}^2 - u_{\Delta Bot}^2) \quad (5)$$

where C_L is the lift coefficient and A is the cross-sectional area of the particle normal to the force. The $u_{\Delta Top}$ and $u_{\Delta Bot}$ are the relative velocities evaluated at the top and bottom of the particle, respectively (Wiberg and Smith, 1985).

The lift coefficient has been related to the drag coefficient by Chepil (1958). He conducted experiments involving evenly-spaced hemispheres and allowed wind to flow over them. He then proceeded to calculate drag, lift, and the ratio of lift to drag for different wind speeds. It was determined that the ratio was approximately equal to 0.85; therefore we assume here that C_L equals 0.85 times C_D .

A. B. Basset (1888) first acknowledged that a particle's history had a role in the present particle path; hence, the Basset history force bears his name. Mei (1995) described the force as

... derived from the diffusion of vorticity generated at the surface of the particle at a rate proportional to the particle's relative acceleration. Since the diffusion rate is finite, this means that the force is dependent on the history of the particle motion.

Consider a sphere in a steady fluid and then instantaneously increasing the flow to some higher value. It takes some time for the boundary layer on the sphere to adjust to the new flow intensity. This time is accounted for through the Basset history force. The Basset force is defined as

$$F_B = 6\rho\sqrt{\pi v} \left(\frac{d}{2}\right)^2 \int_0^{t_s} \frac{d\mathbf{u}}{dt} - \frac{d\mathbf{u}_f}{dt} \frac{dt}{\sqrt{t_s - \tau}} d\tau \tag{6}$$

where \mathbf{u}_f is the fluid velocity, v is the kinematic viscosity, t_s is time, and τ is a dummy variable (Mei, 1994). This force has both a vertical and horizontal component. For steady, shear flow, the fluid acceleration is zero, so the term can be simplified to be a function of the particle acceleration.

In addition to the shear lift force, the Magnus lift force also results from the velocity gradient across the particle. This force, named for Heinrich Magnus who first discovered the phenomenon in 1853, is a pressure force due to the circulation around a spinning sphere (Murphy and Hooshiari, 1982). As a result of viscous effects, angular momentum is supplied to the particle. This force accounts for the different types of pitches in baseball such as the curveball and the slider (Munson, Young, and Okiishi, 1990). The shear flow induces a rotation which causes a particle to saltate higher and further than without the inclusion of this term. If the velocity gradient is positive, the particle will rotate clockwise (cw); hence, an upward lift. If the velocity gradient is negative, the particle will rotate counterclockwise (ccw); hence, a downward lift. For a moving sphere in a shear flow, the force is expressed as

$$F_L(Magnus) = \frac{\pi}{8} d^3 \rho V_r \left(\Omega - \frac{1}{2} \frac{d\mathbf{u}_f}{dz} \right) \tag{7}$$

with Ω as the angular velocity of the particle with units in rad/s (White and Schulz, 1977). This force was developed from the work of Rubinow and Keller (1961). Rubinow and Keller (1961) looked at rotating a moving sphere in a still viscous fluid with low Reynolds numbers only. Based on their analysis, the Magnus force was independent of viscosity. From this they derived the form of the Magnus force and the moment acting on the sphere. The force has been described previously. The moment has the form

$$Moment = I \frac{d\Omega}{dt} = -\pi\mu d^3 \left(\Omega - \frac{1}{2} \frac{d\mathbf{u}_f}{dz} \right) \tag{8}$$

where I is the particle's moment of inertia. This moment equation is solved simultaneously with the equations of motion to constantly adjust the particle rotation to that induced by the fluid. Note that the dynamic viscosity appears in (8). It acts to dampen the effects of the initial particle rotation to that of the fluid. It must be said that the Magnus force and moment equations were derived for small Reynolds numbers. We consider the Magnus force in this shear flow analysis for the purpose of determining whether the effect improves the agreement between experiments and theory.

Applicability of Forces For Different Reynolds Number Ranges

The drag, added mass, shear lift, Magnus lift, and Basset history forces have been formulated as previously published in the literature. The drag force, as defined here, is valid for the entire range of Reynolds numbers encountered. The form of the shear lift force was originally verified for turbulent flow. Also, theoretically a solid sphere in an inviscid fluid has an added mass coefficient value of 0.5; so, the added mass force defined herein is applicable to large Reynolds number flows, too. From Rubinow and Keller (1961), the Magnus force was derived for low Reynolds number flows only. The Basset history force is not well known for low Reynolds number flow (Nino and Garcia, 1992). For analysis purposes, the forces are extended to the entire range of Reynolds numbers. This follows the previous research procedures as done by Wiberg and Smith (1985) and Nino and Garcia (1992) which have yielded satisfactory results.

Equation of Motion

The equation of motion for a saltating particle may be divided into longitudinal and vertical components. The forces acting on a saltating particle are described by the following equations for a steady, horizontal flow.

$$\begin{aligned} \rho_s V \frac{du}{dt} = & -C_D A \frac{1}{2} \rho \sqrt{(u-u_f)^2 + w^2} (u-u_f) - \rho V C_M \frac{du}{dt} - \frac{6\pi\mu \left(\frac{d}{2}\right)^2}{\sqrt{\pi\nu}} \int_0^{T_f} \frac{du}{\sqrt{T_s - \tau}} d\tau \\ & + \frac{\pi}{8} d^3 \rho \sqrt{(u-u_f)^2 + w^2} \left(\Omega - \frac{1}{2} \frac{du_f}{dz} \right) \frac{w}{\sqrt{(u-u_f)^2 + w^2}} + \rho(s-1)gV \sin \beta \end{aligned} \quad (9)$$

and

$$\begin{aligned} \rho_s V \frac{dw}{dt} = & -C_D A \frac{1}{2} \rho \sqrt{(u-u_f)^2 + w^2} (w) - \rho V C_M \frac{dw}{dt} - \frac{6\pi\mu \left(\frac{d}{2}\right)^2}{\sqrt{\pi\nu}} \int_0^{T_f} \frac{dw}{\sqrt{T_s - \tau}} d\tau \\ & - \frac{\pi}{8} d^3 \rho \sqrt{(u-u_f)^2 + w^2} \left(\Omega - \frac{1}{2} \frac{du_f}{dz} \right) \frac{u-u_f}{\sqrt{(u-u_f)^2 + w^2}} \\ & + \frac{\rho}{2} A C_L (u_{\Delta T_{op}}^2 - u_{\Delta B_{ot}}^2) - \rho(s-1)gV \cos \beta \end{aligned} \quad (10)$$

where

$$u_{\Delta T_{op}}^2 = (u - u_{fT_{op}})^2 + w^2 \quad (11)$$

and

$$u_{\Delta B_{ot}}^2 = (u - u_{fB_{ot}})^2 + w^2 \quad (12)$$

The variables, u_{fTop} and u_{fBot} , are the fluid velocities evaluated at the top and bottom of the particle, respectively. The quantities, u and w , are the particle's translational speed parallel and normal to the bed, respectively. All these assume no w -component of fluid velocity. Figure 1 provides a sketch of the particle forces. β is the bed slope as defined in Figure 2.

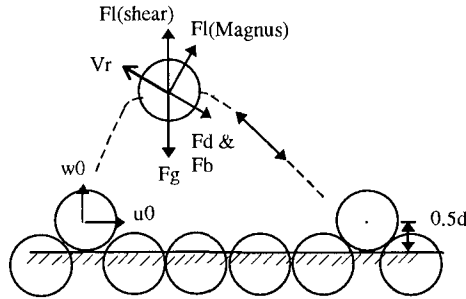


Figure 1 Force definition sketch of particle saltation

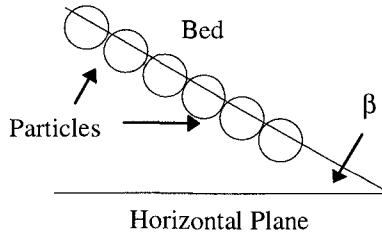


Figure 2 Definition of bed slope

The fluid velocity profile used in the model is the "law of the wall" profile,

$$\frac{\bar{u}}{u_*} = \frac{1}{\kappa} \ln \left(\frac{29.7z}{k_s} + 1 \right) \tag{13}$$

where \bar{u} is the mean fluid velocity, u_* is the fluid friction velocity, κ is Karman's constant, z is height above the "theoretical bed", and k_s is the bed roughness. The "theoretical bed" is located at $z = 0$. Note that the fluid velocity has only a horizontal, or bed-parallel, component.

Boundary Conditions

The "theoretical bed" is assumed to be 0.2 times the particle diameter below the top of the particles as is shown in Figure 3. The initial position of the saltating particle is at one-half a particle diameter above the "theoretical bed". In order to solve the equations of motion given previously, the particle's initial vertical and horizontal velocity components are needed. The values of these components come

from the equations of White and Schulz (1977). They found that the speeds varied from u_* to $2u_*$. In addition, they found that lift-off angles varied from 30 to 70 degrees. When the Magnus force is considered, an initial particle angular velocity is needed. This value is adjusted to yield a best match to a known trajectory.

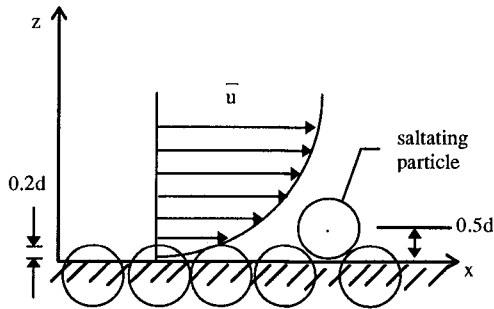


Figure 3 Saltating particle initial position

Method of Solution

The equations of motion along with the moment equation are defined as first order ordinary differential equations. A fourth order Runge Kutta approach is used to yield a vertical and horizontal particle velocity and an angular velocity. The vertical and horizontal velocity components are numerically integrated with a simple Simpson's Rule approach to obtain a particle trajectory. The model includes some adjustable parameters. The bed roughness can be taken to be any multiple of the particle diameter. The initial velocities, angular velocity and the lift-off angle also may be adjusted.

Sensitivity Analysis

This section looks at the relative effect force combinations and initial conditions have in determining the trajectory of a saltating grain. The parameters that are held constant unless otherwise specified through the force sensitivity test are grain diameter, specific gravity, initial particle velocity, initial angle, and bed roughness. They are 0.18 cm, 2.65, $2u_*$, 45 degrees, and $2d$, respectively. The coefficient of lift was taken to be 85% of the coefficient of drag. These are the values that were either used or observed by Fernandez Luque and van Beek (1976). In addition, it needs to be stated that the bed slope was taken to be zero in this case.

The most basic form of the model contains the drag, added mass, and gravity forces. The shear lift force developed by Wiberg and Smith (1985) and the history force from Basset (1888) are successively added to the model. Figure 4 shows the results. For this case, $u_* = 4$ cm/s with $u_0 = w_0 = 2u_*$. The shear lift force increases the length of the trajectory by about one grain diameter while the Basset history

force appears to have a lesser effect on the trajectory. The results with the shear lift force included are consistent with our intuition. Only a small velocity gradient develops across the grain because of its size. As a result, the shear lift has a relatively small effect. The height is increased by less than one-tenth of a grain diameter while the length increased by approximately one-half grain diameter when the Basset term is included. The increase in length is due to the fact that the grain travels higher into the fluid column and thus attains a greater velocity.

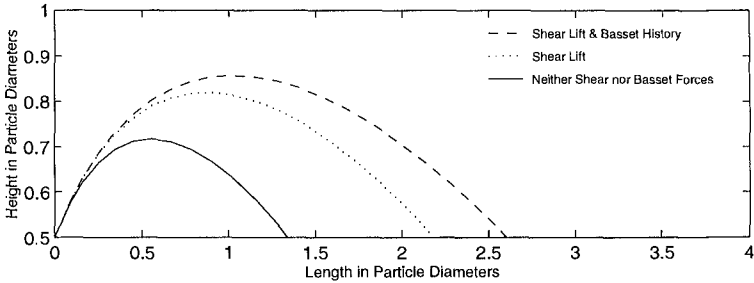


Figure 4 Effect of shear lift and Basset history forces on small particle

We then ran the model with a larger particle size. A diameter of 3.1 cm was chosen, roughly in the gravel regime. The other parameters maintained their same values with the exception of $u_* = 22.84$ cm/s and $\beta = 0.07$ to match the experimental conditions of Nino et al. (1992). Figure 5 shows that the shear lift force had more of an effect than it did with the smaller grain. This result is expected because the velocity gradient is large on a larger particle. The Basset force, however, did not possess the same significance as it did in the other case. This force had little effect on the particle trajectory. The Basset history force had a greater effect on the smaller particle than on the larger particle. This same result was obtained by Nino and Garcia (1992).

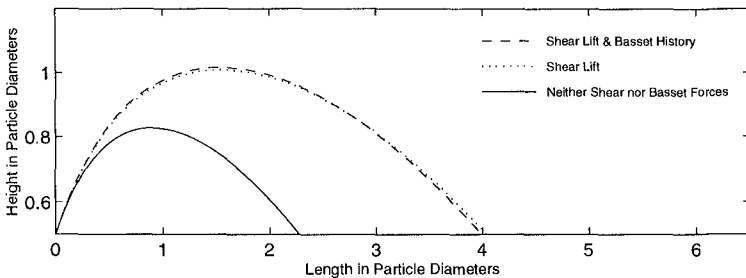


Figure 5 Effect of shear lift and Basset history force on a large particle

The next force to consider adding to the formulation is the Magnus lift force. To review, this force results from grain rotation which is caused in two ways. First, a grain may be transferred an angular velocity from the shear flow. Since the fluid velocity is greater at the top of a grain than at the bottom of a grain, a net torque may

be exerted upon the grain. Second, a grain on the bed may obtain an angular velocity from a collision with another grain. The magnitude of the rotation is dependent on the speed and the placement of the blow that the grain striking the bed delivers. Figure 6 displays the trajectories that result by varying the initial angular velocity. The diameter of the particle is 0.18 cm with $k_s=2d$, $C_L=0.85C_D$, $u_* = 4$ cm/s, $u_0=2u_*$, and $w_0=2u_*$. It is obvious and expected that the trajectories should both increase in length and height with increasing initial angular velocity. The effect of the Magnus force on a particle's path is quite significant. This is a somewhat discouraging result because little is known about the angular velocities of saltating grains. A common practice is to match a known trajectory by "tweaking" the initial angular velocity of the particle.

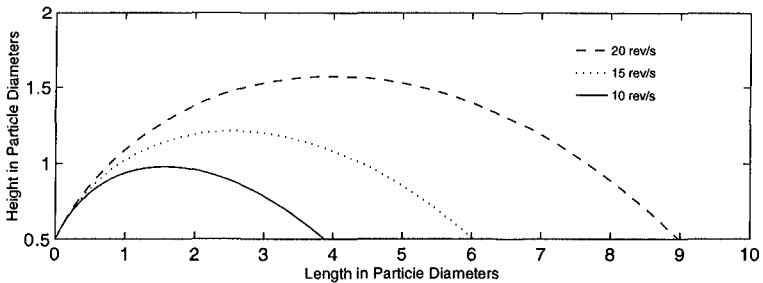


Figure 6 Effect of Magnus force on particle trajectories

The initial angle and velocity of the grain is the next area of interest. Again the grain size used is 0.18 cm. Figure 7 displays the results of varying the take-off angles and maintaining a constant initial velocity. The initial angles are 30, 45, and 60 degrees. The initial longitudinal velocity and initial vertical velocity are both $2u_*$. Figure 8 shows what happens if the velocities are varied and the angles are held constant at 45 degrees. As the lift-off angles increased, the grains saltated farther. Also, the higher the initial velocity, the longer the trajectory. These results are obviously from the fact that the grain attains a higher velocity from the fluid with a larger angle and higher initial velocity.

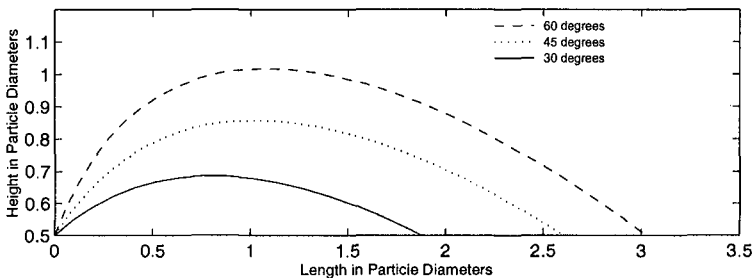


Figure 7 Trajectory sensitivity to particle take-off angle

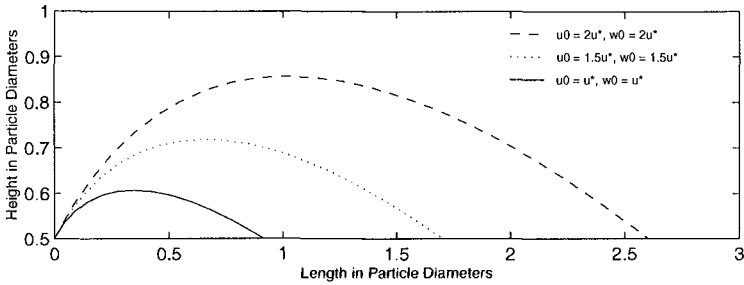


Figure 8 Trajectory sensitivity to particle take-off speed

To summarize, the forces acting on the particle vary significantly with grain size. The shear lift force and the Basset history force vary the greatest of the forces examined. The Magnus effect increases saltation length and height greatly as initial angular particle velocity increases. Finally, the larger the initial velocity and angle, the greater the saltation length and height.

Comparison of Model to Data

The Magnus Effect is neglected for the first comparison with a given data set to see if the shear lift force is sufficient. The trajectory data used for the model comparison is provided by Fernandez Luque and van Beek (1976). The grain diameter was 0.18 cm with a friction velocity of 4 cm/s. The initial conditions for the model were $u_0 = 8$ cm/s, $w_0 = 8$ cm/s, $\beta = 0$, $C_L = 0.85C_D$, and $k_s = 2d$. The trajectory is shown as the solid line in Figure 9. It is easily seen that the shear lift force alone does not adequately describe the motion of the particle as observed by Fernandez Luque and van Beek (1976).

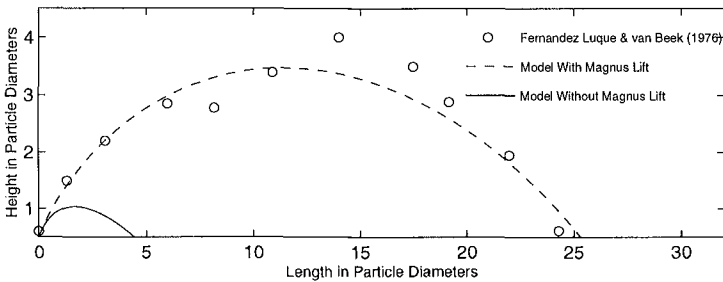


Figure 9 Model comparison to Fernandez Luque and van Beek (1976) observations

Figures 10 through 14 show some of the relevant velocities and forces as predicted by the model. The fluid velocity is always in the rough, turbulent range as shown by the Reynolds number. The drag coefficient was between 0.60 and 0.85. Those quantities are graphically shown in Figure 10 and Figure 11. Figure 12 shows how the particle, fluid, and relative velocities varied over the trajectory length of the saltation. The plot reveals that the particle velocity is continuously increasing

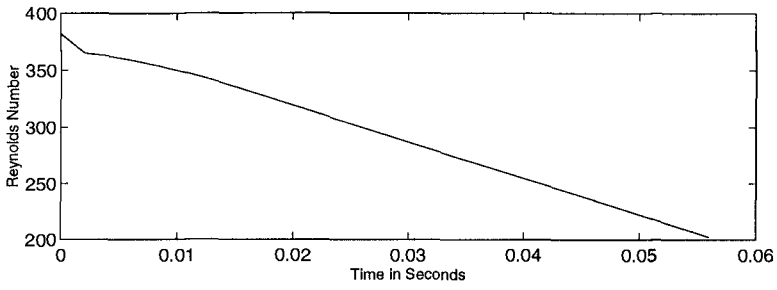


Figure 10 Reynolds number simulated saltation trajectory

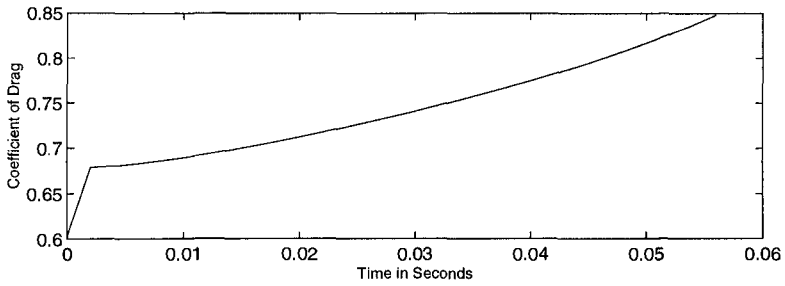


Figure 11 Drag coefficient for simulated saltation trajectory

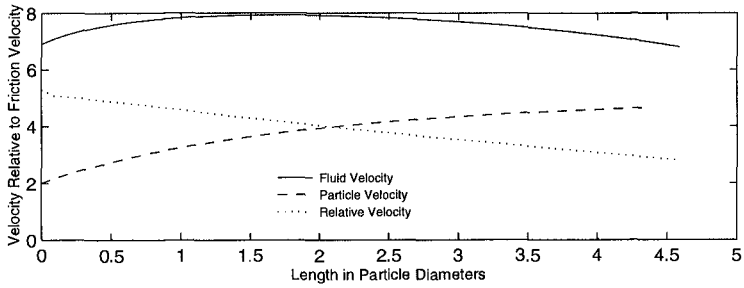


Figure 12 Strength of velocities of simulated particle trajectory

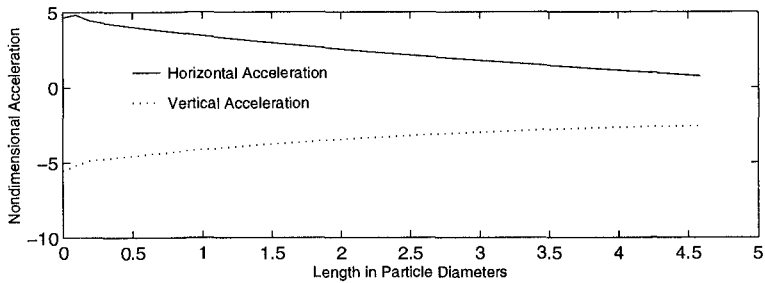


Figure 13 Strength of particle accelerations for a simulated particle trajectory

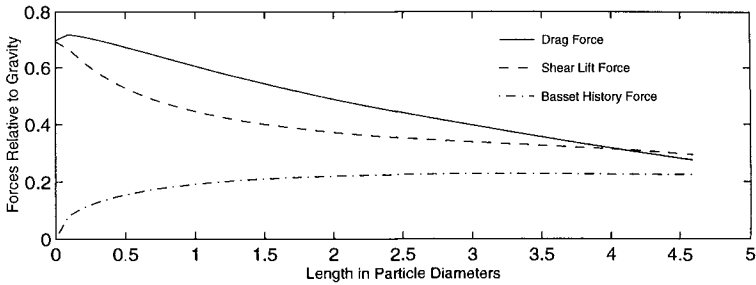


Figure 14 Strength of relevant forces for a simulated particle trajectory

toward that of the fluid velocity. So as a result, the relative velocity is decreasing. This means that the drag and lift forces are both decreasing over the grain trajectory. This is shown in Figure 14. The drag force is represented by the solid line and the shear lift force is represented with a dashed line. The Basset history force is smaller than both the lift force and the drag force for much of the saltation also in Figure 14. These forces in this figure are given relative to gravity. Note that the Basset force continually increases as the particle saltated as a result of the integral nature of the force.

The horizontal acceleration of the particle decreases as the particle velocity approaches the fluid velocity as shown in Figure 13. The vertical acceleration becomes less negative as the particle saltates. The accelerations are non-dimensionalized by multiplying the acceleration by T_s/u_* . The particle decelerates significantly in the rising part of the trajectory and continues to do so until the particle approaches the bed. It accelerates again near the bed because of the aforementioned lift force. This shear lift force is significant when compared to the drag force. It is evident from Figure 9 that the lift force is not providing enough upward thrust for the particle to saltate as observed by Fernandez Luque and van Beek (1976).

The Magnus force was added to the equation of motion to improve the agreement with observations. In addition, the moment equation was added and solved simultaneously with the equation of motion. The initial conditions were maintained with one exception. An initial angular velocity, Ω_0 , of 30 rev/s was added. The model comparison with the data range is displayed in Figure 9. The model now predicts the grain trajectory fairly well and certainly much better than previously. The Magnus force significantly increases the overall lift effect on the particle especially in the rising part of the trajectory according to Figure 15. For this particular case, the Magnus force increased the saltation height by 2.3 grain diameters and the length by 21 grain diameters. Wiberg and Smith (1985) reached a similar conclusion that the Magnus force should be included.

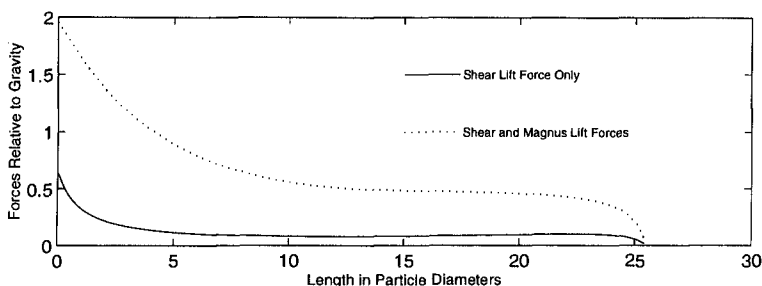


Figure 15 Comparison of shear lift and Magnus forces

Conclusion

The saltation model considered particles from incipient motion through a trajectory and returning to the bed. The saltation model included gravity, added mass, drag, shear lift, Magnus lift, and Basset history forces. The shear lift force is the same as defined by Wiberg and Smith (1985). When the Magnus lift force is applied, the moment equation from White and Schulz (1977) is used to continually update the particle's rotation.

It was found that a particle will saltate farther with increasing take-off speed and angle. The shear lift and Basset history forces vary significantly with particle size. The shear lift force has a greater effect on large particles and Basset history has a greater effect on small particles. The Magnus lift force affects trajectories significantly when included in the model formulation.

The model is able to match observed trajectories from Fernandez Luque and van Beek (1976). It is necessary to include the Magnus lift force to best match their observations. The shear lift force may need further examination. It appears to underpredict the velocity gradient that is expected at the end of a particle's trajectory near bed. These results suggest experiments be conducted to measure the rotation of saltating grains.

Acknowledgments

This work was supported by the U.S. Office of Naval Research, Coastal Sciences Program. Discussions with Renwei Mei are appreciated.

References

- Auton, T.R., Hunt, Jc.R., and Prud'Homme, M., The force exerted on a body in inviscid unsteady nonuniform rotational flow, *J.Fluid Mech.*, 197, 241-257, 1988.
- Abbott, J. E., and Francis, J. R. D., Saltation and suspension trajectories of solid grains in a water stream, *Phil. Trans. R. Soc. London, Ser. A*, 284, 225-254, 1977.

- Bagnold, R. A., The nature of saltation and of 'bed-load' transport in water, Proc. R. Soc. London, Ser A, 332, 473-504, 1973.
- Basset, A. B., A Treatise on Hydrodynamics Volume Two, Dover Publications, New York, 1888.
- Chepil, W. S., The use of evenly spaced hemispheres to evaluate aerodynamic forces on a soil surface, Trans. AGU, 39 (3), 397-404, 1958.
- Einstein, H. A., The bed-load function for sediment transportation in open channel flow, U.S. Dept. Agric., Tech. Bull. no. 1026, 1950.
- Fernandez Luque, R., and van Beek, R., Erosion and transport of bed-load sediment, J. Hydraulic Res., 14 (2), 127-144, 1976.
- Gilbert, G. K., Transportation of debris by running water, U. S. Geol. Survey Prof. Paper, 86, 1914.
- Graf, W.H., Hydraulics of Sediment Transport, Water Resources Publications, Littleton, Colorado, 1984.
- Krecic, M. R., Evaluation and development of particle saltation Models, thesis presented to the University of Florida, Gainesville, FL, in 1995, in partial fulfillment of the requirements for the degree of Master of Science.
- Lee, H. Y., and Hsu, I. S., Investigation of saltating particle motions, J. Hydr. Engrg., 120 (7), 831-845, 1994.
- Mei, R., Flow due to an oscillating sphere and an expression for unsteady drag on the sphere at finite Reynolds number, J. Fluid Mech., 270, 133-174, 1994.
- Morsi, S. A., and Alexander, A. J., An investigation of particle trajectories in two-phase flow systems, J. Fluid Mech., 1972 (part 2), 193-208, 1972.
- Murphy, P. J., and Hooshiari, H., Saltation in water dynamics, J. Hydr. Div., ASCE, 108 (HY11), 1251-1267, 1982.
- Nino, Y., and Garcia, M., Gravel saltation 2. modeling, Water Resour. Res., 30 (6), 1915-1924, 1994.
- Nino, Y., M. Garcia, and L. Ayala, Gravel Saltation 1. Experiments, Water Resour. Res., 30 (6), 1907-1914, 1994.
- Owen, P. R., Saltation of uniform grains in air, J.Fl. Mech., 20(Pt 2), 225-242, 1964.
- Patel, M. H., Dynamics of Offshore Structures, Butterworth & Co. Ltd, NY, 1989.
- Rubinow, S. I., and Keller, J. B., The transverse force on a spinning sphere moving in a viscous fluid, J. Fluid Mech., 447-459, 1961.
- Van Rijn, L. C., Sediment transport, Part I: Bed load transport, J. Hydr. Engrg., 110 (10), 1431-1456, 1984.
- White, B. R., and Schulz, J. C., Magnus effect in saltation, J. Fluid Mech., 81 (part 3), 497-512, 1977.
- Wiberg, P. L., and Smith, A theoretical model for saltating grains in water, J. Geophys. Res., 90, 7341-7354, 1985.

CHAPTER 298

Sediment Movement and Stress Condition in Sea Bed

Yoshihiko Maeno¹, Motoyasu Ishikawa², Kozo Bando³,
Yoshinobu Akiyama⁴ and Kouichi Yabe⁵

ABSTRACT

The stress condition in the sea bed such as effective stress and hydrodynamic condition were measured in the surf zone to understand the detailed mechanism of local and temporal sediment movement. Analysis of the measured data suggests that the large effective stress drop and strong flow in the onshore direction when the wave crest passes are the possible cause for the sand movement in the surf zone. It is also found that the sea bottom elevation change can be evaluated from the effective stress in the sand by a simple equation. The effective stress sensor used in the field measurement was proved to be useful in estimating local and temporal sediment transport.

INTRODUCTION

Sediment transport is usually studied in terms of wave condition and characteristics of bed material. However, in order to understand the detailed mechanism of local and temporal sediment movement, it is important to associate the stress condition in sea bed with wave condition and then to relate the stress to sediment transport. For example, Nago (1982) pointed the relation between the pore pressure and fluidization of the bed.

¹Professor, Dept. of Civil Engineering, Nihon University, 7-24-1 Narashinodai Funabashi, Chiba 274, Japan.

²Research Associate, Dept. of Civil Engineering, Nihon University.

³Chief, Offshore and Hydraulic Engineering Sec., Kajima Technical Research Institute, 19-1 Tobitakuy 2-Chome Chofu, Tokyo 182, Japan.

⁴Senior Research Engineer, Kajima Technical Research Institute.

⁵Manager of Patents, Engineering Dept., Kyowa Electronic Instruments Co., Ltd., 3-5-1, Chofugaoka Chofu, Tokyo 182, Japan.

Maeno and Hasegawa(1985) examined the effects of wave-induced pore pressure in sand bed on liquefaction. Maeno and Tokutomi(1989b) indicated the strong correlation between the liquefaction of sand bed and the mechanisms of sediment transport. Maeno (1992) introduced the experimental results on wave-induced liquefaction and sediment transport, and indicated the needs of the further verification by field observation.

Maeno *et al.*(1993) measured the effective stress, pore pressure and wave conditions outside the surf zone, and concluded that liquefaction occurs by the delayed response of the pore pressure to the surface elevation change. In this research, the similar approach was taken, and the bottom elevation change was tried to relate to the effective stress, pore pressure, wave height and current velocity, which were measured in the surf zone.

This research also attempts to examine the performance of a newly developed effective stress sensor (Maeno *et al.*,1992), which may give the local and temporal information that are hard to obtain by the conventional methods; sand trap, surveying, etc.

FIELD MEASUREMENT

Measurement Site

Measurement was made in a beach at Hazaki-cho, Ibaragi Prefecture, Japan (see Figure 1). This beach is a part of 80 km straight sandy coast facing the Pacific Ocean. There is a 427 m long observation pier on the beach owned by Port and Harbour Research Institute, Ministry of Transport, to study sediment transport. This study made use of the pier, from which various data were taken. Two measurement locations were chosen in the surf zone along the pier: one is 230 m offshore from the shoreline and the other is 260 m offshore. Figure 2 illustrates the measurement locations and the bottom profiles under the pier during the measurement period. The water depth at those locations fluctuated in the range of 1 m, but both the locations remained on a large bar.

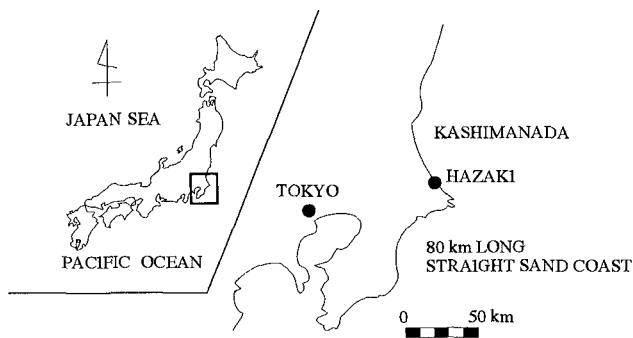


FIG. 1. MEASUREMENT SITE

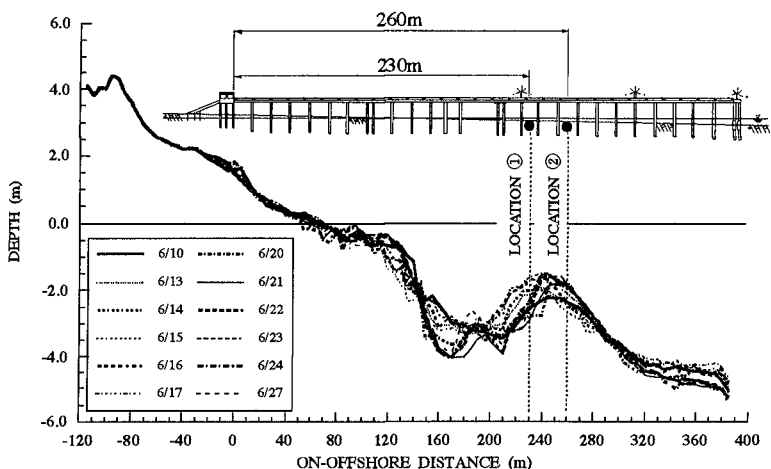


FIG. 2. MEASUREMENTS OF SEA BOTTOM PROFILE

Instruments

The instruments deployed in the measurement locations are listed in Table 1. To install these instruments, a frame structure was put in sea bed at each location as shown in Figure 3. It held an effective stress sensor and a dynamic pore pressure gauge in the sea bed, a pressure gauge on the sea bed, a current meter, and a wave gauge. The effective stress sensor and dynamic pore pressure gauge were the differential type made of the flexible filter (Maeno and Tokutomi, 1989a). Additional data such as sea surface elevation by acoustic wave gauge, wind data, water depth and ground water level were supplied by Port and Harbour Research Institute, who takes these data at the pier on a regular basis. The measured data were recorded at 10 Hz from June 12th to 26th, 1994 for the location 1 and from June 12th to 15th for the location 2. Data acquisition was terminated by the damage to the measurement system due to the high seas.

MECHANISM OF LIQUEFACTION

From a soil mechanical point of view, the sand can be mobilized when the stress acting on it exceeds its capacity. The sand in the zero or negative effective stress condition, which may be called liquefaction, is certainly the case. How liquefaction takes place outside the surf zone was explained (Maeno *et al.*, 1993), and this study focuses on the condition in the surf zone. The mechanism of liquefaction outside the surf zone is reviewed first, and the mechanism in the surf zone found by analyzing the data measured in the present study is followed.

TABLE 1. SUBJECTS FOR MEASUREMENT

MEASURING SUBJECTS	MEASURING EQUIPMENTS	REMARKS
DYNAMIC PORE WATER PRESSURE	DYNAMIC PORE WATER PRESSURE TRANSDUCER	1.0m BELOW SEABED SURFACE
EFFECTIVE EARTH PRESSURE	EFFECTIVE EARTH PRESSURE TRANSDUCER	1.0m BELOW SEABED SURFACE
WATER PRESSURE	WATER PRESSURE TRANSDUCER	1.0 m ABOVE SEABED SURFACE
WAVE PROFILE	ULTRASONIC-TYPE WAVE GAUGE	AIR BEAM TYPE
	CAPACITANCE-TYPE WAVE GAUGE	
VELOCITY	ELECTROMAGNETIC VELOCIMETER	1.0 m ABOVE SEABED SURFACE
WIND DIRECTION AND WIND VELOCITY	PROPELLER-TYPE WIND VANE AND ANEMOMETER	385m OFF SHORELINE
SEA BOTTOM PROFILE	SOUNDING	DAILY MEASURING

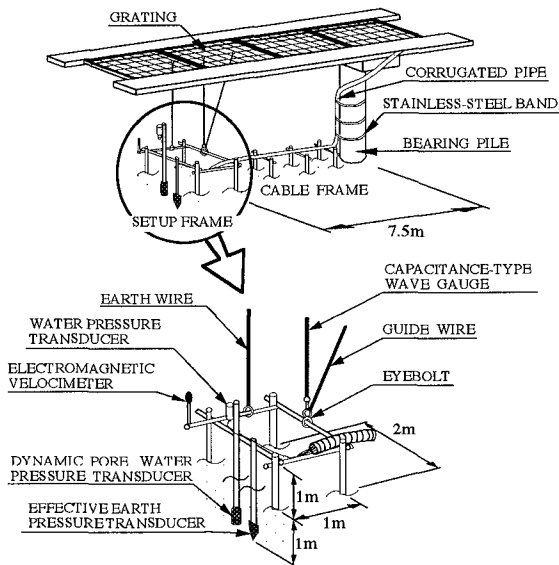


FIG. 3. INSTALLATION OF INSTRUMENTS

Outside Surf Zone

Generally, the dynamic pore pressure and effective stress in the sea bed follow the sea surface elevation change. However, it was found from close observation of these data taken outside the surf zone (Maeno *et al.*, 1993) that the dynamic pore pressure is slightly lagged behind the change of the sea surface elevation. This yields excessive positive effective stress at crest and negative value after the crest passes to compensate

for the insufficient pore pressure response. The negative part of the effective stress gives rise to the liquefaction of the sand, which can be swept away by the currents near the bed. This process is illustrated in Figure 4. Figure 5 shows the time histories of the stresses measured at a depth of 6 m (Maeno *et al.*, 1993). Sharp peaks are observed in the effective stress record due to the late response of the pore pressure to the surface elevation. The magnitude of the negative peak indicates the thickness of the sand layer that was liquidized, and the difference in the stress level before and after the wave is equal to the thickness of the sand layer that was washed away. In this example, the sand in the top 47 cm thick layer was liquidized and the sand layer in the thickness of about 17 cm was carried away.

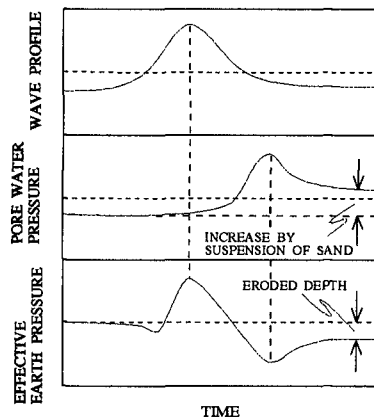


FIG. 4. MECHANISM OF LIQUEFACTION OUTSIDE SURF ZONE

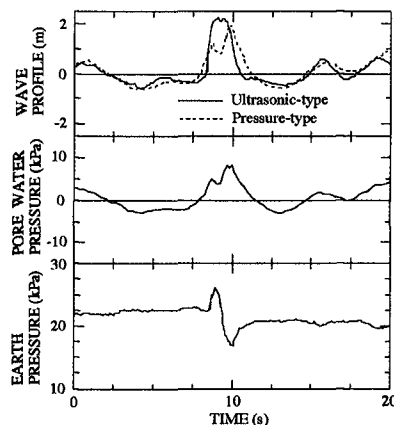


FIG. 5. TIME HISTORIES FOR STEEP AND LARGE WAVE HEIGHT

Inside Surf Zone

In this study the similar kinds of data were collected in the surf zone. Figure 6 shows the responses of those stresses collected at location 2, where waves were steep enough to break. In this case there is little time lag in the response of the pore pressure, which is different from the stress response outside the surf zone. The wave action in the surf zone is severer and the top layer of the sand is more likely to be loose so that the pressure exerted on the sea bottom is transmitted instantaneously to inside.

The response of the effective stress is characterized with the sharp and large drops when the wave crests pass. These drops become larger as the wave height increases. The magnitude of this drop is much smaller than that of the pore pressure, and the negative effective stress may be due to the overshooting response of the pore pressure.

The current data at the sea bottom in Figure 6 show the strong flow in the onshore direction when the crests pass and the effective stress is very low. It is surmised that the loose sand in the top layer where the effective stress is nearly zero may be carried

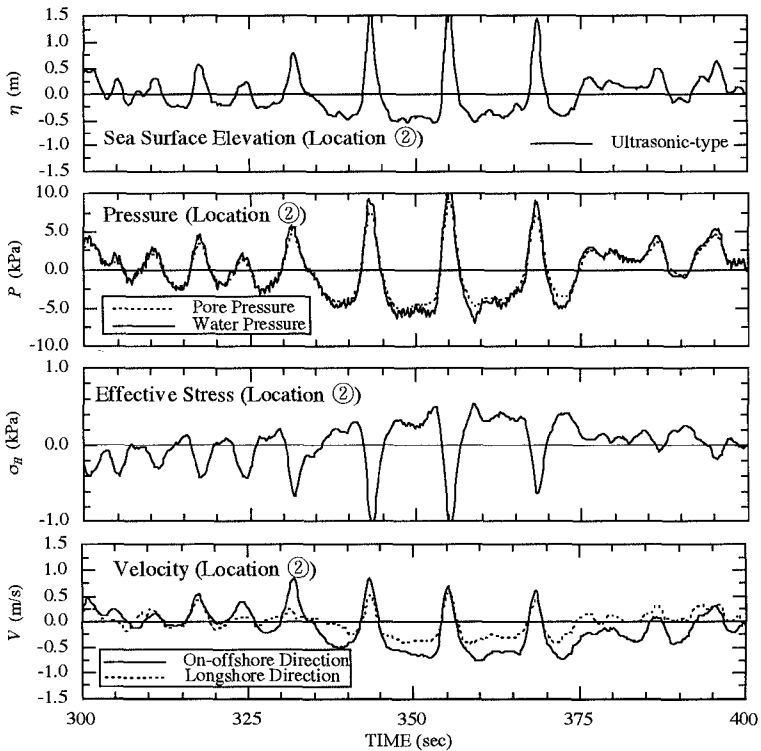


FIG. 6. TIME HISTORY DATA AT LOCATION 2 (6/15/1994 01:17:16)

away by the strong onshore flow. Compared with the condition outside the surf zone, the larger negative effective stress and stronger current due to severer wave action are expected in the surf zone. The condition in the surf zone that large negative effective stress and strong current occur at crest is one of the mechanisms for the sediment movement in the surf zone

ANALYSIS OF FIELD DATA

Wave Condition

The significant wave height and period, and wind information are computed based on 50 minutes-long data to represent the condition at that hour, and are shown in Figure 7. There were two moderate storms with approximately 2 m significant wave height coming in the measuring period: on 15th to 16th and on 19th to 20th. The swells were dominant at the first event, since wind was weak and the wave period was relatively long. On the other hand, the second event was caused by the strong easterly winds.

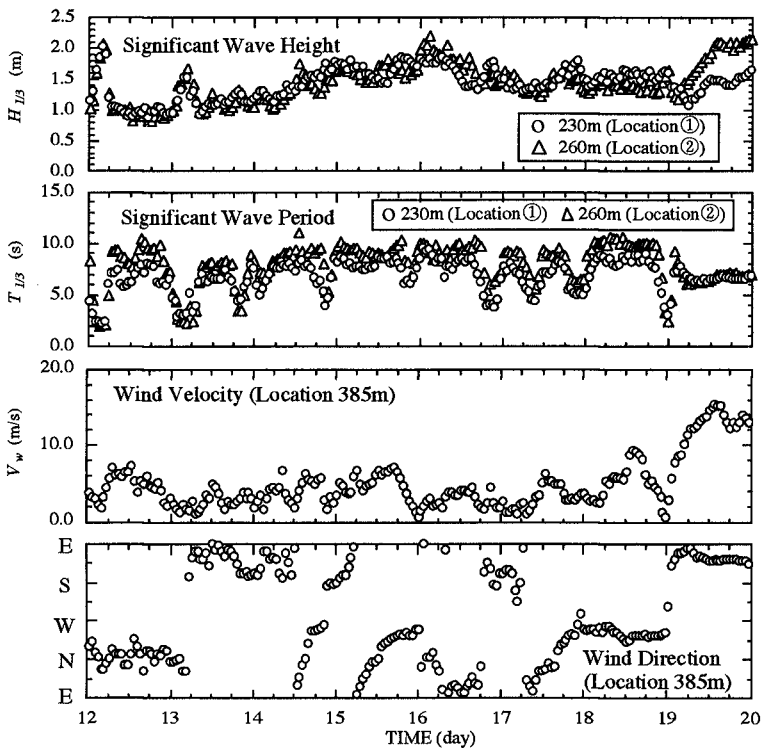


FIG. 7. SIGNIFICANT WAVE HEIGHT AND PERIOD, AND WIND INFORMATION (50 MINUTES-LONG AVERAGED DATA)

Response of Stress in Sand to Wave Action

To compare the stress condition in the sand with the wave condition, the stress data were also processed in the same way as the waves were. Figure 8 illustrates the time histories of the significant pressure, stresses and velocity data. The pressure data can be linearly converted to the sea surface elevation. It is seen that the amplitude of the effective stress change in one wave period becomes larger with the significant wave height. It implies that the effective stress is directly controlled by the wave action.

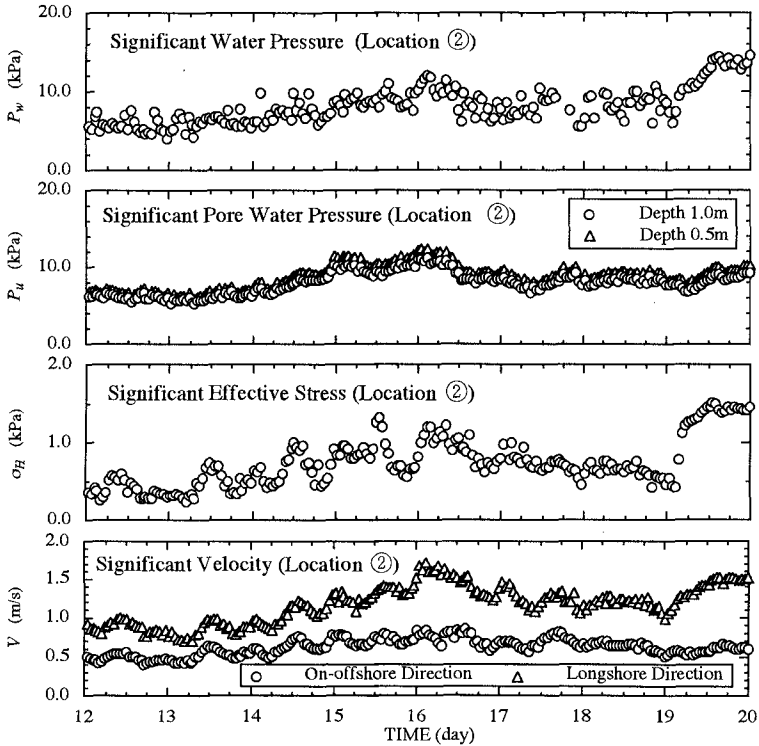


FIG. 8. SIGNIFICANT STRESS AND VELOCITY (50 MINUTES-LONG AVERAGED DATA)

The averaged data are shown in Figure 9. There is a sharp depression everyday in the effective stress data, and it becomes larger with time until 17th. The pore pressure exhibits the similar response but in the positive direction. Then adding them together makes the variation at the time become negligible. It is also seen that the drop in the averaged effective stress occurs at the lowest elevation of the sea surface in each day. Clear cause for these events are not understood, but the non-linearity associated with

shallower water depth may be attributed. Correlation with the wave height is not clear either, since high waves came from 15th evening to 16th morning.

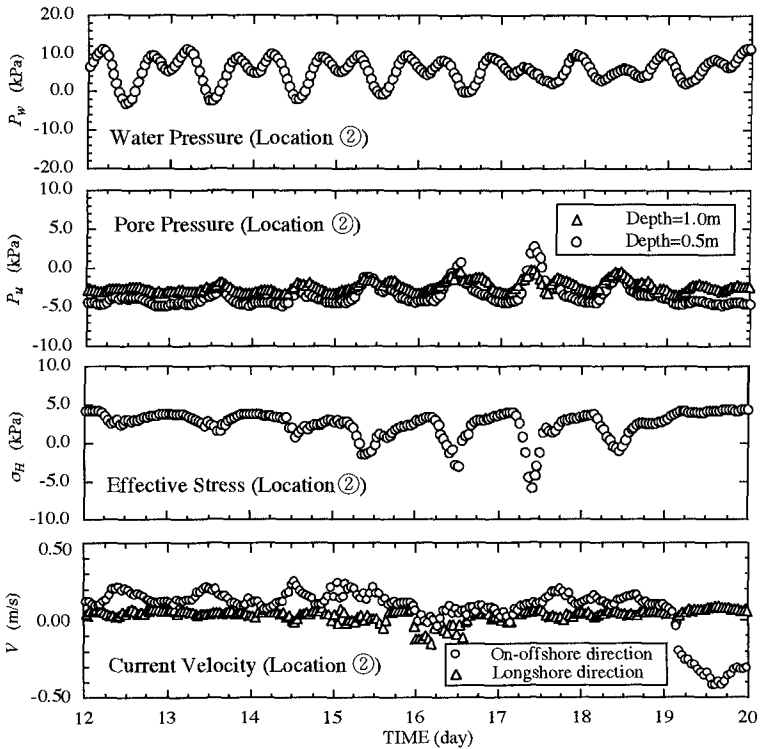


FIG. 9. 50 MINUTES-LONG AVERAGED STRESS AND VELOCITY

Bottom Elevation Change

It is reasonable to assume that the effective stress represents the thickness of the sand above. Then, the vertical location of the effective stress sensor in relation to the sea bottom can be estimated by the following equation (1), and consequently the sea bottom elevation, Δh is evaluated.

$$\Delta h = \frac{\sigma_H}{K_o \{ (1-n)(\rho_s - \rho_w) g \}} \tag{1}$$

where K_o , n , ρ_s , ρ_w and g are coefficient of earth pressure at rest, porosity, density of soil particle, density of sea water and gravity acceleration. The averaged effective stress, σ_H was used in the equation. Note that since there are large drops in the averaged effective stress series as mentioned above, those data was unconsidered. If these data

were converted to the thickness based on equation (1), it turned out to be about 3 m depth change, which is unrealistic. The effective stress change is assumed to be solely by the change of sand layer thickness in equation (1), and those large stress drops are more likely to be caused by other physical factors.

The estimated sea bottom elevation is shown in Figure 10 along with the measured elevation. The estimate appears to oscillate about the measurement. But, considering that the measurement was made only once a day and that the elevation possibly changes within a day, the estimated changes are compared well with the measured data at the corresponding time. This trend is observed both at location 1 and at location 2. Agreement between the measured elevation and the estimate by the effective stress implies that the effective stress is directly related to the sand movement and the sea bed elevation change can be estimated from the information on the effective stress. From this point of view the effective stress sensor employed in this study is found to be one of the most efficient instrument to provide the information on the sediment movement. It also suggests that the bottom elevation may fluctuate in a day and may have to be measured more than once in such a day to understand the actual movement.

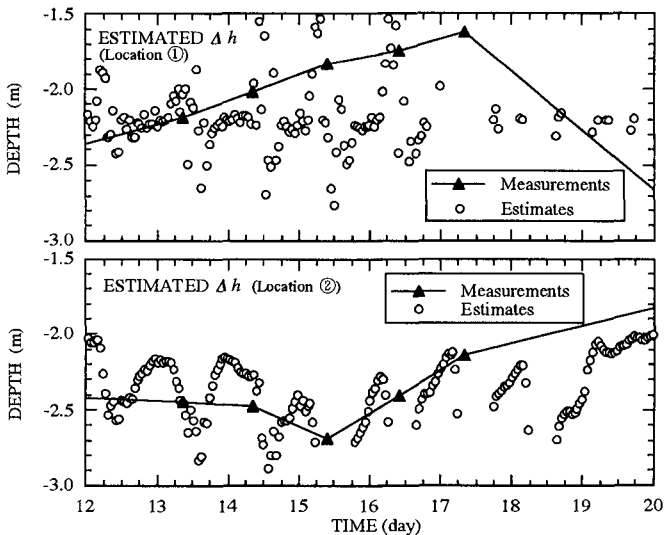


FIG. 10. ELEVATION OF BOTTOM SURFACE

Effect of Ground Water

There are some studies indicating connection between ground water and sediment transport (*e.g.*, Grant, 1948). Since the ground water level near the shoreline was

continuously measured by Port and Harbour Research Institute, its effect was attempted to examine. The sea surface level and ground water table changes are compared in Figure 11. There is a long-period variation in the time history of the ground water level, which is similar to the wave height record in the same period; *i.e.*, the ground water level rose as the wave became higher. There is also oscillations with short periods, responding to the tides. Thus, it is clear that the ground water near the shore is influenced by the sea conditions.

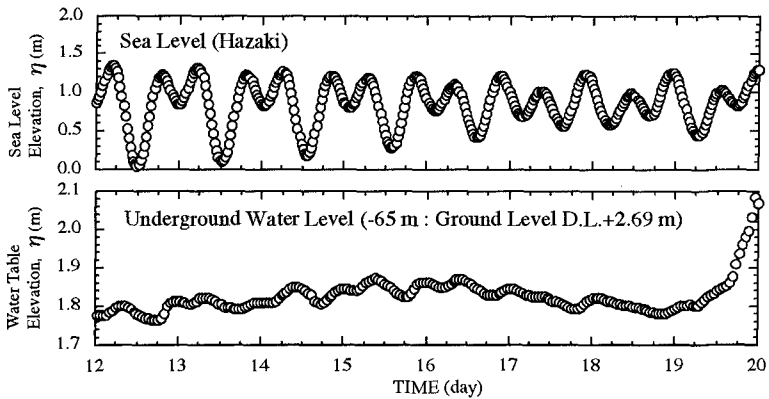


FIG. 11. SEA LEVEL AND WATER TABLE ELEVATIONS

Further, this rise and drop of the ground water level due to the sea condition change may affect the stress condition in the sand bed in the surf zone. Especially, the liquefaction and the sand movement on a bar may be affected by the ground water, because rapid pressure change at bottom by surface wave may cause the discontinuity between that pressure and the pressure defined by ground water.

Effects of Non-Linearity

To examine the non-linear effects of the surface waves on the effective stress, skewness and kurtosis were calculated from the measured sea surface elevation data. When those values in Figure 12 are compared with the time histories of the wave height and effective stress, the skewness becomes slightly bigger with the wave height and the kurtosis remains constant. From these observations clear relation between the non-linearity of the surface waves and the effective stress is not recognized.

Effects of Long-Period Component of Waves

From the spectrum computed from the sea surface data, the long period waves are

estimated and shown in Figure 13. In this study, only the components with the period longer than 30 s are picked. The long-period wave had larger height on 15 th and 16th, the duration of which coincides with that of the higher significant wave. The trend of long-period wave height is also found in the time history of the ground water level. It implies that the ground water near the coast can be affected by the longer waves.

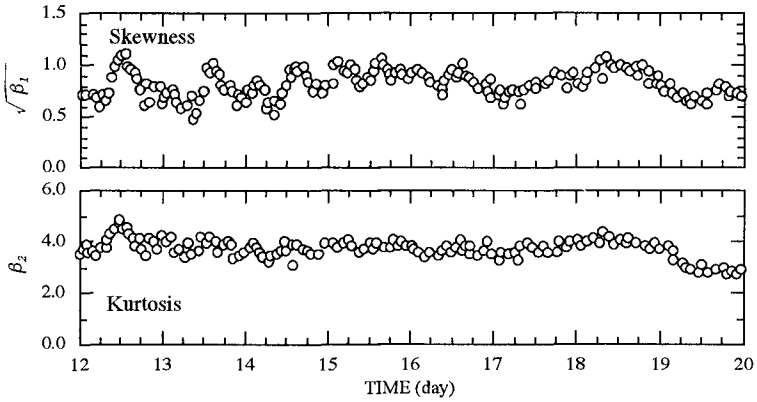


FIG. 12. EFFECTS OF NON-LINEARITY

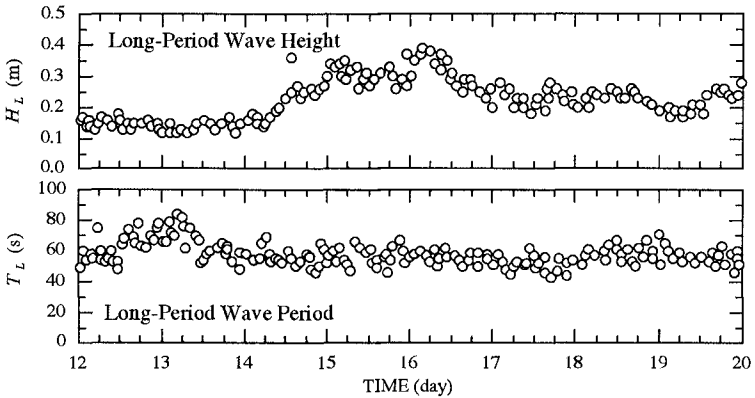


FIG. 13. EFFECTS OF LONG-PERIOD WAVES

Relation between Stresses and Wave Steepness

Using the significant wave height and period, and the corresponding effective stress change, their relation is examined in Figure 14, which exhibits the strong linear relation between them.

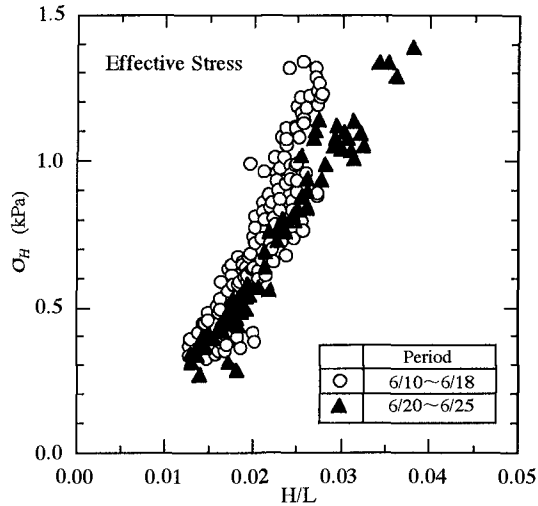


FIG. 14. CORRELATION BETWEEN EFFECTIVE STRESS AND WAVE STEEPNESS

CONCLUSIONS

The effective stress and pore pressure in the surf zone were directly measured to study the relation with the stress, and the wave condition and other factors, and to evaluate the bottom elevation change from the effective stress data. Though the data were collected only 10 days because of difficult installation of the instruments in the surf zone and the damage by high waves, there were two moderate storms in the measuring period. From the careful observation and analysis of the measured data during this period the followings are found.

- (1) The pore pressure and effective stress appears to respond to the water surface elevation without any time lag. The measured area is always attacked by breaking waves and the sand there is anticipated to be loose. Then, the pressure on the bottom transmits almost simultaneously to the pore pressure inside the soil.
- (2) The mechanism of liquefaction in the surf zone seems to be different from that outside the surf zone. The large effective stress drop and strong flow in the onshore direction when the wave crest passes are the possible cause for the sand movement in the surf zone.
- (3) The water depth change estimated from the effective stress records agrees well with the measured depth change. This leads to the following three conclusions.
 - (a) The effective stress in sea bed is closely related to liquidization of sand and then to sand movement.

- (b) The sea bottom elevation change can be evaluated from the effective stress in the sand and equation (1).
- (c) The effective stress sensor was proved to be useful in estimating local and temporal sediment transport.
- (4) Both the pore pressure and effective stress show larger variation when the short waves with large wave steepness pass.
- (5) The currents going offshore were observed when the sea level was low. The effective stress varied corresponding to these currents.
- (6) The averaged effective stress over 50 minutes drops sharply at low tide. The shallower water depth may be a possible cause, and the exact reason for this is still being studied.
- (7) The ground water level near the coast is likely to be affected by the long waves and tidal changes.

ACKNOWLEDGMENTS

The writers gratefully acknowledge the Port and Harbour Research Institute, Ministry of Transport, Japan, for permission to use the observation pier of Hazaki Oceanographical Research Facility.

REFERENCES

- Grant, W. S. (1948). "Influence of the Water Table on Beach Aggradation and Degradation." *J. Marine Res.*, 7(3), 655-660.
- Maeno, Y. and Hasegawa, T. (1985). "Evaluation of Wave-Induced Pore Pressure in Sand Layer by Wave Steepness." *Coastal Engineering in Japan*, JSCE, Vol.28, 31-44.
- Maeno, Y. and Tokutomi, K. (1989a). "Characteristics of Flexible Filter for Pore Pressure Transducer." *IAHR Workshop on Instrumentation for Hydraulics Laboratories*, Ontario, 105-119.
- Maeno, Y. and Tokutomi, K. (1989b). "Measurements of Wave-Induced Pore Pressure by Flexible Filter." *IAHR Workshop on Instrumentation for Hydraulics Laboratories*, Ontario, 121-134+1.
- Maeno, Y. (1992). "Mechanism of Wave-Induced Liquefaction and Densification in Seabed." (Discussion) *Soils and Foundations*, Japanese Society of Soil Mechanics and Foundation Engineering, Vol.32, No.3, 177-181.
- Maeno, Y., Karauchi, H., Yabe, K., and Koketsu, K. (1992). "Development of Transducers for Measuring Effective Stresses and Pore Water Pressure in Seabed." *Proc. of Techno Ocean '92*, Vol.1, 79-85 (in Japanese).
- Maeno, Y., Karauchi, H., Yabe, K., and Suzuki, Y. (1993). "Field Measurements of Wave-Induced Liquefaction and Suspension of Sediments." *Proc. of Coastal Engineering*, JSCE, Vol.40, 576-580 (in Japanese).
- Nago, H. (1982). "Liquefaction of Highly Saturated Sand Layer under Oscillating Water Pressure." *Proc. of the 26th Conference on Hydraulics*, JSCE, 589-594 (in Japanese).

CHAPTER 299

APPLICATION OF THE DEPTH OF CLOSURE CONCEPT

Robert J. Nicholls, ASCE Associate Member¹,
William A. Birkemeier, ASCE Member², and Robert J. Hallermeier³

ABSTRACT

Using data from Duck NC (a wave-dominated, microtidal, sandy oceanic beach), depth of closure is critically evaluated. A meaningful closure is observed for most erosional events, and annual to 30 month time intervals, supporting the application of this concept within coastal engineering. However, the magnitude of depth of closure is sensitive to the definition and analysis approach utilized and estimates of closure need to be explicitly linked to this information.

The limit depth d_l (Hallermeier, 1981) is found to define a conservative bound to the observations of closure during erosional events and in those annual cases where we have data. This confirms the ability to compute a meaningful limit depth simply using extreme wave conditions. At longer time scales there is evidence of a decoupling of the relationship between d_l and observed depth of closure, the observations increase less rapidly than the predictions of d_l . Understanding how closure evolves from individual erosional events to annual and longer time intervals improves the interpretation of sparse surveys and can assist engineering judgement when applying closure predictions.

INTRODUCTION

Depth of closure (DoC) is a widely-used concept within coastal engineering which describes the seaward limit of appreciable depth change (Hallermeier, 1978; 1981; Nicholls *et al.*, in review). It is based on the observation that repetitive beach-nearshore profiles show a decline in vertical variability with increasing depth. Empirically, a closure depth is observed in most high-quality profile data, corresponding to a pinch-out depth

1. School of Geography and Environmental Management, Middlesex University, London EN3 4SF, U.K.

2. US Army Engineer Waterways Experiment Station, Field Research Facility, 1261 Duck Road, Kitty Hawk, NC 27949.

3. Dewberry & Davis, 8401 Arlington Boulevard, Fairfax, VA 22031.

below which depth changes become small (Figure 1). DoC is often used to infer a seaward limit to significant cross-shore sediment transport, leading to applications such as: (1) estimating coastal sediment budgets (e.g., Hands, 1983); (2) numerical modeling of coastal change (e.g., Kraus and Harikai, 1983) and (3) beach nourishment design (e.g., Stive *et al.*, 1991).

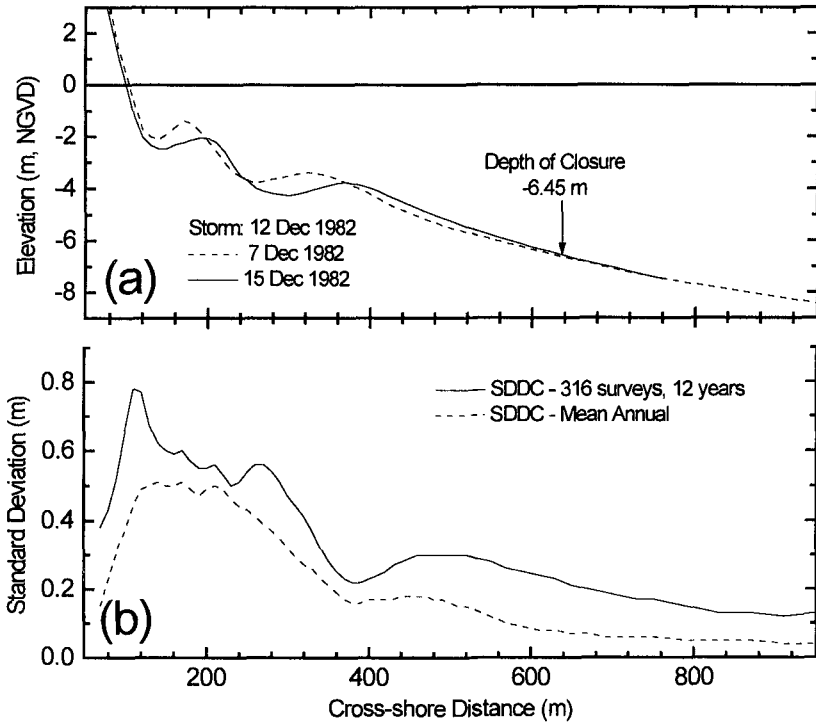


Figure 1. Example of (a) depth of closure produced by single storm, and (b) standard deviation of depth change (SDDC) over a typical year and 12 years. Variability decreases offshore, but increases with time scale. (Profile line 188, Duck, NC).

At sites with repetitive, beach-nearshore profile data, empirical estimates of DoC may be made directly. However, such sites are unusual and DoC is normally estimated using a range of possible indicators (USACE, 1984). The only analytical method to estimate DoC has been proposed by Hallermeier (1978; 1981). Annual DoC is the seaward limit of the littoral zone (depth — d_l) which can be estimated using extreme wave conditions. In a generalized time-dependent form:

$$d_{l,t} = 2.28H_{e,t} - 68.5(H_{e,t}^2/gT_{e,t}^2) \quad (1)$$

where $d_{l,t}$ is the predicted DoC over t years, referenced to Mean Low Water; $H_{e,t}$ is the non-breaking significant wave height that is exceeded 12 hours per t years, $(100/730t)\%$

of the time); $T_{e,t}$ is the associated wave period; and g is the acceleration due to gravity.

The detailed characteristics of DoC, including the validity of Equation 1, have been evaluated (Nicholls *et al.*, in review) using 12 years of profile data collected at the Field Research Facility (FRF) of the U.S. Army Engineer Waterways Experiment Station's, Coastal and Hydraulic Laboratory (formerly the Coastal Engineering Research Center), located in Duck, NC, U.S.A. This paper extends previous analyses, develops additional conclusions, and examines implications for coastal engineering design and practice.

THE DUCK DATA SET

Duck, NC is a wave-dominated, microtidal sandy beach located on the Atlantic Ocean (Birkemeier *et al.*, 1985). The beach-nearshore profile data used in this study were collected to about 8-m depth along four profile lines (58, 62, 188, and 190). On these lines, offshore contours are relatively straight and one or two nearshore bars are usually present. These bars tend to be three-dimensional (Lippmann and Holman, 1990). Surveys are typically collected every two weeks and after most storms, providing pre- and post-storm profiles. Operational survey accuracy is <3 cm (Lee and Birkemeier, 1993).

Wave height and period data were collected every six hours, with hourly measurements during storms. Tidal elevation is also measured on site, with the mean tide range being about 1 m. Mean Low Water (MLW) is 0.42 m below National Geodetic Vertical Datum (NGVD). For more details on the data set see Lee and Birkemeier (1993), Larson and Kraus (1994), Lee *et al.* (1995; in review) and Nicholls *et al.* (in review). All observations of DoC are given relative to MLW as this appears to be an appropriate reference level for DoC estimates based simply on wave dimensions (Hallermeier, 1981; Nicholls *et al.*, in review).

DEFINITION AND INTERPRETATION OF CLOSURE

DoC is a fundamental morphodynamic boundary separating a landward active zone from a seaward less active zone *over the period defined by the profile observations used to define closure*. It is not an absolute cross-shore boundary and some depth change, and hence some cross-shore transport is expected to occur at DoC and further seaward (*cf.* Hallermeier, 1981). The position of DoC depends on several factors, including definition. Time scale is also significant as profile activity increases with time scale and a fixed closure criterion will typically move offshore as time scale increases (*e.g.*, Figure 1(b)). (Note that data accuracy often influences our ability to resolve DoC, but at Duck this is a minor issue). The processes which are observed to control DoC at Duck are the typical annual to decadal storm-accretion processes of the beach-nearshore zone (Lee *et al.*, in review), but at longer time scales, shoreface processes will probably control closure (*cf.* Stive and DeVriend, 1995). Therefore, while the concept of DoC is relatively simple, stating its magnitude at any site as x meters is meaningless without qualification concerning the definition utilized and the pertinent time scale. In some cases, closure may not be susceptible to a practical empirical definition, as observed by Inman *et al.* (1993) in samples of surveys at Oceanside, CA which include major storms in 1982/83.

DoC can be defined for (1) events, such as storms, (2) time-interval (or endpoint) change, which ignore intermediate changes (or in practical terms is equivalent to analysis of a typical sporadic survey program), or (3) time-integrated (or cumulative) change. While events can be related to specific energetic wave conditions and processes (e.g., erosion), time-interval and time-integrated changes are controlled by the balance of erosional processes (rapid offshore transport during high energy wave events) and accretional processes (slow, but continuous onshore transport between erosional events) (Lee *et al.*, in review).

To illustrate and examine the variability of DoC due to different definitions at a site with frequent surveys, annual DoC values from profile lines 62 and 188 at Duck are presented in Table 1. Annual time-interval DoC using three fixed depth change criteria: (6 cm, 10 cm and 15 cm) are considered; In this analysis, profiles are compared proceeding seaward to determine where the profile change consistently declines below the depth change criterion, hence defining closure. Annual time-integrated DoC is measured using the standard deviation of depth change (SDDC) which avoids bias from outliers —

Table 1. Annual closure (m, MLW) derived from three fixed change criteria and from an SDDC analysis, including the annual elevation range shown at closure. Each annual period is July to July (fixed criterion) and July to end June (SDDC). "*" indicates non-closing case.										
Start Year	Profile Line 62					Profile Line 188				
	Fixed Depth -Change Criteria			SDDC		Fixed Depth -Change Criteria			SDDC	
	6 - cm	10- cm	15- cm	Depth (m)	Range (m)	6- cm	10- cm	15- cm	Depth (m)	Range (m)
1981	7.2	6.5	4.4	5.4	0.16	7.9	7.6	7.4	5.8	0.16
1982	8.0	6.1	5.9	6.7	0.12	6.4	6.2	6.0	6.6	0.19
1983	6.4	6.2	6.0	6.2	0.14	7.7	5.9	5.7	6.0	0.13
1984	6.3	5.0	3.8	6.6	0.12	7.3	6.6	6.2	5.1	0.21
1985	8.0	7.5	6.8	5.1	0.20	*	8.3	6.6	4.8	0.20
1986	*	*	8.0	6.9	0.23	*	*	7.7	8.3	0.18
1987	6.3	6.1	5.9	6.1	0.13	6.0	5.8	5.6	6.0	0.12
1988	*	*	*	*	*	*	*	*	7.7	0.43
1989	*	*	*	7.3	0.13	*	*	5.1	7.2	0.20
1990	*	*	5.2	5.7	0.16	*	*	*	6.8	0.24
1991	*	8.1	5.3	5.9	0.22	7.9	7.4	4.8	5.6	0.22
1992	6.9	6.3	6.0	6.8	0.16	5.2	5.0	4.1	6.0	0.14

the DoC then corresponds to the start of a non-zero tail (Kraus and Harikai, 1983). Note that depth change at DoC is a variable defined by the standard deviation envelope and hence there is more potential for an irregular criterion using this approach. Annual SDDC-defined closures from Profile line 62 are illustrated in Figure 2.

The first observation concerning Table 1 is that annual DoC is not always defined within the surveys (≤ 8 -m depth): the 6-cm fixed criterion defines 58% of closures, while SDDC defines 96% of closures. The largest annual DoC is usually given by the 6-cm change criterion: the 10-cm and 15-cm changes are on average about 90% and 80% of the

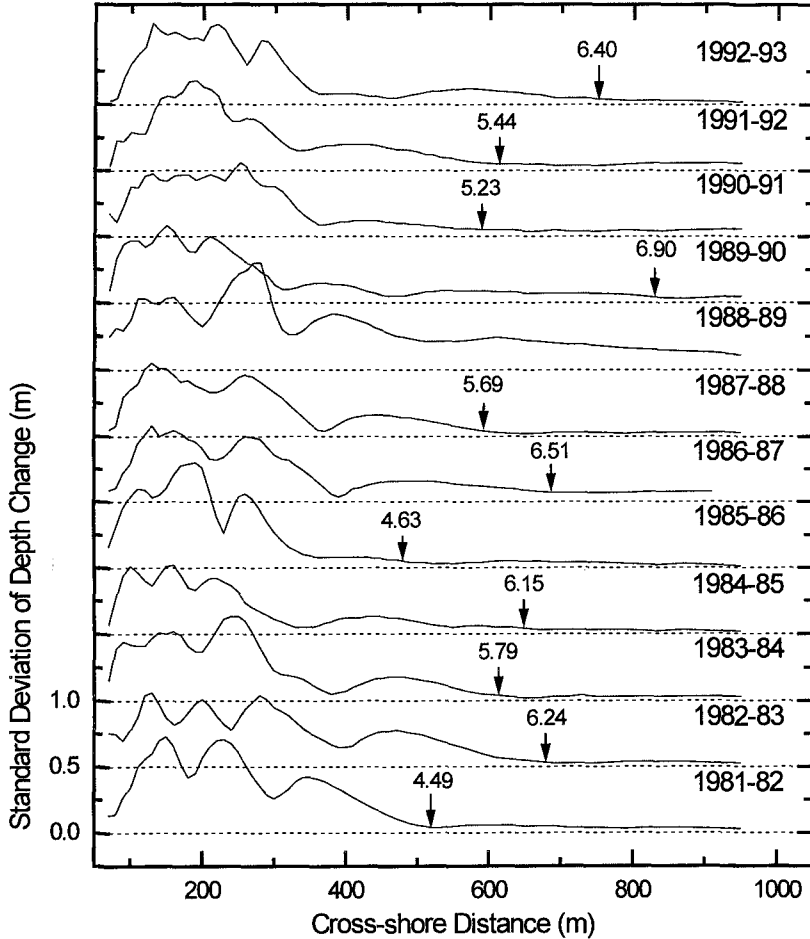


Figure 2. Standard deviation of depth change envelopes for 12 annual periods from July 1981 until end June 1993 (Profile line 62). Arrows mark SDDC-derived closure and are labeled with depths in m below MLW.

6-cm changes, respectively. Clearly, DoC defined with any constant depth change criterion is just one of a family of possible DoCs, depending on the depth change criterion selected. The smaller the depth change criterion, the greater the proportion of the active profile which will be defined.

The SDDC-defined boundary defines most annual DoCs, including periods of significant profile accretion when all the fixed change criteria fail. However, these cases are associated with a larger non-zero tail, indicating larger uniform changes to the seaward limit of the profile envelope than in typical years. On average, the SDDC DoC lies between the 10-cm and 15-cm time-interval DoC, but this relationship is not apparent for the non-closing cases using a fixed change criterion. Therefore, it is concluded that while the SDDC approach is a reasonable empirical method to define DoC, at Duck it shows bias towards smaller annual closure when there are uniform profile changes at the seaward ends of profiles. A fixed, standard deviation criterion (e.g., 10 cm) would provide results more consistent with the fixed change criterion.

It is also noted that these annual SDDC analyses differ from Larson and Kraus (1994). Using all the Duck data from 1981 to 1991, they discriminated a boundary at about 3.6 m below MLW (400 m offshore). However, comparing Figures 1 (b) and 2 shows that while the minimum at 400 m is an intriguing aspect of the survey data, it is part of a larger declining trend to greater depths. Therefore, this position should not be considered the start of a non-zero tail in the sense of the results in Table 1.

Clearly, different definitions for DoC yield different depth estimates, so any stated empirical result needs to make the definitions explicit. Closure at Duck due to erosional events and over annual and longer time scales is now examined in more detail.

DEPTH OF CLOSURE DURING EROSIONAL EVENTS

Predictions Using Hallermeier (1981)

DoC during erosional events, defined by consistent offshore bar migration, was measured for 68 events with high waves (>2 m height) (Nicholls *et al.*, in review) and is henceforth referred to as erosional event-dependent (E-D) DoC. Following the rationale behind Equation 1, which defines a depth where most waves will not have experienced shallow water breaking, analysis of DoC during erosion at Duck shows that a 6-cm change criterion is the best indicator of closure. It is also most consistent with the documented survey accuracy. A 6-cm change criterion is used in all subsequent analysis

Equation 1 is found to define a conservative bound to the observations (Figure 3), agreeing with Hallermeier's (1981) original recommendations concerning input parameters. Below this limit, the observations show considerable scatter which is partly explained by the pre-event bar configuration — the largest DoC appear to be associated with the most dissipative profile morphology, namely, single outer bars (bar crest about 300 m offshore). Three erosional events produced observed DoCs which were near the survey limit (8-m depth), while three erosional events did not close within the measured profile. These results do not contradict Equation 1 as $d_f > 8$ m for those cases which close beyond the survey range.

Using an empirical best-fit approach to the data in Figure 3, a typical erosional

event realizes 69% of the change predicted by Equation 1 (>95% confidence) (Figure 3):

$$d_E = 0.69 d_t \quad (2)$$

where d_E = observed E-D DoC. However, Equation 2 is affected by the fact of missing observations and its validity for other sites is uncertain.

Probability Analysis

The 68 available observations of erosional E-D DoC approximately conform to a lognormal probability distribution, *i.e.* plot near a straight line in Figure 4. The observations have been ranked in ascending order from $i = 1$ to 68, then assigned evenly-spaced probabilities of $(i-0.5)/N$, where $N = (68+3)$; this procedure allows for the three presumably higher missing observations noted in the previous section. A lognormal probability distribution arises "when many random quantities cooperate multiplicatively so that the effect of a random change is in every case proportional to the previous value of the quantity" (Sachs, 1984, p. 107). For these nearshore DoC, the controlling variables include wave height and period and pre-event profile geometry (Nicholls *et al.*, in review).

Such well-behaved observations suggest a coherent sample of erosional events at Duck, so that extrapolation to rarer events than those yet recorded at the site maybe meaningful. One approach to extrapolation is to use annual maxima of the erosional E-D DoC, giving observations a direct basis in annual probabilities. Figure 4 also displays the nine observed annual maxima (three missing) in the same basic format, with these values showing fair conformance to a shifted lognormal probability distribution. The median annual extreme corresponds to 50% annual probability, or a recurrence interval of 2 years. Note that a lognormal distribution yields lower extremes than an exponential distribution, which would typically describe wave heights (USACE, 1984).

Empirical evidence in Figure 4 consistently supports the order-of-magnitude

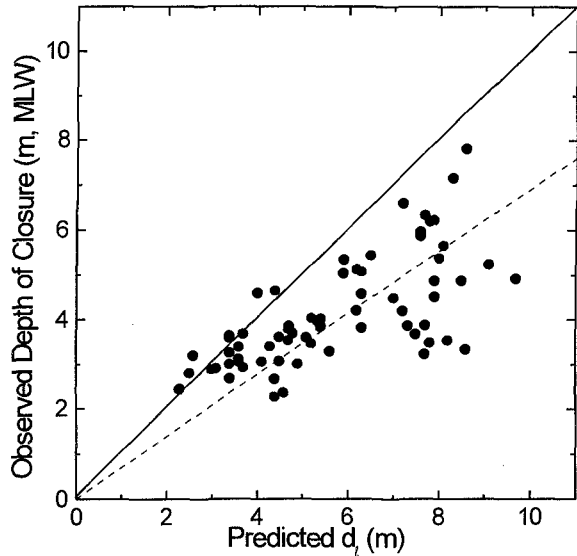


Figure 3. Observed versus predicted depth of closure (averaged alongshore) during 68 storms. The best-fit line (Equation 2) is dashed.

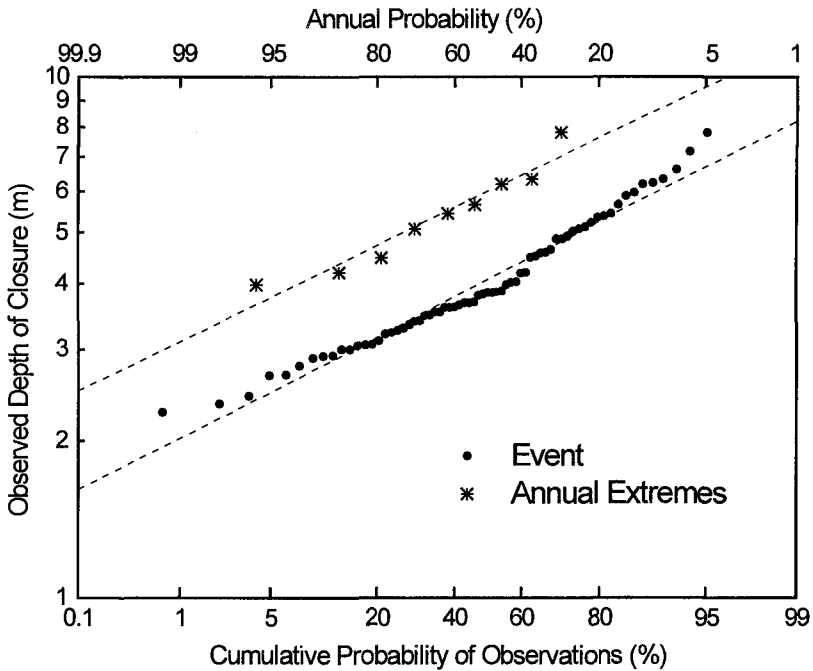


Figure 4. Lognormal distributions of all observed erosional event-dependent cases, comprising all observations (Event), and the nine observed annual extremes estimates for extreme DoC in Table 2. These projections suggest that during more extreme erosional events, advances of DoC into water depths beyond 8- to 9-m depth below MLW are rather rare. This behavior is broadly consistent with (1) the predictions of Equation 1 which suggest that over 12.5 years, DoC during erosional events only exceeded 9-m on four occasions (or 6% of cases), and (2) conclusions about observed DoC in a probabilistic context, derived from an independent analysis of all the Duck survey data from 1981 to 1991 (Larson and Kraus, 1994).

Table 2. Approximate recurrence interval for the annual maximum erosional event-dependent closures based on a probability analysis (see text for more details).					
Closure Depth (m below MLW)	7	8	9	10	11
Approximate Recurrence Interval (years)	2.5	5	12	30	70
Annual Probability (%)	40	20	8	3	1.4

DEPTH OF CLOSURE OVER ANNUAL AND LONGER TIME INTERVALS

This section examines the magnitude of DoC over a range of time intervals (1, 1.5, 2, 2.5, 4 and 8 years), including the applicability of Equation 1. DoC was evaluated using

a time-interval approach (*i.e.*, comparing surveys separated by a fixed time interval, as defined earlier) with a 6-cm change criterion. Surveys three months apart in time over the period July 1981 to October 1993 were selected as the basic data set for analysis. This gave 46 time periods for annual closures, 44 annual time periods for 18-month closure, etc.

Predictions Using Hallermeier (1981)

An important result is that time-interval (T-I) DoC is generally deeper than the largest E-D DoC during the same time period. For the annual case, the residuals (d_t - observed DoC) are about 1 m smaller than the erosional events, as shown in Figure 5. This demonstrates that T-I DoC is an integrated response to both erosional and accretional processes, rather than simply indicating the biggest erosional event during a period. Equation 1 is known to fail under accretional conditions, producing estimates that are generally smaller than the observed DoC (Nicholls *et al.*, in review). Therefore, if erosional processes dominate a period, Equation 1 may have more predictive capability than if accretion dominates the period.

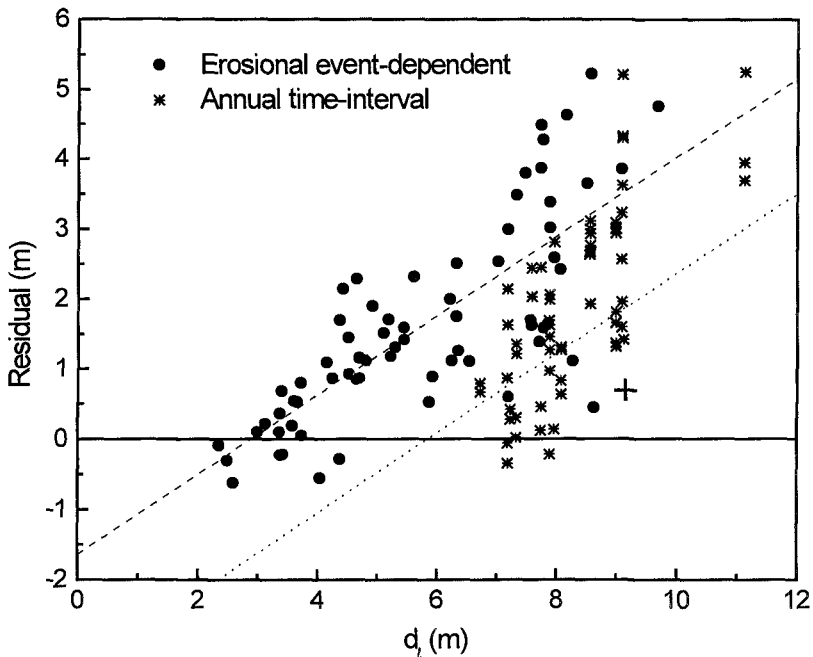


Figure 5. Residuals (d_t - observed DoC) versus d_t for erosional event-dependent closures and annual time-interval closure using a 6-cm change criterion. The dashed line is the best-fit to the erosional data, while the dotted line is the same line offset to pass through the approximate median of the annual time-interval data.

As the time interval between surveys increases, fewer cases close within the surveyed profile range at Duck (≤ 8 -m depth below MLW) — 65% of annual interval cases, 63% of 18-month interval cases, 61% of 2-year interval cases, 51% of 30-month interval cases, 44% of 4-year interval cases and only 3% of 8-year interval cases close. The 8-year intervals always include significant profile movement and hence 6-cm closure is lost, except in one case. In all the non-closing cases, net profile change (>6 cm) is occurring seaward of 8-m depth.

Equation 1 is found to provide a useful conservative bound to those annual DoC which are defined within the survey range, see Figure 6. Using an empirical best-fit approach to the data, over a typical year, 76% of the change predicted by Equation 1 occurs ($>95\%$ confidence):

$$d_{T,1} = 0.76 d_{t,1} \quad (3)$$

where $d_{T,1}$ = observed annual T-I DoC. Note that Equation 3 has a numerical coefficient 10% larger than Equation 2.

Most of the annual cases which do not close are consistent with Equation 1 as $d_{t,1} > 8$ m. However, there are five cases (8%) which are predicted to close but did not within the survey extent. This characteristic is also observed in the 18 month, 2 year and 30 month interval data, comprising 9%, 8% and 17% of cases, respectively. All the time periods where this behavior is observed were characterized by slow near-continuous onshore feed of sand from the upper shoreface (>5 -m depth) (cf. Lee *et al.*, in review). Under these conditions, Equation 1 might be expected to be inapplicable, as already discussed. The large number of missing observations and the scatter in results makes objective assessment of the predictive value of Equation 1 more difficult to assess than for the erosional events.

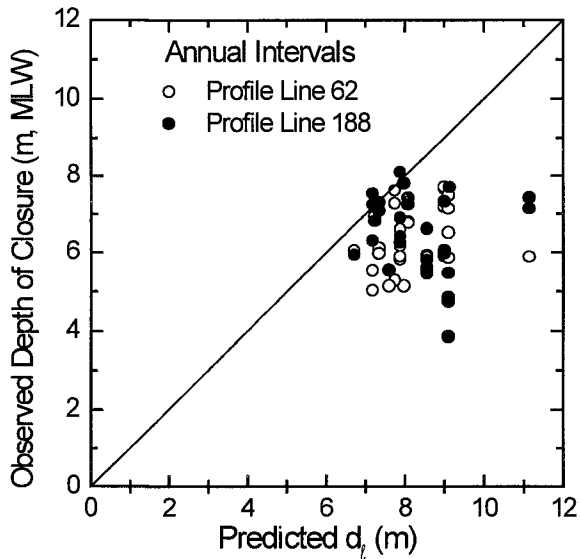


Figure 6. Observed versus predicted annual depth of closure for individual profiles. The dashed line is the best-fit (Equation 3). Of the 32 cases which are not observed to close, $d_{t,1} > 8$ m for 27 cases.

Sensitivity Analysis

The data were examined considering median values to circumvent the missing values, and annual up to 30 month time intervals. (Longer intervals have too few observations to define medians). The cases with d_{θ} of 11.1 m due to the most energetic wave event of record occurring on 31 October 1991, the "Halloween storm," are disarded as outliers not likely to be observed. The remaining data is divided as near equally as possible into a low and high bin, while retaining the capacity to define observational medians: *i.e.*, a meaningful central tendency for measurements. The median for each bin was then determined, treating all missing values as higher than available observations. The sensitivity of observations to predictions is simply the ratio of the difference in observation medians between the two bins, to the difference between the prediction medians. The sensitivity results are presented in Figure 7. Annual observations appear more strongly related to predictions than the erosional event observations. Above the annual time scale, there is a significant decline in sensitivity to negligible levels at 24- and 30-month time intervals.

This indicates that at time intervals longer than one year, the observed closures are increasing much less rapidly than Equation 1 would suggest — *i.e.* the observations and predictions are decoupling. (Of course, Equation 1 still provides estimates of closure that tend to be larger than the observations, so that its predictions have value as a conservative bound.) From this evidence, Equation 1 is interpreted at Duck as being meaningful up to annual time scales, as originally proposed by Hallermeier (1978; 1981).

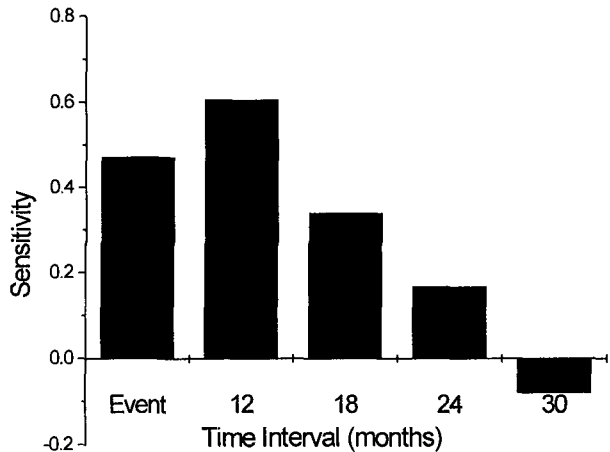


Figure 7. Sensitivity of observation to $d_{\theta,t}$ as a function of time interval: from individual events to a 30-month interval.

DISCUSSION

The time-interval behavior of closures in this extensive database appears to validate a common empirical definition of a useful DoC: such analyses usually group all available surveys of a profile, regardless of the time interval between data (*e.g.*, Inman *et al.*, 1993). The results documented here indicate that a closure estimate from such analysis is meaningful for a site, provided that the time interval of available data includes at least one seasonal profile translation. However, Figure 2 shows that profile variation in any one year

may be a poor description of the statistical properties of a profile and more than one annual cycle of profile data is preferred. Further, a practical DoC may not be evident if the time span included exceptionally energetic wave sequences yielding a permanent profile translation (Inman *et al.*, 1993).

Some previous analyses may appear to be a little misleading about the DoC implications of the Duck profile database. Our analyses focusing on isolated energetic episodes have revealed many cases of resolvable and volumetrically significant changes at water depths well beyond the 4-m or 6-m deduced as limits by Larson and Kraus (1994). In addition, our analysis, focusing on intervals of one year clearly established that, within survey limits, an annual DoC is the prevalent situation at Duck, despite an absence of definite DoC over some longer time spans (Inman *et al.*, 1993). For each type of observation, the seaward limits of profile change are related to extreme wave conditions by Equation 1. Previously repeated conclusions about DoC at Duck are empirically supported by particular analyses addressing certain longer time intervals, but the present findings reflect more detailed and intensive examination of the same database. Additions to and analysis of that database continue at present, and a more coherent picture is expected to emerge progressively.

As Equation 1 provides a robust conservative bound for significant cross-shore sediment transport at Duck for individual erosional events up to the annual time scale, simply knowing the extreme wave conditions will allow estimates of closure to be made at similar microtidal, wave-dominated sites. Interestingly, both Equation 3 and the sensitivity analysis indicate a stronger relationship between annual DoC and Equation 1 than erosional DoC and Equation 1. Given that Equation 1 is an event-based formulation (*i.e.*, based on the biggest event in a period), this is a surprising result. Above an annual time scale, the available evidence suggests that DoC increases less rapidly than Equation 1 would predict. This is an important result which disagrees with earlier work (*e.g.*, Stive *et al.*, 1992) and has important implications for application. While we are unsure about applying Equation 1 to a t -year time interval, we are more confident about applying Equation 1 as a conservative bound with known wave conditions during an t -year erosional event. An estimate of how far sand might be carried offshore during extreme events can assist in analysis of a range of problems. In intervening periods between erosional events when Equation 1 may not be applicable, sand is generally being slowly transported onshore at open-coast sites such as Duck (Lee *et al.*, in review) with beneficial effects for the beach-nearshore sediment budget. In more sheltered sites with more limited swell, this may not be the case.

A key question is the specification of the wave information to use in Equation 1. The predictions presented here are based on 12-hour exceeded wave height and period measurements at a waverider buoy, 6-km offshore at a depth of about 18-m. Therefore, the measurements are shallow water, but well seaward of the breaker zone. In many cases such data are unavailable, although other wave measurements or hindcast wave information may be available. Improved guidance on optimum wave inputs to Equation 1 need to be developed.

Another problem is the variation in $d_{q,1}$ at any site due to variations in annual extreme waves. Twelve years of wave data at Duck show that $d_{q,1}$ can vary by more than 2 meters depending on the annual period selected: the 25th percentile is 7.7 m, the median

is 8.7 m and the 75th percentile is 9.2 m below MLW. Given the apparent tendency for overprediction of closure depth, most attention might be focused on the two lower values. Taking beach nourishment as an example, selecting a smaller DoC will result in a lower initial project cost, but it may be prudent to plan for more frequent renourishment. This type of analysis will help to identify the trade-offs when selecting from the range of legitimate DoC estimates.

Despite the apparent decoupling of Equation 1 and observations with increasing time scale, it is apparent that application of DoC requires a more explicit consideration of time scale. At Duck, longer time scales are associated with greater profile variability at depth (*cf.* Figure 1(b)), implying larger DoC for a constant depth change criterion. The surveys define DoC for 95% of erosion episodes and for 65% of annual intervals, but over the 12-year window they have failed to define a seaward limit of the profile envelope. An important lesson is that when designing long-term, high accuracy, beach monitoring programs to define the profile envelope, the distribution of $d_{\ell,t}$ helps to define a realistic *minimum* target depth for routine surveys. At Duck, the surveys considered in this paper typically only reach the 25th percentile of $d_{\ell,t}$, with the maximum depths attained being less than the median $d_{\ell,t}$. With our present knowledge of Duck, occasional surveys to the 75 percentile of $d_{\ell,t}$ would appear a reasonable target depth for Duck and similar sites.

CONCLUSIONS

A meaningful depth of closure is observed at Duck under erosional events and a range of time intervals from 1 year to 30 months. The depth limit $d_{\ell,t}$ is found to be robust and useful for erosional events and annual time intervals. Therefore, with limited environmental information (the event or annual 12-hour exceeded wave height and period), a reliable closure estimate apparently can be made. However, Equation 1 is a conservative bound to the observed closures and results should be applied with this in mind. At longer time scales, the observations and Equation 1 decouple as observed closure appears to increase more slowly than the predictions of $d_{\ell,t}$ would suggest.

Knowing the nature of Equation 1 and how closure evolves with increasing time scale, coastal engineers can make better judgements when interpreting sparse survey data. They can also optimize application of a closure value by considering the trade-offs in selecting from a range of legitimate estimates for a site. Finally, the Duck data indicates our limited understanding of cross-shore sand exchange between the beach and the upper shoreface. To capture more of the change for extreme cases, routine measurements are required to greater depths. Collection and investigation of the Duck data set continues.

ACKNOWLEDGMENTS

This study is a collaboration between the PACE-project in the framework of the EU-sponsored Marine Science and Technology (MAST-III) under contract no. MAS3-CT95-002 and the Geologic Analysis of Shelf/Beach Sediment Interchange Work Unit under the Coastal Research and Development Program of the US Army Corps of Engineers. Permission was granted by the Chief of Engineers to publish this information.

REFERENCES

- Birkemeier, W.A., Miller, H.C., Wilhelm, S.D., DeWall, A. E. and Gorbics, C. S., 1985. A user's guide to the coastal engineering research center's (CERC's) Field Research Facility. *Instruction Report CERC-85-1*, U.S. Army Corps of Engineers, Waterways Experiment Station, Vicksburg, MI, 121 pp.
- Hallermeier, R. J., 1978. Uses for a calculated limit depth to beach erosion. *Proceedings 16th Coastal Engineering Conference*, ASCE, 1493-1512
- Hallermeier, R. J., 1981. A profile zonation for seasonal sand beaches from wave climate, *Coastal Engineering*, 4, 253-277.
- Hands, E. B., 1983. The Great Lakes as a test model for profile responses to sea level changes. In: Komar, P.D.(ed.), *CRC Handbook of coastal processes and erosion*, CRC Press, Boca Raton, pp.167-189
- Inman, D.L., Hany, M., Elwany, S. and Jenkins, S.A., 1993. Shorerise and bar-berm profiles on ocean beaches. *Journal of Geophysical Research*, 98 (C10), 18181-18199.
- Kraus, N.C. and Harikai, S., 1983. Numerical model of the shoreline change at Oarai beach. *Coastal Engineering*, 7, 1-28
- Larson, M. and Kraus, N.C., 1994. Temporal and spatial scales of beach profile change, Duck, North Carolina, *Marine Geology*, 117, 75-94.
- Lee, G. and Birkemeier, W.A., 1993. Beach and nearshore survey data: 1985-1991, CERC Field Research Facility. *Technical Report-93-3*, US Army Corps of Engineers, Waterways Experiment Station, Vicksburg, MS., 26 pp.
- Lee, G., Nicholls, R. J., Birkemeier, W.A. and Leatherman, S.P., 1995. A conceptual fairweather-storm model of beach-nearshore profile evolution at Duck, North Carolina, U.S.A. *Journal of Coastal Research*, 11, 1157-1166.
- Lee, G., Nicholls, R. J. and Birkemeier, W.A., in review. Storm-driven variability of the beach-nearshore profile at Duck, North Carolina., 1981-1991. *Marine Geology*.
- Lippmann, T. C. and Holman, R.A., 1990. The spatial and temporal variability of sand bar morphology. *Journal of Geophysical Research*, 95(C7), 11575-11590.
- Nicholls, R. J., Birkemeier, W. A. and Lee, G. In review. Evaluation of depth of closure using data from Duck, NC, USA. *Marine Geology*.
- Sachs, L. 1984. *Applied Statistics*, 2nd Edition, Springer-Verlag, New York.
- Stive, M. J. F., Nicholls, R. J. and DeVriend, H. J. 1991. Sea-Level Rise and Shore Nourishment: A Discussion. *Coastal Engineering*, 16, 147-163.
- Stive, M. J. F., DeVriend, H. J., Nicholls, R. J. and Capobianco, M., 1992. Shore nourishment and the active zone; a time scale dependent view. *Proceedings 23rd Coastal Engineering Conference*, ASCE, New York, pp. 2464-2473.
- Stive, M. J. F. and DeVriend, H. J. 1995. Modelling shoreface profile evolution. *Marine Geology*, 126,235-248.
- USACE, 1984. *Shore Protection Manual*, 4th Ed. U.S. Army Corps of Engineers, Waterways Experiment Station, Vicksburg, MI (2 vol.).

CHAPTER 300

Numerical modeling of sediment transport for various mode

Masanobu ONO¹⁾, Ichiro DEGUCHI²⁾ and Toru SAWARAGI³⁾

Abstract

There are various mode of sediment transport on sandy beach. They are bed load, suspended load and sheet flow. Until now, various kinds of numerical model for analyzing these sediment transport have been developed based on the assumption of each mode of sediment transport. Consequently, it is difficult to apply them to different mode of sedimentation.

In this study, we propose a relatively simple numerical model for simulating sediment motion of various mode based on the semi-multi-phase flow model. The applicability of the model to sheet flow transport and suspended load transport is examined by using existing experimental data.

The results show that for the suspended sediment, it is necessary to take into the effect of the vortex to lift up sediment to high position. To construct numerical model for simulating sediment transport phenomena of the various mode, we have to introduce generation, development and disappearance process of bed ripple in this model.

Introduction

Mode of sediment transport continually changes from bed load, suspended load to sheet flow according to the increase in magnitude of agitation force. Until now, various kinds of numerical model for analyzing these sediment transport have been developed. An advection-diffusion equation has been widely used to analyze suspended sediment concentration. Suspended load is expressed as the product of concentration and migration speed of suspended sediment that is assumed to be equivalent to water particle velocity when the concentration is not so high. Concentration of bed load and sheet flow has also been analyzed by solving the advection-diffusion equation and the migration speed is estimated by solving a momentum equation of multi-phase flow. When we analyze sediment motion by these model, we have to know the mode of sediment transport before we determine what kind of model we should use.

1) Research Assoc., and 2) Assoc. Prof., Dept. of Civil Engineering, Osaka University, Yamada-oka, Suita, Osaka, 565, Japan

3) Prof., Dept. of Civil Engineering, Osaka sangyo University, Japan

In this study, we propose a relatively simple numerical model for simulating sediment motion of various mode based on the semi-multi-phase flow model. The applicability of the model to sheet flow transport and suspended load transport is examined by using existing experimental data. The effect of vortex shedding from the rippled bed on the Schmidt number is also investigated numerically.

Numerical simulation method for analyzing sediment transport

(1)Basic equations

Numerical model consists of a horizontal momentum equation of one-phase flow and equations of mass conservation of two-phase flow. There are generally six equations, that is, conservation of mass and conservation of horizontal and vertical momentum flux for sediment phase and fluid phase.

The continuity equations for sediment and water phase are shown by Eq.(1) and Eq.(2).

$$\frac{\partial \rho_s c}{\partial t} + \frac{\partial \rho_s c u_s}{\partial x} + \frac{\partial \rho_s c w_s}{\partial z} = 0 \quad (1)$$

$$\frac{\partial \rho_f (1-c)}{\partial t} + \frac{\partial \rho_f (1-c) u_f}{\partial x} + \frac{\partial \rho_f (1-c) w_f}{\partial z} = 0 \quad (2)$$

where c is volumetric concentration of sediment, ρ_s and ρ_f are the density of sediment and water, u_s and u_f are horizontal velocity of sand and water particle, w_s and w_f are vertical velocity of sand and water particle.

The momentum equations for sediment and water phase are shown by Eqs.(3),(4) and Eqs.(5),(6).

$$\frac{\partial \rho_s c u_s}{\partial t} + \frac{\partial \rho_s c u_s^2}{\partial x} + \frac{\partial \rho_s c u_s w_s}{\partial z} = -c \frac{\partial p}{\partial x} + \frac{\partial r_{xx}}{\partial x} + \frac{\partial r_{zx}}{\partial z} + f_x \quad (3)$$

$$\frac{\partial \rho_s c w_s}{\partial t} + \frac{\partial \rho_s c u_s w_s}{\partial x} + \frac{\partial \rho_s c w_s^2}{\partial z} = -c \frac{\partial p}{\partial z} + \frac{\partial r_{xz}}{\partial x} + \frac{\partial r_{zz}}{\partial z} - \rho_s c g + f_z \quad (4)$$

$$\frac{\partial \rho_f (1-c) u_f}{\partial t} + \frac{\partial \rho_f (1-c) u_f^2}{\partial x} + \frac{\partial \rho_f (1-c) u_f w_f}{\partial z} = -(1-c) \frac{\partial p}{\partial x} - f_x \quad (5)$$

$$\frac{\partial \rho_f (1-c) w_f}{\partial t} + \frac{\partial \rho_f (1-c) u_f w_f}{\partial x} + \frac{\partial \rho_f (1-c) w_f^2}{\partial z} = -(1-c) \frac{\partial p}{\partial z} - \rho_f (1-c) g - f_z \quad (6)$$

where p is pressure, $f_i(i=x,z)$ is the i -th component of interaction force per unit volume between sediment and water, r_{ij} is inter granular stress tensor.

There are six unknowns, p , u_f , w_f , u_s , w_s , and c . However, it is very difficult to get stable numerical results of these equations due to very strong non-linear interaction of each equations, Therefore in our model we use the horizontal momentum equations and mass conservation equations and apply empirical relation for determining vertical velocity of sediment phase.

(2)Numerical simulation method

To construct numerical model we made some assumptions and simplification. One is that the horizontal velocity of moving sand is the same as the horizontal fluid velocity. This implies that we apply single layer model for the sediment larded water and Eqs.(3) and (5) become Eq.(7) as shown below:

$$\begin{aligned} \frac{\partial}{\partial t} \left\{ \rho u - (\rho_s - \rho_f) k_x \frac{\partial c}{\partial x} \right\} + \frac{\partial}{\partial x} \left\{ \rho u^2 - 2u(\rho_s - \rho_f) k_x \frac{\partial c}{\partial x} - (\mu_e + \rho \Omega_x) \frac{\partial u}{\partial x} \right\} \\ + \frac{\partial}{\partial z} \left[\left\{ (1-c) \rho w_f + c \rho_s w_s \right\} u - (\mu_e + \rho \Omega_z) \frac{\partial u}{\partial z} \right. \\ \left. - u(\rho_s - \rho_f) k_z \frac{\partial c}{\partial z} - (\rho_s w_s - \rho_f w_f) k_x \frac{\partial c}{\partial x} \right] = - \frac{\partial p}{\partial x} \quad (7) \end{aligned}$$

where u ($=u_s=u_f$) is the horizontal velocity of sand and fluid particle and μ_e is apparent viscosity of sediment laden water (Savage-McKeown, 1983).

Sediment concentration C is calculated from the continuity equation for the sediment phase Eq. (1) by transforming it into an advection-diffusion equation with diffusion coefficient k_i as follows:

$$\frac{\partial c}{\partial t} + \frac{\partial cu}{\partial x} + \frac{\partial cw_s}{\partial z} = \frac{\partial}{\partial x} \left(k_x \frac{\partial c}{\partial x} \right) + \frac{\partial}{\partial z} \left(k_z \frac{\partial c}{\partial z} \right) \quad (8)$$

Eq.(9) is derived from Eq.(2) by performing the same transform.

$$- \frac{\partial c}{\partial t} + \frac{\partial(1-c)u}{\partial x} + \frac{\partial(1-c)w_f}{\partial z} = - \frac{\partial}{\partial x} \left(k_x \frac{\partial c}{\partial x} \right) - \frac{\partial}{\partial z} \left(k_z \frac{\partial c}{\partial z} \right) \quad (9)$$

The diffusion coefficient is assumed to be proportional to the kinematic eddy viscosity Ω_i by using Schmidt number Sm as follow.

$$k_x = \Omega_x / Sm \quad k_z = \Omega_z / Sm \quad (10)$$

$$\mu_e = 1.2\lambda^2 \mu_0 \quad \lambda = 1 / \left\{ (c_{\max} / c)^{1/3} - 1 \right\} \quad (11)$$

where μ_0 is water viscosity, λ is the Linear concentration, $c_{\max}(=0.65)$ is the maximum possible static concentration of uniform spheres. We used the expression for kinematic eddy viscosity proposed by Nadaoka et al.(1990).

$$\Omega_x = l_{(z)}^2 \left| \frac{\partial u}{\partial x} \right| \quad \Omega_z = l_{(z)}^2 \left| \frac{\partial u}{\partial z} \right| \quad l_{(z)} = \kappa \int_{-\infty}^z (c_{\max} - c) / c_{\max} dz \quad (12)$$

where $l(z)$ is mixing length and κ is Karman constant.

To evaluate the vertical velocity of sediment phase, an empirical expression to relate settling velocity of sand particle and concentration is used.

$$w_s = -w_{s0} \left(1 - c / c_{\max} \right)^{2.3} \quad (13)$$

where w_{s0} is the settling velocity of sand particle in clear water.

Vertical velocity of water particle is calculated by the continuity equation for two phase flow. Eq.(14) is derived from Eqs.(8) and (9).

$$\frac{\partial u}{\partial x} + \frac{\partial}{\partial z} \left\{ cw_s + (1-c)w_f \right\} = 0 \quad (14)$$

Equations (7),(8),(13) and (14) were simultaneously solved by transforming them into finite difference equations. In this model, horizontal phenomena is assumed to be homogeneous in the direction of wave propagation.

(3)Initial and boundary conditions

Z axis is taken upward from the initial sand surface as shown in Fig.1. The up-ward boundary conditions are given by Eqs.(15) and (16) at the boundary layer whose thickness is given by Eq.(17).

$$c w_s + k_z \frac{\partial c}{\partial z} = 0 \quad (15) \qquad u = U_0 \sin(\sigma t) \quad (16)$$

$$\max(D_z) = 4\kappa \max(u^*)/\sigma \qquad u^* = |v_z| \frac{\partial u}{\partial z} \quad (17)$$

The pressure gradient in Eq.(7) is given by the pressure gradient outside the boundary layer using the expression of Eq.(16).

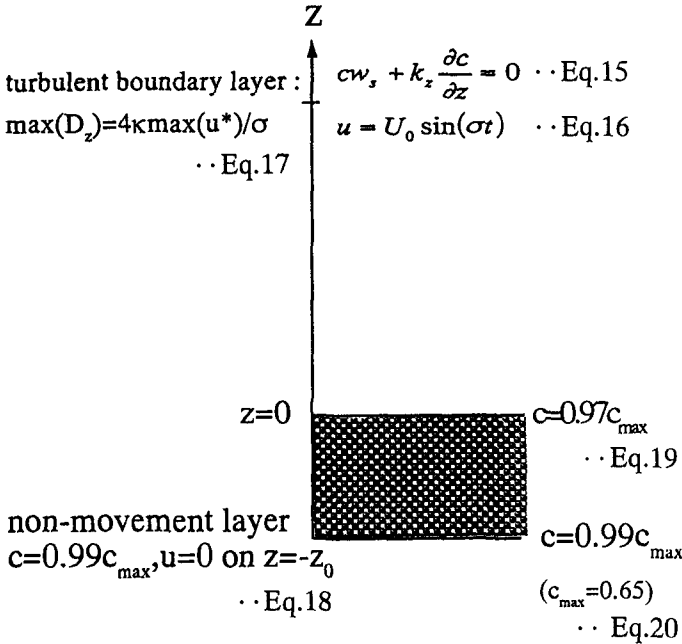


Fig. 1 Coordinate system

Two boundary conditions at the bottom are applied. One is the velocity of sediment laden water is 0 and the other is sediment concentration is $0.99c_{max}$. These are given at assumed initial thickness of sand layer $z=-z_0$. To prevent dispersion of vertical gradient of apparent viscosity near sand surface, we distribute sediment concentration in sand layer from $0.97c_{max}$ to $0.99c_{max}$ between $z=-z_0$ and $z=0$ linearly. Calculations are started from the still water and there is no suspended sediment concentration in the region of z is greater than 0.

The thickness of moving sand layer is determined by using Bagnold's condition as shown by Eq.(21).

$$\mu_e \frac{\partial u}{\partial z} \geq \int_z^{+\infty} (\rho_s - \rho_f) g c \tan \phi dz \quad (21)$$

The friction angle ϕ in Eq. (21) also depends on sediment concentration. When the linear concentration is smaller than 1, there is no resisting force against shear. We assume that the value usually used for ϕ is applicable when the linear concentration is larger than 14. It is said that fluid act as a Newtonian fluid when the linear concentration is smaller than 14. We change the value of ϕ continuously in this region as shown by Eq. (23).

$$\mu_e \frac{\partial u}{\partial z} \geq \int_z^{+\infty} (\rho_s - \rho_f) g c \tan(\alpha\phi) dz \quad (22)$$

$$\alpha = \lambda / \lambda_{14} \quad \lambda \leq 14 (c \leq 0.53)$$

$$\alpha = 1 \quad 14 \leq \lambda (0.53 \leq c) \quad (23)$$

Applicability of the model under sheet flow and suspended sediment conditions

We carried out a series of calculation under various conditions. Here, the calculated results are compared with experimental results under sheet flow condition reported by Horikawa et al.(1982) and experimental results under pure suspension condition given by Nakato et. al.(1977) to examine the applicability of the numerical method. There was not any bottom configuration in the former experiments and there were ripples on the bottom in the latter experiments. Both of the experiments were carried out in oscillatory flow tunnels.

Figures 2 and 3 show the comparisons of calculated and measured horizontal velocity, concentration profile. Fig. 4 is the thickness of moving sand layer under the same experiment (Horikawa et. al.(1982)). In these calculation we assumed that the value of Schmidt number was 10. Measured velocity, concentration and thickness of moving layer are roughly reproduced by the numerical simulation.

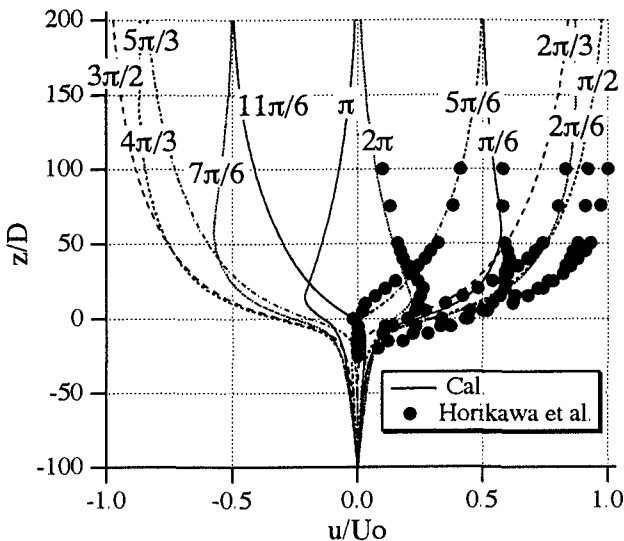


Fig. 2 Comparison between Horikawa's experimental results and calculated results under sheet flow condition (Horizontal velocity profile, Schmidt number :Sm=10)

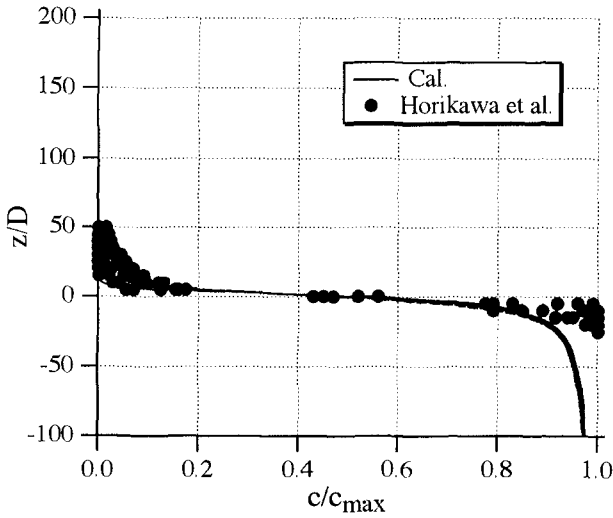


Fig. 3 Comparison between Horikawa's experimental results and calculated results under sheet flow condition (Sediment concentration profile, $Sm=10$)

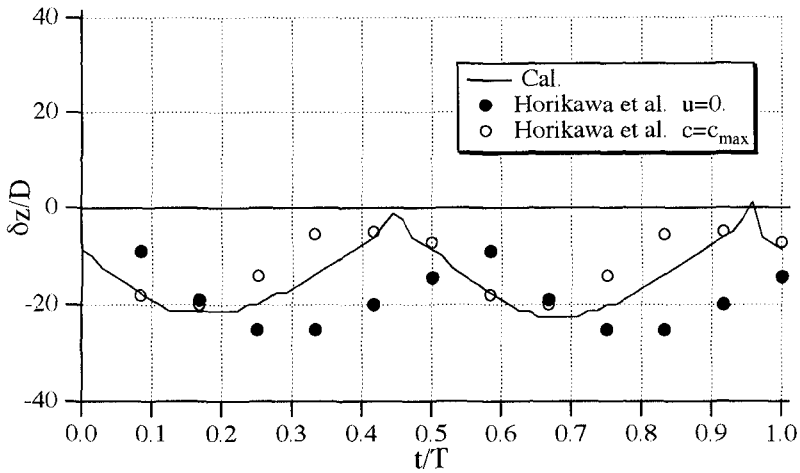


Fig. 4 Comparison between Horikawa's experimental results and calculated results under sheet flow condition (Thickness of moving layer, $Sm=10$)

We calculate the vertical distribution of purely suspended sediment concentration given by Nakato and others by using the same Schmidt number, that is $Sm=10$. In Figs.5 and 6, some examples of calculated results (shown by solid line) are compared with the measured results. As can be seen from this figure, we could not reproduce the measured distribution by the calculation.

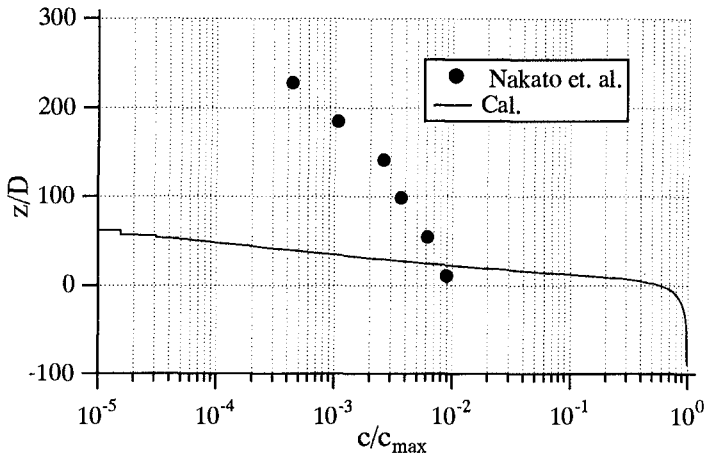


Fig. 5 Comparison between Nakato's experimental results and calculated results under suspended sediment condition (sediment concentration profile ,Case1, $S_m=10$)

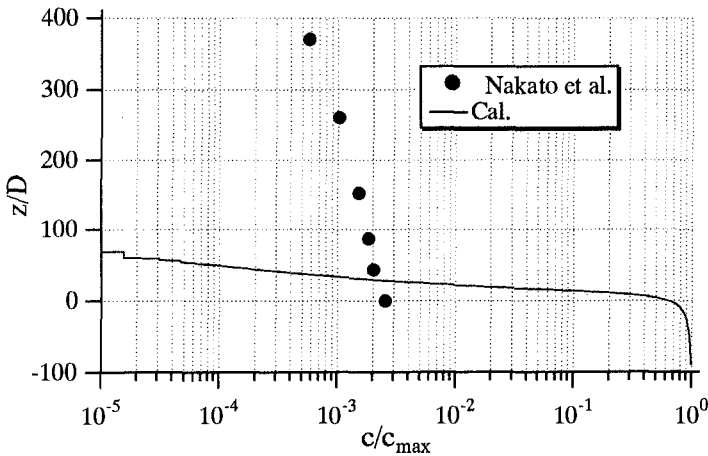


Fig. 6 Comparison between Nakato's experimental results and calculated results under suspended sediment condition (sediment concentration profile ,Case2, $S_m=10$)

The reason for this discrepancy was simply because the kinematic eddy viscosity did not diffuse from the horizontal bottom and diffusion coefficient outside the boundary layer become almost 0. To improve our numerical model, we changed the value of Schmidt number from bed load layer to suspended load layer. In the bed load layer, the same value of Schmidt number as the sheet flow is used and for the suspended load layer, the value is reduced to be 0.5 to increase diffusion coefficient. We defined the bed load layer where the concentration is lower than the reference concentration given by Sawaragi et al.(1985).

The calculated results are shown by broken lines in Figs. 7 and 8. The degree of agreement between measured and calculated concentration is improved. This

implies that the flow field, especially structure of turbulence in the sheet flow region and suspended load layer is perfectly different from each other and systematic vortices generated by the ripples play an important role in the purely suspended load layer.

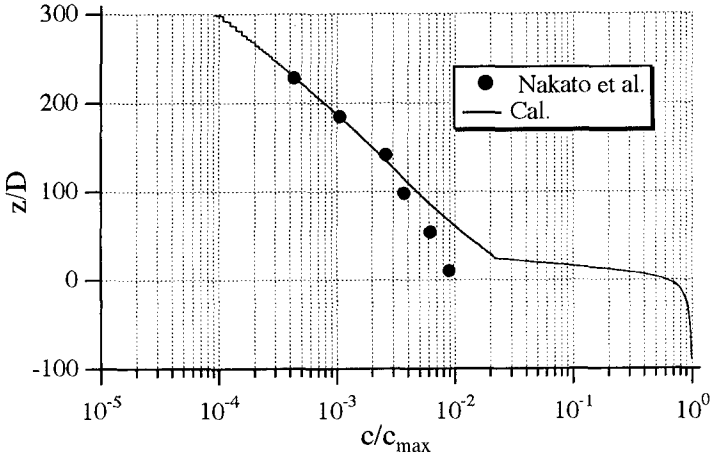


Fig. 7 Comparison between Nakato's experimental results and calculated results under suspended sediment condition (Case1, Suspended load layer : $S_m=0.5$, Bed load layer : $S_m=10$)

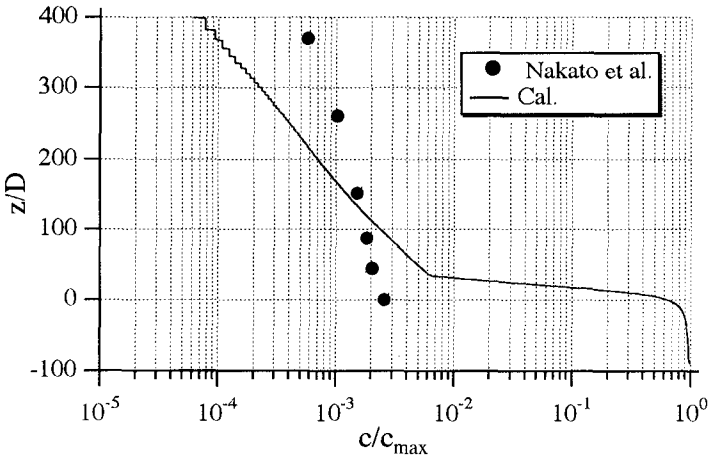


Fig. 8 Comparison between Nakato's experimental results and calculated results under suspended sediment condition (Case2, Suspended load layer : $S_m=0.5$, Bed load layer : $S_m=10$)

Diffusion coefficient of suspended sediment on the ripple bed

To investigate flow field and the effect of the systematic generation of vortex on rippled bottom, we calculated vortex flow field on ripple bed by modified vortex

filament method originally proposed by Longuet-Higgins(1981). We used circular vortex instead of vortex filament to avoid velocity from going infinity. Eqs.(24) and (25) are the complex velocity potential of circular vortex used in the analysis.

$$|W - W_n| > Gr \Rightarrow \frac{\Gamma_n}{2\pi i} \ln(W - W_n) \quad (24)$$

$$|W - W_n| < Gr \Rightarrow \frac{\Gamma_n}{2\pi i} \frac{1}{Gr} (W - W_n) \quad (25)$$

where W is the arbitrary point in the interior of the unit circle on the complex number plane, W_n is the position of circular vortex, Γ_n is the circulation of circular vortex, Gr is the radius of circular vortex that will be determined from the comparison of measured and calculated turbulence intensity of horizontal velocity on the ripples. When the distance between W and W_n is longer than Gr , the complex velocity potential becomes the same equation of vortex filament. But when W_n approaches to W , the complex velocity potential converges to 0.

Decay of circulation of separated vortex is reproduced by decreasing circulation of each circular vortex by assuming the following time variation with the damping coefficient α_G :

$$\Gamma_n = \Gamma_{on} \exp(-\alpha_G t_{0n} / T) \quad (26)$$

where Γ_{on} is the initial circulation of n-th circular vortex, t_{0n} is the elapsed time since n-th circular vortex has been released. The damping coefficient will also be determined from the measured time variation of vortex circulation.

Solid lines in Fig.9 show the calculated time variation of circulation under various values of damping coefficient. In the figure, measured time variation of circulation of separated vortex (Horikawa et al.,1992) is also shown. Fig. 11 shows the comparison of measured turbulent intensity of horizontal velocity on the ripples (Sawamoto et al.,1981) and calculated result by giving various values of radius for the circular vortex. The vertical axis z is the distance upward from the ripple crest.

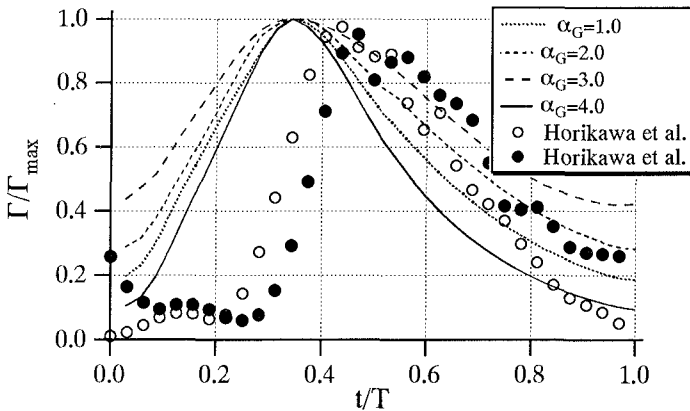


Fig. 9 Time variation of circulation of separated vortex

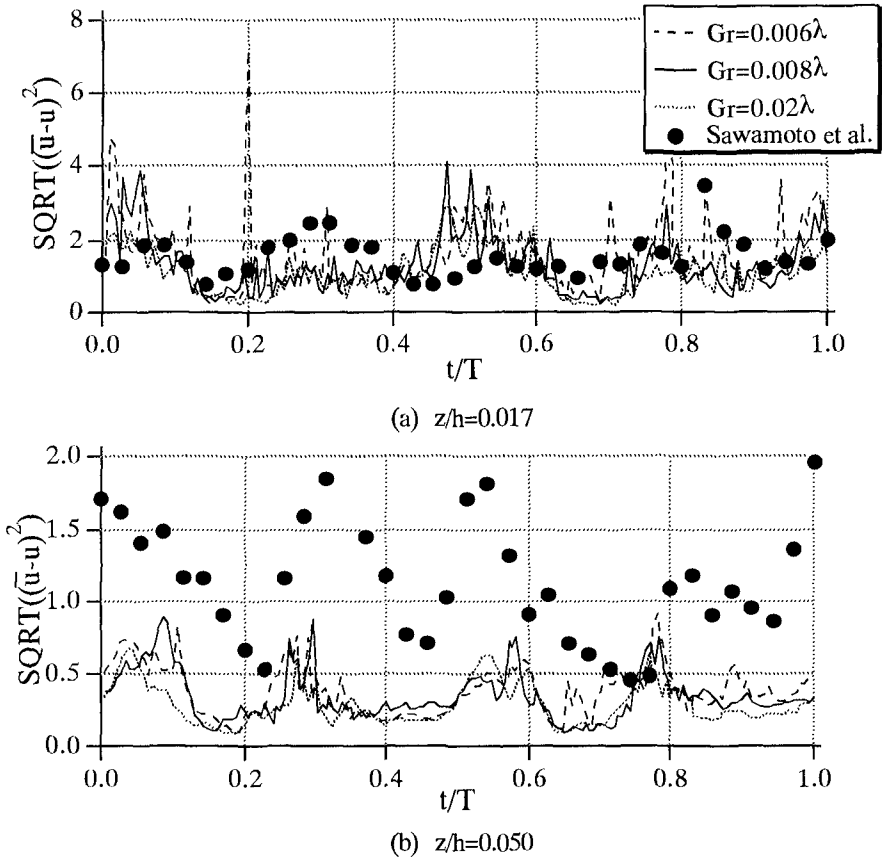


Fig. 10 Vertical distribution of turbulent intensity of horizontal velocity

By comparing calculated and measured result of time decay of circulation and turbulent intensity, circular vortex radius is determined to be 0.8% of ripple length and vortex circulation damping coefficient to be 4.

Calculation of diffusion coefficient of suspended sediment

The motions of suspended sediment are calculated in the flow field obtained on the ripples by an above-mentioned procedure. The governing equations of sediment motion are horizontal and vertical equations of motion as shown in non-dimensional forms by Eqs.(27) and (28) and are solved by using the forth-order Runge-Kutta method.

$$\frac{\partial u_s^*}{\partial t^*} = \frac{3}{4} \frac{1}{\rho_s^* + C_M} C_D K_C |u_f^* - u_s^*| (u_f^* - u_s^*) + \frac{\partial u_f^*}{\partial t^*} \tag{27}$$

$$\frac{\partial w_s^*}{\partial t^*} = \frac{3}{4} \frac{1}{\rho_s^* + C_M} C_D K_C |w_f^* - w_s^*| (w_f^* - w_s^*) + \frac{\partial w_f^*}{\partial t^*} - \frac{\rho_s^* - 1}{\rho_s^* + C_M} g^* \quad (28)$$

$$t^* = t\sigma, (u_s^*, w_s^*) = (u_s, w_s) / w_{s0}, (u_f^*, w_f^*) = (u_f, w_f) / w_{s0},$$

$$\rho_s^* = \rho_s / \rho_f, g^* = g / (w_{s0}\sigma) \quad (29)$$

where $R_e = w_{s0}D/\nu$, $K_C = w_{s0}/D\sigma$, $C_M = 1/2$, g is the gravity acceleration, σ is the angular frequency and C_D is the drag coefficient. The variables with ' in Eqs.(27) and (28) are dimensionless normalized by relation shown by Eq.(29).

To evaluate drag coefficient C_D we adopted the following expression of Molerus and Werther(1968):

$$C_D = \frac{24}{R_e} \left(\frac{1}{|w_f^* - w_s^*|} + \frac{0.152}{\sqrt{|w_f^* - w_s^*|}} + 0.0151R_e \right) \quad (31)$$

Initial positions of sand particles are distributed on the ripples as shown Fig.11. and they are released four cycles after calculation of the flow field where the flow becomes steady and stable. The motion of sand particles is calculated for seven cycles.

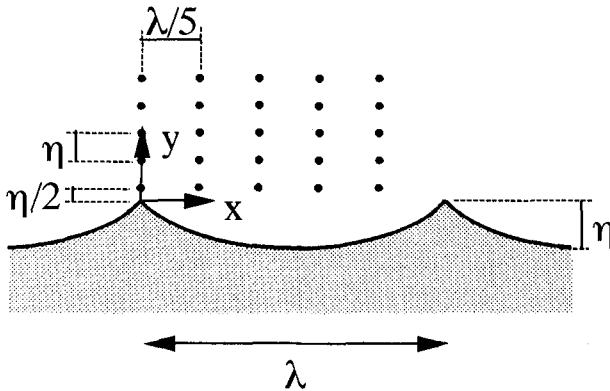


Fig. 11 Coordinate system and initial arrangement of sand particles

Diffusion coefficient of suspended sediment is evaluated by the calculated displacement of sand particles by Eq.(32).

$$k_z(t) = \frac{1}{2} \frac{d}{dt} \left\{ \sum_{i=1}^{25} l_i(t)^2 / 25 \right\} \quad (32)$$

where $l(i)$ is relative position vector of sand particles evaluated by Eq.(33).

$$l_i(t) = s_i(t) - S(t) \quad (33)$$

where $s_i(t)$ is the position of i -th sand particle, $S(t)$ is the average position of all sand particles.

Fig.12 shows the comparison of the calculated and measured diffusion coefficient of suspended sediment. Calculated results show good agreement with the measured diffusion coefficient. This means that systematic vortex shedding from the ripple bed plays very important role in sediment suspension. It is not necessary for the sediment movement under the sheet flow condition that takes place on a flat bed to exist such kind of systematic vortex. For the suspended sediment, it is necessary to take into the effect of the vortex to lift up sediment to high position.

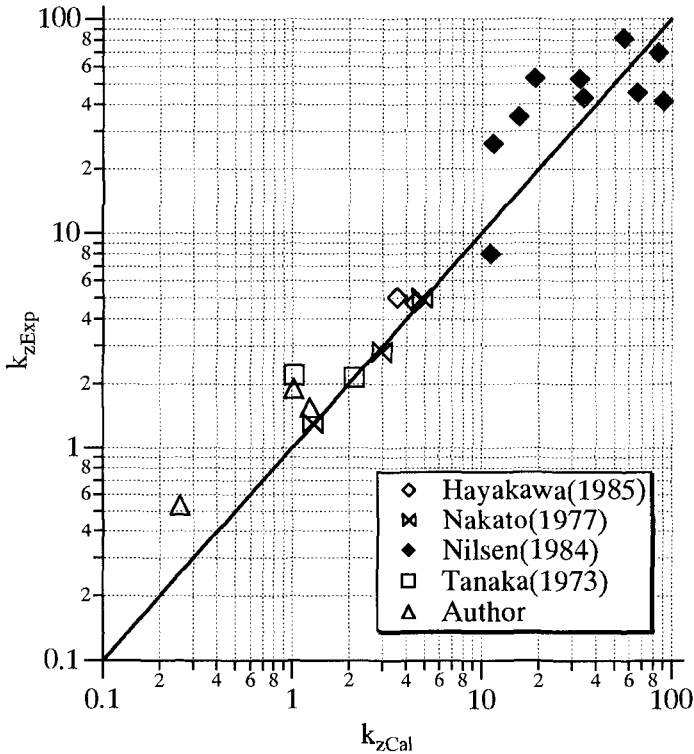


Fig. 12 Comparison of measured and calculated diffusion coefficient

Conclusions

We propose a relatively simple numerical modeling of sediment transport for various mode based on the semi-multi-phase flow model and examine the applicability of the model by using existing experimental results of sheet flow and suspended sediment. Although calculated results roughly reproduce the experimental results under sheet flow condition, we could not predict vertical distribution of the concentration of the suspended sediment.

To investigate this reason, we examine the suspended sand particle motion in vortex flow on the ripples. The diffusion coefficient that is evaluated by analyzing sand particle motions on ripples is coincide with the experimental results. This result implies that systematic vortices generated by the ripples lift up suspended sediment to

high position. Therefore to construct numerical model for various mode of sediment transport, we have to introduce generation, development and disappearance process of bed ripple in the model.

Reference

- Savage S. B. and S. McKeown : Shear stresses developed during rapid shear of concentrated suspensions of large spherical particles between concentric cylinders. *J. Fluid Mech.*, Vol. 127, pp.453-472,1983.
- Nadaoka, K. and H. Yagi: Single-phase fluid modeling of sheet flow toward the development of "Numerical mobile bed", Proc. 22nd Coastal Eng. Conf., ASCE, pp.2346-2359, 1990.
- Horikawa, K., A. Watanabe and S. Katori: Sediment transport under sheet flow condition, Proc. 18th Coastal Eng. Conf., ASCE, pp.1335-1352, 1982.
- Nakato T., F. A. Locher, J. R. Glover and J. F. Kennedy : Wave entrainment of sediment from rippled beds, *A.S.C.E., WW1*, Vol. 103, pp.83-99, 1977.
- Sawaragi T., J. S. Lee, and I. Deguchi: A new model for a prediction of beach deformation around a rivermouth, Proc. Int'l Sympo. on Ocean Space Utilization '85, pp.229-236, 1985.
- Longuet Higgins, M. S.: Oscillating flow over steep sand ripples, *J. Fluid Mech.*, Vol. 107, pp.1-35, 1981.
- Horikawa, K. and S. Mizutani: Oscillatory flow behavior in the vicinity of ripple models, Proc. 23rd Coastal Eng. Conf., ASCE, pp.2122-2135, 1992.
- Sawamoto M., T. Yamashita, and T. Kitamura: Distributions of turbulence intensity and suspended sediment concentration over rippled beds, Proc. 29th Japanese Conf. Coastal Eng., pp.232-236, 1981. (in Japanese)
- Molerus, O. and J. Werther: Berechnung der Sinkbewegung kugeligter teilchen in einem vertikal pulsierenden stromungsfeld, *Chemie-Ingenieur-Technik*, Vol. 40, pp.522-524, 1968.
- Hayakawa, N., G. Tsujimoto and H. Hashimoto, Velocity distribution and suspended sediment concentration over large scale ripple, *Coastal Eng. in Japan*, Vol. 26, pp.91-100,1983.
- Nielsen, P.: Field measurements of time averaged suspended sediment concentration under waves, *Coastal Eng.*, Vol. 8, No. 1, pp.51-72, 1984.
- Tanaka, N., H. Ozawa and A. Ogasawara, Experiments on sand movement by waves and currents, Rept. Port and Harbour Res. Inst., Vol. 12, No.4, pp.2-22,1973,(in Japanese).

CHAPTER 301

Nearbed sediment concentration from tracer studies

Zbigniew PRUSZAK¹, Ryszard WIERZCHNICKI², Andrzej OWCZARCZYK² &
Ryszard B. ZEIDLER¹

ABSTRACT

This paper reports on field investigations, in which the nearbed layer was one of major foci. The study was carried out at the IBW PAN Coastal Research Facility Lubiatowo. The radioactive sand tracer used in the study consisted of iridium glass beads with medium grain diameter D_{50} from 0.2 to 0.25 mm and having physical properties close to their counterparts of natural sand on the Baltic coast of Lubiatowo. Some 150 core samples, each 30 cm long, were taken from the areas where the tracer was set in motion, i.e. bar crests, troughs between bars, and other regions subject to the action of waves and currents. Data analysis shows that sediment movement is characterized by high intermittence reflected in a stratified structure of bedlayer, whereby each sublayer is governed by different forcing factors. For identical external conditions the vertical tracer profiles are different at bar crests and troughs, showing clear diversification of sediment mechanics across the surf zone. Fairly thin sediment sheets, a few millimeters thick, travel at bar crests and troughs, due to high sand speed in one-directional (longshore) movement. The aggregated vertical profile of tracer concentration stems from the superposition of a few quasi-parabolas (close to the injection point) or thin uniform laminas (further away from the tracer source).

1. INTRODUCTION

The surficial layer of seabed is affected by continuous dynamic motion of sea water due to waves and currents. As a result, sediment moves in an unstable and variable moveable layer. Adequate description of the active layer of sediment transport in the sea bed becomes now an urgent but yet controversial problem of coastal dynamics. The thickness of that layer has been assessed in a number of studies to range from a few grain diameters, see Kraus (1984) and Galvin (1987) to several grain diameters (Ingle 1966 and Horikawa et al. 1982) or as much as tens of centimetres (Drapeau et al. 1990). These estimates originate from analyses and investigations having different

¹ Polish Academy of Sciences' Institute of Hydro-Engineering, IBW PAN,
Kościerska 7, 80-953 Gdańsk, Poland

² Institute of Nuclear Chemistry, 16 Dorodna, 03-195 Warsaw, Poland

degree of accuracy, scales and site conditions. Among the conditions bringing about those different estimates of bed layer thickness one can enumerate:

- a) ambiguity of the distinction between bedload and suspended load;
- b) difficulties in determination of real sand grain speed profiles within the entire active layer of sea bed due to variable waves and currents, especially under random field conditions;
- c) problematic delineation of the vertical extension of the movement of single sand grains in sea bed during storms, and controversial singling out individual storm events from aggregated bed thickness due to storm spectrum;
- d) diversified conditions of investigations, analysis and their time and space scales (laboratory versus prototype etc.).

Because of the sophisticated patterns of the transmission of random energy of waves and currents to sea bed and its constituent grains, the problem is complex and highly dependent on scales of the phenomenon. Undistorted relationships between the forces controlling sediment transport stemming from the prototype seem to provide the most reliable and valuable information on the processes investigated here.

This study has aimed at analysing and estimating the bedload thickness in the sea, and its dynamic variability due to random waves and currents.

2. FIELD STUDIES

Our field studies were carried out by the use of radioactive tracers (Ir-192) in the form of iridium glass having geometric and physical properties identical with those of natural sand in the area of investigations (Pruszek & Zeidler 1994).

Some 150 core samples taken from various locations of the cross-shore profile (Fig. 1) were taken all over the area of characteristic coastal features such as sand bars at crests and troughs, under various circumstances created by random waves and currents.

Waves and two components of nearshore currents were measured continuously at two stations D1 and D3 on the cross-shore transect (Fig. 1) every three hours. In addition, wind and sea level oscillations were also recorded every three hours. The results described here stem basically from two measuring series of 23th September to 4th November 93 and 11th May to 30th June 94. Graphical distributions of some hydrodynamic parameters representative of the hydrological background of those situations are shown as examples in Figure 2. The times of core sampling over the area of tracer movement are also indicated on the drawing. Each of the core samples was about 30 cm thick and was subsequently subject to analysis in 2-cm layers with a sensitive apparatus for measurement of low radioactivity.

A special casting box $0.5 \times 0.5 \times 0.25$ m filled up with the radioactive tracer was deployed at the point P1 (Fig. 1). Core samples were taken from that box at intervals of a few hours, in the course of wave and current action. This section of the study was intended as monitoring of the dynamic variability of sea bed in its linkage to changes in the thickness of the active sand layer as a function of time and external factors.

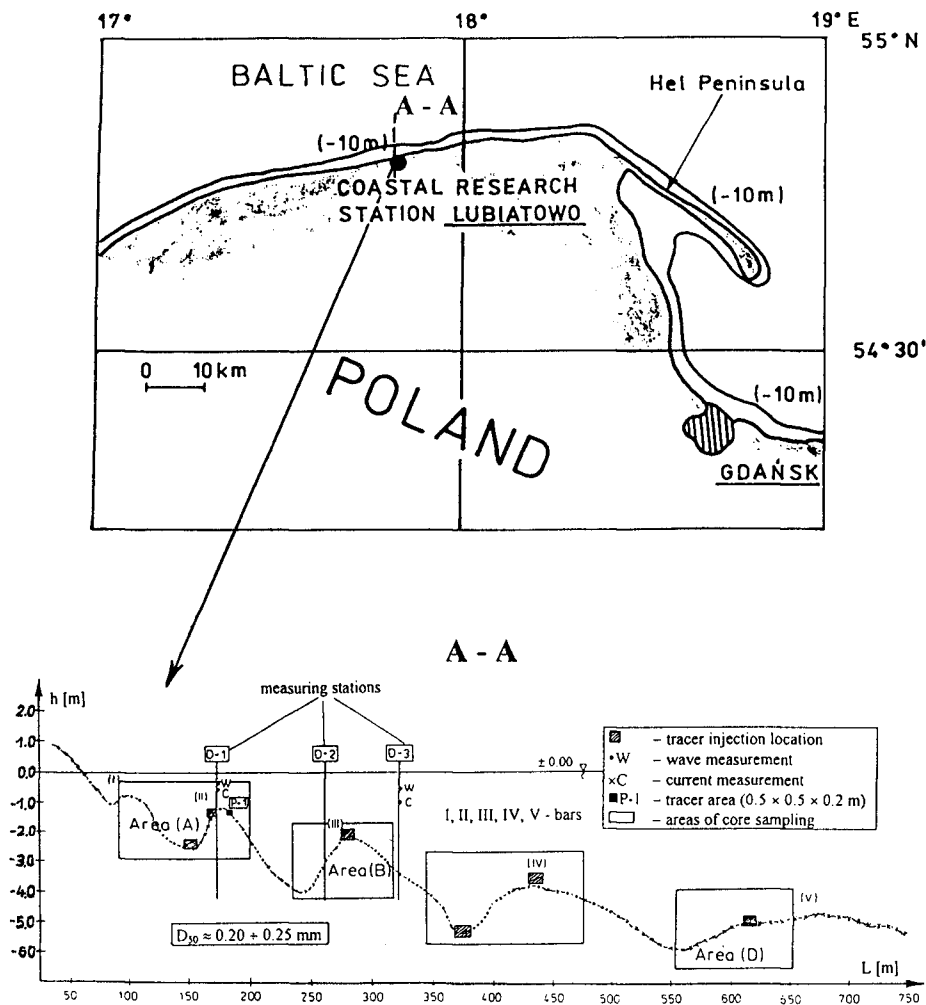


Figure 1. Study area

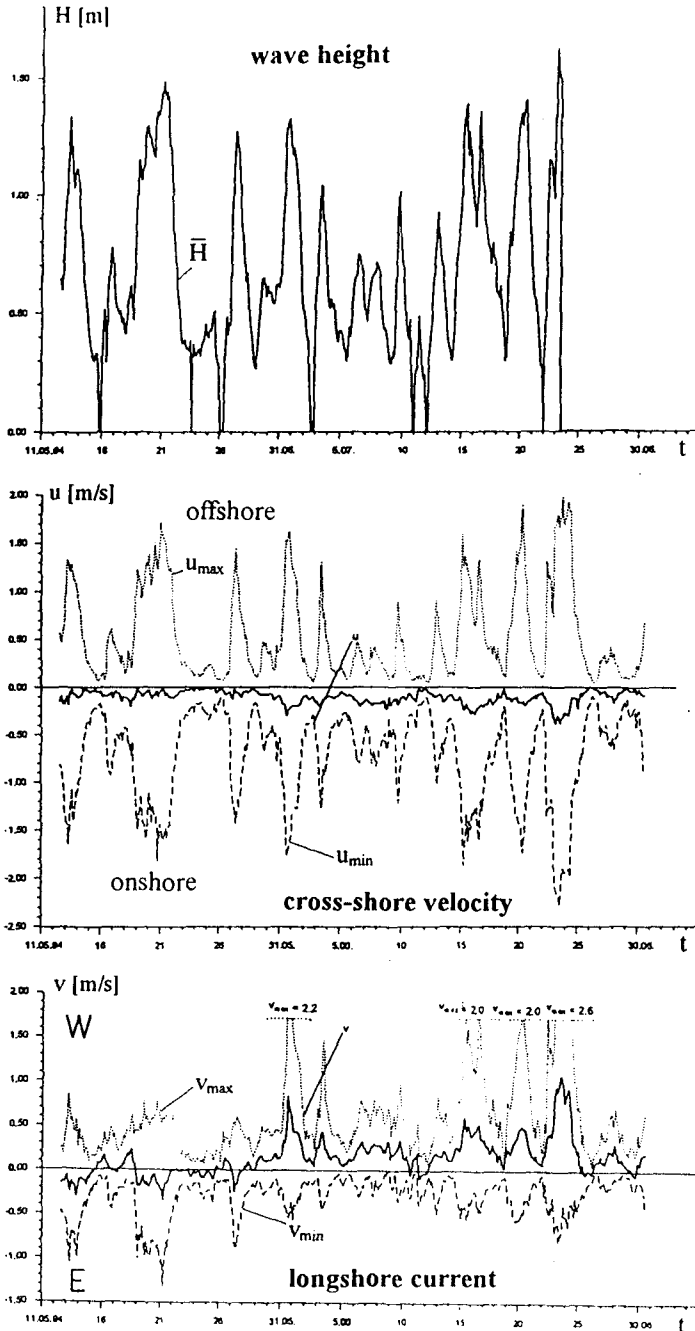


Figure 2. Distribution of wave height and currents at point D-3 during the second series of measurements (1994)

3. ANALYSIS

3.1 TIME AND SPACE CHARACTERISTICS OF THE BEDLOAD LAYER

Geometric characteristics of the variable active layer (primarily its thickness), in the time and space domain, have been analysed by reference to the core samples taken at different locations of the tracer plume. One of the situations tested in area B is illustrated in Figure 3, while the vertical distribution of the tracer concentration, providing insight into the thickness of the active layer with increasing distance from the point of injection, is depicted in Figure 4.

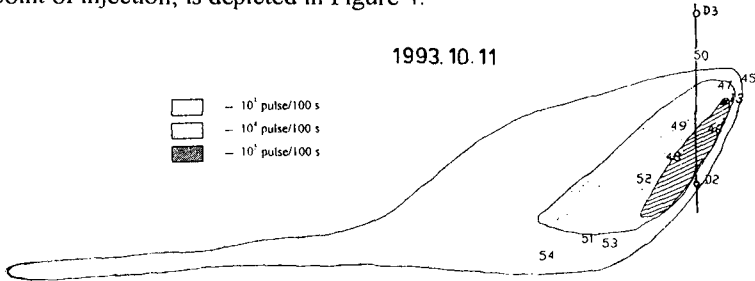


Figure 3. Location of tracer plume in area B during the first series of experiments

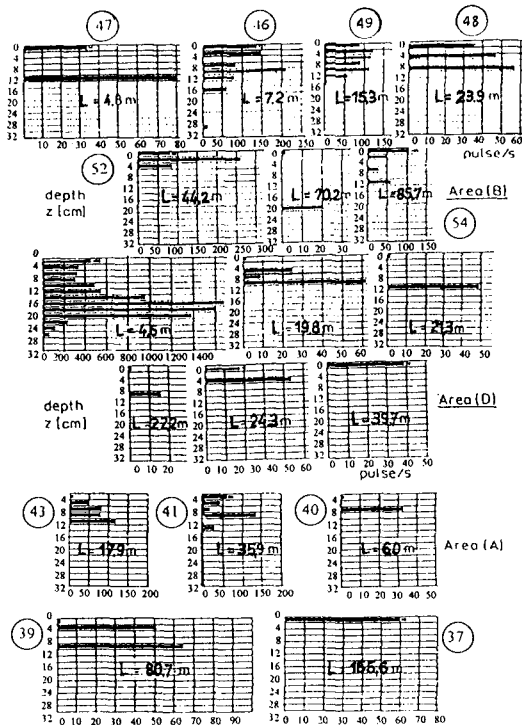


Figure 4. Vertical tracer concentration profiles at various location as a function of spacing L from injection point

Some other vertical profiles, illustrating the wide range of diversity at other locations of the cross-shore transect, are shown in Figure 5. All these results, on the background of the controlling factors have been employed in the determination of characteristic descriptors of the bedload layer.

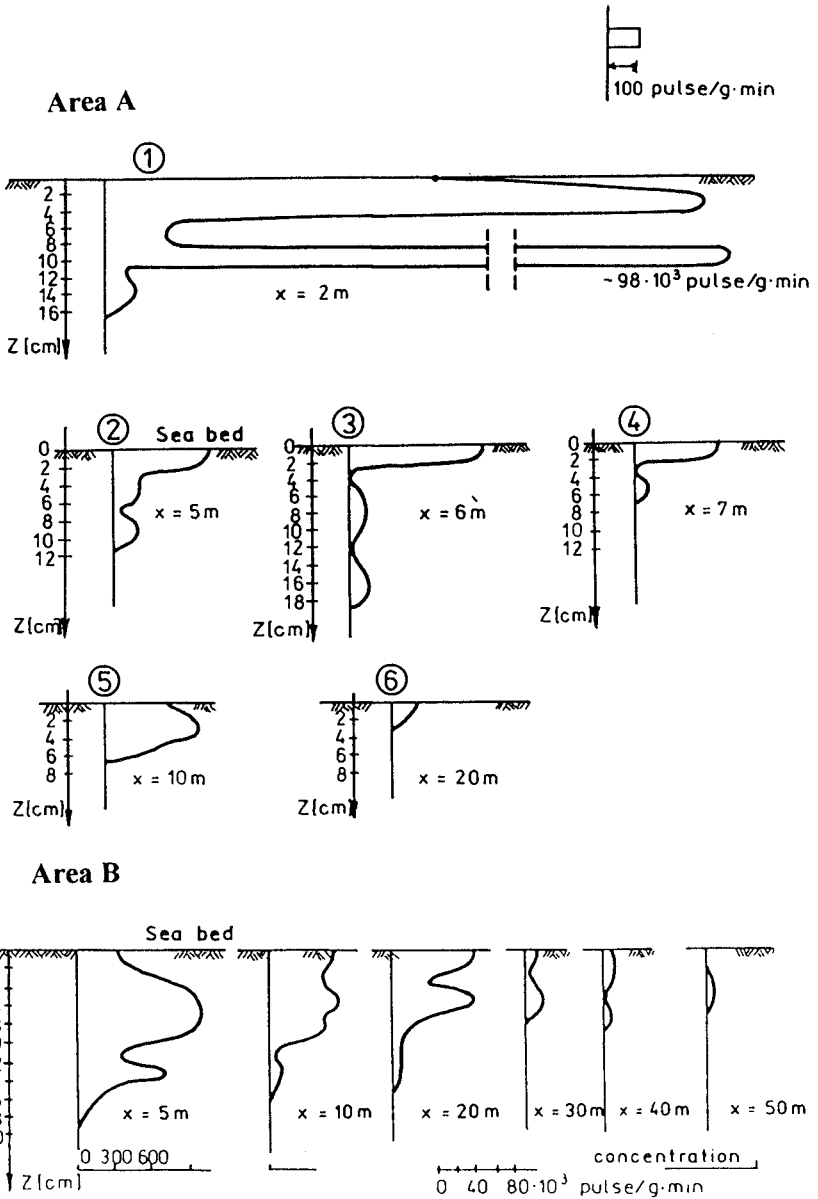


Figure 5. Exemplary types of vertical tracer concentration profiles

As a result of our analysis of the core samples taken in both measuring series it has turned out that there is no prevailing type of vertical concentration within the bedload layer. Among a few possible general types of distribution one can suggest a quasi-parabolic profile resulting from the superposition of two or even three „moving” parabolas and one or a few thin surface layers on top of those parabolas. The schematic representation of that profile is illustrated in Figure 6. The number of components, thus complexity of the profile, depends on the intensity of changes in wave and current climates at a given location. Since every sublayer of the core sample represents a certain instantaneous random hydrodynamic situation cut out of the complex series of events during the measurements, the storm history is obviously reflected in the configuration of the tracer within the core sample. The higher the diversity of the storm history the more complex the core sample.

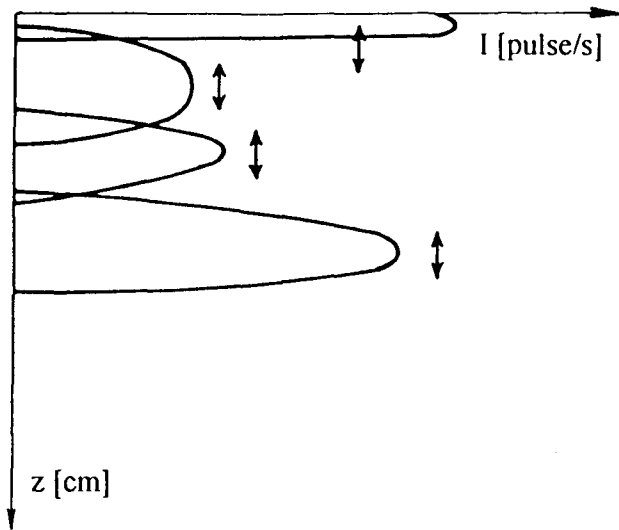


Figure 6. Schematic decomposition of the vertical profile of tracer concentration

Clear-cut variability of the vertical tracer profiles in time and space (distance from the injection point) is visible. In the near field of the injection point, the vertical distribution of the tracer is close to the parabolic type, sometimes with an additional thin surficial sublayer. As one moves away from the injection point, the thickness of the tracer layer decreases and the higher activity „moves” from deeper depth to the sea bed surface.

The shape of the vertical bedload profile depends very much on the shape of sea bed itself and its macroforms such as sand bars. Under the same external conditions, at both crests and troughs the tracer travels in a thin surface layer (Fig. 7). The picture is different at bar slopes and in areas without large bed forms; the vertical profiles of tracer concentrations at those locations are less regular, more variable and close to the types depicted in Figures 4, 5 and 6.

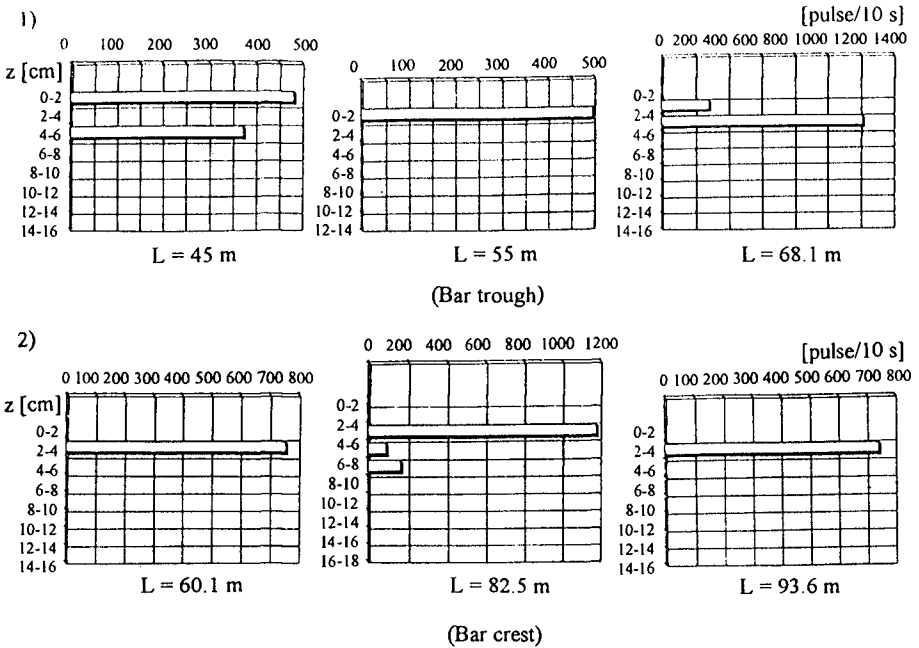


Figure 7. Vertical profile of tracer concentration at bar crests and bar troughs

The core samples tested display a strong nonlinear variability of the bedload thickness as a function of waves and currents. The thickness of each sublayer in the vertical profile, created by various sequences of waves and currents, depends on the intensity and duration of wave motion. Very roughly, it can be described by the general function:

$$a = F(H,t) \approx f(H) \cdot g(b \cdot t/T_{st}) \tag{1}$$

in which T_{st} = time after which stabilisation of the controlling factors takes place and some equilibrium is attained for a given wave situation. This time is estimated as 10 to 100 wave periods T .

The function $f(H)$ stands for the strength of forcing, thus the intensity of sediment transport, while the function $g(b \cdot t/T_{st})$ represents the effect of the time necessary for generation of the bedload layer. After a sufficiently long time $t = T_{st}$ one should get $g(b \cdot t/T_{st}) = 1$ and accordingly $a \approx f(H)$, for a given combination of waves and currents. The vertical profiles of tracer concentration shown in Figures 4 and 5 (or schematically in Figure 6) are thus integrals of the quantity a due to individual segments of the wave and current history.

The thickness a can be estimated from the sediment transport rate $q = (\rho_s - \rho) \cdot v_s \cdot a$ and independent assessments of the average grain speed v_s , both resulting from our

analysis of the tracer movement and core samples. By such procedure one can claim that the thickness a is in the range of 2-4 centimetres during moderate storms.

Theoretical investigations of the bedload layer (Kaczmarek et al. 1995) suggest that the bedload layer thickness a should be smaller. A numerical simulation belonging to those studies is depicted in Figure 8 for the grain diameter D_{50} and wave period T typical of the area of investigation; the thickness a should obviously be a function of wave height and the depth of water.

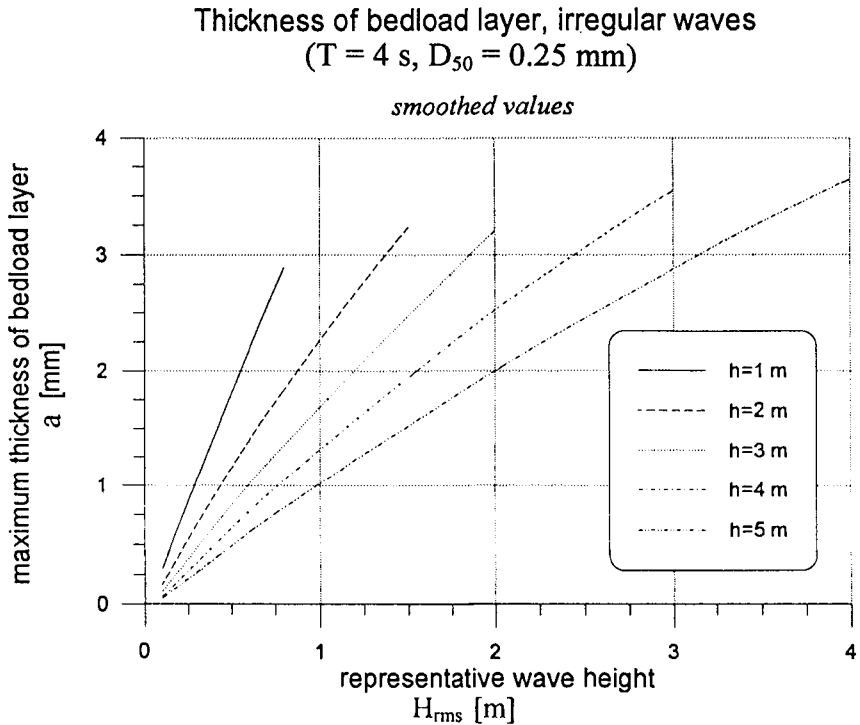


Figure 8. Theoretical bedload layer thickness for wave period $T=4 \text{ s}$ and variable wave height (H_{rms}) and depth of water h (Kaczmarek et al. 1995)

Upon comparison of the simulated quantities and their prototype counterparts it can be inferred that the bedload layer is about a few millimetres thick, thus by one order of magnitude smaller theoretically than under prototype conditions. This disparity can partly be associated with the laboratory origin of the theoretical outcome. More important, the definitions of the bedload layer are different — Kaczmarek et al. (1995) adhere to the classical few grain diameters above and beneath bedline, while in this study the movable bed layer encompasses sheet flow as well.

The function $f(H)$ can be approximated by $f(H) \approx 0.027H_{br}$, as postulated by Kraus et al. (1982) and Pruszek & Zeidler (1994). On the other hand, the function $g(b \cdot t/T_{st})$ can be estimated once T_{st} is given more accurately, which is however beyond the scope of this study.

3.2 LOCAL VARIABILITY OF ACTIVE SAND LAYER

In order to shed light on local variability of the active sand layer as a function of time and variable forcing by waves and currents, the second series of measurements included a special experiment under prototype conditions. The test box denoted by P1 was situated on a depth $h=1.2$ m, on the seaward slope of the sand bar, some 6 m from the bar crest (Fig. 1). The experiment was initiated at 12:00 on 26th May 1994 at calm weather. The tracer concentration on a depth about 25 cm below original sea bed was constant $c=1500$ pulse/s (Fig. 9). Moderate waves were noted between 12:00 and 14:00 (Table 1).

Table 1. Parameters of water and sediment movement at box P1 (depth = 1.2 m, Fig. 1)

Time (t)	Wind		Wave (m)		Current (m/s) Average/ Max		Sea level change (cm)	Depth of mixing (m)	Rate of depth changes	Remarks
	φ	v (m/s)	H	H_{\max}	Long shore	Cross-shore				
26.05.94 13 ⁰⁰ 12 ⁰⁰ -14 ⁰⁰	272°	7.5	0.12	0.44	0.2/0.6	0.01/0.4	0.0	0.04	few D/ 2 h -1cm/4 h	One-point breaking
16 ⁰⁰ 14 ⁰⁰ -18 ⁰⁰	260°	2.2	0.11	0.45	0.2/0.6	0.01/0.4	-2.5	0.04		
19 ⁰⁰	274°	6.8	0.16	0.48	0.2/0.6	0.01/0.4	+5.0			
22 ⁰⁰	328°	2.4	0.2	0.54	0.2/0.5	0.01/0.4	0.0			
27.05.94 1 ⁰⁰ 4 ⁰⁰	19° 38°	4.9 7.5	0.25 0.35	0.96 1.0	0.3/1.1 0.4/1.2	0.01/0.8 0.02/0.9	+1.0 +6.0	a few	mean value = 10cm/10h	Multiple-point wave breaking
7 ⁰⁰	33°	6.5	0.40	1.17	0.4/1.4	0.02/1.1	+20	cm		
10 ⁰⁰	21°	3.0	0.35	1.0	0.4/1.4	0.02/1.0	+20			

Waves broke in a close vicinity of shoreline, far away from the area of investigations. Although quite small, the waves clearly affected the upper sand layer, reaching some 4 cm below original sea bed line. For similar waves and currents between 14:00 and 18:00 the activity of sand movement in the bedload layer was similar, but its intensity was growing, with the maximum at the surface and linear decrease to the depth $h_d = 4$ cm below sea bed line. The latter value can be regarded as the depth of wave effect on sea bed grains; thus it somehow defines the thickness of the active sea bed layer at given external forcing. Substantially thinner bedload thickness, about a few grain diameters, is typical of that period for the grains belonging to the sea bed and being in motion at the same time. As a result of such wave and current forcing the bed was eroded by 1 - 2 centimetres over four hours, (Fig. 9). By the time of the next measurement at 9 o'clock on the next day, waves and currents grew considerably (Tab. 1). Multiple wave breaking was observed at the time

of the next measurements. About the area of the experiment, where one of the wave breaking lines was noted, the breaker height was about $H_{br} = 1.2$ m and the maximum current velocity exceeded 1 m/s. Tracer concentration in the vertical profile decreased substantially and the concentration profile became irregular, close to the parabola shifted by a certain value below sea bed line. The maximum concentration of a tracer some 6-10 cm below sea bed line was much smaller than its initial counterpart (about five times). From thorough observations by scuba divers it can be reported that ripples were not present and strong sediment flux, somehow resembling a moveable sheet a few centimetres thick occurred. It should be stressed that the thickness of sediment movement layer estimated by scuba divers was about 2-4 cm (depending on the accuracy of estimation), but not a few millimetres. Further erosion by 9-10 cm was noted from 18:00 on 26th May to 9:00 on 27th May; the most intensive changes due to growing waves and currents took place most probably about midnight (Tab. 1).

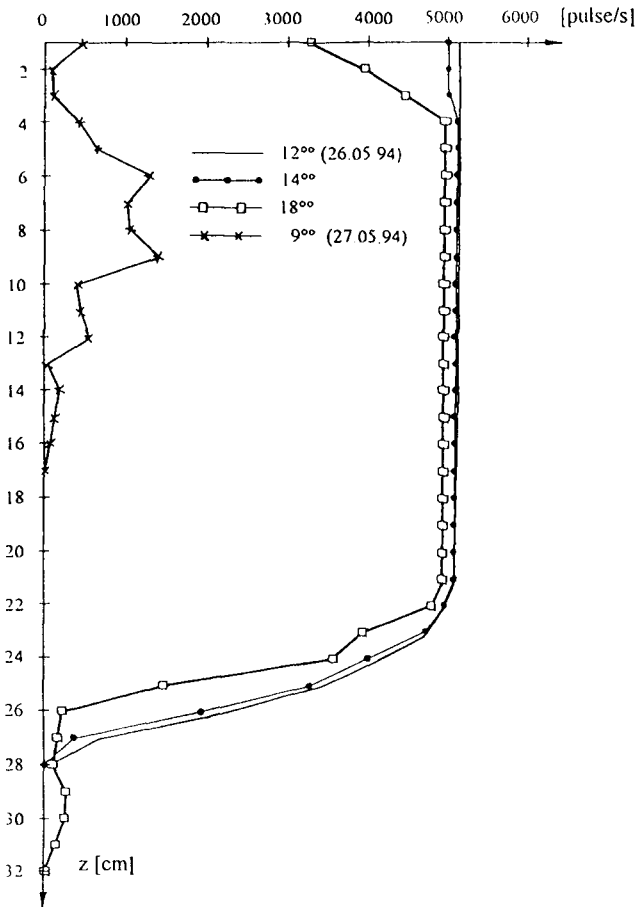


Figure 9. Variability of vertical concentration profile as a function of hydrodynamic parameters

Subsequent measurements were impossible because of the growing storm. After several hours of that medium storm it was realised that the test box was washed away and no tracer was found in its area.

4. CLOSING REMARKS

From our analysis of the tracer distribution and its coupling with waves and currents one can draw some conclusions concerning the bedload layer. The following points should be made:

- sediment movement under dynamic surf zone conditions is characterized by high intermittence reflected in a stratified structure of bedlayer, whereby each sublayer is governed by different forcing factors. The entire vertical profile of tracer concentration represents then a sum of various sublayers, which are correlated with subsequent wave climate changes,
- vertical profile of tracer concentration displays a pronounced variability in time and space, with predominance of quasi - parabolic profile close to the tracer injection point and a thin quasi - uniform one away from the tracer source; being often the superposition of a few thin 'foils',
- for identical external conditions (wave and currents) the vertical tracer profiles are different at bar crests and troughs, showing clear diversification of sediment mechanics across the surf zone. Fairly thin sheets, below 2 cm in thickness, travel at bar crests and in troughs, due to high sand speeds in one directional (longshore) movement,
- the thickness of each sublayer of the nearbed load is a highly nonlinear function of wave and current velocity, depending on intensity (H) and duration (t) of subsequent wave action, $a = f(H,t) \approx f(H) \cdot \log(b \cdot t/T_s)$.

5. REFERENCES

- Drapeau G., Long B., Kamphuis J., W. (1990), *Evolution of radioactive sand tracers to measure longshore sediment transport rates*, Proc. 22nd ICCE, Delft, ASCE, p.2710-2723
- Galvin C. (1987), *Vertical profile of littoral sand tracers from a distribution of waiting times*, Proc. Coastal Sediment's 87, ASCE, p. 436-451
- Horikawa K. A., Watanabe A., Katori S. (1982), *Sediment transport under sheet flow condition*, Proc. 18th ICCE, Cape Town, ASCE, p.1335-1352
- Ingle J., C. (1966), *The movement of beach sand: An analysis using fluorescent grains*, Developments in Sedimentology, No. 5, Elsevier Pub. Company, Amsterdam
- Kaczmarek L., Ostrowski R., Zeidler R. (1995), *Boundary layer theory and field bedload*, Proc. Coastal Dynamics'95, Gdańsk, ASCE, p. 664-675
- Kraus N., C., Isobe M., Igarashi H., Sasaki T., Horikawa K. (1982), *Field experiments on longshore sand transport in surf zone*, Proc. 18th ICCE, Cape Town, ASCE, p.969-988
- Pruszek Z., Zeidler R. (1994), *Sediment transport in various time scales*, Proc. 24th ICCE, Kobe, ASCE, p.2513-2526

CHAPTER 302

A SLOPING DUCT FOR THE STUDY OF SEDIMENT TRANSPORT

Jesper S. Damgaard ¹ , Richard J.S. Whitehouse ¹
and Richard L. Soulsby ¹

Abstract.

The details of a large sloping duct at HR Wallingford Ltd. are presented. The duct is capable of sloping to the angle of $\pm 33^\circ$ which exceeds the angle of repose of normal quartz sand. The duct can be tilted laterally as well as longitudinally so that; 1) the effect of combined slopes can be investigated; 2) the aspect ratio can be inverted. At present the duct operates with a steady flow but it can accommodate a wave piston.

1 Introduction.

An important aspect in modelling coastal morphology is the ability to describe the effects of sloping surfaces on sediment transport rates, for example due to longshore bars, dune and ripple formations, dredged channels and trenches and beaches. The research carried out to date is limited, and to remedy this HR Wallingford Ltd has constructed a unique facility to permit the measurement of sediment transport at steep slopes in a controlled environment.

2 Description.

The sloping sediment duct has been purpose-designed for conducting tests on sediment transport on horizontal beds, and shallow and steep slopes up to the angle of repose for the sediment. It has a maximum longitudinal tilt of $\pm 33^\circ$ and can be tilted, or turned, laterally up to this angle for sediment transport studies where a transverse slope is required. In figure 1 the duct is shown at

¹Marine Sediments Group, HR Wallingford Ltd., Wallingford, Oxon OX10 8BA, UK.

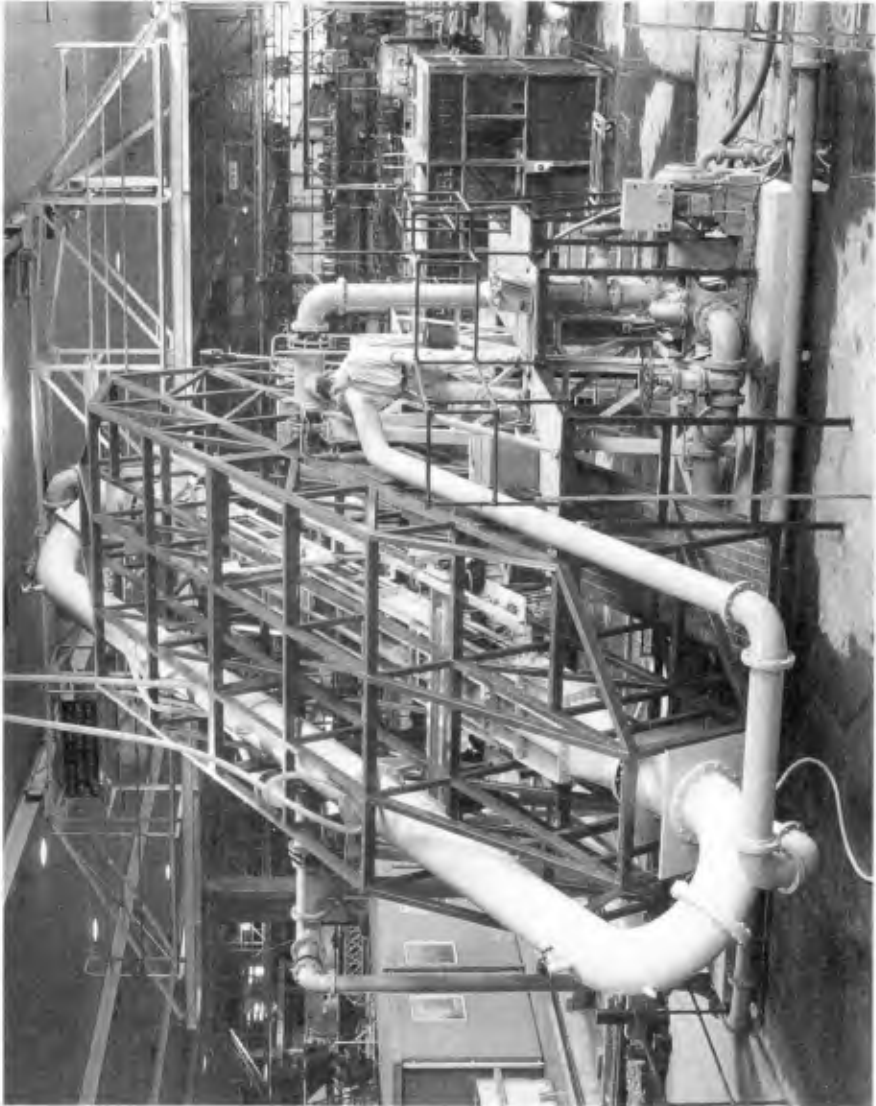


Figure 1: Sloping duct at maximum downslope setting.

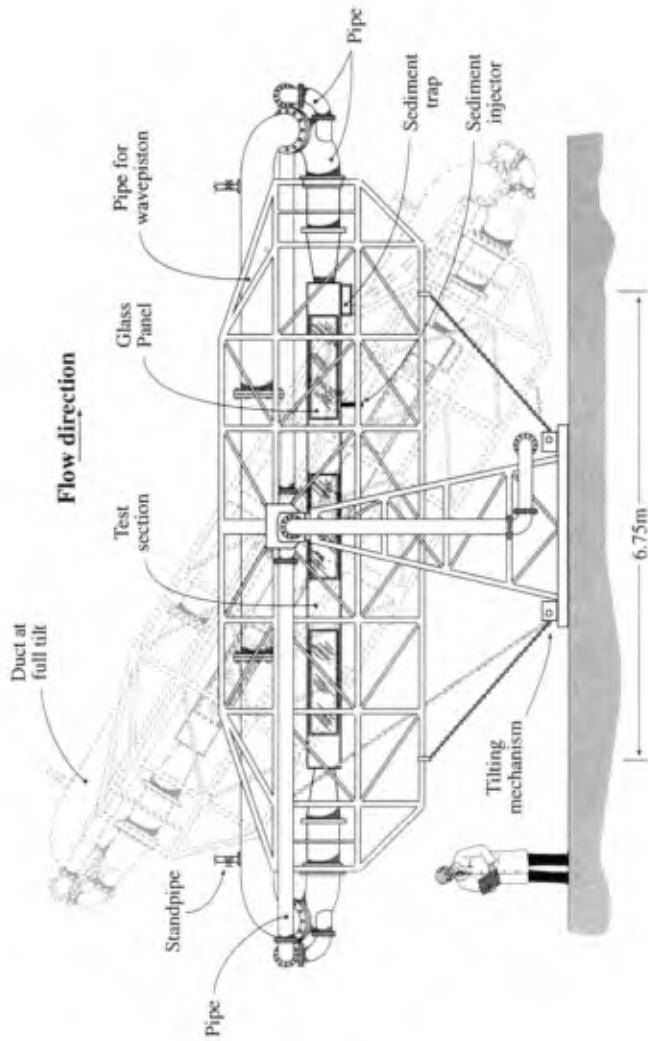


Figure 2: Drawing of sloping duct (not to scale).

full downslope (in the direction of the flow) tilt. The duct consists of a support cage, a test section and a central support on which the support cage pivots. See figure 2.

The dimensions of the test section are 6.75 m long by 0.6 m wide by 0.25 m high with three sections fabricated with glass viewing windows. The ends of the working section have rotating joints, and by tilting the duct laterally through 90° the aspect ratio can be either 1:2.4 or 2.4:1. The downstream end of the duct has a sediment trap which can be emptied by removing a cover plate.

The pump is a P76 centrifugal pump with the following characteristics: maximum head = 13m @ zero flow, design rating = 9m @ $0.17m^3/s$ and head corresponding to the maximum discharge = 5.3m @ $0.21m^3/s$. The maximum discharge corresponds to a mean flow velocity of approximately 1m/s in the duct. The system is a closed conduit with a stand-pipe to avoid water hammer effects.

The flow discharge is measured by an ALTOFLUX K380 electromagnetic flowmeter situated in a straight portion of the 8inch (0.20m) diameter feeder pipework. In each end of the test section there is a small pressure outlet. A Sandhurst Scientific 20mbar differential pressure transducer (GA 64/20E) is used to determine the total head loss in the test section. The distance between the outlets is 5.57m and for a mean velocity of approximately 1m/s, the head loss is of the order 1cm. An absolute pressure transducer (Druck PDCR 930) is installed in the middle of the test section. Provision has been made for mounting a two component Laser Doppler Anemometer (LDA). The laser mounting system rests on rails and can be moved along the test section. An electronically indicating point gauge is installed on the laser mount in order to determine the vertical position of the LDA with an accuracy of $\pm 0.01mm$. Seeding material for boosting the LDA signal can be introduced into the duct while it is operating.

At present the system operates with a steady flow, but it is designed to accommodate a wave piston which will allow oscillatory flows to be generated with periods and amplitudes corresponding to full-scale near-bottom wave motions.

3 Hydrodynamics.

The hydrodynamic properties of the duct have been investigated as a part of the ongoing research. Of particular interest for the sediment transport research is the wall shear stress. For all the experiments that have been conducted so far the floor of the duct has been covered by PVC plates onto which a quartz sand with a median grain diameter of $208\mu m$ has been glued. The sidewall correction method of Vanoni and Brooks (1957) has been used to partition the total pipe friction into wall and bed shear stress. The shear stress has been estimated through head loss measurements obtained by the differential pressure transducer and through LDA measurements in the constant stress layer. It turned out that the variance on the shear stress estimate obtained via head loss measurements was much larger than that of the estimates derived from LDA measurements. Therefore the results

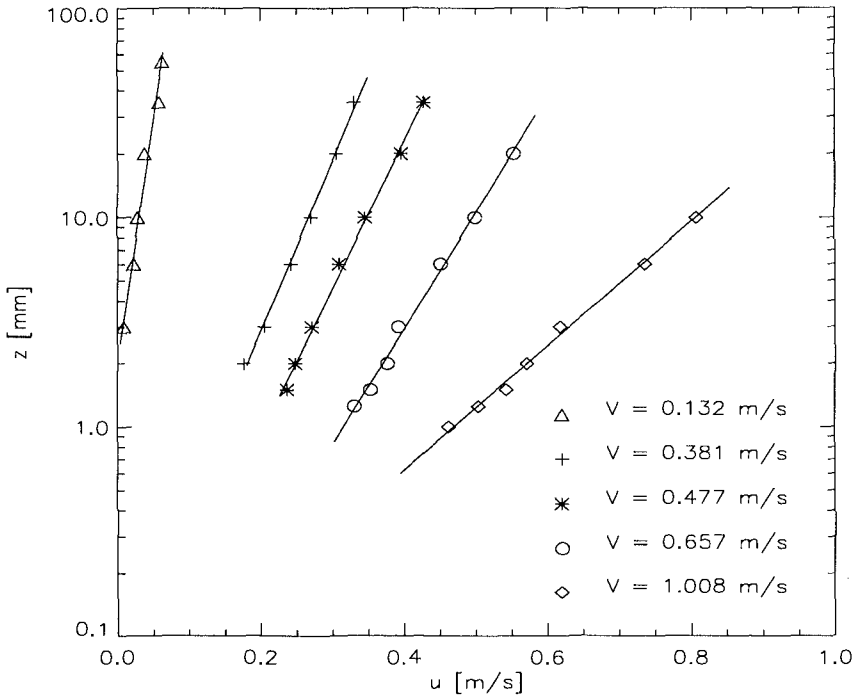


Figure 3: Vertical profiles of mean horizontal velocity measured with the LDA

obtained from the LDA measurements were used to establish the particular pipe friction relation for the duct. The procedure is as follows. First a vertical velocity profile is measured for a range of different discharges. The measuring points in the vertical profile should lie above the viscous sublayer but beneath the core region. See Schlichting (1960) for details. For each discharge the bed friction velocity, u_{*b} , is determined assuming a logarithmic velocity profile

$$\frac{u}{u_{*b}} = \frac{1}{\kappa} \ln \left(\frac{z}{z_0} \right) \quad (1)$$

where u = mean horizontal velocity at distance z above the bed, κ = Von Karman's constant and z_0 = the bed roughness length. A number of velocity profiles are shown in figure 3 for different values of V , mean flow speed, $V = Q/A$, where Q = discharge and A = cross-sectional area.

The bed friction values obtained by equation 1 can be used to estimate the overall pipe friction by applying the sidewall correction method of Vanoni and Brooks (1957). These results have been compared with the Colebrook and White formula (Colebrook, 1939) and a modified version of the C&W formula where the theory of Christoffersen and Jonsson (1985) was used to account for the effect

of uniform grain roughness and where a different value of the constant was used (1.94 rather than 1.74):

$$\frac{1}{\sqrt{\lambda}} = 1.94 - 2 \log \left(\frac{k_s}{R} (1 - e^{-\mathbf{Re}_g/27}) + \frac{18.7}{\mathbf{Re}\sqrt{\lambda}} \right) \quad (2)$$

where λ is the resistance coefficient, $\lambda = 8(u_* / V)^2$, $\mathbf{Re}_g = u_* k_s / \nu$ is the grain Reynolds number, k_s = the Nikuradse equivalent sand roughness, equal to the median grain diameter of bed material, $\mathbf{Re} = 4RV / \nu$ is the pipe Reynolds number and R = hydraulic radius = A/p , p = wetted perimeter. The results are shown in figure 4 using axes based upon Colebrook's original paper.

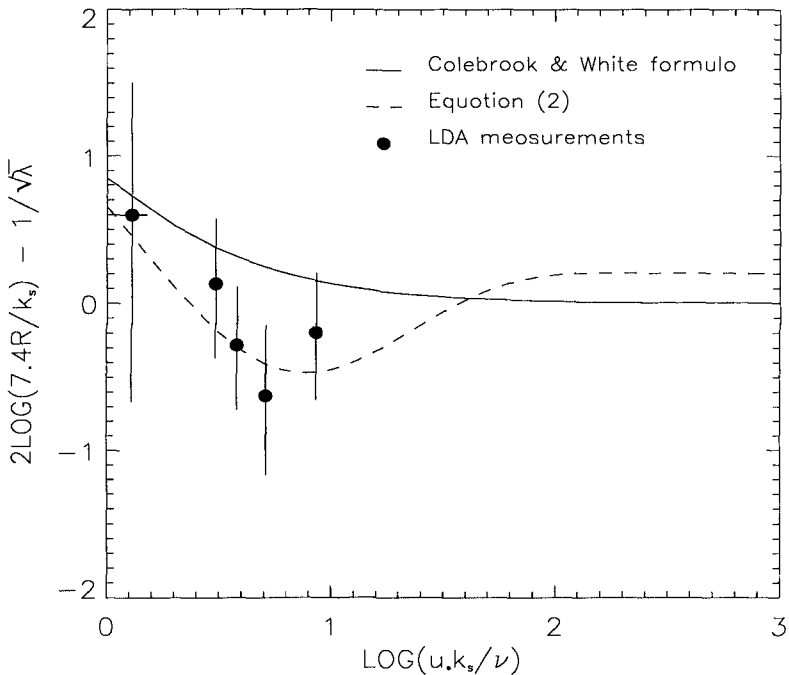


Figure 4: Friction diagram for the sloping duct with a rough floor.

4 Current research.

A study of bed-load transport (erosion rate) on sloping beds in steady flow has been conducted as a part of the MAST G8M Coastal Morphodynamics Project. It is for that purpose that the rough bottom mentioned previously was installed.

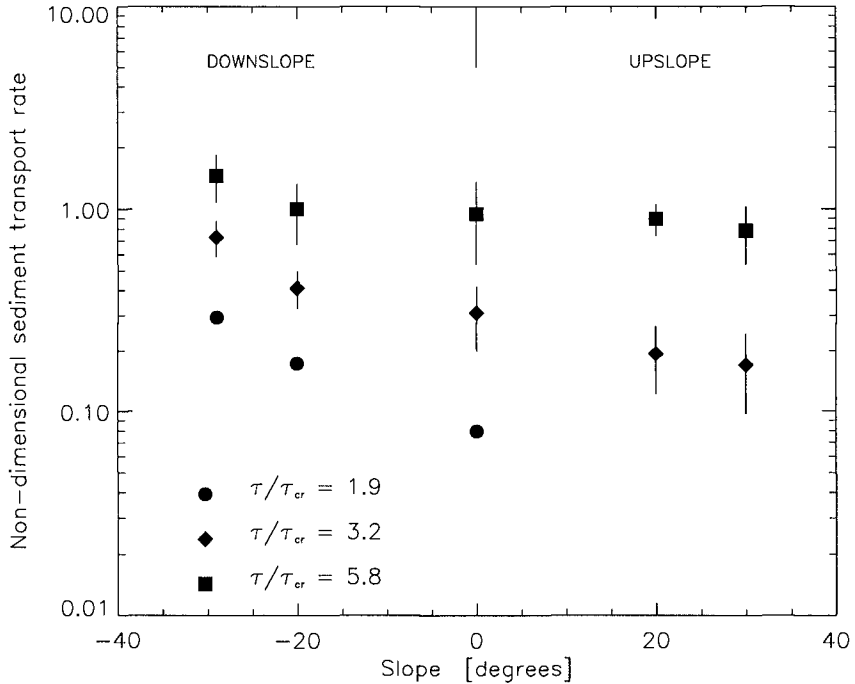


Figure 5: Experiments on slope effect on bed-load sediment transport. The values of τ_{cr} are for a horizontal bed.

An electronically driven sediment injector was installed downstream from the centre of the duct with an inner diameter of 20 mm. This device was used to inject sand into the flow to determine the equilibrium pick-up rate for sediment by the flow. The speed of the piston was adjusted until the rate of delivery of sediment matched the rate of removal by the flow. A porthole in the roof of the duct above the injector could be opened to charge the injector with sand and to make observations. At the downstream end of the test section the sediment trap captured the sediment injected into the flow. Figure 5 contains some results obtained in the duct for a range of bedslopes and shear stresses. The bed shear stress, τ , is given as $\tau = \rho u_{*b}^2$, and τ_{cr} is the critical shear stress for initiation of sediment motion on a horizontal bed. The results of this research are discussed further in Damgaard et al. (1996).

5 Conclusions.

The new sloping duct facility at HR Wallingford Ltd has proven to be suitable for large-scale experimental tests with sediments and can also be used for hydrodynamical research. The unique sloping capability of the facility allows the influence of gravity due to a sloping bed (of an arbitrary angle) on the sediment transport to be investigated for all types of sediment. The recent research has concentrated on a fine sand but the duct would be equally suitable for working with gravels as the flow speed achievable is up to $1m/s$.

It is expected that the duct will continue to be used for steady flow tests and, in the future with the addition of a wave piston, for wave or wave-current sediment or hydrodynamic investigations. The duct is currently available to European researchers through the EC Training and Mobility of Researchers - Access to Large-Scale Facilities - programme and it is anticipated that the facility will become available for wider usage by UK and other researchers in the near future.

Acknowledgements.

The construction of the duct was funded by HR Wallingford Ltd. The funding for parts of the sediment transport research was provided by the Commission of the European Communities Directorate General for Science, Research and Development as part of the MAST2 G8M Coastal Morphodynamics collaborative research programme, under Contract Number MAS2-CT92-0027, and for other parts by the U.K. Ministry of Agriculture, Fisheries and Food (Flood and Coastal Defence Division).

References

- [1] J.B. Christoffersen and I.G. Jonsson. Bed friction and dissipation in a combined current and wave motion. *Coastal Eng.*, 12(5):387-423, 1985.
- [2] C.F. Colebrook. Turbulent flow in pipes, with particular reference to the transition region between smooth and rough pipe laws. *Proc. Inst. Civ. Eng.*, 11:133-156, 1939.
- [3] J.S. Damgaard, R.J.S. Whitehouse, and R.L. Soulsby. Bed-load sediment transport on steep slopes. *accepted for J. Hydr. Eng.*, 1996.
- [4] H. Schlichting. *Boundary layer theory*. McGraw-Hill, New York, Fourth edition, 1960.
- [5] V.A. Vanoni and N.H. Brooks. Laboratory studies of the roughness and suspended load of alluvial streams. Technical Report Report No. E68, California Inst. Tech., Pasadena, California, 1957.

CHAPTER 303

SEDIMENT DYNAMICS AND PROFILE INTERACTIONS: DUCK94

Donald K. Stauble¹ and Mary A. Cialone²

ABSTRACT

Beach profiles and sediment samples were collected on a daily basis along three cross-shore transect lines during the DUCK94 nearshore experiment lasting for 18 days in October 1994. Conditions ranged from near calm during the first week of the experiment to full storm conditions during the second and third weeks, with a two day initiation of beach recovery at the end of the experiment. The profiles responded with similar elevation change, with little morphologic variability during the calm period. During the storm, the bar migrated seaward 70 to 100 m, but the foreshore exhibited little change. The bar began to migrate shoreward at initiation of recovery. Sediment grain-size distributions vary in the cross-shore direction, with medium size grains on the upper foreshore, coarse gravel deposits on the lower foreshore and progressively finer sands in the offshore direction. After the storm, the foreshore and bar/trough samples were coarser with little change in the nearshore sediment distributions.

INTRODUCTION

To quantify sediment distribution response to forcing functions on the foreshore, bar/trough and nearshore along a three-dimensional beach area, a sediment sampling and analysis experiment was conducted as part of the DUCK94 nearshore field experiment (see Birkemeier et al., 1997 for overview of DUCK94 experiment). This experiment was designed to examine the three-dimensional natural sediment distribution and its relationship to profile change at the U.S. Army Engineer, Waterways Experiment Station, Field Research Facility (FRF) at Duck, N.C. (Figure 1). Sediment distribution changes were measured over the short-term (18-day period) during October, 1994. To increase our understanding of sediment distribution, the experiment focused on our knowledge of the short-term 3-D sediment variations of the entire active profile to document relationships between beach morphology and sediment dynamics from the high water line, seaward to closure depth.

Sediment grain-size distributions for different beach environments change as the beach erodes and accretes in response to changes in wave and tidal forcing. A previous long-term study at the FRF along one profile line characterized a cross-shore variability pattern in

¹ Res. Phy. Sci. ² Res. Hyd. Eng., U.S. Army Engineer Waterways Experiment Station, Coastal and Hydraulics Laboratory, 3909 Halls Ferry Road, Vicksburg, Mississippi 39180

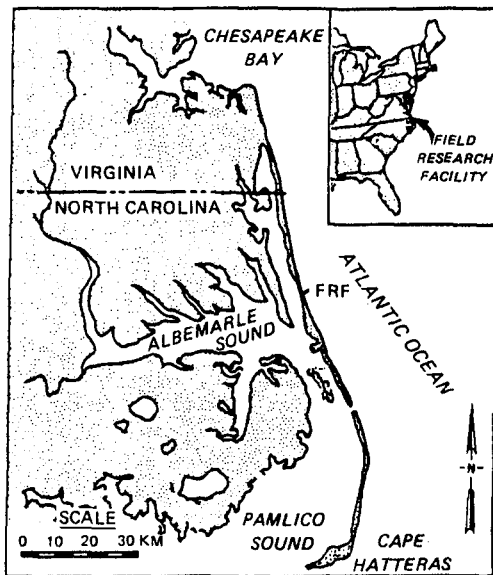


Figure 1. Location map.

grain-size distributions (Stauble, 1992). During the SUPERDUCK (1986) experiment, a short-term storm erosion and recovery study showed a high degree of three-dimensional grain-size variability but was limited to the foreshore and hinted at nearshore control of the foreshore sedimentation (Stauble et al., 1993). A lack of knowledge exists in relating three-dimensional sediment movement on the entire active beach profile during both fair weather and storm periods to the processes that cause the movement. These processes include a) the swash processes on the foreshore, b) wave breaking, longshore currents, and/or cell circulation (rip currents) in the bar and trough area, and c) wave, tidal and wind driven circulation on the nearshore slope out to closure depth and beyond. The variation in grain sizes in each of these environments is indicative of the different active processes.

EXPERIMENT DESIGN

The experiment design included collection of profile data and sediment samples along three lines, approximately 100 m apart, extending from the dune base to the 6-m depth contour (Figure 2). Surface sediment samples were collected at the dune base, mid-berm, berm crest (area around high water), mid-tide, swash (area around low water), trough, bar crest, and the 3-m, 4-m, 5-m, and 6-m depth contours. Shallow surface sediment samples were collected daily with a hand scoop from the foreshore to wading depth and with a grab sampler on subaqueous portion of each profile using the Coastal Research Amphibious Buggy (CRAB), during the beach profile survey. Samples were collected around the time of low tide on the foreshore. The sampling schedule included daily profile and sediment collection of the foreshore and alternate days for the nearshore area sediment collection for a duration of 18 days in October, 1994. The data sampling time period covered physical conditions ranging from near calm to storm conditions.

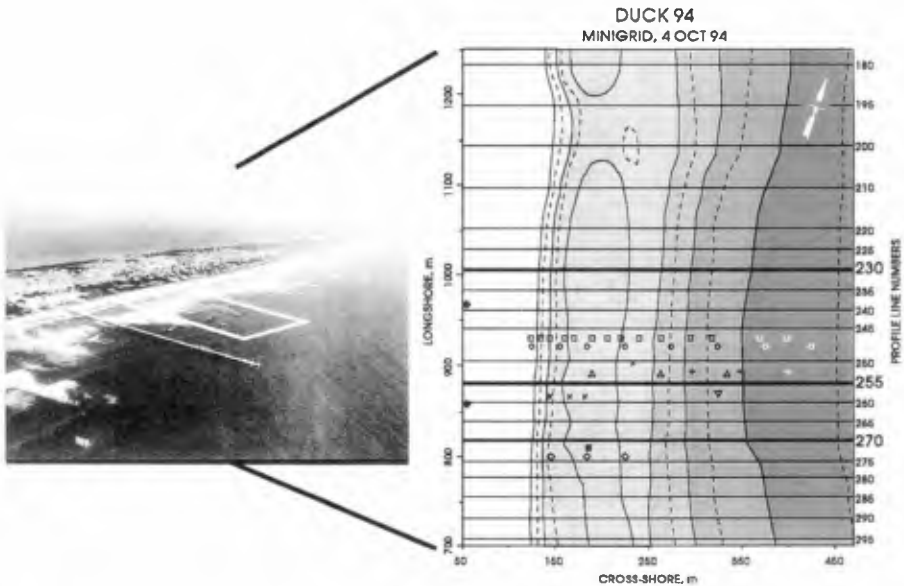


Figure 2. Location of profile transects samples (Lines 230, 255, and 270).

DATA ANALYSIS

Physical data: During the experiment several arrays of wave gauges and current meters were deployed within the study area. An offshore wave gauge array was located in 8 m of water, just offshore of the data collection area. Figure 3 shows the mean wave height (H_{m0}) and peak period (T_p) recorded from 2 to 22 October 1994. Profile and sediment data used in this paper were collected from 4 to 21 October. The experiment began just after a period of high wave activity, as the waves diminished to an average H_{m0} of around 0.5 m and a T_p between 3 and 7 sec. This relatively calm period lasted until 9 October. Currents recorded in the trough area landward of the bar between transects 245 and 250 (Figure 2), indicated that the longshore velocity was near zero and the cross-shore velocity ranged from 0 to 0.2 m/s in the offshore direction during this time period (data courtesy of S. Elgar). At the onset of the storm (10-13 October), H_{m0} rapidly increased to around 2 m and T_p increased from a low of 3 sec to around 7 sec. The longshore currents reached their maximum velocity (around 1.3 m/s) to the south, with a steadily increasing offshore component. The wave gauge recorded its maximum H_{m0} of around 4 m on 15 October as T_p increased to around 11 sec. The longshore currents reversed during this time reaching a peak velocity (1 m/s) to the north as the storm progressed up the coast and wave approach angles switched from a northeasterly direction to a more easterly to southeasterly direction. The offshore velocity component in the trough continued to increase to a maximum of around 0.64 m/s on 19 October. The wave height decreased to around 1.5 to 1.0 m as the experiment ended, but the wave period remained around 14 sec.

Profile Data: Beach profile data were collected from a shore-parallel baseline landward of the dune out to a depth of 6 m, some 700 m seaward of the baseline. All profiles are referenced to the 1929 National Geodetic Vertical Datum (NGVD). Profile data were

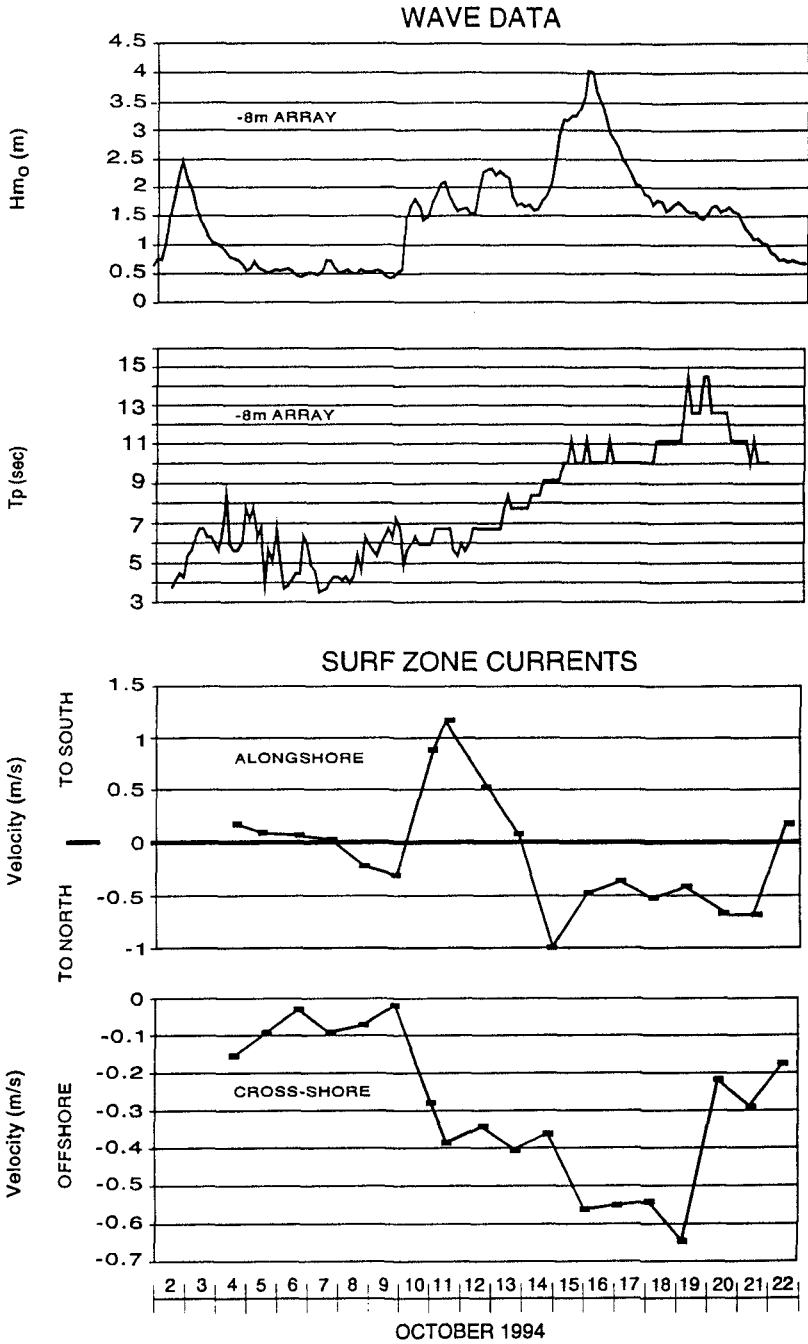


Figure 3. Plot of nearshore wave parameters and surf zone currents in trough.

analyzed and plotted using the Interactive Survey Reduction Program (ISRP) as described by Birkemeier (1984). Plots of the pre-storm beach profile (5 October) at all three transects showed that the bar crest was about 250 m from the baseline (Figure 4). With the increase in wave height beginning on 10 October, the bar migrated seaward. By 15 October the bar had moved to around 280 m seaward of the baseline. Just one day later, at the height of storm wave activity, the bar had moved to between 310 and 350 m offshore. With steadily decreasing wave heights and long period swell (as the storm moved out of the area), the bar migrated back onshore at profile lines 255 and 270. Profile line 230 was the location of a rip current and the bar remained in its seaward position through 21 October. The foreshore did not change significantly in elevation over the study. During the low wave period at the beginning of the experiment the foreshore was planar, but beach cusps developed on 20 and 21 October as the waves subsided.

Sediment Data: A total of 256 sediment samples were collected and sieved using a sonic sifter at quarter-phi ($\frac{1}{4} \phi$) intervals, ranging from -3ϕ (8.0 mm) to 4.25ϕ (0.53 mm), and weight percentages for each interval were computed. Statistical data were calculated using the method of moments (described in Friedman and Sanders, 1978). High variability was found in the cross-shore grain-size distributions, with the foreshore exhibiting the highest variability. This area between the berm crest and low tide swash contained a bimodal gravel component along with sand size fractions. A localized source of coarse relict sediment has been identified in the area of the FRF by previous investigators (Calliari, 1994). The highest variability in profile elevation and sediment distribution occurred in the lower foreshore and trough/bar area, however the gravel component was restricted to the beach foreshore. The grain-size distribution was much more well-sorted and more uniform in mean size in the nearshore, both temporally and spatially. Figure 5a shows an example of the cross-shore sediment distribution on profile line 270 collected just at the beginning of the storm, representative of the sediment distributions deposited during the period of low wave activity. In contrast, at the end of the high wave period on 20 October, the bar had migrated offshore and the trough had widened. The grain-size distributions (Figure 5b) show a coarser and more poorly-sorted sample from the foreshore to the 3-m depth. Little change in nearshore sand distributions were found between low and storm wave conditions, while an increase in coarse material was measured on the foreshore. The finer-sized sediments were removed from the foreshore, trough and bar crest area, leaving behind a coarse lag deposit.

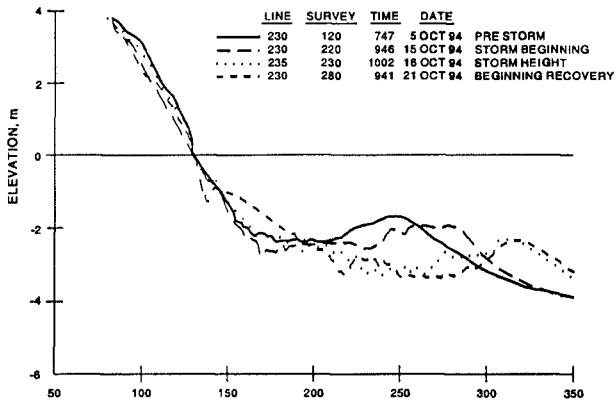
ANALYSIS AND DISCUSSION

Alongshore and cross-shore sediment distribution variability was related to beach morphology changes as a function of wave and current fluctuation. During the October 1994 experiment, the alongshore beach shape was uniform for the low wave period (first six days) and a "linear" beach was the prevalent form. The cross-shore profile elevation change and sediment grain-size distribution exhibited more variability, with a zone of medium size sands on the upper foreshore and coarse material in the lower foreshore. The size distribution became progressively finer in the offshore direction, through the nearshore trough, over a single bar feature, and the sloping nearshore region.

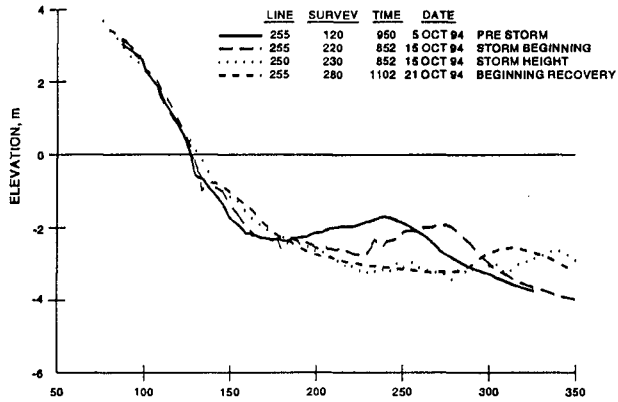
On 10 October, an extratropical storm system developed over the northern Gulf of Mexico and migrated northeastward into the Atlantic Ocean off of Cape Hatteras on 15 October. During this "northeaster", alongshore currents increased to the south and offshore

a.

DUCK 94 PROFILE CHANGE



b.



c.

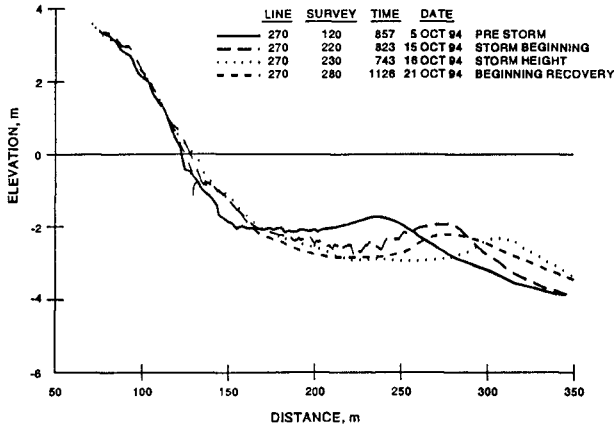


Figure 4. Plot of selected profiles showing bar migration due to storm.
a) line 230, b) line 255, and c) line 270

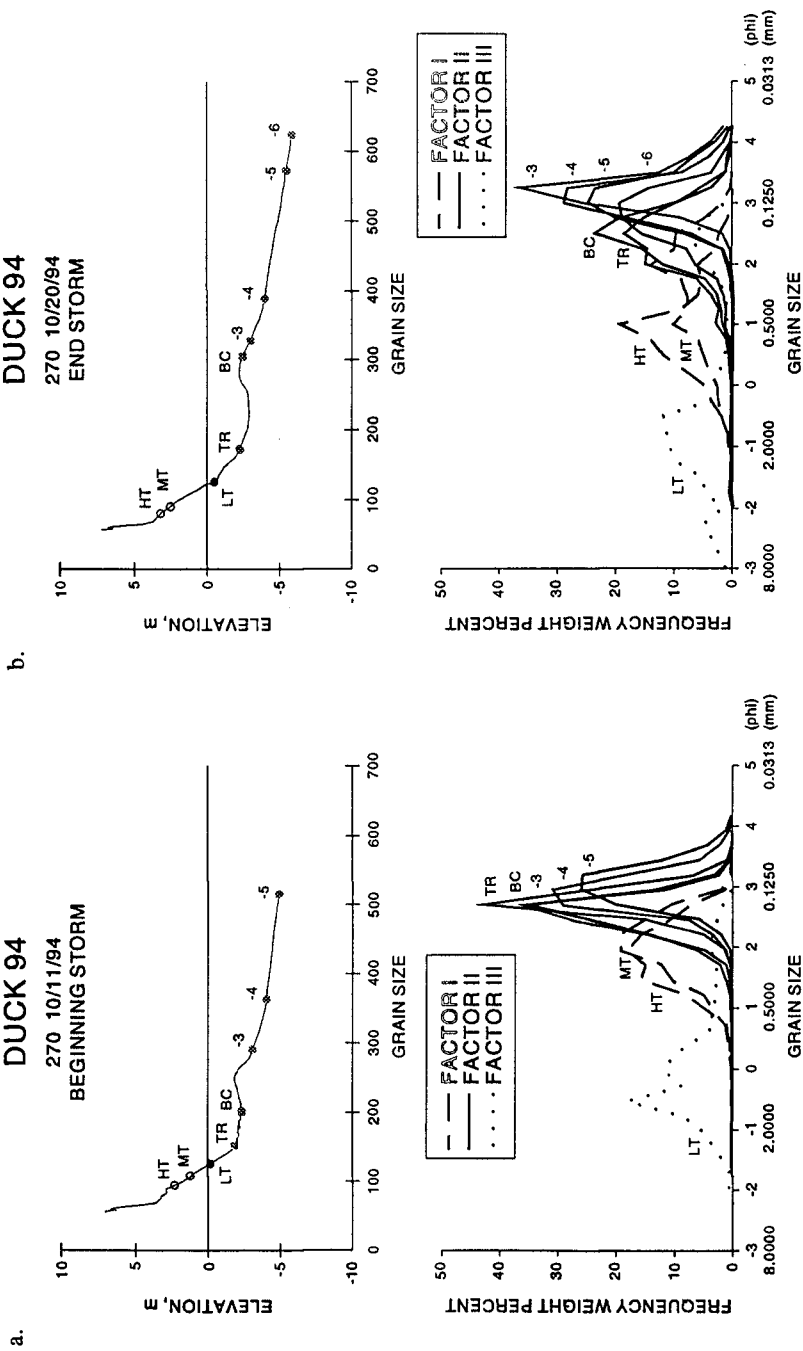


Figure 5. Sediment sample locations and grain-size distributions on line 270 a) pre-storm and b) post-storm

HT = High tide, MT = Mid tide, LT = low tide, TR = trough, BC = bar crest, -3 = 3 meter depth sample, etc. . .

flow increased in the trough area. During this phase of the experiment, the bar feature migrated in the offshore direction, while the foreshore maintained a uniform planar shape along the study area. Wave heights continued to grow and reached a maximum of 4 m at the 8-m depth wave gauge on 15 October.

High pressure developed over the eastern United States on 16 October and continued through the end of the experiment. During this phase of the experiment, the longshore drift switched from a southward to northward direction. In the surf zone, offshore currents reached their peak on 19 October. The profile responded with continued seaward migration of the bar feature and widening of the trough. Wave heights decreased on the last two days of the experiment, as long period swell conditions prevailed. Beach cusps formed and a rip current was present at the northern end of the study area. The beach began to take on more three-dimensional profile features with the bar migrating onshore in the southern region as offshore currents rapidly decreased in velocity.

In order to improve our understanding of both spatial and temporal variability in grain-size distribution during high energy events and compare them with calm periods, foreshore samples were collected and analyzed along all three lines, on a daily basis throughout the experiment. Nearshore sediment data collection was planned on a two-day cycle, but large waves precluded collection in the nearshore during the height of the storm event. However, nearshore samples were taken immediately before and after the storm.

Standard statistical techniques were used to analyze the sediment distribution of each beach and nearshore environment. Mean and standard deviation values were calculated for each sample. In general the coarser samples tended to have poorer sorting. The widest range in mean and sorting values was found in the low tide sediments, where the samples contained coarse shell and gravel components, as well as medium to fine quartz sand material. The upper foreshore (high and mid tide) samples had a coarse to medium-sized sand that was better sorted than the low tide (less of a coarse shell and gravel component). The nearshore (trough to the 6-m depth) had a relatively narrow range of mean grain sizes in the fine sand range, with little shell and no gravel size components.

Analysis of a suite of sediment samples using just the mean and standard deviation values is somewhat limiting. The use of Q-mode factor analysis (Klovan, 1966) provides a method to determine the relationship between grain-size distribution and variability in the 3-D sedimentation of the beach and nearshore. Q-mode factor analysis, as applied to sediment investigation, involves the determination of interrelationship between sediment samples. With this method, a group of sediment samples can be arranged into a meaningful order so that the relationship between each sediment distribution is deduced (Davis 1973). One of the main advantages of Q-mode factor analysis is that the entire grain-size distribution is considered in the analysis, yielding a detailed relationship especially when $\frac{1}{4}$ ϕ sample intervals are used. Using an analytical method to determine statistical relationships is more objective because it does not require arbitrary statistical descriptors or a-priori knowledge of the environment and location of samples (Klovan, 1966). A large number of samples can be objectively analyzed without having to manually compare each pair of curves. This reduces the "human interpretation" in relating large numbers of grain size distributions.

Q-mode factor analysis relies on how similarity between samples is defined (Reyment

et al., 1993). In this application, the technique of Imbrie and Purdy (1962) for defining similarity was used. They defined an index of proportionality, or cosine theta function, to determine the degree of similarity in weight percent in each size class between each pair of samples. The cosine theta matrix shows all the information on the relationship between the sample vectors, but it is difficult to interpret (Klovan, 1966). Factor analysis provides a means of analyzing the cosine theta matrix to determine the minimum number of mutually orthogonal "factor axes" needed to account for most of the information in the cosine theta matrix. The first axis accounts for the majority of the information in the cosine theta matrix, the second axis accounts for most of the remaining information in the matrix, and so forth. Thus, the problem is to determine the number of eigenvalues needed to account for most (95-99%) of the information in the cosine theta matrix. Eigenvalues and eigenvectors were determined for the sediment sample data set. Factor loadings, a measure of each sample's weighting or correlation to each factor, can then be determined from the eigenvectors and eigenvalues. This provides the coordinates of the samples in a space of reduced dimensionality (Syvitski, 1991). Lastly, a varimax method of factor rotation is used to rotate the factor axes to maximize the variance of the factor loadings on each factor axes, while retaining their orthogonality.

The sample's weight percent in each phi-class interval is used to represent the sample distribution and can be used to "place" the sample relative to other samples in the Q-mode analysis. For example, if a sample is sieved into twenty-seven phi intervals, the sample can be defined as a vector in 27-dimensional space whose position is uniquely determined by the amount of sediment in each of the 27 classes (Klovan, 1966). With this technique, similarities and differences between samples can be determined and comparisons from day to day can also be made. Factor analysis relates the sediment distribution curves of similar shape, and dominant grain-size distribution peaks. Three factors accounted for 88.7% of the variance in the sample distributions. Factor I accounted for 57.8% of the variance and represented the medium sands between 1 and 2 ϕ (0.5 and 0.25 mm). Factor II accounted for 18.3% of the variance and represented fine sands with a peak frequency of occurrence between 2 and 3 ϕ (0.25 and 0.125 mm), and Factor III accounted for 12.6% of the variance and represented coarser sands, with a peak between -1 and 0 ϕ (2.0 and 1.0 mm). Figure 6 is a triangular diagram, which illustrates the distribution of the sediment samples within the three factors from the Q-mode analysis. Samples that are at the corners of the triangle represent the "end-members" of each factor group and depict a particular sediment distribution (Klovan 1966). The other samples within the triangle can be considered as a mixture of these three sediment distributions. The sediments from the high and mid tide area were strong in Factor I and embody medium grain-size distributions. The samples collected from the nearshore (trough to -6 m) covered a range from strong Factor II through near Factor I and comprise fine to medium grain-size distributions. The low tide samples were strongest in Factor II and include predominantly coarse sands.

To better understand the temporal changes over the duration of the 18 day experiment, factor analysis was run on each individual group (i.e. all high tide or all 3-m depth samples) within the cross-shore distribution of sediment data set to investigate the differences in grain-size distributions at each profile position over time. The factors will change depending on which sediment distributions are more dominant within each data set. Each cross-shore sediment data set was compared to differentiate the change over the low to high wave activity period. Little change was found in the nearshore sediment groups, with each data set grouping around Factor I (representing the fines) over the study period. A somewhat

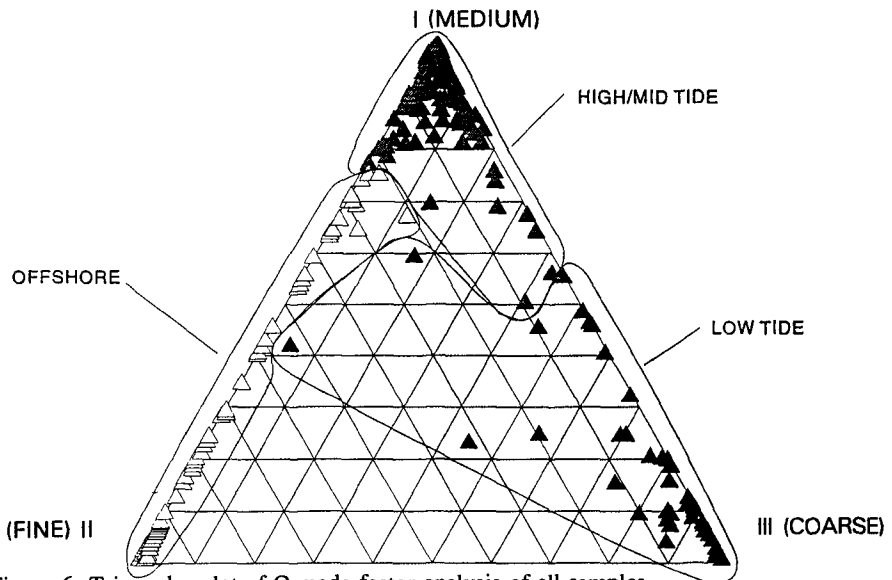


Figure 6. Triangular plot of Q-mode factor analysis of all samples.

more complex grouping was found for the individual foreshore samples over the 18 day study, with the high and mid tide samples grouping more commonly between Factor I (finer) and Factor III (medium), and the low tide samples around Factor II (coarser).

To remove some of the high spatial variability in the foreshore samples, a mathematical composite was made of the high, mid and low tide samples to allow a more clear picture of the temporal change due to storm activity. The 54 composite samples mathematically derived from each of the three profiles per day were analyzed and the grain size variability of the composites was described by three factors representing 94.2% of the variance. Figure 7a shows the triangular plot of the sample distributions within the three factors and representative frequency plots of "end member" samples. Factor I accounted for 79.2% of the variance and represented the finer distributions with peaks around 2ϕ (0.25 mm). Factor II accounted for 12% of the variance and represented coarser grain-size distributions with peaks around -1ϕ (2.0 mm). There was no strong Factor III end member, which accounted for only 3.1% of the variance. Samples that plotted in this area of the diagram had peaks in the medium size range between 1 and 2ϕ (0.5 and 0.25 mm).

To give physical significance of the results of this analysis requires inferring what the end member samples indicate and how the samples group together around these end members. Foreshore composite samples collected from the period of low wave activity (4-10 October) all have a strong grouping toward Factor I. This grain-size distribution is represented by the composite of 9 October on profile line 230 (Figure 7b). All three profile lines exhibited similar composite grain-size distributions. During the period of higher waves (11-19 October) the composites plotted in two groups, one between Factor I and Factor III representing a shift to more medium grain sizes and the second strongly associated with Factor II, the coarse grains. A bi-modal sample from profile line 230 collected on 19 October is representative of this group. Except for the line 230 composite of 20 October

DUCK 94 FORESHORE COMPOSITE

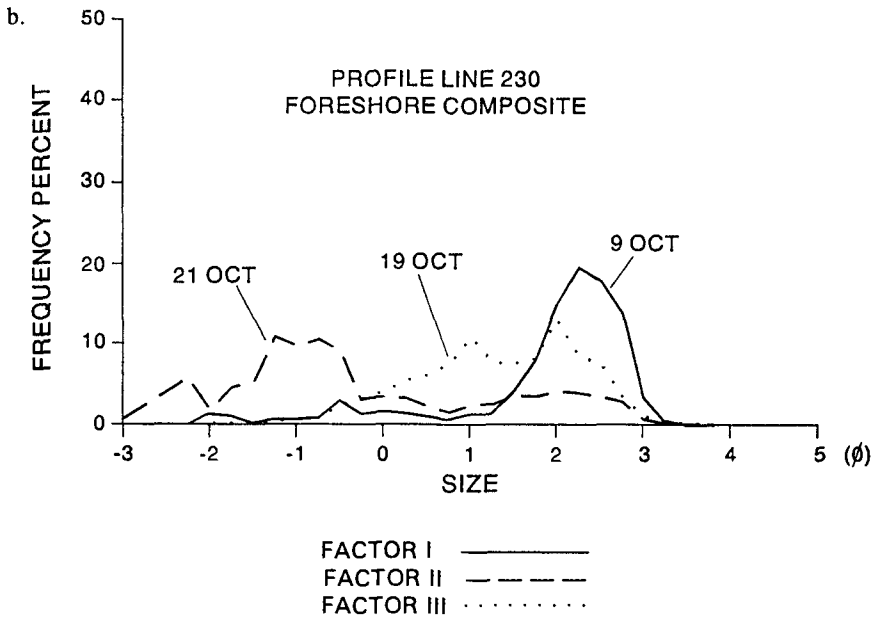
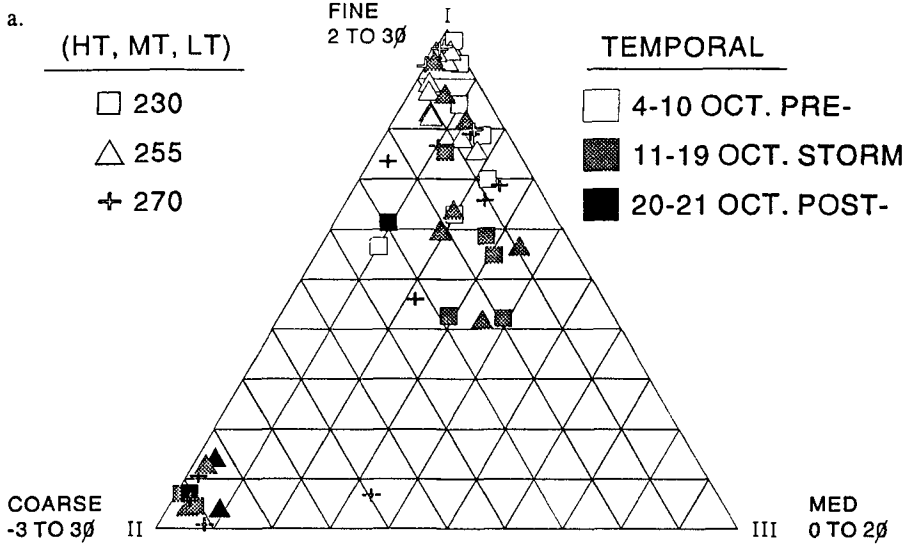


Figure 7. a) Foreshore composite factor analysis and b) examples of grain-size distributions representing Factor I, II and III groups.

all post-high wave samples (20-21 October) plotted strongly as coarse Factor II distributions. The 21 October line 230 sample distribution is an example of this coarse distribution resulting after the storm.

A picture emerges that foreshore and nearshore sediment dynamics are controlled by the wave and current input. During the time of low wave and current activity at the beginning of the experiment, little change was measured on the profile of the foreshore or bar/trough positions and little change in sediment distributions occurred. During the time of high wave and current activity at the latter part of the experiment, the foreshore remained basically unchanged, but the bar migrated seaward and the trough expanded in width. The sediment on the foreshore became coarser and more poorly sorted, particularly in the lower foreshore. Samples from the trough, bar and the 3-m depth also became coarser. Figure 8 illustrates the general trend of the pre- to post-storm sediment distribution change using the mid tide and 3-m depth samples from profile line 270 as an example. A coarse component is present in the grain-size distribution after the storm, possibly a lag deposit of underlying coarse layers exposed as the surficial finer material was removed. Further seaward at the 4-m, 5-m and 6-m depth samples, there was a minimal change in distributions as a result of the storm.

Correlation of sediment data in the trough, bar crest, 3-m, 4-m, and 5-m depth positions, with near real-time physical data such as significant wave height and mean cross-shore and mean longshore currents were possible with an array of sensors positioned 45 m to the north of the center line of sediment sampling. This array of 9 stations extended from the trough seaward over the bar to approximately the 5-m depth contour. The change in longshore current from flow to the south to flow to the north maintained the trough area while strong offshore currents were associated with seaward movement of the bar and the

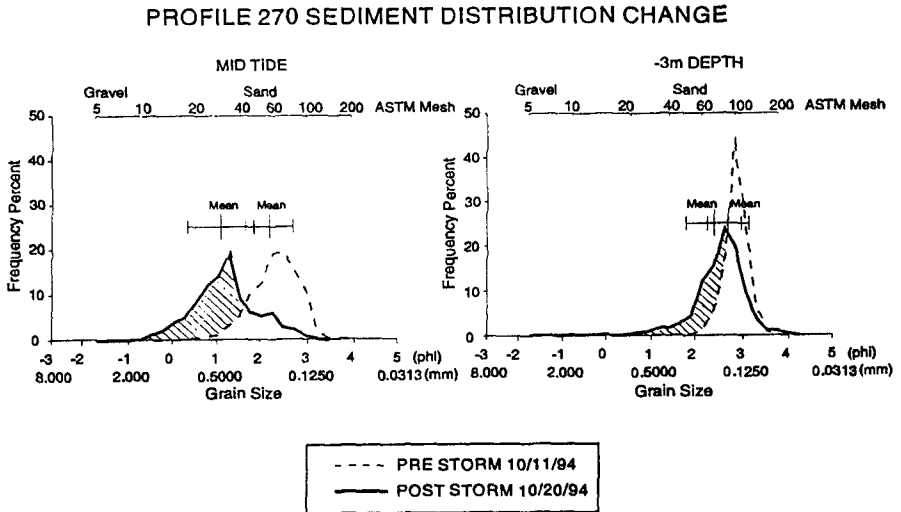


Figure 8. Post-storm coarsening of sediment at mid tide and -3 m depth at profile line 270.

development of a rip current. On the last two days of the experiment the strong currents dissipated and the bar moved landward. The 3-D component of beach morphology was observed with the formation of beach cusps and the rip current at the northern end of the study area. Sediments became much coarser on the foreshore, and a coarser component was present even in the trough, bar and at the 3-m depth position.

CONCLUSION

The dynamics and evolution of sedimentation patterns on beaches and their link to hydrodynamics are poorly understood and present problems in effectively managing erosion control and storm damage reduction. Present research, using sediment statistical data analysis, is proving beneficial to characterize beach sediment distributions and their spatial and temporal deposition patterns. This study afforded a unique opportunity to couple the beach profile evolution, sediment deposition patterns and their resulting grain size distributions with the physical processes active at that coast.

This research examines the interaction of sediment along a three-dimensional active profile during both erosional and accretional events. Previous sediment studies at the FRF were a long term (17.8 month) study limited to one profile (corresponding to Line 230 in this study) (Stauble, 1992) and a 3-D study of a small 50 m wide area of the foreshore during SANDYDUCK (Stauble et. al, 1993). The DUCK 94 profile response covering one storm event was typical of long-term profile response where the most active part of the profile (bar/trough area) alternately moved seaward during storms and landward during fair weather conditions. From the 3-D perspective, the erosion during high wave and strong offshore surf zone currents moves the bar seaward uniformly with a linear foreshore planform. The recovery phase was more three-dimensional. The bar remaining in a fixed seaward position in the presence of a rip current (north end of the study at Line 230), while the bar migrated landward as the wave and surf zone current energy decreased outside of the rip area (southern area of the study at Lines 255 and 270). The foreshore was also very three-dimensional with the formation of beach cusps during this recovery period.

A better understanding of the dynamic processes of sediment deposition and interaction with profile elevation change on a natural beach was documented. The zonation of sediment characteristics over the entire active beach profile provides a picture of cross-shore grain-size data variability, with highest variability on the foreshore. The low tide samples were the most coarse and poorly sorted, with decreasing grain size and better sorting in the offshore direction. Q-mode factor analysis indicated that the foreshore was finer during the calm period at the beginning of the experiment and became coarser during the storm and recovery period. A coarse lag component contributed to the coarsening of the foreshore. The present study provided more detail to similar findings of Stauble (1992) and Stauble et al. (1993). The nearshore became slightly coarser over the bar and out to the 4-m depth. The seaward most sample distributions (5-m, 6-m depth) remained unchanged throughout the study.

Future research needs should focus on the zonation of coarse material and the interaction of the vertical distribution of layered beds on the foreshore/trough area. Conservation of grain-sizes within the three-dimensional beach (cross-shore and alongshore) is still not well understood. A better understanding of sediment processes can provide input into beach profile numerical models. These studies will ultimately help to understand the fate of beach fill material placed anywhere on the beach profile.

ACKNOWLEDGEMENTS

This research was funded through the Coastal Research Program, Geological Analysis of Shelf/Beach Sediment Interchange work unit. The authors would like to thank J.B. Smith, Andrew Morang and the many volunteers who assisted in the field data collection effort. William Birkemeier provided helpful discussion and review, and along with Michael Leffler and the staff of the FRF provided many hours of assistance in collecting and compiling the profile and sediment data. Dr Steven Elgar provided hydrodynamic data in the trough area, Dr Charles Long provided the 8-m array wave data, Kent Hathaway provided video of the beach and Dr Rob Holman provided detailed topographic maps of the foreshore. Sediment analysis was performed by Robert Jones, Chris Murhead and Amy Hampton. Sediment analysis, data reduction and graphics was performed by Johnnie Davenport, with graphics assistance by Robert Chain. Permission to publish was granted by the office Chief of Engineers

REFERENCES

- Birkemeier, W.A., 1984. A User's Guide to ISRP: The Interactive Survey Reduction Program. Instructional Report CERC-84-1, U.S. Army Engineer Waterways Experiment Station, Vicksburg, MS., 114 p.
- Birkemeier, W.A., Long, C.E., and Hathaway, K.K., 1997. DELILAH, DUCK94, SandyDuck: Three Nearshore Field Experiments. *Proceedings 25th International Conference on Coastal Engineering*, Orlando, FL, ASCE, New York, N.Y., (this issue).
- Calliari, L.J., 1994. Cross-shore and Longshore Sediment Size Distribution on Southern Currituck Spit, North Carolina: Implications for Beach Differentiation. *Journal of Coastal Research*, Vol. 10 (2), pp. 360-373.
- Davis, J.C., 1973. *Statistics and Data Analysis in Geology*. John Wiley and Sons, New York, N.Y., 550 p.
- Friedman, G.M. and Sanders, J.E., 1978. *Principals of Sedimentology*. John Wiley and Sons, New York, N.Y., 792 p.
- Imbrie, J., and Purdy, E.G., 1962. Classification of Modern Bahamian Carbonate Sediments. *In*, Ham, W.E. (ed.), *Classification of Carbonate Rocks*, a Symposium, American Association of Petroleum Geologists Memoir 1, pp. 253-272.
- Klovan, J.E., 1966. The Use of Factor Analysis in Determining Depositional Environments from Grain-Size Distributions. *Journal of Sedimentary Petrology*, Vol. 36 (1), pp. 115-125.
- Reyment, R.A., Joreskog, K.G., and Marcus, L.F., 1993. *Applied Factor Analysis in the Natural Sciences*, 2nd Ed. Cambridge University Press, Cambridge, England, 371 p.
- Stable, D.K., 1992. Long Term Profile and Sediment Morphodynamics: Field Research Facility Case History. Technical Report CERC-92-7, U.S. Army Engineer Waterways Experiment Station, Vicksburg, MS., 252 p.
- Stable, D.K., Holem, G.W., Byrnes, M.R., Anders, F.J., and Meisburger, E., 1993. SUPERDUCK Beach Sediment Sample Experiment: Beach Profile Change and Foreshore Sediment Dynamics. Technical Report CERC-93-4, U.S. Army Engineer Waterways Experiment Station, Vicksburg, MS., 41 p.
- Syvitski, J.P.M., 1991. Factor Analysis of Size Frequency Distributions: Significance of Factor Solutions Based on Simulation Experiments. *In*, Syvitski, J.P.M. (ed.), *Principals, Methods, and Application of Particle Size Analysis*, Cambridge University Press, Cambridge, England, pp. 249-263.

CHAPTER 304

A STUDY ON FLOW STRUCTURE AND SUSPENDED SEDIMENT CONCENTRATION OVER SEAWEED BED

Gozo Tsujimoto

ABSTRACT

Numerical calculation of flow structure and the suspended sediment concentration over seaweed bed under surface wave is conducted using the $k-\varepsilon$ turbulence model. Velocity distribution and suspended sediment concentration over seaweed bed, which is made of a plastic sheet, are measured by use of the electromagnetic current meter and a turbidity meter, respectively.

The characteristic phenomenon such as the vortex formation over seaweed bed is simulated and the calculated vertical profile of suspended sediment concentration is similar to that of experiment. The value of drag force coefficient of seaweed is a few times larger than that of rigid seaweed.

I. INTRODUCTION

Seaweed bed in the sea is an important ground for fishes and shellfishes as nursery ground. So method for artificial seaweed bed creation and technique for selecting appropriate site have been studying. But there are many problems to be resolved. One of them is to understand the mechanism of sediment transport induced by the wave motion and the seaweed motion. The seaweed acts against the water body in motion as the drag force, and the flow mechanism is so complicated by that.

Also a study on wave attenuation and control of sediment transport by using the flexible artificial seaweed a like plastic sheet have been investigated recently. This paper presents an experimental approach and a numerical approach on a study of the flow mechanism and the concentration profile of suspended sediment over seaweed beds.

Dr. Eng., Associate Professor, Dept. of Civil Eng., Kobe City College of Tech., 8-3, Gakuen-Higashimachi, Nishiku, Kobe, 651-21, Japan

II. EXPERIMENTAL METHOD

The experiment was performed in a water tank which was 18m long, 0.6m wide and 1.0m high. Since the seaweed motion in the field is very complicated, an artificial flexible roughness element like a plastic sheet is used as the seaweed in this experiment (from now on, it is called seaweed). The plastic sheet is cut at space of 1mm to 10cm in the length, being placed at the bed. Number of seaweed and its settling space were made to change and eight test runs were performed as summarized in Table 1.

For each of the eight test run, capacitance wave gages were used for the measurement of the free surface elevations, the electromagnetic current meter for that of velocity and the turbidity meter for that of suspended sediment concentration. Sand with diameter of 0.014mm was used as bed materials. The bed material was placed in a uniform thickness of 8cm at the tank bottom, about 2.5m long and 0.4m wide. Also the natural frequency of used seaweed is measured by using the oscillating plate, and its value is between 4.5 and 5.5Hz. The output voltages of their measured values were transmitted to personal computer. In table 1, "u" stands for horizontal velocity, "w" for vertical velocity, "c" for concentration, "H" for wave height and "S" for settling space of seaweed. In the follow figures, the settling position of seaweed is marked as "↑" and the wave phase is set to be zero when the flow direction over the seaweed on the offshore side is changed from offshore to onshore.

Table-1 Experimental Conditions

<i>Run</i>	<i>H</i> (<i>cm</i>)	<i>Depth</i> (<i>cm</i>)	<i>Period</i> (<i>sec</i>)	<i>S</i> (<i>cm</i>)	<i>Number</i> <i>Seaweed</i>	<i>Item</i>
1	4.1	30	1.22		1	u, w
2	3.6	21	1.22		1	u,w,c
3	7.3	21	1.22		1	c
4	4.8	21	1.22	10	2	u,w
5	1.1	21	1.72	10	2	u,w,c
6	3.9	21	1.22	10	3	u,w
7	4.6	21	1.22	20	2	u,w
8	4.3	21	1.22	20	3	u,w

III. EXPERIMENTAL RESULTS

3.1 Velocity vector

Figure 1(a) and 1(b) shows the measured velocity over the seaweed without its motion at the wave phase of $t/T=0.25$ for run No.2 and over the seaweed with its motion at that of $t/T=0.5$. A blank space in fig.1(b) shows no data because of the limitation in measurement system. It is thought that formation of vortex over the vertical plate (like fig.1(a)) under the wave motion is seen at the wave phase of a wave crest. Meanwhile the vortex in fig.1(b) with the seaweed motion is formed over seaweed beds at the wave phase when the

flow direction change from onshore to offshore. There is a phase lag of $\pi/2$ on the formation of vortex between both fig.1(a) and (b) and the location of vortex formation in fig.1(b) is lower than that of fig.1(a), and after the vortex in fig.1(b) is expected, following the motion of the free surface.

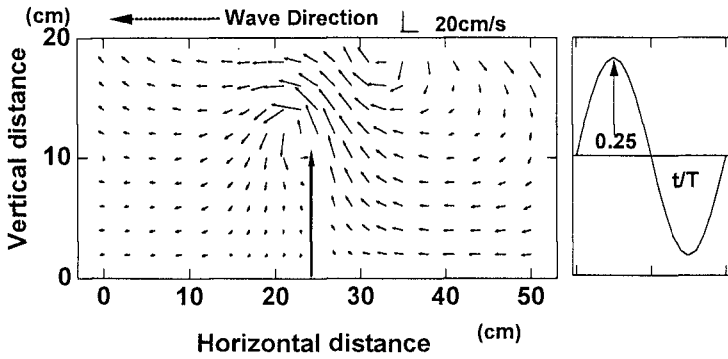


Fig.1(a) Velocity profile over seaweed without motion for run 2

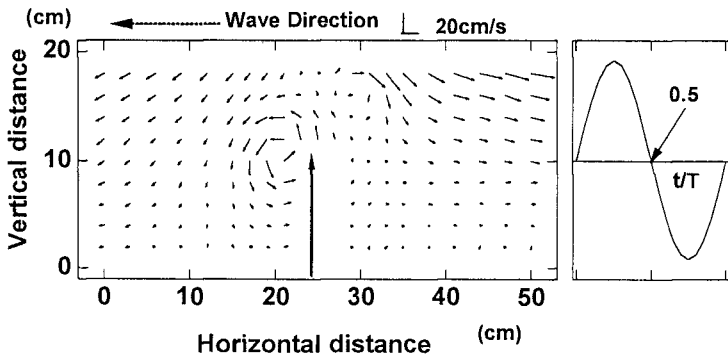


Fig.1(b) Velocity profile over seaweed with motion for run 2

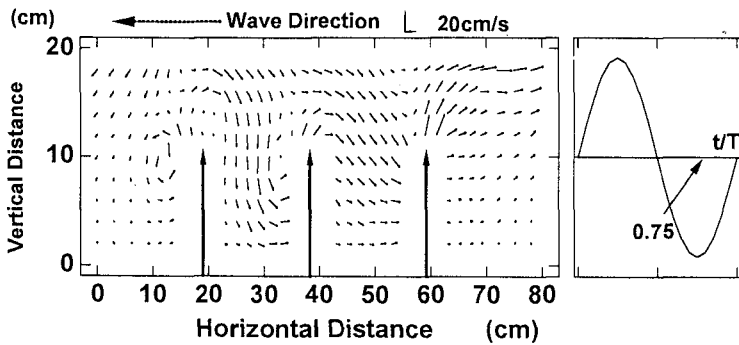


Fig.2. Velocity profile over three seaweed with motion for run 8

Figure 2 show the velocity profile for run No.8. The vortex formation is not seen clearly near the top of seaweed. The counter clockwise vortex, however, is formed over the seaweed bed in the onshore side when the flow direction changes from onshore to offshore and its scale is smaller than that of fig.1(b). Also the other clockwise vortex around there is seen. It is thought that the flow filed produced by the seaweed motion before the half period forms a wavy boundary layer along the top of seaweed, producing this clockwise vortex.

3.2 Steady velocity

Figure.3 shows the measured velocity averaged over a wave period for No.8. The flow profile near the top of seaweed is oscillated wavy. The velocity toward upward direction just over seaweed and the velocity toward downward direction between the seaweed are seen,

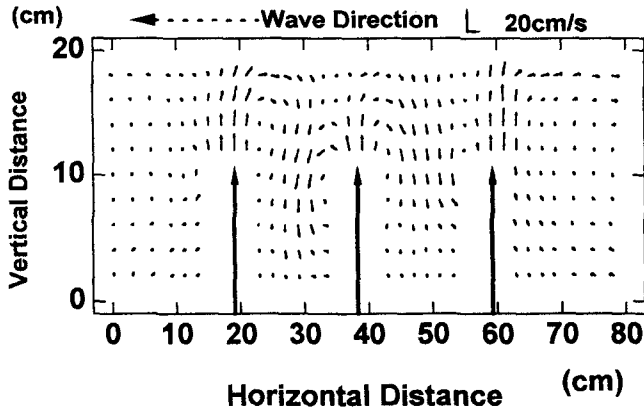


Fig.3 Steady velocity over seaweed for run 8

respectively, so that these flows form a set of circulation flow, having a large scale which compares with the scale of depth. It, therefore, has a effect on the suspension mechanism of sand particles close to the bed among the seaweed. These phenomena are seen in the case of run No.7, too. No vortex, however, is formed for run 4 and 5 in which the distance between both seaweed is half of run 7 or for run No.1,2 and 5 in which the number of seaweed is only one.

3.3 Suspended sediment concentration

It is known that there are three types of the distribution patterns of sediment concentration in the vertical direction, i.e. concave, convex and linear. Under non-breaking wave field, a region of high concentration is produced close to the bed due to the separated vortex over sand ripples and away from the bed surface the mean value of concentration is decreasing.

Figure 4 shows the vertical distribution of mean concentration for run 3 and in which the numbers show the distance from the settling position of seaweed. The distribution patterns of present study, as shown in fig.4, are concave with the turning point in the middle of depth, away from there all profiles reach a constant value. Those are not seen under non-breaking wave condition. Because no turbulent kinematics energy is supplied from the

upper layer unlike the breaking wave and the flow filed by wind shear stress(e.g., Nielsen 1985; Tsujimoto et al.1995). It is thought that the turbulent kinematic energy generated by separated vortex near the top of seaweed can picks up the sand particles from the bed. Especially the separated vortex on the onshore side is conspicuous, having a large scale in space, so that it exerts the major effects on the suspension mechanism of sand particles. Also sand ripples have been formed at the bottom through eight runs.

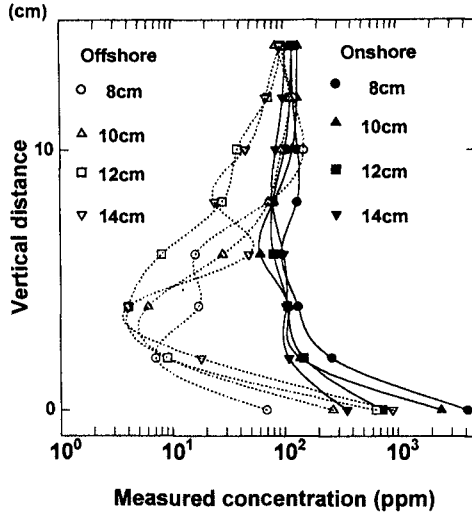


Fig.4 Measured mean concentration of suspended sediment

IV. NUMERICAL APPROACH

4.1 Previous study

Although there are many studies on the flow field with the substance in motion like seaweed, few have considered the mechanism of turbulent flow and sediment transport under wave motion. Asano et al.(1988) investigated the wave damping by using the artificial vegetation. Tsujimoto(1992) studied the mechanism of turbulent flow over an artificial seaweed field using the $k-\epsilon$ turbulent model. The agreement between the calculation and experiment, however, is not satisfactory.

These approaches are characterized by considering the effects of seaweed in the momentum equation as drag force. To calculate the turbulent flow filed over the seaweed bed, the turbulent productions and its dissipation by the seaweed motion should be modeled. There, however, is less knowledge on the production mechanism of turbulence over the seaweed bed under the wave motion and it is not easy for accurate determination on drag coefficient when drag force is adapted in the momentum equation.

4.2 Basic equation

The basic equations describing fluid motion consist of the continuity equation, momentum equations, diffusion equation of suspended sediment and conservation for

turbulent kinematic energy k and its dissipation rate ε . These equations are the same equations as author's used(1991) on calculation of suspended sediment over sand rippled and the effects of seaweed motion includes directly in the calculated grid without estimating that as drag force. These equations are written as follows:

For the continuity

$$\frac{\partial u}{\partial x} + \frac{\partial w}{\partial z} = 0 \quad (1)$$

For the momentum equation in x-direction

$$\begin{aligned} \frac{\partial u}{\partial t} + \frac{\partial u^2}{\partial x} + \frac{\partial uw}{\partial z} = & -\frac{1}{\rho} \frac{\partial p}{\partial x} + \nu \left(\frac{\partial^2 u}{\partial x^2} + \frac{\partial^2 u}{\partial z^2} \right) + \frac{\partial}{\partial x} \left(2\nu_t \frac{\partial u}{\partial x} \right) + \\ & \frac{\partial}{\partial z} \left(\nu_t \left(\frac{\partial u}{\partial z} + \frac{\partial w}{\partial x} \right) \right) \end{aligned} \quad (2)$$

For the momentum equation in z-direction

$$\begin{aligned} \frac{\partial w}{\partial t} + \frac{\partial uw}{\partial x} + \frac{\partial w^2}{\partial z} = & -\frac{1}{\rho} \frac{\partial p}{\partial z} + \nu \left(\frac{\partial^2 w}{\partial x^2} + \frac{\partial^2 w}{\partial z^2} \right) + \frac{\partial}{\partial z} \left(2\nu_t \frac{\partial w}{\partial z} \right) + \\ & \frac{\partial}{\partial x} \left(\nu_t \left(\frac{\partial u}{\partial z} + \frac{\partial w}{\partial x} \right) \right) \end{aligned} \quad (3)$$

For the diffusion equation of the suspended sediment

$$\frac{\partial c}{\partial t} + \frac{\partial uc}{\partial x} + \frac{\partial wc}{\partial z} = -\frac{\partial}{\partial x} \left(\left(\nu + \frac{\nu_t}{\sigma_s} \right) \frac{\partial c}{\partial x} \right) + \frac{\partial}{\partial z} \left(\left(\nu + \frac{\nu_t}{\sigma_s} \right) \frac{\partial c}{\partial z} \right) + \frac{\partial w_o c}{\partial z} \quad (4)$$

For k-equation

$$\frac{\partial k}{\partial t} + \frac{\partial uk}{\partial x} + \frac{\partial wk}{\partial z} = -\frac{\partial}{\partial x} \left\{ \left(\nu + \frac{\nu_t}{\sigma_k} \right) \frac{\partial k}{\partial x} \right\} + \frac{\partial}{\partial z} \left\{ \left(\nu + \frac{\nu_t}{\sigma_k} \right) \frac{\partial k}{\partial z} \right\} + P - \varepsilon \quad (5)$$

For ε -equation

$$\frac{\partial \varepsilon}{\partial t} + \frac{\partial u\varepsilon}{\partial x} + \frac{\partial w\varepsilon}{\partial z} = -\frac{\partial}{\partial x} \left\{ \left(\nu + \frac{\nu_t}{\sigma_\varepsilon} \right) \frac{\partial \varepsilon}{\partial x} \right\} + \frac{\partial}{\partial z} \left\{ \left(\nu + \frac{\nu_t}{\sigma_\varepsilon} \right) \frac{\partial \varepsilon}{\partial z} \right\} + \quad (6)$$

$$C_{1\varepsilon} \frac{\varepsilon}{k} - C_{2\varepsilon} \frac{\varepsilon^2}{k}$$

$$P = 2\nu_t \left\{ \left(\frac{\partial u}{\partial x} \right)^2 + \left(\frac{\partial w}{\partial z} \right)^2 \right\} + \nu_t \left(\frac{\partial u}{\partial z} + \frac{\partial w}{\partial x} \right)^2 \quad (7)$$

$$\nu_t = c_\mu \frac{k^2}{\varepsilon} \quad (8)$$

where x and z are the horizontal axis and the vertical axis, respectively, u and w are velocity in x and z direction, p is the pressure, ρ is the fluid density, ν and ν_t the

molecular and eddy viscosities, c is the suspended sediment concentration, w_0 is the fall velocity of the sediment particle and the constants in these equations are set at the values proposed by Rodi(1980) as given as follows:

$$C_{\mu} = 0.09, C_{1\epsilon} = 1.44, C_{2\epsilon} = 1.92, C_{3\epsilon} = 1.00, \sigma_k = 1.00, \sigma_\epsilon = 1.3, \sigma_t = 1.00 \quad (9)$$

The natural frequency of seaweed is different from that of the experimental wave, so that the oscillation period of seaweed was set to be the same as wave's. The seaweed motion should be coupled from the wave motion in a strict sense, but the experimental value of velocity of seaweed motion are used herein.

There is no relative velocity in the normal direction to the surface of seaweed, and it is given by the following equation;

$$Vn = V'n \quad (10)$$

where n is a unit vector in the normal direction to the seaweed surface, V is the velocity of water particle and V' is the velocity of seaweed motion. The values of V' are given by the displacement of seaweed per a second in the horizontal direction. The displacement of seaweed in the vertical direction is assumed so small that the vertical velocity can be neglected. The boundary conditions at seaweed surface on the turbulent kinematic energy k and its dissipation rate ϵ are the same as that at the bottom and the concentration is set to be zero there. Other boundary conditions are the same as author's(1991).

4.3 Method of calculation

The conditions of calculation are equivalent to that of the experiment as given in Table 1. Forty elements in the vertical direction are used and the number of element in the horizontal direction is changed from forty to one hundred twenty depended on number of seaweed and a fine mesh scheme is employed near the seaweed. The calculation was conducted to investigate the effect to the flow structure when the phase lag between the wave motion and the seaweed motion and the height of seaweed were changed.

V. CALCULATED RESULTS

5.1 Steady flow

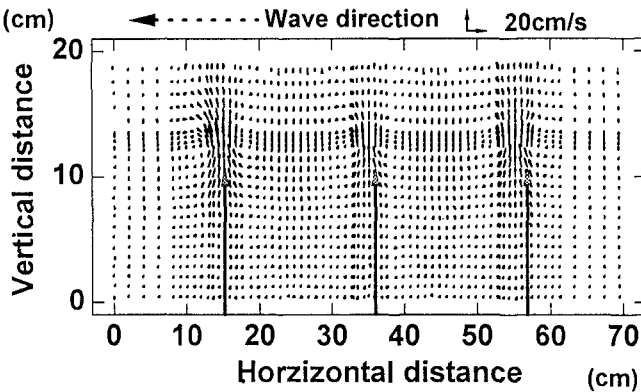


Fig.5 Calculated steady velocity

Figure 5 shows a steady velocity for run 8. The wavy flow near the top of seaweed and the vertical circulation flow between the seaweed are seen as shown in the experimental results (e.g. figure 3). These values are about 20cm/sec and approximately the same value as the experimental one. The calculated values of vertical downward direction, however, are smaller than the experimental values.

5.2 Velocity profile and suspended sediment concentration

Figure 6(a) and (b) show the calculated results on velocity and concentration for run 6. The separated vortex is not seen at the wave phase when a wave crest passes over the seaweed and the wavy flow is only formed near the top of seaweed. So the value of suspended sediment concentration is still low. The suspended sediment cloud is transported from the offshore side to the top of seaweed, but it has little sand particle. A small separated vortex is formed near the top of seaweed for fig 6 (b), but the suspended sediment between the seaweed could not be transported to the upper layer.

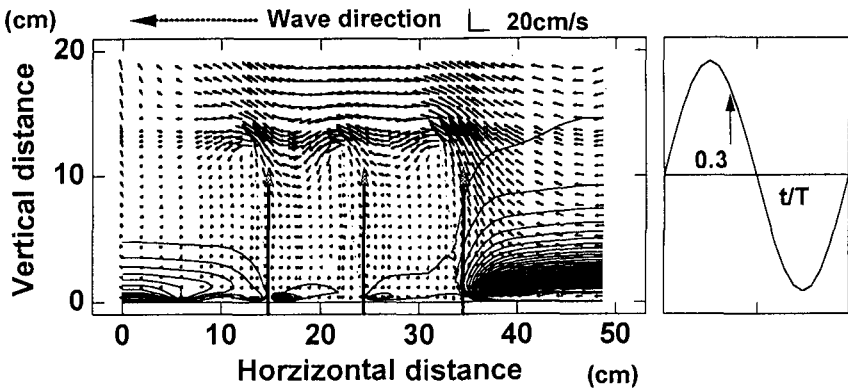


Fig.6(a) Calculated velocity and suspended sediment concentration for run 6

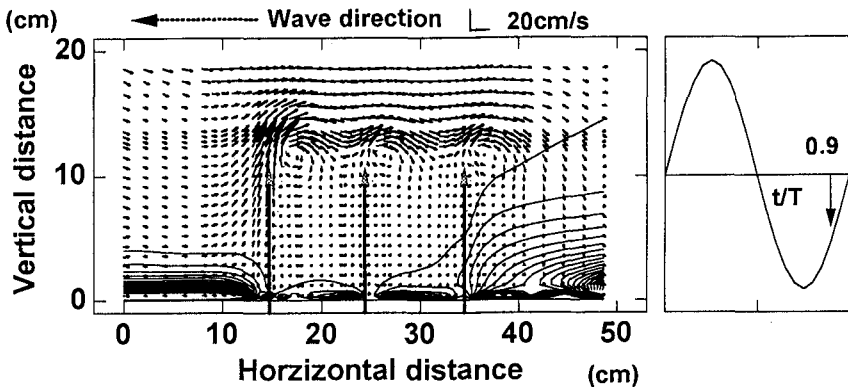


Fig.6(b) Calculated velocity and suspended sediment concentration for run 6

Figure 6(c) shows the calculated results at the same wave phase as that of figure 6 (b) for run 8. The settling space of seaweed in this figure is two times longer than that of figure 6(b). Since the separated vortex grows easily in size, much suspended sediment are transported to upward from the bed. The results of this figure gives an evidence that the settling space of seaweed is very important for suspended sediment transport.

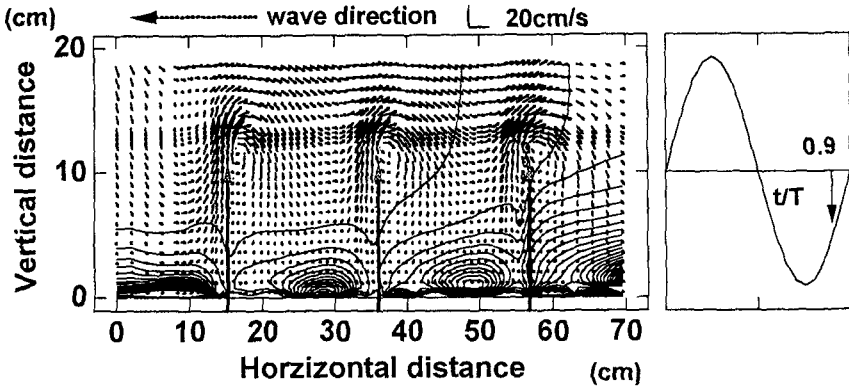


Fig.6(c) Calculated velocity and suspended sediment concentration for run 8

5.3 Suspended sediment concentration

Figure 7 shows the calculated vertical distribution of suspended sediment concentration averaged over a wave period, in which the number shows the distance from the position where the seaweed is located. The value of suspended sediment concentration close to the bed is lower than that of experiment, as the effects of sand ripples are not considered in the present calculation. The calculated results around the top of seaweed are close to the experimental values.

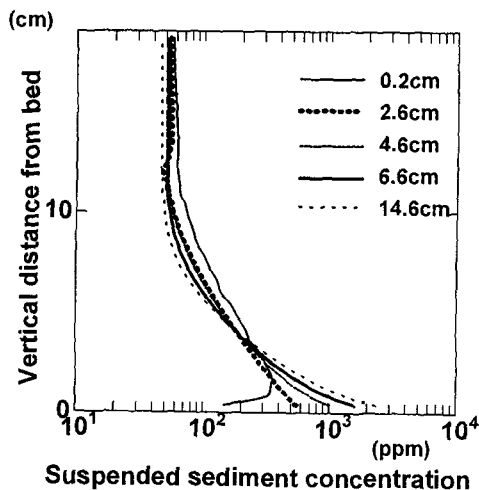


Fig.7 Calculated mean suspended sediment concentration for run 2

The suspended sediment concentration decreases lineally with increasing distance from the bed, whereas away from there it attains a constant value and the distribution pattern is concave. Also a certain level where the slope of the vertical distribution of the sediment concentration changes is approximately equal to the height of seaweed.

5.4 Vorticity

The experimental distribution of vorticity is shown in figure 8 for run 2. The vortex with negative sign at the preceding half period and the vorticity with positive sign at the next half period are seen near the top of seaweed.

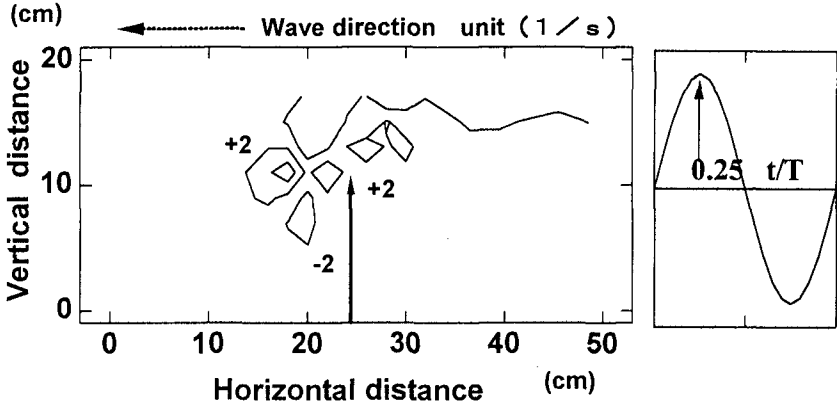


Fig.8 Contour lines of measured vorticity for run 2

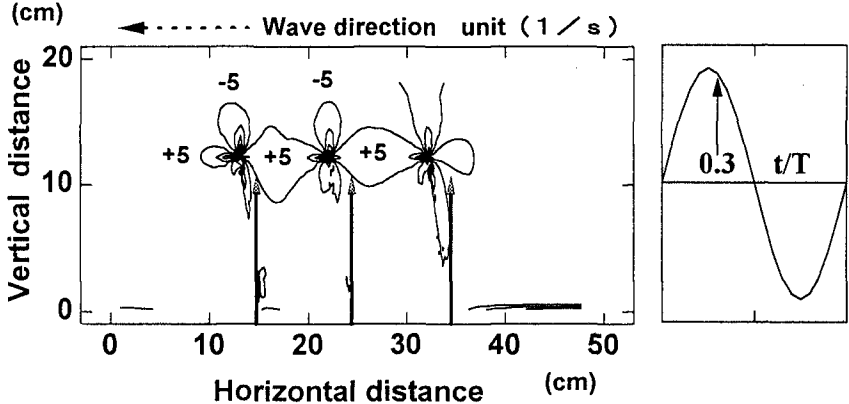


Fig.9 Contour lines of calculated vorticity for run 6

It is thought that the vorticity with positive sign is dominant at this phase; but the seaweed is oscillated at the same frequency of that of water particles toward the same direction, and the vorticity with positive sign are produced late. The similar results are obtained in the present calculation (no figure). The calculated results are shown in figure 9 for run 6. Each vorticity are combined among the seaweed, and they does not grow in size.

5.5 Coefficient of drag force

In the present study the effect of seaweed to the flow mechanism is considered by given the velocity of seaweed motion to calculated mesh. The seaweed field should be considered as the drag force averaged in space in the field, and the estimation on the coefficient of drag force are very important.

Hydrodynamic force $F(t)$ at the each wave phase is calculated by integrated the calculated hydraulic pressure along the seaweed surface, being separated into the drag force and the inertia force as shown eq.(11).

$$F(t) = \frac{1}{2} C_D \rho A u(t) |u(t)| + C_M \rho V \frac{\partial u(t)}{\partial t} \quad (11)$$

in where $u(t)$ is the horizontal velocity just over seaweed close to the free surface, C_D is the coefficient of drag force, C_M is the coefficient of inertia force, A and V are the reference area and volume, respectively. As shown by Ishida(1988), the values of C_D and C_M are assumed to be constant between the adjacent phase and eq.(11) is solved by using the simultaneous equations.

Figure 10 shows the variation of the horizontal velocity and the coefficient of drag force over both the seaweed and the fixed seaweed for run 2. The coefficient of drag force reaches the biggest value at the wave phase when the flow direction changes from onshore to offshore and constant value at other wave phase. Also its value over the seaweed is bigger than that over the fixed seaweed. The drag coefficient C_D is changeable at the each phase, varying from the used value of horizontal velocity. The drag coefficient C_D is generally estimated by the number of the Keulegan-Carpenter number at the wave phase when the wave crest or the wave trough passed over the reference point, when the drag force become maximum.

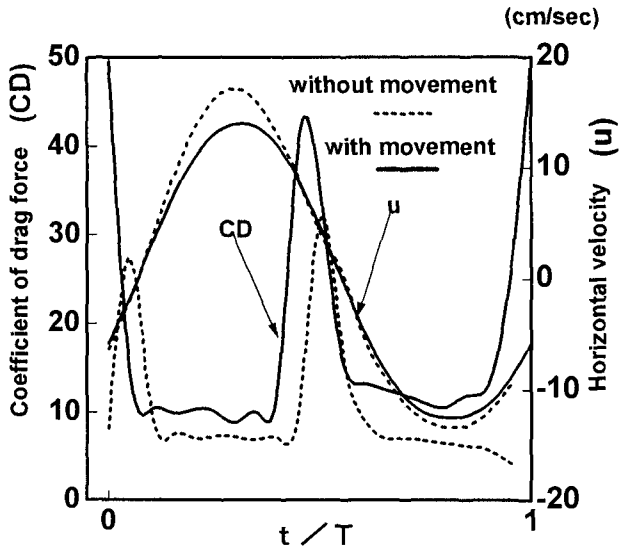


Fig.10 Time history of drag force and horizontal velocity

It is shown through the experiment that the wave phase lag between the seaweed motion and the wave motion is $\pi/2$. The wave phase lag is varied from the wave condition and kinds of seaweed. Figure 11 shows the relationship between the drag coefficient C_D and K.C. number when the wave phase lag between the seaweed motion and the wave motion is changed from 0 to $3\pi/2$. With increasing the value of KC number, the value of KC number attains to about 5. That is similar to Ishida's results, who measured the wave force acting on a pile structure.

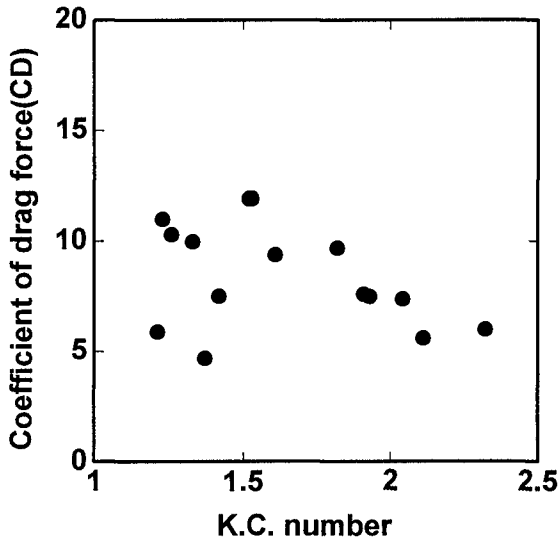


Fig. 11 Drag coefficient and KC number

VI. CONCLUSIONS

The seaweed bed is made of a plastic plate which is oscillated symmetrically with the wave motion and the flow mechanism and suspended sediment concentration over the seaweed bed were investigated by an experimental approach and a numerical simulation. The wavy flow near the top of seaweed and the vertical circulation flow which compared with the scale of water depth are produced by the seaweed motion, respectively. As the separated vortex is formed at the middle of depth, the value of suspended sediment concentration reaches a constant one or increase by the turbulence kinematics energy. That can not be seen under the non-breaking wave.

The turbulent calculation considered the existence of seaweed in the calculated mesh showed as follows:

- 1) The separated vortex over the seaweed is formed later than that over the fixed seaweed.
- 2) The value of suspended sediment concentration attains a constant value away from the bed.
- 3) The settling space between the seaweed and the wave phase lag between wave

motion and seaweed motion have a major effect on the flow mechanism.

- 4) The value of drag coefficient C_D of seaweed estimated as the drag force is several times larger than that of a plate(2.01).

ACKNOWLEDGEMENT

This experiment work was conducted at Kobe City College of Technology. The author wish to express thanks to graduate students; Y.Nagao, H.Arima, Y.Ito and Y.Masuda. A part of this study is supported by the Grant in Aid for Science Research Ministry of Education.

Reference

- Asano T., S. Tsustui, and T. Sakai(1988):Wave damping characteristics due to seaweed,Proc.35th Coastal Eng. Conference in Japan,pp.138-142(in Japanese).
- Ishida, H. and Tamura K.(1988):Coefficient of drag force of a pile structure under separated flow ,Proceeding. of JSCE,No.393,II-9,pp.120-130(in Japanese).
- Nilesen P.(1984):Field measurement of time-averaged suspended sediment concentration under waves, Coastal Engineering,Vol.8,pp.51-72 .
- Tsujimoto G., N. Hayakawa, M. Ichiyama, Y. Fukushima and Y. Nakamura(1991) :A study on suspended sediment concentration and sediment transport mechanism over rippled sand bed using a turbulence model, Coastal Engineering in Japan,Vol.34,No.2,pp. 177-189.
- Tsujimoto G.(1992):Flow and suspended sediment concentration over seaweed field, Proceeding Coastal Eng. of JSCE,Vol.39,pp.276-280(in Japanese).
- Tsujimoto G. and H.G.Stefan(1994):Simulation of sediment resuspension transport by wind driven current in a shallow lake, Research Reports of Kobe City College of Technology No.32,pp.65-72.

CHAPTER 305

An Energetics Approach for Suspended Sand Transport on Macrotidal Ridge and Runnel Beaches

George Voulgaris¹, Travis Mason² and Michael B. Collins²

Abstract

High frequency observations of hydrodynamics and suspended sediment concentration were acquired from the intertidal zone of a macrotidal ridge and runnel beach. The hydrodynamic data from the electromagnetic current meters were used to calculate sediment transport rates according to Bailard's (1981) energetics model. Additionally, suspended sediment fluxes were calculated for the period of data collection. The contribution of long waves, short waves and mean currents to suspended sediment transport was examined. Application of the energetics model suggested that suspended sediment is the dominant mode of transport. Further, it showed that the waves define net sediment transport rate and direction. However, the measurements revealed that the transport due to mean currents was dominant. The discrepancy between the model and measurements was attributed to vortex ripples which were developed in the intertidal zone. Bailard's model failed to predict the oscillatory mode of transport but it was found to predict accurately the mean mode of suspended sediment transport assuming an efficiency factor value of 0.021 is used in the calculations.

Introduction

Sand resuspension under the action of waves and currents is the primary process controlling seabed erodibility. Successful parameterization of this mechanism is the key element for the development of accurate and predictive morphological models. Presently, Bailard's (1981) sediment transport formula is considered one of the best theoretical models for time-dependent, cross-shore sediment transport (Schoonees and Theron, 1995) and is widely used for the prediction of changes in the coastal zone (*e.g.* Scott *et al.*, 1991). The model is based on the importance of various moments of the fluid velocity in determining transport rates. Previous studies examined the various velocity moments

¹Woods Hole Oceanographic Institution, Woods Hole, MA 02543, U.S.A.

²Department of Oceanography, University of Southampton, Southampton Oceanography Centre, European Way, Southampton, SO14 3ZH, U.K.

under either wave (*i.e.*, Guza and Thornton, 1985; Russell *et al.*, 1995) or steady current dominating conditions (*i.e.*, Thornton *et al.*, 1996). Ridge and runnel beaches, however, are found throughout areas with moderate wave conditions (short-fetched seas) and high tidal ranges (King and Williams, 1949; Orford and Wright, 1978). The combination of high tidal currents and moderate wave activity invalidates the assumptions of the previous investigators regarding the dominant forces (*i.e.* waves or steady currents).

In this contribution, high frequency measurements of instantaneous currents and suspended sediment concentration were obtained on a macrotidal ridge and runnel beach. The data collected are used to: (i) examine determine the relative contributions of long waves, short waves and mean currents to suspended sediment transport; (ii) evaluate the energetics sediment transport model (Bailard, 1981) and velocity moments for macrotidal conditions; and (iii) calibrate the energetics model for suspended sand transport.

Energetics Model

Bagnold's (1966) energetics-based total load sediment transport model for streams has been used as a basis for the development of a model of time-varying transport over a plane sloping bed. The idealised equation for the total (*i.e* bedload and suspended load, $\langle I_t \rangle$) time-averaged immersed weight sediment transport is given by Bailard (1981):

$$\begin{aligned} \langle \vec{I}_t \rangle = & \rho C_f \frac{\epsilon_b}{\tan\phi} [\langle |\vec{U}_t|^2 \vec{U}_t \rangle + \frac{\tan\beta}{\tan\phi} \langle |\vec{U}_t|^3 \rangle \vec{i}] \\ & + \rho C_f \frac{\epsilon_s}{W} [\langle |\vec{U}_t|^3 \vec{U}_t \rangle + \frac{\epsilon_s}{W} \tan\beta \langle |\vec{U}_t|^5 \rangle \vec{i}] \end{aligned} \tag{1}$$

where W is the sediment fall velocity; ϵ_b and ϵ_s are the bed load and suspended load efficiency factors, respectively; β is the local bed slope; ϕ is the angle of internal friction of the sediment; i is the unit vector in the down-slope, offshore (-x) direction; and U_t the total instantaneous velocity.

The above general model has been analysed into the cross-shore ($\langle I_x \rangle$) and longshore ($\langle I_y \rangle$) components for application with random waves (Guza and Thornton, 1985):

$$\begin{aligned} \langle I_x \rangle = & \rho C_f U_m^3 \left\{ \frac{\epsilon_B}{\tan\phi} \cdot [\psi_1 \cos\alpha_1 + \delta_u^3 + \delta_u \left(\frac{1}{2} + \cos^2\alpha_2 + \delta_u^2 \right) + \delta_u \sin\alpha_3 \cos\alpha_3 \right. \\ & \left. + \frac{\tan\beta}{\tan\phi} u^3 \right\} + \frac{U_m}{W} \epsilon_s [\psi_2 \cos\alpha_5 + \delta_u \cdot u^3] + \frac{U_m^2}{W^2} \epsilon_s^2 \tan\beta \cdot u^5 \end{aligned} \tag{2}$$

$$\begin{aligned} \langle I_y \rangle = & \rho \cdot C_f \cdot U_m^3 \cdot \left\{ \frac{\epsilon_B}{\tan\phi} \cdot [\psi_1 \sin\alpha_1 + \delta_v^3 + \delta_v \left(\frac{1}{2} + \sin^2\alpha_2 + \delta_u^2 \right) \right. \\ & \left. + \delta_u \sin\alpha_3 \cos\alpha_3 \right] + \frac{U_m}{W} \epsilon_s [\psi_2 \sin\alpha_5 + \delta_v \cdot u^3] \end{aligned} \tag{3}$$

where U_m is the oscillatory velocity (rms) amplitude. δ_u and δ_v are the steady current strength for the cross-shore and longshore directions defined as \bar{u}/U_m and \bar{v}/U_m , respectively. The most important normalised velocity moments are:

$$\psi_1 = \frac{\langle |\vec{U}_t|^2 (u_{osc}, v_{osc}) \rangle}{U_m^3} \quad (4)$$

$$\psi_2 = \frac{\langle |\vec{U}_t|^3 (u_{osc}, v_{osc}) \rangle}{U_m^4} \quad (5)$$

where the symbols $\langle \rangle$ denote a time-averaged quantity. The velocity components are decomposed into an oscillatory (u_{osc} , v_{osc}) and a mean (\bar{u} , \bar{v}) part, so that:

$$|\vec{U}_t| = \sqrt{u_{osc}^2 + v_{osc}^2 + \bar{u}^2 + \bar{v}^2 + 2(u_{osc} \bar{u} + v_{osc} \bar{v})} \quad (6)$$

The definitions of the remaining parameters can be found in Guza and Thornton (1985, see page 251, eqns 35 and 36). Briefly, α_n ($n=1$ to 5) are the angles associated with the directional characteristics of the various flow moments, while u_3^* and u_5^* are the odd moments of the total instantaneous flow, integrated over the whole wave period. Application of the above model requires information on the moments of the instantaneous velocity field.

In order to obtain a quantitative prediction of immersed weight sediment transport rate, values for the drag coefficient (C_D) and the efficiency factors are required. Bowen (1980) proposed a value of 0.005 for the drag coefficient. Here, the drag coefficient is determined by the flow conditions as function of the ratio z_r/h (Soulsby *et al.*, 1993). The efficiency factors used in this model are known to depend on factors such as flow conditions (laminar or turbulent, steady or unsteady, etc), and the grain size characteristics of the sediments. A list of various suggested values is presented in Table 1.

Author	Bedload	Suspended load
Bagnold (1966), steady flow	0.13	0.010
Bailard (1981,1982) longshore	0.21	0.025
Bailard (1981,1982), cross-shore	0.10	0.020
Bowen (1981), cross-shore	$0.15 \tan \phi$	0.010

Table 1. Efficiency parameter values proposed by various investigators.

Guza and Thornton (1985) applied field data to Bailard's cross-shore sediment transport model to determine the dominant terms in the bedload and suspended load modes. They concluded that suspended load dominates sediment transport processes and

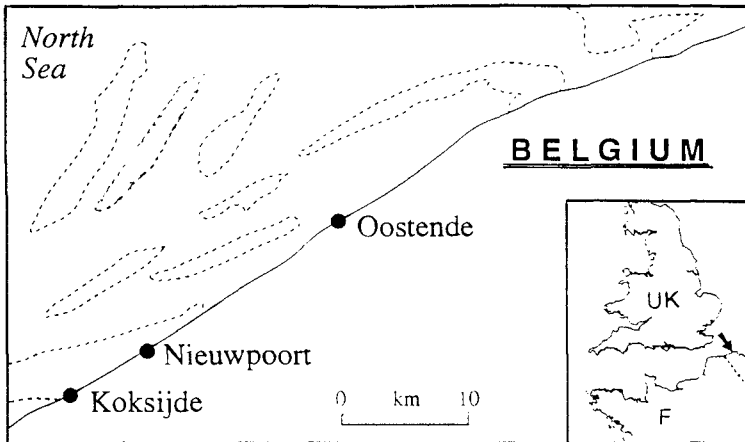


Figure 1. Location of experimental site.

that the normalised velocity moments ψ_2 and $\delta_u u_3^*$ are the most important terms, representing the contribution of the oscillatory and mean flow to suspended sediment transport, respectively.

Bowen (1980), Roelvink and Stive (1989), and Russell et al (1996) have extended Guza and Thornton's (1985) work by examining the relative importance of the long, short period oscillations and mean flow to cross-shore suspended sediment transport. Their analysis was based on the assumption that the longshore currents are much smaller than the orbital velocities ($\bar{v} \ll U_m$). On the other hand, Thornton et al. (1996) presented an expansion of equation (1) which is based on the assumption that mean currents dominate the flow.

Macro-tidal ridge and runnel beaches are found though, throughout areas with moderate wave conditions (short fetched seas); this, combined with the high tidal currents invalidates the assumptions used by the above investigators. In the present analysis the velocity terms of eqns (2) and (3) are examined, assuming that both waves and currents are of equal importance. In addition, almost all of the above studies concentrated on the cross-shore direction only. Due to the importance of the longshore tidally-induced currents found on ridge and runnel beaches it is considered appropriate that both horizontal components (cross-shore and longshore) should be included in the velocity moments analysis.

Experimental Site - Data Collection

The field measurements were obtained at Nieuwpoort-aan-Zee, situated some 13km southwest of Oostende (Fig. 1), from 20th February to 4th March 1994 (Julian days 51-63). The experimental site was outside the influence of any man-made obstructions, such as groynes which are typical elsewhere. The sediment is well sorted, fine/medium sand (mean grain size 0.183mm); at the time of the observations the average beach slope ($\tan\beta$) was 0.012 with an intertidal zone of between 250 and 500m wide. The

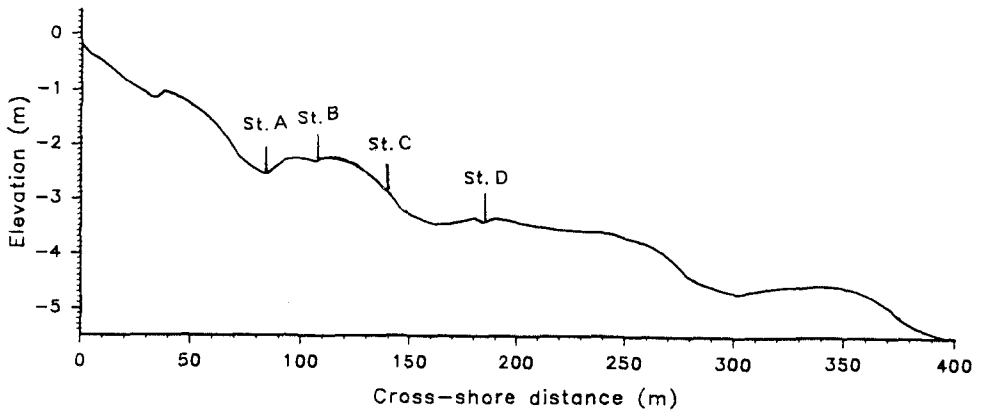


Figure 2. Cross-sectional profile of the intertidal zone and locations of instrument stations (A, B, C and D).

experimental site exhibited typical ridge and runnel beach characteristics (Fig. 2) with up to five well defined ridges exposed at low tide.

Tides in this area are semi-diurnal with a large neap to spring variation of 2.7 to 6.5m during the deployment period. Offshore currents are characterised by elongate and asymmetrical tidal current ellipses, with a northeasterly directed residual flood displacement controlling the sub-tidal sediment transport pathways (De Moor, 1991).

The wave climate of the area is typical of short-fetched seas with wave periods 3 to 6s. However, typical wave periods recorded during the deployment period were between 4 and 12 seconds with offshore wave heights of the order of 0.5 to 1m. Dominant offshore wave direction, extracted from wave hindcasting modelling (U.K. Meteorological Office), is primarily from the west-southwest (23% of the time) and secondarily from the north-northeast (10% of the time).

Four instrumented stations were deployed in the intertidal zone (Fig. 2). The instruments deployed consisted of electromagnetic current meters (Stations A, B, C and D), pressure transducers (Stations B, C and D) and optical backscatter sensors (OBS) for measuring instantaneous suspended sediment concentration (SSC, Stations C and D). The OBS data obtained from station C were of too poor quality to be used for analysis. Therefore, the results presented here are based on the data collected at Station D which was located in the upper mid-tidal zone and on the top of a ridge with a relatively flat crest (Figure 2).

Four 2-axis electromagnetic current meters, 3 OBS sensors and a pressure transducer were deployed at station D. All instruments were cantilevered from a stainless steel pipe, set vertically into the beach sand during low water. Three of the electromagnetic current meters were arranged to measure instantaneous horizontal currents at three levels above the sea bed (21.5, 48 and 108.5cm, respectively). The fourth sensor was orientated to measure vertical currents at 70cm above the sea bed. The OBS sensors were installed at elevations 9, 19 and 34.5cm above the sea bed, respectively. Data were collected when

the instruments were fully submerged and for consecutive time intervals of approximately 17min, spanning flood, high water and ebb tide. The sampling frequency within each burst was 8 Hz.

Sediment from the deployment area was used for the calibration of the OBS sensors. A temporally variable background level of "turbidity" was observed during the data collection period. This was due to fine material in suspension, referred to hereafter as "washload", coming from Nieuwpoort Harbour. To maintain uniformity in data analysis, the offset due to this washload was determined as the 10th percentile of the sample values as suggested by Aagaard and Greenwood (1995). This was the magnitude of concentration which corresponded approximately to a significant break in the cumulative frequency of signal values and best represents the separation between the background signal and sediment resuspension events. As Aagaard and Greenwood (*op. cit.*) noted such an approach may introduce some error in computing absolute magnitudes of sediment transport rates. Laboratory experiments showed that this error is less than 10%.

Hydrodynamic and suspended sediment concentration measurements were obtained during 3 tidal cycles on 3rd and 4th March, 1994 (Julian days 62 and 63, respectively). In particular, 6 data sets (runs) were collected during the flood of the morning flood tide of Julian day 62; 9 runs during the evening of Julian day 62; and finally 12 runs were collected during the morning of Julian day 63.

Time-series of cross-shore and longshore velocity (u, v) and sediment concentration (c) were plotted to check data quality. Statistical descriptions of velocity and sediment concentration were computed (i.e mean and standard deviations). Wave characteristics were computed using the moments of the spectra of the pressure transducer signal after correcting for depth attenuation (Voulgaris, 1992). Significant orbital velocities were estimated from the standard deviation of each time-series ($U_m = (2(u_\sigma^2 + v_\sigma^2))^{1/2}$).

The total fluxes have been analysed into mean and oscillatory modes with the latter being decomposed further into fluxes due to incident short (gravity, subscript s) waves and long period (infragravity, subscript L) flow.

$$\overline{u \cdot c} = \overline{u \cdot c} + \overline{u_{osc} \cdot c_{osc}} = \overline{u \cdot c} + \overline{u_S \cdot c_S} + \overline{u_L \cdot c_L} \quad (7)$$

The mean component was calculated (by averaging the entire 17 minute record), and then subtracted from the record, to obtain the oscillatory component. The infragravity (long) component of the signal (u_L, v_L and c_L) was calculated by applying a low-pass filter (cut-off frequency 0.06Hz) to the oscillatory component. The infragravity component was subtracted from the total oscillatory component, thus giving the gravity contribution.

Local fluxes were calculated for each data run according to eqn. (7), for both the cross-shore and longshore directions and for the three elevations above the sea bed where SSC measurements were obtained. Measurements from the current meter installed at 21.5cm above the sea bed were used for the local flux calculations. Oscillatory currents were assumed to be constant through the water column whilst a logarithmic distribution was assumed for estimating the fluxes due to mean currents.

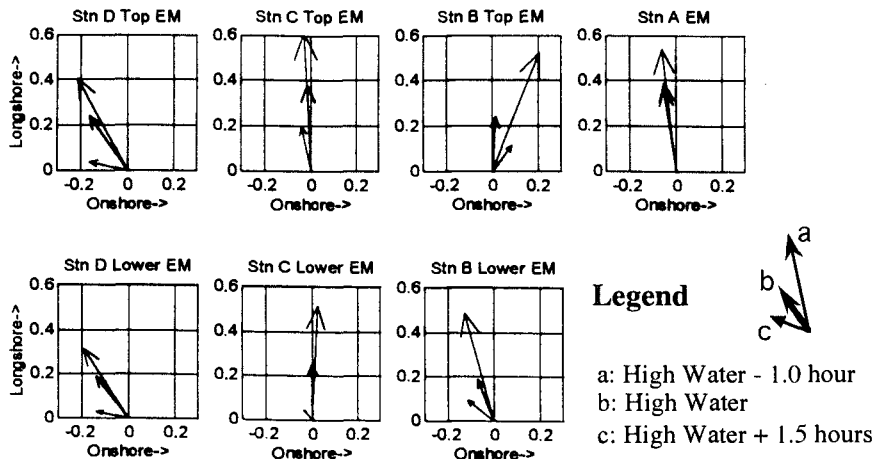


Figure 3. Vector diagrams of mean flow in the intertidal zone (for locations see Fig. 2) at 1 m (top row) and 0.2m (bottom row) above the sea bed (units in m/s).

Results

Overview of Hydrodynamics

In this section an overview of the hydrodynamic conditions in the intertidal zone is presented. This is based on observations from the whole of the experimental period. Typical mean flow patterns in the intertidal zone were found to be tidally-induced. Figure 3 shows the magnitude and direction of the mean current, for a typical tide, before (-1 hour) during and after (+1.5 hours) high water. It is evident that the dominant flow direction is consistently alongshore in the positive (northeast) direction. Maximum longshore flow occurs during the flood stage of the tide and the magnitude of the longshore current reduces as the tide progresses. Preliminary analysis of the hydrodynamic data collected indicates the this behaviour is due to bed friction which causes the longshore currents to lead the tidal elevation inshore. The mean cross-shore flow is generally offshore for all stations. An exception to this is Station B where the currents at 1 m above the bed are generally directed onshore. This station is located at the top of a ridge (see Fig. 2) where the waves exhibit their maximum asymmetry, thus this onshore flow is attributed to onshore mass transport which is balanced by an offshore flow near the seabed.

The wave climate in the intertidal zone exhibits a dependence on tidal stage (ebb, flood, see Figure 4). Local wave height is larger during the flood than during the ebb stage of the tide. This is more enhanced at the offshore stations C and D). This wave height dependence on tidal stage is the result of the interaction of the waves with the tidally-induced longshore currents. During flood, the currents are strongest and are directed toward the northeast. This results in the currents opposing the surface waves which, during the time of observation, were propagating at an angle towards the southwest. This

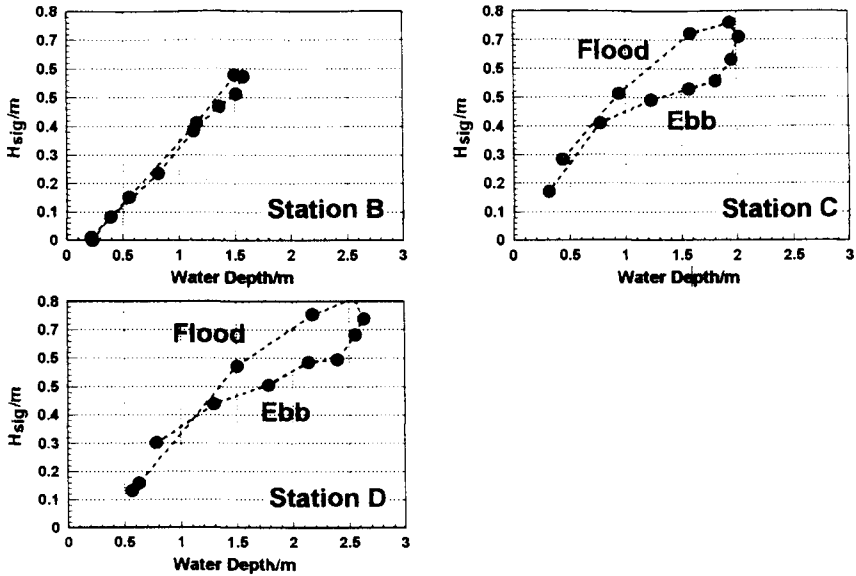


Figure 4. Tidal modulation of the local wave height (H_{sig}) for stations B, C and D (for location see Fig. 2).

opposition of waves and currents resulted in an increased wave steepness. During the ebb stage of the tide, the current strength is significantly reduced (see Figure 3), so that the interaction is much lesser, leading into less steep waves.

Velocity Moments

The relevant flow moments to sediment transport are examined in order to identify the most important terms for macrotidal beaches. Following Guza and Thornton's (1985) approach, the field flow data collected at station D from the lowest current meter are used to estimate the terms of eqns. (2) and (3).

The values of the individual terms such as ψ_1 , ψ_2 , u_3^* , u_5^* , $\delta_{||}$, δ_v and the angles α_1 , α_2 , α_3 , and α_5 have been evaluated for each run during the data collection period and the results are shown in Figure 5. The nonlinear scalar moments ψ_1 and ψ_2 are linked in the transport eqns (2) and (3) to the angles α_1 and α_5 . The moments ψ_1 and ψ_2 , (Fig. 5a) are associated with the wave asymmetry and this is why their variation through the tidal cycles corresponds to the variation in the wave orbital velocity field, as discussed in the previous section (see Fig. 4). However, in the case of a dominant cross-shore oscillatory component, the angles α_1 and α_5 in the case of a dominant cross-shore oscillatory components are expected to be around zero or 180degs (Guza and Thornton, 1985). In the present data set though α_1 varies between -10 and 10 degs with an average value of 5 degs (Figs 5d and e). The angle α_5 is around zero for the first and the last tidal cycles but achieves values of up to 20 degs during the second tidal cycle implying that a significant part of the oscillation occurs in the alongshore direction as well. However these angles are linked to the velocity

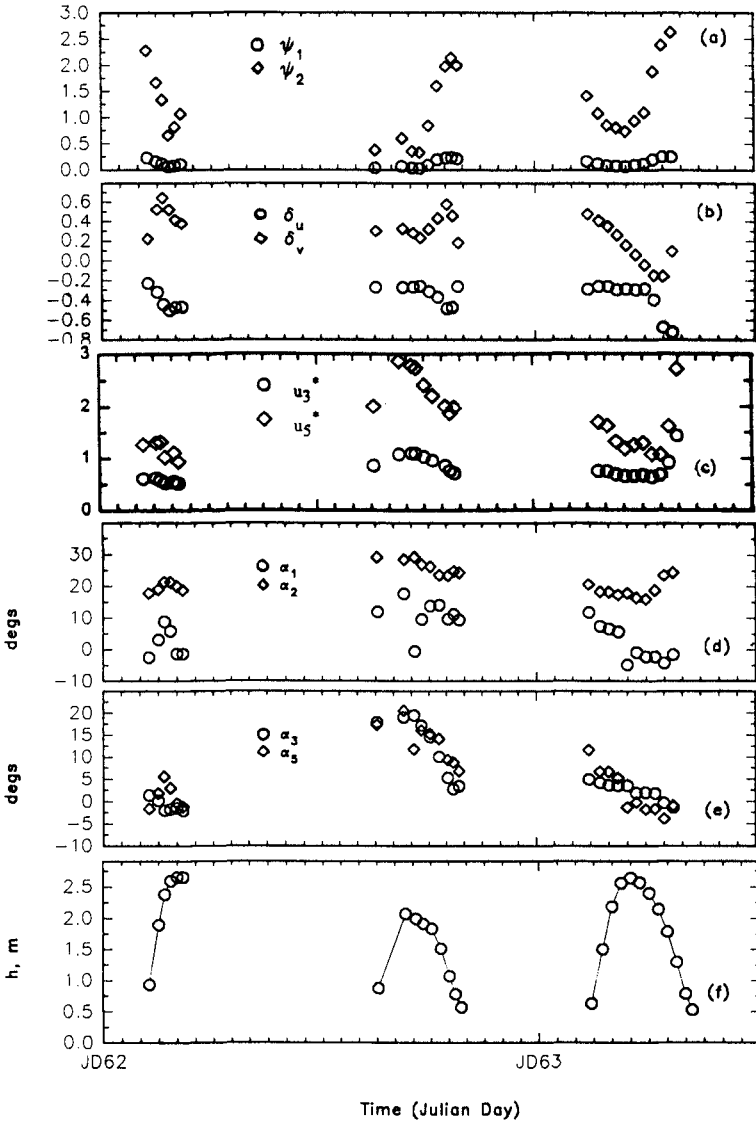


Figure 5. Velocity moment terms used in Bailatd's (1981) energetics sediment transport model (eqs (2) and (3)) as calculated from the measured current velocities from Station D.

moments through their cosine which for the extreme values of 10 and 20degs for the α_1 and α_5 , are 0.98 and 0.94 respectively; this implies that omission of these terms will involve an error of 2 and 6%, respectively in the sediment transport rate attributed to these particular terms.

The relative current strength terms δ_u and δ_v vary in accordance with the mean currents observed at the measuring station. It is characteristic that both terms are very important for ridge and runnel beaches reaching absolute values of up to 0.8 which is significantly higher than the average value of 0.01 observed by Guza and Thornton (1985).

The terms $u3^*$ and $u5^*$ express the contributions of the total currents (mean and oscillatory flow) averaged over the whole wave period. In Guza and Thornton's (1985) studies, these were dominated by contributions from the oscillatory component of the cross-shore currents only. In the present study, both oscillatory and mean currents appear to define these moments. It is characteristic that $u3^*$ is almost constant throughout the data collection period, with an average value of 2.5 (standard deviation 0.34). This value is larger than the theoretical one, derived either assuming a sinusoidal wave ($u3^*=0.42$) or a Gaussian distribution of the wave field ($u3^*=0.56$) with the latter being in good agreement with the field data collected presented by Guza and Thornton (1985). The increased value in the present data set is due to the strong mean flows present which produce an asymmetry of instantaneous flow vector during a wave cycle. The moment $u5^*$ exhibits significant variations throughout the three tidal cycles.

The relative magnitudes of the bedload and suspended load sediment transport and of each individual term of equations (2) and (3) has been examined, assuming that $\epsilon_s=0.025$ and $\epsilon_b=0.20$. Each sediment transport term in eqns (2) and (3) was calculated and then multiplied by the appropriate factor ($\epsilon_b/\tan\phi$, $U_m\epsilon_s/W$). The contribution of each term to the total sediment transport was expressed as a percentage of the total (bedload and suspended load) gross sediment transport rate, with the sign indicating direction of transport. In order to identify any differences in processes under shoaling and breaking waves the analysis was undertaken separately for broken ($H_{ms}/h > 0.20$) and shoaling waves ($H_{ms}/h < 0.20$).

Component	Mode	Term	Contribution
Cross-shore	Suspended	$\psi_2 \cos \alpha_5$	+55%
		$\delta_u u3^*$	-37%
	Bedload	$\delta_u (0.5 + \cos^2 \alpha_2)$	+15%
		$\psi_1 \cos \alpha_1$	+4%
		Others	<4%
Longshore	Suspended	$\delta_v u3^*$	+70%
		$\psi_2 \sin \alpha_5 \cos \alpha_5$	+17%
	Bedload	$\delta_v (0.5 + \sin^2 \alpha_2)$	+16%
		δ_v^3	+7%
		Others	<4

Table 2. Largest terms in energetics sediment transport eqs (2).and (3).

The results suggested that the most important mode of sediment transport is suspended load both in the longshore and cross-shore; this applies to both shoaling and

breaking wave conditions. The most important terms within each mode of transport and for each direction, together with the percentage contribution to the total gross sediment transport rate are shown in Table 2. From these results, it can be seen that suspended load accounts for more than the 80% of the gross sediment transport rate. Thus it can be argued that equations (2) and (3) can be simplified with significant predictive accuracy to:

$$\langle I_x \rangle_s = \frac{\rho \cdot C_f \cdot U_m^4 \cdot \epsilon_s}{W} \cdot (\psi_2 \cos \alpha_s + \delta_u \cdot u_3^*) \tag{8}$$

and

$$\langle I_y \rangle_s = \frac{\rho \cdot C_f \cdot U_m^4 \cdot \epsilon_s}{W} \cdot (\delta_v \cdot u_3^*) \tag{9}$$

for the cross-shore and longshore directions, respectively.

Suspended Sediment Fluxes

Local suspended sediment fluxes from station D and for the lower elevation (9 cm) of SSC measurement are shown in Fig 6 for the cross-shore direction. Mean cross-shore, suspended sediment fluxes dominate; they are directed consistently offshore with maxima occurring at the beginning and the end of the tidal cycle, in shallow water depths where the local resuspension processes are more significant. The absolute values of the mean fluxes are an order of magnitude greater than the oscillatory ones due to gravity and/or infragravity motions. Gravity fluxes are inconsistent; they are directed offshore during the first data cycle, whilst during the second cross-shore suspended sediment flux for the last tidal cycle they are contributing to an onshore flux. Finally, bed contribute to an onshore

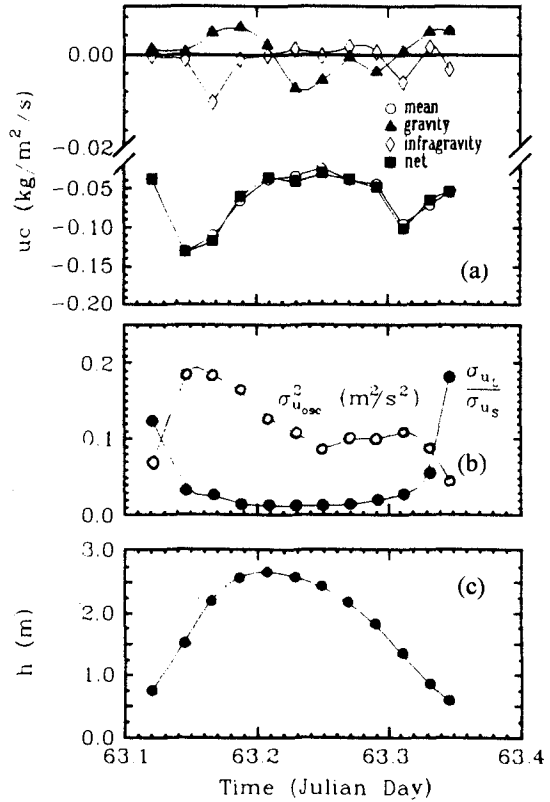


Figure 6. (a) Mean, gravity, infragravity and net local cross-shore suspended sediment flux for the last tidal cycle (Julian day 63) measured at 9 cm above the sea bed. (b) Total variance of oscillatory currents (○) and during the last tidal cycle they ratio of infragravity over gravity kinetic energy (●). (c) Local mean water depth (h).

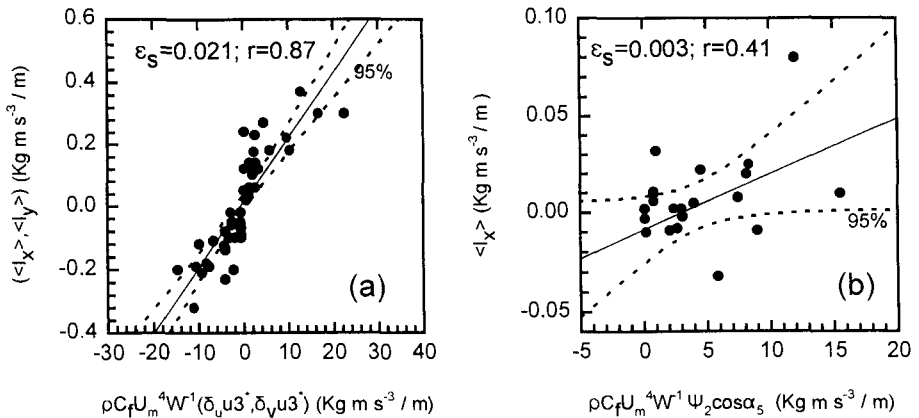


Figure 7. Comparison of measured, depth-integrated immersed weight suspended sediment transport rates with the terms of eqs (2) and (3). (a) Mean mode of suspended sediment transport (cross-shore, $\langle I_x \rangle$ and longshore $\langle I_y \rangle$ data superimposed). (b) Oscillatory mode of transport (cross-shore only).

sediment transport during the flood; during high water the flux is directed offshore and turns again to onshore at the last stage of the ebb tide. The contribution of the infragravity motions is comparable to that of the gravity waves, with the main characteristic being that when the infragravity flux is of any significance it is always directed offshore, in other cases its direction is variable.

Longshore local fluxes (not shown here) are dominated also by the mean fluxes. Both mean and net fluxes are northeasterly (*i.e.* towards the Netherlands). Gravity fluxes although an order of magnitude smaller than the mean, contribute to a northeasterly sediment transport in the direction of wave approach. However, infragravity motions, which result in a southwesterly transport during the first tide, exhibit a variability in direction during the second tidal cycle whilst during the last tidal cycle contribute to a northeasterly transport during the flood and a southwesterly flux during the ebb.

Modelling Suspended Sediment Transport

Depth-integrated values of immersed weight suspended sediment transport rates were obtained by box integrating the measured local suspended sediment fluxes (Voulgaris and Collins, 1996). The lower and upper limits for the integration were the sea bed and 0.5m above the sea bed, respectively. The general patterns observed in the local fluxes analysis were present in the depth-averaged sediment transport rates.

The terms describing sediment transport due to mean currents for both the cross-shore (2nd term in eq. (8)) and longshore directions (eq. (9)) have been combined and

plotted against the predicted mean depth-integrated flux in Figure 6a. A very good agreement was found with a correlation coefficient of 0.87. The efficiency factor (ϵ_s) was determined by regression analysis and was found to be 0.021. The oscillatory component (which is dominated by the gravity mode) of the measured cross-shore suspended sediment transport is plotted against the 2nd term of eq (8) in Figure 7b. There, it can be seen that the correlation is poor; the model always predicts onshore transport due to the waves while the measurements revealed periods of offshore sediment transport. This discrepancy is believed to be due to the presence of vortex ripples which can reverse the sediment transport direction near the bed (Vincent and Green, 1990). Visual observations, during low water, identified ripples with height 0.7cm and wavelength 8.5cm. These were asymmetrical in shape, directed offshore, with curved crests characteristic of ripples occurring under the co-existence of waves and currents. Application of the Wiberg and Harris (1994) model for the period when the intertidal zone was inundated suggested the existence of ripples with height of the order 3 to 5 cm and wavelength 10 to 20cm. The inconsistency between the modelled and visually observed ripple dimensions is attributed to the fact that the latter observations were undertaken during low water when the ripples were washed and flattened out by the swash zone.

Conclusions

In the mid-tidal zone of a macrotidal ridge and runnel beach, under mild conditions, both steady (tidally-induced) and oscillatory currents are equally important for the resuspension of sediment. Their importance is expressed not only in terms of their absolute magnitude but also in terms of wave-current interaction.

Suspended sediment transport is dominated by the mean currents

Bailards (1981) energetics model appears to predict suspended sediment transport due to mean currents quite accurately. However, it fails to predict suspended sediment transport due to wave-induced orbital velocities; this is probably due to the presence of vortex ripples.

The efficiency factor for suspended sediment transport and for the mean mode of transport was found to be 0.021.

Acknowledgments

The authors would like to acknowledge M.P. Wilkin and D.Simmonds for their invaluable assistance. The study was funded by the Commission of the European Community (DG XII) under Contract No. MAS2-CT92-0024-C (C-STAB). This contribution was prepared while G.Voulgaris was at Woods Hole Oceanographic Institution with a Post-Doctoral Award funded by the Mellon Foundation.

References

Aagaard, T. and Greenwood, B.M., 1995. Longshore and Cross-shore Suspended Sediment Transport at Far Infragravity Frequencies in a Barred Environment. *Continental Shelf Research*, 15(10): 1235-1250.

- Bagnold, R.A., 1966. An Approach to the Sediment Transport Problem from General Physics. U.S. Geol. Sur. Prof. Pap. 422-I.
- Bailard, A., 1982. Modelling On-Offshore Sediment Transport in the Surfzone. Proc. ASCE 18th Conf. Coastal Eng.: 1419-1438.
- Bailard, J.A., 1981. An Energetics Total Load Sediment Transport Model for a Plane Sloping Beach. Journal of Geophysical Research, 86:10,938-10,954.
- Bowen, A.J., 1980. Simple Models of Nearshore Sedimentation: Beach Profiles and Alongshore Bars. In: The Coastline of Canada. McCann, S.B. (Editor). Geological Society of Canada, Paper 80-10, Ottawa, pp. 1-11.
- De Moor, G., 1991. The Beach Nourishment of Bredene-De Haan and Its Impact on the Beach Morphology and the Coastal Evolution of the Belgian Coast East of Oostende. Proceedings IGU Symposium "Coastal Protection". Nantes, October, 1991.
- Guza, R.T. and Thornton E.B., 1985. Velocity Moments in the Nearshore. J. Waterway, Port, Coastal & Ocean Eng., 111(2): 235-256.
- King, C.A.M. and Williams, W.E., 1949. The Formation and Movement of Sand Bars by Wave Action. Geographical Journal, 113: 70-85.
- Orford, J.D. and Wright, P., 1978. What's In a Name? - Descriptive or Genetic Implications of "Ridge and Runnel" Topography. Marine Geology, 28: M1-M8.
- Roelvink, J.A. and Stive, M.J.F., 1989. Bar-Generating Cross-Shore Flow Mechanisms on a Beach. Journal of Geophysical Research, 94(C4): 4785-4800.
- Russell, P., Foote, Y. and Huntley, D.A., 1995. An Energetics Approach to Sediment Transport on Macrotidal Beaches. In: Coastal Dynamics '95, ASCE:
- Schoonees, J.S. and Theron, A.K., 1995. Evaluation of 10 Cross-Shore Sediment Transport/Morphological Models. Coastal Engineering, 25: 1-41.
- Soulsby, R.L., Hamm, L., Lopman, G., Myrhaug, D., Simons, R.R. and Thomas, G.P., 1993. Wave-Current Interaction Within and Outside the Bottom Boundary Layer. Coastal Engineering, 21: 41-69.
- Thornton, E.B., Humiston, R.T. and Birkemeier, W., 1996. Bar/Trough Generation on a Natural Beach. Journal of Geophysical Research. 101(C5): 12097-12110.
- Vincent, C.E. and Green, M.O., 1990. Field Measurements of the Suspended Sand Concentration Profiles, and of the Resuspension Coefficient γ over Rippled Bed. Journal Geophysical Research, 95: 15591-15601.
- Voulgaris, G., 1992. Suspended Sediment Transport in the Nearshore Zone. Department of Oceanography, University of Southampton. Unpublished Ph.D. Thesis, 425pp.
- Voulgaris, G. and Collins, M.B., 1996. Suspended Sediment Fluxes. In: B.A. O'Connor (Editor). Project MAS2-CT92-0024, Circulation and Sediment Transport Around Banks, CSTAB. Vol 2. Report No CE/05/96. Department of Civil Engineering, University of Liverpool, pp.495-545.
- Voulgaris, G. and Simmonds, D., 1996. Incident Waves. In: B.A. O'Connor (Editor) Project MAS2-CT92-0024. Circulation and Sediment Transport Around Banks, CSTAB. Vol. 2. Report No CE/05/96. Department of Civil Engineering, University of Liverpool, pp. 451-460..
- Wiberg, P.L. and Harris, C.K., 1994. Ripple Geometry in Wave-Dominated Environments. Journal of Geophysical Research, 99(C1): 775-789.

CHAPTER 306

Field Tests of Suspended-Load Transport Theories Used in Numerical Models

Thomas E. White ¹

Abstract

Surfzone optical-backscatter measurements were conducted at a long, straight sandy beach near Colorado River, Texas, in order to test velocity-based theories for predicting suspended-load sediment transport. Statistical methods were applied that provided estimates of theory performances, independent of any calibration or tuning of the model coefficients. The models of Ackers and White, Bowen, and Roelvink and Stive showed trends opposite that of the data (increasing transport estimates as measured transport decreased). The Bailard model performed very well in the cross-shore, explaining both the trends in transport and most of the variance, as determined by correlation coefficients. Bailard's model did not explain most of the variance in the longshore data, but comparison of the model's performance with other datasets show good correlation in the longshore. When the original coefficients in the unidirectional-flow-based Ackers and White model are used, very low transport estimates are produced. This suggests that this empirical model that was calibrated for unidirectional flows should not be used in coastal areas without considerable recalibration of the coefficients using high-quality datasets.

Introduction

A series of tests of sediment-transport theories has been performed with different data sets for different transport types:

- Bedload theories were tested with small-scale tracer experiments (White, 1987).

¹Coastal Engineering Research Center, USAE Waterways Experiment Station, Attn: CEWES-CD-P, 3909 Halls Ferry Road, Vicksburg, MS 39180-6199, USA

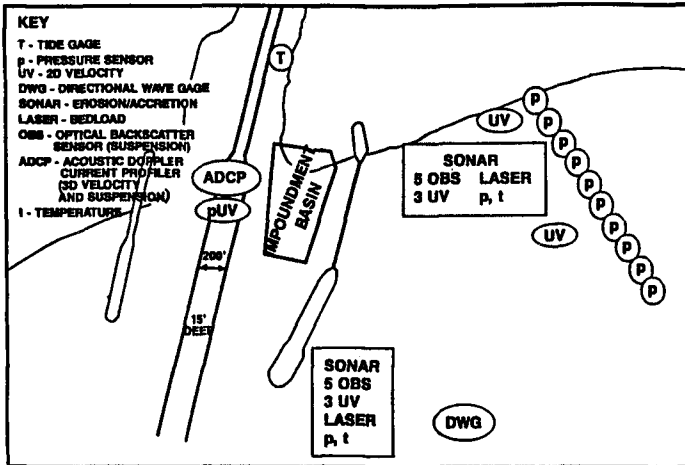
MCCCP COLORADO RIVER, TEXAS

Figure 1: Areas of deployment of each gage type. Gage platforms are not to scale, but for visualization are drawn very large relative to the jetties. The lasers were replaced by micro-OBS gages for bedload.

- The Shore Protection Manual (1984) equation for total longshore transport was tested with large-scale tracer and suspension-trap experiments (White and Inman, 1989).
- Both approximate and exact versions of the SPM longshore-transport formula were tested against each other with surfzone optical-backscatter experiments (White, 1994).
- This paper tests several suspended-load transport equations with optical-backscatter experiments.

Comprehensive arrays of 43 sensors were deployed to measure waves, currents, tides, and sediment transport at a long straight beach with gently-sloping plane-parallel contours near a river outlet, Colorado River, Texas (Figure 1).

This project of monitoring the behavior of the jetty system had several objectives. One was to identify and quantify the sediment budgets for the different parts of the system, in order to evaluate the performance of the sediment-management system of jetties, weir, and dredging (King and Prickett, 1997). Another was to evaluate longshore-transport formulas in the Shore Protection Manual (1984) by comparing the measured longshore sediment transport with the transport estimated from the offshore wave data and the SPM formulas (White, 1994). The topic of this paper is testing suspended-load transport theories at a point, in order to find the best ones to use in numerical models. This paper will describe only the results of this final objective.

Tests of sediment-transport theories can be performed in two very different means on two vastly different scales. Whether to test sediment-transport equations used in numerical models by making measurements at one point ("micro-scale") or by comparing the models' predictions of topographic change with measured topography ("macro-scale") is an ongoing debate. Since the main use of a transport theory is in a numerical model to determine changes in beach topography, one approach is to compare measured topographic change with the changes predicted from each numerical model (Schoonees and Theron, 1995). However, this method incorporates **all** error sources (e.g., grid spacing, coefficients' calibration, "skill" of the modeler, etc.) and cannot **separately** evaluate the transport theory used in the numerical model. It is possible in individual tests that these other factors have more effect than the particular theory that is in the model.

When detailed tests are made of total-load (macro) transport theories, such as the Shore Protection Manual's (1984) well-known longshore-transport formula, the error bars are huge and often larger than the measurements, so that high-confidence objective conclusions can often not be reached (White, 1994; Schoonees and Theron, 1994).

A third problem encountered in testing models with the "macro-scale" method is that individual verification tests invariably test only one model against one set of data. Schoonees and Theron (1995) point out: "Without direct comparative prototype tests the final conclusion as to which are the better models in practice cannot be given."

In this paper, such a direct comparative prototype test is outlined. This approach is to test each theory against transport measured at a single horizontal location. The theory used in the numerical model, not the model itself, is tested.

Experimental Methods

Several state-of-the-art instruments were deployed: an offshore trawler-resistant Directional Wave Gage (DWG), a puv gage of colocated pressure and current sensors, Optical Backscatter Sensors for suspended-sediment concentrations, electromagnetic current meters for velocities, a new cable with internally imbedded pressure sensors for surfzone waves, and Acoustic Doppler Current Profilers for inlet currents and sediment flux.

The surfzone transport was measured by cross-shore integration of the point measurements from three synoptic multi-sensor platform arrays of Optical Backscatter Sensors (OBSs) (Downing, Sternberg, and Lister, 1981) and Electromagnetic Current Meters (ECMs), sonars, and pressure sensors. Figure 1 shows a plan view of the site with various platforms of gages drawn in the general areas where they were deployed. The sediment concentration was measured with OBS2 optical backscatter sensors, which were each calibrated in a flow tank over a wide range of transport values. The sand from the site was sampled prior to each experiment and generally had a median size of 130 microns, with a size distri-

bution that was always single-peaked. The sand from the site was used in the laboratory to calibrate the sensors over a wide range of transport values (from 1 to 300 grams per liter), both prior to and after each of the three experiments.

The currents were measured with standard 1-inch diameter Marsh-McBirney electromagnetic probes, calibrated just prior to use. Pressure sensors were used to determine the range of vertical integration for each platform, and also times when uppermost sensors were out of the water and thus not to be used.

The sediment transport is the direct integration of the product of these two types of calibrated-sensor outputs, as measured in the surfzone:

$$\vec{i} = (\rho_s - \rho)gN_o \int_0^\eta \vec{u}(x, z)c(x, z)dz \quad (1)$$

where \vec{i} is the sediment transport at one horizontal location, ρ_s is the sediment density, ρ the fluid density, g the acceleration of gravity, N_o the solids density (one minus porosity), \vec{u} the fluid velocity, c the sediment concentration, and the integral is taken over the vertical surf depth.

The above integration is first accomplished in the vertical at each platform location by vertically integrating the values of concentration c , longshore velocity v , and vertical range z . See White (1994) for more details. It is important to note that the vertical integration is performed *at each time step of 0.2 seconds*, and is thus unaffected by phenomena with longer time periods, such as bursts of sediment out of the boundary layer. Each sensor measures at one instant, and all the instantaneous products of c , v , and z are vertically summed before moving to the next 0.2s time step.

Theoretical Methods

Theories for computing suspended-sediment transport were obtained via an extensive literature search of several hundred modeling documents (Drake and White, 1995). Five were found to be unique formulas of point transport. Other theories are either variations on these five types, or are not testable with "point" transport measurements. Such other models include (1) diffusion-based theories such as Smith (1977), Grant and Madsen (1979), and Glenn and Grant (1987); (2) the two-layer model of Dally and Dean (1984), and (3) the eddy-viscosity model of Deigaard et al (1986).

The following variables are found in common to many suspended-load theories:
 \vec{i} is the local immersed-weight sediment transport,
 ρ is fluid density, ρ_s is sediment density,
 c_f is a friction coefficient,
 e_s is a suspended-load efficiency, e_b is a bedload efficiency,
 W is sediment fall speed,
 \vec{u} is the fluid velocity,
 ϕ is the sand's angle of internal friction (related to grain size),

h is depth, H is wave height, T is wave period,

g is the acceleration of gravity,

β is the beach slope angle,

\hat{i} is the unit vector in the offshore direction,

x is the cross-shore spatial coordinate, and y is the longshore coordinate.

The value always used for the suspension efficiency was the 0.025 best-fit value found from several experiments, as published by Bailard (1981). A consensus in the literature was reached for a friction coefficient c_f value of 0.007, since to one significant figure, this was the value determined by both Thornton (1970) and Bailard's (1981) experiments.

Three of the models we tested are based on Bagnold's (1966) derivation for both bedload and suspended load in streams. Bagnold's basic concept was that the transport uses a fixed fraction of the available stream power. The derivation of Bagnold's transport relation, along with all of the assumptions may be found in Drake and White (1995).

(1) **Bowen's** (1980) suspended-load model expands Bagnold's basic stream-transport relation using two velocities, an oscillatory and a steady component. Assuming the oscillatory velocity dominates, the formula is expanded in a series and the terms retained yield:

$$\langle \vec{i} \rangle = \rho c_f \frac{e_s}{W} \left[\langle |\vec{u}|^3 \vec{u} \rangle + \frac{\beta}{W} \langle |\vec{u}|^5 \rangle \hat{i} \right] \quad (2)$$

(2) **Bailard** (1981) worked on this problem at the same time as Bowen and independently derived a similar suspended load model. Again expanding in a series and retaining terms yields:

$$\langle \vec{i} \rangle = \rho c_f \frac{e_s}{W} \left[\langle |\vec{u}|^3 \vec{u} \rangle + \frac{e_s \tan \beta}{W} \langle |\vec{u}|^5 \rangle \hat{i} \right] \quad (3)$$

As opposed to Bowen, the reason for the efficiency e_s appearing again in the second term is based on interpretations of Bagnold's claims regarding whether power is contributed through an efficiency factor. For most applications, there is no practical import as to whether β or $\tan \beta$ is used, since the slope is usually small.

(3) **Roelvink and Stive's** (1989) transport model contains transport from two different mechanisms. The stream-power based transport follows the work of Bagnold, Bowen, and Bailard. But they also include transport caused by turbulence from breaking waves:

$$\langle \vec{i} \rangle = \rho c_f \frac{e_s}{W} \left[\langle |\vec{u}|^3 \vec{u} \rangle + K_1 \hat{i} \right] \quad (4)$$

where $K_1 = \beta_d \{ k_t [\exp(h/H_{rms}) - 1]^{-1} \}^{3/2}$

(4) **Larson and Kraus'** (1989) cross-shore transport model extends the energy-dissipation model of Kriebel and Dean (1985) to predict total cross-shore

transport. They add an empirical criterion that determines the **sign** of the transport as either bar growth (offshore transport) or berm growth (onshore transport). Various datasets were used to determine an empirical dividing line between these cases. The resulting model, which forms the basis for CERC's SBEACH cross-shore numerical model is:

$$(i) = \text{sgn} \left\{ M \left[\frac{\langle H_0 \rangle}{WT} \right]^3 - \frac{2\pi \langle H_0 \rangle}{gT^2} \right\} (\rho_s - \rho)gK \left[E - E_{eq} + \frac{\varepsilon_\beta}{K} \frac{dh}{dx} \right] \quad (5)$$

when the rate of energy dissipation is greater than that for an equilibrium beach: $E > E_{eq} - \frac{\varepsilon_\beta}{K} \frac{dh}{dx}$, and zero otherwise.

H_0 is the deep wave height, T the period, W the grain fall velocity, and dh/dx is the beach slope. M , K , and ε_β are empirical constants. The quantity in the first set of brackets is used solely to determine the **direction** of transport, with M the empirical constant dividing their cases of onshore and offshore transport.

The energy dissipation is follows the work of Dean. The dissipation in general and the value for the equilibrium beach are:

$$E = \frac{1}{h} \frac{d}{dx} \left[\frac{1}{8} \rho g H_s^2 \sqrt{gh} \right]; \quad E_{eq} = \frac{5}{24} \rho g^{3/2} \gamma_b^2 A^{3/2}$$

where γ_b is the ratio between wave height and depth, and A is the profile shape parameter.

Note that the Larson and Kraus model requires substantially different measured quantities than the other models. Not only are wave heights and periods used, but their variation across the surf zone must be known.

(5) **Ackers and White's** (1973) river-transport model was not originally developed for or intended for use in an oscillatory flow. However, it has been adapted for use by the Coastal Engineering Research Center for use in modelling the fate of offshore dredge dumps. The fate of these dumps is thought to initially be governed primarily by currents rather than waves. Hence this model was used, and is now being applied to other situations where there is a strong unidirectional (current) component, such as at inlets. Since this model is seeing so many uses in the coastal region, it was included in this testing program.

The unidirectional transport in the original paper is modelled as:

$$(i) = 10^{-6} \frac{\rho_s - \rho}{\rho_s} C_g \left(\frac{F_*}{A_g} - 1 \right)^m \left(\frac{\rho_s D \bar{u}}{\rho h u_*} \right) (\rho \bar{u} h) \quad (6)$$

Some of the final parameters, such as depth h and density ρ cancel. What remains are sediment parameters (density ρ_s and size D) and fluid parameters (ρ , a velocity in the direction of transport \bar{u} , and a friction velocity $u_* = \sqrt{c_f u_T}$). The velocity u_T is the total velocity, and the velocity \bar{u} is the velocity in the direction of transport. So in the cross-shore case, the appropriate instantaneous velocities are the one that appears twice in the numerator, $\bar{u} = u$ (u being the instantaneous cross-shore velocity) and $u_* = \sqrt{c_f (u^2 + v^2)}^{0.5}$ in the denominator.

The remaining parameters are four 'numbers' used in the model. C_g is a function of grain size determined by fitting to Ackers and White's original data set:

$$\log C_g = 2.86 \log D_* - (\log D_*)^2 - 3.53; D_* = D \left[\frac{g(\rho_s - \rho)}{\rho \nu^2} \right]^{1/3}$$

where D_* is a dimensionless grain diameter. The exponent m is another empirically fit number $m = 9.66 D_*^{-1} + 1.34$, as is $A_g = 0.23 D_*^{-1/2} + 0.14$. For fine to medium sediments (suspension) the mobility number F_* is the square root of Shields' number:

$$F_* = \sqrt{\theta} = \frac{\sqrt{\rho} u_*}{[gD(\rho_s - \rho)]^{1/2}}; G_* = C_g \left[\frac{F_*}{A_g} - 1 \right]^m$$

G_* is the so-called transport parameter into which are lumped all the empirical numbers.

Statistical methods

Methods were developed to objectively judge theory performance (White, 1987). The degree of success of the developed theories can be judged by computing correlations between predicted and measured variables by objective statistical techniques. A simple linear regression is performed between measured transport (y) and transport predicted from the models (x):

$$y = mx + b; r = m \frac{\sigma_x}{\sigma_y} \quad (7)$$

where r is the correlation coefficient and σ is the standard deviation using N weighting. Negative values represent anti-correlation. The r^2 values are the fraction of the total variance in the data explained by the method.

For a selected level of confidence, say 90%, confidence limits can be computed. Since the correlation r is not a Gaussian function, it must first be translated into a variable that is Gaussian in order to compute confidence limits. The upper confidence limit is: $w^+ = w + Z/\sqrt{N(N-3)}$ where Z comes from the cumulative normal (Gaussian) distribution tables. The lower limit is computed likewise, except there is a $+$ instead of $-$ before the fraction. The quantity w is from a theorem that determined w is a Gaussian function of the correlation r : $w = \tanh^{-1} r$. The confidence limits allow us to state how confident we are that one theory performs better than another theory. Once translated back into r -space via the inverse of the above equation, we obtain a range of correlations for each theory. If the ranges in correlations r for one theory's performance do not overlap the range computed for another theory's performance, then we may conclude at the specified level of confidence that the theory with the higher r values performs better than the one with lower values. The reason for this

exercise is to show that random variation in small amounts of experimental data have not, by chance, provided an incorrect conclusion. The percent confidence specifies the probability that such incorrect conclusions have not occurred.

The statistical methods separate the issues of calibration and testing. Correlation coefficients determine the degree of success of each theory **without calibrating** to the data; confidence intervals determine which theories are better than which other theories; regression slopes determine appropriate coefficients for each of the theories, independently of the quality or goodness-of-fit issue.

Results

Experiments were performed over a two-week period in January 1992 over greatly varying wave conditions. Each experiment consisted of measurements taken each fifth of a second. The vertically integrated transports were then averaged over the recording time for the experiment, typically one to three hours. This dataset consisted of 81 such cross-shore transport and 36 longshore transport experiments.

Unfortunately, we encountered practical problems when using two of the five theories. The **Larson and Kraus** theory requires somewhat different data than the others: considerable information about wave height and period, and also cross-shore variation in these quantities. The original project had the purpose of measuring transport rates and of testing velocity-based theories. Thus such detailed wave information was not computed in the original dataset. Future work is planned to compute these quantities in order to test this theory.

The **Ackers and White** formula was used but produced extremely small values of transport, by several orders of magnitude. Numerous independent checks of the testing program failed to reveal any programming errors. Another possible explanation is that we are incorrectly surmising how to compute the different velocities required by this unidirectional-flow theory. Of course, it is also quite possible that the results are correct and suggest that such a unidirectional-flow theory was not intended for and should not be used in oscillatory flow. Since we encountered such low values in these cross-shore computations, we did not continue testing this theory with longshore data. Thus their theory does not appear in Table 3.

Correlations between theories and measurements were computed over each time period and are listed in Tables 1 and 2 for cross-shore transport and Table 3 for longshore transport. Confidence limits were also computed in order to determine how confident one can be of conclusions that one theory performs better than another.

Modifications to the theoretical transport equations may be extracted from Tables 1, 2, and 3. The slope m could be used to modify the theory's empirical coefficient or the friction coefficient c_f , *provided* a y-intercept were also added to the equation. So one might compute i from the original formula, and then $i_{new} = mi_{old} + b$.

Table 1: Correlation of Theoretical and Measured CROSS-SHORE Transports for the OUTER Surf Zone

Method being correlated with measured transport:	Measured Transport	Bowen (1980)	Bailard (1981)	Roelvink and Stive (1989)	Ackers and White (1973)
	Outer surf, top water column (number of experiments, N = 15)				
μ Mean, dynes/(cm-s)	-3833.	6178.4	-291.9	2062.5	.00003096
σ Standard Deviation, dynes/(cm-s)	8388.	16373.6	776.2	3395.1	.00008103
m, Regression Slope		-.4612	10.2	-2.2	-93015000.
b, Intercept, dynes/(cm-s)		-983.7	-854.1	778.9	-953.7
r, Correlation Coefficient		-0.900	0.945	-0.905	-0.899
r^2		0.810	0.893	0.819	0.808
Lower 90% Confidence Limit for r		-0.921	0.930	-0.925	-0.920
Upper 90% Confidence Limit for r		-0.874	0.957	-0.880	-0.873
Outer surf, mid water column (number of experiments, N = 15)					
μ Mean, dynes/(cm-s)	-3833.	181.5	-83.5	303.9	.000000982
σ Standard Deviation, dynes/(cm-s)	8388.	221.1	162.7	301.2	.000001599
m, Regression Slope		-19.9	50.7	-12.7	4192780000.
b, Intercept, dynes/(cm-s)		-219.3	397.8	13.8	1008.9
r, Correlation Coefficient		-0.525	0.983	-0.455	-0.799
r^2		0.276	0.966	0.207	0.638
Lower 90% Confidence Limit for r		-0.608	0.978	-0.547	-0.352
Upper 90% Confidence Limit for r		-0.430	0.987	-0.352	-0.750
Outer surf, bottom water column (number of experiments, N = 15)					
μ Mean, dynes/(cm-s)	-3833.	40.4	-21.8	151.0	.000000219
σ Standard Deviation, dynes/(cm-s)	8388.	55.2	40.5	157.9	.000000289
m, Regression Slope		-129.7	203.4	-45.3	27350800000.
b, Intercept, dynes/(cm-s)		1411.8	595.5	3005.1	1168.6
r, Correlation Coefficient		-0.854	0.982	-0.852	-0.942
r^2		0.729	0.964	0.726	0.887
Lower 90% Confidence Limit for r		-0.884	0.977	-0.882	-0.954
Upper 90% Confidence Limit for r		-0.817	0.986	-0.814	-0.926

The computed statistics are reported with far more significant digits than the method justifies, in order to retain digits until the rounding of the final result.

Table 2: Correlation of Theoretical and Measured CROSS-SHORE Transports for the MIDDLE and INNER Surf Zone

Method being correlated with measured transport:	Measured Transport	Bowen (1980)	Bailard (1981)	Roelvink and Stive (1989)	Ackers and White (1973)
	Mid surf, top water column (number of experiments, N = 8)				
μ Mean, dynes/(cm-s)	-24000.	3229.4	-2456.2	1173.7	
σ Standard Deviation, dynes/(cm-s)	12177.	4172.0	3252.4	1303.7	
m, Regression Slope		-1.674	2.038	0.525	
b, Intercept, dynes/(cm-s)		-18595.2	-18994.6	-24616.5	
r, Correlation Coefficient		-0.573	0.544	0.056	
r^2		0.328	0.296	0.003	
Lower 90% Confidence Limit for r		-0.723	0.335	-0.202	
Upper 90% Confidence Limit for r		-0.372	0.702	0.307	
Mid surf, bottom water column (number of experiments, N = 8)					
μ Mean, dynes/(cm-s)	-24000.	3220.2	-2092.6	1498.7	
σ Standard Deviation, dynes/(cm-s)	12177.	3521.5	2986.0	1072.3	
m, Regression Slope		-2.208	2.096	0.932	
b, Intercept, dynes/(cm-s)		-16890.8	-19614.5	-25397.4	
r, Correlation Coefficient		-0.638	0.514	0.284	
r^2		0.407	0.264	0.081	
Lower 90% Confidence Limit for r		-0.768	0.298	0.680	
Upper 90% Confidence Limit for r		-0.457	0.680	0.503	
Inner surf, mid water column (number of experiments, N = 20)					
μ Mean, dynes/(cm-s)	1275.	1024.4	44.9	1188.4	
σ Standard Deviation, dynes/(cm-s)	8076.	1212.8	532.1	1235.5	
m, Regression Slope		2.775	13.800	3.575	
b, Intercept, dynes/(cm-s)		-1567.7	655.9	-2973.4	
r, Correlation Coefficient		0.417	0.909	0.547	
r^2		0.174	0.826	0.299	
Lower 90% Confidence Limit for r		0.341	0.892	0.482	
Upper 90% Confidence Limit for r		0.488	0.923	0.606	

The computed statistics are reported with far more significant digits than the method justifies, in order to retain digits until the rounding of the final result.

Table 3: Correlation of Theoretical and Measured LONG-SHORE Transports

Method being correlated with measured transport:	Measured Bowen and Bailard Transport (same model in the longshore)	
	Mid surf, top water column (number of experiments, N = 8)	
μ Mean, dynes/(cm-s)	-48350.	-3810.0
σ Standard Deviation, dynes/(cm-s)	18563.3	3714.2
m, Regression Slope		2.205
b, Intercept, dynes/(cm-s)		-39950.3
r, Correlation Coefficient		0.441
r^2		0.194
Lower 90% Confidence Limit for r		0.209
Upper 90% Confidence Limit for r		0.626
	Mid surf, bottom water column (number of experiments, N = 8)	
μ Mean, dynes/(cm-s)	-48350.	-3796.4
σ Standard Deviation, dynes/(cm-s)	18563.	3370.2
m, Regression Slope		2.549
b, Intercept, dynes/(cm-s)		-38674.7
r, Correlation Coefficient		0.463
r^2		0.214
Lower 90% Confidence Limit for r		0.235
Upper 90% Confidence Limit for r		0.642
	Inner surf, mid water column (number of experiments, N = 20)	
μ Mean, dynes/(cm-s)	11,505.	736.9
σ Standard Deviation, dynes/(cm-s)	10,792.	761.7
m, Regression Slope		9.417
b, Intercept, dynes/(cm-s)		4564.8
r, Correlation Coefficient		0.665
r^2		0.442
Lower 90% Confidence Limit for r		0.613
Upper 90% Confidence Limit for r		0.712

The computed statistics are reported with far more significant digits than the method justifies, in order to retain digits until the rounding of the final result.

Table 4: Correlations between Model Predictions and Measured Transport

	Bowen (1980)	Bailard (1981)	Roelvink & Stive (1989)	Ackers & White (1973)
January 1992: 81 Experiments for Cross-Shore Transport				
r for outer surf, upper water column	-0.900	0.945	-0.905	-0.899
r for outer surf, mid water column	-0.525	0.983	-0.455	-0.799
r for outer surf, bottom water column	-0.854	0.982	-0.852	-0.942
r for mid surf, upper water column	-0.573	0.544	0.056	
r for mid surf, lower water column	-0.638	0.514	0.284	
r for inner surf	0.417	0.909	0.547	
January 1992: 36 Experiments for Long-Shore Transport				
r for mid surf, upper water column	0.441	0.441		
r for mid surf, lower water column	0.463	0.463		
r for inner surf	0.665	0.665		

All the correlations between models and data are summarized in Table 4. Note that many correlations are negative. This means that the **trend** in the theoretical predictions are opposite the trend in the data. (As measured transport increases, predicted transport decreases.) It does not mean that the direction of the predicted transport is opposite that of measured transport.

Conclusions

Conclusions about model performances can be made from the correlations in Table 4. For the 6 groups of 81 surfzone experiments of 1 to 3 hours length each:

1. The Bailard model performs very well in the cross-shore, predicting most of the variation in cross-shore transport.

Mean $r = 0.81$ and mean $r^2 = 0.70$ (Explains 70% of the variance)

2. The Bowen model and the Roelvink & Stive model do not predict most of the variation in cross-shore transport, and frequently predict the wrong trend (e.g., predicted transport increases as measured transport decreases). The only significant difference between the Bowen and Bailard models is a appearance of the suspended-load efficiency coefficient in the second term, caused by different interpretations of Bagnold's original work on this point by Bowen and Bailard. The results of this study are strong evidence that Bailard's interpretation is correct.

Bowen: mean $r = -0.52$ and mean $r^2 = 0.45$ (45% of the variance)

Roelvink & Stive: mean $r = -0.22$ and $r^2 = 0.36$ (**36% of the variance**)

3. The Ackers and White model performs strangely. Using the coefficients provided in their original publication and making our stated assumptions about how to compute the velocities, results in extremely low values of transport. Results show strong **anti-correlation** with the data. The most likely explanation of the anti-correlation is some local circulation pattern at the outer surf platform, since some of the other models also exhibit this anti-correlation result at that site.

Mean $r = 0.88$ and mean $r^2 = 0.77$ (**Explains 77% of the variance**)

4. The Bowen model and the Bailard model (identical in the longshore) model do not predict most of the variation in longshore transport.

Mean $r = 0.52$ and mean $r^2 = 0.28$ (**Explains 28% of the variance**)

Knowledge of the performance of this model in the longshore is by no means conclusive. Thornton reports in meetings for the Delilah/Duck94 surfzone experiments, that performance levels are similar to what we found here. But we have also tested this model in the longshore against numerous other Shore Protection Manual-type formulas and also other velocity-based formulas in another study using Nearshore Sediment Transport Study sand-tracer data at Santa Barbara, California (White and Grandon, draft). In that study this model performed excellently, with correlations around 0.9.

In another study, the main factor not included in these equations that was found to improve *local* estimates of transport, was inclusion of a sediment threshold-of-motion criterion (White, 1987; White, 1989). In comparing predictions of different local **bedload** transport theories with transport measured by sand tracer, it was found that agreement on direction of transport improved from 70% to 100% of the experiments, once a threshold criterion was added to the theory. We have included threshold subroutines in our testing program and plan to apply such criteria to these suspension models and report the results in a followup paper.

Acknowledgments

The considerable efforts in obtaining the large field data set at Colorado River were performed by the capable staff of the Prototype Measurement and Analysis Branch of CERC, including Mike Carpenter, Bill Grogg, Doug Lee, Rhonda Lofton, Bill Kucharski, Chuck Mayers, Debbie Shafer, and Kerry Taylor. The data-collection systems were designed and built by Ralph Ankeny, Bill Grogg, Gary Howell, and J. Rosati. The analysis of the surfzone time-series data and computation of measured transport were completed by Joon Rhee. Conversion of the author's testing programs to use with OBS data was performed by Rhonda Lofton. Without her considerable programming and data-organization efforts, this paper would not have been possible.

The work presented herein was performed at the Waterways Experiment Station of the US Army Corps of Engineers. Permission was granted by the Chief of Engineers to publish the results.

References

- Ackers, P. and W.R. White, 1973, "Sediment transport: new approach and analysis," *Proc. Hydraulics Div., ASCE*, v 99, n HY11, p 2041-2060.
- Bailard, J.A., 1981, "An energetics total load sediment transport model for a plane sloping beach," *J. Geophys. Res.*, v 86, n C11, p 10938-10954.
- Bowen, A.J., 1980, "Simple models of nearshore sedimentation: beach profiles and longshore bars," *The Coastline of Canada*, Geological Survey of Canada Paper 80-10, ed., S.B. McCann, p 1-11.
- Dally, W.R., and R.G. Dean, 1984, "Suspended sediment transport and beach profile evolution," *J. Waterway, Port, Coastal, and Ocean Engr.*, v 110, n 1, pp. 15-33.
- Deigaard, R., J. Fredsoe, and I.B. Hedegaard, 1986, "Suspended sediment in the surf zone," *J. Waterway, Port, Coastal, and Ocean Engr.*, v 112, n 1, pp. 115-128.
- Downing, J.P., R.W. Sternberg, and C.R.B. Lister, 1981, "New instrumentation for the investigation of sediment suspension processes in the shallow marine environment," *Marine Geology*, v 42, p 19-34.
- Drake, T.G. and T.E. White, 1995, "Compilation of suspended-load point-transport theories," USAE Waterways Experiment Station, Technical Report CERC-95-18, 40pp.
- Glenn, S.M. and W.D. Grant, 1987, "A suspended sediment stratification correction for combined wave and current flows," *J. Geophys. Res.*, v 92, n C8, pp. 8244-8264.
- Grant, W.D. and Madsen, O.S., 1979, "Combined wave and current interaction with a rough bottom," *J. Geophys. Res.*, v 84, pp. 1979-1808.
- King, D.B., Jr., and T.L. Prickett, 1997, "Mouth of the Colorado River, Texas, monitoring program," USAE Waterways Experiment Station Technical Report.
- Kriebel, D.L., and R.G. Dean, 1985, "Numerical simulation of time-dependent beach and dune erosion," *Coastal Engr.*, v 9, n 3, pp. 221-245.
- Larson, M. and N.C. Kraus, 1989, "SBEACH: numerical model for simulating storm-induced beach change," Technical Report CERC-89-9, USAE Waterways Experiment Station, Coastal Engineering Research Center.
- Roelvink, J.A. and M.J.F. Stive, 1989, "Bar-generating cross-shore flow mechanisms on a beach," *J. Geophys. Res.*, v 94, n C4, p 4785-4800.
- Schoonees, J.S. and A.K. Theron, 1994, "Accuracy and applicability of the SPM longshore transport formula," *Proc. 24th ICCE, Kobe, ASCE*, p 2595-2609.
- Schoonees, J.S. and A.K. Theron, 1995, "Evaluation of 10 cross-shore sediment transport-morphological models," *Coastal Engr.*, v 25, p 1-41.
- Shore Protection Manual, 1984, Vol. I, U.S. Army Corps of Engineers' Coastal Engineering Research Center, U.S. Gov't Printing Office.
- Smith, J.D., 1977, "Modeling of sediment transport on continental shelves," in *The Sea*, E.D. Goldberg (Editor), John Wiley, New York, v. 6, pp. 539-577.
- Thornton, E.B., 1970, "Variation of longshore current across the surf zone," *Proc. 12th ICCE, ASCE*, p. 291-308.
- White, T.E., 1987, "Nearshore sand transport," *University of California*, Ph.D. dissertation, 210 pp.
- White, T.E., 1989, "Using sediment-threshold theories in waves and currents," *Proc., Sediment Transport Modeling*, Intl. Symposium, HY Div., ASCE, p 248-253.
- White, T.E., 1994, "Field tests of radiation-stress estimators of longshore sediment transport," *Proc. 24th ICCE, Kobe, ASCE*, p 2799-2812.
- White, T.E. and J. Grandon, draft, "Longshore sediment transport: a comparison of energetics-based total-load models," Technical Report, USAE Waterways Experiment Station, Coastal Engineering Research Center.
- White, T.E. and D.L. Inman, 1989, "Measuring longshore transport with tracers," Chapter 13 of *Nearshore Sediment Transport*, R.J. Seymour, editor, Plenum Pub., New York, p 287-312.

CHAPTER 307

Shore Protection Studies for Ras-Elbar, Egypt

John B. Herbich¹, Fellow ASCE, Abd-Elfattah Elfiky², Abd-Elmohsen Elmongy³
Ali Elbahrawy⁴, Gamal Elsaed⁵, Member ASCE

Introduction and Background of the Coastal Changes Along the Northern Coast of the Nile Delta

The northern coastline of the Egyptian Nile Delta extends some 280 km from a point 30 km west of the City of Alexandria to 30 km east of the City of Portsaid. The coastline is considered to be in a state of continuous change under the action of sea waves and currents.

Over the years the River Nile and its two main branches, Damietta and Rosetta, supplied large volumes of sediment from the mouth of these branches to the sea. This large volume of sediment exceeded the loss of sediment caused by wave and current action; thereby providing natural beach protection and excess sediment to the Nile Delta.

Construction of the Aswan Nile Dam significantly reduced the volume of sediment deposited along the Nile Delta shoreline causing severe erosion. The erosion started after construction of the first Aswan dam, the development of other dams, and the increasing diversion of the river water for irrigation purposes. After closing the Aswan High Dam in 1966, erosion along the Delta coastline accelerated considerably, resulting in loss of several beaches and blockage of estuaries and navigation channels because of accreting sediment and flooding of coastal villages. The erosion had a severe effect on the nearby agricultural areas because of salt water intrusion affecting these areas.

¹Professor Emeritus, Ocean Engineering Program, Department of Civil Engineering, Texas A&M University, College Station, TX 77843, USA.

²Professor, Department of Civil Engineering, Ain Shams University, Cairo, Egypt.

³Professor, Department of Civil Engineering, Ain Shams University, Cairo, Egypt.

⁴Assistant Professor, Department of Civil Engineering, Ain Shams University, Cairo, Egypt.

⁵Researcher, Department of Civil Engineering, Ain Shams University, Cairo, Egypt.

A successful shore protection management plan must be developed for the next twenty years.

Available Data and Description of the Ras-Elbar Area

Ras-Elbar is located at the Damietta branch mouth of the Nile. This popular resort beach has declined severely over the past twenty years due to extensive erosion. Many hectares of beachfront property have been lost since 1965 and erosion is continuing.

The Ras-Elbar area is only five kilometers away from the new Port at Damietta. The development of the port facilities, related industries and new town development will have a significant economic impact upon the coastal erosion at the Ras-Elbar area, and will affect tourism and industrial development in the area.

The Damietta branch of the River Nile was developed during the tenth century. The Nile sediments, directed toward the west and east sides of this branch, developed this area by wave action. The old maps show that the Ras-Elbar-Damietta promontory advanced about three kilometers in the period between 1800 and 1900. At present, the coast is retreating due to sediment supply cut off since 1966 and the permanent closures of the Faraskour Dam some 20 km south of the mouth. Since 1966 erosion has been quite active in this area. The average retreat of the Ras-Elbar Peninsula had been about 30 m/yr before the construction of the western jetty in 1941. This jetty has stabilized the northern part of the Ras-Elbar shoreline, although the rest of the coast continued to erode with a diminishing rate for a distance of 3 km west of the jetty.

In 1970 a series of three short groins were constructed to protect the eastern part of the resort. In 1982 two Dolosse embankments between groins 1 and 2, and 2 and 3 were constructed. The Ras-Elbar nearshore region showed continuous deepening of the water depth and steepening of its underwater shore slope.

Mathematical Studies and Procedure

Computer hardware. The computer used in this study was an IBM 486 DX2 with a 66 MHz clock speed, a 16 MB RAM memory, a 240 MB hard drive memory and a math co-processor. A Hewlett Packard Laser Jet IV P printer and 1 7475A plotter were used. A Numonics 1.0 x 1.20 m digitizer was used to digitize the Ras-Elbar area drawings. The above equipment was proven to be reliable within the range of this study. The average CPU time was 2 hours.

Phases of this study. This study was conducted for the purpose of establishing and examining protection plans for the Ras-Elbar area coastline and

to determine their long-term impact on the shoreline and the volume of sediment transported.

The study was conducted in four main phases. The first phase established the behavior of the initial shoreline subject to the design wave and served as a base reference.

The second phase studied the effect of a system of detached breakwaters on the behavior of the shoreline under the same wave climate conditions. The system proposed by Delft Hydraulics in 1987 was examined for comparative purposes.

The third phase studied the effect of a system of groins on the behavior of the shoreline having the same wave climate conditions.

Finally, the fourth phase evaluated the effect of a combined system of detached breakwaters and groins on the behavior of the shoreline under the same wave climate conditions. All computer runs were conducted for three wave directions.

Simulation Procedure and System Setup. The procedure was as follows:

1. The shoreline data were digitized using the Autocad release 11.0 with a digitized accuracy of 4.16 m. The digitized data were analyzed and extracted using the Quick surf-Cad based program, and the shoreline digitized data were prepared as DXF file. Ras-Elbar shoreline was digitized using Drawing No. 2 prepared by Tetra Tech Inc.
2. The wave data were prepared using the Coastal Research Institute (CRI) and the Suez Canal Authority (SCA) data recorded over various periods of time.
3. A computational program (GENESIS) (Gravens and Kraus 1992) was used to conduct the required simulation. This program was developed by Hanson and Kraus (1982).

Two major tests were conducted:

1. Conducting sensitivity and error analysis runs:
The changes in the output resulting from the intentional change in the input were examined to determine the limitations of different variables. To produce quality results, a knowledge of the sources of errors is important.
2. Conducting sensitivity analysis runs:
Compromise between the efficiency and accuracy of the numerical code while maintaining its stability. To achieve the stability analysis test, several pre-runs were conducted with various conditions and various shore-protection structure alternatives. As a result of these

runs, two parameters were fixed to maintain the stability (without losing either the efficiency or the accuracy of the numerical scheme). The time step was chosen to be 6 hours; 18,992 time steps were calculated. The number of grid cells within the simulation area reach was 60 with a grid spacing of 50 meters.

The start and setup files were selected for each run of the proposed shore plan. If the proposed plan was not successful due to the formation of tombolos, diffracting structures interaction or ineffective structure position, the file had to be redesigned until a successful run was reached. A simulation time of thirteen years was selected for each run to establish a case of relatively-stable state, undergoing minor or moderate changes. The simulation starting date was November 30, 1986, and the ending date was November 30, 1999. The results were calculated and plotted once a year. Figure 1 shows a general layout of the study area.

The following numerical model arrangement was used for all cases:

- a. the total length of simulated coast was 3 km. This length was divided into sixty equal cells, each 50 m in width.
- b. simulation starting date, November 30, 1986 and ending November 30, 1999,
- c. time step used was 6 hours with a total of 18,992 time steps per run,
- d. shoreline position was calculated and presented once a year,
- e. longshore sediment transport coefficients K_1 and K_2 selected were 0.5 and 0.25 respectively (these values are typically $0.5 K_1 < K_2 < 1.5 K_1$ for sandy beaches from experiments and experience),
- f. the depth of the offshore wave input was 10.0 m,
- g. the number of incoming calculated wave cells was four,
- h. only one wave direction was assumed,
- i. the average effective sand diameter was 0.25 mm,
- j. the average height of land above mean water level was 1.5 m, and the limiting depth of profile movement seaward was -6.0 m,
- k. average beach slope was one on twenty,
- l. it was assumed that the breakwaters and groins were impermeable structures, and
- m. it was assumed that there was no wave reflection from the structures.

Analysis

The series of runs conducted were very illustrative in showing the long-term effect of different structures on the shoreline position. The results of the simulation performed can be divided into four different groups:

1. no protection measures,

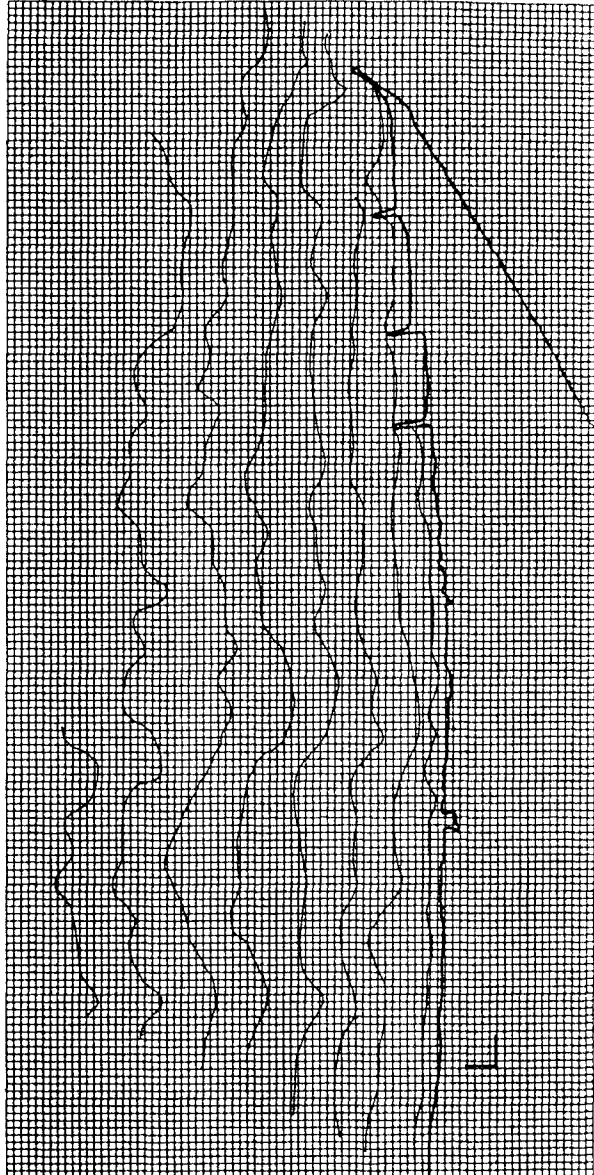


Figure 1. Ras-Elbar Study Area

2. effect of a system of detached breakwaters on the shoreline including the systems proposed by Tetra Tech, Inc. and Delft Hydraulics,
3. effect of a system of groins on the shoreline, and
4. effect of a combined system of detached breakwaters and groins on the shoreline.

For all groups, the final shoreline positions were plotted for each year until reaching a semi-equilibrium state. Relations representing the shoreline change and the average net sediment transport rate for all runs were also provided.

The breaking wave heights and angles were computed for each cell point on the grid. A figure representing the net volumetric change of sediment was prepared to indicate whether a region was gaining or losing sediment.

The different shoreline positions, longshore transport rates, and the shoreline changes from measured values were prepared for each run to illustrate the effect of different parameters and protection plans on the shoreline.

Conclusions

The results of this study were found to be reliable and applicable to a wide range of coastal engineering problems. For the Ras-Elbar area the following conclusions can be made:

1. Large fluctuations in littoral drift were noted.
2. The advantage of being able to vary wave conditions and structural protection plans was clearly apparent throughout this study.
3. A system of offshore detached breakwaters has proven to be the most efficient and reliable plan as a long-term shore protection for long reaches of the coastline.
4. Shore protection planning for a whole region was proven to be useful in providing a continuous interaction plan for the whole coastline.
5. This study has shown that increasing the number of breakwaters (from 4 to 7) for the whole region provided better results than employing a two- or four-breakwater system (Figure 2).
6. The ratio of $G = 1.5 B$ proved to provide a good estimate of the length and the gap of a system of detached breakwaters (where G = distance between two breakwaters, B = length of the breakwater). Four locations of detached breakwaters were studied (165, 294, 445 and 545 m) from the shoreline. At a distance of 294 m from shore, the breakwaters provided minimum shoreline changes. For every case there is an optimum design for the detached breakwater system that will provide minimal or moderate shoreline changes, or cause the formation of tombolos.

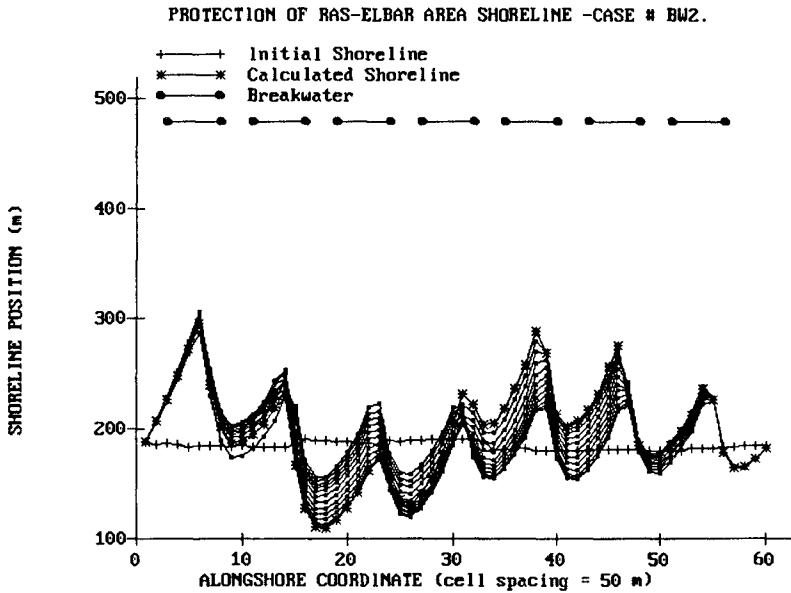
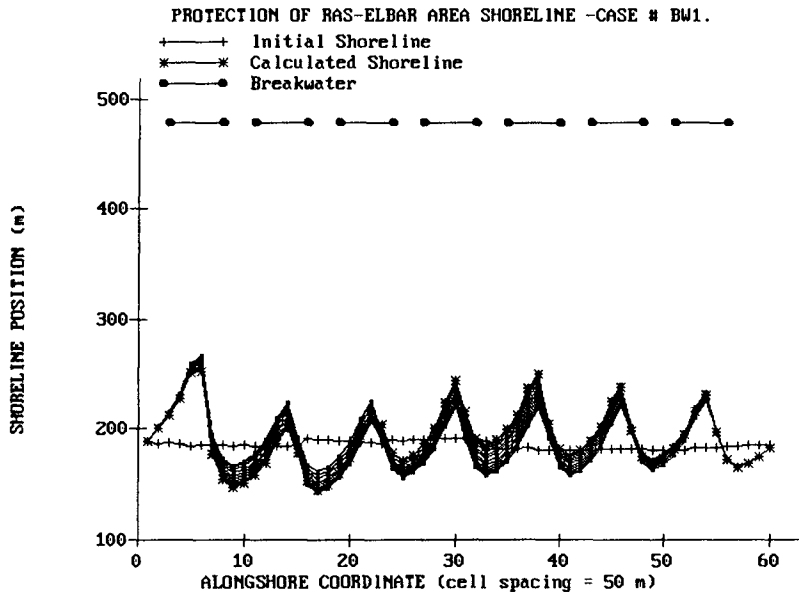


Figure 2. Protection of Ras-Elbar Area Shoreline - Case Numbers BW1 and BW2

7. A system of inclined and staggered breakwaters behaved in a similar manner to the parallel and continuous systems. The higher cost of constructing staggered or inclined offshore structures would make such a system uneconomical.
8. A combined system of offshore detached breakwaters and non-diffracting groins had a fairly similar result to that of using groins only. However, the higher cost involved in construction of two protection systems make it economically unfavorable. Using diffracting groins (which is more realistic) created more problems due to an overlap of the diffracted wave patterns from the groins and the breakwaters.
9. It is concluded that a complete system of detached breakwaters permits the continuation of shore sediment transport and will not affect the coast downstream of the system after equilibrium is reached. At the same time, this system breaks the energy of the incoming waves causing minimum shoreline change in the shadow zones. Sand nourishment should be considered in conjunction with a system of detached breakwaters to accelerate reaching equilibrium and assuring supply of sediment downstream of the system. Moreover the detached breakwater system tends to change the shoreline in a time-dependent manner. A fairly long time will take place to affect and cause changes in the shoreline.

Recommendations

Recommendations for future work are summarized as follows:

1. A uniform numerical grid of 50 m spacing was used, a finer grid spacing less than 50 m should be considered for refinement of the numerical plan.
2. A one-dimensional program employing constant grid spacing and time-step representations was used in this study and proved to be a flexible, reliable and economical method for shoreline change simulation. Higher order two- and three-dimensional schemes with variable grid spacing and time steps should be considered employing a mainframe computer. It should be noted in representing the physics of the flow and the sediment transport process that a compromise between the overall accuracy and the computation costs must be made.
3. As the shore protection structures employed in this study were assumed to be impermeable, consideration of the use of different coefficients of transmissions and permeability are strongly recommended.
4. Use different wave periods and wave heights to study their effect on the shoreline (only one wave height and one wave period were used in this study).

Appendix - References

- Arafa, F. (1981) "Coastal Protection Structures Effect on Northern Coast of Egypt," Report No. 1, Cairo University, MIT.
- Boer, S., De-Vriend, H. and Wind, H. (1984) "System of Mathematical Models for the Simulation of Morphological Processes in the Coastal Area," *Proceedings, Coastal Engineering Conference*, ASCE, pp. 1437-1453.
- CERC (1990) "Shoreline Change and Storm Induced Beach Erosion Modeling," Report No. CERC-90-2 WES, U.S. Army Corps of Engineers, Vicksburg, MS.
- CERC (1984) *Shore Protection Manual*, Volumes I and II, WES, U.S. Army Corps of Engineers, Vicksburg, MS.
- Delft Hydraulics (1987) "Ras-Elbar Shore Protection," Report No. 11500.
- Elsaeed, Gamal H. (1996) "Study of Protection of the Northern Coast of Nile Delta Using Mathematical Models," Ph.D. Dissertation, Faculty of Engineering, Ain Shams University, Cairo.
- Fanos, A., Khafagy, A. and Sharaf-Eldin, S. (1989) "Coastal Changes Along the Egyptian Mediterranean Coast," International Seminar, Egypt.
- Fletcher, C. (1991) *Computational Techniques for Fluid Dynamics*, Volumes 1 and 2, Springer-Verlag.
- Frihy, O., Fanos, A., Khafagy, A. and Komar, P. (1991) "Patterns of Nearshore Sediment Transport Along the Nile Delta Egypt," *International Journal of Coastal Engineering*, Vol. 15, The Netherlands, pp. 409-429.
- Gravens, M. and Kraus, N. (1992) "GENESIS Workbook," Report No. 2, WES U.S. Army Corps of Engineers, Vicksburg, MS.
- Hanson, H. and Kraus, N. (1982) "GENESIS," Technical Reference Report No. 1, WES, U.S. Army Corps of Engineers, Vicksburg, MS.
- Herbich, J.B. (Ed.) (1991-92) *Handbook of Coastal and Ocean Engineering*, Volumes 1, 2 and 3, Gulf Publishing Company, Houston, TX.
- Inman, D. and Jenkins, S. (1984) "The Nile Littoral Cell and Man's Impact on the Coastal Zone of the Southeastern Mediterranean," *Proceedings, Coastal Engineering Conference*, ASCE, pp. 1282-1290.
- Inman, D., Golik, A. and Carmel, Z. (1984) "Transport of Nile Sand Along Southeastern Mediterranean Coast," *Proceedings, Coastal Engineering Conference*, ASCE, pp. 124-173.
- Kadib, A., Shak, A., Mazen, A. and Nader, A. (1986) "Shore Protection Plan for the Nile Delta Coastline," *Proceedings Coastal Engineering Conference*, ASCE, pp. 2530-2544.
- Kraus, N. (1989) "Beach Change Modeling and Coastal Planning Process," *Proceedings, Coastal Zone 1989 Conference*, ASCE, pp. 553-567.
- Kraus, N. and Harikai, S. (1983) "Numerical Model of the Shoreline Change of Oarai Beach," *International Journal of Coastal Engineering*, Vol. 7, The Netherlands.

- Perlin, M. and Dean, R. (1983) "A Numerical Model to Simulate Sediment Transport in the Vicinity of Coastal Structures," WES Report No. 83-10, U.S. Army Corps of Engineers, Vicksburg, MS.
- Tetra Tech, Inc. (1984-85) "Shore Protection Masterplan for the Nile Delta Coast," Reports 1 and 2.
- United Nations Development Program (UNDP) (1973) "Coastal Erosion Studies," Technical Report, Project No. Egy/70/581.

CHAPTER 308

Stabilizing Beaches Downcoast of Harbor Extensions

John R C Hsu¹ and Richard Silvester, M. ASCE²

Abstract

In geomorphological terms, the sandy shoreline of a bay downcoast of a harbor may be stable or in static equilibrium, or could be in dynamic condition, if sediment is still being supplied from upcoast or from downcoast to form a salient predicted by a static bay shape equation. Should commercial expansion demand a larger port, the general solution is to run a breakwater from the headland or existing structure. This has the potential to create a new static equilibrium beach, often with accretion in the lee which is at the expense of beach erosion downcoast. It is strongly recommended that geomorphic approach be incorporated to stabilize downcoast beaches early in the planning stage of a harbor, or as remedial measures. By creating bay beaches in static equilibrium, the potential beach erosion downcoast of a harbor will be kept to a minimum or may be prevented completely.

Introduction

As Inman (1974) has recalled, man has been interfering with river and coastal environments dated back in 1500 BC when the Minoans constructed wharves in Crete and by 480 BC as the Phoenicians built harbors along the coasts of Lebanon and Israel. Fleming (1992) has also discussed the modern history of harbor developments for fishing ports and major maritime trade. Oliveira et al (1982) has reported disappearances of towns in Portugal, as beaches eroded towards their stable shape.

Despite our current understanding of coastal processes there is a missing link as instanced by the many stories of beach erosion still reported in the technical literatures (for example, Ozaki 1964, Dunham 1965, Inman and Frautschy 1965, Herron and Harris 1966, Jordaan 1970, Sato and Irie 1970, Moni 1972, Lepetit 1976, Tanaka and Sato 1976, Nir 1982, Oliveira et al 1982, Komar 1983, Saxena 1983, Kraus et al 1984, Uda et al 1986, Gonzalez et al 1988, Kuo 1988, Moutzouris 1990).

¹ Senior Lecturer, Department of Environmental Engineering, University of Western Australia, Nedlands, WA 6907, Australia E-mail: hsu@cwr.uwa.edu.au

² Honorary Research Fellow, Department of Civil Engineering, University of Western Australia, Nedlands, WA 6907, Australia

The present status of man's abilities in coastal engineering and shore protection has been well summed up by Inman (1974): "In view of man's present extensive intervention in the coastal zone, mostly based on 'brute force' technology, a careful study of the ancients' ability to work with Nature provides valuable insight for today's problems."

In spite of our great knowledge of wave kinematics and sediment movements in marine situations, engineers have not appreciated the macroscopic view of the coast as imposed by Nature. She has transported millions of tonnes of material to sea and back again in a matter of days and also moved it alongshore. More observations are necessary to ascertain the long-term stability of waterlines produced by persistent swell and the aberrations that occur during storm sequences. It is the former which is the concern of this paper.

Many researchers have recognized the effect of harbor construction on sediment transport downcoast, but without adequate quantitative prediction. Herron and Harris (1966) believed that "harbor works are the principal offenders" that have interrupted the balance of natural littoral drift existing over hundreds or thousands of years. Even so, the question of how to predict a stable shoreline in the lee of such structures remains unanswered. It is hoped this situation is overcome with the current submission and other works by Hsu et al (1993) and Silvester and Hsu (1993). In terms of the beach erosion downcoast of harbor extensions, these authors believe it is not so much a need to look back on our achievements but a need to observe natural processes in geomorphological terms and apply them.

Beaches Downcoast of Harbors

In geomorphological terms the stability of a sandy shoreline can assume a bay shape that is *stable* or in *static equilibrium* if the littoral drift is negligible or non-existent, or it can be in *dynamic equilibrium* if drift is still being supplied with sand from upcoast or from within the bay. Whilst this supply is constant the bayed beach can remain in place for decades, but should it decrease the shoreline will recede towards the static equilibrium shape, the final limit to which it will go.

If on a straight sandy length of coast a breakwater or other structure is run out to sea, the immediate result will be interception of littoral drift and the formation of a bay downcoast of the impediment. This will become further indented until sediment bypasses the new structure and dynamic equilibrium is restored. This sudden loss of land instigates the insertion of protective measures such as seawalls or groins, that are usually ineffective since man is fighting with Nature. The walls reflect waves obliquely and so generate short-crested waves (Silvester 1972; Hsu 1990) which expedite the longshore transport. On the other hand, straight groins accelerate drift by forming rip currents during storms that carry vast volumes of material offshore, there to be transmitted downcoast by subsequent swell.

Similar to the eroding beaches on straight coasts, discontinuity or interruption of sediment supply from upcoast has been considered as the main cause of beach erosion downcoast of harbors (Herron and Harris 1966, Komar 1983, Uda et al 1986). This may be attributed to the construction and extension of long breakwaters and dredging of deep access channels.

An additional factor is the potential of salient/bay formation in the lee of the breakwaters, caused by an improper alignment of a new breakwater and the

positioning of its tip. This implies that a large volume of sand is needed, often from the beach downcoast, to build up a salient in the form of a bay. In addition to the evolution of shoreline, it also causes change to the bottom topography in the vicinity of the structures (Sato and Irie 1970). The slopes of beach faces downcoast were found to become steeper with armouring units subsided in front of seawalls. (Uda et al 1986; Hsu et al 1994)

Universal Bay Shape Equation

Crenulate-shaped bays are ubiquitous, occurring as they do on oceanic margins, coasts of enclosed seas, lakes, and even river shorelines. They are indicative of Nature's way of balancing the wave energy with the sediment load to be carried. Bays have thus been maintained in the same position for thousands of years in spite of the fierce storms that hit them infrequently. But for the rocky headlands spaced along the coast, vast indentations would have been formed with the downcoast extremity almost normal to the orthogonals of the most persistent swell (Silvester 1976).

Geographers and geologists have published on bay shapes (Halligans 1906) with the first recognition of this as a stable feature by Jennings (1955), unfortunately without full knowledge of the wave action involved. Davies (1958) observed the importance of wave refraction but not diffraction. Langford-Smith and Thom (1969) noted the zeta-shaped beaches of the New South Wales coasts of Australia, without scientific analysis of their profiles. Although the crenulate shaped bays have received the attention of many scientists (Bird 1984, Carter 1988, Davis 1985, Phillips 1985, Shepard 1973, Zenkovich 1967), their stability has only been examined by engineers (Silvester 1960; Le Blond 1979; Silvester et al 1980). This geomorphic feature has existed for some thousands of years (at least since the last still stand of sealevel), but have become more indented during the past century due to the dearth of sediment for many reasons (Silvester and Hsu 1993). In this relatively short period in geologic time rivers have been harnessed, which results in less supply of sediment to the coast for spreading by wave action. This has resulted in bays approaching their static equilibrium condition, causing greatest erosion at the most indented position of the bay with practically no change at either end.

Yasso (1965) suggested the logarithmic spiral for predicting the shape of the crenulate-shaped bays, which Silvester (1974) adopted for many years. But this was found to be inaccurate for the downcoast region where the beach straightens (Hsu and Evans 1989). A polynomial form resulted from data of a multitude of bays examined as follows:

$$R/R_0 = C_0 + C_1 (\beta/\theta) + C_2 (\beta/\theta)^2 \quad (1)$$

with the variables R , R_0 , β and θ as given in the definition sketch of Figure 1. The values of constants C_0 , C_1 and C_2 are available in Hsu and Evans (1989) and Silvester and Hsu (1993), in tabular and graphical form. It is noted that the wave obliquity (β) is measured between the control line (R_0) and the downcoast beach tangent. For a stable or near stable beach this is normal to the orthogonal of the persistent swell which sculpts the shape. The straight crests of these incoming waves at the point of diffraction, at the other end of the control line, are also angled β to it, from which arcs (R) are drawn at angle θ to it. Thus, by knowing R_0 and β the value of R is determined for a specific θ , so that the complete periphery of the static equilibrium bay can be drawn. It has been shown that the logarithmic spiral

fits only the curved portion of the actual bay, whereas the parabolic formula fits the complete periphery exceedingly well (Hsu and Evans 1989).

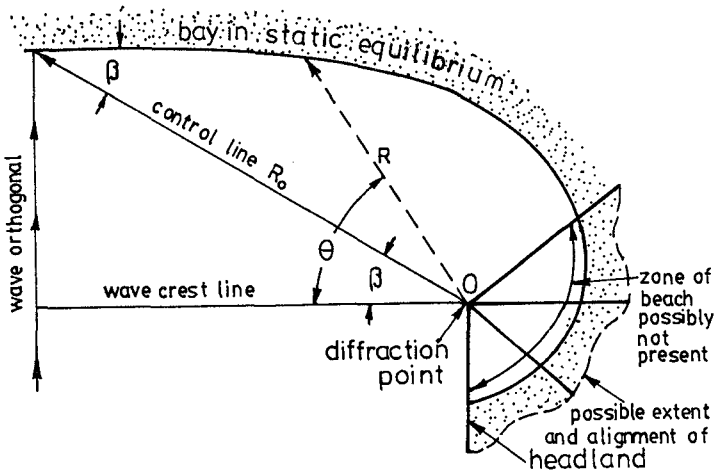


Figure 1. Definition sketch of a new empirical equation for static bay shape.

Besides the shaping of bays in the lee of headlands, equation (1) can be applied to salients behind offshore breakwaters (Hsu and Silvester 1990), as seen in Figure 2. These accretions are not triangular but assume the parabolic curve either side of the apex, as dictated by the diffracting and refracting waves and the associated longshore current circulation. This added land is at the expense of beaches beyond the extremities of the breakwater, if beach nourishment is not carried out.

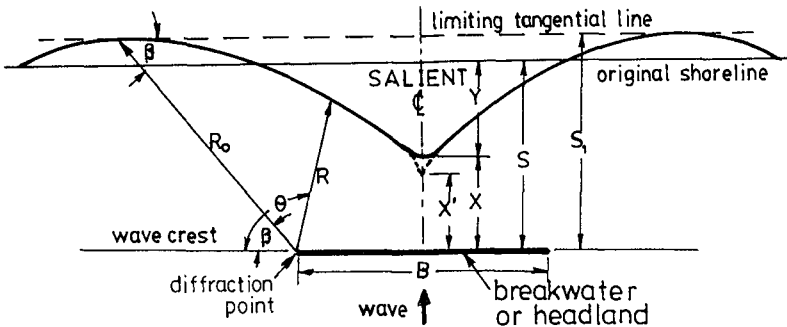


Figure 2. Definition sketch of a salient formed in lee of an offshore breakwater, with normal wave approach, based on the static bay shape equation (1).

Influence of Upcoast Headland Conditions

A natural headland is depicted in Figure 3 a & b as A and the downcoast limit as B in which control line $AB (= R_{01})$ angled to the downcoast tangent by wave obliquity β_1 . When breakwater AC is built the new diffraction point C gives a new control line CB and new angle β_2 , which results in a changed static equilibrium or

stable shape. This natural reshaping will take place inspite of any modest attempts with groins or seawalls to prevent its fruition.

Looking first at Figure 3a, the existing bay may be in dynamic equilibrium, with littoral drift still passing through, as seen by the full line in the figure. The dotted curve denotes the stable shape for control line AB , to which the beach would erode if all sand supply around point A should cease. Now, when the breakwater AC is inserted its length and orientation could be so chosen that diffraction at point C and control line CB , with the static bay for CB being the same as the dynamic for AB . This can be achieved close enough for erosion at all points around the periphery to be negligible. If, however, sand were finally to bypass point C the resulting beach may become dynamic once more with a beachline seawards of this stable shape. But it should be designed for the static condition in case this additional drift ceases in the future.

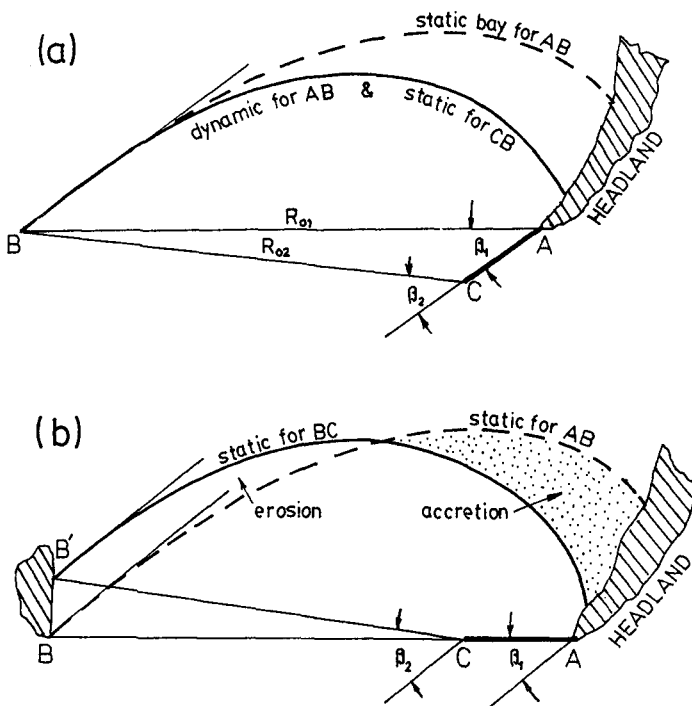


Figure 3. Effect of positioning a breakwater tip (a) in a dynamic bay, and (b) in a static bay, for harbor planning and beach erosion control.

Now turning to Figure 3b, the dotted curve represents the static equilibrium shape for control line AB which is the existing beach. When breakwater AC is added the new control line CB creates a new static beach which involves massive accretion in the lee of headland A . The material for this has to be supplied from the region of B because the beach was originally stable. This causes a new downcoast tangent to operate that determines a new β_2 for equation (1). The situation would detract from the calm water area serving as an anchorage but could be attractive for tourism purposes.

It must be remembered that the stable waterline being predicted applies to swell conditions or calm weather. When storm waves arrive, the beach berms will be removed offshore to form a bar, which take some days to be returned. In the case of static equilibrium the same waterline will result, but all infrastructure should be kept landward of the receded storm limit.

Case Studies of Stabilization

Conventional defense solutions, such as seawalls, groins and offshore breakwaters, have been used to stabilize eroding beaches downcoast of harbors without much success. Sand bypassing and nourishment schemes have also been tried, with some degree of success in the short term. However, the geomorphological approach, involving the construction of stable bay beaches, will be attempted in this paper. This may be regarded as a permanent solution.

Like the medical profession, which prefers to make sick people better by the administration of drugs or surgery, coastal engineers have concentrated on rectifying problems rather than preventing them. Some of these are due to their own mismanagement. Many medicos are now working holistically in looking at the whole person (body, mind and emotions) to find causes rather than remedies as such. In approaching a coastal situation from a geomorphological viewpoint the final trends can be examined which point to a permanent rather than a temporary solution.

As will be seen in many of the cases to be presented, the macroscopic view of the whole coastline gives a better picture of a problem, than looking at a limited section of it. Erosion can be predicted long before it is likely to take place and hence means can be devised to prevent it. In some of the Japanese harbors the breakwater extensions are mammoth, with lengths in terms of kilometers. The incentive may be large current expenditure to generate a larger budget next year. These structures certainly produce many subsidiary problems such as siltation and erosion which demand more money.

1. Durban harbor, South Africa

The erosion of beaches north of Durban harbor on the Indian Ocean of South Africa has been presented by Jordaan (1970). This involved siltation at the port entrance, which is continually dredged and dumped out to sea or along the eroding beaches. The suggested solutions entailed Y or L shaped groins plus two offshore sand breakwaters, each 300 m in length and spaced apart the same amount, and 600 m from the beach. Whether any of these have been implemented does not affect the this exercise to apply the principle of static bay shape.

Using the tip of the outer breakwater as the diffraction point (*A*) the resulting stable bay *A* is shown in Figure 4. This indicates substantial erosion even if minor attempts are made to prevent it. The need is for a new diffraction point to the north in order that a beachline seaward of the present can be established. Such a point (*B*) can be provided by an island breakwater *BD* from which bay *B* is formed. The space between structure *BD* and the existing inner breakwater will permit some wave action to round-off this waterline to the existing (old) breakwater as shown. The beach between it and the main port structure will be reoriented as indicated by the dotted line.

The accretion anticipated for bay beach *B* could be supplied from dredging of the entrance channel that appears to be continuous. Otherwise the siltation would come from beaches to the north. It is expected that the groins will be removed and their stone etc used in the new breakwater *BD*. The offshore sand mounds (if built) could also be removed and perhaps utilized as fill for the beach *B*.

To help overcome the necessity for dredging at the port entrance the outer breakwater could be extended as shown (*AC*) which would reflect waves obliquely. The short-crested system so established would transmit material across the slightly diverted navigation channel and create a shoal near the tip *B*. It would finally find its way to the beaches. This new structure would prevent swell entering the gap between breakwater *B* and the existing structure so that beach *B* would extend to the tip of the old breakwater.

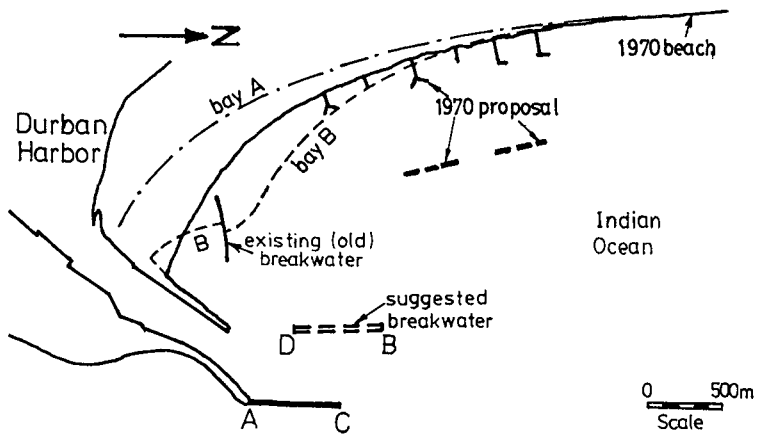


Figure 4. Durban harbor, South Africa

2. Esperance port, Western Australia

Esperance Bay is part of a continuous chain of embayments facing the Southern Ocean in the south of Western Australia. The curved shoreline, in geomorphological terms, was in dynamic equilibrium, implying its stability was maintained by the uninterrupted supply of littoral drift. However, the construction of a breakwater and dredging of an entrance channel for the Port of Esperance between 1962-65, with breakwater extension in 1973-75, has cut off the littoral drift. This has forced the shoreline to recede back to a potential static equilibrium, which is destined by Nature. This limit is landwards of the existing shoreline (see Figure 5). A total of 573,000 m³ of dredged material was placed onto the beach.

The engineering solutions taken to combat with the eroding beach at Esperance has been a low-cost rock groin field with beach renourishment, which has been an ongoing task ever since 1969. Between 1977 and 1995, sand renourishment at an average rate of 23,100 m³/year has been placed on sections of beaches suffering the worst erosion. Two headlands in the shape of a walking sticks with fronting beaches are proposed to achieve the overall stability with one-off beach nourishment to form a bay, rather than a field of short groins or offshore breakwaters with continual renourishment.

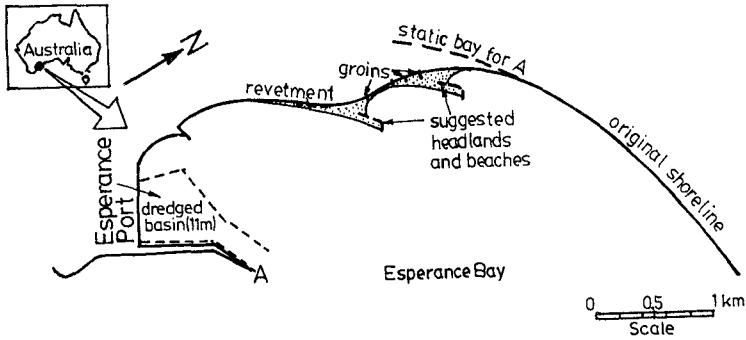


Figure 5. Esperance Bay, Western Australia

3. Hua-Lien harbor, Taiwan

Hua-Lien harbor is located on the Pacific Ocean coast of Taiwan at latitude 24°N. Two breakwaters (*AB* and *CD*) were constructed in 1987, as noted in Figure 6 (Hsu et al 1994). Prior to this extension, erosion of the coast south of the harbor entrance had been experienced, resulting in lengthy seawalls protected by concrete armour units which have steepened the offshore area. The stable beach for breakwater *CD* is shown dotted (bay for *D* in the figure) which is landward of the majority of the protected area, except at the northern tip where accretion would inhibit the discharge of the stream in the lee of breakwater *AB*.

One solution to these two problems is to extend the breakwater from *CD* to *DE*. The new diffraction point at *E* will produce the waterline shown as salient for *DE*, which is seaward of the current shoreline protected by the seawall. The remainder of the beaches will be stabilized, so not requiring other protection such as groins or seawalls. An offshore breakwater *FG* may be constructed which will intercept material in the lee of the main breakwater *DE* to form the secondary curve in the form of a salient to ensure that the stream outlet will not silt up.

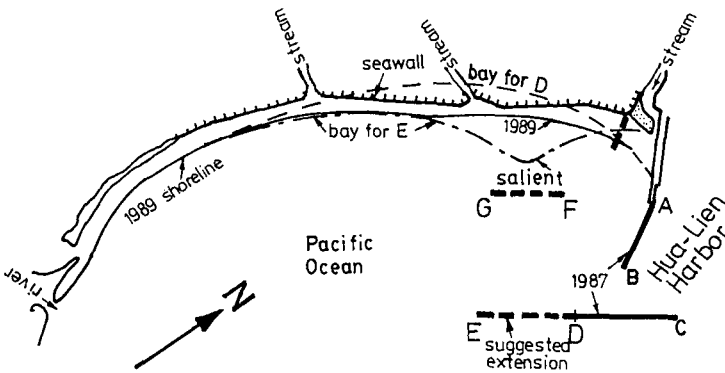


Figure 6. Hua-Lien harbor, Taiwan

4. Ohtsu harbor, Japan

The fishing harbor at Ohtsu on the east coast of Honshu, Japan (see Figure 7 for location), as seen in Figure 8, had a small breakwater complex initially in 1977. It was added to point *A* in 1984, as noted in the figure. The island structure created a new diffraction point *A* that caused accretion west of the groin at Edokomi river and between that and the Satone river outlet. The static equilibrium bay shape for point *A* is seen to match this erosion some distance from the port. To overcome this a revetment was built which suffered undermining and collapsed in places during 1983.

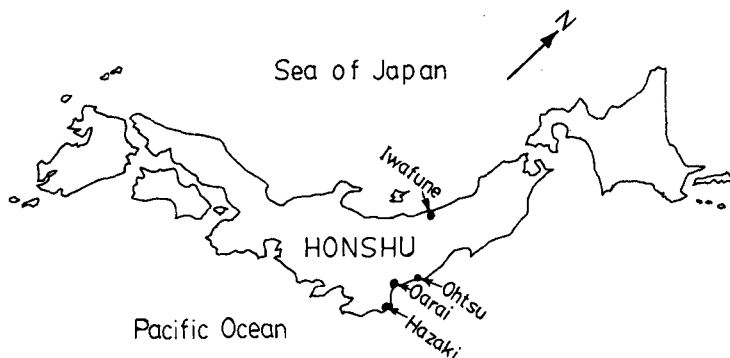


Figure 7. Map of Japan, showing locations of harbors discussed.

Offshore, in the region of the island breakwater, accretion was measured between 1977 and 1984. This was probably due to the oblique reflection of waves from this 600 m long structure that transmitted scoured material to this area. Uda et al (1986) believed these measurements were erroneous soundings. They were aware that the island breakwater had caused the beach accretion but stated: "the current induced the sand movement toward the lee of the breakwater". These authors believe it is the wave direction of approach due to diffraction that generates the new waterline orientation.

Two alternatives are shown in Figure 8 to rectify this problem, namely, either to extend from *A* to *B* or to provide a separate structure *CD*. The new diffraction points *B* and *D* result in stable beaches as shown, which indicate substantial accretion adjacent to the Edokomi river groin but less erosion further west. The additional material required for beach stability could be provided from dredging the outlets of these two rivers, to give the stable beach shown between the two groins. To deal with the slight erosion to the west an offshore breakwater could be constructed from the revetment that should be removed.

5. Oarai harbor, Japan

Oarai harbor on the Honshu coast of Japan (see Figure 7) has had many researchers analyze it (Sato and Irie 1970, Mizumura 1982, Kraus et al 1984 and Uda et al 1986). It was a small port comprising two breakwaters at 45° to the coast which was silted up quickly between 1911 and 1916. By 1976 a new breakwater was built to point *A*, in Figure 9, for which the predictable bay shape (not shown) matched the existing beach at the time (Hsu et al 1993; Silvester and Hsu 1993). In

1981 it was extended to point *B*, and to point *D* by 1985, of which the stable bays for *B* and *D* are shown. This involves massive accretion, which had partially been achieved by 1988. The sediment needed was at the expense of erosion downcoast.

In order to achieve a stable shape more in keeping with the 1988 shoreline, or even the current profile, two extensions to *E* or *F* are suggested, together with their resulting beachlines. It is seen that *F* matches the 1988 shoreline at the groin-type structure, even though it is landward of it towards the south. It is envisaged that the two small groins would be removed, which would permit the sand to find its way back to renourish beaches to the south that have been eroded. The extension of *AB* to *F* infers that breakwater *CD* would be removed as it is no longer needed for wave attenuation.

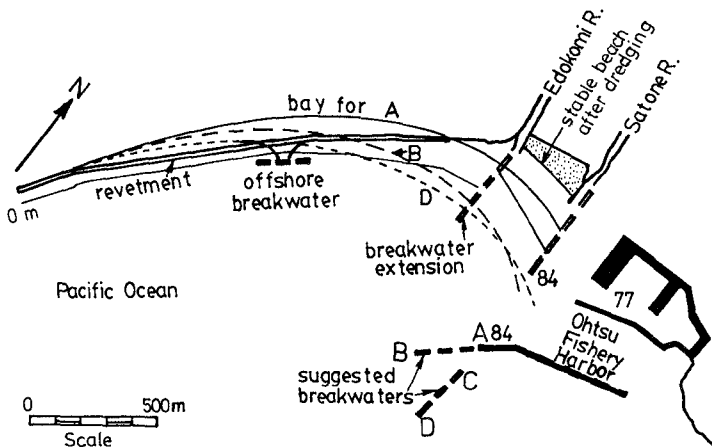


Figure 8. Ohtsu harbor, Japan

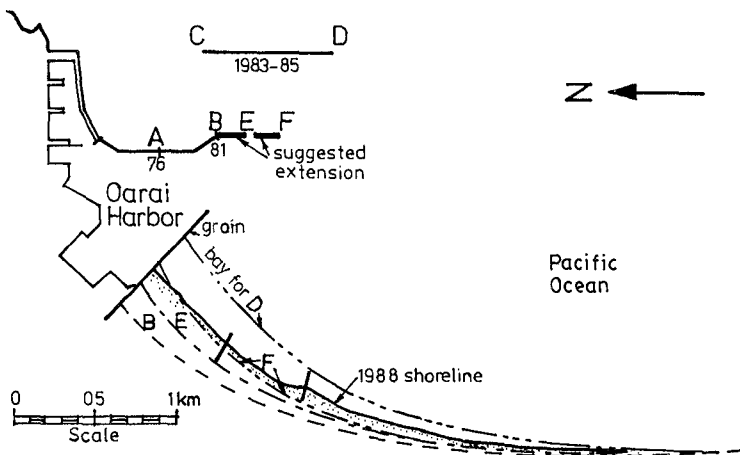


Figure 9. Oarai harbor, Japan

6. Hazaki harbor, Japan

Hazaki fishing harbor is located at the outlet of the Tone river in Honshu, Japan (see Figure 7 for location). As seen in Figure 10, a breakwater was commenced in 1974 and extended in 1976 with another started nearer the mouth. Additions were made to both in 1978 and to the SE one in 1981. By this time erosion had commenced some 600 m from the NE breakwater with accretion adjacent to it. In 1983 a shore parallel section 350 m in length was inserted to calm waters in the harbor, which became silted very quickly. Uda et al (1986) believed this was due to sediment discharge from the Tone river but the actual mechanism was not discussed. These authors believe it was due to waves being reflected obliquely from this shore parallel arm. These transported sand along it, depositing it at the entrance, which subsequently was moved into the harbor. The leg added in 1984 (see Figure 10) did little to prevent this as the mass-transport current of the short-crested wave system would have still formed a shoal at the entrance.

An extension of this leg to point A in the figure would achieve two important objectives. Firstly, continued oblique reflection will transmit sediment from the Tone river in a NW direction to form a shoal beyond the scoured area in proximity to its tip where an access channel can be maintained. This shoal will continually be fed to the downcoast beach. Secondly, the new diffraction point A will create a stable bay shape, as indicated in the figure, which will require no further structures to keep it in place. The accretion already there will thus remain for all time.

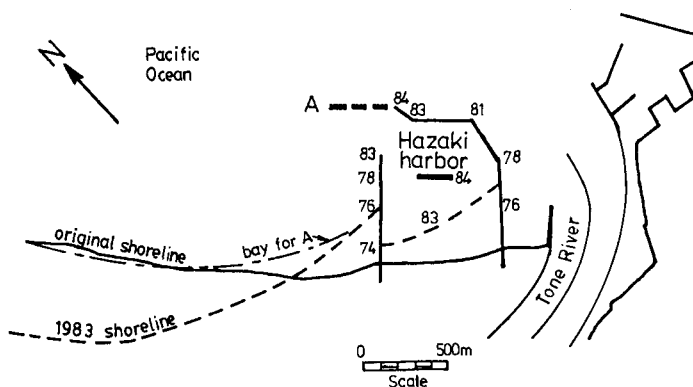


Figure 10. Hazaki harbor, Japan

7. Iwafune harbor, Japan

The shoreline evolution at Iwafune harbor (see Figure 7 for location) has been discussed by Hsu et al (1993) and Silvester and Hsu (1993). As seen in Figure 11 a large triangular land mass had been accreted up to 1988, from having attained to a stable bay shape for A in 1965. The static bay for diffraction point A matched extremely well the waterline at that time. The extensions of the main breakwater from A to B and then to C (by means of a detached structure) relocated the diffraction points for the incoming swell waves. The resulting bay shapes are shown which predict much more siltation if sand is available from the southern beaches. To overcome the present erosion many groins and an offshore breakwater system have been installed with little effect. The reason for this is that littoral drift still

occurs offshore, just after each storm, as the storm bar is being moved back to the beach.

To prevent the transposition of further material from southern beaches it is recommended that two offshore breakwaters be installed (see Figure 11), with concomitant groin removal. The outer structure would have stable bay C pass through its southern tip, with the tombolo curved bay stretching to the tip of the inner breakwater. its curved tombolo would be tangential to the 1988 or present shoreline. The fill required in the lee of and south of each new breakwater could be transported by truck or pipeline from the large triangular landmass, in order to reduce siltation at the harbor mouth.

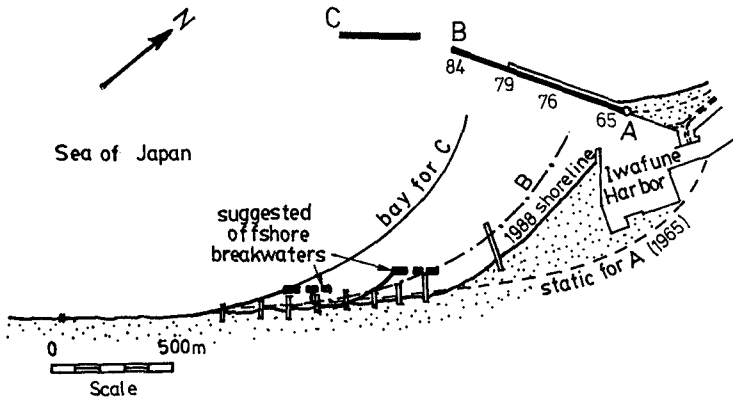


Figure 11. Iwafune harbor, Japan.

Conclusion

1. Bay beaches form downcoast of headlands or man-made structures that can be in dynamic equilibrium (continued littoral drift) or static equilibrium (zero littoral drift).
2. Should the diffraction point for persistent swell waves be altered, the bay as in (1) above will change, which may involve siltation in the lee of the structure and/or erosion downcoast.
3. A bay initially in dynamic equilibrium can be stabilized by a judicious selection of breakwater location, which then does not require any other defense measures.
4. Many major ports have suffered siltation as noted in (2) above after extension of breakwaters, together with erosion of downcoast beaches.
5. There is a dire need for coastal engineers to emulate Nature, who has maintained crenulate-shaped bays for aeons, by taking a geomorphic approach to their problems, both at the planning stage and in remedial measures later.

References

- Bird, E.C.F. (1984). *Coasts: An Introduction to Coastal Geomorphology*. 3rd e d., Aust. National Univ. Press, Canberra.
- Carter, R.W.G. (1988). *Coastal Environments: An Introduction to the Physical, Ecological and Cultural Systems of Coastlines*. Academic Press, London.

- Davies, J.L. (1958). Wave refraction and the evolution of shoreline curves. *Geogr. Stud.*, 5: 1-14.
- Davis, R.A. (ed.) (1985). *Coastal Sedimentary Environments*. 2nd rev. expanded ed., Springer-Verlag, New York.
- Dunham, J.W. (1965). Use of long groins as artificial headlands. *Coastal Eng. Santa Barbara Specialty Conf., ASCE*, 755-762.
- Fleming, C.A. (1992). The development of coastal engineering. In M.G. Barrett (ed.), *Coastal Zone Planning and Management*, Thomas Telford, London, 5-20.
- Gonzalez, J.J.D., Paredes, V.A.E. and Herrando, J.A. (1988). Ria De Foz: Solution for a harbour and coastal problem. *Proc. 21st Int. Conf. Coastal Eng., ASCE*, V. 3, 2896-2907.
- Halligan, G.H. (1906). Sand movement on the New South Wales coast. *Proc. Limn. Soc. N.S.W.*, 31: 619-640.
- Herron, W.J. and Harris, R.L. (1966). Littoral bypassing and beach restoration in the vicinity of Port Hueneme, California. *Proc. 10th Int. Conf. Coastal Eng., ASCE*, V.1, 651-675.
- Ho, S.K. (1971). Crenulate shaped bays. *Master Eng. thesis* No. 346, Asian Inst. Tech., Bangkok.
- Hsu, J.R.C. (1990). Short-Crested Waves. Chapter 3 In *Handbook of Coastal and Ocean Engineering*, (ed. J.B. Herbich), Gulf Publishing Co., Texas, 1: 95-174.
- Hsu, J.R.C. and Evans, C. (1989). Parabolic bay shapes and applications. *Proc. Instn. Civil Engrs.*, London, Part 2, 87: 557-570.
- Hsu, J.R.C. and Silvester, R. (1990). Accretion behind single offshore breakwater. *J. Waterway, Port, Coastal & Ocean Eng.*, ASCE, 116 (3): 362-380.
- Hsu, J.R.C., Silvester, R. and Xia, Y.M. (1989). Generalities on static equilibrium bays. *Coastal Eng.*, 12: 353-369.
- Hsu, J.R.C., Uda, T. and Silvester, R. (1993). Beaches downcoast of harbours in bays. *Coastal Engineering*, 19: 163-181.
- Hsu, T.W., Ou, S.H. and Chang, H.K. (1994). Countermeasures against beach erosion in Hua-Lien coast. *Proc. 16th Ocean Eng. Conf.*, Taiwan, ROC, 186-206.
- Inman, D.L. (1974). Ancient and modern harbors: a repeating phylogeny. *Proc. 14th Int. Conf. Coastal Eng., ASCE*, V. 3, 2049-2967.
- Inman, D.L. and Frautschy, J.D. (1965). Littoral processes and the development of shorelines. *Coastal Eng. Santa Barbara Specialty Conf., ASCE*, 511-536.
- Irie, I., Sakai, M., Nagyu, T. and Katoh, K. (1990). Development of shore protection engineering in Japan. *Proc. 27th Intel. Nav. Congr.*, PIANC, Paper S.II-2-1, 29-45.
- Jennings, J.N. (1955). The influence of wave action on coastal outline in plan. *Aust. Geogr.*, 6: 36-44.
- Jordaan, J.M. Jr. (1970). Study of Durban Harbor silting and beach erosion. *Proc. 12th Int. Conf. Coastal Eng., ASCE*, V. 2, 1097-1116.
- Kraus, N.C., Hanson, H. and Harikai, S. (1984). Shoreline change at Oarai beach: past, present and future. *Proc. 19th Int. Conf. Coastal Eng., ASCE*, V. 2, 2107-2124.
- Kuo, S.D. (1988). Shore protection of Kaohsiung harbour outer breakwater. *Proc. 21st Int. Conf. Coastal Eng., ASCE*, V. 3, 2882-2895.
- Komar, P.D. (1983). Coastal erosion in response to the construction of jetties and breakwaters. In: P.D. Komar (Ed.), *Handbook of Coastal Processes and Erosion*. CRC Press Inc, Boca Raton, Florida, 191-204.
- Langford-Smith, T. and Thom, B.G. (1969). New South Wales coastal geomorphology. *J. Geol. Soc., Aust.*, 16: 672-580.

- Le Blond, P.H. (1979). An explanation of the logarithmic spiral plan shape of headland bay beaches. *J. Sed. Petrology*, 49: 1093-1000.
- Lepetit, J.P. (1976). Impact of yachting marinas on beaches. *Proc. 15th Int. Conf. Coastal Eng., ASCE*, V. 2, 1844-1867.
- Mizumura, K. (1980). Littoral drift of sand near Port of Oarai. *Proc. 17th Int. Conf. Coastal Eng., ASCE*, V. 3, 2159-2173.
- Moni, N.S. (1972). Systematic study of coastal erosion and defence works in the southwest coasts of India. *Proc. 13th Int. Conf. Coastal Eng., ASCE*, V. 2, 1427-1450.
- Moutzouris, C.I. (1990). Effect of harbour works on the geomorphology of three Greek coasts. *Proc. 27th Inter. Nav. Congr.*, PIANC, 17-21.
- Nir, Y. (1982). Offshore artificial structures and their influence on the Israel and Sinai Mediterranean beaches. *Proc. 18th Int. Conf. Coastal Eng., ASCE*, V. 3, 1837-1856.
- Oliveira, I.B.M., Valle, A.J.S.F. and Miranda, F.C.C. (1982). Littoral problems in the Portuguese west coast. *Proc. 18th Int. Conf. Coastal Eng., ASCE*, V. 3, 1950-1969.
- Ozaki, A. (1964). On the effect of an offshore breakwater on the maintenance of a harbour constructed on a sandy beach. *Proc. 9th Int. Conf. Coastal Eng., ASCE*, 323-345.
- Phillips, D.A. (1988). Headland-bay beaches revisited: an example from Sandy Hook, New Jersey. *Marine Geol.*, 65: 21-31.
- Sato, S. and Irie, I. (1970). Variation of topography of sea-bed caused by the construction of breakwaters. *Proc. 12th Int. Conf. Coastal Eng., ASCE*, V. 2, 1301-1319.
- Saxena, P.C. (1983). Role of coastal morphology in the design of layouts of major harbours along the eastern coast of India. *Proc. 8th Inter. Harbour Congr.*, Antwerp, Belgium.
- Shepard, F.P. (1973). *Submarine Geology*. 3rd Ed., Harper & Row, New York.
- Silvester, R. (1960). Stabilization of sedimentary coastlines. Paper 4749, *Nature*, 188: 467-479.
- Silvester, R. (1972). Wave reflection at seawalls and breakwaters. *Proc. Instn. Civil Engrs.*, 51:123-131.
- Silvester, R. (1974). *Coastal Engineering, II*. Elsevier Science, Amsterdam.
- Silvester, R. (1976). Headland defense of coasts. *Proc. 15th Int. Conf. Coastal Eng., ASCE*, V. 2, 1394-1406.
- Silvester, R., Tsuchiya, Y. and Shibano, Y. (1980). Zeta bays, pocket beaches and headland control. *Proc. 17th Inter. Conf. Coastal Eng., ASCE*, V. 2: 1306-1319.
- Silvester, R. and Hsu, J.R.C. (1993). *Coastal Stabilization: Innovative Concepts*. Prentice Hall, Englewood Cliffs, New Jersey, 578 pages.
- Tanaka, N. and Sato, S. (1976). Topographical change resulting from construction of a harbor on a sandy beach: Kashima Port. *Proc. 15th Int. Conf. Coastal Eng., ASCE*, V. 2, 1824-1843.
- Uda, T., Sumiya, M. and Kabayashi, Y. (1986). Analysis of beach erosion around large-scale coastal structures. *Proc. 20th Int. Conf. Coastal Eng., ASCE*, V. 3, 2329-2343.
- Vichetpan, N. (1969). Equilibrium shapes of coastline in plan. *Master Eng. thesis* No. 280, Asian Inst. Tech., Bangkok.
- Yasso, W.E. (1965). Plan geometry of headland bay beaches. *J. Geol.*, 63: 702-714.
- Zenkovich, V.P. (1967). *Processes of Coastal Development*. Ed. J.A. Steers, trans. D.G. Fry, Oliver & Boyd, Edinburgh.

CHAPTER 309

OBSERVATION OF NEARSHORE CURRENTS AND BEACH CHANGES AROUND HEADLANDS BUILT ON THE KASHIMANADA COAST, JAPAN.

Saito, K.* , T.Uda**, K.Yokota*, S.Ohara*, Y.Kawanakajima* and K.Uchida***

ABSTRACT

Nearshore currents and beach changes around headlands built on the Kashimanada coast facing the Pacific Ocean were investigated through the field observation. In order to confirm the effectiveness of headland system to stabilize sandy beach, nearshore current field and shoreline change around headlands were measured as well as the comparison of measured value with the results of numerical simulation of nearshore currents. Comparison of development of a rip current around a completed, anchor-type headland and a groin-type headland under construction was also made and superiority of anchor-type headland to suppress the development of a rip current in the vicinity of the structure was clarified.

I. INTRODUCTION

In recent years, a method to stabilize sandy beach by using headlands has been applying on several coasts in Japan in place of the detached breakwaters and the effectiveness has been confirmed. One of the examples is given on the Kashimanada coast as shown in Photo 1, where headland system was introduced to stabilize coastline(Uda et al., 1988). Now, construction of 40 headlands is underway with 1km intervals. The headland system to stabilize sandy shoreline was originally proposed by Silvester(1976). In his study headland system in which a headland of asymmetric shape is built on the sandy beach, was considered under the obliquely incident wave conditions. On many coasts, however, wave direction varies from season to season. In this condition, symmetric type of headland is more effective to stabilize the sandy beach. On the Kashimanada coast, therefore, headlands of a symmetric shape were built.

In the planning of headland system, due considerations must be paid to the shape and its effect to surrounding nearshore current field. For example, under

* River Dep., Ibaraki Pref. Government, Sannomaru 1-5-38, Mito, Ibaraki 310, Japan(FAX 0292-28-0904).

** Dr. Eng., Res. Coordinator for Hydraulic Structures, Public Works Research Inst., Ministry of Construction, Tsukuba, Ibaraki 305, Japan(FAX 0298-64-1168).

***INA Consultant Co., Ltd., Sekiguchi 1-44-10, Bunkyo-ku, Tokyo 112, Japan (FAX 03-3268-8256).

the obliquely incident wave conditions, a rip current will be developed along the groin-type headland, whereas in case of the T-shape headland, development of a rip current is suppressed because of the sheltering effect of head-part of the headland. These differences deeply relate to the stabilization of sandy beaches between headlands. However, poor experience of constructing headland system on the real coasts prevents these understandings.



Photo 1 Aerial view of headlands on the Kashimanada coast (Dec.1993).

This study aims at the investigation of nearshore currents, beach changes around these headlands, and the confirmation of their effectiveness. To this purpose, the comprehensive field observations and the numerical simulation of nearshore currents were conducted. The study is composed of three contents as shown in Fig.1. First, the results of the field observation on nearshore currents around headlands are described. Field observations were carried out at three times from 1991 to 1993, in which aerial pictures were taken at a constant time interval from a helicopter to investigate diffusion of dyed water. In 1991, pre-observation was done in the vicinity of headlands, aiming at studying the difference between a groin-type and an anchor-type headland. In 1992, observations were done not only near the headland but also in the extensive area between two completed headlands in order to investigate nearshore currents and rip currents. In these observations, however, photographs were taken from a relatively low altitude. Therefore, in 1993, in order to simultaneously investigate current field in extensive area, high altitude photographs were taken from 1,000 m, as well as the bottom sounding.

In addition to these observations, beach stabilizing effect was investigated around a group of headland on the basis of several photographs and soundings,

which have been carried out recurrently. Moreover, numerical simulation of nearshore currents was carried out and results of numerical simulation were compared with the observed nearshore current pattern. Current pattern was well agreed with the observed one.

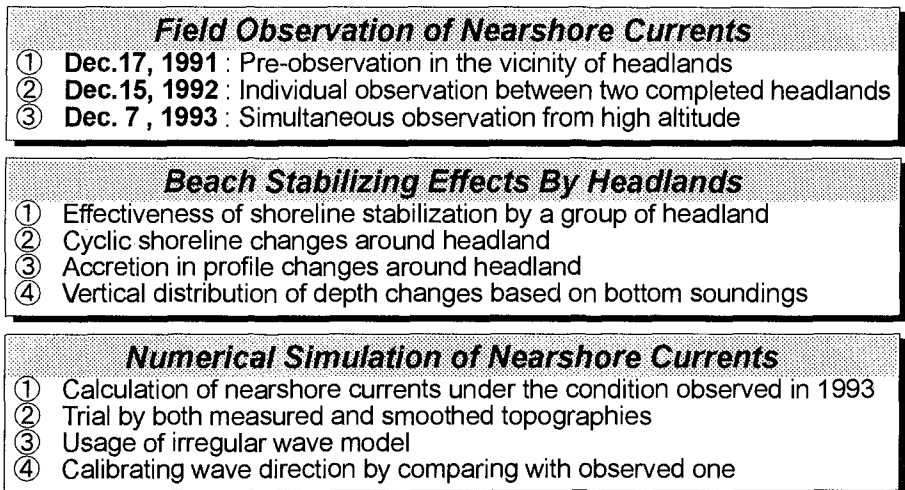


Fig.1 Outline of this study.

II. FIELD OBSERVATION OF NEARSHORE CURRENTS

2.1 GENERAL

Figure 2 shows the location of study site. The Kashimanada coast is located in the southern part of Ibaraki Prefecture facing the Pacific Ocean, where construction of 40 headlands with 1 km intervals is now underway. Construction works were begun in 1984, and by 1995, six sets of headlands were completed. Figure 3 shows the plane shape of the headland. Headland has an anchor-shape, of which offshore length is about 150 m and the head-part length is about 100 m. The head-part has a semi-circular shape and its offshore slope is as mild as 1/3 to reduce wave impact against the structure. The offshore surface of the headland is covered by armor units of 4 tons and the main part is built by natural stones of 1 ton. Field observations were carried out mainly between No.10 and No.11 headlands on the Ono-kashima coast located in the middle of the Kashimanada coast. The Ono-kashima coast is a sandy beach next to Kashima Port and beach slope is about 1/80, and the coastline length is about 12.5 km.

2.2 NEARSHORE CURRENT PATTERN AROUND THE COMPLETED HEADLAND

Photo 2 shows the nearshore current pattern around the completed headland measured on Dec. 17th, 1991, ① : right after the injection of dyestuffs to the foot part of a completed anchor-type headland No.10, ② : 6 minutes after the injection, and ③ : oblique aerial photo after ten minutes. In case of an anchor-type headland, it is realized from the comparison of successive aerial photographs that a nearshore circulation cell was formed on the south side of headland because of the wave dissipating effects of head-part. This is considered to be effective to contain the nearshore currents between headlands.

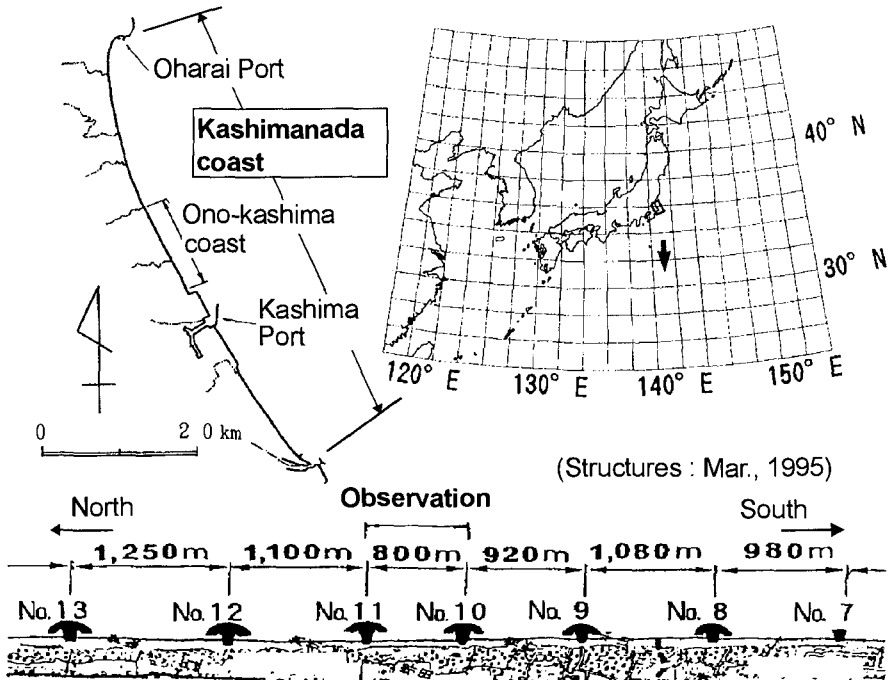


Fig.2 Location of study site.

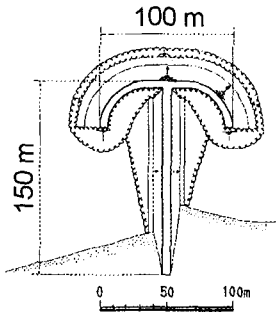


Fig.3 Plane shape of anchor-type headland.

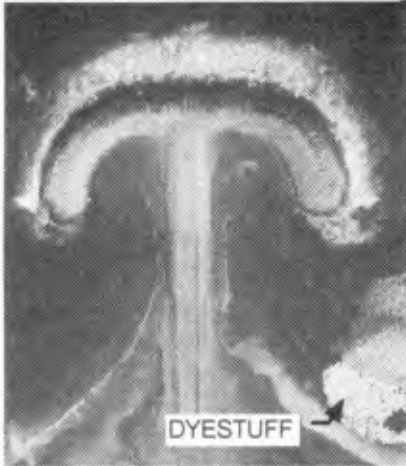
2.3 NEARSHORE CURRENT PATTERN AROUND THE GROIN-TYPE HEADLAND

Photo 3 shows the rip currents developed along the groin-type headland (No.9) under construction observed on Dec. 17th, 1991. In this case, dyed water injected to the foot of the groin-type headland was carried fast along the groin by the rip current. Then, dyed water spread out offshoreward and was diffused, implying that sand will be carried away to downcoast to accelerate the beach erosion on upcoast of the headland.

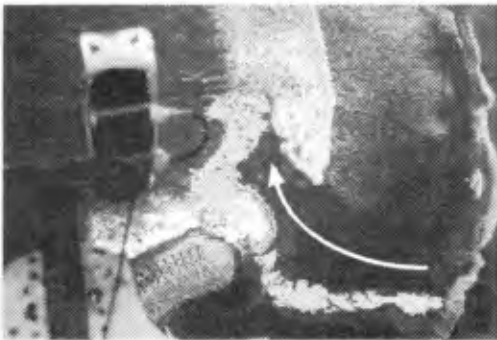
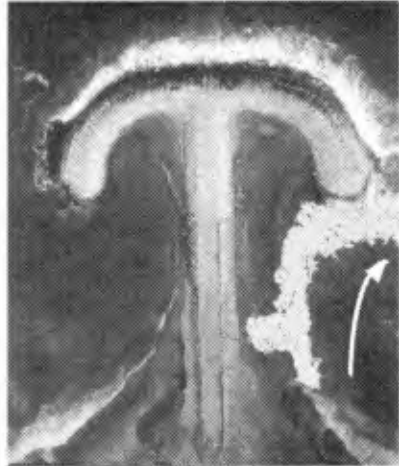
2.4 RESULT OF NEARSHORE CURRENT OBSERVATIONS IN 1992

Figure 4 shows the nearshore current field observed on Dec. 15th in 1992 in the extensive region covering between No.10 and No.11 headlands. The figure shows changes in dyestuff clouds, their moving velocity and wave direction, which were measured from aerial photographs. Diffusion of injected dyed water was traced by the aerial photographing from the helicopter at 15 seconds interval, and the diffusion pattern of dyed water is traced at 1 minute interval.

① RIGHT AFTER THE INJECTION OF DYESTUFFS TO THE FOOT PART.



② 6 MINUTES AFTER THE INJECTION.



③ OBLIQUE AERIAL PHOTO AFTER 10 MINUTES.

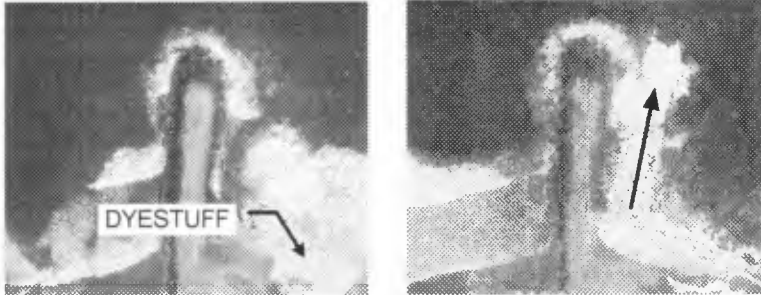
Photo 2 Advection of dyed water around the completed headland of anchor-type (Dec. 17th, 1991).

During the observation, significant wave height was 1.3 m, and the period was 9.1 s due to the wave record measured off Kashima Port by an ultrasonic wave gauge. And also incident wave angle was read to be about 15 degree counterclockwise to the normal to the shoreline from the aerial photograph.

Because of the oblique wave direction, southward longshore currents are predominant and the circulation cell is formed on the north side of No.10 headland. On the other hand, on the north side of No.11 headland, a rip current occurs, which passes over head-part and flows out in the offshore direction. Furthermore, a rip current is occurred at a central part of the beach between No.10 and 11. The position of the rip current is located approximately 500m south of No.11 headland and is a little south from the center of headlands.

When mass flux by waves is considered, it is considered that the flux is mainly heading shoreward from between No.11 headland and the position of the rip current. And it returns to offshore by this strong rip current at central part of the beach. On the contrary, the longshore distance between the rip current in the central part and No.10 headland is short, so that the shoreward mass flux in this area is considered to be small and therefore the strength of the rip current just north of No.10 headland is weak.

- ① RIGHT AFTER THE INJECTION OF DYESTUFFS TO THE FOOT PART ② 2 MINUTES AFTER THE INJECTION



- ③ 6 MINUTES AFTER THE INJECTION ④ 12 MINUTES AFTER THE INJECTION

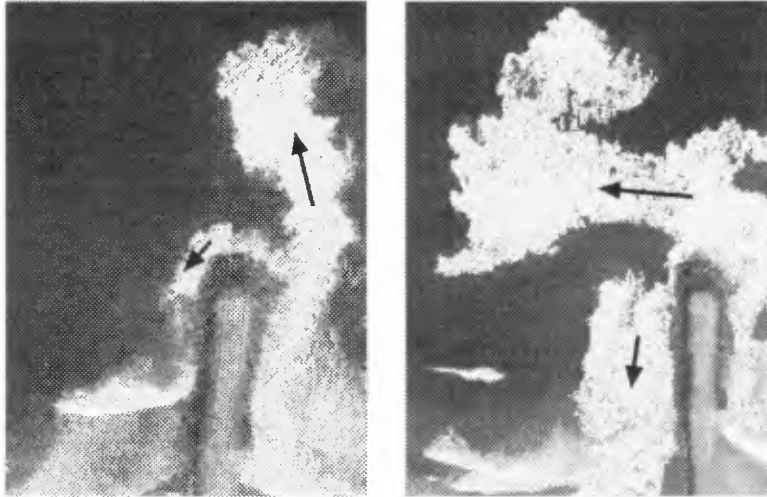


Photo 3 Advection of dyed water around the groin-type headland (Dec. 17th, 1991).

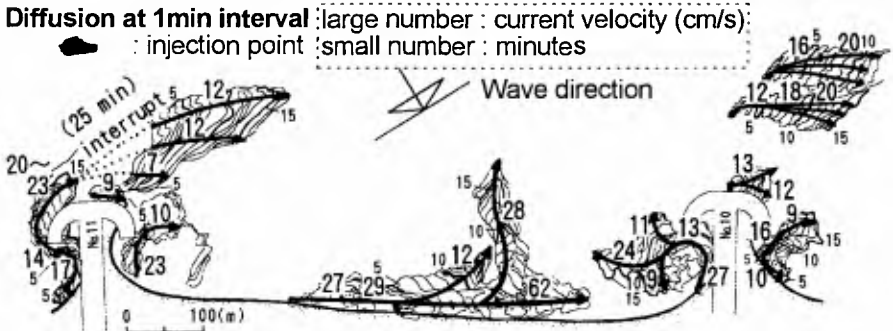


Fig.4 Diffusion of injected dyed water between No.10 and No.11 headlands (Dec. 15th, 1992).

2.5 RESULT OF THE HIGH ALTITUDE PHOTOGRAPHING IN 1993

Figures 5 and 6 show the diffusion process measured on Dec. 7th in 1993. The significant wave height and period were 1.6 m and 7.6 s, and waves were incident from clockwise direction in this observation period as shown in the figure. The condition of this incident wave angle contrasts to the wave characteristics in 1992.

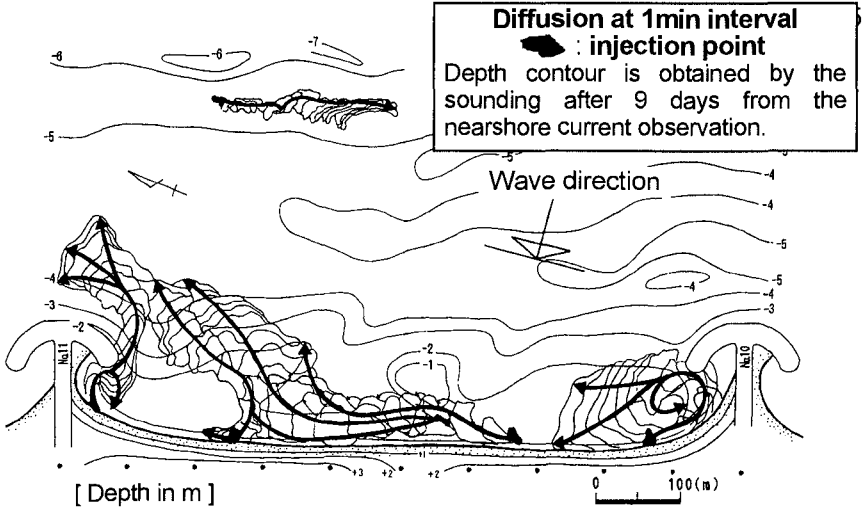


Fig.5 Diffusion of injected dyed water between No.10 and No.11 headlands(Dec. 7th, 1993).

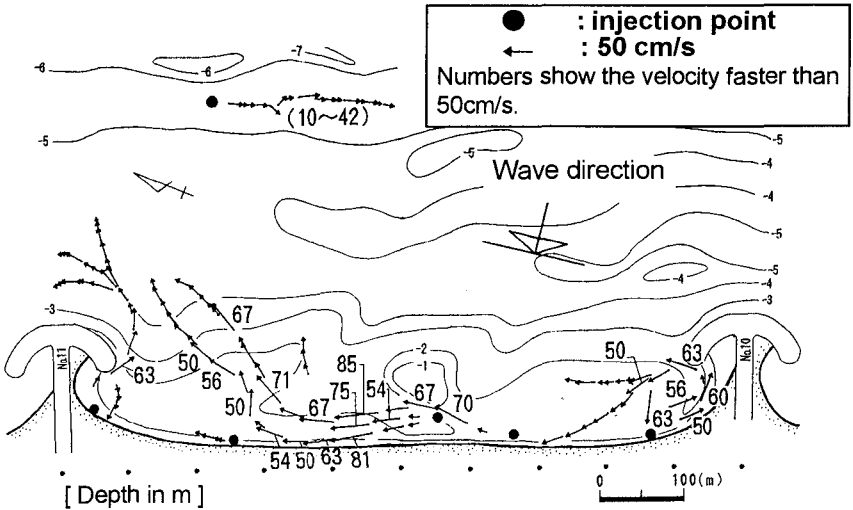


Fig.6 Velocity field of nearshore current determined from advection rate of dyed water front (Dec. 7th, 1993).

As a whole, northward longshore currents were induced, and counterclockwise circulation cell was observed in the vicinity of the north side of No.10. Furthermore, northward longshore currents developed next to this circulation cell. This longshore current is reduced to a rip current at a location of 300m distant from No.11 headland. On the south side of No.11 located on the downcoast, another clockwise circulation cell was formed in the lee side of the headland. A part of this circulation reduces to the rip current and it superimposes the main rip current induced in the central part of the beach. In addition, about 400m off the shoreline, weak southward longshore currents were measured.

These results mean the formation of a large-scale clockwise circulation cell between headlands. Development of this circulation cell is considered to be effective to confine sediment between headlands, and to stabilize the sandy beach.

III. TOPOGRAPHIC CHANGES

3.1 SHORELINE CHANGE

Sea bottom surveys and aerial photographing for monitoring shoreline changes have been recurrently carried out on this coast. Figures 7 and 8 show the shoreline changes around headlands determined from the aerial photographs. As shown in Fig.7, the shoreline retreats in the southern part between headlands and a stepwise shoreline was formed due to the southerly wave incidence, which is the predominant wave direction on this coast. Near the headlands as shown in Fig.8, wide foreshore (tombolo) was formed behind the headland. All these show the effectiveness of headland system to contain sand between headlands, and to form dynamically stable beach between headlands. In this headland system, the interval between them is about 1 km, which is wide enough to keep the coastal scenic beauty on the natural sandy beach. Detached breakwaters are effective against beach erosion. But they have killed scenic beauty of the beach by the dense installation. Usually in Japan, the length is 100m and the opening width is 50m. In the headland system, however, the number of the headlands per unit distance is much less than that of detached breakwaters, thus this system is much more economical.

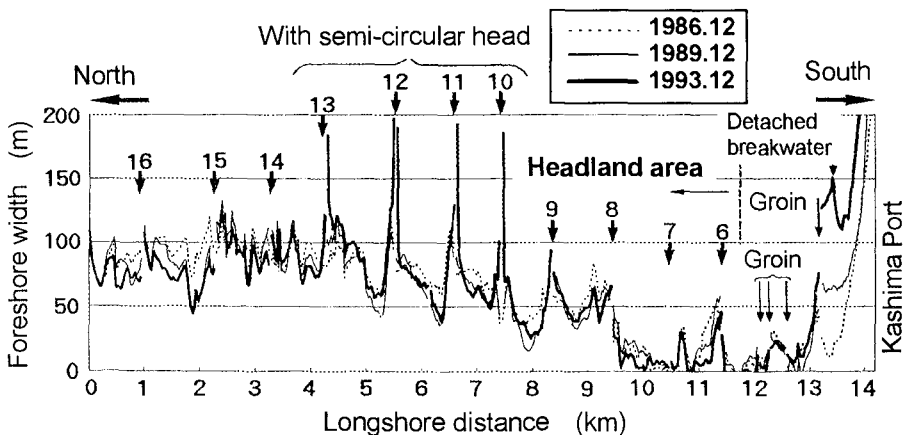


Fig.7 Changes in foreshore width between 1986 and 1993.

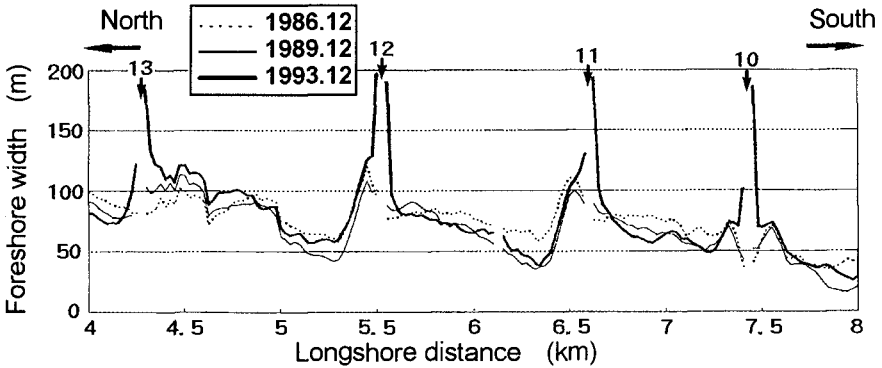


Fig.8 Shoreline changes around completed headlands between 1986 and 1993.

Figure 9 shows the temporal shoreline changes from 1986 to 1993 in the vicinity of No.11 headland. Surveys have been carried out in the same month of December in each year. In this figure, completion time of groin-part and head-part of the headlands are also shown. As shown in this figure, shorelines on the south side (S1~S3) of the headland No.11 change with the same phase, whereas on the north side (N2~N3) of the headland, the opposite mode of shoreline changes occur except the change at N1 located very close to headland and at the concave location. After the construction of the head-part in 1989, shoreline changes turn to the accretion tendency. It is understood that cyclic shoreline change occurs because of the seasonal change in wave direction in the zone next to the structure obstructing longshore sand movement. In short, the north side of headland is eroded and accretion occurs on the south side by southerly waves in summer, and then in winter, opposite phenomenon appears. Furthermore, it is realized that the accretion effect of headland overlaps on the above seasonal changes.

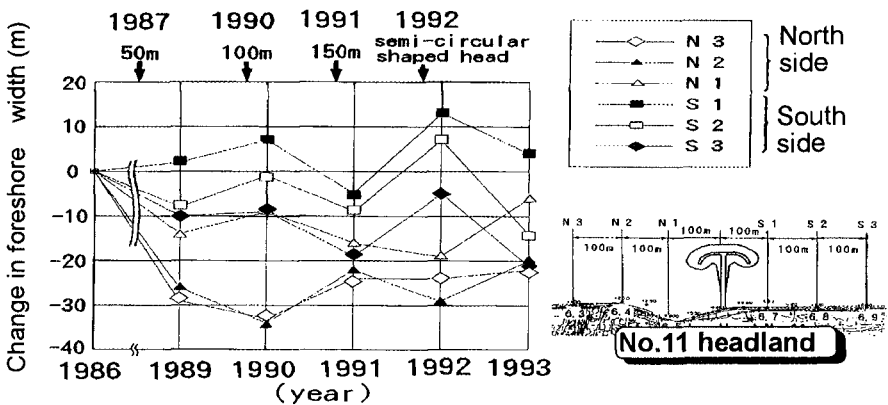


Fig.9 Temporal shoreline changes around headland No.11 between 1986 and 1993.

3.2 PROFILE CHANGES

Regarding the accretive effect of headland, it is also investigated by the bottom soundings along the survey lines arranged with 25m interval. Figure 10 shows the typical cross-shore profile changes around No.10 headland between July, 1987 and August, 1993. On the line of CN100, development of bar-trough topography was seen before the construction, but since 1992 when the head-part had been completed, bar-trough development becomes weak. On CN50 approaching 50m to headland further, because of the wave sheltering effect of the headland, accretion is seen at nearby the shoreline. Then, on CNO nearest to the headland, a large amount of sand is accumulated to form a tombolo. The thickness of accreted sand at a distance of 100m offshore reaches to approximately 3m. On the other hand, a local scouring is not seen off the head, and a gentle slope of approximately 1/100 is formed. Thus, it is confirmed that accretive effect of headland is remarkable around No.10. because of the wave sheltering effect by its head.

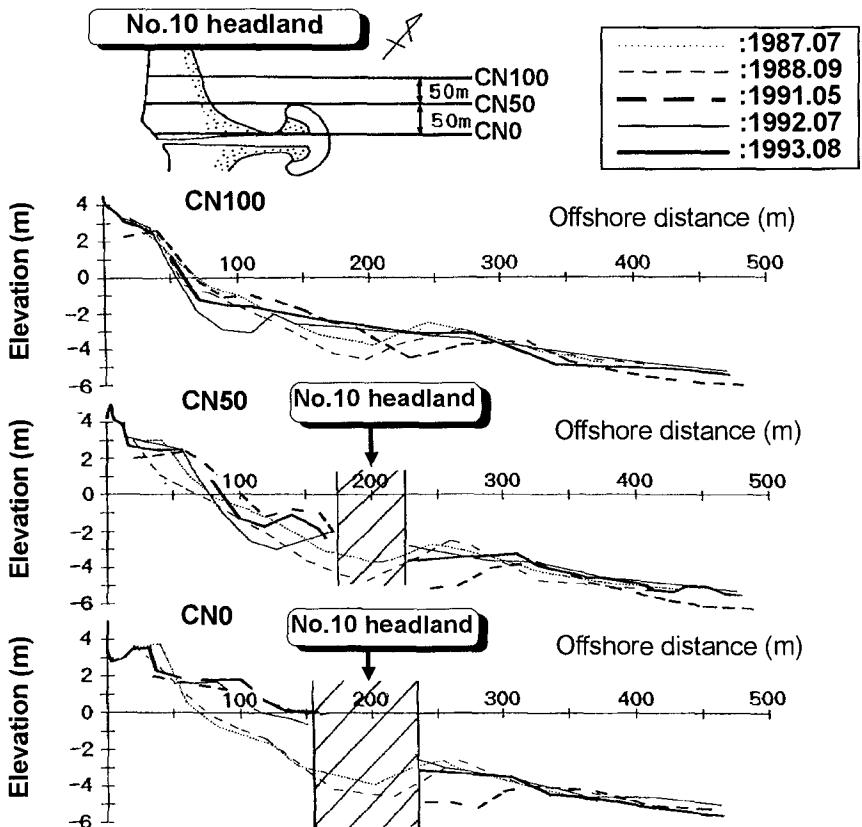


Fig.10 Typical profile changes in a period between July, 1987 and August, 1993.

3.3 VERTICAL DISTRIBUTION OF DEPTH CHANGES

On the basis of the sounding data, a vertical distribution of the standard deviation of the water depth change was examined. Fig. 11 shows the result. The vertical axis indicates the mean depth in meter. They were examined between No.10 and 11 headlands from 1987 to 1993. The significant topographic changes is occurred between -6m to +3m with two peaks at the shoreline and -3m. The peak of -3m is considered to be caused by the changes of bar-trough topography. This distribution shows a range of the remarkable topographic change. And the tip depth of the headland is approximately 3m depth. Therefore, the headland is located at a place which almost contains the range of the remarkable topographic change. This fact means the headlands on this coast is located at a offshore limit for demonstrating its effect.

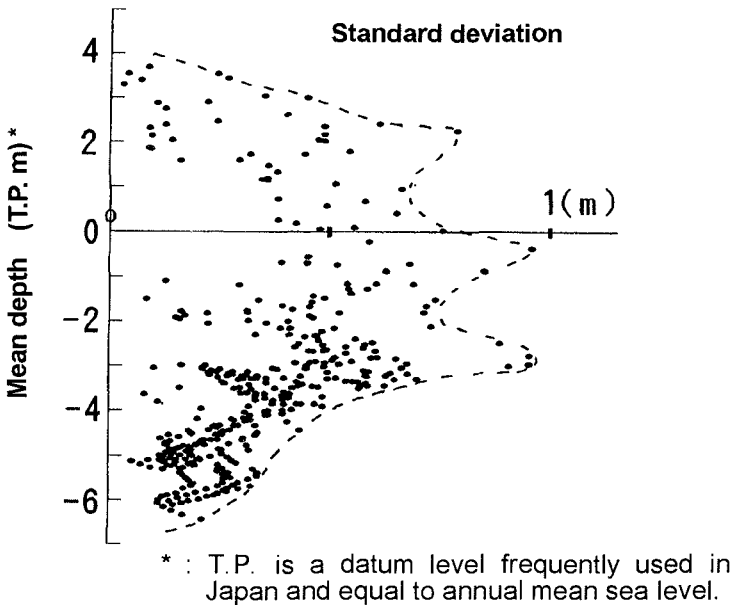


Fig.11 Vertical distribution of depth change between No.10 and No.11.

IV. NUMERICAL SIMULATION OF NEARSHORE CURRENTS

4.1 NUMERICAL MODEL AND COMPUTATIONAL CONDITION

Numerical simulation for the nearshore currents was carried out to compare field data observed in 1993. Table 1 shows the computational condition. In the nearshore current simulation, wave field was first calculated by the irregular wave model. Then, nearshore current field was calculated on the basis of the above wave field and with given some coefficients. On the other hand, regarding the sea bottom topography, two cases of the calculations as described in Table 1 and shown in Figs.12 (Chart 1) and 13 (Chart 2) were carried out. Chart 1 is the original topography data sounded on Dec. 16th, 1993, and Chart 2 is the

smoothed one. The reason using also Chart 2 is why the bottom topography would be changed by the storm continued during 9 days since the above-mentioned nearshore current observation.

Table 1 Computational conditions.

Term	Condition
Computation area	Longshore 2,000 m × Offshore 1,000 m
Mesh size	$\Delta x = \Delta y = 10$ m
Initial topography	Chart 1 : Original bathymetric chart (Dec. 1993) Chart 2 : Smoothed bathymetric chart
Structures	Present (headland No.10 and No.11)
Sea wave conditions	Height and Period : decided from observation at Kashima Port on Dec. 7th, 1993. Direction : Trial in the range of observed direction
Tidal level	T.P.+0.806m
Computation time	1 day
Irregular wave computation	Dividing number of frequency : 5 Dividing number of direction : 11 Directional concentration coefficient : $S_{\max} = 25$
Nearshore current computation	Friction factor : $C_f = 0.01$, Lateral eddy viscosity : $25\text{m}^2/\text{s}$ Time step : $\Delta t = 0.5$ s, Boundary condition : Open

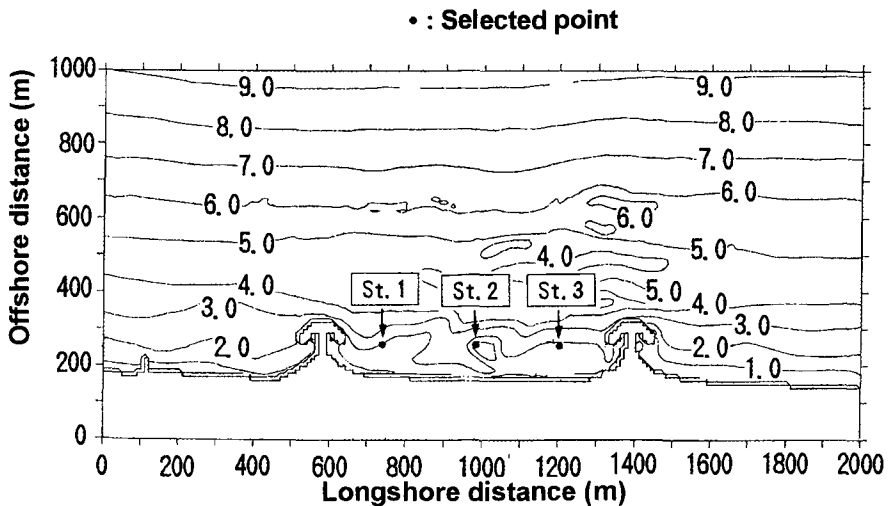


Fig.12 Original bathymetric chart (Chart 1) and selected point for verification of wave direction.

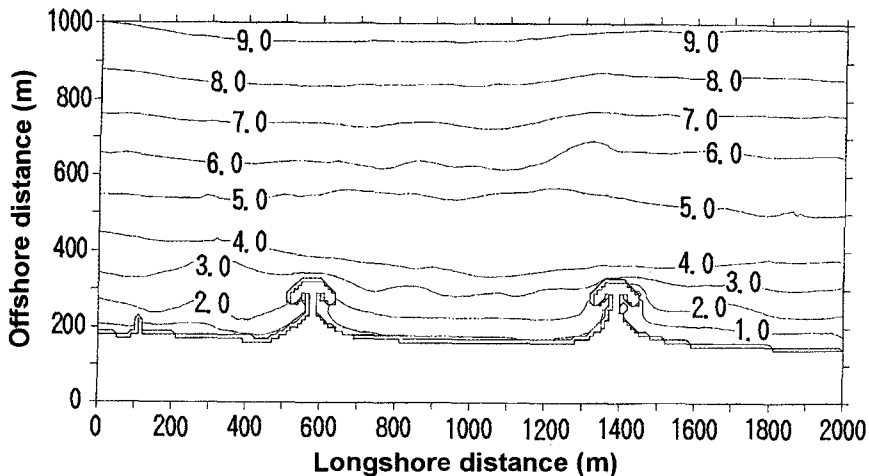


Fig.13 Smoothed contour chart (Chart 2).

4.2 VERIFICATION OF WAVE DIRECTION

First, the wave direction was verified. Table 2 shows the trial cases and results. Besides, as a representative point for verification, St.2 in Fig.12 was selected because it is located in the center, and therefore the influence due to the structures is small enough. As shown in Table 2, in total 8 cases of trials were conducted, and the best fit of the offshore wave direction to reproduce the measured wave direction resulted in -25 degree as case 7 or 8.

Table 2 Measured and calculated wave directions at selected points.

No.	Topography	Wave conditions				Wave directions		
		Height (m)	Period (s)	Direction	Tide level (T.P. m)	St.1	St.2	St.3
1	Chart 1	1.57	7.6	-14.5°	0.806	-1.4°	2.0°	-7.4°
2	"	"	"	-20.0	"	-5.1	-2.1	-9.5
3	"	"	"	-35.0	"	-11.6	-8.2	-14.3
4	"	"	"	-40.0	"	-13.7	-9.5	-16.2
5	Chart 2	"	"	-20.0	"	-11.6	-11.4	-10.5
6	"	"	"	-30.0	"	-15.8	-16.6	-15.4
7	"	"	"	-25.0	"	-13.4	-13.6	-12.8
8	"	2.39	"	-25.0	"	-12.6	-12.8	-11.7
Mean angle measured						-13.7	-13.3	-5.1

4.3 RESULTS OF COMPUTATION

Figure 14 compares calculated current pattern with the observed one. Nearshore circulation cell on the downcoast of No.10, a rip current at the head of No.11, and a rip current at a location of longshore distance 900 m agreed considerably well. On the other hand, in case of using Chart1, a very strong onshore current occurred and discrepancy was large on the shoal located in the middle of the sandy beach.

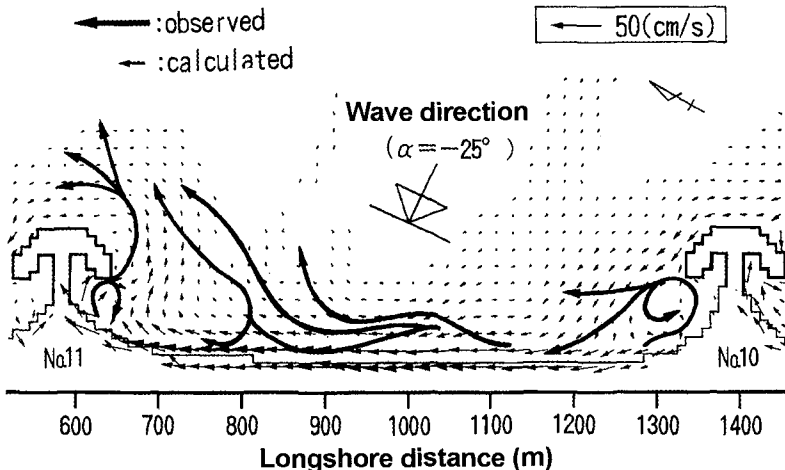


Fig.14 Comparison of observed and calculated nearshore current field.

V. CONCLUSIONS

Main conclusions in this study are summarized as follows :

- ① Nearshore current field with a longshore stretch of about 800m was measured. Development of nearshore circulation cell in the vicinity of headlands was confirmed. And, a rip current induced from the shoreward mass flux were also confirmed.
- ② Due to the shoreline changes around headlands observed by aerial photographs, the shoreline was stabilized to form a step-wise configuration responding to the oblique wave incidence. Furthermore, it was found that seasonal shoreline variation was superimposed to this shoreline to form dynamically stable shoreline.
- ③ Numerical simulation of wave field and nearshore currents were carried out. Results of numerical simulation agreed well with the observed one to show the effectiveness of the wave and current model.
- ④ This study summarizes field experiences regarding headland system in Japan. And this information is thought to be important for further application on the other coast in place of the detached breakwater.

REFERENCES

- Silvester, R. (1976) : Headland defense of coasts, Proc. 15th Coastal Eng. Conf., ASCE, pp.1394-1406.
- Uda, T., M. Sumiya and H. Sakuramoto (1988) : Stabilization of coast by construction of headlands on the Kashimanada coast, Japan, Proc. 21st ICCE, pp.2791-2805.

CHAPTER 310

NOURISHED BEACH CONTROL BETWEEN BALIS AND ARENYS HARBOURS (SPAIN)

F. Javier Escartín⁽¹⁾, Alfonso Vidaor⁽²⁾, A.M. Castañeda⁽³⁾ and Nuria Lupón⁽⁴⁾

ABSTRACT

A description of the monitoring works carried out in the Maresme beaches between Arenys de Mar and Balis Harbour after the completion of the regeneration works consisting on the demolition of the existing groins and the execution of an artificial nourishment is presented.

INTRODUCTION

Maresme beaches are located close to the city of Barcelona (40 km in the northwest) and because of this they are frequently visited all year round.

The zone was suffering an important regression that couldn't be restrained by any attempts of stabilization. So in February of 1992, a regeneration project of this coastal zone was carried out as a part of the works that the Spanish Public Works Ministry has been doing on the Catalan Coast.

The nourishment works began in August 1993 and the first phase of the regeneration was finished in October of the same year, in March of 1994 the second phase ended.

Because of the high investment dedicated to this work, an accurate monitoring of the beaches was planned in order to obtain a better understanding of the beach behaviour with respect to the littoral processes and thus to implement appropriate coastal management strategies.

-
- (1) Senior Engineer; Europrincipia, sl., Centre Tecnològic Europroject, Parc Tecnològic del Vallès, 08290 Cerdanyola, Barcelona, SPAIN; Tel: 34-3-5820187; Fax: 34-3-5824394; e-mail: fjeg@europroject.es
 - (2) Director; Europrincipia, sl., Centre Tecnològic Europroject, Parc Tecnològic del Vallès, 08290 Cerdanyola, Barcelona, SPAIN; Tel: 34-3-5820187; Fax: 34-3-5824394; e-mail: alfonso@europroject.es
 - (3) Projects and Works Service Chief; Catalunya Coasts Demarcation, General Directorate of Coasts, Environment Ministry, Ronda Litoral Mar 36, 08005 Barcelona, SPAIN.
 - (4) Senior Engineer; Europrincipia, sl., Centre Tecnològic Europroject, Parc Tecnològic del Vallès, 08290 Cerdanyola, Barcelona, SPAIN; Tel: 34-3-5820187; Fax: 34-3-5824394; e-mail: nuria @europroject.es

The monitoring has been divided in two different parts:

- A field systematic monitoring of the beaches
- A shoreline evolution analysis using a numerical model of simulation

Following the predicted evolution, the possible actions will be analyzed in order to guarantee the adequate maintenance of the desired stability conditions and quality.

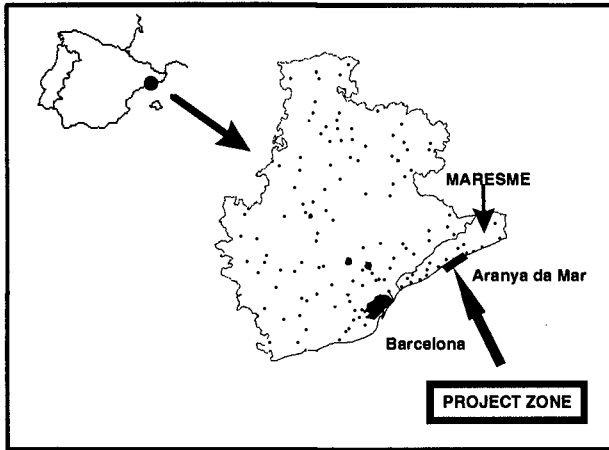


Figure 1: Project location

HISTORY

Maresme littoral is a fisiographic unit which is spread out between Tordera River mouth and Barcelona Harbour.

From the littoral dynamics point of view the working scheme of the stretch, is simple: This area has a NE-SW orientation with a net littoral transport from east to west, and net rates around 40.000 and 100.000 m³/year.

After Arenys Harbour was built in the late forties, littoral dynamics of the beaches in the southwest of the Harbour were strongly modified suffering a regression that could not be restrained by any of the attempts of stabilization carried out. Mainly seawalls and transversal groins.

In the closest zone to Arenys Harbour, a seawall about 2 km long was built to protect the railway line, and far away to the south, for 2.5 km, a set of eleven transversal groins were constructed.

The nourishment project was designed with the double objective of:

- obtaining a great stable beach area
- establishing an important nourishment source for the Maresme beaches in the southwest of Arenys Harbour as far as Barcelona.

The total length of the regeneration was 4.5 km, with a beach width of 70 to 110 m and an elevation of 2.5 m. The mean slope was 1/10.

The total volume of sand was 3.8 million cubic meter. Ten of the eleven transversal groins were demolished.

MONITORING WORKS

Monitoring program consists in bathymetric and topographic works which are performed every six months with the purpose of identifying areas where accretion and erosion occur.

Bathymetric surveys of the whole area were carried out just after the works were completed.

The field data available for this study were those carried out in:

- July 1993 (before regeneration works)
- October 1993 (at the end of the first phase)
- November 1993 (specific survey for the mouth of Arenys Harbour)
- January 1994 (also in the mouth)
- March 1994 (at the end of the second phase)

- February 1995 (first survey)
- July 1995 (second survey)

With these data and employing a digital terrain model, comparative shoreline and isopaches planes, and comparative diagrams of control profiles are obtained.

Some of the results of these works are shown in figure 2 where shorelines corresponding to every bathymetric survey are drawn.

Since the nourishment ends until the february of 1995's monitoring survey, shoreline stepped back around 30 meters along all the study zone except the both ends, westward Balis Harbour and eastward Arenys Harbour. It has been a sediment accumulation which means a shoreline advance, in some points a very significant advance (70 meters close to Arenys Harbour counterdike).

It has also been a shoreline advance in the central part of the stretch, downstream of the Hotel Colon groin.

From February to July 1995, shoreline position has hardly modified what indicates a relative tendency to stabilization. A light tilting takes place at westward beach of Arenys Harbour with an important accretion in the counterdike due to wave diffraction effect.

The control profile analysis also indicates (fig. 3) the local advance and receed of the shoreline. Different studied profiles show how the shoreline has receed 30 meter in profile 82 or has advanced in the other points. It can be seen in any profile that July 95's shoreline tilt around February 95 position with 3 meters variation.

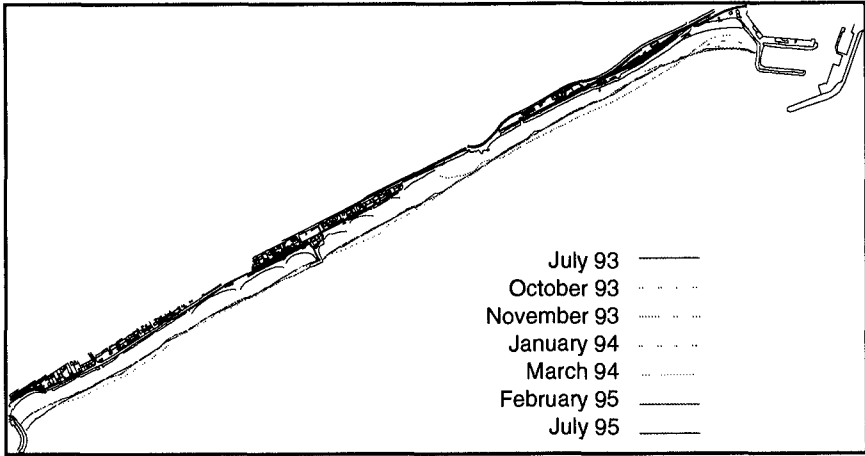


Figure 2: Shoreline evolution

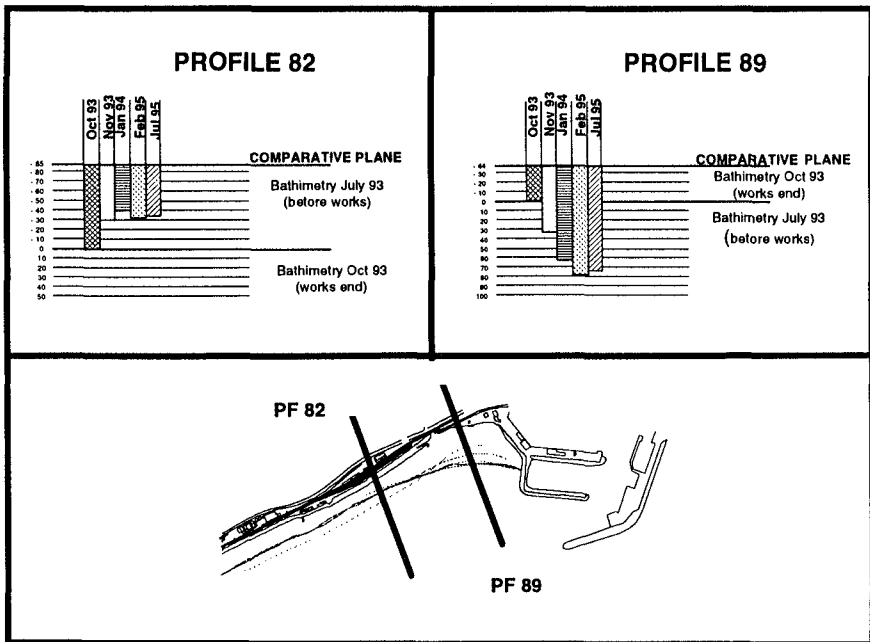


Figure 3: Control profiles evolution

NET SEDIMENT TRANSPORT

A sedimentary budget was done with the purpose of estimating sand volume mobilized by wave action since the completion of the works until July 1995.

Analysing the volumes in the considered cells, the sand quantity lost in this area through the SW extreme during this period was 46,923 m³.

Finally, from these volumes, estimate longshore transport calculations were made.(Figure 4). At this figure two zones can be clearly distinguished:

- In the first zone, from Balis Harbour, and for a length of 3,000 meters, the net sand transport has the NE-SW direction with a maximum value of 89,307 m³/year.
- In the second zone, from this point to Arenys Harbour, the net sand transport has the SW-NE direction with a maximum value of 81,190 m³/year.

In the first zone a relative minimum exists as a consequence of the sand accumulation due to the Hotel Colon groin that acts as a partial barrier.

SHORELINE EVOLUTION NUMERICAL MODELIZATION

Parallel to the monitoring work performed taking account of the field data, a shoreline numerical modelization was executed.

This study was structured in two different parts:

- calibration of numerical model employing the first survey data
In order to obtain good transport coefficients necessary for long term coastal evolution prediction, a calibration was carried out. Then a verification of the obtained coefficients was done.
- simulation of the shoreline behaviour in a 10 year term

The numerical model used for the simulation was GENESIS by CERC.

The main variables involved in one-line shoreline evolution model are wave climate, sediment characteristics, closure depth, coastal structures and boundary conditions.

In this work, different sets of wave data were used. Height and period of wave data proceeded from Tordera escalar buoy, and directions were obtained from visual data of routing ships registered in this sector. With both set of data a continuous register for a year was built up.

The selected boundary conditions were:

- null longitudinal transport in the Arenys Harbour breakwater which means that it acts as a total barrier
- permeable transversal groin in the Balis Harbour breakwater

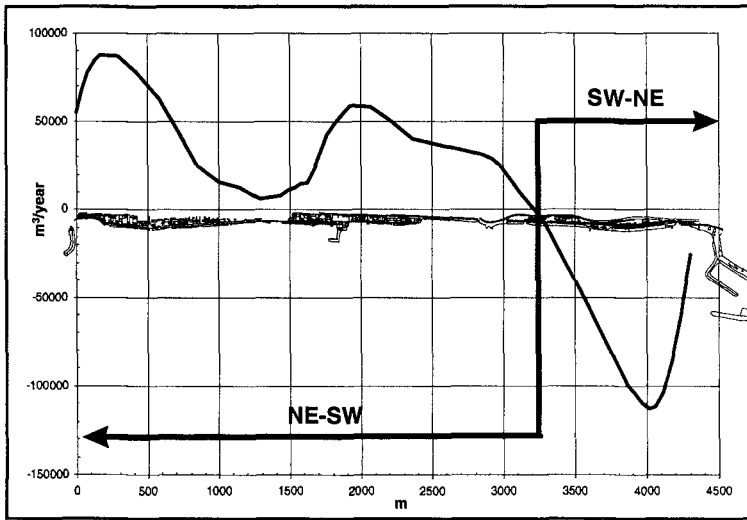


Figure 4: Measured net transport

Some simulations for the period end of the works - February of 1995 period were made, by varying transport parameters k_1 and k_2 , in order to obtain a proper adjustment between the numerical values of the longitudinal transport and shoreline evolution in comparison with the measured values. Values found to agree more accurately were $k_1=0,8$ and $k_2=0,5$.

The net longshore transport distribution along shoreline is shown in figure 5, which can be compared with that obtained from measured values: Both distributions present similar global behaviour with identical peaks of transport.

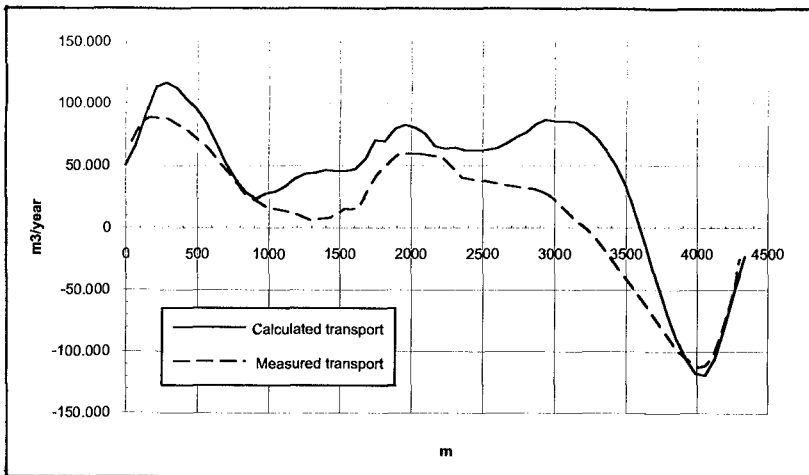


Figure 5: Net transport comparison

The obtained prediction of shoreline evolution is shown in figure 6. A reasonable agreement between measured and predicted shoreline positions can be observed. Both lines present identical accumulation and erosion areas. There is a sediment accumulation close to Balis Harbour and to Arenys Harbour, and sediment erosion in the rest of the stretch, specially downstream of Arenys Harbour.

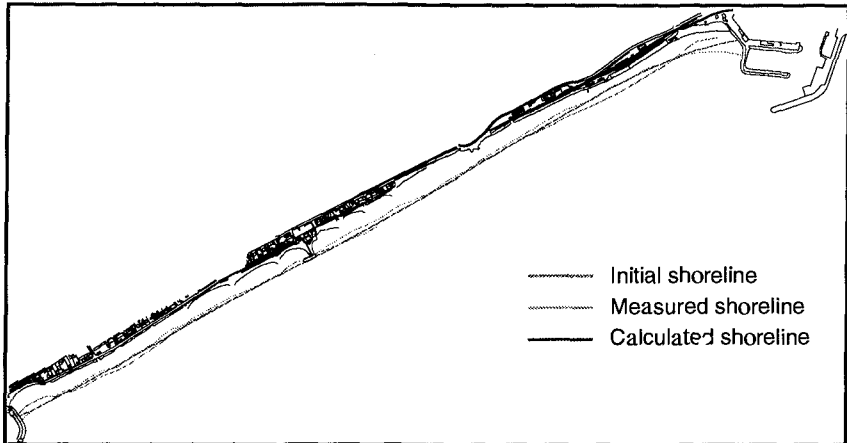


Figure 6: Shoreline prediction

10 YEAR SHORELINE MODELIZATION

Afterwards, with parameters obtained previously, a long term simulation was made in order to find out the beach evolutive trend for the next ten years. In this case a mean climate obtained from visual data is used. Shoreline from July of 1995 is employed as initial position.

Boundary conditions are the same. The existence of a seawall which represents the edge of urbanized area, that can not be overpassed by the shoreline regression, is considered as well.

Figure 7 shows the result. It can be observed that since the 7th year, shoreline has receded, in some points, reaching the edge of the urbanized area. The other points remain rather stable.

Points where regression is maximum are situated downstream of Arenys River Mouth. This zone has been traditionally protected by seawalls.

The most important observations are:

- Westward of Arenys Harbour, shoreline tends to stability but downstream a strong erosion takes place, so after the 6th year less than 10 m of the beach width remains. Points where regression is maximum are situated downstream of Arenys stream outlet. This zone has been traditionally protected by seawalls.

- Hotel Colon Groin doesn't represent, a total barrier to longshore transport and its presence has no influence in the beach behaviour.
- But in the long term, erosive trend of the coast situated downstream of the Arenys stream outlet could move downstream, causing the beach to lie in the Hotel Colon groin.

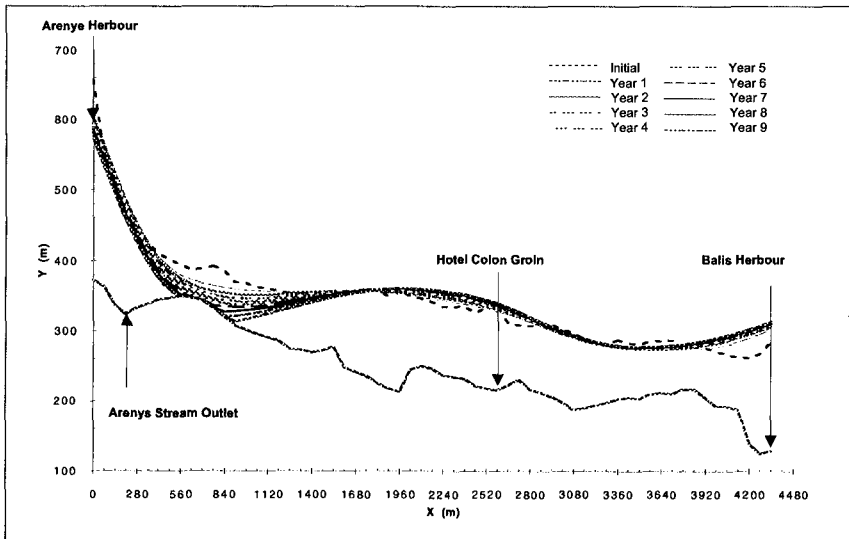


Figure 7: 10 year shoreline evolution

ACTIONS

To restrain the erosive trend of the stretch, two possible actions have been suggested and studied:

- A periodical beach fill, upstream of the stretch (westward of Arenys Harbour)
- Construction of a detached breakwater

Figure 8 shows the first action modelization. As it can be seen in the diagram, an annual beach fill of 40,000 m³ of sand, after the third year, produces stability of the entire beach.

Secondly, with a detached breakwater a salient is generated (figure 9), what means an important increment in the beach surface in this area.

Since there is a possibility of an erosion later on in this point, beach fills are also studied (figure 10). Subsequently the beach would be totally stabilized.

Both solutions satisfy the stabilization objective of the regenerated beach.

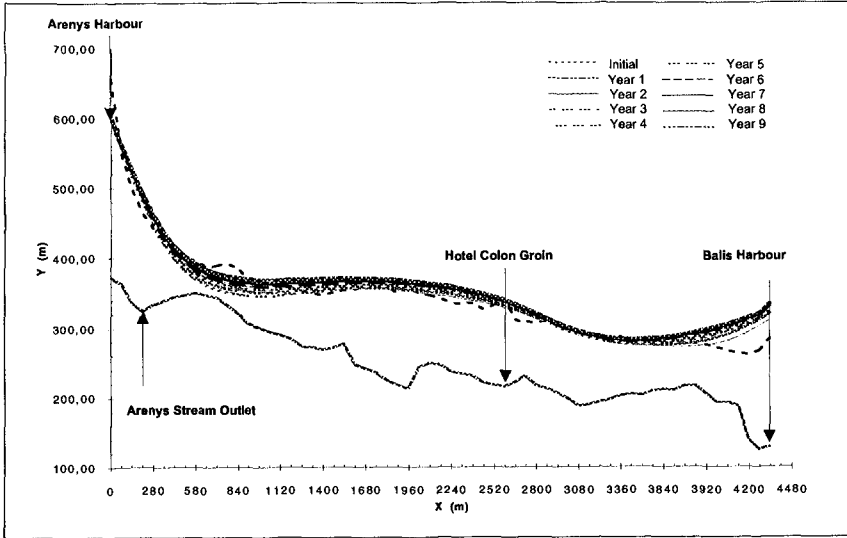


Figure 8: Periodical beach fill modelization

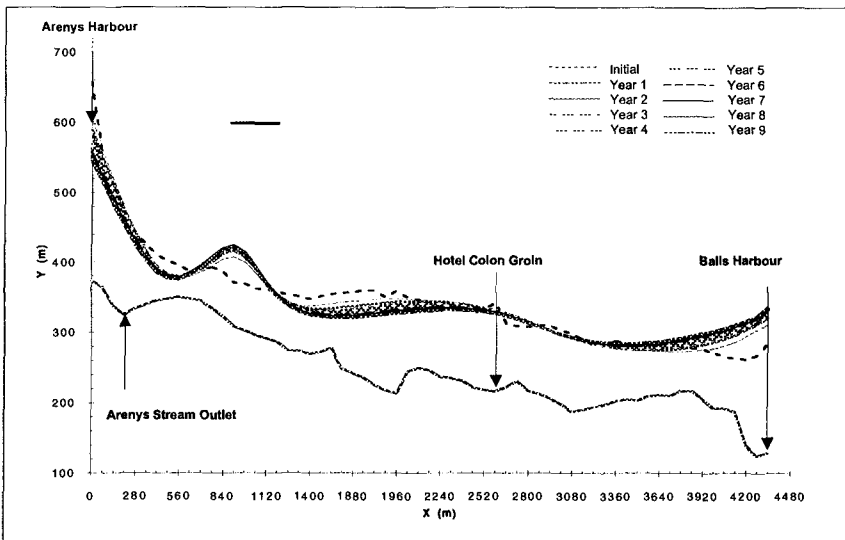


Figure 9: Detached breakwater modelization

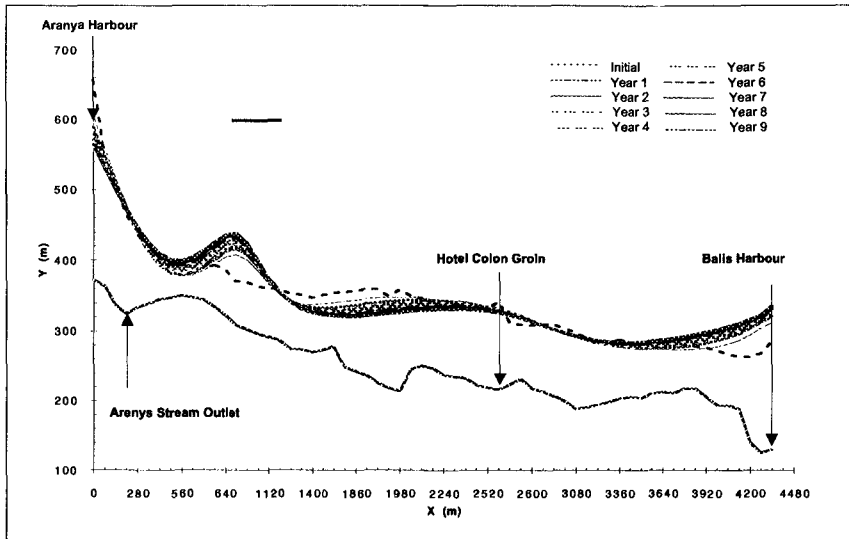


Figure 10: Detached breakwater with periodical beach fill modelization

CONCLUSIONS

- To guarantee extensive coastal zone regeneration, it is very important to carry out monitoring of the shoreline evolution.
- The monitoring and control processes should be completed with simulation models in order to:
 - improve the understanding of littoral processes
 - predict the evolutive trends
 - the necessary actions, their evolution and quantification could therefore be analyzed
- Monitoring continuity will allow the feed back of the calibration of the model and a better adjustment of both, the regenerated beach evolution simulation and the effect of the suggested actions.

CHAPTER 311

NUMERICAL SIMULATION OF SHORELINE CHANGE WITH LONGSHORE SAND WAVES AT GROINS

Hans Hanson¹, M. ASCE, Michelle M. Thevenot², Nicholas C. Kraus³, M. ASCE

ABSTRACT: Longshore sand waves (LSWs) are macro-morphologic features that maintain form while migrating along the shore with speeds on the order of kilometers per year. LSWs can dominate shoreline evolution by causing both apparent long-term erosion and accretion seemingly unrelated to the calculated or estimated net and gross longshore sand transport rates. This paper explores three possible mechanisms, wave asymmetry, form advection, and surf-zone contraction, hypothesized to maintain and translate LSWs. The mechanisms are implemented within the framework of a shoreline change numerical model. Simulations implementing the LSW evolution mechanisms are tested with observations made of LSWs at Southampton, Long Island, New York. Consideration is also given to movement of LSWs at and through groins. It is concluded that fundamental questions remain on processes governing the behavior of LSWs.

INTRODUCTION

Shoreline change can be calculated by one-line numerical simulation models for a wide range of coastal structures, beach fills, waves, and boundary conditions. Such models are based on the continuity equation and a transport rate formula for the particulate movement of sand, such as the CERC formula (SPM 1984). It is well known that the one-line model, with a particulate transport rate formula dependent upon the incident wave angle, reduces to the diffusion equation. The result is that perturbations in

1) Associate Professor, Department of Water Resources Engineering, University of Lund, Box 118, S-221 00 Lund, SWEDEN. (Email: Hans.Hanson@tvrl.lth.se)

2) Deceased. Formerly, Research Hydraulic Engineer, US Army Engineer Waterways Experiment Station, Coastal and Hydraulics Laboratory, 3909 Halls Ferry Road, Vicksburg, MS 39180-6199, USA.

3) Research Physical Scientist, US Army Engineer Waterways Experiment Station, Coastal and Hydraulics Laboratory, 3909 Halls Ferry Road, Vicksburg, MS 39180-6199, USA.

shoreline position will tend to be smoothed, unless controlled or sustained by a boundary condition or another constraint. Particulate transport rate formulas pertain to micro-scale or meso-scale motion (minutes to hours or days) and are stepped through time, typically at 3- to 6-hr intervals, for calculation cell widths typically on the order of 50 to 500 m.

Engineers are becoming aware of morphologic features in the nearshore having much longer time and space scales that may impact project performance. Such features maintain their identities for months to years and move while preserving form. One such collective movement (Sonu 1968) of consequence is that of longshore sand waves (LSWs) (see Thevenot and Kraus (1995) for a literature review of LSWs), large wave-like features that migrate alongshore with a characteristic speed of kilometers per year. Verhagen (1989) examined a 100-year record of LSWs present along 20 km of Dutch coast and concluded that periodic accretion observed in a groin field coincided with the passage of LSWs and not to trapping of littoral (particulate) drift by the groins. LSWs have been associated with intermittency in sand supply, such as the discharge of river sediments, sediments discharged from inlets, artificial injection of a large quantity of sand, and welding of shoals on to the shore.

Recently, Thevenot and Kraus (1995) presented a one-line model that includes both particulate transport and representation of LSWs as a collective motion, and they successfully simulated LSW migration observed at Southampton Beach, Long Island, New York. The purpose of the present paper is to investigate possible mechanisms that maintain and translate LSWs and to extend the one-line model to examine LSW movement in groin fields. The model is tested with data from Southampton Beach.

THEORETICAL CONSIDERATIONS

Here, we discuss three mechanisms we hypothesize might act singly or jointly in the nearshore to preserve LSWs and translate them alongshore. First, basic concepts underlying longshore sand transport and shoreline change calculation are introduced.

General Relations

Shoreline change models have become a standard technique for calculating the long-term evolution of sandy beaches under impressed waves, boundary conditions, and coastal engineering activities (Hanson and Kraus 1989). In these models, the longshore sand transport rate is usually represented by an expression of the form

$$Q = Q_o \sin 2\theta_b = Q_o \sin \left[2 \left(\theta_o - \arctan \left(\frac{\partial y}{\partial x} \right) \right) \right] \quad (1)$$

where Q_o = amplitude of longshore sand transport rate, θ_b = angle of breaking wave crests relative to the shoreline, θ_o = angle of breaking wave crests relative to an axis set parallel to the trend of the shoreline, y = shoreline position, x = distance alongshore, and $\partial y/\partial x$ = local shoreline orientation. For beaches with gentle offshore slopes, it can be

assumed that the breaking wave angle, θ_b , relative to the shoreline and the shoreline orientation, $\partial y/\partial x$, are small. For such a situation, if the amplitude of the longshore sand transport rate and the incident breaking wave angle are constant (independent of x and time t), the equation for the change of shoreline position y reduces to the one-dimensional (1D) diffusion equation (Larson *et al.* (1997)

$$\frac{\partial y}{\partial t} = \epsilon \frac{\partial^2 y}{\partial x^2} \quad (2)$$

in which

$$\epsilon = \frac{2Q_o}{D} \quad (3)$$

where D = sum of depth of profile closure and elevation of the berm. Eq. (2) describes diffusion or spreading of perturbations that might be located along the shoreline, the diffusion acting to obliterate the distinct and persistent shoreline sand forms which are the subject of this study.

In this study, three possible mechanisms are postulated and investigated, by means of a one-line model, which may be responsible for the preservation of the form and translation of the center of mass of LSWs. These mechanisms are (1) wave asymmetry, (2) form advection, and (3) surf-zone contraction.

Wave Asymmetry Mechanism

There are a wide range of expressions for calculating the amplitude of longshore sand transport rate Q_o . For example, the SPM (1984) gives the relation

$$Q_o = \frac{\rho g}{16} H_b^2 C_{gs} \frac{K}{(\rho_s - \rho)\lambda} \quad (4)$$

where H_b = significant breaking wave height, C_{gb} = wave group velocity at breaking, ρ (ρ_s) = density of water (sediment), g = acceleration due to gravity, K = non-dimensional empirical coefficient (approx. 0.5 - 0.8), and λ = porosity of sand (approx. 0.4). Eqs. (1) and (4) show that breaking wave height and direction are the dominant parameters determining the magnitude and direction of the longshore sand transport rate.

Thevenot and Kraus (1995) postulated that a LSW would refract waves toward it, similar to wave convergence at a headland, and this wave asymmetry would tend to "pack" the sand in place on the LSW. Their calculations with a simple 1D wave model showed this phenomenon to be potentially valid. To further evaluate the possible influence of wave asymmetry on LSW migration, breaking wave input for the shoreline change model was calculated with a full 2-dimensional (2D) wave transformation model (Larson and Hanson 1996) that was executed every time step.

The mild-slope equation (Berkhoff 1972) is often employed to describe the transformation of linear water waves. A simplified form of this equation was used in the present study, where diffraction was neglected, but energy dissipation due to depth-limited breaking was included. The dissipation was incorporated as a sink term in the equation for conservation of wave energy flux, and the magnitude of the dissipation was estimated according to the procedure of Dally et al. (1985). The mean water elevation was computed from the cross-shore momentum equation. The wave calculations involved in these simulations were, therefore, much more rigorous than what is normally done for shoreline-change model simulations. A practical limitation in accuracy is the finite grid size, as the breaking wave height and angle are calculated at discrete points across-shore.

Advective Form Mechanism

As shown by Inman (1987) and by Larson and Kraus (1991), the longshore migration of LSWs may be incorporated into Eq. (3) by including a morphologic form-advective term $V(\partial y/\partial x)$ to yield the advection-diffusion equation for a conservative substance

$$\frac{\partial y}{\partial t} + V \frac{\partial y}{\partial x} = \epsilon \frac{\partial^2 y}{\partial x^2} \quad (5)$$

where V = the migration speed of the LSW. Thevenot and Kraus (1995) related V to a longshore water discharge parameter R defined as (Kraus & Dean 1987)

$$R = \frac{1}{2} d_b v_b v_{ls} \quad (6)$$

in which d_b = depth at wave breaking, y_b = the distance from the shoreline to the break point, and v_{ls} = mean velocity of the longshore current. The discharge parameter was considered as an appropriate means to express the form speed because R is a macro-scale quantity, as is V .

The longshore current velocity may, in turn, be calculated using an accepted empirical relation (Komar & Inman 1970)

$$v_{ls} = \frac{1.35}{2} \gamma \sqrt{g d_b} \sin(2\theta_b) \quad (7)$$

in which γ = ratio of wave height to water depth at breaking. Based on these parameters, the volume rate of transport Q_{LSW} may be calculated as (Thevenot and Kraus 1995)

$$(Q_{LSW})_{calc} = \alpha (R - R_{crit}) \quad (8)$$

where α = empirical proportionality coefficient, and R_{crit} = threshold value of R . Both of these values must be determined from field measurements or from inferences made through modeling of shoreline change. On the other hand, based on geometric properties, the volume rate of transport may be estimated as

$$(Q_{LSW})_{est} = \eta DV \quad (9)$$

where η = amplitude of the LSW measured from the ambient shoreline. Elimination of Q_{LSW} between Eqs. (8) and (9) gives an expression for the migration speed of the LSW to be substituted in Eq. (5) as:

$$V = \frac{\alpha(R - R_{crit})}{\eta D} \quad (10)$$

Contracted Surf Zone Mechanism

This analysis is based on the assumption that the presence of a LSW does not alter the alongshore location of depth contours beyond the depth of closure. Under this assumption, because the LSW protrudes seaward from the ambient shoreline, the slope of the profile on the LSW must be steeper than that of the adjacent beach.

The beach profile is assumed to follow a Bruun - Dean equilibrium ($y^{2/3}$) shape. Along the ambient shoreline (unaffected by the LSW), the horizontal distance from the shoreline to D_c is the active width of the surf zone y_c . The equilibrium shape relation for y_c may be expressed as

$$y_c = (D_c/A)^{3/2} \quad (11)$$

where A = empirical scale parameter. Along sections of shore occupied by a LSW, the active width of the surf zone will decrease. If an equilibrium profile is assumed to exist along these sections as well, the steeper profile will be characterized by a modified scale parameter A^* given by

$$A^* = D_c/(y_c^*)^{2/3} \quad (12)$$

where y_c^* is the modified active width, $y_c - \eta$ (Fig. 1). Similarly, the surf-zone width, defined as the distance y_b from the shoreline to the breaker line at depth D_b , may be written as

$$y_b = (D_b/A)^{3/2} \quad (13)$$

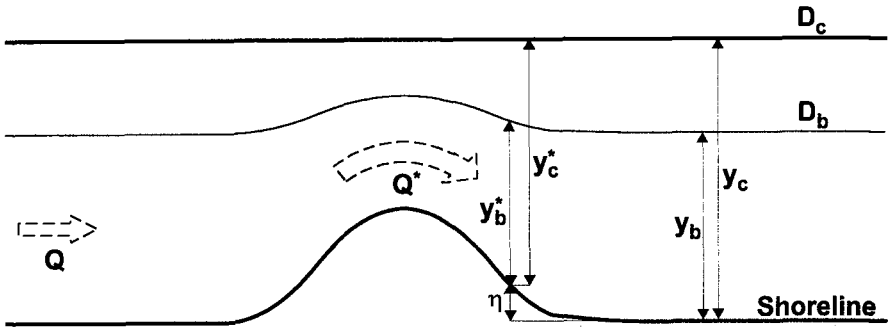


Fig 1. Definition sketch for the contracted surf zone approach.

along ambient beach sections, whereas along the beach at the LSW, the corresponding relation reads:

$$y_b^* = (D_b/A^*)^{3/2} \tag{14}$$

By expressing the longshore sand transport rate Q as an Inman-Bagnold-type relation and applying the continuity equation for the longshore transport of water yields

$$\begin{aligned} Q &\sim v_{ls} H_b^2 & Q^* &\sim v_{ls}^* H_b^{*2} \\ v_{ls} Area_b &= v_{ls}^* Area_b^* \end{aligned} \tag{15}$$

where $Area_b$ = cross-sectional water area between the shoreline and breaker depth, and the superscript * denotes values in the region of the LSW. Based on the unmodified longshore sand transport rate distant from the LSW, the corresponding rate along the LSW is given by

$$\frac{Q^*}{Q} = \frac{A}{A^*} \left(\frac{y_c}{y_c^*} \right)^{5/3} \tag{16}$$

CALCULATION RESULTS

In the following, predictions of the three approaches for maintaining and translating LSW are evaluated through numerical simulation.

Wave Asymmetry Calculation Approach

Starting with a representative single LSW with a length of 5.5 km and an amplitude of 34.2 m (Fig. 2), a standard shoreline change model (particulate transport rate only) was run for 2,000 hr with constant offshore (20-m depth) wave climate of $H = 1.0$ m, wave period $T = 6$ sec, and $\theta = 10$ deg. Other parameters in the simulation were time step $\Delta t = 4$ hr, cell spacing $\Delta x = 50$ m, and $K = 0.7$. As has been shown previously

(Hanson and Larson 1987), wave transformation modules run on assumed locally plane and parallel contours that are typically included in shoreline change models produce wave properties alongshore that results in a high degree of symmetrical transport patterns around a protruding symmetric feature such as a LSW. As a result, the LSW experiences little advection, although the diffusion is significant (Fig 2).

In the 2D wave modeling simulations, the number and size of alongshore calculation cells were the same as in the 1D simulation. The calculation area was divided into 50 sections, each of 20-m spacing across shore. Time step and duration of the simulation were the same as in the 1D case. As seen in Fig. 2, the LSW evolution produced by the 2D wave modeling displays a much greater degree of asymmetry, but there was no significant advective LSW motion, although diffusion was significant.

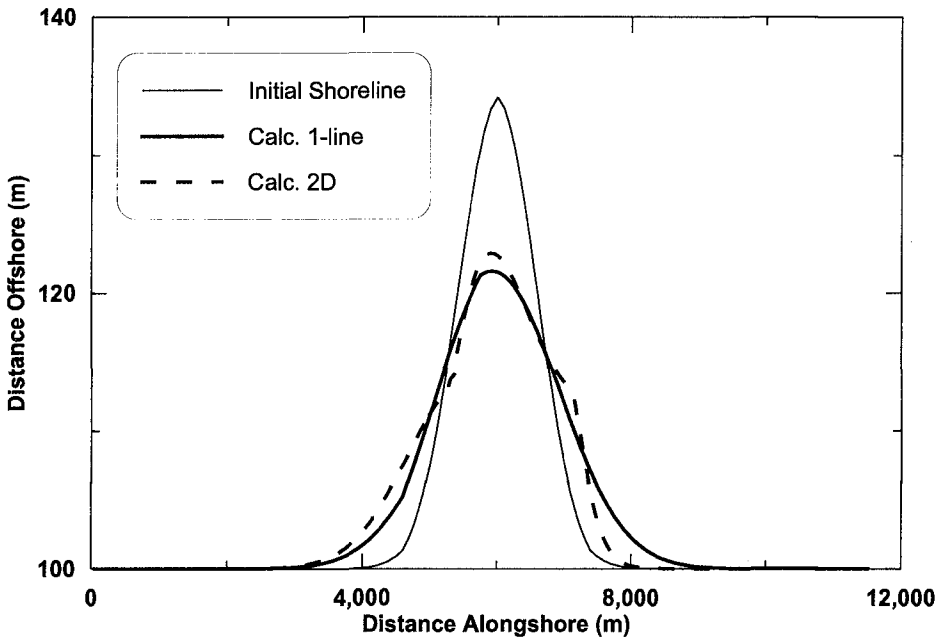


Fig 2. Shoreline change calculated using 1D and 2D wave transformation modeling.

Based on this and other calculations, it is concluded that a 2D wave calculation scheme as run in typical engineering studies will not create enough wave- and associated sand-transport asymmetry around a LSW to cause the LSW to migrate.

Advective Form Calculation Approach

As seen from Eq. (10), the advective speed of any section of a LSW is inversely proportional to its displacement from the baseline. Thus, the center of the initially symmetric LSW in Fig. 3 moves faster than the flanks, resulting in a flatter up-drift plan shape of the LSW and a steeper down-drift flank, in agreement with field observations. From a modeling point of view, the advective speed concept offers significant flexibility. The migration speed is controlled by α and R_{crit} in Eq. (10), whereas the diffusion is controlled by K in Eq. (4).

The initial LSW in Fig. 3 is the same as in the previous figure. In this case, the wave conditions were $H = 1.0$ m, $T = 8$ sec, and $\theta = 20$ deg, and the simulation duration 720 days. The LSW migrates with an average speed of 3 km/yr with a decrease in amplitude of about 50%. Variation of input wave characteristics in several similar simulations (not shown) indicated that the LSW would move in either direction, always migrating in the direction of net sand transport, in agreement with field observations. At the same time,

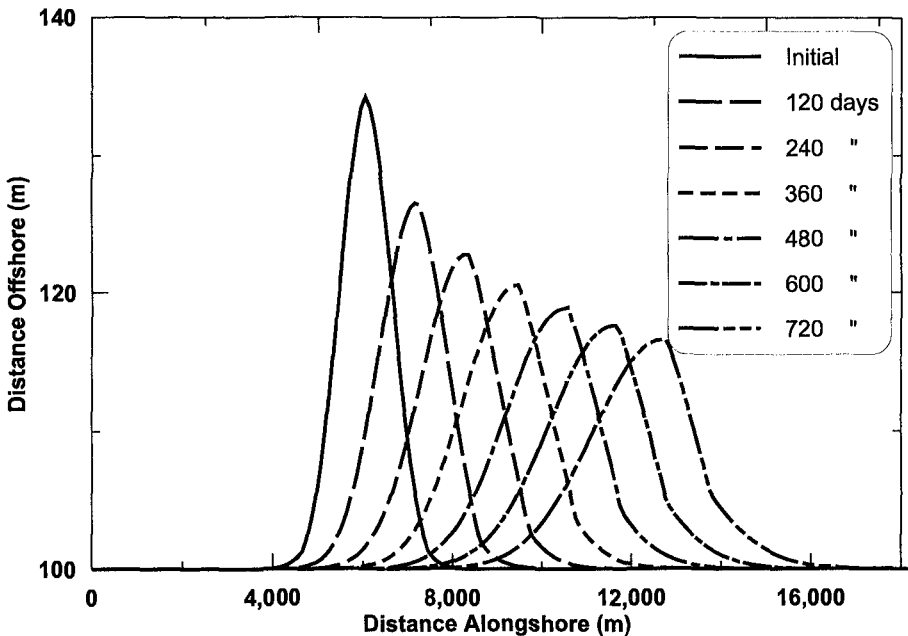


Fig 3. Calculated LSW migration using the advective form approach.

there was always an increase in length of the calculated LSW with time, while its amplitude decreased due to diffusion. Available field observations seem to indicate that LSWs have a more stable amplitude and do not increase in length.

Contracted Surf Zone Calculation Approach

A simulation was performed with the contracted surf zone approach implemented and with identical conditions as in the previous cases. As seen from Fig. 4, the calculated LSW does indeed move downdrift, but with considerably less speed and diffusion than in the previous case. During the simulated 2 years, the LSW moves with an average speed of 0.6 km/yr while maintaining 82% of its amplitude. At this stage, it is not possible to determine which of the two very different results is correct, because both are reasonable.

Distinguishing Advection and Diffusion

One problem both approaches have in common is, however, that any kind of perturbation in the shoreline will move downdrift, which is not reasonable. For example, the local erosion and accretion associated with the presence of a groin are expected to remain in the vicinity of the groin and not to move alongshore as a coherent form.

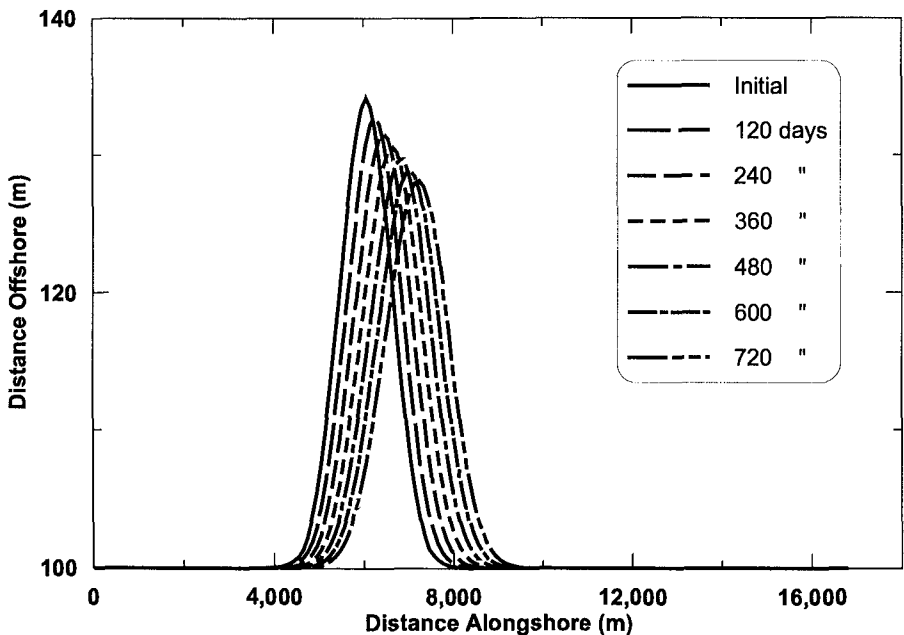


Fig 4. Calculated LSW migration using the contracted surf zone approach.

Fig. 5 shows the situation of an initial LSW identical to that in Fig. 3, calculated with the advective-form approach. The simulation was driven with a Corps of Engineers hindcast wave time series for Southampton Beach, Long Island, New York, that covers the period 1956-75. The simulation started on Jan. 1, 1958, and continued for 1,600 days, chosen to represent a period of unusually strong longshore transport wave conditions and a persistent sediment transport to the west (right). With a groin blocking the sediment transport, impoundment or accretion are expected on its updrift side and corresponding erosion on the opposite side of the structure. However, as these features start to develop, they, too, begin to migrate, resulting in the wavy shoreline shape downdrift of the groin. This behavior is unrealistic.

One *ad-hoc* means of eliminating advection of all perturbations is to *a-priori* identify and specify which features are to migrate. These features will subsequently evolve by advection as well as diffusion. Other features that appear spontaneously in response to constraints or placement of beach fills, such as shoreline displacements near groins, will not be subject to the advective mechanisms and not migrate alongshore. Such an *ad-hoc* specification might be implemented in an engineering application if the results are monitored with caution, but it is not satisfactory because it does not address why some

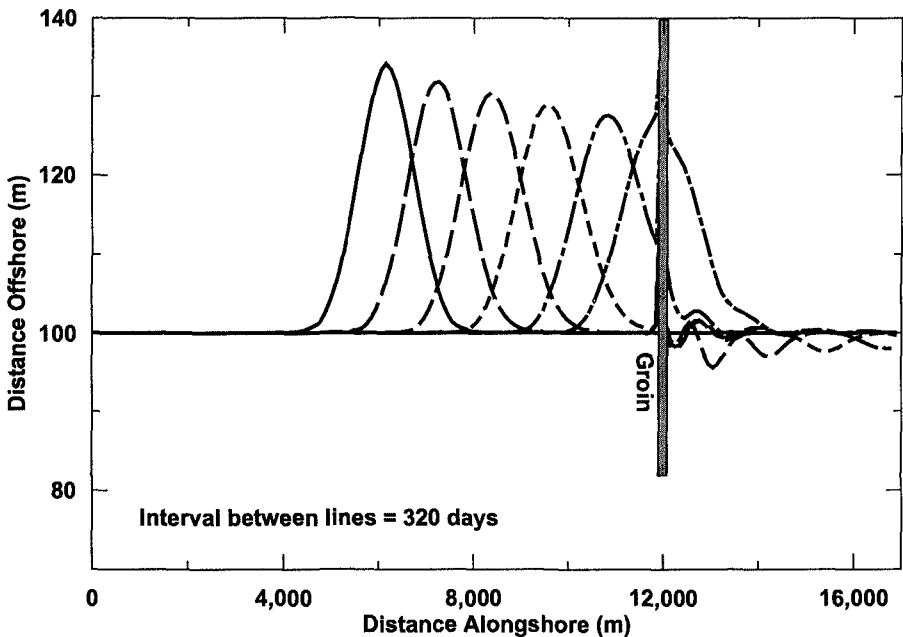


Fig 5. Calculated LSW interaction with a groin using the advective form approach.

shoreline features move and others do not, that is, the physical processes associated with cause and effect of the LSW migration are omitted.

A result of a simulation with such a distinction between advection and diffusion in the advective-form approach is displayed in Fig. 6, representing the same wave conditions as in the previous case, but now only run for 1,200 days. With the LSW distinguishing capability active, accretion as well as erosion adjacent to the groin develop, as expected. With elapsed time, the LSW passes the groin, initially deformed by the presence of the groin, but later resumes its shape as it moves away from the structure.

Application to Southampton Beach

To validate qualitatively the preliminary approach described here to modeling LSW migration, the advective form calculation was applied to the situation at Southampton Beach, Long Island, New York. Here, eleven LSWs present in the early 1990s were identified from aerial photos (Thevenot and Kraus 1995). The LSWs had an average length of 0.75 km, an average amplitude of about 40 m, and an estimated average annual migration speed of 0.35 km/yr. Their speed was found to vary seasonally with the strength of the inferred longshore discharge parameter calculated from the wave hindcast.

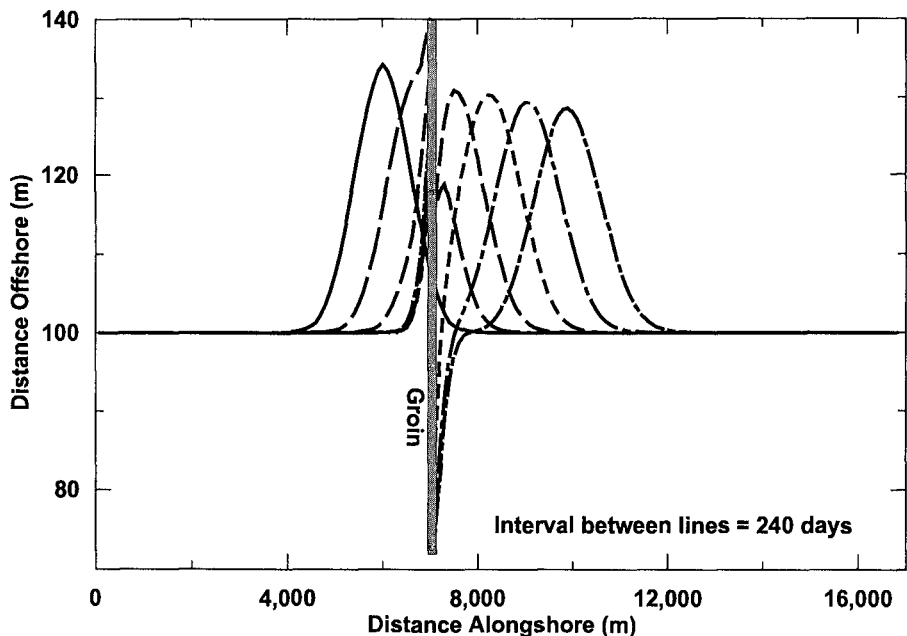


Fig 6. Calculated LSW interaction with a groin using decoupled advection and diffusion.

Available aerial photos dated Sep. 4, 1991, Dec. 20, 1991, and Jan. 2, 1993, served as references for the simulations. The simulated shoreline covers 16.9 km, with a spatial resolution of 100 m and a time step of 3 hr. Results of the simulation are shown in Fig. 7. The same wave hindcast time series as in the above was specified, but now starting on Sep. 4, 1956, and ending Jan. 2, 1958, representing the time period Sep. 4, 1991, to Jan. 2, 1993, because the actual time period of the LSW observation is not covered by the hindcast. The hindcast time period was selected to represent typical conditions at the site.

As expected, the LSWs moved to west (to the right in the simulations). However, it was noted that during the last two weeks of the simulation period, i.e., the end of 1957 (representing the end of 1992), the LSWs moved significantly in the opposite direction, ending on the incorrect side of the intermediate LSW positions. This reversal is an artifact of the wave time series in the hindcast for 1957. The calculations were therefore halted 2 weeks before the end of the simulation period.

The locations of the calculated LSW are in reasonable agreement with most of the LSWs in the photographs. However, representation of the amplitudes is poor. The reason for this is, as indicated previously, that the model cannot produce growth in LSW amplitude,

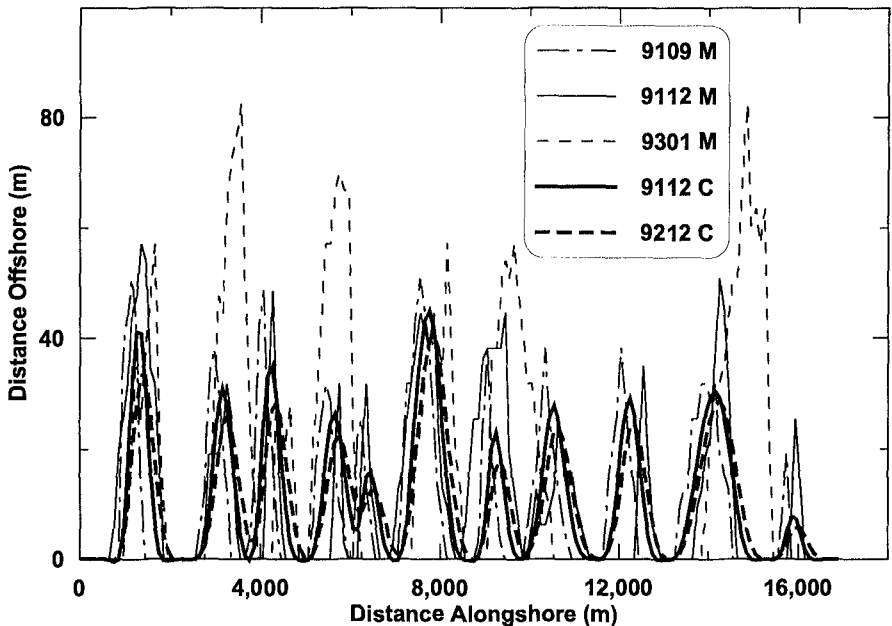


Fig 7. Measured and calculated LSW movement at Southampton Beach, LI, New York.

which appears to be a significant process in the field. It is not known at this point what phenomena are acting to produce a substantial increase in amplitude of the LSWs. It is possible that varying tide level may have contaminated the dimensions of the LSWs measured in the aerial photographs.

CONCLUDING DISCUSSION

Longshore sand waves (LSWs) are a large-scale phenomenon of major significance in coastal engineering and science. The physical processes governing preservation and migration of LSWs have not been firmly identified, no less understood. Predictive models describing LSWs are only at the formative stage, and the present paper has explored three approaches for describing the evolution of LSWs. The interaction between LSWs with groins was also explored.

Comparisons of calculations with measurements of LSWs at Southampton Beach, Long Island, New York, shows that the migration of LSWs may be described by shoreline-change model modified to include a form advection term. However, the temporal and spatial variation in permanence of form and amplitude of the LSWs were not satisfactorily reproduced in the model. Presented results indicate that the advective form calculation approach reproduces the LSW migration better than other methods, whereas the contracted surf zone calculation approach seem. to be superior in preserving LSW amplitude. Further model developments will depend on improved understanding, characterization, and conceptualization of the mechanisms controlling the behavior of LSWs.

ACKNOWLEDGEMENTS

The contribution to this study by H Hanson is based on work in the SAFE-project, performed within the framework of the EU-sponsored Marine Science and Technology Programme (MAST-III), under contract No. MAS3-CT-95-004. N.C. Kraus appreciates permission granted by the Chief of Engineers to publish this information. Our young and talented colleague, Michelle Marie Thevenot passed away on December 21, 1996, after a several-year battle with cancer, and we dedicate this paper to her.

REFERENCES

- Berkhoff, J.C.W. 1972. Computation of Combined Refraction-Diffraction. *Proc. 13th Coastal Engrg. Conf.*, ASCE, 471-490.
- Dally, W.R., Dean, R.G. and Dalrymple, R.A. 1985. Wave Height Variation Across Beaches of Arbitrary Profile. *J. Geophys. Res.*, 90(C6): 11917-11927.
- Hanson, H. and Kraus, N.C., 1989. GENESIS - Generalized Model for Simulating Shoreline Change, Vol. 1: Reference Manual and Users Guide.

- Tech. Rep. CERC-89-19*, US Army Engineer Waterways Experiment Station, Coastal Engineering Research Center, 247 pp.
- Hanson, H. and Larson, M. 1987. Comparison of Analytic and Numerical Solutions of the One-Line Model of Shoreline Change. *Proc. Coastal Sediments '87*, ASCE, 500-514.
- Inman, D.L. 1987. Accretion and Erosion Waves on Beaches. *Shore & Beach*, 55(3 & 4): 61-66.
- Komar, P.D. and Inman, D.L. 1970. Longshore Sand Transport on Beaches. *J. Geophys. Res.* 75(30): 5914-5927.
- Kraus, N.C. and Dean, J.L. 1987. Distribution of the Longshore Sediment Transport Rate Measured by Trap. *Proc. Coastal Sediments '87*, ASCE, 881-896.
- Larson, M and Hanson, H. 1996. Schematized Numerical Model of Three-Dimensional Beach Change. *Proc. 10th Congress of the IAHR Asia and Pacific Division*, Lankawi Island, Malaysia.
- Larson, M. and Kraus, N.C. 1991. Mathematical Modeling of the Fate of Beach Fill. In: H.D. Niemayer, J. van Overeem, and J. van de Graaf, (Eds.), *Artificial Beach Nourishment*, *Coastal Engrg.*, 16,: 83-114.
- Larson, M, Kraus, N C, and Hanson, H. 1997. Analytical Solutions of the One-Line Model of Shoreline Change Near Coastal Structures. *J. Waterway, Port, Coastal and Ocean Engrg.*, ASCE, in press.
- Sonu, C.J. 1968. Collective Movement of Sediment in Littoral Environment. *Proc. 11th Coastal Eng. Conf.*, ASCE, 373-398.
- SPM. 1984. *Shore Protection Manual*, 2nd ed., 2 Vols., US Army Corps of Engineers, Coastal Engrg. Res. Cntr., US Govt. Printing Off., Washington, DC.
- Thevenot, M. M., and Kraus, N. C. 1995. Longshore Sand Waves at Southampton Beach, New York, Observations and Numerical Simulation of Their Movement. *Mar. Geol.*, 126: 249-269.
- Verhagen, H.J. 1989. Sand waves along the Dutch coast. *Coastal Engrg.*, 13: 129-147.

CHAPTER 312

EROSIVE WAVES IN SHORELINE CHANGE DUE TO THE REDUCTION OF A RIVER DELTA

Yoshito Tsuchiya,¹ M. ASCE

ABSTRACT: Using observations of long-term data of shoreline change during the reduction process of a river-mouth delta, space-time shoreline changes and their variations are clarified by the moving-average method. There clearly exist two modes of shoreline changes due to distinct types of erosive wave. The first mode is defined to be an erosive wave propagating down-coast as a diffusion phenomenon. The second was estimated from the variation from the erosive wave and defined to be an erosive wave propagating down-coast as a wave phenomenon. We suggest new terminology for these two kinds of erosive wave. The erosive waves of the first mode are subject to change as positive and negative erosive waves due to the initial and boundary conditions at the river mouth in relation to the sediment input from the river and local change in the submerged river delta. The erosive wave of the second mode propagates down coast faster than the first mode erosive wave. We therefore conclude that shoreline change due to beach erosion can be described as space-time change propagating down-coast as a diffusion phenomenon, upon which shoreline variation propagates as a wave phenomenon faster than the shoreline change. Additionally, a theory for the diffusion-wave phenomenon of shoreline change is attempted using a set of equations of longshore sediment transport rate and continuity of shoreline change to find the dispersion relation of erosive waves.

INTRODUCTION

In the past, it has been considered that shoreline change is a diffusion process, governed by a diffusion-type equation in a one-line theory. It has been observed that, in the reduction process of a river delta, severe shoreline change takes place in the vicinity of the cause of erosion, sometimes with beach collapse, and that shoreline change propagates down-coast like a wave phenomenon. In 1987, Inman defined the propagation velocity of an accretion or erosion wave in terms of the longshore sediment transport rate. By use of this method, Uda and Yamamoto (1994) recently estimated the velocity of a sandy body on the Mihono-matsubara sand spit. In understanding

¹Professor Emeritus, Kyoto University and Professor, Faculty of Urban Science, Meijo University, 4-3-3 Nijigaoka, Kani 509-02, Japan

the shoreline change and establishing methodologies for its control, it is of course very important to recognize whether the shoreline change can be described as a diffusion or a wave phenomenon, or as a diffusion-wave phenomenon.

Recently, Tsuchiya (1995, 1996) studied erosive waves in shoreline change by analyzing long-term shoreline change data from the Shizuoka and Shimoniikawa coasts, using the method of moving average.

In this paper, we analyze data of long-term shoreline change along the Shizuoka Coast facing Suruga Bay by the method of moving average, to find the space-time change of the shoreline and its propagation speed. The narrow, sandy beach was formed on the collision coast due to there being a lot of sediment input from the Abe river. Due to a rapid decrease in sediment input, severe beach erosion and collapse began to take place near the river mouth in 1965. This extends in the direction of longshore sediment transport. The beach erosion can therefore be considered as a reduction process of the river delta. There clearly exist two modes of shoreline change. The first mode is space-time shoreline changes such as positive and negative erosive waves as diffusion phenomena. The second mode is an erosive wave propagating faster than the first mode shoreline change. We demonstrate that shoreline change due to beach erosion must therefore be considered as a diffusion-wave phenomenon.

Additionally, a theory of shoreline change is proposed from a set of equations for longshore sediment transport and continuity of shoreline change. We conclude that the shoreline change can be described by a diffusion-wave phenomenon. The dispersion relation is obtained, and the resulting propagation speed is discussed.

THE DATA

The Shizuoka Coast and Its General Features: Although depth sounding was first performed in 1969, regular surveys of shoreline change and soundings on the

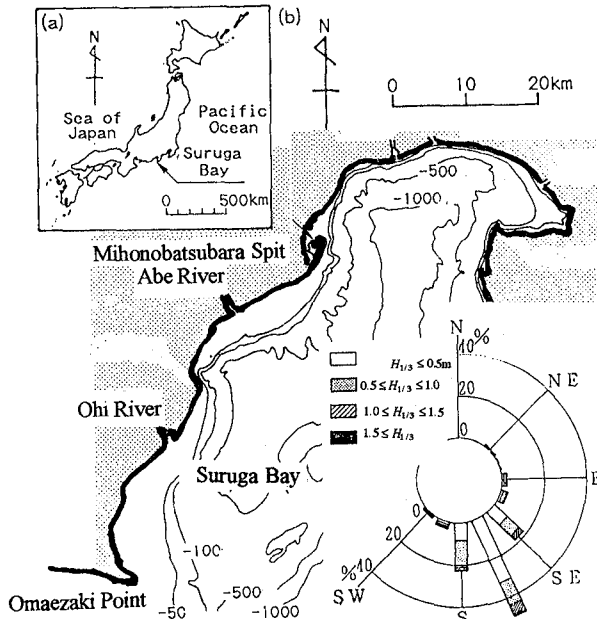


Figure 1. Location of Shizuoka coast and wave rose (Modified from Uda, 1994)

Shizuoka coast have been carried out annually since 1974 by the Shizuoka Prefectural Government.

In this paper, the measured data were used. The Shizuoka coast is one of the Pacific Ocean coasts of the Japanese islands, facing Suruga bay as shown in Figure 1. This coast is a typical collision and mountainous coast according to the coastal classification of Inman and Nordstorm (1971). The width of the coast is very narrow. The beach profiles are very steep and connect with the steep offshore slopes in Suruga bay. Because of the high rate of sediment input from the Abe river, a narrow sandy beach has been formed on the coast by typhoon waves from the south to southeast directions. At the northeast end of the coast, a sand spit called Mihono-batsubara sand spit is beautifully formed by the longshore sediment transport in the northeast direction. Near the sand spit, a sea canyon is located into which part of the longshore sediment is deposited.

Coastal Disasters and the Main Causes of Beach Erosion: Coastal disasters occurred due to the Isewan typhoon in 1959 and Typhoon 6626 in 1966, resulting in

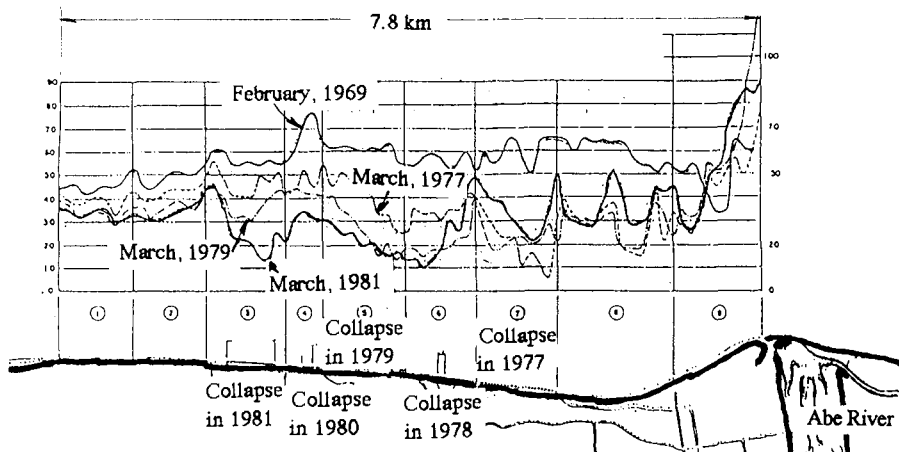


Figure 2. Shoreline changes due to beach erosion and collapse in the initial stages of beach erosion (Toyoshima, Takahashi & Suzuki, 1981).

beach collapse in some locations on the beach north of the river mouth, as shown in Figure 2. Since then sea dikes have been constructed along the coast. Because there was remarkable beach erosion at that time, soundings and shoreline surveys have been carried out along the coast since 1969. The sea dikes were sometimes destroyed and the eroded area extended further along the northeast coast. Therefore offshore breakwaters were begun to be

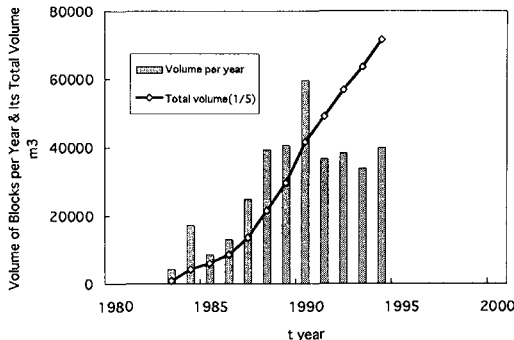


Figure 3. Annual change of total volume of concrete units used for offshore breakwaters.

constructed, and these are now completed along the whole coast. Figure 3 shows the total volume of concrete units used for the offshore breakwaters. In the Abe River sediment mining had been done widely and severely before 1968 for construction works, resulting in severe beach erosion. We therefore conclude that the main cause for beach erosion is due to the decrease in sediment input from the Abe River, and that the beach erosion can be explained as a reduction process of the river delta.

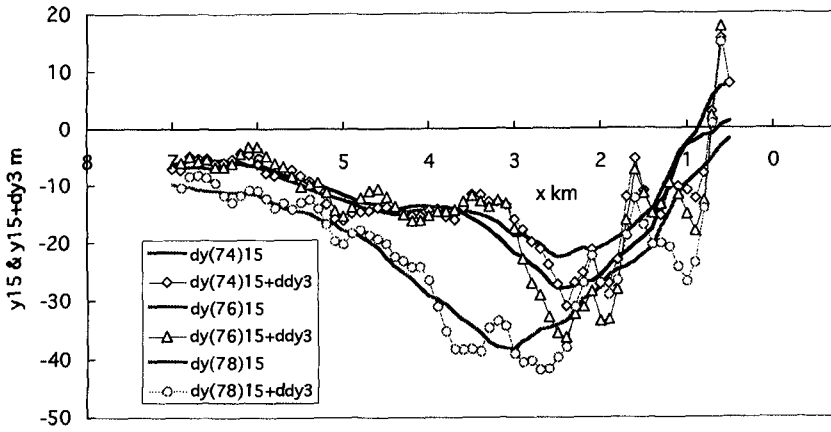
THE METHOD OF DATA ANALYSIS

Purpose of Data Analysis: Shoreline changes are usually measured at intervals of 100m or 200m. As shown in Figure 2, beach collapse takes place locally over several hundred meters, and extends down-coast as it propagates. The spatial magnitude of shoreline change due to beach erosion is wider and reaches sometimes a few kilometers. Therefore, we have to consider shoreline changes extending from several hundred meters up to several kilometers. The shoreline change data include local shoreline changes and some errors in the measurements. In order to clarify the shoreline changes more naturally than we have understood them, it may be effective to analyze the data using spatial smoothing methods.

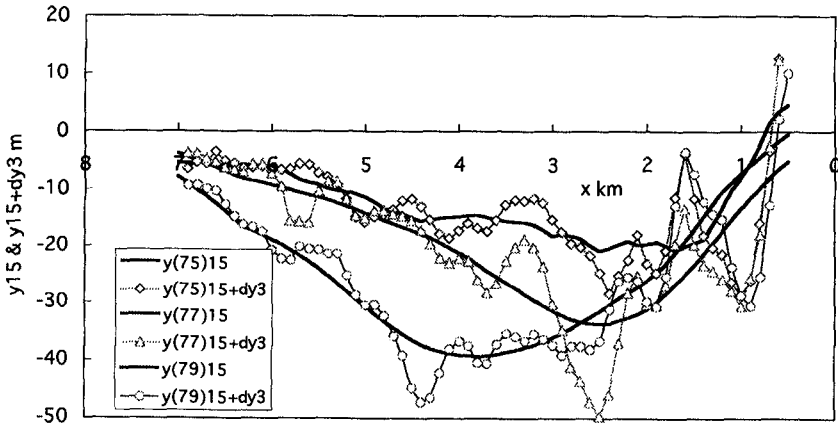
Methods of Data Analysis: We have two traditional methods for smoothing fluctuating data; 1) the triangle-weighting or uniform-weighting method, and 2) the Fourier transform method. Shoreline changes take place not only due to beach erosion, but also by beach collapse under the action of wave concentration, and extend widely along the coast. In this paper, the uniform-weighting method was used. The number of points for weighting was determined by considering whether the phenomena in question can be clearly observed in the smoothed data. 11, 13 and 15 points were used for large-scale shoreline change as a diffusion phenomenon, and 3 points were used for variations from the large-scale shoreline change as a wave phenomenon. The applicability of the smoothing method was established by comparing the results from using different numbers of smoothing points. We conclude that, in the data measured at intervals of 100 m, 13 and 15 smoothing points are suitable for large-scale shoreline change, but 3 points for variations from the shoreline change.

THE CLASSIFICATION OF EROSIIVE WAVES

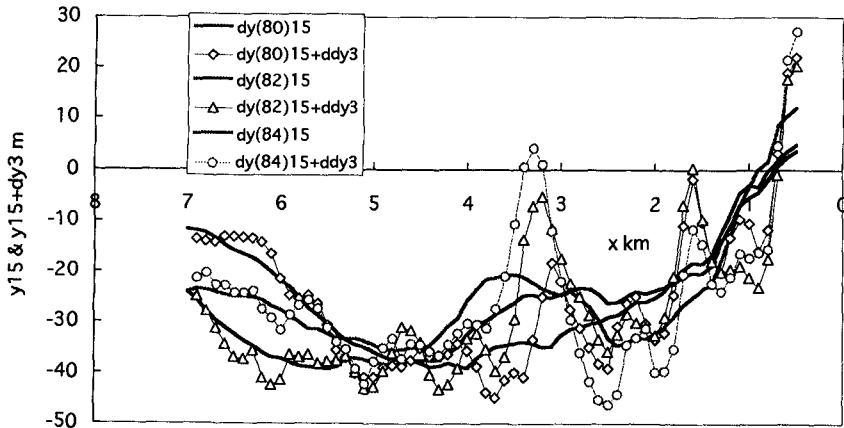
Spatial and Temporal Shoreline Changes: Using the 15-point smoothing method, smoothed shoreline changes and their variations are shown in Figure 4 at intervals of two every years. In the figure there clearly exist two modes of shoreline change. The first mode, indicated by the thick solid curves, is the large-scale shoreline change. The second mode, indicated by the thin curves with marks, is the variation from the first-mode shoreline change. The large-scale shoreline changes show clearly the annual change of shoreline in spatial form from the river mouth of the Abe river. The shoreline change expands widely down-coast in the north-east direction. This shoreline change clearly demonstrates the total shoreline change under the condition of beach erosion, which we understand as a diffusion phenomenon. This shoreline change propagation may correspond to the accretion or erosion wave proposed by Inman (1987). Referring to the cause of beach erosion, which is a decrease in sediment input from the Abe river, this total shoreline change can be understood to be a reduction process of the river delta. However, the boundary condition for the shoreline change at the river



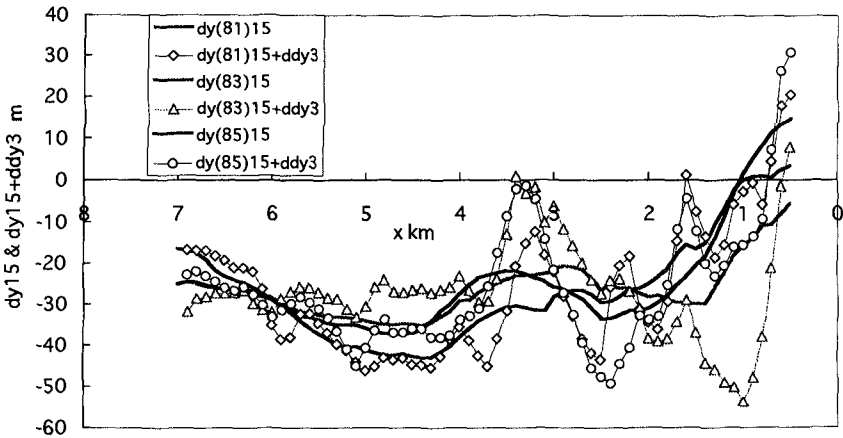
(a) 1974 to 1978.



(b) 1975 to 1979.



(c) 1980 to 1984.

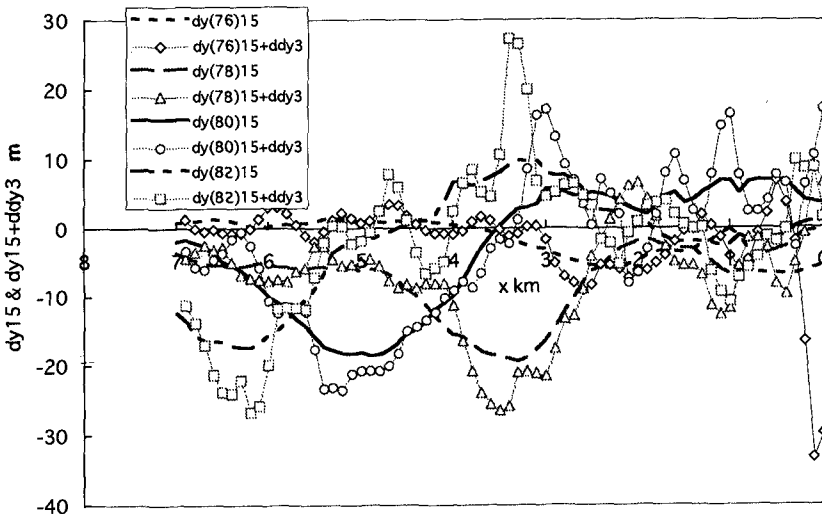


(d) 1981 to 1985.

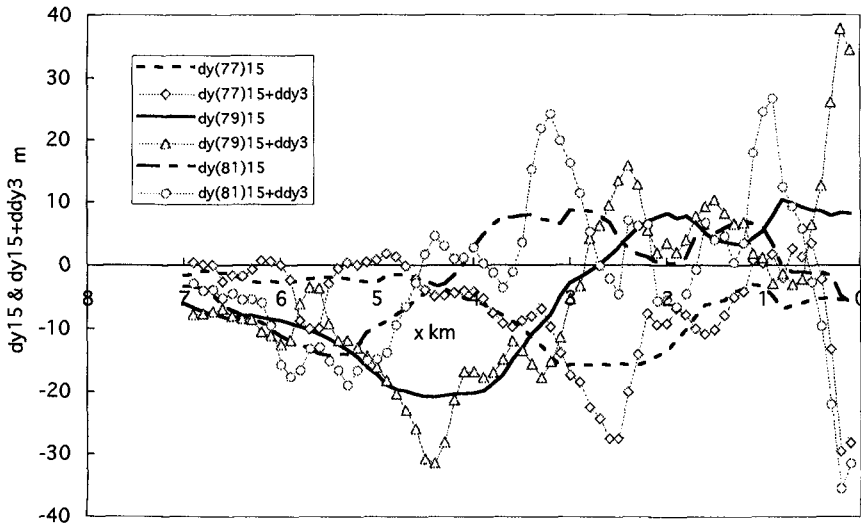
Figure 4. Total shoreline changes with erosive waves (W) down-coast from the river mouth.

mouth will be discussed in relation to the generation of erosive waves, as well as the decrease in sediment input from the river.

Erosive Waves: The thick curves shown in Figure 5 illustrate annual changes in total shoreline change, for which I define an *erosive wave as a diffusion phenomenon*. The erosive wave propagates down-coast, reducing in amplitude gradually. In this case, it has a wave crest defined by a minimum in the spatial shoreline change, and a trough defined by a maximum. Note the fact that the erosive wave is composed of two elementary waves such as positive and negative erosive waves. The positive erosive wave propagates accompanying the negative erosive wave. Further, note that these two waves were generated by different events at the river mouth, probably rapid decrease and increase in sediment input from the river, or their resulting local changes



(a) 1976 to 1982.



(b) 1977 to 1981.

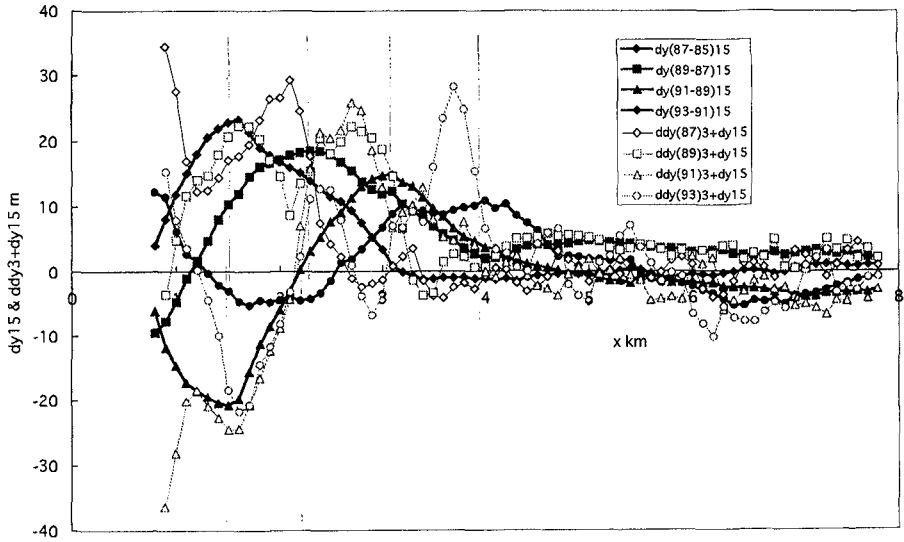
Figure 5. Spatial profiles and propagation of erosive waves (DP) and (DN) with erosive wave (W) before the construction of offshore breakwaters.

in the submerged river delta. Therefore, I define the erosive wave propagating as a diffusion phenomenon as *erosive wave (D)*, and the positive and negative erosive waves as *erosive wave (DP)* and *erosive wave (DN)*, respectively.

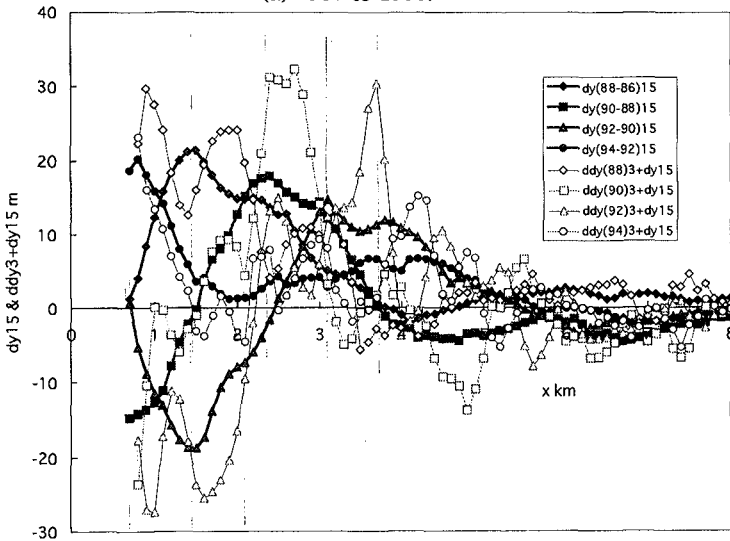
When the erosive waves are specified at the river mouth as the initial and boundary conditions for shoreline change, we may predict the total shoreline change using a common shoreline change model. Actually, beach profiles change in relation to shoreline changes around the river delta, so that the application of the model may need further consideration. The thin curves shown in Figure 6 indicate the variations from the erosive wave (D), for which I define an *erosive wave as a wave phenomenon*. This erosive wave propagates down-coast on the erosive wave (D). Thus, I define it as *erosive wave (W)*. The crest and trough of the erosive wave (W) are denoted as *erosive wave (Wc)* and *(Wt)*, respectively.

THE EROSIIVE WAVE(D) AND ITS PROPAGATION AS A DIFFUSION PHENOMENON

Spatial Profiles and Propagation of the Erosive Waves (D): As previously seen in Figure 5, this erosive wave (D) propagates down-coast accompanying erosive waves (DP) and (DN). Note that the spatial profiles of erosive waves (D) have nearly the same form, but reduce their amplitude gradually as a diffusion phenomenon, until the construction of offshore breakwaters. The erosive waves generated during and after the construction are shown in Figure 6, the thick curves with solid marks indicate the erosive wave (D), and the thin curves with open marks the erosive wave (W) propagating on the erosive wave (D). Note that during this period erosive waves (DN) were generated, and then erosive waves (DP) were then generated. Both the erosive waves propagate slowly down-coast in the same form, but their amplitudes clearly tend to decay down-coast. This fact may be due to the offshore breakwater effect of trapping of longshore sediment.



(a) 1987 to 1993.



(b) 1988 to 1994.

Figure 6. Spatial profiles and propagation of erosive waves (DP) and (DN) with erosive wave (W) during and after the construction of offshore breakwaters.

Propagation Speeds of Erosive Waves (DP) and (DN): The amount of data for the erosive waves is limited. Therefore, by use of the successive spatial profiles corresponding to the crests of erosive waves (DP) and (DN), the positions of the crests can be determined. Figure 7 shows the time-change of the crest positions where the straight line with solid diamond and square marks indicate respectively erosive waves (DP) generated before and during/after the construction of offshore breakwaters. The propagation speeds of erosive waves are obtained from the gradient of the straight lines.

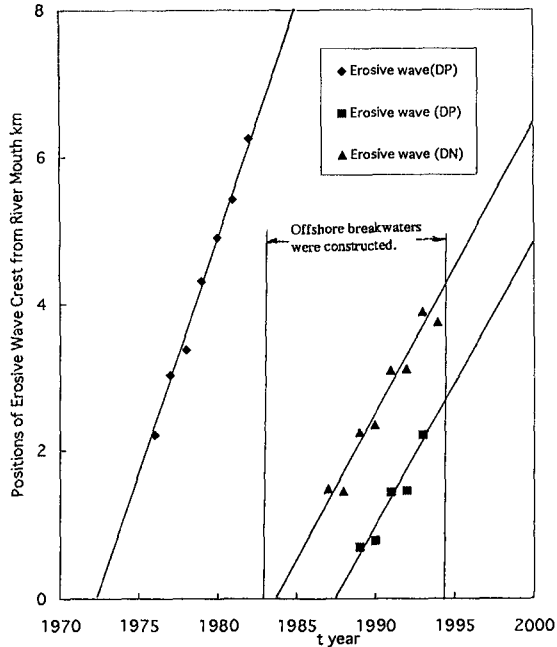


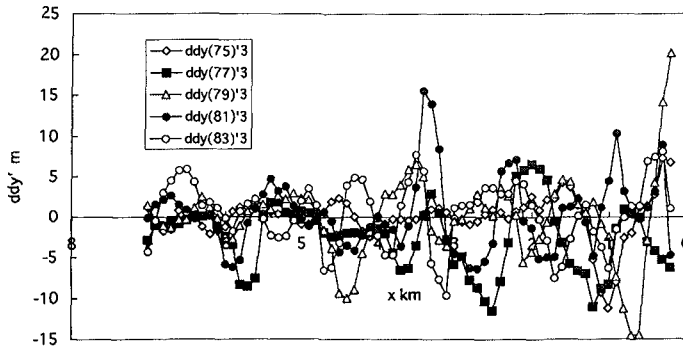
Figure 7. Propagation speed of erosive waves (DP) and (DN) before and during/after the construction of offshore breakwaters.

Note that the propagation speed of erosive waves generated during and after is less than that before the construction. Further, note that the propagation speed of erosive waves (DP) and (DN) are the same. This may explain the fact that the spatial profiles shown in Figure 6 are decaying gradually down-coast, but maintain almost the same form. If the straight line of erosive wave (DP) is extended, the time when the erosive wave was generated is found to be around the year 1972. Alternatively, the times when erosive waves (DP) and (DN) were generated during and after the construction are found to be around the years 1983 and 1987, respectively.

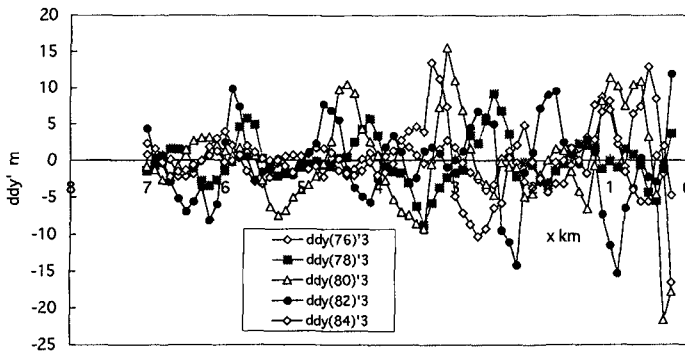
Possible reasons for generation of erosive waves (DP) and (DN): As previously discussed the main cause of beach erosion is due to the decrease in sediment input from the Abe river. Uda, Misawa and Matsui (1996) recently qualified this fact considering river bed changes due to mining of sand and gravel in the river. They conclude that the river bed had been lowered within the alluvial reach near the river mouth during mining until 1968, but changed to deposition of sediment during the period between 1970 and 1973. It therefore seems that within the period, there was no sediment input into the beach, resulting in either the direct generation of the erosive wave(DP) shown in Figure 7, or changing the submerged river delta which may have generated erosive waves. They also described that after the generation of the erosive wave no remarkable floods have been experienced, but a huge flood occurred in 1982, of which the maximum discharge was 3,860 m³/sec. It also seems that the flood generated the erosive wave(DN), and that variations in the submerged river-mouth delta in relation to floods might generate erosive waves .

THE EROSIIVE WAVE(W) AND ITS PROPAGATION AS A WAVE PHENOMENON

Erosive Wave (W) and Its Propagation: Figures 8 and 9 show erosive waves (W) generated before and during/after the construction of offshore breakwaters respectively. A careful inspection shows that the erosive waves (W) propagate down-coast, with some exceptions. Note that the wave amplitudes show their maximum values near the river mouth, and reach over 30 m. Further, note that they decay in their propagation down-coast. It seems that this tendency is the same both before and during/after the construction of offshore breakwaters.



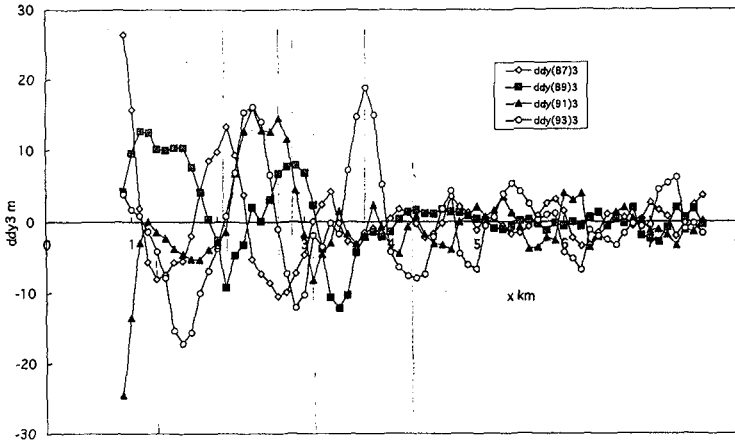
(a) 1975 to 1983.



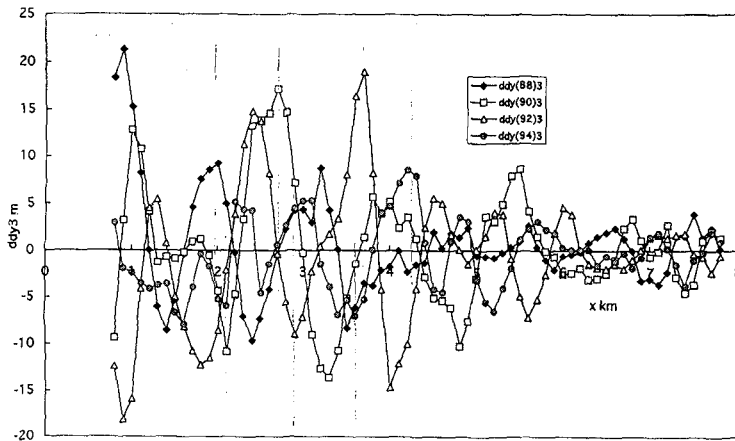
(b) 1976 to 1984.

Figure 8. Erosive waves (W) and their propagation, with wave amplitudes damping down-coast, before the construction of offshore breakwaters.

Wavenumber Spectrum of Erosive Waves (W): The amount of data is not sufficient for calculating wave number spectra of erosive waves (W) accurately. There is also a decay of their wave amplitudes. These may prevent the spectrum from being calculated accurately. However, we tried to estimate them using Mathematica to examine whether a peak wavenumber exists. Figure 10 shows some examples of the spectra. The spectra are not well formed, but there exists a peak wavenumber. The wavelength corresponding to the peak wave number was calculated. Figure 11 shows change in the wave length. It is nearly constant, being about 500 m until 1985, and thereafter varies and increases. This may be due to the trapping effect of longshore



(a) 1987 to 1993.



(b) 1988 to 1994.

Figure 9. Erosive waves (W) and their propagation, with wave amplitudes damping down-coast, during and after the construction of offshore breakwaters.

sediment transport by offshore breakwaters.

Propagation Speed of Erosive Waves (W): From successive crests of erosive waves (W) which were selected from the spatial profiles shown in Figures 8 and 9, the positions of the crests were determined. Figure 12 illustrates time changes of the crest positions of erosive waves (W) where the straight line with solid circles indicates the crest position of erosive wave (DP) and those with open squares and triangles mark the crest and trough positions of erosive waves (Wc) and (Wt), respectively. The propagation speeds of the crest and trough of erosive wave (W) are nearly same, and faster than that of erosive wave (DP). We therefore conclude that the erosive wave (W) propagates faster than the erosive wave (DP). This fact may explain why beach collapse or severe erosion takes place locally at some locations down-coast with the sandy beach being eroded.

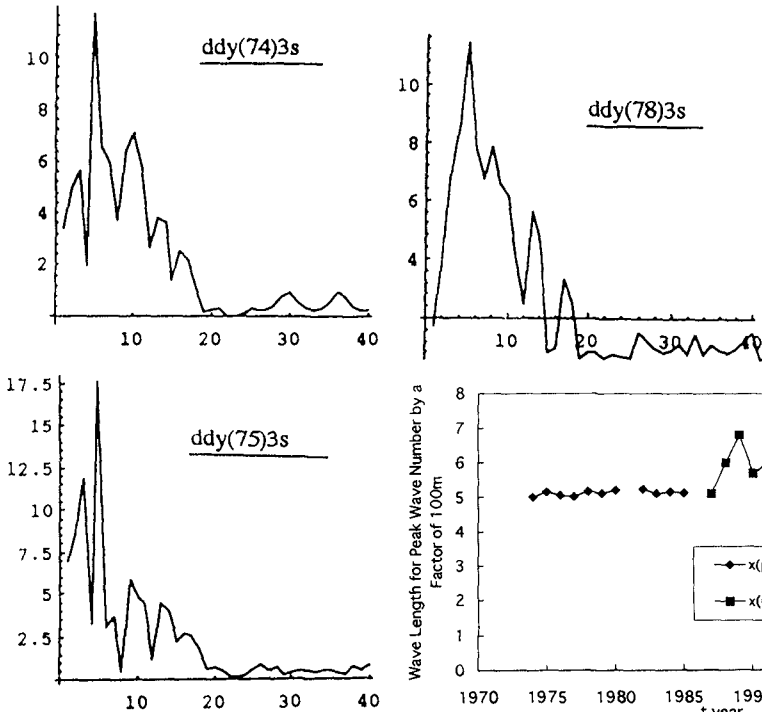


Figure 10. Some examples of wave-number spectra of erosive waves (W).

Figure 11. Changes in wavelength corresponding to the peak wavenumber.

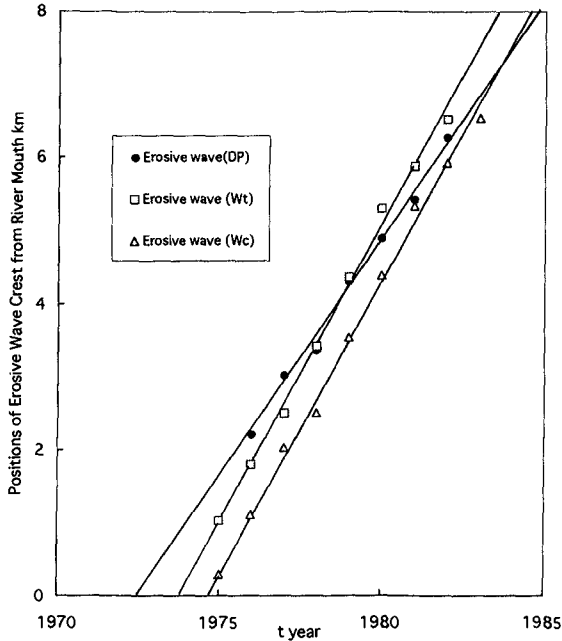


Figure 12. Propagation speed of erosive wave (W) compared with those of erosive waves (DP) and (DN).

Possible Reasons for Generation of Erosive Waves (W): Where there exists a wave phenomenon, there must be a generation force to produce the wave. Such generation forces do exist, such as incoming waves with some frequency of occurrence, but what the restoring forces are should be clarified. As will tentatively be explained later, the local change of shoreline may result in changing the total rate of longshore sediment transport. This may generally result in restoring the shoreline change. Therefore, once a local shoreline change has taken place, the shoreline change propagates down-coast, probably decaying in amplitude.

THE EROSIIVE WAVES AS A DIFFUSION-WAVE PHENOMENON AND THEIR PROPAGATION

So far a set of governing equations for shoreline change, composed of the equation of continuity for shoreline change, the total rate of longshore sediment transport and the geometrical relation of shoreline change has been used to derive a diffusion equation for shoreline change. In order to study a natural phenomenon dynamically, a set of both the equations of motion and continuity must be established. The equations of longshore sediment transport rate and continuity of shoreline change are approximately given by (Refaat and Tsuchiya, 1991)

$$\frac{\partial Q}{\partial t} + a \frac{\partial}{\partial x} \left(\frac{Q}{h_b} \right)^2 = b g h_b^2 \left(\sin 2\alpha_{b0} - 2 \frac{\partial y_0}{\partial x} \right) - e \sqrt{\frac{g}{h_b}} Q \quad (1)$$

$$\frac{\partial y_0}{\partial t} + \frac{1}{(1-\lambda)h_k} \frac{\partial Q}{\partial x} = 0 \quad (2)$$

where y_0 is the shoreline position from the datum line, h_b the breaker depth, h_k the threshold depth of sediment movement, g the acceleration of gravity, λ the porosity of the bottom sediment, and a , b and e are practically constants. The second term in the first term on the right side of (1) demonstrates the restoring force of shoreline change in the wave phenomenon. The linearization of (1) and (2) results in

$$\frac{1}{e} \sqrt{\frac{h_b}{g}} \frac{\partial^2 y_0}{\partial x^2} + \frac{\partial y_0}{\partial t} - \frac{\sqrt{2b}}{e(1-\lambda)} \frac{h_b^2 \sqrt{g h_b}}{h_k} \frac{\partial^2 y_0}{\partial x^2} = 0 \quad (3)$$

which is the linearized wave-diffusion equation for shoreline change. Neglecting the first term the second and third terms reduces to the usual diffusion equation of shoreline change. The dispersion relation of (3) is given by

$$\frac{(\sigma/k)^2}{g h_b} = 2b \left\{ \frac{h_b}{(1-\lambda)h_k} \right\} \frac{1}{1 - e \sqrt{g/\sigma^2 h_b}} \quad (4)$$

The term $g/\sigma^2 h_b$ in (4) describes the diffusion term effect on the dispersion. When the term vanishes (4) demonstrates the wave celerity in the wave equation which can be obtained by neglecting the second term. The wave celerity shows that the wave celerity of erosive waves is proportional to the long-wave velocity evaluated from the breaker

depth and the square root of the ratio of breaker depth to threshold depth of sediment movement.

CONCLUSION

By the use of data on long-term shoreline change in the reduction process of the river delta on the Shizuoka coast, we found that there exist two modes of shoreline change, namely shoreline change as a diffusion phenomenon and variation from shoreline change as a wave phenomenon. We name these erosive waves, which are defined respectively as erosive wave (D) and erosive wave (W) for the two modes of shoreline change. We conclude that the erosive wave (D), the first mode of shoreline change, expands down-coast as a diffusion phenomenon; but the erosive wave (W), the second mode of shoreline change, propagates down-coast as a wave phenomenon faster than the erosive wave (D). The shoreline change in the river delta coast can then be described as a diffusion-wave phenomenon.

The generation of the erosive waves was considered in terms of the sediment input from the river and local change in the submerged river-mouth delta. Finally, a theory for the diffusion-wave phenomenon of shoreline change was attempted using a set of equations of longshore sediment transport rate and continuity of shoreline change. From these the dispersion relation of the phenomenon was found. Further theoretical investigations are now being made to establish a predictive method for shoreline change.

Acknowledgments

I thank Mr. K. Ishida, Chief, Planning Section, Technical Division, Suruga Konsaru Ltd. for his cooperation in the collection of long-term shoreline change data at the Shizuoka coast. Part of this investigation was supported both by Grants-in-Aid for Scientific Research (No. 07555164) from the Ministry of Education, Science, Sports & Culture of Japan, and Research Fund (No. 7-1-4-25) of the Foundation of River and Watershed Environment Management.

References

- Inman, D. L. (1987): Accretion and erosion waves on beaches, *Shore and Beach*, July-October, 61-66.
- Refaat, H.E.A.A. and Y. Tsuchiya (1991): Formation and reduction processes of river deltas; Theory and experiments, *Bul. DPRI, Kyoto Univ.*, Vol. 41, 177-224.
- Toyoshima, O., S. Takahashi and I. Suzuki (1981): On beach erosion of the Shizuoka coast, *Proc. Coastal Eng., JSCE*, Vol. 28, 261-265 (in Japanese).
- Tsuchiya, Y. (1995): Shoreline change due to beach erosion as a wave phenomenon (1) -The Shizuoka coast-, *Proc. Coastal Eng., JSCE*, Vol. 42, 551-555 (in Japanese).
- Tsuchiya, Y. (1996): Shoreline change due to beach erosion as a wave phenomenon (2) -The Shimoniikawa coast-, *Proc. Coastal Eng., JSCE*, Vol. 42, 586-590 (in Japanese).
- Uda, T., T. Suzuki, M. Oishi, Y. Yamamoto and N. Itahashi (1994): Beach change around a sand spit -in special reference to Mihonomatsubara sand spit-, *Proc. Coastal Eng., JSCE*, Vol. 41, 536-540 (in Japanese).
- Uda, T., H. Misawa and H. Matsui (1996): On the initiation of sand body movement in Shizuoka coast, *Proc. Coastal Eng., JSCE*, Vol. 43, 581-585 (in Japanese).

CHAPTER 313

DELILAH, DUCK94 & SandyDuck: Three Nearshore Field Experiments

William A. Birkemeier, M. ASCE, Charles E. Long and Kent K. Hathaway¹

Abstract

Two major field experiments have recently been conducted, and a third is being planned, at Duck, NC, along the mid-Atlantic coast of the USA, to investigate nearshore dynamic processes. Named DELILAH, DUCK94, and SandyDuck, these experiments take advantage of logistical efficiency and relatively uncomplicated, open-coast field conditions provided by the Field Research Facility of the US Army Engineer Waterways Experiment Station. DELILAH occurred in 1990, and emphasized hydrodynamics measurements. DUCK94, in 1994, added measurements of sediment transport and morphologic evolution, and was planned as a comprehensive pilot study for SandyDuck, the most ambitious experiment in the series, scheduled for 1997. Scientific motivation, instrumentation plans, participants, and representative climatic conditions of DELILAH and DUCK94 are described, as are sources of further information and data.

Introduction

Since 1979, the Coastal and Hydraulic Laboratory (formerly the Coastal Engineering Research Center) of the US Army Engineer Waterways Experiment Station has hosted a series of increasingly complex, multi-investigator, multi-agency nearshore field experiments at its Field Research Facility (FRF) located in Duck, North Carolina, USA. Two recent experiments, *DELILAH* and *DUCK94*, and a planned third experiment, *SandyDuck*, all evolved from scientific and pragmatic successes of prior work at this site, and have the basic objectives of improving fundamental understanding and modeling of surf zone physics. The emphasis in *DELILAH* was surf zone hydrodynamics in the presence of a changing barred bathymetry. *DUCK94* and *SandyDuck* have added components to resolve sediment transport and morphologic evolution at bedform scales from ripples to nearshore bars. *DUCK94* was designed as a pilot effort to test instruments and procedures required for the more comprehensive *SandyDuck* experiment. The purpose of this paper is to summarize the two completed experiments, including participants, environmental

1) Authors from US Army Engineer Waterways Experiment Station, Coastal and Hydraulic Laboratory, Field Research Facility, 1261 Duck Road, Kitty Hawk, NC 27949

conditions, data collected, and data availability, and thereby suggest the plan for the future experiment.

DELILAH

The DELILAH (*Duck Experiment on Low-frequency and Incident-band Longshore and Across-shore Hydrodynamics*) design (Figure 1) was to make surf zone hydrodynamics measurements to augment directional wave measurements being made in 8-m water depths by the FRF and in 13-m depths during the concurrent SAMSON (*Sources of Ambient Micro-Seismic Ocean Noise*) experiment (Herbers & Guza, 1994; Nye & Yamamoto, 1994). By agreement among investigators, DELILAH objectives were:

To measure the wave- and wind-forced three-dimensional nearshore dynamics with specific emphasis on infragravity waves, shear waves, mean circulation, set-up, runup, and wave transformation, and to monitor bathymetric response to these processes.

Table 1 lists DELILAH investigators, their organizations at the time of the experiment, and general areas of scientific interest.

The DELILAH array of in situ instruments (Figure 1) consisted of a primary

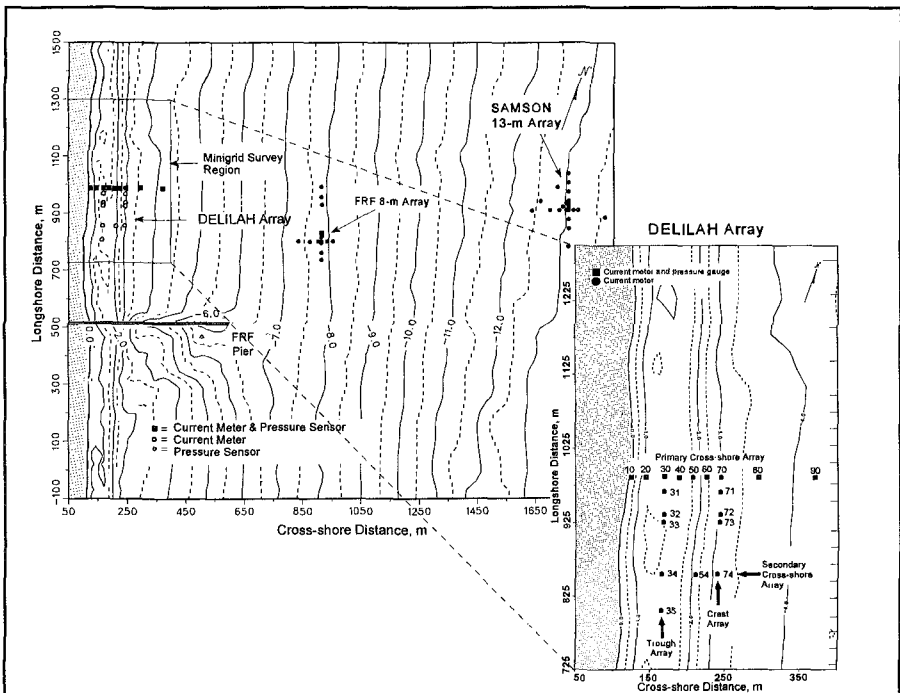


Figure 1. Instrument array locations during the SAMSON & DELILAH experiments

cross-shore array of nine current meters to obtain mean and fluctuating currents, with collocated pressure gauges to enable directional wave measurements. A secondary cross-shore array of three current meters provided long-shore redundancy. Long-shore coverage was provided by an array of six current meters in the nearshore trough, and a second array of five current meters located just seaward of the inner bar crest. Instruments were provided by the Naval Postgraduate School (NPS), Scripps Institution of Oceanography (SIO), and the FRF. The DELILAH array was designed by E. B. Thornton, J. M. Oltman-Shay, and P. A. Howd, with Dr. Thornton having primary responsibility for data collection.

Additional instruments augmented information from the stationary, in situ array. A mobile sled equipped with a vertical array of five current meters, a pressure gauge, and a surface-piercing wave staff was

deployed by J. M. Smith and K. K. Hathaway. Seven video cameras operated by R. A. Holman recorded swash and ocean surface images in the surf zone. D. B. Trizna used five Naval Research Laboratory (NRL) radar systems for remote sensing of waves, currents, and bathymetry. Bathymetric changes were measured daily by the FRF in the 550-m by 400-m minigrad area (Figure 1) using the Coastal Research Amphibious Buggy (CRAB).

A wide range of conditions were encountered during the 21 days of data collection (Figure 2). A short-duration wave event on 1-2 October was followed by several days of low waves ($H_{mo} < 1$ m). On 9-12 October, a "southeaster" built waves of about 2-m height, and induced north-flowing longshore currents that peaked near 1.5 m/s. Passage of Hurricane Lili well offshore on 12-14 October resulted in 2.5-m swell under low-wind conditions. Following Lili, moderately energetic waves and currents continued until the end of the experiment.

In the above conditions, nearshore bathymetry underwent significant changes. Figure 3

Table 1. DELILAH Participants	
US Army Engineer Waterways Experiment Station	William Birkemeier - morphology Kent Hathaway - runup, infragravity waves, morphology, remote sensing Charles Long - incident and reflected directional wave spectra Nicholas Kraus - longshore currents Jane Smith - vertical current profile, 2-D circulation Todd Walton - runup Edward Thompson - surf beat modeling
Naval Postgraduate School	Edward Thornton, Katie Scott - mean circulation, shear waves, rip currents
Naval Research Laboratory	Dennis Trizna - radar measurements of waves and currents
Oregon State University	Rob Holman - morphology, runup, shear waves, infragravity waves, video remote sensing Peter Howd - infragravity waves, morphology Tom Lippmann - morphology, infragravity waves, video remote sensing Todd Holland (also with the US Geological Survey) - runup, cusp formation
Scripps Institution of Oceanography	Robert Guza - cross-shore and longshore currents, infragravity waves, wave transformation, (also SAMSON PI)
Northwest Research Associates	Joan Oltman-Shay - shear waves, infragravity waves (also SAMSON PI)
Washington State University	Steve Elgar - incident and reflected directional wave spectra (also SAMSON PI)

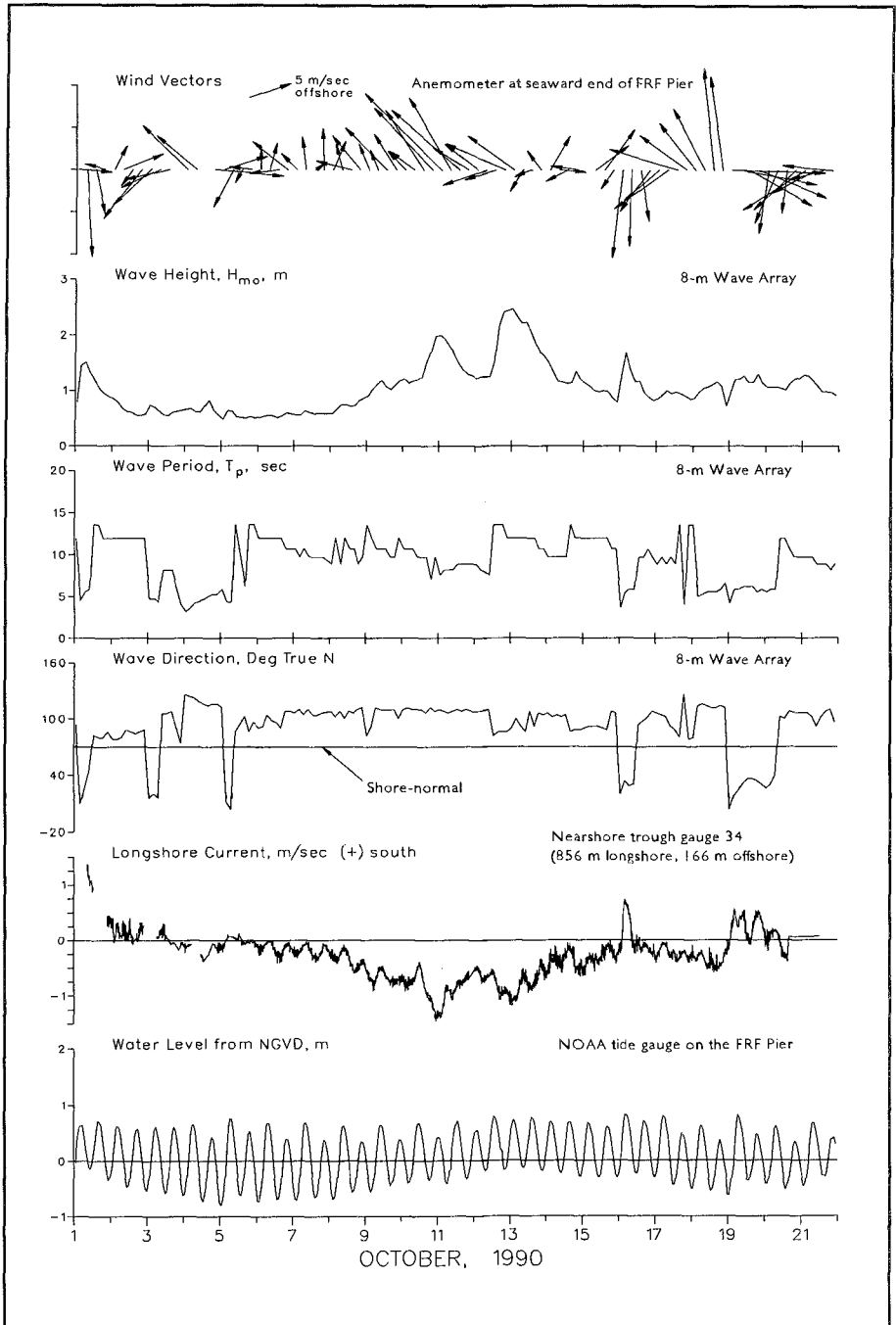


Figure 2. Conditions during DELILAH

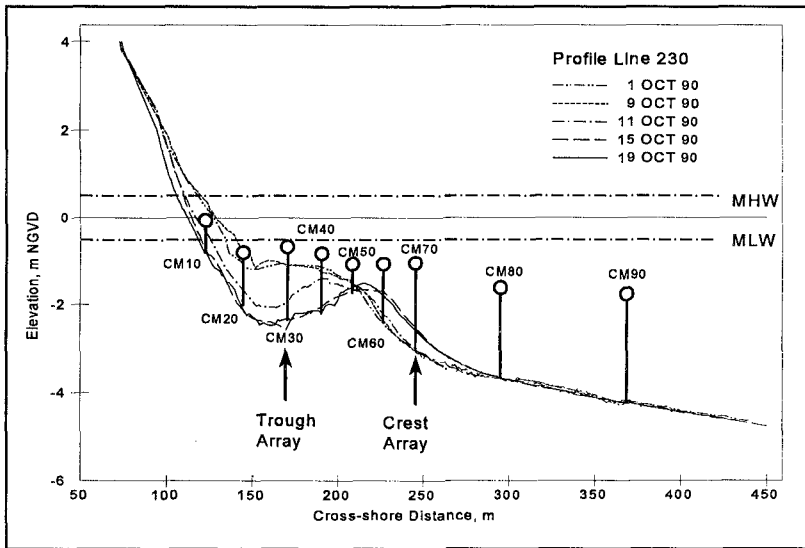


Figure 3. Profile change adjacent to the DELILAH cross-shore array

shows bathymetric profiles along the primary cross-shore array at five times during the experiment, illustrating the offshore migration of the nearshore bar, and notably the extensive deepening of the nearshore trough on 10-13 October. The CRAB surveys also revealed the presence of megaripples in the nearshore trough and on the seaward bar flank. Figure 4 illustrates four of the 20 minigridd surveys. Vertical lines in this figure indicate current meter locations. Bar topography undulated rhythmically in the alongshore direction until 9 October, when it began to assume a more uniform, linear shape. It reached maximum uniformity by 11 October, and retained this shape through the end of the experiment. Well correlated with shoal parts of the nearshore bathymetry in Figure 4 are time exposures of breaking waves patterns shown in Figure 5. Such remote images are used to extend spatial and temporal coverage provided by measured bathymetry.

DUCK94

Success of DELILAH, and the evident need for more detailed information about sediment transport and morphologic evolution that results from hydrodynamic forcing, initiated interest in further field work to be supported by the US Army Corps of Engineers, ONR, and the US Geological Survey. A plan for two additional field experiments developed. The first, DUCK94, was intended as a test run for new instrumentation, a more formal experiment organization, and more complicated logistics in preparation for SandyDuck, the second experiment. DUCK94 was scheduled for August and October 1994 to take advantage of the synergy offered by the National Science Foundation's Coastal Ocean Processes (CoOP) experiment (Butman, 1994), being conducted at the FRF during that time. The following focus topics were established as fundamental to improved understanding of surf zone sediment transport:

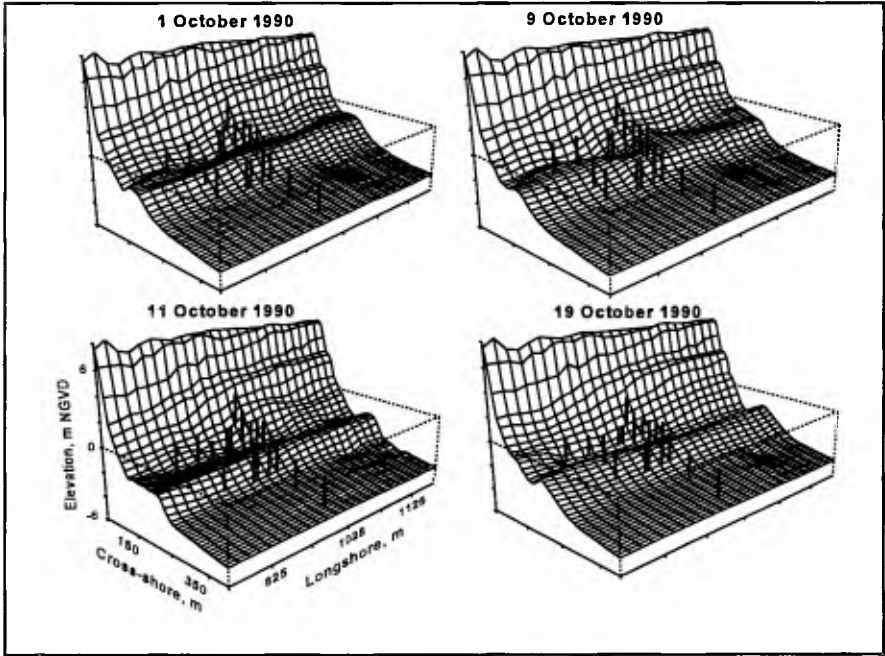


Figure 4. *Minigrid* evolution during DELILAH

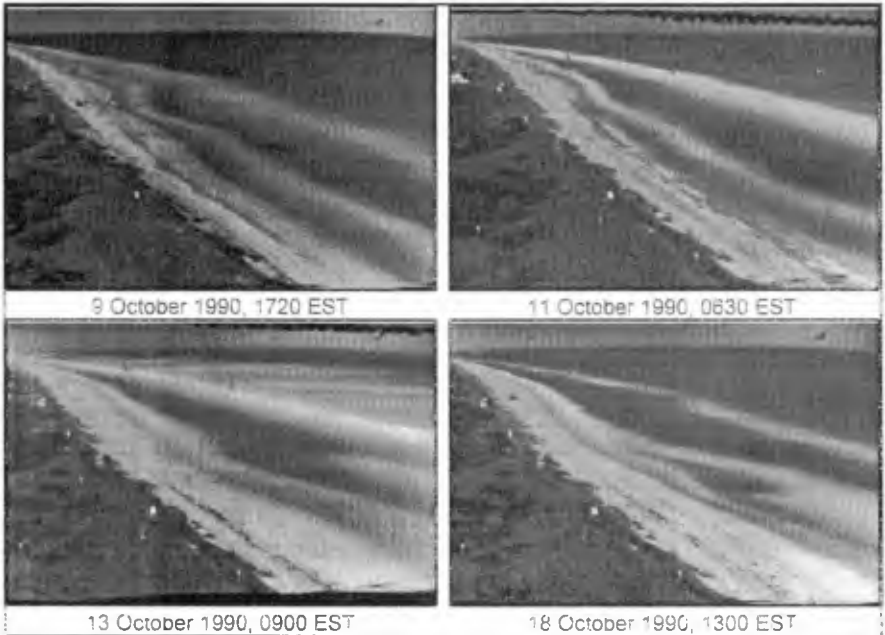


Figure 5. Time-exposure video images showing DELILAH morphology.

- a. *small and medium scale sediment transport and morphology;*
- b. *wave shoaling, wave breaking, and nearshore circulation;*
- c. *swash processes including sediment motion.*

Considerable interest was expressed for DUCK94. Table 2 lists the 19 organizations that conducted 31 experiments involving more than 100 scientists, students, and technicians. Instrument measurements were complemented by observations from ground- and aircraft-based radar and video systems. Table 3 lists the 31 basic studies, along with the principal investigators, their primary focus areas, and experiment durations. The extensive instrumentation resulted from consideration of relevant measurement scales required to address SandyDuck science objectives. Guidance was provided by using measured velocity data from DELILAH and sediment transport modeling. Based on this analysis, a general nearshore instrumentation array was designed (Birkemeier & Thornton, 1994). The full array, shown in

Figure 6, was used during the October phase of DUCK94. An abbreviated form of this array was used in the August segment of the experiment. Formal dates for DUCK94 were 8-24 August and 1-24 October, though some investigations (Table 3) of various durations were underway between June and November.

Agencies	1	US Army Engineer Waterways Experiment Station
	2	United States Geological Survey
	3	Office of Naval Research
	4	Naval Research Laboratory
	5	Naval Postgraduate School
Universities	6	Dalhousie University (Canadian)
	7	Duke University
	8	Oregon State University
	9	North Carolina State University
	10	Memorial University of Newfoundland (Canadian)
	11	Scripps Institution of Oceanography
	12	University of Delaware
	13	University of East-Anglia (United Kingdom)
	14	University of Florida
	15	University of Miami
	16	University of Washington
	17	Washington State University
Companies	18	Areté Associates
	19	Neptune Sciences, Inc.

A wide variety of instrumentation was used in DUCK94. Conventional total-station surveying techniques were used in subaerial morphology studies (29, referring to investigations by experiment number in Table 3), minigrid surveys (15), and positioning of all stationary instruments. Central to the main layout were cross-shore arrays of instrument clusters (11), each containing an electromagnetic current meter, a pressure gauge, an acoustic altimeter, and a thermometer (Fedderson, et al., 1997). The altimeters permitted the first comprehensive real-time measurements of bottom changes (8) (Gallagher, Elgar & Guza, 1997). A large number of suspended sediment concentration gauges were deployed, including optical backscattering sensors (16, 22, 26, 30), and less intrusive fiberoptic backscattering sensors (1). The Coherent Acoustic Sediment Probe (Stanton & Thornton, 1997) was mounted on a mobile sled along with eurrent meters, pressure gauges, scanning sonars, and void fraction sensors (20, 25, 26). The Sensor Insertion System,

Table 3. DUCK94 Experiments (number in parens refers to organization from Table 2)			Participating Months	Wave Shoaling	Nearshore Circulation	Boundary Layers	Swash Processes	Small Scale Sediments	Mesol/laco Morphology	Water Properties
No.	Investigators	Experiment Title								
1	Beach(8), Holman, Stambarg	Sediment dynamics in the nearshore environment	Aug,Oct		X	X		X		
3	Church(4), Elgar, Guza	Mine scour, burial, and migration as a function of wave and current forcing	Sap				X			
4	Draka(9), Smith	Nearshore sedimentary structures	Aug,Oct					X		
5	Dugan(17)	Airborna remote sensing of the environment in the littoral zona	Oct	X	X					
6	Earla(18)	Real-time buoy directional wave measurements for driving surf zone numerical models	Aug,Oct	X						
7	Earle(18), Walsh, Boyd	Scanning radar altimeter sea surface topography & high resolution directional wave measurements	Oct	X						
8	Elgar(16)	Temporal and spatial variability of the bathymetry of a natural beach	Aug,Oct						X	
10	Graber(14), Shay, Haus	An investigation of surfaca currants and internal waves over the inner and mid-shelf	Oct	X	X					
11	Herbers(5), Elgar, Guza, O'Reilly	Surface gravity waves and nearshore circulation	Aug,Oct	X	X					
12	Haines(2), Gelfenbaum	Vertical structure of mean currents & turbulent stresses in the nearshore boundary layer	Aug,Oct		X	X				
13	Hanes(13), Vincent	Near bed intermittent suspension	Aug,Oct		X			X		
14	Hanes(13)	Remote vidad measurement of mesoscale nearshore processes	Aug,Oct				X		X	
15	Hathaway(1), Leflier	Rip current mapping and minigrd surveys	Aug,Oct		X				X	
16	Hay(6), Bowen	Sediment suspension, local morphology, and bubbles	Oct		X			X	X	X
17	Holman(8), Holland, Plant	Foreshore dynamics	Aug,Oct				X			
18	Howd(7), Hathaway	Proccases of shorafaca profila adjustment	Aug,Oct		X				X	
19	Jensen(1)	Evolution of wave spectra in shallow water	Aug,Oct	X						
20	Lippmann(11), Thornton, Stanton, Su	Spatial distribution of wave breaking and turbulence	Aug,Oct	X		X				X
21	Long(1)	Wind wave frequency-direction spectral measurements	Aug,Oct	X						
22	Miller(1)	Longshore sediment transport during storms	Aug,Oct					X		
23	Fabre(19), Wilson, Earle	Wave and surf generated ambient noisa measurements	Aug,Oct							X
24	Staubla(1), Smith, Birkemeier	Sediment dynamics and profile intaractions sampling experiment	Aug,Oct					X		
25	Thornton(5), Dingler	Small-scale morphology in the nearshore	Aug,Oct					X	X	
26	Thornton(5), Stanton	Suspended and bedload sediment transport	Aug,Oct		X			X		
27	Trizna(4)	Radar remote sensing of nearshore processes: bar morphology, directional wave spectra, infragravity waves, wave breaking	Aug,Oct	X	X				X	
28	Walkar(4)	Hyparspectral optical characterization of surf zone bottom/resuspended sediment	Aug					X		X
29	Werner(10), Elgar	Swash zone morphology: field manipulation and simulation	Jun,Sap				X		X	
30	Whita(1)	Field tasts of sadiment transport theories	Aug,Oct		X			X		
31	Livingston(3), Wolf, Pasewark	Wava and surf noise measurements: supplementation	Oct							X

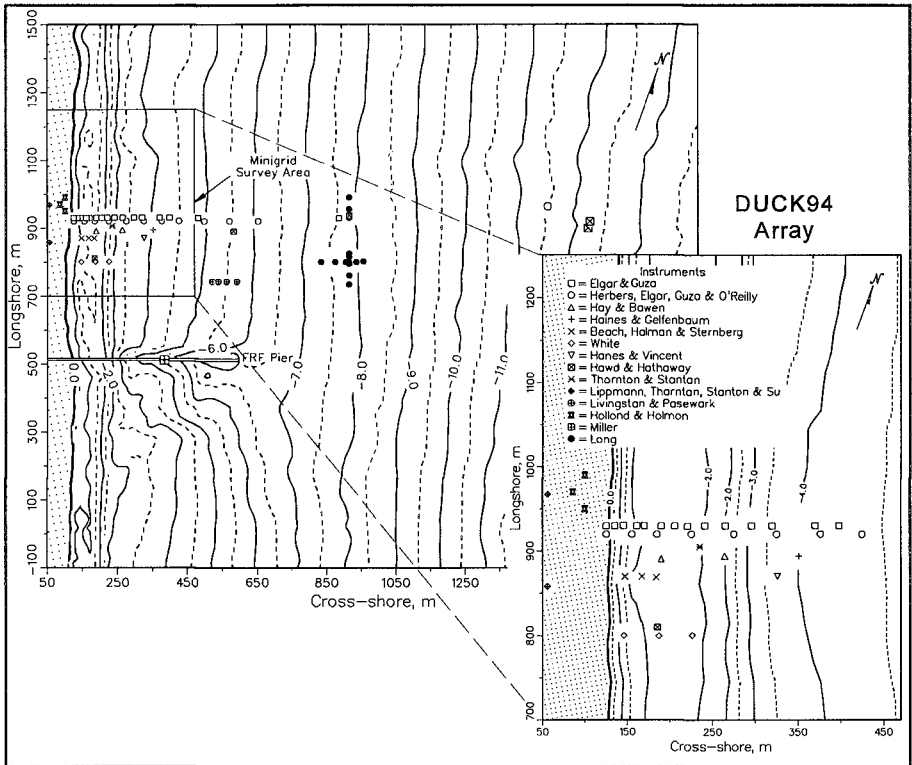


Figure 6. DUCK94 Instrument layout identified by investigator

located on the FRF pier, provided a stable, mobile platform for sediment transport measurements during high-energy conditions (1, 22). In situ (16) and CRAB-mounted (25) side-scan sonars provided observations of bottom bedforms, including megaripples. Most array positions included one or more current meters (1, 3, 11, 12, 13, 15, 16, 18, 22, 26, 30). Incident wave conditions were monitored with directional wave buoys (6, 19), and a direction-sensing array of pressure gauges (21).

Dynamics measurements were complemented by a series of geologic studies that included surface sediment samples (24) (Stauble & Cialone, 1997), short cores, box cores, and vibracores (4). Several remote sensing systems were used. Surf zone and swash processes were observed with tower-mounted video systems (14, 17, 20). Observations were also made with land-based marine radar systems (27), coherent radar systems (10), airborne synthetic aperture radar, topographic lidar, visible and hyperspectral light imaging, and scanning radar altimetry (5, 7, 28). Three studies examined fundamental nearshore acoustic behavior (16, 23, 31).

Environmental conditions during the October phase of DUCK94 are illustrated in Figure 7. Two high-wave events occurred. The first was on 2-4 October, wherein wave

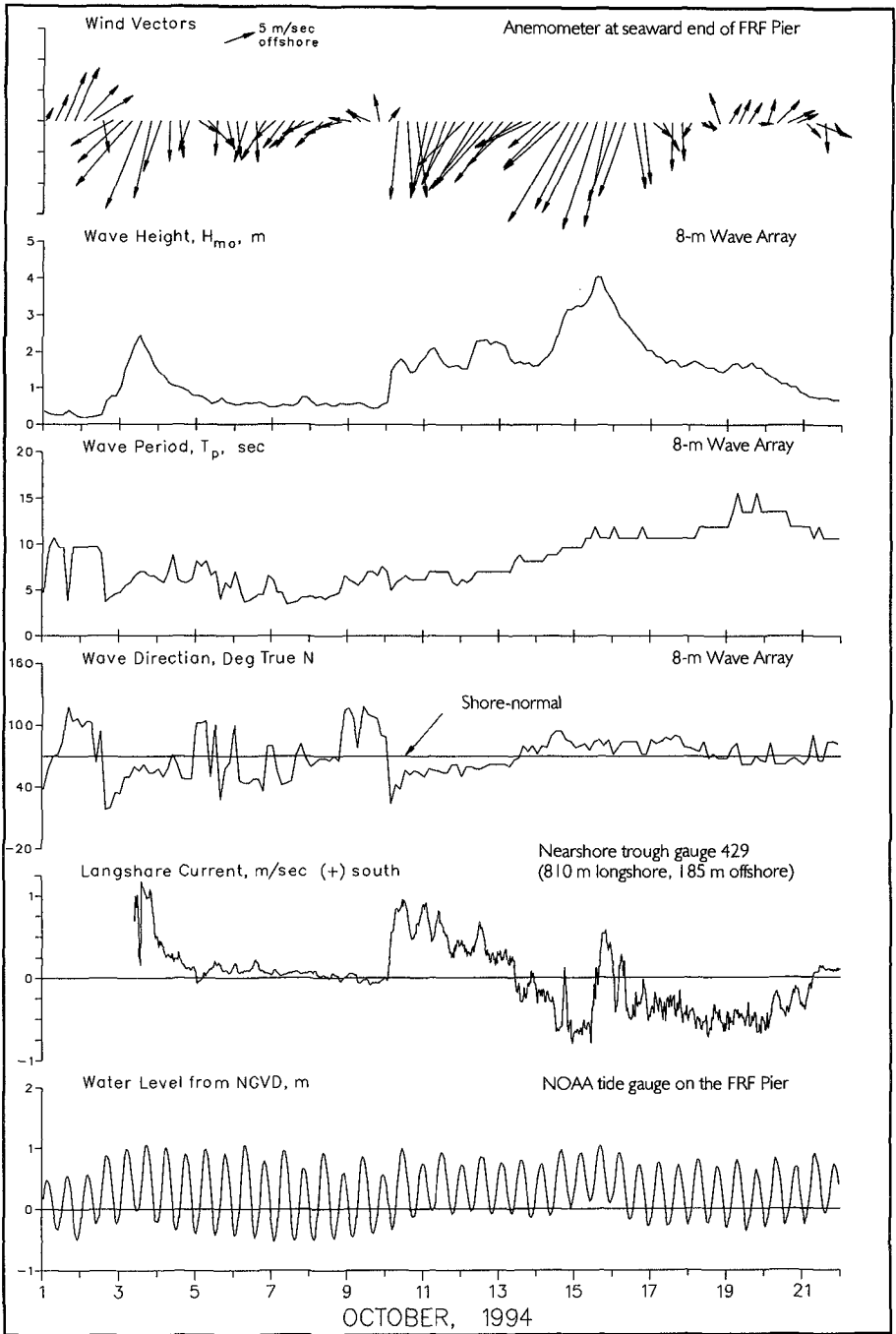


Figure 7. Conditions during the October phase of DUCK94

heights exceeded 2.5 m. Wave heights reached 4.5 m during the second storm, an eight-day event beginning on 10 October. During the larger storm, large bottom changes were accompanied by a complex nearshore circulation pattern wherein wave-driven currents in the surf zone were opposed by strong wind-driven longshore flows offshore. As shown in Figure 7, currents in the nearshore trough changed from about 1 m/s to the south at the beginning of the storm on 10 October to about 1 m/s to the north just prior to the peak of the storm on 15 October.

Figure 8 illustrates four of the 12 minigrad surveys collected during October. Following a pattern similar to that observed in DELILAH, the bar moved offshore and became more linear in the initial part of the 10 October storm. High waves prevented daily surveys until 21 October, when the survey revealed that a very large rip channel had developed. Evolution of this channel is evident in video time exposure images depicted in Figure 9. Sequences of profile data through the region of the rip are shown in Figure 10, where it is seen that the bar crest moved 100 m seaward, causing 1.2 m of deposition at its most seaward observed location on 18 October. By 21 October, the bar crest had begun migrating landward.

DUCK94 data are being analyzed, and research results are beginning to appear in the literature. Preliminary findings were discussed at a post-experiment meeting (summarized by Long & Sallenger, 1995), where adequacy of the DUCK94 experiment plan was also evaluated in preparation for SandyDuck.

SandyDuck

SandyDuck will take place from 22 September to 31 October 1997. Most of the core DUCK94 experiments are being repeated, with improvements based on experience gained in DUCK94, both in keeping with the basic tenets of physics research, and to take advantage of two major improvements in the basic experiment design. DUCK94 revealed that nearshore dynamics is far less uniform alongshore than had previously been assumed. Consequently, instruments will be added to expand longshore coverage of currents, bottom changes, and sediment transport. Missing from all Duck experiments has been accurate, spatially detailed measurements of sea surface elevation, the gradient of which is an $O(1)$ force in the surf zone. As the second change in the experiment plan, new instruments will be deployed to resolve this very important component of nearshore dynamics.

Further Information and Data Availability

More information about these experiments can be found on the World Wide Web at <http://frf.wes.army.mil> under the heading "projects." Summary data and statistics from DELILAH are available through the above web site, or via anonymous FTP at <ftp://frf.wes.army.mil/pub/delilah>. A DELILAH summary report will be published in 1997 by the US Army Engineer Waterways Experiment Station, Vicksburg, MS.

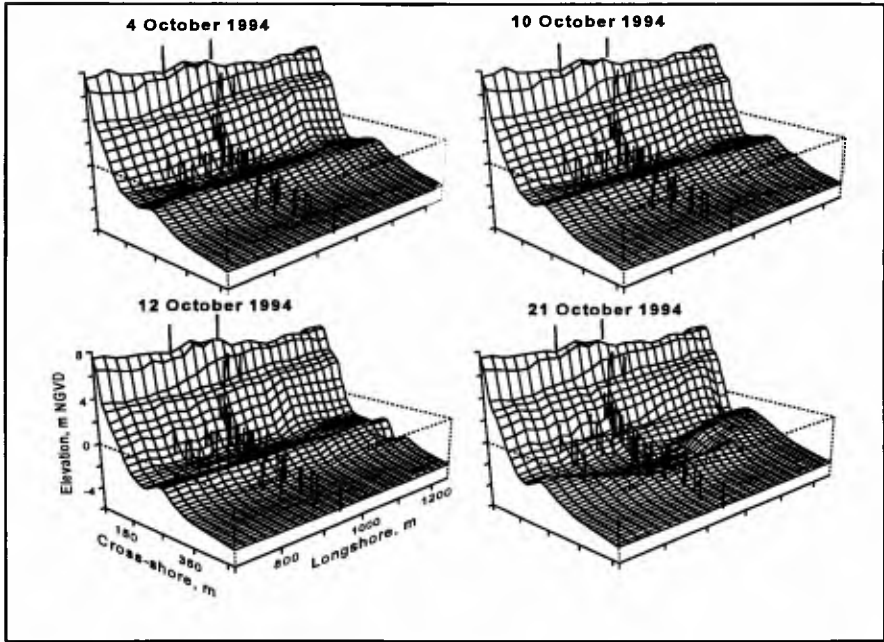


Figure 8. Minigrid evolution during DUCK94

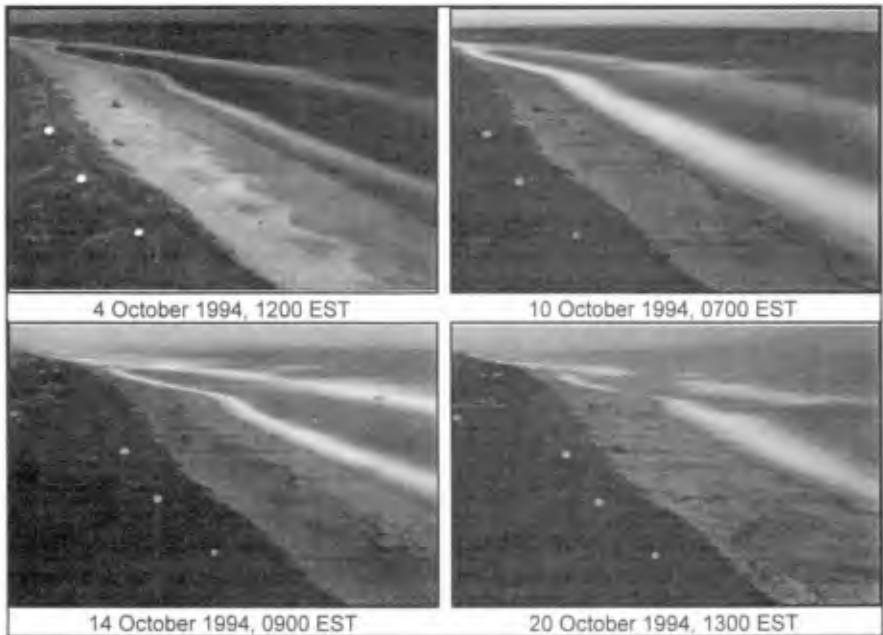


Figure 9. Time-exposure images showing DUCK94 morphology

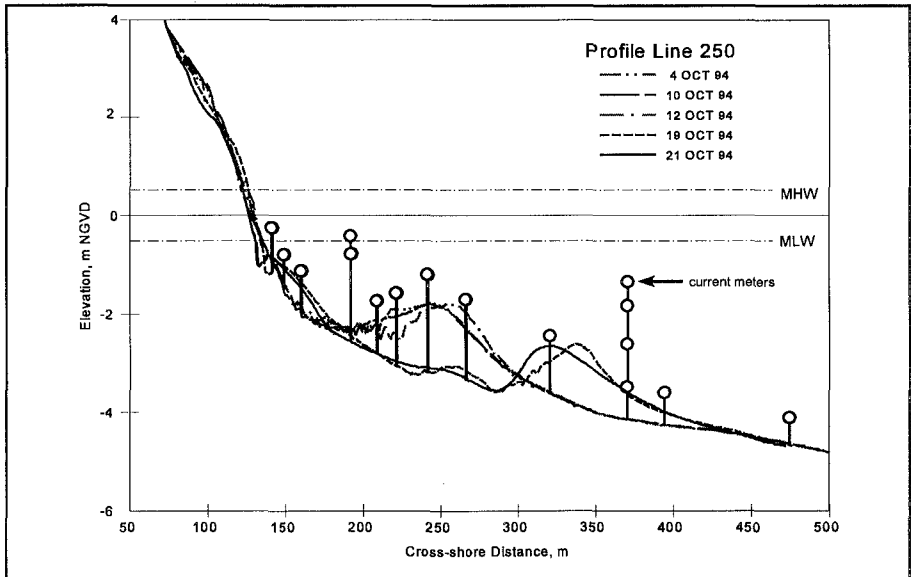


Figure 10. Profile change along the Elgar & Guza cross-shore array during DUCK94

Data from DUCK94 are not yet generally available. The investigators have agreed on a data sharing policy that offers protection of data by collecting investigators, encourages collaboration, and provides for eventual public release. This policy is:

- a. global release of all data three years after the experiment;
- b. responsible investigators will be identified when data sets are used by others;
- c. prior to three-years, data shared by agreement between individual investigators;
- d. any manuscript based on shared data must be approved by all responsible investigators prior to submission;
- e. no third-party data dissemination;
- f. principal investigators control use of their data.

An extensive discussion of the DUCK94 experiments, including tables listing sensors, data sets, and a summary of results, findings and publications, is available through the above web site. It is anticipated that DUCK94 data will become generally available late in 1998, and that SandyDuck data will be released near the turn of the century.

Acknowledgments

This paper was funded through the Field Research Facility Analysis Work Unit of the Coastal Research and Development Program of the US Army Corps of Engineers, Mrs. Carolyn Holmes, program manager, and the Coastal Dynamics Program of the Office of Naval Research, Dr. Thomas Kinder, program manager. We wish to acknowledge the

large group of investigators, students, staff, committee members and others who dedicated incredible amounts of time and effort in pursuit of these experiments. Permission to publish was granted by the office Chief of Engineers.

References

- Birkemeier, W. A. and Thornton, E. B., 1994, "The DUCK94 Nearshore Field Experiment," Proceedings of the Conference on Coastal Dynamics '94, 815-821.
- Butman, C. A., 1994, "CoOP: Coastal Ocean Processes Study," Sea Technology, 35:1, 44-49.
- Fedderson, F., Guza, R. T., Elgar, S., and Herbers, T. H. C., 1997, "Cross-shore Structure of Longshore Currents during DUCK94", Proceedings of the 25th International Conference on Coastal Engineering, Orlando, FL, ASCE.
- Gallagher, E. L., Elgar, S., and Guza, R. T., 1997, "Observations and Predictions of Sand Bar Motion," Proceedings of the 25th International Conference on Coastal Engineering, Orlando, FL, ASCE.
- Herbers, T. H. C., and Guza, R. T., 1994, "Nonlinear Wave Interactions and High-frequency Seafloor Pressure," Journal of Geophysical Research, Vol. 99, No. C5, 10,035-10,048.
- Long, C. E. and Sallenger, A., 1995, "Experiment at Duck, N.C. Explores Nearshore Processes," EOS Transactions of the American Geophysical Union, 76:49.
- Nye, T. and Yamamoto, T., 1994, "Concurrent measurements of the directional spectra of microseismic energy and surface gravity waves," Journal of Geophysical Research, 99:C7, 14321-14338.
- Stanton, T. P. and Thornton, E. B., 1997, "Reynolds Stress and Small-Scale Morphology Measurements during DUCK94," Proceedings of the 25th International Conference on Coastal Engineering, Orlando, FL, ASCE.
- Stauble, D. K., and Cialone, M. A., 1997, "Sediment Dynamics and Profile Interactions: DUCK94," Proceedings of the 25th International Conference on Coastal Engineering, Orlando, FL, ASCE.

CHAPTER 314

EULERIAN MEAN VELOCITIES UNDER NON-BREAKING WAVES ON HORIZONTAL BOTTOMS

Peter Nielsen¹ & Zai-Jin You²

Abstract

A model is presented for the Eulerian time-mean velocities in combined wave-current flows. The typical, measured profiles of weak currents are well modelled. This includes the “toe” of forward drift in the wave boundary layer and the very flat (as opposed to the parabolic shape of laminar models) current profile between the bottom boundary layer and the wave trough. The model relies on a local force balance like Longuet-Higgins’ (1953) diffusion solution rather than on advective influence from the end conditions. This seems justified by experiments, probably because a sufficient amount of turbulent diffusivity is present even for very weak currents. In its present form the model can only handle currents which are so weak that their influence on the wave motion is negligible. However, agreement with measurements of stronger currents can be obtained by modification of the wave Reynolds stress to account the influence of the current on the wave motion. Application to surf zone conditions also require modifications, but the essential structure of the model is globally applicable.

Introduction

Several authors eg. van Doorn & Godefroy (1978), van Doorn (1981), Kemp & Simons (1982), Kaaij & Nieuwjaar (1987), Kampen & Nap (1988), Heiboer (1988), Villaret & Perrier (1992) and Klopman (1994) have found that Eulerian mean velocities under progressive, non breaking waves show different distributions from what has been expected. Following currents reach a maximum value and subsequently decrease towards the surface. See Figure 1. The trend is found for all current strengths as long as the time averaged bed shear stress is in the direction of wave propagation ($d\bar{u} / dz > 0$ for $z \rightarrow 0^+$) but is not found for currents in the opposite direction. Opposing currents show the opposite anomaly. That is, compared with a logarithmic profile, the opposing current grows more rapidly towards the surface.

¹ Reader, Department of Civil Engineering, University of Queensland AUSTRALIA 4072, Fax +61 7 3365 4599, ² Victorian Institute of Marine and Freshwater Resources.

Thus, observations of both following and opposing currents contrast with the existing simple wave current boundary layer models, e.g. Grant and Madsen (1979), Fredsoe (1984), Coffey & Nielsen (1986) or You (1994) which all predict logarithmic, i.e., monotonically increasing current velocities above the wave boundary layer.

It is obvious from Figure 1 that the depth averaged current velocity $\langle \bar{u} \rangle$ may be significantly overpredicted by the old type of models for following currents. The elevation at which the current maximum occurs depends on the relative strength of the current. For very weak currents, e.g. flume experiments with zero net flow, it occurs very close to the bed, i.e., below or near the top of the wave boundary layer. For stronger currents, it occurs closer to the mean water surface. This trend was clearly shown by the measurements of Kemp and Simons (1982). The data in Figure 1 were obtained over a fixed bed but numerous profiles over sand beds, measured by Heijboer (1988) and Villaret & Perrier (1992) show the same trends.

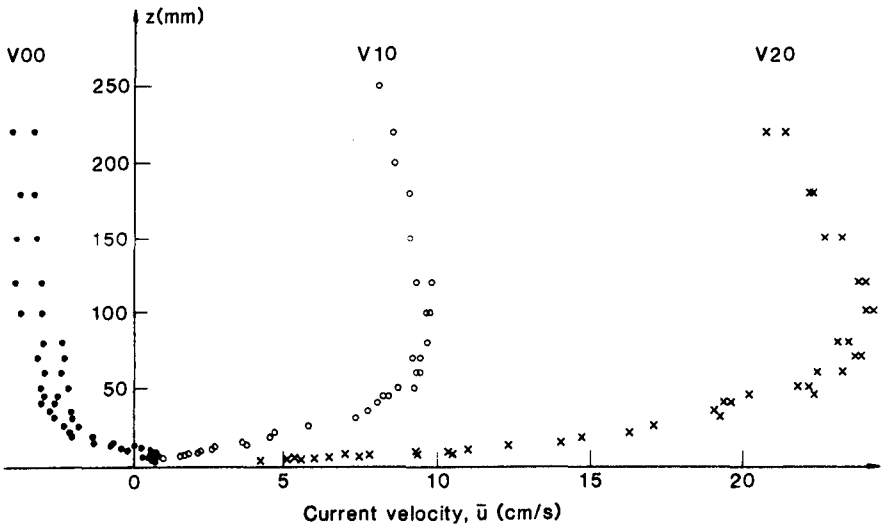


Figure 1: Eulerian mean velocities measured under non breaking waves. van Doorn (1981) test V00, V10, V20. In all tests the wave parameters were $(D, T, H_s) = (0.3m, 2.0s, 0.12m)$, and the bed roughness was artificial ripples with Nikuradse roughness $r = 2.1cm$.

The current maximum is not seen in velocity profiles from U-tube experiments like those of van Doorn (1983). It was therefore suggested by Nielsen (1992) that the profile type in Figure 1 can be understood in terms of the wave Reynolds stress $-\rho \bar{u} \bar{w}$ which exist under a progressive wave with a bottom boundary layer but not in the U-tubes. The tilde indicates periodic components with zero mean, corresponding to the definition $u(t) = \bar{u} + \tilde{u}(t) + u'(t)$.

Figure 2 shows corresponding examples of following and opposing currents superimposed on the same waves (same period and same wave height) measured by Klopman (1994). Klopman's data show very clearly the difference in profile shape

caused by the wave Reynolds stress $-\rho\overline{u'w'}$. Wave basin measurements by Havinga (1992) with angles of 60° , 90° and 120° between current and wave propagation show intermediate stages of this phenomenon.

The following outlines a model of current profiles in the presence of waves which takes $-\rho\overline{u'w'}$ into account explicitly in order to explain the shape of the velocity profiles in Figures 1 and 2. The model can successfully predict the distributions of weak currents as in a flume with no recirculation. For strong currents adjustments are needed to the distribution of $-\rho\overline{u'w'}$ which are as yet not understood. They are most likely due to non linear wave current interaction.

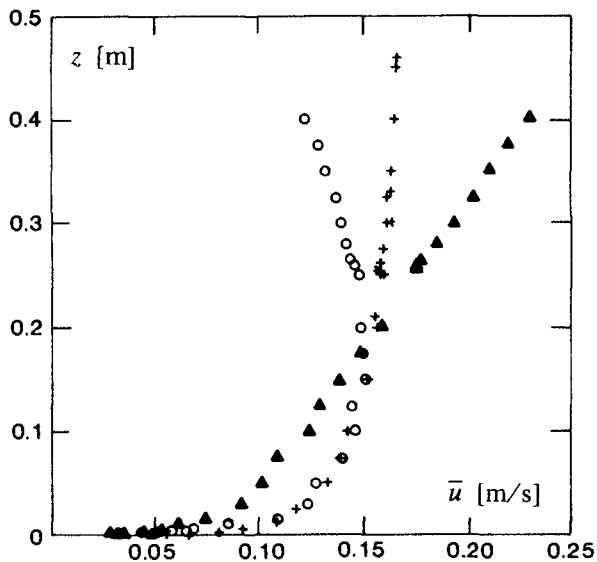


Figure 2: Current profiles in the presence of no waves (+), following waves (o) and opposing waves (triangle) of the same size. Depth $D = 0.5\text{m}$, wave period $T = 1.4\text{s}$ and wave height $H = 0.12\text{m}$. After Klopman (1994).

Shear Stresses and Shear

In the following the notation of Nielsen (1992) will be followed. Thus, the symbol τ represents the total shearing force per unit area of a cross section or the total transfer of x -momentum in the z direction. Hence, in a two dimensional flow with steady, periodic and random velocity components $(u, w) = (\overline{u} + \tilde{u} + u', \overline{w} + \tilde{w} + w')$ in the x and z directions we have

$$\tau = \rho v \frac{d\overline{u}}{dz} - \overline{\rho u w} = \rho v \frac{d\overline{u}}{dz} - \rho \overline{u w} - \rho \overline{u'w'} - \rho \overline{u'w'}$$
 (1)

where, as usual, ν is the kinematic viscosity and ρ is the fluid density. The total normal stress (positive as tension) or horizontal transfer of x -momentum is corresponding given by

$$\overline{\sigma} = -\overline{p} - \rho \overline{u'^2} + \rho v \frac{\partial \overline{u}}{\partial x} = -\overline{p} - \rho \overline{u'^2} - \rho \overline{\tilde{u}^2} - \rho \overline{u'^2} + \rho v \frac{\partial \overline{u}}{\partial x}$$
 (2)

and these two satisfy

$$\frac{\partial \bar{\tau}}{\partial z} + \frac{\partial \bar{\sigma}}{\partial x} = 0 \quad (3)$$

in a steady, two dimensional flow, i e,

$$\frac{\partial}{\partial z} \left[v \frac{d\bar{u}}{dz} - \bar{u}\bar{w} - \overline{u'w'} \right] = \frac{\partial}{\partial x} \left[\frac{\bar{p}}{\rho} + \bar{u}^2 + \overline{u'^2} - v \frac{\partial \bar{u}}{\partial x} \right] \quad (4)$$

Here we assume, for the situation of waves and a weak current, that the second term on the left can be neglected and that the first and the third term are dominant on the right hand side so that we have

$$\frac{\partial}{\partial z} \left[v \frac{d\bar{u}}{dz} - \overline{u'w'} \right] = \frac{\partial}{\partial x} \left[\frac{\bar{p}}{\rho} + \bar{u}^2 \right] \quad (5)$$

which is integrated with the bottom boundary condition $\bar{\tau}(0) = \bar{\tau}_o$ to give

$$v \frac{\partial \bar{u}}{\partial z} - \overline{u'w'} - \overline{u'w'} = \frac{\bar{\tau}_o}{\rho} + \int_0^z \frac{\partial}{\partial x} \left[\frac{\bar{p}}{\rho} + \bar{u}^2 \right] dz \quad (6)$$

Here we may write the first and third terms on the left in terms of a current eddy viscosity ν_c and solve for the current gradient

$$\frac{\partial \bar{u}}{\partial z} = \frac{1}{\nu_c} \left(\frac{\bar{\tau}_o}{\rho} + \int_0^z \frac{\partial}{\partial x} \left[\frac{\bar{p}}{\rho} + \bar{u}^2 \right] dz + \overline{u'w'} \right) \quad (7)$$

This equation will then directly give the current distribution by integrating with the boundary condition $\bar{u}(0) = 0$.

If the main emphasis is on the flow near the bed, it is justified to assume that the mean pressure is hydrostatic. However, in order to get a good representation of the flow closer to the surface it is necessary to use $\bar{p} = \rho g(\bar{\eta} - z) - \rho \bar{w}^2$ in which case Equation (7) can be written.

$$\frac{\partial \bar{u}}{\partial z} = \frac{1}{\nu_c} \left(\frac{\bar{\tau}_o}{\rho} + g \frac{\partial \bar{\eta}}{\partial x} z + \int_0^z \left[\frac{\partial}{\partial x} (\bar{u}^2 - \bar{w}^2) \right] dz + \overline{u'w'} \right) = \frac{1}{\rho \nu_c} \left(\bar{\tau}_o - \int_0^z \frac{\partial \bar{\sigma}}{\partial x} dz + \overline{u'w'} \right) \quad (8)$$

This general expression explains qualitatively the shape of the current profiles in Figure 1. For all three cases, $\bar{\tau}_o$ is positive and hence the current gradient is positive at the bed where the other terms are zero. Those terms will however grow in magnitude with increasing z and they are all initially negative for non-breaking waves over a horizontal bed. Thus, the right hand side and hence the current gradient will change sign at a certain level and the current velocity shows a maximum, see Figure 3.

The mean bed shear stress

The bed shear stress $\tau_o = \bar{\tau}(0)$ can be determined from

$$\tau_o = \tau_w - \rho g D \frac{d\bar{\eta}}{dx} - \frac{d S_{xx}}{dx} \quad (9)$$

where $\bar{\tau}_w$ is the time averaged wind stress, D is the local mean depth, $\bar{\eta}$ is the mean surface elevation and S_{xx} is the wave radiation stress in the direction of wave propagation calculated from a suitable wave theory.

The radiation stress term

Assuming linear wave theory, the radiation stress term of Equation (8) is evaluated as

$$\int_0^z \frac{\partial}{\partial x} [\bar{u}^2 - \bar{w}^2] dz = \int_0^z \left[\frac{1}{2} \frac{\partial}{\partial x} \left(\frac{\pi H}{T \sinh kd} \right)^2 [\cosh^2 kz - \sinh^2 kz] \right] dz$$

$$= H \frac{dH}{dx} \frac{\pi^2}{T^2 \sinh^2 kd} z \tag{10}$$

In general the wave height may also vary due to breaking, refraction, diffraction and shoaling, but if only bottom friction is important, the wave height gradient is given by

$$H \frac{dH}{dx} = - \frac{8}{3\pi g} \frac{f_e (A\omega)^3}{c_{g,r} + \langle \bar{u} \rangle} \tag{11}$$

where f_e is the energy dissipation factor ($\approx f_w$), $c_{g,r}$ is the wave group velocity relative to the current and $\langle \bar{u} \rangle$ is the depth averaged current velocity. See e.g Nielsen (1992) p 77. By inserting into (10) we obtain

$$\int_0^z \left[\frac{\partial}{\partial x} (\bar{u}^2 - \bar{w}^2) \right] dz = \frac{-8\pi}{3gT^2 \sinh^2 kd} \frac{f_e (A\omega)^3}{c_{g,r} + \langle \bar{u} \rangle} z \tag{12}$$

Hence, the radiation stress contribution to the current shear in Equation (8) has the same form as the surface slope term, i.e., both grow linearly in magnitude with distance from the bed. Consequently, the general picture which determines the level of the current maximum ($\frac{\partial \bar{u}}{\partial z} = 0$) is as shown in Figure 3. The current maximum occurs where the terms due to $\frac{\partial \bar{\sigma}}{\partial x}$ and $\bar{\tau}_w$ are balanced by the wave Reynolds stress.

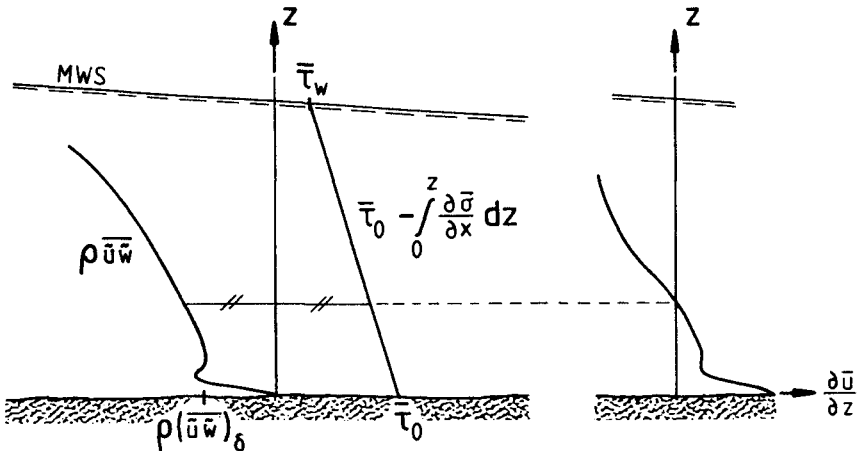


Figure 3: The current shear and the terms that generate it, cf Equation (8), for a typical situation of following current ($\bar{\tau}_0 > 0$). The (lowest) current maximum will occur close to the bed for small $\bar{\tau}_0$ and closer to the MWS for larger $\bar{\tau}_0$, cf the measurements in Figure 1.

The wave Reynolds stress

The wave Reynolds stress $-\rho\overline{u\tilde{w}}$ may be seen as consisting of three components as shown by Bijker et al (1974). One due to the phase shifting of velocities in the boundary layer, one due to wave height decay and one due to bed slope.

Longuet-Higgins (1956) derived an expression for the first one for boundary layers with constant eddy viscosity. It varies through the wave boundary layer as

$$-\rho\overline{u\tilde{w}} = \rho \frac{1}{4} (A\omega)^2 k\delta \left[1 - e^{-\zeta} (2\cos\zeta - e^{-\zeta} + 2\zeta\sin\zeta) \right] \quad (13)$$

where

$$\zeta = \frac{z}{\delta} = \frac{z}{\sqrt{2\nu_t/\omega}} \quad (14)$$

Its asymptotic value above the boundary layer ($z \gg \delta$) is

$$-\rho(\overline{u\tilde{w}})_\delta = -\rho \frac{1}{4} k\delta (A\omega)^2 \quad (15)$$

which can be written in terms of the friction factor as

$$-\rho(\overline{u\tilde{w}})_\delta = \rho \frac{1}{4\sqrt{2}} k A^3 \omega^2 f_w \quad (16)$$

of Nielsen (1992). The wave friction factor may be determined from

$$f_w = \exp \left[5.5 \left(\frac{r}{A} \right)^{0.2} - 6.3 \right] \quad \text{for } r/A < 1 \quad (17)$$

as suggested by Nielsen (1992).

Estimation of $-\rho\overline{u\tilde{w}}$ in and above a turbulent boundary layer

The expression (13) was derived for wave boundary layers that are laminar or which are turbulent with constant eddy viscosity. For turbulent wave boundary layers with moderate relative roughness: $r/A < 0.06$ it is however necessary to adopt a different description, cf Nielsen 1992, p 47. At present we shall adopt the simple, boundary layer model of Nielsen (1985) by which the horizontal velocity under a decaying sine wave can be written as

$$\tilde{u}(z,t) = A\omega \left[\cosh kz - e^{-[1+i]\left(\frac{z}{z_1}\right)^p} \right] e^{i(\omega t - kz)} \quad (18)$$

Provided the boundary layer is thin: $|kz_1| \ll 1$. The wave decay is described by the imaginary part of the wave number $k = k_r + ik_i$. We note that the wave decay is not exactly exponential for a turbulent boundary layer, but we have approximately

$$k_i = \frac{1}{H} \frac{dH}{dx} \approx -H \frac{8\pi^2}{3gT_a^3 (c_{gr} + \langle \bar{u} \rangle) \sinh^3 kd} f_e \quad (19)$$

cf Nielsen (1992), p 78. T_a is the period seen by a fixed observer.

The boundary layer parameters z_1 and p may, for hydraulically rough (roughness r) conditions, be found from the following formulae from Nielsen (1985)

$$z_1 = 0.09 \sqrt{rA} \quad (20)$$

$$p = 0.59 \exp\left(0.59 \frac{1 - (A/38r)^{1.8}}{1 + (A/38r)^{1.8}}\right) \tag{21}$$

This model is likely to be satisfactory for all wave boundary layers in the relative roughness range which has so far been observed with beds of loose sand ($0.015 < r/A < 1$) as discussed by Nielsen (1992). For very rough beds, $p \rightarrow 1$, this model corresponds to constant eddy viscosity.

In order to find the wave Reynolds stress $-\rho \overline{u\tilde{w}}$ we first find the vertical velocity that corresponds to (18) from the continuity principle:

$$\tilde{w} = \int_0^z -\frac{\partial \tilde{u}}{\partial x} dz = A\omega e^{i(\omega t - kx)} [i \sinh k_z z - ik \int_0^z e^{-(1+i)\chi \frac{z}{z_1} p} dz] \tag{22}$$

where $\sinh k_z z \approx \sinh k_r z + i k_i z \cosh k_r z$ for $k_i z \ll 1$ so that

$$\tilde{w} \approx A\omega e^{i(\omega t - kx)} [-k_i z \cosh k_r z + i \sinh k_r z - ik \int_0^z e^{-(1+i)\chi \frac{z}{z_1} p} dz] \tag{23}$$

Similarly the expression (18) for the horizontal velocity can be simplified to

$$\tilde{u} \approx A\omega e^{i(\omega t - kx)} [\cosh k_r z + ik_i z \sinh k_r z - e^{-(1+i)\chi \frac{z}{z_1} p}] \tag{24}$$

Inside the boundary layer where $k_i z \ll k_r z \ll 1$ these expressions lead to an analogous (but very complicated) expression corresponding to (13). For the sake of brevity, we shall use (13) combined with (16) and with ζ replaced by $\xi = (z/z_1)^p$, i.e.

$$(\overline{u\tilde{w}})_{BL} \approx -\frac{1}{4\sqrt{2}} k_r A^3 \omega^2 f_w \cosh k_r z \left[1 - e^{-\xi} (2 \cos \xi - e^{-\xi} + 2\xi \sin \xi)\right] \tag{25}$$

where the subscript BL refers to this term being analogous to the boundary layer term considered by Longuet-Higgins (1956). The cosh factor only makes a difference far above the boundary layer where $\xi \gg 1$.

If we neglect the boundary layer terms (the last terms) in (22) and (23) we get the contribution due to wave decay:

$$(\overline{u\tilde{w}})_{DECAY} \approx -\frac{1}{2} (A\omega)^2 k_i z (\cosh^2 k_r z + \sinh^2 k_r z) = -\frac{1}{2} (A\omega)^2 k_i z \cosh 2k_r z \tag{26}$$

Figure 4 shows the two $\overline{u\tilde{w}}$ -contributions, evaluated for Klopman's (1994) tests.

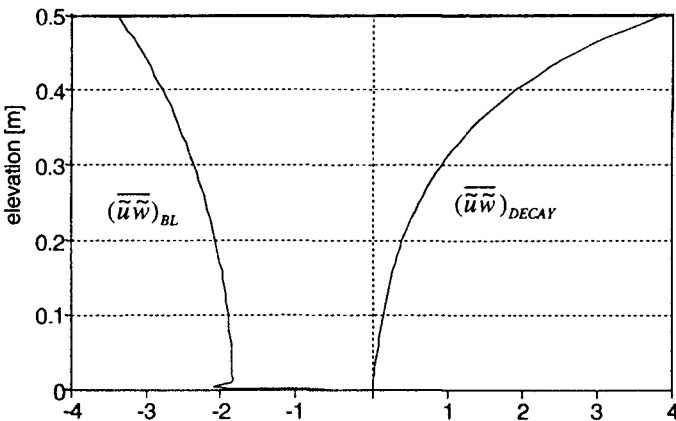


Figure 4: Wave Reynolds stress contributions for $(h, T, H, r) = (0.5\text{m}, 1.4\text{s}, 0.12\text{m}, 0.0012\text{m})$. The units are $\text{m}^2/\text{s}^2 \times 10^{-5}$.

The eddy viscosity distribution

In order to find the \bar{u} -distribution from Equation (8) we must specify the eddy viscosity $\nu_c(z)$ felt by the current. We use the distribution suggested by Nielsen (1992) which consists of a parabolic/constant part based on the current friction velocity $\bar{u}_* = \sqrt{\tau_o / \rho}$ with a square toe added due to wave boundary layer mixing:

$$\nu_c(z) = \text{Max} \left\{ \begin{array}{l} 2\omega z_i^2 \\ 0.4\bar{u}_*z \left(1 - \frac{z}{D}\right) \text{ for } z < D/2, \\ 0.1\bar{u}_*D \text{ for } z > D/2 \end{array} \right\} \quad (27)$$

Discharge considerations

Calculation of the total discharge presents a problem because it must include the discharge which occurs above the wave trough where the velocities are not obtained by integration of Equation (8) as they are for the lower part of the flow. One estimate of the net flow between the wave trough and the crest can be obtained from linear wave theory namely

$$Q_{ic} = \frac{1}{8c} g H^2 \quad (28)$$

where c is the wave speed, see eg. Dean & Dalrymple (1991). It is however not obvious how this irrotational result can be combined with an integral over the lower flow domain ($z < D-H/2$) of the velocities obtained from Equation (8).

Identification	Q_{ic} [m ² /s] based on Eq (28)	Measured $D-H/2$ $\int_0^{\bar{u}} \bar{u} dz$ [m ² /s]	Measured total Q [m ² /s]	Total Q [m ² /s] based on Eq (29)
Klopman 1994	0.010	-0.012	0	-0.06
" - ": monocrom, following	0.010	0.057	0.080	0.080
" - ": monocrom, opposing	0.010	-0.071	-0.080	-0.091
van Doorn & Godefroy, smooth	0.011	-0.0042	0	0.005
van Doorn & Godefroy, rough	0.011	-0.0062	0	0.001
van Doorn V00	0.011	-0.0073	0	0.0004
van Doorn V10	0.011	0.020	0.030	0.041
van Doorn V20	0.011	0.051	0.060	0.087

Table 1

We shall adopt the approach which is illustrated in Figure 5. That is, velocities below the wave trough are found from integration of Equation (8). Above the trough a parabolic velocity distribution corresponding to the flow rate given by Equation (28) is added to the velocity \bar{u}_* at the trough level. The total flow rate is then

$$Q = \int_0^{D-H/2} \bar{u} dz + \frac{gH^2}{8c} + \bar{u}_* H \quad (29)$$

Some comparison between this approach and measurements is afforded by Table 1. There is obviously some scope for improvement but the message from this limited data set is not very clear.

The surface slope

The surface slope $d\bar{\eta}/dx$, albeit very small influences the current distribution and hence the net flow rate per unit width Q . Hence, it is not possible to achieve agreement with experiments if the surface slope is assumed to be zero. Not even for a “no current situation”.

In practical applications it is some times Q which is specified while $d\bar{\eta}/dx$ is not. In such cases the model is easiest applied by trial and error. That is,

1. A reasonable value of $d\bar{\eta}/dx$ is guessed
2. Q is found by integrating Equation (8) and applying (29) to find Q .
3. An improved value of $d\bar{\eta}/dx$ is adopted.

The “necessary” surface slopes to match the usual wave flume conditions with horizontal beds are usually inside the range $\pm 5 \times 10^{-5}$. They are thus hardly measureable.

Comparison with experiments

A comparison of the model above with the “monochromatic waves, no current” experiment of Klopman (1994) is shown in Figure 5.

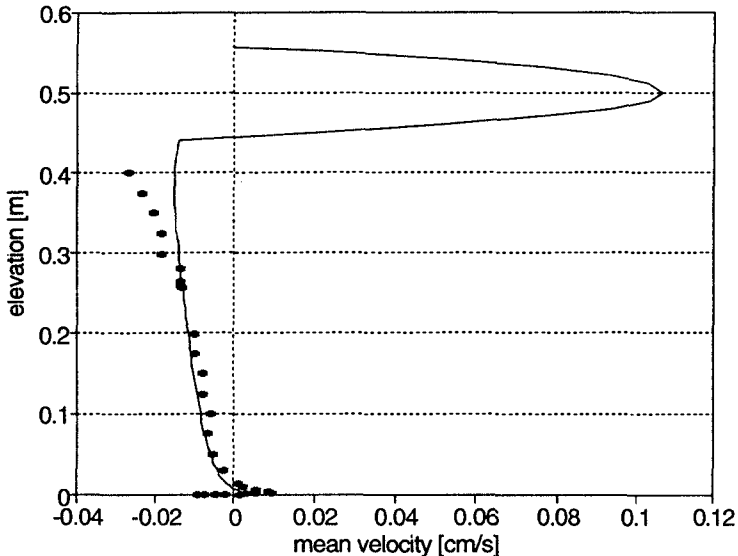


Figure 5: Model comparison with Klopman's data, Monochromatic waves, $D=0.5\text{m}$, $T=1.4\text{s}$, $H=0.12\text{m}$, $Q=0\text{m}^2/\text{s}$. The flume bed was covered with a single layer of 2mm sand giving a Nikuradse roughness of $r=1.2\text{mm}$. In order to achieve zero nett flow with the model, a surface slope of 0.0000017 must be assumed.

Figure 5 shows some discrepancy between the model and the measurements below $z = 6\text{mm}$. Part of this might be corrected by making adjustments to the eddy viscosity distribution in this area. However, the existing detailed data sets: van Doorn & Godefroy (1978), van Doorn (1981), Swan (1990) and Klopman (1994) show quite some variation. In particular, the negative velocities measured by Klopman at $z < 1\text{mm}$ are not paralleled by the other experiments. At any rate, comparison in very great detail is not warranted at levels smaller than the roughness height between this model, which is horizontally uniform, and measurements which, at this level, will depend upon the horizontal position of the probe. Measurements may show horizontal variation both on the scale of individual roughness elements and on the scale of the wave length if some reflection and/or circulation cells occur in the flume.

While the agreement between the model and experiments with weak currents is good as shown by Figure 5, adjustments are necessary in order to model stronger currents. In general the data show a stronger deviation from the logarithmic profile than the model predicts. See Figure 6.

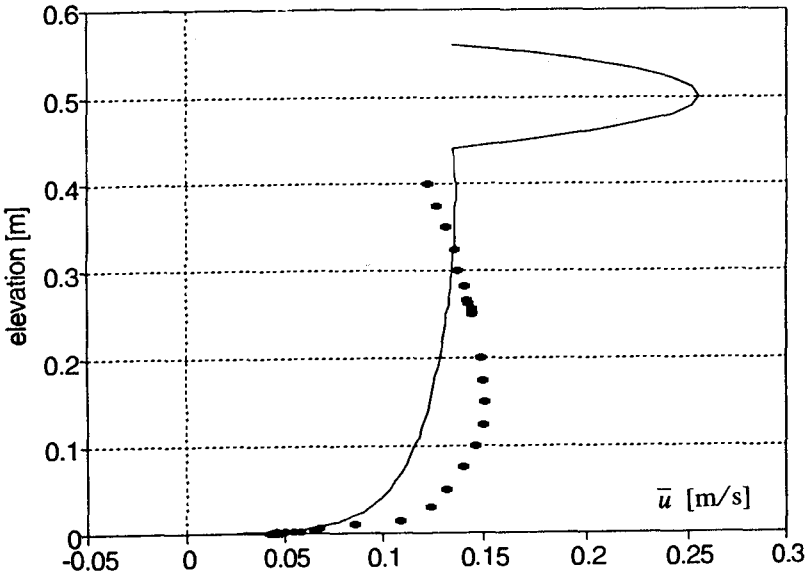


Figure 6: Comparison between the model and the “monochromatic waves, following current” experiment of Klopman (1994). $D=0.5\text{m}$, $T=1.4\text{s}$, $H=0.12\text{m}$, $Q=0.08\text{m}^2/\text{s}$, $r=1.2\text{mm}$. Surface slope -0.00000145 .

Figure 6 shows a clear discrepancy between the model described above and Klopman’s “following current” experiment. The reason is believed to be that this rather strong current ($\langle \bar{u} \rangle = 0.92A\omega$) changes the wave motion and hence $\bar{u}\bar{w}$ in the upper part of the flow. An indication of this change can also be found the direct $\bar{u}\bar{w}$ -measurements of Supharatid et al (1992).

Figure 7 shows an improved model performance obtained by enhancing the wave Reynolds stress component $(\overline{\tilde{u}\tilde{w}})_{BL}$ (Equation 25) by the empirical factor

$$C_{WR} = 1 + 100 \frac{\overline{u_*} z}{A\omega D} \tag{30}$$

while $(\overline{\tilde{u}\tilde{w}})_{DECAY}$ is kept unchanged.

This is a purely empirical adjustment but it is thought to mimic changes to $\overline{\tilde{u}\tilde{w}}$ in the upper part of the flow due to extra vorticity of the wave motion caused by interaction with the strong current. There is little reason to believe that $\overline{\tilde{u}\tilde{w}}$ is changed appreciably inside the wave boundary layer by the current, cf the data Supharatid et al (1992) and Nielsen (1985, 1992). It is noted, however, that the same empirical adjustment would also improve the agreement with the zero-net-flow-data in Figure 5.

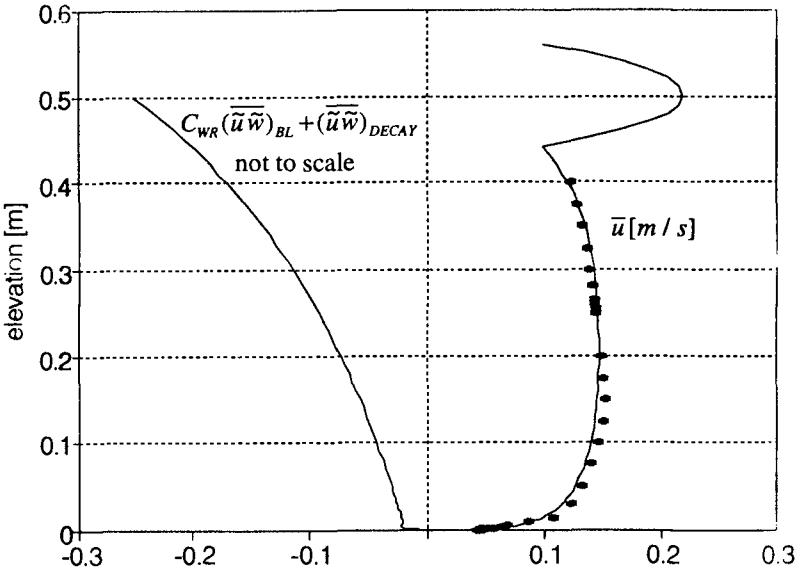


Figure 7: Comparison of the model with empirically enhanced wave Reynolds stress to the same data as in Figure 6. Surface slope -0.000021. The curve on the left shows the enhance distribution of $\overline{\tilde{u}\tilde{w}}$ given by Equations (25), (26) and (30).

Discussion

The magnitude of the eddy viscosity and its capacity to transfer vorticity upwards from the bed influences the nature of the solution as discussed by Longuet-Higgins (1953). If the eddy viscosity is small, the \overline{u} -profile would be strongly influenced by the end conditions through horizontal advection. In that case it would not be determined from the local force balance which leads to Equation (8). However Equation (35) leads to eddy viscosities which are very much larger than the laminar viscosity even in the “no current situations” corresponding to Figure 1a and Figure 4. Thus, in Klopman’s “no current” experiment Equation (9) gives a bed shear stress of

0.015N/m^2 corresponding to an eddy viscosity at mid depth of $0.00039\text{m}^2/\text{s}$, about four hundred times the laminar viscosity. This is probably the reason why “no current” experiments quite consistently show \bar{u} -profiles like to ones in Figure 1a and Figure 5 even though they may have different end conditions.

In other words, it appears that under conditions like those of van Doorn (1981) and Klopman (1994) and even the smooth bed experiments of van Doorn & Godefroy (1978) (D, T, H) = (0.3m, 2s, 0.12m) the eddy viscosity is strong enough that the net flow is governed by the local conditions as expressed by Equation (8). The experimental conditions of Swan (1990), smooth bed and (D, T, H) = (0.369m, 0.893s, 0.06m) are probably close to the limit although he did show (his Figure 5a) a \bar{u} -profile which is qualitatively similar to those observed under more vigorous flow conditions by van Doorn & Godefroy (1978), van Doorn (1981) and by Klopman (1994).

These observations seem to justify the use of Equation (8) as the basis of modelling currents in the presence of waves under field conditions and in most laboratory situations.

The present version of the model is open to a number of refinements. First of all with respect to the treatment of the flow above the wave trough. Secondly, the enhancement of the wave Reynolds stress in the presence of a stronger current should be investigated theoretically.

Application of the model above model to surf zone conditions may require adjustments in three areas:

1. An additional term due to bottom slope may need to be added to $\overline{u\tilde{w}}$,
2. A different expression for the flow above the wave trough, e.g. a roller model may be needed. The eddy viscosity must be enhanced in the upper part of the flow. Guidance in these respects may be found in the measurements of Nadaoka & Kondoh (1982) and Cox et al (1995).

The strength of the present model compared with previous ones is that a detailed description is achieved at the bottom at the same time as a reasonable overall water balance. This is of course necessary in order to model natural situations with movable beds.

References

- Bijker, EW, JP Th Kalkwijk & T Pieters (1974): Mass transport in gravity waves on a sloping bottom. *Proc 14th Int Conf Coastal Eng, ASCE*, pp 447-465.
- Coffey, FC & P Nielsen (1986): The influence of waves on current profiles, *Proc 20th Int Conf Coastal Eng, Taipei*, pp 82-96.
- Cox, D T, N Kobayashi, & A Okayasu (1995): Experimental and numerical modelling of surf zone hydrodynamics. Research report CACR-95-07, Ocean Engineering Laboratory, University of Delaware.
- Fredsoe, J (1984): Turbulent boundary layers in wave-current motion. *J Hydraulic Eng, ASCE Vol 110, No 8*, pp 1103-1120.
- Grant, WD & OS Madsen (1979): Combined wave current interaction with a rough bottom. *J Geophys Res Vol 84 No C4*, pp 1797-1808.

- Havinga, FJ (1992): *Sediment concentrations and sediment transport in case of irregular non-breaking waves with a current*. Draft Thesis, Faculty of Civil Engineering, Delft University of Technology.
- Heijboer, D (1988): *Zandconcentratie- en stroomsnelheidsverdelingen onder golven en stroom, parts I, II and III*, Delft University of Technology.
- Kaaij, Th van der & MWC Nieuwjaar (1987): *Sediment concentrations and sediment transport in case of irregular non-breaking waves with a current, Parts A: Text 104pp and Part B: Tables and Figures*. Delft University of Technology, Faculty of Civil Engineering.
- Kemp, PH and RR Simons (1982): The interaction between waves and a current: waves propagating with the current. *J Fluid Mech Vol 116*, pp 227-250.
- Klopman, G (1994): Vertical structure of the flow due to waves and currents. *Delft Hydraulics Progress Report H 840.30, Part II*, 38pp.
- Longuet-Higgins, MS (1953): Mass transport in Water Waves. *Phil Trans Roy Soc Lond, Vol 245 A*, pp 535-581.
- Longuet-Higgins, MS (1956): The mechanics of the boundary layer near the bottom in a progressive wave. *Proc 6th Int Conf Coastal Eng, ASCE, Miami*, pp 184-193.
- Nadaoka, K & T Kondoh (1982): Laboratory measurements of velocity field structure in the surf zone by LDV. *Coastal Engineering in Japan, Vol 25*, pp 125-146.
- Nielsen, P (1985): On the structure of oscillatory boundary layers. *Coastal Engineering, Vol 9*, pp 261-276.
- Nielsen, P (1992): *Coastal bottom boundary layers and sediment transport*. World scientific, Singapore, 324pp.
- Supharatid, S, H Tanaka & Nshuto (1992): Interactions of waves and current. *Coastal Eng in Japan, Vol 35, No 2*, pp 167-186.
- Swan, C (1990): Convection within an experimental wave flume. *J Hydraulic Res, Vol 28, No 3*, pp 273-282.
- van Doorn, Th (1981): *Experimental investigation of near-bottom velocities in water waves without and with a current. Report no M 1423 part 1*, Delft Hydraulics, 66pp.
- van Doorn, Th & HWHE Godefroy (1978): *Experimental investigation of the bottom boundary layer under periodic progressive water waves. Report no M 1362 part 1*, Delft Hydraulics, 46pp.
- Villaret, C and G Perrier (1992): *Transport of fine sand by combined waves and current: An experimental study. Report no HE-42/92.68*, Electricite de France, 81pp.
- You, Z-J (1994): A simple model for current velocity profiles in combined wave current flows. *Coastal Engineering, Vol 23*, pp 289-304.

CHAPTER 315

REYNOLDS STRESS AND SMALL-SCALE MORPHOLOGY MEASUREMENTS DURING DUCK94

Timothy. P. Stanton and Edward B. Thornton

Department of Oceanography, Naval Postgraduate School, Monterey, CA 93943

Tel: (408) 656 3144, FAX 408 656 2712: email stanton@oc.nps.navy.mil

Abstract

A recently developed Coherent Acoustic Sediment Probe (CASP) was deployed from an instrumented sled during the Duck94 nearshore experiment at Duck, North Carolina, in October 1994. The CASP measured acoustic backscatter profiles and three component velocity vectors in an $O(1\text{ cm}^3)$ volume 25cm in front of the downward-looking instrument package. The CASP was remotely positioned to selected heights to form profiles of velocity and sediment concentration through the bottom boundary layer. A vertical stack of 8, two-axis electromagnetic current meters extended the horizontal measurements to the surface. A co-located scanning pencil-beam sonar and tilt sensors were used to map the small-scale morphology across a 1m by 4m area centered on the CASP measurements, quantifying the local roughness and slope elements down to 4cm scales under low acoustic clutter conditions. It is shown that the stress measured near the bed in a gravity oriented vertical reference system is associated with both the turbulent Reynolds' stresses and a wave stress due the vertical velocity induced by the horizontal wave velocity acting on the sloping bottom being correlated with the horizontal velocity. The wave stress is largest at the bed and decreases towards the surface and can be larger than the turbulent Reynolds' stresses.

DUCK94 Experiment

The data presented herein were obtained during the comprehensive nearshore DUCK94 experiment conducted in October 1994 at the U. S. Army Corps of Engineers Field Research Facility (FRF), Duck, North Carolina. The FRF beach usually is a two-bar system composed of a dynamic inner bar (30-120 m offshore) and a secondary bar of lower amplitude (300-400 m offshore). The mean foreshore slope of the beach is approximately 0.08 (1:12) and the mean slope offshore of the bars is approximately 0.006 (1:170) (Lippmann et al., 1993). Sediments have a wide range of coarse sediment size on the beach and foreshore and fine, well sorted sand within the trough and seaward (mean grain diameter ~ 0.2 mm) (Stauble, 1992). The mean tidal range is approximately 1 m.

Boundary layer stress and velocity profile measurements from 11 October have been chosen to show the structure of the bottom boundary layer under strong wave forcing conditions. Storm waves with significant wave heights of 2m approaching at 16° (in 8m depth) produced

mean longshore currents of 1 ms^{-1} in the surf zone. The resulting bottom boundary layer was composed of both the steady longshore flow and $O(1 \text{ ms}^{-1})$ magnitude cross shore oscillatory flow due to the incoming waves.

Wave, velocity and sediment flux data were acquired using an instrumented sled. A Coherent Acoustic Sediment Probe (CASP) was mounted on a moveable boom (with elevation controlled from shore) deployed from the sled. The CASP measured acoustic backscatter profiles and three-component velocity vectors in an $O(1 \text{ cm}^3)$ volume 25cm in front of the downward-looking instrument package, as it was remotely positioned to selected heights to form profiles of velocity and sediment concentration through the bottom boundary layer. A co-located scanning pencil-beam sonar and tilt sensors were used to map the small-scale morphology across a 1 m by 4 m area centered on the CASP measurements, quantifying the local roughness and slope elements down to 4cm scales under low acoustic clutter conditions

Additional instrumentation on the sled included a vertical stack of eight Marsh-McBirney two-component electromagnetic current meters mounted on a 2.5 m mast to measure vertical profiles of longshore and cross-shore currents. The sled was oriented with the vertical stack of current meters placed on the up-current side to prevent the sled structure from contaminating flow measurements. Surface elevations were measured using an array of five pressure sensors configured in a 3 m square with sensors at the corners and one at the center. For data collection, the sled was towed by the CRAB to its furthest position offshore, dependent upon wave conditions, for the first data run. The sled was tethered to the shore with a chain. A forklift on the beach pulled the sled shoreward approximately 10 to 30 m for each subsequent run. Data were acquired at each location for approximately one hour at four to eight locations. Data were digitized on the sled and transmitted to shore via an armored fibre optic cable married to the chain tether.

Additionally, directional wave spectra were acquired using a linear array of 10 pressure sensors in 8 m depth offshore of the survey area. A fixed current meter in the trough at line 820 m was used to measure longshore currents continuously.

Vertical profiles of the mean longshore currents at various cross-shore location superposed on the bottom profile measured on 11 October are shown in Figure 1. The longshore currents were relatively strong on this day with mean currents exceeding 1 m/s . The bottom profile is barred. The small-scale morphology is near planar on the seaward side and atop the bar and on the foreshore, with well-developed mega-ripples within the trough.

Theory and Analysis

Linear wave theory over a horizontal bed predicts that the horizontal and vertical wave induced velocities are in quadrature, and therefore do not contribute to the Reynolds' stresses. However, for a sloping bottom in a gravity oriented vertical reference system, a vertical velocity is induced at the bed by the horizontal velocity acting on the sloping bottom

$$w = u \tan\beta \quad (1)$$

where u, w are the horizontal and vertical velocities and $\tan B$ is the bottom slope. The vertical

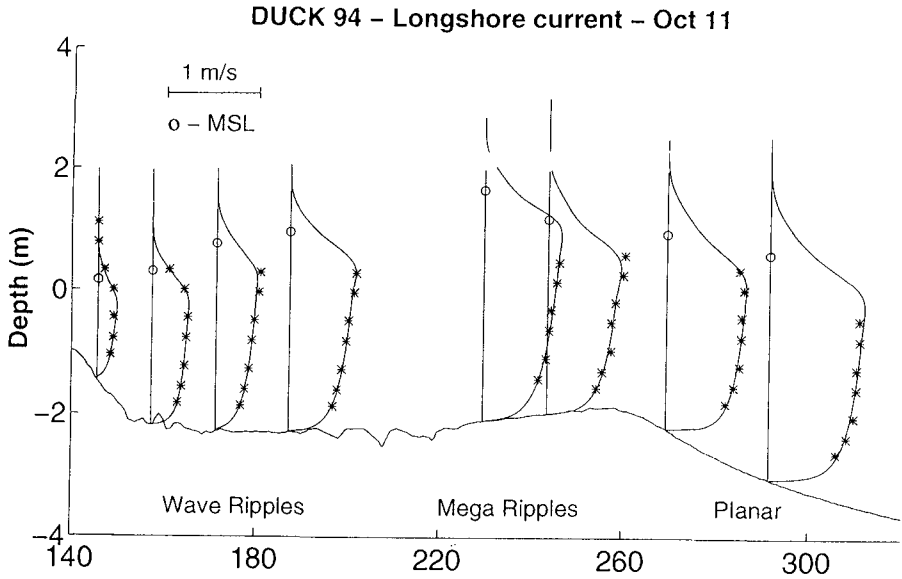


Figure 1. Measured longshore current vertical profiles (*) at various cross-shore locations compared with logarithmic profile (solid line) superposed on the bottom profile.

velocity near the bed will be in-phase with the horizontal velocity, resulting in a contribution to the co-spectrum, $\langle uw \rangle$, which is proportional to the Reynolds' stress. The total stress is composed of an induced wave stress plus the stress due to the friction velocity defined as

$$\frac{\tau}{\rho} = u_{*T}^2 = \langle \bar{u}\bar{w} \rangle = u_{*Friction}^2 + u_{*Wave}^2 \quad (2)$$

It is hypothesized that the appropriate coordinates to measure the Reynold's stresses near the bed are oriented normal to the bottom. However, the bed has a broad range of scales in the near shore (Thornton, et al 1997) ranging from the general bottom profile with horizontal scales $O(10m)$ to mega-ripples and ripples with horizontal scales $O(1m)$. A question then arises as to what is the corresponding scale over which to measure the bottom slope? Instead of trying to measure the appropriate bottom slope, we will use hydrodynamic measures to establish the coordinate system. Hydrodynamically, the velocity normal to the bed goes to zero at the bed. Therefore, the bottom slope in (1) is determined three different ways by minimizing the measured near-bed quantities of covariance between horizontal and vertical velocity, $\langle uw \rangle$, mean vertical velocity, \bar{w} , and vertical velocity variance, $\langle w^2 \rangle$.

Results and Conclusions

Direct estimates of the Reynolds stress components $\langle uw, vw \rangle$ and mean velocity $\langle U, V \rangle$ were formed at each measurement height with averaging times between 4 and 10 minutes. As a vertical profile of these quantities is formed over approximately 1 hour, measurement stations were selected where the mean currents and wave conditions were relatively constant during this time. Profiles of (U, V) vectors, orbital displacement standard deviations in the x, y directions, the friction velocity vector (u^*, v^*) , and the friction velocity magnitude for station 1 (see Figure 1) are shown in Figure 2. The instrument coordinate velocity vector time series was rotated into a vertically orientated coordinate system to a precision of $\pm 0.2^\circ$ before the mean velocity and stress estimates were made. Therefore the true vertical (rather than bed normal) stresses are shown here. Height above the bed was determined to ± 1.6 cm by using the acoustic backscatter profiles. The velocity coordinate system in these plots is $v+$ offshore and $u+$ toward the south, and $w+$ upwards. At both sites, the U/V profiles, which span the lower 0.5m of the bottom boundary layer, show strong offshore and long-shore mean currents decaying toward the bed. The upper CASP-measured mean velocities matched the em-current meter profiles, which extend to the surface (not shown). In the absence of an oscillatory flow component, the stress vectors would be expected to be aligned with the mean current direction within the inner "wall" boundary layer established by the mean flow. However, the mean vertical stress vector has a strong cross-shore wave stress component, increasing toward the bed, which rotates the stress vectors toward the offshore direction (Figure 2). This cross-shore stress is attributed to the wave stress component arising from the shoaling waves interacting with the bottom slope, producing a linearly decreasing wave stress toward the surface (Rivero and Arcilla, 1995). The slight increase in stress in the first 20cm above the bed seen in most of the profiles is likely due to the rotational stress components of the wave boundary layer arising from the strong oscillatory flow and the local bed roughness elements.

An example of the co- and quadrature spectra measured in gravity oriented coordinates at an elevation of 27 cm above the bed is shown in Figure 3. In the gravity oriented vertical reference coordinates, there is a large contribution to both the co- and quadrature spectra (vw, uw) at the wind-wave band of frequencies (0.1 - 0.5 Hz). The co-spectrum is minimized by rotating the coordinates about the x, y axis in 0.1° increments (Figure 4). A definite minimum is found, indicating a mean cross-shore slope of 4.3° and an alongshore slope of 1.6° . The minimized cross-spectra are shown in Figure 5. The co-spectra are greatly reduced, whereas the quadrature spectra are virtually the same, indicating the co-spectral contributions are bottom slope induced, and should not be attributed to turbulent Reynold's stress contributions.

The mean and vertical velocities variance were similarly minimized and the corresponding calculated bottom slopes were essentially the same as calculated from the minimization of the co-spectra. Therefore, the coordinate rotations are based on the minimization of the co-spectra.

The friction velocities calculated at various elevations over the vertical before and after rotations of the coordinates and the cross-shore tilt calculated from the minimization of the co-spectra indicative of the bottom slope are shown for locations offshore the bar and within the trough (Figures 6 and 7). The measured cross-shore bottom slope (averaged over 5m) is also indicated. On the near planar, smooth slope on the seaward side of the bar the calculated slope from the co-spectral minimization corresponds to the bottom slope (averaged over 5m) as the bottom is approached; this indicates that the additional stress is associated with the sloping

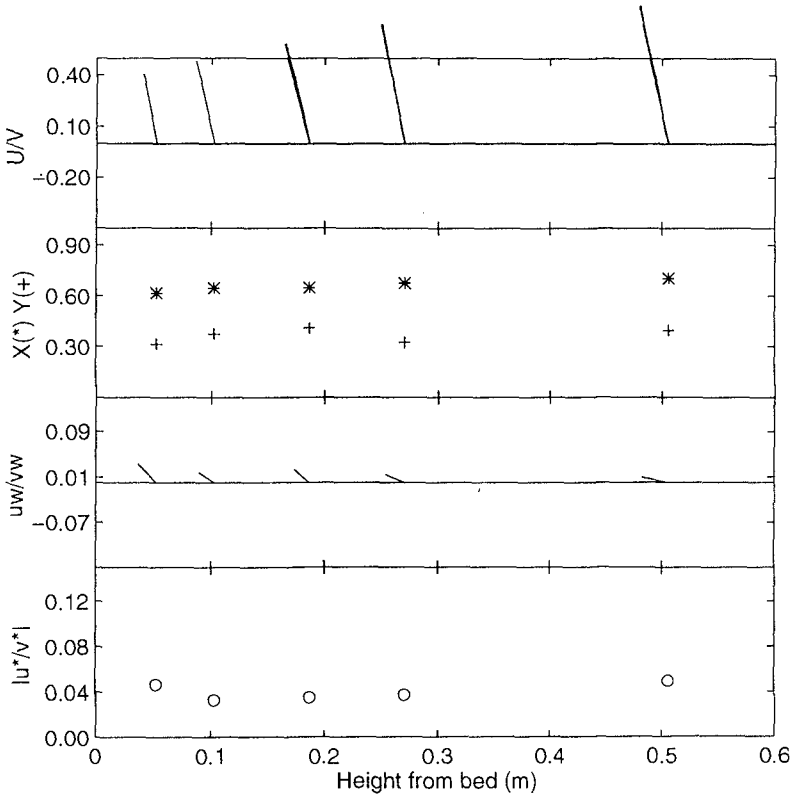


Figure 2. (U,V) mean velocity, orbital displacement magnitudes for x,y components, u^*,v^* friction velocity vector and friction velocity magnitude profiles from 0 to 0.5m above the bed for the offshore station 1 on October 11.

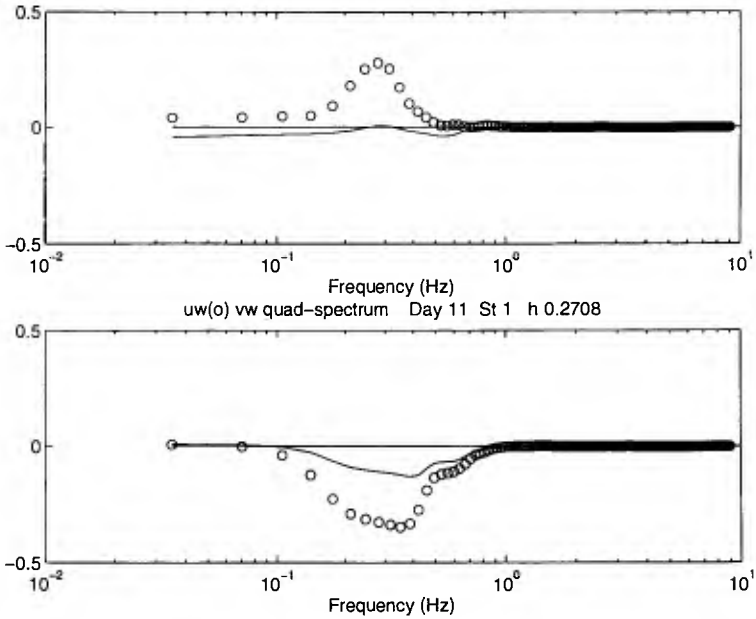


Figure 3. Co-spectra (upper panel) and Quadrature-spectra (lower panel) of uw (o) and vw (-) ($m^2\text{-sec}$) in gravity vertical coordinates, Station 1 at elevation 27cm off the bottom.

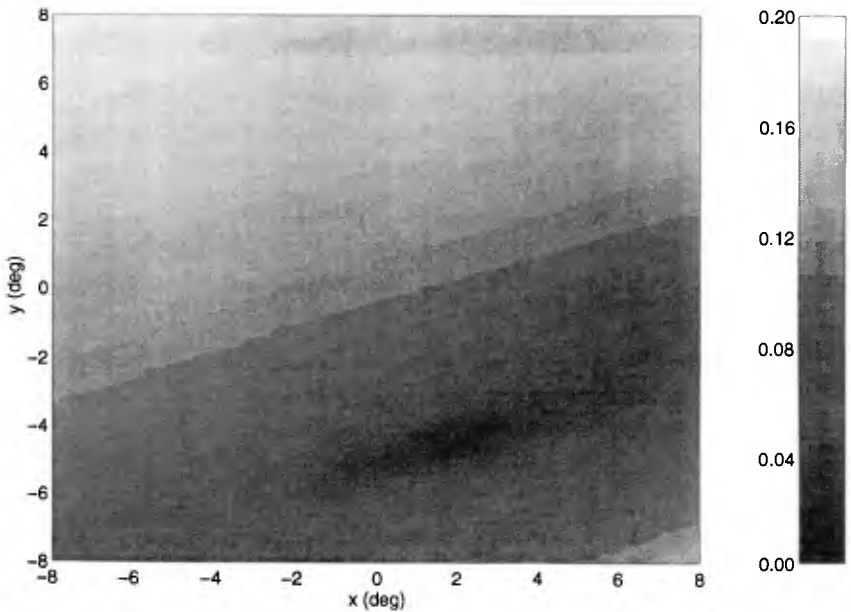


Figure 4. Co-spectra calculated at 0.1 degree rotations in x,y showing minimum, Station 1.

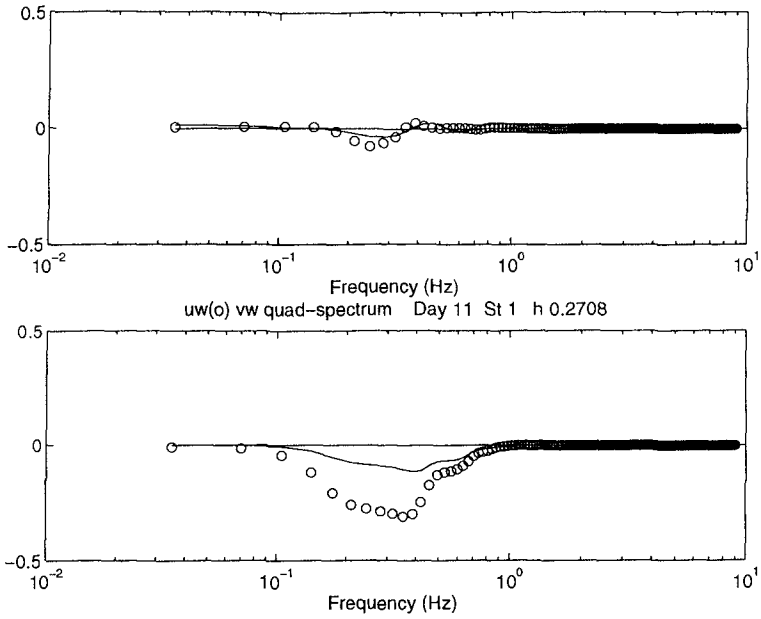


Figure 5. Co-spectra (upper panel) and Quadrature-spectra (lower panel) of uw (o) and vw (-) in rotated coordinates minimizing the co-spectra, Station 1.

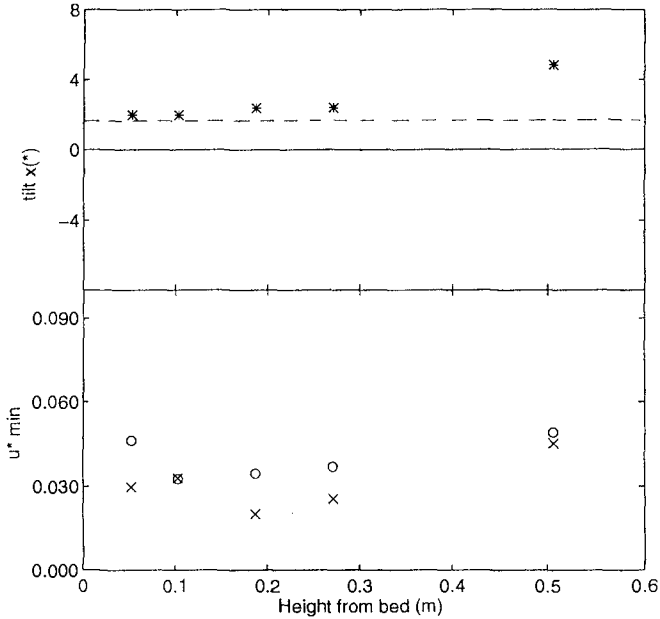


Figure 6. Vertical profiles of cross-shore (x) rotation angles to minimize co-spectra (*) compared with average slope over 5m (-) (upper panel), and total friction velocity (o) and friction velocity in bed normal coordinates (lower panel), Station 1.

bottom. However, within the trough where mega-ripples are prevalent, just the opposite effect is seen where the calculated slope from the minimization of the co-spectra and the bottom slope measure over 5m do not converge until almost 40cm off the bed. The total near bed shear velocities are large. After subtracting u^2_{wave} from the total shear velocity, the residual friction velocities are essential constant over the vertical. The detailed bottom profile at station 5 shows the bottom is composed of mega-ripples with heights of approximately 15cm and wave lengths of about 1m (Figure 7). The location of the CASP is at the vertical dotted line and unfortunately information right beneath the CASP is not available. The mean slope is indicated and it can be seen that is can be quite different that the local slope near the bed as indicated by the tilt values calculated in Figure 6.

Conclusions

The total near-bed friction velocity is viewed as the sum of the friction velocity associated with the turbulent Reynolds' stress and a wave friction velocity induced by the sloping bed. The friction velocity is calculated by minimizing the co-spectra to eliminate the contribution by the horizontal wave velocity acting on the bed to induce an in-phase vertical velocity which contributes to the co-spectrum. The horizontal scale of the bed slope which induces the near-bed vertical velocity due to the waves appears to be related to the distance from the bed. Where a multitude of scales exist very close to the bed, such as when mega-ripples are present, the local bed slope (horizontal scale < 1m) appears to dominate, whereas away from the bed the corresponding bed slope can be much larger. For a smooth, near-planar bed, all horizontal scales have essentially the same slope.

The wave-induced friction velocity is largest near the bed and decreases toward the surface, which agrees with the theoretical work of Rivero and Arcilla (1995). The wave-induced velocity near the bed can be much larger than the turbulent Reynolds' stresses.

Acknowledgments

This work was funded by the Office of Naval Research, Coastal Sciences Branch under contract N00114-95-AF-002. The authors wish to express their appreciation to all those who participated in DUCK94 experiment, particularly the staff of the U.S. Arm Field Research Facility under the direction of B. Birkemeier. In addition, special appreciation is expressed to R. Wyland and J. Stockel for their roles in the acquisition and analysis of the data.

References

- Rivero, F.J. and A.S. Arcilla, 1995, On the vertical distribution of $\langle uw \rangle$, *Coastal Engineering*, 25, 137-152.
- Thornton, E.B., J.L. Swayne and J.R. Dingler, 1997, Small-scale morphology related to waves and currents across the surf zone, (accepted *Marine Geology*).

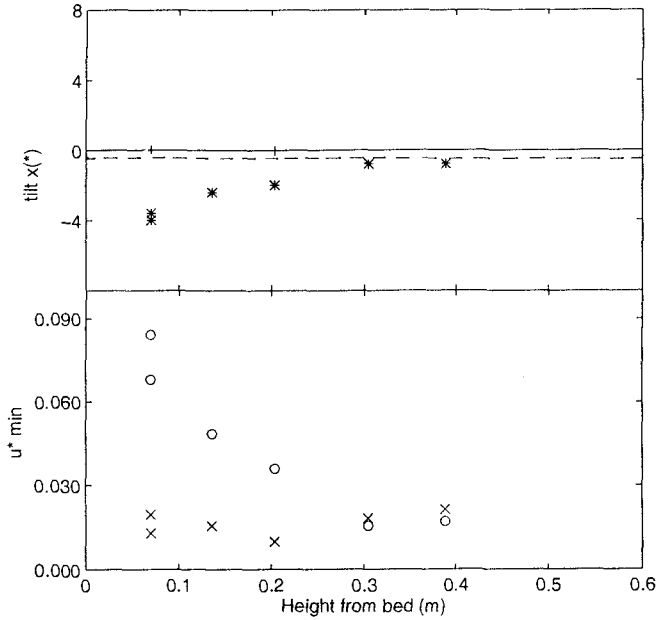


Figure 7. Vertical profiles of cross-shore (x) rotation angles to minimize co-spectra (*) compared with average slope over 5m (-) (upper panel), and total friction velocity (o) and friction velocity in bed normal coordinates (lower-panel), Station 5.

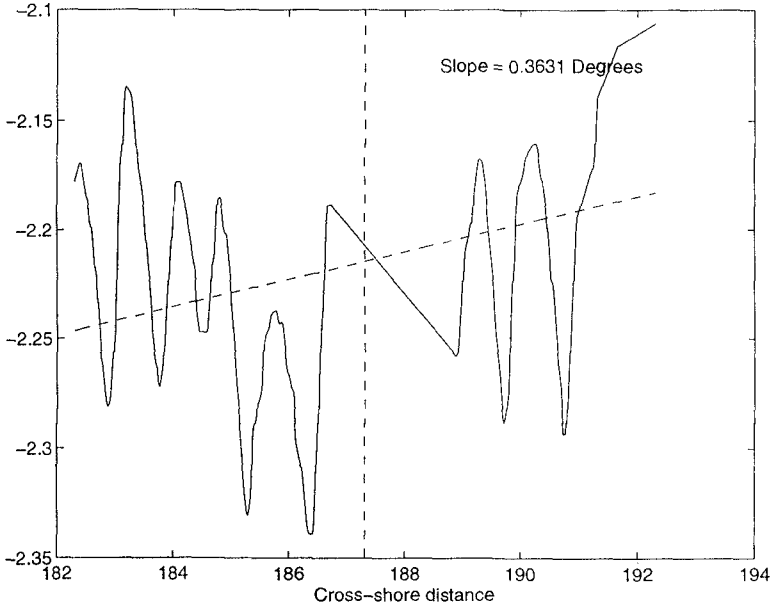


Figure 8. Bottom profile showing mega-ripples superposed on a mean slope (averaged over 5m) of 0.36 degrees.

CHAPTER 316

Studies on the Suspended Concentration in the Surf Zone

Ching-Her Hwang¹ Li-Hung Tsai² Po-Ching Lin² Chin-Chi Tsai³

Abstract

This study is to carry out the field measurements of the suspended concentration by using MTB-16K turbidity records in the surf zone of mild sloping beach (1/144). Then the vertical concentration distributions of the suspended sediment at different water depth d/L_0 and the longitudinal concentration distributions of the suspended sediment across the surf zone are analyzed and discussed respectively in this paper.

Introduction

In order to understand the phenomena of sediment transport in the near shore, it is necessary to investigate the problems of the sediment suspension mechanism induced by waves. Earlier there are many scholars and experts, such as Farichild (1959), Homa and Horikawa (1962), Noda (1967) etc., who had been studied this problems by using siphon, pumped sampler and suspend sampler respectively. In fact, it is difficult to obtain the exact records of suspended sediment variations. Lately there are other researchers such as Homa (1965), Sleath (1974, 1982), Wrigh (1982), Deigaard (1986), Makoto Ifuku (1988), Gotoh (1994), Nielson (1994), Ono (1994) and authors (1993-1995) etc. had also been studied this problems in the laboratory and in the field respectively. And this study is to carry out field measurement of the suspended concentration in the surf zone of mild sloping beach ($S=1/144$) located at the mid-west coast of Taiwan, R.O.C. under the sponsor of the National Science Council for the integrated research program "Coastal Space Utilities".

¹ Chief, the Coastal Engineering Division, Institute of Harbor & Marine Technology, No.83, Lin-Hai Rd., Wuchi, Taichung District, Taiwan, R.O.C.

² Assistant researcher, the Coastal Engineering Division, IHMT.

³ Assist, the Coastal Engineering Division, IHMT.

Field Measurement

Four sets of memory MTB-16K turbidity recorder which set up above the sea-bed 6.5cm, 22cm, 35cm and 76cm etc. near the low water level at the tidal zone are used to measure the vertical concentration distribution of the suspended sediment. Also there are three sets of memory MTB-16K turbidity recorder which set up at a distance of 50m each other and above the sea-bed 6.5cm are used to measure the longitudinal concentration distribution of the suspended sediment across the surf zone. The maximum tidal range is about 5m in this area, hence their concentration distributions of the suspended sediment at different water depth can be measured by the tidal variations. Concurrently a DNW-5M pressure sensor and a UCM 40 Type MKII were also set up respectively near the sea-bed around the low water level and a waverider was set up outside the surf zone to record the oceanography conditions. The schematic diagrams are shown as Fig. 1.

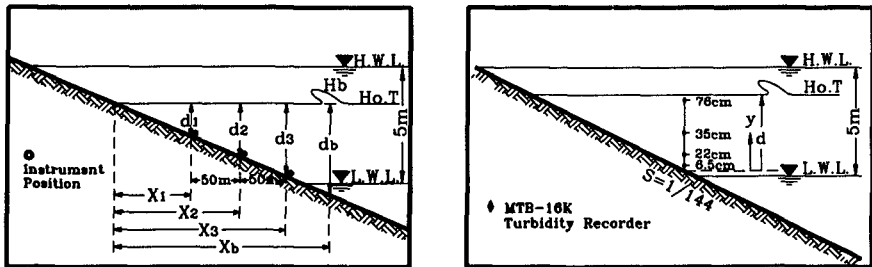


Figure 1 The schematic diagrams of parameters and memory MTB-16K recorders mounted on sea-bed

Field data of wave, water level and suspended concentration are recorded respectively every one hour interval by using the DNW-5M pressure sensor and the MTB-16K turbidity recorder from PM 7, 14 March, 1995 to AM 7, 16 March, 1995. The recorded periods of field data are continuous 10 minutes every times and data is adopted by one second interval.

Data Analysis and Discussions

3.1 The distributions of wave height across the surf zone

Figure 2 shows the parts of time histogram of the wave height and water level field measured data taken from the DNW-5M pressure sensor in the near shore on 14 March, 1995.

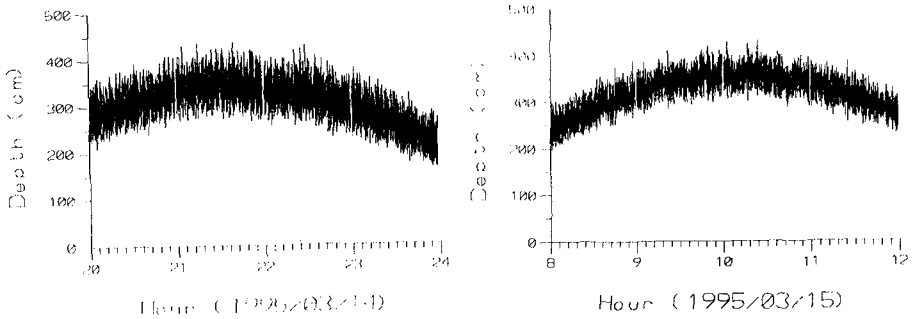


Figure 2 Time series of wave height and water level in the near shore

And the corresponding time series of wave height and wave period taken from the waverider at -20m water depth outside the surf zone are shown as Figure 3.

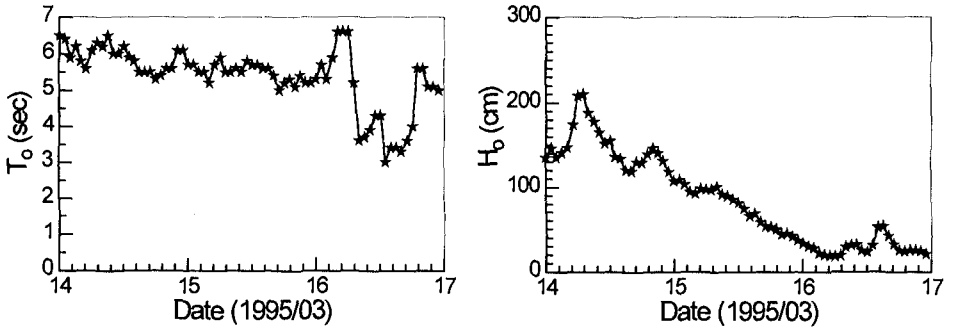


Figure 3 Time series of wave period and wave height at -20m water depth

Results indicate that the distributions of wave height are gradually decreasing from the largest $H_0=2.2\text{m}$ occurred at AM 6, 14 March to the smallest $H_0=0.20\text{m}$ occurred at AM 7, 16 March and its corresponding distributions of wave period are decreasing from 6~7 secs to 3~4 secs during wholly observing periods.

Figure 4 shows the relationship diagram between the local wave height H and its corresponding water depth d by analyzing the field measured data in the surf zone. Various legends such as “□” and “+” etc. represent the results in the flood or in the ebb. Results also indicate that the local wave height is linearly decreasing with water depth when the H/d value is equal to 0.4. If we convert this relationship with the form $H=r(d+H)$, then the empirical constant is $r \cong 0.3$. This means that the distribution of wave height can be expressed as the following empirical form in the surf zone.

$$H = r(d + H) \qquad S = \frac{1}{144} \qquad (1)$$

$$H_0 < 2.2m$$

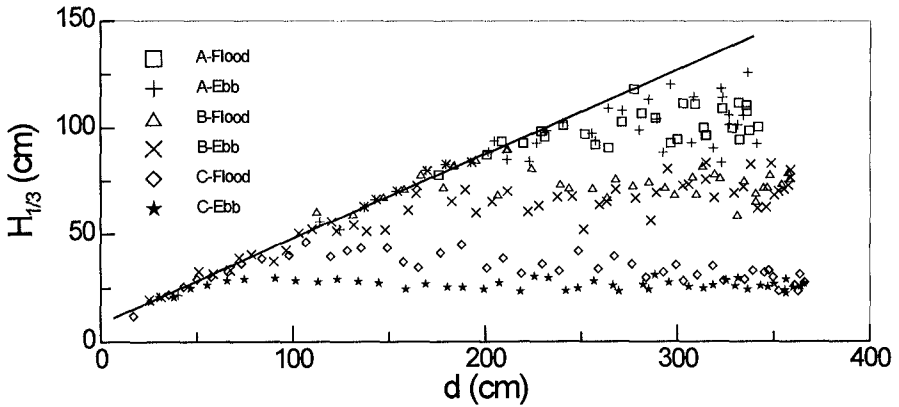


Figure 4 The relationship diagram between wave height and water depth in the surf zone

3.2 The distributions of suspended concentration in the surf zone

3.2.1 The vertical distributions of suspended concentration

Parts of the time series of suspended concentration measured at various positions and its corresponding water level are shown as Figure 5 and Figure 6 respectively.

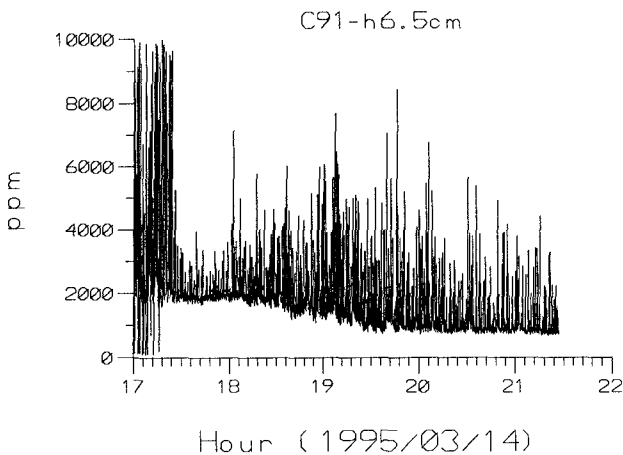


Figure 5 Time series of suspended concentration at various position

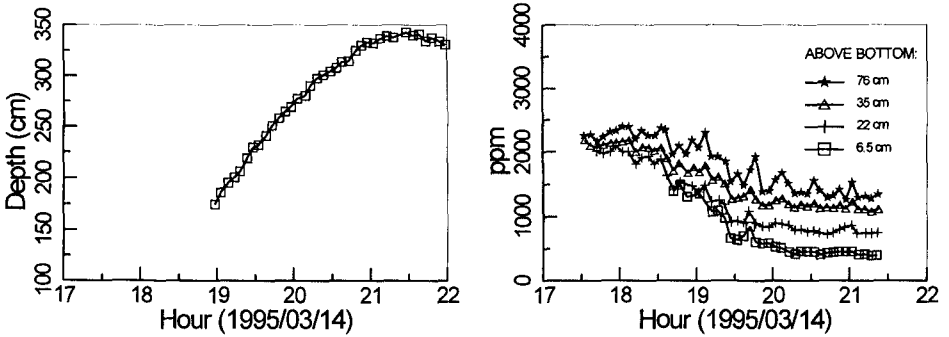


Figure 6 Time series of the water level and its corresponding suspended concentration

Results indicate that the tendency of suspended concentration is decreasing with increasing the water depth. And the higher water depth is, the discrepancy of suspended concentration measured at different height is smaller.

By using the concept of Figure 1 schematic diagram, the concentration distributions of the suspended sediment at different relative water depth d/L_0 can be measured by the tidal variations. Figure 7(a)~(d) shows the vertical distributions of suspended concentration at different relative water depth d/L_0 . The dots and solid line in the Figure 7 represent respectively the field measured data and a regressive curve in this study. Results indicate that the vertical distribution of suspended concentration is more uniform for the smaller relative water depth d/L_0 .

And results also show that the maximum suspended concentration mostly occurs at the bottom for different relative water depth under the same wave conditions. Figure 8(a)~(d) shows the dimensionless relationship between measured relative suspended concentration (C/C_{max}) and different relative water depth d/L_0 .

Then, we can summarize the analyzed results in different way to express the vertical distributions of suspended concentration under various relative water depth d/L_0 as shown in Figure 9.

Moreover, the relationship diagram between the vertical suspended concentration at any relative depth y/d and the relative water depth d/L_0 can be also shown as Figure 10(a)~(c).

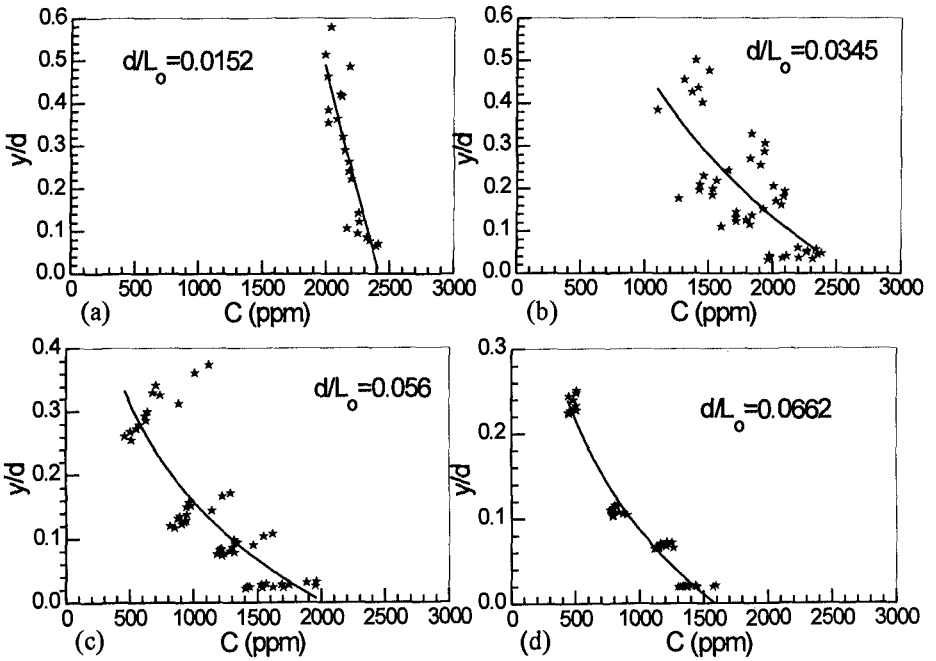


Figure 7 The vertical concentration distribution for the different relative water depth

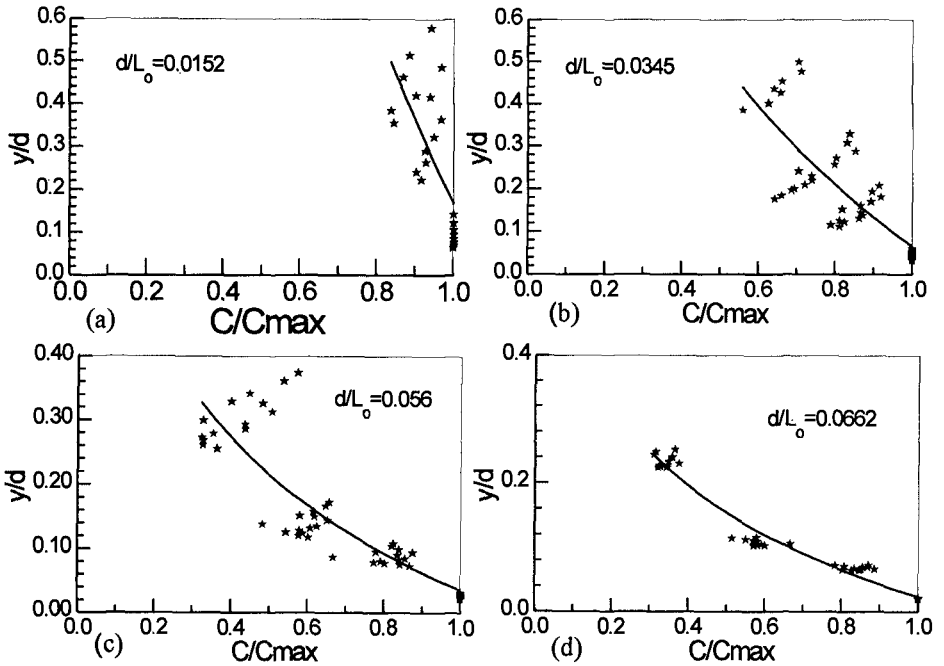


Figure 8 The vertical distribution of dimensionless suspended concentration

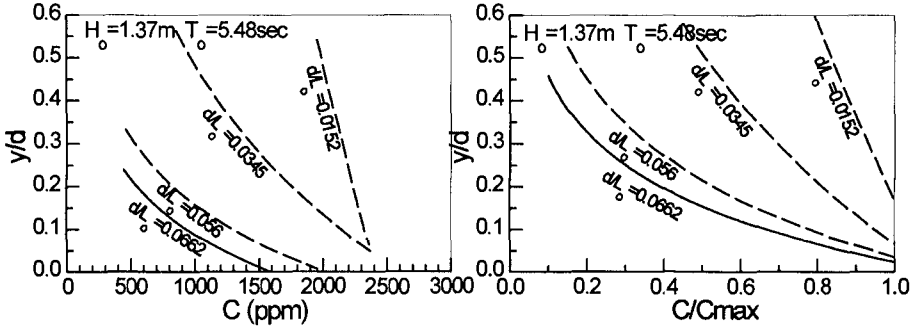


Figure 9 The vertical distributions of suspended concentration under the same wave condition

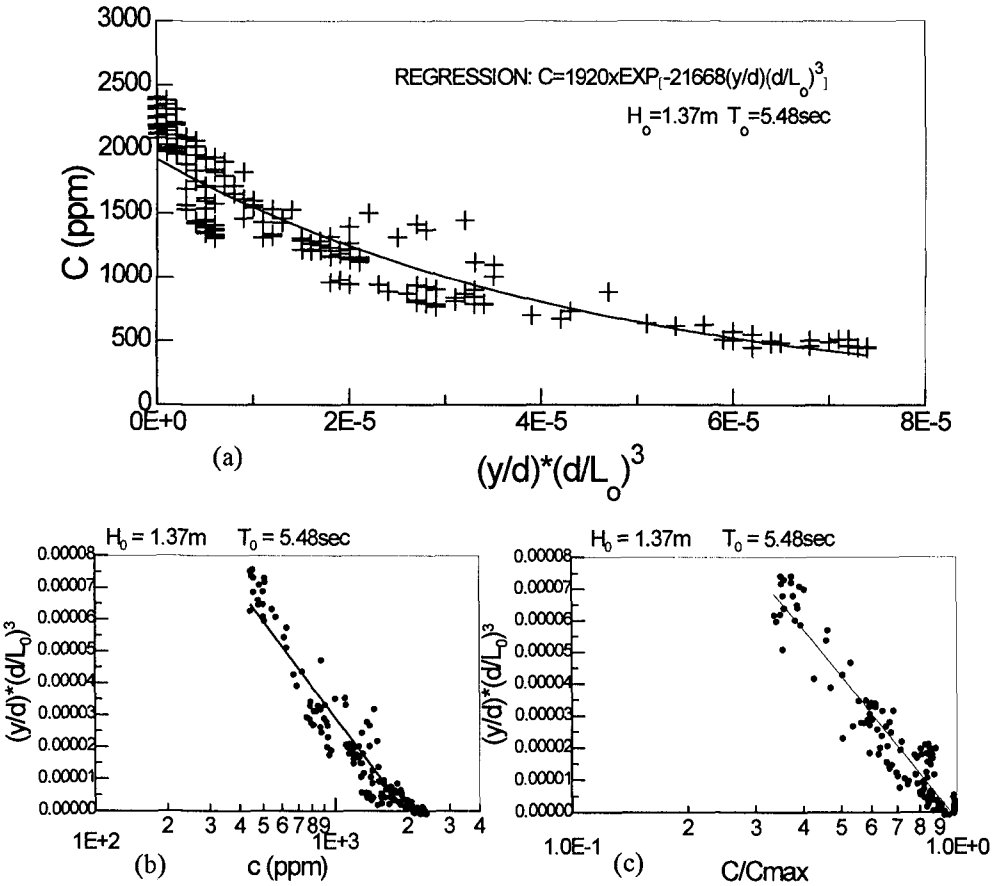


Figure 10 The relationship between suspended concentration C and $(y/d) \cdot (d/L_0)^3$

It means if the water depth d is given, then the suspended concentration at any depth y can be obtained by following regressive formuluss.

$$C = 1920 \cdot e^{-21668 \left(\frac{y}{d}\right) \cdot \left(\frac{d}{L_0}\right)^3} \tag{2}$$

where d : water depth
 y : height from the seabed
 C : suspended concentration, its unit is ppm

3.2.2 Suspended concentration near the seabed across the surf zone

Figure 11(a)~(d) shows the concentration distributions measured near the seabed across the surf zone under various wave steepness H_0/L_0 . The definitions of parameter X and X_b are shown as Figure 1. The width of the surf zone, X_b , is computed by wave theory here. In general, results indicate the maximum values of suspended concentration usually occur around the breaking point for the same wave condition.

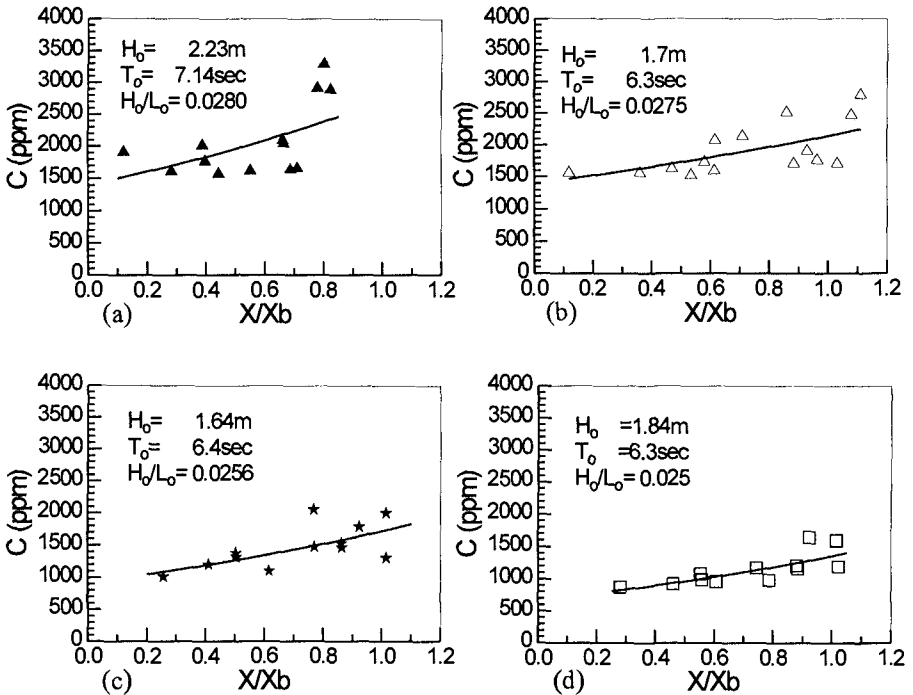


Figure 11 The distributions of concentration near the seabed across the surf zone

We can also summarize above results as Figure 12 under various wave steepness H_0/L_0 . It means that the suspended concentration near the seabed will be decreasing with decreasing the depth. But it will be increasing when the incident wave steepness H_0/L_0 is increasing for the same depth.

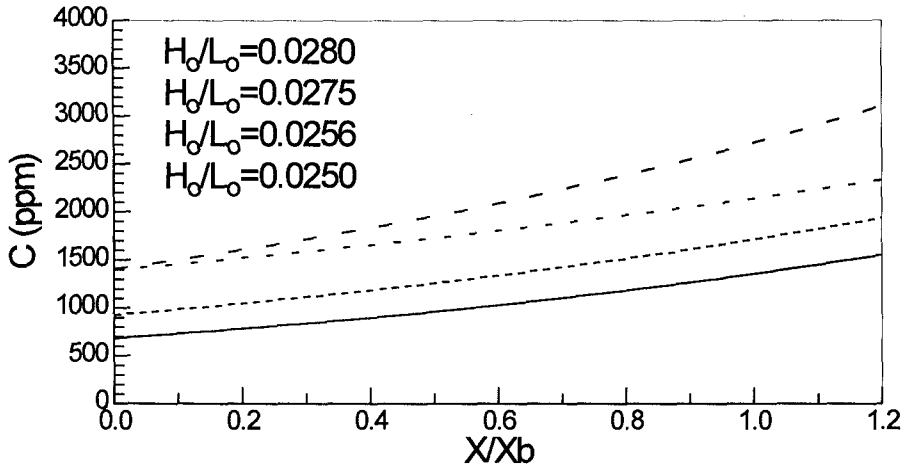


Figure 12 The concentration distributions near the seabed across the surf zone

Conclusions

Summarize above field data analysis and discussions, we can obtain some conclusions as following :

1. All measured field data can be provided as the quantitative basis of the numerical analysis in this study.
2. The local wave height H will be linearly decreasing onshore with depth d when the incoming wave is broken. Its relationship can be expressed as $H=r(d+H)$ when the beach is a mild slop $S=1/144$ and incident wave height H_0 is smaller than 2.2m, then the coefficient is $r \cong 0.3$.
3. The vertical distribution of the suspended concentration C can be computed by equation $C = 1920 \cdot e^{-21668 \left(\frac{y}{d}\right) \cdot \left(\frac{d}{L_0}\right)^3}$ if depth d is known.
4. The distributions of the suspended concentration across the surf zone are related with the incoming wave steepness H_0/L_0 . In general, its maximum value usually occurs around the breaking point.

Acknowledgement

This paper is part of the research projects, which is funded by the National Science Council for the integrated research program "Coastal Space Utilities", under contact NSC 84-2611-E-124-002. Authors also deeply appreciate to Miss Chien, E. J. for typing this manuscript.

References

1. Fairchild, J. C. (1959) : Suspended sediment sampling in oscillatory wave action, Beach Erosion Board, Tech. Memo 115 P.
2. Homma, M. and K. Horikawa (1962) : Suspended sediment due to wave action, proc. 8th coastal Eng. Conf. PP.168-193.
3. Sleath, J. F. A. (1982) : The suspension of sand by waves, J. Hydraul Res., Vol.19, PP.439-452.
4. Makoto Ifuku and Tadao Kakinuma (1988) : Suspended sediment concentration in the surf zone, 21th ICCE, Chap.23, PP.1661-1675, ASCE.
5. P. Nielsen (1994) : Suspended sediment particle motion in coastal flows, Proceedings of 24 ICCE, Chap.174, ASCE.
6. Onoetl (1994) : Suspended sediment concentration profiles under Non-breaking and breaking waves, Proceedings of 24 ICCE, Chap.203, ASCE.
7. C. K. Chang and C. H. Hwang (1995) : Studies on Wave, Current and Suspended Sediment Characteristics at the Surf Zone, Coastal Dynamics'95, ASCE, PP.728-738.

CHAPTER 317

Suspended sediment mixing in the surf zone

José A. Jiménez, Francisco J. Rivero, Agustín Sánchez-Arcilla,
Vicente Gracia and Andrés Rodríguez¹

Abstract

The vertical distribution of suspended sediment in the surf zone is analysed by using field measurements. The analysis focuses in the description of the shape of the profile, *i.e.* mixing coefficient, and to do this, several approaches have been followed: pure diffusion, pure convection and combined diffusion-convection. The obtained results show a strong dependence of the sediment diffusion coefficient with the sediment grain size whereas the convective length scale presented a smaller grain-size influence.

Introduction

The vertical distribution of suspended sediment inside the surf zone may be generally considered as a combination of convective and diffusive processes. The distinction between both can be done in terms of mixing lengths, which in turn depend on the hydrodynamics acting on the sediment. According to Nielsen (1991, 1992), this can be mathematically described in a time averaged form by the convection-diffusion equation

$$w_f c + \varepsilon \frac{dc}{dz} - pF(z) = 0 \quad (1)$$

where w_f is the fall velocity of the sediment, c is the time averaged suspended sediment concentration, z is the elevation above the bottom, ε is the sediment diffusivity, p is the pick-up function and $F(z)$ is the convective entrainment function.

¹ Laboratori d'Enginyeria Marítima (LIM), Catalonia University of Technology (UPC), c/Gran Capitán s/n, 08034 Barcelona, Spain (jimenez@etseccpb.upc.es).

Equation (1) is generally truncated being the pure diffusive description the most common approach (see *e.g.* van de Graff and Roelvink, 1988 among others). In spite of this, the approach may be accurate enough to describe the suspended sediment distribution if sediment is characterised by a mean grain size (without considering the grain size distribution). However, when this distribution is taken into account, a dependence of diffusivity or mixed length with grain size can be often observed (see *e.g.* Nielsen, 1983, van de Graaf and Roelvink, 1988, van Rijn, 1993). Strictly speaking, although a slight variation of the diffusivity of a solid particle (the sediment) with respect to the one of the fluid should be expected (see *e.g.* van Rijn, 1984), large deviations between the sediment diffusivity and the fluid eddy viscosity should indicate that other mechanisms are affecting the sediment mixing.

In this work, the vertical suspended sediment distribution in the surf zone is analysed using field measurements. The analysis focuses on the shape of the distribution from the pure diffusive and/or convective approaches and, an attempt to use the combined diffusion-convection solution is also presented. This last point was introduced due to the observed dependence of the mixing coefficients with sediment characteristics.

Experimental data

The used data were acquired in a field campaign (DELTA' 93) carried out in the Trabucador Bar (Ebro delta, Spanish Mediterranean coast). The measured field data included bathymetry, waves outside and inside the surf zone, mean water levels across the surf zone, velocity field (both horizontal and vertical structure) by means of an instrumented sledge equipped with 6 electromagnetic currentmeters and a step wave gauge (see Rodriguez *et al.* 1995a for a full description of hydrodynamic measurements) and measurements of longshore suspended sediment transport across the surf zone.

Longshore suspended sediment transport were measured by means of portable sediment traps (hereinafter PST) similar to that described in Rosati and Kraus (1989). Each PST was composed by a vertical array of 5 to 6 traps, each one of the cube-type with a nozzle of 5.5x5.5 cm and with a streamer (collection bag) made with a mesh of 100 μm (Ortiz, 1995).

Measurements were taken in the inner part (inside the surf zone in all the cases) of a barred profile under wave conditions characterised by H_{rms} ranging between 0.4 and 0.6 m at 7.5 m depth and with peak periods, T_p , from 5 to 6 sec. Spilling breaking waves were representative of surf zone conditions during all the experiments, with induced longshore currents up to 0.7 m/s.

Figure 1 shows some measured vertical profiles of the longshore current, where it can be seen that for relative depths, $z/d \geq 0.1$, current velocity shows small changes in vertical, *i.e.* is nearly constant in vertical.

Longshore suspended sediment transport measurements were taken in three profiles across the surf zone, with 4 to 5 positions each. In each position, PST were operating during a time period of 2 to 5 min. After that time, PST are carried to shore and collected sand is stored in bags to be weighted and sieved at the laboratory.

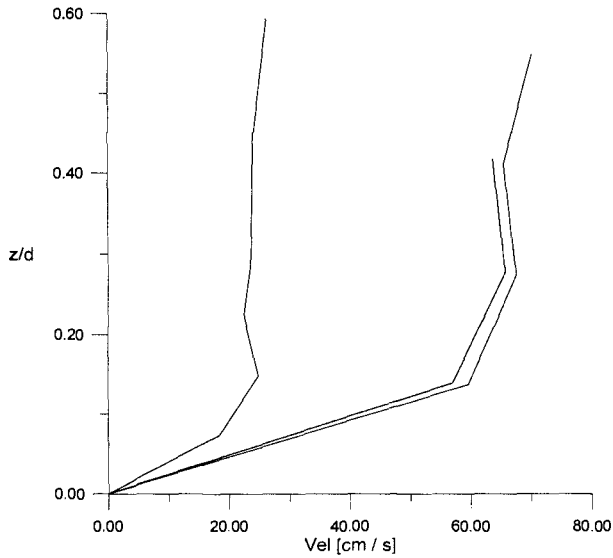


Figure 1. Typical vertical profiles of longshore currents measured during the experiments.

Vertical distribution of suspended sediment concentration

In order to obtain the vertical distribution, the first working hypothesis was that because measurements were acquired inside the surf zone, where a well mixed water column can be assumed, a *constant in vertical* mixing coefficient was considered.

Figure 2 shows the vertical distribution of the vertical eddy viscosity obtained from time series of velocity measurements inside the surf zone (see Rodríguez *et al.* 1995 for further details in the calculation of diffusivity). It can be observed that for relative depths ≤ 0.6 the calculated diffusivity can be considered as constant in vertical, whereas in the upper part of the water column values increase, due to the generation of horizontal turbulent-momentum flux during breaking (Rodríguez *et al.* 1995).

This assumption of a constant in vertical diffusivity leads to an *exponential concentration distribution* (when a pure diffusive process is considered) given by

$$C(z) = C_0 e^{-w_f z / \epsilon}$$

where C_0 is the reference concentration at the bottom, w_f is the fall velocity of the sediment, z is the elevation above the bottom and ϵ diffusion coefficient.

Or in another form (assuming a pure convective process with an exponential function to describe convection, Nielsen, 992) as

$$C(z) = C_0 e^{-z/L}$$

where L is the mixing or length scale.

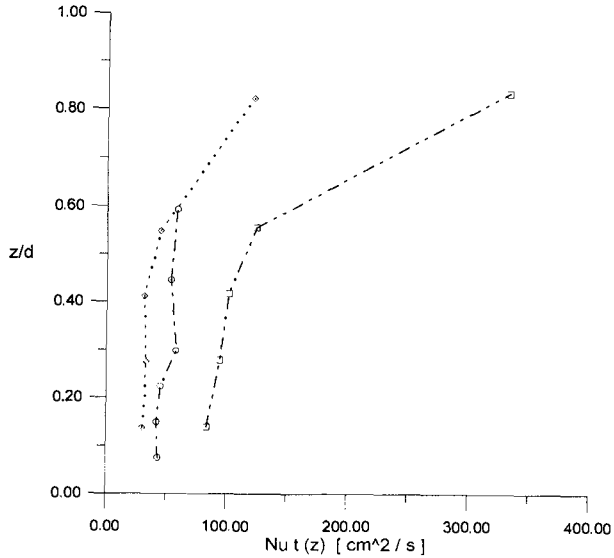


Figure 2. Vertical distribution of eddy viscosity obtained during the experiments.

When experimental profiles were fitted to a vertical distribution given by expressions (2) or (3), a good agreement was obtained. From 15 cases, covering three lines across the surf zone, the mean r^2 value of all the fits was 0.952, with a minimum r^2 value of 0.90 and a maximum of 0.995.

Figure 3 shows an example of the obtained normalised time averaged concentration profiles at different locations across the surf zone with the corresponding exponential fit for one of the monitored cross-shore profiles.

These results indicate that at least during the conditions prevailing during the field experiments, and for measurements taken inside the surf zone, the classical exponential profile describes well the time averaged concentration profiles. In this case, the averaging was done over a relatively long time period (from 20 to 50 waves) and because of this, these results cannot be considered in contradiction to those obtained by Mocke and Smith (1992) since the time scale of their analysis differs.

Cross-shore distribution of mixing coefficient

When the cross-shore distribution of the mixing coefficient was analysed, an increasing diffusivity from the shoreline towards the breaking point was observed for all the analysed cases (as expected). Fig. 4 shows the cross-shore distribution of the mixing length, L , for one of the control lines, where it can be clearly this increase in mixing towards the breakers where reaches the largest value.

Nielsen (1984) analysing the mixing length $-L-$ under non-breaking waves found that it was closely related to the bed ripple height. However, when the surf zone is considered a

different “physical entity” of L should be expected, since the mechanism inducing convection is clearly different.

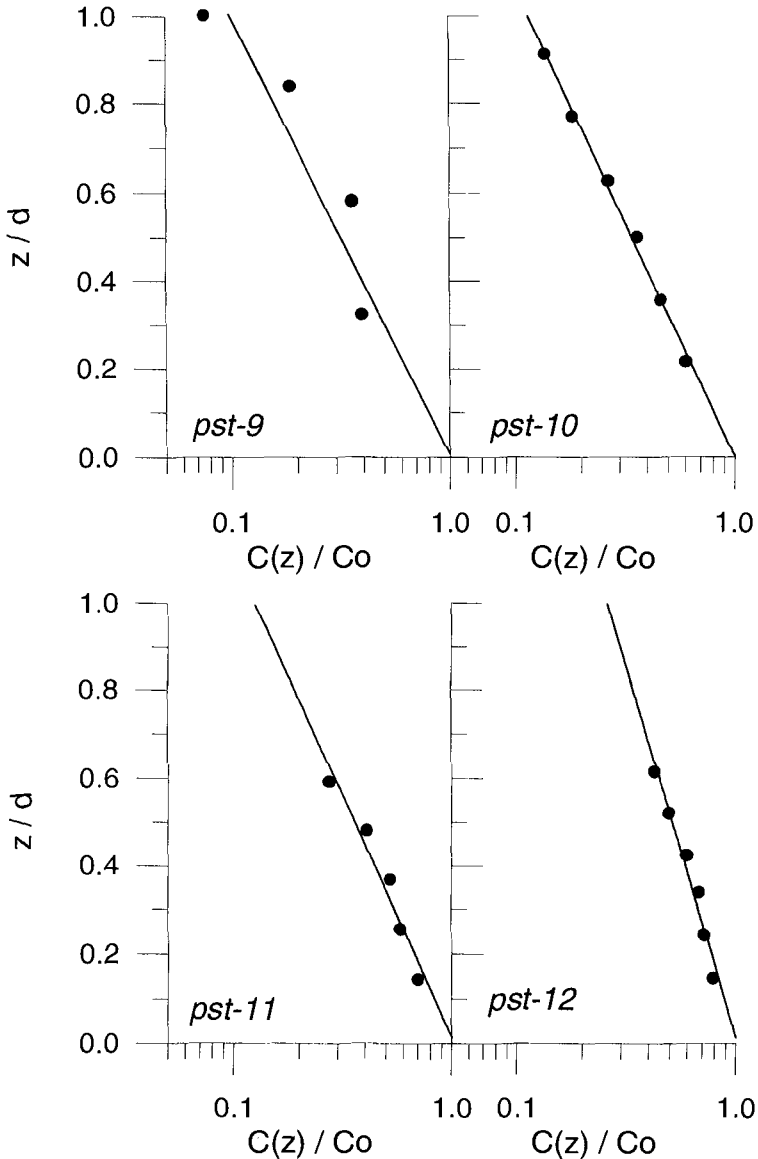


Figure 3. Normalised time averaged concentration profiles at different location across the surf zone.

In this case, it was found that this length scale for convection was closely related to the local H_{rms} (see Figure 4). This fact can be used to validate the assumption of that, inside

the surf zone the sediment is picked-up from the bottom and put in suspension at an elevation above the bottom proportional to the wave height (Dean, 1973).

Thus, for the range of measured conditions and under spilling breakers, the local value of H_{rms} was found to be a good predictor of the magnitude of the convective length scale, L .

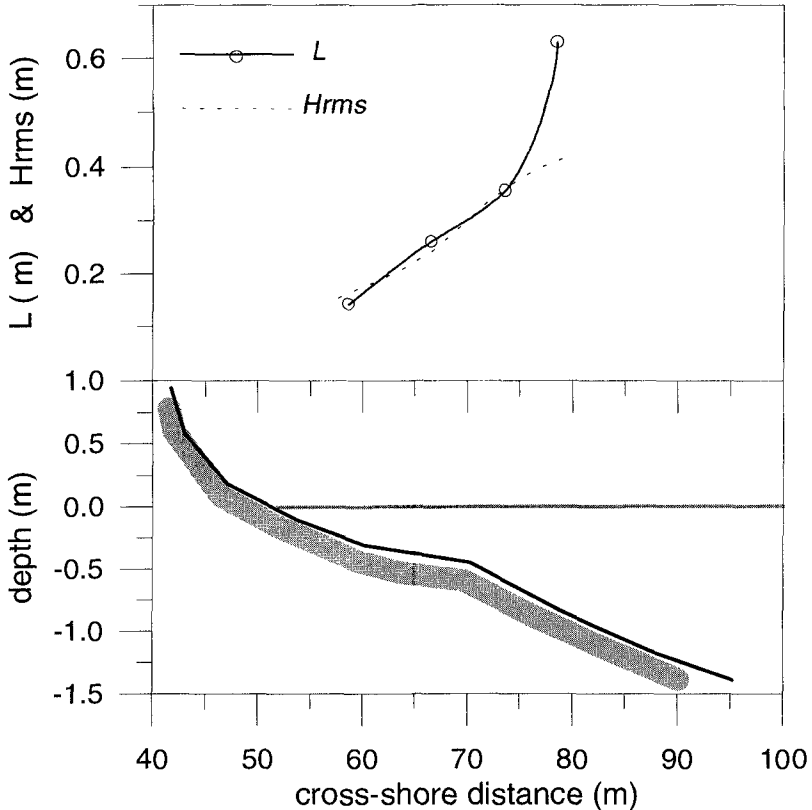


Figure 4. Cross-shore distribution of the mixing length L and H_{rms} .

When the cross-shore distribution of the mixing coefficient is put in terms of sediment diffusion coefficient, ϵ , the same pattern than before is observed (Fig. 5). This was due to that from equations (2) and (3) $L = \epsilon / w_f$, and no significant across-shore variations in sediment grain size was found.

Assuming that this sediment diffusion coefficient must be closely related to the fluid diffusion coefficient, their values should be equivalent to the vertical eddy viscosity for the fluid.

Fig. 5 shows the cross-shore distribution of the eddy viscosity for horizontal mixing using a k-model with production of turbulent energy according to Battjes (1975). It can be seen that both distributions (horizontal and vertical mixing) are qualitatively similar,

although the horizontal mixing coefficient is about two order of magnitude larger than the vertical one (see *e.g.* deVriend and Kitou, 1990). A detailed analysis of this discrepancy may be found in Svendsen and Putrevu (1994).

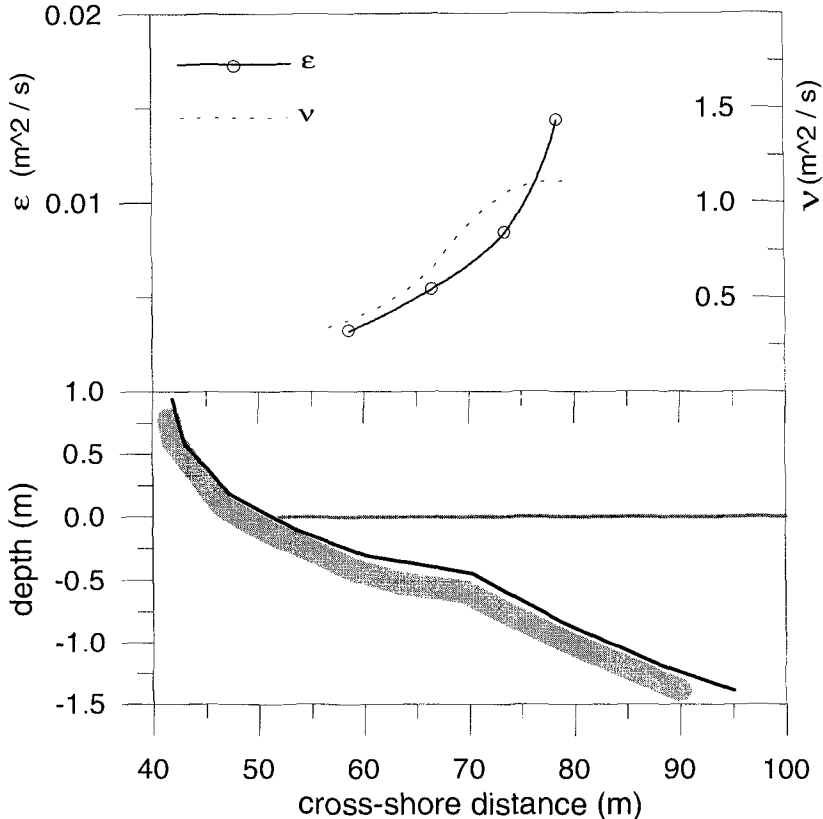


Figure 5. Cross-shore distribution of the sediment diffusion coefficient, ϵ , and calculated horizontal eddy viscosity v .

Effects of the grain size

Once the vertical suspended sediment distributions (assuming pure diffusion and convection) were analysed, the effects of the grain size on the sediment mixing was investigated. To do this, each sample was sieved into a series of fractions and, vertical distributions for each fraction were built. Once these classified vertical profiles were obtained, the same analysis than before was applied, *i.e.* fit to equations (2) and (3) to obtain the corresponding mixing coefficients for each fraction..

Figure 6 shows the obtained sediment diffusion coefficients, ϵ , for the same cases than the ones presented in Fig. 3 but considering different fractions. It can be clearly seen that diffusion coefficient is far from constant for the analysed range.

Focusing on the range of fractions characterised by a sediment fall velocity between 0.02 m/s and 0.06 m/s (out of this range some of the fractions were not statistically representative to build a “classified profile”), a linear relationship between the diffusion coefficient and the fall velocity was found: the larger the fall velocity is, the larger the coefficient will be. Similar results have been obtained for non-breaking waves by van de Graaf and Roelvink (1984) among others (see also Nielsen, 1992).

This result should indicate that for constant fluid diffusion coefficient, the sediment mixing will increase as coarser the sediment is. This discrepancy has been usually explained in terms of a greater influence of the centrifugal forces on the sediment particles with respect to the fluid in a turbulent flow. This would lead to an increase in the effective mixing length and diffusion rate for the sediment (see *e.g.* van Rijn, 1984).

However, although a small change in diffusivity between solid particles and fluid can be expected, the variations shown in figure 6 seems too high to assume that they are due to the above mentioned effect.

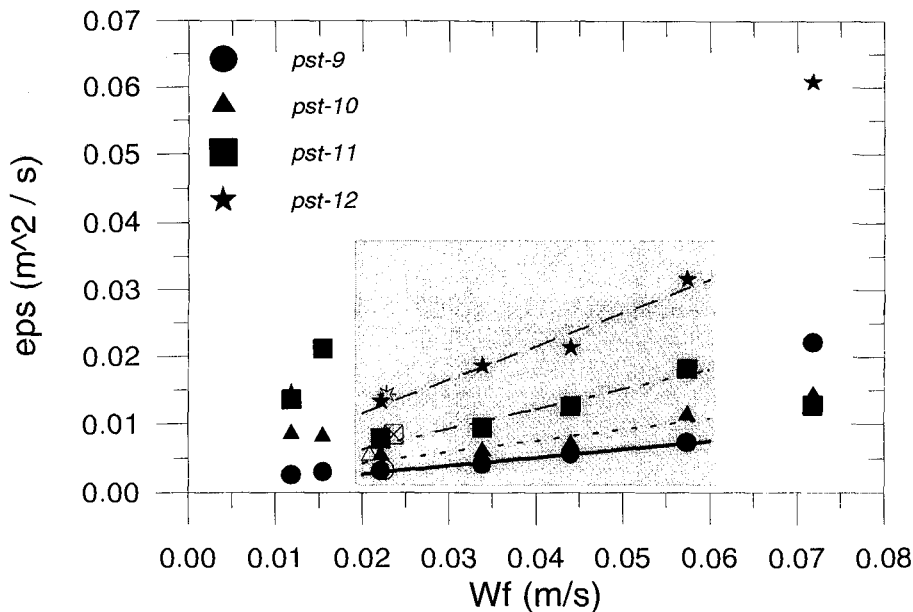


Figure 6. Variation of the diffusion coefficient ϵ_s vs fall velocity of the sediment for different locations across the surf zone. Grey rectangle indicates the range of fall velocities considered in the fit.

In fact, if the variations in diffusivity are measured as

$$\Delta\epsilon = \frac{\epsilon_{(w=0.06)} - \epsilon_{(w=0.02)}}{\epsilon_{(total\ sample)}} 100 \quad (4)$$

a mean value of 138% is obtained (considering the four locations across the surf zone).

From figure 6, it seems that the diffusivity dependence with grain size increases from shoreline (pst-9) towards the breaker point (pst-12). Although this is true in absolute

terms, when this variation is measured in relative terms (e.g. according to eq. 4), they are almost uniform, i.e. it seems to be constant across the surf zone.

Thus, the observed variations in the diffusion coefficient for the sediment mixing due to variations in grain size, introduce an uncertainty about the validity of the pure diffusion model to describe the vertical distribution of suspended sediment inside the surf zone.

Applying the same analysis to the case of pure convection model, i.e. looking to the variations in L when the different fractions are considered, the results depicted in Figure 7 are obtained.

In this case, although a variation in L is also observed, the direction of such variation is opposite to the above described one. Thus, assuming a pure convective process, as coarser the sediment is, smaller the mixing length will be. In other words, for coarser sediments, the mixing will be smaller.

This can be explained assuming that sediment response to convective process induced by wave breaking will be influenced by the sediment "weight". For heavier sediments (coarser), the theoretical distance from the bottom where they will be put in suspension (entrainment level) will be shortened as coarser the sediment is.

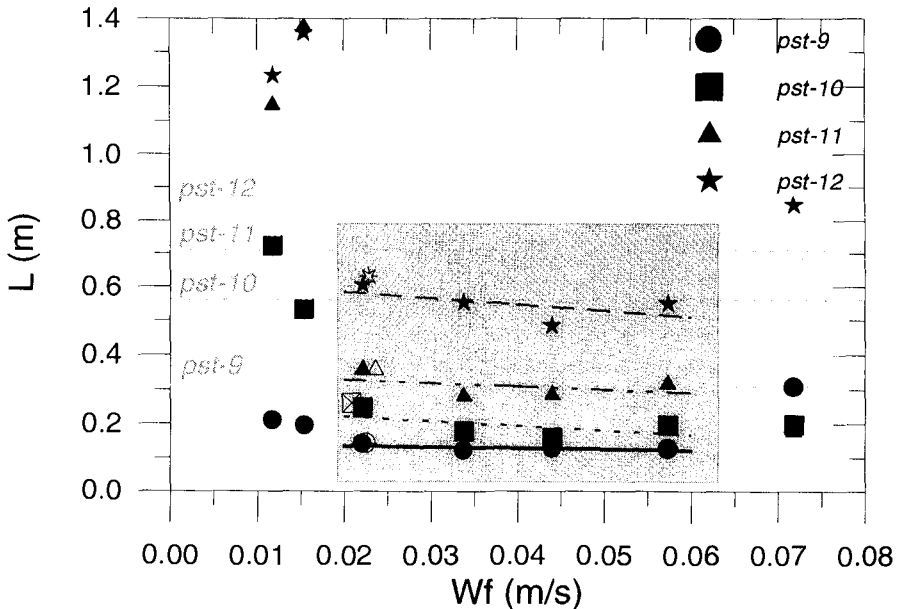


Figure 7. Variation of the length scale, L , vs fall velocity of the sediment for different locations across the surf zone. Grey rectangle indicates the range of fall velocities considered in the fit and grid lines represent largest value of L for each location (equal to the local depth).

Measuring the variations in the convective length scale, L , according to the equation 4, a mean value of 10% is obtained. The relative variations across the surf zone are also constant as it was for the previous case.

The main difference between the variations for diffusive and convective mixing lengths is that the former presented a larger variation than the convective one. In other words, the use of equation (3) to describe the vertical distribution of suspended sediment in the surf zone (assuming a pure convective process) is more "stable" in function of the sediment grain size than the use of a diffusive process. In spite of this, a small variation in the length scale was also found.

If the dominance of the process controlling the vertical distribution is measured in terms of its "stability", the convection process should be dominant under the monitored conditions.

Combined diffusion-convection process

Additionally to the above mentioned effect (variation in mixing coefficients for varying grain sizes), when the profiles for the different fractions were analysed, a change in the shape of the profile was also found. Thus, slight convex upward profiles were found to describe the fine fractions, whereas the coarser ones showed a slight concave upward shape. This change in shape was also explained by Nielsen (1992) as an indication of the presence of a combined diffusion-convection process controlling the sediment suspension.

In order to make a first attempt to describe the obtained suspended sediment profiles by using the combined diffusion-convection approach, a full solution of equation (1) was used.

In this attempt, a constant in vertical diffusion coefficient and a convective function given by an exponential law was selected (see *e.g.* Nielsen, 1992). Although this solution has not to be the best one, it was selected due to its simplicity, although presently other combined solutions are being analysed.

The integration of equation (1) with the selected description of diffusion-convection process leads to (Nielsen, 1992)

$$C = C_0 \left\{ \frac{1}{1 - \frac{\epsilon}{w_f L}} e^{-z/L} + \left(1 - \frac{1}{1 - \frac{\epsilon}{wL}}\right) e^{-wz/\epsilon} \right\} \quad (5)$$

By using the equation (5), the profiles for the different fractions presented in figure 8 were obtained. The main problem to apply this approach is that both diffusion coefficient as well as convective length scale has to be estimated. In this case, it was firstly selected the value of the diffusion coefficient by using the one corresponding to the finest fraction, and afterwards, the convective length was selected by fitting the predicted distribution to the measured profiles. In all the cases, the fitted values of convective length were in a range of 30%-40% of the obtained using a pure convective model.

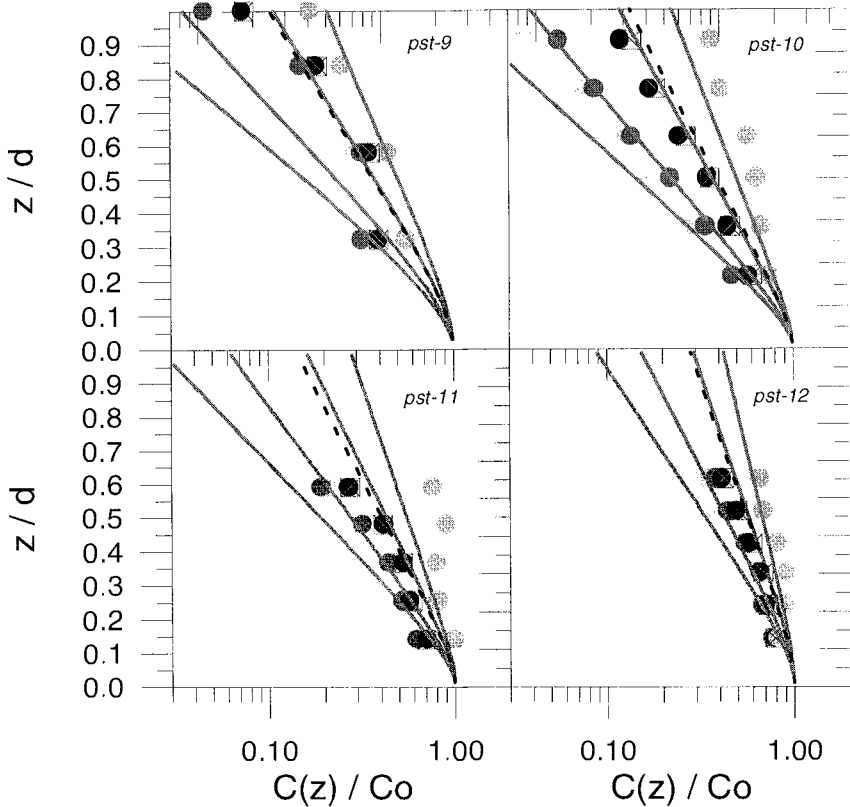


Figure 8. Use of the combined diffusion-convection approach (according to equation 5) to describe the vertical distribution of the different sediment fractions across the surf zone.

Conclusions

For the analysed conditions, several conclusions can be obtained.

- ◆ During the measured conditions, the simple *exponential profile* describes well the time-averaged vertical distribution of suspended sediment in the surf zone.
- ◆ The *length* scale, L , of the distribution can be well represented by the local value of H_{rms} inside the surf zone.
- ◆ The eddy viscosity ν_t for horizontal mixing (obtained using a K-model with production of turbulent energy according to Battjes (1975)) shows a *cross-shore distribution similar* to the vertical mixing coefficient obtained from sediment data, ϵ_s . Obtained values of ν_t are two orders of magnitude higher than ϵ_s .

- ◆ For the analysed field data, the mixing coefficient ϵ_s depends on sediment characteristics, i.e. w_f . In the range of $w_f = 0.02-0.06$ m/s, a linear relationship between ϵ_s and w_f was found. Larger the fall velocity is, larger the diffusion will be.
- ◆ Assuming that the vertical distribution can be described by the length scale, L , a linear dependency with w_f was also found.
- ◆ The magnitude of the measured variation of ϵ_s with w_f was one order of magnitude larger than the obtained for L .
- ◆ These last two conclusions lead to argue the validity of the pure diffusion model to be used in the surf zone.

A first attempt to improve the description of the vertical distribution of suspended sediment considering the different grain has been done. To do this, the approach of Nielsen (1991, 1992) was followed by using a combined solution including diffusion and convection. First results are promising although further works have to be done, specially in the description of the “convective” function.

The generalisation of the obtained conclusions should require additional field data under different energetic conditions. This additional “field effort” is being carried out in the framework of an EU funded Research Project.

Acknowledgements

This work was carried out as part of the *FANS* project. It was supported by the EU *Marine Science and Technology (MAST-III) Programme*, under Contract No. MAS3-CT95-0037. This work was also co-sponsored by the *Spanish Ministry of Education and Research* through *CICYT*. Field data were acquired in the framework of a project funded by *Programa de Clima Marítimo*, *Spanish Ministry of Public Works*. JAJ was partly supported by a travel grant given by the *DPTOP (Generalitat de Catalunya)* through the *ETSECCPB (UPC)*.

References

- Battjes, J. 1975. Modeling of turbulence in the surf zone. *Proc. Symp. on Modeling Techniques*, 1050-1061.
- Dean, R.G. 1973. Heuristic models of sand transport in the surf zone. *Proc. Conf. on Engineering Dynamics in the Surf Zone*, 208-214.
- De Vriend, H.J. and Kitou, N. 1990. Incorporation of wave effects in a 3D hydrostatic mean current model. Delft hydraulics Report H-1295.
- Mocke, G.P. and Smith, G.G. 1992. Wave breaker turbulence as a mechanism for sediment suspension. *Proc. 23rd ICCE, ASCE*, 2279-2292.
- Nielsen, P. 1983. Entrainment and distribution of different sand sizes under water waves. *Journal of Sedimentary Petrology*, 53, 2, 423-428.

- Nielsen, P. 1984. Field measurements of time-averaged suspended sediment concentrations under waves. *Coastal Engineering*, 8, 51-72.
- Nielsen, P. 1991. Combined convection and diffusion: A new framework for suspended sediment modelling. *Coastal Sediments' 91*, ASCE, 418-431.
- Nielsen, P. 1992. *Coastal Bottom Boundary Layers and Sediment Transport*, World Scientific, Singapore, 324 pp.
- Ortiz, V. 1995. *Análisis experimental del transporte longitudinal de sedimento en suspensión en zona de rompientes*. Ms.Sc. Thesis, Catalonia University of Technology, Barcelona.
- Rodríguez, A., Sánchez-Arcilla, A., Bahía, E. and Mosso, C. 1995a. DELTA' 93: Experimental study of surf-zone hydrodynamics at the Ebro delta. *MAST G8M Workshop*, Gdansk.
- Rodríguez, A., Sánchez-Arcilla, A., Gómez, J. and Bahía, E. 1995b. Study of surf-zone macroturbulence and mixing using Delta'93 field data. *Coastal Dynamics' 95*, ASCE, 305-316.
- Rosati, J.D. and Kraus, N.C. 1989. *Development of a portable sand trap for use in the nearshore*. Tech. Rep. CERC-89-11.
- Svendsen, I.A. and Putrevu, U. 1994. Nearshore mixing and dispersion. *Proc. Royal Soc., London, Series A*, 445, 561-576.
- van de Graaf, J. and Roelvink, J.A. 1984. Grading effects in concentration measurements. *Proc. 20th ICCE*, ASCE, 1618-1634.
- van Rijn, L.C. 1984. Sediment transport, part II: suspended load transport. *Journal of Hydraulic Engineering*, 110, 11, 1613-1641.

CHAPTER 318

Sand Suspension Events and Intermittence of Turbulence in the Surf Zone.

R.D. Kos'yan¹, H. Kunz², S.Yu. Kuznetsov³, N.V. Pykhov³, M.V. Krylenko¹

Abstract

The results of the joint field experiment Norderney-94 demonstrates the excellent coincide of fluctuations of suspended sand concentration and kinetic turbulent energy in the nearbottom region of the surf zone. Turbulent fluctuations were separated from the wave induced fluctuations as a part of the motions that are incoherent to the free surface elevation. The time and spatial scales of macroturbulent vortexes had been estimated and discussed.

Introduction

For the prediction of sediment transport in the breaking zone it is necessary to know the distribution of the suspended sediment concentration, of the water velocity and of the cross-correlation between them in the whole frequency spectrum of irregular waves. The analysis of modern approaches to the solutions of this problem published in literature and discussed at the international conferences during the last years (Coastal Dynamics 94, Barcelona/Spain, 1994; 24th Coastal Engineering Conference, Kobe/Japan, 1994; Coastal Dynamics 95, Gdynia/Poland, 1995; MAST 2 - Overall Meeting, Gdynia/Poland, 1995) shows that the most perspective ones are the models based on Boussinesq and Serra equations that afford to adapt these parameters to the time scales of approaching waves and k- ϵ models. But the latter models today allow only to assess mean-time profiles of the suspended sediment concentration in the breaking zone. The possibility to use k- ϵ model for the calculation of the suspended sand fluctuations in time is restricted by the absence of precise descriptions of the physical mechanisms of sediment

¹ *The Southern Branch of the P.P.Shirshov Institute of Oceanology, Russian Academy of Sciences. Gelendzhik-7, 353470 Russia. E-mail: kosyan@sdios.sea.ru;*

² *Coastal Research Station. NLOE-Forschungsstelle Kueste. An der Muehle 5, D-26548, Norderney, Germany. E-mail: kunz.crs@t-online.de*

³ *P.P.Shirshov Institute of Oceanology, Russian Academy of Science, 23, Krasikov str., Moscow, 117851, Russia. E-mail: sergey@shelf.msk.ru; pykhov@coast.msk.ru*

suspension above the bottom, it's distribution in the water column within the breaking zone and by the absence of quantitative correlation between the suspended sediment concentration and parameters of the turbulence for field conditions.

From the physical point of view the presence of instantaneous water flows from the bottom with a velocity that exceeds the sand particle settling velocity is a necessary condition for the occurrence of sediment suspension. In the wave breaking zone such water motions are forced, most probably, by macroturbulent vortexes. Two basic mechanisms of such vortexes formation are possible:

1. Vortexes formation near the water surface under the crests of the breaking waves and its penetration to the bottom. Such a mechanism was observed in laboratory experiments with monochromatic waves above a hard and a movable bottom (Nadaoka, Kondoh, 1989; Zhang et al., 1994). By these experiments it was determined that vortexes were formed as well with horizontal axis as with inclined vertical axis depending on the wave parameters, on the type of their breaking and on the bottom slope. When reaching the bottom, such vortexes, like a tornado, can capture sand from the bottom and suspend it in the flow. The dominant action of this turbulence for sediment suspension is verified by Sato et al. (1990) in a wave flume.

2. Vortexes formation in the bottom boundary layer due to the shear instability of water flow above a plane rough bottom. In this case an explosive character of the generation of turbulent energy and formation of coherent vortexes takes place. Those vortexes are forced from the bottom to the water column. The possibility of realization of such a mechanism has been shown in laboratory experiments (Hino et al., 1983), and its responsibility for the sand suspension is indirectly confirmed in the papers of Foster et al. (1994) and of Pykhov et al. (1995).

The reality of the existence of the first mechanism under field conditions is confirmed by some (not numerous for the present) measurements of the macroturbulence in the surf zone (George et al., 1990; Rodriguez et al., 1995). The results of this research only give a possibility to assess a time-mean value of the turbulent energy, the integral length scale, the turbulent viscosity. But they do not afford to trace the temporal variability of these parameters, which is necessary for the analysis of time fluctuations of the suspended sediment concentration. In spite of the fact that the hypothesis about sediment suspension by such vortexes is shared by the majority of investigators, till now there is no confirmation by direct field measurements.

The aim of our paper based on the data of field measurements is to confirm the existence of turbulent mechanisms of sand suspending by the determination of the scales of fluctuations of turbulent kinetic energy and suspended sand concentration and by ascertaining dependencies between these fluctuations.

Experiment

Field experiment was carried out on a beach section of Norderney Island, North Sea in October 1994 (Fig. 1).

A joint German-Russian team of scientists carried out multipurpose survey at an especially equipped testing site, which is located on the north-western side of the island. In this paper the results of measurements in one point (10 centimeters and more above the bottom) are presented and discussed (Fig. 2). The suspended sand concentration, the free surface elevation and the two horizontal components of water velocity were measured synchronously by optical turbidimeter, pressure gauge and two-component electromagnetic current meter at sampling rate of 18.2 Hz over 20 minutes.

The turbidimeter measures the light beam attenuation at a distance of 6 centimeters that then is recalculated into the suspended sand concentration (Kos'yan et al., 1994). Two-component electromagnetic current meter and pressure sensors (Type NSW) had been used for measuring. Their linear calibration characteristics are in the band of frequency from 0 to 20 Hz. The diameter of the measuring head of the currentmeter is 6 centimeters.

The bed consists of sand with a mean diameter of approximately 0.2 mm. The tidal range of about 2.4 m afforded to produce the measurements at a depth range from 0.5 to 2.5 m. The measurements were carried out in the inner and middle parts of the surf zone under the wind wave and swell conditions. The 25 series of

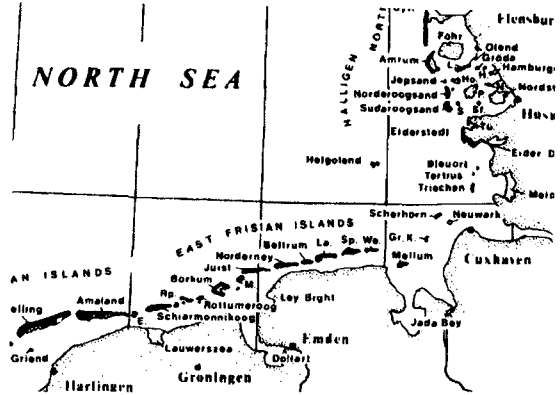


Figure 1. Site of the field experiment.

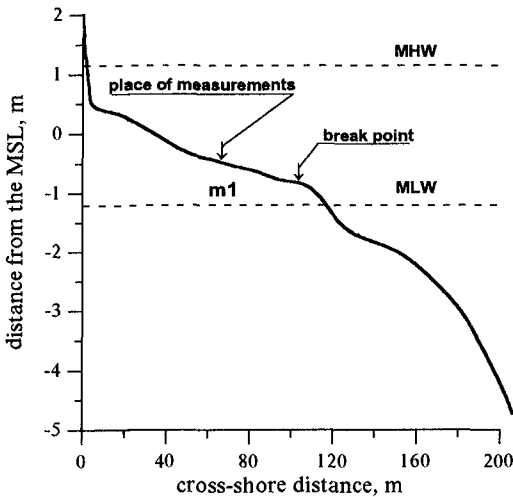


Figure 2. Bottom profile and point of measurements.

recording were obtained during the whole experiment.

Separation of turbulence

We consider the turbulence as a part of water particle fluctuations, which is incoherent to the elevations of the free surface. Spectral and mutual spectral analysis of fluid velocities and free surface elevations show the turbulent fluctuations of the cross- and the long-shore velocities at the frequencies $f > 0.8$ Hz. This is conformed by the absence of the coherence between cross-shore velocity ($u(t)$) and free surface elevations ($H(t)$) at the frequencies $f > 0.8$ Hz and by the change the velocity spectra ($S_u(f)$) gradient from $\sim f^{-4}$ to $\sim f^{-2}$ at $f = 0.8$ Hz (Fig. 3). Turbulent components of the cross-shore $u_t(t)$ and long-shore $v_t(t)$

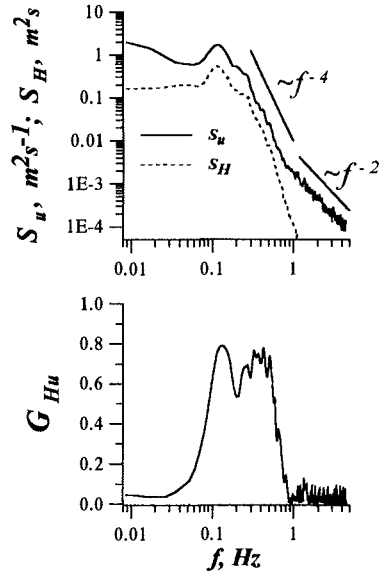


Figure 3. Determination of boundary frequency between waves and turbulence. $f_b=0.8$ Hz. Record 5a. $H_S=1.03$ m, $T_P=8.7$ s, $\bar{h}=1.53$ m, Sp.

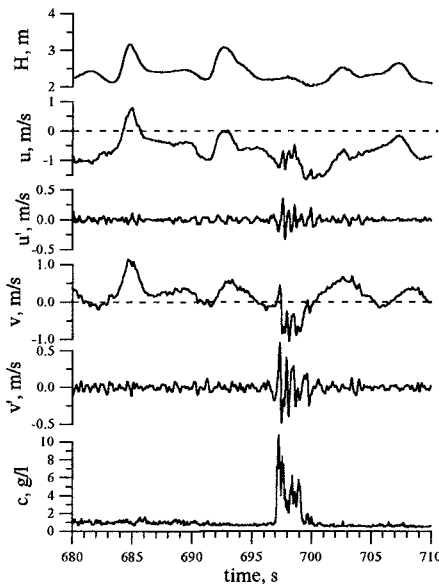


Figure 4. Example of single suspending event. Record 6a. $H_S=1.07$ m, $T_P=8.7$ s, $\bar{h}=1.53$ m, Sp.

velocities were obtained by digital filtering.

Examples of events

Analyses of the records show a rapid appearance and disappearance of suspended sand events, which are well coincided with the appearance and disappearance of turbulent fluctuations of the cross- and long-shore velocities.

A typical example for a single suspending event is given by Figure 4. Recorded are wind waves with a significant height $H_S=1.07$ m, mean period $T_P=8.7$ s, breaking by spilling at the depth $\bar{h}=2.36$ m. $H(t)$ is the free surface elevation, $u(t)$ and $u'(t)$ are the cross-shore velocity and its turbulent component, $v(t)$ and $v'(t)$

are the long-shore velocity and its turbulent component, $C(t)$ is the suspended sand concentration. The splash of turbulent velocity fluctuations and the splash of concentration between 697 to 700 s may be explained by horizontal advection of turbulent vortexes with trapped sand at the sensor array.

Figure 5 shows the two consecutive events of sand suspending for a more intensive wave regime ($H_s=0.90$ m, $T_p=8.7$ s, $\bar{h}=1.62$ m, breaking type is between spilling and plunging). The change of the amplitude of the turbulent fluctuation coincides well in time with the splash of concentration.

Figure 6 demonstrates the intermittence of turbulence and the corresponded events of sand

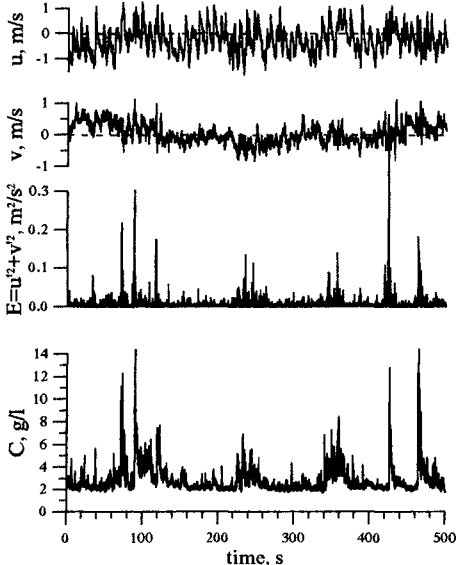


Figure 6. 8-minute fragment of suspending events. Record 7f. $H_s=0.90$ m, $T_p=8.7$ s, $\bar{h}=1.62$ m. Sp-Pl.

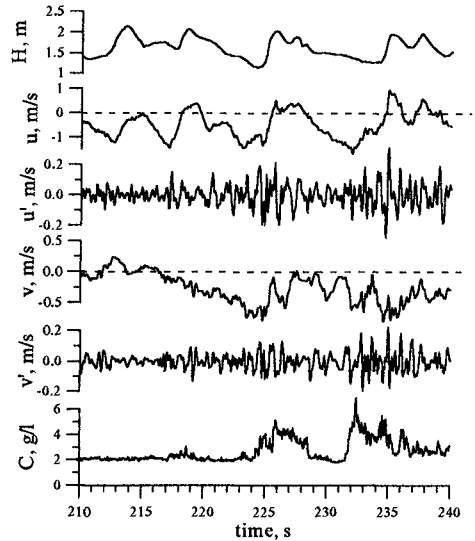


Figure 5. Example of two consecutive events of sand suspending. Record 7f. $H_s=0.90$ m, $T_p=8.7$ s, $\bar{h}=1.62$ m. Sp-Pl.

suspending events during the 500 s for the same record as shown on Figure 5. The fluctuation of turbulent kinetic energy ($E(t)$) coincides well with the fluctuation of suspended sand concentration. Turbulent kinetic energy was calculated as the sum of the squared turbulent velocity components: $E(t) = u'^2(t) + v'^2(t)$

Time scales of the turbulence

The upper parts of Figure 7 show the typical spectra describing the concentration fluctuations $S_C(f)$ and the kinetic turbulent energy variations $S_E(f)$ as function of frequency. Both spectra coincide with increasing frequency. The concentration spectrum has a feebly marked peak at the main wave frequency. Turbulent energy

spectrum is decreasing monotonously with increasing frequency except the peak at the frequency of 1.6 Hz, which is called forth by the method of the turbulence selection, i.e. by the filtering with a boundary frequency of 0.8 Hz, and therefore it has no physical sense (when squaring $(E(t) = u'^2(t) + v'^2(t))$ the frequencies are doubled).

The lower left part of Figure 7 displays the squared coherence function $G_{CE}(f)$. Significant values of the coherence G_{CE} at the frequencies $f < 0.05$ Hz afford to say, that the low frequency suspended sand fluctuations are determined by the bursts of the turbulent velocity fluctuations.

The lower right part of Figure 7 shows for low-frequencies ($f < 0.05$ Hz) the relation between the related components of concentration (C_{low}) and of kinetic turbulent energy (E_{low}). It demonstrates that the deviations from the linear connection are not caused by the nonlinearity, but by random reasons.

Let us consider the regularities of turbulent fluctuations within one suspension event.

Figure 8 presents the chronograms of turbulent components of velocities and their hodograf for a single suspending event, which was demonstrated at Fig. 4. The hodograf shows, how that the end of the vector of turbulent velocity component runs two full circles during one second. This may correspond to the passing of a series of four vortexes, as principally shown in the lower right part of Figure 8. Neighboring vortexes must rotate in opposite directions.

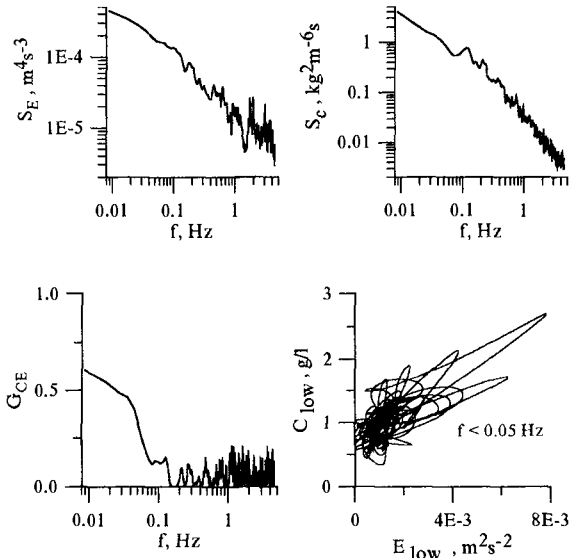


Figure 7. Connection between suspended sand concentration and turbulent energy. Record 5a. $H_S=1.07$ m, $T_p=8.7$ s, $\bar{h}=2.33$ m. Sp.

An assumption about the passing of a series of several consecutive vortices is confirmed by results of laboratory investigations presented at the conference Coastal Dynamics'94 by Zang et al. who presented the nomogram of the type and number of turbulent vortices that are formed in the moments of wave breaking depending on Reynolds number and breaker-type index given by Galvin. The nomogram shows that all our recorded wave regimes occurred in the region of formation of triple oblique vortices.

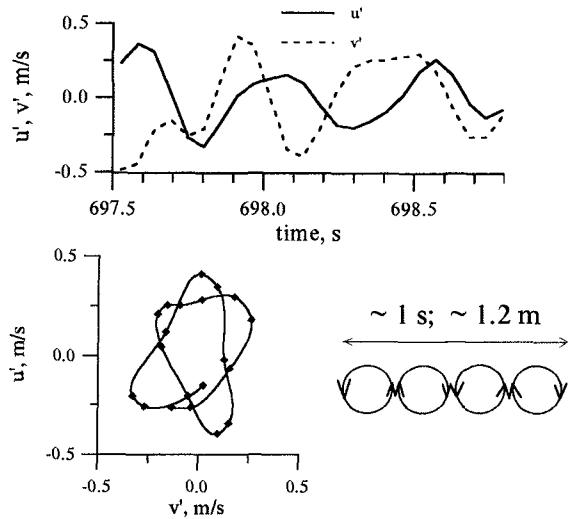


Figure 8. Time scales of turbulent vortices.

Spatial scales of turbulence

To assess spatial scales of turbulence the chronograms of the turbulent velocity fluctuations were recalculated into series of fluctuations along trajectories of the vortex movement according to Taylor's hypothesis "about frozen turbulence". Wave components ($f < 0.8$ Hz) were used as carrier velocities. The obtained series of spatial distribution of turbulent velocity fluctuations are presented as stick diagrams, an example is presented on Figure 9. The zero point of the spatial coordinate has been fixed arbitrarily.

The obtained stick diagrams show that turbulent vortices are grouped in large structures. The passing of these vortex-structures across the point of

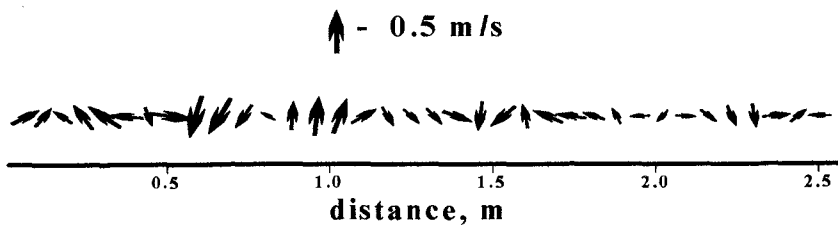


Figure 9. Example of stick-diagram. Record 5a.

measurements coincides with the sand suspending events. The spatial boundaries of such structures were determined visually by using the velocity value of 0.1 m/s as a boundary between the vortex structure and the background turbulence. The length of such structures was varied from 1 to 10 m. Linear scales of vortices in the recorded structures varied from 0.3 to 1.5 m and there were the vortices of different size in one structure. There were also the structures of different size in one series of measurements. Since we had only one velocity gauge in operation, we could not determine whether the central or the outline part of turbulent vortex had been recorded. It was a reason of definite incoherence between wave flow dimensions and vortex size. But if we will consider only the largest vortices in the structures, such correlation becomes obvious.

The dependency between the largest vortex size in a series and a water depth is presented in Figure 10. It demonstrates how the diameter of vortex increases with depth. This dependency confirms the classic idea about a proportionality between sizes of vortices and flow.

To improve the accuracy of the assessment for the turbulent vortex size the next series of experiments will operate several gauges simultaneously, which were be placed at a distance about one meter.

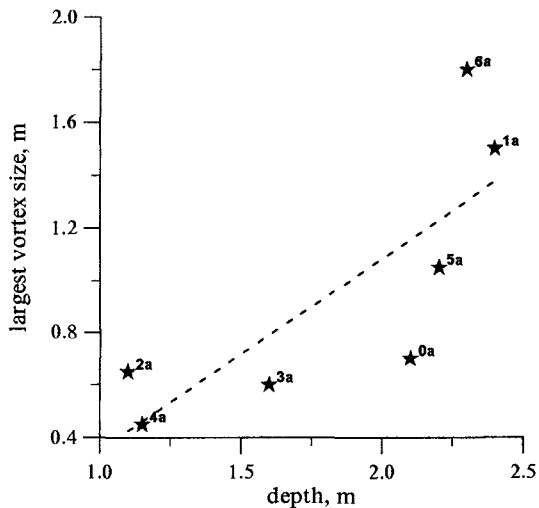


Figure 10. Spatial scales of vortices.

Conclusions

Our results demonstrate that suspension events in the middle and inner parts of a surf zone are determined by macro-turbulent vortices and that the intermittence of turbulence determines the low-frequency fluctuations of suspended sand concentration. In our future investigations we will investigate the connections between intermittence of turbulence and wave parameters and the correlation between parameters of turbulence and the suspended sand concentration.

Acknowledgment

This research was supported by the grant 95-05-14343 from the Russian Foundation for Basic Research and by a grant of the German Federal Ministry for Science, Education, Research and Technology (BMBF).

References

- Foster D.L., R.A. Holman and R.A. Beach (1994). Sediment suspension events and shear instabilities in to bottom boundary layer. *Proc. Int. Conf. "Coastal Dynamics'94", Barcelona*, 712-716.
- George K., R.E. Flick and R.T. Guza (1994). Observation of turbulence in surf zone. *J. of Geoph. Res., Vol. 99, n. C1*, 801-810.
- Hino M., M. Kashivayanagi, A. Nakayama and T Hara (1983). Experiments of the turbulence statistics and the structure of a reciprocating oscillatory flow. *J. of Fluid Mech., Vol. 131*, 363-400.
- Kos'yan R.D., S.Yu. Kuznetsov, I.S. Podymov, N.V. Pykhov and O.V. Pushkarev (1994). Nearshore suspended sediment concentration measuring during storm. In: *"Littoral'94", Proc. of the second International Symposium. V.I. Lisbon*, 445-452.
- Nadaoka K. and T. Kondoh (1989). Turbulent flow field structure of breaking waves in the surf zone. *J. Fluid Mech., Vol. 204*, 359- 387.
- Pykhov N., R. Kos'yan and S. Kuznetsov (1995). Time scales of sand suspending by irregular waves. *Proc. of 2nd Int. Conf. "Medcoast-95", Tarragona, Spain*, 1073-1091.
- Rodrigues A., A. Sanchez-Arcilla, J. Gomez and E. Bahia (1995). Study of surf-zone macroturbulence and mixing using Delta'93 field data. *Proc. Int. Conf. on Coastal Research in Terms of Large Scale Experiments "Coastal Dynamics'95", Gdansk, Poland*, 305-316.
- Sato S., K. Homa and T. Shibayama (1990). Laboratory study on sand suspending due to breaking waves. *Coastal Engineering in Japan, Vol. 33, n. 2*.
- Zhang P., T. Sunamura, Sh. Tanaka and K. Yamamoto (1994). Laboratory experiment of longshore bars produced by breaker-induced vortex action. *Proc. Int. Conf. "Coastal Dynamics'94", Barcelona*, 29-43.

CHAPTER 319

MECHANISMS OF BEACH GROUND WATER AND SWASH INTERACTION

Andrew J. Baird¹, Travis E. Mason², and Diane P. Horn³

ABSTRACT

Previous studies of swash-ground water interactions have given prominence to infiltration of swash and backwash into unsaturated sand as the principal mechanism explaining sedimentation patterns in the inter-tidal zone. Here we consider the role of fluidisation in explaining such sedimentation patterns. It appears that fluidisation due to general ground water outflow from a beach is insufficient to induce fluidisation of surface sand. We propose a different mechanism for explaining fluidisation whereby very small amounts of swash infiltration into the seepage face cause rapid increases in pore water pressure below the beach surface. During the backwash, pressure unloading on the surface causes rapid ground water outflow from the surface sediment. The rate of this outflow is shown, using a simple model, to be sufficient to induce fluidisation. We also consider a model of general beach ground water behaviour and conclude that it can be satisfactorily used to provide boundary conditions for smaller scale models of fluidisation under swash.

1) INTRODUCTION

Grant (1946, 1948) was among the first to suggest a link between beach ground water behaviour and swash zone sediment transport. He proposed that a “dry” beach (one with a low water table, which he equated with unsaturated conditions below the beach surface) allows swash to infiltrate. The reduction in swash depth due to infiltration reduces swash velocity allowing sediment deposition. Therefore, a dry beach promotes accretion. Conversely, on a “wet” beach (one in which the water table is at or near the beach surface) the swash and backwash retain their depth because infiltration is limited. Backwash flows may be augmented by ground water outflow from the beach. Grant (1948) further suggested that the seepage force due to ground water outflow may

¹ Lecturer, Dept. of Geography, University of Sheffield, Sheffield S10 2TN, UK.

² Postgraduate research student, Dept. of Oceanography, Southampton Oceanography Centre, Southampton SO14 3ZH, UK.

³ Lecturer, Dept. of Geography, Birkbeck College, University of London, London W1P 2LL, UK.

cause fluidisation of the sediment at the beach surface and enhance entrainment and sediment transport by backwash.

Infiltration

The logic of Grant's conceptual model has led many researchers to concentrate on the effects of infiltration losses on beach accretion and erosion (e.g. Emery and Foster, 1948; Emery and Gale, 1951; Isaacs and Bascom, 1949; Longuet-Higgins and Parkin, 1962; Duncan, 1964; Strahler, 1966; Harrison 1969,1972; Waddell, 1976; Chappell et al., 1979; Heathershaw, et al. 1981; Lanyon et al., 1982; Carter and Orford, 1993; and Turner 1993). Most of these authors have suggested that infiltration losses during swash provide the main mechanism by which beach accretion occurs above the still water level. However, despite the early suggestion of the importance of infiltration in the swash zone, few attempts have been made to model swash and backwash infiltration. Packwood (1983) developed a numerical model predicting runup due to a single bore incident on an initially dry beach. His justification for the development of this model was based on the assumption that infiltration is the mechanism that controls sediment transport on the beach face. Packwood (1983) argued that, as an incoming tide rises above the water table, the runup advances over dry sand and a proportion of the water mass is lost into the beach. Packwood's results showed that for fine sand (with a porosity, n , of 0.3, and a hydraulic conductivity, K , of 0.01 cm s^{-1}), very little water percolates into the beach. Packwood (1983) found that runup on fine sand and on an impermeable roughened slope are almost the same. In contrast, for medium sand ($n = 0.3$, $K = 0.1 \text{ cm s}^{-1}$), although the maximum runup is reduced very little, the backwash is significantly reduced in depth. This thin backwash layer drains rapidly into the sand, which will have a significant effect on the bed shear stress and the ability of the flow to transport sediment. Packwood (1983) concluded that the effect of a porous bed is seen much more in the backwash than in the swash. However, he did not consider the effect of a water table nearer to the beach surface on the infiltration process.

Fluidisation

In his 1948 paper Grant appears to suggest that the mechanism for fluidisation of sand grains on the beach surface is due to general ground water outflow from the beach associated with a high water table. A number of researchers have considered this effect but none have found convincing evidence of its importance in sand transport. For example, Oh and Dean (1994) used laboratory experiments and numerical modelling to investigate the influence of the beach water table on profile change and concluded that the effect of the upward flow on sediment transport appeared to be small compared with the effects of a steep slope. It seems likely that ground water outflow from a beach in response to a falling tide alone is insufficient to induce fluidisation, since hydraulic gradients under the beach surface will tend to be relatively small. It is proposed here that fluidisation is only generally possible in the presence of swash and that it occurs over relatively short timescales. As a swash flow advances over the saturated beach surface, there will be a relatively rapid increase in pore water pressures

below the beach surface. When under swash flow, the beach sediment behaves like a confined aquifer. The sediment is saturated and movement of water into the beach is extremely limited, since changes in porosity due to expansion and contraction of the mineral 'skeleton' will be minimal. However, because of this limited potential for infiltration, water pressures will propagate rapidly through the sediment. The characteristic time of propagation of any diffusion process is given by

$$t = \frac{x^2}{D} \quad (1)$$

where x is distance (L) and D is the diffusivity ($L^2 T^{-1}$), given by the ratio of hydraulic conductivity, K (LT^{-1}), to specific storage, s (L^{-1}). In a sand in the unconfined case, the specific storage multiplied by depth is called the specific yield and typically has values of between 0.1 and 0.3 per unit depth. In the confined case, which is effectively the case for sand under a swash lens, the specific storage is much lower and a value of the order of 0.002 is more realistic. The hydraulic conductivity of beach sands can be expected to be in the range 0.01 to 0.5 $cm s^{-1}$ (Packwood and Peregrine, 1980). For all of the values in this range, the small value of specific storage will give relatively large values of D and small times of propagation, so that the pressure acting on the sand surface under advancing swash will propagate at least into the surface layers of the beach sediment. As the swash retreats there will be a release of pressure on the beach, giving large hydraulic gradients acting vertically upwards immediately below the surface. The resultant seepage force associated with rapid ground water outflow could be sufficient to induce fluidisation of the sand grains at the beach surface. This may occur during the latter stages of backwash and will provide readily entrainable material that can be carried seaward by the backwash flow. To our knowledge this mechanism has not been previously identified and no attempt has been made at modelling it. Later in this paper, we consider in detail how the propagation of pressure through the beach sediment can be modelled. However, whether infiltration into unsaturated or saturated sand is being considered, a first stage in any modelling exercise is the accurate prediction of the position of the seepage face together with predictions of more general ground water flows and pore water pressures within the beach, since these will act as boundary and initial conditions for infiltration and pressure propagation models. Below we consider how the general ground water behaviour of a beach can be modelled.

2) MODELLING BEACH GROUND WATER BEHAVIOUR

Theory

Recently, we have developed a model capable of predicting water table elevations in, and the extent of the seepage face on, sandy beaches. The model, called **GRIST** (**G**round water **I**nteraction with **S**wash and **T**ides), has been developed as a modular package and is described in Baird and Horn (1996) and Baird et al. (in review). Two approaches, both based on Darcy's Law and the continuity equation, have been used for modelling water table behaviour in response to tidal forcing in sandy beaches in the

GRIST package. The first approach uses the one-dimensional form of the Boussinesq equation given by

$$\frac{\partial h}{\partial t} = \frac{K}{s} \frac{\partial}{\partial x} \left(h \frac{\partial h}{\partial x} \right) \quad (2)$$

where h is the elevation of the water table (L), t is time (T), K is the hydraulic conductivity of the beach sediment (LT^{-1}), s is the specific yield or drainable porosity (dimensionless), and x is horizontal distance (L). The main assumption in using this equation is that ground water flow in a shallow aquifer can be described using the Dupuit-Forchheimer (D-F) approximation. D-F theory states that in a system of shallow gravity flow to a shallow sink when the flow is approximately horizontal, the lines of equal hydraulic head or potential are vertical, and the gradient of hydraulic head is given by the slope of the water table. Using D-F theory, two-dimensional flow to a sink can be approximated as one-dimensional flow, and the resulting differential equation (equation (2)) is more readily solved. In beaches which are underlain by relatively impermeable solid rock or clay deposits it is likely that D-F theory will provide adequate descriptions of ground water flow. The second approach used in the **GRIST** model considers the beach as a two-dimensional flow system in which the water table is a free surface or flow line. The advantage of the second approach is that it can be used to predict radial flow towards the seepage face if such an approach is necessary; for example, in cases where the flow field in the beach suddenly narrows forcing water to the surface.

Both equations have been solved in the **GRIST** package using standard finite-difference methods and are described in detail in Baird et al. (in review). In the 1D model, a block-centred finite-difference scheme is used and tide-water table decoupling is assumed to occur if

$$h_{i,t} + \left(\frac{(Q_i - Q_{i+1})\Delta t}{s_i} \right) > e_i \quad (3)$$

where Q_i is the rate of ground water discharge ($L^3 T^{-1}$) (in a seaward direction) into cell i during Δt (from cell $i-1$), Q_{i+1} is the rate of discharge out of cell i during Δt , and e is the cell height (L). Further details of the model can be found in Baird and Horn (1996).

Field testing of the 1D model

The predictions of the 1D version of the model have been tested against field measurements which are described in detail in Baird et al. (in review). The field measurements were made on a microtidal beach at Canford Cliffs, Poole, Dorset, England. Canford Cliffs beach is a groyned beach and is backed by a sea wall. It has a mean slope of 3.2° ($\tan \beta = 0.056$) on the upper foreshore and a mean slope of 1.5° ($\tan \beta = 0.026$) on the lower foreshore. The tidal range at Canford Cliffs varies between 0.2 and 1.8 m on neap and spring tides respectively. The field measurements which are reported here were taken between the 21st and 28th October 1995 in a period leading from a neap to a spring tide, with a tidal range varying from 0.9 to 1.7

m. The significant wave height (H_s) varied from 0.35 to 0.76 m, while H_{rms} (root mean square wave height) varied between 0.25 and 0.53 m. Zero-crossing period varied between 5.2 and 6 s, and the peak spectral period varied between 5.6 and 9.8 s.

Water table elevations were measured with pressure transducers in ten screened wells placed at distances of 1.9, 3.8, 5.8, 7.8, 9.3, 10.8, 13.1, 15.6, 18.7, and 21.7 m seawards from the sea wall. Wave and tidal frequencies and amplitudes were measured with a seabed-mounted pressure transducer located at the low water mark. All instruments were logged using a PC at the top of the beach and were calibrated before and after the deployment. Beach profiles and instrument locations were measured using a total station. Sediment samples were collected at 0.5 m intervals along a cross-shore transect from the surface of the beach and at a depth of 20 cm for estimation of particle size parameters. Twelve sediment cores were also collected along the cross-shore transect for laboratory determinations of K using a constant head permeameter.

Results

The mean grain diameter of the surface sediments was approximately 0.24 mm (2.06 ϕ), the mean sorting was 0.44 ϕ and the mean skewness was -0.71. Results from 20 cm depth were very similar with a mean grain diameter of 0.22 mm (2.17 ϕ), a mean sorting of 0.36 ϕ and a mean skewness of -0.64. The mean K of the sediment cores was 0.225 cm s⁻¹, with a range from 0.036 to 1.179 cm s⁻¹, and a coefficient of variation of 143 per cent which is typical for this parameter.

The 1D model was run for Canford Cliffs using 40 computational cells with a width of 1 m. Measured values of tidal elevation were used in the simulation. The inland boundary was a no-flow condition at the sea wall. The bottom boundary was a no-flow condition given by the position of an impermeable barrier located 50 cm below Ordnance Datum. The seaward cell was assumed to be permanently saturated; that is, the water table was assumed to be always at the cell surface. A value of K/s of 0.75 cm s⁻¹ was used in the model simulation. This value was calculated using the arithmetic mean of the permeameter measurements of K (0.225 cm s⁻¹) and an assumed value of s of 0.3.

The predictions of the 1D model are shown for each of the wells in Baird et al (in review). Here we show only two examples of the model's predictions, for wells 6 and 10 (9.3 and 1.9 m seaward of the seawall, respectively). In both cases the remarkably good agreement between modelled and observed water table elevations can be seen. The agreement was similarly good for all ten wells. Thus the model was able to predict with some accuracy water table rise and fall at different positions in the beach, giving a good representation of changes in the shore-normal water table profile over time. For most of the wells the model very accurately describes the lag and asymmetry of water table response. The predictions of lag and asymmetry are less good for wells 8 to 10, with the model predicting a later and steeper rise than was observed. The earlier rise of the observed water table may be due to setup and runup above the shoreline causing a greater flow of water into the beach than would occur due to tidal rise alone (see below). This point is discussed in more detail in Baird et al. (in review). It is also possible that the K of the sediment at the back of the beach was lower than that more seaward, giving greater lags than predicted by the model which uses a single value of

K. However, such a pattern of variation in *K* was not evident from the hydraulic conductivity data although it is recognised that surface sand samples may not be representative of sand at depth.

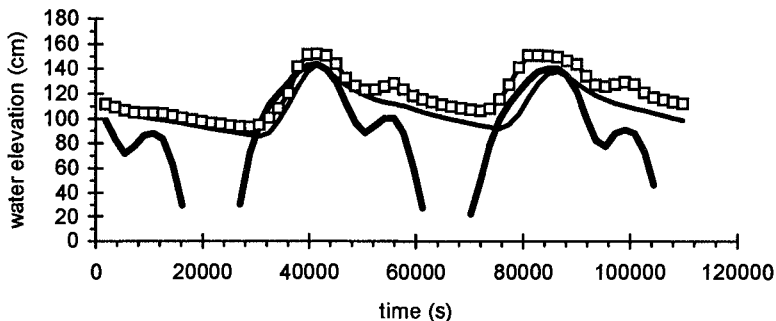


Figure 1. Measured and modelled water table elevations at well 6 (9.3 m seaward of sea wall). Open squares - observed; medium solid line - simulated; thick solid line - observed tide. Elevations given above a datum which represents the position of the impermeable barrier below the beach surface. Time is from 20.00 GMT on 22nd October 1995.

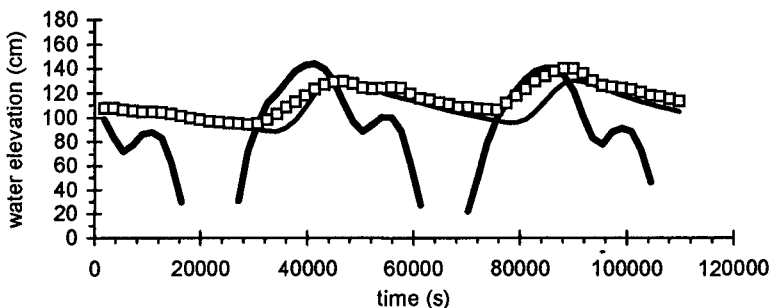


Figure 2. Measured and modelled water table elevations at well 10 (1.9 m seaward of sea wall). Open squares - observed; medium solid line - simulated; thick solid line - observed tide. Elevations given above a datum which represents the position of the impermeable barrier below the beach surface. Time is from 20.00 GMT on 22nd October 1995.

The agreement between observed and simulated water tables is better before high water at 40000 s than after. This is probably due to the fact that wave heights and swash excursions were greater after this time. The wave record shows that through the period of measurement H_s increased from 0.35 to 0.76 m. Setup and swash excursion

can be expected to give higher water tables than would be expected due to the tide alone and this is indeed the case with the observed water tables, with levels in well 6 in particular rising above high tide levels (Figure 1). A water table elevation above the high tide elevation is only possible if an additional source of water, such as rainfall, is entering the beach, or if setup and runup raise the mean water surface causing greater rates of flow into the beach. Greater setup due to the larger wave heights at high tide will increase the elevation of the shoreline. This, in turn, will give rise to greater amounts of seepage into the beach than would occur if the free surface on the beach face were at the tide level. Runup will increase water table levels via vertical infiltration and downward movement of water through the unsaturated zone. No rainfall was recorded during the measurement period reported here, so the source of additional water is most likely to be setup and runup. It is also possible that the increased departure between modelled and observed is due to accumulated error in model predictions since a small error in water table predictions will feed into later predictions. However, error propagation will tend to be cumulative whereas the figures clearly show that the discrepancy between observed and predicted occurs more as a step change during the second high water. Thus setup and runup are the more likely explanation for most of the discrepancy between observed and predicted.

The model based on equation (2) provides a good description of water table dynamics in response to tidal forcing although an allowance should be made in future versions of the model for the effects of setup. We suggest, therefore, that the model can be used to provide satisfactory boundary conditions for swash infiltration and pressure propagation models.

3) THE POSITION OF THE WATER TABLE RELATIVE TO THE BEACH SURFACE

Figure 3 shows the measured position of the water table relative to the sand surface for two positions of the tide, low water at 22800 s and high water at 40000 s. At low water the water table intersected the beach face at a distance of about 32 m from the sea wall (the tide was below the level of the beach shown on the diagram) and tended to approach the beach face at a tangent as suggested by Bear (1972). The water table in wells 1 and 2 fell little during the period between low water and subsequent immersion by the rising tide. Thus during the advance of the tide over the seepage face and later across the zone between 18 and 32 m from the sea wall, where the water table remained close to the beach surface, there would have been little opportunity for significant swash infiltration. Any infiltration that did occur is unlikely to have had an effect on swash and backwash dynamics during these conditions because the beach would have behaved like the impermeable case analysed by Packwood (1983). The water table at high water shows a pronounced landward slope and a superelevation of the water table in wells 6 and 7. This superelevation can be attributed to setup and runup as discussed above, and indicates that infiltration into this part of the beach may have the potential to affect swash and backwash hydraulics in the way described by Packwood (1983) for a permeable beach.

It would appear from the above reasoning that swash and backwash infiltration are only likely to be important in affecting swash/backwash hydraulics on a beach such as

Canford Cliffs during the latter part of the rising tide when some swash and backwash move over an unsaturated beach. However, it is important to stress that even small amounts of swash infiltration into the seepage face followed by rapid ground water outflow could induce fluidisation on middle and lower parts of the beach, and that the interaction between beach ground water behaviour and sediment dynamics may be more subtle than suggested by existing swash/backwash infiltration models such as that of Packwood (1983).

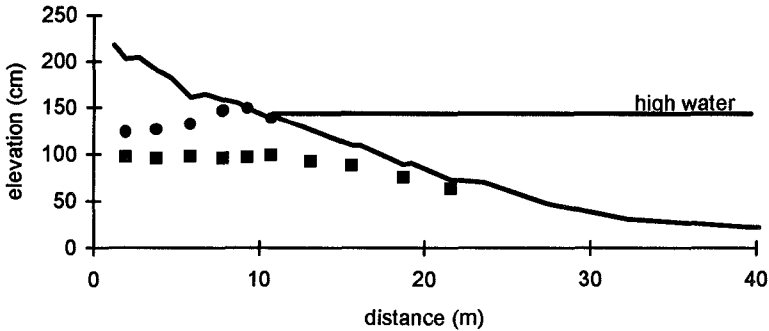


Figure 3. Measured water table elevations along the shore-normal profile at low water after an elapsed time of 22800 s (closed squares), and high water at 40000 s (closed circles).

4) MODELLING FLUIDISATION UNDER SWASH

It was noted earlier that when a swash runs over a saturated beach there will be a relatively rapid increase in pore pressure below the beach surface, and that the pressure release associated with backwash could induce fluidisation of the beach surface. The equation governing water movement through an isotropic and homogeneous saturated beach sediment is

$$\frac{\partial^2 h}{\partial x^2} + \frac{\partial^2 h}{\partial y^2} + \frac{\partial^2 h}{\partial z^2} = \frac{s}{K} \frac{\partial h}{\partial t} \quad (4)$$

where here h is now the hydraulic head (L), and s is the specific storage (L^{-1}). For most purposes this equation can be simplified to its two-dimensional form.

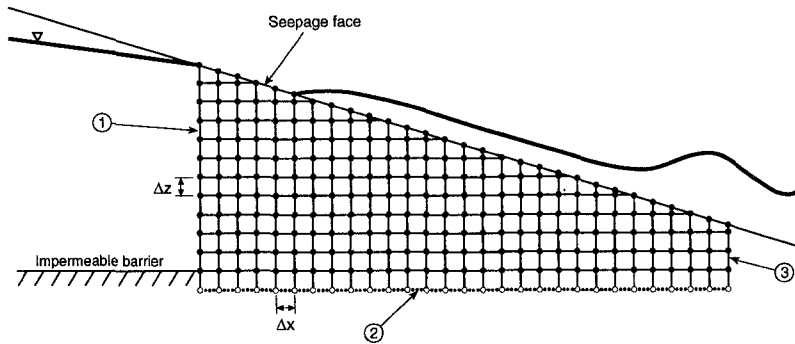


Figure 4. Finite difference grid for the simulation of pressure propagation into a sand bed under swash. ① and ③ are boundaries where the head is given. ② is a no-flow boundary.

The requirements of a two-dimensional model of ground water flow, and therefore pressure propagation, through beach sediment under advancing swash and retreating backwash are shown in Figure 4. The diagram shows a finite-difference, mesh-centred grid representing the body of sand beneath and landward of swash. For the upper boundary condition the model requires a time series of swash depths for that part of the beach face which becomes inundated. It is assumed that the pressure acting on the beach surface at the base of the swash is equivalent to the swash depth; that is, the pressure is hydrostatic. It is this hydrostatic pressure that provides an upper boundary condition to the model. The lower part of the model is assumed to be a no-flow boundary (von Neuman condition) which can be simulated using a set of fictitious nodes shown by open circles. The boundary condition $\partial h/\partial z = 0$ translates in finite-difference form to $h_{i, j-1} = h_{i, j+1}$ assuming an indexing notation whereby j represents row number (z axis - positive upwards) and i column number (x axis - positive to the right of the diagram). The impermeable barrier is given by j so that $j-1$ represents the fictitious nodes. The inland boundary condition is a prescribed head condition (Dirichlet condition) which can be provided either from field measurements or, as noted above, from a larger scale beach ground water model such as **GRIST**. In Figure 4 it is shown as the column of nodes below the exit point. The position of the exit point can also be provided from measurements or modelling. The seaward boundary condition is given by prescribed heads at the nodes. This distribution of heads can be assumed to be hydrostatic and equal to wave height at this point. The initial condition for the internal nodes can be estimated from field measurements or can be assumed to be a hydrostatic distribution of hydraulic heads.

Figure 4 represents an ideal solution to the problem of fluidisation under swash and backwash. In the absence of detailed information on the two-dimensional structure of swash, which we are currently measuring using capacitance probes and video techniques, we consider below the effect of water loading and unloading on a one-dimensional column of saturated sand. A simple explicit finite-difference method was used to solve the one-dimensional form of equation (4). The solution is given by

$$\frac{h_{j+1}^n - 2h_j^n + h_{j-1}^n}{(\Delta z)^2} = \frac{s}{K} \left(\frac{h_j^{n+1} - h_j^n}{\Delta t} \right) \tag{5}$$

where the superscript n refers to time.

Five cases of inundation were considered in the model simulations. In all model runs the initial distribution of hydraulic heads below the surface was assumed to be hydrostatic. Nodes were spaced 2 cm apart and the total column length was 60 cm. The base of the column was a no-flow boundary. The cases were:

Case 1. Step increase in pressure on the upper boundary equivalent to a water depth of 10 cm followed by a step return to a condition of no excess pressure on the surface. The pressure loading lasts for 3 seconds and the simulation lasts for 6 s. $K = 0.1 \text{ cm s}^{-1}$; $s = 0.002 \text{ cm}^{-1}$.

Case 2. As for Case 1 except that $s = 0.004 \text{ cm}^{-1}$.

Case 3. Step increase in pressure on the upper boundary equivalent to a water depth of 5 cm followed by a step return to a condition of no excess pressure. The pressure loading lasts for 3 seconds and the simulation lasts for 6 s. $K = 0.025 \text{ cm s}^{-1}$; $s = 0.002 \text{ cm}^{-1}$.

Case 4. For a more realistic loading and unloading of water on the upper boundary we used Hughes' (1992) measurements of swash on beaches in Sydney, Australia (case 'a' from Figure 7a of Hughes, 1992). The actual swash depths were approximated using a ramp addition lasting for 2 s and a ramp loss of water lasting for 6.5 s, with a maximum water depth of 20 cm and a total period of inundation of 8.5 s. $K = 0.05 \text{ cm s}^{-1}$, $s = 0.002 \text{ cm}^{-1}$.

Case 5. As for Case 4 but with $K=0.02 \text{ cm s}^{-1}$.

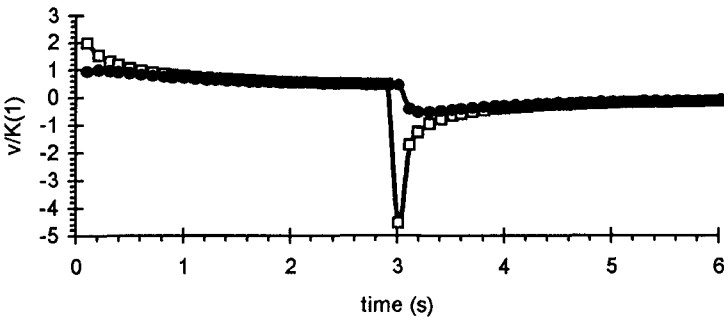


Figure 5. Variations in v/K over time for Case 1 (see text for details).

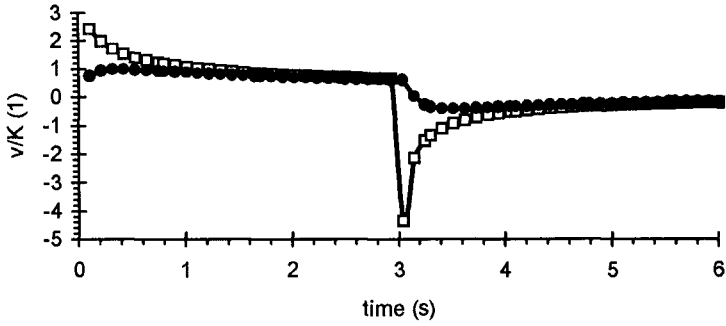


Figure 6. Variations in v/K over time for Case 2 (see text for details).

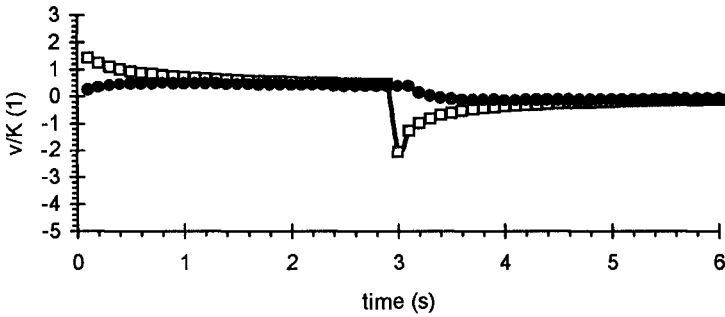


Figure 7. Variations in v/K over time for Case 3 (see text for details).

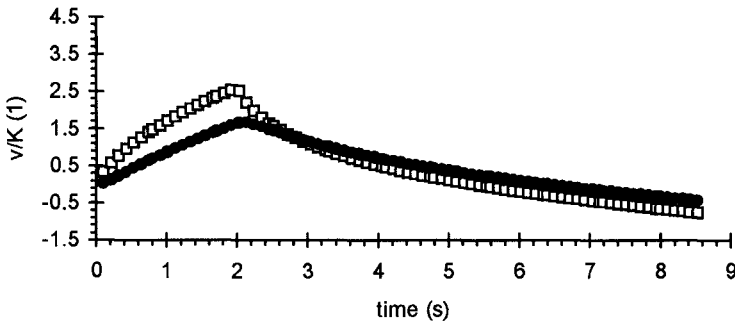


Figure 8. Variations in v/K over time for Case 4 (see text for details). Note the change in axes scales.

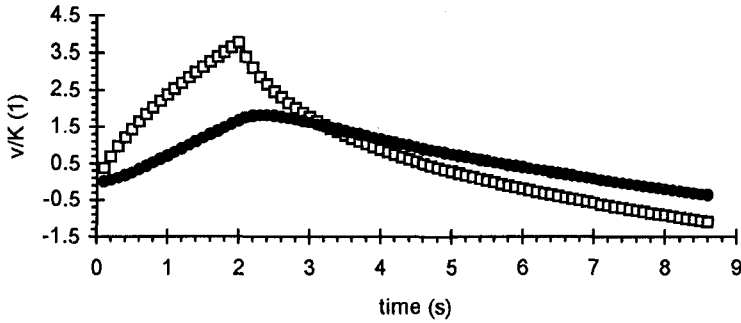


Figure 9. Variations in v/K over time for Case 5 (see text for details).

Cases 1 to 5 are illustrated in Figures 5 to 9, respectively. In each figure, v/K is plotted against time, where v is the specific discharge (cm s^{-1}) through the sand. v/K is equivalent to the hydraulic gradient. Two time series are shown. That with the open squares represents the hydraulic gradient acting between the node 2 cm below the surface and the node representing the beach surface. The closed circles represent the hydraulic gradient between the nodes 4 and 2 cm below the surface. A positive gradient indicates flow downwards into the sand, a negative gradient upward flow. The values of K and s used in Cases 1 to 5 are all within the range of what might be expected for fine to medium sand (see Packwood and Peregrine 1980).

Packwood and Peregrine (1980) noted that for most sands and fine gravels, fluidisation occurs when $v/K < -0.7$ (using the sign convention above). (See also Bear, 1972, pp. 184-189). Fluidisation occurs when the effective stress becomes zero. It should also be noted that downward seepage has the effect of increasing the effective stress and increasing the stability of the sediment. Cases 1 to 3 show that there is an initially large hydraulic gradient associated with the addition of water to the sand surface which declines in an approximately exponential fashion with time. After the removal of the ponded water there is a sudden reversal in the direction of the hydraulic gradient. In all three cases fluidisation can be expected to occur since v/K is less than -0.7 . The period of potential fluidisation lasts for approximately 0.4 to 0.6 s. It is interesting to note that large values of v/K are only present in the uppermost layer of sand.

Under real swash, step loading and unloading is unlikely to occur, with the addition and removal of water being more gradual. As noted above, we used the measurements made by Hughes (1992) as a first approximation to loading and unloading under real swash. In Case 4 fluidisation is not predicted by the model. However, a reduction in the ratio of K/s , as shown in Figure 9 (Case 5), does give predicted fluidisation for approximately the last second of the backwash. Much more information is needed on swash and backwash velocities and shear stresses on the bed to understand the implications of this for sediment movement in the swash zone. However, the simple model is revealing in that it suggests that fluidisation of the bed occurs before the beach surface is exposed so that the entrainment and seaward transport of sediment in the

latter stages of backwash is enhanced. This is consistent with qualitative observations of backwash by Hughes (1992) who, with other workers, notes that as the swash lens thins during backwash it develops into a slurry of fluid and sediment. The one-dimensional model is obviously an over-simplification of pressure propagation through a sand bed under swash, as is the assumption of a single swash passing over the bed in which the initial condition is a hydrostatic distribution of hydraulic head. However, the model does suggest a mechanism for fluidisation in the swash zone apparently not previously considered by other workers, and one that may exert a greater control on sediment movement in the swash zone than infiltration of swash into the unsaturated part of the beach. It is important to stress that, although the mechanism described here involves infiltration into the sand bed, the amount of water lost from swash and backwash is negligible since the specific storage of saturated sand is so low. Thus it appears that infiltration *sensu* Grant (that is, infiltration into unsaturated sand above the water table) is not needed for ground water to have a significant impact on swash sediment dynamics. The mechanism of fluidisation given here is certainly worthy of further investigation, and to elucidate the processes involved we are engaged in measurements of swash/backwash flows and pressure propagation in both the laboratory and the field site at Canford Cliffs. Results from these studies will be reported in due course.

ACKNOWLEDGEMENTS

Most of the funding for this research came from the United Kingdom Natural Environment Research Council (Grant number GR9/01726). The remainder of the funding was from grants from Birkbeck College, University of London, and the University of Sheffield awarded to Horn and Baird respectively. We would like to thank Mike Wilkin, Paul Bentley, Peter Riley, John Cross, Steve Pearce, Matthew Foote, Simon Gaffney, Richard Kelly, Mark Lee, Chris Turner, Jill Ulmanis, and Steve Wallbridge for their help and advice. Finally, we would like to thank Poole Borough Council who kindly allowed us to use the Surf Lifesaving Club building at Canford Cliffs for housing logging equipment.

REFERENCES

- Baird, A.J. and Horn, D.P. 1996. Monitoring and modelling ground water behaviour in sandy beaches. *Journal of Coastal Research* 12(3): 630-640.
- Baird, A.J., Horn, D.P. and Mason, T.E. (in review). Validation of a beach ground water model. Submitted to *Marine Geology*.
- Bear, J. 1972. *Dynamics of Fluids in Porous Media*, Elsevier, New York, 764 pp.
- Carter, R.W.G. and Orford, J.D. 1993. The morphodynamics of coarse clastic beaches and barriers: a short- and long-term perspective. *Journal of Coastal Research* 15: 158-179.
- Chappell, J., Eliot, I.G., Bradshaw, M.P. and Lonsdale, E. 1979. Experimental control of beach face dynamics by water-table pumping. *Engineering Geology* 14: 29-41.
- Duncan, J.R. 1964. The effects of water table and tidal cycle on swash-backwash sediment distribution and beach profile development. *Marine Geology* 2: 186-197.

- Emery, K.O. and Foster, J.F. 1948. Water tables in marine beaches. *Journal of Marine Research* 7: 644-654.
- Emery, K.O. and Gale, J.F. 1951. Swash and swash mark. *Transactions of the American Geophysical Union* 32(1): 31-36.
- Grant, U.S. 1946. Effects of ground water table on beach erosion. *Bulletin of the Geological Society of America* 57: 1252 (abstract).
- Grant, U.S. 1948. Influence of the water table on beach aggradation and degradation. *Journal of Marine Research* 7: 655-660.
- Harrison, W. 1969. Empirical equations for foreshore changes over a tidal cycle. *Marine Geology* 7, 529-551.
- Harrison, W. 1972. Changes in foreshore sand volume on a tidal beach: role of fluctuations in water table and ocean still-water level. *Proceedings of the 24th International Geological Conference, Montreal*: 159-166.
- Heathershaw, A.D., Carr, A.P., Blackley, M.W.L. and Wooldridge, C.F. 1981. Tidal variations in the compaction of beach sediments. *Marine Geology* 41: 223-238.
- Hughes, M.G. 1992. Application of a non-linear shallow water theory to swash following bore collapse on a sandy beach. *Journal of Coastal Research* 8: 562-578.
- Isaaks, J.D. and Bascom, W.N. 1949. Water table elevations in some Pacific coast beaches. *Transactions of the American Geophysical Union* 30: 293-294.
- Lanyon, J.A., Eliot, I.G., and Clarke, D.J. 1982. Observations of shelf waves and bay seiches from tidal and beach ground water-level records. *Marine Geology* 49, 23-42.
- Longuet-Higgins, M.S. and Parkin, D.W. 1962. Sea waves and beach cusps. *Geographical Journal* 128: 194-201.
- Oh, T-M. and Dean, R.G. 1994. Effects of controlled water table on beach profile dynamics. *Proceedings of the 24th International Conference on Coastal Engineering*: 2449-2460.
- Packwood, A.R. 1983. The influence of beach porosity on wave uprush and backwash. *Coastal Engineering* 7: 29-40.
- Packwood, A.R., and Peregrine, D.H. 1980. The propagation of solitary waves and bores over a porous bed. *Coastal Engineering* 3: 221-242.
- Strahler, A.N. 1966. Tidal cycle of changes in an equilibrium beach, Sandy Hook, New Jersey. *Journal of Geology* 74: 247-268.
- Turner, I.L. 1993. The total water content of sandy beaches. *Journal of Coastal Research Special Issue* 15: 11-26.
- Waddell, E. 1976. Swash-ground water-beach profile interactions. In Davis, R.A. and Etherington, R.L. (eds) *Beach and nearshore sedimentation*. Society of Economic and Paleontological Mineralogists Special Publication 24: 115-125.

CHAPTER 320

The equations for integral and mean flow properties in the swash zone

M. Brocchini [†] and D.H. Peregrine [‡]

Abstract

The swash zone is the area of a beach where the waves move the instantaneous shoreline back and forth. This zone is modelled using the nonlinear shallow-water equations (NLSWE) as equations of motion, as is appropriate for gently sloping beaches. Integrated swash zone boundary conditions are derived for wave resolving models: their use gives considerable numerical advantages. Wave-averaged and swash-zone integrated boundary conditions have also been derived. They include numerous terms for which closures are to be found.

Equations and an analytic swash zone solution

In this section we introduce the basic equations used to describe the flow dynamics near the shore. We choose the still water level to be $z = 0$, and define

$$d(x, t) = h(x) + \eta(x, t) \quad (1)$$

where d is the total water depth, $z = -h(x)$ is the seabed, $z = \eta$ is the position of the free surface (see figure 1).

For a plane beach with $h(x) = \alpha x$ the inviscid equations are

$$\begin{aligned} d_{t^*}^* + (d^* u^*)_{x^*} + (d^* v^*)_{y^*} &= 0 \\ u_{t^*}^* + u^* u_{x^*}^* + v^* u_{y^*}^* + g d_{x^*}^* &= -g\alpha \\ v_{t^*}^* + u^* v_{x^*}^* + v^* v_{y^*}^* + g d_{y^*}^* &= 0. \end{aligned} \quad (2)$$

They can be put in a simple dimensionless form with no explicit dependence on the beach slope α (Meyer & Taylor 1972).

The dimensionless variables which eliminate the beach slope α from the equations are:

$$d = \frac{d^*}{\alpha l_0}, \quad u = \frac{u^*}{u_0}, \quad v = \frac{v^*}{u_0}, \quad u_0 = (g l_0 \alpha)^{1/2} \quad (3)$$

$$x = \frac{x^*}{l_0}, \quad y = \frac{y^*}{l_0}, \quad t = \frac{t^*}{t_0}, \quad t_0 = \left(\frac{l_0}{g\alpha} \right)^{1/2} \quad (4)$$

[†]Research Assistant, School of Mathematics, University of Bristol, University Walk, Bristol, BS8 1TW, UK, (*M.Brocchini@bristol.ac.uk*)

[‡]Professor of Applied Mathematics, School of Mathematics, University of Bristol, (*D.H.Peregrine@bristol.ac.uk*)

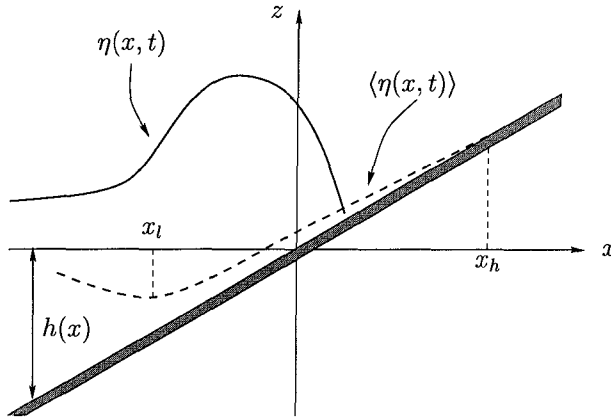


Figure 1: Flow definition in the vicinity of the swash zone.

where l_0 is a reference length which can be specified according to the particular problem under investigation. The equations become:

$$\begin{aligned} d_t + (du)_x + (dv)_y &= 0 \\ u_t + uu_x + vv_y + d_x &= -1 \\ v_t + uv_x + vv_y + d_y &= 0. \end{aligned} \quad (5)$$

For simplicity, friction terms are not included in this analysis and in most of the numerical modelling. Even at laboratory scale they are of secondary importance if beach slope is not too small. Watson et al. (1994) give a quantitative estimate of their importance. On the other hand, the energy dissipation of bores is included in the modelling as discontinuities in the solution.

Equations (5) can be further simplified by approximating for regular waves incident at small angle θ to the beach normal (Ryrie, 1983). We introduce a pseudotime t' and a small parameter ϵ such that:

$$t' = t - \epsilon y \quad (6)$$

gives the only y dependence. It implies that the wave pattern is moving along the shore with phase velocity of $1/\epsilon$. For example, this can occur for a regular train of waves incident towards the shore at a small angle θ to the shore normal, with an alongshore velocity $c/\sin\theta$.

For a weakly three-dimensional flow the following scaling:

$$y' = \epsilon y, \quad v' = v/\epsilon, \quad (7)$$

on substitution into the NLSWE (5), neglecting $\mathcal{O}(\epsilon^2)$ terms and dropping primes, gives the equations:

$$\begin{aligned} d_t + (du)_x &= 0 \\ u_t + uu_x + d_x &= -1 \\ v_t + uv_x - d_t &= 0. \end{aligned} \quad (8)$$

The last of the above set of hyperbolic equations is now decoupled from the first two. The v component of the velocity does not appear in the first two equations of (8) ('onshore problem') and a solution for the third equation ('longshore problem') is found once d and u are known. Characteristic directions in the (x, t) plane for the system (8) are given for the onshore and longshore problem respectively by:

$$\frac{dx}{dt} = u \pm c \quad \text{and} \quad \frac{dx}{dt} = u. \quad (9)$$

Equations (8) can be expressed in characteristic form:

$$\alpha_t + (u + c)\alpha_x = 0, \quad \beta_t + (u - c)\beta_x = 0, \quad \gamma_t + u\gamma_x = 0 \quad (10)$$

where the Riemann invariants are defined as follows:

$$\alpha = 2c + u + t, \quad \beta = 2c - u - t, \quad \gamma = v - \frac{1}{2}u^2 - d - x. \quad (11)$$

Carrier & Greenspan (1958) used a hodograph transformation (velocities are used as coordinates) in solving the onshore problem:

$$\lambda = \alpha - \beta = 2(u + t), \quad \sigma = \alpha + \beta = 4c, \quad u(\sigma, \lambda) = \phi_\sigma / \sigma. \quad (12)$$

The characteristic coordinates (σ, λ) are particularly effective for the moving shoreline since the $\sigma = 0$ contour maps the moving shoreline: $d = c = 0$. We note that σ is a space-like coordinate and λ is a time-like coordinate (e.g. see figure 2(d)). Combining the equations for the onshore problem gives a linear equation in ϕ :

$$(\sigma\phi_\sigma)_\sigma - \sigma\phi_{\lambda\lambda} = 0. \quad (13)$$

The simplest periodic solution is that of Carrier and Greenspan (1958):

$$\eta(\sigma, \lambda) = \frac{1}{4}\phi_\lambda - \frac{1}{2}u^2, \quad x(\sigma, \lambda) = \frac{1}{4}\phi_\lambda - \frac{1}{16}\sigma^2 - \frac{1}{2}u^2, \quad t(\sigma, \lambda) = \frac{1}{2}\lambda - u \quad (14)$$

where

$$\phi(\sigma, \lambda) = AJ_0(\sigma) \sin(\lambda), \quad (15)$$

J_0 is the Bessel function of the first kind. Not all the solutions can be transferred back to the (x, t) plane. This occurs for $A > 1$, i.e. when the Jacobian of the transformation vanishes.

Since the equation for the longshore problem is decoupled we can formally integrate this equation (10c):

$$\gamma_t + u\gamma_x = v_\lambda x_\sigma - v_\sigma x_\lambda + u(v_\sigma t_\lambda - v_\lambda t_\sigma) - (\eta_\lambda x_\sigma - \eta_\sigma x_\lambda) = 0. \quad (16)$$

After some algebra the equation can be rearranged to give a solution valid for any ϕ :

$$v = \frac{1}{4}\phi_\lambda + \text{const.} \quad (17)$$

and setting $\text{const.} = 0$ we get

$$v = \frac{1}{4}AJ_0(\sigma) \cos \lambda. \quad (18)$$

Details on some complicated multi-modal solutions are given in Brocchini & Peregrine (1996).

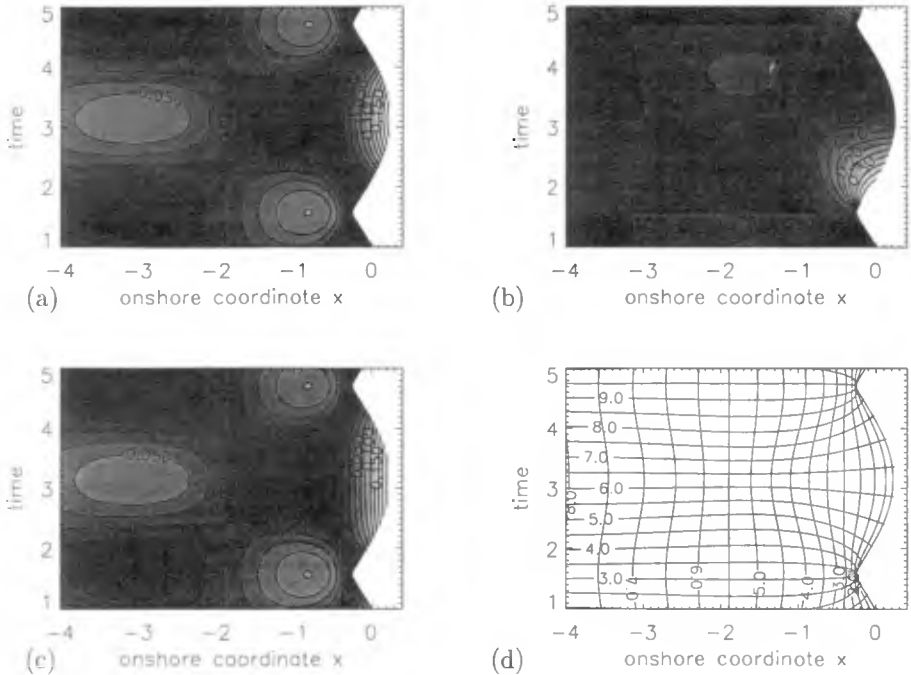


Figure 2: Contour lines for the dimensionless Carrier & Greenspan (1958) solution: (a) the free surface elevation η , (b) the onshore velocity u and (c) the longshore velocity, v , of the weakly three dimensional solution, for the case $A = 1$. Note that the dimensional longshore velocity is a factor ϵ smaller than the dimensionless quantity. (d) shows the (σ, λ) coordinates in the (x, t) plane. Lines of constant λ run from left to right whilst lines of constant σ run from top to bottom.

Contour plots of the free surface elevation and velocity components help visualise the behaviour of the solution, see figure 2. For all the flow properties shown in figure 2 there is a structured pattern of cells. Cells are confined by isolines of zero surface displacement. They also have different sizes and shapes. For all variables the largest values are reached within the most onshore cell. The particular characteristic of the contour structure for u is that it has an antisymmetric cellular pattern within the period. We can therefore state *a priori* that its mean value over a wave period is zero at each $x = const.$ position. This is not true for both the free surface elevation and the longshore velocity. They have similar cell patterns and for both of them, time averaging over a wave period results in a non-zero contribution.

Time averaging of flow properties is rather involved for the Carrier & Greenspan solution because of difficulties in relating (x, t) and (σ, λ) . Let

$$\langle G(x, t) \rangle = \frac{1}{T} \int_T G(x, t) dt = \frac{1}{T} \lim_{t \rightarrow T} H(x, t) \tag{19}$$

be the time average of $G(x, t) = g(\sigma, \lambda)$ where

$$H(x, t) = \int_0^t G(x, s) ds. \quad (20)$$

To evaluate this type of average which is based on time integration on curves of $x = \text{const}$ we solve the following partial differential equation along the curves $x = \text{const}$ in the (σ, λ) plane:

$$\frac{\partial H}{\partial t} = G(x, t) = g(\sigma, \lambda). \quad (21)$$

But for constant x we have

$$\frac{dH}{d\lambda} = \frac{\partial H}{\partial t} \left(\frac{\partial t}{\partial \sigma} \frac{d\sigma}{d\lambda} + \frac{\partial t}{\partial \lambda} \right). \quad (22)$$

Finally a set of two o.d.e.s for $\langle G(x, t) \rangle$ and σ is obtained:

$$\begin{aligned} \frac{d\langle G(x, t) \rangle}{d\lambda} &= \frac{1}{T} \lim_{t \rightarrow T} g(\sigma, \lambda) \left[\frac{\partial t}{\partial \lambda} \left(-\frac{\partial x}{\partial \lambda} / \frac{\partial x}{\partial \sigma} \right) + \frac{\partial t}{\partial \sigma} \right] \\ \frac{d\sigma}{d\lambda} &= -\frac{\partial x}{\partial \lambda} / \frac{\partial x}{\partial \sigma}. \end{aligned} \quad (23)$$

The first equation is the total derivative of $\langle G(x, t) \rangle$ in terms of $G(x, t)$ while the second states that we are integrating along curves where $x = \text{const}$. This method is used to compute the time average of velocities and mass fluxes.

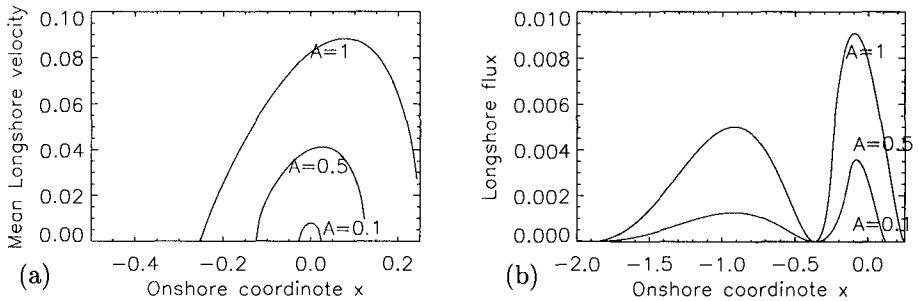


Figure 3: (a) Mean longshore velocity in the swash zone and (b) mean longshore mass flux inside and near to the swash zone for $A = 1$, $A = 0.5$ and $A = 0.1$.

A mean drift is associated with the swash zone width while the average is identically zero outside the swash zone (see figure 3(a)). This closely resembles what happens for the Stokes' drift for 2-D water waves where a mass flux is associated with the motion of the free surface, with zero mass flux below the trough level, and hence is expected. However a more interesting result relates to the mean longshore mass flux (see figure 3(b)). Correlation between solution for the total water depth and the longshore velocity is such that the mean longshore mass flux is non-zero for a wide range of the solution domain.

A more detailed analysis on swash zone mean flow properties is given in Brocchini & Peregrine (1995; 1996).

The model equations for integrated flow properties

In order to average flow properties in the swash zone and to deal with the moving free surface we investigate a model with a boundary chosen at the lower limit of the swash zone.

The swash zone limits are x_l, x_h , the seaward (lower) and shoreward (higher) limits of the swash zone respectively. The seaward boundary may for example be, the lowest limit x_l of the moving shoreline in a group of waves. Integral properties of the water shoreward of that point are considered.

We integrate the basic flow equations across the swash zone. In the following we adopt Einstein's summation convention and use Greek suffices for the two dimensional horizontal flow properties. The general set of equations (5) and the related energy equation are put in conservation form:

$$\begin{aligned}
 d_t + (ud)_x + (vd)_y &= 0 \\
 (ud)_t + \left(u^2d + \frac{1}{2}d^2\right)_x + (uvd)_y + d + \tau_1 &= 0 \\
 (vd)_t + (uvd)_x + \left(v^2d + \frac{1}{2}d^2\right)_y + \tau_2 &= 0 \\
 \frac{1}{2} \left[d(u^2 + v^2) + d^2 \right]_t + \left(\frac{1}{2}u^3d + \frac{1}{2}v^2ud + ud^2 \right)_x \\
 + \left(\frac{1}{2}v^3d + \frac{1}{2}u^2vd + vd^2 \right)_y + u(d + \tau_1) + v\tau_2 &= 0.
 \end{aligned} \tag{24}$$

where a dimensionless bed friction $\tau = (\tau_1, \tau_2)$ is included.

We also assume the wave motion as occurring at a 'fast time scale' t while the swash zone boundaries x_h (run-up) and x_l (run-down) are supposed to vary (if varying in time) on a 'slow time scale' T such as $t = \epsilon T$. We do not use this notation since the separation of the two scales is generally quite clear. Equations (24) are integrated over the swash zone width, with constant x_l , to give:

$$\begin{aligned}
 \frac{\partial V}{\partial t} &= \int_{x_l}^{x_h} d_t dx = Q_1(t)|_{x_l} - \frac{\partial P_2}{\partial y} \\
 \frac{\partial P_1}{\partial t} &= \int_{x_l}^{x_h} (ud)_t dx = S_{11}(t)|_{x_l} - V(t) - \frac{\partial M_{12}}{\partial y} - \Upsilon_1(t) \\
 \frac{\partial P_2}{\partial t} &= \int_{x_l}^{x_h} (vd)_t dx = S_{12}(t)|_{x_l} - \frac{\partial M_{22}}{\partial y} - \Upsilon_2(t) \\
 \frac{\partial E}{\partial t} &= \int_{x_l}^{x_h} \left[\frac{1}{2}(u^2 + v^2)d + d^2 \right]_t dx \\
 &= F(t)Q_1(t)|_{x_l} - P_1(t) - \frac{\partial}{\partial y} \int_{x_l}^{x_h} FQ_2 dx - \Gamma(t).
 \end{aligned} \tag{25}$$

This introduces a number of new flow properties and flow properties integrated over the swash zone. These are listed in table 1 where $\mathbf{u} = (u_1, u_2)$ is the horizontal velocity vector.

The set of equations (25) for the fully three-dimensional motion can be reduced by Ryrie's approximation to a simpler set of equations valid for weakly three-dimensional motion. Second order terms are neglected after the formal substitution (7) is made. Then, at the leading order the set of equations (25)

Name	Explicit expression	Flow property
Q_μ	$u_\mu d$	Local mass flow
$S_{\mu\nu}$	$u_\mu u_\nu d + \delta_{\mu\nu} \frac{1}{2} d^2$	Local momentum flux tensor
F	$\frac{1}{2} \mathbf{u}^2 + d$	Local energy density
V	$\int_{x_1}^{x_h} d \, dx$	Volume of water in swash zone
P_μ	$\int_{x_1}^{x_h} Q_\mu \, dx$	Momentum of water in swash zone
$M_{\mu\nu}$	$\int_{x_1}^{x_h} S_{\mu\nu} \, dx$	Integrated momentum flux tensor
E	$\int_{x_1}^{x_h} (\frac{1}{2} \mathbf{u}^2 d + d^2) \, dx$	Energy of water in swash zone
Υ_μ	$\int_{x_1}^{x_h} \tau_\mu \, dx$	Friction force in swash zone
Γ	$\int_{x_1}^{x_h} u_\mu \tau_\mu \, dx$	Work done by friction in swash zone

Table 1: Definition of the flow properties adopted in equations (25).

becomes:

$$\begin{aligned}
 \frac{\partial V}{\partial t} &= \int_{x_1}^{x_h} d_t \, dx = Q_1(t)|_{x_1} \\
 \frac{\partial P_1}{\partial t} &= \int_{x_1}^{x_h} (ud)_t \, dx = S_{11}(t)|_{x_1} - V(t) - \Upsilon_1(t) \\
 \frac{\partial P_2}{\partial t} &= \int_{x_1}^{x_h} (vd)_t \, dx = S_{12}(t)|_{x_1} + \frac{\partial M_{22}}{\partial t} - \Upsilon_2(t) \\
 \frac{\partial \bar{E}}{\partial t} &= \int_{x_1}^{x_h} (\frac{1}{2} u^2 d + d^2)_t \, dx = \bar{F}(t)Q_1(t)|_{x_1} - P_1(t) - \bar{\Gamma}(t).
 \end{aligned} \tag{26}$$

Table 2 lists definitions which, because of the approximation, differ from those of table 1. We distinguish newly defined flow properties by using overbars in equations (26) and table 2.

Name	Explicit expression	Flow property
\bar{F}	$\frac{1}{2} u_1^2 + d$	Local energy density
\bar{E}	$\int_{x_1}^{x_h} \frac{1}{2} (u_1^2 d + d^2) \, dx$	Energy of water in swash zone
$\bar{\Gamma}$	$\int_{x_1}^{x_h} u_1 \tau_1 \, dx$	Work done by friction in swash zone

Table 2: Definition of some flow properties adopted in equations (26).

In the idealized case of no dissipation ($\Upsilon_1 = \Upsilon_2 = \bar{\Gamma} = 0$) the set of partial differential equations (26) is such that it can be recursively solved for the integral

flow properties in the swash zone (i.e. V , P_1 , P_2 and \bar{E}) once the local flow properties Q_1 , S_{11} , S_{12} and \bar{F} are known at the seaward boundary of the swash zone. The result of the equation for the water volume only depends on the known variable Q_1 . Once this equation is solved for V the result can be substituted into the second equation and so on.

We believe that equations (25) can be used as swash zone boundary conditions for wave resolving models. Use of integrated swash zone properties gives considerable numerical advantage, since adequate modelling of the details of the swash zone flows requires small time steps.

The swash zone boundary conditions for wave-averaged models

A natural extension to averaging the swash zone is to seek appropriate boundary conditions at the seaward swash zone limit for wave-averaged models of the incident motions (both long and short period motions). This requires definition of the contributions to the motion of the boundary $x = x_l$ from both long-period motions (e.g. low frequency waves, currents, etc..) and averaged short-period motions. The problem here is that there is no definitive model for the waves approaching the swash zone, especially for the most usual case where waves are already breaking. The following discussion develops swash-zone boundary conditions by assuming that appropriate short-wave properties are known.

To obtain dynamic equations for wave-averaged flow properties we start with the equations of motion and divide the basic flow properties u , v and d into long-period motions and the short-period wave contributions:

$$u = \langle u \rangle + \tilde{u}, \quad v = \langle v \rangle + \tilde{v}, \quad d = \langle d \rangle + \tilde{d}, \quad \langle \tilde{u} \rangle = \langle \tilde{v} \rangle = \langle \tilde{d} \rangle = 0. \quad (27)$$

Contributions to $\langle u \rangle$, $\langle v \rangle$ and $\langle d \rangle$ come from all motions whose typical time scale is significantly longer than the typical short-wave period. These can be for example either bound long waves associated with the set-down occurring under a group of short-period waves or free long waves caused by a time-varying break-point or any sort of current. On the other hand pure short-period contributions appear as correlations of wave-type terms (e.g. $\langle \tilde{u}\tilde{d} \rangle$, $\langle \tilde{u}\tilde{v} \rangle$, etc..).

By substituting in the shallow water equations (24) in this way for each flow variable and by phase averaging we obtain a set of equations for the long-period flow properties $\langle u \rangle$, $\langle v \rangle$ and $\langle d \rangle$:

$$\frac{\partial \langle d \rangle}{\partial t} + \frac{\partial}{\partial y} [\langle u \rangle \langle d \rangle + \langle \tilde{Q}_1 \rangle] + \frac{\partial}{\partial y} [\langle v \rangle \langle d \rangle + \langle \tilde{Q}_2 \rangle] = 0 \quad (28)$$

$$\frac{\partial}{\partial t} [\langle u \rangle \langle d \rangle + \langle \tilde{Q}_1 \rangle] + \frac{\partial}{\partial y} [\langle d \rangle (\langle u \rangle^2 + \langle \tilde{u}^2 \rangle + \frac{1}{2} \langle d \rangle) + 2 \langle u \rangle \langle \tilde{Q}_1 \rangle + \langle \tilde{S}_{11} \rangle] \quad (29)$$

$$+ \frac{\partial}{\partial y} [\langle d \rangle (\langle u \rangle \langle v \rangle + \langle \tilde{u}\tilde{v} \rangle) + \langle u \rangle \langle \tilde{Q}_2 \rangle + \langle v \rangle \langle \tilde{Q}_1 \rangle + \langle \tilde{S}_{12} \rangle] + \langle d \rangle = 0$$

$$\frac{\partial}{\partial t} [\langle v \rangle \langle d \rangle + \langle \tilde{Q}_2 \rangle] + \frac{\partial}{\partial y} [\langle d \rangle (\langle v \rangle^2 + \langle \tilde{v}^2 \rangle + \frac{1}{2} \langle d \rangle) + 2 \langle v \rangle \langle \tilde{Q}_2 \rangle + \langle \tilde{S}_{22} \rangle] \quad (30)$$

$$+ \frac{\partial}{\partial y} [\langle d \rangle (\langle u \rangle \langle v \rangle + \langle \tilde{u}\tilde{v} \rangle) + \langle v \rangle \langle \tilde{Q}_1 \rangle + \langle u \rangle \langle \tilde{Q}_2 \rangle + \langle \tilde{S}_{12} \rangle] = 0$$

where $\langle \tilde{Q}_\mu \rangle = \langle \tilde{u}_\mu \tilde{d} \rangle$ is the mass flow due to wave motion while the contribution of the momentum flux due to wave motion is given by the radiation stress term $\langle \tilde{S}_{\mu\nu} \rangle$.

The above set can be also written in matrix form in order to clarify the forcing action of the short-period contributions. The set of equations can, thus, be rewritten as:

$$AU_t + BU_x + CU_y + DU = \mathcal{E} \quad (31)$$

where

$$U = \begin{bmatrix} \langle d \rangle \\ \langle u \rangle \\ \langle v \rangle \end{bmatrix} \quad \text{and} \quad \mathcal{E} = - \begin{bmatrix} \langle \tilde{Q}_1 \rangle_x + \langle \tilde{Q}_2 \rangle_y \\ \langle \tilde{Q}_1 \rangle_t + \langle \tilde{S}_{11} \rangle_x + \langle \tilde{S}_{12} \rangle_y + \langle d \rangle \\ \langle \tilde{Q}_2 \rangle_t + \langle \tilde{S}_{12} \rangle_x + \langle \tilde{S}_{22} \rangle_y \end{bmatrix} \quad (32)$$

are respectively the column vector of the unknown variables and the purely short-wave forcing.

This set of equations is not 'closed' unless a particular wave theory for the short-period wave field is adopted to compute terms like the mass flow and the radiation stress. For instance, it is common practice to use linear wave theory while dissipation effects induced by wave-breaking are parameterized in the solution.

However linear wave theory is not a good representation for the wave field near the shore. The Carrier & Greenspan (1958) solutions and their extension described above can be more appropriate. To help crystallise ideas we note that one approach to this problem would be to extend the Carrier & Greenspan solution to $A > 1$ by computing the surf and swash zone behaviour for waves which have incoming Riemann invariants as for the Carrier & Greenspan solution with $A > 1$. The reflection, mass flow, radiation stress and the averaged swash zone properties, V , P and E could be tabulated as functions of the short-wave parameters. We assume that if a suitable model is found for the short-wave motion this can be described in terms of only an amplitude A a frequency ω and a wave number \mathbf{k} once the mean depth and mean flow velocity are given.

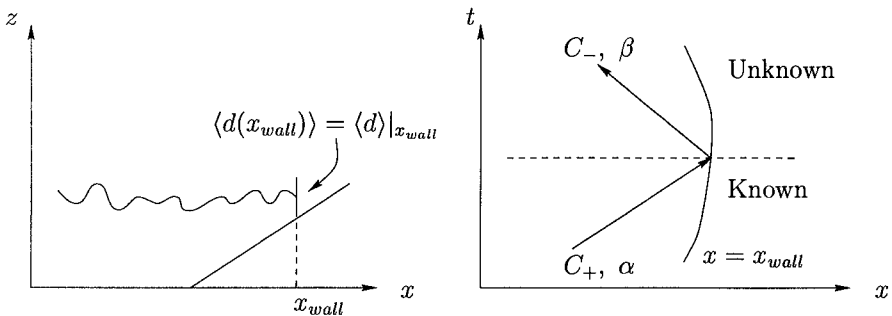


Figure 4: Schematic of: (a) the 'physical' (x, z) plane and (b) the 'characteristic' (x, t) plane for the rigid wall problem.

In order to obtain suitable boundary conditions for wave-averaged models we need to clarify what sort of information is available and what are the unknowns. To achieve this we first use a simple model of a moving boundary that is a rigid wall moving at velocity $U(t)\mathbf{i}$ which varies on a sufficiently slow time scale that its acceleration is unimportant (see figure 4). The flow is one dimensional and the medium is assumed uniform so that A, ω and \mathbf{k} do not depend on (x, t) .

A simple exercise of bookkeeping shows what are known and unknown parameters for both long and short wave motions (see table 3 and figure 4).

Natural boundary conditions for this flow are:

$$\langle d \rangle|_{x_{wall}} = const, \quad \frac{dx_{wall}}{dt} = \langle u \rangle = U(t) \quad (33)$$

Consequently it is possible to explicitly compute the long-period motion variable β (i.e. the outgoing Riemann invariant) from the known incoming variable α

$$\alpha = 2\langle c \rangle + \langle u \rangle, \quad \beta = 2\langle c \rangle - \langle u \rangle, \quad \implies \quad \beta = \alpha - 2U. \quad (34)$$

The incoming waves of amplitude A_{in} , wavenumber \mathbf{k}_{in} frequency ω_{in} may be perfectly reflected at the wall, but to determine the outgoing values of A , \mathbf{k} and ω the local behaviour at the moving wall must be considered.

In a frame of reference moving with the wall, the waves have an unchanging intrinsic frequency σ which is readily found from the Doppler shift:

$$\omega_{in} = \sigma + U\mathbf{i} \cdot \mathbf{k}_{in}. \quad (35)$$

If the waves are perfectly reflected then the outward propagating wave has $A_{out} = A_{in}$ and $\mathbf{k}_{out} = -(\mathbf{k}_{in} \cdot \mathbf{i})\mathbf{i} + (\mathbf{k}_{in} \cdot \mathbf{j})\mathbf{j}$ giving:

$$\omega_{out} = \sigma + U\mathbf{i} \cdot \mathbf{k}_{out} = \sigma - U\mathbf{i} \cdot \mathbf{k}_{in} = \omega_{in} - 2U\mathbf{i} \cdot \mathbf{k}_{in}. \quad (36)$$

	Long-period	Short-period
Known	$\alpha = \alpha(\langle u \rangle, \langle d \rangle), \quad \langle d \rangle _{x_l}$	$A_{in}, \quad \omega_{in}, \quad \mathbf{k}_{in}$
Unknown	$\beta = \beta(\langle u \rangle, \langle d \rangle), \quad x_l(t)$	$A_{out}, \quad \omega_{out}, \quad \mathbf{k}_{out}$

Table 3: Known and unknown flow variables for the rigid wall problem.

In comparing the moving swash zone boundary with the above simple boundary, we note that it is necessary to model the swash zone boundary as a 'leaky wall' such that fluxes of mass and momentum are allowed across $x = x_{wall}$ which for the 'leaky' case may be identified with $x = x_l$. We also note that:

1. sufficient information must be available to determine the motion of the swash zone boundary, $x_l(t)$, as well as to determine β ;
2. as above, a local wave model is needed to determine the properties of the outgoing wave, if any.

We concentrate on the first of these, and look at integration of swash-zone equations similar to (25), or (26), to provide the necessary information. It is clear that in addition to the kinematic type of boundary conditions that occur on the rigid wall (equations 33) a third condition is necessary for the longshore flow in the swash zone.

There is now an important choice to be made: how much of the swash motion, if any, should be assigned to the long time scales? Consideration of the moving

rigid wall example leads us to consider all motion relative to the point $x = x_l(y, t)$ to be short wave motion and $x_l(y, t)$ to be 'driven' by the long-period motions. As a result, we consider all the quantities defined in tables 1 and 2 to be defined with velocities relative to x_l and also to be considered as known once incident short-wave parameters A_{in} , k_{in} and σ are known.

Inside the swash zone most the short-wave quantities averaged over the short wave motion, such as $\langle V \rangle$, $\langle P \rangle$ etc., are to be determined from a short-wave model of the swash. There are exceptions for the longshore current quantities P_2 , M_{p2} which are not entirely dependent on the local waves. When a bore, or flow which was near a bore, enters the swash zone it makes a large contribution to the longshore velocity, which often may only respond to bed friction on the longer time scale, e.g. see Ryrie (1983). This means that a decomposition of long-wave and short-wave contributions is also necessary within the swash zone.

We achieve this decomposition by assuming that swash motion is almost entirely assigned to short-wave contributions and that the only long-wave contribution, other than the motion of x_l , comes from parameterising the longshore drift due to wave-breaking by a longshore current velocity $W = W(y, t)$. In similar fashion to equation (27), which applies outside the swash zone, we separate short-wave from long-wave contribution for the flow properties inside the swash zone:

$$d = \hat{d}, \quad u = \frac{\partial x_l}{\partial t} + \hat{u}, \quad v = W + \hat{v}, \quad (37)$$

where a short-wave property inside the swash zone is defined as \hat{G} rather than \tilde{G} which pertains to short-wave contributions outside the swash zone. This decomposition permits the integrated terms depending on the longshore velocity to be divided between long and short waves:

$$\langle P_2 \rangle = \langle W \hat{V} \rangle + \langle \hat{P}_2 \rangle, \quad (38)$$

$$\langle M_{12} \rangle = \langle W \hat{P}_1 \rangle + \langle \hat{M}_{12} \rangle + \frac{\partial x_l}{\partial t} (\langle W \hat{V} \rangle + \langle \hat{P}_2 \rangle), \quad (39)$$

$$\langle M_{22} \rangle = \langle W^2 \hat{V} \rangle + 2 \langle W \hat{P}_2 \rangle + \langle \hat{M}_{22} \rangle. \quad (40)$$

All the integral properties which are to be considered as short-wave terms have a hat symbol. In principle it is possible to choose a different short-wave solution for the two regions separated by $x = x_l$ also on many sandy beaches there is a strong difference in the character of the bed in the swash zone compared with the bed just outside the swash zone.

In order to avoid greater complexity, the longshore variation of x_l has been assumed to be negligible in the above derivation. This is essentially a geometrical matter, and the above boundary conditions can be interpreted as being applicable when the x direction is normal to the mean lowest boundary of the swash.

To obtain explicit expression of the first boundary condition we consider the flow of mass into the swash zone relative to $x = x_l$. Average of equation (25) is:

$$\frac{\partial \langle V \rangle}{\partial t} + \frac{\partial \langle P_2 \rangle}{\partial y} = \langle Q_1 \rangle|_{x_l} \quad (41)$$

where now the right hand side contains the relative flow velocity ($u - \partial x_l / \partial t$). The left hand side is also rewritten in terms of the local variables inside the

swash zone and then after using (38) for $\langle P_2 \rangle$, after integration across the swash zone width and averaging over the short waves we obtain

$$\frac{\partial \langle \hat{V} \rangle}{\partial t} + \frac{\partial \langle W \hat{V} \rangle}{\partial y} + \frac{\partial \langle \hat{P}_2 \rangle}{\partial y} = \left\langle \left(u - \frac{\partial x_l}{\partial t} \right) d \right\rangle = \langle u \rangle \langle d \rangle + \langle \tilde{u} \tilde{d} \rangle - \frac{\partial x_l}{\partial t} \langle d \rangle. \quad (42)$$

The first term on the left hand side of this equation is the rate of change of the total volume of water in the swash zone; the second and third terms are the change in volume due to the lateral variation of longshore currents respectively associated with the longshore velocity inside the swash zone W and with the wave contribution $\langle \hat{P}_2 \rangle$. The right hand side of (42) is the increase of water in the swash zone through its lower boundary. The right hand side of (42) is evaluated at $x = x_l$ using outer variables.

A similar derivation for the average balance of onshore momentum in the swash zone gives

$$\begin{aligned} & \frac{\partial}{\partial t} \left[\langle \hat{P}_1 \rangle + \frac{\partial x_l}{\partial t} \langle \hat{V} \rangle \right] + \frac{\partial \langle W \hat{P}_1 \rangle}{\partial y} + \frac{\partial \langle \hat{M}_{12} \rangle}{\partial y} \\ & + \frac{\partial x_l}{\partial t} \left[\frac{\partial \langle W \hat{V} \rangle}{\partial y} + \frac{\partial \langle \hat{P}_2 \rangle}{\partial y} \right] + g\alpha \langle \hat{V} \rangle + \langle \Upsilon_1 \rangle = \left\langle \left(u - \frac{\partial x_l}{\partial t} \right)^2 d + \frac{1}{2} g d^2 \right\rangle = \quad (43) \\ & \left(\langle u \rangle - \frac{\partial x_l}{\partial t} \right)^2 \langle d \rangle + \frac{1}{2} g \langle d \rangle^2 + 2 \langle \tilde{u} \tilde{d} \rangle \left(\langle u \rangle - \frac{\partial x_l}{\partial t} \right) + \langle \tilde{u}^2 \rangle \langle d \rangle + \langle \tilde{u} \tilde{d} \rangle + \frac{1}{2} g \langle \tilde{d}^2 \rangle. \end{aligned}$$

In this equation dimensional expressions have been inserted to clarify the origin of terms. The first two terms on the left hand side are the rate of change of the mean momentum in the swash zone. The group of terms with y derivatives are the contribution from longshore velocity gradients which include both long period contributions (terms with W) and short period contributions (terms with $\langle \hat{P}_2 \rangle$ and $\langle \hat{M}_{12} \rangle$). The following terms are the action of gravity and friction on the water in the swash zone. The right hand side is the momentum transfer into the swash zone at $x = x_l$ where the mean flow velocity relative to the swash zone limit appears in both long and short period terms. Finally pure short period contributions appear. Conservation of longshore momentum similarly yields

$$\begin{aligned} & \frac{\partial \langle W \hat{V} \rangle}{\partial t} + \frac{\partial \langle \hat{P}_2 \rangle}{\partial t} + \frac{\partial \langle W^2 \hat{V} \rangle}{\partial y} + 2 \frac{\partial \langle W \hat{P}_2 \rangle}{\partial y} + \frac{\partial \langle \hat{M}_{22} \rangle}{\partial y} + \langle \Upsilon_2 \rangle = \left\langle \left(u - \frac{\partial x_l}{\partial t} \right) v d \right\rangle = \quad (44) \\ & \left(\langle u \rangle - \frac{\partial x_l}{\partial t} \right) \langle v \rangle \langle d \rangle + \langle \tilde{u} \tilde{v} \rangle \langle d \rangle + \langle \tilde{u} \tilde{d} \rangle \langle v \rangle + \langle \tilde{u} \tilde{v} \rangle \langle d \rangle + \langle \tilde{u} \tilde{d} \rangle \langle v \rangle + \langle \tilde{v} \tilde{d} \rangle \left(\langle u \rangle - \frac{\partial x_l}{\partial t} \right) + \langle \tilde{u} \tilde{v} \tilde{d} \rangle. \end{aligned}$$

The above three equations are boundary conditions for the long wave motion and x_l if the short wave properties on each side of $x = x_l$ have 'known' models. Whereas in the rigid wall model only the two boundary conditions are required, now we also need to evaluate the changes in W . In addition, the short-wave models may be chosen to permit the reflection of short waves. Note, the short-wave swash model must be used relative to $x = x_l$, hence the motion of x_l is seen as the long period contribution to the swash zone. A delicate matter concerning the different wave models needed on each side of x_l also needs attention.

The short-wave contribution

In this section we briefly analyse the relevance of the short-wave contributions with particular emphasis on those appearing in the equations (42), (43) and (44) which are used to define the boundary conditions at the lower limit of the swash zone. Computation of the contributions has been performed by integrating the analytical solution for $A \leq 1$ and by integrating the fully numerical solution when wave-breaking occurs, i.e. for $A > 1$.

For waves that break momentum and energy are transferred from the short-waves to the longshore currents hence terms depending on the longshore drift velocity W are to be taken into account as major contributions to the swash zone motions in equations (42), (43) and (44) (see figure 5). Note that the curves have been obtained by joining discrete points which represent the results of single computations. This explains the lack of smoothness in some of the curves.

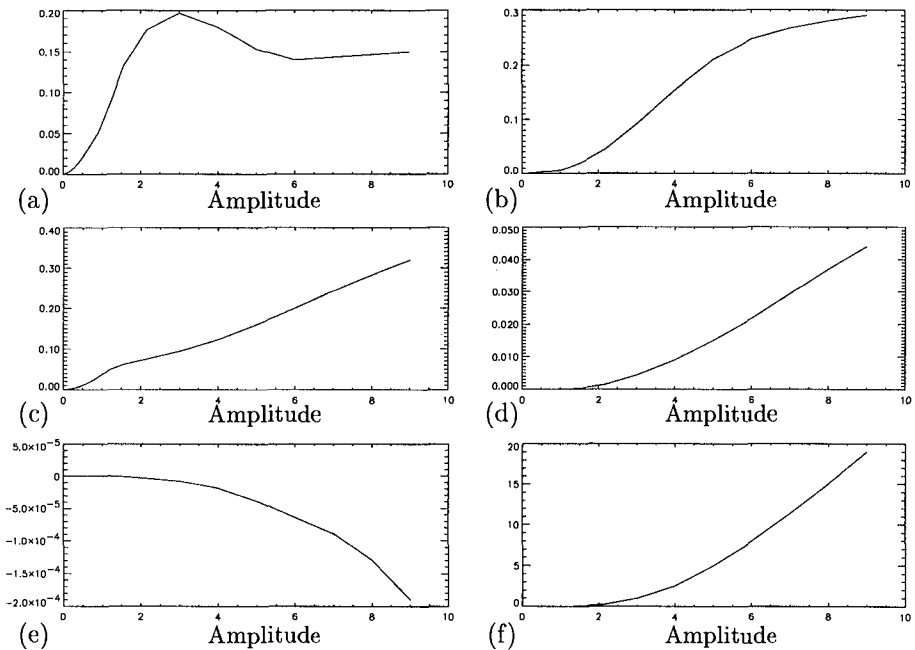


Figure 5: Short-wave contribution at the boundary x_l and inside the swash zone. From top left to bottom right they are the short-wave correlations (a) $\langle \hat{u}^2 \rangle$, (b) $\langle \hat{d}^2 \rangle$ the integral properties (c) $\langle \hat{V} \rangle$, and the rate of change of the three global integral properties (d) $\langle P_2 \rangle$, (e) $\langle M_{12} \rangle$ and (f) $\langle M_{22} \rangle$. Note that for $A \leq 1$ numerical integration of the analytical solution is shown while for $A > 1$ fully numerical solution of the NLSWE is represented.

The input of longshore momentum from the bores is balanced by bed friction but this is generally on the longer time scale. Although bores die out when they meet the shoreline and cause run-up, the water that forms the swash has acquired longshore momentum from the bore before it enters the swash zone. A

fully detailed consideration of this case also awaits further study; here we present the rate of change in time of the quantities $\langle \hat{V} \rangle$, $\langle \hat{P}_2 \rangle$ and $\langle \hat{M}_{22} \rangle$.

The figure presented here indicates that not all the terms that are introduced into the boundary conditions (42, 43 and 44) are necessary. Inspection of figure (5) reveals that the largest term to be retained in case of wave breaking is the rate of change of $\langle \hat{M}_{22} \rangle$. This is not surprising as $\langle \hat{M}_{22} \rangle$ is the only integral term proportional to W^2 (see equations 38) and hence it is more heavily influenced by the longshore drift induced by wave breaking. We can further comment that the non-diagonal contribution $\partial \langle \hat{M}_{12} \rangle / \partial t$ seems to be negligible in this particular case in which we have used $x_l = \text{const}$. However, in view of equation (39), here reported for ease of inspection,

$$\langle M_{12} \rangle = \langle W \hat{P}_1 \rangle + \langle \hat{M}_{12} \rangle + \frac{\partial x_l}{\partial t} (\langle W \hat{V} \rangle + \langle \hat{P}_2 \rangle) \quad (45)$$

we believe that this term may give larger contribution for a time-varying x_l as the rate of change of the boundary position explicitly contributes to this term.

Further investigation should help to clarify both which are the most significant terms when considered in the context of the equations and what are the effects of friction terms.

Acknowledgements

Support from E.U., D.G. XII, contracts : ERBCHBICT930678 and MAS2-CT92-0047 is gratefully acknowledged. We wish to thank Dr Gary Watson for many useful conversations.

References

- BROCCHINI, M. & PEREGRINE, D.H. (1995). Flow properties of the swash zone. *Proc. Coastal Dynamics '95*, ASCE, 221-232.
- BROCCHINI, M. & PEREGRINE, D.H. (1996). Integral flow properties of the swash zone and averaging. *J. of Fluid Mech.* **317**, 241-273.
- CARRIER, G.F. & GREENSPAN, H.P. (1958). Water waves of finite amplitude on a sloping beach. *J. of Fluid Mech.* **4**, 97-109.
- MEYER, R. E. & TAYLOR, A. D. (1972) Run-up on beaches. In *Waves on beaches*. (ed. R. E. Meyer). Academic Press, New York.
- RYRIE, S.C. (1983). Longshore motion generated on beaches by obliquely incident bores. *J. Fluid Mech.* **129**, 193-212.
- WATSON, G., BARNES, T.C.D. & PEREGRINE, D.H. (1994). The generation of low frequency waves by a single wave group incident on a beach. *Proc. 24th Internat. Conf. Coast. Engng., ASCE 1*, 776-790.

CHAPTER 321

Wave Overwash of Subaerial Dunes

Yukiko Tega ¹ and Nobuhisa Kobayashi, M. ASCE ²

Abstract

Small-scale experimental results consisting of 72 runs for minor to major dune overwash are analyzed to improve existing dune erosion models that do not account for wave overwash processes explicitly. The measured cross-shore sediment transport rate is found to vary approximately linearly from the measured rate somewhat below the still water level, which is affected by the overwash intensity, to the overwash rate over the dune crest. The measured overwash sand concentration for the sand with its median diameter of 0.38 mm used in this experiment was in the range of 0.02 to 0.06. The time-dependent one-dimensional numerical model for the overtopping flow combined with two sediment transport formulas indicates that the overwash sand concentration may be on the order of 0.04 except for very fine or coarse sands.

Introduction

The quantitative understanding of wave overwash of dunes is essential for predicting dune erosion as well as coastal flooding hazards during storms. Existing dune erosion models generally assume that the net sediment transport rate may be extrapolated linearly from the value slightly below the still water level (SWL) to zero at the upper limit of wave runup estimated empirically. This linear extrapolation may be necessary for lack of a simple swash model and appears to be a reasonable first approximation for the case of no overwash.

A simple empirical method for predicting the onshore sand transport rate associated with wave overwash of subaerial dunes is presented herein by expanding the experimental study by Hancock and Kobayashi (1994). The experiment was limited to subaerial dunes, while experiments on submerged dunes were conducted by Steetzel and Visser (1992). Kobayashi et al. (1996) showed that the measured reflection coefficient and overtopping rates could be predicted using the empirical formulas developed for coastal structures and adjusted for dunes. This paper examines the cross-shore sand transport on dunes.

Experiment

Fig.1 shows the setup of the dune overwash experiment conducted in a wave tank that was 30 m long, 2.44 m wide, and 1.5 m high. The experiment was

¹Technical Research Institute, Nishimatsu Construction Co.Ltd., 2570-4 Shimotsuruma, Yamato, Kanagawa, 242, Japan

²Professor and Associate Director, Center for Applied Coastal Research, University of Delaware, Newark, DE 19716.

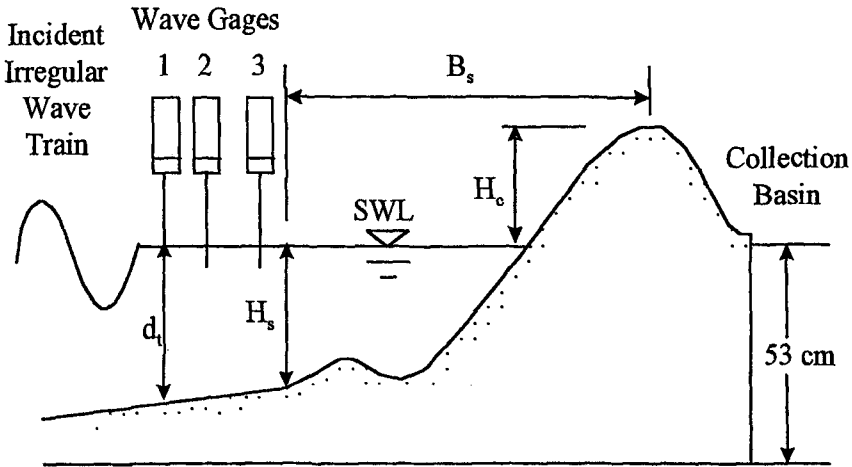


Figure 1: Experimental Setup.

conducted in a 61 cm wide channel by constructing a divider wall to reduce the effects of re-reflection from the wave paddle used to generate irregular waves. The well-sorted sand with a median diameter of 0.38 mm was placed in front of a 53 cm high basin used to collect both overtopped water and overwashed sand. The measured specific gravity, porosity and fall velocity of the sand were 2.66, 0.41 and 5.29 cm/s, respectively. Three wave gages placed immediately seaward of the breaker zone were used to separate the incident and reflected waves at wave gage 1 for each run (Kobayashi and Raichle 1994). The duration of each run was 325 s and the sampling rate for the three gages was 20 Hz.

Seven tests, referred to as tests A to G hereafter, were conducted for minor to major overwash. The dune crest was initially located at approximately 12 cm above SWL and at a horizontal distance of 40 cm from the basin wall. Each test consisted of a series of runs to examine the changes of the overtopping rate per unit width, Q , and the overwash rate per unit width, Q_s , as the beach and dune profile evolved. The overtopping and overwash rates per unit width, Q and Q_s , for each run were obtained by dividing the volumes of water and sand, respectively, collected in the basin by the run duration 325 s and the channel width 61 cm. The value of Q_s is based on the sediment volume only without any void. The test was terminated just before the collection basin wall would become exposed to direct wave action. Beach and dune profiles were measured along three lines using an ultrasound profiler at the beginning and end of each test and after runs of noticeable profile changes. The average profile of the measured three profiles was used to find the dune crest height H_c above SWL, the location where the depth below SWL equals to the significant wave height H_s measured at wave gage 1, and the horizontal distance B_s from the dune crest to this location as shown in Fig. 1. The equivalent uniform slope for wave overtopping, m_o , is assumed to be given by $m_o = (H_c + H_s)/B_s$. The measured values of m_o were interpolated to obtain the value of m_o in the middle of each run.

Table 1 lists the number of runs in each test and the ranges of the incident wave characteristics at wave gage 1, the dune crest height H_c , the equivalent slope m_o , the overtopping rate Q and the overwash rate Q_s for the seven tests. The water depth d_t below SWL at wave gage 1 for each test was constant where the bottom change at wave gage 1 was negligible. The spectral peak period T_p was

Table 1: Ranges of Incident Wave Characteristics, Dune Crest Height, Overtopping, Overwash Rates and Equivalent Slope for 7 Tests

Test	Number of runs	d_t (cm)	T_p (s)	H_s (cm)	H_c (cm)	Q (cm^2/s)	Q_e (cm^2/s)	m_o
A	10	44.3	1.2	11.8-12.2	7.5-12.2	0-0.40	0-0.0148	0.11-0.26
B	9	43.4	1.4	12.2-12.5	7.1-11.1	0.52-1.08	0.024-0.040	0.11-0.25
C	8	44.8	1.6	12.3-12.8	7.0-10.9	1.51-2.61	0.059-0.089	0.11-0.25
D	7	43.7	1.8	12.1-12.4	7.6-11.0	3.33-4.68	0.12-0.16	0.14-0.24
E	5	43.2	2.0	12.4-12.7	6.7-10.7	6.33-8.72	0.30-0.37	0.16-0.25
F	24	43.2	1.4	12.0-12.3	7.9-11.3	0.31-0.47	0.007-0.026	0.09-0.16
G	9	43.2	2.0	12.0-12.4	7.8-11.1	2.89-4.38	0.10-0.16	0.11-0.16

also constant for each test and $T_p = 1.2 - 2.0$ s for the seven tests. The significant wave height, H_s , based on a zero upcrossing method varied little during each test and among the seven tests because the TMA spectra with the spectral significant wave height $H_{m0} = 12.5$ cm and $T_p = 1.2 - 2.0$ s at the wave paddle were used to generate the incident irregular waves. On the other hand, the dune crest height H_c and the equivalent slopes m_o decreased with the increase of run number as the beach and the dune profile evolved. The data from tests A to E consisting of 39 runs were presented by Hancock and Kobayashi (1994). These tests corresponded to high dunes with large storm surge. Two additional tests, F and G, consisting of 33 runs were conducted by placing more sand in front of the initial dune profile used in tests A to E to reduce the water depth at the toe of the dune.

Data Analyses

First, the measured overwash rate Q_o is related to the measured overtopping rate Q in the form

$$Q_o = C_s Q \quad (1)$$

where C_s is the average volumetric sediment concentration in the overwash. The dimensional values of Q_o and Q are plotted in Fig. 2 to show that these values were from the small scale experiment. Fig. 2 shows that the 72 data points fall within the narrow range of $C_s = 0.02 - 0.06$ and that the empirical formula (1) with $C_s \approx 0.04$ may be used to estimate Q_o for Q predicted separately. The subsequent sections will examine whether the assumption of constant C_s holds for field conditions and other sands.

To predict the overtopping rate Q for normally incident breaking waves on dunes, Kobayashi et al. (1996) adjusted the empirical formula for

wave overtopping on coastal structures proposed by Van der Meer and Janssen (1995). The toe of a coastal structure was assumed to correspond to the location of wave gage 1 immediately seaward of the breaker zone. The equivalent uniform slope m_o was assumed to represent the overall slope effect on wave overtopping of dunes. The adjusted formula was shown to yield the agreement between the measured and empirical values of Q almost within the 95 % confidence limits of the original formula based on about 500 data points. Fig. 3 shows the measured overwash rate Q_o as a function of the empirical overtopping rate Q_e based on the adjusted formula by Kobayashi et al. (1996). The formula (1) with Q replaced by Q_e is still reasonable. However, most of the values of C_s are in the range of $C_s = 0.01 - 0.04$ with a typical value of $C_s = 0.02$. These values of C_s are smaller than those of C_s based on Q by a factor of about two. This is because the adjust formula for Q_e tends to overpredict the overtopping rates for the tests with larger

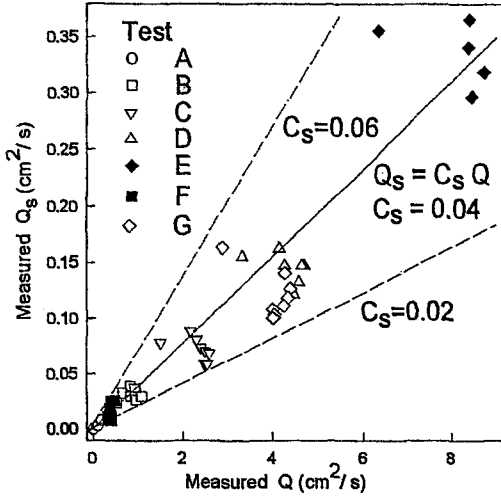


Figure 2: Measured Overwash Rate Q_s vs. Measured Overtopping Rate Q .

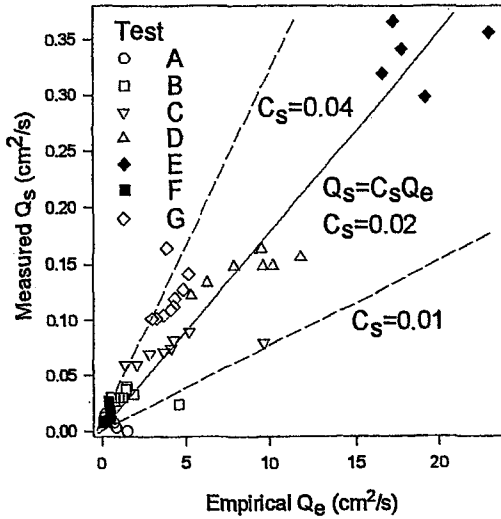


Figure 3: Measured Overwash Rate Q_s vs. Empirical Overtopping Rate Q_e .

overtopping rates. The accurate prediction of Q_s using (1) requires the accurate predictions of C_s and Q . Unfortunately, only the order of magnitude of Q , even for coastal structures, can be predicted at present. Consequently, the present study aims at the prediction of C_s within a factor of about two.

In order to predict the beach and dune profile evolution, the cross-shore variation of the net sediment transport rate is required. The net cross-shore sediment transport rate q_s was calculated using the continuity equation of sediment and the measured profiles starting from the seaward location of no profile change as described by Hancock and Kobayashi (1994). The value of q_s at the landward

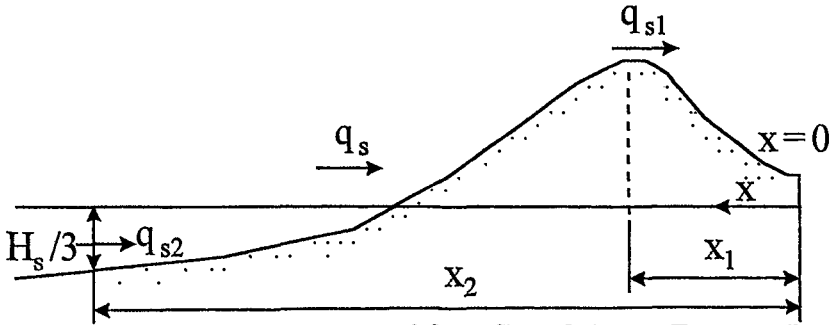


Figure 4: Schematic Representation of Cross-Shore Sediment Transport Rate q_s over Dune

boundary should correspond to the net sediment transport rate into the collection basin but was not exactly the same as the average overwash rate for the same duration calculated from the collected sand because of small profile measurement errors. As a result, the normalized results are presented as explained in the following.

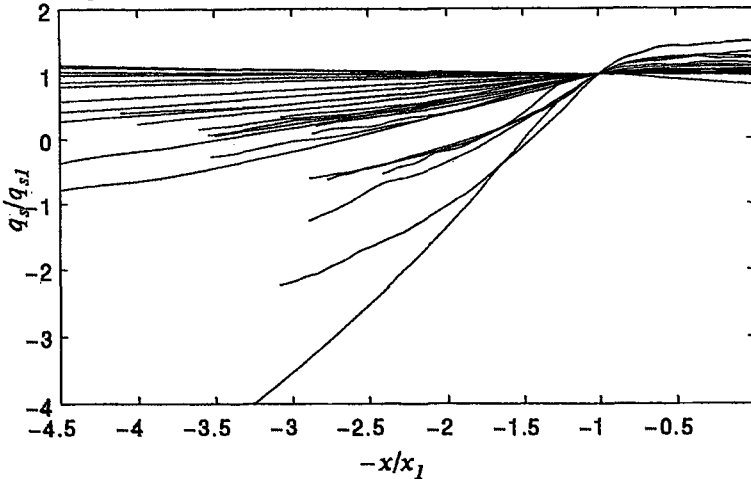


Figure 5: Normalized Cross-Shore Sediment Transport Rate, q_s/q_{s1} , as a Function of $-x/x_1$ with $x = 0$ at Edge of Collection Basin.

The measured cross-shore sediment transport rate q_s is taken to be positive onshore as shown in Fig. 4 where $x =$ cross-shore coordinate taken to be positive seaward with $x = 0$ at the edge of the collection basin. The dune crest is located at $x = x_1$. The seaward limit of this analysis may be taken at the location x_2 where the water depth below SWL equals $H_s/3$ because this depth of $H_s/3$ is larger than the typical smallest depth adopted by existing cross-shore sediment transport models in the surf zone. The values of q_s at $x = x_1$ and x_2 are denoted by q_{s1} and q_{s2} , respectively. The locations of x_1 and x_2 varied somewhat between the two profiles measured consecutively. The first of the two profiles was used to find x_1 and x_2 . The average value of H_s during the runs between the two profile measurements was used for the depth $H_s/3$ for x_2 . The results presented in the

following are not sensitive to the details of the data analysis.

The normalized cross-shore sediment transport rate, q_s/q_{s1} , is plotted in Fig. 5 as a function of $-x/x_1$ in the range $0 < x < x_2$ for all the cross-shore variations of the onshore sand transport rate based on the consecutive profile measurements. Fig. 5 shows that the value of q_s landward of the dune crest is almost constant and may be approximated by the overwash rate Q_s , which is based on the sand volume collected in the basin for each run and should be more accurate than q_s . Furthermore, q_s increases approximately linearly from q_{s2} at $x = x_2$ somewhat below SWL to q_{s1} at the dune crest. Consequently, the cross-shore variation of q_s required for the prediction of the dune profile evolution using the continuity equation for sediment may be represented by $Q_s \simeq q_{s1}$ and q_{s2} where Q_s may be estimated using (1).

Existing dune erosion models estimate the cross-shore sediment transport rate slightly below SWL without regard to wave overwash. To examine the effect of overwash on q_s below SWL, the values of q_{s2}/q_{s1} are plotted as a function of the overtopping rate Q and the overwash rate Q_s in Fig. 6. Since $q_{s1} > 0$ in this experiment, the positive and negative values of q_{s2}/q_{s1} imply the onshore and offshore sediment transport at $x = x_2$ below SWL, respectively. Fig. 6 indicates that the net sediment transport somewhat below SWL in this experiment was offshore for small Q and Q_s but tended to become onshore with the increase of Q and Q_s . This implies that the estimation of q_{s2} will need to account for wave overtopping and overwash.

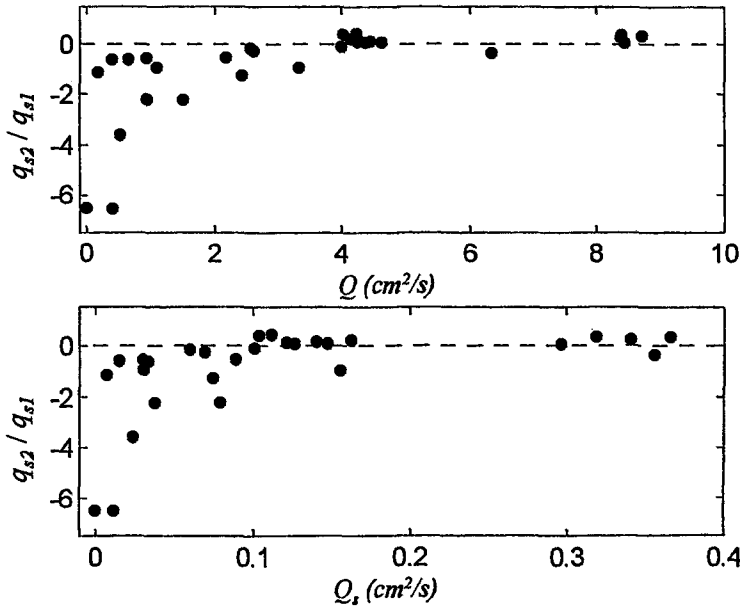


Figure 6: Normalized Sediment Transport Rate q_{s2}/q_{s1} , Somewhat below SWL as a Function of Overtopping Rate Q (top) and Overwash Rate Q_s (bottom)

Numerical Modeling

To elucidate the overwash processes and extrapolate the small-scale experimental results presented above, use is made of the time-dependent one-dimensional numerical model RBREAK2 (Kobayashi and Poff 1994). RBREAK2 was shown

to predict the overtopping rates for revetments in surf zones within about 40 % errors (Kobayashi and Raichle 1994). Two sediment transport formulas are combined with RBREAK2 to predict the net sediment transport rate q_s .

The empirical formula proposed by Trowbridge and Young (1989) for unbroken water waves under sheet flow conditions may be used to express q_s in the form

$$\frac{q_s}{wd} = \frac{A\overline{|u|u}}{g(s-1)d} \quad (2)$$

in which w = fall velocity of the sand particle; g = gravitational acceleration; d = median diameter d_{50} where d is used for brevity; s = specific gravity of the sand; u = instantaneous depth-averaged velocity computed by RBREAK2 ; and A = empirical parameter. The overbar in (2) denotes the time-averaging for the duration of each run. The formula (2) with $A \simeq 0.25$ was employed successfully to predict the onshore sand transport outside the surf zone at the CERC Field Research Facility.

On the other hand, Ribberink and Al-Salem (1994) developed a sediment transport formula using large oscillating water tunnel data. This formula expresses q_s as

$$\frac{q_s}{wd} = af^{1.5} \frac{\overline{u^3}}{w^3} \quad (3)$$

where a = empirical parameter; and f = Jonsson's wave friction factor. The formula with $a = \sqrt{2}$ was shown to yield good agreement with their water tunnel data.

Table 2: Measured and Computed Overtopping Rates for 10 Runs

Test	f	T_p (s)	H_s (cm) (cm)	Measured Q (cm^2/s)	Computed Q_c (cm^2/s)
B6	0.014	1.4	12.36	0.93	0.38
B9	0.014	1.4	12.28	1.08	1.09
B9	0.012	1.4	12.28	1.08	1.06
B9	0.010	1.4	12.28	1.08	0.90
D5	0.012	1.8	12.30	4.63	1.98
D5	0.010	1.8	12.30	4.63	2.19
D7	0.012	1.8	12.29	4.46	1.78
D7	0.010	1.8	12.29	4.46	1.97
E1	0.010	2.0	12.49	6.33	2.16
E2	0.010	2.0	12.67	8.40	3.12
E3	0.010	2.0	12.71	8.38	13.07
G1	0.010	2.0	12.42	2.89	0.12
G2	0.010	2.0	12.34	4.26	0.23
G3	0.010	2.0	12.05	4.38	1.48

The formulas (2) and (3) developed for the sand transport due to prototype large-scale unbroken waves may be applied to the sand transport due to broken waves overtopping on dunes if the empirical parameters A and a are adjusted.

Computations were made for 10 representative runs using the measured profile and incident wave train at wave gage1 as input to RBREAK2 . Table 2 summarizes the computed runs where f = friction factor specified in the computation;

T_p = spectral peak period of the incident waves; H_s = incident significant wave height; Q = measured overtopping rate; and Q_c = computed overtopping rate which is the time-averaged volume flux per unit width at the edge of the collection basin during each run. The friction factor f for the overtopping flow is expected to be different from Jonsson's friction factor. The value of $f \approx 0.01$ is a reasonable estimate from the previous calibration for wave overtopping of revetments performed by Kobayashi and Raichle (1994). RBREAK2 with $f = 0.01 - 0.014$ predicts the order of magnitude of the overtopping rates. For tests E and G, where the overall beach and dune slope was gentler for test G as may be inferred from the range of m_o listed in Table 1, the computed overtopping rates were varied much more than the measured rates for the different profiles of tests E and G and as the profile evolved in each test. This apparent sensitivity of RBREAK2 to the beach and dune profile is not certain for lack of measurements on the depth and velocity of the overtopping flow in this experiment.

The cross-shore variation of the net sediment transport rate q_s is also computed using (2) and (3) where RBREAK2 predicts the temporal and cross-shore variations of the depth-averaged velocity u during each run. The computed cross-shore variation of q_s in the region between the dune crest and the edge of the collection basin is essentially constant and consistent with the measured variation shown in Fig. 5. However, the computed values of q_s seaward of the dune crest vary too rapidly in comparison to these shown in Fig. 5. The assumption of the instantaneous response of sand particles to the depth-averaged velocity u made in (2) and (3) may not be valid seaward of the dune crest. The following analysis is limited to the computed results at the edge of the collection basin which are representative of the computed results landward of the dune crest.

The computed time series of the normalized water depth, $h_* = h/H_s$, where H_s = incident significant wave height for each run, and the normalized depth-averaged velocity, $u_* = u/\sqrt{gH_s}$, are stored at the sampling rate of 20 Hz during each run lasting 325 s. In order to find a relationship between h_* and u_* , the stored values of h_* and u_* for the 10 runs listed in Table 2 are plotted in the form

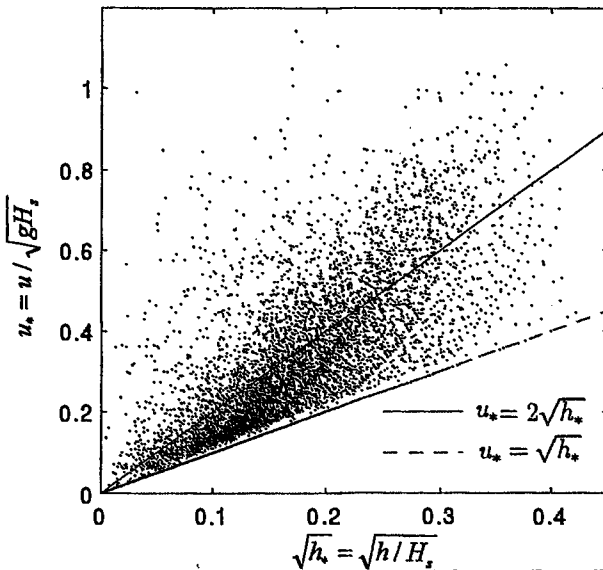


Figure 7: Computed Normalized Velocity, u_* , and Square Root Depth, h_* , of Overwash Flow for 10 Runs

of u_* v.s. $\sqrt{h_*}$ in Fig. 7. RBREAK2 assumes that the overtopping flow at the landward boundary of the computation domain is critical ($u = \sqrt{gh}$ and hence $u_* = \sqrt{h_*}$) or supercritical ($u > \sqrt{gh}$ and hence $u_* > \sqrt{h_*}$). The scattered points in Fig. 7 may be represented crudely by the simple relationship, $u_* \simeq 2\sqrt{h_*}$. This relationship corresponds to that between the bore speed and flow depth on a barrier island measuring using video techniques by Holland et al. (1991) if the celerity and fluid velocity of the bore are assumed to be the same.

The simple relationship of $u_* = 2\sqrt{h_*}$ may describe the overall trend of the overtopping flow but is not accurate enough to predict the instantaneous relationship between u_* and h_* . As an example, Fig. 8 shows the computed time series of u_* and $2\sqrt{h_*}$ for run B9 where $t_* = t/T_p$ is the normalized time with $t_* = 0$ at the beginning of each run. The relationship of $u_* = 2\sqrt{h_*}$ tends to underpredict the peaks of u_* and overpredict the receding segments of u_* .

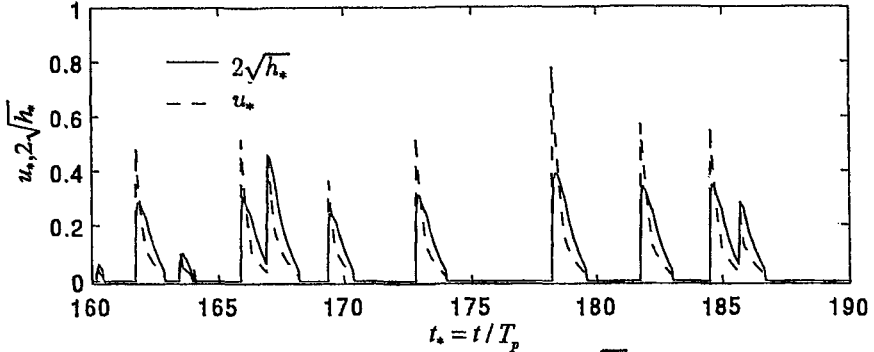


Figure 8: Computed Time Series of u_* and $2\sqrt{h_*}$ for Run B9

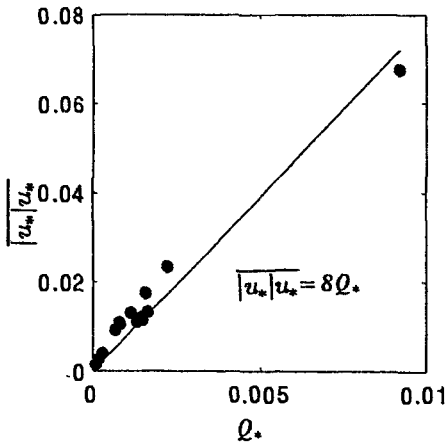


Figure 9: Computed Normalized Velocity Moment $|u_*|u_*$ as a Function of Computed Normalized Overtopping Rate Q_* .

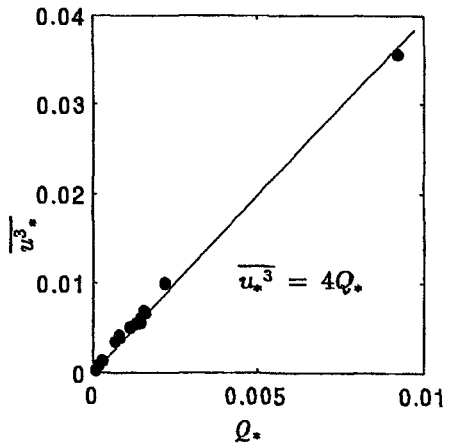


Figure 10: Computed Normalized Velocity Moment u_*^3 as a Function of Computed Normalized Overtopping Rate Q_* .

In order to explain the approximate linear relationship between Q_s and Q expressed by (1) using the formulas (2) and (3), the computed time-averaged values of $\overline{|u_*|u_*}$ and $\overline{u_*^3}$ for each of the runs listed in Table 2 are plotted as a function of the computed normalized overtopping rate, $Q_* = \overline{h_*}u_*$, in Figs. 9 and 10, respectively. The dimensional overtopping rate Q is given by $Q = H_s\sqrt{gH_s}Q_*$. In Fig. 9, $\overline{|u_*|u_*}/Q_* = 7.3 - 18.8$ and the linear regression coefficient is about 8.

In Fig. 10, $\overline{u_*^3}/Q_* = 3.8 - 5.3$ and the relationship of $\overline{u_*^3} = 4Q_*$ based on the assumption of $u_* = 2\sqrt{h_*}$ yields very good agreement. These relationships together with (2) and (3) are used to express the overwash sand concentration C_s in (1) in terms of the sand and wave characteristics.

Overwash Sand Concentration

The overwash rate Q_s is estimated as the values of q_s in (2) and (3) at the edge of the collection basin. Substitution of (1) into (2) and (3) yields the following expressions of C_s :

$$C_s = Av_* \frac{\overline{|u_*|u_*}}{Q_*} \quad ; \quad w_* = \frac{w}{(s-1)\sqrt{gH_s}} \tag{4}$$

and

$$C_s = af^{1.5}d_* \frac{\overline{u_*^3}}{Q_*} \quad ; \quad d_* = \frac{gd}{w^2} \tag{5}$$

where w_* and d_* are the normalized fall velocity and diameter respectively. To calibrate the empirical coefficients A and a in (4) and (5), the measured concentration C_s is plotted as a function of $w_*\overline{|u_*|u_*}/Q_*$ and $f^{1.5}d_*\overline{u_*^3}/Q_*$ in Figs. 11 and 12, respectively, for the computed runs listed in Table 2. Fig. 11 indicates $A \approx 0.1$ in (4) instead of $A \approx 0.25$ calibrated by Trowbridge and Young (1989).

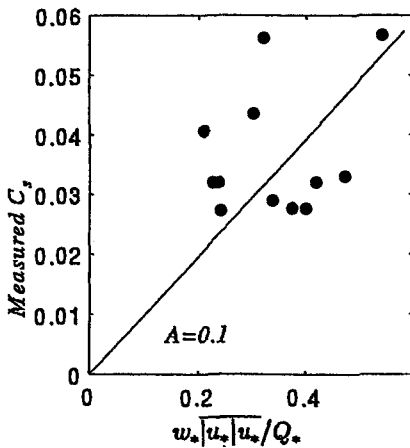


Figure 11: Measured Sand Concentration C_s Compared with Formula (4) with $A = 0.1$

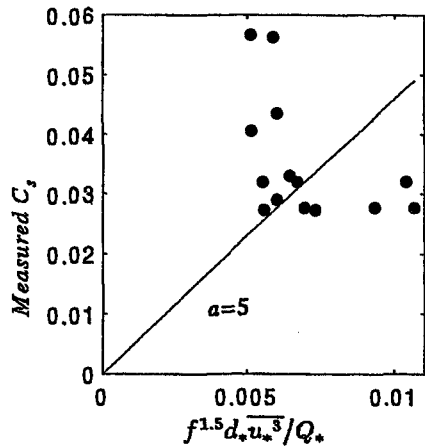


Figure 12: Measured Sand Concentration C_s Compared with Formula (5) with $a = 5$

Fig. 12 suggests $a \approx 5$ instead of $a \approx \sqrt{2}$ obtained by Ribberink and Al-Salem (1994). These order-of-magnitude agreements are encouraging in light of the scale differences (small-scale experiment v.s. field or large-scale experiment) and the different wave conditions (breaking wave overwash of dunes v.s. unbroken waves on essentially horizontal bottoms.). Figs. 11 and 12 also reveal the difficulty in predicting the relatively small variation of C_s .

The formula (4) with $A \approx 0.1$ together with $\overline{u_* u_*} / Q_* \approx 8$ in Fig.9 may be simplified as

$$C_s = Bw_* \tag{6}$$

where B = empirical parameter on the order of 0.8. Furthermore, the formula (5) with $a \approx 5$ and $f \approx 0.01$ along with $\overline{u_*^3} / Q_* \approx 4$ in Fig. 10 may simply be rewritten as

$$C_s = bd_* \tag{7}$$

where b = empirical parameter on the order of 0.02.

For the seven tests consisting of 72 runs listed in Table 1, $d = 0.38$ mm, $w = 5.29$ cm/s, $s = 2.66$ and $H_s \approx 12$ cm. As a result, $w_* \approx 0.03$ and $d_* \approx 1.33$ for this experiment. For the narrow range of the measured values of C_s for the 72 runs, $B = 0.63 - 2.22$ with its mean being 0.8 and $b = 0.014 - 0.049$ with its mean being 0.025. The formulas (6) and (7) are no better than the linear regression between Q_s and Q shown in Fig.2 since w_* is essentially constant and d_* is constant in this experiment. However, (6) and (7) may be applied to estimate C_s for other sands.

The variation of the overwash sand concentration C_s with respect to its median diameter d estimated using (6) with $B = 0.8$ as well as (7) with $b = 0.025$ are shown in Figs. 13 and 14, respectively, where the specific gravity of the sand is assumed to be $s = 2.6$ and its fall velocity w is taken to be equal to that of the spherical particle falling in quiet water whose kinematic viscosity is $\nu = 0.01 \text{ cm}^2/\text{s}$. In Fig.13, use is made of $H_s = 0.1, 1$ and 5 m because w_*

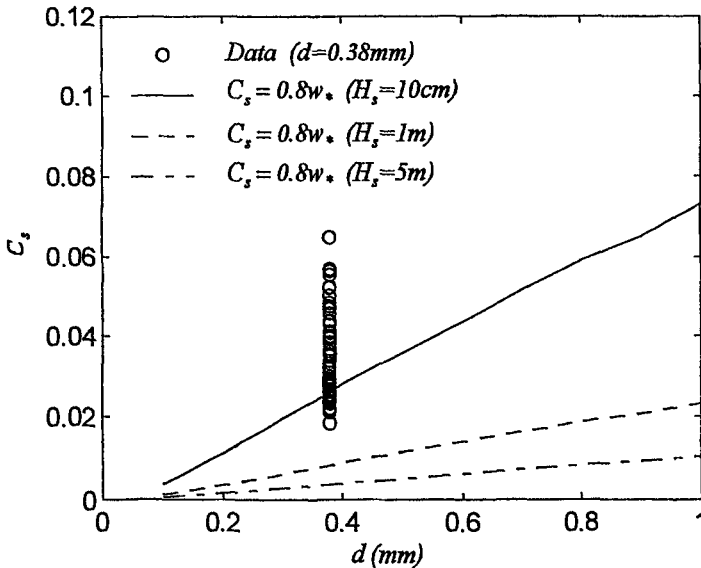


Figure 13: Variation of Sand Concentration C_s with Median Diameter d Estimated by $C_s = 0.8w_*$.

defined in (4) depends on the incident significant wave height H_s . Contrary to our expectation, Fig. 13 suggests the increase of C_s as d is increased and H_s is decreased. This indicates the limitation of the formula (2) proposed by Trowbridge and Young (1989) who stated that their formula might be limited to quartz sand whose diameter should not be too different from 0.2 mm. On the other hand, Fig. 14 indicates the increase of C_s with the decrease of d as expected. The formula (3) proposed by Ribberink and Al-Salem (1994) was compared with the data with $d = 0.2 - 1.8$ mm. The rapid increase of C_s with the decrease of d in the range $d < 0.2$ mm in Fig. 14 appears to be unrealistic in view of the physical upper limit of $C_s \simeq 0.6$. The range of $C_s = 0.018 - 0.065$ for the 72 runs in comparison to the variation of $C_s = 0.025d_s$ for $d = 0.2 - 1.0$ mm in Fig. 14 implies that it will be difficult to detect the effect of d on C_s unless very fine or coarse sands are employed in experiments.

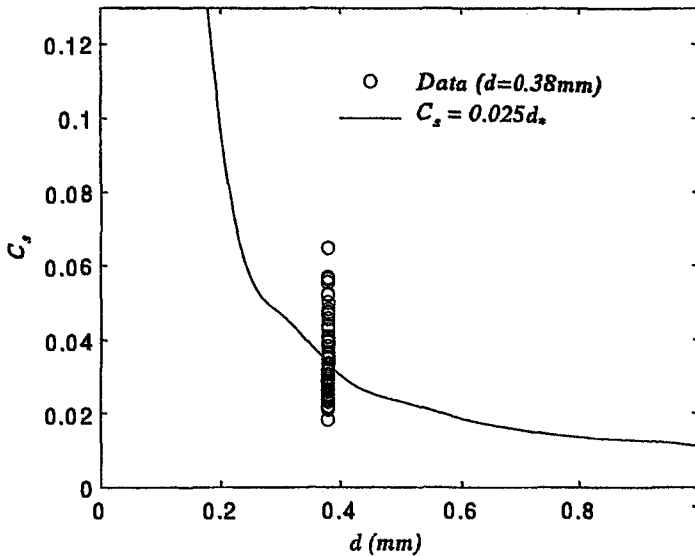


Figure 14: Variation of Sand Concentration C_s with Median Diameter d Estimated by $C_s = 0.025d_s$.

Conclusion

This small-scale experiment on wave overwash of subaerial sand dunes indicates that the net cross-shore sediment transport rate q_s varies approximately linearly from $q_s = q_{s2}$ somewhat below SWL, to $q_s = q_{s1}$ at the dune crest which is approximately the same as the overwash rate Q_s measured at a short distance landward of the dune crest. The transport rate q_{s2} is affected by the overtopping rate Q and may not be assumed to be the same as that for the case of no overtopping. The overwash rate Q_s may be estimated using the simple relationship of $Q_s = C_s Q$ with $C_s \simeq 0.04$ for the median sand diameter $d = 0.38$ mm but the accuracy of this relationship is limited mostly by the accuracy of the empirical formula for Q which predicts only the order of magnitude of Q . In order to extrapolated these small-scale experimental results, the numerical model RBREAK2 for

the overtopping flow is combined with two empirical formulas for C_s . The computed results suggest that C_s is on the order of 0.04 except for very fine or coarse sands. This finding is useful for future experiments.

Acknowledgements

This study is funded by the U.S. Army Research Office, University Research Initiative under Contract No. DAAL03-92-G-0116.

References

- Hancock, M.W. and Kobayashi, N. (1994). "Wave overtopping and sediment transport over dunes." *Proc. 24th Coast. Engrg. Conf.*, ASCE, 2, 2028-2042.
- Holland, K.T., Holman, R.A. and Sallenger, A.H., Jr. (1991). "Estimation of overwash bore velocities using video techniques." *Coastal Sediments '91*, ASCE, 489-497.
- Kobayashi, N. and Poff, M.T. (1994). "Numerical model RBREAK2 for random waves on impermeable coastal structures and beaches." *Res. Rept. CACR-94-12*, Ctr. for Applied Coast. Res., Univ. of Delaware, Newark, Del.
- Kobayashi, N. and Raichle, A.W. (1994). "Irregular wave overtopping of revetments in surf zones." *J. Wtrway. Port, Coast. Oc. Engrg.*, ASCE, 120(1), 56-73.
- Kobayashi, N., Tega, Y. and Hancock, M.W. (1996). "Wave reflection and overwash of dunes." *J. Wtrway. Port, Coast. Oc. Engrg.*, ASCE, 122(3), 150-153.
- Ribberink, J.S. and Al-Salem, A.A. (1994). "Sediment transport in oscillatory boundary layers in cases of rippled beds and sheet flow." *J. Geophys. Res.*, 99(C6), 12707-12727.
- Steezel, H.J. and Visser, P.J. (1992) "Profile development of dunes due to overflow." *Proc. 23rd Coast. Engrg. Conf.*, ASCE, 3, 2669-2769.
- Trowbridge, J. and Young, D. (1989). "Sand transport by unbroken water waves under sheet flow conditions." *J. Geophys. Res.*, 94(C8), 10971-10991.
- Van der Meer, J.W. and Janssen, J.P.F.M. (1995). "Wave run-up and wave overtopping at dikes." *Wave forces on inclined and vertical wall structures*, ASCE, New York, NY, 1- 27.

CHAPTER 322

PRESSURE GRADIENTS WITHIN SEDIMENT BEDS.

Thomas. E. Baldock¹ and Patrick Holmes²

ABSTRACT

A new technique for measuring dynamic pressures and pressure gradients within sediments is developed. The pressure is measured with a series of small diameter steel probes connected to pressure transducers via semi-rigid tubing. The dynamic response of the system was evaluated and found to be satisfactory for typical laboratory wave frequencies. Comparisons with measurements of the pressure gradients obtained from conventional transducers show good agreement. The present technique is demonstrated with pressure measurements at the toe of breakwaters and across the surf zone of model beaches.

1) INTRODUCTION

Pressure gradients induced within sediment beds by surface gravity waves may have a significant influence on the transport of sediment and the stability of coastal structures. The pressure gradients may either be steady or transient. For example, the wave induced set-up of the water level at the shoreline will produce a steady flow within a beach (Longuet-Higgins, 1983). This may be increased by the percolation of swash through the upper part of the beach. Alternatively, transient pressure gradients may locally reduce the effective strength of the sediment, possibly temporarily fluidising the bed material (e.g Madsen, 1974; Yamamoto, 1978). This may lead to higher rates of sediment transport and reduce the stability of structures within the surf zone.

However, considerable uncertainty remains as to the effects of pressure gradients on sediment transport rates and previous work has provided conflicting

1) Research Associate.

2) Professor.

Dept. of Civil Engineering, Imperial College, London, SW7 2BU, UK.

results (Martin, 1970, Oldenzien and Brink, 1974). Loveless (1994) suggested that vertical wave induced pressure gradients were particularly important during toe scour and Conley and Inman (1992) suggested that bed ventilation could be an important aspect in scale modelling. Seepage within the beach may also be an important feature in both long term beach morphology (Turner, 1995) and short term (storm duration) beach evolution. This effect is highlighted by the performance of coastal drainage systems (e.g Vesterby, 1996; Sato et al, 1994). Nevertheless, the mechanism by which the watertable influences the beach dynamics is not immediately apparent. Sato et al (1994) suggest that the drain reduces offshore flows such as the undertow, in addition to increasing percolation into the upper beach, while Vesterby (1996) suggests that an increase in the beach stability and a reduction in wave induced liquefaction are the dominant factors. However, numerical calculations by Oh and Dean (1994) indicated that the pressure gradients induced by changes in the watertable within a beach were generally far too small to influence sediment stability.

Therefore, although the pressures within sediments have been measured by a number of authors (e.g. Sleath, 1970; Yamamoto et al, 1978), measurements of the pressure gradients will enhance the understanding of both sediment transport mechanisms and beach dynamics. The present study addresses this point and outlines the development of a flexible non-intrusive measurement technique. The method allows the pressure gradients at any position within the fluid or sediment bed to be determined quickly and easily, with minimum disturbance of the local flow field. The technique may also be used close to or under structures such as breakwaters, where it may be difficult to obtain results from conventional pressure transducers.

2) MEASUREMENT TECHNIQUE

Conventional pressure transducers have a number of disadvantages when attempting to measure pressure gradients. Firstly, they are relatively large and therefore when mounted close together may significantly disturb the local flow field. Secondly, a large number of transducers are needed to measure the pressure gradients at a number of points without repeatedly disturbing a sediment bed. Finally, the measurement position must be chosen *a priori* and cannot be changed readily. This is a significant drawback when measuring the pressure gradients within model beaches which evolve over time. For example, in order to measure the pressure gradients over either a bar, or at the toe of a beach, it would first be necessary to run a model test to predetermine the measurement positions.

The aim of the present study is to overcome these limitations and develop a measurement method that is as flexible as possible. The technique has been developed from a method used previously to investigate static pressures within

model sand embankments. However, the method has not previously been used to measure either dynamic pressures or pressure gradients. The underlying principle is similar to that proposed by Nielsen et al (1994) and has also been used in medicine to measure blood and lumbar pressures (Kumar et al, 1993).

The pressures within the fluid or sediment are measured by means of a series of 2mm ID steel probes. Each probe is connected to a 0.1 Bar pressure transducer via a three way ball valve and short length of 3mm ID semi-rigid nylon tubing (figure 1). Air may be flushed from the tubing and probe by opening the valve to a small header reservoir mounted above the transducer/valve system. The pressure variation is transmitted into each probe through 12 0.4mm diameter holes drilled into the tip. In order to measure the pressure gradients, five probes are arranged in an array such that both the vertical and horizontal pressure gradients are obtained at a single point. The probes may be moved vertically within the bed by means of a traverse mechanism, with minimal disturbance of the sediment. The probe holder, pressure transducers and header tank are mounted on a carriage running on rails above the flume, which allows the probes to be positioned at any position within the sediment bed.

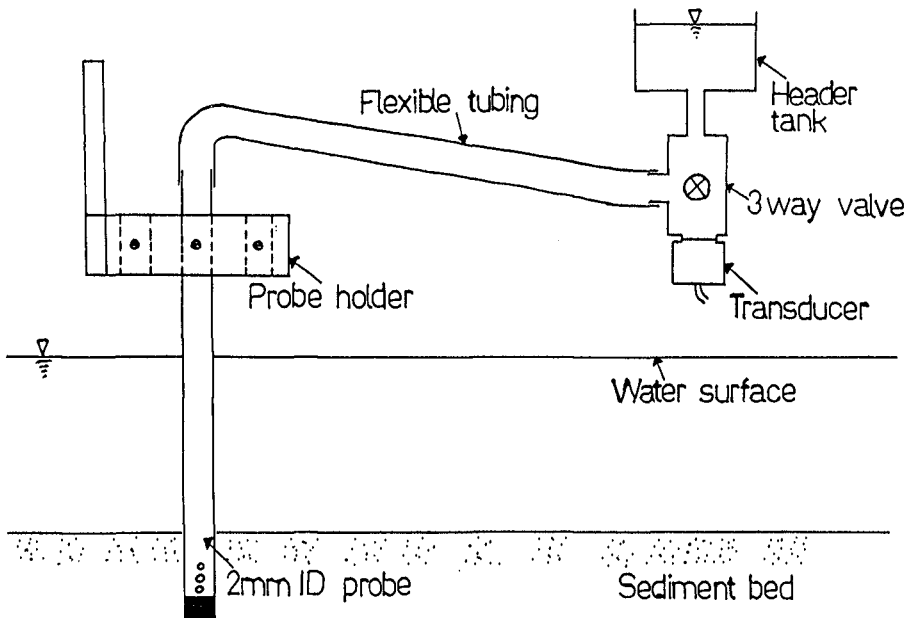


Figure 1. Pressure measurement system.

The static pressure recorded by the probes is the elevation head between the pressure transducers and the mean or still water level. This is generally negative and a variable offset was therefore added to the pressure transducer amplifiers. The “mean pressure” may therefore be set to zero, allowing amplification to be used

when sampling the dynamic pressure. This increases the accuracy of the measurements, since the amplitude of the dynamic pressure may be considerably smaller than the static pressure in many practical circumstances. Note that moving the probes vertically does not change the recorded static pressure and that the probes do not measure a velocity head.

3) EVALUATION / CALIBRATION

For the purpose of measuring mean or steady pressure gradients the probe technique requires no calibration. However, for the purpose of measuring dynamic pressure gradients the dynamic response of the measurement system requires evaluation. The dynamic response depends on the length of the probe and tubing, the geometry of the valve/transducer connection and the speed of the pressure pulse. In order to achieve a satisfactory dynamic response the natural frequency of the system must be as high as possible. If it is assumed that the system behaves as a quarter length resonator (Nielsen et al, 1993) then the natural frequency, f_o , is given by

$$f_o = c / 4L \quad (1)$$

where c is the speed of the pressure pulse and L the length of the probe and tubing. L is consequently kept as small as possible (<1m), while the speed of the pulse should be maximised. The pressure pulse is a one-dimensional wave, whose speed is dependent on the fluid density, ρ , the compressibility of the fluid, C , and the distensibility of the tubing, D (Lighthill, 1978).

$$c = \frac{1}{\sqrt{(\rho(C + D))}} \quad (2)$$

The distensibility of the tubing is given by

$$D = 2a / tE \quad (3)$$

where a is the tube radius, t is the wall thickness and E is the Young's modulus of the tube material ($O \sim 10^9$ N/m²). In the present instance D is of order 10^{-9} m²/N and the compressibility of pure water is approximately $5 \cdot 10^{-10}$ m²/N, giving $c \approx 800$ m/s. However, the presence of small air bubbles within the tube will increase the compressibility of the water significantly. For example, an air content of 0.4% will give a compressibility of $5 \cdot 10^{-8}$ m²/N. Hence, from (2), a few small air bubbles ($O \sim 1$ mm) are sufficient to reduce c to about 150 m/s. This results in a natural frequency of about 35 Hz, far higher than the wave frequencies used in typical laboratory studies (0.5-2 Hz). In order to confirm the estimates above, the speed of

a pressure pulse along a 10m length of tubing was calculated by correlation of this signal with that obtained from a conventional transducer. In this instance the lag along the tube was found to be of order 0.06s, giving a value for c of 150m/s (figure 2). The lag along a 1m length of probe and tubing is therefore less than 0.01s. The difference in lag between probes is inconsequential for the purposes of calculating the pressure gradients (figure 3), although in this figure the ± 0.02 s lag on two of the probes indicates the wave speed.

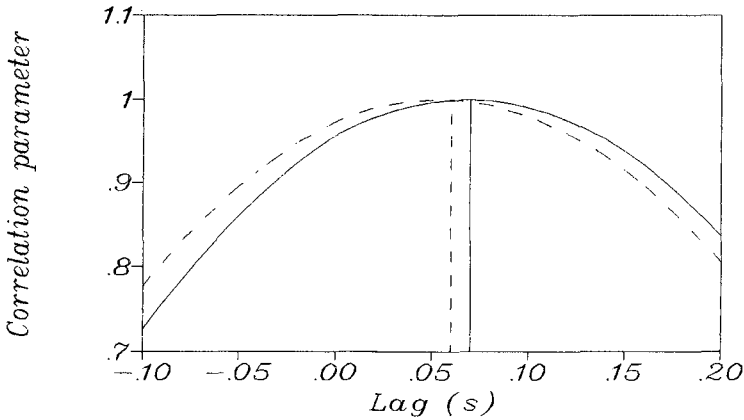


Figure 2. Correlation of the pressure signal from two probes with that from a conventional transducer. $L=10$ m.

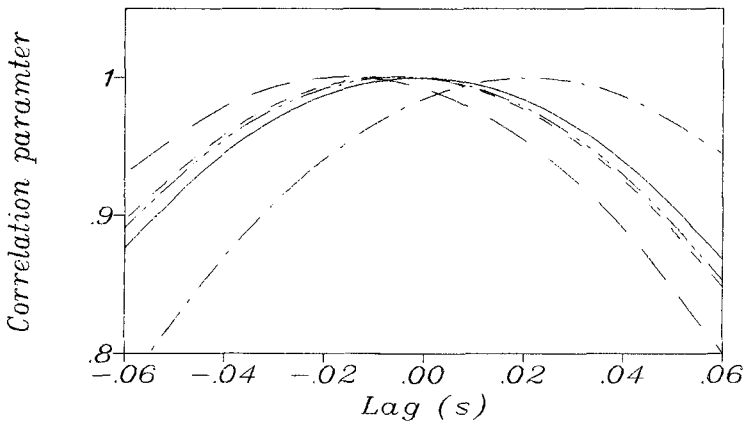


Figure 3. Correlation between the five probes arranged in the measuring array and a conventionally mounted pressure transducer. $L=1$ m.

Regular waves

With a natural frequency of 35Hz, probe/transducer system was expected to have a linear frequency response function and a gain close to 1 over the required

range of wave frequencies. However, some damping is to be expected due to energy losses. In regular wave tests the gain function was evaluated by comparing the amplitude of the signal recorded through the probe/transducer system with that obtained from a conventional transducer. Figure 4 shows the measured response functions for a range of frequencies. In each case the response function is very similar, although some difference is observed in the absolute gain values. This is probably due to slight variations in the concentration of air bubbles in each probe. Therefore, when regular waves are used, each probe is individually calibrated at the beginning of the test session. After calibration, the pressure signal recorded by each probe is very close to that recorded by a conventional pressure transducer (figure 5).

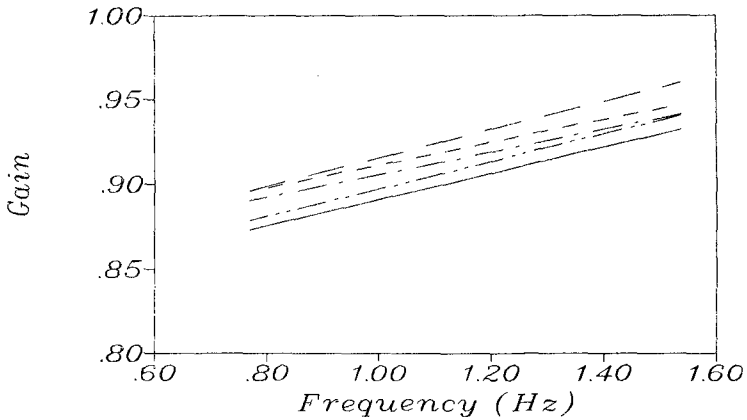


Figure 4. Gain functions measured for each probe/transducer system. $L=1\text{m}$.

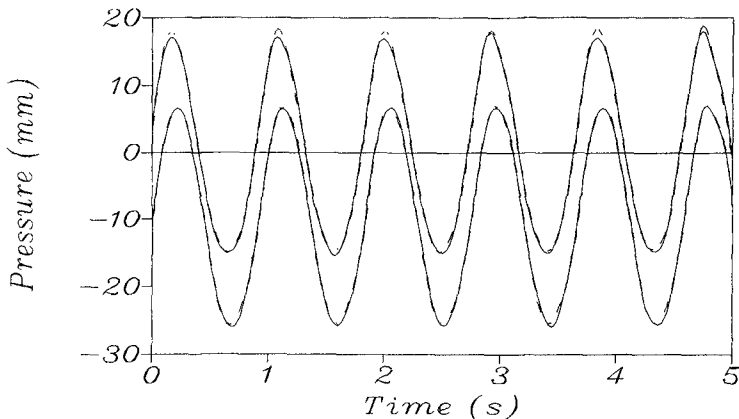


Figure 5. Comparison of the dynamic pressure recorded by two probes with that recorded by conventionally mounted pressure transducers. — Transducers, --- probes.

In order to obtain the pressure gradients, the pressure signals from each probe were first low pass filtered at 5Hz and then the gradients calculated with a simple finite difference scheme. The best results were obtained with a probe spacing of 0.06m in the horizontal direction and 0.02m in the vertical direction. The reduced vertical spacing was necessary to obtain the pressure gradients close to the surface of the sediment bed. A comparison of the dynamic horizontal pressure gradient calculated from probe measurements with that from equally spaced conventional transducers clearly shows good agreement (figure 6). Finally, it was necessary to check the performance of the system with all five probes operating and, in particular, to ensure that the phase relationship between the pressure and pressure gradient was accurately reproduced. Figure 7 shows that this was indeed the case.

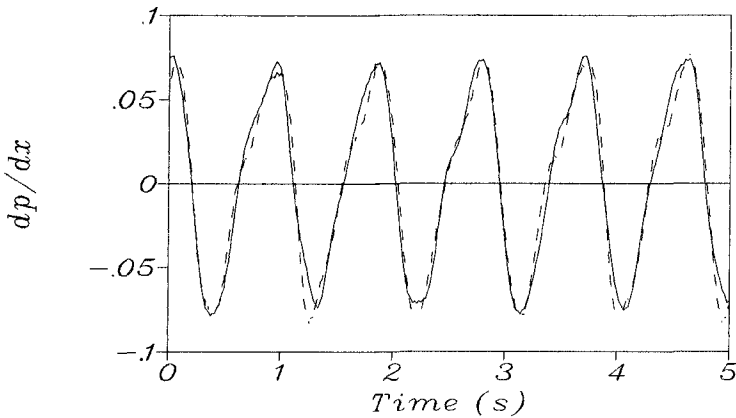


Figure 6. Comparison of the dynamic horizontal pressure gradient.
 — Transducers, --- Probes.

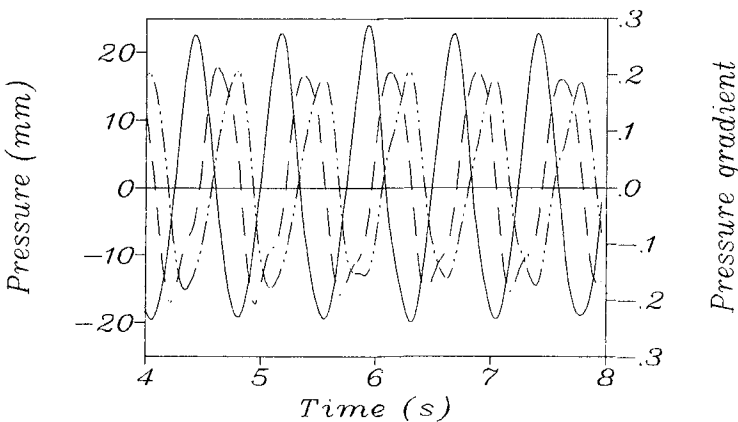


Figure 7. Pressure and pressure gradients within a sand bed.
 — Pressure, --- Horizontal, — · — Vertical.

Random waves

Two approaches are possible when using the present method to measure the pressure variation induced by random waves. The first is simply to calibrate each probe over the appropriate frequency range using regular waves. However, best results are obtained by calibrating the probes at the outset of a model test by using a random wave series and a spectral method. In this instance the pressure signal recorded by each probe is Fourier transformed and compared to the Fourier transform of a pressure signal recorded by a conventional transducer. An impulse response function may then be calculated for each probe and applied to all subsequent measurements. This approach gives gain functions very similar to those for regular waves shown above. Applying the appropriate impulse response function during subsequent tests then results in close agreement between the dynamic pressure obtained from the probe system and that obtained from a conventional transducer.

4) RESULTS / APPLICATIONS

The flexibility of the present technique has considerable advantages for a wide range of pressure measurements. For example, the minimal flow resistance of the probes makes it possible to measure the pressure and pressure gradients at any point within a fluid flow. This is not possible with conventional transducers, which must generally be mounted flush with a surface in order to minimise turbulence effects. A second advantage of the present method is that data may be obtained at a large number of positions within a sediment bed with a minimum number of pressure transducers. This is because the small diameter of each probe allows the probes to be moved vertically within the sediment with virtually no disturbance of the bed material. The variation in the dynamic pressure over the vertical is therefore easily obtained. For example, figure 8 shows measurements of the maximum dynamic pressure within a sand bed and an anthracite bed under regular waves. Data could be collected at a large number of points with only one pressure transducer and gave good agreement with the solution of Sleath (1970).

Pressure gradients

Figures 9 and 10 show the horizontal and vertical pressure gradients at the face of a vertical breakwater and at the toe of a sloping breakwater respectively. The face of the vertical breakwater is an antinode, and therefore the horizontal pressure gradient is small, while the vertical pressure gradient increases rapidly close to the surface of the sediment bed. The sharp discontinuity in the vertical pressure gradient expected at the fluid/sediment interface is also clearly visible, although the finite spacing of the probe tips is apparent. Nevertheless, data of this sort would be difficult to obtain with conventional transducers. The toe of the

sloping breakwater lies between a node and antinode and therefore, in this instance, the horizontal and vertical pressure gradients are of similar magnitude at the sediment surface. However, the present measurement technique is sufficiently accurate to detect the change in the rate of decay of the horizontal pressure gradient at the fluid/sediment interface. This change occurs because the variation in the horizontal pressure gradient within the fluid approaches zero at the interface, while the rate of decay within the bed is proportional to the thickness of the sediment bed (e.g. Sleath, 1970).

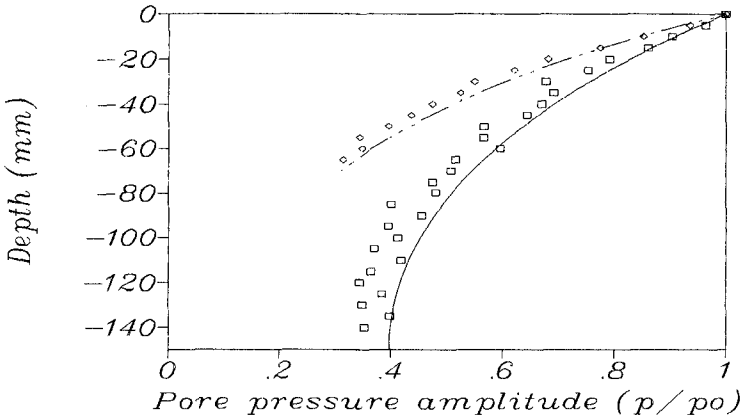


Figure 8. Dynamic pressure within a sand bed and an anthracite bed. □□□□ Sand, $T=0.7s$, ——— Sleath (1970), ◇◇◇◇ Anthracite, $T=0.5s$, — · · — Sleath (1970).

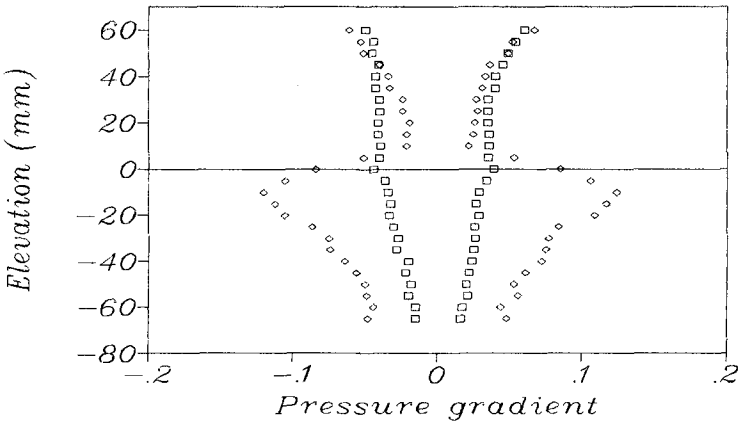


Figure 9. Horizontal and vertical pressure gradients at the face of a vertical porous breakwater. □□□□ Horizontal, ◇◇◇◇ Vertical.

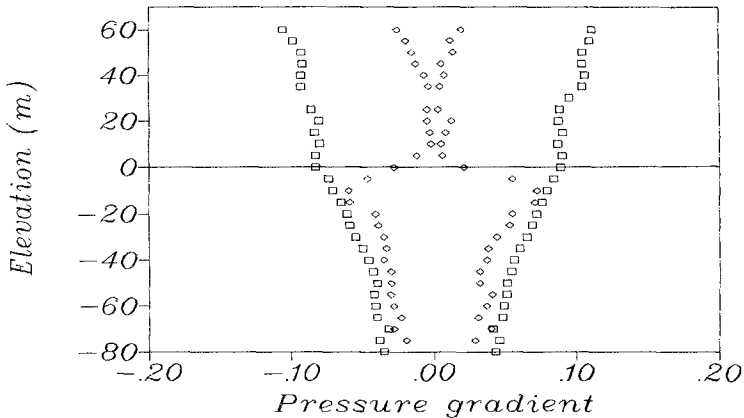


Figure 10. Horizontal and vertical pressure gradients at the toe of a sloping porous breakwater. □□□□ Horizontal, ◇◇◇◇ Vertical.

The pressure gradients within laboratory scale sediment beaches were also investigated with the present measurement technique. The first case considered a coarse sediment beach with a median grain size of 1.5mm and a thickness of 0.1m. Regular waves with a height of 0.1m and wave period of 1.5s were used. Waves were run until the initially plane beach reached a stable shape and the pressure gradients just below the bed surface were then measured at a number of locations across the surf zone. Measurements of this kind would be very difficult to obtain using conventional transducers, which would have to be positioned before the beach attained an equilibrium profile.

Figure 11 shows the mean horizontal pressure gradient increasing across the surf zone due to wave induced set-up and swash zone percolation, reaching a maximum of about 0.1 at the still water level. The vertical pressure gradient has a similar magnitude at this point and is again positive. The flow within the beach is therefore downward and seaward. The vertical pressure gradient reaches a minimum in the middle of the surf zone and, consequently, the flow is out of the beach. However, the mean pressure gradients appear too small to significantly influence the stability of the beach sediment, in general agreement with the numerical calculations of Oh and Dean (1994).

In a second experiment the maximum dynamic pressure gradients were measured across a barred laboratory scale beach. In this instance the beach consisted of sediment with a median grain diameter of 0.5mm and was again 0.1m thick. Regular waves were again run until a stable beach formed and the pressure gradients were measured 20mm below the bed surface in the region of the bar. The data show that both the horizontal and vertical pressure gradients reach a

maximum just seaward of the bar and then decrease rapidly after wave breaking (figure 12).

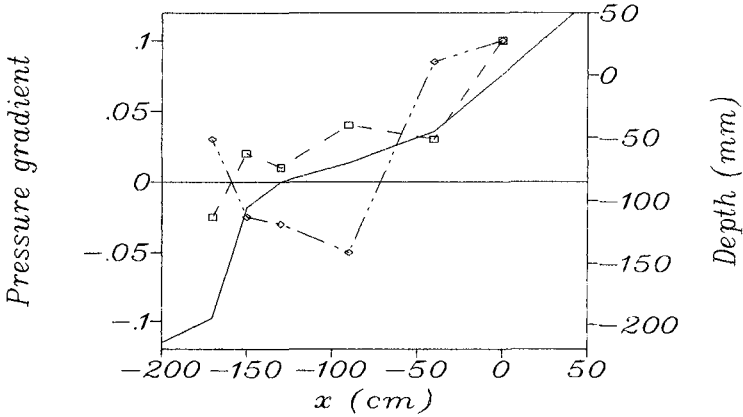


Figure 11. Mean horizontal and vertical pressure gradients within a laboratory scale sand beach. — Water depth, —□—, horizontal, — ·◇· — vertical.

The maximum horizontal gradient does not reach the value required for liquefaction of a sand bed (Madsen, 1974), but is nearly twice that required to initiate the failure of an anthracite bed. The negative horizontal pressure gradient is much larger than the positive gradient, indicating steep wave fronts, while the reverse is the case for the vertical pressure gradients, indicating steep crests and flatter wave troughs (figure 13).

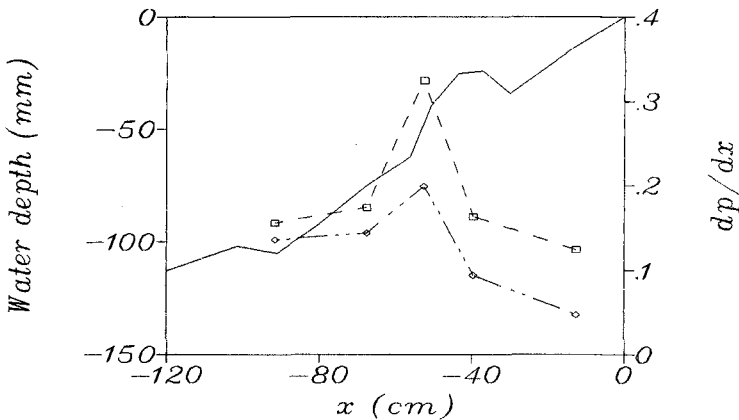


Figure 12. Maximum horizontal dynamic pressure gradient across a laboratory scale sand beach. — Water depth, —□—, negative, — ·◇· — positive.

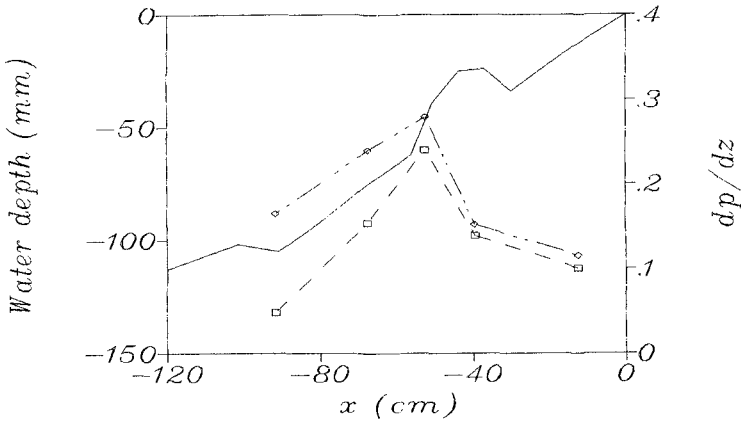


Figure 13. Maximum vertical dynamic pressure gradient across a laboratory scale sand beach.

— Water depth, —□—, negative, —◇—, positive.

CONCLUSIONS

The development of a new technique for measuring the pressure gradients within sediments is presented. The pressure gradients are measured using a series of small diameter steel probes connected to pressure transducers with semi-rigid flexible tubing. This allows the pressure gradients to be determined quickly and easily with minimal disturbance of the sediment. For the purpose of measuring mean pressure gradients the method requires no calibration. The dynamic response of the system was evaluated using both regular and irregular waves and was found to be satisfactory for typical laboratory wave frequencies. A comparison of the pressure gradients obtained by the present technique with those measured using conventional pressure transducers showed good agreement. Measurements of the mean and dynamic pressure gradients within laboratory scale sand beaches have demonstrated the advantages of the system. The measurement technique has already proved useful for investigating the role of pressure gradients in sediment transport mechanics (Baldock and Holmes, 1996) and will aid investigations into the flow pattern within laboratory scale beaches.

REFERENCES

- Baldock, T.E. and Holmes, P., 1996. On the influence of seepage on sediment transport under steady flow and wave motion. Submitted to *J. Hydraulic Research*.
- Conley, D.C. & Inman, D.L., 1992. Field observations of the fluid granular boundary layer under near breaking waves. *J. Geo. Res.*, **97** (C6), 9631-9643.

- Kumar, M., Werner, W. and Murray, M.J., 1993. The fidelity and dynamic response of fluid-filled catheter systems for direct measurement of lumbar cerebrospinal fluid pressure. *J. Clin. Monit.*, **9**, 314-320.
- Lighthill, J., 1978. *Waves in fluids*. Cambridge University Press, Cambridge, UK.
- Longuet-Higgins, M.S., 1983. Wave set-up, percolation and undertow in the surf zone. *Proc. R. Soc. Lond.* **A 390**, 283-291.
- Loveless, J.H., 1994. Modelling toe scour at coastal structures. *Proc. 2nd Int. Conf. on Hydraulic Modelling*, Stratford, UK. BHR Group, 479-489.
- Madsen, O.S., 1974. Stability of a sand bed under breaking waves. *Proc. 14th ICCE*, Copenhagen. ASCE, **2**, 776-794.
- Martin, C.S., 1970. Effect of a porous sand bed on incipient sediment motion. *Water Resources Research*, **6**, (4), 1162-1174.
- Nielsen, P., Hanslow, D. J. and Apelt, C. J., 1993. A new type of nearshore wave gauge. *Proc 11th Australasian Conf. on Coastal and Ocean Engng.*, Townsville, Australia, pp 247-251.
- Oh, T. & Dean, R.G., 1994. Effects of controlled water table on beach profile dynamics. *Proc. 24th ICCE*, Kobe. ASCE, **3**, 2449-2459.
- Oldenzil, D. M. & Brink, W.E., 1974. Influence of suction and blowing on entrainment of sand particles. *J. Hydraulics Div.*, ASCE, **100**, 935-949.
- Sato, M., Hata, S. and Fukushima, M., 1994. An experimental study on beach transformation due to waves under the operation of a coastal drain system. *Proc. 24th ICCE*, Kobe. ASCE, **3**, 2571-2582.
- Sleath, J.F.A., 1970. Wave induced pressures in beds of sand. *J. Hydraulics. Div.*, ASCE, **96**, 367-378.
- Turner, I.L., 1995. Simulating the influence of groundwater seepage on sediment transported by the sweep of the swash zone across micro-tidal beaches. *Marine Geology*, **125**, 153-174.
- Vesterby, H., 1996. Beach drainage - state of the art-. Seminar on Shoreline Management techniques, HR Wallingford, Wallingford, UK.
- Yamamoto, T., 1978. Sea bed instability from waves. *Proc. 10th OTC Conf.*, Houston. ASCE, Paper 3262.
- Yamamoto, T., Koning, H.L., Sellmeijer, H. & van Hijum, E., 1978. On the response of a poro-elastic bed to water waves. *J. Fluid Mech.*, **87**, 193-206.

ACKNOWLEDGEMENTS

The authors gratefully acknowledge the support of the UK Engineering and Physical Sciences Research Council. The advice of Mr Steve Ackerly (Soil Mechanics) on pressure measurement techniques is much appreciated.

CHAPTER 323

Analysis of Mud Mass Transport under Waves Using an Empirical Rheological Model

Qin Jiang¹ and Akira Watanabe²

Abstract

This study is focused on deepening our insight into rheological properties of soft mud under oscillatory forces, on quantifying their effects on the interaction between water waves and mud bed, and especially on the resultant mud mass transport. On the basis of a large number of experiments, an empirical rheological model and formulas for model parameters are proposed. In addition, a simple analytical model for evaluating the temporal change in mud water content ratio under waves is derived. Using these two models, a vertical 2-D numerical model is developed to predict the wave-induced bed mud motion and the resultant mud mass transport velocity. Comparisons between the calculations and measurements are presented.

1. Introduction

Mass transport in a soft mud layer is one of the noteworthy phenomena in a mud bed. Studies on it are of practical importance for both siltation and environmental problems in muddy coasts and estuarine areas.

Variety of theories and models have been proposed to describe the wave-mud interaction and relevant phenomena. The theoretical analysis was initiated by Gade (1958), who assumed that the soft mud would behave as a highly viscous fluid and developed an analytical model for the surface wave attenuation in shallow waters. On the same assumption, Dalrymple and Liu (1978) presented a linear theory for water waves propagating in a two-layer viscous fluid system. Instead of viscous fluid assumption, elastic models were proposed by Mallard and Dalrymple (1977) and Dawson (1978), poro-elastic models by Yamamoto

¹Research Engineer, Penta-Ocean Institute of Technology, 1534-1, Yonku-cho, Nishinasunomachi, Nasu-gun, Tochigi, 329-27, Japan

²Professor, Department of Civil Engineering, University of Tokyo, Hongo 7-3-1, Bunkyo-ku, Tokyo, 113, Japan

et al. (1983, 1987) and Yamamoto and Takahashi (1984), visco-elastic models by Hsiao and Shemdin (1980), Macpherson (1980) and Maa and Mehta (1988, 1990), as well as a Bingham fluid model by Mei and Liu (1987). Recent studies include visco-elasto-plastic models by An *et al.* (1991) and Shibayama and Nguyen (1993).

A primary difference among the above models is in the assumptions of rheological properties of mud. Due to the complexity of the mud properties, it is difficult to judge which of them is most applicable to the wave-mud interaction problems under a certain condition. In addition, many of these models have been proposed either without enough experimental proofs or on the basis of experiments with unidirectional rotary viscometers in which the mud motion is considerably different from the real situation in coastal waters.

On the other hand, Hyunh *et al.* (1990) developed a dynamic rotary shear meter and studied the rheological behaviors of mud under various patterns of loading. Their experiments showed that there existed complicated relationships between the shear stress and shear strain or shear rate when the soft mud was subjected to cyclic loading. Following them, Shen *et al.* (1993) conducted similar experiments and proposed empirical models for the rheological properties and for the mud-wave interaction. However, their experiments only under limited conditions are not sufficient to understand and model the general features of mud behaviors under dynamic wave action.

The present study aims at gaining further understanding on the rheological properties of soft mud under the action of oscillatory forces and the interaction between water waves and a mud bed. An empirical rheological model of soft mud under oscillatory loading will be proposed on the basis of large numbers of measurements. Moreover, a simple analytical model for change in the water content ratio under wave action is derived in order to evaluate its effects on the rheological behaviors and on the motion of bed mud. By incorporating the proposed rheological model as well as the water content ratio model with the linearized Navier-Stokes equations, a vertical 2-D numerical model is constituted for simulating wave-mud interaction and the bed mud motion. Finally, calculated mud mass transport velocities and wave height changes are compared with those measured.

2. Rheological Properties of mud

2.1 Experiments and results

In order to clarify the rheological properties of soft mud under waves, laboratory experiments were conducted for more than 800 runs by using a dynamic rotary shear viscometer that can generate oscillatory forcing like waves (See Hyunh, 1991, for details of the setup). Instead of real seabed mud, pure kaolinite mixed with tap water was used for the test. This is because it has rheological properties similar to and less complicated than those of natural mud in actual coastal areas.

A wide range of conditions was covered in the test, in which the water content

ratio was changed from 120% to 300%, the period of cyclic loading was from 1s to 10s, and its angular amplitude was from 0.5° to 28° . With a series of combinations of the motion of the viscometer and the water content ratio, the measurements were made to examine influences of the angular amplitude and period of the oscillatory shear forces as well as the water content ratio on the rheological behaviors of the mud.

Figures 1 (a) and 1 (b) are the experimental results showing the effects of the angular amplitude A of cyclic forcing, which were obtained under the fixed period T and water content ratio W . Examples indicating the effects of the cyclic loading period and water content ratio are given in Figs. 2 (a) through 3 (b).

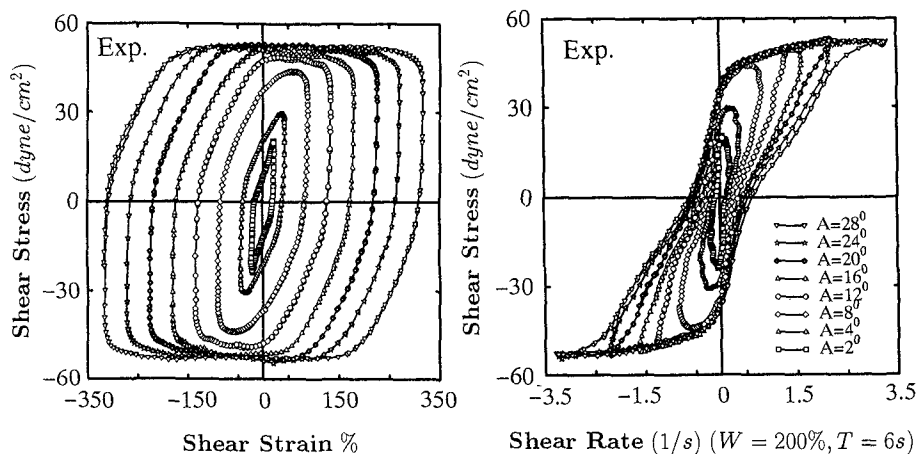


Fig. 1 (a) Shear stress vs. shear strain (effects of the angular amplitude).

Fig. 1 (b) Shear stress vs. shear rate (effects of the angular amplitude).

From these figures, it can be concluded that under the oscillatory action of external forces, the soft mud is characterized by very complicated visco-elasto-plastic properties. The shear stress of the mud is a function of both the shear strain and shear rate with strong nonlinearity featured by remarkable hysteresis in their relationships. In addition, the mud properties are significantly influenced by the water content ratio as well as by the period and amplitude of cyclic loading.

2.2 Constitution equation

On the basis of the above experimental results, a constitution equation of the soft mud is constructed for describing its rheological properties under cyclic loading.

Figures 4 (a) through 4 (g) illustrate a basic concept for constructing the constitution equation. Among these figures, Fig. 4 (a) stands for the hysteresis loop of the shear stress τ versus the shear rate $\dot{\gamma}$. It is obvious that this loop can be separated into two parts, namely, a backbone curve shown in Fig. 4 (b) and a

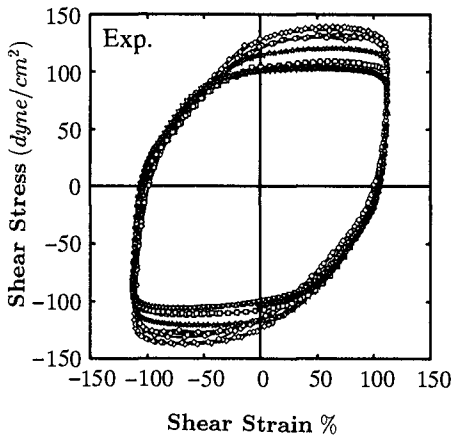


Fig. 2 (a) Shear stress vs. shear strain (effects of the cyclic load period).

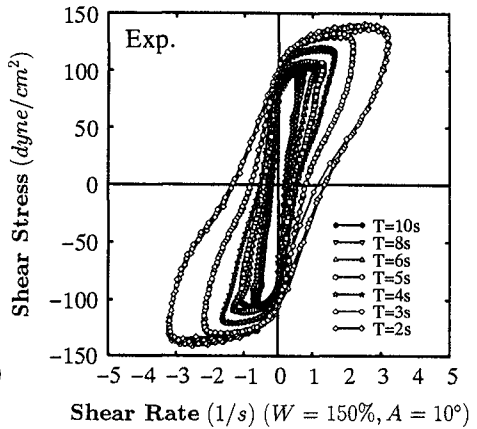


Fig. 2 (b) Shear stress vs. shear rate (effects of the cyclic load period).

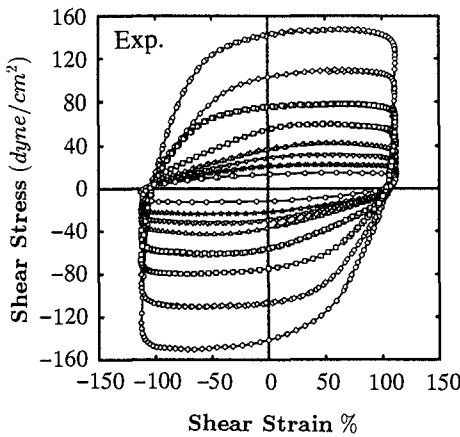


Fig. 3 (a) Shear stress vs. shear strain (effects of the water content).

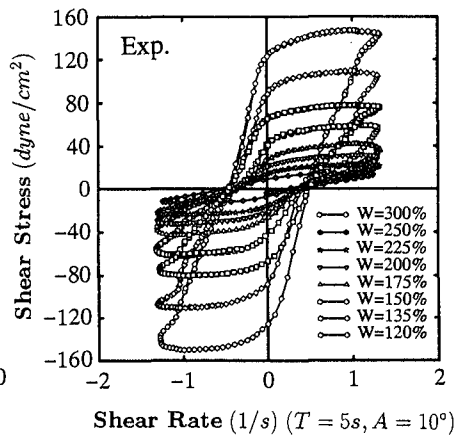


Fig. 3 (b) Shear stress vs. shear rate (effects of the water content).

compensatory curve in Fig. 4 (c). On the other hand, regarding the relationship between the shear stress τ and the shear strain ε shown in Fig. 4 (d), the curves in Fig. 4 (e) and Fig. 4 (f) correspond to Fig. 4 (b) and Fig. 4 (c), respectively, because of the 90° phase lag between the shear strain and shear rate. Namely, combining Fig. 4 (e) and Fig. 4 (f), we obtain Fig. 4 (d) that represents the hysteresis loop of the shear stress versus the shear strain, and Fig. 4 (f) gives the backbone curve for the loop in Fig. 4 (d).

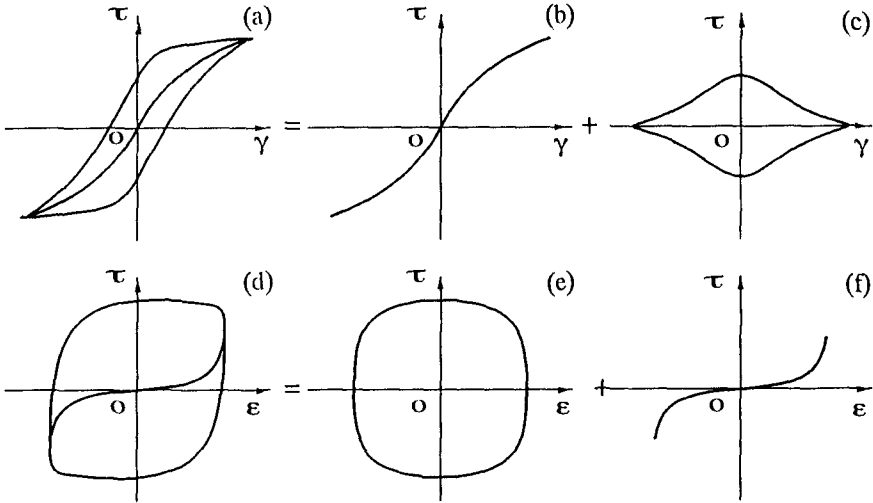


Fig. 4 Definition sketch for the constitution equation.

The concept mentioned above suggests us that if these two backbone curves of the hysteresis loops, Fig. 4 (b) and Fig. 4 (f), are properly determined, the shear stress in mud under waves can be easily obtained through their linear superposition. The constitution equation for the soft mud under the cyclic loading or wave action is thereby written as

$$\tau = \frac{G_0 \varepsilon}{1 - \alpha |\varepsilon|} + \frac{\mu_0 \gamma}{1 + \beta |\gamma|} \quad (1)$$

in which G_0 is the initial shear modulus at $\varepsilon = 0$, μ_0 is the initial viscosity at $\gamma = 0$, and α and β are coefficients determining the shapes of the backbone curves. The applicability of the above proposed model is strongly dependent on these four model parameters. With regression analyses, empirical formulas for them are obtained as follows:

$$\begin{aligned}
 \alpha &= \{1.0 - (0.8 - 5.0 \times 10^{-3} \cdot T) \\
 &\quad \cdot \exp(-[0.75 \cdot \tanh(T/4)] \cdot \varepsilon_{\max})\} / \varepsilon_{\max} \\
 \beta &= (0.45 + 0.11 \cdot T + 0.015 \cdot T^2) \\
 &\quad \cdot \varepsilon_{\max}^{(1.05 - 1.42 \cdot T^{0.2})} \\
 G_0 &= (5.6 \times 10^5 \cdot W^{-2.8}) \\
 &\quad \cdot \{[-7.26 - 560 \cdot (1.0 + \tanh(-0.58 \cdot T))] \\
 &\quad + [81.70 + 707 \cdot (1.0 + \tanh(-0.47 \cdot T))] \\
 &\quad \cdot \alpha^{1.71/[1 + 9.87 \exp(-0.87 \cdot T)]}\} \\
 \mu_0 &= (5.6 \times 10^5 \cdot W^{-2.8}) \cdot \{37.5 \cdot (1.31^T)\} \\
 &\quad \cdot \ln[24.7 \exp(-0.31 \cdot T \cdot \beta + 1.0)]
 \end{aligned}
 \tag{2}$$

where $T(s)$ is the period of the cyclic loading, ε_{\max} ($0.5 \leq \varepsilon_{\max} \leq 4.0$) is the shear strain amplitude, and $W(\%)$ is the water content ratio of the mud. (Here, for convenience, the angular amplitude of cyclic shear load was replaced by the amplitude of shear strain).

Equations (1) and (2) form a thorough rheological model for the soft mud. Their validity was well confirmed both qualitatively and quantitatively through trial hindcasting of experimental data. Examples of the calculated results are shown in Figs. 5, which corresponds to the measurements shown in Fig. 1 in the previous section.

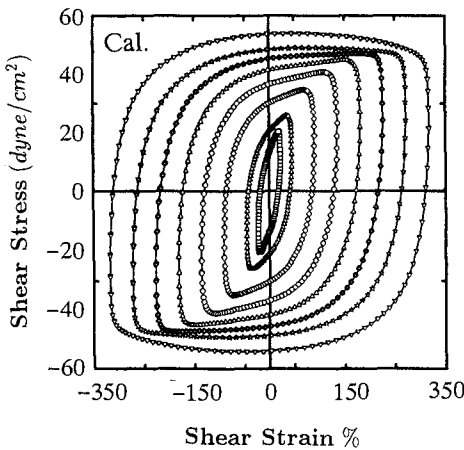


Fig. 5 (a) Shear stress vs. shear strain (effects of the angular amplitude).

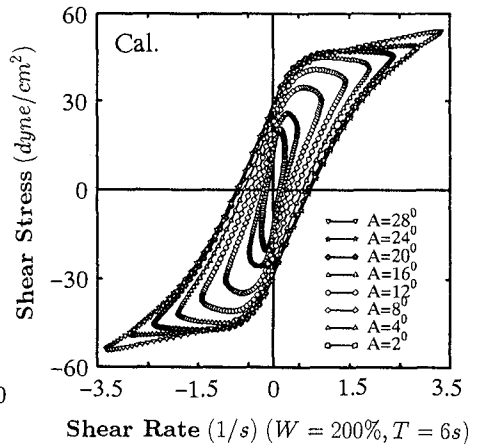


Fig. 5 (b) Shear stress vs. shear rate (effects of the angular amplitude).

3. Water Content Changes in Bed Mud under Waves

The water content ratio is an important factor affecting the rheological properties of the mud. Recent studies revealed that the dynamic change in the water content ratio takes place in a mud bed as a result of wave action. The results of experiments by Shen *et al.* (1993) showed that both the mud self-weight and water waves play significant roles in the variations of water content ratio in mud layers. As compared with the solo consolidation under the self-weight, the wave action causes further complicated change in the water content ratio, including the densification in deeper lower layers of the mud bed and liquefaction or swelling in the near-surface layers. On the basis of these experimental results, a simple analytical model is developed for evaluating the temporal change in water content ratio in bottom mud layers under waves.

3.1 Mechanism of Mud Densification and Liquefaction

Figure 6 illustrates an idealized state of stresses in a mud bed under waves. With consideration for the different effects of wave-induced stresses in mud layers, wave action on a mud bed can be classified into two components which are called "pumping" and "shaking". The pumping means the process of compression and expansion in a mud bed due to the dynamic wave pressure, while shaking refers to the tangential action by the oscillatory bottom shear stresses and the gradient of dynamic pressure in the wave propagation direction.

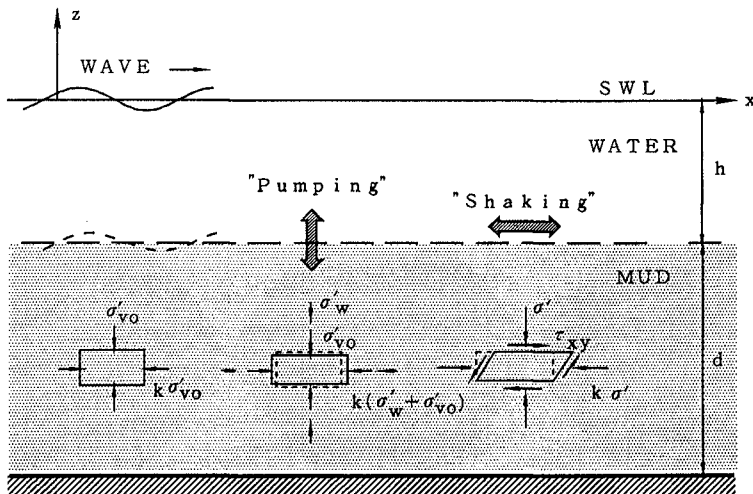


Fig. 6 Idealized stress state in mud bed under waves.

The downward transmission of the pumping and shaking action through the overlying water results in complicated processes in mud layers such as the oscillatory motion of the bed mud, the erosion or settlement of mud particles, and the change of the mud bed structure. Therefore, the water content changes in a

mud bed is regarded as the combined results of the pumping and shaking due to waves.

(a) Densification by the Pumping Action of Waves

It is said and often assumed that the effective stress in the underwater deposits remains unchanged even if the water level varies. However, it is not always true under wave action. According to Zen *et al.* (1993), the excess pore pressure and effective stress will be induced whenever the water surface elevation changes so quickly that the associated water pressure on the interface cannot be entirely transmitted into the deposits as the pore pressure. From this fact, the densification of the mud layers can be regarded as the result of the pumping action due to waves.

In this way the pumping action of waves may generally cause oscillatory change of the normal stress in a mud bed. As a result, the excess pore pressure and effective stresses may vary oscillatorily, and the bed mud is thus forced to condense and expand alternatively responding to the up-and-down motion of the water surface. During every wave period, a process of dewatering or densification may occur since the volume compression rate of the mud is bigger than its expansion rate. The cyclic pumping action of waves will thus induce the densification of the bed mud.

(b) Liquefaction Due to the Shaking Action of Waves

A well-known fact as for noncohesive sediment is that shear loading causes the increase in gross sediment volume, which is called dilatancy. In fact, dilatancy is a general soil property both for noncohesive and for cohesive sediments. Therefore, like the liquefaction of noncohesive sediment, the increase of water content ratio in near-surface mud layers can be reasonably interpreted as the dilatancy effect under the cyclic wave action.

This phenomenon can also be regarded as a result of the exchange of water and mud particles. Parchure and Mehta, *et al.* (1985) has found that the erosion of cohesive sediment occurs if the shear force exerted on mud beds is large enough and it takes place much more easily under the cyclic action of waves. This is because the contacts between mud particles are weakened and the shear strength of the mud decreases under the action of external forces in particular under that of oscillatory forces like waves. Thus the mud particles are entrained into the water part and the water particles enter into the new-born pores where the mud particles lodged, resulting in the increase of the water content ratio in near-surface mud layers with the growth of erosion in the mud bed.

3.2 Water Content Change Model

On the basis of the above discussions, the water content change in a mud bed under wave action e_{s+w} can be divided into three parts, which are the consolidation by the self-weight e_{cs} as well as the densification e_{dw} and liquefaction e_{lw} due to waves. Accordingly, an analytical one-dimensional model is developed for

evaluating the vertical distribution of water content ratio in mud layers by the linear superposition of the three parts.

Since the mud densification is similar to the soil consolidation and the liquefaction can be treated as its reversal process, all of these processes can be expressed by the conventional consolidation equation.

A general equation for the consolidation of soft mud was given by Gibson *et al.* (1967) as

$$\frac{\partial e}{\partial t} - \frac{\partial e}{\partial z} \left[\frac{k}{\rho_f (1+e)} \frac{d\sigma'}{de} \frac{\partial e}{\partial z} \right] + (\rho_s - \rho_f) \frac{d}{de} \left[\frac{k}{\rho_f (1+e)} \right] \frac{\partial e}{\partial z} = 0 \quad (3)$$

in which e is the void ratio of mud, k is the permeability coefficient, σ' is the effective stress, ρ_f and ρ_s are the densities of the water and mud, and z is the vertical coordinate measured from the rigid bottom elevation. Its linearized form can be written as

$$\frac{\partial e}{\partial t} = C_v \frac{\partial^2 e}{\partial z^2} \quad \text{for } 0 \leq z \leq z_0 \quad \text{and} \quad t \geq 0 \quad (4)$$

where $C_v (= k / [\rho_f (1+e)] (d\sigma'/de))$ is the coefficient of consolidation, t denotes the time, z_0 is the thickness of mud layer at $t = 0$.

For the consolidation due to the self-weight and densification caused by the pumping action of waves, the initial and boundary conditions are given as follows.

- 1) Assuming that the distribution of void ratio e_0 at $t = 0$ is uniform, the initial condition is

$$e(z, 0) = e_0 = \text{const.} \quad (5)$$

- 2) On the mud bed surface, the void ratio remains constant because the effective stress is zero, i.e.,

$$e(z_0, t) = e_0 \quad (6)$$

- 3) At the rigid bottom underlying the mud, the impervious boundary condition is

$$\left(\frac{\partial e}{\partial z} \right)_{z=0} = \beta \quad (7)$$

where β is a constant depending on the void ratio distribution at the ultimate state of consolidation by the self-weight and densification due to waves, and is expressed as

$$\beta = \frac{(\rho_s - \rho_f)}{\lambda} + \frac{p_0}{z_0 \lambda} \quad (8)$$

After simple manipulation, the solution of Eq. (4) for the void ratio is obtained as

$$e(z, t) = e_0 - \frac{\beta}{z_0} \left[1 - \frac{z}{z_0} - 2 \sum_{n=0}^{\infty} \frac{\cos \frac{m\pi z}{z_0}}{m^2 \pi^2} \exp \left(-m^2 \pi^2 \frac{C_v t}{z_0^2} \right) \right] \quad (9)$$

where $m = 2n + 1/2$, $\lambda = d\sigma'/de$, and p_0 is the amplitude of wave induced bottom pressure.

Regarding the fact that the volume change of pore water in a mud bed compensates that of the mud eroded from the bed, the swelling of mud by the shaking action of waves can be derived as

$$\Delta e(z, t) = \Delta e_s \left\{ -\frac{z}{z_0} - \frac{2}{\pi} \sum_{n=1}^{\infty} \left[\frac{\sin \frac{n\pi z}{z_0}}{z_0} \exp \left(\left(\frac{n\pi z_0}{z_0} \right)^2 C_i t \right) \right] \right\} \tag{10}$$

where Δe_s is the change of void ratio on the mud surface expressed as in the above equations, $C_i (= k_i/[\rho_f(1 + e)](d\sigma'/de))$ is the coefficient of expansion, N is the number of discretized points in the mud bed layers, and Δz is the grid length in the z direction. The volume of mud particles entrained from the mud bed, V_E , can be estimated by using an empirical formulas for the erosion rate E of mud particles (Parture and Mehta, 1985) as follows:

$$V_E = \sum_{k=1}^K \left(\frac{E\Delta t}{\gamma_s} \right) = \sum_{k=1}^K \left\{ \frac{E_0\Delta t}{\gamma_s} \exp \left[\alpha (\tau_b - \tau_c)^{0.5} \right] \right\} \tag{11}$$

where Δt is time interval, γ_s is the unit weight of the mud, E_0 is the floc erosion rate ($g/cm^2/s$), α is a model constant, τ_b is the wave-induced shear stress on the mud bed, and τ_c is the shear strength of the mud.

From Eqs. (9) and (10), the change in water content ratio W in the mud bed can be calculated from,

$$W(z, t) = e(z, t) \frac{\gamma_s}{S} \tag{12}$$

in which S is the saturation degree of the mud.

The validity of the above model is examined through comparisons of the computations with the measurements by Shen *et al.* (1993). Figure 7 shows comparisons between the calculations and measurements for the temporal change in water content ratio distributions under the conditions listed in Table 1. A good agreement is seen through the overall depth for each time step except for little discrepancy near the rigid bottom, where accurate measurement is generally difficult. Hence it is concluded that if values of the model parameters are properly determined for a mud material of interest, this model can be used to evaluate the temporal change in water content ratio distributions under waves with an acceptable accuracy.

Table 1 Computation conditions.

W_0 (%)	$k/[\rho_f(1 + e)]$ (m^4/kgs)	$k_i/[\rho_f(1 + e)]$ (m^4/kgs)	$\lambda = d\sigma'/de$ (kg/m^2)	T (s)	H_0 (cm)
174	3.6×10^{-11}	2.4×10^{-11}	35.0	1.02	4.5

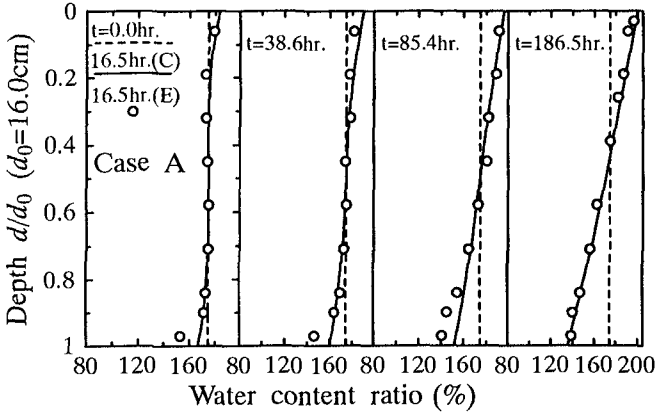


Fig. 7 Comparisons of the change in water content ratio between the calculations and the measurement by Shen *et al.* (1993)

4. Numerical Model of Mud Motion

4.1 Model Equations

A vertical two-dimensional numerical model for the interaction between waves and a mud bed is developed by incorporating the proposed rheological model and the water content ratio model with the Navier-Stokes equations.

On the assumption that the convective acceleration is not significant, the linearized momentum equations and the continuity equation for the incompressible soft mud layer under waves are

$$\rho_m \frac{\partial u}{\partial t} = -\frac{\partial p}{\partial x} + \frac{\partial \tau_{zx}}{\partial z} \tag{13}$$

$$\rho_m \frac{\partial w}{\partial t} = -\frac{\partial p}{\partial z} + \frac{\partial \tau_{xz}}{\partial x} \tag{14}$$

$$\frac{\partial u}{\partial x} + \frac{\partial w}{\partial z} = 0 \tag{15}$$

in which p is the dynamic pressure, u and w are the velocity components in the horizontal x and vertical z directions, ρ_m the mud density, and τ_{xz} and τ_{zx} are the shear stresses which can be obtained by the proposed rheological model Eqs. (1) and (2).

Equations (13) through (15) give a closed set of governing equations for u , w and p . With the non-slip condition ($u_n = w_n = 0$) at the fixed bottom under the mud layers, the zero shear stresses ($\tau_{xz0} = \tau_{zx0} = 0$) and pressure continuity conditions on the mud surface, and the periodic lateral boundary conditions, this

equation system can be solved numerically, for instance, by using the SIMPLEC algorithm.

The coefficient of wave damping along the wave propagating direction, D_H , can be estimated as

$$D_H = -\frac{1}{H} \frac{dH}{dx} = \frac{1}{2EC_g L} \int_x^{x+L} \int_0^d \tau \left(\frac{\partial u}{\partial z} + \frac{\partial w}{\partial x} \right) dz dx \quad (16)$$

The mass transport velocity of mud, U , is given as the summation of the Stokes drift U_S and the mean Eulerian velocity U_E , which are

$$U_S = \overline{\frac{\partial u}{\partial x} \int_0^t u dt'} + \overline{\frac{\partial u}{\partial z} \int_0^t w dt'} \quad (17)$$

$$\mu' \frac{\partial^2 U_E}{\partial z^2} = \overline{\frac{\partial \rho_m u^2}{\partial x}} + \overline{\frac{\partial \rho_m u w}{\partial z}} \quad (18)$$

where μ' is the mean viscosity averaged over one wave period,

$$\mu' = \frac{1}{T} \int_t^{t+T} \frac{\partial \tau}{\partial z} dt = \frac{1}{T} \int_t^{t+T} \frac{\mu_0}{(1 + \beta |\gamma|)^2} dt \quad (19)$$

4.2 Comparisons with Results of Experiment

In order to verify the above-described numerical model, results of calculations are compared with those of experiments by Sakakiyama and Bijker (1989). Figures 8 and 9 give examples of the comparisons with respect to the wave height distribution and the vertical profile of mud mass transport velocity. Agreement is very good for the mass transport velocity distribution, while the wave damping is slightly underestimated by the present model.

To examine the effect of water content ratio on the motion of bed mud, the change of the mud mass transport velocity in response to the temporal change in water content ratio is evaluated as an example. Figure 10 is the predicted mass transport velocity that corresponds to the evolution of water content ratio shown in Fig. 11. It can be seen in these figures that the temporal change in the water content ratio naturally has effect on the mud mass transport but it is not very significant as far as under the conditions in this example.

5. Conclusions

The soft mud is characterized by the very complicated visco-elasto-plastic properties in response to the cyclic action of external forces. In addition, the mud properties are significantly influenced by the water content ratio as well as the period and amplitude of cyclic loading. The proposed empirical rheological model can be regarded more general than most of previous ones, although the formulas for the model parameters may not be directly applicable to actual coastal mud. The temporal change in the mud water content ratio under waves has also been studied and formulated as a simple analytical model. By incorporating these

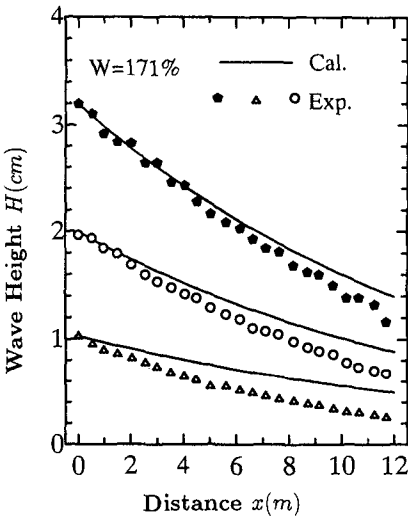


Fig. 8 Comparison between calculated and measured wave damping.

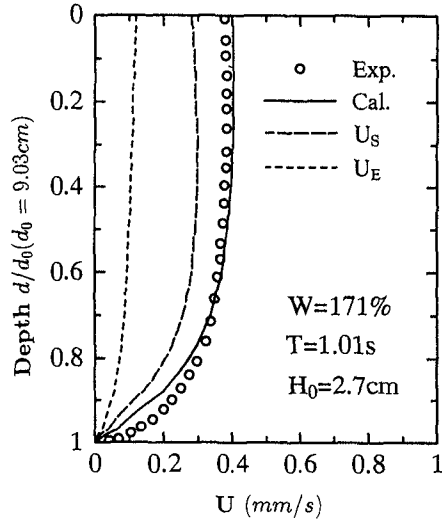


Fig. 9 Calculated and measured mud mass transport velocity.

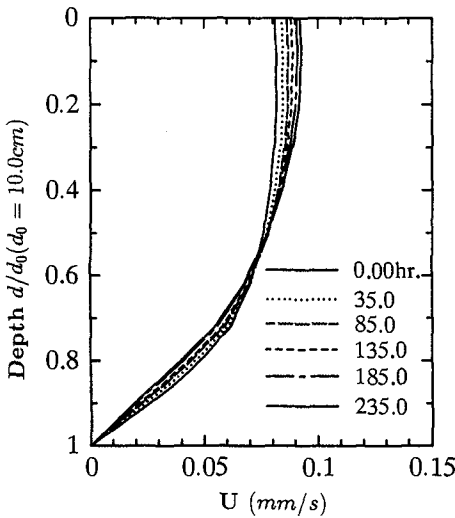


Fig. 10 Temporal changes of mud water content ratio under waves.

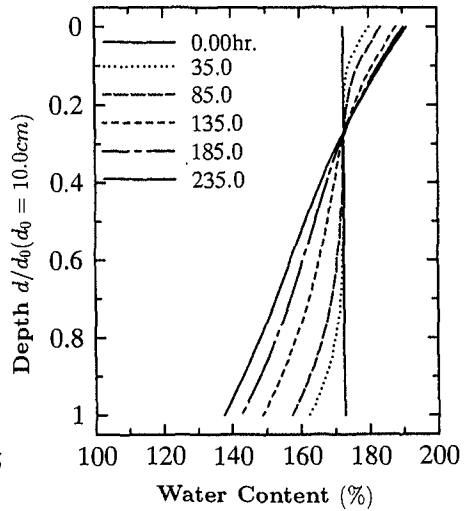


Fig. 11 Evolution of mud mass transport velocity under waves.

models with the Navier-Stokes equations, a vertical two-dimensional numerical model has been constituted to simulate the interaction of waves and mud. It has been verified that the proposed models can reproduce satisfactorily the rheological properties of mud, the temporal change in the water content ratio as well as the mud mass transport velocity under waves.

Acknowledgment

The authors would like to thank Prof. Masahiko Isobe, Department of Civil Engineering, University of Tokyo, for his valuable discussions throughout this study.

References

- Been, K. and G. C. Sills, (1981): Self-weight consolidation of soft soils: an experimental and theoretical study, *Geotechnique*, Vol. 31, No. 4, pp. 519–535.
- Dalrymple, R. A. and P. L.-F. Liu, (1978): Wave over soft muds: a two layer fluid model, *Jour. Phys. Oceanogr.*, Vol. 8, pp. 1121–1131.
- Gibson, R. K., G. L. England, and M. J. L. Hussey, (1967), The theory of one-dimensional consolidation of saturated clays, (i) Finite non-linear consolidation of thick homogeneous layers, *Geotechnique*, Vol. 17, No.26, pp. 251–273.
- Huynh, N. T., M. Isobe, T. Kobayashi, and A. Watanabe, (1990): An experimental study on rheological properties of mud in the coastal waters, *Proc. Coastal Eng., JSCE*, Vol., 37, pp225–229. (in Japanese)
- Jiang, Q. and A. Watanabe, (1995): Rheological properties of soft mud and a numerical model for its motion under waves, *Coastal Engineering in Japan, JSCE*, Vol. 38, No. 2, 195–214.
- Jiang, Q., (1995): Study on the rheological properties and mass transport of soft mud under water waves, Doctoral dissertation submitted to the University of Tokyo.
- Maa, J. P.-Y. and A. J. Mehta, (1990): Soft mud response to water waves, *Jour. Waterway, Port, Coastal and Ocean Eng., ASCE*, Vol. 116, No.5, pp.634–650.
- Macpherson, H., (1980): The attenuation of water waves over a non-rigid bed, *Jour. Fluid Mech.*, Vol. 97, Part 4, pp. 721–742.
- Mei, C. C. and K.-F. Liu, (1987): A Bingham-plastic model for a muddy seabed under long waves, *Jour. Geophys. Res.*, Vol. 92, No. C12, pp. 14,581–14,594.
- Parture, T. M. and A. J. Mehta, (1985): Erosion of soft cohesive sediment deposits. *J. hydraulic Engineering, ASCE*, Vol. 111, pp.1308–1326.
- Sakakiyama, T. and E. W. Bijker, (1989): Mass transport velocity in mud layer due to progressive waves, *J. of Waterways, Ports., Coastal and Ocean Eng., ASCE*, Vol. 115, No. 5, pp.614–633.
- Shibayama. T., and N. A. Nguyen, (1993): A visco-elastic-plastic model for wave-mud interaction, *Coastal Engineering in Japan, JSCE*, Vol. 36, No. 1, pp.67–89.
- Shen, D. S., H. Yokoki, M. Isobe and A. Watanabe, (1993): Mud transport and muddy bottom deformation due to waves, *Proc. Coastal Eng., JSCE*, Vol., 40, pp356–360. (in Japanese)
- Zen, K. K., (1993): Study on the wave-induced liquefaction in seabed, *Tech. Note Port and Harbor Res. Inst., Min. of Transport, Japan*, No. 755. (in Japanese)

CHAPTER 324

COUNTERMEASURES AGAINST WIND-BLOWN SAND ON BEACHES

--- A short summary of the present state-of-the-arts and introduction of new methods ---

Shintaro Hotta*
and
Kiyoshi Horikawa**

Abstract

Characteristics and functionings of prevention works for wind-blown sand are briefly reviewed and discussed. Then, guidelines for their use are given. In addition, new prevention works, including trench, movable porous sand fence, and large-scale sand ripples, are proposed according to the result of recent research.

I. Introduction

One of the important problems in beach stabilization is how to control wind-blown sand. Typical problems concerning blown sand are preservation and promotion of the growth of dunes, prevention of channels, inlet and river mouth closure, protection of residential and cultivated land from contamination by sand, and so on. Many kinds of works for preventing blown sand have been employed all over the world. However, no general criteria or technical standards for the use of prevention works exist at present. Therefore, the main objectives of this study are to summarize the operational characteristics of prevention works for wind-blown sand and to provide specific guidelines for their use.

Attempts are made (1) to systematize and classify prevention works for wind-blown sand according to their functioning, and (2) to evaluate conventional prevention works. In addition, (3) new prevention works are proposed according to studies recently carried out.

II. Functioning and Classification of Prevention Works for Wind-Blown Sand

Prevention works for wind-blown sand might have the following two functions: one is to restrain and stop the generation of blown sand, and the other is to trap the blown sand at the upwind side and to store the blown sand at a given location so that it is not transported further downwind. Hereafter, in short for later convenience, the former function will be known as a restrain function and the latter

* Shintaro Hotta, Dr., Prof. of Dept. of Construction Engrg. Nihon University, Narashino-dai 7-24-1, Funabashi, Chiba Pref., 274, Japan.

** Kiyoshi Horikawa, Dr., Prof. Emeritus of the University of Tokyo and President of Saitama University, Shimo-Okubo, Urawa, Saitama Pref., 255, Japan

function as a trap and fixation function. If a prevention work has a perfect restrain function and can fully stop the generation of blown sand, the work does not need the trap and fixation function. However, it is usually difficult to perfectly stop the generation of blown sand by using a certain prevention work which has the restrain function. It may be expensive or it may prevent an effective use of the beach if we intend to completely stop the generation of blown sand. In such cases, it may be recommendable from an engineering point of view to employ a prevention work which has the trap and fixation function at the downwind site while it may permit the generation of blown sand by decreasing the restrain function, which could be done through changing the kind of prevention work used or downsizing the scale of the prevention work.

The restrain function can be provided by the following methods. One method is to increase the resistance force to the wind which acts on the sand surface and sets sand grains on the surface into motion as blown sand. Another method is to decrease the wind speed that acts near the sand surface to a level so that the sand grains can not begin to move. Examples of methods for increasing the resistance force of the sand surface are spraying water (fresh or salt) or coagulant on the surface and replacement of surface sand. To decrease the wind speed (or the shear stress) that acts on the sand surface, methods to be considered are placing fences, planting shrubs or trees, and covering by grass, nets or mats in order to shut off the wind from direct action on the sand surface.

Two cases are considered for the trap and fixation function. The first case is the forced trap and fixation function that traps coercively blown sand in the air without changing of the basic motion of the sand grains and brings them to rest. The second case involves trapping or bringing to rest the blown sand grains by means of decreasing the wind speed. Cases that catch blown sand grains with streamer-type traps or adhere blown sand grains to a plate coated by an adhesive are considered as cases where the forced trap and fixation function acts. However, it is not possible to trap and store a large amounts of sand by these methods. Thus, these methods can not be employed for engineering use. Another case is where blown sand grains strike a fence stretched by a net with a small mesh and with a high porosity, where the porosity is defined as the ratio of open space area to total projected area, drop and come to rest at the foot of the fence. In this case, we may think of the fence as having the forced trap and fixation function because the fence does not disturb the wind flow and the motion of the sand grains in the air significantly. Such a fence can be applicable for engineering use since the fence can be constructed easily. A trench (which will be described in Section IV) several meters wide and deeper than 1 m can trap almost all blown sand (nearly 100 % of the total amount) without disturbing the wind field (Horikawa *et al.*, 1984). The trench stops coercively the motion of sand grains in the surface creep and saltation at the upwind tip of the trench. Therefore, we may regard the trench as having the forced trap and fixation function. However, inside the trench the wind speed becomes low and sand grains dropped into the trench come to rest. Thus, the trench also has the function of trapping sand by reducing the wind speed.

Prevention works which have the trapping function by reducing the wind speed are fences, foredunes (artificial embankments), planting shrubs, conservation forests for wind-blown sand, artificial large-scale sand ripples, and movable porous fences.

An attempt to systematize and classify the prevention works according to their functioning is given in Fig. 1. In Fig. 1, the prevention works involving trenches, artificial large-scale sand ripples, and movable porous fences are those proposed by the present authors for future use, and they are described in more detail in Section IV.

The prevention works normally employed have both the functions of restrain and of trap and fixation, although some prevention works only have either the function of restrain or trap and fixation. Therefore, the fundamental rule for employment of prevention works is to use more than one type of works, considering the conditions for the generation of blown sand and the general purpose of the works, aiming for the works to perform both functions as effectively as possible.

Functioning and Classification of Prevention Works for Wind-Blown Sand

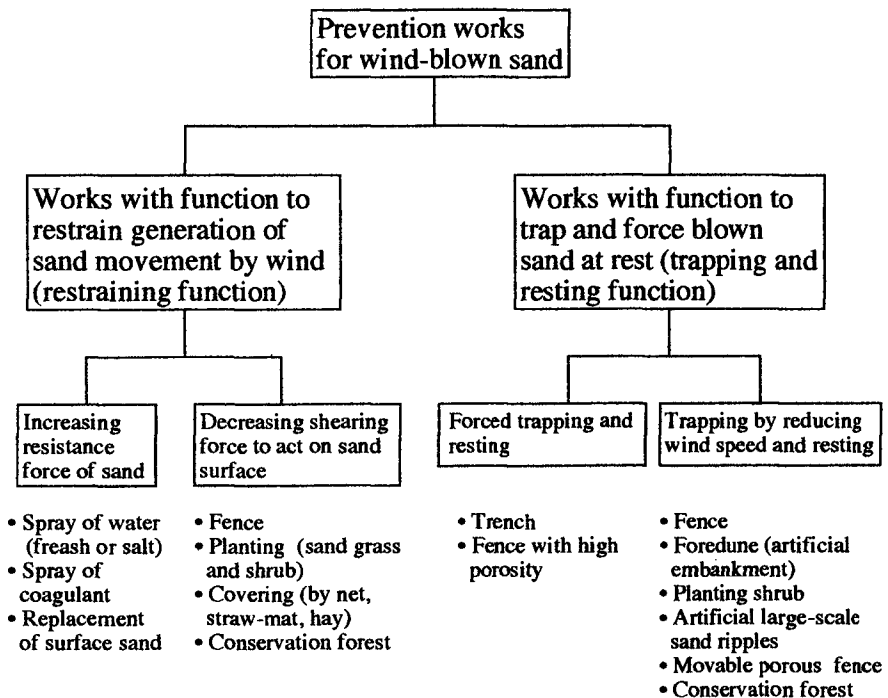


Fig. 1 Functioning and classification of prevention works for wind-blown sand.

III. A Brief Summary of Operational Characteristics and Guidelines for Use of Prevention Works

The prevention works commonly employed worldwide are sand fences, foredunes (including artificial embankment quickly constructed by earthmoving machines), vegetation (planting sand grass or shrubs), and coastal conservation forests. The characteristics and guidelines for practical use of these prevention works are briefly summarized in the following sections.

III.1 Sand Fence

The sand fence is the most commonly employed prevention work throughout the world. Many types of sand fences of varying shape and materials have been designed and employed adapting to the local conditions. The characteristics and guidelines for practical use of sand fences are relatively well understood. Hotta, Kraus and Horikawa (1987) made a critical review of the literature about single row sand fences. They summarized its characteristics and gave guidelines for practical use.

In the guidelines they gave it is recommended to use fence with material of wooden plate, fern, reed, brush, and bamboo which rapidly decompose, expecting that the sand fence will be left in the accumulated sand after the fence is buried. However, if the sand fence is used as a collecting device to interrupt the blown sand intruding into residential area or cultivated land, and if it is planned to remove the accumulated sand for long-term use, it is recommended to use long-life fabrics or metal as the fence material.

For multi-row sand fences, Hotta, Kraus, and Horikawa (1991) also gave a review that concerned the forming of foredunes. Studies regarding multi-row sand fences are limited and many of these studies are not explaining the functioning well. Hotta *et al.* (1992) found important facts about two-row sand fences by means of a wind-tunnel study. The experiment showed that the fence placed downwind would not function to collect blown sand until the fence placed upwind was buried and lost its collecting ability when two-row fences were placed at intervals shorter than $10H$, where H is the height of the fence. This means that two-row fences have no advantage when it comes to collecting blown sand. However, experiments carried out by Manohar and Braun (1970) showed that multi-row sand fences were effective when the wind was strong. Further studies are needed to understand the characteristics of multi-row sand fences and this should be done in the near future.

III.2 Foredune (artificial embankment)

In order to control blown sand, formation of a dune by means of repeated employment of sand fences has been carried out for a long time. The dune formed is usually called a foredune. However, at present formation of a dune is often carried out quickly by using earthmoving machines, and vegetation work is used on the dune surface. A dune formed artificially by construction machines is normally called an artificial embankment.

It is often assumed that the function of a foredune or artificial embankment is almost the same as a non-permeable solid fence. But, the dune has a certain crown width and slopes on both the upwind and downwind sides. Thus, the foredune

probably has a somewhat different function from the non-permeable fence. Figure 2 shows a schematic illustration of the wind flow field and sand accumulation characteristics around an artificial embankment. The wind speed profile begins to distort at a location A affected by the existing embankment. A domain where the wind speed is reduced is formed at the foot of the embankment (around a location B). However, at the upper part of the front slope, the wind will accelerate and the wind speed at the front shoulder of embankment C becomes around 1.2 - 1.8 times of that if no embankment exists. A large circulation cell is formed downwind of the embankment. The wind profile will recover at a location F because of energy supplied from the upper layer. A foredune can catch and store a large amount of blown sand in the wind-reduced domain at the foot, if the foredune is sufficiently high. However, sand is transported beyond the foredune when the wind-reduced domain is filled up by the trapped sand and the storage capacity is lost.

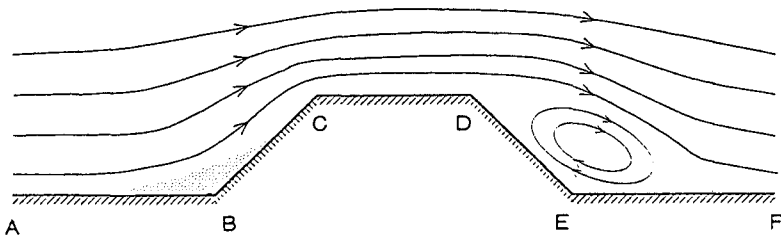


Fig. 2 Schematic illustration of the flow field around an embankment.

There is also a possibility that sand is transported beyond the foredune when the surface of the front slope is bare or paved with some hard material. This can be explained by considering the sand grain motion. A large portion of the sand is transported in a mode of saltation. The sand grains which fall on the hard slope surface can rebound easily and continue the saltation motion. During their stay in the air, sand grains in saltation are accelerated by the wind, and the possibility for the motion to continue increases. Then, sand grains may eventually reach to the top of the foredune. When the surface of the front slope is vegetated by grass or shrubs, the vegetated surface can stop the motion of sand grains and store the grains in the space of the vegetation body. The foredune (or artificial embankment) can control the blown sand as long as the foredune does not lose its storage capacity at the foot and the vegetation on the front slope surface is not buried. Studies concerned with the function of the foredune or embankment for controlling blown sand are limited. Figure 3 shows an example of equi-ratio curves of wind speed reduction in front of an embankment from an experiment by Hotta and Horikawa (1990a). Figure 4 shows the sand accumulation process in front of an embankment under the wind condition corresponding to Fig. 3 (Hotta and Horikawa, 1990b). Note that the scales in the vertical and horizontal directions are not the same in Figs. 3 and 4 and that the figures are distorted.

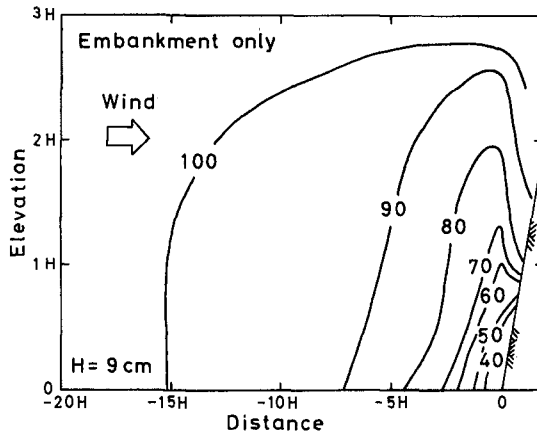


Fig. 3 Equi-ratios curves of wind speed reduction in front of an embankment. (After Hotta and Horikawa, 1990a)

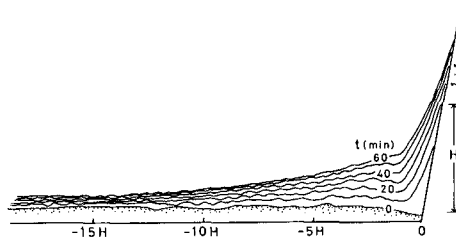


Fig. 4 The sand accumulation process in front of an embankment. (After Hotta and Horikawa, 1990b)

III.3 Vegetation Work

Vegetation is one of the most popular prevention works for controlling blown sand and it has been employed all over the world from early times. Vegetation work has both restrain and trap and fixation functions. Plants (sand grass and shrubs) that cover the sand surface can restrain the generation of blown sand by preventing the wind from acting directly on the surface, and can also trap and fix the blown sand with decreasing wind speed. We can expect a considerable storage capacity for shrubs but not so much for sand grass. The fundamental property required for plants employed in vegetation work is that the rate of growth must be bigger than that of sand accumulation. We can no longer expect any ability for controlling blown sand when plants are buried. There are many previous examples of vegetation works used in the field. The works sometimes succeeded but they occasionally

failed. The circumstances surrounding plant growth involve many factors such as weather condition, bed material, and character of plants. No guidelines for engineering use exist at present. The most suitable plants for selection may be the ones that grow at the site under consideration.

III.4 Coastal Conservation Forest

On many beaches a coastal conservation forest is often planted for several purposes. One of the most important purposes of a conservation forest is to control the wind-blown sand. We can regard the conservation forest as an aggregate of porous fences. Therefore, the function of a conservation forest is almost the same as a porous fence. However, the domain where the wind is reduced is much larger for a conservation forest than for porous fence, since the trees composing the conservation forest are considerably higher than a porous fence, and the forest has a certain width. The boundary towards the beach-end at the seaside edge of the forest is a battle field where the trees fight back against the penetration of blown sand. Therefore, to keep the primary function that a conservation forest should control blown sand, the trees planted at the seaside boundary must grow up above the thickness of the accumulating sand layer occurring during strong winds. Growth of trees is usually slow and trees at the seaside boundary are always exposed to the risk of withering due to the attack of the strong wind, blown sand, and salt transported from the sea. Therefore, it is not wise to only use conservation forests for controlling blown sand. In general, sand fences or a foredune will be placed to prevent the withering of the trees. Then, we may as well consider that a conservation forest provides protection in emergency situations.

Trap and fixation function of a conservation forest depends on the height of the trees, planting distance, kind of tree, and width of forest. To control blown sand satisfactorily, a width of the forest of more than 100 m is required.

III.5 Other Prevention Works

It is a technique commonly employed to spray water on the ground surface to reduce the dust generation when the surface becomes dry and dusty during windy days. Spraying water increases the resistance force against the wind, and suppresses the generation of blown sand, or decreases the amount of sand transported. However, in our review, we could not find any examples where spraying water was employed for controlling wind-blown sand, although we found an example where fresh water was sprayed or showered by sprinkler or portable shower vehicles for washing down salt adhered to leaves of pine trees growing in a conservation forest. Taking care of conservation forests by showering fresh water will be reported in detail by the same authors in the near future. We could not find any examples where coagulant was sprayed for controlling wind-blown sand, although we found several examples of spraying coagulant containing fertilizer for promoting vegetation work. We suppose that usage of coagulant will not be recommended because it may contaminate beach sand and obstruct a comfortable use of the beach.

Covering work by net, hay, straw-mat, and others have often been employed to restrain wind erosion of the ground surface. However, it is difficult to cover a large area of the ground surface, such as the beach, and it is also expected to be costly. We can not ignore that there is an engineering possibility to cover a whole beach surface by a kind of plastic net for effectively controlling blown sand. But, the

problem has not been studied fully yet. Employment of covering work should be limited to small areas.

IV. New Prevention Works

Based on previous studies carried out by the present authors, we would like to propose the following three new prevention works: trench, movable porous fence, and artificial large-scale sand ripples. These three type of works will be discussed in the following sections.

IV.1 Trench

The idea of a trench in prevention work for wind-blown sand is based on long-term experience and results from our previous studies. Iwagaki(1950) studied the phenomenon of blown sand by using diffusion theory. He predicted that (i) the flying distance of a sand grain in saltation motion was rather short, and that (ii) over 97 % of the sand grains in saltation fell within a range of 5 m from the end of the sand bed when the bed abruptly disappeared like at the shoreline. As a verification of his predictions he pointed out that cultivated land in a sandy beach of Tottori Prefecture where it is facing Japan Sea, was protected from the blown sand by excavating a stream upwind, letting sand grains fall into the stream, and returning the sand to the sea. Considering these results, Horikawa *et al.* (1994) tried to measure the sand transport rate by using a trench which was 1 m deep and several meters wide in the field. The measurements showed that the trench trapped almost 100 % of blown sand transported. Hotta and Horikawa (1993) measured the flying distance of sand grains in saltation using a large wind tunnel. They found that the flying distance for an amount of over 95 % of the blown sand was smaller than 1 m. Using the same technique as Hotta and Horikawa, Shiozawa *et al.* (1993) measured the flying distance of blown sand at a real beach. They found the same result as Hotta and Horikawa (1993). Therefore, the present authors concluded that the trench could be employed as a prevention work for wind-blown sand and propose to use a trench practically in the field. However, it is not clear how many meters of trench width that are suitable. Horikawa *et al.* (1996) carried out a wind tunnel experiment and a numerical experiment to determine the flow field in an open cavity. They found that a width of about 5 or 6 meters would be acceptable when the trench is dug deeper than 1 m. An example of how to use a trench for control of blown sand can be seen in Fig. 7.

IV.2 Movable Porous Fence

This method is based on a simple idea. It is an attempt to erect or place a temporary fence, which is not large and can be movable, on the beach sand surface where the blown sand is generated during the windy season. After the windy season has passed, the fence should be removed to a storage for usage the next windy season. When a strong wind blows, blown sand will be generated even though the sand surface is wet (Hotta *et al.*, 1984). The problem with blown sand is usually most serious when the wind blows from the offshore to the inland. Therefore, the fence should be placed near the inland side of the shoreline where the blown sand is generated, although we have to consider the risk that the fence may be attacked by the runup waves during stormy sea conditions. Figure 5 shows a sketch of a test manufacture of a fence.

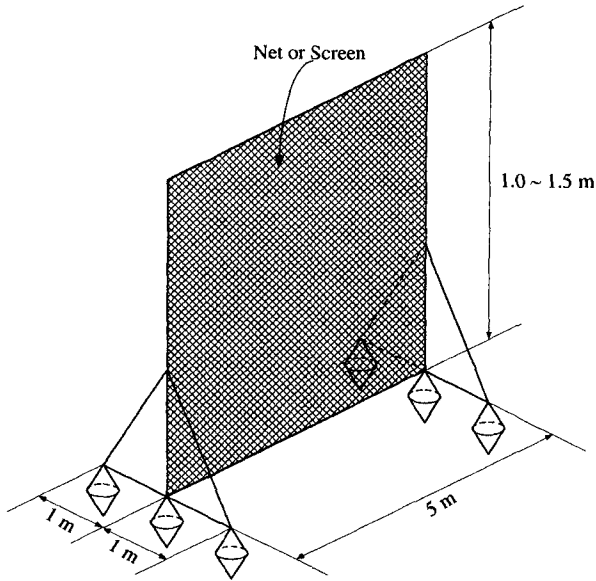


Fig. 5 A test manufacture of a movable porous fence.

IV.3 Artificial Large Scale Sand Ripples

This type of works is based on the same idea as the trench; that is, the flying distance of a sand grain in motion is not so long as described in Section IV.1. The work is simple, and the purpose is only to form giant ripples 2 or 3 m high and several meters long, as shown in Fig. 6, on the beach surface by using earthmoving machines such as power shovels or backhoes. The blown sand generated from the crest part of the giant ripple falls into the following trough part downwind. The sand is not transported beyond the next crest until the trough fills up. The blown sand will be generated on the whole beach surface and the sand will be transported into the inland when the trough is buried. We must form the ripples again as soon as the trough is buried. This type of works means that the blown sand generated from a small area is caught in a short distance downwind and brought back to the original place.

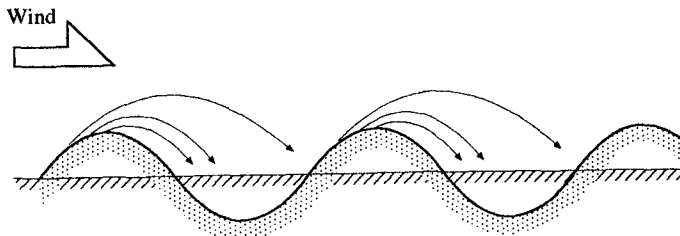


Fig. 6 A schematic illustration of artificial large scale sand ripples.

IV Systematical Use of Prevention Works

Figure 7 shows an example of the systematical use of conventional and new prevention works for wind-blown sand. Movable porous fences are placed on the part of the beach neighboring the shoreline where the blown sand is generated. When fences are buried to more than about two-third of their height, the fences must be pulled up. Then, the fences will recover their restrain and trap and fixation functions. A trench traps the blown sand which pass through the fence field. A fence erected at the downwind tip of the trench with a low fence porosity has a tendency to accumulate sand in front of the fence (Hotta and Horikawa, 1990b). Therefore, we can expect that over 90 % of the amount of the total blown sand can be trapped as far as where the fence is erected at the downwind tip of the trench.

We may remove the sand stored in the trench by using earthmoving machines as a power shovels or backhoes. But, we can also remove sand by using sea water, as described in Fig. 7. The sea water is withdrawn from outside the breaker point, flushing the water in the trench, and draining away the sand at the shoreline. Instead of using seawater, we can also use water from the landside, if enough water is available.

A small amount of blown sand in suspension can be transported beyond the fence. Prevention works arranged behind the trench must control the sand that pass. In the wind field around an embankment, a wind-reduced domain is formed at the foot of the embankment. The domain has a possibility to store the blown sand. Shrubs and grass on the slope of an embankment weaken the wind, and catch and store the blown sand.

The crown of the embankment may be used as a bicycle road or walking road. At the seaside shoulder of the embankment the wind accelerates. To moderate the wind, placement of a fence with a median porosity is recommended. The fence height should be lower than 1 m to maintain a good view.

At the landside shoulder of the crown, placement of a relatively high fence is recommended to reduce the wind and to protect the inland. A low porosity fence is recommended for the upper part of this fence.

V. Concluding Remarks

The characteristics of prevention works for wind-blown sand have mainly been studied in the field of agricultural engineering, forestry, geomorphology and coastal engineering. Studies have been carried out both in the wind tunnel and in the field. The results obtained were qualitative and quantitative evaluations of the effectiveness of the prevention works are scarce. The phenomenon is so complicated that theoretical analysis will be difficult. To evaluate the effectiveness of prevention works quantitatively, systematical and well controlled wind tunnel studies or field studies are needed, although numerical experiment based on the detailed description of the fluid dynamics in computers can assist our understanding.

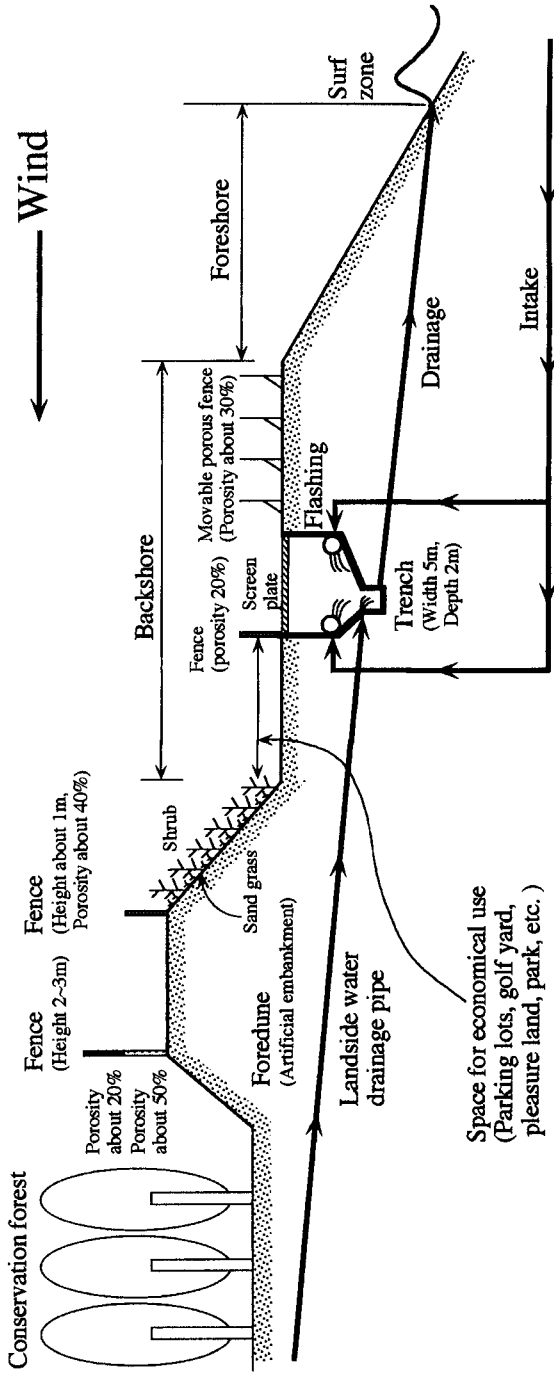


Fig. 7 An example of systematical use of conventional and new prevention works.

References

- Iwagaki, Y. (1950): On the effect of the sand-drift on the coast by wind for sand deposition in Ajiro Harbor, *Journal of JSCE*, Vol. 36 (6), pp. 19-25. (in Japanese)
- Hotta, S. and K. Horikawa (1993): Vertical distribution of sand transport rate by wind, *Coastal Eng. in Japan*, Vol. 36, No. 1, JSCE, pp. 91-110.
- Hotta, S., T. Murata, H. Mori and K. Horikawa (1992): Experimental study on function of two-rows sand fences, *Proc. of Coastal Eng.*, Vol. 39, JSCE, pp. 331-335. (in Japanese)
- Hotta, S., N.C. Kraus and K. Horikawa (1991): Functioning of Multi-row sand fences in forming foredunes, *Proc. Coastal Sediments '91*, ASCE, pp. 261-273.
- Hotta, S. and K. Horikawa (1990a): Function of sand fence placed in front of embankment, *Proc. of Coastal Eng.* Vol. 37, JSCE, pp. 444-448. (in Japanese)
- Hotta, S. and K. Horikawa (1990b): Function of sand fence placed in front of embankment, *Proc. 22nd Coastal Eng. Conf.*, ASCE, pp. 2754-2767.
- Hotta, S., N.C. Kraus and K. Horikawa (1987): Function of sand fences in controlling wind-blown sand, *Proc. Coastal Sediments '87*, ASCE, pp. 772-787.
- Hotta, S., S. Kubota, S. Katori and K. Horikawa (1984): Sand transport by wind on a wet sand surface, *Proc. 19th Coastal Eng. Conf.*, ASCE, pp. 1265-1281.
- Horikawa, K., H. Tanaka, K. Hatanaka, N. Yamaya and S. Hotta (1996): Study on trench trap as a prevention work for wind-blown sand, *Proc. of Coastal Eng.*, Vol. 43, JSCE, pp. 671-675. (in Japanese)
- Horikawa, K., S. Hotta, S. Kubota and S. Katori (1984): Field measurement of blown sand transport rate by trench trap, *Coastal Eng. in Japan*, Vol. 27, JSCE, pp. 213-232.
- Manohar, M. and P. Bruun (1970): Mechanics of dune growth by sand fences, *Dock and Harbour Authority*, Vol. LI, No. 600, October, pp. 243-252.
- Shiozawa, T., S. Nakayauchi, M. Akazawa, S. Tamashiro and K. Kuroki (1993): Observation of the sand transport rate by wind at Niigata West Beach, *Proc. of Coastal Eng.*, Vol. 40, JSCE, pp. 281-285.

CHAPTER 325

Sea breeze Effects on Nearshore Coastal Processes

Charitha Pattiaratchi¹ and Gerhard Masselink²

Abstract

The sea breeze, created by the diurnal solar heating and cooling cycle, is a well known meteorological phenomenon and occurs globally on a regular basis with varying intensity. The impact of the sea breeze system on nearshore coastal processes and sediment budget has received very little attention. In this paper, field data collected from two micro-tidal coastal regions: south-western Australia and Sri Lanka, are presented to illustrate the importance of the sea breeze system in these regions. It is shown that the rapidly changing wave climate, generated by the sea breeze, increases the cross-shore and longshore currents and sediment suspension on the beach. This results in an increase of the longshore sediment flux by up to a factor of 100. The effects of the sea breeze may be present up to 10 hours after the cessation of the sea breeze. The sea breeze system plays a major role in the coastal sediment budget in these regions.

¹ Senior Lecturer, Department of Environmental Engineering, Centre for Water Research, The University of Western Australia, Nedlands 6907, Australia.

² Research Fellow, Department of Environmental Engineering, Centre for Water Research, The University of Western Australia, Nedlands 6907, Australia.

Introduction

On micro-tidal wave dominated beaches, morphological change is primarily induced by variations in the incident wave climate. These variations are usually ascribed to the passage of storms. A neglected source of change to the wave field is the diurnal sea breeze, generated by the differential solar heating of the land and ocean, which could be obscured by the presence of high-wave energy levels or tidal effects. The sea breeze is a dominant feature along tropical and subtropical coastlines and occur along two thirds of the earth's coastlines (Abbs and Physick, 1992; Simpson, 1994). In these areas wind waves generated by the local sea breeze can contribute significantly to the temporal variation in the incident wave climate. In this paper, field studies undertaken in south-western Australia and Sri Lanka are presented to demonstrate the importance of the sea breeze system on the nearshore region and, in particular, the coastal sediment budget.

Data presented in this paper were collected during three field experiments. Two of these experiments were undertaken at City Beach, Western Australia (Figure 1) on 23 January 1992 and 3-9 March 1994. The third experiment was conducted in Ambakandawila, located to the south of Chilaw along the west coast of Sri Lanka (Figure 2). Both sites are located on a relatively straight, north-south oriented shoreline far from any engineering structures and are micro-tidal (tidal range < 0.7 m at spring tides). However, in Western Australia, the tide is diurnal whilst in Sri Lanka the tide is semi-diurnal. The swell waves approach the beach from the south-west at both sites but the direction of the wind (sea breeze) waves differ due to the different direction of the sea breeze. In Western Australia, the sea breeze blows parallel to coastline from the south (an explanation for this effect is given in Pattiaratchi et al., 1997) and thus the sea breeze generated waves approach the beach with a crest of angle 70° (from south-south-west). In Sri Lanka, the sea breeze (in January) blows from north-west and the

sea breeze generated waves also approach from the same quadrant. The occurrence of sea breezes in both of these regions is well known to local residents and fisherman in these regions. In Western Australia, the sea breeze is called the 'Fremantle Doctor' due to cooling effect of the breeze during the summer. In Sri Lanka (in the Chilaw region), the sea breeze is termed Kode by the fisherman.

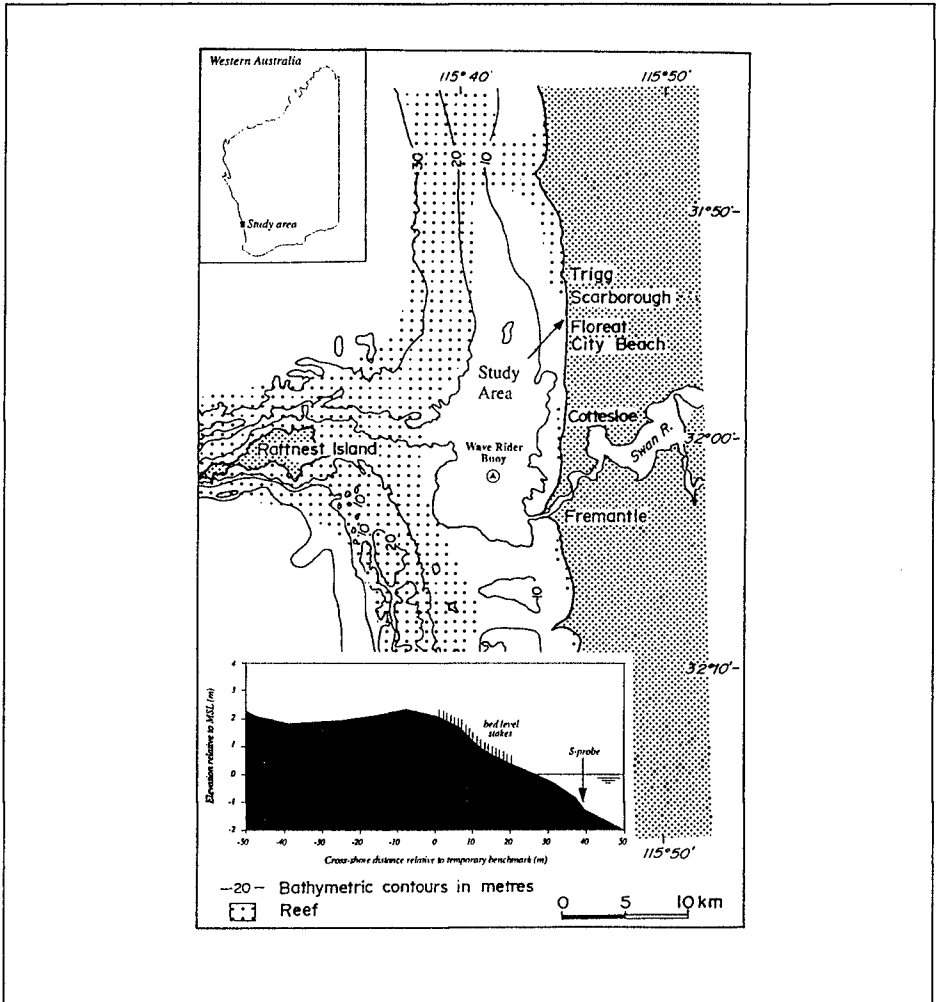


Figure 1 - Location of City Beach, Western Australia

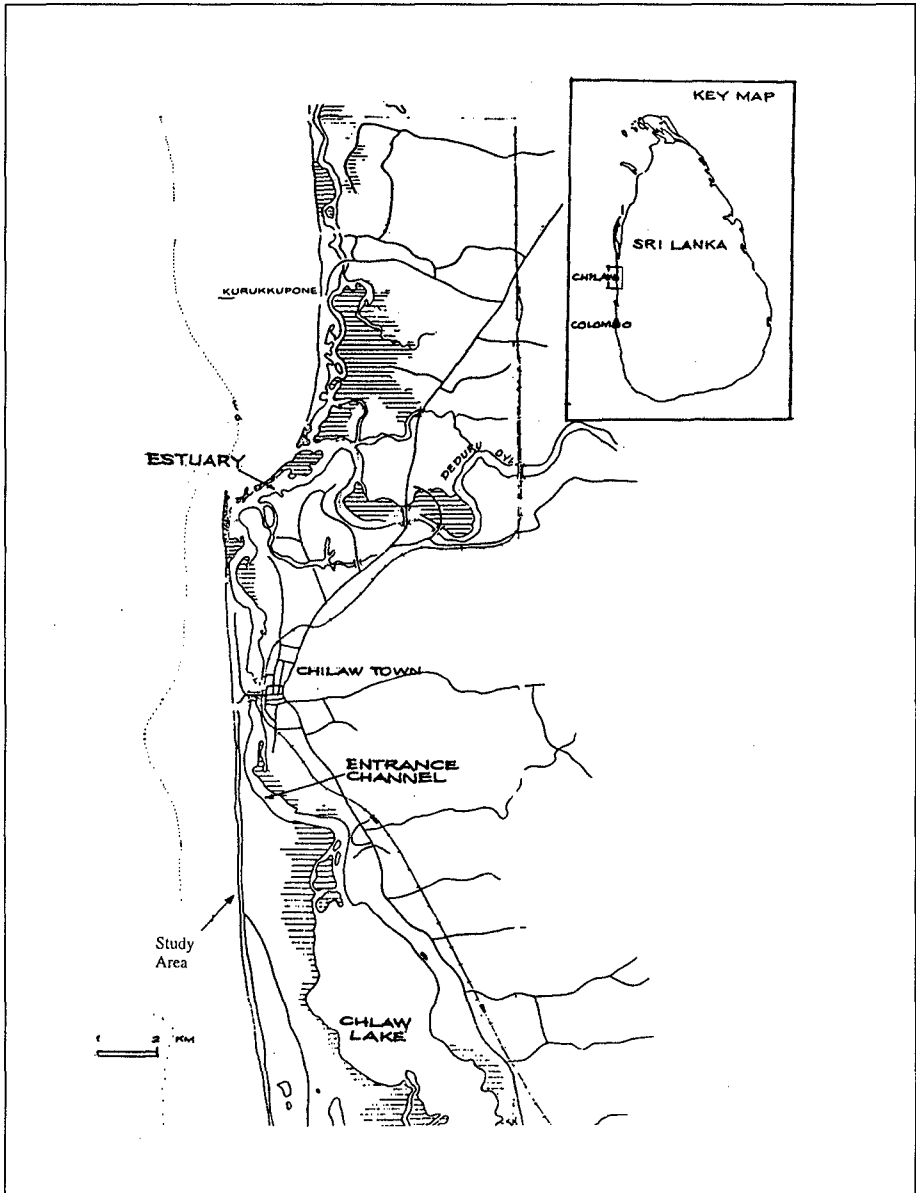


Figure 2 - Location of Ambakandawila, Sri Lanka

Although the sea breeze is a global phenomenon, it's intensity, which depends primarily on the land-ocean temperature gradients, varies geographically. The field data presented in this paper were collected under

sea breeze speeds between 7 and 12 ms^{-1} . To allow comparison with other regions, the following maximum speeds, recorded during the sea breeze, have been reported: 14 ms^{-1} in Barcelona, Spain (Redano et al., 1991); 10 ms^{-1} in Greek waters (Prezerakos, 1986; Balopoulos et al., 1986); 9 ms^{-1} near Kingston, Jamaica (Huntley et al., 1988); 8 ms^{-1} in Tokyo (Yoshikado and Kondo, 1989); 7 ms^{-1} in Monterey, California (Banta, 1995); and, 5 ms^{-1} in Santa Rosa Island, Florida (Sonu et al., 1973).

Methodology

The data presented in this paper were all collected using the 'S-probe', an instrument package, developed at the Centre for Water Research, University of Western Australia. It consists of a Digiquartz pressure sensor, a Neil Brown ACM2 acoustic current meter and three optical backscatterance sensors. The pressure sensor was mounted 0.35 m from the sea bed, whereas the two-dimensional, horizontal current velocity was recorded 0.2 m above the bed. The optical backscatterance (OBS) sensors measured the suspended sediment concentration (SSC) at 0.025 m, 0.125 m and 0.275 m from the bed. The data were transferred via a cable connected to a shore-based computer and logged at a sampling rate of either 5 Hz (exp. 1) or 2 Hz (expts. 2 and 3). The S-probe was deployed in the surf zone at each of the study sites. Calibration of the OBS sensors was conducted with sand samples collected at the survey site, using the methods and apparatus similar to that described by Ludwig and Hanes (1990). Analysis of the water surface elevation, current velocity and suspended sediment concentration records were carried out on time series of 2048 points (approximately 7 or 17 minutes). Although additional data (e.g. offshore wave climate, beach ground water levels, instantaneous shoreline, beach morphology changes etc), have been collected at each of these sites only data collected by the S-probe is presented here. More comprehensive account of the data sets from City Beach may be found in Pattiaratchi et al. (1997),

Masselink and Pattiaratchi, (1997), Masselink et al., (1997).

Data obtained from City Beach on 23 January 1992 (expt 1) is limited to four hours after the onset of the sea breeze. After this time, the S-probe could no longer be maintained in an upright position due to the extremely energetic surf zone conditions. However, continuous data over 3 sea breeze cycles are available from the subsequent survey from City Beach, 3-9 March 1995 (expt 2) and over two days from Ambakandawila, Sri Lanka, 18-20 January 1996 (expt 3).

Results

Experiment 1: City Beach, WA - 23 January 1992

Time series of wind speed and direction obtained on this day indicate a typical sea breeze cycle characterized by weak offshore winds in the morning and early afternoon, and a strong sea breeze starting at 1445 hours which continued into the evening (Figure 3). Wind speeds associated with the sea breeze exceeded 10 ms^{-1} and occur frequently in the summer months in this region. The direction of the sea breeze was consistently from the south and hence the sea breeze was blowing parallel to the shoreline, a feature of the sea breeze system in this region (Pattiaratchi et al., 1997).

Changes in wind speed and direction are reflected in the incident wave field, nearshore currents and suspended sediment concentrations (Figure 3). Prior to the sea breeze, small-amplitude swell ($H_S=0.4 \text{ m}$) with zero-upcrossing periods (T_Z) of 7-8 s were present. Mean cross-shore (offshore) and longshore (northerly) currents were less than 0.05 ms^{-1} and 0.1 ms^{-1} , respectively whilst the mean SCC at a distance of 0.275 m above the bed was about 1 gl^{-1} . Sediment was only re-suspended during the passage of large waves in wave groups. The onset of the sea breeze induced an almost instantaneous change in the nearshore hydrodynamics. The wave height increased ($H_S=0.7 \text{ m}$), the wave period decreased and assumed a constant value ($T_Z=4 \text{ s}$) within

one hour of the start of the sea breeze. Offshore-directed cross-shore currents in the surf zone rapidly increased in strength to a maximum of 0.16 ms^{-1} and the northerly longshore current progressively increased and exceeded 1 ms^{-1} . Sand was continuously re-suspended by the waves and the amount of SSC in the water column (at 0.275 m) increased seven-fold to 7 gl^{-1} . The surf zone averaged northward longshore suspended sediment transport rate increased from approximately 1 kg s^{-1} before the start of the sea breeze to $100\text{--}200 \text{ kg s}^{-1}$ during the sea breeze, an increase by a factor of 100 (Figure 3).

Experiment 2: City Beach, WA - 4-6 March 1995

The results from this experiment are essentially the same as that for experiment 1. However, due to weaker sea breezes (max 7 ms^{-1}), the hydrodynamic changes induced by the sea breeze were less extreme. Continuous measurements of three successive sea breeze cycles were made and these enabled the investigation of the recovery period of the wave conditions after the cessation of the sea breeze. Prior to the sea breezes, offshore winds prevailed with speeds of $2\text{--}3 \text{ ms}^{-1}$. All three sea breezes persisted for approximately 7 hours and a relatively constant wind speed of $5\text{--}7 \text{ ms}^{-1}$ was maintained. After the onset of the sea breeze, immediate changes occurred to the incoming wave field with a decrease in T_z from 10 to 5 s and an increase in the longshore current velocity to $0.15\text{--}0.2 \text{ ms}^{-1}$. Around 2045 hrs each day, the sea breezes stopped. The wind direction gradually shifted back to the east and the wind speed decreased to $< 4 \text{ ms}^{-1}$. T_z increased and the longshore current velocity decreased immediately after the sea breeze had subsided. Around 0600 hrs on the following day, nine hours after the end of the sea breeze, the wave period and the longshore current velocity had reached pre-breeze levels.

Energy spectra of the cross-shore current were computed to construct a three-dimensional time-frequency plot to illustrate the change in spectral signature over the second sea breeze cycle (Figure 4). The cross-shore current data were used, rather than the

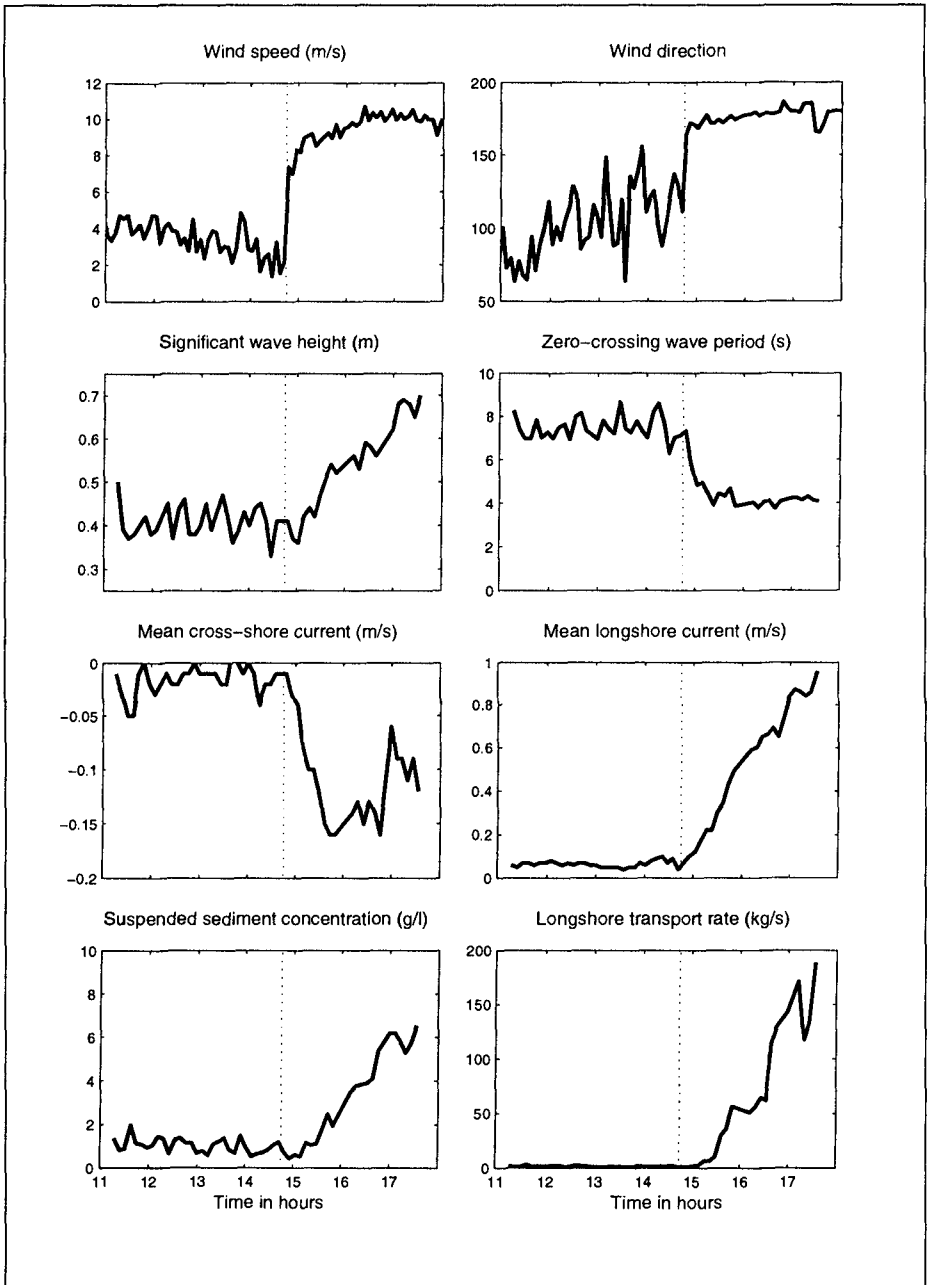


Figure 3 - Time series results for Experiment 1. The vertical dashed line indicates the start of sea breeze.

water surface elevation because they show more clearly the short-period wave energy caused by the sea breeze (frequency > 0.15 Hz). The long-period background swell is present in the time-frequency plot in the form of a linear ridge at frequency 0.07-0.1 Hz. The peak period associated with the swell energy was 12 s and remained relatively constant. After the onset of the sea breeze, wind wave energy begins to emerge at the high-frequency end of the spectra, indicating peak wave periods of 2.5 s. During the sea breeze, the frequency associated with the wind waves decreased progressively, forming a curved ridge in the frequency-time plot. At the end of the sea breeze (2100 hrs), the wind wave energy was concentrated around a frequency of 0.25 Hz, indicating a peak period of 4 s. After the sea breeze had subsided, the wind wave energy gradually decreased, but remained significant. The frequency associated with the wind wave energy decreased to 0.15 Hz, merging with the swell energy. Fifteen hours after the cessation of the sea breeze (1200 hrs 08/03/93), there was still some wave energy present which was generated by the sea breeze in the nearshore zone. This implies that the effect of the sea breeze on the nearshore hydrodynamics may be felt continuously during the sea breeze season (summer).

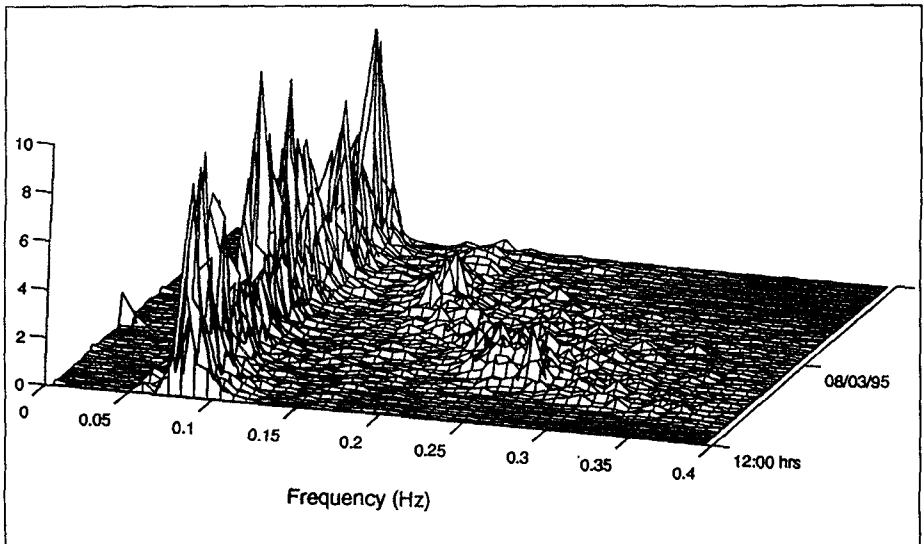


Figure 4- Time frequency plot of cross-shore currents

Experiment 3: Ambakandawila, Sri Lanka - 18-20 January 1996

Data collected from this experiment has not been thoroughly analysed and only a preliminary description is given here. On 18th January 1996, the sea breeze started at 1415 hours and 30 minutes later reached a maximum speed of $10-12 \text{ ms}^{-1}$. Continuous wind data is unavailable at present and the wind speeds quoted here were obtained using a hand-held anemometer on the beach. Coincident with the increase in wind speed, the longshore current increased from 0.05 to 0.75 ms^{-1} and then decreased just before midnight (Figure 5). The cross-shore currents (max = 0.23 ms^{-1}) and SSC (max = 3.8 gl^{-1}) indicated a similar trend (Figure 5). Pre-sea breeze values were reached prior to midnight. The exact time of the sea breeze cessation is unknown at present.

On the following day (19th) the sea breeze started earlier, at 1215 and continued blowing at $6-7 \text{ ms}^{-1}$ throughout the afternoon. Here, although the sea breeze was weaker than the previous day, the recorded maximum values are higher (Figure 5): the longshore current max. is 0.80 ms^{-1} ; max cross shore current 0.35 ms^{-1} ; and, max. SSC 4 gl^{-1} . As per previous day, all values had returned to pre-sea breeze levels before midnight. On both days, the longshore suspended sediment flux (southward) increased by a factor of 60 during the sea breeze.

Discussion

This paper summarizes the results of three field experiments aimed at investigating the impact of sea breeze activity on nearshore processes. The findings are similar to those of Sonu et al. (1973), to date the only other study into sea breeze effects. In summary, the sea breeze results in: (1) an increase of the wave height; (2) a decrease in the wave period; (3) an intensification of the nearshore currents; and, (4) an increase in suspended sediment levels and suspended sediment transport. In Western Australia, due to the predominantly longshore component of the sea breeze,

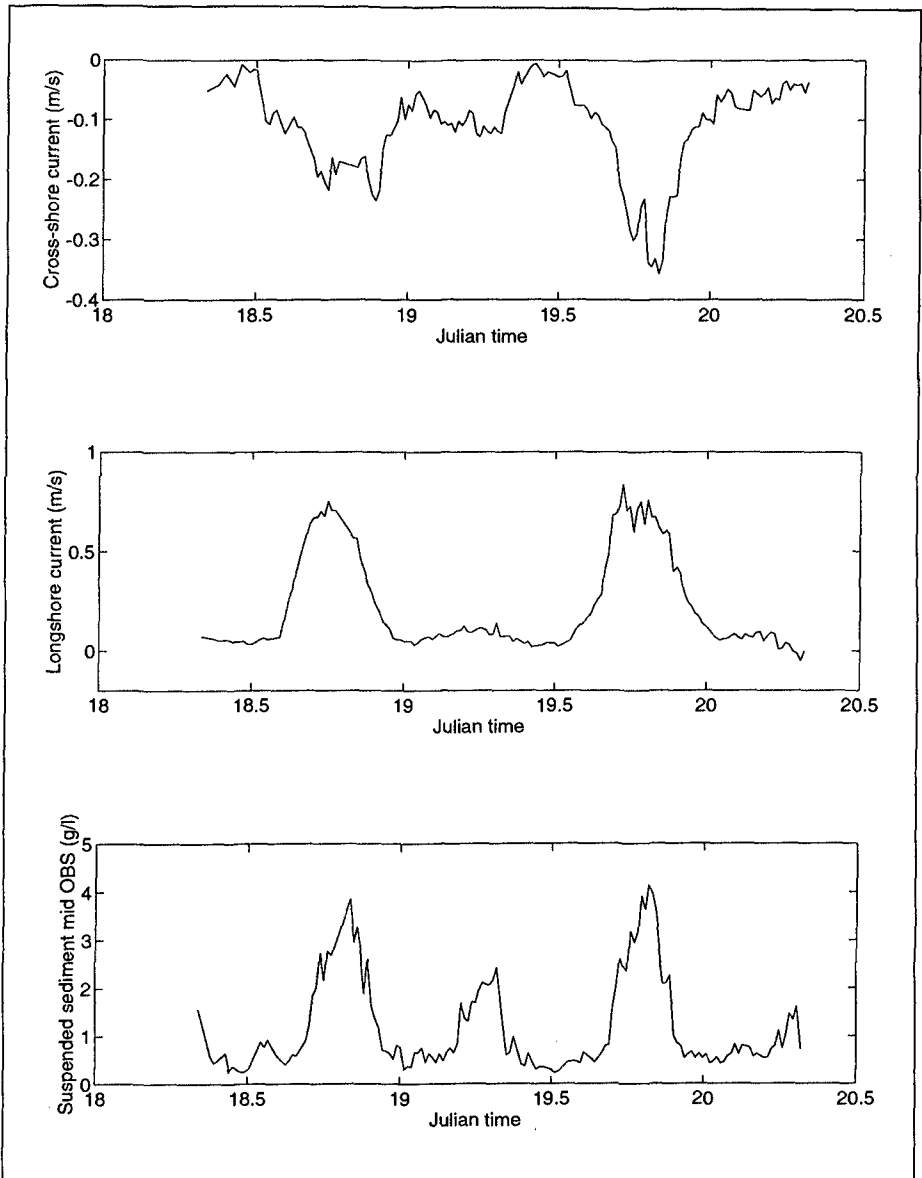


Figure 5 - Time series of cross-shore and longshore currents and SSC from Ambakandawila, Sri Lanka.

the nearshore hydrodynamics are affected long after the sea breeze has ceased to blow. Sonu et al. (1973)

refer to this as the "afterglow effect". Preliminary data from Sri Lanka, shown here, indicate that the impact of the sea breeze did not persist after midnight although visual observations of wave direction on the following morning indicated waves approaching from the direction of the sea breeze. Both the strength and consistency of the sea breeze, and the afterglow effect contribute to the important role that the sea breeze plays on the nearshore processes in both regions.

The sea breeze induces a diurnal cycle of beach change by causing erosion of the upper part of beach and/or planation of beach cusp morphology (Masselink et al., 1997). These changes are reversible in that the beach is usually restored to its pre-breeze state after the cessation of the sea breeze Pattiaratchi et al. (1997). On the larger temporal and spatial scale, the dramatic increase in the longshore sediment transport caused by the sea breeze is important. Masselink and Pattiaratchi (1997) and Pattiaratchi et al. (1997) estimate that along the stable Perth Metropolitan coastline, the annual longshore transport driven by the sea breeze is approximately 100,000 m³. This estimate of longshore transport due to the sea breeze compared favourably with estimates of sediment accumulation at the southern side of Trigg Island (Perth) at the end of the summer. During the winter, the predominant north-westerly storms transport this sand southwards thus completing the seasonal sediment budget. Hence, it is clear that the sea breeze plays a dominant role in the sediment budget of the coastline around Perth.

Similarly, the sea breeze plays an important role in the annual longshore sediment budget along the west coast of Sri Lanka. During the south-west monsoon (May to September), the longshore sediment transport is predominantly northward. The occurrence of the sea breezes during the north-east monsoon period (October to February) would transport some of this sediment southward as shown by the results obtained from this study. Hence, also in this region, the sea breeze plays a dominant role in the annual sediment budget.

Conclusions

Field data presented from two different micro-tidal areas have shown the importance of the sea breeze system on nearshore processes. The sea breeze system induces a diurnal change in the incident wind wave climate (wave height and period) resulting in large increases to longshore and cross velocities and suspended sediment concentrations. The longshore suspended sediment flux can increase by a factor of 100 or more during the sea breeze which is very important in terms of annual sediment budgets.

Acknowledgments

A large number of individuals assisted in the data collection at the West Australian (WA) site and we would particularly like thank Dr Bruce Hegge for his efforts. Funding for the WA experiments was provided by an Individual Research grant awarded by the Division of Engineering and Computer Science at the University of Western Australia (UWA) to CP. Funding for the development of the S-probe was provided by UWA and the Centre for Environmental Fluid Dynamics. The Perth City Council is acknowledged for granting access to the field site. Funding for the field experiments at Ambakandawila (Sri Lanka) was provided by the Ministry of Fisheries and Aquatic Resources (Sri Lanka) as part of the ADB Chilaw Anchorage project to Lanka Hydraulic Institute and the Centre for Water Research. This paper has Centre for Water Research reference ED1243 CP.

References

- Abbs D.J. and Physick W.L. 1992. Sea breeze observations and modelling: a review. *Australian Meteorological Magazine*, 41, 7-19.
- Balopoulos E.Th., Collins M.B. and James A.E. 1986. Satellite images and their use in the numerical modelling of coastal processes. *International J. Rem. Sens.*, 7, 905-919.
- Banta R. 1995. Sea breezes shallow and deep on the California coast. *Monthly Weather Rev.*, 123, 3614-3622.
- Huntley D.A., Hendry M.D., Haines J. and Greenidge B. 1988. Waves and rip currents on a Caribbean pocket beach, Jamaica. *J. Coast. Res.*, 4, 69-79.
- Ludwig K. and Hanes D. 1990. A laboratory evaluation of optical backscatterance suspended sediment solid sensors exposed to sand-mud mixtures. *Marine Geology*, 94, 173-179.
- Masselink G. and Pattiaratchi C.B. 1997. Morphodynamic impact of sea breeze activity on a beach with beach cusp morphology. *J. of Coastal Research*, (in press).
- Masselink G., Hegge B. and Pattiaratchi C.B. 1997. Beach Cusp Morphodynamics. Earth surface processes and landforms, (in press).
- Pattiaratchi C., Hegge B., Gould J and Eliot I. 1997. Impact of sea breeze activity on nearshore and foreshore coastal processes in southwestern Australia. *Continental Shelf Res.* (in press).
- Prezerakos N.G. 1986. Characteristics of the sea breeze in Attica, Greece. *Boundary Layer Meteorology*, 36, 245-266.
- Redano A., Cruz J. and Lorente J. 1991. Main features of the sea breeze in Barcelona. *Meteorology and Atmospheric Physics*, 46, 175-179.
- Simpson J. E. 1994. *Sea Breeze and Local Wind*. Cambridge University Press, 234 pp.
- Sonu C. J., Murray S. P., Hsu S. A., Suhayda J. N. and Waddell E. 1973. Sea breeze and coastal processes. *EOS, Transactions American Geophysical Union* 54:820-833.
- Yoshikado H. and Kondo H. 1989. Inland penetration of the sea breeze over the suburban area of Tokyo. *Boundary Layer Meteorology*, 48, 389-407.

CHAPTER 326

WIND BLOWN SAND AT CASTROVILLE, CALIFORNIA

Douglas J. Sherman¹, Bernard O. Bauer², Paul A. Gares³, Derek W.T. Jackson⁴

ABSTRACT

This paper reports the results of a study designed to evaluate the performance of a set of aeolian transport models, including moisture content corrections, as tested against field measurements. Empirical data were obtained during experiments conducted near Castroville, California, in January, 1993. The comparisons show that the Lettau and Lettau (1977) transport model, coupled with the Belly (1964) moisture correction model, produces estimates most closely approximating measured rates. Nevertheless, the advantages of this approach relative to using an "uncorrected" Bagnold model are small.

INTRODUCTION

Aeolian sand transport is an important component of the sediment budget of many coastal environments. Blowing sand may represent a hazard (Sherman and Nordstrom, 1994) or a resource, especially with regard to dune building and habitat creation (Carter, 1988). For these reasons, it is important to model the aeolian system in a manner consistent with the needs of coastal engineers and resource managers. From a geomorphological perspective, an understanding of the nature of aeolian systems yields insight into fundamental aspects of sediment transport and resulting

¹Professor, Department of Geography, University of Southern California, Los Angeles, CA, 90089-0255, USA.

²Associate Professor, Department of Geography, University of Southern California, Los Angeles, CA, 90089-0255, USA.

³Associate Professor, Department of Geography, East Carolina University, Greenville, NC, 27858-4353, USA

⁴Science Officer, Department of Environmental Studies, University of Ulster, Coleraine, BT52 1SA Northern Ireland

landform change. Determining which model constitutes the most accurate and physically-meaningful approach to aeolian flux prediction is, therefore, a critical challenge.

A number of models have been developed for the purpose of predicting aeolian sand transport rates (see summary by Namikas and Sherman, in press). Those of most practical interest are based on a common set of assumptions: the wind is steady, uniform, and blowing across an unobstructed, horizontal surface of clean, dry, homogeneous sand. These conditions describe the most basic transport systems that one can posit. Models developed from these assumptions have been discussed extensively elsewhere (e.g., Anderson et al. 1991; McEwan and Willetts 1994; Lancaster 1995), and their derivations are not reviewed here. We note, however, that the idealized conditions they describe are seldom, if ever, appropriate to coastal environments. Complicating effects of sediment moisture content and surface slope, in particular, may exert considerable control on the behavior of the transport system.

Previous field experiments aimed at matching observed and predicted transport rates have usually found poor correspondence. Some successes have been reported in cases where empirical constants have been adjusted to improve the model's performance. Because such adjustments are usually site specific, they are of relatively diminished utility when little is known about the transport environment or where field work is impractical. Indeed, if we are always forced to perform field experiments to calibrate the equations, the practical value of modeling is severely constrained. The purpose of this paper is to report the predictive performances of several transport models, in light of field data and in consideration of slope effects and adjustments for moisture content. The objective is to test the models as they appear in the literature and as they might be employed in an engineering or management context.

MODEL DESCRIPTION

Several previous efforts at comparing observed and predicted transport rates have been reviewed recently by Sherman et al. (in press). Typically, these have omitted slope and/or moisture effects, have used liberally the empirical constants in the models, or have been predicated on potentially flawed experimental designs. The Sherman et al. study suggests that, of the five models tested, the best statistical explanation (of the order of 20%) was afforded by the Bagnold (1936) and Zingg (1953) models. These two equations are essentially the same, varying only in the selection of the constant. Their conclusions point to the necessity for similar comparative studies using high quality data sets from other environments.

In the present study, we test the transport models of Bagnold (1936), Kawamura (1951), and Lettau and Lettau (1977). They were selected in conformity with the findings of Sherman et al. (in press) and because they are commonly used in coastal applications. We also considered the moisture-content correction equations

of Belly (1964), Hotta et al. (1984), and Kawata and Tsuchiya (1976). For all tests, we assumed a sediment density, ρ_s , of 2650 kg m^{-3} , an air density, ρ , of 1.23 kg m^{-3} , and a gravity constant, g , of 9.8 ms^{-2} . Sediment flux, q , is in $\text{kg m}^{-1} \text{ s}^{-1}$. A brief description of the models follows.

One of the most frequently used models to predict transport rates is that of Bagnold (1936) who suggested that:

$$q = C \sqrt{\frac{d}{D}} \frac{\rho}{g} u_*^3 \quad (1)$$

where C is a surface-sediment-dependent constant ranging in value from 1.5 to 3.5 ($C = 1.8$ for typical dune sands and this value is used here), d is mean grain diameter, D is a reference grain diameter of 0.25 mm, and u_* is shear velocity.

Kawamura (1951) proposed a model that includes an explicit threshold shear-velocity term, u_{*t} .

$$q = C \frac{\rho}{g} (u_* - u_{*t}) (u_* + u_{*t})^2 \quad (2)$$

In this expression, $C = 2.78$, and we adopt this value even though Horikawa et al. (1984) suggest that $C = 1.0$ might be better.

Lettau and Lettau (1977) proposed an expression with some of the attributes of both previous models:

$$q = C \sqrt{\frac{d}{D}} \frac{\rho}{g} (u_* - u_{*t}) u_*^2 \quad (3)$$

where C in this case has a value of 4.2.

The Kawamura (1951) and Lettau and Lettau (1977) models require the threshold shear velocity to be estimated according to local sediment size characteristics. Bagnold (1936) suggested a Shields-type relation for u_{*t} of the following form:

$$u_{*t} = A \sqrt{gd \left(\frac{\rho_s - \rho}{\rho} \right)} \quad (4)$$

where A is a constant (assumed to be 0.085 during saltation).

When moisture is present in the interstices of surface sands, the resulting surface tension acts as a cohesive force. The shear velocity required to entrain sediments must therefore increase (e.g., review by Namikas and Sherman 1995). We considered three models developed to account for increased threshold shear velocity as a result of moisture content, u_{*tw} .

Belly (1964) proposed an empirical model based upon his wind tunnel experiments:

$$u_{*tw} = u_{*t} (1.8 + 0.6 \log_{10} w) \quad (5)$$

where w is percent moisture content by weight. This model applies to conditions where w does not exceed 4%.

Kawata and Tsuchiya (1976, described in Hotta et al., 1984) developed a model based upon direct consideration of the surface-tension-force distribution between particles:

$$U_{*tw} = U_{*t} \sqrt{1+B} \quad (6)$$

where

$$B = \frac{2\sqrt{6}}{5} \sqrt{\alpha_1 \alpha_2} \sqrt{n_o} \sqrt{\frac{\rho_s}{\rho_w}} \frac{T \sqrt{w} \cos \xi}{(\rho_s - \rho) g d} \quad (7)$$

and α_1 , α_2 are constants, n_o is the number of grain contact points, ρ_w is density of water, ξ is the water/grain contact angle, and T is the surface tension of water.

Hotta et al., (1984) proposed a wind-tunnel-derived empirical relationship for moisture effects:

$$U_{*tw} = U_{*t} + 7.5w \quad (8)$$

The prescribed applicability range for this model is 2% to 8% moisture content and sediment sizes between 0.2 mm and 0.8 mm.

In order to obtain the information necessary to evaluate the above models against prototype conditions, measurements or derivations of the following parameters are required: shear velocity, surface slope, mean grain size, transport rate, and moisture content. In order to attribute differences between observed and predicted transport rates to model performance, substantial care must be taken in experimental design. A field study was designed with the aim of obtaining suitable data.

STUDY SITE

Field experiments were conducted at a site along the coast of Monterey Bay, approximately mid-way between Santa Cruz and Monterey, near the town of Castroville. The site is exposed to open-ocean winds and waves from the southwest to northwest, and aeolian activity is therefore common. Instruments were deployed on the upper, flat portion of a well-developed, high-tide berm (Figure 1) fronting a small foredune system that is essentially continuous from the mouth of the Salinas River (to the south of the site) to Moss Landing (to the north). The upper foreshore is relatively steep and often cusped, and it descends to a much flatter low-tide terrace merging, seaward, with bar topography that is periodically punctuated with rip channels. Morphodynamically, the system falls into the reflective regime during high tide and the dissipative regime during low tide stages. Spring high tides are often associated with foredune scarping and the deposition of flotsam (mostly kelp and woody debris) on the berm flat. Additional details of this site are described in Bauer et al. (1990) and Bauer (1991).



Figure 1: Castroville study site with instrument array.

EXPERIMENTAL DESIGN

Field experiments were conducted over a 30-day period in January, 1993. Only the January 13 data are presented here because this day had the longest duration of continuous sand transport during the study period. Further, winds were blowing

nearly parallel to the shore so that it is reasonable to assume that local equilibria between the velocity profiles and the saltation system existed—that is, conditions were as close to ideal as one might expect for a beach environment. This eliminates complications arising from potential fetch effects (e.g. Nordstrom and Jackson 1992), or from internal-boundary-layer development (e.g. Bauer et al. 1996). Measurements began at 05:45 (PST), and continued for about the next five hours. A total of five data runs were completed, each with three to five u_* - q pairings.

Five sampling locations were established across the berm at 5 m intervals (Figure 2). Gill-type, three cup anemometers were hardwired to a PC-based data acquisition system. All sample runs were of 15 minute duration, with sampling at 1 Hz. Tower 1, near the toe of the foredune, had anemometers at elevations of 0.25, 0.5, 1.0, 2.0, 3.0, and 4.0 m above the sand surface. Towers 2, 3, and 4 had anemometers at 0.2, 0.6, 1.2, and 1.8 m. Tower 5 had anemometers at 0.15, 0.3, 0.6, 1.2, 1.8, and 2.4 m. The lowest Tower 5 anemometer was disabled during this experiment. Wind vanes were installed at the tops of Towers 1 and 5. A set of cylindrical sand traps was deployed adjacent to each tower. Moisture samples were taken at Towers 1 and 3 throughout the experiment, and at Tower 5 only near the end of the data collection, by taking scrapings from the upper 3-5 mm of the sand surface. Topographical slope was measured by rod and level survey.

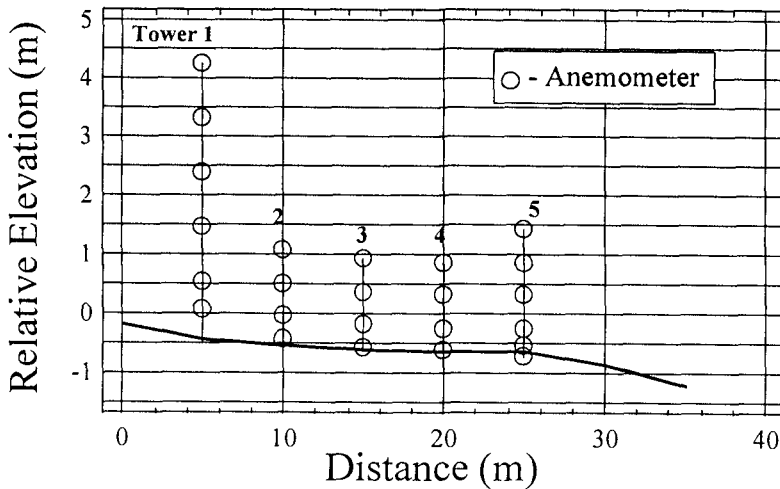


Figure 2: Instrument configuration on January 13, 1993.

Shear Velocity estimates were obtained through analysis of vertical wind-speed profiles. Linear regression was used to obtain “best fit” profile slopes, s , following the methodology described in Bauer et al. (1992). Assuming that the law of the wall applies, estimates of u_* were made using the relationship $u_* = \kappa s$, where κ is von

Karman's constant. To increase the statistical confidence of the u_* estimates, we restricted our analysis to instances where the R^2 associated with the best fit line was greater than 0.98.

Grain Size statistics were estimated using sand samples taken from the sediment traps. Samples were washed, dried, and sieved at 0.25ϕ intervals, and the data were processed according to the method of moments.

Moisture Content was estimated on the basis of pore-water weight relative to dry weight of the sediment sample. Samples were weighed, oven dried, and reweighed in order to solve:

$$w = 100 \left(\frac{W_t - W_d}{W_d} \right) \quad (9)$$

where W_t is total sample weight and W_d is the dry weight of the sample.

Sediment Transport Rates were measured with cylindrical traps (Leatherman 1978; Rosen 1978). Traps were opened for 15-minute periods to correspond with wind sampling. Trapped sands were oven dried and weighed to obtain the transport rate data.

RESULTS AND MODEL EVALUATION

Grain size estimates were obtained from a total of 19 samples taken during the transport event. Grain-size statistics were surprisingly consistent over the entire measurement period with a mean 'd' of 0.12 mm and a standard deviation of 0.007 mm. **Moisture content** was also almost constant, with a mean 'w' for the data set of 6.9 % and a standard deviation of 0.7 %. **Surface slope** upwind of the instrument array was negligible, largely because the predominant wind fetch was oriented parallel to shore. Three shore-parallel lines were surveyed upwind of the instrument array, and they indicated a maximum relief of the berm flat of less than 0.3 m over a 50 m transect. Common slope-correction models indicate that such minor relief affects predicted transport rates by less than 1%. This value is much less than our confidence level for other measurements and estimates, and therefore, we did not investigate slope effects further. **Sediment transport rate** measurements were also obtained for 19 samples. In a recent field experiment, Greeley et al. (1996) found that the efficiency of the cylindrical traps is approximately 30%. Based on that finding, we adjusted our measured transport rates uniformly by 300%.

Our first evaluation was to test the three transport models without moisture (or slope) corrections. Comparison of observed and predicted rates are presented in Figure 3. It can be seen that the Kawamura model over predicts substantially, while the Bagnold and Lettau and Lettau models fit the observations relatively well. There is very little difference in the degree of statistical explanation associated with each

model. With the Bagnold model, $R^2 = 0.50$; for Kawamura, $R^2 = 0.48$; and for Lettau and Lettau, $R^2 = 0.50$. The main difference between the model performances are associated with the slopes and offsets of best-fit lines.

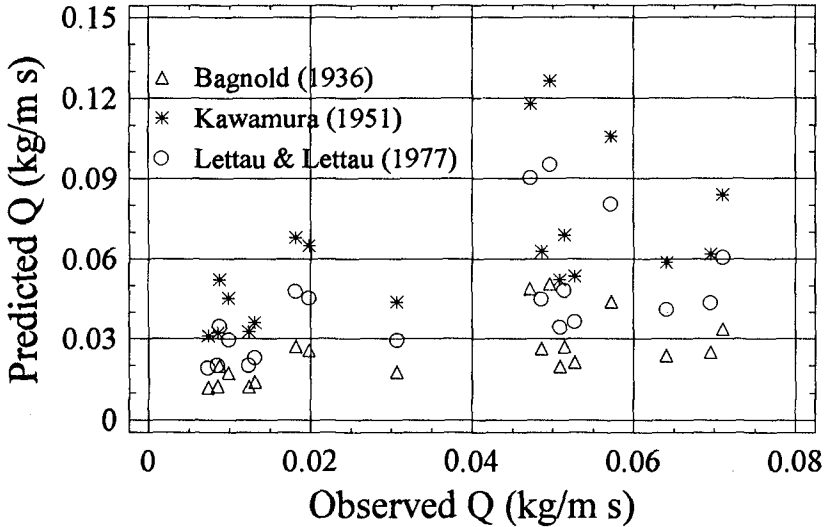


Figure 3: Comparison of observed and predicted transport rates without moisture content adjustments.

A second comparison incorporating moisture-content corrections was made. We evaluated the three moisture models described above (Equations 5 - 8) for their viability with the field data. In several instances, both the Hotta et al. and Kawata and Tsuchiya models yielded predictions of 'no transport' when our measurements clearly showed sediment movement. This peculiar situation arises when the threshold shear velocity predicted by these models on the basis of moisture content is greater than the observed shear velocities. We decided that this was one rational basis upon which the viability of the moisture models, vis-a-vis field data, could be distinguished. Since only the Belly (1964) model was immune to this problem, we used it with the transport equations. Note, however, that because there is no explicit threshold term in the Bagnold model (it is implicit in the parameterization of shear velocity), it was not considered appropriate to apply a moisture correction factor to his equation. Therefore, only the Kawamura and Lettau and Lettau models, with the Belly modification, were compared. Figure 4 shows that there is still considerable scatter in the relationship, with the main effect of accounting for moisture content being an overall reduction in predicted transport rate.

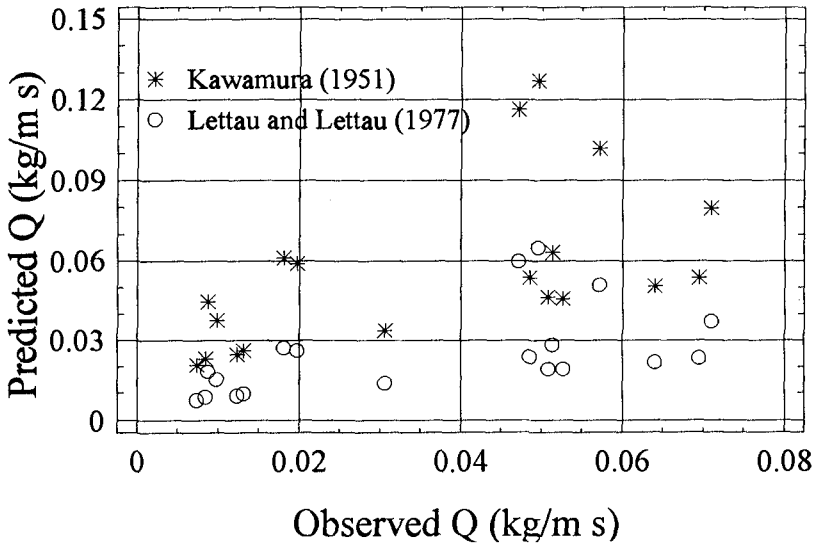


Figure 4: Comparison of observed and predicted transport rates using the Kawamura and Lettau and Lettau models with Belly's moisture model.

Linear regression was used to determine the statistical association between observed and predicted transport rates. On a log-log plot, R^2 for both models was 0.50. However, the Lettau and Lettau/Belly combination yielded predictions that were closer to a one-to-one correspondence with observations. This is best illustrated in Figure 5 using probability density plots (normalized frequency of occurrence) that compare smoothed distributions of ratios of predicted to observed values for both

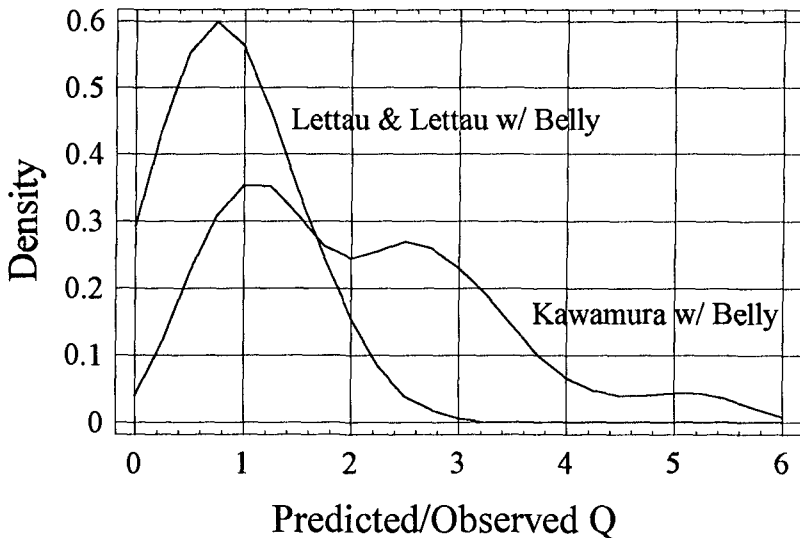


Figure 5: Comparison of ratios of predicted to observed transport rates.

models. An ideal model would have a narrow, peaked distribution centered around one--indicative of a near-one-to-one match between model and prototype conditions. Figure 5 shows that the Lettau and Lettau model, including the moisture content correction, approaches this ideal distribution, whereas the Kawamura and Belly combination over predicts substantially. These distributions of pairwise ratios of observed to predicted transport rates, coupled with the regression analysis, may represent one of the least ambiguous tests of comparative model performances.

DISCUSSION

All statistical comparisons between predicted and measured transport rates show that the scatter around a linear regression fit is approximately the same, regardless of transport model and moisture-content correction (R^2 values range from 0.48 to 0.50). Presumably, this reflects the similarity of the underlying physical bases for the models, and the fact that the variability in sediment moisture content during our experiments was small enough that the Belly model essentially acted as a near-uniform offset in the predictions--that is, all predicted transport rates were approximately uniformly reduced in magnitude.

It is encouraging that, under the conditions reported here, approximately half of the statistical variability in the transport rates monitored can be explained by the models evaluated. The uncertainty regarding the other half of the variability can be ascribed to several sources. First, our estimates of shear velocity were based upon line fitting procedures that, by their very nature, incorporate some degree of statistical uncertainty. Although this uncertainty has been minimized by excluding all wind profiles where R^2 was less than 0.99, it is not totally eliminated (e.g. Bauer et al. 1992). Because errors in estimates of u_* are compounded in the transport models (because third powers of shear velocity are used), 10 % errors translate to about 30% errors in predicted transport rates.

Second, there is substantial uncertainty associated with the measurement of sediment flux using cylindrical-type traps. We implemented a first-order correction to our measurements based on the findings of Greeley et al. (1996), but this is a crude adjustment that forces us to presume that trap efficiency is constant for the range of transport rates. This remains a point of contention.

Third, we feel some degree of unease with the universality of the models themselves and their underlying assumptions concerning grain-size distributions (only mean values are used, and sorting effects are ignored) and the steadiness of the wind field (steady-state conditions are assumed). We are also unable to make substantive distinctions among the physical--theoretical foundations of the different approaches which might provide guidelines as to their applicability. Thus, we are left with statistical performance assessments only.

It is noteworthy that whereas the use of the Lettau and Lettau model with

Belly's moisture correction provides the best predictions of transport for the Castroville system, the results are only marginally better than those obtained using the simple Bagnold model. Figure 6 compares the probability density distributions for the two approaches--the models perform almost identically for this range of conditions. The over-predictions obtained using the Kawamura model may also reflect the use of $C = 2.78$, instead of the more conservative estimate of 1.0 recommended by Horikawa et al. (1984). The latter value brings the Kawamura results into much closer correspondence with the other models and with our observations.

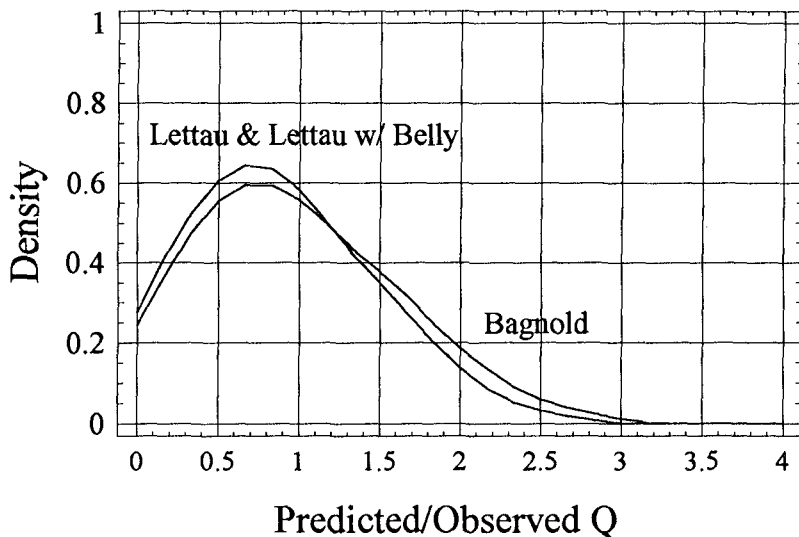


Figure 6: Comparison of ratios of predicted to observed transport rates.

Our results also compare favorably with those of Sherman et al. (in press). In that study of across shore transport conditions, the best models (Bagnold and Zingg) explained only about 20% of the statistical variability found in the observations. The Kawamura and Lettau and Lettau models each accounted for about 15% of the variability in prototype transport rates.

CONCLUSIONS

Conclusions that arise from this study include:

1. Under conditions of relatively uniform slope, grain size, and sediment moisture content, either the Bagnold, Kawamura (with $C = 1.0$), or Lettau and Lettau models provide reasonable estimates of aeolian sand transport. The performance of the Lettau and Lettau model can be enhanced through its coupling with the Belly moisture

model. Any of these model combinations is able to explain about 50% of the variability in transport rates observed during this part of the Castroville experiments.

2. We believe that it is possible, with carefully designed field experiments, to obtain process data of a quality comparable to that obtained in the laboratory. Nevertheless, continued uncertainty regarding the performance of field instrumentation in general and sediment traps in particular confounds our ability to assess accurately aeolian processes across beaches. The inherent complexity of natural systems may never be captured completely.

ACKNOWLEDGMENTS

This project received financial support through a contract from the California Department of Boating and Waterways and a grant from the North Atlantic Treaty Organization. We are also grateful to Andy Smith and the Monterey Dunes Colony Association for pleasant accommodation, and to the California Department of Parks and Recreation for beach access. Able field assistance was provided by Kevin Parnell, John Wolcott, Deming He, Jianchun Yi, Jinkang Wang, James Tyner, and Steven Namikas.

REFERENCES

- Anderson, R.S., M. Sorenson, and B.B. Willetts 1991. A review of recent progress in our understanding of aeolian sediment transport. *Acta Mechanica*, Sup. 1: 1-19.
- Bagnold, R.A. 1936. The Movement of Desert Sand. *Proc. Roy. Soc. London*. A157: 594-620.
- Bauer, B.O. 1991. Aeolian Decoupling of Beach Sediments. *Annals, Association of American Geographers*, 81(2): 290-303.
- Bauer, B.O., R.G.D. Davidson-Arnott, K.F. Nordstrom, J. Ollerhead, and N.L. Jackson. Indeterminacy in aeolian sediment transport across beaches. *J. Coastal Research*, 12: 641-653.
- Bauer, B.O., D.J. Sherman, K.F. Nordstrom, and P.A. Gares. 1990. Aeolian transport and measurement across a beach and dune at Castroville, California. In Nordstrom, K.F., N.P. Psuty, and R.W.G. Carter (eds.), *Coastal Dunes: Form and Process*. New York, Wiley, pp. 39-55.
- Bauer, B.O., D.J. Sherman, and J.F. Wolcott 1992. Sources of uncertainty in shear stress and roughness length estimates derived from velocity profiles. *Professional Geographer* 44: 453-464.
- Belly, P.-Y. 1964. *Sand Movement by Wind*. U.S. Army Corps Eng. CERC. Tech. Mem. 1. Washington D.C. 38 pp.
- Carter, R.W.G. 1988. *Coastal Environments: An Introduction to the Physical, Ecological, and Cultural Systems of Coastlines*. Academic Press, London. 617 pp.

- Gares, P.A. 1988. Factors affecting eolian sediment transport in beach and dune environments. *J. Coastal Research*, SI3: 121-126.
- Greeley, R., D.G. Blumberg, and S.H. Williams 1996. Field measurements of the flux and speed of wind-blown sand. *Sedimentology* 43: 41-52.
- Hesp, P.A. 1988. Surfzone, beach and foredune interactions on the Australian SE coast. *J. Coastal Research* SI3: 15-25.
- Horikawa, K., S. Hotta, S. Kubota, and S. Katori. 1984. Field Measurement of Blown Sand Transport Rate by Trench Trap. *Coastal Eng. Jpn.* 27: 214-232.
- Hotta, S., S. Kubota, S. Katori, and K. Horikawa 1984. Sand transport by wind on a wet sand surface. *Proc., 19th Conf., Coastal Engineering, ASCE., New York*, pp. 1263-1281.
- Kawamura, R. 1951. *Study of Sand Movement by Wind*. Translated (1965) as University of California Hydraulics Engineering Laboratory Report HEL 2-8, Berkeley.
- Kawata, Y., and Y. Tsuchiya 1976. Influence of water content on the threshold of sand movement and the rate of sand transport in blown sand. *Proc., Japanese Soc. Civil Engineers* 249: 95-100 (in Japanese).
- Lancaster, 1995. *Geomorphology of Desert Dunes*, Routledge, London, UK. 290 pp.
- Leatherman, S.P. 1978. A New Aeolian Sand Trap Design. *Sedimentology* 25: 303-6
- Lettau, K., and H. Lettau. 1977. Experimental and Micrometeorological Field Studies of Dune Migration. In K. Lettau and H. Lettau (eds.): *Exploring the World's Driest Climate*. University of Wisconsin-Madison, IES Report 101. 110-147.
- McEwan, I.K., and B.B. Willetts 1994. On the prediction of bed-load sand transport rate in air. *Sedimentology* 41: 1241-1251.
- Namikas, S.L. and D.J. Sherman, in press. AEOLUS II: An interactive aeolian sedimentation simulation program. *Geomorphology*
- Namikas, S.L. and D.J. Sherman 1995. A review of the effects of surface moisture content on aeolian sand transport. In V.P. Tchakerian (ed.), *Desert Aeolian Processes*. New York, Chapman and Hall pp. 269-293.
- Nordstrom, K.F., and N.L. Jackson 1992. Effect of source width and tidal elevation changes on eolian transport on an estuarine beach. *Sedimentology*, 39: 769-778.
- Rosen, P.S. 1978. An efficient, low-cost aeolian sampling system. *Current Res. A. Geol. Surv. Can. Pap.* 78-1A. 531-2.
- Sherman, D.J., D.W.T. Jackson, S.L. Namikas, and J. Wang, in press. Aeolian sediment transport to the coastal dune complex at Inch, Co. Kerry, Ireland. *Geomorphology*.
- Sherman, D.J., and K.F. Nordstrom 1995. Wind-blown sand hazard in the coastal zone: a review. *J. Coastal Research* SI12: 263-275.
- Zingg, A.W. 1953. Wind tunnel studies of the movement of sedimentary material. *Proc. 5th Hydraulics Conf. Bull.* 34. Iowa City: Inst. of Hydraulics. 111-135.



Heavy surf at Golden Gate Park, San Francisco, California.
Photo courtesy of Robert L. Wiegel.

PART V

Coastal, Estuarine and Environmental Problems



Fisher Island adjacent to Miami Beach, Florida. Photo
courtesy of Olsen Associates, Inc.

CHAPTER 327

PIPELINE PROTECTION IN THE SURF ZONE

Gerrit J. Schiereck, Henri L. Fontijn¹

ABSTRACT

Stability relations for rock on a mild slope in breaking waves were investigated, both experimentally and theoretically. Assumptions were made for the influence of turbulence in breaking waves on the load exerted by the wave motion. It appears that with these assumptions, the mechanism is reasonably described in a qualitative way. For design purposes the method is not accurate enough. This is possibly due to the neglect of the (vertical) velocity field near the bottom in a breaking wave, giving an underestimation of the difference in stability in spilling or plunging breakers. The experimental results seem consistent and can be used provisionally for design purposes. An interesting point is that they also are in line with existing relations for stability on steep slopes.

ACKNOWLEDGEMENT

The authors thank prof.dr. Marcel Stive of Delft Hydraulics for his permission to use the wave model ENDEC. ACZ Marine Contractors is thanked for their initiative on the study on pipeline protection and the continuous interest in the progress.

1. INTRODUCTION

Pipelines on the sea bottom are usually protected in order to prevent damage by anchors or erosion. Where a pipeline crosses a beach, it often lays in a dredged trench, see Figure 1, and is covered with stones. For the design of such a protection, which can be seen as an armour layer on a mild slope, a provisional design rule was established, see Schiereck et al., 1994, based on theoretical considerations and experiments. For non-breaking waves on a mild slope, the

¹*Delft University of Technology, Faculty of Civil Engineering,
P.O. Box 5046, 2600 GA Delft, The Netherlands*

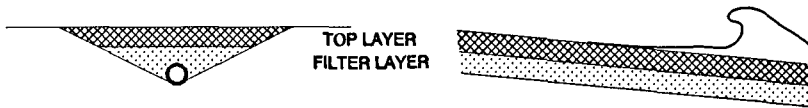


Figure 1 Outfall protection

result was reasonably satisfying. For the stability in breaking waves no theoretical concept was available and the number of experiments was not sufficient to give reliable results. In addition, new experiments were carried out, in which the slope, the stone density and the stone size were varied. Also, an attempt was made to derive a theoretical relationship for the stability of stones in breaking waves. The purpose of this attempt was twofold. First, experimental results that can be explained from theory are better understood, decreasing the danger of misusing empirical relations, while, vice versa, theories that can be verified by experiments get more practical value in hydraulic engineering. The second reason comes from didactics. Hydraulic engineering is still heavily based on empirical relations. Presenting all these relations without a link to the theory on fluid motion is considered a weak point in academical engineering education.

2. APPROACH

Experiments are indispensable to establish design rules in hydraulic engineering, so, laboratory tests are the basis of the research in this paper. But, as already stated in the introduction, the experimental results should be connected with the physical background of forces due to moving water. The creation of a link between the fluid motion and experimental results is tried with a simple, but complete description of the phenomena involved. The stability of stones on a slope is governed by the relation between load and strength. The strength is usually satisfactorily described with the effective weight and the friction of the stones. The load is much more complex. The moving water in a breaking wave will exert forces on a stone. Even in a breaking wave, the orbital velocities will play a role in the velocity field. Also, the breaking will cause turbulent eddies, with their own velocity field. The whole of orbital and turbulent velocity field is responsible for the loading on a stone. Another complicating factor is that waves in nature are irregular. Therefore, some statistical description of the waves is necessary.

In the computations the load will be composed of forces caused by the orbital motion, in combination with turbulent velocities due to breaking. For the stability, existing relations between the load and strength of a stone layer in an oscillating water motion will be used.

3. BASIC EQUATIONS

Orbital motion

The oscillatory flow near the bottom is approached with the linear wave theory:

$$\hat{u}_b = \omega a_b = \frac{\omega H}{2} \frac{1}{\sinh kh} \quad (1)$$

Turbulent velocities

For the turbulent velocities, an approach as given by Battjes, 1975 and Battjes, 1987 is used. Battjes coupled the rate of production of turbulence energy to the rate of dissipation of wave energy due to breaking:

$$q \approx (D_B / \rho_w)^{1/3} \quad (2)$$

in which q is the turbulent velocity scale ($q^2 = u_i u_i$). Figure 2 shows a comparison between measured and computed turbulent velocity scale. In this paper the expression for q , equation (2), will be used as a measure for the turbulent velocity.

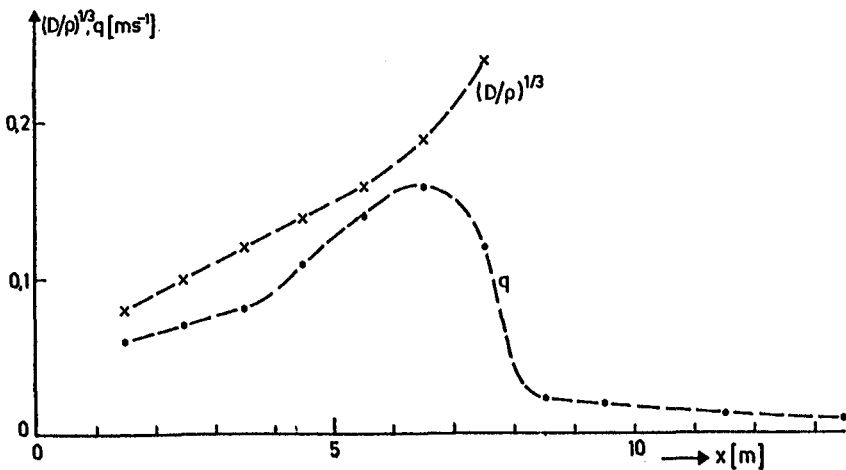


Figure 2 Comparison of computed and measured turbulent velocity scale

The dissipation of wave energy is derived from the analogy between a bore and a breaking wave, see Battjes and Jansen, 1978:

$$D_B = \frac{1}{4} \frac{Q_B}{T_P} \rho_w g H_M^2 \quad (3)$$

in which Q_B is the fraction of the (irregular) waves that are broken, derived

from:

$$\frac{1 - Q_B}{\ln Q_B} = - \left(\frac{H_{RMS}}{H_M} \right)^2 \quad (4)$$

and where H_M is the maximum wave height, given by:

$$H_M = 0.88 * k^{-1} * \tanh(k h) \quad (5)$$

For more details, see Battjes & Janssen, 1978. Several models are available in which this concept is implemented, e.g. the 2-dimensional DUT model HISWA, see Holthuijsen et al, 1989. In this study the 1-dimensional model ENDEC (Delft Hydraulics, see Battjes & Stive, 1985) was used to compute the various wave parameters along the different slopes, since in this model the wave set-up is explicitly computed, which possibly could be important.

Wave height distribution

As a basis for the wave height distribution the Rayleigh distribution is taken. This distribution is also used in Battjes and Janssen, 1978. In shallow water, the wave height distribution deviates from the Rayleigh distribution. $H_{1\%}$ in shallow water, which plays an important role in the stability calculations, is given by, according to Stive, see CUR/CIRIA, 1991:

$$H_{1\% - shallow} = \frac{H_{1\% - Rayleigh}}{(1 + H_s/h)^{1/3}} \approx \frac{1.5 * H_s}{(1 + H_s/h)^{1/3}} \quad (6)$$

Load - strength relations

A simple relation to express the stability of stones in oscillating flow is based on experiments in an oscillating water tunnel by Rance and Warren, 1968 (see also Schiereck et al., 1994):

$$\frac{a_b}{T^2 \Delta g} = 0.025 \left[\frac{a_b}{d_{50}} \right]^{-\frac{2}{3}} \quad (7)$$

Another approach is given by Sleath, 1978. Analogous to the Shields approach in uniform flow, Sleath gives a relation between the shear stress (which is not necessarily the dominant load) and the stone weight, partly based on the experimental data by Rance & Warren (1968). The relation for stones reads:

$$\hat{\tau}_b = 0.056 \cdot (\rho_s - \rho_w) \cdot g \cdot d \quad (8)$$

d is the equivalent spherical diameter, in this paper approximated by d_{50} , the

median sieve diameter, which is easily available and differs only a few percent from the spherical diameter. The shear stress due to orbital velocities can be expressed by:

$$\hat{\tau}_b = \frac{1}{2} \cdot \rho_w \cdot f_w \cdot \hat{u}_b^2 \quad (9)$$

with f_w and \hat{u}_b depending on the wave height, H , and the period, T . The circumflex over a parameter denotes "amplitude of". Given a certain wave height, the longer the period is, the larger the orbital velocity at the bottom, \hat{u}_b . For f_w , the friction coefficient, the opposite holds: the shorter the period, the larger the friction coefficient. In CUR/CIRIA (1991) an expression by Swart is given, based on Jonsson (1966), where f_w is given as a function of the orbital stroke at the bottom, related to the bottom roughness:

$$f_w = \exp[-6 + 5.2 \left(\frac{a_b}{k_s}\right)^{-0.194}] \quad (f_{w \max} = 0.3) \quad (10)$$

Computations

The combination of orbital velocities, turbulent velocities, wave height distribution and load-strength relations into a design procedure can be done in various ways. In section 5, this is further elaborated.

4. EXPERIMENTS

Experiments were done in a wave tank (length 40 m, width 0.8 m, depth 0.9 m) at the Laboratory of Fluid Mechanics, Delft University of Technology (DUT), see Ye, 1996. The slope angles were 1:10 and 1:25. The mass densities of the stones were 2550 and 2850 kg/m³ while the nominal diameters, d_{n50} , varied between 1 and 1.5 cm. The width of the sieve curves of the stones (d_{85}/d_{15}) used in the experiments was about 1.5. 3 to 4 layers of stone were used, in order to ascertain a proper roughness between stones and slope. The difference with the geometry of a real pipeline cover, which has a filter layer under the top layer, is assumed to be negligible with respect to the stability of the top layer.

The stones were laid in coloured strips of 0.25 m (measured in the wave direction) over the full width of the flume. The total number of stones displaced after every test, n , divided by the number of stones in the width of the flume, was used as the total damage S :

$$S = n d_{n50} / w \quad (11)$$

in which w is the width of the flume. An arbitrary damage level of 2 was chosen for incipient motion.

Irregular waves were generated according to a JONSWAP-spectrum; the number of waves tested per spectrum was 2000. The wave heights and spectra were determined at the toe of the slope. The water depth at that location was 0.6 m.

Figure 3 shows the results of the experiments. The stability is expressed as $H_s/\Delta d$, in which H_s is the significant wave height at the toe of the slope. The stability is plotted against the breaker parameter, ξ , the slope angle relative to the wave steepness.

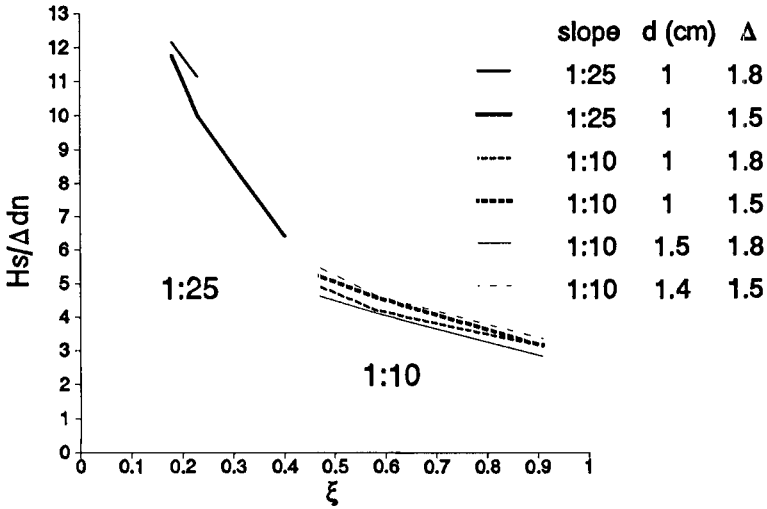


Figure 3 Experimental results

The general tendency is an increase in stability with decreasing ξ . This can partly be explained from the slope angle: the left-hand side of the figure represents the results for the slope 1:25 and the right-hand side those for 1:10. Within the results for each slope angle, there is also clearly an influence of the wave steepness: the larger the wave steepness, the larger the stability. This tendency has to do with the breaker characteristics and was previously found in other experiments, see e.g. Schiereck et al., 1994 and van der Meer, 1988. Within this general tendency, there is some influence of stone density and stone dimension. Whether this is a matter of accuracy or comes from physical reasons, remains to be seen.

5. COMPARISON OF COMPUTATIONS AND EXPERIMENTS

In order to compare the computational results, obtained with the approach described in section 2, with the experimental results, at first the wave parameters along the slope were computed with ENDEC, using the measured wave characteristics at the toe of the slope at the threshold of motion. From previous investigations (see Schiereck et al.,1994) it appeared that in irregular waves, the higher waves are responsible for the incipient motion, in particular the wave height that is exceeded by 1% of the waves. This wave height is computed with equation (6) for various locations along the slope. The orbital velocities at the bottom in these waves were computed with equation (1).

Rance & Warren

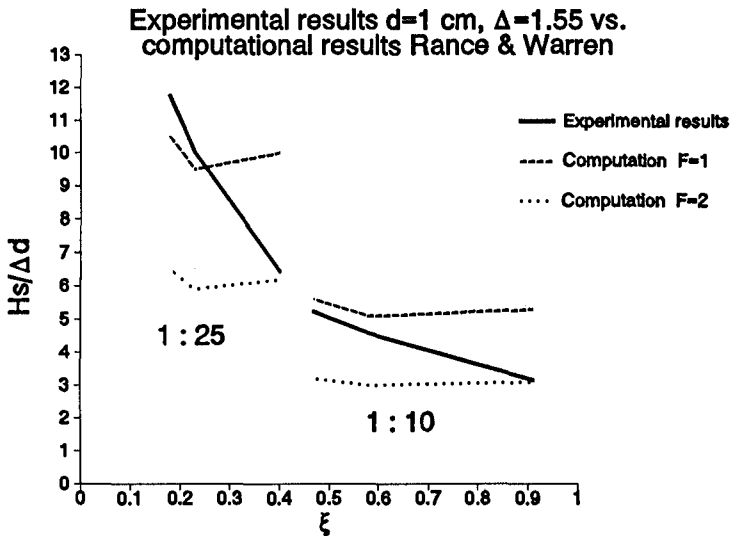


Figure 4 Comparison of experiments with computation according to Rance & Warren

The necessary stone diameter is first computed with the relation of Rance & Warren. With $\hat{u}_b = \omega \cdot a_b$, equation (7) is rewritten as:

$$d_{50} = \frac{2.56 * \hat{u}_b^{2.5}}{\sqrt{T_p} * (\Delta g)^{1.5}} \tag{12}$$

This equation is valid for a horizontal bottom. The diameter in this formula is

the median sieve diameter, d_{50} . In order to compare the computational results with the experiments, the nominal diameter (dn_{50}) is required, which is approximately $0.84 * d_{50}$. The turbulent velocity, from equation (2), is simply added to the orbital velocity from equation (1). Together with a correction for the influence of the slope angle on the stability, the equation finally becomes:

$$dn_{50} = \frac{0.84 * 2.56 * (\hat{u}_b + F * q)^{2.5}}{\sqrt{T_P} * (\Delta g)^{1.5}} * \frac{\sin \phi}{\sin(\phi - \alpha)} \quad (13)$$

in which F is a calibration factor and ϕ is the angle of repose of the stones, here taken as 45° . q , as defined in equation (2), is taken as the turbulent velocity.

With this equation the necessary diameter along the slope is computed. The maximum computed diameter is used, which is equivalent to the use of a total-damage concept in the experiments, regardless of the location of the damage. For comparison, the results of the experiments with $\rho_s = 2550 \text{ kg/m}^3$ and $dn_{50} = 1 \text{ cm}$ are being used. Figure 4 shows the results for $F = 1$ and $F = 2$. The influence of the slope angle, as seen in the experiments, is also found in the computations, but the influence of the wave steepness is not reproduced correctly.

Jonsson/Sleath

The relationship as found from the results of Rance & Warren (equation (7)), expresses the relation between the stroke of the orbital motion and the necessary diameter to prevent the incipient movement of the stones. This implicitly indicates the influence of the inertia of the orbital motion on the stone stability. The simple addition of a turbulent velocity to the orbital velocity, as done in equation (13),

attributes the same influence to the turbulent velocity, which is not logic.

Another approach is the following. Consider the forces on a grain in a flow field, see Figure 5. The shear force is exerted by the orbital movement, described with equations (9), (1) and (10). Equation (8) gives the relation between shear stress and stone size for incipient motion. This equation is now rewritten for the equilibrium of forces, where the turbulent velocity is assumed to generate a lift force, reducing the effective weight of the stone. In this way, the influence of turbulence is treated separately from the orbital motion with its specific relation for the friction factor, equation (10).

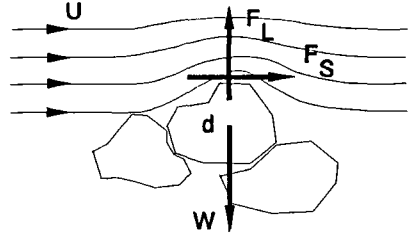


Figure 5 Flow forces on a grain

The equilibrium of forces then leads to the following proportionality:

$$\frac{1}{2} \rho_w f_w u_b^2 A_h \propto (\rho_s - \rho_w) g V - \frac{1}{2} \rho_w C_L A_h q^2 \quad (14)$$

in which A_h is a representative horizontal area, both for shear and lift. V is the volume of a stone and C_L the lift coefficient. Using equation (8), this leads to:

$$\frac{1}{2} \rho_w f_w u_b^2 = 0.056 (\rho_s - \rho_w) g d - \frac{1}{2} \rho_w C_L q^2 \quad (15)$$

giving finally:

$$dn_{50} = \frac{0.84 \frac{1}{2} (f_w \hat{u}_b^2 + F q^2)}{0.056 \Delta g} * \frac{\sin \phi}{\sin (\phi - \alpha)} \quad (16)$$

in which C_L is replaced by F , a calibration factor in which both the lift coefficient and the transfer from wave energy dissipation into turbulence is included.

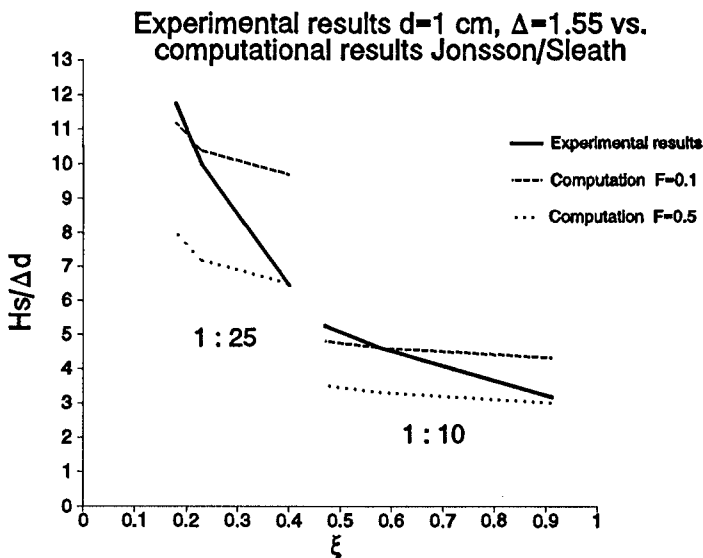


Figure 6 Experimental results compared with computations according to Jonsson/Sleath

Figure 6 shows the results for $F = 0.1$ and $F = 0.5$. The agreement is somewhat better than with the relationship of Rance & Warren. The influence of

the slope angle is represented just as good as for the Rance & Warren relation, while the tendency of the influence of the wave steepness is qualitatively correct. The difference in stability between low and high values of ξ , however, for one value of the slope angle, is too small in the computations.

Variable friction factor in ENDEC

Until now, in ENDEC only one friction factor has been used, viz. 0.05, which is a relatively high value due to the rough bottom. Equation (10) leads to higher friction factors for steeper waves. Using different friction factors for different wave steepness, ($f_w = 0.05, 0.04, 0.03$ for $s = 0.05, 0.03, 0.01$, respectively) is justified, because of equation (10). For the calibration factor F in the computations 0.25 is used, being a value in between the two values of Figure 6.

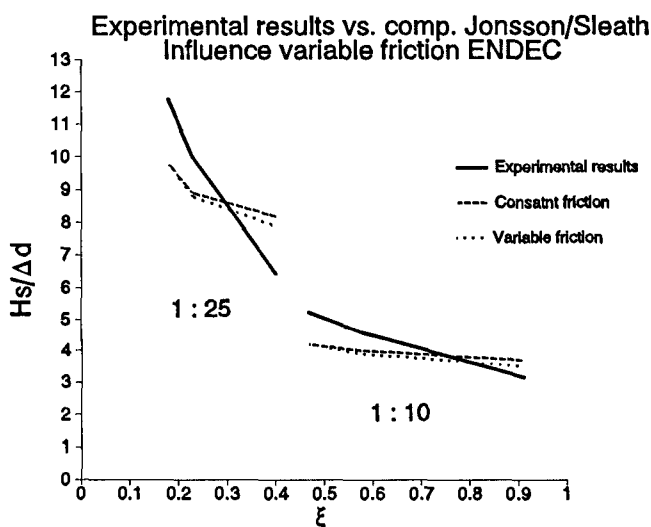


Figure 7 Variable friction factor in ENDEC

The results are now a little bit better, see Figure 7. The models being used are very simple. Considering the fact that the values of the calibration factor F are realistic with respect to the lift coefficient, the description is quite reasonable in a qualitative way. From the point of view of design practice, however, the results are still far from perfect.

The same underestimation of the favourable effect of high wave steepness was found in non-breaking waves, see Schiereck et al., 1994. The explanation has probably to be found in the negelection of the vertical flow pattern in breaking waves. Figure 8 shows a plunging breaker in which a jet obliquely to the bottom occurs, while the jet is absent in a spilling wave. This jet may have an

unfavourable influence on the stone stability, which is not described in the models used here. This difference will only appear when using a 2-dimensional wave model for the wave motion on a slope. The agreement so far is encouraging enough to try to couple the experimental results to the water motion, using a better wave-velocity model.

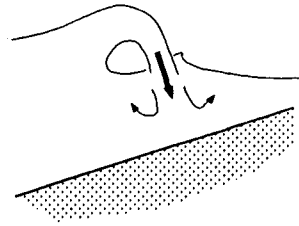


Figure 8 Plunging jet

6. EVALUATION

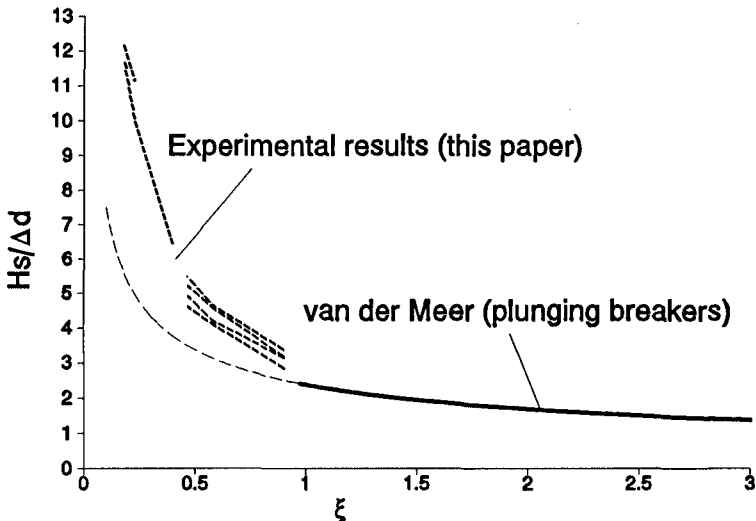


Figure 9 Experimental results compared with van der Meer formula for plunging breakers

Figure 9 shows the experimental results discussed before. The investigations were done in the range $\xi = 0.1 - 1.0$. The figure also shows the relation for stone stability on relatively steep slopes as proposed by van der Meer, 1988. This relation was validated for values $\xi > 1$. The trend for both situations is the same, which encourages further research in this field. Together with a 2-dimensional model, describing the wave motion on a slope in more detail than the models used in this paper, it should be possible in the future to give a satisfactorily accurate description of stone stability in (breaking) waves on slopes. For the time being, the experimental results as presented in this paper can be used as a first approximation for stone stability on mild slopes.

7. CONCLUSIONS

- 1- The computational results give a description that follow the trends of experimental results reasonably well in a qualitative way, when including the following elements from the physical process of the stability of stones in breaking waves on a mild slope:
 - orbital movement (from linear wave theory, equation 1)
 - wave shear stress (according to Jonsson, equation 10 and using equation 9)
 - Rayleigh distribution (with shallow-water correction by Stive, equation 6)
 - wave breaking and energy dissipation (according to Battjes/Janssen, equations 3, 4 and 5)
 - turbulent velocities (according to Battjes, equation 2)
 - stone stability (according to Sleath, equation 8)
 - .
- 2- The computed relation between stone stability ($H_s/\Delta d$) and breaker parameter ($\xi = \tan\alpha\sqrt{H_s/L_0}$), is quantitatively insufficient. Probably the fact that the vertical velocities near the bottom in a plunging breaker were not taken into account, is the main reason for this. Other weak points are possibly the turbulence model used and the influence of turbulence on the stability of a single stone.
- 3- The experimental results seem consistent and are also in line with the (empirical) van der Meer relation for stability of stones on steep slopes. This resemblance can be used as a basis for future research on stone stability in breaking waves on slopes in general.
- 4- The experimental results in this paper can be used for the design of a protective rock layer on a mild slope.

SYMBOLS

a_b	orbital stroke at bottom		m
d_{n50}	median nominal diameter of material	$(d_{n50} = (M_{50}/\rho_s)^{0.33})$	m
d_{50}	median sieve diameter of material		m
D_B	energy dissipation due to breaking of waves		Nm/s/m ²
f_w	friction coefficient in waves		-
F	tuning factor		-
g	acceleration due to gravity		m/s ²
H	wave height		m
H_M	maximum wave height		m
H_s	significant wave height		m
h	water depth		m
k	wave number	$(k = 2\pi/L)$	1/m
k_s	equivalent sand roughness	$(k_s = d_{50})$	m
L_0	deep-water wave length	$(L_0 = gT_p^2/2\pi)$	m
M	mass		kg
n	number of displaced stones		-
q	turbulent velocity scale in breaking waves		m/s
Q_B	percentage of broken waves		-
S	damage		%
s	wave steepness	$(s = H/L_0)$	-
T_p	peak wave period of spectrum		s
\hat{u}_b	amplitude of orbital velocity at bottom		m/s
w	width of flume		m
α	slope angle of structure		-
Δ	relative mass density of material	$(\Delta = (\rho_s - \rho_w)/\rho_w)$	-
ϕ	angle of repose of stones		-
ρ_s	mass density of material		kg/m ³
ρ_w	mass density of water		kg/m ³
ξ	breaker parameter	$(\xi = \tan \alpha \sqrt{H/L_0})$	-
$\hat{\tau}_b$	amplitude of bottom shear stress		N/m ²
ω	angular frequency	$(\omega = 2\pi/T)$	1/s

REFERENCES

- Battjes, J.A., 1975** *Modelling of turbulence in the surf zone*
Symposium on modeling techniques, ASCE, San Francisco
- Battjes, J.A., 1987** *Surfzone turbulence* Seminar on Hydrodynamics of waves in coastal areas, IAHR, Moscow
- Battjes, J.A. and Janssen, J.P.F.M., 1978** *Energy loss and set-up due to breaking in random waves*, Proc. 16th Int. Conf. on Coastal Eng., ASCE, New York
- Battjes, J.A. and Stive, M.J.F., 1985** *Calibration and verification of a dissipation model for random breaking waves*, Jnl. of Geophys. Research, 90
- CUR/CIRIA, 1991** *Manual on the use of rock in coastal and shoreline engineering*, CUR Report 154/CIRIA Special Publication 83, Balkema, Rotterdam, pp. 197, 216, 217, 298
- Holthuijsen, L.A., Booij, N. and Herbers, T.H.C., 1989** *A prediction model for stationary, short-crested waves in shallow water with ambient currents*, Coastal Engineering, 13, pp 23-54
- Jonsson, I.G., 1966** *Wave boundary layers and friction factors*
Proc. 10th Conf. on Coastal Engineering, Tokyo, pp. 127-148
- Meer, J.W. van der, 1988** *Rock Slopes and Gravel Beaches under Wave Attack*
Delft Hydraulics, Publication no. 396, The Netherlands
- Rance, P.J., and Warren, N.F., 1968**, *The threshold of movement of coarse material in oscillatory flow* Proc. 11th Conf. on Coastal Engineering, London, pp. 487-491
- Schiereck, G.J., Fontijn, H.L., Grote, W. and Sistermans, P.G.J., 1994** *Stability of rock on beaches*, Proceedings 21th Int. Conf. on Coastal Eng. ASCE, Kobe
- Sleath, J.F.A., 1978** *Measurements of bed load in oscillatory flow*
Journal of the Waterway, Port, Coastal and Ocean Division, ASCE, Vol.104 no. WW4, pp. 291-307
- Ye, Lei, 1996** *Stability of rock on beaches*
MSc-thesis, Delft University of Technology

CHAPTER 328

Modeling Tidal Circulation in Florida Bay

Y. Peter Sheng¹, Member ASCE, and Justin Davis²

Abstract

A preliminary modeling study on tidal circulation in Florida Bay has been conducted, based on a set of high resolution (20 meters x 20 meters) bathymetric data and a comprehensive set of water level data for Florida Bay obtained by the Everglades National Park in 1993 and 1994. Using the data and a 3-D curvilinear-grid model developed by Sheng (1989, 1994), we conducted preliminary model simulations of tidal, wind-driven and density-driven circulations in Florida Bay (Sheng et al. 1995). This paper presents some results of tidal simulation and comparison with tidal data. The results indicate that the 3-D model is capable of simulating many of the observed circulation features in Florida Bay, including tidal amplitude, tidal phase and residual circulation. Additional work is being conducted with the use of a very fine 50m grid and a robust wetting-and-drying scheme.

Introduction

Florida Bay is a shallow coastal water body located at the southern tip of Florida. It is adjacent to the western Florida Shelf and is separated from the deep Florida Strait by the Florida Keys. In the past few years, Florida Bay has undergone substantial changes in the form of major seagrass die-off and massive algal bloom. Due to the lack of understanding of the extremely complex ecosystem, it is unclear presently as to how Florida Bay can be restored (Johnson and Fennema 1989). One restoration plan, which is based on the assumption that reduced freshwater supply and increase in hypersalinity (salinity reaching up to 35-50 ppt) has caused the seagrass die-off and algal bloom (Figure 1), is to increase the inflow of freshwater into Florida Bay from its northeastern shore. In order to determine the soundness of this

¹Professor, Coastal & Oceanographic Eng. Dept., Univ. of Florida, 32611-6590, USA

²Graduate Assistant, Coastal & Oceanographic Eng. Dept., Univ. of Florida, USA

restoration plan, it is essential to have a quantitative understanding on the circulation and salinity transport in Florida Bay. This paper presents a preliminary study on tidal circulation in Florida Bay. In addition to a comparison between simulated and measured water levels in Florida Bay, we also examine the exchanges between Florida Bay and Florida Strait through the tidal channels along the Florida Keys.

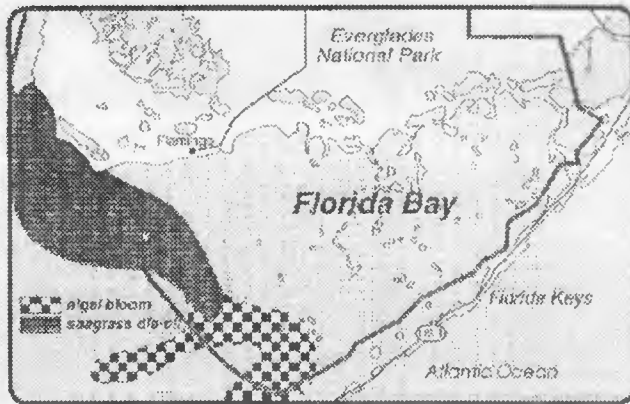


Figure 1. Florida Bay Map with Areas of Massive Algal Bloom and Seagrass Die-off.

Field Data

As a first step, we reviewed a comprehensive set of data which includes the high resolution bathymetric data for Florida Bay and hydrodynamic and hydrographical data at numerous stations in Florida Bay during 1993 and 1994, both compiled by the National Park Service (Sheng et al. 1995). As shown in Figure 2, much of the eastern Florida Bay is less than 1 m deep. Figure 3 shows that mudbanks in Florida Bay actually divide the Bay into numerous lakes during low water. Field data collected in Florida Bay include water level, water temperature, conductivity, rainfall, and evaporation. Water level data were taken at the 27 stations shown in Figure 4. Using these water level data, Smith (1995a) obtained the co-amplitude chart and co-phase chart for the M_2 tide as shown in Figure 5. As can be seen from Figure 5, M_2 tide enters the Florida Bay from both West Florida Shelf and Florida Strait. Diurnal tides such as O_1 and K_1 constituents primarily enter into Florida Bay from West Florida Shelf. Some tide data are from the offshore waters to the south of Florida Keys (Smith 1995b). Wind data are available from 1-2 offshore CMAN stations only. Freshwater discharge data and current meter data are lacking. High evaporation rate often leads to hypersalinity of more than 50 ppt inside Florida Bay even during the wet season.

Using the data indicated above and a 3-D curvilinear-grid model developed by Sheng (1987, 1989, 1994), we conducted model simulations of tidal, wind-driven

and density-driven circulations in Florida Bay (Sheng et al. 1995). In this paper, we present some results of preliminary simulation of tidal circulation. model results.

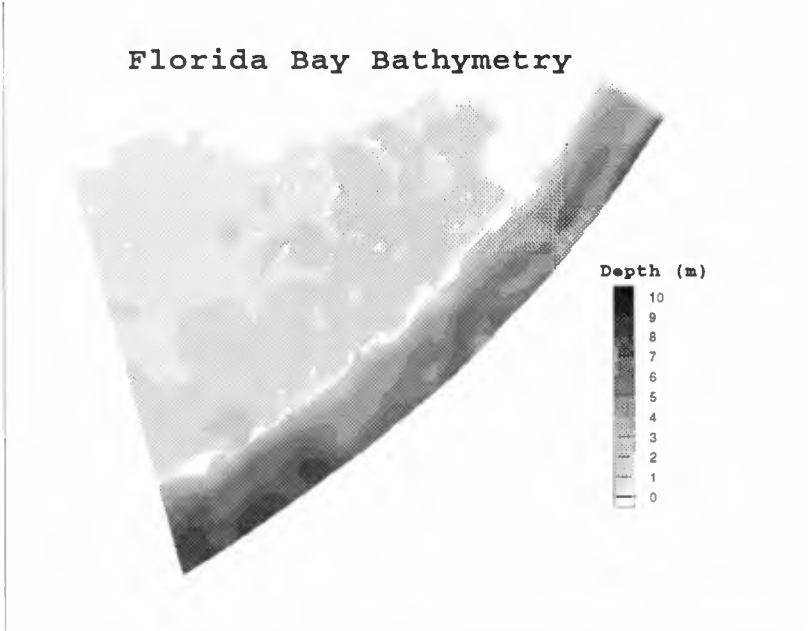


Figure 2. Bathymetry contours in the entire finer-grid model domain. All depths inside the Bay are less than 1-2 meters.

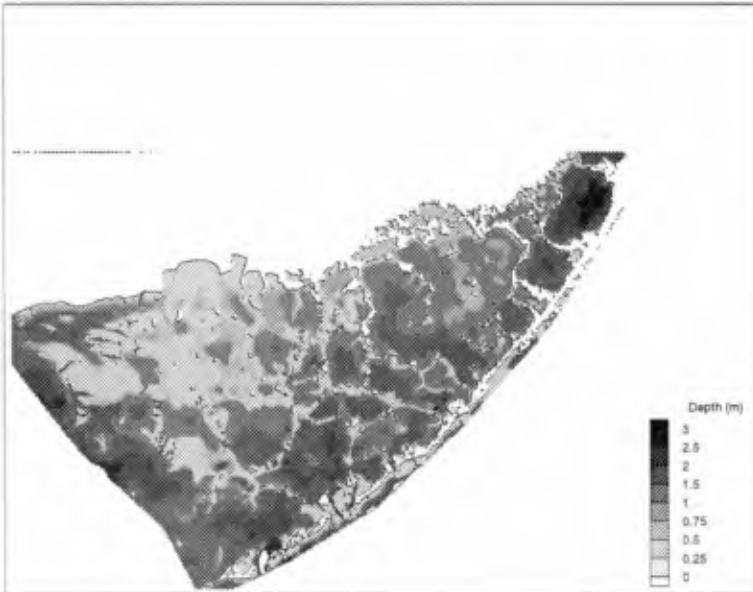


Figure 3. Florida Bay bathymetry provided by Everglades National Park.

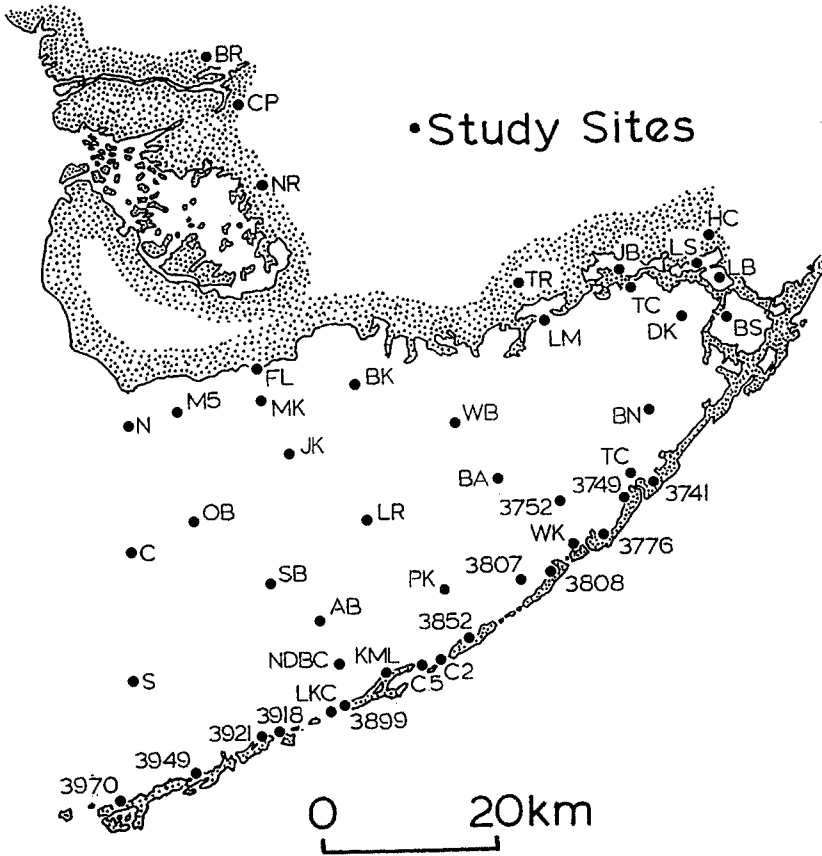


Figure 4. A Map of Monitoring Stations in Florida Bay.

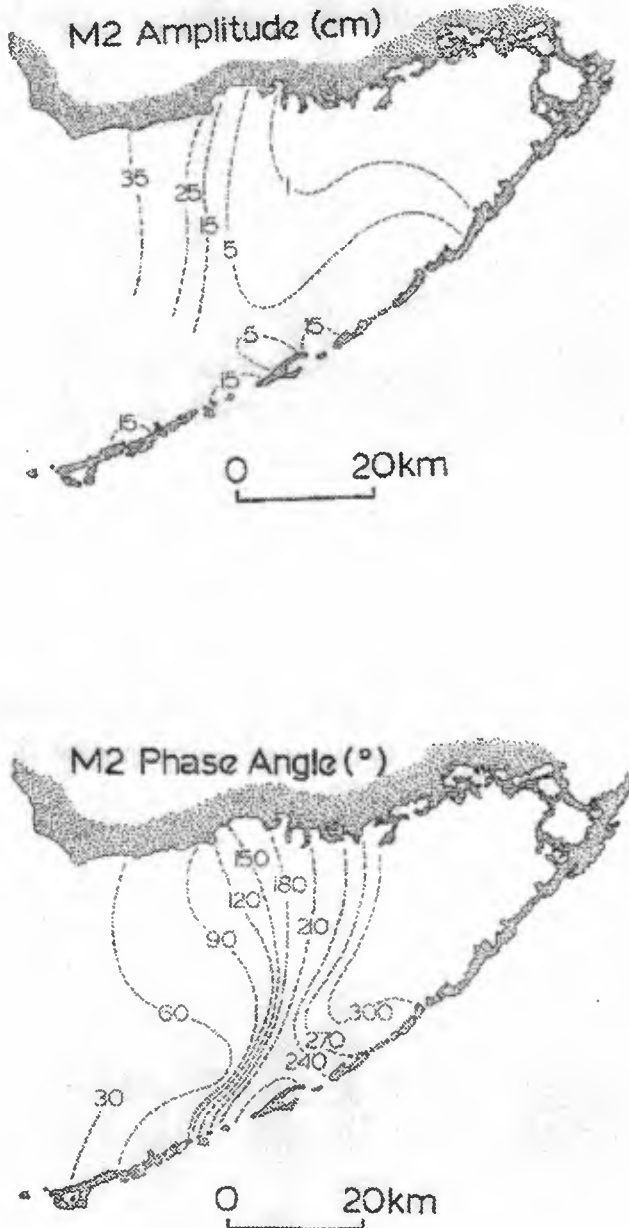


Figure 5. Co-Amplitude and Co-Phase Lines of M_2 Tide in Florida Bay.

Model and Grid

CH3D, the 3-D curvilinear-grid circulation model developed by Sheng (1989, 1994) is modified for application to Florida Bay. In the past few years, through numerous research projects (Chesapeake Bay, James River, Sarasota Bay, Lake Okeechobee, Indian River Lagoon, and Tampa Bay), we have significantly improved the model's features/capabilities for simulating stratified flow, effect of vegetation on circulation, ocean-estuary coupling, and wind-induced flow. The model solves for the three-dimensional equations of motion in terms of the water level and contravariant velocity components. The model solves the vertically-integrated equations of motions as well as the vertical structures of the flow field. Since the same time step is used for the solution of the external mode and the internal mode, the model solutions are consistent with each other and converge. A robust vertical turbulence model (Sheng and Villaret 1989) is used to represent the vertical turbulent mixing. The model allows the use of boundary-fitted grid which can accurately represent the complex shoreline in Florida Bay. In the vertical direction, the sigma grid is used. Sheng et al. (1995) used several boundary-fitted grids to resolve Florida Bay.

The grid shown in Figure 6 includes all the area covered in the detailed bathymetry map in Figure 3 plus the offshore area between the Florida Keys and the reef tract. A total of 98 by 75 grid points are contained in this grid. For 3-D simulations of tidal circulation, a total of 4 vertical cells are generally used.

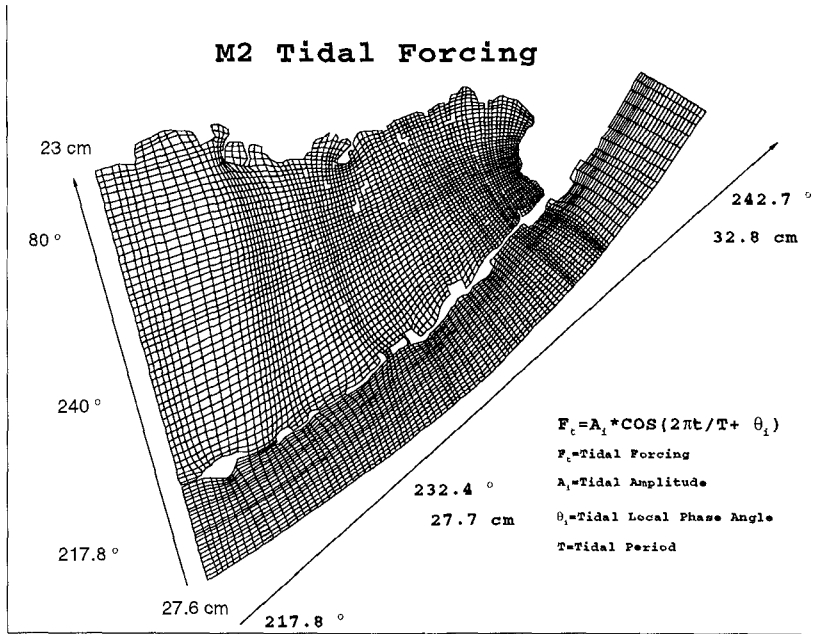


Figure 6. A model grid with 98x75 cells and open boundary conditions for M₂ tide in Florida Bay.

Simulation of Tidal Circulation

Using the horizontal numerical grid shown in Figure 6 and a vertical sigma-grid with 4 cells, we conducted simulations of tidal circulation in Florida Bay with CH3D (Sheng et al. 1995). The major objectives of tidal simulation is to examine the model's ability to simulate tide propagation and dissipation inside Florida Bay, and to examine the simulated residual flow inside the Florida Keys. For the first objective, detailed comparison between model results and data have been made (Sheng et al. 1995). For the second objective, model results can be compared qualitatively with preliminary flow measurement by Smith (1995b) which showed persistent southerly residual flow inside the Florida Keys.

To simulate the tidal dynamics in Florida Bay, it is essential to include part of the offshore water in the numerical grid as shown in Figure 6, since tides in Florida Bay are influenced by tides from the Gulf of Mexico and the Florida Strait. Tidal data along the reef tract were taken at Carysfort Reef, Alligator Reef, Tennessee Reef, Sombrero Key and Sand Key Light. These data were analyzed to produce the amplitudes and phases for various tidal harmonic constituents. Using these data and the tidal data inside Florida Bay, we produced the boundary conditions for the M_2 simulation as shown in Figure 6.

Using the open boundary conditions for M_2 tide described above, the 3-D model CH3D was run for 5 days. The result during the last tidal cycle was then analyzed to produce the maximum water level chart and a corresponding co-phase chart. The simulated maximum water level chart for M_2 tide in Florida Bay is shown in Figure 7. Amplitude in the extremely shallow eastern Florida Bay, where the depth is generally less than 50 cm, is on the order of 1-5 cm only.

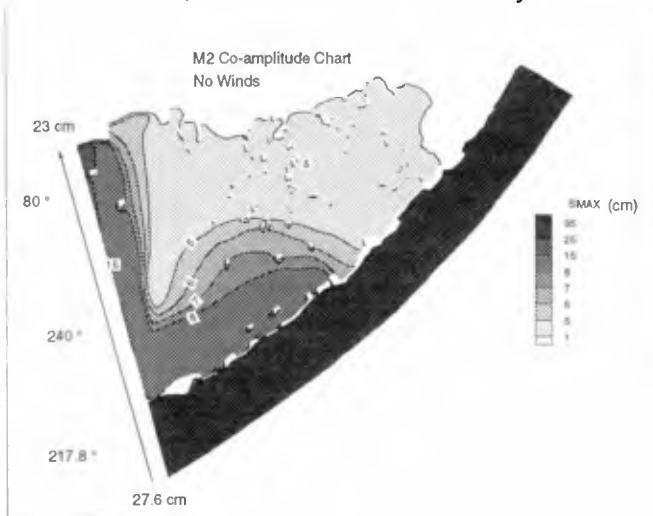


Figure 7. Co-amplitude chart of M_2 tide simulated by the 3-D model.

The results shown in Figure 7 compare favorably with the co-amplitude chart produced from data as shown in Figure 5. The simulated peak water level in the eastern Florida Bay is larger than the observed amplitude, suggesting insufficient tidal dissipation in the model. The simulated co-phase chart, which is presented in Sheng et al. (1995), showed that tides propagated further eastward. This is partly due to the fact that the complicated mudbanks, extremely shallow depths, and narrow Florida Keys in the eastern Florida Bay are not accurately represented in the 3-D model grid and bathymetry. The minimum horizontal grid spacing is approximately 100 meters while a spacing of 20 m may be necessary to represent the detailed bathymetry.

Other reasons for discrepancy between model results and data are that wind and wetting-and-drying were not included in the preliminary simulations. In the absence of wind, the residual (tidally-averaged) water level in the eastern Florida Bay is about 2 cm plus. By including a mild summer wind from the southeast, simulated maximum water level chart as shown in Figure 8 agrees better with the co-tidal chart based on data. In the presence of a summer wind, the residual water level in eastern Florida Bay became approximately -0.5 cm. A robust wetting-and-drying scheme has recently been implemented in CH3D. With the wetting-and-drying scheme and a fine grid (50m minimum grid spacing), we are able to produce much better results with 1 cm tidal amplitude in the eastern Florida Bay.

The tidally-residual vertically-averaged flow field as shown in Figure 9 exhibits significant southerly flow in the Florida Keys, in agreement with recent flow measurement by Smith (1995b). The southerly residual flow results from the higher residual water level in eastern Florida Bay.

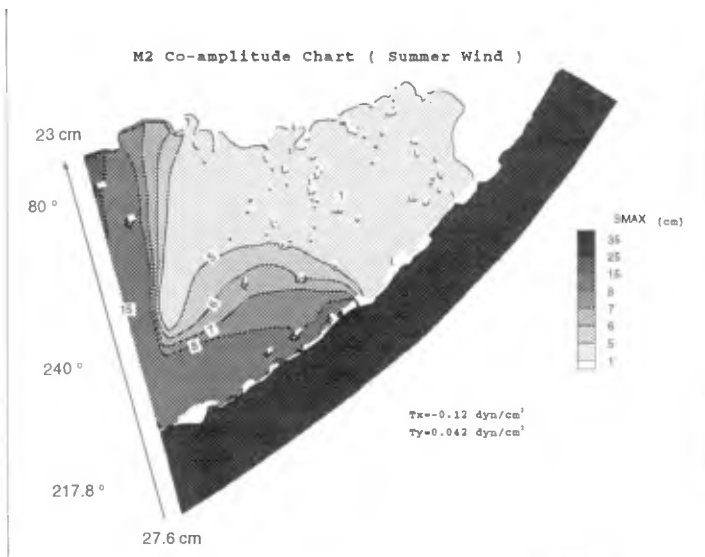


Figure 8. Co-amplitude chart of M_2 tide simulated by the new fine grid model with average summer wind condition.

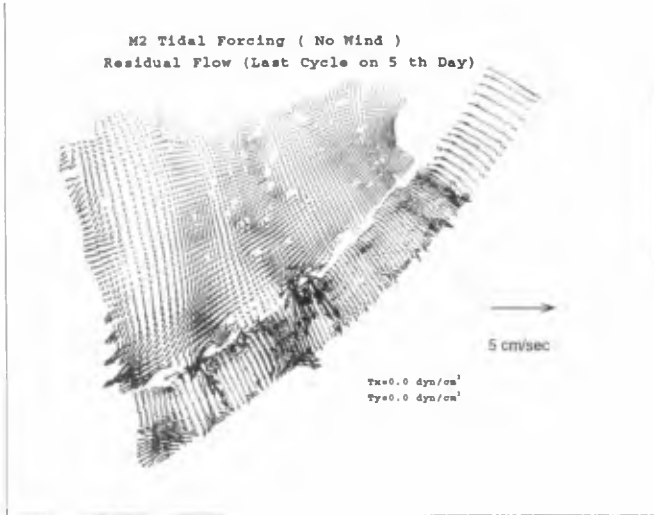


Figure 9. Simulated tidal residual currents in Florida Bay with forcing by pure M_2 tide.

To examine the influence of tides from the southern open boundary, we made a model run with closed Florida Keys. As shown in Figure 10, the maximum water level compares poorly with that in the co-amplitude chart based on the 1-year data. These results also suggest that simulated results in Figure 8 exhibit stronger influence from the southern open boundary than that shown in the data. This could be improved by more accurate representation of the Florida Keys and more accurate open boundary conditions along the southern open boundary.



Figure 10. Simulated maximum water level of M_2 tide in Florida Bay with the Florida Keys closed.

Discussion

A curvilinear-grid 3-D circulation model developed by Sheng (1987, 1989, 1994) has been modified to simulate the tidal circulation in Florida Bay. Tide data collected at 27 stations inside Florida Bay during 1993 and 1994 plus offshore tide data during earlier time periods were analyzed in terms various diurnal (O_1 and K_1) and semi-diurnal (M_2) constituents. Using the tidal constituent data to construct open boundary conditions along the southern and western open boundaries, we conducted numerous model simulations with a number of numerical grids and various forcing conditions: first with tide only, then with tide and wind, and finally with tide, wind and salinity field (Sheng et al. 1995). Due to the dominance of M_2 tide from both the Gulf of Mexico and the Florida Strait, this paper focuses on the simulation of M_2 tide. The simulated maximum water level and co-phase chart compare reasonably well with the co-amplitude and co-phase charts produced from the 1-year tide data. Significant dissipation due to the mudbanks and extremely shallow water depths result in very small tidal amplitude on the order of 1-5 cm in the eastern Florida Bay. The residual (tidally-averaged) model results indicate that there is a setup in the eastern Florida Bay which causes southerly residual flow inside the channels along the Florida Keys, which has been found by recent flow measurement.

Additional model simulations of K_1 and O_1 tides and baroclinic circulation have been conducted by Sheng et al. (1995). Model results suggest that data gap in freshwater inflow and evaporation data prevents longterm (from 1 month to 1 year) simulation of Florida Bay circulation at the present time.

We have continued with the modeling effort. Recently, a robust wetting-and-drying scheme has been implemented in CH3D. A very fine grid, with a minimum grid spacing of 50m, has also been used in recent simulations. This grid gives much better representation of the mudbanks and the complex bathymetry. Using the very fine grid and the wetting-and-drying scheme, we are able to significantly improve the model results in the eastern Florida Bay. Maximum M_2 tidal amplitude in the eastern bay was reduced to 1 cm. Details of the wetting-and-drying scheme and the improved model simulations will be reported in two upcoming papers.

Acknowledgement

This study has been supported by the Everglades National Park of the National Park Service, US Department of Interior, and the University of Florida. Data used for this study have been provided by Dewitt Smith and Ned Smith.

References

Johnson, R.A. and R.J. Fennema, 1989: "Conflicts Over Flood Control and Wetland

Preservation in the Taylor Slough and Eastern Panhandle Basins of Everglades National Park,” in *Wetlands: Concerns and Successes*, American Water Resources Association.

- Sheng, Y.P., 1987: “On Modeling Three-Dimensional Estuarine and Marine Hydrodynamics,” *Three-Dimensional Models of Marine and Estuarine Dynamics* (J.C.J. Nihoul and B.M. Jamart, Eds.), Elsevier Oceanography Series, Elsevier, pp. 35-54.
- Sheng, Y.P., 1989: “Evolution of A 3-D Curvilinear-Grid Hydrodynamic Model: CH3D,” *Estuarine and Coastal Modeling*, (Ed. M. Spaulding), ASCE, 40-49.
- Sheng, Y.P., 1994: “Modeling Hydrodynamics and Water Quality Dynamics in Shallow Waters,” *Keynote Address, International Symposium on Ecology and Engineering (ISEE 1994)*, Taman Negara Resort, Malaysia, 29 Oct. - 3 Nov., 1994.
- Sheng, Y.P., 1995: “On Modeling of Florida Bay Circulation,” *Abstract Book, AGU Chapman Conference on Circulation in Intra-Americas Sea*, La Parguera, Lajos, Puerto Rico, January 22-26, 1995.
- Sheng, Y.P. and C. Villaret, 1989: “Modeling the Effect of Suspended Sediment Stratification on Bottom Exchange Processes,” *Journal of Geophysical Research*, **94:C10**, pp. 14429-14444.
- Sheng, Y.P. and S.J. Peene, 1993: “A Field and Modeling Study of Residual Circulation in Sarasota Bay and Tampa Bay, Florida,” *Coastal & Estuarine Modeling, III*, (Ed. M. Spaulding), ASCE.
- Sheng, Y.P. J. Davis, and Y. Liu, 1995: “Towards the Development of A Comprehensive Model of Circulation and Transport in Florida Bay,” *Proceedings of the 1995 Scientific Symposium on Florida Bay*, Florida Sea Grant.
- Sheng, Y.P. J. Davis, and Y. Liu, 1995: “Development of A Preliminary Numerical Model of Circulation and Transport in Florida Bay,” *Final Report to National Park Service*, Coastal & Oceanographic Engineering Department, University of Florida, Gainesville, FL 32611.
- Smith, N.P., 1995a: “Analysis of Water Level and Current Data in Florida Bay,” *Interim Report to National Park Service*, Harbor Branch Oceanographic Institution.
- Smith, N.P., 1995b: Personal Communication.

CHAPTER 329

RECENT DEVELOPMENTS IN COASTAL DEFENCE POLICY AND GUIDANCE IN ENGLAND

Reg Purnell¹

SUMMARY

In recent years we have seen fundamental changes in the way that coastal defences are planned and implemented. Engineers have recognised the overwhelming public desire to see the environment taken more into account when designing major infrastructure projects and our understanding of coastal processes has improved, allowing the design of coastal defences to become more scientifically based. As a result we have seen attention turn to adapting and supplementing natural coastal processes with the aim of adopting a coastal policy which is both more environmentally acceptable and sustainable in engineering terms.

In England, to reflect these engineering changes, to secure better value for money for our investment in coastal defence and offer a more sustainable approach in the longer term, the Ministry of Agriculture, Fisheries and Food, which has policy responsibility for flood and coastal defences, has invested significant sums of money into research. This has resulted in a better understanding of coastal processes and significant changes to national policy.

INTRODUCTION

As one would expect of a historical maritime nation, England has significant centres of population and economic wealth all around its coastline. The result is that over 5% of the population live in areas which are at risk of coastal flooding, perhaps not significant proportion in international terms. In addition there is an associated risk of coastal erosion which has seen the loss of a significant number of villages and large areas of land over the last few hundred years. The potential economic loss resulting from flooding or erosion is therefore significant in terms of its impact on the GDP. Recognising these risks the UK government spends some \$100m per annum on grant aiding capital improvement works in England to achieve its published overall policy aim which is “to reduce risks to people and the developed and natural environment from flooding and coastal erosion by encouraging the provision of technically, environmentally and economically sound and sustainable defence measures”.

INSTITUTIONAL ARRANGEMENTS

Whilst the Ministry of Agriculture, Fisheries and Food has overall policy responsibility for flood and coastal defences decisions on where and when defences will be provided are left to the local community. Responsibility for the provision of defences

¹Chief Engineer, Flood and Coastal Defence with Emergencies Division, Ministry of Agriculture, Fisheries and Food, Eastbury House, 30/34 Albert Embankment, London SE1 7TL, England.

against flooding are generally with the Environment Agency, which although a national body, makes such decisions on a regional basis with strong local input. Defences against coastal erosion are provided by Local Councils, some of whom also have additional powers with respect to provision of defences against coastal flooding. The boundaries of these bodies generally take no account of coastal processes being based on historical precedent and geography.

Historically these authorities have not generally cooperated in the provision of coastal defences tending to make their decisions on the basis of local needs and precedence.

STRATEGIC PLANNING

In the past defence measures were planned and implemented on a one-off site specific basis, not the most scientifically based approach. Indeed such site by site appraisal not only restricted engineering options but also ensured that not all costs and impacts were taken into account with the result that options were often limited to merely replacing on a like for like basis. This often perpetuated, previous sometimes, inappropriate solutions such as the replacement of hard reflective walls with more of the same. Improvements in the understanding of coastal processes clearly showed that by considering options over a wider area and a longer timescale more lateral thinking was possible, enabling the preparation of schemes that complemented natural processes rather than fighting against them. It was also felt that this more strategic approach would allow the Ministry to more easily meet its own policy objective.

As noted previously the boundaries of the authorities with primary responsibility for the delivery of coastal defences took no account of coastal processes. In addition these authorities had historically made decisions reflecting the needs and wishes of their own electorate and with little consultation with adjoining authorities. Therefore the first policy objective was to encourage these authorities to work together towards more strategic planning such that decisions taken on the basis of engineering knowledge could cross political boundaries. This was achieved by the establishment of voluntary Coastal Defence Groups, encouraged by MAFF, which took account of coastal process cells. To facilitate this a research study was commissioned from HR Wallingford to define logical boundaries of coastal process cells. Cells were defined as lengths of coastline within which the movement of coarse sediment is largely self-contained. Sub-cells within these were also defined on the basis of limited cross boundary influence due to coarse sediment transport.

Once formed these groups allowed authorities on adjoining lengths of coastline to meet and discuss similar problems and solutions and consider joint approaches to the gathering of data etc. Central government also encouraged collaboration between these groups by setting up the Coastal Defence Forum on which all groups in England and Wales are represented.

Central government then provided guidance and encouragement on the production of Shoreline Management Plans which aim to set out a strategy for coastal defences for a specified length of the coast taking account of the natural coastal processes and human and other environmental influences and needs.

The objective in developing these plans was to:

- improve understanding of the coastal processes operating within the sediment cells;
- predict the likely future evolution of the coast;
- identify all the assets within the area covered by the plan which are likely to be effected by coastal change;
- identify the need for regional or sites specific research investigations;

- facilitate consultation between those bodies with an interest in the coastline.

Once the plan was completed the authorities involved in its preparation would then have the means by which they could:

- assess a range of strategic coastal defence options and agree a preferred approach;
- outline future requirements for monitoring, management of data and research related to the shoreline;
- inform the strategic planning process and related coastal zone planning;
- identify opportunities for maintaining and enhancing the natural coastal environment taking account of any specific targets set by legislation or any locally set targets;
- set out arrangements for continued consultation within the group and other interested parties.

BEACH RECHARGE

The practice of recharging beaches as a form of coastal defence has been recognised worldwide for many years, although its use in England has been more limited than in many other countries in Europe. This is partly because of the greater difficulty of predicting beach behaviour due to the variability of beach material and partly because of the difficulty in gaining sufficient suitable material resulting in greatly increased costs.

Improved knowledge of coastal processes and an increasing public desire to take account of environmental effects when designing major infrastructure projects, increased pressure to use beach recharge as a form of coastal defence in England. Such forms of defence were also considered more sustainable in engineering terms. Initial research allowed improvements to modelling techniques which reduced the perceived financial risks and assisted in educating decision makers on the benefits of beach recharge. However, it was soon recognised that recharged beaches needed management if they were to provide a long term sustainable solution. Unfortunately such management works had not previously attracted Central government funding with the costs falling on the local community. Hence the possibility existed that the chosen solution might have more to do with the availability of funding than finding the right engineering solution.

The resulting policy change was to encourage authorities to produce long term beach management plans with the cost of implementing and monitoring for the first time attracting Central government grant. Thus the choice of solution could now more fully depend on science rather than the source of funds. As an additional benefit this change in policy allowed beach management on its own, without the benefit of an initial recharge, to be seen as an effective means of continuing coastal defences along parts of the coastline. With the possibility of Central government finance, operating authorities are now more willing to seek to understand the periodic movements of beach material and manage it for the benefit of improved coastal defences, thereby achieving better value for money and possibly reducing long term capital expenditure.

MANAGED SET-BACK

It was King Canute who first demonstrated to the English population the strength and power of the sea and the need for man to adapt to the wishes of Neptune rather than impose his will on nature. In the intervening years the lesson has been reinforced by the significant loss of land to the sea, recognising that it is not scientifically or economically sensible to protect all 4000 kilometres of our coastline. However, with the change to more naturally sustainable types of defence the option of doing nothing, or more importantly, allowing the

coastline to retreat had to be looked at in a different light. Whilst the retreating of defences did not require any major policy changes, since Mother Nature was doing that already, strategic planning now allowed more informed decisions and the opportunity for environmental enhancement. With improved long term planning it becomes possible to foresee the extent of likely retreat in future years thereby allowing landowners and developers to make more informed decisions but just as importantly the potential beneficial impact of such retreat on other areas of the coastline can be examined.

To compensate for the loss of valuable inter-tidal habitat resulting from coastal squeeze, and man's interference, government also took the opportunity of providing funds to recreate lost tidal wetlands in these setback areas. In areas where setback of the coastline is seen as a viable response mechanism and an opportunity for habitat creation exists, government can now offer payments to landowners for long term management to achieve environmental goals. Obviously merely setting back the coastline may not lead to environmental gain hence a research programme has commenced to determine suitable management regimes.

CARE OF THE ENVIRONMENT

There can be no doubt that flood and coastal defence measures can have a significant impact on the environment with the potential loss of important natural habitats. This is in addition to natural losses which may be exacerbated as a result of the coastline being unable to flexibly respond to natural changes due to man's intervention. These recent changes in coastal defence policy have made it possible to more easily establish the impact of our works on the natural environment and hence consider the possibility of mitigating measures. In addition it may also allow us in the future to understand and quantify some of the natural changes which may result in the loss of important wetland habitat thereby allowing the possibility of adjusting approaches in order to take mitigating measures to retain biodiversity.

FUTURE

As outlined in this paper cooperation between engineers and policymakers has in recent years allowed the scientific advances achieved by coastal engineers to result in consequential policy changes, however, these changes will not necessarily make life any easier for engineers. The move towards long term strategic planning of defences which encourages the maintenance of coastal processes will, without doubt, bring engineers' decisions under closer public scrutiny. Some of their recommendations may not be in accordance with the views of the local population, especially if these include realignment or even the abandonment of some existing defences. With longer term planning an increasing number of people will be involved in decisions affecting the coastline, hence engineers may have to seek consensus views from a wider range of people and interest groups.

The increasing move towards more environmentally friendly solutions to coastal problems will continue to result in change. Earlier in this paper I noted that beach recharge was not as widely used in England as elsewhere in Europe due largely to material supply problems. This is because the material suitable for recharging beaches is also sought by the construction industry. Many prefer to see the use of marine dredged material because of the perceived adverse environmental impact of extracting land based materials whilst the environmental impact of extraction from the sea bed is much less obvious to the general public. Unfortunately in many areas of the North Sea there is now insufficient coarse aggregate to satisfy the long term needs of both the construction industry and beach recharge. Therefore the next policy area that requires consideration is whether the use of marine

aggregate sources should be restricted to allow increased use for beach recharge or to leave it to market forces, as at present.

No matter what the decision on any future restrictions in the use of marine aggregate by the construction industry, demand will, at some time, exceed supply. Engineers' response to this possibility is to seek improvements in the predictive tools for long term sediment movement and developments in coastal morphology. An integrated research project is at present underway which should show some interesting results within a few years. In addition estuaries which are an important but little understood part of the sediment chain are a matter for current review.

The continued move towards more natural forms of defence brings forward questions of risk assessment since decisions are now dependent on a greater number of variables. This has been demonstrated in recent years by the unexpected failure of some soft forms of defence as a result of storm series that were not taken into account in the design process. Our response will be improved techniques in risk assessment leading perhaps to greater use of probabilistic design in coastal defences. An interesting perspective for policymakers.

The move towards strategic planning of coastal defences has resulted in a change of public awareness and perception of coastal engineering problems and as a result the public now takes a fuller part in the decision making process, even questioning the advice of engineers, especially when the "do nothing" option is the preferred choice. This move will, without doubt, bring other areas of coastal use into the decision making process leading to more integrated decisions, although implementation of coastal zone planning in its truest sense is, in my opinion, still some way off.

CONCLUSIONS

It is too early to claim complete success for the recent policy changes in this country, but I have no doubt that we are moving in the right direction and with a speed that has surprised many. Clearly the impact and improvements of recent years has been a lesson to us all and the need for engineers and policymakers to work together remains with us. However, if we are to make the best use of our improved scientific knowledge then it should not always be the policymakers responding to new engineering concepts, but engineers should themselves recognise the pressure on policymakers and be ready to respond with help and advice. Not only should changes in engineering techniques help drive policy but changes in policy need should also feed into engineering research.

REFERENCES

- Strategy for Flood and Coastal Defence in England and Wales. MAFF/Welsh Office (1993): MAFF Publications PB 1471.
- Shoreline Management Plans; a guide for operating authorities. MAFF/Welsh Office (1995): MAFF publication PB 2197.
- Coastal Management: Mapping of Littoral Cells. Report SR 328 Hydraulics Research, Wallingford, January 1993.
- Purnell RG, 1996 - Shoreline Management Plans: National Objectives and Implementation - proceedings of "Coastal Management: putting policy into practice".
- Flood and Coastal Defence Research and Development Implementation Strategy 1994-1998, MAFF publications (1995) ref. PB 2249.
- Beach Recharge Materials - Demand and Resources, 1996, Construction Industry Research and Information Association (CIRIA).
- DoE Circular 30/92, MAFF Circular FD1/92, WO Circular 68/92: Development and Flood Risk, ISBN 0-11-752737-8.
- Planning Policy Guidance Note (PPG) 20: Coastal Planning, DoE/Welsh Office (1992). ISBN 0-11-752711-4.
- Coastal Defence and the Environment: a guide to good practice. MAFF (1993). MAFF Publications PB 1191.
- The EC Habitats Directive: Implications for flood and coastal defence. MAFF (1995).
- MAFF Project Appraisal Guidance Notes for flood and coastal defence. MAFF (1993). MAFF Publications PB 1214.
- Policy Guidelines for the Coast - Discussion draft - DoE (1995).

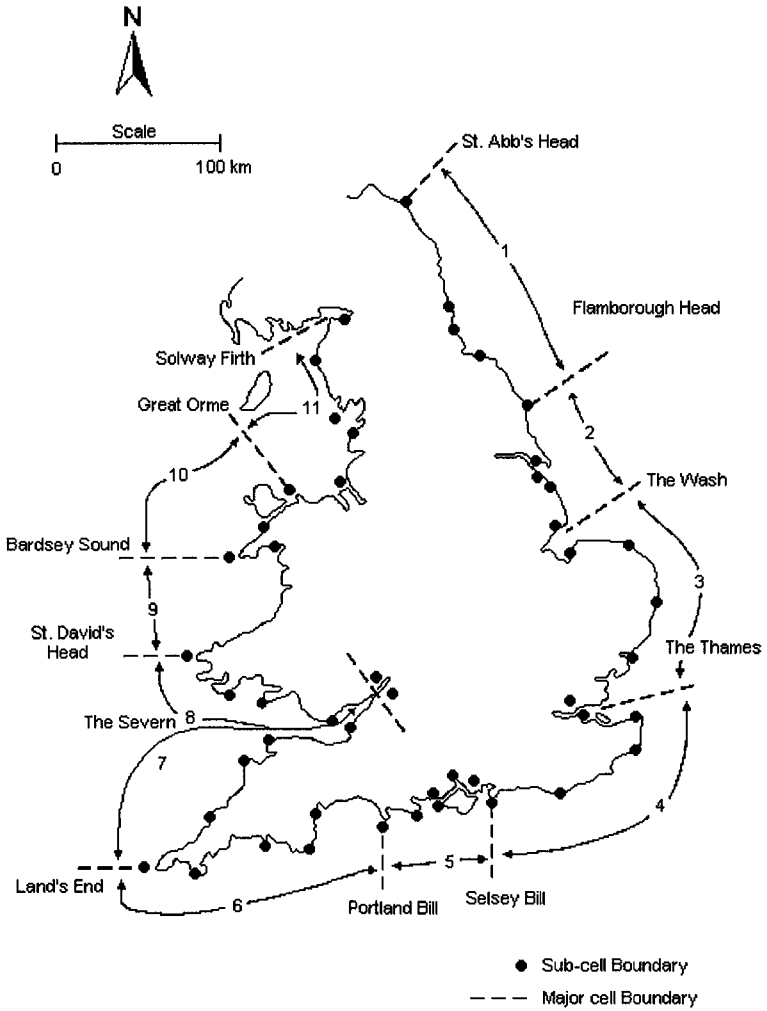


Figure 1: Boundaries of major sediment cells

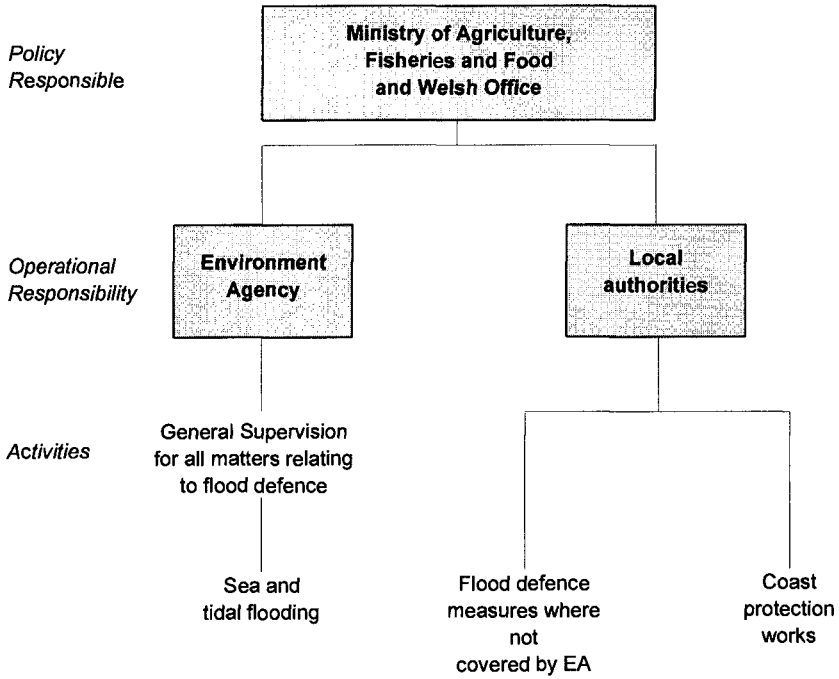


Figure 2 Flood and Coastal Defence: Organisation

CHAPTER 330

STRUCTURAL RESTORATION OF CORAL REEFS DAMAGED BY VESSEL GROUNDINGS

Kevin R. Bodge, Ph.D., P.E.¹

ABSTRACT

In 1995, a unique project was completed in which two coral reef sites in the Florida Keys were structurally restored after having sustained severe damage from the groundings of large vessels. The project, believed to be the world's first major structural restoration of a damaged reef (vs. in-kind mitigation using artificial reefs), demonstrated numerous innovative materials and marine construction techniques. Restoration focused upon the stabilization of coral rubble and large craters which resulted from the vessel groundings. The project's intent was to re-create a stable foundation which closely emulates the adjacent natural seabed and which would foster future recruitment of local biota. Work at one site included the mechanical transfer of coral rubble back into the craters, placement of limerock boulders atop the rubble, and back-filling the boulders' voids with carbonate sand. Work at the other site included excavation of coral rubble and the precision placement of 40 pre-cast reef-replicating armor units into the crater. The gaps between the units and along the crater's perimeter were filled with a specially-designed, non-separable underwater concrete -- into which coral rubble and soft corals were impressed. Design was complicated by the sites' proximity to environmentally sensitive coral beds and shallow depths (2.5 to 11 m). During construction, semi- real-time video images of the underwater work were relayed to the Engineer's office via the Internet to augment construction review. Construction was successfully completed per the engineering plans with no consequent environmental damage amidst a very active tropical storm season.

BACKGROUND

In two separate incidents in 1989, the 40-m *M/V Alec Owen Maitland* and the 142-m *M/V Elpis* went aground upon living coral reefs in the Key Largo National Marine Sanctuary in the Florida Keys, U.S.A. The two sites were within 6.8-km of one another, about 10.4 km offshore of northern Key Largo; and, about 74 km south-southwest of Government Cut at Miami Beach. The Maitland and Elpis sites, respectively, are located in the vicinity of N 25°11'58.776", W 80°13'34.421"; and N 25°8'54.088", W 80°15'9.20" (see Figure 1).

The impact and weight of the vessels upon the reef fractured the underlying coral substrate; and the ships' screws created deep craters in the coralline seabed. Large amounts of coral rubble were created from the fractures and ejected from the craters. Monetary damages were paid by the vessels' operators to the U.S. federal government under the auspices of the National Marine Sanctuaries Act

¹ Sr. Engr, Olsen Assoc., Inc., 4438 Herschel St., Jacksonville, FL 32210 USA; (904) 387-6114.

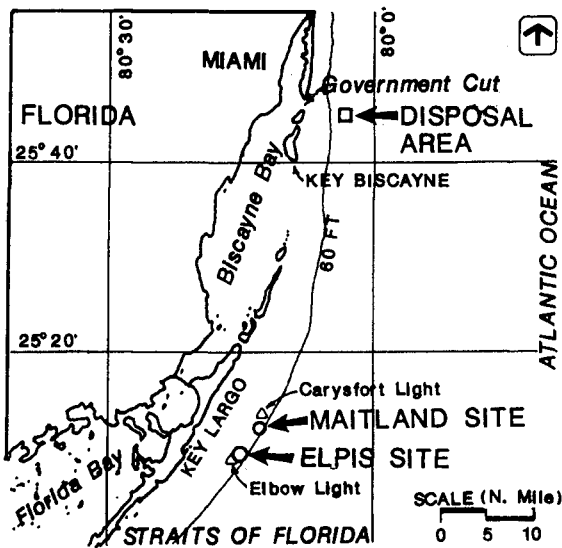


Figure 1:
Location Map

for the purposes of site rehabilitation. The author was retained by the U.S. National Oceanic and Atmospheric Administration (NOAA) to quantitatively assess the sites' structural damage, and to design and supervise engineering works to structurally restore the damaged reefs.

ENGINEERING ASSESSMENT

Site Survey and Conditions. A precision survey of the two damage sites was undertaken in July, 1994 using tightly-gridded fathometer transects and diver measurements involving triangulation and taut-wire cross-sections of the craters' geometry and rubble piles. A multi-beam fathometer (such as SEABAT) would have been ideally suited for the remote survey work, but was not yet commercially available at the time of the study.

Damage at the shallower Maitland site (-1.8 to -3.0 m, MLW) consisted primarily of a 370-m² crater, varying in relief from 0.1 to 1.0 m, relative to the ambient seabed. The crater was formed by the ships' screw when an attempt was made to free the vessel under her own power. Since its creation, the crater had partially infilled with rubble, but had also doubled in size from what was originally two separate holes. The expansion of the crater was due to wave- and current-induced erosion of its coralline perimeter -- a thin (< 1.5-m) semi-continuous crust overlaying 15-m of densely-packed gravelly-sand. The volume of the crater, measured below the ambient seabed grade, was about 115 m³. The seabed of the crater featured a matrix of sand and 7- to 20-cm diameter, loose coral rubble with scattered larger pieces measuring up to 50-cm.

Damage at the deeper Elpis site (about -11 m, MLW) primarily included two adjacent craters, measuring 69 m² and 163 m², likewise formed by the ships' screws as she tried to free herself. The

depth of the craters, below ambient grade, varied from 0.5 to 2.3 m. The volumes measured 127 m³ and 200 m³. The craters' seabed was composed of sand and coral rubble similar to that of the Maitland site, but featured numerous large coralline boulders of up to 1.8-m diameter. The sand fraction was carbonate, with $d_{50} = 0.6$ mm. Adjacent to the craters were three berms consisting entirely of relic *Acropora cervicornes* (elkhorn) coral rubble that had been initially ejected from the craters. This naturally branched rubble, primarily 10- to 25-cm long by 3-cm diameter, was interlocked but easily succumbed to dismantling by hand or jet probe. The berms' relief varied from 0.3 to 1.2 m with crest widths of 0.6 to 1.5 m, and totalled about 30 m³ in volume.

Scattered across a 0.5 by 1.5 km² area centered about the craters were over a dozen patches of fractured coral rubble. These patches, varying in size from 3-m diameter to 230 m², traced the inbound and outbound paths of the *Elpis* as her hull clipped and crushed higher-relief coral spurs. The weight of the vessel upon these spurs caused the coral to fracture deep below its surface. As a result, the surface rubble (about 10 to 20 cm) was loose and fairly easily dislodged by hand or jet probe. However, once exposed, the underlying coral could *also* be dislodged -- to an apparently limitless depth -- because of the dense cracks which permeated the substrate. By volume, the rubble measured about 15% at 18 cm, 30% at 13 cm, 20% at 9 cm, 25% at 5 cm, with the remaining 10% being sand. The total area of the rubble fields was estimated to be over 450 m².

Both sites, being at the seaward edge of the Florida Keys reef tract, were exposed to ocean waves. Annual average heights and periods were hindcast as about 1.0 m and 5.0 seconds. The largest waves, associated with tropical storms, were assumed to be depth-limited conditions, with nominal 2-m storm surge levels. Both sites featured daily tidal currents on the order of about 0.3 m/s. Hourly wind observations for an 8-year period were analyzed to discern those weeks for which the average hourly-sustained wind speeds were less than 5-, 10- and 15- knots. These data were later utilized to determine the statistically optimum window(s) during which on-site construction activities would be best undertaken. (In brief, the optimum window was found to be July 22 - August 18, with the most expansive window being June 17 - September 22.)

Conceptual Design Alternatives. A range of conceptual engineering alternatives was developed for the sites' structural restoration (Bodge and Creed, 1993). These were evaluated by the Sanctuary's Trustees (the National Oceanic and Atmospheric Administration (NOAA)) in terms of stability, construction feasibility, aesthetics, potential for biotic colonization, and probable cost (Sheehy, Bodge, and Finch, 1995).

The no-action alternative was ultimately not favored primarily because (1) there was little indication that the two sites' injuries were rapidly, naturally healing; (2) there was no indication that the shallower Maitland site's crater would cease its expansion; and (3) there was potential for additional injury by mechanical damage associated with the sites' mobile rubble. (That is, in storm conditions, rubble colonized by juvenile coral larvae would overturn and destroy the colonies and, perhaps, other established corals.) Other alternatives considered for the sites, but ultimately declined in favor of the preferred alternative (described below), included a continuous concrete cap, concrete-filled pillow mats, gabions, cable- and non-cable-stayed revetment mats, conventional boulder fills, and soil stabilization. Particularly at the shallower Maitland site, it was essential that the restoration structurally secure the crater's friable perimeter, and that the work physically fit into the shallow and irregular relief of the crater.

The selected alternative for the deeper *Elpis* site involved temporary relocation of the existing coralline boulders (i.e., those with existing biota), from the craters to the surrounding seabed. The coral rubble berms would then be mechanically relocated back into the craters from which the rubble was ejected. An armor layer of 1.2-m marine limerock boulders (totalling 400 tons) would be then placed atop the rubble. The voids were then to be partially filled with aragonite sand (approx: 60 m³). The temporarily relocated coralline boulders, originally salvaged from the crater, would be then replaced atop the imported boulders and sand fill. (See Figure 2.)

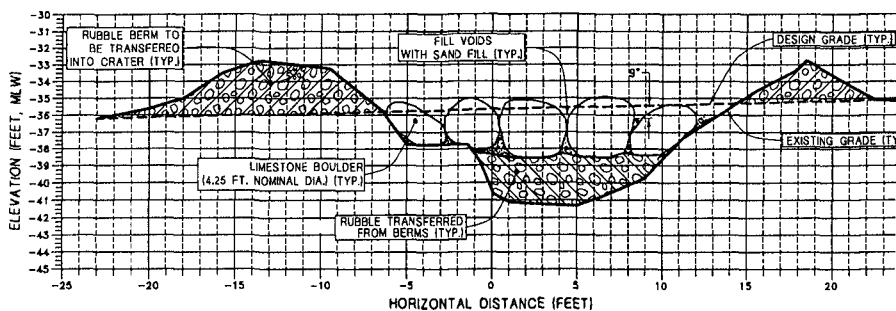


Figure 2: Typical section of Elpis site restoration.

The selected alternative for the shallow *Maitland* site (-2.5 m MLW) involved precision placement of 40 pre-cast "Reef Replicating Armor Units/Living Foundations" (RRAULF's) into the crater, and an underwater pour of specially-designed non-separable concrete (approx. 45 m³) intended to bind the fragile coral perimeter to the armor units and to fill the gaps between the units (Figure 3). The finished elevation of the work was designed to match that of the natural seabed (Figure 4). Steel bar, driven into the seabed, and limerock boulders were to be placed between the units and the crater's perimeter to help secure and dress the concrete, respectively (Figure 5). Limerock gravel and coral berms were to be used as termination forms for the concrete where necessary (Figure 6). As for the Elpis design, the overall stability of the work was designed for a 50-year storm event using stream function wave theory and considerations of drag, inertia, lift and frictional resistance. For stability, the minimum coefficient of friction between an independent armor unit and the seabed was computed as $\mu_f \geq 0.5$ (conservative $C_{Lift} = 0.73$) or $\mu_f \geq 0.38$ ($C_{Lift} = 0.4$).

Each of the 40 armor units featured a highly irregular surface of limerock boulders and exposed aggregate in order to emulate the ambient seabed (Figure 7). The units, each 8300 kg (dry weight), were formed in six different sizes to accommodate the irregular shape and depth of the crater. Steel reinforcement for each unit was designed as a perimeter box beam such that each could be cantilevered 50% in any direction -- in anticipation of the irregular seabed. A standard Portland cement mix was specified for the armor units.

Mix design and specifications for the underwater non-separable concrete were developed by Ben C. Gerwick, Inc. (BCG) of San Francisco, CA. The design mix is summarized in Table 1. Details of the mix design are available from the author, Bodge (1995), or BCG ((415) 398-8972).

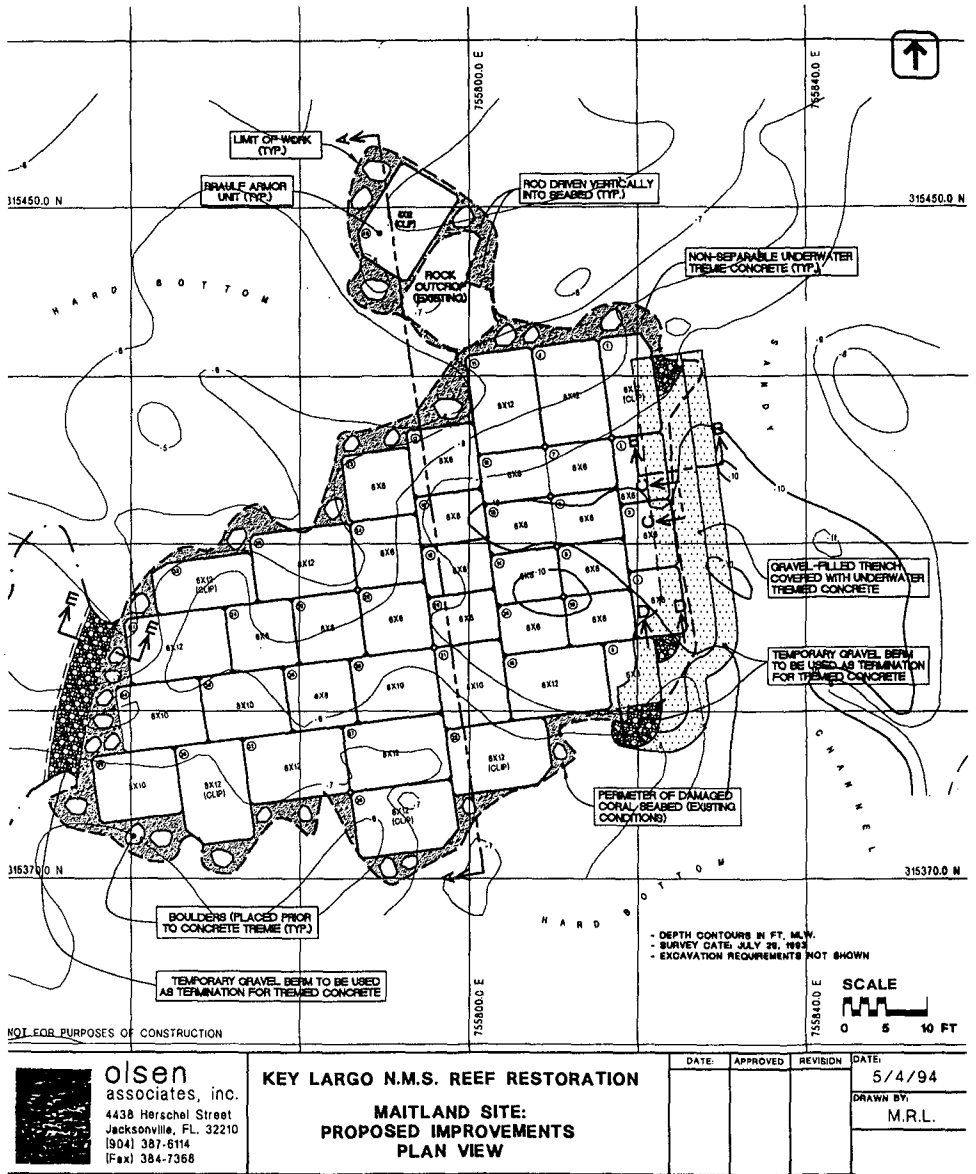


Figure 3: Plan view of Maitland site restoration.

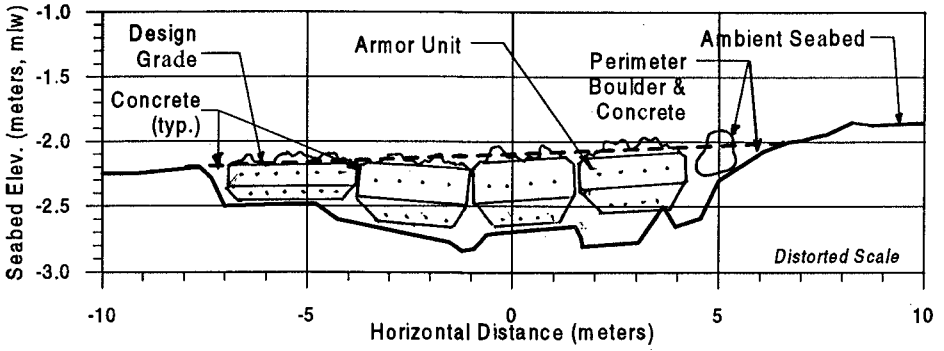


Figure 4: Maitland site restoration (typical section).

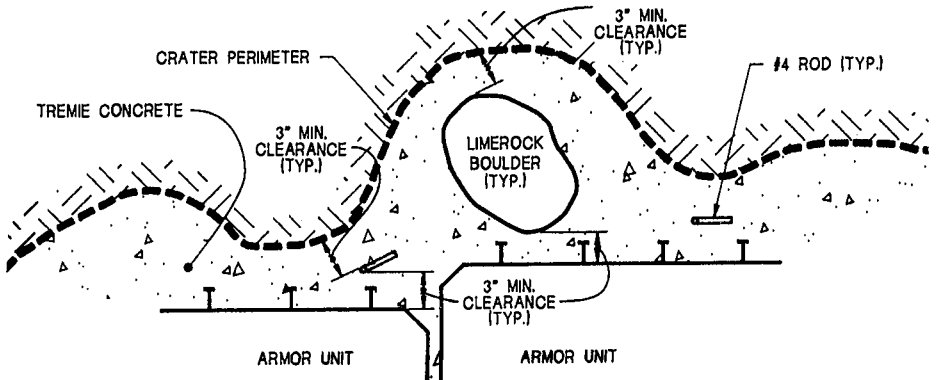


Figure 5: Boulder and re-bar placed between pre-fabricated armor units and crater perimeter.

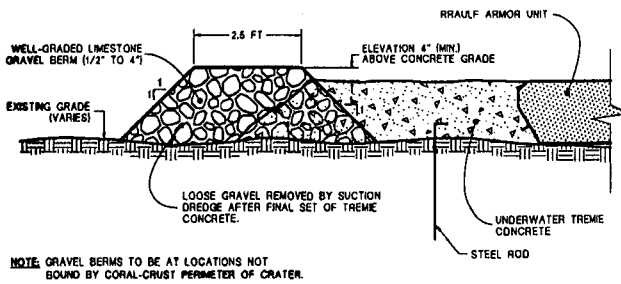


Figure 6: Limerock gravel and coral rubble used as a termination berm for the underwater concrete pour.

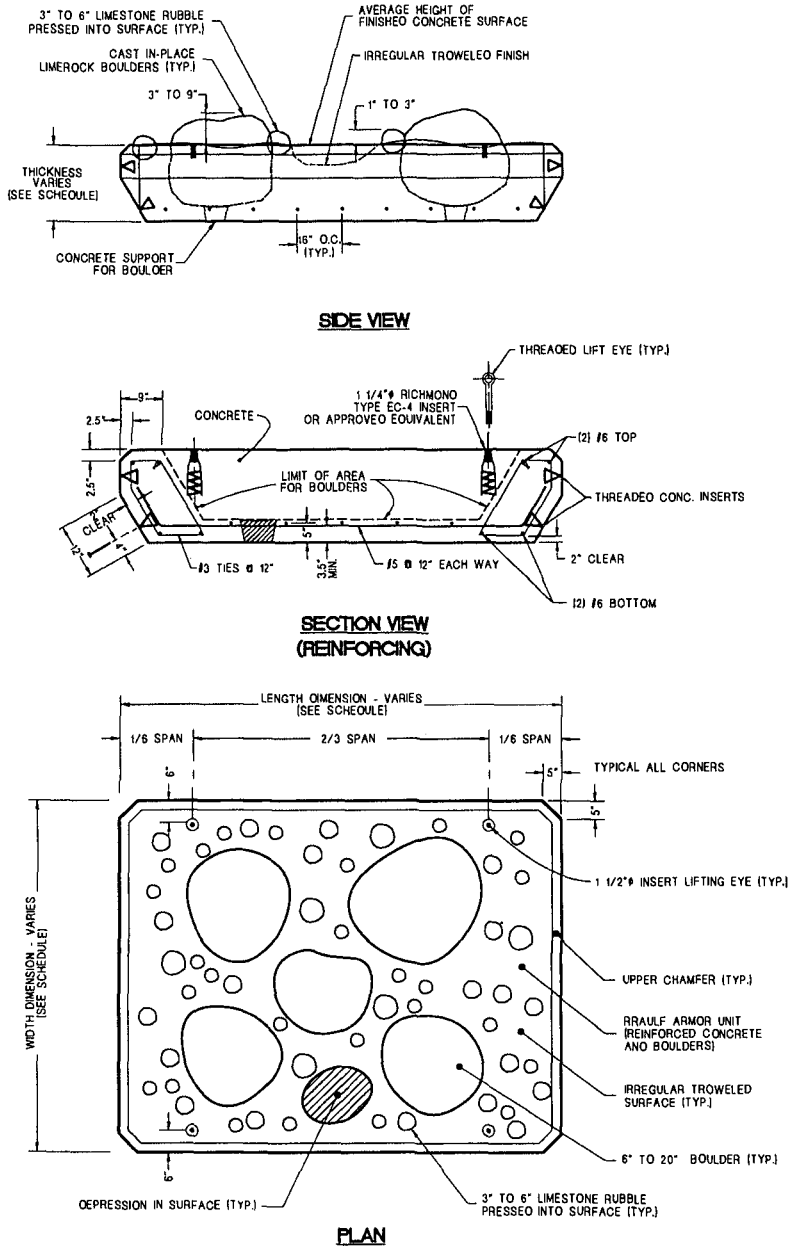


Figure 7: Pre-fabricated (RRAULF) armor unit design for the Maitland site, typical.

IMPLEMENTATION

Permits. Environmental permits for the work were issued by the U. S. Army Corps of Engineers, pursuant to Section 10 of the Rivers and Harbors Act, and Section 103 of the Marine Protection, Research and Sanctuaries Act of 1972. (The latter was required because it was proposed that surplus rubble removed from the sites would be disposed of at an existing ocean disposal site offshore of Miami.) The NOAA Sanctuaries and Reserves Division (SRD) likewise issued a permit for operation within the marine sanctuary. The State of Florida (DEP) was contacted, but did not issue a permit because the activity was outside of State waters (i.e., 4.8-km limit from shore).

Contracting. In mid 1994, NOAA entered into a cooperative agreement with the U. S. Army Corps of Engineers, Jacksonville District, by which the Corps would solicit and manage the construction contract for the work.

Final construction plans and specifications for the work were prepared by the author for the Corps by December, 1994. Procurement was based upon a "best overall value" approach, whereby potential contractors concurrently submitted separate Technical Proposals and Cost Proposals. The former included the Contractor's response, by prescribed form, to specific questions regarding their corporate and personnel experience (among other factors), and their narrative proposals describing their probable technical approach to the work. The offerors' responses were ranked according to prescribed evaluation criteria, previously prepared for the Corps by the author. Cost was to be used only as a "tie-breaker" among the most technically-qualified offerors (which, ultimately, was not necessary). Five proposals were received. The work was awarded to Team Land Development, Inc. of Pompano Beach, FL, in March, 1995.

Construction. Project construction was initiated in April, 1995. The Maitland site's 40 armor units were cast in the Contractor's south Florida yard over a 30-day period using about a dozen wooden forms. The limerock boulders and gravel were locally quarried. The carbonate sand for the Elpis site was oolitic aragonite, imported from the Bahamas and stockpiled in Fort Pierce, FL.

On site, the Contractor utilized conventional shallow draft barge (12 m by 43 m with 1.1-m draft at 150-ton nominal payload), and 27-m tug (1.4 m draft) as the primary work platform. A 10-m pusher tug (0.8 m draft) was used to maneuver the work barge over the shallow Maitland site. At nightfall, the 8- to 12-man work crew bivouaced ashore, at Key Largo, via small workboats.

Table 1: Nominal mix design for underwater, non-separable marine concrete.

Cement	600 lbs./cu.yd.
Fly Ash (class F)	90 lbs./cu.yd.
Silica Fume	43 lbs./cu.yd.
Coarse Aggregate (3/8")	1105 c.y. (40%)
Fine Aggregate	1685 c.y. (60%)
Water	250 lbs/cu.yd.
HRWRA (Sikament 300)	1.3 gals./cu.yd.
AWA (Sikamix 100 SC)	0.6 to 0.9 gals./cu.yd.
Water/Cement Ratio	0.4 ± 0.01
Slump	10" (spec); 9" - 11" (typ.)
Unit Weight (typ.)	142 lb/cu.ft.
% Washout Loss	<1.5%
Initial Setting Time	60 minutes (approx.)
4-day Strength (typ.)	5425 lbs/in ²
28-day Strength (typ.)	6110 lbs/in ²

Virtually all aspects of the work were primarily accomplished or directed by one or two surface-air-supply divers. These divers' communications were audible to the crane operator on the barge deck.

A 3-point mooring was used at the Elpis site, with 120-degree separation at 120-m distance, each, from the work site. Each mooring consisted of a 61-cm, 1.3-cm steel plate anchored to the seabed via four 3-cm, 1.2-m long threaded rods located at the corners of the plate. The rods were anchored to the seabed by pre-drilling deep holes into the coral seabed, placing the rods therein, and grouting with pre-mixed hydraulic cement carried to the seafloor in a 10-cm PVC tube. The plate was secured to the rods by a lockwasher and nut. A padeye was welded to the center of each mooring plate. To each padeye was attached a 3-cm shackle and a buoyant (9-cm polypropylene) mooring line for the barge. Each of the four threaded rods at the corner of each mooring plate was load-tested to vertical pull-out resistance in excess of 66.8 N (15 kip). The barge moorings for the Maitland site consisted of three 61-cm dia. by 1.3-cm wall steel pipes driven approximately 6-m into the seabed by vibro-hammer. Here, the barge was moved offsite at night, during particularly low tides, or in advance of approaching squalls.

At the Elpis site, the rubble berm material was transferred into the craters using both a crane-operated grapple and diver-operated water jet. The latter was more successful, by far, than the former. The limerock armor boulders were placed individually by grapple. The fill sand was placed by a crane-supported, diver-operated 3.5-m³ hopper. Tidal currents carried some of the sand as much as 150-m downcurrent, and resulted in the upcurrent crater being filled with sand to a notably lesser degree than the downcurrent crater (see **Figures 8 and 9**, respectively). As seen in **Figure 9**, local fishes were attracted to the work within hours of its completion.

Attempts were made at the Elpis site to remove unconsolidated coral rubble using both a 15-cm suction dredge with deck-mounted pump and a 10-cm water lift discharging into metal baskets lowered to the seabed. Neither technique proved satisfactory for the work because the rubble was scattered and productivity was very poor. Larger rubble (>8 cm) frequently jammed the intake. [Subsequent rubble removal activities undertaken with suction dredging and water lifts at other grounding sites -- where the rubble was more spatially concentrated and completely unconsolidated (i.e., where the vessel grounding had occurred within the previous year) demonstrated far greater success than at the Elpis site.]

At the Maitland site, the Contractor preferred to use gravel fill to level the crater's seabed (in preparation for the units' placement) rather than excavation. This choice was primarily dictated by the cumbersome difficulty in excavating the dense rubble/sand matrix of the crater's coralline seabed. Excavation around the crater's perimeter, however, was nonetheless necessary to ensure that the upper surface of the perimeter armor units (thickness < 36 cm) would not extend above the adjacent, ambient seabed grade. Coral rubble excavated from within the crater was used to construct a berm around the crater to serve as an additional termination form for the underwater concrete, and to help blend the units' perimeter with the ambient seabed.

After precision placement of the 40 armor units (placed with 5-cm maximum allowable gap between units, and tighter tolerances for vertical differential), and placement of the perimeter boulders and coral/gravel berms, the underwater concrete was placed using a swing-tube pump with 5-cm hose, PVC nozzle, and diver-operable ball-valve. The concrete was batched aboard the barge using a portable ("junior") mixer.

Figure 8:

Photograph of upcurrent Elpis site crater immediately after restoration. Voids between the boulders provided extensive fish habitat and vertical facing for coral larvae recruitment, but resulted in an aesthetic that contrasted with the ambient seabed.

**Figure 9:**

Photograph of downcurrent Elpis site crater immediately after restoration. Voids between the boulders were more effectively filled with carbonate sand, resulting in an excellent aesthetic match with the ambient seabed.



Figure 10 (next page) is a photograph of the *M/V Maitland* hull aground upon the reef in 1989. **Figure 11** depicts one of the pre-cast armor units being lowered from the barge deck to the Maitland site seabed. **Figures 12 and 13** are typical photographs of the Maitland site restoration, taken about a week after the work was completed.

Site work was conducted between June 19 and July 12 at the Elpis site, and between July 13 and September 1, 1995, at the Maitland site. For about half of this time, however, no site work was undertaken because of relentlessly bad seas. In all, the 1995 season was the second worst on record in terms of Atlantic tropical storm activity. At one point in August, there were five tropical storms simultaneously lined-up across the Atlantic, moving toward the Florida peninsula.

Construction Review. Real-time construction review was conducted and coordinated by the Corps, with direct participation of NOAA/SRD personnel and the Design Engineer (Olsen Associates, Inc.). The unique and complex relationship between the project's many parties was facilitated, from the outset, by a 2-day *partnering* conference organized by the Corps prior to construction.

Figure 10:

Photograph of Maitland aground on the reef, 1989. The ship screw is seen resting amidst the coral rubble caused by the grounding.

**Figure 11:**

Photograph of one of the 40 pre-cast reef-replicating armor units being lowered to the seabed. The lifting eyes were unscrewed from the units' threaded inserts after installation.

**Figure 12:**

Photograph of the top surface of the Maitland site repair, taken several days after project completion. The ambient seabed is in the far background. A grouted joint between adjacent armor units is discernible below the fish, in the foreground.



Between site visits, the Engineer (author) was kept abreast of the work by viewing underwater images that had been video-taped by his on-site representative (Mr. Mark Schroeder, Continental Shelf Associates, Inc.). Selected videotape images were captured as a single frame by Mr. Schroeder, then transmitted from his boat via laptop computer, cellular phone, and E-mail to the author's Jacksonville office -- usually within 20- to 30-minutes of the original photography. On

several occasions, the Engineer's access to virtually real-time construction photos permitted timely, cost-saving corrections to the work; or, alerted the Engineer to situations that required an immediate trip to the site and/or instructions to the site-representative.

Environmental Monitoring. Turbidity was monitored using concepts of "exposure" by which "cumulative NTU-hours" were measured and tabulated. There was no observed environmental degradation resulting from the work -- despite the fact that the work was conducted in the midst of sensitive coral resources. Fishes, soft and hard corals have begun re-colonizing the sites (Harold Hudson, NOAA/SRD - personal communication).

Project Cost and Completion. The project's construction cost (bid) was U.S. \$1,047,000, with subsequent change orders resulting in a net additional cost of \$19,600. The total construction cost was about 10% less than the Engineer's estimate. Overall, the project was completed on-time, within budget, in accordance with the design intent, and with no apparent net adverse impact to the environment.



Figure 13:

Photograph of exposed side-face of Maitland restoration, where the repair was terminated adjacent to an existing sandy channel. The restoration is on the left, the ambient seabed is on the right.

CONCLUSION

To the author's knowledge, this experimental project represents the first large-scale, in-situ structural restoration of a coral reef damaged by mechanical impact. Innovative methods introduced, or resurrected, during this project included

- development of structurally sound seabed restoration with emphasis on aesthetic blending with the ambient environment;
- further application of new non-separable underwater marine concretes,

- contract award by the Corps using "best-overall-value" procurement,
- unique cooperation between multiple federal agencies and the private sector, and
- semi-real-time construction review using underwater-taped video images via the Internet among other items. The unfortunate, increasing frequency with which vessels ground upon coral resources -- and other environmentally sensitive seabed resources -- suggest that the lessons learned as part of this project will be of increasing utility to future restoration projects.

ACKNOWLEDGEMENT

The engineering assessment, design, and construction review work described herein were conducted in principal part by Olsen Associates, Inc. under subcontract to Industrial Economics Inc. (IEc), Cambridge, Massachusetts, as authorized by the U. S. Dept. of Commerce, National Oceanic and Atmospheric Administration (NOAA), Contract No. 52-DGNC-1-00007, under Task Order Nos. 50062 and 50089. The leadership of Dr. Dan Sheehy, of IEc, in this project is specifically noted. Initial site survey work was coordinated by Mr. Keith Spring of Continental Shelf Associates, Inc. (CSA), of Jupiter, Florida. The Engineer's on-site technical representative was Mr. Mark Schroeder, also of CSA. Hydrographic survey work was conducted by ARC Surveying & Mapping, Inc., of Jacksonville, FL. Mr. Chris Creed, of Olsen Associates, Inc., greatly assisted in the site survey, data analysis and preparation of the engineering assessment. The innovative internal structural design and specifications for the Maitland site armor units was principally created by Mr. Steve Klecka of SK Engineering, Inc., Jacksonville, FL. The highly successful concrete mix design and specifications were provided by Dr. Dale Berner of Ben C. Gerwick, Inc. (BCG), of San Francisco, California; and then field-reviewed by Mr. Patrick Durnal of BCG. Construction management was executed by the U. S. Army Corps of Engineers, Jacksonville District. Construction review for environmental protection was directed by Messrs. Harold Hudson, Bill Goodwin, and John Halas of the NOAA Sanctuaries and Reserves Division, Key Largo. The construction contractor was Team Land Development, Inc., Pompano Beach, Florida; Mr. Ron Coddington, President. For the contractor, Mr. Charles Calloway was the lead engineer. On behalf of the project's sponsor, NOAA, Mr. Tim Osborn (National Marine Fisheries/Restoration Center), Dr. Charles Wahle (Sanctuaries and Reserves Division), Ms. Darlene Finch (Damage Assessment Center), and Lt. John Tokar (contracting officer) each managed principal aspects of the project, each with great patience and faith.

REFERENCES

- Bodge, K. R., 1995. "Engineering Summary Report: Structural Restoration of the *M/V Alec Owen Maitland* and *M/V Elpis* Vessel Grounding Sites", Prepared for U. S. Dept. of Commerce, National Oceanic and Atmospheric Administration, Silver Spring, MD; by Olsen Associates, Inc., 4439 Herschel St., Jacksonville, FL 32210; December 10, 1995.
- Bodge, K. R. and Creed, C. G., 1994. "Conceptual Engineering Alternatives for Structural Restoration of the Matiland and Elpis Grounding Sites", Prepared for U. S. Dept. of Commerce, National Oceanic and Atmospheric Administration, Silver Spring, MD; by Olsen Associates, Inc., 4439 Herschel St., Jacksonville, FL 32210; 112 pp; Oct. 15, 1993.
- Sheehy, D. J., Bodge, K. R., and Finch, D., 1995. "Coral Reef Restoration Planning: A Decision Analysis Approach", Proc., 1995 Int'l Conf. of the Society for Ecological Restoration, Seattle, WA.

CHAPTER 331

Dredging and Disposal within the Limits of a National Park

H. A. Manzenrieder and J. M. de Vries¹

Abstract

In coastal areas under tidal influence, recurrent dredging is an important part of the maintenance work to secure the nautical situation and the functionality of the harbors. In the past, the orientation of dredging activities was purely economic but since the early 80's, environmental concerns have rapidly increased and these concerns often define the limiting or determining factors that cover all parts of such operations in the marine region. At present, the sometimes quite different interests of engineering and ecological groups are becoming more gentle. Besides the natural learning effect from the changes in general, economic conditions are also an important factor.

This situation especially applies when maintenance dredging takes place within the limits of a national park where environmental concerns have the highest priority.

The scope of the engineering investigations was the estimation of the environmental capacity as a function of hydrology, sedimentation and biology leading to a specific management for dredging and disposal areas.

Introduction

Public awareness concerning the environment was highlighted at the United Nations Conference on the Environment in 1970. This triggered the development of legislation concerning the control of all kinds of waste. In Europe, a need for legal action ensued from the following international agreements, some of which were ratified by Germany:

- Oslo Convention of Feb. 15, 1972, with a supplement of June 12, 1991
- Helsinki Convention of April 9, 1972, with a supplement of June 6, 1992
- London Dumping Convention of Dec. 29, 1972
- Paris Convention of June 4, 1974

¹ Consulting Engineering Office Dr. Manzenrieder and Partner, Brookweg 29, 26127 Oldenburg, Germany

The guidelines for the disposal of dredged sediments are designed to assist contracting parties in the management of dredged sediments in a way that will prevent pollution of the marine environment. The relative importance of the dumping of dredged material within the containment arriving in the North Sea is estimated at approx. 1,600,000 t/y for nitrogen and approx. 10,000 t/y for lead (Neville-Jones 1994).

The guidelines and restrictions apply to the removal as well as the disposal of dredged sediments. A special question is hydraulic injection dredging and transport by the local current capacity.

When making an assessment in general, it will be necessary to consider the central factors as legal requirements, technical aspects, economic considerations, environmental aspects and more complicated subjective local knowledge and emotional aspects or estimations.

In fact, a very important stimulus for this investigation came from the observations of people who have been personally involved in local activities for a long time (even generations), e.g. the tourist guide.

In practice, environmental requirements are reflected in the individual permits which are only valid for a limited time (2-3 years). In Germany, such official permits actually specify the amount of dredging material (sand, mud), the dredging and dumping areas and the duration of dredging and disposal related to the season in the year (preference: winter) and the phase during the astronomic tidal cycle.

The need for investigation which is laid down by the valid guidelines is determined by the pollution load of the dredged material. Guide values r (mg/kg) are respectively defined for the individual heavy metals.

The guide value r results from concentration c related to the 20 μm fraction multiplied with an uncertainty factor α ($r = c \cdot \alpha$), at present $\alpha = 1.5$.

Within the maximum period of three years, the need for investigation is classified by three ranges of values ($c \leq r$, $r < c \leq 5 \cdot r$, $c > 5 \cdot r$).

In addition, permits can also define the need for and determine the scope of investigations on environmental effects as in this case.

Dredging in the National Park

The islands along the southern part of the German North Sea coast, which are predominately oriented to tourism, are located within the eco-system of the National Park's tidal mud flats and have been an important part of this young park, deserving special protection, since 1985.

Based on a mathematical model that gives a rough description of the current field (Dick 1992), the transport system under tidal effects is predominantly from West to East:

The protection status is to safeguard natural development and covers all activities in an area of approx. 2,400 km^2 with some exceptions within the framework of

coastal protection (dikes) and maintenance activities (dredging). In 1993, the National Park became part of the UNESCO-Program "Man and Biosphere" (MAB). This status was the reason for some interesting economical and engineering requirements e.g. when an expensive tunnel was build for a standard pipeline with a diameter of approx. 1 m (Europipe-Project) or the work to raise a dike was suspended during the operation.

Within this protectorate, the navigable channels to the harbors along the coast and the islands lie mainly in areas with continuous sedimentation, the transport processes of which are defined by a regular average tidal range of approx. 2.6 m, superimposed by random storm surges. The consequence of these conditions is the substantial necessity for quasi permanent dredging activities inside the National Park and subsequent dumping. Alternatives, such as disposal outside the protected area or use of the material for beach nourishment in the vicinity are discussed and carried out in part.

Within the National Park, annual dredging quantities of between 300,000 and 500,000 m³ arise from the maintenance of navigation channels. Small suction hopper dredges with a cargo hold capacity of 150 t (mud) to 300 t (sand) are used for dredging and disposal, the limiting factor of which is the allowable draught with a maximum of 3 m determined by the shallow depth of the flat tidal area. As a rule, disposal is carried out gradually over the whole disposal area to achieve an even as possible distribution at the bottom and in the space of the water.

In connection with intensive monitoring of all dredging activities within the National Park, the measures are based on complete modernization of the position finding system based on the highest GPS technics in combination with the continuous recording of basic data to objectively document dredging activity.

With these measures, the efficiency of maintenance dredging is to be increased on the one hand and on the other, complete evidence on the executed dredging and disposal processes are to be ensured.

Effects of Dredging and Disposal

Due to the fact that the main problems concentrate more and more on the disposal of dredged material, the following description will focus on this question. Dependent on material and area specific parameters, the introduction of dredged material into the water space may, as a result, have a variety of effects on the ecological boundary conditions (changes in the environment). This especially applies to the tidal mudflats.

In keeping with the knowledge we have today, an underlying, lasting and negative effect cannot be assumed a priori.

Area specific parameters such as e.g. current conditions, bottom material or sea conditions, are important boundary conditions for the transport and the dispersion behavior of the solid matter introduced into the natural tidal mud flat area by disposal.

The content of suspended solid matter is influenced by a number of parameters:

- Tide (current velocity, water level, turbulence, salinity)
- Meteorology (sea conditions, temperature,) and Climate (duration of ice covering)
- Topography (surrounding tidal mud flats, bottom material, artificial buildings)

In addition, there are chemical parameters such as e.g. oxygen or nutrient content which influence solid matter content, sedimentation behavior and turbidity conditions.

An urgent, independent problem is defining and selecting suitable parameters and characteristic quantities for describing or supplying evidence on the effects against a background of high, natural variance in tidal waters.

In the following, possible effects from the introduction of dredged material into the space of water and therefore the questions associated with it are presented for assessment:

- Local increase of solid matter content
 - Is there a correlation between solid matter content and turbidity?
 - Does a sandblasting effect occur at the bottom in the case of sandy material?
 - Can a natural turbidity or solid matter background be defined?
 - Are changes in light conditions to be evaluated vertically?
 - Is the influence on photosynthesis quantifiable?
 - Will the migration behavior of fish be influenced?
 - Will this reduce the recognition of danger (e.g. fishing nets)?
 - Are there accumulation effects?
- Reduction of oxygen content by introducing oxygen-depleting matter
 - Which material is considered oxygen-depleting?
 - Which depletion potential leads to a reduction in oxygen content?
 - How does the same depletion potential act under dynamic variability?

According to ESSINK (1993), the disposal of dredged material can, among other things, have the following ecological effects:

- Change of the nutrient balance

Example: Phosphate redissolution can have the effect of increasing the growth of phytoplankton (Sea grass can be negatively influenced when algae cover the surface).
- Inhibition of growth

Example: An inhibition of the growth of phytoplankton can occur through increased turbidity resulting in a reduced supply of food for zooplankton and

filtering bottom organisms. Turbidity interferes with the search for food of visual predators (flat fish, ocean swallows)

- Inhibition of respiration

Example: Increased content of suspended solids inhibit gill respiration of fish and invertebrates as well as food intake for zooplankton and filtering organisms (small crabs, mussels)

- Overtaxed adjustment

Increased sedimentation rates have the effect of smothering bottom animals. Sedentary Benthos species have less chance of survival as opposed to mobile species. Fundamental changes in the composition of sediment can increase the damaging effect on bottom fauna.

The processes that take place in the water space and at the bottom are interdependent and have superpositioning effects. Colonization at the bottom can, for example, lead to increased erosion resistance and therefore influence the suspension content (Manzenrieder 1983).

Relevant Publications

In the past years, several papers have been published on the problem of environmental effects caused by dredging and disposal of sedimentary material and International Conferences in particular have provided an opportunity for exchanging ideas and establishing relationships on a wide range, e.g.. DREDGING '94 by the ASCE in Orlando.

Some of the projects include the results of field studies and corresponding theoretical models. In Table 1, a partial list gives short information on selected studies based on the results of field programs covering typical engineering tools (sounding, sampling, sensor measurements, etc.) and an indication of extended results from natural science (Chemistry, Biology). The depth given indicates the depth at the dumping area.

The targets, size and executing institutions and - last not least - financial frame for such programs vary. In general, it can be stated first of all that every dredging and disposal area has its own behavior so that a direct transfer of results is not likely. Experience in engineering practice has often indicated that the respective research must be delegated to basic research and research with a direct reference, the latter of which often has narrow limitations on time and budget. Nevertheless, this is often the appropriate solution.

To answer basic questions concerning mud flats, a very large research program named "Ecosystem-Research" has been underway in Germany since 1989, the main phase expected to end in 1996. Beyond general statements, the results presented could not support the concrete questions formulated in the permits for maintenance dredging.

Table 1: Selected publications on dredging effects with field studies

Literature	Year	Country	Location	Chemistry	Biology
Hübner, H.-J. et al.	1996	Germany	Mudflats	yes	yes
Pejrup, M.	1995	Denmark	Mudflats	no	no
Netzband A. et al.	1995	Germany	Elb River	yes	yes
Borst, W.G. et al.	1994	Netherlands	Haringsvliet	yes	yes
Halka, J. et al.	1994	USA	Chesapeake Bay	no	no
Wiley, M. et al.	1994	USA	Connecticut	no	no
Marsh, J.	1994	U.K.	Cornwall	yes	yes
Stuber, L.M. et al.	1994	USA	Savannah Harbor	yes	yes
Tubman, M. et al.	1994	USA	San Francisco	no	no
Courtney, C.A. et al.	1994	USA	San Francisco	no	no
v. Oostrum, R. et al.	1994	Netherlands		yes	no
Bundesanstalt (BfG)	1993	Germany	Ems River	yes	no
Essink, K. et al.	1993	Netherlands	Ems, Mudflats	no	yes
Thevenot, M. et al.	1992	USA	Tylers Beach	no	no
Paul, J.H. (BfG)	1992	Germany	Weser River	no	no
Dammschneider	1992	Germany	Elb River	yes	no
Gallenne, B.	1989	France	Loire River	yes	yes
Vale, C. et al.	1989	Portugal	Tagus River	yes	yes
Bossinade, J.H. et al.	1988	Netherlands	Eemshaven	no	no
Truitt, C.L.	1986		Duwamish WW	no	no
van der Veer, et al.	1985	Netherlands	Mudflats	no	yes
Tavolaro, J.	1982	USA	New York Bight	no	no
Malherbe, B.	1980	Belgium		no	no
Bokuniewicz, H.J. et al.	1978	USA	Lake Erie/Ontario	no	no
			New York Bay		
			New York Bay		
			Saybrook		
			Elliott Bay		
Sustar, J.; Wakeman, T.	1977		Carquinez	no	no
McCauley, J.E. et al.	1976	USA	Coos Bay	yes	yes
Gordon, R.B.	1974	USA	Long Island	no	no
May, E.B.	1973	USA	Mobile Bay	yes	yes

The various public interests in the results of such (expensive) investigations which include social and political components are often much greater than the knowledge that has been established on the processes. The contrary explanations for the appearance of large areas with a oxygen deficit in the upper mud flat surface, so called "black spots" after a strong winter, was the last remarkable example.

Procedure

The main target of our investigation was and is compliance with the requirements that are a part of the permit, currently valid for a period of 3 years. To achieve this, an investigation program was started in 1994 which is still being executed, the areas of operation being:

- sediments in the subtidal and intertidal flats
- water column
- macrozoobenthos

For a pilot project, disposal sites are selected, which differ in respect to their location within the hydrological units, the quantity of material being disposed as well as the type of disposed material.

In compliance with the concrete time and economic terms of reference and under the responsible coordination of engineering sciences, a pilot study was developed for the interdisciplinary questions, the structure with long-term measurements and detailed surveys was selected as follows:

- Meteorological and hydrological surveys
- Static and dynamic sedimentological surveys
- Biological surveys

To describe biological processes, macrozoobenthos were selected as an indicator group.

Long-term measurements gradually broaden our knowledge and are therefore a part of extended basic research. In view of the investigations listed for the disposal site area, these are primarily oriented to stabilizing the respective causal analysis:

- Analysis of the dredged material (grain distribution, pollutants)
- High resolution topographical surveys using state-of-the-art techniques
- A rough sedimentological and biological survey of the disposal sites
- Taking samples from monitoring stations in the subtidal and intertidal flats
- Sedimentological characterization of surface samples from the mudflats
- Assessment of macrobenthic fauna on the mudflats

The detailed investigations include a great number of individual measurements and are continuously coordinated to developments. Previous investigations have concentrated on the natural variation of turbidity and the change and extension during disposals as well as the changes in oxygen content during disposals.

Previous Results

Part 1: Dredged Material

All objective reflections on the effects of disposal arise from the potential load potential and therefore from the properties of the dredged material with following results:

- The results of laboratory measurements confirm pronounced material-dependent differences.
- As opposed to fine sand, silt (coastal marsh sediments) shows continuously higher depletion rates.
- Silt samples show an up to 45 times higher average depletion activity related to mass than fine sands.
- Depletion curves of the silt samples show a high initial depletion at the beginning which can exceed mean oxygen depletion by 10 times.
- Quantitative results of stabilized laboratory results cannot be directly confirmed by the natural measurements during disposal.
- In individual measurements during the disposal of coastal marsh sediments and sand, no changes in oxygen content beyond the fluctuation margin of measured values before disposal were determined in the space of water over a period of approx. one hour after disposal.
- Heavy metal concentrations determined in the grain size fraction $d < 20 \mu\text{m}$ all range below the defined limiting values in the guidelines used (Figure 1).
- On the basis of this assessment, the examined dredged material can be rated as non-polluted.
- At present, there is no uniform assessment concept for the evaluation of heavy metal content and organic pollutants in dredged material.
- In regard to the area-specific loads from sediments, there is a need for uniform recording of data as a basis for documentation and the evaluation of trends while isolating anthropogenic intervention

Part 2: Disposal Sites

Previously determined results of the engineering and natural science work fields will be presented in abbreviated form.

- Sediment composition and seasonal changes are different at every disposal site.
- Fine and medium grain sands dominate in the sublittoral, the highest variation being shown by the fine grain size fractions.

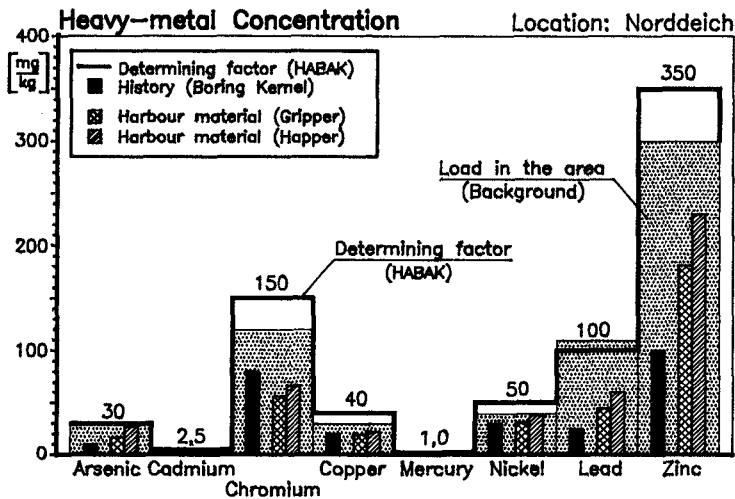


Figure 1. Heavy Metal Concentration and Determining Factors

- With mostly constant main sediment types, changes also occurred on the examined mudflat surfaces during the low-energy summer months in the fine grain areas.
- A sorting of grain size takes place within the immediate disposal site.
- The fine sediment part rises to the edges of a hydraulic/morphological unit (tidal mudflat watershed).

Part 3: Turbidity and Suspension

In order to determine the value range and variation of the natural suspended matter content in connection with current behavior, selective measurements were made over one tide respectively. These results form the basis for an evaluation of concentrated measuring results that were made during the disposal of sand and coastal marsh sediment. The results are characterized as follows:

- The suspension content measured fluctuated during a natural tide cycle (without disposal) in a wide range between 120 mg/l and 660 mg/l. The result over the whole tide was a mean suspension content of $c=225$ mg/l with the maximum values near the bottom.
- Drogues and continuous current measurements in the area of the examined disposal site support a current potential with the highest velocities close to the surface of up to 1.5 m/s at ebb current which, as a whole, dominates over the flood current.
- The measurements made immediately before disposal at lower current velocities comprised recorded values of 2.5 to 30 TE/F (turbidity unit related to Formazin) with respective suspension samples with solid matter contents of 50 to 200 mg/l.

- During disposals, stationary and dynamic measurements were made at a mean water depth of 15 m and in depth steps of 5 m and 10 m in the disposal site and adjacent lee area to survey the spreading cloud of turbidity.
- In Figure 2 a passage of the turbidity cloud during a disposal of sand (d_{50} ca. 0,15 mm) giving a current velocity and water level above the probe is presented. Distance to the input point was approx. 200 m. It was observed that the disposal "trail" clearly stands out against the background values of turbidity. Just a few minutes after input, turbidity values at the selected measuring position rise to approx. 100 TE/F. The mean basic turbidity of approx. 15 TE/F is significantly exceeded over a period of approx. 11 minutes with up to 150 TE/F. After that, the level returns to the level before disposal. At a mean current velocity of 40 cm/s, an extension in the length of the turbidity cloud to approx. 270 m results which corresponds to doubling.
- After the disposal of coastal marsh sediment, the maximum level in the turbidity cloud over a range of 3,000 m was reduced to a third of the measured maximum value.
- The oxygen content within the detected turbidity cloud consistently ranged within the measured natural fluctuation margin.

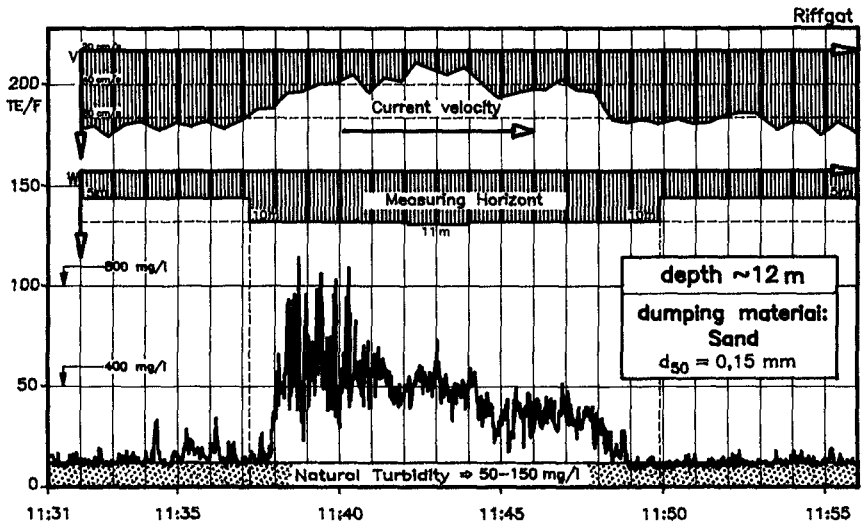


Figure 2. Turbidity Cloud during Dumping passing in the central Lee Side

The newest version of a modern self-sufficient instrument, a so called sand-surface-meter (Manzenrieder 1995) was placed during the disposal of sand and mud direct under the hopper dredger. The real-time history of the stationary measurements is concentrated on Figure 3.

During the observation the disposal of sand is predominant indicated by a stepwise change in the bottom position. The dominant effect of mud disposal is the transient

formation of a cloud with very low particle movement. The stability of the mud clouds was detected between 2 and 6 hours during the measurements.

In-situ measurement during disposal (20.-22.06.1995)

(Below hopper dredger, depth at disposal site: -8 m below chart datum)

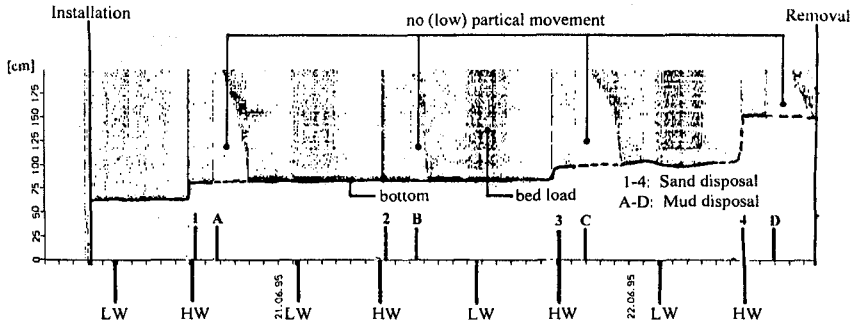


Figure 3. Direct Measurements under a Hopper Dredger during Disposal

Part 4: Benthos Investigations

In the subtidal flats, quantitative samples were taken using van Veen grab sampler supplemented by trawl net catches from a research dredge which were to give a qualitative overview of the epibenthic animal species.

In the intertidal flats, surface samples up to 30 cm in depth were taken respectively. A presentation of the complicated types of analysis and the different extensive groups of results will not be dealt with in this paper.

Assessment (Example)

Since the natural measurements carried out and the model approaches that are available do not form a stable basis for a closed solid matter balance, continuous current and suspension measurements were carried out for a rough model of solid matter loads.

For a defined cross-section in the middle of the disposal site, corresponding suspension loads of 5,800 to 7,700 t per tide phase result for suspension contents of 150 to 200 mg/l. Independent analyses on local bed loads carried by currents show that with an order of magnitude of approx. 10 % of the suspension load, this is a clearly smaller part of the total solid matter load. In Figure 4 the increase of the above presented (natural) suspension transport caused by the input of two dredged material disposals with a quantity of 300 t each is presented for the cross-section of the disposal site. In this case, the first disposal is assumed at approx. 2 hours after the turn of the tide and the second disposal 2 hours before. Under the assumptions made here, both disposals lead to an increase in the quantity of solid matter

transported in suspension during the course of a tide of approx. 10%. This value lies within the documented natural fluctuation margin for the location.

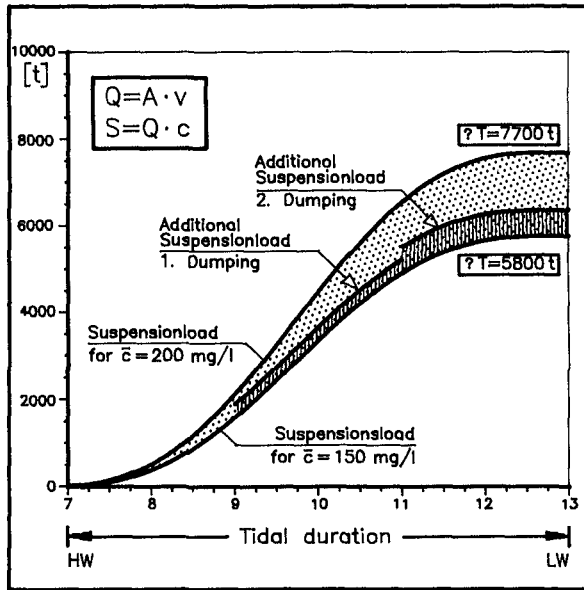


Figure 4. Increase of the natural suspension transport due to 2 disposals (example)

The conditions presented are based as an estimate on assumptions stabilized by measured data and describe the order of magnitude of the solid matter transported. Greater knowledge about natural variation as a result of seasonal fluctuations or meteorological influences as well as secured data concerning the transport of sediment and suspended solids and their distribution for individual tide phases separately are needed for a secured, quantitative assessment of the effect of dredged material disposal. For this, a corresponding picture of current and transport must be described for the area.

Disposal Site Management

Because of the great number of influencing factors that are to be taken into consideration when managing dredged material, especially in shallow water areas, individual disposal site management is to be connected with corresponding ecological requirements. Here, the qualitative and quantitative assessment of specific boundary conditions provides an opportunity to combine the relevant economic and ecological interests into solutions capable of reaching a consensus. Sufficient knowledge on the load potential in connection with the tolerance potential forms the basis for such disposal site management.

The load potential (stress factors) comprises all effective area and material specific effects concentrated in disposal.

The tolerance potential (ecological elasticity) describes the available reaction options of the water ecology and especially the bottom of the body of water under natural and/or anthropogenic loads.

A sensitivity classification as a basis for making decisions which defines limit criteria by stabilized guide parameters and therefore contains e.g. statements on allowable sedimentation dynamics (height, duration) should be the goal for selecting main areas for disposal or disposal sites.

When defining possible disposal sites, the question of whether selective or gradual disposal presents the more economical and ecological solution in the course of a year and for different energy input must be answered.

All of the known or the yet to be determined area and material specific parameters supply a contribution to the effect processes which define the eco-system.

Tolerance potential >> Load potential → Mostly uninfluenced environment

No prolonged change or damage to water ecology and little utilization of loading capacity

Tolerance potential > Load potential → Stable environment

No long-term change or damage to water ecology to be expected for high utilization of loading capacity

Tolerance potential = Load potential → Unstable environment

Unstable limit state of water ecology is reached by full utilization of loading capacity

Tolerance potential < Load potential → Destabilized environment

Prolonged changes or damage to water ecology occur when loading capacity is exceeded

Tolerance potential << Load potential → Changed environment

Comprehensive changes or damage to water ecology by clearly exceeding loading capacity

In the following, an evaluation matrix for the individual monitoring stations has been compiled for a disposal site within the National Park (example).

Based on a measuring program carried out over a period of several years in the area of the disposal site, short-termed, local changes could be quantitatively determined.

Long-term changes or damage to the environment which can be directly attributed to the disposals could not be documented in the dynamic ocean area so far.

A valid assessment of the project dream - "stable environment" - was undertaken according to the presented assessment scheme for the evaluation of intervention in the eco-system which forms the basis for the pending decision of the responsible permit authorities.

Parameter	Retake stations in/around the disposal area in relation to LW												
	above (mudflats)											below	
Bottom Sediments	-	-	/	-	-	/	/	-	/	/	+	/	n
Sedimentary Material	n	n	-	-	-	-	-	+	+	n	-	n	n
Oxygen Content	n	n	/	/	/	/	/	+	/	n	+	n	n
Topography	n	n	+	-	/	-	-	-	-	+	+	n	n
Benthos fauna	n	n	+	-	/	/	n	-	-	/	-	/	n
Turbidity	n	n	n	n	n	n	n	n	n	n	n	+	+
Suspension	n	n	n	n	n	n	n	n	n	n	n	+	+

Values in relation to the natural variation: +:above,/ :boundary,-:below,n:not determined

When objectively viewing the (required) state of knowledge on the manifold influencing factors (cluster), it can be determined that there are considerable deficits. Therefore, qualitative natural observations and quantitative natural measurements will still supply the central contributions.

Conclusion

The quantity of the actual dredged material in the National Park is relatively small in relation to the average annual amount in Germany of 35 million m³. By complying with the defined requirements, the unit price for dredging in the National Park - up to US \$ 13 - has nearly doubled in the past few years. When compared internationally, for example with the United States which has an annual average of 230 million m³, the relation of costs for 1995 is approx. 10:1 (Hales 1995).

The type and nature of the sediment is often different from that in the harbors (mud) and the connecting navigable channel (sand). This is important for dredging and the area influenced by disposal. The strategy and collected results were used as input for characterizing the environmental behavior of each region as a part of a morphological and hydrological unit. To do this, the natural background needed to be described in its seasonal variation, also with regard to the effect of single, extremely energetic storm periods. The assessment will resume on the central question concerning the following relation between the natural tolerance potential and the additional artificial load potential due to dredging and disposal with the simple effects for the concerned environment:

Tolerance potential > Load potential = Stable environment

Tolerance potential ~ Load potential = Unstable environment

Tolerance potential < Load potential = Destabilized environment

Experience from such investigations with an ecological orientation show that not only the formulated requirements and limit values but also the relevant investigations are to be objectively adjusted to the respective questions. In this connection, the results from natural measurements are of central importance with increasing duration of observation.

In this process, the engineering sciences with their optimizing work methodology must actively shape these projects in a major way, also searching for overlapping areas in other sciences as they proceed.

References

- NN (1992). Guiding Rules for the handling of dredged material following the Oslo and Helsinki-Commission (in German), German Authority for Waterways
- NN (1996). Dredging and disposal in the coastal zone, influence on the macrozoobenthos (in German), Mitteilungen der Bundesanstalt für Gewässerkunde (BfG), Heft 11
- ESSINK, K. (1993). Ecological effects of dredging and disposal in the Ems-Dollard estuary and mudflats (in Dutch), Dienst Getijdenwateren, Rijksinstituut voor Kust en Zee Haren
- Hales, L. (1995). Accomplishments of the Corps of Engineers dredging research program, Journal of Coastal Research, No. 11, pp. 68-88
- HÜBNER, H.-J., DE VRIES, J.M., GROTHJAHN, M. (1996). Presentation and first results of a pilot study on the effects of disposal in the coastal zone (in German), Mitteilungen der Bundesanstalt für Gewässerkunde (BfG), Heft 11, pp. 30-44
- Lozan, L.J., et al. (1990). Warning signals in the North Sea (in German), Paul Parey
- Manzenrieder, H. (1983). The biological stabilization of mudflats from an engineering viewpoint (in German), Mitteilungen des Leichtweiß-Instituts der T.U. Braunschweig, No. 79, pp. 135-193
- Manzenrieder, H. (1995). Half-life period of sedimentation - model test on a scale 1:1, Proceedings 24th ICCE 94, pp. 3139 -3153
- Mc Nair, E.C. -Editor- (1994). Proceedings of the 2nd Conference on dredging and dredged material placement, Florida, ASCE
- Neville-Jones, P.; Thompson, G.E. (1994). Coastal pollution, water quality and oil spills, in Abbott, M.B.; Price, W.A.: Coastal estuarial and harbour reference book, pp. 691-703

CHAPTER 332

Storm-Derived Bar/Sill Dynamics in a Dredged Channel

Sean O'Neil, Student Member ASCE,¹ Keith W. Bedford, Member ASCE,² and David P. Podber, Student Member ASCE³

Abstract

The development of sediment bars and sills due to storm-induced flow events in a dredged Great Lakes tributary is studied. The hydrodynamics associated with long-waves from the lake, create flow reversals at the river mouth, and storm runoff produces large sediment loads delivered to the lake. A laterally-averaged numerical model, including a turbulence closure sub-model, is used to simulate the hydrodynamics. A simple sediment settling, resuspension and transport model is coupled to the hydrodynamic model. Model runs are made for flow and temperature conditions which would be typical of the region during the spring season. Runs are made with and without the sediment settling velocity term, which effectively represents the modeling of two grain sizes; clay particles which have extremely small settling velocities and tend to floc together producing neutrally buoyant particles, and silt sizes which have finite settling velocities.

Introduction

Harbor dredging is the necessary result of long term, persistent deposition of watershed-derived sediments. Periodic redredging is required to ameliorate the occurrence of sills and bars which form as a result of the interaction of wave climate, channel geometry, tributary flow and littoral drift. As opposed to the persistent and predictable tidal forcing on coastal harbors, the harbors on the Great Lakes are moderated by random, long-wave effects derived from storms. The storm surges and resulting seiches, coupled with a high sediment influx from watershed runoff, often

¹Graduate Research Associate, ²Professor and Chair, ³Graduate Research Associate. Department of Civil and Environmental Engineering and Geodetic Science, The Ohio State University, 470 Hitchcock Hall, 2070 Neil Avenue, Columbus, OH 43210-1275, USA. email: sean@superior.eng.ohio-state.edu

conspire to yield a two-sill bottom configuration which motivates maintenance dredging.

As part of a study designed to investigate the impacts of dredging operations, the physical processes responsible for the formation of sills and/or bars is explored by the use of detailed numerical models. The models developed as part of this study will also be used to enhance the tributaries portion of Great Lakes Forecasting System (e.g., Bedford and Schwab, 1994) which currently produces nowcasts four times daily and 24-hour daily forecasts of the state (water levels, wave heights, temperature, currents, etc.) of Lake Erie. This contribution details some of the results of the sill dynamics modeling and analysis for conditions marked by flow reversals and stratified flow.

Study Site

Toledo Harbor, on the Maumee River, is the third busiest port in the Great Lakes shipping arena. The site of the model investigation, shown in Figure 1, extends along

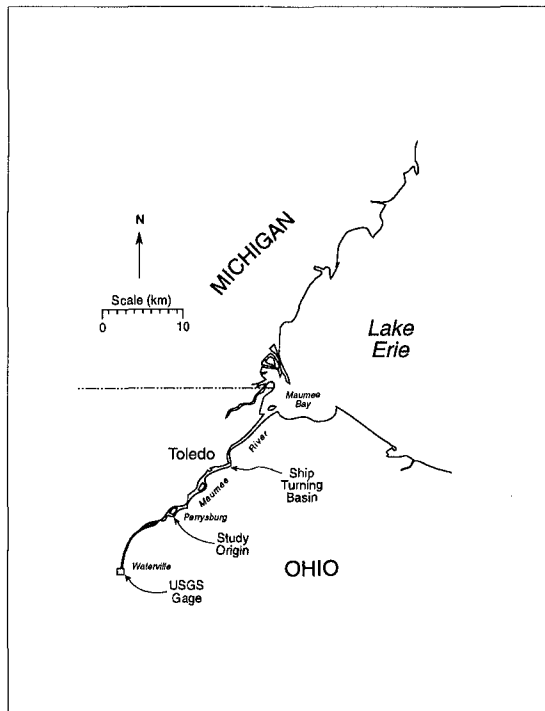


Figure 1: The Maumee River region.

the river, through the Maumee Bay, along a dredged navigation channel. The Maumee River delivers the single largest tributary-derived sediment load to Lake Erie, con-

tributing 44% of the total annual load (Kemp *et al.*, 1976). This high load occurs because 85% of the watershed land use is for agriculture. The extreme shallowness of Maumee Bay, with an average depth 1.5 m (5 ft), and the Western Basin of Lake Erie, average depth 7.6 m (25 ft), necessitates the maintenance of the 152 m (500 ft) wide, 8.5 m (28 ft) deep navigation channel. The dredged portion of the model domain extends from a ship turning basin 9 km upstream in the river, to approximately 6 km into the bay. Figure 2 shows a profile of the modeled portion of the river and navigation channel including the double-silled bathymetric configuration near the mouth of the river.

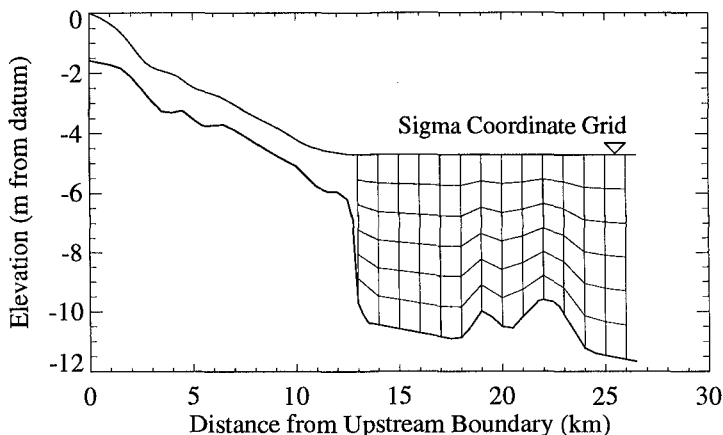


Figure 2: Schematic of model domain profile.

Physical Setting

The physical setting within the Maumee River, Bay and Western Basin of Lake Erie displays all of the features which might be found in a typical marine estuarine system, excluding of course tidal regularity. Storm events in the Lake Erie region occur with a frequency of 5-7 days during the spring and fall, with durations of 1-2 days. The corresponding increase of river flow rate and stage attain values that are significant fractions of the ambient levels.

A typical storm track during these seasons will follow the major axis, west to east, of Lake Erie, producing a significant storm surge at the eastern end of the lake. The storm surge will decay into a lakewide seiche with frequently observed 14.4, 9.1, 5.9 and 4.2 hour longitudinal modes. The seiche typically produces water elevation changes of more than 1 m, which is a significant fraction of the average water depth at Toledo Harbor. After the storm event, the decaying seiche may take 3-4 days to completely disappear. The narrow and deep dredged channel results in a "pipelining" of the excess flow due to runoff into the lake. The oscillations combined with the seasonal variations in water density gradients, here due to temperature differences

between river and lake water, result in a system which behaves like a typical estuary during storms, and like a river during calm conditions. Flow reversals are frequently noted as are internal waves and oscillations.

Numerical Models

The numerical methods and schemes employed for this set of model runs have all been well documented and used by several researchers under a variety of conditions, therefore only a brief outline will be given as to how the model couplings occur. The one-dimensional, hyperbolic de St. Venant equations are solved to determine the river stage and discharge from Waterville, OH to the river mouth at Lake Erie, in this case using the upstream discharge at Waterville and the downstream stage at the lake, as boundary conditions. In turn, the values of discharge and stage are used as the boundary conditions for the two-dimensional hydrodynamic model, which is based on the laterally-averaged, hydrostatic, Navier-Stokes equations. The use of this type of model allows the vertical structure of the flow field to be captured without the expense of a fully three-dimensional model. The use of the model is justified by the fact of the narrow, deep dredged channel. The two-dimensional model is used only from the ship turning basin (see Figure 2) to the lake and uses specified temperature and velocity boundary conditions at the upstream, downstream and bottom. A turbulent closure submodel, the Mellor-Yamada level 2.5 scheme (e.g., Blumberg and Mellor, 1987), is employed to calculate the time-varying vertical eddy viscosities and diffusivities. At the water surface, the flux of velocity and heat are nil, and at the bottom a drag-law based on the square of the horizontal velocity just above the bottom, allows for a shear stress or no-slip condition.

The sediment transport component of the model solves the advection-diffusion equation for suspended sediment concentration using an upwind advection scheme, a size specific constant settling velocity term, and source/sink terms for the erosion and deposition of sediment. The erosion and deposition terms are parameterized using the model of Sheng and Lick (1979), where the deposition of sediment is proportional to the sediment concentration and erosion is proportional to an excess shear stress as compared to the shear stress for sediment resuspension. Boundary conditions are specified to be no sediment flux through the water surface, a well mixed upstream condition giving a constant input sediment concentration, and lake-like concentration and temperature profiles imposed downstream. Empirical parameters in the erosion and deposition terms are based on previous studies performed in the Western Basin of Lake Erie and reported in Sheng and Lick (1979).

Conditions and Assumptions

The specific imposed conditions and assumptions which are applied for the spring season case study are outlined. The boundary conditions at the two ends of the model would normally come from data, or possibly, the output from other models. For the

spring storm conditions of interest, a typical steady river inflow was applied upstream, the magnitude of $141.6 \text{ m}^3/\text{s}$ (5000 cfs) was determined from flow hydrographs obtained during the spring months (Pinsak and Meyer, 1976). To approximate the effect of the lake seiche after a storm, a downstream sinusoidal water elevation with an amplitude of 0.61 m (2 ft) and a period of 14 hours, was applied for four complete cycles. Given the short term nature of the simulation, the bottom was assumed to be fixed, so that the sills were not moving or changing shape. This is justified by the fact that (with the exception of the spring snow melt discharge) the bottom probably doesn't evolve much under the influence of a single storm event, but does over the course of a season or longer.

The river temperature was assumed to be a constant upstream value of 12°C and the lake was assumed to have a temperature of 7°C , typical for spring (Shindel *et al.*, 1993). The upstream sediment concentration was assumed to be $1 \text{ kg}/\text{m}^3$, and downstream a constant concentration profile, with maximum concentration near the bottom of $1 \text{ kg}/\text{m}^3$, imposed if the flow reversed and lake water traveled upstream. However, the form of the profile was found not to affect results in trials with different profile shapes. Model runs were performed for single sediment grain sizes, and two cases were examined. The Stokes' settling velocities were determined to be $1 \times 10^{-5} \text{ m}/\text{s}$ and 0 for the two cases of silt (median diameter 0.004 to 0.06 mm) and clay particles (median diameter $< 0.004 \text{ mm}$).

Results

Analyses examine the impacts of flow reversals introduced by seiches versus regular downchannel river flow during inter-event periods. The following plots depict the water velocity field in the dredged channel as well as the suspended sediment concentration contours. These results were determined at several points within a single seiche cycle, where the cycle fractions are defined as in Figure 3. For brevity, not all of the cycle points designated in Figure 3 will be shown. Depicted in the figures is the third of four complete cycles run due to the fact that the fourth cycle of a run is generally not very different from the third.

The velocity fields shown in Figures 4-7 show that moderate seiche amplitudes are sufficiently strong enough to cause flow reversals in the river, even for riverine flow rates as high as $141 \text{ m}^3/\text{sec}$ (see also Podber and Bedford, 1993). The upstream sill proximity is consistent with its origination from simple channel deposition of sediments introduced upstream, and the downstream sill is located at the furthest up-channel extent of the 14-hr seiche mode excursion distance. During spring conditions a stable gyre is present above the downstream sill and positioned such that horizontal velocities are zero directly above the peak of the downstream sill, as shown in Figures 5 through 7. As the cycle progresses, the gyre appears to move up and then back down in the water column, but maintaining its position above the downstream sill. This may be an extremely important agent in sill formation and migration. Note also that at all times in the cycle the stratification of the water is maintained, where

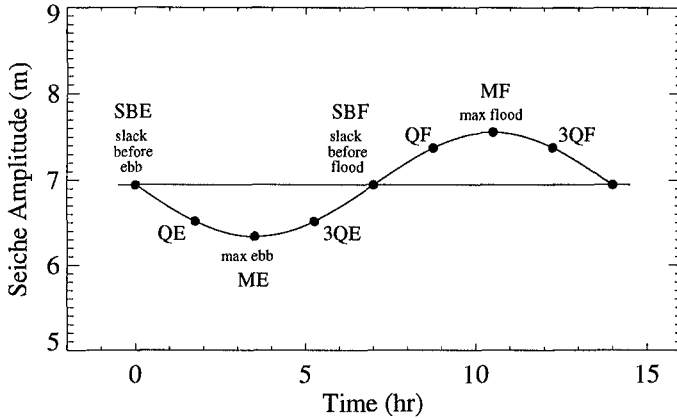


Figure 3: Definitions within a seiche cycle.

the warmer river water flows over the colder lake water. During the fall the inverse situation occurs.

In comparing the suspended sediment contours, it can be seen in all cases that there is a greater mass of the silt sized sediment within the water column than the neutrally buoyant particles. This is seen by fact that the larger valued contours are closer to the bottom and the lake side of the modeled domain. This is most likely due to the fact that neutrally buoyant particles enter the modeled region from the upstream direction, but they can only pass out through the downstream end of the model domain. For the case of the settling silt particles, some portion of the total mass of particles will be settling towards the bottom, and though the flow reversal will bring less sediment-dense water into the river, the settling sediment will tend to push the contours down and closer together. Also note that the extent of the upstream excursion of the intruding lake water has the effect of pushing the neutrally buoyant particles back to the upstream sill, whereas the maximum upstream extent of the silt particles is the downstream sill, which occurs at maximum flood.

Acknowledgements

This research was supported in part by the Coastal Ocean Program of NOAA. The Ohio Supercomputer Center provided computing resources under OSC Grant No. PAS891-1. The support is very much appreciated. This is a contribution from the Great Lakes Forecasting System.

References

Bedford, K. W. and Schwab, D. J. (1994). The Great Lakes Forecasting System: An Overview. In G. V. Cotroneo and R. R. Rumer, editors, *Hydraulic Engineering*

- '94, *Proceedings of the Conference*, pages 197–201, Buffalo, NY. ASCE. See URL <http://superior.eng.ohio-state.edu/>.
- Blumberg, A. F. and Mellor, G. L. (1987). A description of a three-dimensional coastal ocean circulation model. In N. S. Heaps, editor, *Three-dimensional Coastal Ocean Models*, Coastal and Estuarine Sciences 4, pages 1–16. American Geophysical Union.
- Kemp, A. L. W., Thomas, R. L., Dell, C. I., and Jaquet, J.-M. (1976). Cultural impact on the geochemistry of sediments in Lake Erie. *J. Fish. Res. Board Can.*, **33**, 440–462.
- Pinsak, A. P. and Meyer, T. L. (1976). Environmental baseline for Maumee Bay. Maumee River Basin, Level B Study, MRB Series No. 9, Great Lakes Environmental Research Laboratory.
- Podber, D. P. and Bedford, K. W. (1993). Tributary loading with a terrain following coordinate system. In M. L. Spaulding, K. W. Bedford, A. F. Blumberg, R. T. Cheng, and J. C. Swanson, editors, *Estuarine and Coastal Modeling III, Proceedings of the 3rd International Conference*, pages 475–488. ASCE.
- Sheng, Y. P. and Lick, W. (1979). The transport and resuspension of sediments in a shallow lake. *J. Geophys. Res.*, **84**(C4), 1809–1926.
- Shindel, H., Klingler, J., Mangus, J., and Trimble, L. (1993). Water Resources Data – Ohio, 1992. Volume 2, St. Lawrence River Basin. Technical report, U.S. Geological Survey, Water Resources Division.

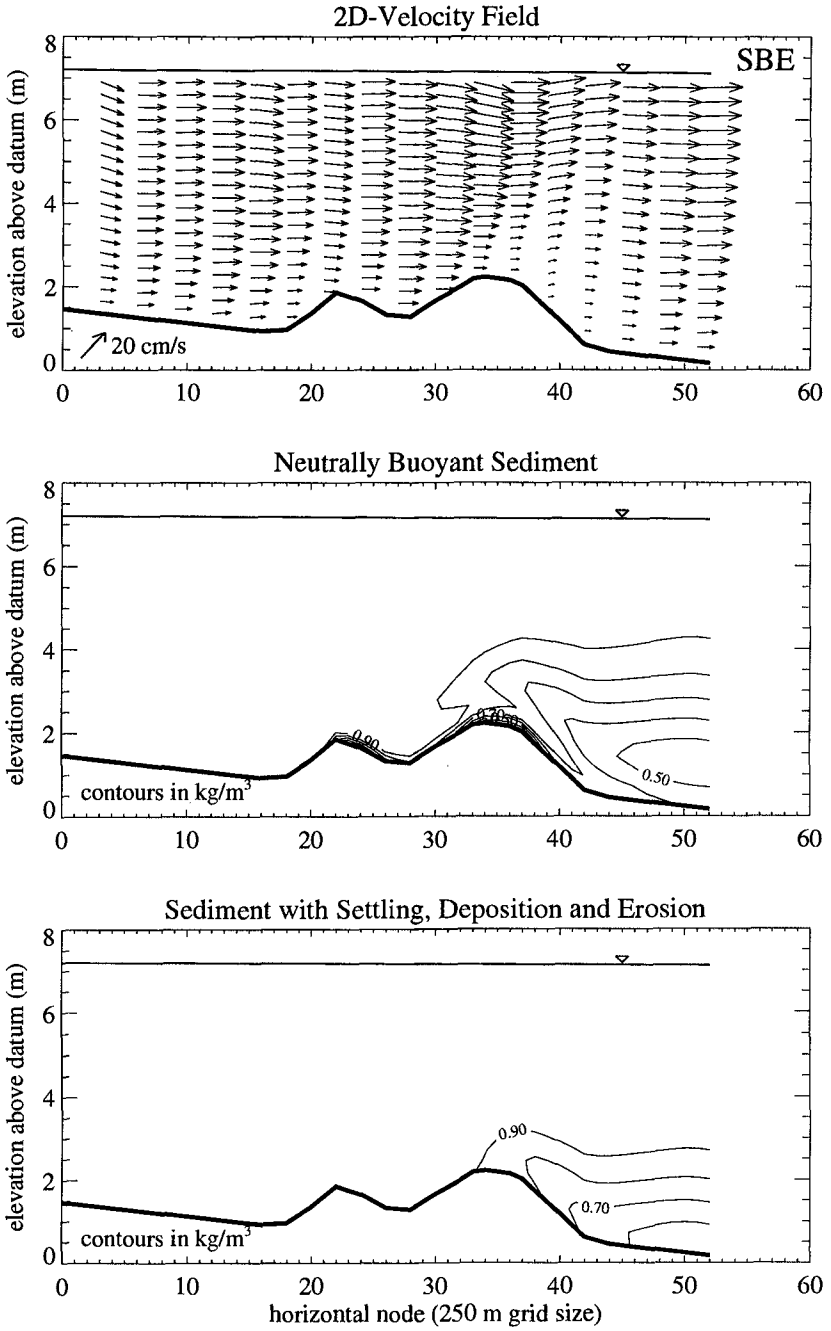


Figure 4: Velocity structure and suspended sediment contours for SBE.

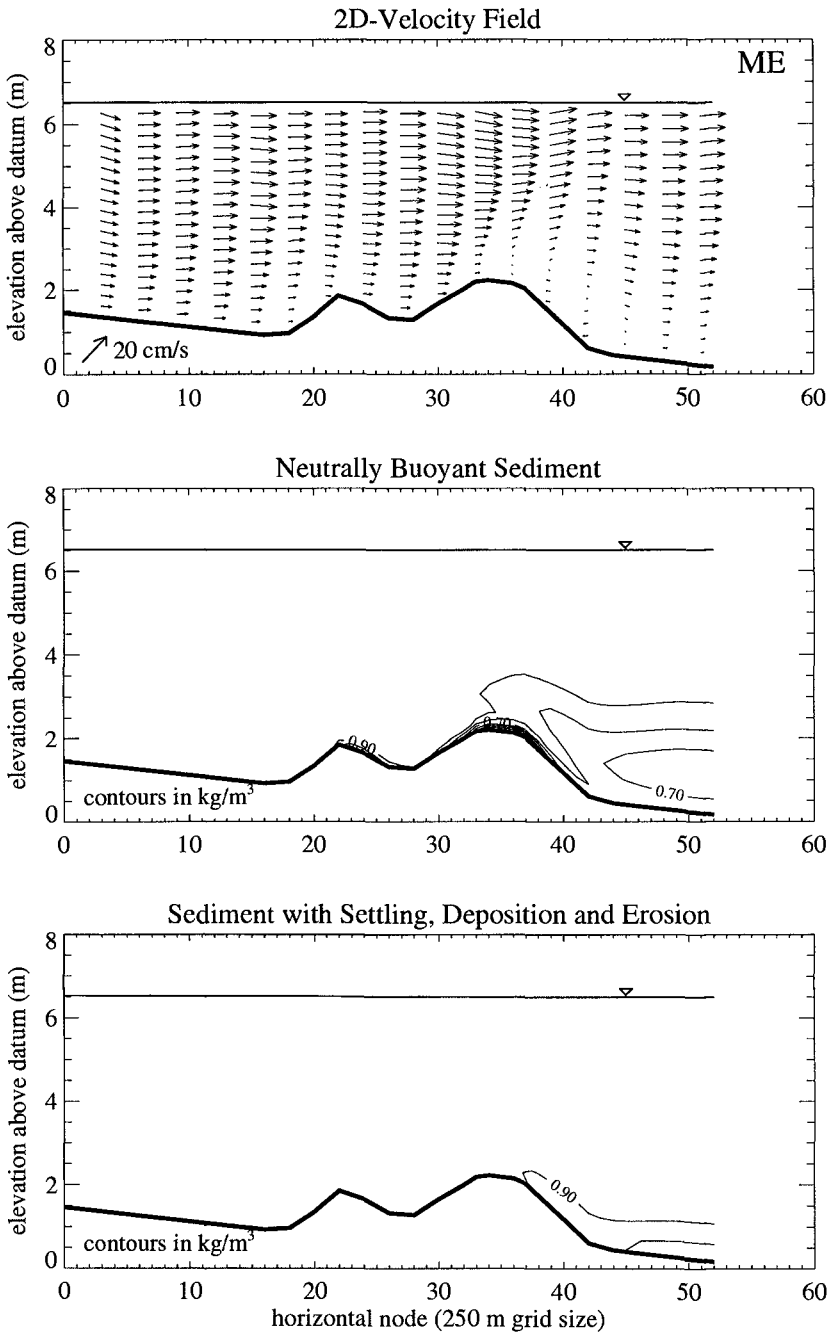


Figure 5: Velocity structure and suspended sediment contours for ME.

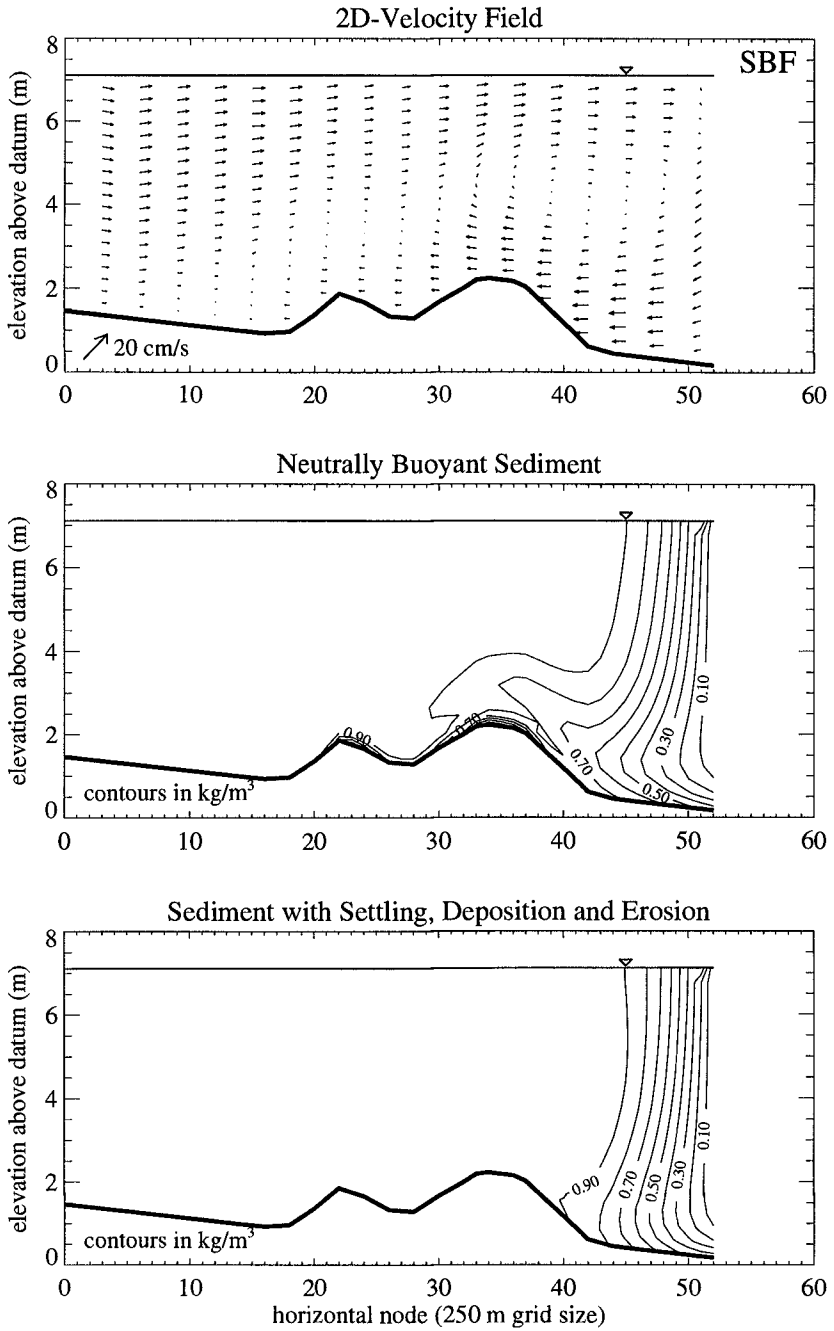


Figure 6: Velocity structure and suspended sediment contours for SBF.

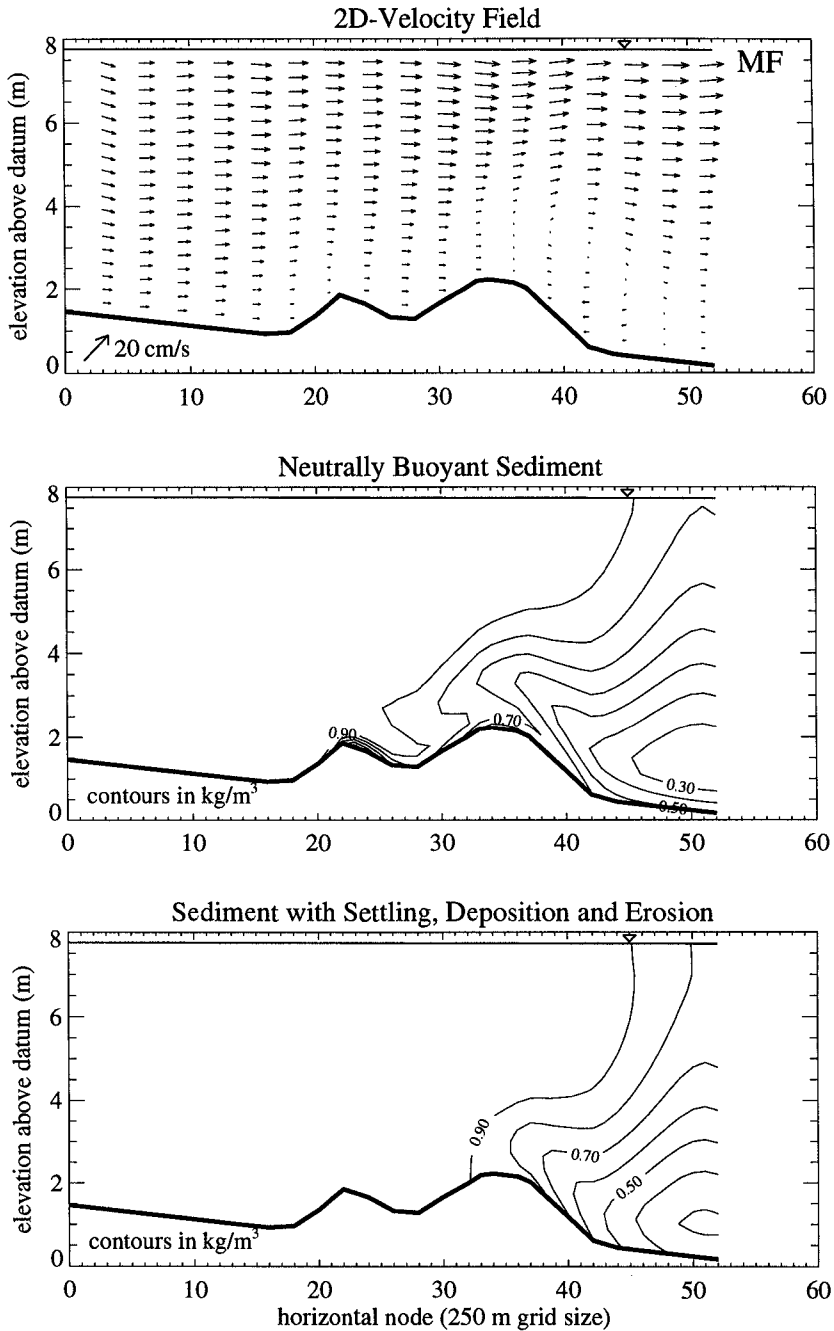


Figure 7: Velocity structure and suspended sediment contours for MF.

CHAPTER 333

Bivalve Habitat Based on Sediment-Transport Mechanics

Hitoshi Gotoh¹ and Tetsuo Sakai², M. ASCE

Abstract

After a storm, thousands of dead bivalves washed upon a beach are sometimes observed. Bivalves are important not only as the marine products but also as the index of the quality of coastal environment. Hence, the field observations of the distribution of bivalves in a coastal zone; and the laboratory experiments on the characteristics of the behavior of bivalves have been performed.

An interesting result is found by Yamashita and Matsuoka (1994) in a laboratory experiment on the burrowing process of bivalves under eroding condition due to the oscillatory flow: even when the descending velocity of a sand surface is sufficiently smaller than the burrowing velocity of bivalves, some bivalves cannot stay in the sand layer and are picked-up by oscillatory flow.

In this study, the physical background of their results are considered from a viewpoint of sediment transport mechanics. Two important aspects are investigated: the one is the stochastic aspect of the burrowing process of bivalves; and the other is the reverse grading phenomena observed in motion of mixed-size grains.

Introduction

Thousands of dead bivalves washed upon beach after a storm have been sometimes observed in the coastal region around Japan. Most of the former field observations and laboratory experiments (Watanabe, 1982; Higano and Yasunaga, 1988; Yamashita and Matsuoka, 1994; and Kuwahara and Higano, 1994) have been performed because

¹ Lecturer, Department of Civil Engineering., Kyoto University
Yoshida Honmachi, Sakyo-ku, Kyoto, 606, Japan

² Professor, Department of Civil Engineering., Kyoto University

of the importance of bivalves as fishery products. Bivalves, or creatures living in sandy beach, are also important as the index of coastal environment.

There are many irregular factors in a moving process of bivalves such as fluctuation of bottom velocity, descending velocity of sand surface due to scoring, size of bivalves, activity, or moving ability, of bivalves and so on. To take these irregularities into consideration, the moving process of bivalves should be treated as a stochastic process.

The other important aspect in the moving process of bivalves is the mode of sediment motion around bivalves. In general, sediment is transported in various modes; bed load, suspended load over sand ripples and sheetflow. Especially, during storm, or under the action of high-shear force, sheetflow should be a dominant transport mode. In the sediment transport in sheetflow regime, the particle/particle interaction, or the momentum transport due to interparticle collision is a mechanism governing the flow structure. To understand the behavior of bivalves in a sediment layer moving in sheetflow regime is an important subject to clarify the mechanism of bivalves-upward motion in a sand layer.

Two important aspects mentioned above are treated in this study based on the numerical model such as the stochastic model for simulating the probabilistic characteristics of bivalve's behavior and the granular material model for the simulation of sediment/sediment and sediment/bivalves interactions.

Laboratory experiment by Yamashita & Matsuoka

Yamashita and Matsuoka (1994) found out very interesting characteristics of bivalves in their laboratory experiment. They performed the experiment on the burrowing process of infant bivalves, or *Spisula sachalinensis*, maximum length of which is more than 5 mm and less than 20 mm, under the oscillatory flow generated by U-tube type oscillating water tunnel. They investigated the probability of the occurrence of the bivalves picked-out-of sand layer under the various values of the ratio of the descending velocity of sand surface, or v_e , to the burrowing velocity of bivalves, or v_s . Figure 1 shows the one of the results of their study on the relation between the probability of the occurrence of the bivalves picked-out-of sand layer and the velocity ratio v_e/v_s .

When the descending velocity of sand surface due to the erosion is larger than the one-thirds of the burrowing velocity of bivalves, namely in the region where the ratio $v_e/v_s \geq 0.3$, whole of the bivalves in a sand layer are picked-out-of sand. In their experiment, the burrowing velocity of bivalves are measured in a still sand layer. To understand the physics of this phenomena, the behavior of bivalves in a streamwise-moving sand layer should be investigated.

In the region $0.1 \leq v_e/v_s < 0.3$, some bivalves are picked-out and others are staying

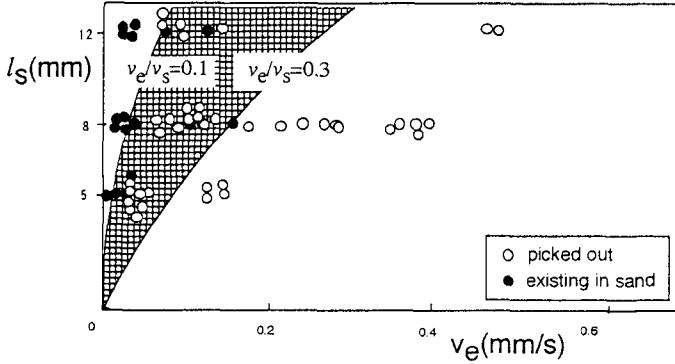


Figure 1. Occurrence of the bivalves picked-out
(Data from Yamashita and Matsuoka, 1994)

in a sand. This means the importance of stochastic consideration of the motion of bivalves to express the probabilistic aspects of the moving process of bivalves.

Stochastic consideration of burrowing process of bivalves

procedures of stochastic calculation

The following assumptions, some of which are based on the previous experiments conducted by Higano, Kimoto and Yasunaga (1993) and Yamashita and Matsuoka (1994), are introduced in this calculation.

(1) The shell length of bivalve $l_s=8$ mm. (2) The bivalve burrows in a sand layer keeping shell-length axis parallel to the vertical direction. (3) Initially, the top edge of bivalve coincide with the surface of sand layer, as schematically shown in Fig. 2.

(4) Bivalve begins to burrow in a sand layer when its top is exposed due to the scouring. The threshold of exposed length at the beginning of bivalve's burrowing is treated as the probabilistic variables based on the experiment by Higano et al (1993). (5) Bivalve rests in sand layer when the clearance between its top edge and the surface of a sand layer is equal to the half of shell length as shown in Fig. 2. The burrowing and the resting are iterated alternately. (6) Bivalve is defined to be picked out of sand layer when the 80% of the shell length are exposed in water as shown in Fig. 2. (7) The cycle of calculation begins at the moment when the condition (5) is satisfied. If the condition (6) has not been satisfied for 2200 s from the beginning, the calculation is terminated. This situation is defined as the survival of bivalves. (8) As it is mentioned above, bivalve is repeating the burrowing process and resting process, the average of the repeating period of which is equal to 2.2 s, according to Yamashita and

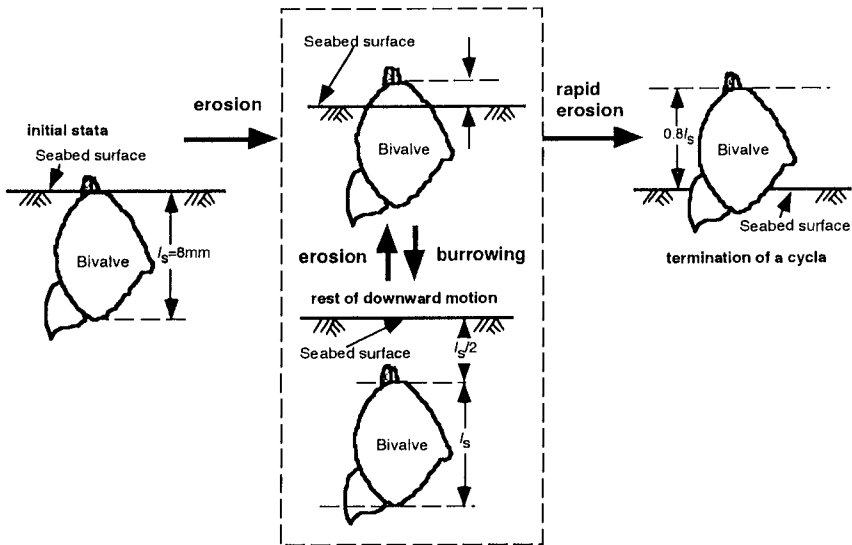


Figure 2. Definition of parameters in bivalves

Matsuoka (1994). They also investigated the distribution of burrowing velocity of bivalves. In this calculation, the burrowing velocity of bivalves changes at every 2.2 s based on the Monte Carlo Method, namely by generating the random numbers following the distribution of the burrowing velocity experimentally investigated. (9) The descending velocity of the surface of sand layer is treated as a probabilistic variables following the normal distribution, the standard deviation of which is equal to one-third of averaged descending velocity, or $\sigma = v_e/3$.

results of the stochastic calculation

Figure 3 shows one of the calculated results of the one-cycle of the burrowing process of bivalves under the condition of $v_e/v_s=1.0$. In this figure, the time series of the existing height of bivalves, elevation of sand-layer surface and the thickness of sand layer above the top of bivalves, or δ , are shown. In this case, the thickness δ is decreasing rapidly during $0.0 \leq tv_s/l_s \leq 1.0$, and on the verge of the picking-out of bivalves. After $tv_s/l_s=1.0$, the thickness δ increases again. In this case, the bivalve survives through one cycle of calculation. If the decreasing velocity of the thickness δ during $0.0 \leq tv_s/l_s \leq 1.0$ is a little more rapidly, this bivalve is picked-out-of sand layer. The survival of bivalve is strongly depends on the accidental-drastic change of the surface elevation of sand layer.

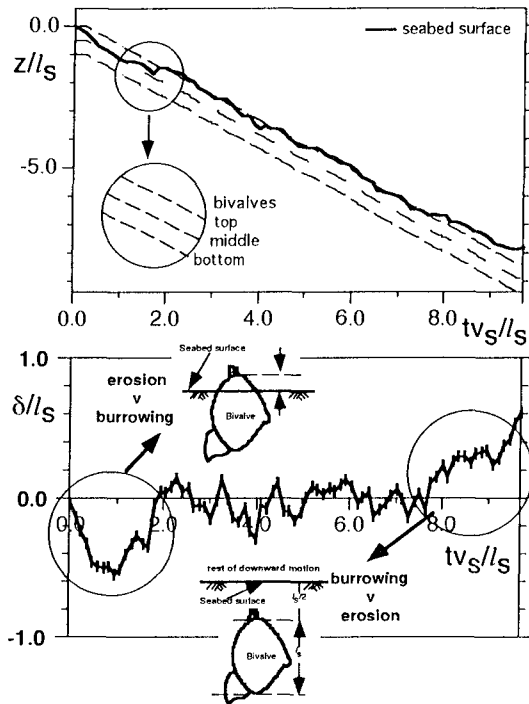


Figure 3. Burrowing process of bivalve

The probability of the survival of bivalves, or P_m , is calculated by continuing the cycle of calculation for m -times with assessing the occurrence of the bivalves picked-out-of a sand layer. Fig. 4 shows the existing probability of bivalves after 100 cycle of calculation, or P_{100} , against the ratio of the descending velocity of sand-bed surface to the burrowing velocity of bivalve, $v_e/v_s (= \alpha)$. Two cases of the calculation are shown in this figure. The one is the calculation in which the probabilistic characteristics of bivalves are only considered; and the other is the calculation in which both of the probabilistic characteristics of bivalves and that of sand-bed surface are considered. The transition range of the probability of the survival of bivalves experimentally investigated by Yamashita and Matsuoka is also shown in this figure.

The transition range of the experiment is $0.1 \leq \alpha \leq 0.3$, while the calculation, in which the probabilistic characteristics of bivalves is only considered, shows the drastic transition around $\alpha=0.9$. The calculation, in which both of the behavior of bivalves and the motion of sand-bed surface are treated as the probabilistic variables, predicts the transition range in $0.6 \leq \alpha \leq 0.75$. But even if the probabilistic characteristics of

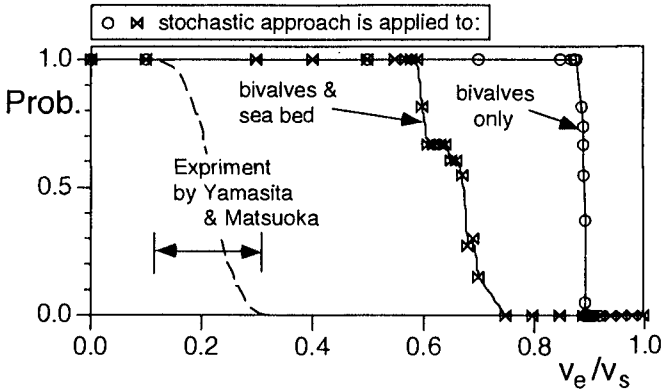


Figure 4. Survival probability of bivalve

sand-bed-surface elevation is considered, the threshold of the emergence of bivalves picked-out-of sand layer are overestimated.

Although the stochastic calculation reproduces the existence of the transition region in the probability of the bivalve's survival against the change of velocity ratio v_e/v_s , the threshold of the bivalve's survival is not reproduced well at least quantitatively. This fact suggests the existence of other mechanism, which promotes the picking-out-of bivalves.

Behavior of bivalves in sheetflow layer

reverse grading as the mechanism of upward vertical motion of bivalves

Boulders are frequently observed to be concentrated at the near-surface region of the front part of debris flow. This phenomenon, namely the existence of the boulders above other grains and gravel, is called reverse grading.

Interparticle collision is the governing mechanism both of debris flow and sediment transport in sheetflow regime. Therefore the same kind of phenomena as the reverse grading of debris flow can be thought to be a mechanism to promote the bivalves to be picked-out-of sand layer. In this study, the behavior of bivalves is traced numerically in the moving sediment particles in sheetflow regime by the distinct element method (=DEM).

distinct element method

Sakai and Gotoh (1995) performed the numerical simulation of the motion of sheared sediment-particle layer based on the distinct element method. In this study,

their simulation is applied to simulate the interactive behavior between bivalve and sediment particles around bivalve by regarding the bivalve as a large and light particle.

governing equations of sediment particles

Sediment particles are modeled by the rigid cylinders with uniform diameter d ; and the bivalve is modeled by the rigid cylinder with diameter D . At inter-cylinder and cylinder-bivalve contacting point, the spring and dashpot systems are introduced, and the equations of motion of cylinder and bivalve are solved by an explicit method.

Equations of motion of the i -th particle or bivalve in the vertically two-dimensional coordinate are as follows:

$$\frac{\pi\sigma_i d_i^2}{4} \frac{d^2 x_i}{dt^2} = \sum_j \left\{ -f_n(t) \cos \alpha_{ij} + f_s(t) \sin \alpha_{ij} \right\}_j + F_{0i} \quad (1)$$

$$\frac{\pi\sigma_i d_i^2}{4} \frac{d^2 y_i}{dt^2} = \sum_j \left\{ -f_n(t) \sin \alpha_{ij} + f_s(t) \cos \alpha_{ij} \right\}_j - \frac{\pi(\sigma_i - \rho) d_i^2 g}{4} \quad (2)$$

$$\frac{\pi\sigma_i d_i^3}{16} \frac{d^2 \phi_i}{dt^2} = \sum_j f_s(t)_j \quad (3)$$

in which f_n, f_s =the forces acting between the i -th and j -th particles; α_{ij} =contacting angle between the i -th and j -th particles; F_{0i} =shear force acting on the i -th particle; σ_i =density of particle; and d_i =diameter of particle; and g =gravitational acceleration. The subscript "n", "s" mean normal and tangential components, respectively.

calculation of interparticle-acting force

Figure 5 shows the schematics of the interaction between two contacting particles. Between two contacting particles, springs and dashpots are introduced to describe the dynamic interparticle relation. The acting force between the i -th and j -th particles in normal and tangential direction, f_n and f_s , can be written as follows:

$$f_n(t) = e_n(t) + d_n(t) \quad ; \quad f_s(t) = e_s(t) + d_s(t) \quad (4)$$

$$e_n(t) = \min \{ e_n(t - \Delta t) + k_n \cdot \Delta \xi_n, e_{n\max} \} \quad ; \quad d_n(t) = \eta_n \cdot \frac{d\Delta \xi_n}{dt} \quad (5)$$

$$e_s(t) = \min \{ e_s(t - \Delta t) + k_s \cdot \Delta \xi_s, e_{s\max} \} \quad ; \quad d_s(t) = \eta_s \cdot \frac{d\Delta \xi_s}{dt} \quad (6)$$

in which e_n, e_s =forces working on springs; d_n, d_s =forces working on dashpots; $\Delta \xi_n, \Delta \xi_s$ =displacement of particle during the time Δt (Δt =time step of the calculation); k_n, k_s =spring constants; and η_n, η_s =damping coefficients. In this simulation, particles

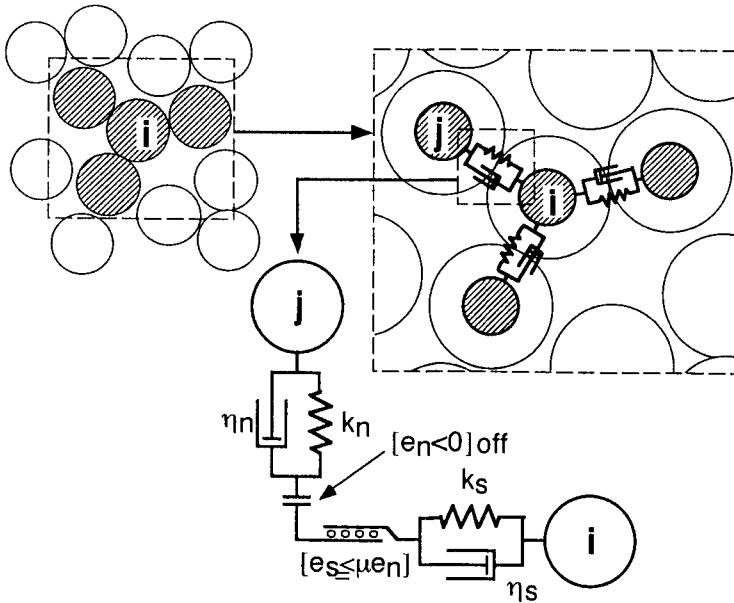


Figure 5. Schematics of the interaction between two contacting particles

are non-cohesive, hence the tensile force does not act between two contacting particles. To describe this characteristics, the joint, which no resistance to the tensile force, is assumed to exist in the normal direction. While, in the tangential direction, the friction force works. To describe this characteristics, the joint, which slips at the limit of the shear stress, is assumed to exist in the tangential direction.

initial conditions and boundary conditions

Figure 6 shows the schematic expression of the calculating domain. In this simulation, streamwise uniform condition is treated, therefore, the both sides of the calculating domain are the periodic boundaries. The bottom boundary is the fixed rough bed constituted by the particles with the same diameter as the moving particles. Before the beginning of the main calculation, the packing to determine the stable initial location of the particles is executed.

The shear stress is distributed to the particles in the neighborhood of the surface of sand layer in a following procedure. Procedure are, firstly, to set the threshold y_{th} (see Fig. 7); secondarily to calculate the area of the particles above the threshold, or

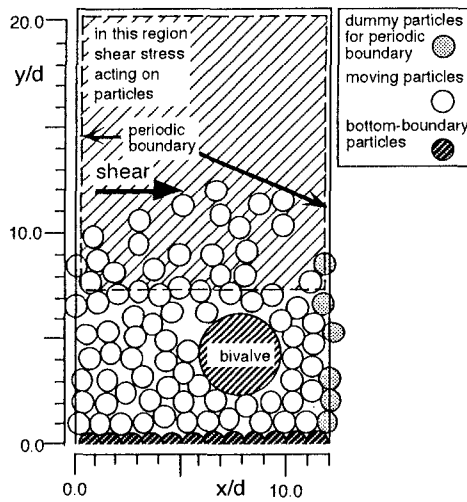


Figure 6. Schematics of calculating domain

the shaded area in Fig. 7, for the particles existing on and above the threshold; and finally to distribute the shear force to the particles existing on and above the threshold with calculating the area of particles above the threshold $S(\theta_i)$ as follows:

$$S(\theta_i) = \begin{cases} \frac{r^2}{4} \left(\pi - \theta_i + \frac{1}{2} \sin 2\theta_i \right) & ; y_i \geq y_{th} \\ \frac{r^2}{4} \left(\theta_i - \frac{1}{2} \sin 2\theta_i \right) & ; y_{th} - \frac{r}{2} < y_i < y_{th} \end{cases} \quad ; \quad \theta_i = \cos^{-1} \left(\frac{y_i - y_{th}}{r} \right) \quad (7)$$

Distributed shear force to the i -th particle is written as

$$F_{0i} = Lw_i\tau_0 \quad ; \quad w_i = S(\theta_i) / \sum_{j=1}^N S(\theta_j) \quad (8)$$

in which L =length of the calculating domain in horizontal direction; τ_0 =bottom shear stress par unit area. The test particle is 0.5 cm in diameter and 2.65 in specific gravity; and the model of bivalve is 2.0 cm in diameter and 1.30 in specific gravity (see Higano et al., 1993). In the calculating domain, 91 particles and 1 bivalve are traced. The model constants are shown in Table 1.

Initially the bivalve is contacting to the bottom constituting particles. The time step of the calculation is 2.0×10^{-5} s and the totally 80,000 cycles of calculation is executed, hence the motion of sediment particles and bivalve for 1.6 s is traced.

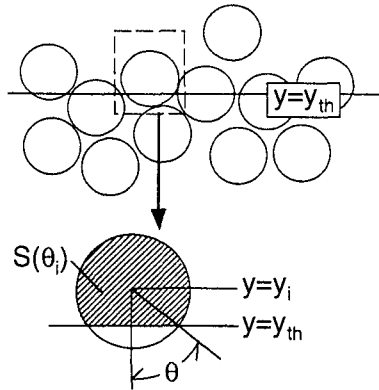


Figure 7. Shear stress distributed to sediment particles

Table 1. Model constants

k_n	9.45×10^6 N/m
k_s	2.36×10^6 N/m
η_n	40.0 Ns/m
η_s	20.0 Ns/m
μ	0.577
e_{nmax}	2.5 N
e_{smax}	0.025 N
Δt	2.0×10^{-5} s

results of simulation

Figure 8 shows the snapshots of the sediment-and-bivalve motion with 0.2 s intervals under the action of the shear stress $\tau^*(\equiv u_*^2 / \sqrt{(\sigma / \rho - 1)gd}) = 1.5$ on the surface of sediment layer. Bivalve, which is initially contacted to the bottom constituting particles, moves upward gradually, and it is picked-out-of a sand layer 0.8 s after the initiation of the shear action. Most of the particles in lower layer has laminar motion, hence the momentum exchange in lower layer is inactive. While, in the upper layer the concentration of sediment particles is less than that in the lower layer, the vertical motion of the sediment particles is less frequently obstructed by the particles in the upper layer than in the lower layer.

To understand the physics of the upward motion of bivalve, following hypothesis is proposed. The bivalve exists in the shear layer, in which the sediment particles

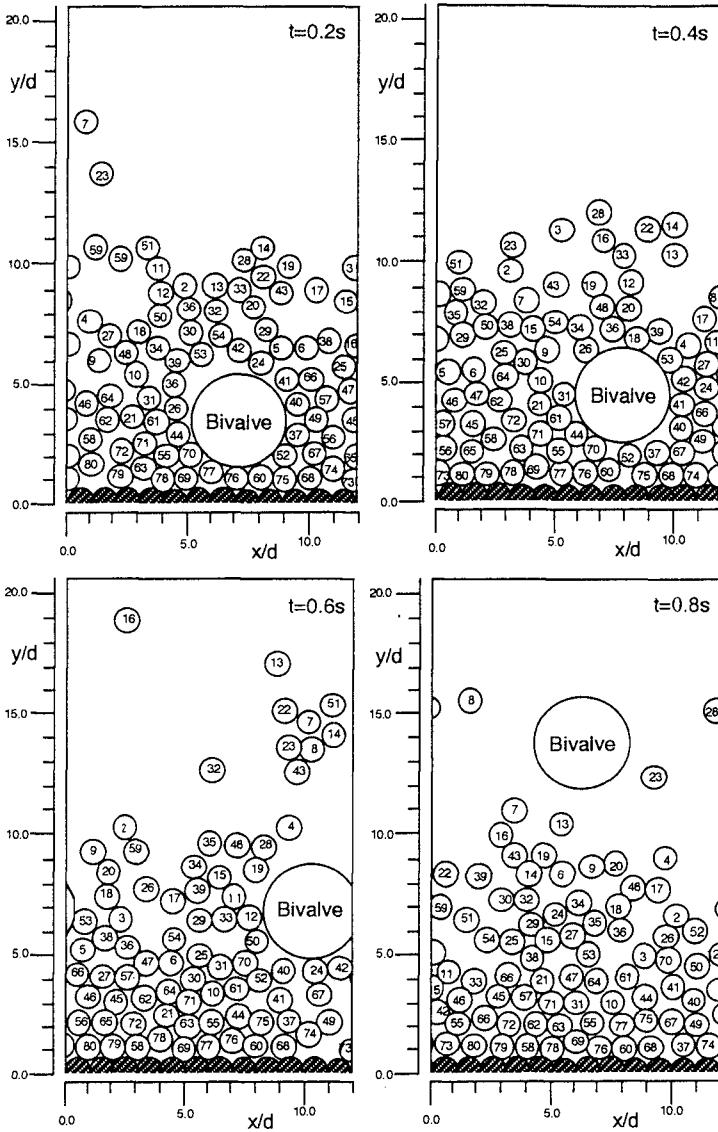


Figure 8. Snapshots of the sediment-and-bivalve motion

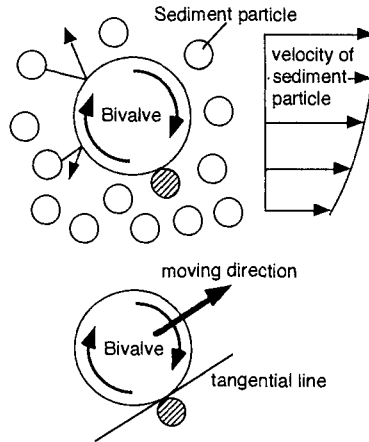


Figure 9. Upward motion of bivalve

have a vertical velocity distribution as schematically shown in Fig.9. Therefore the particle colliding at the upper part of bivalve is faster than that colliding at the lower part of bivalve. This velocity difference of the colliding sediment particles makes the bivalve to rotate in clockwise. Supposing the contacting sediment particle with just the lower part of the bivalve in the downstream section (hatched particle in Fig.9) and the hypothetical plane at the contacting point between bivalve and the particle, the behavior of the bivalve can be simplified as the clockwise rotating cylinder on the slope. And the clockwise rotation moves the cylinder to upward.

Figure 10 shows the time series of the rotating angle, the sign of which is positive in counterclockwise, and the elevation of the centroid of bivalve. The bivalve begins to move upward gradually accelerating the rotational motion. Around 0.6 s, bivalve moves in upward direction drastically, and at the same time the rotational motion is accelerated also drastically. From this fact, the rotational motion of bivalve can be regarded as the driving mechanism of the upward motion of bivalve.

Conclusion

The physical background of the behavior of bivalve in sand layer during storm are considered from a viewpoint of sediment transport mechanics. Two important aspects are investigated: the stochastic aspect of the burrowing process of bivalves and the reverse grading phenomena observed in a motion of mixed-size grains.

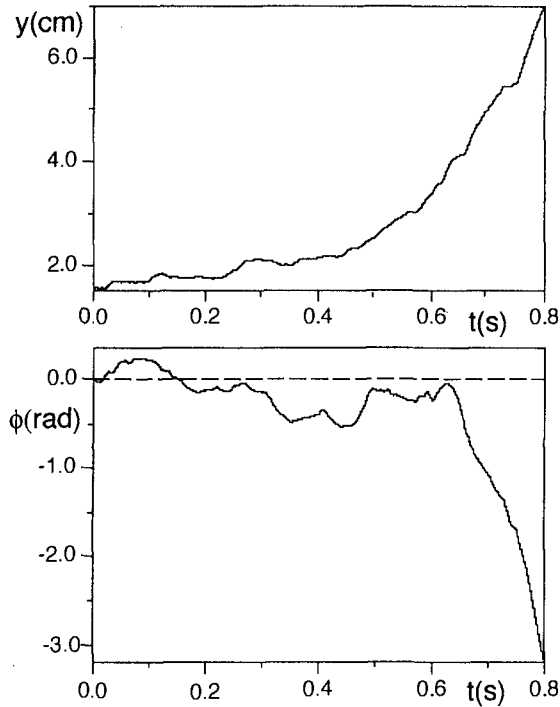


Figure 10. Rotating angle of bivalve

The stochastic model simulates the probabilistic characteristics of environment around bivalves. And the granular material model, or distinct element method, simulates the motion of bivalve in upward direction based on the sediment/sediment and sediment/bivalves interactions.

References

- Higano, J. and Yasunaga, Y. (1988). The change in beach profile and bivalve distribution on a sandy beach facing to open sea. Proc. 35th Japanese Conf. on Coastal Eng. pp.767-771 (in Japanese).
- Higano, J., Kimoto K. and Yasunaga, Y. (1993). Influence on the relation between burrowing behavior and physical environment regarding the distribution of sandy beach bivalves *Meretrix lamarckii* and *Gomphina melanaegis*. Bull. Nat. Res. Inst. Fisheries. Eng. 14, pp.65-87 (in Japanese).

- Kuwahara, H. and Higano, J. (1994). Model of bivalves on/offshore movement by waves. Proc. 24th ICCE, ASCE, pp.3086-3098.
- Sakai, T. and Gotoh, H. (1995). Numerical simulation of sediment transport in sheetflow regime. Proc. XXVIth Cong. IAHR, London, pp.299-304.
- Yamashita, T. and Matsuoka, M. (1994). Experimental study on movement and decline of bivalve by water waves. Proc. Civil Eng. in Ocean, vol. 10, pp. 119-122 (in Japanese).
- Watanabe, E. (1982). Experimental study on the decrease of surf clam under wave action. Monthly report of Inst. Civil Eng., No.351,pp. 3-15 (in Japanese).

CHAPTER 334

Hydraulic Controls on Tidal Wetlands

R. Eric Katmarian, Philip A. McKee, Timothy W. Kana¹

Abstract

Tidal wetlands have long been identified as critical habitats for many species of fish, birds, and other wildlife and are protected areas in many states. For these reasons, coastal projects which impact or destroy wetland areas are difficult to permit and often require substantial mitigation. An hydraulic design procedure is presented for the creation or improvement of wetlands based on flooding duration -- the percentage of time an area is inundated by tidal waters. This is followed by a sample application of the procedure to a recent mitigation project in Savannah, Georgia.

Introduction

Tidal wetlands, sometimes called the oceans' nurseries, contain many habitats for both plants and animals. Among the many habitats that exist, the basic ones include open water, tidal flats, low marsh, high marsh, transitional wetlands, and highland (Fig. 1). These habitats are sensitively balanced for existing tidal conditions, wave climate, daily flooding duration, sedimentation rates, and climate (Kana et al., 1986). Perturbations of these factors over an extended period can result in the transformation of one habitat into another.

Because wetlands tend to exist in areas of limited topographic relief, transitions between habitats can be indistinct and often occur over some distance, making precise location of boundaries difficult. Nevertheless, it is generally recognized that the character of flooding controls species distribution, with some wetland species preferring infrequent and irregular inundation, while others have adapted to frequent flooding. As a result, many studies have been undertaken to define wetland boundaries (Teal, 1958; Redfield, 1972; Nixon, 1982).

¹ Coastal engineer, research assistant, and senior scientist, respectively; CSE-Baird, PO Box 8056, Columbia, SC 29202

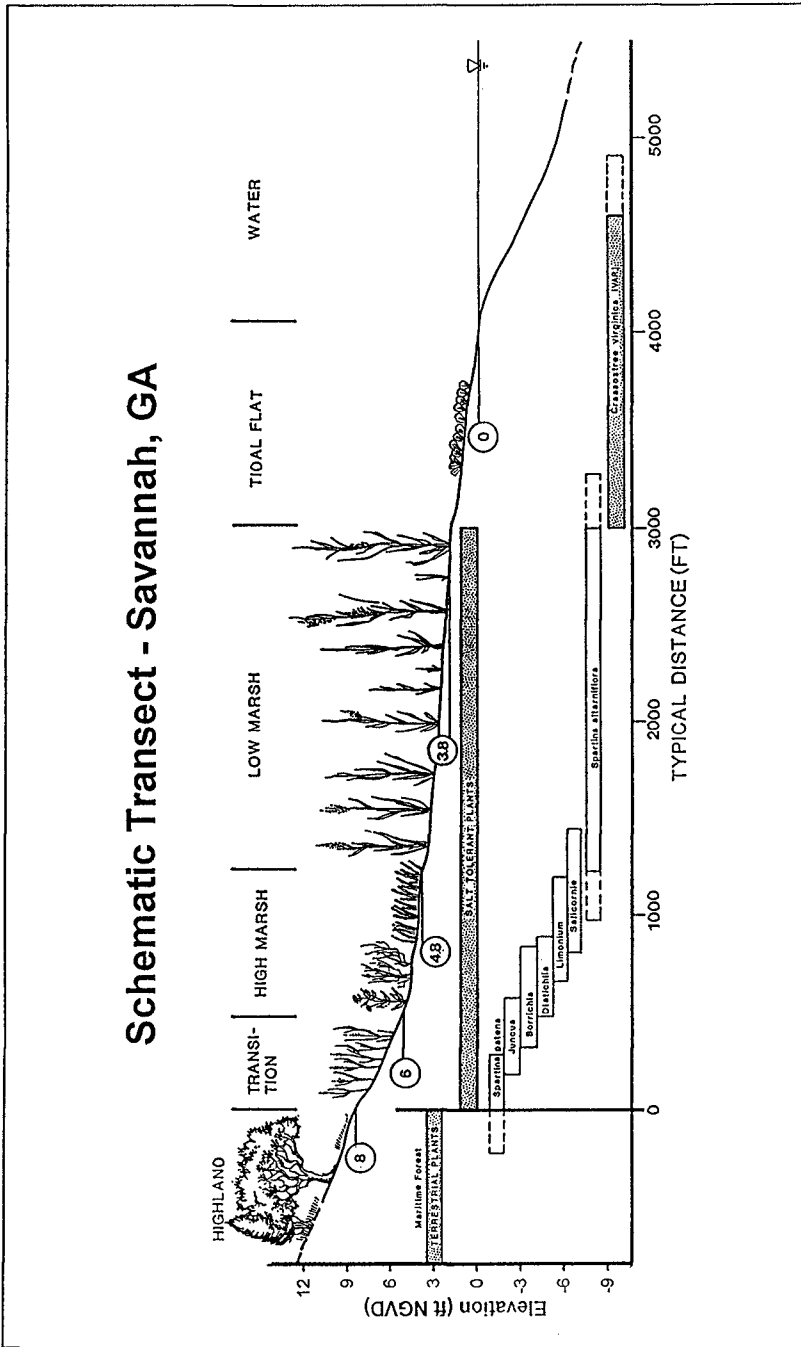


Figure 1. Typical habitats in tidal wetlands near Savannah, Georgia (From CSE 1995).

One method of delineation has been to identify habitats on the basis of flooding frequency – the number of times per day that an area is inundated. On the basis of flooding frequency, the basic habitats occur as follows (Kana et al., 1986):

Highland	-- flooded rarely
Transitional wetlands	-- flooding ranges from biweekly to annually
High marsh	-- flooding ranges from daily to biweekly
Low marsh	-- flooded once or twice daily
Tidal flats	-- flooded up to half the day
Open water	-- flooded more than half the day

Additionally, an often repeated rule of thumb has developed which states that low marsh exists where the substrate elevation is roughly at the mean high water level. However, the above criteria are too general to be incorporated into procedures for quantifying impacts on wetlands or to be used in wetland design criteria.

Many investigators (Adams, 1963 in Lagna, 1975; Kana et al., 1986) have extended the “mean high water” rule, saying that the primary factor controlling the distribution of wetland species is the relationship between marsh substrate elevation and local tidal water levels. Kana et al. (1986) even developed a normalized curve to be applied to arbitrary sites (Fig. 2). To use the normalized curve, a species-specific factor is read from the vertical axis and applied to the local extreme high water level referenced to mean sea level (MSL) datum. For example, for *Spartina alterniflora*, the water level factor is approximately 0.48. Therefore, at a site where extreme high water is 3 meters (m) MSL, *Spartina alterniflora* would be found in low energy environments with a substrate elevation of about 1.44 m MSL. Despite some findings that elevation alone does not control species distribution (Lagna, 1975), the appeal of such simple methods for engineering and environmental applications is clear.

In this paper, the idea of hydraulic controls on tidal wetlands are refined and extended, and a general wetlands design method is proposed.

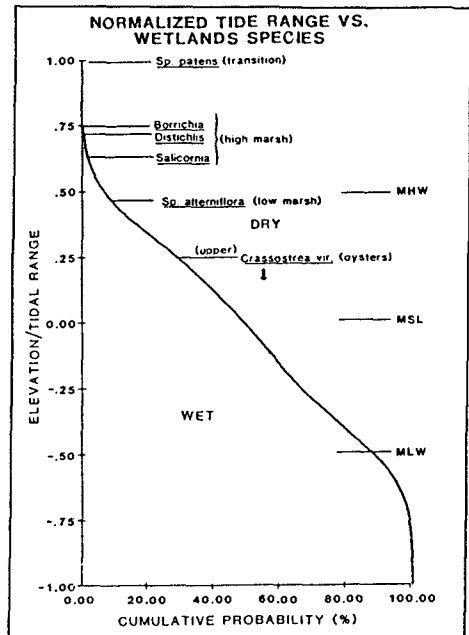


Figure 2. Normalized probability distribution of elevations for various wetland species (From Kana et al., 1986).

Flooding Duration as a Control on Wetland Habitat Distribution

It is generally accepted that character of inundation is the primary factor governing the distribution of wetland species. As described above, previous investigators have chosen to describe inundation in terms of substrate elevation relative to tidal water levels. However, relative elevation does not necessarily represent identical flooding characteristics at sites where tidal signature differs. For example, if two sites have equal tide ranges but one has an attenuated ebb tide, they will be flooded for differing periods for a given elevation (Fig. 3). When the effects of daily inequality, fortnightly cycles, and atmospheric affects are also introduced, relative elevation becomes an even less reliable measure of flooding character.

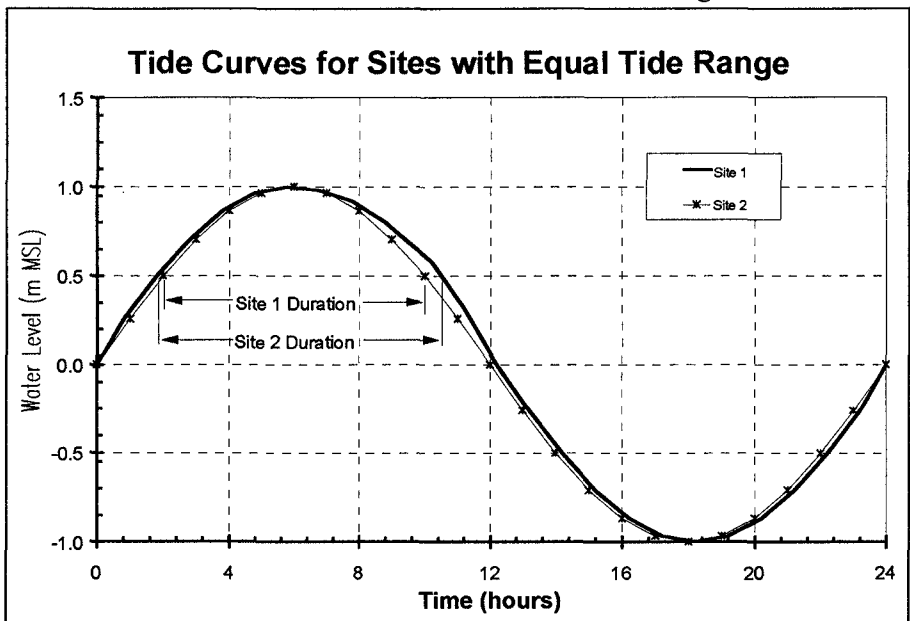


Figure 3. Flooding duration at equal elevations differ at sites where tidal signatures differ.

Flooding duration, the percentage of time that an area is inundated, is proposed as a more accurate measure of flooding character than relative elevation. Flooding duration is applied to species zonation in a manner similar to elevation.

It is assumed that wetland plant species are found in specific ranges of flooding duration. These ranges often overlap, and ranges for some species may be contained in the ranges of others. Indicator species may be chosen to identify specific wetland habitats. Wetland habitats are categorized by flooding duration in Table 1.

The durations listed in Table 1 are based on several wetlands surveys, the project described below, and many years of field observation. Nevertheless, minor variations should be expected on a site-specific basis. Until this method of design has gained wider acceptance, surveys of existing wetlands to confirm flooding durations for specific habitats should be conducted prior to design of new sites.

Table 1. Approximate flooding duration ranges for wetland habitats

Habitat	Flooding Duration
Upland	0 %
Transitional Wetlands	0-2%
High Marsh	2-5%
Low Marsh	5-25%
Tidal Flats	25-50%
Open Water	>50%

Although somewhat cumbersome to use, flooding duration has several advantages over elevation, particularly when broadly applied:

1. The dominant factor controlling species zonation, the character of flooding, is more directly represented by flooding duration.
2. Flooding duration can be more generally applied than relative elevation since variations in tidal signature are accounted for.
3. The effects of frequent inundation due to storm surge or other factors are more accurately accounted for using flooding duration, particularly if a lengthy water level record is available. It is likely that this factor is particularly important where the tide range is relatively small and atmospheric events are more significant.
4. Flooding duration emphasizes the need for relatively long-term, site-specific water level measurements, while elevation data is easily misapplied to areas where the tide is attenuated or otherwise different from open-water conditions (commonly where tide gauges are located).

To calculate flooding duration, *a relatively long-term, site-specific water level record must be used* to account for daily inequality, fortnightly cycles, and irregular variations in water levels. Furthermore, existing tide gauges are generally located in open water where water levels are often significantly different than water levels in wetlands. To obtain an acceptable water level record, a tide gauge may need to be deployed.

The length of the record required will depend on local conditions affecting the variability of the water levels. Judgment must be used in determining the minimum length of record required at a particular site though, in most locations, a 25-day record will suffice.

Once an acceptable water level record is obtained, flooding duration for a given elevation is calculated as:

$$\text{Flooding Duration} = \frac{\text{Cumulative time with water level above elevation}}{\text{Total length of record}} \times 100$$

In some cases, the creation or alteration of a wetland has the potential to significantly change local water levels. This is undesirable since it has the potential to cause habitat transformations in existing wetlands. Additionally, specification of a substrate elevation corresponding to a desired flooding frequency becomes very difficult when postproject water levels are uncertain. Steps must be taken to minimize the impact of projects on local water levels. This can be accomplished by specifying an appropriate substrate elevation for the new wetland or by increasing the hydraulic capacity of connections to open water to accommodate increased flooding areas.

Numerical models can be extremely helpful in predicting postproject water levels when local hydraulics are altered by wetland creation.

Sample Application: Mitigation Site Design

A recent CSE (1995) project involved hydraulic design for a 10-acre wetland at a site previously used for dredge spoil disposal near Savannah, Georgia. The site is approximately 900 m from the Savannah River and has hydraulic connection to the river via a complex network of ditches, culverts and existing wetlands (Fig. 4). The design objective was to create a tidal wetland at the site while minimizing both excavation requirements and impacts to existing wetlands.

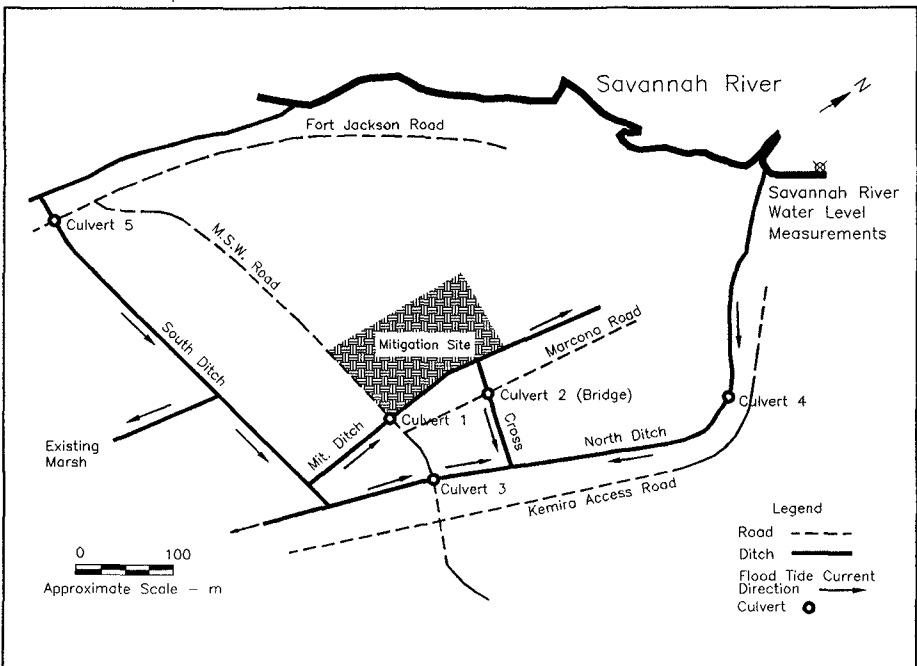


Figure 4. A complicated system of ditches, culverts, and wetlands connected the mitigation site to the Savannah River (From CSE, 1995).

The first step in applying the flooding duration method to the design was to determine the range of flooding duration for the type of wetland desired. A number of transects were surveyed through a nearby "natural" wetland. Elevation and distance were recorded at each point where species changed or where there were noticeable breaks in slope or elevation. Species types were identified with the assistance of a biologist. Elevation for each species was weighted by distance of occurrence to produce an elevation distribution for frequency of occurrence. The elevation data for all observed species were approximately normally distributed.

Local water level data were required to calculate flooding duration for the range of elevations observed for each species. Therefore, water level measurements in the surveyed wetland were taken over several tidal cycles and compared against data from a nearby permanent tide gauge. No significant water levels differences were observed between the surveyed marsh and the permanent gauge, so a 30-day record from the permanent gauge was used for flooding duration calculations. If significant differences had been noted between the marsh and gauge, water levels would have had to be measured at the site for a minimum of 25 days to provide adequate water level data for flooding duration calculations.

Flooding durations were calculated for the average elevation, and average elevation \pm one standard deviation of each species observed (Table 2). Elevations outside this range are attributed to localized variations in water levels and errors introduced by weighting approximations. *Spartina alterniflora* was chosen as the low marsh indicator species, as is the usual practice on the East Coast. Therefore, the observed flooding duration range for local low marsh was found to be approximately 5 to 21 percent.

Table 2. Wetland species flooding durations near Savannah, Georgia (CSE, 1995).

Species	Flooding Duration (% of tidal cycle)		
	Mean	Lower Bound	Upper Bound
<i>Spartina cynosuroides</i>	13.7	8.3	18.5
<i>Spartina alterniflora</i>	12.0	4.5	20.5
<i>Carex</i> sp.	9.3	2.7	19.9
<i>Juncus</i> sp.	6.3	3.2	11.3
<i>Typha augustifolia</i>	3.5	1.3	6.8

With the design flooding duration for low marsh established, the next step was to determine how to achieve this range at the mitigation site. The goal was to specify a substrate elevation range for the mitigation site which would result in the desired flooding frequency, given the hydraulic capacity of the ditch and culvert network. However, it was recognized that the addition of the 40,000 m² wetland to the existing system would change its tidal characteristics, making postproject water levels different than preproject levels. Without good estimates of postproject water levels, accurate determination of flooding duration was impossible. Furthermore, measurements of flows through existing channels and observations of flow restrictions

at culverts indicated that the existing system could not supply adequate tidal exchange to the mitigation site to sustain a low marsh. This meant that improvements would have to be made to the drainage system.

To gain some confidence in postproject conditions, DHI's Mike11 river model was used to simulate the ditch and wetland system. Figure 5 shows a schematic of the model setup. After calibration to existing conditions, the model proved instrumental in arriving at the final design by allowing the effects of ditch and culvert improvements, variation in mitigation site elevation, and impacts to existing wetland areas to be investigated.

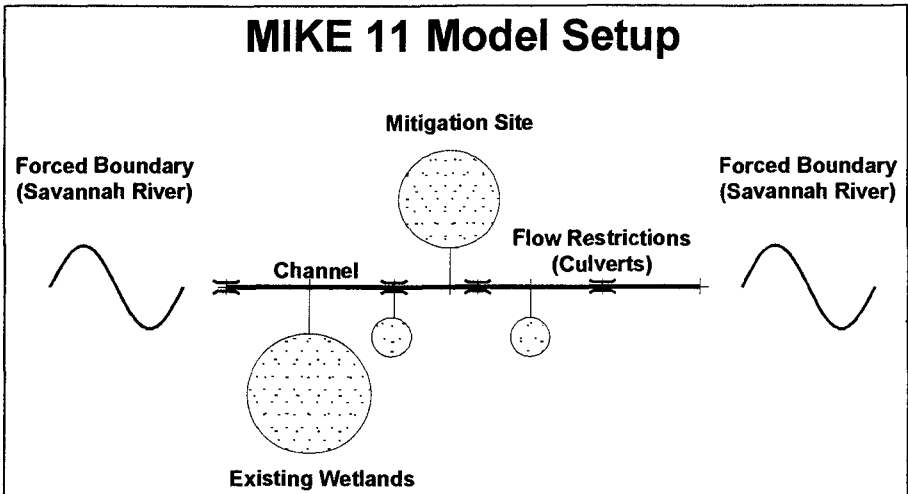


Figure 5. Schematic Mike11 model setup showing the channel/wetlands system modeled (From CSE, 1995).

Model results supported by field observations showed that both the existing wetlands and the site to be mitigated were flooded primarily by the south ditch (Fig. 4). This was primarily due to a topographic high point in the north ditch. With the high point and culvert 4 removed and the north ditch widened, the model showed that flooding of the mitigation site would occur from both the north and south. The model also showed significant increased flooding of the existing wetlands and the potential to convert them to “wetter” habitats. The final design recommendation was to isolate the mitigation site from the existing wetlands by closing culvert 1. Since the north ditch initially provided negligible flooding, the final design did not significantly impact existing wetlands.

With the hydraulic connection set, Mike11 was used to predict postproject water levels at the mitigation site. Using a simulated postproject water level record of 30 days, the variation in flooding duration at the mitigation with mitigation site elevation was established. Mike11 results for water levels at the mitigation site are shown in Figure 6, and corresponding volumetric flow rates in the improved north ditch are given in Figure 7.

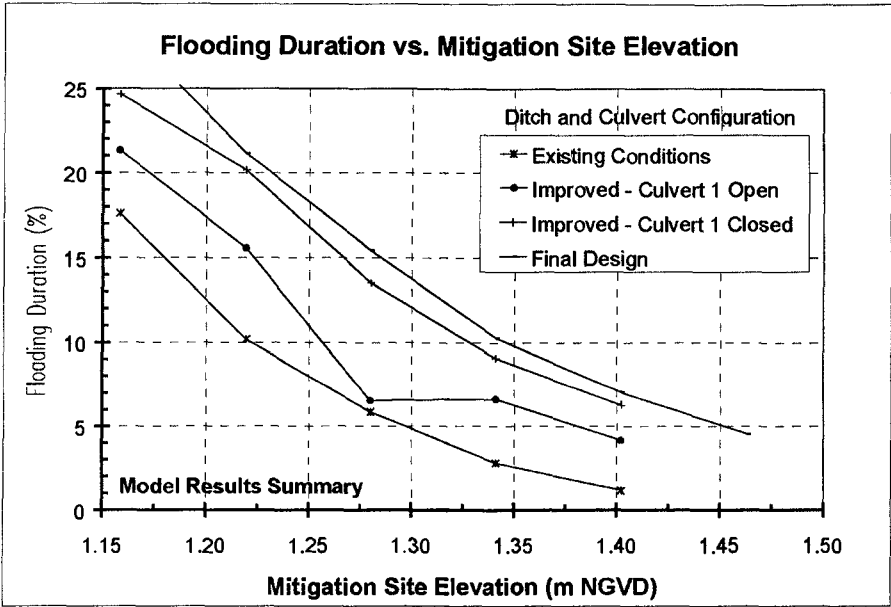


Figure 6. Mike11 model results. Flooding duration variation with mitigation site elevation and ditch/culvert configuration (From CSE, 1995).

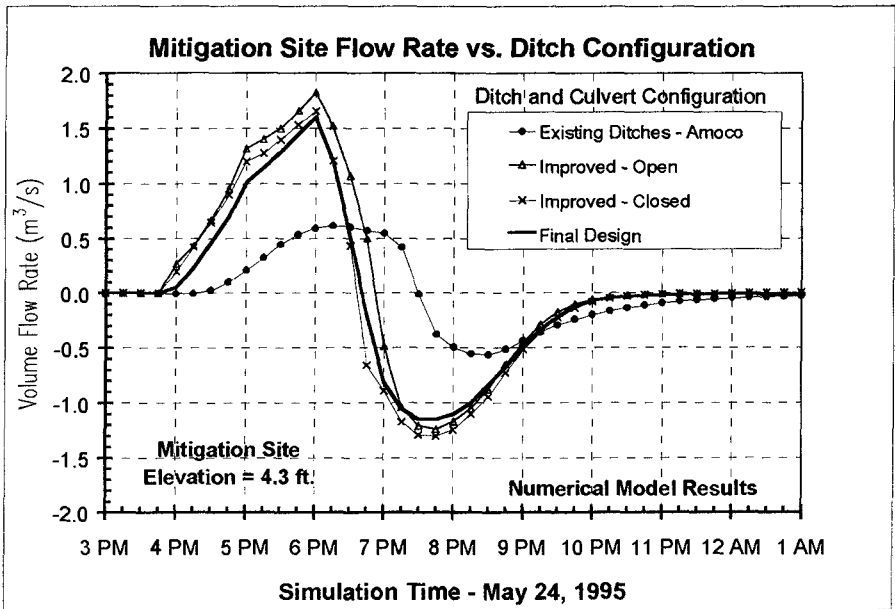


Figure 7. Mike11 model results. Volume flow rates to mitigation site for various ditch and culvert configurations (From CSE, 1995).

Despite the tidal attenuation, the mitigation site elevations were higher than those of the natural marsh. This was a result of greater attenuation of the ebb tide than the flood, which increased flooding duration at the site.

The final design for the mitigation site had the following dimensions:

Wetland area to be created:	40,000 m ²
Wetland substrate elevation:	1.22 m to 1.46 m NGVD
Wetland flooding duration:	5 to 20 %
Length of ditch to Savannah R.:	900 meters
Width of ditch:	3 meters
River to wetland tide attenuation:	0.03 to 0.15 meters
River to wetland phase lag:	30-50 minutes

Conclusions

A procedure for the hydraulic design or improvement of tidal wetlands was proposed based on the principle that wetland plant species inhabit specific ranges of flooding duration. By creating areas with the appropriate flooding duration, desired habitats can be successfully created. When calculating flooding duration, relatively long-term site-specific water levels are required. A 30-day water level record is suggested for typical conditions. Where the creation of wetlands significantly alters local hydraulics, numerical models may be required to predict postproject water levels needed to determine wetland substrate elevations.

References

- CSE. 1995. Kemira wetlands mitigation project: tidal marsh hydraulics & analysis. Report for Kemron Environmental Services. Coastal Science & Engineering, Columbia, S. C., 36pp.
- Kana, T.W., B.J. Baca, and M.L. Williams. 1986. Potential Impacts of Sea Level Rise on Wetlands Around Charleston, South Carolina. EPA Report 230-10-85-014, Washington, D.C., 65pp.
- Lagna, L. 1975. The Relationship of *Spartina Alterniflora* to Mean High Water. New York Sea Grant Institute. NYSSGP-RS-75-002. 43pp.
- Nixon, S.W., 1982. The Ecology of New England High Salt Marshes: A Community Profile. U.S. Fish and Wildlife Serv., Washington, D.C., FWS/OBS-81/55, 70pp.
- Redfield, A.C., 1972. "Development of a New England salt marsh." Ecol. Monogr., Vol. 42, pp. 201-237.
- Teal, J.M., 1958. "Energy flow in the salt marsh ecosystem." In Proc. Salt Marsh Conf., Mar. Inst., Univ. Georgia, pp. 101-107.

CHAPTER 335

Enhanced Mixing Through Perforated Discs on Round Buoyant Jet

Lilun Wu¹, Jiin-Jen Lee²

Abstract

Jets have been widely used in submarine outfall diffuser systems for discharging the sewage effluents into large bodies of sea water to facilitate rapid mixing of the effluent with the ambient water. The primary goal of an outfall diffuser system is to accomplish rapid mixing of the effluent with the ambient water. In an effort to enhance the near field mixing, various obstruction devices may be placed exterior to the diffuser nozzle. This experimental study focuses on the enhanced mixing mechanisms of the jets obstructed with perforated discs.

Experiments are conducted in a deep water tank with glass walls on four sides of the tank. The tank has the dimension of 3.35 m in depth with a square cross-section of 1.15 m. The water particle velocities of the resulting flow field are measured by using a portable four-beam, two-component, fiber-optic Laser-Doppler Velocimeter system (LDV). The concentration of the entrained fluid is measured by using a Laser-Induced Fluorescence system (LIF). The data acquisition system used for obtaining data on the concentration profiles is processed by Labview's programmable virtual instruments software.

The experimental data consist of the axial (vertical) and radial (horizontal) velocities, turbulent intensities, Reynolds stresses and concentrations. It is found that velocity fluctuations in both the axial and radial velocities help to generate vorticity and to induce mixings over a larger area in the neighboring flow region. Moreover, the velocity gradient is significantly increased over the region based on the experimental data involving the perforated discs. The results also show that a large reduction in the concentration of the entrained fluid can be achieved due to the

¹ Graduate Research Assistant, Department of Civil Engineering, University of Southern California, Los Angeles, CA 90089.

² Professor of Civil Engineering, University of Southern California, Los Angeles, CA 90089-2531, Member of ASCE.

obstructing disc. The results demonstrate quite convincingly the ability of the perforated disc to enhance the mixing and entrainment of the discharging fluid with the ambient fluid.

1.0 Introduction

For the removal of municipal sewage, treated or untreated waste water must be disposed of in such a way that will generate minimal effects to the environment. An ocean discharging system is commonly used to discharge sewage effluents into coastal water and to induce mixing of the effluent with the sea water. The systems are generally comprised of embedded pipes, the main outfall, which delivers the waste water to a diffuser system. The length of the main outfall pipes normally range from 1 km to 9 km, depending upon the sea bed topography, ocean currents and environmental requirements.

There are three major factors that affect the mixing of effluent (Fischer et al. 1979). They are: jet parameters, environmental parameters and geometrical factors of the discharging jet. Both the jet parameters and the environmental parameters have been studied extensively in the last four decades. Geometrical factor is an interesting field for the scientists and engineers to study because better geometrical arrangements may result in greater dilution. Increasing dilution in an ocean discharging system would produce significant saving in the construction costs by reducing needed mixing height of the rising plume.

The present experimental investigation includes measurements of axial and radial velocity, turbulent intensity, turbulent shear stress and concentration profiles. The purpose of the measurements is to accurately measure various flow parameters in the flow field of the jets obstructed with perforated disc to provide an answer to the important question posed for the study.

2.0 Experiments

Experiments were performed in a deep water tank system with vertical glass face. The water tank has the dimensions of 335 cm high, 115 cm wide and 115 cm deep. The facilities also included a mixing tank, a constant-head tank, air bubbling hose and a manometer (flow meter). The mixing tank provides a space for adding dye or salt into effluent fluid. The constant-head tank is used for maintaining a steady flow for the effluent fluid, while the air bubbles provide enhance mixing in both the mixing tank and the glass water tank before conducting experiments. Fluid velocity and Rhodamine 6 G dye concentration can be measured by a Laser Doppler Velocimeter (LDV) and a Laser-Induced Fluorescence system (LIF), respectively. For measuring purposes, this glass walled tank is equipped with an instrument

carriage supporting a Laser Doppler Velocimeter or a Laser-Induced Fluorescence device. The carriage is able to move both vertically and horizontally with respect to the tank, thus velocities and concentrations could be measured at various axial and radial locations. The jet nozzle is located on the top of the tank and pointing down. The density of the exit fluid from the jet nozzle is greater (heavier) than that of ambient fluid. Sodium Chloride (salt) is added into the exit fluid to obtain the desired initial density difference between exit fluid and ambient fluid.

A portable four-beam, two component, fiber optic Laser Doppler Velocimeter (LDV) manufactured by TSI, Inc. was used for measuring the water particle velocities. The software of data acquisition for controlling the LDV system, *Flow Information Display (FIND) Data Analysis Package* from TSI, Inc. was used. The concentration is measured by a laser-induced fluorescence system (LIF) at various cross sections downstream from the jet nozzle. This system includes a 2W Argon-Ion laser (Spectra Physics Model 265), a CCD camera (EG&G Reticon LC300A), an analog input/output data acquisition board (National Instrument, AT-MIO-16X) and data acquisition program (Labview). The laser beam is oriented in the direction perpendicular to the centerline of the flow, and it is shot into the water tank across the entire flow field from one side of the tank. A line fluorescence light source is then detected by an array of light-sensitive photo diodes inside the EG&G Reticon LC300A camera. The data acquisition system receives signals from the camera and converts the analog signals to digital data. The data for the concentration profile is processed by Labview's virtual instruments software.

3.0 Results and Discussion

3.1 Velocity Profile and Width of Simple Jets

The results of the velocity measurement conducted for the present work are in agreement with those of Fischer et al (1979) and Papanicolaou and List (1988). This agreement ensures that the instrumentation system used for the present study can yield reliable results. Thus, comparisons can be made between the results conducted for simple jets and for jets obstructed with perforated disc.

Figure 1 shows the normalized diagram by combining all of the velocity profiles of the simple jets into one figure. Data distribution in Figure 1 is a Gaussian distribution. The jet has U_{mean}/U_c value in the range of $|r/z| < 0.2$, beyond this range the U_{mean}/U_c values tend to zero. The normalized diagrams for representing the results of jet obstructed with each perforated disc are presented in Figures 2. Most values of U_{mean}/U_c of each obstructed case are located in between $|r/z| < 0.4$. After comparing the results of velocity profiles for the case of simple jets and the cases of jets obstructed with perforated discs, conclusions can be drawn as follows: (1) For the jets obstructed with different perforated discs compared with the simple

jet (Figures 3), the axial (longitudinal) velocity distributions of the jets with perforated disc have more fluctuations exhibited in each profile. (2) The cases of the jets obstructed with perforated disc have larger plume width on each cross section. (3) For jets obstructed with various perforated disc, the axial velocity distributions are more uniform and broader when compared with the case of simple jets. (4) The centerline velocities of the jets obstructed with perforated disc have relatively smaller value with compared with simple jets.

3.2 *Turbulence Properties*

The axial (vertical) and radial (horizontal) turbulent intensities have been measured simultaneously by LDV for both simple jets and jets obstructed with perforated discs. After comparing the results on the turbulent intensity (both axial and radial) for both simple jets and jets obstructed with perforated discs, general conclusions can be made as follows: (1) Simple jets have larger fluctuations of the axial velocity around the boundary of jet. In the outer region of the cross section (beyond the boundary of the plume width), the percentages of axial turbulent fluctuation of jets with each perforated disc are much greater than those of the simple jets. This shows that jets obstructed with perforated discs can produce more turbulent fluctuation of axial velocity than the simple jets in the outer region of the cross section. (2) The distributions of turbulent fluctuations in the axial and radial component for the jets obstructed with perforated discs are much more uniform and much broader than those of simple jets. (3) The jet obstructed with the 2x8 perforated disc has an overall higher U'_{rms}/U_c value than those for other disc arrangements. (4) The percentages of radial turbulent fluctuation of jet obstructed with perforated disc have higher values than those of simple jets at all of the cross sections within the region of the jet width. Moreover, the overall percentages of radial turbulent fluctuation of jets obstructed with perforated discs are higher than those of simple jets in the region beyond the boundary of the jet for each cross section. This shows that the jets obstructed with perforated discs have higher radial (horizontal) turbulent fluctuation than simple jets beyond the boundary region.

The results from the measurement of turbulent intensity indicate that the jets obstructed with perforated discs will enlarge the region of turbulent fluctuation and resulting in more interaction between ambient and effluent fluid. This also supports the experimental hypothesis that using the perforated discs to obstruct the jets will result in larger areas of axial and radial fluctuations in the flow field.

3.3 *Reynolds Stress*

The shear layer between the effluent fluid and the ambient fluid was proved by Fischer et al (1979) as an important factor to entrain the ambient fluid into effluent fluid and to induce mixing of both fluids. The Reynolds stress ($\overline{U'V'}$ or turbulent shear stress) measurements were conducted for both simple jets and jets obstructed

with perforated discs. Experimental results have been presented in Figure 4 for the simple jets and in Figure 5 for the jets obstructed with perforated discs. Comparisons between the results of simple jets and jets obstructed, can lead to the following conclusions: (1) Fluctuations can be observed on the $\overline{U'V'}$ profiles of the jets obstructed with perforated discs. This is because the effluent fluid flows through the perforated disc (or holes on the disc) and generates many small vortices inside the boundary of the jets. Thus, it creates a larger area of shear layer and induces more entrainments for the entire flow field. (2) Results show that the jets obstructed with perforated discs have higher value of $\overline{U'V'}$ at the region outside of the jets' boundary, and this is the advantage of using the obstructed perforated discs to broaden the extents of the velocity field and the velocity fluctuation. A broader mixing area is created by the obstructing perforated discs, Thus, mixing is enhanced by a broader region possessing certain value of turbulent shear stress.

3.4 Concentrations and Dilutions

The concentration measurements were conducted and included in the present study. The simple jets' maximum concentrations obtained for the present work are in agreement with the previous studies such as Fischer et al. (1979) and Papanicolaou (1984). The widths of concentration profiles of the simple jets measured in the present study are also in agreement with those of Papanicolaou and List (1988).

After comparing the results of concentration measurements for both simple jets and jets obstructed with perforated discs, conclusions can be made as follows: (1) the results of the simple jets are similar to that reported by Fischer et al. (1979) and Papanicolaou and List (1988), (2) the maximum concentration for the cases of the jets obstructed with perforated discs are quite smaller than those of the simple jets, and (3) the concentration widths (b_c) for the jets obstructed with perforated discs are broader than those of the simple jets.

The calculations for the mean dilution achieved for the simple jets and for jets with perforated discs also were performed. The results indicate that (1) the C_{\max}/C_{ave} ratios of the simple jets are in the range of 1.315~1.592, this result is in agreement with that summarized by Fischer et al. (1979) which is 1.4 ± 0.1 , (2) for the jets obstructed with perforated discs, the mean dilution is higher than that of the simple jets, (3) the values of mean dilution reflect that both $\frac{\mu}{Q_0}$ (from velocity measurements) and C_{\max} (observed from concentration measurement) are in consistant trends, (4) the C_{\max}/C_{ave} ratios of the jets obstructed with perforated discs are in the range of 1.052 to 1.369, (5) the μ/Q (mean dilution) versus z/l_Q (normalized distance) of the simple jets and the jets obstructed with perforated discs have been plotted in Figures 6. They show that the jets obstructed with perforated

discs have a higher mean dilution than that of the simple jets for a given z/l_Q . Another measure of the effectiveness of enhanced mixing is to compare the maximum dilution for both the case of simple jet and that for jet obstructed with perforated disc. This is shown in Figures 7. It is found that there is a significant increase of the maximum dilution with perforated disc.

4.0 Conclusions

The results of the present work proved that the jets obstructed with perforated discs have wider profiles of velocity, turbulent intensity, turbulent shear stress and concentration than the simple jets. The normalized diagrams from the experimental results also indicate that the data distributions of the jets obstructed with perforated discs are flatter and broader than those of simple jets in the fields of velocity, turbulent intensity, turbulent shear stress and concentration. All of this provides evidence that jets obstructed by perforated discs have larger areas for mixing than those of the simple jets.

It is clear from the concentration measurements that for the jets obstructed with perforated discs, the concentration of the entrained fluid is greatly reduced and that the region for mixing is significantly enlarged. The results from the calculation of mean dilution and maximum dilution also indicate that the jets with perforated discs can produce significantly increased dilutions when compared with simple jets. The overall experimental results demonstrate quite convincingly the ability of the perforated disc to enhance the mixing and entrainment of the discharging fluid with the ambient fluid.

Acknowledgment

This research study has been supported by University of Southern California Foundation for Cross-Connection Control & Hydraulic Research and the San Gabriel Valley Protective Association. The authors extend special thanks to Professor Fredric Raichlen and Professor John List of the California Institute of Technology for their generosity in granting use of the deep water tank and its associated facilities at W. M. Keck Laboratory of Hydraulics and Water Resources of CalTech for the experiments.

References

1. Chen, C. J. and Rodi, W. (1978), Vertical Turbulent Buoyant Jets - A review of Experimental Data. *HMT Vol. 4, Pergamon Press*, 83 pp.

2. Fan, L. N. (1967), Turbulent Buoyant Jets into Stratified or Flowing Ambient Fluids, *Report No. KH-R-15, W.M. Keck Laboratory of Hydraulics and Water Resources*, California Institute of Technology.
3. Fan, L. N.; Brooks, N. H. (1969), Numerical Solution of Turbulent Buoyant Jet Problems, *Report No. KH-R-18, W.M. Keck Laboratory of Hydraulics and Water Resources*, California Institute of Technology.
4. Fischer, H. B.; List, E. J.; Koh, R.C.Y.; Imberger, J.; and Brooks, N. H. (1979), Mixing in Inland and Coastal Waters, *Academic Press*, New York, N. Y., 483 pp.
5. Hannoum, I. A. and List, E. J. (1988) Turbulent mixing at a shear free density interface. *J. Fluid Mechanics*, 189, 211-34.
6. Koh, R. C. Y. and Brooks, N. H. (1975), Fluid mechanics of wastewater disposal in the ocean. *Ann. Rev. Fluid Mech.*, 7, 187-22.
7. Noutsopoulos, G. C. and Demetriou, J. (1980), The round vertical turbulent buoyant jet impinging on a concentric disc, *Progress Water Technology*, 13, 305-314.
8. Noutsopoulos, G. C. and Yannopoulos, P. C. (1989), Axial dilution in obstructed round buoyant jet. *J. of Hydraulic Engineering*, Vol. 115, No. 1, Jan., 1989. 71-81.
9. Papanicolaou, P. N. and List, E. J. (1987), Statistical and spectral properties of tracer concentration in round buoyant jets. *Int. J. Heat Mass Transfer*, Vol. 30, No. 10, 2059-2071.
10. Papanicolaou, P. N. and List, E. J. (1988), Investigations of round vertical turbulent buoyant jets. *J. Fluid Mech.*, Vol. 195, 341-391.
11. Wallace, R. B. and Wright, S. J. (1984), Spreading layer of two-dimensional buoyant jet, *J. Hydraulic Engineering*, Vol. 110, No. 6, June 1984. 813-828.
12. Wu, Lilun (1996), Enhanced mixing through perforated disc on round buoyant jet, Ph.D Thesis University of Southern California, Los Angeles, CA

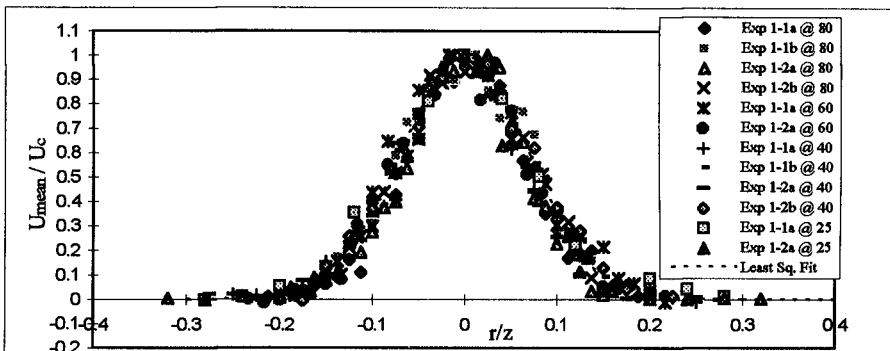


Figure 1 Non-dimensional Mean Axial Velocity Profile for Jets Plotted Against Non-dimensional Distance from Jet Axis, $z/D \geq 50$

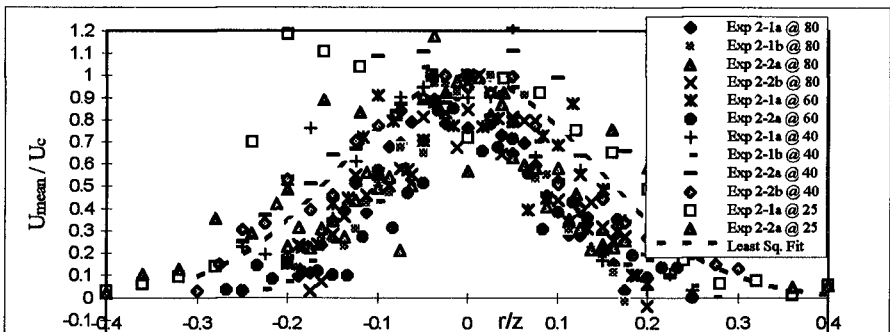


Figure 2a Non-dimensional Mean Axial Velocity Profile for Jet Obstructed with Perforated Disc (2x2) Plotted Against Non-dimensional Distance from Jet Axis, $z/D > 50$

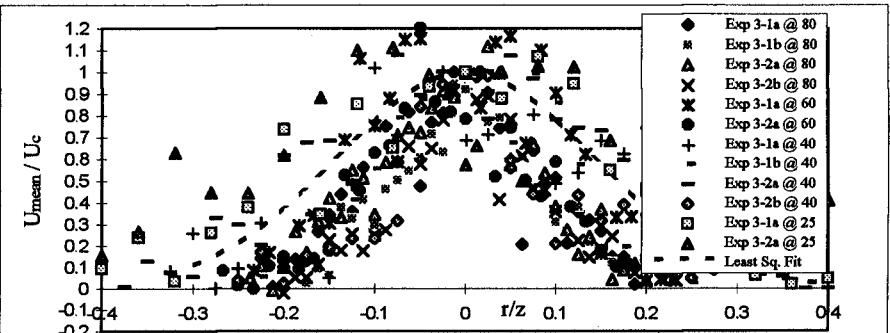


Figure 2b Non-dimensional Mean Axial Velocity Profile for Jet Obstructed with Perforated Disc (2x8) Plotted Against Non-dimensional Distance from Jet Axis, $z/D > 50$

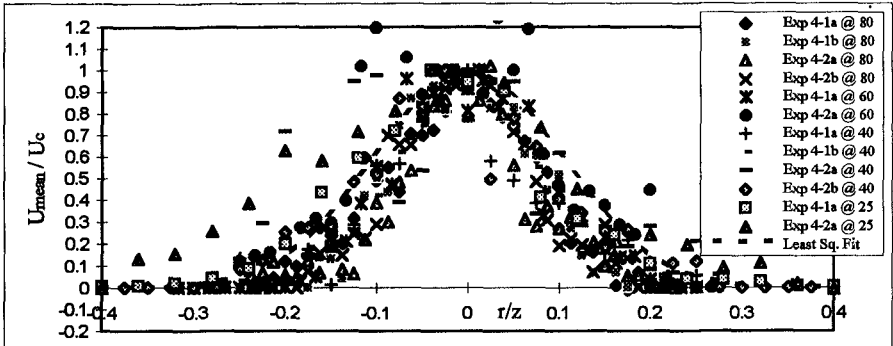


Figure 2c Non-dimensional Mean Axial Velocity Profile for Jet Obstructed with Perforated Disc (B2x8) Plotted Against Non-dimensional Distance from Jet Axis, $z/D > 50$

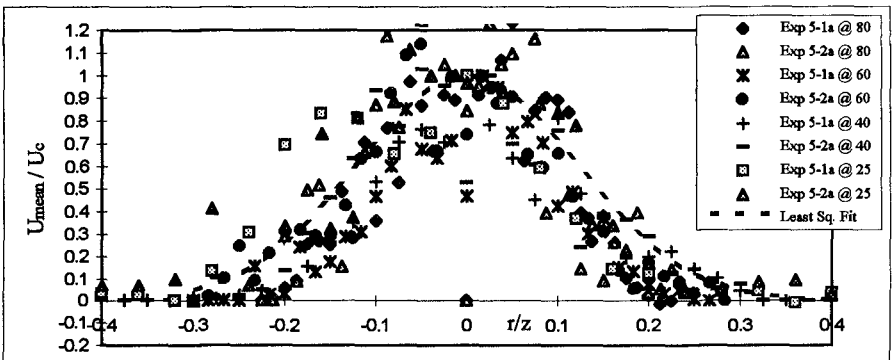


Figure 2d Non-dimensional Mean Axial Velocity Profile for Jet Obstructed with Perforated Disc (323) Plotted Against Non-dimensional Distance from Jet Axis, $z/D > 50$

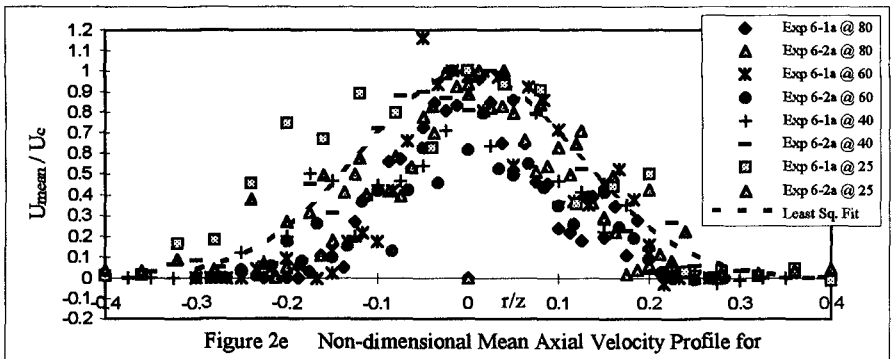


Figure 2e Non-dimensional Mean Axial Velocity Profile for Jet Obstructed with Perforated Disc (4+1) Plotted Against Non-dimensional Distance from Jet Axis, $z/D > 50$

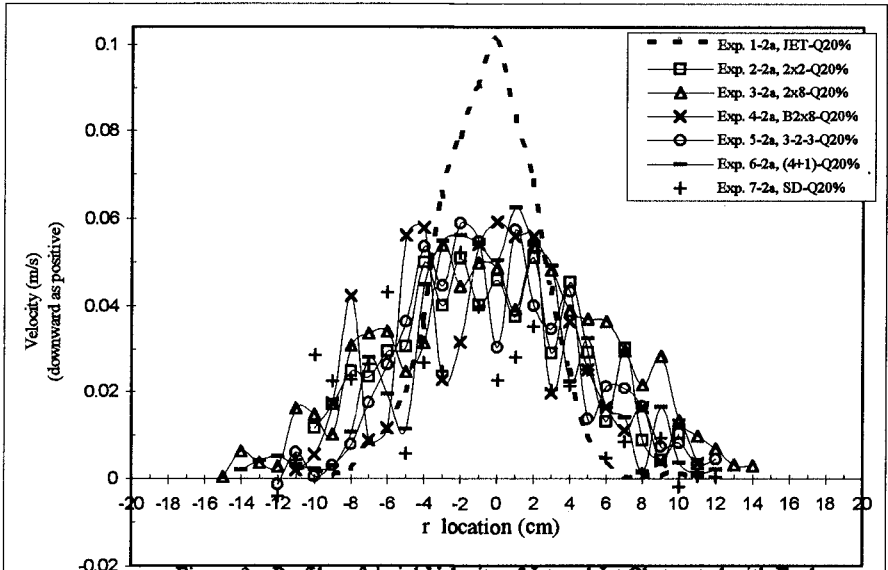


Figure 3a Profiles of Axial Velocity of Jet and Jet Obstructed with Each Perforated Disc at $z=40$ cm for $Q=24.72$ cm³/s

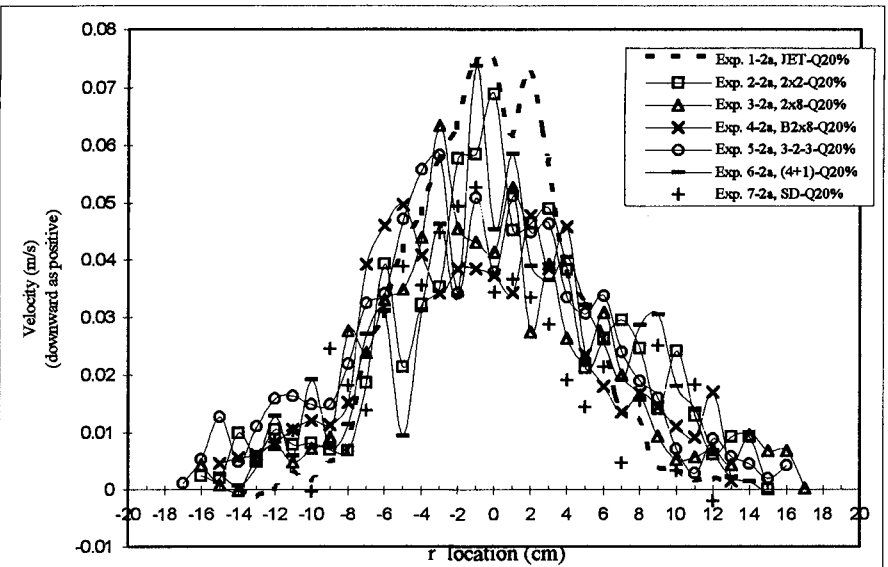
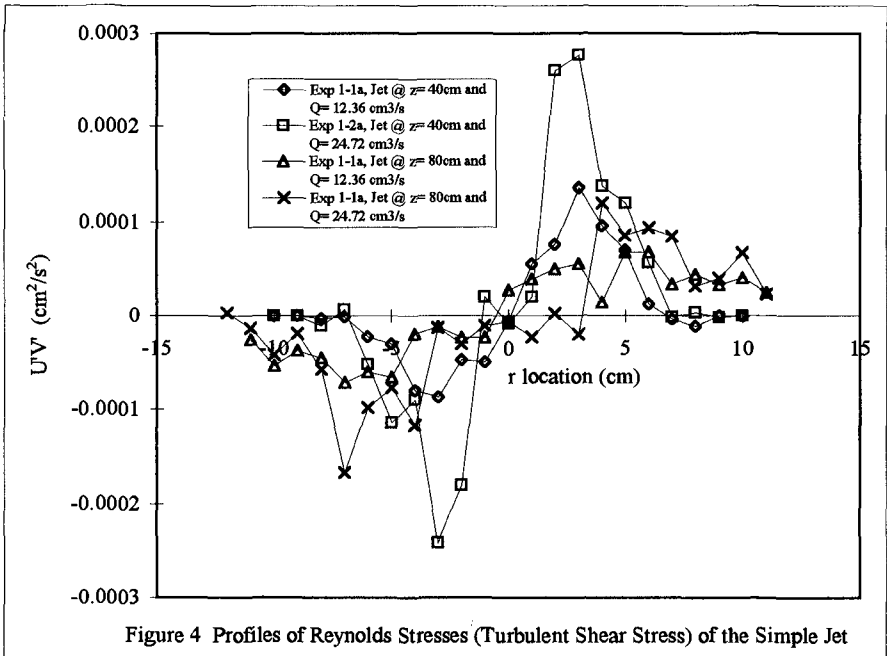
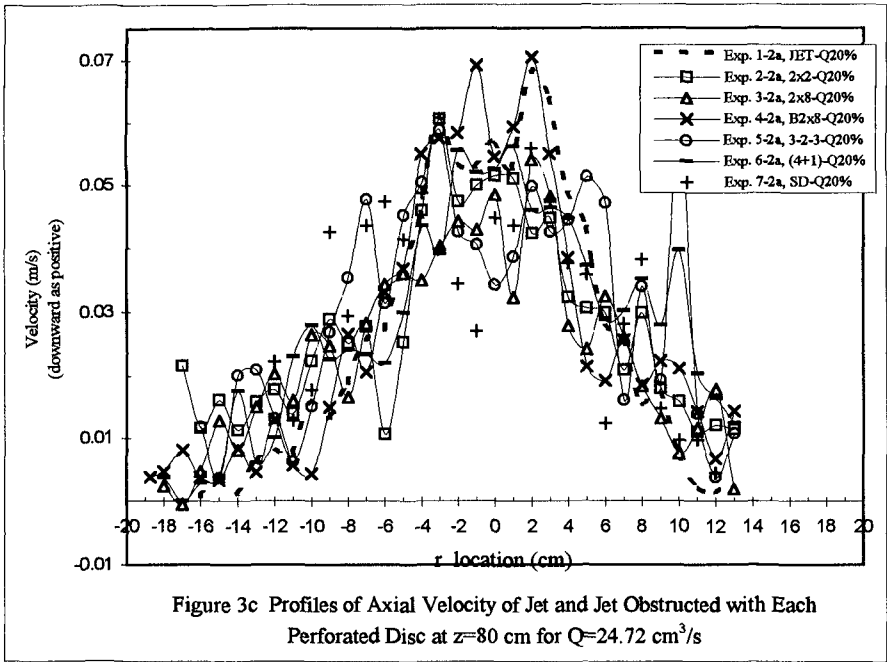


Figure 3b Profiles of Axial Velocity of Jet and Jet Obstructed with Each Perforated Disc at $z=60$ cm for $Q=24.72$ cm³/s



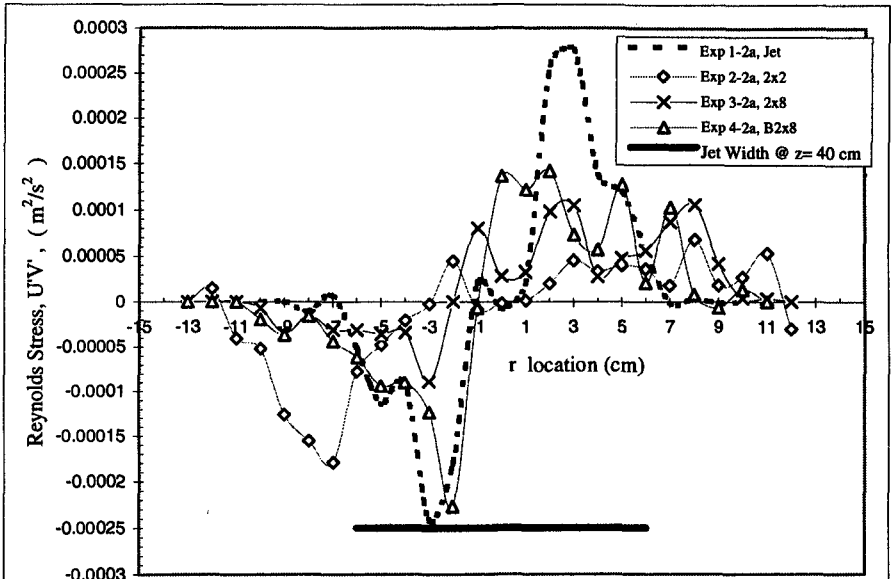


Figure 5a Profiles of Reynolds Stresses (Turbulent Shear Stress) at $z=40$ cm for $Q=24.72$ cm³/s

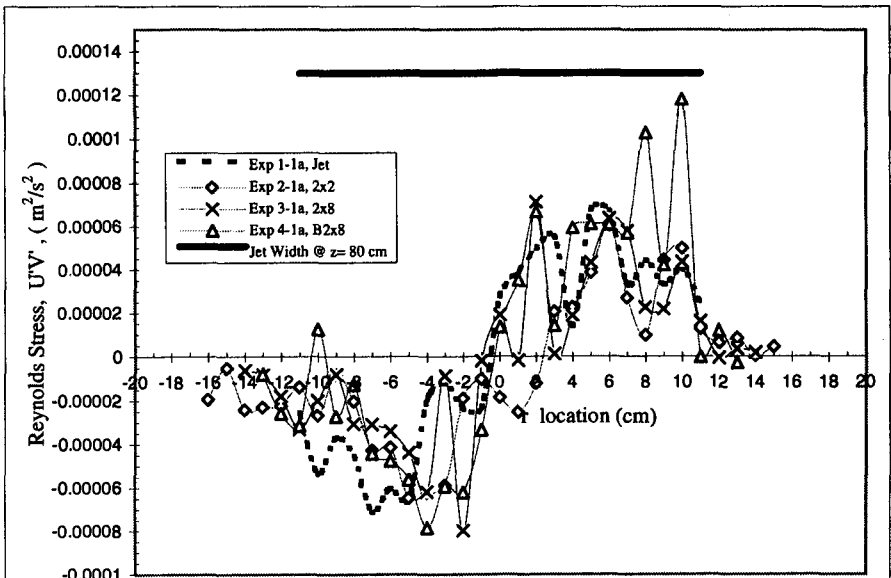
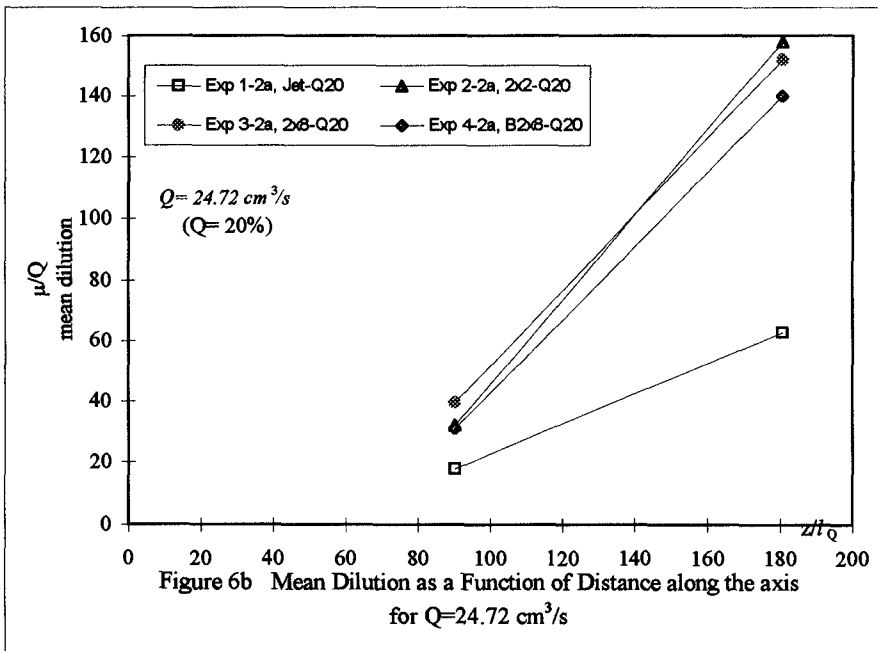
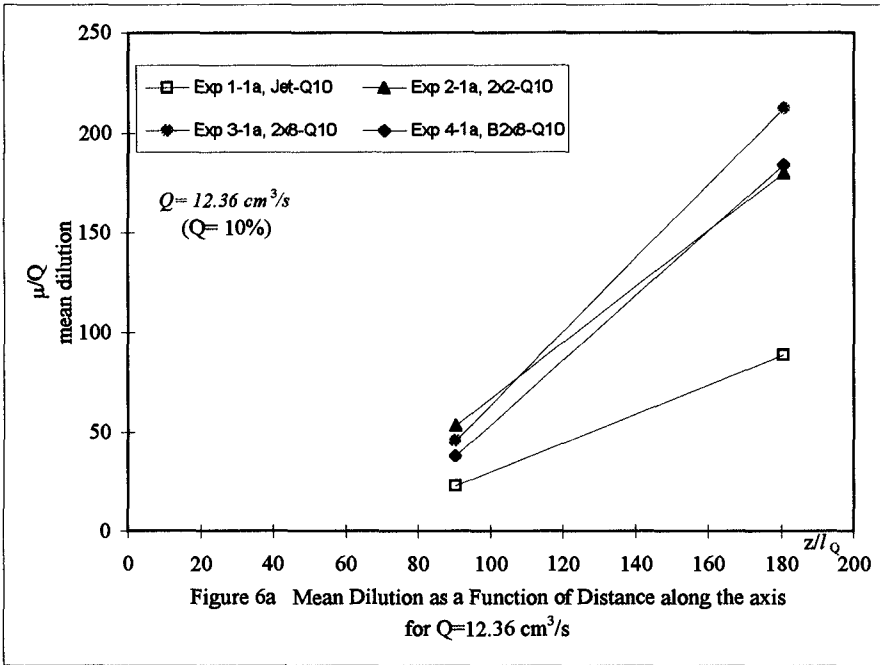
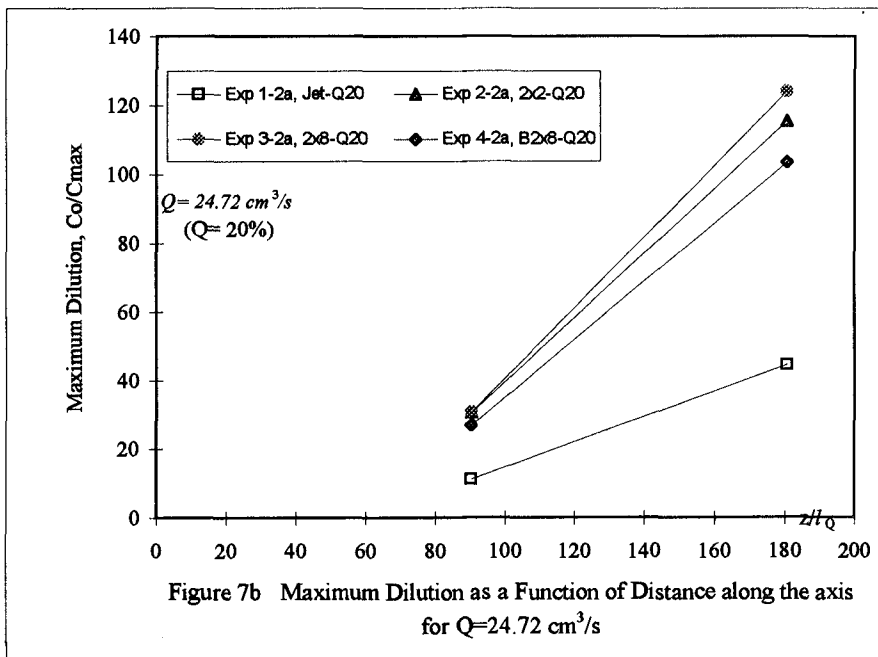
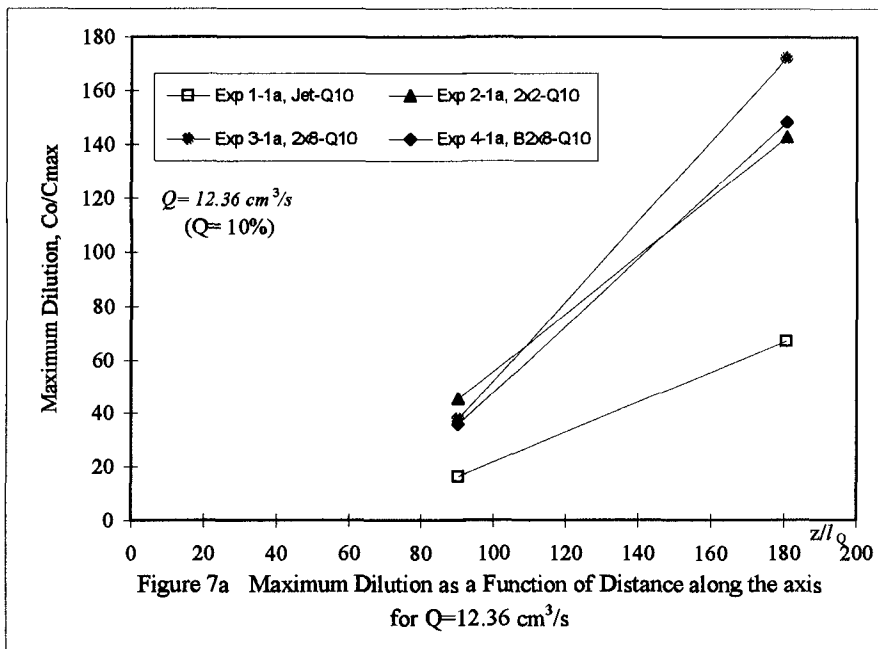


Figure 5b Profiles of Reynolds Stresses (Turbulent Shear Stress) at $z=80$ cm for $Q=24.72$ cm³/s





CHAPTER 336

ASSESSING COASTAL FLOOD RISKS

by Roger Maddrell¹, Chris Fleming¹ and Chris Mounsey²

Abstract

The English and Welsh coasts of the United Kingdom are protected from coastal flooding (as opposed to coastal erosion) by some 1300km of defences, containing about 2000 defence structures. Using data from the sea defence survey of these structures and over 20 years of joint probability data on sea levels and waves, Halcrow assessed the failure risks and coastal flood risks for all these defences. The risks were examined for three Bands or return periods, namely 50 years, 100 years and over 200 years. This analysis included 50 years of relative rise in sea level (isostatic and eustatic changes). The modes of defence failure examined were from overflow, overtopping and toe failure. The results were supplied to the insurance industry, as maps and on disc, as 1km map squares giving the risk band, flood depth and the postal codes in the areas.

Flood risks were shown to be significant and even though reduced when more recent flood defence projects were included, they remain high. The impact of individual storms was later examined and obviously, while the risks were limited to specific areas and coasts, they were still significant. The insurance industry have used these results in order to assess their financial exposure to individual events and to their reinsurers.

Introduction

Potential coastal flood risks areas represent only about 3% of the area of England and Wales, but the value of their insured assets is much higher. Two major storm events in October 1987 and January 1990 sharpened the insurance companies and the "reinsurers" (who insure the insurance companies) concern about their exposure to

¹ Sir William Halcrow & Partners Limited, Burderop Park, Swindon SN4 0QD, UK

² Association of British Insurers, 51 Gresham Street, London, EC2V 7HQ, UK

weather and coastal flooding risks. No one wished to see another 1953 type disaster. Consequently, in 1992 the Association of British Insurers (ABI) asked Halcrow to categorise the flood risk from coastal storm events for the benefit of their 450 members

The ABI membership between them account for over 90% of the UK business. ABI's key objectives are to help insurance companies by representing their interests to Government, particularly on public policy issues; providing them with technical services, in particular in respect of industry statistics, market and regulatory information and reducing the incidence of claims; and promoting insurance and insurance companies generally. It also helps its members at the pre-competitive stage, to improve their chance of success in achieving a balanced underwriting account.

Naturally, ABI are the focus for presenting the industry's concerns on major issues to the Government, ministers and civil servants, MPs, European bodies, the media, consumer bodies and other opinion formers. This responsibility is taken very seriously and it is recognised that their value is diminished if based on inaccurate and illfounded information. Thus, ABI concentrates on resolving real live issues which will affect the industry, of which coastal flooding is particularly relevant.

The areas covered in the Halcrow study were those protected by 1300km of coastal flood defence, the defences of only four main estuaries, namely, Tees, Humber, Thames (Upper and Lower) and Severn, but none of the other estuaries and channels. The pilot study in 1993 examined a detailed approach and one using the sea defence survey (SDS) data from the UK's Environmental Agency (EA). As the results in terms of flood risk were similar, the latter was chosen as it had the shortest completion time and was the most cost effective.

The first main study report was presented to the ABI membership in 1994 and was subsequently updated in 1995 to include for the new and improved defences built since the SDS was published in 1990. Additional studies include the prediction of flood risk from individual storms, using data supplied by the UK's Meteorological Office, examining and reporting on those defence lengths shown to be not performing or at greatest risk and the flood risks to London from combined tidal and high fresh water flows. The latter study is nearing completion.

Study Methodology

The assessment of flood risk needs to examine the integrity of the existing sea defences and assess their likelihood of failure and the extent of the subsequent flood area. There are nearly 1300km of coastal flood defences in England and Wales, containing some 2000

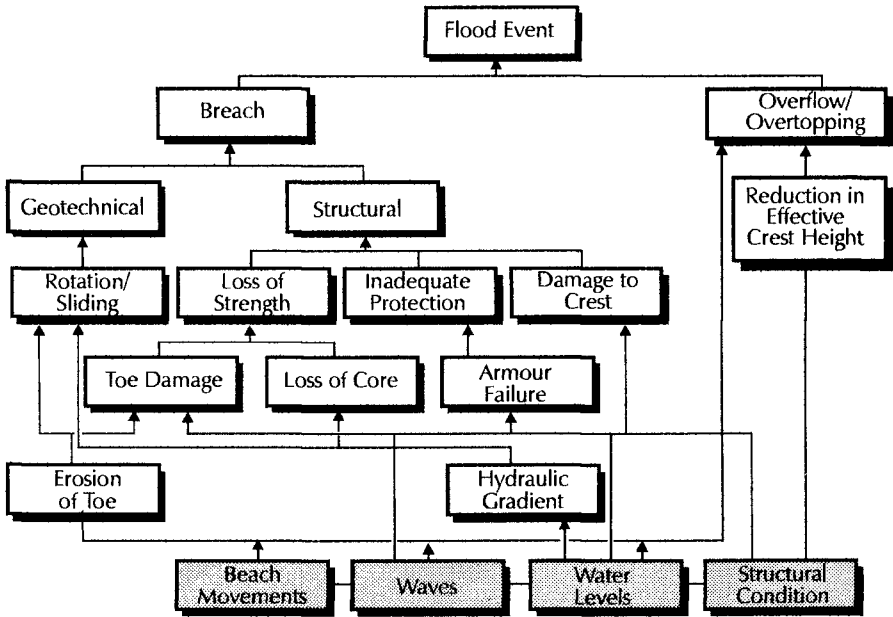


Figure 1. Key failure modes

structures and the integrity of each defence had to be examined. Flood risk can be approached in a number of ways, from highly subjective visual assessments, through to detailed probabilistic analyses based on comprehensive structural data. Whilst detailed probabilistic analyses, including all failure modes, can be applied in specific cases, the pilot study showed it was not economically viable for application on a nationwide basis.

Two methods were examined in the pilot study, which explored the relative costs and the quality of results from each approach. The first method offered a detailed approach, analysing a number of key failure modes (see Figure 1) to provide a quantified assessment of failure risks. This method also incorporated a set of screening tests to reduce the number of defences to be analysed, with the remainder requiring detailed structural information. The major disadvantage of this approach was not the amount of calculation required, which could be automated, but the high costs of acquiring detailed data which could only be acquired through structural inspections (Burgess and Reeve, 1994).

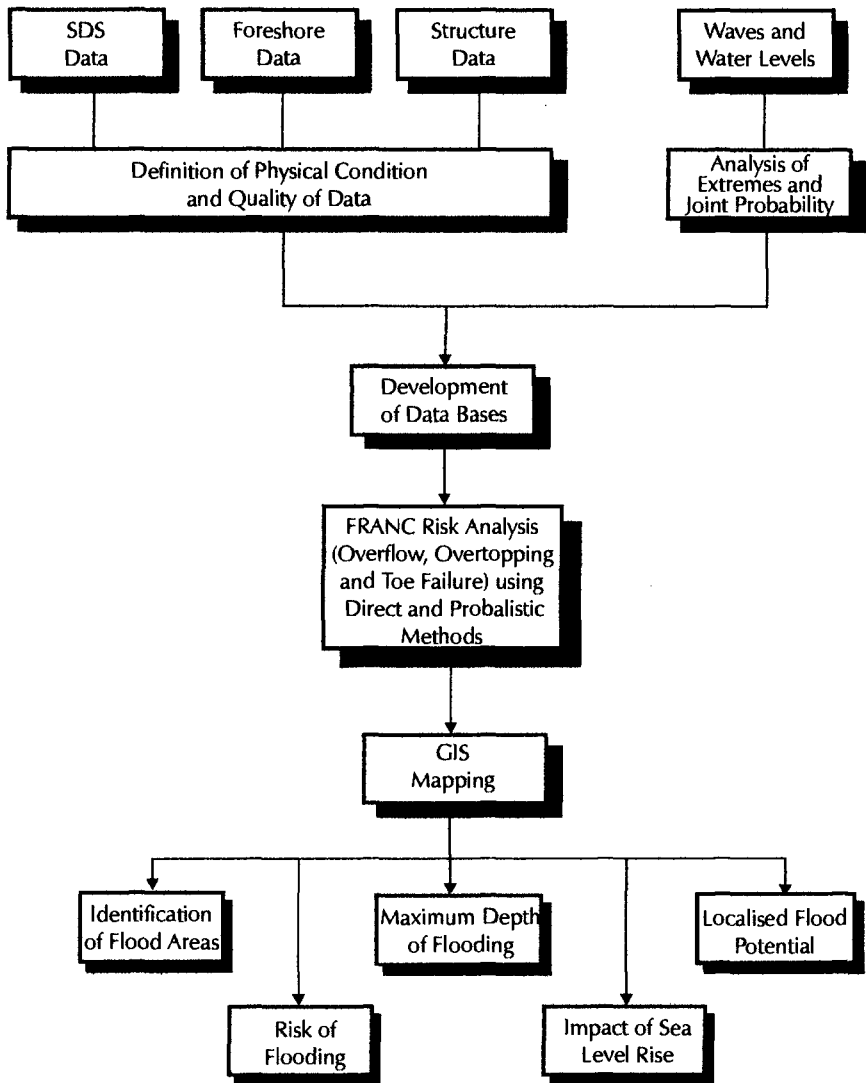


Figure 2. Methodology

The alternative second method made use of information in the UK's Environmental Agency's (EA) sea defence survey (SDS) to estimate risk of failure, supplemented with environmental data. This methodology (see Figure 2) concentrated three primary failure modes namely:

- Overflow - when the still water level exceeds the crest of the defence;

- Overtopping - when the combined effect of waves and water levels results in waves running up and breaking over the defence;
- Toe Failure - when the toe of the structure fails due to low beach levels at the base of the defence (erosion being one of the most common causes of damage to sea defences).

For open coasts, normally overtopping and toe failure and to a certain extent, overflow were critical, but for the estuaries the modes were overflow and toe failure with overtopping being less critical.

The starting point of the study was the 1990 SDS which was a major undertaking and a considerable step forward in flood defence management by updating the original 1980 Herlihy study. An analysis for each defence required a site specific knowledge of waves and water levels. Therefore, inshore study points were defined on the open coast and in the estuaries. Future relative sea level changes were also established. Water level time series covering a period of 30 years were combined with 20 years of offshore wave data, transformed inshore through modelling, to produce marginal and joint probability extremes together with a statistical description of the conditions.

The quality of available structure and beach data was, unfortunately, extremely variable and thus two types of risk assessment were developed for each defence; "direct" and "probabilistic" approaches. In general terms the "direct" approach involved determining the specific conditions and calculating to see whether a particular structure could withstand or would be likely to be at risk of failure under these conditions. The risk of failure and hence flood risk was described by risk bands, with Band 1 defined as a defence potentially vulnerable to a 1 in 50 year event ie with an annual probability of failure greater than 0.02, Band 3 as a defence withstanding conditions with a return period of 200 years, and Band 2 falling between these two limits. The "probabilistic" approach was a first order risk method to calculate the annual probability of failure and defined the risk as Bands 1, 2 or 3, depending on the annual probabilities of failure comparable with the return periods above.

The software package "SANDS" already existed, which could be used for data storage, retrieval and analysis. However, to perform the risk analysis computational software had to be developed for the project, acronym "FRANC", which enabled all three failure modes to be analysed by both the "direct" and "probabilistic" approaches. This was essential given the volume of data and the need to analyse 3 modes of failure for nearly 2000 defences. "FRANC" read the relevant data

direct from the "SANDS" database, performed the calculations, combined the results and assigned the defence classification. The software was designed to establish either an overall probability of failure risk based upon the results of all three mechanisms or to establish the worst case, ie the most likely mode of failure. The results were generated in a format that could be directly linked into the flood area mapping.

To perform the analysis of overflow and overtopping, both wave and water levels were needed. A 30 year water level time series for nearshore locations was obtained from the Proudman Oceanographic Laboratory's (POL) tide and surge model for the United Kingdom. Additional data, including annual maximum levels, were obtained for the Severn, Thames, Tees and Humber estuaries, supplemented by information gathered from the relevant Port Authorities.

Wave data at offshore locations were obtained in the form of a time series output for the North European Storms Study (NESS), which gave wave height and direction for some 32 offshore locations and covered a period of just over 20 years. For the outer areas of the estuaries, wave time series were hindcast from wind measurements covering a period in excess of 14 years for each estuary. Extreme wave heights in the upper estuaries were calculated from monthly maxima wind speeds using shallow water wind-wave hindcasting techniques.

The site specific information on waves and water levels was derived from inshore study points using wave refraction models. This required the digital reproduction of the nearshore bathymetry around the entire English and Welsh coastlines and resulted in the generation of sets of time series wave conditions at each of these locations. Shallow water effects were accounted for by spectral saturation, Bouws et al (1985), whilst wave breaking at each structure related to the beach condition and water level.

In interpolating the water level data to the study points, extreme values were adjusted to reflect the natural variation in Mean High Water Spring (MHWS). Future relative sea level changes in 50 years time for each location required the IPCC's (1990) prediction of global sea level increase due to global warming and isostatic changes described by Shennan (1989).

Extreme values of water levels, wave heights and periods were defined in terms of a return period with the marginal distribution functions determined by fitting a distribution to the data. In this case, the Generalised Extreme Value (GEV) was used to estimate extreme values from the annual maxima of each variable (Carter et al, 1986). Joint extreme values were established empirically from frequencies of occurrence (see Owen, 1980 and Hawkes, 1990), for assessing the risk

of overtopping, where the combination of water levels and waves is important. The results of these data processing exercises were incorporated into the database, for use in the risk assessment.

The results of the risk analysis were transferred to a Geographic Information System (GIS) to relate the risk classification of each defence to its associated flood area. The flood areas were defined by establishing the intersect between predicted extreme water levels and the terrain. Flood depths were established from the interrogation of the Ordnance Surveys (OS) base data and any available drawings to derive ground level estimates. Maps were produced on OS backgrounds using the GIS for 10km by 10km coastal flood areas, showing the risk bands and predicted maximum depth of flooding within each 1km grid square. This size grid was chosen mainly because of the large area that had to be covered in the short time available and the lack of detailed survey data below the 5m contour.

Two characteristics of the sea defences were of relevance to the flood risk mapping; the location of a defence and its risk classification. The location of each defence length was defined by start and end co-ordinates in the SDS database. An automated routine was used to interrogate this information and plot the defences within the GIS. The risk classification output from the defence analysis software was loaded into the GIS database and related to the plotted graphic elements using a unique defence length code identifier. When more than one defence structure existed within a defence length, the highest risk probability amongst those structures was assigned to that length.

The risk assigned to a defence length was then transferred to the area being defended. Again, the rationale of assigning the highest risk was applied so that in cases where a single flood area was bordered by a number of defence lengths of differing risk values, the highest risk value amongst those was transferred to the defended area. The seaward extent of the defended area was taken as being the line of defence and the landward extent that line at which the water level, associated with a given event, intersected the land surface ie the same methodology as that used in the SDS. The accuracy with this line could be determined was largely reliant on the availability of ground level information, some of which was poor.

The variation found in the water levels associated with the 50 and 200 year event typically ranged between 0.1m and 0.5m. This made the differentiation of discrete flood boundaries associated with the 50, 100 and 200 year events problematical, given the quality and quantity of ground level data available from OS sheets.

The protected areas were overlaid with 1km grid squares. Each 1km grid square took on the highest risk classification of any defended areas which it wholly or partially covered. Post code sector

data was provided by the UK's Post Office and the risk was related to the post code sectors.

In addition to the risk classification assigned to each grid square, an attempt was made to assess the depth of flooding using the very limited ground level data available. The approach was generally simple, making a direct interpolation of the depth of flood water calculated at available data points behind the defence and at the inland boundary of the flood water. Where possible, the influence of features such as inland embankments was included.

This method of interpolation obviously created discrepancies when assigning a single flood value across 1km grid squares, which might contain areas of higher relief. Similarly, where the level of the ground was below that defined by drawings or spot heights, underestimation of the depth of flooding occurred.

Results

Each analysis was rigorously checked for its approach and the correctness of numerical results and a further check was carried out to verify the overall output. Direct verification was restricted due to the lack of recorded instances of defence failures, despite obtaining newspaper reports. The "Effective Level of Service" recorded in the SDS provided an alternative measure against which the analysis results could be compared, details of which are given in Table 1.

Classification	SDS (%)	Halcrows' Study (%)
Band 1, 50 year	33	28
Band 2, 50 to 200 years	15	5
Band 3, > 200 years	52	67

Table 1. Overflow classification results, percentages of defences at risk

The results from the original study showed a good agreement for overflow with those in the SDS (only overflow was examined in the SDS) with 64% of all structures analysed having the same risk classification. Of the remaining 36%, the majority had a lower classification than that given by the SDS. However, notwithstanding the differences in analysis and classification techniques, a slightly lower result is expected as the Halcrow study used probabilistic calculation where possible, in preference to a direct method of determination.



Figure 3. Coastline of England and Wales, outlined by Band 1 risk areas

Consequently, the overall result was considered satisfactory and was confirmed by major coastal flood events. Consequently, the overall results was considered satisfactory and was confirmed by recent major coastal flood events such as those at Towyn in North Wales, which were shown to be in Band 1.

Toe failure results were spread between the risk bands although 22% of them fell within Band 1. Given the widespread erosion of many of the UK's beaches, this was perhaps not too surprising. Of possibly greater significance was the high percentage of defences apparently at risk from overtopping. Whilst the risk criteria were based upon well established and universally accepted overtopping thresholds (see Owen, 1980 and Hawkes, 1990), the question of whether critical damage would only result from sustained overtopping over a reasonable duration, was examined. To take account of this, the risk thresholds were therefore set an order of magnitude higher, ie assuming the defence could withstand ten times the established criteria before failure could occur. All the areas falling into Band 1 are shown on Figure 3.

It should also be noted that, with the Band 3 risk threshold as a 1 in 200 year event, the total number of potentially defences at risk falling within Band 2, was only 12%. This percentage could only be increased if the upper and lower thresholds for Band 2 were an order of magnitude apart ie taking Band 1 as a 20 year event.

The initial study was based upon the structural data in the SDS and did not include new defences or remedial works carried out since 1990. However, minor updating of the SDS information was undertaken where possible, and Halcrows recently completed an updated study for the ABI following liaison and co-operation from the EA Regions. The results, which included the most recent defence improvements, showed a reduction of 7% in the structures vulnerable to Band 1 events.

The maps produced for ABI only indicate the flood areas associated with the defined sea defences and the named estuaries. Other potential risk areas, eg the Fens inland of the Wash and other estuaries were not within the defined scope of this study and were therefore not included on the maps. In addition, the available OS maps were not up to date and recent urban developments may have been missed.

Whilst many defences and thus coastal areas were given a Band 1 classification, this did not mean that all defences protecting such areas had an equivalent risk as, in reality, the failure of only a relatively short length of defence could lead to widespread flooding. As described earlier, the weakest link in any flood area frontage was taken to represent the risk associated with that area, although the majority of the defences might have had a much greater integrity and a relatively minor amount of remedial works could be sufficient to move the areas into Bands 2 or 3.

The results provide a relative measure of flood area risks and the risk of failure does not necessarily imply that a total functional failure of a defence and subsequent flooding would definitely occur. It

simply indicates potential risks and vulnerability under particular conditions. No account could be taken of remedial or emergency action, which might occur prior to or after an event. Because of constraints in time, the impact of successive tides could not be taken into account, nor the likely time for breach repair or flood duration.

The 1:10,000 maps and Figure 3 show very large areas of the coast and specified estuaries as Risk Band 1, ie being at risk to inundation from a 50 year storm event, it does not mean that all these areas are susceptible to any one single event, simply that they have a greater probability of being affected. Thus, while a major storm event could affect large areas of the East, South and West coastal areas of England and Wales, it will not affect all coastal areas as its impact will be limited to relatively short lengths of coastline, particularly on the South and West coasts. On the East coast a major event could affect larger areas, as experienced during the disastrous 1953 event.

The impact of individual storms was therefore examined following on after the two earlier studies. As described above, the coasts of England and Wales were divided into three coastal areas: West, South and East. Meteorological records going back to the last century were analysed by the UK's Meteorological Office in order to determine generic storm types. In all, the two storms likely to have the most significant impact on each of the coasts and their associated wave and surge conditions were defined for each section of coast. Significant storms affecting more than one section of coast were also defined. While it is possible to define wave and surge levels in terms of their probability of occurrence, it is not possible with storms. This is because they are made up of many different elements eg air pressure, density and spacing of isobars, storm track direction etc, each of which can influence the other. The impact of the conditions produced (wave and surge) also varies along the coast, say being 1 in 50 year near its centre decreasing to 1 in 1 year towards its edge.

The storms produced varying conditions along the coastline and thus assigning a particular return period to an individual storm is problematical. A prime example is the 1953 East coast storm, where shoreline conditions experienced in Yorkshire were estimated to be in the order of 1 in 50 years, whilst by the time the storm surge had been driven south to Lincolnshire and East Anglia, it represented a 1 in 500 year condition.

The analysis defined the impact of potentially different storm types for each coastal area rather than specific storms. Detailed comparison of the analysis against past events was not possible, but a qualitative comparison of results and newspaper reports of flooding was made.

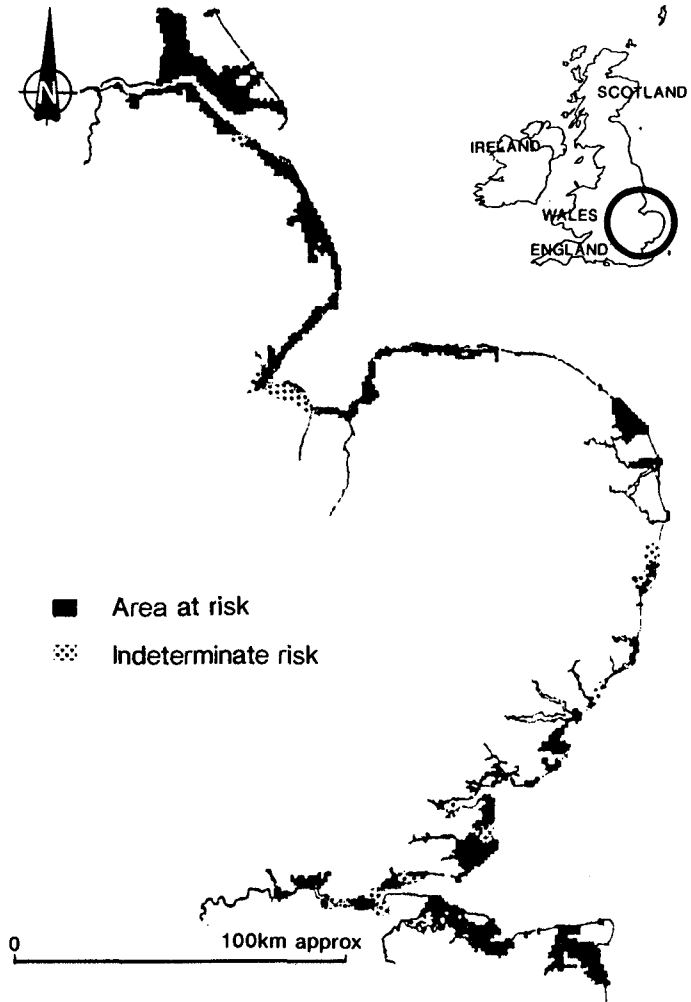


Figure 4. Flood risk areas resulting from a major East coast storm

Two storms affecting individual coasts were examined, together with one affecting both the East and South coasts, one affecting both the West and South coasts and one hypothetical storm for each coast. The hypothetical storms represent small changes of previous storms to modify the timing of the storm surge to coincide with high water. These were then compared as a way of establishing the storm scenarios with the greatest impacts.

Typical variations in the wave and water level conditions adopted for the single storms and the two earlier studies were examined, including the probabilistic wave heights and water levels for return periods of 50, 100 and 200 years. The comparison showed variation in wave height for the East coast locations were markedly different and other differences along the remaining coasts were also apparent. The variations were smaller for water levels.

The results produced by "FRANC" for these storms showed that one of the East coast storm produced the highest number of defences at risk ie 36.5% (see Figure 4) The percentages at risk from the other two East coast storms were very similar, although their distribution was different.

The South coast storms indicate that a high percentage of defences were at risk (approximately 70%). Both have an eastbound surge associated with waves of between 9m and 13m, generated by gale force winds sweeping in from the Atlantic. On the West coast, the hypothetical storm produced the worst conditions with 383 defences at risk (48.1%). Had it been coincident with high tide, the results would have been more severe.

The Insurance Industry's Application of the Results

The information from the studies was applied by the Insurance Industry in two basic ways, namely;

- the practical application of the project output data in overall portfolio exposure and in underwriting individual property risks on a geographic basis according to flood risk; and
- strategic use of the valuable data (which supplements and refines the existing knowledge base) to assist Government, through its agencies (MAFF and the EA), to target resources to exposed locations, always recognising the need for cost/benefit analyses.

The individual insurers try to obtain sufficient premium to cover their potential exposure and to do this they need to understand the underlying risk. The output of the project was therefore applied to this end by analysing the areas at risk against the locations and post codes of the insured properties to establish their aggregate portfolio exposure.

Insurers usually also have to operate with the support of reinsurers (who are also subject to the same regulatory approach) to give them added capacity or to reduce the financial consequences of a catastrophic loss eg 1987/90 storms or coastal flood. These reinsurers need to be satisfied that the insurers they are backing are

not themselves overexposed and also require some technical evidence these studies provided in order to take on these risks.

The data analyses from the study were therefore able to assist the insurers to:

- assess their overall exposure;
- determine whether correct rates are being charged; and
- provide information to reinsurers to gain their “capacity” and “catastrophe” support.

It also allows them to put pressure on the relevant Government Departments and to consider their exposure globally.

References

Bouws E, Gunther H, Rosenthal W and Vincent C, 1985. Similarity of the wind wave spectrum in finite depth water. J Geophys Res 90 (C1).

Carter, D J T et al, 1986. Estimating wave climate parameters for engineering applications, Department of Energy Offshore Technology Report OTH 86 228, HMSO.

Diment R P and Deakin R, 1994. The role of GIS in risk assessment, European Geographic Information Systems Conference '94, Paris.

Hawkes P J, 1990. Joint probability of waves and water levels on the north Wales coast, Hydraulics Research Limited, Report EX 2133.

IPCC (Intergovernmental Panel for Climatic Change), 1990. Climate Change, Cambridge University Press.

Herbert D M, 1993. Wave overtopping of vertical walls, Hydraulics Research Wallingford, Report SR316.

Maddrell R J, Burgess K A and Mounsey C, 1995. Coastal flooding: assessing the risks for the insurance industry, ICE Conference, Bournemouth, p167 - 184.

Owen M W, 1980. Design of seawalls allowing for wave overtopping, Hydraulics Research Station Wallingford, Report EX 924.

Shennan I, 1989. Holocene crustal movements and sea level change in Great Britain, Journal of Quaternary Science.

CHAPTER 337

EXPERIMENTAL STUDY ON THE BEHAVIOR OF BIVALVES BY OSCILLATORY FLOW

Toshihiko Yamashita¹, Akira Wada², Gaku Matsuoka³,
Kenji Yano⁴ and Sadamitsu Akeda⁵

ABSTRACT

To improve propagation of bivalves living in exposed sandy beach, we need to clarify the behavior of bivalves affected by water waves. Using a U-shape tube, the behavior of bivalves (surf clam and sunray surf clam) in an oscillatory flow was experimentally studied. It was found that the critical condition at which bivalves are forced out of the sand into the water is determined by the ratio between the velocity of bed erosion and the burrowing rate of bivalves, and until the bivalves are forced out into the water their own movement is significant. Also the experimental values measuring their behavior on a smooth surface fixed bed was found to be theoretically explained by setting C_D (drag coefficient), C_M (added mass coefficient) and μ (coefficient of dynamic friction) at 1.0, 0.5 and 0.1, respectively. After the bivalves are forced out into the water from the sand, therefore, their behavior is hardly affected by their own movement and we can regard them as inanimate objects.

INTRODUCTION

Japanese surf clam (*Pseudocardium sybillae*) and sunray surf clam (*Macrta cinensis*), which live in open sandy beaches along the coast of northern Japan are important fishery resources. However, there is a high mortality rate among young

¹Associate Professor, Department of Civil Engineering, Hokkaido University, N-13, W-8, Sapporo 060, JAPAN

^{2,3}Graduate Student, Department of Civil Engineering, Hokkaido University

^{4,5}Head of section, Civil Engineering Research Institute, Hokkaido Development Bureau, 1-3, Hiragishi, Sapporo 062, JAPAN

bivalves, which must be minimized to ensure their propagation.

There have been reports showing an increase in young bivalves of surf clams in tranquil areas around newly constructed ports (for example, Hayase and Miyamoto , 1985). A large number of young bivalves are often cast onto the shore by high waves in winter (Photo. 1). From these examples and other on-site investigations of the clam's population (Watanabe , 1980), waves, especially high waves during winter, have been thought to be one of the major factors responsible for the mortality of young bivalves. Therefore, the process of mortality and the behavior of young live bivalves due to waves must be clarified. As the first example above shows, bivalves are deeply related to structures built on coastlines. Therefore, for the designe of coastal structures with consideration to the surrounding environment, the influence on the bivalves by waves must be clarified.

The effects of the bivalves' own active movements (burrowing) are important for investigating the behavior of bivalves due to waves. Although some experimental studies have been carried out on the behavior of dead bivalves (Watanabe ,1982; Kuwahara ,1993,1994), except for our previous studies (Yamashita et al. 1994a,1994b,1995), very few experimental studies have been carried out on the behavior and mortality of live bivalves due to waves. The effects of the bivalves' own active movements (burrowing) under water waves have still not been estimated quantitatively.

Bivalves usually dig themselves into the sand. According to our previous studies, when the sea bed erosion and accumulation occurs due to the action of waves, the bivalves keep digging into the sand by reacting to the deformation of the sea bed. However they are sometimes forced out of the sand into the water by a sudden deformation due to high waves. This movement is thought to be the first phase in the mortality process.

In this study, the following five points were investigated in order to understand the first phase of the mortality process: (1) the critical condition of release, (2) the critical condition of burrowing, (3) the burrowing rate of bivalves, (4) the bed erosion velocity and (5) the moving velocity of bivalves on a fixed bed.

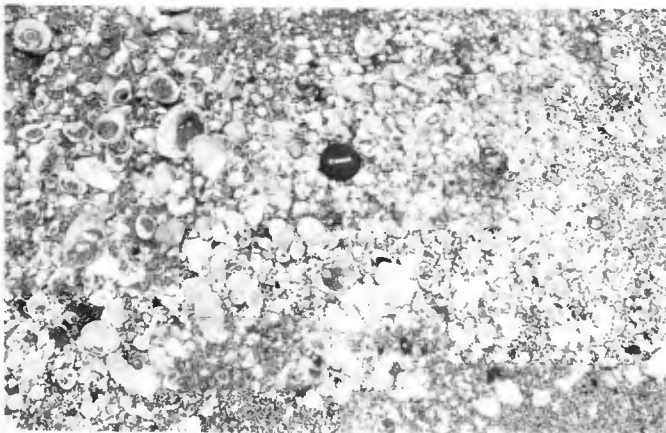


Photo.1 Young bivalves cast onto the shore in winter

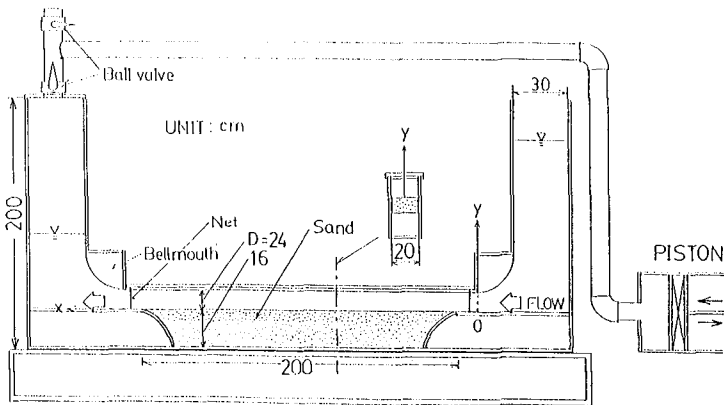


Fig.1 Schematical view of the U-shape tube

EXPERIMENTS

For the experiments, a U-shape oscillatory flow tube made of acrylic resin was used (Fig. 1). Sea water and sand were put into it. In the movable bed experiments, a 16cm-deep layer of sand, with a grain size of 0.3mm, was made at the bottom of the tube. In the fixed bed experiment, a plate made of acrylic resin with a smooth surface was used. Young live bivalves (surf clam and sunray surf clam), 5mm~40mm in size, were used in the experiments. The wave period was set at either 3 sec. or 3.5 sec. The amplitude of the flow velocity (U_m) ranged from 20 cm/s to 90 cm/s. The water temperature was set at 16°C~22°C.

The following were investigated:

- (1)the critical condition at which bivalves are forced out of the sand into the water
- (2)the critical condition at which bivalves forced out into the water can burrow back into the sand again
- (3)the decrease in the energy (burrowing rate) of bivalves due to a drop in water temperature
- (4)the bed erosion velocity at which sand ripples are formed
- (5)the behavior of bivalves forced out into the water on a fixed bed with a smooth surface.

Experiments were conducted according to the following methods. Experiment (1): After the bivalves had dug themselves into the sand, we generated an oscillatory flow, and the deformation of the bed and behavior of bivalves were recorded by video camera. Experiment (2): To measure the critical flow velocity at which bivalves can burrow into the sand, bivalves were put into water where stable sand ripples had formed by varying the flow velocity. Experiment (3): We measured the burrowing rate of bivalves by changing the water temperature from 20°C to 5°C every 5°C in a controlled temperature room, and investigated the relationship

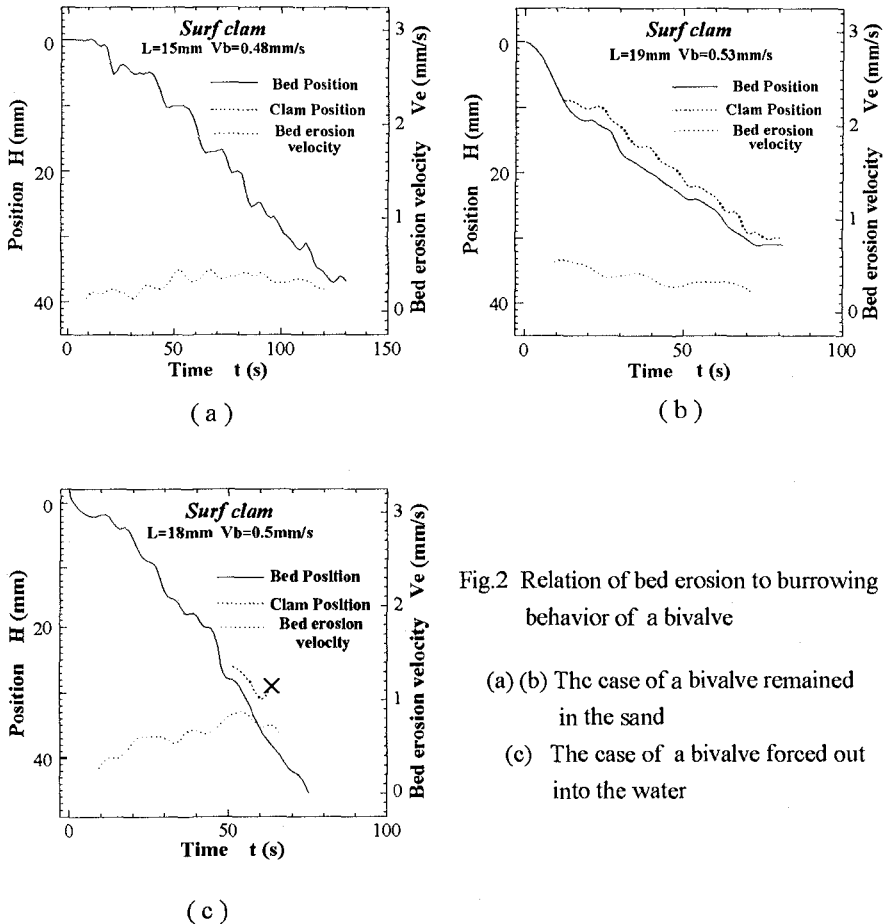


Fig.2 Relation of bed erosion to burrowing behavior of a bivalve

- (a) (b) The case of a bivalve remained in the sand
- (c) The case of a bivalve forced out into the water

between water temperature and burrowing rate of bivalves after adapting bivalves to each water temperature for three days. Experiment (4): We measured the bed erosion velocity at which sand ripples were formed from a flat condition using a video camera. Experiment (5): We measured the moving velocities of bivalves, and compared the theoretical and experimental values.

RESULTS

(1) Critical Condition of Release

Fig.2 shows typical examples of sea bed deformation and the behavior of the bivalves. The velocity of the sea bed erosion was calculated hourly from the variation in bed form. Fig.2(a) shows an example where the bivalve kept digging into the sand and remained there despite erosion of the sea bed, because the velocity of the

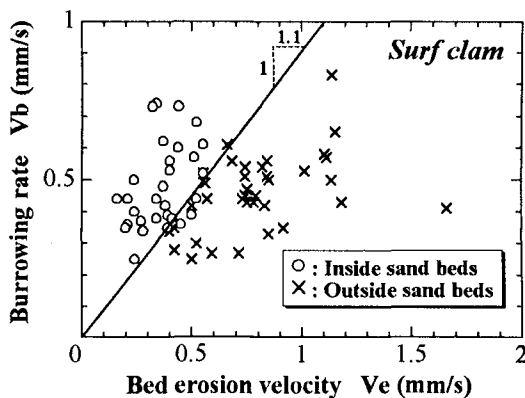


Fig.3 Critical condition at which bivalves are forced out of the sand into the water by the flow

sea bed erosion (V_e) was lower than the burrowing rate of the bivalve (V_b). Fig.2(b) shows another result. At the beginning of the experiment, the velocity of the deformation of the bed exceeded the burrowing rate of the bivalve, and only one-fifth of the shell length of the bivalve was washed out of the sand. However, later as the velocity of the bed erosion became lower than the burrowing rate of the bivalve, the bivalve remained in the sand. Fig.2(c) shows the following example. At the beginning of the experiment, the deformation of the sea bed occurred at a velocity almost equal to the burrowing rate of the bivalve, and the bivalve kept digging into the sand and remained there for 43 sec. after the experiment started. Later, as the velocity of the deformation of the bed exceeded the burrowing rate of the bivalve, the bivalve was at first partly washed out, and then completely forced out into the water. Fig.2 clearly shows that the critical condition at which the bivalves were forced out into the water is related to the bivalves' burrowing rate (V_b) and the velocity of deformation of the sea bed (V_e).

Fig.3 shows the relation between V_e and V_b based on data from 80 samples, using surf clams as Fig.2. Fig.3 shows the conditions of the bivalves with a certain burrowing rate at a certain velocity of deformation of the sea bed, which are categorized into the following: ○ indicates bivalves that remained in the sand completely, and × indicates bivalves that were completely forced out into the water. When the bivalves were washed out of the sand by about half the length of their shell, they tended to be completely forced out of the sand. Thus, the velocity of the deformation of the bed can be defined as the maximum value (V_{max}) in the experiment of the mean erosion velocity at which erosion of the sea bed occurred at a depth of half of the shell length. The burrowing rate of bivalves (V_b) can be calculated by dividing the shell length (L) by the time taken for bivalves to burrow into the sand.

Fig.3 shows that the critical condition at which bivalves are forced out of the sand into the water by the flow is determined by the ratio between V_e and V_b , i.e. 1.1. The present experimental results were higher than those using dead bivalves placed on the sand. Thus, until the bivalves are forced out into the water, their own movement is important.

(2) Critical Condition of Burrowing

Fig.4 shows the results using sunray surf clams of the critical condition at which bivalves forced out into the water can burrow back into the sand. In Fig.4, \circ indicates bivalves that could burrow into the sand under the water flow, and \times indicates bivalves that couldn't. The oblique line in the figure shows the critical condition. The critical flow velocity at which a bivalve with a certain burrowing rate can burrow into the sand is quantitatively obtained from this figure. It was found that when the burrowing rates of the bivalves increased, they can burrow back into the sand by themselves against higher flow velocities.

The critical flow velocity obtained in this experiment is the value that usually occurs at the sea bottom. Therefore, it seems to be difficult for bivalves which are forced out of the sand to burrow into the sand again under a rough sea for several days.

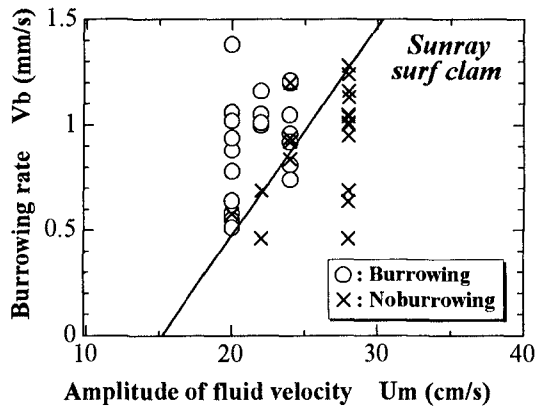


Fig.4 Critical condition at which bivalves forced out into the water can burrow back into sand again

(3) Borrowing Rate of Bivalves

The ability of the bivalves to dig into the sand by themselves greatly affects both the critical conditions at which the bivalves are forced out of the sand into the water and at which the bivalves can burrow back into the sand. Fig.5 shows one example (surf clam) of the experimental results concerning the burrowing rates of bivalves

with varying water temperatures from 20°C to 5°C. The straight lines in the figure indicate regression lines that coincide with the origin under each temperature. The result of the experiment was that the burrowing rate of bivalves below a certain water temperature is roughly proportional to the length of the shell, and decreases with a fall in water temperature.

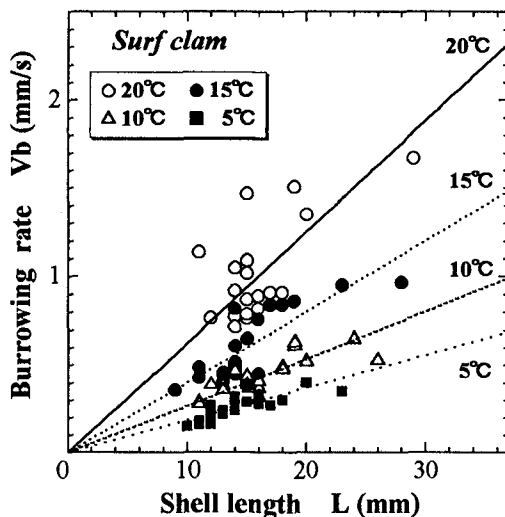


Fig.5 Relation of shel length to burrowing rate

(4) Bed Erosion Velocity

It was observed in Experiment (1) that the critical condition at which bivalves are forced out of the sand into the water was related to the velocity of the sea bed erosion. Bivalves tend to be forced out of the sand when sand bed are eroded about shell length in depth for a short time. Major examples of local deformation at a high velocity of topography by waves are the erosion and accumulation of sand resulting from the formation of sand ripples, the movement of sand ripples, and the large scale vortex caused by wave breaking. In this experiment, we first measured the bed erosion velocity under which sand ripples were formed from a flat condition to clarify the bed erosion velocity under which sand ripples were formed by an oscillatory flow, and then the amplitude of the flow velocity $U_m = 20, 40, 60, 80$ cm/s.

Under the condition where sand ripples were formed, the erosion and accumulation of the sea bed occurred complexly. The pattern of deformation of the topography showed a wide variation from 50 sec. to 2000 sec.. The release of bivalves out of the sand into the water depended on whether the velocity of the deformation of the bed exceeded the burrowing rate of the bivalves. Therefore, the probability of the

bivalves being released is related locally to the probability of maximum bed erosion velocity occurring. Fig.6 shows the local probability of the maximum bed erosion velocity at which it exceeded a certain erosion velocity of the bed. In the calculation, as in Experiment (1), the maximum bed erosion velocity is defined as the maximum value in the experiment of the mean bed erosion velocity at which the erosion of the bed occurred at a depth of half of the shell length.

Fig.6(a) shows an example of the experimental results of the maximum bed erosion velocity for the bivalve with a shell length of 10mm. Fig.6(b) shows another example of the bivalve with a shell length of 30mm. These figures indicate that under the condition where the same flow velocity or deformation of the bed occurred, the shorter the length of the bivalve, the higher the bed erosion velocity related to the release of the bivalve became. Fig.6 quantitatively shows that as the amplitude of the flow velocity increased, the maximum erosion velocity of the bed increased.

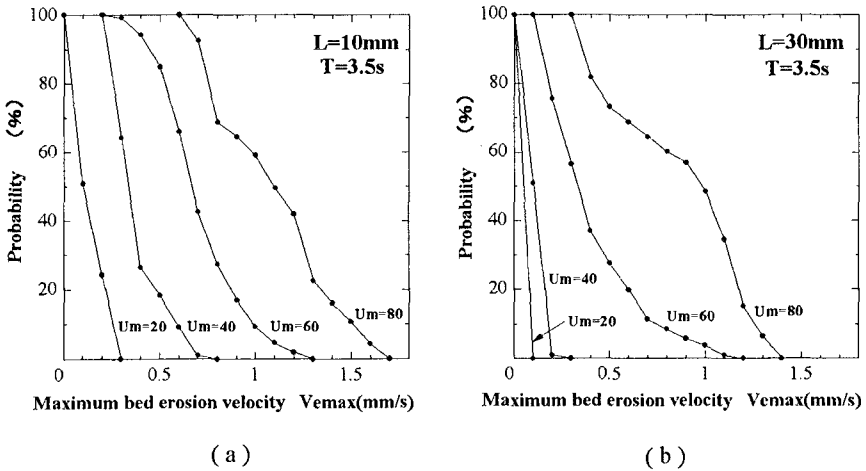


Fig.6 Probability of maximum bed erosion velocity occurring

(5) Moving Velocity of Bivalves on a Fixed Bed

We measured the velocity of moving bivalves which had been forced out into the water from the sand due to the flow, using a fixed bed with a smooth surface. Fig.7 shows a comparison between the experimental and theoretical results. The theoretical values were calculated by the following equation, and we regarded the behavior of bivalves as that of inanimate objects, which can not move by themselves.

$$M \frac{dUs}{dt} + C_m m \frac{d(Us - u)}{dt} = m \frac{du}{dt} + \frac{1}{2} C_D \rho_w A |u - Us| (u - Us) - \mu' (M - m) g \frac{Us}{|Us|}$$

Where, M is the mass of a bivalve, m is the mass of water equal to the volume of the bivalve, Us is the velocity of the moving bivalves and u is the water particle

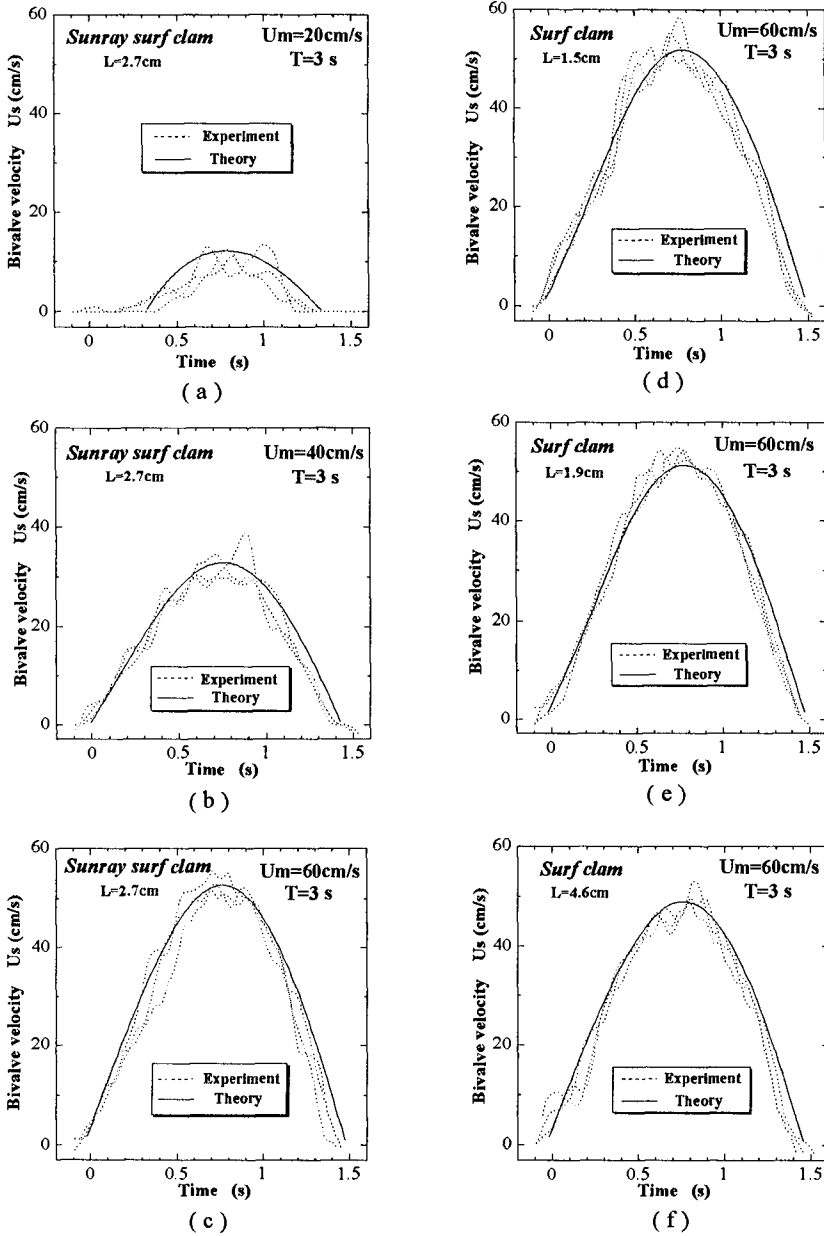


Fig.7 Moving velocity of the bivalves on a smooth surface fixed bed
 (a)(b)(c) The case of using sunray surf clams at three different amplitude of the flow velocity
 (d)(e)(f) The case of using surf clams of three different sizes

velocity. In the calculation, (1) the volume of a bivalve is converted into a globe and its projected area is regarded as the projected area A of the bivalve in the direction of the flow; (2) the drag coefficient $C_D = 1.0$; (3) the added mass coefficient $C_M = 0.5$; and (4) the coefficient of dynamic friction $\mu' = 0.1$. Fig.7(a), Fig.7(b) and Fig.7(c) show the results of experiments using sunray surf clams at three different amplitudes of the flow velocity. Fig.7(d), Fig.7(e) and Fig.7(f) show the results of experiments using surf clams of three different sizes.

The zero on the hour axis indicates the time when the main stream was reversed. The experimental values of three different velocities of moving bivalves in a one-half wave period were plotted. Turbulence was observed from experimental values because, while the flow acts on the bivalves, they turn around in various directions. However, in general, the theoretical values and experimental values agreed well.

Fig.7(a), Fig.7(b) and Fig.7(c) indicate that bivalves began moving at an early phase as the amplitude of the flow velocity became higher, and the ratio between the maximum value of the moving bivalves' velocity (U_{sm}) and the amplitude of flow velocity (U_m) approached 1.0. Fig.7(d), Fig.7(e) and Fig.7(f) indicate that the longer the shell length of the bivalves is, the lower U_{sm} becomes, although there were few differences between shell lengths because of the high flow velocity.

The results of the present study showed that once bivalves are forced out into the water from the sand, there is little effect of their own movement. Therefore, they can be regarded as inanimate objects.

CONCLUSIONS

- [1]The critical condition for which bivalves (surf clam) forced out of the sand and into the water by the water flow was determined by the ratio between V_e and V_b , which are the velocity of bed erosion and the burrowing rate of bivalves, respectively. V_e/V_b is approximately 1.1.
- [2]The critical flow velocity at which bivalves can borrow into the sand increases as the burrowing rate rises.
- [3]The burrowing rate of bivalves is related to both critical conditions, and the effects of the bivalves' own active movements (burrowing) were found to be significant for these conditions.
- [4]The burrowing rate of bivalves below a certain water temperature is roughly proportional to the length of the shell, and decreases with a fall in water temperature between 20°C and 5°C.
- [5]Under conditions where sand ripples are formed, as the amplitude of the flow velocity increases, the probability of a higher bed erosion velocity increases.
- [6]The behavior of bivalves which are forced out of sand are hardly affected by their active movements, and they can be regarded as inanimate objects. Supposing that the volume of a bivalve is converted into a globe, the behavior of bivalves could be theoretically explained by setting C_D (drag coefficient), C_M (added mass coefficient) and μ' (coefficient of dynamic friction) to 1.0, 0.5 and 0.1, respectively.
- [7]The shorter the length of the bivalves, the lower the water temperature, and the

higher the wave height, the more easily the bivalves are forced out of the sand into the water by the water flow. These are considered to be one of the major factors affecting the mortality of young bivalves due to waves in winter.

ACKNOWLEDGEMENTS

We wish to thank Hokkaido Central Fisheries Experimental Station, Muroran Branch-Hakodate Fisheries Experimental Station, and National Research Institute of Fisheries Engineering for advice on the ecology of bivalves and cooperation of the collection of bivalves.

REFERENCES

- Hayase, Y. and Miyamoto, Y.(1985): Formative Mechanism of *Spisula Sachalinensis* Fishery by Coastal Structure, Monthly Report of the Civil Engineering Research Institute, Hokkaido Development Bureau, No.386, pp.1-11
- Kuwahara, H. and Higano, J.(1993): Analysis Method on On-Off Shore Movement of Bivalves by Waves, Proc. Coastal Eng., JSCE, Vol.40, pp.311-315
- Kuwahara, H., Higano, J., Nakamura, Y. and Mimura, N.(1994): Study on mechanism of bivalve movement by wave and validity of numerical method, Proc. Coastal Eng., JSCE, Vol.41, pp.376-380
- Watanabe, E.(1980): The relationship between the decrease of surf clam and environmental factors, Monthly Report of the Civil Engineering Research Institute, Hokkaido Development Bureau, No.325, pp.1-12
- Watanabe, E.(1982): Experimental Study on the Decrease of Surf Clam under Wave Action, Monthly Report of the Civil Engineering Research Institute, Hokkaido Development Bureau, No.351, pp.3-15
- Yamashita, T., Matsuoka, G., Yano, K. and Akeda, S.(1994): Experimental Study on Movement and Decline of Bivalve under Oscillatory Flow, Proc. The Japanese Society of Fisheries Engineering, pp.57-58
- Yamashita, T. and Matsuoka, G.(1994): Experimental Study on Movement and Decline of Bivalve by Water Waves, Proc. Civil Engineering in the Ocean, JSCE, Vol.10, pp.119-122
- Yamashita, T., Wada, A. Matsuoka, G., Yano, K. and Akeda, S.(1995): Experimental Study on Behavior of Bivalves under Oscillatory Flow, Proc. Coastal Eng., JSCE, Vol.42(1), pp.506-510

CHAPTER 338

Wind- and Sea Level-Induced Shore Evolution in Poland

Ryszard B. Zeidler, Marek Skaja, Grzegorz Różyński & Jarka Kaczmarek ¹

Abstract

The effect of climate change factors on Polish shoreline is investigated in meso-scales of decades and tens of kilometres along the entire Baltic coast, with emphasis on the selected segment from Ustka to Łeba. Intensification of westerly wind circulation and sea level rise (SLR) are quantified as an input in computations of shoreline change by a one-line model. Joint probability distributions of wind and sea level derived under an extensive programme employing field data are used to produce input for computations of shoreline change due to rare events. The computations prove that the effects of both wind change and SLR can be perceptible in mesoscales, although it is difficult to clearly single out one from the other. In general, the westerly intensification of wind climate along the Polish coast seems to be slightly less important than SLR. A separate qualitative analysis of the acceleration of Polish shore retreat noted in recent years points to wind change as one of the possible causes.

1. Introduction: Coastal Climate Change (CCC)

The present coastal climate in the Baltic area, including Poland, is believed to undergo perceptible change due to global warming. The sea level rise, an increase in storminess and annual sea level maxima, and the changing patterns of wind circulation are the most pronounced change features affecting the coastal processes. The potential changes in precipitation, evaporation, transpiration, and their various outcomes over the Baltic coast and its drainage area, are also investigated although they are not easy to predict reliably and accurately.

An analysis of the variation of the zonal and meridional components of the geostrophic wind vector allows one to draw conclusions on the change of both components in the 40-year period from 1951 to 1990. For the more pronounced zonal component, this appears to be a trend of 0.0125 m/yr having a 95-% confidence level. By and large, one may note an intensification of the westerly air flow over the Polish coast, reflected in a shift of predominant wind directions towards W and NW, at the expense of the SW-W sector. A schematic change in the wind direction rose postulated for 50 years from 1995 to 2045 is

¹Professor, Snr Eng, Snr Res Assoc, Snr Asst, respectively; Institute of Hydro-Engineering IBW PAN; 7 Kosciarska, 80-953 Gdansk, Poland

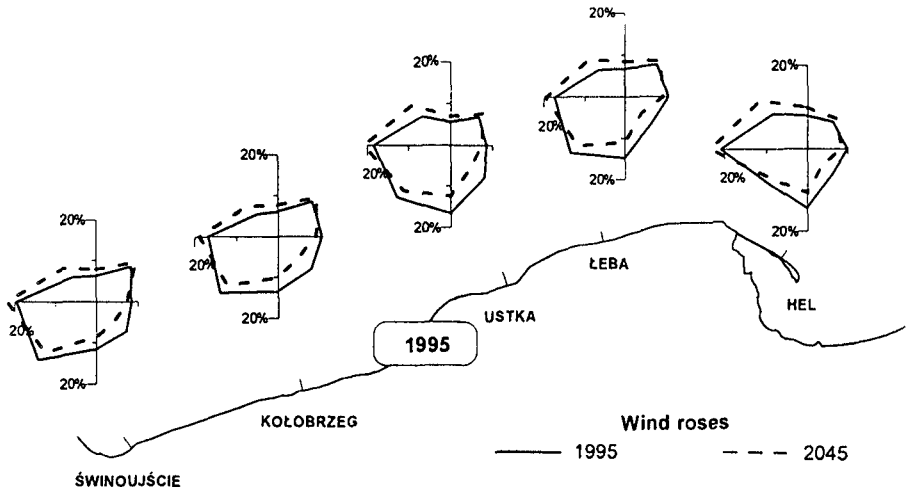


Figure 1. Frequencies of wind along the Polish coastline in 1995 (solid line) and postulated for the year 2045 (dash line).

depicted in Figure 1. In seasonal terms, the intensification of the westerly sector is particularly conspicuous in the winter season from October to March.

The mean sea level (SL) rise in Poland is presently estimated below 30 cm per century but its acceleration due to the greenhouse effect is taken into consideration (Zeidler 1995).

Another factor of climate change, i.e. storm intensity or 'storminess' can be analysed in terms of the annual sea level maximum (occurring once per year). One can prove that such storminess clearly increases over recent decades (Zeidler 1995). The growth trend of annual sea level maxima (ASLM) along the Polish coast is estimated about 10 cm per century.

It is also worthwhile to recollect that sea level increments Δh (four- or six-hourly at the Polish stations) display a certain long-term trend (Zeidler 1995). Moreover, they have been found to be correlated with high sea levels.

The present practice identifies as storm surges the events at which high sea levels alone occur, which brings about ambiguities. In order to determine the linkage between high sea levels and significant sea level increments, an analysis of the two quantities has been carried out (Wróblewski et al. 1996), with the primary objective as the derivation of statistical and probabilistic characteristics for both datasets and subsequent identification of their common features. Taken as a criterion of similarity was the condition that the numbers of occurrences of both quantities (SL and SL increments) are nearly equal. Such similarity has been concluded for 4-hourly SL increments greater than 21 cm at Ustka and Gdańsk (Nowy Port) or 26 cm at Swinoujście, versus $h \geq 563$ cm at Swinoujście and Gdańsk and $h \geq 560$ cm at Ustka (mean sea level being 500 cm). Within the above approach, regressional relationships between the time series for SL and their increments have been established.

Further on, the trend of storm winds could have been determined on the

basis of the sea level increments measured at Swinoujscie, Ustka and Gdańsk (Wróblewski et al. 1996). This was done by relying on relationships between Δh and storm winds in selected areas; a detailed analysis of statistical characteristics of storm winds and identification of their trend would have required processing of thousands of synoptic maps (e.g. above 100,000 maps taken every 4 hours in the investigated time span of 1955-1990).

The two major factors of CCC, i.e. wind and sea level in Poland are dealt with in this study while other CCC effects (primarily temperature, precipitation and groundwater changes) are incorporated in a coastal management programme led by the first author, where they contribute to changes in land-use patterns, flooding of coastal lowlands, cliff stability and other phenomena.

The basic objective of this study is to determine the effects of wind change and sea level change on the evolution of the Polish coastline.

It is interesting to note that the intensification of the westerly circulation has also been noted along the Danish coast. Figure 2 provides evidence for a time span of 100 years, showing increasing frequency of high wind speeds of the westerlies. The atmospheric circulation in Denmark has been shown to change by enhancement of the westerly winds and the clockwise turning of the predominant winds (from W to NW along the Jutland Peninsula coast investigated by Christiansen and Bowman, 1990). The wind change is accompanied by a more severe wave attack and retreat of the more exposed coastline segments.

In this paper, description of the climate change precedes shore evolution computations, from which conclusions can be drawn as to the evolution of the Polish coast in decadal scales, and these findings can be compared with the prototype data available.

The entire Polish coast measures five hundred kilometers between the mouth of the Oder (Odra) River and Poland's eastern border with Russia across the Vistula Spit. All over the Polish coast one encounters coastal lakes/lagoons of glacial origin. The same origin is assigned to the Hel Peninsula, a spectacular yet vulnerable to storms and climate change 30-km barrier separating the Gulf of Gdańsk from the open sea. Although the large-scale evolution of the Hel Peninsula is also investigated, this paper describes only some results obtained for the coastal stretch from Ustka to Łeba, belonging in part to the former category (lagoonal barrier).

The primary objectives of the study discussed in this paper consist in assessing the effects of climate change on the evolution of Polish coastline. The two basic effects tested are sea level change and wind change, treated both separately and jointly.

2. Joint Characteristics of Coastal Phenomena

In an investigation of shore evolution due to climate change one faces the necessity of focusing on joint characteristics of coastal phenomena, such as waves, sea level and wind. Also, extreme cases of coast evolution should be looked at. The selection and definition of extreme cases brings one to the problem of joint probability distributions for coastal quantities (such as sea level, wave parameter(s), wind etc.). By using the software produced for this programme one is able to compute shoreline changes or coastal evolution for every situation (sea level, wind speed and direction and at the same time the respective wave climate and other derivatives) but the open question remains how wave parameters are correlated with wind and sea level, and which combinations thereof are representative for extreme cases.

Hence four-dimensional probability distributions of wind (speed and di-

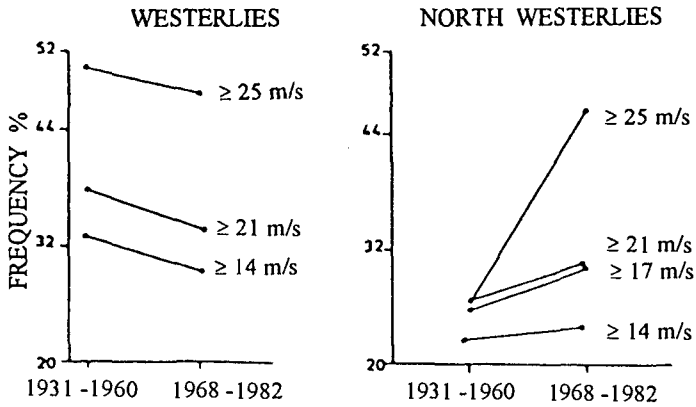


Figure 2. Change in wind direction along a latitudinal segment of NW Jutland (Klitmoller to Blokhus) shown by Christiansen and Bowman (1990).

rection), wave height and sea level have been investigated by the use of a large database for the Polish coastal weather stations, covering the years 1955–1990. At the beginning of the investigations it was realised that the probability of higher sea levels (exceeding 60 cm above the multiyearly mean value) might depend on wind direction. This would mean *inter alia* that the local growth of the mean sea level along the Polish coast due to the expected changes in wind circulation patterns could be quite pronounced by the year 2050.

As the study proceeded, wind-wave parameters were found to be correlated with wind direction as well, which is linked to the effect of fetch. At the same time, the correlation of wave height and sea level is low (about 0.2 for the stations of Hel and Gdynia) for all wind directions lumped, but a clear dependence on particular wind directions is displayed in some classes of water levels.

Figure 3 illustrates the cumulative joint probability of wind speed and sea level for N and NW winds at Hel, while Figure 4 shows the counterparts for Gdańsk (North Harbour). The two graphs stem from different datasets, not only for their locations but also because of the concept by which they were selected. The data for Hel in Figure 3 were taken for all events, i.e. at regular time steps, every three hours over nearly 5 years from 1976 to 1981 (11,500 events). The data for Gdańsk were purposefully biased to represent the impact of storm events (defined as those with significant wave height above 1 m); they also cover a shorter time lapse (1991 to 1992 and some months of 1995; about 4,500 events).

The correlations between sea level and wind speed were tested in eight principal classes of wind directions. Sea levels were arranged in sets exceeding the numbers indicated in the top lines of the tables in Figures 3 and 4. In order to examine the dependence on wind strength, the datasets were truncated in the sense that all events with wind speed below 6 or 8 m/s were rejected.

The correlations at Hel have been found very low in general; they seldom exceed 0.6 (the rightmost figures in the tables are not conclusive because of the low counts of data in those classes). The findings are certainly affected by the

Hel. Correlations sea level (L) - wind speed (v), truncated at v=6m/s

	500	510	520	530	540	550	560	570	580
N	0,253	0,177	0,146	0,016	-0,03	-0,23	-0,03	0,408	x
NE	0,271	0,326	0,123	0,021	0,017	0,288	0,444	x	x
E	0,131	0,12	0,248	0,071	0,228	0,375	0,431	x	x
SE	-0,02	0,04	0,249	0,041	x	x	x	x	x
S.	0,017	0,087	0,093	0,156	0,478	0,424	x	x	x
SW	0,073	0,104	0,155	0,141	0,232	0,262	-0,06	x	x
W	0,277	0,293	0,306	0,266	0,321	0,335	0,326	0,408	0,116
NW	0,301	0,301	0,281	0,269	0,268	0,267	0,259	0,146	0,319
	N	NE	E	SE	S	SW	W	NW	
L - V	0,287	0,199	-0,13	-0,24	-0,11	0,051	0,244	0,246	

Hel. Correlations sea level (L) - wind speed (v), truncated at v=8m/s.

	500	510	520	530	540	550	560	570	580
N	0,222	0,137	0,097	0,057	0,13	-0,11	0,422	x	x
NE	0,095	0,146	0,062	-0,08	0,163	-0,53	-0,4	x	x
E	0,13	0,06	0,237	0,034	0,251	0,424	0,41	x	x
SE	0,308	0,187	0,622	0,614	x	x	x	x	x
S.	0,069	0,097	0,266	0,264	0,702	x	x	x	x
SW	0,088	0,143	0,195	0,308	0,329	0,29	0,918	x	x
W	0,298	0,316	0,367	0,18	0,359	0,453	0,417	0,225	0,116
NW	0,35	0,333	0,276	0,278	0,301	0,322	0,253	0,041	0,687
	N	NE	E	SE	S	SW	W	NW	
L - V	0,238	-0,05	-0,15	-0,18	-0,05	0,049	0,254	0,218	

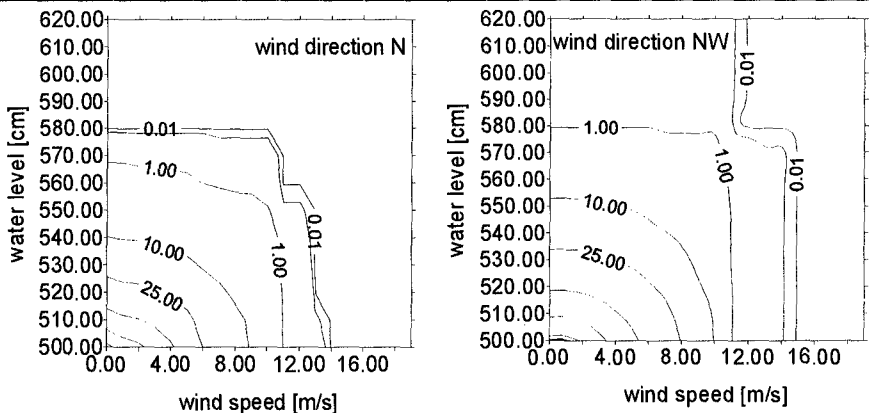


Figure 3. Correlation tables and cumulative exceedance graph for sea level and wind speed at the station of Hel, 1976-1981.

North Harbour. Correlations sea level (L) - wind speed (v), truncated at v=6m/s

	500	510	520	530	540	550	560	570	580
N	x	0,27	0,13	0,17	0,20	-0,20	-0,31	-0,35	x
NE	0,35	0,35	0,35	0,17	0,64	0,41	0,44	-0,24	x
E	0,47	0,39	0,34	0,54	0,54	0,50	-0,57	x	x
SE	-0,05	x	x	x	x	x	x	x	x
S.	-0,05	-0,23	0,45	x	x	x	x	x	x
SW	0,03	-0,27	-0,76	x	x	x	x	x	x
W	0,21	0,47	0,41	0,34	0,06	-0,37	x	x	x
NW	0,29	0,26	0,20	0,07	-0,15	-0,05	x	x	x
	N	NE	E	SE	S	SW	W	NW	
L - V	0,66	0,52	0,31	0,01	0,13	0,15	0,23	0,31	

North Harbour. Correlations sea level (L) - wind speed (v), truncated at v=8m/s.

	500	510	520	530	540	550	560	570	580
N	x	0,18	0,07	0,10	0,04	-0,20	-0,31	-0,35	x
NE	-0,09	-0,09	-0,09	0,03	0,03	0,61	0,55	-0,24	x
E	0,39	0,19	0,17	0,54	0,54	0,50	-0,57	x	x
SE	x	x	x	x	x	x	x	x	x
S.	-0,17	-0,05	x	x	x	x	x	x	x
SW	0,22	0,12	-0,52	x	x	x	x	x	x
W	-0,07	0,21	0,19	-0,07	-0,24	-0,37	x	x	x
NW	0,21	0,20	0,17	0,05	-0,11	-0,05	x	x	x
	N	NE	E	SE	S	SW	W	NW	
L - V	0,66	0,54	0,33	-0,07	-0,13	0,21	0,13	0,25	

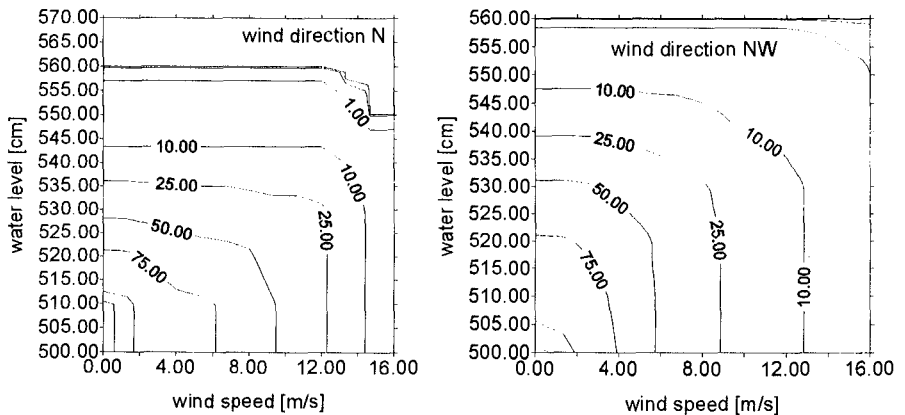


Figure 4. Correlation tables and cumulative exceedance graph for sea level and wind speed at the station of Gdańsk (North Harbour, 1991-1992..1995).

very specific location of the station and the complex nature of the controlling hydrodynamic phenomena.

For the North Harbour, the correlations become significant for NE winds. The relatively high marginal correlations with both N and NE winds (given at the bottom of table) are linked to the fact that all sea levels were taken into account there (also those below 500, i.e. below MSL).

In representation of some characteristic rare events in the subsequent shoreline evolution computations, reference should be made to the exceedance graphs of the type shown in Figures 3 and 4. The following couples of wind and sea level were chosen for the selected isolines of the exceedance probability F :

- (a1) wind N 9 m/s + SL 545 ($F=2\%$);
- (a2) wind N 16 m/s + SL 500 ($F=0.01\%$);
- (b1) wind NW 9 m/s + SL 555 ($F=2\%$);
- (b2) wind NW 17 m/s + SL 500 ($F=0.01\%$);
- (c1) wind E 7 m/s + SL 535 ($F=2\%$);
- (c2) wind E 12 m/s + SL 500 ($F=0.01\%$).

3. Shore Evolution Computations

The wind change trends alone have been taken for granted by Zeidler (1995), who computed the respective sediment transport along the Polish coast in the 50-year time span, and drew conclusions on shoreline evolution. Despite a sharp change in wind direction (but not speed) the alteration of sediment transport rate and the subsequent shoreline evolution was not found dramatic, due to the wind change alone. Yet it was concluded that shoreline change might become quite conspicuous if the wind change is added to the accompanying storm surge or a sea level rise.

The shoreline computations in this study are founded on the one-line theory, which ends up with the diffusion-type equation

$$\frac{dy}{dt} = A \frac{d^2y}{dx^2} - B \quad (1)$$

in which

$$A = \frac{2}{(1-p)h_c} \frac{\partial Q_l}{\partial \varphi}$$

$$B = \frac{2}{(1-p)h_c} \left(\frac{\partial Q_l}{\partial x} + q_c \right)$$

h_c = depth of closure,

p = porosity of bed sediment,

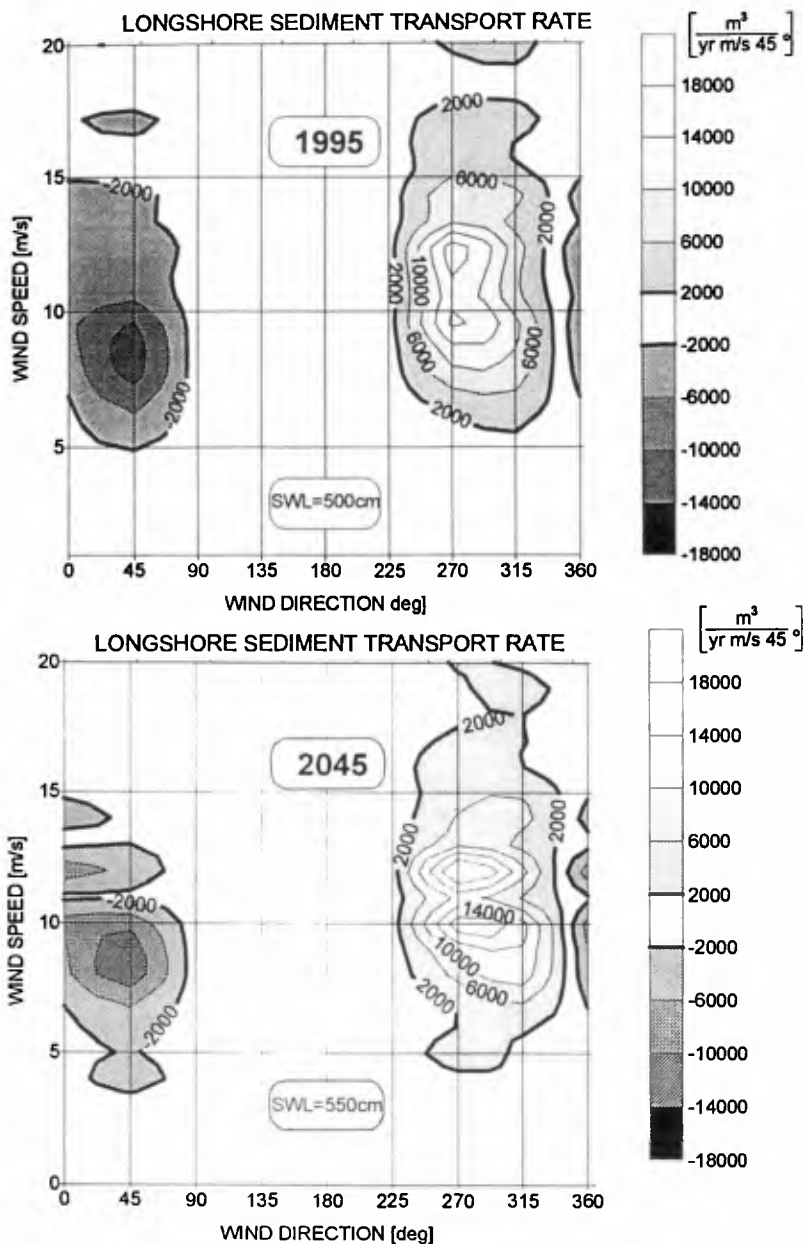
Q_l = longshore sediment transport rate,

q_c = cross-shore transport rate per unit length along shore,

t = time,

x, y = longshore and cross-shore coordinate of shoreline.

In order to determine the long-term shore evolution due to changes in wind, waves and sea level, by the above one-line scheme, an extensive computational procedure had to be employed. It encompasses five major subroutines: (1) preparation of input data with CCC quantities (wind, wind-induced waves and sea level); (2) arrangement of probability distributions for wave height and sea level in the format accepting CCC; (3) computations of sediment transport for the whole domain of wave height and sea level occurrence; (4) integration of sediment transport rate over representative time spans, with their probability distributions; (5) one-line type assessment of shore evolution over the time span of CCC.



SEDIMENT TRANSPORT VS. WIND, ĽEBA

Figure 5. Longshore sediment transport rate as a function of wind speed and direction at Ľeba, for the years 1995 (SWL datum 500, top) and 2045 (SL rising by 50 cm to SWL datum 550, bottom).

Waves are computed routinely by Krylov's 'spectral' method calibrated against field data. A Battjes/Jansen-type algorithm for irregular wave transformation is used as an input of the IBW PAN program for wave-induced currents, and the sediment transport formulae are Bijker-type for longshore movement and IBW PAN modified Bailard-type for cross-shore transport. Sea level controls the shore evolution at the places where shoaling and the closure depth intervene but is not included in nonlinear interactions with waves.

Hence in our routine, the input wind change leads to wave climate change, waves producing currents and then sediment transport. On the basis of that input, together with sea level rise, shore evolution patterns are produced.

The results of our computations of the longshore transport are depicted in Figure 5. For every cell of particular wind speed and direction one has the sediment transport rate computed for the present situation (1995) and for the future (2045). It should be noted that the future situation can arise in two versions — wind change only and wind change plus sea level rise. Hence at present one has the status shown at the top of the drawing, while in the future one may face two different situations with sediment transport for sea level change and for wind climate change.

The coefficients A and B in the one-line equation are functions of longshore sediment transport rate (partial derivatives) and cross-shore rates as well (per unit length along the shore). Those coefficients were assessed separately for every location of the study area, with respective closure depths, wave incidence angles, breaking parameters etc.

The study area was confined to the coastal stretch between Ustka and Łeba. Various climate input situations were tested. In addition to the rare cases selected from the joint probability graphs as described in Section 2 (situations a1–c2), the average year was also simulated. The latter encompassed aggregated westerly winds and aggregated easterly winds, for which one obviously had different sediment transport rates, different angles of wave attack etc.

The program USTLEB was compiled for computations of shoreline change in accordance with the one-line model, and was validated against the known analytical solutions (i.a. Larson et al. 1996). It is based on an explicit finite-difference scheme, where instability problems do not arise in practice. Some peculiarities emerge at points of discontinuity (of sediment transport rate, shoreline position) but the difficulties are overcome by locally decreasing space steps and iterative finding of shoreline derivatives. Estimates of the partial derivatives of the longshore transport rate must also be reasonably derived in a practical way.

In the computations by USTLEB for the 45-km segment Ustka–Łeba, the following conditions were adopted:

- (i) the time span 1995–2045 divided in 25 time steps 2 years each;
- (ii) two basic versions of climate change: (a) wind climate change only, (b) wind change + sea level change, 50 cm per 50 years;
- (iii) 'average year' and 'rare cases' a1–c2 as specified above for the wind ... sediment transport input.

Some results of the shoreline change computations are illustrated in Figure 6. Only the aggregated annual effects are shown to highlight the basic differences resulting from the impacts of the two major directional sectors of wind action along the Polish coast — from west to east (top) and east to west (bottom). The two annual components of shoreline change are strikingly different. The wind change effect is negligible vs. the sea level rise effect for the westerlies, and becomes of the same magnitude for the easterlies. The absolute magnitude of shoreline change is greater for the westerlies than for the winds

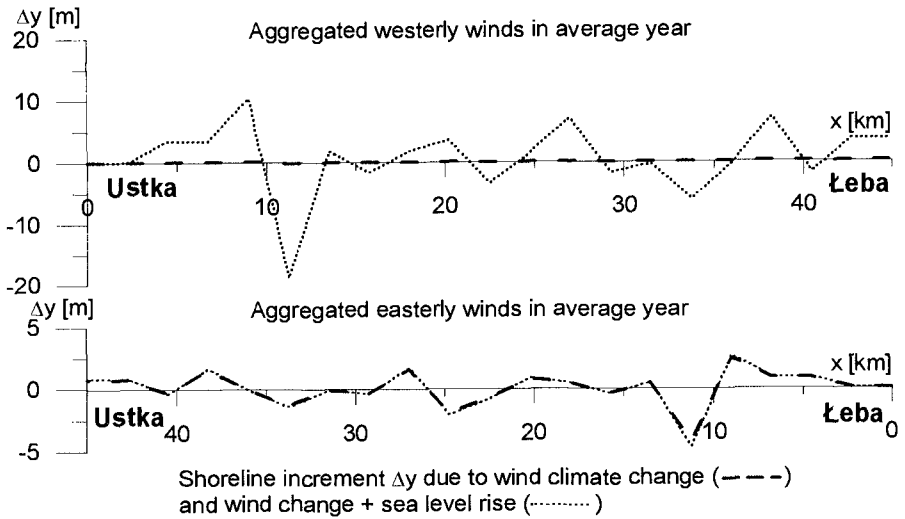


Figure 6. Results of one-line computations for the Polish coast segment from Ustka to Łeba, showing the 50-yr climate change effects — wind change only and wind change + SL change.

blowing from the eastern sector. If one takes into account that the former are more frequent than the latter, then one may venture the conclusion that the effect of wind change on the shoreline change is generally weaker than the impact of sea level rise.

Yet it is appropriate to note that the above conclusion is not so straightforward for the individual 'rare events' (a1–c2) tested in this study. Moreover, the contribution of the cross-shore transport to results of the computations by USTLEB also remains unclear so far. Attempts with various predictors of the cross-shore transport integrated along the shore transects (26 from Ustka to Łeba) have been inconclusive, and therefore are not reflected in Figure 6. More complementary research is required to shed light on the cross-shore effects. Needless to say, the latter may turn out fairly diversified along the Polish coast, if the research is extended far beyond the segment from Ustka to Łeba.

4. Prototype Data and Comparison with Computations

In preparation for the extended research on the entire Polish coast, as signalled at the end of Section 3, one may turn to the prototype evidence collected to date. On the basis of this data one can then venture some general observations and hypotheses relating to the evolution of the Polish coast in large scales of decades and hundreds of kilometres. Similarly, postulates can be formulated for the effects on shoreline of sea level rise and wind climate change.

For a period of slightly above one hundred years, Zawadzka-Kahlau (1994) retrieved the data on the position of Polish beach and shore features. The basic core of that collection consists of a vast database for shoreline ('waterline') and cliff/dune toe stemming from cartographic mapping dating back to

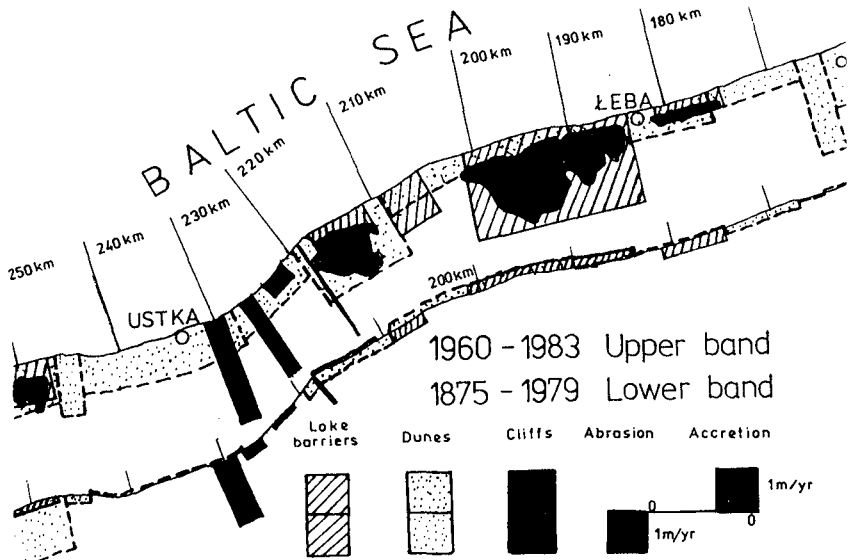


Figure 7. Decadal shoreline change along the coast segment from Ustka to Łeba (Zawadzka-Kahlau 1994).

the 19th century and extending over most of the Polish coastline. The statistical estimates obtained by processing of that database provide an opportunity of verifying the quantities resulting from our computations.

Under this study the database has been re-arranged graphically in the form illustrated in Figure 7 for the area Ustka-Łeba (although the same format was applied to the entire coast). Hence the shoreline change undergone in the years from 1875 till 1979 is shown in the lower band, while that in the more recent 20 years (1960-1983) is presented in the upper band. The purpose of such rearrangement is to provide insight into the general trends and to determine whether one faces some more conspicuous, dramatic shoreline changes in the recent years and if these changes are somehow linked to the change in wind circulation patterns and sea level change.

Consider the intensification of westerly winds, i.e. decadal increase in the frequency of W and NW winds depicted in Figure 1. More pronounced abrasion of concave shore segments could be expected, although to a different degree, depending on the coast type i.e. lake/lagoon barriers, dunes and cliffs. Indeed, such a trend is visible on many Polish coast segments. For majority of concave shore segments it can be concluded that more erosion is encountered in the recent years. There are a number of locations on concave segments where this can be claimed and where dramatic shift from accretion to erosion is noted. As a sound hypothesis, such behaviour can be assigned to the intensification of the westerly circulation. Unfortunately, this qualitative finding suffers i.a. from being embedded in the effect of sea level change. Unless differentiated more clearly, the two effects should be considered equally probable.

Figure 7 has been drawn for the stretch from Ustka to Łeba only. Accretion and erosion have been marked for three different shore types, accretion

lines progressing towards the sea and erosion being marked as lines of landward retreat. One very conspicuous feature visible in the drawing is the clear growth of the erosion rate in the years 1960–1983. Identification of the nature and cause of that accelerated growth remains a task of future investigations — the combined effects of the westerly intensification and SL change are slightly more likely than decadal cyclicity of shore evolution change.

5. Summary and Conclusions

The effect of climate change factors (wind and sea level) on Polish shoreline has been investigated in mesoscales of decades and tens of kilometres along the entire Baltic coast. Emphasis has been placed on the selected segment from Ustka to Łeba. Intensification of westerly wind circulation and sea level rise (SLR) have been quantified as an input in computations of shoreline change by a one-line model. Joint probability distributions of wind and sea level derived under an extensive programme employing field data have been used to produce input for computations of shoreline change due to rare events.

The computations carried out in this study prove that the effects of both wind change and SLR can be perceptible in mesoscales, although it is difficult to clearly single out one from the other, and/or from other natural and man-induced effects. In general, the westerly intensification of wind climate along the Polish coast seems to be less important than SLR alone, in terms of decadal and centennial coast evolution patterns. Simple one-line computations of Polish coast evolution confirm the potential effects of wind change and SLR in both interannual coast evolution and extreme events (SLR + Wind Change). Both effects are also equally probable in the light of field data for Polish shore covering the period of more than one century.

The software routine worked out in this study provides a useful tool of long-term coastal planning facing coastal climate change. The data input (wind, wave, sea level, bathymetry) and the software itself pave way for more complex investigations of coast evolution, including the modelling of joint wind, wave and sea level input and chronology effects.

ACKNOWLEDGEMENTS

This paper is based on the work done in the PACE project, in the framework of the EU-sponsored Marine Science and Technology Programme (MAST-III), under contract MAS3-CT95-0002. The work was cosponsored by the Polish Academy of Sciences (PAN) under the programme IBWPAN-Gr-tem-2-96.

REFERENCES

- Christiansen Ch. & D. Bowman 1990. Long-term beach and shoreface changes in NW Jutland, Denmark: effects of change in wind direction. *Expected effects of climatic change on marine coastal ecosystems* (J.J. Beukema, ed), 113-122. Kluwer Acad. Publ.
- Larson M., H. Hanson & N.C. Kraus 1996. Analytical solutions of the one-line model for shoreline change near coastal structures. *Jour. Waterway, Port, Coastal and Ocean Eng.* (in press).
- Wróblewski A., R.B. Zeidler & J. Kaczmarek 1996. Analysis of storm surges, sea level and atmospheric pressure for the Polish Baltic coast. *Arch. Hydr. Envir. Engng Gdańsk* (in press).
- Zawadzka-Kahlau E. 1994. *Coast evolution trends on the Polish Baltic* (in Polish). Ph.D. Thesis. Gdańsk University.
- Zeidler R.B. 1995. Sea level rise and coast evolution in Poland. *Proceedings 24th Intern. Conf. Coastal Eng.* 3462–3475. ASCE, New York.

CHAPTER 339

ASHDOD PORT'S EFFECT ON THE SHORELINE, SEABED AND SEDIMENT

Abraham Golik¹, Dov S. Rosen¹-MASCE, Arik Golan¹,
Maxim Shoshany², Dan DiCastro³ and Pinkhas Harari³

Abstract

During its 35 years of existence, Ashdod Port, Israel, caused changes to its physical environment. Analysis of aerial photographs and bathymetric surveys show that the port served as a sediment trap, blocking the natural northward sediment transport. Between 1958, prior to the port construction, and 1992 the beach to the south of the port underwent accretion which increased in magnitude from zero, at a distance of 2.5 km south of the port, to more than 100 m near the main breakwater. On the northern side of the port the shoreline was stable during that period. It was found that the beach north of the port did not suffer erosion because the sand of that beach was mined for building purposes prior to the port's construction. When the port was built, it was already a rocky beach.

Comparison between bathymetric surveys, which were carried out in the vicinity of the port, at various periods since prior to its construction until 1995, show that the port has trapped some 4.5 million m³ of sediments on its southern side. Of these, about 2.2 million m³ were deposited during the period of 1985-1995. It is estimated that more than half of this volume was deposited in 1992 during three very severe storms. On the basis of the depositional pattern in the vicinity of the port, and assumptions related to the net longshore sediment transport, it is estimated that more than half of the sediment volume bypasses the port northward.

¹National Institute of Oceanography, Israel Oceanographic & Limnological Research, POB 8030, Tel Shikmona, HAIFA 31080, ISRAEL, Fax: +972 48511911

²Department of Geography, Bar-Ilan University, Ramat-Gan, Israel

³Ports and Railways Authority-Israel, 74 Dereh Petah-Tikva Ave., Tel Aviv, Israel

Introduction

Ashdod Port is located on the Mediterranean coast of Israel some 30 km south of Tel-Aviv. It was built between 1961 and 1964 on a straight sandy beach backed by sand dunes. About 200 m south of the main breakwater of the port Lakhish River discharges into the sea. The length of the existing main breakwater is 2,200 m and that of the lee breakwater is 900 m. The head of the main breakwater is at a water depth of 15 m, and the entrance of the port was 13 m deep when it was built. The port penetrates seaward from the shore to a distance of about 1,000 m.

Since the beginning of its operation in 1964, the volume of traffic in this port has continuously increased. Presently (1996), it handles some 13.7 million tons of cargo a year, but projections are for 15.4 million in the year 2000 and 16.6 million tons a year in 2010. It is therefore planned to expand the port by extending its main breakwater by 1,150 m to a water depth of about 21 m (Figure 1).

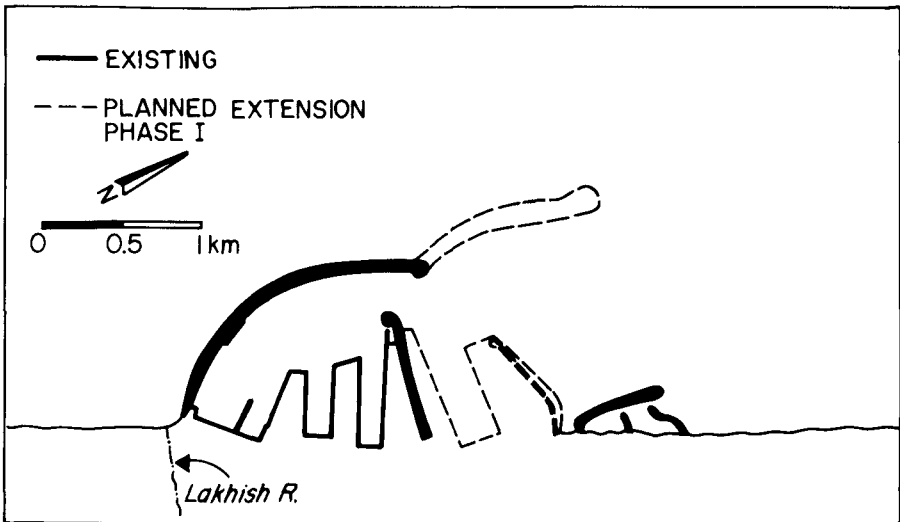


Figure 1. General plan for the planned expansion of Ashdod Port, phase I.

The increasing concern in Israel, as in the rest of the world, regarding the effect of coastal construction on the marine environment, led the authorities in Israel to impose preparation of environmental impact statements (EIS) for each major coastal structure. As part of the requests of the EIS for the expansion of Ashdod port, a numerical sedimentological model had to be carried out. This model should predict the effect of the port's expansion on the environment, and in particular on the nearby bathymetry, coastline and sediments. The present study was carried out in order to gather available information on the sedimentological development resulting from the

construction of the existing Ashdod Port, and to evaluate the effect of its breakwaters on the sedimentological balance in the area and the stability, in terms of erosion or accretion, of the seabed and of the shoreline. The results of this study should be used to calibrate and verify the above mentioned model.

Previous studies on the effect of Ashdod Port on the sedimentological processes in its vicinity were carried out by Kran (1980) who analyzed bathymetric profiles which were surveyed between 1964 and 1971 in the vicinity of the breakwaters. Computations of changes in the volume of sediment in the vicinity of the port between 1959 and 1975 were made by Finkelstein (1980) and between 1959 and 1985 by Vajda et al. (1988). Rosen (1985) assessed the longshore sediment transport rate at Ashdod on the basis of wave energy flux calculation.

Three data bases were used for this study:

- (a) Aerial photographs, taken since prior to the construction of the port until the present. They enabled to detect shoreline erosion and accretion caused by the port,
- (b) Bottom charts and profiles which were prepared before and after the port was built. These were used in order to evaluate changes in the seabed which were caused by the port.
- (c) Wave climate resulting from wave observations and measurements carried out near the port since 1957. These were used to evaluate the natural rate of sediment transport in the area, and in particular the longshore transport.

Methodology

Analysis of Aerial Photographs

The changes in shoreline position which resulted from the construction of the port were measured by comparing aerial photographs, which have been taken on different dates since prior to the port construction until 1992. To avoid errors resulting from seasonal changes in the shoreline, only photographs taken during the autumn season were used. This season was selected because the sea is calm and the beach face is steep at that period. Therefore, horizontal change in the waterline due to sea level fluctuations, is rather limited. Also, wave records showed that during the photography sortie and the days preceding it, wave height was less than 1 m. Eight aerial photographic sorties from the years 1958, 1964, 1971, 1976, 1980, 1983, 1988 and 1992 were selected for this study.

The analysis of aerial photographs was that adopted by Shoshany and Degani (1992). The analog format of the photographs was transformed into a digital one using a digital scanner. Prominent objects in the photographs were used to relate photographs from different dates into a uniform geographic system.

The line which separates the wet part of the beach from the dry one was selected to represent the shoreline because it is clear and sharp on the photograph. Also, this line does not fluctuate momentarily as the water line does. This line was further

accentuated by enhancing the brightness contrast. The 1988 sortie was selected as a reference sortie, because it contained a large number of common reference points which were seen on photographs from preceding and succeeding sorties. These reference points were used to rectify the aerial photographs and remove distortions from them. Once this was done, the shoreline was digitized for each sortie. It is estimated that the error involved in determination of the shoreline position is less than 10 m.

Bathymetric Analysis

Bathymetric surveys in the vicinity of the port, which were conducted in 1957, 1959, 1970, 1975, 1980, 1983, 1985 and 1995, were used for this study. The surveying methods which were employed in these surveys changed during this period. Until the early 1970's, navigation was carried out by sextant readings from the boat to reference points on the beach, and depth was measured using a Kelvin Hughes surveying echo sounder. After 1972 navigation was carried out by an electronic system, Decca Trisponder, and later by Miniranger. Data processing, interpolation of boat position and depth reading, and collation of these data, were carried out manually until the beginning of the 1980's and gradually changed to computer processing in the early 1980's. The survey of 1995 was carried out using a differential GPS system for navigation and a digital Odom echosounder. The collation of depth and position was carried out on board the surveying boat, using the OCEANOGRAPHER navigation and mapping computer software system, developed and written for such purposes by the third author. The charts were digitized and an interpolated grid of depth points for each survey was prepared. Each grid was subtracted from its predecessor, and depth differential maps which show the magnitude and spatial distribution of deposition or erosion on the seabed were prepared.

Wave Data and Computation of Longshore Sediment Transport

Wave data have been collected from Ashdod Port region since 1957. Some of the data (1957-1975) were based on visual observations, some (1978-1992) on a combination of instrumental measurement (wave height and frequency) and visual observation (wave direction), and for three years, 1992-1995, wave height, frequency and direction were instrumentally measured. In view of the low reliability of the wave directions of the old wave data, the final computation of the longshore sediment transport rate, was based on the April 1992 - March 1995 wave data, gathered off Ashdod with a Datawell Wavec buoy at 3 hour intervals. These data were used as an input in computer programs using the formulas of longshore sediment transport known as the CERC (USArmy CERC-1984), Komar (Komar-1977), LCHF (Migniot et Manoujan-1983) and Bijker (Bijker-1972) formulae. The longshore sediment transport was computed for each sedimentological year, namely years starting in April on one year and ending in March of the following year, to comply with the sedimentological seasonal wave regime in this region.

To account for the longshore sediment transport taking place beyond the surf zone, the joint contribution of wave stirring and geostrophic current transport, current data statistics gathered by Israel Oceanographic & Limnological Research off Ashkelon, in 27 m water depth, were used in combination with the Bijker formula.

Results

Shoreline Position

Examination of the position of the shoreline south and north of the port, as derived from the aerial photographs analysis, reveals two phenomena. First, the distance between the positions of the shorelines of 1958, prior to the construction of the port, and 1964, when it was almost completed, is very small and falls within the resolution magnitude of the analysis. The second, is the change with time in the shoreline position south of the port versus those north of it. South of the port, a distinct accretion of the shore with time is noticed, whereas north of the port, the shoreline position is relatively stable with the exception of the sector in the immediate vicinity of the lee breakwater.

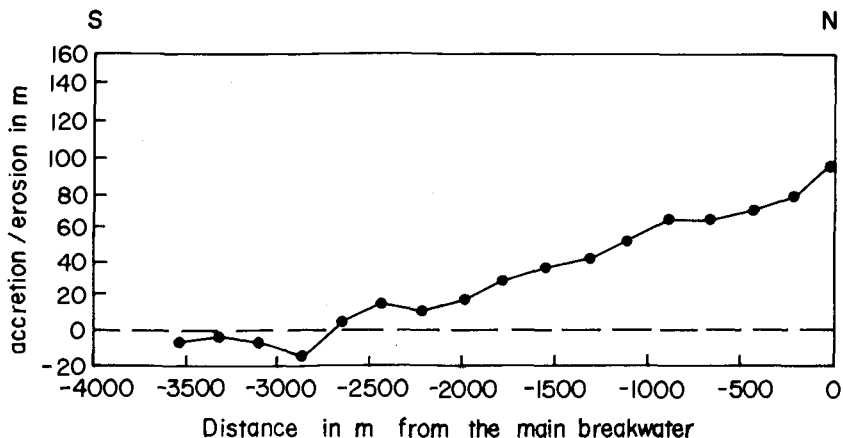


Figure 2. Difference in m between the mean position of the shoreline in 1958-1964 and that of 1983-1992 south of Ashdod Port.

Figures 2 and 3 were prepared with the purpose of showing the general trend in the development of the coastline, south and north of the port. It shows the distance between the mean position of the shoreline in the years 1958 and 1964 and that of the years 1983-1992. Figure 2 shows that during the study period the shoreline has advanced westward gradually from zero at 2,500 m south of the main (southern) breakwater to about 100 m near it. North of the port, Figure 3 shows that accretion has occurred very close to the lee (northern) breakwater, to a distance of about 300 m

north of it, but from there on northward, the position of the shoreline was rather stable during the study period.

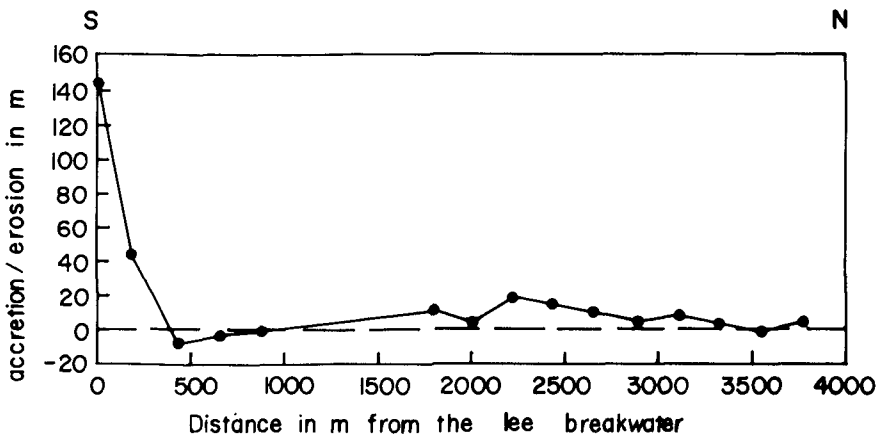


Figure 3. Difference in m between the mean position of the shoreline in 1958-1964 and that of 1983-1992 north of Ashdod Port.

Bathymetric Changes

Examination of the depth differential maps which resulted from the analysis of the bathymetric charts shows that the first impact of the port on the seabed was a severe erosion, up to 2.5 m, north of the port and deposition of up to 3.0 m next to the lee breakwater. With some fluctuations in magnitude, these effects remained throughout the history of the port.

Another phenomenon, which also started following the port's construction, is the increase of deposition near the beach south of the port as well as near the head of the main breakwater. Deposition increased both in thickness as well as in space with time. In 1975, sediment was "creeping" along the main breakwater reaching about a third of its length. In 1980, the depositional area south of the main breakwater increased, and the accumulation at the head of the breakwater increased in thickness. In 1983, deposition followed the same pattern but increased in thickness. Between 1983 and 1985, minor changes occurred in the sea bottom, but between 1985 and 1995, an impressive deposition took place along the southern part of the main breakwater and south of it, parallel to the beach, at a distance of between 700 and 1,000 m. The thickness of this deposition is mostly up to 2.0 m but in restricted areas up to 3.0 m. 4.5 million m³ of sediment have accumulated in the studied area south of the main

breakwater between 1957 and 1995. Of these, 2.3 million m^3 between 1957 and 1985, and 2.2 million m^3 between 1985 and 1995.

Assessment of Wave Climate and Longshore Sediment Transport

Figures 4-6 show the average yearly marginal distributions of the deep water wave characteristics off Ashdod during sedimentological years 1993-1995 (04/1992 -03/95) using data bases of 3 hours data, noon daily data and maximum daily data. Figure 4 shows the marginal distribution of deep water characteristic wave heights, Figure 5 shows the marginal distribution of peak wave periods, and Figure 6 shows the marginal distribution of deep water wave directions for the mentioned period.

Figures 7 and 8 provide the average yearly marginal distributions of the general current characteristics off Ashkelon (15 Km south of Ashdod Port) which were measured in 1992-1993 (Rosen, 1993). The current was measured at a water depth of 27 m, 10 m below the sea surface. Figure 7 shows the marginal distribution of hourly averaged current speeds, and the marginal distribution of hourly averaged current directions is presented in Figure 8.

On the basis of these data and the various formulas mentioned before estimates of the longshore transport were obtained. As can be seen in Figure 9, there are differences of up to four times among the various formulas. The evaluation using the CERC formulae of the net transport is about 3 times larger (720,000 m^3 /year) than that of Bijker formula (230,000 m^3 /year) without accounting for the presence of currents

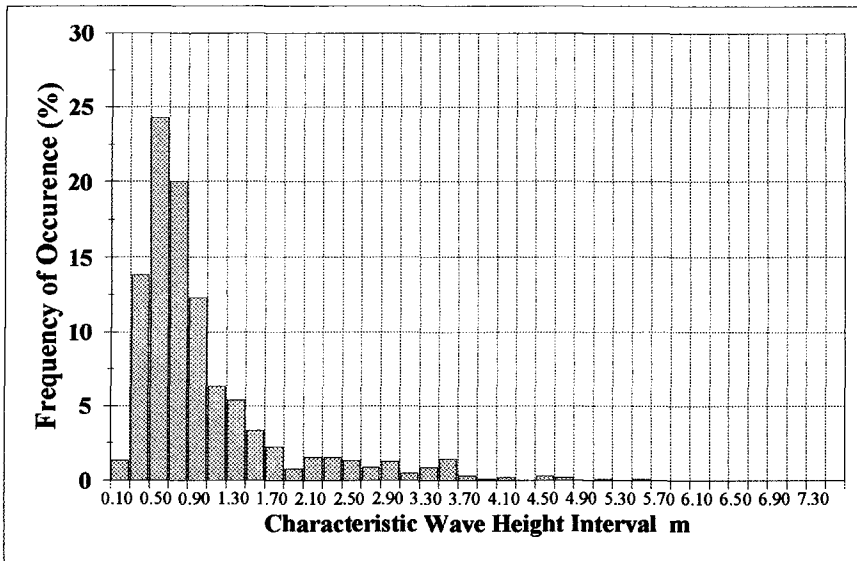


Figure 4. Yearly deep water distribution of characteristic wave height (04/92-03/95).

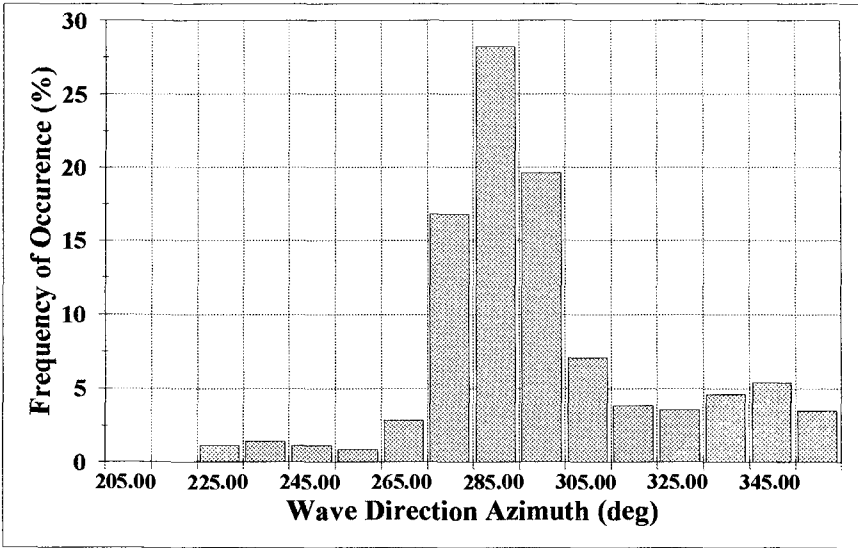


Figure 5. Yearly deep water distribution of peak wave periods (04/92-03/95).

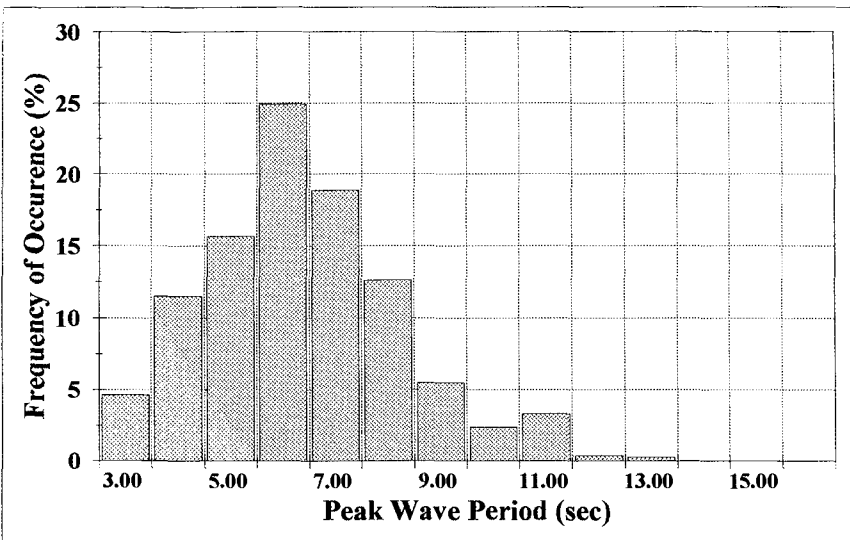


Figure 6. Yearly deep water distribution of wave directions (04/92-03/95).

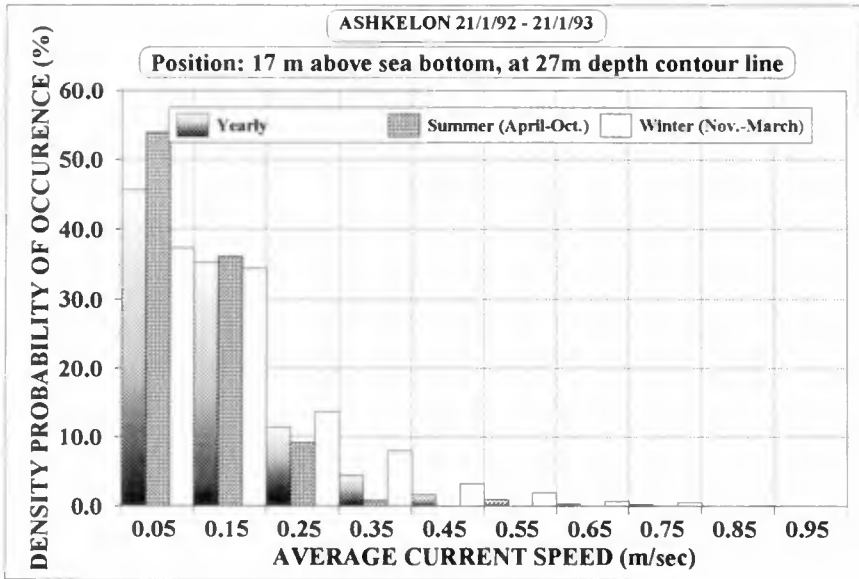


Figure 7. Current speed distribution offshore Ashkelon.

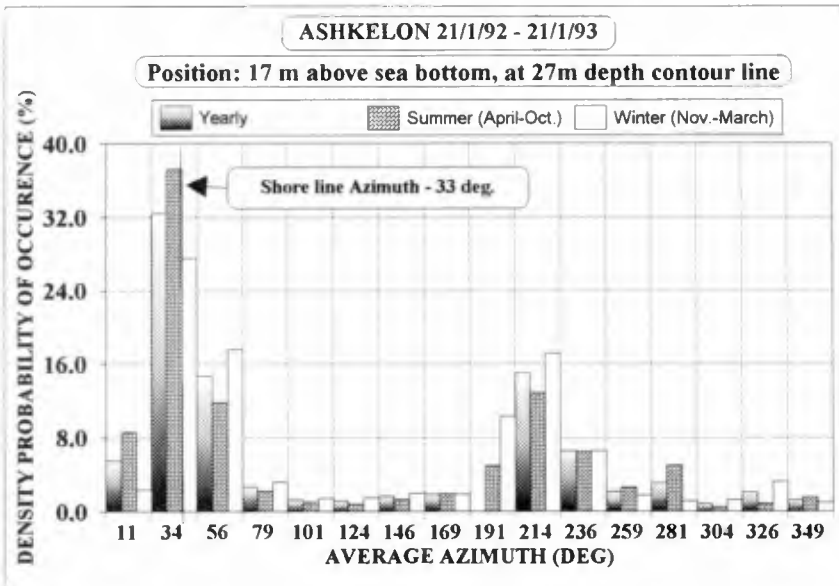


Figure 8. Current direction distribution offshore Ashkelon.

beyond the surf zone. The LCHF provides a value which is about 0.75 of the Bijker formula without currents beyond the surf zone. The comparison between the estimate of the transport with and without accounting for the currents beyond the surf zone is also presented in the same Figure. As one may see, the transport assessment including currents beyond the surf zone on the basis of the current statistics given in Figures 6 and 7 leads to volumes comparable to those of the CERC formula. In Figure 10 the yearly average longshore sediment transport distribution across the shore at Ashdod, based on the period 04/92-03/95, is presented.

ASHDOD YEARLY NET LONGSHORE SAND TRANSPORT
Averaged over the period 04/92-03/95

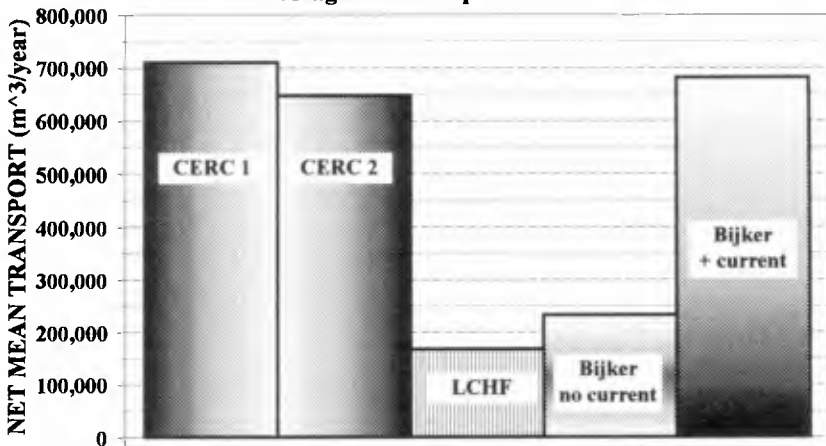


Figure 9. Comparison among methods of evaluation using the 3 hours data set.

Considering the fact that the assessment using currents was based by one year of currents data, during a harsher weather than in the following two years, the average longshore net transport was assessed on a weighted average between assessment with currents and assessment without currents. Thus, an yearly net longshore transport of 350,000 m³ to the North was assessed as the most probable rate for a normal year.

Discussion

Shoreline Changes

The results of the shoreline analysis clearly indicate that the net sediment transport in the area of Ashdod Port is northward. Under these conditions, one would expect erosion to occur north of Ashdod Port, but no such erosion of the shoreline is noticed from the analysis of the aerial photographs. The reason for this is the sand mining activity which was very intensive on this beach until 1964. This can be seen in Figure 11, which is an aerial photograph taken in 1958, prior to the port construction. The

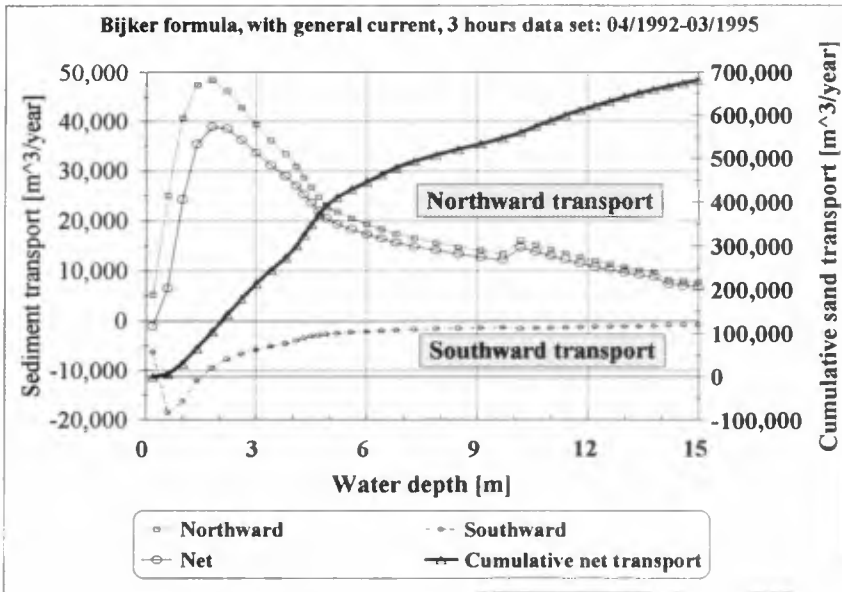


Figure 10. Yearly cross-shore sand transport profile at Ashdod (with currents).

scars of the sand mining are clearly seen on this picture, as well as on aerial photographs taken from the coast both north and south of this point. More than 5 million m³ of sand were mined between 1949 and 1963 from the beaches stretching along some 30-40 km of the Ashdod coastline (Zifzif Committee, 1964).



Figure 11. Aerial photograph taken in 1958 showing the scars of beach mining along the Ashdod shoreline.

This mining must have left the coast either devoid of loose sand, or close to it. The sand trapped south of the port after its construction "healed" these scars and widened the beach. However, north of the port, the beach was already rocky before the port construction, lacking sand to be removed by erosion, and this is why the position of the shoreline remained stable. The rocky beach extends today to some 3.5 km north of the port, and from there on northward, sand becomes gradually more ubiquitous on the beach.

Bathymetric Changes

The most striking finding of the analysis of the sea bottom changes is the massive accumulation of sediment, more than 2 million m³, which took place between 1985 and 1995. This raises a few questions: Was this accumulation a gradual one or an episodic event? What caused this rapid accumulation? Where did the sediment come from?

It was found that a bathymetric survey which was carried out in 1991 offshore Ashdod city, overlapped a small part of our study area in the south. Depth differential maps for the period 1985-1991 and 1991-1995 clearly showed that sediment accumulation which occurred in that area was greater in the period of 1991-1995 by many times than in 1985-1991. This indicates that the massive accumulation of sediment seen in the depth differential map for the period 1985-1995 occurred sometime between 1991 and 1995. The most prominent event that occurred in the period of 1991-1995 is a series of very severe storms which occurred in December 1991, February 1992 and December 1992. In one of them, February 1992, the deep water characteristic wave height was 7.2 m and in the others more than 5 m. Computation of longshore sediment transport rate using a simulated storm with waves of this magnitude resulted in a net transport of up to 400,000 m³ per storm. The storms of 1991-1992 are therefore responsible for the large deposition of sediment which was detected in the 1985-1995 depth differential map.

There was, however, another source of sediment input into the area. The Lakhish River, which discharges into the sea just south of Ashdod Port, has flooded during the storms, particularly during that of February 1992. According to Hydrological Survey of Israel, the water flow of this river in 1992 was the largest ever to be recorded. Figure 12, which is an aerial photograph taken 10 days after the flood, shows an extensive shoal in front of the river mouth which was formed, at least partly, by the sediment brought by the river to this area.

Sediment Bypass of Ashdod Port

The issue of sediment bypass of Ashdod Port is an important one because it implies to what degree the port acts as an obstacle to the natural transport of sand to the northern beaches of Israel. However, the evidence for such a bypass is only an indirect one. The depth differential map for the period of the port's existence clearly



Figure 12. Aerial photograph taken on 14 February 1992, 10 days after the flooding of Lakhish River, showing the shoal which was formed in front of the river's mouth.

shows that the pattern of accumulation of sediment south of the port, follows the contour of the main breakwater, surrounds it, and there are areas north of the port in which sediment accumulation is already noticed. According to reports of the Ports and Railways Authority the entrance channel to Ashdod Port is undergoing siltation. As it is unlikely that this siltation results from an on-offshore transport at this depth, it is another confirmation to the sediment bypass of the port.

It is difficult to provide the rate of sediment bypass because there is no direct way to measure it and we do not have quantitative information for all the parameters which control it. Nevertheless, an attempt was made to come up with an estimate which is based on assumptions and estimates. For the 10 year period between 1985 and 1995 some 3.5 million m^3 entered into the area as a result of the normal net yearly longshore sediment transport ($350,000 m^3/yr \times 10$ years). In addition, the storms of 1992 yielded some 0.9 million m^3 ($400,000 m^3/feb.92$ storm + $2 \times 250,000 m^3$ for the other 2 storms). It is estimated that Lakhish River contributed 0.25 million m^3 during the flood of 1992. All these add up to about 4.6 million m^3 that were input into the area south of Ashdod Port during that period of time. At that time 2.2 million m^3 of sediment were trapped in the area south of the port implying that 2.45 million m^3 , i.e. more than 50% of the sediment managed to bypass the port during that decade.

Acknowledgments

This study was supported by the Ports and Railways Authority, Israel. Wave data from Ashdod were provided by the Coastal & Marine Engineering Research Institute, Haifa, Israel. The authors wish to express their gratitude to E. Kit and J. Zwamborn for their constructive criticism.

References

- Bijker E.W., 1972. Lecture notes for Topics in Coastal Engineering, Delft Technical Univ., pp. 20-78.
- Finkelstein, A., 1980. Development of Ashdod Port, research in a sedimentological model; model calibration. CAMERI - Coastal and Marine Engineering Research Institute, Report No. P.M. 74/80: 1-49 (in Hebrew).
- Kran, N. 1980. Analysis of bathymetric data and sedimentation near Ashdod Harbor (1964-1971). Geol. Surv. Israel Report MG/6/80: 1-9.
- Komar P.D., 1977. Beach Sand Transport: Distribution and Total Drift *J. Waterway, Port Coastal and Ocean Div.*, ASCE, **103**, WW2, pp. 225-240 (May 1977).
- Manoujan S., and Mignot C., 1983, Ashdod Port Extension, Final Report, Laboratoire Centrale de'Hydraulique de France, Paris, 79p.
- Rosen, D.S., 1985. Assessment and Consultation on the Operability of the Coal Unloading Terminal at Ashdod Port North - Stage A, Final Report, CAMERI, PN. 160/85, pp. 13-15. (in Hebrew).
- Rosen D.S., 1993, Offshore Coal Unloading Terminal for Rutenberg Power Station Ashkelon Wave and Current Monitoring Program, Reporting Period 21/01/92 - 21/01/93, IOLR, P.N. H5/93.
- Shoshany, M. and Degani, A., 1992. Shoreline detection by digital image processing of aerial photography. *J. Coastal Res.*, **8**, 29-34.
- U.S. Army Corps of Engineers, Coastal Engineering Research Center, 1984, Shore Protection Manual, vol I,II, 2nd ed.
- Vajda, M., Mechrez, E. and Etrog, U., 1988. Disposal of sand from deepening dredging in Ashdod Port in connection with the construction of quay no. 9; examination of alternative solution and analysis of the port impact on the environment. CAMERI - Coastal and Marine Engineering Research Institute, Report No. P.M. 201/88: 1-46 (in Hebrew).
- Zifzif Committee, 1964. Zifzif Committee Report. Ministry of Development and Housing (in Hebrew).

CHAPTER 340

Tweed River Sand Bypass: Concepts and Progress

Russell J. Murray,¹ R.P. (Jock) Brodie,² Mark Porter,³ David A. Robinson⁴

ABSTRACT: The objectives of the Tweed River Entrance Sand Bypassing Project on Australia's east coast are to establish and maintain a navigable entrance to the Tweed River and to enhance and maintain the southern Gold Coast beaches, with the objectives to be achieved in perpetuity. The joint project of the New South Wales and Queensland State Governments with the support of the Gold Coast City Council offers the opportunity to achieve this co-operatively in partnership. Agreements have been established. The environmental impact assessment of the first stage (initial dredging and nourishment) has been completed, and the first component of these works involving over 2.2Mm³ of sand was successfully completed in August 1996. Environmental impact assessment and design studies for the second stage (the permanent bypassing system) are in progress. The paper describes the overall project and its key features, the investigations and analyses undertaken to date, the identified impacts, the initial dredging and nourishment works, and the issues being investigated for the permanent system.

INTRODUCTION

The Gold Coast-Tweed Heads region (28°S, 153.5°E) on Australia's east coast is a major international and national tourism destination, and a significant growing recreational and residential area, with a unique coastal environment. The beaches are subject to cyclonic(hurricane) and storm waves, and are characterised by a

-
- 1) Project Director, Queensland Dept. of Environment, PO Box 155 Brisbane Albert Street, Qld 4002, Australia.
 - 2) Project Director, New South Wales Dept. of Land and Water Conservation, McKell Building, Level 12, 2-24 Rawson Place, Sydney, NSW 2000, Australia.
 - 3) Manager Coastal, New South Wales Dept. of Land and Water Conservation (as above).
 - 4) Manager Coastal Resource Assessment, Qld Dept. of Environment (as above).

predominantly northwards longshore sand transport averaging 0.5 million cubic metres (Mm^3) per year net, which is driven mainly by the predominant easterly and south-easterly waves (median significant waveheight: 1.4m, median peak period 9s). The beaches are composed of clean fine-grained quartz sand with median diameter of 0.22mm. Mean spring tidal range is 1.3m.

The Tweed River entrance which influences the continuity of the natural littoral system has been plagued by mobile sandbars which have endangered navigation since the early 19th century. Entrance training walls (rock jetties) started in 1890 offered only short-term relief. From 1962 to 1965, the training walls were extended seaward 380m to aid navigation of the entrance. These walls reduced sand transport past the entrance, Letitia Spit to the south of the entrance accreted (total accretion to 1995 of over $7Mm^3$ has filled the walls), and the downdrift southern-most beaches of the Gold Coast experienced erosion (Macdonald and Patterson, 1984). Major beach nourishments totalling over $6Mm^3$ have been successful in substantially offsetting the erosion of these beaches (Murray et al, 1993 and 1994).

Following separate and joint studies by the responsible authorities, and complex negotiations with four jurisdictions, agreement was concluded between the State of New South Wales and the State of Queensland to undertake the Tweed River Entrance Sand Bypassing Project which impacts on both States. It is being supported by the local city, the City of the Gold Coast (Murray, Brodie et al, 1995).

The project agreements are:

- (a) the Heads of Agreement signed on 31 March 1994 by the Premiers of New South Wales and Queensland; and
- (b) the formal legally-binding Deed of Agreement signed by the responsible Ministers on 2 March 1995.

The New South Wales Parliament has enacted ratifying legislation (the *Tweed River Entrance Sand Bypassing Act 1995* (NSW)), and similar legislation is proposed in Queensland.

OBJECTIVES, PRINCIPLES, AND BENEFITS

The objectives of this joint project (to be achieved in perpetuity) are to:

- (a) improve and maintain the navigability of the Tweed River entrance (in New South Wales); and
- (b) improve and maintain the southern Gold Coast beaches (in Queensland).

The project comprises two inter-related components:

- (a) an initial dredging of the bar and entrance area and beach nourishment; and
- (b) an artificial sand bypassing system, to operate in perpetuity.

The benefits are anticipated to include:

- (a) the improvement in the safety of navigation of the river entrance with the consequent benefits to recreational boating, tourism, property values and the fishing industry;
- (b) improved tidal flushing of the river estuary, improved water quality, and mitigation of flooding; and
- (c) the restoration, widening and long-term maintenance of the beaches, with associated benefits to tourism, recreation, property values and the reduction of erosion threats.

To achieve early benefit, initial dredging and nourishment was scheduled to be undertaken while permanent bypassing system options and impacts were being investigated and assessed.

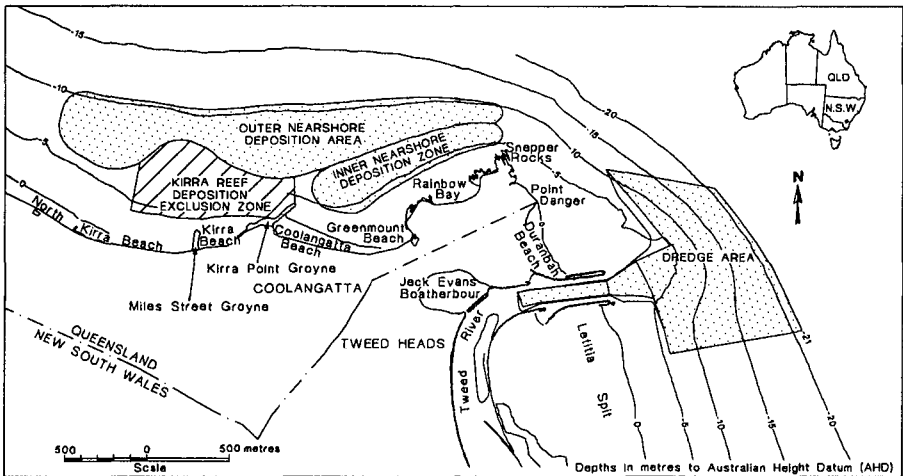


Figure 1: Location diagram, showing approximate dredging and nourishment areas

INITIAL DREDGING AND NOURISHMENT (STAGE 1)

The initial dredging and nourishment involves about 2.5Mm³ of sand to be dredged from the entrance and placed on the beaches. The environmental impact statement (EIS) was prepared to comply with the requirements of both States. Following exhibition of the document, public meetings and the receipt of twenty-six submissions, an EIS Submission Review Report addressed the submissions received and made recommendations for actions, monitoring and an Environmental Management Plan.

Impacts and issues identified included:

- (a) increased operational window for fishing trawlers traversing the bar;
- (b) improved ability of beaches of Rainbow Bay, Greenmount, Coolangatta, Kirra and North Kirra to withstand storm erosion;
- (c) improved flushing of the lower estuary, to result in improvement in water clarity, nutrients and bacterial loads;
- (d) restoration of nearshore bathymetry to a condition similar to pre-1960s (pre-wall extensions) condition enhancing conditions for beach users;
- (e) slightly increased tidal range in the estuary (high waters increased by up to 0.04m with possible impact on saltmarsh habitat and roosting and nesting sites for birds, and low waters lowered by up to 0.12m with possible impact on seagrass areas);
- (f) erosion of up to 75m from the previously accreted shoreline at the northern end of Letitia Spit;
- (g) changed surfing conditions;
- (h) concern regarding possible effects on the rocky reef community of Kirra reef if the nourishment produced conditions outside the natural range of seabed fluctuations;
- (i) potential disturbance by noise from booster pumps and mechanical equipment during upper beach nourishment; and
- (j) possible wrecks in the dredge area.

Each of these issues has been considered in detail and, where appropriate, modifications have been made to the scope and extent of the work (Brodie et al, 1995).

The lowest of six tenders(bids) from Australian and international companies for the first part of the initial dredging and nourishment (Stage 1A) was accepted. Dredeco undertook the work using three dredgers in successive campaigns from 26 April 1995 to 20 August 1996, transferring over 2.2Mm³ of sand.

The greater proportion of the work was carried out by the (144m long) *Pearl River*, the world's then largest trailing suction hopper dredger. In a six week campaign, it dredged up to approximately 9,000m³ of sand each load in typically four sweeps. The original design slope was modified to allow bench dredging to a similar volume and shape. The *Pearl River* dredged the bar and entrance area to the limits set by its draft. It deposited 0.93Mm³ through the bottom-opening doors to a predetermined profile in the outer nearshore deposition area with an upper level of minus 7m Australian Height Datum (AHD, approximately mean sea level). A further 0.59Mm³ was pumped onto the upper beaches through a single point mooring connected to a 750m long, one metre diameter submerged pipe, which came ashore at Kirra Point, and linked to alongshore pipelines which extended from Kirra Point to the limits of beach nourishment at Rainbow Bay and North Kirra.

The shallower bar areas were dredged by the smaller trailing suction hopper dredger, the *Ngamotu* which has a length of 61m, draft of 3.5m fully laden and a hopper capacity of 490m³. The *Ngamotu* established a channel through the bar, increasing the ruling depth over the bar from less than 4m AHD to more than 6m AHD, thus allowing access by larger dredgers. During suitable conditions from May to November 1995, it dredged 0.17Mm³ and placed this sand in the inner nearshore deposition area to an upper level of minus 4.5m AHD.

Subsequently, in two campaigns in January/February and July/August 1996, the 2,300m³ capacity split-hull trailing suction hopper dredger, the *Krankeloon*, removed a further 0.56Mm³ and placed this in the inner nearshore deposition zone (0.12Mm³), the outer nearshore deposition zone (0.39Mm³), and an eastwards extension of the nearshore deposition zones around Snapper Rocks (0.05Mm³).

Further dredging and nourishment (Stage 1B) is expected to be carried out in late 1997 following monitoring of the results of this work and assessment of maintenance requirements.

PERMANENT BYPASSING SYSTEM (STAGE 2)

The permanent bypassing component consists of the design, manufacture, supply, delivery and commissioning of a sand bypassing system and the continuing operation of that system including replacement of the capital equipment. Its purpose is to facilitate the natural littoral sand movement processes by conveying past the river entrance the net littoral transport which occurs at the northern portion of Letitia Spit, so as to maintain a clear navigation channel of at least 4.5m AHD and maintain a continuing supply of sand to the beaches.

Artificial sand bypassing alternatives include jetty(pier)-based systems, mobile (jack-up) systems, floating plant, and traditional dredgers. A mobile system could overdredge a buffer during low transport periods to assist in intercepting some of the sand which would otherwise be missed. A mobile system should in principle be capable of bypassing 500,000m³ per year, even though some is missed from time to time. Fixed jet-pump bypassing system options (such as used at the Gold Coast Seaway 28km to the north where 4.5Mm³ has been bypassed in the first 10 years) would require fundamental modification or augmentation because there is no buffer sand trap at the project site as, for example, provided by the Seaway training walls (Coughlan and Robinson, 1990), and fixed systems rely on, and are limited by, natural processes in bringing sand to the intakes. No system can be totally effective in intercepting all of the sand transport, particularly during storm/cyclone events when operations may have to be curtailed and sand transport may be very high. Some allowance will have to be made for sand not captured by the system before it reaches the Tweed entrance or which escapes from the operational area of the system. (Robinson, 1993).

The delivery locations are expected to be Snapper Rocks (major quantity), Kirra Point (possible on demand capability), and Duranbah Beach (possible minor quantity capability). As natural sand transport around Snapper Rocks and across the Rainbow Bay and Greenmount/Coolangatta beaches is characterised by some slug-like spurts overlying a more regular transport, there are likely to be some beach management advantages if sand can be discharged on demand at Kirra, where local shortages of sand occur from time to time. However Snapper Rocks could be a sufficient discharge site, provided a suitable discharge mechanism was designed, and operation of the bypassing rate was managed in accordance with changing transport rates. The long term average net littoral transport rate is currently understood to be 500,000m³ per year, but analysis suggests that it can vary between 270,000m³ and 900,000m³ in any single year. The delivery of sand will match the long term average net littoral transport, but will take account of the annual variations in quantities of sand delivered by natural processes to Letitia Spit and the specific objectives of the project, including coastal process issues of the beaches and the entrance, beach usage and navigation requirements. If the long term average net littoral transport rate changes, the rate of delivery will be changed accordingly.

Other issues to be considered for the system include:

- (a) system reliability and safety in the high-energy, corrosive, abrasive environment;
- (b) outlet design;
- (c) water discolouration (though the sand is clean);
- (d) public safety (for beach and waterway users);
- (e) effects on beach usage (including swimmers, surfers, and anglers);
- (f) visual impact;
- (g) noise;
- (h) operational scheduling;
- (i) performance criteria;
- (j) commercial and contractual arrangements; and
- (k) operational management.

Actions already implemented include the assembly and evaluation of the performance of the Gold Coast Seaway and other existing and planned bypassing systems, a value management study, and the incorporation of data requirements for the permanent system in the current data collection and monitoring program. A comprehensive environmental impact assessment study is in progress, and is scheduled for completion in mid-1997.

CONCLUSIONS

The objectives of the Tweed River Entrance Sand Bypassing Project are to establish and maintain a navigable entrance to the Tweed River and to enhance and maintain the southern Gold Coast beaches, with the objectives to be achieved in perpetuity. The joint project offers the opportunity to achieve this co-operatively in partnership.

The project is located on an open high-energy coastline subject to variable natural forces, in a highly-valued environment, subject to intensive usage. Accordingly, it is recognised that the project must be designed, evaluated and implemented prudently using best practice and in an environmentally sensitive way, if the long-term benefits are to be effectively achieved.

The complex bar dredging and beach nourishment have provided initial benefits, have satisfied strict environmental criteria, and have received widespread public support. Extensive environmental monitoring and public consultation has been incorporated.

The significant engineering, environmental and contractual challenges facing the permanent bypassing system are being progressively addressed.

REFERENCES

- Brodie, R.P., Murray, R.J., Porter, M., Robinson, D.A., and Lawson, S. (1995) 'Implementing the Tweed River Entrance Sand Bypassing Project', Proc. NSW Coastal Conf., Tweed Heads, Oct.
- Coughlan P. M. and Robinson D.A. (1990) 'The Gold Coast Seaway Queensland, Australia', Shore and Beach, Vol 58, No.1, Jan.
- Macdonald, H.V. and Patterson, D.C. (1984) 'Beach Response to Coastal Works, Gold Coast, Australia', Proc. 19th Coastal Eng. Conf., ASCE, Houston. pp 1522-1538.
- Murray, R.J., Brodie, R.P., Jackson, L.A., Porter, M., Robinson, D.A., Lawson, S. and Perry, M.P., (1995) 'Tweed River Entrance Sand Bypassing Project: Principles and Progress', 12th Australasian Conf. on Coastal and Ocean Engineering, The Institution of Engineers Australia, Melbourne, 29 May - 2 June, pp7-12.
- Murray, R.J., Robinson, D.A, and Soward, C.L. (1993) 'Monitoring of the Southern Gold Coast Beach Nourishment Project', 11th Australasian Conf. on Coastal and Ocean Engineering, The Institution of Engineers Australia, Townsville, 23-27 August, 1993, pp119-125.
- Murray, R.J., Robinson, D.A, and Soward, C.L. (1994) 'Southern Gold Coast Beach Nourishment Project: Implementation, Results, Effectiveness', *Terra et Aqua*, 56, Sept. 1994, pp12-23.
- Robinson, D.A. (1993) 'Tweed Heads Sand Bypassing System', Bruun Workshop: Beach Nourishment & Sand Bypassing, Dept of Civil Eng., Uni. of Qld, 28-29 Jan.

CHAPTER 341

DESIGN CONSIDERATIONS FOR COASTAL PROJECTS IN COLD REGIONS

Craig B. Leidersdorf, M. ASCE¹

Peter E. Gadd, M. ASCE¹

Kennon D. Vaudrey, M. ASCE²

ABSTRACT

Design considerations for coastal projects in cold regions include not only the oceanographic factors that tend to assume primary importance in temperate climates, but also ice and thermal factors. This paper reviews the current understanding of each of these three types of design considerations, with emphasis on the lessons learned from recent project experience in the Alaskan Beaufort Sea. It is concluded that the environmental influences unique to cold regions introduce both increased complexities and increased uncertainties into the design process for coastal structures. In consequence, a conservative approach that incorporates damage-tolerant components and non-catastrophic failure modes is recommended for the design of sensitive facilities.

INTRODUCTION

During the past two decades, the number of coastal and nearshore projects constructed in cold regions has increased significantly. The primary motivation for these projects has been petroleum-related activities, which have resulted in the installation of more than 50 artificial islands, causeways, and coastal pads off the Arctic coasts of Alaska and Canada. Public works projects also have been undertaken by communities such as Barrow, Alaska, where bluff stabilization and beach nourishment programs have been carried out in recent years (Wiegel, 1995).

For purposes of this paper, a "cold region" is defined as an area in which the sea surface remains ice-covered for a significant portion of each year. Important

¹ Principal, Coastal Frontiers Corp., 9420 Topanga Canyon Blvd., Ste. 101, Chatsworth, CA 91311

² President, Vaudrey & Associates, Inc., 1540 Marsh Street, Ste. 105, San Luis Obispo, CA 93401

design considerations for coastal projects in cold regions include not only the oceanographic factors that tend to assume primary importance in temperate climates, but also ice and thermal factors.

The objective of this paper is to review the current understanding of ice, oceanographic, and thermal design considerations for coastal projects in cold regions. Particular emphasis will be placed on recounting the lessons learned from recent project experience in the Alaskan Beaufort Sea.

ICE DESIGN CONSIDERATIONS

Ice-related factors that may warrant consideration in the design of coastal and nearshore facilities include horizontal loads, encroachment onto the structure work surface, gouging of the sea floor by ice floe keels, and "strudel scouring" of the sea bottom by the drainage of river outflow through holes in the ice. The first two factors, horizontal loads and encroachment, can exert a major influence on structures that extend above the sea surface, such as islands, causeways, and coastal pads. The last two factors, ice gouging and strudel scouring, are particularly relevant to engineering works constructed on the sea floor, such as pipelines and toe protection.

Horizontal Ice Loads

The horizontal loads that result from ice movement can be segregated into two categories: global ice loads, which act on large structures such as gravel islands, and local ice loads, which act on small structural elements such as sheet pile walls and caissons. Global ice loads vary with the ice thickness, strength, and mode of failure. In turn, the failure mode depends on the type of ice feature impacting the structure. For exposed locations in the Beaufort Sea in water depths of 10 to 15 m, the governing global ice load is likely to be produced by encounters with multiyear floes (floes that have survived at least one open-water season). For protected locations between the shoreline and the 10-m isobath, the design global ice load results from first-year sheet ice. Such loads can be calculated probabilistically or deterministically, with the methodology for each presented in the American Petroleum Institute Recommended Practice 2N (API RP2N; 1995), and in Sanderson (1988).

In the case of exposed structures such as man-made islands, it is assumed that the kinetic energy of the moving multiyear floe is totally dissipated in ice crushing as the floe either comes to rest against the island or continues moving past while developing a maximum contact width equal to the maximum waterline dimension of the island. If a floe of mass m is traveling at velocity v , it will come to rest after a total penetration X , when:

$$\frac{1}{2}mv^2 = \int_0^X P(x)dx \quad (1)$$

where $P(x)$ is the total force exerted when the floe has moved a distance x after initial contact. The load $P(x)$ may be expressed as:

$$P(x) = \sigma(A) A(x) \quad (2)$$

where the contact area $A(x)$ varies with the penetration distance and $\sigma(A)$ is the average ice failure pressure associated with this contact area. It is assumed that the largest global ice load for any multiyear floe impact will occur at the point of maximum penetration. In order to solve Equations (1) and (2), values are required for the ice floe mass m , the initial velocity v , and the failure pressure $\sigma(A)$. The contact area $A(x)$ is determined from the interaction geometry of the floe and the structure.

Using the above ice loading scenario and Equations (1) and (2), global ice loads can be computed probabilistically by considering the input parameters as random variables. Independent distribution functions are required for the multiyear floe thickness, the floe diameter, the floe velocity, and the ice failure pressure to determine the annual probability distribution of the total ice load P acting against the structure. The maximum annual load developed from an appropriate random sampling of the four input parameters is assumed to approximate an extreme value (e.g., Type I or Gumbel) distribution, from which a design value can be determined. In the Alaskan Beaufort Sea, representative design global ice loads associated with multiyear floe impacts range from 5 to 6 MN per meter of island exposure width for a return period of 100 years.

In the case of protected sites such as coastal pads, the maximum global load P exerted by sheet ice can be estimated on the basis of an ice crushing failure using a modified version of the Korzhavin equation (API, 1995):

$$P/D = p t \quad (3)$$

where P represents the total horizontal ice force acting against the maximum exposure width D of the structure, t represents the ice thickness, and p represents the effective ice crushing or failure pressure (which varies with the ice type, temperature, movement rate, and contact area).

The maximum annual load usually will occur in late winter, when the ice temperature and thickness produce the strongest ice. Values ranging from 1 to 1.5 MPa for the effective ice failure pressure p and 0.5 to 2 m for the ice thickness t are representative of the nearshore first-year ice conditions utilized for design purposes in the Alaskan Beaufort Sea. The resulting global ice loads range from 0.5 to 3 MN per meter of exposure width for a return period of 100 years.

Small structural elements such as sheet pile walls and caissons must be designed to withstand ice pressures exerted over areas of several square meters. These local ice failure pressures can be much larger than the uniaxial compressive ice

strength because of the confinement provided by the surrounding ice. In consequence, the design local ice loads on small structural elements always exceed the global loads exerted by the same ice conditions on large structures.

As suggested by Figure 1, local ice pressures increase with decreasing contact areas. The two curves in Figure 1 represent recommended upper and lower bounds derived from an empirical local ice pressure-area relationship set forth in the API RP2N (1995). The lower bound is based upon the mean plus two standard deviations ("M+2SD"), while the upper bound is based upon the mean plus three standard deviations ("M+3SD"). Because these curves were developed from measurements acquired throughout the Arctic, site-specific experience should be taken into consideration when they are applied to specific projects. In addition, the curves should be utilized only for contact areas less than 10 m²; the product of the local ice pressure and the contact area always should exceed the global ice load calculated according to the appropriate method described above; and the local ice pressure should be regarded as acting normal to the exposed face of the structure.

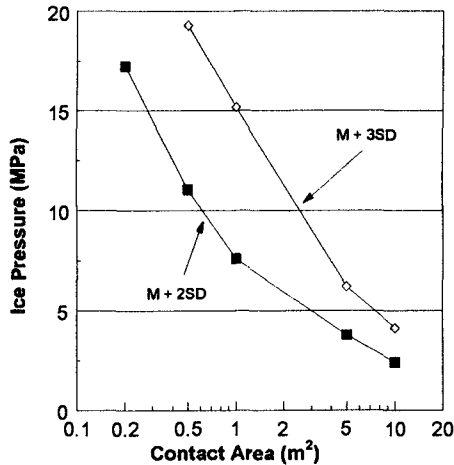


Figure 1. Pressure-Area Curves for Small Structural Elements

Ice Encroachment

In the context of this paper, encroachment refers to the movement of an ice sheet or individual ice blocks onto the work surface of a man-made island or coastal pad (Plate 1). If the sheet ice is driven up the side slope intact by a storm wind, the phenomenon is considered ice "ride-up". If the ice fails in buckling or bending and breaks up into individual blocks, an ice "pile-up" is formed on the side slope. In the Beaufort Sea, ride-up and pile-up events can occur during both freeze-up (early October through mid-December) and break-up (early June through mid-July).



Plate 1. Ice Encroachment on Endeavor Island, Alaska (1982)

A number of factors influence the susceptibility of a given location to ice ride-up, pile-up, and possible encroachment. Although ice movement results from wind stress, the single most important factor in initiating a ride-up or pile-up event is the loss of confinement of the ice sheet. Reversal of the wind direction is the usual cause of confinement loss, due to the formation of cracks or small leads in the nearshore ice. An easterly wind may produce the cracks or leads in the ice, for example, after which a westerly wind can drive the relatively unconfined ice up the slope of a pad or island.

While loss of confinement represents the dominant influence on ice ride-up and pile-up events, the ice thickness and the intensity and duration of storms constitute important secondary influences. The greater the ice thickness, the larger the driving force that will be required to initiate motion. Once the ice begins to move, severe storms of long-duration will maintain sufficient driving force to keep the ice in motion. The ice typically moves at a rate of 100 to 200 m/hr during the formation of a shoreline ice pile-up. Motion ceases when the driving force is balanced by the resistance of an "infinitely" wide obstruction, such as a shoreline.

The most common encroachment event, a combination of ride-up and pile-up, occurs when the sheet ice rides up the structure slope until increasing frictional resistance or a change in slope causes the ice to rubble and form a pile-up. If the pile-up attains sufficient height, ice blocks at the top of the pile can tumble down onto the work surface. Such an event occurred in October 1982 on Endeavor Island, which is

located in a water depth of 3.7 m in the Alaskan Beaufort Sea. As is evident in Plate 1, a southwesterly storm with wind speeds of 15-20 m/s created a 7.6 m high pile-up and caused 20-cm thick ice blocks to encroach up to 5 m onto the island work surface (Vaudrey, 1983).

Because our present understanding of pile-up mechanics is limited, encroachment estimates must be based upon statistical extrapolations of pile-up characteristics observed in the general project area. The method involves four primary steps: (1) compiling a database of historical pile-up events; (2) performing an extremal analysis to estimate the pile-up height associated with the desired return period; (3) estimating the pile-up geometry; and (4) computing the encroachment distance based on the structure geometry (Figure 2). A conservative lower bound of 30° is recommended for the slope angle β of the landward side of the pile-up. This value is based on shoreline pile-ups observed on the Alaskan Beaufort Sea coast and on the west coast of Banks Island, Canada, by Kovacs and Sodhi (1980). In the Alaskan Beaufort Sea, the predicted 100-year return period ice encroachment distances typically range from 8 to 16 m for work surface elevations of 3 to 6 m above mean sea level. A buffer zone exceeding the predicted encroachment distance can be maintained around the perimeter of the work surface to insure that sensitive facilities are not impacted.

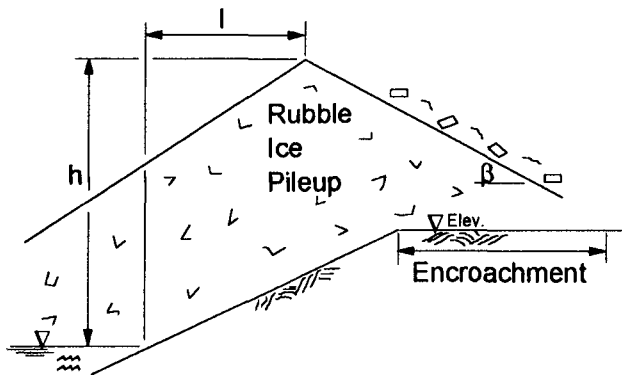


Figure 2. Ice Encroachment Geometry

Ice Gouging

The term “ice gouging” refers to the distinctive furrowing of the sea floor that results from the plowing action of ice keels. A representative example is provided in Figure 3, which displays a multi-beam sonar image of several gouges detected off the Alaskan Beaufort Sea coast in a water depth of 11 m. The single gouges were formed by individual ice keels, while the “gouge multiplet” is believed to have been caused by a multi-keeled ice feature.

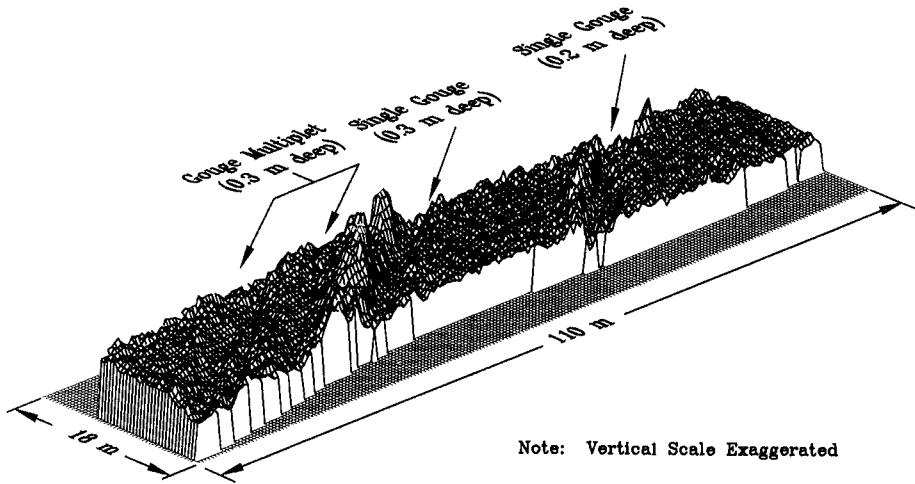


Figure 3. Multi-Beam Sonar Image of Ice Gouges in the Alaskan Beaufort Sea

The frequency and severity of gouging depend upon complex interactions between the dynamic ice environment and the sea floor sediments. Although our knowledge of the process is far from complete, key parameters appear to include the ice movement characteristics, the soil characteristics, the sea floor slope, and the water depth. From a study of ice keel structure and available driving forces, Kovacs and Mellor (1974) concluded that virtually all ice keels possess sufficient strength for gouging.

Extensive ice gouge measurement programs were conducted in the Alaskan Beaufort Sea from 1970 to the mid-1980's by the U.S. Geological Survey (USGS). Based on an analysis of more than 100,000 gouges, Barnes, *et al.* (1984), reported an average gouge density of $70/\text{km}^2$ and a maximum density of $490/\text{km}^2$. The mean incision depth for individual gouges was 0.56 m (measured below the original sea floor), while the maximum measured value was 4.0 m. The dominant gouge orientation was found to be slightly onshore of contour-parallel. Additional findings from the USGS programs of potential relevance to engineering projects such as subsea pipelines include the following: (1) gouge characteristics (density, depth, and width) attain their maximum values in the zone of active ice rubble formation known as the "stamukhi zone"; (2) sea floor morphology influences the intensity of gouging, with shallower gouges typically occurring in areas protected by offshore shoals; (3) gouge frequency and size are extremely variable from year to year in any one area, and from area to area in any one year (Rearic, 1986; Rearic and Ticken, 1988).

In view of the spatial and temporal variability inherent the gouging process, repeated annual surveys are advisable to obtain an accurate statistical characterization

of the gouge population at a particular project site. Multi-beam sonar, when used in conjunction with differentially-corrected Global Positioning System (GPS) position data, has proven to be a valuable tool for such surveys. Based on two successive field programs performed in support of a planned pipeline project near Prudhoe Bay, Alaska, multi-beam sonar is capable of mapping gouge features with a resolution of less than 0.1 m.

Strudel Scour

Strudel scour depressions in the sea floor are formed in the spring, when the breakup of river ice precedes the breakup of ice in the nearshore zone. If the sea ice in the river deltas is frozen to the sea floor (as occurs in the Alaskan Beaufort Sea to a depth of 2 m), this "bottomfast" ice forms a dam that causes overflowing of the river water. The overflow water, typically 0.5 to 1.5 m deep, spreads offshore and drains through discontinuities in the ice sheet caused by tidal cracks, thermal cracks, and seal breathing holes. Such "strudel zones" usually are located immediately offshore of the river deltas, in water depths of 2 to 9 m.

In those instances where the overflow rate is high, the drainage holes become enlarged and powerful strudel jets develop. Sizable scour depressions in the sea floor can result, particularly in the area immediately seaward of the bottom fast ice where the attenuating effect of the water column on the strudel jet is minimal. Although the depressions tend to be circular in plan form, clustered scours and extended linear scours also have been detected. The probable cause of these multiple and extended scours is drainage through linear fractures in the ice sheet, such as tidal cracks.

Measurements of strudel scour characteristics, unlike those of ice gouges, have been extremely sparse. Studies conducted by the USGS in 1972 (Reimnitz, *et al.*, 1974), and 1978-80 (Reimnitz and Kempema, 1982) documented three scour depressions in the vicinity of Prudhoe Bay in water depths of 3.0 to 3.5 m. The scour depths ranged from 1.2 to 4.3 m below the original sea floor, while the maximum horizontal dimensions ranged from 12 to 25 m. Of interest for the design of nearshore structures is the data set acquired by BP Exploration (Alaska) Inc. in the vicinity of Resolution Island, which is located in 2.3 m of water off Alaska's Sagavanirktok River. Annual bathymetric surveys conducted from 1985 through 1995 revealed the formation of seven strudel scours in proximity to the island toe (Coastal Frontiers, 1996). The deepest, 2.8 m below the sea floor, re-filled with sediment to the point that it was no longer detectable five years after its discovery. A probable explanation for the high frequency of strudel scouring at this location is the tendency for the island to induce cracks in the surrounding ice sheet. The primary implication for coastal projects is that the lower slope and toe of a nearshore structure may require additional protection to withstand the strudel jets caused by the presence of that structure.

OCEANOGRAPHIC DESIGN CONSIDERATIONS

Oceanographic design considerations in cold regions are analogous to those in temperate climates, with water levels, waves, and currents often constituting the key parameters. Complications can arise, however, from factors that include a paucity of measured data and exceptionally large storm surges.

Due to low population densities, low volumes of vessel traffic, and the difficulties associated with obtaining measurements in ice-infested waters, oceanographic data tend to be sparse or non-existent in many cold regions. Of particular concern is the situation that arises in areas like the Beaufort Sea, where the most severe storm events of the open-water season often occur just prior to freeze-up. If bottom-mounted instruments such as wave gauges or current meters are removed in advance of this period, the data may be skewed toward milder conditions. Conversely, if the instruments are allowed to remain in place until after freeze-up and then recovered through the ice, the probability of damage or loss from ice keel impacts increases substantially.

In the absence of reliable measurements, the database needed to estimate extreme events at coastal project sites must be derived from hindcast analyses. Difficulties may be encountered in a number of areas, beginning with a lack of meteorological data from which to specify the wind fields. Also problematic is the influence of sea ice, whose damping effect on wave generation and propagation is not fully understood. Specification of the fetch for wave generation is further complicated by the mobility of the ice edge during storm events.

Despite these difficulties, the hindcast approach has proven to be both reliable and cost-effective in the Alaskan Beaufort Sea, where storm surge and wave models were used to hindcast the 16 most severe storms occurring between 1949 and 1980 (Oceanweather, 1982). Initially, the models were implemented for the entire region, with the surge model utilizing a grid spacing of 4.6 km (2.5 nautical miles) and the wave model a grid spacing of 37 km (20 nautical miles). Subsequently, nested grids have been used to predict extreme conditions at numerous individual project sites.

Because Coriolis force increases with the sine of the latitude, coast-parallel winds at high latitude produce storm surges and setdowns of greater magnitude than would occur under similar conditions at low latitude. One obvious implication is that flooding constitutes a major design consideration for many coastal projects in cold regions. In the Beaufort Sea, for example, the predicted 100-year surge heights are typically on the order of 2 m, and driftwood strand lines have been observed as high as 3.4 m above mean sea level (Reimnitz and Maurer, 1979).

Surge-altered water levels are important not only for their direct impact on coastal flooding, but also for their indirect influence on wave and current conditions. In those areas where the wave heights are depth-limited, the elevated water levels

that result from storm surge can cause substantial increases in design wave heights. To properly account for this phenomenon in hindcast analyses, a time-series history of water levels should be developed for each historical storm and then utilized when modeling the wave conditions for that event.

The pronounced surge and setdown events that occur at high latitude can induce accelerated coastal boundary currents. As water either builds up or draws down at the coastline, a sloping sea surface is created in the shore-perpendicular direction. The resulting pressure gradient couples geostrophically with Coriolis force to produce a strong shore-parallel flow known as a barotropic coastal jet (Csanady, 1982). Indirect evidence supporting the existence of such currents is provided by ice floe velocities recorded in the Alaskan Beaufort Sea during the 1984 open-water season (Tekmarine, *et al.*, 1985). The floe velocities measured landward of the 30-m isobath during periods of accelerating winds averaged approximately 5% of the wind speed, which is substantially higher than the value of 2 to 3% that might be expected in deep water. The implications of these accelerated currents for the design of nearshore structures include higher velocities for ice floe impacts during periods of open water, and an increased potential for current-induced scour.

THERMAL DESIGN CONSIDERATIONS

Of the many thermal design considerations unique to cold regions, those of particular importance to coastal projects include thermal erosion of ice-bonded bluff sediments, and low-temperature effects on construction materials. In the case of thermally-induced erosion, bluff retreat can result not only from sea water thawing the base of the bluff (Kobayashi and Reimnitz, 1988), but also from elevated air temperatures thawing ice lenses embedded in the bluff face.

Insight into the process of thermal erosion has been provided by an on-going monitoring program at Heald Point Peninsula, which constitutes the northeast boundary of Prudhoe Bay, Alaska. From an analysis of aerial photographs obtained periodically between 1949 and 1988, and survey data acquired annually between 1989 and 1994, it was determined that the central portion of the 5-m high western bluff was retreating at an average rate of 1.6 m/yr. The adjacent bluff areas, by comparison, were retreating at less than 0.5 m/yr (Figure 4). Annual inspections revealed the cause of the accelerated erosion to be the melting of a 2-m thick ice lens embedded in the bluff face near the top of the bluff (Plate 2). Notwithstanding the importance of factors such as wave-induced erosion of the bluff toe and the degree of soil cover on the ice lens, the dominant influence over the annual retreat rate was found to be the summer air temperature. In 1989, for example, when exceptionally high mean monthly temperatures were recorded during the summer season, the bluff edge in the area occupied by the ice lens retreated by up to 7.2 m.

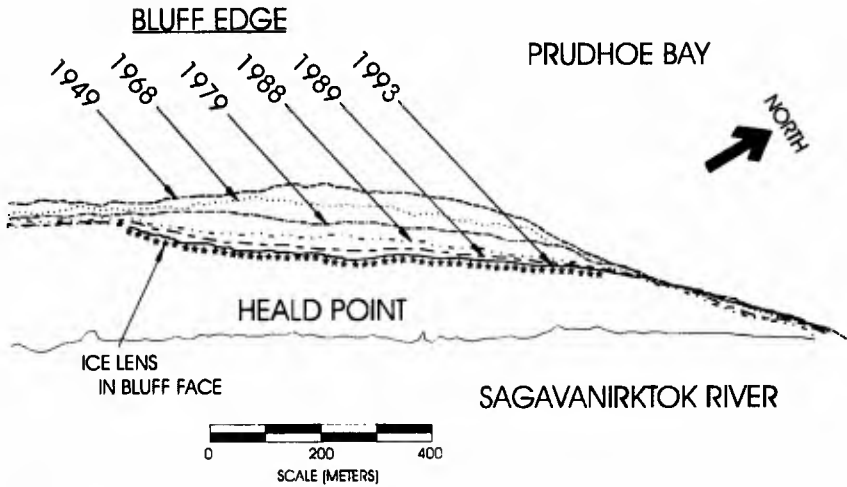


Figure 4. Historical Bluff Edge Retreat at Heald Point, Alaska



Plate 2. Thermal Erosion of Ice Lens in Heald Point Bluff Face (1993)

A particular concern with subaerial melting is that erosion can occur even in the absence of severe oceanographic events. Fortunately, however, the experience acquired with a gravel pad constructed on Heald Point suggests that the problem can be addressed by insulating the bluff face with granular fill material. Since 1993, when

gravel was installed from the blufftop to the waterline at a slope of 7(H):1(V), thermal erosion of the western bluff edge has been negligible.

Among the low temperature effects on construction materials encountered in cold regions, freeze-thaw stressing and brittle failure often assume importance for the design of coastal structures. Prior to freeze-up, when air temperatures are sub-freezing but the sea remains unfrozen, materials in the splash zone can be subjected to repeated freeze-thaw cycles. To minimize the impact on concrete structures or armor units, the concrete should be made as impermeable as possible through the use of a high cement factor, a low water-cement ratio, and pozzolan or silica fume (Leidersdorf, *et al.*, 1982). Air entrainment of 6% to 9% is recommended to limit cracking. In addition, sufficient reinforcing steel must be provided to insure that the cracks which do occur will not progressively widen.

Steel components that will be subject to impact or vibration, such as lifting eyes, should remain ductile at the lowest temperatures anticipated. Although corrosion losses over the design life must be taken into consideration, data obtained on Resolution Island suggest that corrosion rates in the Alaskan Beaufort Sea are modest. During a 4-year period in which exposed carbon steel rebar was monitored in the splash zone, corrosion rates were found to be less than 0.05 mm/yr.

CONCLUSIONS

The design of coastal projects in cold regions often is complicated by the need to consider ice and thermal factors as well as oceanographic factors. In some cases, the design process involves identifying a single governing influence; in others, the potential interactions between factors must be taken into account. A representative example of the former situation arises in determining an appropriate work surface elevation for a coastal facility. Two distinctly different phenomena, wave overtopping and ice encroachment, must be evaluated independently before selecting an appropriate minimum value. A situation where interactive environmental factors assume primary importance is in designing a slope protection system that must withstand wave and ice attack. Prototype observations have indicated that ice impacts can predispose the armor to damage under wave conditions that otherwise would be considered benign (Gadd and Leidersdorf, 1990; Leidersdorf, *et al.*, 1990).

In addition to increased complexities, the environmental influences unique to cold regions often introduce increased uncertainties into the design process. At the present level of understanding, quantitative predictions of phenomena that include ice gouging, strudel scouring, and thermal erosion can be derived only from statistical treatments of limited historical databases. In consequence, a conservative approach that incorporates damage-tolerant components and non-catastrophic failure modes is recommended for the design of sensitive facilities.

REFERENCES

- American Petroleum Institute, (1995), *Recommended Practice for Planning, Designing, and Constructing Structures and Pipelines for Arctic Conditions* (API RP2N), Dallas, TX.
- Barnes, P.W., D.M. Rearic, and E. Reimnitz, 1984, "Ice Gouging Characteristics and Processes", in Barnes, P.W., D.M. Schell and E. Reimnitz, *The Alaskan Beaufort Sea: Ecosystems and Environments*, Academic Press, Orlando, FL, p. 185-214.
- Coastal Frontiers Corporation, 1996, "1995 Resolution Island Inspection Program", Chatsworth, CA, 51 pp. + appen.
- Csanady, G.P., 1982: *Circulation in the Coastal Ocean*, D. Riedel Publishing Co., Boston, MA, 279 pp.
- Gadd, P.E., and C.B. Leidersdorf, 1990, "Recent Performance of Linked Concrete Mat Armor Under Wave and Ice Impact", in Edge, B.L., ed., *Proc. 22nd Coastal Engineering Conference*, ASCE, New York, NY, p. 2768-2781.
- Kobayashi, N, and E. Reimnitz, 1988, "Thermal and Mechanical Erosion of Slopes and Beaches", in Chen, A.T. and C.B. Leidersdorf, eds., *Arctic Coastal Processes and Slope Protection Design*, ASCE, New York, NY, p. 46-62.
- Kovacs, A. and M. Mellor, 1974, "Sea Ice Morphology and Ice as a Geologic Agent in the Southern Beaufort Sea", in J. Reed and J. Sater, *The Coast and Shelf of the Beaufort Sea*, Arctic Institute of North America, Arlington, VA, p. 113-161.
- Kovacs, A. and D. Sodhi, 1980, "Shore Ice Pileup and Rideup", *Cold Regions Science and Technology*, v. 2, p. 209-288.
- Leidersdorf, C.B., P.E. Gadd, and W.G. McDougal, 1990, "Arctic Slope Protection Methods, in Edge, B.L., ed., *Proc. 22nd Coastal Engineering Conference*, ASCE, New York, NY, p. 1687-1701.
- Leidersdorf, C.B., R.E. Potter, B.C. Gerwick, Jr., and Y.Y. Hsu, 1982, "Modular Slope Protection for the Arctic Environment", in *Proc 14th Offshore Technology Conference*, Houston, TX, p. 689-704.
- Oceanweather, Inc., 1992, "Beaufort Sea Wave Hindcast Study: Prudhoe Bay/Sag Delta and Harrison Bay", White Plains, NY, 103 pp. + appen.
- Rearic, D.M., 1986, "Temporal and Spatial Character of Newly Formed Ice Gouges in Eastern Harrison Bay, Alaska, 1977-1982", Open-File Report 86-391, U.S. Geological Survey, Menlo Park, CA, 52 pp.
- Rearic, D.M., and E.J. Ticken, 1988, "Ice Gouge Processes in the Alaskan Beaufort Sea", in Chen, A.C.T., and C.B. Leidersdorf, eds., *Arctic Coastal Processes and Slope Protection Design*, ASCE, New York, NY, p. 85-107.

- Reimnitz, E., and E. Kempema, 1982, "High Rates of Bedload Transport Measured from Infilling Rate of Large Strudel Scour Craters in the Beaufort Sea", *Continental Shelf Research*, v. 1, n. 4, p. 237-252.
- Reimnitz, E., and D.K. Maurer, 1979, "Effects of Storm Surges on the Beaufort Sea Coast, Northern Alaska", *Arctic*, v. 32, n. 4, p. 329-344.
- Reimnitz, E., C. Roderick, and S. Wolf, 1974, "Strudel Scour: A Unique Arctic Marine Geologic Phenomenon", *Journal of Sedimentary Petrology*, v. 44, n. 2, p. 409-420.
- Tekmarine, Inc., Polar Alpine, Inc., and Offshore and Coastal Technologies, Inc., 1985, "1984 Beaufort Sea Multiyear Ice Floe Tracking Study", AOGA Project No. 280, Sierra Madre, CA 233 pp. + appen.
- Sanderson, T. 1988, *Ice Mechanics: Risks to Offshore Structures*, Graham & Trotman, London, UK.
- Vaudrey, K., 1983, "1982 Freezeup Study of the Barrier Island Chain and Harrison Bay", AOGA Project No. 200, Vaudrey & Associates, Inc., San Luis Obispo, CA..
- Wiegel, R.L., 1995, "Shore & Beach Observations, Alaska", *Shore & Beach*, v. 63, n. 2, p. 2, 37.

CHAPTER 342

EXPERIMENTAL STUDY ON DEFORMATION AND FRACTURE OF ICE SHEET BY PROPAGATING WATER WAVE

Shigeki Sakai¹, Xiaodong Liu², Makoto Sasamoto³
Shigeo Kanada⁴, Koh Izumiyama⁵

ABSTRACT

A criteria of ice sheet fracture by propagating waves is proposed based on an elastic bending theory. Experiments with a model ice are carried out to examine the validity of the criteria. Comparisons with experimental results show that the proposed criteria is available for a wide range of ice properties. The crack span induced by waves is between $1/4$ and $1/2$ of wave length in ice.

INTRODUCTION

In the sub-Arctic sea, wave-induced motion of ice is a dominant factor causing many coastal problems; e.g. damages to structures by ice impact forces, or beach erosion by ice drift. To estimate the wave energy inside the ice zone, it is necessary to understand how waves transform under the ice cover. Previous studies show that the presence of ice causes wave energy attenuation, and the attenuation rate depends on the ice floe size and concentration. If some floes are fractured by waves, the distribution of floe sizes will be changed, and then the effects of the ice zone on waves will also vary. Therefore, for estimation of wave energy inside an ice zone, it is important to consider the ice deformation and fracture caused by waves.

-
- 1) Associate Professor, Department of Civil and Environmental Eng.,
Iwate University, 4-3-5 Ueda, Morioka, 020 Japan
 - 2) Graduated Student, Ditto
 - 3) Research Associate, Ditto
 - 4) Researcher, Ship Research Institute, Ministry of Transport
6-38-1 Shinkawa, Mitaka, Tokyo, 181 Japan
 - 5) Senior Researcher, Ditto

Ice-wave interaction has been mainly investigated by field observations, however it is very difficult to observe the deformation and fracture of ice since these occur in stormy sea conditions. A few experiments have been carried out, while in most of them plastic sheets were used as a model ice, and the effects of the difference in material properties between ice and plastic have not been examined. Furthermore, ice fracture cannot be simulated in the experiment with plastic sheets. In the present study, experiments with a model ice were carried out to examine wave-induced deformation of ice sheet and to verify the availability of the ice fracture criterion described hereafter.

EXPERIMENTS

Experimental Equipment and Procedure

Experiments were carried out in an ice tank which is 35m long, 6m wide and 1.8m deep, as illustrated in Figure 1. Water in the tank was doped with a solution of propylene glycol to weaken the ice which would be formed on the water surface. It took 10 hours or more to form an ice sheet of 25mm thickness and another 10 hours to set up experimental equipments, to test material properties and to observe the ice sheet deformation and fracture. Totally, 2 days were needed to perform one experiment, and one more day was necessary for the experiment with the ice sheet of 50mm thickness. The bending strength and the elastic modulus of ice were measured by a cantilever beam failure test and Plate Deflection Method, respectively.

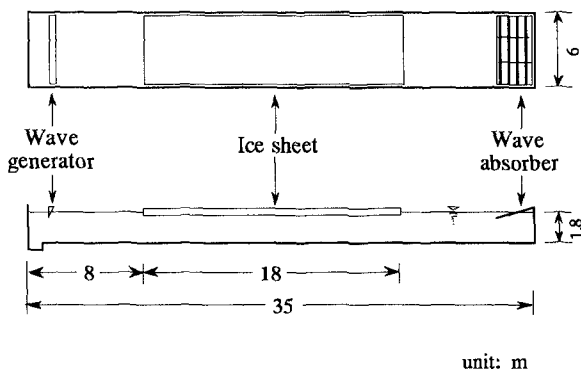


Figure 1 Experimental equipment

The wave was generated by a plunger type wave generator. At the far end of tank, a wave absorber was set up to decrease wave reflection. The vertical displacement of the ice sheet was measured at several points along the center of the tank, by using laser sensors and ultra-sonic sensors. Each experiments

started with a very small incident wave height. If the ice sheet fracture was not observed in this condition, another experiment with a little larger wave height was carried out. This procedure was repeated till the ice sheet fracture occurred. After the occurrence of the first fracture, the above procedure was also continued to observe proceeding fracture of ice sheet. The conditions of the incident wave and the material properties of ice are listed in Table 1.

Table 1 Experimental condition

Case No.	Wave Period T(s)	Wave Height in Open Water H_0 (mm)	Ice Thickness h_i (mm)	Bending Strength of Ice σ_i (kPa)	Elastic Modulus of Ice E (MPa)
1	1.19	20.5~30.2	49.2	35.1	21.8
2	0.80	20.6~26.1	25.2	22.6	5.3
3	0.79	12.3~32.0	28.4	36.0	31.4
4	0.80	18.9~32.2	53.3	39.7	29.3
5	0.99	29.7	53.3	39.7	29.3
6	1.40	20.6~27.7	53.3	39.7	29.3
7	1.20	27.7~29.7	54.2	38.1	34.3
8	1.40	14.3~26.7	23.2	119.3	125.4
9	1.20	17.9~23.8	24.3	137.4	202.5
10	1.00	18.4~26.0	23.2	87.9	201.5

Experimental Results

As the incident wave penetrates into the ice-covered water, the wave height changes significantly near the ice edge and attenuates gradually under the ice. Figure 2 shows the effects of incident wave height on the change of

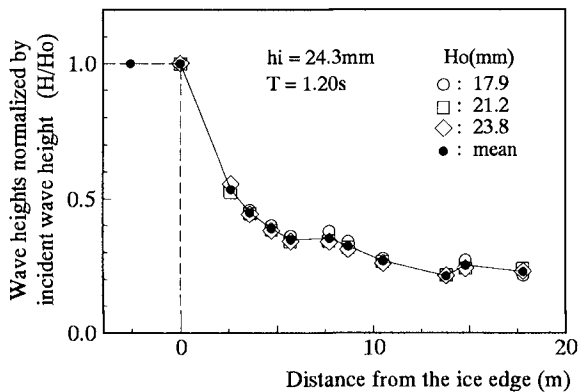


Figure 2 Wave height under ice sheet

wave height under the ice. The wave heights in this figure were normalized by the wave height in the open water. This ratio does not contain the effects of reflected wave from the ice edge since the wave height in the open water were estimated by subtracting reflected wave energy from incident wave energy. Generally, non-linear effects appear clearly with increasing of wave steepness, however there cannot exist steep waves under ice sheet since such waves cause ice sheet fracture. Figure 2 indicates that there is no effect of wave steepness on the wave height change under ice sheet in the condition where the ice sheet fracture does not occur. So, it can be concluded that the non-linearity of waves under ice sheet is to be negligible. Figure 3 gives an example of wave profile under ice sheet. The measured profile is described by a trigonometric function.

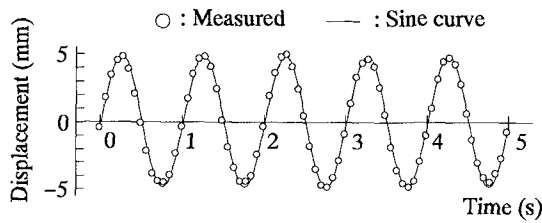


Figure 3 Example of wave profile under ice sheet

The wave celerity under ice sheet differs from that in open water and is almost constant over ice sheet, as shown in Figure 4. The non-linear effects of wave steepness on wave celerity is negligible, as well as on wave height change. A linear theory for waves under elastic plate gives a good explanation to experimental results of wave celerity under ice sheet(see Figure 5).

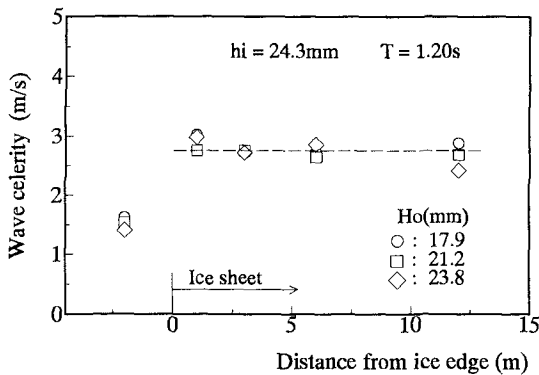


Figure 4 Wave celerity under ice sheet

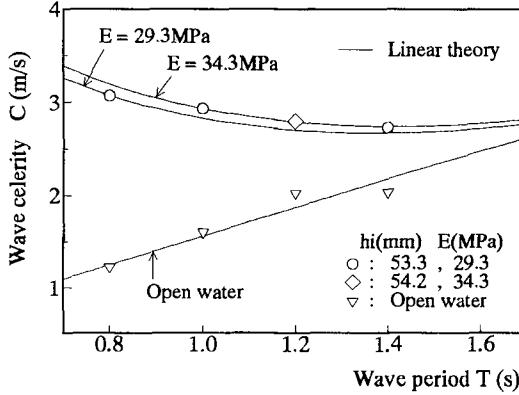


Figure 5 Comparison between measured and calculated wave celerity

THEORY

Ice sheet fracture is to be analyzed based on an elasto-plasticity fracture mechanics. However, it will be helpful for simple theoretical analysis on ice sheet fracture to consider how the elasticity or the plasticity of ice influences on ice-wave interactions. Liu and Sakai(1996) compared the numerical calculation of wave under elastic plate with experimental results of waves under elasto-plastic plate. Their comparisons showed that the calculated wave height near the edge agrees with experimental data fairly well and that the calculated values become somewhat larger than measured one as waves penetrate deeper in the plate. This discrepancy might be brought by a lack of plasticity effects in the numerical calculation. Wadhams(1973) explained the attenuation of wave height under ice sheet by energy loss due to a time dependent plastic strain (creep), and showed that this theory gives a good explanation for field observations of wave height attenuation in sea ice. These studies indicate that the deformation of ice sheet by waves is essentially elastic and the plasticity of ice cannot be negligible with increasing of penetration. Generally, ice sheet fracture by waves occurs near the ice edge. Therefore, it is reasonable to regard ice sheet fracture as a results of elastic deformation induced by waves.

An elastic bending theory gives a stress on the ice sheet surface as;

$$\sigma = \frac{Eh_i}{2(1-\nu^2)} \frac{\partial^2 \zeta}{\partial^2 x} \tag{1}$$

where E is elastic modulus of ice, h_i is ice thickness, ν is Poisson's ratio(=0.3), ζ is wave profile of ice sheet and x is direction of wave propagation.

As shown in Figure 3, a wave profile is expressed by a trigonometric function as follows;

$$\zeta = \frac{H}{2} \sin(kx - \omega t) \tag{2}$$

where H is wave height in ice, k is wave number ($= 2\pi/L_i$, L_i is wave length in ice), ω is angular frequency ($= 2\pi/T$, T is wave period) and t is time.

When the bending stress on the surface reaches the bending strength σ_f , ice sheet fracture occurs. Therefore, a fracture criterion is expressed as follows;

$$\frac{Hh_i}{L_i^2} = \frac{1 - \nu^2}{\pi^2} \frac{1}{E/\sigma_f} \tag{3}$$

VALIDITY OF ICE FRACTURE CRITERIA

The measured wave height is not accurate since the ice separated from the main part of ice sheet moves as an ice floe, not as a continuous ice sheet, and this floe dissipates wave energy penetrating into the ice sheet. The wave height can be estimated from the wave height in open water and the distance of fracture point from the ice edge, since the ratio of wave height in ice to that in open water does not depend on the incident wave height for a given wave period, as illustrated in Figure 2. Another quantities in Equation (3) were directly measured in the experiment. The wave length in ice can be also calculated from a linear theory for wave under elastic plate, which gives a good estimation for wave celerity, as shown in Figure 5.

Figure 6 shows that the ice fracture criteria proposed herein is available over a wide range of the ratio of elastic modulus to bending strength of ice. This agreement of the criteria based on an elastic bending theory with experimental results also ensures the applicability of the elastic bending theory for analysis on ice fracture by waves.

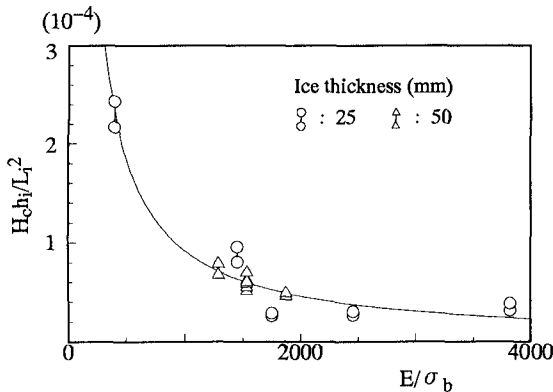


Figure 6 Ice fracture criteria compared with experimental results

CRACK SPAN IN ICE

The cracks in ice are almost perpendicular to the direction of the wave propagation, and the crack span is within $1/4$ and $1/2$ of the wave length under the ice sheet, as shown in Figure 7. The splits of ice were fractured laterally, resulting in rectangular pieces of almost same size. This regular pattern of ice fracture is also observed in the actual sea ice.

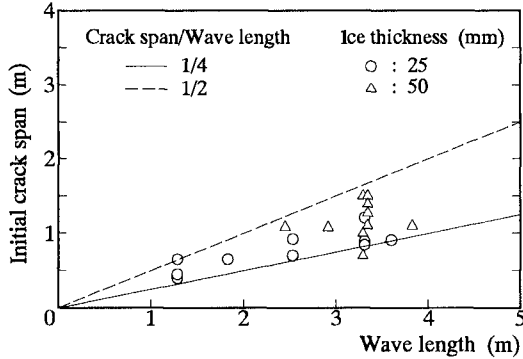


Figure 7 Relation between crack span and wave length in ice

REFERENCES

- Liu, X.D. and Sakai, S. (1996): Analysis on the Interaction of Waves with Flexible Floating Structure by BE-FE Combined Method, Proc. of 25th I.C.C.E., (in print)
- Wadhams, P. (1973): Attenuation of Swell by Sea Ice, J.G.R., Vol. 78, No. 18, pp. 3552-3563

CHAPTER 343

An Attempt to Determine the Spanish Public Domain Border

R. Medina¹, I.J. Losada¹, F. Méndez², A.J. Fernández³

Abstract

In this paper the problem of the determination of the Spanish maritime-land public domain border is analyzed. The Spanish public domain border is defined by the Spanish Law as the limit where the waves reach during the worst storm in the area. The law also establishes that this limit must be calculated taking into account the effects of the astronomical tide, the storm surge and the wave run-up. Since the storm surge and the wave run-up are random variables, the extreme flooding level determination is carried out by means of an extension of the joint probability method, first proposed by (Pugh and Vassie, 1978), which includes the effect of the wave run-up. The proposed theoretical approach is applied to a case study of a beach located in the North Coast of Spain.

Introduction

In Spain not only the sea, but also the shoreline is considered to be public property. This consideration is linked to our cultural and legal tradition and can be found in the ancient Roman and medieval Spanish Law.

In the 6th century, for instance, Justiniano established that: *“According to the natural law, the air, the running water, the sea and its shore are common to everybody. These shores have no owner...”*. Later, in the 13th century King Alfonso X, also known as Alfonso “The Wise”, ruled that: *“The things that communally belong to all creatures living in this world are: the air, the rainwater, the sea and its shore. No building can be undertaken on the seashore that could restrain the communal use of the people”*.

The present Spanish Legislation on Coasts, passed in 1988, also protects the shore-line and defines what is called the Maritime-Land Public Domain: *“The public domain stretches as far as the waves reach (maximum flooding level) during the worst storm in the area, and it includes beaches, dunes, cliffs, swamps and other low wetlands”*.

No type of trade activities can be allowed in this property. The Legislation on Coasts extends its influence to the private lands adjacent to the public property, Fig. 1,

¹Associate Professor, ² Graduate Student, Ocean & Coastal Research Group. Universidad de Cantabria. Dpto. Ciencias y Técnicas del Agua y del Medio Ambiente. Avda. de los Castros s/n. 39005 Santander

³ Formerly, State Coast Office. Ministry of the Environment. Paseo de la Castellana, 67. 28071 Madrid.

to avoid any use carried out on those areas which could be harmful to this space of high environmental value, (M.O.P.T.M.A., 1994). Therefore, in order to implement this policy, the Ministry of Public Works has undertaken a series of programs of actions with the first being the need to complete a precise identification of the public domain maritime-land assets in accordance to the definition set down in the Legislation on Coasts. This process has given rise to the current Property Survey Plan, whose purpose it is to fix public domain boundaries throughout the whole of the Spanish coast. This approach to the management of the coast in an integral manner has to embrace all territorial and political levels of government such as central government, states and city councils, as well as any individual with private interest on the coast.

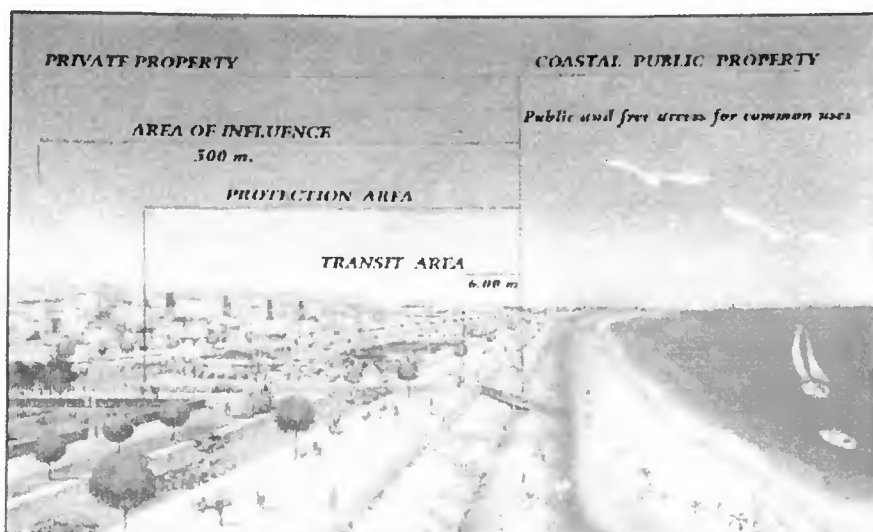


Figure 1. Public and private uses of shoreline

For this reason, the determination of the Spanish maritime-land public domain border is an extremely important element in the Program of Coastal Actions initiated by the Spanish Government, and in the last years it has become a key reason for many law suits between the different agents with interest in the coastal area.

Public Domain Border Determination

In order to determine the limit where “the waves reach during the worst storm in the area”, the 1988 Law established the maritime and meteorological dynamics that must be taken into account. In particular, the law established that the calculation of the maximum flooding level must account for the effects of the: (1) astronomical tide, (2) storm surge and (3) wave run-up, Fig. 2. Episodic events such as tsunamis must be omitted from the calculation, and the influence of long term effects such as sea level rise is not explicitly considered in the law.

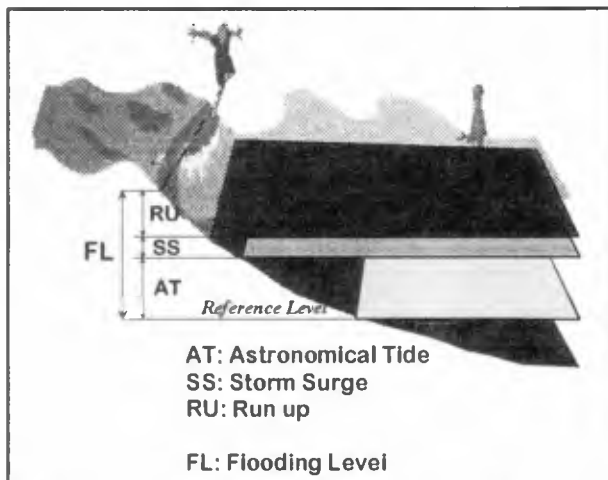


Figure 2. Dynamics to be considered in the determination of the public domain border

Since the storm surge and the wave run-up are random variables, the flooding level is also a random variable. Consequently, the determination of the public domain border is a stochastic extreme problem.

One of the consequences of being a stochastic problem is that there is not a deterministic "limit where the waves reach during the worst storm" but each level will have "a probability of being exceeded during a given storm". This probabilistic aspect is not considered in the law in which the public domain border is thought of as a deterministic line.

In this paper the extreme flooding level determination problem is analyzed by means of the joint probability method, (Pugh and Vassie, 1978), which has to be modified to include the effect of the wave run-up. The theoretical approach proposed to determine the public domain border is then applied to a case study in a beach located in the North Coast of Spain. In this case study, the probabilistic problem is also analyzed and a maritime-land public domain border is proposed.

Theoretical Approach

The existing methods for estimating the distribution of extreme sea-level at a site, using field data, can be divided into: (1) Direct Methods - in which extremes of the observed water level are analysed-, and (2) Indirect Methods - in which the constituent processes (i.e. tides, surges and waves) are modeled separately and the extreme water level is inferred.

Direct Methods

The direct methods are, mainly, the classical annual maxima approach and the r-largest annual events method.

Annual Maxima Method: The best known, simplest, and most widely used method of analysis of extreme distributions is the annual maxima method, (Gumbel, 1958). This approach has been previously used by several investigators to determine extreme sea-

levels, eg. (Lennon, 1963), (Suthons, 1963) and (Graff, 1981).

According to (Tawn and Vassie, 1991), this method is highly inefficient in its use of data and provides inaccurate results. These authors remarked that the assumptions made in using the annual maxima method are namely that hourly sea level heights are (1) independent, (2) identically distributed, and (3) that the number of hours in a year is large enough for the asymptotic approximations to hold. However, because of the nature of the tide and the dependence on the surge sequence, it is clear that (1) and (2) do not hold.

R-largest Annual Events Method: Several proposals have been made to extend the annual maxima method to incorporate all independent extreme sea-level observations into the estimation of the annual maxima distribution: (1) the peaks over thresholds method, (Davison and Smith, 1990); (2) the r-largest events method, (Tawn, 1988); and (3) the point process method, (Smith, 1989).

These methods are based on extreme value limit theory for stationary random sequences and, consequently, it is assumed the r-largest annual extreme levels are from stationary data. This assumption is critical since, due to the tide, the water level is highly non-stationary. According to this argument, the r-largest annual events method is not appropriate to determine extreme sea-levels, (Dixon and Tawn, 1994).

Indirect Methods

The existing indirect approaches, the joint probability method (Pugh and Vassie, 1978) and the revised joint probability method, (Tawn and Vassie, 1991) are the only viable options for estimating extreme levels when short data sets are available.

The main advantage of these methods is to exploit our knowledge of the tide in short data sets to which the annual maxima method could not be applied. Basically, these methods seek the probability distribution function (p.d.f.) of the different variables involved and calculate the sea level p.d.f. by combining those p.d.f.s. The nature of the combination of the p.d.f.s depends on whether there is dependence between the variable sequences.

The joint probability method assumes that extreme hourly water levels are independent. Clearly hourly water levels are not independent, but extreme levels may be only weakly dependent. (Tawn and Vassie, 1989) studied this feature and found that the assumption was false but led only to small overestimation of return levels.

In the revised joint probability method the temporal dependence of the variables is considered to be a parameter, called extremal index, θ , which is determined empirically from the data.

Although the revised joint probability method results hold for temporal dependence between variables, the existing records are not long enough to have data in the regions of both extreme tides and surges and, consequently, the external index determination is, many times, impossible.

From the previous analysis it can be concluded that direct methods cannot be used to determine extreme sea levels due to the lack of long records. Furthermore, the revised joint probability method also needs a long enough series in order to estimate θ . Consequently, the only methodology capable of giving reasonable results to the problem

under study is the joint probability method.

The Joint Probability Method (J.P.M.)

This method was first introduced by (Pugh and Vassie, 1978) to calculate extreme sea-levels due to the combined effect of tides and storm surges. At any time the observed sea level, after averaging out surface waves, has three components: mean sea level, tidal and storm surge level. Using standard methods, the first two of these components can be removed from the sea level sequence leaving the surge sequence.

Because the tidal sequence is deterministic, the p.d.f. for all tidal levels can be generated from tidal predictions, while the p.d.f. for the surge level is determined from the nontidal residual.

The p.d.f. of the sea level is finally calculated using the tidal and surge p.d.f.s'. Assuming that the tide and the surge can be considered independent, then

$$p(z) = \int_{-\infty}^{\infty} p_T(z - y) p_S(y) dy$$

where $p_T(z - y)$, $p_S(y)$ and $p(z)$ are the probability density functions for tide, surge and sea levels respectively.

Wave-Surge Joint Modelling

As stated previously, wave run-up is an important factor that must be included when determining the maximum flooding level on a beach. The inclusion of wave run-up leads to a two stochastic variables problem, surge and wave run-up, extending the J.P.M. developed by (Pugh and Vassie, 1978), which considers the surge only.

This new problem is one of bivariate extremes and the extrapolation of the distribution tail is required for both the surge and the wave run-up. Furthermore, the dependence between the extremes of these variables must be accounted for.

If surge and wave run-up are related, the probability density function for the sea level (flooding level) can be written as:

$$p(z) = \int_{-\infty}^{\infty} \int_{-\infty}^{\infty} p_T(z - y - x) p_{S,Ru}(y, x) dx dy$$

where $p_{S,Ru}(y, x)$ is the combined p.d.f. of surge and wave run-up.

If surge and wave run-up are independent, then

$$p(z) = \int_{-\infty}^{\infty} \int_{-\infty}^{\infty} p_T(z - y - x) p_S(y) p_{Ru}(x) dx dy$$

It should be noted that the availability of wave run-up data for a particular beach is usually scarce and, consequently, wave run-up p.d.f. must be inferred from wave data and wave run-up theory.

The study of wave run-up on artificial and natural beaches has received considerable attention by researchers over the last several years; e.g. (Guza and Thornton, 1981), (Holman, 1986), (Nielsen and Hanslow, 1991), (Holland and Holman, 1993).

In this study, (Nielsen and Hanslow, 1991) results for wave run-up distribution on a natural beach are used. Using run-up distributions measured on a wide spectrum of sandy beaches, these authors showed that, for a sea state, the Rayleigh distribution is a reasonable statistical model for the maximum level reached by individual waves. This result was also obtained theoretically by (Battjes, 1971) for the special case of perfect correlation between wave height, H and wave period, T . That is,

$$F(R_{\text{run}} \geq R) = \exp \left[- \left(\frac{R - R_{100}}{L_{R_{\text{run}}}} \right)^2 \right]$$

where R_{100} is the highest level transgressed by 100% of the waves and $L_{R_{\text{run}}}$ is the vertical scale of the distribution.

For extreme wave conditions, the beach can be assumed to be dissipative and, $L_{R_{\text{run}}} \approx 0,05 (H_{\text{rms}} L_o)^{0,5}$ where H_{rms} is the mean squared root wave height and L_o is the deep water wave length. Notice that for a typical relationship $T_s = \alpha_1 H_s^{0,5}$, $L_{R_{\text{run}}} \approx \alpha_2 H_s$ where α_1 and α_2 are two constants, depending on the wave climate of a given region.

Notice that the wave run-up p.d.f. is a Rayleigh distribution that depends on a random variable H_s , which has its own p.d.f. (e.g. Weibull), consequently the flooding level p.d.f. can be written as:

$$p(z) = \int_{-\infty}^{\infty} \int_{-\infty}^{\infty} p_T(z - y - x) p_S(y) p_{Ru}(x) dx dy$$

with

$$p_{Ru}(x) = \int_{-\infty}^{\infty} p_{Ru}^*(x, H_s) p_{H_s}(H_s) dH_s$$

$p_{Ru}^*()$ where is the Rayleigh $p_{H_s}()$ p.d.f., and is the significant wave height p.d.f.

Application

In this section, the wave-surge joint modelling is applied to a beach located on the North Coast of Spain.

Study Site

The study site is Oyambre Beach, located close to the city of Santander, on the Cantabrian coast of Spain, Gulf of Biscay, Fig. 3.

The northern coast of Spain is divided into a series of pocket beaches and small inlets isolated between rocky headlands. Most of the headlands extend into deep water and appear to be effective in confining littoral sand to the embayments. Therefore, the coast can be analyzed as a series of littoral cells.

One of these littoral cells is the beach of Oyambre. The beach is bound westward by Cape Oyambre and eastward by Cape El Moro. Several reefs can be found in intermediate water as part of Cape Oyambre along the northwest part of the beach (e.g. La Molar Shoal, San Francisco Shoal, Fig. 3).

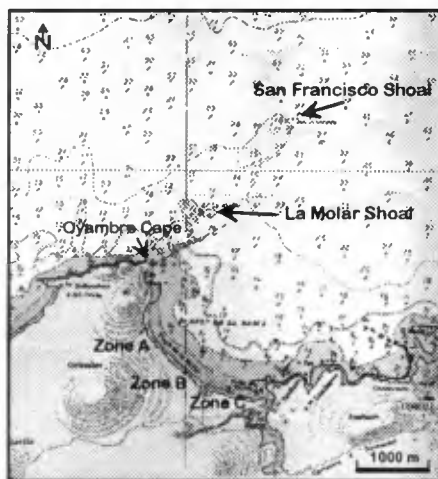


Figure 3. Location Map

More than three-quarters of the deep-water waves approach Oyambre Beach from the northern - northwestern sector. The annual average significant wave height is about 1 m with typical winter storms waves of $H_s \sim 4 + 6$ m. Tides at Oyambre Beach are semidiurnal with a mean tidal range of 3 m and spring tidal range of 5 m.

Maritime and Meteorological Data

In order to apply the methodology presented in section "Wave-Surge Joint Modelling", different data sets of waves and sea-level were analyzed. These data sets are continuously recorded by the Spanish Network for Maritime Recording and are presented in several publications from the Ministry of Public Works, Transportation and Environment, called R.O.M., (Losada et al, 1996).

Sea-Level Data

Sea-level data used in this study were recorded at Santander. This sea-level data set consists of hourly sea-level measured during the last five years and include three additive components: mean sea-level, tidal, and surge level.

Standard tidal analysis, (Godin 1978), is used to separate the astronomical tide and the surge from the sea-level data. The astronomical tide distribution shown by a probability density function in Fig. 4, is bi-modal. This kind of distribution is typical of

semi-diurnal dominated tides, with the modes occurring at levels corresponding to mean high and low water tides.

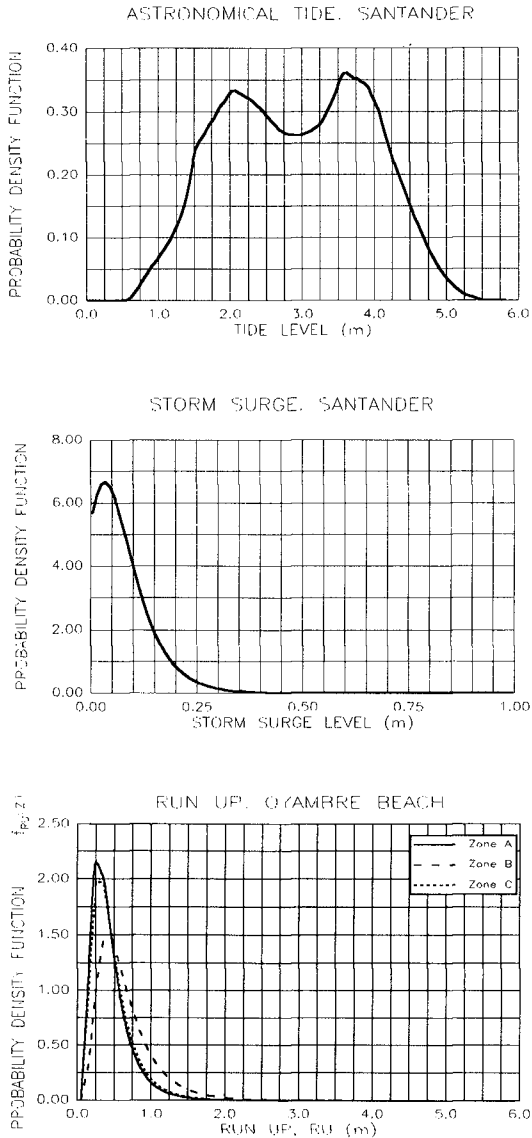


Figure 4. Tide, surge and wave run-up p.d.f.'s

The surge series is defined as the residual of the tidal series; i.e. the difference

between the observed sea-level and the predicted tide. The difference between observed levels and tidal predictions is due to meteorological forcing in the form of changes in air pressure and winds which constitutes the surges forcing.

Due to the location of the tidal gauge, inside Santander Bay and in water depth of about 10 m, most of the surge is caused by air pressure. This hypothesis was further corroborated by correlating the 5 year surge data to air pressure data. Using this correlation, a probability density function of the surge was estimated by means of pressure data from the last 50 years, Fig. 4. The surge distribution is uni-modal, with the mode close to zero, and is positively skewed, leading to large positive surge levels being more likely than large negative surges (not shown).

Wind surge cannot be determined from Santander sea-level data. Furthermore, since the variability of wind-surge from coast to coast due to local bathymetry is so high, theoretical wind-surge estimation from wind data is the only feasible way to determine wind-surge at Oyambre Beach. Different simulations were run to estimate the combined surge due to air pressure and wind at Oyambre Beach. The main conclusion was that wind surge can be considered negligible when compared to air pressure surge, especially in extreme events when a low pressure is close to Oyambre. This characteristic of the surge at Oyambre Beach is due to the kind of low pressure reaching the northern Spanish coast and the bathymetry of Oyambre Beach and cannot be generalized for other locations.

Wave Data

Wave data used in this study was recorded at Gijón (about 100 km west of Oyambre). These data are deep water measurements of wave characteristics monitored by the Spanish Network mentioned above. Wave characteristics were propagated to the study area using a numerical wave propagation model. The model used, called REF/DIF, (Kirby and Dalrymple, 1985), solves the parabolic approximation of the mild slope equation and is adequate to estimate the effect of the different shoals located northwestward the beach, Fig. 3.

Since the wave characteristics varies from point to point along the beach, a zoning was made in order to set zones in which the wave characteristics can be assumed to be homogeneous. At Oyambre Beach this classification led to three areas called A, B and C, shown in Fig. 3.

For these three areas, different combinations of wave height, H_s , and wave period, T , at deep water were propagated in order to obtain the wave height distribution at shallow water in front of zones A, B and C. Using this wave distribution and (Nielsen and Hanslow, 1991) empirical distribution for wave run-up, the wave run-up p.d.f. at the different zones is calculated Fig. 4. The wave run-up distributions are also uni-modal and positively skewed. Zone C, which is exposed, has higher run-up probabilities than zones A and B.

Maximum Flooding Level

Using the p.d.f.s shown in Fig. 4 and the Joint Probability method described above, the flooding level p.d.f. is estimated, Fig. 5. The probability that the flooding level is less than x is:

$$F(z) = \int_{-\infty}^z p(x) dx$$

FLOODING LEVEL

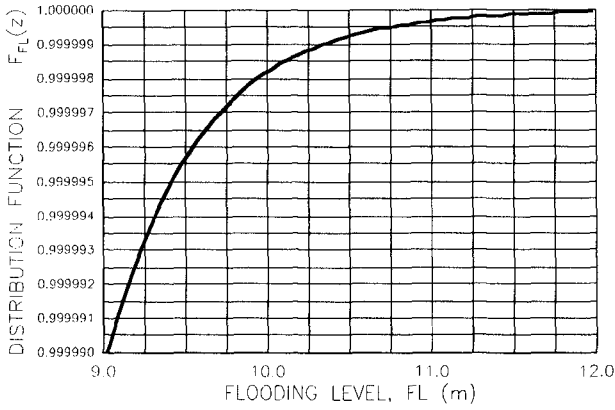


Figure 5. Flooding level p.d.f.

This distribution function $F(z)$ is shown, for the maxima, in Fig. 6.

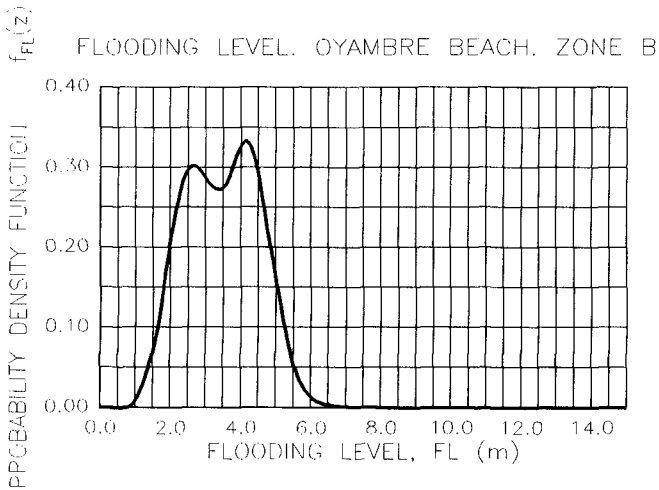


Figure 6. Flooding level distribution function

Although the probability of a level to be exceeded by the combination of tide,

surge and wave run-up can be determined from Fig. 6, the application of the results to the determination of the public domain border is not straightforward since the law is not expressed in terms of probability but in terms of number of waves. ("The limit as far as the wave reach during the worst storm").

Changing flooding probability into number of waves is a straightforward technique but it adds a new random variable to the problem; i.e. the number of waves in a given period of time. This new variable can also be determined by means of the data from the wave buoy network.

In Fig. 7, the flooding level distribution, in terms of number of waves, is presented for zone B of Oyambre Beach. If the number of waves is limited to "one wave" we will obtain the limit reached by one wave in a mean year.

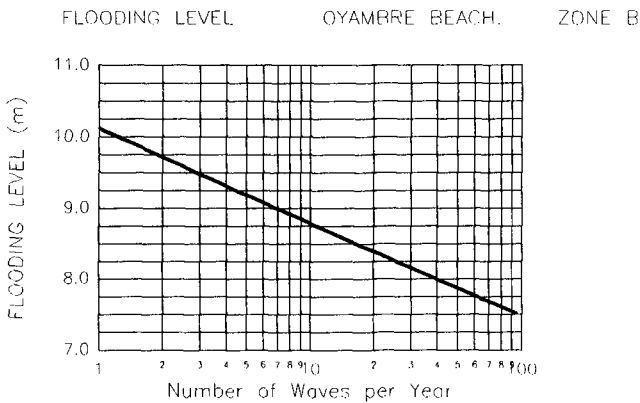


Figure 7. Flooding level distribution in terms of number of waves

Upper flooding levels will have an exceeding probability average less than "one wave per year" but they can be exceeded if we increase the number of years of observation. In this way we can determine the return period (years) of a level to be exceeded by one wave, Fig. 8.

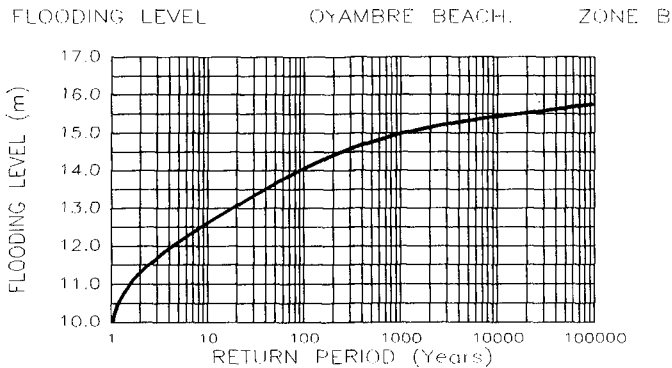


Figure 8. Flooding level exceeded by one wave versus return period (years)

Public Domain Border

From Fig. 8 it is clear that, a given flooding level will be exceeded if we have enough years of observations. At this point a criteria must be selected in order to establish the return period to be adopted in the calculation of the public domain border.

Since the Law of 1988 does not fix that criteria, the Spanish Recommendations for Coastal Works R.O.M. 02-90, (Puertos del Estado, 1990) is used. These recommendations give the designer an estimate of the minimum life and the risk to be adopted as a function of the type of maritime work and the security level demanded. With these two parameters, the return period can be calculated. For a public domain border determination, a mean return period of 500 years has been estimated.

Conclusions

This paper presents a methodology to determine the Spanish public domain border, which is the theoretical line that separates the public and the private properties in the Spanish coastal zone.

The methodology is based on the joint probability method (J.P.M.) first introduced by (Pugh and Vassie, 1978) to estimate extreme sea-levels due to the combined effect of tides and storm surge. In this paper an extension of the J.P.M. has been developed in order to include the wave run-up on a beach.

To account for the probabilistic character of the problem a methodology is presented consistent with other Spanish coastal works recommendations. The given methodology provides an engineering tool to determine the public domain border based on available field data and on hand numerical models.

Acknowledgements

The authors would like to acknowledge the funding provided by the Dirección General de Costas (Ministry of the Environment) and the Comisión Interministerial de Ciencia y Tecnología (CICYT) under grant number MAR96-1135.

References

- Battjes, J.A., 1971. Run-up distributions of waves breaking on slopes. *Journal of the Waterways, Harbours and Coastal Eng. Div., ASCE*, Vol. 97, ww1, pp. 91-114.
- Davison, A.C. and R.L. Smith, 1990. Models for exceedances over high thresholds. *J. Roy Statist. Soc. B.*, Vol. 52, pp. 339-442.
- Dixon, M.J. and J.A. Tawn, 1994. Extreme sea-levels at the UK A-class sites: Site-by-site analyses. Proudman Oceanographic Laboratory internal document N° 65.
- Godin, G., 1991. The analysis of tides and currents. In *tidal Hydrodynamics*. Bruce B. Parker, ed. John Wiley & Sons, Inc. pp. 675-709.
- Graff, J., 1981. An investigation of the frequency distributions of annual sea level maxima at ports around Great Britain. *Estuarine, Coastal and Shelf Science*, Vol. 18, pp. 389-449.
- Gumbel, E.J., 1958. *Statistics of extremes*. New York: Columbia University Press.
- Guza, R.T., and E.B. Thornton, 1981. Wave set-up on a natural beach. *Journal of Geophysical Research*, Vol. 86 (C5), pp. 4133-4137.
- Holman, R.A., 1986. Extreme value statistics for wave run-up on a natural beach. *Coastal Eng.* Vol. 9, pp. 527-544.

- Holland and R.A. Holman, 1993. The statistical distribution of swash maxima on natural beaches. *Journal of Geophysical Research*, Vol. 98, N° C6, pp. 10271-10278.
- Kirby, J.T. and Dalrymple, R.A., 1993. Combined refraction/diffraction model REF/DIF1. Documentation and user's manual. Report N.° CACR-92-04. Center for Applied Coastal Research. University of Delaware, 106 pp.
- Lennon, G.W. , 1963. A frequency investigation of abnormally high tidal levels at certain west coast ports. *Proc. Instn. Civ. Engrs.*, Vol. 25, pp. 451-484.
- Losada, M.A., R. Medina, C. Vidal and I.J. Losada, 1996. History of coastal eng. in Spain. In *History and Heritage of Coastal Eng.* ed. N. Kraus. ASCE, pp. 465-449.
- M.O.P.T.M.A., 1994. Recovering the coast. Spanish Ministry of Works, Transportation and Environment report. NIPU: 161-93-019-2.
- Nielsen, P., and D.J. Hanslow, 1991. Wave run-up distributions on natural beaches. *Journal of Coastal Research*. Vol. 7, N° 4, pp. 1139-1152.
- Puertos del Estado, 1990. R.O.M. 02-90. Actions in the design of maritime and harbor works. M.O.P.T.M.A. Madrid. 264 pp
- Pugh, D.T., and J.M. Vassie, 1978. Extreme sea level from tide and surge probability. *Proc. 16th Coastal Eng. Conference, Hamburg*. ASCE, Vol. 1, pp. 911-930.
- Smith, R.L., 1989. Extreme value analysis of environmental time series: an application to trend detection in ground level ozone. *Statist. Sci.* Vol. 4, pp. 367-393.
- Suthons, C.T., 1963. Frequency of occurrence of abnormally high sea levels on the east and south coast of England. *Proc. Instn. Civ. Engrs.*, Vol. 25, pp. 443-449.
- Tawn, J.A., 1988. An extreme value theory model for dependent observations, *J. Hyd.* Vol. 101, pp. 227-250.
- Tawn, J.A. and J.M. Vassie, 1989. Extreme sea-levels: the joint probabilities method revisited and revised. *Proc. Instn. Civ. Engr. Part. 2*, Vol. 87, pp. 429-442.
- Tawn, S.A., and J.M. Vassie, 1991. Recent Improvements in the joint probability method for estimating extreme sea levels. In *tidal Hydrodynamics*. Ed. Bruce B. Parker John Wiley & Sons, Inc. pp. 813-828.

CHAPTER 344

EDUCATION OF COASTAL ENGINEERS FOR THE 50th ICCE

Henk Jan Verhagen¹

INTRODUCTION

In general the problem in education is that we teach nowadays students the knowledge from five years ago, to be applied in the next 5 to 15 years (I admit, the student of today will have reached his retirement when he will participate in the 50th ICCE, the title is exaggerating reality). When one analyses the developments in the profession, it is clear that teaching present day facts is not very useful. We have to teach approaches, design-philosophy, concepts, etc. What the meaning is for education of coastal engineers will be worked out in this paper.

CHANGES

In the past engineers only had to look at the technical aspects. Nowadays, the impact on society and environment, the costs and the sustainability are at least as important. The consequence of this is that the role of coastal engineers has changed considerably in the past few years. Recently a joint IAHR-UNESCO panel addressed the current developments in hydraulic engineering and their implications for the education of hydraulic engineers [KOBUS *ET AL.*, 1994]. Being specialized hydraulic engineers, many of the conclusions of this panel are also valid for Coastal Engineers. With reference to the UNCED '92, the panel concluded that "hydraulic engineering should be taught in a broad context of the natural and social environment and must enhance the *engineer's sense of responsibility* for sustainable water development within environmental and societal limitations."

Fortunately, also the tools for the engineers have changed considerably. In the past much was done based on experience, engineering judgement and empirical formula. Verification was usually only possible by means of measuring in prototype or by physical modelling. Worldwide research in coastal sciences and coastal engineering has shown the following two developments:

- a considerable increase in the domain knowledge (knowledge of coastal processes);

¹ Associate professor in coastal engineering, Int. Inst. for Infrastructural, Hydraulic and Environmental Engineering (IHE-Delft), P.O. Box 3015, 2601 DA Delft, The Netherlands

- advanced tools have been developed like mathematical models (in various dimensions) and decision support systems. For design and project development the role of the physical models is almost completely taken over by the mathematical models.

A general trend can be observed from applying rules to more conceptual thinking. Rules will change fast, so it is more important for an engineer to know the design philosophy. Also engineers have to learn where to find the most up-to-date knowledge regarding the design which he is making at a certain moment. Because the increased growth in science, rules are outdated faster than in the past; this means that in most cases engineers should not apply the rules they have learned in university. So they should be trained always first to verify if the design method they learned in university is still valid.

Engineers should be trained in a flexible application of the design methodologies they have learned.

For design purposes the use of complicated computer software is increasing. The packages become more and more user friendly, but the insight in the computational process becomes less. This means that the direct link between output and input is less obvious. Engineers have to become more and more aware of the need of checking the output of these programs in inconsistencies (rather than on numerical accuracy). Because of the high quality of presentation methods of modern software, input inconsistencies are often not recognised in time. Engineers have to be trained to become more and more keen on this problem.

TYPES OF ENGINEERS

Because of this development one may distinguish nowadays three types of coastal engineers:

- the research-engineers, involved in expanding the understanding of the coastal processes; using advanced analysis of field data and sophisticated physical models;
- the "toolmakers", engineers involved in translating the newly gained knowledge into mathematical models and encapsulate this knowledge in various knowledge based systems (Hydroinformatics, see ABBOTT [1994]);
- the design engineers (the tool-users), contributing in solving the coastal problems in a multi-disciplinary team.

The first two types of engineers produce products which can be used globally. Results from research done in Australia can easily be used in Iceland. Also (the better) tools can be used anywhere. Tools, developed in the Netherlands can easily be used in Sri Lanka. However, applying the tools for solving local problems requires the specific local knowledge of the various parameters of the system. In his keynote speech to Copedec IV, professor Hildebrando [HILDEBRANDO, 1995] gave an overview of the labour market for coastal engineers (based on Brazilian experiences), and he came to the conclusion that the demand for coastal engineers will grow in the following main fields of activities: Design, Construction, Operation and Research. He came also to the conclusion that the demand for researchers is relatively limited, compared to the other fields.

WHAT IS A (COASTAL) ENGINEER ?

An engineer is a trained person, able to solve practical problems in society (and in our case of course related to the coast), using technical means. In this paper I focus on the engineer with an academic education. From such an engineer it is expected that he is able to solve problems which cannot be solved by applying standard handbook solutions. Therefore he has to be able to understand the problem (analyze the cause of the problem), find in a creative way a path towards a solution of the problem, and implement that solution

(make a "construction", however in this sense a "construction" is not necessarily concrete and steel, it may also be a beach nourishment or the implementation of a set-back system). Usually this process is called "design".

An important point is that the academically trained engineer has to bear "design responsibility". This means that he is responsible for the effect of the construction on the human and non-human environment. This includes of course the aimed effects (an erosion protection should protect against erosion), but also not non-aimed effects (an erosion protection should not increase downstream erosion without consultation with the downstream coastal manager).

So the main objective of the engineer is to solve the problem, only understanding is not sufficient. Understanding is only an intermediate step.

At this moment the process description in our profession is in many cases weaker than in other engineering professions. Many formulas used in coastal engineering are empirical or have important empirical coefficients (examples are the sediment transport formulas and the formulas for the stability of armour units). Apart from this, we usually have to work with considerably unreliable input data (e.g. wave data, waterlevels). And last but not least, the materials used in coastal engineering (rock) have a highly variable strength. The result of this all is that the main art of coastal engineering is the handling of uncertainties.

Because uncertainties are so important (and even will become more important in the future), a coastal engineer should have a good knowledge of statistics and probabilistic methods. In many engineering professions uncertainties can be handled by using a "safety-coefficient" or the use of a characteristic value (like the 95% value used in concrete engineering). However, because of the wide standard deviations in the distributions of the parameters common in coastal engineering, often only a full probabilistic approach leads towards acceptable solutions.

In coastal engineering the "client" is often the government. Especially when considering coastal protection works (notably beach nourishments), the link between the paying organisation and the beneficiaries are sometimes unclear. This makes that financing coastal protection works is sometimes quite difficult and prone to an other form of uncertainties.

SCIENCE AND ENGINEERING

This also shows the main difference between a scientist and an engineer. The objective of a scientist is to understand the world. For a coastal scientist it means understanding the coastal processes. Sometimes this understanding is expressed in models. Some scientists think they understand a system when they are able to model the system (usually with mathematical descriptions). Personally I think models can help to understand the process, but the fact that you are able to model a process does not necessarily means that you understand the system. The aim of a scientist is to make this understanding as complete as possible. Also an engineer needs understanding, otherwise he is not able to solve any problem. But his research will be focused towards the needed solution of the problem, not towards a full understanding of the process.

An important point to mention is the worldwide focus on the "pure science" in coastal engineering. Much research in coastal engineering leads to longer formulas, not to better applicable formulas, as is proclaimed by SMITH [1994]. Reviewing most journals on coastal

engineering, he came to the conclusion that only very few papers were focusing on engineering, while most papers were focused on coastal science.

TRAINING

At most universities emphasis is put on the study of various coastal sciences for increasing our knowledge of the coastal processes. This is very important work, that has to be continued; however the consequence is that most students are only trained for this kind of research, and much less for practical engineering. So, in fact, we are mainly training the first 2 types of engineers, and neglecting the type 3 (the design engineer). Therefore it is necessary that apart from the education of coastal researchers attention is also paid to the education of engineers, i.e. people who are able to solve practical problems and design solutions.

When one analyzes "problem coasts", in most cases the coastal engineer is confronted with several types of problems. Among others, the following types can be distinguished:

- the "obvious" mistake;
- lack of data (no accurate boundary conditions);
- no accurate design method available.

The most usual problem is the "obvious" mistake. For example, buildings constructed too near to the waterline at an eroding coastline, undesirable effects of downstream erosion due to coastal works, etc. In these cases the origin of the problem is not really an engineering problem, but absence of awareness of coastal behaviour at (political) decision making level. It is more a political problem than a technical problem. A better technical training of engineers will never solve this kind of problems, one has to create coastal awareness at the group of clients. This requires communicative skills and the ability to compose clear and understandable reports. Usually this is a weak point of technical people, therefore special attention has to be paid to this point in the education of engineers.

Also very often no detailed input data are available for making an appropriate design. Accurate long-term wave data are very scarce. This means for an engineer:

- he has to learn how to "generate" data (hindcasting, combining several sources of data, etc.)
- he has to learn to make the design in such a way that the influence of unreliable input data is as minimal as possible (for example using probabilistic methods).

In order to solve the third kind of problem (no design method available to the designer), he first has to find out, if such a design method exists somewhere in the world. This means that he should be trained in searching this type of information. And finally in those cases where no design method is available, our engineer has to perform his own research (or write an research assignment to be executed by a specialized institute). In some cases this is necessary. But in 90 % (or more) of the design cases, this is not relevant.

Having made a (far from complete) overview of academic coastal education in the world, the conclusion is that in those universities where coastal engineering is presented, it is usually a specialisation of civil (or hydraulic) engineering, offering only a few graduate courses really in coastal engineering. The most common situation is that in the final year, the hydraulic engineer can follow a few lectures in specialised coastal engineering topics, followed by a thesis on the subject. In the very few more specialized universities, in the last year of the programme more coastal topics are presented and the thesis is usually linked to the current faculty research programme of the institute. Hardly anywhere an M.Sc.-

programme is offered, focusing on coastal engineering only, and give the student the possibility to gather real engineering (design) qualifications.

For a practising engineer, working in a multi-disciplinary team, it is vital to know the physical processes instead of only knowing the mathematical approximation of these processes². In education this point is often underexposed. Especially in the education of engineers from developing countries attention has to be paid to the education of the design (type 3) engineers, see VERHAGEN [1995].

GENERAL REQUIREMENTS FOR COASTAL ENGINEERS

In our institute we have 39 years of experience in giving coastal engineering courses to participants from countries which do not have a tradition in training of coastal engineers. The conclusion is that there is a great need for engineers who are able to plan, design, construct, maintain and manage coastal structures. The need for engineers with abilities to design coastal structures of a very complicated technical nature is much less. Although the interest of both universities and politicians is often different, maintenance and management of coastal structures are important and costly matters. It is important to include maintenance and management aspects already in the design phase, see VERHAGEN AND YAP [1992]. Based on our experience we came to the conclusion that for the design engineers the following requirements are the most important ones:

- good understanding of the basics of the physical processes;
- insight in the effect of reliability of data, used in the design processes (also including the ability to design a construction as less as sensitive to uncertain input data);
- select the appropriate tools for analyzing the problem and designing a solution;
- develop capabilities to organise the design work in a straightforward way, given the limited resources available;
- develop to ability to cooperate with specialists from other disciplines in a inter-disciplinary coastal zone management project;
- develop capabilities to come to practical solutions given the local constraints;
- the ability to formulate research assignments.

Because, according to our experience, the engineering qualities and the design and management skills are the most important requirements for coastal (design) engineers, we started to define the required qualities and skills, instead of a list of subjects to be taught. For the engineering qualities and the design and management skills, we have worked this out into the following general objectives:

Engineering qualities:

The coastal engineer:

- has a good quality engineering attitude, i.e. he is able to analyze practical problems in his profession, is able to generate solutions and is able to implement the engineering

² A clear example can be found in wave-mechanics. Often teaching starts with the dispersion equation for gravity surface waves (in fact a mathematical model description). And then, for example, refraction is explained by combining the dispersion equation with the continuity of wave crests in order to get a formula for the ray curvature. Usually this is not very clarifying for students with an engineering attitude.

solutions in a sound way; doing this the engineer is knowledgeable with respect to his profession, but also aware of the surroundings and the environments of the project, and is able to organize the solving the problem and implementing the solution in a interdisciplinary environment.

- has some knowledge of technical and scientific developments in fields adjacent to his own field and is able to communicate with experts in those fields; examples for coastal engineers are: river engineering aspects, inland navigation, merchant shipping, port management, information technology, environmental sciences.
- has knowledge of modern design methodologies, like the probabilistic approach and the policy analysis approach to select alternatives, and is able to apply them.
- is aware of the fact that hydraulic engineering structures always have a large impact on the environment in its widest meaning; the engineer has to be able to make an inventory the impacts of his work with the aid of specialists in environmental sciences and to execute an environmental impact assessment.
- is able to define the required input data for his problem; he is able to judge the required accuracy of the data; he is able to compose an adequate dataset from an ambiguous dataset.
- is able to search in international literature and databases for relevant design methodologies.

design skills

The coastal engineer is able to:

- analyze coastal (erosion) problems, to generate alternative coastal protection methods (including "soft" methods), to select a protection method, to design the protection and to supervise the construction of the protection.
- protect low-lying coastal areas from flooding by means of the construction of dikes and revetments; he is able to determine the functional requirements of the protection, to generate alternative flood protection methods, to select a protection method, to design the protection and to supervise the construction of the protection.
- evaluate the necessity and to design closure dams, causeways, etc. in a coastal, tidal environment; he is able to determine the functional requirements of the dam, to generate alternative lay-outs and construction methods, to select an alternative, to design it and to supervise the construction of the dam.
- design the entrance to a harbour, i.e. the design of the access-channel and the design of the breakwater; he is able to determine the design boundary conditions, to generate alternative solutions, make a selection, make the detailed design and supervise the construction.
- design mooring facilities, both at offshore jetties as along quay-walls, he is able to develop and select alternatives and is able to design the structure; he is able to specify the boundary conditions for quay-wall and jetty construction; he is able to design a jetty and a quay-wall.
- design earth structures and foundations in the coastal zone (dikes, sheetpiles, soil improvement techniques), the coastal engineer has a workable knowledge of pile foundations.

managerial skills

The coastal engineer:

- is able to organize and cooperate in a multi-disciplinary group to set-up and implement an integrated coastal zone management plan.

- has specific knowledge of construction methods specific for coastal engineering, i.e. wet and dry earth moving; related to dredging he has to be able to define the working method, to know the possibilities of the industry, to prepare terms-of-reference and contract and price estimate; he is able to select the contractor and to supervise the work.
- is able in case of environmental emergencies in the coastal zone (oil-spills, hurricanes, etc) to organize the appropriate actions to mitigate the impact.
- has some knowledge regarding the organization of the profession, the international institutions, the organization of large contractors and consultants.

Having defined these more general qualities and skills, the next step is to define the required knowledge for individual subjects, like "design of breakwaters" or "short waves". Only those aspects of the several subjects should be taught, when they contribute to the general qualities and skills, as defined above. If one neglects this point, the result is usually a programme which consists of a set of hobbies of the teachers. Because of the limited scope of this paper, this step will not be worked out.

ATTAINMENT TARGETS

Of course these objectives, but also a list of topics within a series of lectures gives no information regarding the level, depth or orientation of the subject. Often one sees in curricula of universities descriptions like:

Short waves

linear and non-linear regular gravity waves, wave properties and transformation in shallow water, forecasting and hindcasting of waves.

In fact, such a description gives not very much information. For example, after having followed this course, is the student able to derive refraction equations, is he able to make a refraction calculation by hand, is he able to interpret the results of a refraction calculation by a computer programme, is he able to define whether a refraction calculation is necessary or not, and if yes, what are the input variables ???

Therefore it is more appropriate to describe as detailed as possible the attainment targets a student has to meet in order to get his diploma. For "refraction", such targets could be described as follows:

- *Know the phenomenon of refraction, be able to calculate refraction in case of parallel depth contours, using Snell's law, be able to determine refraction in a qualitative way in case of non-parallel depth contours, know the advantages and problems of ray-refraction programs, be able to interpret two-dimensional wave penetration programs.*

Attainment targets can be worked out for all course objectives, mentioned above. As an example the attainment targets for the design capabilities are given below:

Attainment targets for design capabilities

- be able to translate a vague (political) question into exact requirements and formulate them in terms-of-reference for a study to be performed
- be able to analyze the problem on main aspects and distinguish between essentials and matter of secondary importance
- to be able to analyze the functional requirement of the construction needed, in order to determine design criteria

- be able to collect data for a (real world) project from the general available data sources (like libraries, information retrieval systems, already existing consultancy reports)
- be able to analyze the above mentioned data and to be able to use them in order to come to a complete, relevant and unambiguous set of boundary conditions (including the reliability of the given figures)
- be able to determine scenarios to describe unknown future effects
- be able to determine alternative designs
- be able to make global designs of the alternatives, in order to make a selection; be able to make a choice between the various available computational and design methods; be able to apply these methods
- evaluate the designs on at least the following aspects
 - costs
 - environmental acceptance
 - social acceptance
 - maintenance cost
 - robustness of the design
 - executionability
- be able to read technical drawings, to be aware of the effects of distorted scales (especially in coastal profiles)
- be able to make a bill of quantities given the design drawings
- be able to make a set-up for an Environmental Impact Assessment for the design
- be able to write a systematic report on the design process followed
- be able to write readable well-structured reports, with clear set-up, and with a good quality lay-out.
- be able to organize the design work, define various subtasks and have these subtasks executed by various group members
- be able to make a time planning for a design work, and be able to produce the design report; i.e. to deliver the report (1) in time, (2) with the subjects as determined in the original plan, (3) with the required quality; the sequence of these points is important
- be able to present the results of a study or design work orally in a short period (10-30 minutes) for various types of audiences (such as technical experts, decision makers, financial experts); be able to make good quality overhead sheets (both from a viewpoint of contents as lay-out)
- be able to gather additional skills and knowledge on a rather specialistic field (not treated in detail in the teaching programme) in order to solve the design problem.

THE MASTER DEGREE

The engineering study is usually completed with a Master degree. Unfortunately there is not really a world-wide standard for a master degree. Especially for students from developing countries this is a real problem. For most of them their career depends completely on the fact if they have paper indicating a Master degree, and not on their knowledge or skills. So in fact it is for them very unattractive to follow a high quality course. Usually these courses are long (and therefore costly), with a high risk of failure for the candidate; so why not go to an easy course ? This strong focus on "paper" degrees is a clear problem in the developing world. But on the other hand, for an outsider it is indeed difficult to assess the quality of a diploma. Therefore the detailed described attainment targets can be very useful. In fact, by issuing the diploma, we guarantee that the candidate has reached all the described attainment targets, so a future employer can easily see what is the knowledge and skill of the degree-holder.

There is a variety of Master titles, a taught masters, a master by thesis, a master of engineering, a master of science, etc. In our institute we provide two types, a Taught

Masters and a Master of Science. The first is given to a student who has followed the complete (2000 study hours) program, has done all exercises sufficiently and who has passed all examinations. Students with sufficient high marks for the Taught Masters programme are academically admitted to the Master of Science programme, which consists of an additional individual assignment of approx. 1000 hours. This individual assignment can be a research work, but can also be a design work. Of course not all design work automatically has sufficient level for M.Sc. We use the following list of requirements for a subject for design-work at M.Sc.-level

- It has to be a complex problem, i.e.:
 - The boundary conditions are ill-defined
The criteria are not clear on beforehand
 - There are several, complex scenarios.
- The technical solution is complicated, this means that it is not possible to apply straightforward existing design formulas.
- It is not possible to determine the best alternative by a simple (one-dimensional) computation.
- The problem has to be realistic and relevant, preferably for the home-country of the participant.

CONCLUSIONS

Because of the focus on research in most universities of the world, the training and education of design engineers is somewhat problematic. Many design engineers have been trained as researchers. In future there is a need for trained designers with understanding of coastal processes, the ability to design in a flexible way coastal "constructions" and able to communicate with others. Training programs can be improved considerably by defining the attainment targets which have to met by the students at the end of their education, and not only by defining the subjects to be dealt with in the curriculum.

REFERENCES

- ABBOTT, M.B. [1994] Hydroinformatics: A Copernican revolution in hydraulics; *J. of Hydraulic Research*, vol 32, extra Issue, pp 3-13
- HILDEBRANDO DE A. GÓES FILHO [1995] Profile of the new coastal and port engineering technician at the end of the 20th century; *Invited Paper, Copedec IV*, Rio de Janeiro, Brazil
- KOBUS, H., PLATE, E., HSIEH, WEN-SHEN, SZÖLLÖSI-NAGI, A. [1994] Education of Hydraulic Engineers; *J. of Hydraulic Research*, vol32, nr2, pp 163-181
- SMITH, A.W.S. [1994] The coastal engineering literature and the field engineer; *J. of Coastal Research*, vol 10, no2, pp iii-viii
- VERHAGEN, H.J. [1995] The requirements for Coastal Engineers in Integrated Coastal Zone Management; *Copedec IV*, Rio de Janeiro, Brazil
- VERHAGEN, H.J. & YAP, J. [1992] Coastal Zone Management with relation to Low Investment Solutions; *proceedings Second seminar on Ports and Inland Waterways in Developing Countries*, PIANC-PCDC; Surabaya 1992

CHAPTER 345

Risk-Based Analysis of Coastal Projects

Edward F. Thompson¹, Member, ASCE, Michael Wutkowski², Member, ASCE,
and Norman W. Scheffner¹, Member, ASCE

Abstract

Coastal engineering usually embodies large uncertainties about attacking forces and coastal/structure response. The coastal engineer must address these uncertainties with judgement and experience, supplemented with some level of direct probability analysis. The nature and scope of risks related to coastal projects are reviewed. Analysis approaches developed for wider engineering application, where risks are usually better defined (e.g. Ang and Tang 1975, 1984; Harr 1987), may be less effective in coastal engineering. Two accepted general approaches for risk-based analysis of coastal projects are discussed. The approaches are illustrated with an example shore protection project.

Introduction

The approach for analyzing coastal projects is undergoing some fundamental changes, shifting from the traditional deterministic emphasis to a more comprehensive probabilistic, risk-based methodology. The changes strongly impact both planning and engineering phases of project formulation and design.

The changes, which can be expected to be distilled into a new standard for coastal practice by the end of the decade, are driven by several progressive developments. First, our understanding of probabilistic coastal processes continues to advance, particularly due to advances in field measurement, physical modeling, and numerical modeling.

¹ Research Hydraulic Engineer, US Army Engineer Waterways Experiment Station, CEWES-CR, 3909 Halls Ferry Road, Vicksburg, Mississippi 39180-6133, USA.

² Civil Engineer/Programmer, US Army Engineer District, Wilmington, CESAW-EN-C, P.O. Box 1890, Wilmington, NC 28402-1890, USA.

Second, standard computing capabilities are increasing rapidly, facilitating lengthy probabilistic calculations which would have been impractical in the past. Third, engineers, cognizant of limitations in the traditional approach, are often eager to implement better procedures, provided that they are well-founded and clearly improve the analysis. Finally, the public is becoming more aware and concerned about coastal project performance, and they expect realistic project analyses. In the U.S., public involvement in coastal projects is further intensified by legislation which increases the proportion of costs borne by the client (typically state or local government) in Federal projects.

Traditional vs. Risk-Based Analysis

Traditional analysis treats a coastal project in deterministic terms. The forces of nature are often represented as a design significant wave height, period, and direction, a design water level, etc. Coastal response is described as *the* response if no project is implemented, *the* response if one plan is implemented, *the* response if another plan is implemented, etc., without much formal recognition of the wide variation in possible responses.

In contrast to traditional analysis, some significant developments in probabilistic treatment of coastal projects have appeared during the 1990's. Most relate to coastal structure design (CIRIA/CUR 1991, ICCE 1992). Within the U.S. Army Corps of Engineers (CE), water resource planning guidance has moved from a deterministic to a risk-based approach, which incorporates considerations of risk and uncertainty. Similar concepts are now being adapted to CE coastal engineering studies (U.S. Army Corps of Engineers 1996).

Reasons for Risk-Based Analysis

There are a number of reasons why coastal projects in the broader sense, not just structure design, may be effectively analyzed from a risk-based point of view, as follows (Table 1):

1) *Coastal forcing is probabilistic.* Wave characteristics vary greatly both over short term (individual waves) and long term (from one sea state to another). Similar considerations arise with winds, water levels, infragravity waves, and currents.

2) *Coastal engineering embodies major uncertainties.* Knowledge of both the forcing processes and coastal response usually involves major uncertainties.

Table 1. Reasons for Risk-Based Analysis of Coastal Projects

- | |
|--|
| <ol style="list-style-type: none"> 1) Forcing is probabilistic 2) Major uncertainties in behavior 3) Damage & functional performance change incrementally 4) Benefits & risks not fully represented in deterministic terms 5) Uncertain effects on adjacent areas |
|--|

Deterministic representations mask the uncertainties and can be misleading.

3) *Damage and functional performance change incrementally.* Coastal projects rarely progress from the design condition to total failure during a single storm event. Damage usually occurs incrementally. For example, damage to a rubble mound breakwater (when it occurs) typically begins during an unusually severe storm and progresses during subsequent severe storms until repairs are done. Similarly, beach fills erode incrementally in response to storms over a period of years. Coastal projects often continue to provide some measure of functional benefit even in a damaged state. A damaged breakwater continues to provide some protection from incident waves; a partially eroded beach fill continues to reduce coastal flooding risks.

4) *Benefits and risks not fully represented in deterministic terms.* Because of the above factors, positive impacts and risks of coastal projects cannot be fully represented in deterministic terms. Some projects provide benefits beyond the design configuration, which are generally ignored in traditional practice. For example, a nearshore berm which is over-built to allow for progressive deterioration provides increased coastal protection during its early life. Another example is an over-dredged entrance channel giving increased vessel access depths until it shoals to the design depth.

5) *Uncertain effects on adjacent areas.* In addition to the uncertainties associated directly with coastal projects, the projects can introduce significant possibilities for changing adjacent areas. While projects are designed with the intent of minimizing adverse impacts on adjacent areas, it is important to recognize that uncertainties and risks can increase beyond the without-project condition. In effect, a project can transfer risk from one area or party to another. When the risks of *all* major aspects of a project are represented as best they can be determined, better-informed final decisions can be made.

Experienced coastal engineers are well-aware of the concerns in Table 1. Even with deterministic methods, they can be expected to produce project plans which include a large measure of professional judgement to insure a technically successful project. However, the ultimate fate of a project can depend upon higher level decision-makers who must weigh technical concerns against economic, environmental, aesthetic, social, and political concerns. By quantifying risks, the coastal engineer can better pass his or her experience and judgement on to other decision-makers, who may not have coastal expertise.

Considerations for Including Risk-Based Analysis in Project Design

Objectives. The main objectives of adopting a risk-based analysis approach rather than a traditional approach are to explicitly identify uncertainties, provide improved information for assessing tradeoffs between risks and cost, and improve decision-making

for project optimization (Table 2).

Key Variables. Although a large number of variables affect any coastal project, a small subset can usually be identified as *key variables*, that is variables which strongly relate to project performance. The key variables will embody the

main forcing mechanisms, project sizing, and project response. For example, some of the key variables for a beach nourishment project might be significant wave height (forcing), beach fill width (project size), and erosion width (response).

Professional Judgement. Coastal engineering requires an unusually large measure of professional judgement because of the number and complexity of processes and responses involved. Analytical and modeling tools help to represent the variability affecting coastal projects, but the judgement of an experienced engineer is a vital ingredient in risk assessment and project optimization.

Resistance and Functional Performance Vary with Time. Both the resistance to damage and functional performance often vary significantly over a coastal project's design life. For example, the resistance (or structural strength) of a rubble mound breakwater may decrease in time due to deterioration of stone such as loss of angular corners, cracking, and breaking. Resistance may also decrease due to displacement of stone and exposure of underlayers to wave attack, which would also decrease protection provided by the breakwater (functional performance). For a beach nourishment project, loss of material to storms decreases the resistance of the beach to future storms. The effectiveness of the beach as a deterrent to coastal flooding is also decreased (functional performance). In some cases, resistance *increases* with time, as in the progressive growth of protective vegetation on coastal dunes and natural cementation of beach sediments rich in calcium carbonate.

Construction Season and Mobilization Concerns. Often maintenance of coastal projects requires major mobilization efforts and is confined to a *construction season* dictated by climate and environmental factors. Therefore the risk during the *interval between construction seasons* rather than during a single storm becomes a key concern. During an unusually stormy winter (such as the winter of 1987-88 in southern California), this risk can be significantly greater than that for individual storms.

Environmental, Aesthetic, Social, and Political Concerns. The role of environmental, aesthetic, social, and political factors in the ultimate planning and design of a coastal project is often at least as important as the technical engineering factors. An optimized final design includes appropriate consideration of these factors and their

Table 2. Objectives of Risk-Based Analysis

- Explicitly identify uncertainties
- Provide improved information for assessing risk vs. cost tradeoffs
- Improve decision-making for project optimization

associated risks and uncertainty.

Frequency-Based vs. Life Cycle Approach

Risk-based analysis of coastal projects can be done by either of two fundamentally different approaches. The *frequency-based approach* deals with frequency-of-occurrence relationships among the key variables. By combining key forcing variables with various occurrence frequencies, information about the frequency-of-occurrence of key project responses can be developed. For example, a traditional stage (water level) vs. frequency curve and a stage-damage curve can be combined to generate a damage vs. frequency curve. This approach can be applied as an add-on to traditional planning and design procedures.

The *life cycle approach* deals with multiple realizations of possible evolution of the project with *time* during the span of its design life. The suite of life cycle realizations is constructed with consideration of the probabilities of key variables. For example, the realistic time variation of key forcing and response variables during a 50-yr life cycle can be generated for 1000 different possible life cycles. Uncertainty in the data and models relating natural forcing to coastal response can be represented as another source of variability. Probabilities and risks associated with the project are then compiled by analyzing project performance over the 1000 life cycles.

An example shore protection project helps to illustrate the life cycle approach in comparison to a more traditional frequency-based approach. The project area is a relatively uniform stretch of beach with several rows of houses along the shore (Fig. 1). The example project is a beach nourishment to widen the existing beach and dune (Fig. 2). The frequency-based approach used for this example is based on a set of six storms representing 5-, 10-, 25-, 50-, 100-, and 500-year events. Expected erosion of the existing or project beach profile and property damages are calculated for each storm. An average annual damage is calculated by integrating over the range of storm probabilities. For each year of the project life span, the shoreline is retreated according to a long term erosion rate and calculations of annual damage are repeated. Total damage over the project life span is the sum of the annual damages. This more traditional approach produces a single result based on a single set of storms and response parameters. There is no indication of confidence level of the answer. The example project shows net benefits of \$980,000 over a 50-year life span and a benefit/cost ratio of 2.4.

The life cycle approach in this example embodies sequences of storms (including provisions for multiple storms of varying intensity during each year of the life cycle), erosion and post-storm recovery during each event, partial and complete property damage during each event (depending on water level, waves, extent of storm erosion, and type of building construction), cumulative property damage due to a succession of storms, optional repair or rebuilding after a suitable time lag (with conformance to any stricter building codes in effect), and periodic renourishment of the beach when needed

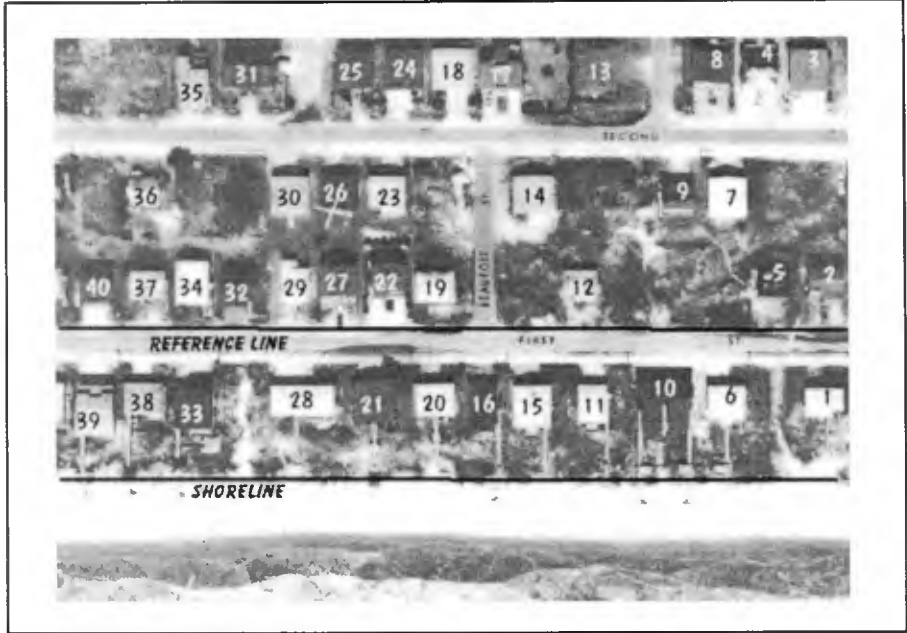


FIG. 1. Sample Section of Coastline

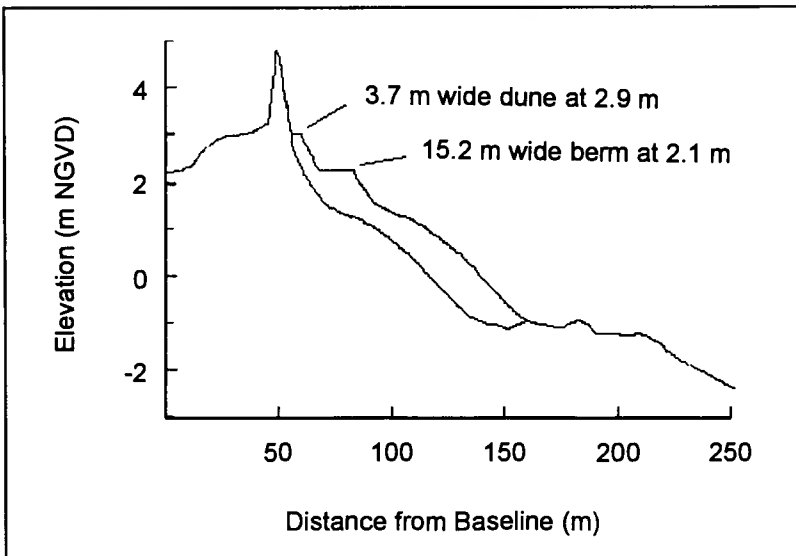


FIG. 2. Example Project Profile

and feasible during the life cycle. A key result from this analysis is the renourishment required during each life cycle, which can be converted to an economic present worth dollar value. The costs and net benefits in this example vary over a wide range, depending on the occurrence of major storms during the life cycle simulation (Fig. 3). The expected cost and economic risks associated with maintaining the beach can be realistically assessed by condensing information from many different life cycle simulations (Figs. 4 and 5). The mode and mean net benefits are \$275,000 and \$814,000, respectively (Table 3). There is a 65% probability that the net benefits will be less than the \$980,000 amount calculated by the more traditional frequency-based approach. There is a 7% probability that the net benefits will be negative (cost of the project exceeds the damages prevented). Negative benefits come from simulations with mild storm climates. While net benefits are used to optimize a project, the benefit/cost ratio is also of interest (Table 3 and Fig. 6).

Statistic	Net Benefits (\$1,000)	Benefit Cost Ratio
Mode	275	1.50
Mean	814	3.09
Standard deviation	649	1.59
Maximum value	3557	8.92
Minimum value	-119	0.67
Number of cases	7000	7000

The life cycle approach appears better suited to most coastal engineering applications. Variation with time is an essential ingredient in most coastal projects, and it is directly incorporated into the life cycle approach. Time variation of resistance and functional performance, constraints imposed by construction season and mobilization, even some economic, environmental, and political factors, can be conveniently and flexibly introduced into the life cycle approach. This approach leads to a unified analysis of technical performance and many economic factors which are critical to project success. As illustrated in the above example, the life cycle approach provides valuable information relative to the objectives of risk-based analysis (Table 2). In addition to its technical and economic strengths, the life cycle approach is more easily understood by nontechnical parties involved with a project. This type of approach is evident in the Empirical Simulation Technique (Scheffner et al. 1996) and CE guidance in preparation (U.S. Army Corps of Engineers 1996).

Typical Project Elements

Risk-based analysis can be integrated into the major planning steps of a coastal engineering project. Typical project elements which are especially well-suited to

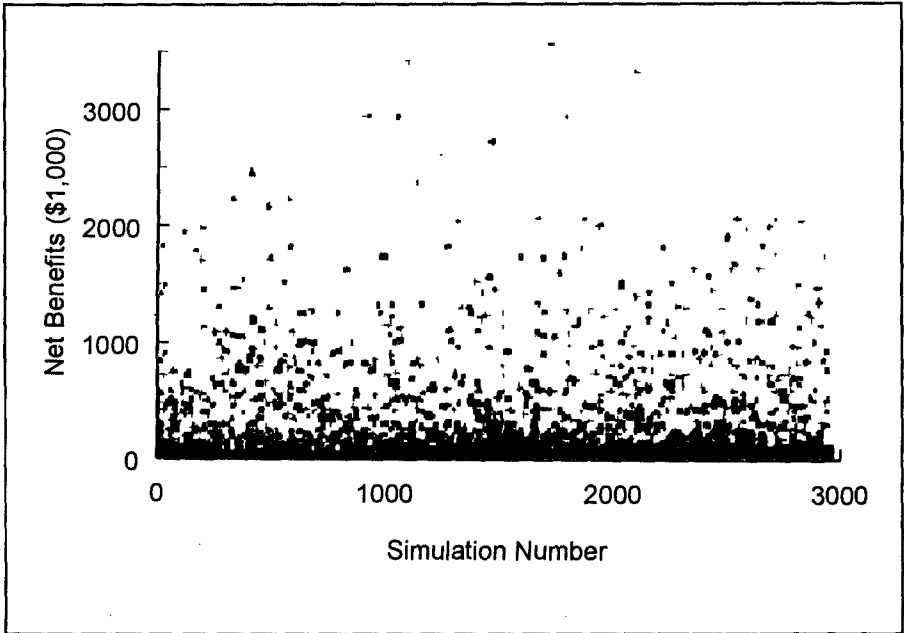


FIG. 3. Unsorted Risk Results

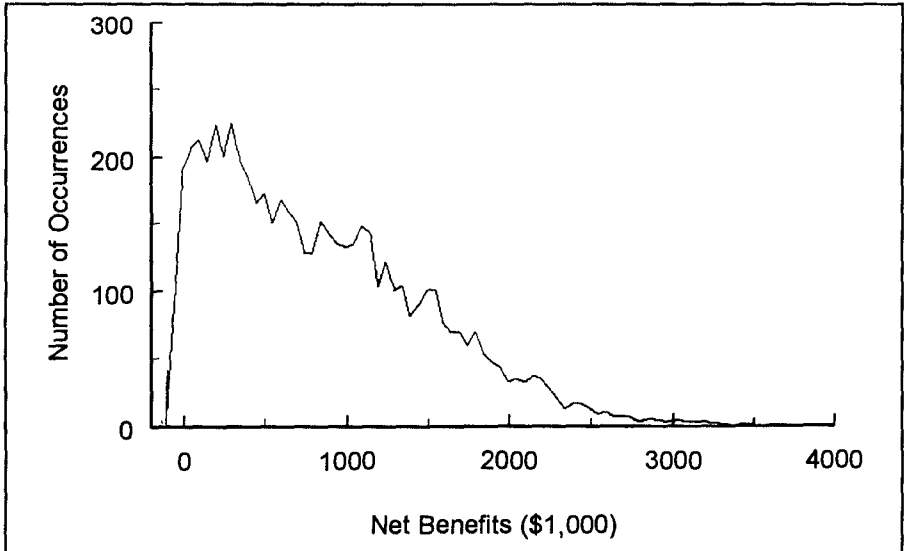


FIG. 4. Net Benefits, Probability Density Distribution

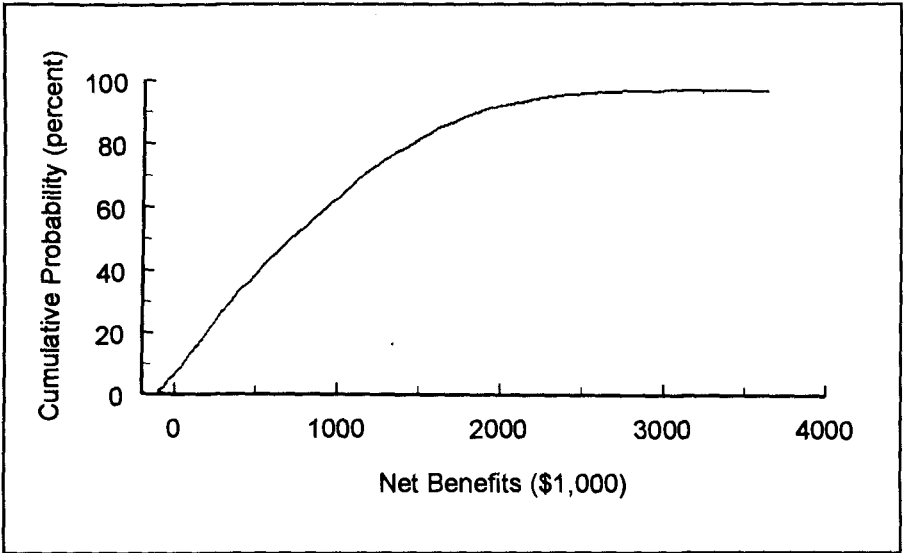


FIG. 5. Net Benefits, Cumulative Probability Distribution

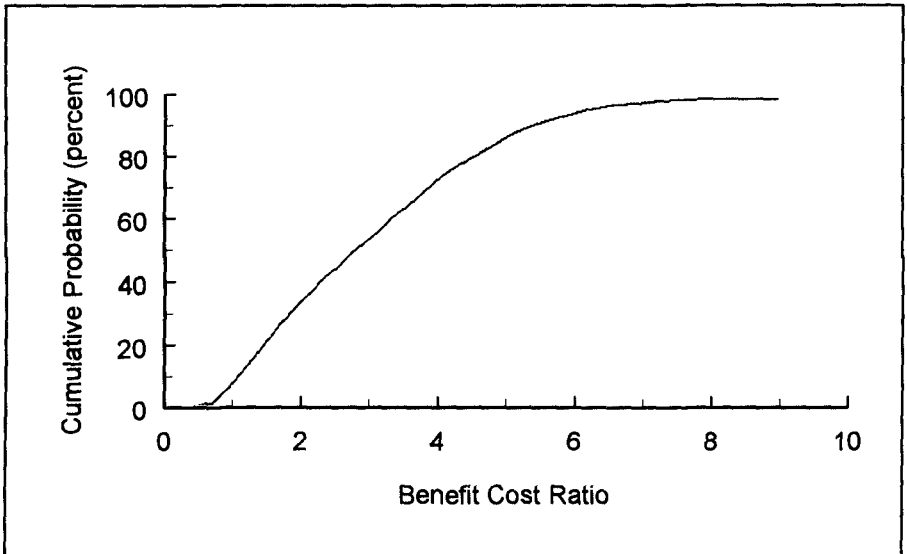


FIG. 6. Benefit Cost Ratio, Cumulative Probability Distribution

risk-based analysis include the following:

Site Characterization. Significant uncertainty can arise in documenting past and present behavior at a site. The uncertainty can be estimated based on data quality and quantity, methodologies used, observed variability, etc.

Without Plan Alternative. Evaluation of what would happen in the future if no project were built involves speculation about the natural processes and human interventions which would affect the site during the proposed project life. The impact of the *without plan* alternative is conveniently described in probabilistic terms.

Formulate, Evaluate, and Compare Alternative Plans. Risk-based analysis can be a powerful tool for formulating and comparing alternative plans. It enables decision-makers to intercompare not only the expected level of performance, but also the probabilities of enhanced or reduced performance levels, which can differ greatly among alternatives. Typically, alternatives involve hard structures (such as walls, revetments, breakwaters, and jetties) and/or soft structures (such as beach nourishment projects, coastal dunes, and nearshore berms). Risk-based analysis of hard structures is increasingly being considered in planning and design (CIRIA/CUR 1991, ICCE 1992). Soft structures involve calculated risks about the movement of sediment through time and the need for future maintenance. Uncertainties arise in forcing processes, sequencing of storms, initial state of nearshore profile when storms occur, and evolution and recovery of storm profiles (especially three-dimensional aspects). The life cycle approach to risk analysis has been shown to be a powerful tool in this type of application.

Conclusions

The following conclusions are reached regarding risk-based analysis of coastal projects:

- Risk-based approaches provide a powerful tool for analyzing coastal projects.
- Risk-based analyses can lead to improved decision-making for project optimization.
- The life cycle approach is especially well-suited to coastal engineering.

Acknowledgements

The work presented herein, unless otherwise noted, was supported by the Coastal Navigation Research Program of the U.S. Army Engineer Waterways Experiment Station, Coastal and Hydraulics Laboratory, under the Coastal Engineering Manual

work unit of Coastal Structure Evaluation and Design. The example project was developed by the U.S. Army Engineer District, Wilmington (SAW). Mr. J. T. Jarrett, SAW, contributed significantly to the example project. The work of Dr. David A. Moser, U.S. Army Corps of Engineers (USACE), Institute for Water Resources, and Mr. Steve R. Cone, USACE Headquarters, in developing CE guidance on risk-based analysis is acknowledged. Permission was granted by the Chief of Engineers to publish this information.

Appendix. References

Ang, A. H.-S., and Tang, W. H. (1975). *Probability concepts in engineering planning and design; Volume I: Basic principles*. Wiley, New York, NY.

Ang, A. H.-S., and Tang, W. H. (1984). *Probability concepts in engineering planning and design; Volume II: Decision, risk, and reliability*. Wiley, New York, NY.

CIRIA/CUR. (1991). *Manual on the use of rock in coastal and shoreline engineering*. CIRIA Special Publication 83, Construction Industry Research and Information Association, London, UK; and CUR Report 154, Centre for Civil Engineering Research and Codes, Gouda, The Netherlands.

Harr, M. E. (1987). *Reliability based design in civil engineering*. McGraw-Hill, New York, NY.

ICCE. (1992). *Design and reliability of coastal structures*. Proceedings of a short course attached to the 23rd International Conference on Coastal Engineering, Venice, Italy.

Scheffner, N. W., Borgman, L. E., and Mark, D. J. (1996). "Empirical simulation technique based storm surge frequency analyses." *J. Wtrwy., Port, Coast. and Oc. Engrg.*, 122(2), 93-101.

U.S. Army Corps of Engineers. (1996). "Risk-based analysis for evaluation of hydrology/hydraulics and economics in shore protection studies." *Circular No. 1105-2-xxx* (in preparation), Washington, DC.

CHAPTER 346

DESIGNING FOR PROPELLER ACTION IN HARBOURS

G.A. HAMILL ¹, J.A. MCGARVEY ²

Abstract

The scour produced by the action of a ship's propeller is an increasing problem. There is a need for an accurate method of velocity prediction so that adequate steps can be taken to design suitable bed protection systems. The velocity characteristics of the jet produced by the rotating propeller are presented as an aid to the engineer.

Introduction

One consequence of the increases in ship size, installed engine power, and volume of marine transport is an increase attack by propeller slipstreams on the bed and banks of harbour basins and navigation channels. In restricted waterways the situation has been exacerbated since the introduction of bow thrusters in the 1960's which has increased the navigability of large ships to such an extent that they can now operate without tug assistance.

A ship's propeller produces thrust by drawing in water, accelerating it and discharging it in the form of a wash. This wash is a highly turbulent submerged jet, the velocities within which depend upon the operating characteristics of the propeller and the speed of advance of the ship. The wash entrains the surrounding water and so the velocities within it decay with distance from the propeller. In this way the jet expands and dissipates its energy by diffusion. If the ship is moving in a confined area, for example in the shallow waters of a harbour basin, the diffusion process within the wash will be restricted and the energy remaining within the jet may cause damage to the bed and nearby quay structures.

Related Research

A survey of harbours in Sweden (Bergh 1981) has shown that 16 out of the 18 ports surveyed have suffered propeller induced damage in recent years. Similar problems have been encountered in several United Kingdom ports and the British Ports Association commissioned a review (Prosser 1986) of existing knowledge. In a survey of all British ports in 1994, Qurrain (1994) found that 42% of these encountered scouring as a result of propeller action, of which 29% regarded this scouring to be a serious problem causing damage to quays, with expensive remedial repairs and costly facility downtime. The diffusion characteristics of a propeller jet have been examined by numerous authors. Investigation which include the influence of the rudder on the diffusion process however, are not extensive and the majority of all predictive equations do not allow for it's inclusion.

1) Lecturer 2) Research Student

The Queen's University of Belfast, Department of Civil Engineering, N. Ireland

Robakiewicz (1966), Verhey (1983) and Fuehrer (1985) have studied the velocities within the propeller jet in the presence of a rudder, and presented equations for estimating bottom velocities. These equations are limited in that a full velocity distribution cannot be calculated and they are related to an efflux velocity equation, i.e. the maximum velocity on the propeller face, which has been found to be up to 20% in error.

Experimental Set-up

Detailed velocity measurements were taken within the diffusing jets, produced by two propellers with differing characteristics, up to a distance of 10 diameters from the propeller plane. Four jets, corresponding to four speeds of rotation, were investigated for the first propeller which was 0.076m in diameter, while three jets were investigated for a second propeller 0.131m in diameter. Axial and radial measurements of velocity were taken using a twin component Laser Doppler Anemometry system.

Rudder Effect

The magnitudes of the axial and radial velocity components within the wash were measured within the formation stages of the propeller jet, i.e. up to $2.0 D_p$. To provide a better understanding of the jet diffusion, velocity vector diagrams were plotted for all experimental results with and without the rudder present. These provided a 2D schematic representation of the flow within the propeller jet. Figures 1(a) to 1(c) are typical of those obtained during the current investigation.

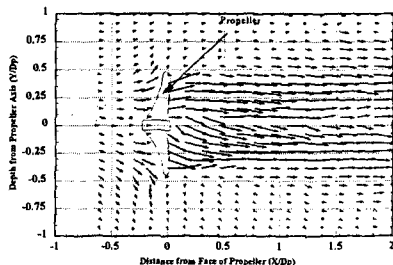


FIGURE 1(a) Resultant velocity vectors (without rudder)

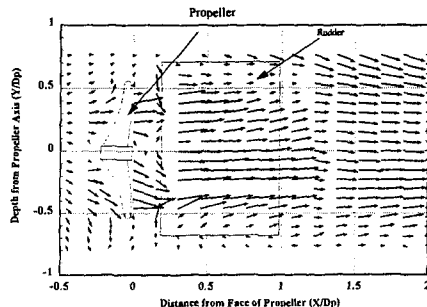


FIGURE 1(b) Resultant Velocity Vectors (Rudder at Zero Degrees)

Figure 1(a) shows the velocity distributions obtained without the rudder. The magnitude of the velocities at the hub is lower than across the blades, and the jet is diffusing away from the propeller centreline due to the radial velocity component. It can be seen that the vectors revert to the horizontal with distance from the propeller, indicating the reduction in the magnitude of the radial velocity component. The velocity distribution at each vertical section from the propeller is approximately symmetrical through the propeller axis which confirms the results of previous work. The results obtained with the rudder situated at zero rudder angle or midships position is shown in figure 1(b).

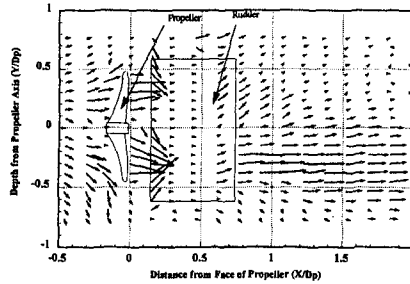


FIGURE 1 (c) Resultant Velocity Vectors (Rudder at +35 Degrees)

It can be seen that the resultant velocity distribution at the face of the propeller is similar to the distribution obtained without the rudder present. There is a significant change in the flow with distance from the propeller, as the jet is circulated around the rudder. There is a rapid reduction in the magnitudes of the velocities at the first section behind the propeller. In subsequent sections the velocities are greater as the flow moves along the sides of the rudder.

It can also be seen that the vectors in subsequent section along the rudder are almost to the horizontal. This indicates that the magnitudes of the radial velocities are insignificant, and that the rudder has a straightening effect on the jet. The velocity distribution appears to vary at each section and it can be seen in some sections that there are higher velocities below the propeller centreline than at the corresponding position above the centreline.

Figure 1(c) shows the results obtained when the rudder is placed at an angle of 35 degrees to the propeller axis. The velocities at the face of the propeller are approximately symmetrical through the propeller axis and therefore appear to be unaffected by the rudder. It is the distributions in the subsequent sections that are interesting as the magnitude of the velocity below the centreline can be seen to be greater than above the centreline. This is due to the effects of splitting of the flow by the rudder. The vectors shown represent the velocities in a stream directed towards the bottom. The distribution shows that there is only one position of maximum velocity, unlike the axi-symmetrical profiles found in the absence of the rudder.

In order to provide a better understanding of the propeller diffusion characteristics with the rudder present, velocities were measured throughout the jet using a system of pitot tubes. These results were then plotted in the form of an isovel plot for each speed of rotation, which provided contours of the velocity distribution within the propeller jet. Figures 2(a) to 2(d) show the sequence of isovel plots with the rudder positioned at zero degrees, and is typical of the velocity distributions obtained for all the jets tested at this angle. Figure 2(a) shows the velocities obtained at a distance of $0.46 D_p$ behind the propeller, at the location of the rudder. The velocities obtained at this section are unlike those obtained for the jet without a rudder as the velocities are not symmetrical through the propeller axis (Stewart 1992). The rudder splits the main wash into two separate streams of jets. one jet is directed towards the water surface, while the other is deflected towards the sea bed. The jets are just forming at this position and the bottom jet below the centreline is clearly defined, with the

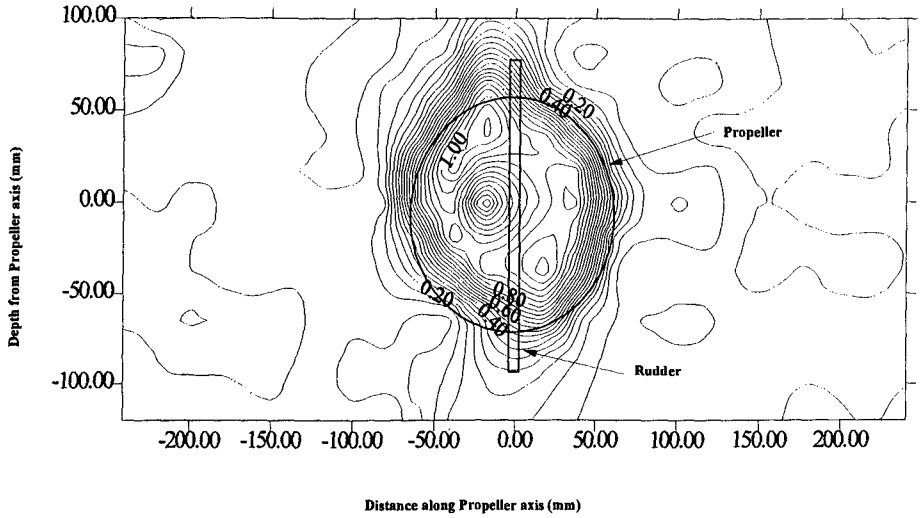


FIGURE 2(a) Isovels at 0.46 D_p for zero rudder angle

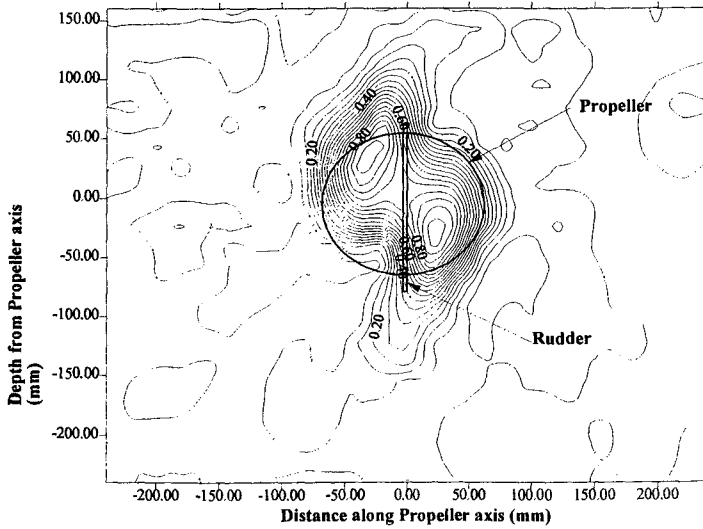


FIGURE 2 (b) Isovels at 0.92 D_p for zero rudder angle

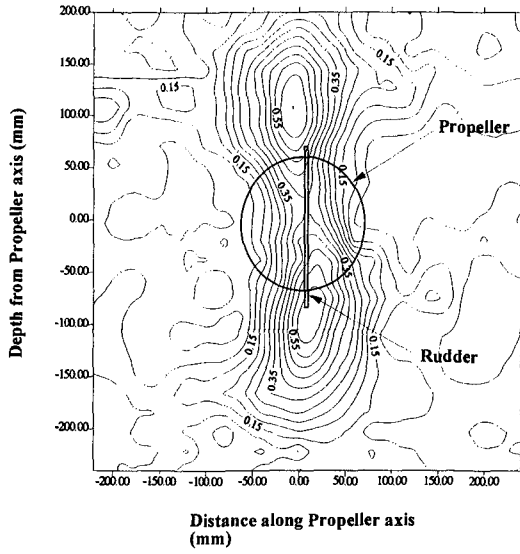


FIGURE 2(c) Isovels at 3.05 Dp for zero rudder angle

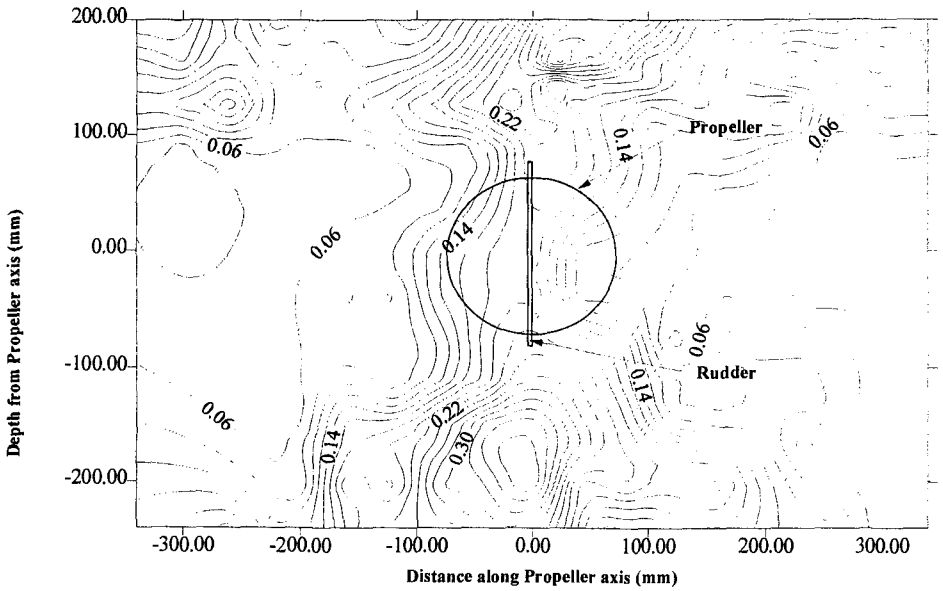


FIGURE 2(d) Isovels at 6.95 Dp for zero rudder angle

surface stream just becoming visible. Figure 2(b) which is located at a section subsequent to the location of the end of the rudder, shows the formation of the two streams, represented by the two high velocity peaks shown on each side of the rudder. This trend continues with distance from the propeller and the two streams are visible at $3.05 D_p$, as shown in figure 2(c). This position has previously been termed the end of the zone of flow establishment for the jet without a rudder, at which location the maximum velocity would be located on the propeller centreline. It can be seen that with distance from the propeller there is a gradual increase in the distance between the streams, and therefore the maximum velocity is not likely to revert to the propeller centreline. The divergence of the streams continues and this is confirmed in figure 2(d), at $7 D_p$, where the two jets are still separating.

It has been shown that the rudder splits the jet into two streams and their deviation continues throughout the remainder of the diffusing jet. The rudder has the effect of altering the diffusion characteristics of a propeller jet and this has resulted in the formation of a different type of jet. There is no further alteration of the streams, other than by natural diffusion with the surrounding fluid, once they have been established. The zone of established flow could therefore be considered to commence at the position of the formation of the two streams. Figure 2(a) showed the formation of the two streams, although not clearly defined. However, it can be seen in figure 2(b) that the two streams are clearly defined and diverging away from each other. This position represents approximately the end of the rudder. It can therefore be concluded that the jet is fully established from the location of the trailing edge of the rudder.

It is evident from the findings of this investigation that the processes of formation and diffusion of a propeller wash, under the influence of a rudder, can in no way be described by the predictive equations that are currently available as the two streams formed by the rudder have been shown to behave as independent jets.

Characteristics of a propeller jet

Efflux Velocity Distribution

The magnitudes of all velocities within the wash produced by the rotating propeller are dependent on the magnitude of the initial velocity within the wash. This velocity, termed the efflux velocity, is found on the cutting edge of the propeller. As can be seen from figure 1 the velocity distribution along the cutting edge, or the efflux distribution, remains unchanged in the presence of the rudder, with an axi-symmetric distribution being developed. It is this initial distribution, along with the subsequent rudder interaction, which forms the wash. The velocity distribution at efflux will be proportional to the thrust developed by the propeller blade. The thrust produced by a ships propeller depends on the geometry of the propeller blades and the speed of rotation. The main characteristics which influence the developed thrust include the pitch and chord length. These characteristics vary with radial distance from the hub, and hence the thrust and therefore the velocity must also vary with distance along the blade.

The position along a propeller blade at which the greatest thrust is produced generally corresponds to the position of maximum velocity, termed the efflux velocity, V_0 . Several authors have proposed equations which determine the magnitude of the efflux velocity. The original efflux velocity equation, as reported by Blaauw et al (1978) and adopted by most authors, was based on the Froude momentum theory,

$$V_0 = 1.59nD_p\sqrt{C_t}$$

The assumptions made in the momentum theory have been shown to be invalid. These short-falls in the theory have led to modifications of the theoretical efflux equation by Stewart (1992). These modifications take account of the propeller characteristics as follows,

$$V_o = E_o n D_p \sqrt{C_t} \quad 1$$

where

$$E_o = \left[\frac{D_p}{D_h} \right]^{-0.323} [C_t]^{-0.1459} [P]^{0.44} [\beta]^{0.513}$$

The magnitude of the axial velocities at the face of the propeller have to date been estimated by solving equations developed by Albertson (1950). He proposed that the velocity distribution within the jet, close to the propeller, follows the Gaussian normal probability function.

Stewart modified the Gaussian equation and presented the following equation, to describe the axial velocity distributions within the propeller jet, based on his own investigations:

$$\frac{V_{xr}}{V_{\max}} = EXP\left(-\frac{1}{2} \frac{(r - R_{mo})^2}{\sigma^2}\right) \quad 2$$

where the standard deviation of velocity, σ , was equal to $0.5 R_{mo}$ and the maximum velocity, V_{\max} at the face of the propeller is equal to the efflux velocity, V_o . Berger et al. (1981) proposed that the distance to the position of the maximum velocity at the face of the propeller, R_{mo} , could be determined as follows,

$$R_{mo} = 0.67 R_p - R_h \quad 3$$

where R_h is the radius of the hub and R_p is the propeller radius.

The velocity distribution along the face of the propeller can be determined by solving equations 1,2 and 3. Velocity profiles were plotted comparing the results obtained from existing equations and the measured data. The profiles, as shown in figures 3 and 4, indicate that the measured velocity increases from the hub to a distance of approximately $0.7 R_p$ along the blade, and then decreases rapidly to the blade tips. This is in contrast to the profile predicted by existing equations, where the velocity increases to approximately $0.5 R_p$ and then gradually decreases to the blade tips. The position of the maximum velocity can also be seen to vary greatly from that determined from existing equations, when compared to the measured velocities. The distance to the maximum velocity, in all of the profiles that were plotted using existing equations, was underestimated when compared to the measured results. The existing equations, which are based on the momentum theory, have been revised and updated on several occasions by replacing the experimental constant. The magnitude of the constant varied in several investigations using different propellers, more recently Stewart updated the equation to relate the constant to the propeller characteristics. This was a calibration of a theory, which is inherently flawed, to suit experimental results. It was decided to investigate a more realistic method by which the magnitude of the axial velocities along the face of the propeller could be obtained.

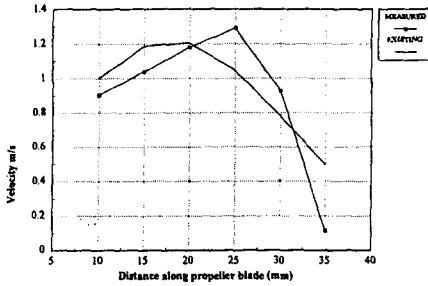


FIGURE 3 Velocity Distribution Comparison for 76mm propeller

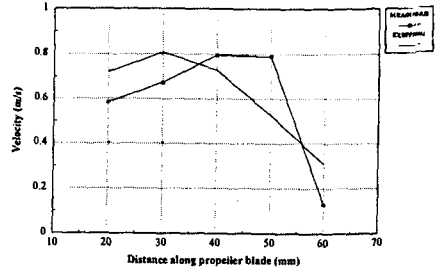


FIGURE 4 Velocity Distribution Comparison for 131mm propeller

A literature survey revealed that Koumbis (1981) investigated the thrust produced by a ship's propeller and developed a computer program which relates the thrust to the characteristics of the propeller blades. The program is based on the Vortice Lattice theory.. In designing a propeller the naval architect determines the most suitable characteristics to provide the optimum thrust for each blade. It therefore seemed reasonable to relate the distribution of velocity on the propeller face to the characteristics which produce this thrust.

The blade cross sections, as shown in figure 5, were obtained for positions along the propeller blade where the velocity measurements had been recorded. It was decided to attempt the derivation of a relationship in which the magnitude of the axial velocity could be expressed in terms of the characteristics of the propeller blades.

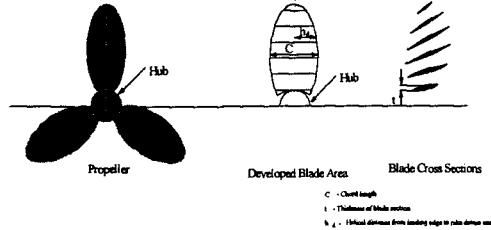


Figure 5 Propeller Blade Characteristics

A literature survey provided detailed information on the design of a propeller, and revealed the properties considered by the naval architect in designing the geometry of the propeller blade. Considering the axial velocity V_{ax} , it can be written as:

$$V_{ax} = f(n, N, r, \mu, \rho, p, t, c, h_D, h_T)$$

- where n = number of rev/sec N = number of blades
- r = radius of propeller μ = kinematic viscosity
- ρ = density of fluid p = pitch of blade
- t = thickness of blade c = chord length
- h_D = helical distance from blade section leading edge to rake datum line
- h_T = helical distance from blade section leading edge to position of maximum thickness

Using the Pi theorem the equation can be written as:

$$\frac{V_{ax}}{Nnr} = f\left(\frac{\rho nr^2}{\mu}, \frac{p}{r}, \frac{c}{r}, \frac{t}{r}, \frac{h_d}{r}, \frac{h_r}{c}\right)$$

It was found from the literature survey that the effect of viscosity could be neglected if the Reynolds number of the jet was greater than 10^4 . In the present investigation the Reynolds numbers were greater than 10^4 , and could therefore be neglected from further analysis. This analysis resulted in an equation with a correlation coefficient R^2 of 0.985:

$$\begin{aligned} \frac{V_{ax}}{Nnr} = & 1.261 - 0.974\left(\frac{p}{r}\right) + 0.733\left(\frac{c}{r}\right) + 18.527\left(\frac{t}{r}\right) + 5.028\left(\frac{h_d}{r}\right) \\ & + 0.106\left(\frac{p}{r}\right)^2 - 7.277\left(\frac{h_d}{r}\right)^2 - 4.093\left(\frac{h_r}{c}\right)^2 \end{aligned} \quad 4$$

The high correlation obtained for the experimental data shows the assumption that the velocity distribution along the blade was a function of the varying blade characteristics was valid. The velocity distribution obtained from equation 4 and the results obtained from existing equations, were plotted with the experimental results. Figure 6 is typical of that found for the present investigation. It can be seen that there is a significant improvement in the correlation with the measured data, when compared to the results of existing equations. This was found to be the trend of the results obtained for all experiments.

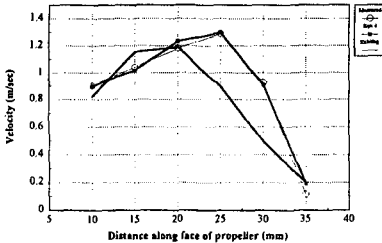


FIGURE 6 COMPARISON OF EXPERIMENTAL DATA WITH THE RESULTS FROM EXISTING AND PROPOSED EQUATION

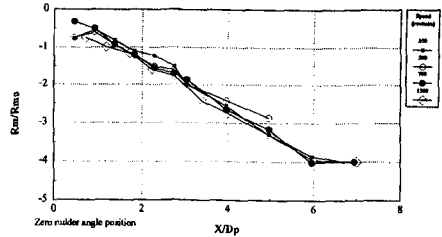


FIGURE 7 LOCATION OF THE MAXIMUM AXIAL VELOCITY WITHIN THE BOTTOM STREAM OF THE DIFFUSING JET

The magnitude of the axial velocity distribution at the face of the propeller can now be determined by solving a single equation, equation 4, instead of the three equations as proposed by existing work. The derivation of this equation is based on the physical properties of the propeller blades rather than the momentum theory which is inherently flawed. Equation 4 will accurately determine the magnitude of the maximum velocity, V_0 , and the position at which it occurs along the blade. Its use beyond the scope of the current experimental programme will require further verification. However, when compared to the equations which are currently used, which themselves are based on a limited test programme, it shows great potential.

Location of the maximum velocity

The location of the maximum velocity within the bottom stream was plotted with distance from the propeller. Figure 7 shows the location of the maximum velocity in the bottom stream for each speed of rotation for a zero rudder angle. It can be seen that there is

no significant variation in the location of the maximum velocity, with an inclination of approximately 12 degrees observed towards the bottom for each speed of rotation. This is in sharp contrast to that obtained when there was no rudder fitted where the maximum velocity was located along the horizontal propeller axis. It would therefore appear that for a zero rudder angle the location of the maximum velocity is independent of propeller speed of rotation.

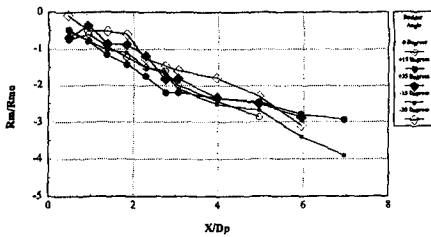


FIGURE 8. LOCATION OF THE MAXIMUM AXIAL VELOCITY WITHIN THE BOTTOM STREAM OF THE DIFFUSING PROPELLER JET FOR CHANGES IN RUDDER CONFIGURATION

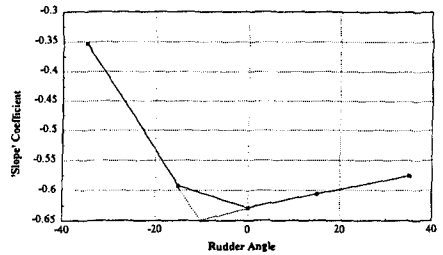


FIGURE 9. EXPERIMENTAL CONSTANT 'C' VS. RUDDER ANGLE

The vertical location of the maximum velocity in the bottom stream of the jet was then plotted for all experiments and the results obtained for a typical rotational speed, with a varying rudder angle, are as shown in figure 8. The location of the maximum velocity appears to diverge at approximately the same rate for each rudder angle. The greatest depth to the maximum velocity was observed when the rudder is placed at 15 degrees up to a distance of 3 D_p and generally thereafter is greater when the rudder is positioned at zero degrees. The divergence angle was found to be approximately 12 degrees and this was found to be the general trend for this propeller at different rudder angles. The general trend showed that the greatest depths to the maximum velocity were observed when the rudder was placed at positive rudder angles. It can therefore be concluded that the depth to the maximum velocity is dependent of the rudder angle.

Equation for location of maximum velocity

Analysis of the change in position of the maximum velocity showed that its location could best be described by a linear decay equation of the type

$$\frac{R_{mx}}{R_{m0}} = Const. \left(\frac{X}{D_p} \right)$$

where R_{mx} is the maximum velocity location at any distance X from the propeller.

It was obvious that the constant term was a function of the rudder angle, as the location was seen to shift as the rudder angle changed. Figure 9 shows a plot of these constant values against the rudder angle, and it is clear that a significant variation can be observed between the positive and negative rudder angles. This is to be expected as the

negative angles cause the rudder to be turned into the bottom stream therefore hindering the flow, while with positive angles the stream is free to expand. Based on this physical interference two separate equations have been developed by which the position of the maximum velocity can be obtained, and these depend on the rudder angle range as follows;

Rudder angle range $-10 < \theta < +35$ degrees

$$\frac{R_{mx}}{R_{mo}} = (-0.659 + 0.002\theta) \left(\frac{X}{D_p} \right)$$

Rudder angle range $-35 < \theta < -10$ degrees

$$\frac{R_{mx}}{R_{mo}} = (-0.772 - 0.012\theta) \left(\frac{X}{D_p} \right)$$

These equations are a first approximation based on the current experimental investigation and further work would be recommended to provide a clearer understanding of the influence of the rudder on the location of the maximum velocity between the zero and -15 degree rudder position.

Decay of Maximum Axial Velocity

It has been shown that for a jet without a rudder, the decay of the maximum axial velocity is not constant throughout the jet, Qurrain. The present investigation has shown that the jet is fully established from the location of the end of the rudder and therefore a single relationship must be considered to describe the decay of the maximum velocity within the propeller jet with a rudder present.

The rate of decay of the maximum velocity was found to be independent of propeller rotational speed. The rate of decay of the maximum velocity however, varies significantly when compared to previous work due to the presence of the rudder. In order to establish a relationship for the rate of decay, the values of the maximum velocity, V_{max} , within the jet were non-dimensionalised with the maximum velocity at the face of the propeller, V_o , and the distance from the propeller, X , was divided by the propeller diameter, D_p . Analysis of the results was carried out on all the data and it was found that the following type of equation provided the best correlation for the results, as can be seen in figure 10.

$$\frac{V_{max}}{V_o} = A + B \left(LN \frac{X}{D_p} \right)$$

It was found for all tests that the B coefficient was constant and equal to 0.293. This shows that the actual rate of decay is independent of the rudder angle. There was however a significant variation observed in the values found for the A coefficients. This indicated that although the rudder had no influence on the rate of decay of velocity it clearly was influential in the initial magnitude of the maximum velocity. As was the case in the location of the maximum velocity the A coefficients were compared to the respective rudder angles and again positive and negative angles were seen to influence the magnitude of velocity. Again this is not unreasonable as has already been discussed. As before two equations by which this coefficient should be determined have been produced, again depending on the rudder angle considered.

Rudder angle range $-10 < \theta < +35$ degrees

$$A = 0.915 - 0.004(\theta)$$

Rudder angle range $-10 < \theta < -35$ degrees

$$A = 1.0 - 0.007(\theta)$$

Concluding Comments

The present investigation has studied the influence of the rudder within a ship's propeller jet, and has confirmed the formation of two high velocity streams, one directed upwards to the surface and the other directed downwards towards the bottom.

The axial velocity distribution at the face of the propeller could only be determined by solving a number of equations based on the results of previous work. The present investigation found that the velocity along the face of the propeller was related to the characteristics of the propeller blade. An equation was developed which related the magnitude of the axial velocity at any point along the blade to the properties of the blade at that point.

It was found that there was an increase in magnitude of the axial velocities by as much as 30% with the rudder present when compared to the jet without a rudder.

The location of the maximum velocity within the propeller jet was on the axis of each stream which were established from the position of the rudder. This led to a redefinition of the zone of established flow. Equations are presented which locate the maximum velocity in the vertical direction allowing for changes in rudder position. The maximum deflection of the bottom stream was observed for the zero rudder angle position and was found to be approximately 14 degrees.

Results have shown that the decay of the maximum velocity within each of the streams was the same at each of the angles tested and was independent of the propeller rotational speed. It was found that there was a logarithmic decay of the maximum velocity at each of the rudder angles tested and the magnitude of the velocity encountered was found to be dependent on rudder position.

By using the equations presented it is now possible for the engineer to establish the maximum velocity at any depth below a rotating propeller. Given the bed clearance conditions it is therefore possible to predict the magnitude of the velocity which will impact on the sea bed. Knowing this velocity, and an understanding of sediment movement prediction techniques, it is possible to design either suitable bed armour units or to predict eroded depths.

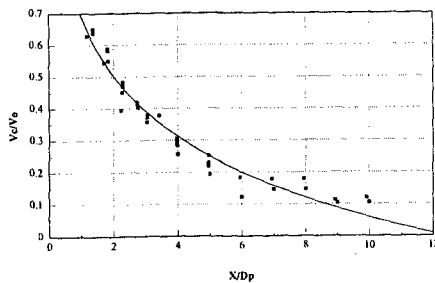


FIGURE 10 DECAY OF THE MAXIMUM AXIAL VELOCITY ALONG THE PROPELLER AXIS FOR ALL EXPERIMENTS AT ZERO RUDDER ANGLE

APPENDIX**REFERENCES**

- ALBERTSON, M.L.**, (1950) "Diffusion of submerged jets", Transcript of the A.S.C.E., Paper No. 2409, Vol. 115, pp 639-697.
- BERGER, W., FELKEL K., HAGER M., OEBIUS., SCHALE E.**,(1981) "Courant rovoque par les bateaux. Protection des berges et solution pour eviter l'erosion du lit du Haut Rhin" PIANC 25th Congress, Edinburgh, 1981, Section I-1
- BERGH H., CEDERWALL K.**, (1981), "Propeller erosion in harbours", Bulletin No. TRITA-VBI-107, Hydraulics Laboratory, Royal Institute of Technology Stockholm, Sweden.
- BLAAUW, H.G., KAA, E.J. van de**, (1978)," Erosion of bottom and sloping banks caused by the screw race of manoeuvring ships ", Publication No.202, July 1978, Delft Hydraulics Laboratory, Netherlands.
- FUEHRER, M., ROMISCH, K.**, (1985), Dimensionierung von Sohlen- und oschungs-befestigungen an Schiffahrtkanalen. Mitteilungen der Forschungsanstalt fur Schiffhart, Wasser und Grundbau, Berlin. Schriftenreihe Wasser und Grundbau, Heft 45
- KOUMBIS A.**, (1981) "An improved mathematical modek of the action of open and ducted thrusters", PhD. thesis, University of Newcastle upon Tyne, 1981.
- PROSSER, M.J.**, (1986), "Propeller induced scour", BHRA report for the British Ports Authority, February 1986.
- QURRAIN, R.M.M.** (1994), "Influence of the sea bed and berth geometry on the hydrodynamics of the wash from a ship's propeller", Thesis submitted to the Queen's University of Belfast for the degree of Ph.D. 1994.
- ROBAKIEWICZ, W.**, (1966), Wplyw dzialania strumienia zasrubowego na dno przy nabrzezu stanowiska prob na uwiezi na przykladzie baden model owychiernowych ztrawlerem B 20. Rosprawy Hydrotechniczne 19.
- STEWART, D.P.J.**,(1992), " Characteristics of a ships screw wash and the influence of quay wall proximity ", Thesis submitted to the Queens University of Belfast for theDegree of Doctor of Philosophy.
- VERHEY, H.J.**, (1983), The stability of bottom and banks subjected to the velocities in the propeller jet behind ships. Delft Hydraulics laboratory. Publication No 303

CHAPTER 347

MODELING INLET SAND BYPASSING

Christopher G. Creed¹

Abstract

Consideration of the magnitude and phasing of sand bypassing events with respect to incident wave conditions is necessary when modeling shoreline change adjacent to tidal inlets where sand bypassing occurs. Likewise, the effects of wave transformation over nearshore bathymetric features (i.e., ebb tidal shoals, bypassing bars, etc.) and the resulting variations in alongshore sand transport rates relative to bypass discharge locations should also be considered. This paper presents a method for developing time-dependent inlet sand bypassing data for use in predicting future shoreline change. The method includes developing a relationship between the local offshore wave climate, longshore sand transport regime and inlet sand bypassing utilizing coincident time series of (1) local wave climate and (2) sand bypassing. The proposed model is compared to two other typical sand bypassing models to demonstrate the importance of relating the wave climate and bypassing. The proposed method was used successfully to create a representative time series of both mechanical and natural sand bypassing data for a shoreline change study conducted for the downdrift shoreline of South Lake Worth Inlet, Florida.

Introduction

Shoreline change adjacent to inlets where sand bypassing occurs is directly related to the characteristics of bypassing conditions. Specifically, sand bypassing is responsible, in part, for the manner in which both the updrift and downdrift shorelines of an inlet respond to the offshore wave climate and longshore sand transport regime. That is, the rate at which sand is removed from an updrift shoreline or added to a downdrift shoreline relative to the magnitude of the longshore transport potential affects the rate of shoreline change. For example, if the bypassing rate is below average during

¹ Coastal Engineer, Olsen Associates, Inc., 4438 Herschel Street, Jacksonville, FL 32210.

above average transport conditions, the net effect would be an impoundment of sand along the updrift shoreline and erosion along the downdrift shoreline. Therefore, when modeling shoreline change adjacent to inlets where sand bypassing occurs, it is important to represent both longshore transport and bypassing conditions accurately. This requires that the magnitude and phasing of sand bypassing events with respect to incident wave conditions be considered.

Background

Shoreline change models are typically used to predict future response of shorelines where a beach fill or coastal structure may be constructed. The characteristics of the mechanisms which contribute to future shoreline change (i.e., the wave climate, longshore transport regime, updrift sand supply, bypassing, etc.), however, are generally not known *apriori*. Therefore, accurate prediction of future shoreline change requires assumptions regarding the future characteristics of mechanisms which contribute to shoreline change. Typically, the assumption is made that future conditions can be represented by average historical conditions.

In the instance where a time-dependent model is used, annual and seasonal variations in the shoreline change mechanisms are also represented. Time-dependent shoreline change models often require a time series of input conditions to represent the annual and seasonal variations in shoreline change. For example, a shoreline change model may require a wave time series to represent wave conditions. In predicting future shoreline change, wave conditions may be representative of historical average annual and seasonal conditions.

When modeling shoreline change for a shoreline adjacent to a tidal inlet where sand bypassing occurs, the time dependent nature of bypassing events and the relationship of sand bypassing to incident wave climate and transport regime must also be considered. It is known that inlet sand bypassing events, both mechanical and natural, are related to the incident wave climate and the resulting longshore sand transport regime. Considering this relationship, a *sand bypassing time series* which is correlated to the incident wave climate and resulting longshore sand transport regime is required to represent bypassing conditions accurately.

In instances where it is known that shoreline change adjacent to an inlet is directly affected by bypassing activities, bypassing data must be developed which are representative of the magnitude of bypassing quantities and a function of the incident wave climate. Developing representative wave and bypassing data, without consideration of their interdependence, may not produce an accurate representation of the mechanisms which contribute to shoreline change. A method for the development of this data is presented in the following.

Method

The purpose of the proposed method is to determine the relationship between wave conditions, longshore transport conditions, and sand bypassing. The method is therefore based upon the assumption that sand bypassing around an inlet is a function of both the incident wave climate and the resulting longshore sand transport regime. That is, it is assumed that sand bypassing occurs only when the wave and longshore transport conditions are such that a sufficient volume of material is transported toward an inlet which is mechanical or natural bypassing.

The method requires that coincident time series of historical wave and bypassing data are available. The wave data times series can be either from measured or hindcast sources. Bypassing data may be available from bypass plant records or other measurement efforts. Application of the method results in a correlation expression which describes the relationship between the magnitude and occurrence of bypassing events relative to that of wave and longshore sand transport events. This relationship can then be used along with an assumed representative wave data to formulate bypassing data for use in predicting future shoreline change.

Application of the method includes computing longshore transport conditions from offshore wave time series which correspond to the period for which sand bypassing data are available. Simplistically, the transport conditions may be computed with a longshore sand transport equation such as the CERC formula (Shore Protection Manual, 1984). The general CERC formula can be expressed as

$$Q = K H_b^{\frac{5}{2}} \sin 2\theta_b \quad (1)$$

where Q is the longshore sand transport rate, H_b is the incipient breaking wave height, θ_b is the local breaking wave angle relative to shore normal and K is a calibration coefficient. Incipient breaking wave heights can be computed from the offshore wave data assuming the wave climate is linear and monochromatic and the offshore bathymetric contours are straight and parallel. A time series of longshore transport data can then be compiled to correspond to the period and frequency of the bypassing data. The resulting longshore sand transport time series can be calibrated with the coefficient, K , to produce average annual transport conditions equivalent to known quantities for the region.

To determine the relationship between the transport and bypassing, the data are plotted and a best-fit expression is derived. This resulting expression implicitly describes the phasing and magnitude of bypassing relative to the offshore wave data.

Alternate Method. In instances where historical bypassing records are not available, an inlet sediment budget may be utilized along with the assumption that bypassing is proportionately related to the local longshore sand transport potential. Although this method does not strictly include the relationship between actual wave and bypassing data, it generally describes annual and seasonal variations in the wave climate and bypassing for modeling purposes. The technique simply describes bypassing as a fraction of longshore sand transport.

Once the relationship between transport and bypassing is determined, the wave time series may be applied to the expression to develop a corresponding bypassing time series which represents future bypassing conditions. This technique was applied for a shoreline change investigation described below.

Application

The proposed method was applied during a shoreline change model study conducted for South Lake Worth Inlet in South Florida. The intent of model study was to simulate shoreline change along approximately 12,000 feet of shoreline immediately downdrift of the inlet for purposes of formulating a Federal Shore Protection Project for the Town of Ocean Ridge, Florida ("Palm" 1996). Analysis of historical shoreline change data, as well as the general morphology and littoral transport patterns, suggested that sand bypassing across the inlet, both mechanical and natural, strongly influenced the downdrift shoreline. The shoreline change model GENESIS, developed by Hanson (1987) and Hanson and Kraus (1989), was used for the investigation. GENESIS is a one-line shoreline change model which computes time-dependent shoreline change using a time series of input wave and sand bypassing conditions. Realizing the importance of sand bypassing to the study shoreline, both mechanical and natural sand bypassing which occur at the inlet were modeled as input to the updrift boundary condition.

Background. South Lake Worth Inlet is located in southern Palm Beach County on the southeastern coast of Florida (Figure 1). The inlet was mechanically cut through the sandy barrier which separates the Atlantic Ocean and Lake Worth in 1927. The inlet is stabilized by two jetties; the north jetty extends about 122 meters farther seaward than the south jetty and is curved towards the southeast. In 1967, the inlet was modified to its current configuration in an attempt to improve its bypassing capacity and reduce interior shoaling. The regional net sand transport in the vicinity of the inlet is from north to south, with approximately eighty-five percent of the gross transport being southerly directed.

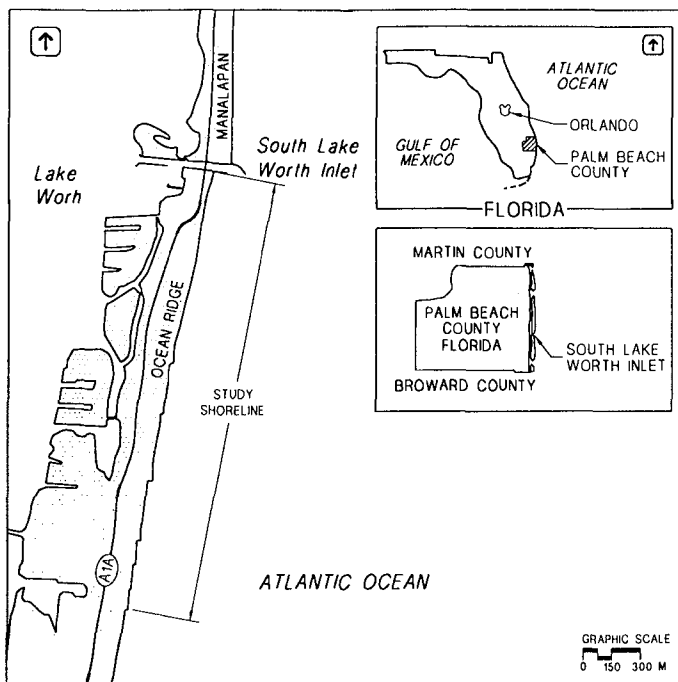


Figure 1: Location of South Lake Worth Inlet, Florida.

Despite natural and mechanical sand bypassing, the inlet acts as a partial littoral barrier to the net southerly drift of sand along Florida's southeast coast. Sand which drifts towards the inlet from the north is intercepted by the inlet's north jetty or diverted to the inlet's ebb and flood tidal shoals. Sand intercepted by the inlet's north jetty is impounded either in the fillet along the northern shoreline or mechanically bypassed to the southern shoreline. Sand diverted to the ebb shoal is stored either in the shoal platform, transported to the flood shoal and sand trap, or naturally bypassed to the southern shoreline. It is estimated that approximately 18 percent of the net southerly drift is intercepted and lost to the inlet system, resulting in a net sediment deficit along the downdrift shoreline. The net southerly sand transport in the vicinity of the inlet may vary between 134,000 and 172,000 cubic meters per year.

Sediment Budget. To quantify sand transport in the vicinity of South Lake Worth Inlet, Olsen Associates, Inc. (1990) developed a detailed nine-component sediment budget which quantitatively described sediment transport paths at South Lake Worth Inlet. The sediment transport components of the sediment budget are highlighted in Figure 2. Six of the nine sediment transport components of the sediment budget were

developed from available data. Using these values and the governing equations of the sediment budget, estimates of the natural bar bypassing and the net drift rate south of the inlet were calculated for a range of net littoral drift rates north of the inlet.

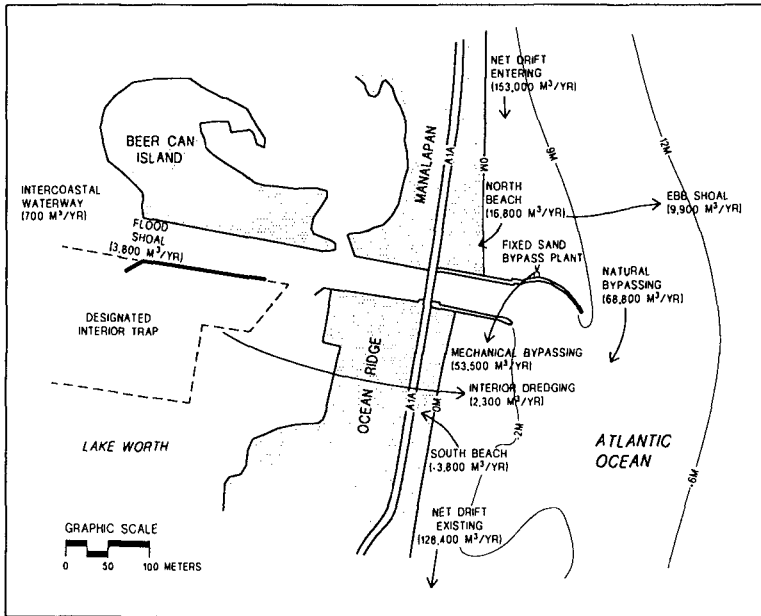


Figure 2: Sediment transport components for South Lake Worth Inlet, Florida.

Data collected since the 1967 modifications suggest that approximately 45 percent of the southerly net drift is bypassed across the ebb tidal shoal and bypassing bar. An additional 35 percent of the net southerly drift is bypassed by the fixed sand transfer plant.

Mechanical bypassing at the inlet is achieved with the inlet's sand transfer plant, which transports sand from the northern shoreline to a location between 60 and 150 meters south of the inlet. The plant is located atop the north jetty and bypasses sand from the northern to southern shoreline at a typical rate of about 53,500 cubic meters per year. Natural sand bypassing occurs along the inlet's ebb tidal shoal and bypassing bar platform. The bypassing bar attaches to the southern shoreline about 600 to 900 meters south of the inlet.

Because approximately 80 percent of the net transport is bypassed across the inlet, it was essential that this input to the study shoreline be included in model simulations.

Therefore, both mechanical and natural sand bypassing data (which were assumed to represent future bypassing conditions) were developed with the method described herein.

Mechanical Sand Bypassing Data. The relationship used to develop mechanical sand bypassing data representative of future conditions was determined from comparison of longshore sand transport data -- computed from offshore wave hindcast data -- and historical sand bypassing records. Mechanical bypassing records are available for the South Lake Worth Inlet sand transfer plant for the period from 1967 to the present. The bypassing rates are compiled from operation records and measured bypassing rates at the plant. WIS hindcast data are available for the area offshore of South Lake Worth Inlet for the period from 1956 to 1995. A time series of longshore sand transport was computed using these WIS hindcast wave data. The period for which the two databases overlap and are most reliable is 1970 to 1990. Therefore, it is this twenty year period for which longshore sand transport and mechanical sand bypassing data were compared.

The sand bypassing data were compared to both the net and southerly longshore transport components. This comparison revealed that mechanical bypassing is more closely correlated to the southerly transport component than the local net transport rate. (In fact, the mechanical sand bypassing plant operates only during periods of southerly directed transport.) The computed southerly transport data are plotted against the measured bypassing data in Figure 3. These data represent the twenty year period from 1970 to 1990. Inspection of the figure suggests a general trend in the data, where the magnitude of bypassing is related to the magnitude of southerly directed sand transport. The best-fit curve is of the form:

$$MB = aQ^b \quad (2)$$

where Q is the computed southerly transport rate from Eq. 1 (with $K=1.0$), MB is the reported mechanical bypassing rate, each in units of cubic meters per month, and a and b are coefficients. In this instance, the coefficients a and b were 29.0 and 0.54, respectively.

To demonstrate the effectiveness of this expression to represent actual mechanical sand bypassing data, a 9-year time series of southerly sand transport was applied to the expression to create a predicted 9-year time series of mechanical bypassing. The actual and predicted bypassing data for this period are presented in Figure 4. It is noted that areas of disagreement between actual and predicted bypassing records (such as the predicted spike in the latter part of 1974) may result from operational limitations of the sand bypass plant. Nonetheless, the comparison suggests that the mechanical sand bypassing at the inlet is correlated reasonably well with the incident wave climate.

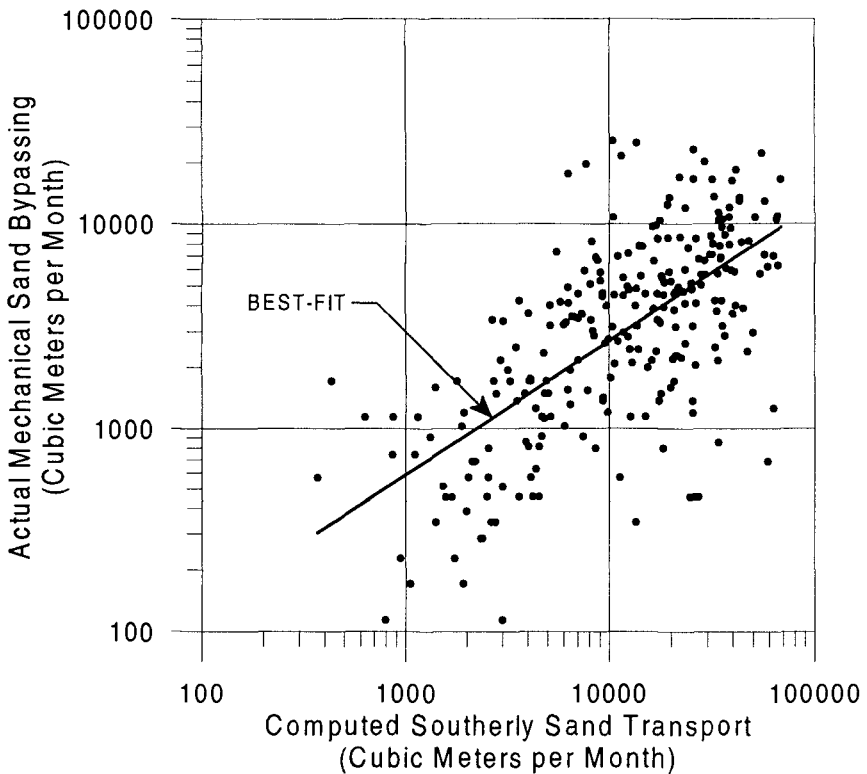


Figure 3: Correlation between actual mechanical sand bypassing (1967-1990) and computed southerly sand transport at South Lake Worth Inlet, Florida.

Natural Sand Bypassing Data. A time series of natural sand bypassing related to the longshore sand transport time series was also required as input to the shoreline change model. Actual measurements of the quantity and occurrence of natural bypassing, however, are not available at most inlets, including South Lake Worth Inlet. Therefore, the inlet's sediment budget and the assumption that natural bypassing occurs only during periods of southerly directed transport were used to formulate a natural bypassing time series. That is, the "natural bypassing" time series was developed by assuming that north to south sand transport across the bypassing bar is proportionately correlated to the southerly longshore sand transport component. This assumption was based, in part, upon the comparison of computed southerly sand transport and recorded mechanical sand bypassing. The proportionality constant for natural bypassing (0.45) was determined from the inlet's sediment budget (Figure 2); i.e.,

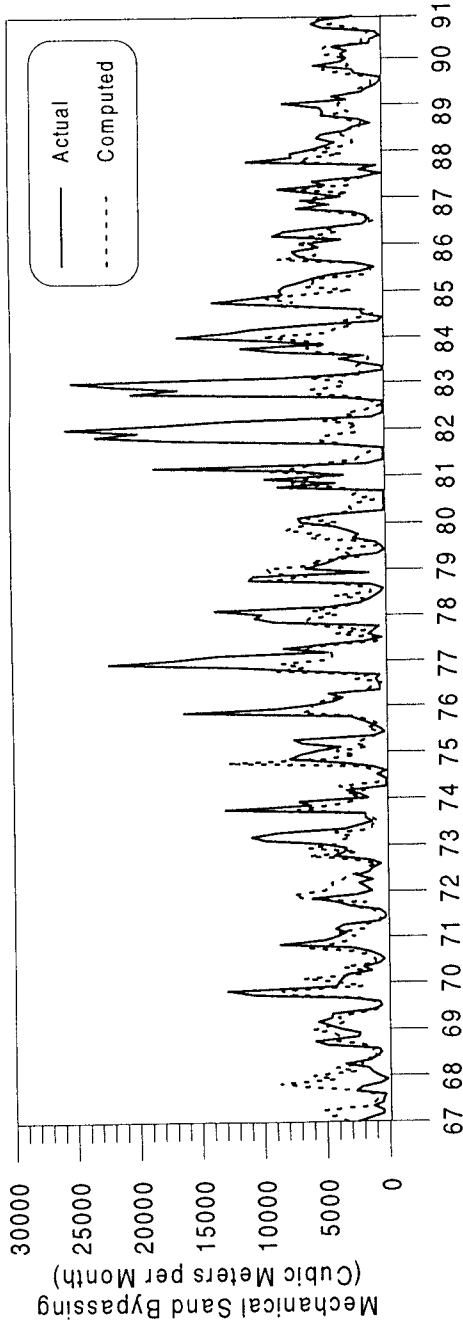


Figure 4: Time Series of actual and computed mechanical sand bypassing at South Lake Worth Inlet, Florida.

$$NB = 0.45 Q \quad (3)$$

where NB is the rate of natural bypassing and Q is computed southerly transport rate from Eq. 1 (with $K=1.0$).

Shoreline Change Simulations. For purposes of predicting future shoreline change, a representative four year wave time series was developed for input to the GENESIS model. This time series was selected from the entire 38 year WIS hindcast time database as being most representative of average annual and seasonal variations in wave conditions offshore of the study site. Using this representative wave time series, corresponding mechanical and natural bypassing time series were computed using Eqs. 2 and 3, respectively. Both the wave and bypassing time series were used as input to the GENESIS for model simulations.

Bypassing Locations. The locations along which bypassed sand is supplied to the shoreline were also considered in the shoreline change investigation. As noted above, the study shoreline is supplied with bypassed material along two general areas. The sand which is mechanically bypassed is supplied to the shoreline within 60 to 150 meters south of the inlet. The sand which is bypassed naturally is supplied to the shoreline at the point where the natural bypassing bar attaches to the shoreline. This attachment point is some 600 to 900 meters south of the inlet.

Consideration of the locations along which the sand is supplied to the study shoreline was necessary because the alongshore distribution of sand transport is characterized by extreme accelerations and decelerations due to the effects of the inlet's ebb tidal shoal and bypassing bar on the incident wave climate. Because of these variations, shoreline change is strongly influenced by the locations along which bypassed material is supplied to the shoreline. To accommodate this sensitivity, sand was added to the model at the locations representative of the mechanical sand bypass plant discharge points and the average location at which the natural bypassing bar attaches to the shoreline.

As configured, the GENESIS model does not consider changes to the wave climate caused by such shallow features at South Lake Worth Inlet's ebb tidal shoal and bypassing bar. Because these changes to the wave climate are important to shoreline change and the movement of bypassed sand, a method was developed by Bodge, et.al. (1996) to consider the effects of nearshore bathymetric features on the wave climate. Briefly, the method computes the breaking waves conditions through a grid-based refraction analysis for wave conditions which are representative of the offshore time series. The breaking wave information is then "back-refracted" to a nearshore wave reference line which the GENESIS model is designed to accept. This technique,

therefore, includes the variations in breaking wave conditions created by nearshore bathymetric features (such as ebb tidal shoals and bypassing bars) in the wave data input to the GENESIS model. This provides for more accurate representation of the local transport conditions in the areas where sand is supplied to the shoreline through bypassing.

Comparison Bypass Model Comparison. To demonstrate the necessity of accurately representing the relationship between longshore sand transport and sand bypassing, two other representations of sand bypassing were developed. These include assuming that an annual equivalent volume of bypassing is supplied to the shoreline at a constant rate (*uniform*). The other assumes that an annual equivalent volume of bypass sand is supplied at the beginning of each year (*plug*). A graphical representation of these concepts is provided in Figure 5.

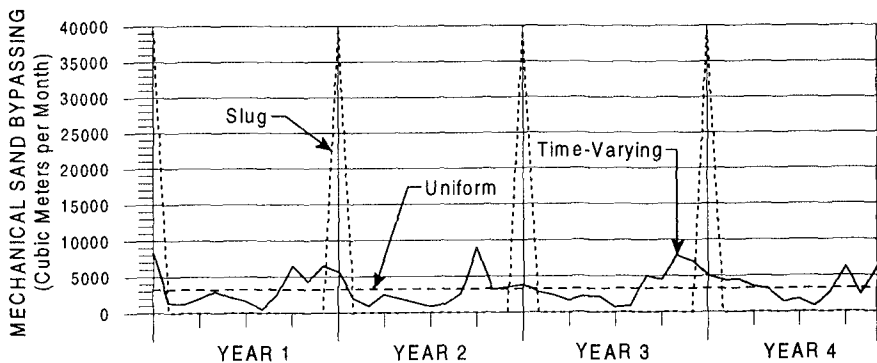


Figure 5: Concept of sand bypassing models.

These two bypassing models along with the bypassing model proposed herein (*time-varying*) were used to develop bypassing data for comparative model simulations. The representative four year wave time series described above was used to develop the bypassing data. Each representation of bypassing supplies an equivalent volume of sand to the model domain over the simulation period. For verification purposes, where both initial and final measured shorelines are available, model simulations were conducted for the 18 year period between 1975 and 1993. The results of the three comparative simulations are shown in Figure 6. In the figure, it is clear that the *time-varying* bypassing model provides a more accurate representation of measured shoreline change. The *uniform* and *slug* bypassing models fall short of the time-varying model by producing a significant build of sand along the northernmost section of the study shoreline. This is due to sand being supplied to the shoreline during periods of inactive longshore transport; thus allowing a build up of material which is not transported away when transport becomes active. To more clearly demonstrate these results, the differences between measured and computed shorelines are provided in Figure 7.

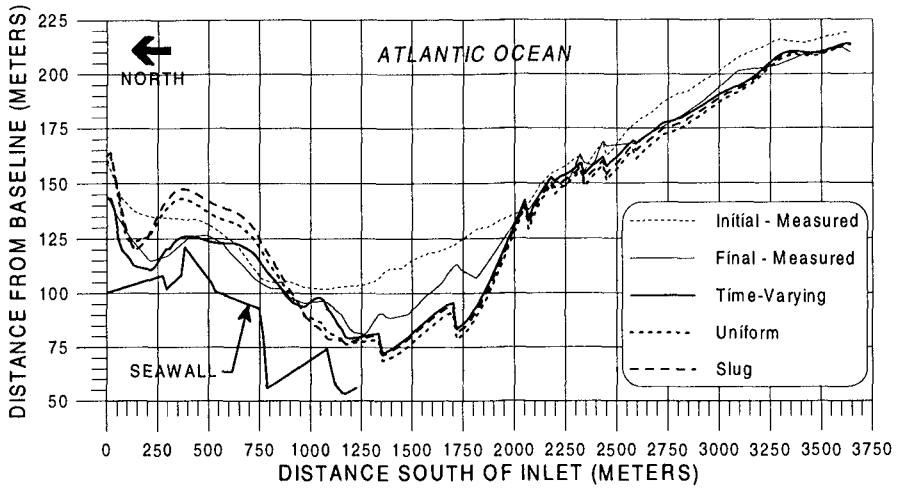


Figure 6: GENESIS shoreline change results using three sand bypassing models.

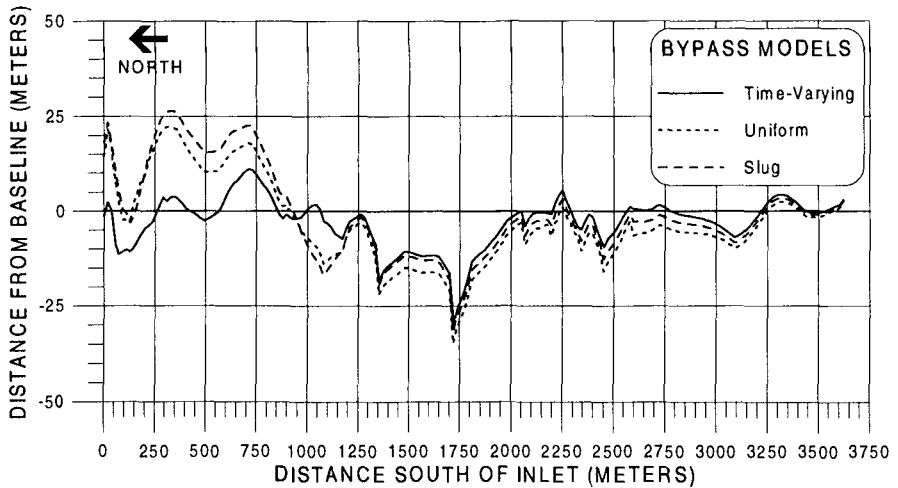


Figure 7: Difference between measured and computed shorelines.

Conclusions

A method is proposed to relate mechanical and natural inlet sand bypassing to the incident wave climate and develop a time series of bypassing for use as input to shoreline change models. Data requirements for the method include coincident time series of (1) local wave climate and (2) sand bypassing are required. Application of the model indicates that the magnitude and phasing of sand bypassing events with respect to incident wave conditions should be considered when modeling shoreline change adjacent to tidal inlets where sand bypassing occurs. The proposed method was used to successfully simulate shoreline change for the downdrift shoreline of South Lake Worth Inlet, Florida. U.S.A.

Acknowledgment

The author is sincerely grateful to Dr. Kevin R. Bodge of Olsen Associates, Inc. for his technical insight and guidance during this investigation.

References

- Bodge, K.R., C.G. Creed, and A.W. Raichle, (1996). "Improving input wave data for use with shoreline change models," Technical Note, *J. Wtrwy., Port, Coast., and Oc. Engrg*, ASCE, 122 (5), 259-263.
- Hanson, H., (1987). "GENESIS, a generalized shoreline change model for engineering use," Report No. 1007, Department of Water Resources Engineering, University of Lund, Lund, Sweden, 1987.
- Hanson, H. and N.C. Kraus, (1989). "GENESIS: generalized model for simulating shoreline change," Technical Reference, Report 1, Coastal Engineering Research Center, U.S. Army Corps of Engineers Waterways Experiment Station, Vicksburg, MS, December, 1989.
- Olsen Associates, Inc. (1990)., "South Lake Worth Inlet Sand Management Plan," Submitted to the Palm Beach Board of County Commissioners, Olsen Associates, Inc., Jacksonville, FL.
- U.S. Army Corps of Engineers, (1984). "Shore Protection Manual," U.S. Army Corps of Engineers, Coastal Engineering Research Center, U.S. Government Printing Office, Washington, D.C.
- "Palm Beach County, Florida, Shore Protection Project, General Design Memorandum for Ocean Ridge Segment," *Rep. Prepared for U.S. Army Corps of Engineers*, Jacksonville, Fla.

CHAPTER 348

AN APPROACH TO MODELING INLET AND BEACH EVOLUTION

Mark B. Gravens¹, A. M., ASCE

Abstract

Improved understanding of the physical processes controlling inlet and adjacent beach morphology is required to manage sand resources in the vicinity of tidal inlets and to reduce costs associated with structural rehabilitation, maintenance dredging of navigation channels, and mitigation of adverse impacts on adjacent shores. A quantitative modeling capability for estimating sediment fluxes, morphology evolution, and the interaction between the inlet and adjacent beaches is a goal of engineering research. This paper presents the initial phase of work aimed at developing empirical relationships between the physical processes and resulting inlet morphologic response, which are needed to formulate a modeling capability. First, the technical and computational requirements of the model are outlined. Then, a conceptual model of inlet sediment bypassing and a brief overview of a recently developed model (De Vriend et al. 1994) which appears to satisfy most of the model requirements is given. Finally, preliminary results of an empirical analysis of inlet ebb shoal geometric characteristics are presented.

Introduction

The presence of tidal inlets along a mainland or barrier island sandy shoreline represents a major morphological perturbation in the otherwise generally linear features (dune, berm, shoreline, longshore bar) that make up the coastal zone. The shoreface morphology at tidal inlets is a product of the changes in the physical forces that form the beachface. In the vicinity of tidal inlets, longshore currents generated by waves breaking at oblique angles to the shoreline interact with concentrated cross-shore currents that pass through the inlet gorge. Littoral sediments carried in the longshore current are swept into the inlet interior or are jetted offshore by the tidal currents. Over time, if the

¹ Research Hydraulic Engineer, U.S. Army Engineer Waterways Experiment Station, Coastal and Hydraulics Laboratory, 3909 Halls Ferry Rd., Vicksburg, MS, 39180-6199, USA.

inlet cross-section is stable, depositional shoal features will develop. Walton and Adams (1976), Marino and Mehta (1987), and others have shown that the ebb shoal tends toward an equilibrium volume which can be related to the tidal prism. If flood shoal volumes are also assumed to approach an equilibrium condition or a near constant growth rate, then it follows that under natural conditions, an inlet system could form and in time (10's to 100 years), reach a near-equilibrium condition, in which a large percentage of the littoral drift bypasses the inlet to downdrift shorelines.

However, because navigable tidal inlets represent an important economic resource, many inlets have been stabilized with jetties or improved for navigation by dredging. Inlet stabilization by jetties has been shown to produce a seaward displacement of the ebb shoal (Kraus et al. 1994). Seaward movement of the ebb-tidal shoal can result in an increase in the volume of material comprising the shoal. Dean (1993) presented a conceptual model together with field examples that indicate that maintaining a channel through a tidal inlet that is deeper than the natural channel depth causes sediment to flow into the maintained channel, which comes at the expense of volumetric erosion of the beaches adjacent to the inlet. Consequently, engineering practices involving inlet stabilization by jetties and navigation channel dredging are increasingly cited for their role in the observed persistent erosion of adjacent shorelines.

In the United States, federal responsibility for the design, operation, and maintenance of inlet stabilization structures and navigation channels lies with the U.S. Army Corps of Engineers. Improved sand management in the vicinity of tidal inlets will reduce costs associated with structural rehabilitation, maintenance dredging, and mitigation of adverse shoreline impacts. However, a better understanding of the physical processes controlling inlet morphology is required, including estimating sediment fluxes, morphology evolution, and the interaction between the inlet and adjacent beaches. A quantitative modeling capability can help improve our understanding of the interaction between an inlet system and its adjacent beaches. The model to be developed is intended to aid in the analysis and prediction of inlet adjacent shoreline evolution over mid- to long-term time scales (1 to 10's of years), and spatial scales up to 10's of kilometers.

Model Requirements

Goals and Development Philosophy. The primary goal of the research discussed in this paper is to develop a predictive methodology to estimate quantitatively the potential impacts of engineering activities on shorelines adjacent to modified or engineered inlet systems. The desired use of the numerical model is to predict shoreline response within the reach of shoreline influenced by the inlet in response to different engineering activities. An inlet-shoreline response model is recognized for its value in providing a quantitative basis for the comparison of alternatives. Procedures for application also will include guidance for producing an ensemble of solutions based on Monte Carlo-type simulations produced from a combination of plausible input

conditions. The ensemble of solutions then may be examined to determine the range and the frequency of the outcomes within that solution set. Because this model is being designed for use by practicing coastal engineers, model development is being undertaken with the expressed intent of capturing the evolutionary trends of the shoreline and maximizing range of applicability. This development philosophy stems from the observation that models the engineer is most likely to use are those which he or she can understand and defend, and those which require minimum adjustment of calibration parameters. Traditional approaches to coastal engineering design are expected to become more reliable with the addition of objective and quantitative estimates of an inlet's total littoral impact, which will be provided by the numerical model.

Prediction Requirements. Inlets impact adjacent shores primarily by their action as a sediment sink; therefore, a fundamental requirement of the model is the capability to predict whether and to what degree an action will change the net volume of sand lost (trapped against stabilization structures or otherwise stored in inlet associated shoal features) from the adjacent shorelines. A related requirement is the need to predict the distribution of that sand deficit along the adjacent beaches. Furthermore, regulatory agencies asking for a prediction of project performance resulting from both natural and engineered site changes leads to the requirement for model prediction of, for example, sea-level rise, extended mechanical failure of bypassing equipment, and/or planned or unexpected delays in renourishing a project or performing routine maintenance dredging of a navigation channel. The parameter of primary interest in many situations and therefore required from the model predictions is the shoreline location. For other situations the profile geometry is also of keen interest and less frequently sediment volume in various locations around the inlet-adjacent beach system are required. Table 1 provides a list of specific model requirements. Predictions are required for engineering time scales (1 to 10's of years) and spatial scales corresponding with the total longshore extent of the inlet's impact (up to 10's of kilometers).

Physical Processes. Conceptually, inlets impact adjacent shorelines in two fundamental ways. One impact is the inlet channel as a sediment sink which results in a net loss of sediment from the adjacent beach systems. The second impact is the altering of wave and current patterns, which results in a change in sediment transport patterns. Therefore, the physical processes responsible for these fundamental functions of an inlet system must be captured in the numerical model at some appropriate level. The physical processes important to determining an inlet's overall impact to the littoral system are those which result in net sediment impoundment, jetty leakage, channel shoaling, and shoal formation. Sediment conservation requires that the net volumetric impact to the adjacent shorelines equal the net volume of sediment lost to the inlet. To be useful (to estimate the inlet's impact on adjacent shores), the model must compute the rate at which sediment is delivered to the inlet, the rate at which sediment is moved through the inlet (along its axis), and the rate at which sediment is transported across, around and away from the inlet. These quantities will enable estimation of that fraction of the littoral drift which bypasses the inlet from that which is trapped within

Table 1. Model Requirements

Model Requirement	Comments
Foreshore slope changes	Beach profile slopes at stabilized tidal inlets are typically steeper updrift of the inlet and milder downdrift of the inlet as compared to beach profiles not influenced by inlet system.
Sediment point/line source and sink capabilities	To effectively evaluate many typical engineering activities (e.g., sand bypassing, beach nourishment), the capability to model point and/or line sediment sources and sinks is required.
Structure specification	To evaluate the influence of modifying inlet stabilization structures, the model must be sensitive to user-specified characteristics of the structures (e.g., length, orientation and configuration, permeability, weir sections, elevation, etc.).
Wave transformation and the possibility of multiple wave breaker lines	Wave transformation, including shoaling, refraction, diffraction and the possibility of multiple wave breaker lines with differing breaker characteristics, is required to capture the influence of the ebb shoal feature on the incident wave climate.
Hindcast capability	To demonstrate reasonability in predictions, the model must be able to simulate pre-project adjacent beach evolution.
Forecast capability	To be useful in evaluating the relative merits of competing design alternatives, the model must be able to provide mid- to long-term (1 to 10's of years) existing- condition forecasts as well as with-project forecasts.
Scoping mode / design mode applications	To quickly and efficiently provide estimates of the impact of preliminary design considerations, as well as to provide detailed estimates of refined design alternatives, the model is required to have the capability of being operated with differing levels of sophistication and data requirements.
Input data requirements	Data required to operate the model must be consistent with typically available data and/or data which can be reasonably collected.
Compatible with sediment budget methodology	Model input and output should be compatible with classical sediment budget methodologies (e.g., sediment budget information can be input to the model and model outputs can be integrated back into the sediment budget).

the inlet or is otherwise lost to the littoral system. How the net volumetric impact of the inlet is distributed along the adjacent shores is determined by hydrodynamic and sediment transport processes which exist away from the inlet. In short, modeling sediment movement in the vicinity of inlets ultimately involves essentially all of the most complicated processes of coastal sediment transport.

Target Inlet Type and Behavior. In nature, inlet systems vary widely in their characteristics and behaviors, and it is doubtful that one model or even one modeling approach would be equally applicable to all inlet systems. It is expected that the developed model will not be able to adequately predict all inlet behaviors and, therefore, will be more applicable to certain types of inlets than to others. Consequently, it is essential that the target inlet type and behavior are clearly defined. The inlet systems for which the model is being developed may be characterized as being relatively stable, often the result of stabilization structures for the purpose of providing safe navigation. The system is viewed as being in a state of dynamic equilibrium, meaning that the inlet system responds to seasonal variations in the wave and water level climate as well as to storm events. However, it is assumed that these responses are short-term or seasonal variations imposed upon an underlying state of equilibrium and do not have a destabilizing effect on the inlet system nor do they significantly alter the underlying equilibrium state. Engineering activities, on the other hand, can both temporarily displace the system from its equilibrium condition (e.g., sand mining from the ebb shoal) and in some cases change the inlet's equilibrium state (e.g., by changing the tidal prism). In either case, the inlet system will evolve toward either its old or new equilibrium state with impacts ultimately occurring on the adjacent beaches. Natural sediment bypassing is assumed to be a semi-continuous process, and the possibility of random or periodic bar welding on downdrift shorelines is excluded. The model will not allow the inlet to migrate as many natural inlet systems do. Furthermore, because sediment transport along the outer ebb delta is computed as a function of the incident wave energy the model will be more applicable to wave dominated and mixed-energy inlets than it will to tide dominated inlets.

Conceptual Model of Inlet Sediment Bypassing

Inlet sediment bypassing is the process by which littoral material delivered to the inlet from the updrift beach makes its way across the inlet system and is integrated into the littoral material on the downdrift beach. In a series of papers (Bruun and Gerritsen 1959, Bruun 1967, and Bruun 1978), a model has been presented that describes two possible pathways for inlet sediment bypassing by natural action: 1) bypassing on an offshore bar, and 2) bypassing by tidal flow action. In bar bypassing, littoral material that is delivered to the inlet from the updrift shorelines is transported along a submerged bar in front of the inlet system and delivered to the downdrift shoreline. In tidal flow bypassing littoral material is pulled through the inlet by flood currents and then discharged out of the inlet by ebb currents in the downdrift direction. Though sediment may cycle several times through the inlet, it is ultimately bypassed to the downdrift

shoreline. Bruun indicated that in most cases a combination of both of these mechanisms for natural bypassing is active but that the dominant process could be identified by examining the ratio of the tidal prism over the total littoral drift.

FitzGerald (1988) presented three conceptual models to explain inlet sediment bypassing along mixed energy coasts. These models are categorized according to the stability of the inlet throat and movement of the main ebb channel. These are: 1) inlet migration and spit breaching, 2) stable inlet processes, and 3) ebb-tidal delta breaching. In the first model, the entire inlet migrates downcoast leaving a trailing spit extending from the updrift barrier. The resulting elongation of the inlet channel becomes hydraulically inefficient for tidal flow between the ocean and the bay. Ultimately the spit is breached during a storm and the new channel which provides a shorter route for tidal exchange will normally remain open while the less efficient old inlet channel closes. In the second model, the inlet throat position and the main ebb channel do not migrate. Sand bypassing at these inlets occurs through the formation, landward migration and welding of large bar complexes to the downdrift shoreline. In the third model, the location of the inlet throat is stable, but the main ebb channel migrates. The dominant direction of longshore sediment transport causes a preferential accumulation of sand on the updrift side of the ebb-tidal delta which results in a deflection of the main ebb channel. Similar to the first model, the migration of the ebb channel ultimately results in a hydraulically inefficient channel and a new channel breaches through an updrift spillover lobe channel. Ebb-tidal delta breaching results in the bypassing of a large portion of the ebb delta sand bodies. Some of this sand fills the abandoned channel while the rest forms a large bar complex that ultimately migrates onshore and attaches to the downdrift shoreline. FitzGerald summarized by indicating that during the history of a particular inlet, all three bypassing processes may dominate at one time or another. He also states that Bruun and Gerritsen's (1959) bar-bypassing mechanism (the movement of sand around an inlet by wave action along the terminal lobe of the ebb-tidal shoal) is an active but secondary process at most mixed-energy tidal inlet systems.

For the target inlet type and behavior described previously we believe that the bypassing models of Bruun and Gerritsen (1959) are more applicable than those of FitzGerald (1988). From a long-term (10's of years) perspective the net effect of FitzGerald's bypassing models could be idealized as a sediment drift along the outer edge or crest of the ebb delta from the updrift to the downdrift island. However, for shorter time periods (up to 10 years) which are of interest to us, FitzGerald's models are not compatible with the approach we have adopted. For the development of a computational model for inlet adjacent beach evolution the mid- to long-term (1 to 10's of years), net transport patterns near the inlet are idealized as shown in Figure 1. This idealization is a substantial simplification of the real situation, but it is consistent with typically available data, the level of schematization envisioned for the computational model and our capability to estimate details of sand transport at tidal inlets.

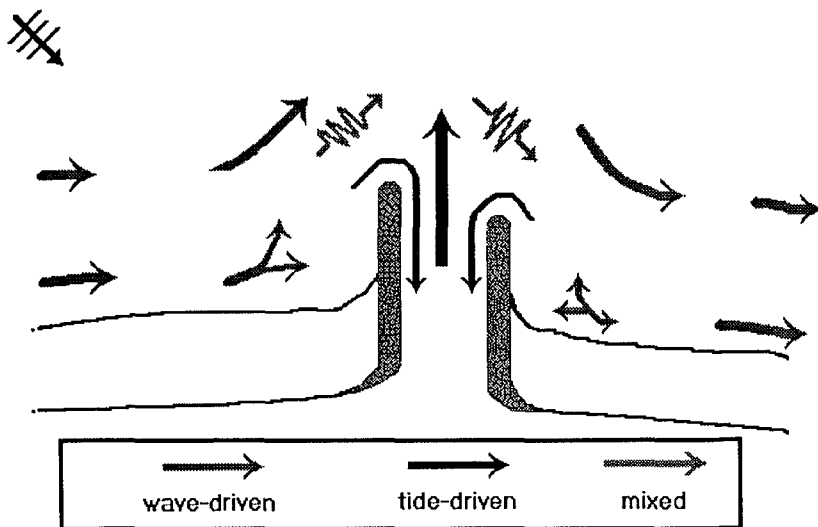


Figure 1. Conceptual model of inlet sediment bypassing.

Computational Approach

The computational approach selected for development of the inlet and adjacent beach evolution model falls into the class of models described by Kraus (1989) as multi-contour line models. This class of model was selected because the capabilities and characteristics of the model best satisfied the needs identified in a requirements analysis for inlet adjacent beach evolution modeling (Truitt and Bodge 1995). The initial development of a morphological behavior model for the outer delta of mixed-energy tidal inlets (De Vriend et al. 1994) tends to confirm that the selected computational approach has some merit and the interest of researchers. In the outer delta model, the two-line model concept of Bakker (1968) is extended to a situation where the coast is interrupted by a tidal inlet. The behavior of adjacent island coasts are modeled directly utilizing a two-line modeling approach (evolution of a beach line and a foreshore line); at the inlet, the beach line is discontinued because there is no subaerial beach profile at this location. The foreshore or inshore line, however, protrudes seaward at the location of the inlet, thereby representing the inlet delta or ebb shoal. Based on empirical relationships for the equilibrium state of the ebb shoal, the protrusion distance and geometric configuration of the ebb shoal are determined. The inlet-adjacent beach system and its evolution are described by: 1) computed wave-driven sediment fluxes along the adjacent island coasts and along the seaward edge of the ebb shoal, 2) specified net sediment fluxes through the inlet channel, and 3) the requirement for sediment continuity at six locations.

The outer delta model includes consideration of sediment fluxes through the main ebb channel as well as sediment fluxes through flood channels located near the beaches adjacent to the inlet. Sediment flux through the flood channels is fed by both the beach line and the inshore line. The equilibrium state of the delta (volume, seaward protrusion) is described using empirical relationships. A sediment balance is maintained throughout the evolution, and the sediment demand or supply by the basin is taken into account as an input parameter. The model output consists of the cross-shore positions of the beach line and the inshore line as a function of time and the longshore coordinate. It is noted, however, that the model developers (De Vriend et al. 1994) caution that the model results should be interpreted at a higher aggregation level (e.g., the trend of predicted change should be given more weight than the predicted magnitude of change). For more details on the outer delta model and its validation the reader is referred to the Master's thesis of Bilse (1993).

Empirical Analysis

Goals. To refine and expand on the initial model developed by De Vriend et al. (1994), a focused empirical analysis and parameterization of inlet geometry and processes has been undertaken. The goal of this research is to characterize the volume, geometric shape, and general location of the ebb shoal based on estimable quantities such as tidal prism, magnitude of net and gross longshore sand transport rates, and tidal range. U.S. inlets with rich temporal and spatial historical data sets are being analyzed. Specific analysis to be conducted include: 1) confirmation of the ebb shoal volume tidal prism relationship proposed by Walton and Adams (1976), 2) investigate the shoal volume to shoal protrusion relationship assumed by De Vriend et al. (1994), 3) the correlation, between the ebb shoal aspect ratio (longshore extent/cross-shore extent) and the tidal prism and/or net or gross longshore sand transport rates, 4) the relative stability of updrift and downdrift shoreline offsets, and 5) the correlation, between ebb shoal skewness (offset between ebb shoal centroid and inlet throat at jetty tips) and net and gross longshore sand transport rates.

Status. At present this analysis has included the geometric analysis of four tidal inlets along the eastern US Atlantic coast. The four inlets are: 1) Ocean City Inlet located in Ocean City, Maryland, 2) Barnegat Inlet located in central New Jersey, 3) Moriches Inlet located between Fire Island and Westhampton Beach on Long Island, New York, and 4) Shinnecock Inlet located between Tiana Beach and Southampton Beach on Long Island, New York. The analysis has not progressed to the point where new or refined empirical relationships can be proposed, but procedures for the geometric analyses of ebb tidal shoals have been developed, and their application to the four inlet systems will be discussed in the remainder of this paper. (We plan to extend this geometric analysis to a number of other inlet systems in the future at which time a database of the physical driving forces will be integrated for the development of new or updated empirical relationships.)

Methods. The bathymetry data were obtained by three methods, standard hydrographic surveys using a vessel mounted fathometer, sea-sled beach profile surveys, and airborne LIDAR (L*ight* D*etection* A*nd* R*anging*) surveys obtained using the helicopter based SHOALS (S*canning* H*ydrographic* O*perational* A*irborne* L*idar* S*urvey*) system. In all cases some combination of these survey methods were used to obtain the complete bathymetric coverage data sets. The procedure begins by developing a digital terrain model (DTM) using the original bathymetric data as input. Contours were then generated with reference to the National Geodetic Vertical Datum (NGVD). A polygon was then drawn around the ebb shoal. Typically, the offshore boundary of the polygon followed along the 10- to 11-m NGVD contour (the landward most contour that does not protrude seaward at the ebb shoal). The landward boundary followed along the 0-m NGVD contour. The lateral boundaries were selected at an alongshore location corresponding to where the contours began to protrude seaward around the shoal. A least-squares best-fit line was computed for contours at 1-m intervals outside the ebb shoal polygon. These computed best-fit contours on either side of the ebb shoal polygon were joined and then smoothed using the cubic B-spline method. The “no ebb shoal” bathymetry was estimated by digitizing the smoothed best-fit contours and then generating a DTM of the result. The next step involved taking the difference between the idealized “no ebb shoal” DTM and the original bathymetry DTM within the ebb shoal polygon. The result of this differencing operation is a DTM that we will refer to as the “residual” ebb shoal topography. This terminology describes the morphological residual of the formation of the ebb-tidal shoal; topography is used because the residual is described in terms of positive elevations and no longer represents a bathymetry. The residual ebb shoal topography was used to estimate the volume and geometric configuration of the ebb shoal. Figure 2 provides plots of the ebb shoal bathymetry, the idealized no ebb shoal bathymetry, and the residual ebb shoal topography for each of the four inlet systems examined. This procedure is similar to that used by Dean and Walton (1973) but employs modern terrain modeling software which, to some extent, reduces the subjectivity of the analysis.

Results. Figures 3-6 are contour plots of the residual ebb shoal topography with the extracted geometric characteristics indicated for Barnegat, Ocean City, Shinnecock, and Moriches inlets, respectively. Shown in the figures are the 1-, 3-, and 5-m contours of the residual ebb shoal topography with their alongshore and offshore dimensions. Also indicated is the location of the centroid of the residual ebb shoal topography with respect to the inlet throat at the tips of the inlet jetties. Without examination of the site-specific physical driving forces (e.g., tidal prism, tide range, wave energy, net and gross longshore sand transport rates etc.), we are unable at this time to draw conclusions or explain the differences in the geometric configuration of these four inlet systems.

Conclusion

This paper documents the initial phase of work that has been undertaken to develop a needed modeling capability in the vicinity of tidal inlets. The requirements

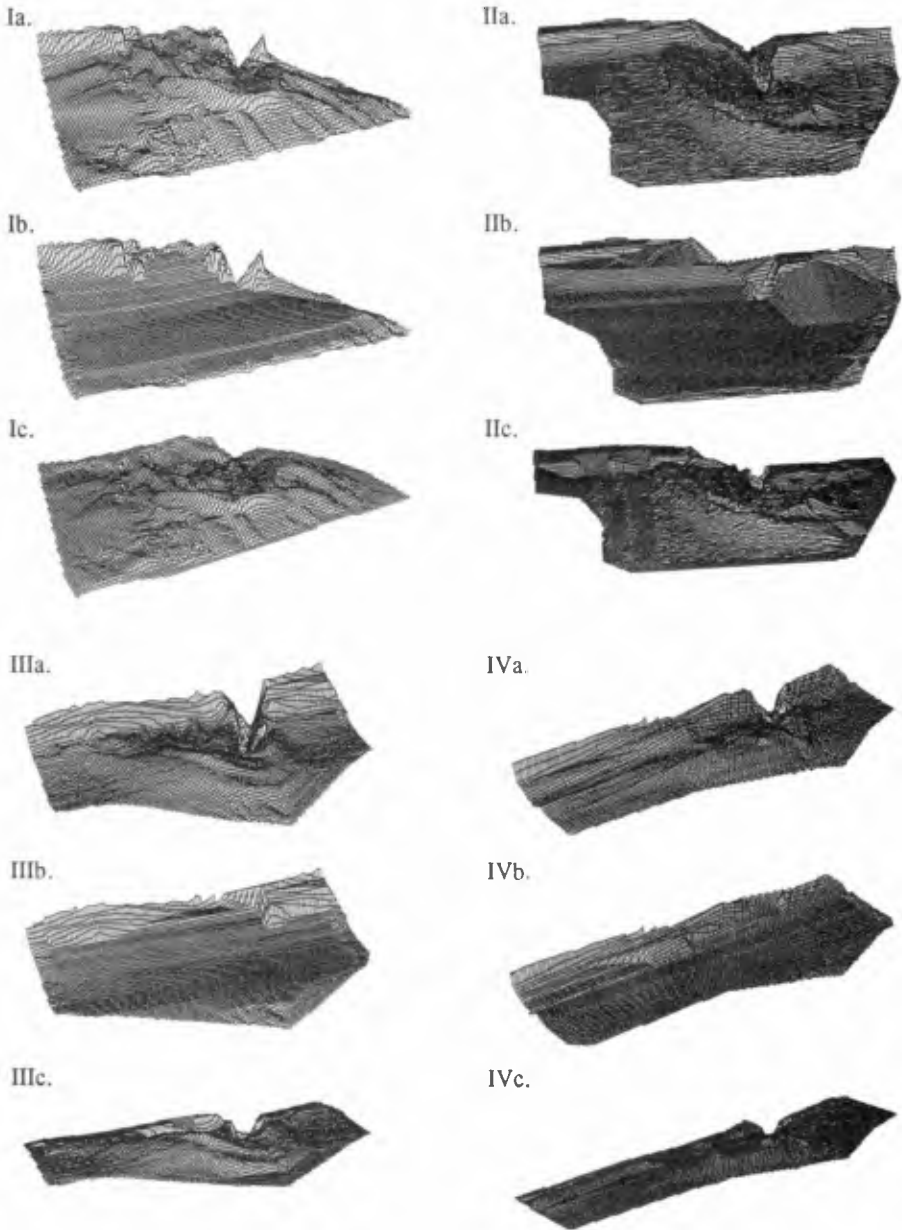


Figure 2. Plots of ebb shoal at Barnegat (I), Ocean City (II), Shinnecock (III), and Moriches (IV) inlets. (a) ebb shoal bathymetry, (b) idealized no ebb shoal bathymetry, and (c) residual ebb shoal topography.

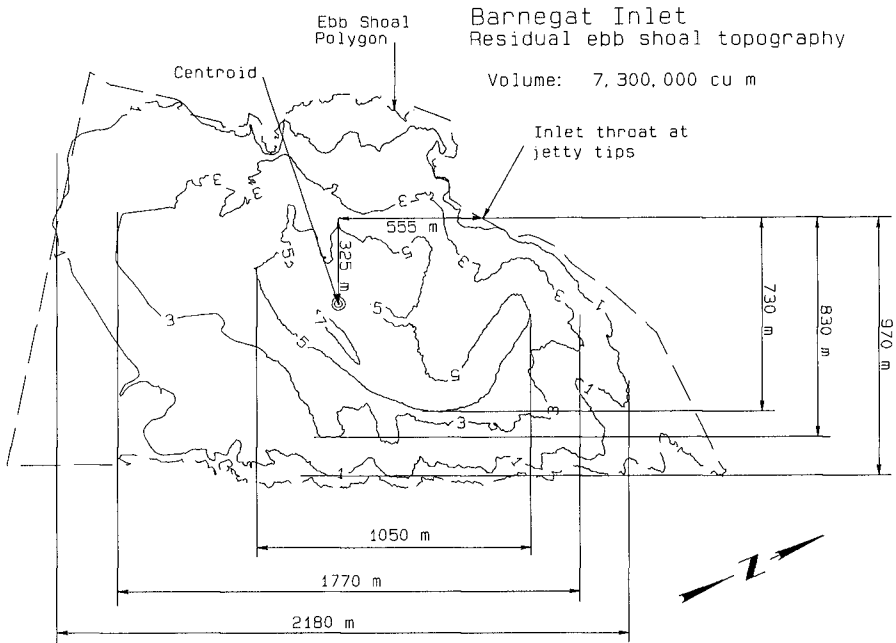


Figure 3. Barnegat Inlet residual ebb shoal topography and geometric attributes.

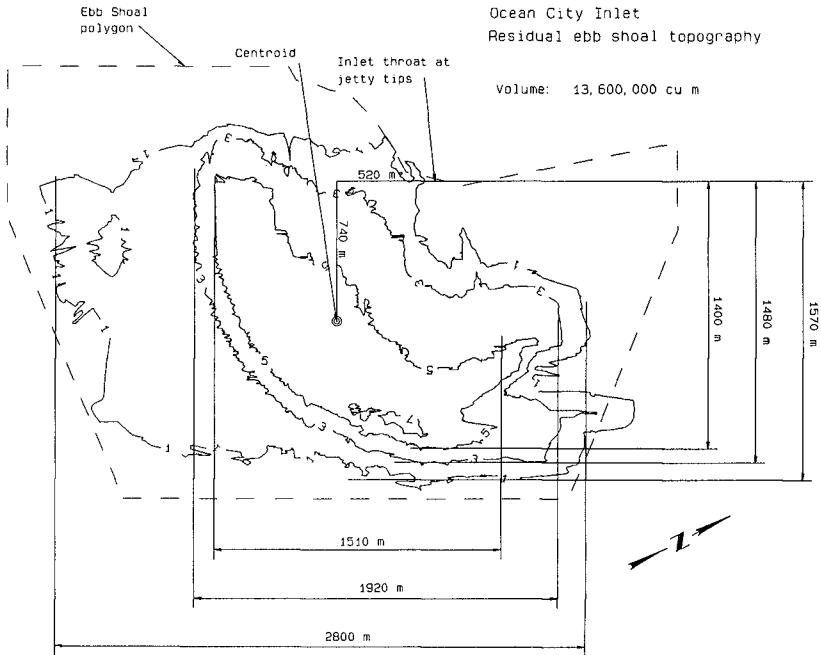


Figure 4. Ocean City Inlet residual ebb shoal topography and geometric attributes.

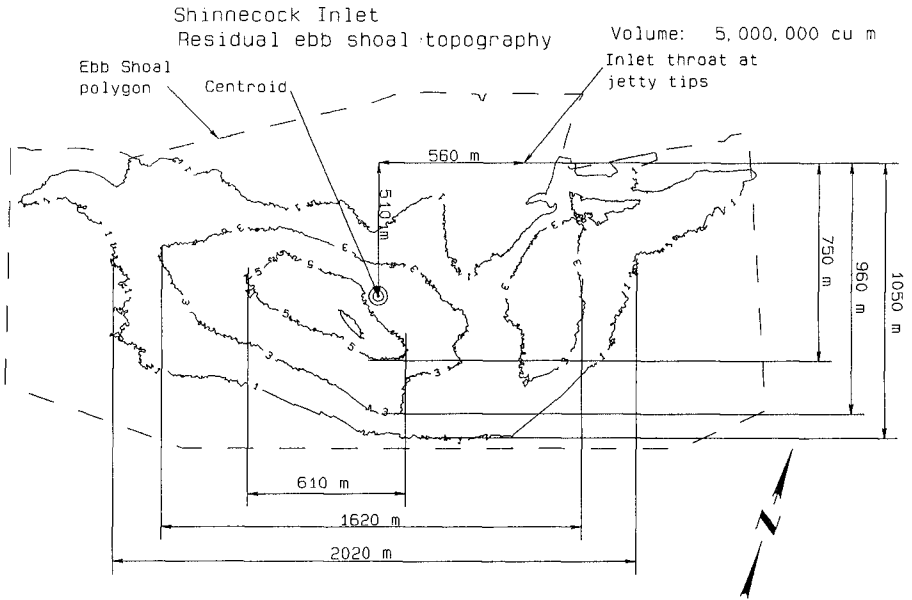


Figure 5. Shinnecock Inlet residual ebb shoal topography and geometric attributes.

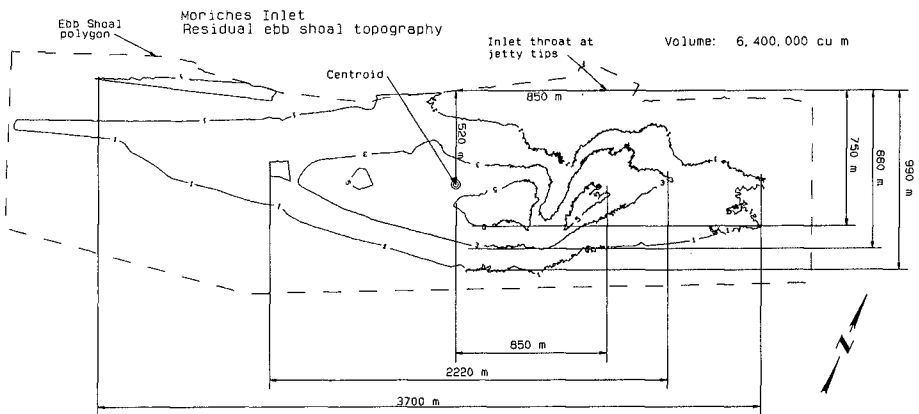


Figure 6. Moriches Inlet residual ebb shoal topography and geometric attributes.

of the numerical model from a philosophical and practical standpoint were documented. The characteristics of the inlet system for which the tool is expected to be applicable were identified. A conceptual model of inlet sediment bypassing consistent with the envisioned computational model and sediment budget methodology was presented. A recently proposed computational approach to modeling the behavior of inlet and adjacent beach systems that appears to satisfy many of the model requirements defined herein and, which we plan to extend through this research, was briefly reviewed. Procedures for characterizing the geometry of an inlet system were presented together with the application of those procedures to four inlet systems located along the central U.S. Atlantic coast.

Acknowledgments

This study was performed under the work unit *Shoreline Change Adjacent to Inlets* of the Coastal Inlets Research Program of the U.S. Army Corps of Engineers, Waterways Experiment Station. Permission was granted by the Chief of Engineers to publish this information.

References

- Bakker, W. T. 1968. "The Dynamics of a Coast with a Groyne System," *Proceedings*, 11th International Conference on Coastal Engineering, ASCE, New York, NY. pp. 492-517.
- Bilse, D. P. 1993. "A Large Scale Model of the Morphological Behaviour of the Outer Delta of Tidal Inlets," Master Thesis, The International Institute for Infrastructural, Hydraulic and Environmental Engineering, Delft, The Netherlands.
- Bruun, P. 1967. "Tidal Inlet Housekeeping," *Journal Hydraulics Division*, ASCE, Vol 93, No. HY5, pp. 167-184.
- Bruun, P. 1978. "Stability of Tidal Inlets: Theory and Engineering," *Developments in Geotechnical Engineering* 23, Elsevier Scientific Pub. Co., New York, 510 p.
- Bruun, P., and Gerritsen, F. 1959. "Natural By-passing of Sand at Coastal Inlets," *Journal Waterways and Harbors Division*, ASCE, Vol 85, WW4, pp75-107.
- Dean, R. G. 1993. "Terminal Structures at Ends of Littoral Systems", *Journal of Coastal Research*, SI 18, pp.195-210.
- Dean, R. G., and Walton, T. L. 1973. "Sediment Transport Processes in the Vicinity of Inlets with Special Reference to Sand Trapping," *Proceedings*, Second International Estuarine Research Conference, Academic Press, 129-149.
- De Vriend, H. J., Bakker, W. T., and Bilse, D. P. 1994. "A Morphological Behaviour Model for the Outer Delta of Mixed-Energy Tidal Inlets," *Coastal Engineering*, 23: 305-327.
- FitzGerald, D. M. 1988. "Shoreline Erosional-Depositional Processes Associated with Tidal Inlets," In: Aubrey, D. G. and Wisler, L, (eds.), 1988. *Hydrodynamics and Sediment Dynamics of Tidal Inlets. Lecture Notes on Coastal and Estuarine Studies*, Vol 29, Springer Verlag, New York, 454 pp.

- Kraus, N. C. 1989. "Beach Change Modeling and the Coastal Planning Process," *Proceedings*, Coastal Zone '89, ASCE, New York, NY. pp.553-567.
- Kraus, N. C., Gorman, L. T., and Pope, J. 1994. "Kings Bay Coastal and Estuarine Physical Monitoring and Evaluation Program: Coastal Studies," Technical Report CERC-94-9, Volumes I and II, US Army Engineer Waterways Experiment Station, Vicksburg, MS.
- Marino, J. N., and Mehta, A. J. 1987. "Inlet Ebb Shoals Related to Coastal Parameters," *Proceedings*, Coastal Sediments '87, ASCE, New York, NY. pp. 1608-1623.
- Truitt, C., and Bodge, K. R. 1995. "Requirements Analysis for Inlet Adjacent Beach Evolution Research," Mote Marine Laboratory Technical Rep. No. 421, Sarasota, FL.
- Walton, T. L., and Adams, W. D. 1976. "Capacity of Inlet Outer Bars to Store Sand," *Proceedings*, 15th International Conference on Coastal Engineering, ASCE, New York, NY. pp. 1919-1937.

CHAPTER 349

Hydrodynamics of a bar in a flood channel - the Westerschelde estuary

Claire Jeuken¹

Abstract

Several long-term current meter observations (30 days) over a complex flood shield, i.e. an estuarine bar, display major temporal and spatial variations in current asymmetry. The variations in current asymmetry indicate the presence of small-scale circulations of sediment that are induced by smaller channels that penetrate the bar. The current meter observations and depth-averaged current patterns obtained with an ADCP revealed processes of advective flow acceleration and deceleration, as well as flow convergence and divergence, over the bars in the small channels.

Introduction

Estuaries are important coastal systems, providing natural navigation channels as well as habitats for marine flora and fauna, and recreational space. The Westerschelde forms the seaward, marine part (length 60 km) of the Schelde estuary (total length 160 km) and has a well-developed system of channels and intertidal shoals (Fig. 1a). The meandering ebb channels form the main navigation channel for ocean shipping to the harbours of Antwerpen and Gent. The shorter, straight flood channels are only suitable for small ships as the landward channel-margin of the flood channels is marked by a shallow extensive bar. Moreover, the bars in the flood channels display a complex topography due the presence of migrating connecting channels, the smaller channels that penetrate the bar and connect the main ebb and flood channel. To maintain the shipping lane dredging is carried out at the deeper bars in the main ebb channels. At present approximately $8 \cdot 10^6$ m³ of sediment is dredged annually. A further deepening of the bars, to enable the passage of larger ships, is planned for the near future. A better understanding of the morphodynamics of channels and shoals and the processes over bars in tidal channels in particular, is important for the management of the estuarine system and for determining the optimal dredging strategies. Recent developments in understanding the morphodynamics of channels and shoals have resulted in the formulation of different types of models (De Vriend (1996), De Vriend and Ribberink (1996)). Bars in tidal channels are however still understudied (Dalrymple and Rhodes, 1995 for a review).

¹ Institute for Marine and Atmospheric Research, Utrecht University, Department of Physical Geography, PO box 80.115, 3508 TC, Utrecht, The Netherlands.
c/o Ministry of Transport and Public Works, Directorate Zeeland PO box 5014, 4330 KA Middelburg, The Netherlands.

This paper discusses the hydrodynamics of a complex bar at the end of a main flood channel, based on field observations. Flow computations with a 1D-network model indicate that this bar largely determines the distribution of tidal flow between the main ebb and flood channels during the periods of maximum flow (Jeuken, submitted). Objective of this study is to identify spatial and temporal variations of the tidal flow that are important for bar morphology and sediment transport patterns over the bar. Herein two aspects of tidal flow are considered: 1) Spatial velocity gradients and 2) differences between the velocity during ebb and flood, often referred to as current asymmetry. Spatial velocity gradients largely control processes of erosion and sedimentation. In literature tidal current asymmetry is often used as a first indicator for the direction of net sediment transport (e.g. Aubrey, 1986; Dronkers, 1986; Friederichs and Aubrey, 1988; Van de Kreeke and Robaczewska, 1993; Lessa and Masselink, 1995). In most studies current asymmetry is based on the amplitude of velocity components, often derived from a harmonic analysis of the velocity record. In this study a different approach is used to quantify variations in current asymmetry.

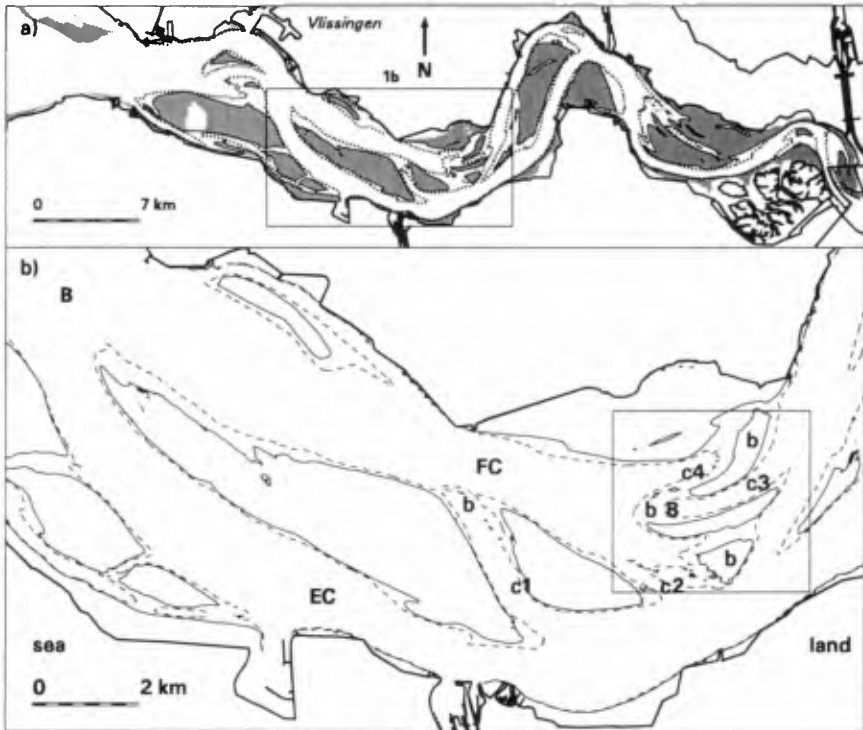


Figure 1 Location and channel configuration in the study area. a) the Westerschelde, b) the main study area. FC= main flood channel, EC=main ebb channel, c#=connecting channel (#=number), B= bar in main channel, b= bar in connecting channel.

The study area

An overview of the general hydraulic and morphologic evolution of the Schelde estuary is given by Van den Berg et.al. (in press). The main characteristics are described in this section. The Schelde is a tide-dominated meso-tidal estuary. The vertical tide displays a general asymmetry characterized by a faster rise than fall. This asymmetry increases in landward direction. In addition the vertical tide shows a pronounced neap-spring tidal variation as do the surface gradients and tidal currents. Maximum depth-averaged current velocities are in the order of 1-1.5m/s.

The larger channels in the Westerschelde display a regular returning pattern consisting of a meander-shaped ebb channel and a straight flood channel, separated by shoals (Fig. 1b). The shoals are bisected by smaller channels. These so called connecting channels form connections between the main ebb and flood channel and owe their existence to water level differences between the channels. Most connecting channels occur in the area of the bar in the main flood channel and tend to display a cyclic behaviour on the timescale of one to several decades. The shallow bar in the main flood channel is marked by various connecting channels, that originated and developed from 1986/1987. The small bars in the connecting channels are superimposed on the large bar in the main flood channel. The connecting channels C3 and C4 together reflect the morphologic characteristics of the main ebb and flood channel with respect to channel alignment and location and depth of the bars. At present (september 1996) channel C3 is rapidly degenerating. A new connecting channel has formed north of connecting channel C4.

Field observations

'Flachsee' impeller-type current meters were deployed at several locations during five measurement campaigns between April 1994 and February 1996 (Fig. 2). The current meters registered current velocity and direction for periods of thirty days with a sampling interval of ten minutes and a sampling period of one minute. At each location two current meters were deployed at the same measurement height, for validation purposes. A comparison of the double current meter deployments revealed an average difference in speed of about five percent, whereas the average difference in current direction approximated three degrees.

Detailed observations of the flow response over the small bars in two connecting channels were obtained in the summer of 1995 with a ship-borne, broad-banded two pulse Acoustic Doppler Current Profiler (ADCP). Measurements were carried out along a straight transect, oriented parallel to the general alignment of each channel, for a period of thirteen hours (Fig. 2b). The measurements along transect 1 were carried out during mean tide in June 1995. The measurements along transect 2 were obtained during spring tide in August 1995. The settings and instrumental accuracy of the ADCP during the two surveys are summarized in Table 1.

Table 1 System configuration of the ADCP during the two surveys

Transect	1	2
Acoustic frequency (kHz)	600	600
Pings per ensemble	5	20
Horizontal sampling interval (m)	10-15	40-50
Vertical bin size (m)	0.5	0.5
Depth range (m)	2.74-20	2.85-20
Velocity precision (m/s)	0.06	0.03
Compass precision (°)	1	1

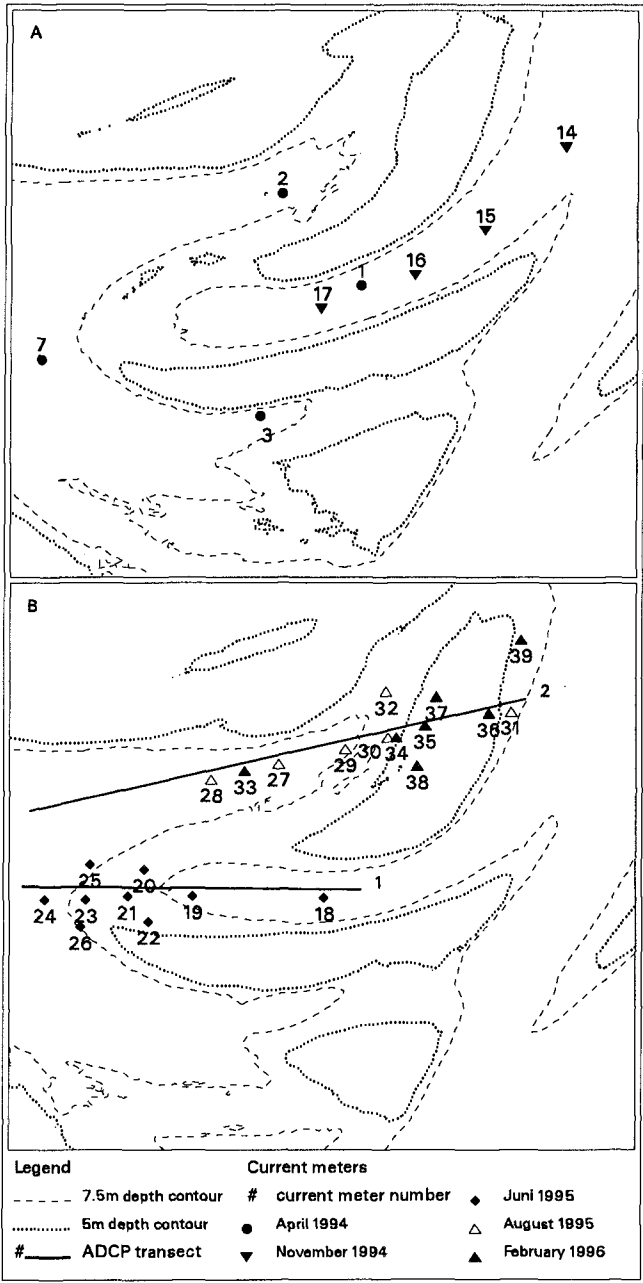


Figure 2 Locations of measurements. a) measurements in 1994 b) measurements in 1995 and 1996. For location of the bar see inset in Figure 1b.

Data-analysis

The current meter data were used to quantify temporal and spatial variations in current asymmetry and to characterize the current patterns over the small bars in the connecting channels. Prior to further analysis, the noise in the velocity data was reduced by applying a low-pass smoothing filter to the North-South and East-West velocity components.

The relative height of the current meters changed with time as a result of the large tidal range (3.3-4.75m) and the small water depths (5-13m). This variation in measurement height inhibit a comparison of measured ebb and flood velocities. Therefore measured current velocities (not direction) were converted to depth-averaged values, by assuming the logarithmic velocity profile of steady and uniform flow and an averaged roughness length based on bedform dimensions ($z_0=0.033k_s$, $k_s=0.4m$). In areas of major advective flow acceleration and deceleration this results in under-estimated (flow deceleration) and over-estimated (accelerating flow) depth-averaged velocities. These effects were not taken into account. The obtained time-series of the depth-averaged velocity vectors were then used to compute significant current vectors for each ebb and flood period. The significant velocity is defined as the mean of the 1/3 highest current velocities and represents the conditions near maximum flow over a period of about two hours. For each current meter location relationships between significant velocity (ebb and flood) and observed tidal range were determined by applying a linear regression analysis. The linear relationships were then used to compute significant ebb and flood velocities during mean, neap and spring tide. This was done by substituting the tidal range for neap, mean and spring tide in the linear relationships. Current asymmetry was then defined as the natural logarithm of the ratio of significant ebb velocity over significant flood velocity. A positive current asymmetry indicates ebb-dominated flow. A negative asymmetry indicates flood-dominated flow. The advantage of the significant velocity is, that it gives a better weighting of the tidal variation of current velocities than the often used maximum velocity.

The ADCP observations were used to determine variations in the depth-averaged flow patterns over the small bars in the connecting channels. Prior to further analysis the noise in the ADCP data was reduced by applying a low-pass, infinite impulse response filter to the North-South and East-West velocity components (Stanley et.al. 1984).

The computation of depth-averaged velocities implies extrapolation of the velocity profiles towards bottom and water surface. Extrapolation of the velocity profile was done by fitting a series of three shapefunctions through the data using a least squares method. This method has been derived from the shapefunction approach described by Zitman (1992) and has been previously applied by Van de Meene (1994). As winds were low during the ADCP measurements, the contribution of wind stress to the current velocity was neglected. Then the vertical velocity profile in North-South and East-West direction can be expressed as (Zitman, 1992):

$$u(\zeta) = \sum_{k=1}^m F_k \cdot f_k(\zeta) \quad (1)$$

where f_k is the series of shapefunctions, ζ is the dimensionless vertical coordinate and m is the number of shapefunctions ($m=3$ in the present analysis). The weights F_k are the unknowns to be determined using the measured velocity profile $u(\zeta)$. Figure 3 shows the applied shapefunctions together with an example of a curve fitted through observations. The shapefunction approach was used only as a statistical, curve-fitting tool, essentially to compute the depth-averaged current vectors in an objective way. The advantage of this approach is that it is possible to

describe velocity profiles that deviate from e.g. a parabolic profile.

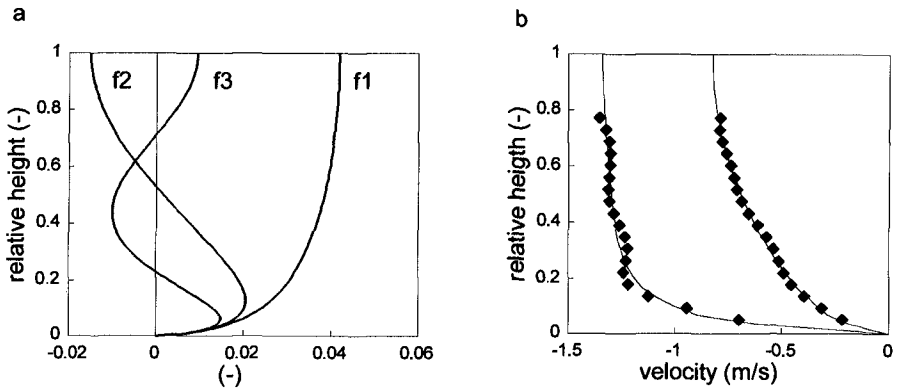


Figure 3 Shapefunction approach. a) the three shapefunctions used in the analysis, b) comparison of measured velocity components (\blacklozenge) and fit (-).

Variations of current asymmetry over the bar in the main flood channel

Figure 4 shows spatial patterns of current asymmetry over the bar in the main flood channel for mean, neap and spring tide. The spatial variation of current asymmetry in Figure 4a is related to the presence and morphology of the connecting channels. In the connecting ebb channel and at the landward side of the bar in the connecting flood channel current asymmetry ranges between 0 and 0.11, indicating that ebb velocities exceed flood velocities by about 0 to 12 percent. In the connecting flood channels and at the seaward side of the bar in the connecting ebb channel, negative current asymmetries of -0.12 to -0.31 occur, indicating flood-dominated flow. In these areas flood velocities are 12 to 40 percent stronger than the ebb velocities. The bars in the connecting channels form the transition zones between ebb-dominated and flood-dominated flow. Current asymmetry changes with tidal range (Fig.4b). In the connecting ebb channel and at the landward side of the bar in the connecting flood channel, current asymmetry decreases with 6 to 25 percent when tidal range increases from 3.3 to 4.75m. At some locations in the connecting ebb channel tidal flow becomes even slightly flood-dominated during spring tide (locations 15, 20, 21 and 22 in Fig. 2). In the connecting flood channels and at the seaward side of the bar in the connecting ebb channel current asymmetry increases with 10 to 34 percent with increasing tidal range.

The spatial variation in current asymmetry indicates small-scale circulations of net sediment transport over the bar in the main flood channel, that are induced by connecting ebb and flood channels (Fig. 5a). This means net ebb transports in the ebb channel and net flood transports in the flood channel. The circulations confirm the concept of mutually evasive ebb and flood channels of Van Veen (1950), who identified the presence of ebb-dominated and flood-dominated channels on the basis of net water transports and the location of the bars in tidal channels. The changes in current asymmetry with tidal range, has two important implications for the small-scale circulations (Fig. 5b): 1) The intensity of the circulation is not constant in time and 2) the circulation is not closed. The changes in current asymmetry over the neap-spring tidal cycle indicate that the magnitude of net sediment transport, the intensity,

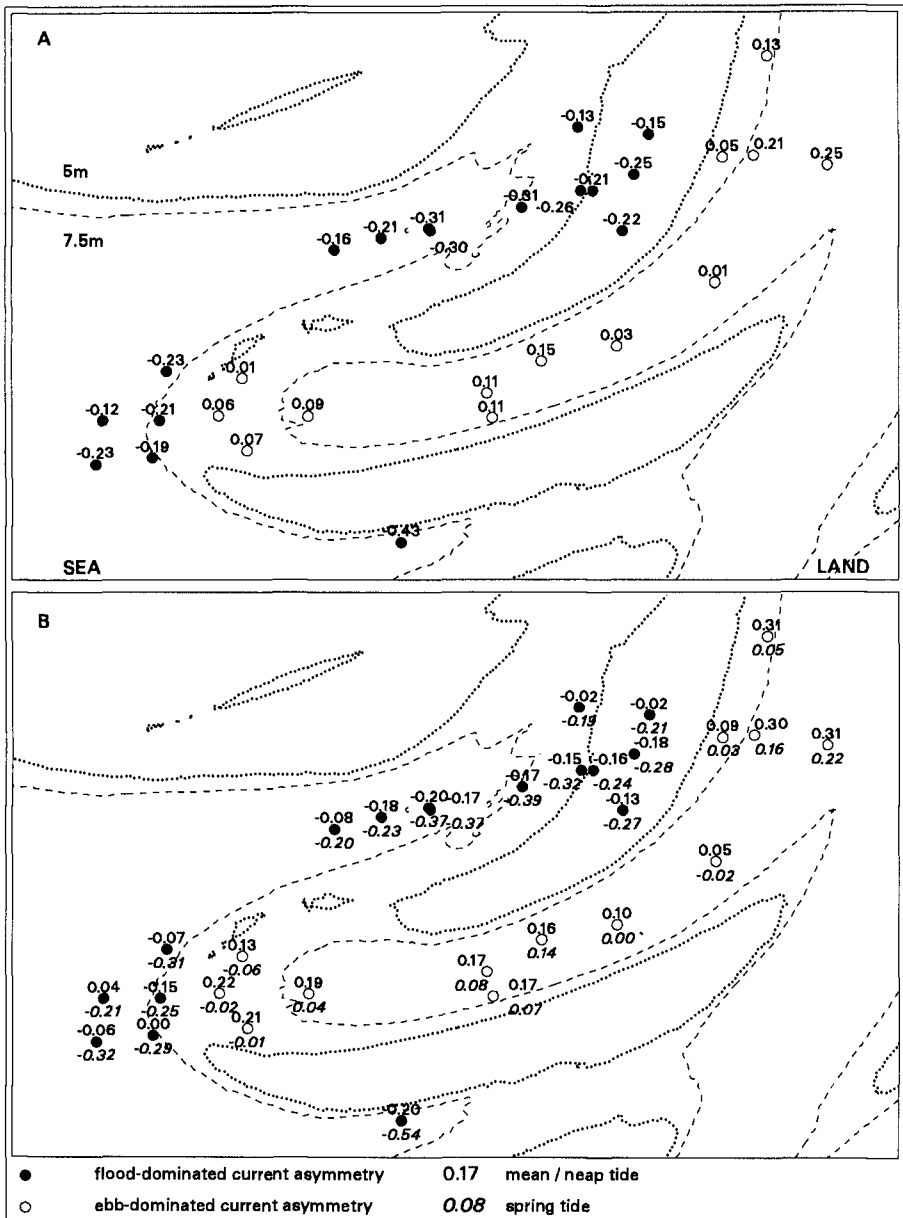


Figure 4 Patterns of current asymmetry. a) mean tide, b) neap and spring tide

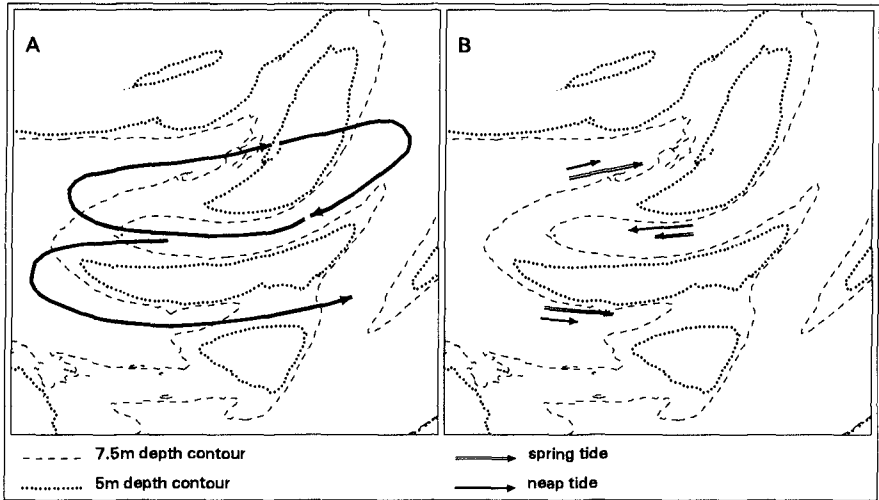


Fig. 5 Implications of the variations in current asymmetry for the patterns of net sediment transport. a) Small-scale circulations, b) the relative magnitude of net sediment transports during neap and spring tide

changes with tidal range. The decrease in current asymmetry in the ebb channel with increasing tidal range indicates larger net ebb transports in the ebb channel during neap tide than during spring tide. The increase of current asymmetry in the flood channel indicates smaller net flood transports during neap tide than during spring tide. This difference between ebb and flood channel means that the circulation is not closed. A net flood-dominated component that increases with tidal range is likely as the flood-dominated current asymmetry is larger than the ebb-dominated current asymmetry. Moreover the morphology of the bar is dominated by connecting flood channels. Computed sediment transports (not shown), based on the current observations, confirm the above inferred spatial and temporal variations in net sediment transport.

Flow response over the bars in two connecting channels

Figure 6 and 7 summarize the flow characteristics over the bar in the connecting ebb channel during mean tidal conditions. Figure 6 shows the pattern of significant current vectors in June 1995. Figure 7 displays the pattern of depth-averaged along-transect and cross-transect velocities during accelerating, maximum and decelerating tidal flow. During ebb the pattern of significant current vectors displays an ebb flow flowing around the bar (Fig. 6a). At the upstream side of the bar the ebb flow diverges and shows minor flow decelerations towards the bar of about 7 percent (0.08m/s). Significant current directions at location 20 and 22 differ by twenty degrees (see Fig. 2b for locations). At the downstream side of the bar the ebb flow converges and strongly decelerates with about 25 percent (0.25m/s). The ADCP observations confirm the patterns of flow deceleration (Fig. 7). The depth-averaged velocity pattern shows an instantaneous drop in current velocity as soon as the ebb flow passes the top of the bar. The depth-averaged velocity reduces with 28 percent (0.3m/s) on average. The flow reduction tends to increase with time and decreasing

water level. In addition the ADCP observations show a tendency towards small flow acceleration just before the top of the bar during maximum and decelerating ebb flow. The small cross-channel velocity component, both during ebb and flood, indicates tidal flow approximately parallel to the ADCP-transect (with 5°). Thus the ebb flow diverges and decelerates towards the bar, slightly accelerates near the top of the bar and converges and strongly decelerates after passing the top of the bar.

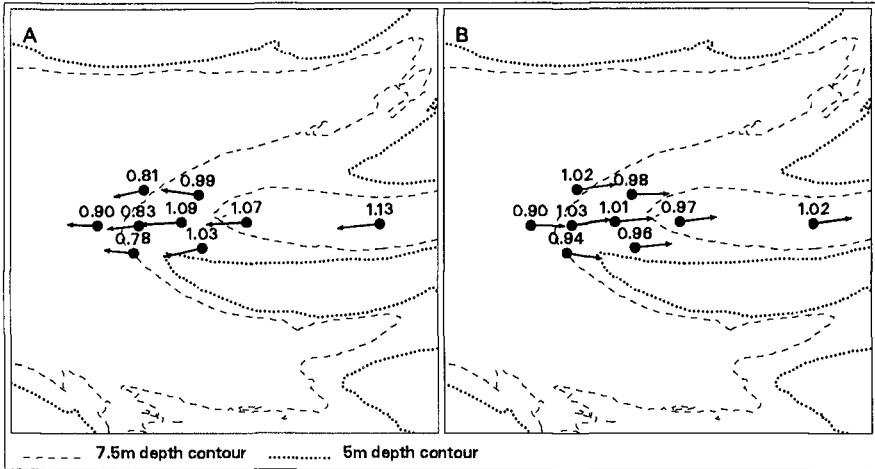


Fig. 6 Mean significant current vectors over the bar in the connecting ebb channel during mean tide in June 1995. a) ebb, b) flood.

The flood displays a small tendency towards flow around the bar (Fig. 6b). The pattern of significant current vectors shows flow divergence at the upstream (seaward) side of the bar that is accompanied by an increase in current velocities of about 14 percent (0.13m/s). At the downstream side of the bar the current vectors are aligned more or less parallel and only minor velocity gradients are observed. The ADCP observations also display flow acceleration at the upstream side of the bar (Fig.7). Depth-averaged velocities increase with about 10 percent (0.1m/s). At the downstream side, between 500 and 1200 meters, reductions in current velocity of about 10 percent (0.1m/s) are observed. Thus the flood flow slightly diverges and accelerates over the bar.

The characteristics of the flow pattern over the bar in the connecting flood channel during spring tide, measured in August 1995 and February 1996, are summarized in Figures 8 and 9. During ebb the significant current pattern displays flow deceleration over the bar (Fig 8a). At the downstream side of the bar current velocities are 15 to 30 percent smaller than near the top of the bar (location 36, Fig. 2b). The gradual change in current direction between locations 37 and 38 of fourteen degrees, indicates a tendency towards flow convergence. The ADCP observations (Fig.9) reveal deflection of the ebb flow at the upstream side of the bar, where the current vectors are inclined towards the ADCP-transect by 15-25 degrees (not shown). Despite this current deflection a major velocity gradient over the bar can be identified. On average current velocities at the top of the bar exceed currents at the upstream and downstream side of the bar by 30 percent (0.4-0.5m/s). These large velocity differences indicate flow acceleration at the upstream side of the bar and

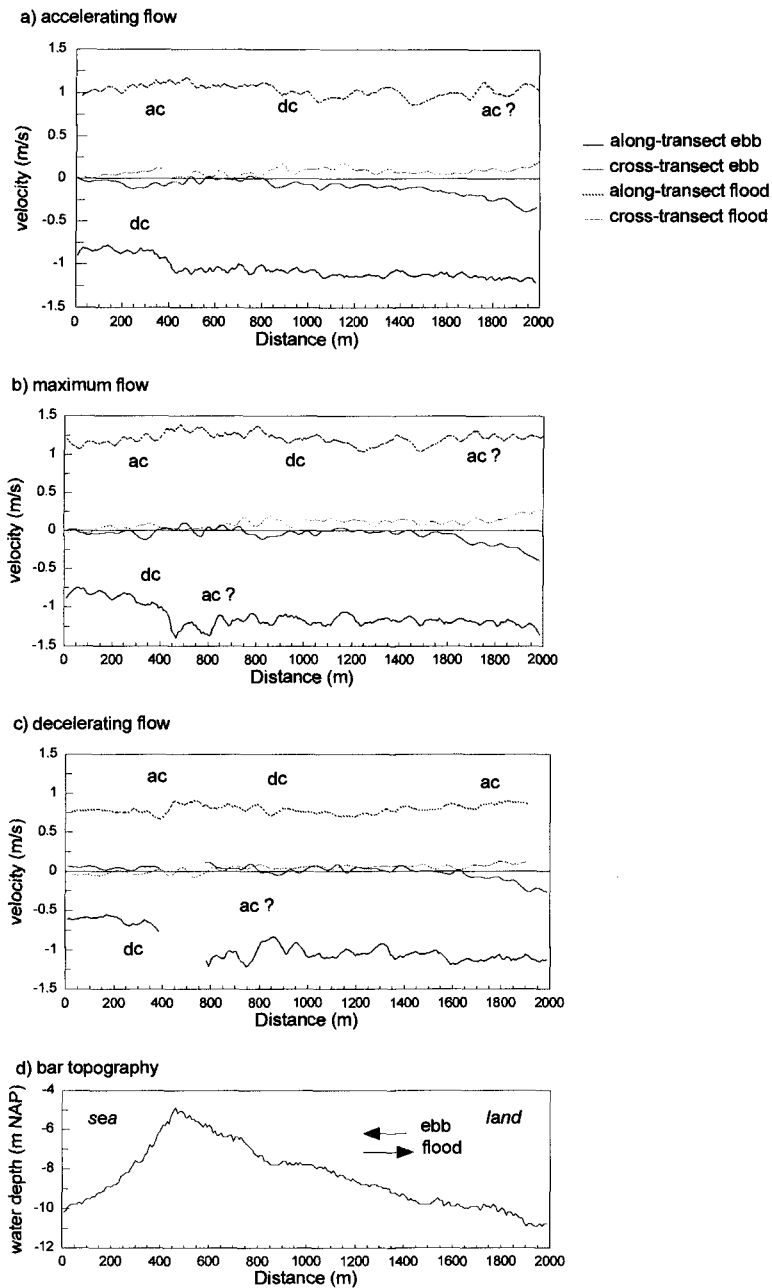


Figure 7 Depth-averaged along-transect and cross-transect velocity over the bar in the connecting ebb channel during ebb and flood on 29 June 1995. Ebb is negative, flood is positive, ac=acceleration, dc=deceleration.

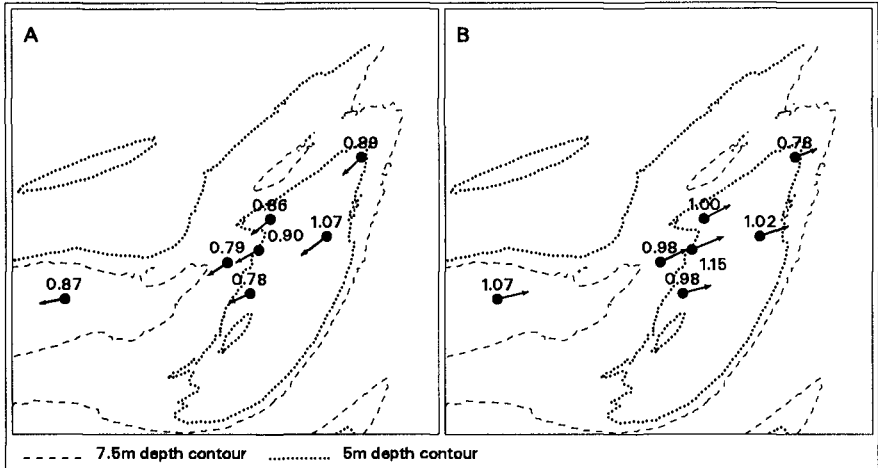


Figure 8 Mean significant current vectors over the bar in the connecting flood channel during spring tide in February 1996. a) ebb, b) flood.

flow deceleration at the downstream side of the bar. Thus the ebb flow accelerates towards the top of the bar and decelerates and converges at the downstream side of the bar. During flood the significant current vectors show a flow acceleration of about 17 percent (0.17m/s) at the upstream side of the bar (Fig. 8b). Significant current directions gradually change with twelve degrees between locations 37 and 38 (see Fig. 2b for locations), indicating minor flow divergence. The current velocity at the upstream side of the bar is 12 to 22 percent ($0.13\text{-}0.22\text{m/s}$) stronger than at the downstream side of the bar. This means that the flood flow decelerates over the bar. The ADCP observations show a flow deceleration of about 20 percent just before the bar (between 1700 and 2200m , Fig.9), where the flood flow diverges (not shown). At the upstream side of the bar the flood flow accelerates with about 30 percent ($0.3\text{-}0.4\text{m/s}$). At the downstream side flow decelerations of 40 to 50 percent ($0.5\text{-}0.7\text{m/s}$) are observed. The cross-transect velocity components indicate that the flood flow is less deflected by the topography of the bar than the ebb flow (inclination of $6\text{-}12^\circ$ with respect to the ADCP-transect, not shown). Thus the flood flow diverges and decelerates towards the bar, accelerates near the top of the bar and strongly decelerates after passing the top of the bar.

The ADCP observations are marked by second-order fluctuations. The amplitude and length scale of these fluctuations increase with time and decreasing water level. The unfiltered velocity data display similar fluctuations. The cause of the fluctuations is not clear. Both turbulence and depth variations may cause such fluctuations.

The pronounced topography of the small bars in the connecting channels is reflected in the hydrodynamics: 1) The bars in these channels demarcate the transition zones between ebb-dominated and flood-dominated flow, 2) Neap-spring tidal variations in current asymmetry change over the bar and 3) The ebb and flood flow tend to flow around the bars of the channels and display non-uniform velocity patterns. In the connecting ebb channel largest velocity gradients are observed during ebb. In the connecting flood channel largest velocities and velocity gradients tend to occur during flood. Fluid continuity across the bar may explain the observed flow

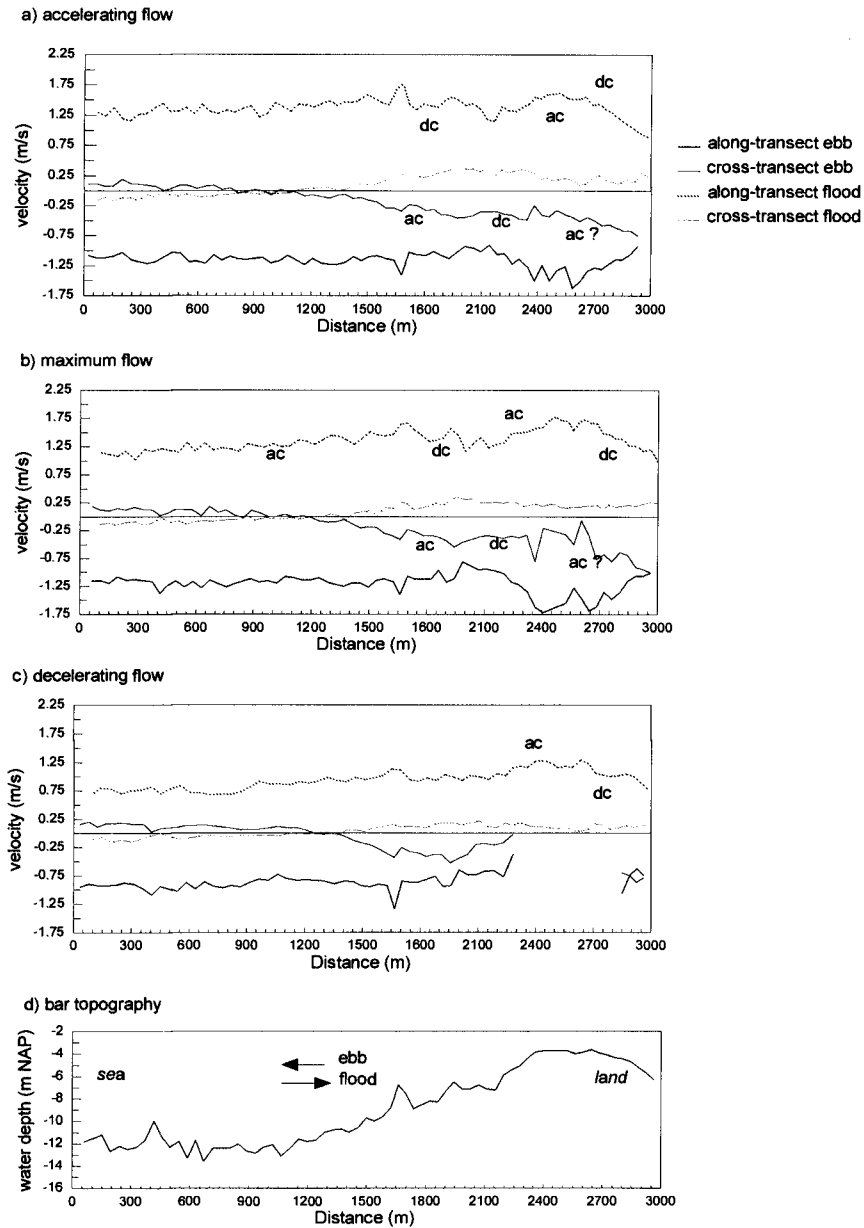


Figure 9 Depth-averaged along-transect and cross-transect velocity over the bar in the connecting flood channel during ebb and flood on 30 August 1995. Ebb is negative, flood is positive, ac=acceleration, dc=deceleration.

around the bars. Fluid continuity implies that the discharge Q (m^3/s) does not change much across the bar. The overall discharge Q is defined as $Q=b\cdot\bar{u}\cdot h$, where b is the width of the imaginary stream tube (m), \bar{u} is the depth-averaged current velocity and h is the water depth. The changes in channel depth over the bar may result in changes in the width of the stream tube and the depth-averaged velocity. At the upstream side of the bars the flow diverges. The width of the stream tube increases. At the downstream side the flow converges. The width of the stream tube decreases. In addition to these changes in width the depth-averaged velocity increases and decreases across the bars, whereas the water depth increases and decreases. The flow over the bars shows a tendency towards flow deceleration and accelerations at the upstream side of the bar and deceleration at the downstream side. The pattern reverses every tidal phase. The implications of these flow phenomena for sediment transports, the patterns of erosion and sedimentation and the net effect over e.g. one semi-diurnal period are not evident. The implications depend on the magnitude and duration of flow accelerations and decelerations, as well as the effect of variations in stream tube width and water depth, differences in current asymmetry and the dominant sediment transport mode. The small bars are stable morphological features despite the observed flow accelerations and decelerations. This indicates that relaxation of the suspended transport may be important for the maintenance of the estuarine bars.

Conclusions

Variations of the tidal flow over the bar in the main flood channel are strongly determined by connecting channels:

- 1) Spatial variations in current asymmetry indicate the presence of small-scale net circulations of tidal flow and sediment transports over the bar, that are induced by connecting ebb and flood channels.
- 2) The changes in current asymmetry with tidal range indicate that the intensity of the circulations is not constant and that the circulations are not closed.

The flow over the small bars in the connecting channels is non-uniform and displays tendencies towards divergence, decelerations and accelerations of the flow at the upstream side of the bar and convergence and deceleration of the flow at the downstream side of the bar. The implications of the flow patterns for sediment transports and the maintenance of the bars are not evident and will be further elaborated on the basis of computations with a mathematical model and morphological analysis.

Acknowledgements

This study was funded by Directorate Zealand of the Ministry of Transport Public Works and Water Management. The measurements were carried out by the survey department of Directorate Zealand. Ir A. Langerak, drs A. Van Kleef and dr J.R. Van de Berg are greatly acknowledged for their useful comments.

Appendix

Aubrey, D.G. (1986). Hydrodynamic Controls on Sediment Transport in Well-mixed Bays and Estuaries. In: J. Van de Kreeke (ed.). Physics of shallow estuaries and Bays, p. 245-258.

Dalrymple, R.W. and R.N. Rhodes (1995). In: G.M.E. Perillo (ed.), Estuarine dunes and bars. *Geomorphology and Sedimentology of Estuaries. Developments in Sedimentology* 53, p. 359-422.

De Vriend, H.J. (1996). Mathematical Modelling of meso-tidal barrier island coasts. Part 1: empirical and semi-empirical models. In: P.L.F. Liu (ed.), *Advances in coastal and ocean engineering* (2), p.115-149.

De Vriend, J. and J.S. Ribberink (1996) Mathematical Modelling of meso-tidal barrier island coasts. Part II: process-based simulation models. In: P.L.F. Liu (ed.), *Advances in coastal and ocean engineering* (2), p.151-197

Dronkers, J. (1986). Tidal asymmetry and estuarine morphology. *Neth. Jour. of Sea Res.* 20 (2/3), p. 117-131.

Friederichs C.T. and D. Aubrey (1988). Non-linear Tidal Distortion in Shallow Well-mixed Estuaries: a Synthesis. *Est. Coast. and Shelf Sci.*(27), p. 521-545.

Jeuken, M.C.J.L. (submitted for review). Morphodynamics of connecting channels in the Westerschelde estuary (the Netherlands). *Proc. Conf. Physics of Estuaries and Coastal Seas, The Hague, 1996.*

Lessa, G. and G. Masselink (1995). Morphodynamic evolution of a macro-tidal barrier island. *Marine Geology* 129: 25-46.

Stanley, D.W., G.R. Dougherty and R. Dougherty (1984). *Digital Signal Processing*, Prentice Hall, 514 p.

Van de Kreeke, J. and K. Robaczewska (1993). Tide-induced residual transport on coarse sediment: application to the Ems estuary. *Neth. Jour. of Sea Res.* 31 (3), p.209-220.

Van de Meene, J.W.H. (1994). The shoreface-connected ridges along the central Dutch coast, Ph.D. thesis, IMAU, Utrecht Univ., *Neth. Geogr. Studies* 174, KNAG, Utrecht, 256 p.

Van den Berg, J.H., M.C.J.L. Jeuken and A. F. van der Spek (in press). Hydraulic processes affecting the morphology and evolution of the Westerschelde estuary. In: K.F. Nordstrom and C.J. Roman (eds.). *Estuarine Shores: Evolution, Environments and Human Alterations.*

Van Veen, J. (1950). Eb- en vloedcharen in de Nederlandse getijwateren. *Tijdschr. Kon. Ned. Aardr. Gen.* 67, p. 303-335 (in Dutch).

Zitman, T.J. (1992). Quasi three dimensional current modelling based on a modified version of Davies' shapefunction approach. *Cont. Shelf Res.*, 12(1), p. 143-158.

CHAPTER 350

Interactions between a Sand Barrier and Flood Terrace at the Abukuma River Mouth

Akira Mano ¹and Masaki Sawamoto ¹

Abstract

The sand barrier at the Abukuma River mouth flushed by floods in autumn firmly recovered within a half year by stretching its tip to the cross river direction. However, the direction suddenly changed upstream since 1993. This paper analysis the mechanism of the change.

The river has a large terrace formed by the flood in 1986, the maximum in the observed floods over fifty years. Bathymetric data sounded once a year reveal gradual development of a channel on the terrace off the river axis. From wave ray analyses, it is shown the development accompanies change of the refraction characteristics of waves. The channel becomes to function as a half mirror; reflecting waves incoming from one direction and transmitting from the other direction. This is shown to modify direction of dominant waves near the barrier and to turn the stretch direction of the barrier.

The channel evolution is also shown to correlate with the flood outflow.

1 Introduction

Development of sand barriers at river mouths has close influences on the river management such as flood passage and voyage. The barriers also control water salinity inside the river, which relates with water resources and ecological environments. Although the barrier has important roles in the various aspects near the mouth, the mechanism of the development or deformation is not well known.

The difficulties to find the mechanism may mainly come from complexity of the dual external forces of river flows and waves. The complicated topographies inherent to the mouth like flood terraces and sand barriers also tangle the affair, because they cause flow fields and wave fields to considerably deform. Furthermore broadness of the time scale band on the topography change, which would

¹Department of Civil Engineering, Tohoku University, Sendai 980-77, Japan

relate with the characteristics of the external forces, requires vast set of observed data in the analyses.

Over twelve years, we have been surveying the sand barrier at the Abukuma River mouth in Japan. The details of the observations on the Abukuma River and the characteristics of the barrier deformation in various time scales have been reported (Mano et al. 1995). This river has a catchment of 5,400 km² and a main channel of 239 km. The maximum flood over fifty years of observation by Ministry of Construction occurred on August 1986 with the peak discharge of $Q=7,900\text{m}^3/\text{s}$ near the mouth. This flood flushed out the sand barrier so far and made a large flood terrace off the mouth.

After the flush by the flood, the barrier started to recover. The tip of the barrier advanced in the cross river direction. Then within a half year, it reached equilibrium such that the minimum opening width at the mouth is maintained by the usual river flows and tides. This elongation is the earliest process in the recovery then thickening barrier followed until the next year's flush caused mainly by typhoons in autumn. After the 1986 event, this cycle of flush and recover had continue for seven years always accompanying transverse elongation of the barrier.

However in 1993, the barrier changed its development from cross-river direction to upstream direction. The typical shapes are shown in Fig.1 (a) and (b).



(a) March, 1991.



(b) April 1994.

Fig. 1: Aerial photographs for the typical sand barrier shapes.

After a lapse of more than a half year, both photographs show the fully developed barriers in length. However the shapes are quite different. Figure 1 (a) shows the barrier stretching transversely from the right side bank and very narrow opening width, about 70 m. However Fig.1 (b) exhibits the barrier stretching upstream and the widely opened mouth. Waves are intruding inside the river and two typical arced beaches are formed in the river.

The barrier as Fig.1 (b) has less resistance for the flood passage and provides safer routes for the voyage. Therefore it looks like as if the nature is helping river management since then. The purpose of this paper is to find the mechanism that the sand barrier that had firmly stretched in the cross river direction for seven years changed the direction.

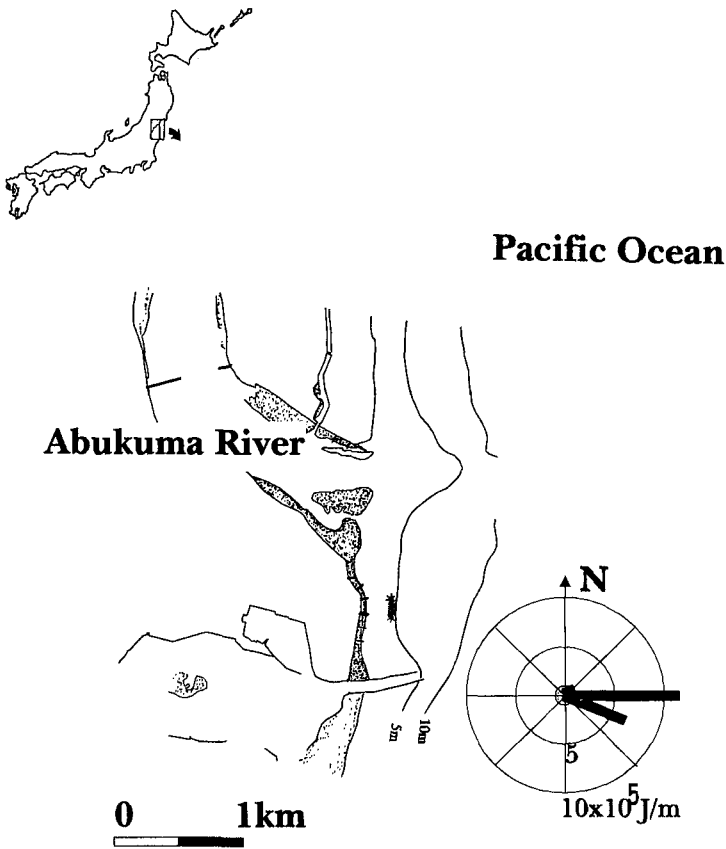


Fig. 2: Topography near the Abukuma River mouth.

2 Topography near the mouth

The Abukuma River flows into the Pacific Ocean, crossing the coast line that has the azimuth, N5°E as shown in Fig.2. No jetties are constructed about the mouth. Waves are observed by the Ministry of Transport off the Sendai Harbor that locates about 25 km north of the mouth. Annual deep water wave energies that are the integration of the energy flux in a year and the averaged values in the period, 1984 to 1992 are also plotted in this figure. The most dominant waves are those of E and have the energy of 11×10^5 J/m that is about 60 % of the total energy. The next dominant waves are those of ESE sharing 35 %. Depending on the directional distribution of the wave energy, the longshore drift around the coast orients north.

The bathymetric charts near the mouth are shown in Fig. 3 (a), (b), (c), and (d) for various stages. Before the 1986 flood, there existed a small terrace in front of the sand barrier and a small channel off the opening, while the barrier was thick. These characteristics correspond to the history of flood activity. Fig. 3 (b), sounded one month after the 1986 flood, showed formation of a large terrace. The top surface of the terrace was very flat with the depth, 4 m. The foot of the terrace reached as deep as 13 m. The mouth was still widely opened.

In 1988, although outline of the terrace was preserved, several deformations were advancing. The shoulder part of the terrace was rounded and the front part of the barrier became shallower. The most remarkable change is the development of a channel on the terrace in the offshore direction from the opening. The opening was usually fixed next to the left side bank by the transverse stretch of the barrier. On the other hand, the terrace was formed along the center line of the river since it was formed by the huge flood that flushed the barrier thoroughly. The position of the channel, therefore, shifted northward from the center of the terrace. In 1993, the channel on the terrace extended offshore.

3 Refraction analysis

To know the influences of the topographic deformations, we have executed wave refraction analysis. Among several numerical methods dealing with the refraction, the wave ray method is especially superior in grasping physical images moreover has the advantage in computational feasibility. Thus we employed the wave ray equation (Mei, 1983) and the refraction coefficient equation (Munk et al., 1952) as follows;

$$\frac{dy}{dx} = \pm \frac{K}{\sqrt{k^2 - K^2}} \quad (1)$$

$$\frac{d^2\beta}{ds^2} + p \frac{d\beta}{ds} + q\beta = 0 \quad (2)$$

$$K = k_o \sin \alpha_o, p = p(c, \alpha), q = q(c, \alpha), K_r = 1/\sqrt{\beta}. \quad (3)$$

Where, x is the local coordinate taken to the steepest gradient of the bottom, y is perpendicular to x , s is the coordinate taken along a wave ray, α is direction

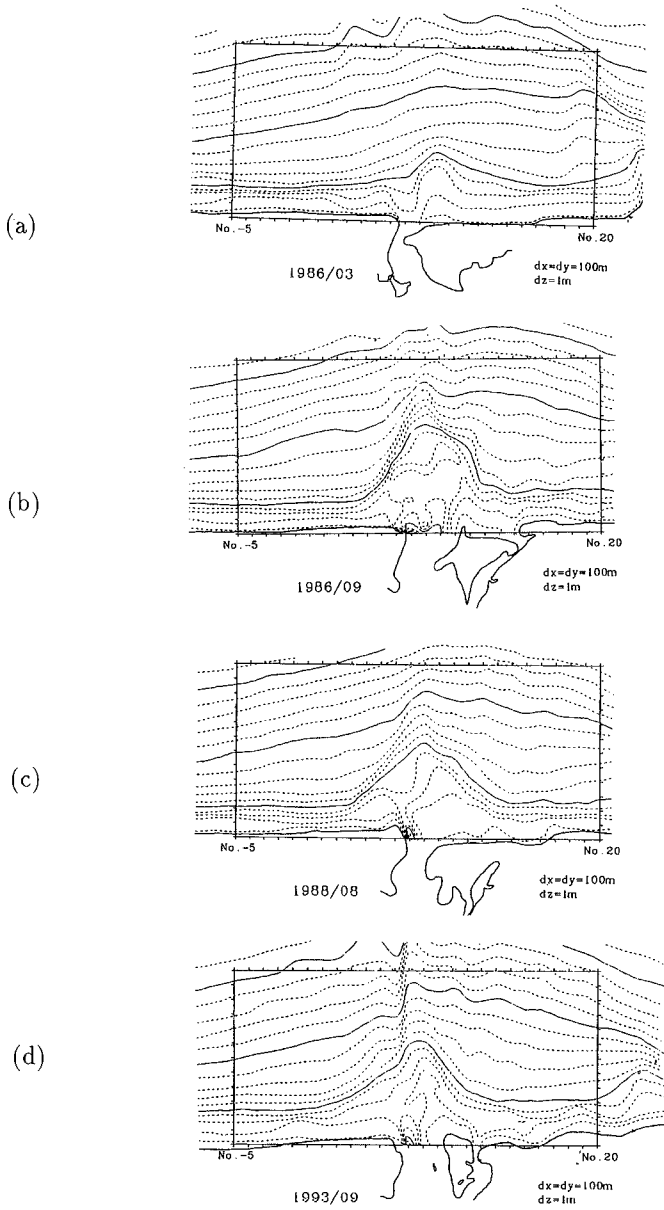


Fig. 3: Bathymetric charts at various stages.(a): March, 1986,(b): September 1986,(c): August 1988,(d): September 1993.

of wave ray, k is the wave number, c is the phase velocity, K_r is the refraction coefficient, and subscript o denotes the boundary value. These equations are solved together with the dispersion relation and boundary conditions by the finite difference method. The employment of the local coordinate x has such an advantage that it is required to solve only once the dispersion relation for each space step marching.

After digitizing the contour lines of the bathymetric charts, we made bathymetric mesh data and expressed the topography by the sets of plane triangle elements. The wave rays started from the offshore boundary were advanced step by step through the integration of the equations with the local coordinate system.

For the topographies mentioned in Figs. 3 and the corresponding annual mean waves, wave rays were computed as shown in Figs. 4 (a), (b), (c), and (d). The incident wave height and period are 0.77 to 0.88 m and 7.4 to 8.4 s respectively. The breaking point for each wave ray was evaluated by using the breaking index (Goda, 1970) and plotted by the filled circle near the shoreline.

In Fig. 4 (a) indicating wave refraction before the 1986 flood, the wave rays approaches uniformly in the longshore direction except very near the river mouth. The small terrace in front of the barrier gathers the wave rays and focuses at the barrier. While for the topography just after the flood, the large terrace gathers more wave rays and focuses about the middle of the terrace. Most of the wave rays passed the focus reach the north coast of the river. Local focuses are again formed. The sand barrier is outside such wave rays and reached rather direct waves that make the barrier stretch in the transverse direction.

In Fig.4 (c), according to the deformation of the terrace, the wave refraction changes. The sand barrier becomes to get two wave groups; direct waves that are almost straight incident and reflected wave at the channel on the terrace. The intensity of the reflection increases with the development of the channel as shown in Fig.4 (d). Along the long channel from the mouth to the contour of 10 m, caustic, that is, the envelop of the wave rays, is formed. Almost all the wave rays reflected at the channel concentrate at the tip of the barrier in such a way that these waves prevent the crosswise stretch or promote the upstream elongation.

Figures 5 (a), (b), (c), (d), and (e) show the effect of the off shore wave direction for the topography of 1993. Here the direction is taken anti-clockwise from the normal to the coastline. For the positive directions, (a) and (b), although the terrace refracts wave rays complicatedly, it transmits the wave rays and makes them concentrate at the tip of the barrier. On the other hand, for the normal to the negative directions, the caustic is firmly formed along the channel moreover makes concentration at the tip of the barrier. Therefore for the waves of positive direction, the terrace is transparent and acts like a convex lens. However for the waves of negative directions it functions as concave reflector. As a whole, the channel functions like a half mirror. Thus the deformed terrace gathers waves of all direction and focuses at the tip. This an-isotropic characteristic of the refraction comes mainly from the position of the channel that is shifted north

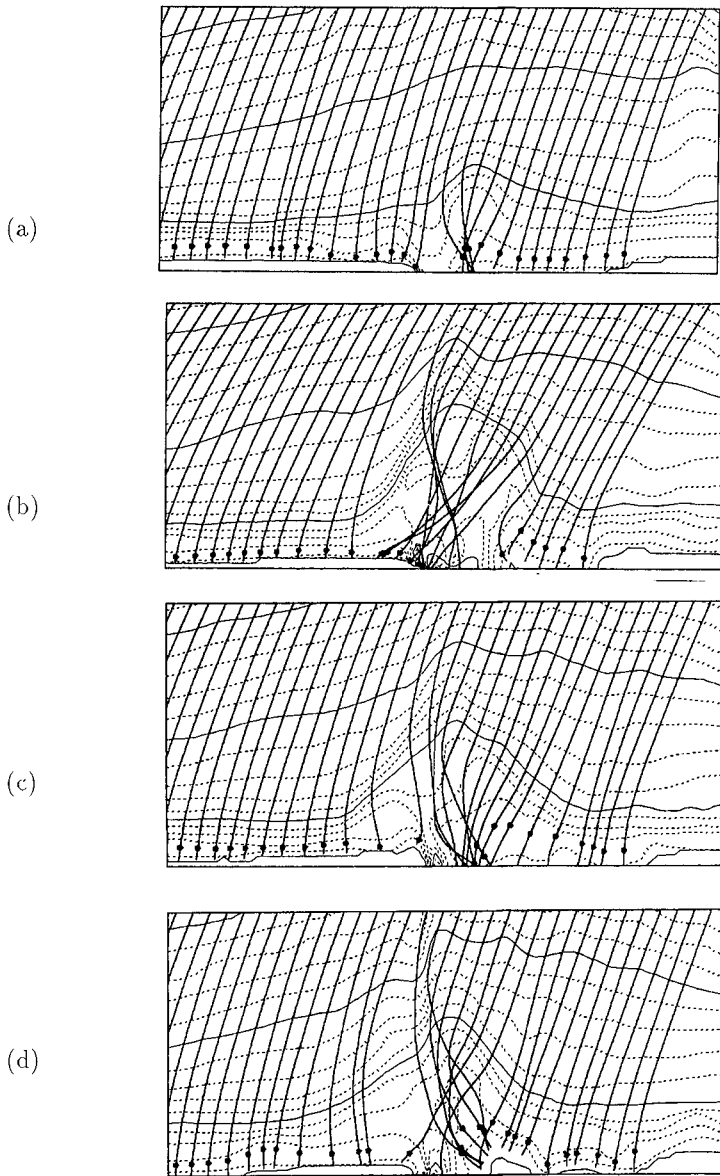


Fig. 4: Wave rays for the topographies at various stages.(a): March, 1986,(b): September 1986,(c): August 1988,(d): September 1993.

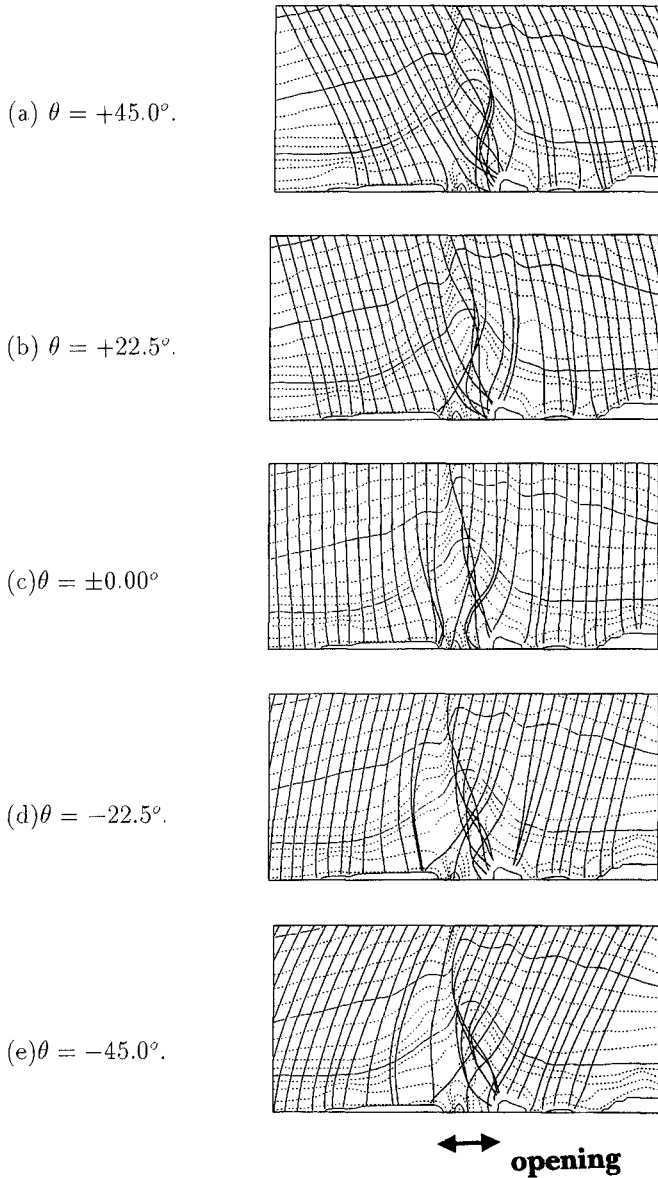
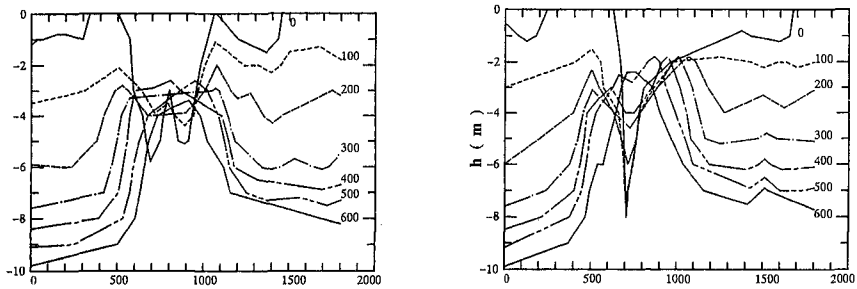


Fig. 5: Effect of wave directions.

from the center of the terrace as stated before.

4 Channel evolution

The next step is to examine how the channel has been developed. The cross sections of the terrace along shore are shown in Figs .6 (a) and (b) for each off shore distance y . The initial shape of the terrace formed by the 1986 flood was almost trapezoidal. Near the mouth there was a broad channel with banks in both sides. Then the banks were disappeared at $y = 400\text{m}$ and a very flat and horizontal surface appeared. The depth was about 3 m here.



(a) September, 1986.

(b) January 1992.

Fig. 6: Profiles of the terrace.

As time passing, the shoulder parts and the banks near the mouth were eroded to become round and the channel on the terrace was developed. The cross sections on January 1992 (Fig. 6 (b)) indicate a wide and triangular channel on the terrace. By using these profiles, we calculated the channel area that is bordered by the line connecting apexes at both sides. Then the volume of the channel was obtained by integrating the area to the offshore direction till $y = 600\text{ m}$, beyond which the evaluation of the area is not so precise.

Time histories of the volume and the outflow that is the integration of the discharge during the flood are shown in Fig. 7. This figure reveals correlation between the flood activity and the channel evolution. In 1991, we had many floods including large one and the channel volume remarkably increased after the floods. While for the inactive year in the floods, the change of the volume is small. Here the case for the 1986 flood is exceptional. After the largest flood of 1986, the increase of the channel was not so large. This is because the 1986 flood mainly deposited considerable amount of sediment off the mouth. The counted volume was due to the local score very near the mouth and bank formation on the terrace near the mouth.

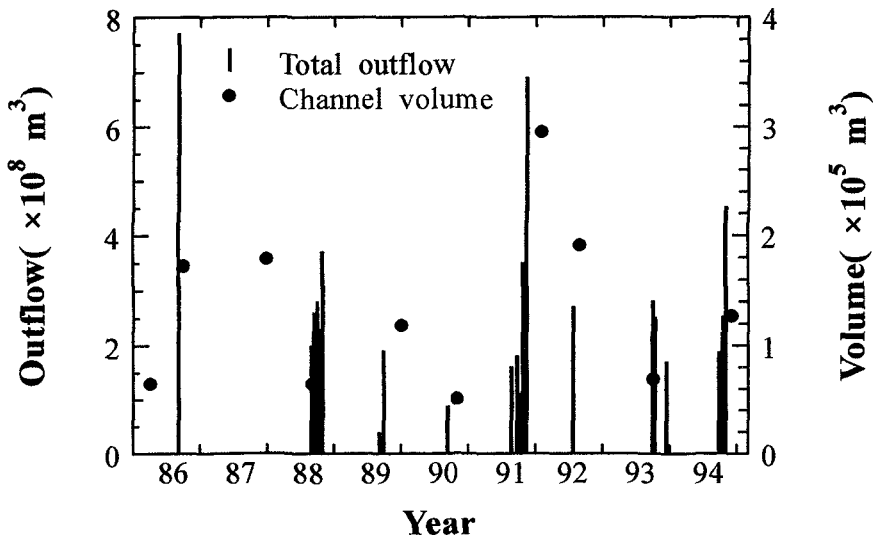


Fig. 7: History of floods and channel evolution.

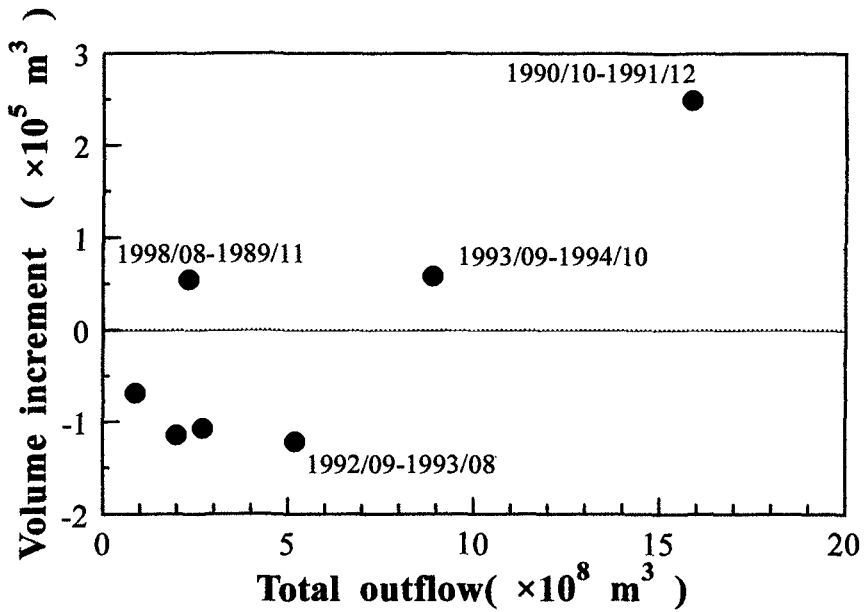


Fig. 8: Correlation between the outflow of the floods and increment of the channel volume.

The correlation between the flood activity and the increase of the volume is examined in Fig. 8. The ordinate indicates the increment of the channel volume obtained from the successive bathymetric charts. The abscissa is the sum of the outflow in the corresponding period. For the large value of the outflow, these two quantities are in linear relationship. While for the small value, the decrement of the channel volume appears, which would correspond to the deposition by waves. Thus the evolution of the channel on the terrace is related with passage of the small to middle scale of floods, except such a huge flood as to make a terrace.

5 Considerations

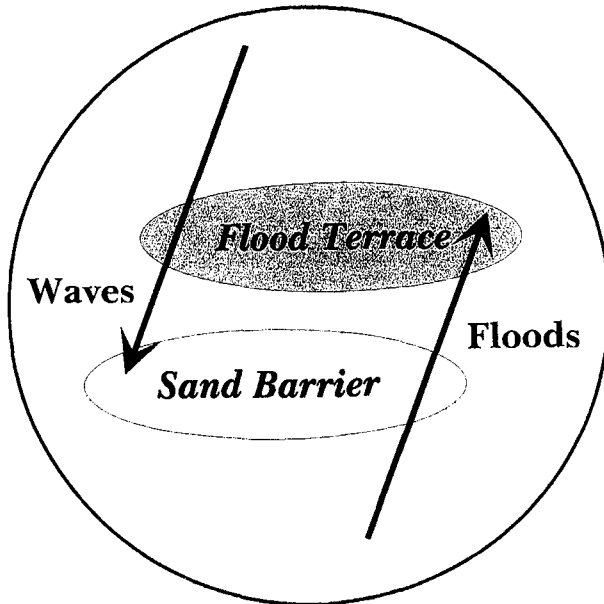


Fig. 9: The river mouth system at the Abukuma River

Starting from the terrace formation by the 1986 flood as an initial stage, here we summarize the flow of the cause and effect in the morphological change in the river mouth system. In the early stage after the terracc formation, the large terrace refracts waves to stretch the sand barrier in the cross river direction. The stretch takes half a year at most. Thus till spring, the opening of the mouth reaches equilibrium maintained by tides and usual river flows with narrow width. Then it is forced to lie adjoining the left bank of the river. Then thickening of the barrier as the following step of the development continues until next flood season. In autumn we have several floods mainly caused by the rainfall due to typhoon. For the small to middle size of floods, they may flush the barrier partly, however the major part of the flow runs out through the old opening. Then it erodes the terrace. The channel on the terrace gradually evolves along the flow axes.

The evolution of the channel also changes the refraction characteristics on the terrace. The reflected waves at the channel are gradually intensified and gathers at the tip of the barrier such a way as to suppress the cross ward stretch. When the reflected waves become dominant to the direct waves, the barrier stops transverse stretch and turns to the upstream direction. The transverse stretch lasted about seven years, while the fixation of the opening to the left bank contributes the channel evolution.

After the turning point, since the opening remained widely open, the reflected waves intrude inside the river and transport the sediment upstream. The waves also make the circular shore lines as shown Fig. 1 (b).

Figure 9 summarizes the interactions between the typical topographies; the sand barrier and flood terrace under the action of the external forces; floods and waves.

6 Conclusions

Based on the bathymetric chart, sand barrier survey, hydro-graphs of floods and wave data over ten years as well as the refraction analysis, we have shown the interactions between the sand barrier and flood terrace under the action of floods and waves. The different time scales on the deformation of these topography also have roles on turning the stretch direction of the barrier.

Acknowledgements

We are grateful for the permission to use the data observed by the Ministry of Transport and the Ministry of Construction in Japan. Our field work was funded by Grant-in-Aid by the Ministry of Education, Science, Sports and Culture in Japan and was partly sponsored by Tohoku Regional Bureau, the Ministry of Construction. We would like to thank for their awards and sponsorships.

References

- [1] Goda, Y. (1974): New wave pressure formulae for composite breakwater, 14 th Int. Conf. Coastal Engineering, pp.1702-1720.
- [2] Mano A. and M. Sawamoto, and M. Nagao (1995): Response characteristics of river mouth topography in wide time scale range, Proc. 24th Inter. Conf. Coastal Engineering, pp.3126-3138.
- [3] Mei, C.C.(1983):The Applied Dynamics of Ocean Waves, John Wiley & Sons.
- [4] Munk, W.H. and Arthur, R.S.(1952):Wave intensity along a refracted ray, Natl. Bur. Stand., U.S. , Circ., 521, Gravity Waves.

CHAPTER 351

A Unique Look at Oregon Inlet, NC USA

Herman C. Miller¹, M ASCE, William A. Dennis², M ASCE, and
Michael J. Wutkowski²

Abstract

Oregon Inlet (OI) in North Carolina (NC), the only inlet along a 170 km stretch of coast, supports an active commercial fishing and recreational boating industry. Severe erosion, because of the ongoing migration of OI, resulted in NC constructing a terminal groin to prevent the highway from being severed from the south side of the OI bridge. Construction of this structure provided a unique opportunity to monitor and assess project impacts which could be directly related to the twin jetties which are proposed for this site. The monitoring program included a directional wave gauge, aerial photography, and semi-annual sled-surveys extending 6 km north and south of the inlet. The terminal groin returned the shoreline to its pre-1986 position and has successfully protected the highway abutment to the bridge through many severe storms. This paper presents the results of 6 years of monitoring the morphologic changes. The results document how the coast has adjusted to the construction, a multi-year wave climate reversal, and placement of 1.5 million m³ of dredged material on the beach. The surveyed area generally lost material both on the up and downdrift sides, much of which apparently has been deposited in the inlet. The effect of these changes on the coast and the inlet's stability are discussed.

Introduction

Oregon Inlet (OI) is the only inlet along a 170 km stretch of coast from Cape Hatteras, North Carolina (NC) to the south, to Rudee Inlet in Virginia to the north, as

¹US Army Engineer Waterways Experiment Station Coastal & Hydraulics Laboratory Field Research Facility, 1261 Duck Road, Kitty Hawk, NC 27949, USA

²US Army Engineer Wilmington District, Coastal, Hydrology, & Hydraulics Section, PO Box 1890, Wilmington, NC 28402, USA

shown in Fig 1. The inlet provides an important link between the Atlantic Ocean water and the expansive estuarine Albemarle/Pamlico/Currituck Sound system. The inlet supports an active commercial fishing and recreational boating industry.

During the peak summer months, over 12,000 vehicles a day use the bridge across OI to work and enjoy the beaches in the Cape Hatteras National Seashore. OI and Roanoke Inlet before it, have been migrating south at a rate exceeding 2 km per century. By 1989 this ongoing southerly migration threatened to sever the southern abutment of the bridge to the highway that provides the only land route to the southern beaches. In 1990, NC Department of Transportation (NCDOT) constructed a 953 m rubble mound terminal groin to stabilize the south shoulder of OI. The terminal groin was intended to create a fillet in its lee and return the shoreline to the pre-1986 position. Documenting how the adjacent shoreline and nearshore waters adjusted to construction of the terminal groin was important to the local residents, NC, and the US Army Corps of Engineers (USACE).

This construction provided a unique opportunity to monitor and assess project impacts which could be directly related to the twin jetties which are proposed for this site. Although the function of the terminal groin and jetties (which provide for safe navigation through the inlet) is quite different, it was believed that information gathered concerning the project induced changes resulting from stopping the southerly migration of the inlet would be extremely beneficial in the planning and design of the jetties.

With local and state support for funding, the USACE Wilmington District and the USACE Waterways Experiment Station Coastal and Hydraulics Laboratory, Field Research Facility (FRF) jointly developed a monitoring program to assess the impacts of the terminal groin. The close proximity of OI to the FRF, located in Duck, NC, made it possible to take advantage of the equipment and experienced staff to conduct a long-term monitoring program.

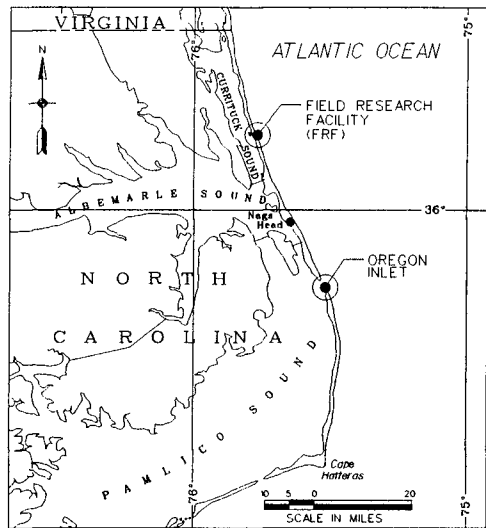


Fig. 1. Site Location. Note, location of USACE Field Research Facility 48 km north of OI. (Kilometers = Miles * 1.61)

This paper presents the results of 6 years of monitoring. In addition to the presence of the terminal groin during that time, there was an unusual long-term wave climate reversal, and material dredged from the inlet was disposed of on the beach on four occasions. The paper organization is generally as follows: monitoring program, monitoring results which document the response of the coast, a discussion of the effect on the inlet stability, and conclusions.

Monitoring Program

The OI area is subject to both hurricanes and northeasters and has one of the highest wave climates on the US east coast. The average annual significant wave height and period for the area are 1 m and 9 sec, respectively (Leffler, et al, 1996). The mean tide range on the open coast is 1.2 m and 0.7 m for the inlet gorge (NOAA 1996). OI separates Bodie Island to the north from Pea Island to the south. The monitoring program consisted of semi-annual nearshore sled-surveys along a portion of the coast extending approximately 6 km on both Bodie and Pea Islands. These surveys were conducted along 38 profile lines spaced at 300 m intervals, Fig 2. The profiles begin behind the dune and extend to the 9 m depth contour. All of the profiles are surveyed in January during the winter storm season and July during the summer recovery season. In addition to these surveys, a directional wave gauge has been operated at the inlet since 1990. Also, aerial photographs were collected approximately every other month.

The sled-survey system (Miller, 1991) consists of an amphibious vehicle and a sled with an 11 m tall mast, Fig 3. The sled, which slides across the ocean bottom virtually unaffected by waves and currents, carries a ring of reflective target-prisms. HYPACK software on a PC is used to collect position and depth measurements every 1 m along a profile using a Geodimeter 140T tracking total-station that is aimed at the prisms. Processing the profile data was facilitated by the Interactive Survey Reduction Program (Birkemeier, 1991). Summaries were generated using Intergraph Inroads/Insite software.

Results

By Halloween in October, 1991, the terminal groin was completed, the fillet had formed, and the shoreline had been returned to the desired location, just in time for a major storm, Fig 4. The road and bridge abutment was protected, accomplishing the primary function of the construction (Dennis and Miller, 1993). As can be seen, the breaking waves define a well formed ebb-shoal which is the main pathway for sand to bypass the inlet. Seeing that this natural pathway was well established, it was not expected that the terminal groin would have a major impact on sediment transport past the inlet. What was expected was that the inlet would narrow, since only the downdrift shoulder was stabilized. The effect of this realignment on the hydraulics of the inlet and on the adjacent coast was of primary interest.

The results are summarized by showing the changes that occurred from the winter of 1991 through the winter of 1994, then from the winter of 1994 through the winter of 1996. This separation shows the different responses of the coast to apparently different processes resulting from an infrequent long-term annual wave climate reversal during 1991 through 1993.

Figure 5 shows the elevation changes over 3 years on the Pea Island (south) side of OI. Every other profile is numbered starting with "15" closest to the inlet and ending with "239," 6.8 km to the south. The February, 1994 shoreline position is included to distinguish the sub-aerial from the

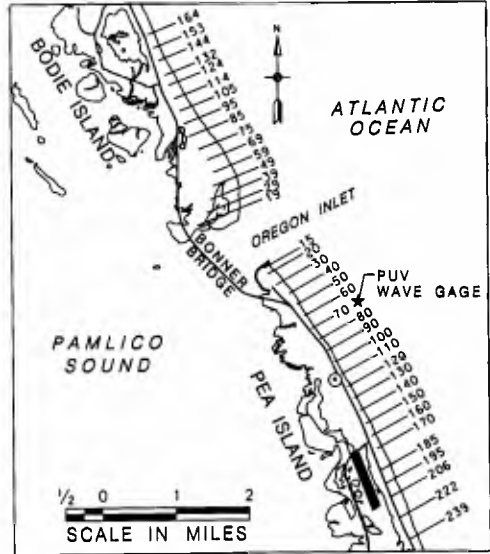


Fig. 2. Sled-survey profile lines. Note, directional wave gauge location at end of Profile #70 off of Pea Island. (Kilometers=Miles* 1.61)



Fig. 3. Survey sled and amphibious vehicle. The sled mast carries the prism array at an 11m elevation.



Fig. 4. OI during "Halloween Storm" on 31 October, 1991. Surge from 4 m, 22 sec. waves have flooded fillet behind the terminal groin at end of the old ferry landing road.

sub-aqueous portions. The terminal groin extends from the "Feb 94" shoreline position at "15" approximately 1 km to the west. The inlet would be to the north (right side) of the terminal groin. Positive elevation changes indicate accretion and are shown as light shaded contour areas. Negative contours in the dark shaded portion of the figure are areas of erosion.

From March, 1991 to February, 1994, near the inlet, there was inshore accretion and offshore erosion along the ebb-shoal. South of "140" there was nearshore erosion that resulted in shoreline retreat, overwash, and destruction of some dunes that were 60 years old. However, the overwhelming feature in the area during this time was the 1.5 million m³ of dredged material disposed of on the beach between profile lines 50 and 130. As can be seen, much of the disposal material moved offshore. Material also moved north along the inshore bar and trough into the fillet and around the terminal groin into the inlet.

More recently, from February, 1994 to April, 1996, Fig 6, the pattern of changes is quite different in comparison to the earlier time shown in Fig 5. Now the inshore erosion is along the entire length of the survey area. However, there is accretion offshore along a pathway consistent with transport along the ebb shoal toward the south.

Corresponding changes on the Bodie Island (north) side of OI from March, 1991 to February, 1994 are shown in Fig 7. For orientation, the inlet is 0.6 km south (to the left) of "39." Clearly, changes during this time are quite different than those for the Pea Island side shown above. Erosion pervades almost the entire area with the exception of an area of sub-aerial accretion near "59."

An almost opposite response is seen from February, 1994 to April, 1996 as shown in Fig 8. During those 2 years there is sub-aerial and sub-aqueous accretion over most of the area. One exception is the shoreline retreat south of "85" which corresponds to a swing of the Bodie Island spit toward the west. To document what was responsible for these different adjustments before and after February, 1994, it is informative to look at the wave data.

Historic estimates of the annual rate of sediment transport along this portion of coast, (Jarrett, 1978, Birkemeier, et al, 1985, Inman & Dolan, 1989, USAEDW, 1995),

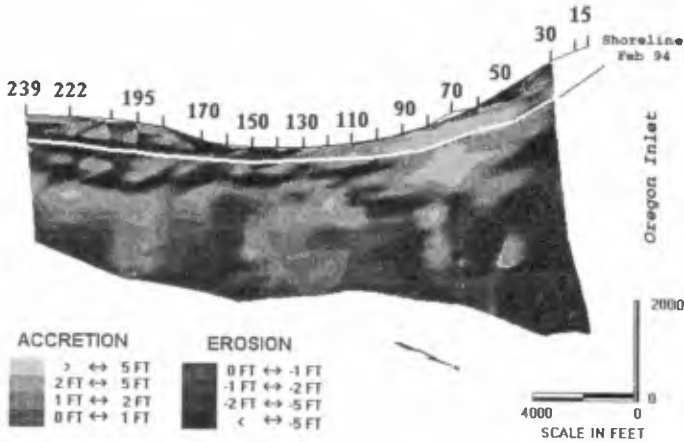


Fig. 5. Pea Island elevation changes from March, 1991 to February, 1994. Terminal groin is at profile 15; inlet is to the north (to right). (Meters = Feet*.3048)

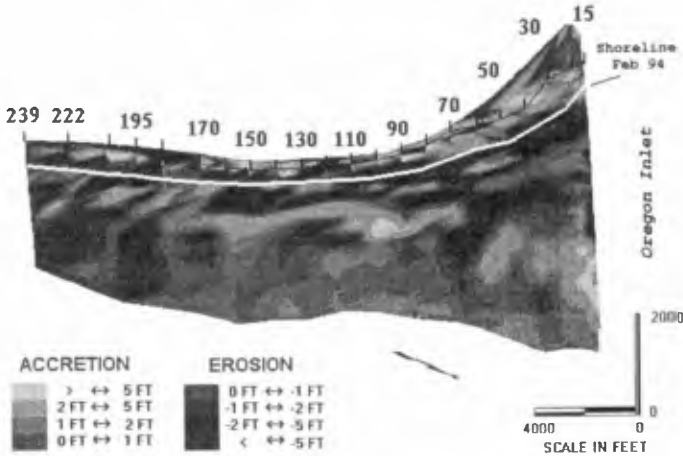


Fig. 6. Pea Island elevation changes from February, 1994 to April, 1996. (M=Ft*.3048)

show that annually approximately 1.5 million m³ of sediment moves south primarily during the Fall and Winter storm seasons; 800,000 m³ moves north during the Spring and Summer, for a net southerly transport rate of 700,000 m³ per year. Potential longshore transport volumes using the energy flux method in the Shore Protection Manual (SPM, 1984) based on hindcasted wave data since 1956 (WIS, 1993), historic wave climatic summaries (Thompson, 1971), and FRF measurements (see FRF WWW page at HTTP://FRF.WES.ARMY.MIL) show that this trend of net annual southerly longshore transport has been consistent over the past 4 decades with one exception in the early 1980's when the southward and northward transport approximately balanced.

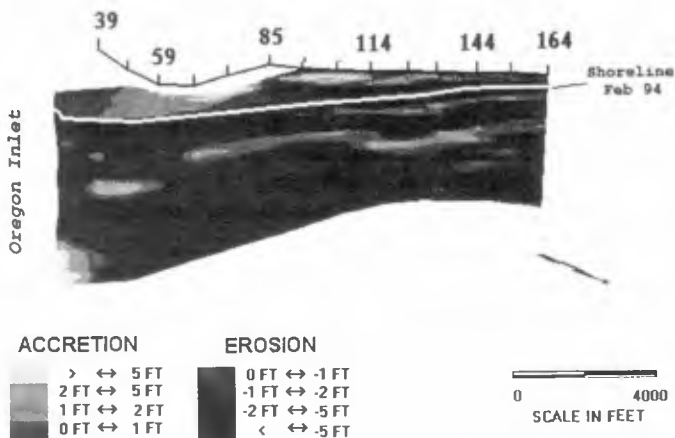


Fig. 7. Bodie Island elevation changes from March, 1991 to February, 1994. Inlet is 2 km south (to left) of Profile #39. (Meters = Feet * .3048)

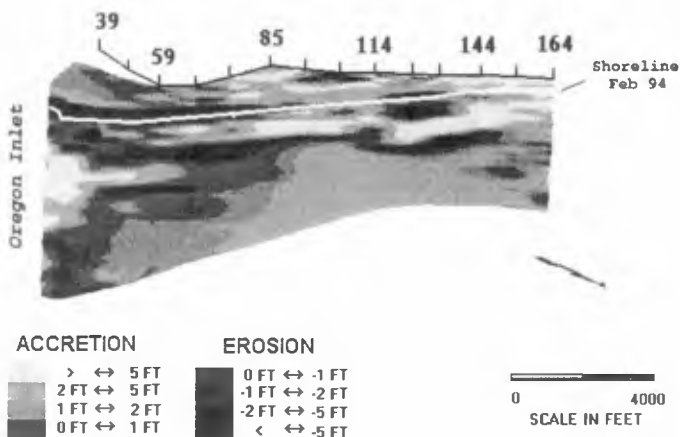


Fig. 8. Bodie Island elevation changes from February, 1994 to April, 1996. Shoreline retreat near inlet accompanied growth of spit toward south. (Meters = Feet * .3048)

Computations based on the FRF's linear directional wave array, (Long and Oltman-Shay, 1991), are shown in Fig 9. The complete data record from the FRF was used, instead of the directional measurement from the self-recording gauge at OI, because of intermittent gaps in the OI data. However, comparison of computations from both gauges, (Miller and Dennis, in prep.), show the wave climate summaries at the FRF are representative of the wave climate at OI. From January, 1990 through February, 1991 and from 1994 through 1996 there is southward transport during the storm seasons, consistent with historic trends. However, during 1991 through 1993, with only a few exceptions, each month the net transport is toward the north. It can also be seen that beginning with the Halloween 1991 storm, frequently, the northward transport rates were quite high. The annual net transport rates during these years approached 2 million m^3 toward the north. One explanation we have considered for this is that there was a long El Nino event in the Pacific Ocean during that time which may have diverted the "jet stream" across the United States causing mid-Atlantic extratropical storms to move inland south of OI instead of typically moving up the coast to the north. Whatever the cause, it provided a unique opportunity to study how the coast adjusted to the changing coastal processes.

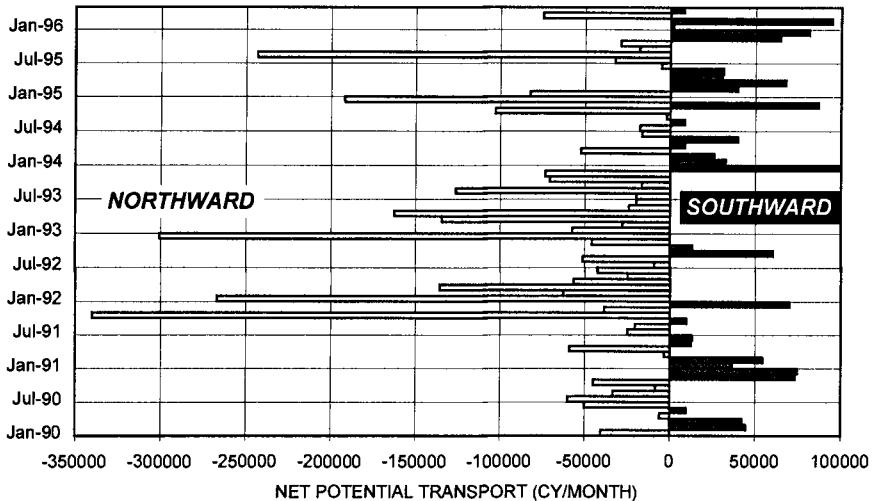


Fig. 9. Monthly net potential transport. Wave climate during 1991-1993 resulted in predominately northward net transport close to 2 million m^3 per year. ($M^3=Yd^3*.028$)

The effect of an inlet is often categorized in terms of the up drift or downdrift sides of the inlet. Figure 10 summarizes the adjustments of the coast at OI in light of the wave climate reversal that caused the up/downdrift categories to change during the monitoring period. Cumulative volume changes for each of the semi-annual surveys are presented for both Pea and Bodie Islands. During 1991 through 1993, Bodie Island is in the lee because of the wave climate reversal and shows a consistent loss of volume.

By the summer of 1994 the wave climate is more climatologically consistent and the volume shows signs of recovery. On the other hand, the Pea Island side remains approximately neutral through 1994 with some indication of a trend toward loss of material more recently while in the lee of the inlet. However, recall that 1.5 million m³ of material was deposited on the Pea Island side prior to 1995, and so it too lost volume during the monitoring period. So both sides lost volume, particularly during the times when in the lee of the inlet. Where did the sand go? We believe it went into the inlet. Unfortunately, we do not have volume changes in the inlet. However, using the aerial photography it is possible to gain some insight into the inlet's stability during this time.

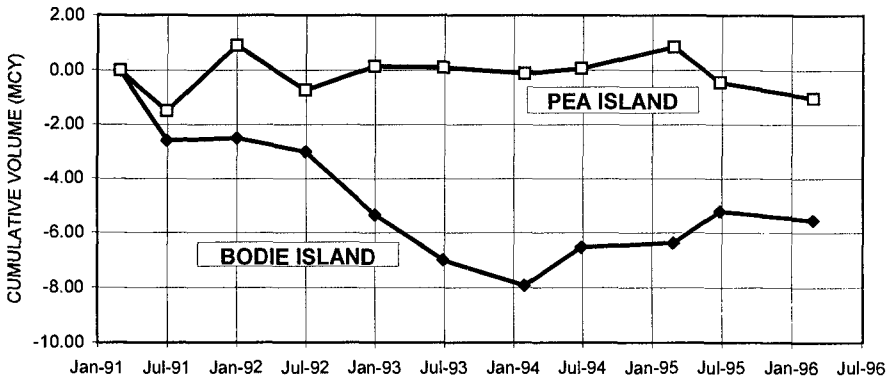


Fig. 10. Pea and Bodie Islands volume changes. Note, while Bodie Island shows loss of volume through July, 1994, Pea Island remains unchanged because of 1.5 million m³ of dredged material placed on the beach. (M³ = Yd³ * .028)

Figure 11 was constructed from photography taken on 13 April, 1992. Notice the width of the channel under the bridge. For reference note the “dark spot” on the bridge. This is a repaired section caused by a dredge that washed through the bridge during a storm in October, 1990. Also, note the shape of the ebb shoal. It has a parabolic “flattened bell” shape with a wide base that is asymmetric on the Bodie Island side.

Figure 12 is 1.5 years later on 11 November, 1993. The spit has grown to well south of the repaired bridge section. The Bodie Island side continues to move south as has been the tendency for the past 150 years since OI opened. The narrowing and realignment of the inlet can be seen in the shape of the ebb shoal, which now has an “arrow head” form, less wide at the beach and asymmetric on the Pea Island side. However, the shoal does not extend any further offshore. Higher currents associated with a decreasing inlet cross-section would tend to wash the shoal further offshore which is not seen at this time. The pond in the middle of the fillet behind the terminal groin is the result of mining 250,000 m³ of sand which was placed on the beach south of the monitoring area.

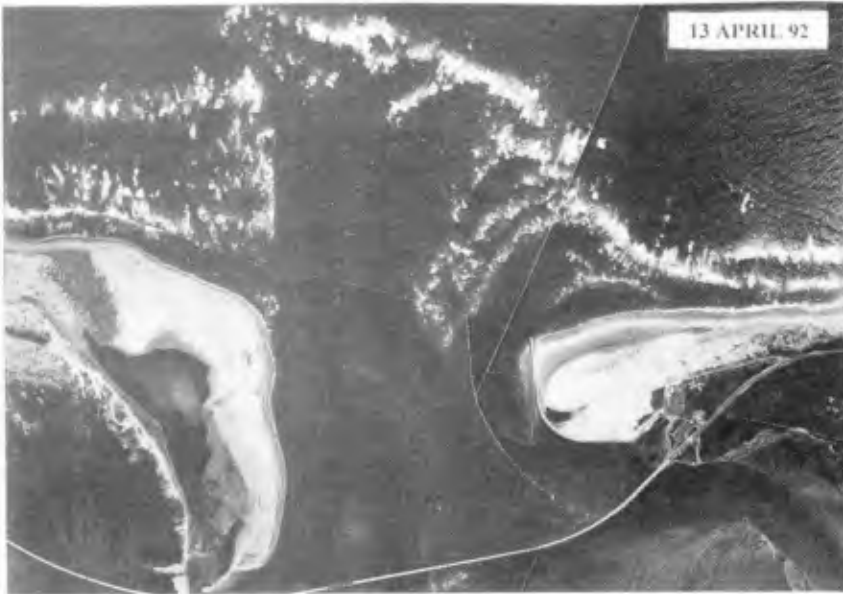


Fig. 11. Mosaic of aerial photography of OI taken on 13 April, 1992.

More recently, as seen in Fig 13 taken on 23 May, 1996, the spit is very near the navigation span under the bridge and an island has formed between the south “Davis” slough and the main OI channel. The volume of material in the inlet, although unknown, appears to have increased dramatically in comparison to Fig 11. We believe this accounts for a large part of the volume losses off of Pea and Bodie Islands.

Inlet Stability

The growth of the Bodie Island spit and development of the shoals have had an effect on the inlet stability. The effect of the shoal under the bridge is that instead of having to dredge to keep the authorized 4.3 m depth in the navigation channel at the bridge, as during the 1991 disposal projects, the depth has now approached 20 m. This equates to approximately 15 m of scour primarily over the past 3 years. Although scour in the navigation channel is unusual, scour has been a problem at OI in the past and has required that remedial measures be taken to reinforce the bridge at “Davis” slough on the south end. The deep scour has not, as yet, been measured in the inlet on the ocean side east of the bridge. In May, 1996 the inlet width, using the traditional method of measuring the minimum distance from the Bodie Island spit to the south side of the inlet (now to the terminal groin), is 820 m. This is the narrowest it has been since 1983, yet the inlet has been more narrow, on a few occasions, such as in 1975 when it was just 640 m wide (USAEDW, 1977). Since the inlet in recent years appears to have maintained a consistent cross-sectional area, (McCafferty, 1996), and is expected to continue to narrow, additional scour can be expected.

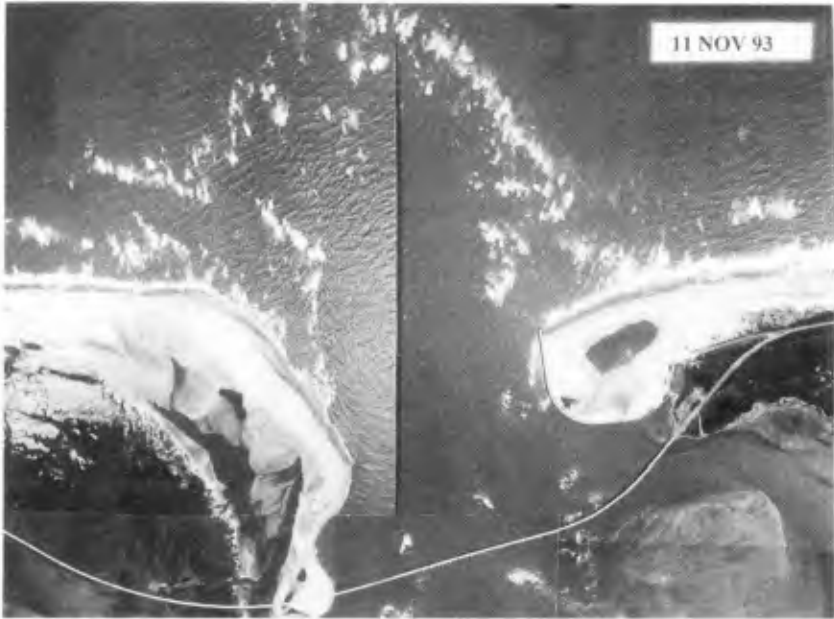


Fig. 12. Aerial photography of OI taken on 11 November, 1993. Note spit now well south of "dark spot" on bridge.

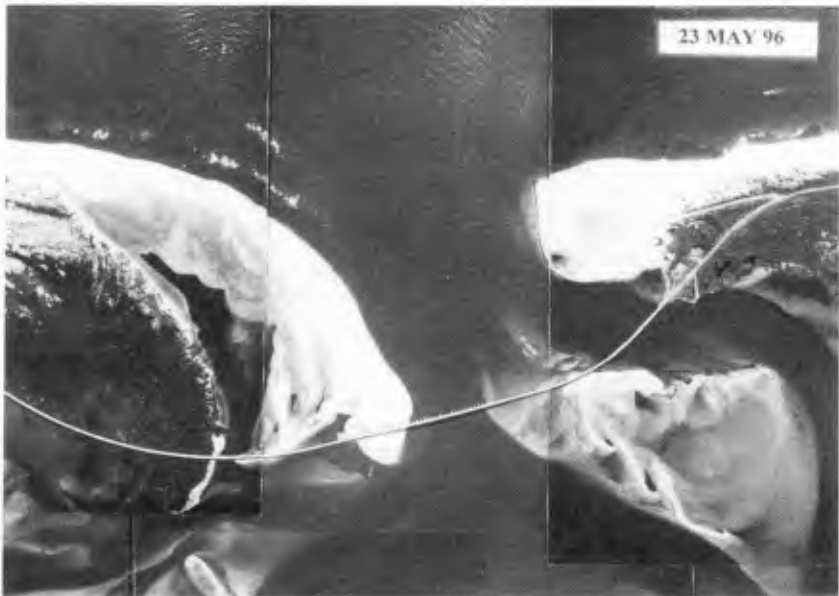


Fig. 13. Aerial photography of OI taken on 23 May, 1996. Development of shoal under bridge has resulted in 15 m of scour in navigation channel.

However, the scour in the navigation channel under the bridge suggests the inlet may be more narrow there. The “effective width” of the inlet might be considered the width measured at the bridge. Considering the shoal, that width is 720 m at this time. As the material continues to enter the inlet and the spit continues to migrate toward the south, it is possible that the main flow channel will shift to “Davis” slough. Should that occur, the spit and island under the bridge would tend to coalesce making it very difficult to maintain the navigation channel at the narrow navigation span of the existing bridge. Also, as the channel moves up against the terminal groin, the scour could increase, possibly, putting the structure in danger. The terminal groin was designed, however, anticipating the channel moving toward the structure by adding a 12 m wide scour apron along the inlet toe.

OI has always been an effective sink for sediment as evidenced by the extensive shoals west of the bridge. The inlet’s stability and downdrift beach erosion rates are highly dependant on the natural bypassing of material past the inlet. Unfortunately, with or without the terminal groin, natural bypassing is not efficient at OI. Dredging, in the past used primarily for maintaining the navigation channel, may become an almost mandatory bypassing supplement. This may not be satisfactory since dredging is also not efficient. It requires dredging quantities approaching the annual gross transport of material, which is more than three times the net. An alternative would be to stabilize the inlet with jetties that would prevent the material from entering the inlet and mechanically bypassing the net transport as needed on the downdrift beaches.

Conclusions

A terminal groin was constructed at OI to prevent the important only highway route to popular beaches from being severed from the bridge. The construction was intended to establish a fillet in its lee that would return the shoreline to the pre-1986 position. The structure has been well tested by many large storms and has been very successful.

A long term measurement program, including semi-annual sled surveys, has documented the response of the coast to the construction. Measurements made over the past 6 years captured the unique response of the inlet to an unusual wave climate reversal. During the reversal, erosion was measured on both the up drift and downdrift sides. Since the processes have returned to more normal conditions, there has been recovery on the up drift side and the ebb-shoal is accreting on the downdrift side. However, erosion on both sides indicates that natural bypassing continues to be insufficient at OI.

Apparently, the eroded material is ending up in the inlet. The inlet has adjusted by the growth of the spit toward the south and the rapid development of a shoal under the bridge. The “effective width” of the inlet is now 720 m, near the minimum in half a century, which has caused 15 m of scour in the main channel under the bridge.

The monitoring program at OI has been successful documenting the adjustment of the inlet and adjacent coastal region to construction of the terminal groin. Future efforts will include quantifying the volume changes within the inlet particularly on the shoals. Continued monitoring, as the Bodie Island Spit moves further south, will provide valuable data for future engineering activities that seem inevitable at OI.

References

- Birkemeier, W. (1991). "A User's Guide to ISRP: The Interactive Survey Reduction Program." Tech. Rpt. CERC-IR-84-1, Coast. Engrg. Res. Ctr., US Army Eng. Waterways Exp. Stn., Vicksburg, Miss.
- Birkemeier, W., Miller, H., Wilhelm, S., DeWall, A., and Gorbics, C. (1985). "A User's Guide to the Coast. Engrg Res. Ctr's (CERC's) Field Research Facility." Tech. Rep. CERC-85-1, US Army Eng. Waterways Exp. Stn., Vicksburg, Miss.
- Dennis, W. and Miller, H. (1993). "Shoreline Response Oregon Inlet Terminal Groin Construction." Proc. The Hilton Head Is. S. Carolina USA Int. Coast. Symp. Jour. or Coast. Res., Royal Palm Beach, FL
- Inman, D. and Dolan, R. (1989). "The Outer Banks of North Carolina: Budget of Sediment and Inlet Dynamics Along a Migrating Barrier System." Journal of Coastal Research. Vol. 5, No. 2, pp193-237.
- Jarrett, J. (1978). "Coastal Processes at Oregon Inlet, North Carolina." Proc. of the 16th Conf. on Coast. Eng., American Society of Civil Engineers.
- Leffler, M., Baron, C., Scarborough, B., Hathaway, K., Hodges, P., and Townsend, C. (1996). "Annual Data Sum. for 1994 CERC Field Research Facility." 2 Vols, Tech. Rep. CERC-96-6, Coast. Engrg. Res. Ctr., US Army Eng. Waterways Exp. Stn., Vicksburg, Miss.
- Long, C. and Oltman-Shay, J. (1991). "Directional Characteristics of Waves In Shallow Water." Tech. Rep. CERC-91-1, Coast. Engrg. Res. Ctr., US Army Eng. Waterways Exp. Stn., Vicksburg, Miss.
- McCafferty, H. (1996) "A Comparative Analysis of The Effects of Storms Upon A Tidal Inlet: Pre- and Post Inlet Stabilization Effects Oregon Inlet, North Carolina." Masters Thesis, Dept. of Env. Sci., Univ. of Virginia.
- Miller, H. (1991). "A Topographic Survey System For The Surf and Nearshore." Proc. US Army Corps of Eng. Survey Conf. US Army Eng. Topo. Lab., Ft. Belvoir, VA
- Miller, H. and Dennis, W. (in prep). "Predicting Longshore Trans. From Near and Far." National Oceanic and Atmospheric Administration. (1996). "Tide Tables 1992 East Coast of North and South America." US Dept. of Commerce, National Ocean Service, Silver Spring, Maryland
- Shore Protection Manual. (1984). 4th Edition, 2 Vols, US Army Eng. Waterways Exp. Station, Coast. Engrg Res. Ctr., US Government Printing Office, Wash., DC.

- Thompson, E. (1971). "Wave Climate at Selected Locations Along U.S. Coasts." Tech. Rep. CERC-77-1, Coast. Engrg. Res. Ctr., US Army Eng. Waterways Exp. Stn., Vicksburg, Miss.
- US Army Eng. Dist. Wilmington. (1977). "Manteo (Shallowbag) Bay North Carolina General Design Memorandum Phase 1 Plan Formation."
- US Army Eng. Dist. Wilmington. (1995). "Manteo (Shallowbag) Bay North Carolina Feature Design Memorandum Sand Bypassing (Management)."
- Wave Information Studies of US Coastlines. (1993). "Hindcast Wave Information For the US Atlantic Coast." WIS Rep. 30. Coast. Engrg. Res. Ctr., US Army Eng. Waterways Exp. Stn., Vicksburg, Miss.

Approvals

The authors would like to acknowledge the late, Robert Williams, Chairman of the Oregon Inlet and Waterways Commission, for his support for the monitoring program, efforts to fund the study, and open mind concerning the findings...he will be missed. Permission to publish this paper was granted by the Chief of Engineers.

CHAPTER 352

IMPACTS OF INLET STRUCTURES ON CHANNEL LOCATION

William C. Seabergh¹, Mary A. Cialone¹, Donald K. Stauble²

Abstract

Barnegat Inlet, New Jersey, has undergone a variety of structural changes in an attempt to provide a navigable channel from bay to ocean. These structures have included shoreline revetments, arrowhead jetties with their crest elevation at mean tide level, a sand dike to better align interior channel flow, a raised impermeable jetty, and now parallel jetties. Each of these structures has had significant influence on inlet hydraulics and sedimentation, which in turn has impacted channel location.

Introduction and Historical Overview

Barnegat Inlet, New Jersey (Figure 1), is an inlet worth detailed examination as it is rich in history of man's struggle to control nature's scheme. A paper written in the 1970's about the inlet entitled "Barnegat Inlet, Nature Prevails" (Caccese and Spies, 1977) expressed the frustration an inlet can cause coastal engineers and scientists. The natural inlet migrated to the south 1600 m from 1839 to 1932. An inlet shoulder revetment and groin to protect Barnegat lighthouse anchored the south side of the inlet. A pair of "arrowhead" jetties was constructed in the late 1930's, followed in 1943 by a sand dike in the adjacent bay that caused a redirection of flow. Important in understanding the response of the inlet channel in this time frame were the jetties' low crest elevations at mean tide level. These jetties were functioning as "weir jetties," which allowed tidal flow, wave-generated currents, and sand to be transported over these inlet structures. This resulted in creation of sand spits at the inlet gorge and became a new control for channel location, withstanding many dredging attempts to control channel position. During a twenty year period the sinuous channel was completely inverted as this new regime interacted with structural controls.

¹Research Hydraulic Engineer,² Research Physical Scientist, U.S. Army Engineer Waterways Experiment Station, Coastal Engineering Research Center, 3909 Halls Ferry Road, Vicksburg, Mississippi 39180-6199

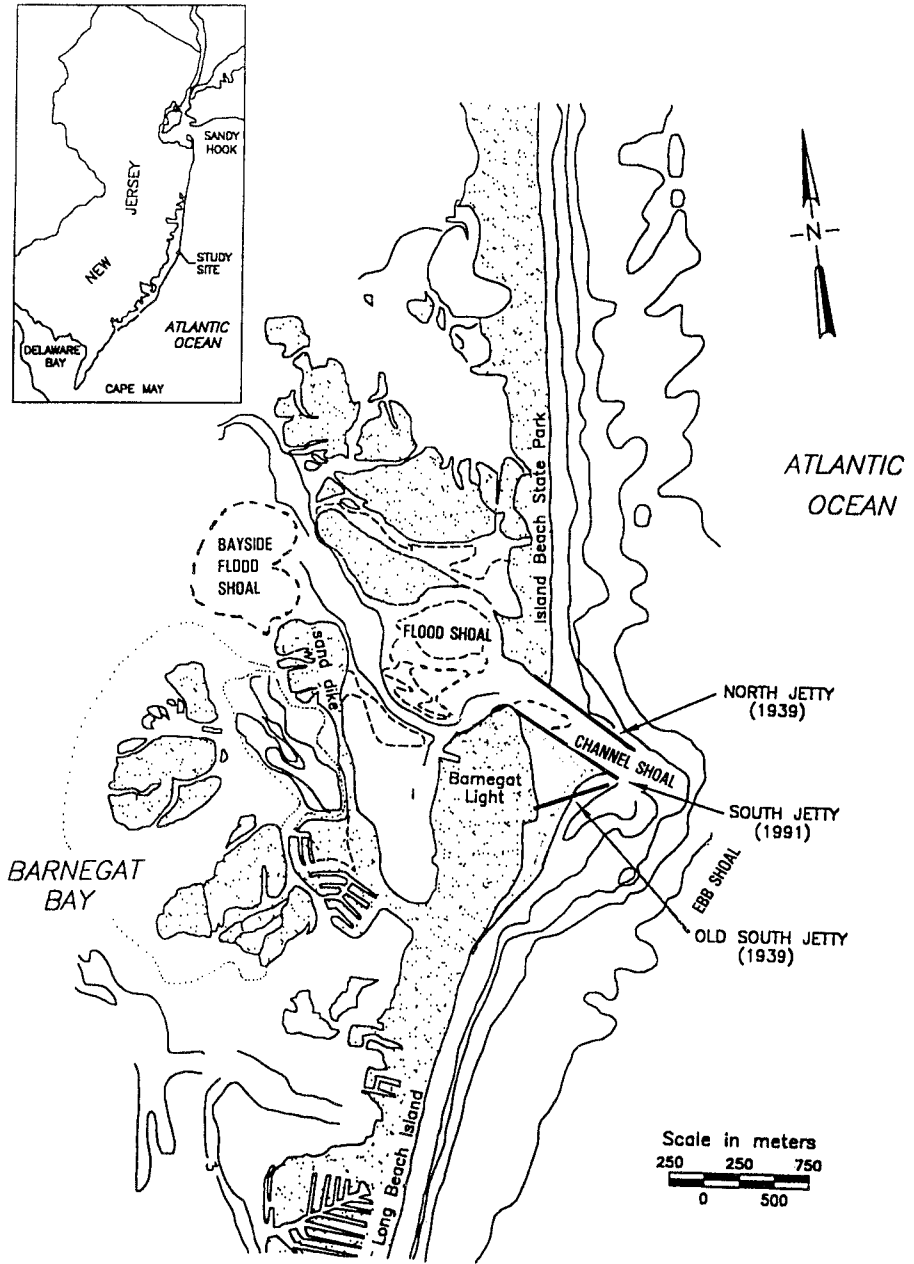


Figure 1. Barnegat Inlet, New Jersey location map and project elements.

In the early 1970's, a sequence of steps to improve channel dynamics was developed from a physical model study (Sager and Hollyfield, 1974) which included raising the north jetty and making it impermeable plus the addition of a new south jetty paralleling the existing north jetty. In 1972-74, the north jetty was raised 1.8 m. Sand was diverted offshore along the impermeable jetty and growth of the ebb shoal resulted. The channels adjusted to a reduction of sediment from the north beach.

A significant amount of dredging was done in the late 1970's to maintain the channel at the inlet throat. However, the increase in ebb shoal volume created additional maintenance dredging in that location. Another phase suggested by the model study was implemented beginning in 1989, with the construction of a new south jetty located within the arrowhead system. This jetty paralleled the original north jetty and served as a replacement to the original low south jetty. Upon completion of the project, a monitoring study was initiated to understand the response of the navigation channel to the most recent inlet structures, but, in doing so, an understanding of the historic interaction of the channel and structures was also necessary.

Physical Factors

The inlet separates Island Beach, a spit to the north, from Long Beach Island, a barrier island to the south. These barriers are characterized by medium to fine sands. Within the inlet region, medium to fine sands (0.25-0.5 mm) are on the ebb and flood shoals and coarser sands (0.50-1.0 mm) are in the deeper channel areas (Stauble and Cialone, 1995). The inlet provides access for commercial fisherman, day fishing excursion boats and small craft. The inlet's design channel is 91.5 m wide by 3 m deep (relative to mean low water), extending through the ebb shoal. The mean ocean tide range is 1.28 m and mean wave height is 1.20 m. Littoral transport estimates at the inlet are 840,000 cubic meters gross transport, with a net of 110,000 cubic meters to the south. These estimates are based on wave heights hindcasted at the 20-m contour near the inlet.

Effect of Inlet Hydraulics on Channel Dynamics

Throughout the recent history of Barnegat Inlet there has been the interaction of structures, changing sedimentation patterns and inlet hydrodynamics. The inlet system now contains four consecutive, fully-developed shoal features (compared to typical one ebb/one flood shoal), with an ebb shoal seaward of the jetties, a shoal in the intra-jetty region (particularly evident for the arrowhead configuration), a large flood shoal contained by the sand dike and finally a bayside flood tidal delta where flow exits into Barnegat Bay (Figure 1). Development of these shoals initially created a higher friction environment, which with the initial structural configuration, created increased sedimentation and a gradual decrease in tidal prism. Raising the north jetty reduced sediment input from the north beach, and coupled with dredging, and the construction of the new south jetty, some flow efficiency was regained as evidenced by increased tidal prism.

Important in relating the channel response to inlet structures is an understanding of the inlet's hydrodynamics. This inlet has maximum flood currents near high water elevations and maximum ebb currents near low water and is typical for an inlet lagoon which has very large surface area relative to channel cross-sectional area. Essentially the lagoon level fluctuates very little and the ocean tide range oscillates about that level, resulting in maximum head differences across the inlet near high and low waters. This phasing of flow relative to structure crest elevation and flow over shallow shoal areas is important to channel location. Figure 2 shows flow patterns for maximum ebb and flood flows as determined for 1968 conditions from a physical model study (Sager and Hollyfield, 1974). For the mean tide level elevation jetties, maximum flood currents (strongest near high water) had a great potential for introducing sediment to the inlet system and thus the development of a large flood shoal complex. Low water ebb currents are more channelized. This permits shoals to be more effective ebb shields; that is, ebb flow will tend to be deflected around the shoal area if the shoal elevation is higher than low water. Also, maximum ebb flows at low water elevation can lead to incising of channels.

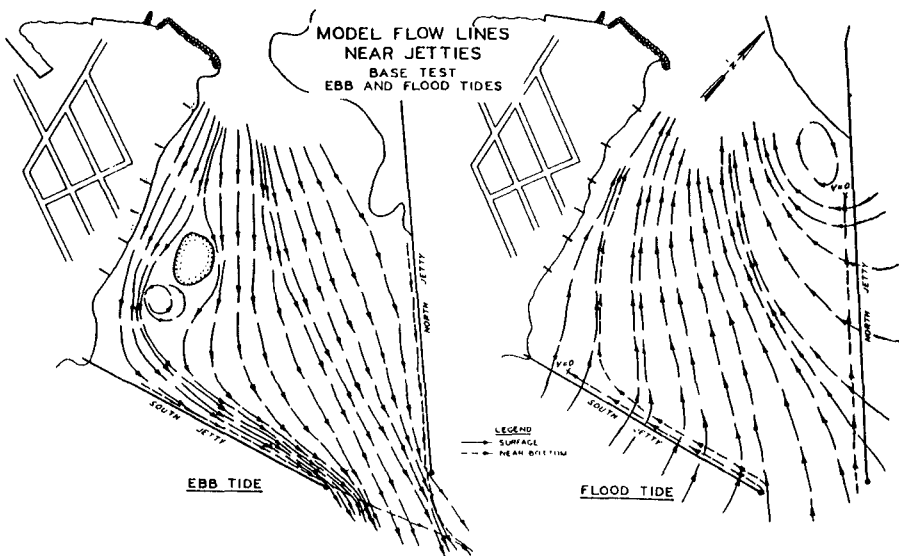


Figure 2. Model study flowlines, ebb and flood currents.(Sager and Hollyfield, 1974)

Historic Bathymetric Analysis

A review of historical bathymetry was performed to provide a basis for interpreting recent bathymetric changes at Barnegat Inlet and in providing guidance to anticipate future changes. Some historical information was derived from US Army Engineer District, Philadelphia, (1981) and Fields and Ashley (1987).

Pre-jetties In 1937 (Figure 3a) the pre-jetty inlet bathymetry shows that the interior channel swept south then turned east to northeast to exit the inlet, then turned southeast, on the ebb shoal, in response to predominant waves from the northeast. The 1937 interior channel was more than 460 m southeast of its current position (1996). The channel probably owed its large curvature to the infilling of the natural inlet on its north side as the inlet and channel both migrated south. The predominant portion of the tidal prism exited the bay from the north, channelizing around the large flood shoals due to a strong ebb shield factor resulting from this inlet's hydraulic phasing.

Arrowhead Jetties In 1939 arrowhead jetties were constructed and a channel, about parallel to the north jetty, was dredged into the bay in an attempt to provide a more direct route to the bay. Figure 3b shows the new interior channel in 1941. Also note the deflection of the ocean channel resulting from having the south jetty placed directly in its path.

Sand Dike By 1943 (Figure 3c), the sand dike was constructed in order to cut off the strong ebb flow from the dominant interior channel which was causing excessive scour on the inside shoulder of the inlet behind the lighthouse. It was anticipated that flow would be diverted to the straight interior channel, providing a deeper direct channel connecting ocean and bay. In addition, groins were constructed along the ocean shoreline inside the south jetty to mitigate shoreline erosion.

The 1946 bathymetry (Figure 4a) indicated a slight deflection of the navigation channel at the inlet's intersection with the shoreline as sediment moved over the low jetties at this location. On the south side of this region there was a shoal extending seaward from the lighthouse area, probably derived from sediment moving toward the inlet gorge along the shoreline inside the south jetty, then deflecting seaward on ebb. A buildup of sand at the shoreline is noted just inside the south jetty indicating an influx from the south beaches.

By 1953 (Figure 4b) the main navigation channel had shifted slightly south and rotated somewhat to the southeast. Sediment was moving over the low north jetty into the inlet gorge region. The interior region between the inlet gorge and the north tip of the sand dike contained flood shoals and three smaller channels. On the ocean side of the inlet, the navigation channel was close to the north jetty, as it had been for the previous ten years.

As of 1959 (Figure 4c) the navigation channel through the inlet gorge rotated away from the north jetty to the south and a scour area reappeared adjacent to the outer portion of the south jetty. The influx of sediment over the north jetty contributed to this rotation. Interesting to note was the shifting of the deepest area at the bayward end of the sand dike, which moved to the southeast side (compared with earlier conditions).

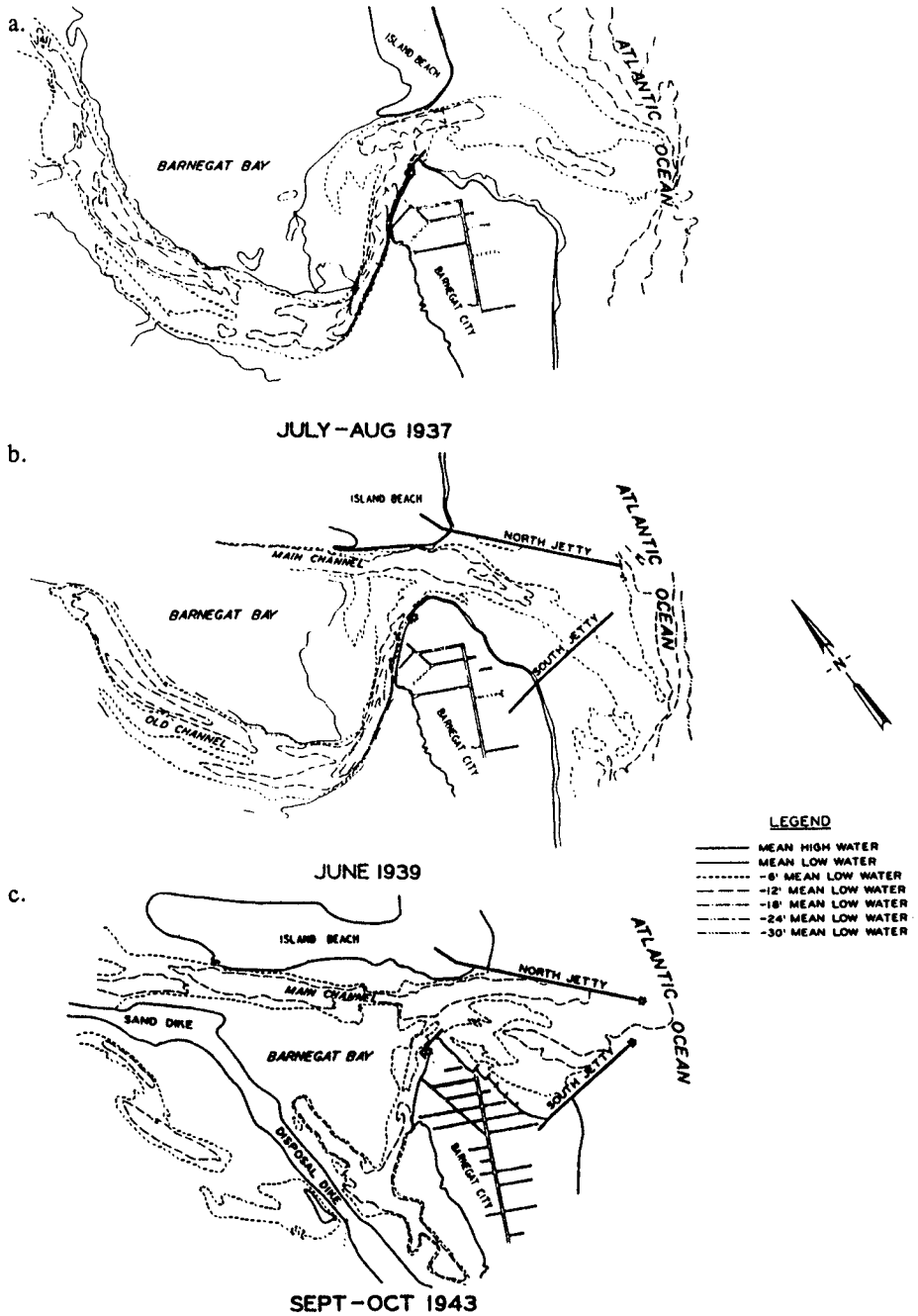
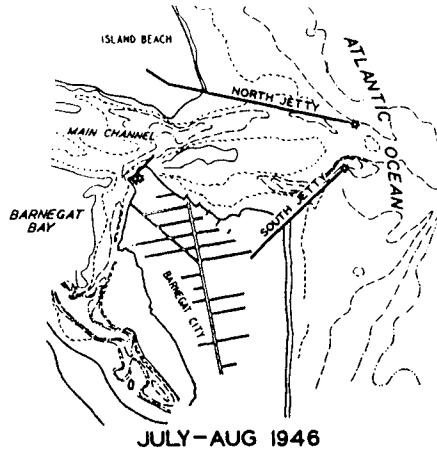
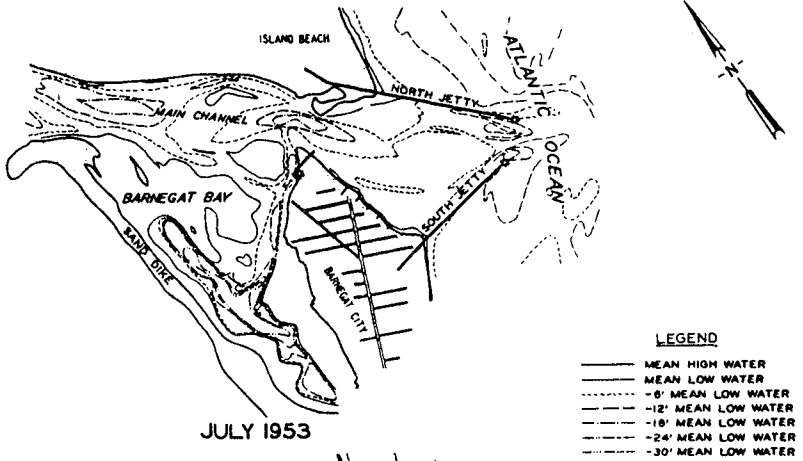


Figure 3. Barnegat Inlet bathymetry, July-August 1937, June 1939 and Sept-October 1943.

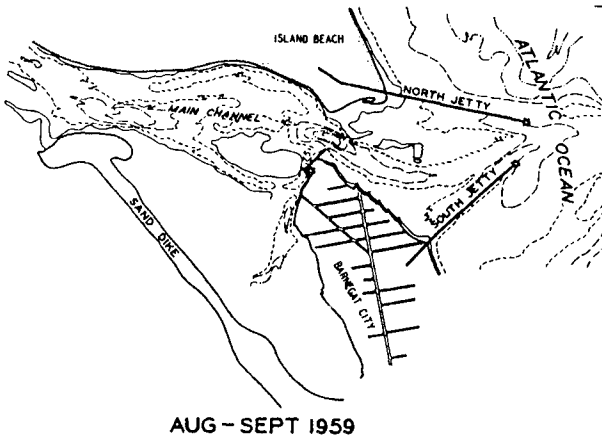
a.



b.



c.



LEGEND

—————	MEAN HIGH WATER
—————	MEAN LOW WATER
.....	-6' MEAN LOW WATER
-----	-12' MEAN LOW WATER
-----	-18' MEAN LOW WATER
-----	-24' MEAN LOW WATER
-----	-30' MEAN LOW WATER

Figure 4. Barnegat Inlet bathymetry, July-August 1946, July 1953 and August-September 1959.

Nineteen-sixty-two (Figure 5a) showed a new part of the flood shoal developing from sediment stripped from a spit which extended further from the north beachline into the inlet gorge. The minimum width of the inlet was reduced considerably due to sediment movement over the north jetty. The seaward portion of the channel migrated against the south jetty.

By 1968 (Figure 5b), the flood shoal occupied the location of the original dredged interior navigation channel. The interior channel was still bifurcated, but the region south of the flood shoal was widening and becoming the main interior ebb channel. It was forming in a similar configuration as was seen for the pre-jetties condition, except not as far southeast due to the presence of the sand dike. Sediment movement over the north jetty almost closed off the inlet gorge. The region between the arrowhead jetties was shoaling considerably except for the channel which had migrated against the south jetty. This sinuous channel was eroding the ocean-facing shoreline inside the south jetty and creating toe erosion which endangered the integrity of the oceanward portion of the south jetty. The trend of flood shoal growth and interior channel shifting south continued until the north jetty was raised 1.8 m from its original mean tide level crest elevation in the 1972-74 period.

Raised North Jetty The 1975 bathymetry (Figure 5c) indicated a major reorientation of the navigation channel through the jetty region. Dredging at the inlet gorge combined with cutting off sediment input by raising the north jetty permitted a straighter channel which was more in alignment with and closer to the north jetty. This channel orientation is reinforced by a concept presented by Keislich (1981) where a channel at a single-jettied inlet migrates toward the structure independent of whether or not the jetty structure is situated on the side of stronger longshore sediment drift. The Barnegat system probably can be considered a single jetty system in this respect due to the free flow of sediment and currents over the mean tide level south jetty, which helps move the channel toward the "single" north jetty.

Raising the north jetty caused a significant change in sediment pathways. The ebb shoal began to increase in magnitude (Figure 6a). This most likely can be attributed to the movement of sediment along the outside of the north jetty which previously had passed over the landward end of the low north jetty and contributed to flood shoal building and the movement of the inlet gorge towards the south. The same trend of channel alignment seen in the 1970's continued through the 1980's (Figure 6b). The interior navigation channel moved more towards its pre-project (1930's) location and the channel between the jetties was concentrated on the north side adjacent to the raised north jetty. This configuration was maintained until the construction of a new south jetty which occurred between late 1987 and 1991.

Hydraulic Response to New South Jetty

In order to build the new south jetty (Figure 7) from the revetted region on the south shoulder of the inlet beneath the lighthouse, shallow shoals were removed from

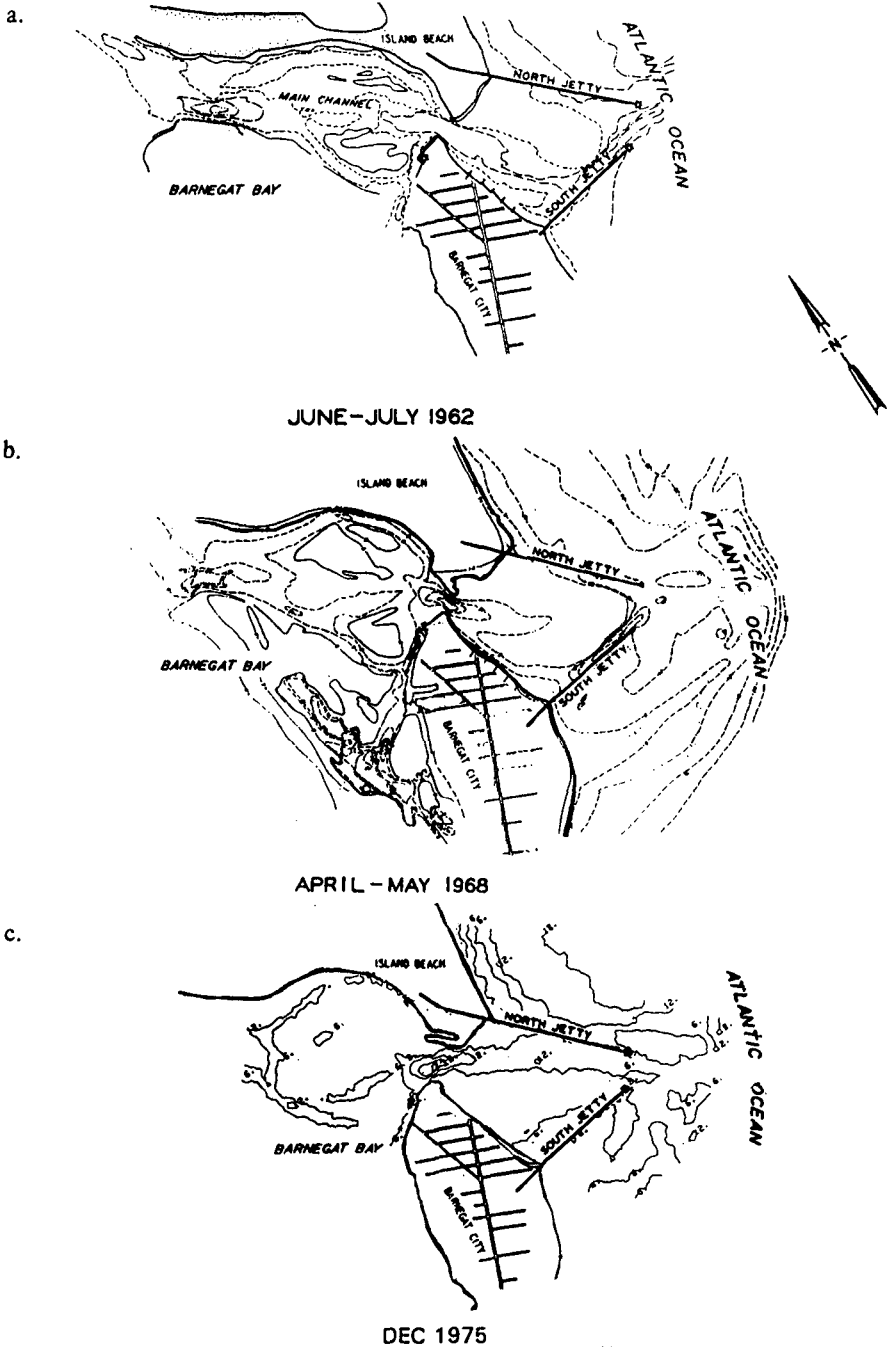


Figure 5. Barnegat Inlet bathymetry, June-July 1962, April-May 1968 and December 1975.

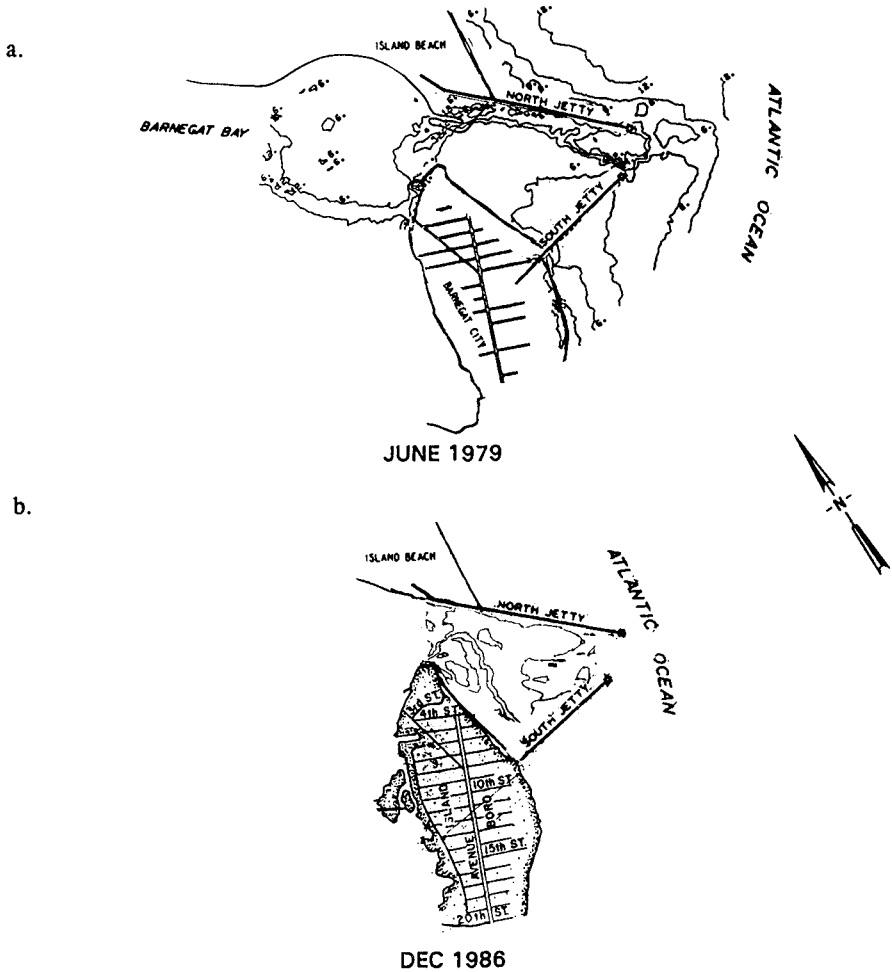


Figure 6. Barnegat Inlet bathymetry, June 1979 and December 1986.

this region. The inlet system became more efficient hydraulically due to an increase in minimum cross-sectional area which resulted from this shoal removal. This follows from O'Brien's (1969) relation between minimum inlet area, A_C (m^2) and tidal prism, P (m^3) at dual jettied systems: $A_C = 7.489 \times 10^{-4} P^{0.86}$. With minimal sediment entering the inlet system the increase in prism has been maintained since completion of the new south jetty. Figure 8 shows the variation in prism for the duration of the project. After the construction of jetties (1941), the inlet initially had the same tidal prism as the natural inlet, but the addition of the inside sand dike (Figure 1) lengthened the inlet channel and the newly dredged interior navigation channel had a reduced channel area compared to the old sinuous one. Sediment influx reduced areas and thus prism. The new south jetty prevented the influx of sediments that had previously occurred for the low south jetty and so the new, larger, minimum area has been maintained.

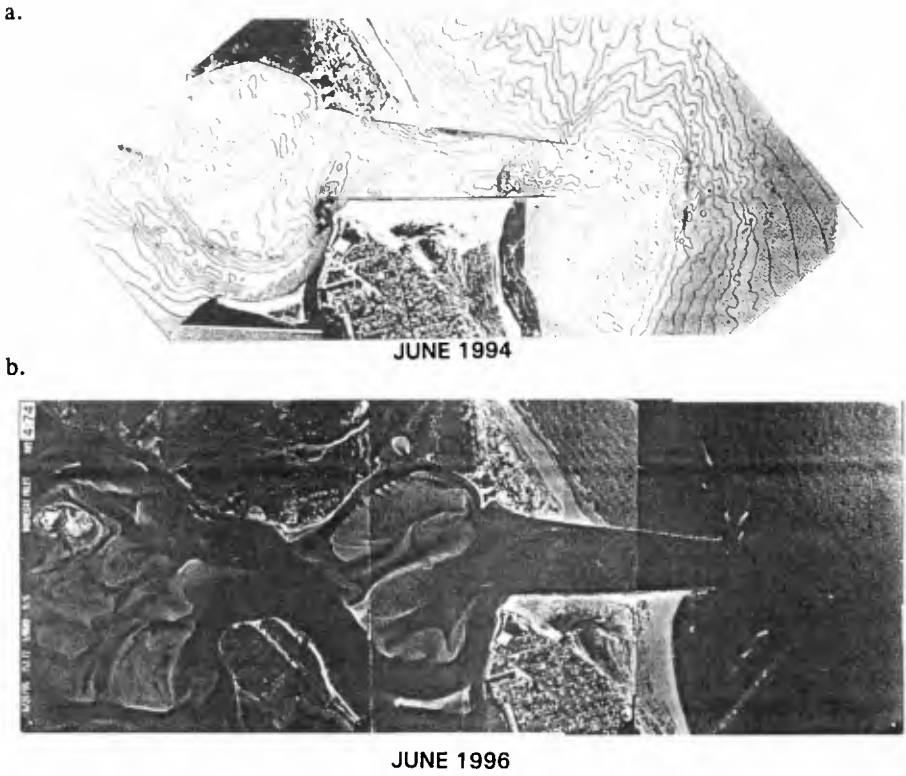


Figure 7. Barnegat Inlet 1994 bathymetry and 1996 air photograph.

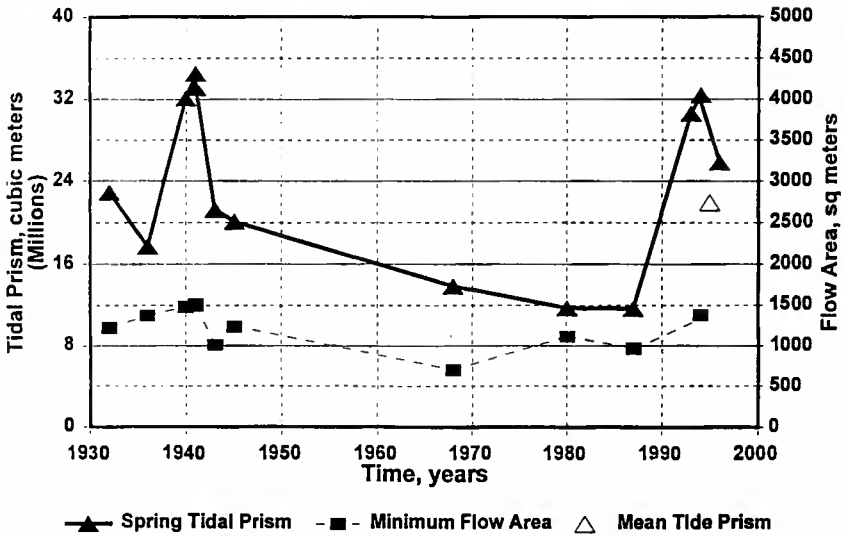


Figure 8. Historical measured tidal prism variation.

Channel Response To New South Jetty

Analysis of the channel response to the most recent addition of the new 1250-m long south jetty reveals what appears to be an evolutionary change in channel depth in the region between the north jetty and new south jetty (Figure 9). The net sediment

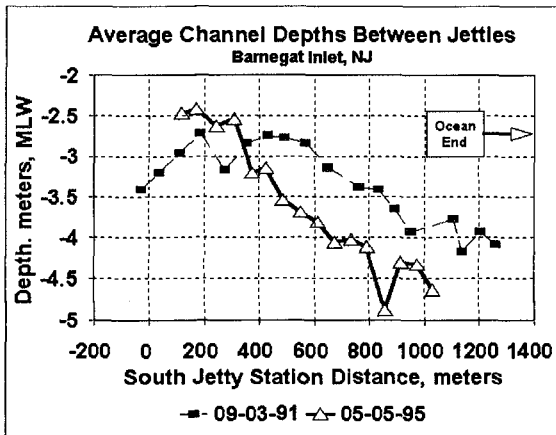


Figure 9. Average channel depths between jetties, 1991 and 1995.

mass is translating bayward in the region of the parallel jetties. An important aspect of this is the flood dominance of currents on the south side of the intra-jetty region of the channel. Flood currents tend to enter the inlet region from the north jetty side (due to greater ebb shoal depth on the north and shallower ebb shoal depth on the south side, Figure 7a) and sweep toward the south jetty. Also the outer 305 m of the north jetty remains at the mean tide level elevation, permitting maximum flood currents to flow over this low section into the channel perpendicular to flow coming through the oceanward jetty tips. This also helps guide flood currents to the south side of the intra-jetty region. The occurrence of a shoal region between stations 200 and 400 is essentially a nodal point between ebb and flood flow dominance. Flood flow pushes sediment through the channel mostly on the south side, (based on velocity distribution measurements taken in 1994-96 by the authors). Ebb currents from the curved interior channel shear this shoal and sediment moves along the north side of the shoal (where ebb flows are concentrated) towards the ocean. Dredging of the channel shoal and, evidently, a net oceanward sediment circulation out of the intra-jetty region have caused a progressively deeper channel.

The interior navigation channel is moving southward, as the flood shoal flattens out since sediment is not reaching it from the north or south adjacent shorelines or the ebb shoal. This channel has migrated south about 90 m in the last three years (1994-96). Flood currents plus ocean waves traveling with the currents move sediment towards the bayside of the flood shoal. On ebb, the current shears off sediments from the back edge of the flood shoal and moves it counter-clockwise along the edge of the shoal. Sediment settles out on the south edge of the flood shoal as strong ebb currents move away from the shoal to the outside of the curved channel. This spreading out of sediment may decrease the effectiveness of the flood shoal as an ebb shield and gradually permit more ebb flow over the shoal. Some incised cutting of the center of the flood shoal can be noted in Figure 7b.

Lessons Learned

The concept of arrowhead jetties to provide concentration of ebb flows at the oceanward terminus (in order to cut through the ebb shoal) and for wave attenuation due to diffraction as waves propagated into the expansion area, were positive design attributes. The hydraulics of such a system with regard to the velocity phasing at Barnegat Inlet (maximum flood currents near high water and max ebb near low water) combined with mean tide level jetties would permit broad, less concentrated flood currents to approach the inlet, presumably having less potential to carry sediments into the inlet. Strong ebb flow concentration in the navigation channel would flush sediments out of the channel as water surface elevation dropped. However, the sediment influx over these low jetties overshadowed the positive elements of the plan. Apparently most of the sediment movement was at the shoreline intersection with the jetties.

It was learned from the historical analysis of bathymetries that the interior navigation channel moved back to its pre-structure alignment, probably due to the influx of sand coming over the low north jetty, which enlarged the flood shoal significantly and helped deflect ebb currents coming from the bay towards the southeast. There was a similar situation for the natural inlet, which had been migrating south, thus infilling on the north side and accumulating sediments to help deflect ebb currents to the south.

Raising of the north jetty crest elevation cut off direct sediment influx from the north but sediments from the south maintained the same minimum area at the inlet gorge. Channel migration to the now dominant north jetty, plus dredging, cut off input to the flood shoal and redirected beach sediments to the ebb shoal.

The effects of sediment input into an inlet system in equilibrium usually is balanced by sediment moving out. At Barnegat Inlet, initially structural changes effectively lengthened the channel which led to increased friction, reduced currents, followed by sedimentation and reduction in tidal prism. The addition of a new higher south jetty paralleling the north jetty along with an increase of minimum channel area due to dredging and the prevention of sediments entering from the south into the inlet gorge permitted a larger tidal prism.

It took over 20 years (1941 to 1965) for the straight interior navigation channel to move to the south back to its historic curved configuration. However, recent incising of the flood shoal and the apparent reduction in sediment supply to the flood shoal indicates a potential for ebb currents to eventually "short-cut" across the flood shoal and deepen a channel there.

Conclusions

Inlet channel location is a complex function of inlet hydraulics, littoral influx to the channel system, and inlet structures. Historic analysis of structural effects has provided a clear picture of inlet response and impacts on channel location. Initially low arrowhead jetties followed by an interior sand dike, then sand tightening of one jetty with increased jetty elevation, and finally conversion to a parallel jetty system, affected inlet hydraulics and sediment input, which in turn changed shoaling patterns and thus channel location. With the low arrowhead jetty system, sedimentation reduced channel cross-sectional area with a corresponding reduction in tidal prism. Today's inlet, which is still adjusting to the new parallel south jetty, appears to allow a more stable channel to exist due to the restriction of sediment input into the navigation channel. These factors along with an increase in minimum channel area due to dredging have changed the tidal prism back to pre-structure conditions.

Acknowledgments

The work was funded through the Monitoring Completed Navigation Projects Program and the Coastal Inlets Research program. Assistance of Mr. Keith Watson and others at the US Army Engineer District, Philadelphia, is appreciated. Work performed by previous co-investigators, Ms. Monica Chasten and Mr. John McCormick, is also recognized. Permission to publish was granted by the Office, Chief of Engineers.

References

- Caccese, L.A. and Spies, H.R. 1977.** "Barnegat Inlet, Nature Prevails" *Proceedings, Coastal Sediments '77*, American Society of Civil Engineers, Charleston, SC, pp 305-310.
- Fields, M.L. and Ashley, G.M. 1987.** "Barnegat Inlet, New Jersey - A Stabilized Inlet," *Proceedings, Coastal Sediments '87*, American Society of Civil Engineers, New Orleans, LA, pp 2006-2021.
- Kieslich, J.M. 1981.** "Tidal Inlet Response to Jetty Construction," GITI Report 19, U.S. Army, Corps of Engineers, Coastal Engineering Research Center, Fort Belvoir, VA, and U.S. Army Engineer Waterways Experiment Station, Vicksburg, MS.
- O'Brien, M.P. 1969.** "Equilibrium Flow Areas of Inlets on Sandy Coasts, *Journal of the Waterways and Harbors Division*, ASCE, Vol 95, No. WW1, pp 43-52.
- Sager, R.A. and Hollyfield, N.W. 1974.** "Navigation Channel Improvements, Barnegat Inlet, New Jersey; Hydraulic Model Investigation," Technical Report H-74-1, US Army Engineer Waterways Experiment Station, Vicksburg, MS.
- Stauble, D.K. and Cialone, M.A. 1995.** "Analysis of Sediment Grain Size Trends For Defining Inlet Sediment Processes," *Proceedings of the 8th Annual National Conference on Beach Preservation Technology*, FSBPA, Tallahassee, FL, pp 211-226.
- US Army Engineer District, Philadelphia. 1981.** Barnegat Inlet, New Jersey, Phase- I General Design Memorandum, Philadelphia, PA.

CHAPTER 353

Complete Closure of The Nanakita River Mouth in 1994

Hitoshi Tanaka¹, Fumihiko Takahashi² and Atsushi Takahashi³

ABSTRACT

Very severe draught occurred in Japan during the dry season in 1994. Due to considerably reduced river discharge, complete closure was induced five times at the Nanakita River mouth in Japan during this period. Detailed field observations were carried out immediately before and after the closures. By analyzing hydraulic characteristics measured at the mouth, date of the closure occurrence can be estimated. An analytical solution is derived for predicting time-variation of river mouth width under the combined influence of incoming waves and effluent river discharge.

1. INTRODUCTION

There have been a lot of field measurements of topography change at a river mouth in connection with practical problems such as flood control and maintenance of a navigation channel. Most of them are, however, made at relatively large rivers due to their practical importance, and, consequently, very few attention has been paid to small ones.

The authors have been conducting field measurement of topography change at the mouth of the Nanakita River, one of typical small rivers in Japan, since 1988 (Tanaka and Shuto, 1989, 1991, 1992; Tanaka, Kabutoyama and Shuto, 1995; Tanaka and Ito, 1996). The Nanakita River originates at the northern part of Sendai and pours into the Pacific Ocean as shown in Fig.1. The catchment area and the length of the river are 229km² and 45km, respectively.

From 1988 to 1993, the complete closure at the Nanakita River mouth has been observed only twice (Tanaka and Shuto, 1991), whereas in 1994, the closure

¹ Professor, Department of Civil Engineering, Tohoku University, Aoba, Sendai 980-77, JAPAN.
e-mail: tanaka@tsunami2.civil.tohoku.ac.jp

² Civil Engineer, Penta-Ocean Construction Co. Ltd., Koraku, Bunkyoku, Tokyo 125, JAPAN.

³ Civil Engineer, Niigata Prefecture, 4-1, Sinkocho, Niigata 950, JAPAN.

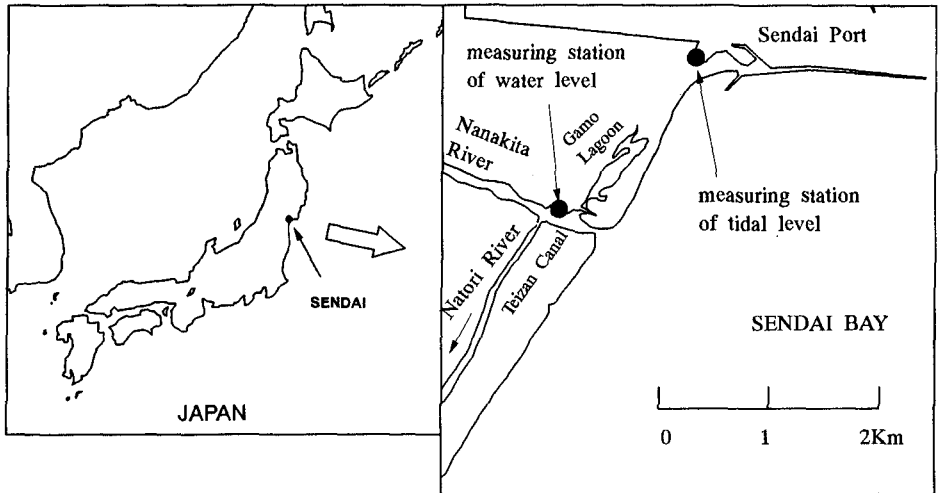


Fig. 1 Location map of the Nanakita River mouth

occurred five times in contrast, probably due to remarkable reduction of the fresh water discharge during the dry season. In this paper, results of detailed field surveying of the topography change will be firstly shown along with corresponding external forces acting at the river mouth. Furthermore, a mathematical model, considering littoral drift by waves and sediment flushing due to river discharge, will be applied to the Nanakita River in order to reproduce the change in the river mouth width.

2. RESULTS OF FIELD OBSERVATION

Figure 2 shows the significant wave height H , the wave period T , the wave incident direction θ measured clockwise from the north, and the river discharge Q_r . The wave characteristics are measured 4 km offshore from the river mouth at the mean depth of 20m, while the fresh water discharge is measured at a gauge station 9km upstream. In Fig2, the dates when the river mouth closure was firstly observed are also drawn by thick arrows. It should be noted that these are not the dates when each closure occurred, but the dates when the authors firstly noticed the closure. It is seen that the river discharge is considerably small due to draught as compared with other years (Tanaka and Shuto, 1989, 1991) and that very high waves immediately before each closure are common to all events.

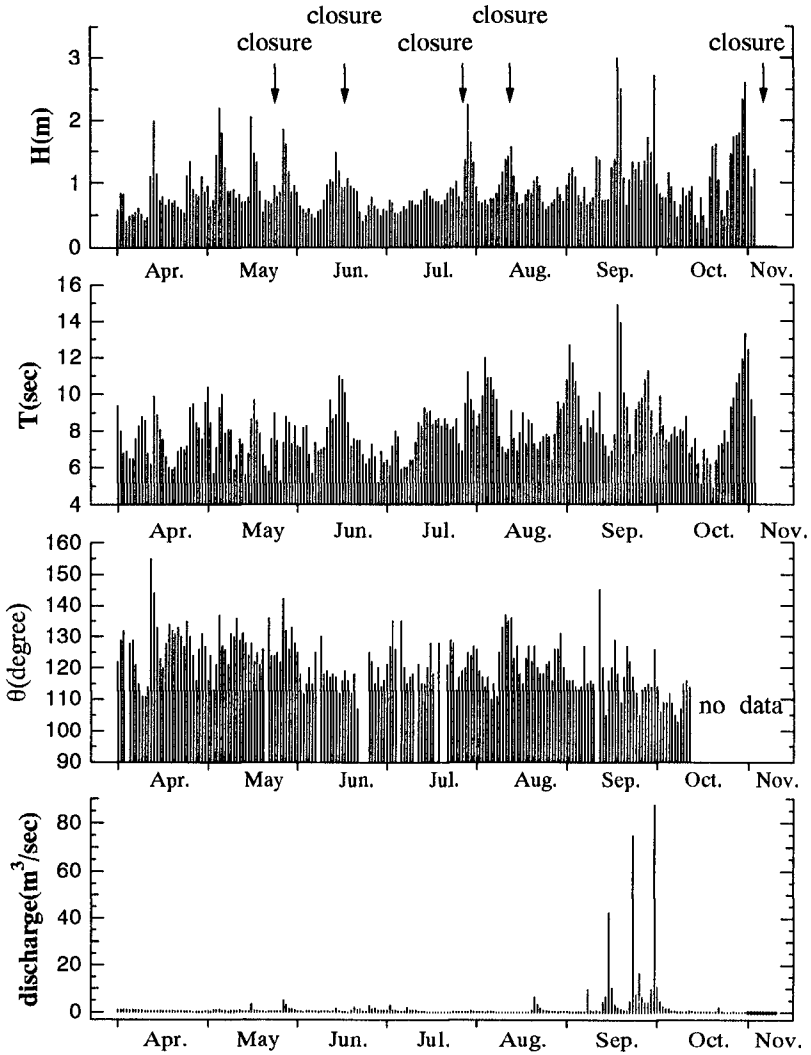


Fig. 2 Time-variation of waves and river discharge

According to Tanaka and Shuto's (1991) study on river mouth closure at the Nanakita River, the incoming waves with incident angle of about 100° are the most unfavorable for keeping the mouth open, suggesting that onshore sediment transport is more effective for the river mouth closure than the longshore sediment movement. In 1994 data set shown in Fig.2, though, such a relationship between the occurrence of closure and the wave incident angle can not be observed.

Water level variation in the mouth is shown in Figs.3 and 4 for June and November respectively, along with the tidal variation measured in the Sendai Port. The location of the measuring stations can be found in Fig.1.

In June, the closure was firstly observed on 17th, and artificial excavation was carried out on 20th. The water level in the mouth shows less variation before and after 17th and is always higher than the tidal level. Even after the closure, slight time-variation can be seen in the Nanakita River mouth. This is due to the tide propagated through the Teizan Canal shown in Fig.1, which connects the Nanakita and Natori River mouths.

The closure in November was firstly observed on 6th. However, judging from Fig.4, it seems that the closure of the mouth progressed gradually from the end of October. Figure 5 shows a temporal variation of the shoreline in the process of river mouth closure in November. Since it can be confirmed that the topography change affected much the water level inside the mouth (Tanaka and Shuto, 1991), the ratio

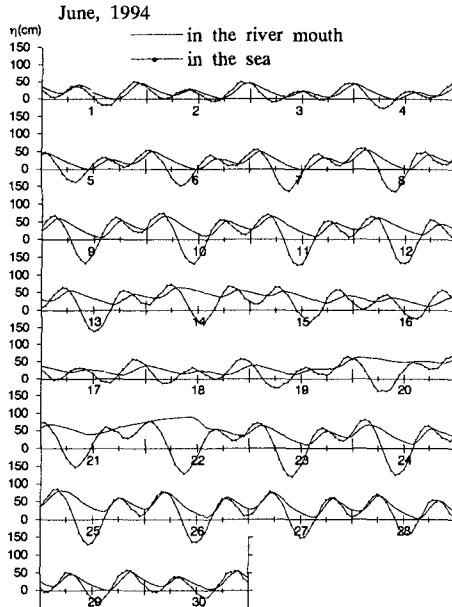


Fig. 3 Water level variation in June

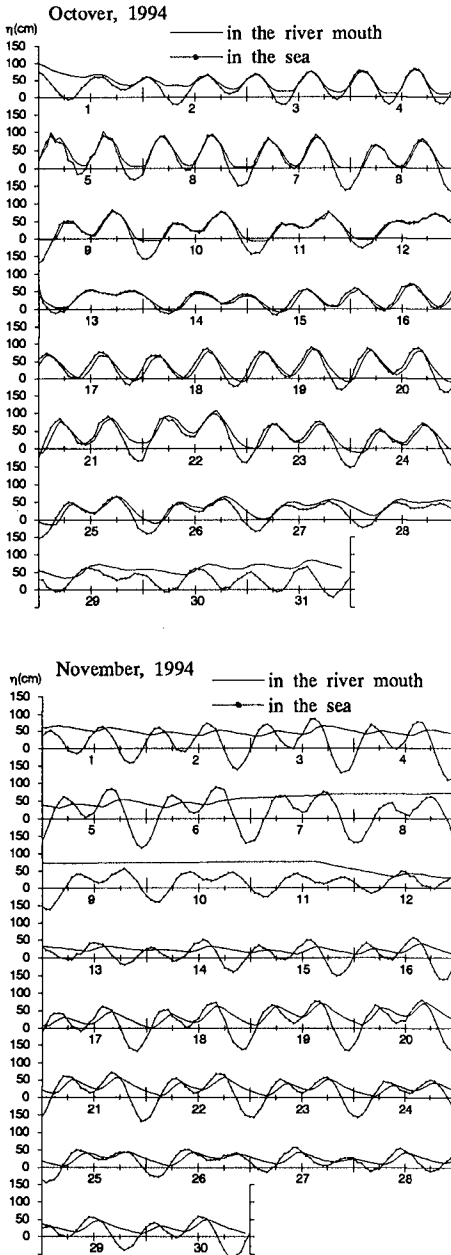


Fig. 4 Water level variation in October and November

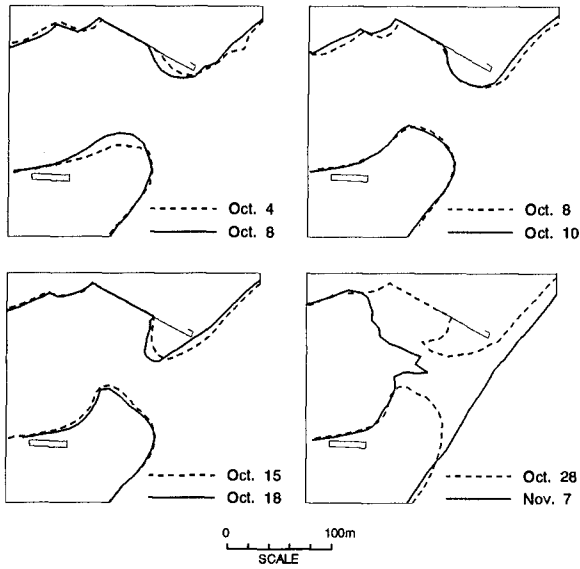


Fig. 5 Shoreline change at the Nanakita River mouth

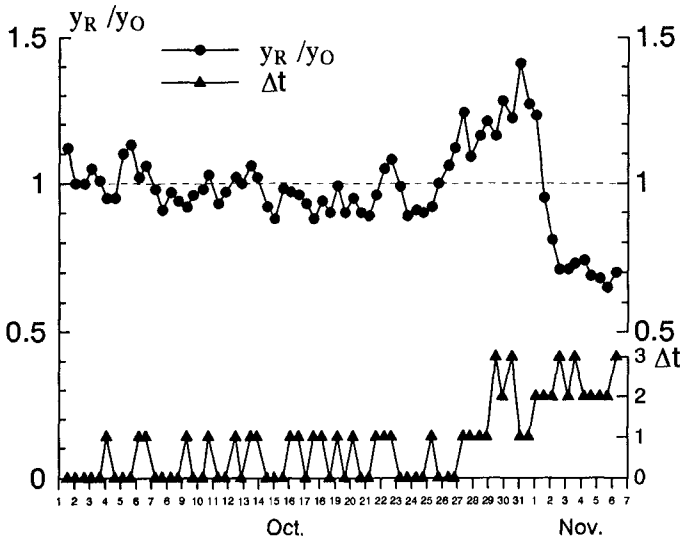


Fig. 6 Water level ratio and lag time

y_R/y_O and the lag time Δt are plotted in Fig.6, where y_R and y_O the daily highest water levels in the river mouth and the sea, respectively, and Δt the time difference between y_R and y_O . At first, the water level ratio shows gradual increase from 1.0 on October 26th to 1.4 on November 1st, and then distinctly decreased to 0.6 on November 3rd, while Δt shows an increase from 0 hour up to 3 hours. Thus, this figure suggests that the river mouth closure was completed on November 3rd. The water level rise in the mouth immediately before the closure in Fig.6 was induced by wave set-up due to wave breaking in front of the river mouth (Tanaka and Shuto, 1992), and the wave set-up height measured in the mouth shows close relationship with the wave height.

3. MATHEMATICAL MODELING

3.1 Governing Equations

A mathematical model proposed by Ogawa et al. (1984) will be employed for predicting closing process at a river mouth owing to predominant wave motion. It is assumed that the wave motion is responsible for the intrusion of sediment into the mouth, while the river discharge is effective for flushing sediment out of the mouth as illustrated in Fig.7. Thus, the corresponding governing equation is expressed as follows (Ogawa et al., 1984).

$$(1 - \lambda)Lh \frac{dB}{dt} = e_r q_r B - e_w (1 - \lambda) Q_w \quad (1)$$

where λ the porosity of sand, L the width of sand spit, h the water depth at a mouth, B the width of a river mouth, and e_r and e_w the efficiency of sediment inflow by waves and that of sediment outflow by current, respectively. The sediment transport rate due to current, q_r , and that induced by wave motion, Q_w , can be evaluated by means of conventional formulae, Eq.(2) (Brown, 1950) and Eq.(3) (CERC, 1984), respectively.

$$q_r = K \left(\frac{u_*}{sgd} \right)^m u_* d \quad (2)$$

$$Q_w = \alpha (Ec_g)_b \sin \theta_b \cos \theta_b \quad (3)$$

where K is the constant (=10.0), u_* the shear velocity, s the immersed specific weight

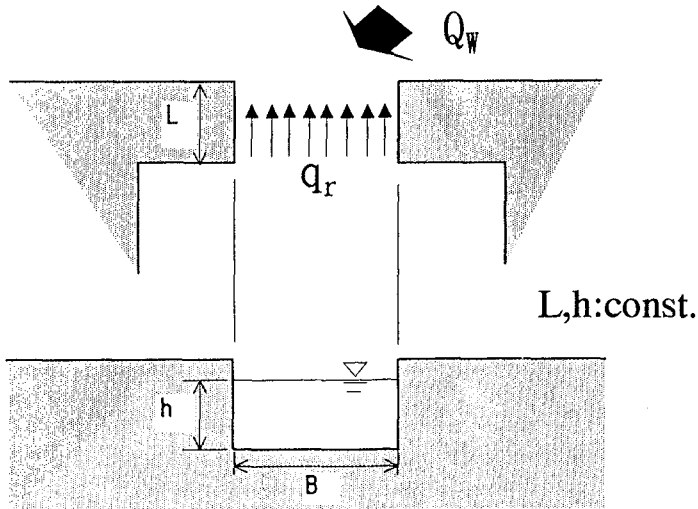


Fig. 7 Schematic explanation for the model

of sediment, g the gravitational acceleration, d the grain diameter, m the power (≈ 2.0), α the empirical coefficient, $(Ec_g)_b$ the incident wave energy flux evaluated at the breaker line, and θ_b the breaking wave angle to the shoreline. The coefficient α in Eq.(3) has already been evaluated to be 0.05 by Tanaka and Shuto (1991) by applying the one-line model to shoreline change adjacent to the Nanakita River mouth.

3.2 Analytical Solution

The following exact solution can be derived from Eq.(1), assuming the wave condition and the river discharge are constant.

$$(B^* - 1) + \frac{A_1^*}{4} \log \left| \frac{(B^* - A_1^*)(1 + A_1^*)}{(B^* + A_1^*)(1 - A_1^*)} \right| - \frac{A_1^*}{2} \left[\tan^{-1} \left(\frac{B^*}{A_1^*} \right) - \tan^{-1} \left(\frac{1}{A_1^*} \right) \right] = -t^* \quad (4)$$

where the dimensionless quantities in Eq.(4) are defined as

$$B^* = \frac{B}{B_0}, \quad A_1^* = 4 \sqrt{\frac{A_1/A_2}{B_0}}, \quad t^* = \frac{A_2 t}{B_0} \quad (5)$$

$$A_1 = \frac{e_r K d (\sqrt{gnQ})^{2m+1}}{(1-\lambda)Lh(sgd)^m h^{7(2m+1)/6}} \tag{6}$$

$$A_2 = \frac{e_w Q_w}{Lh} \tag{7}$$

in which B_0 denotes the initial river width, n the Manning's friction coefficient and Q the effluent discharge consists of fresh water and tidal prism.

Some interesting asymptotic behaviors of a river width can be derived from Eq.(4). First of all, if the river discharge is zero, substitution of $A_1^*=0$ into Eq.(4) yields the following simplification.

$$B^* = 1 - t_* \tag{8}$$

Namely, the dimensionless river width shows linear reduction with the passage of time until it closes completely at $t_*=1$. Secondly, the width of equilibrium stage can be easily obtained by substituting $dB/dt=0$ in Eq.(1). The dimensionless form normalized by B_0 is

$$B_\infty^* = \frac{B_\infty}{B_0} = A_1^* \tag{9}$$

According to Eq.(4), it takes infinite duration to reach equilibrium width, though, t_∞ will be herewith defined as the duration when B becomes $0.99 B_\infty$. A dimensionless form for t_∞ can be derived from Eq.(4).

$$t_\infty^* = A_1^* \left\{ a^* - \frac{1}{4} \log \left| \frac{1+A_1^*}{1-A_1^*} \right| - \frac{1}{2} \tan^{-1} \left(\frac{1}{A_1^*} \right) \right\} + 1 \tag{10}$$

where $a^*=0.722$ for $A_1^*>1$ and $a^*=0.711$ for $0<A_1^*<1$. As A_1^* approaches infinity, Eq.(10) can be approximated by the simple expression,

$$t_\infty^* = 0.723A_1^* \tag{11}$$

Time-variation of dimensionless width, B^* , computed from Eq.(4) is depicted in Fig.8. The parameter A_1^* denotes the ratio of sediment transport rate out of a river mouth due to river discharge to sediment intrusion into a river mouth caused by wave

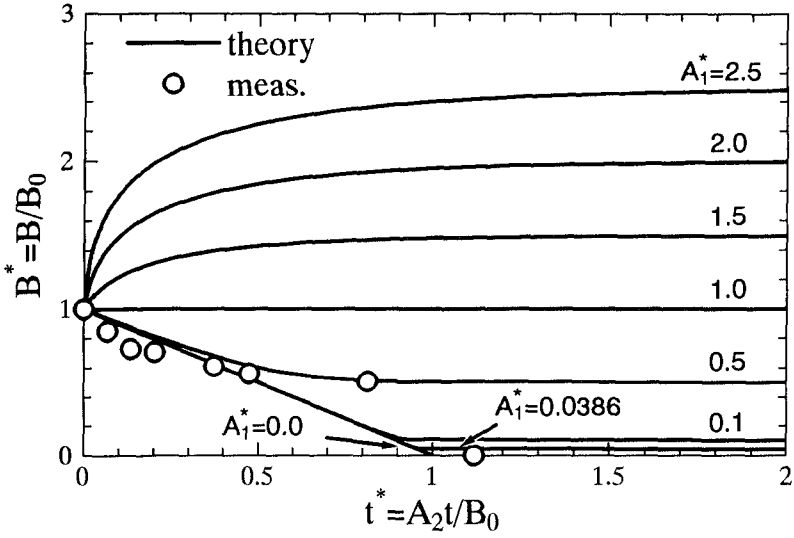


Fig. 8 Time-variation of river mouth width

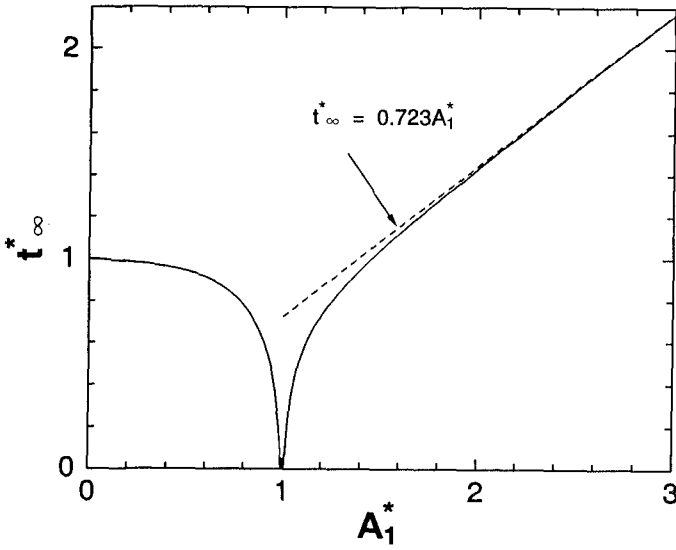


Fig. 9 Relationship between t^*_∞ and A_1^*

motion, as defined by Eq.(5). Thus, the horizontal line for $A_I^*=1.0$ in Fig.8 corresponds to dynamic equilibrium state, in which sediment transport rates out of and into a river mouth are balanced, whereas the family of curves for $A_I^*>1.0$ and $A_I^*<1.0$ represents widening and reduction processes of river mouth. In case of $A_I^*=0.0$, the river mouth closes completely at $t^*=1.0$ as mentioned earlier because of no sediment flushing out of a river mouth. According to the existing theory for river mouth closure without sediment outflow from a river mouth, the solution is given in terms of exponential function, denoting that infinite duration is needed for completion of closure (Tsujimoto et al, 1989). It seems that the present solution, in which closure can be completed within finite duration, is more realistic.

Figure 9 shows the relationship between t_{∞}^* and A_I^* obtained from Eqs.(10) and (11). At $A_I^*=0$, sediment movement at the mouth is in dynamic equilibrium state as described before. Therefore, t_{∞}^* is exactly zero at $A_I^*=0$. The accuracy of Eq.(10) is sufficient as long as A_I^* is higher than 2.0.

3.3 Comparison with Field Observation

The measured shoreline change at the river mouth shown in Fig.5 can be now compared with the present theory. The open circles in Fig.8 denote measured data at the Nanakita River mouth in 1994. Since the wave characteristics and the fresh water discharge are assumed to be constant in the theory, the quantities shown in Fig.2 except wave direction are averaged from October 4th through November 7th, whereas the averaging of wave direction is done from October 4th through November 12th due to lack of the data after November 13th as depicted in Fig.2. As for the coefficients, e_r and e_w in Eq.(1), the values determined by one of the authors (Tanaka, Kabutoyama and Shuto, 1995) are used for the present computation. It is observed that the measured change in the river mouth width shows reasonable agreement with the present theory.

4. CONCLUSIONS

River mouth closure was observed five times at the Nanakita River mouth in Japan in 1994. Conclusions drawn from this study can be summarized as follows:

- (1) One of the authors has already reported that the closures of the Nanakita River mouth in 1988 and 1989 were induced by high waves having a incident angle 100° . In 1994, however, the incident angle of high waves which caused the closure did not show this tendency.
- (2) By analyzing the ratio and lag time between the water level measured in the mouth and that in the ocean, the date when the closure had completed can be determined. Distinct rise of water level in the mouth caused by wave set-up can be observed immediately before the completion of the closure.
- (3) A mathematical model proposed by Ogawa et al. (1984) is used for predicting

time-variation of width at a river mouth under the combined influence of incoming waves and effluent river discharge. Analytical solution can be obtained, assuming constant wave characteristics and fresh water discharge. The measurements and the theory showed reasonable agreement.

5. ACKNOWLEDGMENT

The authors would like to express their grateful thanks to the members of River Engineering Laboratory and Tsunami Engineering Laboratory, Tohoku University, for their cooperation during the course of the field measurements. Their appreciation should be extended to the Shiogama Construction Office, Ministry of Transport, and the Higashi Sendai Construction Office, Miyagi Prefectural Government, for their offer of the field data. A part of this study was supported by a Grant-in-Aid for Scientific Research from the Ministry of Education, Science and Culture of Japan.

6. REFERENCES

- Brown, C.B., Sediment Transportation, In H. Rouse (ed.), *Engineering Hydraulics*, pp.769-857, John Wiley & Sons, Inc., New York, 1950.
- Coastal Engineering Research Center, *Shore Protection Manual*, U.S. Army Corps of Engineers, 1984.
- Ogawa, Y., Fujita, Y. and Shuto, N.: Change in the cross-sectional area and topography at river mouth, *Coastal Eng. in Japan*, Vol.27, pp.233-247, 1984.
- Tanaka, H. and Ito, T.: An estimation method of gorge section at a river mouth, *Coast. Eng. in Japan*, Vol.39, No.1, pp.27-38, 1996.
- Tanaka, H., Kabutoyama, H. and Shuto, N.: Numerical model for predicting seasonal migration of a river mouth, *Computer Modelling of Seas and Coastal Regions II*, pp.345-352, 1995.
- Tanaka, H. and Shuto, N.: Field measurement of topography change at a river mouth, *Proc. Int. Symp. Sediment Transport Modeling*, pp.480-485, 1989.
- Tanaka, H. and Shuto, N.: Field measurement of the complete closure at the Nanakita River mouth in Japan, *Proc. Int. Symp. Natural Disaster Reduction and Civil Eng.*, pp.67-76, 1991.
- Tanaka, H. and Shuto, N.: Field investigation at a mouth of small river, *Proc. 23rd Int. Conf. Coastal Eng.*, pp.2486-2499, 1992.
- Tsujimoto, T., Mori, A., Okabe, T. and Ohmoto, T.: Non-equilibrium sediment transport, *Proc. 33rd Japanese Conf. on Hydr.*, pp.445-461, 1989. (in Japanese)

CHAPTER 354

THE EROSION OF A SALT WEDGE TRAPPED BEHIND A BARRAGE ACROSS AN ESTUARY

Walker¹, S.A., Hamill², G.A. , Johnston³,H.T.

Abstract

The problems associated with the stratification of fluids, particularly in estuaries, are of growing concern. Based on water quality problems which occurred at the River Lagan, N. Ireland, an experimental investigation was undertaken into the fluid mixing process within a stratified flow. High quality temporal measurements have been used to examine the processes of erosion of a saline stratification trapped behind a barrage. Two distinct mechanisms of wedge erosion have been identified, both of which involve the formation of a mixed layer.

Introduction

Density stratification in fluids occur due to variations in momentum, temperature and salinity. Mixing between such strata plays a critical role in various phenomena of meteorology, hydraulics and oceanography. Barrages are now frequently used to improve the visual appearance of estuaries by controlling water levels in a semi-tidal impoundment. In such impoundments fresh river water and salt water from the sea normally mix. However, under certain circumstances a stable stratification occurs between the two fluids. When the flow in a river is low, there is little mixing and therefore limited transfer of oxygen between the fresh and salt water layers. This can lead to oxygen depletion and possibly anaerobic conditions at the bed, with subsequent damage to the aquatic environment.

¹ Research student, ² Lecturer, ³ Senior Lecturer

Department of Civil Engineering, The Queen's University of Belfast, David Keir Building, Stranmillis Road, Belfast. BT7 1NN

Background

Belfast developed along a tidal reach of the River Lagan and many industries were established along the banks of the river. At low tide extensive areas of unsightly mudflats were exposed and so a weir was constructed across the river in 1934 to create, on part of the river, a semi-tidal pond which would cover the muds at all tide states. However, the construction of this weir led to periodic water quality problems. During periods of low river flows, the fresh and saline waters entering the pond from the river and the tidal flow stratified, and there was little flushing of the denser saline water trapped behind the weir. The oxygen content of the trapped water was rapidly depleted by the decomposition of organics in the water and the bed muds. This damaged the fish and plant life in the river and led to the production of hydrogen sulphide.

The demise of riverside industries and the poor river water quality resulted in the city turning away from the river front which rapidly became polluted. The result was that extensive inner city areas were blighted and had little development potential.

In 1969 the construction of a new weir downstream of the Queen's Bridge was proposed to regulate river levels and create an attractive water environment. This proposal was renewed by the River Lagan Working Group in the 1970s and specialist studies were instigated. In 1988, the Civil Engineering Department of The Queen's University of Belfast was commissioned to undertake a study seeking to establish design parameters for a structure which would control the water levels, protect the city against tidal flooding and improve the water quality in the river. The proposed impoundment was just under 5 km. in length with a surface area of 40 ha. This pond would have river flow and urban drainage inputs, some of which would have high biochemical oxygen demand levels.

Research Programme

A research programme was undertaken in which a physical model of some 8 km. of the tidal channel and harbour area, including the proposed impoundment, was constructed to a horizontal scale of 1:150 to establish design and operation parameters for the weir. A scale distortion factor of three was used to ensure adequate depths for the study of salinity profiles in the model.

In conjunction with the construction of the physical model a monitoring programme was established on the River Lagan. Velocity and salinity measurements were taken at a number of stations on the river for use in calibrating the model. The measurements were taken for river conditions ranging from low to flood flows, and at a variety of tidal conditions. The velocity measurements were used to establish boundary roughness values in the model at different water levels. The model was then validated by reproducing salinity profiles measured in the river at different tide states.

Salinity profiles at high tide, established after a number of tide cycles in the model, behind the existing weir showed that for a river flow of 2 cumecs the stratification was well defined and extended over the full length of the impounded reach. When the river flow was increased to 5 cumecs, the entrapped wedge retreated

showing a significant reduction in both volume and concentration. A new weir placed at the proposed downstream site resulted in a pond with characteristics similar to that behind the existing weir. This showed that the construction of a fixed crest weir at the new site would simply replicate the problems of water quality being experienced behind the existing weir.

An active weir design was considered whereby the impoundment would be controlled by a gated weir structure incorporating a system for withdrawal of water at a low level. A gated weir would have the added advantage of being able to exclude high tides as well as controlling water levels in the impoundment. It was decided to use a gate system which would be able to exclude surge tide levels above that which would be reasonable expected at present but which might occur if there was a rise in tide levels due to global warming.

A low level withdrawal system was included to evacuate saline water from behind the weir on an ebb tide, when stratification problems were present in the impoundment. On a flood tide, the weir would allow saline water into the impoundment over the lowered gates. At high tide, the gates would be raised and the low level withdrawal system would be opened. This would allow drawdown of the impoundment, during the ebb tide period, through the low level withdrawal system which would have a capacity of 25 cumecs.

It became clear from the model study that the mixing process involved in this highly stratified situation was unclear. The lack of information for the design engineers to predict the quantity of saline material which would be removed under normal flow conditions indicated the need for a fundamental investigation of the process. This programme of work commenced in 1993, and the initial findings are reported in this paper.

Related research

It has already been established that the entrainment of the salt water is a function of the Richardson number, Ri , of the flow (Ellison 1959). The Richardson number is a measure of the ratio of the gravity forces to the inertial forces in a shear flow having a vertical density gradient. It is widely used as a measure of the stability of the flow with regards to vertical mixing. It generally takes one of two forms, the bulk Richardson number

$$Ri_b = g \frac{\Delta\rho H}{\rho V^2}$$

where $\Delta\rho$ is the density difference, H is the depth of fresh water and V is the average velocity, and the gradient Richardson number

$$Ri_g = -g / \rho \frac{\delta\rho / \delta z}{[\delta v / \delta z]^2}$$

where $\delta\rho/\delta z$ is the density gradient and $\delta v/\delta z$ is the velocity gradient. Turner (1973) and Christodolou (1985) further classified the type of mixing to be dependent on the magnitude of the Richardson number. A critical gradient Richardson number of 0.25 was found to be the limiting criteria between stable and unstable flow.

Experimental facility

To allow a wide test range, upto prototype conditions, a new facility was constructed within the Civil Engineering Department. This new facility consisted of a testing area 20m long, 0.75m wide and 0.75m deep a schematic of which is shown in Figure 1. The salt water was retained between two baffles which were 17.5 m apart. The salt water depth was kept constant at 0.25m whilst the fresh water depths were varied by means of an adjustable weir. The ability to produce conditions in which the saline water was either stationary or flowing, either with or against the prevailing river flow, was included thus allowing the simulation of tidal movements. The results

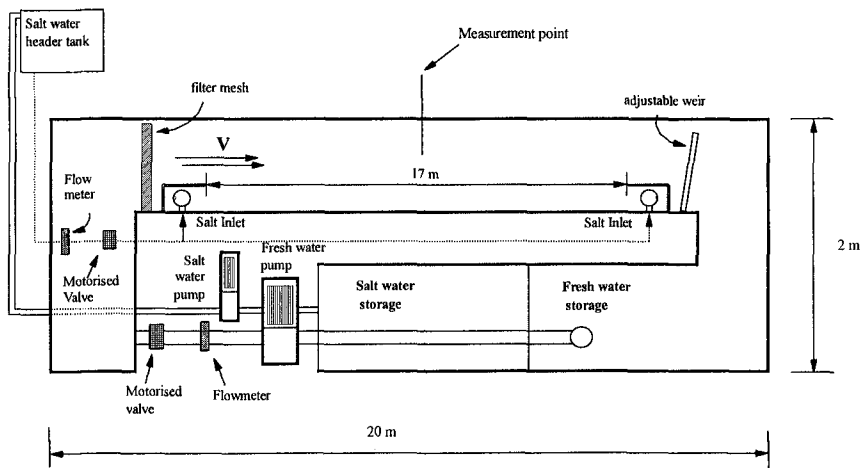


Figure 1 Experimental Facility

presented here represent the condition of a fully trapped saline wedge. Fresh water was mixed with dried salt and dye in the storage tanks and then pumped into the salt water impoundment to a depth of 0.25m. Fresh water was then filled slowly on top, over the course of 12 to 15 hours. Flow was initiated slowly in the upper layer by starting the fresh water pump. Once the flow had reached the required rate the water in the storage tanks was changed slowly by opening the waste valve and filling from the supply. This was necessary due to the contamination of the fresh water which occurred as a result of mixing. The degree of contamination was relatively small in most cases, but large enough to change the salinity of the fresh water over a substantial time period.

The scanning process was commenced after flow was initiated. Velocity and density profiles were obtained at the centre of the channel. Velocity measurements were obtained using LDA with a fibre optic attachment to limit the effect of differing refractive indices. Density measurements were obtained using a conductivity probe with small measuring volume. The probe consisted of two wires 5 mm thick which

were completely covered except for 2 rings, 2mm thick, near the bottom. Both probes were mounted on a linear actuator which was computer automated. The probes were placed in the salt water, usually about 20 to 30mm below the interface in order to obtain a reading of maximum salinity. An average was taken over a period of 30 seconds and the probes were then moved in a 5 mm step so that the vertical density profile could be obtained. Due to the temporal nature of the experimental investigation it was necessary to obtain as many profiles per hour as possible. The profile obtained was therefore not a full vertical traverse but was limited to 120mm around the interface. With time the interface moved downwards, as salt water was removed by entrainment from the impoundment, and it was necessary to incorporate movement of the base profile position into the scanning program.

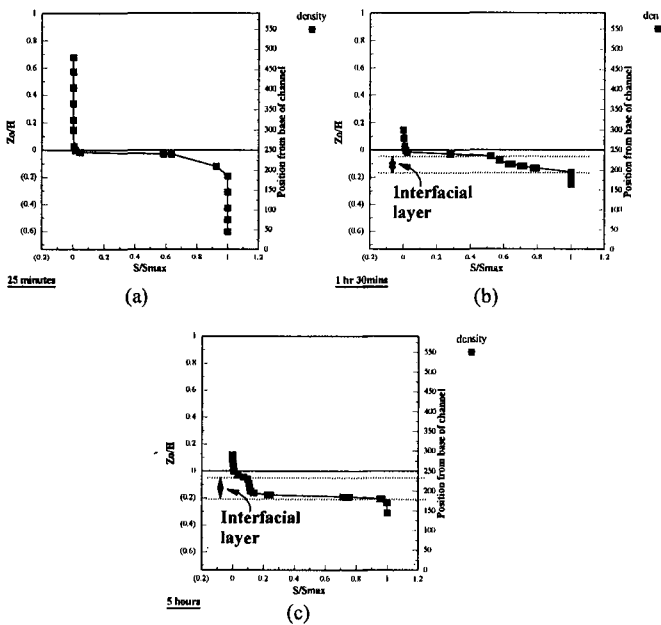


Figure 2 Density profiles (a) After 25 minutes (b) After 1 hour 30 minutes (c) After 5 hours

Development of Interfacial Layer.

The development of the mixing interfacial layer, as fresh water was allowed to flow across the stationary salt wedge, was studied with time. Figure 2 (a) shows the initial condition used in all tests. It clearly displays the fresh and salt water zones. Figures 2 (b) and 2 (c) are for the same situation, but with time having advanced to 1 hour 30 minutes and 5 hours respectively. The presence of a flow in the fresh water can be seen to have developed an interfacial layer, in that there is no longer a clear distinction between the fresh and salt water. It is from within this interfacial layer that the majority of entrainment of the saline liquid takes place.

This is clearly visible by the changing density gradient within the interface. The density within the interfacial layer was taken to be the average value within the density gradient of the layer. Figure 3 shows the interfacial layer in detail. It can be seen that the layer is defined by that position of the mixing region over which the variation of density occurred, this variation being taken as linear for purposes of analysis. The thickness of the interfacial layer was also obtained on this basis.

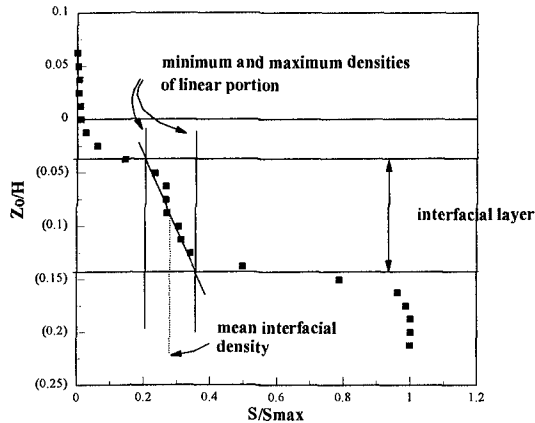


Figure 3 Definition of interfacial layer

It was found that the behaviour of this layer varied with certain combinations of flow, depth and density difference, and two mechanisms of erosion existed. In the first of these the wedge was eroded by sequential stripping of the interfacial layer, this process was labelled as oscillating due to the cyclic nature of the event. The second mechanism showed no such cyclic behaviour, with the density of the mixing layer decreasing to a steady state value. This mechanism was labelled as being non-oscillating. Significant differences in the temporal development and entrainment process was found for each mechanism.

Oscillating mechanism

Using the density profiles obtained from the experimental investigation, the layer position was plotted with time. Figure 4 represents a typical test which displayed the cyclic behaviour. On it can be seen the change, with time, in thickness of the interfacial layer and the density within that layer. The decrease in layer density corresponds with an increase in the layer thickness, this is as would be expected and closely mirrors the initial stage of the steady state condition. However, a critical point is reached where upon the density within the layer starts to increase again, with a corresponding decrease in the layer thickness. This corresponded to a period of rapid upper boundary movement when part of the layer was washed out. When the layer was at its thinnest there appeared to be an increase in the lower boundary movement,

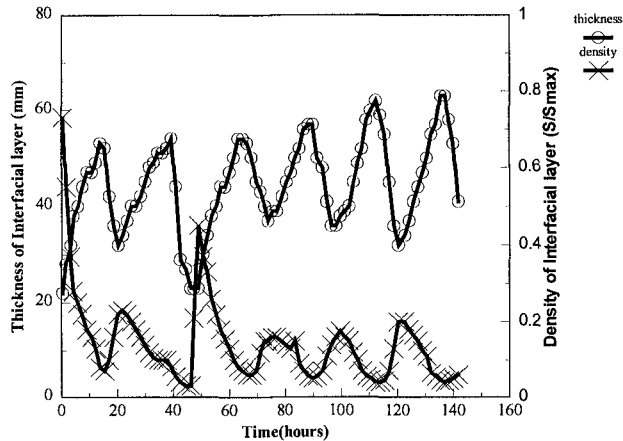


Figure 4 Relative interfacial layer density and thickness (oscillating mechanism)

as the free stream was now much closer to this boundary. This resulted in entrainment from the salt pool within the wedge. It would appear that for the oscillating process as the density of the layer decreases, the interfacial slope increases in order to resist the interfacial shear stresses. Figure 5 shows the variation of typical velocity and density gradients. These also show a definite cyclic behaviour with the maximum velocity gradients occurring when the layer was most dense.

If the change in the gradient Richardson number is examined, as shown on Figure 6, it can be seen that when the upper part of the layer was removed, the value of Ri dropped to approximately 0.25. As this represents the critical Richardson number it implies that the flow becomes unstable at these times, and this was confirmed by the presence of large amplitude breaking waves.

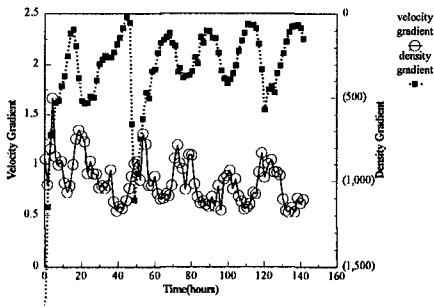


Figure 5 Interfacial velocity and density gradients (oscillating mechanism)

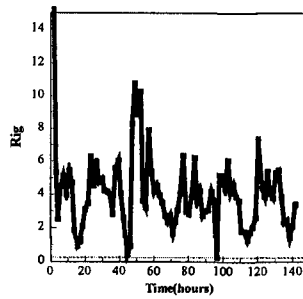


Figure 6 Variation of gradient Richardson number (oscillating mechanism)

Non Oscillating mechanism

Whenever no oscillation of the mixing layer characteristics occurred the removal of the trapped saline solution progressed steadily with time. The time taken to achieve this varied with the magnitude of the circulation velocity within the mixing layer. Figure 7 shows the typical variation of the interfacial density and layer thickness for those tests which eroded at a steady rate. An initial high growth rate of the mixing layer occurred both in thickness and density, where upon almost constant conditions prevailed, and the saline pool was steadily depleted. Comparison with the equivalent figure for the oscillating test (figure 4) shows clearly the different mechanism of erosion in action. The velocity and density gradients also can be seen, in figure 8, to remain constant once the layer became established, as did the gradient Richardson number. Figure 9 gives an indication of typical variations in the Richardson number for non oscillating tests. The accepted threshold of instability in the flow occurs when the Richardson number fall below a value of 0.25.

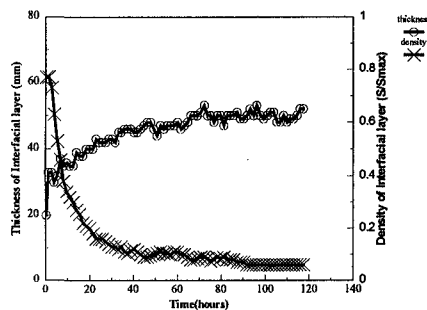


Figure 7 Relative interfacial density and thickness (non oscillating mechanism)

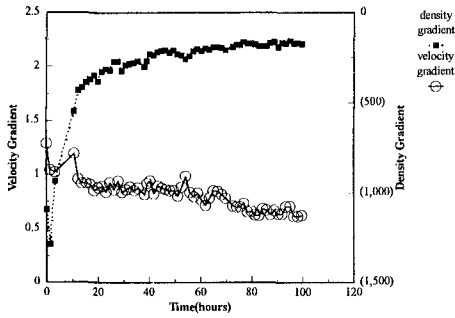


Figure 8 Interfacial velocity and density gradients (non oscillating)

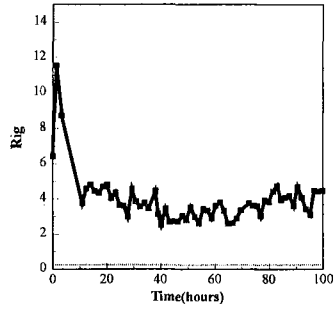


Figure 9 Variation of gradient Richardson number (non oscillating)

At no point during any of the tests which showed no oscillation did the Ri_g number approach this threshold. The key to the two mechanisms is therefore clearly a function of the flow instability.

Transport Rates

The changes in the density profiles obtained at different times during each test were used to determine the rate of erosion of the salt water impoundment. Transport across the upper boundary gave the overall rate of salt water removal during the test. This was calculated by approximating the profile, as can be seen in Figure 10, based on the position of the boundaries and the density of the layer. This allowed the volume of salt to be calculated very easily, with the differences between profiles at different times being taken as the as the volume of salt water transported. Any change in density of the interfacial layer, or drop in position of the upper boundary, was deemed to be due to transport across the boundary. Transport rates across the lower boundary were determined in a similar manner.

Based on a dimensional analysis, a dimensionless form of transport was used. This dimensionless transport, T, was defined as

$$T = \frac{t}{\Delta\rho V H}$$

where t is the average transport (kg/s), $\Delta\rho$ the initial density difference, V the initial average fresh water velocity and H the initial fresh water depth.

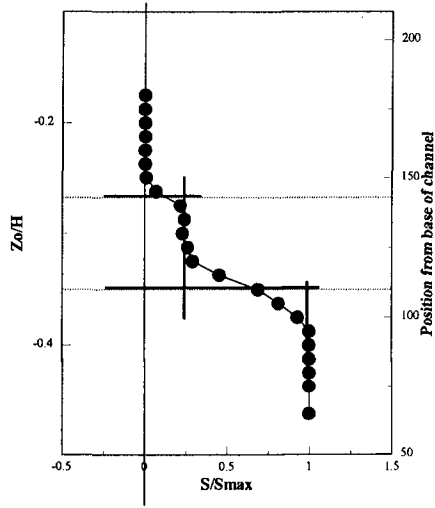


Figure 10 Stepped approximation for density profile

Figures 11 and 12 show the average transport rates obtained for the oscillating and non oscillating mechanisms respectively, plotted against the bulk Richardson number. It can be seen that in each case there exists a strong linear relationship between the rate T , and the Ri_b value, and that the rate obtained for each mechanism is similar, with the major difference occurring in the rates across the upper and lower boundaries.

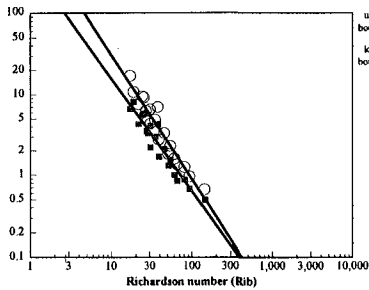


Figure 11 Dimensionless transport rates (oscillating mechanism)

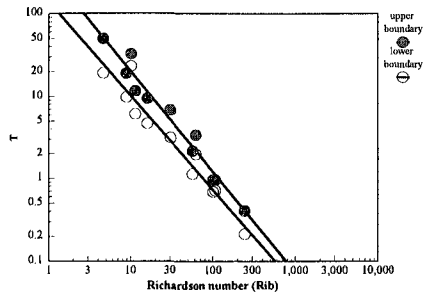


Figure 12 Dimensionless transport rates (non oscillating mechanism)

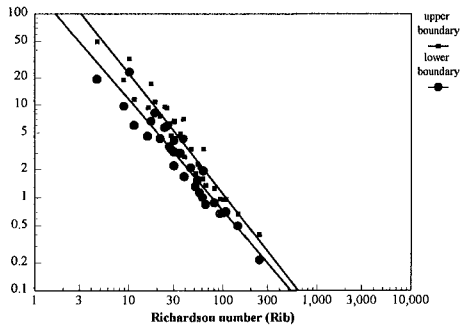


Figure 13 Dimensionless tranport rates for both mechanisms

Figure 13 is a combined plot for the transport rates obtained for both mechanisms of erosion. It can be seen that within each mechanism the transport rates were similar and could be best described by equations of the form

$$T_u = 447.2 Ri_b^{-1.303}$$

for the transport across the upper boundary and

$$T_l = 184.2 Ri_b^{-1.2}$$

for the transport across the lower boundary.

Conclusion

In all cases interfacial mixing resulted in the formation of an interfacial or mixed layer which was around 30 to 40 mm thick. Only those tests conducted with low values of Reynolds number (i.e. <2000) showed no mixing.

Two mechanisms of erosion have been observed. These were classified as oscillating and non-oscillating, depending on the behaviour of the layer in terms of its relative density and thickness. In some tests the density of the layer decreased rapidly, and then remained constant and these were classified as non-oscillating. In a number of cases the density within the layer decreased initially and then increased again after the upper part of the layer was removed. These tests were classified as oscillating as a cyclic behaviour was observed in the layer density.

The gradient Richardson number remained approximately constant during those tests which did not oscillate, indicating a stable flow. For those tests which showed the oscillating behaviour, the value of Rig was found to show a cyclic behaviour. When the layer was washed out, the value of Rig dropped towards 0.25, indicating unstable flow. Mixing occurred as a result of large amplitude breaking interfacial waves.

After the start of a test greater rates of transport were observed at the upper boundary as the layer formed. This resulted in a decrease in density until the layer washed out and a peak rate was observed at the upper boundary. Greater rates of transport were observed at the lower boundary when the layer was thinnest. This caused the density of the layer to increase with time.

Average transport rates were calculated during each test from the change in density profiles. Rates were averaged over the duration of the test and calculated for both boundaries. Dimensionless transport rates were found to be best related to the bulk Richardson number (Rib) with higher rates of transport for low values of Rib .

It is hoped that the ability to estimate the removal rate of trapped salt water will aid the process of barrage design, and act as a tool for river management schemes by which the inducement of natural mixing can be accounted for.

References

Christodolou, C.G. (1985) "Interfacial mixing in stratified flows" J. Hyd. Research, Vol. 24, No. 2, pp 77-92

Ellison, T.H. and Turner, J.S., (1959) "Turbulent entrainment in stratified flows" J. Fluid Mech., Vol. 6, pp 423-448

Turner, J.S., (1973) "Buoyancy effects in fluids" Cambridge University Press.

CHAPTER 355

Near-Field Measurements of a Buoyant Jet in Waves and Currents.

K.H. Kwan¹ & C. Swan².

Abstract.

The present paper concerns the near-field characteristics of a jet discharged into a wave environment, and contrasts the results of two new experimental studies with a modified integral solution based upon a quasi-Lagrangian description of the flow field. This solution differs from previous attempts to model near-field wave mixing (namely Koole and Swan, 1994) in that it is formulated within an absolute frame of reference, and therefore adequately incorporates the momentum flux associated with the entrained fluid. Having implemented this important modification, the Lagrangian model is shown to provide a good quantitative description of a buoyant hot-water jet discharged into either a steady current or an unsteady wave field. In particular, there is no uncertainty regarding the magnitude of the entrainment coefficients, and as such the model is suitable for design calculations. In addition, detailed comparisons between the temperature profiles ensemble-averaged with respect to the phase of the wave cycle hint at a new mixing mechanism. Experimental data is presented which suggests that the wave-induced oscillatory motion leads to the division of the jet at certain phases of the wave cycle. If this effect is indeed important, then it implies that the average dilution will be enhanced when a jet is discharged into the plane of the wave motion.

Introduction.

Under most practical conditions outfalls discharge their pollutants, whether it be unwanted heat or partially treated effluent, into coastal waters which are dominated by the effects of wave action. However, present design practice largely ignores the wave motion and applies a simplistic approach in which both the

¹ Research student & ² lecturer, Department of Civil Engineering, Imperial College, London. SW7 2BU. United Kingdom.

concentrations and the velocities arising within the near-field are predicted using some form of integral solution (Morton et al, 1956) based upon the conservation of mass, momentum, and where appropriate species concentration. This approach is often justified on the basis that the wave motion will, at worst, produce additional mixing and thus the design calculations are conservative. Unfortunately, recent studies (Koole and Swan, 1995) have shown that this does not necessarily follow, and that under some circumstances the wave motion may produce local increases in the concentration levels. Furthermore, previous studies have also clearly demonstrated that the occurrence of any additional wave-induced mixing is critically dependent upon the flow conditions at the exit nozzle. In particular, the ratio of the exit velocity to the local wave-induced velocity is a significant parameter. This in itself has important design implications given the increasing tendency to build long-outfalls. These are constructed so that firstly, the source of the pollutant is far removed from the adjacent coastline; and secondly, it is discharged in deeper water so as to reduce the pollutant concentrations arising at the water surface. Although, at first sight, these objectives appear desirable, the construction of a long-outfall may inadvertently move the pollutant source to a location at which the effective wave-induced mixing is negligible. As a result, the increased construction costs may actually produce higher concentrations at the water surface, and therefore potentially increase the risk of pollutant contamination arising on an adjacent coastline.

However, in order to incorporate these effects within the design process, and thereby optimise the efficiency of a given outfall design, one first requires a quantitative model capable of predicting the additional wave effects within the near-field. Although previous studies (notably Chin, 1988 and Koole and Swan, 1994) have considered this problem, quantitative comparisons with laboratory data are at best inconclusive. The present paper addresses this point, and provides a brief description of a corrected model which is subsequently shown to be in good quantitative agreement with new laboratory data describing a buoyant hot-water jet discharged into both a steady current and an unsteady (or time-dependent) wave field.

Background.

Although previous studies have clearly demonstrated the potential importance of wave-induced mixing (Sharp (1986), Chyan et al. (1991) and Hwung et al. (1995)); the only papers to have considered an appropriate mixing model are Chin (1988), Koole and Swan (1994) and more recently Chu and Lee (1996). In the first two cases the models were written with the specific intention of incorporating wave effects, while the latter model has to date only been applied to the description of pollutants discharged in a steady current. However, each of these models are similar in that they apply a quasi-Lagrangian representation of the flow field in which elements of the pollutant jet are tracked within the ambient flow.

Detailed comparisons with laboratory data involving both two-dimensional plane jets and three-dimensional round jets suggest that the model outlined by Koole and Swan (1994 and 1995) provides a good qualitative description of a jet discharged in waves. In particular, this model provides a plausible explanation for the non-Gaussian characteristics of the time-averaged radial distributions (both in terms of velocities $u(r)$ and concentrations $C(r)$), and suggests that the occurrence of a bi-peaked or flat-topped distribution is simply dependent upon the local ratio of the jet diameter to the wave-induced displacement of the jet axis. Furthermore, the multi-stage centre line decay (i.e. $u(z)$ or $C(z)$ at $r=0$) first noted by Chyan et al. (1991) may also be explained (at least qualitatively) by the wave-induced displacements, and is a clear consequence of applying a time-averaged representation of a cyclic process.

Unfortunately, quantitative comparisons between the laboratory data and the model predictions proved more difficult. In particular, Koole and Swan (1995) demonstrated that good agreement along the time-averaged jet axis could only be obtained if the coefficient of forced entrainment (Winiarski and Frick, 1976) was set at $\beta=1.0$; and, in addition, the coefficient of radial entrainment was increased three-fold with respect to the value typically adopted in a stagnant ambient (i.e. $\alpha=3 \times 0.055$). The first of these points is consistent with previous studies, and stresses the importance of forced entrainment in non-stagnant ambients. However, the three-fold increase in the coefficient of radial entrainment is perhaps more difficult to explain. Koole and Swan (1994) argued that this change was justified by the large increase in the turbulent shear stresses ($\rho u'v'$) measured along the boundary of the jet discharged in a wave environment. However, no attempt was made to correlate the Reynold's stresses with the increased entrainment, and consequently it remains unclear whether a large increase in the coefficient of radial entrainment represents a genuine increase in the rate of mixing, or merely arises due to some inadequacy within the model formulation.

To help clarify this point the Lagrangian model proposed by Koole and Swan (1994) was applied to the case of a vertical jet discharged in a steady cross-flow (i.e., the ambient fluid flow is perpendicular to the initial jet axis). Although a Lagrangian model is equally applicable to this case, or indeed any other, there is a clear distinction between the cross-flow and waves cases in that previous researchers (Lee and Cheung, 1990) have already confirmed that for the case of a jet discharged into a steady cross-flow the appropriate entrainment coefficients are given by $\beta=1.0$ and $\alpha=0.055$. In other words, in this case it is well known that the ambient flow has no effect upon the coefficient of radial entrainment.

If (x,y,z) represent the usual Cartesian coordinates in which (x,y) defines a horizontal plane and z is measured vertically upwards; the trajectory of a vertical jet subject to a cross-flow orientated along the x axis may be represented on the (x,z) plane. Figure 1 concerns four such cases corresponding to $u_j/u_a=45.1, 20.0, 16.2$ and 11.7 ; where u_j is the exit jet velocity and u_a is the ambient cross-flow velocity. In each of these cases laboratory data describing the jet trajectory (Patrick, 1967) is

compared with the results of the Lagrangian model proposed by Koole and Swan (1994) in which the entrainment coefficients are defined as $\alpha=0.055$ and $\beta=1.0$. The agreement between the measured data and the model predictions is clearly very poor, and suggests (at least in this case) that this Lagrangian description of the flow field is fundamentally incorrect.

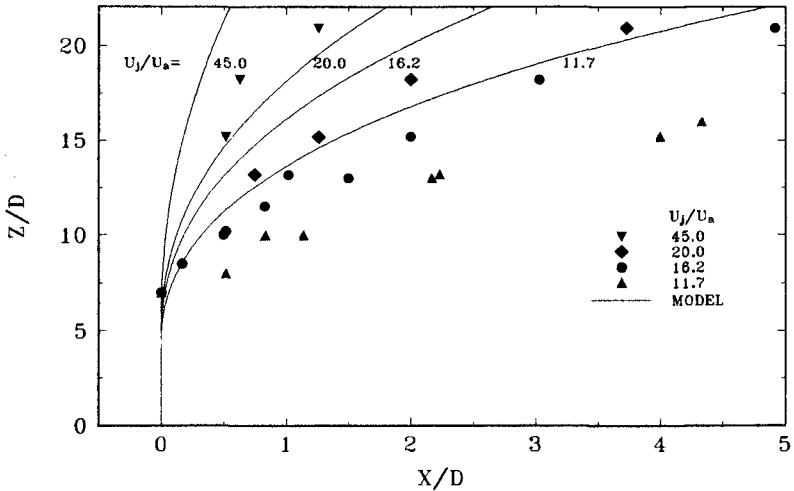


Figure 1. Jet trajectory: comparisons with a Lagrangian model formulated in a relative frame of reference.

Improved Integral Formulation.

In attempting to explain the apparent inadequacy of the previous Lagrangian models (namely Chin 1988 and Koole and Swan 1994) the recent formulation proposed by Chu and Lee (1996) was noted. Although there are many similarities between these three models, the latter solution is quite distinct in that the integral equations are formulated in an absolute frame of reference. The distinction between this and the relative frame of reference, used in the former models, is shown to be very important and in particular accounts for discrepancies within the momentum conservation equation. Figure 2 concerns a simple jet element of area A_j which has a velocity u_j measured relative to the ambient fluid, which itself has a velocity u_a . The vector sum of u_j and u_a defines the instantaneous jet axis such that u_j and u_a are respectively at angles of γ and δ to the ξ -axis. In a relative frame of reference, or one moving with the ambient flow, the conservation equations relating to mass and momentum are given by:

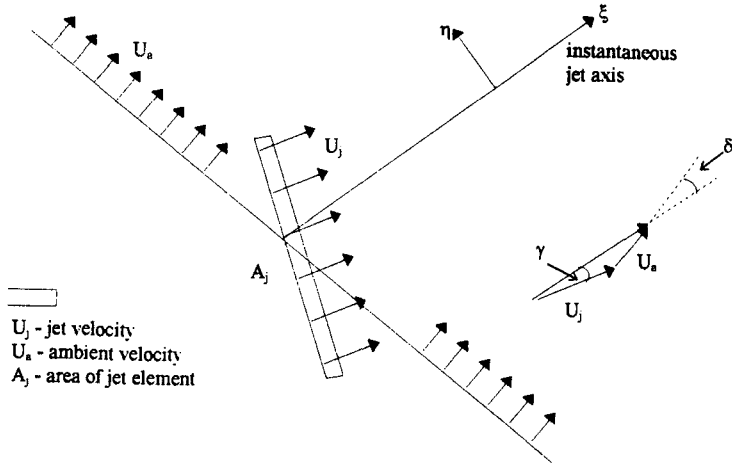


Figure 2. Definition sketch.

$$\frac{\partial}{\partial \xi} \int_{A_j} u_j \cos \gamma d\eta = \alpha u_j 2\pi b_j \cos \gamma + 2b_j \beta |u_j \sin \gamma|$$

1a.

$$\frac{\partial}{\partial \xi} \int_{A_j} (u_j \cos \gamma)^2 d\eta = 0$$

1b.

where again α is the coefficient of radial entrainment, β is the coefficient of forced entrainment and b_j is related to the radius of the jet element. In contrast, the same conservation equations written within an absolute frame of reference are given by:

$$\frac{\partial}{\partial \xi} \int_{A_j} u_j \cos \gamma d\eta = \alpha u_j 2\pi b_j \cos \gamma + 2b_j \beta |u_j \sin \gamma|$$

2a.

$$\frac{\partial}{\partial \xi} \int_{A_j} (u_j \cos \gamma + u_a \cos \delta)^2 d\eta = u_a E$$

2b.

where E corresponds to the total mass of fluid entrained into the jet element, and is given by the right hand side of equation 2a (or 1a). Comparisons between these equations immediately confirm that while the mass conservation equation is unaltered (since the entrainment of fluid is dependant upon a relative velocity effect), the equations defining the conservation of momentum (1b and 2b) differ significantly. In particular, equation 2b incorporates the momentum of the entrained fluid.

In light of these differences a new Lagrangian model was written in which the integral equations were formulated in an absolute frame of reference. A complete description of this model is beyond the scope of the present paper (see Kwan and Swan, 1997), but comparisons with the previously noted cross-flow data (Patrick, 1967) suggest that this modification is sufficient to explain the inadequacy of the previous model highlighted in figure 1. Indeed, figure 3 shows a similar set of comparisons with the new model, and confirms that a good description of the jet trajectory can indeed be achieved with the previously recorded entrainment coefficients ($\alpha=0.055$ and $\beta=1.0$).

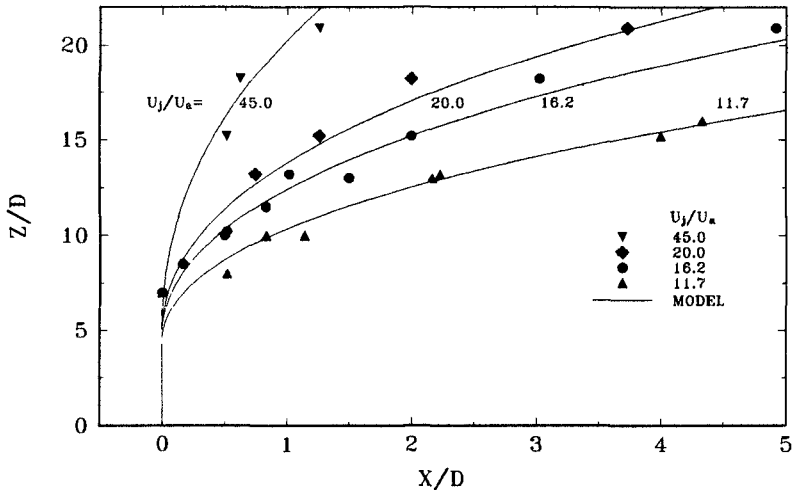
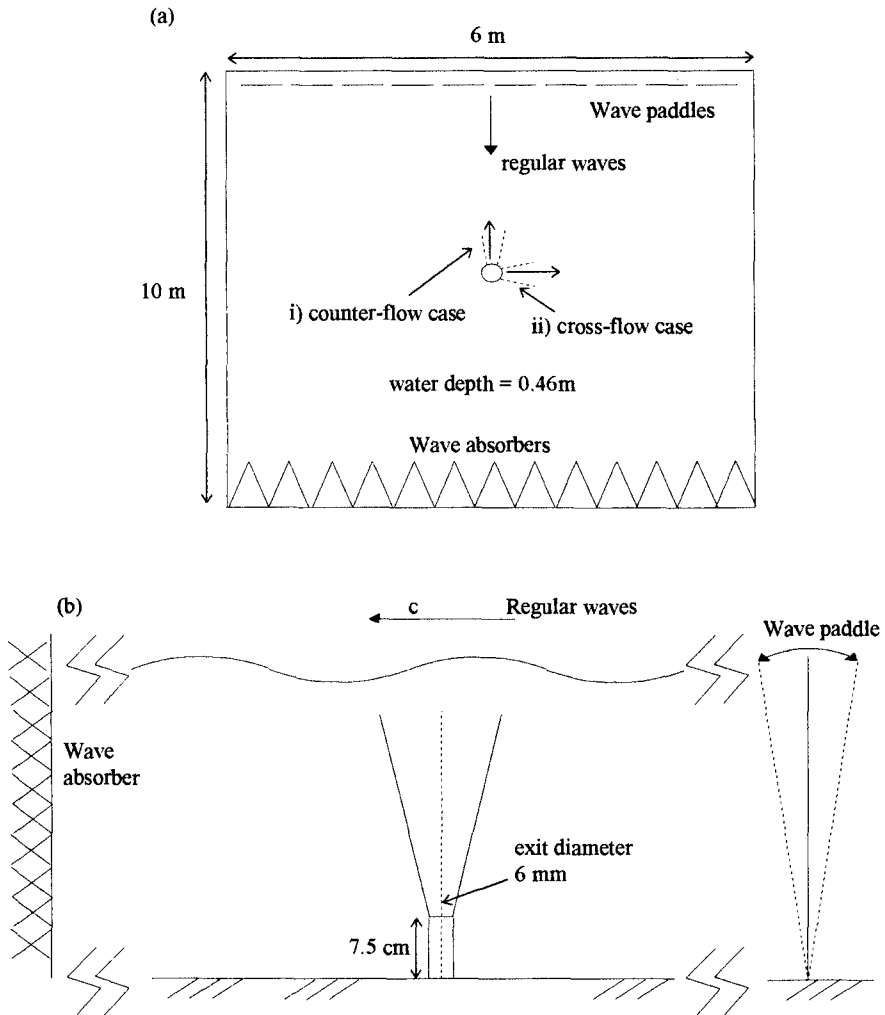


Figure 3. Jet trajectory: comparisons with a Lagrangian model formulated in an absolute frame of reference.

Experimental Work.

To further clarify the near-field behaviour of a jet discharged into a wave environment a new experimental programme was undertaken. In the first stage a buoyant hot-water jet was discharged horizontally beneath a series of regular waves having a period of $T=1$ s and a wave amplitude of $a=0.032$ m. These measurements were undertaken within a small wave basin located in the hydraulics laboratory within the Civil Engineering Department at Imperial College. This facility has a plan area of 6m x 10m, and has an effective working depth of 0.46m. At the upstream end of the basin the waves were generated by 10 individually controlled random wave paddles each 0.6m wide; while at the downstream end the wave energy was dissipated on a one in ten sloping beach, with further passive absorption provided by several large blocks of poly-ether foam. The hot-water jet was introduced in the centre of the wave basin through a horizontal nozzle of diameter $D=6$ mm, with its centre line

located 150mm above the bottom boundary. Although several orientations of the jet relative to the direction of wave propagation were considered, the present paper only addresses one case in which the jet was discharged perpendicular to the plane of the wave motion. In this case the exit characteristics of the jet were such that its temperature was 17°C above the ambient water temperature, and its velocity was 0.76m/s. These conditions correspond to a densimetric Froude number of $F_{ro}=45$ and a velocity ratio of $u_j/u_a=10.9$, where u_a now represents the maximum wave-induced ambient velocity at the elevation of the discharge nozzle. A sketch describing the layout of this test case is given on figure 4a.



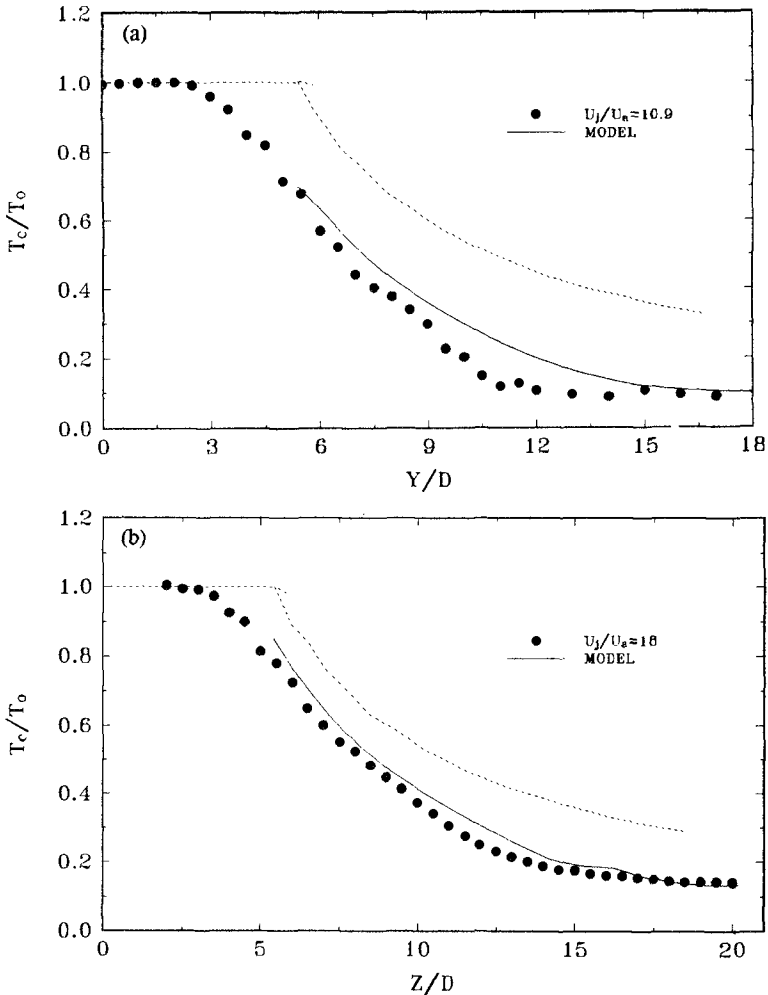
Figures 4a-4b. Experimental apparatus: (a) horizontal jet, and (b) vertical jet.

In a second series of tests a vertical hot-water jet was discharged from a similar nozzle located 75mm above the bed of a two-dimensional wave flume. This facility, which is again located in the Civil Engineering Department at Imperial College, is 25m long, 0.3m wide, and (for the duration of the present tests) had a working depth of 0.62m. The wave conditions again consisted of a regular wave train having a period of $T=1.0$ s and wave amplitude of $a=0.3$ m. Likewise, the exit temperature of the jet was again 17°C above the ambient water temperature and the exit velocity was 0.76 m/s. These conditions are similar to those occurring in the previous test case, and correspond to a densimetric Froude number of $F_{\rho}=37.8$ and velocity ratio of $u_j/u_a=18$. A sketch showing the layout of this case is given on figure 4b.

In both test cases the near-field mixing was quantified using an array of thermocouples. These were supported in a two-dimensional traverse having a positional accuracy of ± 0.5 mm in both the horizontal and the vertical directions. Each thermocouple was constructed from k-type thermocouple wires having an external diameter of 3 microns, and fused at one end to produce a measuring volume with a diameter of $\phi \leq 0.2$ mm. Although probes of this type were difficult to handle, their size was essential to ensure the required accuracy and response (0.1°C in 0.01 s). After careful calibration this measuring apparatus was able to resolve the temperature fluctuations within an individual wave cycle, and was thus deemed appropriate to determine the nature of the mixing processes.

Discussion of Results.

Figures 5a and 5b respectively concern the horizontal and vertical jets discussed above, and describe the decay in the time-averaged temperatures measured on the central axis of the jet. In both cases the measured data is compared with two models. The first, indicated by a dashed line, represents a standard integral solution based upon the assumption that the jets were discharged into a stagnant ambient; while the second, indicated by a solid line, represents the results of the new Lagrangian model outlined above. In this latter case it is important to note that although the Lagrangian model is not in perfect agreement with the laboratory data, it provides a significant improvement over the stagnant ambient model. Furthermore, unlike the previous formulations proposed by Koole and Swan (1994), there is no uncertainty with regard the entrainment coefficients (α , β). Indeed, the calculations presented on figures 5a and 5b are based upon the widely accepted entrainment coefficients commonly applied in both stagnant and steady flows (i.e. $\alpha=0.055$ and $\beta=1.0$).



Figures 5a-5b. Centre-line temperature decay: (a) horizontal jet and (b) vertical jet.

To further examine the success of the Lagrangian solution figure 6 concerns the time-averaged temperature profiles at five elevations above the vertical jet, and contrasts the measured data with the model predications. These comparisons clearly suggest that the modified Lagrangian solution is, in general, in good quantitative agreement with the laboratory data. However, on closer inspection it is apparent that the temperature profiles become increasingly asymmetric at higher elevations above the discharge orifice. This pattern has been observed in several other test cases and is, at first sight, very difficult to explain since one would assume that the cyclic nature of the wave motion effects both sides of the jet in an identical manner. However, if one considers that the central core of the jet, at least in the near-field region, provides

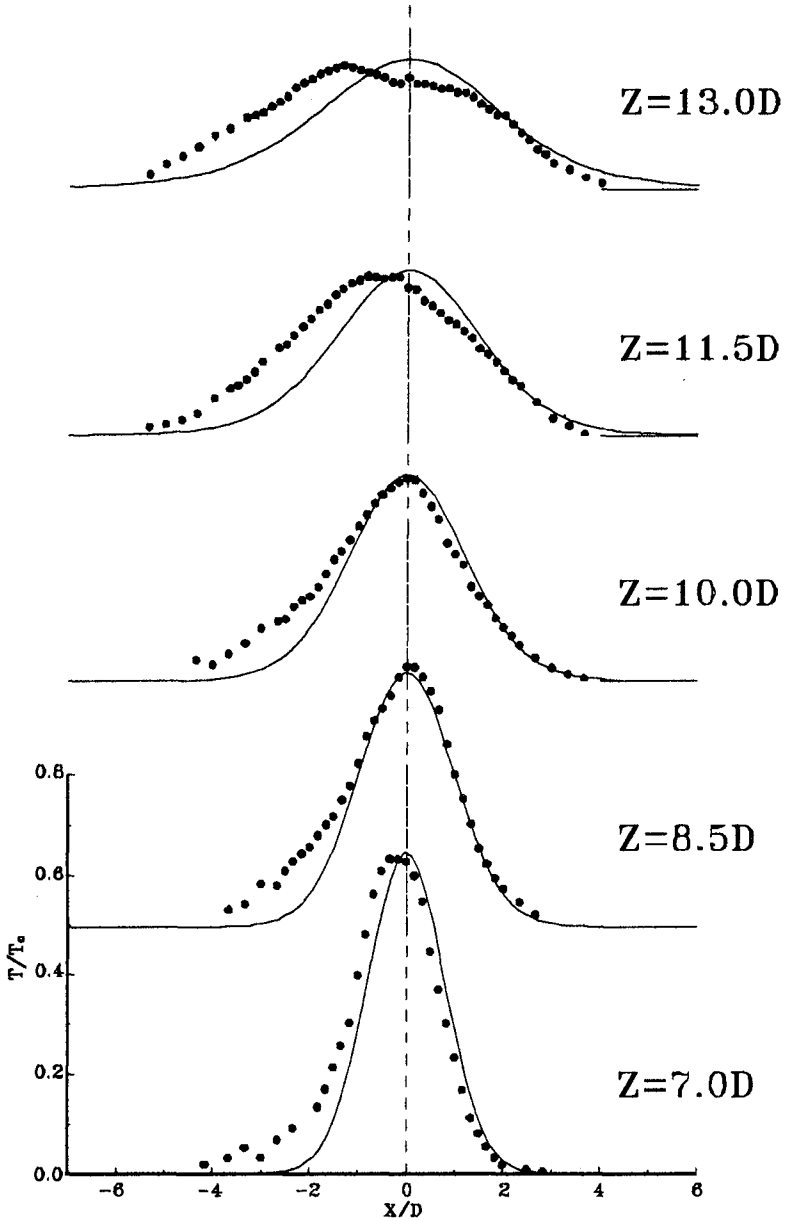


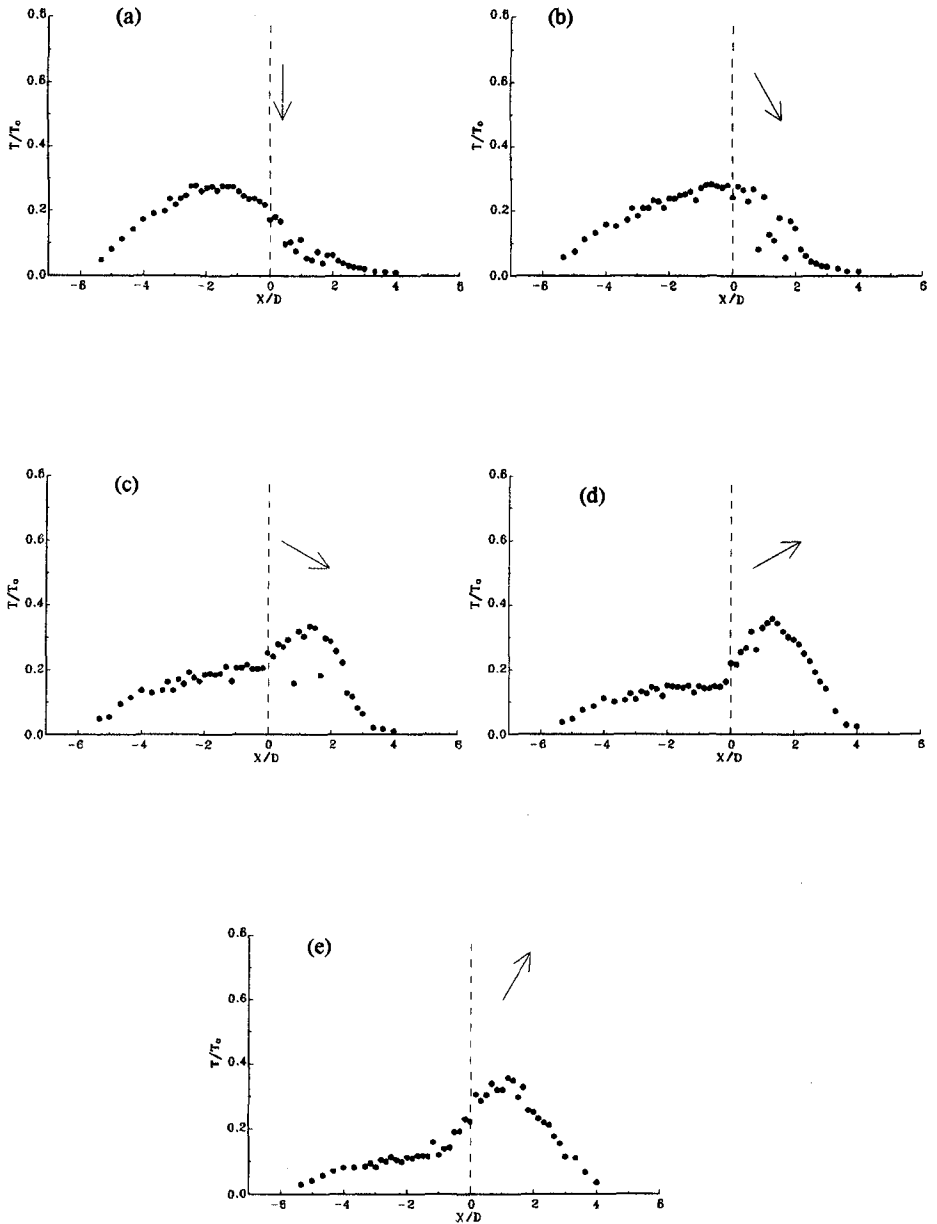
Figure 6. Time-averaged temperature profiles measured above the vertical jet.
● laboratory data, — Lagrangian model.

an effective barrier to the wave motion in the vicinity of the jet, it becomes apparent that the upstream and downstream sides of the jet (measured relative to the direction of wave propagation) experience very different flow regimes. Adopting the usual notation whereby a co-flow corresponds to the movement of ambient fluid in the same direction as the jet velocity, and a counter-flow opposes the jet velocity, it can easily be shown that the upstream side of the jet is subject to a transition from a co-flow to a cross-flow, while the downstream side of the jet experiences a transition from a counter-flow to a cross-flow. These changes occur between phase angles $0 \leq \theta \leq 0.25$ and $0.5 \leq \theta \leq 0.75$ respectively, where $\theta=0$ corresponds to a zero up-crossing. The difference between these regimes provides a plausible explanation for the jet asymmetry observed in figure 6.

Indeed, if one further considers the temperature profiles in a phase-averaged sense (or ensemble-averaged at specific phases of the wave cycle) there is evidence of a new wave-induced mixing mechanism which specifically effects the downstream side of the evolving jet. Figures 7a-7e describe the ensemble-averaged temperature profiles at $\theta=0.5, 0.6, 0.7, 0.8$ and 0.9 respectively, where $\theta=0.5$ corresponds to a zero down-crossing and $\theta=0.75$ is in phase with the wave trough. During this portion of the wave cycle, the vertical jet is first subject to a counter-flow ($\theta=0.5$), followed by an increasing cross-flow which is orientated towards the downstream side of the jet. In each of these five figures the large arrow positioned above the temperature data indicates the approximate direction of the ambient flow. In this case the effect of the ambient motion appears to divide the jet so that although a large proportion of the jet is swept upstream (in the positive x direction), a significant proportion also appears to remain almost static. This apparent division of the jet only arises during this stage of the wave cycle, and in particular does not occur 180° later, when the jet is subject to a co-flow ($\theta=0$) followed by an increasing cross-flow orientated towards the upstream face. In this latter case the entire jet is swept downstream (in the negative x direction), and thus the pattern looks very different to that presented on figures 7a-7e.

Concluding Remarks.

The present study has addressed the case of a buoyant hot-water jet discharged in a wave environment, and has sought a quantitative description of the near-field mixing based upon a quasi-Lagrangian formulation of the integral equations. Previous attempts at a solution of this type have provided a good qualitative representation of the flow field, but detailed quantitative comparisons have been limited due to the apparent uncertainty in the entrainment coefficients. In particular, a three-fold increase in the coefficient of radial entrainment was necessary to model the centre-line decay. To investigate this point an existing Lagrangian model, formulated in a relative frame of reference, was used to describe a vertical jet discharged in a steady cross-flow. Although in this case there is no ambiguity regarding the entrainment coefficients, the agreement between the model predictions



Figures 7a-7e. Phase-averaged temperature profiles at $z=13D$.

(a) $\theta=0.5$, (b) $\theta=0.6$, (c) $\theta=0.7$, (d) $\theta=0.8$, (e) $\theta=0.9$.

and laboratory data were poor. On closer inspection, it has been shown that a Lagrangian model formulated in a relative frame of reference neglects the momentum flux associated with the entrained fluid. In contrast, an alternative model, formulated in an absolute frame of reference, is shown to be in good agreement with all cases involving buoyant jets discharged in both steady currents and unsteady wave fields.

To further validate this latter model, new experimental studies were undertaken in which both horizontal and vertical jets were discharged within a wave environment. Laboratory data describing the near-field mixing is shown to be in good agreement with the modified Lagrangian solution, and perhaps most importantly there is no ambiguity with regard the entrainment coefficients. As a result, the proposed solution is appropriate to design applications. Furthermore, detailed consideration of the phase-averaged temperature data measured within the near-field provides evidence of a new wave-induced mixing mechanism. This effect provides a plausible explanation for the development of non-symmetric time-averaged temperature profiles. More importantly, it provides the first quantitative evidence which suggest that the average dilution will be enhanced if a pollutant is discharged in the plane of the wave motion.

Acknowledgements.

The authors gratefully acknowledge the financial support provided by the Croucher Foundation, Hong Kong.

References.

- Chin, D.A. 1988. Model of buoyant-jet-surface-wave interaction. *J. Waterway, Port, Coastal, and Ocean Eng.*, ASCE, **114**(3), 331-345.
- Chu, V.H. & Lee, J.H.W. 1996. General Integral Formulation of the turbulent buoyant jets in cross-flow. *J. Hyd. Eng.*, ASCE, **122**, No. 1, 27-34.
- Chyan, J.M., Hwung, H.H. & Chang, Y.H. 1991. Wave effects on the mean flow characteristics of turbulent round jets. In: *Environmental Hydraulics*, Eds. Lee, J.H.W. & Cheung, Y.K. **1**, 109-114.
- Hwung, H.H., Chyan, J.M., Chang, C.Y. & Chen, Y.F. 1995. The dilution processes of alternative horizontal buoyant jets in wave motions. *Proc. 24th Int. Con. Coastal Engineering*, **3**, 3045-3059. Kobe, Japan 1994.
- Kwan, S.H. & Swan, C. 1997. Near-field modelling of a buoyant jet in a wave environment. Submitted to *Coastal Engng.*
- Koole, R. & Swan, C. 1994. Measurements of a 2-D non-buoyant jet in a wave environment. *Coastal Eng.*, **24**, 151-169.
- Koole, R. & Swan, C. 1995. Dispersion of pollution in a wave environment. *Proc. 24th Int. Con. Coastal Engineering*, **3**, 3071-3085. Kobe, Japan 1994.

- Lee, J.H.W. & Cheung, Y.K. 1990. Generalised Lagrangian model for buoyant jets in current. *J. Envir. Eng., ASCE*, **116**(6), 1085-1106.
- Morton, B.R., Taylor, G.I. & Turner, J.S. 1956. Turbulent gravitation convection from maintained and instantaneous sources. *Proc. Roy. Soc. Lon., SerA*: **234**, 1-23.
- Patrick, M.A. 1967. Experimental investigation of the mixing and penetration of a round turbulent jet injected perpendicularly into a transverse stream. *Trans. Inst. Chem. Eng.*, **45**, 16-31.
- Sharp, J.J. 1986. The effects of waves on buoyant jets. *Proc. Inst. Civ. Eng.*, **81** (2), 471-475.
- Winiarski, L.D. & Frick, W.E. 1976. Cooling tower plume model. US EPA, Ecological Res. Series, EPA-600/3-76-100, Corvallis, OR.

CHAPTER 356

COST EFFECTIVENESS OF WAVE POWER EXTRACTION AT EROSIIVE COASTS

HIDEO KONDO*

ABSTRACT

Cost of wave power extraction is investigated for the coasts where erosion has been continuing without suitable countermeasures. By a wave power extraction, a shoreline accretion is expected due to the mean sea level drop. Cost effectiveness is discussed with the concept of total cost instead of the generation cost only.

INTRODUCTION

Wave power utilization has not essentially been commercialized yet except small size navigation buoys though remarkable progress has been achieved in the last two decades. The reason is simply that the cost of electricity from waves is still much higher compared with those from fossil fuels and of nuclear. However, it is required to remove unfavorable gases like CO₂ etc. exhausted in the process of burning fuels from the standpoint of global environmental protection. This process needs an additional cost which we may call the environmental cost. The cost is known presently to be no less than that of power production itself.

Meanwhile continuous retreat of coasts by wave and meteorological tidal actions has become serious at most coastal countries in the world. Coastal engineers have worked extensively to solve the problems by constructing coastal structures or by feeding sand in eroding beaches. Extraction of wave power decreases apparently the transmitted wave power shoreward and will weaken beach erosion with similar actions as the above two methods do.

In the present study the author proposes an approach to evaluate the total cost as well as the production cost of wave power extraction at erosive coasts which is subsequently examined for case studies.

* Department of Civil Engineering & Architecture, Muroran Institute of Technology,
27-1 Mizumoto-Cho, Muroran, Hokkaido, 050 Japan

TOTAL COST ESTIMATION

The total cost Pt (¥/ kWh) consists of the market or generation cost Pm , the environmental cost Pe and the social cost Ps as (Kondo et al,1991 and 1993),

$$Pt = Pm + Pe + Ps \quad (1)$$

Pm is estimated with conventional procedures. Defining $E_{p,j}$ as the environmental value of j th factor, Pe , the cost to repair the environmental damages occurred in power production process is estimated as,

$$Pe = \sum \Delta P_{i,j} = \sum \frac{\partial E_{p,j}}{\partial x_i} \Delta x_i \quad (2)$$

In the above equation $\Delta P_{i,j}$ is the repair cost brought by the variation of j th environmental factor by the variation of the environmental factor i in the course of production. Pe of fossil-fired electricity includes expense of removing and treatment of harmful waste gases such as CO₂.

The environmental cost is positive for the cases of fossil-fired and nuclear powers. For the cases of renewable energies it can be minus when they bring better environment than that without extraction. The social cost Ps may be the expenses of moving houses and structures, compensation for damaging fishing industry, and the expenses dispatching troops to keep the sea-lane safe to tankers for imported oil, etc.

WAVE POWER BUDGET AND DEFORMATION

The incident wave power through the extracting device and structure is divided to the reflected, the power extracted, the loss by extracting process and structure, and the transmitted shoreward. The ratios of these depends on types of device, structure and the operating conditions. Approximate figures for the extracted and the transmitted are estimated for later calculation as in the following.

TABLE-1 WAVE POWER BUDGET (Extracted / Transmitted)

TYPE OF SYSTEM	IN OPERATION	STOPPED
Floating (OWC)	30 / 50	0 / 100
Bottom Fixed(Pendolor)	50 / 20	0 / 50

SHORELINE ACCRETION BY MSL DROP

Continuous retreat of shoreline by wave and meteorological tidal action has become one of the most serious problems in all coastal countries. It has been accelerated by the remarkable trend of mean sea level (MSL) rise. The power extraction from waves in offshore or inshore zone decreases the incident power and the height of transmitted wave and the size of MSL.

We know that a MSL rise brings a retreat of shoreline more than that anticipated from the static geometry in sandy coasts. Thus we may apply the relationship between the MSL rise versus the shoreline retreat to MSL drop at beach versus shoreline accretion by the wave power extraction. Several approaches have been proposed for the relationship between MSL rise and beach retreat we will use the one by Mimura et al (1994) for later calculation.

The environmental cost for the wave power extraction is minus since it makes natural beaches wider or saves constructing revetments on shores.

PENDULOR WAVE POWER EXTRACTOR

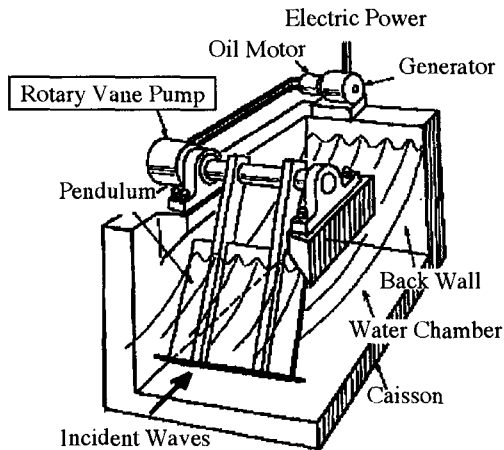
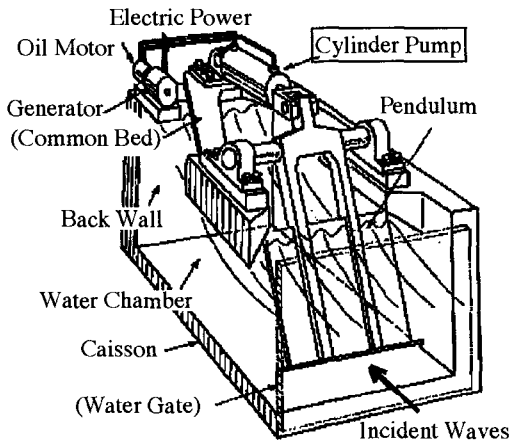


Fig.1 Pendulum Wave Power Extractor in Caisson

We have studied Pendolor power extractor of bottom standing type which can be installed in upright caisson breakwaters since 1980 (Kondo et al, 1984, Yano et al,1985, and Watabe, 1993). Two basic types of it are sketched in Fig.1. It consists of pendulum plate in a concrete caisson with seaside open and a hydraulic power transmission system. A back wall, two side walls and the bottom plate of caisson together with the pendulum plate forms a water chamber where a standing wave system is generated by oscillation of the plate.

Originally it had been developed as the cylinder pump type (the upper one in Fig.1). Laboratory and field experiments has proved it to have high efficiency and to lower the cost compared with the other kinds of extractors (Watabe, 1993).

The rotary pump type, the lower one in Fig. 1, was proposed later and has been being studied (Watabe et al, 1996).

STUDIED LOCATIONS

Three locations of Japanese coast which are typical ones at Hokkaido, Touhoku and Kantou area, respectively of different wave climate have been chosen to estimate the total cost for electric power production employing Pendolor system.

TABLE -2 WAVE CLIMATE OF THREE TYPICAL COASTS

COASTS (Oceans)	AVERAGE WAVE			DESIGN WAVE	
	H1/3	T1/3	W	H1/3	T1/3
Hokkaidou (Japan Sea)	1.1(m)	4.9(sec.)	5.3(kWh/m)	7.5 (m)	12.0(sec.)
Touhoku (Pacific)	1.0	7.4	6.3	7.5	14.0
Kantou (Pacific)	1.5	7.4	11.5	11.0	15.0

COMPUTATION PROCEDURE

The generation or market cost P_m was computed according to a conventional way for the case of electricity in Japan. Table-3 presents the computational process for the case of KANTOU coast.

The environmental cost has been computed from the two approaches:

- (a) From the difference of expenses to construct a revetment at shoreline.

The revetments are designed for the two cases of with and without power extraction to the design waves shown in Table-2. The expense to construct a

revetment is estimated from which P_e is computed.

(b) From the expense of filling the eroded shores every year.

The volume of beach eroded by the average annual wave shown in Table-2 is estimated for each location. Then the cost of sand filling to eroded shore is estimated from which P_e is computed.

TABLE - 3 Estimation of Market Cost, P_m (KANTOU COAST)

(1) DESIGN CONDITION

Water Depth:	10 m below LWL
Tidal Range:	1 m
Mean Wave Power:	11.5 kW/m
Design Wave;	$H_{1/3} = 11$ m, $T_{1/3} = 15$ sec.
Extrator:	Pendulor in Bottom Standing Caisson
Overall Efficiency:	0.5
Caisson:	Unit Length of 20 m
Rating Output per Unit:	$11.5 * 20 * 0.5 = 115$

(2) EXPENSE AND COST (Debt Financing Rate 6 % per Year)

A: Cost of Caisson =	$12 (M\text{¥}/m) * 100 = 1200 M\text{¥}$
B: Cost of Generating System =	$60 M\text{¥} * 5 = 300 M\text{¥}$
C: Total Construction Cost =	$1500 M\text{¥}$
D: Specific Cost = C/ Output =	$1500/575 = 2.6 M\text{¥}/kW$
E: Fixed Cost = Total Cost * Equivalent Coefficient	$= 1500 * 0.07581 = 114 M\text{¥}/Year$
F: Operation Cost = B * 0.05 =	$15 M\text{¥}/Yea$
G: Expenditure = E + F =	$129 M\text{¥}/Year$
H: Amount of Generated Electricity	$= \text{Output } 24hr * 365day * \text{Workig Rate}$
	$= 575 * 24 * 365 * 0.58 = 2.72 * 10^6 kWh/Year$

(3) MARKET COST

I: Cost of Electricity = G/H =	$44 \text{ ¥}/kWh$
--------------------------------	--------------------

The result of estimation is shown in Table 4 which reveals that Kantou area shows the lowest market cost, Pm of 44(¥/kWh). It is still about three times than that of oil-fired as of 1994. It is sensitive to the debt financing rate which is 6 % in present estimation. For the case of 2% rate, Pm decreases to 30(¥/kWh).

The total costs, Pt, however, becomes close to it at Kantou area (Table - 5). For the case of the debt ratio of 2 % it becomes less than that of oil-fired.

TABLE - 4 COST OF ELECRCITY FROM WAVE in ¥/kWh

LOCATION	Pm	Pe	Ps	Pt
HOKKAIDOU	62	(a) -18	1	45
	40	(b) - 5	1	58
TOUHOKU	59	(a) -16	1	44
	38	(b) -11	1	49
KANTOU	44	(a) -11	1	34
	30	(b) -13	1	32

In addition to the wave power, the other two ocean energies, namely current and tide, and wind are also investigated for the cost analysis at promising locations in Japan, the costs of which are considerably higher than those of wave power as shown in Table-5, except wind. -5.

TABLE - 5 COST OF ELECTRICITY BY RENEWABLE ENEGIES
IN ¥ /kWh (Ratio to Oil-Fired)

ENERGY	LOCATION	Pm	Pe	Ps	Pt
WAVE	KANTOU	44	-13	1	32 (1.3)
CURRENT	TSUGARU STRAIGHT	33	3	1	37 (1.5)
TIDE	ARIAKE BAY	73	3	2	78 (3.1)
WIND	MURORAN	48	-14	1	35 (1.4)
OIL - FIRED	KANTOU	12	12	1	25 (1)

CONCLUSIONS

The present study has revealed that wave power utilization at erosive coasts is found to be a promising way to get inexpensive clean energy in Japan and may be so for most coastal countries though the cost depends on heavily domestic natural and economical condition. The utilization will restore invaluable fossil fuels, and precious beaches for the future generation.

ACKNOWLEDGMENTS

The author would like to thank Dr. Tomiji WATABE, T-Wave Consulting Volunteer and Mr. Senji OSANAI, formerly Manager of Cold Region Port & Harbor Engineering Research Center for their constant support to the wave power study at Muroran Institute of Technology.

Thanks must go to Miss Hiromi HAMATSU, former student who had done a part of this study for her B. E. Thesis and Mr. Noriyuki OOTA, the technical staff who assisted for preparing the manuscript at Department of Civil Eng. & Architecture of the institute.

REFERENCES

- KONDO, H. T. WATABE and K. YANO (1984): Wave power extraction at coastal structure by means of *moving body in the chamber*, *Proc. of 19th International Conf. on Coastal Eng., Vol. 4*, ASCE, pp. 2875-2891.
- KONDO, H., I. SUGIOKA, S. OSANAI and S. OZAWA (1992): Application of the new cost analysis to wave power extraction at breakwaters, *Renewable Energy, Technology and the Environment, Proc. 2nd World Renewable Energy Congress, 5*, Pergamon Press, pp. 2829-2833.
- KONDO, H., I. SUGIOKA, S. and OSANAI (1993): The concept of true cost of energy and its application to ocean energies, *Proc. of International Symposium on Ocean Energy Development*, Muroran Inst. Tech. and Cold Region Port & Harbor Eng. Research Center, pp. 101-106.
- KONDO, Hideo (1997): A hybrid system of wave power extraction and shore protection, *Proc. of 27th IAHR Congress* (submitted).
- Mimura, N., H. IKUYO and K. INOUE: Evaluation of effect on sandy shores of the mean sea level rise, *Proc. of 40th Japanese Conf. on Coastal Engineering*, JSCE, pp. 1046-1050 (in Japanese).
- OSANAI, S., H. KONDO, Y. MIZUNO and T. WATABE (1997): Feasibility Tests of new Pendular-type wave energy conversion apparatus, *Proc. of 25th International Conf. on Coastal Eng.*, (in press).

Seymour, Richard. J.[Edit.] (1992): *Ocean Energy Recovery - The state of the art-*, ASCE, 309p.

WATABE, Tomiji (1993): Pendular wave power convertor -15 years study and its future prospect -, *Proc. of International Symposium on Ocean Energy Development*, Muroran Inst. Tech. and Cold Region Port & Harbor Eng. Research Center, pp.101-106.

Watabe, T., H.KONDO, M.NARITA, K.SEINO and E.AKAMA (1996): Studies on a large displacement pump for ocean wave power converter, *JHPS International Symposium on Fluid Power, Yokohama*, JHPS(in press).

YANO, K., H.KONDO and T.WATABE (1985): A device for wave power extraction in coastal structures - Field test of a pendular system - , *Coastal Engineering in Japan*, 28. JSCE, 243- 254.

CHAPTER 357

FAESIBILITY TESTS OF NEW PENDULAR-TYPE WAVE ENERGY CONVERSION APPARATUS

Senji Osanai¹, Hideo Kondo², Yuzo Mizuno³ and Tomiji Watabe⁴

Abstract

In order to utilize natural energy, it is essential to develop a fully compatible system, instead of conventional power-generating systems.

The authors proposed a new pendular-type wave power generation device. Design criteria for a new rotary vane pump systems (NRVP) was studied for several years and a 5-kW-model test plant with a large displacement of 45.9 l/rev pump was established. This simplified pendular system was considered to limit the investment costs. This paper describes the new pendular-type converter and its components, and presents observation data obtained in field tests conducted at sea.

1. Introduction

As Japan is largely dependent on fossil fuels such as coal and petroleum for energy, transition to nuclear power and others non-fossil fuels is being undertaken. Efforts should be made to find energy-saving techniques or new energy sources in order to ensure future development while protecting the earth's environment. It is essential to switch to clean and natural energy sources such as solar radiation, wind power and wave power.

.....
1) Adviser, North Japan Port and Harbor Consultants Co., Ltd. (Formerly, Cold Region Port and Harbor Engineering Research Center) 18-N11 Heiwadori-2 Shiroishi-ku, Sapporo, 003, Japan

2) Professor, Muroran Institute of Technology, 27-1 Mizumototyō, Muroran, 050, Japan

3) Dr., Civil Engineering Research Institute, Hokkaido Development Bureau, 1-3 Hiragishi, Sapporo 062, Japan

4) Dr., T-Wave Consulting Volunteer, 5-23-3 Misono, Noboribetsu, 059, Japan

However, these sources have problems regarding cost and generation capacity limitations. The biggest obstacle to the practical use of clean and natural energy sources is their generating costs compared with those of fossil fuels.

To address this problem, a new, pendular-type wave energy conversion device, named Pendular by the authors, was developed.

In 1981, the first device^{1), 3)} (20 kW) was installed on a breakwater at the Port of Mashike in a collaborative development project involving the Town of Mashike, the Muroran Institute of Technology and Hitachi Zosen corp. Full-scale feasibility tests were conducted.

Following these tests, in 1983 a research group from the Muroran Institute of Technology made the first experimental test device by improving the existing one, and conducted test plant experiments. The tests achieved the expected results and the device was proved to be efficient in wave energy conversion. But it was absolutely necessary to further reduce the power generation costs. Therefore, based on the past research and development results, a new, remarkably improved wave energy conversion device was built under a new research plan. Field tests were conducted at sea.

2. Outline of new pendular device

Wave energy conversion devices can be largely classified into OWC(Oscillating-wave-column) and pendular-types. The principal of the device is shown Fig.1.

Horizontal standing wave motion is converted to motion of the pendular plate, which is then converted to reciprocating rotary motion of a vane-type rotary pump directly connected to the pendulum. This rotation feeds hydraulic oil to the hydraulic motor and drives the generator.

Figure 2 shows the original pendular device^{4), 8)} which had a cylinder pump. It was used to drive an oil motor-generated set.

Since the pendulum actuated the pump, both were fixed on a common bed lest the caisson suffer from the huge reaction of the pump. When the pump and pendulum were coupled together at sea, the system became dangerous because

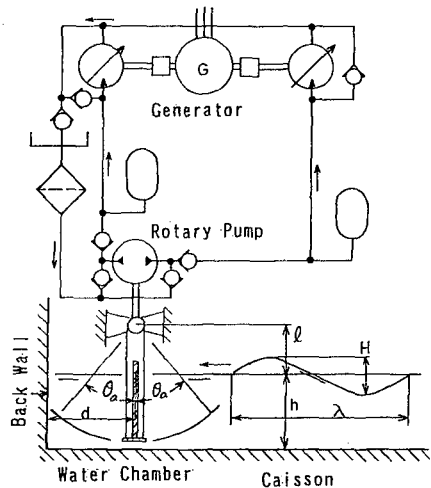


Fig. 1 Principle of the device

the pendulum moved whenever incident waves exited it. A water gate as illustrated as in the figure was required.

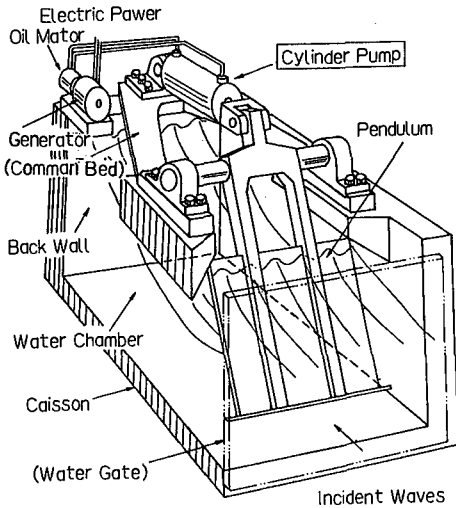


Fig.2 Original pendular device

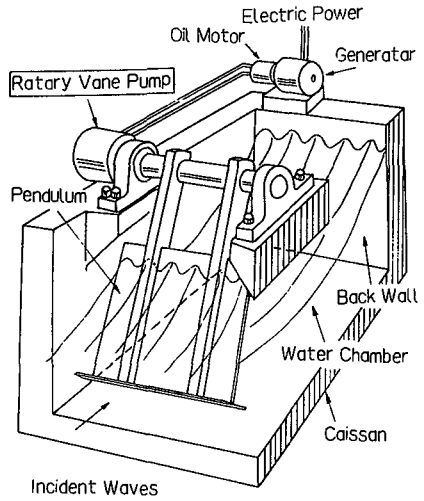


Fig.3 New pendular device

In order to improve cost efficiency, simple combined feature was invented in which a rotary vane pump was coupled with the pendulum.

A long shaft was used to support both the pump rotor and the pendulum, having no coupling component. There were 3 bearings on the shaft, 2 of which were for the pendulum. This combination makes for easier installation work than with the previous model. This system was called a new pendular device^{2),5),6)} as seen in Fig.3.

This large-capacity vane -type pump offers the following advantages:

- 1) The features of the pendular system can be simplified through an integrated pendular plate and rotary vane-type pump.
- 2) Energy generation costs can be reduced through simplification of installation work at sea.
- 3) High-wave resistance of the pendular system is also improved.

3. Design of new rotary pump and pendulum

3.1. Rotary pump

Displacement D_p of the pump, which consists of 2 vanes, is described in the following equation, assuming it is the same as the previous pump.

where D_p displacement of the pump

$$D_p = \frac{\pi}{2} (d_1^2 - d_2^2) B = 2 \pi A_p r$$

d_1 vane tip diameter
 d_2 rotor cylinder diameter
 B vane width
 A_p piston area (cylinder pump) = $98.17 \times 10^{-4} \text{ m}^2$ r arm radius = 0.6 m

The leakage is prevented by the metal seals. As leakage is proportional to the total seal length L_p , a pump having greater value of D_p/L_p (displacement/total seal length) can operate more efficiently. D_p/L_p is shown in the next equation⁷⁾:

$$\frac{D_p}{L_s} = \frac{\pi ((d_1/d_2)^2 - 1) d_1^2}{4 \left(2 \frac{d_1}{d_2} + \frac{d_1}{W} \left(\pi + \frac{d_1}{d_2} - 1 \right) \right)}$$

where W vane width

Through the results of the research, the following equation was determined to provide the optimal profile of the pump⁷⁾:

$$\frac{d_1}{d_2} = \sqrt{\frac{(0.36 \sim 0.46) (d_2/W) \tau_s}{P_{\max}} + 1}$$

where $d_2/W = 1.0 \sim 1.2$, τ_s is shearing stress of the shaft, P_{\max} is maximum delivery pressure of the pump.

Applying the research results, the test pump shown in Fig.4 was designed.

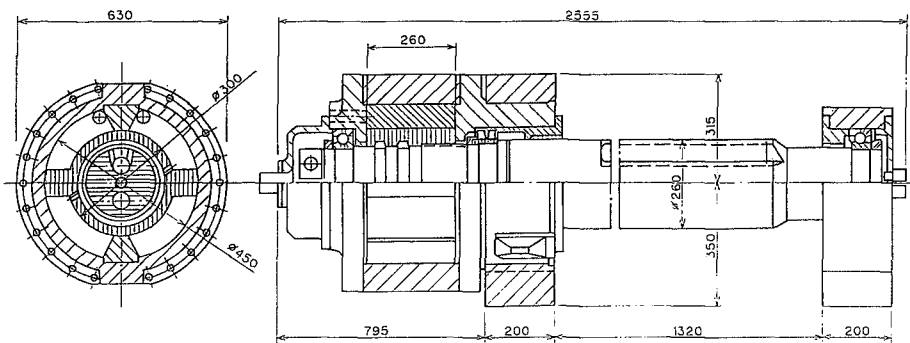


Fig.4 New rotary pump

Its specifications are arranged in Table 1.

Table 1 Specification of the NRVP

Input: $\eta_1 E_1 = 16.6 \text{ kW}$	Displacement: $D_p = 0.0459 \text{ m}^3/\text{rev}$
Vane tip diameter: $d_1 = 0.45 \text{ m}$	Rotor cylinder diameter: $d_2 = 0.30 \text{ m}$
Vane Width: $W = 0.26 \text{ m}$	Shaft diameter: $d_s = 0.232 \text{ m}$
Movable angle: $\theta_{\text{max}} = 65^\circ$ (both sides)	
Pressure (mean/max.): $P_{\text{mean}}/P_{\text{max}} = 12.8/25 \text{ MPa}$	

3.2. Pendulum

The power E_1 produced by the pendulum can be determined with the following equation⁷⁾:

$$E_1 = 1/8 \times \rho \ g \ H^2 \ C_g \ B \ \eta_1$$

where H is wave height = 1.5m, ρ is density of water = 1,030kg/m³, g is acceleration of gravity = 9.81 m/sec², C_g is group speed of the incident waves = 3.46m/s (wave period 4s, water depth: $h = 2.75 \text{ m}$), B is width of the pendulum in water = 2m, η_1 is conversion ratio from wave power to pendular power = 80%.

In this case, these parameters were adopted in the design, and then it was decided that $E_1 = 16.6 \text{ kW}$.

In design, amplitude of pendular motion θ_a was established using the following values.

$$\theta_a = M / (\omega N) = 0.285 \text{ rad} (16.3^\circ) \text{ at no load operation}$$

$$\theta_a = 16.30^\circ \times 0.625 = 10.20^\circ \text{ at optimal load operation}$$

where M is amplitude of exiting moment = 370kNm, N is load factor by wave generation = 828kNms, ω is circular frequency of wave = 1.571rad/s ($T = 4 \text{ s}$).

As seen in the pendular device shown in Fig.5, the basic style was not changed significantly, though the pendulum is more durable in storms with its rubber tires of heavy track's, it can swing wider

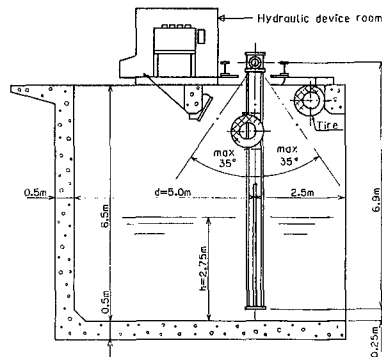


Fig.5 Test pendular device

and more reliable to absorbing shock loads. It is expecting to be relatively maintenance free.

In order to prevent electro-chemical corrosion, the shaft was connected to the earth through brushes and zinc plate were fixed to the pendulum surface and incorporated into the vane- type rotary pump.

3.3. Installation

The device was installed using a large crane in August 1994, on the caisson of the Muroan Institute of Technology around the exterior of the south breakwater in the Etomo area of Muroan. The installation was completed within 2 hours, not included preparation of a gate.

Muroan is centrally located on the middle of Hokkaido and faces the Pacific Ocean. The water in front of the breakwater is approximately 4.0 m in depth. Because of the port's location in a bay, incoming waves are small. The largest significant wave was 2.7 m high and its period was 5.4 second. The mean wave direction was west northwest. Photo 1 shows the installation of the device. Fig. 6 shows the location of the port of Muroan.



Photo 1 Installation work

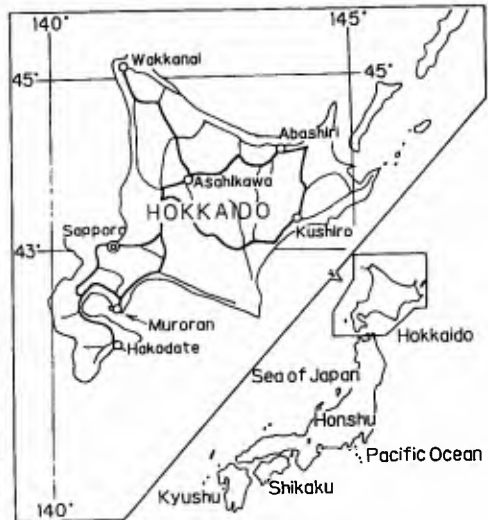


Fig. 6 Location of Muroan port

4. Measurement of the new pendular-type wave conversion device

Measurement were made at 8 points: ① Pump pressure (4 points). ② Motor

axis torque (1 point), ③ Motor axis rotation speed (1 point), ④ Pendulum gradient (1 point), ⑤ Wave recorder (1 point).

Eight patterns were successively measured, with load condition changed every 20 minutes. The data was stored on a CVS-type disk. Figure 7 shows the interior structure of the observation system.

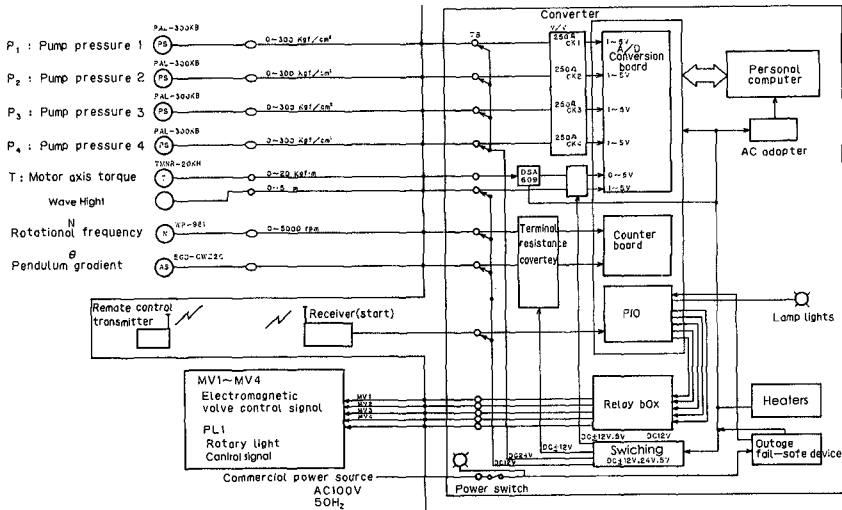


Fig.7 Observation instruments and wiring diagram

5. Observation of the new pendular-type wave energy conversion device

The new pendular-type wave energy conversion device was produced and tested in accordance with the development schedule shown in Fig.8.

The device was produced in 1993 and 1994. It was installed at the site, along with observation instruments, and ancillary electrical work was carried out before conducting observations.

	1993	1994	1995	1996	97~98
Development of device	—				
Testing		—	—	—	—
Data analysis					—
Other					

Fig.8 Research and development schedule

The device was installed in August 1994 in front of the port of Muroran shown fig-6. Since then, tests have been conducted for 20 months. In order to analyze efficiency , measurements were conducted at 8 points during operation. The data is presented in Table1. Figure 9 shows spectrum response of the system . Two spectrums, wave and angular displacement of the pendulum, showed a close correlation.

Year / Date	95 11.8	95 11.8	96 1.04	96 1.07
H $\frac{1}{2}$ (m)	2.52	2.53	2.36	2.63
T $\frac{1}{2}$ (sec)	6.45	6.57	6.04	5.93
Wave Power (kw)	14.426	14.727	14.125	18.401
Primary Conversion Efficiency (%)	61.71	56.0	53.55	42.16

H $\frac{1}{2}$ Wave Height, T $\frac{1}{2}$ Wave Period

Table 1 Observation data

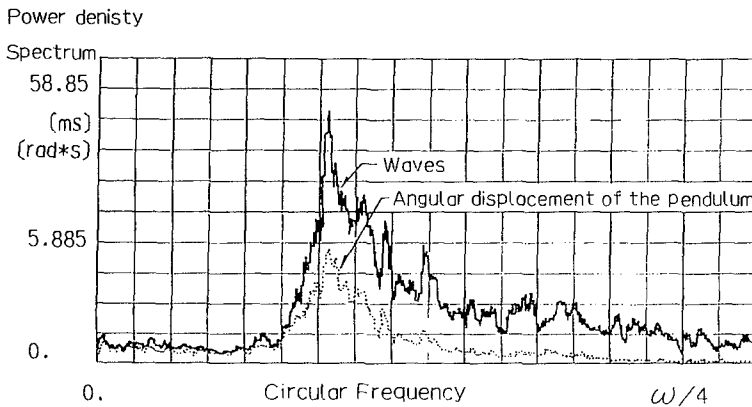


Fig.9 Responsiveness of the system

Figure 10 shows the efficiency of the new pendulum. The efficiency η_1 is shown in relation to wave period, $T_{1,3}$. It can be seen that $\eta_1 = 0.5 \sim 0.9$, and it reaches peak value at approximately $T_{1,3} = 4.5 \sim 5.2$ second.

During the field test ,the pump operated without a breakdown, but pump effi-

ciency was only 27-37%.

No contamination of the oil has been observed, so it is presumed the cause of low efficiency may be malfunction of the seal .

Besides the power conversion test, remarkable durability of the pump has been proved .There were no troubles around the pendulum or the pump such as loosening of bolts , leaking of oil or wear of sliding parts.

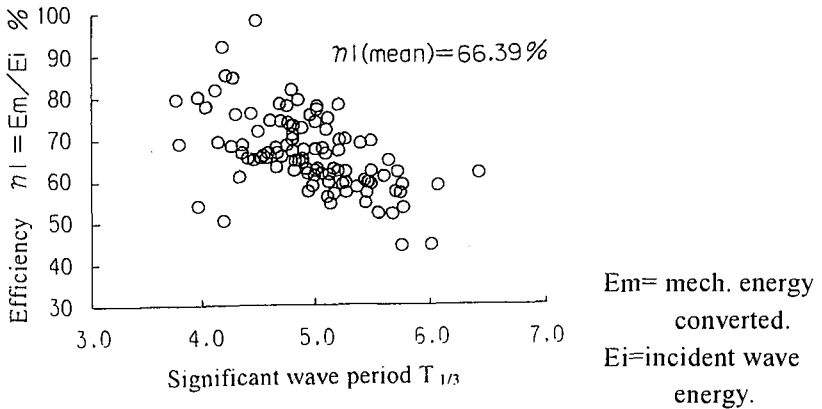


Fig.10 Efficiency of the new pendulor

6. Conclusions

Through testing of the new pendular device , the following conclusions were obtained.

- 1) The new rotary-vane pump system proposed for the pendulor makes installation easier, without the need for a water gate. It can lower energy costs.
- 2) The new pendular system improves durability not only for the pump, but also for the pendulor.
- 3) Efficiency of the new pendular was approximately 50~70 % (It was the same as the old pendulor coupled with a cylinder pump.)
- 4) Pump efficiency did not achieve the predicted value, as derived in the indoor test.

Therefore, there is still the need to solve the problems regarding pump efficiency and the seals on the pump unit. Further research to this end is expected .

After a great deal of research and development, the new pendular system was realized. It employed unique technique developed in Hokkaido, and which must be further developed. To put the device to practical use, we must continue field tests. Observation data, particularly that for durability and efficiency versus load, will be collected for application in design.

Acknowledgments

The authors would like to express their sincere gratitude to Mr. Seino, Muroran works of Narasaki Co. Ltd., and the Port Authority of Muroran for their contributions in the installation of the measuring instruments and to the 1st Regional Marine Safety Headquarters for their cooperation in the use of a power source.

References

- 1) M.Kuroi (1982), Wave Power Generation at the Port of Mashike. Sea and Port, Hokkaido Port and Coastal Research Assn.,pp.79~80.
- 2)S.Osanai, H.Kondo, Y.Mizuno, T.Watabe, K.Seino(1995), Development of a New Model of Wave Conversion Apparatus, Proc.of the Hokkaido Civil Engineering Lectures. pp.308~311
- 3) T.watabe, H.Kondo, K.Yano, H.Takeda and M.Kuroi(1982), Research on Wave Energy Absorption Devices Attached to Breakwater. Proc.of the 29th Coastal Engineering lectures, pp486~490.
- 4)T.Watabe(1993), Pendulor Wave Power Conversion:15 years Study and Future Prospect, Pro.of International Symposium on Ocean Energy Development, Muroran,pp41~52.
- 5)T.Watabe, H.Kondo, H.Shirai, K.Seino(1994), Remolding of Muroran Wave Test Plant, ISOPE 94. pp.353~358
- 6)T.Watabe, H.Kondo, M.Narita, E.Matumoto, K.Seino, M.Inoya and F.Akama(1995),New Pendulor and its Field Test, Pro.of 2nd European Wave Power Conference, Lisbon. (in printing)
- 7)T.Watabe, H.kondo, M.Narita, K.Seino(1996), Studies on a large Displacement Pump for a Ocean Wave Power Converter, JHPS International Symposium on Fluid.
- 8) K.Yano(1992), Study of Methods for Pendulum-type Wave energy conversion Device, Report of the Civil Engineering Research Institute, Hokkaido Development Bureau, No.97. pp1~48.

CHAPTER 358

Watertable Dynamics in Coastal Areas

Hong-Yoon Kang¹ and Peter Nielsen²

Abstract

Fresh water lens measured under the coastal barrier is much thinner than that predicted by the classical Ghyben-Herzberg theory. Landward downsloping watertable which is usually seen at coastal areas results in a landward flow of salty water or waste water released into aquifer. Comparison between the laboratory experiments with regular waves and no tides and the field data has revealed significant difference in magnitudes of the infiltration velocity. It is obvious that the tidal phase is very important. Infiltration velocities are large when the shoreline moves landward on a partially saturated beach on a rising tide. General magnitudes of U , are $0.08K$ for steady laboratory conditions to $0.45K$ for field conditions during the rising tides. A mathematical model of the watertable which includes the effects of runup infiltration is obtained in a steady state. A finite-difference numerical model of the watertable is also presented with the glassy/dry boundary as a boundary condition.

Introduction

Watertable dynamics in coastal areas are of obvious interest in relation to problems such as salt water intrusion to the aquifer and wastewater disposal from coastal developments, but research into these processes has been scarce. In addition, the modeling of swash zone sediment transport requires a better knowledge of the beach groundwater dynamics.

Extensive field studies along the east coast of Australia have revealed that the overheight in the coastal watertable due to wave runup and tidal action on the ocean side are sufficient to create a steady drift of salty ground water under narrow coastal islands

¹Center for Applied Coastal Research, University of Delaware, Delaware 19716, USA
Fax: +1 (302) 831 1228, Email: Kang@coastal.udel.edu

²Department of Civil Engineering, University of Queensland, Brisbane 4072, Australia
Fax: +61 (7) 3365 4599, Email: nielsen@uq_civil.civil.uq.oz.au

and barriers. Figure 1 details a typical situation showing the landward downsloping watertable and the very thin fresh water lens monitored at the narrow northern end of Bribie Island near Brisbane, Australia.

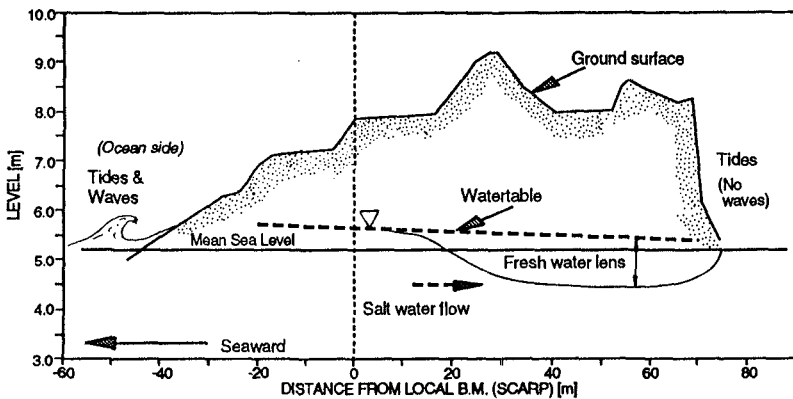


Figure 1. Field data showing the landward downsloping watertable and the thin fresh water lens (Bribie Island North, 14 July 1994).

In this case, the difference in groundwater level between the ocean side which is exposed to waves and the landward side which is relatively sheltered from waves is 0.4 meters. The magnitude of difference varies depending on the wave conditions, the slopes on the two sides and the landmass width. These features are important for understanding ecosystems in these areas and for pollution control. The difference in groundwater levels shown in Figure 1 is due to the combined effect of tides and waves.

The fresh water lens observed at the barrier island is seen to be much thinner than that predicted by the classical Ghyben-Herzberg (see Domenico and Schwartz, 1990) theory. The Ghyben-Herzberg result was obtained from simple hydrostatics with no consideration of the details of the wave runup infiltration near the high water mark. The measured fresh water lens under the barrier also shows an asymmetry, i.e. it opens up gradually on the ocean side, but closes abruptly on the landward side.

This paper outlines the recently developed theory for wave effects significantly affecting coastal watertable dynamics and presents comparison with field and laboratory measurements. Watertable modeling is also given mathematically and numerically.

Wave Induced Watertable Overheights

Ocean waves raise the coastal watertable through their lifting of the free mean water surface seaward of the shoreline, i.e. wave setup, and due to the infiltration from wave runup landward of the shoreline. See Figure 2.

Wave Setup

The phenomenon of wave setup has been treated extensively in the water wave

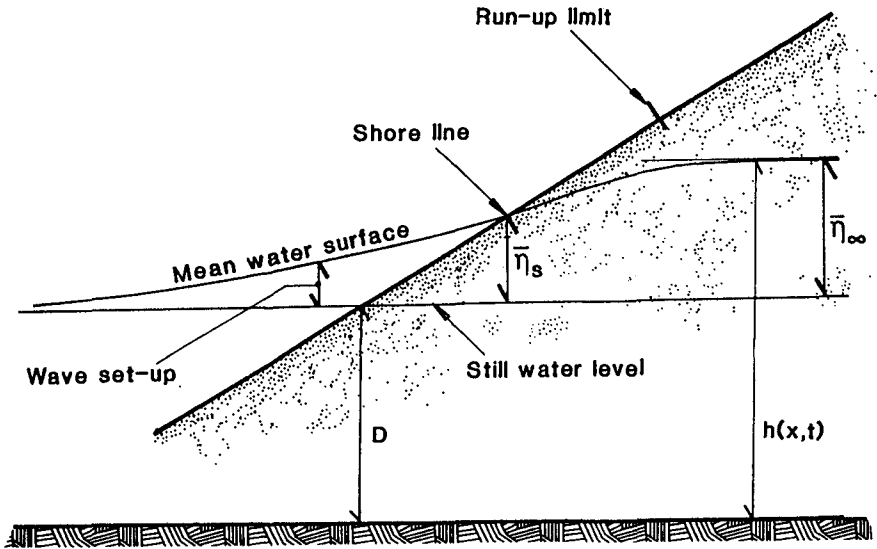


Figure 2. Definition sketch

literature. Extensive field data have been reported by Nielsen [1988] and Hanslow and Nielsen [1993]. They indicate that the shoreline setup $\bar{\eta}_s$

$$\bar{\eta}_s = 0.38H_{orms} \tag{1}$$

or

$$\bar{\eta}_s = 0.048\sqrt{H_{orms}L_o} \tag{2}$$

where H_{orms} is the root mean square deep water wave height and L_o the deep water wave length ($L_o = gT^2/2\pi$, where T is the wave period).

Regular Waves, No Tide

Experimental studies were undertaken in a wave flume with regular waves and no tide to gain insight into process of infiltration from wave runup and the resulting watertable overheight as reported by Kang et al. (1994). It was found from the flume experiments that the asymptotic inland overheight $\bar{\eta}_\infty$ depends on the beach profile, the wave height H_i and the wave period T , but not directly on the hydraulic conductivity K of the beach material. Kang et al. [1994] recommended the following formula in relation

to Hunt's [1959] formula for the runup of regular waves:

$$\bar{\eta}_\infty = 0.62(Z_R - SWL) = 0.62 \tan\beta_F \sqrt{H_i L_o} \tag{3}$$

where Z_R is the level of maximum runup, SWL the still water level and $\tan\beta$ the beachface slope. This indicates that the asymptotic inland overheight amounts to be 62% of the runup height irrespective of sand size. However, separate regression lines for coarse and fine sands, as seen in the relation between the inland overheight scaled on the wave height ($h_\infty - SWL/H_i$) and the surf similarity parameter $\xi (= \tan\beta_F (L_o/H_i)^{0.5})$ (see Figure 3), show a weak effect/correlation of sand size, indicating that the watertable overheight is larger for larger sands, in the range of wave conditions of $1.2 \text{sec} \leq T \leq 2.8 \text{sec}$ and $58 \text{mm} \leq H_i \leq 200 \text{mm}$ with aquifer depths ranging from 372mm to 436mm (regression coefficients: 0.64 with $r^2=0.73$ for coarse sands and 0.48 with $r^2=0.86$ for fine sands). This trend is consistent with Gourlay's [1985] data. The fact that the watertable overheight is larger for coarser sands may not be caused directly by different sand sizes, but by different beach profile shapes associated with different breaker types and different beach materials (see Rector, 1954; Gourlay, 1980; 1985). In general, finer sands form characteristically flatter foreshore beach profiles (with an outer bar formed at the breaking point of the waves), and more energy is dissipated through the surf zone than for beaches with coarse sands for the same wave conditions. The former results in less runup on the beach face than the latter. Smaller wave runup heights hence produce less watertable overheight.

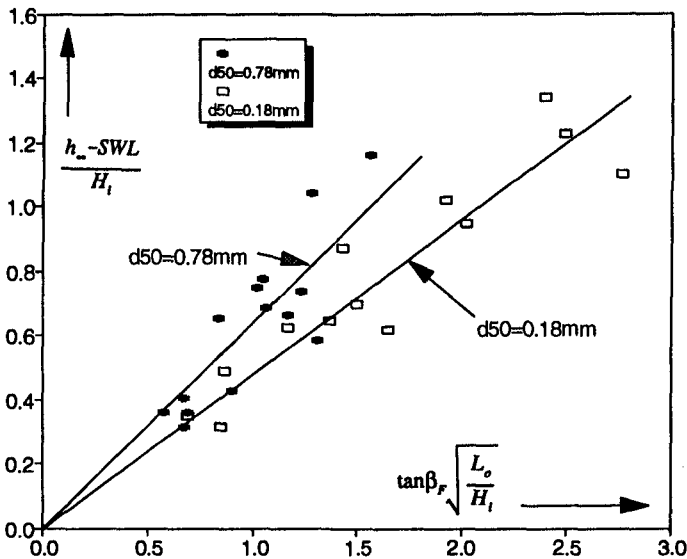


Figure 3. The normalized inland overheight as a function of the surf similarity parameter $\xi (= \tan\beta_F (L_o/H_i)^{0.5})$.

On the other hand, the present result is not directly consistent with Gourlay's [1992] example for a flat wave ($H/L_o=0.007$) which shows that the elevation of the watertable increased as the hydraulic conductivity of the beach material decreased. Equation (3) may apply when the breaking waves are not surging (for $H/L_o > 0.01$: see Figure 4 of Gourlay [1985]) and the beach material is sand, but it may not hold for very flat waves ($H/L_o < 0.01$). The wave steepness is an important factor governing onshore or offshore movement of beach material which determines the beach profile and breaking point/characteristic. It thus influences the beach watertable elevation/profile.

Wave Runup Infiltration

Recently, the wave runup infiltration contributing to significant lifting of the coastal watertable was stressed by several researchers (e.g. Nielsen et al., 1988; Hegge and Masselink, 1991 and Kang et al., 1994). Figure 4 outlines the processes of wave runup/infiltration and the coastal watertable.

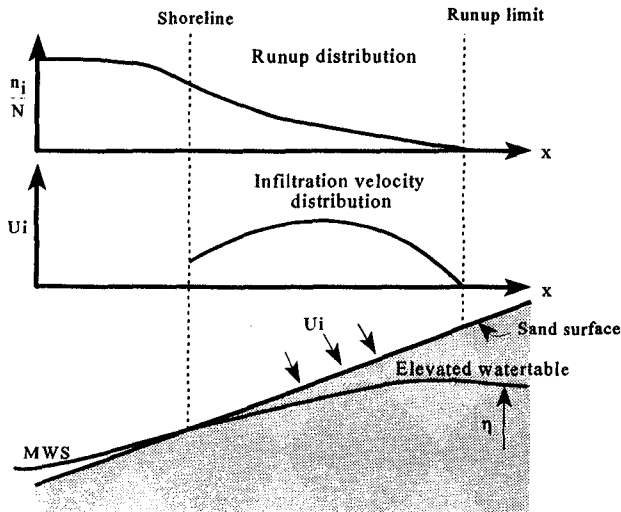


Figure 4. Relationships between wave runup, infiltration and the coastal watertable.

The top part of the figure shows the runup distribution (transgression statistics) of irregular waves, i.e. the fraction of the waves which transgressed certain points during the recording interval. The middle part shows the infiltration velocity distribution from wave runup, and the bottom part shows the corresponding elevated coastal watertable. With no sinks or sources landward of the runup limit the watertable will be horizontal landward of the runup limit.

Runup infiltration velocities indirectly determined from the watertable measurements and the parameters n and K of the porous medium, using the Finite

Difference approach, have maximum values roughly midway between the shoreline and the runup limit from both the field and laboratory data (see Kang et al., 1994 and Kang, 1996). General magnitudes of the infiltration velocity U_i are $0.08K$ for the steady laboratory conditions to $0.45K$ for field conditions during the rising tides. This difference is probably due to the fact that the field data were taken during rising tides where the beach is less saturated than in the steady state of the laboratory experiments. These magnitudes may vary according to characteristics of the porous medium.

Mathematical Modeling of the Coastal Watertable

Consider homogeneous sand body, with the specific yield n and the hydraulic conductivity K overlying a horizontal impermeable stratum at depth D . Under the Dupuit-Forchhermer assumption, the local height h of the watertable above the impermeable layer obeys the Boussinesq equation:

$$n \frac{\partial h}{\partial t} = K \frac{\partial}{\partial x} \left(h \frac{\partial h}{\partial x} \right) \quad (4)$$

In order to model the watertable in the zone of runup infiltration, the modified Boussinesq equation or the corresponding linearized equation (5) which includes the runup infiltration effect should be used as reported by Nielsen et al. (1988) and Kang et al. (1994):

$$n \frac{\partial h}{\partial t} = KD \frac{\partial^2 h}{\partial x^2} + U_f(x,t) \quad (5)$$

where $U_f(x,t)$ is the infiltration velocity averaged over numerous uprush-backwash cycles or the infiltration flow rate per unit area.

For steady flume condition (pure wave forcing, no tide), equation (2) leads to:

$$\frac{\partial^2 h}{\partial x^2} = -\frac{1}{KD} U_f(x) \quad (6)$$

The nature of $U_f(x)$ may reasonably be expected to be:

$$U_f(x) = \begin{cases} C_f K f(x) & \text{for } x_s \leq x \leq x_R \\ 0 & \text{for } x > x_R \end{cases} \quad (7)$$

where C is a dimensionless infiltration coefficient and $f(x)$ is a dimensionless function of x . x_s and x_R are the horizontal shoreline and the runup limit coordinates, respectively.

In order to define the solution for equation (6) under the steady laboratory

conditions, consider a simple situation where the infiltration velocity $U_f(x)$ is distributed evenly between the shoreline x_s and the runup limit x_R . That is

$$U_f(x) \equiv U_I \tag{8}$$

Then equation (8) is written as:

$$\frac{\partial^2 h}{\partial x^2} = -\frac{U_I}{KD} \tag{9}$$

The boundary condition at the runup limit ($x=x_R$) may be written as:

$$\frac{dh}{dx} \Big|_{x=x_R} = 0 \tag{10}$$

and the boundary condition at the shoreline can be stated as:

$$h_{x=x_s} = D + \bar{\eta}_s \tag{11}$$

The solution to equation (9) with the boundary conditions (10) and (11) is :

$$h(x) = D + \bar{\eta}_s + \frac{U_I(x_R-x_s)^2}{KD} \left[\frac{x-x_s}{x_R-x_s} - \frac{1}{2} \left(\frac{x-x_s}{x_R-x_s} \right)^2 \right], \quad x_s \leq x \leq x_R \tag{12}$$

and for $x=x_R$, the asymptotic inland overheight is obtained as:

$$h_\infty = h_{x=x_R} = D + \bar{\eta}_s + \frac{1}{2} \frac{U_I(x_R-x_s)^2}{KD} \tag{13}$$

Hence we see that the asymptotic inland overheight is proportional to $(x_R-x_s)^2/D$. If $U_f(x)$ is always distributed in the same way between x_s and x_R , i.e.

$$U_f = KF \left(\frac{x-x_s}{x_R-x_s} \right) \tag{14}$$

where F is a universal function, equation (13) can be written as:

$$h_w = D + \bar{\eta}_s + C \frac{(x_R - x_S)^2}{D} \quad (15)$$

where C is a constant. A universal function F would give a universal constant C .

Numerical Modeling of the Watertable

Model Formulation

The numerical technique used here is the finite-difference approach. Consider the typical four-node grid with node spacings of δ_x and δ_t in each coordinate direction. The dependent variable $h(x, t + \delta_t)$ will be obtained from the following equation, which is a Taylor series expansion about node $h(x, t)$:

$$h(x, t + \delta_t) = h(x, t) + \delta_t \left(\frac{\partial h}{\partial t} \right) \quad (16)$$

By substituting the watertable equation (4) into (16), we get the governing equation:

$$h(x, t) = h(x, t) + \delta_t \frac{K}{n} \frac{\partial}{\partial x} \left(h \frac{\partial h}{\partial x} \right) \quad (17)$$

for the groundwater surface level h . In this way one equation is obtained for each node, which can be used to find $h(x, t + \delta_t)$.

In order to get the solution for the most seaward and landward wells, we need two boundary conditions. The first of these can be obtained using the glassy/dry boundary (G/D) which corresponds to the watertable exit point, as the seaward watertable boundary condition (see Figure 5). Hence, since the G/D is moving horizontally as well as vertically, the spacing δ_x from the G/D to the first well is not constant, i.e.

$$\delta_{x1} = \delta_{x2}, \quad \text{for the first well landward of MSS} \quad (18)$$

where δ_{x1} is the distance between the glassy/dry boundary and the first well landward of MSS, δ_{x2} is the distance between the first and second well landward of MSS and MSS defines the intersection between the mean sea level (MSL) and the beachface (cf. Figure 5).

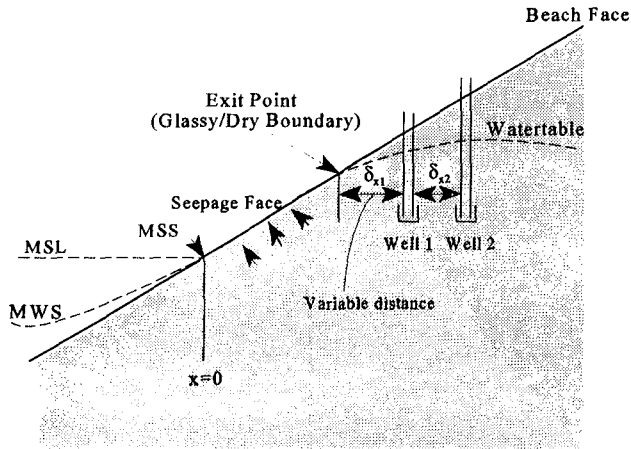


Figure 5. The moving glassy/dry boundary as the seaward watertable boundary condition

Secondly, at the landward boundary, a reflecting, no flux boundary condition is imposed. This is reasonably realistic since the watertable waves decay exponentially with distance from the shore. That is

$$h(x - \delta_x, t) = h(x + \delta_x, t) , \quad \text{for } x \rightarrow \infty \quad (19)$$

Numerical solution of equation (17) subject to the periodic boundary condition at the ocean and to (19) is then readily obtained by iteration. That is, in order to overcome the influence of the initial conditions, the model is run for several tidal cycles.

Comparison with Experiments

As an example, the watertable data measured for 25 hours from Kings Beach, Queensland are used because tides were approximately sinusoidal at the time of measurement.

Figures 6 and 7 show the time variations of simulated and measured watertables at 15m, 20m and 30m landward from the mean sea level shoreline with the variation of glassy/dry boundaries during two semidiurnal tidal cycles (25 hours period), respectively. The amplitudes of the watertable variation from the model give quite good agreement with those of the measured watertable. It is however seen that the simulated watertable levels always sit a bit higher than the measured watertable levels. This difference may be reduced by using the shoreline as a boundary condition because the shoreline always sits lower than the glassy/dry boundary level. Some improvement may also be obtained by varying hydraulic conductivity *K* and aquifer depth *D* at each well. The compactness of the beach sand body may vary in the shorenormal direction and hence hydraulic conductivity may vary shorenormally.

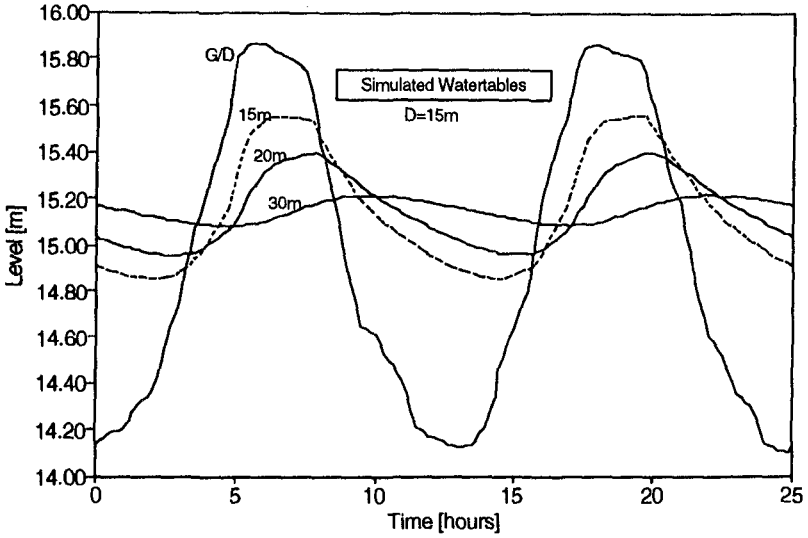


Figure 6. Simulated watertable variations during two semidiurnal tidal cycles at wells landward of the mean sea level shoreline. The numbers on the curves indicate distances landward from MSS.

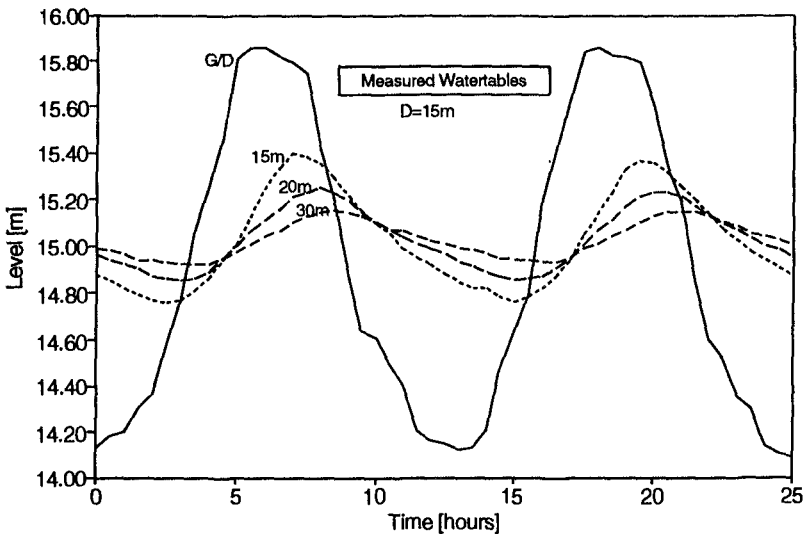


Figure 7. Measured watertable variations at the wells landward of the mean sea level shoreline from Kings Beach (Nov. 24-25, 1991).

Conclusions

Field measurements of groundwater dynamics in coastal barriers show landward downsloping watertable which results in a landward flow of salt water or waste water released into aquifer. Fresh water lens under the barrier tends to be much thinner than that predicted by the classical Ghyben-Herzberg principle.

Comparison between the laboratory experiments with regular waves and no tides and the field data (see Kang, 1996) has revealed significant difference in magnitudes of the infiltration velocity. It is obvious that the tidal phase is very important. Infiltration velocities are large when the shoreline moves landward on a partially saturated beach on a rising tide. General magnitudes of U_f are $0.08K$ for the steady laboratory conditions and $0.45K$ for field conditions during the rising tides.

A mathematical model of the watertable which includes the effects of wave runup infiltration was obtained in a steady state. The development of the numerical watertable model was also attempted with the glassy/dry boundary as a boundary condition. However, the numerical model of the watertable in this study is based on tidal fluctuations with the use of the wave-influenced G/D boundary condition.

References

- Domenico P.A. and Schwartz F.W. (1990): Physical and chemical hydrogeology, *John Wiley & Sons, Inc.*, 824pp.
- Gourlay M.R. (1980): Beaches: profiles, processes, permeability, *Proc. 17th International Conf. On Coastal Engrg*, ASCE, Sydney, pp 1320-1339.
- Gourlay M.R. (1985): Beaches: states, sediments and set-up, *Preprints 1985 (7th Australasian Conf. Coastal and Ocean Engrg*, Vol.1, Christchurch, pp 347-356.
- Gourlay M.R. (1992): Wave set-up, wave runup and beach water table: Interaction between surf zone hydraulics and groundwater hydraulics, *J. Coastal Engineering*, 17, pp 93-144.
- Hanslow D.J. and Nielsen P. (1993): Shoreline setup on natural beaches. *J. Coastal Research*, Special Issue 15, pp 1-10.
- Hegge B.J. and Masselink G. (1991): Groundwater-table responses to wave runup: an experimental study from Western Australia, *J. Coastal Res.*, 7(3), pp 623-634.
- Hunt I.A. (1959): Design of sea walls and breakwaters, *Proc. Paper 2172*, ASCE, Vol.85 No.WW3, pp 123-152.
- Kang H.Y., Nielsen P. and Hanslow D.J. (1994): Watertable overheight due to wave runup on a sandy beach, *Proc. 24th International Conf. On Coastal Engineering*, ASCE, Kobe, pp 2115-2124.
- Kang H.Y. (1996): Watertable dynamics forced by waves, *PhD thesis*, Department of Civil Engineering, University of Queensland, Australia, 200pp.
- Nielsen P., Davis G.A., Winterbourne J. And Elias G. (1988): Wave setup and the watertable in sandy beaches, *Tech. Memo.*, 88/1, NSW Public Works Department, Australia, 132pp.
- Nielsen P. (1988): Wave setup: a field study. *J. Geophys Res*, Vol 93, No C12, pp 15643-15652.

Rector R.L.(1954): Laboratory study of equilibrium profiles of beaches, *Technical Memo.* No.41, Beach Erosion Board, U.S. Army Corps of Engineers, pp 1-38.

CHAPTER 359

LONG RANGE POSITIVE EFFECTS OF THE DELRAY BEACH NOURISHMENT PROGRAM

Kim E. Beachler, P.E.¹
and
Douglas W. Mann, P.E.²

INTRODUCTION

The success of beach nourishment projects is often questioned due to the observed losses of sand from the fill area and what appears to be a loss of benefits. Observations made by the authors indicate that there have been noticeable advances in the shoreline both to the north and the south of the Delray Beach, Florida beach nourishment project. The purpose of this evaluation is to show that much of the sand which moves out of the project can actually be accounted for and benefits the neighboring beaches.

The City of Delray Beach is located on the southeast coast of Florida approximately 80 kilometers north of Miami (Figure 1). A portion of the City encompasses about 4.8 km of the barrier island. The nourishment project is maintained over a distance of 4.3 km.

BACKGROUND HISTORY

In the 1960's, the Delray Beach shoreline was experiencing severe erosion. The public beach was almost non-existent and State Road A1A was damaged annually in winter storms (Figure 2). To combat this problem, the City constructed concrete and rock revetments along the public beach. In 1971, the concrete revetment failed and the City initiated a beach nourishment program.

The initial beach nourishment was completed in 1973. The project totaled 1,249,739 cubic meters of sand which was dredged from an offshore borrow area and placed in the project area. Subsequent to the initial nourishment the project area was renourished in 1978, 1984 and 1992 using sand volumes of 536,000, 994,000 and 770,000 cubic meters, respectively. The location of the various fill placements is shown in Figure 2.

The annualized cost of the beach nourishment program is approximately US\$980,000 (Coastal Planning & Engineering, Inc., 1991). The program is a Federally authorized shore protection project. As a result, the nourishments are designed consistent with Federal (U.S. Army Corps of Engineers) standards and are funded at both the federal, and local level.

The variation of fill volumes in this program (1973 to the present) is indicative of the expanded knowledge gained from both the monitoring of the beach fill and the advancement in beach nourishment design over this time period. A review of the initial 1973 fill placement has indicated that only enough material was placed to construct the design (storm protection) section of the beach. Virtually no sand was placed to account for end losses or background erosion losses (advanced nourishment). Subsequent nourishments have placed sufficient sand in an advanced nourishment section to maintain the design section through the nourishment interval. This design procedure is consistent with the National Research Council (NRC) recommendations (NRC, 1995).

¹ Formerly, Vice President, Coastal Planning & Engineering, Inc., 2481 NW Boca Raton Blvd., Boca Raton, FL 33431, USA.

² Coastal Engineer, Coastal Planning & Engineering, Inc., 2481 NW Boca Raton Blvd., Boca Raton, FL 33431, USA.

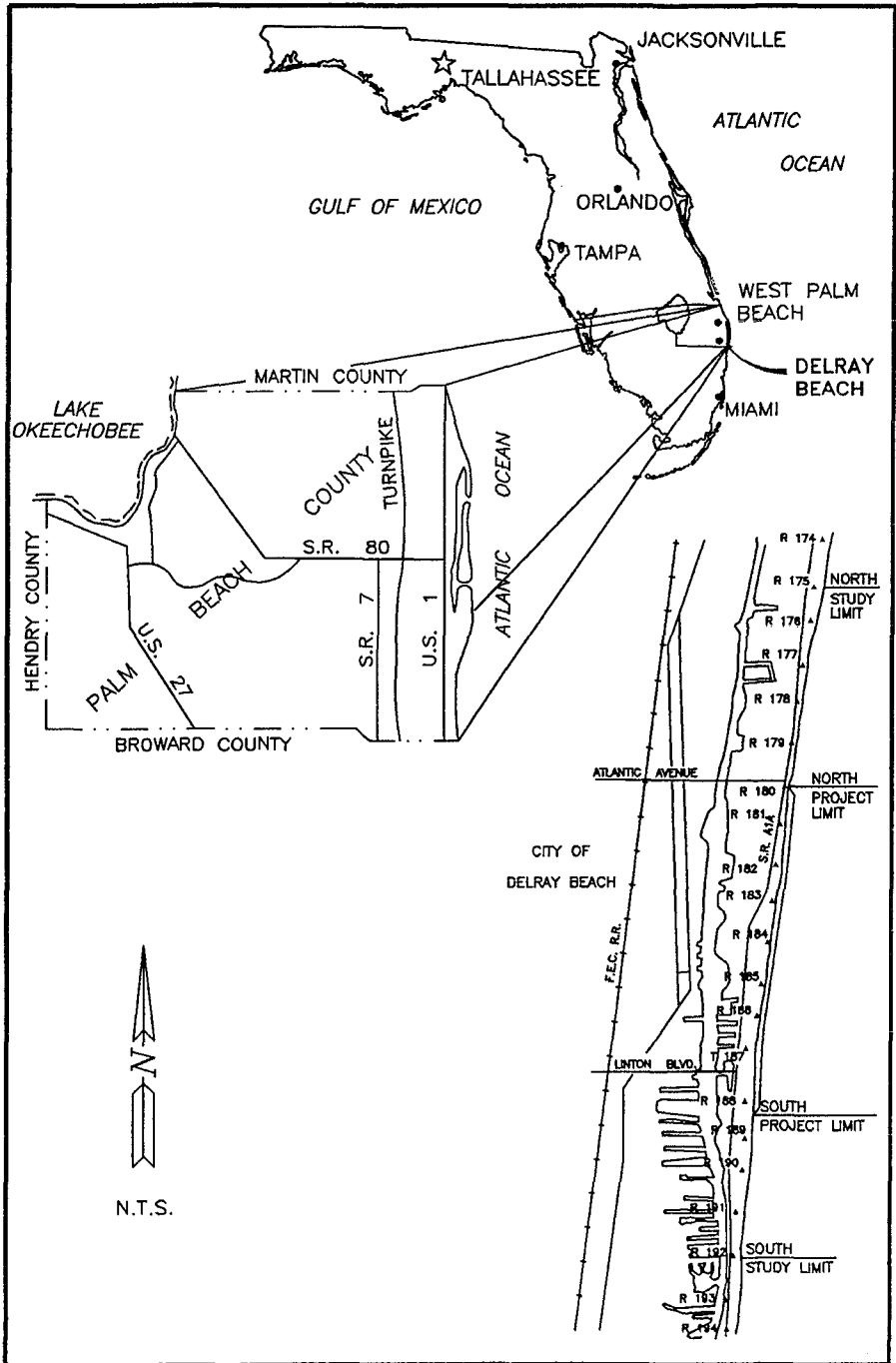


FIGURE 1

BEACH MONITORING, ANALYSIS, AND RESULTS

Annual monitoring studies have been conducted by the City of Delray Beach since the initial restoration, providing data for the performance assessment. Survey data from the State of Florida Department of Environmental Protection collected in 1974, 1990, and 1995 was used to evaluate changes outside of the project area. The State of Florida maintains a series of beach profiles which are spaced approximately every 330 meters along the sandy shoreline of the State. The profiles in the fill area are shown in Figure 2. All beach profiles are surveyed from the upland limit to the depth of closure (approximately -10 meters).

Figure 3 shows the mean high water shoreline changes from 1974 to 1995 both within the fill area and on the adjacent shorelines. While the initial fill project occurred in 1973, no beach profiles were measured on the adjacent shorelines until 1974. As a result, the shoreline response in Figure 3 is not complete; nevertheless, the survey comparison represents one of the few extended (spatially and temporally) monitorings of a beach nourishment program.

The beach fill plan form demonstrates end loss or diffusion characteristics which are similar to those predicted by Pelnard-Consideré (1956) though a direct comparison has not been made. Accretion outside of the fill area is highest immediately adjacent to the fill and tapers to lesser amounts further from the fill (Figure 3). The length of the taper to the south is longer than the taper to the north which is consistent with the net littoral transport to the south. There are distinct points to the north (R165) and south (R201) where the data showed no change or erosion over the 21-year comparison. These end points are used as the lateral limits of the impact of the beach fill on adjacent beaches. It is probable that the beach fill impacts beaches further to the south, but that the accretion due to the fill is less than the existing erosion. The north limit is in the vicinity of a large natural limestone rock outcrop which tends to act as a groin and divides the beach into small littoral cells.

The monitoring data indicates that some of the sand from the nourishment project has moved about 3 kilometers north and south of the fill limits. This movement results in an advancement of the shoreline as well as increased volumes of sand on the beaches within the neighboring towns of Gulfstream and Highland Beach. The nourishment program has placed about 3.5 million cubic meters of sand on Delray Beach between 1973 and 1992. The beach profiles indicate that a total of 43% of that sand, about 1.5 million cubic meters, has been eroded from the fill area; however, the analysis found that 1.3 million cubic meters (85%) of that sand could be located between 2.7 km north of the project to 3.5 km south of the project. The total volume accreted to the north is 629,000 cubic meters over 2.7 km and to the south the accretion is 673,000 cubic meters over 3.5 km. Therefore, the majority of the sand that has eroded from the project has not been "lost" but rather has been deposited on adjacent beaches.

Nourishment Interval

The nourishment interval for the Delray Beach nourishment project has increased from 5 years to the present 8 years (1984 to 1992). The design of the fill places an economically optimum amount of advanced nourishment on the beach. Currently, the advanced nourishment is designed to last 9 years (U. S. Army Corps of Engineers, 1992). The increase in the actual nourishment interval is a result of better estimation of end losses and the spreading of the beach fill. The diffusion theory indicates that a longer fill project will last longer than a shorter fill project. The accretion of sand on adjacent beaches has extended the "effective" length of the beach and has resulted in less diffusion loss and a longer nourishment interval.

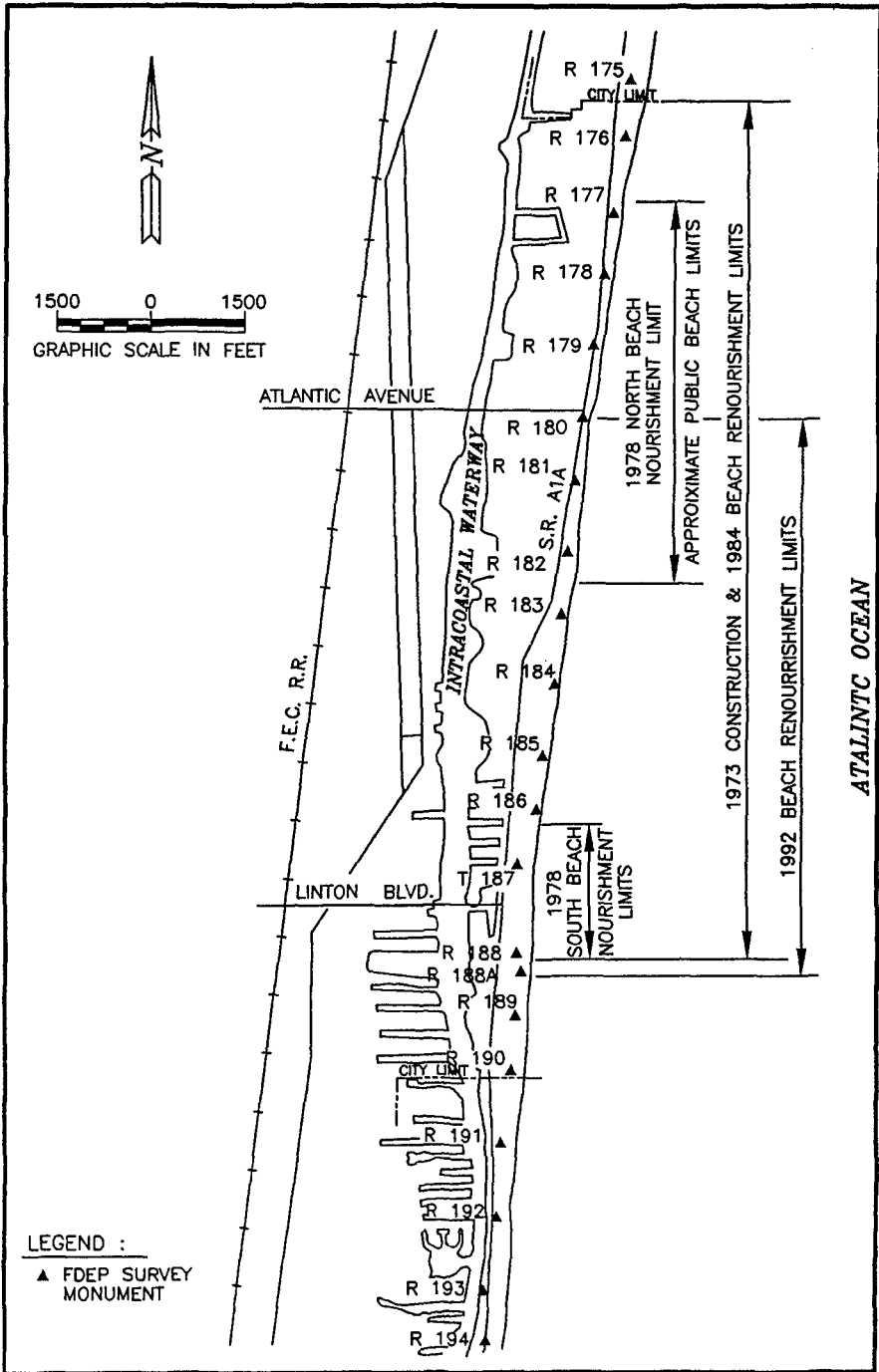


FIGURE 2

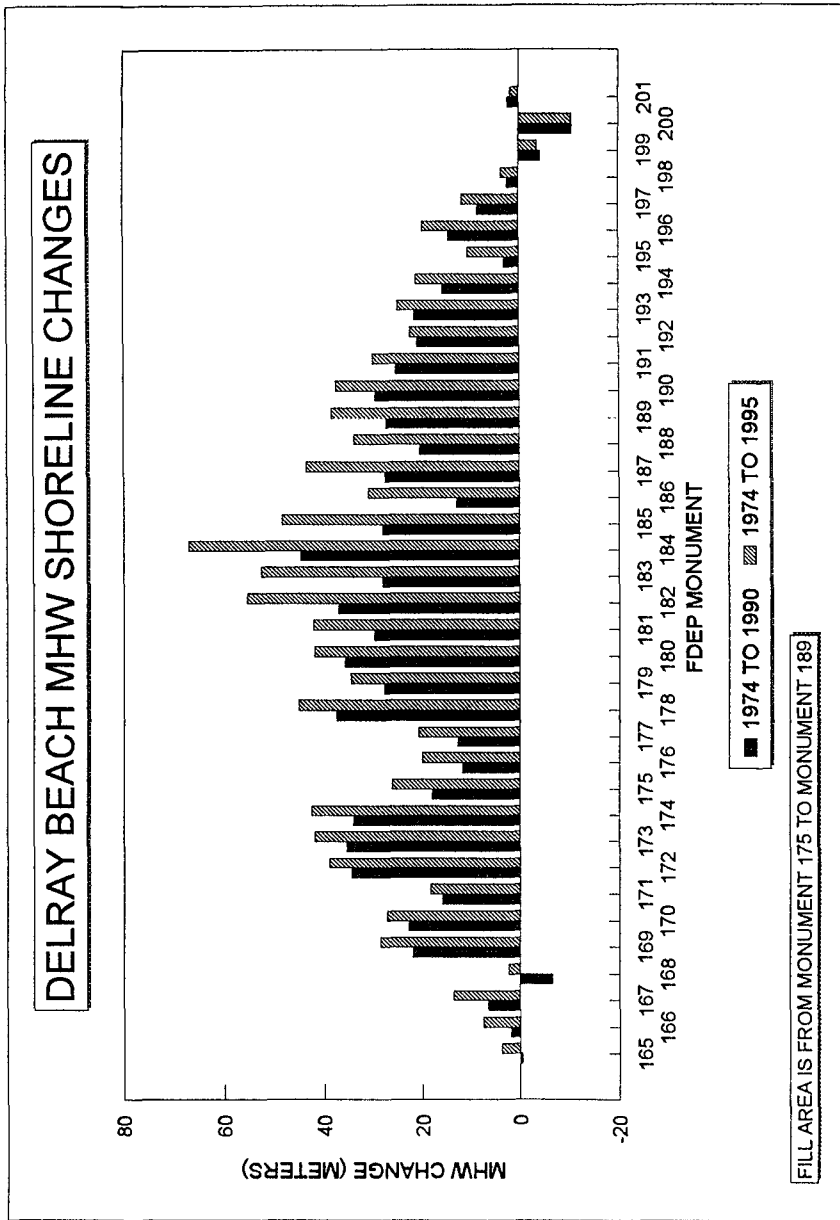


Figure 3

PROJECT BENEFITS

Benefits of a beach nourishment project are attained in several ways. The most important are the protection of upland properties from coastal storm damage, the improved recreational value of the maintained beaches and the resulting increase in property values. The City of Delray Beach, who manages its beach program, requested that these benefits be determined to understand the positive impact of the beach program on the local economy.

Storm Damage Reduction

Storm damage prevention benefits presented in this paper are limited to those that are recognized by the U.S. Army Corps of Engineers in their evaluation of Federal participation. Storm damage reduction benefits are estimated by comparing the with project damage to the with out project damage. Damages are limited to structural damage to upland structures and roads, the loss of fill from upland areas from extreme events, the loss of land from long term recession of the beach profile, and the damage to existing coastal armoring. In addition, the prevention of coastal armoring is also included as a benefit. The Florida coast is susceptible to large storm surge and wave events associated with tropical storms and hurricanes. As these storms are acknowledged to be random events, storm damages are calculated in a probabilistic method. The method of computing the storm damages is generally described by Bodge(1991). For this analysis, the computer program of Thomas(1990) was utilized. An interest rate of 7.625 percent was assumed for the economic calculations. While this interest rate is about twice the U.S. rate of inflation, it is the rate prescribed by the U.S. Army Corps of Engineers and results in conservative benefits estimates. All economic data is calculated in U.S. dollars.

The storm damage prevention benefits were calculated using land and property values from the 1995 tax appraisers roll. For the fill area only(R175 to R189), the storm damage reduction benefits are \$3,819,800 annually. The annual storm damage reduction benefit of the Delray Beach nourishment projects on the adjacent beaches is \$5,863,000. This can be further divided; \$2,552,500 for properties in Gulfstream to the north and \$3,310,500 for properties to the south in Highland Beach.

The storm damage reduction benefits are thus greater outside the fill area than inside the fill area. While this may appear counterintuitive since the fill material is placed only in Delray Beach, the benefits are higher due to the level of upland development in each area. The City of Delray Beach maintains a public beach which is accessed by a beach front road. The adjacent communities of Highland Beach and Gulfstream are heavily developed along the ocean with expensive private homes and multi-unit condominiums. In addition, the Town of Gulfstream was heavily eroded in the early 1970's. The accretion of sand on a heavily eroded and heavily developed beach generates significant storm damage reduction benefits.

Property Value Enhancement

Recent beach nourishments within the state of Florida have resulted in increased property values. This increase in property values results in beach front owners receiving higher profits from their real estate investments as well as increasing the local property tax. A recent analysis of the study area was performed by Regional Research Associates(1996). They compared the unit property values(\$/square meter) for similar properties located on the barrier island and on the mainland(Figure 1). The Delray Beach nourishment project has resulted in beachfront properties costing 15-20% more than mainland properties due to the maintained beach. This increase is \$109.6 million within the fill area, \$31.0 million and \$58.4 million in Gulfstream and Highland Beach, respectively. The property value increase results in annual local taxes

of \$2.8 million, \$1.1 million, and \$1.9 million for Delray Beach, Gulfstream and Highland Beach, respectively.

Recreation Benefits

Recreational benefits attributed to a beach nourishment project are due to the increase in available beach space. The Corps of Engineers limits the recreational benefits by the demand to go to the beach and by the availability of public parking. The maintenance of the beach nourishment results in the annual benefits of \$496,000 in Delray Beach (Coastal Planning & Engineering, Inc., 1991). Because there is no public parking or access within Gulfstream or Highland Beach, no recreational benefits accrue due to the project.

Benefit Summary

The Delray Beach beach maintenance program generates approximately \$10.2 million annually in storm damage reduction benefits and recreational benefits to the City of Delray Beach and the adjacent towns of Highland Beach and Gulfstream. A common economic decision making principle is the ratio of annual benefits to annual costs. For this project, the benefit to cost ratio is 10.4. This excludes the increase in annual tax revenues due to the effect of the beach on property values.

CONCLUSIONS

The Delray Beach nourishment program has had a positive effect on a total of 11.3 km of shoreline as a result of filling about 4.3 km on a periodic basis. The analysis showed average shoreline advances of 28.3 meters to the north of the fill and 23.1 monitoring to the south. This was confirmed by an analysis of total volume change over the 23-year life of this project. The study accounted for 85% of the sand lost from the nourishment project.

As a result of this accretion outside of the fill area in neighboring cities, it was found that storm damage prevention benefits amounted to \$3,819,800 within the fill area and \$5,863,000 outside of the fill area but as a direct result of sand moving from Delray Beach to neighboring shorelines. The fact that there is a beach in place within the fill area provides an increase of 15 to 20 percent in property values.

ACKNOWLEDGMENT

The property value analysis data from Regional Research Associates is appreciated.

REFERENCES

Pelnard-Considere', R., "Essai de Theorie de l'Evolution des forms de Rivage en Plage de Sable et de Galets," *4th Journees de l'Hydraulique*, Les Energies de la Mer, Question III, No. 1, pp.289-298, 1956.

Bodge, K., "Damage Benefits and Cost Sharing for Shore Protection Projects", *Shore and Beach*, Vol 59, No. 2, pp. 11-18, April 1991.

Coastal Planning & Engineering, Inc., "Palm Beach County, Florida From Martin County Line to Lake Worth Inlet and from South Lake Worth Inlet to Broward County Line, General Design Memorandum Addendum for Third Periodic Nourishment at Delray Beach," report to the City of Delray Beach, 1991.

National Research Council, *Beach Nourishment and Protection*, National Academy Press, Washington D.C., 1995.

Regional Research Associates, "The Economic and Fiscal Impact of the Delray Beach Maintenance Program on Delray Beach, Gulfstream and Highland Beach Barrier Island Properties", unpublished report to the City of Delray Beach , 1996.

Thomas, C., "STORM02, Shore Protection Project Economic Analysis," copyrighted software, 1990.

CHAPTER 360

EFFECTIVENESS OF A COMBINED BEACH AND SHOREFACE NOURISHMENT ON THE ISLAND OF NORDERNEY/EAST FRISIA, GERMANY

Hanz D. Niemeyer¹, Ralf Kaiser¹ & Heiko Knaack¹

Abstract

In order to improve the effectiveness of artificial nourishments a replenishment outside of the beach itself was taken into consideration for a prototype test. Contradictory to the earlier six conventional beach nourishments the material was deposited both on the shoreface and on the beach. The fate of the combined shoreface and beach nourishment was as well as that of the preceding conventional beach replenishment intensively monitored including field investigations of bathymetry, hydro- and sediment dynamics. On the basis of these data and additional application of mathematical models the effectiveness of this new type of nourishment has been evaluated in comparison with a conventional beach replenishment.

Introduction

The East Frisian island of Norderney experiences structural erosion in its western parts since the beginning of last century which is caused primarily by large scale tidal inlet and ebb delta migration [LUCK 1977; NIEMEYER 1995] and secondary by a gradient in long shore transport in the generally west-eastern directed drift [KRAMER 1960; NIEMEYER 1991]. In addition to earlier erected solid structures eight beach nourishments have been executed here since 1951/52 [KRAMER 1960; KUNZ 1991; NIEMEYER et al. 1995a]. Hydro- and morphodynamical boundary conditions have already been described in earlier publications [NIEMEYER 1991].

In 1992 a combined beach and shoreface nourishment was chosen as an alternative to conventional beach nourishments (fig. 1) [NIEMEYER et al. 1995a]. In order to evaluate its effectiveness an intensive monitoring programme including sedimentological, morphological and hydrodynamical site

¹Coastal Research Station of the Lower Saxonian Central State Board for Ecology, P.O. Box 1221, 26534 Norderney/East Frisia, Germany

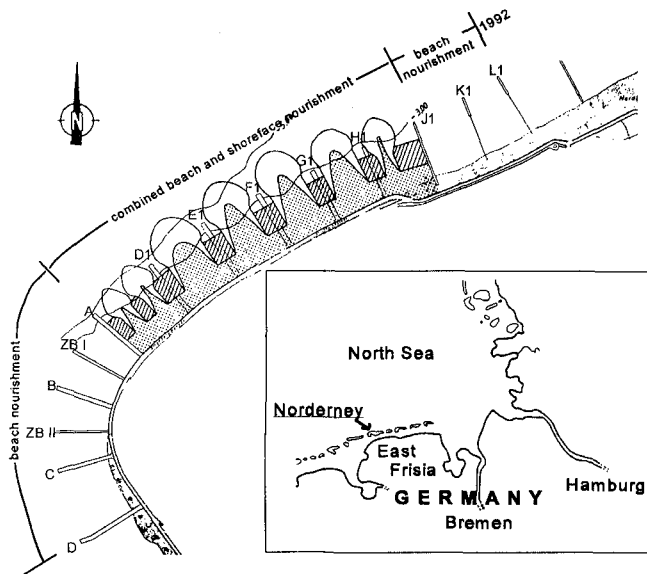


Figure 1. Island of Norderney/East Frisia in the southern North Sea; placements of the combined beach and shoreface nourishment in 1992 and of the preceding conventional beach replenishment in 1989

measurements has been carried out [KNAACK et al. 1996] as well as for the preceding conventional beach nourishment [KUNZ 1991; NIEMEYER 1991]. The investigations were carried out in cooperation with Danish and Dutch partners in the project "Innovative nourishment techniques evaluation (NOURTEC)" in the framework of the MAST II-programme of the European Communities and are additionally funded on a national basis. Results of the investigations carried out in respect to the combined shoreface and beach nourishment on the island of Norderney are subject of this paper focussing on its effectiveness by comparison with the preceding conventional one.

Design and initial behavior of the combined beach and shoreface nourishment

On the western and northwestern beaches of Norderney structural erosion is counterbalanced by artificial beach nourishments since 1951 [KRAMER 1960; KUNZ 1991; NIEMEYER 1991] though already between 1899 and 1909 dredging material has been dumped on the shoreface of the western beaches in order to improve beach stability [NIEMEYER et al. 1996]. In 1992

both nourishment techniques were combined for the replenishment of the northwestern beaches whereas on the western beaches only the beach was nourished (fig. 1). Basic idea of the deposition of material on the shoreface was to benefit from observed transport mechanisms explaining the pending of material between beach and shoreface [NIEMEYER 1991]. On the western beaches a deposition on the steep shoreface was considered as inconvenient; high initial irreversible losses into the close deep inlet channel were anticipated. A pure shoreface nourishment on the northwestern beaches was excluded because its execution by dumping or the rainbow-method on the shoreface between the groynes was regarded as dangerous for the executing vessels. Therefore the nourishment of the shoreface was carried out similar to that of the beach after finishing there the replenishment: the pipes were lengthened in the middle of the groyne fields and large humps were pumped into that area (fig. 2). It was anticipated that the local hydodynamical forces would create a dispersion of the sand stored in the artificial humps across the whole shoreface within a few weeks leading to its more or less uniform distribution.

Explanatory the reshaping of the hump in the groyne field E_1-F_1 is documented here by depth lines with reference to German datum = NN which is approximately equivalent to mean sea-level whereas mean high tide is about NN + 1,2 m and mean low tide about NN - 1,3 m (fig. 3): It is evident that the hump is lesser pronounced on the shoreface than on the beach. The highest initial losses occur therefore also on the intertidal beach and not on the shoreface which lower parts even benefit, but to a much lesser extent than the reduction of the hump's volume on the beach. A suitable explanation might be



Figure 2. Execution of the shoreface nourishment by pumping humps of sand from the shore

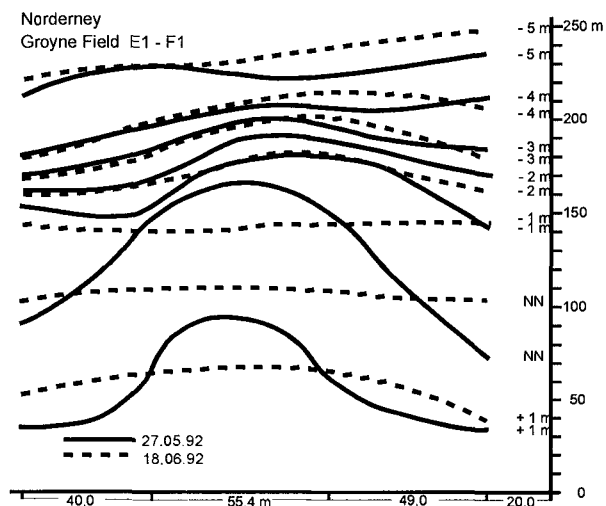


Figure 3. Reshaping of a sand hump after nourishment execution

that the geometry of the humps enforced the initialization of strong ripp currents evacuating large amounts of the nourished material from the beach across the shoreface directly offshore being there unavailable for the anticipated pending between beach and shoreface.

Behavior of the combined beach and shoreface nourishment

Behavior of the total nourishment

The analysis of the behavior of the nourished beaches is focussed on the areas where the replenishment has been carried out both on the beach and on the shoreface. For this area also the corresponding data of the preceding conventional nourishment are taken into consideration in order to compare the effectiveness of both replenishment techniques. A comparison for the relative volumes per m beach length of the two replenishments above certain levels with reference to NN across the whole stretch between the groynes A and J₁ (fig. 1) highlights again that in the case of the combined nourishment the volumes on the shoreface below NN -1,5 m are not significantly large in relation to that ones on the beach, particularly not if compared with volumes of the preceding conventional replenishment (fig. 4a). This fact is evidently confirmed by a comparison of the volumes between the chosen levels (fig. 4b): the relative volumes on the beach of the combined nourishment are higher than those of the conventional one. But nevertheless the data highlight also that a comparison of the two distinct nourishment on the basis of their lifetime will remain insufficient, because the remaining relative volumes of the combined beach and shoreface nourishments were at the end of its lifetime in 1994 higher than those of the preceding conventional one in its final stage.

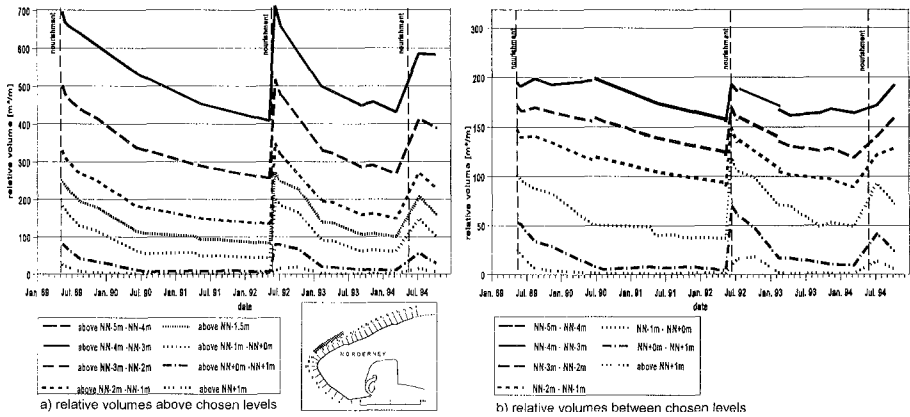


Fig. 4: Relative volumes per m beach length between the groynes A and J₁ after the conventional beach replenishment in 1989 and the combined beach and shoreface nourishment in 1992

Behavior of the nourishment in specific groyne fields

In order to get a deeper insight into the behavior of the two nourishments the development of their volumes in specific groyne fields has been evaluated with reference to the differences of shape and relative volumes. In the groyne field A-D₁ (fig. 1) at the downdrift edge of the combined beach and shoreface nourishment the relative volumes become between nearly all levels continuously smaller after the conventional beach nourishment of 1989. Only a slight increase occurred in the lower part of the shoreface in the very beginning and on the intertidal beach after a lifetime of more than two years (fig. 5). Contradictory the relative volumes of the lower shoreface increase during the whole lifetime of the combined nourishment and there is after initial erosion accretion on the upper part of the beach above mean sea-level during the first autumn and winter after implementation of the nourishment.

In the updrift succeeding groyne field D₁-E₁ (fig. 1) the intertidal beach loses relative volume immediately after the conventional beach replenishment in 1989 (fig. 6). After the first winter following the implementation of the nourishment here the relative volumes have again the same order of magnitude as before. They remain on the lower part of the intertidal beach then rather stable and decrease slightly in the final stage of the lifetime. The relative volumes on the shoreface increased during the first stage of the lifetime or experienced even a transient increase. After a period of about one year in coincidence with reduction of the relative volumes on the beach to the pre-nourishment level a continuous erosion of the shoreface started. It is itself suggesting that probable losses on the shoreface might have been compensated by eroded material from the beach as long as this source was available.

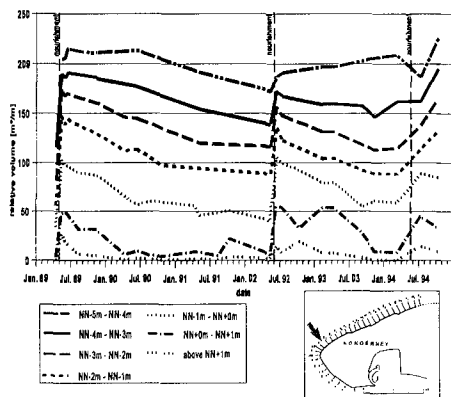


Fig. 5: Relative volumes per m beach length between the groynes A and D₁ between distinct levels after the conventional beach replenishment in 1989 and the combined beach and shoreface nourishment in 1992

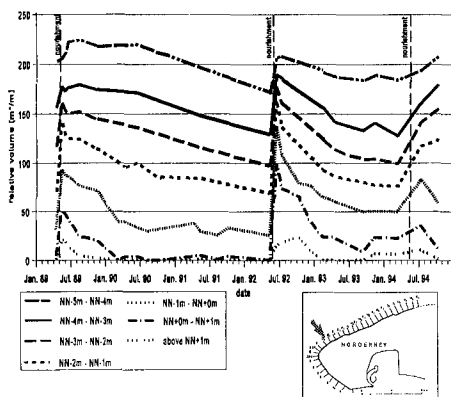


Fig. 6: Relative volumes per m beach length between the groynes D₁ and E₁ between distinct levels after the conventional beach replenishment in 1989 and the combined beach and shoreface nourishment in 1992

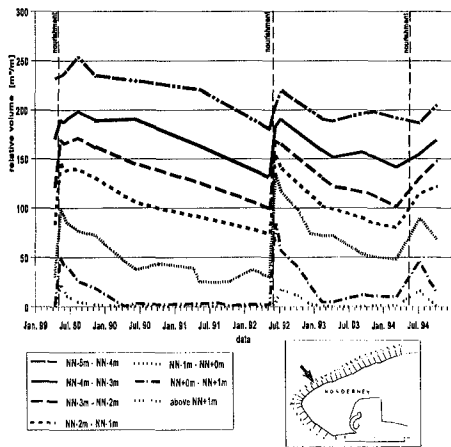


Fig. 7: Relative volumes per m beach length between the groynes E₁ and F₁ between distinct levels after the conventional beach replenishment in 1989 and the combined beach and shoreface nourishment in 1992

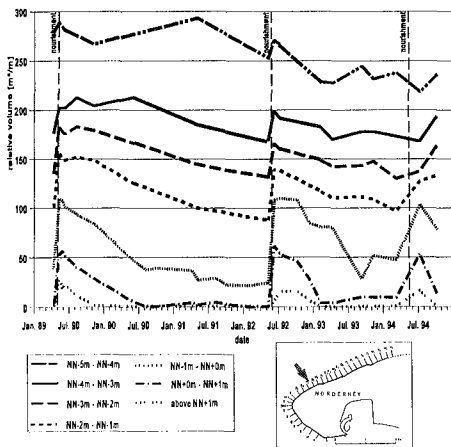


Fig. 8: Relative volumes per m beach length between the groynes F₁ and G₁ between distinct levels after the conventional beach replenishment in 1989 and the combined beach and shoreface nourishment in 1992

The nourished volumes in this groyne field have been larger for the subsequent combined nourishment leading to remarkable initial losses beside a slight increase on the highest part of the beach during the following five months. But after more than one year of lifetime a stabilization occurred on a

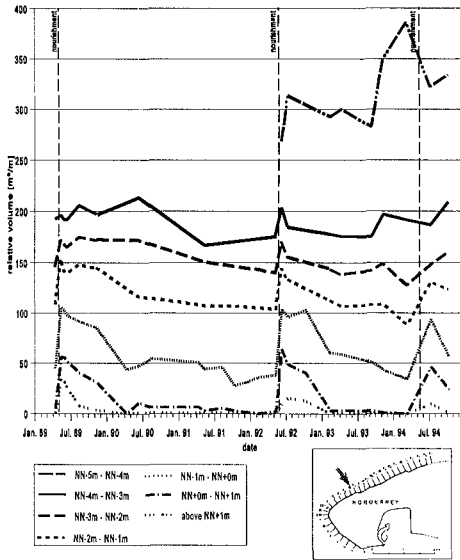


Fig. 9: Relative volumes per m beach length between the groynes G_1 and H_1 between distinct levels after the conventional beach replenishment in 1989 and the combined beach and shoreface nourishment in 1992

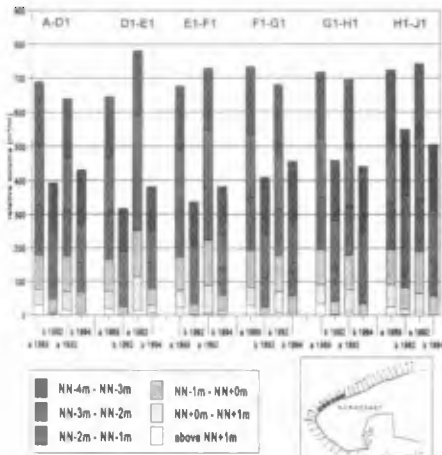
level significantly higher than the one before the implementation of the nourishment. Moreover the higher parts of the beaches recovered where the material is in respect of the primary aim to reduce wave loads more effective than anywhere else in the profile. This highlights once more that the morphological situation did not demand for the subsequent nourishment in 1994.

Similar results are gained for the next two groyne fields in updrift direction $E_1 - F_1$ and $F_1 - G_1$ (fig. 1) though less pronounced than for $D_1 - E_1$: There are both on the upper part of the beach as well as on the lower shoreface transient phases with accretion after initial erosion (fig. 7 + 8). Particularly on the lower part of the beach the relative volumes are significant larger at the final stage of the combined beach and shoreface nourishment than before.

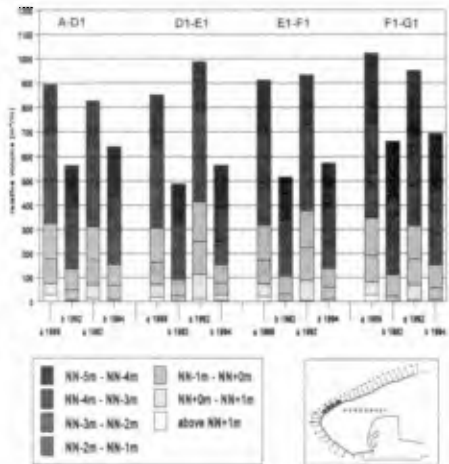
Contradictory the relative volumes after the combined nourishment in the groyne field $G_1 - H_1$ follow another tendency. Whereas their values remain rather stable or increase even on the lower shoreface those on the beach reflect continuous erosion. Particularly there the preceding conventional beach replenishment has not experienced a higher amount of erosion though its lifetime lasted longer (fig. 9). This effect requires further explanation, because the behavior of the nourished beach and foreshore in this area has changed in comparison with preceding nourishments. Erosion has become relatively higher with respect to the rates in the groyne fields being located updrift.

Total balance

For all groyne fields the relative volumes between certain levels have been determined as well for the combined beach and shoreface nourishment in 1992 as for the preceding conventional beach replenishment in 1989 on the following basis: total amount before and after execution (fig. 10.1 + 10.2), losses and nourished volume (fig. 11.1 + 10.2). The relative volumes after the execution of the combined nourishment are higher than after the implementation of the preceding conventional one in the groyne field $E_1 - F_1$, $H_1 - J_1$ and particularly in $D_1 - E_1$. According to the relative volumes before



10.1 Groyne fields A-D1 to H1-J1 above NN -4m

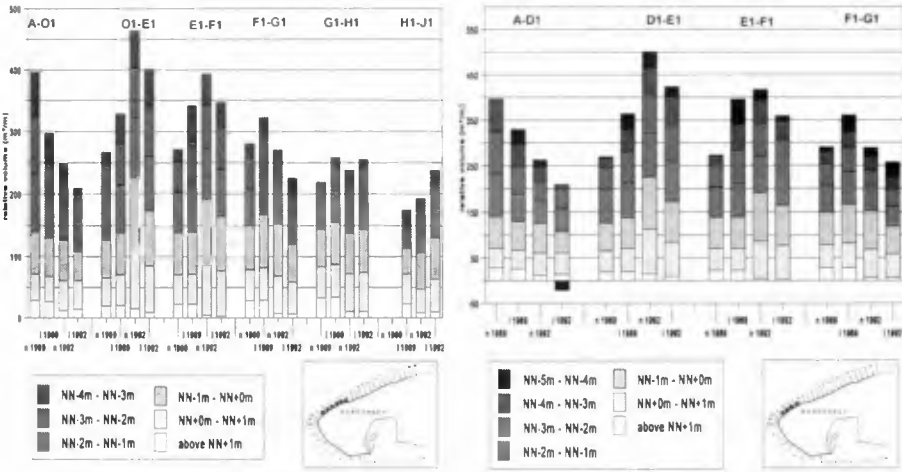


10.2 Groyne fields A-D1 to F1-G1 above NN -5m

Fig. 10: Relative volumes per m beach length between distinct levels after implementation (a) and at the end of the lifetime (b) for the nourishments in 1989 and 1992

implementation this was aimed at counterbalancing an anticipated higher rate of erosion in these areas (fig. 10.1 + 10.2). The same design procedure has been applied for the replenishment in 1989 (fig. 11.1) for the groyne field A-D₁ which has been rather successful if the remaining relative volumes in total are taken into consideration. In the groyne fields A-D₁, F₁-G₁ and G₁-H₁ the total relative volumes have been smaller for the combined nourishment in comparison to that one in 1989. The remaining relative volumes at the end of the lifetime of the combined nourishment are higher at that of the conventional replenishment between the groynes A and G₁ and smaller in the two following groyne fields G₁-H₁ and H₁-J₁ (fig. 10). Of high importance with respect to the primary aim to reduce wave attack at the seawall are the significantly higher remaining relative volumes on the beach and there particularly in the upper part above mean sea-level in the area between the groynes A and F₁ and to a lesser extent in the groyne field F₁-G₁. With respect to the necessity of a subsequent nourishment a comparison of the remaining relative volumes at the end of the lifetime of both nourishments makes evident that the minimum values existing before the combined beach and shoreface nourishment were still by about 25% and more exceeded in any place at the end of its lifetime (fig. 10)

Beside the groyne field A-D₁ the losses after the conventional beach nourishment exceed the nourished relative volumes (fig. 11). Though the losses in A-D₁ were not compensated by the combined nourishment it delivered on overish of which is particularly evident for the lower shoreface where instead of losses a net win has taken place (fig. 11.2). The comparison



11.1 Groyne fields A-D1 to H1-J1 above NN -4m

11.2 Groyne fields A-D1 to F1-G1 above NN -5m

Fig. 11: Relative nourished volumes (n) and afterward losses (l) per m beach length between distinct levels for the nourishments in 1989 and 1992

between nourished relative volumes and subsequent losses makes evident that particular for the stretch between the groynes A and G_1 where for both nourishments the highest losses occur the combined beach and nourishment left over an overshot of material at the end of its lifetime. In the groyne fields A-D₁, F₁-G₁, G₁-H₁ (fig. 11) and if the lower part of the shoreface is included even in the groyne field E₁-F₁ the total losses after the implementation of the combined nourishment have been remarkably smaller than for the preceding conventional beach replenishment. Only in the groyne fields D₁-E₁ and H₁-J₁ the total losses after the execution of the combined nourishment have been larger than those of the preceding one (fig. 11.1). The difference decreases by about 50 % for the groyne field D₁-E₁ if the lower shoreface is taken into consideration (fig. 11.2). With respect to of the major purpose of artificial nourishments in this place to reduce wave attack on the seawall it is of high importance to check the losses on the upper part of the beach. The behavior of combined beach and shoreface nourishment in the area with the largest losses makes evident that particularly there the relation between nourished and lost relative volumes above mean sea-level is favourable in comparison to that of the preceding conventional beach replenishment (fig. 11).

Impacts of changing local wave climate

measurements in the offshore area and on the shoreface of the island of Norderney highlighted enormous changes in wave damping on the ebb delta of the tidal inlet. In comparison to results from earlier investigations [NIEMEYER 1987] waves are lesser attenuated when propagating across the ebb delta, even for conditions with no remarkable set-up on mean high tide the

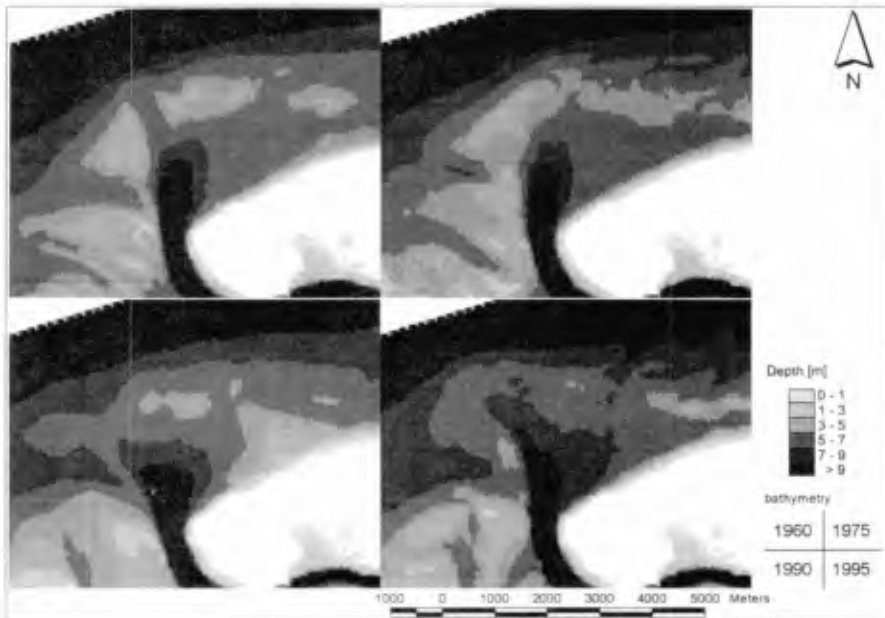


Fig. 12: Topography for the area seaward of the tidal inlet and the northwestern shore of the island of Norderney according to surveys in 1960, 1975, 1990 and 1995

shelter effect of the ebb delta for the northwestern beaches of the island of Norderney was remarkably reduced. In order to get a deeper and more systematic insight into background on these processes runs with the mathematical wave model HISWA [HOLTHUIJSEN & BOOIJ 1987; BOOIJ & HOLTHUIJSEN 1992] have been carried out for four distinct morphological situations of the area seaward of the tidal inlet and the northwestern shore of the island of Norderney (fig. 12): the bathymetries of 1960, 1975, 1990 and 1995 were used as a basis for model topography. The model HISWA has already been successfully applied to this specific area and similar ones and is regarded as a suitable tool for the anticipated purpose [DEN ADEL et al. 1991; NIEMEYER et al. 1995b].

Already the simple comparison of the topography for the distinct four situations makes significant morphological changes evident (fig. 12): Whereas the ebb delta is becoming even more pronounced after 1960 with a climax in 1975 the later surveys in 1990 and 1995 make a reduction of the shallows with heights above NN - m evident. Accompanied is this process by a migration and seaward directed deepening of the main channel of the inlet between 1990 and 1995: Both morphological changes enhance onshore wave penetration in direction of the island's northwestern shores.

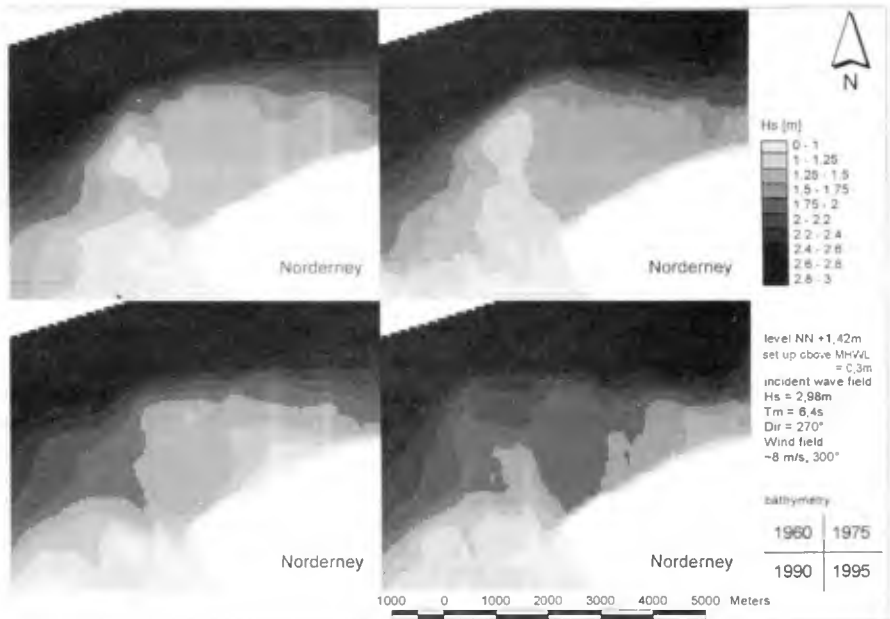


Fig. 13: Significant wave heights for the area seaward of the tidal inlet and the northwestern shore of the island of Norderney according to the bathymetry in 1960, 1975, 1990 and 1995 (computed with HISWA)

The model runs confirm this first estimate with respect to penetration of higher waves into the northwestern shoreface of the island of Norderney (fig. 13): For the situations of 1960 and 1975 no significant changes occur. But already for the topography of 1990 higher waves with $1,75 \text{ m} \leq H_s \leq 2,00 \text{ m}$ propagate across the ebb delta though not appearing nearshore. For the topography of 1995 waves with heights with this order of magnitude occur on a large part of the shoreface. This increase in nearshore wave energy is not only confirmed by prototype data; the measured wave heights on the shoreface are even higher than those being computed with the model for the same offshore conditions. Additional investigations have shown that this effect does not increase for storm surges with higher set-up and higher waves. The higher waves enforce also a more intensive wave energy dissipation due to breaking in the ebb delta area.

In order to make the effect of this change in local wave climate for the dynamics on the northwestern shoreface and beaches of the island of Norderney more evident the computed significant wave heights for all four morphological situations are compared at 26 selected points at the edge of shoreface and beach parallel to the island's northwestern shore (fig. 14). For the situations of 1960 and 1975 there are no remarkable changes in wave climate. The significant wave heights are of the same order of magnitude on

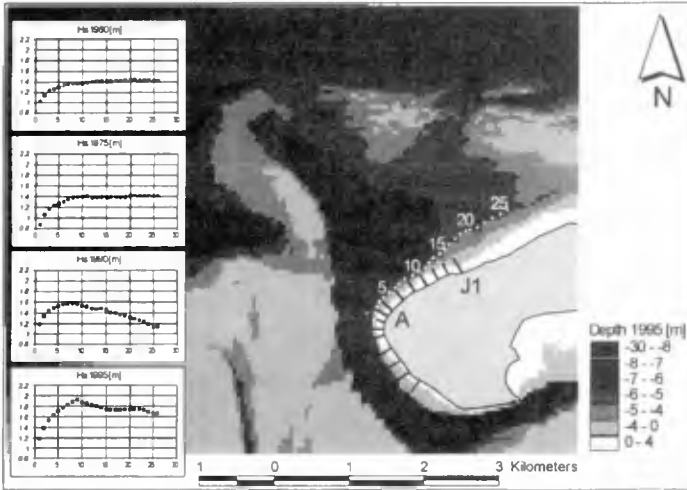


Fig. 14: Significant wave heights at the edge of shoreface and beach parallel to the northwestern shore of the island of Norderney according to the bathymetry in 1960, 1975, 1990 and 1995 (computed with HISWA)

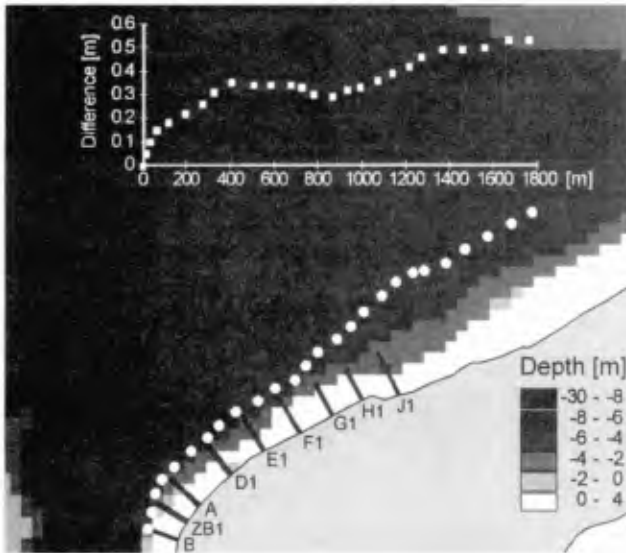


Fig. 15: Differences of significant wave heights at the edge of shoreface and beach parallel to the northwestern shore of the island of Norderney according to the bathymetry in 1990 and 1995 (computed with HISWA)

the whole stretch of the northwestern shoreface. In 1990 there is an increase of wave heights particularly in the stretch between the groynes A and F₁ but they decrease further downdrift. In 1995 wave height have increased in all places downdrift of groyne A (fig. 15). This comparison highlights that the combined nourishment experience for the same offshore conditions higher wave loads with stronger driving forces than the preceding conventional one. This unfavorable boundary conditions are another indication for the superior effectiveness of the combined nourishment. The change in wave climate explains also the higher losses occurring after the implementation of the combined beach and shoreface nourishment in the area downdrift of groyne H₁.

Conclusions

The comparison between the combined beach and shoreface nourishment and the preceding conventional replenishment with respect to their effectiveness has lead to the following conclusions:

1. Lifetime is in this case no suitable measure for comparing the effectiveness because the remaining relative volumes are for the combined nourishment in any place larger than the accepted minimum values for the preceding conventional for which no damages of the seawall occurred.
2. High initial losses of the combined nourishment might be credited to the chosen execution method with the deposition of humps which might have provoked strong ripp currents in the groyne fields. A less concentrated dumping of supply material on the shoreface could improve the measure.
3. Relatively higher losses in the downdrift part of the combined nourishment in comparison to the preceding conventional one do not occur due to the changes in the execution method. They are enforced by changes in local wave climate due to migration of the ebb delta leading to an increase of the driving forces for longshore currents and littoral drift.
4. The application of reliable mathematical wave models in combination with available actual bathymetries is suitable to make changing wave loads evident allowing an optimized adaption of the spatial distribution of relative nourished volumes in distinct groyne fields.
5. Particularly in the area with high rates of erosion the behavior of the combined nourishment delivered indications for the anticipated pending of the sand between shoreface and beach leading there to a recovery of the upper part of the beach which is beneficial with respect to the major aim of these nourishments to enforce wave energy dissipation in front of the landward placed seawall.

6. An further optimization of artificial nourishments on the northwestern shore of the island of Norderney requires a definition of acceptable wave loads for the existing seawall in order to evaluate the ultimately necessary minimum of relative volumes on the beach for sufficient wave energy dissipation.

Acknowledgement

This investigations have been carried out in the framework of the NOURTEC project of THE COMMISSION OF THE EUROPEAN COMMUNITIES (Contract MAS-CT93-0049) and additionally benefitted from national funds of the GERMAN FEDERAL MINISTRY FOR EDUCATION AND RESEARCH and the LOWER SAXONIAN MINISTRY FOR THE ENVIRONMENT. The authors have substantially benefitted from the joint cooperation in this European project with their Danish and Dutch partners. They are also very grateful for the assistance and support by Mr. Günther Brandt, Detlef Glaser, Thomas Hartkens, Peter Heddinga, Holger Karow, and Georg Münkewarf.

References

- den Adel, J.D., H.D. Niemeier, A.F. Franken, N. Booij, J. Dekker, J.A. Vogel [1991]: Wave model application in a Wadden Sea area. Proc. 22nd Int. Conf. o. Coast. Eng. Delft, ASCE, New York
- Booij, N. & L.H. Holthuijsen [1992]: HISWA user manual. Prediction of stationary, short-crested waves with ambient currents. TU Delft, Faculteit d. Civ. Techn.
- Holthuijsen, L.H. & N. Booij [1992]: A grid model for shallow water waves. Proc. 20th Intern. Conf. o. Coast. Eng. Taipei, ASCE, New York
- Knaack, H., R. Kaiser, H.D. Niemeier [1996]: Behaviour and effectiveness of the NOURTEC experimental test sites - Norderney case. Rep. MAS II-CT93-0049 (unpubl.)
- Kramer, J. (1960): Beach Rehabilitation by Use of Beach Fills and Further Plans for the Protection of the Island of Norderney. Proc. 7th Conf. o. Coast. Eng. Richmond, ASCE
- Kunz, H. [1991]: Artificial Beach Nourishment on Norderney, a Case Study. Proc. 22nd Int. Conf. o. Coast. Eng. Delft, ASCE, New York
- Lastrup, C., H. Toxvig Madsen, P. Sørensen, I. Bröker [1997]: Comparison of beach and shoreface nourishment-Torsminde Tange, Denmark. Proc. 25th Intern. Conf. o. Coast. Eng. Orlando/Fl., USA, ASCE, New York
- Luck, G. [1977]: Long-termed development of tidal inlets between Eastfrisian islands. Proc. 15th Intern. Conf. o. Coast. Eng. Honolulu, ASCE, New York
- Mulder, J.P.M., J. van de Kreeke, P. v. Vesseem [1995]: Experimental shoreface nourishment, Terschelling (NL). Proc. 24th Intern. Conf. o. Coast. Eng. Kobe/Japan, ASCE, New York
- Niemeier, H. D. [1987]: Changing of wave climate due to breaking on a tidal inlet bar. Proc. 20th Intern. Conf. o. Coast. Eng. Taipei, ASCE, New York
- Niemeier, H.D. [1991]: Field measurements and analysis of wave-induced nearshore currents. Proc. 22nd Intern. Conf. o. Coast. Eng. Delft/The Netherlands, ASCE, New York
- Niemeier, H.D. [1995]: Long-term morphodynamical development of East Frisian Islands and Coast. Proc. 24th Intern. Conf. o. Coast. Eng. Kobe/Japan, ASCE, New York
- Niemeier, H.D. & R. Kaiser [1994]: NOURTEC-design report: Combined shoreface and beach nourishment, island of Norderney, East Frisia. Com. Europ. Comm. - MAST II-Progr., MAS 2-CT93-0049
- Niemeier, H.D., R. Kaiser, J.D. den Adel [1995b]: Anwendung des mathematischen Seegangmodells HISWA auf Wattenmeerbereiche. Die Küste, H. 57
- Niemeier, H.D., E. Biegel, R. Kaiser, H. Knaack, C. Lastrup, J.P.M. Mulder, R. Spannhof, H. Toxvig [1995a]: General aims of the NOURTEC project -effectiveness and execution of beach and shoreface nourishments-. Proc. 4th Conf. o. Coast. & Port Eng. i. Develop. Countr., Rio de Janeiro/Brazil
- Niemeier, H.D., H. Rohde & H. Eiben [1996]: History and heritage of German coastal engineering. In: N. Kraus (ed.): History and heritage of coastal engineering. ASCE, New York



Lake Worth sand bypass plant, Palm Beach, Florida.
Photo courtesy of Billy L. Edge.

PART VI

Case Studies



Hillsboro Inlet, Hillsboro, Florida. Photo courtesy of
Coastal Systems International, Inc.

CHAPTER 361

Nearshore Berm Performance at Newport Beach, California, USA

Chuck Mesa¹

Abstract

In 1992, approximately 1,276,000 cubic yards of littoral material was hydraulically placed into a berm configuration in nearshore water depths at Newport Beach, California, USA. A monitoring program conducted included directional wave measurements, beach and bathymetric profiles, surficial sediment sampling, and controlled aerial photography. Analysis of the bathymetric profiles collectively indicate the berm is experiencing a shoreward-directed dispersal; there is no evidence suggesting offshore or alongshore directed berm movement. Sediment physical characteristics and grain size distribution indicating the berm effects on the seabed are discussed. Recently proposed models for berm stable/active categorization and migration rate are examined. Surfing at the site was significantly enhanced; the berm created breaking wave conditions never before experienced at this location.

Introduction

This paper describes a nearshore disposal monitoring project at Newport Beach, California, USA. The nearshore placement activity was conducted during the period Jan-Nov 1992. Approximately 1,276,000 cubic

1

U.S. Army Corps of Engineers, Los Angeles District, P.O. Box 2711, Los Angeles, CA, 90053, USA

yards of suitable littoral material was hydraulically placed into a berm configuration in water depths ranging from -5 ft to -30 ft MLLW (Note: All elevations and/or depths cited herein are in feet referred to Mean Lower Low Water (MLLW)). These depths are both within and outside the day-to-day surf zone. The purpose of the monitoring plan was to determine the fate of the disposal berm by providing a quantitative and qualitative description of the movement of disposal material in the cross-shore and alongshore directions. The material was obtained as the result of the Lower Santa Ana River flood control channel expansion project.

The project site is located in the City of Newport Beach, California, USA. The shoreline immediately landward of the disposal area is a mixed use area of recreation and residential development. Coastal structures in the project area include three shore perpendicular jetties at the mouth of the Santa Ana River, and a field of eight groins. The disposal site was selected to confine the material between the river mouth system and the groin field.

Monitoring Plan

The monitoring program conducted during the period Dec 91 - May 95 included directional wave measurements, beach and bathymetric profiles, surficial sediment sampling, and controlled aerial photography of the project area (Fig 1).

The nearshore directional wave climate was monitored by installation of a S_{xy} slope array wave recording instrument during the period 3/92 - present. The slope array was placed offshore of Huntington Beach approximately 1.5 miles northwest of the project site at a water depth of 33 ft.

The 24 beach and bathymetric profile lines were established as follows: 8 lines placed throughout the groin field system; 11 higher spatial resolution lines placed at 300 ft intervals over the disposal area; 1 line placed over the Santa Ana River delta; 3 lines spaced at even intervals; 1 line (control) placed

approximately 1.5 miles northwest of the project area. The control line is not expected to be influenced by movements of the nearshore disposal material, and acts as an indicator for seasonal or gross shoreline movements. Profiles were measured from a fixed point on the backshore to depths of greater than -40 ft. Profile survey dates were: 12/91 pre-construction; 5/92 1st interim; 7/92 2nd interim; 11/92 1st post-construction; 3/93 2nd post-construction; 5/93 3rd post-construction; 1/94 4th post-construction; 11/94 5th post-construction; and 5/95 6th post-construction.

Sediment samples were obtained by surficial grab sampling techniques along 6 profile lines (Line 1, Line 5, Line 9, Line 14, Line 19, Line 24) at 8 elevations corresponding to +6 ft, 0 ft, -6 ft, -12 ft, -18 ft, -24 ft, -30 ft, and -36 ft.

Controlled aerial photography flown over the project area included: 12/91, 6/92, 11/92, 12/92, 3/93, and 5/93.

Wave Climate Description

Directional wave measurements indicate a multi-directional, seasonally dependent, sea/swell climate is experienced at the project site. The nearshore slope array recorded 6905 observations during the measurement period. The sample histogram of wave heights included a maximum measured wave of 10.6 ft; the mean, mode, and standard deviation are given as 2.7 ft, 2.5 ft and 0.9 ft respectively. The sample histogram of spectral peak period indicates double peaks at $T=7$ sec and $T=15$ sec. In southern California this is typically associated with sea and swell respectively (not withstanding the respective classical definitions dependent on the point of origin). The combined sea/swell climate was assumed a priori; a double peaked distribution of wave climate was expected.

Profile Comparison

Repeated bathymetric mapping of the cross-shore profiles indicates the nearshore disposal material

formed a significant clearly distinguishable feature on the local seabed relative to the pre-project profile.

Fig 2 illustrates a time series of the cross-shore distribution of berm material at Line 19 (located at the disposal area northwestern boundary). Fig 2 indicates the berm is distributed along the profile approximately between depths of -2 ft and -32 ft. The berm toe appears located at the -32 ft contour; the berm indicates a relatively sharp relief on the seaward side and is diffused gradually towards shallower water. The berm maximum vertical relief (e.g. "centroid") appears located at a depth of -29 ft.

Fig 3 is a time series comparison of the profile *differences* developed by subtraction of the pre-project profile from the post-construction profiles. Inspection of Fig 3 clearly illustrates the berm cross-shore behavior. The berm centroid is located 1900 ft from the survey baseline, or about 1200 ft from the beach. The berm had a maximum vertical relief of 14.5 ft from the pre-project seabed, diminishing successively to 11.5 ft, 9.0 ft, 8.5 ft, and finally diminishing to 8.0 ft by the sixth survey episode (31 months). Thus, the berm vertical relief appears to diminish rapidly initially, with the deflation rate decreasing over time. Close inspection of Fig 3 indicates as the berm crest erodes, the crest material is sheared off in the *landward* direction. The survey data indicates there is significant accretion of material throughout the region between the berm and the foreshore. This landward directed movement is particularly indicated by the accretion of material in a bar formation as indicated in the 5/93 survey episode. Further inspection of Fig 3 indicates the berm centroid location is stationary, and not migratory as the berm erodes. There is no indication the berm migrates as a solitary feature; migration is measured as a function of the crest material dispersal. This observation is relevant to the following discussion of berm migration rate.

There is no evidence in the data to suggest offshore or alongshore directed movement of the berm material. Analysis of all measured profiles indicates

no signal within the resolution of the survey data which substantiates seaward berm movement. There is little or no indication of significant alongshore movement of the berm. Due to the prevailing wave climate, net sediment transport is a priori expected to be in the southeasterly direction. Analysis of the profile closest to the disposal area southeastern boundary (Line 8 within the groin field) indicates no signal to substantiate southeasterly alongshore movement. Likewise, there is no significant indication of berm migration in the northwesterly direction. This is unambiguously no movement across the northwesterly control line. The profile closet to the northwestern boundary exhibits some accretionary signal, however, that was determined to be remnant storm flow material from the Santa Ana River.

Sediment Physical Characteristics and Distribution

The sediment characteristics of the nearshore disposal material are known from pre-project geotechnical analyses. The material was approximately 83% sand and 17% fines (defined as passing the #200 U.S. Std sieve), with a d_{50} median diameter of approximately 0.27 mm which is classified as fine sand under the Unified Soils Classification.

Fig 4 illustrates a time series comparison of sediment grain size distribution along a selected profile (Line 19) and depth (-24 ft). The pre-project (12/91) sediment distribution is a poorly graded fine sand material, approximately 17% fines, with a d_{50} median diameter of 0.09 mm. Fig 4 indicates a well behaved coarsening of the grain size distribution between the 1st, 2nd, and 5th survey episodes. At the 5th survey episode (11/94) the sediment achieved its coarsest distribution, a poorly graded fine sand, 1% fines, with a d_{50} median diameter of 0.22 mm. There appears to be a rebound of the grain size distribution at the 6th survey episode.

Fig 5 illustrates a cross-shore time series comparison of d_{50} median diameters at Line 19. The data is fairly well behaved and indicates the coarsest

fraction is located on the upper portions of the profile while the fine grained fraction is dispersed towards deeper water. The berm material is coarser than the pre-project seabed and appears to be maintaining its position on the seabed.

Fig 6 illustrates a cross-shore time series comparison of percent fines at Line 19. The data clearly shows the percent fines is significantly higher in water depths greater than -24 ft. Over time the percent fines remain less than or approximately equal to the pre-project seabed condition.

Berm Categorization

Hands & Allison (1991) present a empirically based method to categorize stable or active nearshore berms. The method calculates the long-term distribution of wave-induced, near-bed velocities as an appropriate criterion to discriminate between stable and active behavior. Used conjunctively with the Hallermeier proposed inner and outer limits of profile zonation, the method successfully discriminates between stable and active berms in the "buffer" zone bounded by the inner and outer limits.

The results of the present analysis, shown in Fig 7, delineates the regions of berm stability or activity based on the wave-induced near-bed velocities. The berm in the present analysis is classified as *stable*, particularly at the 75-95 percentile which Hands & Allison describe as possessing the best correlation with berm behavior. It is worth noting that the present berm velocity distribution crosses the boundary delineating the stable-active regions, and also tends to converge towards the active classification near the 99-percentile (indicating a tendency for berm movement during extreme events).

The results using the Hallermeier profile zonation limits, shown in Fig 8, indicate the berm falls in the "buffer" zone. Hands & Allison further showed that berms stable in the buffer zone were less than 50% below the outer limit, while active berms were more than 50%

above the outer limit. Thus, with this methodology the Newport Beach berm gains an active classification. This directly contradicts the previously determined *stable* classification based on near-bed velocities. However, it should be noted that the berm could be considered weakly active based on its relative position as slightly greater than the 50% outer limit within the buffer zone.

Berm Migration Rate

Douglass (1995) proposed a model for landward migration rate estimation of nearshore sand berms. The model is formulated on the assumption that net shoreward sediment transport is due primarily to the velocity asymmetry characteristics of finite amplitude waves. The model parameters can be estimated using a joint probability density function (height-period, direction is assumed onshore) of site-specific wave climate data. The "expected value" of berm migration rate can be estimated as a function of depth.

The results estimate the berm migration rate to be approximately 100 ft/yr (Fig 9). Douglass provides no guidelines for choosing a depth from the functional relationship to use for berm migration estimation. An observation made during this analysis indicates that the results are critically dependent on the depth chosen. The depth used in the current study is the depth at the berm center of mass. However, this depth no longer exists after berm placement. Since the method is based on the velocity asymmetry of finite amplitude waves, the depth used should be the depth at the berm crest. This appears to be an inherent inconsistency, yet still the model appears to produce results that are in reasonable agreement with observed values and are the correct order of magnitude. The decaying semi-logarithmic function of depth appears intuitively correct. However, with decreasing depths at the shore, the model expected value approaches unrealistically high values. The model also assumes landward migration only and does not consider offshore movement.

Surfing

The nearshore berm disposal project temporarily significantly enhanced conditions for the recreational sport of surfing. This study photographically recorded breaking waves never before experienced at this location. The pre-project wave-breaking condition typically consisted of long crested swell waves propagating over straight and parallel contours with wave breaking occurring relatively close to shore. Typical pre-project surfing can be described as beach-break resulting in short, fast spilling/plunging "lefts" and "rights".

The hydraulic placement techniques employed by the construction contractor resulted in a series of small mounds constructed throughout the disposal area footprint. These disposal mounds were dispersed cross-shore throughout the nearshore zone, from near the typical breaker line to upwards of 1,200 feet offshore. Refraction effects focused the wave energy directly onto the individual mounds, which were effectively a severe perturbation to the straight and parallel bathymetric contours, tending to scatter the local wave field (Photo 1). The result was many wave "peaks" throughout the nearshore zone. Due to the extremely sharp relief of the mounds, waves tended to shoal extremely quick, increasing the local wave steepness, and creating a very "fast", "hollow" surfing wave (Photo 2). The surf lasted throughout the period of nearshore disposal, and several months thereafter. The surf was best at lower tidal levels with longer period swell.

Conclusions

In 1992, approximately 1,276,000 cubic yards of littoral material was hydraulically placed into a nearshore berm configuration at Newport Beach, California, USA. The monitoring program established included directional wave measurements, beach and bathymetric profiles, surficial sediment sampling, and controlled aerial photography. Bathymetry measurements indicate the berm is eroding by undergoing dispersal of the crest material shoreward. The berm base appears

stable. There is no evidence suggesting either offshore or alongshore movement of the berm material. Sediment physical characteristics indicate the coarser sediments are remaining within the active littoral system, while the berm is not adversely affecting the percentage of fines. Results using recently proposed models for berm stable/active categorization and migration rate are mixed. The berm gained both a stable and active classification. A calculated migration rate of 100 ft/yr appears correct in order of magnitude, but some question remains on functional application based on selection of appropriate water depth. Surfing at the site was significantly improved. Berm influence on the local wave field created shoaling and breaking conditions never before experienced at this location.

Acknowledgments

The author wishes to acknowledge the Commander, U.S. Army Corps of Engineers Los Angeles District, for authorizing publication of this paper. It was prepared as a result of the Lower Santa Ana River Flood Control Improvement study. I would like to thank the following individuals for their assistance and participation in this project: Dr. Scott L. Douglass at the University of South Alabama and Mr. Edward B. Hands at the Coastal Engineering Research Center. A special thanks is expressed to the boys at The Frog House Surf Shop.

References

- Douglass, Scott L. (1995). "Estimating Landward Migration of Nearshore Constructed Sand Mounds." *Journal of Waterway, Port, Coastal, and Ocean Engineering.*, ASCE, New York, N.Y., Vol 121, No. 5.
- Hands, E.B., and Allison, M.C. (1991). "Mound Migration in Deeper Water and Methods of Categorizing Active and Stable Depths." *Proceedings, Coastal Sediments 91 Conference.*, ASCE, New York, N.Y., Vol. 2, 1985-1999.

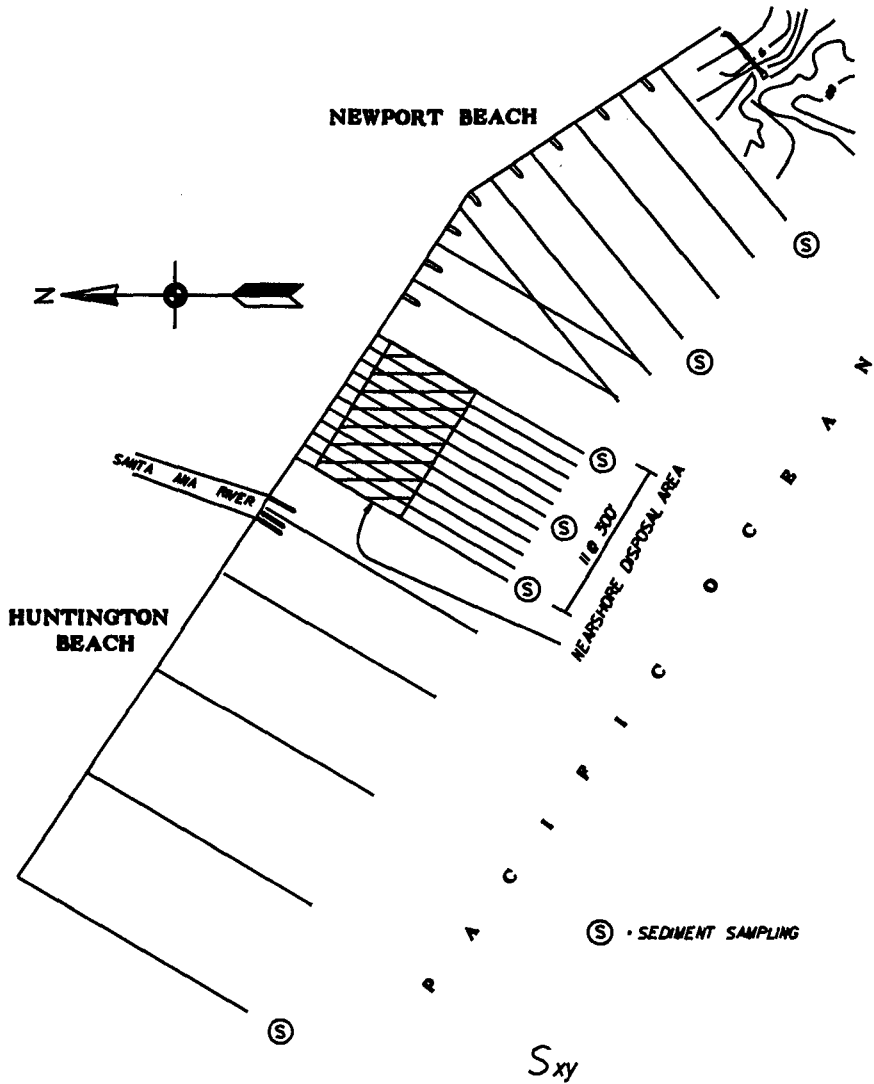


Figure 1. Monitoring Program Schematic.

Note: Survey lines numbered sequentially 1-24 from southeast to northwest.

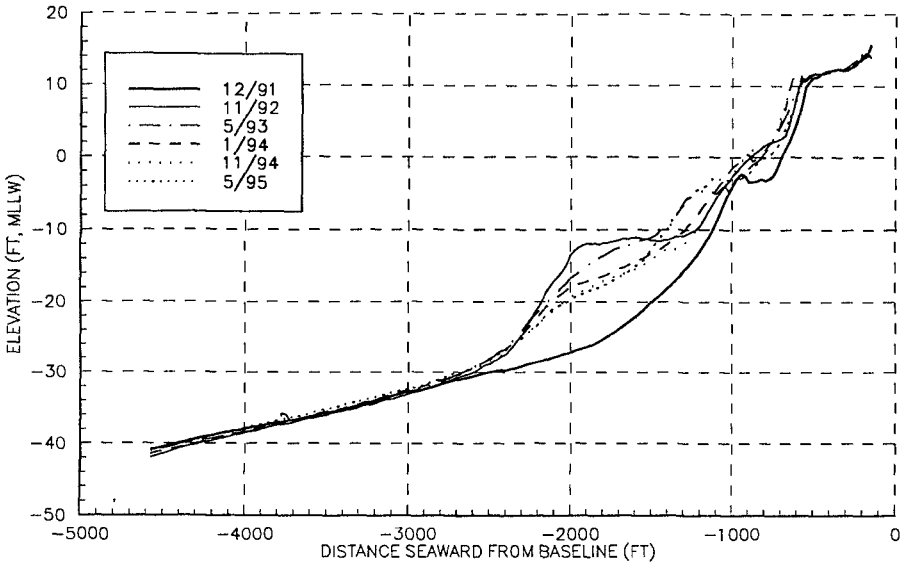


Figure 2. Comparison of Profiles at Line 19.

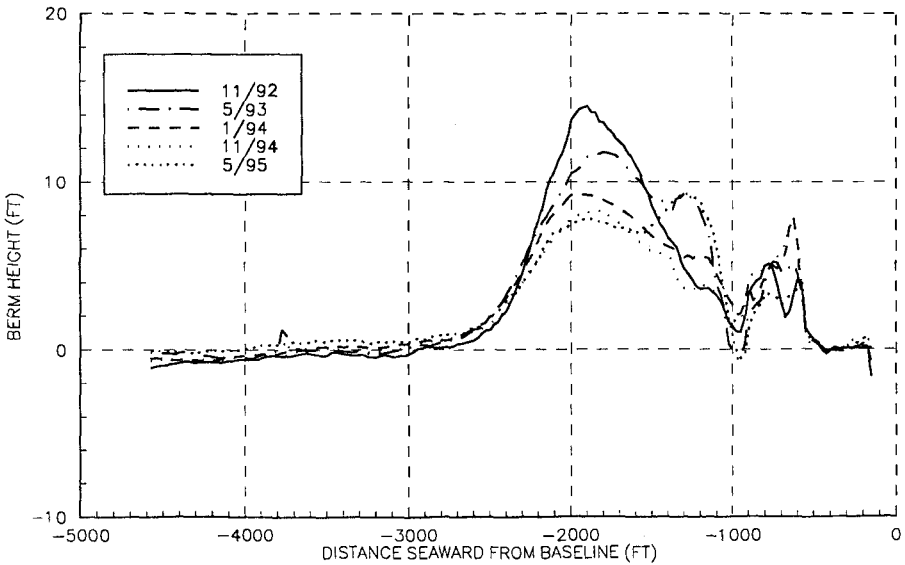


Figure 3. Comparison of Profile Differences at Line 19 Relative to Pre-project Condition (12/91).

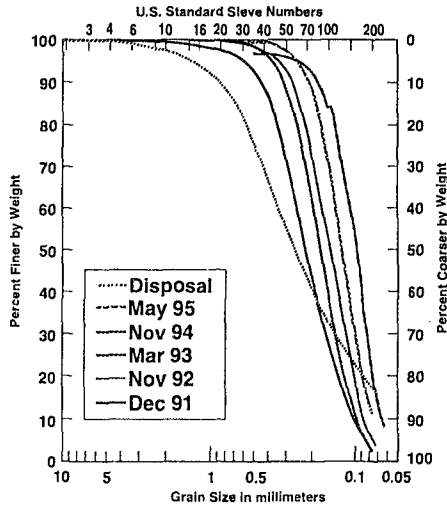


Figure 4. Grain Size Distribution Comparison, Line 19, $d = -24$ ft

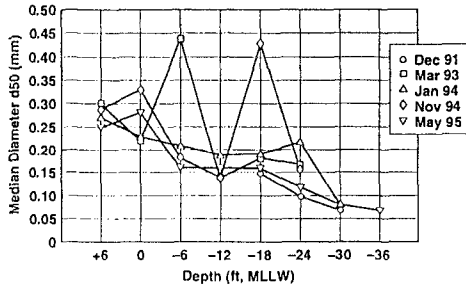


Figure 5. Cross-shore Comparison of d_{50} Median Diameter, Line 19

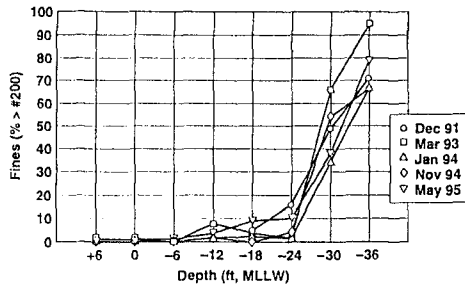


Figure 6. Cross-shore Comparison of Percent Fines, Line 19

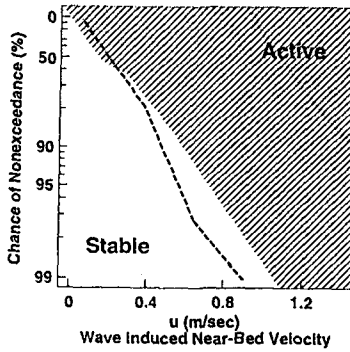


Figure 7. Berm Categorization Based on Wave Induced Near-bed Velocity. Adapted from Hands & Allison (1991).

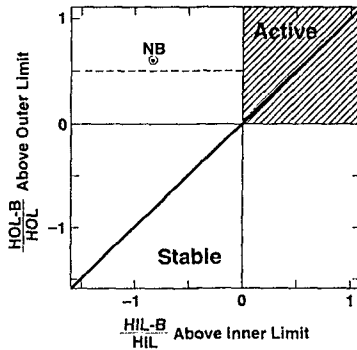


Figure 8. Berm Categorization Based on Hallermeier Limits. Adapted from Hands & Allison (1991).

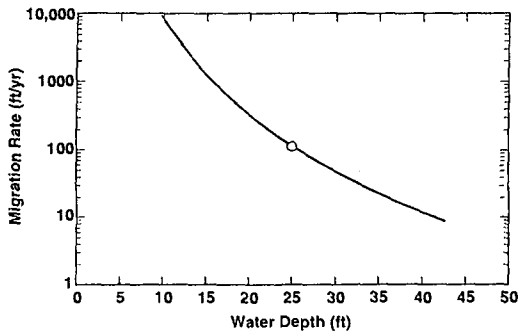


Figure 9. Berm Migration Rate.



Photo 1. Wave Refraction due to Nearshore Berm. 12/92.



Photo 2. Wave Breaking due to Nearshore Berm. Summer 1992.

CHAPTER 362

San Gabriel River to Newport Bay Erosion Control Project Orange County, California 30 Years of Periodic Beach Replenishment

Arthur T. Shak, P.E.¹, M. ASCE and Joseph A. Ryan, P.E.²

Abstract: Monitoring of a Beach Erosion Control project consisting of a protective and feeder beach with periodic beach nourishment in Orange County, California is assisted with Computer Aided Design and Drafting technology. Time series of depth changes and profile volumes are analyzed, and predicted renourishment requirements compared to 31 years of project history.

Introduction

The U.S. Congress authorized an erosion control project in 1962, recognizing the impacts of flood works, coastal harbors and other factors in causing beach erosion along the northern Orange County, California shoreline. With legislatively established cost-sharing between the State and federal government, an initial beachfill was constructed in 1964, with periodic nourishment in 1971, 1979, 1984, 1989-90 and 1996-97. Future beachfills are projected to be needed on a 5 year cycle, indefinitely.

The construction of the project was modified from the originally formulated plan with the use of sand sources of opportunity, the addition of a groin field, and deferring a detached breakwater/sand trap feature. A comprehensive analysis was performed of available profile data to compute the shoreline and volumetric history from pre- and post project to the present. This analysis was compiled by meticulously reconstructing historic data from the 1960's to the present to create controlled digital terrain maps which can easily be analyzed with CADD software.

1) Civil Engineer, U.S. Army Corps of Engineers, Los Angeles District, Los Angeles, California 90053.

2) Civil Engineer, U.S. Army Corps of Engineers, Los Angeles District, Los Angeles, California 90053.

Project History

The erosion control project formulated in the 1960's consisted of a protective and feeder beach to be located at the updrift end of the littoral cell at Surfside and Sunset Beach, with periodic beach nourishment by back-passing from the downdrift end of the cell near the Santa Ana River. The project area of approximately 20 km alongshore had a planned fill volume of three million cubic yards (mcy) for the initial protective beach, and a projected periodic renourishment rate of 1.75 mcy every five years. A detached offshore breakwater was also planned as a sand trap to be located at the downdrift location. The overall project plan is shown on Figure 1.

The initial protective and feeder beach was built in 1964 with four mcy of material from the adjacent Anaheim Bay/Seal Beach Naval Weapons Station (NWS). Between the initial fill and 1995, four renourishment cycles and three dredging projects of the NWS placed 8.6 mcy of dredge material - measured at the dredge site - at the feeder beach, as listed in Table 1. Of dredge material, 5.0 mcy were borrowed from offshore dredge pits. Photos 1 and 2 show typical pre and post beachfill conditions.

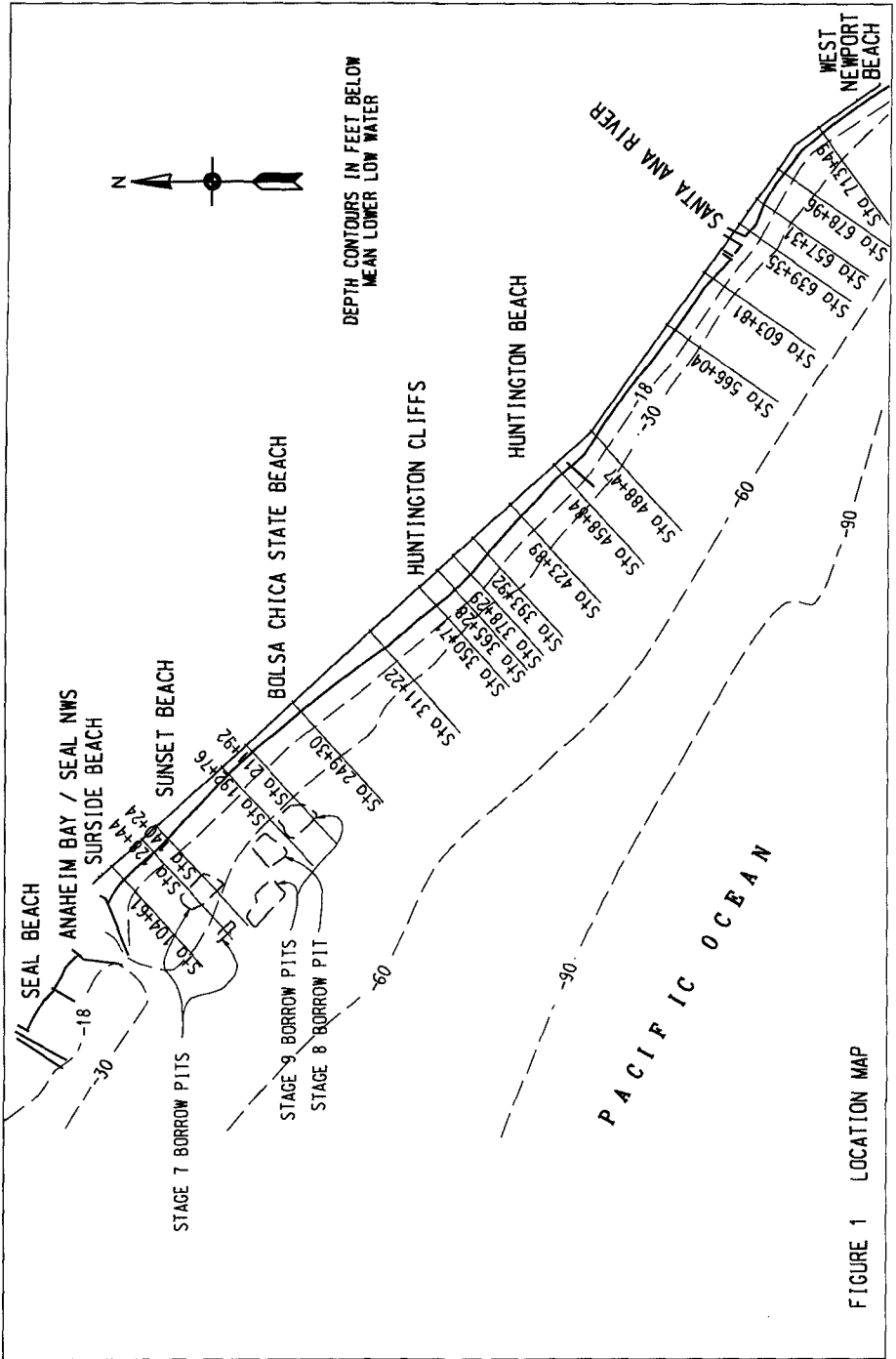
Construction of the detached breakwater/sand trap is deferred pending a demonstration of need, and no backpassing from the downdrift beach area has been performed. A groin field and beachfill at west Newport Beach was added to the project and constructed between 1969 and 1973. Eight groins were constructed and their cells filled with about 1.5 mcy of beachfill from the Santa Ana River or the adjacent Balboa peninsula.

Table 1 Surfside-Sunset Beach Fills (1963-90)

Completion Date	Dredge Volume (cy)	Cumulative Volume (cy)	Description /Borrow Sit
June 1964	4,000,000	4,000,000	Stage 1/Seal Beach NWS
May 1971	2,260,000	6,260,000	Stage 4A/Seal Beach NWS
June 1979	1,644,000	7,904,000	Stage 7/Offshore Borrow Pit
May 1983	400,000	8,304,000	Deepening NWS Channel
April 1984	1,500,000	9,804,000	Stage 8/Offshore Borrow Pit
April 1984	783,000	10,587,000	Seal Beach NWS
March 1989	180,000	10,767,000	Deepening NWS Channel
June 1990	1,300,000	12,067,000	Stage 9/Offshore Borrow Pit
Sep 1990	522,000	12,589,000	Stage 9/Offshore Borrow Pit

Analysis Methodology

Commercial Computer Aided Drafting and Design (CADD) software, MicroStation and InXpress from Bentley Systems, Inc., were utilized in creating digital terrain models (DTM) of the beach and nearshore hydrography. The CADD design files (.dgn) and digital terrain models (.dtm) are full scale models referenced to the California State Plane Coordinate System (SPCS27, Zone 6) as described in Stem(1989). The coordinate system was chosen for compatibility with an existing Geographic Information System (GIS) database made





**PHOTO 1 Feeder Beach Area - Post Stage 7 Beachfill
(Oct 31, 1979)**

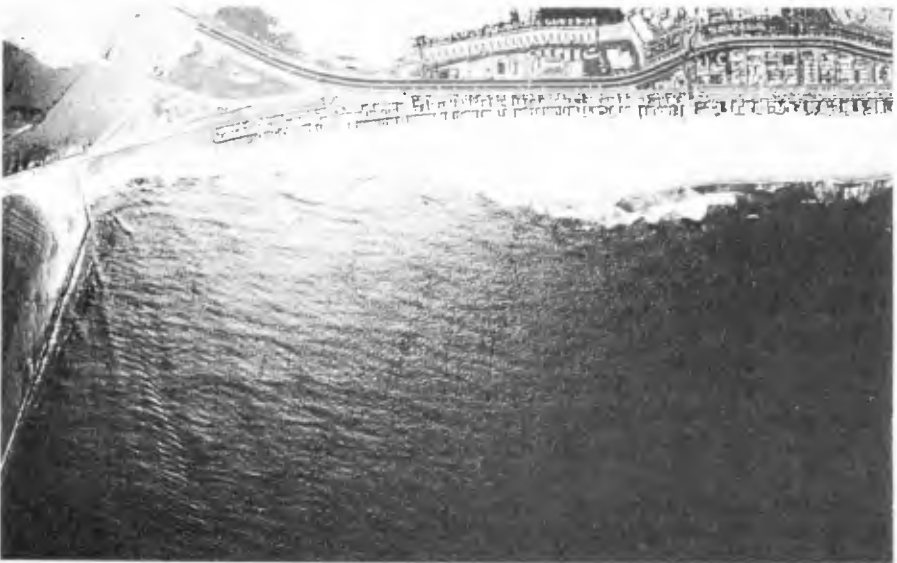


**PHOTO 2 Feeder Beach Area - Pre Stage 8 Beachfill
(April 16, 1982)**

available by Orange County, California, allowing overlays of the beach profile data to map data having property line resolution and orthogonally rectified aerial photography. Programs, such as CORPSCON developed by the U.S. Army Corps of Engineers Topographic Engineering Center, are available for conversion to any of the common horizontal datums with an accuracy as good as the original positioning data. The vertical datum used for all of the analysis is mean lower low water.

Available surveys used to construct DTM models, also referred to as Triangulated Irregular Network (TIN) models, include condition surveys, and pre- and post construction surveys of the San Gabriel River to Newport Bay Beach Erosion Control project; dredging of the Seal Beach NWS; the Santa Ana River Mainstem (SAR) project; the Coast of California Storm and Tidal Wave Study (CCSTWS); and surveys of the National Ocean Survey (NOS) conducted along the coasts in 1934 and 1975-77. Surveys were performed with varying degrees of spatial coverage and resolution, as well as duration. The recent profile surveys (1990's) were collected in time periods as short as a week while the 1960's surveys were collected over several months and the NOS surveys collected over multiple years. A tabulation of surveys utilized are listed in Tables 2 and 3.

After the tedium of reconstructing survey notes to the SPCS27 datum and data input into the DTM models, analysis alignments or baselines and control volumes were established. Volume estimates can be made with three different computational methods: 1) surface to surface comparisons between each facet of TIN models, 2) comparison of gridded surfaces fit to the TIN models, and 3) the traditional average-end area method applied to cross-sections of an alongshore alignment. The surface to surface approach provides the most numerically precise computation of the available data, however, the most useable volumetric comparisons were provided by the average-end area method with carefully selected sections located near surveyed profile lines. The reason that the surface to surface or gridded model computed erroneous results were due to differences in alongshore spacing of profiles between the different surveys resulting in the comparison of measured to interpolated surfaces. Interpolation of the beach profile across even slight embayments can result in large errors. The location of the selected sections used are shown on Figure 1. Sample cross-sections generated from the TIN model are shown on Figure 2.

Closure Depth and Profile Control Volume

The depth of closure, "pinch-out" depth, or location where measurable depth changes do not occur could not be readily found in the profile comparisons. Some reasons why the profiles have significant depth changes in deeper than typical depth of closure water depths are the dredge borrow pits, nearshore dredge material disposal, and subsidence associated with mineral extraction, besides natural sediment transport occurring on the nearshore shelf. The depth of closure concept defined as the seaward limit of significant sediment transport is a misnomer since near-bottom wave induced currents do mobilize large volumes of sediment, and small depth changes on the nearshore shelf result in large volume changes in comparison to the volumes contained on the beach and within the limits of the surf zone. Utilizing a depth of closure concept as a control volume boundary in plan, with its location determined from an abrupt change in the standard deviation of a time series of elevation is a more useful definition along this coastline. This boundary approximates the seaward limit of "significant" wave generated longshore currents and is numerically more consistent with

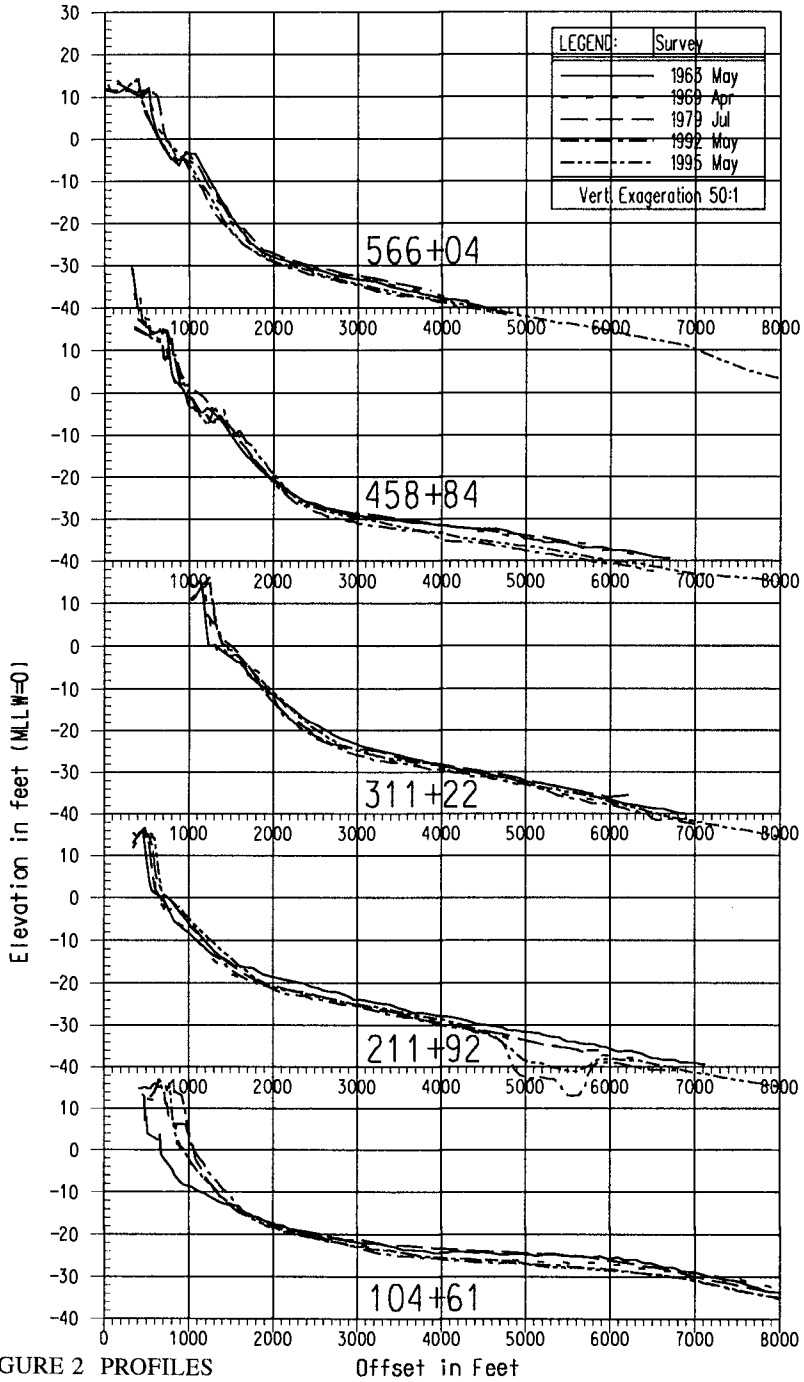


FIGURE 2 PROFILES

Offset in Feet

values estimated from formulae and wave statistics, ie. the 12-hour annual wave at Huntington Beach of 233 cm based on four years of observation results in a computed depth of closure of 16 feet (Hallermier, 1981). It also does not have to assume a priori insignificant sediment transport across the boundary.

Table 2 Surveys between 1963 and 1993

<u>Date of Survey</u>	<u>Construction Activity and Survey Coverage</u>
1963 May-August	Pre-Stage 1. Seal Beach to Newport Bay.
1964 July	Post Stage 1. Surfside to Bolsa Chica.
1966 October	Condition Survey. Seal Beach to Newport Bay.
1969 April	Condition Survey. Seal Beach to Newport Bay.
1971 June	Post Stage 4A. Surfside to Bolsa Chica.
1973 May	Post Stage 5. Bolsa Chica St. Beach to Newport Bay.
1978-79 Dec-Jan	Pre-Stage 7. Surfside to Newport Bay.
1979 June	Post-Stage 7. Surfside to Newport Bay.
1982 April	Condition Survey. Seal Beach to Newport Bay.
1982-83 Dec-Jan	Condition Survey. Seal Beach to Newport Bay.
1987 December	Condition surveys and
1988 October	pre- and post-dredge
1989 March	surveys of Anaheim Bay and the
1993 October	approach channel to Anaheim Bay
1990 January	Stage 9 Borrow Pit pre-dredge.
1990 June	Stage 9 Borrow Pit interim post-dredge.
1990 July	Stage 9 interim pre-dredge and beachfill.
1990 September	Stage 9 Borrow Pit post-dredge.
1993 October	Surfside nearshore condition survey.

Table 3 CCSTWS and SAR Survey Dates

<u>Coast of California Surveys</u>	<u>Santa Ana River Surveys</u>
1992 February	1991 December
1992 May	1992 May
1992 November	1992 July
1993 May	1992 November
1993 October	1993 Mar
1994 April	1993 May
1994 November	1994 January
1995 May	1994 November

Figure 3 shows the mean, range and standard deviation of elevation along a profile through the feeder beach at Surfside Beach. Elevation statistics were computed separately for the Feb 1992 to May 1995 time period and the 1963 to 1983 time period because of the differences in collection methodology and sampling interval between the two data sequences

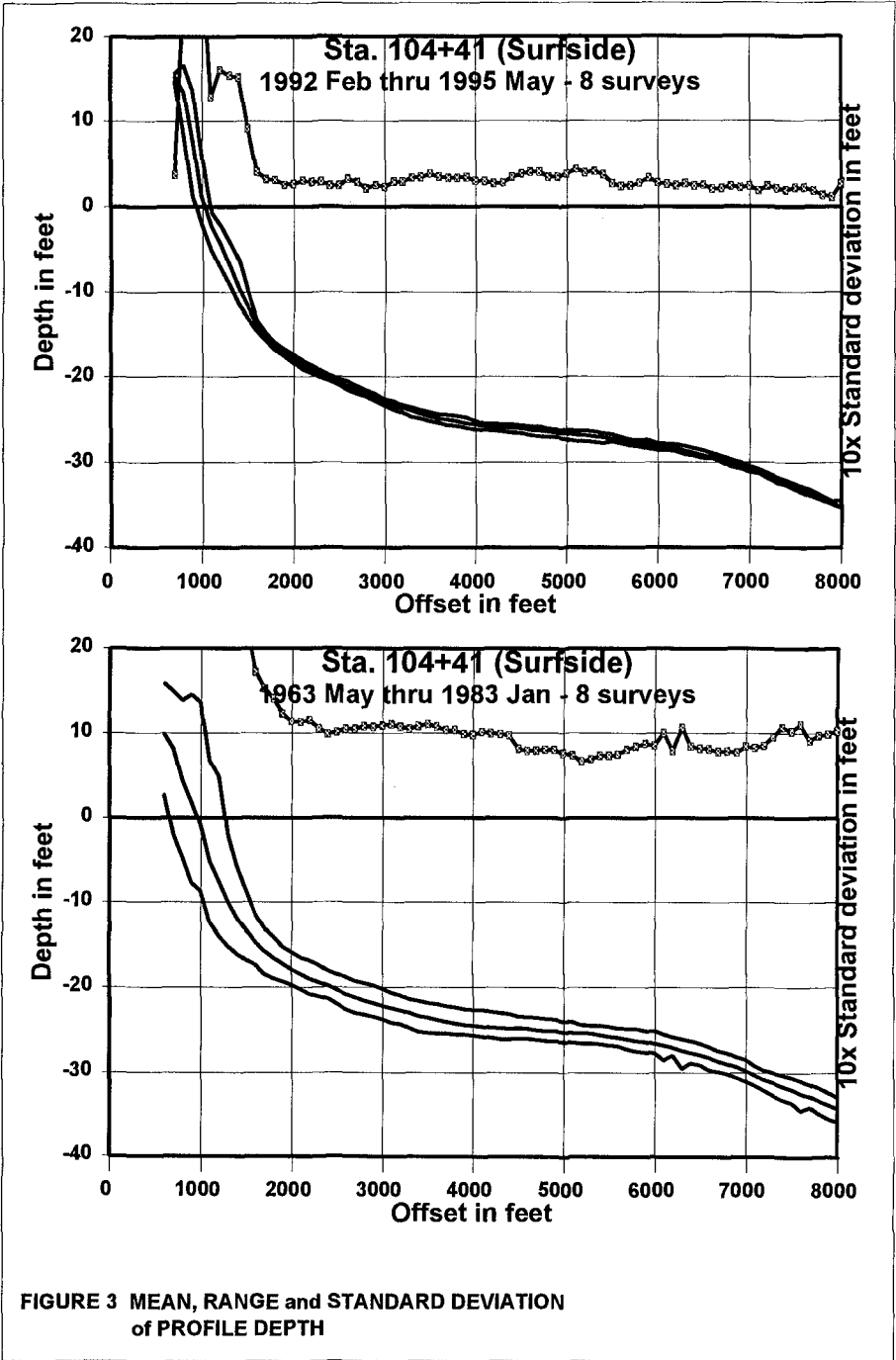


**FIGURE 3 MEAN, RANGE and STANDARD DEVIATION
of PROFILE DEPTH**

-- ie. multiple surveys per year compared to multiple years per survey. For the recent 3-year period, a depth of closure boundary is at approximately -16 feet, while for the 20-year period it is at approximately -20 feet. This depth of closure also coincides with the boundary between the shoreface and nearshore shelf. Alongshore variation of depth of closure ranges from about -16 to -28 feet, the deepest being located offshore of Huntington Cliffs and Huntington Beach.

A control plan area was defined for profile volume computation. This area is bounded by the landward limit of overlapping survey coverage on the back beach, but below the toe of the coastal cliffs, and the location of the 20-foot depth contour of the 1963 survey -- although a seaward boundary that varies with depth by alongshore location could have also been applied.

Profile Volume and Volumetric Changes

Profile volumes, contained within the control volume plan limits defined by the survey limit along the beach backshore and the -20 foot contour, are averaged with ranges and deviations computed as shown on Figure 4 by alongshore stationing. These profile volumes, in cubic yards per alongshore foot of beach, have a zero mean over the available surveys. Relatively large standard deviations in profile volume occurs for sections through the Surfside-Sunset feeder beach (Sta 100 to Sta 140) and south of the Santa Ana River Mouth (Sta 630) with values of about 190 cy/ft and 110 cy/ft, respectively. These large variations are due primarily to beach nourishment, groin field and nearshore berm construction (see Mesa, Paper No. 330). Along the remainder of the shoreline, where natural transport processes predominate, the standard deviation of profile volume averages approximately 60 cy/ft.

End-area volumes contained in the control volume described above and relative to the 1963 survey are shown in the format of a mass-haul diagram in Figure 5. Volumes, by date, are cumulative alongshore starting at Anaheim Bay (Sta 97+71) progressing southeasterly to West Newport Beach and the Newport submarine canyon (Sta 757+74). A positive, flat or negative slope of the diagram indicates an accreted, stable or eroded profile volume, respectively, relative to pre-project condition in 1963. The effects of the initial 4 mcy beachfill can be seen in the July 1964 survey, which shows a profile volume gain of about 3 mcy along Surfside-Sunset Beach (Sta 100 to Sta 200). Other general observations from this diagram are that the total profile volume accreted between Anaheim Bay and the Santa Ana River (Sta 100 to 630) for all surveys compared to 1963; a slight erosional trend is observed in the Huntington Cliffs area (Sta 350 to 410); and with the exception of Dec 78 and Jan 83, both abnormally severe storm years in addition to being surveys before renourishment stages, the profile volume along most of the shoreline has been stable or accretional. The sharp increase in alongshore volume at the Santa Ana River mouth in 1969 is the result of a broad delta created by the flood flows earlier that year. A similar increase shown in the 1992 through 1995 surveys are due to construction of a 1.3 mcy nearshore berm (1992), and groin field and beachfill (1970's) at West Newport Beach.

Other control volumes were defined such as the area bounded by the back beach and the MLLW datum plane (dry beach volume), and the nearshore shelf area bound by the -20 and -30 foot contour in 1963. The dry beach volume follows similar trends to that of the profile

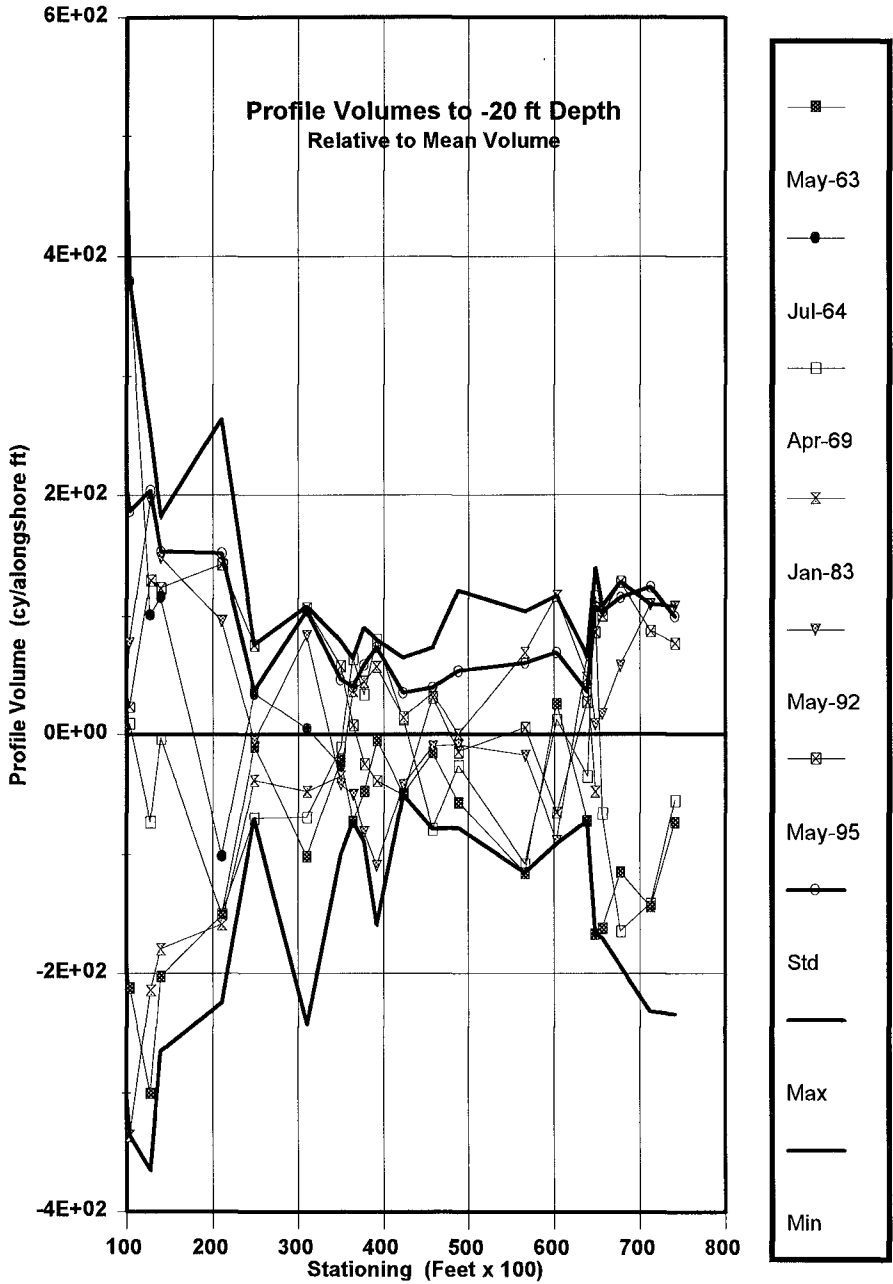


FIGURE 4 PROFILE VOLUMES

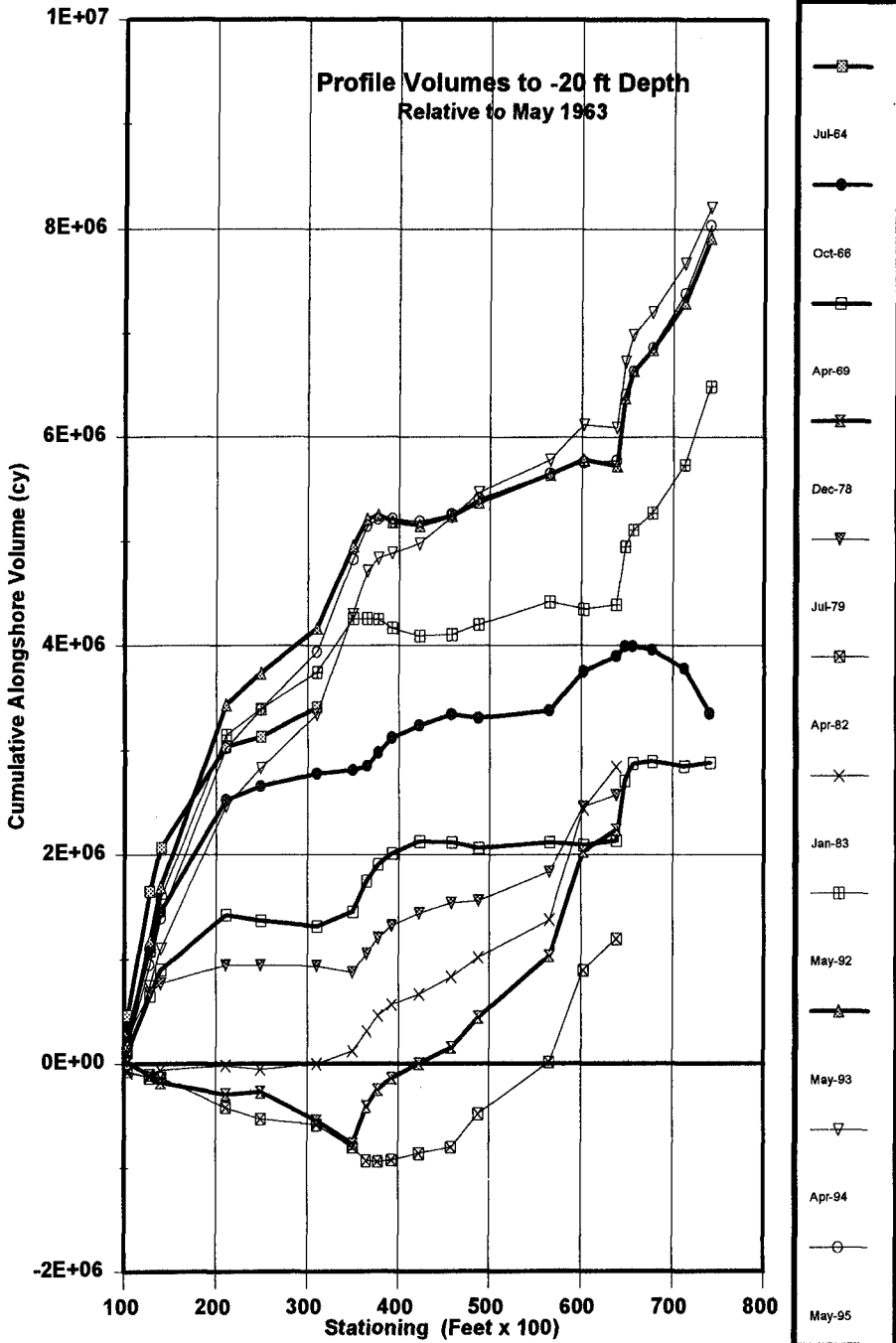


FIGURE 5 CUMULATIVE PROFILE VOLUMES

volume of the -20 foot depth, whereas, the nearshore shelf (-20 to -30 ft) has experienced deepening over a large portion of this coastal segment. Some of this deepening is the direct result of sand mining for beach replenishment while other deepened areas appear to be directly related to subsidence associated with mineral extraction. The latter has been documented through differential leveling along the coast highway and is most evident in comparison of the 1934 to 1975 NOS nearshore hydrography.

Conclusions

Available surveys for the northern Orange County coastal segment have been analyzed with the use of CADD and triangulated irregular network models. Historic surveys with U.S. Coast and Geodetic Survey control can be reduced and used to build a shoreline and profile history database accessible to GIS systems. State Plane Coordinate Systems can be easily related to geodetic coordinates allowing utilization of data from multiple historic sources. Once the TIN models are created, time series of depths, volumes and shoreline positions can be queried for analysis.

As for the San Gabriel River to Newport Bay Erosion Control Project, monitoring over 30 years of beach nourishment has shown a transport rate from the feeder beach to be remarkably close to the originally projected beachfill requirements published by the U.S. Army Engineer District, Los Angeles(1962). Comparison of profiles generally show wider beaches and a deepening of the nearshore. By comparison to the pre-project condition, artificial beach fills have created a protective and feeder beach such that the profile volume has always been above that which existed in 1963, except during the severe winter seasons of 1978 and 1982-83. At the feeder beach location, 772,000 more cubic yards existed on the beach above MLLW datum in May 1995 than in 1963, and 1.39 million cubic yards more existed within the profile volume bound by the beach and historic -20 foot contour. The initial beach construction, NWS channel deepening and four nourishment cycles placed dredge material totaling 12.6 mcy on the feeder beach. Assuming 15 percent of the dredge prism to be composed of fine grain sediments which would quickly wash away, a beach nourishment volume of 10.8 mcy can be estimated. Only 1.4 mcy remain within the profile volume of the feeder beach after 31 years, yielding an average loss rate of 303,000 cy/year. The predicted periodic renourishment volume of 1.75 mcy about every five years in the 1962 study was based on an annual loss of 350,000 cy/year, consisting of 300,000 cy/yr loss from the littoral cell and 50,000 cy/yr loss to the offshore, wind and other causes.

While periodic beach nourishment has maintained profile volumes above pre-project levels, protective beach widths are not always provided for all locations. This is particularly true for about 3,000 feet adjacent to the Anaheim Bay East Jetty (sta 100+00 to 130+00) which appears to have a component of southeasterly directed longshore transport from westerly swells and reflected southerly swell as can be seen in the approaching wave fronts of Photos 3 and 4.

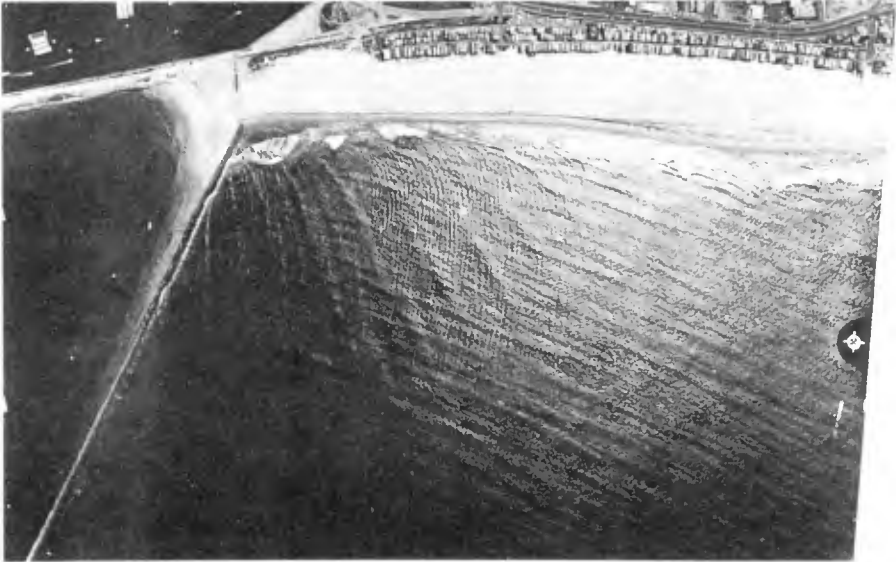


**PHOTO 3 Surfside Beach with a South Swell Wave Pattern
(June 7 , 1980)**



**PHOTO 4 Surfside Beach with a West Swell Wave Pattern
(April 17, 1981) Sunset Gage: 0904, Hs=110.3 cm; Tp=13s.**

Acknowledgements

The authors are grateful to their predecessors in the Los Angeles District and the Beach Erosion Board who collected the historic profile data and had the foresight of using national datums with documented survey control. We also acknowledge the National Ocean Surveys for providing their hydrographic database, the Coastal Data Information Program for making wave data available online, and Orange County Beaches and Harbors Department and Survey Department for providing the GIS database and performing the recent surveys.

References

- Hallermeir, R. J. (1981). "Seaward Limit of Significant Sand Transport by Waves: an Annual Zonation for Seasonal Profiles." Coast. Engr. Tech. Aid No. 81-2, Coast. Engrg. Res. Ctr., U.S. Army Engr. Wtrwys. Exp. Sta., Vicksburg, Miss.
- Stem, James E. (1989). "State Plane Coordinate System of 1983." NOAA Manual NOS NGS 5, U.S. Dept. of Commerce, NOAA, NOS, Charting and Geodetic Services, (Reprinted Jan. 1993), Rockville, MD.
- U.S. Army Engineer District, Los Angeles (1962). "Beach Erosion Control Report on Cooperative Study of Orange County, California." Appendix V, Phase 2, (Mar. 1), Los Angeles, California.

CHAPTER 363

A Ten-Year History of Dolos Monitoring at Crescent City

William S. Appleton¹, Thomas Kendall¹, M. ASCE,
and Jeffrey A. Melby², M. ASCE

ABSTRACT

Ten years of monitoring data are now available from the Crescent City dolos monitoring program. This extensive field data collection program was initiated in 1986, following the rehabilitation of the dolos section of the main stem of the Crescent City Outer Breakwater. The rehabilitation involved the placement of 680, fiber-reinforced, 38-tonne dolosse. Unique field monitoring techniques have been employed to collect data at Crescent City: movement data have been collected with ground-truthed, low-altitude (helicopter) photogrammetric survey techniques and stress data have been derived from strain gages mounted internally in select dolosse grouped together near the center of the dolos field. Results presented in this paper include 10 year histories on: wave climate, dolos movement/breakage, stress build up within dolosse, and concrete strength and fatigue. In addition, internal strain gage instrumentation verification test results are presented.

INTRODUCTION

The hydraulic stability of dolos armor units has been a large factor in their success as an armor unit. For this reason, the use of dolos armor units has helped to allow for the construction and long-term stability of shore and navigation protection structures sited in extremely energetic wave environments. The use of dolos armor units has been extensive and in most cases these armor units have performed well; however, due to the slender nature of the dolos design, these units are susceptible to breakage especially as the size of the units increases. To gain further insight into the mechanisms which govern the design life of these

¹USACE, San Francisco District, 333 Market Street, San Francisco, CA 94105-2197, USA

²USACE, Waterways Experiment Station, 3909 Halls Ferry Road, Vicksburg, MS 39180-199, USA

breakwater armor units, the Corps has collected an extensive data set from the dolos armor layer located on the Crescent City, California Outer Breakwater.

There are now 10 years worth of monitoring data available addressing the role of dolos movement, breakage, fatigue, and static stress build-up which provide insight into mechanisms affecting the life of these armor units.

BACKGROUND

The Crescent City Outer Breakwater has had a history of being badly damaged since it was lengthened in 1930 to include the section which now contains dolos armoring. In particular, the last 100 meters of the structure's main stem have been especially difficult to maintain and, consequently, dolosse have been used in this section for the past 22 years. The most recent round of extensive maintenance work came in 1986 when, following years of wave damage from winter storms, the dolos section of the breakwater was rehabilitated. The rehabilitation work involved the placement of 680, 38-tonne fiber-reinforced dolosse on the seaward slope of the structure (Figure 1) and 80 on the lee side slope for future use. Placement of the armor units was aimed at recreating, to the extent possible, the design tested in physical model studies which included the use of trenching and buttressing (with stone) along the dolosse southern perimeter for increased stability at the dolosse-stone transition. A thorough background description of the project site can be found in Kendall (1988) and Kendall and Melby (1989).

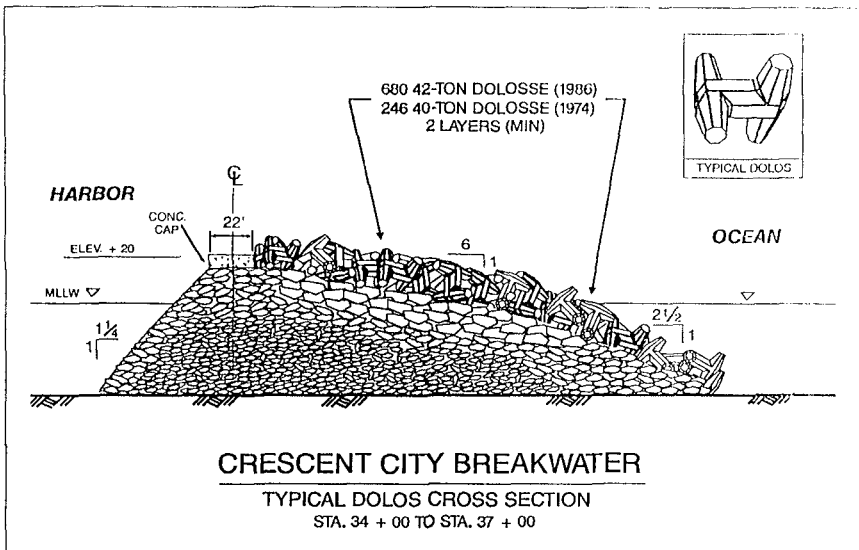


Figure 1: Typical cross-section through the dolos section of the Crescent City Outer Breakwater.

MONITORING TECHNIQUES

Displacement and Breakage Monitoring

Dolos displacements and breakage have been monitored since the completion of the rehabilitation project. Targeted and non-targeted dolos displacements have been detected and assessed using photogrammetric techniques. A helicopter continues to be used as the platform for mapping photography work; this technique allows for the measurement of targeted dolos displacements to be reported with an accuracy of ± 2 cm and non-targeted dolos displacements with an accuracy of ± 15 cm. This work has been previously reported by Kendall (1988) and Kendall and Melby (1992). Changes in the subsurface slope and toe of the structure are monitored using both side scan sonar and diving inspections. However, given the conditions under which this work is conducted, only gross estimates of subsurface displacements can be made.

Dolos breakage counts are monitored through walk-over inspections of the dolos field as well as by helicopter reconnaissance. To date, no techniques have been identified which would allow for determining subsurface breakage.

Static Stress Monitoring

As part of the 1986 rehabilitation work, 20 of the dolosse were instrumented with internal strain gauges mounted on rebar rosettes. An internal microprocessor allowed for data to be digitized within the dolos. The instrumentation measures two moments and a torque, which are then used to compute stresses at the shank-fluke interface. The data stream from the internal microprocessors is sampled at a rate of 1 Hz for six minutes and only data that has passed a series of reliability tests is retained for analysis. Instrumented units that repeatedly fail the reliability tests are removed from the sampling rotation and are no longer retained as part of the sample set. Further details of the data acquisition system and summary of the static stress monitoring program are provided by Kendall and Melby (1992) and Melby and Turk (1995).

Of the 20 instrumented dolosse, 17 were found to be functioning properly during the first round of sampling in 1987. Since then, the number of instrumented dolosse returning data which passes the reliability tests has dwindled to three, all of which are located in the top of the armor layer.

Artificial Loading of Dolos

Upon reviewing the time history of average static stress in the instrumented dolosse through 1994, it was anticipated that future stress readings might begin to fall outside of a range which could be explained through observed boundary conditions. Therefore, a testing method was developed and implemented in 1995 on one dolos (dolos C), to determine if the instrumentation was giving false readings. Dolos C was selected because it had a low RMS error on the data channels, the magnitude of the recorded displacements were not very reasonable and the dolos was resting on the top layer with the upper surface of the shank nearly horizontal.

A steel load frame was bolted onto the shank of the dolos and designed to allow for the placement of a load on the extreme end of the dolos fluke equivalent to the full weight of another dolos. A 90.6-tonne (100-ton) hydraulic jack was used to apply the load, which was done in increments of 6.9 MPa (1000psi) corresponding to a force of 8,858 kg (19,511 lbs).

Fatigue and Concrete Strength

Given the constant cyclical loadings experienced by concrete armor units placed in the near-shore wave environment, the question of what role, if any, fatigue plays in the life of concrete armor units, was asked. In the most recent round of monitoring activities, this question was addressed.

Although fatigue testing in its formal sense, strength versus number of blows and destructive testing, was not carried out on the armor units, 7.6 cm (3 in) diameter core samples were taken from dolosse placed in both 1974 and 1986 to determine changes in the concrete strength over time. If the armor units were experiencing significant fatigue, it was expected that the compressive and flexural-tensile strength of the samples would reflect it. Both of the armor units were located near the cap since heavy sampling equipment presented a significant mobility limitation.

WAVE CLIMATE

Presented in Figure 2 is a time history of wave power off of Crescent City. Buoy data, taken primarily from the Point St. George buoy #46026 (41.9° latitude, 124.4° longitude, 60 m of water), was used to generate the plot shown. Nearby buoys were used to fill in gaps in the Point St. George Buoy data set. The extreme local wave energetics that the structure is subjected to annually are clearly evidenced in Figure 2.

Hales (1985) provides a thorough description of depth-limited waves at the outer breakwater at Crescent City. Hales applied RCPWAVE, a numerical model which calculates the combined wave refraction/diffraction/shoaling effects in shallow water, using the bathymetry off Crescent City and tidal stages of -0.3 m (-1 ft) mean lower low water (MLLW) and +3.04 m (+10 ft) to obtain the design wave criteria for the 1986 rehabilitation. Based on Hales work, a depth-limited breaking wave of approximately 10.5 m was determined to be the design wave for the structure. Hale's work as well as comparison with a small data set from a buoy placed just offshore of the structure in 12 m of water, indicated that wave transformation coefficients are on the order of unity or greater for typical storm events out of the west to west-southwest directions.

Approximately 10 years of buoy data (buoy # 46014) were analyzed to determine whether the structure has in fact seen its design wave. Presented in Table 1 are the probabilities of exceedence for wave heights (H) greater than 5 m for measured significant wave heights (H_s) equal to or exceeding 5m. It was assumed that the wave heights were Rayleigh distributed. The buoy data set was filtered for events generating significant wave heights greater than 5m, of which 29 were found for a total of 80 hours. Given the near unity wave transformation

coefficients, deep water wave heights were likely to have existed just seaward of the structure as well. The maximum tidal stage was then found for each of the events using standard tide tables. Presented in Figure 3 is a plot of the results of this analysis.

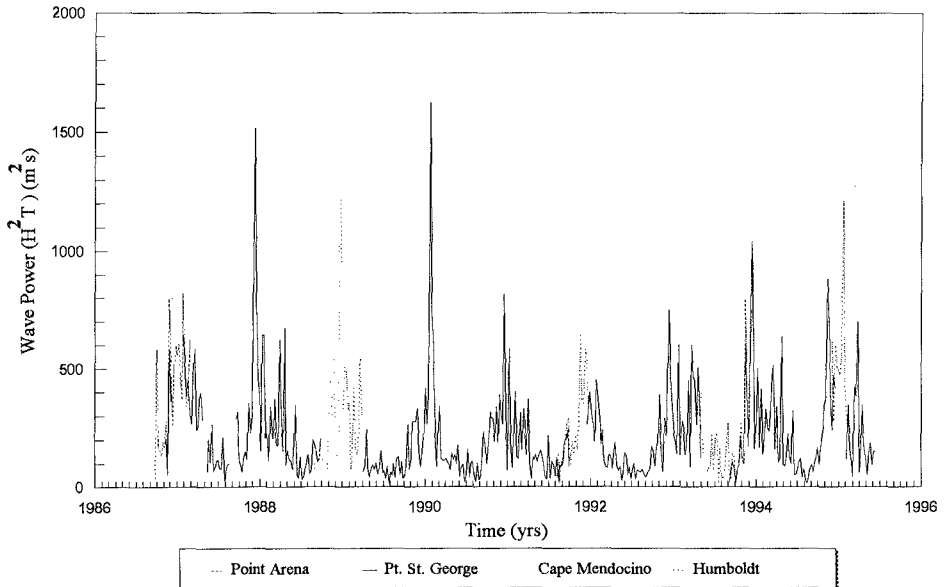


Figure 2: Time history of wave power off Crescent City, California.

Table 1: Probability of exceedence for wave heights for a Rayleigh distribution.

Significant Wave Height (H_s), meters	Wave Height (H)					
	5 m	6 m	7 m	8 m	9 m	10 m
5 m	13.5 %	5.6 %	1.9 %	0.6 %	0.15 %	0.03 %
6 m	24.9 %	13.5 %	6.6 %	2.9 %	1.1 %	0.39 %
7 m	36.0 %	23.0 %	13.5 %	7.3 %	3.7 %	1.7 %
8 m	45.8 %	32.5 %	21.6 %	13.5 %	8.0 %	4.4 %
9 m	53.9 %	41.1 %	29.8 %	20.6 %	13.5 %	8.5 %
10 m	60.7 %	48.7 %	37.5 %	27.8 %	19.8 %	13.5 %

Of the 29 extreme events identified, 9 of them, or approximately 30%, occurred during peak tidal stages that equaled or exceeded +1.8 m (6 ft), giving a minimum water depth at the toe of the repair section of 10.6 m (35 ft). The storm setup contribution to the water depth at the structure during the events is not known since measured tidal records at Crescent City have not yet been analyzed, however, it is reasonable to assume that the storm setup contribution would be on the order of at least a half meter. Therefore, there have been at least 9 events to-

date which may have generated waves equaling and possibly exceeding the design wave in water depths that would have allowed these waves to reach the structure prior to breaking. Generally speaking, the above events correspond with wave power readings in excess of $800 \text{ m}^2\text{s}$ in Figure 2.

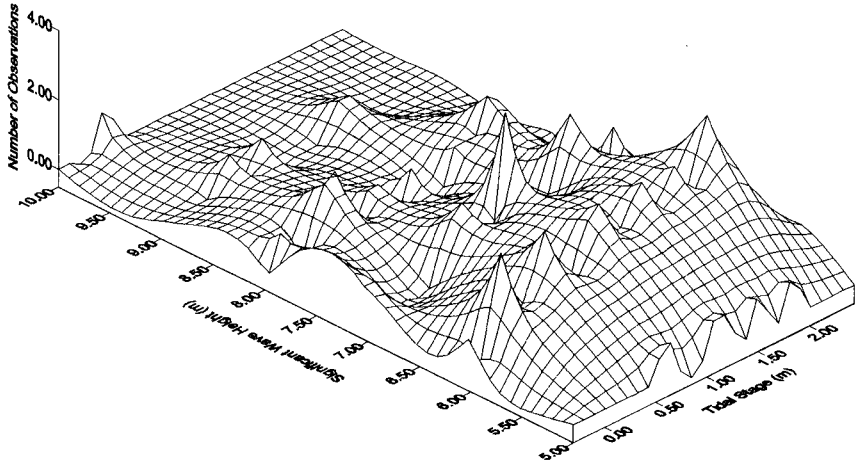


Figure 3: Number of significant wave events and corresponding tidal stage.

MONITORING RESULTS THROUGH THE TENTH YEAR

Evidence of Long-term Nesting

The history of average cumulative dolos displacement is shown in Figure 4. Kendall and Melby (1992) reported that for those units having undergone translation, the dominant direction of movement was up-slope. For those units having experienced rotation, the dominant axis about which rotation occurred was the z axis (yaw). Since 1992, significant displacements have occurred for four units, one in 1994 and three in 1996. In all four cases, translation up-slope was observed, however there did not appear to be an indication that rotation about the z axis was more prevalent than rotation about any of the other axes. It is interesting to note that while the curve describing average cumulative translations continues to behave as one might expect for a fully nested structure, the jump in the cumulative rotation curve is not as intuitive. It would appear that as equilibrium nesting conditions are approached, significant rotations are more likely to occur than significant translations. In other words, a nested quasi-equilibrium state is more apt to allow for rotations than translations of the armor units. A similar jump in the cumulative rotation curve corresponding with a relatively flat translation curve was seen in the 1992-1993 data as well. Considering that translation requires that the centroid of the unit be displaced, while rotations can occur via a pivot point, it is understandable that rotations should be more likely to occur under nested conditions. Results appear to indicate that despite near equilibrium nesting conditions, movements, especially

rotations, will continue to occur although they seem to be small enough not to be considered significant.

Side scan sonar records as well as dive inspections indicate that there were no significant changes in the position of the toe or slope of the dolos rehabilitation section.

Breakage

Prior to 1993, the last year in which any new broken dolosse were found was in 1988 (one unit was found). However, as presented in Figure 5, a comparatively large number of broken units were found in 1993. But, as also shown in Figure 5, it is uncertain when these units actually were broken, and it is thought, given the appearance of the breaks, that they could have occurred much earlier, but were simply not visible from the helicopter surveys used almost exclusively up until 1993.

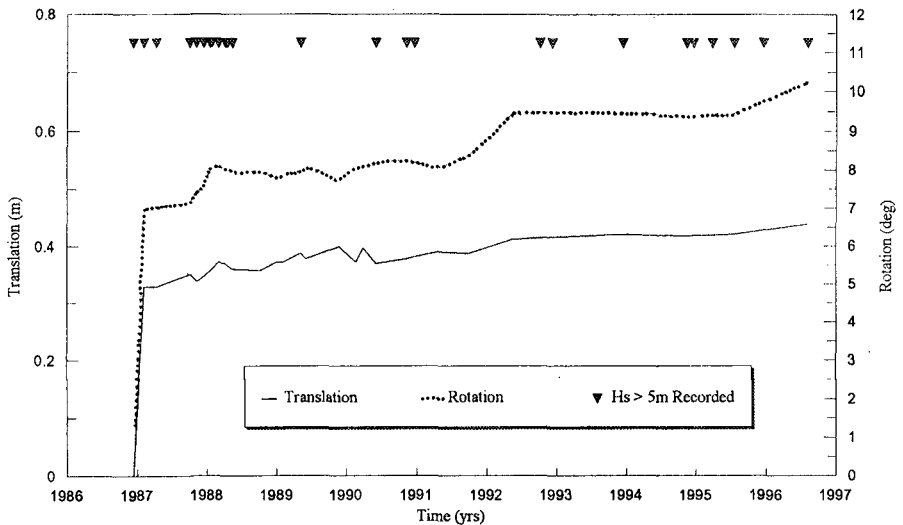


Figure 4: Time history of cumulative dolos displacement.

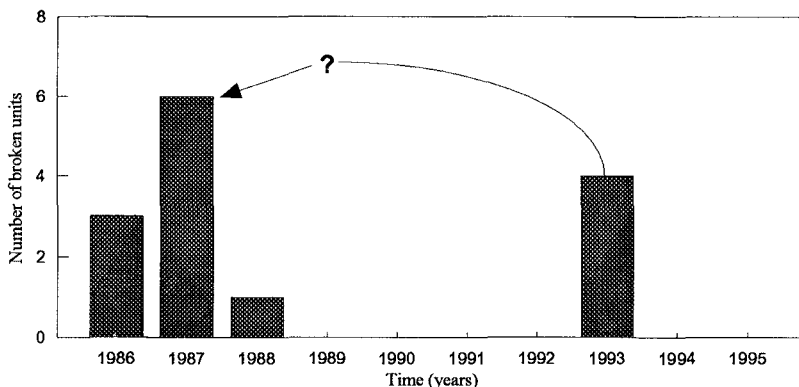


Figure 5: Dolos breakage results.

Static Stress History

Burcharth (1988) defined the various loads on armor units, the three primary loads being static loads, impact loads and pulsating loads. The history of average static stress measured within the dolosse is presented in Figure 6. Each data point represents an average of all of the reporting units on that date. Also shown in Figure 6 is the dwindling sample set from which these readings were taken. Initial measurements, made in 1987, were taken from 17 units, 3 in the lower armor layer and 14 in the top layer. 1995 measurements were taken from 3 units, all of which were located in the top layer. The average static stress for the three (3) reporting units was found to be approximately 3 MPa (434 psi). The trend in this curve is not an artifact of the dwindling sample size as the history of the three remaining units reflects the same trend exhibited.

The newest data point appears to be consistent with the trend apparent in the data from prior years, showing a linear increase in static stress. However, the continuing linear increase in static stress levels within the dolosse is cause for concern, since boundary conditions leading to such stress levels are not at all apparent. Therefore a check was made to determine if the static stress levels being reported by the instrumentation were reasonable. An extreme boundary condition was considered, one where a dolos was assumed to be loaded at the extreme end of a fluke by the weight of another 38-tonne unit. Simple beam theory was applied to obtain an approximation of the normal stress at the section A - A shown in Figure 7. This simple calculation showed that the maximum normal stress (located at the extreme fibers of the cross section) for the boundary condition shown is approximately 2.5 MPa (358 psi). Hence, the latest stress reading has exceeded the estimated "full dolos loading" level.

If the post nesting growth of static stress within the dolosse is to be believed, then the flexural-tensile strength of the concrete is rapidly being approached. The slope of the plot in Figure 6 indicates that the reserve concrete strength is being consumed at a rate of approximately 3% per year. However, if this was in fact

true, given the wave events that these units are being subjected to, one would

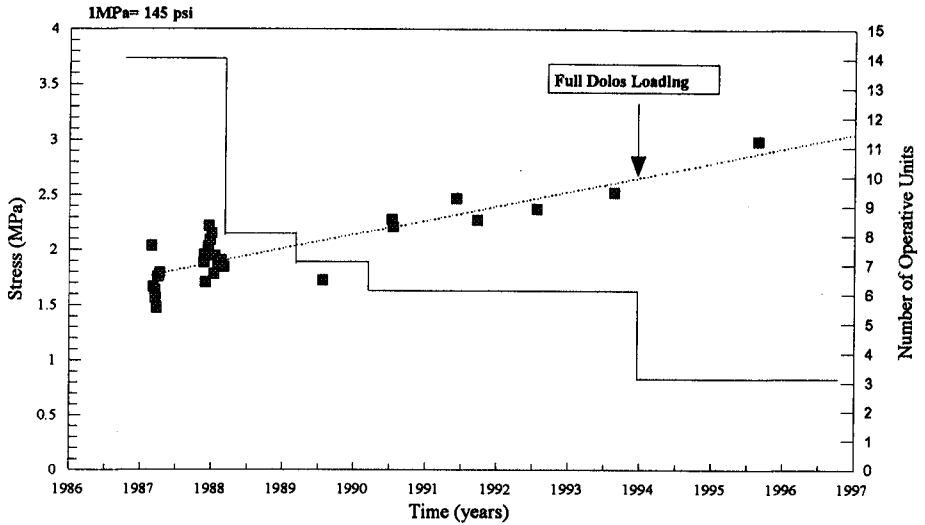


Figure 6: Time history of average static stress levels

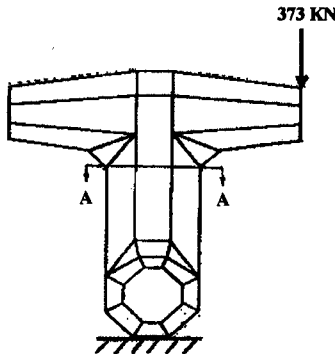


Figure 7: Caricature of dolos loading

expect a much higher rate of breakage in recent years than what has been observed. In order for the instrumentation to be functioning properly while still returning data that indicates a continuing rise in static stress, the concrete must be relaxing while the strain gauges continue to deform. Shrinkage, thermal contraction/expansion and creep were considered as mechanisms that may be

responsible for creating permanent strains on the instrumentation, while at the same time allowing the concrete to recover via plastic deformations. Creep or some form of plastic deformation within the concrete is the only plausible explanation. However, as pointed out by Neville and Brooks (1987), the effectiveness of stress relaxation by creep is reduced with time. Most stress that is relieved via creep is done so in the very early stages of concrete curing. Shrinkage, swelling and thermal expansions/contractions may have influenced the static stress trend during the first year, but after that they would play a very minimal role in any static stress buildup. Therefore, material properties of concrete and boundary conditions are unable to fully explain the recorded high measurements of static stress.

Artificial Load Testing

Results from the artificial load testing showed that the recorded strain was of the correct order of magnitude given the load, but half what one would expect from an analytical check using simple beam theory. Since the actual moment arm length is difficult to quantify due to unknown boundary conditions and since the dolos is not a slender beam, the difference between the analytical check and the measured value is considered to be within reason (Melby and Turk, 1995).

Fatigue and Concrete Strength

Core samples that were returned to the lab for testing were subjected to traditional compressive and tensile testing methods. The compressive tests were done in accordance with American Standard for Testing Materials (ASTM) C 39, the splitting in accordance with ASTM 496 and the flexure in accordance with ASTM C 293. Shown in Table 2 are the concrete strength test results.

Table 2: Concrete strength test results from core samples taken in 1995.

Dolos/Core Number	Compressive Strength (MPa)	Flexural Tensile Strength (MPa)	Splitting Tensile Strength (MPa)
559 / N1	-	9.79	4.31
559 / N2	53.24	8.55	2.14
559 / N3	56.41	-	4.59
752 / N1	70.69	-	4.48
752 / N2a	-	11.93	3.48
752 / N2b	-	-	3.03
752 / N4	60.00	10.03	3.48
752 / N6	73.45	-	-
236 / N1	52.34	-	4.17
236 / N2	-	8.76	-
236 / N3	62.83	7.55	4.14
236 / N4	-	-	2.93

Non-shaded area contains data obtained from 1986 dolosse and the shaded area is data obtained from 1974 dolosse.

Lab results indicated that on average, the flexural-tensile strength of the

concrete samples from the 1986 dolosse had increased 48% and the compressive strength had increased 70%. These increases in concrete strength are based upon a 28-day compressive strength of 36.4 MPa (5,280 psi) reported by Bevins (1989) and a 28-day flexural-tensile strength of 6.8 MPa (984 psi) reported by Gutsehow (1989). For standard type II cement, a 50% increase in 28-day compressive strength after five years can be expected. Therefore, although the concrete used in the dolos is steel-fiber reinforced, the 70% increase over 10 years is significant considering that most of the changes within concrete occur in the first five years.

Conclusions regarding the compressive and flexural-tensile strength of the concrete used in the 1974 dolos could not be made due to a lack of data prior to 1995. However, the compressive strength of the cores tested was within 2% of the average compressive strength obtained from the 1986 dolos concrete samples while the average flexural-tensile strength was within 20% of the 1986 values.

CONCLUSIONS

- It is highly likely that the dolos section of the Crescent City Outer Breakwater has been subjected to its design wave and possible that it has experienced design wave conditions as many as nine time.
- While the time history of dolos displacements does continue to show some rotational displacements, the dolos field is believed to have reached a relatively nested state following the first storm season.
- Strain gages in the tested dolos were shown to be functional within acceptable parameters. Moments measured were on the same order as those predicted by simple linear beam theory.
- Although the internal instrumentation within dolos C was found to be functional and recorded strain readings brought about by artificial loading were within reason, static stress readings still need to be questioned. The material properties of concrete, i.e. creep, shrinkage/swelling, thermal expansion/contraction, do not appear to explain the observed measurements.
- Both compressive and flexural-tensile concrete strengths measured in 1995 on the 1986 dolosse, were found to be significantly higher than design strengths (28-day); 70% and 48%, respectively.
- Fatigue weakening within dolosse does not appear to be significant.

RECOMMENDATIONS

- Conduct aerial photogrammetric work every 2 years. Exceptions would be made following extremely energetic winters having repeated events during which there is a greater than 1% chance of the design wave occurring (approximately when $H_s^2 T > 800 \text{ m}^2\text{s}$).

- Investigate the possibility of picking up a dolos and measuring static stress rebound as an additional step in verifying internal instrumentation measurements.

ACKNOWLEDGEMENTS

The work described in this paper has been conducted as part of the Operations and Maintenance program of the U.S. Army Corps of Engineers (USACE) San Francisco District.

REFERENCES

- Bevins, T.L., 1989, U.S. Army Engineer Waterways Experiment Station, Vicksburg, MS, personal communication.
- Burcharth, H. F. and Howell, G.L., 1988. "On Methods of Establishing Design Diagrams for Structural Integrity of Slender Complex Types of Breakwater Armor Units," Seminaire International Entreien des Infrastructure Maritimes, Casablanca, Morocco.
- Gutschow, R., 1989, U.S. Army Engineer District, Los Angeles, CA, personal communication.
- Hales, L.Z., 1985. Water Wave Refraction/Diffraction/Shoaling Investigation, Crescent City, California, Miscellaneous Paper CERC-85-3, U.S. Army Engineer Waterways Experiment Station, Vicksburg, MS.
- Kendall, T.R., 1988. "Analysis of 42-Ton Dolos Motions at Crescent City," Coastal Engineering, 1988 Proceedings of the International Conference, ASCE, New York, NY.
- Kendall, T.R. and Melby, J.A., 1989. "Continued Monitoring of 42-Ton Dolos Movements and Static Stresses at Crescent City," Proceeding of Stresses in Concrete Armor Units, Vicksburg, MS, ASCE, New York, NY.
- Kendall, T.R. and Melby, J.A., 1992. "Movements and Static Stresses in Dolosse: Six Years of Field Monitoring at Crescent City," Coastal Engineering, 1992 Proceeding of the International Conference, ASCE, New York, NY.
- Melby, J.A. and Turk, G., 1995. "Crescent City, California, Breakwater, Dolos Structural Response Study," Letter Report, U.S. Army Corps of Engineers Waterways Experiment Station, Vicksburg, MS.
- Neville, A.M. and Brooks, J.J., 1987. "Concrete Technology", Longman Scientific & Technical, New York, NY.

CHAPTER 364

BREAKWATER DAMAGE IN OKUSHIRI PORT DUE TO THE HOKKAIDO NANSEI-OKI EARTHQUAKE TSUNAMI

Katsutoshi KIMURA¹
Yuzo MIZUNO¹
Hiroichi TSURUYA²
Yasuyuki NAKAGAWA²

Abstract

A tsunami caused by the Hokkaido-Nansei-oki earthquake struck Okushiri Island and the southwest coast of Hokkaido damaging many port facilities. This paper describes typical breakwater damage at Okushiri Port and the applicability of Tanimoto's formula for tsunami wave forces on vertical walls based on prototype failure analyses and the result of numerical simulations. The armor stability and the rubble mound scourings were examined from the results of 3-D model tests at a scale of 1/15. The damage patterns at the narrow opening of breakwaters were reproduced by the tests. The necessary weight of armor blocks and foot-protection blocks for breakwater heads were calculated by the C.E.R.C. formula using averaged flow speed at the peak of tsunami.

Introduction

The Hokkaido Nansei-oki earthquake of July 12, 1993, had a Richter scale magnitude of 7.8, and generated a huge tsunami. Okushiri Island, 70 km from the seismic center, was struck by the tsunami. In addition to a death toll exceeding 200, the tsunami damaged many public facilities in the coastal areas and port facilities, mainly breakwaters.

In general, breakwater damage from tsunamis are classified into the following two patterns;

- Sliding of caissons by tsunami wave forces
- Scouring of rubble mound foundations at breakwater heads by the strong tsunami flows

-
- 1) Civil Engineering Research Institute, Hokkaido Development Bureau, 1-3 Hiragishi, Sapporo, 062, JAPAN
 - 2) Port and Harbour Research Institute, Ministry of Transport, 3-1-1 Nagase, Yokosuka, 239, JAPAN

The caissons of the Kawaragi breakwaters in Hachinohe Port were damaged along a total length of 328m in the 1968 Tokachi-oki Earthquake. Ito et al. (1968) analyzed the tsunami height by numerical simulations and confirmed that the difference in the water level between the inside and outside of the breakwater led to the damage. In Noshiro Port, the offshore seawalls of a power plant were heavily damaged by the 1983 Nihonkai-Chubu earthquake tsunami. Tanimoto et al. (1983) analyzed the tsunami wave forces based on the field survey and model tests. In Okushiri Port at the eastern side of Okushiri Island, similar damage patterns appeared in the north breakwater. In this paper, the relationship between the sliding distances and tsunami height is examined from the results of numerical simulations

The armor stability at the breakwater head is a very important factor for the design of tsunami protection breakwaters. Tanimoto et al. (1988) made the three-dimensional (3-D) model tests for the offshore breakwaters in Kamaishi Port, and proposed armor stability coefficients for practical design. A remarkable aspect of tsunami damage appeared at the narrow opening between the outer east breakwater and the east breakwater in Okushiri Port. The head caissons of both breakwaters

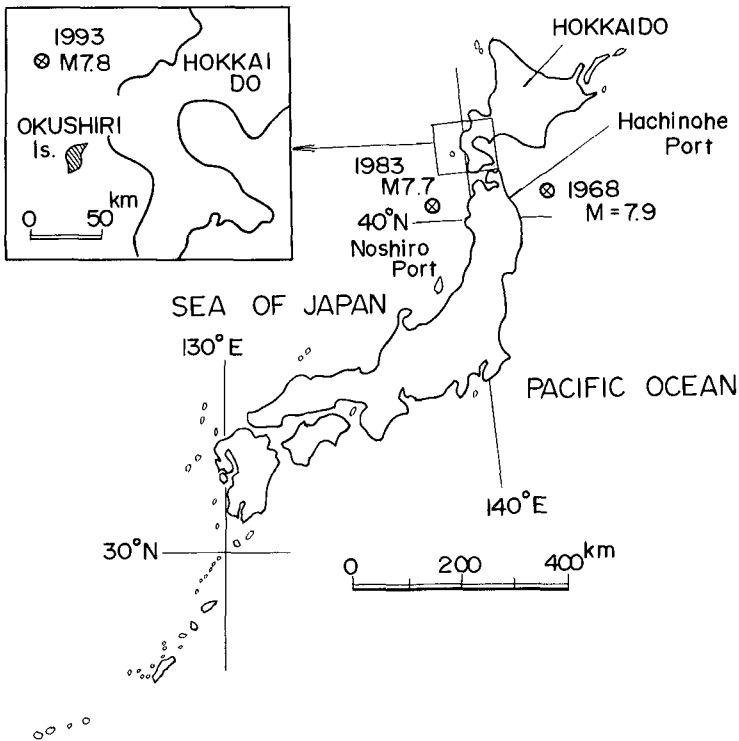


Figure 1. Location of Epicenter

collapsed due to scourings of rubble mound covered with armor blocks by the strong tsunami flow. To reproduce the damage pattern, large-scale 3-D hydraulic model tests were made at a model scale of 1/15. In this paper, the relationship between the flow speed and the damage ratio is examined from test results, and the applicability of armor stability coefficients is confirmed for the practical design of breakwaters against tsunamis.

Outline of breakwater damages

On 12 July 1993, a tsunami, caused by seismic disturbance at latitude $42^{\circ} 47'$ and longitude $139^{\circ} 12'$ struck Okushiri Island and along the southwest coast of Hokkaido. Figure 1 shows the location of the epicenter and Okushiri Island.

Okushiri Port on the eastern side of Okushiri Island is the only port of the island, and includes the ferry terminal to mainland Hokkaido. Figure 2 shows the breakwaters and port facilities in Okushiri port. The outer east breakwater and the east breakwater are the main barriers against wind waves. The opening between the outer east breakwater and the north breakwater is used for the main waterway, and a narrow opening between the outer east breakwater and the east breakwater is also used for a waterway for small craft.

Figure 3 shows the damage pattern of the north breakwater. Sections A, B, C, and D are caisson-type composite breakwaters, and section E is a concrete block type. According to the eyewitnesses, the tsunami waves propagated parallel to the shore line and attacked vertically against sections, C, D, and E of the north breakwater. In contrast, caissons slid little in sections A and B near the head of the breakwater.

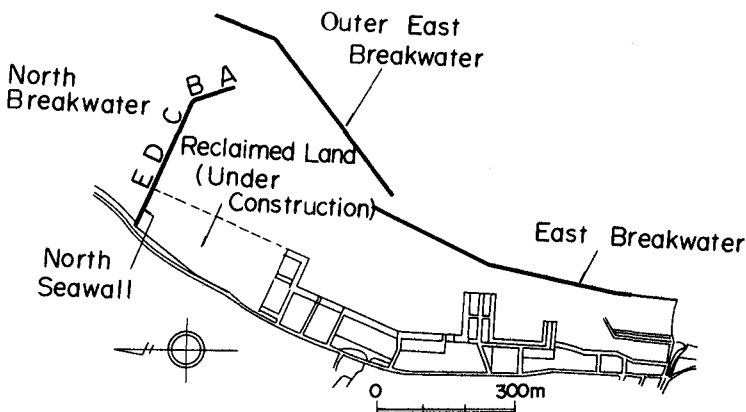


Figure 2. Breakwaters in Okushiri Port

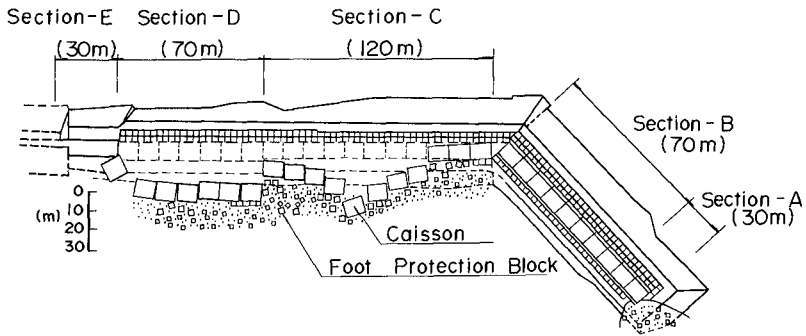


Figure 3. Caisson Sliding at the North Breakwater

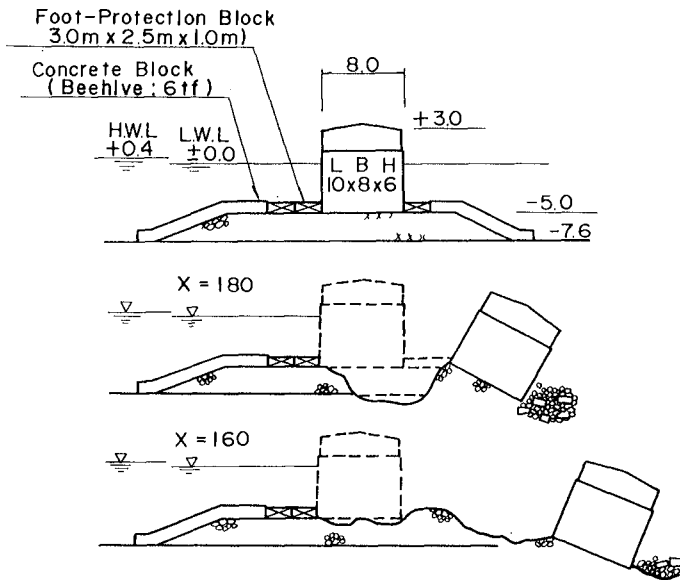


Figure 4. Damage Patterns of Section C of the North Breakwater

Figure 4 (upper diagram) shows a standard cross section of section C. The depth was 7.6m and the caisson was settled at a depth of 5.0m. Figure 4 (lower diagrams) shows typical damage patterns. At the position of X=180 m, the caissons slid 20m and pushed foot-protection blocks (3.0m long, 2.5m wide and 1.0m thick) and concrete blocks (6tf beehive). The scouring of rubble stones (30~300kg)

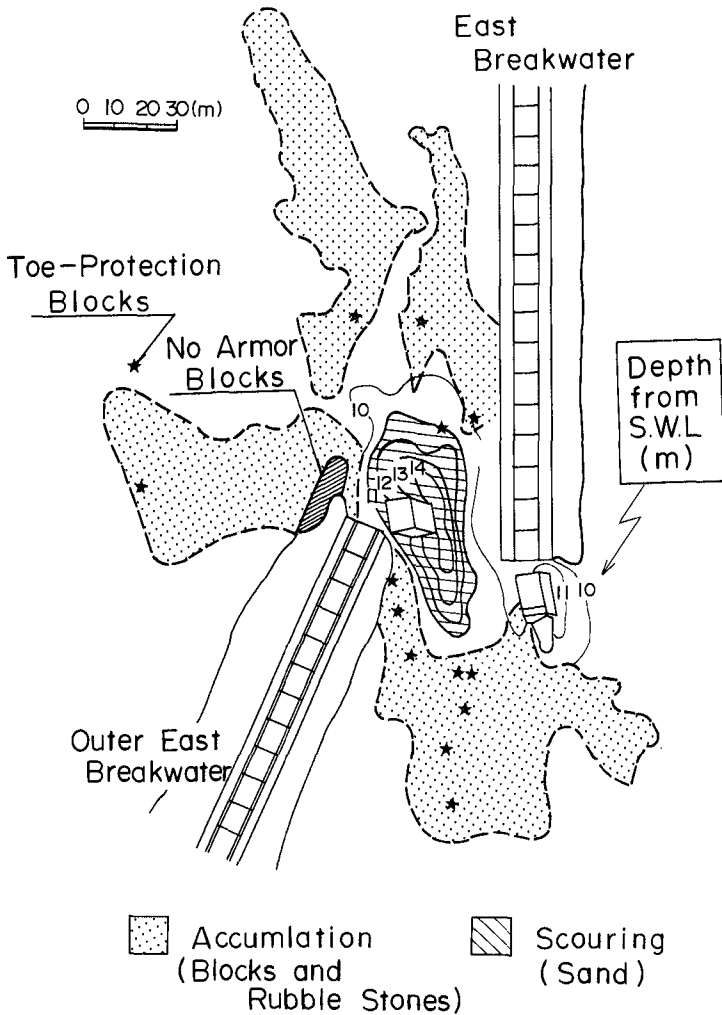


Figure 5. Scouring at the Narrow Opening

progressed along with the action of tsunami waves even after the caissons had slid, and mound rubble collected at $X = 160$ m.

Figure 5 shows the scouring at the narrow opening between the east and the outer east breakwaters. The width of the opening is 35m and the depth was 10m. Rubble mounds of both breakwaters were covered by concrete blocks (1 tf beehive) and foot-protection blocks (1.5m wide, 2.5m long and 1.5m thick). These armor

blocks were moved and scattered as shown in Fig. 5. The maximum scouring depth was 4 m from the original sea bed, and the head caissons at both breakwaters collapsed.

Tsunami forces on vertical walls

The lower part of Fig.6 shows the sliding distance S of each section in the north breakwater. The upright structures of Section E (seawalls for reclaimed land) were heavily damaged, because the sand fillings were not completed when the tsunami struck. Other sections were caisson breakwaters with depths of 5~11 m, and widths of 7.5~9.0 m.

Tanimoto (1983) proposed tsunami wave pressure distributions (Fig.7). The pressure intensity under the still water level p_1 and the crest tsunami height η^* can be calculated as follows:

$$p_1 = 2.2w_0a_I \quad \text{-----(1)}$$

$$\eta^* = 3.0a_I \quad \text{-----(2)}$$

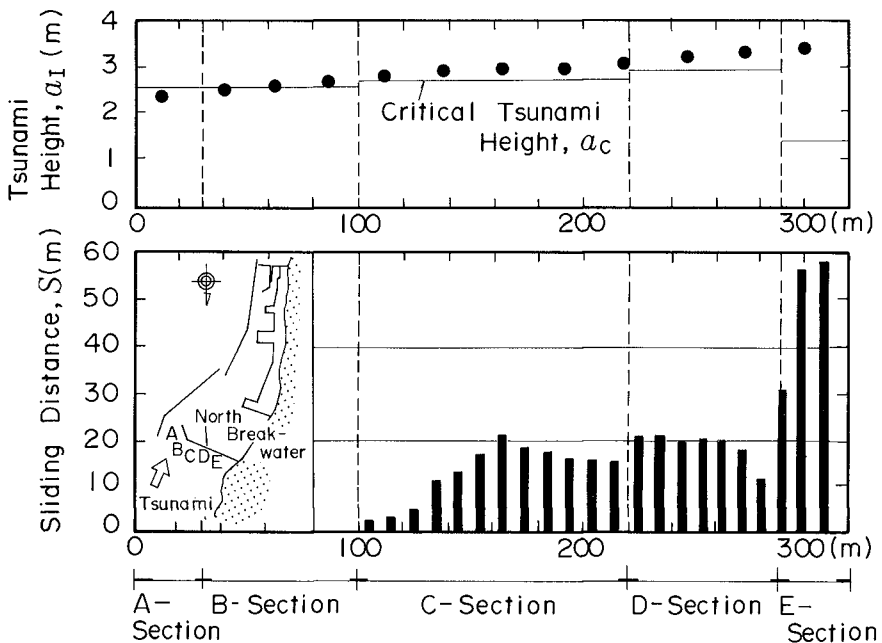


Figure 6. Tsunami Heights and Sliding Distances of the North Breakwater

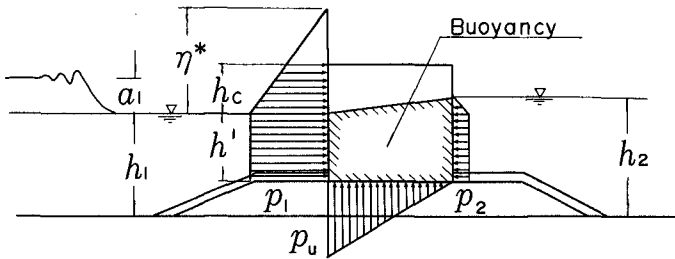


Figure 7. Tsunami Wave Pressure Distribution

where a_I is the incident tsunami height and w_0 is the unit weight of water. h_1 and h_2 are the depth at the offshore side and the harbor side, respectively.

The upper part of Fig.6 shows the critical tsunami heights a_c (horizontal lines) calculated by Tanimoto's formula, and the incident tsunami heights a_I (solid circles) estimated by 3-D numerical simulations. The sliding distances S increase when $a_I \geq a_c$, which confirms the applicability of Tanimoto's formula for prototype failures.

The distance between Okushiri Port and mainland Hokkaido is about 30km. Because the wind fetch is short, the design wave height for the breakwater H_{\max} was 3.5 ~ 5.1 m. However, the design wave height in most ports and harbors facing the Sea of Japan exceeds H_{\max} of 10 m. The small design wave height for Okushiri Port seems to have contributed to the extensive damages.

Experiments on scouring by strong tsunami flows

Large-scale hydraulic model tests with a scale of 1/15 were also made in the 3-D basin (50 m long, 20 m wide and 3.5 m deep) at the Port and Harbour Research Institute (Fig.8). Four axial flow pumps were installed in the basin so that tsunami waves could be reproduced by the action of the flow. By changing the rotation direction and cycles of the axial pumps, the flow direction and speed could be changed according to the analog signals.

The breakwater models were placed in the center of the basin (Fig.9). The scourings of rubble mounds and successive caisson failures at the narrow opening were reproduced. The depth was 66cm, the average depth of this area considering the tidal conditions. The upright section of breakwaters were made of reinforced concrete box (66.7cm long, 56.7cm wide and 73.3cm high) and their weights were adjusted by the filling materials. Concrete blocks (296gf beehive) and foot protection blocks (10cm wide, 16.7cm long and 6.7cm thick) were produced to scale. To facilitate the observations, concrete blocks were classified into four areas (Fig.9) and painted different colors.

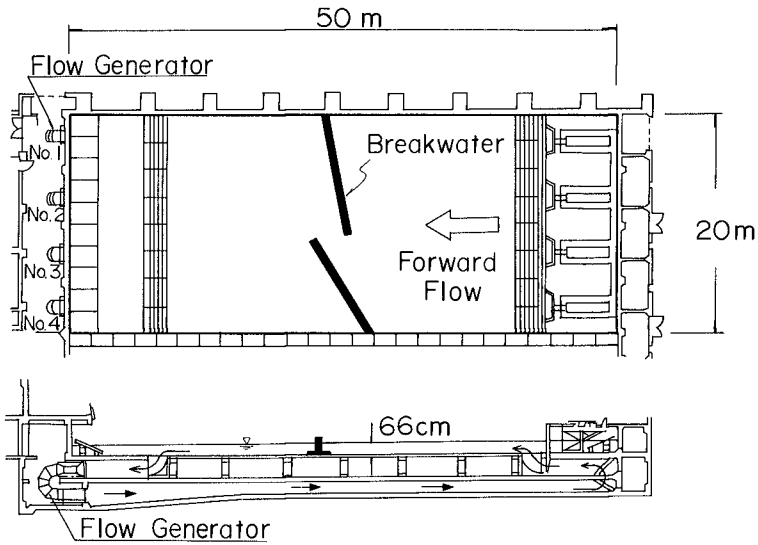


Figure 8. 3-D Basin with Flow Generators

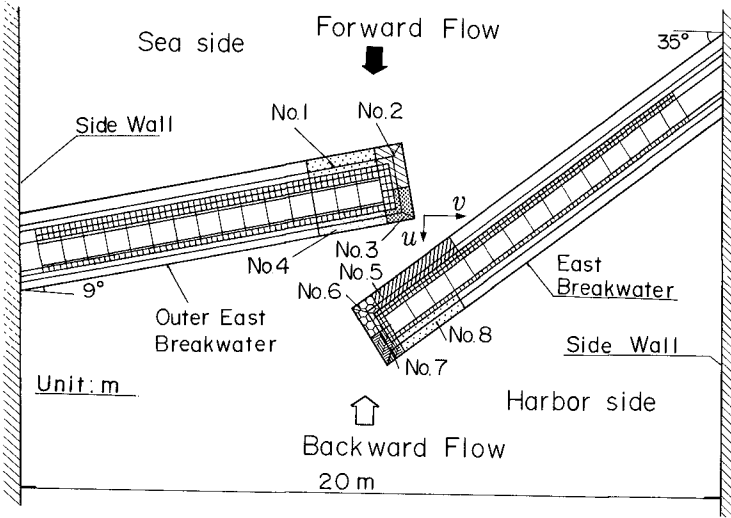


Figure 9. Breakwater Model in the 3-D Basin

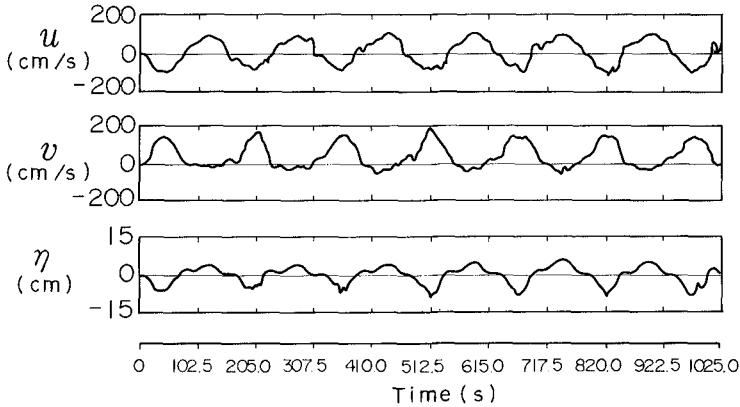


Figure 10. Flow and Water Level at the Center of Opening

Tsunami waves were simulated by generating oscillatory flows with the observed tsunami period of 10 minutes (prototype scale). The forward direction is defined as flow coming into the harbor. The flow speed was monitored at the center of the opening (Fig. 8) with a 2-D electromagnetic flow meter at the depth of 10 cm above the still water level. The peak flow speed of the tsunami (U_0) was defined as the square root of each flow components. The water level was also measured at the same point by a wave gauge.

Five kinds of tsunami flow with different peak speeds ($U_0 = 112, 151, 169, 180$ and 196 cm/s) were used for stability tests. How many tsunami waves attacked this area is not clear, but at least three waves are certain to have covered this area from information given by witnesses. In this experiment, tsunami waves corresponding to a duration of 6.5 times as long as the wave period were created to observe the displacement of the armor blocks and caissons. Figure 10 shows the flow and water level changes at $U_0 = 196$ cm/s.

Damage patterns around breakwater heads

Armor damage was found first at area No.3 in the outer east breakwater at a flow rate $U_0 = 151$ cm/s. The number of blocks moved was 18, and the damage ratio in this area was 20 %. The damage of foot-protection blocks was not observed at this flow rate. Tanimoto et al. (1988) examined the flow patterns at the mouth of tsunami protection breakwaters in 3-D model tests. They pointed out that the armor damage was heavier at the projecting head for the flow direction. In our experiment, the damage pattern for the forward flow was the same as for the experiments of Tanimoto. However, for the backward flow, no damage was observed at the area of No.7 of the east breakwater, probably because the opening ratio of our experiment was much lower than usual for tsunami protection breakwaters



Photo 1. Damaged Caisson and Mound of the Outer East Breakwater

At the flow rate $U_0=169$ cm/s (6.5 m/s in prototype), all armor blocks were damaged at the outer east breakwater and rubble stones were also scattered. At the east breakwater, 80% of the armor blocks were damaged. The damage of foot protection blocks was observed as 80% at the head of the outer east breakwater.

At the flow rate $U_0=196$ cm/s (7.6 m/s in prototype), the first tsunami wave scoured most of rubble stones around the head caissons, and the head caissons of both breakwaters tilted due to the scouring of the rubble mound. In the outer east breakwater, the damage progressed further to the head caisson failure by the second tsunami wave. The maximum flow rate at the failure was recorded to be 2.3 m/s (8.9 m/s in prototype). Photo 1 shows the damaged caisson and mound of the outer east breakwater after the experiment. The prototype damage around the breakwater heads as shown in Fig. 5 was successfully reproduced by these model tests.

Necessary weight of Armors

The weight required to withstand the flow can be calculated by the following Coastal Engineering Research Center (C.E.R.C.:1984) formula;

$$W = \frac{\pi w U_0^6}{48y^6 g^3 (w/w_0 - 1)^3 (\cos \theta - \sin \theta)^3} \quad (3)$$

where W is the weight of armor unit, U_0 is the flow speed, w_0 is the unit weight of fluid, w is the unit weight of armor units, g is the acceleration of gravity and θ is the angle of mound slope. This equation (3) is commonly accepted as giving the

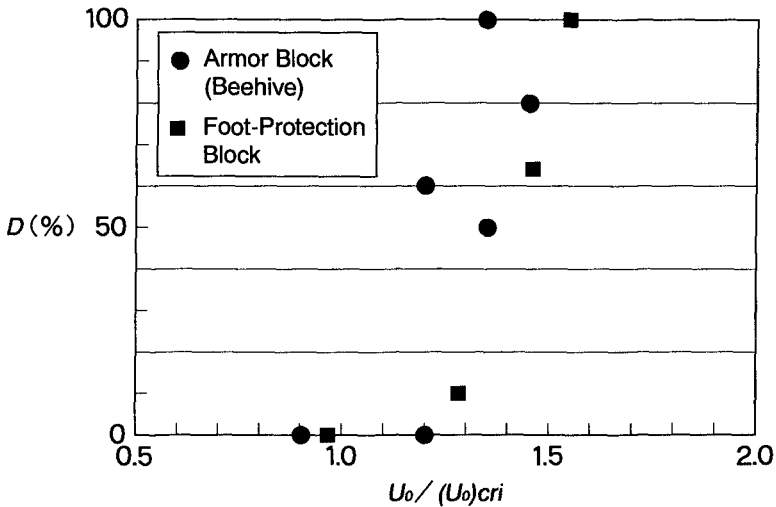


Figure 11. Damage Ratios of Armor Blocks and Foot-Protection Blocks

necessary weight of stones and armor blocks to withstand steady flows. Tanimoto et al.(1988) carried out the armor stability tests of tsunami protection breakwaters, and showed the applicability of this formula for tsunami flows.

Tsuruya et. al. (1994) recommended that the Isbash parameter γ for beehive blocks should be 1.2 in the actual settled condition, and 0.967 for individual blocks separately settled on the sea bottom. Kimura(1995) proposed that $\gamma=0.6\sim 0.7$ can be used based on the previous tsunami damage for foot-protection blocks.

In the 3-D model test for breakwater heads, damage ratios were also observed for each tsunami flows. Figure 11 shows the damage ratio of beehive and foot-protection blocks for $U_0=151, 169, 180$ and 196 cm/s. The critical flow speed $(U_0)_{cri}$ is calculated from Eq.(3) for beehive ($\gamma = 1.2$) and foot-protection block ($\gamma = 0.65$). Damage starts from $U_0/(U_0)_{cri} = 1.0$, and therefore the applicability of these coefficients is proved.

Conclusions

The damage analyses of breakwaters in Okushiri Port due to the 1993 Hokkaido Nansei-oki earthquake tsunami gave the following results and conclusions;

- The caisson breakwaters, whose design wave height due to storm waves were small, were damaged by the tsunami attack.
- The applicability of Tanimoto's formulae for tsunami forces on vertical walls was confirmed by the prototype failure analyses of the north breakwaters in Okushiri Port.

- The failure at breakwaters heads was reproduced by the 3-D model tests. The maximum flow speed of the tsunami was estimated as 8.9 m/s in the prototype.
- The necessary weight of armors around the head of breakwaters can be estimated by the C.E.R.C. formula using the Izbash parameter of previous model tests.

The 3-D experiment in this report did not reproduce the scouring of sandy sea beds. The sea bed was possibly scoured at a smaller flow velocity than indicated in this report, which resulted in the destruction of mounds and in turn led to the collapse of caissons at the breakwater head. Future studies should consider the influence of sediment movement.

Acknowledgments

The field survey on breakwater damages was made by the Port and Harbor Division of Hokkaido Development Bureau and the Cold Region Port and Harbor Engineering Research Center. The authors would like to express their gratitude to Professor N. Shuto at Tohoku University for advice on the numerical calculations on tsunami height.

References

- Coastal Engineering Research Center(1984): Shore Protection Manual, Volume II, pp.7-253.
- Ito, Y., Tanimoto, K., and Kihara, T.(1969): Desital computation on the effect of breakwaters against long-period waves(5th Report), Repot of Port and Harbour Res. Inst., Vol.8, No.3, pp.16~46.
- Kimura, K. (1995): Stability of rubble mound foundation for composite breakwaters against storm waves and tsunamis, Report of Civil Engineering Res. Inst., No. 110, pp. 82.
- Tanimoto, K.(1983): On the Hydraulic Aspects of Tsunami Breakwaters in Japan, Proc. of the International Tsunami Symposium by IUGG Tsunami Commission, pp.423~435.
- Tanimoto, K., et al. (1983): Field and laboratory investigations of tsunami caused by 1983 Nihonkai Chubu Earthquake, Technical Note of the Port and Harbour Res. Inst., No. 470, 299p.
- Tanimoto, K., Kimura, K., Ikegami, M. and Miyazaki, K. (1988): Study on stability of submerged dike at the opening section of tsunami protection breakwaters, Report of Port and Harbor Res. Inst., Vol.27, No.4, pp.93~121.

Tsuruya, H. and Nakagawa, Y. (1994): Model experiment for reproduction of disaster at Okushiri-Higashi breakwater by Hokkaido-Nanseioki earthquake Tsunami, Technical Note of the Port and Harbour Res. Inst., No.789, 19p.

CHAPTER 365

RICHARDS BAY NORTH BREAKWATER - REPAIR OF A ROUNDHEAD: MONITORING, MODEL TESTING, DESIGN AND CONSTRUCTION

D Phelp¹ , A M^cClarty² and A Bartels³

ABSTRACT

The head section of the north breakwater, at the entrance to the Port of Richards Bay, has suffered some damage since its construction in 1973. This paper briefly discusses the changes in the design conditions, the first unsuccessful repair in 1986/87, using 15t dolosse, the annual photographic monitoring results showing the rates of damage to the roundhead since then, and the model testing of various repair options, using available spare 20t and 30t dolosse. Finally the construction of the optimal repair, carried out in 1996, using a heavy duty mobile crane (with 48m boom reach) and DGPS positioning, is described. Construction was still in progress at the time of publishing this paper.

INTRODUCTION

The Port of Richards Bay, on the east coast of South Africa, has two dolos breakwaters, a shorter straight breakwater on the northern side of the harbour entrance channel and a longer curved breakwater on the southern side. The north breakwater consists of a straight rubble mound structure, constructed in 1973, which stretches for approximately 600m perpendicular to the coastline. The original armouring on this breakwater consists mainly of 5t dolosse on both sides of the trunk, but includes 15t dolosse on the roundhead (Figure 1). Like many similar breakwaters, the neck of the roundhead was found to have experienced the worst damage to the armour layer.

¹ Environmentek, CSIR, P O Box 320, Stellenbosch 7600 South Africa

² Portnet, Port of Richards Bay, P O Box 464, Richards Bay 3600 (SA)

³ Entech Consultants (Pty) Ltd, P O Box 752, Stellenbosch 7600 (SA)

Annual photographic monitoring of the north breakwater showed an increase in damage in localised areas on the head, particularly on the southern side (Figures 1 and 2), despite temporary repairs using 15t dolosse, carried out by Portnet in 1986/87. A previous model study (CSIR, 1992a) indicated that the spare 20t and 30t dolosse, available from a stockpile of spare dolosse at the root of the south breakwater, would be suitable for the repairs. It was therefore decided to test various repair options using 20t and 30t dolosse.

In June 1994 the CSIR was commissioned by Portnet to carry out a physical model study to determine the most cost effective design for the repair work. These included repair solutions in which a toe of anchored 30t dolosse was constructed around the head and 20t dolosse were placed in the cusps and over the anchor chains. After an initial calibration run, a total of four different repair options were tested. Due to delays in the commissioning of a suitable crane, the construction of the final repair was delayed to the end of 1996. This paper does however include construction details of a temporary repair using 5t dolosse (placed using an available smaller crane) and the start of the final repair, using the 20t and 30t dolosse.



FIGURE 1: View of North Breakwater and Cross-Section through head.

MONITORING RESULTS

The crane/helicopter photographic survey method (Phelp *et al*, 1994) was used to annually monitor the breakwater. The photographic survey stations are spaced at 25m intervals, and both sides of the breakwater are monitored; the breakwater was however already 13 years old before annual photographic monitoring was commenced. The areas with the highest damage (over 25% breakage) continued to

deteriorate the fastest. At stations P2 and P3 on the round-head, the damage was mostly localized in cusps, which are visible in Figure 1. A sharp increase in the rate of damage in the worst areas, since 1992 (72 months), can be seen in Figure 2. This damage has mainly been attributed to bottom scour resulting in increased wave heights reaching the breakwater, ie. increased depth limited wave heights. Station P1 also lies at the transition between the 5t and 15t dolosse, which is at an inherent weak point in the armouring.

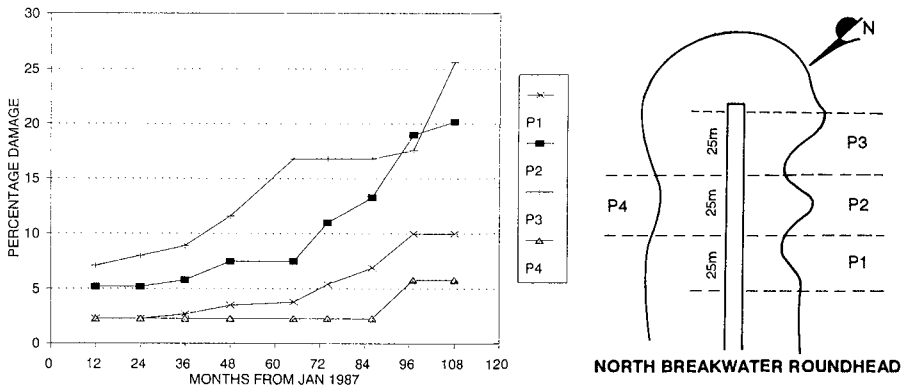


FIGURE 2: Rates of Damage to the Dolos Armouring Since 1987.

FACTORS CONTRIBUTING TO THE HIGH DAMAGE

The occurrence of low pressure cyclonic storms (cyclones Demoina and Emboa in 1984) subjected the breakwater to wave heights exceeding the 7,9m 1:50 year design H_{mo} . Storm wave and low atmospheric pressure set-up associated with these storms also had the effect of raising the water level, thereby raising the depth limited wave heights reaching the breakwater. A previous model study on wave penetration in the entrance channel (CSIR 1974) also showed, based on wave refraction that wave conditions between SE and S (deep sea) result in the worst conditions opposite the north breakwater head.

Bathometric surveys carried out regularly by Portnet revealed a general erosion of sand, of up to 2m, around the head and seawards of the breakwater, especially between 1989 and 1994. This would have resulted in further increasing the depth limited heights of the waves reaching the breakwater. Besides the scour at the toe (seismic surveys carried out by CSIR in August 1993 confirmed the toe erosion) the breakwater was also subjected to severe storms in October 1990 (max H_{mo} of 6.1m) and moderate storms since then, resulting in accelerated damage to the dolos armouring behind the weakened toe.

Like many similar breakwaters, both sides of the neck of the roundhead were found to have experienced the worst damage to the armour layer. Jensen (Jensen, 1984) found that for tetrapods, relative to the stability coefficients for the breakwater trunk, the roundhead area at 135° from the wave direction showed the lowest stability. This indicates that some of the damage found on the southern side of the north breakwater could also have been caused by more northerly waves. Model tests also showed evidence of eddies on the lee-side of the roundhead where toe dolosse were pulled off the slope.

Repairs which were carried out in 1986/87 using 200 additional 15t dolosse have proved unsuccessful, mainly due to the toe damage and sea-bed erosion mentioned above. No model tests were done for these initial repairs. The area where the 15t dolosse on the roundhead meet the 5t dolos trunk (Figure 1) has also been a focus of damage, likely as a result of poor interlocking between the different sized units.

RESULTS OF MODEL TESTS

Constraints to the Repair Design

Model tests were carried out in an existing 3D model of Richards Bay (CSIR, 1995), to save both time and costs. This available model was built at a scale of 1:110 and covered the harbour entrance and part of the inner channel. The model test options were restricted to using available 200 20t and 100 30t dolosse, which have been brought across the harbour from a stockpile near the southern breakwater. The proposed repair consists of a double row of 30t dolosse at the toe, with a double layer of 20t dolosse behind. 5t dolosse were also available to wedge into the gaps behind the 20t repair and between the existing 5t slope where the repair overlapped the breakwater trunk section.

The removal of rubble and pre-repair slope preparation was limited to the removal of only large broken dolos pieces (assisted by divers), and the filling of holes at the toe of the armour slope. The crane reach was limited to 45m for a 30t dolos, which was achieved by using a specially designed crane which could fit onto the 6m wide mass-concrete capping of the north breakwater.

Choice of Model Scale

The scale of 1:110 used for the tests gives a Reynolds number of approximately 1×10^4 , which is just within the minimum range recommended by Van der Meer (Van der Meer, 1988) but less than the

value recommended by CERC. Some scale effects should therefore be expected, especially on the 5t dolosse, but these scale effects have been found (Oumeraci, 1984) to make the model results conservative. The scale effects, being similar for all the test runs, still allowed the comparisons made between the options tested. The results were however interpreted as giving an indication rather than an exact prediction of the possible damage. The calibration test showed that the hindcast of the damage which occurred in the 1990 storm is in qualitative agreement with the observed prototype damage confirming the validity of the physical model. A plan of the model is shown in Figure 3 and the "as-built" cross-section through the head in Figure 1.

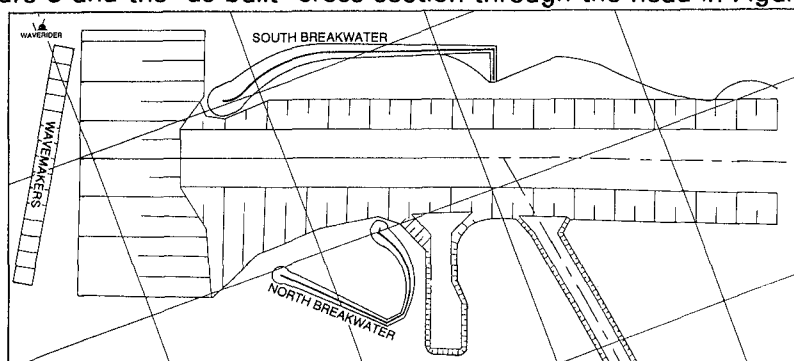


FIGURE 3: Plan showing Model Layout

Wave Generation and Measurement

Eight standard wire resistance wave probes were used which were coupled so that measurements could be carried out over prescribed areas. The wave generator bank was 9,75 m long situated at the 1 km mark (Figure 3). The direction of the generators was 30° N, ie: waves coming perpendicularly out of the wave boxes have a direction of 120° . Based on a review of existing data, the following main test conditions:

- Wave direction, entrance area (12s) 145°
- Storm input, Richards Bay Spectrum, $\gamma = 2,74$ with the following approximate steps $H_{mo} = 4, 5, 6, 8$ m with following wave per respectively: $T_p = 10, 12, 13, 15,5$ s
- Water level for main test MHWS = 2,0 m CD

DESCRIPTION OF THE TESTS

Test procedure

In order to calibrate the physical model, a calibration test was carried out in which the prototype damage resulting from the 1990

storm was reproduced in the model. A number of repair options were then investigated, starting with the simplest option and then extending the repair until a stable solution was found. Before each repair option was constructed, the original damage (after the 1990 storm) was replicated in the model. The repaired breakwater was then exposed to the five different wave conditions described above. After each test, the repair dolosse were removed and the 1990 damage reconstructed, after which the next repair option was implemented.

Measurement of Damage

Movements of Dolosse

The number of dolos movements was determined by comparing the photographs taken before and after each run. A number of swing tests were carried out on full-scale 9t dolosse to determine the degree of movement these dolosse could sustain without breakage (Zwamborn and Phelp, 1989). Based on the results of these tests it was recommended that all movements greater than half the height of a dolos be included as damage. The number of dolosse which moved was determined separately for a number of zones located at the head of the breakwater. The damage was then expressed as a percentage of the number of dolosse placed in each zone.

Rocking Dolosse

In addition to determining the movements, the number of dolosse which were rocking was estimated visually during each test. However due to the difficulty in observing these movements over the whole test area, it was decided to use the small movements (less than $h/2$), which were measured from the photographs, as an estimation of rocking dolosse. In (CSIR, 1992b) this alternative approach was also adopted, where it was found that dividing the movements less than $h/2$ by nine, would give a reliable estimation of the number of rocking dolosse.

DETAILS OF THE REPAIR OPTIONS TESTED

Discussion on the Repair Strategy Followed

The strategy of placing 20t or 30t dolosse on top of the damaged 5t and 15t dolosse was originally tested and found to be feasible in previous model tests (CSIR, 1992a and 1992b). Static tests on dolosse have shown that a dolos can carry 4 to 6 times its own weight without breaking; this implies that a number of layers can be constructed without breakage under static load. Thus it was considered feasible to place a 1 to 2 layer thick 20t dolos strengthening layer, safely on top of the

existing damaged 15t dolosse. Although the quality of the underlying 15t dolosse is questionable, the dynamic loading over the past 8 years has caused the weaker dolosse to break, and careful placing of new dolosse should not result in significant further breakages. However, since most parts of the repair sections will consist of already broken units, the repair itself was designed as well interlocked armour, finished to a uniform slope, which should be able to stand on its own.

Although stresses cannot be modelled, extensive prototype observations and structural tests on full size dolosse support the above conclusions. For example the main breakwater at Gansbaai, on the South African southern coast, consists of an original layer of 4.5t dolosse covered by one layer of 12.4t units, covered by one layer of 17.1t dolosse overlapped with a double layer of 25t dolosse. This repair has thus far proved to be successful.

Repair Option 1

The first repair option tested involved the filling of the cusps with the minimum number of dolosse, ie. starting with the simplest option and then extending the repair until a stable solution was found. This was a temporary (intermediate) repair solution to protect the breakwater core from further damage, but would also eventually form part of a more permanent repair. The number of repair dolosse per hole was approximately 10 30t and 20 to 30 20t dolosse. The total number of dolosse needed to repair all the cusps (northern and southern sides) was approximately 40 30t and 150 20t. The 30t dolosse were used to construct a toe at the bottom in front of the cusps to anchor the 20t dolosse filling up the cusps behind.

Repair Option 2

After repair option 1 had shown extensive damage to the edges of the repaired areas, it was decided to extend the repaired area to provide a more uniform profile. The second repair option was similar to the first repair option but with a more continuous row of 30t dolosse at the toe around the whole breakwater head. The construction of a toe with a double layer of 30t dolosse was an attempt to increase the stability of the repaired slope. The 20t repair layer was then placed on top of the 15t dolosse. The shape of the head was modified slightly to have a slightly flatter slope. Approximately 80 30t and 200 20t dolosse were used.

Repair Option 3

In this repair option the cusps were also filled with 20t dolosse, but the 30t dolosse on the southern-side of the breakwater were fixed

using anchor chains (scrap, ship's anchor chains). First, a double row of 30t dolosse were placed to construct the toe, after which the 20t dolosse were used to repair the cusps and to cover the chains. This method proved to be very successful in the construction of the Port of Cape Town breakwater where similar conditions exist at the toe (CSIR, 1985 and Zwamborn *et al*, 1990). As was done in Cape Town, the end of the chains should be connected to a piece of scrap rail to provide improved anchorage. Approximately the same number of dolosse were used as for the temporary repair option (option 1). The chains used to fix the 30t dolosse can be clearly seen. Figure 4 shows the anchor chains in the model and as used in prototype.

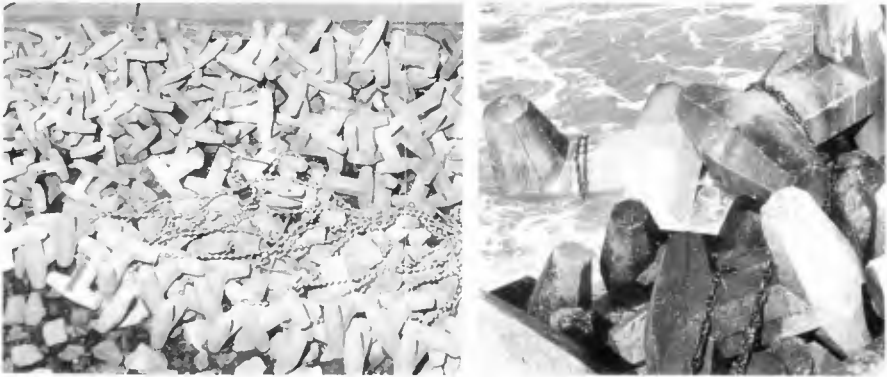


FIGURE 4: Anchor Chains used to Secure 30t Toe Dolosse

Repair Option 4

In this repair option, a double row of anchored 30t dolosse was used to construct the toe around a slightly wider head. The 20t dolosse were then placed in the cusps and over the chains. Also, before the 20t dolosse were placed on top of the 15t dolosse, the damaged slope beneath the repair was reprofiled to allow for a double layer of 20t dolosse, to provide a more uniform repair slope. In this last repair option all the 30t dolosse were fixed by anchor chains.

INTERPRETATION OF RESULTS

Comparison of Damage to the Repair Options Tested

A comparison of the damage at the end of each run is shown graphically in Figure 5. The x-axis presents the section of the breakwater which starts at the northern-side of the breakwater, around the head to the southern side of the breakwater. These location numbers are given in Figure 5. Repair Option 4 is clearly the best option.

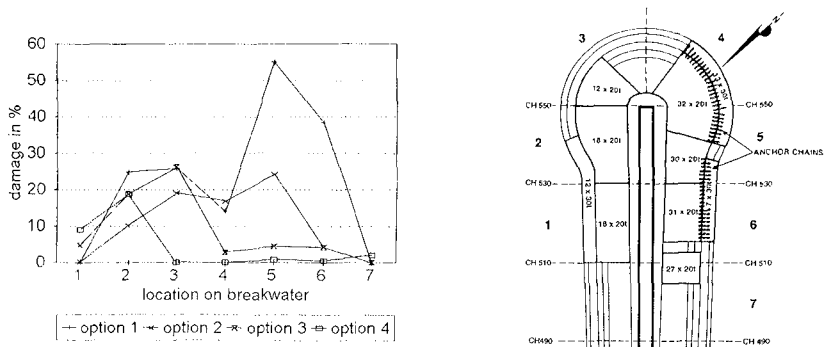


FIGURE 5: Comparison of Damage to the Repair Options Tested

For all the repair options, the existing 15t dolosse were well protected by the additional dolosse. For repair options 1 and 2 it was clear that again, similar to the prototype, the highest damage could be observed just behind the head at the southern side of the breakwater. The eddies caused by the waves passing around the head were responsible for rolling the toe dolosse along the surface of the rubble. Once a dolos had been extracted from the slope it was easily rolled along by big waves.

The 30t dolosse, which were fixed by anchor chains, reduced the damage in that specific area considerably. Repair Option 4 showed acceptable damage levels for all the repair dolosse, apart from the area on the northern side of the head where the 20t dolosse showed higher damage - poor interlocking of this section may have been the cause. The damaged 15 t dolosse on this side were not reprofiled as was done on the southern side, which meant that the 20t repair dolosse were not interlocked properly in a double layer. Although the original prototype damage (CSIR, 1994) on the northern side of the head is less than one third of that on the southern side, it is felt that the repairs would have been more effective if the whole northern side had also been properly prepared (reprofiled) before the repair.

Based on the results of the model study and from previous experience, the following recommendations for the repair works were made:

- a) Before any repairs, as many as possible of the broken pieces of dolosse should be removed without disturbing adjacent dolosse.
- b) Crane and ball surveys should be used to identify all underwater depressions, both before and during construction of the repair.
- c) Particular care should be taken when placing the dolosse to ensure that dolosse interlock as well as possible with the

underlying dolosse. Re-slinging of a newly placed dolos is worth the effort if a better interlocking is obtained.

- d) For the placing of dolosse, both above and below water, a predetermined grid pattern should be developed with angles and distances for the crane, or x,y references for DGPS positioning.
- e) The 30t toe dolosse should be anchored by chains.

CONSTRUCTION OF THE OPTIMUM REPAIR

Construction Methods

Based on the results of the model tests, 20t and chained 30t dolosse were to be used for the repair. The 20t and 30t dolosse were brought across from the south side of the entrance channel to a stockpile at the root of the north breakwater, while the 5t dolosse were also already available from a part of the root of the original breakwater which was now covered with sand. Three double direction trailers were then used to transport the dolosse onto the breakwater. These trailers could only pass when unloaded, which meant that only one 20t or 30t dolos could be brought onto the breakwater at any one time (Figure 6).



Initial crane and ball surveys were done with 5m profile intervals over the damaged areas. A certain amount of reprofiling was then carried out to remove irregularities in the overall profile. Broken pieces of dolosse were removed and placed in erosion holes. Another crane and ball survey was then carried out to get the underlayer profile, from which the repair dolos placing grid could be calculated. The smoother the underlayer profile, the easier it was to set a placing grid with uniform packing density.

The repair dolosse were then placed, starting with the double row of chained 30t dolosse at the toe. The chains, which were lifted on a separate hook were laid at an angle of 45° seawards along the toe of

the slope, later to be covered with 20t dolosse. The crane hook was fitted with a 15m sling (to ensure the hook and pulley remained out of the seawater), a quick release hook (Figure 6) and a double cable sling. The double slings which support the dolosse were hand spliced (instead of swage joined) to allow easy removal of the slings once the dolos was in position. The quick release hook was hung from a swivel and fitted with two torque bars, which allowed easy rotation of the dolosse to ensure good interlocking. The torque bars were attached to 10mm nylon (light and water resistant) ropes, which were pulled perpendicularly from the mass capping to orientate the dolosse.

It was found that to ensure correct packing density, the dolos placing must be kept as close as possible to the grid coordinates. The final orientation and positioning of the dolos is then done by eye to ensure good interlocking. Dolosse are placed with a minimum of three contact points to reduce the change of rocking under wave action. After all the grid positions were full, it was found that up to 10% additional dolosse had to be placed "in holes" to ensure a well interlocked uniform profile. To identify these "holes" it is advisable to get an aerial view of the slope from a helicopter, or from a basket hung from the crane.

DGPS for Crane Positioning

For both the crane and ball surveys of the slope profiles, and the correct placing of the dolosse, there was a need to accurately position the hook of the crane. The original method used was triangulation from two theodolites, but this proved labourious and time consuming. Another method was to fit the crane with a pendulum boom angle indicator and a horizontal slew protractor whereby the horizontal and vertical angles of the boom could be measured and converted from polar to x,y grid coordinates.

Recently a differential GPS system has been introduced using satellite positioning linked to a portable computer onboard the crane (Figure 7). The satellite receiver is positioned on top of the crane boom, directly above the position of the hook. The pre-determined positions are entered into AutoCAD software on the computer, and standard survey software enters the real time navigation parameters which indicate the position of the boom. By entering the standing position of the crane along the breakwater, the boom reach and safety circle can also be indicated on the screen. The crane operator can then immediately see which dolosse can be placed from the present position of the crane. The AutoCAD dolos placing grid is shown in Figure 8.



The positioning software includes the following useful features:

- Zoom in and out, and centring the cranes position on the screen.
- The entry of up to 20 predetermined crane standing positions on the breakwater, including facility to orientate and offset.
- The entry of up to 500 top and 500 bottom layer dolosse, including an indication of size and numbering (colour options)
- The facility to import and editing of an AutoCAD or other CAD drawing of the breakwater eg: the "as-built" layout.
- Indication and editing of the safe radius of the cranes reach.
- The input and storage of the placed positions of the dolosse.
- A backup system where the polar coordinates can be entered to position the crane, should the DGPS signal fail.

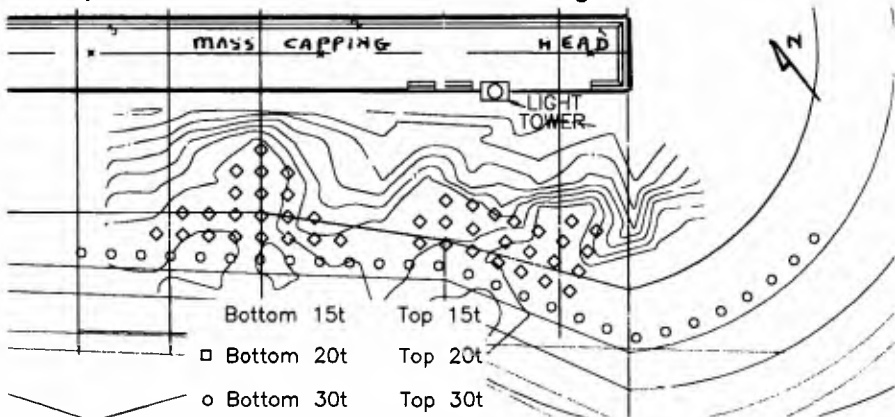


FIGURE 8: Example of DGPS AutoCAD Dolos Placing Grid

Emergency Temporary Repair and Final Repair

Planning for the repair was well underway by mid 1996, when a breakdown of the special crane (the only crane which could fit onto the breakwater and have sufficient reach for placing the 30t dolos toe) resulted in having to delay the final repair to the end of 1996. As the localised damage on the southern side of the roundhead was starting to

expose the underlayer rock, it was decided to carry out emergency temporary repairs. These took the form of filling the cusps with 5t dolosse (which could be placed with a smaller mobile crane). This repair was not extended further than the original slope profile so that it would form part of the underlayer of the final repair. The same construction method was used as described above. Figure 9 shows this section before and after the emergency repair. Figure 10 shows the chained 30t dolosse at the start of the final repair in December 1996.



ACKNOWLEDGEMENTS

The first author would like to thank Mr M^cClarty of Portnet and Mr Bartels of Entech for their contributions to this paper and for the team spirit which prevailed between Portnet, the Client/Port Authority, Entech, the Coastal Consulting Engineers and the CSIR Research Laboratory.

REFERENCES

- CSIR (1974). Design of Richards Bay Harbour Entrance Wave Model Tests on Entrance Layout. CSIR report C/SEA 74/2.
- CERC (1984). shore protection manual. US Army Coastal Engineering Research Centre, Vol. 2. US Government Printing Office, WashingtonDC
- CSIR (1992a). Port of Richards Bay: Model Study to Optimise Breakwater Repairs. CSIR report EMAS-C 93049.
- CSIR (1992b). Mossel Bay Breakwater: Model Study of Repair Options. CSIR report EMAS-C 92051.
- CSIR (1994). Port of Richards Bay: Photographic crane and helicopter surveys of the north and south breakwaters, March 1994. CSIR report EMA/C 94115.
- CSIR (1995). Port of Richards Bay - North Breakwater Repair: Results of Model Tests. CSIR Report EMAS-C 95033, Stellenbosch.
- Jensen (1984). A Monograph on Rubble Mound Breakwaters, O. Juul Jensen, DHI, Denmark. November 1984.
- Oumeraci H (1984). Scale effects in coastal hydraulic models. Symposium on scale effects in modelling hydraulic structures. International Association for Hydraulic Research.
- Phelp *et al* (1994). Results of Extensive Field Monitoring of Dolos Breakwaters. 24 ICCE 1994, Kobe, Japan.
- Van der Meer J (1988). Rock slopes and gravel beaches under wave attack. Doctoral thesis. Delft University of Technology.
- Zwamborn J A and Phelp D (1989). Structural tests on dolosse. Seminar on stresses in concrete armour units. Vicksburg, USA.
- Zwamborn *et al* (1990). Redesign, Repair, and Monitoring of the Table Bay Breakwater. 26 PIANC 1990, Osaka, Japan.

CHAPTER 366

THYBORØN COASTAL INVESTIGATIONS 1995: NEW LESSONS FROM AN OLD COASTAL PROBLEM

by
I. Brøker¹, J.A. Zyserman² and Per Roed Jakobsen³

INTRODUCTION AND BACKGROUND

Thyborøn channel is located on the West coast of Jutland, Denmark, and connects the Limfjord with the North Sea, see figure 1. The channel was naturally opened following a major storm event in 1862. In the years after the opening of the channel, the neighbouring coasts experienced substantial erosion, which put the town of Thyborøn at risk. For historical background and previous investigations and analysis, please see References.

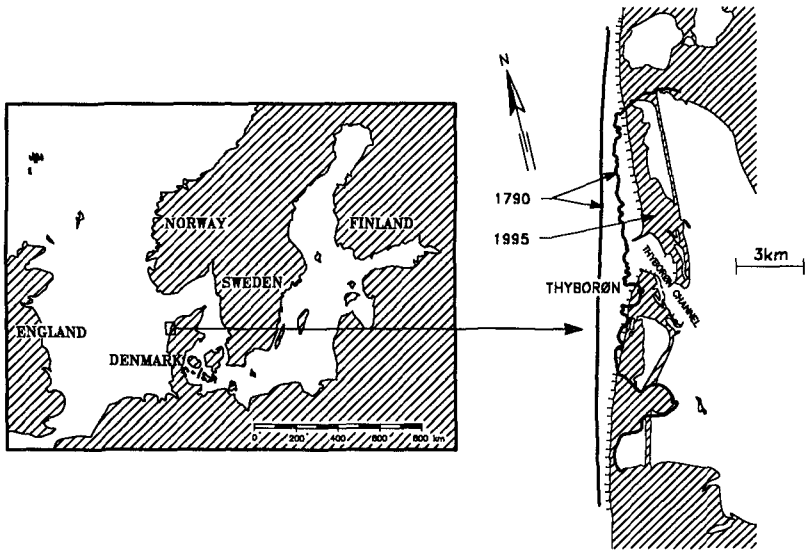


Figure 1 Location map, including indication of development over 205 years

¹ Chief Engineer, Danish Hydraulic Institute (DHI), Agern Allé 5, DK-2970 Hørsholm, Denmark

² Coastal Engineer, Danish Hydraulic Institute (DHI), Agern Allé 5, DK-2970 Hørsholm, Denmark

³ Director, Danish Coastal Authority, Højbovej 1, DK-7620 Lemvig, Denmark

The geology in the area can be briefly described as postglacial sediments, mostly fine to medium sand, overlaying hard clay in depths of 10 to 12 m below seabed level. The area is exposed to severe storms from directions between southwest and northwest. Along the coast the conditions are influenced by a northgoing sea current. In the inlet area the currents are determined by the differences in water level across the peninsula of Jutland. The tidal variations are small, with a maximum tidal range of ~ 40 cm. The yearly net sediment transport along the narrow barrier beaches is directed towards the inlet from both sides. The undisturbed net transport rates are of the order of magnitude of 1 million m^3/year . A dense groyne system reduces the longshore sediment transport rates to about 2-300,000 m^3/year from each side; the sediment transported into the channel ends up on large shoals inside the Limfjord, giving a yearly deposition of approximately 0.5 mill m^3 .

The groynes along the coast have decreased the rate of shoreline retreat to about 50% of the natural erosion. This means that the land ends of the groynes have to be extended inland in pace with the erosion. The tips of the groynes experience continuous deterioration due to severe pressure arising from the wave action. The submerged groyne elements are left on the seabed as they are still considered as active parts of the coastal system.

NUMERICAL MODELLING STUDIES

As a part of the study of the processes around this inlet numerical models were established, both for the quantification of the overall sediment budget along the barrier beaches, and for the study of the details of the morphological evolution under storm conditions inside and around the inlet.

Sediment budget along the barrier beaches

The sediment budget along the barrier beaches has been studied by the LITPACK model, and the details around the inlet by a morphological model constructed from various modules of MIKE 21. **LITPACK** is a model complex for calculation of waves, wave-driven currents (possibly coupled with a general sea current) and longshore sediment transport on an arbitrary coastal profile. A basic assumption of quasi-uniform conditions in the longshore direction allows for simulation of all combinations of waves, water levels and sea currents and establishment of a complete sediment budget. The calculated budget is illustrated in figure 2. The budget was validated through comparisons with the transport rates derived from measured erosion/deposition during 15 years.

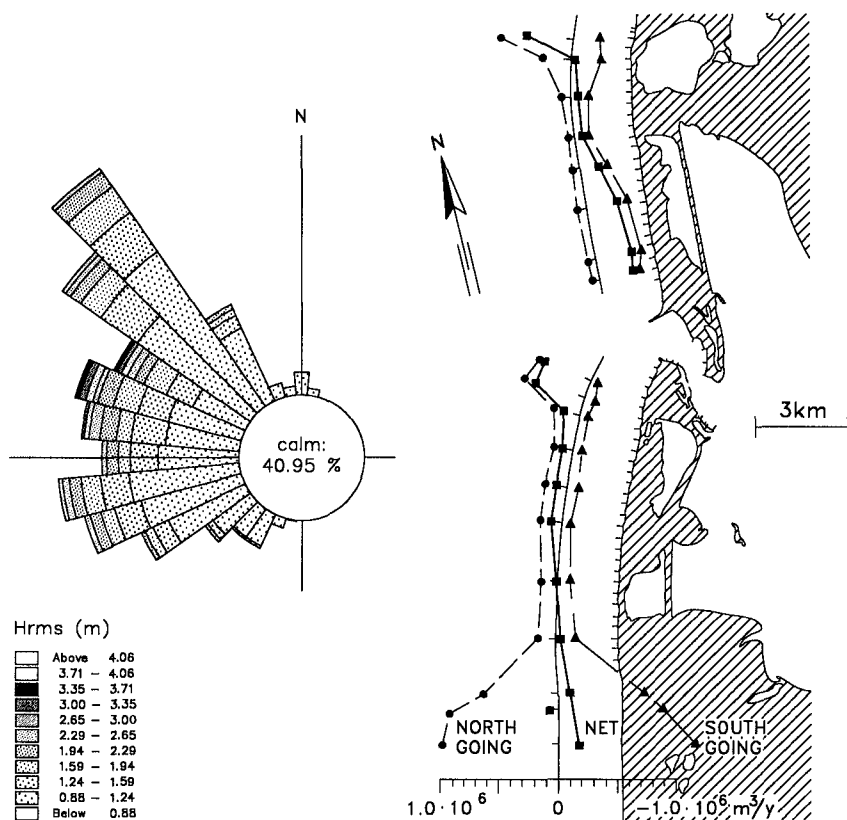


Figure 2 Left: Illustration of wave statistics
 Right: Sediment budget along the barrier beaches

Wave level, wind and directional wave data were available for a three-year period. Two characteristic storms (Storm 1 and Storm 3) were selected for detailed studies of sediment transport and morphological evolution in the area around the inlet. Furthermore, the littoral transport along the barrier islands during each storm was calculated using LITPACK to give an indication of the representativeness of the two storms. The distributions of the littoral drift in the longshore direction and along a selected profile are shown in figure 3. The comparison showed that the storms represented approx. 20 % and 15 % of the southgoing and northgoing yearly transport, respectively. The distribution along the coastal profile is, however, more concentrated over the bars under storm conditions than in average over the year.

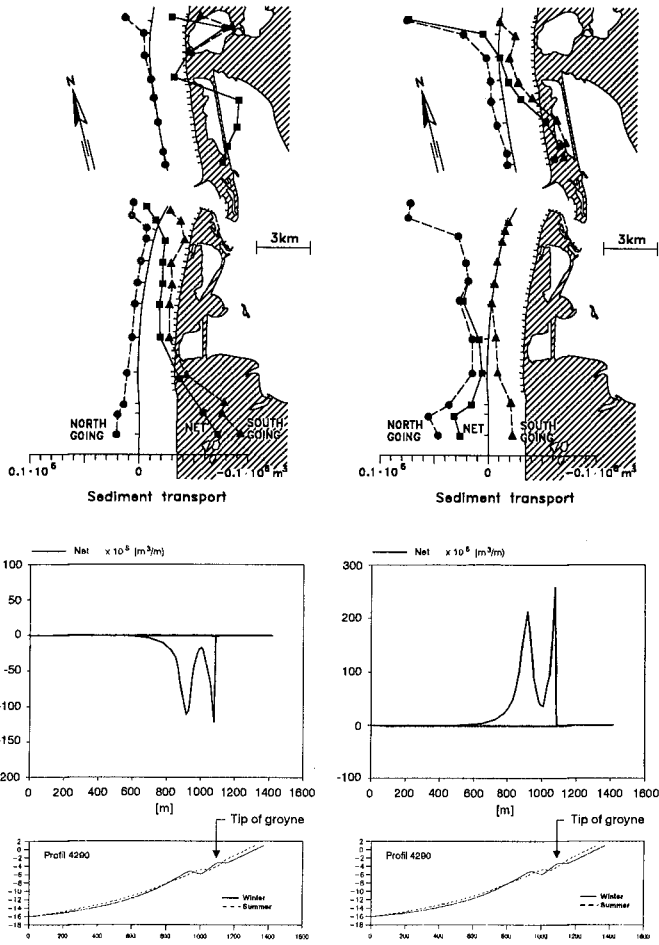


Figure 3 Upper, left: Storm 1, littoral drift along the coasts
 Upper, right: Storm 3, littoral drift along the coasts
 Lower, left: Storm 1, littoral transport along a profile
 Lower, right: Storm 3, littoral transport along a profile

Detailed studies around the inlet

Model setup and boundary conditions for the morphological model

A comprehensive set of models was established in order to transfer measured data into boundary conditions for a morphological model covering the area of interest. The measured data comprised: directional wave measurements at Fjaltring, water levels at Thorsminde, Thyborøn, Aalborg and Hanstholm, wind at Thyborøn and Aalborg, see figure 4. Current speed and direction were measured in the channel during one month for calibration purposes. The model areas and the positions of measurements are indicated in figure 4. It

must be noted that the fluxes across the eastern boundary of the general hydrodynamic model are calculated from a 1D river model, MIKE 11, which covers the entire Limfjord from Thyborøn to Aalborg, see Figure 4.

The general and the regional hydrodynamic models have a resolution of 400 m and 100 m respectively. The model is MIKE 21 HD, which is depth-integrated. In the general model the driving forces are wind and variations in tidal levels and fluxes along the boundaries. The effect of Coriolis force is included.

The regional wave model is a parameterised, spectral wind wave model, MIKE 21 NSW.

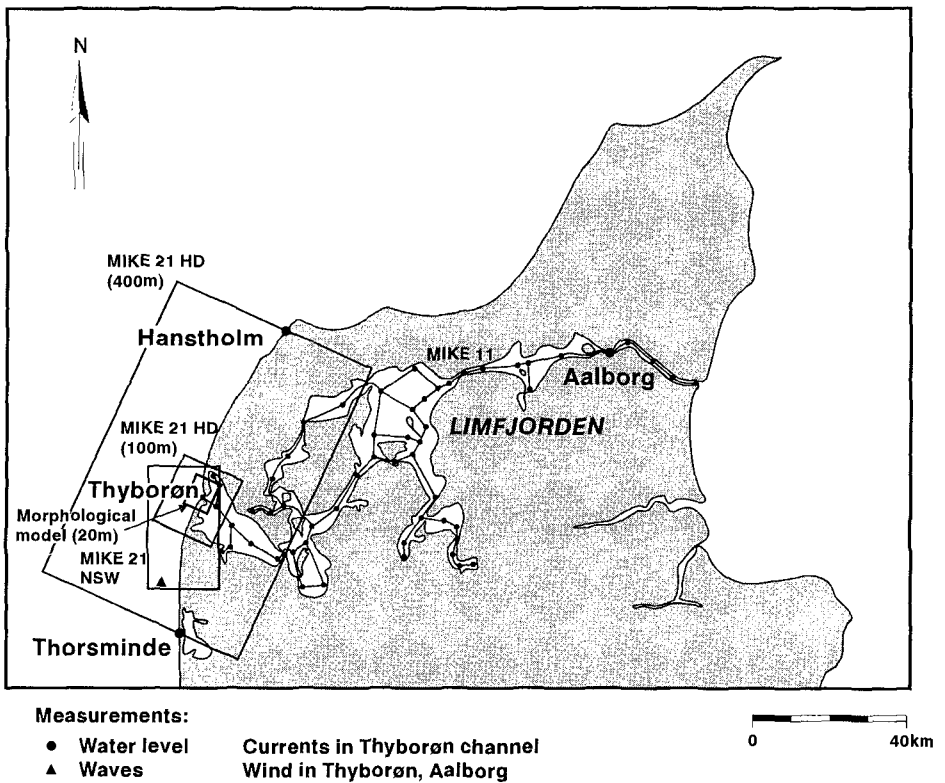


Figure 4 Areas covered by the general and regional hydrodynamic model
 Area covered by the regional wave model
 Area covered by the morphological model
 Locations of measured water levels, wind, waves, currents

The regional models give boundary conditions to the morphological model, see figure 4 for the extent of this model. In the morphological model, wave-, current- and sediment transport modules are coupled as described below. A mild-slope wave model, based on the parabolic approach, was applied in the morphological model complex. Inside the morphological model area, the time- and space-varying radiation stresses were included as an extra forcing term for the hydrodynamic model. The resolution within the morphological model area is 20 m.

Brief description of the morphological modelling complex

DHI's morphological modelling complex is centred around the hydrodynamic model. A morphological simulation is 'warmed up' by calculation of initial wave and current fields on a fixed bed. After the 'warm-up period' the sediment transport field and the corresponding rates of bed level change rates, $\partial z/\partial t$, are calculated. $\partial z/\partial t$ is incorporated in the continuity equation of the hydrodynamic model, and the hydrodynamic simulation proceeds for a period of time corresponding to a so-called 'morphological timestep', which is determined so that the maximum Courant number for the migration of bed forms is less than 1. At the end of this (typically short) period of time the sediment transport field is recalculated using the bathymetry evolved within the morphological timestep. The wave field is recalculated every k'th morphological timestep, where k is an arbitrary integer. (In the present simulation k equals 3). A second-order accurate finite-difference method is used for the calculation of $\partial z/\partial t$ and the truncation errors are eliminated by a modified Lax-Wendroff scheme.

This setup meets the requirements of offering the capability of running with time-varying boundary conditions, and of minimizing the computational effort by avoiding recalculation in the hydrodynamic model. A block flow chart of the morphological model complex is shown in Figure 5.

Three different types of **wave models** are presently built into the morphological complex: an elliptic mild slope model, MIKE 21 EMS, a parabolic mild slope model, MIKE 21 PMS, and a spectral nearshore wind wave model, MIKE 21 NSW. The second one was used in the simulations described here.

The **hydrodynamic module** in the morphological modelling complex is MIKE 21 HD, which solves the vertically integrated equations of conservation of mass and momentum in two horizontal dimensions. The hydrodynamic model operates with a space- and time-varying hydraulic roughness, accounting for the apparent bed resistance in combined waves and current. This apparent roughness is updated every morphological time step.

The deterministic intra-wave period model for **transport of non-cohesive sediment**, STP, is applied. The model covers the range from pure current to combined current and waves (breaking or non-breaking), see Deigaard et al (1986). It is a basic assumption in the present model complex that the transport capacity is a function of the local conditions.

The hard-clay layer described in the Introduction section was included in the model as a non-erodible surface over which transport was allowed to take place.

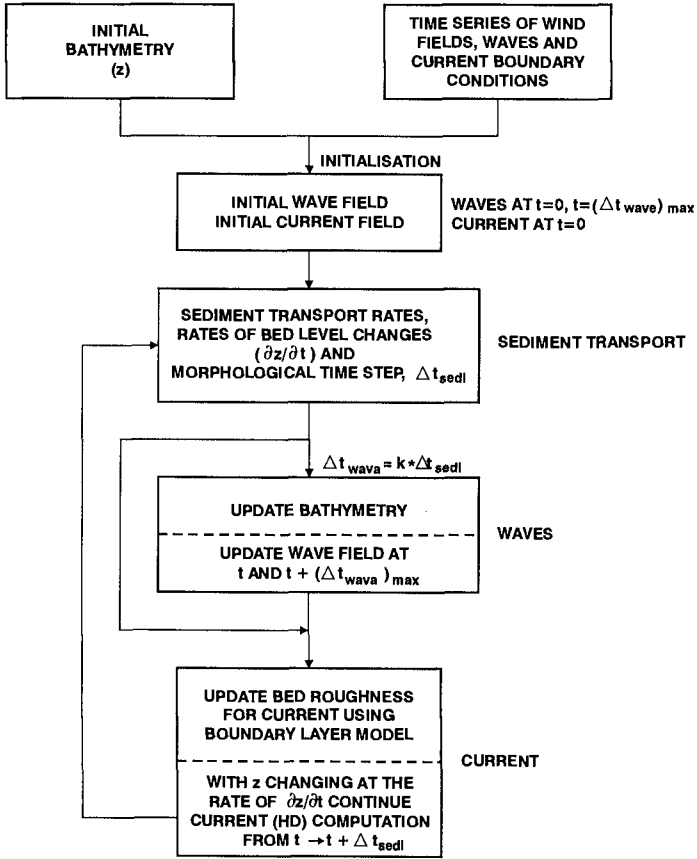


Figure 5 Block flow chart for the morphological modelling complex

Examples of results from the morphological modelling

As mentioned above, two historical storms, each of a duration of 4 days, were modelled in detail. The two storms represented typical storms from the two dominant directions, namely southwest and northwest.

Results from one of the storms, covering the period 20/1/1993 0:00 - 24/1/1993 0:00, are presented in figures 7 and 8. Figure 6 gives a brief overview of some of the important parameters, i.e. water levels at 3 stations, wind speed and direction and wave height and direction. Figure 7 shows wave-, current and sediment transport patterns at the peak of the storm, 22/1/1993 12:00. Figure 8 shows the bed level changes after 1 day, 2 days, 3 days and 4 days. The results show that sediment is 'sucked' out of the cells between the groynes, some of it is deposited off the groyne system in this storm, but most of it, as well as littoral drift which enters the model area, is trapped in the inlet area.

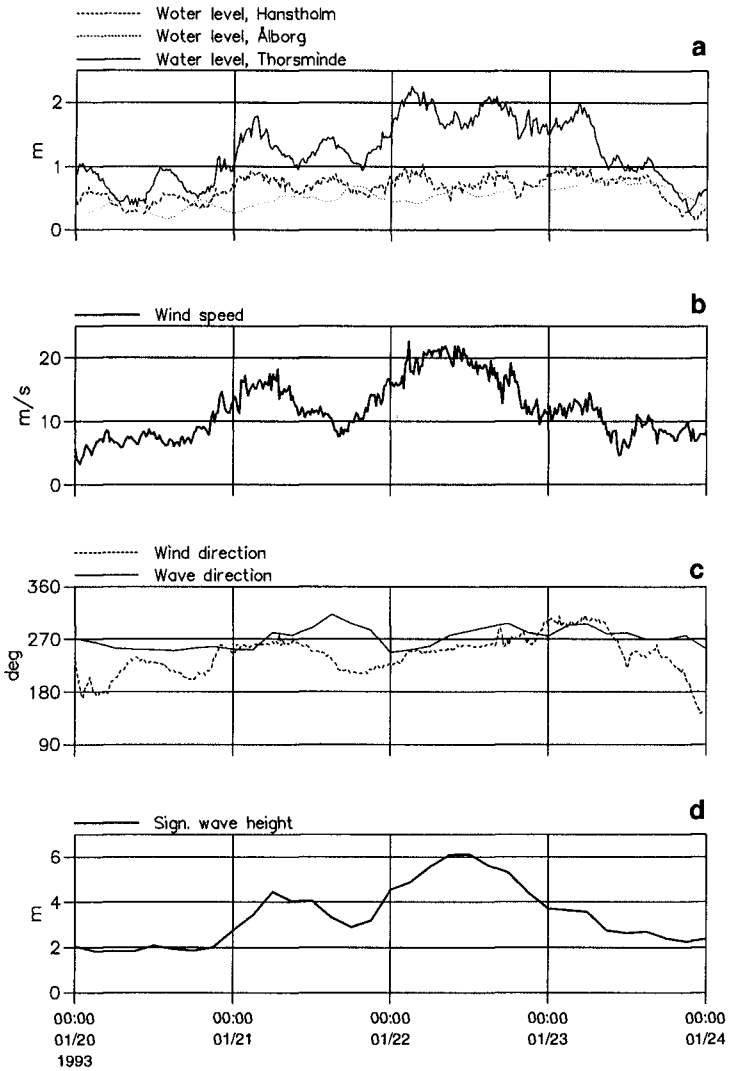


Figure 6 Time series of: a) water levels at Thorsminde, Thyborøn, Hanstholm and Aalborg
 b) wind speed at Thyborøn
 c) wind direction at Thyborøn, wave direction at Fjaltring
 d) wave height at Fjaltring

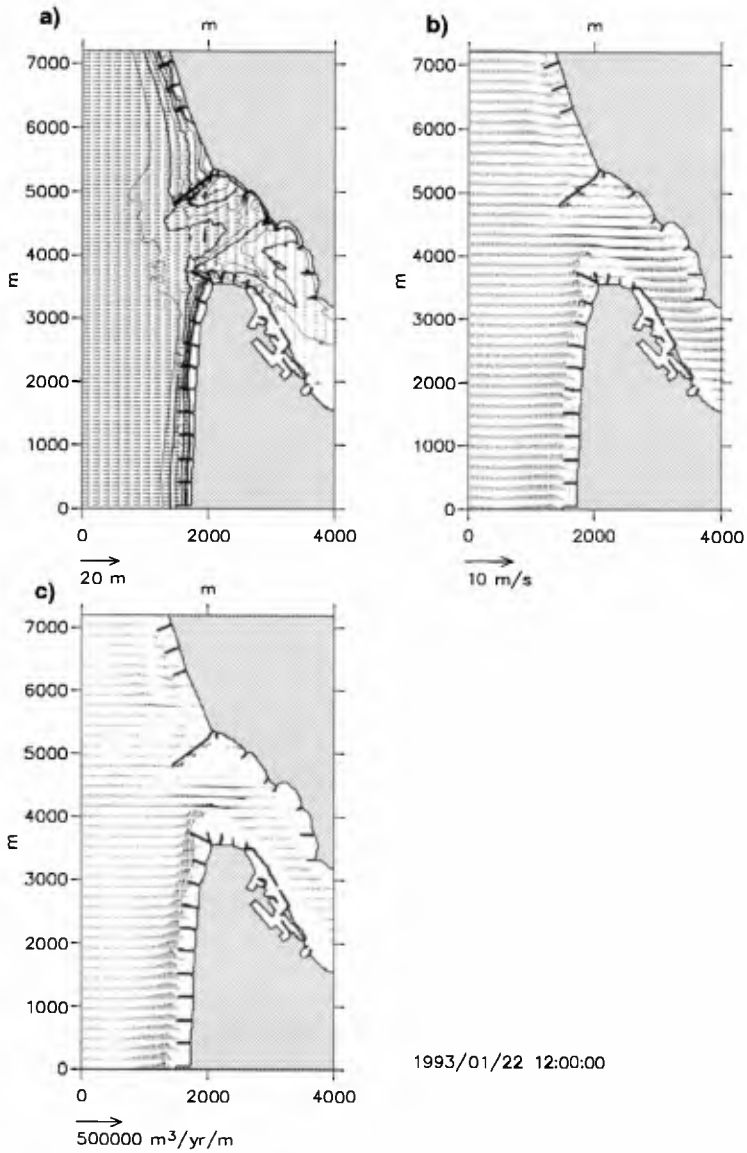


Figure 7 a) Calculated wave field, 22/1 1993 12:00
 b) Calculated flow field, 22/1 1993 12:00
 c) Calculated sediment transport field, 22/1 1993 12:00

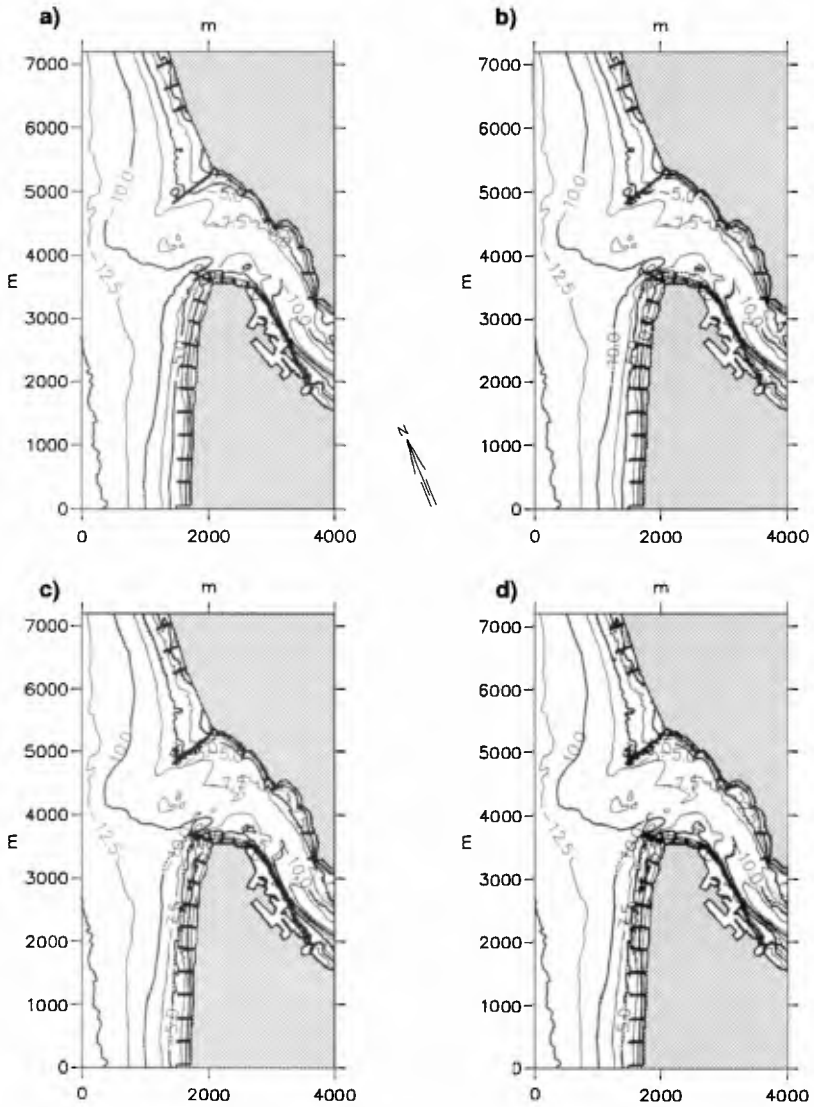


Figure 8 Calculated morphological evolution

- a) From 20/1 1993 0:00 to 21/1 1993 0:00
- b) From 20/1 1993 0:00 to 22/1 1993 0:00
- c) From 20/1 1993 0:00 to 23/1 1993 0:00
- d) From 20/1 1993 0:00 to 24/1 1993 0:00

New understanding of the complicated processes in the area was gained from the modelling work. Examples of details which were learned from the simulations are given below.

One example is the fact that the inlet over the last years has started to erode more severely on the opposite side, (the east side) to that where erosion previously occurred. It was clearly seen from the modelling that storms from southwest were responsible for this development, and over the last years the intensity of these storms has actually increased.

This effect becomes more clear if the model is run without any non-erodible clay layer. Figure 9 shows the comparison of the accumulated bed level changes over 4 days with and without the clay layer. It appears that a potential for erosion at the east side exists. (It should be mentioned that erosion does take place in the clay, just at a much slower pace than for sand. Erosion in the clay is therefore not included in the present model.) One effect of the clay layer on the sediment transport is seen from figure 10, where the accumulated transport across the western limit of Thyborøn channel, defined by the tips of the breakwaters, is compared for Storm 3 with and without the clay layer. It appears that the transport capacity is larger when the clay layer is included than when this is not the case. This is connected to the fact that the transport capacity decreases for increasing depth for constant flux.

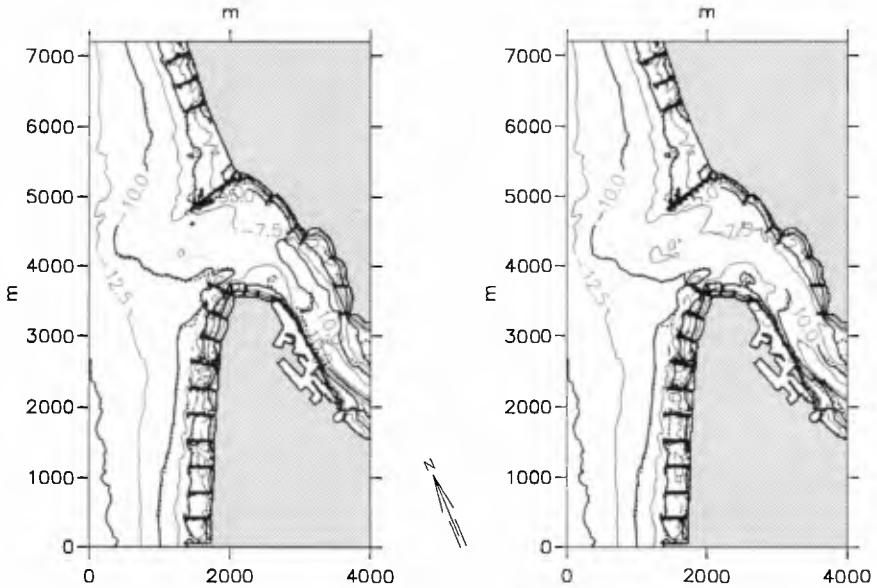


Figure 9 Comparison of accumulated bed level changes over 4 days.
 Left: without clay layer
 Right: with clay layer

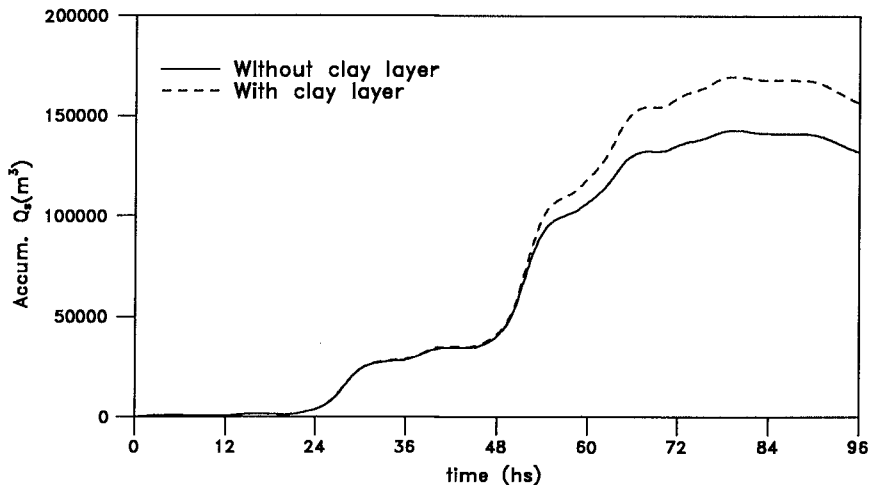


Figure 10 Comparison of sediment transport through the inlet with and without the clay layer

Another example was the observed tendency for more severe wave overtopping along the harbour protection works, which has moved further inside the channel than earlier observed. This could now be explained by the deposition and erosion patterns related to the predominant southwesterly storms which permitted the waves from northwesterly directions to penetrate further into the channel.

Sensitivity to the length of the groynes

The groyne system at Thyborøn was constructed about 100 years ago. Due to the ongoing erosion, the coastal profiles have steepened off the tips of the groynes with the result that the ends of the groynes have collapsed, and rocks from the old structures have been left at the sea bottom. The length of today's groyne system and the way in which its submerged part influences the littoral transport are therefore not known. The effect of the groynes on the morphological evolution has consequently been investigated for the two extremes: the original length of the groynes and today's length, as determined from the overwater part of the groynes.

Figure 11 shows the sediment transport on 22/1/1993 15:00 and the morphological response in the vicinity of some of the groynes in the two cases: original length of the groynes, and present length of the groynes. It appears that the flow and the sediment transport patterns and thereby the morphological response are very different for the two configurations. The example demonstrates the capability of the modelling complex to represent the interaction between the longshore current that is generated within the cells and forms a rip current along the updrift side of each groyne and the eddies generated in the lee of each groyne.

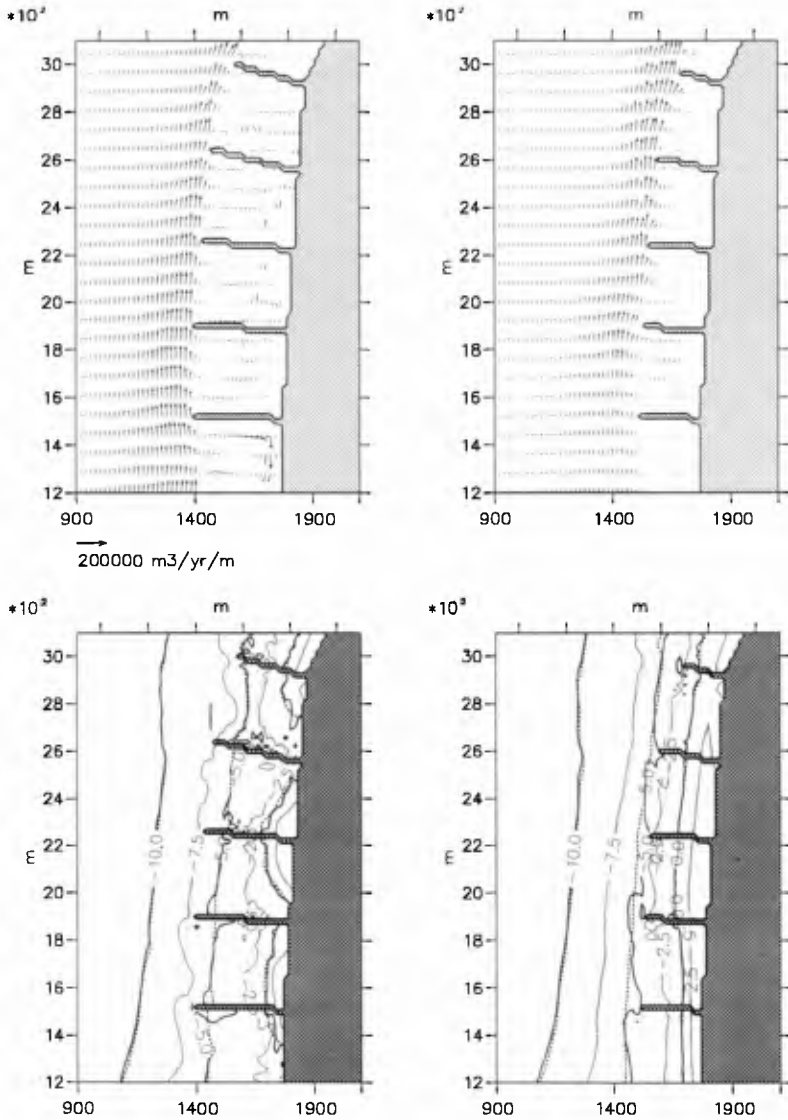


Figure 11 Sediment transport (instantaneous) and morphological response (20/1/1993 0:00 - 22/1/1993 15:00) in a groyne field during a storm. Two different lengths of the groynes are tested

CONCLUSIONS AND FUTURE PROSPECTS OF THE STUDY

Use of mathematical coastal models has cast new light on well-known coastal problems in the area and has allowed to quantify important parameters such as transport rates, spatial distributions of wave heights and current speeds, etc.

The results from the models have been useful in understanding some of the observed processes, cf. changes in erosion patterns in the channel and increased wave overtopping along the harbour structures.

Numerical models have proved to be an important tool for the analysis of different situations such as length of the groynes, existence of a non-erodible surface underlying the sandy bottom, etc.

The work around Thyborøn is still in progress, November 1996.

More historical storms are planned to be modelled. The intention is to simulate a large enough number of different storms to reproduce both the observed sediment transport through the inlet and the development along the barrier beaches through a suitable combination of the storm events. At the present stage, only very scarce information is available on the current statistics in the inlet. A measuring campaign has been planned based on the model results, and this has now been initiated.

The model complex will be used to guide the design of possible coastal protection structures and to evaluate the effect of different nourishment schemes.

REFERENCES

- Bruun, Per (1954): Coast Stability. Atelier Elektra, Copenhagen.
- Danish Hydraulic Institute (1995): Thyborøn Investigations 1995. Simulation of Sediment Transport and Morphological Evolution (in Danish), May 1995 for the Danish Coastal Authority.
- Deigaard, R., Fredsøe, J., Brøker Hedegaard, J. (1986). Suspended Sediment in the Surf Zone, *Journal of the Waterway, Port, Coastal and Ocean Eng.* ASCE, Vol 112, No 1, pp 115-128.
- Johnson, H.K., Brøker, I. and Zyserman, J.A. (1994): Identification of some Relevant Processes in Coastal Morphological Modelling. *Proceedings of the 24th International Conference on Coastal Engineering*, Kobe, Japan, pp. 2871-2885.
- Johnson, H.K., Brøker, I., Zyserman, J.A. and Mangor, K. (1995): Morphological Response in the Vicinity of Offshore Breakwaters. *Proceedings of the IV COPEDEC Conference*, Rio de Janeiro, Brazil.
- Coastal Engineering Laboratory, Technical University of Denmark (1959): Coastal Morphology of the Barrier Beaches of the Limfjord (in Danish). Report No 3 to the Thyborøn Commission of 1957.
- Mikkelsen, Søren, C. (1997): The Effect of Groynes on Beach Erosion and Channel Stability at the Limfjord Barriers, Denmark. To appear in *Coastal Sediments 1997*.
- Sørensen, Torben (1961): The Development of Coastal Profiles on a Receding Coast Protected by Groynes. *Proceedings 7th International Conference on Coastal Engineering (ICCE)*, The Hague, Netherlands, pp. 836-846.

CHAPTER 367

Probabilistic Risk Assessment of Beach Erosion at Pevensey Bay in England

Ping Dong¹ and Keith J Riddell²

Abstract

This paper presents a comprehensive case study in which probabilistic methods were applied to assess the risk of damage to properties protected by a shingle beach on the south coast of England. Both the short term storm response and longer-term longshore drift effects were considered. The mathematical model was calibrated against data from an extensive series of physical model tests and was used to predict the shoreline evolution for a number of beach management design options. A full cost-benefit analysis was carried out based on the predicted damage probabilities. The general methodology developed is believed to be applicable to other situations with different beach material types and various design options.

Introduction

In recent years, the limitations of a conventional semi-probabilistic approach in coastline studies and scheme development have become more widely recognised. In studying beach processes, hydraulic parameters such as extreme waves, tides and surges are usually specified in terms of single parameter return periods or joint return periods. The safety of the structure, or the level of protection it provides, is ensured by selecting design conditions (generally waves and water levels) which, individually and/or in combination, have a sufficiently remote chance of occurring. No explicit reliability calculations are undertaken and the precise level of damages over the design life, due to overtopping, breaching and erosion, is unknown. Consequently, the standard of protection that coastal defence schemes may be expected to achieve

¹ Formerly Principal Engineer, Babbie Group Ltd, now Lecturer, Department of Civil Engineering, University of Dundee, Dundee DD1 4HN, United Kingdom

² Divisional Director, Babbie Group Ltd, Simpson House, 6 Cherry Orchard Road, Croydon, Surrey, CR9 6BE, United Kingdom

can only be given in terms of the return periods of these input parameters rather than the damages which may be expected to occur. The success of such an approach would require that the return period of any damages is not lower than the return periods of the corresponding input parameters, a condition that can not be guaranteed *a priori* in a non-linear multi-parameter dynamic system such as a beach. By comparison with traditional methods, a direct technique which aims at evaluating the probabilities of occurrence of the beach processes that are actually responsible for the flood damages gives more meaningful design conditions. It also enables the evaluation of the variabilities and uncertainties in the damage estimates and provides a rational basis for cost-benefit assessment to be used as an integral part of scheme development.

The probabilistic design concept in coastal engineering is not new. It has been used in the design of breakwaters, seawalls and sand dunes as shown in a recent review on probabilistic design of flood defences by Vrijling (1990). Nearly all of the previous applications were restricted to dealing with the short term response of coastal defence structures under extreme forcing conditions, and the methodology used was largely based upon standard theories and techniques developed for the reliability of structures. Only very recently has some attention been paid to longshore processes. Vrijling and Swart (1992) presented a probability Level II method for berm breakwater design to evaluate the cumulative damage to the breakwater as the result of the longshore transport of rocks under extreme angular wave attack. Both Level II and Level III methods were employed by Vrijling and Meijer (1992) to assess long term shoreline evolution using a one-line shoreline model as the transfer function. Both the practical value of such approaches in engineering assessment and the uncertainties involved were highlighted by these workers.

The advantages of adopting a probabilistic approach and some important practical issues concerning its application in scheme development were presented by Riddell (1993). Probably, due to the lack of quality long term data and the perceived complexity of probability methods, the coastal engineering community are still showing signs of reluctance in adopting such methods in the design of beach management schemes. However, this situation is about to change in the UK with the introduction of new design guidelines from the Government which emphasise the need for rational cost-benefit analysis, the long term sustainability of engineering works and the need for all coastal works to be carefully evaluated in the light of global considerations.

The paper presents a comprehensive case study in which a probabilistic methodology was applied to assess the risk of damage to properties protected by a shingle beach on the south coast of England. Both the short term storm response and longer-term longshore drift effects were considered. The mathematical model was calibrated against data from an extensive series of physical model tests and was used to predict the shoreline evolution for a number of beach management design options. A full cost-benefit analysis was carried out based on the predicted damage

probabilities. The general methodology developed is believed to be applicable to other situations with different beach material types and various design options.

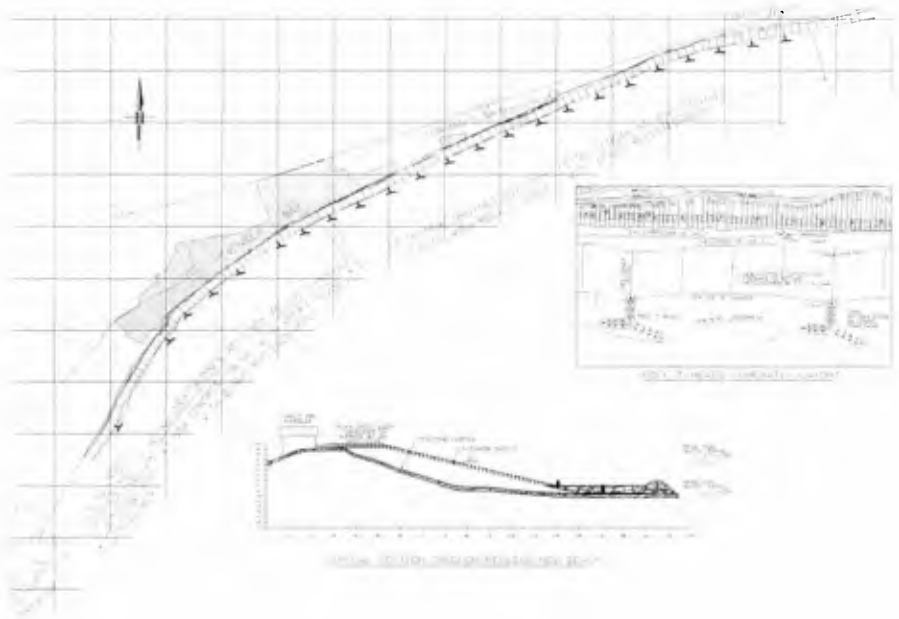


Figure 1 - Site Plan of Pevensey Bay

Site characteristics and design objectives

Pevensey Bay (Figure 1) has a shoreline 9km in length curving from a north/south alignment to east/west in a fairly classical bay configuration. Its beach is formed by shingle material above the mean water level grading rapidly to sand below this point. The shingle ridges, which are generally low and narrow, stand as a fragile



Figure 2

line of defence to the moderately well-developed low lying areas immediately behind the beach crest. Along several sections of the frontage, the beach has suffered from severe depletion of the mobile material and a large part of the existing timber groyne system has also been badly damaged, being, effectively, near the end of its useful life. Over the last twenty years extreme storms, combined with high tides, have, on a number of occasions, resulted in overtopping, beach crest recession and even small-scale breaching. These events have brought about considerable damages, not least of which were the costs of mobilising emergency services and carrying out rehabilitation measures to ensure some continued standard of protection. This situation can be best illustrated by an aerial view and a land-based photograph (Figure 2) of one of many critical locations showing the close proximity of housing to the crest of the shingle beach.

The threat of much larger breaching of the defences in the near future led the former National Rivers Authority (now part of the Environment Agency) to engage Babbie Group to carry out a comprehensive study of the Pevensy frontage lasting for a period of well over four years (1991-1995). During the first phase of this project, extensive data (both contemporary and historic) were collected and analysed with regard to waves, currents, sediment characteristics, beach profiles and past damages. Deterministic mathematical models were used to predict the beach response during extreme storm attack and the long term shoreline evolution over many years of average wave climate. These field data and predictions were used in an approximate cost-benefit analysis and for the preliminary design of a range of management options. During the second phase of the project, a detailed assessment of a limited number of potential scheme options was carried out, involving an extensive physical modelling programme and numerical model predictions.

Having realised the deficiencies of the deterministic methods that were used in the first phase, the decision was made to apply probabilistic techniques for both beach recession predictions and cost-benefit analysis. In this paper some of the work carried out in the second phase of the project is presented, with special emphasis on the use and validation of the probabilistic methods for beach recession predictions and cost-benefit analysis.

Methodology

General approach

The study methodology identified storm beach response as the primary process to be assessed in order to determine the type and severity of erosion, breach and levels of flooding. The probabilistic approach used for crest recession and overtopping was a simplified version of a full Level III approach with the erosion due to long-term longshore drift gradient being treated as an independent addition to the short-term crest recession.

Extensive physical model tests were carried out in the random wave flume and wave basin at HR Wallingford. The purpose of these tests was to assess the beach response under selected design storm waves and average morphological conditions over a period of 5 years. For the flume tests, 9 conditions were tested having estimated joint wave and water level return periods ranging from 1 in 1 year to 1 in 250 years. These tests were carried out on three profiles and two different gradings of beach material. Beach profile development for each test condition was recorded and used to calibrate a mathematical model. In the basin tests, one morphological condition and three (two for some cases) storm conditions were used. The full wave climate was represented by four equivalent wave spectra with increasing energy but decreasing probability of occurrence. The water levels were controlled to follow a predetermined tidal cycle. The data from the physical model tests were used to adjust the predictions made by the mathematical models. The return periods of overtopping and crest recession were calculated using a twenty year hindcast joint wave and water level time series, both including and excluding an allowance for long term sea level rise.

From wave refraction analysis and inshore monitoring results, it was found that the inshore wave climate exhibits considerable change from one end of the frontage to the other. In order to account for this variation, the use of different design wave conditions at different sections of frontage, for the purpose of cross-shore process analysis, was necessary. Due to these longshore changes of wave climate, as well as the change in shoreline orientation, large gradients in littoral drift exist at a number of sections of the shoreline. The effect of this was confirmed by observations that these beaches were known to be prone to erosion and required continuous maintenance. Therefore, longshore structural erosion was included in the overall risk analysis.

In developing design options, the probability of various levels of damage was determined for each beach management scenario, and these probabilities were then used to carry out a comprehensive cost-benefit analysis. This methodology is summarised in Box 1.

Transfer functions

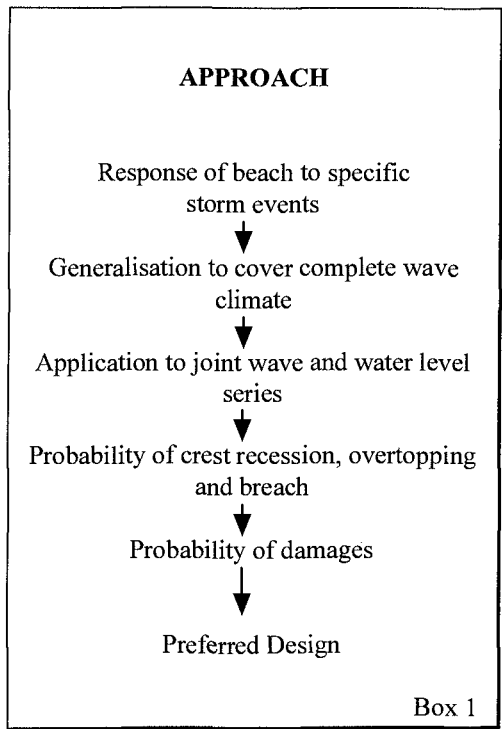
A key element in the design methodology is the transfer function which determines the response of the system for a given set of input parameters. In coastal engineering, the transfer functions are usually in the form of empirical equations or models or process-based mathematical models. Deterministic beach profile responses during storms have been parameterised by Dean (1972), Van der Meer (1991) and Powell (1991). Among these models the **Beach Profile Prediction Model** by Powell was developed specifically for shingle beaches based on extensive physical model tests and validated against a certain amount of (mainly UK) field data. This was therefore selected for the present work.

In order to limit the number of random variables that have to be considered, the model parameters were treated as deterministic and adjustable to give the best fit to the site specific data from the flume tests. In the case of Pevensey Bay such adjustments were required for only one of the three profiles considered. This was largely due to the influence of the limited thickness of the shingle layer at the location of this profile. It should be pointed out that the relationship as described by the BPPM model, between the equilibrium profile shapes and the input wave and water-level parameters, is highly non-linear and dependent upon the characteristics of the initial profile. Therefore, the predicted probability distribution of crest recession for different profiles could be quite different not just in terms of numeric values but also in the shape of the overall distribution.

Input Data

The input data can be classified into two main types: hydraulic data and morphological data. The hydraulic data consisted of a twenty year inshore joint wave and high water level time series, obtained by transferring a hindcast offshore time series to a number of inshore locations using a spectral back-tracking model (OUTRAY by HR Wallingford). The hindcasting model was calibrated against one year of offshore directional wave data obtained at the site during the study period. The refraction model was calibrated against simultaneous inshore records obtained at two locations.

The morphological data consists of surveyed beach profiles, sediment sizes and shoreline positions. Cross-sections at 150m intervals of this and adjacent frontages had been taken annually for a period of twenty years and were used for the detailed assessment of recent shoreline evolution and sediment budget considerations. For simplicity of modelling, the morphological inputs were treated as deterministic. The appropriate mean values and variations for these morphological input data were derived using historical charts and the long term beach survey data.



Prediction procedures

When considering cross-shore processes, it is important to preserve the essential correlation in the wave and water time series. This rules out a probability Level II method which assumes the parameters to be independent and to follow Gaussian distributions. All the wave and water level records in the time series, apart from some small waves deemed to be insignificant, were directly input into the calibrated BPPM model to obtain a single time series for the beach crest movement. The predicted beach movements were then ranked and fitted with appropriate logarithmic distributions. The same calculations were performed for each of the three profiles, taken as being representative of sections of frontage, using the appropriate time series for different inshore points.

Longshore processes are more difficult to deal with, because they essentially have two time scales; one for long-term average movements of sediment and the other for short-term storm effects. Although the techniques of Vrijling and Swart (1992) could, at least in principle, be adopted for predicting the probability of long term average shoreline changes, difficulties arise when trying to combine the two sets of recession probabilities from cross-shore and alongshore calculations. The short-term effects due to oblique storm waves on the coastline development would also need to be determined separately.

Short of using a 3D or quasi-3D model as a transfer function, further assumptions on the potential correlation between short- and long-term processes and between cross-shore and longshore effects have to be made. Due to the lack of research concerning the above problems, longshore processes were treated as deterministic. As a result, the crest recession probabilities would be invariant although the reference shoreline position would change with time as predicted by a one-line model. The corrections to the reference shoreline position were introduced in the design assessment based on the basin test results.

Predictions of crest recession

Model calibration

In order to ensure that the transfer function used was reliable the numerical model (BPPM) was firstly calibrated against the crest recession data from the flume tests. It was found that the model predictions agreed well with the measurements from Profiles 2 and 3 but some adjustment was necessary for Profile 1 in order to achieve best overall fit. Similarly the one-line model predictions were also compared with the actual shoreline positions determined from the annual surveys for the same data period (20 years). To achieve best agreement, it was found that the transport parameter in the CERC formula 'K' should be about 0.04 assuming the existing groynes are virtually ineffective.

Cross-shore beach crest recession

Assuming that an equilibrium beach profile can be established over the period of one tidal cycle, under given wave and water level conditions, the time series of crest recession and overtopping rates can be calculated for a given beach configuration. The exceedance probability and the return periods of crest recession can then be determined using ranking statistics. Some of the results are shown in Figures 3 and 4. It can be seen that the active crest tends to establish seaward of the initial crest for most wave conditions during the twenty year record period whilst

crest retreat takes place during only a small number of severe events. In order to determine the extreme crest recession, a logarithmic curve was fitted to the computational data. The crest recessions for the more extreme events such as 1 in 250 year, can be obtained by extrapolation of the fitted recession curves.

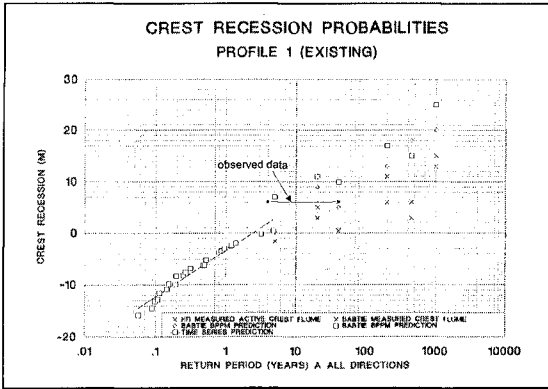


Figure 3

the joint probability density of wave and water level and then calculating the overtopping and crest recession for the extended records. This is due to the fact that the joint probability density function is very irregular at small values, and it is difficult to find a sensible surface to fit to these values. Whatever probability distributions is assumed, large errors are unavoidable in extrapolation.

In general, the accuracy of the simpler method has been shown to depend on the data length, regularity of crest movement and the transfer functions adopted. From the model tests it was found that the

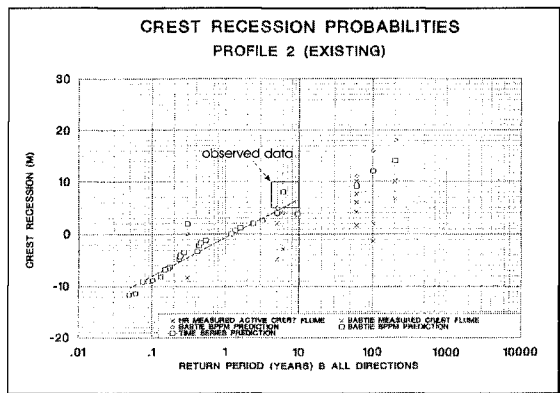


Figure 4

beach can be 'washed off' by overtopping when its crest is very thin. This means that extrapolation of the predicted recession probability can not be extended indefinitely because the crest movement can change from progressive erosion to wash-out with only a very small change of input hydraulic conditions. A minimum crest width has been assumed on the basis of the model tests which represents this change of mode of beach damage. A 250 year return period was determined to be the upper cut-off limit for the extrapolation of beach processes at the study frontage.

Figures 3 and 4 also show the observed recession ranges during previous observed storms. Although the data are rather limited, and the quality of these data is far from ideal, it was quite satisfying to note that the predictions were consistent with the field data on all three profiles. Since the numerical model was only calibrated against data from the physical model, and for only a limited number of extreme storm conditions, the predictions obtained are considered to be remarkably good.

Effects Of Long Term Shoreline Evolution

Although the storm response of the beach is dominant in the determination of the level of risk at any particular point in time, the long-term shoreline evolution trend must be taken into account if the true risk level of a particular section of the

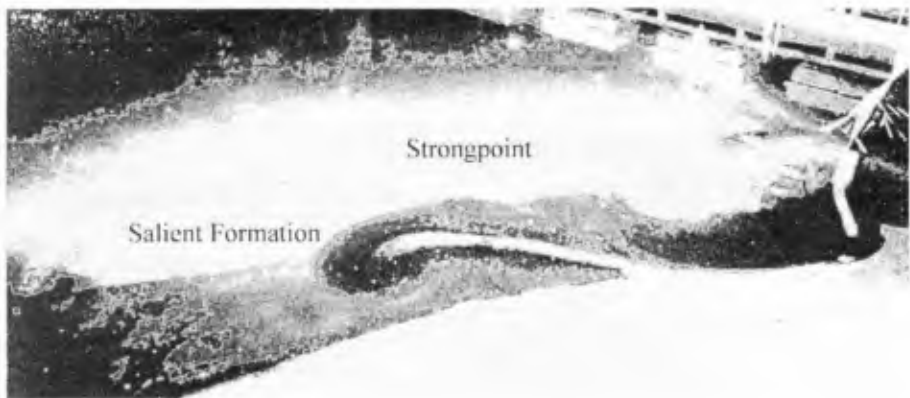


Figure 5, Strongpoint Basin Test in Progress

coastline, over a significant length of time, is to be established. For an open beach, the long term erosion due to the longshore transport gradient is usually fairly regular at a given site, depending, primarily, on the average wave climate, the supply of material and local shoreline orientation. The mean erosion rates for the Pevensey Bay frontage were calculated using a standard one-line model. In order to account for variability in the predictions of wave climate and sediment supply, the average shoreline position was determined for 5, 10, 20 and 50 year periods. The storm wave

response probability was assumed to be invariant at any time within the design life of the defence. Although it is possible to introduce a higher level of probabilistic representation for the shoreline position than that used, such an approach was rejected on the grounds that the transfer function would have become too complicated to be practicable and no suitable method was found which was capable of dealing with the correlation between longshore and cross-shore processes in a consistent and robust way.

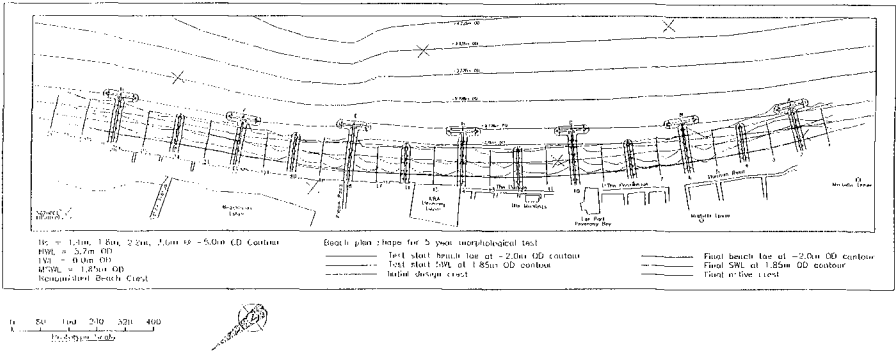


Figure 6 - Basin Test Results for mixed Rock T-head and Groyne Scheme

In developing the scheme options a number of beach management scenarios, ranging from timber groynes to large shore-attached rock structures, were tested in the wave basin. The crest movements under morphological and extreme storm conditions were obtained. Using similar techniques as described for the open beach case, the crest recession probabilities for each of the beach management options were estimated, taking into account the effects of the longshore gradient of drift rates during storm events. An example of a test in progress is shown in Figure 5 and an example of scheme test results in Figure 6. A comparison of the effect of different

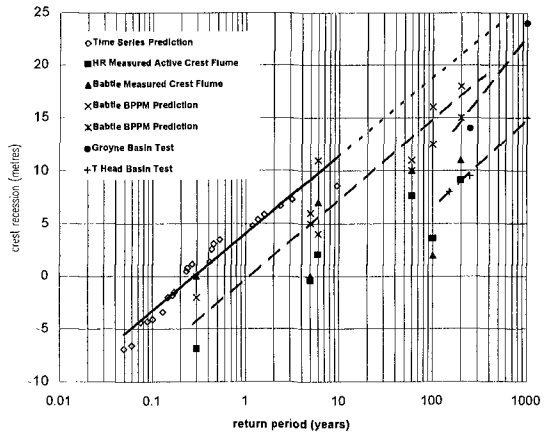


Figure 7 - Crest Recessions for various schemes

management options on the probability distribution of crest recession is shown in Figure 7.

Cost Benefit Analysis

The ultimate aim of all the preceding analyses is to generate damage probability graphs for all kinds of damage/loss considered. A typical graph for an open beach 'do-nothing' option is shown in Figure 8. In developing various design options, losses due to erosion, overtopping and breaching were all included wherever appropriate. The damage cost was assessed for each year during a nominal 50 year design life using appropriate discount factors. Since the total loss for any area is not always the simple sum of all probable losses, depending on the physical characteristics and economic values of the shoreline and hinterlands, and the interaction between them, care must be taken in deriving the total losses/damages.

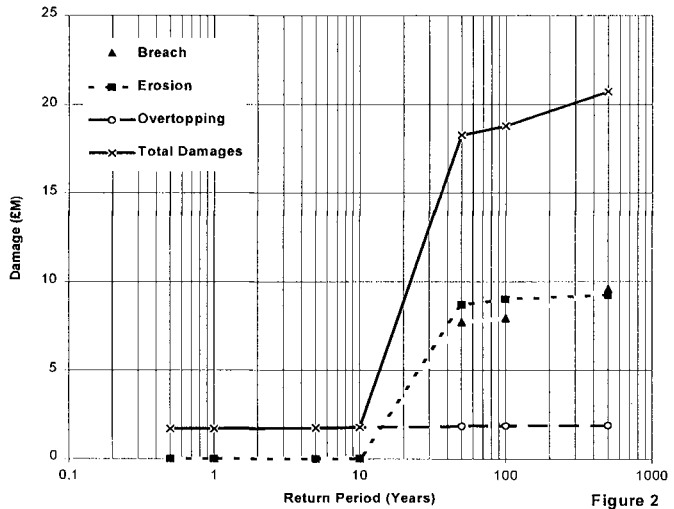


Figure 8 - Damage / Probability Profile

Discussion And Conclusions

A probabilistic design methodology has been developed which can be applied to shoreline studies, scheme design and the selection of management options. It provides a rational basis for the assessment of flooding risk and the standard of protection.

As long as the joint time series of wave and water level can be made available, it is straightforward to calculate the probability of run-up, overtopping and breaching using either empirical formulae or mathematical models. Physical modelling significant confidence to the results of the above and is essential for the consideration of non-standard situations.

Beach response is not just dependent on waves and water levels. Many other parameters are important such as the initial beach profile, material variability and storm duration and sequencing. A true probabilistic design methodology needs to take into account all of these parameters on a physical basis including systematic sensitivity assessments.

The transfer functions which provide the link between hydraulic parameters and beach processes are dependent on the configuration of the beach and detailed material properties. Great care must be taken when applying a transfer function developed for one type of beach condition to another.

Based on this study the following conclusions can be drawn

1. Predicted erosion probabilities are consistent with experimental data and some limited field observations.
2. The probabilistic method is no more difficult to apply than a conventional method, although it does require more long-term data and is therefore more time consuming.
3. Predictions are site dependent and sensitive to changes in the parameters characterising the beach and within the numerical model transfer function.
4. The damage modes treated in this study were limited and many other damage modes such as scouring, abrasion and offshore loss of beach material could be important at other beaches. Hence, design decisions made at one site should not be transferred to another site despite apparently similar features.
5. It has been found to be virtually impossible to deal with both long term and short term processes using the same high level of probabilistic techniques and within the prediction framework adopted. Research in this area is urgently required.

References

CIRIA, 1995 Beach Management Manual.

HR Wallingford, 1995, Langney Point to Cooden Sea Defences-Physical Model Studies,

HR Wallingford, 1995, Report No. EX3241.

Riddell, K.J., 1993, Probabilistic Methods in Scheme Development, Proceedings of MAFF River and Coastal Engineering Conference.

Vrijling, J.K. and G.J. Meijer, 1992, Probabilistic coastline position computations, Coastal Engineering, 17, pp. 1-23.

Vrijling, J.K. and P.F. de Swart, 1992, Berm breakwater design - the longshore transport case: a probabilistic approach, Coastal Structures and Breakwaters, Thomas Telford, London, pp. 513-525.

Vrijling, J.K., 1990, Probabilistic Design of Flood Defences, in Coastal Protection (ed. K.W Pilarczyk), Publisher: AA Balkema 1990.

CHAPTER 368

BEACH NOURISHMENT IN ALTAFULLA, SPAIN: VERIFICATION OF THEORETICAL MODELS

J. Galofré¹, F. J. Montoya² and R. Medina³

ABSTRACT

This paper describes the comparison between results from theoretical methods and field data measurements on a beach nourishment project, in Altafulla beach, Spain. A brief review of the processes involved in the behaviour of beach nourishment projects are made in order to analyse beach evolution after filling it. Theoretical results can be obtained applying theoretical methods. A monitoring program was carried out after nourishment works and field data measurements were taken in order to verify theoretical models. Capability, application and validity of models to the prediction of a project performance are discussed comparing with field data results.

The conclusion of the comparison is made for the Altafulla case study and a discussion of the results is included in order to understand beach evolution method by field data results.

1.- INTRODUCTION

Beach nourishment works, as an integrated coastal zone management plan, are used as a coastal engineering tool in order to guarantee the functions of a beach. The most important functions of a beach are: - Energy dissipation mechanism and Useful free space for every one.

Theoretical, technical-empirical and numerical methods are needed in order to design the solution and optimize nourishment efficiency. They must be calibrated in order to know the right beach parameters and analyze their behaviour.

-
- 1) Coastal Civil Engineer. Tarragona Coastal Service. Environment Ministry. Pl.Imperial Tarraco 4-4^a. 43005 Tarragona, Spain.
 - 2) Coastal Civil Engineer. Head of Tarragona Coastal Service. Environment Ministry. Pl. Imperial Tarraco 4-4^a. 43005 Tarragona, Spain.
 - 3) Associated professor. Ocean & Coastal Research Group. Universidad de Cantabria. Avda. de los Castros s/n. Santander 39005. Spain.

Analysis of beach behaviour has received considerable attention during the last decades. Although the sediment processes involved in the changes of a beach are non linear and have great variability both in space and time, the comparative analysis of beach evolution with theoretical models and field data is necessary in order to know how powerful the predictive models are. These models can be used to assist in the determination of project design and/or beach evolution. Furthermore, models describing the response of beaches to different coastal forcings have become increasingly numerous and sophisticated in recent years (see Work and Dean 1995, as a general reference). At present, however, there is no model that can be used to solve all the spatial and temporal scales of variability involved in beach nourishment evolution and, consequently, different models must be used. Monitoring field data are needed in order to calibrate and verify the models. It is necessary to know how well every model works and when it can be used.

The goal of this paper is to analyse the theoretical and real behaviour of Altafulla beach, comparing monitoring field data to technical-empirical and numerical model results. Various types of models are used, they are classified by their spatial and temporal domains of applicability.

2.- ANALYSIS METHOD

The analysis of processes, scales and tools is necessary in order to advance the knowledge of beach behaviour.

In order to understand beach performance it is necessary to analyse the beach forcings that are acting on the beach, these are the cause of all the processes.

The beach responses are the consequence of the beach forcings, they are the phenomena that appear along the coast. Beach behaviour analysis implies many methods working with the forcings and responses give a comprehension of beach performance.

Erosion, accretion and beach change in offshore bottom topography are controlled by beach forcings described in table 1. They are divided into three time scales of variability: Short term (less than 15 days), middle term (15 days to 6 months) and long term (years). The space scale considered is the meso scale that has a range from 100 m to 10 km shoreline. There are others spatial scales like microscale, less than 100 m shoreline, and macroscale, more than 10 km shoreline. This case study involves the mesoscale. The responses of beaches to these perturbations and variable forcings can be found in a wide range of time scales, see table 2.

Besides the wide range of temporal and spatial scales of variability, coastal evolution processes are often three-dimensional. In spite of this, important aspects of the coastal behaviour can be understood and prediction on the bases of lower-

PROCESS - FORCINGS		
SHORT TERM	MIDDLE TERM	LONG TERM
<ul style="list-style-type: none"> • Waves • Tides • Wave currents • Wind • Atmospheric pressure • Sediment budget 	<ul style="list-style-type: none"> • Platform-Currents • Fortnight-Tides • Storms • Sediment budget 	<ul style="list-style-type: none"> • Winter-Summer waves • Platform-Currents • M.S.L. Variation • Sediment budget

TABLE 1 FORCINGS INVOLVED IN BEACHES

RESPONSES		
SMALL SCALE	MESO SCALE	LARGE SCALE
<ul style="list-style-type: none"> • Bed forms: <ul style="list-style-type: none"> • Beach cusps • Bars • Morphological changes • Sediment transportation and distribution 	<ul style="list-style-type: none"> • Profile changes • Planform changes • Shoreline changes • Crescentic bars • Morphodynamic states variation • Sediment distribution 	<ul style="list-style-type: none"> • Coastline accretion-erosion • Beach equilibrium planform • Beach equilibrium profile • Sediment distribution • Eustatic reponse

TABLE 2 RESPONSES INVOLVED BEACHES

MODELS			
	SHORT TERM	MIDDLE TERM	LONG TERM
	SMALL SCALE	MESO SCALE	LARGE SCALE
FORCINGS	<ul style="list-style-type: none"> • Wave propagation • Tide propagation • Wave - currents 	<ul style="list-style-type: none"> • Wave propagation • Tide propagation • Wave - currents 	<ul style="list-style-type: none"> • Wave propagation • Tide propagation • Waves - currents
RESPONSES	<ul style="list-style-type: none"> • Profile models • Local sediment transport 	<ul style="list-style-type: none"> • Profile models • N-Lines models • Sediment transport 	<ul style="list-style-type: none"> • Parametric Models (plan, profile and granulometric) • N-Lines models • Sediment transport • Statistic models

TABLE 3 MODELS USEFULS IN BEACH BEHAVIOUR ANALYSIS

dimensional models. These models take advantage of the circumstance that the response of a beach often exhibits a different behaviour with essentially different length scales in three mutually orthogonal space directions (vertical, cross-shore and longshore), De Vriend, (1992).

The next point is to define the models that it is possible to use for the analysis of the forcings and responses. Table 3 shows a wide range of different models.

To improve predictive models for beach responses, an accurate description of the forcings is necessary. From table 3, it can be seen that existing hydrodynamic models (wave, tide propagation and wave induced currents) can be used for solving the forcings at almost all spatial scales of interest. The choice of a particular model should be made in relation to the response model to be used.

When selecting a response model, several physical facts must be taken into account. Cross-shore transport is very important just after the fill. A nourishment beach reaches its equilibrium profile within the first year after the fill (Kamphuis and Moir 1977). Several existing models can describe the post-fill evolution of the profile (usually neglecting longshore transport). However, cross-shore transport at greater time scales (months to years) remains a challenging problem that has not received a great deal of attention (Work and Dean 1995).

Longshore sediment transport is found to be important near the shoulders of the fill in the beginning. The effects of the longshore gradients propagate afterwards into the nourished region. N-line models can represent these coastline changes in the mid-long term. The one-line approach imposes limitations by neglecting the influence of cross-shore transport. However, this can be overcome if the model is calibrated adequately (Hanson and Kraus 1977). Technical empirical models can be useful in order to know beach equilibrium planform (Hsu et al, 1989) and profile equilibrium form (Dean, 1995). For the long term evolution prediction, parametric models (e.g. equilibrium profile-coast line models) and statistical models (e.g. P.C.A. models) can help N-line models.

The next step is to analyse this wide range of models and select the most interesting in order to know the beach behavior. In beach analysis from input data with the analysis method, must be obtained the output data. In table 4 an analysis model is proposed for it.

The case study will compare the models propounded in table 4 with the field data obtained from the monitoring program.

INPUT DATA			
Historical analysis Maritime climate data Topobaltimetry Granulometric data			

A N A L Y S I S			
	SHORT TERM	MIDDLE TERM	LONG TERM
<i>TECHNICAL- EMPIRICAL METHODS</i>		Morphodynamics state distribution	Shoreline equilibrium model Profile equilibrium model Grain size distribution study Empirical evolution methods
<i>NUMERICAL METHODS</i>	Waves propagation Breaking current system Sediment transport		Numerical evolution shoreline methods (One line) Statistical model (3PCA)

OUTPUT DATA
Beach Evolution Behaviour: - Beach planform - Beach profile form - Grain size

TABLE 4 ANALYSIS METHOD IN BEACH BEHAVIOUR

3.- FIELD SITE AND DATA COLLECTION

The site of the field study is Altafulla (Fig.1), a sandy beach located 10 km north of Tarragona and 80 km south of Barcelona, in Catalonia, on the Mediterranean Coast of Spain. Altafulla is a half-opened beach 2.3 km long located between two capes, "Els Munts" to the east and "Tamarit" to the west. A small river flows during storms in the middle of the beach.

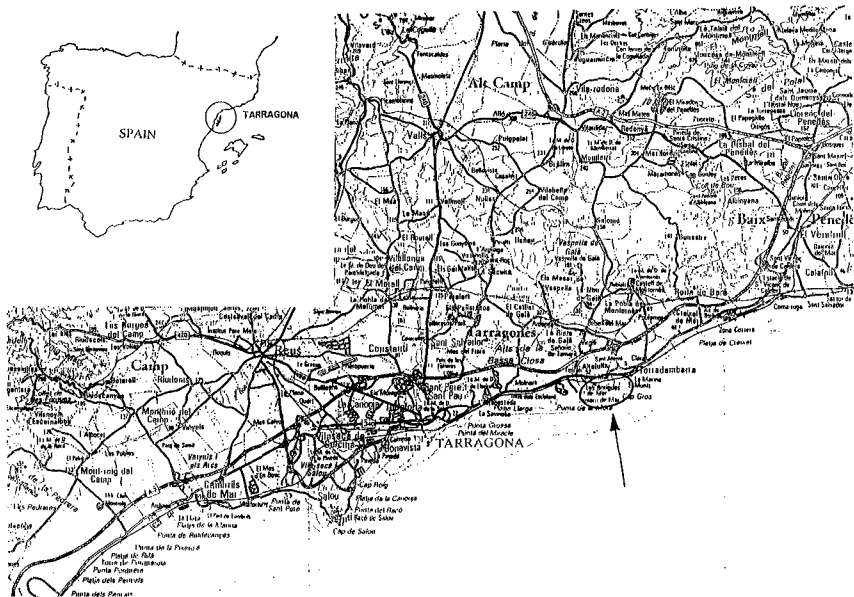


FIGURE 1 SITE LOCATION MAP

There are two predominant directions of wave approach: SW and E. More than three quarters of deep water waves approach Altafulla from those sectors. The annual average significant wave height is about 0.5 m with typical winter storm waves of H_s of about 3.0 meters. Tides at Altafulla are negligible. In figure 3 a visual wave distribution is made and the affected area is shown, sea and swell limits are defined.

The native beach sand had a mean diameter between $D_{50} = 0.12$ to 0.2 mm and the beach profile slope changed from 1.2 % to 2.0 % from shoreline to bathymetric -5 meters. This value contour is considered the profile closure depth at Altafulla. The bottom of the sea is sandy up to the 10 m bathymetric contour line.

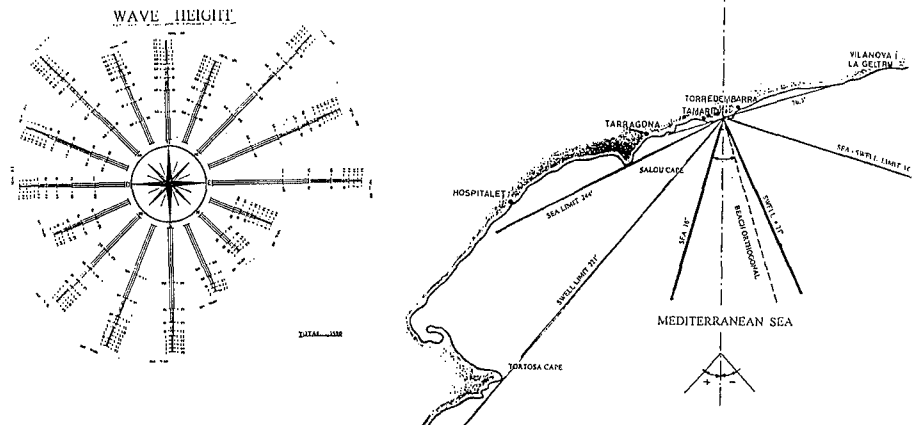


FIGURE 2) WAVE CLIMATE. SEA AND SWELL LIMITS

4.- BEACH NOURISHMENT AND MONITORING PROGRAM

In figure 3, a bathymetric map is shown in order to present beach problems and their solution.

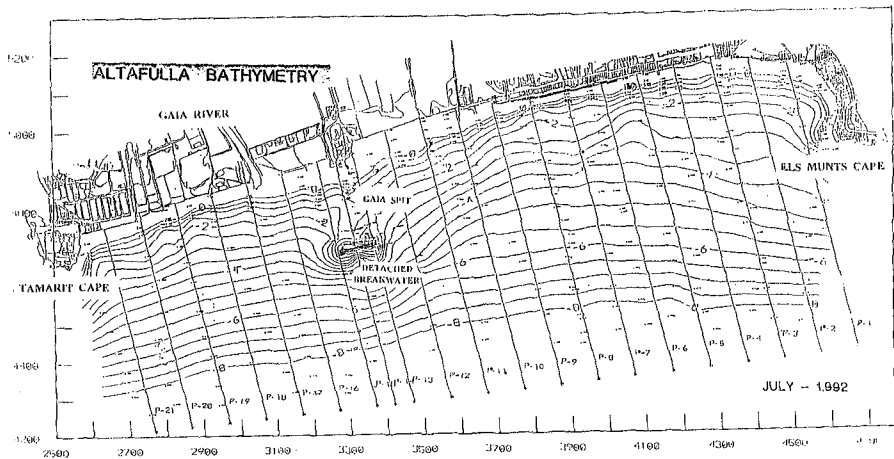


FIGURE 3 MORPHOLOGICAL AND BATHYMETRIC MAP

Several erosion problems occurred in the northern part of the beach. A seawall was built to prevent backshore building damage. Southward littoral drift reduction of sediment appeared because of the construction of a dam 8 km up to the Gaià river and sand extraction during the 50's and 60's for construction works and filling the surrounding marsh. These have been theorized as major factors in the erosion that has been witnessed in Altafulla. A beach nourishment project was undertaken in 1989. Beach nourishment started in late 1990 and was completed in 1991. The beach nourishment works consisted of 160.000 m³ of borrowed sand volume. The borrowed sand had a median diameter averaging $D_{50} = 0.6$ mm. A detached breakwater was also built in the middle of the beach, see figure 3. The breakwater was 110 m long and was placed at the -5 m bathymetric contour line.

A monitoring project was carried out to evaluate the evolution of the fill. The monitoring program started in July 1991, at the conclusion of the fill, and finished in December 1993, before renourishment works. The field program includes bathymetric beach profile every survey and sediment samples on some surveys. Six profile surveys were taken in this period. Each profile was surveyed from permanent monuments landward to a depth of approximately 10 meters. Sediment samples were taken in the last survey and samples were collected along three profiles simultaneous with beach equilibrium planform and profile survey.

Historical aerial pictures and visual maritime climate data are used with monitoring data in the comparison with the models.

5.- MODEL VERIFICATION

In table 3 a wide range of models which affect forcings and responses have been described. In table 4, a selection of these models have been chosen in order to define the analysis method to study beach nourishment evolution. Beach planform, beach profile form and grain size distribution can be obtained from historical analysis, maritime climate data, topobatymetric and granulometric data using the analysis methods.

The field data are needed in order to validate the models, some data are input, some are used to calibrate the models and others are output data. A planform and profile form are analysed in order to know their equilibrium. Grain size distribution is evaluated.

Qualitative and quantitative verification have been made. Qualitative results have been obtained studying beach dynamics and comparing with aerial pictures and topobatymetrics. Beach dynamics were computed by means of the numerical models.

Computations were carried out for conditions before and after the fill and construction of the detached breakwater. Different wave heights, wave periods and wave approach directions were used applying the REFDIF program, from Kirby and Dalrymple (1983-1986) computed by the parabolic wave propagation model.

Different wave heights were composed, the refraction and diffraction phenomena were combined. By analysing aerial pictures, the protected areas behaviour, predicted by the models, can be observed. Figure 4 shows the wave induced currents determined from the wave field, as shown in the last figure. It can be seen that the breaking waves currents direction, induced by different wave height, change near the capes and the breakwater by diffracting phenomena. Aerial pictures

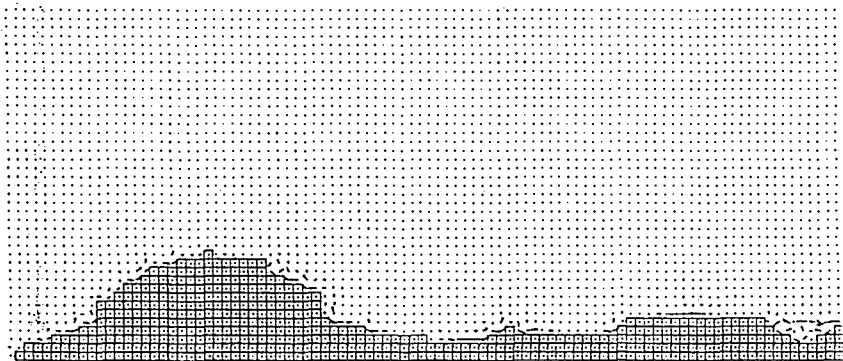


FIGURE 4.a) WAVE INDICED CURRENTS $H=0.5$ m; $\alpha = +45^\circ$; $T = 10$ s.

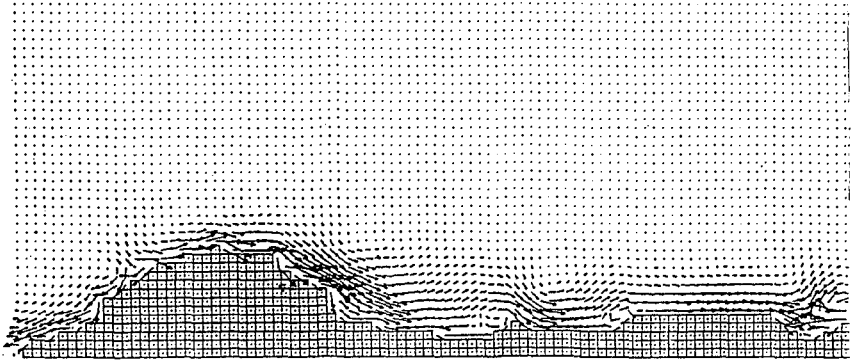


FIGURE 4.b) WAVE INDUCED CURRENTS $H = 3.0$ m; $\alpha = +45^\circ$; $T = 10$ s.

confirm these results showing sand accumulation in the calm areas. The spit formation landward of the breakwater can be explained with these results as is shown in the monitoring bathymetry.

Quantitative verification can be made in order to analyse beach behaviour. Beach profile, planform and prediction methods are verified.

Beach field data profiles were compared with theoretical profiles before and after nourishment works. The Dean profile was used and compared with field data. The beach profile before nourishment can be approached by $y = A \cdot X^{2/3}$, with the corresponding A according with $D_{50} = 0.16$ mm., the average of D_{50} in the native beach. After nourishment the beach profile can be approached by the same formula with A corresponding with $D_{50} = 0.35$ mm., the average of D_{50} in the nourished beach in the last topobathymetry field data.

Closure depth profile is calculated by the Birkermeier formula and compared with monitoring field data. Bathymetric -5 m. contour is considered the closure depth at Altafulla. This value was determined from the monitoring profiles and by technical-empirical model.

Planform was analysed by technical-empirical and numerical models and the results have been compared with monitoring field data results. The technical-empirical Hsu and Silvester method was used for analysing planform on the east part of the beach. Figure 5 shows the results with a great similarity with theoretical and field data results. The spit formed landward of the detached breakwater built in the middle of the beach is analysed using the method proposed by Gonzalez (1995), to calculate spits and tombolos. Figure 6 shows the application of this method and the conclusion is compared with the results of the monitoring field data results.

Numerical models can be used in order to understand beach performance and beach evolution. The basic procedures followed in this case study to analyse the beach nourishment evolution were the one-line model and statistical model. Field data are needed in order to calibrate and verify the one-line model and as input data for statistical models that can show theoretical tendencies from field data.

The one-line model used was GENESIS, (Hanson and Krauss, 1991). The model was calibrated with the profile evolution data following the procedure by Hanson and Krauss (1989). The climate waves were taken from visual data and calibrated from Tarragona harbour buoy data. Figure 7 shows the results of the shoreline position obtained from the model. The field data used for the calibration was 92 - 02 - 28 to 93 - 10 - 17.

The one-line model is a powerful tool that must be used carefully. To model the reality means to simplify the problem in order to reach some logical results that represent because two capes exist at the ends of the beach. These capes are not very long but it is not know if sand bypassed them.

In the model the capes are represented by two diffracting groings 550 m long. This hypothesis works well in a small and mesotime scale. It was calibrated and verified using two years monitoring field data and the results were quite reasonable. But if we apply long-term scales, more than 10 years, the results must be discussed more accurately. The boundary conditions are critical, especially for the evaluation of the sand beach losing outside the study stretch. Extra data are needed in order to calibrate the program better. Length, sand bypassing and sand transmission must be discussed in order to apply long term.

Wave climate is another data that must be chosen carefully. In this case visual data, calibrated with Tarragona harbour buoy data, were used. During the monitoring period not many storms occurred. This means that the medium wave climate that visual data represent was not absolutley according to real wave climate.

Sand granulometry is another aspect to consider. In the GENESIS model and program homogeneous sand is used, in this case it was supposed that all the sand had $D_{50} = 0,35$ mm. Before restoration $D_{50} = 0,2$ mm and in the mouth os the Gaià river a lot of rocks and gravel existed. This phenomena was not considered in the GENESIS program. In the places where gravel exists erosion problems are less than in sandy areas. In long term analysis these aspects have importance and the results must be taken carefully.

Combined phenomena, boundary conditions, wave climate and sand granulometry have incidences in the prediction results in long term scale and it is difficult to plan long term future by this kind of program in this case.

EQUILIBRIUM PLANFORM

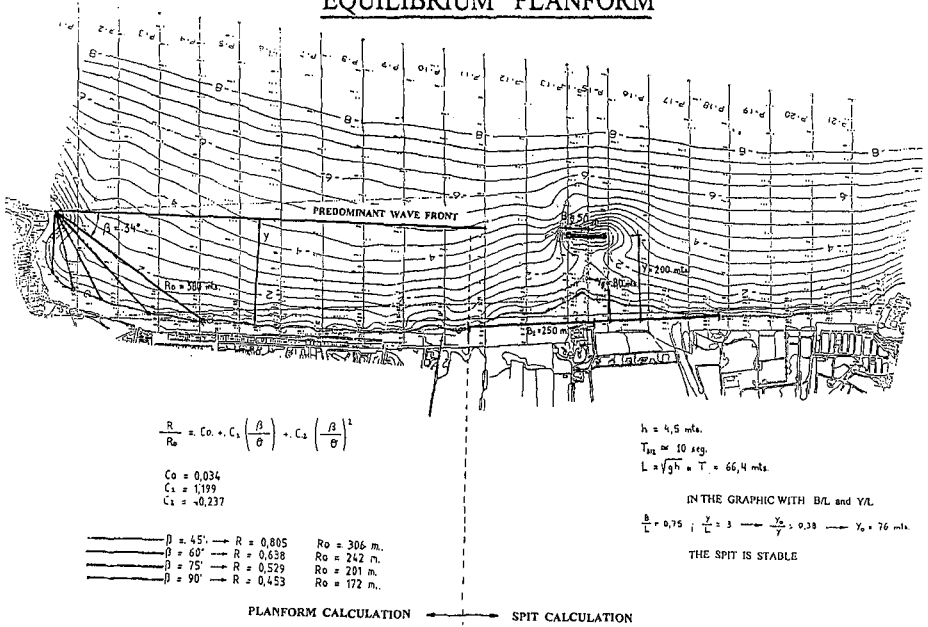


FIGURE 5 THECNICAL-EMPIRICAL METHODS INPLANFORM EVALUATION

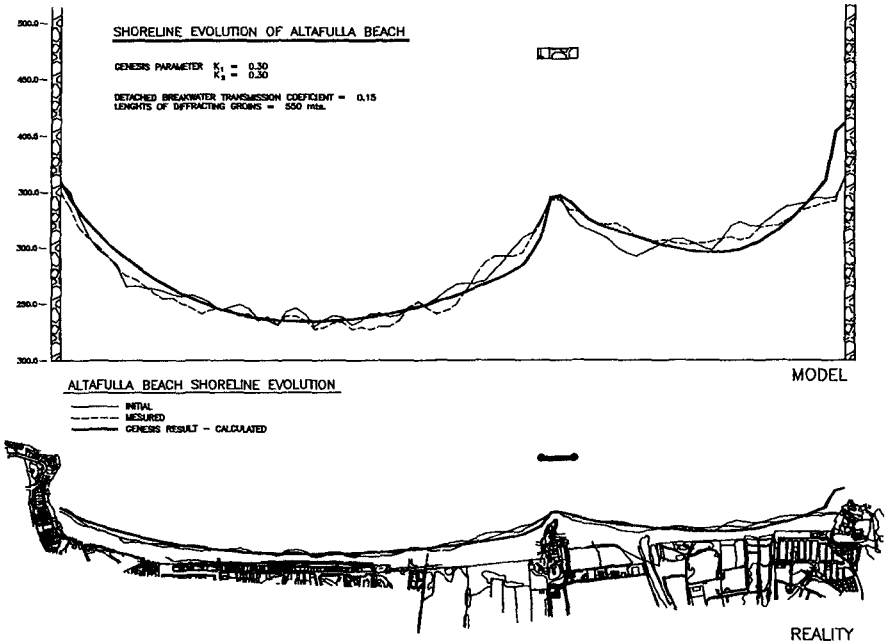


FIGURE 6 NUMERICAL METHOD, GENESIS, FOR SHORELINE EVOLUTION ANALYSIS

In order to understand beach behaviour, after the analysis of beach profiles and planform, a brief study of longshore transport was made. Theoretical formulas can be used, some of them only consider oblique wave incidence: CERC, KOMAR, etc. In this case height wave gradient, because of diffraction phenomena, are also important. That is why it is necessary to use models that consider both phenomena. The GENESIS program also calculates longshore transport ratios along the shoreline and the average transport ratio considering obliquity wave incidence and height wave gradient. In this calculation initial and final shoreline data were used to calibrate the model. The average of long shore transport is about 5.000-9.000 m³/year, this result agrees with some theoretical studies made near this area.

A statistical model was used computing the monitoring topobathymetry field data in order to find the tendencies of beach behaviour. The statistical model used was Principal Component Analysis (three way PCA). The method was used to objectively separate the spatial and temporal variability of the beach profile, planform and the sediment grain size data, as described by Medina et al 1994. The results show a seasonal variability in the beach profile data and a long-term trend. The bases of these statistical methods are the concentration of all topobathymetric information and to find some intrinsic information that can explain the trend of the beach evolution.

Three-way PCA is a statistical tool that can be used in the knowledge of beach behaviour. In Figure 7 the first, second and third cross-shore components, eigenvector are shown. The first one defines the mean of the variable, in this case representing the medium average profile. The second cross-shore eigenvector is very important in the upper part of the profile and it will play an important role in determining the upper profile slope. The third cross-shore eigenvector shows a berm-bar variability. In our case the second and third eigenvectors have influence on the detached breakwater comparing COMPL Ø and COMPL 1. A similar analysis can be made for long-shore eigenvectors.

The shows temporal eigenvectors, have been calculated the first one represents medium average temporal variation. The second one represents a seasonal dependence. Both of these are constant, and in the case of a two-year monitoring program, the temporal variability is not important. This means that the beach is in a quite equilibrium position with this wave climate. The combination of these eigenvectors explains most of the variability of the evolution of the beach. In order to combine them we will use the corresponding Bartussek core matrix values and the percentage of variation explained. This matrix shows how to combine eigenvectors. In order to better interpret the variability they account for, it is useful to examine the profile or the bathymetry that is obtained by the product or one alongshore eigenvector with one cross-shore eigenvector, and use the corresponding temporal function to determine how the obtained profile or bathymetry evolves in time.

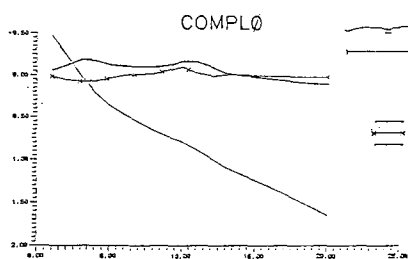


FIGURE 7 a) CROSS-SHORE EIGENVECTOR AFTER NOURISHMENT WORKS

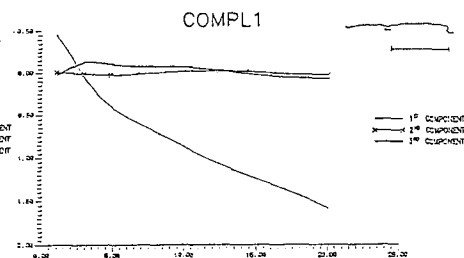


FIGURE 7 b) CROSS-SHORE EIGENVECTORS BEFORE NOURISHMENT WORKS

6.- CONCLUSION AND DISCUSSION

1.- Good data is needed in order to know the beach behaviour. It is the most important aspect for Coastal Engineers.

1.1 Wave climate must be obtained from:, Directional buoy, Non directional bouy with the direction data, Non directional buoy, Visual climate data.

This is the classification from the most valuable data to the least. Also, it depends on the range of information that it is possible to use. It is necessary to check different data information, if possible, and analyse it carefully before choosing the calculation data.

1.2 Topobathymetry data are the physical suport of Coastal Engineers. Accurate data is necessary for all kind of model. It is necessary to control: Study are limits, Profile distance, Profile length, Points per profile, Position system and errors, Bathymetric and althymetric measurement system and errors, Working weather conditions, Technical and worker personnel, Data analysis and computation, Topobathymetry frequency.

1.3 Sand sampling is needed as a basic component of beach performance. It is necessary to control: Study area limits, Sampling points, Sampling system, Sampling analysis and computation, Sampling frequency.

2.- Technical empirical models are easy to use and give important qualitative and some quantitative results. Data errors can be detected.

3.- Numerical models are more complicated to use than technical-empirical and sometimes can take data errors obtaining results with more errors.

4.- No model, technical-empirical or numerical, gives good results with bad data.

- 5.- Numerical models need a lot of data, a calibration step and a verification step. The whole process requires a lot of time and money. For this reason, it is necessary to be rigorous choosing them on quantity and quality.
- 6.- Statistical models must be studied in depth in order to find the beach trends.
- 7.- Altafulla beach has been studied comparing monitoring field data and theoretical models. It is a quite stable beach with a sand drift of 5.000 m³/year, from east to west. Sand is accumulated in calm areas and eroded in open areas.

REFERENCES

- * Dean R.G., 1995. "Equilibrium Beach Profiles: Characteristics and Application" *J. Coastal Research*, vol. 7 n° 1, pp. 53-84.
- * González E.M., 1995. "Morfología de playas en equilibrio: Planta y Perfil". Universidad de Cantabria, p.p. 183-198.
- * Hanson, H. and N.C. Kraus, 1991. "Comparison of Shoreline Change obtained with Physical and Numerical Models". *Proc. Coastal Sediments'91*, ASCE, pp. 1785-1799.
- * Hanson, H. and N.C. Kraus, 1989. "GENESIS-Generalized Model for Simulating Shoreline Change", vol. 1. Reference Manual and Users Guide, Tech. Report CERC-89-19, U.S. Army of Engineers, Waterway Experiment Station, 247 pp.
- * Hsu, J.R.C., Silvester R., Yi-Min Xia 1989. "Static Equilibrium Bays: New Relationship". *Journal of Waterway, Port, Coastal, and Ocean Engineering*, vol. 115, n° 3, pp. 285-298.
- * Kamphuis, J.W. and J.R. Moir, 1977. "Mean Diameter Distribution of Sediment Sizes before and after Artificial Beach Nourishment". *Proc. Coastal Sediments'77*. ASCE, New York, pp. 115-125.
- * Medina, R., M.A. Losada, I.J. Losada and C. Vidal, 1994. "Temporal and Spatial Relationship between Sediment Grain Size and Beach Profile". *Marine Geology*, 118, pp. 195-206.
- * de Vriend, H.J., 1992. "Mathematic Modelling of 3D Coastal Morphology". *Proc. Short Course on Design and Reliability of Coastal Structure*. 23rd I.C.C.E. Venecia, Chapter 10, 25 pp.
- * Work, P.A. and R.G. Dean 1995. "Assessment and Prediction of Beach-Nourishment Evolution". *Journal of Waterway, Port, Coastal and Ocean Engineering*, vol. 121, n° 3, May/June, pp. 182-189.

CHAPTER 369

ALTERNATIVES TO BEACH STABILIZATION: CAMBRILS COAST CASE STUDY (SPAIN)

Nuria Lupón⁽¹⁾, Alfonso Vidaor⁽²⁾, Jordi Galofré⁽³⁾ and F. Javier Escartín⁽⁴⁾

ABSTRACT

A study of alternatives including a shoreline evolution numerical modelization has been carried out in order to both diagnose the erosion problem at the beaches located between Cambrils Harbour and Pixerota delta (Tarragona, Spain) and select nourishment alternatives.

INTRODUCTION

Cambrils and Montroig are two villages located in a zone of big tourism growth in the Tarragona coast (northeast of Spain) 35 km from Tarragona and 125 km from Barcelona, very well communicated by road, motorway and railway (see figure 1).

Due to the importance of this tourist zone the Spanish Ministry planned a beach nourishment project for the area, including six beaches (6,000 meter long): Verge del Camí, Llosa, Torrent d'en Gené, Ardiaca, Riudecanyes and Pixerota.

The Cambrils Harbour construction in the thirties with a breakwater reaching the active depth, acting as a sediment transport barrier, strongly modified the littoral dynamics on beaches located southwest, suffering a severe regression only partially controlled by stabilization works carried out, which consisted basically in the construction of detached breakwaters and sand contribution. The efficiency of those works wasn't completely satisfactory, and the coastal zone between Cambrils Harbour and Pixerota delta presents nowadays a clear lack of stability with a general trend to regression.

-
- (1) Senior Engineer; Europrincipia, sl., Centre Tecnològic Europroject, Parc Tecnològic del Vallès, 08290 Cerdanyola, Barcelona, SPAIN; Tel: 34-3-5820187; Fax: 34-3-5824394; e-mail: nuria@europroject.es
 - (2) Director; Europrincipia, sl., Centre Tecnològic Europroject, Parc Tecnològic del Vallès, 08290 Cerdanyola, Barcelona, SPAIN; Tel: 34-3-5820187; Fax: 34-3-5824394; e-mail: alfonso@europroject.es
 - (3) Projects and Works Service Chief; Tarragona Coasts Demarcation, General Directorate of Coasts, Environment Ministry, Plaza Imperial Tarraco 4, 43005 Tarragona, SPAIN.
 - (4) Senior Engineer; Europrincipia, sl., Centre Tecnològic Europroject, Parc Tecnològic del Vallès, 08290 Cerdanyola, Barcelona, SPAIN; Tel: 34-3-5820187; Fax: 34-3-5824394; e-mail: fjeg@europroject.es

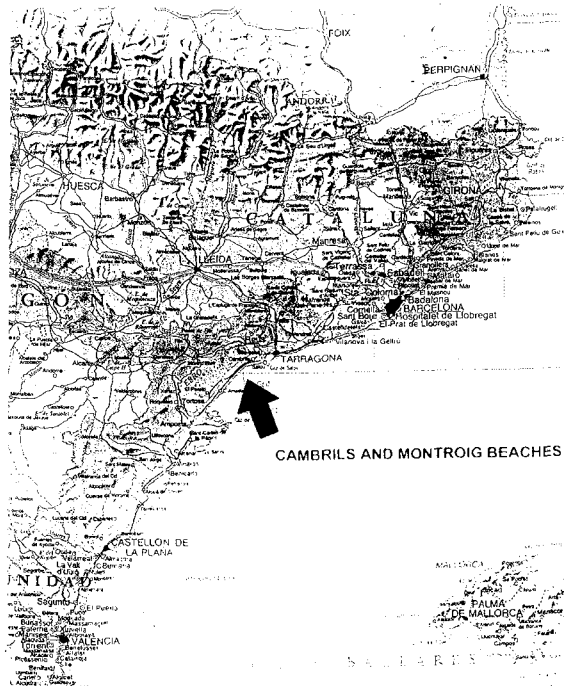


Figure 1: Location plan

MARITIME CLIMATE

The wave data used were:

- Cap Tortosa directional buoy, belonging to the General Directorate of Ports and Coasts of the Catalonia Autonomous Government during the interval 90/6 to 93/6, located at $0^{\circ}58'6''$ E, $40^{\circ}44'6''$ N coordinates in a depth of 45 m.
- Visual data registered at Casablanca oil platform during the interval 1983-1988, located at $1^{\circ}21'30''$ E, $40^{\circ}43'3''$ N coordinates in a depth of 170 m.
- Visual data registered by ships in the zone $0^{\circ}-2^{\circ}20'$ E, $40^{\circ}-41^{\circ}30'$ N and treated by the National Oceanic and Atmospheric Administration in Asheville.

The three data are valid though each of them presents some inconvenients:

- The Cap Tortosa buoy data have great reliability for being instrumental registers, but encompass a period of only three years.
- The ship visual data present a longer temporal interval, enough to represent the average zonal climate, but they have lesser reliability because of their origin.
- The Casablanca visual data present an intermediate reliability compared to other data.

NATIVE SAND GRANULOMETRIC ANALYSIS

A complete topographic and bathymetric survey of the studied zone was made including from dry beach to depth -13, deeper than active depth. At the same time a native seabed sand sampling campaign was performed: sixty sand samples in twelve profiles at five depths (+2.5, ± 0.0 , -3.0, -5.0 and -8.0) were analyzed obtaining the results shown in table 1.

Sample	D ₁₆ (mm)	D ₅₀ (mm)	D ₈₄ (mm)
+2.5	1.568	0.549	0.290
±0.0	1.684	0.553	0.296
-3.0	0.453	0.299	0.180
-5.0	0.439	0.312	0.221
-8.0	0.439	0.311	0.212
Total	0.859	0.390	0.232

Table 1: Native sand granulometry

BORROW SAND GRANULOMETRIC ANALYSIS

Studies performed in the last years verified the existence of submarine sand banks close to the project area, capable of being used for beach nourishment (as in the L'Hospitalet de l'Infant beach regeneration).

Another possible source for borrow sand was the material originated by the granite meteorization, locally known as "sauló". There existed four quarries near the project area that had been already used by the Ministry with satisfactory results.

The representative mixture granulometric characteristics for the two borrow sand types are shown in the table 2

	D ₁₆ (mm)	D ₅₀ (mm)	D ₈₄ (mm)
"Sauló"	1.568	0.549	0.290
Seabed sand	1.684	0.553	0.296

Table 2: Borrow sand granulometry

REGENERATION CHARACTERISTICS

There isn't a general rule that relates submerged beach slope with sand granulometry. However it's known that the slope proportionally increases with the average sand grain size.

R. Silvester in his classical publication "Coastal Engineering" showed relationships between the beach slope and the sand size for three types of beaches: protected, semi-exposed and exposed.

For the different native sand samples the relation between beach slope and grain size was analyzed, obtaining figure 2, in which the three theoretical curves before mentioned were drawn, too. The values measured in Cambrils and Montroig beaches were located on the curves, representing exposed beaches. The borrow sand average size (0.42 or 0.92 mm) was located in the upper zone of the figure, where an additional dotted line representing Cambrils and Montroig beaches was drawn.

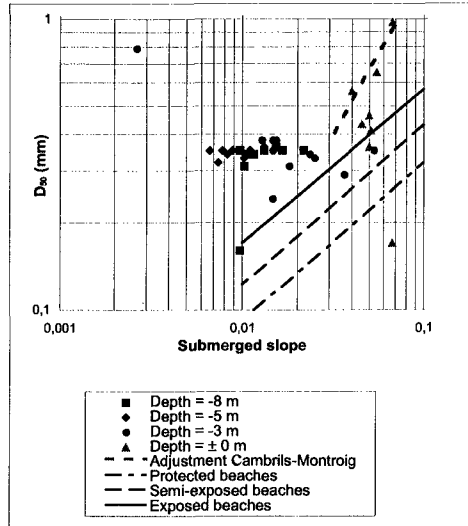


Figure 2: Submerged beach slope vs. Average grain size

In 1984 Garau and Friedman suggested a beach profile model for the case of sand classified by littoral processes for open beaches in the Mediterranean. The beach slope could be calculated using the average diameter D_{50} by means of the expression

$$m = 0.075 + 0.035 \cdot \ln D_{50}$$

Finally, from eroded profiles analysis Vellinga (1984) got a relationship between beach slope (with a certain granulometry) and slope (with another grain size):

$$m_1 = m_2 \left(\frac{w_1}{w_2} \right)^{0,56}$$

where w is the grain fall velocity. Once known the Cambrils and Montroig beaches grain sizes ($D_{50} = 0.39$ mm) and slopes (between 1V:30H and 1V:57H) and borrow sand sizes ($D_{50} = 0.42$ or 0.92 mm) the design beach slope could be calculated. The Ministry finally chose the seabed sand option with 1V:50H as submerged slope.

The estimation of longshore sediment transport rate induced by breaking wave action was used to obtain the zero transport direction, that is the shoreline orientation for which the average sand movement is zero.

A first estimation using the Komar's formulation was made in the assumption of straight uniform beach. The calculations were made for different shoreline orientations between 10°N and 115°N and for the three wave data (see figure 3). It can be noticed that the differences between the ship and Casablanca visual data curves are relatively little whereas the Tortosa buoy data curve differs much more (this is probably due to

that the differences between the ship and Casablanca visual data curves are relatively little whereas the Tortosa buoy data curve differs much more (this is probably due to the shorter time interval which could be not completely representative of average local climate). It can be observed too, that for the real shoreline orientation (around 60° N) the transport direction is NE-SW, as it could be deduced from sand accumulation north of Cambrils Harbour (that acts as total barrier to sediment transport). A further analysis indicated that sediment transport values estimated with the ship visual data seemed to be overestimated, specially gross transport, so the most representative data appeared to be those obtained from the Casablanca data. In this case the zero transport orientation was approximately 38° N.

The average incident wave direction was also estimated according to

$$D_{av} = \frac{\sum_i D_i \cdot p_i}{\sum_i p_i}$$

where p_i is the presentation probability, obtaining a value $D_{av} = 135,1^\circ$ N, very close to the zero net transport direction. Therefore this was considered as the average wave direction, value very similar to the perpendicular to the shoreline orientation north of Cambrils Harbour, were there is no sand movement.

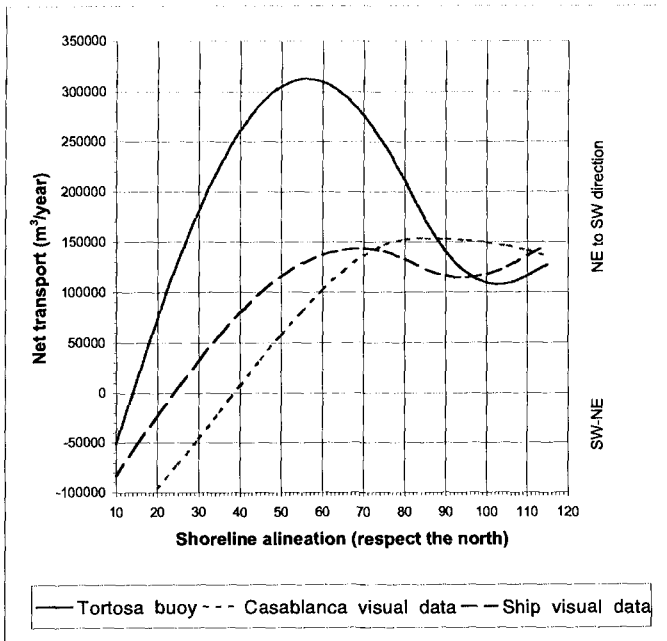


Figure 3: Net sediment transport

HISTORICAL EVOLUTION

A previous step to alternatives study was the shoreline historical evolution analysis in order to know the situation in the area between Cambrils Harbour and Pixierota delta, and how the existing beaches were formed. Five aerial photographs restitutions corresponding to 1947 (February), 1957 (June), 1965 (August), 1973 (June) and 1977 (March), two aerial photographs (not restituted, for qualitative estimation, June of 1983 and May of 1990) and May 1994 bathymetry were used for the analysis.

Historically the Cambrils and Montroig coast presented a continuous beach nourished by the sand transported by littoral drift in NE-SW direction. The Cambrils Harbour, built in the late thirties, became the main artificial barrier to sediment transport.

The main local sedimentary sources are the existing streams (Alforja, Verge del Camí, Torrent d'en Gené, Riudecanyes and Pixierota) characterized by a discontinuous flow, only important during storms periods. Some of them have created small deltaic formations with coarser material (gravels).

The correspondence between the beaches located south of the harbour and its distance or kilometric point (KP) is

Verge del Camí (V)	100 to 900	L'Ardiaca (A)	2300 to 2800
Llosa (L)	900 to 1800	Riudecanyes (R)	2800 to 3400
Torrent d'en Gené (T)	1800 to 2300	Pixierota (P)	3400 to 5400

The 1947 shoreline included the Cambrils Harbour presence and became the comparison base for the study. In the period 1947-1957 the V, L, T and A beaches eroded in average 2.7, 2.8, 1.8 and 2.1 meters/year respectively, although the first 200 meters of V beach advanced 0.8 m/year. The first 400 meters of R beach eroded 1 m/year whereas its last 200 meters advanced 0.4 m/year. P beach eroded an average of 0.9 m/year. The cause of this behaviour was the interruption of sediment transport by Cambrils Harbour that in the zone had the NE-SW direction: therefore beaches located SW of the port became the main nourish source for the littoral current, so its erosion process started.

Between 1957 and 1965 the generalized erosion process continued with an absolute lower value in the northern half. The average regressions were 0.7, 1.4, 1.1, 1.1 and 1.1 m/year respectively, though the first 350 meters of V beach advanced 1.5 m/year. The first 200 meters of P beach advanced 0.4 m/year whereas the rest eroded in average 1.1 m/year.

In the period 1965-1973 the V, L, T, A and R beaches eroded an average of 1.4, 1.9, 1.9, 1.3 and 0.2 m/year respectively, although the first 300 meters of R beach advanced 0.3 m/year. The first 200 meters of P beach advanced 0.5 m/year whereas the rest eroded 1.0 m/year.

This means that in 1973 the average shoreline erosion for the sector was between 20 and 55 meters in comparison to 1947 (with extreme values of 70 meters). So in 1976 the first stabilization project was performed, consisting in the construction of four detached breakwaters, the enlargement of an existing breakwater and the nourishment of sand to generate tombolos behind the detached breakwaters that stabilized the V, L, and T beaches. Nevertheless the lack of sediment proceeding from the three first beaches which in the past had nourished partially the littoral current accelerated the

erosion process in the rest of beaches: the **A**, **R** and **P** beaches eroded in average 1.7, 3.6 and 1.9 m/year.

Thus, in 1985 a second stabilization project was carried out, with the construction of two additional detached breakwaters to protect the **A** and **R** beaches and six artificial islands between the detached breakwaters and the coastline to optimize its behaviour that had caused important erosions at the center of the protected beaches. Since then the northern beaches shoreline position hasn't varied substantially, indicating its stability, while the Riudecanyes delta and **P** beach have continued to erode with an average of 0.6 and 1.6 meters/year.

All this values are summarised in table 3 whereas all the shoreline evolution is represented in figure 4.

Beach	Verge del Camí		Llosa	Torrent d'en Gené	L'Ardiaca	Riudecanyes		Pixerota
1947-57	+0.8	-2.7	-2.8	-1.8	-2.1	-1.0	+0.4	-0.9
1957-65	1.5	-0.7	-1.4	-1.1	-1.1	-1.1		+0.4 -1.1
1965-73	-1.4		-1.9	-1.9	-1.3	+0.3	-0.2	+0.5 -1.0
1973-77	Tombolos generation		Tombolos generation	Tombolos generation	-1.7	-3.6		-1.9
1977-94	Tombolos generation		Tombolos generation	Tombolos generation	Tombolos generation	Tomb. gen.	-0.6	-1.6

Table 3: Average annual accretion and erosion summary

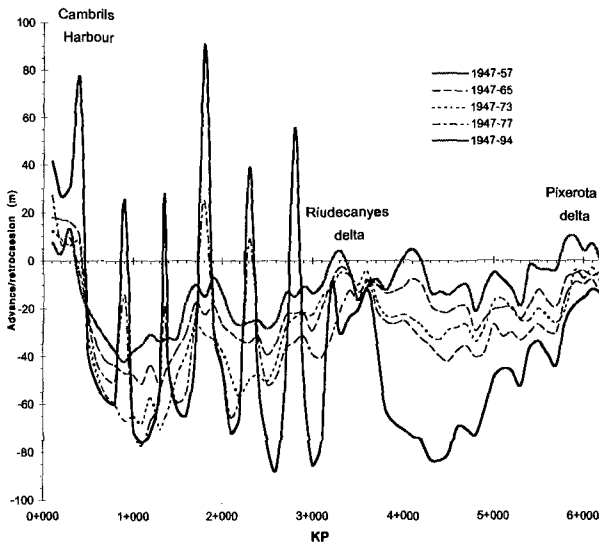


Figure 4: Shoreline evolution between Cambrils Harbour and Pixerota delta

From shoreline variations the volume of sand mobilized by wave action between Cambrils Harbour and Pixerota delta was estimated in 35,000 m³/year with a direction NE-SW.

ALTERNATIVES STUDY

In the study carried out nine stabilization alternatives were analysed, taking into account flexible solutions (just sand nourishment) and rigid ones (new breakwaters). All of them included the demolition of the existing detached groins until the depth -2.0 and considered a minimum dry beach width of 60 meters (see figure 5). The quarry and sand volumes required and budgets for each alternative are presented in table 4.

- *Alternative 0*: It consisted exclusively in sand contribution between Cambrils Harbour and Pixerota delta. From the historical shoreline evolution study it was estimated that 8 years after nourishment the erosion in the northern beach would be important enough (about 20 m) to consider a periodical sand contribution south of the harbour at a rate of 35,000 m³/year.
- *Alternative 1*: Compared to alternative 0 it included a 142 m long groin at the Pixerota delta to ensure a beach support. The groin was designed short enough to let the sediment pass (and nourish southern beaches as Rifà and Porquerola), so the same periodical contributions that in alternative 0 were necessary.
- *Alternatives 1a, 2, 2a*: Compared to option 1, they incorporated one, two and three groins respectively with the same purpose, being also permeables to sand movement.
- *Alternative 2b*: In this case the groins position was very similar to alternative 2a, but they were much longer and included submerged toes in order to stabilize completely the new three northern beaches (until Riudecanyes delta), as littoral transport was completely interrupted. The southern groin (at Pixerota delta) was the same than in alternatives 0 to 2a. From historical shoreline evolution study it was estimated that 17,500 sand m³/year would be mobilized in direction NE-SW between Riudecanyes and Pixerota deltas and would cross the last groin to nourish partially the southern beaches (Rifà, Porquerola...). Therefore there would exist in those beaches an insufficiency of 17,500 m³/year that should be added periodically south of Pixerota delta to avoid its erosion. Moreover, the sand mobilized along the new Pixerota beach would produce important erosions in the northern part, so it was estimated that 8 years after the regeneration periodical sand contributions (17,500 m³/year) south of Riudecanyes delta would be necessary.

Alternative	0	1	1a	2	2a	2b	3	4	5
KTn of demolished quarry	183	183	183	183	183	183	183	183	183
KTn of quarry for new groins	0	15	37	53	76	352	379	350	291
Km ³ of sand for initial nourishm.	1,695	1,930	2,613	2,684	2,742	3,954	2,841	2,691	2,699
Km ³ of sand for periodical contributions	770	770	770	770	770	787.5	787.5	787.5	787.5
Budget (M\$)	13.3	14.3	17.0	17.3	17.6	24.3	20.4	19.5	19.0

Table 4: Quarry and sand volumes required and budgets

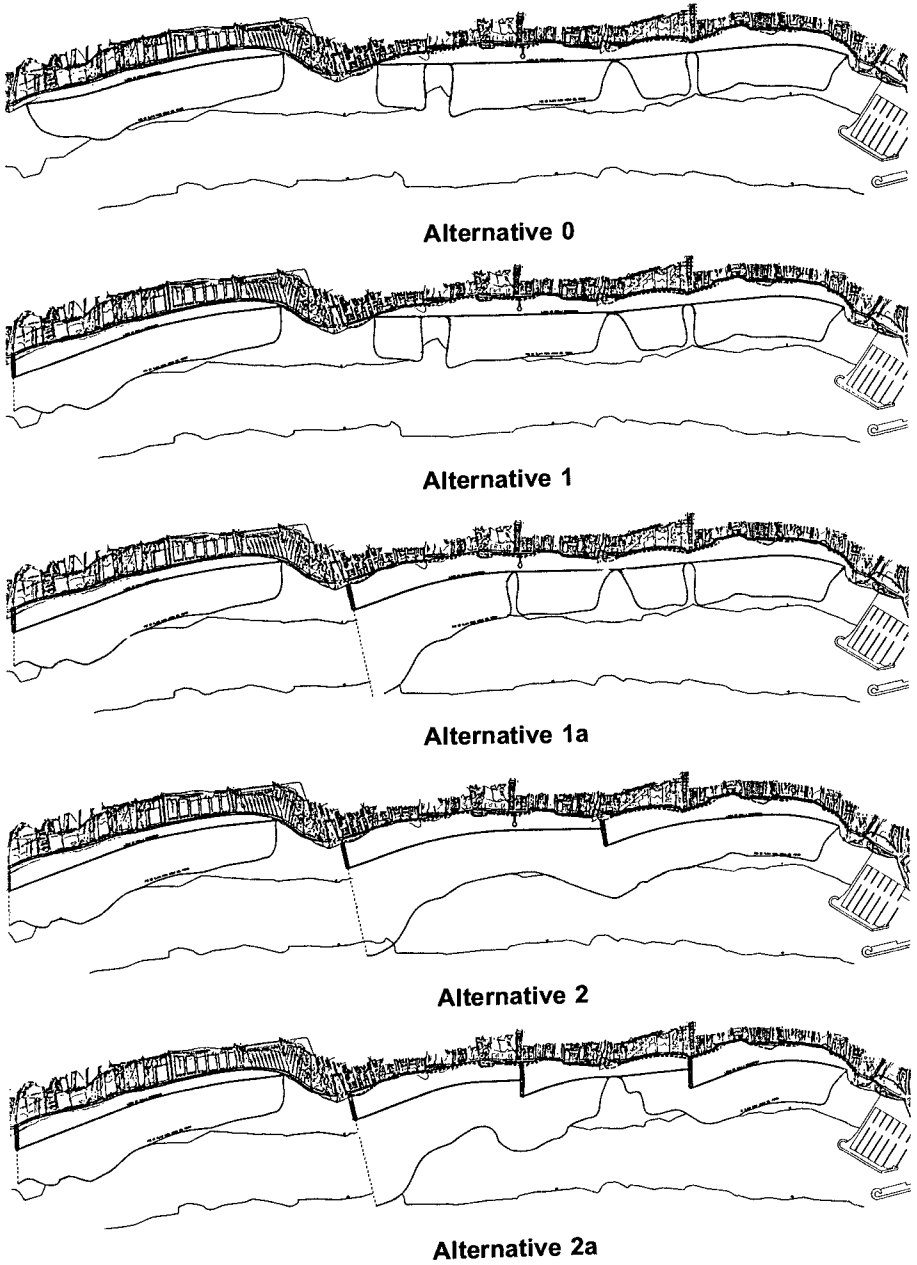
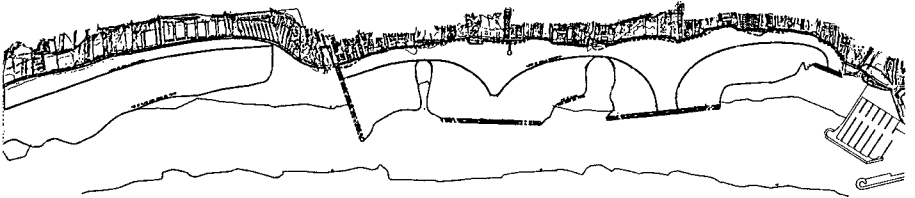


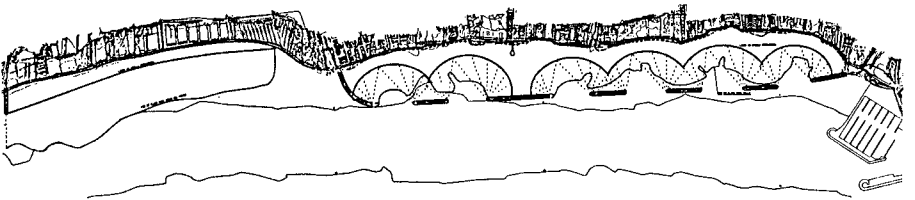
Figure 5a: Suggested regeneration alternatives



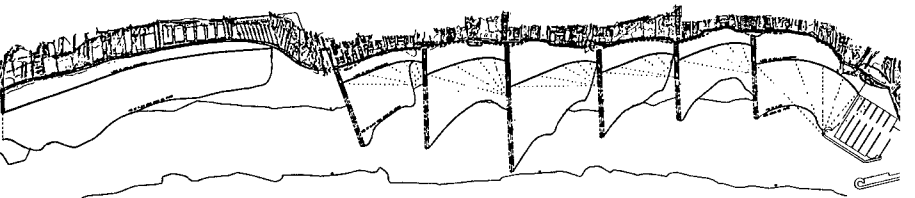
Alternative 2b



Alternative 3



Alternative 4



Alternative 5

Figure 5b: Suggested regeneration alternatives

- *Alternatives 3, 4 and 5:* They had the same purpose than the previous alternative but the complete stabilization of the northern beaches was obtained respectively by means of: *a)* two long detached groins and one transversal groin with a submerged toe, *b)* seven detached groins and *c)* six transversal groins between 157 and 214 meters long with submerged toes respectively. In the Pixerotha delta the same groin than in alternative 2b was designed.

SHORELINE EVOLUTION NUMERICAL MODELIZATION

After having presented the nourishment alternatives, the shoreline evolution numerical modelization for three of them (1, 1a and 5) was carried out with the GENESIS v 3.0 program.

A thorough calibration process was done in order to obtain transport coefficients for the area, necessary for long term coastal evolution predictions of the alternatives selected. For calibration the 1947 and 1957 shorelines were used. Different simulations were made by varying the formulation parameters until obtaining a proper adjustment between the numerical values of the longitudinal transport and shoreline evolution in comparison with measured values. This adjustment was obtained for $K_1 = 0.40$ and $K_2 = 0.20$

Long term simulations (10 years) were made in order to estimate the beach evolutive trend for the three alternatives. In figure 6 results for the alternative 1 modelization are presented. It can be noticed the main problem is that the shoreline erodes half of the beach amplitude (won with the nourishment) five years after the regeneration at certain points. Therefore a second prediction including periodical sand contributions was made (figure 7). After some tests it was estimated that a 38,000 m³/year contribution stabilized the beach. This value was very similar to that estimated in the alternatives study. At Riudecanyes and Pixerotha deltas the maximum erosion was limited due to its granulometric characteristics (gravels and boulders). This methodology was repeated for the 1a and 5 alternatives.

CONCLUSIONS

The alternative 1a was selected by the Ministry and a construction detailed design was developed in order to prepare the tendency of the works. Main quantities and budget for the project are:

Tn of quarry demolished from existing groins:	193,000
Tn of quarry for new groins:	81,000
m ³ of sand for initial beach nourishment:	2,616,000
Total budget (M\$):	15.6
Length of beach stabilized:	5.2 km

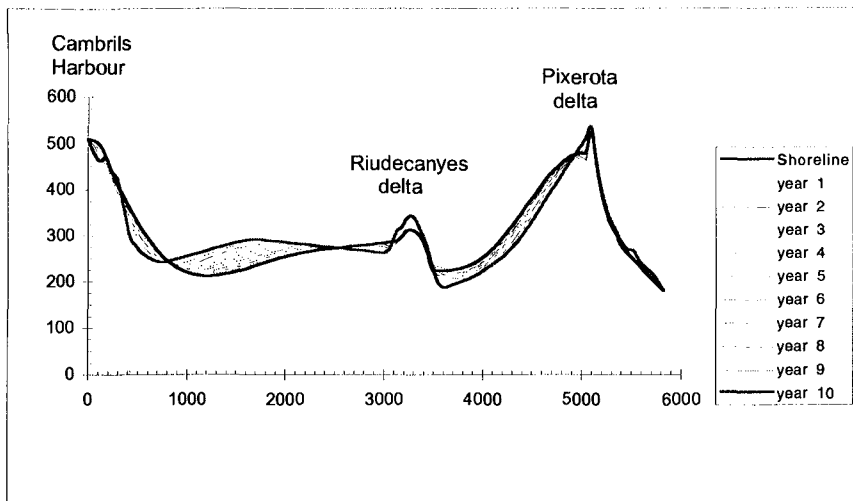


Figure 6: Alternative 1 shoreline evolution prediction without periodical sand contributions

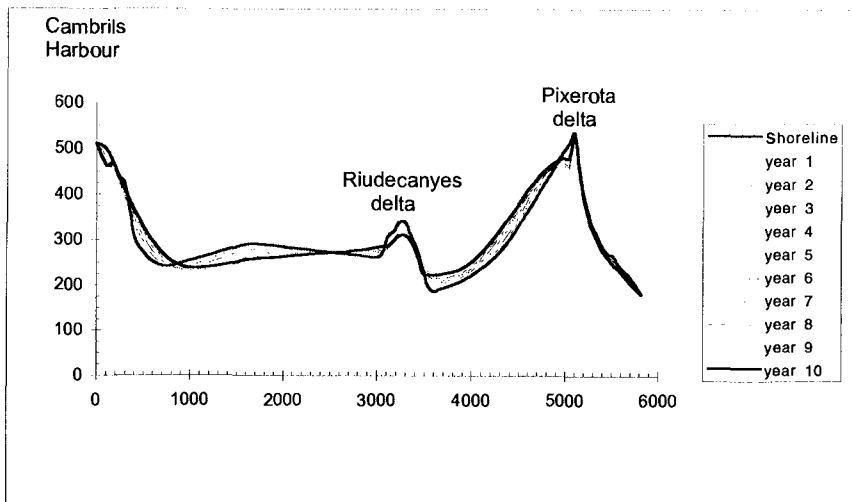


Figure 7: Alternative 1 shoreline evolution prediction with periodical sand contributions

CHAPTER 370

THE EFFECT OF GRAIN SORTING ON PROFILE STABILITY OF NOURISHED BEACHES

Ram K. Mohan, Ph.D., P.E.¹ and Timothy W. Kana, Ph.D., P.G.²

Abstract

Dean's (1983) model is often used to predict the profile shape and berm width after nourishment. Ideally, if the borrow sediment is identical to native sediment, the adjusted profile will take on the same shape as the existing profile. But, if the borrow sediment is coarser than native, the nourished profile will adjust to a steeper configuration, producing a wider dry beach. If borrow sediments are finer, the fill will adjust to a gentler slope, producing a narrow dry beach. A conceptual model of the effect of grain sorting on nourished profile stability is presented in this paper and verified by comparison with actual beach measurements. The results indicate that the post-nourishment performance can be improved measurably by minor variations in grain size distribution, specifically where a coarse fraction is present (i.e., negative skewness). Fill placement technique and other environmental factors, of course, also impact performance.

Introduction

Numerous researchers have developed empirical models for beach profile stability and equilibrium slopes (Brunn, 1954; Dean, 1983 and 1991; Hands, 1981; and Krumbein and James, 1965). However, these models relate primarily to environmental factors such as wave steepness, wave energy, tide levels, and sea-level changes. Historical data from numerous beaches indicate a trend of increasing slope with grain size and decreasing slope with increasing wave energy (Wiegel, 1964). The general relationship of wave energy, grain size, and beach face slope on sand beaches is illustrated in Figure 1. Empirical data from numerous beaches confirm the trend of increasing slope with grain size and decreasing slope with

¹ Senior Engineer, Gahagan & Bryant Associates, Inc., 9008-0 Yellow Brick Road, Baltimore, MD 21237, USA.

² Senior Scientist, CSE-Baird, A division of W.F. Baird & Associates, Ltd., P.O. Box 8056, Columbia, SC 29210, USA.

increasing wave energy (Wiegel, 1964). Larger grain sizes allow increased percolation of wave uprush and a corresponding decrease in backrush volumes (Waddell, 1973). This results in steeper beach face slopes with increasing grain size.

Intense mixing under breaking waves will further affect the distribution of grain sizes over the shore face. Coarsest material is common at the breakpoint ("step" at the toe of the beach face), and fining will occur in either direction: toward the foredunes and back shore (Mason and Folk, 1958; Fox et al., 1966) and toward the lower foreshore (Swift et al., 1971). Multimodal size distributions across the beach occur in some areas [e.g., Duck, North Carolina (Kana et al., 1980)], but more commonly, a single mode distribution occurs. Data from Swift et al. (1971) revised by Swift (1976) show variations in the modal grain size from the berm to the lower shoreface (Figure 2). Sediment coarsening near the breaker line is reflected in the size distribution in Swift's transect B, as well as by coarse-skewed distributions for this zone of profile in transects A and C. As Swift's data show, sorting is generally good across the shoreface. Dean (1983; 1991) performed extensive work in modeling equilibrium profiles, assuming a uniform grain size distribution across the active profile.

Work and Dean (1991) suggest that varying the grain size across the profile within limited size ranges typical for beaches does not significantly improve the simpler, and often used, profile model (Brunn, 1954; Dean, 1983):

$$h(y) = Ay^{0.667}$$

where h is the water depth at a distance y offshore of the mean water line and A is a scale parameter dependent on sediment characteristics.

Dean's model (Dean, 1983; 1991) has been used to predict the resulting profile shape and berm width (dry beach width) after nourishment. In simple terms, if borrow sediment is identical to the native size distribution, the adjusted profile will take on the same shape as the existing profile. But if the borrow sediment is coarser than native, the nourishment profile will adjust to a steeper configuration, leaving more sand along the back shore (and producing a wider dry beach). If borrow sediments are finer, the fill will adjust to a gentler slope with more material shifting offshore (producing a narrow dry beach) as shown in Figure 3. As a result of these important relationships, the Shore Protection Manual (USACE, 1984) and common practice recommends use of the same or slightly coarser size distribution for nourishment purposes. The authors followed these guidelines for selecting the borrow area for the 1991 Hunting Island nourishment project (CSE, 1991). The borrow area sediments for this project contained slightly coarser sands and the grain size distributions confirmed the negative skewness of the samples produced by the presence of broken shells. Overfill ratios for this project were

favorable in the range 1.10 to 1.20 and the percentage mud was relatively low at 5 percent. Based on these results and the findings of other investigators just outlined, some changes in the profile shape and slope after nourishment would be expected. This change would be due to a general coarsening of the beach sediment, or due to a change in the grain size distributions across the shoreface after nourishment.

A conceptual model of the grain size distribution shift for hydraulic nourishment projects will be presented in this paper and verified by comparison with actual beach measurements taken after the fifth Hunting Island beach nourishment project.

Effect of Method of Placement on Profile Stability

Given a different size distribution of borrow sediments compared to the native sediments, the method of placement would affect the size distribution across the profile. Fill by trucks along intertidal and dry beach is likely to produce uniform admixtures which are gradually eroded along the seaward margin. Back shore fill in this case may initially contain the same distribution of fines as the borrow area. In fact, a legitimate concern with such projects is the possibility of creating hard pan because of the binding effect of muddy sediment in the mixture (Siah et al., 1985; Kana and Jones, 1988). These fines may not erode until large storms occur or more seaward material has shifted downslope through profile adjustment.

For projects built by pipeline dredge, the response will be different. Studies on dredged material disposal (Montgomery, 1978; Palermo et al., 1978) show that coarse material settles closest to the discharge point, whereas the fine material moves further away in the slurry. If the pipeline is placed along the back shore, this leads to sorting down-profile, with coarse material concentrating along the berm and finer material settling downslope. The result will be a systematic shift in the grain size distributions from the back shore to the lower foreshore.

Conceptual Model of Nourished Beach Profile Stability

A conceptual model of the grain size distribution shift for hydraulic nourishment projects is presented in Figure 4. As the material is discharged onto the beach, the coarser fraction settles in the upper beach face. This modifies the pre-nourished grain size frequency curve by shifting it to the left, thereby indicating that the coarser fraction has increased (Figure 4a). The mid-sized fraction moves further down the beach profile and settles along the beach face. Since the grain size distribution of this section of the beach is very similar to the modal size fraction, the pre-nourished grain size frequency curve retains its shape more or less (Figure 4b). The finer fraction moves further down the profile and eventually settles at the lower foreshore. This modifies the pre-nourished

grain size frequency curve by shifting it right, thereby indicating that the finer fraction has increased (Figure 4c).

An important consequence of this is that the upper beach face and berm becomes more stable and wider than would occur if the borrow area sediments matched the native beach. This means that the recreational life may be longer as well because dry-beach width often defines recreational benefits. A negative consequence of such a shift in the grain size distributions is the possibility of accelerated erosion of the lower shoreface.

Comparison with Actual Beach Observations

Comparison of pre-nourished (1990) and post-nourished (1993) grain size distribution curves for the fifth Hunting Island beach nourishment project (Figure 5) show a clear trend of the sediments at the berm becoming coarser after nourishment while those along the beach face becoming finer after nourishment. The 1993 beach samples retained a coarse tail but the proportion of coarse material decreases with distance offshore. The bulk of the sample population is seen to shift toward finer sized down profile and has a smaller modal size than native in the lower shoreface.

Two schemes of statistical analysis were used to compare the native beach (1990) and nourished beach (1993) sediments (Krishna Mohan et al., 1993). In the first method (Method A), coarse sand, very coarse sand and gravel were grouped together to form percent coarse material (i.e., <1.0 Phi). Similarly, very fine sand, silt, and clay were grouped together to form percent fine material (i.e., >3.0 Phi). According to this scheme, the total sediment volume of the borrow area (757,644 cy) consisted of 15.35 percent (116,298 cy) coarse material and 19.17 percent (145,240 cy) fines. While the results of this analysis (see Table 1) show the expected trend of increased coarsening in the berm and increased fines in the lower beach, they do not include a large portion of the fill represented by size classes 1.0 Phi to 3.0 Phi. Therefore, the authors prepared a second analysis whereby the entire sediment grain size range was divided into two broad subdivisions comprising of coarse and fine groups.

In the second method of analysis (Method B), materials with grain sizes less than 2.5 Phi were classified as coarse and those with grain sizes greater than 2.5 Phi were classified as fines. Accordingly, most fine sands, medium sands, coarse sands, very coarse sands and gravel fall into the "coarse" category. Similarly, some fine sands, very fine sands, silts and clays fall into the "fine" category. According to this scheme, the total sediment volume of the borrow area (757,644 cy) is comprised of about 51.44 percent (389,732 cy) coarse material and about 48.56 percent (367,912 cy) fines. Table 2 summarizes the results obtained by this method which clearly supports the propositions of the conceptual model. A close

examination of Table 2 indicates that coarse sediments in the berm increased from 36 percent to about 78 percent of the sample population after nourishment, whereas those at the beach face decreased from 56 percent to about 42 percent of the sample population. These trends correspond to the leftward shift of the upper beach sediments and the rightward shift of the lower beach sediments as predicted by the conceptual model. The grain size statistics in Tables 1 and 2 confirm these trends but also show that two years after nourishment the fill retains a coarse tail and is more graded. Sorting decreased significantly between 1990 prefill and 1993 postfill conditions (about 0.4 Phi to 1.0 Phi, respectively); and skewness became more negative in the 1993 samples. Skewness after nourishment was higher on the beach face than on the berm or lower foreshore.

Table 1. Comparison of native beach (1990) versus nourished beach (1993) composite samples. [Coarse <1.0 ϕ ; fine >3.0 ϕ]

Location	Mean Grain Size		%Coarse		%Fine	
	[1990]	[1993]	[1990]	[1993]	[1990]	[1993]
Berm	2.73	1.57	0.20	32.52	26.70	4.35
UBF	--	1.93	--	23.05	--	11.39
LBF	2.49	2.41	0.80	8.66	9.15	17.01
LSF	--	2.56	--	0.31	--	12.83

Note:UBF=Upper Beach Face; LBF=Lower Beach Face; LSF=Lower Shore Face.

Kana and Andrassy (1993) conducted a volume change analysis for the postnourished beach profile which showed that there has been a rapid loss of sand in the project area. By April 1993, north beach had lost 50 percent of the fill, and south beach had lost almost 80 percent of its fill. The central project area compartment lost about 45 percent of the fill by April 1993. Figure 6 (lower) illustrates the average unit volume beach change since nourishment (February 1991) as a function of contour interval within the project area. The dry beach to MHW (+10 ft to +3.2 ft NGVD) within the project area retained 70 percent of the fill through April 1993. The intertidal beach (MHW to MLW; ie., +3.2 ft to -2.2 ft NGVD) retained about 45 percent of the fill two years later. In contrast, the underwater lenses (-2.2 ft to -12.0 ft NGVD) retained only 27 percent of the fill by April 1993. A close review of these results reveals an interesting factor: the loss rate for the upper beach lenses was much lower. These results support the predictions of the conceptual model that more fill is retained at the berm than on the lower beach.

Table 2. Comparison of native beach (1990) versus nourished beach (1993) composite samples. [Coarse 2.5ϕ; fine >math>2.5\phi</math>]

Location	Mean Grain Size		%Coarse		%Fine	
	[1990]	[1993]	[1990]	[1993]	[1990]	[1993]
Berm	2.73	1.57	35.98	78.04	64.02	21.96
UBF	--	1.93	--	60.71	--	39.29
LBF	2.49	2.41	56.02	43.25	43.98	56.75
LSF	--	2.56	--	46.28	--	53.72
<i>Sorting (ϕ)</i>						
Berm	0.42	1.13				
UBF	--	1.14				
LBF	0.41	0.82				
LSF	--	0.41				
<i>Skewness</i>						
Berm	0.02	-0.29				
UBF	--	-0.48				
LBF	-0.58	-0.91				
LSF	--	-0.13				

Note:UBF=Upper Beach Face; LBF=Lower Beach Face; LSF=Lower Shore Face.

Comparison with Previous Projects

Unpublished profile data following the December 1968 and December 1971 federal projects at Hunting Island were used to develop an estimate of the average fill volumes remaining (Figure 6 top and middle). The reported mean grain sizes prior to nourishment are given in Tabel 3.

Table 3. Mean Grain Size of Native Beach and Borrow Area Sediments.

Project Year	Native Beach Grain Size (mm)	Borrow Area Grain Size (mm)
1968	0.16	0.18
1971	0.16-0.21	0.18
1975	--	--
1980	0.14-0.20	--
1991	0.20	0.20-0.23

A review of Figure 6 indicates that fill losses have been exceedingly rapid after all projects. However, the proportion of fill remaining above low water has been many times higher following the 1991 nourishment. In fact, upwards of 75% of the fill remaining following the 1991 project has been situated above the low water contour. In contrast, most of the fill above low water was lost soon after the 1968 and 1971 projects.

Conclusions

A conceptual model of profile stability for beach nourishment projects was presented in this paper. The model predicts a trend of sediments in the upper beach becoming coarser by means of selective sorting at the discharge point (hydraulic nourishment) along the back shore, while those at the lower beach become finer after nourishment. While the conceptual model of nourished profile stability is not quantitative, it can be used as a basis for predicting trends and formulating alternatives. Comparison with actual beach observations support this prediction since the actual (observed) data showed the berm sediments becoming measurably coarser in both mean grain size and degree of grading (i.e., poor sorting). Comparative profiles and a detailed volume change analysis revealed that the dry beach retained 70 percent of its fill whereas the underwater lenses retained only 27 percent of their fill after two years. This further supports the idea that use of coarser borrow material will improve longevity of the upper beach. Profiles, in this case, became steeper after nourishment. In conclusion, three factors become important in controlling the postnourishment grain size distribution and profile stability (in order): (i) *Grain size distribution*: This fundamentally controls the overall slope and distribution as predicted by equilibrium profile theory. Basic engineering logic suggests increasing coarse material tends to improve beach profile stability. The finer fraction washes out faster, thereby decreasing longevity and, hence, should be kept to a bare minimum whenever possible; (ii) *Placement of fill material*: The most common method of placement of fill material in a nourishment project is by the use of pipelines. If discharge is along the back shore, coarse material will settle near the berm and fines will shift downslope with the slurry. This type of placement improves berm longevity. If the discharge point is along the lower foreshore (i.e., profile nourishment, Brunn, 1988), coarse material will have less chance of concentrating on the berm; and, (iii) *Environmental factors*: These include the magnitude and interrelationship of the following variables: background erosion rates, shoreline morphology, waves, currents, tides, and storm frequency. These factors produce site-specific responses and are independent variables in nourishment design.

References

- Brunn, P. 1954. Coastal Erosion and the Development of Beach Profiles. Tech. Memorandum No. 44, Beach Erosion Board, Washington, D.C.
CSE. 1991. Geotechnical Studies for the Hunting Island Beach Nourishment

- Project. Coastal Science & Engineering, Inc., Columbia, SC.
- Dean, R.G. 1983. Principles of Beach Nourishment. In *Handbk. of Coastal Processes and Erosion* (Komar, ed.), CRC Press, Boca Raton, FL.
- Dean, R.G. 1991. Equilibrium Beach Profiles: Characteristics and Applications. *Journal of Coastal Research*, Vol. 7(1).
- Fox, W.T., J.W. Ladd, and M.K. Martin. 1966. A Profile of the Four Moment Measures Perpendicular to a Shoreline. *Journal of Sediment Petrology*, Vol. 36(4).
- Hands, E.B. 1981. Predicting Adjustments in Shore and Offshore Sand Profiles on the Great Lakes. CETA81-4, U.S. Army Corps of Engineers, Coastal Engineering Research Center, Ft. Belvoir, VA.
- Kana, T.W., and C.J. Andrassy. 1993. Hunting Island State Park 1991 Beach Nourishment Report. Coastal Science & Engg., Columbia, SC.
- Kana, T.W., and C.P. Jones. 1988. Myrtle Beach Nourishment Project. Coastal Science & Engineering, Inc., Columbia, SC.
- Kana, T.W., L.G. Ward., and H.M. Johnson. 1980. Suspended Sediment Transport at Duck, NC. Coastal Science & Engg., Inc., Columbia, SC.
- Komar, P.D. 1976. *Beach Processes and Sedimentation*. Prentice Hall, Englewood Cliffs, N.J.
- Krishna Mohan, R., Kana, T.W., and C.J. Andrassy. 1993. Comparison of Geotechnical Properties of Beach Fill Versus Borrow Area Sediments for the Fifth Hunting Island (SC) Beach Nourishment Project. Coastal Science & Engineering, Inc., Columbia, SC.
- Krumbein, W.D., and W.R. James. 1965. A Lognormal Size Distribution Model for Estimating Stability of Beach Fill Material. Tech. Memo. No. 16, U.S. Army Corps of Engineers, Vicksburg, MS.
- Mason, C.C., and R.K. Folk. 1958. Differentiation of Beach, Dune and Aeolian Flats by Size Analysis. *J. of Sediment Petrology*, Vol. 28(2).
- Montgomery, R.L. 1978. Methodology for Design of Fine-Grained Dredged Material Containment Areas for Solids Retention. TR D-78-56, U.S. Army Corps of Engg., Waterways Experiment Station, Vicksburg, MS.
- Palermo, M.R., R.L. Montgomery, and M.E. Poindexter. 1978. Guidelines for Designing, Operating and Managing Dredged Material Containment Areas. TR DS-78-10, U.S. Army Corps of Engineers, Vicksburg, MS.
- Siah, S.J., E.J. Olsen, and T.W. Kana. 1985. Myrtle Beach Nourishment Project. Coastal Science & Engg, Inc., Columbia, SC.
- Swift, D.J.P. 1976. Coastal Sedimentation. In *Marine Sediment Transport and Environmental Mgmt.* (Stanley & Swift, ed.), Wiley & Sons, N.Y.
- Swift, D.J.P., R.B. Sanford, C.E. Dill, Jr., and N.F. Avignone. 1971. Textural Differentiation on the Shoreface During Erosional Retreat of an Unconsolidated Coast. *Sedimentology*, Vol. 16.
- USACE. 1984. *Shore Protection Manual*. U.S. Army Corps of Engineers, Washington, DC.
- Waddell, E. 1973. Dynamics of Swash and its Implications to Beach Response. Louisiana State University, Baton Rouge, LA.
- Wiegel, R.L. 1964. *Oceanographical Engg.* Prentice Hall, Engle Cliffs, NJ.
- Work, P.A., and R.G. Dean. 1991. Effect of Varying Sediment Size on Equilibrium Beach Profiles. *ASCE Coastal Sediments'91*, New York, NY.

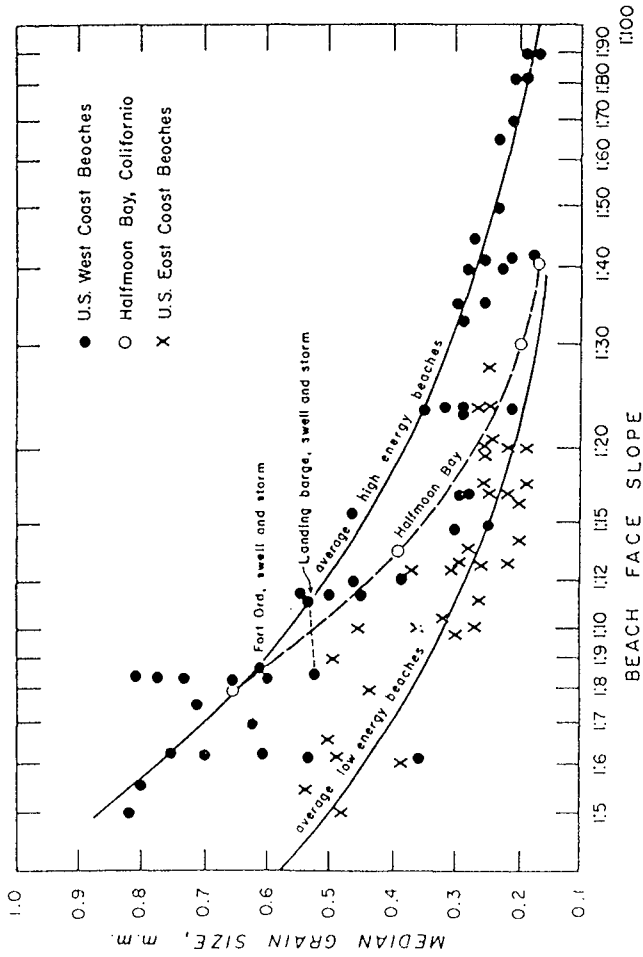


Figure 1. Relationship of grain size, wave energy, and beach face slope [from Komar, 1976]

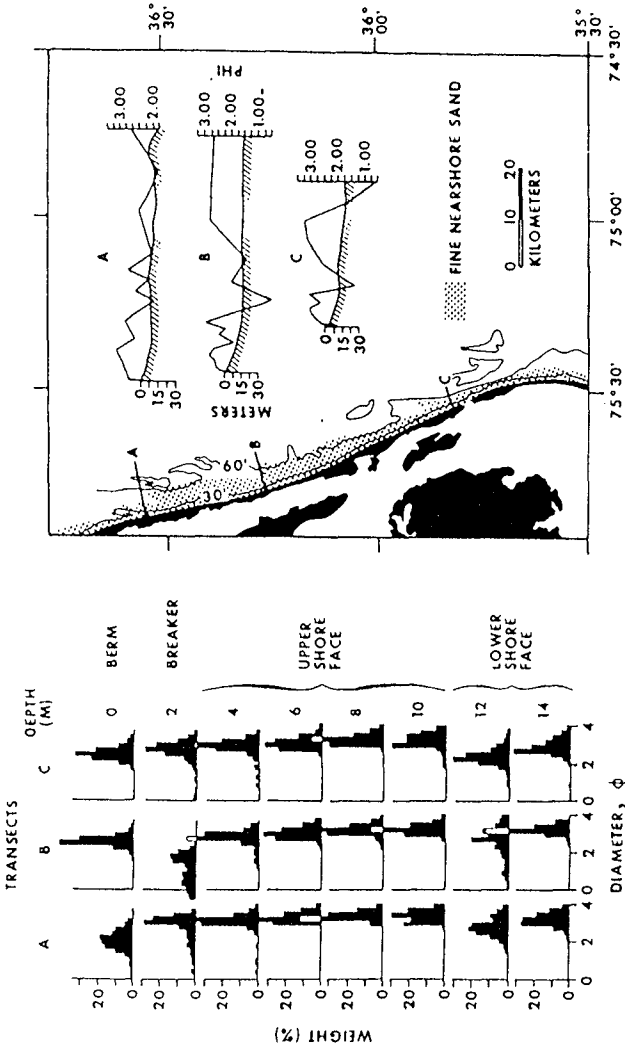


Figure 2. Distribution of grain sizes (in Phi units) along three shoreface transects of Virginia-North Carolina coast [from USACE, 1984, after Swift et al, 1971]

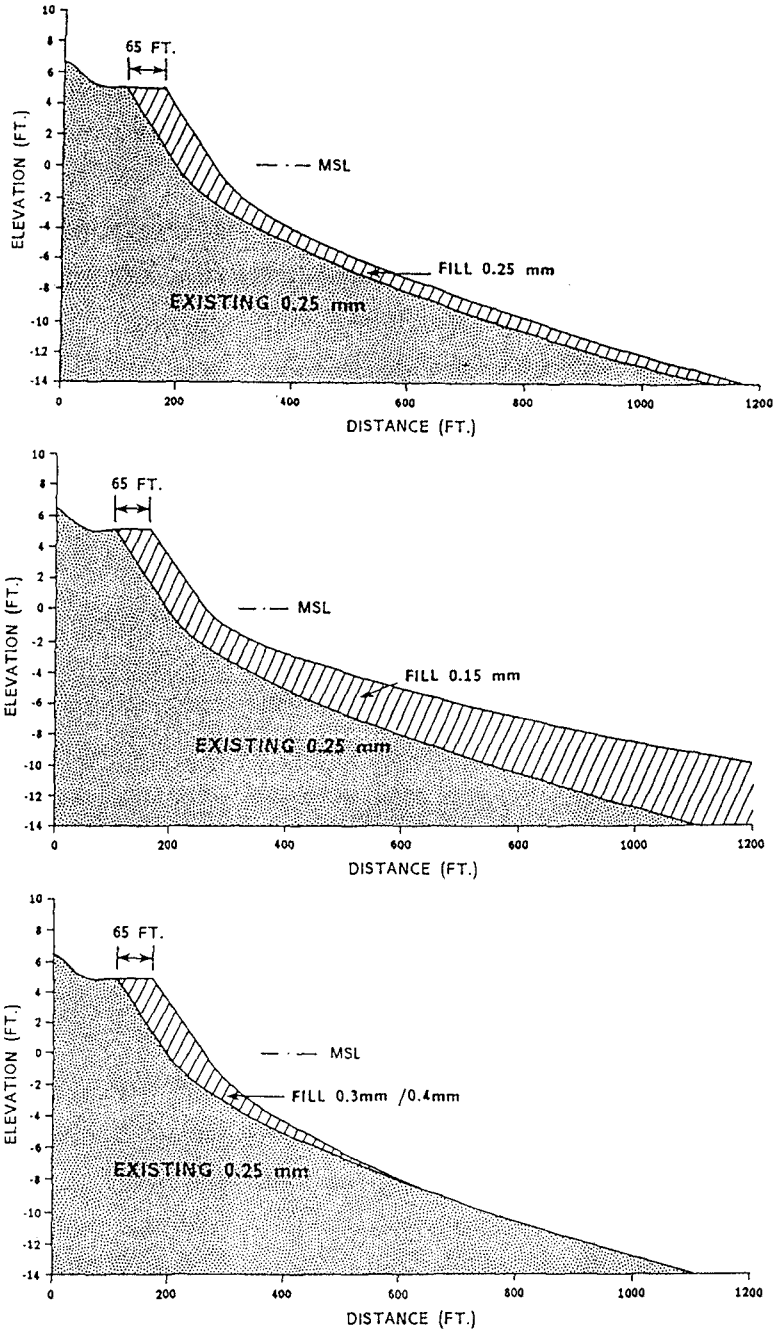


Figure 3. Theoretical equilibrium profiles to produce a uniform berm width using borrow sediments that: matches native sediment (top), is finer than native sediment (middle), and, is coarser than native sediment (bottom) [from Siah et al., 1985, after Dean, 1983]

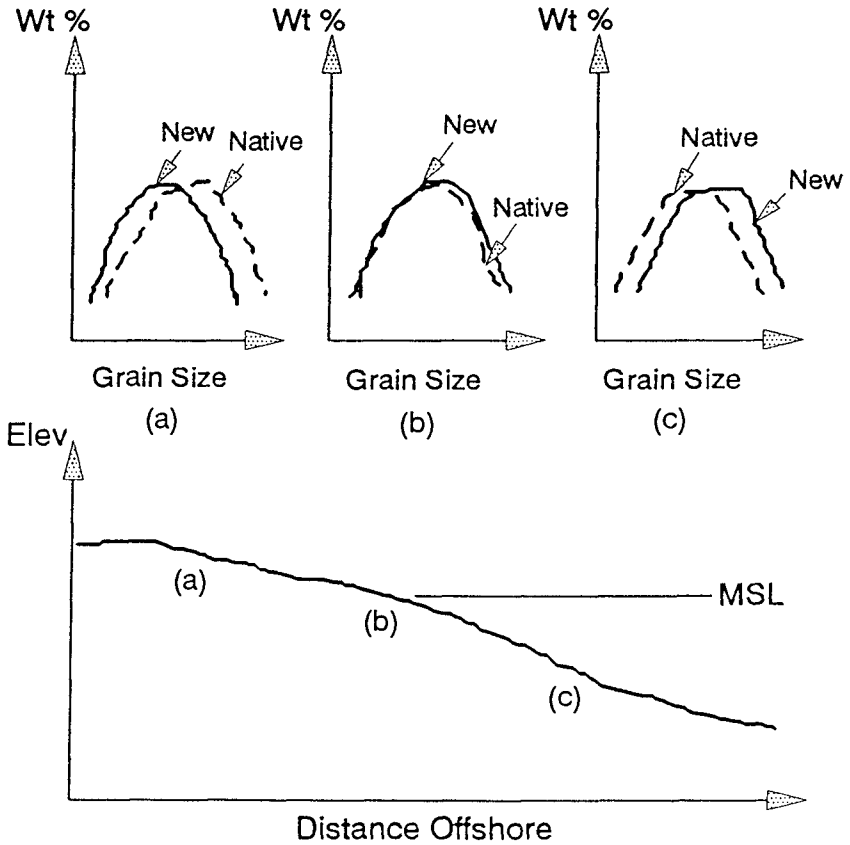


Figure 4. Schematic of the conceptual model relating to a shift in grain size distribution under a hydraulic fill with discharge along the back shore. [This assumes that the borrow source contains some fraction of sediment which is coarser than the native sediment]

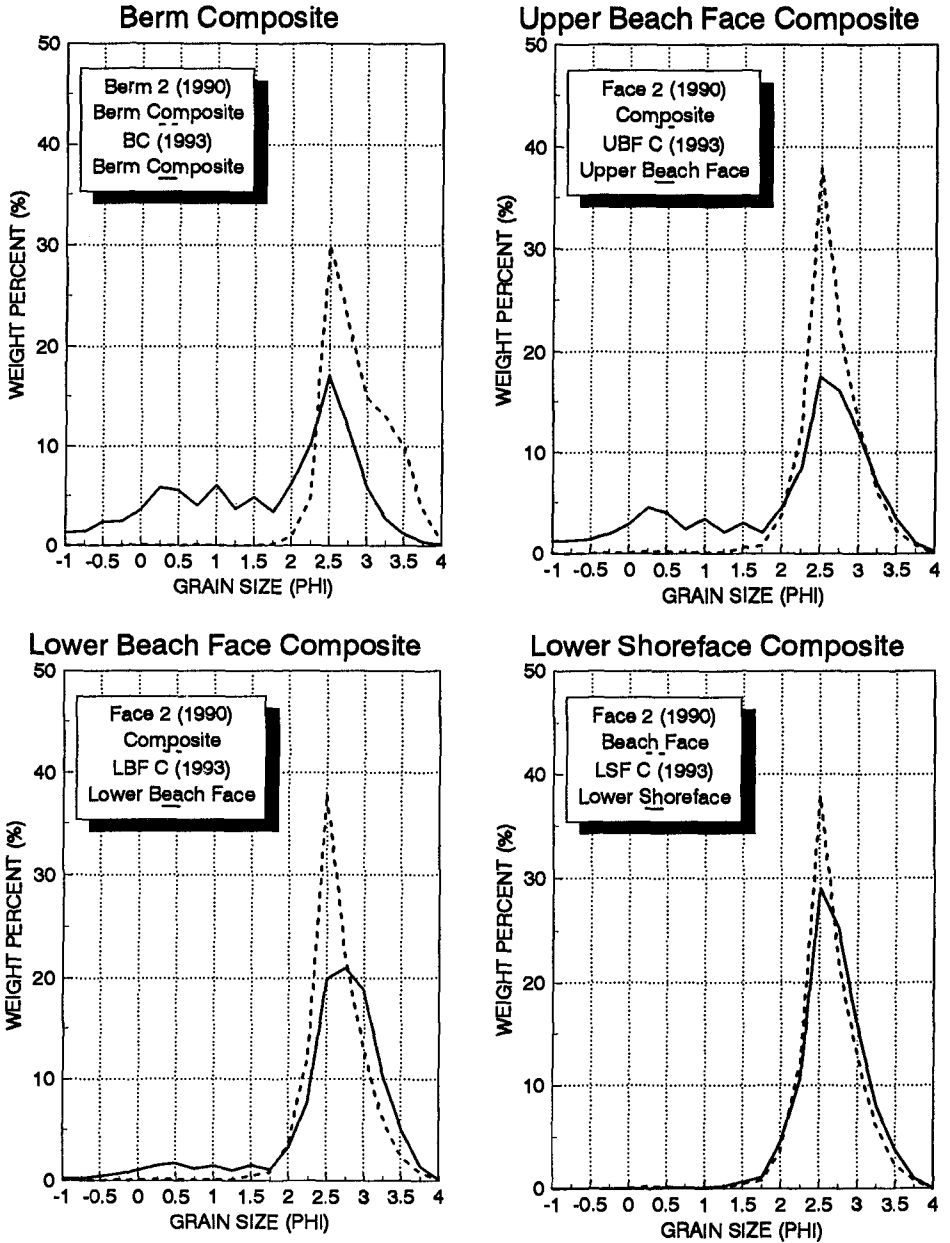


Figure 5. Grain-size comparison plots of 1990 versus 1993 beach composites for the Hunting Island beach nourishment project.

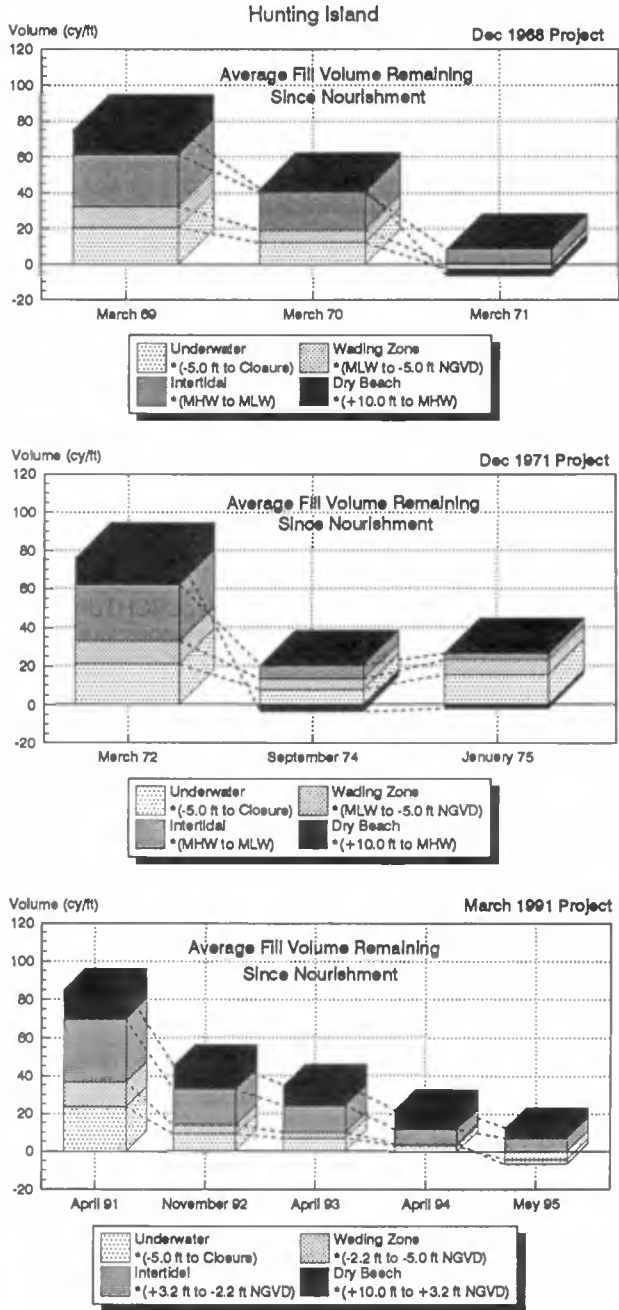


Figure 6. Estimated average unit volume fill remaining after the December 1968, December 1971, and March 1991 nourishment projects as a function of contour interval* within the Hunting Island project limits (based on surveys by USACE and CSE).

CHAPTER 371

The Use of Data Assimilation to Improve Wave Hindcast Results

Jon M. Hubertz¹

Abstract

A sequential data assimilation scheme was used to assimilate wind speed and direction measured at land and buoy platforms into a modeled wind field over the Gulf of Mexico during January 1996. The resulting wind field is more accurate than the modeled field alone for locations near the coast where winds are affected locally by transition from land to water. The assimilated winds result in improved hindcasts of wave height over modeled winds alone when compared to wave measurements from buoys.

Introduction

Data assimilation is the process of incorporating observations of a dynamic system into a model of the system. In the context of wave modeling, this is the process of incorporating observed wind and/or wave information into a wave model or the results from a wave model. At this stage of wave model development, the most significant and timely improvement in the accuracy of model results lies in the combination of measurements and model results.

The Wave Information Study (WIS) at the Coastal and Hydraulics Laboratory (CHL) has developed and is applying a WIS Data Assimilation System (WDAS) to make optimal use of data collected under the Coastal Field Data Collection Program at CHL. The objective is to improve the accuracy of hindcast results, especially in high energy events where available wind fields and/or present wave models are sometimes not sufficiently accurate.

¹Coastal and Hydraulics Laboratory, U.S. Army Engineer Waterways Experiment Station, 3909 Halls Ferry Road, Vicksburg, MS 39180-6199

Accuracy of Present Wave Models

Cardone et al. (1996) conclude that first, second, and third generation wave models presently in use give equivalent results when used to hindcast extreme wave heights in two severe storms off the U.S. East Coast. Their conclusion is based on comparison of model results to measurements from nine buoys. They also note that all models underestimate the highest waves over 12 m. Tracy and Cialone (1996) provide statistics from comparison of results from the same second generation model used by Cardone et al. to 16 buoys off the U.S. East Coast for one year, 1994. They conclude there is little bias in wave height and peak period results from the model compared to measurements, and root mean square differences are about 0.5 m and 2 sec, respectively. Until a significant improvement in wave modeling emerges, the most expedient approach to improved accuracy is the use of data assimilation in wave hindcasting.

Assimilation Techniques

All data assimilation techniques attempt to improve the results of a model by using some method to minimize the difference between model results and a set of observations of model variables, spaced closely in location and time to model values and considered more accurate than model values. Data assimilation approaches can be grouped into two general categories. One is referred to as sequential and the other variational.

Sequential techniques use observations to improve model results only at the time the observations occur; that is, current observations are discarded as soon as assimilated. Their success increases with the number of observations in space each time data are assimilated. A number of different approaches are included in the sequential method. These are, in ascending order of complexity, direct insertion, blending, nudging, optimal interpolation, successive corrections, and Kalman filtering.

The adjoint method is a commonly used variational approach. It considers a set of observations in space over a certain time interval which by ergodicity is equivalent to a distribution in probability space. Again, the objective is to minimize the difference between model results and observations or a cost function. This is done by solving a set of equations consisting of the model equations and adjoint equations. The adjoint equations are formed by differentiating the cost functions with respect to a control variable and setting the result equal to zero. This differentiation can be very difficult due to the dynamical coupling between state variables in the cost function and control variables, for example, wave height and wind speed, respectively.

Hubertz, Thompson, and Wang (1996) provide a summary of recent studies which employed these techniques to improve wind, wave, and water level/current model results. The WDAS employs a sequential technique similar to optimal interpolation which allows assimilation of vector or scalar measurements from random points on a

latitude, longitude grid with model data and interpolation to a target grid using minimization of a quadratic form to provide fit and smoothness.

WIS Data Assimilation System

Application of the system consists of three steps. First, available measurements pass through a quality control filter to ensure only valid data are used and they are consistent in characteristics, e.g., units, conventions, elevation, etc. Second, a target grid is specified upon which the results of the assimilation process will be available for use. Randomly spaced measurements and/or data from a model are interpolated to this target grid. Finally, a set of equations (one for each target grid point) is solved which minimizes the difference between input data and final values on the target grid. The equations allow a weight for data type if one type of data is considered more important, and a smoothing weight on a derivative constraint to control smoothness of the final field. The equations to be solved have the form

$$w_d(F_d - F)^2 + \beta^2[(\delta F/\delta x)^2 + (\delta F/\delta y)^2] = \text{Minimum}$$

where F refers to a vector or scalar variable, d to input data, w a weight, β a smoothing parameter, δ the derivative operator, and x , y the longitudinal and latitudinal directions, respectively. The equations are solved with a Gauss-Seidel iteration scheme. Details of the system are provided by Oceanweather Inc. (1996).

Results - Time Series at a Point

Wind speed and direction from buoys and coastal land stations in the Gulf of Mexico were assimilated into an approximate 1 degree latitude, longitude background wind field from the National Meteorological Center (NMC) during January 1996. Figure 1 shows the locations of measured and modeled wind data. Measured data locations are indicated by either the alphabetic Coastal-Marine Automated Network (CMAN) designation or the National Data Buoy Center (NDBC) numeric identifier. Modeled National Center for Environmental Prediction (NCEP) wind results are indicated by the meteorological wind barb symbols.

Measured data are available every hour while NCEP data are available at a 6-hour interval. The NCEP data are interpolated in time to every hour. NCEP values are removed within a specified radius of measured values to give added influence to the measured data. Figure 2 provides an example of the difference between modeled NCEP data, measured data from the buoy and the assimilation product WDAS using both NCEP modeled and buoy data at the grid point closest to the buoy. The WDAS and buoy data are almost identical reflecting the influence of the assimilation process at the grid point closest to the buoy. The NCEP model data depart from the other two most

notably at times of higher wind speeds, which in these cases are due to fronts moving offshore. These are at approximately hours 175, 275, 450, and 650 in Figure 2.

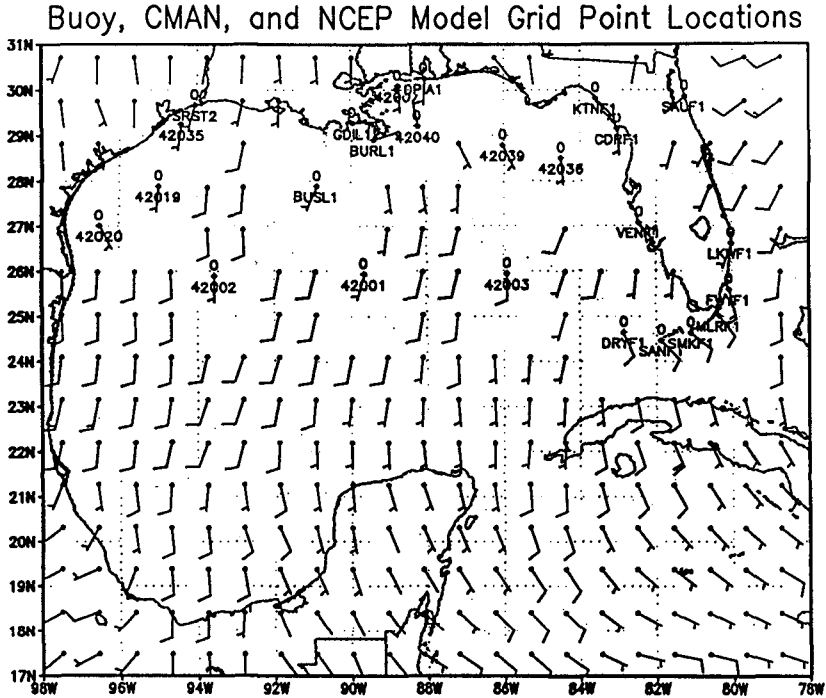


Figure 1. Locations of Measured and Modeled Wind Data

Wind fields from NCEP and from the assimilation process were input to the WISWAVE model to hindcast wave conditions over the Gulf of Mexico during January 1996. The hindcast results were then compared to wave measurements made at the buoys shown in Figure 1. Hindcast wave height results at the grid point closest to the buoy and measured values at the buoy are compared in Figure 3. Wave heights are overestimated at the same times wind speeds are overestimated, the NCEP winds being higher with respect to hindcast values using assimilation with measurements at the buoy. The first 50-75 hours in Figure 3 represent the “spin-up” of the model and should not be used to compare differences in wind input. At other times there is little difference between using NCEP winds and the assimilated wind product.

In general there was little improvement in hindcast wave height and peak period using the assimilated winds over using the NCEP winds alone, as measured by monthly values of bias and root mean square differences at the eight buoys recording wave information during January 1996. However, these monthly statistics mask cases where

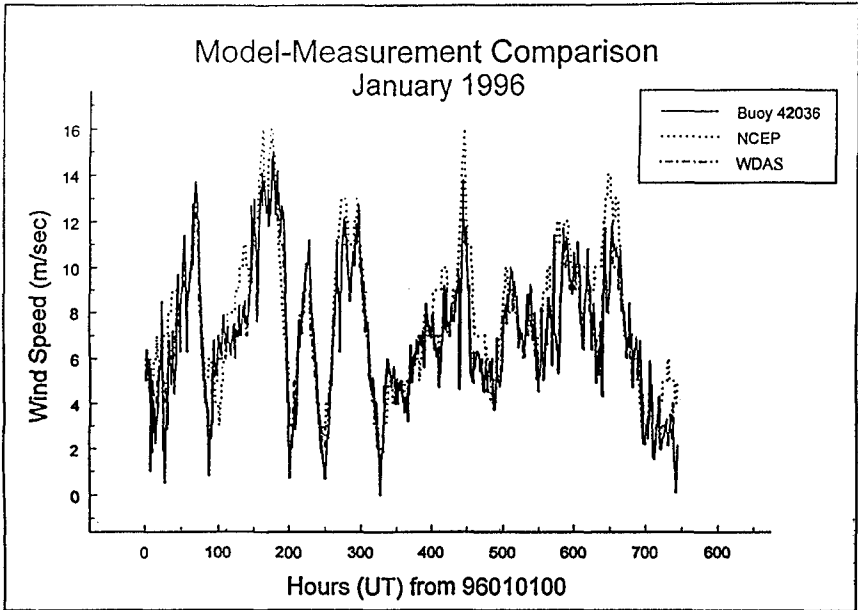


Figure 2. Wind Speed Versus Time at Buoy 42036 for Measured, Modeled, and Assimilated Data

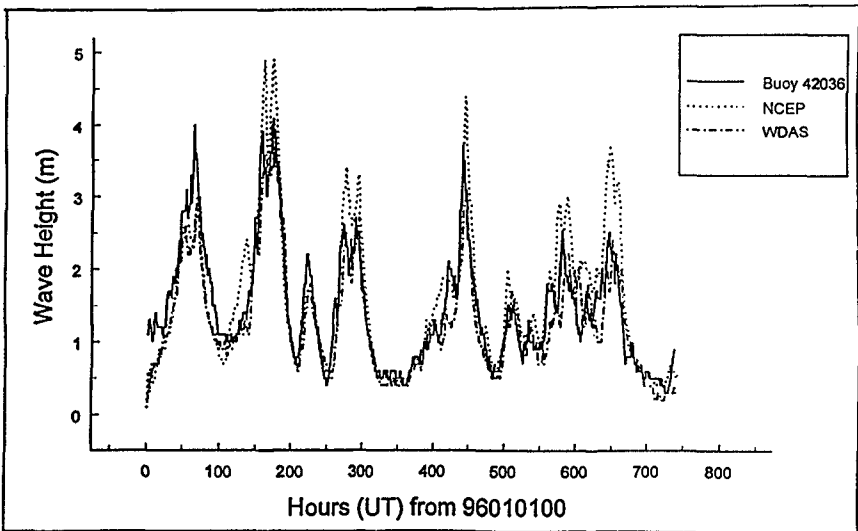


Figure 3. Wave Height Versus Time from WISWAVE Model Using Wind Input from NCEP Model and Winds from WDAS Compared to Measurements from Buoy

the NCEP winds did not accurately represent local wind speeds and directions. In these cases, improved hindcast values of wave height and peak period were obtained.

Results - Wave Height on Grid at One Time

Next, differences in hindcast wave heights over the entire grid at one time are shown for the case of using NCEP winds alone and using the product of the assimilation process. Figure 4 shows the winds over the Gulf of Mexico at 0100 UT on January 28, 1996. This corresponds to hour 650 on the previous time series plots. The contour interval is 1 m/s. Wind speed is relatively high (10 m/s) and offshore along the northwest coast of Florida. It was in this area assimilated winds were lower than NCEP winds (Figure 2) and resulted in lower wave heights of about 1 m (Figure 3).

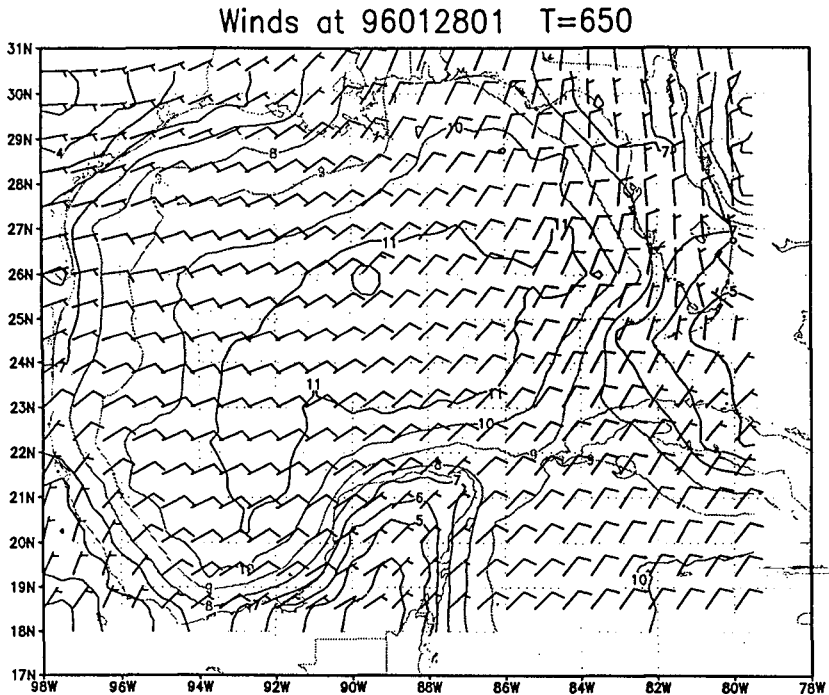


Figure 4. NCEP Wind Field Over Gulf of Mexico at 0100 UT, January 28, 1996

The difference in hindcast wave height using NCEP winds as input and using the assimilated winds as input over the whole Gulf at hour 650 is shown in Figure 5. The contour interval is 0.4 m. Most of the difference is in the northeast Gulf where the land/water boundary has an influence on offshore winds. These differences illustrate the spatial effect of assimilating data when the NCEP winds do not accurately model local

conditions. Note, that in other areas differences are small indicating there is little effect of using assimilation. In these areas at this time, the NCEP winds provide accurate wave results.

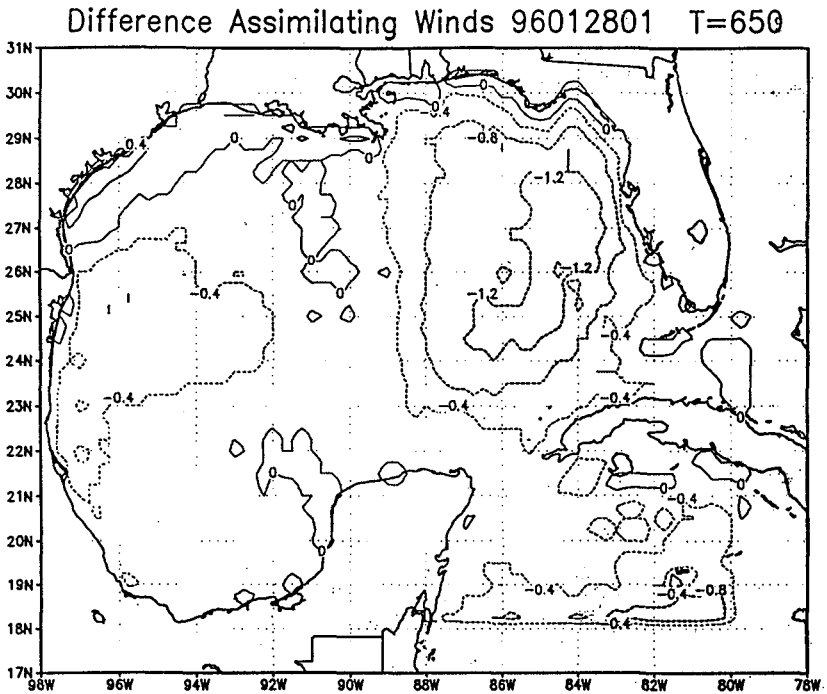


Figure 5. Hindcast Wave Heights Using NCEP Winds as Input Minus Hindcast Wave Heights Using Assimilation Winds as Input (Contour Interval 0.4)

The above applications assume correcting a wind field will lead to acceptable wave model results. If this is not the case, then the wave model is deficient, and accurate hindcast results can only be obtained by fixing the model or modifying the results by assimilating measured wave data. The WIS system can also be used in this mode using either scalar input such as wave height and peak period or vector input from wave height and direction values.

This approach can also be extended to modifying wave spectra. Typically, a WIS hindcast spectra has 20 frequency bands. For a given wave model grid over a geographic region at a given time, one has 20 stacked grids of energy densities representing the energy spectrum at each grid point. Measured energy density corresponding to model bands can be assimilated over the grid at each frequency level. This amounts to applying the system 20 times in a scalar mode using energy density. The resulting volume of data

accurately reproduces the measured spectrum near the measurement point and spreads to surrounding points based on the value of a smoothing parameter.

Conclusions

At this time, first, second, and third generation wave models in use give equally good or bad results. Until advances in the theories of wave models are made, the most expedient improvement in the accuracy of wave hindcast results lies in the use of available measurements to either improve wind input or modeled wave results through data assimilation. Since accurate wave hindcast results are critically dependent on accurate winds, a system has been developed to improve hindcast wind input. The system was tested in the Gulf of Mexico using one month of modeled hindcast winds and available wind measurements from land and buoy platforms.

The system was successful in improving hindcast wave heights for certain times and locations dependent on the land/water boundary and weather systems. Improvements of up to 1 m in wave height were realized. The system will be implemented in the WIS nowcast procedure in a test mode in 1997.

Acknowledgment

This work was carried out under the Coastal Field Data Collection Program, Coastal Engineering Functional Area of Civil Works Research and Development. The Office of the Chief of Engineers, U.S. Army Corps of Engineers is acknowledged for authorizing publication of this paper.

References

- Cardone, V. J., Jensen, R. E., Resio, D. T., Swail, V. R., Cox, A. T. (1996). "Evaluation of Contemporary Ocean Wave Models in Rare Extreme Events: The Halloween Storm of October 1991 and the Storm of the Century of March 1993," Journal of Atmospheric and Oceanic Technology, Vol. 13, No. 1 pp.198-230.
- Hubertz, J. M., Thompson, E. T., Wang, H. V. (1996). "Annotated Bibliography on Coastal and Ocean Data Assimilation," WIS Report 36, U.S. Army Corps of Engineers Waterways Experiment Station, 3909 Halls Ferry Road, Vicksburg, MS 39180-6199.
- Oceanweather Inc. (1996). "Interactive Objective Kinematic Analysis Program for Marine Surface Wind Field Analysis, Documentation and User's Guide," Contractor's Report, Wave Information Study, U.S. Army Corps of Engineers Waterways Experiment Station, Vicksburg, MS 39180-6199.

Tracy, B. T., Cialone, A. (1996). "Wave Information Study Annual Summary Report, Atlantic 1994," WIS Report 34, U.S. Army Corps of Engineers Waterways Experiment Station, 3909 Halls Ferry Road, Vicksburg, MS 39180-6199.

CHAPTER 372

Grain-size influence on sand transport in oscillatory sheet flow

C. Marjolein Janssen¹, Jan S. Ribberink²

Abstract

Experimental investigations (Ribberink & Chen, 1993; Ribberink & Al-Salem, 1994; Katopodi et al., 1994) indicated that the grain diameter is an important parameter for the prediction of the *net* (time-averaged) transport rates in oscillatory sheet flow. As only little is known about the influence of the grain diameter on the net transport rates and the transport mechanisms, new experiments with fine sand ($D_{50} = 0.13$ mm) were carried out in the Large Oscillating Water Tunnel (LOWT) of Delft Hydraulics. Since 1992 the LOWT is equipped with a recirculation system, such that experiments with combined wave-current flow can be performed at full scale (1:1).

Several existing transport models are based on the assumption that the transport can be described in a quasi-steady way (see Janssen, 1995). In order to investigate whether or not this assumption is valid, both a 'quasi-steady' (Baillard, 1981) and a 'semi-unsteady' (Dibajnia & Watanabe, 1992) transport model are verified with existing and new experimental data.

Description of two existing sand transport models

a) Baillard (1981)

The first model described here, is the one developed by Baillard (1981), which is one of the 'quasi-steady' models. These models are based on the assumption that the transport rates under oscillatory flow can be described in a quasi-steady

-
- 1) PhD-student, Delft University of Technology, Dep. of Civil Engineering, p/a Delft Hydraulics, PO Box 152, 8300 AD Emmeloord, The Netherlands.
e-mail: marjolein.janssen@wldelft.nl
 - 2) Formerly Delft Hydraulics; University of Twente, Section Civil Engineering and Management, PO Box 217, 7500 AE Enschede, The Netherlands.
e-mail: j.s.ribberink@sms.utwente.nl

way, which means that it is assumed that the sand transport reacts immediately to changes in flow condition. Therefore a direct relation exists between the instantaneous near-bed free stream velocity or instantaneous bed shear stress and the instantaneous transport rate. The assumption of quasi-steadiness is often applied in sheet flow conditions, where the majority of the sand transport takes place in a thin layer close to the bed and a quick sediment response to the oscillatory flow can be expected (see Ribberink et al., 1994).

The model of Bailard consists of a bed-load and a suspended-load part. Both parts contain a term which depends on the bed slope. Because the model is compared with measurements of sand transport above a horizontal bed, these terms become zero. In order to calculate the *net* sand transport rate, the equation is averaged over the wave-period, resulting in:

$$\langle q_s \rangle = \frac{\rho_w c_f}{(\rho_s - \rho_w) g} \frac{\varepsilon_b}{\tan\varphi} \langle u^3 \rangle + \frac{\rho_w c_f}{(\rho_s - \rho_w) g} \frac{\varepsilon_s}{w_s} \langle |u|^3 u \rangle \quad (1)$$

Where $\langle \dots \rangle$ means time-averaging over the wave period, q_s is the sand transport rate per unit width (m^2/s), ρ_w and ρ_s are the density of the water and the sediment (kg/m^3), c_f is a friction coefficient (-), g is the gravity acceleration (m/s^2), ε_b and ε_s are efficiency factors for the bed-load and the suspended-load transport (-), $\tan\varphi$ is the tangent of the dynamic friction angle (-), w_s is the settling velocity of the sediment (m/s) and u is the horizontal near-bed velocity, directly above the wave boundary layer (m/s).

Because of the assumption of quasi-steadiness *and* the fact that q_s is related to the third- and fourth-power velocity moment, the *net* sand transport rate, predicted by this model, will always be in the direction of the largest velocity, i.e. under real asymmetric waves, generally this will be in the onshore direction.

b) Dibajnia & Watanabe (1992)

Dibajnia & Watanabe developed a 'semi-unsteady' model, which is able to take into account unsteady effects, like the time-lag between velocity and concentration, although it does not contain fully unsteady equations. Considering the amount of sand which is entrained during a positive half wave cycle, the model determines the part which will be transported directly by the positive half cycle and the part that will still be in suspension as the flow reverses and will therefore be transported by the negative velocity, during the successive half cycle. The relative magnitude of these parameters depends on the ratio of the fall time of the particles (determined by their settling velocity and the height to which the particles are suspended) and the period of the positive half wave cycle. Of course the same is valid for the negative half cycle. The net sediment transport rate is the difference between the two contributions in positive and the two contributions in negative direction. For the exact formulations, the reader is referred to the original paper.

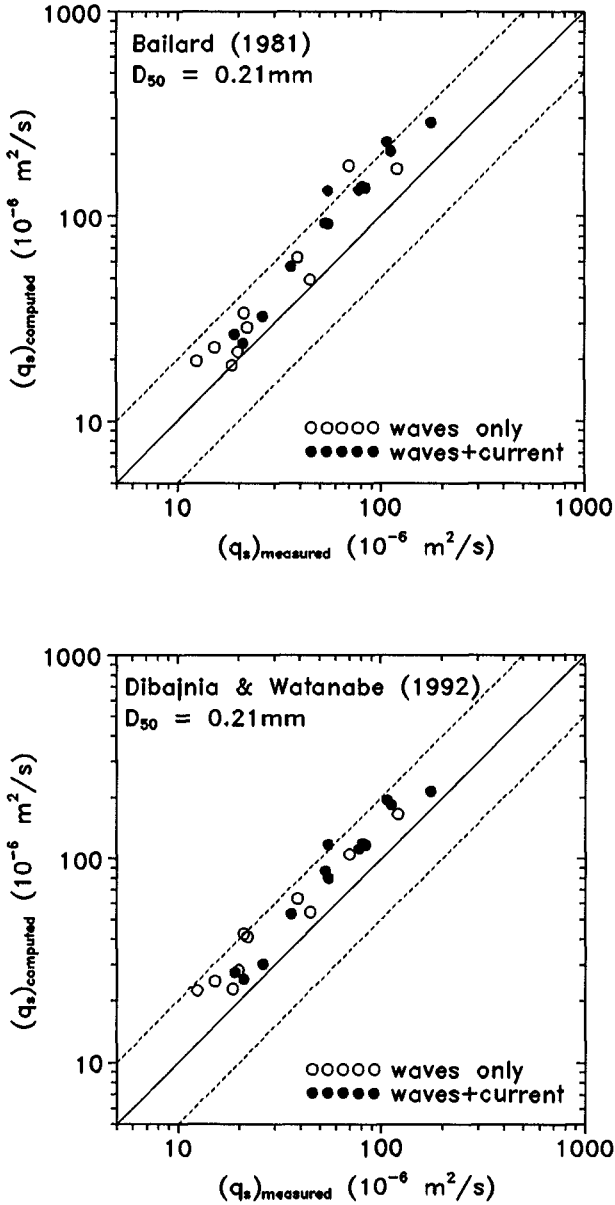


Figure 1: Comparison between measured and calculated net transport rates for sand with $D_{50} = 0.21 \text{ mm}$. Model results of Bailard (1981) and Dibajnia & Watanabe (1992).

Comparison between two models and existing data

In order to verify the two transport models and to check whether the assumption of quasi-steadiness is always valid in sheet flow conditions, predicted net transport rates were compared with measurements, performed in the Large Oscillating Water Tunnel (LOWT) of Delft Hydraulics. This facility enables experiments to be performed at full scale and is able to generate oscillatory flows with net currents superimposed. Net transport rates are derived from a mass-conservation technique by measuring the bed level before and after a test and determining the weight of sand collected during the test in the sand traps. (For a more detailed description see the following pages).

Fig.1 shows the measured and calculated transport rates on log-log scale for the models of Bailard and Dibajnia & Watanabe, respectively. All data are for sand with a mean diameter $D_{50} = 0.21$ mm (settling velocity $w_s = 0.026$ m/s) and both experiments with purely oscillatory flow (Ribberink & Al-Salem, 1994) and combined wave-current flow (Ribberink et al., 1994) are included. All conditions were in the sheet-flow regime. For the model of Bailard the following values of the input parameters are used: $\varepsilon_b = 0.1$, $\varepsilon_s = 0.02$, $\tan\varphi = 0.625$. For the case of purely oscillatory flow c_f is calculated as the friction factor of Jonsson, slightly modified by Swart (1974) with $k_s = D_{50}$. For the case of combined wave-current flow, c_f is calculated as a combined wave-current flow friction factor, developed by Ribberink & Van Rijn and described by Koelewijn (1994). The model of Dibajnia & Watanabe does not require any further input parameters. The solid lines represent perfect agreement between the predicted and the measured transport rates, while the dashed lines represent a factor two difference. It is clear that both models perform similarly, with almost all predictions within a factor two of the measurements. Apparently, the assumption of quasi-steadiness is reasonable in this case of sheet flow conditions and relatively coarse sand.

However, the situation is completely different for transport rates of sand with a mean grain diameter D_{50} of 0.13 mm. Fig.2 shows a comparison between the experimental data (Ribberink & Chen, 1993) and the predictions by the two models. The test conditions of these experiments concerned purely oscillatory, asymmetric (2nd-order Stokes) flow. It must be emphasized that again all test conditions were in the sheet-flow regime. The experiments show the surprising behaviour of a negative net transport rate for increasing root-mean-square velocity (U_{rms}), corresponding to increasing oscillatory velocities. This means that for large oscillatory velocities the *net* sand transport rate is opposite to the direction of the largest velocity (i.e. in 'offshore' direction). Because of the assumption of quasi-steadiness, the model of Bailard is not capable to predict this behaviour and apparently, the assumption of quasi-steadiness is not valid for this fine sand.

In contrast to the model of Bailard, the model of Dibajnia & Watanabe predicts decreasing and even negative net transport rates for increasing oscillatory velocities. This is caused by the part of the entrained sand which remains in suspension and is transported in opposite direction. Due to the asymmetry of the

flow this results in negative net transport rates. Although the trend shown in the data is followed much better by the model of Dibajnia & Watanabe, the magnitudes are still different.

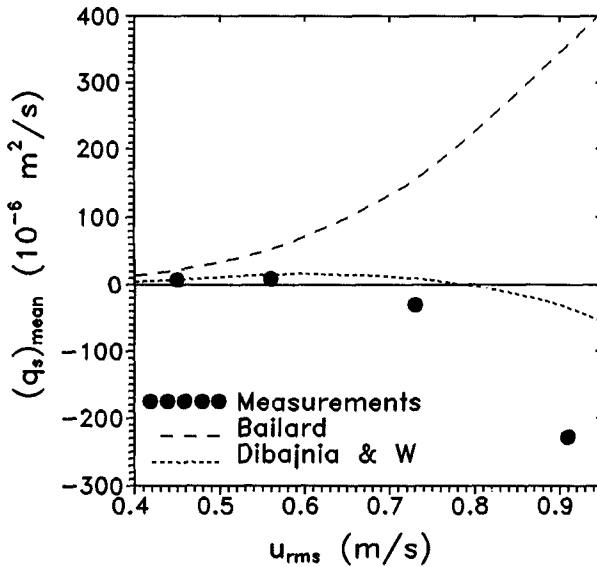


Figure 2: Net transport rates as a function of the root-mean-square velocity (U_{rms}). Measurements by Ribberink & Chen (1993), model results of Bailard (1981) and Dibajnia & Watanabe (1992)

New experiments

From the previous section it is clear that the grain diameter is an important parameter in the prediction of the net transport rate. Apparently, the assumption of quasi-steadiness is not valid in the case of sand transport of very fine sand in purely oscillatory sheet flow conditions. In order to investigate the influence of the grain diameter on the net transport rates and the transport mechanisms in *combined wave-current flow*, a new set of experiments with fine sand ($D_{50} = 0.13$ mm) was performed in the LOWT of Delft Hydraulics. The experimental research was carried out between October 1995 and January 1996 and consisted of two parts. In the first part, net sand transport rates were measured and in the second part, detailed time-dependent measurements of velocity and concentration were performed. This paper focuses on the first part of the experiments, i.e. the net transport measurements.

i) The Large Oscillating Water Tunnel

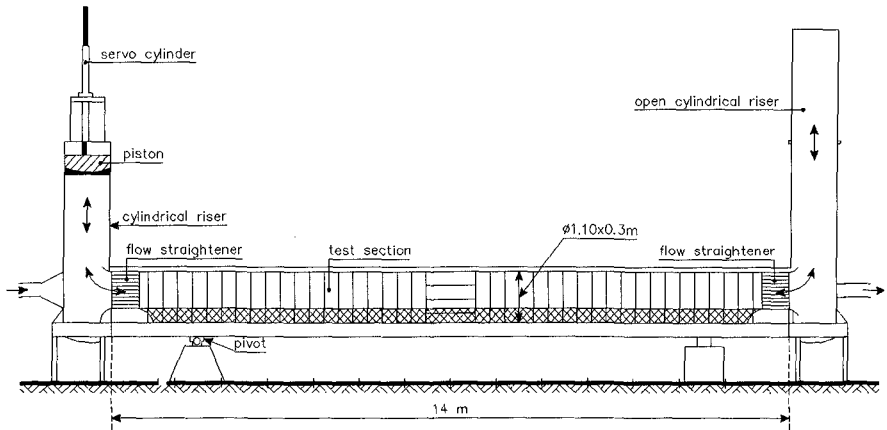


Figure 3: General outline of the Large Oscillating Water Tunnel of Delft Hydraulics.

Fig.3 shows a general outline of the LOWT. The tunnel has the shape of a vertical U-tube with a rectangular horizontal test section and two cylindrical risers on either end. The desired oscillatory water motion inside the test section is imposed by a steel piston in one of the risers. The other riser is open to the atmosphere. The test section is 14 m long, 1.1 m high and 0.3 m wide and is provided with flow straighteners on either end. A 0.3 m thick sand bed can be brought into the test section, leaving 0.8 m height for the flow above the bed. Two sand traps are located underneath the cylindrical risers.

The maximum piston amplitude is 0.75 m, which means a maximum semi-ex-cursion length of the water particles in the test section of 2.45 m. The range of velocity amplitudes is 0.2 - 1.8 m/s and the range of oscillation periods is 4 - 15 seconds. It is possible to generate purely sinusoidal, regular asymmetric and irregular oscillatory motions with the piston.

In 1992 the tunnel was extended with a recirculating flow system connected to the cylindrical risers, so that a steady current can be superimposed onto the oscillatory motion. The maximum superimposed current velocity in the test section of the tunnel is 0.5 m/s. The recirculating flow system is also provided with a sand trap, consisting of a 12 m long pipe with a diameter of 1.2 m. The trap was designed for trapping 90% of the suspended sediments (minimum grain size 100 microns) at maximum flow discharge.

ii) Measurement procedure

During these experiments net transport rates as well as near-bed velocities were measured. The velocities were measured at 10 cm above the bed, using a 2D forward scatter Laser-Doppler system, developed by Delft Hydraulics.

Net transport rates were derived from a mass-conservation technique. Therefore the bed level along the test section is measured before and after the test and the weight of sand, collected in the traps during the test, is determined.

The bed levels in earlier experiments were measured by hand. However, for the present experiments a bed level profiling system (BLPS) was built. The BLPS consists of three bed profilers, mounted on a measurement carriage, which can be moved along the test section. The bed level measurement technique is based on a conductivity measurement. The profilers measure the bed level every cm along the test section, accurate to about 0.4 mm in the vertical. From the difference between the bed level before and after a test, the total volume of sand, eroded from the test section (including pores), can be determined. This sand is collected in the three sandtraps and weighed under water, giving the total volume (without pores).

The transport rate in the middle undisturbed part of the test section can now be calculated by solving the continuity equation for the sediment over the test section, starting either from the left- or from the right-hand side, resulting in two estimates of the net transport rates.

iii) Test conditions

Table 1 Test conditions present experiments

Condition	T (s)	U_m (m/s)	U_a (m/s)
H2	7.2	0.23	0.70
H3	7.2	0.23	0.95
H4	7.2	0.23	1.10
H5	7.2	0.23	1.30
H6	7.2	0.23	1.47
H7	7.2	0.44	0.50
H8	7.2	0.44	0.70
H9	7.2	0.44	0.95
H24	4.0	0.23	0.70
H4S	4.0	0.23	1.10
H12	12.0	0.23	0.70
H12S	12.0	0.23	1.10

The test conditions of the present experiments consisted of combinations of sinusoidal oscillatory flow, with varying amplitudes of the velocity (U_a) and varying oscillation periods (T), superimposed onto varying net current velocities (U_m). Again all test conditions are in the sheet-flow regime. The test conditions

are summarized in Table 1, where the italic typed conditions represent the two test conditions which are equal to the test conditions of earlier experiments with coarser sand (Katopodi et al., 1994).

Results of new experiments in comparison with model predictions

Fig.4 shows the measured net transport rates of the new experiments ($D_{50} = 0.13$ mm) in comparison with the predictions of the two models. The results for a constant net current velocity (U_m) of 0.23 m/s and a constant wave period (T) of 7.2 s are shown as a function of the amplitude of the oscillatory velocity (U_a).

Because of the assumption of quasi-steadiness in the model of Bailard, this model predicts strongly increasing net transport rates for increasing oscillatory velocities. The measured net transport rates have much smaller values and show a weaker increase for increasing oscillatory velocities. The predictions of the model of Dibajnia & Watanabe are much closer to the measured values. However, a more detailed comparison (Fig.4b) shows that this model predicts *decreasing* transport rates for amplitudes of the oscillatory velocity larger than about 1.1 m/s. This is again caused by the unsteady effects. Although the increase in the measured net transport rates is much smaller than predicted by the quasi-steady model, the measurements do not yet show a decrease in transport rate. Thus apparently the unsteady effects are smaller than predicted by the model of Dibajnia & Watanabe. This is opposite to the situation for purely oscillatory flow, where the measurements showed a larger unsteady effect, than predicted by the model of Dibajnia & Watanabe (see Fig.2).

Fig.5 shows a comparison between the measured and calculated net transport rates as a function of the wave period (T), for a constant amplitude of the oscillatory velocity (U_a) of 1.1 m/s and a constant net current velocity (U_m) of 0.23 m/s. In the quasi-steady model of Bailard the wave period only has an effect on the friction factor. Increasing wave periods lead to decreasing friction factors, resulting in decreasing sand transport rates, as shown in Fig.5. However, the measurements show decreasing net transport rates for *decreasing* oscillation periods. The same trend is predicted by the model of Dibajnia & Watanabe. It is caused by the fact that the unsteady effects become relatively more important for decreasing wave periods.

Grain-size influence on net sand transport rates in sheet flow conditions.

The influence of the grain size can be analyzed by just comparing the experimental data and by analyzing the performance of both models for all data of fine and coarser sand. In Fig.6 the net sand transport rates are plotted as a function of the third power velocity moment for all experiments in combined wave-current flow (Ribberink et al., 1994 and present tests). From this figure it is clear that the net transport rates of fine sand are smaller than those of coarser sand. This is completely opposite to the behaviour in uni-directional steady flow, where finer sediments would result in larger transport rates. The decrease in net transport rate

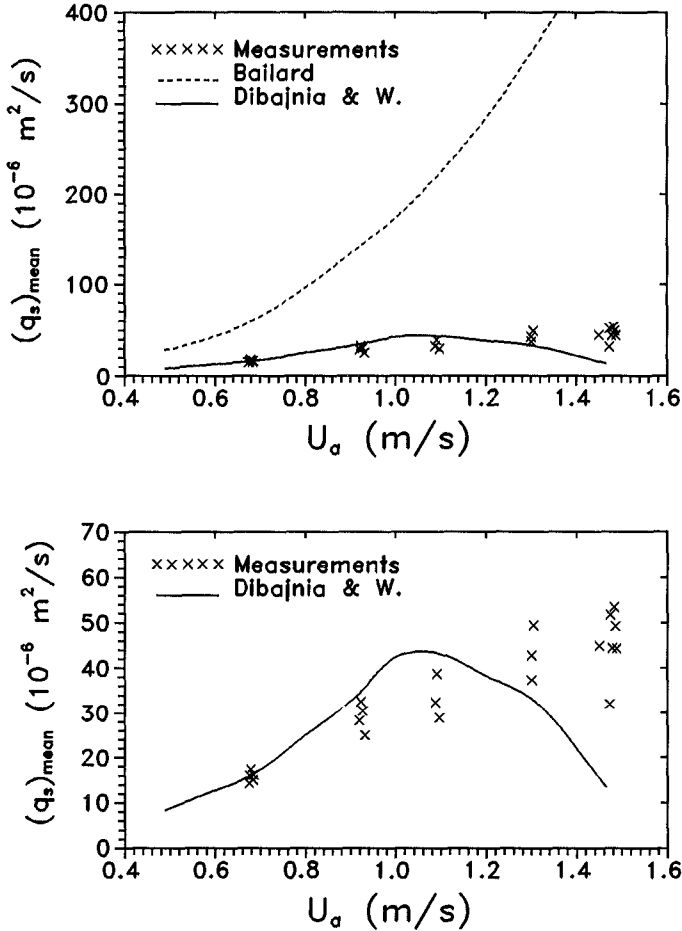


Figure 4: Net transport rates as a function of the amplitude of the oscillatory velocity U_a , for $U_m = 0.23$ m/s and $T = 7.2$ s. Present tests compared with model results of Bailard (1981) and Dibajnia & Watanabe (1992).

is caused by the unsteadiness, as the amount of sand in motion (or gross transport rate) will be larger for the finer sand. However, part of the sand remains suspended and is transported in opposite direction, resulting in smaller net transport rates.

Fig.7 is similar to Fig.1, but now also includes the data for fine sand. The two tests with negative transport rates in purely oscillatory flow (see Fig.2) are left out, because they cannot be plotted on a log scale. As observed before, both

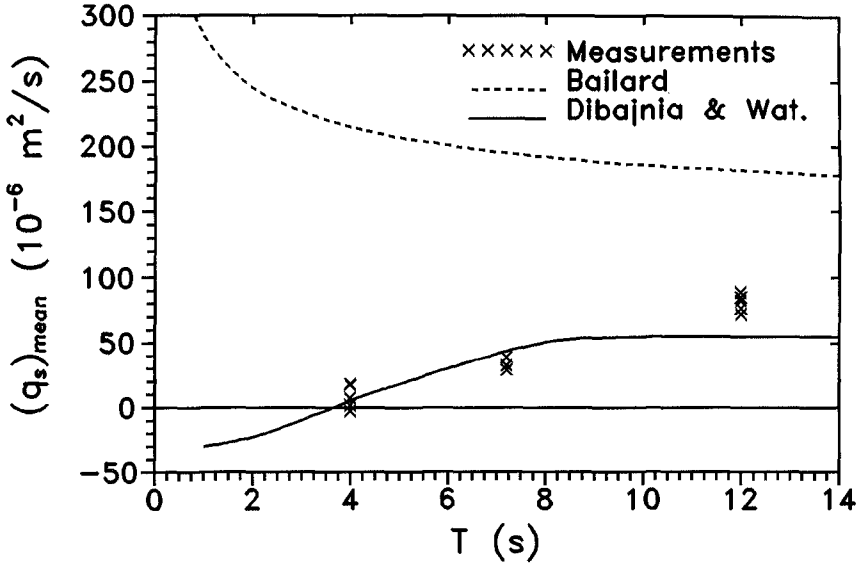


Figure 5: Net transport rates as a function of the oscillation period T, for $U_m = 0.23$ m/s and $U_a = 1.08$ m/s. Present tests compared with model results of Bailard (1981) and Dibajnia & Watanabe (1992).

models show a similar kind of agreement with the experimental data for sand with a mean grain diameter of 0.21 mm. However, the 'quasi-steady' model of Bailard largely overpredicts the measured transport rates of fine sand. Due to the inclusion of unsteady effects in the model of Dibajnia & Watanabe, predictions by the latter model for fine sand are much better. This confirms the fact, already observed for the purely oscillatory flow data, that even in sheet flow conditions the assumption of quasi-steadiness of the transport rates is not always valid for fine sand.

Analysis of unsteady behaviour of net transport rate of fine sand

In order to analyze the unsteady behaviour of the transport rate of fine sand, use is made of the results from the second part of the experiments (time-dependent measurements of velocity and concentration). The net sand transport rate can be calculated from:

$$\langle q_s \rangle = \int_0^h \langle u(z,t) * c(z,t) \rangle dz = \int_0^h \langle \phi(z,t) \rangle dz \tag{2}$$

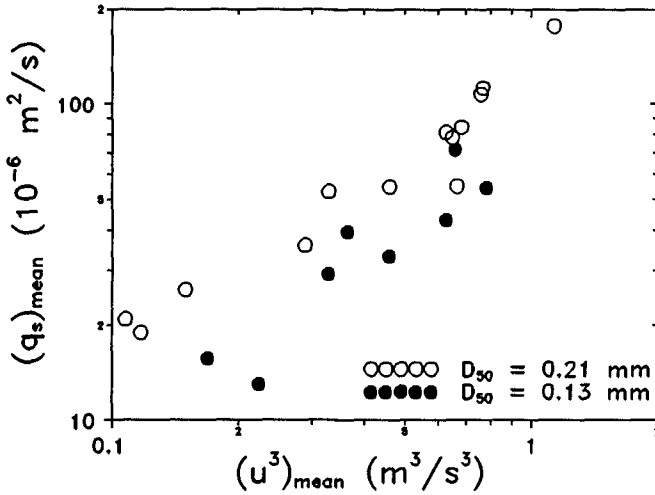


Figure 6: Measured net transport rates for fine ($D_{50} = 0.13$ mm) and coarse ($D_{50} = 0.21$ mm) sand as a function of the third-power velocity moment.

Where c is the sediment concentration (m^3/m^3), φ is the sediment flux (m/s), z is the height above the bed (m), t is time (s) and h is the water depth (m).

Because both the velocity and concentration consist of a time-averaged ($\langle \dots \rangle$) and an oscillatory (\sim) component, the time-averaged sediment flux $\langle \varphi(z) \rangle$ can be split up into a current-related $\langle \varphi_c(z) \rangle$ and a wave-related $\langle \varphi_w(z) \rangle$ contribution, as follows:

$$\langle \mathbf{u}(z, t) * c(z, t) \rangle = \langle \mathbf{u}(z) \rangle * \langle c(z) \rangle + \langle \tilde{\mathbf{u}}(z, t) * \tilde{c}(z, t) \rangle = \langle \varphi_c \rangle + \langle \varphi_w \rangle \quad (3)$$

The vertical distributions of these two contributions, as well as the total (time-averaged) flux profile, are shown in Fig.8 (for more detail about the time-dependent measurements, see Janssen et al., 1996). The results are for test condition H6 (see Table 1). It is clear that the total net transport rate (derived by integrating the total flux profile over the height), will be positive (i.e. in the direction of the net current). Of course the current-related contribution is positive everywhere, because it is just the product of the time-averaged velocity (which is positive by definition, because it is the velocity of the net current) and the time-averaged concentration. However, the wave-related contribution has a value which is of the same order of magnitude, but in opposite direction (against the net current). This must be caused by a time-lag effect between the oscillatory component of the concentration and the oscillatory velocity. Because of this negative wave-related transport rate, the total net transport rate will be much smaller than

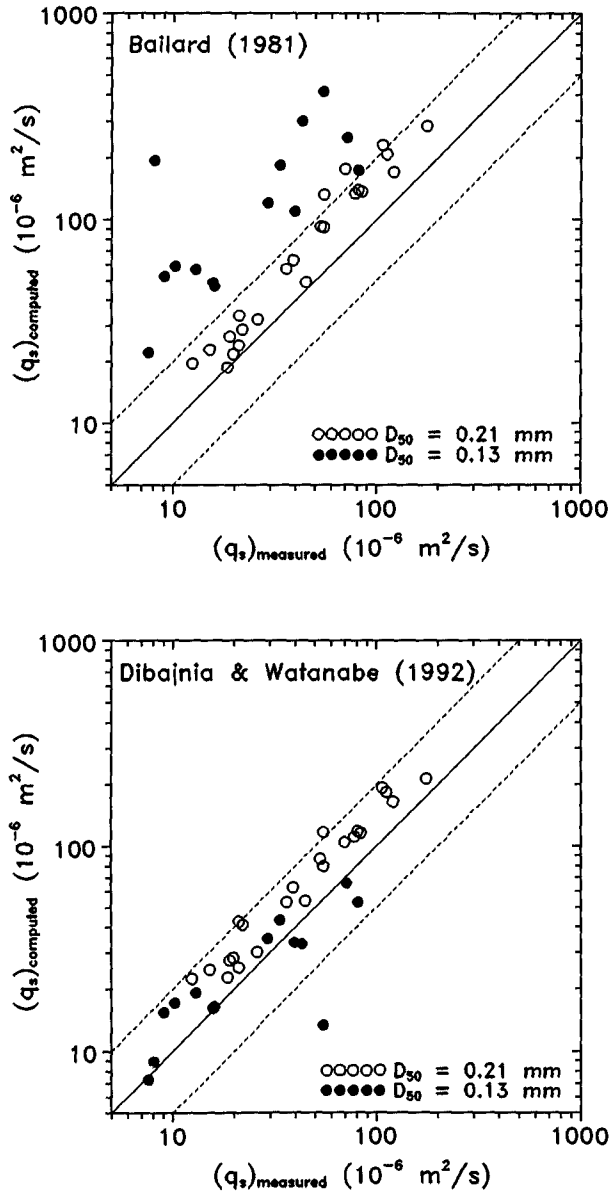


Figure 7: Comparison between measured and calculated net transport rates for fine sand ($D_{50} = 0.13$ mm) and coarse sand ($D_{50} = 0.21$ mm). Model results of Bailard (1981) and Dibajnia & Watanabe (1992).

predicted by the 'quasi-steady' model, which does not include this effect. Additionally, the total net transport rate will be smaller than in the case of coarser sand, where the larger particles result in a smaller time-lag between concentration and velocity and therefore less negative wave-related transport rates. So apparently, the behaviour, as present in the concept of the model of Dibajnia & Watanabe is not only occurring in rippled bed conditions, but also occurs in sheet flow conditions with fine sand.

Conclusions

Modelling the sand transport in a quasi-steady way leads to the following predictions for net sand transport rates: i) increasing net transport rates for decreasing grain diameter, ii) largely increasing net transport rates for increasing oscillatory velocities and iii) increasing net transport rates for decreasing wave periods. However, experimental data of net transport rates in oscillatory sheet flow show the following results:

- *Smaller* net transport rates for 0.13 mm sand than for 0.21 mm sand.
- A much *weaker increase* in net transport rates for 0.13 mm sand than for 0.21 mm sand, with increasing oscillatory velocities.
- *Decreasing* net transport rates with decreasing wave periods for sand with $D_{50} = 0.13$ mm and conditions with sufficiently large oscillatory velocities.

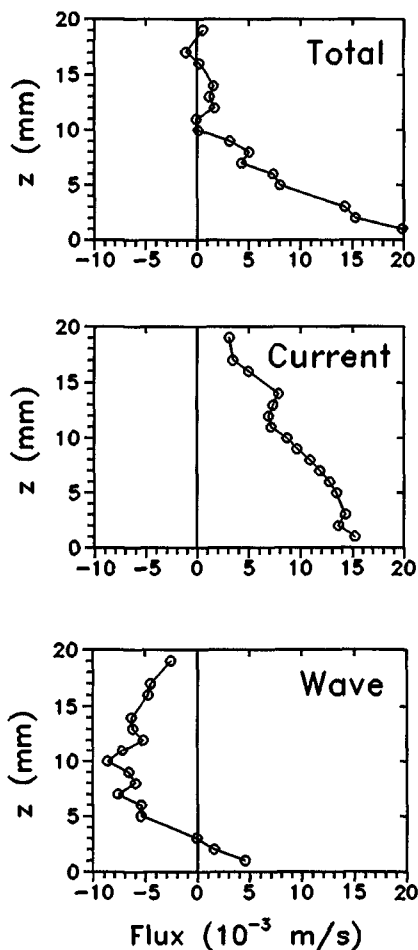


Figure 8: Vertical distribution of time-averaged total, current- and wave-related sediment flux, determined from time-dependent velocity and concentration measurements (experiment H6).

All these 'unsteady effects' are caused by a time-lag between velocity and concentration, resulting in negative wave-related transport rates and therefore smaller total net transport rates than without these effects. Apparently, even in sheet flow conditions, the net sand transport rate cannot always be described in a quasi-steady way. Obviously, the quasi-steady model of Bailard (1981) is not able to predict these phenomena. The 'semi-unsteady' model of Dibajnia & Watanabe (1992) is at least able to predict the behaviour qualitatively. However, this model underpredicts the unsteady effects in purely oscillatory asymmetric flow and overpredicts the unsteady effects in the case of combined wave-current flow (compare Fig.2 and Fig.4b).

Acknowledgements

The authors want to thank the Dutch Ministry of Transport and Public Works (RIKZ), for the financial support to perform the experiments. The help of Mr. W.N. Hassan and Mr. R.J. v.d. Wal during the experiments and the data-processing is greatly appreciated. The first author also wants to thank the Technology Foundation (STW) for their financial support during the complete research project.

References

- Bailard, J.A. (1981). An energetics total load sediment transport model for a plane sloping beach. *J. Geoph. Res.*, Vol. 86, No. C11, pp. 10938-10954.
- Dibajnia, M. & A. Watanabe (1992). Sheet flow under nonlinear waves and currents. *Proc. 23rd ICCE, Venice*, pp. 2015-2028.
- Janssen, C.M. (1995). Sand transport in oscillatory sheet-flow; a literature review. Delft University of Technology, Communications on Hydraulic and Geotechnical Engineering, Rep. No. 95-6, ISSN 0169-6548.
- Janssen, C.M., W.N. Hassan, R. v.d. Wal, J.S. Ribberink (1996). Net sand transport rates and transport mechanisms of fine sand in combined wave-current sheet flow conditions. *Delft Hydraulics, Data report H2462, Part IV*.
- Katopodi, I., J.S. Ribberink, P. Ruol & C. Lodahl (1994). Sediment transport measurements in combined wave-current flows. *Proc. Coast. Dyn.'94, Spain*.
- Ribberink, J.S. & Z. Chen (1993). Sediment transport of fine sand under asymmetric oscillatory flow. *Rep. H840, Part VII, Jan 1993, Delft Hydraulics*.
- Ribberink, J.S. & A.A. Al-Salem (1994). Sediment transport in oscillatory boundary layers in cases of rippled bed and sheet-flow. *J.Geoph.Res.*, Vol.99, C6.
- Ribberink, J.S., I. Katopodi, K.A.H. Ramadan, R. Koelewijn & S. Longo (1994). Sediment transport under (non)linear waves and currents. *Proc.24th ICCE*.
- Jonsson, I.G. (1966): Wave boundary layers and friction factors. *Proc.10th ICCE*.
- Koelewijn, H. (1994): Sediment transport under sheet-flow conditions. *M.Sc. Thesis, Delft University of Technology, October 1994, 98 pp*.
- Swart, D.H. (1974): Offshore sediment transport and equilibrium beach profiles. *Delft Hydr. Lab. Publ., No. 131, Delft Hydraulics, The Netherlands*.

CHAPTER 373

Cross-shore sediment transport mechanisms in the surfzone on a timescale of months to years

Klaas T. Houwman¹ and Gerben Ruessink¹

Abstract

The relevance of several cross-shore sediment transport mechanisms on a timescale of months to years was studied. Data from a large measuring campaign carried out in the outer surfzone of a barred surfzone was used to calculate sediment fluxes. The transport rates were calculated using the measured near bed velocities and sediment concentrations, and two sediment transport models. Both fluxes and the transport rates are only significant during breaking waves. The high-frequency fluxes/transportations are onshore directed, the mean fluxes/transportations are offshore directed, and the low frequency waves also give offshore directed fluxes/transportations. Taking into account the frequency of occurrence of the conditions, the breaking wave conditions turned out to be the most important for the cross-shore sediment transport on a timescale of a year. The cross-shore sediment transport is a delicate balance between the onshore directed high frequency term and the offshore directed mean term. Therefore the smaller terms, like the low frequency term and the bedload term, may still be of importance to the net sediment transport.

Introduction

In the surfzone mean currents and high- and low frequency waves are responsible for sediment transport. Most field experiments presented in literature have focussed a typical time scale of a single storm-event. It is therefore unknown whether sediment transport on the scale of months to years is dominated by infrequent high energy conditions or by the often occurring calm to moderate conditions. In the frame work of the NOURTEC-project (Hoekstra et al., 1994) a shoreface nourishment was carried out in the multiple bar system of the Dutch island of Terschelling. A large-scale field measuring program, started to monitor this nourishment, offered an opportunity to determine the most important sediment

¹ Institute for Marine and Atmospheric Research, Utrecht University, Department of Physical Geography, P.O.Box 80.115, 3508 TC Utrecht, The Netherlands.

transport mechanisms at different locations in a barred surfzone and to evaluate the relevance of these mechanisms on a time scale of months to years. The sediment transport mechanisms were evaluated in the following way. Firstly, sediment fluxes were calculated using the measured velocity and sediment concentrations to determine the importance of mean currents, and high- and low-frequency waves to the *suspended* sediment transport on a time scale of a few weeks. These fluxes were related to the ratio of the local wave height and the local waterdepth (H_{m0}/h), incorporating both changes in wave conditions and tidal water levels. Secondly, the Bailard (1981)-approach was used to evaluate the relative importance of currents, high- and low frequency waves to the suspended sediment transport. The calculated contributions of the currents and waves were combined with a probability density function of H_{m0}/h to obtain insight in the effects on a timescale of years. Finally, a convection-diffusion sediment transport model (Van Rijn, 1993) was used, again in combination with probability density functions to evaluate the influence of waves and currents.

The Terschelling field site and data acquisition

The field experiment site is fully exposed to the North Sea with an annual mean significant offshore wave height of 1.1m (Van Beek, 1995). The tide is semidiurnal with a range of 1.5 and 2.5m during neap and spring tide, respectively. The nearshore area can be described as very dissipative with a very mild overall slope (1:200) and is characterized by the presence of several breaker bars (Hoekstra et al., 1994). In the period May 1994 to November 1995 three measuring campaigns were carried out: T2- (May and June 1994), T3- (October and November 1994), and the T4- (October and November 1995) campaign of five weeks each. The offshore significant wave height during the whole period ranged from 0.2 to 5m. During these campaigns four tripods (F2 to F5) were positioned in a cross-shore array (see Figure 1). Each tripod was equipped with two electro-magnetic flow meters (EMF) at an initial height of 0.25 and 1.2m above the bed and with a pressure sensor at 2.2m above the bed. On the tripods F3, F4 and F5 also two optical back scatter sensors (OBS) at 0.15m and 0.25m above the bed were installed. Timeseries were acquired with a sampling frequency of 2 Hz for 2048 seconds per hour. During the whole period from May 1994 to November 1995 the tripod F3 operated continuously (however without OBSs). At a waterdepth of 15m a wave directional buoy (WAVEC) was operational during the same period. The morphology landward of F4 evolved from a more or less alongshore uniform bar-trough system during the T2 and T3 campaigns to a three dimensional bar system during the T4 campaign. Seaward of F4 no large morphological changes were observed.

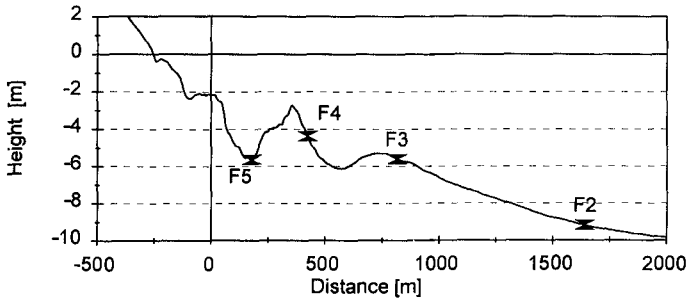


Figure 1. Instrumented positions and cross-shore profile of June 1994

Field observations of suspended sediment fluxes

Method

Fluxes were calculated from the measured timeseries of the cross-shore velocity u and concentration c . These timeseries were divided into a mean- and a high and low frequency oscillating term.

$$\langle u.c \rangle = \langle \bar{u}.\bar{c} \rangle + \langle \tilde{u}_h.\tilde{c}_h \rangle + \langle \tilde{u}_l.\tilde{c}_l \rangle \quad (1)$$

The left-hand side of (1) is the net suspended sediment flux; the first term on the right-hand side is the mean flux and the second and the third one are the high frequency and low frequency oscillating flux, respectively. The brackets denote time-averaged values. A positive flux is directed onshore. The separation frequency between high- and low-frequency waves was set to 0.04 Hz. Because of the different height at which u and c were measured, a correction for \bar{u} had to be applied. Here, a simple engineering rule was used (Van Rijn, 1991), which reads as

$$\bar{u}_1 = \bar{u}_2 \left(\frac{z_1}{z_2} \right)^{0.25} \quad (2)$$

As a result, \bar{u} at $z = 0.15$ m was about 88% of that at $z = 0.25$ m. Very small offsets in \bar{c} ($< 1 \text{ kgm}^{-3}$) were encountered and corrected for. For this reason, the background concentration equaled 0 kgm^{-3} .

Results

Burst-averaged values of the high- and low-frequency oscillating fluxes at $z = 0.15$ m at F3 (T2 and T4-), F4 (T2 +T3-) and F5 (T2 campaign) are plotted in Figure 2 as a function of the local relative wave height (spectral wave height based on short wave

band) H_{m0}/h . A study of Van Enckevort and Reincke (1996) made in the intertidal zone of the same cross-shore transect showed that initial wave breaking starts at $H_{m0}/h = 0.33$. In other words, the highest wave in a wavegroup is breaking at this local relative wave height. Assuming that this relationship holds for the deeper parts of the nearshore zone, a distinction can be made between transport under breaking and nonbreaking wave conditions.

F3: At F3 non-zero fluxes only occurred for H_{m0}/h values larger than about 0.3 - 0.35 at the lower sensor (Figure 2) and 0.35 - 0.4 at the upper one (not shown). In other words; when wave breaking occurs at that location. High-frequency fluxes were onshore directed and were associated with the horizontal asymmetry of the incident short waves, i.e. the difference in magnitude between onshore and offshore orbital motion. Low-frequency fluxes were rather small and seaward directed and were likely related to bound long waves.

For $H_{m0}/h < 0.3$ sediment was not resuspended on the time scale of individual short waves nor on that of wave groups. The negligible oscillating fluxes for $H_{m0}/h < 0.3$ thus seemed to be mainly due to a lack of coherence between u and c for almost all frequencies. In addition, the variance in c was very low at both sensors compared to more energetic events.

For $H_{m0}/h > 0.3$ sediment was stirred on both the individual short-wave and wavegroup time scale. The co-spectrum between u and c showed the 'classic' shape of a large positive (onshore) peak at the peak frequency of the short waves and a broad negative (offshore) peak at infragravity frequencies (cf. Huntley and Hanes, 1987). The phases at the peak frequency were between -45 and 0 degrees, which indicates that c lagged u slightly. Phase lags between both sensors were, in general, negligible at both high and low frequencies.

The oscillating fluxes at $z = 0.25$ m were considerably smaller than at $z = 0.15$ m. The sediment fluxes at the upper OBS were about 29 % and 4 % of that at the lower OBS for the high- and low-frequency sediment flux, respectively.

Time-averaged values of the mean flux at $z = 0.15$ m are also shown in Figure 2 as a function of H_{m0}/h . The largest fluxes, which were in a seaward direction, occurred for conditions with H_{m0}/h above 0.3 to 0.35. This indicates that these negative fluxes were associated with wave-driven undertows.

F4: The same pattern for the oscillating fluxes and the mean fluxes were also found at F4. However, during one wave event offshore directed high frequency fluxes occurred as well, caused by phase lags between \tilde{u}_h and \tilde{c}_h larger than 90 degrees. The reason for these large phase lags is not fully understood. In general, phase lags are ascribed to the presence of ripples (e.g., Vincent and Green, 1990), though they have also been observed in the sheetflow regime (e.g., Ribberink and Al-Salem, 1995). Why such large phase lags developed during this particular storm (presumably sheet flow conditions) and not during other ones or at other positions is unknown. The mean fluxes at F4 were not only offshore directed due to undertows, but also onshore directed velocities and fluxes were observed (Figure 2). The origin of these onshore currents is not clear. On average, the mean fluxes were offshore directed and the averaged high-frequency fluxes onshore.

F5: In the trough at F5, no breaking wave conditions occurred ($H_{m0}/h < 0.3$). Although some scatter is present at the high frequency fluxes (Figure 2), no systematic contribution of this term was found. The scatter at the mean fluxes was not the result of enhanced cross-shore currents, but was caused by high sediment concentrations unrelated to the cross-shore velocity signal. These high sediment concentrations were probably the result of the tidal longshore currents in combination with bedforms.

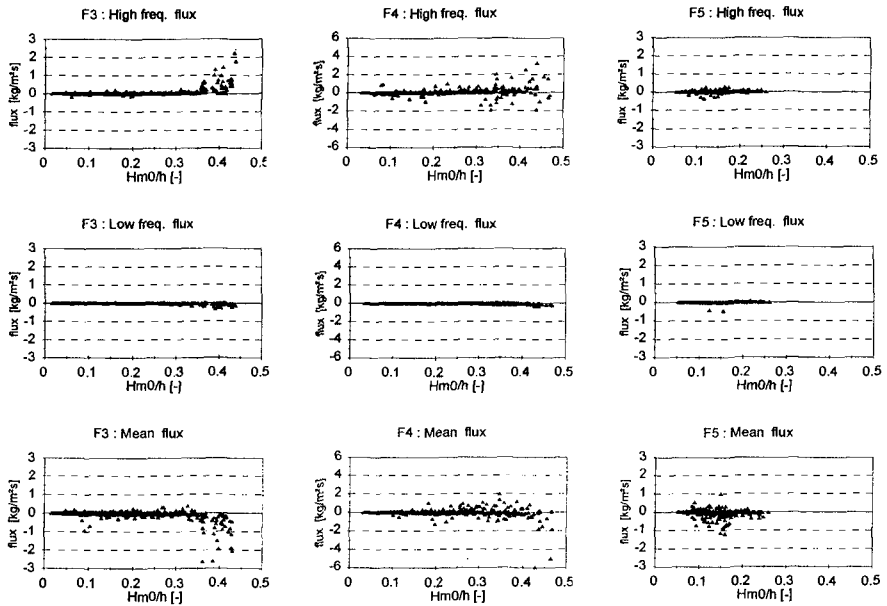


Figure 2. Measured fluxes at 15 cm above the bed at F3, F4 and F5

Long-term suspended sediment transport: an energetics approach

Introduction

The analysis of the suspended sediment fluxes at a height z above the bed has given important insight into the magnitude, direction and relative importance of different processes to the total suspended sediment transport. However, the findings strictly apply to the height z and are, therefore, not necessarily representative for the depth-averaged fluxes. Furthermore, the analysis presented so far has not taken the long-term distribution of the hydrodynamical conditions into account. The magnitude of the fluxes increased with H_{m0}/h , but this does not necessarily mean that on a time scale of months to years the sediment transport is limited to conditions which occurrence in time is only infrequent. The cumulative effect of small, but often

occurring transports may outweigh that of large, but rarely present ones. The cross-shore transport rate under mean and oscillating flows can relatively simple be modelled with a formulation in which the sediment transport rate is assumed to respond instantaneously to fluctuations in velocity above the bed (Bowen, 1980; Bailard, 1981). This rate is then expressed as a linear combination of terms containing products of the three different velocity components \bar{u} , \bar{u}_h and \bar{u}_l . These terms, referred to as 'velocity moments', represent the depth-averaged sediment fluxes.

Roelvink and Stive (1989) showed that the most important contributions to the magnitude and the direction of suspended load transport is given by the term $\langle |u(t)|^3 u(t) \rangle$. This term can be expanded in several terms after replacing the instantaneous velocity $u(t)$ by a sum of the mean, high and the low frequency oscillating velocity. The most important terms (Roelvink and Stive, 1989) are:

$$\langle |u|^3 u \rangle = 4 \langle |\bar{u}_h|^3 \bar{u} \rangle + \langle |\bar{u}_h|^3 \bar{u}_h \rangle + 4 \langle |\bar{u}_h|^3 \bar{u}_l \rangle \quad (3)$$

In these terms the stirring of sand is proportional to $|\bar{u}_h|^3$. The sediment is then transported by any mean current, by high-frequency (HF) and low-frequency (LF) oscillations. Under breaking wave conditions in shallow water other velocity moments, such as those related to the stirring of sediment by long waves ($|\bar{u}_l|^3$), may become of importance as well (Foote et al., 1994; Kroon, 1994), but these terms are neglected in the present analysis. The velocity moments were scaled with the inverse of the fall velocity w to investigate their cross-shore variability. The drag - and the efficiency coefficient (Roelvink and Stive, 1989) were assumed to be constant over the profile. The median sediment fall velocity at F2, F3, F4 and F5 were 15.1, 17.7, 27.6 and 20.5 mm/s, respectively (Guillén and Hoekstra, 1996). The velocities of the lower EMF were used to calculate the velocity moments. It should be emphasized that the energetics approach is only applied to investigate trends; quantitative information on the time-averaged transport rates is not a subject of this section.

Results

The w^{-1} -scaled velocity moments are shown in Figure 3 as a function of H_{m0}/h . The lines shown in Figure 3 are based on the average values of a particular H_{m0}/h -class (width = 0.02). At each position the w^{-1} -scaled velocity moments were clearly related to H_{m0}/h , and the growth of the velocity moments start at $H_{m0}/h=0.3$. In general, the contribution of $\langle |\bar{u}_h|^3 \bar{u}_h \rangle$ (HF) and $\langle |\bar{u}_h|^3 \bar{u} \rangle$ (mean) to the total fourth-order velocity moment were about equal, but of opposite sign. Consequently, the LF-term $\langle |\bar{u}_h|^3 \bar{u}_l \rangle$, which had a negative sign and was smaller than both $\langle |\bar{u}_h|^3 \bar{u}_h \rangle$ and $\langle |\bar{u}_h|^3 \bar{u} \rangle$, often strongly influenced the size and the direction of the net fourth-order velocity moment. The fourth-order velocity moments at F5 were minimal compared to those at the other positions indicating negligible suspended sediment transport in the middle trough.

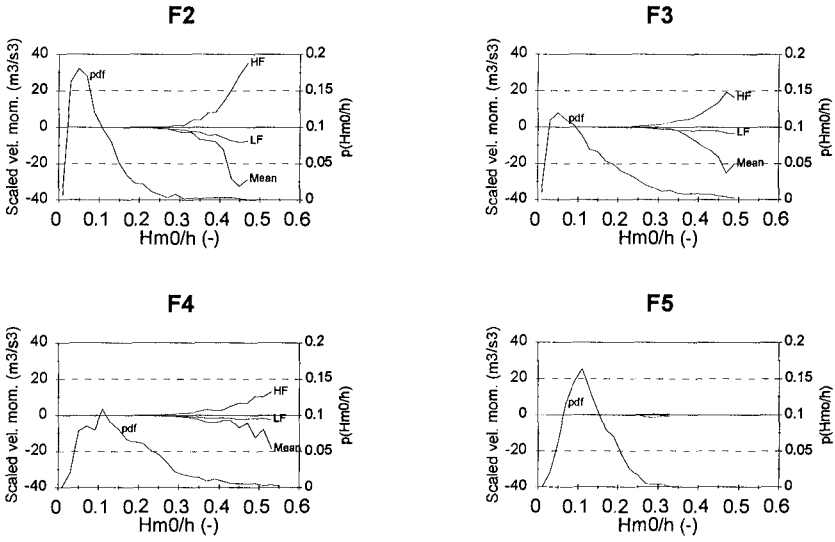


Figure 3. Measured scaled velocity moments and probability density function of ($Hm0/h$)

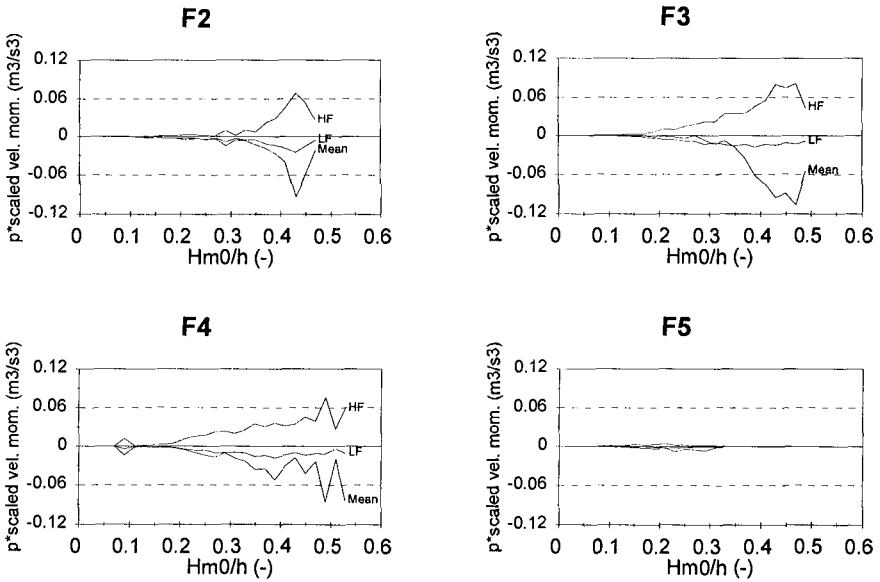


Figure 4. Long term transport rates weighted for the frequency of occurrence

An impression of the long-term effect, i.e. on the time scale of months to a few years, can be obtained by multiplying the H_{m0}/h -dependence of the velocity moments with the probability density function of H_{m0}/h at that location. At each location the frequency of occurrence of H_{m0}/h is known from the measurements. Figure 3 also shows the probability density function (pdf) of H_{m0}/h ($p(H_{m0}/h)$) at each position. The pdf of F2, F3, F4 and F5 are determined based on measured data of 2682, 9220, 1551 and 1541 hours, respectively.

The product of the pdf and the w^{-1} -scaled velocity moments is shown in Figure 4. Significant contributions of the separate processes to the long-term suspended sediment transport started from a value of $H_{m0}/h = 0.25$ at F2, and of $H_{m0}/h = 0.15$ at F3 and F4, which means that the suspended sediment transport was restricted to 3.4%, 32% and 51% in time at F2, F3 and F4, respectively. The majority of the suspended sediment transport (about 70 to 90 %) took place, however, when wave breaking occurred at that location ($H_{m0}/h > 0.33$) and as a consequence, was limited to a much smaller amount in time (1.8, 5.6 and 8.5% in time respectively). This does not imply that the long-term suspended sediment transport is restricted to truly extreme events, except perhaps at F2. For decreasing water depths the occurrence of the long-term suspended sediment transport shifts towards more common conditions, although it remains largely restricted to conditions with breaking waves.

The products of the pdf and the velocity moments are in the same order at F2, F3 and F4 and much smaller at F5. The approximately equal net long-term suspended sediment transports at F2, F3 and F4 are caused by the fact that the two largest contributions, viz. the high-frequency oscillating and current-related one, are nearly the same and, therefore, cancel out. This implies that the cross-shore suspended sediment transport is a delicate balance between contributions by mean currents, and by high- and low-frequency waves. The present results have also indicated that the long-term suspended sediment transport in the middle trough is very small.

Long-term sediment transport: the Van Rijn/Ribberink model

Method

The Van Rijn/Ribberink model (Van Rijn, 1993) was used to calculate the sediment transport. This model is a combination of two different submodels: a suspended load (Van Rijn, a convection-diffusion model) and a bedload one (Ribberink). In the suspended load model the stirring of the sediment is the result of both waves and currents. However, the suspended sediment is only transported by mean currents; oscillating suspended load transport is not included. The bedload model, however, is an instantaneous model. As a result, the sediment can be transported due to both waves (short and long waves) and currents. The model has been modified in such a way that timeseries of measured velocities and waterlevels can be used as input instead of the vertical mean velocity and wave height (Houwman and Hoekstra, 1994). Timeseries of the T2- and T4-campaigns at position F2, F3, F4 and F5 were

used to calculate the sediment transport. The measured timeseries of velocities u and v (at 0.25 m above the bed) and the measured waterlevels (measured by the pressure sensor at 2.2 m above bed) were used as input into the model. From these velocity signals the near bed velocity distribution was constructed assuming a logarithmic velocity profile for the mean current and a constant orbital velocity distribution in the vertical. Only measured velocity signals were used, therefore the effect of the wave induced near bed velocity ('Longuet-Higgins streaming') was not included in the computations. For the computations the local median grain size was used (d_{50} is 154, 163, 172 and 178 μm for F2, F3, F4 and F5 respectively) and a constant bed roughness height $k_s = 0.3$ cm.

The previous analysis of the fluxes and the velocity moments showed that the high-frequency suspended load transport cannot be neglected. To get insight in contribution of this term to the net transport, the Van Rijn model is modified in the following way. The model produces a time-averaged sediment concentration distribution over the vertical. At a certain height above the bed this mean sediment concentration is thought to be the time averaged value of two sediment concentration peaks per wave cycle, one during the onshore directed wave motion and the other during the offshore directed peak. According to the velocity moments approach the shape of the sediment concentration peaks can be assumed to be equal to the shape of $|u(t)|^3$. If one also assumes that each half wave cycle can be described with linear wave theory with different amplitudes but with equal duration, equation (4) is derived.

$$\begin{aligned} \bar{c}(z) &= k \left[\left| \frac{2}{T} \int_0^{T/2} U_{on}^3 \sin^3 \omega t dt \right| + \left| \frac{2}{T} \int_{T/2}^T U_{off}^3 \sin^3 \omega t dt \right| \right] \\ &= k * [U_{on}^3 + U_{off}^3] * \left[\frac{2}{T} \int_0^{T/2} \sin^3 \omega t dt \right] \end{aligned} \quad (4)$$

In equation (4), the left term is the time averaged sediment concentration at height z above the bed, U_{on} and U_{off} refer to the onshore and offshore peak orbital velocity, T and ω are the wave period and angular frequency, respectively and k is a constant. The oscillating suspended flux at a certain height z above the bed can be related to the fourth order moment $u^*|u^3|$. The wave averaged oscillating sediment transport rate $S(z)$ through a layer dz is then described by (5):

$$S(z) = \frac{1}{T} \int_0^T k * u(t) |u(t)^3| dt dz = k [U_{on}^4 - U_{off}^4] dz * \frac{1}{T} \int_0^T \sin^4 \omega t dt \quad (5)$$

$$S(z) = k' * \bar{c}(z) * \frac{U_{on}^4 - U_{off}^4}{U_{on}^3 + U_{off}^3} * dz$$

$$with : k' = \frac{1}{2} \int_0^T \sin^4 \omega t dt * \left[\int_0^{T/2} \sin^3 \omega t dt \right]^{-1} \approx 0.884$$

After integration over the vertical the oscillating suspended sediment transport can be obtained. The mean concentration at height z above the bed is calculated with the Van Rijn/Ribberink model, and the measured significant onshore and offshore orbital motions can be used.

This approach gives an upper limit for the suspended oscillating sediment transport, because one assumes that there are no phase lags present between $u(t)$ and $c(t)$ and that the sediment always responds instantaneously to the third power of the orbital velocity. However, the measurements have shown that phase lags were present and it is unclear if the sediment always responded to $u(t)^3$. Therefore, the parameter k' in (5) is replaced by a new parameter, the "efficiency coefficient" (eff) which incorporates these effects. This parameter was determined from the OBS data.

The measured fluxes were divided by the mean concentration for both OBSs at F3 and were related to the significant orbital velocity. The relative (to the mean) response of the sediment is important, because the mean concentration $c(z)$ is obtained from the model. The values are averaged for an orbital velocity class (width of 0.1m/s), based on data of the T2, T3 and T4 campaigns. A comparison between the measured values and the values of the fourth-order moment show that no fixed k' values can be taken. Based on the two lines from both OBSs the efficiency coefficient was determined as:

$$eff(U_{on}, z) = [(2.5 * z - 0.292) * U_{on}^{-3} * z + 0.42] * \tanh(6.5(z_{max} - z)) \quad (6)$$

$$IF \quad eff(U_{on}, z) < 0 \rightarrow eff(U_{on}, z) = 0$$

To prevent that large oscillating fluxes are calculated far away from the bottom, a tanh function was used to force the efficiency coefficient down to zero again at a particular height (z_{max}) above the bed. The model outcomes were not very sensitive for the values of z_{max} . In the calculations a value of 0.6 m was chosen for z_{max} . A comparison between the 'theoretical' efficiency coefficient k' and the 'observed' efficiency coefficient makes clear that the theoretical one is significantly higher than the observed one. At a height of 0.25 m above the bed the observed efficiency coefficient ranges from 0 to 0.2 (at $U_{on} = 1.6$ m/s) instead of having a fixed value of

0.884. The oscillating suspended load sediment transport was also calculated at F4 using the same formulation for the efficiency coefficient. The observed values were described reasonably by the model. Therefore the approach described above was used for all tripods.

Results

From the calculated cross-shore transport rates an average sediment transport can be calculated for a particular relative wave height class (H_{m0}/h). Figure 5 shows the transport rates calculated at four locations and split up into the contribution of the three transport mechanisms: bed(load), mean- and osc(illating suspended load) transport. The $p(H_{m0}/h)$ for each position are also given. At F2, F3 and F4 the mean and oscillating suspended load transport increased rapidly for situations with a relative wave height larger than 0.3.

The 'yearly-averaged' transport rates shown in Figure 6 were created in a similar way with the pdfs as for the velocity moments. For both F2 and F3 the oscillating and mean suspended load sediment transport were very high during breaking wave conditions ($H_{m0}/h > 0.33$). The yearly net sediment transport is a sensitive balance between the offshore directed mean suspended load transport and the onshore directed oscillating suspended load transport, the contribution of the bedload transport at these positions is only small. However, the difference between the relative large contributions of the suspended load terms may also be very small and, consequently the influence of the bedload transport on the net transport is not clear yet. Again at location F4 the mean suspended load is neutralized by the oscillating suspended load component. The magnitudes of the different yearly averaged transport rates at F2, F3 and F4 were of the same order of magnitude.

In the trough at the position F5 the cross-shore sediment transport rates were much lower and offshore directed. The lack of any onshore transport mechanism in the trough region indicates that no large onshore exchange of sediment across the trough may be expected.

Discussion and conclusions

The field measurements at Terschelling have shown that high- and low-frequency waves, as well as mean currents, contribute to the net suspended sediment transport. In general, the high-frequency oscillating transport is onshore directed and is caused by the positive skewness of the short waves. The low-frequency oscillating transport is in a seaward direction owing to the dominance of bound long waves in the total long wave field and the stirring of sediment on the wave-group time scale. The current-related flux is in an offshore direction in most cases and is caused by wave-driven undertows.

The "measured" fluxes start to increase at a relative wave height $H_{m0}/h > 0.33$, which coincides with breaking wave conditions. The velocity moments are increasing at a lower H_{m0}/h ratio (0.15 - 0.25) but also here the highest transport rates were found during breaking wave conditions. The suspended load transport rates calculated with

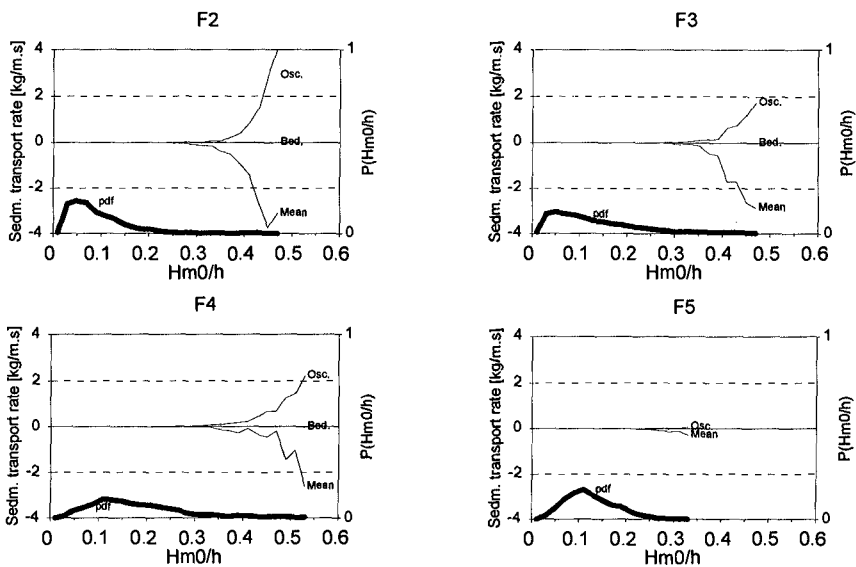


Figure 5. Modelled transport rates with pdf

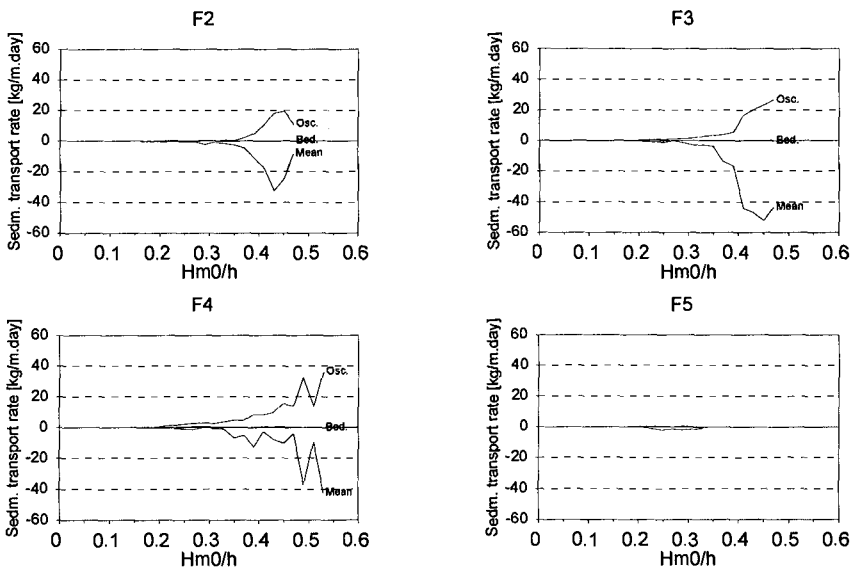


Figure 6. Long term transport rates weighted for the frequency of occurrence

the Van Rijn model were only non-zero during these conditions ($H_{m0}/h > 0.33$) as well. In general, the suspended load transport rates are well related to the relative wave heights H_{m0}/h .

All three applied methods show that the contributions of the onshore directed oscillating suspended load transport or flux is more or less balanced by the offshore directed mean transport/flux.

The combination of a local probability density function (pdf) and the calculated velocity moments and transport rates gives insight in the long term contributions of different transport mechanisms. The yearly averaged suspended load transport rates obtained in this way, start to increase at $H_{m0}/h > 0.33$ for F2, F3 and F4. This indicates that on the long run only breaking wave conditions are important at these positions. But again, at this time scale the suspended sediment transport is a delicate balance between the onshore directed (short wave) oscillating transport and the offshore directed mean transport.

The contribution of the low frequency suspended load transport is rather small compared to the high frequency and mean transport but is systematic and therefore still significant. The calculations of the bedload transport have shown that this contribution is very small compared to the other terms. Although the contributions of the low frequency suspended transport and the bedload transport are small their importance will increase when the mean suspended transport is neutralized by the oscillating high frequency transport.

The results obtained from the calculated long term transport rates are not in agreement with the beach-shoreface exchange mechanism proposed by Niederoda et al. (1984). They found an offshore directed sediment transport from the beach/inner surfzone to the upper shoreface ($h > 4\text{m}$) during a storm and a slow return of this sediment during low energetic conditions in response of asymmetric waves propagating to the coast. If this mechanism is also valid for the Terschelling coast one expects a large contribution of the short wave transport during non-breaking wave conditions ($H_{m0}/h < 0.33$) and a clear dominance of the mean transport during breaking wave conditions. However, for the whole range of H_{m0}/h values the terms are in balance and no clear dominance of a term at a particular H_{m0}/h value has been found. In addition, the morphological observations do not support the theory of such a systematic exchange mechanism between beach and deeper water.

The lack of significant sediment transport in the trough at location F5 also prevents a large exchange between the shallow water and deep water region. In the trough no waves break, and the calculated transport rates are very low. It seems that the landward-located trough acts as a barrier against cross-shore sediment transport.

References

- Bailard, J.A., 1981. An energetics total load sediment transport model for a plane sloping beach. *Journal of Geophysical Research*, 86 (C11), p. 10938-10954.
- Bowen, A.J., 1980. Simple models of nearshore sedimentation; beach profiles and longshore bars. In: McCann, S.B. (ed.), *The coastline of Canada*, Geological Survey Canada, Paper 80-10, p.1-11.
- Foote, Y.L.M. and Huntley, D.A., 1994. Velocity moments on a macrotidal intermediate beach. *Proc. of Coastal Dynamics'94*, ASCE, p. 794-808.
- Guillén, J. and Hoekstra, P., 1996. The "equilibrium" distribution of grain size fractions and its implications for cross-shore sediment transport: a conceptual model. *Marine Geology* (in press).
- Hoekstra, P., Houwman, K.T., Kroon, A., Van Vessem, P., Ruessink, B.G., 1994. The Nourtec experiment of Terschelling: process-oriented monitoring of a shoreface nourishment (1993-1996), *Proc. of Coastal Dynamics'94*, ASCE, p. 402-416.
- Houwman, K.T., and Hoekstra, P., 1994. Shoreface sediment dynamics; Field measurements Egmond aan Zee, IMAU R94-3, Utrecht University, 25 pp.
- Huntley, D.A. and Hanes, D.M., 1987. Direct measurement of suspended sediment transport. *Proc. of Coastal Sediments'87*, ASCE, p. 723-737.
- Kroon, A., 1994. Sediment transport and morphodynamics of the beach and nearshore zone near Egmond, the Netherlands, PhD Thesis, Utrecht University, 275 pp.
- Niedoroda, A.W., Swift, D.J.P., Sawyer Hopkins, T. and Chen-Mean Ma, 1984. Shoreface morphodynamics on wave-dominated coasts, *Marine Geology*, 60, p. 331-354.
- Ribberink, J.S. and Al-Salem, A.A., 1995. Sheet flow and suspension of sand in oscillatory boundary layers. *Coastal Engineering*, 25, p. 205-225.
- Roelvink, J.A. and Stive, M.J.F., 1989. Bar-generating cross-shore flows on a beach. *Journal of Geophysical Research*, 94 (C4), p. 4785-4800.
- Van Beek, L.P.H., 1995. Wave climate of Terschelling. A statistical analysis for the Nourtec project. IMAU R 95-10, Utrecht University, 48 pp.
- Van Enckevort, I. and Reincke, E., 1996. Longshore currents in the intertidal zone of Terschelling. IMAU V96.09, Utrecht University, 62 pp.
- Van Rijn, L.C., 1991. Database sand concentrations and sand transport in currents and/or waves. Delft Hydraulics, Report H1148-04/05.
- Van Rijn, L.C., 1993. Principles of sediment transport in rivers, estuaries and coastal seas, Aqua Publications, Amsterdam, The Netherlands, 614 pp
- Van Rijn, L.C. and Havinga, F.J., 1995. Transport of fine sands by currents and waves. II., *Journal of Waterway, Port, Coastal, and Ocean Engineering*, p. 123-133.
- Vincent, C.E. and Green, M.O., 1990. Field measurements of the suspended sand concentration profiles and fluxes and of the resuspension coefficient γ_0 over a rippled bed. *Journal of Geophysical Research*, 95 (C7), p. 11591-11601.

CHAPTER 374

NUMERICAL PREDICTION OF BREAKING WAVES AND CURRENTS WITH A BOUSSINESQ MODEL

Okey George Nwogu¹

ABSTRACT

This paper describes the extension of a comprehensive numerical model for simulating the propagation and transformation of ocean waves in coastal regions and harbours to include wave breaking, runup and breaking-induced currents. The numerical model is based on a time-domain solution of a fully nonlinear set of Boussinesq-type equations for wave propagation in intermediate and shallow water depths. The equations are able to describe most of the phenomena of interest in the nearshore zone including shoaling, refraction, diffraction, reflection, wave directionality and nonlinear wave-wave interactions. The Boussinesq model is extended to the surf and swash zones by coupling the mass and momentum equations with a one-equation model for the temporal and spatial evolution of the turbulent kinetic energy produced by wave breaking. The waves are assumed to start breaking when the horizontal component of the orbital velocity at the wave crest exceeds the phase velocity of the waves. Numerical and experimental results are presented for the shoaling and runup of regular and irregular waves on a constant slope beach and wave-induced currents behind a detached breakwater.

1. INTRODUCTION

The processes of wave breaking, runup, setdown and setup of the mean water level, turbulent energy production, generation of nearshore currents and generation of infragravity waves are important driving mechanisms for the transport of sediments and pollutants in coastal regions. A full mathematical description of the complex hydrodynamics in the surf and swash zones is difficult due to the highly nonlinear and turbulent nature of flow. By making different simplifying assumptions, however, numerous mathematical models have been developed which reproduce with varying degrees of success the different hydrodynamic phenomena that occur in the surf and swash zones.

For waves propagating over simple bathymetries where shoaling, refraction and breaking are the dominant wave transformation processes, models based on the conservation of energy flux with an appropriate energy dissipation term have successfully been used to model the wave height variation in the surf zone (e.g. Battjes and Janssen 1978, Dally et al. 1985). Battjes and Janssen (1978) used a hydraulic jump analogy to derive

¹Canadian Hydraulics Centre, National Research Council, Ottawa, Canada K1A 0R6

the form of dissipation term while Dally et al. (1985) assumed that the dissipation rate was proportional to the difference between the local energy flux and a stable energy flux. Similar energy dissipation terms have also been incorporated into the mild-slope equation (e.g. Isobe 1987, Özkan and Kirby 1993).

Most surf zone wave transformation models are based on time-averaged integral wave properties and do not follow the breaking process in a time dependent manner. For applications such as irregular wave propagation and sediment transport over barred beaches, time domain modeling provides a more accurate description of the breaking and reformation process. A time-dependent breaking model is also able to simulate the transition region after the onset of wave breaking, where there is a rapid decay in wave energy with almost no change in the setdown of the mean water level. The transition zone plays an important role in the prediction of wave-induced currents and sediment transport in the surf zone (Nairn et al., 1990).

Time-dependent numerical models based Boussinesq-type equations have successfully been used to simulate the nonlinear transformation of multidirectional ocean waves in intermediate and shallow water depths (e.g. Nwogu, 1994). Boussinesq equations can accurately describe most wave transformation processes outside the surf zone including shoaling, refraction, diffraction, reflection and nonlinear wave-wave interactions. Recently, several authors have extended Boussinesq models to simulate wave breaking in the surf zone including Zelt (1991), Karambas and Koutitas (1992), Schäffer et al. (1993), and Sato and Kabiling (1994). The models essentially incorporate a dissipative term due to turbulence stresses or the presence of a surface roller into the momentum equation. The models differ on how they treat the onset of breaking and the rate of wave energy dissipation.

In this paper, we employ a one-equation turbulence model to describe the temporal and spatial evolution of the turbulent kinetic energy produced by wave breaking. The waves are assumed to start breaking when the horizontal component of the orbital velocity at the wave crest exceeds the phase velocity of the waves. The rate of production of turbulent kinetic energy is assumed to be proportional to the vertical gradient of the horizontal water particle velocity at the wave crest. The time-dependent model is applicable to both periodic and non-periodic unidirectional and multidirectional waves.

One advantage of extending Boussinesq-type models to the surf zone is the ability to implicitly model interactions between hydrodynamic processes occurring at different time scales. Wave-induced currents and mean water level fluctuations are implicitly included in the wave propagation model and are derived from a time-average of the predicted velocities and surface elevation respectively, without having to explicitly calculate radiation stresses and separately solve a time-averaged hydrodynamic model.

2. THEORETICAL MODEL

2.1 Fully Nonlinear Boussinesq Equations

Boussinesq equations represent the depth-integrated equations for the conservation of mass and momentum for nonlinear dispersive waves, propagating in water of variable depth. The velocity potential, ϕ , can be expanded as power series in the vertical coordinate, z . An approximation is introduced for frequency dispersion by truncating the series at second-order, resulting in a quadratic variation for the horizontal velocity over depth, and a linear variation for the vertical velocity:

$$\begin{aligned} \mathbf{u}(z) = & \mathbf{u}_\alpha + (z_\alpha - z)[\nabla(\mathbf{u}_\alpha \cdot \nabla h) + (\nabla \cdot \mathbf{u}_\alpha)\nabla h] \\ & + \left[\frac{(z_\alpha + h)^2}{2} - \frac{(z + h)^2}{2} \right] \nabla(\nabla \cdot \mathbf{u}_\alpha) \end{aligned} \quad (1)$$

$$w(z) = -[\mathbf{u}_\alpha \cdot \nabla h + (z + h)\nabla \cdot \mathbf{u}_\alpha] \quad (2)$$

where $\nabla = (\partial/\partial x, \partial/\partial y)$, $h(\mathbf{x})$ is the water depth and $\mathbf{u}_\alpha = \nabla\phi|_{z=z_\alpha}$. Given a vertical profile for the flow field (Eqns. 1 & 2), the governing equations of fluid motion can be integrated over depth, reducing the three-dimensional problem to a two-dimensional one. The depth-integrated mass conservation equation can be written as:

$$\eta_t + \nabla \cdot \int_{-h}^{\eta} \mathbf{u} dz = 0, \quad (3)$$

where $\eta(\mathbf{x}, t)$ is the free surface elevation. Although Boussinesq equations were originally derived for weakly nonlinear waves, a fully nonlinear variant of the equations was recently derived by Wei et al. (1995). The momentum equation, fully nonlinear up to the order of truncation of the dispersive terms, is derived from the dynamic boundary condition at the free surface as:

$$\begin{aligned} & \mathbf{u}_{\alpha t} + g\nabla\eta + (z_\alpha - \eta)[\nabla(\mathbf{u}_{\alpha t} \cdot \nabla h) + (\nabla \cdot \mathbf{u}_{\alpha t})\nabla h] \\ & + \left[\frac{(z_\alpha + h)^2}{2} - \frac{(h + \eta)^2}{2} \right] \nabla(\nabla \cdot \mathbf{u}_{\alpha t}) + \frac{1}{2}\nabla(\mathbf{u}_s \cdot \mathbf{u}_s + w_s^2) \\ & - [(\mathbf{u}_{\alpha t} \cdot \nabla h) + (h + \eta)(\nabla \cdot \mathbf{u}_{\alpha t})]\nabla\eta + \frac{f_w}{(h + \eta)}\mathbf{u}_b|\mathbf{u}_b| + \frac{\partial}{\partial z}(\overline{\mathbf{u}'w'}) = 0 \end{aligned} \quad (4)$$

where g is the gravitational acceleration, $\mathbf{u}_b = \mathbf{u}(-h)$, $\mathbf{u}_s = \mathbf{u}(\eta)$ and $w_s = w(\eta)$. Two additional terms have been introduced into the momentum equation to simulate the dissipation of wave energy due to bottom friction and wave breaking. f_w is an empirical bottom friction factor while $\overline{\mathbf{u}'w'}$ represents the shear stress due to breaking-induced turbulent velocity fluctuations (u', v', w'). A semi-empirical turbulence closure model (Section 2.2) is used to relate the turbulence stresses to the wave orbital velocities.

The elevation of the velocity variable z_α is a free parameter and is chosen to minimize the differences between the linear dispersion characteristics of the Boussinesq model and linear theory. An optimum depth for the velocity variable, $z_\alpha = -0.53h$, gives errors of less than 2% in the phase speed from shallow water depths up to the deep water depth limit.

2.2 Turbulence Model

Several turbulence models have been proposed for fluid flow problems (see review by Rodi, 1980). In this paper, the standard one-equation turbulence model is used to describe the spatial and temporal evolution of the turbulent kinetic energy, k , produced by wave breaking. We do not attempt to model details of the turbulent motion, but rather, investigate the effect of turbulence on the wave field.

The key assumptions made in developing the model are:

1. the breaking process is assumed to be "spilling"
2. turbulence is initiated in the wave crest region due to large vertical gradients of the horizontal velocity, $\partial \mathbf{u} / \partial z$
3. turbulence is produced only when the horizontal velocity at the wave crest exceeds the phase velocity of the waves
4. the rate of production of turbulent kinetic energy is proportional to the vertical gradient of the horizontal velocity at the wave crest
5. turbulence is primarily convected in the crest front region with the horizontal component of the orbital velocity at the crest

The Boussinesq eddy viscosity concept can be used to relate the turbulence shear stresses to the velocity gradients:

$$\overline{\mathbf{u}'w'} = -\nu_t \frac{\partial \mathbf{u}}{\partial z} \quad (5)$$

where ν_t is the eddy viscosity. By substituting the expression for $\mathbf{u}(z)$ given in equation (1), the dissipative term in the momentum equation (Eqn. 4) becomes:

$$\frac{\partial}{\partial z} (\overline{\mathbf{u}'w'}) = -\frac{\partial}{\partial z} \left(\nu_t \frac{\partial \mathbf{u}}{\partial z} \right) = \nu_t \nabla (\nabla \cdot \mathbf{u}_\alpha) \quad (6)$$

The rate of wave energy dissipation is thus governed by the magnitude of the eddy viscosity which is related to the turbulent kinetic energy, k , and a turbulence length scale, ℓ_t , by:

$$\nu_t = \sqrt{k} \ell_t \quad (7)$$

The turbulent kinetic energy is determined from a semi-empirical transport equation with a source term for turbulent kinetic energy production by wave breaking:

$$k_t + \mathbf{u}_s \cdot \nabla k = \nu_k \nabla^2 k + B \nu_t \left[\left(\frac{\partial u}{\partial z} \right)^2 + \left(\frac{\partial v}{\partial z} \right)^2 \right]_{z=\eta} - C_D \frac{k^{3/2}}{\ell_t} \quad (8)$$

The first term on the right hand side represents the horizontal diffusion of turbulent kinetic energy. This term is usually much smaller than the convective term, $\mathbf{u}_s \cdot \nabla k$. The second term represents the production of turbulent kinetic energy due to wave breaking. The parameter B is introduced to ensure that turbulence is produced only when horizontal velocity at the wave crest, u_s , exceeds the phase velocity of the waves, C , i.e.

$$B = \begin{cases} 0 & |u_s| < C \\ 1 & |u_s| \geq C \end{cases} \quad (9)$$

This criterion is valid for progressive waves and has been found to accurately predict the breaker location observed in experiments with regular waves shoaling on a constant slope beach. For irregular waves, an approximate phase velocity can be calculated using the average zero-crossing period, although an instantaneous phase velocity can also be determined using $C = -\eta_t / |\nabla \eta|$.

The last term on the right hand side of the transport equation (8) represents the dissipation of turbulent kinetic energy into heat. C_D is an empirical constant with a representative value of 0.08 for most turbulent shear flows (Rodi, 1980).

The rate of production of turbulent kinetic energy depends on ν_t which initially is unknown. Using the mixing length hypothesis which assumes a local balance between production and dissipation of turbulent kinetic energy, the value of ν_t for the production term is determined as:

$$\nu_t = \frac{\ell_t^2}{\sqrt{C_D}} \left[\left(\frac{\partial u}{\partial z} \right)^2 + \left(\frac{\partial v}{\partial z} \right)^2 \right]_{z=\eta}^{1/2} \quad (10)$$

By choosing an arbitrary value for C_D , the turbulence length scale ℓ_t becomes the only free parameter in the turbulence model which governs the rate of wave energy dissipation and turbulent kinetic energy production. ℓ_t is expected to be of the order of the wave height and is determined from comparisons of the numerical model results with experimental results.

2.3 Numerical Solution

The governing Boussinesq equations have been solved with an iterative Crank-Nicolson finite difference method, with a predictor-corrector scheme used to provide the initial estimate. The computational domain is discretized using a rectangular grid, with the dependent variables η , u_α and v_α defined at the grid points in a staggered

manner. The numerical solution procedure consists of solving an algebraic expression for η at all grid points, tridiagonal matrices for u_α along lines in the x direction and tridiagonal matrices for v_α along lines in the y direction at every time step. An explicit second-order scheme is used for the turbulence transport equation. Details of the numerical solution technique can be found in Nwogu (1996).

The boundaries of the computational domain may be specified as wave input boundaries or solid walls. Along external or internal wave generation boundaries, time histories of $(u_\alpha, u_{\alpha,xx}, v_{\alpha,xy})$ or $(v_\alpha, v_{\alpha,yy}, u_{\alpha,xy})$, corresponding to periodic or non-periodic unidirectional or multidirectional sea states are input. Waves propagating out of the domain are artificially absorbed in damping regions placed next to solid wall boundaries. Artificial damping of wave energy is accomplished by introducing terms out of phase with the surface velocity and fluid acceleration into the continuity and momentum equations respectively.

A simple extrapolation scheme is used to simulate wave runup. Consider the one-dimensional case where the shoreline boundary condition is given by zero mass flux, or equivalently, $\eta_x = 0$. When the water surface elevation η_i at grid point i exceeds the elevation of an adjacent land point, h_{i+1} , we assume that the land point will be flooded at the next time step. The initial value of the water level on the the land point for the next time step is then extrapolated from the surface elevation at adjacent water points:

$$\eta_{i+1} = 4\eta_i - 3\eta_{i-1} \quad \text{if } \eta_i > -h_{i+1} \quad (11)$$

Outputs of the numerical model are time histories of the surface elevation and two components of the horizontal velocity at desired grid points in the computational domain, corresponding frequency and directional wave spectra at those locations, the instantaneous water surface elevation at specified time steps, and the significant wave height distribution and time-averaged horizontal velocities over the entire computational domain.

3. NUMERICAL AND EXPERIMENTAL RESULTS

The numerical model was initially evaluated using data obtained from experiments carried out by Nwogu (1993) in the three-dimensional wave basin of the Canadian Hydraulics Center. A 1:25 constant slope concrete beach was constructed in the 30 m \times 20 m \times 3 m basin, equipped with a 60-segment directional wave generator. The toe of the slope was located 4.6 m away from the wave boards. The water depth in the constant depth portion of the basin was 0.56 m. Tests were carried out for a wide variety of regular and irregular, unidirectional and multidirectional waves. The water surface elevation along the centerline of the basin was measured with a linear array of 23 water level gauges. The experimental setup is described in greater detail by Nwogu (1993).

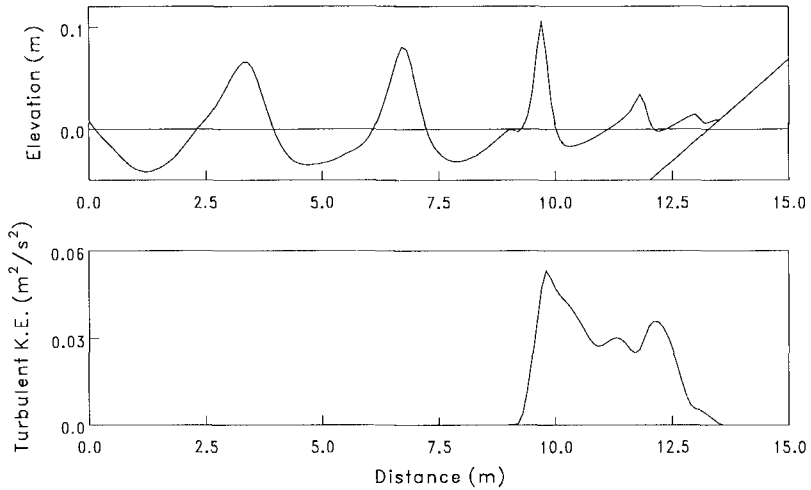


Figure 1. Breaking and runup of a regular wave ($T = 2$ s) on a 1:25 beach.

3.1 Shoaling of Regular Waves

The numerical model was used to investigate the shoaling and breaking of a regular wave with period, $T = 2$ s, and height, $H = 0.09$ m, on a 1:25 beach. The computations were carried out using a grid size $\Delta x = 0.1$ m and time step size $\Delta t = 0.04$ s. A bottom friction coefficient, $f_w = 0.01$, was used for all the computations. Figure 1 shows the spatial profile of the water surface elevation at an instant of time and the corresponding turbulent kinetic energy distribution. The turbulent kinetic energy is maximum close to the breaker location and decreases towards the shoreline. The turbulent kinetic energy exhibits an oscillatory behaviour in space due to the periodic nature of the production of turbulence from each breaking wave event.

Figure 2 shows a comparison of the measured and predicted time histories of the surface elevation at four water depths, both outside and inside the breaker zone. The numerical model is able to reproduce the highly asymmetric wave profile in the surf zone. The spatial variation of the average zero-crossing wave height and mean water level are plotted in Figure 3. Fairly good agreement is obtained between the numerical and experimental results. A turbulence length scale $l_t = 0.35$ m with $C_D = 0.08$ gave the best match of rate of wave energy decay through the surf zone. The solution is not unique, however, as other combinations of C_D , l_t , and the breaking criterion also give reasonable matches of the wave height decay. An extensive investigation is presently being carried out to recommend optimum values of the turbulence model parameters as a function of incident wave parameters.

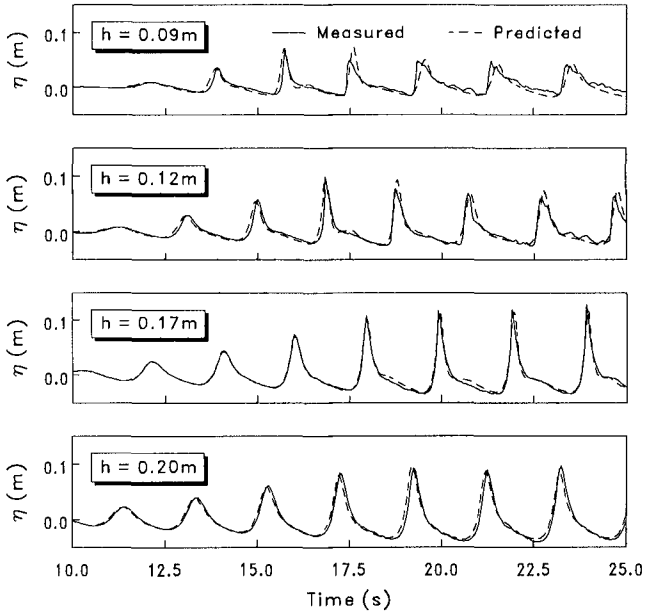


Figure 2. Measured and predicted time histories for a regular wave ($T = 2$ s) shoaling on a 1:25 beach.

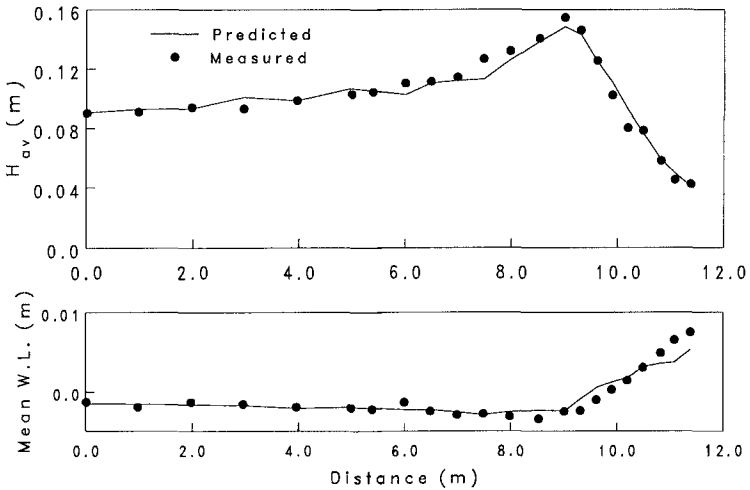


Figure 3. Measured and predicted spatial variation in wave height for a regular wave ($T = 2$ s) shoaling on a 1:25 beach.

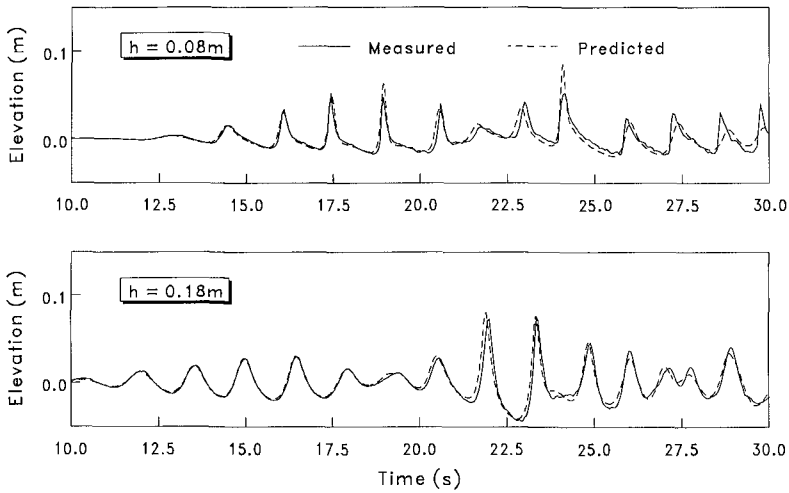


Figure 4. Measured and predicted water surface elevations for an irregular wave with $T_p = 1.5$ s shoaling on a 1:25 beach.

3.2 Shoaling of Irregular Waves

The numerical model was applied to the shoaling of an irregular wave train on the 1:25 beach. A sea state with a duration of 819.2 s was synthesized from a JONSWAP spectrum with significant wave height, $H_{mo} = 0.09$ m, peak period, $T_p = 1.5$ s, and peak enhancement factor, $\gamma = 3.3$, using the random phase method. The computations were carried out using $\Delta x = 0.075$ m, $\Delta t = 0.025$ s and $l_t = 0.1$ m. Figure 4 shows a comparison of the measured and predicted water surface elevations at two shallow water depths. The numerical model is able to reproduce reasonably well the time-domain characteristics of individual wave breaking in an irregular wave train.

The spectral densities of the measured and predicted water surface elevation time histories at different water depths are compared in Figure 5. The spectral estimates were averaged over 0.04 Hz frequency bands. Fairly good agreement is obtained between the measured and predicted wave spectra. The numerical model is able to accurately describe the cross-spectral transfer of energy due to nonlinear wave-wave interactions as well as the decrease in wave energy through the surf zone.

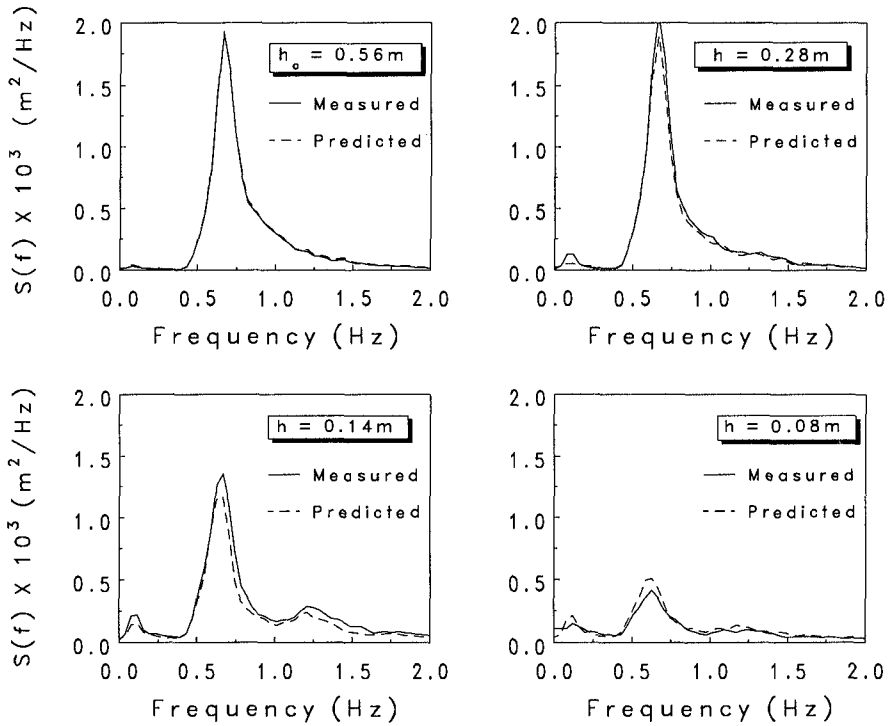


Figure 5. Spectral densities of surface elevation for an irregular wave with $T_p = 1.5$ s shoaling on a 1:25 beach.

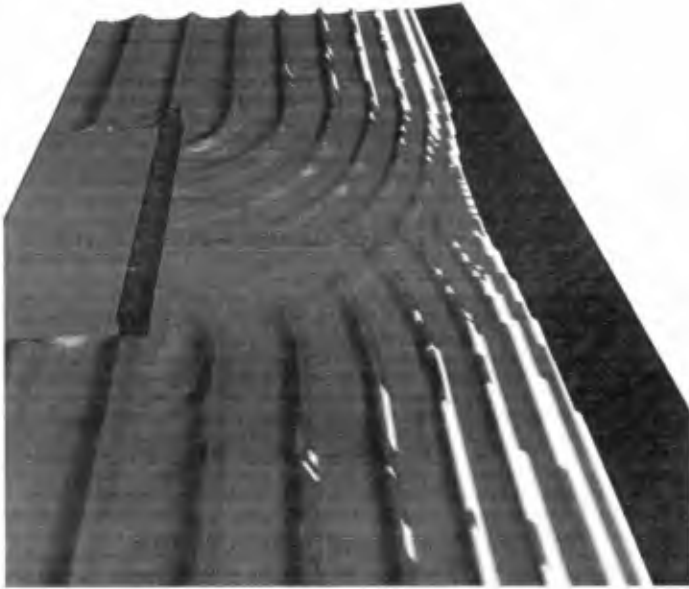


Figure 6. Three-dimensional view of the instantaneous water surface elevation around an offshore breakwater a 1:50 beach.

3.3 Wave-Induced Currents behind a Detached Breakwater

The calculation of currents induced by breaking waves is important in modeling the transport of sediments and pollutants in the surf zone. The two-dimensional Boussinesq model was used to investigate the generation of currents behind an offshore breakwater on a constant slope beach by shoaling and breaking waves. A generic example was used with a 400 m long breakwater placed 350 m from the shoreline on a 1:50 beach. A normally incident regular wave with period $T = 10$ s and height $H = 2$ m was generated at the 10 m depth. The computations were carried out with $\Delta x = \Delta y = 5$ m, $\Delta t = 0.2$ s, and $f_w = 0.01$.

Figure 6 shows a three-dimensional view of the instantaneous water surface elevation around the offshore breakwater. Regions of the crest front with turbulent kinetic energy present have been highlighted in white. The predicted wave height distribution is shown in Figure 7 while the time and depth-averaged velocity pattern is shown in Figure 8. Two circulation cells are observed behind the detached breakwater. This pattern is qualitatively consistent with known observations of wave-induced currents and the formation of tombolos behind offshore breakwaters.

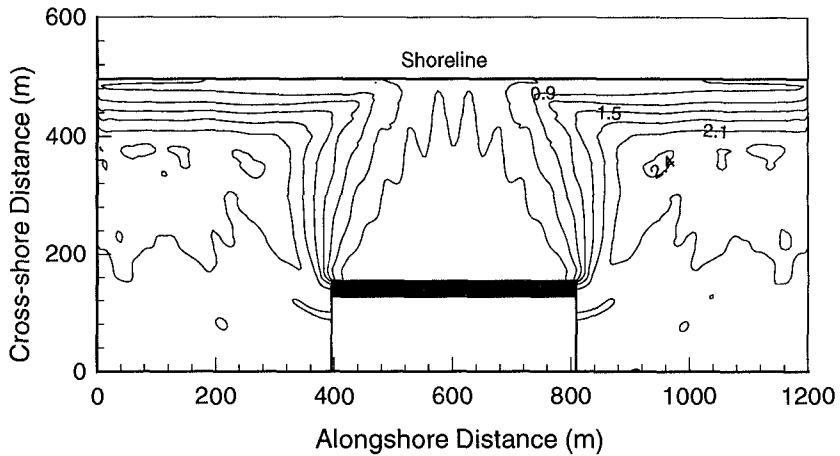


Figure 7. Average wave height distribution behind an offshore breakwater for a regular wave ($T = 10$ s, $H = 2$ m) shoaling on a 1:50 beach.

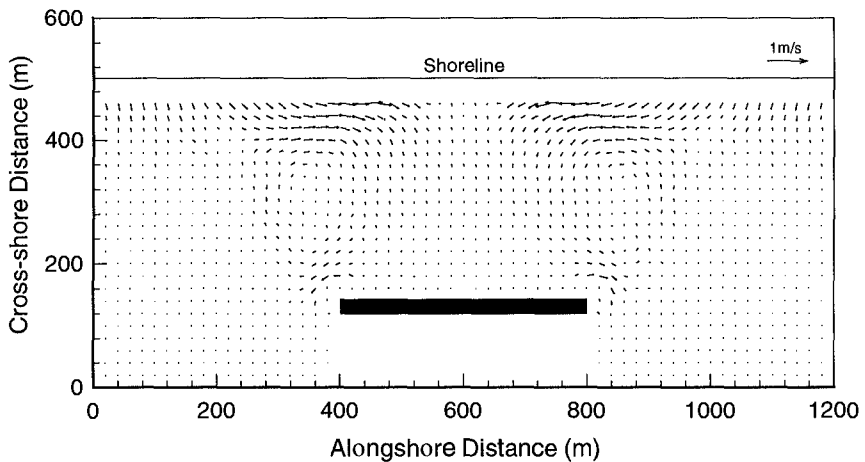


Figure 8. Predicted time and depth-averaged velocity behind an offshore breakwater for a regular wave ($T = 10$ s, $H = 2$ m) shoaling on a 1:50 beach.

4. CONCLUSIONS

A fully nonlinear Boussinesq wave propagation model has been extended to the surf and swash zones by coupling the mass and momentum equations with a one-equation turbulent kinetic energy transport model. The waves are assumed to start breaking when the horizontal velocity at the wave crest exceeds the phase velocity of the waves. The rate of production of turbulent kinetic energy is assumed to be proportional to the vertical gradient of the horizontal velocity at the wave crest. The numerical model has been compared to experimental data for the shoaling of regular and irregular waves on 1:25 beach. The model is able to reproduce reasonably well the frequency and time domain characteristics of waves in the surf zone. The results presented in this paper are of preliminary nature and further work is being carried to compare the numerical model with measured data on the spatial and temporal evolution of turbulence induced by wave breaking, the vertical distribution of currents in the surf zone, wave runup and nearshore circulation patterns.

REFERENCES

- Battjes, J.A. and Janssen, J.P.F.M. 1978. Energy loss and setup due to breaking of random waves. *Proc. of the 16th Int. Conference on Coastal Engineering*, ASCE, Hamburg, 569-589.
- Dally, W.R., Dean, R.G., and Dalrymple, R.A. 1985. Wave height variation across beaches of arbitrary profile. *Journal of Geophysical Research*, **90**(C6), 11917-11927.
- Isobe, K. 1987. A parabolic equation model for transformation of irregular waves due to refraction, diffraction and breaking. *Coastal Engineering in Japan*, **30**, 33-47.
- Karambas, Th. V. and Koutitas, C. 1992. A breaking wave propagation model based on Boussinesq equations. *Coastal Engineering*, **18**, 1-19.
- Nairn, R.B., Roelvink, J.A., and Southgate, H.N. 1990. Transition zone width and implications for modelling surfzone hydrodynamics. *Proc. of the 22nd Int. Conference on Coastal Engineering*, ASCE, Delft, 68-81.
- Nwogu, O. 1993. Alternative form of Boussinesq equations for nearshore wave propagation. *Journal of Waterway, Port, Coastal and Ocean Engineering*, ASCE, **119**(6), 618-638.
- Nwogu, O. 1994. Nonlinear evolution of directional wave spectra in shallow water. *Proc. of the 24th Int. Conference on Coastal Engineering*, ASCE, Kobe, 467-481.
- Nwogu, O. 1996. WaveSimTM - A comprehensive wave simulation model for coastal regions and harbours. *Canadian Hydraulics Centre Technical Report*, National Research Council, Canada (in preparation).

Rodi, W. 1980. Turbulence models and their application in hydraulics - A state of the art review. International Association for Hydraulic Research, Delft.

Sato, S., and Kabiling, M.B. 1994. A numerical simulation of beach evolution based on a nonlinear dispersive wave-current model. *Proc. of the 24th Int. Conference on Coastal Engineering*, ASCE, Kobe, 2557-2570.

Schäffer, H.A., Madsen, P.A., and Deigaard, R. 1993. A Boussinesq model for waves breaking in shallow water. *Coastal Engineering*, **20**, 185-202.

Özkan, H.T. and Kirby, J.T. 1993. Evolution of breaking directional spectral waves in the nearshore zone. *Proc. of the 2nd Int. Symposium on Ocean Wave Measurement and Analysis*, WAVES '93, ASCE, 849-863.

Wei, G., Kirby, J.T., Grilli, S.T., and Subramanya, R. 1995. A fully nonlinear Boussinesq model for surface waves. Part 1. Highly nonlinear unsteady waves. *Journal of Fluid Mechanics*, **294**, 71-92.

Zelt J.A. 1991. The run-up of nonbreaking and breaking solitary waves. *Coastal Engineering*, **15**, 205-246.

CHAPTER 375

THE EFFECT OF THE CL-VORTEX FORCE IN 3D WAVE-CURRENT INTERACTION

M.W. Dingemans¹, J.A.Th.M. van Kester², A.C. Radder³ and
R.E. Uittenbogaard²

Abstract

Experiments in flumes (i.e., Kemp and Simons, 1982, 1983, and Klopman, 1994) have shown that the mean current profile for following waves is more uniformly distributed than the corresponding current-only case, whereas the case of an opposing current leads to a more straight profile. This paper is concerned with proving that inclusion of the so-called Craik-Leibovich (CL) vortex force in the mean-current equation gives, at least for a part, an explanation of this phenomenon.

Introduction

For coastal dynamics applications it is essential to have an accurate prediction of the vertical structure of the mean current. The mean current, however, is strongly influenced by the free surface wave motion. Experiments in flumes (i.e., Kemp and Simons, 1982, 1983, and Klopman, 1994) have shown that the mean-current profile for following waves is more uniformly distributed than the corresponding current-only case, whereas the case of an opposing current leads to a more straight profile (see Figure 1). The purpose of this paper is to give a possible explanation of this behaviour. Hereto we consider the so-called Craik-Leibovich (CL) equation, derived by Craik and Leibovich (1976) in which a vortex force is present. The effect of this vortex force on the underlying flow is studied.

First we consider the CL-equation. As it is essential to have shear in the velocity profile, the used turbulence-closure model is subsequently described. Because the CL-equation is also used to describe the formation of Langmuir circulation cells, some properties of these are succinctly described next. For numerical evaluations the treatment of the vertical momentum equation is possible in a number

¹Senior Researcher, Delft Hydraulics, P.O. Box 152, 8300 AD Emmeloord, The Netherlands

²Senior Researcher, Delft Hydraulics, P.O. Box 177, 2600 MH Delft, The Netherlands

³Senior Researcher, Rijkswaterstaat-RIKZ, P.O. Box 20907, 2500 EX The Hague, The Netherlands

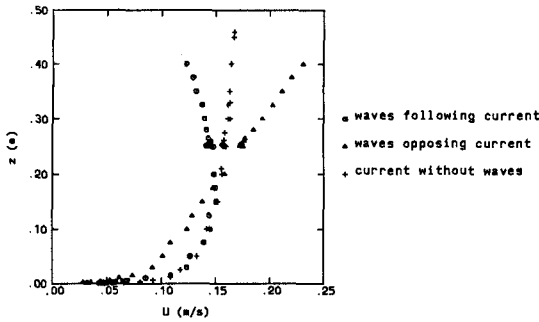


Figure 1: Mean current profiles, after Klopman (1994).

of ways. The most accurate one is described next. Finally the results of some numerical experiments are shown and compared with Klopman's measurements.

The CL equation

When deriving the mean-current equations in so-called Generalised Lagrangian Mean (GLM) coordinates, the following equation is obtained (see Andrews and McIntyre, 1978, Eq. (3.8)):

$$\overline{D}^L(\overline{u}_i^L) + \frac{1}{\rho_0} \frac{\partial \overline{p}^L}{\partial x_i} - \frac{\overline{\rho}^L}{\rho_0} g_i = \overline{D}^L(\overline{P}_i^L) + \frac{\partial}{\partial x_i} \left(\frac{1}{2} \overline{(u_m^L u_m^L)} \right) + \overline{P}_k^L \frac{\partial \overline{u}_k^L}{\partial x_i}, \quad (1)$$

where \overline{P}_i^L is the pseudo-momentum and $\overline{(\)}^L$ is the Generalised Lagrangian mean, i.e. the mean over the perturbed position. Summation over repeated indices is used, i.e., the Einstein convention is applied.

Leibovich (1980) has shown that under mild conditions, Eq. (1) reduces to the so-called Craik-Leibovich equation in Eulerian coordinates, which can be written as

$$\frac{\partial \overline{\mathbf{u}}}{\partial t} + (\overline{\mathbf{u}} \cdot \text{grad}) \overline{\mathbf{u}} + \text{grad} \overline{\pi} = \overline{\mathbf{u}}^S \wedge \text{curl} \overline{\mathbf{u}}, \quad (2)$$

where the pressure term $\overline{\pi}$ is given by $\overline{\pi} = \frac{\overline{p}}{\rho} + gz + \left\langle \frac{1}{2} \tilde{\mathbf{u}} \cdot \tilde{\mathbf{u}} \right\rangle$, $\overline{\mathbf{u}}$ is the (Eulerian) mean velocity and $\tilde{\mathbf{u}}$ is the wave part of the velocity. The so-called mild conditions for which the approximations are valid, amount to the condition that the waves are primarily dominated by their irrotational part. This implies that either the mean shear or the mean current is relatively weak and we thus have to impose the condition that the current is small with respect to the orbital velocity.

Notice that with $\overline{\mathbf{u}}^S = (\overline{u}^S, \overline{v}^S, 0)^T$ and $\overline{\mathbf{u}} = (\overline{u}, \overline{v}, \overline{w})^T$ we have, writing $\overline{\boldsymbol{\omega}} = \text{curl} \overline{\mathbf{u}}$,

$$\overline{\mathbf{T}} = \overline{\mathbf{u}}^S \wedge \overline{\boldsymbol{\omega}} =$$

$$\begin{aligned}
&= \left(\bar{v}^S \left(\frac{\partial \bar{v}}{\partial x} - \frac{\partial \bar{u}}{\partial y} \right), -\bar{u}^S \left(\frac{\partial \bar{v}}{\partial x} - \frac{\partial \bar{u}}{\partial y} \right), \bar{u}^S \left(\frac{\partial \bar{u}}{\partial z} - \frac{\partial \bar{w}}{\partial x} \right) - \bar{v}^S \left(\frac{\partial \bar{w}}{\partial y} - \frac{\partial \bar{v}}{\partial z} \right) \right)^T \\
&\cong \left(0, \bar{u}^S \frac{\partial \bar{u}}{\partial y}, \bar{u}^S \frac{\partial \bar{u}}{\partial z} \right)^T \equiv \bar{\mathbf{T}}_0, \quad (3)
\end{aligned}$$

where the latter approximations are those of Craik (1982), valid for a flume with x directed along the flume.

Although the inclusion of viscosity is not directly needed, it is needed in an indirect way, otherwise no shear would be present in the mean-current profile. Moreover, once generated vortices should remain bounded in magnitude and this is achieved by taking viscosity into account. Also in view of the application to a wave flume, where the lateral boundary conditions play an important role, we include the viscous stress tensor in the description. Equation (2) then is extended to

$$\frac{\partial \bar{\mathbf{u}}}{\partial t} + (\bar{\mathbf{u}} \cdot \text{grad}) \bar{\mathbf{u}} + \text{grad} \left(gz + \frac{\bar{p}}{\rho} + \left\langle \frac{1}{2} \tilde{\mathbf{u}} \cdot \tilde{\mathbf{u}} \right\rangle \right) = \bar{\mathbf{u}}^S \wedge \bar{\boldsymbol{\omega}} + \frac{1}{\rho} \text{div} \bar{\boldsymbol{\sigma}}', \quad (4)$$

where $\text{div} \bar{\boldsymbol{\sigma}}' \equiv \partial \bar{\sigma}'_{ki} / \partial x_k$ and $\bar{\sigma}'_{ki}$ is given by $\bar{\sigma}'_{ki} = (\eta^{(i)} \partial u_k / \partial x_i + \eta^{(k)} \partial u_i / \partial x_k)$, while no summation over the indices on η should be performed and the viscosity is usually non-isentropic. However, we take the (eddy) viscosity coefficient to be isentropic because of the scales on which the flow occurs here and the directions. Applying the Boussinesq-hypothesis, the stresses $\bar{\sigma}'_{ki}$ are approximated as

$$\bar{\sigma}'_{ki} = \nu_T \left(\frac{\partial \bar{u}_i}{\partial x_k} + \frac{\partial \bar{u}_k}{\partial x_i} \right), \quad (5)$$

while the eddy viscosity ν_T has still to be determined. In the present case we consider a cross section of the flume, i.e., we take $\partial_{x_1} \equiv 0$.

The turbulence-closure model

For the specification of the eddy-viscosity coefficient ν_T three possibilities were considered.

1. For a constant eddy-viscosity coefficient the velocity profiles near the bottom and the side walls are parabolic. This is physically not correct as for such situations the profiles should be logarithmic; ν_T should be flow-dependent.
2. Prandtl mixing-length model.

In the Prandtl mixing-length model, the mixing length ℓ is prescribed as a function of the geometry. Because in our case the lateral boundaries are

also of importance, the following variation of Bakhmetev's (1932) choice for shallow-water models is used for the mixing length:

$$\ell = \kappa y (b - y) (z + h) \left(1 - \frac{z + h}{h + \zeta} \right)^{1/2}, \quad (6)$$

where b is the width of the flume, h is the still-water depth, ζ is the free-surface elevation and κ is von Karman's constant. This choice for ℓ yields a parabolic profile near the boundaries. As ℓ only depends on the distance to the boundaries, it is independent of the secondary circulations induced by the CL vortex force \overline{T}_0 . No results from this model are shown.

3. $k - \epsilon$ model.

In our application of the $k - \epsilon$ model the advection and dissipation terms in the direction of the flume (the x -direction) have been neglected. The transport equations for the kinetic energy k and the dissipation ϵ are then given by

$$\frac{Dk}{Dt} = \nabla \cdot \left[\left(\nu + \frac{\nu_T}{\sigma_k} \right) \nabla k \right] + P_k - \epsilon \quad (7a)$$

$$\frac{D\epsilon}{Dt} = \nabla \cdot \left[\left(\nu + \frac{\nu_T}{\sigma_\epsilon} \right) \nabla \epsilon \right] + P_\epsilon - c_{2\epsilon} \frac{\epsilon^2}{k}, \quad (7b)$$

where

$$D/Dt \equiv \partial/\partial t + \mathbf{v} \cdot \nabla, \quad \nabla = (0, \partial_y, \partial_z)^T, \quad \mathbf{v} = (0, v, w)^T, \quad (7c)$$

$$P_k = \frac{1}{2} \nu_T \left| \frac{\partial \overline{u}_k}{\partial x_j} + \frac{\partial \overline{u}_i}{\partial x_k} \right|^2 \quad \text{with} \quad \partial_{x_1} \equiv 0, \quad (7d)$$

$$P_\epsilon = c_{1\epsilon} \frac{\epsilon}{k} P_k \quad \text{and} \quad \nu_T = c_\mu \frac{k^2}{\epsilon} \quad (7e)$$

and the constants are given by the standard setting:

$$c_\mu = 0.09, \quad c_{1\epsilon} = 1.44, \quad c_{2\epsilon} = 1.92, \quad \sigma_k = 1 \quad \text{and} \quad \sigma_\epsilon = 1.3. \quad (7f)$$

Boundary conditions for the $k - \epsilon$ model

The turbulent kinetic energy is imposed both at the side walls and the bed. The pertinent value is obtained by applying local equilibrium between production and dissipation of kinetic energy. This leads to the Dirichlet boundary conditions

$$k|_{y=0} = k|_{y=b} = (u_*^s)^2 / \sqrt{c_\mu} \quad \text{and} \quad k|_{z=-h} = (u_*^b)^2 / \sqrt{c_\mu} \quad (8a)$$

with u_*^s and u_*^b the shear-stress velocity at the sidewalls and the bottom respectively. The shear-stress velocity u_* is obtained by applying the logarithmic

boundary law for the velocity point nearest to the boundary. With δ half the grid size near the side walls and the bed and z_0 the roughness length, the following relations hold

$$\frac{\bar{u}(\delta)}{u_*} = \frac{1}{\kappa} \log \left(\frac{\delta}{z_0} \right) \quad \text{for a rough wall} \quad (8b)$$

and

$$\frac{\bar{u}(\delta)}{u_*} = \frac{1}{\kappa} \log \left(\frac{\delta u_*}{\nu} \right) + 5.2 \quad \text{for a smooth wall,} \quad (8c)$$

where \log is the natural logarithm. In the latter case the value u_* is found by iteration. Because a staggered grid is used, the velocity $\bar{u}(\delta)$ is indeed known at the previous time step. At the free surface we take $k = 0$.

For the transport equation for dissipation rate ϵ we take the following Neumann-type boundary condition:

$$\frac{\partial \epsilon}{\partial z} \Big|_{\delta} = -\frac{u_*^3}{\kappa \delta^2}, \quad (8d)$$

and at the free surface is taken $\epsilon = 0$.

Langmuir circulations

Equation (4) is basic to the generation of Langmuir circulations by an instability mechanism (Leibovich, 1983). The essential point is that a combination of a 2D shear flow in the vertical xz plane with an irrotational Stokes drift of the wave field in the same direction is unstable to spanwise (i.e., in y) disturbances. Write now the vorticity vector as $\boldsymbol{\omega} = (\omega_x, \omega_y, \omega_z)^T$. Two different forms of CL-instability are recognised:

1. **CL1-type** in which the vorticity-component ω_x can be generated by a Stokes drift which varies in the lateral direction
2. **CL2-type** in which the vorticity component ω_x may be generated by a lateral uniform Stokes drift acting on a pre-existing vertical vorticity ω_z .

The CL2-type instability is described by Leibovich (1977) and amounts to the following. It is supposed that the wind stress has produced a parallel shear flow $\bar{u}(z)$ and a Stokes drift $\bar{u}^S(z)$. A perturbation of the shear flow is now considered such that the total flow is described by $(\bar{u}(z) + \hat{u}, \hat{v}, \hat{w})^T$. A perturbation of the pressure is not needed here. Then, the following behaviour of the perturbations is considered:

$$\begin{aligned} \hat{w} &= \phi(z) \exp[\sigma t + i(my + kz)] \quad , \quad \hat{u} = \frac{1}{(m^2 + k^2)} \left(ik\hat{w}_z - m^2\hat{w} \frac{\hat{u}}{f} \right) \\ \hat{v} &= \frac{m}{(m^2 + k^2)} \left(i\hat{w}_z + k\hat{w} \frac{\hat{u}}{f} \right) \quad , \quad f = \sigma + ik(\bar{u} + \bar{u}^S) \quad , \end{aligned}$$

with \tilde{u} being the wave part of the current. For $\phi(z)$ then is obtained in the non-viscous approximation the Rayleigh equation

$$\frac{\partial^2 \phi}{\partial z^2} - (m^2 + k^2) \phi + \left\{ \frac{k}{if} \frac{\partial^2 \bar{u}}{\partial z^2} + \frac{m^2}{f^2} \frac{\partial \bar{u}}{\partial z} \frac{\partial \bar{u}^S}{\partial z} \right\} \phi = 0. \quad (9)$$

With the further simplification of rolls aligned with the mean flow (i.e., $k = 0$) we get

$$\sigma^2 \left(\frac{\partial^2 \phi}{\partial z^2} - m^2 \phi \right) + m^2 \mathcal{M}(z) \phi = 0 \quad \text{with} \quad \mathcal{M}(z) = \frac{\partial \bar{u}^S}{\partial z} \frac{\partial \bar{u}}{\partial z}. \quad (10)$$

The condition for instability now reads $\mathcal{M}(z) > 0$ anywhere in the interval for z . The corresponding maximum growth is $\mathcal{M}^{1/2}(0)$. For the growth of Langmuir circulations it is thus necessary that $\mathcal{M}(z)$ is positive anywhere in the fluid, in other words, a positive shear of the current is required because the Stokes drift diminishes for increasing depth. However, Nepf and Monismith (1991) found experimentally, in a flume, that vortices developed for both $\mathcal{M}(z) > 0$ and $\mathcal{M}(z) < 0$, see also the discussion in Nepf et al. (1995).

Manipulation of the vertical momentum equation

The numerical evaluation will be performed within an existing free-surface flow model in which the treatment of the vertical momentum equation will be worked out in a number of ways.

Hydrostatic approach

For the handling of the vertical momentum equation several possibilities exist. A very simple one consists of ignoring the vertical momentum equation altogether and determining the vertical velocity afterwards by an integration of the continuity equation in which the solutions u and v from the horizontal momentum equations are used. These horizontal momentum equations in most simple form are

$$\frac{du}{dt} + \frac{\partial \bar{\pi}}{\partial x} = \frac{1}{\rho} \frac{\partial \bar{\sigma}'_{k1}}{\partial x_k} \quad \text{and} \quad \frac{dv}{dt} + \frac{\partial \bar{\pi}}{\partial y} = \frac{1}{\rho} \frac{\partial \bar{\sigma}'_{k2}}{\partial x_k} + \bar{u}^S \frac{\partial u}{\partial y}. \quad (11)$$

One of the ways of explaining the measured mean current profiles is the following qualitative one. We consider waves and current in a laboratory flume. In the lateral (y) direction, changes in the velocity field should occur. This has to be generated by the wall effects. The basic idea is as follows. Suppose that a circulation cell has developed. Suppose that the cell is such that in the middle of the flume the flow is in downward direction. The situation is as sketched in Figure 2. In the upper part of the fluid, water with a small amount of momentum is transported towards the middle of the flume and consequently decelerates, while in the lower part of the fluid the reverse situation occurs. In the upper half of

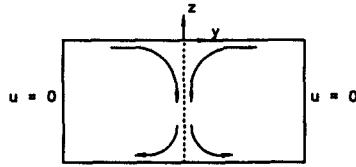


Figure 2: Flow in a lateral vertical section

the fluid the downward velocity increases and in the lower half it decreases. In the middle of the flume $\partial v / \partial y = 0$ because of symmetry. From the continuity equation $u_x + w_z = 0$ in the middle of the flume then follows that $\partial u / \partial x < 0$ in the upper half and $\partial u / \partial x > 0$ in the lower half of the fluid. Consequently, the profile $u(z)$ turns back in the upper part of the fluid and increases in the lower part. The result is a more uniform horizontal velocity profile in the vertical.

A semi-Poisson approach

A more precise formulation consists of splitting the pressure in a hydrostatic and a non-hydrostatic part. The solution procedure then consists of two steps. In the first step only the hydrostatic part of the pressure is used and in the second step a Poisson equation for the non-hydrostatic part has to be solved. Such a method has also been used by Casulli (1995). We write the pressure as the sum of a hydrostatic part p_h and a non-hydrostatic part q : $p = p_h + q$. The computation is split in two parts.

Step 1

Consider the continuity equation and for the momentum equations we only use the hydrostatic part of the pressure. These momentum equations, which are to be solved in the first step then are, in vectorial form

$$\frac{d\bar{\mathbf{u}}}{dt} + \frac{1}{\rho} \text{grad } p_h = -\mathbf{g} + \frac{1}{\rho} \text{div } \bar{\boldsymbol{\sigma}}' \quad \text{with } \mathbf{g} = (0, 0, -g)^T. \quad (12)$$

Step 2

In the second step we consider the momentum equations without the convective terms and we only account for the non-hydrostatic part of the pressure. Furthermore the vortex force is accounted for here. We then have the system:

$$\frac{\partial \bar{\mathbf{u}}}{\partial t} + \frac{1}{\rho} \text{grad } q = \bar{\mathbf{T}}_0 \quad (13)$$

with the vortex force $\bar{\mathbf{T}}_0$ given by (3).

We now apply the operation div on (13). For the velocities it is mandatory that $\text{div } \bar{\mathbf{u}} = 0$ (i.e., the continuity equation is applied as a side condition because it was already used in the first step). The result is a Poisson equation for the

non-hydrostatic part of the pressure:

$$\operatorname{div} \left(\frac{1}{\rho} \operatorname{grad} q \right) = \operatorname{div} \left[\left(0, \bar{u}^S \frac{\partial u}{\partial y}, \bar{u}^S \frac{\partial u}{\partial z} \right)^T \right] \quad (14)$$

After solving the pressure part q of this Poisson equation, the solution q is substituted in Eq. (13) yielding new estimates for the velocities. This completes step 2.

Notice that the splitting is such that in step 1 a usual free-surface flow computation is performed. The second step gives the correction to the hydrostatic pressure, which correction is due to the vortex force. The vortex force, figuring at the right-hand side of the Poisson equation, is computed with the velocities estimated in the first step.

Numerical experiments

We now perform some computations to compare with the results of measurements of Klopman's physical experiments in the so-called Scheldt flume, which has a width of 1 m while the mean water depth in the experiments is 0.5 m. The walls of the flume are made of glass and are therefore hydraulically smooth. The bed was roughened with sand with a grain size of approximately 2 mm. The roughness of the bed was determined experimentally and the Nikuradse roughness was found to be 1 mm. The experimental set-up consists of two wave boards near each end of the flume; both wave boards generated waves and, at the same time, absorbed reflected waves. A discharge was generated with a constant outflow of 80 litres/s. For further details about the lay-out of these experiments we refer to Klopman (1994).

We only consider the regular-wave experiments. The main parameters are

wave period	$T = 1.44 \text{ s}$
wave amplitude	$a = 0.06 \text{ m}$
current velocity	$\bar{u} = 0.16 \text{ m/s}$
mean depth	$h = 0.50 \text{ m}$
bottom roughness height	$z_0 = 0.04 \text{ mm}$

Following waves

In order to obtain enough shear for the CL-vortex force to be effective, the computations are started first without the CL force included and as initial value a uniform velocity of 0.16 m/s is used, whereas the turbulent kinetic energy k and the dissipation ϵ are initially taken to be zero. After 200 s the turbulent logarithmic shear flow has developed sufficiently for the CL-vortex force to be effective. From that moment on the CL-vortex force is included in the computations. At $t = 300 \text{ s}$ a new steady state is obtained with two eddies in the cross-section of

the flume. For the situation of waves following the current, the velocity profile in a cross section of the flume has been shown in Fig. 3. The development of the

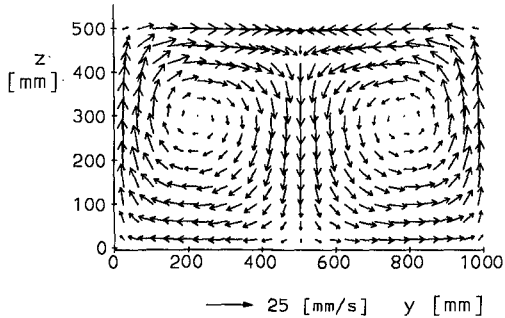


Figure 3: Velocity field in cross section at time $t = 300$ s.

vertical profile of the horizontal velocity in time is shown at the left-hand side of Fig. 4; the time that logarithmic profile is developed is now taken as the origin of the time-axis for the further discussion.

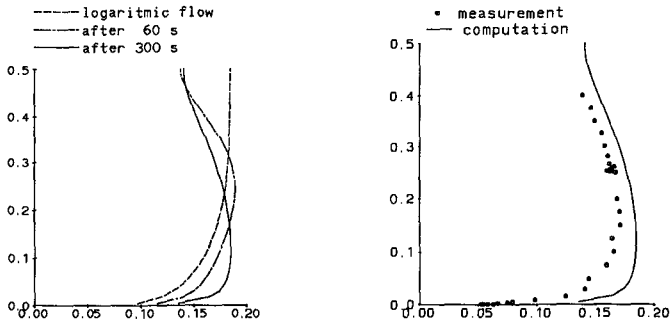


Figure 4: Development in time of the vertical profile of the horizontal velocity for the situation of waves following the current (*left*); Comparison of the vertical profile for following waves with the measured profile (*right*).

Because in the measurements a reference velocity, averaged over the depth, was based on the total flow, with the assumption of uniform flow over the width of the flume, a correction procedure is necessary now to account for the side-wall effects. For the situation of current alone (no waves) the computed vertically averaged horizontal velocity, evaluated in the centre of the flume, was taken as reference for the vertically averaged velocity as resulting from the measurements, likewise taken in the centre of the flume. This requires an enlargement of the measured velocity in the centre of the flume by a factor 1.135. This factor has been applied to all measurements, also those with following and opposing waves. The comparison of the vertical profile of the computation and the measurement with this correction is shown at the right-hand side of Fig. 4. The inclusion

of the CL-vortex force thus has, for following waves, the effect of increasing the near-bottom horizontal velocity and decreasing the horizontal velocity near the free surface, as was also measured. The profile of the current over the width of the flume is shown for a height of 5 cm above the bottom at the left-hand side of Fig. 5. At the right-hand side is shown the development of the vertical current in the centre of the flume.

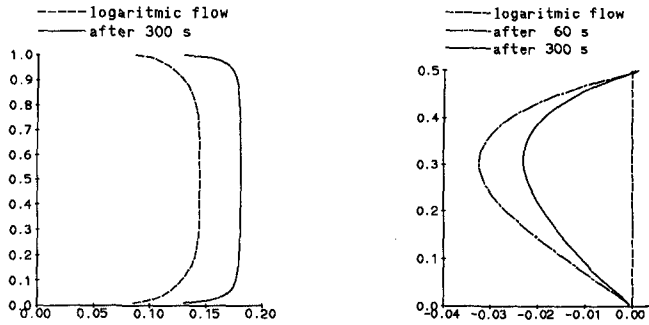


Figure 5: The horizontal current across the width of the flume for following waves, without waves (the logarithmic profile) and 300 s later (with waves); development in time of the vertical profile of the vertical velocity for the situation of waves following the current (*right*); Comparison of the vertical profile for following waves with the measured profile (*right*).

A test on the possibility of Langmuir circulations was devised by taking a very wide flume with otherwise the same parameters. In this situation also only two circulation cells developed and therefore the possibility of obtaining true Langmuir circulations is ruled out for this situation. In the present situation the flow is boundary-driven. The rigid side walls act as an agent for the development of the circulation cells.

Waves propagating against the current

Also in this case two eddies are generated, rotating in opposite directions as those generated for waves propagating in the same direction as the current. This is as was expected. The development of the vertical profile for the horizontal current is shown in Fig. 6. This shows that the flow near the bed is reduced, and that the flow near the free surface is not increased as was to be expected. Notice that Nepf and Monismith (1991) found from measurements in a flume for both waves following and against the current that circulation cells developed. This is also the case in the present computations. Why almost no effect on the current profile is found for opposing waves is not yet clear. This deserves further investigation.

Conclusion

The numerical experiments lead to the following conclusions.

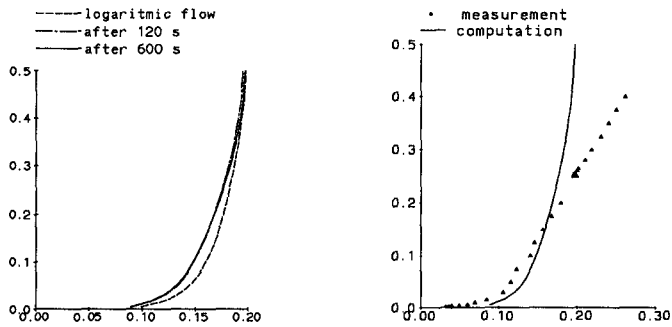


Figure 6: Development in time of the vertical profile of the horizontal velocity for the situation of waves propagating against the current (*left*); Comparison of the vertical profile of the horizontal velocity for waves propagating against the current with the measured profile (*right*).

1. Because also for a very wide flume only two circulation cells will develop, we conclude that the possibility of Langmuir circulation is ruled out for this situation. The flow is boundary-driven.
2. The principal mechanism of change of the near-surface velocities is the lateral transport of low-momentum fluid from the rigid side walls to the centre of the flume. Therefore, we conclude that the CL-vortex force is, at least partly, responsible for the observed change in velocities due to waves upon currents.
3. For both following and opposing waves circulation cells are found in the computations, which is in accord with the experiments of Nepf et al. (1995). Why the case for opposing waves has so little effect on the change of the current profile compared to the case without waves is not yet clear and deserves further investigation.

Acknowledgement

This work was commissioned by the National Institute for Coastal and Marine Management/RIKZ of the Dutch Public Works Department.

References

- [1] Andrews, D.G. and McIntyre, M.E. (1978). An exact theory of non-linear waves on a Lagrangian-mean flow. *J. Fluid Mech.* **89**(4), pp. 609-646.
- [2] Bakhmetev, B.A., 1932. *Hydraulics of Open Channels*, Eng. Soc. Monograph, McGraw-Hill.

- [3] **Casulli, V., 1995.** Recent developments in semi-implicit numerical methods for free surface hydrodynamics. In: *Advances in Hydrosience and Engineering*, Vol. II, March 1995, Beijing, China, 8 pp.
- [4] **Craik, A.D.D. and Leibovich, S., 1976.** A rational model for Langmuir circulations. *J. Fluid Mech.* **73(3)**, pp. 401-426.
- [5] **Craik, A.D.D., 1982.** The generalized Lagrangian-mean equation and hydrodynamic stability. *J. Fluid Mech.* **125**, pp. 27-35.
- [6] **Kemp, P.H. and Simons, R.R., 1982.** The interaction between waves and a turbulent current: waves propagating with the current. *J. Fluid Mech.* **116**, pp. 227-250.
- [7] **Kemp, P.H. and Simons, R.R., 1983.** The interaction between waves and a turbulent current: waves propagating against the current. *J. Fluid Mech.* **130**, pp. 73-89.
- [8] **Klopman, G. (1994).** Vertical Structure of the flow due to waves and currents; Laser-Doppler flow measurements for waves following or opposing a current. *Delft Hydraulics*, Report **H840.30, Part II**.
- [9] **Leibovich, S., 1977.** Convective instability of stably stratified water in the ocean. *J. Fluid Mech.* **82(3)**, pp. 561-581.
- [10] **Leibovich, S., 1980.** On wave-current interaction theories of Langmuir circulations. *J. Fluid Mech.* **99(4)**, pp. 715-724.
- [11] **Leibovich, S., 1983.** The form and dynamics of Langmuir circulations. *Annual Review of Fluid Mechanics* **15**, pp. 391-427.
- [12] **Nepf, H.M. and Monismith, S.G., 1991.** Experimental study of wave-induced longitudinal vortices. *J. of Hydraulic Engineering* **117(12)**, pp. 1639-1649.
- [13] **Nepf, H.M., Cowen, E.A., Kimmel, S.J. and Monismith, S.G., 1991.** Longitudinal vortices beneath breaking waves. *J. Geophys. Res.* **100(C8)**, pp. 16211-16221.

SUBJECT INDEX

Page number refers to the first page of paper

- Abrasives, 2166
Absorption, 55
Accretion, 2955, 4038
Accuracy, 2, 4770
Acoustic measurement, 275
Advection, 4024
Aeolian sands, 4214
Aerial surveys, 1944
Aging, 1888
Alaska, 1293
Algorithms, 914
Analytical techniques, 575, 1762, 1985
Anchorages, 1631
Anemometers, 602
Aquatic habitats, 4300
Armor units, 1542, 1583, 1617, 1640, 1665, 1679, 1721, 1735, 1748, 1789, 1803, 1862, 1944, 2377, 2418, 2522, 3006, 3791, 4228
Artificial islands, 754, 1862, 2298
Asymmetry, 3183, 3467
Australia, 4200, 4390

Backfills, 3231, 4261
Baltic Sea, 2142
Barrier beaches, 247, 2732, 3391, 3546
Barrier islands, 2128, 2732, 2756, 2897, 4621
Barriers, 2087, 2352, 2470, 4505, 4601
Bars, 3680, 4289
Bars, riverine, 2884, 2897, 3546, 3588, 3600, 3666, 4491
Bathymetry, 731, 3521, 4376

Bays, 4242, 4531
Beach erosion, 1349, 1985, 2352, 2666, 2691, 2705, 2718, 2732, 2756, 2770, 2820, 2857, 2871, 2884, 2911, 2918, 2955, 2982, 3115, 3295, 3378, 3442, 3521, 3874, 3976, 3986, 4038, 4583, 4613, 4650, 4717, 4744, 4756
Beach nourishment, 2746, 2770, 2857, 2897, 2911, 2918, 2927, 2941, 2955, 2982, 3115, 3642, 3708, 3722, 4014, 4390, 4440, 4613, 4621, 4650, 4730, 4756
Beaches, 151, 233, 261, 275, 602, 616, 717, 889, 955, 981, 1130, 2036, 2050, 2128, 2142, 2152, 2284, 2612, 2640, 2654, 2677, 2779, 2829, 2843, 2969, 2994, 3006, 3020, 3062, 3090, 3104, 3169, 3349, 3405, 3442, 3560, 3666, 3680, 3736, 3750, 3770, 3888, 3921, 3948, 3962, 3986, 4000, 4079, 4088, 4120, 4161, 4188, 4228, 4353, 4376, 4477
Bed load, 3467, 3913
Bed load movement, 3614
Bed movements, 3495
Bed ripples, 3129, 3183, 4079
Bed roughness, 3143
Bedforms, 3129, 3169, 3391, 3784
Belgium, 836
Benefit cost ratios, 2927, 4717
Berms, 1528, 1542, 1617, 1693, 1735, 1826, 1930, 2192, 2897, 2982, 3708, 3722, 4636
Blocks, 1888

Volume 1 1-1254, Volume 2 1255-2572, Volume 3 2573-3804, Volume 4 3805-4832

- Boundary conditions, 3770, 4120, 4134
- Boundary element method, 165, 1516, 2377, 2548
- Boundary layer, 3194, 3207, 3818
- Boundary layer flow, 3183, 3219, 4779
- Boussinesq equations, 95, 109, 123, 493, 589, 955, 1060, 1116, 1144, 1178, 1192, 1491, 3048, 3349, 4807
- Breaking, 1876
- Breaking waves, 2, 109, 151, 186, 200, 214, 233, 247, 261, 275, 286, 403, 527, 551, 602, 657, 754, 1144, 1156, 1178, 1192, 1219, 1321, 1403, 1803, 1826, 2216, 2244, 2298, 2338, 2366, 2442, 2456, 2484, 2598, 3104, 3194, 3588, 3805, 4228, 4793, 4807
- Breakwaters, 137, 186, 300, 767, 1280, 1528, 1542, 1589, 1640, 1652, 1665, 1693, 1707, 1721, 1735, 1789, 1803, 1816, 1826, 1852, 1930, 1998, 2008, 2022, 2036, 2050, 2063, 2178, 2192, 2216, 2312, 2324, 2352, 2366, 2377, 2391, 2404, 2428, 2470, 2494, 2508, 2522, 2534, 2584, 2770, 2871, 3830, 3976, 3986, 4664, 4676, 4689, 4744
- Bridges, piers, 2230
- Buoyant jets, 4325, 4569
- Buoys, 616, 743, 2087
- Caissons, 1516, 1902, 2008, 2584, 4583
- Calibration, 247, 1102, 3614
- California, 4214, 4636
- Canada, 2230
- Case reports, 1293, 2404, 2732, 3986, 4717
- Channel flow, 4491
- Channel improvements, 3323
- Channels, waterways, 1074, 4531, 4703
- Chaos, 864
- China, People's Republic of, 354
- Climatic changes, 314, 1349, 4364
- Climatic data, 81
- Closed form solutions, 3244
- Cnoidal waves, 2598
- Coastal engineering, 2, 67, 109, 286, 314, 328, 340, 354, 457, 465, 616, 1034, 1465, 1707, 2114, 3652, 3680, 4431
- Coastal environment, 314, 689, 794, 836, 1022, 1478, 2244, 3270, 3363, 3962, 4300, 4807
- Coastal management, 864, 1008, 1375, 2666, 2677, 2793, 2820, 2884, 2911, 2927, 3020, 3431, 4000, 4014, 4253, 4339, 4418, 4440, 4636, 4703, 4744
- Coastal morphology, 1349, 1417, 2770, 2806, 2829, 2897, 2955, 3048, 3090, 3391, 3521, 3534, 3560, 3574, 3600, 3750, 3762, 3830, 3913, 4024, 4038, 4079, 4477, 4517
- Coastal processes, 214, 2022, 2036, 2691, 2779, 2871, 3295, 3378, 3481, 3495, 3600, 3614, 3642, 3666, 3708, 3750, 3805, 3874, 3888, 4052, 4200, 4364, 4464, 4477, 4545, 4583, 4703, 4821
- Coastal structures, 43, 55, 214, 221, 314, 380, 389, 403, 616, 743, 981, 1452, 1569, 1735, 1852, 1862, 1876, 1957, 1971, 2008, 2114, 2128, 2142, 2152, 2166, 2178,

- 2206, 2216, 2258, 2272, 2284,
2338, 2352, 2391, 2404, 2418,
2456, 2560, 2573, 2718, 2918,
2969, 3507, 4397, 4440, 4531
- Coefficients, 1516
- Cohesive sediment, 3337
- Cold weather construction, 4397
- Colorado River, 3309
- Composite structures, 1707
- Computation, 537, 1102, 1130
- Computer aided design, 4650
- Computer aided drafting (CAD),
4650
- Computer networks, 1443
- Concrete blocks, 1652, 1665
- Concrete structures, 1556
- Configuration, 1735, 1816, 3155,
4636
- Construction, 4689
- Control, 493, 1998
- Control systems, 55
- Convection, 3784, 4098
- Coral reefs, 3143, 4261
- Core, 1735
- Corrosion, 2166
- Cost effectiveness, 2114, 4583
- Costs, 1735
- Cracks, 4411
- Crossflow, 175, 3378, 3405, 3666
- Currents, 30, 67, 95, 354, 629, 1060,
1219, 1247, 2391, 3363, 3431,
4066, 4079, 4569, 4730, 4807,
4821
- Curtain walls, 2470, 2484
- Cylinders, 380, 415
- Damage, 1233, 1789, 2969, 4261,
4676
- Damping, 2298, 2626, 3143, 4174
- Dams, 1233
- Dams, earth, 2101
- Data banks, 3652
- Data collection, 81, 137, 368, 629,
643, 677, 1916, 3722, 4200
- Data processing, 4770
- Databases, 81, 2418
- Decay, 300
- Decks, 2573
- Deep water, 2494
- Deflection, 2456
- Deformation, 261, 2338, 3062, 4411
- Deltas, 2806, 2820, 3270, 3284,
3976, 4505, 4545
- Denmark, 2927, 4703
- Density stratification, 4557
- Design, 314, 616, 1280, 1403, 1617,
1631, 1640, 1665, 1748, 1776,
1826, 1971, 2036, 2114, 2128,
2508, 2584, 2897, 2927, 3034,
3628, 4261, 4440, 4451, 4689,
4717
- Design criteria, 221, 354, 2352,
2534, 4397, 4431, 4591
- Design improvements, 2101
- Design waves, 328, 1233, 2494,
2560
- Dewatering, 2677
- Diffusers, 4325
- Diffusion, 3784, 4098
- Digital techniques, 657
- Dikes, 994, 1008, 1233, 1876, 1888,
2746, 2820
- Discharge, 3309
- Docks, 1293
- Documentation, 1443
- Dolos, 4664
- Doppler systems, 527, 629, 1060
- Drag, 3846
- Drag coefficient, 3363
- Drainage, 3507
- Drainage systems, 2640, 2654
- Drains, 2666, 2677
- Dredge spoil, 3708

- Dredging, 3284, 3708, 4274, 4289, 4390
- Ducts, 3913
- Dunes, 2793, 2884, 2955, 2969, 3034, 3115, 4148
- Dynamic response, 2456, 2584
- Dynamic stability, 1930, 2534
- Dynamics, 1178, 2955, 3560, 3805, 3846, 3921, 4052, 4364, 4601
- Earthfill, 2101
- Earthquakes, 1478
- Ecology, 4274
- Eddy viscosity, 200, 3194, 3419
- Education, 1443, 4431
- Effluents, 4325
- Egypt, 3976
- Eigenvalues, 1074, 2470
- Eigenvectors, 2829, 4730
- Embankments, 1707, 4188
- Energy conversion, 4591
- Energy dissipation, 261, 836, 1088, 1192, 1247, 2626, 3062
- Engineers, 4431
- Entropy, 643
- Environmental impact statements, 4274
- Equations of motion, 3846
- Equipment, 4591
- Erosion, 214, 1693, 2230, 2404, 3034, 4052, 4148, 4353, 4397, 4451, 4557, 4621, 4703
- Erosion control, 2666, 2677, 2820, 4038
- Estimates, 328, 3453
- Estimating, 16, 43, 2508
- Estimation, 30, 689, 794, 900, 981, 1389, 1503
- Estuaries, 2691, 4289, 4491, 4557
- Europe, 1375
- Evaluation, 340, 2036, 2677, 2857, 3652
- Experimentation, 443, 479, 516, 1617, 1840, 2640, 2746
- Extraction procedures, 4583
- Failure modes, 1902
- Failures, 1542, 1589
- Fatigue, 4664
- Feasibility studies, 4591
- Field investigations, 137, 994, 1652, 1876, 3600, 3901, 4000, 4491
- Field tests, 516, 689, 2077, 2612, 2654, 3257, 3323, 3962, 4052, 4111, 4591
- Finite element method, 2548
- Finite elements, 465
- Fisheries, 4253
- Floating breakwaters, 1631
- Floating structures, 2548
- Flood control, 2820, 4253, 4339, 4505
- Flood plain insurance, 4339
- Flooding, 1349, 2244, 2746, 4314, 4339, 4418
- Floods, 2258, 2705, 3284, 4491
- Florida, 2312, 3323, 3642, 4242, 4613
- Flow characteristics, 67
- Flow patterns, 4134
- Fluid flow, 3546
- Fluidizing, 4161
- Flumes, 300, 493, 575, 968, 1542, 1816, 1826, 1902, 2428, 3076, 3442
- Forecasting, 340, 743, 864
- Foundation performance, 3507
- Fourier analysis, 968, 1034
- Fourier transform, 3762
- Fractures, 4411
- Free surfaces, 389
- Frequency analysis, 123, 1144
- Frequency distribution, 16

- Friction, 836
Friction factor, 3143, 3495
- Gaging stations, 1465
Geographic information systems, 4650
Geometry, 1280
Georgia, 4314
Geotextiles, 1902, 2114
Germany, 2128, 3534, 4621
Gradient, 4161
Grain size, 4756, 4779
Gravel, 981
Gravity, 2640, 2654
Gravity waves, 1335
Great Lakes, 2705, 4289
Groins, structures, 2128, 2142, 2770, 3976, 4024, 4517, 4744
Ground water, 2152, 2654, 4120, 4601
Ground-water flow, 2640
Guidelines, 1748, 4188, 4253
Gulf of Mexico, 4770
- Harbors, 864, 889, 1256, 1268, 1280, 1491, 1816, 3284, 3986, 4014, 4451, 4744
Head loss, 1776
History, 457
Human factors, 275
Hurricanes, 781, 2756, 2982
Hydraulic design, 4314
Hydraulic models, 221, 443, 3169
Hydraulic performance, 1721
Hydraulic roughness, 3143
Hydraulics, 1679, 4531, 4545
Hydrodynamics, 109, 415, 668, 3419, 3546, 3680, 3948, 4289, 4491
Hydrology, 4274
- Ice forces, 4397
Ice loads, 4397
Ice sheets, 4411
Impact, 1640, 2022, 2442, 2573, 2779
Impact forces, 2456
Impact loads, 2508, 2522, 2534, 2584
Incipient motion, 1803
Indonesia, 1443
Infiltration, 2654
Inlets, waterways, 1219, 2258, 2779, 3270, 3284, 3295, 3323, 3642, 4464, 4477, 4517, 4531
Installation, 1631
Interactions, 1060, 1219, 2377, 2548, 3694, 4120, 4821
Ireland, 4557
Islands, 1452
Italy, 2404
- Japan, 137, 794, 1349, 1389, 1465, 1491, 4000, 4038, 4545, 4676
Jets, 4451
Jetties, 1852, 2573, 3295, 3309, 4531
- Kinematics, 502, 537, 565, 1034, 1247, 1776, 2442, 3481
- Laboratory tests, 43, 493, 927, 1022, 1307, 1321, 1583, 1631, 2077, 2626, 2746, 3295, 3628
Lagrangian functions, 4569
Landslides, 1293, 1478
Large structures, 380
Lasers, 527, 602
Leakage, 1556
Limit analysis, 3874
Liquefaction, 1902, 3860
Littoral currents, 175, 233, 602, 1361, 3391, 3419, 3481, 3560, 3628, 3666, 3860

- Littoral deposits, 2779
 Littoral drift, 1998, 2871, 2897,
 3270, 3309, 3628, 3652, 3830,
 4390, 4464, 4545
 Loading, 3507
 Long waves, 151, 493, 1307, 1321,
 1431, 1452, 1478, 3076, 3090
 Louisiana, 2756

 Maintenance, 1852, 2770
 Maintenance costs, 2969
 Mass transport, 4174
 Mathematical models, 589, 2941,
 3104
 Measurement, 286, 1762, 1916,
 3129, 3169, 3391, 3431, 3588,
 4079, 4098, 4161, 4569
 Measuring instruments, 643
 Mechanics, 4300
 Membranes, 2087
 Meteorology, 703, 822, 4200
 Mixing, 175, 3419, 4098, 4325, 4569
 Model studies, 1748, 4242
 Model tests, 1431, 1528, 1693, 1971,
 2428, 2484, 2534, 4689
 Model verification, 2806, 4730
 Modeling, 109, 186, 286, 565, 889,
 1205, 1247, 1375, 2036, 2230,
 2857, 2982, 2994, 3805, 3913,
 4120, 4464, 4477, 4621, 4821
 Models, 2, 81, 123, 165, 247, 403,
 429, 502, 703, 767, 781, 794,
 1048, 1060, 1116, 1144, 1168,
 1192, 1307, 1335, 1417, 1589,
 2008, 2022, 2178, 2298, 2456,
 2494, 3062, 3115, 3207, 3257,
 3405, 3419, 3467, 3574, 3784,
 3935, 4066, 4214, 4569, 4756,
 4770, 4779
 Momentum transfer, 175
 Monitoring, 889, 1944, 2312, 2871,
 4014, 4664, 4689, 4730

 Monte Carlo method, 822, 900, 1665
 Morphology, 3231
 Movable bed models, 1998, 2258,
 2428, 3169, 3295, 3495, 3628
 Mud, 3337, 4174

 Navier-Stokes equations, 200
 Navigation, 1074, 3231, 3284, 3323,
 4390, 4531
 Nearshore circulation, 808, 822, 878,
 1205, 1335, 1361, 1417, 2391,
 2843, 3020, 3694, 3722, 3830,
 4000, 4052, 4242
 Netherlands, 1876, 3600
 Networks, 616
 New Zealand, 3284
 Noise measurement, 275
 Nomographs, 781
 Nonlinear analysis, 165, 589
 Nonlinear response, 95, 717, 731,
 767, 850, 927, 955, 1034, 1048,
 1088, 1130, 1156, 1178
 Nonlinear systems, 657, 1491
 North Carolina, 3521, 3588, 3666,
 4517
 Numerical analysis, 575, 754, 927,
 1130, 1361, 1516, 2548
 Numerical models, 30, 95, 137, 200,
 233, 300, 340, 389, 465, 551, 668,
 941, 1074, 1219, 1256, 1268,
 1876, 1930, 2050, 2324, 2338,
 2666, 2746, 2770, 2969, 3614,
 3722, 3736, 3818, 3830, 3888,
 3962, 4174, 4289, 4601, 4807

 Ocean engineering, 457, 565
 Ocean waves, 16, 1465, 1789
 Oceanography, 3090
 Offshore structures, 1603
 Optimal design, 1589
 Optimization, 479
 Oregon, 2718

- Oscillations, 1268, 1491, 2884
Oscillatory flow, 3183, 3244, 3495,
4353, 4779
Outfall sewers, 4228
Outflows, 4120
Outwash, 4148
Overtopping, 1721, 1816, 1840,
1862, 2178, 2192, 2206, 2216,
2598
Oxygen transfer, 403
- Parks, 4274
Particle motion, 3846
Peak values, 900, 2484
Performance, 1852, 4636
Performance evaluation, 2087
Permeability, 2142
Photogrammetry, 3750, 4664
Piers, 2573
Piles, 2142
Pipelines, 3231, 4228
Planning, 3986
Plunging flow, 2442
Polynomials, 1130
Ponding, 2312
Pore pressure, 1916, 3219, 3860
Porosity, 2366
Porous materials, 2063
Porous media, 2377
Ports, 1707, 4376, 4676
Predictions, 123, 314, 429, 502, 703,
743, 864, 878, 941, 1321, 1417,
2077, 2230, 2338, 2806, 2941,
3231, 3378, 3405, 3574, 3652,
4650, 4807, 4821
Pressure measurement, 429, 1034
Pressures, 4161
Probabilistic methods, 2793, 4717
Probabilistic models, 808
Probability, 2560, 4418, 4440
Probability density functions, 368,
850, 4793
- Probability distribution, 328, 2272
Professional development, 4431
Profiles, 2829, 2982, 2994, 3006,
3020, 3048, 3104, 3169, 3194,
3349, 3405, 3442, 3736, 3750,
3784, 3901, 3921, 4052, 4650,
4756
Programs, 4613
Progressive waves, 3183
Projects, 1375, 2941
Propellers, 4451
Protective structures, 1403
Prototypes, 1762
Public land, 4418
Public opinion, 4253
Pumps, 4591
- Quality control, 643
Quays, 4451
- Radioactive tracers, 3901
Random waves, 2, 16, 30, 43, 261,
415, 537, 657, 754, 850, 914, 927,
1144, 1247, 2272, 3006, 3034,
3076, 3442
Ratings, 1852
Rayleigh waves, 914, 2272
Reaeration, 403
Recirculation, 3628
Recreational facilities, 2770
Reefs, 2298
Regulation, 2391
Reliability, 1589
Remote sensing, 1944
Repairing, 4689
Research, 286, 994, 1375, 1876,
1888, 3481
Reservoirs, 1233, 1748, 2101, 2918
Resonance, 1583
Resonators, 1280
Restoration, 4261

- Revetments, 1008, 1556, 1583, 1888,
2206, 2718
- Reynolds stress, 200, 4079
- Rheological properties, 4174
- Rip currents, 1361, 2142, 3391,
3680, 3694, 4000
- Riprap, 1233, 1748, 2101
- Risk analysis, 4339, 4440, 4717
- River flow, 4505
- River systems, 2244
- Rivers, 1349, 4545, 4557
- Rock structures, 2077
- Rocks, 1957
- Rotational flow, 2178
- Roughness, 3129, 3495
- Rubble-mound breakwaters, 1516,
1569, 1589, 1603, 1617, 1679,
1776, 1916, 1944, 1957, 1971,
2418
- Russia, 2918
- Salt water, 1022
- Salt water intrusion, 4601
- Sand, 981, 1876, 2050, 2166, 2927,
3034, 3219, 3600, 3642, 3770,
3874, 3888, 3962, 4353, 4390,
4505, 4613
- Sand transport, 137, 2284, 2829,
2871, 2911, 2994, 3708, 3736,
3784, 3791, 3846, 3948, 4111,
4148, 4188, 4214, 4464, 4779
- Sand waves, 3183, 3521, 3574, 4024
- Satellite mapping, 81
- Satellite photography, 3762
- Scale effect, 403, 1762, 2152, 2192,
2522
- Scale models, 1762, 1888, 2101,
2152, 2941
- Scattering, 941
- Scour, 2152, 2230, 2258, 4397, 4517
- Scouring, 1652, 4451, 4676
- Screens, 1762
- Sea cliffs, 2793
- Sea floor, 941, 955, 2230, 3129,
3155, 3207, 3378, 3507, 3860,
4376
- Sea level, 1349, 1503, 3860, 4364,
4418, 4583
- Sea state, 703
- Sea walls, 1022, 1403, 1840, 1862,
1902, 1985, 2192, 2216, 2442,
2456, 2508, 2612, 2718, 4621
- Sea water, 354
- Sediment, 2152, 2732, 4161
- Sediment concentration, 3901, 3935,
4088
- Sediment deposits, 4200, 4214
- Sediment transport, 214, 1321, 2022,
2612, 2691, 2756, 2843, 2941,
2994, 3006, 3048, 3062, 3076,
3104, 3115, 3155, 3194, 3231,
3309, 3337, 3349, 3363, 3378,
3405, 3467, 3534, 3546, 3560,
3614, 3628, 3642, 3652, 3736,
3770, 3791, 3805, 3818, 3860,
3888, 3901, 3913, 3921, 4014,
4289, 4300, 4376, 4545, 4744,
4793
- Sediment yield, 2391
- Sedimentation, 3231
- Sedimentology, 2050
- Sensitivity analysis, 2746
- Sensors, 3453
- Settlement analysis, 1902
- Sewage disposal, 4325
- Shallow water, 95, 109, 123, 221,
465, 502, 551, 589, 602, 668, 878,
889, 955, 1088, 1452, 1930, 2192
- Shape, 1957
- Shear, 175, 3207
- Shear stress, 1168, 3155, 3194, 3337,
3467, 3481, 3913, 4325
- Shellfish, 4300, 4353
- Ship motion, 1268

- Ships, 4261
- Shoaling, 2, 95, 151, 247, 537, 717, 754, 955, 1130, 3295, 4517
- Shore protection, 2063, 2114, 2128, 2206, 2312, 2352, 2391, 2404, 2418, 2428, 2470, 2640, 2654, 2705, 2718, 2911, 2918, 3034, 3976, 4440
- Shoreline changes, 1985, 2404, 2732, 2756, 2779, 2820, 2829, 2843, 2857, 2884, 2927, 3405, 3521, 3588, 3750, 3770, 3874, 3921, 4000, 4024, 4038, 4364, 4376, 4464, 4613, 4744
- Simulation, 16, 389, 657, 900, 914, 1431, 1789, 3442, 3560, 3818, 3976, 4024, 4242
- Simulation models, 67, 731, 2806
- Slope stability, 1556, 1603
- Slopes, 941, 3913
- Small structures, 380
- Soil mechanics, 1603
- Soil-structure interaction, 3507
- Solitary wave, 1156
- Sonar, 1944
- South Africa, 340
- Spain, 1816, 2806, 2871, 4014, 4418, 4730, 4744
- Spectral analysis, 43, 175
- Spraying, 994, 1022, 1840
- Sri Lanka, 4200
- Stability, 1583, 1617, 1640, 1652, 1665, 1679, 1721, 1748, 1776, 1789, 1803, 1826, 1862, 1888, 1957, 1971, 3534, 4161, 4228, 4664, 4756
- Stabilization, 2640, 2654, 2718, 2829, 3986
- Standing waves, 151, 3090
- Statistical analysis, 900, 914, 1985, 2560
- Statistical models, 1088
- Statistics, 123, 794, 808, 822, 1375, 1503
- Steel pipe piles, 2166
- Stochastic models, 1389, 4300
- Stochastic processes, 878
- Stones, 1583, 1640, 1693
- Storm surges, 822, 994, 1268, 1389, 1403, 1417, 4397
- Storms, 703, 743, 781, 1789, 2982, 3034, 3115, 3257, 3874, 3921, 4300, 4339, 4703
- Stratified flow, 4557
- Streams, 3183
- Stress, 3453
- Stress analysis, 4274
- Structural elements, 4261
- Structural response, 1617
- Submerged flow, 927
- Surf zone, 109, 151, 200, 214, 233, 286, 537, 551, 602, 1178, 1321, 1361, 1431, 3048, 3076, 3104, 3431, 3453, 3694, 3805, 3901, 4066, 4088, 4098, 4111, 4228, 4793
- Surface dynamics, 389
- Surface waves, 565, 1048, 3244, 3935
- Surveys, 2114, 3020
- Suspended sediments, 2612, 3076, 3207, 3257, 3736, 3784, 3791, 3888, 3935, 3948, 3962, 4088, 4098, 4111, 4793
- Tests, 30, 221, 286, 968, 1542, 1816, 3442, 3680
- Texas, 3736
- Theories, 443, 864, 3962
- Three-dimensional analysis, 1102
- Three-dimensional models, 233, 2843
- Tidal currents, 2691, 3722, 4491
- Tidal effects, 2994, 3090, 3574

- Tidal energy, 1478
 Tidal flats, 994
 Tidal waters, 3270, 3284, 3295,
 3323, 3534, 3948, 4242, 4314,
 4477, 4491
 Tides, 629, 1603, 1707, 3431, 3442
 Time studies, 1307
 Toe aprons, 1971
 Topography, 1349, 1417, 1452, 1998,
 3534, 3560, 3762, 4545
 Transducers, 3129
 Trenches, 3231, 4188
 Tributaries, 4289
 Tsunamis, 1443, 1465, 1478, 1707,
 4676
 Turbidity, 4088
 Turbulence, 186, 200, 214, 3207,
 3818, 3935, 4111, 4228, 4325
 Turbulent boundary layers, 3244
 Turbulent diffusion, 4066
 Turbulent flow, 200, 3453
 Two-dimensional models, 3846
 Typhoons, 1389, 1417, 1491

 Uncertainty analysis, 1256, 2560
 Undertow, 3006, 3048, 3062, 3194,
 3419, 3830
 Underwater structures, 380, 927,
 1998, 2312, 2324
 Uniformity, 479
 United Kingdom, 286, 3614, 4253,
 4339
 United States, 3020, 3708
 Uplift pressure, 2008

 Validation, 551, 794, 1256, 3574
 Vegetation, 2626, 3935, 4188
 Velocity, 629, 677, 1116, 1168, 1803,
 2666, 3244, 3431, 3453, 3818,
 4066, 4353, 4793
 Velocity distribution, 565, 1569
 Velocity profile, 109, 527, 551

 Vietnam, 2820
 Virginia, 1985
 Viscosity, 2178
 Vortices, 186, 1168, 3183, 3888,
 3935, 4111, 4821

 Waste disposal, 4274
 Water depth, 516, 677, 878, 1116,
 2324, 3257
 Water levels, 1205, 1826, 2244,
 2793, 4148
 Water pressure, 1603, 3155
 Water quality, 403, 2677, 4557
 Water surface, 850
 Water surface profiles, 629
 Water table, 3860, 4120, 4601
 Water waves, 55, 81, 186, 275, 340,
 457, 465, 502, 516, 527, 589, 657,
 677, 717, 731, 878, 889, 1022,
 1034, 1074, 1088, 1156, 1168,
 1205, 1219, 1256, 1268, 1280,
 1375, 1417, 1478, 1528, 1542,
 1776, 1862, 2063, 2087, 2166,
 2178, 2192, 2377, 2470, 2573,
 3020, 3155, 3363, 4174, 4353,
 4411
 Wave action, 137, 175, 221, 380,
 389, 415, 1603, 1679, 1693, 1930,
 3048, 3337, 3507, 3784, 3791,
 3948, 4038, 4088
 Wave attenuation, 1022, 1916, 3349
 Wave climatology, 314, 328, 575,
 689, 808, 864, 1008, 1233, 1503,
 1789, 2022, 2312, 4464, 4517,
 4621
 Wave diffraction, 2, 731, 754, 1048,
 1862, 2063, 2366
 Wave dispersion, 95, 300, 668, 767,
 836, 941, 1048, 1060, 1116, 1144,
 1631, 1652, 1665, 1840, 2077,
 2298

- Wave energy, 261, 731, 767, 836,
1156, 1205, 2484, 2598, 2626,
3270, 4583, 4591
- Wave equations, 1452, 2324, 2366
- Wave forces, 415, 1168, 1528, 2008,
2050, 2377, 2494, 2508, 2522,
2534, 2548, 2573, 2584, 3129,
3155, 3467, 3481, 3495, 3507,
3694, 4676
- Wave generation, 55, 165, 443, 479,
493, 668, 677, 1293, 1307, 1321,
1335, 2338
- Wave groups, 151, 165, 493, 677,
1178, 1307, 1335, 1491, 1503,
3006, 3143, 3257, 3546
- Wave height, 67, 221, 247, 261, 300,
328, 368, 537, 689, 717, 743, 767,
794, 808, 850, 900, 1192, 1205,
1389, 1431, 1583, 1679, 2272,
2298, 2560, 2640, 2705, 3270,
4770
- Wave measurement, 354, 368, 429,
527, 537, 565, 616, 629, 643, 689,
703, 781, 1034, 1465, 4636, 4770
- Wave pressure, 575, 1403, 1556,
1762, 2442, 2484, 2522
- Wave propagation, 123, 165, 457,
589, 668, 878, 889, 1074, 1102,
1130, 1156, 1335, 1569, 1998,
2626, 3244, 4134, 4411, 4807
- Wave reflection, 43, 55, 443, 955,
968, 1516, 2077, 2284, 2338,
2366, 2418, 2470, 2598, 2612
- Wave refraction, 2, 754, 1048, 2324,
2366, 2691, 3762, 4505
- Wave runup, 233, 551, 981, 994,
1008, 1431, 1452, 1556, 1916,
2206, 2244, 2793, 3104, 3349,
3770, 4120, 4134, 4601
- Wave spectra, 16, 30, 43, 175, 368,
516, 629, 643, 689, 781, 822, 914,
927, 968, 1247, 2272, 3762
- Wave tanks, 479, 717, 1840, 2428,
3034, 3219, 3680, 3830
- Wave velocity, 502, 1569, 1776
- Waves, 3207, 3219, 3378, 3560,
3722, 4066, 4079, 4148, 4569,
4821
- Weibull density functions, 2272
- Weirs, 3309
- Wetlands, 4314
- Wildlife habitats, 4314
- Wind, 354, 1233
- Wind forces, 781, 2206, 2216, 3363,
4188, 4200, 4214, 4364
- Wind speed, 429, 4770
- Wind velocity, 2705
- Wind waves, 30, 429, 1088, 3363
- Yield strength, 3337

AUTHOR INDEX

Page number refers to the first page of paper

- Ahn, Kyungmo, 657
Ahn, Sung Mo., 1516
Ahrens, John P., 981, 3378
Akeda, Sadamitsu, 4353
Akiyama, Yoshinobu, 3860
Alikhani, A., 1528
Alikhani, Amir, 1693
Allsop, N. W. H., 2508, 2522
Allsop, N. William H., 389
Aminti, P., 1542
Andersen, Henning, 968, 1679
Anglin, C. D., 2230
Annandale, G. W., 2230
Aono, Toshio, 2298
Appleton, William S., 4664
Araki, Hideo, 275
Archetti, Renata, 1693
Arès, Raymond, 2101
Arntsen, Øivind A., 565
Asano, Toshiyuki, 3770
Axe, Philip, 2036
Azarmsa, Seyed Ali, 2442
- Baird, Andrew J., 4120
Bakker, Willem T., 1876, 2857
Baldock, Thomas E., 3006, 4161
Bando, Kozo, 3860
Banijamali, B., 95
Barker, Christopher H., 1034
Barnes, T. C. D., 186, 214
Bartels, A., 4689
Basco, David R., 1060, 1985, 2969
Bascom, Willard N., 3020
Battalio, Robert T., P.E., 2691
Battjes, J. A., 109, 1088, 3337
Battjes, Jurjen A., 175
Bauer, Bernard O., 4214
- Bazhenov, Yuri, 2918
Beach, R. A., 2793, 3207
Beachler, Kim E., P.E., 4613
Beale, Robert G., 389
Becq, Françoise, 465
Bedford, Keith W., 4289
Beji, Serdar, 1048
Benoit, Michel, 465, 1617
Berlamont, Jean, 836
Bian, J., 354
Bird, Paul A. D., 2077
Birkemeier, William A., 3874, 4052
Black, Kerry, 3284
Boczar-Karakiewicz, B., 3546
Bodge, Kevin R., P.E., 4261
Bollmann, Chad A., 2470
Bona, J. L., 3546
Booij, N., 668, 743
Bos, K. J., 2022
Bosboom, J., 109
Bosma, Kirk F., 2829
Bowen, A. J., 3207
Breeding, J. Ernest, Jr., 677
Breteler, M. Klein, 1556
Breteler, Mark Klein, 1888
Briggs, Michael, 1631
Briggs, Michael J., 1219
Brocchini, M., 186, 4134
Brodie, R. P. (Jock), 4390
Brøker, I., 3048, 4703
Brøker, Ida, 2927, 3805
Browder, Albert E., 2312
Brunone, Bruno, 1569
Bullock, Geoff N., 2077
Bullock, Geoffrey N., 2584
Burcharth, H. F., 1589, 1640

- Burcharth, Hans F., 2560
Burger, G., 1957
- Cadevall, Cristina, 1816
Caires, S., 743
Camfield, Fred E., 1583
Capobianco, Michele, 2884
Caron, Octave, 1233, 1748
Castañeda, A. M., 4014
Chadwick, Andrew, 2036
Chae, J. W., 1268
Chakrabarti, Subrata K., 380
Chakrabarti, Sumita, 380
Chan, Ray T. C., 3006
Chang, Kuang-An, 527
Chawla, Arun, 2
Chen, Qin, 1060
Chen, Renjie, 2312
Cho, Yong-Sik, 955
Christiani, E., 1589
Christopoulos, Spiros, 689
Cialone, Mary A., 3921, 4531
Cieslikiewicz, Witold, 703, 1375
Cinotto, Charles M., 2206
Claessen, Edward W. M., 2428
Clark, Stephen, 3784
Coates, L. E., 3257
Collins, Michael B., 3948
Cook, Benjamin, 1443
Cornett, A. M., 2230
Cox, Daniel T., 551, 3194
Craig, Kenneth R., II, 602
Creed, Christopher G., 4464
Cruz, Eric C., 2298
Curtis, William R., 2677
- Dally, W. R., 808
Dally, William R., 3419
Dalrymple, Robert A., 731, 1074,
2829
Damgaard, Jesper S., 3614, 3913
d'Angremond, Kees, 1971, 2418
- Davidson, Mark A., 2077
Davies, Michael H., 1679, 1748,
3507
Davies, P., 214
Davis, J. P., 2522
Davis, Jack E., 2677
Davis, Justin, 4242
Davis, Richard A., Jr., 2982
de Haas, Paul, 165
de Jong, Rutger J., 2418
de la Peña, Jose M., 889
de Lange, Willem, 3284
de Loeff, A. P., 2770
de Loeff, Harry, 2746
de Rouck, Julien, 1603, 1916, 1944
de Somer, Marc, 1916
de Vries, J. M., 4274
de Waal, Johannes P., 2216
Dean, Robert G., 2312, 3115, 3680
Deguchi, Ichiro, 3349, 3888
Deigaard, R., 3048
Deigaard, Rolf, 3805
Demirbilek, Zeki, 1219, 1256
Dennis, John M., 389
Dennis, William A., 4517
Dette, Hans-H., 3442
Diaz Rato, J. L., 1762
Dibajnia, Mohammad, 3104, 3791
DiCastro, Dan, 4376
Dingemans, M. W., 1156, 2022, 4821
Dingemans, Maarten, 165
Dombrowski, Michael R., 3270
Dong, Lifen, 2324
Dong, Ping, 4717
Donnars, Philippe, 1617
Douglass, Scott L., 3708
Dubi, Alfonse, 2626
Dunaszegi, L., 2230
Dupuis, Pierre, 1233, 2101
Duy, Nguyen The, 200

- Ebersole, Bruce A., 2779
Edge, B. L., 2087
Edge, Billy L., 941, 3309
Elbahrawy, Ali, 3976
Eldeberky, Y., 1088
Elfiky, Abd-Elfattah, 3976
Elfrink, Berry, 3805
Elgar, Steve, 3666
Elmongy, Abd-Elmohsen, 3976
Elsaeed, Gamal, 3976
Elwany, M. Hany S., 314
Escartín, F. Javier, 4014, 4744
- Falqués, Albert, 3560
Faria, A. F. Garcez, 3391
Feddersen, Falk, 3666
Fenton, J. D., 1130
Fenton, John D., 575, 1102
Fernández, A. J., 4418
Fisher, John S., 3750
Fisher, Paul R., 2994
Fleming, Chris, 4339
Fontijn, Henri L., 4228
Foster, D. L., 3207
Fowler, Jimmy, 1631
Fowler, Jimmy E., 3628
Franco, Claudio, 2008
Franco, Leopoldo, 2008
Fredsoe, Jørgen, 3231
Frigaard, P., 1640
Fujiwara, Ryuichi, 16, 1516
Fukumoto, Tadashi, 300
Fukunaga, Masahiko, 2666
Fukushima, Tadahiro, 2666
- Gadd, Peter E., 4397
Galofré, J., 4730
Galofré, Jordi, 4744
García, Cristina, 1816
Gares, Paul A., 4214
Gelfenbaum, Guy, 3453
Glodenis, Marina, 2918
- Gobbi, Maurício F., 1116
Goda, Yoshimi, 261, 629
Golan, Arik, 4376
Goldenbogen, Roland, 3534
Golik, Abraham, 4376
Gomyoh, Michio, 1652
Göricke, Frank, 2142
Gotoh, Hitoshi, 3155, 4300
Gouloumis, Spiros M., 429
Gracia, Vicente, 4098
Graff, Jerzy, 703, 1375
Grant, Geoffrey T., 2152
Gravens, Mark B., 4477
Greated, C. A., 214
Green, Debra R., 1219
Greenwood, B., 3546
Grilli, Stéphan T., 717
Groenewoud, Martin D., 2428, 2857
Grønbech, John, 968, 1679
Grüne, Joachim, 994, 1008
Guillen, Jorge, 2884
Guo, Lulin, 731
Guza, R. T., 3666
- Haines, John W., 3453
Hald, T., 1640
Hallermeier, Robert J., 2705, 3874
Hamill, G. A., 4451, 4557
Hamilton, David G., 3628
Hamm, Luc, 537
Hands, Edward B., 3378
Hanes, Daniel M., 3129, 3846
Hann, D. B., 214
Hansen, Erik Asp, 3805
Hansen, Mark E., 2756
Hanslow, David J., 2244
Hanson, Hans, 4024
Hanzawa, Minoru, 479, 1665
Harari, Pinkhas, 4376
Harcastle, P. J., 3257
Hasegawa, Iwao, 2640
Hashida, Misao, 1022, 3363

- Hashimoto, Noriaki, 30, 629, 1465
Hatada, Yoshio, 1389
Hathaway, Kent K., 4052
Hattori, Masatato, 2456
Haydon, T. R., 214
Healy, Terry, 3284
Hearon, G. E., 2718
Heilman, Daniel J., 3309
Hemsley, J. Michael, P.E., 616
Herbers, T. H. C., 3666
Herbich, John B., 3976
Hewson, Peter J., 2584
Hibbert, Kevin, 2244
Hinata, Hirofumi, 3431
Hoekstra, P., 2897
Holman, R. A., 3207
Holman, Rob, 3521
Holman, Rob A., 3588
Holmes, Patrick, 3006, 4161
Holthuijsen, L. H., 668, 743, 1247
Horikawa, Kiyoshi, 3405, 4188
Horn, Diane P., 4120
Horrillo, Juan, 717
Hosoi, Yoshihiko, 275
Hotta, Shintaro, 4188
Housley, John G., P.E., 2911
Houwman, K. T., 2897
Houwman, Klaas T., 4793
Howarth, M. W., 2522
Howell, Gary L., 3323
Hsu, John R. C., 3986
Huan, Nguyen Ngoc, 2820
Hubertz, Jon M., 4770
Hughes, Steven A., 2258
Hulscher, S. J. M. H., 3574
Humphery, J. D., 3257
Huntley, David A., 2077, 2612, 3090
Hwang, Ching-Her, 4088
Hwang, K. S., 3219
Hwung, H. H., 3219
Ikeno, Masaaki, 3076
Ilic, Suzana, 2036
Inman, Douglas L., 314
Iranzo, Vicente, 3560
Irie, I., 1840
Irie, Isao, 1022, 1998, 2391
Irish, Jennifer L., 3736
Ishii, Toshimasa, 754
Ishikawa, Motoyasu, 3860
Isobe, Masahiko, 16, 43, 443, 754, 767, 2324
Itabashi, Naoki, 137
Ito, Kazunori, 443
Ito, Shinichi, 2166
Itoh, Sadahiko, 275
Ivanova, Nadya, 2918
Iwata, Koichiro, 2338
Izumiyama, Koh, 4411
Jackson, Derek W. T., 4214
Jaffe, Bruce E., 2756
Jakobsen, Per Roed, 4703
Janssen, C. Marjolein, 4779
Jenkins, Scott A., 314
Jensen, Jacob Hjelmager, 3231
Jensen, Robert E., 781
Jensen, Thomas, 968, 1679
Jeong, W. M., 1268
Jervis, M., 2192
Jetté, Christopher D., 3129
Jeuken, Claire, 4491
Jiang, Qin, 4174
Jiménez, José A., 2806, 4098
Johanson, Hans, 1888
Johnson, Bradley D., 551
Johnston, H. T., 4557
Jones, Bryan N., 1985
Jones, R. J., 2522
Juang, Jea Tzyy, 3762
Juhl, J., 1528
Juhl, Jørgen, 1693

- Jung, K. T., 1268
Justesen, Peter, 3805
- Kaczmarek, Jarka, 4364
Kaczmarek, Leszek M., 3467
Kaihatu, James M., 123, 1144
Kaiser, Ralf, 4621
Kajima, R., 1862
Kakuno, Shohachi, 1516
Kamikubo, Y., 1840
Kamphuis, J. William, 221, 1431,
2258
Kana, Timothy W., 2732, 4314, 4756
Kanada, Shigeo, 4411
Kanazawa, Hiroshi, 2640
Kang, Hong-Yoon, 4601
Kânog'lu, Utku, 1452
Kant, G., 2770, 2820
Kariyazono, Yoshihisa, 2166
Karjadi, Entin A., 233
Karlsson, Robert I., 2152
Kaskevitch, Liya, 2918
Katmarian, R. Eric, 4314
Kato, Hajime, 794, 2391
Kato, Kazumasa, 2640, 2654
Katori, Sadakazu, 3818
Katsui, Hidehiro, 443, 3183
Kawaguchi, Eiichi, 1349
Kawakami, Hiroshi, 3363
Kawamori, Akira, 1707
Kawanakajima, Y., 4000
Kawasaki, Koji, 2338
Kee, S. T., 2087
Kendall, Thomas, 4664
Kennedy, A. B., 1130
Kennedy, Andrew B., 1102
Khabidov, Alexander, 2918
Kim, Do-Sam, 2338
Kim, M. H., 2087
Kim, Taerim, 3830
Kimura, Akira, 864, 1776, 2272,
2366
- Kimura, Katsutoshi, 4676
Kimura, Yoshiaki, 1707
Kioka, Wataru, 1491
Kirby, James T., 2, 123, 1116, 1144,
1361
Kitamura, Fujio, 1465
Klammer, P., 2534
Klopman, G., 109
Klopman, Gert, 165
Knaack, Heiko, 4621
Kobayashi, N., 1721, 1803
Kobayashi, Nobuhisa, 233, 551,
3194, 4148
Kojima, Haruyuki, 927
Komar, P. D., 2718, 2793
Kondo, Hideo, 1707, 4583, 4591
Konicki, Kathryn M., 3588
Kortenhaus, A., 1403, 2534
Kos'yan, R. D., 4111
Koyabu, Tsuyoshi, 275
Kraak, Arie W., 2746
Kranenburg, C., 3337
Kraus, Nicholas C., 3020, 3034,
4024
Krecic, Michael R., 3846
Kriebel, David L., 2470
Kroon, A., 2897
Krylenko, M. V., 4111
Kudale, M. D., 1721
Kumagai, Takahiro, 2843
Kunz, H., 4111
Kunz, Hans, 2128, 3534
Kurata, Katsuhiko, 1516
Kuriyama, Yoshiaki, 247
Kuwabara, Shinji, 1707
Kuznetsov, S. Yu., 4111
Kwan, K. H., 4569
Kweon, Hyuck-Min, 261
- Lai, M.-Y., 914
Lamberti, A., 1542
Lamberti, Alberto, 2352

- Larson, Magnus, 3244
Lastrup, Christian, 2857, 2927
Lee, B. H., 3219
Lee, Jiin Jen, 1293
Lee, Jiin-Jen, 2178, 4325
Lee, Jong-In, 955
Lee, Jong-Kyu, 955
Leidersdorf, Craig B., 4397
Lesnik, John, 1852
Leyden, V. M., 808
Li, Li, 1074
Liaw, S.-R., 2494
Lillycrop, W. Jeff, 3736
Lin, Lihwa, 643, 3295
Lin, Paul C.-P., P.E., 3642
Lin, Po-Ching, 4088
Lissev, Nikolay, 1735
List, Jeffrey H., 2756
Liu, Paul C., 457
Liu, Philip L.-F., 527, 589
Liu, Xiaodong, 2548, 4411
Liu, Zhou, 2560
Long, Charles E., 4052
Losada, I. J., 4418
Losada, M. A., 1762
Loveless, John H., 2152
Lozano, José, 889
Lu, Chia-Chi, 822
Luo, Weimin, 836
Lupón, Nuria, 4014, 4744
- MacIver, Ruairi D., 3481
Maddrell, Roger, 4339
Madsen, Holger Toxvig, 2927
Madsen, P. A., 95, 1178, 3048
Madsen, Per A., 1060
Maeno, Yoshihiko, 3860
Mancinelli, Alessandro, 2352
Mann, Douglas W., P.E., 4613
Mano, Akira, 4505
Mansard, Etienne P. D., 1679, 1748
Manzenrieder, H. A., 4274
- Marcos, Frédéric, 465
Marinski, Jordan, 2484
Martens, Jean-Pierre, 1916
Martin, F. L., 1762
Mase, Hajime, 2366
Mason, Travis, 3948
Mason, Travis E., 4120
Masselink, Gerhard, 4200
Mathew, Joseph, 3284
Matsukawa, Fumihiko, 2640
Matsumi, Yoshiharu, 1776
Matsumoto, Akira, 479
Matsumoto, Teruki, 1321
Matsunaga, Hiroshi, 1516
Matsunaga, Nobuhiro, 1022, 3363
Matsuoka, Gaku, 2166, 4353
McClarty, A., 4689
McDougal, W. G., 2377, 2718, 2793
McGarvey, J. A., 4451
McKee, Philip A., 4314
McKenna, J. E., 2508
Medina, Josep R., 328, 1789, 2871
Medina, R., 4418, 4730
Mehta, Ashish J., 3270
Melby, J. A., 1803
Melby, Jeffrey A., 4664
Méndez, F., 4418
Mesa, Chuck, 4636
Miles, Jonathon R., 2612
Miller, C., 1403
Miller, Herman C., 4517
Mimura, Nobuo, 1349, 2391
Mitsui, Masao, 629
Mizuguchi, M., 493
Mizuguchi, Masaru, 1307, 2598, 3818
Mizuno, Yuzo, 4591, 4676
Mizutani, N., 2377
Mlynarski, Jeffrey M., 1074
Mochizuki, Hitoshi, 1280
Mochizuki, Masashi, 443
Mocke, G. P., 1205

- Moe, Geir, 565
Mohan, Ram K., P.E., 4756
Mohan, Ram Krishna, P.E., 2732
Monbaliu, Jaak, 836
Monsó, José Luis, 1816
Montoto, Amadeu, 3560
Montoya, F. J., 4730
Moores, S. P., 3257
Mori, Nobuhito, 850
Morita, Satoshi, 1280
Moriya, Yoichi, 2598
Mostafa, A. M., 2377
Mounsey, Chris, 4339
Moutzouris, C. I., 403, 1826
Murakami, Hitoshi, 275
Murakami, Keisuke, 927, 1840
Murray, Russell J., 4390
Mutsuda, Hidemi, 300, 2442
- Nadaoka, Kazuo, 1048, 3183, 3431
Nagai, Toshihiko, 629, 1465
Nagase, Satoru, 1307
Naim, R. B., 2230
Nakagawa, Yasuyuki, 30, 4676
Nakamura, Satoshi, 1503
Nakamura, Takayuki, 1280
Nelson, Raymond C., 3143
Neshaei, M. Ahmad L., 3006
Newe, Jürgen, 3442
Nicholls, Robert J., 3874
Nielsen, Peter, 2244, 3495, 3784,
4066, 4601
Niemeyer, Hanz D., 4621
Nishi, Ryuichiro, 2666, 3034
Nobuoka, Hisamichi, 794, 2391
Nolten, R., 2770
Nwogu, Okey George, 4807
- Ochi, Michel K., 878
O'Donoghue, Tom, 2284
Oh, Tae-Myoung, 3680
Ohara, S., 4000
- O'Hare, Tim J., 2994, 3090
Ohno, Kenichi, 1776
Ohta, Takao, 864, 2272
Okayasu, Akio, 200, 1321
Oliver, John, 1852
O'Neil, Sean, 4289
Ono, Masanobu, 3349, 3888
Osanai, Senji, 4591
Osiecki, Daniel A., 3419
Ostrowski, Rafaxl, 3467
Otay, Emre N., 3722
Otta, A. K., 1156
Oumeraci, H., 1403, 2534
Overton, Margery F., 3750
Owczarczyk, Andrzej, 3901
Oya, Atsushi, 300
Özkan-Haller, H. Tuba, 2, 1361
- Palao, Ian M., 368
Panchang, Vijay, 1256
Panchang, Vijay G., 81
Park, W. S., 1268
Parson, Larry E., 3736
Pattiaratchi, Charitha, 4200
Péchon, Philippe, 2050
Peregrine, D. H., 186, 2192, 2573,
4134
Peters, Karsten, 3442
Petroff, Catherine, 1293, 1443
Phelp, D., 340, 4689
Pilarczyk, K. W., 1556
Pilarczyk, Krystian W., 2114
Pirie, Douglas, 1852
Plant, Nathaniel, 3521
Plotkin, Don, 1852
Pluijm, M., 2770
Podber, David P., 4289
Pollock, Cheryl, 1631
Polnikov, V., 1088
Porter, Mark, 4390
Pruszek, Z., 2820
Pruszek, Zbigniew, 3901

- Purnell, Reg, 4253
Pykhov, N. V., 4111
- Radder, A. C., 1156, 4821
Raichlen, Fredric, 1293
Rakha, K. A., 3048
Raudkivi, Arved J., 2142
Reniers, Ad, 175
Resio, Donald, 1631
Resio, Donald T., 3378
Ribberink, Jan S., 4779
Riddell, Keith J., 4717
Ris, R. C., 668, 1247
Rivero, Francisco J., 1168, 4098
Robillard, David J., 878
Robinson, David A., 4390
Rodríguez, Andrés, 4098
Roelvink, J. A., 109, 2022, 2897
Rogers, W. Erick, 2941
Romańczyk, W., 3546
Rønberg, J. K., 3048
Rosati, Julie D., 3628
Rosati, Julie Dean, 2779
Rose, C. P., 3257
Rosen, Dov S., 4376
Rossouw, Jan, 328
Rossouw, M., 340
Róz'yiński, Grzegorz, 4364
Ruessink, B. G., 2897
Ruessink, Gerben, 4793
Ruggiero, P., 2793
Russell, Paul E., 2612
Ryan, Joseph A., P.E., 4650
Rybak, Oleg, 2918
- Sabeur, Zoheir A., 389
Saeki, Hiroshi, 2166
Saito, K., 4000
Sakai, Kazuhiko, 1652
Sakai, Shigeki, 2548, 4411
Sakai, Tetsuo, 3155, 4300
Sakakibara, Hiroshi, 2366
- Sakakiyama, T., 1862
Saleh, Wameidh M., 3481
Sallenger, Asbury H., Jr., 2756
Sánchez-Arcilla, Agustín, 2806, 4098
Sancho, F. E., 1335
Santás, José C., 889
S.-Arcilla, Agustín, 1168
Sasamoto, Makoto, 4411
Sasso, R. Harvey, P.E., 3642
Sato, Hirokazu, 1665
Sato, Koichi, 2166
Sato, Michio, 2666
Savkin, Valery, 2918
Sawamoto, Masaki, 4505
Sawaragi, Toru, 3349, 3888
Schäffer, H. A., 95, 1178
Schäffer, Hemming A., 55
Scheffner, Norman W., 4440
Schiereck, Gerrit J., 1971, 4228
Schofield, Sidney, 643
Schoonees, J. S., 3652
Schroeder, Ernst, 3534
Seabergh, William C., 4531
Seaman, Roy C., 2284
Seelig, William N., 981
Serra, José, 2871
Shah, Adam M., 1431
Shak, Arthur T., P.E., 4650
Sharma, Jagat N., 354
Sheng, Y. Peter, 4242
Shepherd, Ian E., 3169
Sherman, Douglas J., 4214
Shibayama, Tomoya, 200, 3062
Shimizu, Kazuyoshi, 1465
Shimizu, Takao, 3076
Shimizu, Takuzo, 2843
Shimosako, Kenichiro, 1665
Shimosako, Ken-ichiro, 1902
Shin, Cheol S., 2969
Shoshany, Maxim, 4376
Siddabathula, M., 81
Sigurdarson, Sigurdur, 1640

- Silvester, Richard, 3986
Simmonds, David J., 3090
Simons, Richard R., 3481
Skaja, Marek, 4364
Skourup, Jesper, 55
Sloth, Peter, 1693
Smit, F., 1205
Smith, Jane M., 3628
Smith, Susan, 502
Soares, C. Guedes, 743
Sobey, Rodney J., 67, 1034
Solomonidis, Christos, 689
Somers, Christel, 1876
Sørensen, J. Dalsgaard, 1589
Sørensen, O. R., 95, 1178
Sørensen, Ole R., 1060
Sørensen, Per, 2927
Soulsby, Richard L., 3614, 3913
Southgate, Howard N., 286
Spanhoff, R., 2897
Spanhoff, Ruud, 2857
Stansby, P. K., 186
Stanton, T. P., 3391
Stanton, Timothy P., 4079
Stauble, Donald K., 3921, 4531
Steetzel, Henk J., 2746
Stelling, Guus S., 1876
Stive, Marcel J. F., 2884
Stoutjesdijk, Theo, 1888
Strange, R. Rea, III, 822
Stripling, Stuart, 286
Suriamihardja, D. A., 3694
Suzuki, Kojiro, 1652, 1902
Suzuki, Yasuyuki, 1321
Svendsen, I. A., 151, 1192, 1335
Swan, C., 4569
Swan, Christopher, 502
Synolakis, Costas Emmanuel, 1452,
1478

Tada, Akihideo, 300
Tadepalli, Srinivas, 1478

Takahashi, Atsushi, 4545
Takahashi, Fumihiko, 4545
Takahashi, Shigeo, 1652, 1665, 1902
Takahashi, Tomoharu, 629
Takayama, Tomotsuka, 1665
Takayama, Tomotuka, 1652
Takewaka, Satoshi, 1998
Tanaka, Hitoshi, 4545
Tanimoto, Katsutoshi, 1665, 3405
Tega, Yukiko, 4148
Teisson, Charles, 2050
Teng, Chung-Chu, 368
Theron, A. K., 3652
Thevenot, Michelle M., 4024
Thieke, Robert J., 602
Thompson, Edward F., 4440
Thorne, P. D., 3257
Thornton, E. B., 3391
Thornton, Edward B., 4079
Togashi, Hiroyoshi, 2063
Toita, H., 493
Tokubuchi, Katsumasa, 1902
Tomasicchio, G. R., 1528
Tomasicchio, Giuseppe R., 1569
Tomasicchio, Ugo, 2404
Tönjes, Patrick, 2216
Tørum, Alf, 1735, 2626
Toue, Takao, 3183
Tournier, Jean-Pierre, 1233, 2101
Townsend, Murray, 575
Trampenau, Thomas, 2142
Trivedi, Dilip, P.E., 2691
Trizno, Anatoly, 2918
Troch, Peter, 1916
Tryggestad, S., 354
Tsai, Chin-Chi, 4088
Tsai, Li-Hung, 4088
Tsay, Ting-Kuei, 589
Tsoukala, V. K., 403
Tsuchiya, Yoshito, 3694, 4038
Tsujiimoto, Gozo, 3935
Tsujioka, Nobuaki, 2456

- Tsuruya, Hiroichi, 30, 4676
Turner, Ian L., 2677
Turnham, J., 2230
Tutuarima, W. H., 1957
Tzang, S.-Y., 2494
- Uchida, K., 4000
Uda, T., 4000
Uda, Takaaki, 137
Uittenbogaard, R. E., 4821
- van Damme, Luc, 1603, 1916, 1944
van de Graaff, Jan, 2428, 2857
van der Biezen, Stephan C., 2428
van der Meer, Jentsje W., 1957,
2008, 2216, 2418
van der Meulen, Ton, 1971
Van Dongeren, A. R., 1335
van Endt, M., 743
van Gent, Marcel R. A., 1930
van Hove, Conan, 1916
van Kessel, Thijs, 3337
van Kester, J. A. Th. M., 4821
van Kuik, Christine, 1876
Vann, A. M., 2522
Vaudrey, Kennon D., 4397
Veeramony, J., 151, 1192
Verhagen, Henk Jan, 4431
Verhagen, L. A., 516
Vermeir, Dierik, 1916
Vicinanza, D., 2508
Vidal, C., 1762
Vidaor, Alfonso, 1816, 4014, 4744
Vincent, Charles L., 781
Vinh, Ton That, 2820
Voulgaris, George, 3948
- Wada, Akira, 4353
Walkden, Michael J. A., 2584
Walker, S. A., 4557
Walstra, D. J. R., 1205
Wang, Hsiang, 643, 3295, 3830
Wang, Ping, 2982
Wang, Xu, 3295
Wang, Zeya, 1008
Ward, Donald L., 2206
Watabe, Tomiji, 4591
Watanabe, Akira, 754, 767, 2324,
2843, 3104, 3791, 3818, 4174
Watson, Gary, 1417
Watts, Philip, 1293
West, J. R., 3257
White, Thomas E., 3962
Whitehouse, Richard J. S., 3913
Whittaker, T. T. J., 2508
Wibner, Christopher G., 2206
Wiegel, Robert L., 3020
Wierzchnicki, Ryszard, 3901
Wijnberg, Kathelijne M., 3600
Williams, J. J., 3257
Wilson, D. J., 3257
Winyu, Rattanapitikon, 3062
Wood, D. J., 2573
Work, Paul A., 2941, 3722
Wu, Ji, 3762
Wu, Lilun, 4325
Wu, Nan-Jing, 589
Wutkowski, Michael, 4440
Wutkowski, Michael J., 4517
- Xu, Bingyi, 1256
Xu, Jianlu, 67
- Yabe, Kouichi, 3860
Yagi, Hiroshi, 3431
Yamaguchi, Masataka, 900, 1389
Yamaji, Kosuke, 137
Yamamoto, Shogo, 767
Yamamoto, Yoshimichi, 137, 3405
Yamashiro, Masaru, 927
Yamashita, Takao, 1417
Yamashita, Toshihiko, 2166, 4353
Yanagishima, Shin-ichi, 2654
Yano, Kenji, 4353

- Yasuda, Takashi, 300, 850, 2442
Yedapin, Veniamin, 2918
Yim, John Z., 914
Yokoki, Hiromune, 43
Yokota, K., 4000
Yoshida, Akinori, 927
You, Zai-Jin, 3495, 4066
Young, I. R., 516
Yu, Ke, 1192
Yu, Xiping, 2063
Yu, Yu-xiu, 415
Zawadzka, Elz'bieta, 2955
Zeidler, Ryszard B., 3901, 4364
Zelensky, Grigory, 2918
Zhang, Jun, 2206
Zhang, L., 2087
Zhang, Libang, 941
Zhang, Ning-chuan, 415
Zhao, Qun, 415
Zheng, Jie, 3115
Zhuang, Fei, 2178
Zyserman, J. A., 4703